

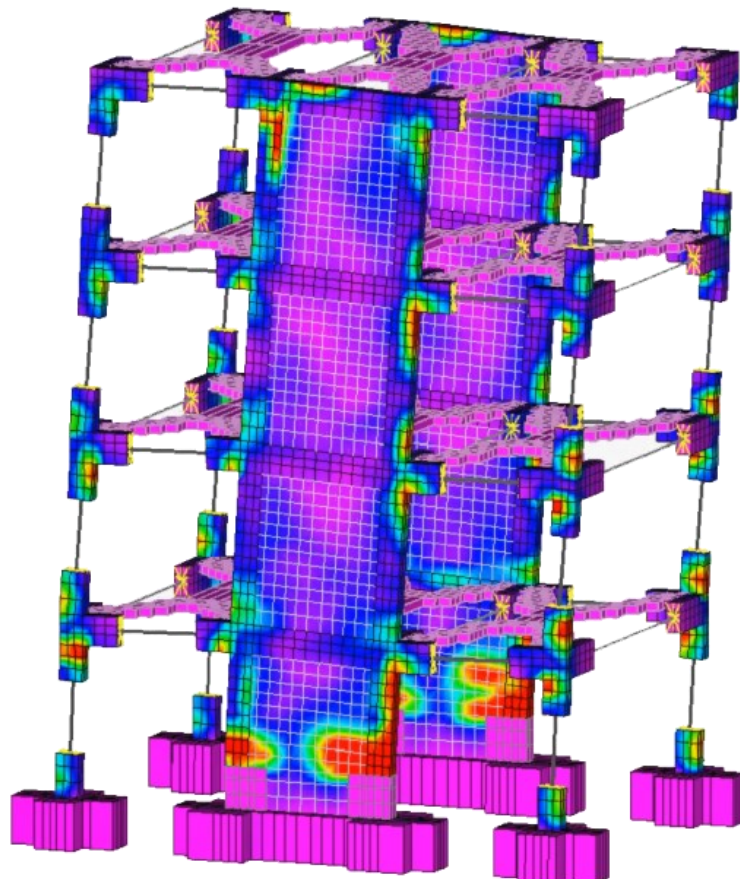
COMPDYN 2021

*8th International Conference
on Computational Methods in Structural Dynamics
and Earthquake Engineering*

PROCEEDINGS

Volume I

M. Papadrakakis, M. Fragiadakis (Eds.)



COMPDYN 2021

Computational Methods in Structural Dynamics and Earthquake Engineering

Proceedings of the 8th International Conference on Computational
Methods in Structural Dynamics and Earthquake Engineering
Streamed from Athens, Greece
28-30 June 2021

Edited by:

M. Papadrakakis

National Technical University of Athens, Greece

M. Fragiadakis

National Technical University of Athens, Greece

A publication of:

Institute of Structural Analysis and Antiseismic Research
School of Civil Engineering
National Technical University of Athens (NTUA)
Greece

COMPDYN 2021

Computational Methods in Structural Dynamics and Earthquake Engineering

M. Papadrakakis, M. Fragiadakis (Eds.)

First Edition, September 2021

© The authors

ISBN (set): **978-618-85072-5-8**

ISBN (vol I): **978-618-85072-3-4**

PREFACE

This volume contains the full-length papers presented in the 8th International Conference on Computational Methods in Structural Dynamics and Earthquake Engineering (COMPDYN 2021) that was streamed from Athens, Greece on June 28-30, 2021.

COMPDYN 2021 is one of the 32 Thematic Conferences of the European Community on Computational Methods in Applied Sciences (ECCOMAS) which were held in 2021 and is also a Special Interest Conference of the International Association for Computational Mechanics (IACM). The purpose of this Conference series is to bring together the scientific communities of Computational Mechanics, Structural Dynamics and Earthquake Engineering, to act as a forum for exchanging ideas in topics of mutual interests and to enhance the links between research groups with complementary activities. We believe that the communities of Structural Dynamics and Earthquake Engineering will benefit from their exposure to advanced computational methods and software tools which can highly assist in tackling complex problems in dynamic and seismic analysis and design of structures, while also giving the opportunity to the Computational Mechanics community to be exposed to very important engineering problems of great social interest.

The COMPDYN 2021 Conference is supported by the National Technical University of Athens (NTUA), the European Association for Structural Dynamics (EASD), the European Association for Earthquake Engineering (EAEE), the Greek Association for Computational Mechanics (GRACM).

The editors of this volume would like to thank all authors for their contributions. Special thanks go to the colleagues who contributed to the organization of the Minisymposia and to the reviewers who, with their work, contributed to the scientific quality of this e-book.

M. Papadrakakis

National Technical University of Athens, Greece

M. Fragiadakis

National Technical University of Athens, Greece

ACKNOWLEDGEMENTS

The conference organizers acknowledge the support towards the organization of the “8th International Conference on Computational Methods in Structural Dynamics and Earthquake Engineering”, to the following organizations:

- European Community on Computational Methods in Applied Sciences (ECCOMAS)
- International Association for Computational Mechanics (IACM)
- European Association for Structural Dynamics (EASD)
- European Association for Earthquake Engineering (EAEE)
- Greek Association for Computational Mechanics (GRACM)
- Hellenic Society for Earthquake Engineering (HSEE)
- School of Civil Engineering, National University of Athens (NTUA)

Plenary Speakers and Invited Session Organizers

We would also like to thank the Plenary and Semi-Plenary Speakers and the Minisymposia Organizers for their help in the setting up of a high standard Scientific Programme.

Plenary Speakers: Sondipon Adhikari, Peter Betsch, Hong Hao, Boris Jeremic, Geert Lombaert , Gabriele Milani , Shinobu Yoshimura

Semi-Plenary Speakers: Denis Duhamel, Fernando Fraternali, Muneo Hori, Alexander Idesman , Jean-Mathieu Mencik, Giuseppe Muscolino

MS Organizers: Christoph Adam, Hamid Ahmadi, Ada Amendola, Giulia Angelucci, António Arêde, Davide Arezzo, Nikolaos P. Bakas, Rui Carneiro Barros, Manuel Braz-César, Bruno Briseghella, Eleonora Bruschi, Bruno Calderoni, Guido Camata, Luca Caracoglia, Sandro Carbonari, Donatello Cardone, Claudia Casapulla, Serena Cattari, Nicola Cavallaghi, Liborio Cavaleri, Dimitrios Chronopoulos, Francesco Clementi, Marco Gaetani d’Aragona, Mario D’Aniello, Dario De Domenico, Maria Teresa De Risi, Matt DeJong, Carlo Del Gaudio, Ciro Del Vecchio, Pedro Delgado, Mariano Di Domenico, Raffaele Di Laora, Marco Di Ludovico, Luigi Di Sarno, Fabio Di Trapani, Beatrice Faggiano, Marco Filippo Ferrotto, Amedeo Flora, Antonio Formisano, Michalis Fragiadakis, Fernando Fraternali, Fabio Freddi, André Furtado, Stefano Galassi, Emanuele Gandelli, Linda Giresini, José A. González, Chiara Iacovino, Alper Ilki, Maria Iovino, Konstantinos Katakalo, Jin-Gyun Kim, Radek Kolman, Daniele Losanno, George C. Manos, Giuseppe Carlo Marano, George Markou, Angelo Masi, Konstantinos G. Megalooikonomou, Gabriele Milani, Lucia Minnucci, Fabrizio Mollaioli, Michele Morici, Lukas Moschen, Jiří Náprstek, Vanni Nicoletti, Ehsan Noroozinejad, Roger Ohayon, K. C. Park, Carlo Pettorruso, Vagelis Plevris, Maria Polese, Virginio Quaglini, Giuseppe Quaranta, Laura Ragni, Gian Andera Rassati, Paolo Ricci, Hugo Rodrigues, Emmanouil Rovithis, Juan Chiachío Ruano, Manuel Chiachío Ruano, Antonio Sandoli, Fabrizio Scozzese, Salvatore Sessa, Anastasios Sextos, P. Benson Shing, Castorina Silva Vieira, Aram Soroushian, Enrico Spacone, James Swanson, Francesca Taddei, Kumar Tamma, Marco Tanganelli, Roberto Tartaglia, Anton Tkachuk, Savvas Triantafyllou, Grigorios Tsinidis, Yiannis Tsompanakis, Enrico Tubaldi, Filippo Ubertini, Nicolò Vaiana, Humberto Varum, Michalis Vassiliou, Ilaria Venanzi, Gerardo M. Verderame, Stefania Viti, Marco Vona

SUMMARY

Preface	iii
Acknowledgements	iv
Contents	ix

VOLUME I

PLENARY	1
SEMI-PLENARY	28

Minisymposia

MS 1: INFLUENCE OF INFILL MASONRY WALLS IN THE RESPONSE AND SAFETY OF BUILDINGS	63
<i>Organized by Humberto Varum, Hugo Rodrigues, Enrico Spacone</i>	
MS 2: REPAIR AND RETROFIT OF STRUCTURES	111
<i>Organized by Ciro Del Vecchio, Marco Di Ludovico, Alper Ilki</i>	
MS 3: RECENT ADVANCES AND CHALLENGES IN GEOTECHNICAL EARTHQUAKE ENGINEERING	202
<i>Organized by Castorina Silva Vieira, Yiannis Tsompanakis</i>	
MS 4: ADVANCEMENTS IN NUMERICAL MODELLING AND SEISMIC INTERVENTION TECHNIQUES OF HISTORICAL MASONRY STRUCTURES	231
<i>Organized by Francesco Clementi, Nicola Cavalagli, Antonio Formisano, Gabriele Milani, Vagelis Plevris</i>	
MS 6: ADVANCES ON SEISMIC ASSESSMENT AND LOCAL COLLAPSE MECHANISMS OF RIGID BLOCKS IN STRUCTURES AND INFRASTRUCTURES	637
<i>Organized by Claudia Casapulla, Linda Giresini, Francesca Taddei, Ehsan Noroozinejad</i>	
MS 7: NEW ADVANCES IN COMPUTATIONAL MODELLING AND EXPERIMENTAL TESTING OF INFILLED FRAMES (2ND EDITION)	779
<i>Organized by Fabio Di Trapani, Liborio Cavaleri, Guido Camata, P. Benson Shing</i>	
MS 8: A MATTER OF SCALE: FROM REAL-TIME MONITORING TO AREA-WIDE SEISMIC RISK ASSESSMENT	987
<i>Organized by Konstantinos G. Megalooikonomou</i>	
MS 9: NONLINEAR MODELLING AND ASSESSMENT OF EXISTING REINFORCED CONCRETE ELEMENTS	1016
<i>Organized by Mariano Di Domenico, Paolo Ricci, Gerardo M. Verderame</i>	

MS 10: VULNERABILITY OF MUSEUM'S COLLECTIONS DYNAMIC RESPONSE, SAFETY ASSESSMENT AND DIGITAL INNOVATIONS	1125
<i>Organized by Stefania Viti, Marco Tanganelli, Stefano Galassi</i>	
MS 11: RECENT FINDINGS AND OPEN ISSUES IN SEISMIC PERFORMANCE ASSESSMENT OF AS-BUILT AND RETROFITTED EXISTING RC BUILDINGS	1188
<i>Organized by Maria Teresa De Risi, Carlo Del Gaudio, André Furtado, Gerardo M. Verderame, Humberto Varum</i>	
MS 12: ADVANCES IN COMPUTATIONAL MODELLING, EXPERIMENTAL TESTING AND OPTIMIZATION OF SEISMIC RETROFITTING.....	1322
<i>Organized by Liborio Cavaleri, Marco Filippo Ferrotto, Fabio Di Trapani, Giuseppe Carlo Marano</i>	
MS 13: MODELLING AND SOLUTION STRATEGIES FOR DYNAMIC PROBLEMS	1416
<i>Organized by Aram Soroushian, Kumar Tamma</i>	
MS 14: SEISMIC ASSESSMENT AND RETROFITTING OF EXISTING STEEL STRUCTURES	1492
<i>Organized by Luigi Di Sarno, Fabio Freddi, Mario D'Aniello</i>	
MS 16: DYNAMIC RESPONSE ASSESSMENT IN RAIL TRACK ENGINEERING	1550
<i>Organized by Lukas Moschen, Grigorios Tsinidis, Christoph Adam, Anastasios Sextos</i>	
MS 17: RECENT DEVELOPMENTS IN ROCKING STRUCTURES	1574
<i>Organized by Matt DeJong, Michalis Vassiliou</i>	
MS 19: ADVANCES IN THE OPTIMUM DESIGN AND CONTROL OF LARGE STRUCTURES UNDER DYNAMIC LOADS	1712
<i>Organized by Fabrizio Mollaioli, Giulia Angelucci, Bruno Briseghella, Giuseppe Carlo Marano, Giuseppe Quaranta</i>	
MS 20: COMPUTATIONAL DESIGN AND MODELING OF TENSEGRITY SYSTEMS FOR APPLICATIONS IN SCIENCE AND ENGINEERING	1825
<i>Organized by Fernando Fraternali, Ada Amendola</i>	
MS 22: CONDITION BASED MAINTENANCE AND POST-PROGNOSTICS OF COMPOSITE STRUCTURES: AN ENHANCED PLATFORM	1874
<i>Organized by Dimitrios Chronopoulos, Savvas Triantafyllou, Juan Chiachío Ruano, Manuel Chiachío Ruano</i>	
MS 23: ADVANCED MODELS AND NUMERICAL METHODS IN DYNAMICS, WAVE PROPAGATION AND COUPLED PROBLEMS	1892
<i>Organized by José A. González, Radek Kolman, Anton Tkachuk, Jiří Náprstek, K. C. Park</i>	
MS 24: LIFE-CYCLE RISK-BASED STRUCTURAL ASSESSMENT AND COST ANALYSIS	1941
<i>Organized by Ilaria Venanzi, Filippo Ubertini, Luca Caracoglia</i>	
MS 25: MONITORING, IDENTIFICATION AND VIBRATION CONTROL OF STRUCTURES	2014
<i>Organized by Rui Carneiro Barros, Manuel Braz-César</i>	
MS 26: SEISMIC SAFETY ASSESSMENT OF STRUCTURES	2157
<i>Organized by Pedro Delgado, António Arêde</i>	

MS 27: TIMBER-BASED ELEMENTS: RECENT ADVANCEMENTS FOR NEW AND EXISTING SEISMIC-RESISTANT STRUCTURES	2195
<i>Organized by Antonio Sandoli, Bruno Calderoni, Beatrice Faggiano</i>	
MS 29: SEISMIC PROTECTION OF NON-STRUCTURAL COMPONENTS: RECENT DEVELOPMENTS AND FUTURE CHALLENGES	2388
<i>Organized by Luigi Di Sarno, Michalis Fragiadakis</i>	
MS 30: DYNAMIC PROTECTION SYSTEMS AND DEVICES: EXPERIMENTAL TESTS, MATHEMATICAL MODELING AND DESIGN METHODS	2435
<i>Organized by Nicolò Vaiana, Daniele Losanno, Salvatore Sessa</i>	
MS 32: SIMPLIFIED METHODOLOGIES FOR PERFORMANCE AND LOSS ASSESSMENT AT BUILDING OR TERRITORIAL SCALE	2557
<i>Organized by Maria Polese, Marco Gaetani d'Aragona</i>	

VOLUME II

Minisymposia

MS 33: EXPERIMENTAL MEASUREMENTS AND NUMERICAL SIMULATION ON PROBLEMS IN THE FIELD OF EARTHQUAKE ENGINEERING AND STRUCTURAL DYNAMICS	2718
<i>Organized by George C. Manos, Konstantinos Katakalos</i>	
MS 34: FRAGILITY CURVES FOR EXISTING BUILDINGS: OPEN CHALLENGES IN THEIR DEFINITION AND USE FOR SEISMIC RISK ANALYSES	3059
<i>Organized by Serena Cattari, Angelo Masi</i>	
MS 35: RECENT ADVANCES IN SEISMIC ISOLATION AND SUPPLEMENTAL DAMPING SYSTEMS FOR VIBRATION CONTROL	3187
<i>Organized by Virginio Quaglini, Eleonora Bruschi, Emanuele Gandelli, Carlo Pettoruso</i>	
MS 36: METHODOLOGIES AND ADVANCED TOOLS FOR SEISMIC RISK ASSESSMENT, MANAGEMENT, AND MITIGATION: ADVANCES AND OPEN CHALLENGES	3305
<i>Organized by Marco Vona, Donatello Cardone, Amedeo Flora, Chiara Iacovino</i>	
MS 37: RISK ASSESSMENT OF BRIDGES AND ROAD NETWORKS SUBJECTED TO NATURAL HAZARDS	3377
<i>Organized by Michele Morici, Fabrizio Scozzese, Lucia Minnucci</i>	
MS 38: DYNAMIC SOIL-FOUNDATION-STRUCTURE INTERACTION: DEVELOPMENTS AND EMERGING ISSUES	3577
<i>Organized by Emmanouil Rovithis, Raffaele Di Laora, Maria Iovino</i>	
MS 39: THE CONTRIBUTION OF DYNAMIC TESTS AND STRUCTURAL MONITORING ON THE SEISMIC RISK ASSESSMENT AND MITIGATION	3697
<i>Organized by Davide Arezzo, Sandro Carbonari, Vanni Nicoletti</i>	

MS 40: ARTIFICIAL INTELLIGENCE & MACHINE LEARNING IN DESIGN AND ASSESSMENT OF STRUCTURES	3795
<i>Organized by George Markou, Nikolaos P. Bakas</i>	

MS 41: SEISMIC PERFORMANCE OF STRUCTURES WITH ISOLATION AND/OR ENERGY DISSIPATION DEVICES	3912
<i>Organized by Enrico Tubaldi, Laura Ragni, Dario De Domenico, Hamid Ahmadi</i>	

MS 42: ADVANCES IN MODEL REDUCTION TECHNIQUES OF COMPUTATIONAL AND STRUCTURAL DYNAMICS	4111
<i>Organized by Jin-Gyun Kim, K. C. Park, Roger Ohayon</i>	

MS 43: ANALYSES AND DESIGN OF STEEL JOINTS UNDER CYCLIC ACTION	4134
<i>Organized by Roberto Tartaglia, Mario D'Aniello, Gian Andera Rassati, James Swanson</i>	

Thematic Sessions

TS 5: DYNAMICS OF CONCRETE AND MASONRY STRUCTURES	4226
TS 14: NUMERICAL SIMULATION METHODS FOR DYNAMIC PROBLEMS	4331
TS 15: OPTIMUM DESIGN AND CONTROL IN STRUCTURAL DYNAMICS AND EARTHQUAKE ENGINEERING	4428
TS 17: PERFORMANCE-BASED EARTHQUAKE ENGINEERING	4558
TS 19: REPAIR AND RETROFIT OF STRUCTURES	4729
TS 20: SEISMIC ISOLATION	4816
TS 21: SEISMIC RISK AND RELIABILITY ANALYSIS	4853
TS 27: STEEL STRUCTURES.....	4906
TS 28: STOCHASTIC DYNAMICS.....	4926
TS 31: NUMERICAL SIMULATION OF GEOTECHNICAL PROBLEMS.....	4946
TS 32: DYNAMICS OF STEEL AND SLENDER STRUCTURES.....	5108
TS 33: AEROELASTICITY, SOUND AND VIBRATION AND BRIDGE DYNAMICS	5179
TS 34: NONLINEAR AND IMPACT DYNAMICS.....	5307

CONTENTS

VOLUME I

PLENARY

SEISMIC VULNERABILITY OF MASONRY HISTORICAL STRUCTURES: A SIMPLE ADAPTIVE NURBS FE APPROACH FOR THE LIMIT AND THE SUBSEQUENT NON-LINEAR STATIC ANALYSIS WITH FEW DOFS	1
<i>Nicola Grillanda, Gabriele Milani</i>	

SEMI-PLENARY

SOME RECENT ADVANCES IN THE WAVE FINITE ELEMENT METHOD	28
<i>Denis Duhamel, B. Claudet, T. Hoang, G. Foret, Jean-Mathieu Mencik</i>	
DYNAMIC ANALYSIS OF PERIODIC STRUCTURES AND METAMATERIALS VIA WAVE APPROACHES AND FINITE ELEMENT PROCEDURES	42
<i>Jean-Mathieu Mencik, Denis Duhamel</i>	

Minisymposia

MS 1: INFLUENCE OF INFILL MASONRY WALLS IN THE RESPONSE AND SAFETY OF BUILDINGS

IMPACT OF MASONRY INFILL VARIABILITY ON THE ESTIMATION OF FLOOR RESPONSE SPECTRA IN RC BUILDINGS	63
<i>Gianrocco Mucedero, Daniele Perrone, Emanuele Brunesi, Ricardo Monteiro</i>	
EFFECT OF IN-PLANE/OUT-OF-PLANE INTERACTION IN INFILL WALLS ON THE FLOOR SPECTRA OF REINFORCED CONCRETE BUILDINGS	84
<i>Mariano Di Domenico, Paolo Ricci, Gerardo M. Verderame</i>	
SEISMIC LOSS ANALYSIS OF A CODE-DESIGNED INFILLED RC BUILDING ACCOUNTING FOR INFILL MODEL CLASS UNCERTAINTY	102
<i>Fabio Romano, Mohammad S. Alam, Maria Zucconi, Marco Faggella, Andre R. Barbosa, Barbara Ferracuti</i>	

MS 2: REPAIR AND RETROFIT OF STRUCTURES

SEISMIC BEHAVIOR OF SUBSTANDARD EXTENDED RECTANGULAR RC COLUMNS JACKETED WITH SPRAYED GFRM	111
<i>Muhsin Can Lülecı, Bilal Sari, Ugur Demir, Muhammed Maraslı, Alper İlki</i>	
DAMAGE EVOLUTION FOR REPAIRABILITY OF SUBSTANDARD BEAM-COLUMN JOINTS	120
<i>Özgür Yurdakul, Ciro Del Vecchio, Marco Di Ludovico, Ladislav Řoutil, Özgür Avşar</i>	

EXPERIMENTAL RESPONSE AND NUMERICAL MODELLING OF TWO-STOREY INFILLED RC FRAME	131
<i>Ciro Del Vecchio, C. Moliterno, Marco Di Ludovico, Gerardo Mario Verderame, Andrea Prota, Gaetano Manfredi</i>	
DEFENCE OF ARCHITECTURAL HERITAGE: EXPERIMENTAL CAMPAIGN ON MASONRIES REINFORCED WITH NATURAL FRCM COMPOSITE MATERIALS	141
<i>Riccardo Liberotti, Nicola Cavalagli, Federico Cluni, Massimiliano Gioffrè, Chiara Pepi, Vittorio Gusella</i>	
NUMERICAL MODELLING AND ANALYSIS OF ECCENTRIC BRACING WITH VERTICAL SHEAR LINKS	151
<i>Gaetano Cantisani, Emilio Rodontini, Gaetano Della Corte</i>	
PERFORMANCE OF EXISTING REINFORCED CONCRETE ARCH BRIDGES UNDER CURRENT NON SEISMIC LOADS	164
<i>Giovanni Crisci, Francesca Ceroni, Gian Piero Lignola, Andrea Prota</i>	
A SUSTAINABLE SOLUTION FOR THE SEISMIC STRENGTHENING OF RC EXISTING BUILDINGS THROUGH THE HPDF SYSTEM (HPDF): A CASE STUDY	180
<i>Giuseppe Ventura, Vincenzo Manfredi, Angelo Masi, Giuseppe Santarsiero, Andrea Digrisolo</i>	
APPLICATION OF C-FRP SHEETS FOR STRUCTURAL REPAIRING OF RC BEAM-COLUMN CONNECTIONS DAMAGED UNDER CYCLIC LOADING – EXPERIMENTAL STUDY	191
<i>Emmanouil Golias, Stavroula Katsimante, Eirini Ziavra, Konstantinos Kirtsonis, Constantin E. Chaliotis, Chris C. Karayannis</i>	
 MS 3: RECENT ADVANCES AND CHALLENGES IN GEOTECHNICAL EARTHQUAKE ENGINEERING	
SEISMIC VULNERABILITY OF SHALLOW UNDERGROUND CAVITIES IN SOFT ROCK	202
<i>Stefania Fabozzi, Filomena De Silva, Marco Nocentini, Edoardo Peronace, Emilio Bilotta, Massimiliano Moscatelli</i>	
EFFICIENCY OF SEISMIC LIQUEFACTION MITIGATION METHODS FOR EXISTING STRUCTURES	212
<i>Alexandros Valsamis, Taxiarchoula Limnaiou, Achilleas Papadimitriou</i>	
PREDICTING RAILWAY TRACK DISPLACEMENTS WITH THE HARDENING SOIL SMALL STRAIN MODEL NEAR CRITICAL SPEED	222
<i>Jesús Fernández-Ruiz, Pedro Alves Costa</i>	
 MS 4: ADVANCEMENTS IN NUMERICAL MODELLING AND SEISMIC INTERVENTION TECHNIQUES OF HISTORICAL MASONRY STRUCTURES	
NON-DESTRUCTIVE AND DESTRUCTIVE TESTS ON OPUS INCERTUM MASONRY PANELS	231
<i>Francesca Autiero, Giuseppina De Martino, Marco Di Ludovico, Andrea Prota</i>	
PRELIMINARY NONLINEAR STATIC AND DYNAMIC ANALYSIS OF THE MAIN PYRAMID OF HUACA DE LA LUNA, PERU	244
<i>Selman Tezcan, Miguel a. Pando, Rafael Aguilar, Benjamin Castañeda, Carol Rojas, Renato Perucchio</i>	

MODELING STRATEGIES FOR NON-LINEAR SEISMIC ANALYSES: COMPARISON AMONG EFM AND FEM RESULTS ON AN EXISTING URM CASE STUDY	258
<i>Marco Pegoraro, Elisa Saler, Matteo Salvalaggio, Maria Rosa Valluzzi</i>	
ANALYSIS OF THE DAMAGE STATE OF A MONUMENTAL BUILDING BY CONSIDERING THE VARIATIONS IN SOIL CONDITIONS	268
<i>Erica Lenticchia, Gaetano Miraglia, Stefania Coccimiglio, Rosario Ceravolo</i>	
ADVANCED NUMERICAL PREDICTION OF UNREINFORCED U-SHAPED MASONRY WALLS LOADED OUT-OF-PLANE	278
<i>Jacopo Scacco, Luís C. Silva, Graça Vasconcelos, Gabriele Milani, Paulo B. Lourenço</i>	
LOW-COST BASE ISOLATION SYSTEMS FOR UNREINFORCED MASONRY BUILDINGS IN DEVELOPING COUNTRIES	286
<i>Nagavinothini Ravichandran, Daniele Losanno, Fulvio Parisi</i>	
NONLINEAR STATIC ANALYSIS OF MASONRY BUILDINGS THROUGH FIBRE-BASED CAPACITY MODELLING	298
<i>Elia Acconcia, Valentina Buonocunto, Fulvio Parisi</i>	
A DISCRETE-MACRO-ELEMENT-MODEL FOR THE IN-PLANE ANALYSIS OF MASONRY STRUCTURES STRENGTHENED BY FRCMS	309
<i>Paolo Zampieri, Riccardo Piazzon, Bartolomeo Pantò, Carlo Pellegrino</i>	
NUMERICAL MODELLING OF DIAGONAL COMPRESSION TESTS ON MASONRY PANELS STRENGTHENED BY FRCM	318
<i>Francesca Ferretti, Francesco Saverio Murgo, Claudio Mazzotti</i>	
EMPIRICAL AND MECHANICAL ANALYSIS METHODS FOR SEISMIC VULNERABILITY ASSESSMENT OF CLUSTERED BUILDINGS OF HISTORICAL CENTRES: A CASE STUDY	331
<i>Antonio Formisano, Giovanni Mochi, Nicola Chieffo</i>	
SETTLEMENT-INDUCED DAMAGE ASSESSMENT IN UNILATERAL MASONRY-LIKE STRUCTURES: A PIECEWISE RIGID DISPLACEMENT APPROACH	338
<i>Ida Mascolo, Antonio Fortunato</i>	
ON THE USE OF DIGITAL TWINS FOR SEISMIC STRUCTURAL HEALTH MONITORING OF A MONUMENTAL MASONRY TOWER	346
<i>Alban Kita, Nicola Cavalagli, Ilaria Venanzi, Filippo Ubertini</i>	
MICROMECHANICAL ANALYSIS OF UNREINFORCED AND REINFORCED MASONRY ARCHES	354
<i>Daniela Addressi, Cristina Gatta, Mariacarla Nocera, Domenico Liberatore</i>	
ANALYTICAL AND NUMERICAL ANALYSIS OF S. MARTINO'S DEI GUALDESI CHURCH DAMAGED DURING THE 2016 CENTRAL ITALY SEISMIC SEQUENCE	367
<i>Ivis Cescatti, Michol Rampado, Veronica Follador, Francesca da Porto, Claudio Modena</i>	
A NURBS-BASED NUMERICAL APPROACH FOR THE ASSESSMENT OF MASONRY VAULTS UNDERGOING DIFFERENTIAL SETTLEMENTS	380
<i>Andrea Chiozzi, Nicola Grillanda, Gabriele Milani, Antonio Tralli</i>	

NUMERICAL MODELLING OF BONDED BRICKWORK UNDER CYCLIC COMPRESSION LOADING	387
<i>Mohammad Asad, Tatheer Zahra, Julian Thamboo</i>	
FULL 3D CAD PROCEDURE FOR THE LIMIT ANALYSIS OF LONGHU PAGODA IN CHINA	398
<i>Peixuan Wang, Alessandro De lasio, Jacopo Scacco, Gabriele Milani, Shengcai Li</i>	
ROLE OF REPEATED SEISMIC EVENTS ON THE COLLAPSE OF TWO CALIDARIA IN ROME DATING BACK TO THE IMPERIAL AGE	406
<i>Francesca Faleri, Nicola Grillanda, Selman Tezcan, Renato Perucchio, Gabriele Milani</i>	
3D ADVANCED NUMERICAL MODELLING OF A CATALAN-LAYERED MASONRY VAULT UNREINFORCED AND REINFORCED WITH GLASS-TRM MATERIALS AND SUBJECTED TO VERTICAL SUPPORT MOVEMENTS	415
<i>Elisa Bertolesi, Gabriele Milani, José M. Adam, Pedro A. Calderón</i>	
DYNAMIC ANALYSIS OF MASONRY CHIMNEYS BY MEANS OF A SIMPLE RIGID BEAM MODEL	423
<i>Daniele Baraldi, Gabriele Milani, Vasilis Sarhosis</i>	
COMPARATIVE ANALYSIS AMONG DIFFERENT ANALYSIS PROGRAMS FOR SEISMIC VULNERABILITY EVALUATION OF A MASONRY BUILDING COMPOUND IN THE DISTRICT OF NAPLES	433
<i>Generoso Vaiano, Antonio Formisano</i>	
TERRITORIAL ANALYSIS OF SEISMIC PERFORMANCE OF ANCIENT CHURCHES: METHODS AND APPLICATION TO CASE STUDIES	447
<i>Michele D'Amato, R. Laguardia, Rosario Gigliotti, Antonio Formisano</i>	
FE MODELING OF A SEISMIC ISOLATOR MADE OF HDR AND REGENERATED EPDM	456
<i>Gaetano Pianese, Gabriele Milani, Antonio Formisano</i>	
INFLUENCE OF CROSSLINKING ON THE SEISMIC PERFORMANCE OF UNBONDED FIBER REINFORCED ELASTOMERIC ISOLATORS (UFREI) MADE OF REGENERATED RUBBER	463
<i>Gaetano Pianese, Davide Torrini, Gabriele Milani, Antonio Formisano</i>	
COMBINING OPERATIONAL MODAL ANALYSIS AND GENETIC ALGORITHMS TO UNDERSTAND THE ACTUAL STRUCTURAL BEHAVIOR OF HISTORICAL CONSTRUCTIONS	470
<i>Gianluca Standoli, Georgios Panagiotis Salachoris, Maria Giovanna Masciotta, Francesco Clementi</i>	
SEISMIC ASSESSMENT OF MASONRY CROSS VAULTS THROUGH NON-LINEAR STATIC ANALYSES	487
<i>Marco Alforno, Alessia Monaco, Fiammetta Venuti, Chiara Calderini</i>	
“SCAGLIA ROSSA” EXPERIMENTAL CAMPAIGN AND MODEL UPDATING FOR NUMERICAL DAMAGE EVALUATION	497
<i>Georgios Panagiotis Salachoris, Erica Magagnini, Francesco Clementi</i>	
BEHAVIOUR FACTOR ASSESSMENT OF ANCIENT MASONRY TOWERS THROUGH AN INNOVATIVE SIMPLIFIED PUSHOVER METHOD	508
<i>Alessandro De lasio, Peixuan Wang, Gabriele Milani, Bahman Ghiassi</i>	

FE PUSHOVER ANALYSES OF A 20TH-CENTURY MASONRY CHIMNEY IN SPAIN: COLLAPSE BEHAVIOR AND NUMERICAL UNCERTAINTIES	519
<i>Alessandro De Iasio, Gabriele Milani, Jose M. Adam</i>	
FINITE ELEMENT ANALYSIS OF JUMA MOSQUE IN UZBEKISTAN BASED ON LASER SCANNING AND AMBIENT STUDIES	530
<i>Shakhzod Takhirov, Bahodir Rakhmonov</i>	
CONTINUOUS AND DISCONTINUOUS DESCRIPTIONS OF BLOCKED STRUCTURES: THE CASE STUDY OF SANTISSIMO CROCIFISSO CHURCHES IN PRETARE (ITALY)	539
<i>Francesco Clementi, Angela Ferrante, Ersilia Giordano, Stefano Lenci</i>	
LATTICE DISCRETE MODELING OF OUT-OF-PLANE BEHAVIOR OF IRREGULAR MASONRY	546
<i>Micaela Mercuri, Madura Pathirage, Amedeo Gregori, Gianluca Cusatis</i>	
NUMERICAL STUDY ON SEISMIC RETROFIT OF URM WALLS USING TIMBER PANELS	563
<i>Davide Cassol, Ivan Giongo, Maurizio Piazza</i>	
OPTIMIZATION OF EMPIRICAL SEISMIC VULNERABILITY ASSESSMENT FOR MASONRY BUILDINGS FOLLOWING NONLINEAR ANALYSIS	581
<i>Eugen Onescu, Iasmina Onescu, Marius Mosoarca</i>	
NONLINEAR SIMULATION OF MASONRY VAULTS UNDER EARTHQUAKE LOADING	595
<i>Adam Plavsic, Bartolomeo Pantò, Corrado Chisari, Lorenzo Macorini, Bassam A. Izzuddin, Ingrid Boem, Natalino Gattesco</i>	
LOW-COST RUBBER COMPOUNDS FOR FIBER-REINFORCED ELASTOMERIC ISOLATORS: RECOVERED POWDERS AND WASTE OILS FROM RUBBER MANUFACTURING PROCESSES	607
<i>Gaetano Pianese, Gabriele Milani, Federico Milani, Ahmad Basshofi Habieb</i>	
HORIZONTAL FORCE CAPACITY OF A HEMI-SPHERICAL DOME	614
<i>Carlo Olivieri, Anna Castellano, Isabella Elia, Antonio Fortunato, Ida Mascolo</i>	
SEISMIC RETROFITTING TECHNIQUES FOR EXISTING MASONRY BUILDINGS	626
<i>Ida Mascolo, Antonio Fortunato, Carlo Olivieri, Antonio Gesualdo</i>	
 MS 6: ADVANCES ON SEISMIC ASSESSMENT AND LOCAL COLLAPSE MECHANISMS OF RIGID BLOCKS IN STRUCTURES AND INFRASTRUCTURES	
PRELIMINARY DESIGN METHOD FOR ROCKING AND NEGATIVE STIFFNESS SYSTEMS	637
<i>Natalia Reggiani Manzo, Michalis Vassiliou</i>	
PREFABRICATED REINFORCED CONCRETE CLADDING PANELS SUPPORTS: DESIGN AND NUMERICAL MODELLING	649
<i>Flavio Stochino, Fausto Mistretta, Mario Lucio Puppio, Mauro Sassu</i>	

INFLUENCE OF THE ELASTO-PLASTIC BEHAVIOR OF TIE-RODS IN THE RESPONSE OF ROCKING MASONRY WALLS THROUGH SEISMIC DEMAND HAZARD CURVES	664
<i>Fabio Solarino, Linda Giresini, Pietro Croce</i>	
GRAPHICAL METHODS, KINEMATIC AND FINITE ELEMENT ANALYSIS OF THE PREMILCUORE MASONRY BRIDGE ...	682
<i>Linda Giresini, Daniela De Paola, Mario Lucio Puppio, Giovanni Buratti</i>	
REDUCTION OF HOUSNER'S COEFFICIENT OF RESTITUTION FOR MASONRY WALLS UNDER ONE-SIDED ROCKING	702
<i>Linda Giresini, Pietro Croce</i>	
AN EQUIVALENT VISCOUS DAMPING PROPOSAL FOR BLOCK-BASED ROCKING MODELS	717
<i>Georgios Vlachakis, Carla Colombo, Anastasios Giouvanidis, Anjali Mehrotra, Nathanael Savalle, Paulo B. Lourenço</i>	
PROBABILISTIC SEISMIC FRAGILITY FOR ROCKING MASONRY FAÇADES USING CLOUD ANALYSIS	727
<i>Armando Benenato, Stefania Imperatore, Gian Piero Lignola, Barbara Ferracuti</i>	
MODELLING OF THE OUT-OF-PLANE BEHAVIOUR OF UNREINFORCED MASONRY PANELS USING THE DISCRETE MACRO-ELEMENT METHOD (DMEM)	738
<i>Valeria Cusmano, Bartolomeo Pantò, Ivo Calì, Paulo B. Lourenço</i>	
VISUAL PROGRAMMING FOR MACRO-BLOCK ANALYSIS OF MULTI-STOREY MASONRY BUILDINGS	752
<i>Elham Mousavian, Luca Umberto Argiento, Claudia Casapulla</i>	
OUT-OF-PLANE RESPONSE OF T-SHAPED MASONRY WALLS STRENGTHENED WITH CFRP INJECTED ANCHORS: MODELLING AND DESIGN PROVISIONS	764
<i>Alessandra Maione, Claudia Casapulla, Francesca Ceroni, Marco Di Ludovico, Andrea Prota</i>	
MS 7: NEW ADVANCES IN COMPUTATIONAL MODELLING AND EXPERIMENTAL TESTING OF INFILLED FRAMES (2ND EDITION)	
NUMERICAL MESO-MODEL FOR REINFORCED CONCRETE FRAMES WITH RETROFITTED MASONRY INFILL	779
<i>Gianni Blasi, Daniele Perrone, Maria Antonietta Aiello</i>	
ASSESSMENT OF OUT-OF-PLANE STRENGTH OF MASONRY INFILLS ACCORDING TO EC6	795
<i>Laura Liberatore</i>	
INFLUENCE OF PRIOR IN-PLANE DAMAGE ON THE OUT-OF-PLANE RESPONSE OF NON-LOAD BEARING UNREINFORCED MASONRY WALLS UNDER SEISMIC LOAD	808
<i>Bogdan Šakić, Aleksa Milijaš, Marko Marinković, Christoph Butenweg, Sven Klinkel</i>	
EXPERIMENTAL INVESTIGATION OF BEHAVIOUR OF MASONRY INFILLED RC FRAMES UNDER OUT-OF-PLANE LOADING	829
<i>Aleksa Milijaš, Bogdan Šakić, Marko Marinković, Christoph Butenweg, Sven Klinkel</i>	
STRUCTURAL CONCEPTS IN THE DESIGN OF MASONRY-INFILLED STEEL FRAMES	847
<i>Dario Sokic, Damir Markulak, Tihomir Doksanovic, Ivan Radic</i>	

A SIMPLE METHODOLOGY FOR THE INFILL MASONRY WALL STIFFNESS ESTIMATION	860
<i>Vanni Nicoletti, Davide Arezzo, Sandro Carbonari, Fabrizio Gara</i>	
ASSESSMENT OF DAMAGE TO MODERN REINFORCED CONCRETE BUILDINGS – ENGINEERING ANALYSIS OF THE M6.4 ALBANIA EARTHQUAKE, 26TH OF NOV. 2019	871
<i>Lars Abrahamczyk, Davorin Penava, Melad Haweyou, Filip Anić, Arturo E. Schultz, Jeff Rautenberg</i>	
INFLUENCE OF THE INFILL TYPOLOGY IN THE EVALUATION OF THE ANNUAL LOSSES OF RC STRUCTURES THROUGH THE APPLICATION OF A NEW METHOD	886
<i>Andrea Rossi, Paolo Morandi, Riccardo R Milanese, Guido Magenes</i>	
LOCAL EFFECTS DUE TO THE SEISMIC INTERACTION BETWEEN INNOVATIVE DUCTILE MASONRY INFILLS AND RC ELEMENTS	899
<i>Riccardo R. Milanese, Valentino Bolis, Simone Pelucco, Paolo Morandi, Guido Magenes, Marco Preti</i>	
A DEGRADING BOUC-WEN DATA-DRIVEN MODEL FOR THE CYCLIC BEHAVIOR OF MASONRY INFILLED RC FRAMES	913
<i>Matteo Pellicciari, Stefano Sirotti, Fabio Di Trapani, Bruno Briseghella, Giuseppe Carlo Marano, Camillo Nuti, Angelo Marcello Tarantino</i>	
SEISMIC PERFORMANCE OF PAKISTANI-TECHNIQUE INFILLED REINFORCED CONCRETE FRAMES	923
<i>Nisar Ali Khan, Alessandro Vittorio Bergami, Camillo Nuti, Giorgio Monti, Marco Vailati, Bruno Briseghella</i>	
GENERATION OF OUT-OF-PLANE FRAGILITY FUNCTIONS FOR IN-PLANE DAMAGED UNREINFORCED MASONRY INFILLS	935
<i>Bharat Pradhan, Liborio Cavaleri, Vasilis Sarhosis, Marco Filippo Ferrotto</i>	
EMPIRICAL FORMULATION OF THE OUT-OF-PLANE RESISTANCE OF INFILLED FRAMES	955
<i>Fabio Di Trapani, Alessandro Vizzino, Giovanni Tomaselli, P. Benson Shing</i>	
MECHANICAL VS EMPIRICAL MODELS FOR MODELS IN-PLANE RESPONSE OF INFILLED FRAMES: RELIABILITY 7 COMPARISON AND VALIDATION OF A NEW DATA-DRIVEN MODEL	970
<i>Fabio Di Trapani, Giovanni Tomaselli, Gabriele Bertagnoli</i>	
 MS 8: A MATTER OF SCALE: FROM REAL-TIME MONITORING TO AREA-WIDE SEISMIC RISK ASSESSMENT	
EARTHQUAKE EARLY WARNING AND RAPID RESPONSE SYSTEM BASED ON SMART SEISMIC AND MONITORING SENSORS EMBEDDED IN A COMMUNICATION PLATFORM AND COUPLED WITH BIM MODELS	987
<i>Georgios Balaskas, Benno Hoffmeister, Christoph Butenweg, Marco Pilz, Anna Bauer</i>	
MONITORING OF A PRESTRESSED BRIDGE MODEL BY ULTRASONIC MEASUREMENT AND VIBRATION RECORDINGS	999
<i>Chun-Man Liao, Falk Hille, Daniel Fontoura Barroso, Ernst Niederleithinger</i>	

COMPARATIVE NON-STRUCTURAL VULNERABILITY ASSESSMENT METHODS FOR HISTORICAL RESIDENTIAL MASONRY BUILDINGS	1008
<i>Filippos Alogdianakis, Konstantinos G. Megalooikonomou, Georgios S. Papavasileiou</i>	

MS 9: NONLINEAR MODELLING AND ASSESSMENT OF EXISTING REINFORCED CONCRETE ELEMENTS

STUDY OF BIAXIAL SHEAR FAILURE ENVELOPE OF REINFORCED CONCRETE COLUMNS	1016
<i>Beatrice Belletti, Simone Ravasini, Andrea Alberici</i>	

EVALUATION OF THE SEISMIC VULNERABILITY OF EXISTING PRE-CODE RC CORE STRUCTURAL SYSTEMS THROUGH NON-LINEAR PUSHOVER ANALYSES	1027
<i>Beatrice Belletti, Enzo Martinelli, Elena Michelin, Francesca Vecchi</i>	

CALIBRATION AND VALIDATION OF AN OVERDAMPED DISPLACEMENT ADAPTIVE PROCEDURE FOR SEISMIC ASSESSMENT OF INFILLED RC FRAMES	1039
<i>Francesca Barbagallo, Melina Bosco, Aurelio Gherzi, Edoardo Michele Marino, Pier Paolo Rossi</i>	

CYCLIC TESTING OF 1:40 SCALE CANTILEVER RC ELEMENTS WITH DIGITALLY MANUFACTURED REINFORCEMENT	1053
<i>Lorenzo Del Giudice, Rafal Wrobel, Antonios Katsamakas, Christian Leinenbach, Michalis Vassiliou</i>	

R/C COLUMN MODELLING USING ANSYS AND LOADING RATE AND MESH METHOD INFLUENCE STUDIES	1063
<i>Theodora Mitkou, Theodoros Chrysanidis</i>	

CALIBRATION AND NUMERICAL MODELING OF RC BEAM-COLUMN JOINTS DESIGNED FOR GRAVITY LOADS	1085
<i>Marcello Sabene, Maria Zucconi, Stefano Pampanin, Barbara Ferracuti</i>	

ASSESSMENT OF THE RESPONSE ENVELOPE OF REINFORCED CONCRETE MEMBERS WITH DIFFERENT FAILURE MODES	1097
<i>Mariano Di Domenico, Paolo Ricci, Gerardo M. Verderame</i>	

SEISMIC ASSESSMENT OF AN EXISTING RC BUILDING AFFECTED BY SLOW-MOVING LANDSLIDES INDUCED DISPLACEMENTS MONITORED BY REMOTE SENSING TECHNIQUE	1112
<i>Annalisa Mele, Andrea Miano, Diego Di Martire, Donato Infante, Andrea Prota, Massimo Ramondini</i>	

MS 10: VULNERABILITY OF MUSEUM'S COLLECTIONS DYNAMIC RESPONSE, SAFETY ASSESSMENT AND DIGITAL INNOVATIONS

VULNERABILITY OF ART WORKS TO BLAST HAZARD: THE FOUNTAIN OF NEPTUNE IN FLORENCE	1125
<i>Marco Domaneschi, Marco Tanganelli, Stefania Viti, Gian Paolo Cimellaro</i>	

SIMPLIFIED ANALYSES FOR THE MODEL SETTING OF SCULPTURES: THE "OCEANO" BY GIAMBOLOGNA	1135
<i>Marco Tanganelli, Stefano Galassi, Stefania Viti</i>	

VULNERABILITY ASSESSMENT OF MONUMENTAL ARTWORKS USING CONTACT TIME-HISTORY ANALYSIS	1145
<i>Raffaele Gagliardo, Michele Godio, Lucrezia Cascini, Francesco Portioli, Raffaele Landolfo</i>	

THE TARANTOLA ETRUSCAN PEDIMENT: NDT AND 3D MODEL CONTENT	1153
<i>Anna Livia Ciuffreda, Massimo Coli, Tessa Donigaglia, Paola Ilaria Mariotti, Teresa Salvatici, Gabriela Simoni</i>	
CORRELATION OF VULNERABILITY AND CONSERVATION BETWEEN ARTISTIC ASSETS AND STRUCTURAL ELEMENTS: CAMPAIGN OF THERMOGRAPHIC SURVEYS ON THE FRESCOS OF THE TEMPLAR CHURCH OF SAN BEVIGNATE	1170
<i>Riccardo Liberotti, Federico Cluni, F. Faralli, Vittorio Gusella</i>	
 MS 11: RECENT FINDINGS AND OPEN ISSUES IN SEISMIC PERFORMANCE ASSESSMENT OF AS-BUILT AND RETROFITTED EXISTING RC BUILDINGS	
EVALUATION OF A NUMERICAL MODELLING APPROACH FOR THE SIMULATION OF RETROFITTED RC ELEMENTS	1188
<i>Ines Sousa, Rita Couto, Rita Peres, José Miguel Castro, Rita Bento</i>	
EXPERIMENTAL INVESTIGATION ON ANCHORAGE PERFORMANCE OF EMBEDDED SMOOTH REBARS SUBJECTED TO CYCLICNG LOADING	1201
<i>Anthony Paderno, Simone Pelucco, Marco Preti</i>	
OUT-OF-PLANE TESTING OF MASONRY INFILL WALLS MADE WITH LIGHTWEIGHT CONCRETE BLOCKS	1212
<i>M. Agante, André Furtado, Hugo Rodrigues, António Arêde, P. Fernandes, Humberto Varum</i>	
SELECTION OF OPTIMAL SEISMIC RETROFITTING FOR EXISTING SCHOOL BUILDINGS THROUGH MULTI- CRITERIA DECISION MAKING	1223
<i>Wilson Carofilis, Nicholas Clemett, Giammaria Gabbianelli, Gerard O'Reilly, Ricardo Monteiro</i>	
NUMERICAL INVESTIGATIONS ON THE RESIDUAL CAPACITY AND ECONOMIC LOSSES OF EARTHQUAKE- DAMAGED REINFORCED CONCRETE WALL STRUCTURES	1242
<i>Cristiana Ceccarelli, Simona Bianchi, Livio Pedone, Stefano Pampanin</i>	
SIMPLIFIED LOSS ESTIMATION IN INFILLED RC BUILDINGS: MECHANICAL METHOD AND VALIDATION	1261
<i>Carlo Del Gaudio, Maria Teresa De Risi, Gerardo Mario Verderame</i>	
SEISMIC PERFORMANCE ASSESSMENT OF AS-BUILT AND RETROFITTED RC BUILDINGS CONSIDERING THE INFLUENCE OF INFILLS: PRE-'70 LOW-MIDE RISE CASE-STUDIES	1275
<i>Maria Teresa De Risi, Santa Anna Scala, Carlo Del Gaudio, Gerardo Mario Verderame</i>	
MAPPING PERFORMANCE-TARGETED RETROFITTING TO SEISMIC FRAGILITY REDUCTION	1301
<i>Karim Aljawhari, Roberto Gentile, Carmine Galasso</i>	

MS 12: ADVANCES IN COMPUTATIONAL MODELLING, EXPERIMENTAL TESTING AND OPTIMIZATION OF SEISMIC RETROFITTING

EXPERIMENTAL STUDY ON THE IN-PLANE RESPONSE OF ADOBE MASONRY WALLS STRENGTHENED WITH TEXTILE REINFORCED MATRIX SYSTEMS	1322
<i>Paolino Cassese, Luigi Fenu, Domenico Asprone, Antonio Occhiuzzi, Fulvio Parisi</i>	
GENETIC OPTIMIZATION FOR THE DESIGN OF SEISMIC RETROFITTING OF PLANE RC FRAMES WITH BUCKLING RESTRAINED BRACES (BRBS)	1333
<i>Giovanni Minafò, Gaetano Camarda</i>	
INFLUENCE OF THE EFFECTIVENESS FACTORS IN ASSESSING THE SHEAR CAPACITY OF RC BEAMS STRENGTHENED WITH FRP	1345
<i>Piero Colajanni, Salvatore Pagnotta</i>	
OPTIMIZATION OF STEEL-JACKETING RETROFITTING OF SHEAR-CRITICAL AND DUCTILITY CRITICAL RC FRAME STRUCTURES BY A NOVEL GENETIC ALGORITHM FRAMEWORK	1368
<i>Antonio Pio Sberna, Fabio Di Trapani, Giuseppe Carlo Marano</i>	
EXPECTED ANNUAL LOSS ORIENTED SEISMIC RETROFITTING OPTIMIZATION OF RC FRAME STRUCTURES USING A NEW AI-BASED FRAMEWORK	1383
<i>Fabio Di Trapani, Antonio Pio Sberna, Giuseppe Carlo Marano</i>	
THE ROLE OF THE SUSTAINED LOADS ON THE BEARING CAPACITY OF REINFORCED CONCRETE COLUMNS RETROFITTED BY STEEL JACKETS	1401
<i>Marco Filippo Ferrotto, Bharat Pradhan, Liborio Cavaleri</i>	

MS 13: MODELLING AND SOLUTION STRATEGIES FOR DYNAMIC PROBLEMS

CASE STUDY OF CONNECTIVITY OF DIGITAL TWINS AND EXPERIMENTAL SYSTEMS	1416
<i>Matthew Bonney, Paul Gardner, David Wagg, Robin Mills</i>	
AN ADAPTIVE FAST NONLINEAR ANALYSIS (AFNA) ALGORITHM FOR RAPID TIME HISTORY ANALYSIS	1426
<i>Bowei Li, Wei-Chu Chuang, Seymour M.J. Spence</i>	
A NOVEL METHOD FOR THE GENERATION OF FULLY NON-STATIONARY SPECTRUM COMPATIBLE ARTIFICIAL ACCELEROGRAMS	1437
<i>Federica Genovese, Giuseppe Muscolino, G. Biondi, E. Cascone</i>	
AN APPLICATION OF THE PROPER ORTHOGONAL DECOMPOSITION METHOD FOR NONLINEAR DYNAMIC ANALYSIS OF REINFORCED CONCRETE STRUCTURES SUBJECTED TO EARTHQUAKES	1445
<i>Naim Ayoub, Walid Labri, Joseph Pais, Lucie Rouleau, Jean-François Deu</i>	
MULTI-RESOLUTION FINITE WAVELET DOMAIN METHOD FOR FAST TRANSIENT DYNAMIC ANALYSIS IN HOMOGENEOUS AND HETEROGENEOUS RODS AND BEAMS	1458
<i>Dimitris K. Dimitriou, Christos V. Nastos, Dimitris A. Saravanos</i>	

A TECHNIQUE FOR TIME INTEGRATION WITH STEPS LARGER THAN THE EXCITATION STEPS: REVIEW OF THE PAST AND ADDRESSING THE EXISTING CHALLENGES AND A PERSPECTIVE OF THE FUTURE	1476
<i>Aram Soroushian</i>	

MS 14: SEISMIC ASSESSMENT AND RETROFITTING OF EXISTING STEEL STRUCTURES

A SIMPLIFIED APPROACH FOR THE ESTIMATION OF SEISMIC VULNERABILITY OF STEEL MOMENT RESISTING FRAMES	1492
<i>Rosario Montuori, Elide Nastri, Vincenzo Piluso, Paolo Todisco</i>	

PRELIMINARY NUMERICAL ANALYSIS OF THE SEISMIC RESPONSE OF STEEL FRAMES WITH MASONRY INFILLS RETROFITTED BY BUCKLING RESTRAINED BRACES	1506
<i>Fernando Gutiérrez-Urzúa, Fabio Freddi, Luigi Di Sarno, Jing-Ren Wu, Mario D'Aniello, Raffaele Landolfo, Stathis Bousias</i>	

NUMERICAL MODELLING OF MASONRY INFILL WALLS IN EXISTING STEEL FRAMES	1519
<i>Luigi Di Sarno, Jing-Ren Wu, Fabio Freddi, Mario D'Aniello, Stathis Bousias, Fernando Gutiérrez-Urzúa, Raffaele Landolfo, Nikolaos Stathas</i>	

HYBRID COLD-FORMED/TUBULAR MODULAR STRUCTURAL SYSTEM WITH INNOVATIVE JOINTS	1532
<i>Luís Carlos Silva, Hélder David Craviero, Trayana Tankova, Rui Simões, Ricardo Costa, Mario D'Aniello, Raffaele Landolfo, Luís Simões da Silva</i>	

SEISMIC ASSESSMENT OF BEAM-TO-COLUMN JOINTS FOR A NON-CONFORMING MRF EXISTING STRUCTURE	1542
<i>Roberto Tartaglia, Mario D'Aniello, Aldo Milone, Raffaele Landolfo</i>	

MS 16: DYNAMIC RESPONSE ASSESSMENT IN RAIL TRACK ENGINEERING

APPLICATION AND ASSESSMENT OF A DYNAMIC SOIL-BRIDGE-TRAIN INTERACTION MODEL	1550
<i>Benjamin Hirzinger, Christoph Adam</i>	

SEISMIC FRAGILITY ANALYSIS OF RAILWAY RC BRIDGES. ACCOUNTING FOR BRIDGE-TRAIN INTERACTION BASED ON A NOVEL FORMULATION FOR CONSTRAINED DYNAMICAL SYSTEMS AND A CO-SIMULATION TECHNIQUE	1562
<i>Sotiria Stefanidou, Elias Paraskevopoulos</i>	

MS 17: RECENT DEVELOPMENTS IN ROCKING STRUCTURES

REDUCTION OF LOCAL DAMAGES IN PRECAST POST-TENSIONED SEGMENTAL BRIDGE PIERS	1574
<i>Parya Ahmadi, Ehsan Ahmadi, Mohammad M. Kashani</i>	

BASE VERSUS TOP ACTIVE CONTROL TO IMPROVE DYNAMIC AND SEISMIC PERFORMANCES OF RIGID BLOCKS .	1583
<i>Angelo Di Egidio, Alessandro Contento, Stefano Pagliaro</i>	

UNIFORM RISK SPECTRA FOR NEGATIVE STIFFNESS SYSTEMS	1596
<i>Natalia Reggiani Manzo, Christos Lachanas, Michalis Vassiliou, Dimitrios Vamvatsikos</i>	
SEISMIC BEHAVIOR OF ARCHAEOLOGICAL MULTIDRUM COLUMNS AT THE POMPEII SITE	1607
<i>Francesca Autiero, Giuseppina De Martino, Marco Di Ludovico, Andrea Prota</i>	
THE INFLUENCE OF IMPACT MODELLING ASSUMPTIONS ON THE DYNAMIC BEHAVIOUR OF FLEXIBLE ROCKING OSCILLATORS	1618
<i>Huanian Zhu, Manolis Chatzis, Sinan Acikgoz</i>	
QUANTIFYING SEISMIC RESILIENCE OF SINGLE-COLUMN ROCKING BRIDGES – A COMPARATIVE STUDY	1626
<i>Anastasios Giouvanidis, You Dong</i>	
DYNAMIC RESPONSE OF MULTI-STOREY STRUCTURES SEISMICALLY ISOLATED USING KINEMATIC BEARINGS	1641
<i>Kosmas E. Bantilas, Ioannis E. Kavvadias, Lazaros Vasiliadis, Anaxagoras Elenas</i>	
THE EFFECT OF IMPACT MODELING ON THE SEISMIC RESPONSE OF MULTI-STOREY PODIUM STRUCTURES	1657
<i>Ioannis E. Kavvadias, Kosmas E. Bantilas, Lazaros Vasiliadis, Anaxagoras Elenas</i>	
3D ROCKING MOTION: BLIND PREDICTION CONTEST RESULTS AND INFLUENCE OF EVALUATION METRIC ON THE RANKINGS	1672
<i>Michalis F. Vassiliou, Marco Broccardo, Cihan Cengiz, Matt Dietz, Luiza Dihoru, Selim Gunay, Khalid M. Mosalam, George Mylonakis, Anastasios Sextos, Bozidar Stojadinovic</i>	
FINITE ELEMENT MODELLING OF A RC ROCKING WALL WITH ADDITIONAL STEEL REBARS	1688
<i>Michele Egidio Bressanelli, Andrea Belleri, Jose Ignacio Restrepo</i>	
CYCLIC TEST OF A PRECAST BRIDGE COLUMN FOR SUSTAINABLE BRIDGE DESIGN	1700
<i>Natalia Reggiani Manzo, Michalis Vassiliou</i>	
 MS 19: ADVANCES IN THE OPTIMUM DESIGN AND CONTROL OF LARGE STRUCTURES UNDER DYNAMIC LOADS	
STUDY OF THE INFLUENCE OF SEISMIC ACTION ON THE CONSTRUCTION COST OF THE LOAD-BEARING STRUCTURE OF A TEN-STOREY R/C BUILDING	1712
<i>Panagiotis Sioulas, Theodoros Chrysanidis, Nikolaos Alamanis, Grigorios Papageorgiou</i>	
ASSESSMENT AND RETROFITTING OF A RC BUILDING THROUGH A MULTI-HAZARD APPROACH: SEISMIC RESISTANCE AND ROBUSTNESS	1725
<i>Martina Scalvenzi, Fabio Freddi, Fulvio Parisi</i>	
OPTIMAL LATERAL RESISTING SYSTEMS FOR HIGH-RISE BUILDINGS UNDER SEISMIC EXCITATIONS	1737
<i>Giulia Angelucci, Giuseppe Quaranta, Fabrizio Mollaioli</i>	
NON-INVASIVE VIBRATING CONTROL OF THE ZOSER PYRAMID	1751
<i>Masoud Shadlou, Pierfrancesco Cacciola, Ashraf Ayoub, Youssef Rashed, Alessandro Tombari</i>	

OPTIMUM DESIGN OF A HYBRID ISOLATION DEVICE FOR SERVER RACKS USING CONSTRAINED DIFFERENTIAL EVOLUTION ALGORITHM	1767
<i>Luca Aceto, Giuseppe Quaranta, Guido Camata, Bruno Briseghella, Enrico Spacone</i>	
INNOVATIVE MASS-DAMPING-BASED APPROACHES FOR SEISMIC DESIGN OF TALL BUILDINGS	1778
<i>Elena Mele, Diana Faiella, Mario Argenziano</i>	
DIAGRID SYSTEM COUPLED WITH SHEAR WALLS: ANALYTICAL INVESTIGATION ON THE DYNAMICAL RESPONSE IN TALL BUILDINGS	1793
<i>Giuseppe Lacidogna, Giuseppe Nitti, Domenico Scaramozzino, Alberto Carpinteri</i>	
OPTIMUM DAMPING OF SLENDER MONOPOLE TOWERS BY GYROSCOPIC STABILIZER	1803
<i>Gian Felice Giaccu, Luigi Fenu, Bruno Briseghella, Camillo Nuti</i>	
VIBRATION CONTROL OF WIND TURBINE TOWERS WITH KDAMPER-BASED DESIGNS	1812
<i>Konstantinos Kapasakalis, Ioannis Antoniadis, Evangelos Sapountzakis</i>	
 MS 20: COMPUTATIONAL DESIGN AND MODELING OF TENSEGRITY SYSTEMS FOR APPLICATIONS IN SCIENCE AND ENGINEERING	
ADAPTIVE BENDING-ACTIVE MODULES FOR A TENSILE SOLAR SHADING SYSTEM	1825
<i>Alessandro D'Ambrosio, Maria Matheou, Rosario Montuori, Elide Nastri</i>	
A MESOSCALE TENSEGRITY MODEL OF SPIDER DRAGLINE SILK FIBER	1834
<i>Ada Amendola, Narinder Singh, Cornelia Rodenburg, Chris Holland, Fernando Fraternali</i>	
GEOMETRIC PATTERNS AND DYNAMICS OF FOLDABLE MODULI FOR ADAPTIVE FAÇADES	1840
<i>Veronica Abbate, Enrico Babilio, Filipe Amarante dos Santos, Narinder Singh, Fernando Fraternali</i>	
MODELING AND DESIGN OF PERIODIC LATTICES WITH TENSEGRITY ARCHITECTURE AND HIGHLY NONLINEAR RESPONSE	1848
<i>Andrea Micheletti, Claudio Intrigila, Nicola Nodargi, Edoardo Artioli, Fernando Fraternali, Paolo Bisegna</i>	
A DYNAMIC-STIFFNESS APPROACH FOR DAMPED LOCALLY-RESONANT TIMOSHENKO BEAMS	1856
<i>Andrea Francesco Russillo, Giuseppe Failla, Antonina Pirrotta, Fernando Fraternali</i>	
SEISMIC METAMATERIALS WITH TENSEGRITY ARCHITECTURE	1867
<i>Filipe Santos, Narinder Singh, Ada Amendola, Fernando Fraternali, Andrea Micheletti</i>	
 MS 22: CONDITION BASED MAINTENANCE AND POST-PROGNOSTICS OF COMPOSITE STRUCTURES: AN ENHANCED PLATFORM	
RECONSTRUCTION OF MATERIAL STIFFNESS PROPERTIES FROM DISPERSION RELATIONS USING GENETIC ALGORITHMS	1874
<i>Victor Thierry, Wen Wu, Dimitrios Chronopoulos, Sergio Cantero-Chinchilla</i>	

PARTICLE FILTER-BASED HYBRID DAMAGE PROGNOSIS CONSIDERING BIAS	1881
<i>Tianzhi Li, Francesco Cadini, Claudio Sbarufatti</i>	

MS 23: ADVANCED MODELS AND NUMERICAL METHODS IN DYNAMICS, WAVE PROPAGATION AND COUPLED PROBLEMS

DISPERSION ANALYSIS OF BULK ACOUSTIC WAVES IN PIEZOELECTRIC MEDIA DISCRETIZED BY ENERGY-ORTHOGONAL FINITE ELEMENTS	1892
<i>Francisco J. Brito Castro</i>	

DISPERSION DESIGN OF 1D PERIODIC DISCRETE SYSTEMS USING LOG-DET HEURISTICS	1922
<i>Anton Tkachuk, Mykola Tkachuk</i>	

AN EFFICIENT PRECONDITIONER FOR MODAL FREQUENCY RESPONSE	1934
<i>Tobias Willerding</i>	

MS 24: LIFE-CYCLE RISK-BASED STRUCTURAL ASSESSMENT AND COST ANALYSIS

FRAGILITY ASSESSMENT OF WIND-EXCITED VIDEO SCREEN ROOMS IN HIGH-RISE BUILDINGS	1941
<i>Fabio Rizzo, Laura Ierimonti, Stefano Sacconi, Ilaria Venanzi</i>	

FRAGILITY OF EXISTING ITALIAN BRIDGES TO TRAFFIC LOADS	1950
<i>Giacomo Miluccio, Daniele Losanno, Fulvio Parisi, Edoardo Cosenza</i>	

TOWARDS THE DEVELOPMENT OF A COMPREHENSIVE FRAMEWORK FOR LIFE CYCLE COST ANALYSIS OF BRIDGES SUBJECTED TO MULTIPLE HAZARDS	1961
<i>Stefano Sacconi, Laura Ierimonti, Ilaria Venanzi, Filippo Ubertini</i>	

LIFE-CYCLE COST ANALYSIS OF TALL BUILDINGS IN SYNOPTIC, MIXED WIND LOAD CLIMATES BY LAYERED STOCHASTIC APPROXIMATION MONTE-CARLO METHOD	1973
<i>Lei Zhang, Luca Caracoglia</i>	

APPLICATION OF BAYESIAN FE MODEL SELECTION FOR SHM OF A MONUMENTAL MASONRY PALACE THROUGH SEMI-SUPERVISED LEARNING	1988
<i>Laura Ierimonti, Nicola Cavalagli, Enrique García-Macías, Ilaria Venanzi, Filippo Ubertini</i>	

A NEURAL NETWORK-BASED APPROACH FOR SEISMIC-INDUCED DAMAGE ASSESSMENT OF STEEL LIQUID STORAGE TANKS	2003
<i>Laura Micheli, Mahmoud Faytarouni</i>	

MS 25: MONITORING, IDENTIFICATION AND VIBRATION CONTROL OF STRUCTURES

APPLICATION OF WAVELET TRANSFORMS ON ACCELERATION RECORDS: PRACTICAL APPROACH	2014
<i>Vladimir Vukobratović, Trevor Yeow, Koichi Kusunoki</i>	

NUMERICAL INVESTIGATION ON THE PRINCIPAL STRESS ROTATION EFFECT UNDER EARTHQUAKE LOADINGS ..	2022
<i>Zhe Wang, Yunming Yang</i>	
ENRICHED BEAM FINITE ELEMENT MODELS WITH TORSION AND SHEAR WARPING FOR DYNAMIC ANALYSIS OF FRAME STRUCTURES	2033
<i>Daniela Addessi, Paolo Di Re, Cristina Gatta</i>	
EARTHQUAKE-INDUCED STRUCTURAL POUNDING BETWEEN TWO INELASTIC SDOF STRUCTURAL SYSTEMS	2058
<i>Pedro Folhento, Rui Barros, Manuel Braz-César</i>	
INFLUENCE OF STRUCTURAL INELASTIC BEHAVIOR IN THE STUDY OF COLLIDING SDOF STRUCTURES	2085
<i>Pedro Folhento, Rui Barros, Manuel Braz-César</i>	
VIRTUAL SENSING AND STRAIN ESTIMATION ON AN OFFSHORE WIND TURBINE USING SUPERVISED LEARNING	2112
<i>Marius Tarpø, Sandro Amador, Evangelos Katsanos, Mattias Skog, Johan Gjødvad, Rune Brincker</i>	
SIMPLIFIED METHODS FOR FREQUENCY ESTIMATION OF SMALL WIND TURBINE TOWER	2121
<i>Anelise Dick, Rui Carneiro-Barros, Manuel Braz-César</i>	
FINITE ELEMENT MODEL CALIBRATION EFFECTS ON THE STATIC AND DYNAMIC RESPONSE OF A METALLIC HOLLOW TOWER	2132
<i>Anelise Dick, Rui Carneiro-Barros, Manuel Braz-César</i>	
PARAMETRIC STUDY OF LATTICE TOWERS ON THE INFLUENCE OF WIND ACTION FOR DIFFERENT TYPOLOGIES OF BRACING	2143
<i>Rui Carneiro-Barros, Luís Barros</i>	
 MS 26: SEISMIC SAFETY ASSESSMENT OF STRUCTURES	
EXPERIMENTAL IN-PLANE LATERAL RESPONSE OF A FULL-SCALE ADOBE MASONRY WALL WITH OPENING	2157
<i>Paolino Cassese, Luigi Fenu, Domenico Asprone, Antonio Occhiuzzi, Fulvio Parisi</i>	
INFLUENCE OF BEAM-TO-COLUMN CONNECTIONS IN SEISMIC VULNERABILITY ASSESSMENT OF STEEL STRUCTURES	2170
<i>Giammaria Gabbianelli, Daniele Perrone, Emanuele Brunesi</i>	
ASSESSMENT OF RC HOLLOW-PIERS FOR SEISMIC LIMIT STATE OF DAMAGE - DIRECT REPAIR COSTS	2185
<i>Pedro Delgado, Naiara Silva, Mário Marques, António Arêde</i>	
 MS 27: TIMBER-BASED ELEMENTS: RECENT ADVANCEMENTS FOR NEW AND EXISTING SEISMIC-RESISTANT STRUCTURES	
OPTIMIZATION OF THE SLIP FORCE IN A NOVEL FRICTION-BASED CONNECTION FOR THE E-CLT TECHNOLOGY ..	2195
<i>Angelo Aloisio, Francesco Boggian, Roberto Tomasi</i>	

EXPERIMENTAL AND NUMERICAL INVESTIGATION OF INNOVATIVE DUCTILE AND REPLACEABLE ANCHORING SYSTEMS FOR WOOD SHEAR WALLS UNDER SEISMIC LOADS	2211
<i>Georgios Balaskas, Vera Wilden, Benno Hoffmeister</i>	
ANALYTICAL AND NUMERICAL MODELLING OF THE IN-PLANE RESPONSE OF TIMBER DIAPHRAGMS RETROFITTED WITH PLYWOOD PANELS	2227
<i>Michele Mirra, Marianthi Sousamli, Michele Longo, Geert Ravenshorst</i>	
MOMENT-CURVATURE DIAGRAMS FOR CLT PANELS ACCOUNTING FOR ORTOGONAL TO GRAIN COMPRESSION TIMBER PROPERTIES	2254
<i>Antonio Sandoli, Claudio D'Ambra, Maria Lippiello, Carla Ceraldi, Bruno Calderoni, Andrea Prota</i>	
REINFORCING STOP-SPLAYED SCARF JOINTS WITH TIMBER PEG: ROLE OF SLENDERNESS	2272
<i>Carla Ceraldi, Claudio D'Ambra, Maria Lippiello, Antonio Sandoli, Andrea Prota</i>	
IMPACT OF RETROFIT OF RC FRAMES BY CLT PANELS AND FRICTION DAMPERS	2287
<i>Francesca Barbagallo, Giuseppe Margani, Edoardo M. Marino, A. Moretti, Carola Tardo</i>	
SEISMIC STRENGTHENING OF EXISTING URM STRUCTURES THROUGH CLT ELEMENTS: NUMERICAL ANALYSIS OF THE APPLICATION OF A NOVEL INTERVENTION TECHNIQUE	2300
<i>Matteo Salvalaggio, Marco Pegoraro, Elisa Saler, Umberto Turrini, Maria Rosa Valluzzi</i>	
POST-TENSIONED LOW DAMAGE TIMBER WALLS WITH DISSIPATIVE DEVICES BEHAVIOUR: NUMERICAL PREDICTION	2314
<i>Valentina Tomei, Maria Zucconi, Barbara Ferracuti</i>	
MANSORY-INFILLED RC FRAMES STRENGTHENED WITH CROSS-LAMINATED TIMBER PANELS	2323
<i>Zabih Mehdipour, Jorge Branco, Iztok Sustersic, Leonardo Filipe Rodrigues, Paulo Lourenço</i>	
INFLUENCE OF PERPENDICULAR WALLS ON THE LATERAL STIFFNESS OF CLT SHEAR WALLS	2336
<i>Elisabetta Maria Ruggeri, Giuseppe D'Arenzo, Marinella Fossetti, Werner Seim</i>	
POST-TENSIONED LOW DAMAGE CLT WALLS WITH REPLACEABLE HYSTERETIC DEVICES – CONCEPT, EXPERIMENTAL AND NUMERICAL CHARACTERIZATION	2352
<i>Luca Pozza, Luca Benedetti, Valentina Tomei, Barbara Ferracuti, Maria Zucconi, Claudio Mazzotti</i>	
TIMBER BEAM-TO-COLUMN JOINT WITH STEEL LINK: DESIGN AND MECHANICAL CHARACTERIZATION THROUGH NUMERICAL INVESTIGATION	2359
<i>Giacomo Iovane, Beatrice Faggiano</i>	
A NUMERICAL STUDY ON A TIMBER-BASED SEISMIC RETROFIT INTERVENTION FOR MASONRY INFILLED CONCRETE FRAMES	2366
<i>Francesco Smirolto, Davide Viel, Ivan Giongo, Maurizio Piazza</i>	

MS 29: SEISMIC PROTECTION OF NON-STRUCTURAL COMPONENTS: RECENT DEVELOPMENTS AND FUTURE CHALLENGES

COMPREHENSIVE NONLINEAR ANALYSIS OF FAILURES OF FIRE-SPRINKLER SYSTEM BASED ON FINITE ELEMENT MODELLING AND AMBIENT VIBRATION TESTS	2388
<i>Shakhzod Takhirov, Amir Gilani</i>	
IMPROVEMENT OF DYNAMIC AND SEISMIC BEHAVIOUR OF CABINETS THROUGH CONTROLLED DEFORMATION	2396
<i>Stefano Pagliaro, Angelo Di Egidio, Alessandro Contento</i>	
NUMERICAL MODELING OF ROCKING AND SLIDING CYLINDRICAL COLUMNS UNDER SEISMIC EXCITATION	2408
<i>Antonios Katsamakas, Michalis Vassiliou</i>	
SEISMIC RISK ASSESSMENT OF ROCKING BUILDING CONTENTS	2421
<i>Michalis Fragiadakis, Spyridon Diamantopoulos</i>	

MS 30: DYNAMIC PROTECTION SYSTEMS AND DEVICES: EXPERIMENTAL TESTS, MATHEMATICAL MODELING AND DESIGN METHODS

SOME RECENT ADVANCES ON THE MODELING OF THE HYSTERETIC BEHAVIOR OF RATE-INDEPENDENT PASSIVE ENERGY DISSIPATION DEVICES	2435
<i>Nicolò Vaiana, Ciro Napolitano, Luciano Rosati</i>	
SEISMIC PROTECTION OF CULTURAL HERITAGE ARTEFACTS BY MEANS OF ELASTOMERIC ISOLATORS: A CASE STUDY	2446
<i>Davide Pellecchia, Stefania Lo Feudo, Nicolo Vaiana, Jean-Luc Dion, Luciano Rosati</i>	
TUNING THE LATERAL RESPONSE OF UNBONDED FIBER REINFORCED ELASTOMERIC ISOLATORS (U-FREIS): EXPERIMENTAL-NUMERICAL FINDINGS	2456
<i>Simone Galano, Andrea Calabrese, Daniele Losanno</i>	
ON THE VERTICAL RESPONSE OF FIBER REINFORCED ELASTOMERIC ISOLATORS (FREIS) UNDER COMBINED VERTICAL AND LATERAL LOADING	2468
<i>Simone Galano</i>	
SEISMIC ISOLATION OF LIGHTWEIGHT STRUCTURES THROUGH WIRE ROPE DEVICES: PRELIMINARY EXPERIMENTAL RESULTS AND SIMULATION	2488
<i>Mariacristina Spizzuoco, Giorgio Serino</i>	
REAL-TIME HYBRID SIMULATION OF A STRUCTURE WITH CIRCULAR FIBER REINFORCED ISOLATORS	2498
<i>Carlos Riascos, Semion Klopov, Johannio Marulanda, Peter Thomson, Giorgio Serino</i>	
A COMPARATIVE STUDY ON THE ACCURACY AND EFFICIENCY OF TWO BIAXIAL HYSTERETIC MODELS SUITABLE FOR ELASTOMERIC BEARINGS	2511
<i>Nagavinothini Ravichandran</i>	

LABORATORY CHARACTERIZATION OF A RECLAIMED RUBBER COMPOUND FOR LOW-COST ELASTOMERIC ISOLATORS	2525
<i>Fabrizia Cilento, Daniele Losanno, Luigi Piga</i>	
EFFECT OF EXTREMELY LOW TEMPERATURE ON MECHANICAL PROPERTIES OF A LARGE SIZE LRB	2536
<i>Gokhan Ozdemir, Esengul Cavdar, Volkan Karuk</i>	
STIFF DYNAMIC ABSORBERS FOR THE VERTICAL SEISMIC PROTECTION OF STRUCTURES	2543
<i>Marina Kalogerakou, Konstantinos Kapasakalis, Ioannis Antoniadis, Evangelos Sapountzakis</i>	
 MS 32: SIMPLIFIED METHODOLOGIES FOR PERFORMANCE AND LOSS ASSESSMENT AT BUILDING OR TERRITORIAL SCALE	
ACCURATE COLLAPSE CAPACITY QUANTIFICATION FOR INFILLED RC FRAME BUILDINGS	2557
<i>Al Mouayed Bellah Nafeh, Gerard O'Reilly</i>	
DEVELOPMENT OF A PYTHON-BASED STOREY LOSS FUNCTION GENERATOR	2573
<i>Davit Shahnazaryan, Gerard O'Reilly, Ricardo Monteiro</i>	
ASSESSMENT OF POST-EARTHQUAKE DAMAGES ON ITALIAN SCHOOL BUILDINGS PORTFOLIO OVER THE LAST 50 YEARS	2591
<i>Sergio Ruggieri, Chiara Tosto, Daniele Perrone, Giuseppina Uva, Maria Antonietta Aiello</i>	
SEISMIC RISK ASSESSMENT FOR THE ITALIAN RESIDENTIAL MASONRY BUILT STOCK AND EFFECTIVENESS OF DIFFERENT MITIGATION STRATEGIES	2606
<i>Pietro Carpanese, Veronica Follador, Elisa Saler, Francesca da Porto</i>	
THE USE OF STICK-IT MODEL FOR EDP ASSESSMENT IN EXISTING RC INFILLED TYPOLOGIES	2619
<i>Marco Gaetani d'Aragona, Maria Polese, Marco Di Ludovico, Andrea Prota</i>	
APPLICATION OF THE EMPIRICAL PREDICTIVE DAMAGE MODEL OF HISTORICAL CHURCHES	2631
<i>Claudia Canuti, Michele Morici, Andrea Dall'Asta, Graziano Leoni</i>	
A SEISMIC RISK ASSESSMENT FRAMEWORK FOR LOSS ESTIMATION OF CRITICAL INFRASTRUCTURE – HOSPITALS CASE	2643
<i>Paolo Basso, Saimir Osmani, Matteo Scolari, Ruben Valsecchi</i>	
CAESAR II: AN ITALIAN DECISION SUPPORT TOOL FOR THE SEISMIC RISK. THE CASE STUDY OF TORRE PELLICE, VILLAR PELLICE AND PINEROLO MUNICIPALITIES	2659
<i>Giulio Zuccaro, Francesca Linda Perelli, Daniela De Gregorio, Daniele Masi</i>	
OPEN MODELS AND SOFTWARE FOR ASSESSING THE VULNERABILITY OF THE EUROPEAN BUILDING STOCK	2678
<i>Helen Crowley, Vitor Silva, Luis Martins, Xavier Romão, Nuno Pereira</i>	

PELL-SCHOOLS A STANDARDIZED AND INTEROPERABLE PLATFORM FOR THE SEISMIC VULNERABILITY AND ENERGY EFFICIENCY DATA MANAGEMENT OF ITALIAN SCHOOLS	2689
<i>Laura Blaso, Sonia Giovinazzi, Simona Bianchi, Livio Pedone, Chiara Ormando, Paolo Clemente, Stefano Pampanin, Nicoletta Gozo, Giuseppina Giuliani, Maurizio Pollino</i>	

EFFECT OF BUILDING SAMPLE SELECTION ON SEISMIC FRAGILITY CURVES FOR RC BUILDINGS AT TERRITORIAL SCALE	2707
<i>Maria Zucconi, Fabio Romano, Barbara Ferracuti</i>	

VOLUME II

Minisymposia

MS 33: EXPERIMENTAL MEASUREMENTS AND NUMERICAL SIMULATION ON PROBLEMS IN THE FIELD OF EARTHQUAKE ENGINEERING AND STRUCTURAL DYNAMICS

ANALYTICAL INVESTIGATION OF THE TENSILE EXPERIMENTS MODELING THE ELONGATION DEGREE OF R/C WALLS FOR STUDYING THE LATERAL BUCKLING PHENOMENON	2718
<i>Theodoros Chrysanidis, Vassilis Panoskaltsis</i>	

ANALYTICAL INVESTIGATION OF THE TENSILE EXPERIMENTS TO PRISMS WITH VARYING LONGITUDINAL RATIO FOR STUDYING THE LATERAL BUCKLING OF R/C WALLS	2730
<i>Theodoros Chrysanidis, Vassilis Panoskaltsis</i>	

PRELIMINARY CONSIDERATIONS ON THE LOSS OF SUPPORT FOR PRECAST BEAM ELEMENTS	2744
<i>Marius Eteme Minkada, Simone Labò, Alessandra Marini, Andrea Belleri</i>	

SEISMIC PERFORMANCE OF BELL TOWERS	2754
<i>George C. Manos</i>	

STUDYING THE PERFORMANCE OF STONE MASONRY ARCH BRIDGES EMPLOYING IN-SITU MEASUREMENTS AND NUMERICAL PREDICTIONS	2769
<i>George C. Manos, N. Simos</i>	

EXPERIMENTAL IDENTIFICATION OF MECHANICAL AND DYNAMIC CHARACTERISTICS OF 3D PRINTING SPECIMENS	2791
<i>Ioannis E. Kavvadias, Konstantinos Tsongas, Dimitrios Tzetzis, Kosmas E. Bantilas, Lazaros Vasiliadis, Anaxagoras Elenas</i>	

INVESTIGATION OF LOW COST SMAS UNDER ELEVATED TEMPERATURES	2800
<i>Sofia Piliafa, Lazaros Melidis, Lambros Kotoulas, Nikolaos Makris, Konstantinos Katakalos</i>	

EXPERIMENTAL AND NUMERICAL INVESTIGATION OF THE PLASTIC CYCLIC BEHAVIOUR OF SIMPLE STEEL COUPONS	2808
<i>Alexandra Nalmpantidou, George C. Manos</i>	

EXPERIMENTAL TESTS AND NUMERICAL STUDY OF THE PLASTIC CYCLIC BEHAVIOUR OF A STEEL BEAM-TO-COLUMN CONNECTION	2824
<i>George C. Manos, Alexandra Nalmpantidou</i>	
DYNAMIC AND VIBROACOUSTIC RESPONSE OF TIMBER FLOOR PANELS. MEASUREMENTS AND NON-LINEAR NUMERICAL SIMULATIONS	2843
<i>Magdalini Titirla, Sarah Benakli, Walid Larbi</i>	
THE USE OF INTELLIGENT FACADES FOR UPGRADING ENERGY AND SEISMIC DEMANDS OF EXISTING R/C STRUCTURE	2852
<i>Lazaros Melidis, Efthymios A. Kechagias, Konstantinos Katakalos, George C. Manos</i>	
EXPERIMENTAL AND NUMERICAL INVESTIGATION OF FRP STRENGTHENED R/C BEAM-TO-COLUMN JOINTS SUBJECTED TO CYCLIC SEISMIC-TYPE LOADING	2863
<i>Lazaros Melidis, George C. Manos, J. Maranos, Konstantinos Katakalos</i>	
THE BEHAVIOR OF PARTIALLY GROUTED MASONRY WALLS SUBJECTED TO OUT OF PLANE SEISMIC TYPE LOADS. LABORATORY MEASUREMENTS AND NUMERICAL SIMULATIONS	2875
<i>George C. Manos, Lazaros Melidis, Lampros Kotoulas, Konstantinos Katakalos</i>	
IN PLANE BEHAVIOR OF PARTIALLY GROUTED MASONRY WALLS USING A NEW CLAY UNIT. LABORATORY MEASUREMENTS AND NUMERICAL SIMULATIONS	2885
<i>George C. Manos, Lazaros Melidis, Lampros Kotoulas, Konstantinos Katakalos</i>	
EXPERIMENTAL AND NUMERICAL INVESTIGATION OF THE OUT OF PLANE BEHAVIOR OF THERMAL INSULATED MASONRY WALLS	2895
<i>George C. Manos, Lazaros Melidis, Konstantinos Katakalos, Anthimos Anastasiadis</i>	
EXPERIMENTAL & NUMERICAL INVESTIGATION OF LAP-SPLICED R/C COLUMNS UNDER THREE POINT BENDING & AXIAL COMPRESSION	2903
<i>Pelagia Kastiza, Lazaros Melidis, Konstantinos Katakalos</i>	
DEVELOPMENT OF AN EXPERIMENTAL SETUP FOR MEASURING THE EFFECTIVENESS OF STRENGTHENED PRESTRESSED CONCRETE CYLINDER PIPES (PCCP)	2913
<i>Sofia Gkaraklova, Lazaros Melidis, George C. Manos, Konstantinos Katakalos</i>	
MECHANICAL PROPERTIES CHARACTERISATION OF FRPS UNDER ELEVATED TEMPERATURES	2922
<i>Christina Papadimitriou, Lambros Kotoulas, Nikolaos Makris, Lazaros Melidis, Konstantinos Katakalos</i>	
EXPERIMENTAL TESTING CAMPAIGN AND NUMERICAL MODELLING OF AN INNOVATIVE BASE-PLATE CONNECTION FOR PALLET RACKING SYSTEMS	2934
<i>Bonaventura Tagliaferro, Rosario Montuori, Ioannis Vayas, Sofia Antonodimitraki, Magdalini D. Titirla, Marco Simoncelli, Xenophon Lignos</i>	
STUDY OF THE INFLUENCE OF UNDERLYING SOFT-SOIL LAYERS ON THE DYNAMIC AND EARTHQUAKE RESPONSE OF BELL TOWERS	2943
<i>George C. Manos</i>	

THE INFLUENCE OF WOODEN ROOF CONNECTION ON THE DYNAMIC AND EARTHQUAKE RESPONSE OF OLD INDUSTRIAL STONE MASONRY BUILDINGS	2965
<i>George C. Manos, Lampros Kotoulas</i>	
EXPERIMENTAL AND ANALYTICAL INVESTIGATION OF THE STRENGTHENING OF TRADITIONAL TIMBER FRAMES	2983
<i>Ioannis Stavrou, Panayiotis Demosthenous, Stelios Papastilianou, Milton Demosthenous</i>	
NUMERICAL SIMULATIONS OF THE EXPERIMENTAL RESULTS OF STEEL FRAME MODEL WITH ROOF ROLLER SYSTEM SUBJECTED TO DYNAMIC BASE EXCITATIONS	2997
<i>Nikodemos Kouroufexis, Milton Demosthenous</i>	
EXPERIMENTAL AND NUMERICAL INVESTIGATION OF A MASONRY MODEL BUILDING SUBJECTED TO DYNAMIC BASE EXCITATIONS	3007
<i>Stefania Demosthenous, Milton Demosthenous</i>	
PASSIVE CONTROL ISSUES ON THE LONGITUDINAL AND TRANSVERSE VIBRATIONS OF FLEXIBLE PYLONS	3021
<i>George Manolis, George Dadoulis</i>	
PSEUDO-DYNAMIC ANALYSES OF INFILLED REINFORCED CONCRETE FRAMED STRUCTURES WITH PRIOR DAMAGES AFTER ADVANCED RETROFIT	3036
<i>Theodoros Rousakis, Evgenia Anagnostou, Theodora Fanaradelli</i>	
EXPERIMENTAL AND NUMERICAL STUDY OF SELF-SUPPORTING DOUBLE SKIN METAL FACED MINERAL WOOL PANELS	3049
<i>Sofia Gkaraklova, Lazaros Melidis, George C. Manos, Konstantinos Katakalos</i>	
 MS 34: FRAGILITY CURVES FOR EXISTING BUILDINGS: OPEN CHALLENGES IN THEIR DEFINITION AND USE FOR SEISMIC RISK ANALYSES	
SEISMIC FRAGILITY ASSESSMENT FOR A CLASS OF RC SCHOOL BUILDINGS IN ITALY LEVERAGING DETAILED AND REDUCED-ORDER MODELS	3059
<i>Sergio Ruggieri, Giuseppina Uva</i>	
FRAGILITY CURVES FOR RC FRAMED BUILDINGS CONSIDERING CUMULATIVE DAMAGE DUE TO EARTHQUAKE GROUND MOTION AND SLOW-MOVING LANDSLIDES	3073
<i>Fulvio Parisi, Elia Acconcia</i>	
FRAGILITY CURVES FOR ITALIAN RESIDENTIAL MASONRY BUILDINGS WITH RETROFIT INTERVENTIONS	3083
<i>Veronica Follador, Marco Donà, Pietro Carpanese, Francesca da Porto</i>	
FRAGILITY MODELS FOR EXISTING MASONRY INFILLED RC FRAMES IN THE EMILIA AREA	3098
<i>Gianluca Salamida, Nicola Buratti</i>	
FRAGILITY ASSESSMENT OF THE ITALIAN MASONRY SCHOOL BUILDING ASSET FOR RISK EVALUATION AT NATIONAL SCALE	3113
<i>Elisa Saler, Veronica Follador, Pietro Carpanese, Francesca da Porto</i>	

DERIVATION OF SEISMIC FRAGILITY CURVES OF A GRAVITY-LOAD DESIGNED RC SCHOOL BUILDING THROUGH NLTHA	3127
<i>Elisa Saler, Pietro Carpanese, Veronica Follador, Francesca da Porto</i>	
TYPOLOGICAL ANALYSIS AND VULNERABILITY CURVES FOR MASONRY CHURCHES	3141
<i>Elvis Cescatti, Veronica Follador, Francesca da Porto</i>	
COMPARATIVE STUDY ON TWO ANALYTICAL MECHANICAL-BASED METHODS FOR DERIVING FRAGILITY CURVES TARGETED TO MASONRY SCHOOL BUILDINGS	3155
<i>Serena Cattari, Sara Alfano, Daria Ottonelli, Elisa Saler, Francesca da Porto</i>	
ROLE OF DESIGN LEVEL AND INFILL ARRANGEMENT ON THE SEISMIC FRAGILITY CURVES OF ITALIAN RC EXISTING BUILDINGS	3176
<i>Angelo Masi, Vincenzo Manfredi, Giuseppe Nicodemo, Andrea Digrisolo</i>	
 MS 35: RECENT ADVANCES IN SEISMIC ISOLATION AND SUPPLEMENTAL DAMPING SYSTEMS FOR VIBRATION CONTROL	
EXPERIMENTAL AND NUMERICAL ASSESSMENT OF ISOLATION SEISMIC DEVICE FOR RETROFIT OF INDUSTRIAL EXISTING SHED	3187
<i>Luca Mari, Virginio Quaglini, Carlo Pettoruso, Eleonora Bruschi</i>	
INVESTIGATION OF THE BREAKAWAY FRICTION INFLUENCE ON THE SEISMIC RESPONSE OF BUILDINGS ISOLATED WITH CURVED SURFACE SLIDERS	3204
<i>Eleonora Bruschi, Virginio Quaglini, Emanuele Gandelli</i>	
SUPPLEMENTAL ENERGY DISSIPATION WITH PRESTRESSED LEAD EXTRUSION DAMPERS (P-LED): EXPERIMENTS AND MODELING	3216
<i>Carlo Pettoruso, Eleonora Bruschi, Virginio Quaglini</i>	
AN INNOVATIVE STEEL DAMPER WITH ADAPTIVE HYSTERETIC BEHAVIOR	3230
<i>Emanuele Gandelli, Johan Distl, Peter Huber, Christian Braun</i>	
INVESTIGATIONS ON INTER-STOREY SEISMIC ISOLATION AS A TECHNIQUE FOR ADDING UPPER STOREYS	3248
<i>Enrico Bernardi, Marco Donà, Francesca da Porto, Ping Tan</i>	
FUNCTIONAL ACCEPTANCE TESTS FOR THE SEISMIC ISOLATION DEVICES OF THE NEW SAN GIORGIO BRIDGE IN GENOA	3267
<i>Marcello Cademartori, Andrea Miano, Antimo Fiorillo, Alessandro Aliotta, Marco Di Ludovico, Andrea Prota, Simone Dellacasagrande, Alaeddine Fatnassi, Daniele Pastorelli</i>	
MODELING STRATEGIES FOR THE LATERAL RESPONSE OF CURVED SURFACE SLIDER DEVICES UNDER EXTREME DISPLACEMENT DEMANDS	3281
<i>Marco Furinghetti, Alberto Pavese</i>	
ASSESSMENT OF THE SHEAR PROPERTIES OF HDRBS UNDER DIFFERENT COMPRESSION LEVELS	3294
<i>Eleonora Bruschi, Emanuele Gandelli, Carlo Pettoruso, Virginio Quaglini</i>	

MS 36: METHODOLOGIES AND ADVANCED TOOLS FOR SEISMIC RISK ASSESSMENT, MANAGEMENT, AND MITIGATION: ADVANCES AND OPEN CHALLENGES

A FRAMEWORK FOR THE ASSESSMENT OF SEISMIC DAMAGE SCENARIOS IN THE EMILIA-ROMAGNA REGION, ITALY	3305
<i>Elena Simoni, Nicola Buratti, Claudio Mazzotti</i>	
THE USE OF AN INTEGRATED APPROACH FOR BUILDING INVENTORY AND EFFECTS ON RISK ESTIMATIONS AT THE TERRITORIAL SCALE	3323
<i>Maria Polese, Marco Di Ludovico, Gabriella Tocchi, Andrea Prota</i>	
SEISMIC ASSESSMENT OF MASONRY BUILDINGS AT TERRITORIAL SCALE	3338
<i>Chiara Iacovino, Amedeo Flora, Donatello Cardone, Marco Vona</i>	
INVESTIGATING GROUND-MOTION DURATION EFFECTS ON BUILDING PORTFOLIO LOSS ESTIMATES	3360
<i>Kenneth Otárola, Roberto Gentile, Luis Sousa, Carmine Galasso</i>	

MS 37: RISK ASSESSMENT OF BRIDGES AND ROAD NETWORKS SUBJECTED TO NATURAL HAZARDS

RELIABILITY-BASED ASSESSMENT OF A MASONRY ARCH BRIDGE UNDER FLOOD EVENTS	3377
<i>Carlos Andres Mendoza Cabanzo, Monica Patricia Santamaria Ariza, Hélder S. Sousa, Jose Antonio Campos e Matos</i>	
SIMPLIFIED FRAGILITY ANALYSIS OF MULTI-SPAN ISOSTATIC RC-BRIDGES CONSIDERING AN INCOMPLETE KNOWLEDGE LEVEL	3389
<i>Andrea Nettis, Domenico Raffaele, Giuseppina Uva</i>	
SCOUR-INDUCED DYNAMIC PROPERTIES MODIFICATION OF MASONRY ARCH BRIDGES WITH DIFFERENT GEOMETRY	3407
<i>Fabrizio Scozzese, Laura Ragni, Enrico Tubaldi, Fabrizio Gara</i>	
INFLUENCE OF THE PIERS' HEIGHT ON THE FRAGILITY ASSESSMENT OF ITALIAN R.C. LINK SLAB BRIDGES	3418
<i>Lucia Minnucci, Fabrizio Scozzese, Andrea Dall'Asta, Sandro Carbonari, Fabrizio Gara</i>	
PERFORMANCE-BASED EARTHQUAKE ENGINEERING ANALYSIS OF SHORT-MEDIUM SPAN STEEL-CONCRETE COMPOSITE BRIDGES	3430
<i>Daniele Corritore, Fabrizio Paolacci</i>	
SEISMIC VULNERABILITY ANALYSIS OF THE HISTORICAL SS FILIPPO E GIACOMO MASONRY ARCH BRIDGE IN ASCOLI PICENO (ITALY)	3445
<i>Graziano Leoni, Fabrizio Gara, Michele Morici</i>	
ROC-BASED PERFORMANCE EVALUATION OF DATA CLEANSING TECHNIQUES FOR FALSE ALARM RISK REDUCTION IN CONTINUOUSLY MONITORED BRIDGES	3458
<i>Valentina Giglioni, Enrique García-Macías, Ilaria Venanzi, Laura Ierimonti, Filippo Ubertini</i>	
RC TIED-ARCH BRIDGES: TYPOLOGICAL ANALYSIS FOR THE DEFINITION OF RETROFIT INTERVENTIONS	3470
<i>Valentina Pernechele, Elisa Saler, Francesca da Porto, Claudio Modena</i>	

APPLICATION TO AN URBAN BRIDGE STOCK OF A PRIORITIZATION PROCEDURE BASED ON SEISMIC ASSESSMENT COMPARED WITH THE NOVEL ITALIAN GUIDELINES	3484
<i>Elisa Saler, Valentina Pernechele, Giovanni Tecchio, Francesca da Porto</i>	
ANALYTICAL PROBABILISTIC RESILIENCE ESTIMATION FOR BRIDGES UNDER NEAR-FAULT EARTHQUAKES	3499
<i>Yang Liu, Da-Gang Lu, Fabrizio Paolacci</i>	
SIMPLIFIED ANALYTICAL-MECHANICAL METHODOLOGY FOR STRUCTURAL-SEISMIC SAFETY ASSESSMENT OVER TIME OF RC BRIDGES AFFECTED BY CORROSION PHENOMENA	3520
<i>Matteo Gentile, Filippo Molaioni, Stefano Pampanin</i>	
REAL-TIME ASSESSMENT OF PERFORMANCE INDICATORS FOR BRIDGES TO SUPPORT ROAD NETWORK MANAGEMENT IN THE AFTERMATHS OF EARTHQUAKE EVENTS	3536
<i>Chiara Ormando, Ugo Ianniruberto, Paolo Clemente, Sonia Giovinnazzi, Maurizio Pollino, Vittorio Rosato</i>	
DIAGNOSTICS OF HISTORICAL STEEL BRIDGES: THE CASE OF THE VALENCIAN RAILROAD NETWORK	3551
<i>Valentino Sangiorgio, Andrea Nettis, Giuseppina Uva, Juan A. García-Cerezo, Pedro A. Calderón, Humberto Varum, Jose M. Adam</i>	
TOWARDS A UNIFIED SEISMIC- FLOOD HAZARD MODEL FOR RISK ASSESSMENT OF ROADWAY NETWORKS IN GREECE	3569
<i>Anna Karatzetzou, Sotiria Stefanidou, Stefanos Stefanidis, Grigorios Tsinidis, Dimitrios Pitilakis</i>	
MS 38: DYNAMIC SOIL-FOUNDATION-STRUCTURE INTERACTION: DEVELOPMENTS AND EMERGING ISSUES	
DYNAMIC CROSS-INTERACTION BETWEEN TWO CLOSELY-SPACED SHALLOW FOUNDATIONS	3577
<i>Enza Zeolla, Filomena de Silva, Stefania Sica</i>	
ON THE SITE-AMPLIFICATION AND SOIL-STRUCTURE INTERACTION IN URM STRUCTURES: USE OF FRAGILITY CURVES TO ASSESS THE SIMPLIFIED CODE-APPROACH	3589
<i>Andrea Brunelli, Filomena de Silva, Serena Cattari</i>	
ELASTODYNAMIC ANALYSIS OF LATERALLY LOADED PILES: MODIFICATIONS TO A SIMPLIFIED ENERGY APPROACH	3605
<i>Jamie J. Crispin, George Mylonakis</i>	
ON THE EFFECTIVENESS OF EXPERIMENTALLY-DERIVED FOUNDATION IMPEDANCE FUNCTIONS	3617
<i>Chiara Amendola, Filomena de Silva, Dimitrios Pitilakis, Francesco Silvestri</i>	
NUMERICAL ANALYSIS ON THE INFLUENCE OF DYNAMIC SOIL-STRUCTURE INTERACTION IN SORIA ARCH DAM: A CASE STUDY	3633
<i>J.C. Galván, L.A. Padrón, J.J. Aznárez, O. Maeso</i>	
SOIL-CAISSON-BRIDGE PIER-DECK DYNAMIC INTERACTION UNDER STRONG EARTHQUAKES: THE INFLUENCE OF PRIMARY AND SECONDARY SOIL NONLINEARITIES	3645
<i>Domenico Gaudio, Sebastiano Rampello</i>	

INFLUENCE OF SCOUR ON DYNAMIC IMPEDANCES OF BRIDGE SHALLOW FOUNDATIONS	3658
<i>Christos Antonopoulos, Enrico Tubaldi, Sandro Carbonari, Fabrizio Gara, Francesca Dezi</i>	

KINEMATIC PILE-HEAD BENDING UNDER LARGE EARTHQUAKE-INDUCED SHEAR STRAINS	3671
<i>Stefano Stacul, Emmanouil Rovithis, Raffaele Di Laora</i>	

ASPECTS OF SEISMIC SOIL-PILE-STRUCTURE INTERACTION IN SOFT CLAY BY CENTRIFUGE TESTING	3685
<i>Maria Iovino, Emmanouil Rovithis, Raffaele Di Laora, Cristiano D'Alterio, Luca de Sanctis, Thejesh K. Garala, Stuart Haigh, Gopal S. Madabhushi</i>	

MS 39: THE CONTRIBUTION OF DYNAMIC TESTS AND STRUCTURAL MONITORING ON THE SEISMIC RISK ASSESSMENT AND MITIGATION

LONG TERM MONITORING OF THE SANTA MARIA DI COLLEMAGGIO BASILICA	3697
<i>Angelo Aloisio, Riccardo Cirella, Antonacci Elena, Rocco Alaggio</i>	

AMBIENT VIBRATION TEST ON AN EXISTING PRESTRESSED CONCRETE BRIDGE	3720
<i>Alessandra De Angelis, Giacomo Esposito, Giuseppe Maddaloni, Edoardo Cosenza, Maria Rosaria Pecce</i>	

MODAL ANALYSIS OF THE HISTORICAL SS FILIPPO E GIACOMO MASONRY ARCH BRIDGE IN ASCOLI PICENO (ITALY)	3731
<i>Fabrizio Gara, Graziano Leoni, Michele Morici</i>	

THE TRACKING OF MODAL PARAMETERS FOR A REINFORCED CONCRETE BUILDING DURING LOW-MEDIUM INTENSITY EARTHQUAKES	3743
<i>Davide Arezzo, Vanni Nicoletti, Sandro Carbonari, Fabrizio Gara</i>	

FIRST RESULTS OF LONG-TERM MONITORING OF PORTICO VARANO IN THE CAMERINO DUCAL PALACE (ITALY)	3752
<i>Leonardo Cipriani, Andrea Dall'Asta, Graziano Leoni, Michele Morici, Alessandro Zona</i>	

DEVELOPMENT OF LOW COST SENSORS FOR MONITORING OF STRUCTURES	3762
<i>Giuseppe Maddaloni, Alessandra De Angelis, Francesco Minicozzi, Claudio Martino, Maria Rosaria Pecce</i>	

CALIBRATION OF NUMERICAL MODELS TO SUPPORT SHM: THE CONSOLI PALACE OF GUBBIO, ITALY	3778
<i>Serena Cattari, Daniele Sivori, Sara Alfano, Laura Ierimonti, Nicola Cavalagli, Ilaria Venanzi, Filippo Ubertini</i>	

MS 40: ARTIFICIAL INTELLIGENCE & MACHINE LEARNING IN DESIGN AND ASSESSMENT OF STRUCTURES

RAPID DESIGN OF R/C COLUMNS USING MACHINE LEARNING TECHNIQUES	3795
<i>Vassilis Papanikolaou, Aristotelis Charalampakis</i>	

DEVELOPMENT OF A NEW FUNDAMENTAL PERIOD FORMULA BY CONSIDERING SOIL-STRUCTURE INTERACTION WITH THE USE OF MACHINE LEARNING ALGORITHMS	3801
<i>Vicky-Lee Taljaard, Dewald Z. Gravett, Christos Mourtas, George Markou, Nikolaos Bakas, Manolis Papadrakakis</i>	
PREDICTING THE SHEAR CAPACITY OF REINFORCED CONCRETE SLENDER BEAMS WITHOUT STIRRUPS BY APPLYING ARTIFICIAL INTELLIGENCE ALGORITHMS	3810
<i>Zelda Spijkerman, Nikolaos Bakas, George Markou, Manolis Papadrakakis</i>	
STRUCTURAL DAMAGE PREDICTION UNDER SEISMIC SEQUENCE USING NEURAL NETWORKS	3820
<i>Petros C. Lazaridis, Ioannis E. Kavvadias, Konstantinos Demertzis, Lazaros Iliadis, Antonios Papaleonidas, Lazaros K. Vasiliadis, Anaxagoras Elenas</i>	
AUTOMATED ESTIMATION OF BUILDING HEIGHT THROUGH IMAGE PROCESSING	3837
<i>Pietro Carpanese, Marco Donà, Francesca da Porto</i>	
MACHINE LEARNING TECHNIQUES FOR THE ESTIMATION OF LIMIT STATE THRESHOLDS AND BRIDGE-SPECIFIC FRAGILITY ANALYSIS OF R/C BRIDGES	3848
<i>Sotiria Stefanidou, Vassilis Papanikolaou, Elias Paraskevopoulos, Andreas Kappos</i>	
LINKS OF AESTHETIC VALUE OF MULTI-CURVATURE ARTIFACTS, WITH THEIR STRUCTURAL BEHAVIOR, UTILIZING MACHINE LEARNING ALGORITHMS	3857
<i>Nikolaos Bakas, Neofytos Christofi, John Bellos, Dimitrios Antoniou, George Markou</i>	
PERFORMANCE AND SCALABILITY OF DEEP LEARNING MODELS TRAINED ON A HYBRID SUPERCOMPUTER: APPLICATION IN THE PREDICTION OF THE SHEAR STRENGTH OF SLENDER RC BEAMS	3878
<i>Nikolaos Bakas, George Markou, Dimos Charmpis, Kyriakos Hadjiyiannakou</i>	
PREDICTION OF THE EIGENPERIODS OF MDOF SHEAR BUILDINGS USING NEURAL NETWORKS	3894
<i>Vagelis Plevris, German Solorzano</i>	
 MS 41: SEISMIC PERFORMANCE OF STRUCTURES WITH ISOLATION AND/OR ENERGY DISSIPATION DEVICES	
SEISMIC PERFORMANCE OF STRUCTURES EQUIPPED WITH BRB	3912
<i>Paolo Castaldo, Enrico Tubaldi, Laura Gioiella</i>	
EFFECT OF LEAD RUBBER BEARING (LRB) MODELING TECHNIQUE ON THE SEISMIC RESPONSE OF BASE-ISOLATED BRIDGES	3930
<i>Vahid Aghaeidoost, Ahm Muntasir Billah</i>	
AN ADVANCED MODEL FOR THE FLUID VISCOUS DAMPER BRITTLE FAILURE	3942
<i>Laura Gioiella, Fabrizio Scozzese, Enrico Tubaldi, Laura Ragni, Andrea Dall'Asta</i>	
SEISMIC PERFORMANCE OF STEEL MRFS RETROFITTED WITH BRBS: INFLUENCE OF THE DESIGN DECISIONS FOR THE DEVICES	3957
<i>Fernando Gutiérrez-Urzuá, Fabio Freddi</i>	

EXPERIMENTAL INVESTIGATION OF SPHERICAL RUBBER SEISMIC ISOLATION BEARINGS	3970
<i>Antonios Katsamakas, Gabriel Belser, Michalis Vassiliou, M. Blondet, Božidar Stojadinovic</i>	
EXPERIMENTAL SEISMIC POST-TENSIONING PERFORMANCE AND LONG-TERM EFFECTS OF A POST-TENSIONED TIMBER FRAMED MODEL WITH DISSIPATIVE SYSTEMS	3982
<i>Antonio Di Cesare, Felice Carlo Ponzo, Nicla Lamarucciola, Domenico Nigro</i>	
EXPERIMENTAL COMPARISON BETWEEN FLAT AND CURVED SLIDING CONDITIONS FOR THE RESPONSE EVALUATION OF CURVED SURFACE SLIDER DEVICES	3992
<i>Alberto Pavese, Marco Furinghetti</i>	
THE NEW CAMERINO UNIVERSITY RESEARCH CENTER: DESIGN OF THE BASE-ISOLATED BUILDING AND DYNAMIC TESTING	4005
<i>Andrea Dall'Asta, Graziano Leoni, Fabio Micozzi, Laura Gioiella, N. Ceccolini, Laura Ragni</i>	
VARIATION IN RESPONSE OF A BRIDGE SEISMICALLY ISOLATED WITH LRBS UNDER THE EFFECT OF LOW AMBIENT TEMPERATURE	4015
<i>Esengul Cavdar, Volkan Karuk, Gokhan Ozdemir</i>	
SEISMIC PROTECTION OF MULTI-STORY STRUCTURES WITH NOVEL VIBRATION ABSORPTION DEVICES COMBINING NEGATIVE STIFFNESS AND INERTER	4026
<i>Konstantinos Kapasakalis, Georgios Florakis, Ioannis Antoniadis, Evangelos Sapountzakis</i>	
MULTI-LEVEL OPTIMISATION OF NONLINEAR VISCOUS DAMPERS FOR SEISMIC RETROFIT OF SUBSTANDARD STEEL FRAMES	4046
<i>Dario De Domenico, Iman Hajirasouliha</i>	
SEISMIC RETROFIT OF EXISTING PRECAST RC BUILDINGS WITH DISSIPATIVE DEVICES BASED ON CARBON WRAPPED STEEL TUBES	4058
<i>Lucia Praticò, Andrea Vittorio Pollini, Devis Sonda, Nicola Buratti</i>	
METAMODELING CHOICES FOR SEISMIC VULNERABILITY ASSESSMENT OF BRB-RETROFITTED LOW-DUCTILITY RC FRAMES	4078
<i>Jayadipta Ghosh, Fabio Freddi</i>	
NUMERICAL INVESTIGATION OF RUBBER BEARINGS WITH LOW SHAPE FACTOR UNDER SEISMIC EXCITATION	4091
<i>Alessandra Orfeo, Enrico Tubaldi, Alan Muhr, Daniele Losanno</i>	
INELASTIC RESPONSE MODES OF SEISMICALLY ISOLATED STRUCTURES: FAILURE OF THE ISOLATORS OR DAMAGE IN THE ISOLATED STRUCTURE?	4100
<i>Anastasios Tsiavos, Tomislav Markić, David Schlatter, Božidar Stojadinović</i>	
 MS 42: ADVANCES IN MODEL REDUCTION TECHNIQUES OF COMPUTATIONAL AND STRUCTURAL DYNAMICS	
A NEW PARALLEL ALGORITHM FOR THE OPTIMUM EMBEDDED REBAR MESH GENERATION FOR LARGE-SCALE REINFORCED CONCRETE STRUCTURES	4111
<i>Dewald Gravett, George Markou</i>	

ON THE APPLICATION OF GENERALISED SCHUR COMPLEMENTS TO SUBSYSTEM-LEVEL VARIABILITY QUANTIFICATION	4120
<i>Vladimir Yotov</i>	

MS 43: ANALYSES AND DESIGN OF STEEL JOINTS UNDER CYCLIC ACTION

BEHAVIOUR OF LAP SHEAR RIVETED CONNECTIONS WITH CONSTRUCTIONAL IMPERFECTIONS	4134
<i>Aldo Milone, A. De Martino</i>	
BEHAVIOR OF INNO3D JOINTS UNDER MONOTONIC AND CYCLIC LOADING	4142
<i>Arash Poursadrollah, A. De Martino</i>	
DESIGN AND ANALYSIS OF FREEDAM FRAMES: COMPARISON WITH TRADITIONAL CONNECTIONS	4149
<i>Maria Maglio, Camilla Naddei, Elide Nastri, Rosaria Russo, Paolo Todisco</i>	
COMPONENT MODELLING OF CONNECTIONS BETWEEN CIRCULAR-HOLLOW-SECTIONS AND THROUGH- ALL MEMBERS	4177
<i>A. Saldutti, Sabatino Di Benedetto, Massimo Latour, Gianvittorio Rizzano</i>	
SEISMIC RESPONSE OF INNOVATIVE CFS WALLS BRACED WITH UHS STEEL BARS: EXPERIMENTAL INVESTIGATION	4185
<i>Alessia Campiche</i>	
VALIDATION OF NOVEL SEISMIC DESIGN CRITERIA FOR LIGHTWEIGHT STEEL BUILDING IN EUROPE	4199
<i>Sarmad Shakeel, Marica Navarra, Alessia Campiche</i>	
BEHAVIOUR OF T-STUB UNDER MODE 2 AND 3 WITH HV AND HR BOLTS	4212
<i>Roberto Tartaglia, Mario D'Aniello</i>	
INFLUENCE OF THE JOINT BEHAVIOUR ON THE PERFORMANCE OF ORTHOGONAL EXOSKELETONS FOR SEISMIC RETROFIT	4219
<i>Roberto Tartaglia, Gianmaria Di Lorenzo, Antonio Formisano, Raffaele Landolfo</i>	

Thematic Sessions

TS 5: DYNAMICS OF CONCRETE AND MASONRY STRUCTURES

EVALUATION OF THE SEISMIC BEHAVIOR OF HISTORICAL CHURCHES REINFORCED BY CROSS-LAM ROOF- STRUCTURES	4226
<i>Nicola Longarini, Pietro Crespi, Marco Zucca</i>	
SEISMIC RESPONSE OF SEVEN EXISTING REINFORCED CONCRETE CHIMNEYS EQUIPPED WITH TUNED MASS DAMPERS UNDER FIVE STRONG SEISMIC EVENTS	4248
<i>Pietro Giuseppe Crespi, Nicola Longarini, Marco Valente, Marco Zucca</i>	

SHAKING TABLE TEST ON THE EFFECTS OF SHEAR WALLS FOR LONG-SPAN KOREAN TRADITIONAL TIMBER STRUCTURE	4262
<i>Yeong-Min Kim</i>	
INVESTIGATION OF THE IMPACT OF SEISMIC ZONE TO THE COST OF CONSTRUCTION OF A 5-STOREY R/C BUILDING	4272
<i>Theodoros Chrysanidis, Nikolaos Alamanis, Grigorios Papageorgiou, Georgia Kaouri</i>	
FLEXURAL PERFORMANCE OF CONCRETE BEAMS UNDER CYCLIC LOADING	4283
<i>Waseem Khan, Saleem Akhtar, Aruna Rawat, Anindya Basu</i>	
A MULTILAYER SHELL ELEMENT FOR NONLINEAR ANALYSIS OF R/C SHEAR WALLS	4294
<i>Vassilis Papanikolaou, Christos Karakostas, Konstantinos Morfidis, Emmanouil Baboukas</i>	
COMPARISON OF THE EFFICIENCY OF MINIMUM-THICKNESS CIRCULAR AND PARABOLIC ARCHES FOR VARIOUS GRAVITY CONDITIONS	4302
<i>Nicos Kalapodis, Georgios Kampas, Thomas McLean, Christian Malaga-Chuquitaype</i>	
LARGE-DISPLACEMENT RESPONSE OF UNREINFORCED MASONRY STRUCTURES: COMPARISON BETWEEN ANALYTICAL SOLUTIONS AND DEM MODELS INCLUDING OPEN-SOURCE SOFTWARE	4317
<i>Igor Bouckaert, Michele Godio, João Pacheco de Almeida</i>	
TS 14: NUMERICAL SIMULATION METHODS FOR DYNAMIC PROBLEMS	
NONLINEAR FINITE ELEMENT MODELS FOR EMBEDDED BASE CONNECTIONS	4331
<i>Nicolas Mora Bowen, Pablo Torres Rodas</i>	
LOCAL SCALE DAMPING MODEL FOR REINFORCED CONCRETE ELEMENTS	4341
<i>Clotilde Chambreuil, Cédric Giry, Frédéric Ragueneau, Pierre Léger</i>	
NUMERICAL STUDY ON THE DAMPING CHARACTERISTICS OF A SHOCK ABSORBER VALVE UTILIZING DIFFERENT VELOCITIES THROUGH CFD ANALYSIS	4353
<i>Yousif Badri, Thaer Syam, Sadok Sassi, Mohammed Hussein, Jamil Renno, Saud Ghani</i>	
ENERGY HARVESTING FROM RAILWAY VIBRATIONS – A NUMERICAL STUDY BASED ON BEAM-ON-ELASTIC-FOUNDATION UNDER QUASI-STATIC LOADING	4363
<i>Shahd Elshafei, Mohammed Hussein, Jamil Renno, Asan Mutalif</i>	
IMPACT FACTORS DERIVED FROM INTERNAL FORCES IN TIMOSHENKO BEAMS SUBJECTED TO CONCENTRATED MOVING LOADS	4373
<i>Benjamín Pinazo, Salvador Monleón, Carlos Lázaro, Pedro Museros</i>	
ON THE DEVELOPMENT OF A NOVEL APPROACH FOR SIMULATING ELASTIC BEAMS IN DUALSPHYSICS WITH THE USE OF THE PROJECT CHRONO LIBRARY	4385
<i>Salvatore Capasso, Bonaventura Tagliafierro, Iván Martínez-Estévez, José M. Domínguez, Joe El Rahi, Vasiliki Stratigaki, Alejandro J.C. Crespo, Rosario Montuori, Peter Troch, Moncho Gómez-Gesteira, Giacomo Viccione</i>	

DIGITAL SIMULATION OF WIND FIELD VELOCITY FOR EVALUATING PROPER STIFFNESS INDICATORS OF WINDOW MULLIONS	4400
<i>Gian Felice Giaccu, Antonio Cazzani</i>	
ANALYTICAL/NUMERICAL SOLUTIONS TO THE PROBLEM OF THE DYNAMIC RESPONSE OF AN ELASTIC PLATE ON A CONTINUOUSLY NON-HOMOGENEOUS CROSS-ANISOTROPIC VISCOELASTIC SOIL TO A MOVING LOAD	4407
<i>Niki D. Beskou, Edmond V. Muho</i>	
 TS 15: OPTIMUM DESIGN AND CONTROL IN STRUCTURAL DYNAMICS AND EARTHQUAKE ENGINEERING	
OPTIMAL DESIGN OF TID-BASED SYSTEM FOR THE CONTROL OF WIND-INDUCED VIBRATION IN TALL BUILDINGS THROUGH CULTURAL ALGORITHM	4428
<i>Luis Lara-Valencia, Mateo Ramírez-Acevedo, José Brito, Daniel Caicedo, Yosef Farbiarz</i>	
A PARAMETRIC ANALYSIS OF THE SEISMIC PERFORMANCE OF BRIDGES AS A FUNCTION OF THE DCFP DEVICE PROPERTIES	4439
<i>Paolo Castaldo, Guglielmo Amendola</i>	
SEISMIC PERFORMANCE OF BRIDGES ISOLATED WITH FPS	4452
<i>Paolo Castaldo, Guglielmo Amendola</i>	
CRITICAL ACCELERATION, SEISMIC SLIDING DISPLACEMENT AND SMART DESIGN OF CANTILEVER WALLS	4467
<i>Loukas C. Katsenlis, Constantine A. Stamatopoulos, Vassilis P. Panoskaltsis</i>	
COMPARISON OF CONTROL ALGORITHMS APPLIED TO AN HYBRID MASS DAMPER ATTACHED TO AN WIND TURBINE TOWER	4481
<i>Pedro Rocha, Suzana Avila</i>	
PRELIMINARY STUDY OF AN ARDUINO CONTROLLED SHAKE TABLE TO LOW-FREQUENCY TEST	4494
<i>Ledyamar F. Moreno, Marcus V. G. de Moraes, Suzana M. Avila</i>	
EFFICIENT DAMPER DESIGN METHOD FOR ELASTIC-PLASTIC MDOF STRUCTURES UNDER CONSECUTIVE-LEVEL EARTHQUAKES	4508
<i>Hiroki Akehashi, Izuru Takewaki</i>	
DIFFERENTIATION OF THE CONSTRUCTION COST OF A FIFTEEN STOREY R/C BUILDING DEPENDING ON THE SEISMIC HAZARD ZONE	4520
<i>Paulina Tselempi, Theodoros Chrysanidis</i>	
DOES THE SEISMICITY OF THE AREA HAVE AN IMPACT ON THE CONSTRUCTION COST OF THE LOAD-BEARING STRUCTURE OF R/C BUILDINGS?	4535
<i>Thomas-Erik Makris, Theodoros Chrysanidis</i>	

IMPROVING ENERGY DISSIPATION CAPACITY OF NATURALLY BUCKLING BRACES UNDER LOW-CYCLE FATIGUE LOADS	4547
<i>Shadiya Jamshiyas, Kazuhiro Hayashi, Xiaopo Yang, Konstantinos Skalomenos</i>	

TS 17: PERFORMANCE-BASED EARTHQUAKE ENGINEERING

NUMERICAL MODELING OF SLIP RESPONSE OF LATERALLY SWAYING BRIDGE PIERS' TENSILE REINFORCEMENT	4558
<i>Konstantinos G. Megalooikonomou</i>	

SEISMIC RISK ASSESSMENT OF A PROCESS PLANT UNIT ACCOUNTING FOR DYNAMIC INTERACTION	4568
<i>George Karagiannakis, Luigi di Sarno</i>	

A COMPARATIVE STUDY ON SEISMIC RESPONSE OF A SUPER HIGH-RISE BUILDING USING CONVENTIONAL AND MODAL PUSHOVER ANALYSIS	4582
<i>Xianlong Zhang, Hao Wu, Qiao Yu, Yang Liu, Lingzhi Li, Wannan Xu, Junyan Zhou</i>	

NUMERICAL PARAMETRIC STUDY OF GRILLE-TYPE STEEL CONCRETE COMPOSITE SHEAR WALL FOR SEISMIC REGIONS	4593
<i>Tian Wang, Qiao Yu, Hao Wu, Yang Liu, Lingzhi Li, Xianlong Zhang</i>	

SEISMIC RELIABILITY OF BRIDGES ISOLATED WITH FPS	4607
<i>Paolo Castaldo, Guglielmo Amendola, Luca Giordano, Diego Gino, Elena Miceli</i>	

INTENSITY MEASURES PROPERTIES AND SELECTION FOR RISK ANALYSIS ON STRUCTURES SUBJECTED TO EARTHQUAKE INDUCED BUILDING POUNDING WITH A NON SMOOTH CONTACT DYNAMICS METHOD	4621
<i>Thomas Langlade, David Bertrand, Stéphane Grange, Gabriel Candia, Juan Carlos de la Llera</i>	

ESTIMATION OF DUCTILITY IN ASYMMETRIC-PLAN STRUCTURES	4633
<i>Kaan Kaatsiz, Halûk Sucuoğlu</i>	

A MULTI-OBJECTIVE DISPLACEMENT-BASED DESIGN PROCEDURE OF VISCOUS AND HYSTERETIC DAMPED BRACES FOR THE SEISMIC PROTECTION OF RC BUILDINGS	4646
<i>Fabio Mazza, Carlo Pasceri</i>	

EFFECT OF THE DAMPING RATIO OF THE NON-STRUCTURAL COMPONENTS ON FLOOR ACCELERATION DEMANDS IN TORSIONALLY IRREGULAR BUILDINGS	4660
<i>Ankur Jain, Mitesh Surana</i>	

EXPLORING THE EXPECTED INCREASE OF COSTS AND LOSS REDUCTION BY RAISING THE BAR IN SEISMIC DESIGN: COMPARISON OF ALTERNATIVE DESIGN METHODOLOGIES AND EARTHQUAKE-RESISTANT TECHNOLOGIES	4670
<i>Francesca Gentili, Jonathan Ciurlanti, Simona Bianchi, Stefano Pampanin</i>	

SEISMIC RESPONSE OF A TRANSPARENT PAVILION MADE OF STRUCTURAL GLASS	4688
<i>Dimitra V. Achillopoulou, Nikoleta K. Stamataki</i>	

ON THE USE OF INSTANTANEOUS POWER FOR NEAR-FAULT RECORD MODIFICATION	4697
<i>Esra Zengin, Norman Abrahamson</i>	
SEISMIC DESIGN OF STEEL FRAMES WITH INTENTIONALLY ECCENTRIC INDUCTION-HEAT TREATED STEEL BRACES	4706
<i>Thomas Whittall, Konstantinos A. Skalomenos</i>	
AN EFFICIENT RECORD-TRUNCATION SCHEME FOR PULSE-LIKE RECORDS USING A WAVELET-BASED APPROACH	4720
<i>Vicky Dimakopoulou, Michalis Fragiadakis, Ioannis Taflampas</i>	
 TS 19: REPAIR AND RETROFIT OF STRUCTURES	
NUMERICAL MODELLING OF SHEAR BOND TESTS ON EXTERNALLY STRENGTHENED MASONRY SPECIMENS	4729
<i>Ottavio Tamborrino, Daniele Perrone, Marianovella Leone</i>	
A DISPLACEMENT-BASED DESIGN PROCEDURE OF VISCOUS DAMPED STEEL EXOSKELETONS FOR THE SEISMIC RETROFITTING OF RC FRAMED BUILDINGS	4742
<i>Fabio Mazza, Egidio Mollo</i>	
DEBONDING ANALYSIS OF FRCM COMPOSITES FOR STRUCTURAL UPGRADING OF RC STRUCTURES	4758
<i>Maria Teresa Cristofaro, Angelo D'Ambrisi, Francesco Focacci, Raffaele Nudo, Gianfranco Stipo, Marco Tanganelli, Mario De Stefano</i>	
NODAL DISSIPATIVE DEVICES FOR SEISMIC PROTECTION OF PRECAST RC STRUCTURES	4772
<i>Fabrizio Comodini, Angelo D'Ambrisi, Marco Mezzi</i>	
INVESTIGATION OF THE RESPONSE OF INTERFACES OF CFRP SHEET STRENGTHENING SCHEMES ENHANCED WITH TOUGHENED EPOXY ADHESIVE LAYERS APPLIED IN CORRODED CONCRETE SUBSTRATES	4782
<i>Dimitra Achillopoulou</i>	
SEISMIC RETROFITTING OF SINGLE-STORY RC PRECAST BUILDINGS THROUGH A NOVEL METALLIC HYSTERETIC DEVICE	4789
<i>Chiara Di Salvatore, Gennaro Magliulo, Maria G. Castellano, Nicola Caterino</i>	
COMPRESSIVE STRENGTH EVALUATION OF BLUE MOSQUE MINARET STONES WITH ULTRASONIC TESTING	4800
<i>Gulen Uncu, Şahin Dede, Eser Çaktı</i>	
EXPERIMENTAL INVESTIGATION OF SHEAR STRENGTH OF SOLID BRICK URM WALLS RETROFITTED WITH TRM JACKET	4808
<i>Athanasia Thomoglou, Athanasios Karabinis</i>	

TS 20: SEISMIC ISOLATION

METAFoundation AS A NEW APPROACH FOR SEISMIC ISOLATION OF BUILDINGS	4816
<i>Stefania Fiore, Domenico Magisano, Giovanni Finocchio, Massimo Chiappini</i>	

SEISMIC PERFORMANCE OF DOUBLE FRICTION PENDULUM BEARINGS UNDER HORIZONTAL AND VERTICAL EXCITATION	4824
<i>Ioannis E. Kavvadias</i>	

SEISMIC DEVICES FOR STEEL STORAGE STRUCTURES	4834
<i>Marco Simoncelli, Bonaventura Tagliaferro, Rosario Montuori</i>	

ANALYSIS OF THE PARTICLES DISTRIBUTION INFLUENCE ON THE RECYCLED RUBBER PROPERTIES TO BE USED AS A MATRIX OF LOW-COST SEISMIC ISOLATORS	4845
<i>Carolina Rojas Cabrera, Lizeth F. Ortega Escobar, Ingrid E. Madera Sierra, Daniele Lossano, Albert R. Ortíz Lasprilla</i>	

TS 21: SEISMIC RISK AND RELIABILITY ANALYSIS

THE EFFECT OF SOIL-STRUCTURE INTERACTION AND LIQUEFACTION ON THE SEISMIC VULNERABILITY OF TYPICAL PORT STEEL LIGHT-FRAME WAREHOUSES	4853
<i>Stella Karafagka, Stavroula Fotopoulou, Anna Karatzetzou, Giorgos Malliotakis, Dimitrios Pitilakis</i>	

COMPARATIVE ASSESSMENT OF EMPIRICAL AND MECHANICAL APPROACHES FOR THE ESTIMATION OF THE SEISMIC FRAGILITY OF ORDINARY MASONRY BUILDINGS TYPE IN THE INNER CENTRAL ITALY	4869
<i>Ilaria Capanna, Franco Di Fabio, Massimo Fragiocomo</i>	

EVALUATION OF SEISMIC RESILIENCE OF RC-BUILDINGS SUBJECTED TO REPEATED EARTHQUAKE USING RESILIENT INDEX AND FRAGILITY SURFACE FUNCTIONS	4880
<i>Moustafa Moufid Kassem, Fadzli Mohamed Nazri, Ahmad Mohamad El-Maissi</i>	

A SIMPLIFIED APPROACH FOR THE VULNERABILITY ASSESSMENT OF REGULAR AND IRREGULAR REINFORCED CONCRETE BUILDINGS AT THE LARGE SCALE	4896
<i>Valentina Blasone, Alberto Basaglia, Raffaele De Risi, Flavia De Luca, Enrico Spacone</i>	

TS 27: STEEL STRUCTURES

GENERALIZED MACROELEMENT FOR GEOMETRIC AND MATERIALLY NON-LINEAR ANALYSIS OF STEEL MEMBERS	4906
<i>Konstantinos Morfidis</i>	

TS 28: STOCHASTIC DYNAMICS

GAUSSIAN AND NON-GAUSSIAN WIND TUNNEL PROCESSES	4926
<i>Marco Di Giovanni, Piero D'Asdia</i>	

RANDOM PROCESS PEAKS PREDICTION: A LITERATURE OVERVIEW	4934
<i>Marco Di Giovanni, Piero D'Asdia</i>	
 TS 31: NUMERICAL SIMULATION OF GEOTECHNICAL PROBLEMS	
EFFECT OF SOIL PROFILE CHARACTERISTICS ON THE SEISMIC SLIDING DISPLACEMENT OF SLOPES	4946
<i>Loukas C. Katsenis, Constantine A. Stamatopoulos, Vassilis P. Panoskaltsis</i>	
EFFECT OF 1D VERTICAL VARIABILITY OF SHEAR MODULUS ON THE SEISMIC RESPONSE OF SITES	4963
<i>Mounia Menoun Hadj Brahim, Hamid Afra</i>	
A PARAMETRIC STUDY OF “WEAK LAYER” EFFECTS ON THE SEISMIC RESPONSE OF LIQUEFIABLE SOIL PROFILES	4973
<i>Yannis Tsiapas, Maria Spanea, George Bouckovalas</i>	
COUPLED ANALYSIS OF SEISMIC PILE-TENDON-PLATFORM INTERACTION IN LIQUEFIABLE SEABED	4983
<i>Yannis Chaloulos, Yannis Tsiapas, George Bouckovalas, Konstantinos Bazaios</i>	
STATE-OF-THE-ART INVESTIGATION OF WIND TURBINE STRUCTURES BY CONSIDERING THE SOIL- STRUCTURE INTERACTION PHENOMENON	4993
<i>Dewald Gravett, George Markou</i>	
MODELLING THE IMPACT OF GAPPING BEHAVIOUR ON MONOPILE MOUNTED OFFSHORE WIND TURBINE DYNAMICS	5005
<i>Stephen Williams, Loizos Pelecanos, Antony Darby</i>	
SOIL-STRUCTURE INTERACTION IN THE SEISMIC VULNERABILITY ANALYSIS OF RC BUILDINGS. APPLICATION TO A CASE STUDY BUILDING LOCATED IN SOUTHWESTERN SPAIN	5015
<i>Maria-Victoria Requena-Garcia-Cruz, Antonio Morales-Esteban, Percy Durand-Neyra, Emilio Romero-Sanchez</i>	
FREE VIBRATION RESPONSE OF LONG MULTI-SPAN BRIDGES ACCOUNTING FOR SOIL-STRUCTURE INTERACTION	5028
<i>Pieter Reumers, Geert Lombaert, Geert Degrande</i>	
THREE DIMENSIONAL DYNAMIC INTERACTION OF ADJACENT FOUNDATIONS ON A HALFSpace WITH LOCAL INHOMOGENITY APPLYING A COUPLED ITM-FEM APPROACH	5039
<i>Julian Freisinger, Gerhard Müller</i>	
NUMERICAL ANALYSIS ON SHALLOW FOUNDATIONS LATERAL DISCONNECTION	5066
<i>Fausto Somma, Alessandro Flora, Emilio Bilotta, Giulia Viggiani</i>	
INFLUENCE OF THE DYNAMIC SOIL-STRUCTURE INTERACTION IN CONCRETE FRAMES WITH INCORPORATED VISCOUS DAMPERS	5078
<i>Andrés Mauricio Cortés Arias, Francisco Peña Ocampo, Orlando Cundumí Sánchez</i>	

COMPUTATIONAL MODELING AND PARAMETRIC STUDY OF PILE GROUPS	5093
<i>Mariana Lazarini, Miguel Paula, Manuel Braz-César</i>	

TS 32: DYNAMICS OF STEEL AND SLENDER STRUCTURES

ADVANCES IN COMPUTATIONAL AND ANALYTICAL MODELS FOR COLUMN BASE CONNECTIONS	5108
<i>Pablo Torres-Rodas</i>	
INFLUENCE OF EARTHQUAKE MECHANISMS TO THE SEISMIC RESPONSE OF STEEL MOMENT FRAMES	5124
<i>Liseth Campos, Pablo Torres-Rodas, Pablo Quinde, Fabricio Yopez</i>	
SEISMIC ACTION COMBINATION RULES FOR THE DESIGN OF AZIMUTH-INDEPENDENT STRUCTURES	5134
<i>Nikolaos Karaferis, Dimitrios Vamvatsikos</i>	
INVESTIGATING THE OVERTURNING STABILITY OF UNANCHORED CONTAINERS WITH FINITE ELEMENT SIMULATIONS	5142
<i>Stefanos Gkatzogiannis, Peter Knoedel, Thomas Ummenhofer</i>	
GREEN BANK RADIO TELESCOPE: WIND INDUCED EFFECTS ON FEED-ARM	5159
<i>Gian Felice Giaccu, Luca Gallisai, Steven White, Richard Prestage, Luca Caracoglia</i>	
PARAMETRIC STUDY OF STEEL COLUMN-BASE CONNECTION SUBJECTED TO BIDIRECTIONAL BENDING AND AXIAL COMPRESSION	5165
<i>Md. Asif Bin Kabir, Ahm Muntasir Billah</i>	

TS 33: AEROELASTICITY, SOUND AND VIBRATION AND BRIDGE DYNAMICS

GEOMETRICALLY NON-LINEAR FREE IN-PLANE VIBRATION OF FUNCTIONALLY GRADED CIRCULAR ARCH WITH UNIFORM CROSS SECTION	5179
<i>Omar Outassafte, Ahmed Adri, Yassine El Khouddar, Said Rifai, Rhali Benamar</i>	
ANALYSIS OF GEOMETRICALLY NON-LINEAR FREE VIBRATIONS OF FUNCTIONAL GRADED BEAMS IN A THERMAL ENVIRONMENT	5191
<i>Yassine El Khouddar, Ahmed Adri, Omar Outassafte, Issam El Hantati, Said Rifai, Rhali Benamar</i>	
PERSPECTIVES ON THE ACCELERATION OF THE NUMERICAL ASSESSMENT OF FLUTTER AND BUFFETING RESPONSE OF BRIDGE DECKS	5201
<i>Julien Heremans, Anass Mayou, Vincent Denoël</i>	
SIMULATING LOW FREQUENCY SOUND TRANSMISSION LOSS OF MOUNTED PANELS	5214
<i>Moris Kalderon, Andreas Paradeisiotis, Ioannis Antoniadis</i>	
INVESTIGATION OF A METHODOLOGY FOR DESCRIBING FAN BLADE FLUTTER LIMITATIONS INDUCED BY NON-LINEAR FRICTION AT BLADE ROOTS	5232
<i>Nicolas Ombret, Maxime De Pret, Alain Dugeai, Fabrice Thouverez, Laurent Blanc, Thomas Berthelon</i>	

GEOMETRICALLY NON-LINEAR FREE IN-PLANE VIBRATION OF STEPPED CIRCULAR ARCH	5255
<i>Omar Outassafte, Ahmed Adri, Yassine El Khouddar, Said Rifai, Rhali Benamar</i>	
SIMPLE AND COMPLEX MODELLING OF SEAT-TYPE ABUTMENT-BACKFILL SYSTEMS	5266
<i>Ioannis G. Mikes, Andreas J. Kappos</i>	
INFLUENCE OF THE CONTINUITY OF THE BALLASTED TRACK ON THE DYNAMIC RESPONSE OF A SIMPLY SUPPORTED HIGH SPEED RAILWAY BRIDGES	5283
<i>Said El Hankari, Rachid Dkiouak, Khalid Roky</i>	
A FRAMEWORK ON THE DYNAMIC RESPONSE OF TALL STRUCTURES TO NON-STATIONARY WIND USING DESIGN SPECTRUM	5299
<i>Jing Song, Pedro Martinez-Vazquez, Konstantinos A. Skalomenos</i>	
 TS 34: NONLINEAR AND IMPACT DYNAMICS	
GEOMETRICALLY NONLINEAR FORCED TRANSVER VIBRATIONS ANALYSIS OF TAPERED EULER-BERNOULLI BEAMS	5307
<i>Issam El Hantati, Ahmed Adri, Hatim Fakhreddine, Said Rifai, Rhali Benamar</i>	
POWDER SNOW IMPACT OF TALL VIBRATING STRUCTURES	5318
<i>Andrin Caviezel, Stefan Margreth, Kseniya Ivanova, Betty Sovilla, Perry Bartelt</i>	
GEOMETRICALLY NONLINEAR FREE VIBRATIONS OF FULLY CLAMPED MULTI-STEPPED BEAMS CARRYING MULTIPLE MASSES	5331
<i>Issam El Hantati, Ahmed Adri, Hatim Fakhreddine, Said Rifai, Rhali Benamar</i>	
COMPARISON BETWEEN DYNAMIC NONLINEAR ANALYSIS WITH ASCE 7-10 AND ASCE 7-16 IN CONCRETE FRAMES WITH VISCOUS DAMPERS INCORPORATED	5342
<i>Juan Sebastián Cundumí García, Orlando Cundumí Sánchez</i>	
FRAGILITY CURVES DEFINITION OF EXISTING REINFORCED CONCRETE BUILDINGS DESIGNED FOR GRAVITY LOADS	5357
<i>Alberto Basaglia, Marco Terrenzi, Enrico Spacone</i>	
STOCHASTIC NONLINEAR RESPONSE OF STRUCTURAL SYSTEMS ENDOWED WITH SINGULAR MATRICES SUBJECT TO COMBINED PERIODIC AND STOCHASTIC EXCITATIONS	5367
<i>Ioannis P. Mitseas, Peihua Ni, Vasileios C. Fragkoulis, Fan Kong, Michael Beer, Michalis Fragiadakis</i>	

SEISMIC VULNERABILITY OF MASONRY HISTORICAL STRUCTURES: A SIMPLE ADAPTIVE NURBS FE APPROACH FOR THE LIMIT AND THE SUBSEQUENT NON-LINEAR STATIC ANALYSIS WITH FEW DOFS

Nicola Grillanda¹ and Gabriele Milani¹

¹ Department of Architecture, Built Environment and Construction Engineering (ABCE), Polytechnic University of Milan
Piazza Leonardo Da Vinci 32, 20133 Milan (Italy)
email: nicola.grillanda@polimi.it, gabriele.milani@polimi.it

Abstract

The present contribution deals with an innovative evaluation of the vulnerability and static seismic behavior of existing masonry structures and monumental buildings. For a given masonry construction, a discretization through few NURBS surfaces is realized. NURBS surfaces are converted into shell elements which are assumed rigid and infinitely resistant. The non-linearities typical of the masonry material (almost no tensile strength, frictional behavior in shear, and relatively larger resistance in compression) are imposed at interfaces between adjacent elements, which represent in this way possible fracture lines. Once defined a horizontal load configuration, an adaptive upper bound limit analysis is applied. As final result, the collapse mechanism and the collapse load multiplier are found. Then, to provide the complete non-linear structural response, a FE model composed of elastic elements representing macro-blocks and non-linear contact-based interfaces or plastic damaging strips corresponding to the cracks is derived. On such model, static non-linear analyses can be performed easily at a fraction of the computational burden needed by standard approaches. Several examples including masonry churches, vaults, and buildings are presented. Finally, a novel limit analysis computational technique based on a discretization through NURBS solid elements is introduced and future perspectives of the research are drawn.

Keywords: Masonry, seismic vulnerability, NURBS, limit analysis, non-linear analysis.

1 INTRODUCTION

The prediction of the load bearing capacity and ultimate displacements in the framework of a displacement-based design for existing masonry structures and monumental buildings is a very difficult task and at present a hot topic for the specialized scientific community, especially for earthquake prone masonry countries.

As a matter of fact, a huge amount of different modelling strategies have been developed in the last decades [1] to deal with the multitude of challenges that characterize the analysis of such structures in the non-linear range. Indeed, masonry is characterized by heterogeneity, strongly non-linear behavior even at low levels of both horizontal and vertical loads, anisotropic response, complex geometries and an infinite variability of the textures.

Classically, we can distinguish two main analysis approaches for masonry structures subjected to horizontal loads [2], namely (i) limit analysis-based and (ii) incremental-evolutionary approaches.

Numerical techniques based on limit analysis are quite diffused nowadays because it is well-known their reliability for the realistic determination of both collapse mechanisms and ultimate load carrying capacity. Limit analysis applied to masonry has a long tradition and is basically due to the seminal work by Heyman [3]. In the last four decades, many different approaches have been developed grounded on the utilization of both the lower bound [4]-[8] and the upper bound [9]-[11] theorem, removing also in some cases the associativity of the flow rule. When embedded in a FE formulation, limit analysis becomes very intuitive in its upper bound formulation and kinematic approaches are generally preferred in the literature [12]-[14]. Within the FE upper bound formulation, different models have been proposed, assuming that the inelastic deformation occurs only inside elements, only at the interfaces between adjoining elements or on both interfaces and elements, as firstly proposed in [15] for geotechnical problems. When the plastic dissipation is constrained to occur only on interfaces, then the problem becomes strongly mesh dependent and either remeshing or mesh adaptation algorithms are needed [16]. The advantage is that the number of variables is limited and, if the adaptation scheme is efficient, the computational burden remains rather limited [17]-[19]. However, as well known limit analysis typically does not provide any information regarding displacements, although this would be essential in a displacement-based design, which is considered the standard for any seismic analysis [20].

Incremental-evolutionary approaches are widely utilized tools for the step-by-step investigation of the structural equilibrium in nonlinear iterative analysis frameworks, often used in pushover analyses for the seismic assessment of masonry structures [21]. These approaches can be used within three classic modelling strategies that proved to be effective for masonry structures:

- Macro-element models or simplified models in general (see e.g. [22]-[27]), widely used in common engineering practice due to their simplicity, although typically limited to ordinary buildings and not applicable for complex monumental structures;
- Block-based models (see e.g. [28]-[32]) where masonry is modelled block-by-block (typically into Finite Elements) and the interaction between blocks can be accounted for through various formulations, being the most diffused the utilization of mortar interfaces. Although potentially highly accurate, their main drawback is the huge computational effort needed even for small and medium size structures;
- Continuum models (see e.g. [33]-[35]) where masonry is modelled through a deformable continuum and the constitutive law can be defined directly or through a multi-scale framework. These models, although interesting and potentially very effective, could be computationally expensive or could find difficulties in representing the post-peak response due to

convergence issues, as well as the collapse mechanism predicted could be, in general, not fully clear and somewhat smeared [35].

- Discrete element models -or restricting the family of the approaches proposed, Distinct Element Methods DEMs- (as for instance those presented in [36]-[44] without being exhaustive) where masonry is modelled with rigid or elastic blocks and all non-linearity is lumped on joints typically assumed with a cohesive frictional behaviour [43][44]. Such approach is conceived mainly for Non Linear Dynamic Analyses NLDAs [45]-[47] but it can be adapted also to static non linear analyses, or in presence of foundation settlements, albeit requiring typically huge computational efforts. There are obviously other important drawbacks that cannot be summarized in few words in this introduction, but it is interesting to point out how they have recently inspired the implementation of FEM combined with DEM for large scale computations (see for instance [48]-[49]).

Accordingly, both limit analysis-based and incremental-evolutive approaches present either advantages or disadvantages, and their coupling would represent a favourable solution. The research initially conceived by one of the authors of this paper [50] represented a first attempt to couple limit analysis to displacement-based strategies. In particular, in [50] the collapse mechanism deduced by a genetic algorithm-based GA adaptive limit analysis has been used in a pushover-based framework using two different approaches to introduce nonlinearities in the model. The first one considered 3D plastic damaging strips governed by a nonlinear continuum constitutive law, while the second exploited zero-thickness contact-based interfaces governed by a cohesive-frictional contact behaviour. Both approaches proved a good performance in simulating not only the separate in- and out-of-plane behaviour of masonry structures, but also than of full 3D buildings, having the advantage of requiring for such analyses a considerably low computational demand.

Returning to deal with classic limit analysis, it can be affirmed that its adoption, when the procedure grounds basically on the pioneering paper by Heyman [3] is still very suitable; it is not a case indeed that it has been recently applied in a very successful manner, because the approach is very straightforward, relatively simple and quite accurate in predicting load carrying capacities and failure mechanisms. This is probably the reason why many other researchers developed in the last four decades interesting different limit-analysis procedures, in the majority of the cases basing on a FE discretization (that goes well with limit analysis) -both homogeneous and heterogeneous-, using less the static theorem [4]-[8] and slightly more the kinematic theorem [51]-[56] approach. This is not a case; it is indeed opinion of the authors that, from an implementation point of view, limit analysis procedures which use finite elements (FEs) are typically easier to implement when based on the upper bound theorem, i.e. in a kinematic framework. For cohesive-frictional materials (e.g. masonry) the solution can be found easily also in presence of a non associated flow rule and therefore it appears particularly flexible, especially in all those cases where dissipation occurs only on interfaces between contiguous elements, i.e. failure is due to the formation of a kinematic chain formed by large rigid blocks, an intuition which follows the idea originally proposed in [57]. Nowadays, limit analysis-based solutions are considered trustworthy to investigate collapse mechanisms and the ultimate load in masonry structures [3].

The present paper discusses the following important key issues related to an adaptive limit analysis of existing masonry buildings in general (including also masonry aggregates), masonry curved structures and monumental buildings;

- 1) The most suitable and stable adaptive limit analysis algorithm to use to obtain results quickly with a high confidence on the correctness of the estimated collapse accelerations and failure mechanisms.

- 2) The flexibility of the approach, intended as its utilization in a variety of different limit analysis problems, which includes also the possibility to take into account the orthotropy of the material (when present), the possible presence of multi-leaf walls, double curvature structures or the analysis of complex masonry aggregates exhibiting good or bad interlocking at the intersection between perpendicular walls, also in presence of any kind of strengthening device, such as tie rods, FRP strips, continuous FRCM reinforcement, etc.
- 3) The extension to non-linear static analyses, i.e. a newly conceived two-step methodology where ultimate displacements can be predicted after a preliminary limit analysis. The main idea of the procedure proposed is shown schematically in Figure 1. For a given masonry construction, a discretization through few NURBS surfaces is realized. NURBS surfaces are converted into shell elements which are assumed rigid and infinitely resistant. The non-linearities typical of the masonry material (almost no tensile strength, frictional behavior in shear, and relatively larger resistance in compression) are imposed at interfaces between adjacent elements, which represent in this way possible fracture lines. Once defined a horizontal load configuration, an adaptive upper bound limit analysis is applied. As final result, the collapse mechanism and the collapse load multiplier are found. Then, to provide the complete non-linear structural response, a FE model composed of elastic elements representing macro-blocks and non-linear contact-based interfaces or plastic damaging strips corresponding to the cracks is derived. On such model, static non-linear analyses can be performed easily at a fraction of the computational burden needed by standard approaches.

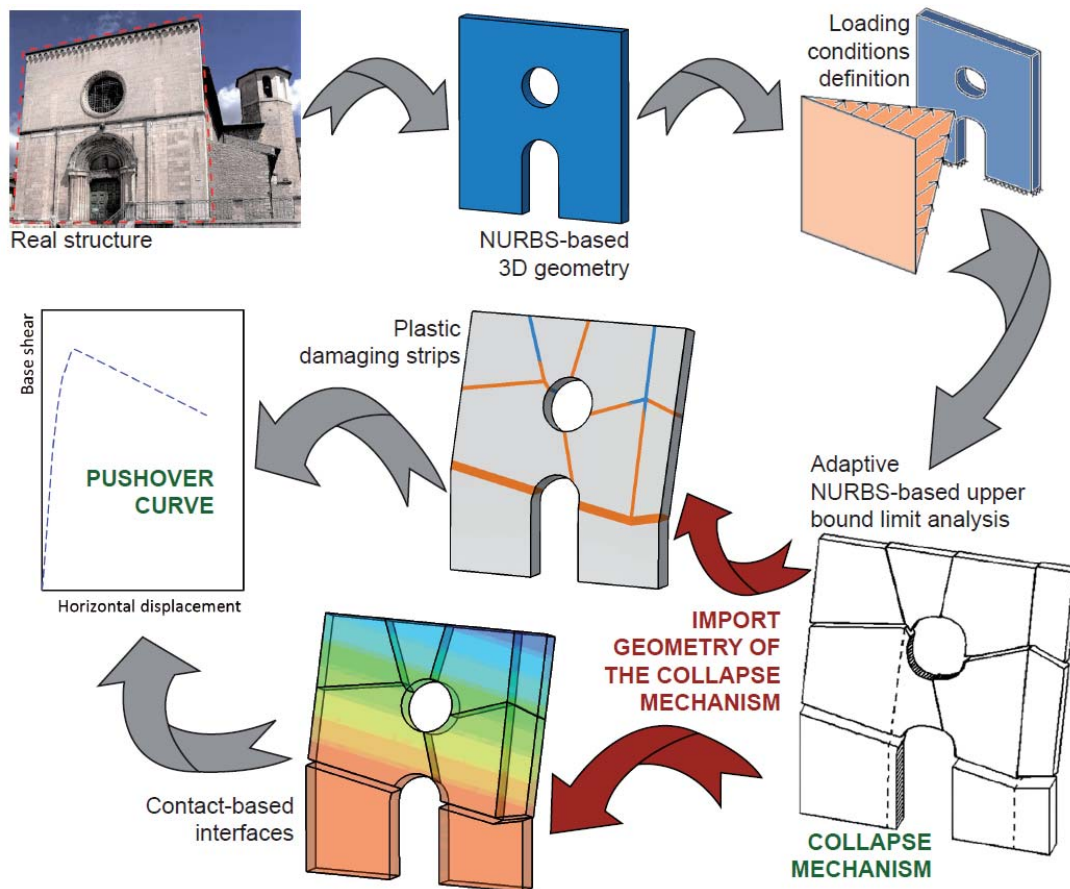


Figure 1. two-step approach used to provide quickly pushover curves for complex masonry structures.

In the present paper, several examples including masonry churches, vaults, and buildings are discussed in detail. Finally, a novel limit analysis computational technique based on a discretization through NURBS solid elements is introduced and future perspectives of the research are drawn.

2 THE THEORETICAL METHOD ADOPTED

In the present Section, the main features of the theoretical model adopted for the adaptive limit analysis and the subsequent simplified pushover analysis are recalled and commented, discussing also the efficiency of different meta-heuristic approaches used for the mesh adaptation.

2.1 Adaptive NURBS-based upper bound limit analysis

For a given masonry structure, a model composed by curved or planar NURBS surfaces is realized within the Rhinoceros environment. NURBS surfaces (Non-Uniform Rational Bezier Spline [58]) are parametric surfaces whose basis functions are piecewise polynomial rational functions obtained starting from the traditional spline basis function. In this approach, NURBS properties are used to both represent exactly curved geometries and facilitate mesh adaptation procedures.

The NURBS model of the whole masonry structure is imported within MATLAB, where each surface is here converted into a 3D shell element through the definition of a thickness value. By using the properties of NURBS, a mesh can be defined by subdividing each initial surface into few trimmed surfaces: each one generates a single element that is still a NURBS surface and the overall geometry is not altered. Elements are supposed to behave as rigid blocks with internal dissipation allowed only along their interfaces. With the aim of finding a failure mechanism constituted exclusively by macro-blocks, the NURBS elements constitute the macro-blocks involved in the mechanism and interfaces are possible fracture lines or hinges.

An upper bound limit analysis is applied. Given a load configuration $[\mathbf{q}_0, \lambda \mathbf{q}]$, in which \mathbf{q}_0 are permanent loads and \mathbf{q} are live loads depending on a multiplier λ , a mechanism involving the few rigid elements composing the initial mesh can be identified by solving a linear programming problem. The mechanism is described by a velocity field $\dot{\mathbf{u}}$ that contains the six velocity components (three translational and three rotational) of each centroid of a NURBS macro-block, which at the edges exhibits discontinuities (i.e. velocity jumps) with respect to the contiguous elements. To properly quantify the velocity jumps, rigid-plastic interfaces are defined at the common boundaries between adjacent elements. Each interface is discretized through collocation points to which the associative flow rule is imposed:

$$\Delta \tilde{\mathbf{u}} = \dot{\lambda} \frac{\partial f}{\partial \boldsymbol{\sigma}} \quad (1)$$

where $\Delta \tilde{\mathbf{u}}$ are the velocity jumps defined in the local reference system, $\dot{\lambda}$ are the non-negative plastic multipliers, $\boldsymbol{\sigma}$ is the stress vector, and f is the linearized three-dimensional yield domain defined in the space of the local stress. For the masonry material, f can be represented by using a three-dimensional Mohr-Coulomb failure criterion defined through a cohesion value c and a friction angle φ . A tension cut-off and a linear cap in compression are included to limit respectively the maximum tensile strength f_t , otherwise equal to $c/\tan(\varphi)$, and the maximum compression strength f_c that masonry can undergo. The failure surface can be in any case changed at user's discretion, for instance utilizing the homogenization theory in the rigid plastic case to take into account in a rigorous manner orthotropy [59]. Alternatively, to reproduce the orthotropic behavior of masonry, a much more straightforward strategy is to

assign two different sets of resistance values along two orthogonal directions of each NURBS surface (e.g. following the directions of bed and head joints): for each inclined interface, a Mohr-Coulomb domain is thus determined by combining the resistance values proportionally to the inclination angle.

Once defined the internal and the external power in reference to the overall vector of unknowns $\mathbf{x} = [\dot{\mathbf{u}}, \dot{\boldsymbol{\lambda}}]$, the linear programming problem that solves the upper-bound formulation is summarized as follows:

$$\min \lambda = \mathbf{c}^T \mathbf{x} \text{ such that } \begin{cases} \mathbf{A}\mathbf{x} = \mathbf{b} \\ \dot{\boldsymbol{\lambda}} \geq \mathbf{0} \end{cases} \quad (2)$$

in which \mathbf{A} is the global matrix of constraints (geometric, compatibility, and normality condition), \mathbf{b} is the vector of known terms in the equality equations (basically a zero-vector with a unitary value as the last term), and \mathbf{c} is the vector of coefficients derived from the Principle of Virtual Powers. The solution vector \mathbf{x} contains the discontinuous velocity field that describes the mechanism obtained starting from the adopted mesh. Eventually, the linear programming problem can be modified into a sequential linear programming to take into account a non-associative behavior in shear (see [51]).

However, the use of a reduced number of macro-elements makes the problem highly mesh-dependent. According to the upper bound theorem of limit analysis, the collapse load multiplier is the minimum of the kinematic load multipliers and it is associated to the real collapse mechanism, which is properly identified only if the interfaces between adjacent elements coincide with the real position of fracture lines. Therefore, a procedure of mesh adaptation is finally applied: the initial mesh is iteratively adjusted until the absolute minimum of the kinematic load is found. For this operation, a meta-heuristic approach is used. Among the several available meta-heuristic algorithm [52], a Genetic Algorithm (GA) is generally applied, because considered sufficiently stable and reliable, as demonstrated in the following Section.

A representative scheme of adaptive limit analysis procedure (step 1 of Figure 1) is depicted schematically in Figure 2. This limit analysis procedure has been used to study several typologies of masonry structures in the last years by the authors, ranging from in-plane and out-of-plane loaded panels to double curvature structures and masonry aggregates [18][19][51]-[56].

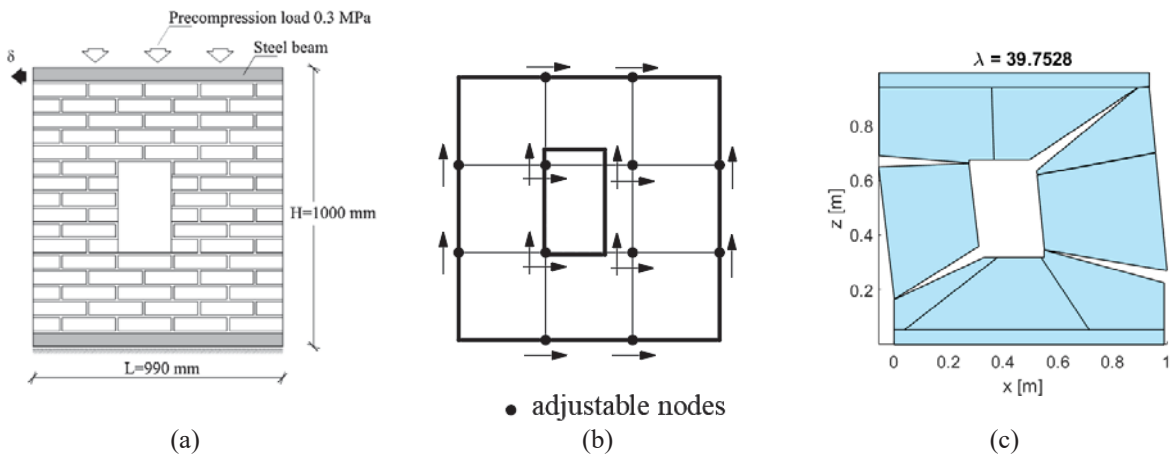


Figure 2. Adaptive upper bound limit analysis tool: (a) original geometry and load condition, (b) NURBS model with initial mesh, (c) collapse mechanism and collapse load multiplier.

2.2 Efficiency test for different meta-heuristic approaches for double curvature structures

The adaptive meta-heuristic approach previously mentioned has been tested on 4 double curvature structures utilizing 4 different algorithms in [52], namely using a specifically devised Prey Predator Algorithm (PPA), a Particle Swarm Optimization (PSO) Algorithm, a Firefly Algorithm (FA) and a specifically crafted Genetic Algorithm (GA). The reader interested into the details of the procedures adopted is referred to [52] for the sake of conciseness. In particular, here it is worth mentioning that the 4 benchmarks considered are a circular skew arch (test #1), a parabolic straight arch (test #2), a parabolic skew barrel vault (test #3) and a ribbed cross vault (test #4). Here we focus almost exclusively on test #3, i.e. on the parabolic skew barrel vault, see Figure 3, for the sake of conciseness. The skew geometry forces the vault to fail non-symmetrically, displaying a mixed interaction of bending and torsional deformation modes. Therefore, the NURBS mesh of the vaulted surface is generated by four moving interfaces in the parameters space. As it can be easily predicted, the failure mechanism is more complex than a failure mechanism formed by four hinges as it occurs for straight arches. In particular, interfaces are not anymore constrained to remain orthogonal to the vault shape: in fact, they can rotate, so that the placement of each interface in the parameters space is governed by two parameters (i.e. the location of the yield lines extremes). It follows that the problem at hand is governed by eight parameters, as depicted in Figure 3(b). Therefore, the NURBS mesh of the vaulted surface is generated by eight moving interfaces in the parameters space. Nonlinear finite element analyses on this case study have been performed in [60] and they are used for comparison purposes. A population of 40 individuals has been adopted in all the meta-heuristics approaches. The number of total iterations is 50. Figure 4(a) depicts convergence plots for the 4 discussed meta-heuristic algorithms, whereas Figure 4 (b-c) illustrate the computational time needed to solve the problem. Similarly to the other benchmarks treated in [52] (i.e tests #1, 2 and 4), PPA seems to guarantee a slightly faster convergence to the optimal solution when compared to the other three proposed meta-heuristic algorithms; furthermore, the error in the estimation of the collapse load multiplier is less than 5% after only 7 iterations, computed in 82 seconds. However, in general and also in this case, the performance of PPA is approximately equivalent to that provided by GA algorithm, which is able to furnish a very good approximation of the final solution after only 11 iterations. Table 1 summarizes the results in terms of computational time, number of iterations and number of function evaluations required for all the benchmarks discussed in [52]. Finally Figure 5 and Figure 6 show respectively the last iteration crack patterns associated to the collapse mechanisms for the four examples discussed in [52] and a comparison between the collapse mechanisms obtained by means of the proposed meta-heuristic NURBS-based limit analysis schemes and the ones obtained in the literature through both homogenized finite element limit analysis and experiments.

From the numerical tests carried out in [52], it can be affirmed that all meta-heuristic approaches are able to furnish engineering meaningful results at a fraction of standard FE limit analysis computations carried out with many elements. However, GA seems globally slightly more efficient and always in agreement with experimental evidences: such reasons are at the base of the preference given to GA in the two-step numerical procedure proposed in this work.

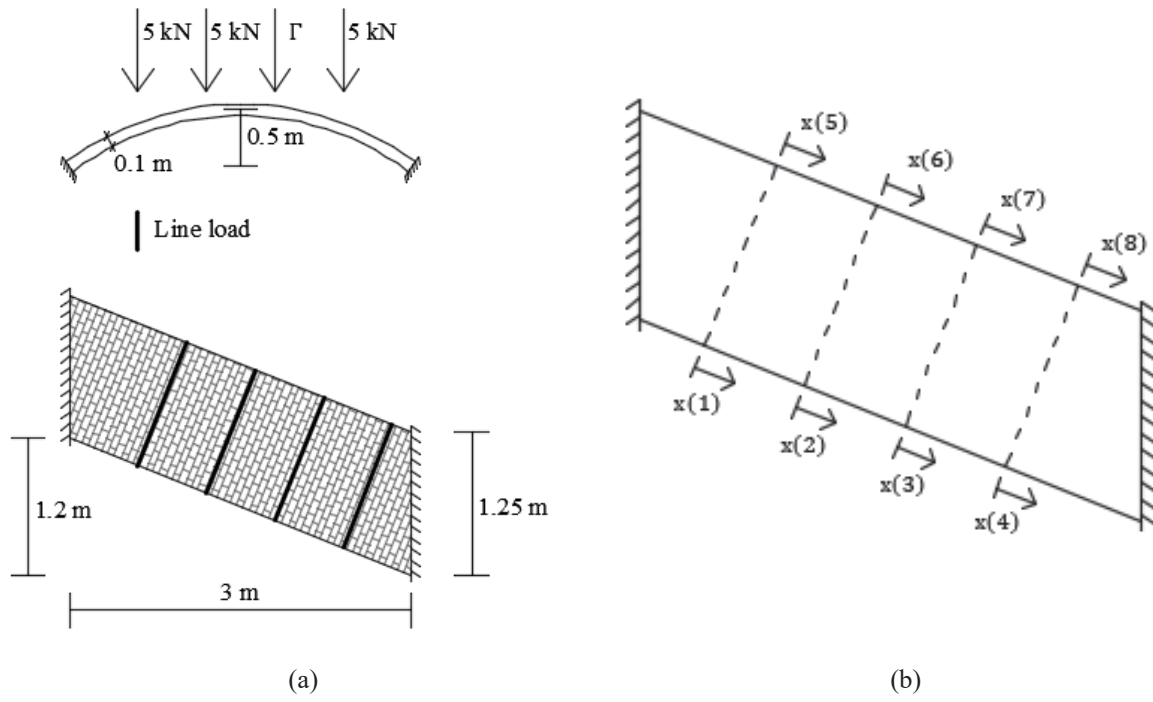


Figure 3. Skew barrel vault: (a) geometry and load condition, (b) eight parameters describing collapse mechanism.

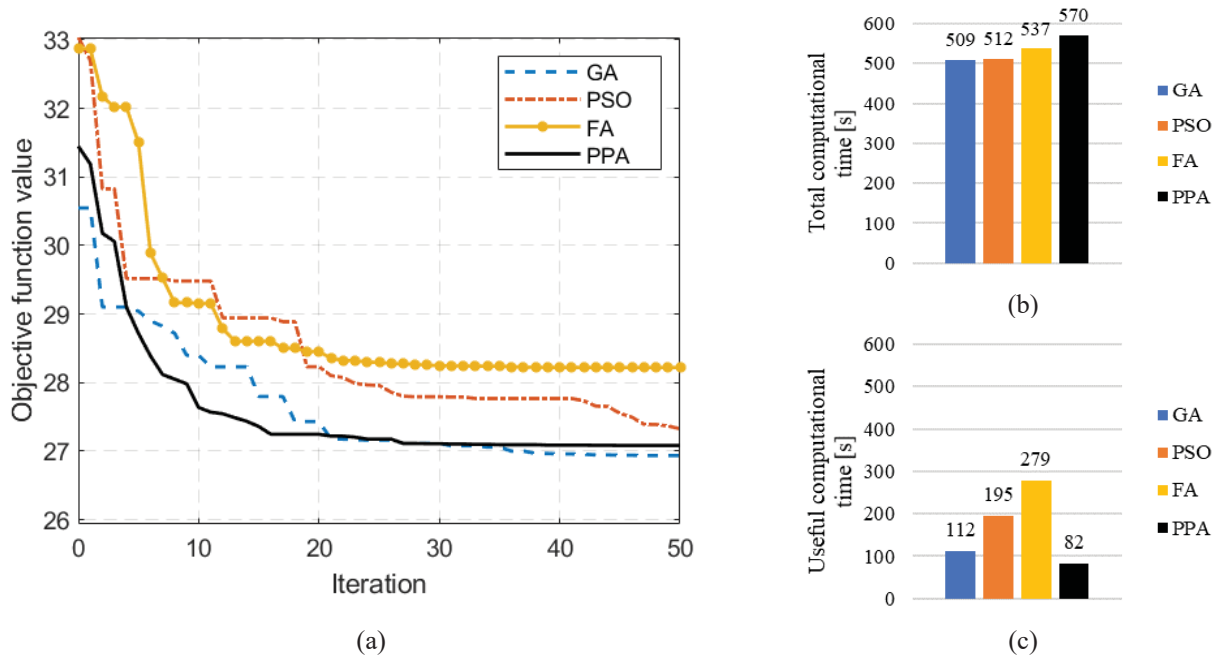


Figure 4. Skew barrel vault: comparison between the four different proposed meta-heuristic schemes; (a) convergence plots, (b) total computational time and (c) time spent for reaching the optimal solution within a 5% error.

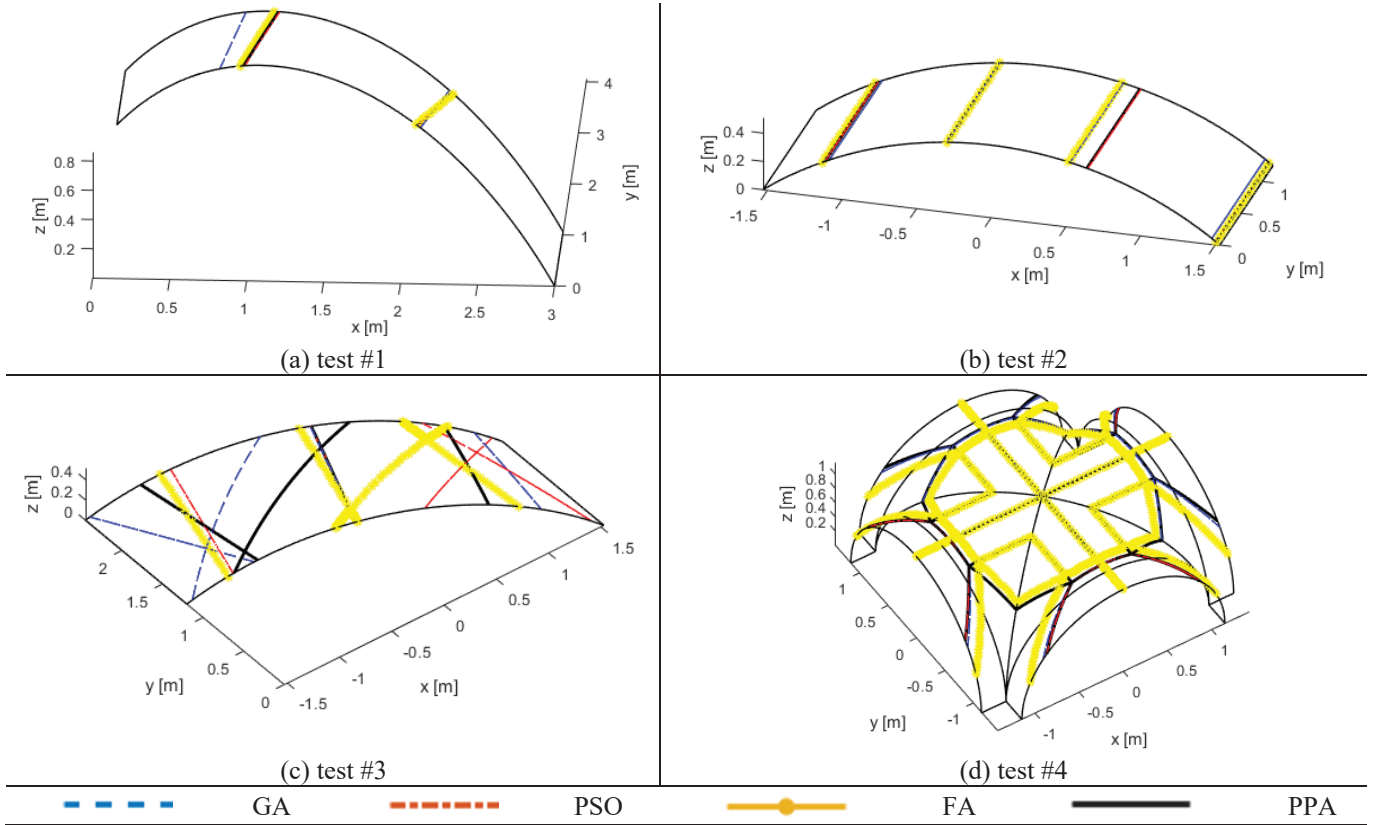


Figure 5. Final crack patterns associated to the collapse mechanisms for the four benchmark tested in [52], one of them re-discussed here (test #3), obtained by applying four different meta-heuristic approaches to a NURBS-based limit analysis scheme: (a) circular skew arch test #1, (b) parabolic straight arch test #2, (c) skew barrel vault test #3, (d) ribbed cross vault test #4.

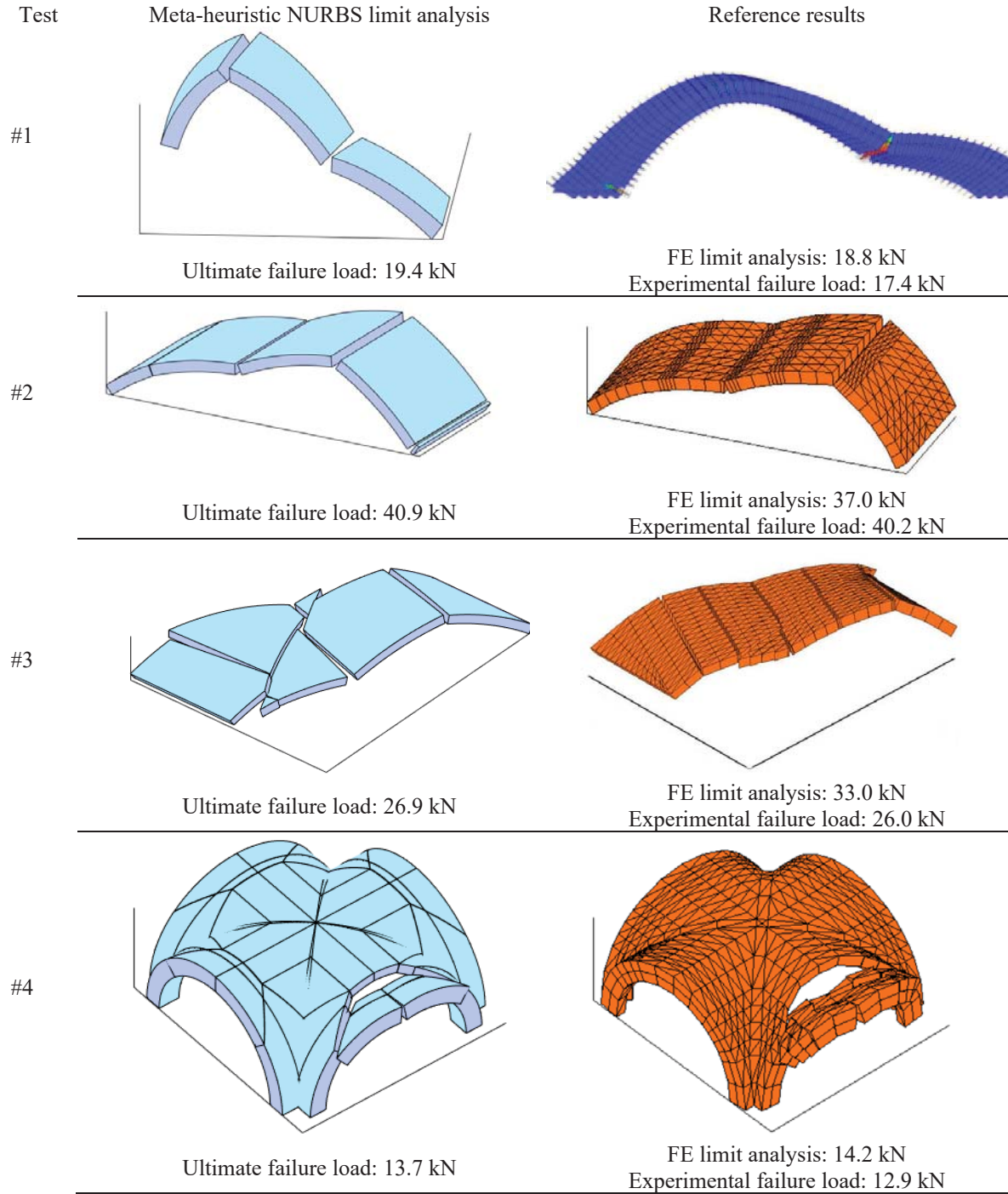


Figure 6. Comparison between the collapse mechanisms obtained in [52] by means of the proposed meta-heuristic NURBS-based limit analysis approach and the ones obtained in the literature through both homogenized finite element limit analysis and experiments.

Table 1. Summary of results obtained in [52] for four different benchmarks on curved structures

Test#	Algorithm	Computing time [s]	Collapse load multiplier Γ	# Function evaluations	Efficiency: 1.05 · min(Γ) obtained after		
					# iterations	time [s]	# function evaluations
1	GA	63	20.449	765	>50	>63	>765
	PSO	55	19.389	765	6	7	105
	FA	57	19.607	765	11	13	180
	PPA	60	19.377	858	2	3	45
2	GA	47	45.626	1020	>50	>47	>1020
	PSO	46	40.895	1020	8	8	180
	FA	53	43.150	1020	>50	>53	>1020
	PPA	54	40.901	1164	3	4	84
3	GA	509	26.936	2040	11	112	480
	PSO	512	27.329	2040	19	195	800
	FA	537	28.219	2040	26	279	1080
	PPA	570	27.083	2324	7	82	335
4	GA	3408	13.960	1020	46	3133	940
	PSO	3441	13.733	1020	4	275	100
	FA	2998	16.302	1020	>50	>2998	>1020
	PPA	3715	13.733	1154	7	541	168
NOTES: circular skew arch test #1, parabolic straight arch test #2, skew barrel vault test #3, ribbed cross vault test #4. Prey Predator Algorithm (PPA), Particle Swarm Optimization (PSO) Algorithm, Firefly Algorithm (FA) and specifically crafted Genetic Algorithm (GA).							

2.3 FE model with few DOFS and non-linear analyses

Once the optimized position of fracture lines has been found, the NURBS mesh is imported in a FE software where non-linear static and dynamic analyses can be performed. A FE model governed by few degrees of freedom (dofs) is built starting from the NURBS geometry by using a properly defined subroutine [61]. Each shell rigid element is converted into a mesh of elastic tetrahedral finite elements (12 dofs for each one). Then, cohesive-frictional contact-based interfaces are automatically inserted in the cracks of the collapse mechanism formerly obtained. In alternative, plastic damaging strips can be used as well, according to the general scheme depicted in Figure 1. Such failure criterion has been implemented in Abaqus through an automatic user-defined subroutine but any FE code can be utilized for such purpose. In this way, a non-linear constitutive law under interface tangential and tensile stresses is imposed along the contact-based interfaces. Moreover, the potential effects of masonry crushing failure

can be accounted for inside the macro-blocks assuming for their constituent material any non-linear continuum plastic-damage constitutive law. For Abaqus, for instance, the standard concrete damaged plasticity (CDP) model appears very suited and has been considered in the simulations reported in this paper, see [62][63] for the constitutive laws adopted.

An incremental-evolutive approach is adopted to derive the full load-displacement curves of any kind of masonry structure. It is important to observe that, having non-linearities mainly imposed just at the contact-based interfaces, the computational burden required by this FE model is much lower in comparison with fully non-linear FE models. At the same time, any mesh dependency effect is avoided thanks to the previous adaptive limit analysis that allows defining the exact position of the cracks. The procedure, initially proposed for out-of-plane loaded walls, has been recently extended to in-plane loaded walls and 3D buildings [61]. Figure 7 shows a schematization of the proposed procedure (corresponding to step 2 of the full procedure depicted in Figure 1).

Alternatively, the FE model can be realized by following an approach [50] based on discrete elements recently proposed for masonry vaults in [64]. This allows extending the two-steps procedure for double curvature masonry elements.

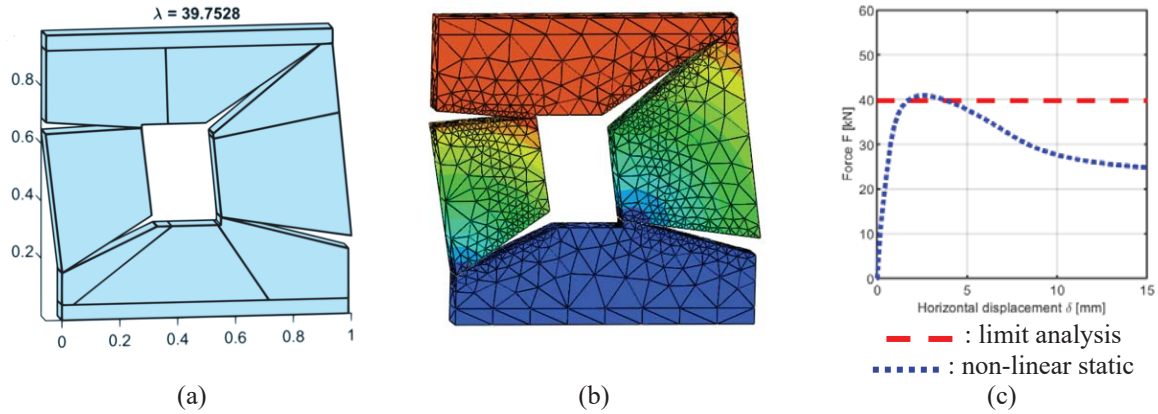


Figure 7. Step 2: non-linear static analysis with few dofs: (a) collapse mechanism obtained from limit analysis, (b) FE model derived from the NURBS model, (c) collapse load multiplier and pushover curve.

3 NUMERICAL EXAMPLES

Some numerical examples involving monumental masonry constructions are here presented.

The first structure considered is the Church of Natività di Maria Vergine, in Bondeno (Italy), a single nave church with lateral chapels (Figure 8a), approximately 36 meters long and 22 meters wide. The façade is 19 meters high and is built with a typical Romanesque style. The original plant dates back to the Middle Age (1100), but exception made for the apse and the bell tower, the rest was re-built more recently, from the end of 1600 to the end of 1800. The medieval semi-octagonal apse is covered by irregular ribbed gothic cross vaults, which are original of that period. Vaults are realized with thin single leaf common clay bricks.

Numerical results can be obtained by representing the whole construction with few NURBS elements. Mechanical properties for clay bricks and mortar joints masonry have been adopted according to prescriptions contained in the Italian code: in particular, a vanishing tensile stress is adopted, with a cohesion of the non-linear interfaces and friction angle equal to 0.06 MPa and 22° (corresponding to a friction coefficient equal to 0.4) respectively.

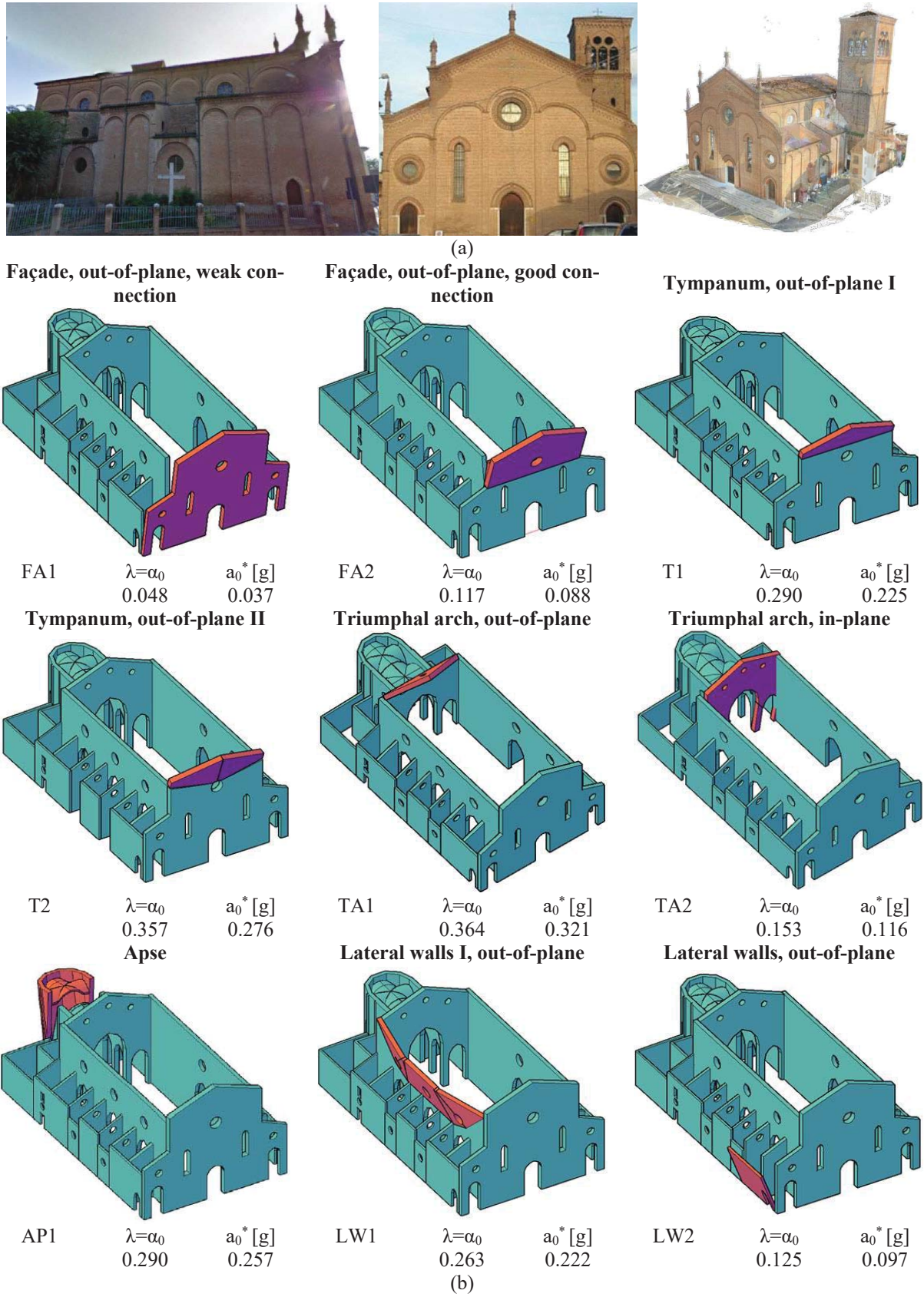


Figure 8. (a) The Church of Natività di Maria Vergine in Bondeno (Italy), (b) failure mechanisms obtained through adaptive limit analysis assuming different directions of the seismic action and interlocking between walls.

A compression strength cap equal to 2.4 MPa has been also used. As prescribed, these values have been furtherly reduced according to a factor equal to 1.35. In the present simulations, a constant horizontal force distribution along the height of the building is assumed.

The resultant failure mechanisms are depicted in Figure 8b. In the same figure, for the sake of completeness, values of α_0 and a_0^* are also reported, where α_0 is the horizontal load multiplier λ from limit analysis and a_0^* the corresponding spectral acceleration (normalized against g). In general, the obtained mechanisms are in good agreement with the pre-assigned failures suggested by the Italian Guidelines for the Cultural Heritage.

The second example here presented is the seismic behavior of the dome of the Church of Anime Sante, which was severely damaged on 6th April 2009 during the L'Aquila seismic sequence (maximum seismic event with the following characteristic: $M_w = 6.3$, $ML = 5.8$). Attributed to Giuseppe Valadier, the dome (Figure 9a) was completed in parallel with the realization of the church in 1805. After the earthquake, both the lantern and the dome collapsed, and the still standing parts of the drum and the dome are visible from photos reported in Figure 9b.

Some simulation results under the application of two distributions of horizontal loads, one linear and the other constant along the height, are here presented. Even in this case, in absence of specific data to assign to masonry mechanical properties, resistance values have been chosen in agreement with the Italian code for existing buildings: null value of tensile stress, 2.4 MPa for compression strength, 0.06 MPa for cohesion and 22° degrees for interfaces friction angle.

The results obtained in terms of both collapse mechanisms and normalized acceleration are reported in Figure 9c. The failure mechanism does not change too much with the distribution of horizontal loads applied, conversely the collapse acceleration is very sensitive to the actual distribution of accelerations. It is interesting to observe that the still standing portion of dome and drum obtained through the NURBS limit analysis reproduces quite closely the situation observed after L'Aquila earthquake.

The identification of such a clear collapse mechanism is also useful to perform non-linear static analyses by simply re-meshing the structure with elastic elements and non-linear interfaces where the yield lines are located (as described in the previous Section). This procedure is followed in the benchmark discussed next.

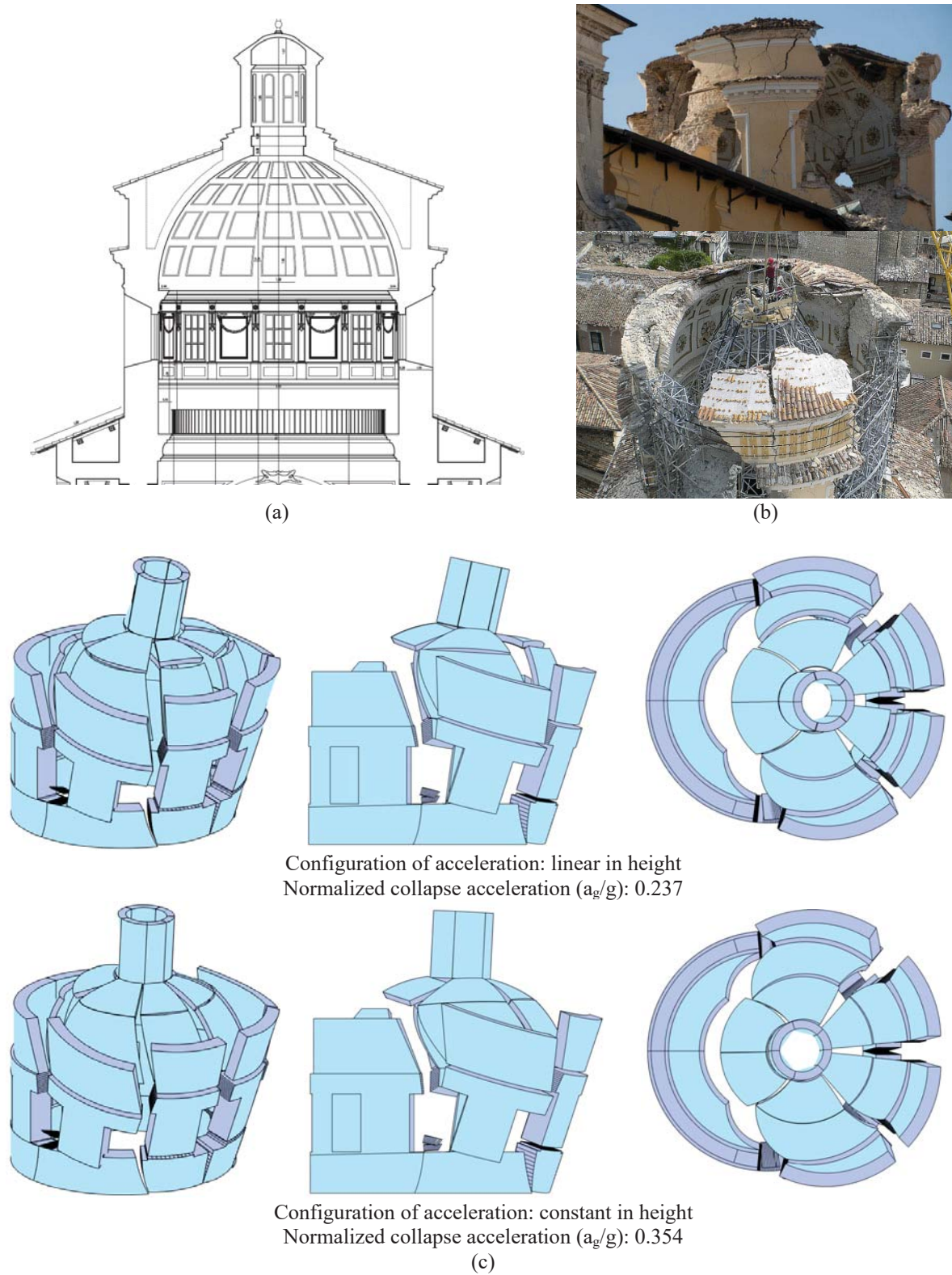


Figure 9. Dome of the Anime Sante Church, in L'Aquila (Italy): (a) geometry before the earthquake, (b) still standing parts after the collapse, (c) collapse mechanisms obtained under linear and constant in height horizontal acceleration (perspective, lateral and plan views).

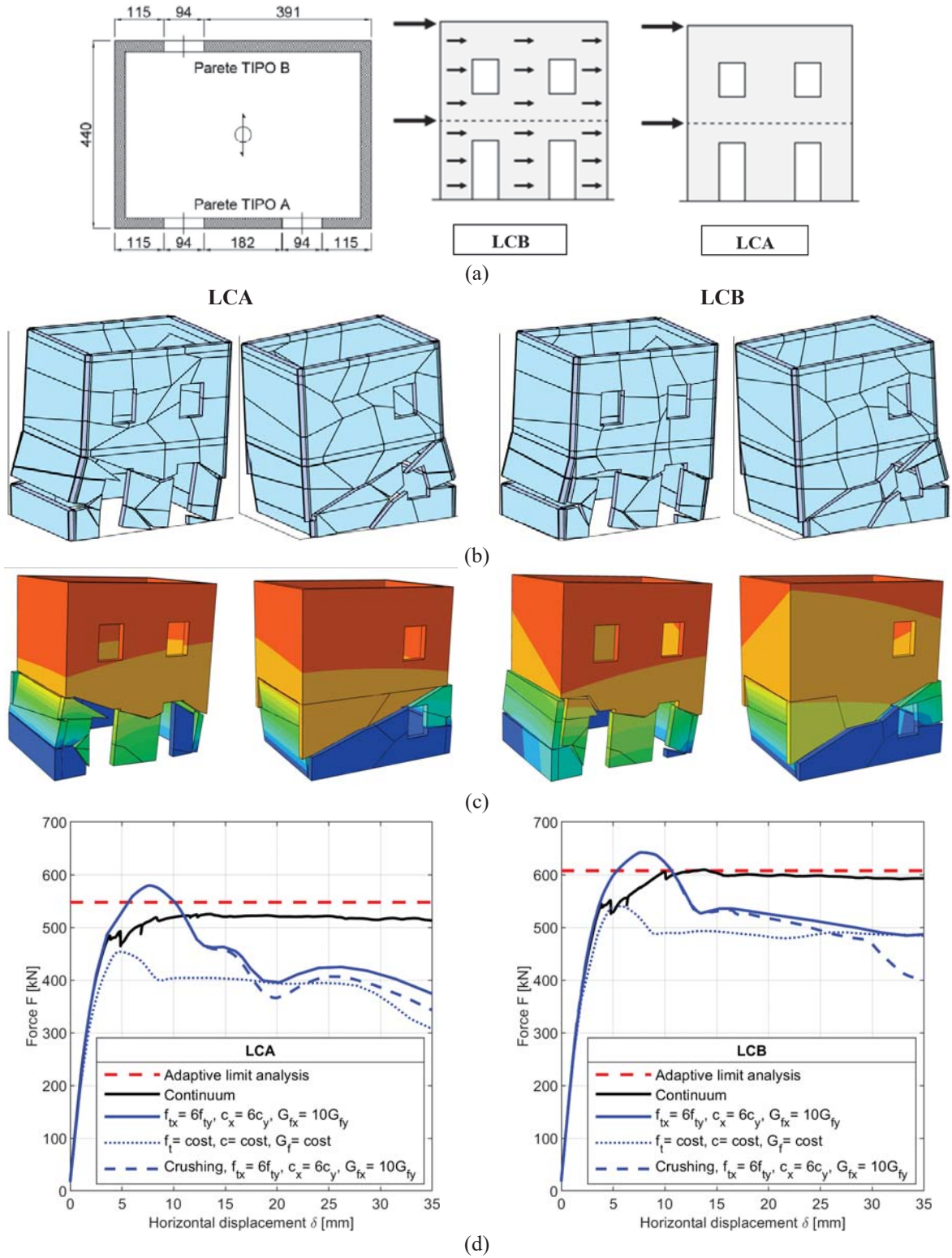


Figure 10. Two-storey masonry building: (a) geometry and load conditions, (b) collapse mechanisms obtained through limit analysis, (c) non-linear static deformed shape, and (d) comparison of results (in b-d, LCA on the left and LCB on the right).

Such benchmark relies on the application of the aforementioned two-step procedure to a simple laboratory two-storey masonry building. As depicted in Figure 10a, the horizontal projection of the construction is completely described by the 4 perimeter walls, each one 0.25 m

thick. Some openings are present on the two longitudinal walls. Both storeys are characterized by rigid horizontal floors, carried by the longitudinal walls and connected by concrete edgings. From here on the longitudinal direction term will be referred to that direction parallel to the long walls (i.e. the horizontal direction in Figure 10a). The vertical load given by the floors is equal to 10 kN/m^2 . It is worth mentioning that this benchmark has been extensively analyzed by the authors within a research project supported by the Italian network of University laboratories of seismic engineering (ReLUIIS).

The small two-storey house is analyzed under the application of two different horizontal load distributions, directed along the longitudinal direction (i.e. parallelly to the longest walls) and labelled as LCA and LCB. LCA is characterized by horizontal forces concentrated at floor levels, whereas LCB by distributed forces along the height of the structure (see Figure 10a). A NURBS model of this full-scale 3D case study has been realized. Limit analyses have been performed by assuming 0.04 MPa as tensile strength f_t , 6.2 MPa as compression strength f_c , a cohesion c equal to 0.163 MPa and a friction coefficient for the interfaces equal to 0.58 . Moreover, a specific weight equal to 17.5 kN/m^3 has been also adopted. With the aim of providing a more realistic representation of the masonry behavior in shear, a non-associative flow rule has been used in this example. The final results obtained are depicted in Figure 10b-d in terms of collapse mechanism and collapse base shear. It can be observed that cracks spread mainly on piers at the ground floor, where both flexural damage and sliding cracks appear on all four perimeter walls.

Non-linear static analyses on the derived FE model are now presented. Four hypotheses have been considered as regards material properties: (i) linear material with constant contact properties, i.e. the same resistance values assigned in limit analysis plus contact fracture energy $G_f = 500 \text{ N/m}$, (ii) linear material with variable contact properties, for which $f_{tx} = 6f_t$, $f_{ty} = f_t$, $G_{fx} = 6G_f$, $G_{fy} = G_f$, $c_x = 6c$, $c_y = c$, (iii) variable contact properties as above and material with finite compressive strength (called “crushing” model in what follows), and (iv) continuum approach introduced for comparison.

The results of the present modeling procedure (Figure 10c) show a good agreement with the base shear values obtained with limit analysis and with those obtained through a continuum approach, in terms of both pushover curves (presented in Figure 10d) and damage pattern (the continuum damage pattern is not shown here for sake of brevity). Concerning the post-peak response, the continuum model exhibits a plateau, while a considerable softening is shown by the variants of the proposed approach, which is further accentuated in the case with crushing. Accordingly, the proposed approach appears significantly robust and able to account for a softening behavior without particular numerical issues.

The proposed procedure resulted computationally efficient, particularly if compared to standard continuum FE models. Therefore, the adaptive NURBS limit analysis combined suitably with a FE non-linear static analysis can be considered an effective and efficient tool for the seismic assessment of historic and monumental masonry buildings.

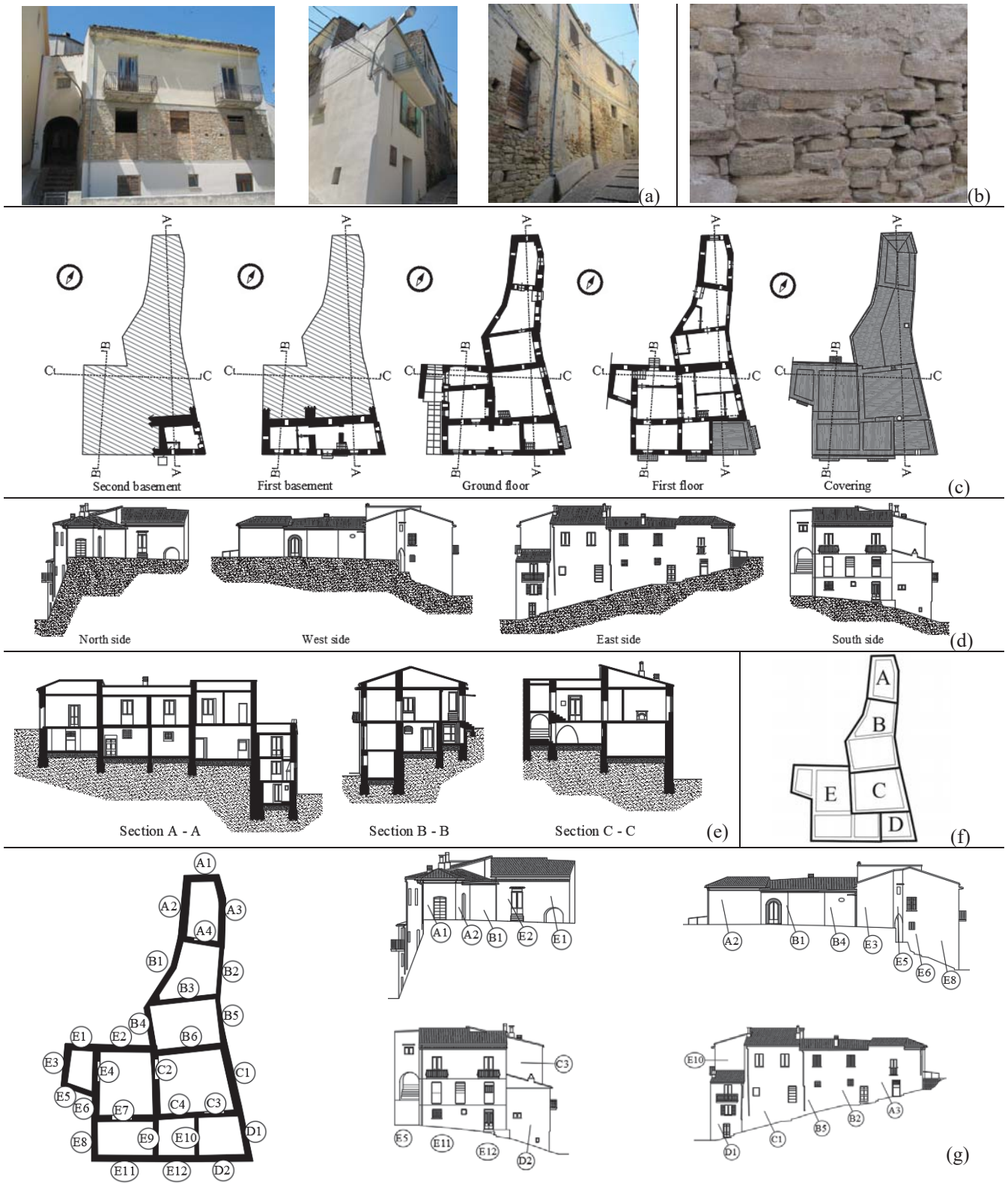


Figure 11. Aggregate “La Vecchia Forestale”: (a) pictures of South and East sides, (b) particular of the irregular masonry texture, (c) plan views, (d) perspective views, (e) sections, (f) identification and notation of structural units, and (g) nomenclature here adopted for each wall.

The fourth numerical example deals with a masonry aggregate called “La Vecchia Forestale” (Figure 11). In Figure 11 (a) some pictures of the aggregate are reported. The

building is characterized by an irregular masonry texture, composed of irregular stones and low quality mortar, as it can be seen on several masonry walls (see Figure 11(b)). The maximum length is about 25 m, which is referred to the East side, whereas, in the orthogonal direction, the width is almost equal to 14.2 m for the South side and 3.8 m for the North side. Strong irregularities can be observed both in plan and elevation. There is a total of four floors, two of which are basements defining different foundation levels. The maximum and the minimum height are respectively equal to 11.8 m on the East side and 3.9 m in the North-West corner, both measured in relation to the local ground level. The plan of different levels, perspective views, and some sections are reported in Figure 11(c-e). Five different structural units, which have been named by using the letters from A to E, have been identified. In Figure 11(f), the distinction of each structural unit is depicted: only units C, D, and E are residential, whereas units A and B are used as storage rooms. Different types of horizontal floors are present and no chains or concrete edgings are reported: the roof is made with light wood elements.

Finally, in Figure 11(g) the notation here adopted for each wall is reported. Basically, each wall is named with a letter, representing the unit to which it belongs, and a number: therefore, for example, A1 is the wall number 1 belonging to structural unit A.

Figure 12 shows the analyses on structural unit A considering two directions of the horizontal load; a relatively good interlocking between perpendicular walls is considered. In Figure 12(a) the horizontal load has been applied along the North direction. As it can be seen, the collapse occurs through the overturning of wall A1 together with some triangular portions of the transversal walls A2 and A3. Moreover, a vertical fracture line opens on wall A1: such a fracture line is probably due to the different geometries of walls A2 and A3, resulting in a non-symmetrical contribution to the failure mechanism. A value of α_0 equal to 0.772 has been obtained for the horizontal load multiplier, which is much higher when compared with the simple overturning of wall A1. Such a result is mainly due to the internal dissipation in tension and shear related to the formation of inclined fracture lines, a consequence of the good interlocking hypothesis. In Figure 12(b) the horizontal load has been applied along the East direction. In this case, the final result mainly consists of an overturning of the out-of-plane loaded wall including a single triangular portion of the transversal wall A1. Since wall A4 is thinner than wall A1, the fracture line is almost vertical and therefore no triangular blocks from this element are involved in the mechanism. Despite the similarities with the simple overturning of wall A3 evaluated in [56], a value of α_0 equal to 0.319 has been obtained: such higher value is due to the internal dissipation included in the computations.

In Figure 13 the analysis of structural unit B is reported. A total of 4 walls has been selected, as it can be seen in the plan view. The walls adjacent to other structural units have been supposed as disconnected in the contact-edge. Therefore, only one of the out-of-plane loaded walls is involved in the collapse mechanisms. The collapse takes place through an overturning of wall B2 along an inclined fracture line, due to the different constraint conditions applied on the vertical edges of wall B2 (good connection with walls B3 and B5, no connection with walls A4 and A3). The associated α_0 is equal to 0.156.

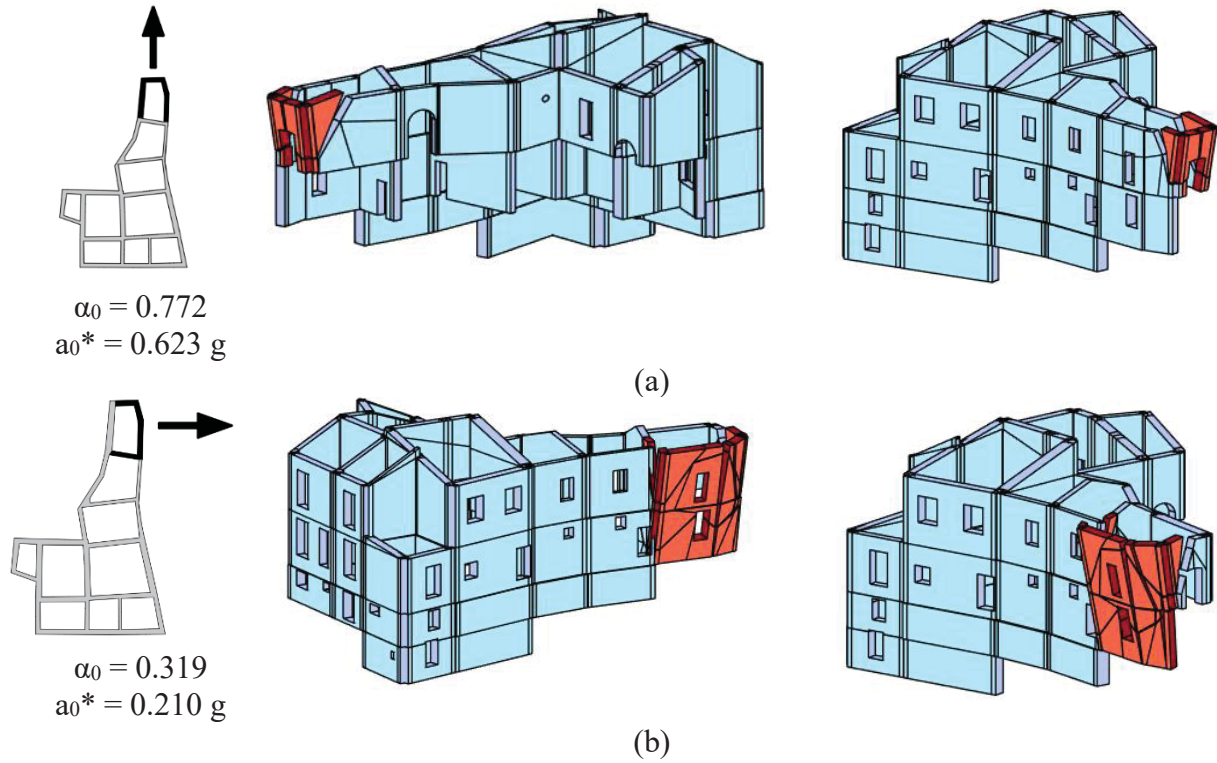


Figure 12. Aggregate, unit A, analyses with good interlocking: horizontal load applied along (a) the North and (b) the East directions.

A similar behavior has been observed for wall C1, as it can be seen in Figure 14. Even in this case, wall C1 is well connected only to the transversal wall C3. The collapse mechanism is again an overturning with inclined fracture line: however, in this case the fracture line starts at the bottom of the last storey. This is due to the lower thickness of wall C3 at the last storey with respect to the bottom part, resulting in a partial participation of this weaker portion of wall C3 in the failure mechanism.

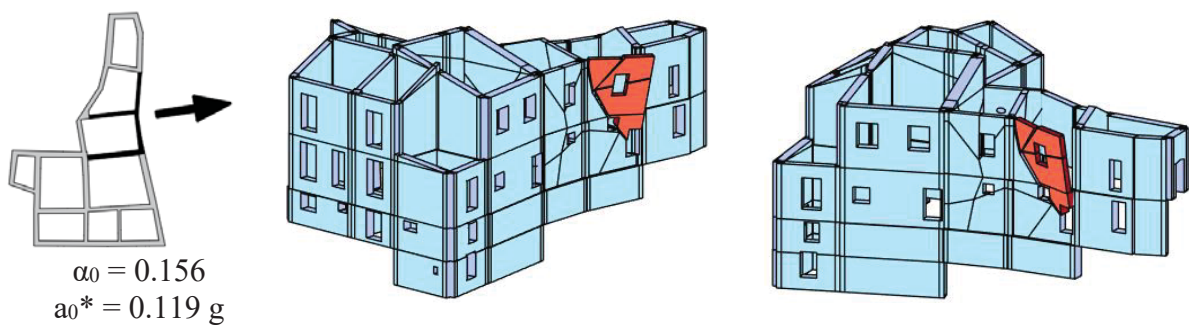


Figure 13. Aggregate, unit B, analyses with good interlocking.

Similar results are obtained for units D and E, not reported here for the sake of conciseness. The interested reader is referred to [56] for further details.

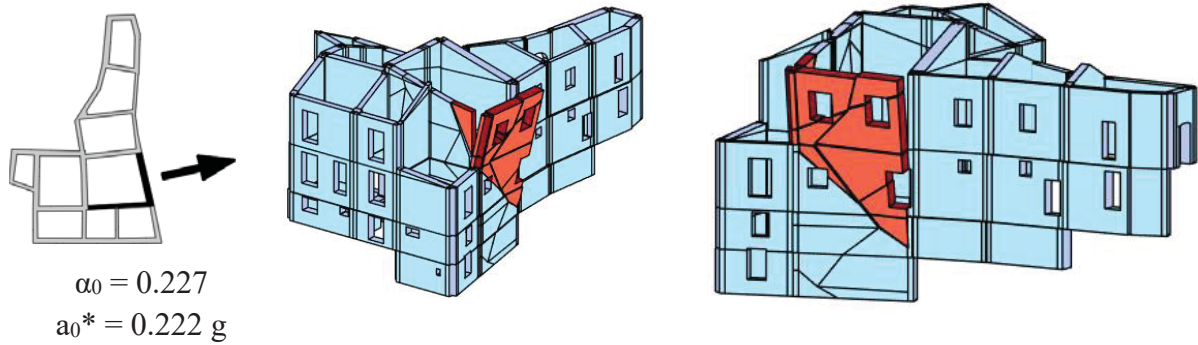


Figure 14. Aggregate, unit C, analyses with good interlocking.

As final example, a quite complex 3D limit analysis approach conceived for monumental constructions characterized by complex curved shapes is here presented. This approach consists of a limit analysis in which the structure is discretized through NURBS solids. A NURBS solid is a closed region of space delimited by NURBS boundary surfaces. NURBS solids are used to represent the rigid elements involved in the mechanism. By using NURBS surfaces to describe the external boundary of each block, this approach allows extending the study to structures that do not behave as shell-like elements, thus resulting as a generalization of the kinematic limit analysis for curved three-dimensional rigid block structures.

The Carmo Convent, in Lisbon (Portugal), is here analyzed through the NURBS solids-based limit analysis. The conventual church, see Figure 15a, presents a Gothic style composed of a nave, two longitudinal aisles, one transept, a main chapel and four side chapels, distributed onto a Latin cross. Considering the huge complexity of the case, the analysis is here focused on the triumphal arch located in the transept. Some structural elements cannot be properly represented without a NURBS solid representation: Gothic arches present a non-rectangular and curved cross-section, whereas limestone columns have a multi-circular cross-section.

The transept is analyzed under the application of an out-of-plane directed horizontal load. A comparison with FE non-linear static analyses previously presented by Scacco and colleagues [65] is also shown. Materials parameters have been assumed in agreement with those indicated in [65]. In particular a compression strength equal to 27 MPa, a friction angle equal to 30° , a cohesion equal to 0.05 MPa, and null tensile strength are adopted. Similarly to the example of the masonry dome, a constant (Load Case 1, LC1) and a linear along the height (Load Case 2, LC2) distribution of horizontal accelerations are considered. In addition, kinematic non-linear analyses aimed at including a softening behavior in tension (initial tensile strength of 0.15 MPa, fracture energy equal to 0.015 N/mm) are performed using a sequential linear programming approach where displacements at the end of the simulations are found with a procedure fully described in [66].

The results obtained are reported in Figure 15b. The failure mechanism involves the overturning of the central columns with the participation of arches at the top. Moreover, arches at the top show a combined in- and out-of-plane mechanism. A load multiplier equal to $1.19 \cdot 10^{-1}$ has been found for LC1 distribution. The resultant horizontal loads at collapse normalized for the total weight (i.e. the load multiplier) are compared with the pushover curve derived in [65], finding again a very good agreement even in such very complex case where the geometry reproduction of the sections is particularly demanding.

With this last example, it can be affirmed that the presented approach is promising in terms of efficiency and reliability to perform limit and non-linear static analysis for complex exist-

ing masonry buildings, historical structures and monumental constructions, even when very complex 3D massive curved geometries are present.

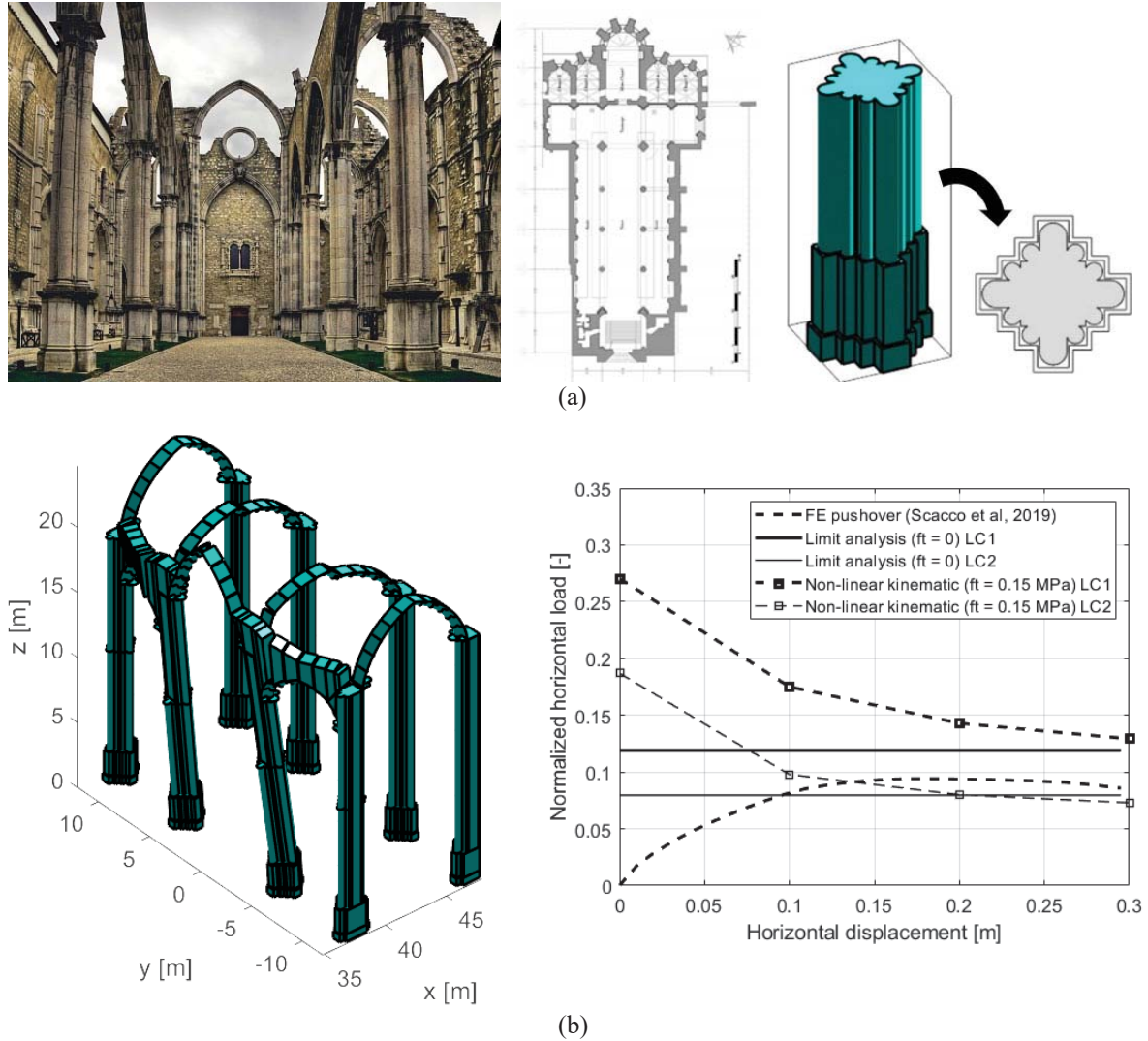


Figure 15. Analysis of the transept of the Carmo Convent (Lisbon, Portugal): (a) photo of the church as it appears now, plane view and multi-circular column in the transept, (b) collapse mechanism and results compared with previous FE non-linear static analyses reported in [65].

4 CONCLUSIONS

The present research paper was intended to show a short synopsis of the results obtained by the authors in the evaluation of the ultimate load bearing capacity and the non-linear static behavior of complex historical or existing masonry structures using non conventional software. Such approach is based on a two-step procedure, where the structures are first analyzed in the limit analysis case with adaptive 2D and 3D NURBS meshes and then with non-linear FEs where non linearity is lumped on the crack patterns found using the adaptive limit analysis. A particularly interesting recent improvement of the approach proposed is the utilization of 3D NURBS and Sequential Linear programming to predict also displacements during the formation of the failure mechanism, as shown in the last example (Carmo Convent in Lisbon). Future research streams will include (but they will not limited to) the adaptive NURBS limit analysis of massive historical masonry structures (e.g. towers and pagodas) and the extension

to non-linear dynamic loads, which include not only seismic actions but also extreme events such as explosions and floods.

REFERENCES

- [1] A. M. D'Altri, V. Sarhosis, G. Milani, J. Rots, S. Cattari, S. Lagomarsino, E. Sacco, A. Tralli, G. Castellazzi and S. de Miranda, "Modeling strategies for the computational analysis of unreinforced masonry structures: review and classification," *Archives of Computational Methods in Engineering*, vol. 27, pp. 1153-1185, 2020.
- [2] M. Malena, F. Portioli, R. Gagliardo, G. Tomaselli, L. Cascini and G. de Felice, "Collapse mechanism analysis of historic masonry structures subjected to lateral loads: A comparison between continuous and discrete models," *Computers & Structures*, vol. 220, pp. 14-31, 2019.
- [3] J. Heyman, "The stone skeleton," *International Journal of Solids and Structures*, vol. 2, no. 2, p. 249-279, 1966.
- [4] M. Angelillo, "Static analysis of a Guastavino helical stair as a layered masonry shell," *Composite Structures*, vol. 119, p. 298-304, 2015.
- [5] F. Marmo and L. Rosati, "Reformulation and extension of the thrust network analysis," *Computers & Structures*, vol. 182, p. 104-118, 2017.
- [6] P. Block and J. Ochsendorf, "Thrust network analysis: A new methodology for three-dimensional equilibrium," *Journal of the International Association for shell and spatial structures*, vol. 48, no. 3, pp. 167-173, 2007.
- [7] F. Fraternali, "A thrust network approach to the equilibrium problem of unreinforced masonry vaults via polyhedral stress functions," *Mechanics Research Communications*, vol. 37, no. 2, p. 198-204, 2010.
- [8] A. Iannuzzo, A. Dell'Endice, T. Van Mele and P. Block, "Numerical limit analysis-based modelling of masonry structures subjected to large displacements," *Computers & Structures*, vol. 242, p. 106372, 2021.
- [9] F. Portioli, C. Casapulla, M. Gilbert and L. Cascini, "Limit analysis of 3D masonry block structures with non-associative frictional joints using cone programming," *Computers & Structures*, vol. 143, p. 108-121, 2014.
- [10] C. Baggio and P. Trovalusci, "Limit analysis for no-tension and frictional three-dimensional discrete systems," *Journal of Structural Mechanics*, vol. 26, no. 3, pp. 287-304, 1998.
- [11] M. Rossi, C. Calderini, B. Di Napoli, L. Cascini and F. Portioli, "Structural analysis of masonry vaulted staircases through rigid block limit analysis," *Structures*, vol. 23, pp. 180-190, 2020.
- [12] G. Milani, "3D Upper Bound Limit Analysis of Multi-Leaf Masonry Walls," *International Journal of Mechanical Sciences*, vol. 50, no. 4, p. 817-836, 2008.
- [13] G. Milani and P. Lourenço, "A simplified homogenized limit analysis model for randomly assembled blocks out-of-plane loaded," *Computers & Structures*, vol. 88, p. 690-717, 2010.
- [14] A. Cavicchi and L. Gambarotta, "Two-dimensional finite element upper bound limit analysis of masonry bridges," *Computers & structures*, vol. 84, no. 31-32, pp. 2316-2328, 2006.
- [15] S. Sloan and P. Kleeman, "Upper Bound Limit Analysis Using Discontinuous Velocity Fields," *Computer Methods in Applied Mechanics and Engineering*, vol. 127, no. 1-4, pp. 293-314, 1995.

- [16] G. Milani, P.B. Lourenço “A discontinuous quasi-upper bound limit analysis approach with sequential linear programming mesh adaptation,” *International Journal of Mechanical Sciences*, vol. 51, no. 1, pp. 89-104, 2009.
- [17] G. Milani, “Upper bound sequential linear programming mesh adaptation scheme for collapse analysis of masonry vaults,” *Advances in Engineering Software*, vol. 79, p. 91–110, 2015.
- [18] A. Chiozzi, G. Milani and A. Tralli, “A Genetic Algorithm NURBS-based new approach for fast kinematic limit analysis of masonry vaults,” *Computers & Structures*, vol. 182, p. 187–204, 2017.
- [19] A. Chiozzi, G. Milani, N. Grillanda and A. Tralli, “A fast and general upper-bound limit analysis approach for out-of-plane loaded masonry walls,” *Meccanica*, vol. 53, no. 7, pp. 1875-1898, 2018.
- [20] M. Godio and K. Beyer, “Evaluation of force-based and displacement-based out-of-plane seismic assessment methods for unreinforced masonry walls through refined model simulations,” *Earthquake Engineering & Structural Dynamics*, vol. 48, no. 4, p. 454–475, 2018.
- [21] C. Chácará, F. Cannizzaro, B. Pantò, I. Calìo and P. B. Lourenço, “Seismic vulnerability of URM structures based on a Discrete Macro-Element Modeling (DMEM) approach,” *Engineering Structures*, vol. 201, p. 109715, 2019.
- [22] S. Lagomarsino, A. Penna, A. Galasco and S. Cattari, “TREMURI program: An equivalent frame model for the nonlinear seismic analysis of masonry buildings,” *Engineering Structures*, vol. 56, p. 1787–1799, 2013.
- [23] N. Chieffo, F. Clementi, A. Formisano and S. Lenci, “Comparative fragility methods for seismic assessment of masonry buildings located in Muccia (Italy),” *Journal of Building Engineering*, vol. 25, p. art. no. 100813 , 2019.
- [24] G. Chiumiento and A. Formisano, “Simplified and refined analyses for seismic investigation of historical masonry clusters: Comparison of results and influence of the structural units position,” *Frontiers in Built Environment*, vol. 5, p. art. no. 84, 2019.
- [25] A. Formisano and A. Massimilla, “A Novel Procedure for Simplified Nonlinear Numerical Modeling of Structural Units in Masonry Aggregates,” *International Journal of Architectural Heritage*, vol. 12, no. 7-8, pp. 1162-1170, 2018.
- [26] A. Formisano and A. Marzo, “Simplified and refined methods for seismic vulnerability assessment and retrofitting of an Italian cultural heritage masonry building,” *Computers and Structures*, vol. 180, pp. 13-26, 2017.
- [27] D. Malomo and M. J. DeJong, “A Macro-Distinct Element Model (M-DEM) for simulating the in-plane cyclic behavior of URM structures,” *Engineering Structures*, vol. 227, p. 111428, 2021.
- [28] D. Baraldi and A. Cecchi, “Discrete Approaches for the Nonlinear Analysis of in Plane Loaded Masonry Walls: Molecular Dynamic and Static Algorithm Solutions,” *European Journal of Mechanics - A/Solids*, vol. 57, p. 165–177, 2016.
- [29] A.M. D'Altri, F. Messali, J. Rots, G. Castellazzi and S. de Miranda, “A damaging block-based model for the analysis of the cyclic behaviour of full-scale masonry structures,” *Engineering Fracture Mechanics*, vol. 209, pp. 423-448, 2019.
- [30] R. Serpieri, M. Albarella and E. Sacco, “A 3D Microstructured Cohesive–frictional Interface Model and Its Rational Calibration for the Analysis of Masonry Panels,” *International Journal of Solids and Structures*, vol. 122–123, p. 110–127, 2017.
- [31] L. Cascini, F. Portioli and R. Landolfo, “3D Rigid block micro-modelling of a full-scale unreinforced brick masonry building using mathematical programming,” *International Journal of Masonry Research and Innovation*, vol. 1, no. 3, pp. 189-206, 2016.

- [32] M. Angelillo, A. Fortunato, A. Gesualdo, A. Iannuzzo and G. Zuccaro, "Rigid block models for masonry structures," *International Journal of Masonry Research and Innovation*, vol. 3, no. 4, pp. 349-368, 2018.
- [33] D. Addessi and E. Sacco, "Nonlinear analysis of masonry panels using a kinematic enriched plane state formulation," *International Journal of Solids and Structures*, vol. 90, pp. 194-214, 2016.
- [34] M. Petracca, L. Pelà, R. Rossi, S. Oller, G. Camata and E. Spacone, "Regularization of first order computational homogenization for multiscale analysis of masonry structures," *Computational Mechanics*, vol. 57, no. 2, pp. 257-276, 2015.
- [35] M. Valente, G. Milani, E. Grande and A. Formisano, "Historical masonry building aggregates: advanced numerical insight for an effective seismic assessment on two row housing compounds," *Engineering Structures*, vol. 190, pp. 360-379, 2019.
- [36] T. Forgács, V. Sarhosis and K. Bagi, "Influence of construction method on the load bearing capacity of skew masonry arches," *Engineering Structures*, vol. 168, no. 1, pp. 612-627, 2018.
- [37] A. Ferrante, F. Clementi and G. Milani, "Advanced numerical analyses by the Non-Smooth Contact Dynamics method of an ancient masonry bell tower," *Mathematical Methods in the Applied Sciences*, vol. 43, no. 13, pp. 7706-7725, 2020.
- [38] J. Lemos, "Contact representation in rigid block models of masonry," *International Journal of Masonry Research and Innovation*, vol. 4, no. 321-334, p. 2, 2017.
- [39] F. Clementi, A. Ferrante, E. Giordano, F. Dubois and S. Lenci, "Damage assessment of ancient masonry churches stroked by the Central Italy earthquakes of 2016 by the non-smooth contact dynamics method," *Bulletin of Earthquake Engineering*, vol. 18, no. 2, pp. 455-486, 2020.
- [40] V. Sarhosis and J. Lemos, "A detailed micro-modelling approach for the structural analysis of masonry assemblages," *Computers and Structures*, vol. 206, no. 1, pp. 66-81, 2018.
- [41] V. Sarhosis, S. Garrity and Y. Sheng, "Influence of brick-mortar interface on the mechanical behaviour of low bond strength masonry brickwork lintels," *Engineering Structures*, vol. 88, no. 1, pp. 1-11, 2015.
- [42] G. Uva, V. Tateo and S. Casolo, "Presentation and validation of a specific RBSM approach for the meso-scale modelling of in-plane masonry-infills in RC frames," *International Journal of Masonry Research and Innovation*, vol. 5, no. 3, pp. 366-395, 2020.
- [43] Ž. Nikolić, H. Smoljanović and N. Živaljić, "Numerical analysis of masonry structures by finite-discrete element model," *International Journal of Masonry Research and Innovation*, vol. 1, no. 4, pp. 330-350, 2016.
- [44] V. Sarhosis, K. Tsavdaridis and I. Giannopoulos, "Discrete element modelling of masonry infilled steel frames with multiple window openings subjected to lateral load variations," *Open Construction and Building Technology Journal*, vol. 8, no. 1, pp. 93-103, 2014.
- [45] V. Gazzani, M. Poiani, F. Clementi, G. Milani and S. Lenci, "Modal parameters identification with environmental tests and advanced numerical analyses for masonry bell towers: a meaningful case study," *Procedia Structural Integrity*, vol. 11, pp. 306-313, 2018.
- [46] A. Ferrante, D. Loverdos, F. Clementi, G. Milani, A. Formisano, S. Lenci and V. Sarhosis, "Discontinuous approaches for nonlinear dynamic analyses of an ancient masonry tower," *Engineering Structures*, vol. 230, p. 111626, 2021.
- [47] F. Clementi, G. Milani, A. Ferrante, M. Valente and S. Lenci, "Crumbling of Amatrice clock tower during 2016 Central Italy seismic sequence: Advanced numerical insights," *Frattura Ed Integrità Strutturale*, vol. 14, no. 51, p. 313-335, 2019.

- [48] M. Pepe, M. Pingaro, P. Trovalusci, E. Reccia and L. Leonetti, "Micromodels for the in-plane failure analysis of masonry walls: Limit analysis, FEM and FEM/DEM approaches," *Frattura e Integrità Strutturale*, vol. 14, no. 51, pp. 504-516, 2020.
- [49] D. Baraldi, E. Reccia and A. Cecchi, "In plane loaded masonry walls: DEM and FEM/DEM models. A critical review," *Meccanica*, vol. 53, no. 7, pp. 1613-1628, 2018.
- [50] A.M. D'Altri, S. de Miranda, G. Milani and G. Castellazzi, "A numerical procedure for the force-displacement description of out-of-plane collapse mechanisms in masonry structures," *Computers & Structures*, vol. 233, #106234, 2020.
- [51] N. Grillanda, A. Chiozzi, G. Milani, A. Tralli, "Tilting plane tests for the ultimate shear capacity evaluation of perforated dry joint masonry panels. Part II: Numerical analyses," *Eng Struct*, vol. 228, #111460, 2021. doi:10.1016/j.engstruct.2020.111460.
- [52] N. Grillanda, A. Chiozzi, G. Milani, A. Tralli, "Efficient meta-heuristic mesh adaptation strategies for NURBS-based upper-bound limit analysis of general curved three-dimensional masonry structures," *Computers and Structures* vol. 236, #106271, 2020. doi:10.1016/j.compstruc.2020.106271.
- [53] A. Chiozzi, N. Grillanda, G. Milani, A. Tralli, "UB-ALMANAC: An adaptive limit analysis NURBS-based program for the automatic assessment of partial failure mechanisms in masonry churches," *Engineering Failure Analysis*, vol. 85, pp. 201–220, 2018. doi:10.1016/j.engfailanal.2017.11.013.
- [54] N. Grillanda, A. Chiozzi, G. Milani, A. Tralli, "On Collapse Behavior of Reinforced Masonry Domes under Seismic Loads," *Key Engineering Materials*, vol. 817, pp. 275–282, 2019. doi:10.4028/www.scientific.net/KEM.817.275.
- [55] N. Grillanda, M. Valente, G. Milani, A. Chiozzi, A. Tralli, "Advanced numerical strategies for seismic assessment of historical masonry aggregates," *Engineering Structures*, vol. 212, #110441, 2020. doi:10.1016/j.engstruct.2020.110441.
- [56] N. Grillanda, M. Valente, G. Milani, "ANUB-Aggregates: a fully automatic NURBS-based software for advanced local failure analyses of historical masonry aggregates," *Bulletin of Earthquake Engineering*, vol. 18, pp. 3935–2961, 2020. doi:10.1007/s10518-020-00848-6.
- [57] A. Giuffrè, "Safety and conservation of historical centres: the case of Ortigia", Laterza, Rome, 1993, (in Italian).
- [58] L. Piegł, W. Tiller, "The NURBS Book," Berlin: Springer; 1995. doi:10.1007/978-3-642-59223-2.
- [59] G. Milani, P.B. Lourenco, A. Tralli, "Homogenised limit analysis of masonry walls, Part I: failure surfaces," *Computers and Structures*, vol., no. (3-4), pp. 166-180, 2006.
- [60] E. Milani, G. Milani, A. Tralli, "Limit analysis of masonry vaults by means of curved shell finite elements and homogenization," *International Journal of Solids and Structures*, vol. 45, pp. 5258–5288, 2008. doi:10.1016/j.ijsolstr.2008.05.019.
- [61] A.M. D'Altri, N. Lo Presti, N. Grillanda, G. Castellazzi, S. de Miranda, G. Milani, "A two-step automated procedure based on adaptive limit and pushover analyses for the seismic assessment of masonry structures", *Computers and Structures*, in press, 2021. doi: 10.1016/j.compstruc.2021.106561
- [62] J. Lubliner, J. Oliver, S. Oller, E. Oñate, "A plastic-damage model for concrete," *International Journal of Solids and Structures*, vol. 25, pp. 299-326, 1989.
- [63] J. Lee, G.L. Fenves, "Plastic-Damage Model for Cyclic Loading of Concrete Structures," *Journal of Engineering Mechanics*, vol. 124, pp. 892-900, 1998.
- [64] J. Scacco, G. Milani, P.B. Lourenço, "Automatic mesh generator for the non-linear homogenized analysis of double curvature masonry structures", *Advances in Engineering Software*, vol., 150, #102919, 2020. doi:10.1016/j.advengsoft.2020.102919.

- [65] J. Scacco, G. Salazar, N. Bianchini, N. Mendes, C. Cullimore, L. Jain, “Seismic assessment of the church of Carmo convent,” in Proc. of the Congress on Métodos Numéricos em Eng., 2019.
- [66] A. Tralli, A. Chiozzi, N. Grillanda, G. Milani, “Masonry structures in the presence of foundation settlements and unilateral contact problems,” International Journal of Solids and Structures, vol. 191-192, pp. 187-201, 2020.

SOME RECENT ADVANCES IN THE WAVE FINITE ELEMENT METHOD

D. Duhamel¹, B. Claudet¹, T. Hoang¹, G. Foret¹ and J.-M. Mencik²

¹Ecole des Ponts, laboratoire Navier,
6 et 8 Avenue Blaise Pascal, Cité Descartes, Champs sur Marne,
77 455 Marne la Vallée, cedex 2, France
e-mail: {denis.duhamel,benjamin.claudet,tien.hoang,gilles.foret}@enpc.fr

² INSA Centre Val de Loire, Université d'Orléans,
Université de Tours, Laboratoire de Mécanique Gabriel Lamé,
Rue de la Chocolaterie, 41000 Blois, France
e-mail: jean-mathieu.mencik@insa-cvl.fr

Keywords: Wave Finite Element, Periodic Structures, Structural Dynamics, Distributed Loads, Numerical Methods, Time Response, Absorbing Boundary Conditions.

Abstract. *The wave finite element (WFE) method is now an established numerical method for obtaining the structural response of periodic structures. From a model of a substructure obtained from any finite element software, it allows to get dispersion curves and responses of finite periodic structures with a low calculation cost. Here, we consider some recent improvements of the method. First of all, the original WFE is often formulated with some point loads on the structure, but we show that it is possible to extend this to the consideration of general loads as pressure waves or moving loads for which external loads are applied on each substructure. Second, the classical WFE deals with structures in the frequency domain. It would be interesting to consider the analysis of periodic structures in the time domain, for instance to deal with blast loads. We present here one possibility to do so by computing absorbing boundary conditions in the time domain. By considering supplementary variables at the boundary, a new formulation can be obtained and a classical equation with extended mass, damping and stiffness matrices can be formulated in the time domain and solved by classical algorithms like the Newmark scheme.*

1 INTRODUCTION

The wave finite element method (WFE) is often used to predict the dynamic response of periodic structures under harmonic loading like railway tracks, pipelines, ribbed plates, tires, reinforced panels or metamaterials. This consists in computing wave modes (propagation constants, wave shapes) of a periodic structure from the finite element (FE) model of a substructure and its related mass, damping and stiffness matrices which can be obtained from any FE software. Afterwards, these wave modes can be used to calculate the harmonic response of periodic structures in an efficient way, i.e., by computing small matrix systems for one substructure, or a few of them, see for instance the works in [1, 2, 3, 4].

First of all, the original WFE considers mainly some points loads on the structure, but we show here that it is possible to extend this to the consideration of general loads as pressure waves or moving loads for which external loads are applied on each substructure. Several applications of this are possible. At first is the computation of civil engineering structures such as bridges which have extended loads and various displacement and reaction forces at supports, or the computation of structures under moving loads such as railways tracks under the dynamic loads of a train.

Second, it is a matter of fact that the classical WFE deals with structures in the frequency domain. But it would also be interesting to consider the analysis of periodic structures in the time domain, for instance to deal with shocks or blast loads. We present here one possibility to do so by computing absorbing boundary conditions in the time domain. For dispersive media like beams [5], multi-layered systems [6] or general periodic structures [7], absorbing BCs can be formulated in terms of boundary operators involving complicated functions of the frequency — e.g., square roots of the frequency — which, as such, cannot be converted to simple functions of time after inverse Fourier transforms. To solve this issue, the impedance relation at the boundary of a periodic structure is first written in the frequency domain, then this impedance frequency function is decomposed as a rational function for which poles and residues are computed. By considering supplementary variables at the boundary, a formulation in the time domain can be obtained. Finally, a classical equation with extended mass, damping and stiffness matrices can be formulated in the time domain and solved by classical algorithms like the Newmark scheme.

The rest of this paper is organized as follows. In section 2, the main steps of the WFE method are recalled. In section 3, the case of complex and moving loads are considered. Then section 4 is concerned with the formulation of time domain absorbing boundary conditions for periodic structures and the solution of time domain structural dynamics problems. Numerical comparisons with analytical or an equivalent infinite full FE model are presented. Concluding remarks are finally brought in section 5.

2 WFE method

The present paper investigates the dynamic response of infinite 1D periodic structures subject to harmonic or time-dependent loadings. For instance, a schematic of a periodic structure made up of identical substructures is shown in Fig. 1. The substructures under concern can be of arbitrary shape and are supposed to be linear, elastic, isotropic and damped (viscous damping). Also, the excitations are applied on the structure encompassing those substructures which can be infinite or bounded by two left and right boundaries.

The wave propagation analysis in 1D periodic structures can be conducted with the WFE method [2, 4, 8]. The basics of the method are recalled hereafter. Let us consider infinite structures under harmonic disturbance $e^{i\omega t}$ which are built from identical substructures as shown

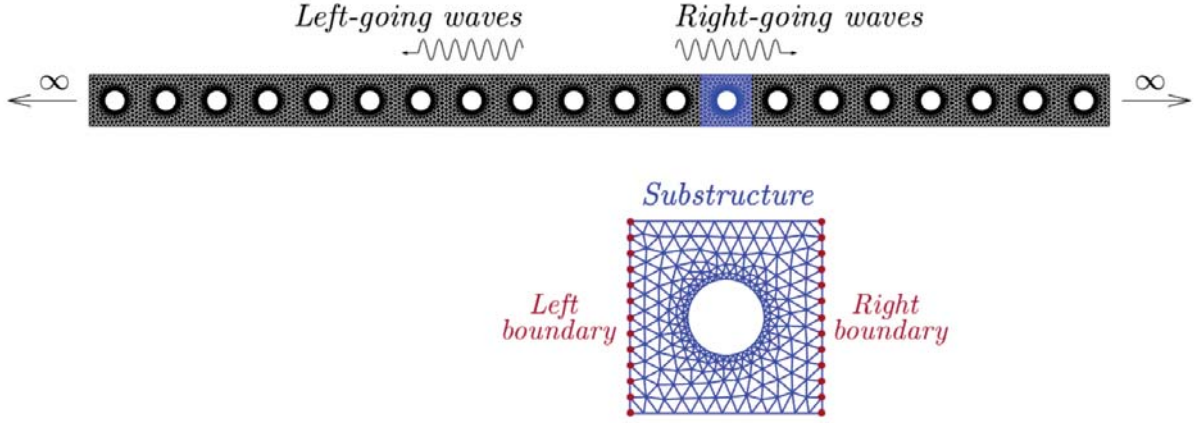


Figure 1: Periodic structure of infinite length, and FE mesh of a substructure.

in Fig. 1, are supposed to share the same FE mesh, and are modelled by means of identical mass, damping and stiffness matrices \mathbf{M} , \mathbf{C} and \mathbf{K} . The related dynamic equilibrium equation is given by:

$$\begin{bmatrix} \mathbf{D}_{II} & \mathbf{D}_{IL} & \mathbf{D}_{IR} \\ \mathbf{D}_{LI} & \mathbf{D}_{LL} & \mathbf{D}_{LR} \\ \mathbf{D}_{RI} & \mathbf{D}_{RL} & \mathbf{D}_{RR} \end{bmatrix} \begin{bmatrix} \mathbf{q}_I \\ \mathbf{q}_L \\ \mathbf{q}_R \end{bmatrix} = \begin{bmatrix} \mathbf{F}_I \\ \mathbf{F}_L \\ \mathbf{F}_R \end{bmatrix} \quad (1)$$

where \mathbf{q} and \mathbf{F} refer to the displacement vector and the force vector (respectively), and where \mathbf{D} is the dynamic stiffness matrix of the substructures (similar for all the substructures) expressed by $\mathbf{D} = -\omega^2 \mathbf{M} + i\omega \mathbf{C} + \mathbf{K}$. The FE mesh of a substructure is shown in Fig. 1, and involves internal (I) degrees of freedom (DOFs), left (L) and right (R) boundaries which are described with the same number n of DOFs. If we assume that the internal DOFs are free from excitation, e.g., $\mathbf{F}_I = \mathbf{0}$, we can remove \mathbf{q}_I and rearrange Eq. (1) to yield the following transfer matrix relation between the right and left boundaries of the substructure:

$$\mathbf{u}_R = \mathbf{S} \mathbf{u}_L, \quad (2)$$

where \mathbf{u}_R and \mathbf{u}_L are $2n \times 1$ state vectors expressed by:

$$\mathbf{u}_R = \begin{bmatrix} \mathbf{q}_R \\ \mathbf{F}_R \end{bmatrix}, \quad \mathbf{u}_L = \begin{bmatrix} \mathbf{q}_L \\ -\mathbf{F}_L \end{bmatrix}. \quad (3)$$

Also, \mathbf{S} is a symplectic $2n \times 2n$ matrix (also called transfer matrix) expressed by:

$$\mathbf{S} = \left[\begin{array}{c|c} -(\mathbf{D}_{LR}^*)^{-1} \mathbf{D}_{LL}^* & -(\mathbf{D}_{LR}^*)^{-1} \\ \hline \mathbf{D}_{RL}^* - \mathbf{D}_{RR}^* (\mathbf{D}_{LR}^*)^{-1} \mathbf{D}_{LL}^* & -\mathbf{D}_{RR}^* (\mathbf{D}_{LR}^*)^{-1} \end{array} \right], \quad (4)$$

where \mathbf{D}^* refers to the dynamic stiffness matrix of the substructure condensed on the left and right boundaries [9].

The eigenvalues and eigenvectors of the transfer matrix \mathbf{S} occur in pairs as (μ_j, ϕ_j) and $(\mu_j^* = 1/\mu_j, \phi_j^*)$ with $|\mu_j| < 1$ (see [3] for further details about the computation of the eigensolutions of \mathbf{S}). Also, the eigenvectors ϕ_j (resp. ϕ_j^*) have the meaning of wave shapes, for the waves traveling to the right and left directions (respectively) of the periodic structure. Those vectors of wave shapes are of size $2n \times 1$ and are usually partitioned as follows:

$$\phi_j = \begin{bmatrix} \phi_{qj} \\ \phi_{Fj} \end{bmatrix}, \quad \phi_j^* = \begin{bmatrix} \phi_{qj}^* \\ \phi_{Fj}^* \end{bmatrix}, \quad (5)$$

where ϕ_{qj} and ϕ_{qj}^* (resp. ϕ_{Fj} and ϕ_{Fj}^*) are $n \times 1$ vectors involving displacement (resp. force) components. The related $n \times n$ matrices of wave shapes — namely, Φ_q , Φ_q^* , Φ_F and Φ_F^* — are given by:

$$\Phi_q = [\phi_{q1} \cdots \phi_{qn}], \quad \Phi_q^* = [\phi_{q1}^* \cdots \phi_{qn}^*], \quad \Phi_F = [\phi_{F1} \cdots \phi_{Fn}], \quad \Phi_F^* = [\phi_{F1}^* \cdots \phi_{Fn}^*]. \quad (6)$$

A state vector at any substructure interface can then be decomposed on these wave modes by

$$\mathbf{u} = \sum_{j=1}^{j=n} Q_j \phi_j + \sum_{j=1}^{j=n} Q_j^* \phi_j^* \quad (7)$$

where Q_j and Q_j^* are respectively the amplitudes of the right and left propagating waves in the considered section.

3 WFE with complex loads

3.1 Equations

We consider now the case where the structure is under a distributed load that can be applied on each substructure. For loads inside a substructure, relation (1) yields

$$\mathbf{q}_I = \mathbf{D}_{II}^{-1} [\mathbf{F}_I - \mathbf{D}_{IL}\mathbf{q}_L - \mathbf{D}_{IR}\mathbf{q}_R] \quad (8)$$

and so relation (2) is transformed to a relation linking the state vector in sections n (between substructures $n - 1$ and n) and the state vector in section $n + 1$ (see [10] for details)

$$\mathbf{u}^{(n+1)} = \mathbf{S}\mathbf{u}^{(n)} + \mathbf{b}^{(n)}, \quad (9)$$

with

$$\mathbf{u}^{(n)} = \begin{bmatrix} \mathbf{q}^{(n)} \\ -\mathbf{F}_L^{(n)} \end{bmatrix}, \quad \mathbf{b}^{(n)} = \begin{bmatrix} \mathbf{D}_{qI}\mathbf{F}_I \\ \mathbf{D}_{fI}\mathbf{F}_I - \mathbf{F}_R^{ext} \end{bmatrix} \quad (10)$$

where \mathbf{F}_R^{ext} is the external load applied in section $n + 1$ and

$$\begin{bmatrix} \mathbf{D}_{qI} \\ \mathbf{D}_{fI} \end{bmatrix} = \begin{bmatrix} -(\mathbf{D}_{LR}^*)^{-1}\mathbf{D}_{LI}^* \\ \mathbf{D}_{RI}^* - \mathbf{D}_{RR}^*(\mathbf{D}_{LR}^*)^{-1}\mathbf{D}_{LI}^* \end{bmatrix} \quad (11)$$

where the superscript $*$ means that the matrix is condensed on the boundary, for instance,

$$\begin{aligned} \mathbf{D}_{LR}^* &= \mathbf{D}_{LR} - \mathbf{D}_{LI}\mathbf{D}_{II}^{-1}\mathbf{D}_{IR} \\ \mathbf{D}_{LI}^* &= \mathbf{D}_{LI}\mathbf{D}_{II}^{-1} \end{aligned} \quad (12)$$

Finally, the state vector in section n is related to the state vectors of sections 1 and $N + 1$ by

$$\mathbf{u}^{(n)} = \mathbf{S}^{n-1}\mathbf{u}^{(1)} + \sum_{k=1}^{n-1} \mathbf{S}^{n-k-1}\mathbf{b}^{(k)} \quad (13)$$

or

$$\mathbf{u}^{(N+1)} = \mathbf{S}^{N-n+1}\mathbf{u}^{(n)} + \sum_{k=n}^N \mathbf{S}^{N-k}\mathbf{b}^{(k)} \quad (14)$$

where the sum including $\mathbf{b}^{(k)}$ allows to take into account all the loads applied between the two sections. Projecting on the wave modes, the state vector $\mathbf{u}^{(n)}$ in section n and load vector $\mathbf{b}^{(k)}$ in section k can also be written in terms of wave amplitudes by

$$\begin{aligned} \mathbf{u}^{(n)} &= \Phi \mathbf{Q}^{(n)} + \Phi^* \mathbf{Q}^{*(n)} \\ \mathbf{b}^{(k)} &= \Phi \mathbf{Q}_E^{(k)} + \Phi^* \mathbf{Q}_E^{*(k)} \end{aligned} \quad (15)$$

3.2 Case of moving loads

An interesting case concerns moving loads. For a moving load at speed v , with a substructure of length L , the amplitude of the load in section (k) is related to the amplitude of the load in section (0) by

$$\begin{aligned} \mathbf{Q}_E^{*(k)} &= e^{-ik\frac{\omega L}{v}} \mathbf{Q}_E^{*(0)} \\ \mathbf{Q}_E^{(-k)} &= e^{ik\frac{\omega L}{v}} \mathbf{Q}_E^{(0)} \end{aligned} \quad (16)$$

because the loads on the different substructures are related by $f_n(t) = f_{n-1}(t - L/v)$. From relations (13) and (15), one gets

$$\begin{aligned} \mathbf{u}^{(n)} &= \Phi \mathbf{Q}^{(n)} + \Phi^* \mathbf{Q}^{*(n)} \\ &= \Phi \mu^n \left(\mathbf{Q} + \sum_{k=0}^{n-1} \mu^{k+1} \mathbf{Q}_E^{(k)} \right) + \Phi^* \mu^{-n} \left(\mathbf{Q}^* + \sum_{k=0}^{n-1} \mu^{k+1} \mathbf{Q}_E^{*(k)} \right) \end{aligned} \quad (17)$$

with μ the diagonal matrix made of the propagation constants μ_j on the diagonal and \mathbf{Q} , \mathbf{Q}^* are free wave amplitudes in the structure determined by the boundary conditions. As the precedent relation should be bounded for $n \rightarrow \infty$, we get

$$\mathbf{Q}^* = - \sum_{k=0}^{\infty} \mu^{k+1} \mathbf{Q}_E^{*(k)} = - \frac{\mu}{1 - \mu e^{-i\frac{\omega L}{v}}} \mathbf{Q}_E^{*(0)} \quad (18)$$

For the left side, we get

$$\mathbf{Q} = \sum_{k=1}^{\infty} \mu^{k-1} \mathbf{Q}_E^{(-k)} = \frac{e^{i\frac{\omega L}{v}}}{1 - \mu e^{i\frac{\omega L}{v}}} \mathbf{Q}_E^{(0)} \quad (19)$$

Finally, one gets

$$\mathbf{u}^{(0)} = \frac{e^{i\frac{\omega L}{v}}}{1 - \mu e^{i\frac{\omega L}{v}}} \mathbf{Q}_E^{(0)} \Phi - \frac{\mu}{1 - \mu e^{-i\frac{\omega L}{v}}} \mathbf{Q}_E^{*(0)} \Phi^* \quad (20)$$

3.3 A simple example

Consider the very simple example of a bar undergoing a longitudinal displacement subject to a moving force

$$\rho \frac{\partial^2 u}{\partial t^2} = E u'' + f \quad (21)$$

We have $k = \sqrt{\frac{\rho \omega^2}{E}} = \frac{\omega}{c}$, $c = \sqrt{\frac{E}{\rho}}$, $f(x, t) = \delta(x - vt)$ and the wave modes are

$$\Phi = \begin{bmatrix} 1 \\ -ikE \end{bmatrix}, \quad \Phi^* = \begin{bmatrix} 1 \\ ikE \end{bmatrix} \quad (22)$$

The propagation constant is $\mu = e^{-ikL}$ and the load amplitudes are obtained from the load in the period $[0, L]$. The solution of (21) such that $u(0) = u'(0) = 0$ is given by

$$u(x) = - \int_0^x \frac{1}{kE} \sin(k(x-t)) f(t) dt \quad (23)$$

So that for $x = L$ and $f(t) = \frac{1}{v}e^{-i\omega t/v}$, one gets

$$\begin{aligned} u(L) &= -\frac{1}{2ikEv} \int_0^L (e^{ik(L-t)} - e^{-ik(L-t)}) e^{-i\omega t/v} dt \\ &= -\frac{1}{2ikEv} \left(\frac{e^{-i\omega L/v} - e^{ikL}}{-ik - i\omega/v} - \frac{e^{-i\omega L/v} - e^{-ikL}}{ik - i\omega/v} \right) \end{aligned} \quad (24)$$

and

$$Eu'(L) = -\frac{1}{2ikv} \left(\frac{\frac{-i\omega}{v} e^{-i\omega L/v} - ik e^{ikL}}{-ik - i\omega/v} - \frac{\frac{-i\omega}{v} e^{-i\omega L/v} + ik e^{-ikL}}{ik - i\omega/v} \right) \quad (25)$$

Using relation (9) and the solution of (21) such that $\mathbf{b} = {}^T[u(L) \quad Eu'(L)]$, the load amplitudes are obtained by decomposing the solution at $x = L$ on the wave modes by

$$\begin{aligned} Q_E^{(0)} &= \frac{{}^T\Phi^* \mathbf{J} \mathbf{b}}{{}^T\Phi^* \mathbf{J} \Phi} \\ &= -\frac{e^{-i\omega \frac{L}{v}} - e^{-ikL}}{2kEv(k - \frac{\omega}{v})} \\ Q_E^{*(0)} &= \frac{{}^T\Phi \mathbf{J} \mathbf{b}}{{}^T\Phi \mathbf{J} \Phi^*} \\ &= -\frac{e^{-i\omega \frac{L}{v}} - e^{ikL}}{2kEv(k + \frac{\omega}{v})} \end{aligned} \quad (26)$$

with

$$\mathbf{J} = \begin{bmatrix} 0 & 1 \\ -1 & 0 \end{bmatrix} \quad (27)$$

The amplitudes of the right-going and left-going waves are thus given by, using (20),

$$\begin{aligned} Q &= -\frac{1}{2kEv(k - \frac{\omega}{v})} \\ Q^* &= -\frac{1}{2kEv(k + \frac{\omega}{v})} \end{aligned} \quad (28)$$

and we recover the displacement at $x = 0$ by

$$\begin{aligned} u &= -\frac{1}{2kEv(k - \frac{\omega}{v})} - \frac{1}{2kEv(k + \frac{\omega}{v})} \\ &= -\frac{1}{Ev(k^2 - \frac{\omega^2}{v^2})} \\ &= -\frac{1}{Ev\omega^2(\frac{1}{c^2} - \frac{1}{v^2})} \end{aligned} \quad (29)$$

which is the analytical solution of (21). Following the same procedure, this can be extended to more complex structures with many DOFs in each section.

4 Absorbing boundary conditions in the time domain

4.1 WFE formulation

Consider now a periodic structure involving a finite number N of substructures which is enclosed between two left and right boundaries S_L and S_R where absorbing BCs are considered (see Fig. 2). Such BCs are used to describe the coupling effect between the periodic structure and two semi-infinite periodic structures, that would expand to the left and right directions. The related impedance matrices for the left and right boundaries S_L and S_R — namely, \mathbf{Z}_L and \mathbf{Z}_R — can be defined, in the frequency domain, as follows:

$$\mathbf{F}_L = \mathbf{Z}_L \mathbf{q}_L, \quad \mathbf{F}_R = \mathbf{Z}_R \mathbf{q}_R, \quad (30)$$

where \mathbf{q}_L and \mathbf{q}_R (resp. \mathbf{F}_L and \mathbf{F}_R) are the displacement (resp. force) vectors (size $n \times 1$) for the periodic structure on S_L and S_R . Following the WFE procedure and expanding those vectors on the basis of wave shapes, this yields [9]:

$$\mathbf{q}_L = \Phi_q^* \mathbf{Q}_L^*, \quad \mathbf{q}_R = \Phi_q \mathbf{Q}_R, \quad (31)$$

and

$$\mathbf{F}_L = -\Phi_F^* \mathbf{Q}_L^*, \quad \mathbf{F}_R = \Phi_F \mathbf{Q}_R, \quad (32)$$

where \mathbf{Q}_L^* (resp. \mathbf{Q}_R) is the vector of wave amplitudes, at position S_L (resp. S_R), for the waves traveling to the left (resp. right) direction of the structure. The fact that left-going (resp. right-going) waves are only considered at S_L (resp. S_R) results from the absorbing BC, i.e., the fact that no wave comes from infinity. So we get the following expressions for the impedance matrices:

$$\mathbf{Z}_L = -\Phi_F^* (\Phi_q^*)^{-1}, \quad \mathbf{Z}_R = \Phi_F (\Phi_q)^{-1}. \quad (33)$$

Let us decompose the impedance matrices \mathbf{Z}_L and \mathbf{Z}_R which are complicated functions of frequency that do not generally possess an analytical expression, via rational approximations like in [7]:

$$\mathbf{Z}_L = \sum_{k=1}^P \frac{\mathbf{R}_{Lk}}{i\omega - p_{Lk}} + \mathbf{K}_L, \quad \mathbf{Z}_R = \sum_{k=1}^P \frac{\mathbf{R}_{Rk}}{i\omega - p_{Rk}} + \mathbf{K}_R, \quad (34)$$

where p_{Lk} and p_{Rk} denote poles ($k = 1, \dots, P$), and \mathbf{R}_{Lk} and \mathbf{R}_{Rk} denote matrices of residues. Some of these usually appear in conjugate pairs, i.e., $(p_{Lk}, \overline{p_{Lk}})$ and $(p_{Rk}, \overline{p_{Rk}})$, and $(\mathbf{R}_{Lk}, \overline{\mathbf{R}_{Lk}})$ and $(\mathbf{R}_{Rk}, \overline{\mathbf{R}_{Rk}})$. As a result, Eq. (34) leads to:

$$\mathbf{Z}_L = \sum_{k=1}^Q 2 \frac{i\omega \Re\{\mathbf{R}_{L(2k)}\} - \Re\{\overline{p_{L(2k)}} \mathbf{R}_{L(2k)}\}}{-\omega^2 - 2i\omega \Re\{p_{L(2k)}\} + |p_{L(2k)}|^2} + \sum_{k=2Q+1}^P \frac{\mathbf{R}_{Lk}}{i\omega - p_{Lk}} + \mathbf{K}_L \quad (35)$$

where $2Q < P$. Only the left impedance is described as the right impedance follows similar expression by replacing the subscript L by R . To remove the denominator terms in Eq. (35), let us introduce $n \times 1$ vectors of supplementary variables \mathbf{X}_{Lk} and \mathbf{X}_{Rk} , and let us rewrite Eq. (30) by means of Eq. (35) as follows:

$$\mathbf{F}_L = \sum_{k=1}^Q 2 (i\omega \Re\{\mathbf{R}_{L(2k)}\} - \Re\{\overline{p_{L(2k)}} \mathbf{R}_{L(2k)}\}) \mathbf{X}_{Lk} + \sum_{k=2Q+1}^P \mathbf{R}_{Lk} (i\omega) \mathbf{X}_{L(k-Q)} + \mathbf{K}_L \mathbf{q}_L \quad (36)$$

where:

$$\begin{aligned} (-\omega^2 - 2i\omega\Re\{p_{L(2k)}\} + |p_{L(2k)}|^2) \mathbf{X}_{Lk} &= \mathbf{q}_L & \text{for } k = 1, \dots, Q, \\ (-\omega^2 - i\omega p_{Lk}) \mathbf{X}_{L(k-Q)} &= \mathbf{q}_L & \text{for } k = (2Q+1), \dots, P, \end{aligned} \quad (37)$$

Finally, let us introduce the following $(P-Q)n \times 1$ vector \mathbf{X}_L defined by:

$$\mathbf{X}_L = \begin{bmatrix} \mathbf{X}_{L1} \\ \vdots \\ \mathbf{X}_{LQ} \\ \mathbf{X}_{L(Q+1)} \\ \vdots \\ \mathbf{X}_{L(P-Q)} \end{bmatrix}. \quad (38)$$

The block components of the matrices occurring in Eqs. (36) and (37) represent polynomials of $i\omega$ of orders 0, 1 or 2, which as such can be simply and quickly converted to the time domain (see hereafter). By separating the terms of identical powers of $i\omega$, and by invoking the classical time-frequency transforms $\mathbf{q}(\omega) \rightarrow \mathbf{q}(t)$, $i\omega\mathbf{q} \rightarrow \dot{\mathbf{q}}$, $-\omega^2\mathbf{q} \rightarrow \ddot{\mathbf{q}}$ and $\mathbf{X}(\omega) \rightarrow \mathbf{X}(t)$, $i\omega\mathbf{X} \rightarrow \dot{\mathbf{X}}$, $-\omega^2\mathbf{X} \rightarrow \ddot{\mathbf{X}}$ (where dot and double-dot notations mean single and double time derivatives, respectively), this yields:

$$\mathbb{M}_L \begin{bmatrix} \ddot{\mathbf{X}}_L \\ \dot{\mathbf{X}}_L \\ \mathbf{X}_L \end{bmatrix} + \mathbb{C}_L \begin{bmatrix} \dot{\mathbf{X}}_L \\ \mathbf{X}_L \end{bmatrix} + \mathbb{K}_L \begin{bmatrix} \mathbf{q}_L \\ \mathbf{X}_L \end{bmatrix} = \begin{bmatrix} \mathbf{F}_L \\ \mathbf{0} \end{bmatrix} \quad (39)$$

where:

$$\begin{aligned} \mathbb{M}_L &= \begin{bmatrix} \mathbf{0} & \mathbf{0} & \mathbf{0} \\ \mathbf{0} & \text{blkdiag}\{\mathbf{I}_n\}_{k=1}^Q & \mathbf{0} \\ \mathbf{0} & \mathbf{0} & \text{blkdiag}\{\mathbf{I}_n\}_{k=2Q+1}^P \end{bmatrix}, \\ \mathbb{C}_L &= \begin{bmatrix} \mathbf{0} & 2\Re\{\mathbf{R}_{L(2)} \cdots \mathbf{R}_{L(2Q)}\} & [\mathbf{R}_{L(2Q+1)} \cdots \mathbf{R}_{LP}] \\ \mathbf{0} & \text{blkdiag}\{-2\Re\{p_{L(2k)}\}\mathbf{I}_n\}_{k=1}^Q & \mathbf{0} \\ \mathbf{0} & \mathbf{0} & \text{blkdiag}\{-p_{Lk}\mathbf{I}_n\}_{k=2Q+1}^P \end{bmatrix}, \\ \mathbb{K}_L &= \begin{bmatrix} \mathbf{K}_L & -2\Re\{\overline{p_{L(2)}}\mathbf{R}_{L(2)} \cdots \overline{p_{L(2Q)}}\mathbf{R}_{L(2Q)}\} & \mathbf{0} \\ -\mathbb{1}_{Q \times 1} \otimes \mathbf{I}_n & \text{blkdiag}\{|p_{L(2k)}|^2\mathbf{I}_n\}_{k=1}^Q & \mathbf{0} \\ -\mathbb{1}_{(P-2Q) \times 1} \otimes \mathbf{I}_n & \mathbf{0} & \mathbf{0} \end{bmatrix}, \end{aligned} \quad (40)$$

where \otimes denotes the Kronecker product.

Let us denote by \mathbf{M} , \mathbf{C} and \mathbf{K} the mass, damping and stiffness matrices of the periodic structure (N substructures), and let us write the related equation of motion as follows:

$$\mathbf{M}\ddot{\mathbf{q}} + \mathbf{C}\dot{\mathbf{q}} + \mathbf{K}\mathbf{q} = \mathbf{F}, \quad (41)$$

where $\mathbf{q} = \mathbf{q}(t)$ and $\mathbf{F} = \mathbf{F}(t)$ are the displacement and force vectors, respectively. In this case, the force vector is expressed by $\mathbf{F} = [\mathbf{F}_I^T \mathbf{F}_L^T \mathbf{F}_R^T]^T$ where \mathbf{F}_L and \mathbf{F}_R refer to the force vectors on S_L and S_R (absorbing BCs), and \mathbf{F}_I refers the force vector for the internal DOFs (I) of the structure. Also, the displacement vector is expressed by $\mathbf{q} = [\mathbf{q}_I^T \mathbf{q}_L^T \mathbf{q}_R^T]^T$ where \mathbf{q}_I is the displacement vector for the internal DOFs. By considering the absorbing BCs (Eq. (39)), this yields:

$$\mathbf{M}_{\text{tot}} \ddot{\mathbf{y}} + \mathbf{C}_{\text{tot}} \dot{\mathbf{y}} + \mathbf{K}_{\text{tot}} \mathbf{y} = \mathbf{f}. \quad (42)$$

with

$$\mathbf{y} = \begin{bmatrix} \mathbf{q}_I \\ \mathbf{q}_L \\ \mathbf{q}_R \\ \mathbf{X}_L \\ \mathbf{X}_R \end{bmatrix}, \quad \mathbf{f} = \begin{bmatrix} \mathbf{F}_I \\ \mathbf{0} \\ \mathbf{0} \\ \mathbf{0} \\ \mathbf{0} \end{bmatrix} \quad (43)$$

In (42), the matrices \mathbf{M}_{tot} , \mathbf{C}_{tot} and \mathbf{K}_{tot} are given by:

$$\begin{aligned} \mathbf{M}_{\text{tot}} &= \begin{bmatrix} \mathbf{M}_{II} & \mathbf{M}_{IL} & \mathbf{M}_{IR} & \mathbf{0} & \mathbf{0} \\ \mathbf{M}_{LI} & \mathbf{M}_{LL} & \mathbf{M}_{LR} & \mathbf{0} & \mathbf{0} \\ \mathbf{M}_{RI} & \mathbf{M}_{RL} & \mathbf{M}_{RR} & \mathbf{0} & \mathbf{0} \\ \mathbf{0} & \mathbf{0} & \mathbf{0} & \mathbb{M}_{L(XX)} & \mathbf{0} \\ \mathbf{0} & \mathbf{0} & \mathbf{0} & \mathbf{0} & \mathbb{M}_{R(XX)} \end{bmatrix}, \\ \mathbf{C}_{\text{tot}} &= \begin{bmatrix} \mathbf{C}_{II} & \mathbf{C}_{IL} & \mathbf{C}_{IR} & \mathbf{0} & \mathbf{0} \\ \mathbf{C}_{LI} & \mathbf{C}_{LL} & \mathbf{C}_{LR} & -\mathbb{C}_{L(qX)} & \mathbf{0} \\ \mathbf{C}_{RI} & \mathbf{C}_{RL} & \mathbf{C}_{RR} & \mathbf{0} & -\mathbb{C}_{R(qX)} \\ \mathbf{0} & \mathbf{0} & \mathbf{0} & \mathbb{C}_{L(XX)} & \mathbf{0} \\ \mathbf{0} & \mathbf{0} & \mathbf{0} & \mathbf{0} & \mathbb{C}_{R(XX)} \end{bmatrix}, \\ \mathbf{K}_{\text{tot}} &= \begin{bmatrix} \mathbf{K}_{II} & \mathbf{K}_{IL} & \mathbf{K}_{IR} & \mathbf{0} & \mathbf{0} \\ \mathbf{K}_{LI} & \mathbf{K}_{LL} - \mathbb{K}_{L(qq)} & \mathbf{K}_{LR} & -\mathbb{K}_{L(qX)} & \mathbf{0} \\ \mathbf{K}_{RI} & \mathbf{K}_{RL} & \mathbf{K}_{RR} - \mathbb{K}_{R(qq)} & \mathbf{0} & -\mathbb{K}_{R(qX)} \\ \mathbf{0} & \mathbb{K}_{L(Xq)} & \mathbf{0} & \mathbb{K}_{L(XX)} & \mathbf{0} \\ \mathbf{0} & \mathbf{0} & \mathbb{K}_{R(Xq)} & \mathbf{0} & \mathbb{K}_{R(XX)} \end{bmatrix}, \end{aligned} \quad (44)$$

where:

$$\begin{aligned}
\mathbb{M}_{L(XX)} &= \left[\begin{array}{c|c} \text{blkdiag} \{ \mathbf{I}_n \}_{k=1}^Q & \mathbf{0} \\ \hline \mathbf{0} & \text{blkdiag} \{ \mathbf{I}_n \}_{k=2Q+1}^P \end{array} \right], \\
\mathbb{C}_{L(qX)} &= \left[\begin{array}{c} 2\Re \{ [\mathbf{R}_{L(2)} \cdots \mathbf{R}_{L(2Q)}] \} \\ \hline [\mathbf{R}_{L(2Q+1)} \cdots \mathbf{R}_{LN}] \end{array} \right], \\
\mathbb{C}_{L(XX)} &= \left[\begin{array}{c|c} \text{blkdiag} \{ -2\Re \{ p_{L(2k)} \} \mathbf{I}_n \}_{k=1}^Q & \mathbf{0} \\ \hline \mathbf{0} & \text{blkdiag} \{ -p_{Lk} \mathbf{I}_n \}_{k=2Q+1}^P \end{array} \right], \\
\mathbb{K}_{L(qq)} &= \mathbf{K}_L, \\
\mathbb{K}_{L(qX)} &= \left[\begin{array}{c} -2\Re \{ [\overline{p_{L(2)}} \mathbf{R}_{L(2)} \cdots \overline{p_{L(2Q)}} \mathbf{R}_{L(2Q)}] \} \\ \hline \mathbf{0} \end{array} \right], \\
\mathbb{K}_{L(Xq)} &= \left[\begin{array}{c} -\mathbb{1}_{Q \times 1} \otimes \mathbf{I}_n \\ \hline -\mathbb{1}_{(P-2Q) \times 1} \otimes \mathbf{I}_n \end{array} \right], \\
\mathbb{K}_{L(XX)} &= \left[\begin{array}{c|c} \text{blkdiag} \{ |p_{L(2k)}|^2 \mathbf{I}_n \}_{k=1}^Q & \mathbf{0} \\ \hline \mathbf{0} & \mathbf{0} \end{array} \right], \tag{45}
\end{aligned}$$

and similar expressions for the right boundary.

Eq. (42) represents a second-order differential matrix equation for the displacement vector \mathbf{q} and the vector of supplementary variables $\mathbf{X} = [\mathbf{X}_L^T \mathbf{X}_R^T]^T$. This indeed represents a classical dynamic equation, in the time domain, of a structure with absorbing BCs and subject to an input force vector $\mathbf{F}_I = \mathbf{F}_I(t)$, with the only modification that supplementary DOFs are added at the boundaries. Therefore, this equation can be solved in a standard way via a time integration numerical scheme (e.g., Newmark scheme).

4.2 Euler-Bernoulli beam on an elastic foundation

We consider the example of the dynamic response of an infinite Euler-Bernoulli beam lying on an elastic foundation as shown in Fig. 2 and subject to some forces $f(x, t)$. The governing equation of motion of the beam is given by:

$$\rho S \ddot{v} + EI \left(\frac{\partial^4 v}{\partial x^4} + \xi \frac{\partial^4 \dot{v}}{\partial x^4} \right) + k_F v = f(x, t), \tag{46}$$

where $v = v(x, t)$ represents the transverse displacement, ρ is the density, S is the cross-sectional area, E is the Young's modulus, I is the inertia moment, and ξ is a damping parameter. For harmonic disturbance of the form $f(x) e^{i\omega t}$, Eq. (46) leads to:

$$(-\rho S \omega^2 + k_F) v + EI(1 + i\omega \xi) \frac{\partial^4 v}{\partial x^4} = f(x), \tag{47}$$

For this simple case, there exist analytical expressions of the matrices of wave shapes Φ_q , Φ_q^* , Φ_F and Φ_F^* , see Eq. (6). Hence, by expressing the transverse displacement v together with the rotation $\theta = \partial v / \partial x$, this yields:

$$\begin{bmatrix} v \\ \theta \end{bmatrix} = \Phi_q \begin{bmatrix} e^{-ikx} & 0 \\ 0 & e^{-kx} \end{bmatrix} \begin{bmatrix} Q_1 \\ Q_2 \end{bmatrix} + \Phi_q^* \begin{bmatrix} e^{ikx} & 0 \\ 0 & e^{kx} \end{bmatrix} \begin{bmatrix} Q_1^* \\ Q_2^* \end{bmatrix}, \tag{48}$$

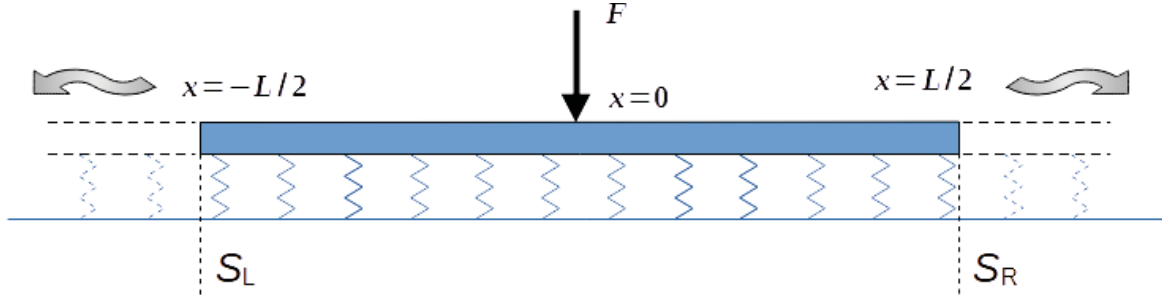


Figure 2: Infinite flexural beam on an elastic foundation.

where:

$$\Phi_q = \begin{bmatrix} 1 & 1 \\ -ik & -k \end{bmatrix}, \quad \Phi_q^* = \begin{bmatrix} 1 & 1 \\ ik & k \end{bmatrix}, \quad k = \left(\frac{\rho S \omega^2 - k_F}{EI(1 + i\omega\xi)} \right)^{1/4}. \quad (49)$$

Also, by expressing the shearing force $V = -EI(\partial^3 v / \partial x^3)$ and the bending moment $M = EI(\partial^2 v / \partial x^2)$, this yields:

$$\Phi_F = EI k^2 \begin{bmatrix} -ik & k \\ -1 & 1 \end{bmatrix}, \quad \Phi_F^* = EI k^2 \begin{bmatrix} ik & -k \\ -1 & 1 \end{bmatrix}. \quad (50)$$

Therefore, the impedance matrices are written as:

$$\mathbf{Z}_L = -\Phi_F^* (\Phi_q^*)^{-1} = -\frac{EI k^2}{1 - i} \begin{bmatrix} 2ik & -(1 + i) \\ -(1 + i) & \frac{2}{k} \end{bmatrix}, \quad (51)$$

and

$$\mathbf{Z}_R = \Phi_F (\Phi_q)^{-1} = -\frac{EI k^2}{1 - i} \begin{bmatrix} 2ik & 1 + i \\ 1 + i & \frac{2}{k} \end{bmatrix}. \quad (52)$$

These are analytical expressions of the impedance matrices that could also have been obtained numerically by means of the WFE method.

Consider an infinite beam of rectangular cross-section having the following parameters: height $h = 0.001$ m, width $b = 0.01$ m, Young's modulus $E = 2.2 \times 10^{11}$ Pa, density $\rho = 7800$ kg/m³, damping parameter $\xi = 0.001$ s. Also, the lineic stiffness of the elastic foundation is $k_F = 1$ N/m². The system is at rest at time $t = 0$ — i.e., $v(x, 0) = 0$ and $\dot{v}(x, 0) = 0$ — and, for $t \geq 0$, it is excited by a point harmonic force of frequency $f_0 = 5$ Hz (at $x = 0$):

$$f(x, t) = \cos(2\pi f_0 t) \delta(x) \quad \text{for } t \geq 0. \quad (53)$$

A beam of finite length L — i.e., $x \in [-L/2, L/2]$ where, for instance, $L = 5$ m — excited at $x = 0$ (Eq. (53)) is considered as shown in Fig. 2. Here, the system beam-foundation is modeled by means of 500 identical substructures that represent identical two-node Hermitian beam elements of length $d = 0.01$ m. The rational approximations of the impedance matrices \mathbf{Z}_L and \mathbf{Z}_R with $P = 12$ poles/residues (see Eqs. (34)) are computed with the MATLAB rationalfit function.

The differential matrix equation (42) is solved with the Newmark algorithm where $\Delta t = 0.01$ s, $\mathbf{y}^0 = \mathbf{0}$ and $\dot{\mathbf{y}}^0 = \mathbf{0}$. The related transverse displacement field, at $t = 20$ s, is shown in the left of Fig. 3 along with the analytical harmonic solution. In this case, the proposed solution closely matches the analytical one, as expected. Finally, the right of Fig. 3 shows the history of the displacement solution at position $x = L/2$. Again, it is seen that, after a certain time (transient period), the solution issued from the proposed approach stabilizes towards the harmonic solution.

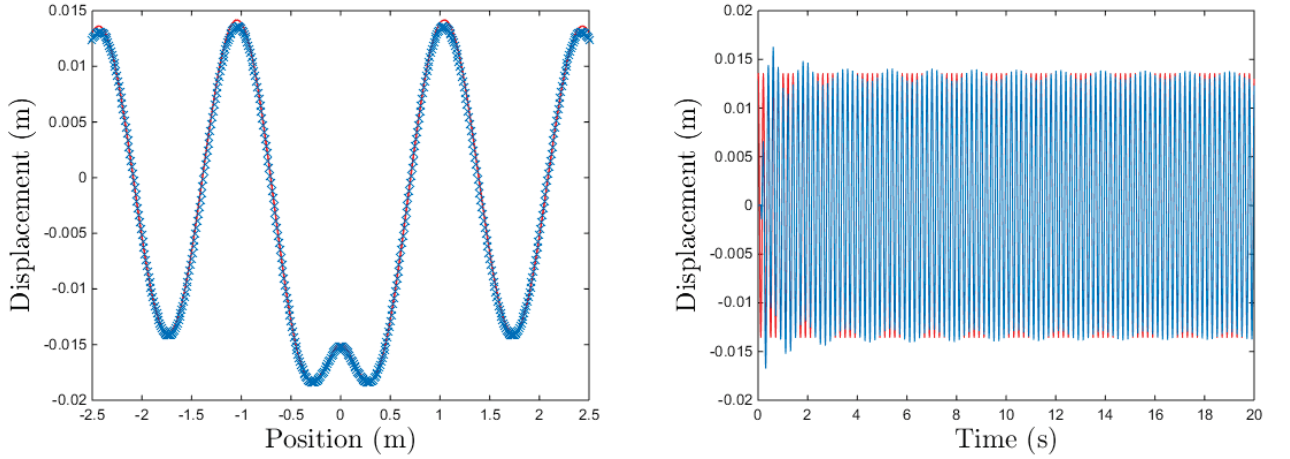


Figure 3: Transverse displacement field of the beam on the elastic foundation at $t = 20$ s (left): (blue crosses) Proposed approach; (red line) analytical harmonic solution and time response at $x=L/2$ for $t \in [0, 20]$ s (right) (blue line and crosses) Proposed approach; (red line) analytical theory, harmonic response.

4.3 Periodic structure with 2D substructures

We consider now a 2D beam with periodic distributions of holes and elastic supports (springs of stiffness K_s) as shown in Fig. 4. Here, square substructures of dimensions 2×2 m² with holes of radius 0.4 m are considered which are similar to those depicted in Fig. 1. Regarding the modeling of the periodic supports, a nodal stiffness of $K_s/2$ (vertical direction) is added to the FE model of the substructures at the left and right boundaries (bottom node). Other substructure parameters are: thickness $e = 0.005$ m, Young's modulus $E = 7 \times 10^{10}$ Pa, Poisson's ratio $\nu = 0.35$, density $\rho = 2700$ kg/m³, and stiffness $K_s = 10^5$ N/m. Rayleigh-type damping matrices $\mathbf{C} = a\mathbf{M} + b\mathbf{K}$ are also considered where $a = 0.01$ s⁻¹ and $b = 5 \times 10^{-5}$ s.

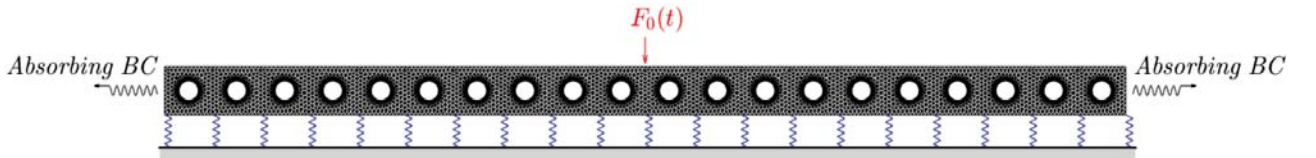


Figure 4: Schematic of an infinite periodic structure with periodic elastic supports.

The time response of the infinite periodic structure subject to a vertical point force $F_0(t)$ at $x = 0$ (top node) is analyzed. Within the framework of the proposed approach, a periodic structure involving $N = 20$ substructures and absorbing BCs is considered as shown in Fig. 4. In this case, the structure has a length of $L = 40$ m. The rational approximations of the impedance matrices \mathbf{Z}_L and \mathbf{Z}_R (Eq. (34)) are expressed by means of $P = 15$ poles/residues. The time response of the structure is computed over a time range of $[0, 0.1]$ s by solving the differential matrix equation (42) with the Newmark algorithm where $\Delta t = 10^{-4}$ s, $\mathbf{y}^0 = \mathbf{0}$ and $\dot{\mathbf{y}}^0 = \mathbf{0}$. For comparison purpose, an equivalent FE model of an “infinite” structure with a larger number of substructures (200) is considered and simulated over the time range $[0, 0.1]$ s which is supposed to be small enough to prevent wave reflections (free boundaries). Consider a harmonic point force of magnitude $F_0(t) = 10^4 \cos(2\pi \times 100t)$ acting at $x = 0$, and assume that the structure is at rest at $t = 0$. The time response is analyzed over a time range of $[0, 0.1]$ s which is supposed to be broad enough to include several oscillations (10 in this case) and cover

the transient phase. Especially, the time variation of the transverse displacement at $x = 20$ m (right boundary, top node) can be computed as shown in Fig. 5. It is shown that the proposed solution perfectly matches the reference one over the whole time range. It is also numerically stable, i.e., a smooth curve that well predicts the oscillating nature of the signal.

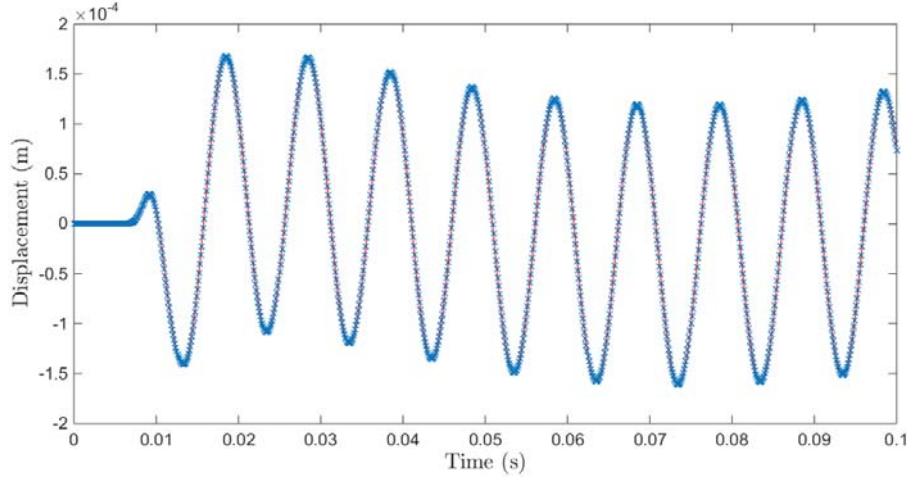


Figure 5: Harmonic force: time response at $x=L/2$ (top node, vertical displacement). (blue crosses) Proposed approach; (red line) reference FE method.

5 Conclusion

A FE procedure has been proposed to model infinite periodic structures subject to distributed or moving loads, or localized time-dependent excitations. For instance, in the case of moving loads, the load is applied on each substructure. Concerning time domain problems, first, using the WFE method to express the absorbing BCs by means of impedance matrices, in the frequency domain, impedance matrices have been rewritten in terms of polynomials of the frequency $i\omega$ up to order 2. Then, they are simply converted to the time domain and the global dynamic equation is solved by the Newmark algorithm. Follow-on works could include the analysis of infinite periodic structures with localized nonlinear effects.

REFERENCES

- [1] B. Mace, D. Duhamel, M. Brennan, L. Hinke, Finite element prediction of wave motion in structural waveguides, *Journal of the Acoustical Society of America* 117 (2005) 2835–2843.
- [2] D. Duhamel, B. R. Mace, M. J. Brennan, Finite element analysis of the vibrations of waveguides and periodic structures, *Journal of Sound and Vibration* 294 (1-2) (2006) 205–220.
- [3] J.-M. Mencik, D. Duhamel, A wave-based model reduction technique for the description of the dynamic behavior of periodic structures involving arbitrary-shaped substructures and large-sized finite element models, *Finite Elements in Analysis and Design* 101 (2015) 1–14.

- [4] J.-M. Mencik, M. N. Ichchou, Multi-mode propagation and diffusion in structures through finite elements, *European Journal of Mechanics - A/Solids* 24 (5) (2005) 877–898.
- [5] P. Ruge, C. Birk, A comparison of infinite Timoshenko and Euler-Bernoulli beam models on Winkler foundation in the frequency- and time-domain, *Journal of Sound and Vibration* 304 (3) (2007) 932 – 947.
- [6] M. Zhao, L. Wu, X. Du, Z. Zhong, C. Xu, L. Li, Stable high-order absorbing boundary condition based on new continued fraction for scalar wave propagation in unbounded multilayer media, *Computer Methods in Applied Mechanics and Engineering* 334 (2018) 111 – 137.
- [7] D. Duhamel, J. Mencik, Time response analysis of periodic structures via wave-based absorbing boundary conditions, *European Journal of Mechanics - A/Solids* (submitted).
- [8] W. X. Zhong, F. W. Williams, On the direct solution of wave propagation for repetitive structures, *Journal of Sound and Vibration* 181 (3) (1995) 485–501.
- [9] J.-M. Mencik, New advances in the forced response computation of periodic structures using the wave finite element (WFE) method, *Computational Mechanics* 54 (3) (2014) 789–801.
- [10] T. Hoang, D. Duhamel, G. Foret, Wave finite element method for waveguides and periodic structures subjected to arbitrary loads, *Finite Elements in Analysis and Design* 179 (2020) 103437.

DYNAMIC ANALYSIS OF PERIODIC STRUCTURES AND METAMATERIALS VIA WAVE APPROACHES AND FINITE ELEMENT PROCEDURES

J.-M. Mencik¹ and D. Duhamel²

¹INSA Centre Val de Loire,
Université d'Orléans, Université de Tours,
Laboratoire de Mécanique Gabriel Lamé, EA 7494,
Rue de la Chocolaterie, 41000 Blois, France
e-mail: jean-mathieu.mencik@insa-cvl.fr

²Ecole des Ponts, laboratoire Navier,
6 et 8 Avenue Blaise Pascal, Cité Descartes, Champs sur Marne,
77455 Marne la Vallée, cedex 2, France
e-mail: denis.duhamel@enpc.fr

Keywords: Periodic Structures, Metamaterials, Wave Approaches, Finite Elements, Model Reduction, Nearly Periodic Structures.

Abstract. *Two kinds of numerical approaches able to predict the dynamic response of periodic structures and metamaterials are presented. Both of them are model reduction techniques which can be used to obtain the response functions of the structures at a low computational cost. The first kind of approaches employs the wave finite element (WFE) method for modeling 1D periodic structures made up of complex substructures, e.g., 2D cells of arbitrary shapes. Resonant metamaterials are particular cases of periodic structures where the substructures possess local resonances — e.g., layered substructures involving soft layers and heavy layers/core —, which in turn lead to band gap effects and low vibration levels. Although well-suited for modeling periodic structures in the frequency domain, the WFE method also works for periodic structures subject to time-dependent excitations. The second kind of approaches employs finite element (FE) procedures for modeling 2D periodic structures, and 2D nearly periodic structures involving substructures with slightly varying (random) geometrical properties. For nearly periodic structures like plates with disordered resonant 2D cells, results show that the vibrational energy is localized around the excitation sources.*

1 INTRODUCTION

Periodic structures are frequently encountered in engineering applications, e.g., in the aeronautic (fuselages, turbines) and railway industries. Also, they appear interesting to passively control the vibration levels of mechanical systems. Metamaterials are periodic structures which possess such interesting features, i.e., the fact that they do not convey vibrational energies on some frequency bands (band gaps) which as such yield low vibration levels. Well-known examples of metamaterials are periodic structures made up of resonant cells where band gaps occur in the vicinity of the resonance frequencies of the cells. There exist plenty of works in the literature about the analysis of the wave propagation in 1D or 2D periodic structures and the related band gap effects [11, 10, 9, 12, 29, 25, 4, 28]. However, the forced response analysis of periodic structures is much less reported. This especially means developing numerical models able to predict the dynamic response of periodic structures of finite dimensions with various kinds of boundary conditions, or assemblies of finite dimensions involving several periodic structures and other non-periodic components which are systems of practical interest in engineering applications. In this case, the analysis of the band gap effects does not only rely on the wave propagation properties, but also on the boundary and coupling conditions which induce energy conversion between waves.

This paper aims at investigating the modeling of 1D and 2D periodic structures, of finite dimensions, subject to various kinds of excitations and boundary conditions. Periodic structures made up of complex cells — i.e., substructures which can be of various shapes and which are modeled with a moderately high number of degrees of freedom (DOFs) — are especially dealt with. Numerical results are brought which concern the dynamic response of periodic structures and resonant metamaterials.

The paper starts with an overview of the wave finite element (WFE) method and its recent applications. The method is well suited for modeling 1D periodic structures, i.e., structures made up of identical substructures which are connected to each other along a straight or circumferential direction. The WFE method works by considering the FE model of a substructure, and computing the eigenvalues and eigenvectors of the related transfer matrix to determine the waves traveling along a periodic structure. To predict the forced response of periodic structures, the WFE method involves expanding the displacement and force vectors on the basis of the eigenvectors (wave shapes) of the transfer matrix of a substructure. The methodology is detailed in [16, 18] (see also [30, 6, 32, 15]). Among the recent extensions of the method are: the development of model reduction strategies based on reduced wave bases to target substructures with large-sized FE models [22]; the modeling of periodic structures with cyclic symmetry, such as turbines [19]; the time response analysis of periodic structures via wave-based absorbing boundary conditions [7].

Aside from the study of 1D periodic structures, 2D periodic structures with resonant substructures are well-known examples of metamaterials to passively control the vibration levels of mechanical systems. As mentioned earlier, the analysis of the wave propagation (e.g., Bloch waves) in 2D periodic structures is well documented in the literature. However, contrary to the study of 1D periodic structures, the forced response analysis of 2D periodic structures of finite dimensions, based on wave expansion (displacement and force vectors), is prone to tough theoretical and numerical modeling issues which make it difficult even impossible to carry out. The issue is linked to the multi-directional behavior of the propagating waves, and the description of the wave reflection at boundaries that arise from these multi-directional waves. Here, two FE-based approaches are proposed as alternative model reduction techniques. The first

one is standard and makes use of the Craig-Bampton (CB) method and the related fixed interface modes of the substructures for modeling purely periodic structures. The second approach targets the modeling of 2D nearly periodic structures made up of resonant substructures with slightly varying geometrical properties [20]. Plates with disordered resonant 2D cells, made up of soft layers and heavy layers/core with random geometrical properties, are examples of 2D nearly periodic structures. Such structures possess interesting features, e.g., the fact that the vibrational energy remains localized around the excitation points. The proposed strategy involves computing the reduced matrices of the substructures for some particular distorted FE meshes (a few number), and interpolating these matrices between these “interpolation points” for modeling substructures with random FE meshes.

2 WFE METHOD FOR 1D PERIODIC STRUCTURES

2.1 Wave propagation

The WFE method originates from the transfer matrix theory and the Bloch’s theorem. Let us first consider an infinite periodic structure under harmonic disturbance $e^{i\omega t}$ made up of identical substructures with similar FE meshes as shown in Fig. 1. Also, let us denote by \mathbf{M} , \mathbf{C} and \mathbf{K} the conventional mass, damping and stiffness matrices of the substructures (identical for all the substructures). From the practical point of view, these matrices can be obtained via usual FE softwares, Matlab FE mesh generators (e.g., DistMesh [27]) or Matlab in-house FE codes. The related dynamic equilibrium equation, for a given substructure k , is given by:

$$\mathbf{D}\mathbf{q}^k = \mathbf{F}^k, \quad (1)$$

where \mathbf{q}^k and \mathbf{F}^k refer to the displacement vector and the force vector (respectively) of the substructure k ; \mathbf{D} is the dynamic stiffness matrix expressed by $\mathbf{D} = -\omega^2\mathbf{M} + i\omega\mathbf{C} + \mathbf{K}$.

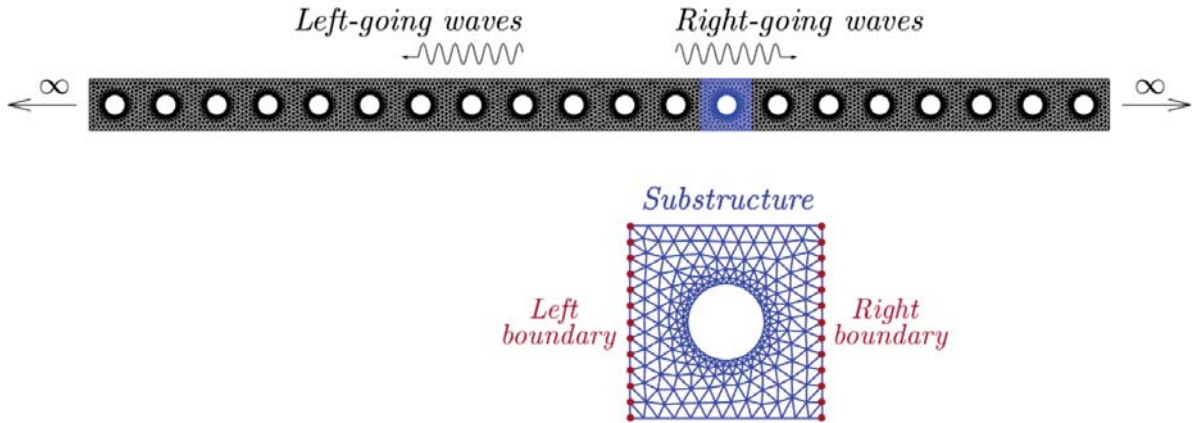


Figure 1: Periodic structure of infinite length, and FE mesh of a substructure.

The FE mesh of the substructure involves left (L) and right (R) boundaries (see Fig. 1) which are here assumed to be described with a same number n of DOFs. From Eq. (1), the following transfer matrix relation between the right and left boundaries can be proposed:

$$\begin{bmatrix} \mathbf{q}_R^k \\ \mathbf{F}_R^k \end{bmatrix} = \mathbf{S} \begin{bmatrix} \mathbf{q}_L^k \\ -\mathbf{F}_L^k \end{bmatrix}, \quad (2)$$

where \mathbf{S} is the so-called transfer matrix (size of $2n \times 2n$), expressed by:

$$\mathbf{S} = \left[\begin{array}{c|c} -(\mathbf{D}_{\text{LR}}^*)^{-1}\mathbf{D}_{\text{LL}}^* & -(\mathbf{D}_{\text{LR}}^*)^{-1} \\ \hline \mathbf{D}_{\text{RL}}^* - \mathbf{D}_{\text{RR}}^*(\mathbf{D}_{\text{LR}}^*)^{-1}\mathbf{D}_{\text{LL}}^* & -\mathbf{D}_{\text{RR}}^*(\mathbf{D}_{\text{LR}}^*)^{-1} \end{array} \right]. \quad (3)$$

Here, \mathbf{D}^* represents the condensed dynamic stiffness matrix, i.e., on the left and right boundaries of the substructure [18]. Let us consider two consecutive substructures k and $k+1$ which are rigidly connected at a common interface. In this case, the coupling conditions write $\mathbf{q}_{\text{R}}^k = \mathbf{q}_{\text{L}}^{k+1}$ and $\mathbf{F}_{\text{R}}^k = -\mathbf{F}_{\text{L}}^{k+1}$, and Eq. (2) gives:

$$\begin{bmatrix} \mathbf{q}_{\text{L}}^{k+1} \\ -\mathbf{F}_{\text{L}}^{k+1} \end{bmatrix} = \mathbf{S} \begin{bmatrix} \mathbf{q}_{\text{L}}^k \\ -\mathbf{F}_{\text{L}}^k \end{bmatrix} \quad \text{and also} \quad \begin{bmatrix} \mathbf{q}_{\text{R}}^{k+1} \\ \mathbf{F}_{\text{R}}^{k+1} \end{bmatrix} = \mathbf{S} \begin{bmatrix} \mathbf{q}_{\text{R}}^k \\ \mathbf{F}_{\text{R}}^k \end{bmatrix}, \quad (4)$$

which relates the displacement and force vectors between two consecutive substructures k and $k+1$.

It can be proven that the transfer matrix \mathbf{S} is symplectic [23], which means that its eigenvalues and eigenvectors come in pairs (μ_j, ϕ_j) and $(\mu_j^* = 1/\mu_j, \phi_j^*)$ with $|\mu_j| < 1$. Numerical issues about the computation of the eigensolutions of \mathbf{S} are discussed in [22, 32, 36]. According to the Bloch's theorem [34], the eigenvalues of \mathbf{S} have the meaning of wave parameters which are given by $\mu_j = e^{-i\beta_j d}$ for the waves traveling to the right direction (β_j : wave number for a wave j ; d : substructure length) and $\mu_j^* = e^{i\beta_j d}$ for the waves traveling to the left direction. Also, the eigenvectors ϕ_j and ϕ_j^* have the meaning of wave shapes for the waves traveling to the right and left directions, respectively. These are vectors of size $2n \times 1$, expressed by:

$$\phi_j = \begin{bmatrix} \phi_{\text{q}j} \\ \phi_{\text{F}j} \end{bmatrix}, \quad \phi_j^* = \begin{bmatrix} \phi_{\text{q}j}^* \\ \phi_{\text{F}j}^* \end{bmatrix}, \quad (5)$$

where $\phi_{\text{q}j}$ and $\phi_{\text{q}j}^*$ (resp. $\phi_{\text{F}j}$ and $\phi_{\text{F}j}^*$) are $n \times 1$ displacement (resp. force) component vectors for the right-going and left-going waves. In matrix form, these vectors give:

$$\Phi_{\text{q}} = [\phi_{\text{q}1} \cdots \phi_{\text{q}n}], \quad \Phi_{\text{q}}^* = [\phi_{\text{q}1}^* \cdots \phi_{\text{q}n}^*], \quad \Phi_{\text{F}} = [\phi_{\text{F}1} \cdots \phi_{\text{F}n}], \quad \Phi_{\text{F}}^* = [\phi_{\text{F}1}^* \cdots \phi_{\text{F}n}^*]. \quad (6)$$

2.2 Forced response

The analysis of the harmonic response of periodic structures of finite length — i.e., with a finite number N of substructures — can be easily performed with the WFE method. The advantage, against the conventional FE method, is in the modeling of a whole periodic structure via a small matrix system of size $2n \times 2n$ that is linked to the number of DOFs on the left and right boundaries of a substructure. In comparison, the FE method would involve assembling the condensed dynamic stiffness matrices of all the substructures, yielding a bigger matrix system of size $(N+1)n \times (N+1)n$ whose computation is likely to take much more time. The main idea behind the WFE modeling is to expand the displacement and force vectors, on a particular interface (k) connecting two substructures $k-1$ and k , on the wave shapes $\phi_{\text{q}j}$ and $\phi_{\text{q}j}^*$, and $\phi_{\text{F}j}$ and $\phi_{\text{F}j}^*$, of a periodic structure [16, 18]:

$$\mathbf{q}_{\text{L}}^{(k)} = \mathbf{q}_{\text{R}}^{(k)} = \Phi_{\text{q}} \boldsymbol{\mu}^{k-1} \mathbf{Q} + \Phi_{\text{q}}^* \boldsymbol{\mu}^{N-k+1} \mathbf{Q}^* \quad k = 1, \dots, N+1, \quad (7)$$

$$-\mathbf{F}_{\text{L}}^{(k)} = \mathbf{F}_{\text{R}}^{(k)} = \Phi_{\text{F}} \boldsymbol{\mu}^{k-1} \mathbf{Q} + \Phi_{\text{F}}^* \boldsymbol{\mu}^{N-k+1} \mathbf{Q}^* \quad k = 1, \dots, N+1. \quad (8)$$

Here, $\mathbf{q}_L^{(k)}$ and $\mathbf{F}_L^{(k)}$ represent the displacement and force vectors at the left boundary of the substructure k for $k = 1, \dots, N$; $\mathbf{q}_R^{(k)}$ and $\mathbf{F}_R^{(k)}$ represent the displacement and force vectors at the right boundary of the substructure $k-1$ for $k = 2, \dots, N+1$; \mathbf{Q} is the wave amplitude vector for the right-going waves at the substructure interface (1) (left end of the periodic structure); \mathbf{Q}^* is the wave amplitude vector for the left-going waves at the substructure interface ($N+1$) (right end of the periodic structure). Finally, $\boldsymbol{\mu} = \text{diag}\{\mu_j\}_{j=1}^n$ is the diagonal matrix of the wave parameters μ_j for the right-going waves, with the property that $\|\boldsymbol{\mu}\|_2 < 1$ [16].

Consider for the sake of clarity a finite periodic structure as shown in Fig. 2 whose left end is excited by some forces (vector \mathbf{F}_0), and whose right end is constrained by prescribed displacement vector \mathbf{q}_0^* . In this case, by considering Eqs. (7) and (8), the boundary conditions write $-\mathbf{F}_0 = \boldsymbol{\Phi}_F \mathbf{Q} + \boldsymbol{\Phi}_F^* \boldsymbol{\mu}^N \mathbf{Q}^*$ and $\mathbf{q}_0^* = \boldsymbol{\Phi}_q \boldsymbol{\mu}^N \mathbf{Q} + \boldsymbol{\Phi}_q^* \mathbf{Q}^*$ which, after some simple manipulations, yield the following wave-based matrix equation (size $2n \times 2n$):

$$\begin{bmatrix} \mathbf{I}_n & (\boldsymbol{\Phi}_F)^{-1} \boldsymbol{\Phi}_F^* \boldsymbol{\mu}^N \\ (\boldsymbol{\Phi}_q^*)^{-1} \boldsymbol{\Phi}_q \boldsymbol{\mu}^N & \mathbf{I}_n \end{bmatrix} \begin{bmatrix} \mathbf{Q} \\ \mathbf{Q}^* \end{bmatrix} = \begin{bmatrix} -(\boldsymbol{\Phi}_F)^{-1} \mathbf{F}_0 \\ (\boldsymbol{\Phi}_q^*)^{-1} \mathbf{q}_0^* \end{bmatrix}. \quad (9)$$

Solving the wave-based matrix equation (9) yields the wave amplitude vectors \mathbf{Q} and \mathbf{Q}^* . The determination of the displacement and force vectors, at any substructure interface (k), follows from Eqs. (7) and (8). If needed, the displacements at the internal nodes (I) of the substructures can be retrieved by considering the full dynamic stiffness matrix, i.e., $\mathbf{q}_I = -(\mathbf{D}_{II})^{-1}(\mathbf{D}_{IL} \mathbf{q}_L^{(k)} + \mathbf{D}_{IR} \mathbf{q}_R^{(k+1)})$ for a substructure enclosed between two interfaces (k) and ($k+1$).

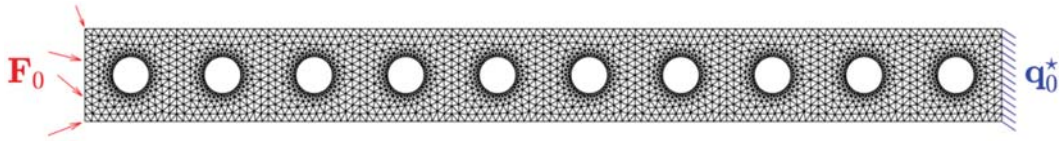


Figure 2: Finite periodic structure with prescribed forces \mathbf{F}_0 (left end) and prescribed displacements \mathbf{q}_0^* (right end).

The main numerical tasks involved in the WFE method may be summed up as follows:

- (i) Computation of the condensed dynamic stiffness matrix \mathbf{D}^* of a substructure;
- (ii) Computation of the eigensolutions of the transfer matrix \mathbf{S} ;
- (iii) Computation of the matrix system (9).

Task (iii) is not computationally cumbersome given that the matrix system (9) has a small size, as explained earlier. As for the computation of the condensed dynamic stiffness matrix \mathbf{D}^* (task (i)), this can be easily performed via the CB method [18]. For periodic structures involving substructures whose number of boundary DOFs is not excessive (e.g., smaller than 300), task (ii) is not cumbersome too. Things are more complicated for substructures with large-sized FE models, and in this case, it is advised to only compute a few low-order waves (rather than all the waves) using appropriate eigensolvers like the Lanczos algorithm [22].

The WFE method can be advantageously applied to structural assemblies made up of different periodic structures and other non-periodic structural components, i.e., mechanical systems which are of practical interest in engineering. The reader is referred to [23, 24, 17, 30]. The

WFE modeling of those structural assemblies involves considering coupling conditions between periodic structures (two or more), across a rigid interface c or a non-periodic structural component c (coupling element), which in wave-based form are written as:

$$\mathbf{Q}^{c*} = \mathbb{C}^c \mathbf{Q}^c + \mathbb{F}^c, \quad (10)$$

where \mathbf{Q}^c and \mathbf{Q}^{c*} represent the wave amplitudes vectors for the outgoing waves and incoming waves, respectively, for the periodic structures connected at interface c or coupling element c ; \mathbb{C}^c is the so-called scattering matrix (reflection and transmission coefficients); \mathbb{F}^c is a vector representing the excitation sources imposed at the interface or inside the coupling element. Hence, a global wave-based matrix equation which takes into account coupling conditions between several periodic structures, and classical boundary conditions (prescribed forces or displacements), can be proposed whose size is not big, i.e., linked to the numbers of boundary DOFs of the substructures used for modeling the periodic structures.

2.3 Some recent and ongoing works

1D periodic structures are often considered as straight structures, made up of simple or more complicated substructures, vibrating under harmonic disturbance. The purpose here is to show that the WFE method can handle more sophisticated engineering problems. Two examples of recent WFE strategies are proposed. The purpose is to give the main ideas and outlines of these strategies rather than fully detailing all the theoretical developments (see [19, 7]).

2.3.1 Periodic structures with cyclic symmetry

The first kind of problems concerns the analysis of multi-stage bladed disks, which is well known in the aeronautic industry. The proposed approach involves computing the dynamic flexibility modes of a given periodic structure (cyclic symmetry) via the WFE method, and modeling assemblies made up of several periodic structures via dynamic substructuring [19].

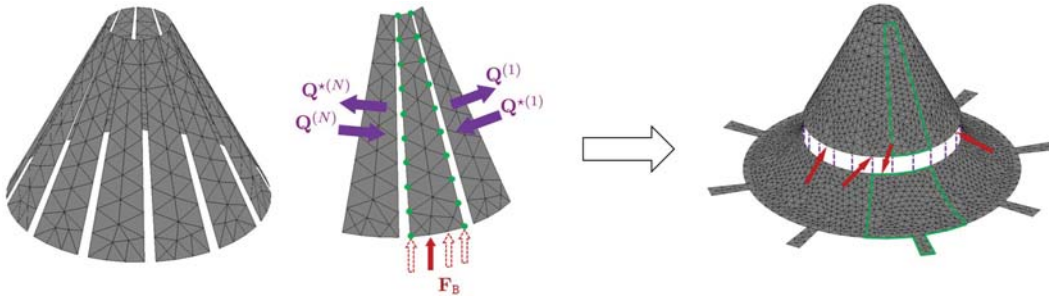


Figure 3: (left) Periodic structure with one of its substructures subject to one unit force on the boundary. (right) Two connected periodic structures with arbitrary forces applied to the coupling interface.

A dynamic flexibility mode of a periodic structure (N substructures) represents the displacement vector that results from applying one unit force to a given DOF of the boundary, the others being free (see Fig. 3). For instance, assume that the unit force (force vector \mathbf{F}_B) is applied to a boundary DOF i of a substructure enclosed between two substructure interfaces (N) and (1).

The resulting dynamic flexibility mode is given by:

$$\mathbf{x}_i^{(N)} = \begin{bmatrix} (\mathbf{I}_{(n+n_{\text{I|B}})/3} \otimes \mathcal{R}) \mathbf{q}^{(1)} \\ (\mathbf{I}_{(n+n_{\text{I|B}})/3} \otimes \mathcal{R}^2) \mathbf{q}^{(2)} \\ \vdots \\ (\mathbf{I}_{(n+n_{\text{I|B}})/3} \otimes \mathcal{R}^N) \mathbf{q}^{(N)} \end{bmatrix}, \quad (11)$$

where $\mathbf{q}^{(k)}$ ($k = 1, \dots, N-1$) represents the displacement vector of a substructure enclosed between two substructure interfaces (k) and ($k+1$) and expressed in the local cartesian coordinate system of the substructure; \mathcal{R} is the 3×3 rotation matrix for the angle $-2\pi/N$, with $\mathcal{R}^N = \mathbf{I}_3$; n is the number of interface DOFs (between the substructures), and $n_{\text{I|B}}$ is the number of internal DOFs which belong to the boundary. Recall that the unit force is applied to the boundary of a substructure enclosed between interfaces (N) and (1). The displacement vector of this substructure is denoted by $\mathbf{q}^{(N)}$ and is given by:

$$\mathbf{q}^{(N)} = \begin{bmatrix} \mathbf{I}_n & \mathbf{0} \\ \mathbf{X}_{\text{st|B}} - \tilde{\mathbf{X}}_{\text{el|B}} \tilde{\mathbf{D}}_{\text{el-e1}}^{-1} \tilde{\mathbf{D}}_{\text{st-e1}}^T \end{bmatrix} \mathcal{H}^T \begin{bmatrix} \Phi_{\mathbf{q}} \boldsymbol{\mu}^{N-1} & \Phi_{\mathbf{q}}^* \boldsymbol{\mu}^{N-1} \\ \Phi_{\mathbf{q}} & \Phi_{\mathbf{q}}^* \boldsymbol{\mu}^{N-1} \end{bmatrix} \begin{bmatrix} \mathbf{Q} \\ \mathbf{Q}^* \end{bmatrix} + \begin{bmatrix} \mathbf{0} \\ \tilde{\mathbf{X}}_{\text{el|B}} \tilde{\mathbf{D}}_{\text{el-e1}}^{-1} \tilde{\mathbf{X}}_{\text{el}}^T \mathcal{L}_{\text{IB}} \end{bmatrix} \mathbf{F}_{\text{B}}. \quad (12)$$

Here, \mathbf{X}_{st} and $\tilde{\mathbf{X}}_{\text{el}}$ are, respectively, the matrices of static modes and fixed interface modes of the substructure (CB method), $\tilde{\mathbf{D}}_{\text{el-e1}}$ represents the dynamic stiffness matrix of the substructure “projected” on $\tilde{\mathbf{X}}_{\text{el}}$, and \mathcal{H} is a transformation matrix which relates the unit vectors in cylindrical coordinates (i.e., \vec{e}_r , \vec{e}_θ and \vec{e}_z) to those in cartesian coordinates (i.e., \vec{e}_x , \vec{e}_y and \vec{e}_z) at the interface nodes of the substructure. Also, for a non-excited substructure, one has:

$$\mathbf{q}^{(k)} = \begin{bmatrix} \mathbf{I}_n & \mathbf{0} \\ \mathbf{X}_{\text{st|B}} - \tilde{\mathbf{X}}_{\text{el|B}} \tilde{\mathbf{D}}_{\text{el-e1}}^{-1} \tilde{\mathbf{D}}_{\text{st-e1}}^T \end{bmatrix} \mathcal{H}^T \begin{bmatrix} \Phi_{\mathbf{q}} \boldsymbol{\mu}^{k-1} & \Phi_{\mathbf{q}}^* \boldsymbol{\mu}^{N-k} \\ \Phi_{\mathbf{q}} \boldsymbol{\mu}^k & \Phi_{\mathbf{q}}^* \boldsymbol{\mu}^{N-k-1} \end{bmatrix} \begin{bmatrix} \mathbf{Q} \\ \mathbf{Q}^* \end{bmatrix} \quad \text{for } k \neq N. \quad (13)$$

In Eqs. (12) and (13), $\mathbf{Q} = \mathbf{Q}^{(1)}$ and $\mathbf{Q}^* = \mathbf{Q}^{*(N)}$ are wave amplitude vectors, expressed at substructure boundaries (1) and (N) (see Fig. 3) and obtained via WFE procedure. The matrix of flexibility modes which results from applying successive unit forces to the boundary DOFs of the substructure enclosed between interfaces (N) and (1) is given by $\mathbf{X}^{(N)} = [\mathbf{x}_1^{(N)} \mathbf{x}_2^{(N)} \dots \mathbf{x}_{n_{\text{B}}}^{(N)}]$ where n_{B} is the number of boundary DOFs of a substructure. The whole matrix of flexibility modes which results from applying successive unit forces to the boundary DOFs of the whole periodic structure follows as $\mathbf{X} = [\mathbf{X}^{(1)} \mathbf{X}^{(2)} \dots \mathbf{X}^{(N)}]$, where:

$$\mathbf{X}^{(k)} = (\mathbf{I}_{n_{\text{T}}/3} \otimes \mathcal{R}^k) \mathcal{P}^{(k)} \mathbf{X}^{(N)} (\mathbf{I}_{n_{\text{B}}/3} \otimes \mathcal{R}^k)^T, \quad (14)$$

where $\mathcal{P}^{(k)}$ is a permutation matrix, and $n_{\text{T}} = N(n + n_{\text{I|B}})$. The modeling of several periodic structures with cyclic symmetry follows from domain decomposition procedure. For instance, for two structures (displacement vectors \mathbf{q}_1 and \mathbf{q}_2) subject to force vectors \mathbf{F}_{B1} and \mathbf{F}_{B2} on their boundaries, this yields:

$$\begin{bmatrix} \mathbf{I} & \mathbf{0} & -\mathbf{X}_1 \mathcal{L}_{\text{B1}}^T \\ \mathbf{0} & \mathbf{I} & \mathbf{X}_2 \mathcal{L}_{\text{B2}}^T \\ \mathcal{L}_1 & -\mathcal{L}_2 & \mathbf{0} \end{bmatrix} \begin{bmatrix} \mathbf{q}_1 \\ \mathbf{q}_2 \\ \boldsymbol{\lambda} \end{bmatrix} = \begin{bmatrix} \mathbf{X}_1 \mathbf{F}_{\text{B1}} \\ \mathbf{X}_2 \mathbf{F}_{\text{B2}} \\ \mathbf{0} \end{bmatrix}, \quad (15)$$

where \mathbf{X}_1 and \mathbf{X}_2 are the matrices of flexibility modes of the structures, and $\mathcal{L}_1, \mathcal{L}_2, \mathcal{L}_{B1}, \mathcal{L}_{B2}$ are localization matrices. Also, $\boldsymbol{\lambda}$ represents a vector of Lagrange multipliers to enforce the displacement continuity conditions (i.e., $\mathcal{L}_1 \mathbf{q}_1 - \mathcal{L}_2 \mathbf{q}_2 = \mathbf{0}$) for some nodes of the boundaries of the structures. Solving Eq. (15) yields:

$$\boldsymbol{\lambda} = -(\mathcal{L}_1 \mathbf{X}_1 \mathcal{L}_{B1}^T + \mathcal{L}_2 \mathbf{X}_2 \mathcal{L}_{B2}^T)^{-1}(\mathcal{L}_1 \mathbf{X}_1 \mathbf{F}_{B1} - \mathcal{L}_2 \mathbf{X}_2 \mathbf{F}_{B2}). \quad (16)$$

The displacement vectors of the structures follow as $\mathbf{q}_1 = \mathbf{X}_1(\mathbf{F}_{B1} + \mathcal{L}_{B1}^T \boldsymbol{\lambda})$ and $\mathbf{q}_2 = \mathbf{X}_2(\mathbf{F}_{B2} - \mathcal{L}_{B2}^T \boldsymbol{\lambda})$.

Some results are proposed hereafter which concern two coupled bladed disks 1 and 2 (two stages) with $N_1 = 36$ and $N_2 = 60$ substructures (respectively), excited by non-symmetric forces. Here, the harmonic response function (transverse displacement) at some node at the tip of one blade of structure 1 is assessed up to 10,000 Hz (see Fig. 4), which is high enough to include local resonance effects for each blade. Those results show that the proposed approach perfectly agrees with the conventional FE method.

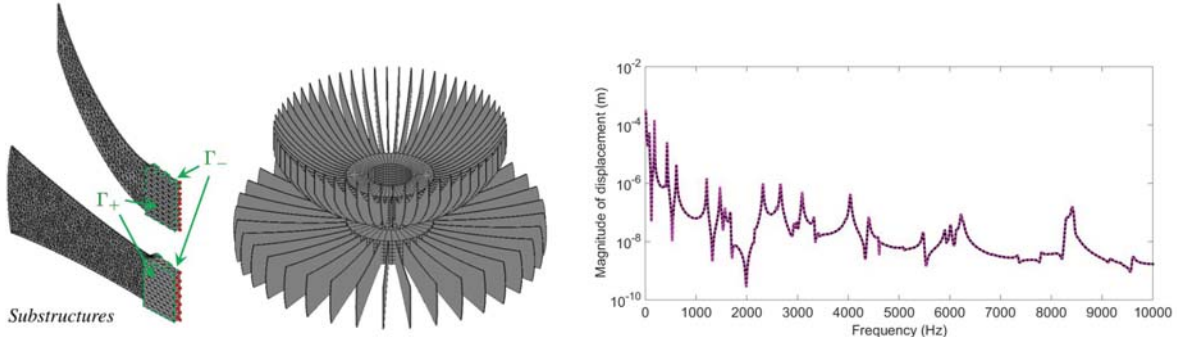


Figure 4: (left) Two periodic structures and FE meshes of the related substructures (Γ_- and Γ_+ are coupling interfaces with previous and subsequent substructures). (right) Response functions, conventional FE (black solid line) and WFE (pink dotted line).

2.3.2 Time response of periodic structures via wave-based absorbing boundary conditions

The second kind of problems concerns the modeling of infinite periodic structures (or periodic structures which are supposed to be long enough) subject to localized time-dependent loadings. Potential applications could be, for instance, structures like pipelines or tanks subject to shocks. A periodic structure with a finite number N of substructures and subject to time dependent forces (vector $\mathbf{F}(t)$) is shown in Fig. 5. The semi-infinite behavior at the left and right ends — i.e., the fact that no wave is coming from infinity — is described by means of absorbing boundary conditions expressed in the time domain [7]. Although easy to understand in the frequency domain, the determination of absorbing conditions for time response analysis is not a straightforward task and, for this reason, this study hasn't been conducted extensively so far.

The proposed approach can be summarized as follows. Let us start with the impedance matrices (frequency domain) at the left (L) and right (R) ends of a periodic structure (N substructures), which can be simply obtained via the WFE method as follows:

$$\mathbf{Z}_L = -\Phi_F^*(\Phi_q^*)^{-1}, \quad \mathbf{Z}_R = \Phi_F(\Phi_q)^{-1}. \quad (17)$$

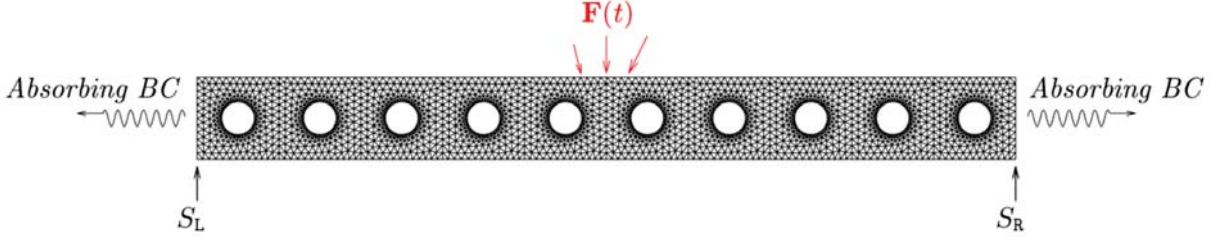


Figure 5: Schematic of a periodic structure with N substructures subject to time-dependent forces and semi-infinite boundary conditions.

Then, decompose the impedance matrices \mathbf{Z}_L and \mathbf{Z}_R via rational approximations:

$$\begin{aligned}\mathbf{Z}_L &= \sum_{k=1}^Q 2 \frac{i\omega \Re\{\mathbf{R}_{L(2k)}\} - \Re\{\overline{p_{L(2k)}} \mathbf{R}_{L(2k)}\}}{-\omega^2 - 2i\omega \Re\{p_{L(2k)}\} + |p_{L(2k)}|^2} + \sum_{k=2Q+1}^P \frac{\mathbf{R}_{Lk}}{i\omega - p_{Lk}} + \mathbf{K}_L, \\ \mathbf{Z}_R &= \sum_{k=1}^Q 2 \frac{i\omega \Re\{\mathbf{R}_{R(2k)}\} - \Re\{\overline{p_{R(2k)}} \mathbf{R}_{R(2k)}\}}{-\omega^2 - 2i\omega \Re\{p_{R(2k)}\} + |p_{R(2k)}|^2} + \sum_{k=2Q+1}^P \frac{\mathbf{R}_{Rk}}{i\omega - p_{Rk}} + \mathbf{K}_R,\end{aligned}\quad (18)$$

where (p_{Lk}, p_{Rk}) and $(\mathbf{R}_{Lk}, \mathbf{R}_{Rk})$ denote poles and matrices of residues ($k = 1, \dots, P$), respectively. Usually, some of these terms appear in conjugate pairs, say, for $k = 1, \dots, Q$. In the frequency domain, the absorbing boundary conditions are expressed by $\mathbf{F}_L = \mathbf{Z}_L \mathbf{q}_L$ and $\mathbf{F}_R = \mathbf{Z}_R \mathbf{q}_R$ where \mathbf{q}_L (resp. \mathbf{q}_R) and \mathbf{F}_L (resp. \mathbf{F}_R) are the displacement vector and force vector at the left (resp. right) end of the structure, respectively. By considering vectors of supplementary variables \mathbf{X}_{Lk} and \mathbf{X}_{Rk} together with Eq. (18), it can be shown that the absorbing conditions can be rewritten as follows:

$$\begin{aligned}\mathbf{F}_L &= \sum_{k=1}^Q 2 (i\omega \Re\{\mathbf{R}_{L(2k)}\} - \Re\{\overline{p_{L(2k)}} \mathbf{R}_{L(2k)}\}) \mathbf{X}_{Lk} + \sum_{k=2Q+1}^P \mathbf{R}_{Lk}(i\omega) \mathbf{X}_{L(k-Q)} + \mathbf{K}_L \mathbf{q}_L, \\ \mathbf{F}_R &= \sum_{k=1}^Q 2 (i\omega \Re\{\mathbf{R}_{R(2k)}\} - \Re\{\overline{p_{R(2k)}} \mathbf{R}_{R(2k)}\}) \mathbf{X}_{Rk} + \sum_{k=2Q+1}^P \mathbf{R}_{Rk}(i\omega) \mathbf{X}_{R(k-Q)} + \mathbf{K}_R \mathbf{q}_R,\end{aligned}\quad (19)$$

where:

$$\begin{aligned}(-\omega^2 - 2i\omega \Re\{p_{L(2k)}\} + |p_{L(2k)}|^2) \mathbf{X}_{Lk} &= \mathbf{q}_L & \text{for } k = 1, \dots, Q, \\ (-\omega^2 - 2i\omega \Re\{p_{R(2k)}\} + |p_{R(2k)}|^2) \mathbf{X}_{Rk} &= \mathbf{q}_R & \text{for } k = 1, \dots, Q, \\ (-\omega^2 - i\omega p_{Lk}) \mathbf{X}_{L(k-Q)} &= \mathbf{q}_L & \text{for } k = (2Q+1), \dots, P, \\ (-\omega^2 - i\omega p_{Rk}) \mathbf{X}_{R(k-Q)} &= \mathbf{q}_R & \text{for } k = (2Q+1), \dots, P.\end{aligned}\quad (20)$$

The interesting feature of Eq. (19) is that the force vectors are described in terms of polynomials of $i\omega$, of order 1. In comparison, Eq. (18) is more complicated with rational terms of $i\omega$. As for Eq. (20) — i.e., the relations between the displacement vectors and the vectors of supplementary variables — it also involves polynomials of $i\omega$ (up to order 2). By separating the terms of identical powers of $i\omega$ in Eqs. (19) and (20), and by invoking the classical time-frequency transforms $\mathbf{q}(\omega) \rightarrow \mathbf{q}(t)$, $i\omega \mathbf{q} \rightarrow \dot{\mathbf{q}}$, $-\omega^2 \mathbf{q} \rightarrow \ddot{\mathbf{q}}$ and $\mathbf{X}(\omega) \rightarrow \mathbf{X}(t)$, $i\omega \mathbf{X} \rightarrow \dot{\mathbf{X}}$, $-\omega^2 \mathbf{X} \rightarrow \ddot{\mathbf{X}}$

(where dot and double-dot notations mean single and double time derivatives, respectively), two classical second-order differential equations can be obtained:

$$\mathbb{M}_L \begin{bmatrix} \ddot{\mathbf{q}}_L \\ \ddot{\mathbf{x}}_L \end{bmatrix} + \mathbb{C}_L \begin{bmatrix} \dot{\mathbf{q}}_L \\ \dot{\mathbf{x}}_L \end{bmatrix} + \mathbb{K}_L \begin{bmatrix} \mathbf{q}_L \\ \mathbf{x}_L \end{bmatrix} = \begin{bmatrix} \mathbf{F}_L \\ \mathbf{0} \end{bmatrix}, \quad \mathbb{M}_R \begin{bmatrix} \ddot{\mathbf{q}}_R \\ \ddot{\mathbf{x}}_R \end{bmatrix} + \mathbb{C}_R \begin{bmatrix} \dot{\mathbf{q}}_R \\ \dot{\mathbf{x}}_R \end{bmatrix} + \mathbb{K}_R \begin{bmatrix} \mathbf{q}_R \\ \mathbf{x}_R \end{bmatrix} = \begin{bmatrix} \mathbf{F}_R \\ \mathbf{0} \end{bmatrix}, \quad (21)$$

where \mathbf{X}_L and \mathbf{X}_R are vectors built from all the vectors of supplementary variables \mathbf{X}_{Lk} and \mathbf{X}_{Rk} . Eq. (21) can be simply integrated into a FE model of a periodic structure (N substructures). Thus, the FE model of a periodic structure with absorbing boundary conditions can be written in the time domain as follows:

$$\mathbf{M}_{\text{tot}} \ddot{\mathbf{y}} + \mathbf{C}_{\text{tot}} \dot{\mathbf{y}} + \mathbf{K}_{\text{tot}} \mathbf{y} = \mathbf{F}_{\text{tot}}, \quad (22)$$

where

$$\mathbf{y} = \mathbf{y}(t) = \begin{bmatrix} \mathbf{q}_I(t) \\ \mathbf{q}_L(t) \\ \mathbf{q}_R(t) \\ \mathbf{X}_L(t) \\ \mathbf{X}_R(t) \end{bmatrix}, \quad \mathbf{F}_{\text{tot}} = \mathbf{F}_{\text{tot}}(t) = \begin{bmatrix} \mathbf{F}_I(t) \\ \mathbf{0} \\ \mathbf{0} \\ \mathbf{0} \\ \mathbf{0} \end{bmatrix}, \quad (23)$$

where \mathbf{q}_I and \mathbf{F}_I represent the displacement vector and force vector (time loadings) for the internal DOFs (between the left and right ends). Eq. (22) is a classical second-order differential equation which can be solved in a standard way via time integration numerical schemes (e.g., Newmark scheme). For instance, the time response of an infinite periodic structure, with 2D substructures, subject at its center to a shock (transverse Ricker wavelet force pulse) is analyzed. Here, a periodic structure consisting of only 20 substructures (squares with holes, meshed with 2D plane stress triangular elements) is considered. Absorbing boundary conditions are invoked at the left and right ends of the periodic structure, as discussed earlier. For comparison purposes, a FE model of a much longer periodic structure with free ends and 200 substructures, aiming at modeling an infinite structure, is simulated. Results are shown in Fig. 6 for the time history and the displacement field at $t = 0.01$ s, which fully validate the proposed approach.

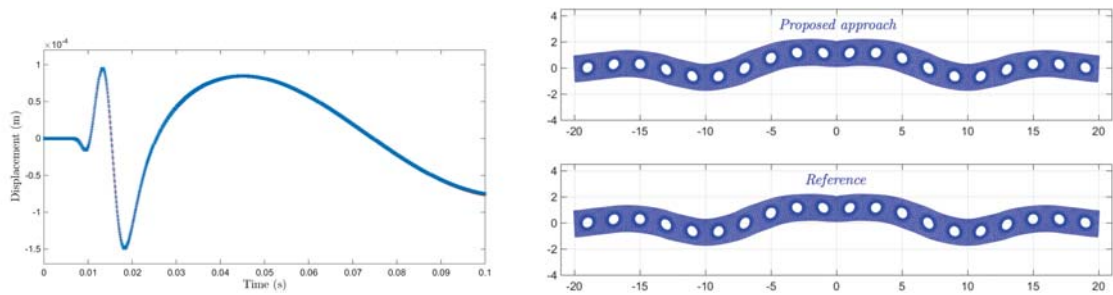


Figure 6: Time response of the periodic structure: (left) time history at the right end (reference FE: red line; proposed approach: blue crosses); (right) deformed shape.

2.4 Some results about locally resonant metamaterials

The analysis and design of locally resonant metamaterials is a research topic of growing interest, which is mostly due to their ability to create band gaps and strongly attenuate the vibration levels of structures [31, 1, 35, 8, 33]. Band gaps refer to frequency bands in which

one or several waves do not propagate, and which are here induced by the local resonances of the substructures (cells).

Among the resonant metamaterials are those made up of multi-layered continuous substructures combining soft and heavy materials (e.g., soft and stiff/heavy layers/core) which behave like a single or multi-DOF mass-spring system. For instance, a periodic structure with periodic inclusions of viscoelastic layers (spring and damping effects) and heavy parts (mass effect) is shown in Fig. 7. The goal of the present study is to analyze the band gap effect in such periodic structures. Also, it aims at investigating whether periodic structures with viscoelastic properties can be used to create band gaps with larger bandwidths (compared to when purely elastic properties are considered), to make them useful for a wider range of engineering applications.

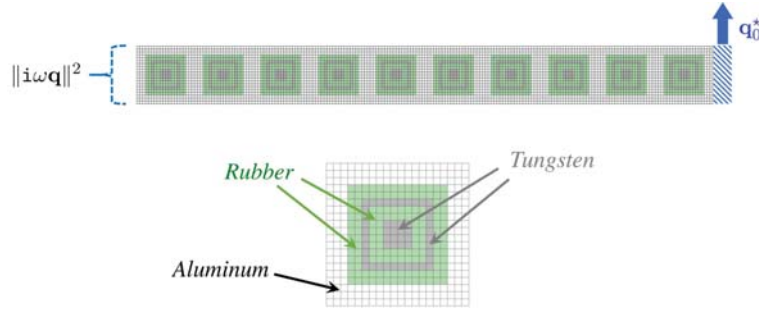


Figure 7: Periodic structure with $N = 10$ squared substructures with two viscoelastic layers (rubber), a heavy layer and a heavy core (tungsten).

Following the WFE procedure, the wave properties of the periodic structure and the related forced response can be obtained straightforwardly. Attention must be paid, however, to the FE modeling of the viscoelastic layers and the fact that their stiffness matrices depend on the frequency (see [21] for further details):

$$\mathbf{K}_v^{\text{vel}}(\omega) = \mathbf{K}_{v\infty} + \sum_{i=1}^{n_v} \mathbf{K}_{vi} \left(\frac{\omega^2 \tau_i^2}{1 + \omega^2 \tau_i^2} + i \frac{\omega \tau_i}{1 + \omega^2 \tau_i^2} \right), \quad (24)$$

where τ_i are relaxation times with $\tau_i = 10^{-i}$ s for $i = 1, 2, \dots, n_v$. The stiffness matrix of a whole substructure involves assembling several FE viscoelastic layers (v) together with FE elastic layers (e), i.e.:

$$\mathbf{K}(\omega) = \mathbf{K}_1 + \mathbf{K}_2(\omega), \quad (25)$$

where

$$\mathbf{K}_1 = \sum_{e=1}^{N^{\text{el}}} (1 + i\eta_e^{\text{el}}) (\mathcal{L}_e^{\text{el}})^T \mathbf{K}_e^{\text{el}} \mathcal{L}_e^{\text{el}} + \sum_{v=1}^{N^{\text{vel}}} (\mathcal{L}_v^{\text{vel}})^T \mathbf{K}_{v\infty} \mathcal{L}_v^{\text{vel}}, \quad (26)$$

and

$$\mathbf{K}_2(\omega) = \sum_{v=1}^{N^{\text{vel}}} \sum_{i=1}^{n_v} (\mathcal{L}_v^{\text{vel}})^T \mathbf{K}_{vi} \mathcal{L}_v^{\text{vel}} \left(\frac{\omega^2 \tau_i^2}{1 + \omega^2 \tau_i^2} + i \frac{\omega \tau_i}{1 + \omega^2 \tau_i^2} \right), \quad (27)$$

where $\mathcal{L}_e^{\text{el}}$ and $\mathcal{L}_v^{\text{vel}}$ are localization (Boolean) matrices, and η_e^{el} denotes the loss factors of the elastic parts. As it turns out, the dynamic stiffness matrix of the substructure is expressed by $\mathbf{D} = -\omega^2 \mathbf{M} + \mathbf{K}_1 + \mathbf{K}_2(\omega)$. Numerical issues about the condensation of the dynamic stiffness matrix on the left and right boundaries of the substructure (see Sec. 2.1) are discussed in [21]. Results about the dispersion curves of the bending wave are shown in Fig. 8, e.g., when $n_v = 5$

(number of terms in the series in Eq. (24)) and $\mathbf{K}_{vi} = 0.05 \times \mathbf{K}_{v\infty}$ ($i = 1, \dots, 5$). The structure of interest is shown in Fig. 7. Here, squared substructures with two viscoelastic layers (rubber, $N^{\text{ve}1} = 2$) and elastic parts including an external layer in aluminum, a central layer and a core in tungsten ($N^{\text{el}} = 3$), are considered. Here, each substructure is meshed using 20×20 eight-node plane stress quad elements. For comparison purposes, a purely equivalent elastic structure, when $\mathbf{K}_v^{\text{ve}1} = \mathbf{K}_{v\infty}(1 + 5 \times 0.05)$, is also considered.

Band gaps occur when the real parts of the wavenumbers are equal to 0 or π/d (d being the substructure length). The dispersion curves displayed in Fig. 8 represent plots of the functions $\omega \mapsto \Re\{\beta d\}$ and $\omega \mapsto \Im\{\beta d\}$ where β is the wavenumber for the bending wave. Associated to the band gap behavior — when $\Re\{\beta d\} = 0$ or $\Re\{\beta d\} = \pi$ — are local increases of the magnitude of the imaginary part of the wavenumber, which means that the wave is becoming evanescent. The band gap effect in resonant metamaterials mostly relies on the presence of substructure local modes. For instance, the fixed interface mode shapes of a purely equivalent elastic substructure are shown in Fig. 8, which could help understand the physical behavior of the structure in the vicinity of band gaps. As expected, band gap phenomena yield strong reduction of the vibration levels of the structure. Here, a structure with $N = 10$ substructures with prescribed transverse harmonic displacement at the right end is considered. For instance, two locally resonant band gaps appear at 742 Hz and 984 Hz which are close to each other. In the purely elastic case, the vibration levels show two local minima around these frequencies which appear to be well separated to each other. The interesting feature in the viscoelastic case is that these frequency bands with minimum vibration levels tend to merge to produce a wide frequency band (i.e., between 700 Hz and 1100 Hz) where, overall, the vibration levels remain low. This opens interesting prospects for the passive vibration control of structures.

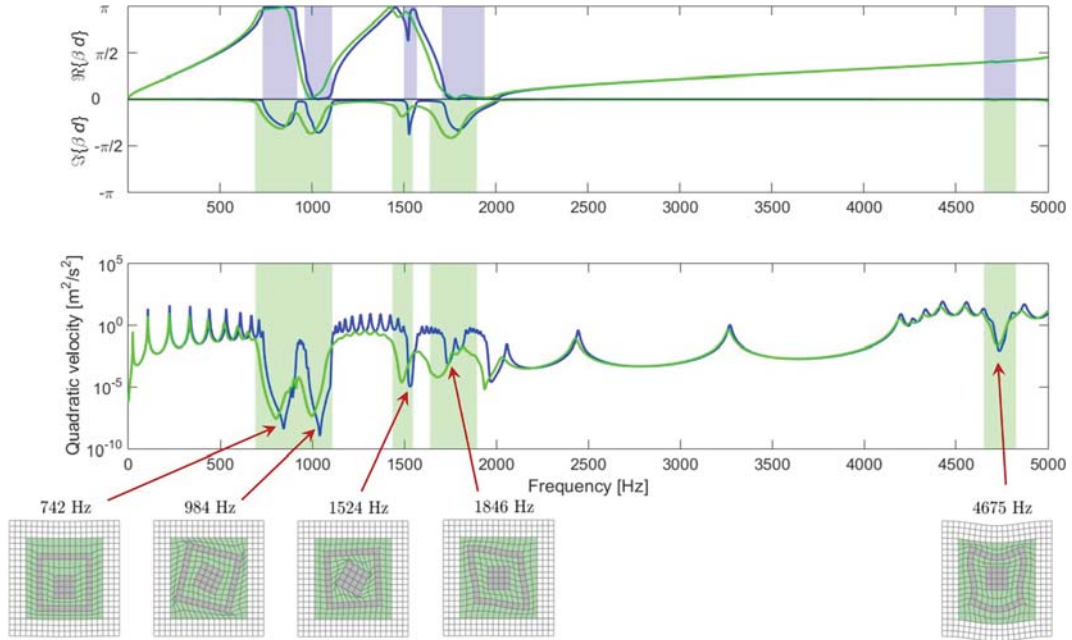


Figure 8: Periodic structure with $N = 10$ substructures. (top) Dispersion curves (elastic: blue line, viscoelastic: green line); (middle) Quadratic velocity at the left end; (bottom) fixed interface modes of the substructures.

Additional results about 1D periodic structures and resonant or non-resonant (Bragg) band gaps can be found in [30] (aircraft structures) and [2] (rotating phononic crystal ring).

3 2D PERIODIC STRUCTURES

3.1 Wave approaches and the modeling of structures of finite dimensions

The dynamic analysis of 2D periodic structures like metamaterial plates with resonant substructures constitutes a research topic of growing interest which mostly rely, with the era of 3D printing, on the ability to design and manufacture such structures at a low cost. A schematic of a 2D periodic structure made up of resonant layered substructures (soft layer and heavy core) is shown in Fig. 9. From the FE point of view, there exist plenty of works analyzing the propagation of Bloch waves in infinite 2D periodic structures and the related band gap effects. These approaches can be classified in two ways:

1. Those where a Bloch solution $\mathbf{u}(\mathbf{x}, \boldsymbol{\beta}, t) = \tilde{\mathbf{u}}(\mathbf{x}, \boldsymbol{\beta})e^{i(\omega t - \boldsymbol{\beta}^T \mathbf{x})}$ ($\boldsymbol{\beta} = [\beta_x \beta_y 0]^T$: wavenumber vector with $\beta_x = \beta \cos(\theta)$ and $\beta_y = \beta \sin(\theta)$; $\mathbf{x} = [x \ y \ z]^T$: position vector; $\tilde{\mathbf{u}}(\mathbf{x}, \boldsymbol{\beta})$: periodic function) is considered in the dynamic equilibrium equation of a cell (see for instance [9, 4]). The resulting dynamic equation of the cell together with the periodicity conditions for $\tilde{\mathbf{u}}(\mathbf{x}, \boldsymbol{\beta})$ are then converted into a FE model (Galerkin method), yielding a generalized eigenproblem of the form $\mathbf{A}(\beta_x, \beta_y)\tilde{\mathbf{q}} = \omega^2 \mathbf{B}(\beta_x, \beta_y)\tilde{\mathbf{q}}$ for the eigenvalue ω^2 and the eigenvector $\tilde{\mathbf{q}}$. The computation of the so-called band diagrams then involves plotting the pulsation ω for some pre-determined values of β_x and β_y following the first irreducible Brillouin zone.
2. Those where a FE model of a substructure is considered and where pseudo-periodic conditions are applied to its boundary. For substructures with rectangular boundaries (e.g., of lengths L_x and L_y), the pseudo-periodic conditions write $\mathbf{q}_R = e^{-i\beta_x L_x} \mathbf{q}_L$ between the left (L) and right (R) edges, $\mathbf{q}_T = e^{-i\beta_y L_y} \mathbf{q}_B$ between the bottom (B) and top (T) edges, $\mathbf{q}_{RB} = e^{-i\beta_x L_x} \mathbf{q}_{LB}$ between the left-bottom and right-bottom corners, $\mathbf{q}_{LT} = e^{-i\beta_y L_y} \mathbf{q}_{LB}$ between the left-bottom and left-top corners, and $\mathbf{q}_{RT} = e^{-i(\beta_x L_x + \beta_y L_y)} \mathbf{q}_{LB}$ between the left-bottom and right-top corners (see for instance [14, 25]). By considering the FE model of a substructure together with these pseudo-periodic conditions, a generalized eigenproblem of the form $\mathbf{A}(\beta_x, \beta_y)\tilde{\mathbf{q}} = \omega^2 \mathbf{B}(\beta_x, \beta_y)\tilde{\mathbf{q}}$ can be proposed (again) for computing the band diagrams of the structure.

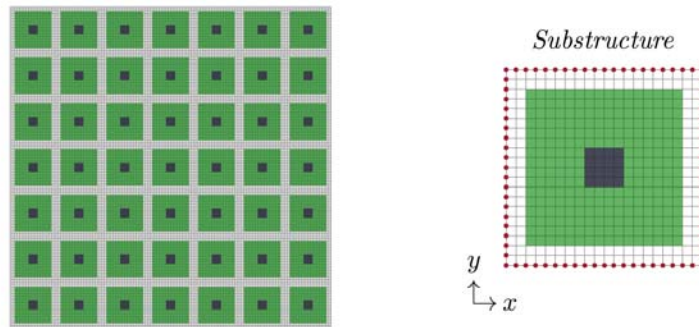


Figure 9: 2D periodic structure and FE mesh of a substructure (red spots highlight boundary nodes).

Although well detailed in the literature, the dynamic analysis of 2D periodic structures that uses wave approaches appears quite restricted to infinite systems where waves are supposed to

propagate freely, or infinite systems subject to point forces (see for instance [5]). In contrast, the analysis of 2D periodic structures of finite dimensions — i.e., systems which are frequently encountered in engineering applications — is not well reported. The thing is, the modeling of 2D periodic structures of finite dimensions via wave approaches appears to be a tough task (as opposed to the 1D periodic case) mostly due to the multi-directional behavior of the propagating waves, and the description of the boundary conditions (or coupling conditions) using these multi-directional waves.

Fortunately, there remain several FE-based reduced models which can be used to simulate the dynamic behavior of finite periodic structures, at a low computational cost. Indeed, by considering the periodicity hypothesis into account, the FE models of the substructures are identical and, therefore, they can be efficiently reduced via component mode synthesis like the Craig Bampton (CB) method. In fact, since the substructures are identical, their component modes are identical too which means that they only have to be computed once, i.e., regardless of the number of substructures considered. Hence, the following transformation matrix, for all the substructures, can be proposed [20]:

$$\tilde{\mathbf{T}} = \begin{bmatrix} \mathbf{I}_{N_B} & \mathbf{0} \\ -(\mathbf{K}_{II})^{-1}\mathbf{K}_{IB} & \tilde{\mathbf{X}} \end{bmatrix}, \quad (28)$$

where $-(\mathbf{K}_{II})^{-1}\mathbf{K}_{IB}$ and $\tilde{\mathbf{X}}$ are the matrix of static modes and the matrix of fixed interface modes (a reduced set) of the substructures, respectively; N_B is the number of boundary DOFs of the substructures. The reduced dynamic equation of a substructure s follows as:

$$\left[(-\omega^2 + i\omega a)\tilde{\mathbf{M}} + (i\omega b + 1)\tilde{\mathbf{K}} \right] \begin{bmatrix} \tilde{\mathbf{u}}_B^s \\ \tilde{\boldsymbol{\alpha}}^s \end{bmatrix} = \begin{bmatrix} \mathbf{F}_B^s - \mathbf{K}_{BI}(\mathbf{K}_{II})^{-1}\mathbf{F}_I^s \\ \tilde{\mathbf{X}}^T \mathbf{F}_I^s \end{bmatrix}, \quad (29)$$

where notation “ \mathbf{u} ” is used to denote displacement vectors (instead of “ \mathbf{q} ”); $\tilde{\mathbf{u}}_B^s$ is the approximated displacement vector for the boundary nodes; $\tilde{\boldsymbol{\alpha}}^s$ is a vector of generalized coordinates; \mathbf{F}_B^s and \mathbf{F}_I^s are force vectors for the boundary and internal nodes (respectively); a and b are damping coefficients (Rayleigh damping). Also, $\tilde{\mathbf{M}}$ and $\tilde{\mathbf{K}}$ are the reduced mass and stiffness matrices of the substructure (similar for all the substructures), expressed by:

$$\tilde{\mathbf{M}} = \tilde{\mathbf{T}}^T \mathbf{M} \tilde{\mathbf{T}}, \quad \tilde{\mathbf{K}} = \tilde{\mathbf{T}}^T \mathbf{K} \tilde{\mathbf{T}}. \quad (30)$$

The reduced global mass and stiffness matrices of a whole 2D periodic structure — namely, $\tilde{\mathbf{M}}_{\text{per}}$ and $\tilde{\mathbf{K}}_{\text{per}}$ — follow from conventional FE assembly procedures by considering the displacement continuity conditions at the boundary DOFs. The global dynamic equation of the periodic structure follows as:

$$\left[(-\omega^2 + i\omega a)\tilde{\mathbf{M}}_{\text{per}} + (i\omega b + 1)\tilde{\mathbf{K}}_{\text{per}} \right] \begin{bmatrix} (\tilde{\mathbf{u}}_B)_{\text{per}} \\ \tilde{\boldsymbol{\alpha}}_{\text{per}} \end{bmatrix} = \tilde{\mathbf{F}}_{\text{per}}, \quad (31)$$

where $(\tilde{\mathbf{u}}_B)_{\text{per}}$ is the displacement vector of the boundary/interface nodes of the substructures. In addition, the boundary conditions of the periodic structure may be written in a general way as:

$$\mathbf{Y}_B(\tilde{\mathbf{u}}_B)_{\text{per}} + \mathbf{Z}_B(\tilde{\mathbf{F}}_B)_{\text{per}} = \mathbf{Y}_B^0(\tilde{\mathbf{u}}_B)_{\text{per}}^0 + \mathbf{Z}_B^0(\tilde{\mathbf{F}}_B)_{\text{per}}^0, \quad (32)$$

where $(\tilde{\mathbf{u}}_B)_{\text{per}}^0$ and $(\tilde{\mathbf{F}}_B)_{\text{per}}^0$ are vectors of prescribed displacements and prescribed forces, respectively, and where \mathbf{Y}_B , \mathbf{Z}_B , \mathbf{Y}_B^0 and \mathbf{Z}_B^0 are matrices whose expressions depend on the kind of applications considered. A second reduced mode expansion can be proposed to speed up the computation of the matrix system (31) by expressing the displacement vector $(\tilde{\mathbf{u}}_B)_{\text{per}}$ on some “boundary modes” (eigenvectors) for the matrix pencil $((\tilde{\mathbf{K}}_{BB})_{\text{per}}, (\tilde{\mathbf{M}}_{BB})_{\text{per}})$.

3.2 2D nearly periodic structures

It is well known that nearly periodic structures — e.g., periodic structures with disordered resonant substructures with slightly varying geometrical properties — possess interesting properties, e.g., the fact that the vibrational energy is localized around the excitation points [3, 13]. For instance, a schematic of a nearly periodic plate with layered substructures (soft layer and heavy core), embedded in a floor panel, is shown in Fig. 10.

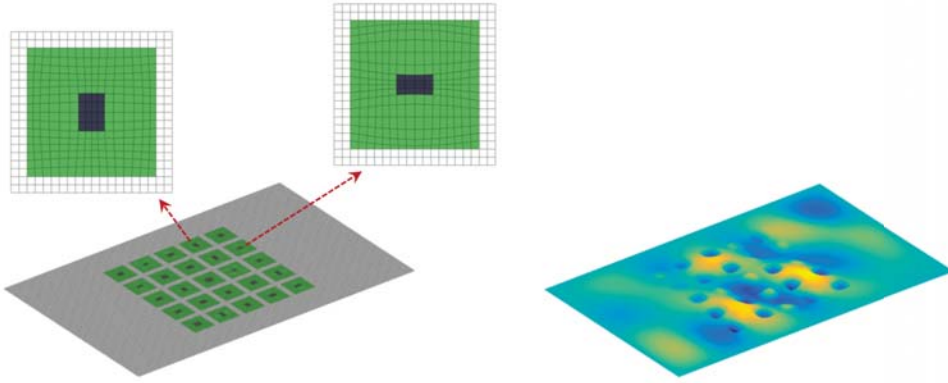


Figure 10: 2D nearly periodic plate embedded in a floor panel, and related transverse displacement field resulting from harmonic excitations.

A strategy for modeling such nearly periodic structures has been recently proposed in [20] and is briefly summarized here. The key idea for describing disordered substructures is to make use of distorted FE meshes, with node positions which randomly vary around a baseline (undistorted) mesh:

$$x_j^{se} = x_j^e + \epsilon_x^s f_x(x_j^e, y_j^e) \quad , \quad y_j^{se} = y_j^e + \epsilon_y^s f_y(x_j^e, y_j^e), \quad (33)$$

where (x_j^{se}, y_j^{se}) and (x_j^e, y_j^e) are the node coordinates of the distorted and undistorted meshes, respectively; ϵ_x^s and ϵ_y^s are uniform random variables with support $[-\delta, \delta]$ where δ is a dispersion parameter; $f_x(x, y)$ and $f_y(x, y)$ are two arbitrary deterministic functions of (x, y) , identical for all the substructures, which are supposed to cancel out on the boundary. Examples of distorted substructures are highlighted in Fig. 10.

When it comes to nearly periodic structures, the modeling of substructures raises two main issues compared to the purely periodic case. First, since the substructures are not identical, their mass and stiffness matrices \mathbf{M}^s and \mathbf{K}^s have to be computed several times (as many times as the number of substructures considered); second, the matrices of static modes and fixed interface modes $-(\mathbf{K}_{II}^s)^{-1}\mathbf{K}_{IB}^s$ and $\tilde{\mathbf{X}}^s$, and also the reduced mass and stiffness matrices $\tilde{\mathbf{M}}^s$ and $\tilde{\mathbf{K}}^s$ (matrix multiplications with the transformation matrix, see Eq. (30)), have to be computed several times. For structures with many substructures, this makes the CB method ineffective. To address these issues — i.e., to avoid computing the reduced mass and stiffness matrices many times — it is proposed to compute these matrices at some points $\epsilon_x^s = (\epsilon_x)_p$ and $\epsilon_y^s = (\epsilon_y)_p$ (a small number) for some particular distorted FE meshes of the substructures, and approximate these matrices between these points via matrix interpolation for any distortion ϵ_x^s and ϵ_y^s . Although easy to understand, the procedure for interpolating matrices is not straightforward, however, and requires the reduced matrices to be expressed using coordinate systems which are

compatible to each other [26]. For this task, the following alternative reduced matrices of fixed interface modes, at the interpolation points, can be considered [20]:

$$\widehat{\mathbf{X}}_p = \widetilde{\mathbf{X}}_p (\Psi^T \widetilde{\mathbf{X}}_p)^{-1}, \quad (34)$$

where

$$\Psi = \left((\mathbf{M}_{\text{II}}^0)^{\frac{1}{2}} \right)^T \widetilde{\mathbf{X}}^0. \quad (35)$$

Here, notations \mathbf{M}_{II}^0 and $\widetilde{\mathbf{X}}^0$ mean that the matrices \mathbf{M}_{II}^s and $\widetilde{\mathbf{X}}^s$ are expressed at $\epsilon_x^s = 0$ and $\epsilon_y^s = 0$. As a result, the following transformation matrix, reduced mass matrix and reduced stiffness matrix can be proposed:

$$\widehat{\mathbf{T}}_p = \begin{bmatrix} \mathbf{I}_{N_B} & \mathbf{0} \\ -(\mathbf{K}_{\text{II}})_p^{-1} (\mathbf{K}_{\text{IB}})_p & \widehat{\mathbf{X}}_p \end{bmatrix}, \quad (36)$$

$$\widehat{\mathbf{M}}_p = \widehat{\mathbf{T}}_p^T \mathbf{M}_p \widehat{\mathbf{T}}_p, \quad \widehat{\mathbf{K}}_p = \widehat{\mathbf{T}}_p^T \mathbf{K}_p \widehat{\mathbf{T}}_p. \quad (37)$$

The determination of the interpolated reduced mass and stiffness matrices — namely, $\widehat{\mathbf{M}}^s$ and $\widehat{\mathbf{K}}^s$ — for any substructure s with mesh parameters (ξ^s, η^s) follows from classic interpolation, e.g., using an interpolation scheme based on eight interpolation points (ξ_p, η_p) and eight Serendipity interpolation functions $N_p(\xi^s, \eta^s)$, as shown in Fig. 11. Thus:

$$\widehat{\mathbf{M}}^s = \sum_{p=1}^8 N_p(\xi^s, \eta^s) \widehat{\mathbf{M}}_p, \quad \widehat{\mathbf{K}}^s = \sum_{p=1}^8 N_p(\xi^s, \eta^s) \widehat{\mathbf{K}}_p, \quad (38)$$

where :

$$\xi^s = \sqrt{2} \frac{\epsilon_x^s}{\delta}, \quad \eta^s = \sqrt{2} \frac{\epsilon_y^s}{\delta}. \quad (39)$$

The modeling of a whole 2D nearly periodic structure follows from classic FE assembly procedure, as reported earlier.

Numerical experiments can be carried out to validate the proposed strategy. Let us consider, for instance, a nearly periodic plate with 8×4 substructures embedded in a floor panel and subject to random forces, as shown in Fig. 12 where simply supported boundary conditions are considered. Typical distorted substructures are shown in Fig. 10 and are meshed using 20×20 isoparametric quadratic Mindlin elements. Concerning the distorted meshes of the substructures, $f_x(x_j^e, y_j^e)$ and $f_y(x_j^e, y_j^e)$ are chosen as trigonometric functions, while $\delta = 0.01$ m (mesh dispersion).

The frequency responses of the structure (quadratic velocities at the location of the excitation points) over a frequency band of $[0, 150]$ Hz, obtained from the interpolation strategy and the conventional FE modeling, are shown in Fig. 13 where good matches are observed. The eigenfrequencies of the undistorted substructures (fixed interfaces) are shown with dotted vertical red lines. For the purely periodic case, these frequencies correspond to band gap effects where vibration levels are low.

Also, the transverse displacement fields of the plate/panel at 125 Hz are shown in Fig. 14 for the nearly and purely periodic cases. For the nearly periodic case, the displacement field shows localized peaks of high magnitude in the plate, and small displacement levels in the floor. In comparison, the periodic case involves uniform (diffuse) field in the plate, and higher displacement levels in the floor. In this sense, the nearly periodic plate appears to be a suitable means to passively control the vibration levels of the floor. Finally, in terms of computational times, the interpolation strategy provides an overall time reduction of 82% compared to the FE method.

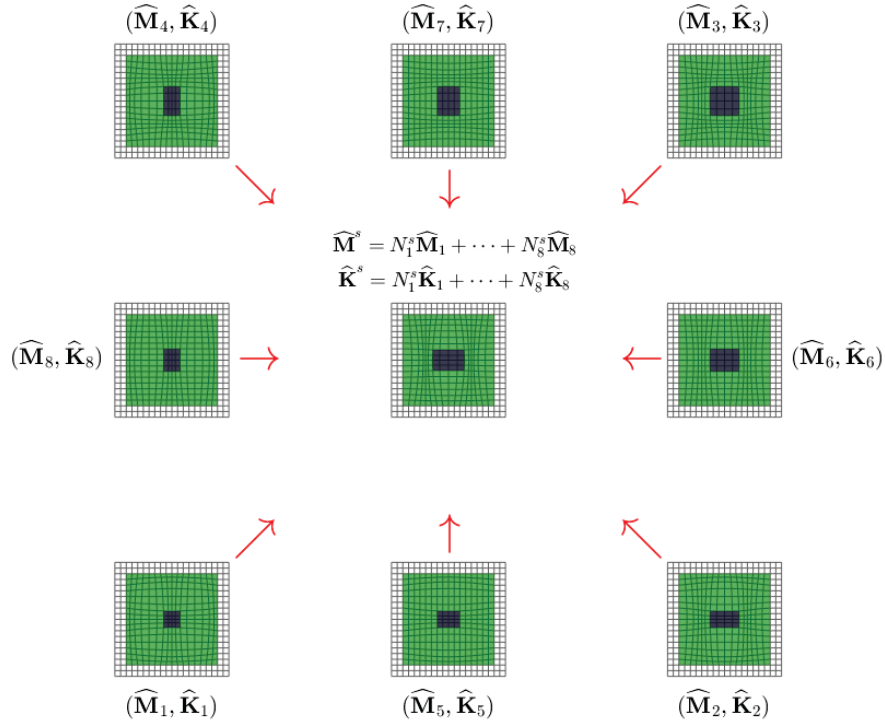


Figure 11: Eight point interpolation scheme based on serendipity interpolation functions $N_p(\xi^s, \eta^s)$ ($p = 1, \dots, 8$).

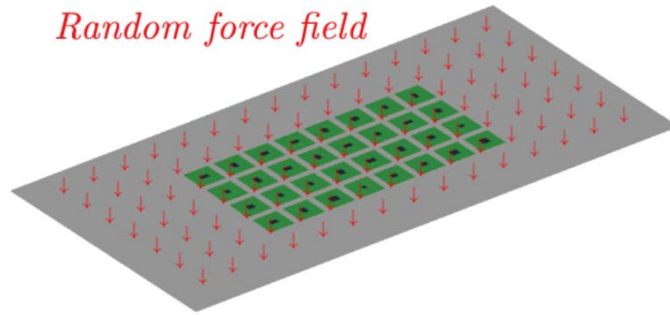


Figure 12: Schematic of a nearly periodic plate with 8×4 substructures with a floor panel subject to random forces.

4 CONCLUSION

An overview of some wave approaches and FE-based procedures, for modeling periodic structures and metamaterials, has been proposed. For 1D periodic structures, the WFE method has been investigated and some recent advances in this field have been presented. For 2D periodic structures, a reduced FE modeling of the substructures based on the CB method has been proposed. The procedure has been extended to the dynamic analysis of 2D nearly periodic structures (with substructures having randomly varying geometrical properties) via the use of distorted FE meshes and the interpolation of the reduced matrices of the substructures between “interpolation points” (some particular distorted meshes). Those wave approaches and FE procedures have been proven relevant for predicting the dynamic behavior of periodic structures including metamaterials with resonant cells that could be of various shapes. The dynamic analysis of periodic structures is a research topic in constant progress. This concerns the wave

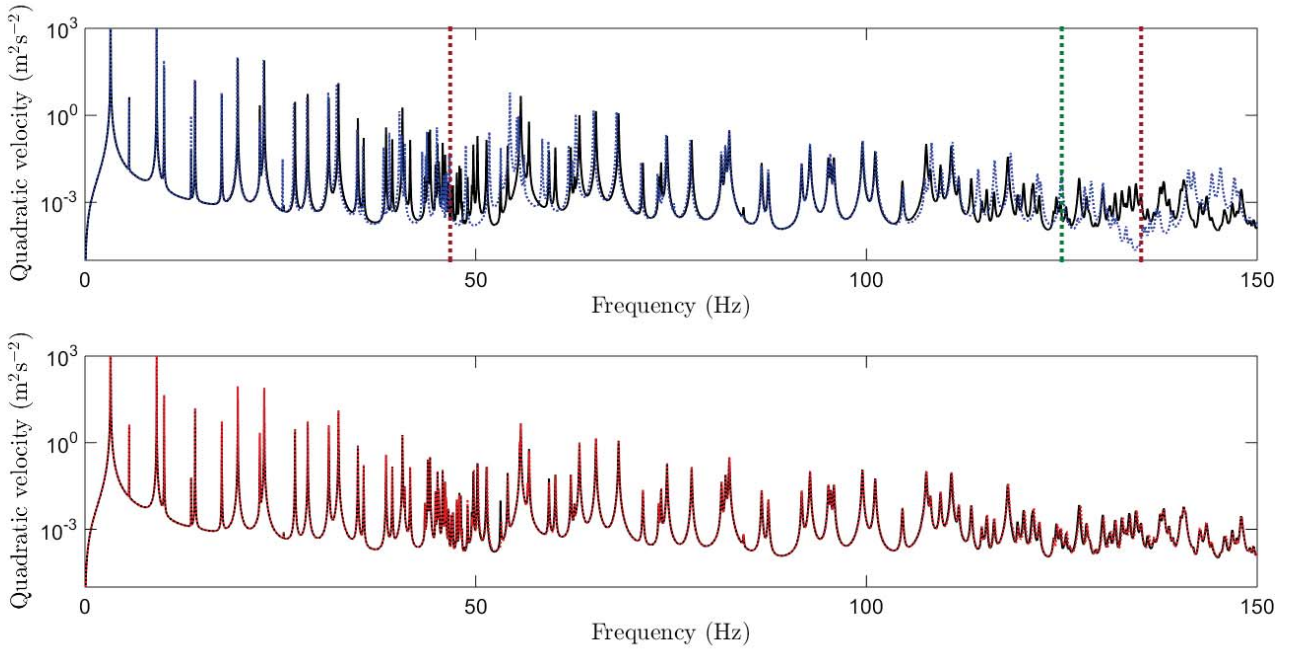


Figure 13: FRF (mean value of the quadratic velocity) of the plate with 8×4 substructures with the floor panel. (black solid line) FE method, nearly periodic structure; (red dotted line) interpolation strategy, nearly periodic structure; (blue dotted line) FE method, purely periodic structure.



Figure 14: Transverse displacement field (real part) of the plate with 8×4 substructures with the floor panel at 125 Hz, obtained with the interpolation strategy. (left) Periodic case; (right) nearly periodic case.

propagation analysis in infinite systems, but also, the study of systems of finite dimensions (one or several, possibly coupled together). Follow-on works could include the analysis of periodic structures with localized nonlinear effects, e.g., metamaterials with local nonlinear resonant devices, or structures locally subject to fast loadings of high magnitudes (shocks, blast).

REFERENCES

- [1] D. Beli, A.T. Fabro, M. Ruzzene, and J.R.F. Arruda. Wave attenuation and trapping in 3D printed cantilever-in-mass metamaterials with spatially correlated variability. *Scientific Reports*, 9:5617, 2019.
- [2] D. Beli, J.-M. Mencik, P.B. Silva, and J.R.F. Arruda. A projection-based model reduction strategy for the wave and vibration analysis of rotating periodic structures. *Computational Mechanics*, 62:1511–1528, 2018.

- [3] M.P. Castanier and C. Pierre. Individual and interactive mechanisms for localization and dissipation in a mono-coupled nearly-periodic structure. *Journal of Sound and Vibration*, 168(3):479–505, 1993.
- [4] M. Collet, M. Ouisse, M. Ruzzene, and M.N. Ichchou. Floquet-Bloch decomposition for the computation of dispersion of two-dimensional periodic, damped mechanical systems. *International Journal of Solids and Structures*, 48(20):2837–2848, 2011.
- [5] D. Duhamel. Finite element computation of Green’s functions. *Engineering Analysis with Boundary Elements*, 31(11):919–930, 2007.
- [6] D. Duhamel, B.R. Mace, and M. J. Brennan. Finite element analysis of the vibrations of waveguides and periodic structures. *Journal of Sound and Vibration*, 294(1-2):205–220, 2006.
- [7] D. Duhamel and J.-M. Mencik. Time response analysis of periodic structures via wave-based absorbing boundary conditions. *European Journal of Mechanics - A/Solids (submitted)*, 2021.
- [8] G.L. Huang and C.T. Sun. Band Gaps in a Multiresonator Acoustic Metamaterial. *Journal of Vibration and Acoustics*, 132:031003, 2010.
- [9] M.I. Hussein. Reduced Bloch mode expansion for periodic media band structure calculations. *Proceedings of the Royal Society A*, 465:2825–2848, 2009.
- [10] M.I. Hussein, G.M. Hulbert, and R.A. Scott. Dispersive elastodynamics of 1D banded materials and structures: Design. *Journal of Sound and Vibration*, 307:865–893, 2007.
- [11] J.S. Jensen. Phononic band gaps and vibrations in one- and two-dimensional mass-spring structures. *Journal of Sound and Vibration*, 266:1053–1078, 2003.
- [12] D. Krattiger and M.I. Hussein. Generalized Bloch mode synthesis for accelerated calculation of elastic band structures. *Journal of Computational Physics*, 357:183–205, 2018.
- [13] F.-M. Li and Y.-S. Wang. Study on wave localization in disordered periodic layered piezoelectric composite structures. *International Journal of Solids and Structures*, 42:6457–6474, 2005.
- [14] B.R. Mace and E. Manconi. Modelling wave propagation in two-dimensional structures using finite element analysis. *Journal of Sound and Vibration*, 318(4-5):884–902, 2008.
- [15] D.J. Mead. The forced vibration of one-dimensional multi-coupled periodic structures: An application to finite element analysis. *Journal of Sound and Vibration*, 319:282–304, 2009.
- [16] J.-M. Mencik. On the low- and mid-frequency forced response of elastic systems using wave finite elements with one-dimensional propagation. *Computers and Structures*, 88(11-12):674–689, 2010.
- [17] J.-M. Mencik. A wave finite element-based formulation for computing the forced response of structures involving rectangular flat shells. *International Journal for Numerical Methods in Engineering*, 95(2):91–120, 2013.

- [18] J.-M. Mencik. New advances in the forced response computation of periodic structures using the wave finite element (WFE) method. *Computational Mechanics*, 54(3):789–801, 2014.
- [19] J.-M. Mencik. A wave finite element approach for the analysis of periodic structures with cyclic symmetry in dynamic substructuring. *Journal of Sound and Vibration*, 431:441–457, 2018.
- [20] J.-M. Mencik. Model reduction based on matrix interpolation and distorted finite element meshes for dynamic analysis of 2D nearly periodic structures. *Finite Elements in Analysis and Design*, 188:103518, 2021.
- [21] J.-M. Mencik, V. Denis, M. Caliez, and S. Méo. Application of the wave finite element method to the analysis of locally resonant band gaps in periodic structures with viscoelastic properties. *Proceedings of the 28th International Conference on Noise and Vibration engineering (ISMA2018), Leuven, Belgium*, pages 2469–2481, 2018.
- [22] J.-M. Mencik and D. Duhamel. A wave-based model reduction technique for the description of the dynamic behavior of periodic structures involving arbitrary-shaped substructures and large-sized finite element models. *Finite Elements in Analysis and Design*, 101:1–14, 2015.
- [23] J.-M. Mencik and M. N. Ichchou. Multi-mode propagation and diffusion in structures through finite elements. *European Journal of Mechanics - A/Solids*, 24(5):877–898, 2005.
- [24] J.-M. Mencik, M. N. Ichchou, and L. Jézéquel. Propagation multimodale dans les systèmes périodiques couplés (in French). *Revue Européenne de Mécanique Numérique*, 15(1-3):293–306, 2006.
- [25] A. Palermo and A. Marzani. Extended Bloch mode synthesis: Ultrafast method for the computation of complex band structures in phononic media. *International Journal of Solids and Structures*, 100–101:29–40, 2016.
- [26] H. Panzer, J. Mohring, R. Eid, and B. Lohmann. Parametric model order reduction by matrix interpolation. *at-Automatisierungstechnik*, 58(8):475–484, 2010.
- [27] P.-O. Persson and G. Strang. A Simple Mesh Generator in MATLAB. *SIAM Rev.*, 46(2):329–345, 2004.
- [28] A.S. Phani, J. Woodhouse, and N. Fleck. Wave propagation in two-dimensional periodic lattices. *The Journal of the Acoustical Society of America*, 119(4):1995–2005, 2006.
- [29] V.F. Dal Poggeto and A.L. Serpa. Flexural wave band gaps in a ternary periodic meta-material plate using the plane wave expansion method. *Journal of Sound and Vibration*, 495:115909, 2021.
- [30] P.B. Silva, J.-M. Mencik, and J.R.F. Arruda. Wave finite element-based superelements for forced response analysis of coupled systems via dynamic substructuring. *International Journal for Numerical Methods in Engineering*, 107(6):453–476, 2016.

- [31] C. Sugino, Y. Xia, S. Leadenham, M. Ruzzene, and A. Erturk. A general theory for bandgap estimation in locally resonant metastructures. *Journal of Sound and Vibration*, 406:104–123, 2017.
- [32] Y. Waki, B.R. Mace, and M.J. Brennan. Numerical issues concerning the wave and finite element method for free and forced vibrations of waveguides. *Journal of Sound and Vibration*, 327(1-2):92–108, 2009.
- [33] Z. Wang, P. Zhang, and Y. Zhang. Locally Resonant Band Gaps in Flexural Vibrations of a Timoshenko Beam with Periodically Attached Multioscillators. *Mathematical Problems in Engineering*, Article ID 146975:104110, 2013.
- [34] K. Willcox and J. Peraire. Balanced model reduction via the proper orthogonal decomposition. *AIAA Journal*, 40(11):2323–2330, 2002.
- [35] Y. Xiao, B.R.Mace, J. Wen, and X. Wen. Formation and coupling of band gaps in a locally resonant elastic system comprising a string with attached resonators. *Physics Letters A*, 375:1485–1491, 2011.
- [36] W. X. Zhong and F. W. Williams. On the direct solution of wave propagation for repetitive structures. *Journal of Sound and Vibration*, 181(3):485–501, 1995.

IMPACT OF MASONRY INFILL VARIABILITY ON THE ESTIMATION OF FLOOR RESPONSE SPECTRA IN RC BUILDINGS

G. Mucedero¹, D. Perrone^{1,2}, E. Brunesi³ and R. Monteiro¹

¹ University School for Advanced Studies IUSS
{gianrocco.mucedero,daniele.perrone,ricardo.monteiro}@iusspavia.it

² University of Salento
daniele.perrone@unisalento.it

³ European Centre for Training and Research in Earthquake Engineering
emanuele.brunesi@eucentre.it

Abstract

Although the seismic performance of non-structural elements is currently recognised as a key issue in the seismic behaviour and loss estimation of buildings, both at the individual and portfolio level, the accurate evaluation of the seismic demand to which the former are subjected is still an open issue. Code formulations, as well as simplified methodologies for regional scale applications, are often based on inaccurate distributions of peak floor accelerations and floor spectral accelerations. In this respect, one of the main shortcomings in the formulations available in the literature is related to the effect of masonry infills on Floor Response Spectra (FRS), which is generally neglected, even in recently proposed design/assessment-oriented simplified methodologies. This study highlights and quantifies the impact of different masonry infill typologies on FRS estimates in existing infilled reinforced concrete (RC) frames. Nonlinear time history analyses are carried out for different case-study RC frames, selected from a fully integrated building portfolio, representative of buildings designed according to the Italian codes in force between 1970 and 1980. To account for the infill-related uncertainty, a macro-level distinction of common infill types, in terms of shear strength, was used. Moreover, the influence of the geometrical configuration and the number of storeys was also investigated. Acceleration FRS were then computed and statistically characterised, based on the observed infill-to-infill-related variability.

Keywords: Floor response spectra; Buildings portfolio; Masonry infills; Non-structural elements; Regional risk models.

1 INTRODUCTION

The earthquake related economic losses observed in the last decades were often attributed, for a good share, to damage to non-structural elements (NSEs), as reported in post-earthquake surveys [1,2]. NSEs represent all the systems and elements attached to the floors and walls of a building that are not part of the vertical and lateral load-bearing structural systems [3] but that are subjected to the same dynamic excitation during a seismic event. As reported by Miranda and Taghavi [4], NSEs represent the largest portion of the total investment in typical buildings. At the same time, the damage to NSEs can also represent a threat to life mostly because of falling hazards. Due to the numerous typologies of NSEs installed in a building, their vulnerability could significantly affect the immediate functionality because they generally exhibit damage at low (serviceability) seismic intensities, while the supporting structures respond mainly in the elastic range. This issue is paramount for strategic facilities, such as hospitals and schools that should remain operational in post-earthquake emergency situations. In Italy, for instance, the actual repair costs of reinforced concrete (RC) residential buildings damaged by the 2009 L'Aquila Earthquake, involved majorly the repair of infills and partitions [1,5-7]. Indeed, hollow clay brick walls, typical of Mediterranean construction standards, are characterised by brittle behaviour, which resulted in significant earthquake damage [5]. In particular, the costs related to structural elements did not exceed the 10% of the total repair costs; the remaining 90% was related to NSEs, such as infill walls and partitions (about 47%), plumbing and electrical systems, which are commonly incorporated in hollow clay brick (around 16%), windows and doors (around 22%), and other elements (15% approximately). Similar observations were made following the 2012 Emilia Earthquake and the 2016 Amatrice Earthquake [1,5-7], where it was reported that most of the NSE failures were related to partition walls experiencing large in-plane drifts and/or out-of-plane collapse (OOP), as well as damage to storage rack systems and ceiling systems [1,8].

NSEs are generally classified into different performance groups, according to their sensitivity to a specific engineering demand parameter (EDP); the main distinction is between acceleration-sensitive and drift-sensitive NSEs. For example, infill walls, partition walls and glazing systems are vulnerable to storey drifts whereas bookshelves, suspended ceilings, light fixtures, piping systems and rigidly attached elements are examples of acceleration sensitive NSEs. It is worth mentioning that infill and partition walls are also vulnerable to OOP collapse, which could be caused by floor accelerations. Consequently, the seismic performance assessment of NSEs requires the characterisation of the structural response in terms of inter-storey drifts and absolute acceleration floor response spectra (FRS), respectively, for drift-sensitive and acceleration-sensitive NSEs.

The lack, or in some cases the questionable accuracy, of code prescriptions and code-compliant guidelines [9,10], has oriented the recent past research efforts towards the development of simplified methodologies to predict absolute acceleration and displacement FRS for elastic and inelastic single-degree-of-freedom (SDOF) and multi-degree-of-freedom (MDOF) systems [11–18]. Such methodologies are particularly useful, given that accurate FRS estimates require complex and demanding nonlinear time-history analysis (NLTHA). Petrone et al. [11] proposed a methodology to predict absolute acceleration FRS calibrated using a set of RC moment resisting frames designed according to Eurocode 8 [9] and subjected to frequent (serviceability-level) earthquake ground motions. Sullivan et al. [12] proposed a simplified approach to predict absolute acceleration FRS for linear and nonlinear SDOF structures, which was subsequently extended to linear and nonlinear MDOF systems [13,14]. Another approach, proposed by Vukobratovic and Fajfar [15], was calibrated for both elastic and inelastic SDOF and MDOF structures. In the case of MDOF structural systems, the resulting FRS were obtained

by a combination of the FRS obtained for individual vibration modes; a significant influence of higher modes on FRS was observed. Recently, other methodologies were also developed by Calvi [16] to evaluate relative-displacement FRS and by Merino et al. [17] to predict consistent absolute acceleration and relative displacement FRS, which can be used within displacement-based seismic design of NSEs [18].

2 RESEARCH METHODOLOGY

It was highlighted in the Introduction how the performance of new and existing buildings is strictly related to that of NSEs and how, for such reasons, research efforts have been made with the aim to develop simplified methodologies to predict absolute acceleration and displacement FRS for elastic and inelastic SDOF and MDOF systems [11–18]. As also previously discussed, some simplified methods are available in the literature to predict the FRS of RC buildings [11,14,15] but the influence of masonry infills, which are typically present in Italy and other Mediterranean countries, was not considered in any of them.

Few studies have investigated the influence of masonry infills on FRS in RC buildings [19,20]. Lucchini et al. [19] investigated the influence of masonry infills and damping models on FRS in nonlinearly analysed buildings, pointing out how the infill walls can significantly affect the peak floor acceleration profile at a given intensity, as well as the FRS at all storeys in terms of spectral acceleration and shape. More recently, Surana et al. [20] studied the effect of unreinforced masonry infills on the inelastic FRS of RC frame buildings; the outcomes demonstrated that the influence of masonry infills cannot be neglected in the evaluation of FRS in RC frames, especially for frequent earthquakes, for which cracking developing in the masonry is generally not expected and the uncracked stiffness of the infills tends to be considered. Recently, Perrone et al. [21], by means of Monte Carlo simulation, analysed a database of European masonry-infilled RC frames and computed absolute acceleration and relative displacement FRS at different floor levels for both bare and infilled frame archetypes using NLTHA. As a result, a first model was proposed for regional scale application, to evaluate the seismic demand to which the NSEs are subjected, taking the effect of masonry infills explicitly into account.

With such considerations in mind, this paper deals with the evaluation of absolute acceleration FRS of bare and infilled frames, with the aim of (i) highlighting the difference between the results for these two structural configurations and (ii) quantifying the impact of masonry infills on the FRS. A fully integrated building stock, recently assessed by means of nonlinear static analysis in [22], is considered as case-study. In particular, the RC buildings built between 1970 and 1980, one of the decades with massive construction in Italy, are focused on. Figure 1 presents the research approach workflow of the study, while more information related to the case-study building portfolio can be found in [22]. Once the building stock was defined, NLTHAs were performed to record the accelerations at two different floor levels (first and roof floor) and the FRS were then computed from floor acceleration time-histories recorded along the structure's height. Finally, the comparison of FRS at two intensity levels, corresponding to Serviceability Limit State (SLS) and Life Safety Limit State (LSLS), are presented for both infilled and bare frames.

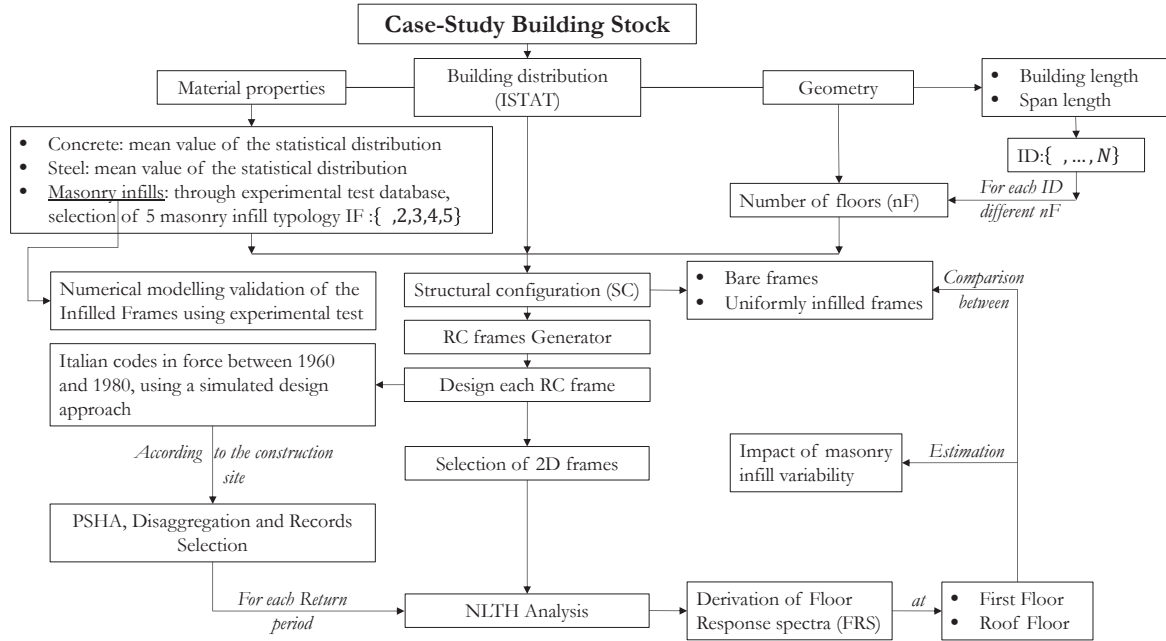


Figure 1: Research approach workflow.

3 RESEARCH METHODOLOGY

A building portfolio representing existing masonry-infilled RC residential buildings in Italy has been analysed in this study. It accounts for both the building geometrical layout and infills variability, characterised from statistical data collected from ISTAT [23] and from databases comprising information regarding experimental tests carried out on different masonry infill typologies [24-26]. According to the data provided by ISTAT [23], in Italy, there are 3 594 695 RC residential buildings, representing around 30% of the entire building stock, whereas 57% are in masonry and 13% correspond to other structural typologies (e.g. steel, precast). These buildings can be disaggregated as a function of the construction year, which allows to identify the building codes employed for their design, the material properties, the construction practice and the structural detailing. Most of the RC residential buildings in Italy were built before 1990 and, analysing the ISTAT database, no correlation between period of construction and geographical area has been found, demonstrating a quasi-uniform building construction trend over the national territory. Following such a preliminary analysis, this study is focused on RC buildings built between 1960 and 1980, decades with massive construction of such a building typology and during which an update of the seismic design guidelines was introduced. In order to fully develop the building portfolio, the variability in the following parameters has been considered: plan dimension, number of floors, inter-storey height, span length, material properties of RC elements and of masonry infills.

3.1 Building stock

In this section, the development of the building portfolio is summarised while interested readers can refer to Mucedero et al. [22] for full details. With the aim to define a statistically representative building stock, the data provided by ISTAT [23] was used, however, specific information, such as the material properties, number of floors, building height and plan dimensions, were aggregated or were not reported. For example, the ISTAT database does not provide information about the buildings' plan dimension; however, for residential buildings, it could be estimated using data from urbanistic directives and population distribution. Combining

this information with satellite images [27] for different geographical areas in Italy, a more precise and accurate definition of the plan dimensions was achieved. In particular, the range of variation of the plan dimensions in the longest and shortest dimensions (L_x and L_y) was estimated as in between 10-50 m and 8-25 m, respectively. Regarding the number of floors, including the ground floor, almost half of the buildings consist of two storeys, whilst only 10% have four or more storeys. Furthermore, the data provided by ISTAT [23] aggregated all the buildings with more than four storeys into a single class, making a further disaggregation difficult. As such, the defined building stock consists of RC frames with a number of storeys varying from one to six. Considering the design practice and common architectural trends, the inter-storey height was fixed at 3.0 m and span lengths were limited to the range of 3.0-5.0 m. Since no information is provided in ISTAT [23] about structural element properties, additional information was collected analysing the codes in force during the selected construction period, as well as original drawings of residential buildings from different geographical areas in Italy.

The mechanical properties of the materials used in the selected construction period (1970-1980) were obtained from the results of in-situ tests on existing buildings or from data collected in laboratory archives [28,29]. Considering the wide range of steel properties adopted in the reference construction period, it was chosen to use a yielding strength of 350 MPa. The ratio between the ultimate and the yielding strength was assumed as 1.4 [28]. Regarding the diameter of the longitudinal bars, 14 mm was chosen according to the mean value provided in Verderame *et al.* [28]. For what concerns the concrete strength, exhaustive information is presented in Masi *et al.* [29], from a large database of test results on concrete cores extracted from about 300 RC public buildings located in the Basilicata region (Italy), for which the mean strength and dispersion for different construction periods were provided. The test results showed mean values of concrete strength in the construction periods 1961–1971 and 1972–1981 of 19.53 MPa and 21.03 MPa, respectively. Although these tests were based on concrete strength of hospital and school buildings, this information was deemed suitable for residential buildings thus 20 MPa was considered as mean concrete strength in the period 1970-1980. The assumption of mean values for the concrete strength and for the ultimate and yielding strength of steel reinforcements is in accordance with the results pointed out in Celarec *et al.* [30], Dolšek [31], Mohammad *et al.* [32], in which it was showed that those parameters have limited effect on the dispersion when compared to other sources of uncertainty.

Despite the high-level of uncertainty surrounding the masonry infill properties, constant mechanical and geometrical properties of the masonry infills are typically assumed in seismic risk assessment studies of single buildings or at regional scale. To the authors' best knowledge, results of in-situ tests on masonry infills are not available; hence, the results of experimental studies [33-36], also reported in recent databases dealing with the definition of the mechanical properties of masonry infills [24,26], are taken into account to define a range of variability. Such variability is related to many parameters, such as the maximum shear strength of the panel, the stiffness of the panel, the relative stiffness between the panel and the surrounding frame, the vertical/horizontal compressive strength of the masonry, vertical/horizontal modulus of elasticity and thickness of the masonry.

This study considered, firstly, based on the results provided by Mucedero *et al.* [37], a macro-level distinction of the infills in terms of shear strength, which, according to the results of the works by Blasi *et al.* [38] and Mohammad *et al.* [32], is one of the most important, affecting the lateral capacity of RC frames and that could also lead to local shear failure (e.g. shear failure of columns that were built without particular construction details). Five masonry infill typologies, from weak to strong, classified according to the shear strength (Table 1) were thus selected as representative of the existing masonry infill typologies used in RC residential buildings built between 1970 and 1980 in Italy.

References	Type	Macro classification	t_w [mm]	E_{wv} [MPa]	E_{wh} [MPa]	G_w [MPa]	f_{wv} [MPa]	f_{wlat} [MPa]	f_{wu} [MPa]
Calvi and Bolognini [33]	1	Weak	80	1873	991	1089	2.02	1.18	0.44
Hak <i>et.al</i> [36]	2	Weak-Medium	240	1873	991	1873	1.5	1.11	0.25
Hak <i>et.al</i> [36]	3	Medium-Strong	300	3240	1050	1296	3.51	1.5	0.3
Morandi <i>et.al</i> [34]	4	Medium-Strong	350	5299	494	2120	4.64	1.08	0.359
Cavaleri and Di Trapani [35]	5	Strong	150	6401	5038	2547	8.66	4.18	1.07

t_w : thickness; E_{wv} : elastic modulus vertical direction; E_{wh} : elastic modulus horizontal direction; G_w : shear modulus; f_{wv} : vertical strength; f_{wlat} : lateral strength; f_{wu} : shear sliding strength.

Table 1: Representative masonry infills.

Considering the wide spectrum of characteristics of the selected infill typologies, it is believed that, even if some typologies that can be found in existing buildings are not represented, due for example to the variation in the thickness of the panels, the combination of five different masonry infill typologies is representative enough. Moreover, comparing the ranges of minimum and maximum values of the main mechanical properties (Young's modulus (E_w), shear modulus (G_w), peak load (F_{peak}) and the cracking strength (F_{cr})) provided in the database by De Risi *et al.* [26], it is possible to see that the selected masonry infill typologies cover the entire range of variation.

The design of the buildings was then carried out using a simulated design approach, according to the codes in force between 1970 and 1980 [39,40]. Table 2 summarises the main geometrical and material parameters considered in this study to define the building portfolio. The results of the simulated design are in good agreement with those provided in Bal *et al.* [41] and Silva *et al.* [42].

The case-study building portfolio comprised a total of 108 geometrical configurations, given by the combination of the different variables. In specific, the number of bays and the length of the analysed 2D masonry infilled RC frames vary according to the data reported in Table 2 for L_y (8-25 m). The span length varies between 3 m and 5 m, with increments of 1 m, while the height of the buildings varies between 3 m and 18 m, with increments of 3 m (the inter-storey height). Seven discrete building lengths were selected from the range of L_y (8-25 m) and combined with equally discrete possible different span lengths, leading to 18 different geometrical configurations (labelled as ID-1 to ID-18). Each of these was then combined with six different building heights, leading to 108 geometrical configurations, and with the five masonry infill typologies, leading to a total of 648 RC frames, subdivided as follows: 108 bare frames and 540 uniformly infilled frames.

<i>Description</i>	<i>Variable</i>	<i>Range</i>
Building length X direction	L_x	[10-50] m
Building length Y direction	L_y	[8-25] m
Span length	b_x or b_y	[3-5] m
Number of storeys	n	[1-6]
Interstorey height	h	3.0 m
Steel yield strength	f_y	350 MPa
Longitudinal rebar diameter	ϕ_l	14 mm
Stirrup diameter	ϕ_s	8 mm
Concrete compressive strength	f_c	20 MPa
Concrete cover	c	20 mm
Column height	h_c	[300-550] mm
Beam height	h_b	[300-400] mm
Column or beam width	b_c or b_b	300 mm
Masonry infill	IF	Type: [1-5]

Table 2: Geometrical and material parameters, together with corresponding ranges, considered for the definition of the case-study building portfolio.

3.2 Numerical Modelling

An advanced nonlinear numerical model was developed to account for the many phenomena that may occur in the buildings during an earthquake, such as: material and geometrical nonlinearity, bar slippage, flexible joints with likely shear failure, behaviour of poorly detailed and non-ductile RC frame members, premature shear failure, deficiencies in concrete core confinement due to stirrup spacing, inelasticity concentrated in the structural element ends, amongst others. To account for any potential structural deficiencies, the modelling approach proposed by O'Reilly *et al.* [43] and Perrone *et al.* [44] for older RC frames was followed, as shown in Figure 2. The numerical models were developed using OpenSees [45]. The flexural elements (i.e. beams and columns) were modelled through force-based beam-column elements with a modified Radau plastic hinge integration scheme, as suggested by Scott & Fenves [46], where the nonlinearity is lumped at the ends of the element and an aggregation section [45], V- γ and M- Θ , was introduced. The flexural behaviour was thus defined through the moment-curvature relationships proposed in [47], whereas the shear behaviour was modelled according to Zimos *et al.* [48], in which the backbone shear deformation curve consists of four phases, namely: initial elastic behaviour, post-cracking, peak response and strength degradation. To capture the nonlinear behaviour of joints, a zero-length spring coupled with a rotational hinge was adopted, which represents the shear joint behaviour; its hysteretic behaviour was calibrated according to different experimental tests [49-52]. Regarding damping, 5% tangent stiffness proportional Rayleigh damping at the fundamental periods was adopted.

The uniaxial nonlinear Pinching4 Material model has been adopted to simulate the hysteretic behaviour of the masonry infills; all the parameters defining the equivalent strut's hysteretic behaviour were not selected a priori but rather calibrated considering the specific features of each masonry infill typology, defined according to the numerical modelling validation recently carried out by Mucedero *et al.* [37]. More details on the numerical modelling approach and validation of the response of both bare and masonry infilled RC frames using experimental testing results are provided in [37].

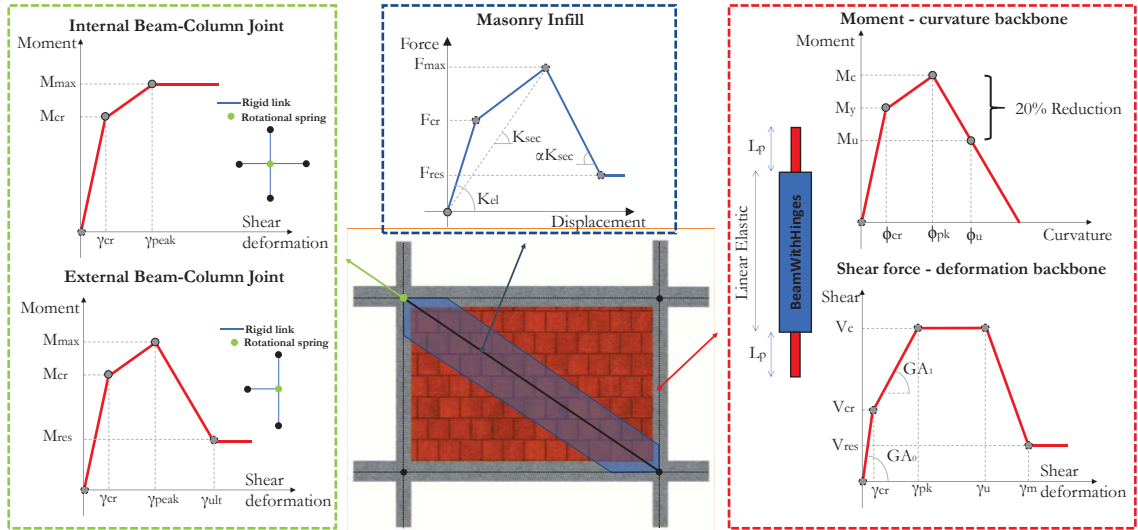


Figure 2: Numerical modelling of RC members, beam-column joints and masonry infills.

3.3 Seismic Hazard modelling and ground motion Record Selection

The OpenQuake [53] software was used to perform the seismic hazard computations, adopting the SHARE Project [54] source model and the GMPE proposed by Boore & Atkinson [55]. The hazard curve corresponding to the average spectral acceleration (AvgSa), the chosen intensity measure (IM), for the period range 0.01-2.0 s for the city of L'Aquila (Italy) was derived and, accordingly, a total of 30 pairs of ground motion records were selected, for each IM level, from the PEER NGA-West database [56]. Two IM levels were selected according to the limit states defined in [57], namely Serviceability Limit State (SLS) and Life Safety Limit State (LSLS), corresponding to return periods (T_r) of 50 and 475 years, respectively. Figure 3 illustrates the two target spectra and the corresponding empirically derived conditional spectra (CS) of the selected record ensembles based on CS(AvgSa). It is worth mentioning that the two presented limit states are of paramount importance in the Italian “Guidelines for the seismic risk classification of constructions,” in which technical principles for exploiting tax deductions with respect to seismic strengthening interventions on existing buildings (Sismabonus) have been defined [58].

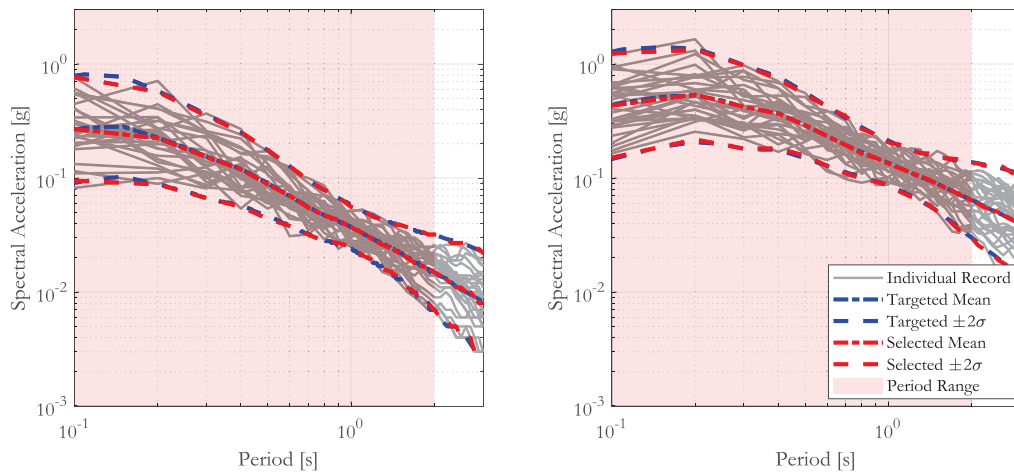


Figure 3: Comparison between the two target spectra and the corresponding empirically derived conditional spectra of the selected record ensembles based on CS(AvgSa): (left) Serviceability Limit State (SLS) and (right) Life Safety Limit State (LSLS)

4 DERIVATION OF FLOOR RESPONSE SPECTRA

The results of NLTHAs of the 2D frame buildings were used to derive absolute acceleration FRS (AFRS). The 5%-damped AFRS were evaluated by subjecting the building portfolio to the selected set of ground motions and then using numerical techniques to compute the FRS from floor acceleration time-histories recorded along the structure's height, for the two structural configurations (i.e. bare and infilled frames). For the sake of brevity, only the AFRS of the first and roof storeys, for the two selected IM levels, are presented; in the case of the one-storey RC frames, the AFRS are not plotted for the first storey because the first and roof storeys coincide.

4.1 Bare frames

Figure 4 plots the AFRS for the bare frames for the SLS return period. The dynamic properties of the RC frames in the case-study building portfolio are comprehensively presented in [22], in particular, the median, 16th and 84th percentile of the first elastic period of vibration (T_1). For the complete building portfolio, T_1 varies in the range of [0.44-1.99 s]. For each plot in Figure 4, the median acceleration floor response spectra (MAFRS) taken across the ground motions ensemble are presented in bold, while the grey-filled area represents the envelope defined by the 16th and 84th percentiles, representing both the record-to-record variability and the geometrical layout variability.

Analysing the first storey AFRS (Figure 4a), it is possible to observe that the floor spectral acceleration (S_a) in correspondence of higher modes is governing the response, except for the two-storey buildings, in which S_a at the fundamental period is still relevant. As regards the AFRS at the roof level (Figure 4b), one-storey buildings are characterised by a single peak that lies at a period close to the fundamental period of the structure, whereas when increasing the number of storeys, the higher modes have a significant impact on the shape of MAFRS. In the MAFRS, the S_a values are higher in correspondence of higher modes, except for the two-storey buildings for which S_a at the fundamental period is still higher than the ones due to the higher modes. For three- to six-storey buildings, the shape of the MAFRS is quite similar and the peaks are less pronounced. For all the buildings, for periods longer than the fundamental period, the S_a tends to reduce and it is close to zero for long periods. For both first and roof levels the record-to-record-related variability and the geometrical layout variability is low and quite similar when varying the number of storeys, as would be somehow expected for such a low return period.

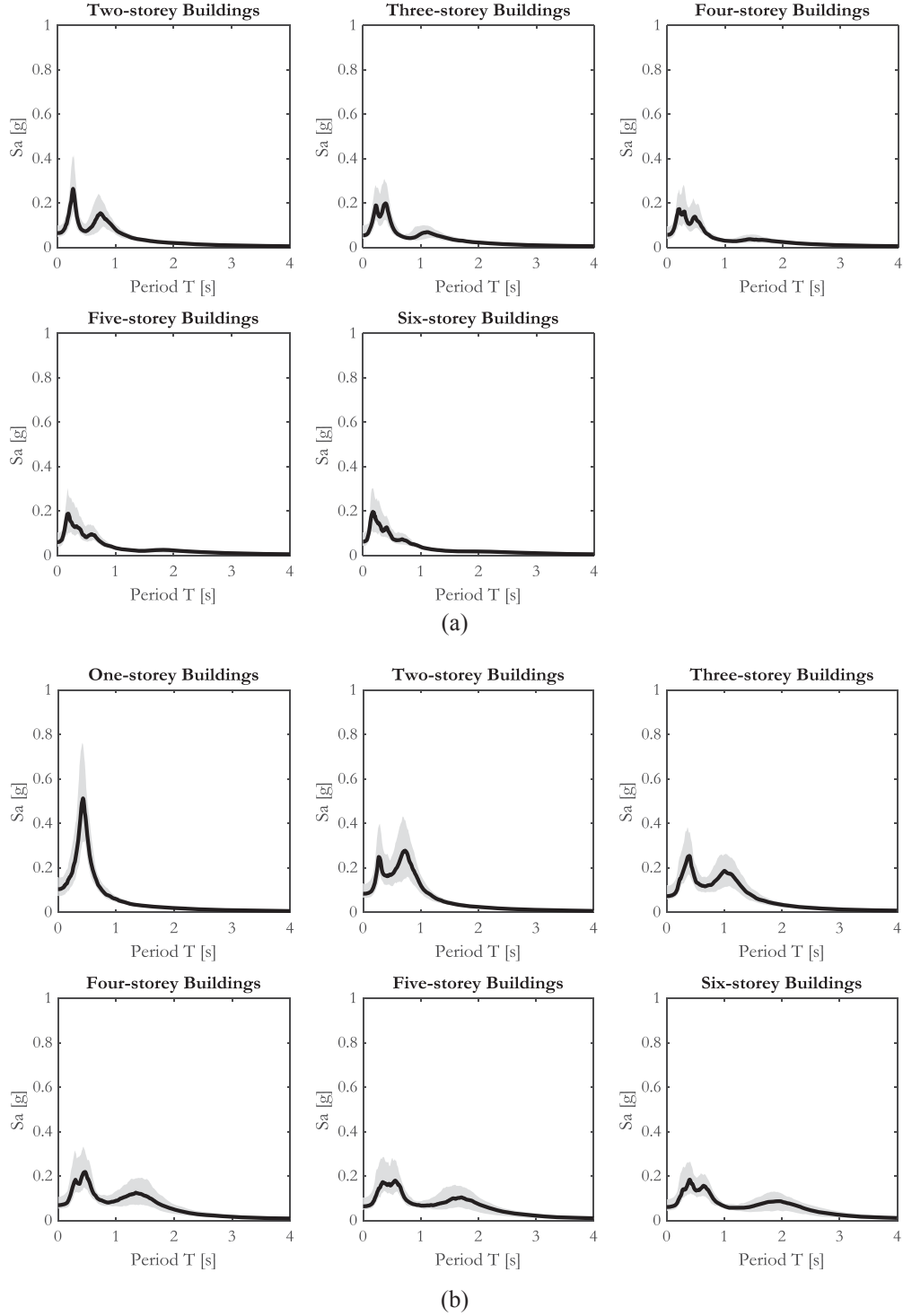
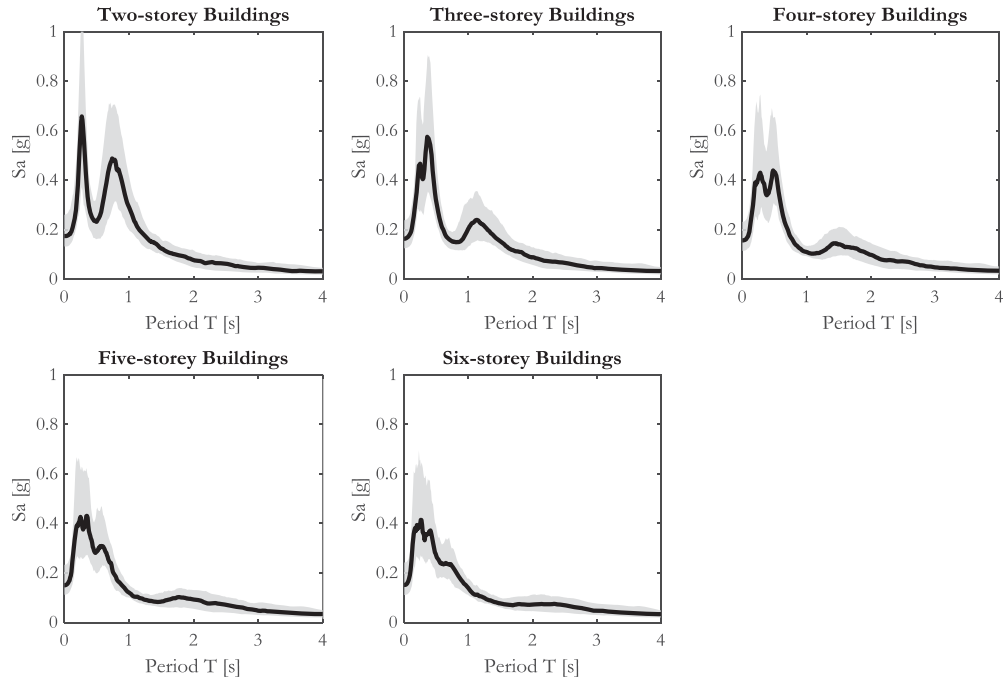


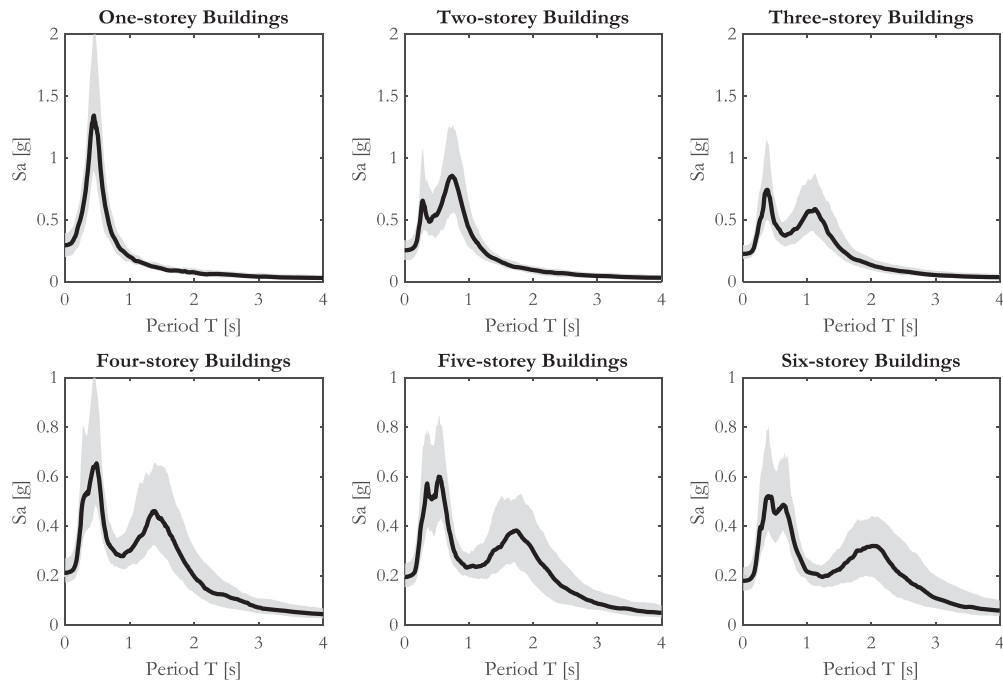
Figure 4: Acceleration floor response spectra, $\xi=5\%$, at (a) first level and (b) roof level for the bare frame structural typology at SLS ($T_r = 50$ years). Median values (black line), envelope (grey-filled area) of 16th and 84th percentile of AFRS over the entire building portfolio, by aggregating the IDs.

Increasing the ground motion IM level, considerations similar to those reported for the SLS can be made (see Figure 5), albeit the surrounding variability is higher. As expected, the amplitudes of S_a significantly increase, whereas the MAFRS shape is almost unaffected. Also, for LSLs, the MAFRS of the five- and six-storey buildings at the roof level exhibit a smoother shape with a plateau in correspondence of the higher modes, in contrast to the other

configurations, for which a well-defined peak is obtained. The large influence of the higher modes is the consequence of the long fundamental periods associated with the bare configurations, in particular for RC frames with more than three storeys.



(a)



(b)

Figure 5: Acceleration floor response spectra, $\xi=5\%$, at (a) first level and (b) roof level for the bare frame structural typology at SLSL ($T_r = 475$ years). Median values (black line), envelope (grey filled area) of 16th and 84th percentile of AFRS over the entire building portfolio, by aggregating the IDs.

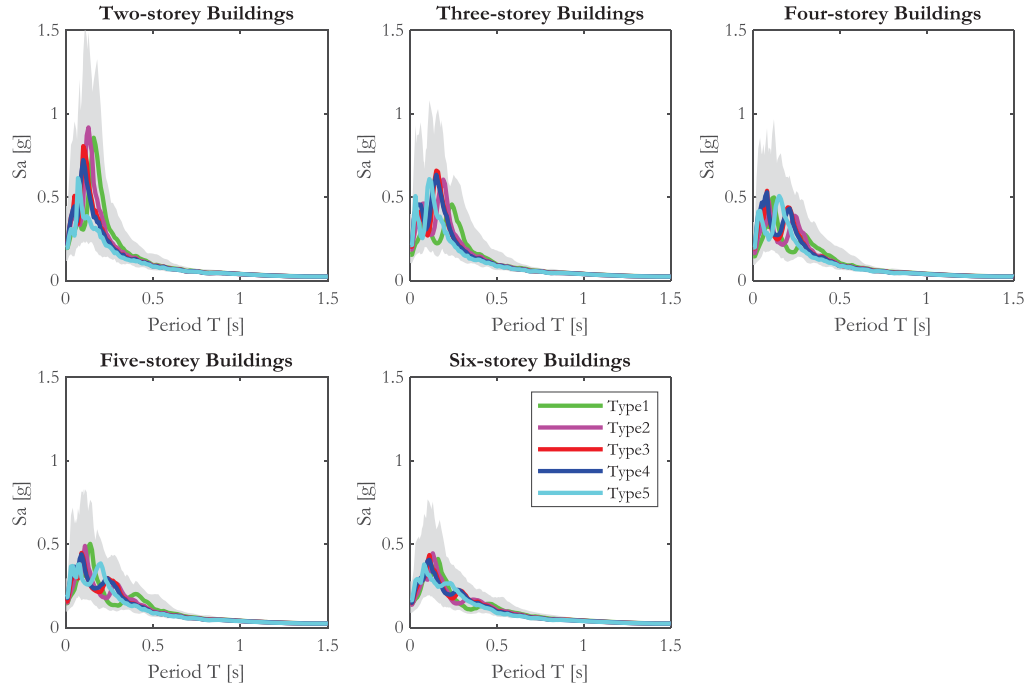
4.2 Infilled frames

For what concerns the AFRS for the infilled configurations, the macro-level distinction of the infills in terms of shear strength, based on the results provided in Mucedero *et al.* [22], is used. The results of the eigenvalue analyses carried out to characterise the dynamic properties of the case-study building portfolio, as well as the variability due to different typologies of masonry infills, are comprehensively presented in [22], through median, 16th and 84th percentiles of the first elastic period of vibration, T_1 . This period varies in the range [0.04-0.075 s] and [0.194-0.374 s] for single-storey and six-storey buildings, respectively. This highlights the significant impact of the masonry infills and their variability on the fundamental period of the case-study RC frames. Figures 6 and 7 plot the MAFRS and the area defined by the 16th and 84th percentiles for the first (Figures 6a and 7a) and roof (Figure 6b and 7b) levels, considering both seismic intensity levels (SLS in Figure 6 and SLSL in Figure 7). The MAFRS are reported for all considered masonry infill typologies. In contrast to Figure 4, the grey-filled areas in Figure 6 and Figure 7 are representative of the record-to-record variability, the geometry variability and the variability due to the masonry infill typology.

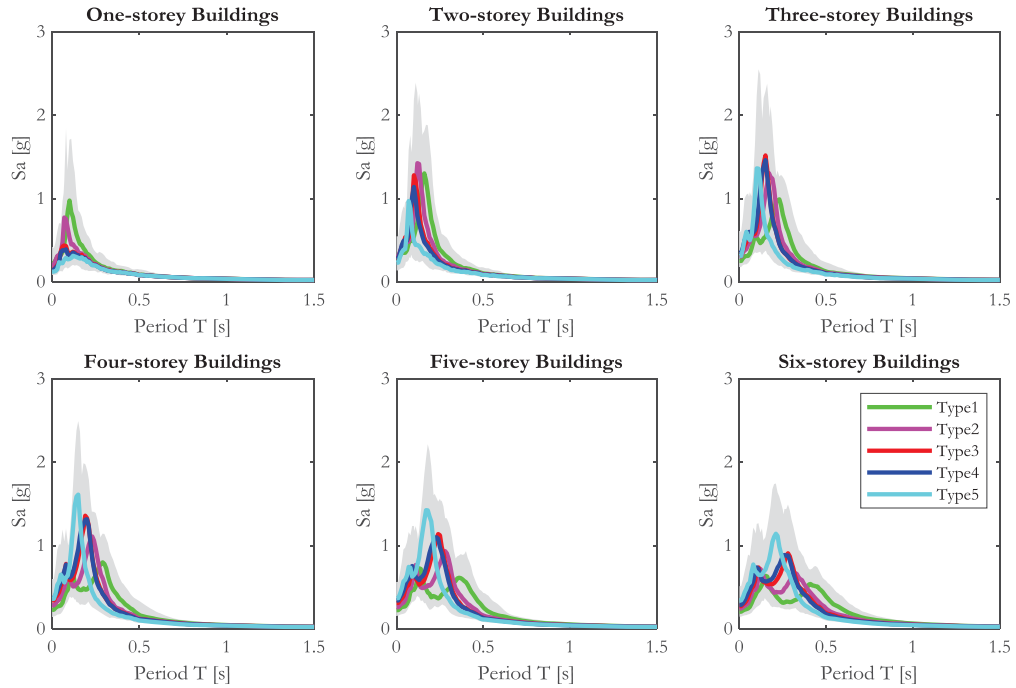
Looking at the first-storey AFRS (Figure 6a), the S_a values in correspondence of the higher modes are well evident, exception made for the two- and three-storey buildings, in which S_a at the fundamental period is also relevant. The impact of different masonry infill typologies is quite evident for low-rise buildings, whereas, for taller buildings, the AFRS at the first storey are less affected by the masonry infill typology, resulting in more similar trends and comparable values. Considering the AFRS at the roof level (Figure 6b), the influence of higher modes, in terms of maximum S_a , is reduced with respect to the AFRS at the first storey, whereas the higher S_a values are close to T_1 . Moreover, the differences coming from the masonry infill typology are more remarkable. For lower buildings, the higher S_a values are due to the weak and weak-to-medium masonry infills, whereas increasing the number of storeys, this trend is reversed, with the higher S_a values observed for the medium-to-strong and strong masonry infills.

In both cases, the envelope of the 16th and 84th percentiles, is quite wide; the differences of median MAFRS values, as a function of the masonry infill typology, are higher at the roof level than those at the first storey. For instance, considering the four-storey buildings, when changing infill type 5 to infill type 1, the median values of MAFRS at first storey decrease of only 4%, whereas the decrease is close to 50% when the roof-level MAFRS are taken as reference.

Moreover, considering the six-storey buildings, the peak value of MAFRS at roof level decreases of almost 44%, when comparing infill type 5 (strong) with infill type 1 (weak). This trend is quite similar also in case of four- and five-storey buildings, with the peak value of MAFRS that decreases of almost 48÷50%, when comparing the aforementioned infill typologies. For three-storey buildings, the MAFRS decreases of almost 27%, changing infill type 5 to infill type 1. The trend is reversed for lower buildings: for one- and two-storey buildings, comparing infill type 1 with infill type 5, the MAFRS ordinates decrease of almost 68% and 26%, respectively. The median S_a , as a function of the considered masonry infills, is in the range of [0.37÷0.85g] and [0.3÷1.61g] for AFRS at first and roof levels, respectively.



(a)



(b)

Figure 6: Acceleration floor response spectra, $\xi=5\%$, at (a) first level and (b) roof level for the infilled frame structural typology at SLS ($T_r = 50$ years). Median values of FRS for each infill typology over the entire buildings, by aggregating all the IDs, and envelope (grey-filled area) of 16th and 84th percentile for each infill typology.

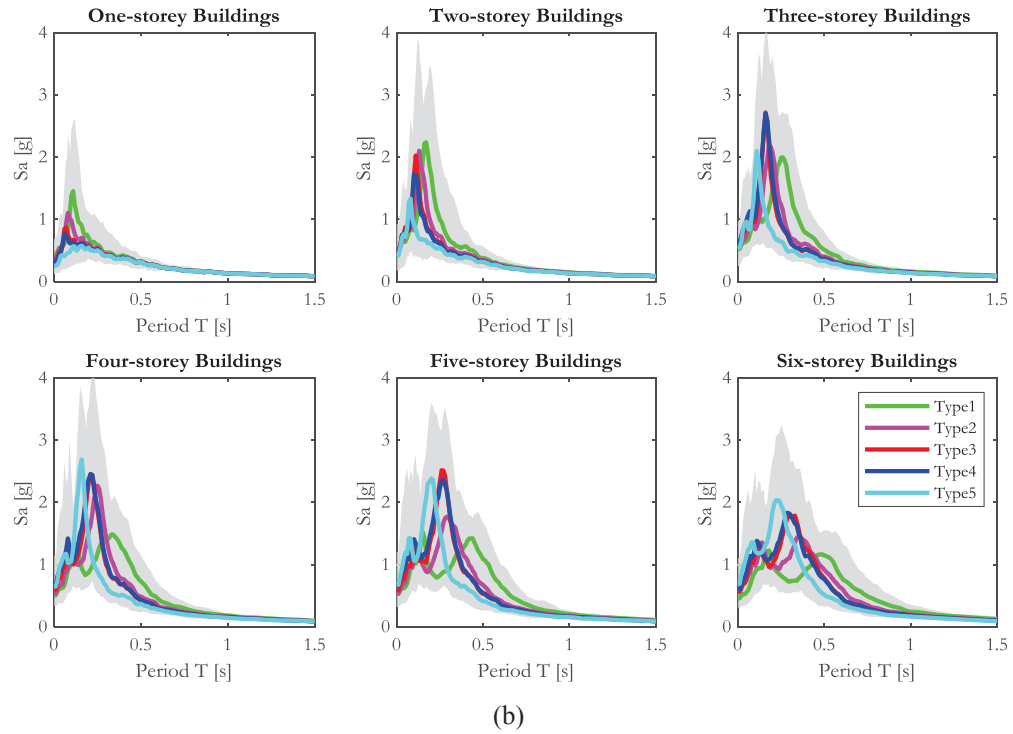
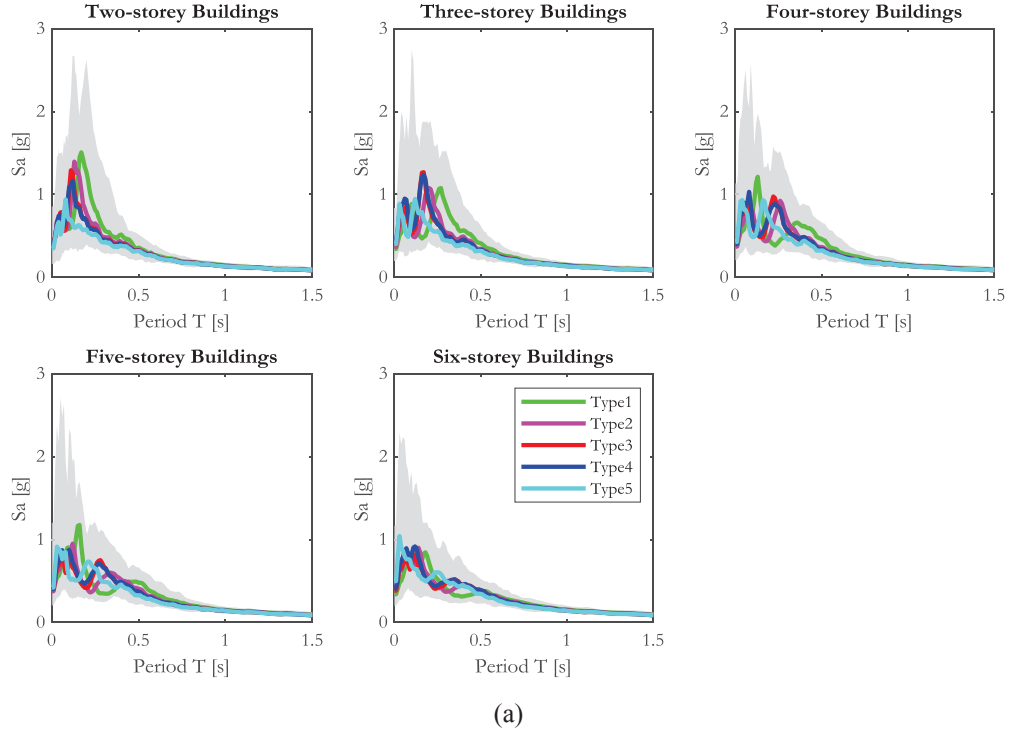


Figure 7: Acceleration floor response spectra, $\xi=5\%$, at (a) first level and (b) roof level for the infilled frame structural typology at SLSL ($T_r = 475$ years). Median values of FRS for each infill typology over the entire building portfolio, by aggregating all the IDs, and envelope (grey-filled area) of 16th and 84th percentile for each infill typology.

Regarding the AFRS at LSLs (Figure 7), with respect to the results at SLS, no significant changes are observed in terms of AFRS shape. As expected, the median S_a values are higher than those at the SLS. Also for the LSLs, the impact of masonry infill properties is less significant for the AFRS at first storey, except for one- and two-storey RC frames, while it is

significant at roof level. Also in this case, for lower-rise buildings, the higher values of the S_a are due to weak and weak-to-medium masonry infills, whereas for taller buildings the trend is reversed, with the higher values generated by medium-to-strong and strong masonry infills. The median S_a , as a function of infill typology, is in the range of $[0.91 \div 1.51g]$ and $[0.57 \div 2.69g]$, respectively, for AFRS at first and roof level. Moreover, as regards the envelope of the 16th and 84th percentiles, the variability is quite different as a function of the period of the NSEs considered. Given three different periods T and considering the AFRS recorded at roof level for the SLSL, the maximum differences between the 16th and 84th percentiles are in the following ranges: (i) $[0.74 \div 3.02g]$ for $S_a(T=0.2s)$, (ii) $[0.19 \div 1.4g]$ for $S_a(T=0.5s)$, and (iii) $[0.007 \div 0.23g]$ for $S_a(T=1.0s)$. This variability also increases with the number of storeys, particularly for the shorter periods.

Considering the six-storey buildings, the peak value of MAFRS at the roof level decreases of almost 43%, when comparing infill type 5 (strong) with infill type 1 (weak). This trend is quite similar also in the case of four- and five-storey buildings, with peak values of MAFRS that decrease almost 40÷44%, when comparing infill type 5 with infill type 1. For three-storey buildings, the MAFRS peak decreases of around 5%, going from infill type 5 to infill type 1. Conversely, for lower buildings (one- and two-storey buildings), when changing infill type 1 to infill type 5, the MAFRS peak decreases of almost 60% and 40%, respectively. Regardless of the LS considered, for both first and roof storeys, the variability surrounding the MAFRS is quite significant. Additionally, regardless of the IM investigated, the variability due to masonry infills' properties is less significant for periods longer than 1 s.

4.3 Comparison of MAFRS for bare and infilled frame configurations

For completeness, and to further highlight the differences in the shape and on the S_a intensity at different periods between the two structural configurations, the results of MAFRS for infilled and bare frames are compared herein. Figure 8 illustrates the 5%-damped MAFRS at the first and roof levels for SLSL, for both structural configurations. Regardless of the selected masonry infill type, the shape of the FRS for the infilled frames is quite different from the ones derived for the bare frame configurations. The S_a peaks are in the range of $0 \div 0.5$ [s] in the case of infilled frames, whereas in case of bare frames, due to a longer first elastic period, the S_a peaks are not restricted to a limited range of periods but are rather associated with a wider period range of $0.2 \div 2$ [s]. Moreover, it is noteworthy that for the bare frame's portfolio analysed, the S_a peaks, due to higher mode effects, are in the range of $0 \div 0.7$ [s], depending on the number of storeys. In the latter range, the S_a intensity of the bare frame configuration is lower than the one of the infilled frame configurations for the vast majority of cases.

As regards the S_a at different periods, a quite relevant impact of the masonry infills on the AFRS is observed, especially until 0.5 s, whereas for higher periods the S_a of bare frames are most often higher than those of the infilled frames. There are some expected implications of such differences in terms of seismic risk, at both single-building and portfolio scale. For instance, if for an infilled frame the acceleration sensitive non-structural components are characterised by a period of vibration in the range of $0 \div 0.5$ [s], the seismic demand in terms of acceleration on those components would be completely different and much higher than that derived from a bare frame configuration. Moreover, since the simplified methods available in the literature do not account for the presence of masonry infills, the impact of the latter on the shape and on the S_a magnitude itself could be underestimated, even significantly, in comparison with NLTHA-driven counterparts.

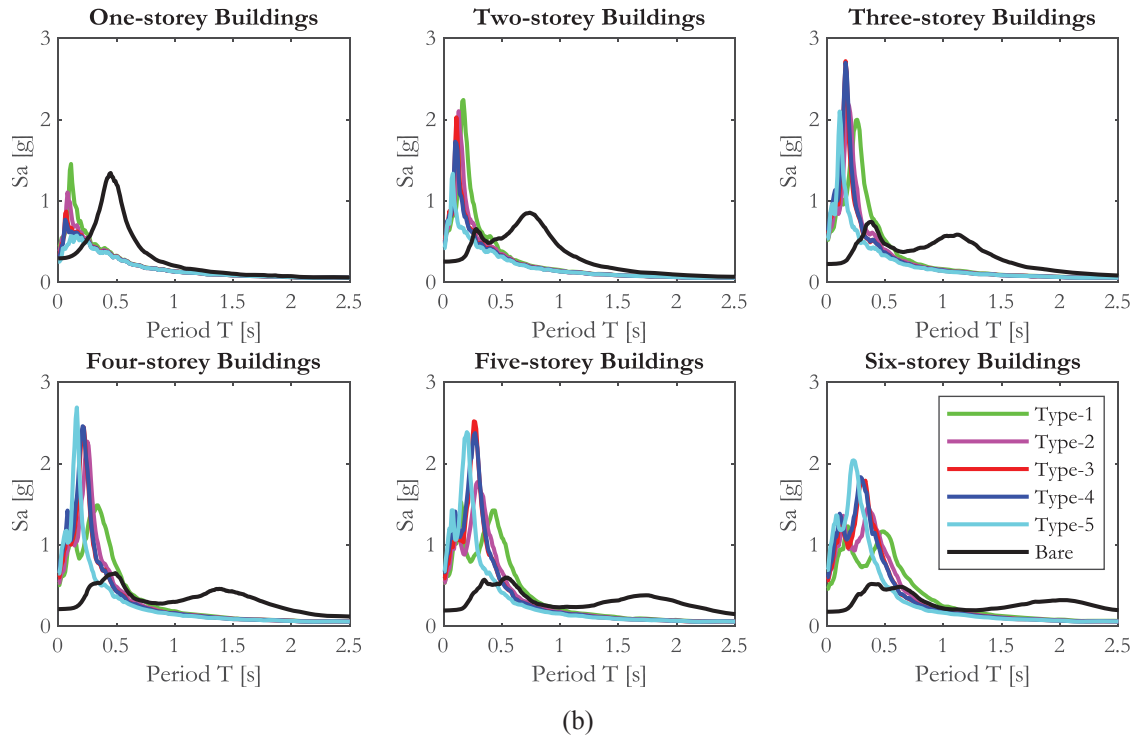
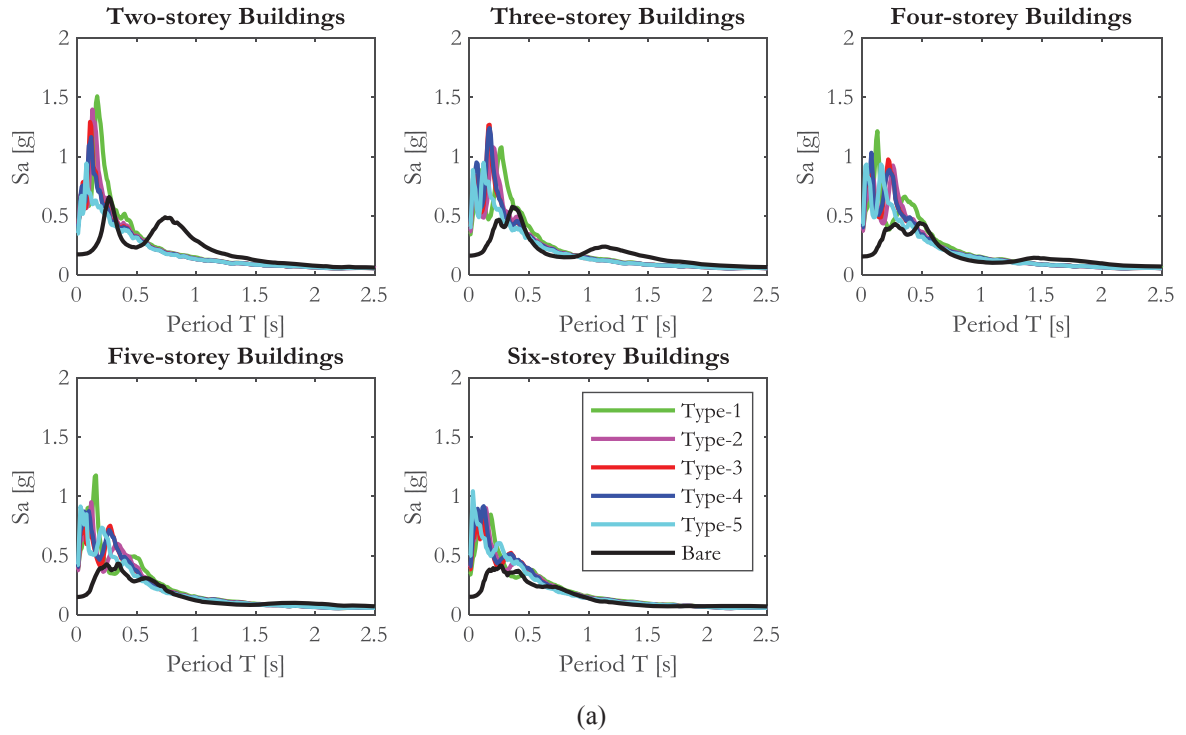


Figure 8:MAFRS for both infilled and bare frame structural typology, $\xi=5\%$, at (a) first level and (b) roof level for SLSL.

5 CONCLUSIONS

Significant efforts have been made in the recent past to investigate the influence of masonry infills on the seismic performance of existing RC buildings. However, less attention has been paid to the evaluation of the role of their variability on peak floor accelerations and floor response spectra. To address this gap, this study investigates the influence of different typologies of masonry infills on the acceleration floor response spectra (AFRS), as well as the differences in terms of S_a intensity and shape of AFRS between infilled and bare frames. In particular, a macro-level distinction of masonry infills that defines five typologies, representative of the infill properties commonly adopted in the European context, has been used.

The results of this study quantitatively pointed out how the seismic demand to which the NSEs are subjected is significantly affected by the interaction of the masonry infills with the surrounding RC frames and by the variability in their mechanical properties. Neglecting the masonry infills in the numerical modelling should therefore be avoided, paying careful attention to the structural details of the analysed building (i.e. masonry infills connected or disconnected to surrounding frame). The AFRS have been compared in detail for two different storeys and considering two seismic intensity levels. The floor spectral accelerations (S_a) recorded in the infilled frames are significantly higher than those observed in the bare frames, for both considered storey levels and seismic intensities. In terms of AFRS shape, the ones for bare frame are generally smoother, while in the infilled frames the S_a peaks that lay at the fundamental periods of the RC frames are more evident. The impact of the variability in the masonry infills is evident, although different trends are observed for low-rise and medium-rise buildings. In particular, for lower buildings, the higher S_a values are due to weak and weak-to-medium masonry infills, whereas for taller buildings the trend is reversed, with the higher values generated by medium-to-strong and strong masonry infills.

These results can be used, for instance, to correctly define the seismic demand imposed on NSEs and, consequently, to realistically perform the design or assess expected annual losses. Moreover, this study further demonstrates that the variability related to the masonry infills induces significant dispersion on the AFRS and sheds light into how neglecting the masonry infill variability can be highly misleading and lead to results that are not realistic, particularly for seismic demand on NSEs in regional-scale frameworks. Although some simplified methods are available in the literature and codes to predict the FRS of RC buildings, the influence of masonry infills, which are typically present in the Italian and European building portfolios, has not yet been comprehensively accounted for. For this reason, it is evident that further efforts are still required to improve such simplified methodologies.

REFERENCES

- [1] D. Perrone, P.M. Calvi, R. Nascimbene, E.C. Fischer, G. Magliulo, Seismic performance of non-structural elements during the 2016 central Italy earthquake. *Bull Earthquake Eng* 2018. <https://doi.org/10.1007/s10518-018-0361-5>.
- [2] G.J. O'Reilly, D. Perrone, M. Fox, R. Monteiro, A. Filiatrault, Seismic assessment and loss estimation of existing school buildings in Italy. *Eng Struct* 2018;168(1):142–62.
- [3] R. Villaverde, Seismic design of secondary structures: state of the art. *J Struct Eng* 1997;123(8):1011–9.

- [4] E. Miranda, S. Taghavi, Estimation of Seismic Demands on Acceleration-sensitive Nonstructural Components in Critical Facilities, Proceedings of the Seminar on Seismic Design, Performance, and Retrofit of Nonstructural Components in Critical Facilities, ATC 29-2, Newport Beach, CA, 347-360 2003.
- [5] C. Del Vecchio, M.D. Ludovico, A. Prota, Repair costs of reinforced concrete building components: from actual data analysis to calibrated consequence functions. *Earthquake Spectra*. 2020;36(1):353-377. doi:10.1177/8755293019878194
- [6] P. Ricci, F. De Luca, G.M. Verderame, L'Aquila earthquake, Italy: reinforced concrete building performance. *Bull Earthq Eng* 2011;8:285-305.
- [7] A. Belleri, E. Brunesi, R. Nascimbene, M. Pagani, P. Riva, Seismic performance of precast industrial facilities following major earthquakes in the Italian territory. *J Performance Construct Facility ASCE* 2015;29(5):04014135.
- [8] W. Salvatore, S. Caprili, V. Barberi, Rapporto dei danni provocati dall'evento sismico del 6 Aprile sugli edifici scolastici del centro storico dell'Aquila, available online: <http://www.reluis.it/>; 2009.
- [9] CEN, Eurocode 8 – Design provisions for earthquake resistant structures, EN-1998-1:2004, Comité Européen de Normalization, Brussels, Belgium.
- [10] ASCE, Minimum design loads for buildings and other structures, ASCE/SEI Standard 7-10, American Society of civil engineers, Reston.
- [11] C. Petrone, G. Magliulo, G. Manfredi, Seismic demand on light acceleration-sensitive nonstructural components in European reinforced concrete buildings. *Earthquake Eng Struct Dyn* 2015;8(10):1203-17.
- [12] T.J. Sullivan, P.M. Calvi, R. Nascimbene, Towards improved floor spectra estimates for seismic design. *Earthquakes Struct* 2013;4(1):109-32.
- [13] D.P. Welch, T.J. Sullivan, Illustration a new possibility for the estimation of floor spectra in nonlinear multi-degree of freedom systems, 16th World Conference on Earthquake Engineering, Santiago, Chile, 9-13 January 2017, Paper N°2632.
- [14] P.M. Calvi, T.J. Sullivan Estimating floor spectra in multiple degree of freedom systems. *Earthquake Struct* 2014;7(1):17-38.
- [15] V. Vukobratovic, P. Fajfar, A method for the direct estimation of floor acceleration spectra for elastic and inelastic MDOF structures. *Earthquake Eng Struct Dyn* 2016;45(15):2495-511.
- [16] P.M. Calvi Relative displacement floor spectra for seismic design of non structural elements. *J Earthquake Eng* 2014;18(7):1037-59.
- [17] R. Merino, D. Perrone, A. Filiatrault (2020) "Consistent floor response spectra for performance-based seismic design of non-structural elements". *Earthquake Engineering and Structural Dynamics*, 49(3), 261-284, <https://doi.org/10.1002/eqe.3236>
- [18] A. Filiatrault, D. Perrone, R. Merino, G.M. Calvi Performance-Based Seismic Design of Non-Structural Building Elements. *J Earthquake Eng* 2018. <https://doi.org/10.1080/13632469.2018.1512910>.
- [19] A. Lucchini, F. Mollaioli., P. Bazzurro Floor response spectra for bare and infilled reinforced concrete frames. *J Earthquake Eng* 2014;18(7):1060-82.

- [20] M. Surana, M. Pisode, Y. Singh, D.H. Lang, Effect of URM infills on inelastic floor response of RC frame buildings. *Eng Struct* 2018;175:861–78.
- [21] D. Perrone, E. Brunesi, A. Filiatrault, R. Nascimbene, Probabilistic estimation of floor response spectra in masonry infilled reinforced concrete building portfolio, *Engineering Structures*, 20, 109842, <https://doi.org/10.1016/j.engstruct.2019.109842>
- [22] G. Mucedero, D. Perrone, R. Monteiro, Nonlinear static characterisation of masonry-infilled RC building portfolios accounting for variability of infill properties. *Bull Earthquake Eng* 19, 2597–2641 (2021). <https://doi.org/10.1007/s10518-021-01068-2>
- [23] <http://dati-censimentopopolazione.istat.it/Index.aspx>
- [24] F. De Luca, E. Morciano, D. Perrone, Aiello M.A., MID1.0: Masonry Infilled RC Frame Experimental Database. In: di Prisco M, Menegotto M (eds) *Proceedings of Italian Concrete Days 2016. ICD 2016. Lecture Notes in Civil Engineering*, vol 10. Springer, Cham.
- [25] K. Sassun, T.J. Sullivan, P. Morandi, D. Cardone, Characterising the In-Plane Seismic Performance of Infill Masonry. *Bulletin of the New Zealand Society for Earthquake Engineering*.
- [26] M.T. De Risi, C. Del Gaudio, P. Ricci, G.M. Verderame, In-plane behaviour and damage assessment of masonry infills with hollow clay bricks in RC frames. *Eng Struct* 168:257–275,2018.
- [27] <https://www.google.com/maps>
- [28] G.M. Verderame, P. Ricci, M. Esposito, F.C. Sansiviero, Le caratteristiche meccaniche degli acciai impiegati nelle strutture in c.a. realizzate dal 1950 al 1980. *Atti del XXVI Convegno Nazionale AICAP Le prospettive di sviluppo delle opere in calcestruzzo strutturale nel terzo millennio (in Italian)*, Padua, Italy, 2011.
- [29] A. Masi, A. Digrisolo, G. Santarsiero, Concrete strength variability in Italian RC buildings: Analysis of a large database of core tests. *Appl. Mech. Mater.*, 597, 283–290, 2014
- [30] D. Celarec, P. Ricci, M. Dolšek, The sensitivity of seismic response parameters to the uncertain modelling variables of masonry-infilled reinforced concrete frames. *Engineering Structures*, Vol. 35, pp. 165–177, 2012.
- [31] M. Dolšek, Simplified method for seismic risk assessment of buildings with consideration of aleatory and epistemic uncertainty. *Structure and Infrastructure Engineering: Maintenance, Management, Life-Cycle Design and Performance*, Vol. 8, No.10, pp. 939–953, 2012.
- [32] A.F. Mohammad, M. Faggella, R. Gigliotti, E. Spacone, Probabilistic seismic response sensitivity of nonlinear frame bending-shear and infill model parameters for an existing infilled reinforced concrete structure. In: *Proceedings of the Twelfth International Conference on Computational Structures Technology* B.H.V. Topping and P. Iványi, (Editors), Civil-Comp Press, Stirlingshire, Scotland, 2014.
- [33] G.M. Calvi, D. Bolognini, Seismic response of RC frames infilled with weakly reinforced masonry panels. *Journal of Earthquake Engineering*, 5(02), 153-85, 2001.

- [34] P. Morandi, S. Hak, G. Magenes, Performance-based interpretation of in-plane cyclic tests on RC frames with strong masonry infills. *Engineering Structures*, 156, 503–521,2018.
- [35] L. Cavaleri, F. Di Trapani, Cyclic response of masonry infilled RC frames: Experimental results and simplified modeling. *Soil Dynamics and Earthquake Engineering*, 65, 224-242,2014.
- [36] S. Hak, P. Morandi, G. Magenes, T.J Sullivan, Damage control for clay masonry infills in the design of RC frame structures. *Journal of Earthquake Engineering*, 16(S1), 1-35,2012.
- [37] G. Mucedero, D. Perrone, E. Brunesi, R. Monteiro, Numerical Modelling and Validation of the Response of Masonry Infilled RC Frames Using Experimental Testing Results. *Buildings* 10:182,2020
- [38] G. Blasi, D. Perrone, M.A. Aiello, Fragility functions and floor spectra of RC masonry infilled frames: influence of mechanical properties of masonry infills”. *Bulletin of Earthquake Engineering*, 16: 6105-6130,2018, <https://doi.org/10.1007/s10518-018-0435-4>
- [39] Ministerial Decree (D.M. 30/05/1972): Design code of reinforced concrete, prestressed concrete and steel structures, (in Italian).
- [40] Ministerial Decree (D.M. 05/07/1975) Amendments to ministerial instructions June 20, 1896, relating to the minimum height and to the main sanitation requirements of the living quarters, (in Italian).
- [41] I.E. Bal, H. Crowley, R. Pinho, G. Gulay, Structural characteristics of Turkish building stock in Northern Marmara Region for Loss Assessment Applications. ROSE Research Report 2007/03, IUSS Press,Pavia, Italy.
- [42] V. Silva, H. Crowley, H. Varum, R. Pinho, L. Sousa, Investigation of the characteristics of Portuguese regular moment-frame RC buildings and development of a vulnerability model,2014.
- [43] G.J. O'Reilly, T.J. Sullivan, Modeling techniques for the seismic assessment of the existing Italian RC Frame Structures. *Journal of Earthquake Engineering*, DOI: 10.1080/13632469.2017.1360224. *Bulletin of Earthquake Engineering*, 13(5),1-36,2017.
- [44] D. Perrone, G.J. O'Reilly, R. Monteiro, A. Filiatrault, Assessing seismic risk in typical Italian school buildings: from in-situ survey to loss estimation. *International Journal Disaster Risk Reduction* 44:101448,2020.
- [45] F. McKenna, G. Fenves, F.C. Filippou, S. Mazzoni (2000) Open system for earthquake engineering simulation (OpenSees), http://opensees.berkeley.edu/wiki/index.php/Main_Page
- [46] M.H. Scott, G.L. Fenves (2006) Plastic hinge integration methods for force-based beam–column elements. *ASCE Journal of Structural Engineering*, Vol. 132, No. 2, 244-252.
- [47] G.J. O'Reilly, Performance-Based Seismic Assessment and Retrofit of Existing RC Frame Buildings in Italy, PhD Thesis, IUSS Pavia, Italy,2016.
- [48] D.K. Zimos, P.E. Mergos, A.J. Kappos, Shear hysteresis model for reinforced concrete elements including the post-peak range. *COMPdyn 2015-5th ECCOMAS Thematic*

- Conference on Computational Methods in Structural Dynamics and Earthquake Engineering, Crete Island, Greece, 2015.
- [49] S. Pampanin, G. Magenes, A. Carr, Modelling of shear hinge mechanism in poorly detailed RC beam column joints. *Concrete Structures in Seismic Regions*, Athens, Greece, 2003.
- [50] F. Braga, R. Gigliotti, M. Laterza, R/C Existing Structures with Smooth Reinforcing Bars: Experimental Behaviour of Beam-Column Joints Subject to Cyclic Lateral Loads. *Open Constr. Build. Technol. J.*, 3, 52–67, 2009
- [51] J. Melo, H. Varum, T. Rossetto, A. Costa, Cyclic response of RC beam-column joints reinforced with plain bars: An experimental testing campaign. In *Proceedings of the 15th World Conference on Earthquake Engineering*, Lisbon, Portugal, 24–28 September 2012.
- [52] C. Beschi, P. Riva, G. Metelli, A. Meda, HPFRC Jacketing of Non Seismically Detailed RC Corner Joints. *J. Earth. Eng.*, 19, 25–47, 2014
- [53] D. Monelli, M. Pagani, G. Weatherill, V. Silva, H. Crowley, The hazard component of OpenQuake: The calculation engine of the Global Earthquake Model. *15th World Conference on Earthquake Engineering*, Lisbon, Portugal, 2012
- [54] Giardini D. et al., Seismic Hazard Harmonization in Europe (SHARE). Online data resource, Swiss Seismological Service, 2013: p. ETH Zurich, Zurich, Switzerland, [<http://www.efehr.org:8080/jetspeed/>].
- [55] D.M. Boore, G.M. Atkinson, Ground-motion prediction equations for the average horizontal component of PGA, PGV, and 5%-Damped PSA at spectral periods between 0.01 s and 10.0 s. *Earthquake Spectra*, 24 (1), 99–138, 2008.
- [56] PEER 2013/03 – PEER NGA-West2 Database by Timothy D. Ancheta, Robert B. Darragh, Jonathan P. Stewart, Emel Seyhan, Walter J. Silva, Brian S.J. Chiou, Katie E. Wooddell, Robert W. Graves, Albert R. Kottke, David M. Boore, Tadahiro Kishida, and Jennifer L. Donahue
- [57] Ministry Decree n.58 28/02/2017 Allegato A: linee guida per la classificazione del rischio sismico delle costruzioni (in Italian). Italian Ministry of Infrastructures and Transport, Italy. <http://www.mit.gov.it/normativa/decreto-ministeriale-numero-58-del-28022017>
- [58] E. Cosenza, C. Del Vecchio, M. Di Ludovico, et al., The Italian guidelines for seismic risk classification of constructions: technical principles and validation. *Bull Earthquake Eng* 16, 5905–5935, 2018. <https://doi.org/10.1007/s10518-018-0431-8>

EFFECT OF IN-PLANE/OUT-OF-PLANE INTERACTION IN INFILL WALLS ON THE FLOOR SPECTRA OF REINFORCED CONCRETE BUILDINGS

Mariano Di Domenico¹, Paolo Ricci¹, and Gerardo M. Verderame¹

¹ Department of Structures for Engineering and Architecture, University of Naples Federico II
Via Claudio 21 – 80125 – Naples, Italy
e-mail: {mariano.didomenico, paolo.ricci, verderam}@unina.it

Abstract

Currently, in the framework of performance-based earthquake engineering, the seismic assessment of buildings should be performed by considering the safety of non-structural components. This is necessary to protect human life safety from their collapse, as well as to limit the economic losses associated with their damage. Typically, the safety assessment of non-structural components is performed with a force-based approach, i.e., by comparing their force/acceleration capacity with the expected force/acceleration demand under the design earthquake scenario, i.e., with reference to different limit states.

Different acceleration demand models, i.e., floor response spectra, exist, but relatively few of them were defined by considering the influence on the structural response of the in-plane response of infill walls, and none of them by considering the so-called “in-plane/out-of-plane interaction” effects. In other words, it is nowadays well known that the out-of-plane damage of unreinforced masonry infills affects their in-plane response, thus influencing the seismic response (and the floor response spectra) of the supporting structure.

In this paper, non-linear time-history analyses are performed on reinforced concrete framed buildings with different number of storeys, design level, and infill wall layout. The analyses are performed on the bare structure as well as on the infilled structure by considering and by not considering the in-plane/out-of-plane interaction effects in the infill wall model. The acceleration floor spectra derived from the analyses are compared, thus investigating the potential effect of the in-plane/out-of-plane interaction effect on the expected acceleration demand acting on infill walls.

Keywords: RC structure, infill wall, out-of-plane, seismic assessment, floor spectrum.

1 INTRODUCTION

In the framework of performance-based earthquake engineering, the seismic assessment of nonstructural components is a paramount issue: in fact, most of the earthquake-induced damage to buildings and the consequent economic losses is related to the response of nonstructural elements. Nonetheless, the heavy damage of certain nonstructural components, such as infill walls, may even threaten human life safety. For these reasons, there is need for the development of robust and reliable models for the assessment of capacity and demand associated with nonstructural elements. This work is focused on the definition of the acceleration demand acting on them, i.e., on floor response spectra.

Floor response spectra are a useful tool for the assessment of the pseudo-acceleration demand acting on acceleration-sensitive nonstructural components within a linear force-based approach, which is typical of the design process of new buildings. To understand what a floor spectrum is, the simplest way is considering the usual approach to the seismic analysis of a building. It is well-known that a structure subjected to a certain earthquake, i.e., to a certain ground motion acceleration time-history, will experience a certain maximum acceleration demand which is different from the maximum acceleration demand at its base, which is also known as Peak Ground Acceleration (PGA). This occurs since the ground motion is filtered by the structure through its mass, deformability and damping properties, thus resulting in an acceleration response history of the structure different from that applied to the base and in a maximum pseudo-acceleration demand named pseudo-spectral acceleration (S_a) different from PGA. The S_a acting on a certain structure represented by an equivalent Single Degree of Freedom (SDOF) system characterized by vibration period T and damping ratio ξ can be simply calculated through the pseudo-acceleration response spectrum of the ground motion. Similarly, the maximum pseudo-spectral acceleration, herein identified as PSA, acting on a nonstructural component represented by an SDOF system with vibration period T_a and damping ratio ξ_a supported by a certain floor of a structure can be calculated through the pseudo-acceleration response spectrum of the acceleration time-history of the supporting floor. This pseudo-acceleration response spectrum is known as floor response spectrum.

In other words, a stiff nonstructural component (i.e., a nonstructural component with $T_a=0$) attached to a certain floor of a structure will experience a PSA equal to the maximum acceleration demand of that floor, which is named Peak Floor Acceleration (PFA) and is different from the PGA. If T_a is higher than zero, the PSA will be different from the PFA dependently on T_a and ξ_a . These concepts are summarized in Figure 1.

So, based on the above discussion, the seismic demand acting on a certain nonstructural component supported by a certain floor of the structure can be known if the PFA of that floor and the floor spectral shape are known. In addition, based on the above discussion, it is possible to define some parameters that, intuitively, are expected to have an influence on the PFA and on the spectral shape. Regarding the PFA, one can expect its dependence on the PGA value (the higher the PGA, the higher the PFA) and on the height of the specific floor considered, z , potentially normalized with respect to the total building height, H . Regarding the spectral shape, one can expect that the PSA is amplified or de-amplified with respect to the PFA, with the maximum amplification expected due to resonance of the nonstructural component and of the structure, i.e., when T_a is closer to the fundamental vibration period(s) of the supporting structure. As will be shown later in this paper, further parameters may have a paramount influence on both the PFA distribution along the building height and the floor spectral shape.

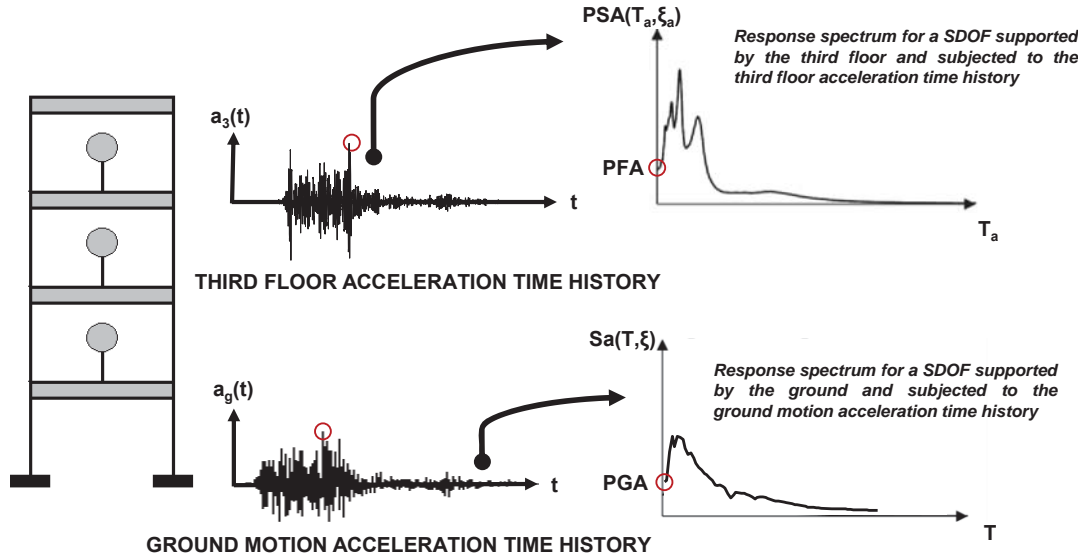


Figure 1: Concept of floor response spectrum.

In this study, the state-of-the-art of current code and literature formulations is presented, mainly to define a systematic review of the geometric and mechanical structural parameters which are expected to influence the PFA distribution along the building height and the floor spectral shape. Second, nonlinear models of bare and infilled case-study reinforced concrete framed buildings with 2, 4, 6 and 8 storeys designed for different PGA levels (0.05 g, 0.15 g, 0.25 g and 0.35 g) according to Eurocodes are defined. Then, nonlinear time history analyses are performed on the case-study buildings to evaluate floor response spectra. The numerical outcomes are compared in order to analyze the effect of the presence of infill walls on floor response spectra considering and not considering the out-of-plane response of infill walls and the mutual interaction between their in-plane and out-of-plane response (i.e., the in-plane/out-of-plane interaction). To this aim, a recent out-of-plane and in-plane/out-of-plane interaction model proposed by the Authors of this study is updated in order to account for the potential softening and cyclic degradation of the out-of-plane response of infill walls. Note that modelling the out-of-plane response of infills and the in-plane/out-of-plane interaction is a novelty element for studies dedicated to floor spectra assessment, which rarely have been dedicated to infilled buildings in general.

2 SUMMARY OF EXISTING FORMULATIONS

Several studies have been dedicated to floor response spectra in past and recent times. Comprehensive state-of-the-art reviews are proposed by Rodriguez et al. [1] and by Vukobratović [2]. In this section, for the sake of conciseness, the discussion is focused on recent practice-oriented proposals available in the literature, as well as on main code prescriptions regarding this topic.

2.1 Code proposals

Eurocode 8 [3], in section 4.3.5, proposes an expression for the PSA as shown, with some manipulation in the nomenclature, in Equation 1.

$$PSA = PGA \left[\frac{3(1 + z/H)}{1 + (1 - T_a/T_1)^2} - 0.5 \right] \quad (1)$$

In Equation 1, T_a is the non-structural element vibration period and T_1 is the fundamental vibration period of the structure. If T_a equals zero, a linear PFA distribution along the building height is obtained at varying z/H ratio. PFA ranges from PGA (at z equal to zero) to 2.5PGA (at z equal to H). On the other hand, the maximum PSA is obtained if T_a equals T_1 . In this case, the maximum PSA ranges from 2.5PGA (at z equal to zero) to 5.5PGA (at z equal to H). It should be noted that this formulation returns a maximum PSA/PFA ratio different for each floor. This will be observed also from the numerical analyses performed in this study.

ASCE/SEI 7-10 [4], in section 13.3.1, proposes an expression for the PSA as shown, with some manipulation in the nomenclature, in Equation 2.

$$PSA = PGA \left(1 + 2 \frac{z}{H} \right) a_p \quad (2)$$

In Equation 2, a_p is a factor accounting for the amplification of accelerations due to the deformability of the non-structural element reported in Table 13.5-1 of the code. It is worth noting that the American approach, with this factor, simplifies the calculation of the seismic demand acting on non-structural elements, as there is no need of a more or less detailed dynamic characterization of the nonstructural element required for the determination of its period, T_a , which enters Eurocode 8 [3] formulation. Exterior non-structural wall elements, such as unreinforced masonry infills, are associated with an a_p factor equal to 1.00.

Also according to the ASCE/SEI 7-10 [4] approach, the PFA varies linearly along the building height. It ranges from PGA (at z equal to zero) to 3PGA (at z equal to H). The maximum value of a_p reported in Table 13.5-1 of the code is equal to 2.5. Hence, the maximum possible PSA value is always equal to 2.5PFA, independently on the floor considered.

The New Zealand code NZSEE2017 [5], in section C7.6.2, refers to the loading code NZS 1170.5 [6] for the calculation of floor response spectra. NZS 1170.5 [6], in section 8.5.1, provides the formulation reported, with some manipulation in the nomenclature, in Equation 3 to calculate the PSA.

$$PSA = PGAC_{Hi}C_i(T_a) \quad (3)$$

C_{Hi} is calculated through the formulations reported in Equation 4 and defines the PFA distribution along the building height which is, in this case, multilinear. The PFA ranges from PGA (at z equal to zero) to 3PGA (at z equal to H).

$$C_{Hi} = \left(1 + \frac{z}{6} \right) \quad \text{for all } z < 12 \text{ m} \quad (4a)$$

$$C_{Hi} = \left(1 + 10 \frac{z}{H} \right) \quad \text{for } z < 0.2H \quad (4b)$$

$$C_{Hi} = 3.0 \quad \text{for } z \geq 0.2H \quad (4c)$$

In Equation 3, $C_i(T_a)$ is the spectral shape coefficient. $C_i(T_a)$ is expressed as a function of the period T_a and ranges from 0.5 for T_a higher than 1.50 s to 2.0 for T_a lower than 0.75 s. Hence, the maximum possible PSA value is always equal to 2PFA, independently on the floor considered. It is worth noting that, in this case, the maximum PSA value depends on the “absolute” value of T_a , i.e., it does not depend on T_a/T_1 ratio.

As above shown, the previous code prescriptions generally relate the PFA linear or multilinear distribution along the building height to the floor height normalized with respect to the building height (i.e., the higher z/H , the higher the PFA) and the PSA spectral shape to the ratio between the T_a and T_1 . From both these features, it can be assumed that they relate the floor response spectra to the elastic response of the structure to its first vibration mode.

The commentary (Circolare 2019, [7]) to the current Italian building code (NTC2018, [8]) defines a “rigorous” approach for the assessment of floor response spectra as well a simplified approach specific for framed reinforced concrete structures. Both account for multi-modal contributions and for the effect on floor response spectra of structural nonlinearity. In fact, structural nonlinearity limits the maximum force acting on a structure: hence, it also may limit the maximum acceleration acting at its floors. Both topics have been also highlighted in recent literature, as will be shown in the next subsection.

The rigorous approach accounts for multi-modal contributions based on simple considerations related to structural dynamics. In fact, the PFA_{ij} acting at the j -th floor of the structure associated with its i -th vibration mode is determined by means of Equation 5.

$$PFA_{ij} = \Gamma_i \varphi_{ij} S_a(T_i) \quad (5)$$

In Equation 5, Γ_i is the modal participation factor of the i -th vibration mode, φ_{ij} is the modal displacement of the j -th storey for the i -th vibration mode, $S_a(T_i)$ is the spectral acceleration of the structure associated with its i -th vibration period, potentially reduced by means of the structure behaviour factor. The PSA is obtained, for each floor and for each vibration mode contribution, by amplifying or de-amplifying the PFA through an R factor (which equals PSA_{ij}/PFA_{ij}) calculated by means of Equation 6.

$$R_{ij} = \frac{PSA_{ij}}{PFA_{ij}} = \left(\sqrt{\left(2\xi_a \frac{T_a}{T_i} \right)^2 + \left(1 - \frac{T_a}{T_i} \right)^2} \right)^{-1} \quad (6)$$

Equation 6 returns a PSA_{ij} value equal to $1/2\xi_a$ times PFA_{ij} for $T_a=T_i$. The value of the maximum amplification is a classical result of the dynamic of the damped SDOF system (Chopra [9]). For each storey, the floor spectrum can be obtained by combining multi-modal contributions through the SRSS rule, thus resulting in a spectral shape with multiple peaks corresponding to the number of significant modes considered. Implicitly, also the PFA at the j -th floor can be obtained through the SRSS combination of the different modal contributions, thus resulting in a potentially non-monotonic distribution along the building height. Both circumstances will be observed also from the analyses results presented in this study.

Regarding the PFA distribution, it is worth noting that Equation 6 may yield to a de-amplification of the PFA with respect to the PGA value, especially in bottom floors of high-rise structures. This circumstance has been observed by some authors (e.g., Rodriguez et al. [1], Petrone et al. [10], Surana et al. [11]), especially when analyzing elastic models, but not by other authors and never in the analyses performed in this study. A comment to this issue will be given in the next subsection, when describing the approach proposed by Calvi and Sullivan [12].

The simplified approach proposed by the Italian regulation for framed reinforced concrete structures is borrowed by the work by Petrone et al [10]. Since this proposal is based on numerical analyses on nonlinear models of reinforced concrete framed structures, it implicitly account

for both multi-modal contributions and structural nonlinearity effect. The proposed formulations are reported, with some manipulation in the nomenclature, in Equation 7.

$$PSA = \begin{cases} PGA \left(1 + \frac{z}{H}\right) \left[\frac{a_p}{1 + (a_p - 1) \left(1 - \frac{T_a}{aT_1}\right)^2} \right] \geq PGA & \text{for } T_a < aT_1 \\ PGA \left(1 + \frac{z}{H}\right) a_p & \text{for } aT_1 \leq T_a < bT_1 \\ PGA \left(1 + \frac{z}{H}\right) \left[\frac{a_p}{1 + (a_p - 1) \left(1 - \frac{T_a}{bT_1}\right)^2} \right] \geq PGA & \text{for } T_a \geq bT_1 \end{cases} \quad (7)$$

In Equation 7, a , b , and a_p are coefficients depending on T_1 that account for higher modes effects (a), resonance period elongation due to nonlinearity (b) and effect of nonlinearity of the maximum PSA value (a_p). If T_a equals zero, a linear PFA distribution along the building height is obtained. PFA ranges from PGA (at z equal to zero) to 2PGA (at z equal to H). On the other hand, the maximum PSA is obtained if T_a is between aT_1 and bT_1 . In this case, the floor spectral acceleration ranges from 2.5PFA to 5PFA, dependently on a_p value.

It is worth noting that none of the proposals discussed in this subsection explicitly refers to infilled buildings, as if the presence of infills may be considered only through T_1 value, i.e., as if the presence of infills only affects the resonance period at which the maximum PSA is attained, except for the simplified proposal of the Italian regulation, in which also the maximum PSA value depends on T_1 and attains its maximum potential value for small values of the period (i.e., $a_p=5$ when T_1 is lower than 0.5 s). In other words, based on this approach, an infilled building is expected to experience an equal or higher maximum PSA value, at a certain floor, with respect to an identical but bare structure. This is also generally observed in the numerical analyses shown in this paper.

2.2 Literature formulations

Calvi and Sullivan [12] propose an approach for the assessment of floor response spectra for SDOF systems extended to Multi-Degree of Freedom systems and validated against the results of numerical time-history analyses on reinforced concrete wall structures. The PSA value for each floor and for each modal contribution is calculated by means of Equation 8.

$$PSA_{ij} = \Gamma_i \varphi_{ij} a_{m,i} \quad (8)$$

In Equation 8, $a_{m,i}$ is a spectral shape function given by Equation 9.

$$a_{m,i}(T_a) = \begin{cases} \frac{T_a}{T_i} [a_{max,i}(DAF_{max} - 1) + a_{max,i}] & \text{for } T_a < T_i \\ a_{max,i} DAF_{max} & \text{for } T_i \leq T_a < T_{i,eff} \\ a_{max,i} DAF_i & \text{for } T_a \geq T_{i,eff} \end{cases} \quad (9)$$

In Equation 9, $a_{\max,i}$ is the minimum between $S_a(T_i)$ and the S_a corresponding to global yielding of the structure (S_{ay} , potentially determined by means of a nonlinear static analysis), DAF is given by Equation 10, with DAF_{\max} obtained for $T_a=T_{i,eff}$.

$$DAF_i = \left(\sqrt{\left(1 - \frac{T_a}{T_{i,eff}}\right)^2 + \xi_a} \right)^{-1} \quad (10)$$

In Equations 9 and 10, $T_{i,eff}$ is the effective period of the structure (which is assumed potentially different from the elastic vibration period only for the first vibration mode), potentially evaluated through a nonlinear static analysis.

This approach accounts for the effect of multiple vibration modes contributions, which can be combined through the SRSS rule. Also, it accounts for structural nonlinearity effects in terms of resonance period elongation and limitation of the maximum PSA. Also in this case, as highlighted when discussing the Italian regulation “rigorous” approach, the PFA value may result lower than PGA. Since this is only seldom observed as a result of numerical analyses, due to, according to Calvi and Sullivan [12], the interaction between the ground motion typical frequency content and the structure dynamic properties, they suggest that the PFA value should never be assumed lower than PGA at bottom floors and that, at the same floors, the floor response spectrum should never return PSA values lower than those associated with the ground motion response spectrum.

Vukobratović and Fajfar [13, 14] propose a theoretical-based (except for the determination of the maximum PSA value, which is empirical) approach for the assessment of floor response spectra validated against the results of numerical time-history analyses on reinforced concrete frames. The PSA value for each floor and for each modal contribution is calculated by means of Equation 11.

$$PSA_{ij} = \frac{F_i \varphi_{ij}}{\left| \left(\frac{T_a}{T_{i,eff}} \right)^2 - 1 \right|} \sqrt{\left(\frac{S_a(T_{i,eff})}{R_{\mu,i}} \right)^2 + \left(\left(\frac{T_a}{T_{i,eff}} \right)^2 S_a(T_a) \right)^2} \leq AMP_i F_i \varphi_{ij} \frac{S_a(T_{i,eff})}{R_{\mu,i}} \quad (11)$$

In Equation 11, $T_{i,eff}$ is different from the elastic period only for the first vibration mode and can be calculated by means of a nonlinear static analysis; $R_{\mu,i}$ is the reduction factor due to the nonlinear behaviour of the structure and is equal to the maximum between 1 and the ratio between $S_a(T_{i,eff})$ and S_{ay} (potentially determined by means of a nonlinear static analysis) for the first vibration mode, while it is equal to 1 for higher vibration modes; AMP_i is the maximum PSA_{ij}/PFA_{ij} value and is expressed as a function of the damping ratio similarly to the approach proposed by Calvi and Sullivan [12]. The effects of multiple modes are combined by applying ALGSUM combination rule in the post-resonance region, with the SRSS rule otherwise.

3 DESIGN AND MODELLING OF THE CASE-STUDY STRUCTURES

The 2-, 4-, 6-, and 8-storey case-study reinforced concrete moment resisting frames have regular rectangular plan defined by five and three bays in the longitudinal and transverse direction, respectively. Beams are 4.5 m long; columns are 3.0 m high. The buildings were designed according to Eurocode 2 [15] and Eurocode 8 [3] for four different design PGA values at Life Safety Limit State (0.05 g, 0.15 g, 0.25 g and 0.35 g) in “High” Ductility Class (DCH). The materials used for design are class C28/35 concrete with characteristic compressive strength of

the cylinder equal to 28 N/mm² and steel rebars with characteristic yielding stress equal to 450 N/mm². It is assumed that floor slabs have a diaphragmatic behaviour. During the design and the analysis process, second-order geometric effects are neglected. Further details on the design of the case-study RC frames are available in Di Domenico [16] and in Ricci et al. [17]. For the analyses, the reinforced concrete elements' non-linearity is modelled by adopting a lumped-plasticity approach in OpenSees [18] by using ModIMKPeakOriented Material with response parameters determined according to Haselton et al. [19] and with the introduction of the cracking point. In the modelling process, average material properties are used, namely a compressive strength for concrete equal to 36 N/mm² determined according to Eurocode 2 [15], and a steel yielding stress equal to 517.5 N/mm² determined according to Fardis et al. [20].

Two different unreinforced masonry infill layouts are considered. The first is constituted by a two-leaf (thickness: 80+120 mm) 'weak' infill wall (weak layout, WL), the second is constituted by a one-leaf (thickness: 300 mm) 'strong' infill wall (strong layout, SL). Note that the two-leaf infills are constituted by independent non-interacting panels. In other words, the in-plane and the out-of-plane responses of each leaf are determined (and modelled) independently on those associated with the other leaf.

The mechanical properties of these infills are those calculated for the masonry wallets tested by Calvi and Bolognini [21] for the WL and those by Guidi et al. [22] for the SL. Each infill leaf is introduced in the structural model by using a couple of equivalent no-tension struts.

The in-plane non-linear behaviour is modelled, separately for each leaf, based on the proposal by Panagiotakos and Fardis [23]. According to this modelling approach, only the slope of the softening branch of the force-displacement in-plane behaviour relationship is an open parameter, and it should be set to a fraction α of the infill initial elastic stiffness. In Fardis [24] it is suggested to set α to a value between -1.5% and -5%. For the 80-, 120-mm thick leaves α is set to -1.6% while for the 300-mm thick leaf it is set to -3.6% in order to reproduce the experimental evidences shown by Calvi and Bolognini [21] and by Guidi et al. [22]. The two layouts analyzed are characterized by similar elastic in-plane stiffness but by different in-plane and out-of-plane strength capacity. In other words, buildings with WL and SL infills have similar elastic period, but those with WL infills are more likely to experience nonlinearity due to infills' cracking.

Regarding the out-of-plane response, the modelling strategy proposed by Ricci et al. [25] is adopted in order to account for the in-plane/out-of-plane interaction effects, i.e., the degradation of the out-of-plane strength and stiffness due to in-plane damage and of the in-plane strength and stiffness due to out-of-plane damage. The equations adopted for modelling the out-of-plane response are those proposed in Ricci et al. [17] for infills in which the out-of-plane response is governed by two-way arching effect strength mechanism, except for those associated with some response parameters. In fact, for this study, the out-of-plane response model is improved and updated.

First, the empirical equation for the assessment of the out-of-plane first macro-cracking force, F_{crack} , is updated to account for recent experimental evidences proposed by De Risi et al. [26] and by Di Domenico et al. [27] The new formulation is reported in Equation 12.

$$F_{crack} = 5.90 f_{mv}^{0.11} \frac{t^{0.83}}{h^{1.44}} wh \quad (12)$$

In Equation 12, forces are expressed in Newtons and lengths are expressed in millimeters. In addition, the formulations proposed by Di Domenico et al. [27] are used to model the in-plane/out-of-plane interaction effects. In these formulations, the reduction of the out-of-plane strength and stiffness capacity is related not only to the in-plane interstorey drift ratio demand

and to the infill wall vertical slenderness (i.e., the h/t ratio), but also to the infill wall aspect ratio w/h .

However, the most important and significant improvement of the out-of-plane response model is the introduction of the softening branch in the out-of-plane response backbone, as shown in Figure 2a, and the assessment of the cyclic degradation of the response envelope. As shown in Figure 2a, the out-of-plane response backbone adopted in Ricci et al. [17] was trilinear with a plastic branch after the peak load point up to the attainment of the displacement, equal to 0.30 times the infill thickness, corresponding, on average and based on experimental tests, to the 20% degradation of the maximum out-of-plane strength, which is a usual threshold associated with conventional collapse of structural members. In this study, the “conventional” ultimate point is retained at a displacement equal to 0.30 times the infill thickness. However, a bilinear softening branch is modelled. The first part of the softening branch goes from the peak load point to the “conventional” ultimate point set at a force equal to 80% of the predicted maximum strength capacity. The second part goes from the “conventional” ultimate point to the “collapse displacement” point corresponding to zero out-of-plane strength capacity, i.e., at vanishing of arching action strength mechanism. As demonstrated in Angel et al. [28] and further explained in Di Domenico et al. [29], vanishing of both vertical and horizontal arching effect is expected, based on geometrical considerations, at an out-of-plane central displacement of the infill wall equal to 0.80 times the infill thickness. So, the out-of-plane collapse displacement is set, in this study, to this value.

The quadri-linear response envelope shown in Figure 2a is modelled in OpenSees [18] by adopting Pinching4 Material. Pinching4 Material also allows modelling the hysteretic degradation of strength, unloading and reloading stiffness, as well as the so-called “pinching” effect. Further details on the nature and meaning of the hysteretic parameters governing Pinching4 Material response are available in Lowes et al. [30]. A preliminary calibration of these parameters has been performed by carrying out at the laboratory of the Department of Structures for Engineering and Architecture of University of Naples Federico II (DIST-UNINA) a cyclic out-of-plane test on an unreinforced masonry infill with thickness equal to 120 mm and poor mechanical properties (i.e., nominally identical to those monotonically tested in Di Domenico et al., [31]), whose out-of-plane force (F_{OOP})-displacement (d_{OOP}) response is shown in Figure 2b. Further details on this experimental test are available in [16].

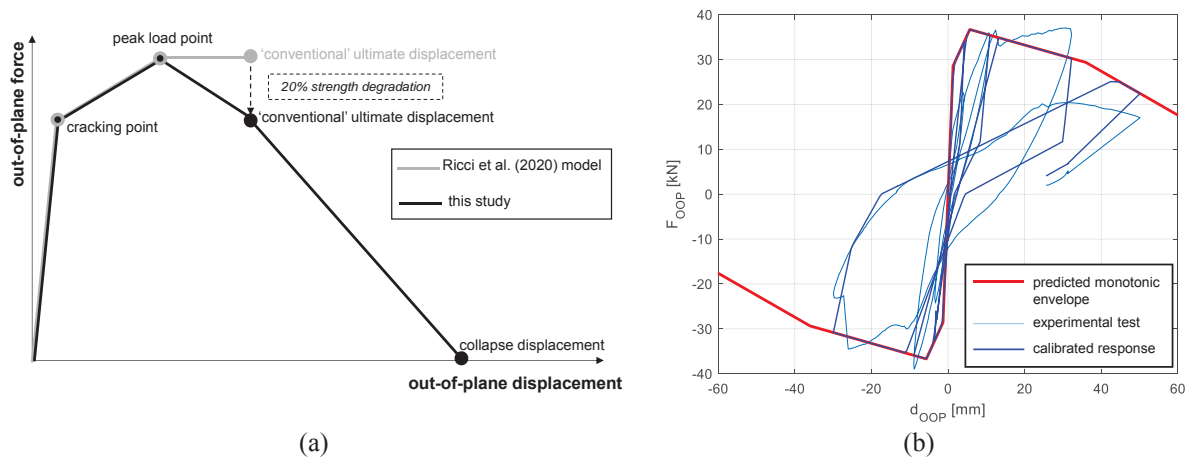


Figure 2: Updating of the out-of-plane response model: (a) new response envelope and (b) calibration of Pinching4 Material hysteretic parameters based on the cyclic test performed at DIST-UNINA.

The Pinching4 Material hysteretic parameters have been calibrated by setting damage degradation type to “energy” and in order to minimize the distance between the experimental and the predicted energy dissipation history during the entire experimental test. They have been calibrated by neglecting the force cyclic degradation, since the limited number of comparisons between monotonic and cyclic experimental tests available (e.g., [16, 32]) shows that no significant strength degradation is observed when comparing monotonic and cyclic out-of-plane tests. The calibrated parameters are $gK1=2.00$, $gK2=0.55$; $gK3=1.50$; $gK4=0$; $gD1=0.45$; $gD2=0.85$; $gD3=0.45$; $gD4=0.50$; $gF1=gF2=gF3=gF4=0$; $gKLim=1$; $gDLim=1$; $gFLim=0$; $gE=100$; $rDispP=rDispN=-0.40$; $rForceP=rForceN=-1.00$; $uForceP=uForceN=-0.40$. As already highlighted, the number of cyclic out-of-plane experimental tests is very limited. Further experimentation is needed to achieve a more robust and reliable calibration of the hysteretic parameters of the out-of-plane response of unreinforced masonry infills, also characterized by different geometric and mechanical properties.

4 NONLINEAR ANALYSIS PROCEDURE

The nonlinear time-history analyses have been performed by scaling up to the design PGA of each case-study building ten bidirectional ground motions selected in the European Strong Motion (ESM) Database [33]. The selected records were registered on stiff and horizontal soils (i.e., type A soils according to Eurocode 8 [3]). Both components of the selected records were simultaneously matched to the 5%-damped design spectrum at Life Safety Limit State by using wavelets and the RspMatchBi software [34]. The record component registered in the NS direction was applied along the longitudinal global direction, while the component registered in the EW direction was applied along the transverse global direction. Further details on record selection are available in [16].

Nonlinear time-history analyses were performed on the Bare Frame (BF) models, on the infilled frame models with WL infills and SL infills but modelling only their in-plane response (WL and SL models), and on the infilled frame models with WL infills and SL infills with modelling both the out-of-plane response and the in-plane/out-of-plane interaction effects (WLOOP and SLOOP models). In the following, each case-study building is identified using an acronym, such as XPY_Z , in which X is the number of storeys, Y the design PGA at Life Safety Limit State expressed in $g/100$, Z the model identifier (BF, WL, SL, WLOOP, and SLOOP).

Consistently with the design process, a 5% damping ratio was used to calculate damping forces during the analyses. More specifically, mass- and tangent stiffness-proportional Rayleigh damping model was adopted.

5 TIME-HISTORY ANALYSIS RESULTS

In this section, the results of the time-history analyses are presented and discussed. Namely, the outcomes in terms of PFA/PGA profiles and PSA/PFA spectral shapes are shown. The spectral shapes are calculated by assuming a code-consistent value of the damping ratio equal to 5%. For each case-study building, the results shown are obtained as the average of the results obtained from the ten time-history analyses performed under the action of the ten bidirectional ground motions selected. For the sake of brevity, only some significant results are shown. These results can be considered representative of the general trends observed from the outcomes of all the numerical analyses. Then, these outcomes are compared with the results of the application of code and literature proposals previously described.

5.1 PFA/PGA profiles

The PFA/PGA profiles along the longitudinal direction for a selection of case-study buildings are shown in Figure 3.

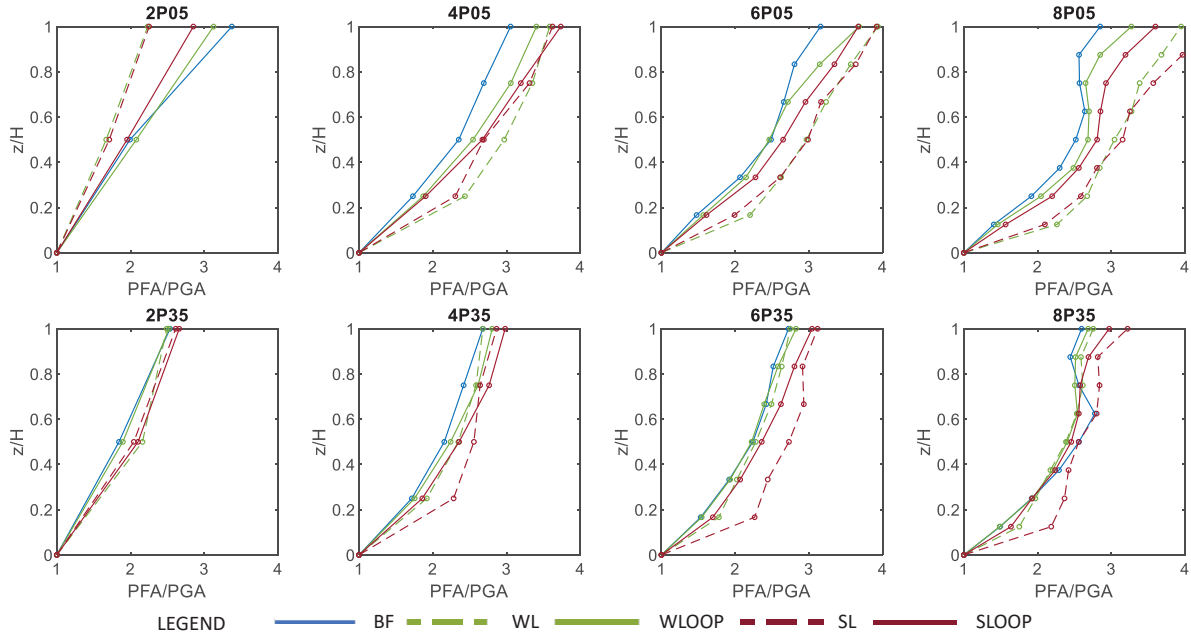


Figure 3: PFA/PGA profile along the longitudinal direction of a selection of case-study buildings.

Some considerations can be drawn:

- i. The maximum value of PFA/PGA is generally between 3 and 4, it is registered at top floors and is lower for buildings designed and analyzed for higher PGA (see point v. for comments on this). Among code and literature formulations, NZSEE2017 [5] approach returns a maximum PFA/PGA value equal to 3 at the top floors of buildings; in addition, a maximum PFA/PGA ratio equal to 4 was expected at top storeys according to Uniform Building Code [35]. Hence, the PFA/PGA maximum values obtained from the analyses can be deemed reasonable.
- ii. The shape of the profiles is roughly linear for 2-storey buildings, while it becomes multilinear for the other buildings and non-monotonic for taller (6- and 8-storey) buildings. This is an effect of the influence of higher vibration modes, which, as it is well-known, is more significant in high-rise structures. This is expected based on the more refined code and literature proposals discussed in section 2. The effect of higher modes appears also more visible and significant for infilled structures than for bare structures, as well as in presence of higher nonlinearity (i.e., for higher PGA demand).
- iii. Generally, at fixed building and at fixed floor, the maximum PFA/PGA value is registered for infilled buildings without modelling of out-of-plane response and in-plane/out-of-plane interaction, except for the 2-storey buildings. This occurs due to the dependence of the PFA on $S_a(T_1)$. In fact, in 4-, 6-, and 8-storey buildings, $S_a(T_1)$ is generally higher for infilled buildings, since T_1 is lower for infilled buildings and T_1 for bare frames is higher than the corner period T_C equal to 0.40 s; on the contrary, T_1 for 2-storey bare structures is lower than T_C , so, infilled buildings, which are always characterized by lower T_1 than bare buildings, are characterized, in this case,

- also by lower $S_a(T_1)$. The dependency of the PFA values on $S_a(T)$ is expected based on the more refined code and literature proposals discussed in section 2.
- iv. Generally, at fixed building, the PFA/PGA profiles for infilled buildings with out-of-plane response of infills and in-plane/out-of-plane interaction modelled tend to approach the profile obtained for the bare structures. This is expected, since when the in-plane/out-of-plane interaction is modelled, the in-plane response of the infill deteriorates, in terms of both stiffness and strength capacity, due to the out-of-plane displacement demand. So, the general behaviour of the building results intermediate between those of the bare and of the infilled (with in-plane response only of infills modelled) buildings.
 - v. Generally, the trends described above are confirmed when passing from the buildings designed and analyzed for PGA equal to 0.05 g to those designed and analyzed for PGA equal to 0.35 g. However, they are sometimes disturbed due to structural nonlinearity, which in general, yields to a reduction of the PFA/PGA demand in the case-study buildings. This is expected based on the more refined code and literature proposals discussed in section 2. Note that due to the modelling approach adopted (see section 3.1), the case-study buildings experience nonlinearity (in terms of tangent stiffness variation during the analysis) due to elements'/infills' cracking, while their elements do not yield. In other words, the reduction of PFA at increasing demand PGA and, as will be shown in the following, period elongation and PSA reduction at increasing demand PGA is mainly due to elements'/infills' cracking. This has been observed also by Petrone et al. [10].

Based on the above considerations, which are corroborated by the discussion of literature and code proposals presented in section 2, it can be concluded that, with reference to the set of case-study buildings analyzed for this study, the significant parameters influencing the values of PFA/PGA ratios are the $S_a(T)$ acting on the structure and on the PGA value itself (which is representative of the level of expected nonlinearity in the structure), both referred to the ground motion. On the other hand, the shape of the PFA/PGA profile depends on the importance of higher modes, which is higher for taller buildings than for lower buildings, as well as for infilled buildings than for bare buildings.

5.2 PSA/PFA spectral shapes

The PSA/PFA spectral shapes obtained along the longitudinal direction for a selection of floors of a selection of case-study buildings are shown in Figure 4. The value of T_1 used to normalize the period T_a is the period of the bare frame for WLOOP and SLOOP models: in fact, as previously discussed, due to the in-plane/out-of-plane interaction effects, the behaviour of models in which the out-of-plane response of infills is modelled is intermediate between the behaviour of the bare structural model and that of the infilled structural model with only the in-plane response of infills considered; for bare and WL/SL models, the period adopted for normalization is the one calculated by means of modal analysis of the elastic uncracked model.

Some considerations can be drawn:

- i. The maximum value of PSA/PFA is significantly variable from floor to floor, as some of the code and literature models described in section 2 show. In general, it appears dependent on the PFA/PGA value: the higher the PFA/PGA, the higher the maximum value of PSA/PFA. The maximum observed value of the PSA/PFA ratio is roughly equal to 5.5, which is consistent with the maximum value, equal to 5, predicted by the proposal by Petrone et al. [10] adopted also by the Italian code.

- ii. The spectral shapes are characterized, in general, by multiple peaks corresponding to the different vibration modes of the structure. This is quite evident in taller buildings, in which the maximum value of PSA/PFA associated with the higher modes (i.e., at T_a/T_1 significantly lower than the unit) may be even higher than that associated with the first vibration mode (i.e., at T_a similar to T_1). In 2-storey buildings, the effect of higher modes is visible only at the first floor, at which, actually, the maximum influence of the second vibration mode is expected. On the other hand, in the 8-storey buildings, peaks of PSA/PFA associated with higher modes are visible at different T_a/T_1 values dependently on the floor considered. This occurs because at bottom floors the predominant effect among higher modes may be associated with different higher modes from floor to floor (e.g., the second or the third vibration mode of the structure).
- iii. In general, infilled buildings are characterized by higher values of the maximum PSA/PFA ratio associated with the first vibration mode with respect to bare buildings, except for the 2-storey buildings. This occurs, most likely, because $S_a(T_a=T_1)$ is higher for infilled buildings with respect to $S_a(T_a=T_1)$ for bare buildings, since T_1 of the infilled building is lower than T_1 of the bare building, which, in tune, is higher than T_C . As already explained when discussing maximum PFA/PGA trends, this is not true for 2-storey buildings, since in this case $S_a(T_a=T_1)$ is lower for infilled buildings than for bare buildings. This occurs because T_1 of the infilled building is still lower than T_1 of the bare building, but T_1 of the bare building is lower than T_C . The dependence of the maximum PSA/PFA value on $S_a(T_a=T_1)$ may be also expressed by relating it directly to the period T_1 , as done by Petrone et al. [10].
- iv. As also shown when discussing the PFA/PGA profiles, also the spectral shapes for infilled buildings with modelling of the out-of-plane response of infills and of the in-plane/out-of-plane interaction effects are intermediate between those obtained for the bare models and those obtained for the infilled models with modelling of the in-plane response only of the infill walls. The fact that for WLOOP and SLOOP models the peak of PSA/PFA due to resonance with the first vibration mode occurs at $T_a/T_1 < 1$ is due to the fact that, in this case, T_a is normalized with respect to T_1 of the bare frame, while the real resonance period is lower than it, being intermediate between the bare and the infilled structure elastic vibration period.
- v. Generally, the trends described above are confirmed when passing from the buildings designed and analyzed for PGA equal to 0.05 g to those designed and analyzed for PGA equal to 0.35 g. However, the peak PSA/PFA associated with the first vibration mode of the structure is noticeably reduced due to the effect of structural nonlinearity; in addition, the resonance period is higher than T_1 for the period elongation due to structural nonlinearity. Remember that, as previously highlighted, this effect is mainly due to elements'/infills' cracking. Both effects of structural nonlinearity are expected also by applying the more refined literature proposals discussed in section 2. Also note that, even if with a lower impact, also the peaks associated with higher vibration modes may be reduced due to structural nonlinearity. This was observed also by Surana et al. [11].

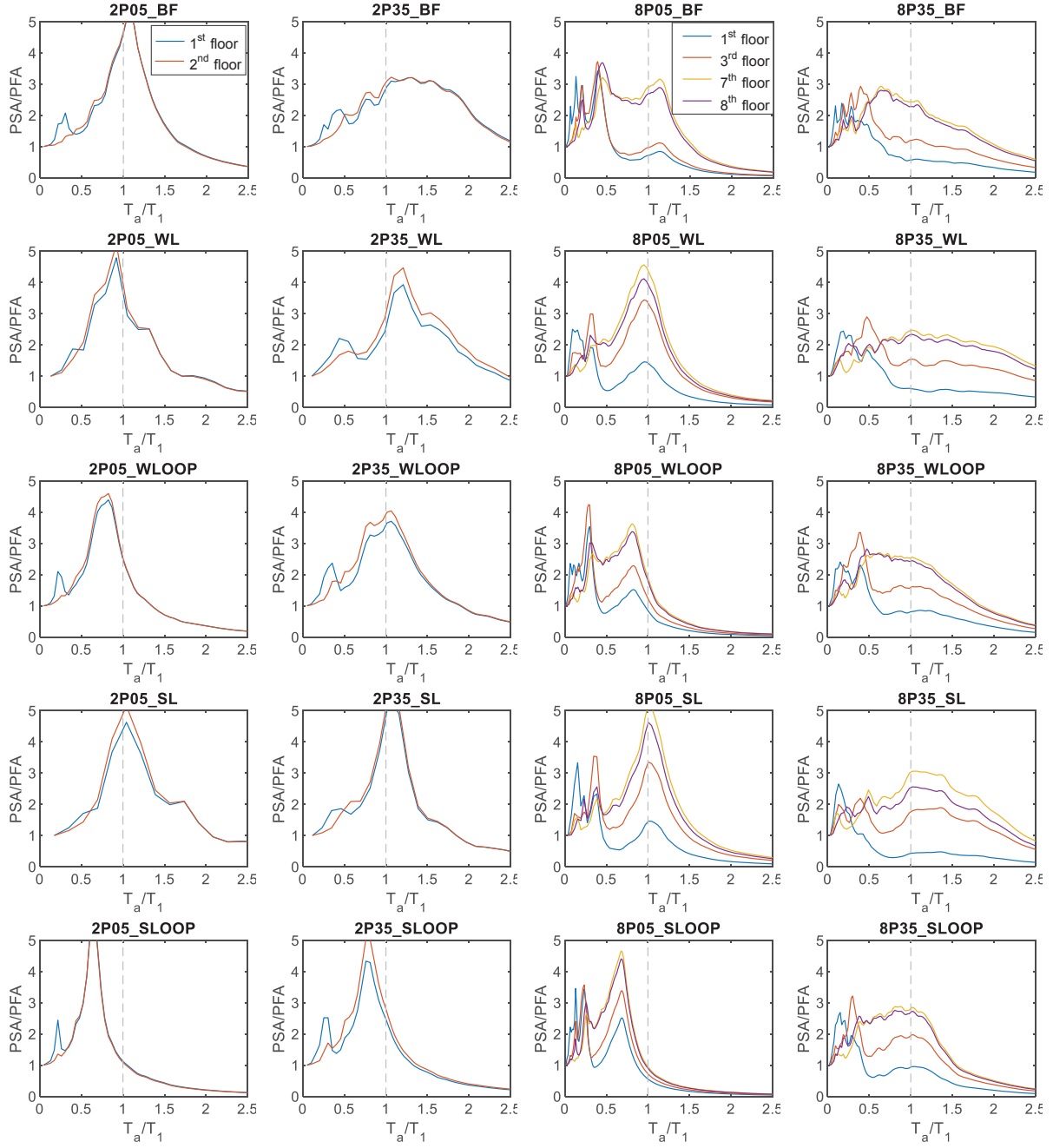


Figure 4: PSA/PFA spectral shapes along the longitudinal direction of a selection of case-study buildings.

Based on the above considerations, which are corroborated by the discussion of literature and code proposals presented in section 2, it can be concluded that, with reference to the set of case-study buildings analyzed for this study, the significant parameters influencing the values of the maximum PSA/PFA ratios associated with the resonance with the i -th vibration mode at a certain floor are the PFA/PGA value at that floor, the $S_a(T_a=T_i)$ value, potentially substituted directly by T_i , and the PGA value (which is representative of the level of expected nonlinearity in the structure). On the other hand, the shape of the PSA/PFA profile is characterized by a peak associated with the resonance with the structure first vibration mode and with a group of close peaks associated with the resonance with the structure higher modes.

6 CONCLUSIONS

- Floor response spectra are a useful tool for the assessment of the seismic demand on non-structural components, whose safety check is a paramount issue in performance-based earthquake engineering. This study was dedicated to the assessment via nonlinear time-history analyses of floor response spectra of case-study reinforced concrete framed structures designed according to Eurocodes for four different levels of design peak ground acceleration at Life Safety Limit State. The case-study bare structures have also been analyzed by including in the model two different kinds of uniformly-distributed infill walls. The main novelty of this study is not only the assessment of floor spectra for infilled reinforced concrete buildings, which has been rarely addressed in the past, but above all the fact that infill walls are modelled by considering their in-plane response, as usual, and their out-of-plane response, as well as the in-plane/out-of-plane interaction, i.e., the degradation of the in-plane response due to the out-of-plane seismic demand and vice-versa.
- Based on literature and code existing formulations, the main parameters which are expected to influence floor response spectra have been identified, namely the floor height normalized with respect to the building height, the pseudo-spectral accelerations acting on the considered building, the vibration periods of the considered building and the shape of its vibration modes, the building height, the expected peak ground acceleration demand. Moreover, floor spectra shape is strongly influenced by higher vibration modes and by the nonlinearity demand experienced by the structure.
- Generally, at fixed building, the PFA/PGA profiles for infilled buildings with out-of-plane response of infills and in-plane/out-of-plane interaction modelled tend to approach the profile obtained for the bare structures. This is expected, since when the in-plane/out-of-plane interaction is modelled, the in-plane response of the infill deteriorates, in terms of both stiffness and strength capacity, due to the out-of-plane displacement demand. So, the general behaviour of the building results intermediate between those of the bare and of the infilled (with in-plane response only of infills modelled) buildings.
- Also the spectral shapes for infilled buildings with modelling of the out-of-plane response of infills and of the in-plane/out-of-plane interaction effects are intermediate between those obtained for the bare models and those obtained for the infilled models with modelling of the in-plane response only of the infill walls.
- Based on the above discussion, formulations for the assessment of floor response spectra have will be proposed for both bare and infilled buildings in future studies.

ACKNOWLEDGMENTS

This work was developed under the financial support of ReLUIS-DPC 2019-2021 funded by the Italian Department of Civil Protection (DPC). This support is gratefully acknowledged.

REFERENCES

- [1] M.E. Rodriguez, J.I. Restrepo, A.J. Carr, Earthquake-induced floor horizontal accelerations in buildings. *Earthquake Engineering and Structural Dynamics* 200, **31**, 693-718, 2002.

- [2] V. Vukobratović. *The influence of nonlinear seismic response of structures on the floor acceleration spectra*. Doctoral thesis, University of Ljubljana, Faculty of Civil and Geodetic Engineering, Ljubljana, Slovenia, 2015.
- [3] CEN, *Eurocode 8. Design of structures for Earthquake Resistance. Part 1-1: General Rules, Seismic Actions and Rules for Buildings*. Brussels, 2004.
- [4] ASCE/SEI 7-10, *Minimum Design Loads for Buildings and Other Structures*. ASCE 7-10. Reston, VA: ASCE, 2010.
- [5] New Zealand Society for Earthquake Engineering (NZSEE), Structural Engineering Society New Zealand Inc. (SESOC), New Zealand Geotechnical Society Inc., Ministry of Business, Innovation and Employment, Earthquake Commission, *The Seismic Assessment of Existing Buildings (the Guidelines), Part C – Detailed Seismic Assessment*, 2017.
- [6] New Zealand Society for Earthquake Engineering (NZSEE), *NZS 1170.5:2004. Structural design actions. Earthquake design Actions*, 2004.
- [7] Ministero delle Infrastrutture e dei Trasporti, *Circolare esplicativa delle Norme Tecniche per le Costruzioni*. Supplemento ordinario n. 5 Gazzetta Ufficiale 11 febbraio 2019. (in Italian).
- [8] Ministero delle Infrastrutture e dei Trasporti, *Decreto ministeriale 17 gennaio 2018 - Norme Tecniche per le Costruzioni*. Supplemento ordinario n. 42 Gazzetta Ufficiale 20 febbraio 2018. (in Italian).
- [9] A.K. Chopra. *Dynamics of Structures, 5th edition*, Pearson, London, United Kingdom, 2017.
- [10] C. Petrone, G. Magliulo, G. Manfredi, Seismic demand on light acceleration-sensitive nonstructural components in European reinforced concrete buildings. *Earthquake Engineering and Structural Dynamics*, **44**, 1203-1217, 2015.
- [11] M. Surana, M. Pisode, Y. Singh, D.H. Lang, Effect of URM infills on inelastic floor response of RC frame buildings. *Engineering Structures*, **175**, 861-878, 2018.
- [12] P.M. Calvi, T.J. Sullivan, Estimating floor spectra in multiple degree of freedom systems. *Earthquakes and Structures*, **7**(1), 17-38, 2014.
- [13] V. Vukobratović, P. Fajfar, A method for the direct estimation of floor acceleration spectra for elastic and inelastic MDOF structures. *Earthquake Engineering and Structural Dynamics*, **45**, 2495–2511, 2016.
- [14] V. Vukobratović, P. Fajfar, Code-oriented floor acceleration spectra for building structures. *Bulletin of Earthquake Engineering*, **15**(7), 3013-3026, 2017.
- [15] CEN, *Eurocode 2. Design of Concrete Structures. Part 1-1: General Rules and Rules for Buildings*. Brussels, 2004.
- [16] M. Di Domenico, *Out-of-plane seismic response and modelling of unreinforced masonry infills*. PhD Dissertation. University of Naples Federico II, Naples, Italy, 2018.
- [17] P. Ricci, M. Di Domenico, G.M. Verderame, Effects of the in-plane/out-of-plane interaction in URM infills on the seismic performance of RC buildings designed to Eurocodes. *Journal of Earthquake Engineering*, 2020. doi: 10.1080/13632469.2020.1733137.

- [18] F. McKenna, G.L. Fenves, M.H. Scott, OpenSees: *Open System for Earthquake Engineering Simulation*. Pacific Earthquake Engineering Research Center. University of California, Berkeley, CA, USA, 2004.
- [19] C.B. Haselton, A.B. Liel, S. Taylor-Lange, G.G. Deierlein, *Beam-column element model calibrated for predicting flexural response leading to global collapse of RC frame buildings*. PEER Report No. 2007/03. Pacific Earthquake Engineering Research Center, University of California, Berkeley, CA, USA, 2008.
- [20] M.N. Fardis, A. Papailia, G. Tsionis, Seismic fragility of RC framed and wall-frame buildings designed to the EN-Eurocodes. *Bulletin of Earthquake Engineering*, **10**(6), 1767-1793, 2012.
- [21] G.M. Calvi, D. Bolognini, Seismic response of reinforced concrete frames infilled with weakly reinforced masonry panels. *Journal of Earthquake Engineering*, **5**(2), 153-185, 2001.
- [22] G. Guidi, F. da Porto, M. Dalla Benetta, N. Verlato, C. Modena, Comportamento sperimentale nel piano e fuori piano di tamponamenti in muratura armata e rinforzata. *Proceedings of the XV ANIDIS, L'Ingegneria Sismica in Italia*, Padua, Italy, 2013. (in Italian).
- [23] T.B. Panagiotakos, M.N. Fardis, Seismic response of infilled RC frames structures. *11th World Conference on Earthquake Engineering*. June 23-28, Acapulco, México, 1996.
- [24] M.N. Fardis (editor). *Experimental and numerical investigations on the seismic response of RC infilled frames and recommendations for code provisions*. ECOEST/PREC8 Report No.6. Laboratorio Nacional de Engenharia Civil Publications, Lisbon, 1996.
- [25] P. Ricci, M. Di Domenico, G.M. Verderame. Empirical-based out-of-plane URM infill wall model accounting for the interaction with in-plane demand. *Earthquake Engineering and Structural Dynamics*, **47**(3), 802-827, 2018.
- [26] M.T. De Risi, M. Di Domenico, P. Ricci, G.M. Verderame, G. Manfredi, Experimental investigation on the influence of the aspect ratio on the in-plane/out-of-plane interaction for masonry infills in RC frames. *Engineering Structures*, **189**, 523-540, 2019.
- [27] M. Di Domenico, M.T. De Risi, P. Ricci, G.M. Verderame, G. Manfredi, Empirical prediction of the in-plane/out-of-plane interaction effects in clay brick unreinforced masonry infill walls. *Engineering Structures*, **227**, 2021.
- [28] R. Angel, D.P. Abrams, D. Shapiro, J. Uzarski, M. Webster, *Behaviour of reinforced concrete frames with masonry infills*. University of Illinois Engineering Experiment Station. College of Engineering. University of Illinois at Urbana-Champaign, 1994.
- [29] M. Di Domenico, P. Ricci, G.M. Verderame, Experimental assessment of the influence of boundary conditions on the out-of-plane response of unreinforced masonry infill walls. *Journal of Earthquake Engineering*, **24**(6), 881-919, 2020.
- [30] L.N. Lowes, N. Mitra, A. Altoontash, *A beam-column joint model for simulating the earthquake response of reinforced concrete frames*. PEER Report No. 2003/10. Pacific Earthquake Engineering Research Center, University of California, Berkeley, CA, USA, 2004.
- [31] M. Di Domenico, P. Ricci, G.M. Verderame, Experimental assessment of the out-of-plane strength of URM infill walls with different slenderness and boundary conditions. *Bulletin of Earthquake Engineering*, **17**(7), 3959-3993, 2019.

- [32] A. Furtado, H. Rodrigues, A. Arêde, H. Varum, Experimental evaluation of out-of-plane capacity of masonry infill walls. *Engineering Structures*, **111**, 48-63, 2016.
- [33] L. Luzi, R. Puglia, E. Russo & ORFEUS WG5, *Engineering Strong Motion Database, version 1.0*. Istituto Nazionale di Geofisica e Vulcanologia, Observatories & Research Facilities for European Seismology, 2016.
- [34] D.N. Grant, Response spectral matching of two horizontal ground-motion components. *Journal of Structural Engineering*, **137**(3), 289-297, 2010.
- [35] International Conference of Building Officials, *Uniform Building Code*. Whittier, CA, USA, 1997.

SEISMIC LOSS ANALYSIS OF A CODE-DESIGNED INFILLED RC BUILDING ACCOUNTING FOR INFILL MODEL CLASS UNCERTAINTY

Fabio Romano¹, Mohammad S. Alam², Maria Zucconi¹, Marco Faggella^{3,4}, Andre Barbosa^{2,5}, Barbara Ferracuti¹

¹ Niccolò Cusano University, Via Don Carlo Gnocchi 3, Rome, Italy
{fabio.romano, maria.zucconi, barbara.ferracuti}@unicusano.it

² Oregon State University, 101 Kearney Hall, Corvallis, OR 97331, USA
{alammo, andre.barbosa}@oregonstate.edu

³ Sapienza University of Rome, Via Eudossiana 18, Rome, Italy

⁴ University of Porto, 4200-465, Porto, Portugal
mfaggella@gmail.com

⁵ University of Bristol, Queen's Building, University Walk, Bristol, BS8 1TR, UK
andre.barbosa@bristol.ac.uk

Abstract

Several sources of uncertainty affect seismic loss analysis results, and investigating their influence is crucial to obtain reliable quantitative estimates of the building performance under seismic excitations. The present study propagates uncertainties from seismic hazard to annualized seismic losses of a code-designed unreinforced masonry infilled reinforced concrete moment resisting frame building. Uncertainties were considered in the ground motion record-to-record variability and in model class uncertainty of masonry infill walls that originates from two equivalent strut macro-model classes used and uncertainties in their backbone model parameters. A large set of finite element models (FEMs) was generated for each infill strut model class by Latin hypercube sampling (LHS) of the statistical distribution of experimentally fitted backbone parameters. Each finite element model was subjected to multiple-stripe based nonlinear response history analyses to estimate the structural response parameters of interest. The propagation of uncertainties from structural response to repair costs was evaluated considering mean values and dispersion in repair cost at the selected seismic hazard levels for two building performance models. Moreover, the contribution of different structural and non-structural elements of the studied building to the expected annualized losses was evaluated.

Keywords: expected annual losses; FEMA P-58; model class uncertainty; seismic risk analysis; URM infill.

1 INTRODUCTION

Reinforced concrete (RC) moment-resisting frames with unreinforced masonry (URM) infills represent a predominant typology of buildings worldwide. Understanding the performance of such building typology to seismic actions is crucial to assess the impact of their potential damage on the economic and societal losses [1–6]. To this end, performance-based earthquake engineering (PBEE) methods and tools can be used to evaluate the seismic risk of existing or newly designed structures through targeted seismic loss analysis. Seismic loss analysis is a very complex process, whereby a robust assessment of the seismic performance is needed and requires propagation of relevant sources of uncertainty [7]. In particular, uncertainties in numerical modeling of structural and non-structural elements and damage mechanisms considerably affect the seismic response, such as those related to the modeling of infill panels. Even though, several research efforts addressed the effect of modeling parameter uncertainty of URM infill walls on the seismic structural response of RC buildings [8–10], only a limited number of studies focused on the impact of model class uncertainty on estimated losses. Model class uncertainty [11, 12] incorporates the uncertainty in modeling parameters and the uncertainty in the selection of appropriate models to describe a general physical phenomenon.

This paper deals with the impact of incorporating model class uncertainty related to URM infills on seismic loss assessment results. Model class uncertainty is described via two equivalent infill strut models and considering the uncertainty in their backbone parameters by generating 200 realizations of the infill strut backbone for each infill model. Nonlinear response history analyses (NRHAs) were carried out using the multiple-stripe analysis (MSA) approach [13], with a different set of 30 ground motion (GM) records selected for each seismic intensity level. The FEMA P-58 methodology [14], which finds several applications in the literature for building-specific seismic loss analyses [15, 16], was adopted to evaluate the monetary performance of the considered building. This was achieved through the building performance models developed incorporating the NRHAs results of the two selected infill model classes and considering necessary information on elements damage and loss characteristics. In particular, the recently validated SP3 web-tool [17] has been used for the seismic loss analysis. Results highlight the impact of model class uncertainty for URM walls by comparing mean repair costs and mean annualized costs obtained for the two selected model classes.

2 DESCRIPTION OF BUILDING

An existing code-conforming RC URM building is selected to evaluate the effect of infill-strut model class uncertainty on seismic loss assessment. The building is an irregular six-story structure infilled with URM walls, with three bays in the Y-direction (transverse) and five bays in the X-direction (longitudinal), as shown in Figure 1(a). The lateral force resisting system consists of RC special moment-resisting frames in both longitudinal and transverse directions. The concrete used has expected compressive strength of $f'_{ce} = 30$ MPa, and the reinforcing steel with expected yield strength of $f_y = 496$ MPa. Figure 1(b) shows the elevation view of the internal frames for grid lines B to E, where infill walls are used as partitions in second and third stories. Solid clay bricks are used for infill wall panels. Detailed information regarding the building description is reported in [18].

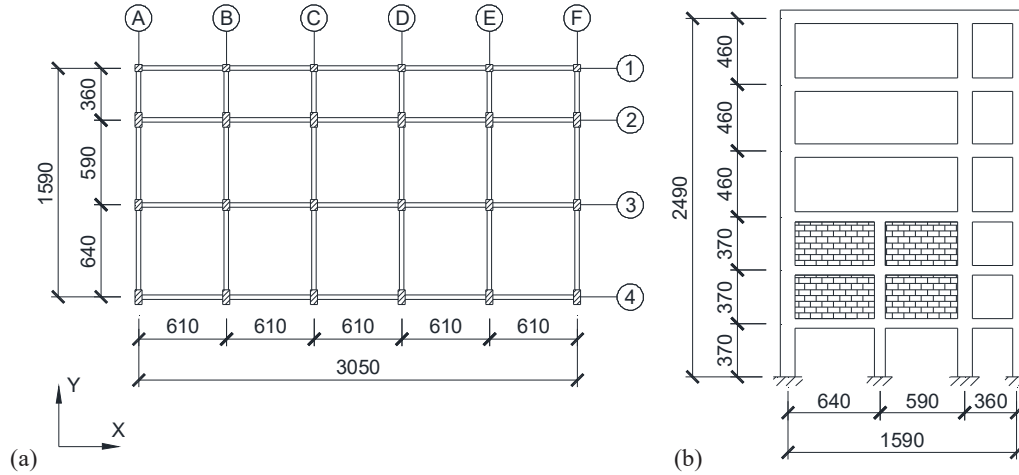


Figure 1: Code-designed infilled RC URM building: (a) second-story plan view of structural RC frames, (b) elevation view along Y-direction (transverse direction) of internal frames, (dimensions in cm).

3 NUMERICAL MODELING AND STRUCTURAL ANALYSIS

3.1 RC frame and infill strut modeling

A two-dimensional model of the building internal RC frame in the transverse direction is developed in OpenSees [19]. The graphical representation of the numerical modeling scheme is presented in Figure 2. Beams and columns of the RC frame are modeled as fiber-section force-based finite length plastic hinge elements [1, 2, 5, 6]. The uniaxial stress-strain response of the concrete fibers is modeled using the model by Yassin [20], while the reinforcing steel bars are modeled with an elastoplastic with linear hardening model. Geometric nonlinearity ($P - \Delta$) are explicitly considered. A strength-based nonlinear zero-length shear spring is considered near the column end offsets to capture potential column shear failures due to infill-frame interaction. The details of the shear-spring model implemented are described elsewhere [21].

Infill panels are modeled through equivalent strut macro-models. Among the numerous infill strut macro models available in the literature to model infill panels [22–25], the infill strut models proposed by (1) Sattar and Liel [26], and (2) Burton and Deierlein [27] are adopted and hereafter referred to as SL10 and BD14, respectively. The SL10 is composed of a single diagonal concentric strut. In contrast, the BD14 model consists of a diagonal concentric strut and an off-diagonal strut, the latter connected at the end of the column end offsets. Figure 2(c) shows the two-infill strut model backbone curves, based on expected infill model parameters. The differences in the infill strut backbones arise from the different failure mechanisms considered by each infill strut model and the relative strength of the infill and surrounding RC frame.

To account for uncertainty in infill model constitutive parameters, 200 finite element model (FEM) realizations of the infill strut backbones are generated for each infill model, considering five models to experiment bias ratio parameters for the infill strut backbones as basic random variables, including: (1) bias in peak strength, $V_{cap,model}/V_{cap,exp}$, (2) bias in initial stiffness, $K_{e,model}/K_{e,exp}$, (3) ratio of experiment measured peak strength to yield strength, $V_{cap,exp}/V_{y,exp}$, (4) ratio of experiment measured capping drift to yield drift, $\Delta_{cap,exp}/\Delta_{y,exp}$, and (5) ratio of experiment measured residual strength to peak strength, $V_{r,exp}/V_{cap,exp}$. Statistics on model bias are determined based on the approach and results presented in Burton and Deierlein [27] and FEMA 307 [28].

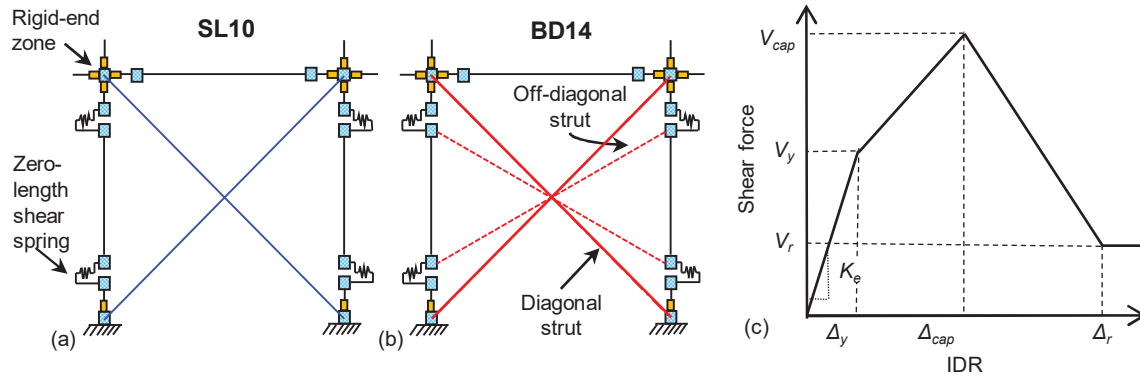


Figure 2: Infilled RC frame modeling: (a) SL10; (b) BD14; (c) infill strut backbone parameters.

3.2 Structural analysis results

The uncertainty in ground shaking is considered by simulating nonlinear response history analyses (NRHAs) with 30 natural GM records at eight seismic intensity levels, corresponding to exceedance probabilities of 50%, 30%, 10%, 5%, 2%, and 1% in 50 years, 1% in 100 years, and 1% in 200 years, respectively. Within the MSA approach [13], for each seismic hazard level (HL), a different GM records suite is selected for a soil site class D in Salem, Oregon, USA. Two-dimensional structural analyses are performed on the 200 FEM realizations of the two considered model classes representing an internal building RC frame. The suite of analyses is carried out by using high-performance parallel computing [29].

The summary of the results of NRHAs is presented in Figure 3, in which median profiles for peak interstory drift ratio (PIDR) are reported. It can be seen from Figure 3 that there is a notable reduction of the drift demands at the second and third stories, which are the stories in which the infill panels are located. The comparison between the results for the two model classes indicates a lower PIDR demand in lower stories when the BD14 infill strut model is adopted.

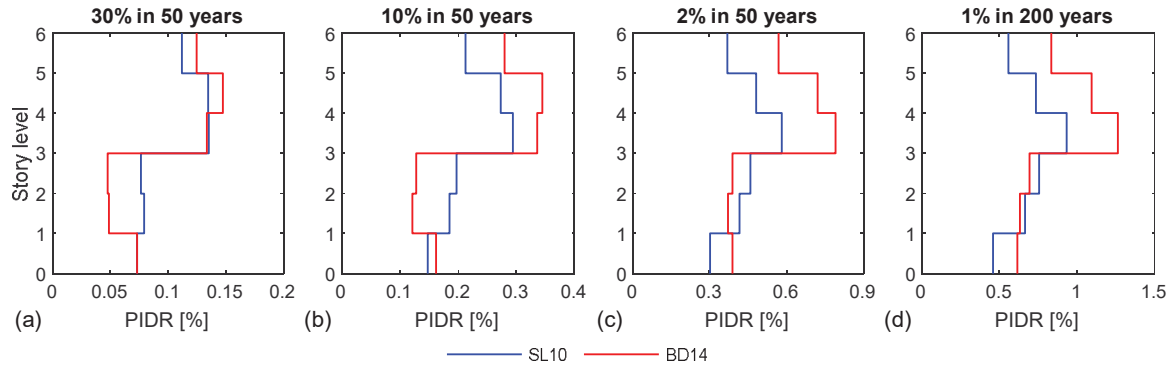


Figure 3: Median PIDR profiles for the two selected model classes, SL10 and BD14, at 30%, 10%, 2% in 50 years HLs and 1% in 200 years hazard levels.

4 LOSS ANALYSIS RESULTS

The building seismic loss analysis is evaluated via the FEMA P-58 loss methodology on a three-dimensional performance model of the building, where the information related to the geometrical building characteristics, the structural response results, as well as the damage and loss description of the elements, is required. In particular, the demand distribution generated from the NRHAs is used as input data for the damage analysis of damageable structural and non-structural elements at each selected HL. In this paper, the seismic loss analysis is carried out for two building performance models, each one corresponding to one of the two selected infill

strut model classes. The correspondence is expressed using the specific PIDR demand resulting from the NRHAs of the 200 FEM realizations of that infill strut model class. In other words, the two performance models have a different PIDR distribution, reported in the previous section in Figure 3. In order to appreciate the influence of infill modeling uncertainty, the fragility and loss functions of the structural and nonstructural elements are the same for the two performance models. Figure 4 reports the mean repair cost values at the selected seismic intensities for the two performance models, normalized by the total replacement cost of the building. The element category deaggregation of mean repair cost is also reported. The seismic risk due to collapse is much less relevant than those from element damage analysis, which is partly explained by the fact that a modern code-designed building is considered in this study. The figure shows that the most substantial contribution to the risk is from the masonry infill walls, whereas repair costs from MEP (mechanical, electric, and plumbing) elements are less relevant at higher HLs. In addition, repair costs due to collapse for the BD14 model class become progressively more important with increasing HLs and even though a similar trend is observed for the SL10 model class, the contribution of collapse to the risk is less for the latter model class.

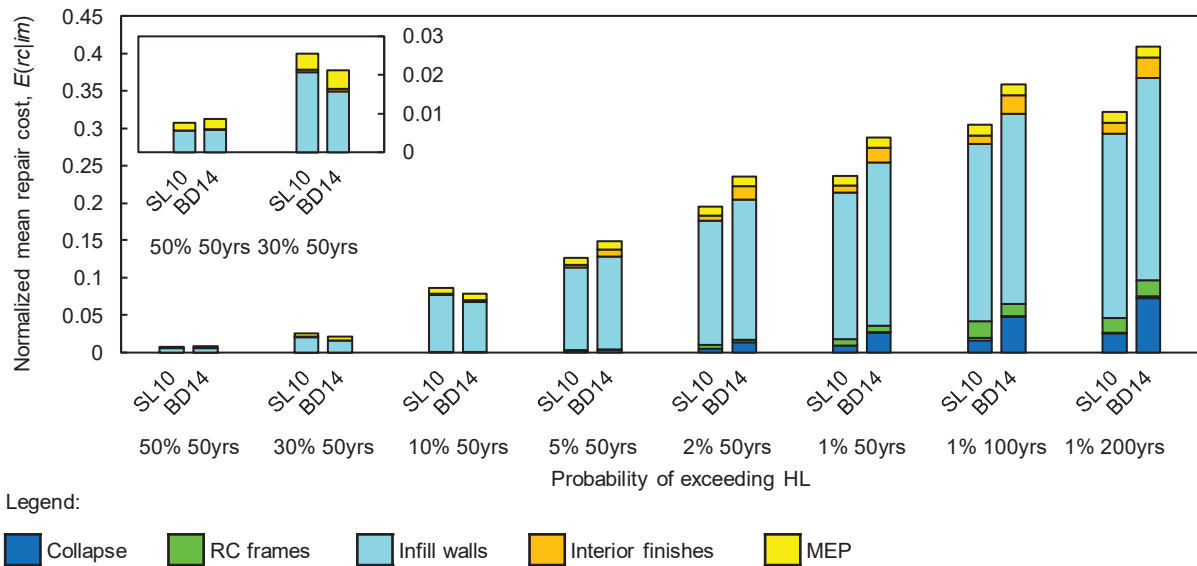


Figure 4: Effect of model class uncertainty on the mean total repair cost, deaggregated by the different structural and nonstructural elements contribution, for the two implemented performance models, SL10 and BD14.

To illustrate the propagation of the uncertainty from the structural response to losses, the dispersions of the maximum PIDR over all the building stories ($MIDR$), β_{MIDR} , and repair cost dispersions, β_{RC} , are compared at the selected HLs. Figure 5 reveals an amplification of repair cost dispersions compared to $MIDR$ dispersions, and results in Figure 5(b) indicate that dispersions of seismic loss in terms of repair costs decrease as seismic intensity increases, probably because higher values of the EDP imply that elements damage condition tend to concentrate at the higher damage states, hence the same for subsequent elements loss. This observation is consistent with the results presented in Kohrangi et al. [30].

Within a more comprehensive seismic loss analysis, the expected annualized losses (EAL) are computed as a percentage of the total replacement cost. The estimated EAL values are very similar, 0.0728 % and 0.0738% for the SL10 model class and BD14 model class, respectively, revealing a negligible influence of infill strut model class uncertainty on annualized losses for the present case-study modern RC building. Moreover, these values are relatively low when compared with studies on older RC frame buildings [15, 31, 32].

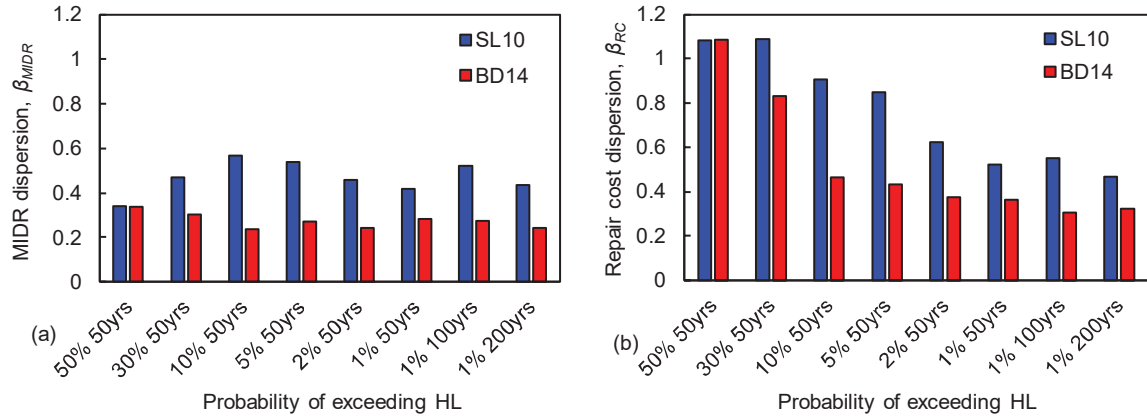


Figure 5: Logarithmic standard deviation for the two implemented performance models, SL10 and BD14: (a) maximum peak inter-story drift ratio, β_{MIDR} ; (b) repair cost, β_{RC}

The EAL percentage deaggregation in terms of replacement losses and damageable element category losses reported in the bar chart in Figure 6 confirms the predominant contribution from masonry infill walls, whereas MEP elements contributed to approximately 15% of EAL. The structural damage contribution to the risk is negligible, highlighting the importance of using modern building codes to reduce seismic risk.

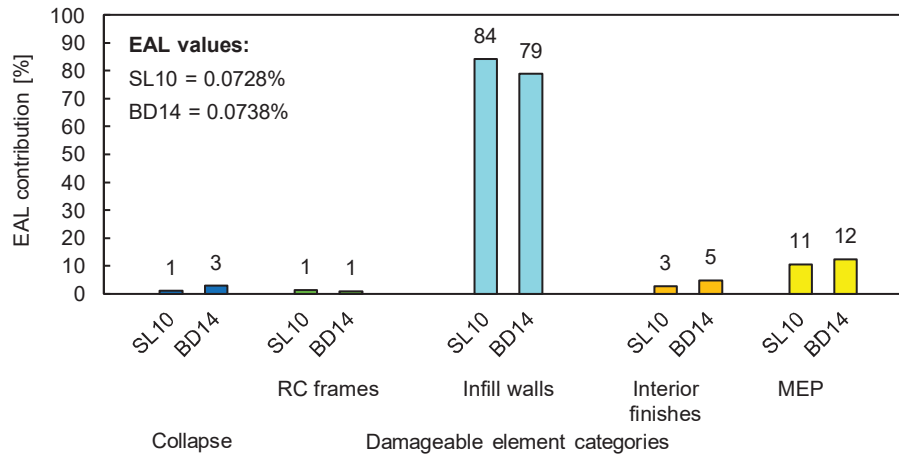


Figure 6: Contributions of collapse and damageable element losses to expected annualized loss for the two implemented performance models, SL10 and BD14.

5 CONCLUSIONS

This paper aims to assess the effect of model class uncertainty related to URM infills modeling on seismic risk of a modern RC building by using two different equivalent strut models, namely SL10 and DB14, and the uncertainty in the infill strut backbone parameters. NRHAs were performed at eight hazard levels for 200 FEM realizations of each of the two selected infill strut backbones, obtained through Latin hypercube sampling of the backbone parameters. The key findings of the study are as follows:

- Comparison between uncertainties in NRHAs results and loss analysis results shows a strong amplification of repair cost dispersions compared to maximum PIDR (MIDR) dispersion at low and medium HLs, which reduce at higher HLs, for both the infill-strut model class used.

- The results of the loss analysis reveal the influence of model class selection for URM walls on mean repair costs; in fact, the SL10 model class experiences larger losses at low and medium HLs, whereas repair costs for the BD14 model class become progressively predominant at increasing HLs due to the higher contribution of collapse losses.
- The EAL values for the two implemented performance models are very similar. Moreover, the EAL deaggregation indicates the predominant contribution from the masonry infill walls and other nonstructural elements, while the contribution from RC frames and collapse is negligible.

Summarizing, model class uncertainty for URM infills has significant effects on repair costs and mostly on repair costs dispersions, whereas the impact on annualized costs is less relevant. Such consideration is valid for the present case-study modern RC building, and further work should be performed to validate the results.

6 ACKNOWLEDGEMENT

The first, the third, and the last author wish to acknowledge the financial support received by the Italian Department of Civil Protection (ReLUIS Grant – Reinforced Concrete Structures). The second and fifth authors would like to acknowledge that part of the funding for this study was provided as part of the cooperative agreement 70NANB15H044 between the National Institute of Standards and Technology (NIST) and Colorado State University through a subaward to Oregon State University. The contents expressed in this paper are the views of the authors and do not necessarily represent the opinions or views of NIST or the US Department of Commerce.

REFERENCES

- [1] F.L.A. Ribeiro, L.A.C. Neves, A.R. Barbosa, Implementation and Calibration of Finite-Length Plastic Hinge Elements for Use in Seismic Structural Collapse Analysis. *Journal of Earthquake Engineering*, **21**, 1197–1219, 2017.
- [2] H. Varum, R. Dumaru, A. Furtado, A.R. Barbosa, D. Gautam, H. Rodrigues, Seismic Performance of Buildings in Nepal After the Gorkha Earthquake. *Impacts and Insights of Gorkha Earthquake in Nepal*, Elsevier, 2018.
- [3] M. Faggella, R. Gigliotti, G. Mezzacapo, E. Spacone, Graphic dynamic prediction of polarized earthquake incidence response for plan-irregular single story buildings. *Bulletin of Earthquake Engineering*, **16**, 4971–5001, 2018.
- [4] A.F. Mohammad, M. Faggella, R. Gigliotti, E. Spacone, Effects of bond-slip and masonry infills interaction on seismic performance of older R/C frame structures. *Soil Dynamics and Earthquake Engineering*, **109**, 251–265, 2018.
- [5] F. Romano, M. Zucconi, B. Ferracuti, Seismic fragility curves for RC buildings at territorial scale. *Proceedings of the 7th International Conference on Computational Methods in Structural Dynamics and Earthquake Engineering (COMPDYN 2019)*, Hersonissos, Crete, Greece, June, 24-26, 2019.
- [6] M. Zucconi, R. Ferlito, L. Sorrentino, Validation and extension of a statistical usability model for unreinforced masonry buildings with different ground motion intensity measures. *Bulletin of Earthquake Engineering*, **18**, 767–795, 2020.

- [7] H. Crowley, J.J. Bommer, R. Pinho, J. Bird, The impact of epistemic uncertainty on an earthquake loss model. *Earthquake Engineering and Structural Dynamics*, **34**, 1653–1685, 2005.
- [8] D. Celarec, P. Ricci, M. Dolšek, The sensitivity of seismic response parameters to the uncertain modelling variables of masonry-infilled reinforced concrete frames. *Engineering Structures*, **35**, 165–177, 2012.
- [9] A.F. Mohammad, M. Faggella, R. Gigliotti, E. Spacone, Probabilistic seismic response sensitivity of nonlinear frame bending-shear and infill model parameters for an existing infilled reinforced concrete structure. *Proceedings of the twelfth International Conference on Computational Structures Technology*, 2014.
- [10] A. Muratovic, N. Ademovic, Influence of masonry infill on reinforced concrete frame structures' seismic response. *Coupled systems mechanics*, **4**, 173–189, 2015.
- [11] J.L. Beck, K.-V. Yuen, Model Selection Using Response Measurements: Bayesian Probabilistic Approach. *Journal of Engineering Mechanics*, **130**, 192–203, 2004.
- [12] B.A. Bradley, A critical examination of seismic response uncertainty analysis in earthquake engineering. *Earthquake Engineering & Structural Dynamics*, **42**, 1717–1729, 2013.
- [13] F. Jalayer, *Direct probabilistic seismic analysis: implementing non-linear dynamic assessments*. Department of Civil and Environmental Engineering, Stanford University, 2003.
- [14] FEMA, *FEMA P-58-1: Seismic performance assessment of buildings - Methodology*. Federal Emergency Management Agency, 2012.
- [15] F. Romano, M. Faggella, R. Gigliotti, M. Zucconi, B. Ferracuti, Comparative seismic loss analysis of an existing non-ductile RC building based on element fragility functions proposals. *Engineering Structures*, **177**, 707–723, 2018.
- [16] C. Del Vecchio, M. Di Ludovico, S. Pampanin, A. Prota, Repair Costs of Existing RC Buildings Damaged by the L'Aquila Earthquake and Comparison with FEMA P-58 Predictions. *Earthquake Spectra*, **34**, 237–263, 2018.
- [17] D. Cook, K. Wade, C. Haselton, J. Baker, D.J. Debock, A structural response prediction engine to support advanced seismic risk assessment. *Proceedings of the 11th U.S. National Conference on Earthquake Engineering*, Los Angeles, California, June 25-29, 2018.
- [18] F. Romano, M.S. Alam, M. Zucconi, M. Faggella, A.R. Barbosa, B. Ferracuti, Seismic demand model class uncertainty in seismic loss analysis for a code-designed URM infilled RC frame building. *Bulletin of Earthquake Engineering*, **19**, 429–462, 2021.
- [19] F. McKenna, M.H. Scott, G.L. Fenves, Nonlinear Finite-Element Analysis Software Architecture Using Object Composition. *Journal of Computing in Civil Engineering*, **24**, 95–107, 2010.
- [20] M.H.M. Yassin, *Nonlinear analysis of prestressed concrete structures under monotonic and cyclic loads*. University of California, Berkeley, 1994.
- [21] M.S. Alam, A.R. Barbosa, Probabilistic seismic demand assessment accounting for finite element model class uncertainty: Application to a code-designed URM infilled reinforced concrete frame building. *Earthquake Engineering & Structural Dynamics*,

- 47, 2901–2920, 2018.
- [22] M.N. Fardis, Experimental and numerical investigations on the seismic response of RC infilled frames and recommendations for code provisions. *Report ECOEST-PREC8 No. 6*, 1996.
 - [23] W.W. El-Dakhakhni, M. Elgaaly, A.A. Hamid, Three-Strut Model for Concrete Masonry-Infilled Steel Frames. *Journal of Structural Engineering*, **129**, 177–185, 2003.
 - [24] F.J. Crisafulli, A.J. Carr, Proposed Macro-Model for the Analysis of Infilled Frame Structures. *Bulletin of the New Zealand Society for Earthquake Engineering*, **40**, 69–77, 2007.
 - [25] A. Stavridis, *Analytical and experimental study of seismic performance of reinforced concrete frames infilled with masonry walls*. University of California, San Diego, 2009.
 - [26] S. Sattar, A.B. Liel, Seismic performance of reinforced concrete frame structures with and without infill walls. *9th US National and 10th Canadian Conference on Earthquake Engineering*, Toronto, Canada, 2010.
 - [27] H. Burton, G. Deierlein, Simulation of Seismic Collapse in Nonductile Reinforced Concrete Frame Buildings with Masonry Infills. *Journal of Structural Engineering*, **140**, A4014016, 2014.
 - [28] FEMA, *FEMA 307: Evaluation of earthquake damaged concrete and masonry wall buildings - technical resources*. Federal Emergency Management Agency, 1998.
 - [29] M. Faggella, A. Barbosa, J.P. Conte, E. Spacone, J.I. Restrepo, Seismic Assessment of R/C Building Structure through Nonlinear Probabilistic Analysis with High-performance Computing. *AIP Conference Proceedings*, AIP, 2008.
 - [30] M. Kohrangi, D. Vamvatsikos, P. Bazzurro, Implications of Intensity Measure selection for seismic loss assessment of 3-D buildings. *Earthquake Spectra*, **32**, 2167–2189, 2016.
 - [31] C.B. Haselton, C.A. Goulet, J. Mitrani-reiser, J.L. Beck, G.G. Deierlein, K.A. Porter, J.P. Stewart, An Assessment to Benchmark the Seismic Performance of a Code-Conforming Reinforced Concrete Moment-Frame Building. 2008.
 - [32] C.M. Ramirez, E. Miranda, *Building-specific loss estimation methods & tools for simplified performance-based earthquake engineering*. The John A. Blume Earthquake Engineering Center Department of Civil and Environmental Engineering Stanford University, 2009.

SEISMIC BEHAVIOR OF SUBSTANDARD EXTENDED RECTANGULAR RC COLUMNS JACKETED WITH SPRAYED GFRM

Muhsin Can Luleci^{1A}, Bilal Sari^{1B}, Ugur Demir², Muhammed Marasli³ and Alper Ilki⁴

¹ MSc Student

Istanbul Technical University, 34469, Maslak, Istanbul
e-mail: A: luleci19@itu.edu.tr; B: sarib19@itu.edu.tr

² PhD, Research Assistant

Hakkari University, Hakkari
e-mail: udemir@itu.edu.tr

³ Member of Board of Directors

Fibrobeton Yapi Elemanlari, 34810, Kavacik, Istanbul
e-mail: muhammed@fibrobeton.com.tr

⁴ Professor

Istanbul Technical University, 34469, Maslak, Istanbul
e-mail: ailki@itu.edu.tr

Abstract

In earthquake prone areas, columns of many relatively old RC (reinforced concrete) structures do not comply with the current seismic design codes, particularly in developing countries. Low concrete strength, improper seismic detailing of transverse reinforcement and high axial stresses on the columns are common problems causing lack of sufficient ductility under seismic forces. External jacketing of substandard columns by spraying GFRM (glass fiber reinforced mortar) is a new, practical and feasible method to overcome these deficiencies, particularly for the cases where access to the structural members is limited. In this study, the effects of cross-sectional aspect ratio (h/b) of columns on effectiveness of external jacketing with sprayed GFRM are investigated experimentally. For this purpose, four full scale RC columns were tested under constant axial load ($0.35f_c A_g$) and cyclic lateral displacement reversals before and after seismic retrofit with sprayed GFRM jacket. The cross-sectional aspect ratios of two columns were 2.0, whereas the cross-sectional aspect ratio was 4.0 for the other two columns. The structural responses of the columns are discussed through hysteretic and envelope load-displacement curves. The test results show that sprayed GFRM jacketing improves lateral ductility of the substandard columns significantly. It is also shown that the method is effective for the columns with high cross-sectional aspect ratios.

Keywords: Column, GFRM, Reinforced Concrete, Seismic

1 INTRODUCTION

There are many buildings all over the world that do not comply with the requirements of current seismic design codes or with the requirements of their construction times. The poor seismic performance of buildings with typical deficiencies of structural members (i.e. columns) such as low strength concrete, inadequate detailing and insufficient transverse reinforcement may cause a considerable number of casualties and economic losses during severe earthquakes. Previous devastating earthquakes (i.e. 1994 Northridge, 1995 Kobe, 1999 Kocaeli, 2011 Van, 2020 Elazig and Izmir earthquakes) have also demonstrated the vulnerability of substandard RC columns exposed to seismic actions demanding large inelastic deformations [1-2]. To mitigate this risk, many studies on seismic retrofitting of substandard columns were conducted in the last decades. Because the major problem for the substandard building stock stems from the lack of lateral strength, ductility and stiffness, the external jacketing method using fiber reinforced polymers (FRPs) has gained popularity for the enhancement of the seismic performance of substandard RC members [e.g. 3-9]. The proven efficiency of this innovative solution in terms of providing additional confinement, leads to improved seismic resistance in terms of lateral load capacity and inelastic deformation capabilities of substandard RC members. Recent researches have shown that usage of other innovative materials such as textile reinforced mortar [e.g. 10-11] or fiber reinforced mortar [12] for external confinement is also a promising retrofitting solution for reinforced concrete and masonry members [13].

Therefore, this paper is aimed at improving the seismic resistance of extended rectangular substandard RC columns through sprayed GFRM (glass fiber reinforced mortar) jacketing. Towards this aim, preliminary results of an experimental study conducted on full-scale substandard RC columns of different cross-sectional aspect ratios (2.0 and 4.0) are presented in this paper. The study examines the impact of reversed cyclic lateral loading on the columns before and after application of proposed external jacketing method.

2 EXPERIMENTAL WORK

2.1 Specimen details and test setup

In the scope of the study, a total of 4 cantilever columns were cast to assess the efficiency of sprayed GFRM jacketing on seismic behavior of substandard RC columns. The columns had dimensions of 200 mm×400 mm and 200 mm×800 mm, corresponding to cross-sectional aspect ratio (h/b) of 2.0 and 4.0, respectively. The columns with h/b of 2.0 and 4.0 were cast having a height of 1750 and 2100 mm, respectively. For each aspect ratio, two columns were cast, one to be a reference column and the other with purpose of retrofitting. Each column incorporated an RC foundation block with dimensions of 900 mm×1300 mm ($h/b=2.0$) or 1300 mm×1700 mm ($h/b=4.0$) and height of 700 mm. Columns were reinforced with 4 of 16 mm ($h/b=2.0$) or 8 of 16 mm ($h/b=4.0$) diameter longitudinal steel plain bars placed at the corners with a 30 mm concrete cover from the edge of the specimen to the outside of the longitudinal bars (Fig. 1). These bars had a yield strength of 292 MPa. Transverse reinforcement was provided in the form of plain bars with 10 mm diameter, which had a yield strength of 312 MPa. These bars were formed at 200 mm spacing center-to-center with 90 degrees hook angle at the test region representing existing substandard building stock. The geometric ratio of longitudinal reinforcement ratio was 1% and volumetric ratio of transverse reinforcements was 0.22% ($h/b=2.0$) or 0.1% ($h/b=4.0$), respectively, which were calculated according to current Turkish Building Earthquake Code [14]. All columns were constructed so as to be representative of

the substandard columns not complying to any design codes. Concrete compressive strength at 28th day after casting was around 12 MPa, and at around the seismic test day (six months after casting) it was 14.1 MPa, which were obtained from 150 mm×300 mm standard cylinders. The columns were tagged as C2 (reference specimen with $h/b=2.0$), C2-R (retrofitted specimen with $h/b=2.0$), C4 (reference specimen with $h/b=4.0$) and C4-R (retrofitted specimen with $h/b=4.0$). The columns were strengthened with sprayed GFRM that had 4.5% glass fiber content by weight. The average 28-day compressive strength of five standard 50 mm cubic GFRM specimens was obtained in accordance with ASTM C109 [15] as 41.4 MPa.

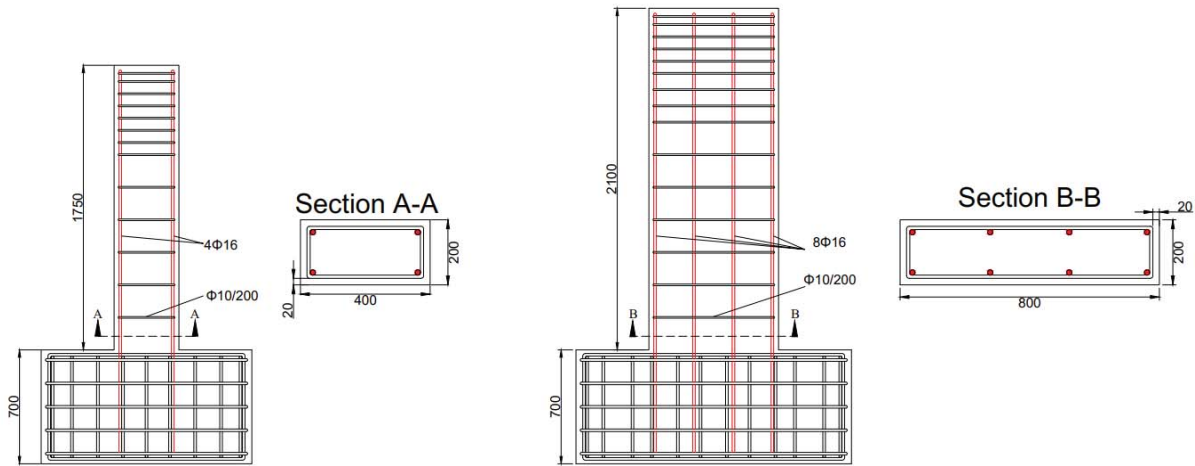


Figure 1: Reinforcement details of the columns. Note: All dimensions are in mm

The general view of the test setup and measurement system consisting of load cells, potentiometers and strain gauges are shown in Fig. 2. The data from the potentiometers, load cells, and electrical resistance strain gauges were collected by means of a data logger. TML YFLA-5 post-yield strain-gauges and TML FLA-5 foil strain-gauges were mounted on longitudinal and transverse reinforcements, respectively. The types and measurement lengths of potentiometers are shown in Fig. 2. In this figure, for instance, SLPS 50 denotes the potentiometer with a 50 mm stroke length. Specimens were fixed to the strong floor of the laboratory by means of six high strength 36 mm diameter bolts. Prior to the seismic tests, the axial load was applied by means of a manually force-controlled hydraulic jack with 2200 kN capacity. After application of vertical constant load, reversed cyclic lateral displacement protocol was applied to the column by means of a horizontal hydraulic actuator with a ± 300 kN and ± 400 mm force and displacement capacity, respectively. Each target displacement had two repeated cycles. The reversed cyclic lateral loading was applied considering increasing drift ratios in pushing and pulling directions that corresponded to ± 0.0005 , ± 0.001 , ± 0.002 , ± 0.003 , ± 0.004 , ± 0.005 , ± 0.0075 , ± 0.01 , ± 0.015 , ± 0.02 , ± 0.025 , ± 0.03 , ± 0.04 , ± 0.05 , ± 0.06 and ± 0.07 drift ratios according to ACI 374.2R-13 [16]. Tests were not terminated until the failure (at least 25% loss of axial and/or lateral load capacities) was observed.

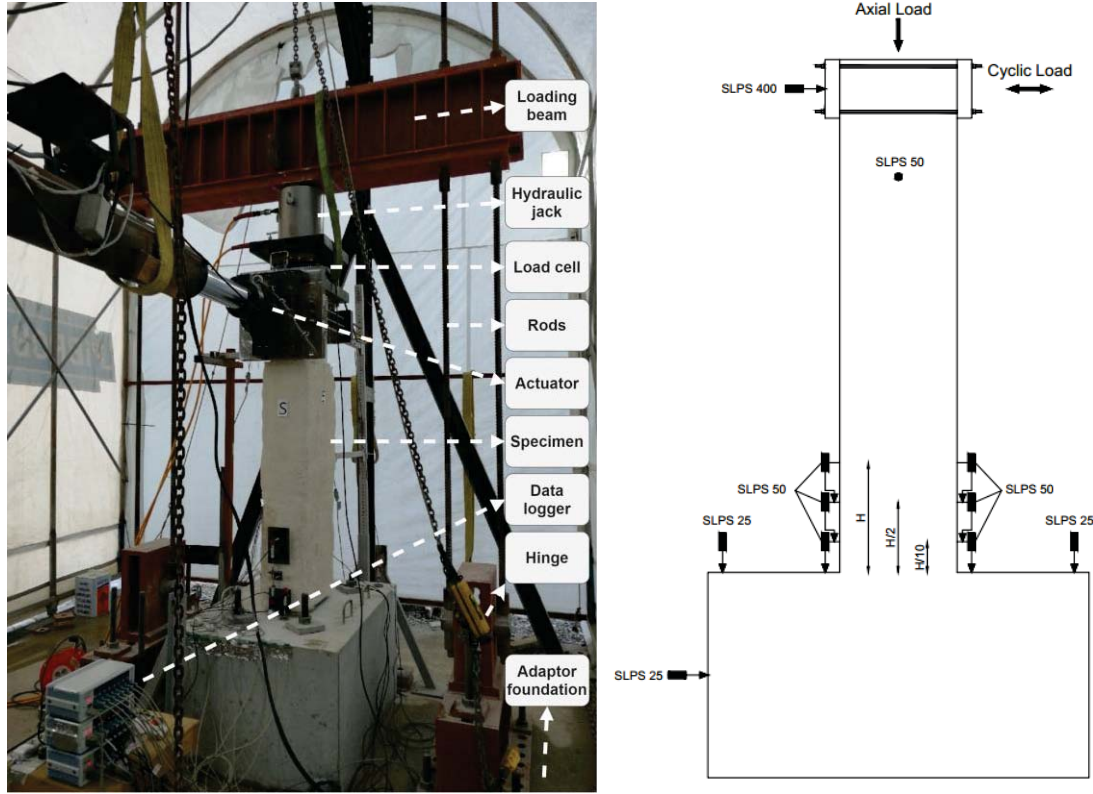


Figure 2: Seismic test setup and instrumentation

2.2 Retrofitting procedure

The columns C2-R and C4-R were prepared to be strengthened by rounding off their corners with a radius of 30 mm. After preparing the surface by cleaning the dust to provide saturation between concrete and GFRM, spraying of GFRM started. Then, GFRM was sprayed by using a spraying gun to the surface of the column. The thickness of GFRM jacket for the column C2-R varied between 25 mm and 35 mm, whereas for the column C4-R, this thickness was between 25 mm and 45 mm. This enlarging thicknesses towards the center of the column edges were proposed to enhance the lateral confinement pressure provided by the jacket. Chopped glass fibers of 32 mm length were used in this composite material. Technical properties of the fibers provided by the manufacturer are shown in Table 1. In order to avoid local damages in the GFRM near the column foundation, a 30 mm of vertical gap was left between the GFRM and the column-foundation interface. The process of strengthening is shown in Fig. 3.

Table 1: Chopped glass fiber technical properties

Properties	Value
Average Filament Diameter (μm)	19
Specific Gravity (gr/m^3)	2.68
Thickness (mm)	0.8-0.9
Tensile Strength (MPa)	1000-1700
Elastic Modulus (GPa)	72



Figure 3: Strengthening process of the columns with GFRM a) rounding off the corners, b) rolling GFRM to distribute uniformly, c) spraying

2.3 Test results

The columns were tested under constant axial load and reversal cyclic lateral loading about six months after casting. During the tests, axial load was kept constant at $0.35f'_c b h$ for all specimens, where f'_c is the compressive strength of concrete, b and h are the width and depth of the column cross-sections. The lateral load-displacement hysteretic curves of the columns and their envelopes are shown in Figs. 4 and 5. The maximum lateral load capacities in pushing and pulling directions are shown in Table 2. For the reference columns C2 and C4, peak lateral loads were achieved at around 1% and 0.75% drift ratio, respectively. The damage progressed for these columns sequentially with crushing and spalling of concrete cover which was followed by buckling of longitudinal rebars. Yielding of longitudinal reinforcement did not occur in these columns. For the reference columns, tests were terminated with 68% and 77% loss of lateral strength, respectively. On the other hand, due to the additional confinement provided by sprayed GFRM, retrofitted columns C2-R and C4-R exhibited a more ductile behavior with respect to their reference counterparts. This additional confinement led to delayed buckling of longitudinal bars which results with more ductility. Moreover, longitudinal reinforcements of strengthened specimens yielded before strength degradation, indicating that failure was not governed by crushing of concrete merely. For retrofitted columns C2-R and C4-R, peak loads were achieved at 1% drift ratio and 0.75% drift ratio, respectively. After this point, strength loss initiated due to an increase in crack widths at the edges of the GFRM jacket. Finally, these cracks extended along the height up to the middle of the column leading to the failure of the column. Jacketing of the specimens with sprayed GFRM enhanced the lateral load capacity of the columns with aspect ratio 2.0 and 4.0, around 6% and 10%, respectively. On the other hand, maximum drift ratio experienced in the seismic tests for these columns were 7% and 4%, respectively. The increase in maximum drift of the columns C2-R and C4-R were around 250% and 166%, respectively, with respect to their reference columns. The damages of the columns after tests are shown in Fig. 6.

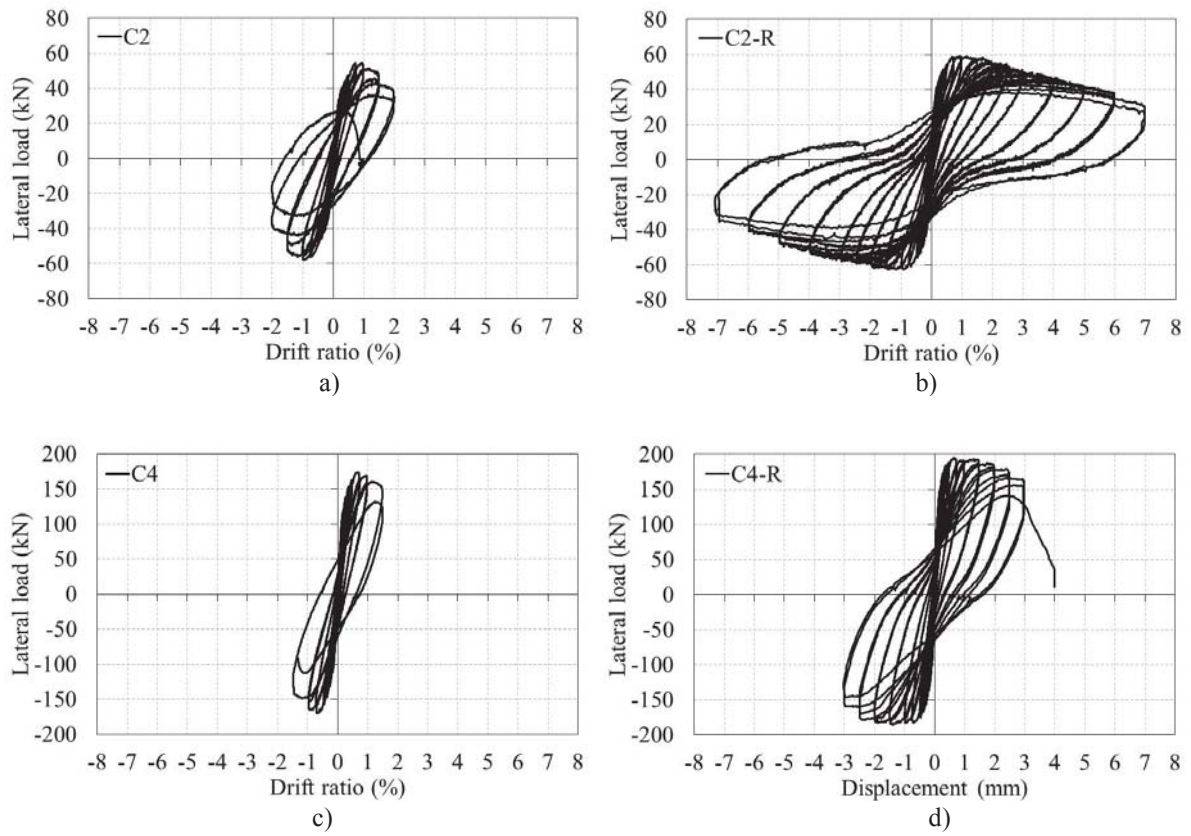


Figure 4: Hysteretic response of the columns a) C2, b) C2-R, c) C4 and d) C4-R

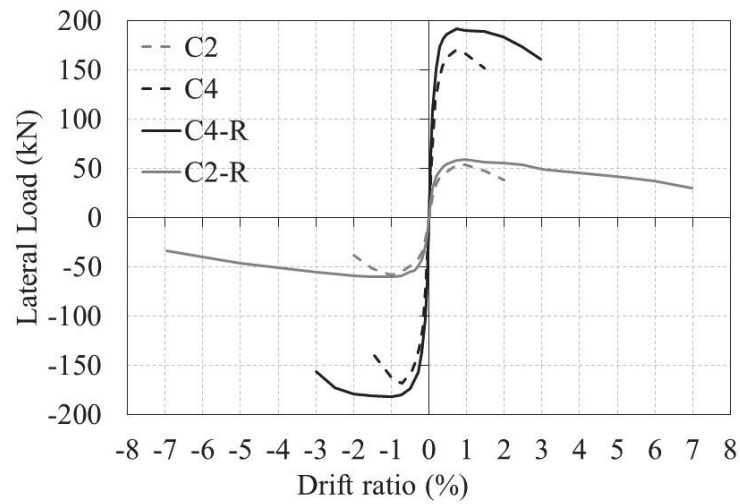


Figure 5: Envelope curves of the columns

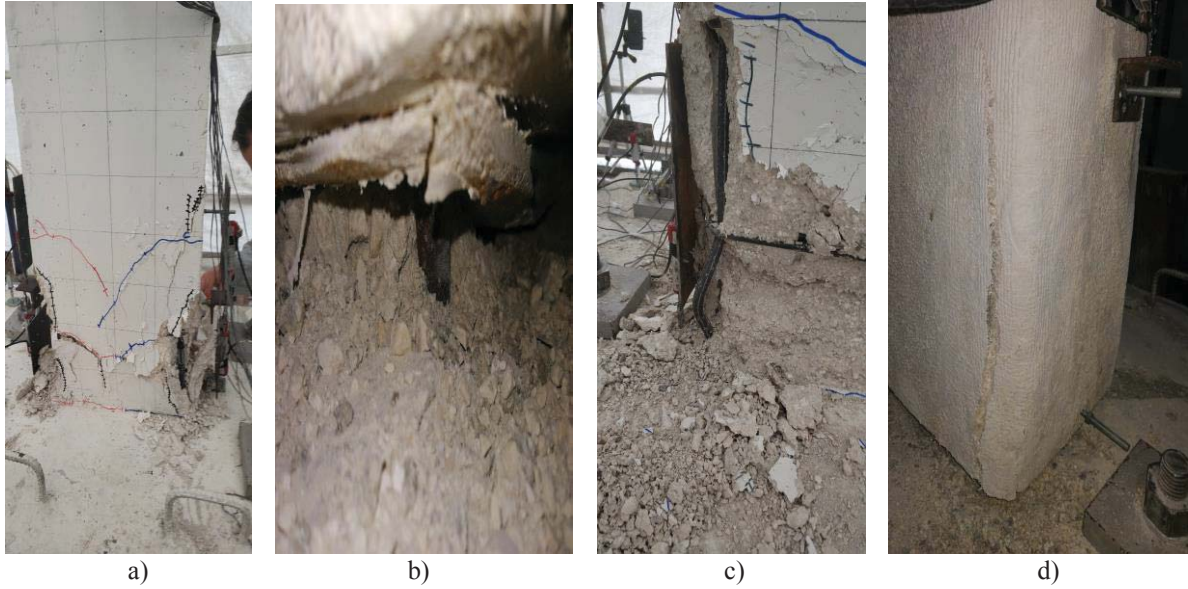


Figure 6: Damages of the columns a) C2, b) C2-R c) C4 and d) C4-R at the end of the tests

Table 2: Summary of the test results

Specimen	Failure drift ^a (%)	Maximum lateral load in pushing (kN)	Maximum lateral load in pulling (kN)	Yield displacement, Δ_1 (mm)	Ultimate displacement, Δ_2 (mm)	Ductility factor, μ_Δ
C2	1.8	58.1	53.2	5.8	28.9	5.0
C2-R	3.6	60.2	58.6	6.6	59.4	9.0
C4	1.5	168.7	170.0	4.4	30	6.8
C4-R	3	181.7	191.4	4.0	60	15.0

^a drift corresponding to ultimate displacement (when the lateral strength was reduced to 80% of the peak value)

For a better comparison of the column performances in terms of ductility, displacement ductility factors (μ_Δ) are calculated as an indicator of deformability. Displacement ductility factors are defined in this study as the ratio of ultimate displacement to the yield displacement. Yield displacement, Δ_y , is the lateral displacement obtained from lateral load-lateral displacement ($P-\Delta$) curve corresponding to the maximum lateral load on straight line joining origin and the point at 75% of the peak lateral load on ascending portion of the average envelope curve, and Δ_u is the ultimate lateral displacement obtained from $P-\Delta$ curve corresponding to 80% of the peak load on descending portion of average envelope curve. The yield and ultimate displacements are shown in Table 2 as well as corresponding displacement ductility factors. As seen in this table, sprayed GFRM jacketing of the columns doubled the ductility of the columns irrespective of the cross-sectional aspect ratio.

3 CONCLUSIONS

The main objective of this study is to investigate the efficiency of sprayed GFRM jacketing in terms of improving seismic performance of substandard columns with extended rectangular cross-sections. In accordance with this purpose, the preliminary results of an ongoing study are presented herein. Two reference and two sprayed GFRM jacketed sub-standard RC columns were tested under seismic loading with cross-sectional aspect ratios of 2.0 and 4.0. The following conclusions can be drawn from the study.

- Application of sprayed GFRM jacketing resulted with a 6-10% increase in lateral load capacity of the substandard columns.
- Due to the effective confinement provided by sprayed GFRM jacketing, the drift capacities of the columns were approximately doubled corresponding to 80 and 120% increase of displacement ductility for the columns with cross-sectional aspect ratios of 2.0 and 4.0, respectively.

Further numerical and experimental studies are under progress for different cross-sections to shed some more light on the behavior of sprayed GFRM strengthening for substandard extended rectangular columns. The current results show that this cost-effective and easily-applicable technique is promising for future practical applications.

ACKNOWLEDGMENTS

This research was granted in the scope of the bilateral collaboration between the research councils of Turkey (TUBITAK) and the Pakistan (PSF) under the grant number 118M261. The authors are most thankful to the Fibrobeton company for their continuous support from the construction phase of the specimens to the testing stage. The contributions of Dr. Cem Demir, Alihan Baltaci, Safiye Gundogan and Erkan Tore are also gratefully acknowledged.

REFERENCES

- [1] R. D. Iacobucci, S. A. Sheikh, and O. Bayrak, Retrofit of square concrete columns with carbon fiber-reinforced polymer for seismic resistance. *ACI Structural Journal*, **100** (6), 785-794, 2003.
- [2] M. Tapan, M. Comert, C. Demir, Y. Sayan, K. Orakcal and A. Ilki, Failures of structures during the October 23, 2011 Tabanlı (Van) and November 9, 2011 Edremit (Van) earthquakes in Turkey. *Engineering Failure Analysis* **34**, 606-628, 2013.
- [3] S. N. Bousias, T. C. Triantafillou, M. N. Fardis and L. Spathis, Fiber-reinforced polymer retrofitting of rectangular reinforced concrete columns with or without corrosion. *ACI Structural Journal*, **101** (4), 512-520, 2004.
- [4] M. S. Memon, and S. A. Sheikh, Seismic resistance of square concrete columns retrofitted with glass fiber-reinforced polymer. *ACI Structural Journal*, **102** (5), 774, 2005.
- [5] A. Ilki, C. Demir, I. Bedirhanoglu and N. Kumbasar, Seismic retrofit of brittle and low strength RC columns using fiber reinforced polymer and cementitious composites. *Advances in Structural Engineering* **12** (3), 325-347, 2009.
- [6] H.F. Ghatte, M. Comert, C. Demir, M. Akbaba and A Ilki, Seismic retrofit of full-scale substandard extended rectangular RC columns through CFRP jacketing: test results and design recommendations, *Journal of Composites for Construction* **23** (1), 2018.
- [7] M. Di Ludovico, A. Prota, G. Manfredi and E. Cosenza, Seismic strengthening of an under-designed RC structure with FRP. *Earthquake Engineering & Structural Dynamics*, **37** (1), 141-162, 2008.
- [8] M. Comert, C. Demir, A.O. Ates, K. Orakcal, and A. Ilki, "Seismic performance of three-storey full-scale sub-standard reinforced concrete buildings" *Bulletin of Earthquake Engineering*, **15** (8), 3293-3320, 2017.

- [9] E. Tore, M. Comert, C. Demir, A. Ilki, Collapse testing of full-scale RC buildings with or without seismic retrofit of columns with FRP jackets, TU1207 End of Action Conference, Budapest, 3-5 April, 2017.
- [10] T.C. Triantafillou, C.G. Papanicolaou, P. Zissimopoulos, T. Laourdekis, Concrete confinement with textile reinforced mortar jackets. *ACI Structural Journal*, **103** (1), 2006.
- [11] D.A. Bournas, P.V. Lontou, C.G. Papanicolaou, T.C. Triantafillou, Textile-reinforced mortar versus fiber reinforced polymer confinement in reinforced concrete columns. *ACI Structural Journal*, **104** (6), 2007.
- [12] A.O. Ates, S. Khoshkholghi, E. Tore, M. Marasli, A. Ilki, Sprayed glass fiber reinforced mortar with or without basalt textile reinforcement for jacketing of low strength concrete prisms, ASCE, *Journal of Composites for Construction*, **23** (2), April, 2019.
- [13] P.E. Mezrea, I.A. Yilmaz, E. Binbir, M. Ispir, I.E. Bal, and A. Ilki, External jacketing of unreinforced historical masonry piers with open-grid basalt reinforced mortar, *ASCE Journal of Composites for Construction*, **21** (3), Article Number: 04016110, 2017.
- [14] Turkish Building Earthquake Code (TBEC), Disaster & Emergency Management Authority, Ankara, Turkey, 2018.
- [15] ASTM C109/109M-16a, Standard test method for compressive strength of hydraulic cement mortars. American Society for Testing and Materials. West Conshohocken, PA. Sec.4, Volume 04.01, 2016.
- [16] ACI 374. 2R-13, Guide for testing reinforced concrete structural elements under slowly applied simulated seismic loads. American Concrete Institute, Farmington Hills, MI., 2013.

DAMAGE EVOLUTION FOR REPAIRABILITY OF SUBSTANDARD BEAM-COLUMN JOINTS

Özgür Yurdakul¹, Ciro Del Vecchio², Marco Di Ludovico³
Ladislav Řoutil¹, and Özgür Avşar⁴

¹ University of Pardubice
Department of Transport Structures, Faculty of Transport Engineering
(ozgur.yurdakul, ladislav.routil)@upce.cz

² University of Sannio
Department of Engineering
cdelvechio@unisannio.it

³ University of Napoli Federico II
Department of Structures for Engineering and Architecture
diludovi@unina.it

⁴ Eskişehir Technical University
Department of Civil Engineering, Engineering Faculty
ozguravsar@eskisehir.edu.tr

Abstract

Substandard reinforced concrete (RC) joints often exhibited poor seismic performance even under moderate intensity earthquakes, which is due to the lack of earthquake-resistant design detailing. Premature joint cracking often compromises the seismic performance of the entire building, initiating local collapses or global failure mechanisms. The quantification of the joint repairability in terms of reduction of the structural damage as well as expected economic losses is still a challenging task. This is due to the uncertainties in the assessment of residual and maximum crack widths. This study deals with the evaluation of crack by the increasing drift level. To this end, available numerical and experimental cyclic data on the substandard beam-column joints are collected. The variability in material properties is considered and the correlation between residual and maximum crack width is obtained. These data are then used to obtain residual-to-maximum crack width ratio by increasing drift level. The available repairability thresholds are then compared with the residual-to-maximum crack width ratio curve.

Keywords: Crack width, Repair, Probabilistic, Beam-column joints, Substandard

1 INTRODUCTION

Existing reinforced concrete buildings designed according to former code provisions lack several earthquake-resistant design detailing. This makes these buildings vulnerable to seismic actions. The poor energy dissipation and sudden strength and stiffness degradation are the main consequences of the brittle failures of such vulnerable structural members. Beam-column joints deserve special interest in existing buildings because they can be the critical and possibly the weakest link according to the capacity design principles or hierarchy of strength considerations [1]. Such an unfavorable seismic behavior of joints obviously compromises the structural integrity of the whole system. Therefore, the experimental performance of the deficient joints has attracted considerable research interest [2–7]. The response of beam-column joints under a multi-axial complex stress field is also reproduced by the computer-aided nonlinear analysis [8–12]. The refined and validated numerical models are also combined with the stochastic approach requiring a solution with randomized material properties to improve the accuracy of the analysis results [13–15]. The repair of deficient joints has attracted considerable research interest [16–20]. However, the building repair is usually limited by the high repair cost of drift-sensitive members [21], and massive reconstruction and intrusive repair procedures [22]. Besides, the repair procedure and type are fairly sensitive to damage level (i.e., light, moderate or severe damage). The damage indicators characterizing the severity and extent are usually associated with the crack width for light/moderate damage level and macroscopic concrete and reinforcing bar damage for severe damage state [23–29]. Therefore, the selection of a suitable repair procedure usually depends on damage level and crack width. The evolution of the crack width by the increasing drift level, the correlation between maximum and residual crack width are important parameters in assessing the level of damage (and the repair actions). The effect of randomness at the material level should be also considered when obtaining such engineering demand parameters (EDPs). This study mainly deals with the evolution of crack at imposed drift and residual crack width by the increasing drift level. The residual-to-maximum crack width ratio at imposed drift ratio is obtained to show the crack closure effect. Then, this ratio is compared with current repairability thresholds to obtain proper relationships suitable for on-site engineering applications.

2 METHODOLOGY

The deformation limit of serviceability and its corresponding crack width are usually considered as a threshold for the building repairability considering conventional repair actions (i.e., crack filling, concrete patching, or cover replacement). On the other hand, it should not be beyond economical repair. FEMA P-58 [30] specifies a threshold value of 50% of building cost when contemplating whether a damaged structure should be replaced or repaired. Light to moderate damage can be identified as the threshold for the feasibility of repair. Here, light damage corresponds to hairline cracks or cracks that can be repaired with surface finishing/epoxy resin while moderate damage refers to remarkable wide cracks, concrete cover spalling, local concrete crushing, and reinforcement yielding [30, 31]. The use of fiber-reinforced polymers (FRP) for the repair and rehabilitation of heavily damaged RC members is an efficient solution [23–28]. The indicators for the detection of damage at light to moderate damage levels are also identified for in-situ inspections in terms of residual crack width. Therefore, the residual crack width can be useful for the detection of the damage during post-earthquake damage inspections for the feasible repair action. The available standards and guidelines also refer to the use of residual crack width for repairability [23, 25, 27, 32]. On the other hand, special attention should be given to assess the residual crack width as the scatter in the residual crack width is high.

Note that, Maximum Inter-story Drift Ratio (IDR) is commonly accepted to be a key engineering demand parameter. The residual story drift is also one of the global acceptance criteria for repairability [32], however large variability could be associated to this parameter and residual crack width. Besides, it is more sensitive to hysteretic unloading and reloading response in moderately damaged reinforced concrete plastic hinges [31]. In the case of brittle behavior of joint, limiting the residual displacements (and so the residual crack width) as a means of increasing the probability that the building can be repaired following earthquake ground shaking is also an efficient solution. Therefore, the damage evolution could be represented by the crack width at maximum and residual IDR.

This research proposes relationships between residual crack width and maximum crack width together with the correlation to maximum drift. This allows the reader to obtain the relationship between residual and maximum crack width together with the evolution of the crack width by the increasing drift level. To address this scope, the outcomes of stochastic analyses developed on validated FEM numerical models are used. The substandard beam-column joint specimen with low strength concrete and plain round bar is first tested (i.e., specimen EJ_R) [22]. Then, the progress of crack developments, its patterns, and global hysteretic response is reproduced in ATENA Science [33] finite element method (FEM) software. The modeling approach, the constitutive law of the materials and its parameters suitable for application to substandard beam-column joint, modeling accuracy and effectiveness in reproducing the experimental behavior, modeling advantages-disadvantages, difficulties in the modeling of substandard joints are discussed in detail in Yurdakul *et al.* [12]. The simulation of the randomness at the material level (i.e., concrete and reinforcing steel) is accounted by computational stochastic mechanics. The mechanical properties of concrete and reinforcing steel are described as random variables to consider the variability in material properties [14]. Thus, the effect of material parameters on the cracking response is found. The residual crack width and maximum crack width at the imposed drift with their scatter are obtained from the numerical analyses. In many cases, the cracking mechanism at the joint back, joint core and interface occur simultaneously. The most critical cases for the most unfavorable situation are taken into account when evaluating the crack width at each location of the joint region. More detailed information about the cracking response can be found in Yurdakul *et al.* [13].

3 RESULTS AND DISCUSSION

The outcomes of numerical analyses in terms of the crack width vs. maximum or residual IDR are reported in Figure 1a and b, respectively. The data can be fitted with a linear relationship with an acceptable level of accuracy. The correlation among datasets (i.e., imposed/residual drift and imposed/residual crack width), referred as the coefficient of determination R^2 in the graphs is high, demonstrating the accuracy of the fitting. When both imposed and residual crack widths at the interface are considered, a higher scatter in fitting the data can be observed.

As mentioned in the previous section, the uncertainty in the residual crack width is high. Therefore, the reliability of setting a crack repairability limit based on the residual drift (and so crack width) should be further investigated. The correlation between the residual crack widths and maximum crack widths is presented to validate the range of application of the considerations for joint repairability based on residual crack width. For this purpose, the data are fitted with a linear relationship, and the correlation between the residual crack widths and crack widths at imposed drift is obtained for 30 samples (see Figure 2). The graph indicates the correlation at each imposed and residual drift ratio.

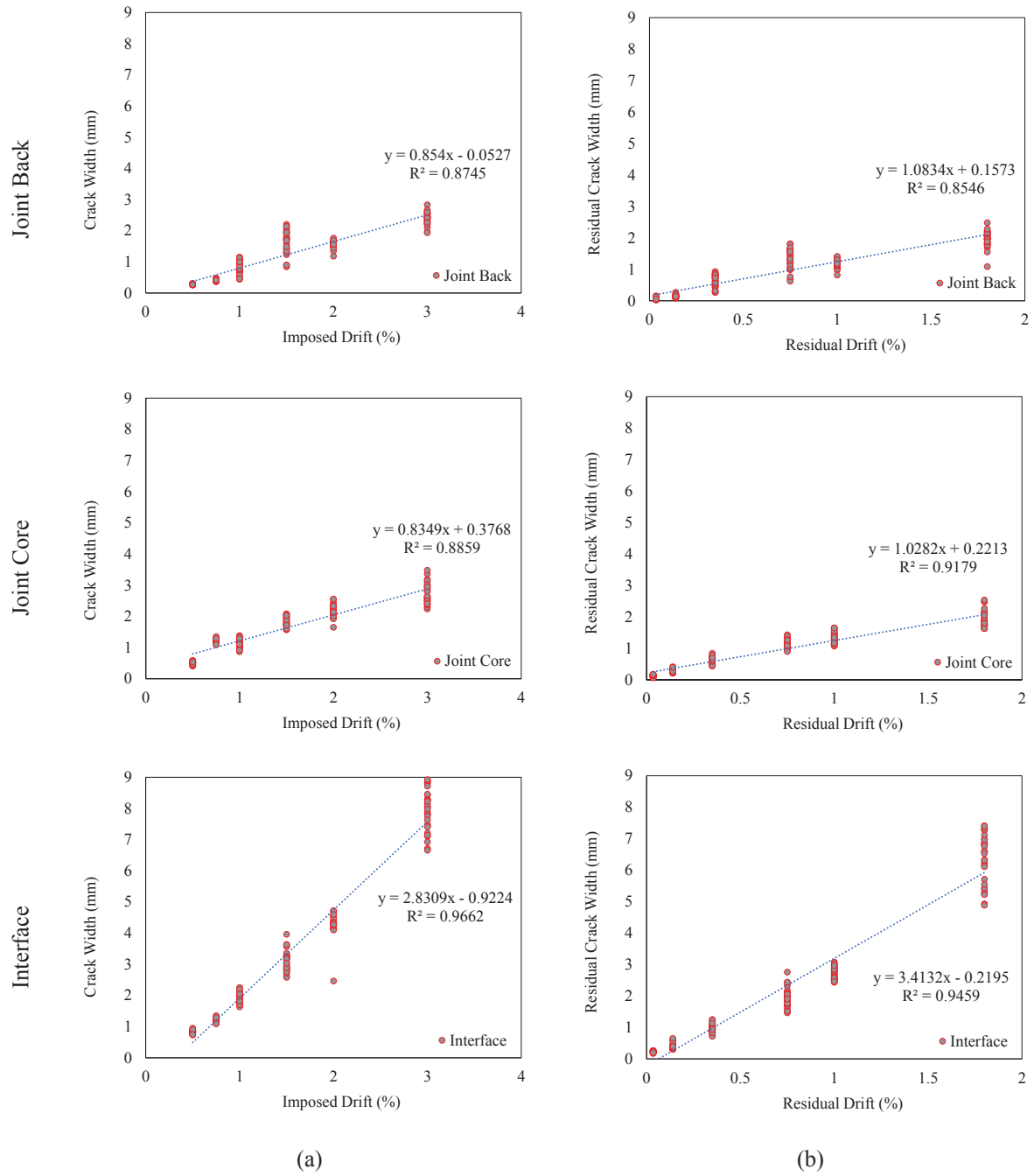
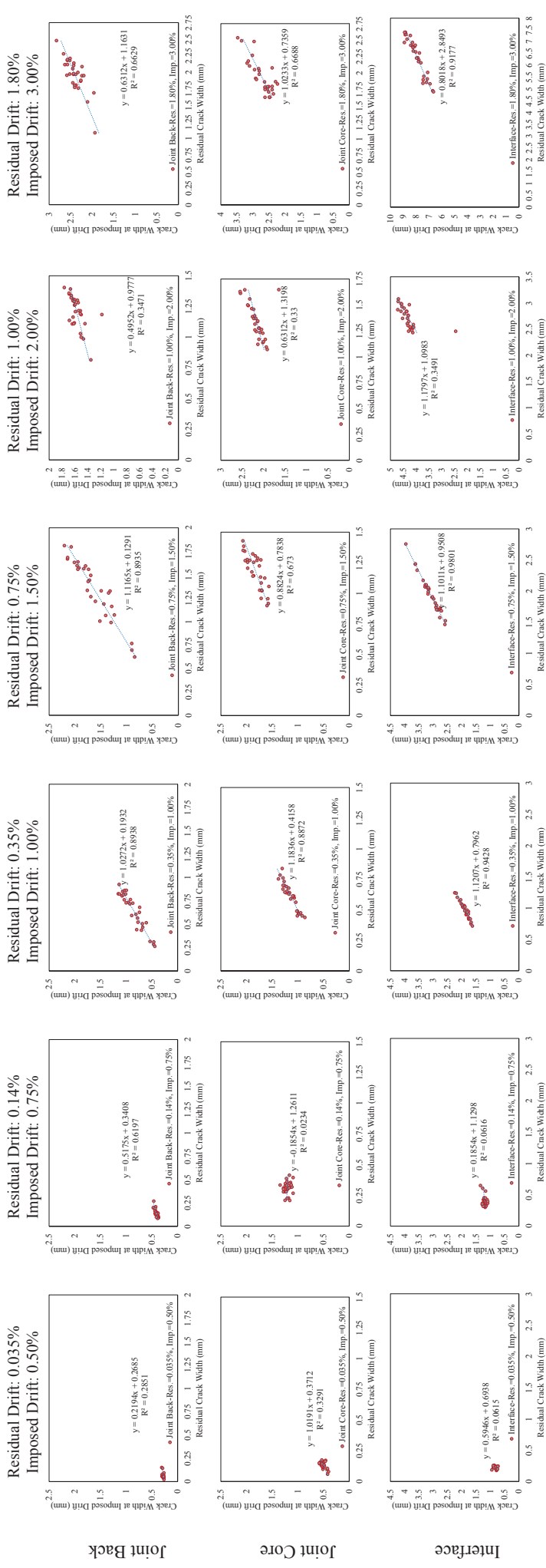


Figure 1. Correlation between (a) maximum crack width and imposed drift (b) residual crack width and residual drift (EJ_R)



Res: Residual Drift, Imp: Imposed Drift

Figure 2. Correlation between imposed/residual crack width (specimen EJ-R)

The evolution of the correlation coefficient, referred as a coefficient of determination R^2 , at each drift level in Figure 2 is presented in Figure 3. A low correlation between peak and residual crack width is found at low imposed drifts (i.e., 0.50 and 0.75%). This is due to the sensitivity of the crack width to the tensile strength of concrete at low joint shear stress demand [14]. Indeed, a high variability of concrete tensile strength is widely recognized [34, 35]. The R^2 values indicate the acceptable level of correlation between the residual crack widths and crack widths at imposed drift at 0.35% residual drift (corresponding to the imposed drift of 1.00%) and 0.75% residual drift (corresponding to the imposed drift of 1.50%). It should be noted that FEMA P58 [30] refers to the residual drift ratio of 0.5% as a threshold for the feasible repair action. The residual drifts of 0.35% and 0.75% are the closest values to 0.5% residual drift ratio representing the threshold limit as per FEMA P58 [30]. The correlation then drops to a certain level in the subsequent drift levels. This could be due to excessive damage in subsequent drift levels.

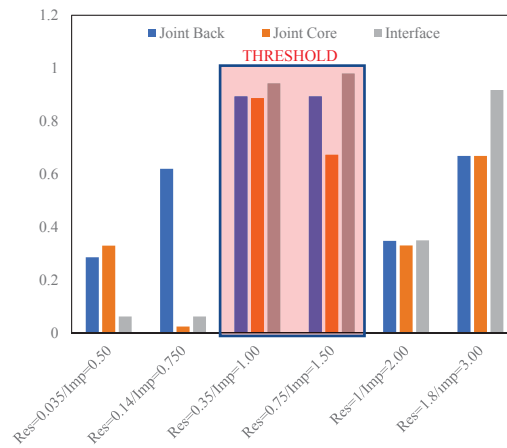


Figure 3. Coefficient of determination R^2 of the linear fitting of maximum vs residual crack width at increasing drift demand.

The change in the residual-to-maximum crack width ratio by the increasing imposed drift is presented in Figure 4a-c. If one of the parameters in Figure 4a-c is known, the other parameters can be estimated from the presented equations. For instance, the proposed relationships allow the calculation of the maximum crack width by knowing the residual crack width and maximum inter-story drift (that can be estimated with a numerical model). Thus, it allows correlating two of the most important EDP to assess building reparability.

An in-depth analysis of the results reported in Figure 4a-c allows to draw important consideration on the feasible reparability and crack closure effect for RC beam-column joints. An ascending linear trend is followed by a second linear trend with a lower steepness. The change of steepness approximately takes place between 1.00% and 1.50% imposed drift. With the less steep curve, the residual-to-maximum crack width ratio gets close to 1.00. Namely, the cracks become large enough, which are not closing, and exhibit large residual cracks. Therefore, the breakpoint of the curve where it changes the characteristics can be assumed as a feasible reparability threshold value. Note that the residual drifts of 0.35% (corresponding to 1.00% imposed drift) and 0.75% (corresponding to 1.50% imposed drift) are the closest values to residual drift ratio of 0.5% being a threshold for feasible repair according to FEMA P58 [30]. Overall, the change in the characteristics of the multilinear curve takes place between 1.00% and 1.50% drift ratio, being the corresponding imposed drifts closest to the feasible repair threshold.

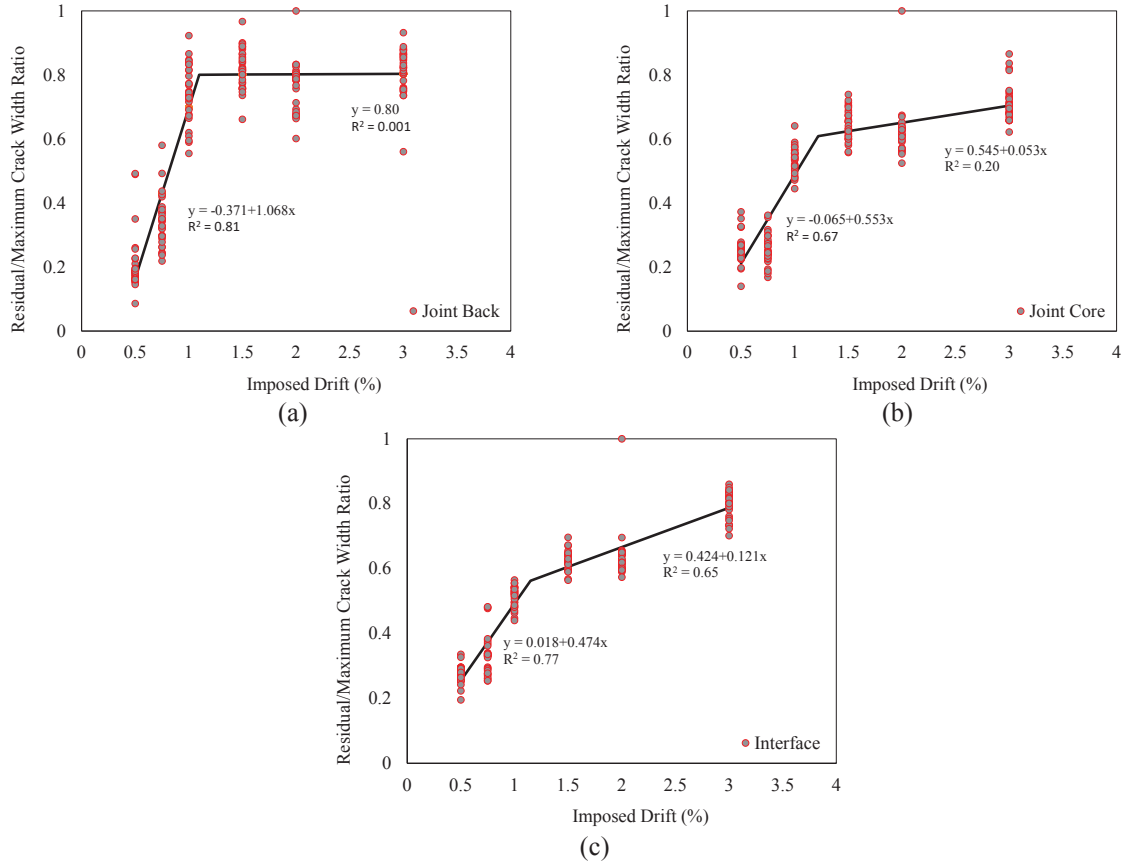
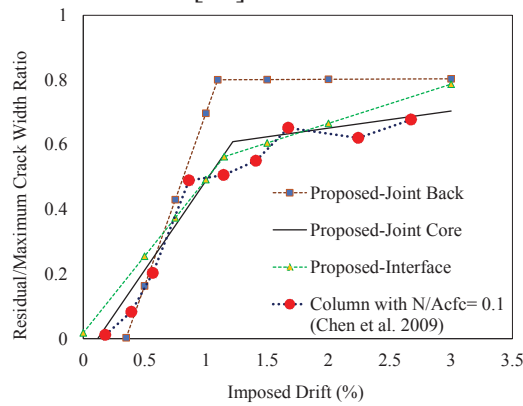


Figure 4. Residual to maximum crack width ratio at different residual drift levels

The proposed residual-to-maximum crack width curves are compared with each other as well as with the curve available in the literature (Figure 5). The trend of the proposed curve for the joint back crack is far from the experimental observations of Chen *et al.* [36]. That of interface predicts the experimental observations of Chen *et al.* [36] with a rather low accuracy, in turn, the proposed curve for joint core closely characterizes the experimental observations of Chen *et al.* [36]. The trend obtained for the joint core is best among all data in reproducing the experimental observations of Chen *et al.* [36].



Data retrieved from Chen *et al.* [36]

Figure 5. Comparison of residual to imposed crack width ratio

4 COMMENTS ON REPAIRABILITY

The apparent macroscopic damage at RC components, which covers wide cracks, the onset of concrete spalling, and local concrete crushing, is usually associated to the repairability threshold. Proper repair actions can restore the strength and stiffness of the component that experienced such a damage level. A comprehensive literature review of codes, standards, and guidelines [30, 37] showed a high scatter in the definition of the repairability threshold. FEMA P-58 [30] refers to DS1 (with corresponding maximum drift ratio of 1.75%) for non-conforming beam-column joints (under the condition that residual crack width is smaller than 1.50 mm) while HAZUS MR4 [37] associates the imposed drift with 0.60% for moderate structural damage. Besides, FEMA P-58 [30] also refers to residual drift ratio of 0.5% for the repairability threshold. As mentioned previously, the residual drifts of 0.35% and 0.75% are the closest values to 0.5% residual drift ratio representing the threshold limit as per FEMA P58 [30]. The imposed drifts are 1.00% and 1.50%, respectively. The change in the curve characteristics lies between imposed drifts of 1.00% and 1.50%, corresponding to the threshold value of residual drifts in FEMA P-58 [30] (Figure 6). To conclude, the breakpoint of the curve where it changes the characteristics can be assumed as a feasible repairability threshold value, which is between 1.00% and 1.50% imposed drift.

The correlated most important EDPs, which are residual and maximum crack width, allows the calculation of the maximum crack width. The maximum crack width can be calculated by the proposed curves if the residual crack width (which is a quantifiable parameter after an earthquake) and maximum inter-story drift (which can be estimated with a numerical model) are known. It should be also noted that this study relies on the numerical and stochastic assessment of the substandard beam-column joint. The specimen represents the substandard RC member with low strength concrete and plain round bar. The scatter in the stochastic analysis is considered only for material uncertainties. Besides, the resulting failure mode is shear failure together with slippage of the beam longitudinal reinforcement. A further study is required accounting for geometrical uncertainties together with different failure modes.

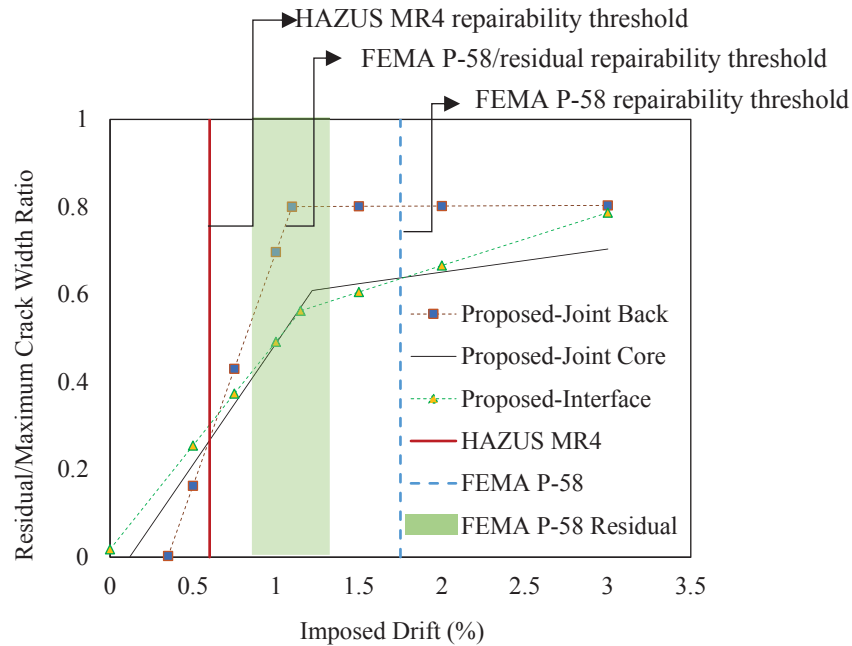


Figure 6. Repairability thresholds on residual-to-maximum crack width plots

5 CONCLUSION

Existing reinforced concrete buildings are vulnerable to seismic actions due to lack of earthquake-resistant design detailing. The poor energy dissipation and sudden strength and stiffness degradation may result in devastating brittle failure for beam-column joints. Furthermore, the lack of transverse reinforcement does not allow to keep the integrity of joint panel, often resulting in marked cracking difficult to repair. Determining widely recognized acceptance criteria for feasible repair is challenging. Limiting the residual drift is commonly accepted since it is a measurable quantity after an earthquake (i.e., the residual story drift and so residual crack). On the other hand, the maximum inter-story drift allows making proper consideration on the achieved damage state by using available fragility curves. However, this requires a reliable numerical model. Based on the results of numerical analyses by using a validated numerical FEM model, this study proposes a correlation between residual and maximum crack width as well as evaluation of both maximum and residual crack width.

Based on the obtained results, the following preliminary conclusions can be drawn;

- The reliability of setting a crack reparability limit based on the residual drift (and so crack width) is validated via the correlation between the residual crack widths and maximum crack widths.
- The data fitted with a linear relationship has enough accuracy. The correlation among datasets (i.e., imposed/residual drift and imposed/residual crack width), referred as the coefficient of determination R^2 in the graphs, is high demonstrating an acceptable level of accuracy of the data fitting at 1.00% and 1.50% imposed drifts corresponding to 0.35% and 0.75% residual drifts, respectively. Those are the closest values to 0.5% which is considered a feasible threshold value for repair according to FEMA P-58 [30].
- The residual-to-maximum crack width ratio graphs allow to draw important consideration on the feasible reparability and crack closure effect for RC beam-column joints. The change of steepness approximately takes place between 1.00% and 1.50% imposed drift. With the less steep curve, the residual-to-maximum crack width ratio gets close to 1.00. Namely, the cracks become large enough, which are not closing, and exhibit large residual cracks. Therefore, the breakpoint of the curve where it changes the characteristics can be assumed as the feasible reparability threshold value.
- The study relies on the numerical and stochastic assessment of the substandard beam-column joint with low strength concrete and plain round bar. The shear failure together with slippage of the beam longitudinal reinforcement is the resulting failure mode. A further study is required accounting for geometrical uncertainties together with different failure modes.

ACKNOWLEDGMENTS

This study was performed within the framework of the PE2019–2021 joint program DPC-ReLUIIS. Also, it was accomplished with the support of the Educational and Research Centre in Transport, Faculty of Transport Engineering, University of Pardubice.

REFERENCES

- [1] Pampanin, S., Christopoulos, C., Chen, T.-H., Development and validation of a metallic haunch seismic retrofit solution for existing under-designed RC frame buildings. *Earthquake Engineering & Structural Dynamics*, **35**, 2006.

- [2] Bedirhanoglu, I., Ilki, A., Pujol, S., Kumbasar, N., Seismic behavior of joints built with plain bars and low-strength concrete. *ACI Structural Journal*, 2010.
- [3] Yurdakul, Ö., Avşar, Ö., Strengthening of substandard reinforced concrete beam-column joints by external post-tension rods. *Engineering Structures*, **107**, 2016.
- [4] Yurdakul, Ö., Tunaboyu, O., Avşar, Ö., Retrofit of non-seismically designed beam-column joints by post-tensioned superelastic shape memory alloy bars. *Bulletin of Earthquake Engineering*, **16**, 2018.
- [5] Del Vecchio, C., Di Ludovico, M., Balsamo, A., Prota, A., Seismic retrofit of real beam-column joints using fiber-reinforced cement composites. *Journal of Structural Engineering*, **144**, 2018.
- [6] Hassan, W.M., Moehle, J.P., Shear strength of exterior and corner beam-column joints without transverse reinforcement. *ACI Structural Journal*, **115**, 2018.
- [7] De Risi, M.T., Del Vecchio, C., Ricci, P., Di Ludovico, M., et al., Light FRP strengthening of poorly detailed reinforced concrete exterior beam-column joints. *J. Compos. Constr.*, **24**, 2020.
- [8] Haach, V.G., Lúcia Homce De Cresce El Debs, A., Khalil El Debs, M., Evaluation of the influence of the column axial load on the behavior of monotonically loaded R/C exterior beam-column joints through numerical simulations. *Engineering Structures*, **30**, 2008.
- [9] Kulkarni, S.A., Li, B., Yip, W.K., Finite element analysis of precast hybrid-steel concrete connections under cyclic loading. *Journal of Constructional Steel Research*, **64**, 2008.
- [10] Del Vecchio, C., Di Ludovico, M., Prota, A., Manfredi, G., Modelling beam-column joints and FRP strengthening in the seismic performance assessment of RC existing frames. *Composite Structures*, **142**, 2016.
- [11] Najafgholipour, M.A., Dehghan, S.M., Dooshabi, A., Niroomandi, A., Finite element analysis of reinforced concrete beam-column connections with governing joint shear failure mode. *Latin American Journal of Solids and Structures*, **14**, 2017.
- [12] Yurdakul, Ö., Del Vecchio, C., Di Ludovico, M., Avsar, Ö., Numerical simulation of substandard beam-column joints with different failure mechanisms. *Structural Concrete*, 2020.
- [13] Yurdakul, O., Del Vecchio, C., Di Ludovico, M., Routil, L., et al., Sensitivity of cyclic response of substandard beam-column joints to material properties, in: *Computational Methods in Structural Dynamics and Earthquake Engineering (COMPDYN 2019)*, Crete, Greece., 2019.
- [14] Yurdakul, Ö., Tunaboyu, O., Routil, L., Avşar, Ö., Parameter sensitivity of CFRP retrofitted substandard joints by stochastic computational mechanics. *Composite Structures*, **238**, 2020.
- [15] Shayanfar, J., Hemmati, A., Bengar, H.A., A simplified numerical model to simulate RC beam-column joints collapse. *Bull Earthquake Eng.*, **17**, 2019.
- [16] El-Amoury, T., Ghobarah, A., Seismic rehabilitation of beam-column joint using GFRP sheets. *Engineering Structures*, **24**, 2002.
- [17] Ilki, A., Bedirhanoglu, I., Kumbasar, N., Behavior of FRP-retrofitted joints built with plain bars and low-strength concrete. *Journal of Composites for Construction*, **15**, 2011.
- [18] Sezen, H., Repair and Strengthening of Reinforced Concrete Beam-Column Joints with Fiber-Reinforced Polymer Composites. *J. Compos. Constr.*, **16**, 2012.
- [19] Garcia, R., Pilakoutas, K., Hajirasouliha, I., Guadagnini, M., et al., Seismic retrofitting of RC buildings using CFRP and post-tensioned metal straps: shake table tests. *Bulletin of Earthquake Engineering*, **15**, 2017.

- [20] Faleschini, F., Gonzalez-Libreros, J., Zanini, M.A., Hofer, L., et al., Repair of severely-damaged RC exterior beam-column joints with FRP and FRCM composites. *Composite Structures*, **207**, 2019.
- [21] Del Vecchio, C., Eeri, M., Di Ludovico, M., Prota, A., Repair costs of RC building components: From actual data analysis to calibrated consequence functions. *Earthquake Spectra*, **36**, 2020.
- [22] Yurdakul, O., Avsar, O., Structural repairing of damaged reinforced concrete beam-column assemblies with CFRPs. *Structural Engineering and Mechanics*, **54**, 2015.
- [23] JBDPA, Guideline for post-earthquake damage evaluation and rehabilitation, The Japan Building Disaster Prevention Association (JBDPA), Japan, 2001.
- [24] fib, Displacement-based seismic design of reinforced concrete buildings. State-of-art report. Fédération Internationale du Béton (fib), fib Bulletin No. 25. Lausanne, Switzerland., 2003.
- [25] European Commission & Joint Research Centre, Field Manual for post-earthquake damage and safety assessment and short-term countermeasures (AeDES), Institute for the Protection and Security of the Citizen, Joint Research Centre, European Commission, 2007.
- [26] Cardone, D., Fragility curves and loss functions for RC structural components with smooth rebars. *Earthquakes and Structures*, **10**, 2016.
- [27] FEMA 306, Evaluation of earthquake damaged concrete and masonry wall buildings: Basic procedures manual (FEMA 306), Federal Emergency Management Agency, USA, 1998.
- [28] Pagni, C.A., Lowes, L.N., Fragility functions for older reinforced concrete beam-column joints. *Earthquake Spectra*, **22**, 2006.
- [29] Di Ludovico, M., Polese, M., Gaetani d'Aragona, M., Prota, A., et al., A proposal for plastic hinges modification factors for damaged RC columns. *Engineering Structures*, **51**, 2013.
- [30] FEMA P58, Seismic performance assessment of buildings (FEMA P58), Federal Emergency Management Agency, USA, 2018.
- [31] Marder, K., Elwood, K.J., Motter, C.J., Clifton, G.C., Post-earthquake assessment of moderately damaged reinforced concrete plastic hinges. *Earthquake Spectra*, **36**, 2020.
- [32] TBI, Guidelines for Performance - Based Seismic Design of Tall Buildings, Version 2.03, Pacific Earthquake Engineering Center Report No. 2017/06, 2017.
- [33] ATENA Program Documentation, Part 8., User's manuel for ATENA-GID interface, 2015.
- [34] Pukl, R., Sajdlova, T., Routil, L., Novák, D., et al., Case study – Nonlinear reliability analysis of a concrete bridge., in: *Maintenance, Monitoring, Safety, Risk and Resilience of Bridges and Bridge Networks: Proceedings of the 8th International Conference on Bridge Maintenance, Safety and Management (IABMAS2016)*, 2016.
- [35] Joint Committee on Structural Safety, Probabilistic model code, Part 3: Material properties, <https://www.jcss-lc.org/>, 2000.
- [36] Chen, L., Lu, X., Jiang, H., Zheng, J., Experimental investigation of damage behavior of RC frame members including non-seismically designed columns. *Earthq. Eng. Eng. Vib.*, **8**, 2009.
- [37] HAZUS MR4, Multi-hazard loss estimation methodology. Earthquake Model (HAZUS MH. MR4) Technical Manual. Department of Homeland Security, Emergency Preparedness and Response Directorate, FEMA, 2003.

EXPERIMENTAL RESPONSE AND NUMERICAL MODELLING OF TWO-STOREY INFILLED RC FRAME

C. Del Vecchio¹, C. Moliterno², M. Di Ludovico², G.M. Verderame², A. Prota², G. Manfredi²

¹ Dept. of Engineering, University of Sannio, piazza Roma, 21, 82100, Benevento, Italy
e-mail: cdelvecchio@unisannio.it

² Dept. of Structures for Engineering and Architecture, University of Napoli Federico II, via Claudio
21, 80125, Napoli, Italy
carmine.moliterno@unina.it, diludovi@unina.it, verderam@unina.it, apota@unina.it

Abstract

Recent devastating earthquakes pointed out the high vulnerability of existing reinforced concrete (RC) buildings and the critical role of infills. The presence of stiff infills may significantly modify the lateral response of RC moment resisting frame buildings and cause severe damage on the surrounding RC members due to seismic actions transmitted at level of beam-column joints. Furthermore, due to their brittle response, they commonly exhibited severe damage often leading to high economic losses. In this context, effective seismic retrofit strategies should aim at both increasing the shear strength of RC members and reducing the damage to infills. However only few tests are available in literature addressing the seismic strengthening of existing RC frames accounting for the infill-to-structure interaction. To fill this gap a comprehensive experimental program of pseudo-dynamic tests on full-scale two-storey infilled RC frames has been designed and is currently ongoing at the full-scale laboratory testing of the University of Napoli Federico II.

This paper reports the preliminary experimental results and numerical analyses carried out by using available non-linear models accounting for the infills contribution. The comparison between theoretical predictions and experimental results provides useful insights to improve the numerical models to reproduce the infill-to-strut interaction. Finally, a retrofit strategy to improve the seismic performance of the structural system and reducing the expected damage to infills is herein outlined.

Keywords: pseudo-dynamic, full-scale, shear failure, FRP

1 INTRODUCTION

Recent devastating earthquake pointed out the high vulnerability of existing reinforced concrete (RC) buildings designed with obsolete code provisions. This resulted in number of fatalities, injuries and massive economic losses [1]. Severe damage were commonly found on hollow clay brick infills (see Figure 1a) [2] and at level of beam-column joints with marked shear cracks involving in many cases also the top end of the columns; this latter effect is caused by the interaction with stiff infills (see Figure 1b). Thus, stiff infills have a crucial role in the seismic response of existing RC buildings, modifying their dynamic response [3–5], increasing the shear actions transmitted to surrounding RC members [6], and, last but not least, experiencing significant damage and high economic losses due to their brittle response [7]. This remarks the need to properly account for the infill contribution to the lateral response of RC buildings and for the infill-to-structure interaction that may lead to premature shear failure of poorly detailed columns.



Figure 1: Case study building: front view (a); damage to RC column due to infill-to-structure interaction (b).

In the last decades, a significant research effort was devoted to the experimental testing [3,6,8–10] and numerical modelling of RC building or frames with hollow clay brick infill and partitions [5,6,11,12]. This resulted in number of analytical and numerical approaches to assess the infill contribution to the lateral response of RC buildings. Nowadays different numerical models are available [3,6,9,13–16]. They can be used to assess the damage state of the infills and the action transmitted to the surrounding frames. Furthermore, refined analytical models are recently proposed to capture the column shear failure due to the infill-to-frame interaction.

Although number of studies can be found in literature to assess the contribution of infills to the lateral response of RC buildings, only few researches addressed the experimental behavior of full-scale RC frames and their seismic strengthening to resist the infill action [17,18]. This paper presents the preliminary results of pseudo-dynamic experimental tests carried out on infilled full-scale RC frames. The experimental outcomes are reported and compared with the preliminary results of a numerical model. Then, the model is used to assess internal actions in RC members that can be used for the design of suitable strengthening solutions.

2 EXPERIMENTAL PROGRAM

The experimental program consists of pseudo-dynamic tests on a full-scale two storey infilled RC frame (see Figure 2). The frame reproduces a perimetral frame of a real building damaged during the L'Aquila earthquake (2009), see Figure 1, and re-built due economic inconvenience of repair and structural retrofit [1]. Indeed, the severe damage to structural and non-structural components (see Figure 1) resulted in very high repair costs.



Figure 2: Front view of the prototype infilled RC frame.

The selected frame is extracted from the building depicted in Figure 1. It is 6.86 m high and 4.50 m long. The interstorey height is about 3.10 m and the foundation block is 0.56 m high. The square columns, 0.40 m side, are reinforced with 8 ϕ 16 mm longitudinal bars and ϕ 8 mm transverse reinforcement 250 mm spaced. The beam is 0.55 m high and 0.40 m width reinforced with 6 ϕ 16 mm and 4 ϕ 16 mm bars at top and bottom side, respectively. The joint panel have no transverse reinforcements as commonly observed in existing buildings built in the last century in the Mediterranean area.

The concrete compressive strength of the tested frame is about 8 MPa corresponding to a very poor-quality concrete as often found in many existing buildings in the Mediterranean area [19].

Hollow clay brick stiff infills are used at both floors. Square bricks with 250 mm side and 200 mm thick are used. Furthermore, 10 mm joints of M10 class mortar are used to build the infill walls. The mechanical characterization tests on wall samples showed a shear strength of about 0.35 MPa.

The experimental program consists of pseudo-dynamic tests at increasing intensities. In particular, the AQG record in the Est direction ($PGA=0.45$ g) of the 2009 L'Aquila earthquake is used as input acceleration. The Alpha-OS [20] integration algorithm is used for the numerical solution of the equation of motion and calculate step-by-step the displacement profile to apply at the different floors. The mass matrix is defined considering two lumped mass at the level of

the two floors. They are calculated making simple considerations on the substructuring of the test. In particular, it is assumed that the portion of the floor mass belonging to each frame is function of the elastic stiffness of the frame. In this case, exterior frames are considered infilled and interior frame bare. The test results in terms of recorded displacement histories at the two floors as well as in terms of global hysteretic response are reported in the following and compared with the numerical predictions.

3 NUMERICAL MODELLING

A non-linear FEM model has been developed in the SAP2000 environment [21]. An overview of the adopted model is reported in Figure 3 along with the selected capacity models used to characterize the structural members and the infill walls.

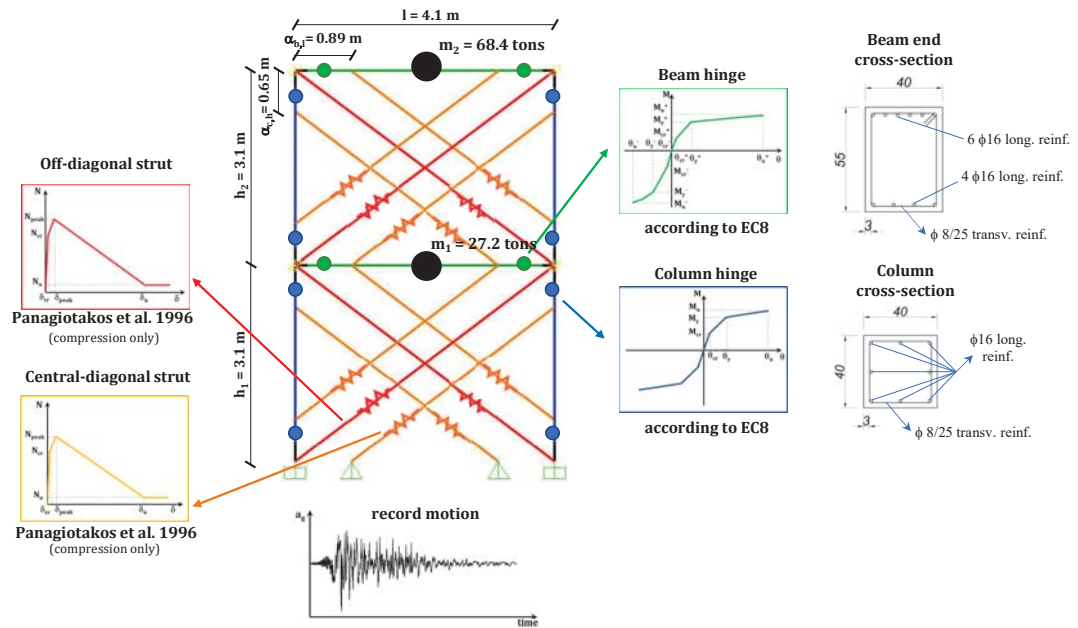


Figure 3: Overview of the adopted numerical model.

The frame is represented by using the member axis. All the nonlinearities are lumped at the member ends. The plastic hinge properties are characterized by using the capacity models suggested by the Eurocode 8 [22] and Italian building code [23,24] for the plastic hinge rotation at the yielding and at the ultimate limit state. The contribution of the joint non-linear response to the building lateral deformation is neglected at this stage. The infill walls are included in the model by means of diagonal compression struts in the perimetral frames. A three-strut model is considered for this study. Indeed, it is demonstrated that this model can reproduce the actual force distribution transmitted by the infills to the surrounding frame members [6]. The mechanical properties of the strut are defined according to the Panagiotakos and Fardis model [3]. The mechanical properties of the hollow clay brick masonry wall are assumed according to mechanical characterization tests (i.e. $\tau_{cr} = 0.35$ Mpa). The distribution of the portion of the infill lateral load absorbed by each strut assumed in this work is compliant with the proposal by Jeon, Park, and DesRoches [25], while the mechanical characterization of the off-diagonal struts have been reproduced according to the proposal by Chrysostomou et al. [26]. Furthermore, the use of a three-strut model allow to identify the ac-

tual distribution of shear on the column due to the interaction of the RC frame with the infill walls [6]. Nonlinear time-history analyses (NLTH) are carried out imposing the input motion at the base and concentrating the masses in the center of the beam. A mass of about 27.2 tons is applied at the first level, while a mass of 68.4 tons at the second level. The reference mass of the selected frame is calculated distributing the total floor mass of the reference building (see Figure 1) as function of the elastic stiffness of the frame respect to the total floor stiffness of the building. The masses of the third and forth floor are lumped at the second level assuming that they behaved as rigid floor. This assumption is made according to those made in the substructuring of the pseudo-dynamic test as discussed in the previous section.

4 COMPARISON OF EXPERIMENTAL AND NUMERICAL RESULTS

A direct comparison of the experimental and numerical response in terms of measured top displacement, d_2 , during the pseudo-dynamic test at 50% and 100% of the 2009 L'Aquila earthquake is depicted in Figure 4.

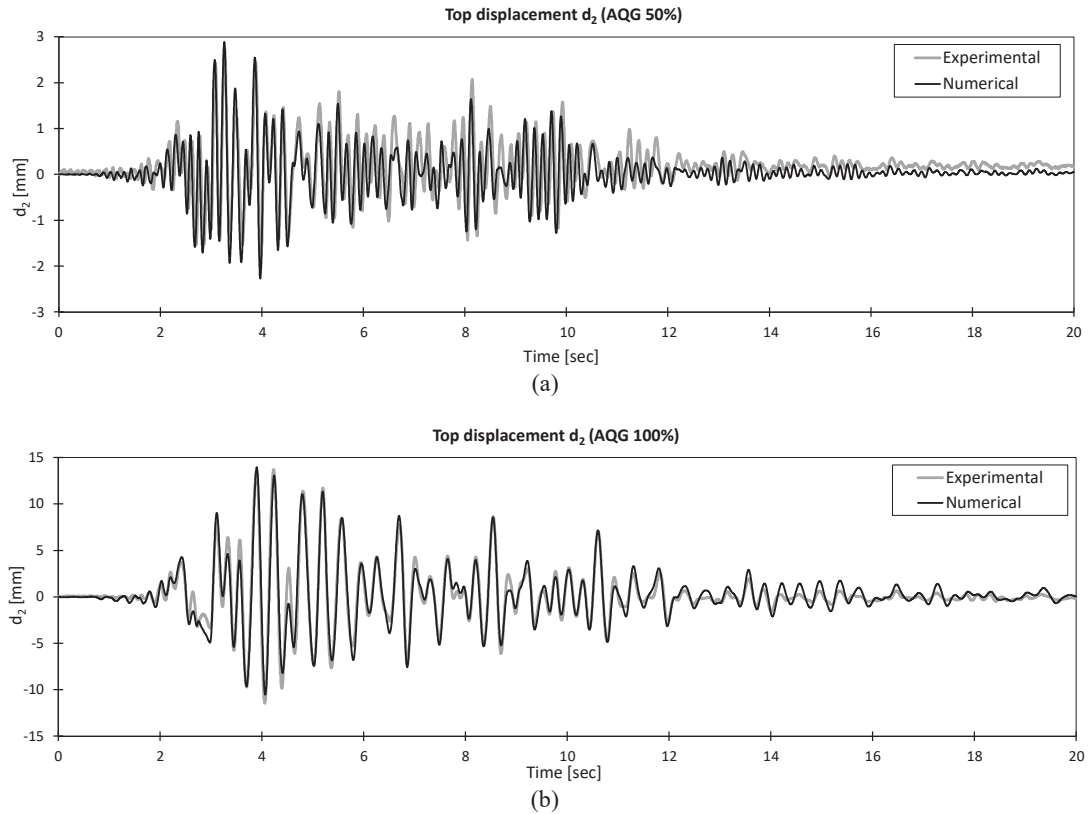


Figure 4: Comparison of experimental and numerical results in terms of top displacement: 50% of the selected record motion (a); 100% of the selected record motion (b).

The comparison outlines the accuracy of the proposed modelling procedure that is capable of providing reliable estimations of the top displacement at all the steps of the test. In particular, the best match between experimental response and theoretical model at 50% of the earthquake intensity (Figure 4b) is attained in the first 5 seconds of the test. Also, the peak displacement of about 3 mm is well captured by the model. In the following time steps, the model predicts a displacement lower than the experimental one as a consequence of a theoretical stiffness higher than the actual one. This can be clearly observed comparing the experimental and

global stiffness expressed as the ratio of the base shear and the top displacement showed in Figure 5a. Although a quite good matching can be observed also in the hysteretic response, the numerical model have a post peak degraded stiffness higher than the experimental one in the range 0-1 mm. This results in an underestimation of the top displacement in the post peak after 5 s in the time-history response.

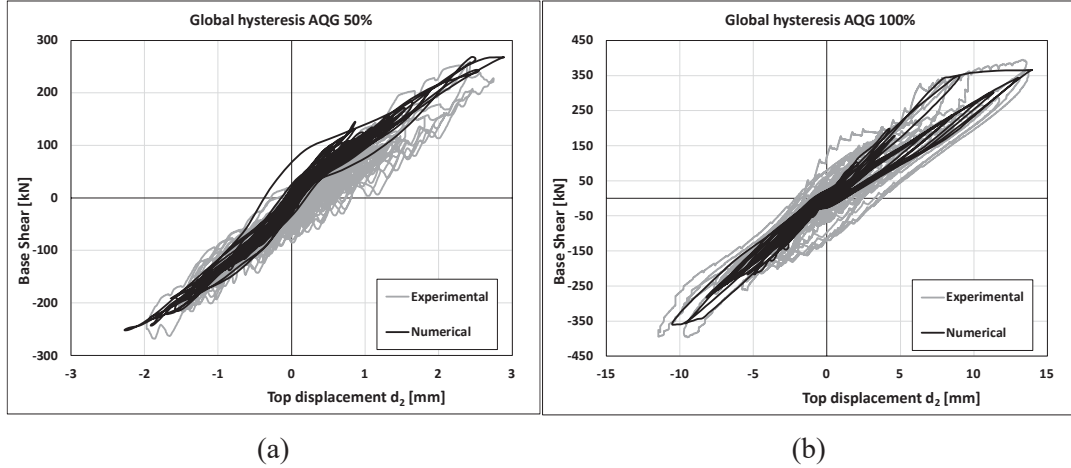


Figure 5: Comparison of experimental and numerical results in terms of global hysteretic response: 50% of the selected record motion (a); 100% of the selected record motion (b).

With reference to the test at 100% intensity of the L'Aquila 2009 earthquake, a top displacement of about 13.5 mm is achieved. It is significantly larger than the double of the one achieved at 50% due to the stiffness degradation in the infill walls. This can be clearly observed comparing the two responses in Figure 5, where a drop of the experimental secant stiffness of about 1/3 to 1/4 can be observed. The numerical model well captures both the displacement time history and hysteretic response resulting in an good accuracy of the predicted displacement and base shear during the test.

5 STRUCTURAL DAMAGE AND RETROFIT STRATEGY

During the test at 100% of the earthquake intensity a significant shear cracking at top of the ground floor columns was observed. This is related to the infill-to-structure interaction and could be triggering of a shear failure and collapse as observed in the post-earthquake inspections in many exiting RC buildings. In order to assess the reliability of the proposed modelling procedure to assess the shear failure at the top of the columns due to the infill-to-structure interaction, the model proposed by Verderame et al. [6] is used to evaluate the shear strength. According to experimental evidences and other available literature models [27,28], the shear strength degrades as function of the inelastic demand at the top of the column. Despite other degrading models, it allows to account for the actual internal force distribution due to the interaction with the off-diagonal infill strut insisting on the column. The overlapping of the shear strength with the shear demand at the top of the column due to the infill action is depicted in Figure 6. The intersection between capacity and demand allows to recognize the shear failure detected at a top displacement at the ground column of about 4.15 mm corresponding to about 0.2% drift. This result clearly remarks the key role of such failure mode to properly assess the seismic response and the structural safety of existing infilled RC buildings. In order to avoid such a kind of failure, different strengthening solutions can be found in literature [17,29,30]. However, it should be considered that recent financial incentives provided by the

Italian government, consisting in 100% tax deduction of the cost of seismic strengthening interventions, exacerbated the need to have light strengthening intervention that can be applied to the structural system with a minimum level of disruption [31,32].

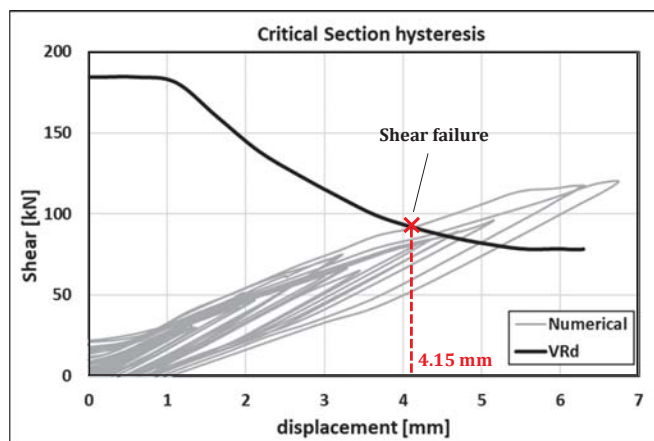


Figure 6: Comparison of the shear demand at the ground floor column top end and shear capacity

This will help the widespread of seismic strengthening interventions to large scale and may fulfill the needs to significantly improve the seismic response with the low disruption to occupants. In this context composite materials may represent a sound solution because they combine the advantage related to the easy installation procedure with their high performances to increase the shear capacity of RC members and beam column joint panels [33]. In light of the observed damage and the structural weaknesses outlined from numerical analyses, the strengthening layout proposed in Figure 7 is initially outlined.

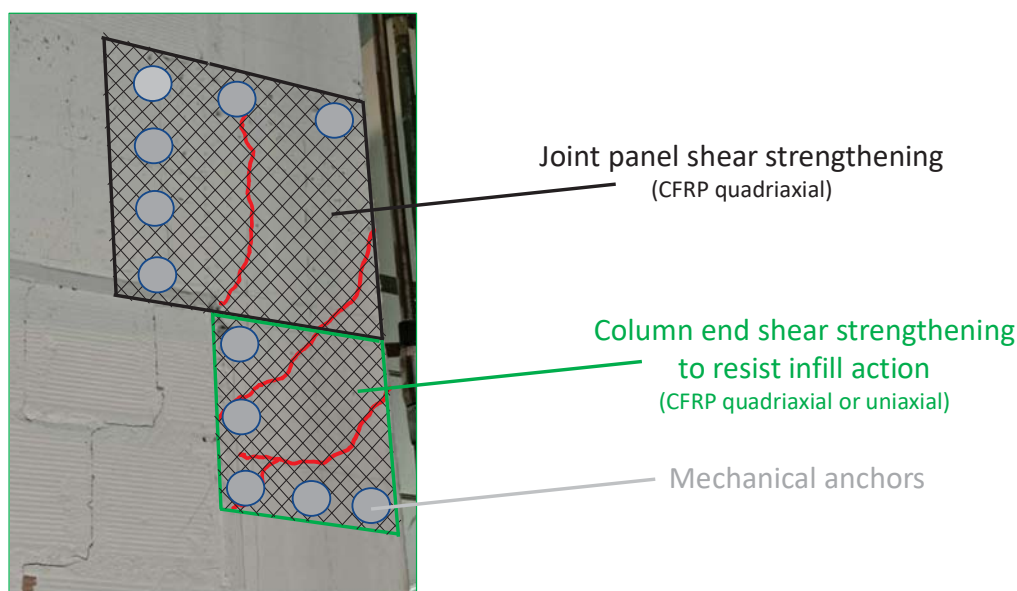


Figure 7: Strengthening system for the RC frame.

It consists of the column end shear strengthening by using Quadriaxial or uniaxial CFRP wrapped around the column on the two sides. This is in line with the strengthening system proposed in the ReLUIIS guidelines [29] to resist the infill action. Then quadriaxial fabric is

also outlined on the joint panel serving as joint shear strengthening to avoid the joint panel shear cracking, which are commonly observed in poorly detailed subassemblies. Number of layers of quadriaxial fabric on the joint panel can be designed according to the formulation proposed in the fib bulletin 90 [34] properly developed and validated on experimental data [29]. The novelty of this new proposal consists in the use of FRP mechanical anchors to replace the commonly adopted U-wrap on beams and columns useful to avoid end-debonding. This may further reduce the disruption to occupants in real field applications. This is a promising technique [32] that requires further experimental investigation to validate its use at large scale. Ongoing experimental tests will show the advantages and limitations of such strengthening solution.

6 CONCLUSIONS

This research focuses on the design and analysis of an experimental pseudodynamic tests on a full scale infilled RC frame representative of a portion of an existing RC building damaged by the L'Aquila 2009 earthquake. The analytical modelling of the specimen behavior under seismic actions is also presented. In particular, the experimental results in terms of time histories of the top displacement and global hysteretic response are showed and compared with the results of a non-linear FEM model. The following preliminary conclusions can be drawn:

- the experimental tests remarked the role of stiff infills in the lateral response of existing RC frames. They increase the stiffness of the building resulting in a reduction of the displacement demand and in an increase of the seismic forces that will be transmitted to surrounding RC members;
- the proposed non-linear numerical model consisting in a lumped plasticity model for the RC frame and in a three-strut model to reproduce the infill contribution well captured the global displacement and hysteretic response occurred in the experimental tests;
- the proposed numerical model allowed to quantify the actual internal force distribution with particular emphasis on the shear actions transferred from the infill to the RC columns;
- literature shear strength capacity models properly developed to account for the top column shear failure due to infill-to-structure interaction allows to accurately predict the failure mechanism and to provide useful insights for the design of an effective strengthening intervention.

ACKNOWLEDGMENTS

This study was performed within the framework of the PE2019–2021 joint program DPC-ReLUIIS, WP5: “Fast and Integrated Retrofit Interventions” and of the reSTART-school research project funded by the UNINA - Compagnia San Paolo STAR 2018 program.

REFERENCES

- [1] M. Di Ludovico, A. Prota, C. Moroni, G. Manfredi, M. Dolce, Reconstruction process of damaged residential buildings outside historical centres after the L'Aquila earthquake: part II—“heavy damage” reconstruction, Springer Netherlands, 2017.

- <https://doi.org/10.1007/s10518-016-9979-3>.
- [2] C. Del Vecchio, M. Di Ludovico, S. Pampanin, A. Prota, Repair costs of existing rc buildings damaged by the l'aquila earthquake and comparison with FEMA P-58 predictions, *Earthq. Spectra*. (2018). <https://doi.org/10.1193/122916EQS257M>.
 - [3] T.B. Panagiotakos, M.N. Fardis, Seismic response of infilled RC frame structures, in: *Proc. 11th World Conf. Earthq. Eng.*, 1996: pp. 1–8.
 - [4] F. Colangelo, Pseudo-Dynamic Seismic Response of Reinforced Concrete Frames Infilled with Non-Structural Brick Masonry, *Earthq. Eng. Struct. D.* 34 (2005) 1219–41.
 - [5] G. Magenes, S. Pampanin, Seismic response of gravity-load design frames with masonry infills, *13th World Conf. Earthq. Eng.* (2004).
 - [6] G.M. Verderame, P. Ricci, M.T. De Risi, C. Del Gaudio, Experimental Assessment and Numerical Modelling of Conforming and Non-Conforming RC Frames with and without Infills, *J. Earthq. Eng.* 00 (2019) 1–42. <https://doi.org/10.1080/13632469.2019.1692098>.
 - [7] C. Del Vecchio, M. Di Ludovico, A. Prota, Repair costs of reinforced concrete building components: from actual data analysis to calibrated consequence functions, *Earthq. Spectra*. (2020) 1–25. <https://doi.org/10.1177/8755293019878194>.
 - [8] A.D. Dautaj, Q. Kadiri, N. Kabashi, Experimental study on the contribution of masonry infill in the behavior of RC frame under seismic loading, *Eng. Struct.* 165 (2018) 27–37. <https://doi.org/10.1016/j.engstruct.2018.03.013>.
 - [9] L. Cavaleri, F. Di Trapani, Cyclic response of masonry infilled RC frames: Experimental results and simplified modeling, *Soil Dyn. Earthq. Eng.* 65 (2014) 224–242. <https://doi.org/10.1016/j.soildyn.2014.06.016>.
 - [10] G.M. Calvi, D. Bolognini, Seismic response of reinforced concrete frames infilled with weakly reinforced masonry panels, *J. Earthq. Eng.* 5 (2001) 153–185. <https://doi.org/10.1080/13632460109350390>.
 - [11] L. Liberatore, F. Noto, F. Mollaioli, P. Franchin, In-plane response of masonry infill walls: Comprehensive experimentally-based equivalent strut model for deterministic and probabilistic analysis, *Eng. Struct.* 167 (2018) 533–548. <https://doi.org/10.1016/j.engstruct.2018.04.057>.
 - [12] A. De Angelis, M.R. Pecce, The Role of Infill Walls in the Dynamic Behavior and Seismic Upgrade of a Reinforced Concrete Framed Building, *Front. Built Environ.* 6 (2020). <https://doi.org/10.3389/fbuil.2020.590114>.
 - [13] A.M.B. Nafeh, G.J. O'Reilly, R. Monteiro, Simplified seismic assessment of infilled RC frame structures, *Springer Neth*, 2020. <https://doi.org/10.1007/s10518-019-00758-2>.
 - [14] G. Mucedero, D. Perrone, E. Brunesi, R. Monteiro, Numerical modelling and validation of the response of masonry infilled rc frames using experimental testing results, *Buildings*. 10 (2020) 1–30. <https://doi.org/10.3390/buildings10100182>.
 - [15] M. Galli, Evaluation of the Seismic Response of Existing R . C . Frame Buildings With Masonry Infills, *Response*. (2006).
 - [16] F. da Porto, M. Donà, N. Verlato, G. Guidi, Experimental Testing and Numerical Modeling of Robust Unreinforced and Reinforced Clay Masonry Infill Walls, With and Without Openings, *Front. Built Environ.* 6 (2020). <https://doi.org/10.3389/fbuil.2020.591985>.
 - [17] L. Koutas, S.N. Bousias, T.C. Triantafillou, Seismic Strengthening of Masonry-Infilled RC Frames with TRM: Experimental Study, *J. Compos. Constr.* 19 (2015) 04014048. [https://doi.org/10.1061/\(asce\)cc.1943-5614.0000507](https://doi.org/10.1061/(asce)cc.1943-5614.0000507).
 - [18] F. Bianchi, R. Nascimbene, A. Pavese, Experimental vs. Numerical Simulations: Seismic Response of a Half Scale Three-Storey Infilled RC Building Strengthened

- Using FRP Retrofit, *Open Civ. Eng. J.* 11 (2018) 1158–1169.
<https://doi.org/10.2174/1874149501711011158>.
- [19] I.E. Bal, H. Crowley, R. Pinho, F.G. Gülay, Detailed assessment of structural characteristics of Turkish RC building stock for loss assessment models, *Soil Dyn. Earthq. Eng.* 28 (2008) 914–932. <https://doi.org/10.1016/j.soildyn.2007.10.005>.
- [20] D. Combescure, P. Pegon, A-Operator Splitting Time Integration Technique for Pseudodynamic Testing Error Propagation Analysis, *Soil Dyn. Earthq. Eng.* 16 (1997) 427–443. [https://doi.org/10.1016/S0267-7261\(97\)00017-1](https://doi.org/10.1016/S0267-7261(97)00017-1).
- [21] C.S.I. Computers and Structures Inc., SAP 2000, Static and Dynamic Finite Element Analysis of Structures, (2004).
- [22] CEN, “Design of structures for earthquake resistance - Part 3: Assessment and retrofitting of buildings” EN-1998-3, Eurocode 8., European Committee for Standardization, Brussels, 2005.
- [23] MIT, Aggiornamento delle «Norme tecniche per le costruzioni» (in Italian). Supplemento ordinario n. 8 alla GAZZETTA UFFICIALE del 20-2-2018, Italy, 2018.
- [24] MIT, Istruzioni per l’applicazione dell’«Aggiornamento delle “Norme tecniche per le costruzioni”» di cui al decreto ministeriale 17 gennaio 2018., Italy, 2019.
- [25] J.S. Jeon, J.H. Park, R. DesRoches, Seismic fragility of lightly reinforced concrete frames with masonry infills, *Earthq. Eng. Struct. Dyn.* 44 (2015) 1783–1803. <https://doi.org/10.1002/eqe.2555>.
- [26] C.Z. Chrysostomou, P. Gergely, J.F. Abel, A six-strut model for nonlinear dynamic analysis of steel infilled frames, *Int. J. Struct. Stab. Dyn.* 2 (2002) 335–353. <https://doi.org/10.1142/S0219455402000567>.
- [27] D.E. Biskinis, G.K. Roupakias, M.N. Fardis, Degradation of shear strength of reinforced concrete members with inelastic cyclic displacements, *ACI Struct. J.* 101 (2004) 773–783. <https://doi.org/10.14359/13452>.
- [28] C. Del Vecchio, M. Del Zoppo, M. Di Ludovico, G.M. Verderame, A. Prota, Comparison of available shear strength models for non-conforming reinforced concrete columns, *Eng. Struct.* (2017). <https://doi.org/10.1016/j.engstruct.2017.06.045>.
- [29] DPC-ReLUIS, Linee Guida Per Riparazione E Rafforzamento Di Elementi Strutturali, Tamponature E Partizioni (in Italian), Doppiavoce, 2011.
- [30] V. Bolis, A. Paderno, M. Preti, Experimental assessment of an innovative isolation technique for the seismic downgrade of existing masonry infills, in: *Brick Block Mason. - From Hist. to Sustain. Mason.*, 2020: pp. 935–942. <https://doi.org/10.1201/9781003098508-133>.
- [31] C. Menna, C. Del Vecchio, M. Di Ludovico, G.M. Mauro, F. Ascione, A. Prota, Conceptual design of integrated seismic and energy retrofit interventions, *J. Build. Eng.* 38 (2021). <https://doi.org/10.1016/j.jobbe.2021.102190>.
- [32] M.T. De Risi, C. Del Vecchio, P. Ricci, M. Di Ludovico, A. Prota, G.M. Verderame, Light FRP strengthening of poorly detailed reinforced concrete exterior beam-column joints, *ASCE J. Compos. Constr.* (in press) (2020). [https://doi.org/10.1061/\(ASCE\)CC.1943-5614.0001022](https://doi.org/10.1061/(ASCE)CC.1943-5614.0001022).
- [33] C.E. Bakis, L.C. Bank, V.L. Brown, E. Cosenza, J.F. Davalos, J.J. Lesko, A. Machida, S.H. Rizkalla, T.C. Triantafillou, Fiber-reinforced polymer composites for construction - State-of-the-art review, *J. Compos. Constr.* 6 (2002) 73–87. [https://doi.org/10.1061/\(ASCE\)1090-0268\(2002\)6:2\(73\)](https://doi.org/10.1061/(ASCE)1090-0268(2002)6:2(73)).
- [34] fib bulletin 90, Externally applied FRP reinforcement for concrete structures, *Fédération internationale du béton (fib)*, 2019, 2019. <https://doi.org/doi.org/10.35789/fib.BULL.0090>.

DEFENCE OF ARCHITECTURAL HERITAGE: EXPERIMENTAL CAMPAIGN ON MASONRIES REINFORCED WITH NATURAL FRCM COMPOSITE MATERIALS

R. Liberotti, N. Cavalagli, F. Cluni, M. Giofrè, C. Pepi and V. Gusella

Department of Civil and Environmental Engineering
University of Perugia 06125 Perugia, Italy
e-mail: riccardo.liberotti@studenti.unipg.it

e-mail: {[nicola.cavalagli](mailto:nicola.cavalagli@unipg.it), [federico.cluni](mailto:federico.cluni@unipg.it), [massimiliano.gioffre](mailto:massimiliano.gioffre@unipg.it), [chiara.pepi](mailto:chiara.pepi@unipg.it), [vittorio.gusella](mailto:vittorio.gusella@unipg.it)}@unipg.it

Keywords: Heritage, FRCM, Retrofit, Composite Materials, Masonry.

Abstract. *In this contribution are reported the first results of an experimental campaign conceived to evaluate the performance of FRCM (Fiber Reinforced Cementitious Matrix) composite materials for the recovery and restoration field of heritage buildings. With reference to the risks of seismic collapse concerning ancient masonry buildings, the peculiar structural behaviour of “in falso” walls, a typology of load-bearing masonries built without a direct load path to the foundations, has been examined. The tests have been conducted, through an experimental set-up specially designed, on two rectangular walls characterized by the same basic traits: the first one in unreinforced masonry, the second presenting a non-canonical “truss-like” application of bands of composites. Alongside the progression of the experimental campaign - delayed due to the COVID outbreak - that in the near future will engage other two masonry panels enhanced by different applications of the FRCM, the creation of a FEM will be achieved gathering data from the new tests in order to replicate the complex mechanical behaviour of the FRCM composites with reference to the skills and time required for different installation modalities.*

1 INTRODUCTION

For any country, the conservation of heritage buildings is a primary goal: it is a reflection of the society and a basic tool to transfer its cultural and educational values. These purposes require an inclusive and interdisciplinary approach to masonry structures' reinforcement that involves, among the others, structural engineering, non-destructive techniques of survey, numerical modelling and architectural design [1, 3, 4]. In this regard, as part of an ongoing research, a peculiar focus is dedicated to the study of the mechanical behaviour of natural FRCM composite materials in the field of the innovative strengthening techniques, since they are compatible with the architectural value of historic surfaces and are, to a large extent, reversible, biodegradable and eco-friendly; however, their numerical modelling represents a complex task, due to the interactions between fibers, matrix and masonry. Moreover, a previous experience, that covered the seismic assessment and the restoration plan of an architectural complex designed by Luigi Vanvitelli, pointed out a recurrent feature affecting the structural safety of Italian heritage architectures: the presence of "in falso" walls, consisting of load bearing walls built without a direct load path to the ground and standing on top of masonry vaults [2, 5]. That occurrence, in case of seismic action, could trigger a "domino effect", due to the possible collapse of underlying masonry vaults, then compromising the safety of the entire heritage structure. However, it should be noted that the investigation for the mechanical behaviour of the such walls, that struggle to perform like masonry beam structures, is not adequately investigated by the scientific literature. In order to improve the knowledge about such topic and to investigate new applications of FRCM technology, an experimental campaign has been started in partnership with a company, the Kimia S.p.a., to evaluate the effectiveness of composites regarding the prevention of in-plane collapses described above.

2 THE EXPERIMENTAL CAMPAIGN

2.1 The setup implementation: an experimental test designed "ad hoc"

The FRCM systems represent an innovative class of fiber-reinforced composites, which are becoming broadly used concerning heritage constructions. The key feature of this emergent technology is the replacement of the classical polymeric matrix with an inorganic one, making them particularly effective in retrofitting of historical masonries given their chemical, physical, and mechanical compatibility to the ancient substrates. Such new-gen. methodologies allow to fulfil the strengthening and the architectural reconfiguration of historical masonry buildings in compliance with the cultural and social context. On this, the benefits of FRCM materials are the following:

- Good mechanical properties in the face of low thickness and little weight;
- Easy installation modalities ensuring the continuity of the building's activities;
- Use of inorganic mortar (less aggressive than the epoxy resins) that is useful in order to apply first aid enhancements whilst and at the same time permits a better transpiration to masonry;
- Chance to recycle, considering the natural origin of nets and the matrix characteristics.

Several experimental investigations have been carried out so far - during previous experiences - both at the scale of the composite material and of the single components, reaching an adequate level of experimental mechanical characterization of the materials used for the campaign

in question; for further details refer to such data [6]. Even so, in this contribution the beneficial effects of composites on walls subjected to gravity loads and earthquake actions in peculiar conditions are highlighted, also with reference to the installation modalities. Indeed, the outcomes deriving from an experimental test on an ordinary masonry wall and another one retrofitted according to non-canonical criteria are compared. In order to evaluate the influence of FRCM in the prevention of knock-on collapses a specific experimental set-up has been conceived, and realized, to engage life-sized masonry walls with action similar to the ones ascribed in case of collapse of the below vaults on which they rest: masonry panels inferiorly suspended, except for lateral supports of reduced length, Figure 1. Therefore, with the aim of bringing a single brick wall to failure, a steel contrast portal has been designed - and realized - to make a self-balanced closed system.

2.2 Preparation of the specimens

The masonry specimens are walls of the dimensions 2.4m wide for 1.2m high, made of a single wythe of solid bricks, of dimensions 12x24x5.5 (respectively thickness, width and height), and recalling the wall's dimensions provided by the Italian Building Code for the shear verification [7]. Concerning the materials' features of the walls, solid bricks and lime mortar were used and with reference to the latter a "shoddy" lime inorganic mortar (M 2.5) with poor mechanical properties was created from the company in order to simulate the structural behaviour of a historical masonry.

Concerning the composite materials, the fiber net *Kimitech BS ST 200* and the matrix *MALTA M15/F* have been used. In particular, has been used a bidirectional basaltic fiber net characterized by a size of the square knitting interaxle spacing of 20mm between the strands (of 4mm wide). The matrix is a lime inorganic mortar with maximum 1.20 mm particle size distribution. The samples' preparation, concerning the application of the composites, required:

- the cleaning of the surface of the masonry substrate and its saturation and wetting (condition s.s.a.);
- application of a first layer of mortar Basic MALTA M15/F;
- positioning of the fiber net Kimitech BS ST 200;
- application of a second layer of mortar Basic MALTA M15/F.

As mentioned so far regarding the reinforced wall, for this non-conventional reinforcement a specific intervention was designed - since generally this type of composite material is applied evenly on the wall's surface - devising the application of FRCM bands each 20cm wide, a measure that represents a multiple of one meter, the dimension with which the meshes in basaltic fiber are produced [8].

The goal was to reinforce the weakest areas of the wall thus using less composite material than in the classic applications: the diagonals subject to traction, two shorter diagonals parallel to the main ones but placed below, the lower band of the masonry panel and, moreover, three vertical bands useful for maintaining adhered to the wall the ends of the other strips of composite material. The reinforcement intervention was applied with the same criteria on both sides of the wall. After the curing period exceeding 56 days - 28 days for the walls plus the same duration for the FRCM - the experimental tests were performed. All the material's mechanical features are available in the aforementioned contribution [6].

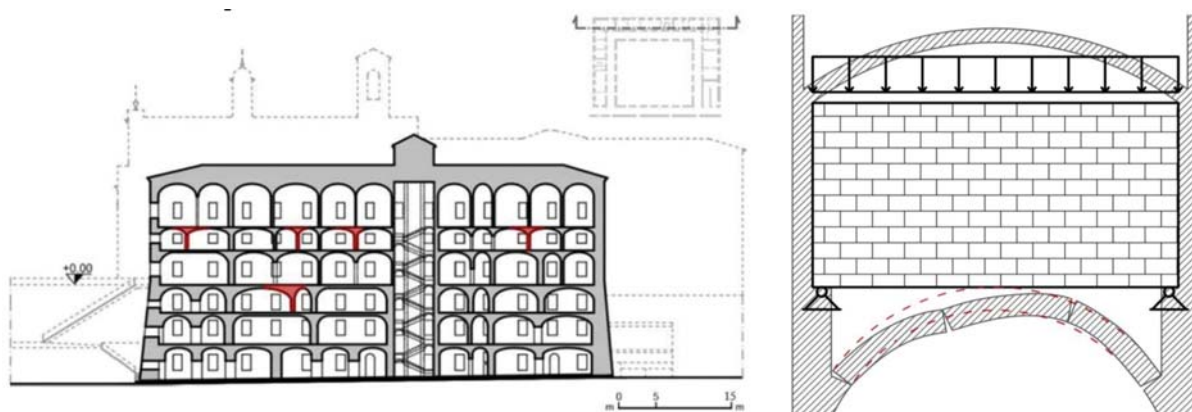


Figure 1: On the right, the “in falso” walls of Palazzo Murena. On the left, a schematization of the walls in the vault’s collapse scenario.

2.3 Boundary conditions and acquisition systems

In the scientific literature there are several references to experimental tests, both codified and innovative ones for these materials, but there is no one similar to the one presented in such contribution [9, 10]. The specimens were built directly on top of steel temporary supports, designed with a dual function: the first reason to facilitate their movement on the portal-shaped steel frame, the other to prop-up the walls themselves until the beginning of the test; in both cases without causing damages or deformations to the samples. Thanks to a forklift it was possible to remove the support - separated from the rest thanks to plastic sheets - and begin the test with the walls, already equipped with sensors, resting only on the remaining permanent lateral supports (Figures 2 and 3); such constraint condition is addressing the described above damage scenario (Figure 1). Concerning the load conditions, the load was applied gradually by means of a hydraulic jack placed on the top of a load cell. About the modalities, force distribution steel beams were used to create a load concentrated in two points, by means of two steel plates, similar to an equivalent distributed load. Moreover, an active sensor system has been implemented. A total of 8 Linear Variable Displacement Transducer (LVDT) sensors was installed on the wall - 4 for each side - as indicated in Figure 4. The measured lengths were extended by means of diagonal support rods anchored to the specimens through rocker like constraints. Those sensors along with the load cell, aimed at measure the applied load, were connected to an acquisition system.

3 THE TWO EXPERIMENTAL TESTS

In this Section will be discussed, and finally compared, the results of the aforementioned first two tests, in the order: ordinary masonry and masonry reinforced on both faces with a truss-like application of FRCM designed to reinforce the diagonals subjected to tension and other significant parts [11].

3.1 Experimental test on the ordinary wall

Both tests lasted less than 15 minutes. The breakage, as can be seen in Figure 3, occurred due to the separation and breakage of the mortar joints. In test led to breaking the masonry sample with the damages starting at a load of about 40KN.

As far as possible, the load was applied gradually with the hydraulic jack by controlling the load cell connected to the acquisition system.

Due to the structural relaxation, even before the removal of the sensor's support rods, a further collapse and the effective damage pattern came forward. From the critical interpretation of this latter, a “arched” stress redistribution mechanism is observable, comparable to the one to which are subject the weakly reinforced concrete beams, Figure 3. Moreover, concerning the data acquisitions, it is observable that the sensors sg2 with sg6 and sg3 with sg7 record consistently even if, however they mate on opposite faces, not all manifest the same trend. For example, it is noted that, possibly due to a manufacturing defects on the wall, the sensors sg1 and sg4 were in traction (negative sign on the acquisitions), Figures 4 and 5, perhaps implies a flexural behaviour out of plane of the wall. Considering that is an innovative and non-codified type of test, such results have been used as a basis for the subsequent test which, except for the application of the composite materials, in every part has been analogous to this one. The purpose is to evaluate, by comparison, the influence of FRCM on the structural behaviour due to seismic damages to the vaulted underlying masonry elements. Therefore, the same procedure will always be respected also in the future tests, also in terms of points of view for the photos.

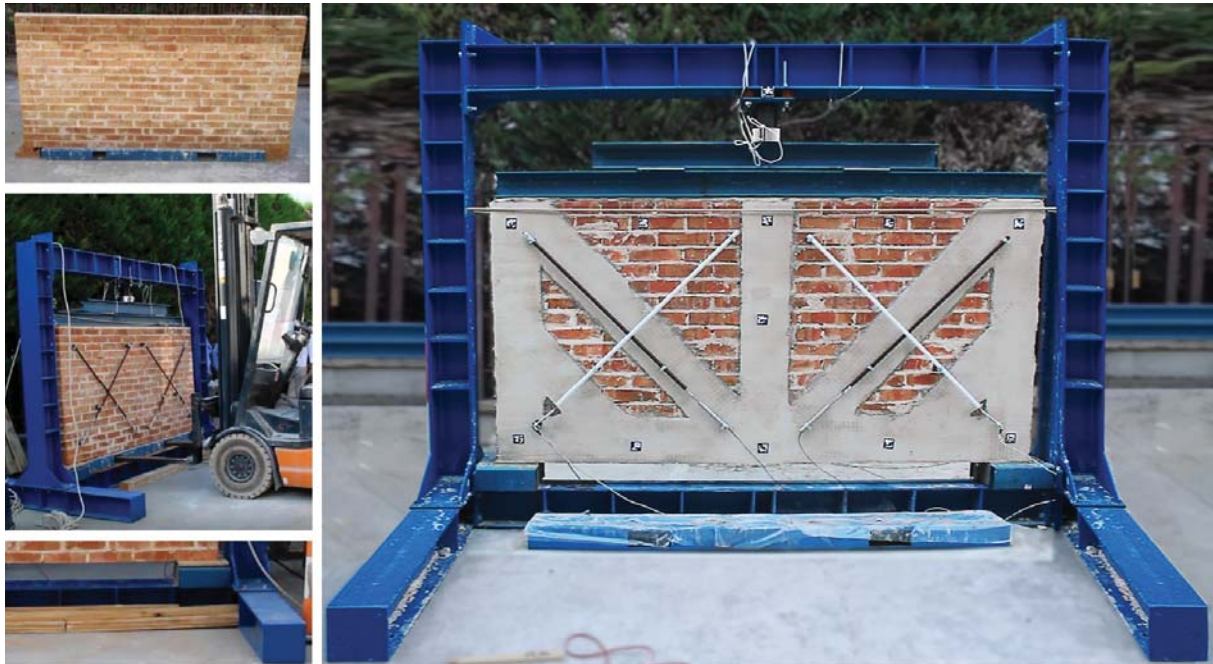


Figure 2: On the right starting with the top row, the ordinary wall ready to be moved, handling of the same and the subsequent removal of the steel support, zoom on one of the two remaining supports. On the left, masonry wall reinforced with truss-like application of FRCM at the start of the test, all components of the setup.

3.2 Experimental test on the wall reinforced with FRCM

In this case it was possible to witness a peculiar collapse phenomenon which manifested itself first with partial lesions on the composite reinforcements and then led to the collapse through the breaking of bricks (and not by the separation of the courses, as seen in the first test). Moreover, were necessary about 140KN to break this wall, compared to the 40KN needed to breach the unreinforced one in the very first test.

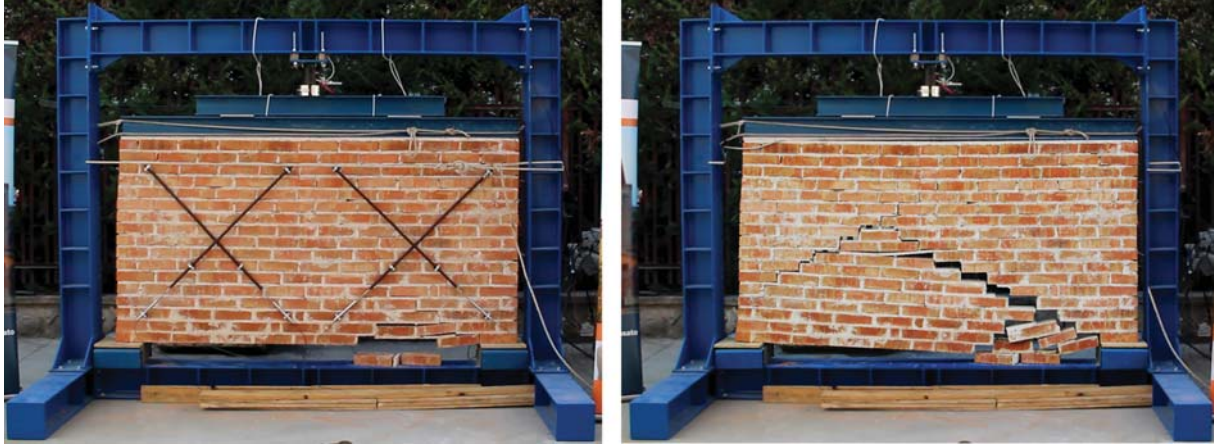


Figure 3: On the right, tearing of the wall at the end of the test. On the left, photo of the experimental setup at few minutes later the completion of the test.

Although the beginning of a fracture in the lower left reinforcement band has been observed during the test, the presence of the vertical strip in composite probably led to an asymmetry in the damage pattern of the wall that has collapsed because of a large crack located on the right side of the wall, that evidently was weaker (Figure 6). It is observed how the instruments that match each other on the opposite faces of the reinforced wall (sg1-sg5, sg2-sg6, sg3-sg7, sg4-sg8) seem to acquire data consistently and in parallel. In particular the diagonals with sensors sg1, sg4, sg5 and sg8 worked at traction, Figure 7. From the previous and further data processing (Figure 8) it is clear that during such test the expected behaviour of the diagonals, in terms of displacements related to compressive and tensile deformations, was confirmed. Among the readings of the instruments, the one of inferior quality this time concerned only that of the sensor marked as sg1. For purposes of comparison, the averages of the sensor readings with positions sg3 and sg7 (Figures 5 and 8) were plotted in relation to the applied load path, which in the authors' opinion represent reliable measurements in both the experimental tests, Figure 9.

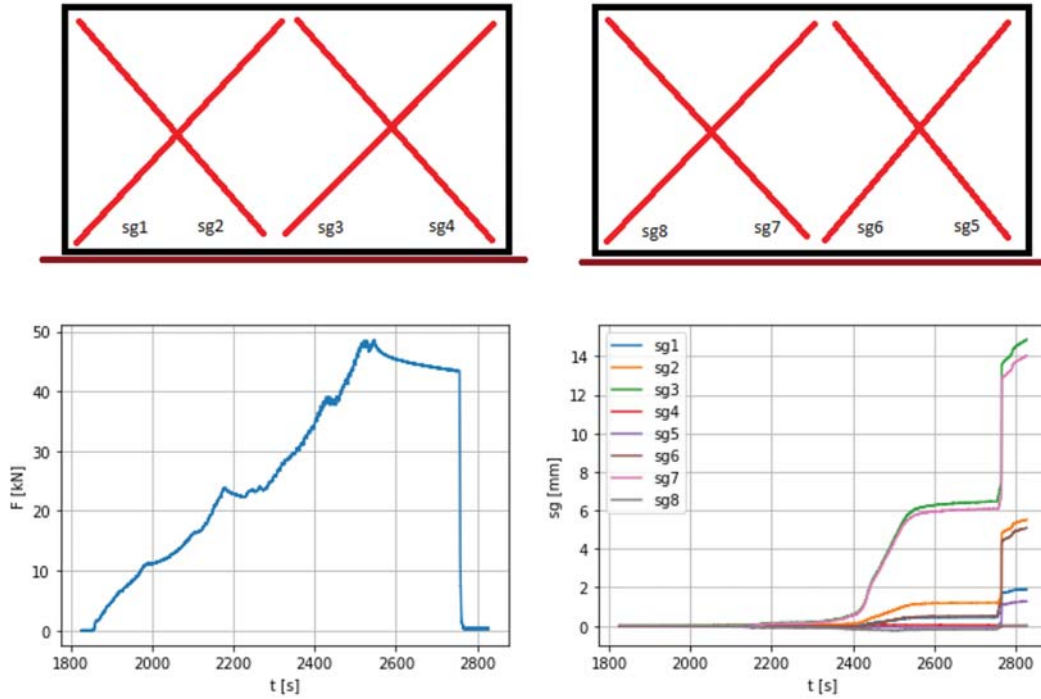


Figure 4: On the top the positions of the sensors on the wall (the picture on the right presents the same point of view of the photos reported in Figure 3). Below, respectively the force and displacement diagrams against time.

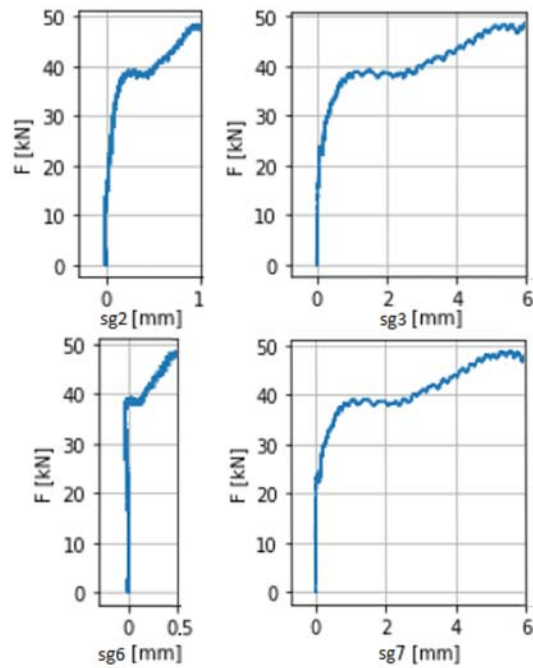


Figure 5: For the sensors subjected to tension, force-displacement graphs for collapse incipient.

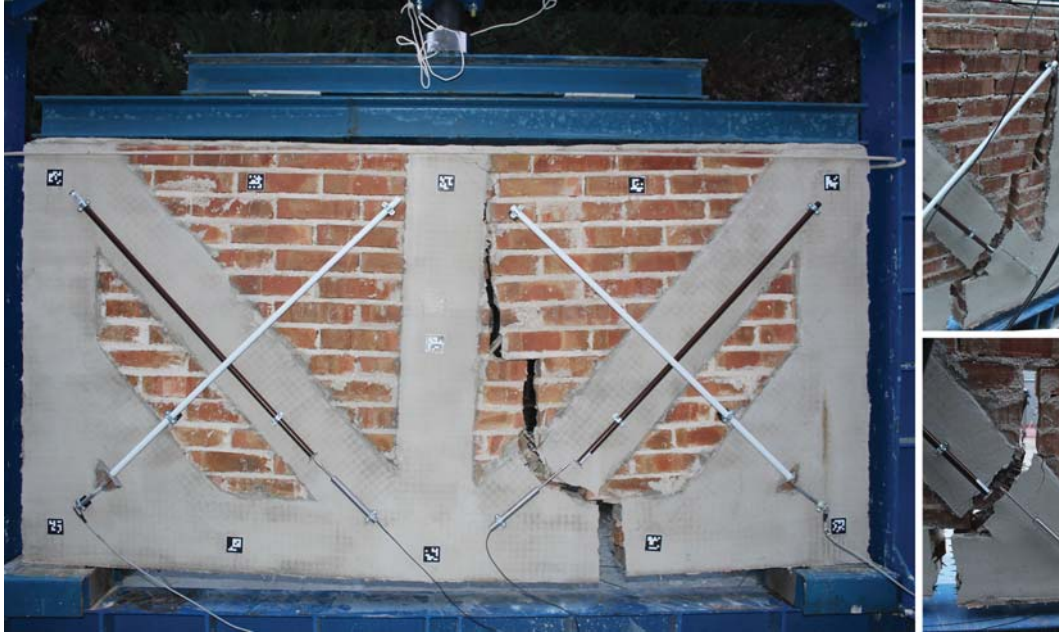


Figure 6: On the right, tearing of the wall at the end of the test. On the left, two closer photos of the crack taken on the opposite face than the previous photo.

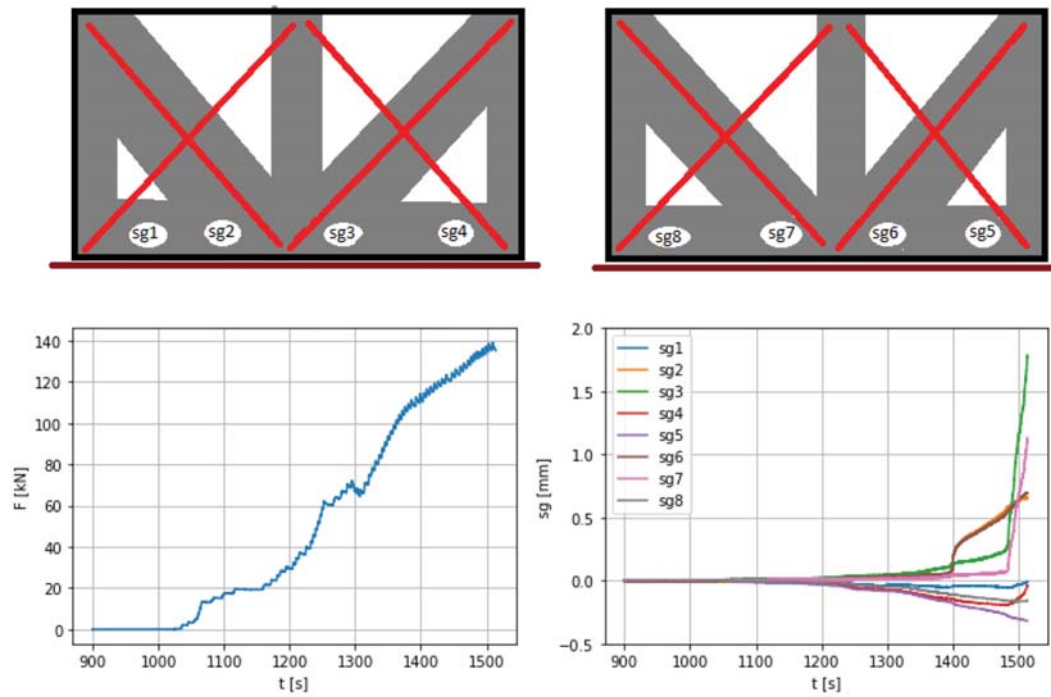


Figure 7: On the top the positions of the sensors on the reinforced wall (the picture on the right presents the same point of view of the photos in Figures 4). Below, respectively the force and displacement diagrams against time.

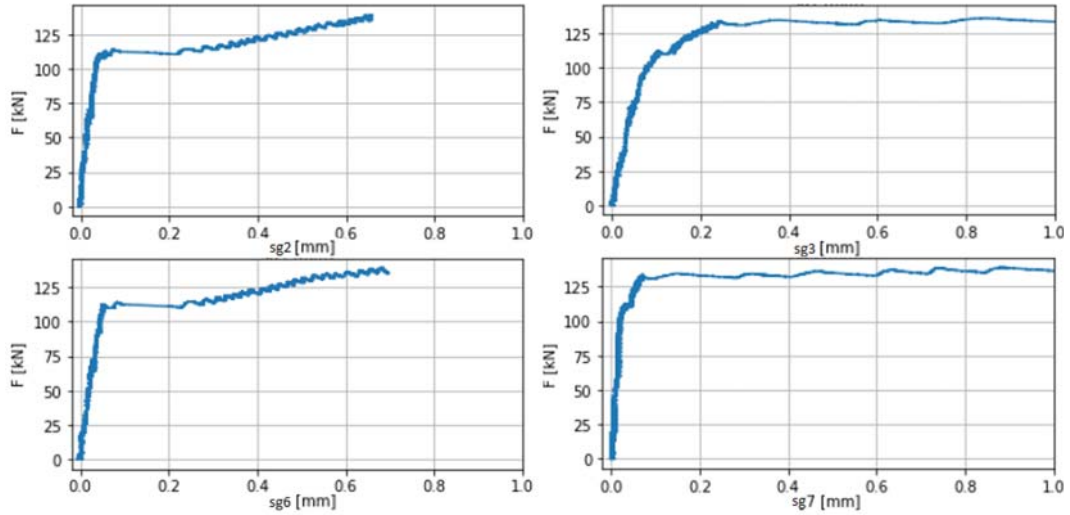


Figure 8: For the sensors subjected to tension, force-displacement graphs.

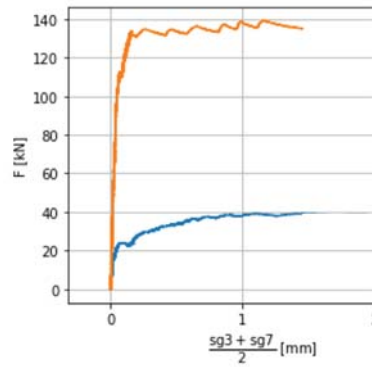


Figure 9: A comparison diagram between the two tests: unreinforced masonry in blue lines, the reinforced wall in orange lines.

4 CONCLUSIONS

- A focus on the study of the mechanical behaviour of natural FRCM composite materials was carried out in the field of the innovative strengthening techniques on masonry structures, since they are more compatible with the architectural value and specificities of heritage buildings;
- A experimental setup has been designed and realized in order to evaluate the influence of FRCM in the prevention of knock-on collapses in heritage buildings and to, in a future perspective, achieve the creation of a Finite Element Model gathering data from the tests;
- The first two tests have been made, involving an unreinforced masonry panel and a reinforced one, whose allowed to analyse the good functioning of the experimental setup designed and to evaluate the loads necessary to break the prototype and observe the stress redistribution mechanism due to the peculiar constraint conditions.

REFERENCES

- [1] V. Gusella, F. Cluni, R. Liberotti, Feasibility of a Thermography Nondestructive Technique for Determining the Quality of Historical Frescoed Masonries: Applications on the Templar Church of San Bevignate. *Appl. Sci.*, **11**, 281, 2021. <https://doi.org/10.3390/app11010281>
- [2] V. Gusella, R. Liberotti, Seismic Vulnerability of Sub-Structures: Vantitelli's Modulus in Murena Palace. *Buildings*, **10(9)**, 164, 2020.
- [3] C. Pepi, N. Cavalagli, V. Gusella, M. Giofrè, An integrated approach for the numerical modeling of severely damaged historic structures: Application to a masonry bridge. *Advances in Engineering Software*, **151**, 102935, 2021, ISSN 0965-9978, <https://doi.org/10.1016/j.advengsoft.2020.102935>.
- [4] C. Pepi, N. Cavalagli, V. Gusella, M. Giofrè, Damage detection via modal analysis of masonry structures using shaking table tests. *Earthquake Engng Struct Dyn.*, 1–21, 2021. <https://doi.org/10.1002/eqe.3431>
- [5] R. Liberotti, F. Cluni, V. Gusella, Vulnerability and seismic improvement of architectural heritage: The case of Palazzo Murena. *Earthquakes and Structures*, **18(3)**, 321–335, 2020.
- [6] R. Liberotti, N. Cavalagli, V. Gusella, Experimental Tests On Frcm And Fe Modelling For The Heritage Structure's Reuse. P. Roca, L. Pelà and C. Molins eds. *Proceeding of 12th International Conference on Structural Analysis of Historical Constructions SAHC 2020*, under process of publication.
- [7] NTC Decreto Ministeriale 14 Gennaio 2018. Aggiornamento Delle Norme tecniche Per Le Costruzioni. Supplemento Ordinario Alla "Gazzetta Ufficiale"; N. 42 Del 20 Febbraio 2018—Serie Generale; Ministero Delle Infrastrutture E Dei Trasporti: Roma, Italy, 2018.
- [8] RELUIS - WP 2, Compositi a matrice cementizia (FRCM) - Prove di distacco di sistemi di rinforzi FRCM da supporto in muratura-Istruzioni per l'esecuzione delle prove, Luglio 2017.
- [9] P. Zampieri, J. Gonzalez-Libreros, N. Simoncello, C. Pellegrino, Strengthening of Masonry Arches with FRCM Composites: A Review. *Key Engineering Materials*, **817**, 251—258, 2019.
- [10] C.B. De Carvalho Bello, I. Boem, A. Cecchi, N. Gattesco, D.V. Oliveira, Experimental tests for the characterization of sisal fiber reinforced cementitious matrix for strengthening masonry structures. *Construction and Building Materials*, **219**, 44—55, 2019.
- [11] A. Monaco, G. Minafò, J. D'Anna, M. C. Oddo, L. La Mendola, Constitutive Numerical Model of FRCM Strips Under Traction, *Frontiers in Built Environment*, **6**, 60, 2020.

NUMERICAL MODELLING AND ANALYSIS OF ECCENTRIC BRACING WITH VERTICAL SHEAR LINKS

G. Cantisani¹, E. Rodontini¹, and G. Della Corte¹

¹ Department of Structures for Engineering and Architecture, University of Naples Federico II
Naples, Italy
e-mail: {gaetano.cantisani, gaetano.dellacorte}@unina.it, emilio.rodontini@gmail.com

Abstract

Eccentric steel bracing with a vertical shear link is a type of seismic force resisting system that could be selected for seismic retrofitting or upgrading of existing structures. Previous studies have shown that short links with relatively small sections could develop peak shear forces larger than usually predicted values, because of a combination of geometrical characteristics of the link cross section, the link length and the boundary conditions. The peak shear force could be limited by the ductility demand as well as by the occurrence of local and/or global buckling phenomena. This paper explores the response of eccentric bracing comprising the link as well as the diagonal members, looking for the overall behavior. To this end, realistic eccentric bracing systems have been first designed. The case studies were generated starting from the analysis of an existing RC school building in Italy. The existing building was selected within an Italian research project sponsored by the ReLUIS consortium and the Department of Civil Protection in Italy. The response of the existing RC structure was upgraded by designing a steel eccentric bracing system to fulfil the design criteria of the Italian seismic code. Then, the steel bracing system was modelled by means of the finite element (FE) method. This paper describes shortly the design criteria and the consequent results. Then, the FE models and the analyses are described in detail, especially discussing the global behavior in terms of steel strain hardening and overall system stability at the peak inelastic deformation demand estimated at the design stage.

Keywords: Building, brace, buckling, FEM, link, upgrading.

1 INTRODUCTION

Older reinforced concrete (RC) buildings usually suffer from known structural deficiencies which typically lead to poor seismic performance. In fact, several structural and non-structural damages were observed during past and more recent earthquakes [1]. Nowadays, because of the severe difficulties in upgrading existing buildings, the Italian seismic code allows designing for a minimum performance. In fact, the code introduces a conventional risk measuring parameter (ζ_E), defined as the ratio between the maximum seismic intensity that the building is predicted to resist and the design intensity that it should resist if it were a new building. The ratio ζ_E is accepted to be less than unity, but not less than a minimum value; for example, in case of school buildings $\zeta_E \geq 0.60$. In this context, retrofit solutions which maximize the building resistance and ductility while increasing the lateral stiffness are worth to be studied, addressing designers in using less conservative assessment procedures and designing structural details for which one can have both numerical and experimental validations. The technical literature has proposed several technical solutions based on using additional steel elements. Y-bracing with vertical shear links is one possibility, allowing to increase the building lateral stiffness, resistance and being inherently ductile [2,3,4]. In fact, steel braces do generally provide significant increase of the global system stiffness, thus contributing to reduce the deformation demand to existing members and joints. Besides, the use of yielding links allows the additional forces introduced into the existing system to be limited to selected upper bounds, so that the existing structure could sustain the change in the loading system. In case of eccentric bracing, the use of short links is usually preferable, because short links allow maximizing the increase of global system stiffness while minimizing the moment demand to the connections between the link and the existing RC frame members.

Therefore, the paper describes an investigation into a few design and analysis issues for Y-bracing systems with short links, by adopting an existing school building as a case study. Numerical modelling issues are discussed concerning both global and local behaviors, especially referring to the out-of-plane stability of the bracing system.

2 CASE STUDY STRUCTURE AND DESIGN OF THE BRACING SYSTEM

The case study structure is taken from an existing school building located in a small town in Italy (Loro Piceno, MC). Figure 1 summarizes the structural layout with plan and elevation views. The building has moment-resisting (MR) frames in the transverse (X-) direction, while both MR frames and RC walls exist in the longitudinal (Y-) direction. The RC walls evidently originate some irregular dynamic response. In fact, the modal analysis results for the as-built structure show that the first vibration mode is mainly torsional, while the second mode was a combination of translation in the X-direction and torsion. On the contrary, because of the relatively large lateral stiffness of the RC walls, the Y-translational mode of vibration was essentially uncoupled from the torsional response. Structural deficiencies were found in beams and columns, as well as in beam-to-column joints, leading to premature shear failures. Therefore, the need for some local reinforcements to ensure a global ductile failure mode was apparent from the analysis of the as-built structure [5, 6]. However, to improve the overall system performance (i.e., to reduce damage to non-structural elements), a global bracing system was also needed to keep the displacement demand into an acceptable range.

Figure 1 shows an overall view of the designed bracing system. The figure highlights also the plan location of the braces. Design of the additional steel members was carried out according to [7, 8, 9]. Two alternative design solutions were analyzed: (i) short links with HE cross sections and (ii) short links with built-up square hollow sections (B-SHS). In both cases, diagonal members were designed using HE cross sections. In Figure 1, information concerning

the RC beam and column dimensions are also summarized. Eventually, the figure shows the link and brace cross sections.

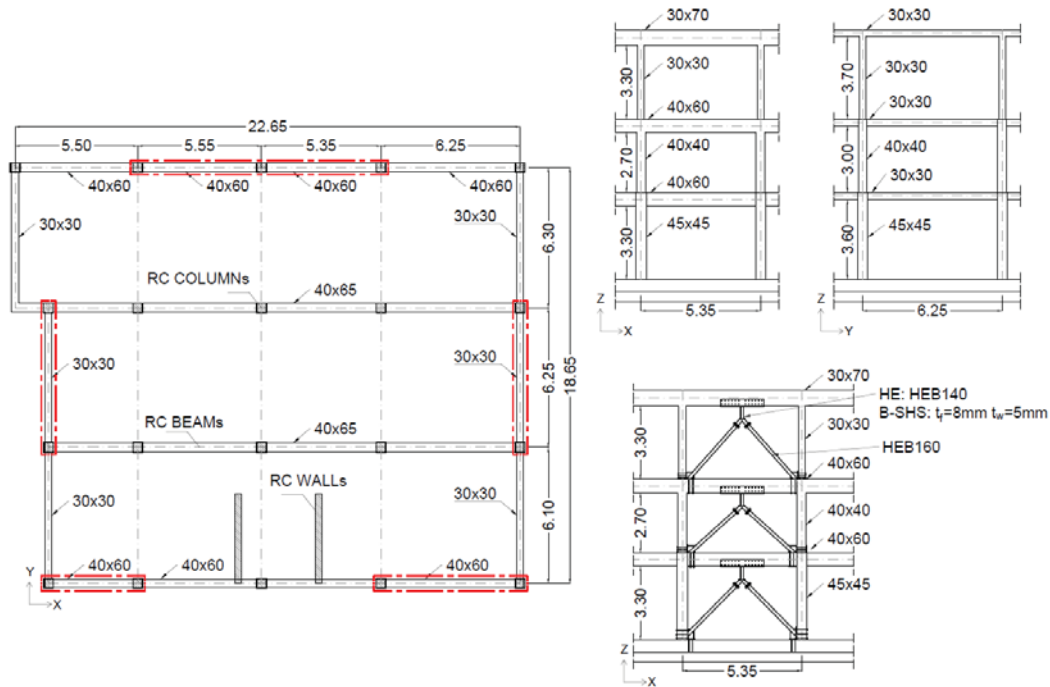


Figure 1: Plan and elevation views of the structural layout.

The design of connections was carried out according to [10]. Capacity design rules and strain hardening of the steel links, as well as uncertainties in the definition of the link yielding strength, were considered according to [7, 8]. Figure 2 shows examples of typical connection details for the considered case study. Particularly, Figure 2(a) and Figure 2(b) show examples of link to RC beam connections, for the HE and the B-SHS design solutions respectively. In both cases, link to RC beam connections were strongly affected by the concrete edge failure mode [11, 12], thus resulting in multiple anchors to allow for sufficient connection overstrength, especially for the HE links (Figure 2(a)). A smaller number of connectors was needed for the B-SHS links because of the smaller link length producing smaller moment demand to the connection (Figure 2(b)).

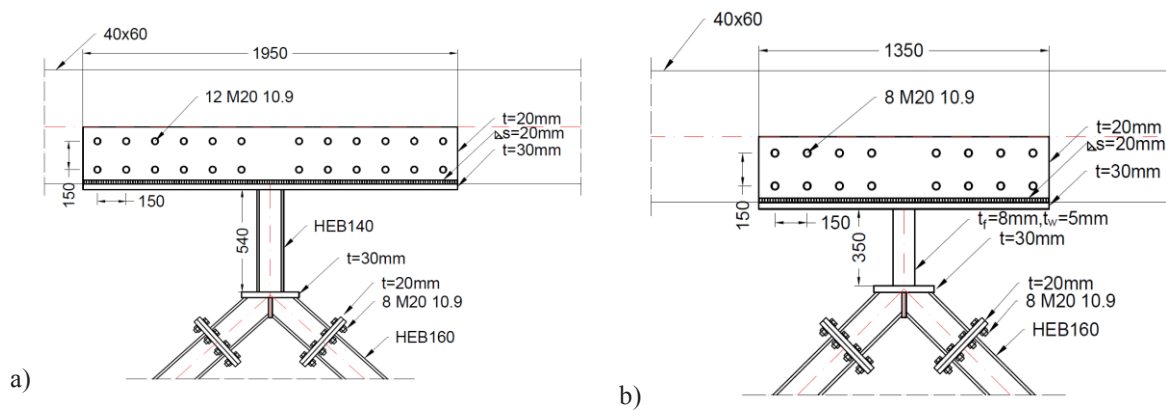


Figure 2: Link-to-beam connections: (a) HE; (b) B-SHS.

Figure 3(a) shows the connection between the brace and the RC beam-column joint, while Figure 3(b) shows the brace connection to the RC column and foundation beam. In every case, brace connections were designed assuming fixed ends for the diagonal members, thus conservatively evaluating the bending moment demand.

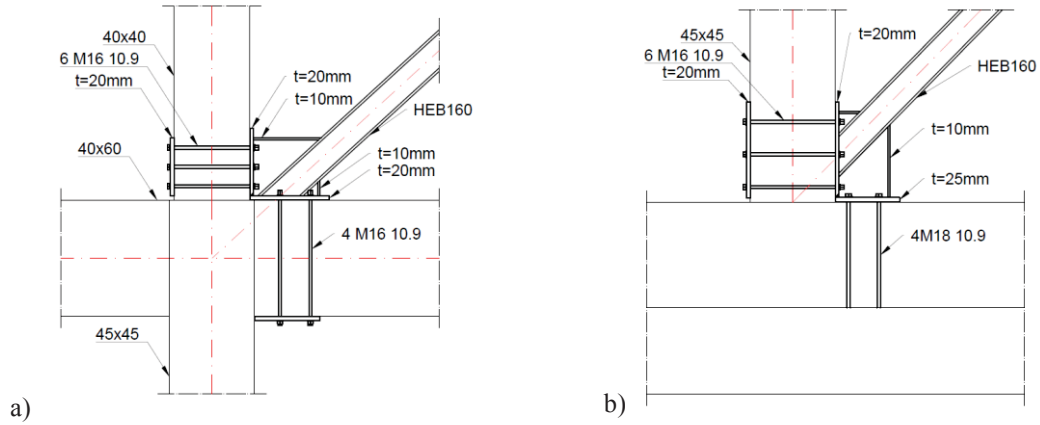


Figure 3: Brace to frame connections: (a) at a beam to column joint, (b) at a foundation beam joint.

3 ASSESSMENT OF THE EXISTING STRUCTURE AND DESIGN OF THE BRACING SYSTEM

3.1 Numerical models

The global seismic response assessment was carried out by developing a 3D non-linear model in SAP2000 [13]. All the RC members were modelled non-linearly with a concentrated plasticity approach [6]. Diagonal brace members were modelled as elastic beam-column elements, while a shear plastic hinge was used to consider link yielding and cyclic hardening. Figure 4 shows the link shear force (V_l) vs. link chord rotation (θ) relationship adopted for the global structural assessment. The link shear force was normalized by the design resistance of the link ($V_{l,Rd}$). Other backbone parameters were obtained by applying the ASCE-SEI standard rules [14]. According to the Italian code [7], the maximum link rotation should not exceed $\theta_u = 0.08 \text{ rad}$.

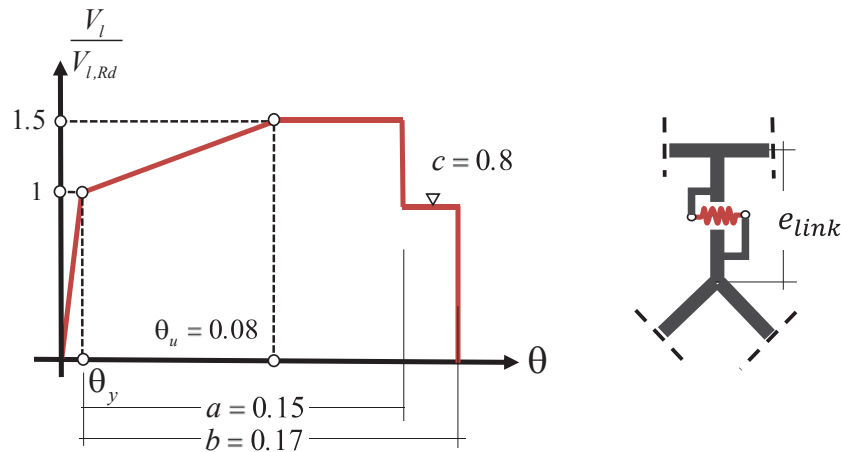


Figure 4: Modelling the shear links for design purposes.

3.2 Analysis results

Pushover analysis results are summarized in Figure 5. Two force distributions were used for the analysis: (i) a modal force pattern (MP) and (ii) a uniform force pattern (UP). The worst structural response was always observed in the Y-direction. The ratios between the lateral stiffness considering the EBs and the bare RC frame model resulted equal to 2.4 and 1.3 for the X- and Y-direction, respectively. The ratio between the base shear force resistance of the structure equipped with EBs and that of the bare RC frame was equal to approximately 1.5 for every building directions and link sections. In the figure, ductile failures of members are highlighted with empty circles ($\zeta_{E,min} > 1$). Empty triangles in the plots highlight brittle shear failure of RC columns. In the case of the structure with EBs, such condition was reached with a value of $\zeta_E = 1$, i.e. with a fully satisfactory performance.

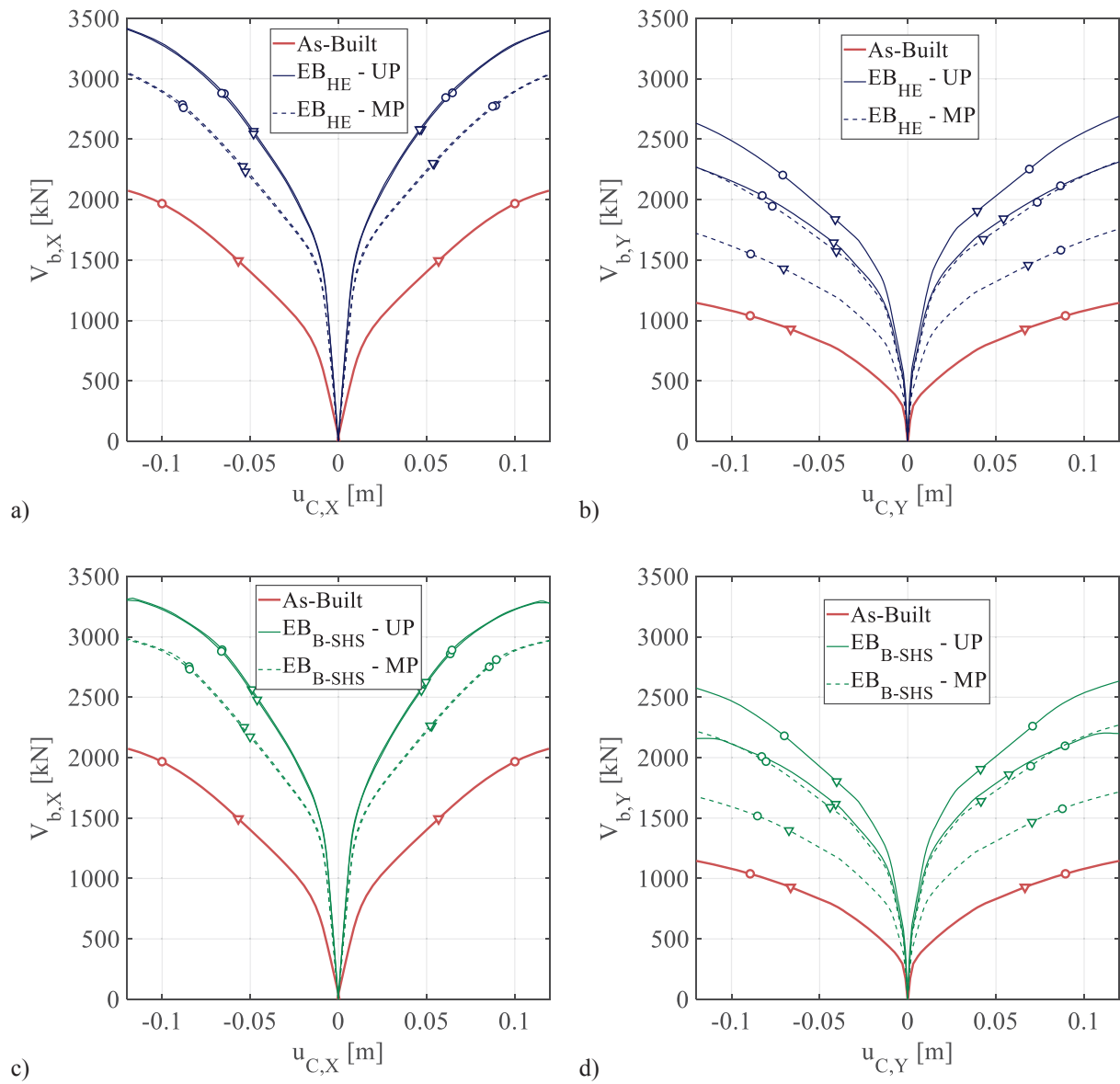


Figure 5: Pushover analysis results:
EB with HE links in X- (a) and Y- (b) directions; EB with B-SHS links in X- (c) and Y- (d) directions.

4 ANALYSIS OF THE BRACING SYSTEM RESPONSE

4.1 Numerical models

The out-of-plane (OoP) stability of the bracing system and the effects of various models for the steel strain-hardening response were investigated using finite element (FE) models of a couple of braces and the corresponding vertical link. The models were built by using non-linear shell elements. Two FE software packages were adopted to perform the analysis and compare the results: (i) *SAP2000* and (ii) the open-source software *Code_Aster* [15]. The two software packages were used to perform elastic, linear buckling and non-linear static analyses. The assumed in-plane boundary conditions are shown in Figure 6(a). Both out-of-plane displacements and rotations were fixed at the boundaries. Regarding the length of the brace members, two models were considered: (i) a node-to-node length (N, Figure 6(b)); (ii) a shorter brace member, considering the RC beam and column sizes (C, Figure 6(c)). The analyses were carried out for the EBs with links having the HE cross sections.

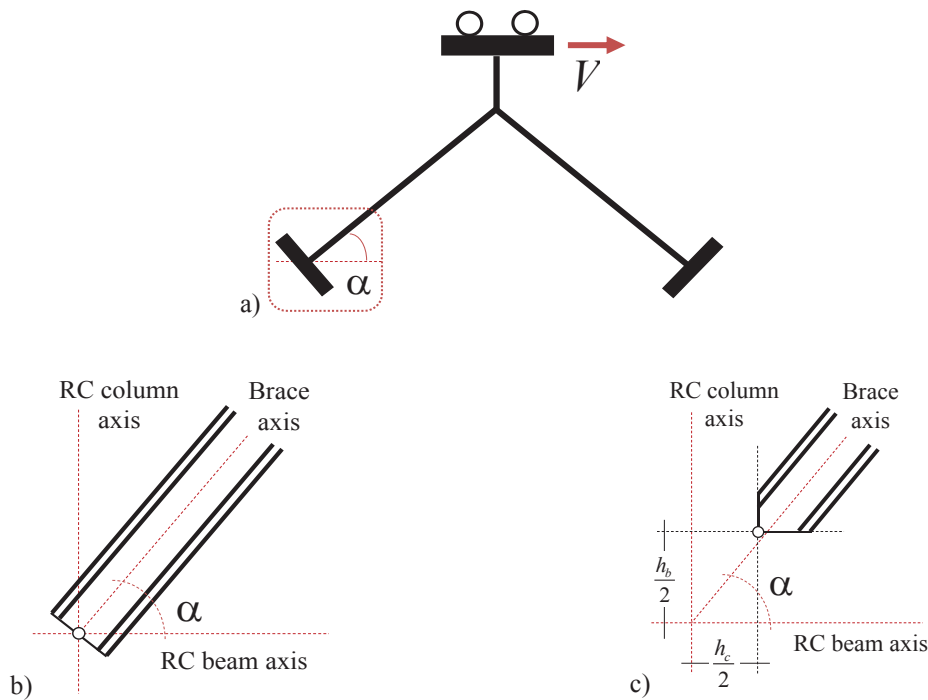


Figure 6: EB model: (a) boundary conditions; (b) Node-to-node (N) model; (c) model considering the finite size of the concrete (C) members.

Three steel stress-strain relationships were used to investigate the role of the steel strain hardening model. First, a simple bilinear stress-strain relationship with kinematic hardening (KH) was considered. The yielding strength was assumed equal to the expected value ($f_{ym} = 343.75$ MPa), while the ultimate strength and strain were assumed equal to the design nominal values ($f_u = 430$ MPa, $\varepsilon_u = 0.20$). Such bilinear relationship was implemented for all the brace geometries both in *SAP2000* and *Code_Aster*. The KH model is shown in Figure 8(a). Second, the numerical data used by Della Corte *et al.* [4] were adopted to fit a numerical stress-strain relationship to the stress-strain experimental data. The considered experimental stress-strain relationships are shown in Figure 8(a), where both monotonic (M, dashed line) and cyclic (C, dotted line) test data are reported according to [4]. The numerical calibration was carried out

using the cyclic response data, because the non-linear static analysis was used to assess the envelope response for a cyclic loading history (i.e., to properly include the steel cyclic strain hardening). The non-linear isotropic saturation hardening (SH) model available in *SAP2000* was used. The SH model has two parameters: (i) the ratio of the ultimate stress to the yield stress (k); (ii) the hardening rate (δ), which controls the rate of approaching the ultimate stress with an exponential decay function. Equation (1) shows the SH model for the uniaxial stress-strain case, in which ε_p represents the uniaxial plastic strain.

$$\sigma(\varepsilon_p) = f_y + f_y \cdot (k - 1) \cdot (1 - e^{-\delta \varepsilon_p}) \quad (1)$$

In Figure 8(a), the curve labelled as SH1 assumes $k = 1.78$ and $\delta = 20$. This curve was taken as a best fit of the non-linear behavior for strain values larger than 0.10. The curve labelled as SH2 assumes $k = 1.60$ and $\delta = 50$, which was taken as a best fit of the non-linear behavior for strain values smaller than 0.10.

In the *SAP2000* model, both the shell “thick” and shell “thin” mechanical formulations were used, which do respectively consider or exclude the deformability to shear forces transverse to the shell thickness. Within *Code_Aster*, similar mechanical formulations are available (called DST and DKT respectively). Two different meshing strategies were considered for the *SAP2000* and *Code_Aster* models as shown for example in Figure 7 with reference to one of the examined links. The mesh for the *SAP2000* model was manually generated, to minimize the number of triangular elements needed to mesh locally the geometry at the intersections of the link and the two diagonal members (Figure 7(a)). On the contrary, within *Code_Aster* the mesh was generated automatically by one of the algorithms available within the graphical pre-processor *Salome* [16] (*NETGEN 1D-2D*). Consequently, the number of triangular elements is automatically generated by the software (Figure 7(b)).

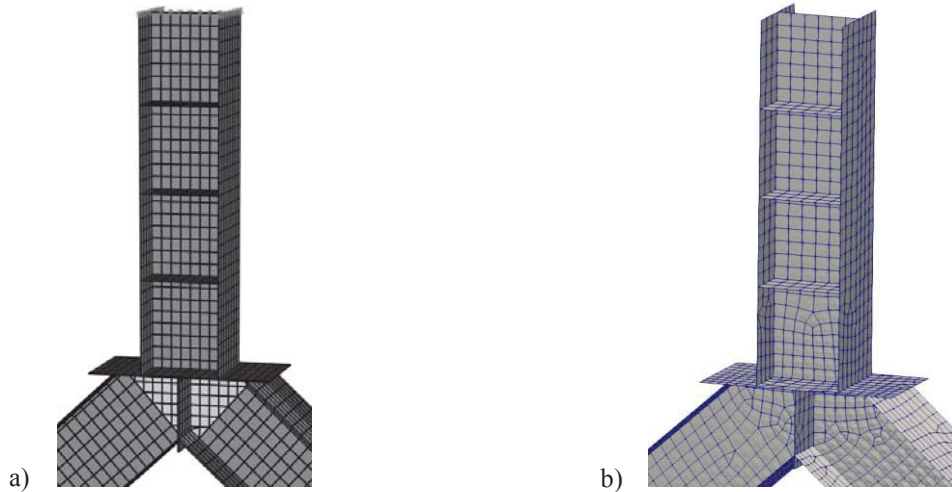


Figure 7: Example of generated meshes with (a) *SAP2000* and (b) *Code_Aster*.

An analysis of the sensitivity to the mesh density was carried out, to select the maximum permissible size of the finite elements and to evaluate the effect of the different mechanical formulations (“thin” or “thick” elements). Results are summarized in Figure 8(b) by plotting the horizontal displacement at the top end cross section of the link (u_{top}) as a function of the mesh geometrical parameter (i.e., the characteristic size of the generic shell element). The hor-

horizontal displacement was calculated by performing a static analysis of the bracing system subjected to a horizontal force equal to the link plastic shear resistance. To have a reference solution, a geometrically equivalent frame model (i.e., with only beam-column elements) was also built and analyzed in *SAP2000*. The frame model had the same boundary conditions as the refined shell model (Figure 6(a)). The solution from the frame model is depicted in the plot with a dashed line. As one can see, analysis results show a small increase of the elastic displacement varying the mesh size. A relatively small difference is also shown by varying the shell mechanical formulation, as well as the considered FE software. In every case, the frame model was found to be stiffer than the corresponding shell models. A mesh characteristic size equal to 20 mm was chosen for the subsequent nonlinear analysis.

Three different bracing were extracted from the design results, to evaluate any change in response due to changes in the diagonal member inclinations and lengths.

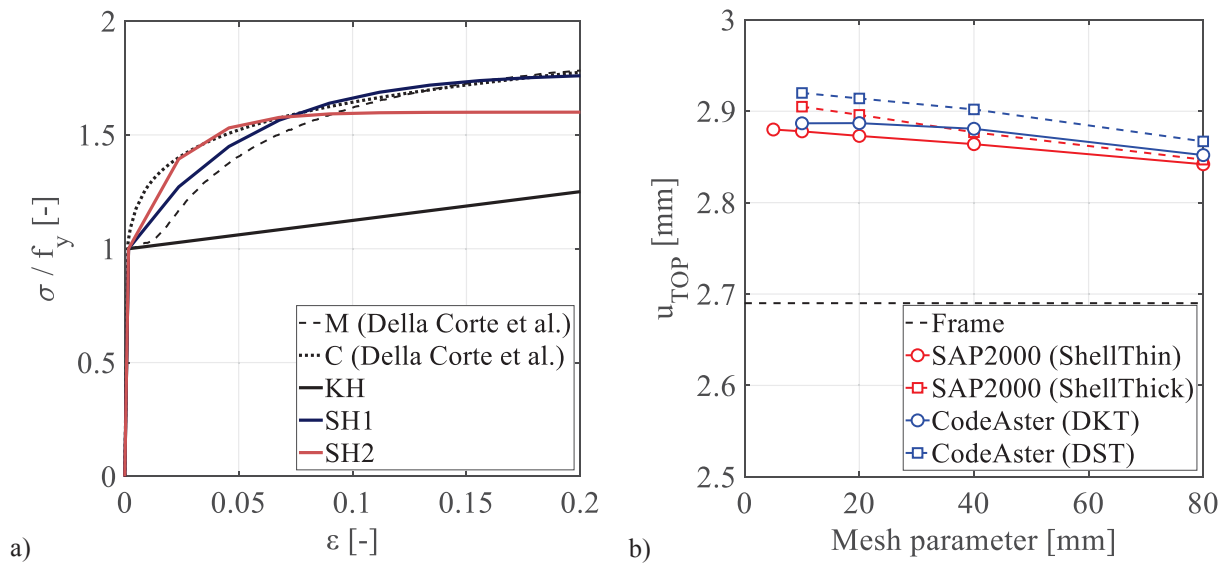


Figure 8: (a) Steel stress-strain relationship; (b) mesh sensitivity analysis.

4.2 Linear buckling analysis results

The linear buckling analyses were carried out to investigate the OoP stability of the bracing system, as well as to identify the shape of the imperfections to use for the non-linear static analyses.

Numerical results from *SAP2000* are summarized in Table 1 for all the examined cases. Particularly, the table provides information concerning the brace length (L_{br}), the brace inclination with respect to the horizontal axis (α , as shown in Figure 4), the (elastic) critical link shear force (V_{cr}), and the global slenderness for OoP buckling (λ_{op}) which was evaluated according to EC3 [9]. In the worst examined case, the elastic critical load multiplier was equal to 18, with respect to the shear yielding strength of the link. The corresponding global slenderness λ_{op} was equal to 0.23 for the N model and 0.22 for the C model. Such values are slightly larger than the EC3-stipulated limit (0.2) for predicting yielding prior to buckling.

Figure 9(a) and Figure 9(b) show first-mode buckling shapes, for the N1 and C1 models respectively, with respect to a sample geometry among all the examined cases. Similar results were obtained for the other geometries. The first buckling modes show lateral-torsional buck-

ling of the compressed brace, along with some out-of-plane (OoP) link displacements mainly concentrated at its bottom end cross section.

For the N1 case study, a linear buckling analysis was performed also using *Code_Aster* for comparison purposes. The analysis results from the *Code_Aster* model shows the same first mode of buckling as obtained with *SAP2000* (Figure 10), thus confirming the lateral-torsional buckling of the compressed brace.

MODEL	L_{br} [m]	α [°]	V_{cr} [kN]	λ_{op} [-]
N1	3.60	42	3896.64	0.19
N2	4.52	46	2598.87	0.23
N3	3.66	57	2924.13	0.22
C1	3.16	42	4619.4	0.18
C2	4.30	46	2876.35	0.22
C3	3.30	57	3468.39	0.20

Table 1: Buckling analysis results.

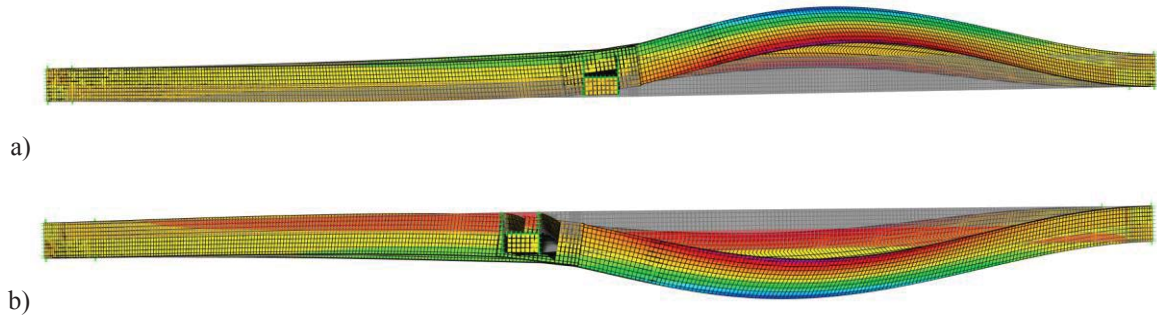


Figure 9: First mode buckling shapes with *SAP2000*: (a) N-EB model; (b) C-EB model.

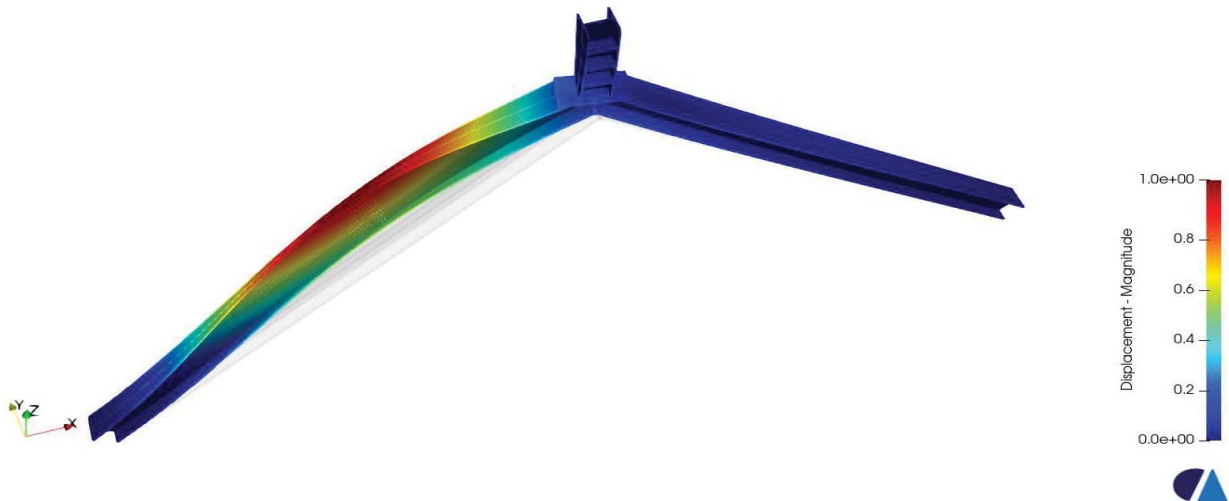


Figure 10: First mode buckling shape with *Code_Aster* for the N1-EB model.

4.3 Non-linear static analysis results

Non-linear static analyses were performed to investigate the OoP stability and the non-linear link behavior. The previously described FE model based on shell elements was used for these analyses. An imperfect geometry was considered, by using the buckling shape obtained by means of the linear buckling analysis results previously discussed. The amplitude of the imperfection was assumed equal to 1/1000 of the brace length. Results are summarized in Figure 11 by plotting the link shear force, normalized with respect to the expected plastic shear resistance, $V/V_{l,Re}$, as a function of horizontal displacement of the top end cross section of the link (u_{top}). Particularly, Figure 11(a) shows a comparison between the results obtained by using either *SAP2000* or *Code_Aster* with the KH non-linear stress-strain model. In *Code_Aster*, the analysis was performed either considering or neglecting non-linear geometrical effects (NLG). Analysis shows identical results up to yielding of the link. After such non-linear event, non-linear geometrical effects took place along with the strain hardening, thus increasing the shear strength. Results suggest minor differences between *Code_Aster* and *SAP2000* in the non-linear branch of the curve.

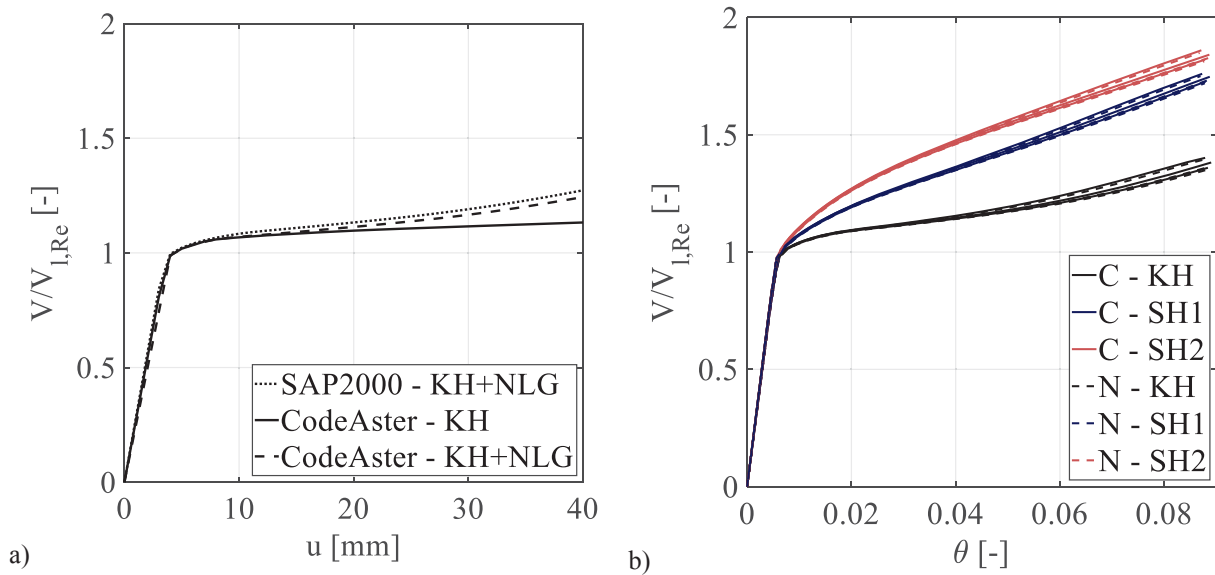


Figure 11: Non-linear static analysis results: (a) *SAP2000* vs. *Code_Aster*; (b) strain hardening model.

Figure 11(b) shows all the numerical analyses carried out with *SAP2000* by using the three previously described stress-strain relationships (i.e., KH, SH1 and SH2) and, by varying the considered model geometry (C and N models, Figure 6). The results are shown by plotting the normalized link shear force as a function of the link chord rotation (θ). All the performed numerical analyses show that both link and brace stability are ensured up to drift angles equal to at least $\theta_u = 0.08$ rad. Therefore, the results from the linear buckling analyses appear to provide conservative results for the assessment of the brace stability. In fact, the global slenderness for OoP stability was slightly larger than 0.2, that is the code stipulated limit to avoid OoP buckling. Besides, the non-linear static analysis results show negligible differences between the N and C geometrical modelling options. Particularly, the pushover curves were practically coincident in the elastic response range, whilst negligible differences were observed in the inelastic response range.

Focusing on the link overstrength, the analysis results show that the KH model significantly underestimates the inelastic link shear forces. In fact, the ratio between the link peak shear force developed for $\theta = 0.08 \text{ rad}$ and the expected plastic shear resistance is equal to 1.30 for the KH model, 1.67 for the SH1 model, and 1.77 for the SH2 model (the values reported here are the mean values among the six examined structures per each considered non-linear stress strain relationship). The basic link overstrength factor that is stipulated by the current Italian code is 1.50, which the code increases to 1.65 (multiplying 1.5 by a factor of 1.1) for capacity design of “non-dissipative” members and connections adjacent to the yielding link. Since the analysis results predicted peak strains smaller than 0.10 for $\theta = 0.08 \text{ rad}$, the SH2 model should be considered in comparing the code-stipulated overstrength factors with those obtained by the numerical analysis. Therefore, the ratios between the code-stipulated overstrength factors and the numerical results are equal to $1.65/1.77=0.93$ and $1.5/1.77=0.85$.

Figure 12(a) shows an example of a contour plot of the equivalent Von-Mises stresses in the link and the plates connecting the braces to the link. Considering that very close results were obtained by varying the brace geometry, the C1 model was selected as an example. The results in Figure 14(a) are for a link rotation $\theta = 0.01 \text{ rad}$, which approximately corresponds to $V_l = V_{l,Re}$. The Von Mises stresses show that yielding develops almost uniformly within the link web. Yielding occurs also in the link flanges close to the bottom and top end cross sections. On the contrary, the Von Mises stresses were always smaller than the yielding strength in the horizontal and vertical plates, as well as in the brace members.

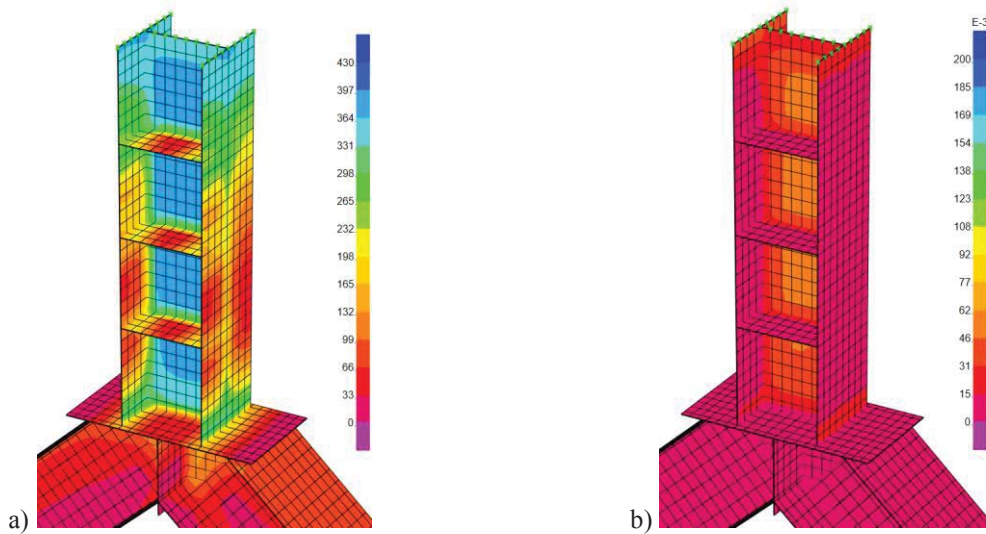


Figure 12: Example of (a) Von-Mises equivalent stresses and (b) equivalent strains in the link.

Figure 12(b) shows an example of the equivalent Von Mises strains in the link and the plates connecting the braces to the link. The equivalent Von Mises strains are used in *SAP2000* as a measure of the plastic deformation intensity. Again, the C1 model was selected as an example. The analysis step corresponds to a link rotation equal to $\theta = 0.08 \text{ rad}$, i.e. considering the ultimate limit state for the link element according to the Italian code. Values of the equivalent strains are smaller than 0.10 everywhere in the link web. Plastic strains can be observed also in the link flanges at its top and bottom cross sections, consistently with the Von Mises stresses depicted in Figure 12(a).

Figure 13 shows examples of deformed shape for the considered C1 model. Hence, Figure 13(a) shows the deformed shape corresponding to a link rotation equal to $\theta = 0.01 \text{ rad}$. The

contour plot highlights out-of-plane displacements (values in the plot are in mm). The compressed brace on the left-side shows OoP displacements with a maximum value approximately equal to 0.3 mm . On the contrary, the tensile brace on the right-side shows negligible OoP displacements if compared with the compressed brace (the maximum value is smaller than 0.07 mm). Figure 13(b) shows the deformed shape corresponding to a link rotation equal to $\theta = 0.08\text{ rad}$. The results show the same distribution of OoP displacements as previously discussed, thus confirming the brace stability for the whole range of the investigated structural response.

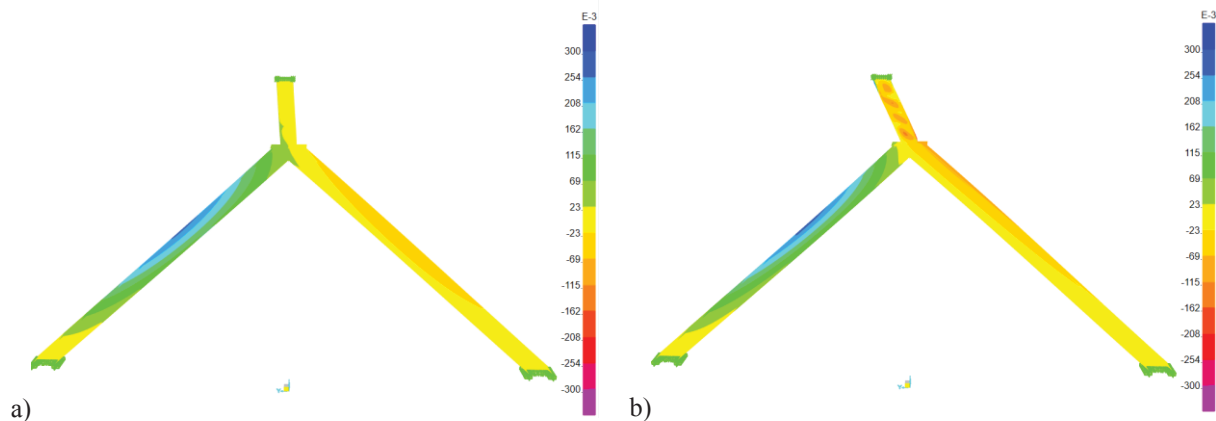


Figure 13: Example of deformed shapes with out-of-plane displacement contour plot:
(a) $\theta = 0.01\text{ rad}$; (b) $\theta = 0.08\text{ rad}$.

Overall, the static non-linear analysis results confirm the validity of the assumed design procedure which adopted member-based buckling checks and capacity design rules for the design of both braces and connections. Further studies with FE models explicitly including connections between brace members will be considered to evaluate the influence on the OoP stability.

5 CONCLUSIONS

The paper presented a numerical study on steel eccentric braces with vertical shear links used for seismic retrofitting of older reinforced concrete (RC) structures. The study mainly focused on the numerical modelling and analysis of the bracing members. Particularly, the paper presented an investigation into the out-of-plane stability of the bracing system, and the peak inelastic forces developed by the link. The investigation was carried out by means of various finite element (FE) models analyzed with different FE software packages. The out-of-plane stability was assessed by performing two types of analysis: 1) linear buckling analysis, coupled with the general method for stability verification proposed by Eurocode 3; 2) non-linear static analyses with imperfect geometrical models. The first analysis method yielded conservative results compared with the static non-linear analysis. The non-linear static analysis has shown a stable behavior of the bracing system up to the ultimate link chord rotation stipulated by the current Italian code. Regarding the plastic overstrength of the shear links, the numerical results indicates that the currently suggested rules by the Italian code could underestimate the peak shear strength. However, effects such as the loading history and the steel strain hardening models still need further investigations to make conclusive comments on this aspect of the code.

ACKNOWLEDGMENTS

Authors gratefully acknowledge the financial support from the RELUIS-DPC 2019–2021 project, funded by the Italian Department for Civil Protection.

REFERENCES

- [1] Del Vecchio C., Di Ludovico M., Pampanin S., Prota A., Repair cost of existing rc buildings damaged by the L'Aquila earthquake and comparison with FEMA P-58 predictions. *Earthquake Spectra*, **34**, 237-26, 2018.
- [2] Ghobarah A., Elfath Abou H., Rehabilitation of a reinforced concrete frame using eccentric steel bracing. *Engineering Structures*, **23**, 745 – 755, 2001.
- [3] Mazzolani F.M., Della Corte G., D'Aniello M., Experimental analysis of steel dissipative bracing systems for seismic upgrading. *J. Civ. Eng. Management*, **15**(1), 7-19, 2009.
- [4] Della Corte G., D'Aniello M., Landolfo R.: Analytical and numerical study of plastic overstrength of shear links. *Journal of Constructional Steel Research*, **82**, 19-32, 2013.
- [5] Frascadore R., Di Ludovico M., Prota A. et al., Local strengthening of reinforced concrete structures as a strategy for seismic risk mitigation at regional scale. *Earthquake Spectra*, **31**(2), 1083–1102, 2015.
- [6] Progetto DPC-ReLUIS 2019-2021, WP5: Interventi di rapida esecuzione e a basso impatto ed integrati. Caso studio 2: Edificio scolastico in cemento armato. *ReLUIS report*, ReLUIS, Naples, Italy, 2020. Available at <http://www.reluis.it/>.
- [7] CS.LL.PP. Aggiornamento delle norme tecniche per le costruzioni. Gazzetta Ufficiale della Repubblica Italiana 42, 2018.
- [8] CEN, Eurocode 8: Design of structures for earthquake resistance – Part 1: General rules, seismic actions and rules for buildings. European Committee for Standardization, Brussels, Belgium, 2003.
- [9] CEN, EN 1993-1-1 Design of steel structure – part 1-1: General rules and rules for buildings. European Committee for Standardization, Brussels, Belgium, 2005.
- [10] CEN, Eurocode 3, Design of steel structures – Part 1-8: Design of joints. European Committee for Standardization, Brussels, Belgium, 2009.
- [11] Della Corte G., Landolfo R., Lateral loading tests of built-up battened column with semi-continuous base plate connections. *Journal of Constructional Steel Research*, **138**, 783-798, 2017.
- [12] Della Corte G., Cantisani G., Landolfo R., Battened Steel Columns with Semi-Continuous Base Plate Connections: Experimental Results vs. Theoretical Predictions. *Key Engineering Materials*, **763**, 243-250, 2018.
- [13] CSI, SAP2000 Linear and Nonlinear Static and Dynamic Analysis and Design of Three-Dimensional Structures. CSI Computer & Structures, Berkeley, California, 2011.
- [14] ASCE-SEI 41-17, Seismic evaluation and retrofit of existing buildings, 2017.
- [15] EDF Electricité de France, Code_Aster, Analysis of Structures and Thermomechanics for Studies & Research. 1989. Open source on www.code-aster.com.
- [16] Open CASCADE, SALOME: The Open-Source Integration Platform for Numerical Simulation. Open source on www.salome-platform.org.

PERFORMANCE OF EXISTING REINFORCED CONCRETE ARCH BRIDGES UNDER CURRENT NON SEISMIC LOADS

Giovanni Crisci¹, Francesca Ceroni¹, Gian Piero Lignola² and Andrea Prota²

¹Engineering Department, University of Naples “Parthenope”,
Centro Direzionale is. C4, 80143, Napoli, Italy
{giovanni.crisci, francesca.ceroni}@uniparthenope.it

²Department of Structures for Engineering and Architecture, University of Napoli “Federico II”,
Via Claudio, 21, 80125, Napoli, Italy,
{glignola, aprota}@unina.it

Abstract

The present analytical work deals with the assessment of the performances of Reinforced Concrete (RC) Deck Arch Bridges under the non-seismic loading conditions required by the current mandatory Italian codes. In particular, the attention is focused on a specific RC deck arch bridge typology, better known as the “Maillart Type Arch Bridge”, which is characterized by a very stiff deck beam and a slender and wide vault. As well as other existing RC structures which were designed under only gravity loads and without specific structural details, such as lower limits for longitudinal and transverse reinforcement bars, these bridges could be damaged by loading conditions not considered at the time of design. For the evaluation of the main critical issues related to the current performance of such bridges under the current non-seismic loading conditions, it has been defined a large inventory of simulated arch bridges in accordance to the design procedures usually adopted in 1950s which considered only gravitational loads, i.e. self-weight and moving loads. Each bridge of the inventory is modelled and studied by means of a Linear Gravitational analysis implemented in the structural software SAP2000, with support of an Application Programming Interface (API), such as Matlab.

Due to the differences between the current loads and those considered at the design time and to the approximations of the design strategies of the time, a performance – based analysis of the existing bridges under non-seismic loads is important for the stakeholders as much as for the decision – makers in order to plan risk mitigation programs and prioritize eventual retrofit interventions for risk reduction.

Keywords: RC Arch Bridges, Maillart Bridges, Gravitational loads, Vulnerability Analysis.

1 INTRODUCTION

In recent years, considerations and rehabilitations of existing bridges have been an ongoing problem for the bridge administrations and for their owners in almost all countries. The performance level of an existing bridge is often inadequate: indeed, the always increasing number of vehicles and of traffic and the heavier weight loads, have made the structural safety of existing infrastructure system progressively insufficient even under vertical loads only.

In Italy, the Reinforced Concrete (RC) arch bridges are today still one of the most important part of the transportation system. Such bridges, designed and built around 50s, and in most cases under-designed for the nowadays serviceability conditions, require particularly attention due to their specific peculiarities that make exceptionally complex the assessment of their behavior under both static and dynamic actions. In addition to the previous “vulnerabilities”, most of these structures were designed only for gravitational loads: indeed, the seismic hazard has only recently been recognized by national structural codes ([1], [2]) and this means that their current vulnerability may be much more important.

In this study, the attention is focused on a specific arch bridge typology: the “Maillart-Type Arch Bridges” or “Deck Stiffened Arch Bridges” ([3], [4], [5]), which are characterized by a very stiff deck beam and a slender and wide vault (with a low moment of inertia), connected the one to the other by means of slender piers, often wall-like and lightened by central windows (Figure 1). The name of this bridge typology comes from the Swiss civil engineer Robert Maillart, who first introduced a very revolutionary concept: he reversed the classic arch-to-deck stiffness ratio, realizing in this way a significant reduction of the bending moment and of the shear forces in the arch in favor of a mainly compression stress status in the arch. This led to the fact that, being the structure hyperstatic, the stiffest element also bears the highest stresses and, thus, the deck beam becomes the key element of the whole bridge, since it has to bear the most bending moments and shear forces ([6], [7]).

Nowadays, as mentioned previously, some of RC Deck Stiffened Arch Bridges built in the last century need a structural strengthening due to several environmental factors such as corrosion and degradation of materials and/or anthropological factors such as the always increasing traffic loads under serviceability conditions and/or poor maintenance [8].

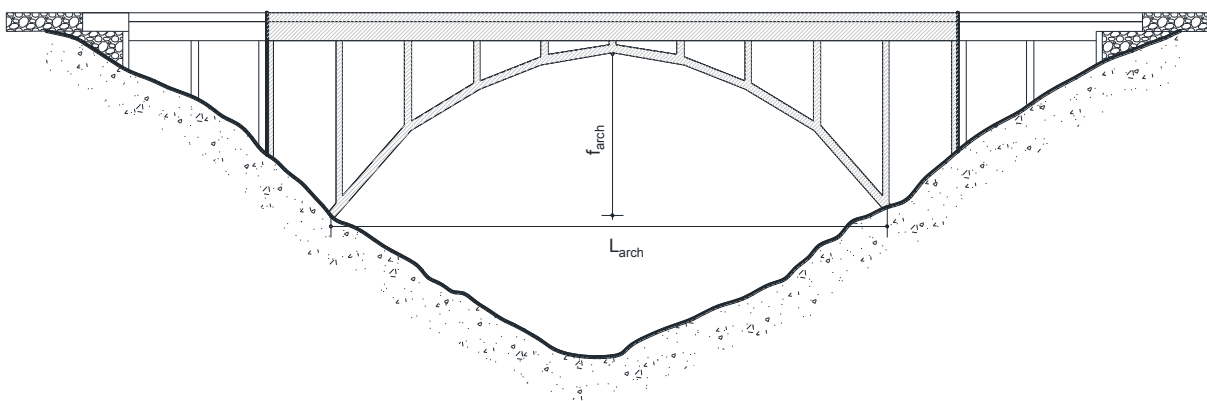


Figure 1: General view of a RC Deck Stiffened Arch Bridge.

It is worth to note that a fundamental problem in Italy is represented by the absence of a detailed database of existing infrastructures; indeed, the lack of exact information makes the role of managing entities even more difficult. An example of the particularity of the Italian

scenario is that, in February 2019, there were about 1000 bridges whose ownership was not even known [9].

Therefore, information about damage and/or structural deficiencies of bridges is also quite rare and, additionally, details about dimensions, type and amount of materials of real structures are not available for a large number of these bridges.

The present study focusses attention on the assessment of the safety conditions of RC Deck Stiffened Arch Bridges under the current static loading conditions defined by the Italian codes ([10], [11]). Despite several bridges of this typology have been recognized in Italy, due to the lack of detailed information about them, the structural analyses herein presented have been performed with reference to a large building inventory of simulated “Maillart – Type” Arch Bridges, characterized by geometry and material properties varying in the ranges typical of the real structures. Firstly, a simulated design procedure according to the current codes at the age of construction has been used for creating the geometrical models and define the internal steel reinforcements. Then, structural analysis and safety verifications have been carried out for the samples of the collected inventory under the static loads provided by the current Italian codes ([10], [11]).

2 CREATION OF THE BRIDGES INVENTORY

2.1 Characteristics of existing “Maillart – Type” Arch Bridges in Italy

Although the typology of girder bridges is certainly the most widespread in Italy, examples of arch bridges are also frequent. In Crisci et al., 2021 [12], after careful investigations based on examination of old projects, books and online resources, several existing RC arch bridges (about 90) were collected and recognized on the Italian territory. Unfortunately for most of them, it was only possible to retrieve general information on geometry, such as span length L_{arch} and the rise of arch f_{arch} . This study allowed to identify the variability of the main geometric parameters of such structures; indeed, most of the bridges are characterized by an arch span L_{arch} ranging between 50 and 90 m, while a low percentage is found for the case 90-110 m (Figure 2a). It is worth noting that these distributions are representative of the only collected available data and, thus, they might be not fully representative of the real situation in Italy or worldwide.

Similar considerations can be summarized for the arch rise f_{arch} : a good percentage of bridges, approximately 50%, are characterized by an arch rise ranging between 10-20 m, whereas a lower percentage is concentrated around the values of 20-30 m and 30-40 m (Figure 2b). In Figure 2c, the frequency distribution of the ratio f_{arch}/L is also plotted.

In addition to the arch, the structural elements of each bridge consist of a regular grid of main and secondary RC beams with rectangular cross sections, connected the one to the other by means of a slab. Finally, slender piers connect the vault to the deck beam. Detailed information about the dimensions of the various structural elements or the reinforcement ratios are more difficult to determine or collect, and they would require ad hoc investigations and inspections. For such reason, in Crisci et al. 2021 [12], thanks to historical documents and old designs, the typical variability of the secondary geometric characteristics has been presented, such as the dimensions of piers, beams, reinforcement ratios for the vault, piers, etc...

Thus, for the generation of the inventory, the following ranges were fixed for the main geometrical parameters:

- 50 - 120 m for the arch span, L ;
- 10 - 40 m for the arch rise, f_{arch} ;
- 0.2 - 0.3 for the ratio, f_{arch}/L ;

- 0.30 - 0.45 m for the base of piers, B_p ;
- 0.30 - 0.45 m for the base of the main beams, $B_{b,I}$;
- 1.0 - 1.6 m for the height of the main beams, $H_{b,I}$;

Note that for the parameters plotted in Figure 2, the ranges have been defined by considering the minimum and maximum values relative to the cases with greater frequency.

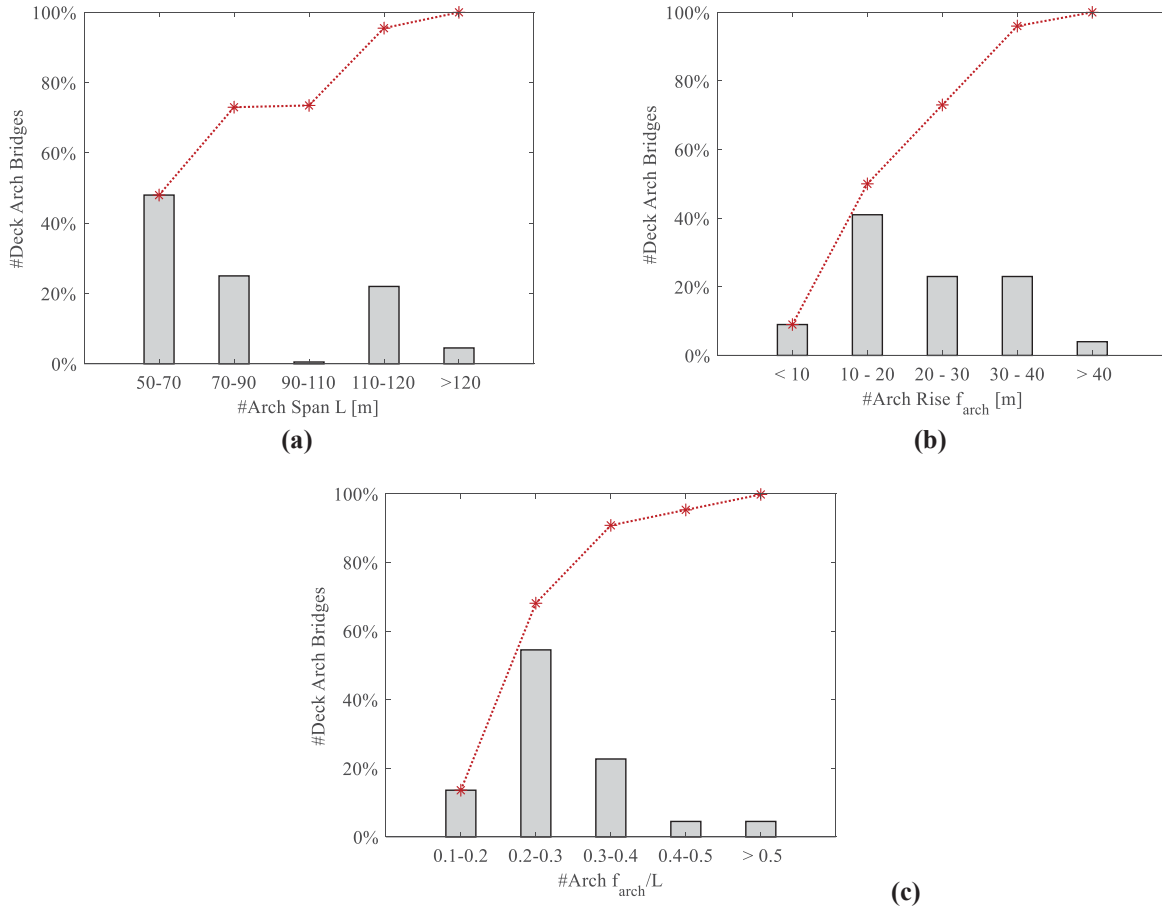


Figure 2: Distribution and cumulative percentage of bridges as: (a) function of Arch Span, L ; (b) function of Arch Rise, f_{arch} ; (c) function of ratio between f_{arch}/L .

About the mechanical characteristics of the materials, historical and documented sources evidenced that it was customary to use concrete with a cubic characteristic compressive strength R_{ck} of at least 36 MPa, whereas for the steel reinforcement, usually the one known as TOR60 was adopted with an average yielding stress of about 600 MPa.

A proper Bridge Inventory of more than 1500 structures has been, thus, defined by means of the Monte Carlo simulation procedure ([13]). The generation of a proper dataset is, indeed, very useful in order to study the average behaviour of a homogeneous class of structures at large scale with regards to a certain demand, that for the present study will be represented by the static loads provided by the current Italian codes.

The bridge inventory was, thus, built by changing some significant parameters such as geometrical data, mechanical and reinforcement percentages in the fixed ranges discussed previously. As regard the reinforcement percentages, they were established in accordance with the minimum values indicated by the mandatory codes of the time ([14]) and with reference to a few designs of real bridges. In particular, for the vault and the piers, the minimum

reinforcement percentage was, on average, equal to 0.8% of the area of the concrete cross section. For the elements subjected to bending moment, on average, the reinforcement percentage varied between 0.1% and 2%. Moreover, it was customary to use a transverse reinforcement (e.g. stirrups) with a very scattered distance, i.e. variable between 150 and 250 mm.

In particular, with regard to the dimensions of the piers, it is worth to note that only the lower dimension of the vertical piers has been defined, because it is linked to the base of the main beams for geometric reasons. As regard the larger dimension, e.g. the one parallel to the longitudinal direction of the bridge, it has been obtained as a function of the slenderness, λ , of the structural element. Indeed, in order to reduce the effects of the second order, it was usual at the time to set the slenderness of the piers to a limit value of 50.

Generally, the extraction of the parameters should take place with reference to a probability distribution, but, due to the limited number of known reference structures and, thus, to the limited knowledge of the actual distribution of each parameter in the real structures, the parameters have been drawn assuming a uniform probability distribution for each of them.

Moreover, in order to exclude the combinations of geometric and mechanical parameters which could lead to bridges structurally not verified nor realistic, each generated arch bridge was subsequently verified with reference to the vertical loads of the time, i.e. according to the mandatory codes of the time. These verifications, explained in the following, have been carried out according to the structural schemes and analysis procedures of the time that were simpler in comparison with those adopted nowadays thanks to the aid of numerical software.

2.2 Verifications of “Maillart – Type” Arch Bridges according to the codes of the time

Once the bridge inventory has been defined, the geometric and mechanical characteristics of each structure are known, such as arch span and rise, dimensions of piers, principal and secondary beams, steel reinforcement ratio, and so on. For each bridge, a simulated design has been carried out according to the mandatory codes at the time of design in order to verify the correct size and the reinforcement layers assigned to the various structural elements (Crisci et al. 2021 [12]) and to exclude non-realistic combinations of geometric and mechanical parameters. In this section the steps followed for carrying out these verifications are described.

The starting point for building the geometry of a deck arch bridge is the definition of its arch; a common practice of the time consisted into design the axis of the arch in order to be funicular of the gravitational loads corresponding to the self-weight only of the entire structure. This means that the arch is subjected to axial compression force only, without any bending moment and shear force. The calculation of the stresses acting on each arch has been done considering a simplified model in agreement with the assumptions commonly done by the designers of the time, i.e., an equivalent two-dimensional structure, characterized by a continuous deck beam supported by the piers, a hinged arch at both springings, and axially rigid piers connected to both the arch and the deck beam by means of hinges.

The load combinations were fixed with reference to the mandatory codes in force at the time, in particular the Royal Decree of 1939 [14] and the Circular n. 6018 concerning the loads on bridges of 1945 [15]. In particular, two different types of loading schemes were adopted:

1. Two or more undefined trains of trucks weighing 12 tons (about 120 kN) side by side;
2. Two compressor rollers weighing 18 tons each (about 180 kN) side by side.

In addition, a compact crowd was expected on the sidewalks next to the driveway.

The assessment of maximum stresses was carried out by placing the moving loads, given by the loading condition 1 [15], in the most unfavourable position on the deck, which was

found by means of the Influence Lines. Figure 3 shows some of the influence lines adopted for the verification of the structural elements of bridges, i.e. the influence lines of bending moments for moving vertical loads in one cross section of the deck (magenta line) and of the horizontal thrust in the arch (yellow line).

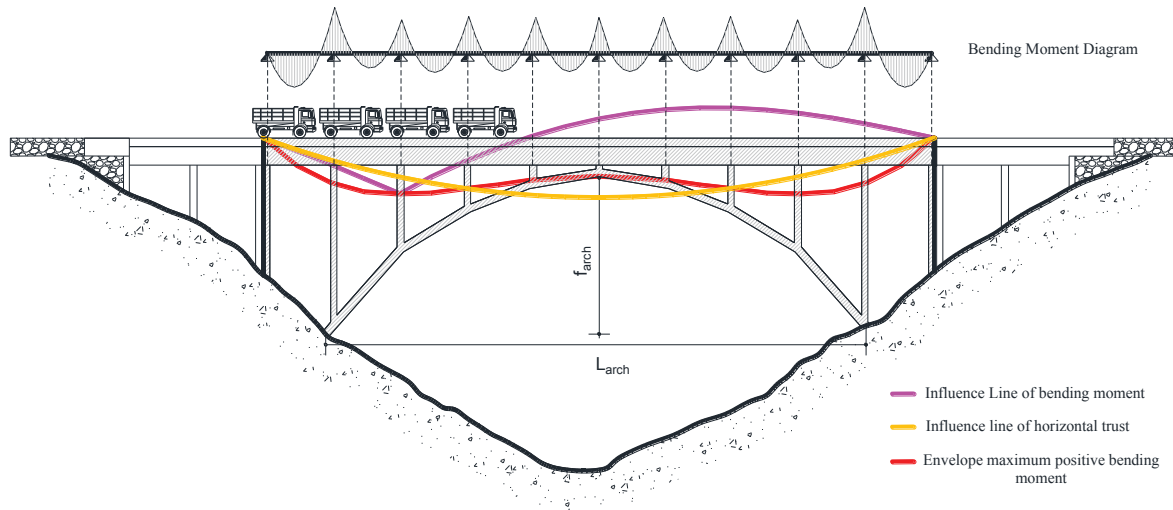


Figure 3: Examples of influence line of bending moment on the deck, horizontal thrust and position of moving loads able to maximize the bending stress.

It is worth to note that the position of the moving loads giving the maximum bending moment on the deck does not yield the maximum horizontal thrust in the arch as well. Indeed, in order to maximize the horizontal thrust, H , and so the compression force, N , in the arch as well, the moving loads must be applied on the whole entire deck. Under this latter load condition, the piers were verified as well.

The envelope of all the positive and negative peaks of each magenta line represents the diagram of the maximum and minimum bending moments from which it is possible to identify the cross section and, therefore, the position of the moving loads able to maximize the bending moment on the deck beam. For simplicity, in Figure 3, the only envelope of the maximum positive bending moments is plotted (red line); the envelope of the minimum negative bending moments is, indeed, mirrored to this one.

Conversely, the secondary beams have been verified with reference to their tributary area to define the entity of the gravitational loads (uniformly distributed loads) and with reference to the worst condition for the moving loads, i.e. when the axis of the vehicle is just on the secondary beam. Moreover, the constraint conditions at the ends of the secondary beams have been assumed as ranging between a simple supported beam and a fully fixed beam, in order to maximize the positive and negative bending moments along the element.

According to the Royal Decree of 1939 [14], the design of steel reinforcement in the beams was made with respect to “*Allowable Stress Method (ASM)*” [16], where the working stress is defined as the 5% percentile strength divided by a safety factor, equal to 3 for concrete and 2 for steel. On the basis of the stress distributions in each element under the previously cited load combinations, each generated arch bridge has been verified with reference to both flexural, normal and shear stresses. If some verifications are not satisfied, the bridge has been excluded from the database under the assumption that the casual combinations of the parameters have led to hypothesize a structure not in agreement with design rules and loads of the time and, thus, not representative of an existing bridge. Clearly, for the not verified

samples, a different choice of some parameters, as, for example, the reinforcement percentage or the dimensions of some structural elements, might lead to a representative structure, but lacking more detailed information on these parameters, this option was not pursued. Therefore, in place of the excluded cases, other bridges were extracted, as long as the sample size was satisfactory and the geometrical parameters assumed for the generation of the sample were equally distributed.

2.3 Creation of 3D Finite Element Models

Once each geometric model has been designed and verified according to a simplified methodology and in agreement with the loads and rules of the time, a 3D Finite Element Model (FEM) is implemented using the software SAP2000 [17]. Two node – frame elements, i.e. beam elements with three translational and three rotational degrees-of-freedom (DOF) at each node have been used to model the beams, the piers and the arch. Moreover, the eccentricities of the piers with regard to the axis of the vault have been taken into account by means of rigid offsets and massless links. In Crisci et al., 2020 [6] it was, indeed, verified that no significant differences in the stresses in all structural elements occur if the vault is modelled by two-dimensional elements instead of frame elements with offsets. This latter solution was preferred in order to reduce the computational effort also in view of the analyses under seismic actions.

About the constraint conditions of the piers, it is worth to remember that usually at the time of design the piers were modelled as pendulums, i.e. simply hinged at both ends, under the gravitational loads and, thus, they resulted subjected to axial loads only. The choice of modelling the piers as pendulums was related to the reduction of the hyperstatic unknowns and, thus, of the complexity of the solution of the structural scheme of the bridge, but, at the same time, led also to a reduction of the differences in stiffness of the deck beam and the vault. However, some design documents of the time have evidenced that in many cases the piers were realized as fixed at the end, as testified by constructive details, and were, thus, subjected to some shear and bending actions as well. For this reason, in the SAP2000 model the piers have been considered fixed constrained at their both ends and not connected by simple hinges to the arch and the deck. It is worth noting that the entity of the shear and bending actions transferred to the piers under gravitational loads was limited due to the high difference of stiffness between the deck and the arch and, thus, between deck and piers [6].

The deck slab, on the contrary, has been considered only in terms of loads acting on the main beams, while a “diaphragm” constraint has been used to simulate its behaviour on the bridge deck. Fixed supports at ends of the arch have been assumed; this assumption is well accepted when bridge foundation is over bedrock sites, i.e. ground type A [10], as it is the case for the majority of this type of bridges. With reference to the deck constraints, the generic bridge was assumed to be constrained along the longitudinal direction in order to simulate the presence of abutments or of other roads which could limit its displacement, whereas it was considered free along the out – of – plane direction.

Each structural element is modelled as elastic and, in order to take into account the development of cracking phenomena in the concrete, the effective moment of inertia of the beams has been reduced by 50%, while by only 25% for the vertical piers and the arch according to the prevalent compression forces in the elements ([10], [18]). No reduction of the transverse area, torsion and shear area has been considered [19]. This procedure was automatized adopting specific software such as MATLAB [20], where by means of Open Application Programming Interface (OAPI), it is possible to integrate with structural software, such as SAP2000 [17], to run analysis on a multitude of several models.

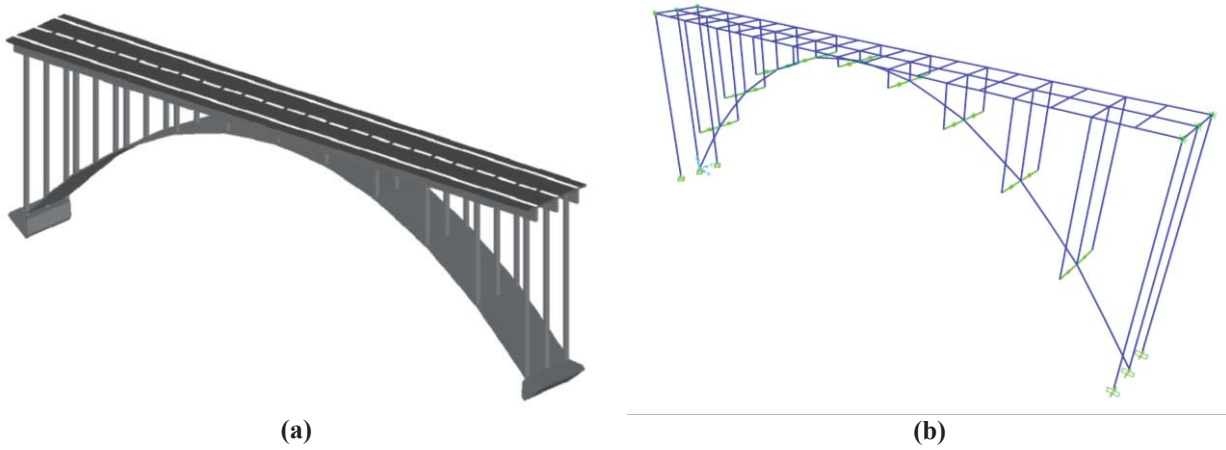


Figure 4: (a) Geometric model of RC Deck Stiffened Arch Bridge; (b) Three Dimensional (3D) FEM.

3 ASSESSEMENT OF TRAFFIC LOADS ACCORDING TO ITALIAN CODES

As reported in section 1, the demand in terms of traffic loading is very different nowadays if compared to the past. This study is, indeed, aimed to highlight which are the main structural deficiencies of existing bridges, especially for arch bridges designed and built with regards to the rules of 40s, under the non-seismic loads prescribed by the current codes, i.e. the new guidelines for existing bridges [11] and the Italian code for structures [10]. This is a fundamental aspect that has to be investigated prior to proceed with the verifications under seismic actions. It is worth to note that, for structural purposes, according to new guidelines [11], each generated arch bridge was assumed to be classified as CC3, i.e. Consequences Class 3, that means “*high consequence for loss of human life, or economic, social or environmental consequences very great, such as bridges, public buildings, where consequences of failure are high*”. The structural verifications were carried out considering the loads according to the new guidelines for bridges [11], that entail to assume the same partial safety coefficients prescribed by [10].

The structural analyses were performed considering, in addition to the structural and non - structural weights, e.g. road pavement, the moving loads schemes in accordance with [10]. The latter, shown in Figure 5, also include the dynamic effects due to the passage of vehicles on the structures, and they are the reference schemes that have to be used for the global structural verifications of the bridge structures.

Q_{ik} Q_{ik} q_{ik}		
		Lane 1
		$Q_{1k}=300\text{kN}$ $q_{1k}=9\text{kN/m}^2$
		Lane 2
		$Q_{2k}=200\text{kN}$ $q_{2k}=2.5\text{kN/m}^2$
		Lane 3
		$Q_{3k}=100\text{kN}$ $q_{3k}=2.5\text{kN/m}^2$
		Remaining part $q_k=2.5\text{kN/m}^2$

Figure 5: Moving loads according to Italian Building Code 2018 [10].

Moreover, it has been considered the braking actions of the vehicles, which are applied as uniformly distributed loads on the axis of the lane. In addition to the moving loads, the loads

related to temperature, wind and snow have been considered as well, assuming for simplicity a climatic zone III and an altitude of less than 200m [10].

In order to define the characteristic values (i.e. the 5% percentile values) of the traffic loads, the loading schemes have been combined by considering two groups of actions, respectively the group 1 and the group 2a, as reported in [10]. The first group considers the characteristic values of the moving loads without taking into account the braking actions. The group 2a, on the other hand, considers the frequent values of the moving loads and takes into account the characteristic values of the braking actions. Finally, the various actions have been combined with the fundamental combination at the Ultimate Limit State, obtaining a total of 9 individual load combinations, as Table 1 shows.

Tab 1: Load combinations at the Ultimate Limit State according to ([10], [11])

ID	G _{k1}	G _{k2}	Q _k			Wind	Snow	Temperature
			Q _{ik}	q _{ik}	Braking			
1	1.35	1.5	1.35	1.35	-	0.9	-	0.72
2	1.35	1.5	1.01	0.54	1.35	0.9	-	0.72
3	1.35	1.5	1.01	0.54	-	1.5	-	0.72
4	1.35	1.5	1.01	0.54	0.54	1.5	-	0.72
5	1.35	1.5	1.01	0.54	-	0.9	1.5	0.72
6	1.35	1.5	1.01	0.54	0.54	0.9	1.5	0.72
7	1.35	1.5	1.01	0.54	-	0.9	-	1.20
8	1.35	1.5	1.01	0.54	0.54	0.9	-	1.20
9	1.35	1.5	-	-	-	0.9	-	0.72

The structural verifications have been carried out with reference to both the ductile (flexural verifications) and brittle mechanisms (shear verifications) in terms of capacity at the Ultimate Limit State (ULS), in accordance to [10]. For the flexural capacity, in order to take into account the presence of biaxial bending moments, the following Bresler's equation has been adopted:

$$\left(\frac{M_{Ed,x}}{M_{Rd,x}}\right)^{\alpha} + \left(\frac{M_{Ed,y}}{M_{Rd,y}}\right)^{\beta} \leq 1 \quad (1)$$

being $M_{Ed,x}$ and $M_{Ed,y}$ the bending moments around the two principal axes, x and y, of the cross sections and come from the 9 loads combinations, $M_{Rd,x}$ and $M_{Rd,y}$ the flexural capacity of the section evaluated with respect to the x and y axis respectively, α and β two shape coefficients, which for rectangular cross section have been assumed equal to 1.5.

As regard the shear capacity, two different approaches have been considered for the arch and for the beams. Due to the presence of longitudinal steel reinforcement only, for the arch the shear strength for members without shear reinforcement given by ([10], [18]) has been used, while for the piers and the beams, which are supposed to have steel stirrups, the shear capacity has been evaluated according to the strength model proposed by [21] in order to take into account the significant benefit of the compression force in the piers on their ultimate shear capacity.

4 DISCUSSION OF RESULTS

Each simulated bridge has been studied with reference to the several combinations of loads discussed above; in particular, the results are represented in terms of DCR, i.e. Demand over

Capacity Ratio, where the Demand and the Capacity are represented by bending moment, shear or axial force. It is worth to point out that, as more than 1500 Maillart-Type Arch Bridges have been generated and verified, the results will be represented in the following in terms of maximum DCR ratio for each bridge with reference to the main stress acting in the various structural elements, e.g. arch, piers and beams, and with reference to the considered load combinations. This means that for each structural element the worst safety condition is represented.

The Figure 6 shows the trend of the maximum DCR for the arch, in the case of flexural and shear verifications, as a function of the span (6a and 6b) and the rise of the arch (6c and 6d); it is clear that structural problems do not arise in any case for the arch. In particular, the maximum DCR, for flexural verifications, is about 0.8, whereas it is about 0.5 for shear verifications. In order to better read the trend of DCR, a linear regression line has been represented too: it is observed that the average trend, as function of both the span and the rise, is increasing in the case of flexural verifications (minimum value of about 0.2 and maximum value of about 0.6), while it is rather constant for shear verifications (approximately 0.4).

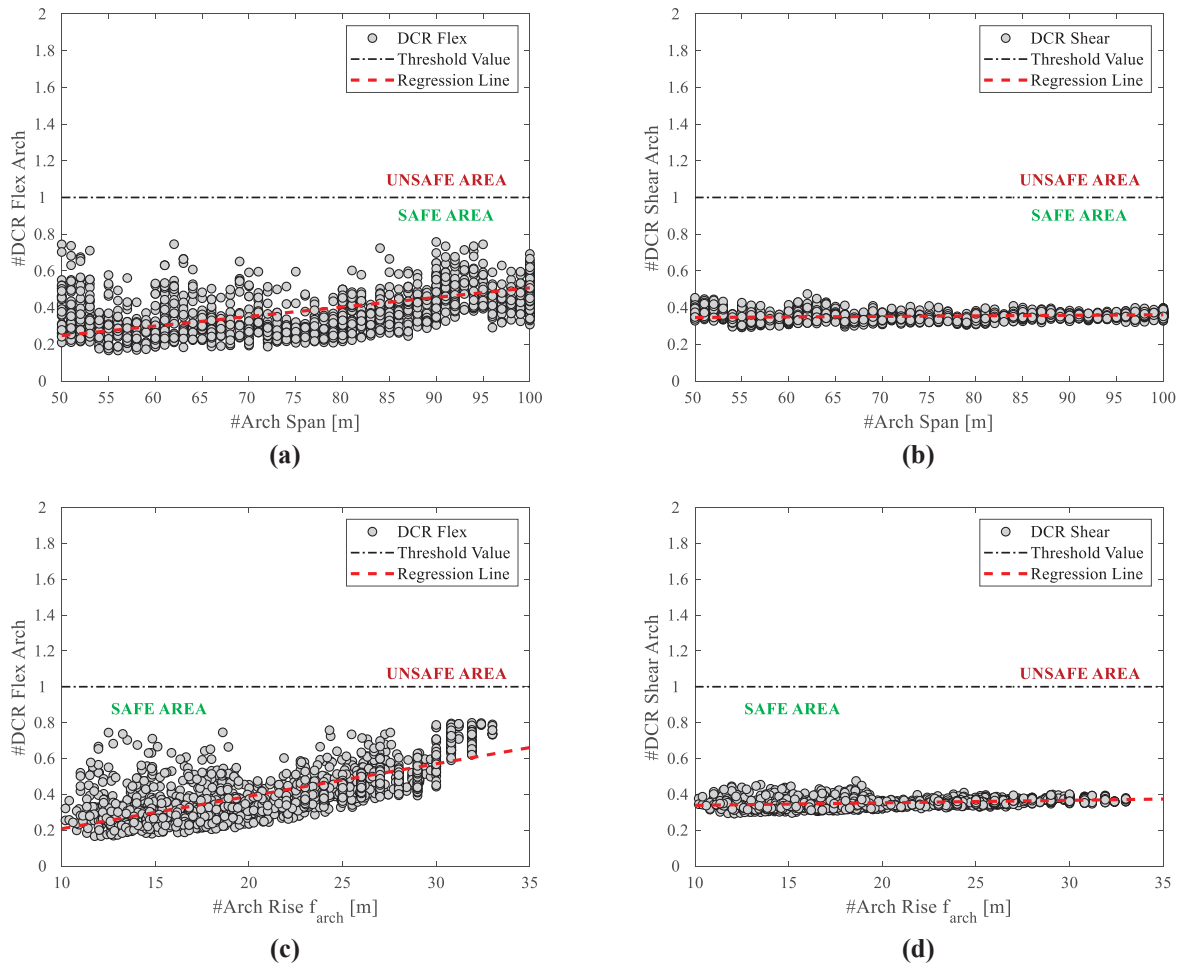


Figure 6: Demand over Capacity Ratio (DCR) distribution in the arch for flexural and shear failure, respectively, vs. : a)-b) Arch Span, L ; c)-d) Arch Rise, f_{arch} .

Figure 7 shows the trend of the maximum DCR for the piers in function of arch span length and arch rise with reference to flexural (Figure 7a-c) and shear (Figure 7b-d) failures. It can be noted that the flexural problems are very prominent if compared to the shear ones,

especially as the span and the rise of the arch increases. This is due to the fact that the piers, as previously mentioned, were verified in section 2.2 under axial forces only due to the assumption of simple hinges at their ends, according to a common practise of the time. This means that, under only axial forces, a fairly lower percentage of steel was required to satisfy the verifications if compared to the case of elements subjected to shear and bending moment.

However, in many real cases details were built at the ends in order to let the piers work as fixed elements and not as pendulums. As previously discussed, the presence of the pendulums drastically reduced, indeed, the hyperstatic unknowns and, thus, the complexity of the solution of the structural scheme of the bridge, but, at the same time, the relevant differences in the stiffness of the deck beam and the vault ensured that, under gravitational loads only, the neglected stresses were however limited even considering the hinges at the ends.

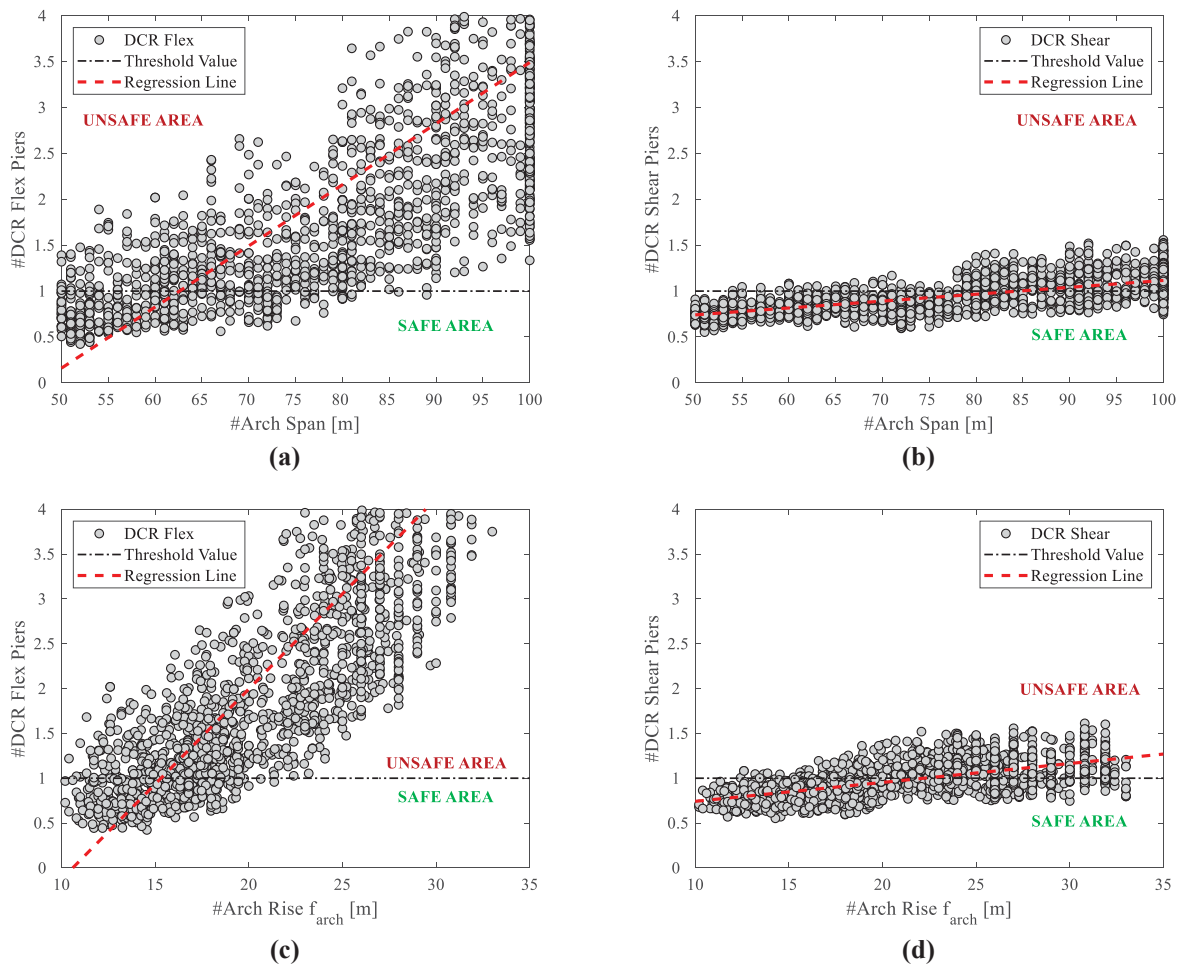


Figure 7: Demand over Capacity Ratio distribution in the piers for flexural and shear failure vs.: a)-b) Arch Span, L ; c)-d) Arch Rise, f_{arch} .

Clearly, in addition to the different constraining conditions introduced in the SAP model, the loads combinations adopted in the verifications herein presented, being more demanding than those considered at the design time both in terms of gravitational loads and of presence of horizontal actions, as the braking and acceleration forces, not considered in the past, have also contributed to have values of DCR in the piers higher than 1. This topic will become even more important for the verifications of the piers under seismic actions because they

became mandatory only in the most modern regulatory codes and, thus, it is expected that higher stresses would be present in the piers for the acceleration loads provided by the current codes. Therefore, under the design seismic actions, the constraint conditions at the ends of the piers will make even more the difference. For the beams of the deck, for the sake of simplicity, the distributions of the maximum DCR have not been reported, because, as for the arch, there aren't criticisms related to bending or shear failures. It is worth to remember that the deck of these bridges, and therefore the beams, are characterized by a high flexural stiffness in comparison with the arch. Thus, if the moment of inertia of the deck and of the vault cross section are denoted as I_d and I_a , for a "Maillart – Type" Arch Bridge, the ratio I_d/I_a is very large: in particular, manuals and historical sources indicate that the minimum value of this parameter has to be about 50 ([4]) for such a bridge typology.

Finally, the analysis of the Demand-to-Capacity ratios highlighted that, under the current vertical loading conditions, for "Maillart – Type" Arch Bridge the piers are the most vulnerable structural elements. In particular, the maximum DCR ratio is attained for flexural failure in the outermost piers with respect to the crown of the arch, i.e., the slenderest ones. It is worth noting that, although the ratios f_{arch}/L range in 0.2-0.3, for spans of 80-100 m, there are piers with a length of about 20 m, which are characterized by a very important bending demand. These piers, on the contrary, are characterized by a flexural capacity not very adequate, because, as previously discussed, they were designed to bear only compression force.

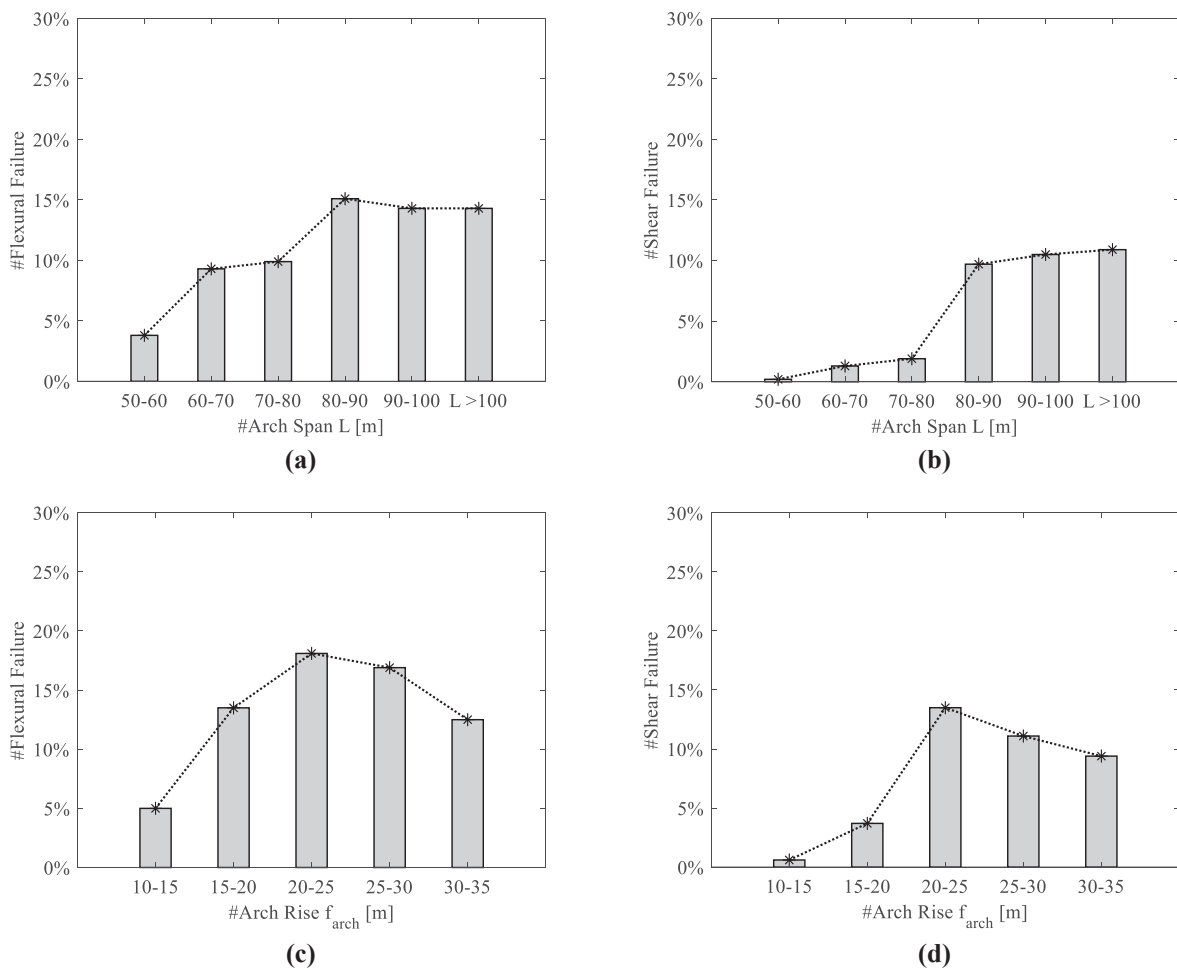


Figure 8: Distribution of failures for flexural and shear failure vs. a)-b) Arch Span L ; c)-d) Arch Rise, f_{arch} .

A global view of the obtained results for the examined numerical database of 1500 bridges can be represented by the percentages of failures, differentiated according to the type of failure and distributed in the variation ranges of span and arch rise in the inventory. Figures 8a and 8b report, indeed, the failure percentage with reference to flexural and shear failures, respectively, versus the arch span, L . Analogously, Figures 8c and 8d report the failure percentage versus the arch rise. It is worth noting that the number of analysed structures, for each subclass of the rise and span of arch within the selected ranges, is fairly uniform, as it is evidenced in the diagrams of Figures 9 and 10 that report the number of failed bridges (for flexure in Figure 9 and for shear in Figure 10) and the number of the generated ones for the fixed ranges of arch rise and arch span.

Representations shown in Figures 8, 9 and 10 are very useful to highlight how many structures, for each subclass, have showed at least one failure on the total number of bridges of the subclass. It is worth to remember, once again, that the sample of bridges was generated and verified through a simulated design, adopting, thus, reinforcement ratios indicated in the regulations of the time, defined and controlled also according to some original designs and drawings. Therefore, such results necessarily reflect the characteristics of the inventory of bridges defined in the previous section, and provide, for that inventory, an idea of damages that may affect such typology of bridges.

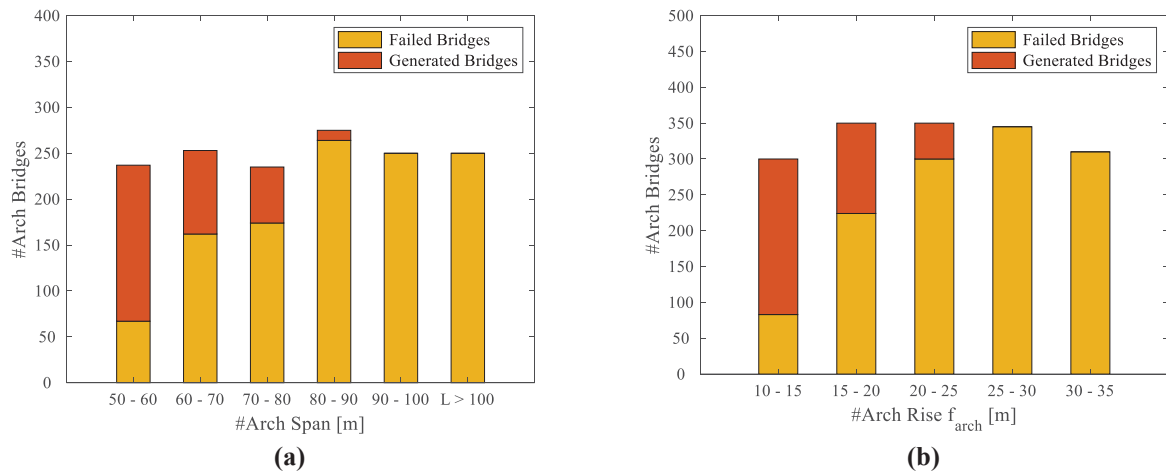


Figure 9: Distribution of failed bridges compared to generated bridges (flexural failure).

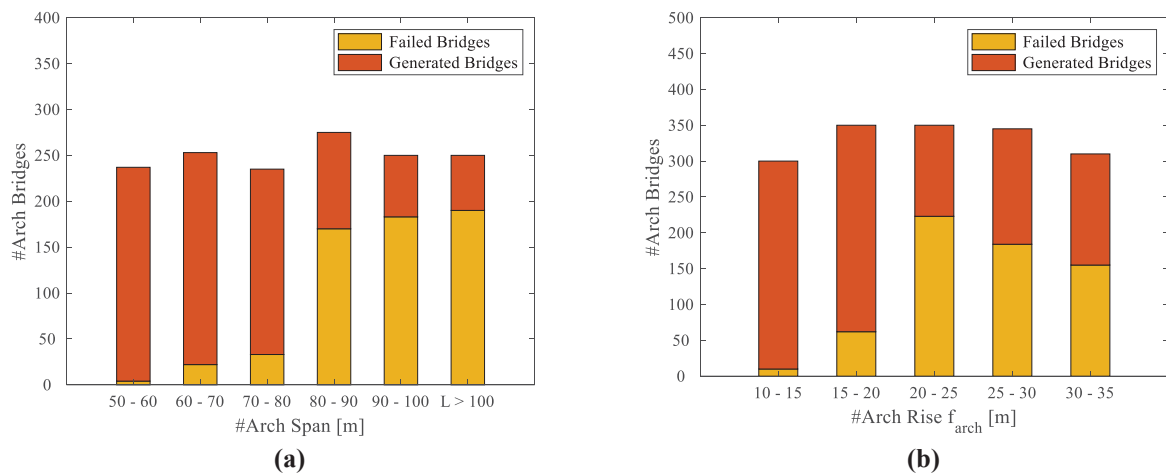


Figure 10: Distribution of failed bridges compared to generated bridges (shear failures).

The study of the behaviour of these structures at large scale is, indeed, a crucial point for planning risk mitigation programs and for understanding how to prioritise the interventions for risk reduction. Moreover, since the failures are localized at the piers, above all at their ends for flexural problems and along the element for the short piers at the arch keystone, the structural reinforcement of these bridges through the use of FRP, i.e. Fiber Reinforced Polymers, could represent an efficient solution that would allow to realize non-invasive and reversible interventions for improving the structural performance ([22], [23]). Clearly, further studies are in progress aimed to assess the performance of the same inventory of bridges under the design seismic actions provided by the current codes and verify if the critical elements are the same identified in the analysis under the load combinations herein presented.

5 CONCLUSIONS

The paper presents the performance of Reinforced Concrete “Maillart-Type” Arch Bridges, also known as “RC Deck – Stiffened” Arch Bridges, under the gravitational and the moving loads prescribed by the current mandatory codes for bridges.

The structural performance has been evaluated by means of a linear analysis implemented in a Finite Element (FE) model for a Bridge Inventory made of more than 1500 structures, which have been generated by means of the Monte Carlo simulation method considering fixed variation ranges of several geometrical parameters. Each bridge within the inventory has been verified based on the typical design approaches adopted in the 50s and under the loading conditions required by the Codes of the time (i.e. only gravitational loads). Successively, according to current guidelines (Italian Building Code and New Guidelines for existing bridges), the performance of the designed bridges has been assessed considering the current non seismic design actions.

The analyses evidenced that at the Ultimate Limit State, flexural failures occur in the most external piers, which are also the slenderest ones, while shear failures occur mainly in the short piers at the arch keystone. This is due to the fact that the piers were designed only for axial forces and schematized as pendulums even if, in many cases, they were built as fixed elements at both ends and with some additional steel reinforcements. Therefore, the design assumption of pendulum scheme led to a fairly lower percentage of steel if compared to elements subjected to shear and bending moment. Conversely, no flexural or shear failures occur in the arch and in the beams of the deck.

This study allowed to identify the main vulnerabilities of this type of bridge under the current gravitational and moving loads and to highlight the opportunity for future developments, which could include the definition of different structural strengthening systems in order to improve the structural capabilities of such bridges. Further studies will investigate the same bridge inventory, herein defined, under the seismic actions provided by the current Italian codes to better understand the global vulnerability of such bridges under both static and seismic loading conditions.

6 ACKNOWLEDGEMENTS

This paper was developed under the financial support of “ReLUIs DPC 2019/2021–WP4/Task 5.4 – *Interventi di rapida esecuzione a basso impatto ed integrati per ponti esis-*

tenti”, funded by the Italian Department of Civil Protection (DPC). This financial support is gratefully acknowledged.

7 REFERENCES

- [1] Gentile R, Nettis A, Raffaele D. Effectiveness of the Displacement-Based seismic performance Assessment for continuous RC bridges and proposed extensions. *Eng Struct* 2020;221:110910. <https://doi.org/10.1016/j.engstruct.2020.110910>.
- [2] Modena, C., Tecchio, G., Pellegrino, C., da Porto, F., Donà, M., Zampieri, P., & Zanini, M. A. (2015). Reinforced concrete and masonry arch bridges in seismic areas: typical deficiencies and retrofitting strategies. *Structure and Infrastructure Engineering*, 11(4), 415-442.
- [3] Billington, D. P. (1973). Deck-Stiffened Arch Bridges of Robert Maillart. *Journal of the Structural Division*. 99(7):1527 – 1539.
- [4] Franciosi, V. *Scienza delle Costruzioni*, Volume 3, Tomo 2. 1971. (Liguori Editore) (in Italian).
- [5] Billington, D. (2000). “The revolutionary bridges of Robert Maillart”. *Scientific American*, 283(1), 84-91.
- [6] Crisci G., Ceroni F., Lignola G.P., Prota A. (2020). Structural peculiarities of Maillart Type Arch Bridges. In *Proceedings of Italian Concrete Days 2020*.
- [7] Crisci G., Ceroni F., Lignola G.P., Prota A. (2020). Seismic Response of RC Deck – Stiffened Arch Existing Bridges. In *Proceedings of the 18th International Conference of Numerical Analysis and Applied Mathematics*, Rhodes, Greece, 17–23 September 2020.
- [8] Bossio, A., Fabbrocino, F., Monetta, T., Lignola, G.P., Prota, A., Manfredi, G., Bellucci, F. Corrosion effects on seismic capacity of reinforced concrete structures (2019) *Corrosion Reviews*, 37 (1), pp. 45-56. DOI: 10.1515/correv-2018-0044.
- [9] De Matteis G., Bencivenga P., Zizi M., Del Prete A.; 2019: Rischio strutturale di ponti esistenti: considerazioni preliminari sullo scenario in provincia di Caserta. In *Proc. XVIII Convegno ANIDIS*, Ascoli Piceno, Italy.
- [10] Italian Building Code Aggiornamento sulle Norme Tecniche per le Costruzioni, D.M; Italian Ministry of Infrastructures and Transportation: Rome, Italy, 2018.
- [11] Linee guida per la classificazione e gestione del rischio, la valutazione della sicurezza ed il monitoraggio dei ponti esistenti, Italian Ministry of Infrastructures and Transportation: Rome, Italy, 2020.
- [12] Crisci G., Ceroni F., Lignola G. P., Prota A. Vulnerability of Existing RC Deck Stiffened Arch Bridges under Seismic Actions.
- [13] Gentle, J. E. (2006). *Random number generation and Monte Carlo methods*. Springer Science & Business Media.
- [14] Royal Decree n° 2229, “Norme per la esecuzione delle opere in conglomerato cementizio semplice ed armato”, November 11th 1939. (in Italian).

- [15] Ministry of Public Works: circular n° 6018, “Carichi da considerare nel calcolo dei ponti”, June 9th 1945, (in Italian).
- [16] Weiwei L and Teruhiko Y Bridge Engineering Classifications Design Loading and Analysis Methods (Butterworth Heinemann).
- [17] Computer & Structures Inc. (CSI) SAP2000 Integrated Software for Structural Analysis and Design Computers and Structures Inc. Berkeley California.
- [18] European Committee for Standardization. Eurocode 2: Design of concrete structures – Part 1: General rules and rules for buildings. BS EN 1998-1: 2004.
- [19] Álvarez, J. J., Aparicio, A. C., Jara, J. M., & Jara, M. (2012). Seismic assessment of a longspan arch bridge considering the variation in axial forces induced by earthquakes. *Engineering Structures*, 34, 69-80.
- [20] Matlab. (2018). Version 9.4.0.813654 (R2018a). Natick, Massachusetts: The MathWorks Inc.
- [21] Biskinis, DE, Roupakias GK and Fardis MN., 2004, Degradation of shear strength of reinforced concrete members with inelastic cyclic displacement, *ACI Structural Journal*, 101(6), 773-783.
- [22] Zinno, A., Lignola, G.P., Prota, A., Manfredi, G., Cosenza, E. “Influence of free edge stress concentration on effectiveness of FRP confinement “(2010) *Composites Part B: Engineering*, 41 (7), pp. 523-532. DOI: 10.1016/j.compositesb.2010.07.003
- [23] Lignola, G.P., Nardone, F., Prota, A., Manfredi, G. “Analytical model for the effective strain in FRP-wrapped circular RC columns” (2012) *Composites Part B: Engineering*, 43 (8), pp. 3208-3218. DOI: 10.1016/j.compositesb.2012.04.007

A SUSTAINABLE SOLUTION FOR THE SEISMIC STRENGTHENING OF RC EXISTING BUILDINGS THROUGH THE HPDF SYSTEM (HPDF): A CASE STUDY

**Giuseppe Ventura, Vincenzo Manfredi, Angelo Masi, Giuseppe Santarsiero,
Andrea Digrisolo**

School of Engineering, University of Basilicata
via dell'Ateneo Lucano, 10, Potenza, Italy
{vincenzo.manfredi, giuseppe.santarsiero, angelo.masi, giuseppe.ventura, an-
drea.digrisolo}@unibas.it;

Abstract

The large number of existing buildings for which seismic rehabilitation interventions are required highlights the need of sustainable techniques able to reduce costs and downtime. To this purpose, a new strengthening technique named High-Performance Dissipating Frame (HPDF) was developed. It consists of new framed structures applied from the outside thus reducing the impact and relocation needs of tenants. This is even more important for strategic (e.g. hospitals) and other public buildings (e.g. schools) due to the social and economic effects deriving from their interruption of use. HPDF system consists of external precast RC frames (i.e. exoskeletons) rigidly connected to the existing structure and equipped with both shear and flexural damper devices to provide a high dissipation capacity in case of seismic actions and then to protect existing building. In the paper, the HPDF system has been applied to a Reinforced Concrete (RC) school building designed only to gravity loads. After a brief description of the building under study and the HPDF system, the stiffness, strength, and dissipation properties have been determined using an iterative displacement-based design procedure purposely set up. Results show that the considered strengthening technique increases seismic performance of the existing building according to different targets involving both structural and non-structural components, also avoiding any other local intervention.

Keywords: Seismic Strengthening, Existing Buildings, RC Structures, Exoskeleton System, Energy Dissipation.

1 INTRODUCTION

The large number of existing buildings in Italy without adequate seismic protection [1] requires the definition of sustainable intervention techniques, able to reduce time and costs, and to limit the interruption of use. Specifically, regarding existing reinforced concrete (RC) structures, most of the gap is due to inadequate detailing and poor behavior of fragile elements like beam-column joints [2] as clearly demonstrated by recent earthquakes [3].

Sustainable strengthening techniques were and are being developed, at both local and global level, within the activities of the Work Package 5 “Integrated and Sustainable Interventions for the Requalification of Existing Buildings” (WP5) carried out in the framework of the 2019-21 research program funded by the Italian Dept. of Civil Protection (DPC) and carried out by the Network of Laboratories of Earthquake Engineering (ReLUIS). Among others, a patented local seismic strengthening system was developed in order to allow cheap interventions only from the outside [4].

Also, new techniques were developed to perform upgrading interventions at global level as for example that based on RC exoskeletons [5, 6, 7]. This solution is frequently coupled with further interventions devoted to reducing energy consumption of buildings, thus increasing their sustainability [8, 9].

In [10] a strengthening solution based on the use of precast RC exoskeletons connected to the existing structure to provide it with additional seismic capacity, is proposed. Further, the possibility of adding dissipative capacity to this kind of intervention technique has been studied [11, 12], in order to enhance global performance and therefore optimize the required intervention costs. The strengthening solution named HPDF (High Performing Dissipation Frame) was developed in order to optimize the position of dissipative elements coinciding with the centreline of the beams. This makes it possible to maximise the deformation to which the dissipative elements are subjected, which is amplified with respect to the inter-storey displacement. Therefore, an increased effectiveness is expected with respect to dissipative bracing systems, where hysteretic dissipation elements work on the interstorey displacement due to seismic actions.

As a first step of the development process, the HPDF frames were applied to simple structural models [11] in order to identify the parameters that most influence their behaviour and effectiveness in increasing the seismic capacity of the structure under intervention. Moreover, the iterative design process was outlined starting from the push-over curve of the existing structure and the identification of the seismic capacity gap to be covered by the strengthening technique.

The present study, relying on the design method set-up in [11], is devoted to applying the strengthening solution to a real case study represented by the “Santini school building” located in the small town of Loro Piceno town, province of Macerata, Italy. The building is an old RC structure dating back to early ‘60s designed only to gravity loads. The application of the HPDF system to a real case study is helpful in identifying the potential advantages and disadvantages of the technique and to better evaluate its effectiveness.

2 DESCRIPTION OF THE STRENGTHENING SYSTEM

As can be seen in Figure 1a, the HPDF system is made up of two main components each one made up of a column and a half beam. At the beam end, the shear dissipative devices are placed to work under the relative displacements (S hinges). Moreover, at the base of the column, flexural dissipative hinges are inserted working under the rotation of column members. It can be noted that when the span length is two times the interstorey height, the relative dis-

placement of the S hinge is equal to 2Δ , where Δ is the interstorey displacement. This highlights the advantage with respect to other devices whose dissipative capacity is related to the interstorey displacement Δ as, for example, in the case of bracing systems.

A suitable working mechanism of the HPDF system is obtained when the framing elements behave in a suitably stiff manner. In fact, in order to maximize the relative displacement of the S hinge, small or no deformations of the beam members are needed. This is strongly dependent on the bay length and makes the system not effectively applicable in case of large values of the span length, which would require large cross-sections of beams and columns. In these cases, an additional bracing system may be introduced to reduce RC members deformations thus increasing the effectiveness of the HPDF system (see Fig. 1b)

The new frames of the HPDF system have to be connected to the existing structure by means of shear connectors, grouted with epoxy resin and designed to resist the (inertial) shear forces that are transferred from the existing structure to the new frames. In order to allow the dissipative kinematics, the connections must be such that only vertical displacements are allowed.

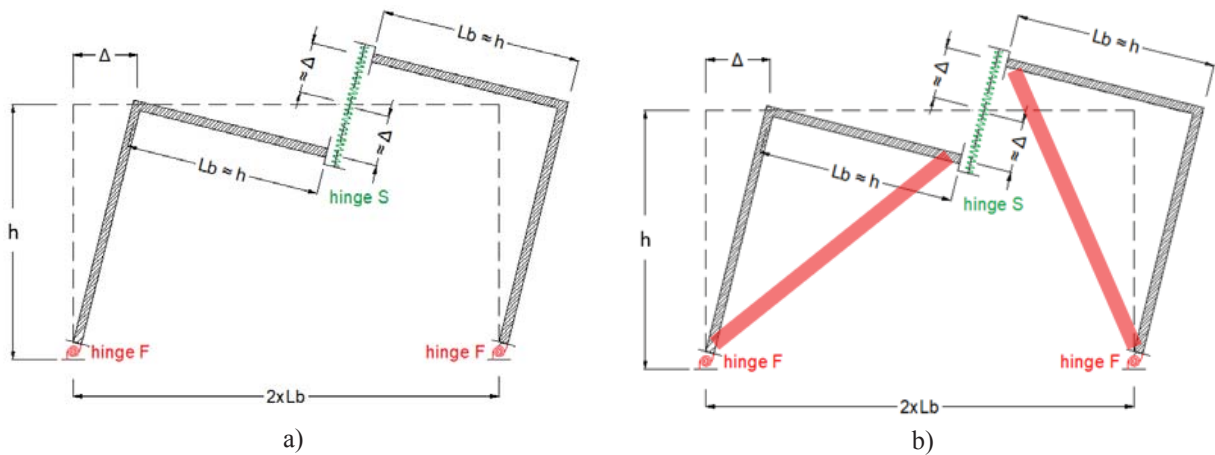


Figure 1: Position of the bending (F) and shear (S) hinges for a single-bay frame a); HPDF system with addition bracing members b).

The connection between the HPDF system and the existing structure must be present only at beam column joints in order to allow a rigid body behavior of new frames with respect to the existing one. Details of the connection system are reported in [11].

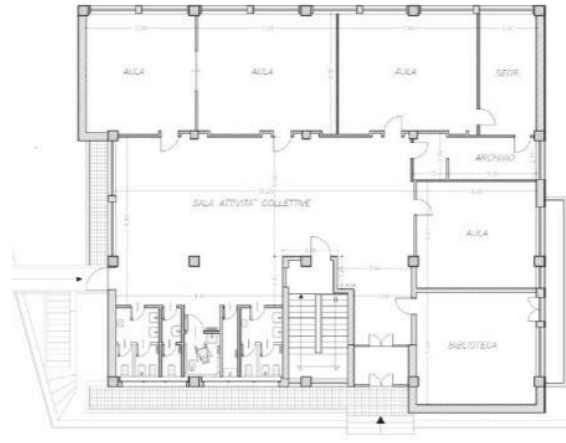
3 DESCRIPTION AND ASSESMENT OF THE CASE STUDY

In order to apply a reinforcement technique from the outside, by means of an exoskeleton, the Primary School "Pietro Santini" (Fig. 2a) in Loro Piceno (Macerata) was selected as a case study. The building was damaged by the 2016-2017 Central Italy seismic sequence.

The school building has RC structure, rectangular plan with three stories (Fig. 2b), two of which are below the ground level (south side), while only one storey is visible on the north side, which faces the main road. The building has a floor area of about 400 m² and it reaches a total height of about 12 m. The structure has a regular mesh of columns, with the exception of a small plan irregularity. The structural arrangement shows the presence of a series of one-way frames (Fig. 2b). The staircase, made of two RC walls, is eccentric with respect to the building's center of mass. In order to verify the effectiveness of the proposed technique, the modelling activity first focused on the development and calibration of the FEM model of the building in SAP2000 for assessment purposes.

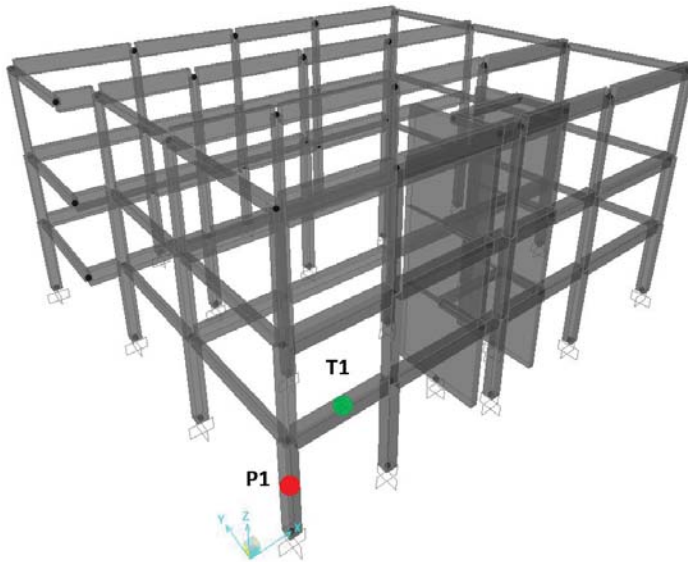


a)



b)

Figure 2: The "Pietro Santini" school buildings case study in Loro Piceno: a) photo of building; b) floor plan.



Mode	Type	T (sec.)	Mass (%)
1	Rotat. (z)	0.81	50
2	Transl. (x)	0.64	51
3	Transl. (y)	0.41	73

Storey seismic masses			
Storey	Ux [ton.]	Uy [ton.]	Rz [ton.*m ²]
I	452	452	38741
II	444	444	37893
III	472	472	40173

Figure 3: 3D finite element model and dynamic characteristics of the structure.

The material properties were determined through destructive and non-destructive tests in accordance with the code NTC 2018 [13]. In particular, the mechanical characterisation of the compressive strength of concrete was obtained from compressive tests on cores drilled from the structure. From these tests a mean cylindrical compressive strength $f_{cm} = 10.9$ MPa has been found. The yield strength of the reinforcing steel was obtained from tensile tests on reinforcement bars. These tests resulted in an average yield strength $f_{ym} = 370$ MPa. It is worth noting that the material properties found in the Santini school are essentially consistent with the expected values reported in [14] for the same construction period.

Figure 4 shows the reinforcement arrangement and moment-rotation relationships of typical column (Fig. 4a) and beam (Fig. 4b) members. The column cross-section dimension is generally 46x46 cm (related to column P1 in Fig. 3), while beams have 40x65 cm section (beam T1 in Fig. 3).

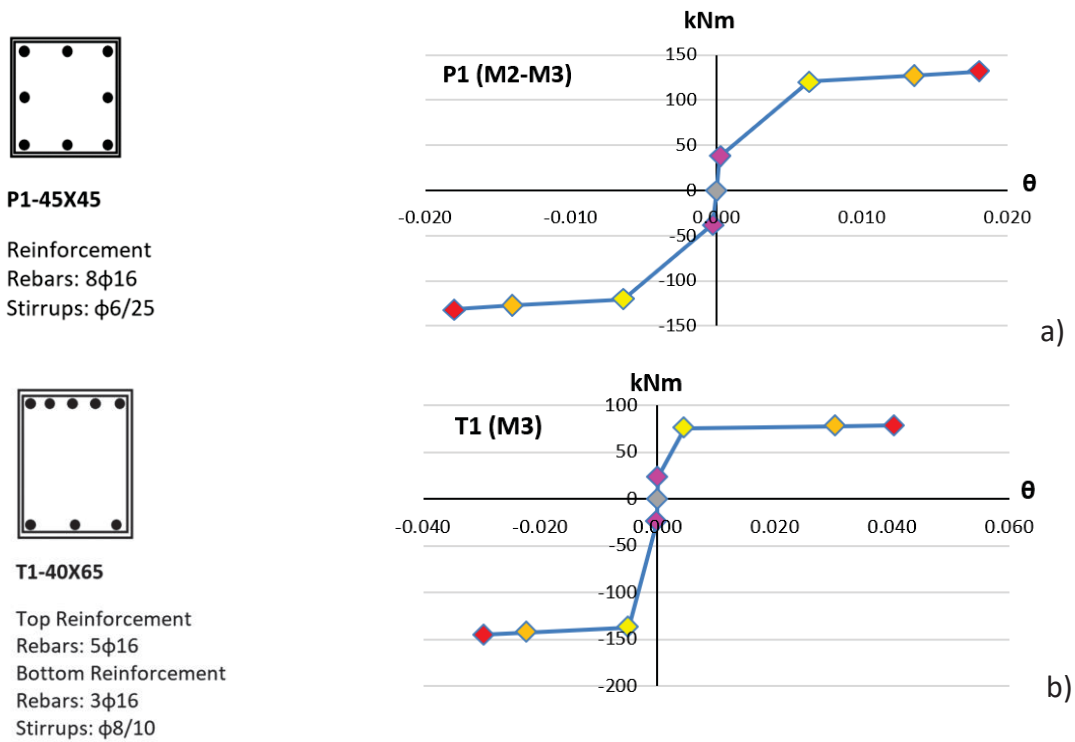


Figure 4: Plastic hinge modelling of column (P1) and beam (T1).

Figure 5 shows the capacity curve of the structure, determined through push-over analysis in the X direction considering a pseudo-triangular eccentric load distribution. The analysis was pushed up to a displacement of 120mm (evaluated at the top of the structure) where the seismic capacity/demand ratio is equal to $\zeta_E=1$. The capacity curve does not account for possible brittle failures but only for ductile ones related to the exceedance of the rotation capacity of flexural hinges in RC members. The identification of brittle failures in RC members was made *ex-post* by comparing shear stresses on beams, columns and beam-column joints with the related capacity. Therefore, the displacement (and related base shear) that causes the first fragile crisis was determined equal to $d=11$ mm to which a $\zeta_E=0.12$ is obtained.

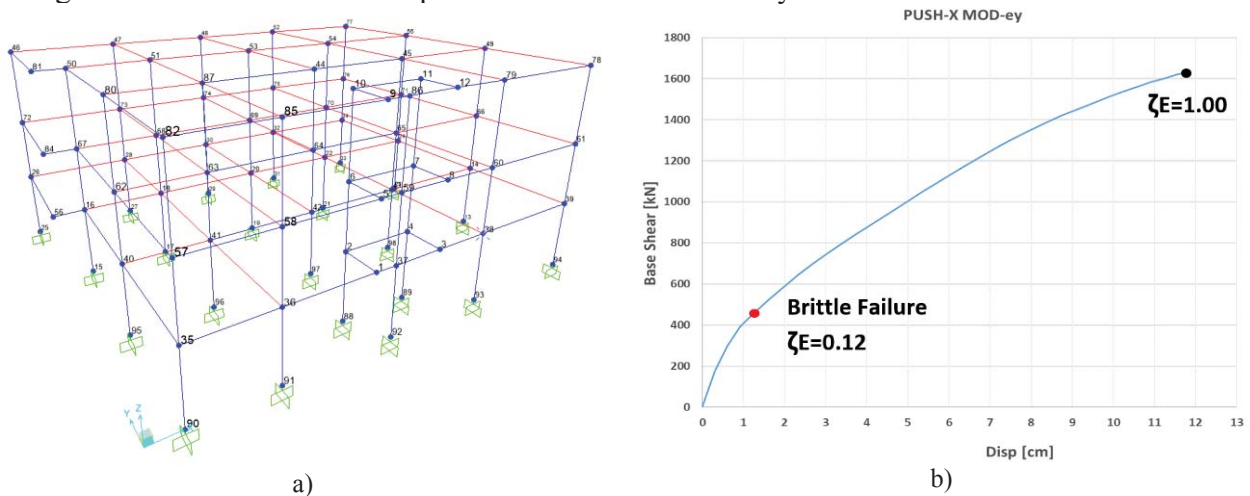


Figure 5: Structural model a); Push-over analysis in the X direction b).

4 THE STRENGTHENING INTERVENTION

In order to design the strengthening intervention, all the HPDF frame elements were considered as elastic and substantially rigid, while the dampers were modelled as elasto-plastic, without hardening behaviour. Starting from the push-over (PO) curve [15, 16], obtained for the X-direction (Fig. 5), the equivalent bilinear behaviour was reported in the ADRS format along with the 5% damping demand spectrum, according to the current code NTC-2018 [13]. In the first design phase, the achievement of seismic upgrading (conventionally related to a value $\zeta_E=0.6$) was set for the structure, therefore the demand spectrum was properly reduced. The target displacement was assumed to be equal to the displacement at which the existing structure achieves the first fragile collapse ($d_{y,EX} = 11\text{mm}$ $d_{y,EY} = 13\text{mm}$, for the X and Y directions respectively). This latter means that the HPDF system is designed to prevent any fragile collapse in the existing structure, in order to also avoid local interventions to strengthen RC members. The displacement value is reported on the demand spectrum to evaluate the stiffness value of the complete dissipative frame structure ($K_{EX} + K_{HPDF}$). The stiffness is given by the slope of the straight line connecting the origin of the ADRS plane and the intercept on the demand spectrum (Fig. 6). By reporting the target displacement on the reduced spectrum (damping $\xi=30\%$), both the force and the yield displacement of the HPDF-frame reinforced structure are determined. In this case the ductility demand is approximately equal to 2.0.

After defining the $K_{EX} + K_{HPDF}$ stiffness of the coupled system (green line in Fig. 6), the stiffness of the dissipative system alone (1) is obtained as follows:

$$K_{HPDF} = K_{(EX+HPDF)} - K_{EX} \quad (1)$$

The stiffness and strength properties of shear (S) and flexural (F) hinges are linked together and contribute to the global stiffness K_{HPDF} according to equation (2).

As reported in [11] the contribution to the global stiffness and strength of F hinges is lower than that of S hinges which are usually more numerous. In some cases, the contribution of F hinges could be also neglected by realizing a pinned connection at bottom end of the first story columns.

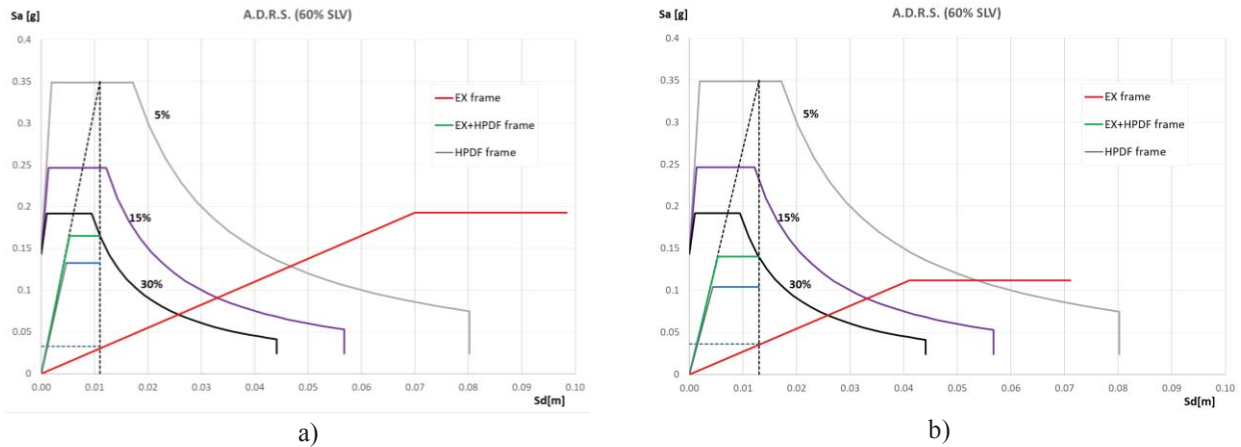


Figure 6: Demand and capacity spectra according to ADRS format for x-direction a) and y-direction b).

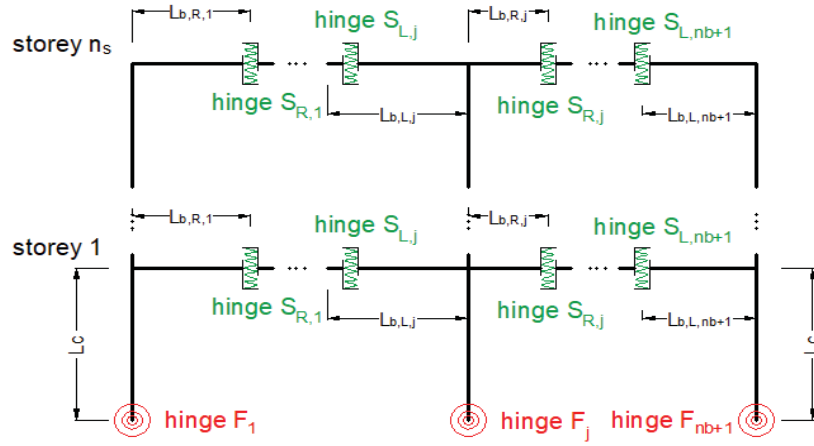


Figure 7: Stiffness of the dissipative system as a function of the stiffnesses of the individual devices in shear and bending.

$$K_{HPDF,i} = \sum_{j=1}^{n_b+1} \frac{K_{F,j,i}}{n_s^2 \cdot L_c^2} + 2 \cdot \frac{K_{SL,i,j} \cdot L_{bL,j,i}^2}{n_s \cdot L_c^2} + 2 \cdot \frac{K_{SR,i,j} \cdot L_{bR,j,i}^2}{n_s \cdot L_c^2} \quad (2)$$

4.1 Assessment of the upgraded structure

The new HPDF frames are placed only externally, along the existing structure perimeter (Fig. 8). The upgraded structure is made of two RC frames working in parallel. New frames are devoted to subtracting seismic action from the existing ones in order to limit their stresses and deformations. However, frames along one side only work in their own plane, so their contribution is negligible in orthogonal direction. Therefore, post-intervention structural assessment can be made by means of separate PO analyses for the two plan directions.

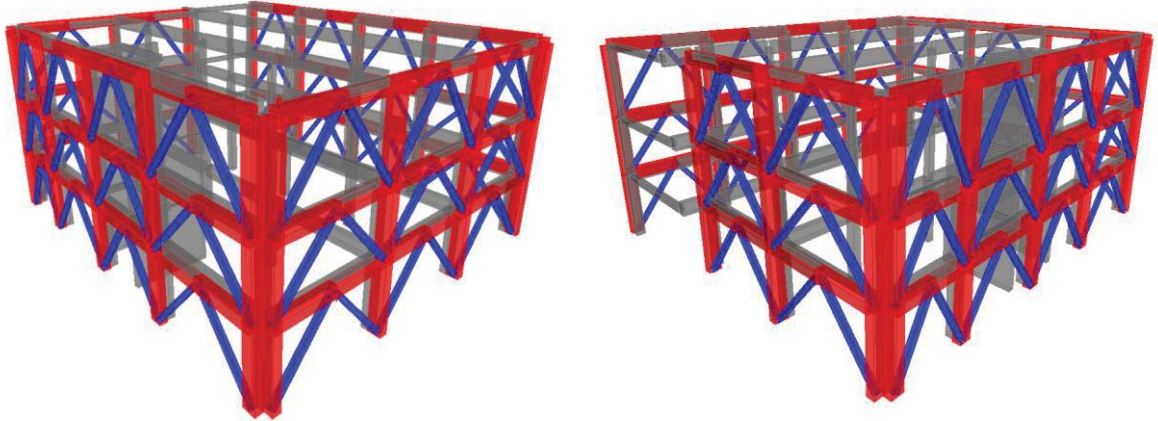


Figure 8: Exoskeleton defined by four HPDF frames.

The proposed methodology, which refers to the N2 method [17], is applied for each of the two main directions of analysis and is based on an iterative procedure [11]. That procedure allows the stiffness of dissipative elements to be calibrated according to the stiffness of the system (HPDF+existing structure) and the equivalent damping ξ . For each step of the analysis, the damping value must be compared to that one assumed, and to this purpose, the expression provided by Mazza and Vulcano [18] was adopted. Figure 6 shows the results in the final configuration at 30% damping.

The first results showed that the flexural dampers provide a small contribution, so the frames were considered to have a pinned connection at the base. The characteristics of the shear dampers are shown in Figure 9.

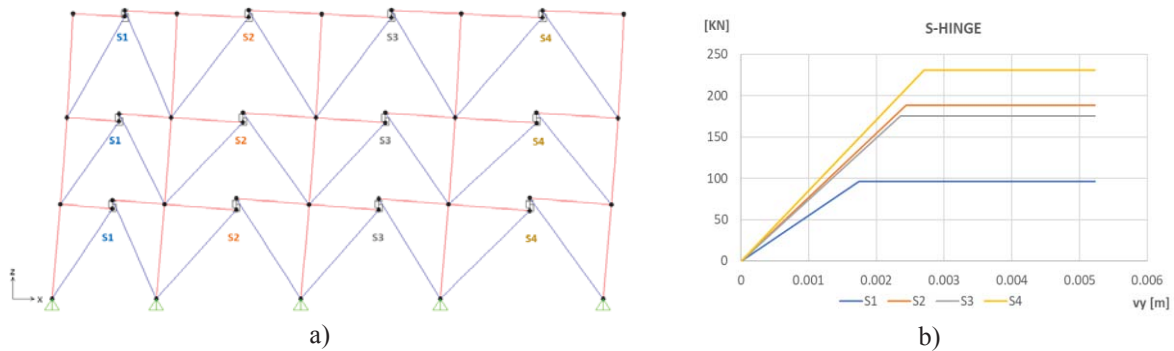


Figure 9: Shear hinges on X frames a); Load-deformation relations of shear hinges b).

The four HPDF frames (Fig. 8) are defined by RC beam and column elements (concrete class C28/35) with a 40x60cm rectangular cross-section. The braces are HEB300 and HEB240 steel profiles (structural steel of class S275), for the X-direction and Y-direction frames, respectively.

Figure 10 shows the capacity curves ante and post intervention for the X and Y plan directions. As can be seen, a large stiffness increase for both directions and a consequent increase in the base shear capacity at the target displacement are visible.

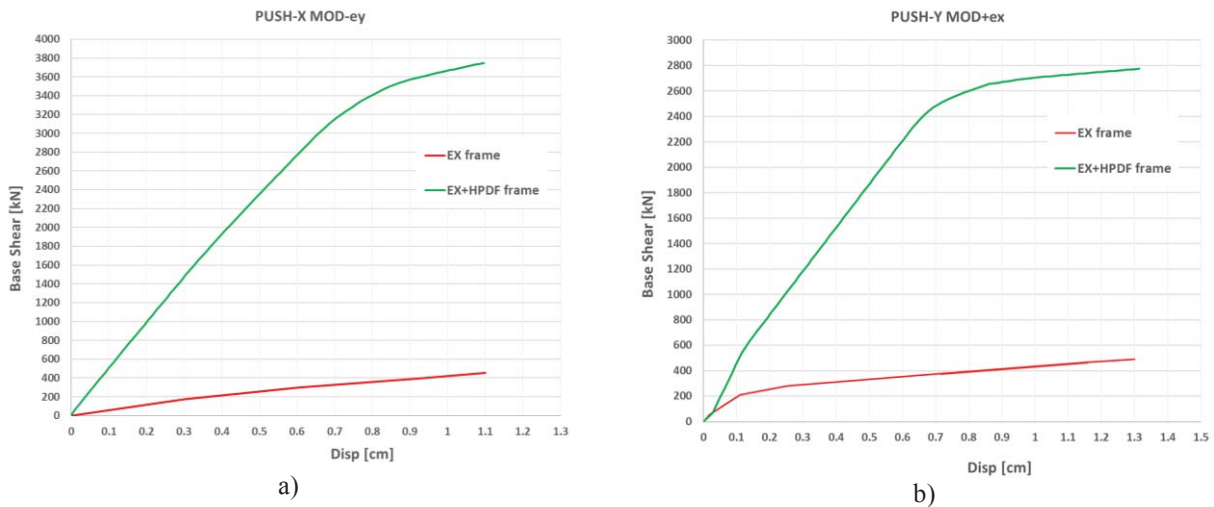


Figure 10: Push-over pre and post intervention in x-direction a) and y-direction b).

Figure 11 shows the capacity-demand comparison in the ADSSR format for the X and Y directions. As can be seen, a clearly larger stiffness is provided by the upgraded structure (HPDF + existing structure). The base shear has a higher value with respect to the assumption made in the design phase. This latter could be attributed to the existing structure irregularity that behave in a little different way when upgraded with the HPDF system, modifying the assumed distribution of base shear between the existing and the upgrading frames. However, this does not affect the effectiveness of the HPDF system, which relying on a 30% damping is able to lead the structure to the wanted performance displacement.

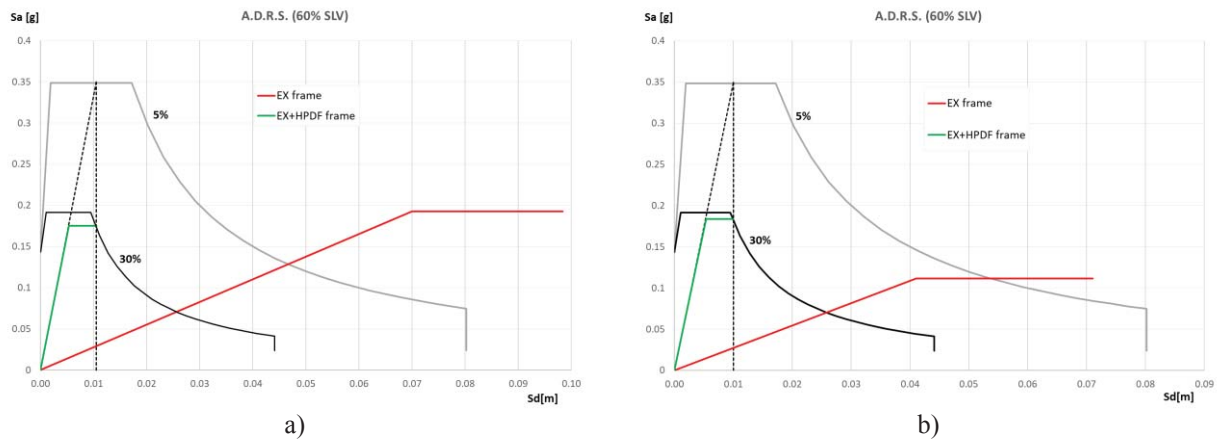


Figure 11: Post-intervention structure capacity according to ADRS format in x-direction a) and y-direction b).

5 CONCLUSIONS

Seismic strengthening techniques based on exoskeletons allow to operate only from the outside without interrupting the building use. Moreover, the demolition and restoration of non-structural elements (e.g. plugging, flooring, infills, etc.) which cause considerable inconvenience to the occupants of the buildings is avoided.

The main aim of this study was to apply the HPDF system to a real case study building, which was so far developed and applied to simple structural schemes. The mentioned case study allowed to recognize that in case of large span length of the existing structures it appears advisable modifying the basic configuration adopted for the HPDF system. In fact, to increase the system effectiveness, it is suggested the installation of steel braces to reduce the beam and column deformability. This allows to fully exploit the relative displacement between beam ends, maximizing the global seismic performance. Moreover, in such a way, the RC members' cross section can be kept under dimensions more suitable from both the economic and aesthetic point of view.

The intervention was designed to upgrade the seismic capacity of the case study building that, in the as-built condition, was equal to 12% of the seismic demand ($\zeta_E = 0.12$). The entire assessment process was performed in accordance to the current Italian seismic code with respect to the life safety limit state. The existing structure capacity is referred to the first fragile collapse and the upgrading system was designed to prevent it. This intervention approach favourably allows to apply only the HPDF system without any other local intervention to achieve the strengthening target.

Using an iterative design procedure, all the elements of the upgrading system were designed starting from the dissipative hinges up to the RC members and bracing steel members. The needed performance point was attained by providing a damping value of 30%, which is usual for hysteretic devices like those used in the HPDF system.

The case study analysed in the present paper contributed to optimise the HPDF system for its application to real buildings showing the need of some layout modifications under the occurrence of specific structural configurations like, for example, the presence of long frame spans.

ACKNOWLEDGMENTS

This study was partially developed under the financial support of the Italian Department of Civil Protection, within the ReLUIS-DPC 2019–2021 project, Research Line WP5. This support is gratefully acknowledged.

REFERENCES

- [1] ISTAT. 2011: *XV Censimento Generale della Popolazione e delle Abitazioni*. Available online: www.istat.it.
- [2] Santarsiero G., Masi, A. Key mechanisms of the seismic behaviour of external RC wide beam–column joints. *Open Construction and Building Technology Journal*. 13(1), pp. 36–51, 2019.
- [3] Rossetto T., Peiris N., Alarcon J.E., So E., Sargeant S., Free M., Sword-Daniels V., Del Re D., Libberton C., Verrucci E., *Field observations from the Aquila, Italy Earthquake of April 6, 2009*. *Bull Earthq Eng* 9:11–37, 2011.
- [4] Santarsiero G., Manfredi V. & Masi, A. Numerical Evaluation of the Steel Plate Energy Absorption Device (SPEAD) for Seismic Strengthening of RC Frame Structures. *Int J Civ Eng* 18, 835–850, 2020. <https://doi.org/10.1007/s40999-020-00510-x>.
- [5] Labò S., Passoni C., Marini, A., Belleri A. Design of diagrid exoskeletons for the retrofit of existing RC buildings. *Eng. Struct.*, 220, 110899, 2020.
- [6] Di Lorenzo G., Colacurcio E., Di Filippo A., Formisano A., Massimilla A., Landolfo R., Steel exoskeletons for seismic retrofitting of existing reinforced concrete buildings: State-of-the art and a case study. *XVIII ANIDIS Conference*, Ascoli Piceno, Italy, 15–18 sept, 2019.
- [7] Di Lorenzo G., Colacurcio E., Di Filippo A., Formisano A., Massimilla A., Landolfo R. State-of-the-art on steel exoskeletons for seismic retrofit of existing RC buildings. *Ingegneria Sismica*, 37(1):50, 2020.
- [8] Del Vecchio C., Frascadore R., Menna C, Mauro G.M, Di Ludovico M, Di Sarno L, Bianco N., Prota A., Dolce M. An integrated design approach for the retrofit of existing RC school buildings, *XVIII ANIDIS Conference*, Ascoli Piceno, Italy, 15–18 Sept. 2019.
- [9] Menna C., Del Vecchio C., Di Ludovico M., Mauro G.M., Ascione F., Prota A. Conceptual design of integrated seismic and energy retrofit interventions. *Journal of Building Engineering*, 38, 2021.
- [10] Manfredi V., Masi A., Ventura G., Chiauzzi L., Digrisolo A., Santarsiero G., Rafforzamento sismico degli edifici esistenti in c.a. una soluzione innovativa per interventi integrati e sostenibili. *Structural*, 215 gennaio/febbraio. De Lettera Editore, 2018 (in Italian).
- [11] Manfredi V., Santarsiero G., Masi A., Ventura, G., The High-Performance Dissipating Frame (HPDF) System for the Seismic Strengthening of RC Existing Buildings. *Sustainability*, 13, 1864, <https://doi.org/10.3390/su13041864>, 2021.
- [12] Passoni C., Guo J., Christopoulos C., Marini A., Riva P. Design of dissipative and elastic high-strength exoskeleton solutions for sustainable seismic upgrades of existing RC buildings, *Engineering Structures*, Volume 221, 15 October 2020.

- [13] Ministero delle Infrastrutture, “NTC 2018-Decreto Ministeriale 17/1/2018 - Aggiornamento delle norme tecniche per le costruzioni”.
- [14] Masi A., Digrisolo A., Santarsiero G. Analysis of a large database of concrete core tests with emphasis on within-structure variability. *Materials*, 12(12),1985, 2019.
- [15] Antoniou, S. Pinho R. Development and verification of a displacement-based adaptive pushover procedure. *Journal of Earthquake Engineering* 2004, 8:5, 643-661.
- [16] Chopra A.K. Goel R.K. A modal pushover analysis procedure for estimating seismic demands for buildings. *Earthquake Engineering and Structural Dynamics* 2002, 31, 561-582.
- [17] Fajfar P. A nonlinear analysis method for performance based seismic design. *Earthquake Spectra*, 2000, Vol 16, No.3, pp 573-592, August 2000.
- [18] Mazza F., Vulcano A. Displacement-based design procedure of damped braces for the seismic ret-rofitting of R.C. framed buildings. *Bull Earthquake Eng* 2015, 13, 2121–2143.

APPLICATION OF C-FRP SHEETS FOR STRUCTURAL REPAIRING OF RC BEAM-COLUMN CONNECTIONS DAMAGED UNDER CYCLIC LOADING – EXPERIMENTAL STUDY

Emmanouil Golias¹, Stavroula Katsimene², Eirini Ziavra², Konstantinos Kirtsonis²,
Constantin E. Chalioris³, and Chris C. Karayannis⁴

¹ Dr. Civil Engineer

Democritus University of Thrace, Department of Civil Engineering,
Division of Structural Engineering, Xanthi 67100, GREECE
e-mail: egkolias@civil.duth.gr

² Graduate students

Democritus University of Thrace, Department of Civil Engineering,
Division of Structural Engineering, Xanthi 67100, GREECE
e-mails: lkats12@yahoo.gr , eiriniziavra1@gmail.com , kyrkost@outlook.com

³ Associate Professor

Democritus University of Thrace, Department of Civil Engineering,
Division of Structural Engineering, Xanthi 67100, GREECE
e- mail: chaliori@civil.duth.gr

⁴ Professor

Democritus University of Thrace, Department of Civil Engineering,
Division of Structural Engineering, Xanthi 67100, GREECE
e-mail: karayan@civil.duth.gr

Abstract

The effectiveness of externally applied Carbon Fiber-Reinforced-Polymer (C-FRP) sheets for the retrofitting of damaged Reinforced Concrete (RC) beam-column connections is experimentally investigated. Two real-scale exterior RC beam-column connection specimens are tested under reverse cyclic deformation. The damaged specimens have been repaired using C-FRP sheets superficial placed as surface reinforcement after the sealing of the developed cracks with high strength resin paste. The retrofitted joints re-tested under the same reverse cyclic deformation loading. The retrofitted specimens in comparison with the original ones exhibited more or less similar load capacity and stiffness level with respect to the original ones.

Keywords: Reinforced Concrete, Beam-column connections, C-FRP sheets, Cyclic tests, Hysteretic response.

1 INTRODUCTION

Structural repair and upgrading of Reinforced Concrete (RC) beam-column joints in damaged RC frame structures after seismic excitations is a common problem in seismic prone regions. Researchers have published during the last decades valuable research on the post-earthquake rehabilitation procedures of damaged beam column joints [1], [2]. Many efforts have been done so far for the introduction and the establishment of techniques that are based on the promising material of Fiber-Reinforced Plastics (FRP) sheets [3], [4], [5], [6], [7].

A well-known efficient rehabilitation technique of RC beam-column joints damaged during earthquake excitations is the application of FRP sheets in combination with resin injections. It includes thin resin infusion under pressure in the cracks of the damaged area prior to the application of FRP sheets on the damaged body. The efficacy of this combined procedure of resin injection and FRP sheets for the strengthening of damaged beam-column connections has also been the subject of the experimental project by Karayannis and Sirkelis (2008) [4] and Tsonos et al (2017) [2]. Nevertheless, the increasing interest in the use of FRP sheets, due to the immediate and easy-to-apply nature of the required intervention, was the main motive behind the simplification of the rehabilitation technique by omitting the use of resin injections prior to the application of the FRP sheets [8]. Addressing the issue of the efficiency of any strengthening technique it is important to remember that the seismic behavior of reinforced concrete connections involves the interaction of complex phenomena such as bond, shear, confinement, fatigue which have not been yet well understood [9], [10], [11]. Since many unanswered questions remain about the traditionally reinforced connections it is justifiable to consent for a certain measure of uncertainty for the mechanics of joints with superficially applied C-FRP sheets as external strengthening reinforcement [12], [13]. Despite all the uncertainties and based on the justified thought that a structural member can adequately be re-designed and strengthened to resist seismic loading even without full knowledge of all the involving interacting phenomena, this easy-to-apply technique is experimentally investigated.

This simplified technique is usually adopted in areas after damaging earthquakes due to the fast and easy-to-apply required procedure. This treatment of the damaged beam column joints has been mainly based on the generally accepted concept that in all reported cases the application of FRP sheets has been proved rather successful. In this direction, the experimental study presented herein investigates the efficacy of the rehabilitation of damaged beam-column connections using FRP sheets after a meticulous but superficial repair of the cavities and cracks of the damaged area using resin paste. The investigation presents experimental results of 4 real-scale beam column specimens; two original specimens and two retrofitted ones. The original two joint specimens first were subjected to cyclic loading and then repaired with C-FRP sheets. The reteofitted specimens were re-subjected to the same cyclic loading and the observed results are used for the evaluation of the efficiency of the applied repair technique.

2 CHARACTERISTICS OF THE SPECIMENS

Cross-sections, dimensions, materials and reinforcement arrangements of the specimens were chosen in the way that the first specimen (BJB-S1) represents common RC buildings designed according to earlier codes without the proper shear reinforcement in the joint body (only one stirrup in the joint area) whereas the second specimen (BJB-BX) represents cases with X-type reinforcement in the joint without stirrups.

The maximum joint shear that can be developed in the joint body by the steel bars of the beam is 0.32 MN and consequently shear stress equal to 3.67MPa. The ratio $\Sigma M_c / \Sigma M_b$ is almost 1.40 (a little higher) and therefore cracks are expected to be developed both in the joint body and the part of the beam near the joint (ACI 318).

Name	Geometry and Reinforcement (in mm)				
	Joint area	Beam		Column	
	Steel	Cross-section	Steel	Cross-section	Steel
BJB-S1	Ø8	{350×250}	$\left\{ \begin{array}{l} 4\text{Ø}14 \text{ up} \\ 4\text{Ø}14 \text{ bot.} \\ \text{Ø}8/100 \end{array} \right\}$	{350×350}	$\left\{ \begin{array}{l} 4\text{Ø}14 \\ \text{Ø}8/100 \end{array} \right\}$
BJB-S1-R	Ø8 + FRP				
BJB-XV	X2Ø12	{350×250}	$\left\{ \begin{array}{l} 4\text{Ø}12 \text{ up} \\ 4\text{Ø}12 \text{ bot.} \\ \text{Ø}8/100 \end{array} \right\}$	{350×250}	$\left\{ \begin{array}{l} 4\text{Ø}14 \\ \text{Ø}8/100 \end{array} \right\}$
BJB-XV-R	X2Ø12 + FRP				

Table 1: Geometrical and reinforcement characteristics of the tested exterior beam-column joint specimens.

The total length and cross-section of the column are 3.0m and 350/250cm, respectively, whereas the free length and the cross-section of the beam are 1.875m and 350/250cm, respectively. The list of the tested beam column specimens, their names, the geometrical characteristics and the reinforcement arrangements are presented in Table 1.

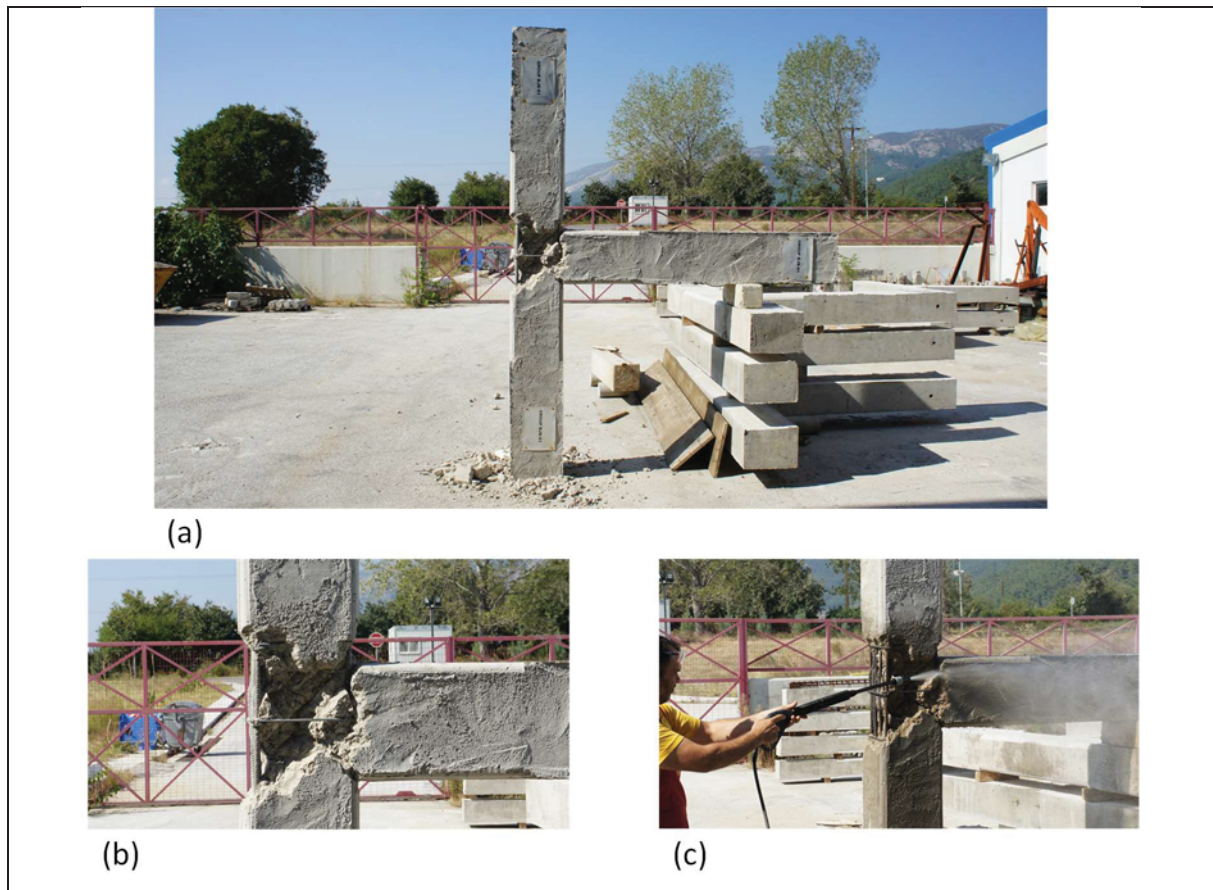


Figure 1: Damage of the joint (a, b). Cleaning (c) of the damage area and removal of loose material.

2.1 Application of the C-FRP sheets

The FRP sheets are applied to the body of the damaged joints after a superficial repair of the damage. First, cleaning and removal of the loose concrete material takes place (Figure 1). Right

after, meticulous filling of the cavities and the developed cracks is performed with high strength resin paste (Figure 2). Prior to the application of the C-FRP sheets abrasion of the surfaces is absolutely necessary (Figure 2c).

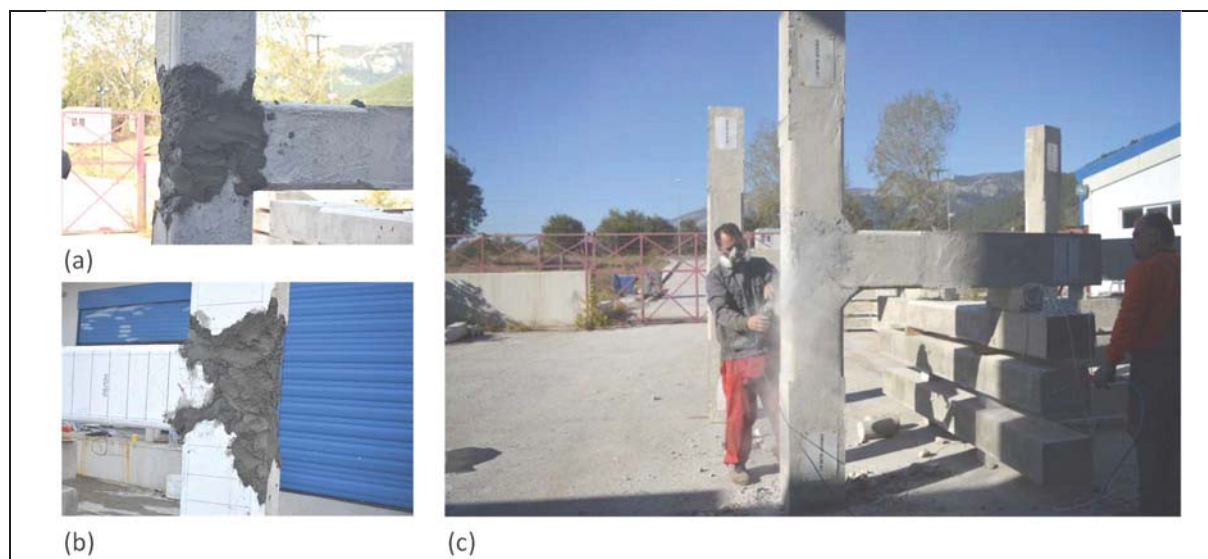


Figure 2: Filling of the developed cavities and cracks with high strength resin paste (a, b) and meticulous abrasion of the surfaces (c) prior to the C-FRP application.

The positions of the applied C-FRP sheets are schematically shown in Figure 3a and application works in Figures 3b and c. As presented in Figure 3a the C-FRP sheets are placed round the joint body and round the critical parts of the upper and down column and the beam.

2.2 Materials

The concrete's cylinder compressive strength was 34MPa whereas the yield tensile strength of the longitudinal steel bars and the stirrups was 550MPa. The type of the fiber-reinforced plastics sheets was Carbon FRP sheets. The characteristics of the used C-FRP sheets as given by the manufacturer were: Thickness of the sheets 0.168mm, tensile strength 4300MPa and tensile modulus of elasticity 240GPa.

2.3 Loading procedure and test setup

The loading procedure of the specimens includes full reverse cyclic deformations that are applied near the free end of the beam. The examined beam column subassemblages are subjected to seven loading steps and each step comprised three full cycles as shown in Figure 4. The used loading program permits the evaluation of the structural performance parameters of the specimens.

The experimental setup and the instrumentation are shown in Figure 5. Each beam-column joint specimen is placed after 90° counter clockwise rotation in the way that the column is in the horizontal direction whereas the beam is in the vertical direction. The specimen is supported by rotational devices that allow rotation to simulate the inflection points of the real columns in the middle of their heights.

Compressive axial load equal to 150kN is applied to the horizontally placed column element throughout the testing procedure. This loading is almost equal to 5% of the nominal strength of the concrete section of the column ($0.05A_c f_c$).

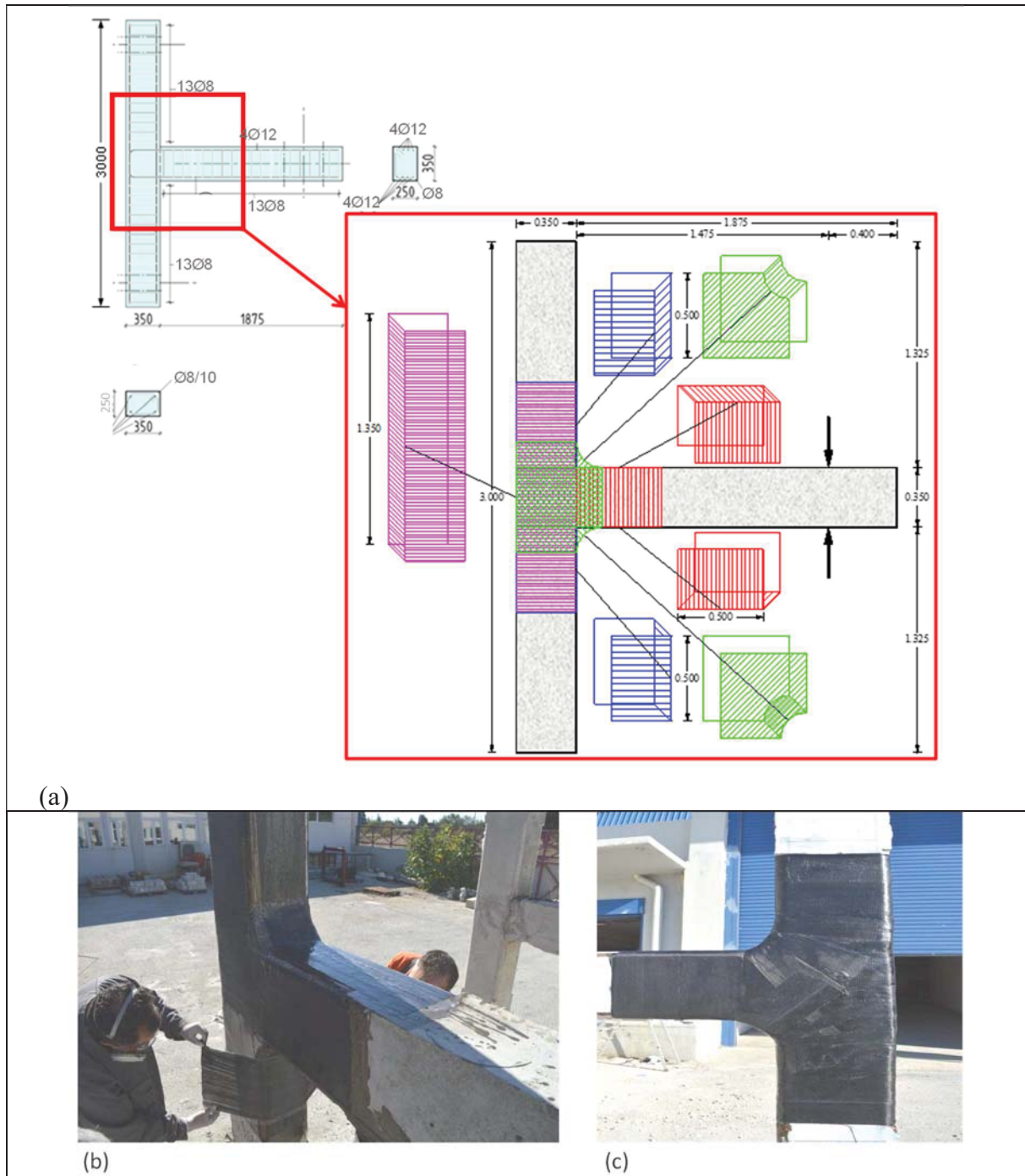


Figure 3: Schematic application of the C-FRP sheets (a) and application works of the C-FRP sheets (b, c).

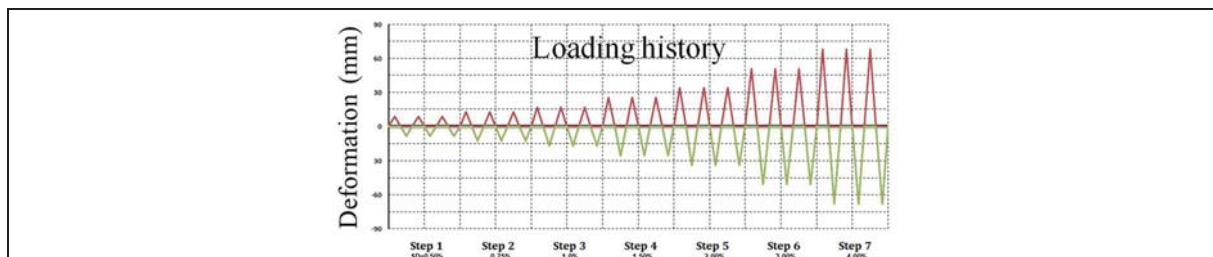


Figure 4: Loading procedure

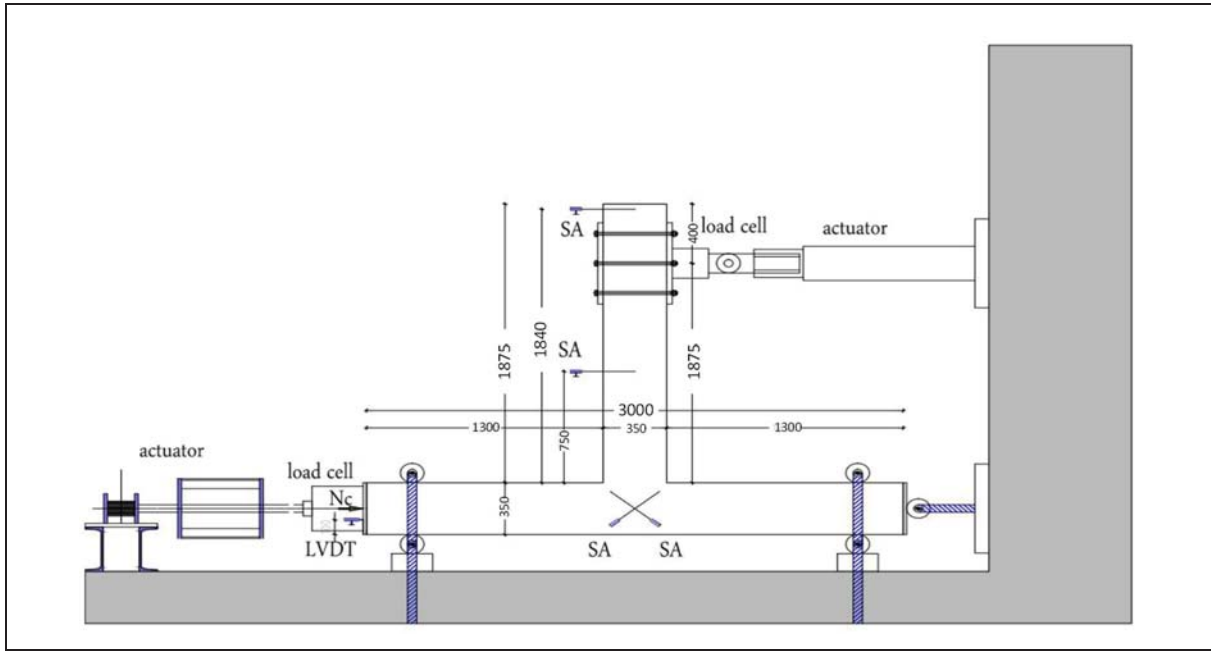


Figure 5: Test setup.

3 TEST RESULTS AND DISCUSSION

For the evaluation of the efficiency of the studied retrofitting procedure the overall performance of each original beam column joint is examined and compared to the performance of the corresponding retrofitted one in terms of hysteretic responses and energy dissipation curves.

3.1 Hysteretic responses - Load carrying capacity

The hysteretic responses of the original joint BJB-S1 and the corresponding retrofitted one BJB-S1-R are presented in Figures 6a and 6b, respectively. Further, the cracking patterns of these specimens at the end of the loading sequence are presented in Figures 6c and 6d, respectively. For comparisons purposes the envelope curves for the three full cycles per loading step, of these two tested specimens, BJB-S1 and BJB-S1-R, are shown in Figures 7a and 7b, respectively. The comparison of the hysteretic curves and the envelope curves obtained from the original joint and the corresponding ones obtained from the testing of retrofitted joint indicates that the application of C-FRP sheets restored the capacity values of the damaged joint in respect to those of the original specimen, to a great degree.

The hysteretic responses of the original joint BJB-XV and the corresponding retrofitted one BJB-XV-R are presented in Figures 8a and 8b, respectively. Further, the cracking patterns of these specimens at the end of the loading sequence are presented in Figures 8c and 8d, respectively. For comparisons purposes the envelope curves for the three full cycles per loading step, of these two tested specimens, BJB-XV and BJB-XV-R, are shown in Figures 9a and 9b, respectively. The comparison of the hysteretic curves and the envelope curves obtained from the original joint and the corresponding ones obtained from the testing of retrofitted joint indicates that the application of C-FRP sheets restored the capacity values of the damaged joint in respect to those of the original specimen, to a great degree.

Nevertheless, from the observations it is concluded that there are some reservations for the efficiency of the technique in the restoration of the load bearing capacity in cases of high levels of loading or high levels of initial damage.

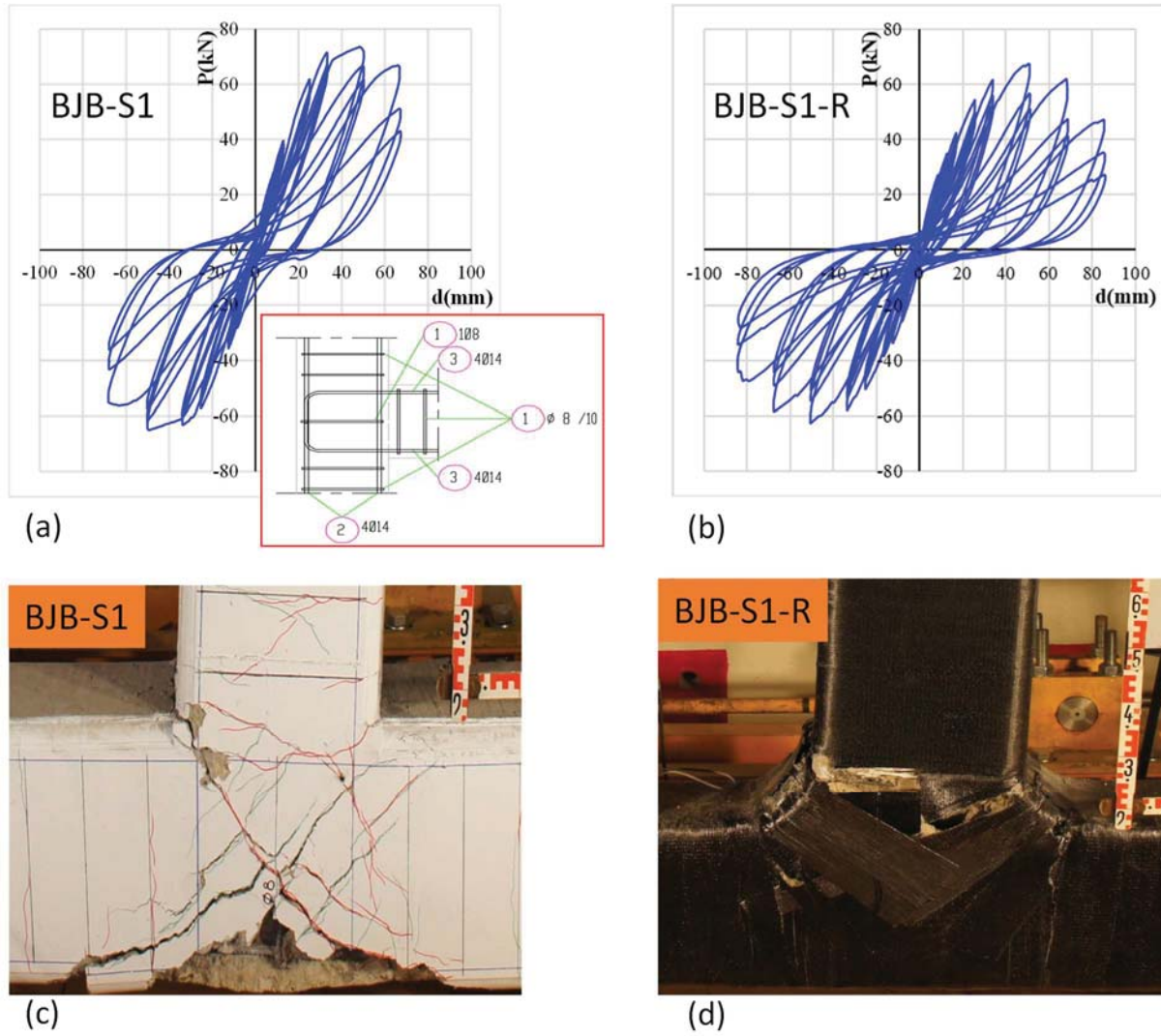


Figure 6: Hysteretic response (a) of the specimen BJB-S1 and hysteretic response (b) of the corresponding repaired specimen BJB-S1-R and cracking pattern at the end of loading of the same specimens (c, d).

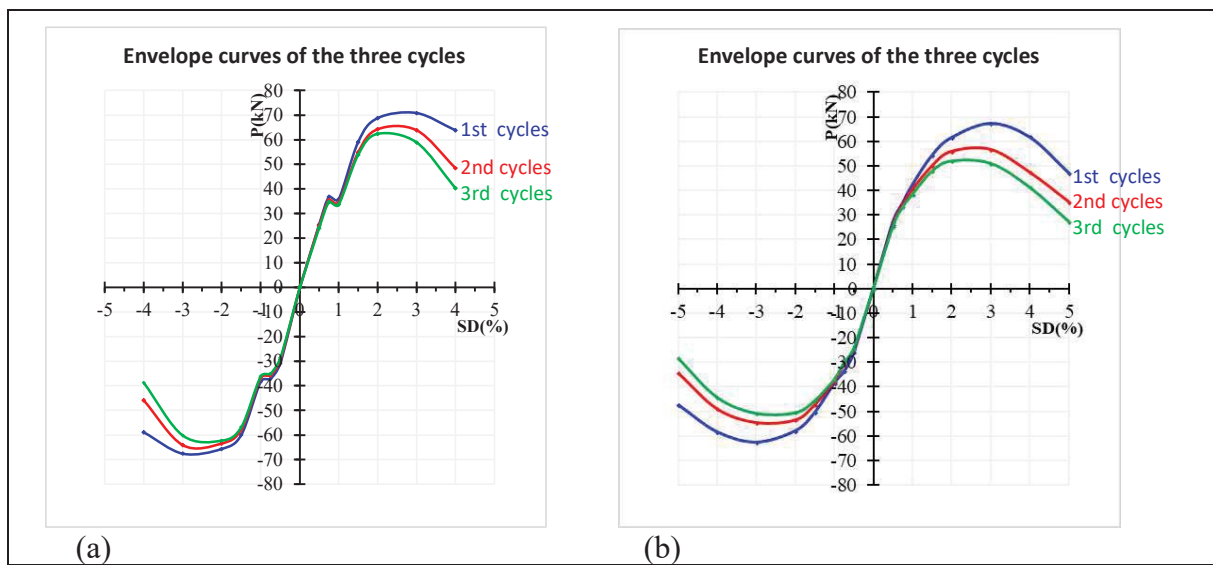


Figure 7: Envelop curves of the hysteretic responses (a) of the specimen BJB-S1 and (b) of the corresponding repaired specimen BJB-S1-R.

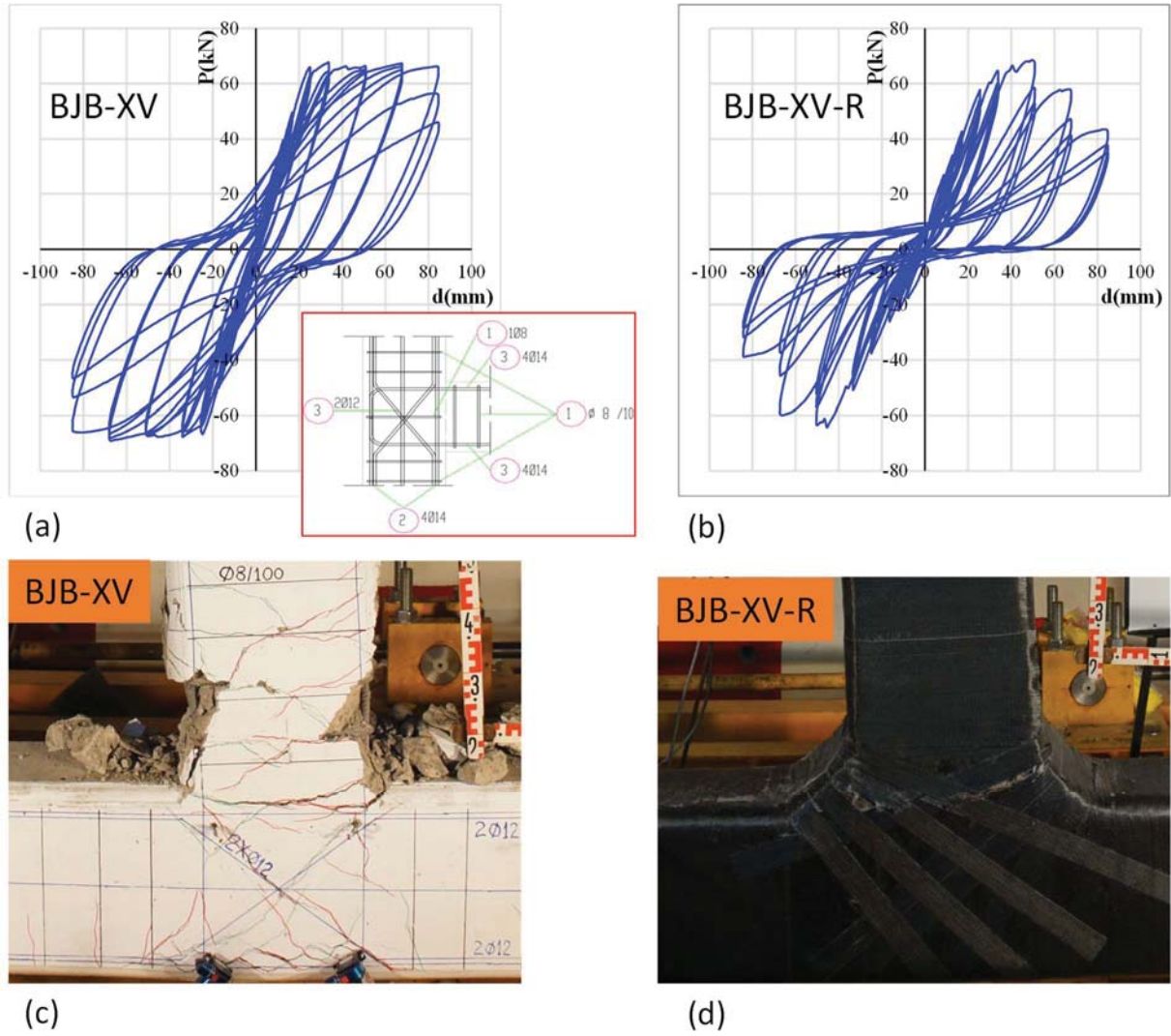


Figure 8: Hysteretic response (a) of the specimen BJB-XV and hysteretic response (b) of the corresponding repaired specimen BJB-XV-R and cracking pattern at the end of loading of the same specimens (c, d).

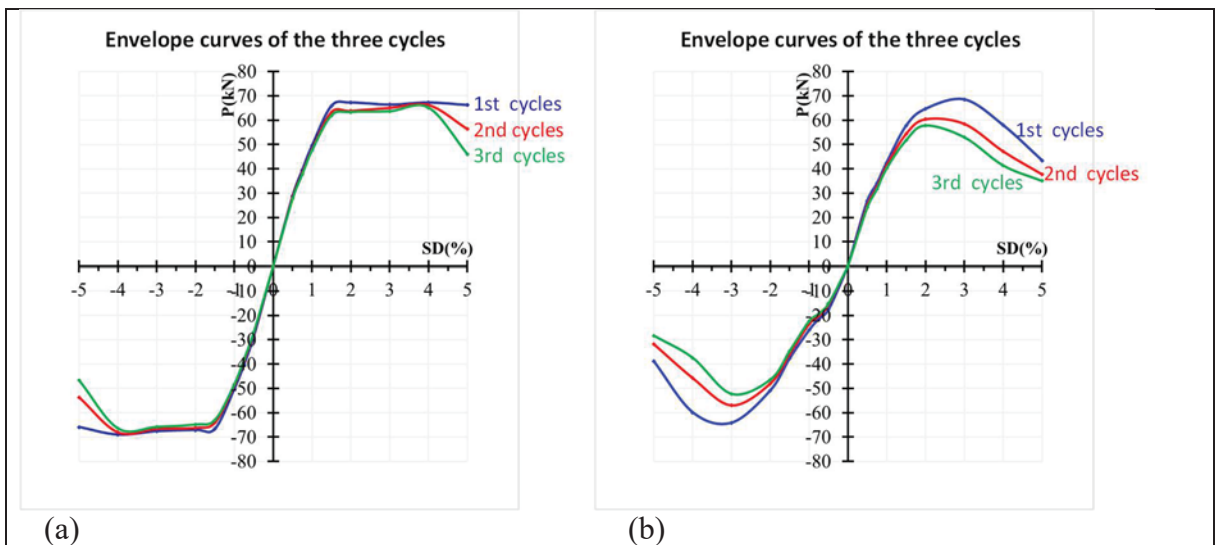


Figure 9: Envelope curves of the hysteretic responses (a) of the specimen BJB-XV and (b) of the corresponding repaired specimen BJB-XV-R.

3.2 Dissipated energy capacity

A measurement for the assessment of the efficacy of the applied retrofitting technique can be the observed dissipated energy capacity in terms of the area of the hysteresis loops. Energy dissipation is an indication of the structural element capacity to be strained and it defines the energy that can be absorbed before the loss of the system stability.

The dissipated energy at 1st, 2nd and 3rd cycles of each loading step as measured in terms of the area of the corresponding hysteresis loops of the original specimen BJB-S1 are presented in Figure 10a. Further, the dissipated energy at 1st, 2nd and 3rd cycles of each loading step as measured in terms of the area of the corresponding hysteresis loops of the retrofitted specimen BJB-S1-R are presented in Figure 10b. Comparing the diagrams of retrofitted specimen with the corresponding diagrams of the original specimen it is deduced that the applied technique can rather adequately restore the energy dissipating capacity for the specimen designed according to earlier codes without the proper shear reinforcement in the joint body (only one stirrup in the joint area).

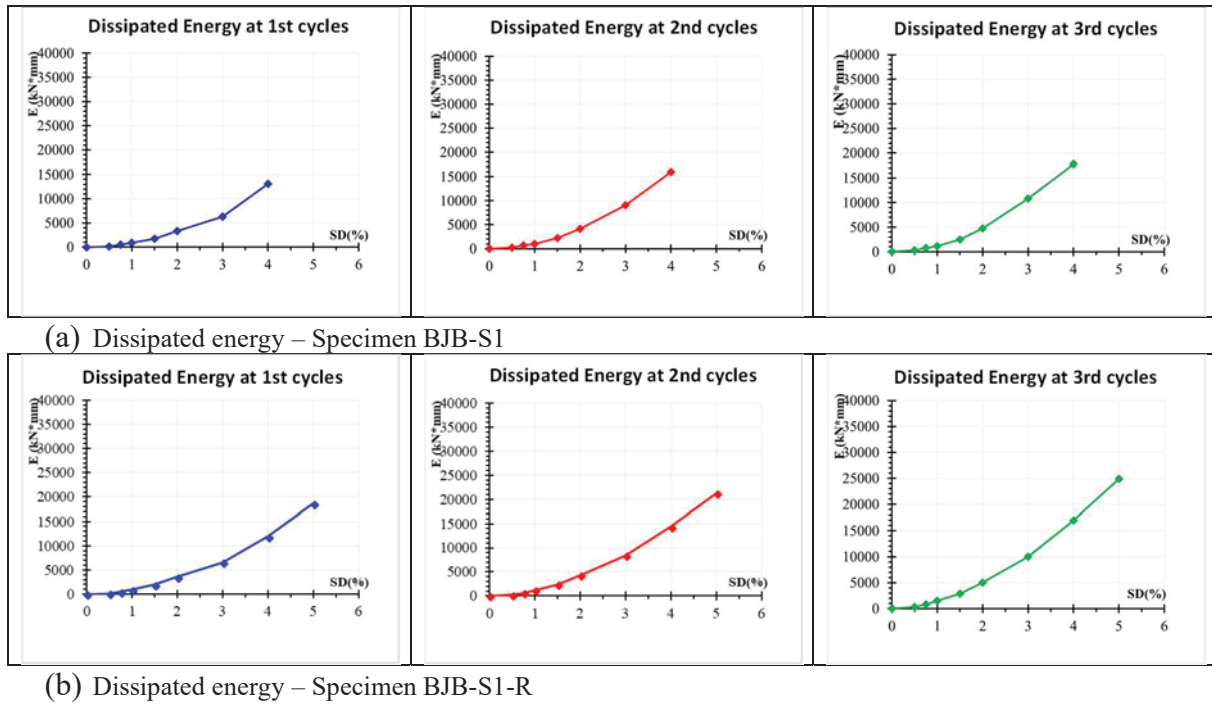


Figure 10: Energy dissipation per each loading step (a) of the specimen BJB-S1 and (b) of the corresponding retrofitted specimen BJB-S1-R.

The dissipated energy at 1st, 2nd and 3rd cycles of each loading step as measured in terms of the area of the corresponding hysteresis loops of the original specimen BJB-XV are presented in Figure 11a. Further, the dissipated energy at 1st, 2nd and 3rd cycles of each loading step as measured in terms of the area of the corresponding hysteresis loops of the retrofitted specimen BJB-XV-R are presented in Figure 11b. Comparing the diagrams of retrofitted specimen with the corresponding diagrams of the original specimen it is deduced that the applied technique can rather adequately restore the energy dissipating capacity for the specimen with X-type reinforcement in the joint (without stirrups).

However, from Figures 9 and 10 it can be observed that there are reservations about the efficiency of the technique in the restoration of the energy dissipation capacity in high levels of loading or high degree of initial damage.

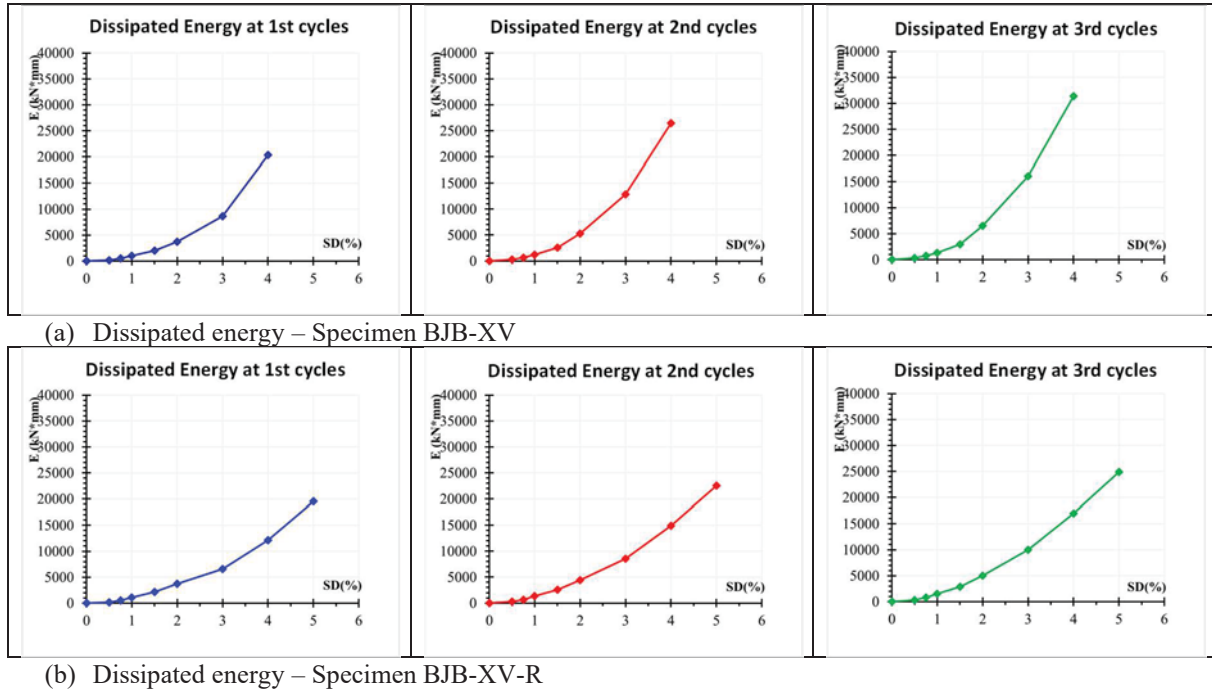


Figure 11: Energy dissipation per each loading step (a) of the specimen BJB-XV and (b) of the corresponding retrofitted specimen BJB-XV-R.

4 CONCLUSIONS

The efficacy of using C-FRP sheets for the retrofitting of damaged external beam column joints after seismic excitations is experimental studied. In the repair technique under investigation in this work, the C-FRP sheets are applied after a meticulous filling of the developing cavities and cracks but without the infusion of thin resin into the cracking system of the damaged area.

From the comparisons of the hysteretic responses of the original specimens with the hysteretic responses of the retrofitted ones it is deduced that in both cases the load bearing capacity values of all the retrofitted joints were almost equal to the ones of the original specimens in every loading step of the loading history.

Further, from the comparisons of the dissipated energy at 1st, 2nd and 3rd cycles of each loading step of the original specimens with the dissipated energy at 1st, 2nd and 3rd cycles of each loading step of the corresponding retrofitted ones it is deduced that the applied technique has rather adequately restored the energy dissipating capacity in the examined cases.

Finally, there are reservations for the efficiency of the technique in the restoration of the load bearing capacity and energy dissipation in cases of high level of loading or high degree of initial damage.

REFERENCES

- [1] C.G. Karayannis, C.E. Chalioris, K.K. Sideris, Effectiveness of RC beam-column connection repair using epoxy resin injections. *J. of Earthquake Engineering*, 2(2), 217-240, 1998.

- [2] A.G. Tsonos, G.I. Kalogeropoulos, P.E. Iakovidis, D. Konstantinidis, Seismic retrofitting of pre-1970 RC bridge columns using innovative jackets., *Int.J. of Structural Engineering*, **8**(2), 133-147, 2017.
- [3] A.G. Tsonos, Effectiveness of CFRP-jackets in post-earthquake and pre-earthquake retrofitting of beam-column subassemblages. *Structural Engineering and Mechanics*, **27**(4), 393-408, 2007.
- [4] C.G. Karayannis, G.M. Sirkelis, Strengthening and rehabilitation of RC beam-column joints using carbon-FRP jacketing and epoxy resin injection. *Earthquake Engineering and Structural Dynamics*, **37**, 769-790, 2008.
- [5] A.G. Tsonos, Effectiveness of CFRP-jackets and RC-jackets in post-earthquake and pre-earthquake retrofitting of beam-column sub assemblages. *Engineering Structures*, **30**(3), 777-793, 2008.
- [6] D.J. Kakaletsis, K.N. David, C.G. Karayannis, Effectiveness of some conventional seismic retrofitting techniques for bare and infilled R/C frames. *Structural Engineering and Mechanics*, **39**(4), 499-520, 2011. <https://doi10.12989/sem.2011.39.4.499>
- [7] C. Marthong, Rehabilitation and strengthening of exterior RC beam-column connections using epoxy resin injection and FRP sheet wrapping: Experimental study. *Structural Engineering and Mechanics*, **72**(6), 723-736, 2019. <https://doi.org/10.12989/sem.2019.72.6.723>
- [8] C.G. Karayannis, E. Golias, Full scale tests of RC Joints with minor to moderate damage repaired using C-FRP sheets. *Earthquakes and Structures*, **15**(6), 617-627, 2018. <https://doi:10.12989/eas.2018.15.6.617>
- [9] C.G. Karayannis, (2015), Mechanics of external RC beam-column joints with rectangular spiral shear reinforcement: experimental verification. *Meccanica*, **50**(2), 311-322, 2015. <https://doi:10.1007/s11012-014-9953-6>
- [10] C.G. Karayannis, B.A. Izzuddin, A.S. Elnashai, Application of adaptive analysis to reinforced concrete frames. *J. Structural Engineering*, ASCE, **120**(10), 2935-2957, 1994. [https://doi:10.1061/\(ASCE\)07339445\(1994\)120:10\(2935\)](https://doi:10.1061/(ASCE)07339445(1994)120:10(2935))
- [11] E. Golias, H. Lindenthal, F.-H. Schlüter, A.I. Karabinis, Ertüchtigung seismisch beschädigter Rahmenknoten aus Stahlbeton mittels FRP-Filamentbündelverbindungen. *Bautechnik*, **97**(4), 268-278, 2020. <https://doi.org/10.1002/bate.201900085>
- [12] C.E. Chalioris, A.G. Zapis, C.G. Karayannis, U-jacketing applications of fiber-reinforced polymers in reinforced concrete T-beams against shear - Tests and design, *Fibers*, **8**(2), 13, 2020. <https://doi.org/10.3390/fib8020013>
- [13] G.I. Kalogeropoulos, A.D. Tsonos, Cyclic performance of RC columns with inadequate lap splices strengthened with CFRP jackets, *Fibers*, **8**(6), 39, 2020. <https://doi.org/10.3390/fib8060039>

SEISMIC VULNERABILITY OF SHALLOW UNDERGROUND CAVITIES IN SOFT ROCK

S. Fabozzi¹, F. de Silva², M. Nocentini¹, E. Peronace¹, E. Bilotta², M. Moscatelli¹

¹ Institute of Environmental Geology and Geoengineering - National Research Council of Italy
Area della Ricerca Roma, 1, Monterotondo RM, Italy
{stefania.fabozzi,marco.nocentini,edoardo.peronace,massimiliano.moscatelli}@igag.cnr.it

² Department of Civil, Architectural & Environmental Engineering - University of Naples Federico II
Via Claudio 21 Napoli, Italy
{filomena.desilva,emilio.bilotta}@unina.it

Abstract

The instability risk of underground cavities is issue of concern particularly for areas densely urbanized as the case of many historical centers in Italy. Among the possible causes of the cavity damages up to collapse, the proposed work considers a particular triggering factor that is the dynamic loading induced by an earthquake. Thus, the seismic vulnerability of shallow cavities in soft rock is addressed by proposing a methodology based on an extensive parametric two-dimensional finite element analysis. The proposed methodology is extended to a significant number of realistic cases, considering the effect of the variability of some predisposing and triggering factors on the cavity stability like roof thickness and cavity width, presence of overburden on the top of the rock layer, seismic signal intensity. The seismic vulnerability of the studied cases is assessed through the minimum Factor of Safety calculated during the whole length of the dynamic analysis. Finally, the results of the parametric study are rearranged into 'seismic stability charts for cavities in soft rock' proposed to be adopted as preliminary level of screening, to assess the seismic vulnerability of shallow underground cavities in soft rock. The results of screening enable to identify the critical zones that need a detailed analysis, in consideration of their possible interaction with above-ground structures, infrastructures and human activities.

Keywords: FEM, full dynamic analysis, underground cavities, soft rock, Factor of Safety

1 INTRODUCTION

Shallow underground anthropogenic cavities are frequently spread over the most urbanized areas in many Italian regions whereby their stability represents matter of concern leading to potential risk for buildings, infrastructures, and population. Different causes can induce cavity instability: starting from their excavation, the initial static stability can worsen over time due to an unexpected overloading, water recharge, water table fluctuation and other particular conditions that can result in progressive damage up to the global collapse. Furthermore, seismic actions can represent source of instability for underground cavities as documented by numerical studies in literature [1, 2] and historic observations in some Italian database of co-seismic effects (CFTI5Med, <http://storing.ingv.it/cfti/cfti5/> [3]; CEDIT, http://www.ceri.uniroma1.it/index_cedit.html, [4]).

In the present work we focused our attention on the seismic behavior of cavities, proposing a methodology to assess their stability. The proposal was tested in a specific soft rock type, that is the Neapolitan Yellow Tuff where it is very recurrent to find anthropogenic cavities excavated for different needs during years and with different features (e.g. cavity shape, dimension, cover, other loads). Some studies in the technical literature are dedicated to such cavities, that consider their stability under static and seismic actions [5, 6, 7, 8, 9, 10].

The proposed methodology, described in detail afterwards, is extended to a significant number of realistic cases, taking into account the variability of some different predisposing and triggering factors of the cavity instability (*i.e.* the width and depth of cavity, the overburden stress, the intensity of the seismic action). A parametric study via numerical dynamic analyses was conducted in plane strain conditions using the finite element code Plaxis 2D, on simplified rectangular shapes of shallow cavity. The ground shaking was simulated by applying several time histories of acceleration at the base of the numerical model.

The cavity stability was evaluated by assuming the rock cover above the cavity roof as a beam and quantifying the so-called Factor of Safety (FoS) calculated as the ratio between the resistant moment (M_r) and the loading moment (M_{load}) in correspondence of the most critical vertical sections. The considered FoS is the lowest one experienced during each shaking. The obtained results are presented and discussed in terms of variation of FoS as a function of the ratio L/H (with 'L' equal to cavity width and 'H' equal to the depth of the cavity roof, or rock cover), of PGA_{input} and of the overburden above the rock cover, q .

Although the analyzed conditions are simplified, the parametric study provides a methodological approach to be adopted as a preliminary level of screening to assess the seismic vulnerability of shallow underground cavities in soft rock. The results of screening enable to identify the critical zones that need a detailed analysis, in consideration of their possible interaction with the above structures, infrastructures and human activities.

2 METHODOLOGY

The preliminary stability assessment of underground cavities in soft rock under seismic actions is proposed upon the results of a significant number of parametric two-dimensional finite-element analyses carried out for realistic cases of underground cavities. A rectangular shape cavity was adopted for the analyses that is, with good approximation, representative of many shallow cavities excavated in soft rock. Therefore, for the specific case of rectangular shallow cavities, the parametric study was built considering: *i*) the effect of varying the width of the cavity (L); *ii*) the effect of stress acting in the rock, by varying the depth of the cavity roof (H) and the entity of the load applied above the rock cover (q); *iii*) the intensity of the seismic action by varying the PGA and the frequency content of the input signals selected

among unscaled records of real earthquakes. Table 1 shows all the geometries considered for the analyses: in total 10 geometrical layouts were analysed, defined by varying H from a minimum of 2 m up to a maximum of 10 m, and L from a minimum of 2 m up to a maximum of 10 m. For each layout, two loading conditions were considered ($q_1=50$ kN/m, $q_2=150$ kN/m), reaching a total number of cases equal to 20. The minimum cavity dimensions were selected to obtain a value of the slenderness of the roof, L/H , higher or at least equal to 1 while the maximum dimensions were set in order to guarantee the static stability of the cavity. The vertical load applied at the model surface intends to simulate the presence of soil layers and fills and above the rock cover and structures or infrastructures at the ground surface.

layout #	H (m)	L (m)	L/H (-)	q_1, q_2 (kN/m)
1.1	2	2	1	50, 150
1.2		5	2.5	
1.3		10	5	
2.1	5	5	1	
2.2		10	2	
2.3		15	3	
2.4		20	4	
3.1	10	10	1	
3.2		15	1.5	
3.3		20	2	

Table 1: Geometric and loading properties of realistic cavity models.

The variability of the seismic action was considered by varying the peak ground acceleration and the frequency content of the input signals as shown in Table 2: 12 unscaled accelerograms of real earthquakes were extracted from the Italian database ITACA (<http://itaca.mi.ingv.it/>) and, for the classes with higher energy content, from the international PEER database (<https://ngawest2.berkeley.edu/>), considering PGA_{max} values ranging from a minimum of 0.118g up to a maximum equal to 0.367g and f_{max} values ranging from a minimum of 0.51Hz up to a maximum equal to 11.26Hz. The signals were subjected to a band-pass filtering in the range of 0.1–25 Hz prior to the seismic response analyses.

Finally, 240 analyses (10 cavity geometries x 2 load conditions x 12 signals) were performed.

Figure 1 shows, as an example, the numerical model implemented in Plaxis 2D for the layout #3.1 (see Table 1). The cavity was excavated in Neapolitan Yellow Tuff that was modelled with a simple linear elastic-perfectly plastic model with a Mohr-Coulomb failure envelope [5]: the tuff unit weight (γ_t) equal to 16 kN/m³, the cohesion (c') equal to 866 kPa, the friction angle (ϕ') equal to 30°, the angle of dilatancy (ψ) equal to 0°, the uniaxial compressive strength (σ_c) equal to 3 MPa, the Poisson ratio (ν) equal to 0.3, the Young modulus (E) equal to 2000 MPa, a tension cut-off of σ_t equal to $0.1\sigma_c$.

An amount of viscous damping equal to 5% was added to the model through the well-known Rayleigh formulation, calibrating the mass and stiffness matrix coefficients by means of the double frequency approach. Moreover, the hysteretic behavior of tuff under dynamic loading was not modelled, given the high linearity threshold measured experimentally by [11].

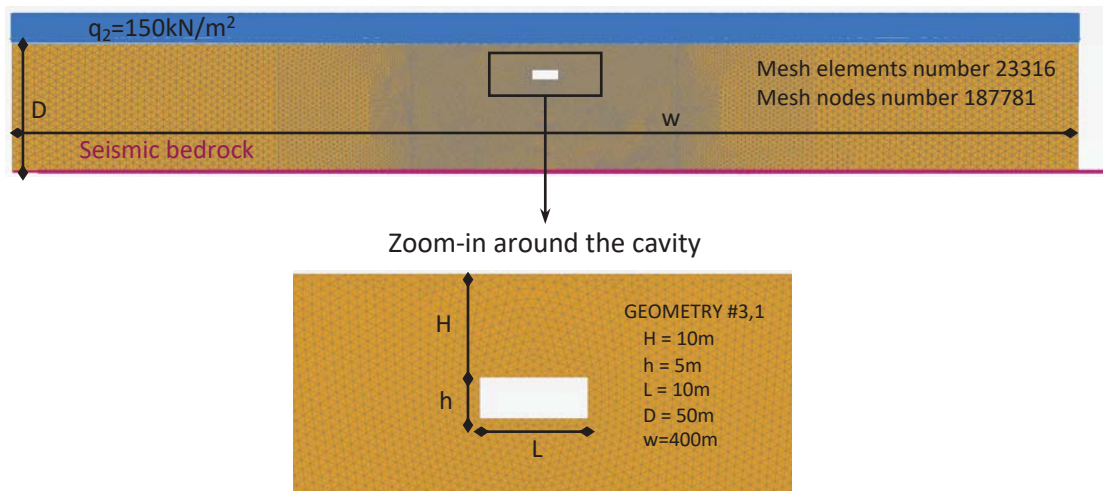


Figure 1: Example of numerical mesh for layout #3.1 implemented in Plaxis 2D.

Event	Date	Mw	PGA _{max} (g)	f _{max} (Hz)
-	-	-	-	-
Greece	07/09/99	5.8	0.118	2.33
L'Aquila (Italy)	09/04/09	5.4	0.146	11.26
Southern Italy	09/09/98	5.6	0.161	1.56
Cosenza (Italy)	25/10/12	5.0	0.182	3.48
Central Italy	26/10/16	5.4	0.192	2.91
Central Italy - Visso	26/10/16	5.9	0.210	1.06
Southern Greece	15/09/86	4.8	0.232	1.34
Central Italy - Norcia	30/10/16	6.5	0.264	0.88
Greece	15/10/16	5.5	0.287	2.68
Imperial Valley	15/10/79	6.4	0.315	1.90
Friuli 3 th shock (Italy)	15/09/76	6.0	0.341	5.10
Loma Prieta	18/10/89	6.9	0.367	0.51

Table 2: Natural accelerograms selected for the seismic analyses.

The numerical analyses consist of three calculation stages [12, 13]:

- first stage: initialization of the initial stress state within the soft rock mass domain;
- second stage: simulation of the cavity excavation by means of the deactivation of the cavity volume. When possible, generally for lower value of L/H , single step excavation solution was assumed as conservative assumption, while for higher values of L/H multiple steps excavation solution were adopted;
- third stage: full dynamic analyses in the time domain, simulating all the selected earthquake recordings in Table 2.

It is worth noting that the same FE mesh used for static analysis (see Fig. 1) was used for the full dynamic analysis. The width of such numerical model in fact, was originally optimized by a series of sensitivity analyses, in order to reach a true free-field condition at the lateral borders and to minimize the influence of vertical boundaries [13]. Also, the mesh was refined to achieve a reliable propagation of the minimum significant wavelength of the input

signals [14]. The lateral boundary conditions consist of fixed displacements in the horizontal direction perpendicular to the vertical sides of the mesh in static condition; viscous dashpots are applied during dynamic stages of analysis [14]; the base of the model, 50 m deep, is fixed both in vertical and in horizontal directions; the nodes at the top surface are free.

The cavity stability was assessed by means of the Factor of Safety (FoS), calculated as the ratio between the ultimate resistant moment ($M_{r,ULS}$) corresponding to the achievement of the compressive, σ_c , and tensile, σ_t , strengths in the compression and tensile zones and the loading moment (M_{load}) acting in correspondence of the most critical vertical section of the roof beam and calculated by integrating the horizontal stress component, σ_{xx} , acting on the considered sections. The FoS_{static} is computed at the end of the second stage of analysis, while FoS_{dyn} is computed at the end of the full dynamic analyses at stage three, as the lower value experienced during the dynamic analysis under each input signal.

3 RESULTS

Figures 2 and 3 show, for the case of layout #3.1, the horizontal stress distribution acting around the cavity (assuming negative the compressive stress) in correspondence of three reference sections of the roof beam (central section in red, the right and left sections at pillars edges in green and light blue, respectively) after its excavation and during Loma Prieta earthquake considered as example.

After the cavity excavation (Figure 2), the roof tends to behave as a beam subjected to uniform distributed load, not completely bounded at the edges of the pillars: in the upper portion of the vault, the compression area assumes the typical arched profile over the underlying tension area; the separation curve between the compression and tension zones represents the location of the neutral axes of the different sections of the roof beam that assumes an approximately parabolic shape. Definitely, the central section is stretched in the bottom, in correspondence of the roof cavity extrados, and compressed at the top while the lateral reference sections at the intersection with pillars are totally compressed. Similar behavior was observed also in the other cavity layouts (see Table 1); a tensile zone in correspondence of the lateral section in the upper portion closer to the ground surface has been sometimes calculated for shallower cavities, depending on the roof slenderness (the ratio between the cavity width and cover).

For the proposed example in Figure 2, the horizontal stress distributions in correspondence on the central and the lateral sections produce a value of loading moment equal to $M_{load,cx}=3432$ kNm and $M_{load,left=right}=1144$ kNm respectively. By comparing the loading moments with the resistant moment $M_{r,ULS}=13727$ kNm of the roof resistant section, FoS_{static} equal to 4 and 12 was calculated for the central and the lateral section respectively. As expected, after the cavity excavation, the central roof section is the most loaded one exhibiting the lowest value of FoS.

Starting from this stress distribution induced by the cavity excavation, thus from this initial equilibrium condition, the seismic excitation starts, producing in the surrounding cavity a continuous redistribution of the stresses during ground shaking. As example of the time history of σ_{xx} in some points of the cavity roof—selected each 1 m along the central and the right sections of the roof beam—is shown in Figure 3,

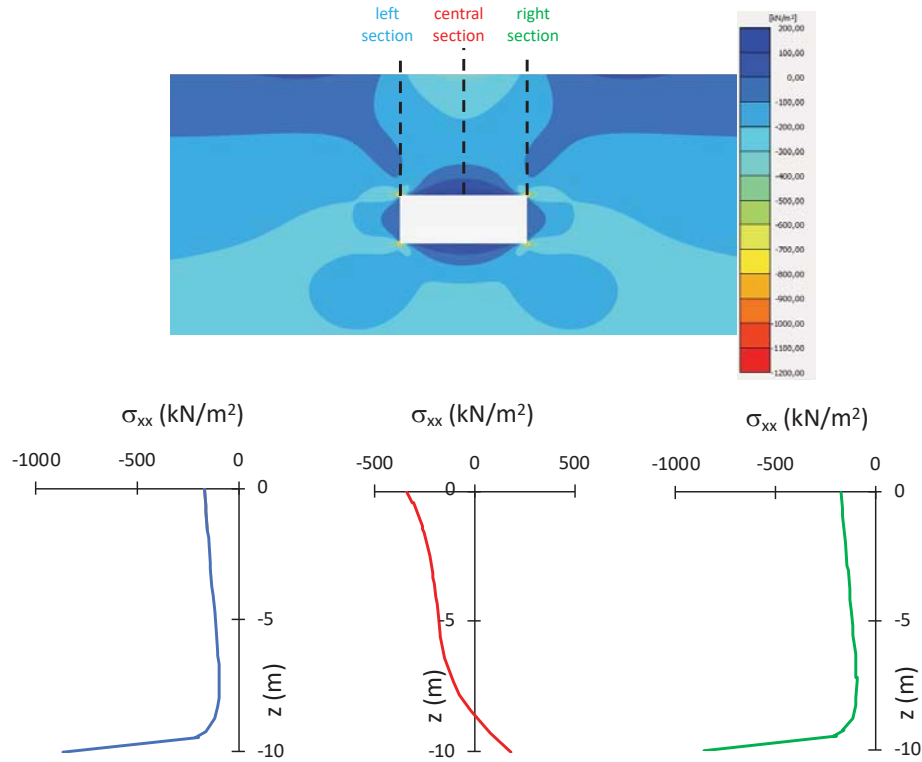


Figure 2: Horizontal stress distribution after the cavity (layout #3.1) excavation.

Consistently with the expected ground deformation under shaking, the lateral sections of the cavity roof experience higher stress variation than the central section. This implies a different modification of the FoS in the considered sections during shaking.

In the central section, starting from $FoS_{static} = 4$, a minimum value of $FoS_{dyn_min} = 3.6$ occurred at the instant $t = 6.15$ s of the time history and a value of $FoS_{dyn_final} = 4.3$ is computed at the end of the shaking; in the left and right sections, starting from $FoS_{static} = 12$, a minimum value of $FoS_{dyn_min} = 1.6$ occurred at the instant $t = 6.15$ s of the time history and a value of $FoS_{dyn_final} = 8$ is computed at the end of the shaking.

Therefore, the initial static conditions of the central section do not change substantially during the shaking, actually a slight increase of FoS occurs at the end shaking due to the redistribution of stress. Such aspect was already observed with reference to a more complex case study by [10]. Conversely, an important reduction of FoS is observed in the lateral sections both during and at the end of the shaking (a reduction of FoS_{static} about equal to 86% and 25% is calculated respectively) due to the high seismic intensity of the selected earthquake, highlighting the effect of earthquake-induced modifications of the static equilibrium under gravity loads. Fortunately, the FoS after earthquake increases in the section (the central) where FoS_{static} was lower and does not reduce down to unity in the lateral sections, hence the roof stability of the selected cavity is not compromised.

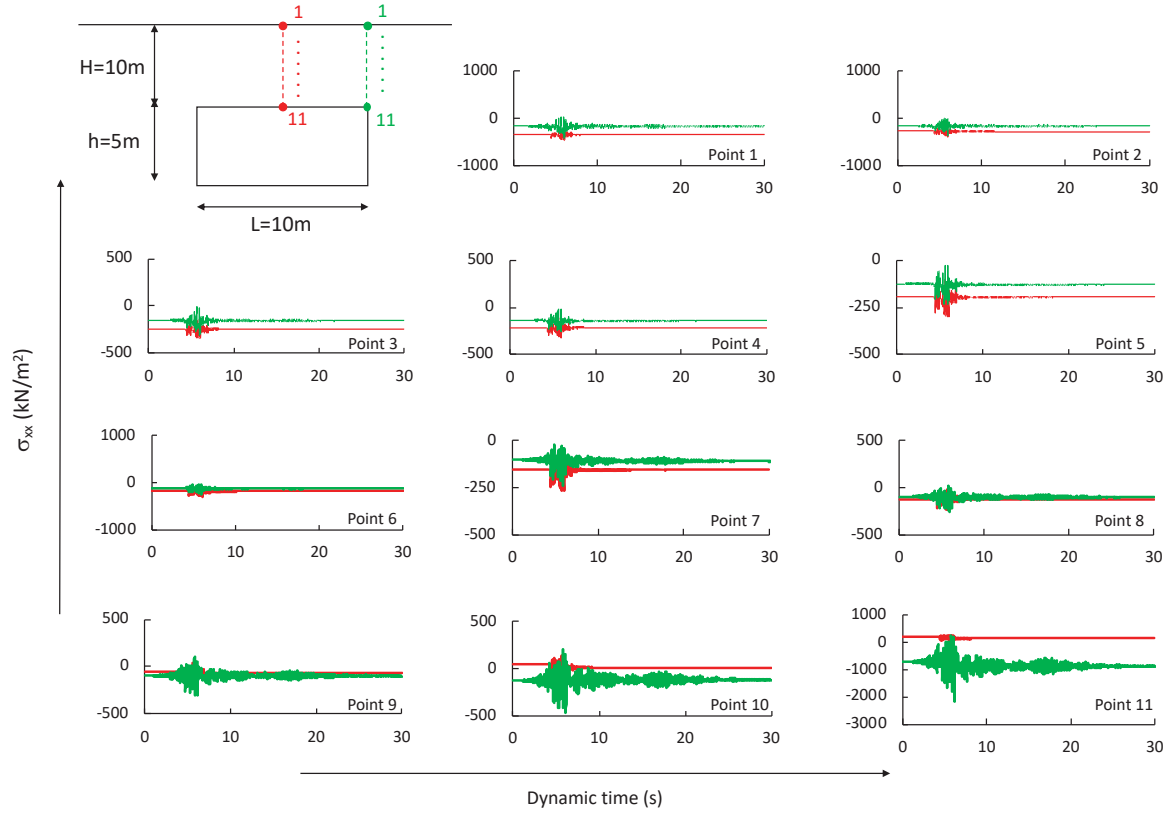


Figure 3: Horizontal stress time history in correspondence of selected points of the cavity roof (layout #3.1) during Loma Prieta earthquake 1989 earthquake.

To generalize the outcome of the proposed parametric study, the FoS values calculated for all cases as the minimum between the central and lateral sections, were processed as function of the increasing intensity of PGA in the proposed Seismic Stability Charts for Cavities, SSCCs (Figure 4). Each chart refers to a specific cavity geometry including both considered loading combinations (q_1 black lines/points, q_2 grey lines/points). In particular, the first row of Figure 4 represents the three cases in which H is set equal to 2 m while L varies from 2 m to 10 m (Figs 4a,b,c respectively), the second row of Figure 4 represents the four cases in which H is set equal to 5 m while L varies from 5 m to 20 m (Figs 4d,e,f,g respectively), the third row of Figure 4 represents the three cases in which H is set equal to 10 m while L varies from 10 m to 20 m (Figs 4h,i,j respectively).

The general trend of the results shown in the figure leads to the following considerations:

1. FoS tends to decrease with the increasing of the seismic loading intensity, here expressed as function of PGA;
2. higher FoS is expected for q_1 loading combination compared to q_2 , because a lower vertical stress is initially induced by a lower overburden; however, with increasing cavity depth such effect vanishes as expected;
3. shallower (lower depth H with same width L) and wider (larger width L with same depth H) cavities exhibit a lower level of safety (FoS) compared with the deeper and narrower ones, when the seismic intensity (PGA) increases.

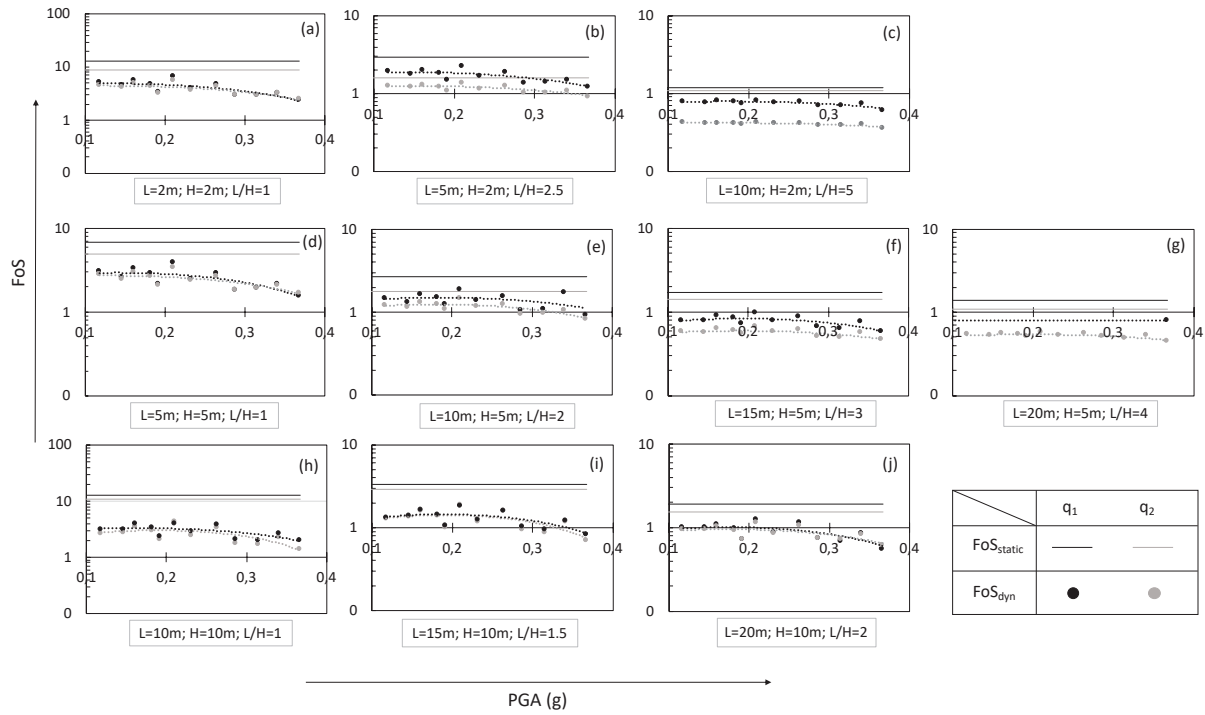


Figure 4: Seismic Stability Charts for Cavities (SSCCs) when $H=2$ m (a,b,c), $H=5$ m (d,e,f,g), $H=10$ m (h,i,j).

It is worth noting that, for the considered layouts, instability conditions (i.e. $FoS < 1$) are achieved, independently of the amplitude of the input motion, when $H=2$ m and $L/H > 5$, $H=5$ m and $L/H > 3$, while failure occurs only under the highest PGA when $H=10$ m and $L/H > 1.5$.

The proposed charts can be adopted as a preliminary level of screening to assess the seismic vulnerability of shallow underground cavities in soft rock, by comparing the so calculated FoS values with a threshold expressing the accepted damage level (i.e. the well-known limit state): “damage limit state” occurring when the FoS is lower than 3; “collapse limit state” associated to FoS lower than 1.5 [10]. In this way, a reconnaissance of possible critical zones that need a more detailed and site-specific analysis can be accomplished.

However, the basic hypotheses of the present study – that constrain the use of the proposed charts to a specific field of applicability – should be here underlined: i) the charts are valid for cavities with approximate flat roof, which are the most widespread in urban areas, hence their applications to arch roof could lead to an underestimation of FoS; ii) the charts are valid in presence of cavity excavated into a homogeneous lithotype rock, therefore they are not strictly applicable in presence of multiple lithotypes that may imply different site effects [15]. Any simplification in the use of the proposed charts outside the hypotheses under which they were obtained, can reduce their reliability.

4 CONCLUSIONS

The seismic actions represent a source of instability for underground cavities, bringing to their damage up to the global collapse. This possibility represents matter of concern leading to potential risk situations for buildings, infrastructures and population. In this scenario the present work represents an attempt to frame the problem at large scale, proposing a methodologi-

cal approach that provides stability charts to assess the seismic vulnerability of shallow underground cavities in soft rock, as preliminary level of screening.

The charts evaluate the cavity seismic stability by means of the proposed Factor of Safety ($FoS = M_{r,ULS}/M_{load}$ of the most vulnerable roof beam sections) as a function of some controlling parameters: the width of the cavity, the depth of the cavity roof, the PGA of the earthquake and the overburden stress on the top of the rock layer. By comparing the estimated FoS values with threshold values expressing the admissible damage level, possible instable cavities can be identified, that require a detailed site analysis.

The discussed results represent a preliminary outcome of a larger ongoing research project that is aimed to extend the methodological approach proposed in this paper to study a large number of cases, including different geometrical layouts and rock mechanical characteristics, in order to widen the applicability of the proposed charts.

ACKNOWLEDGEMENT

This research was supported by the Italian Civil Protection Department within the project “Contratto concernente l’affidamento di servizi per il programma per il supporto al rafforzamento della Governance in materia di riduzione del rischio sismico e vulcanico ai fini di protezione civile nell’ambito del PON Governance e Capacita Istituzionale 2014-2020 CIG6980737E65”.

REFERENCES

- [1] Evangelista L, de Silva F, d’Onofrio A, et al. Application of ERT and GPR geophysical testing to the subsoil characterization of cultural heritage sites in Napoli (Italy). *Measurement*. 2016;104:326–335.
- [2] Santo A., Ascione A., Del Prete S., Di Crescenzo G., Santangelo N. (2011) Collapse sinkholes distribution in the carbonate massifs of Central and Southern Apennines. *Acta Carsologica* 40 (1), 95–112. <https://doi.org/10.3986/ac.v40i1.31>.
- [3] Guidoboni E., Ferrari G., Tarabusi G., Sgattoni G., Comastri A., Mariotti D., Ciuccarelli C., Bianchi M.G., Valensise G. (2019) CFTI5Med, the new release of the catalogue of strong earthquakes in Italy and in the Mediterranean area. *Scientific Data* 6, 80. doi: <https://doi.org/10.1038/s41597-019-0091-9>.
- [4] Fortunato C., Martino S., Prestininzi A., Romeo R.W., coauthors Fantini A., Sanandrea P. (2012) New release of the Italian catalogue of earthquake-induced ground failures (CEDIT). *Italian Journal of Engineering Geology and Environment*, DOI: 10.4408/IJEGE.2012-02.O-05.
- [5] Evangelista A., Feola A., Flora A., Lirer S., Maiorano R.M.S. (2000) Numerical analysis of roof failure mechanisms in a soft rock. *GEOEng 2000*. Melbourne.
- [6] Evangelista A, Flora A, Lirer S, de Sanctis F, Lombardi G. Studi ed interventi per la tutela di un patrimonio sotterraneo: l’esempio delle cavità di Napoli. In: *Proceedings of 21st Geotechnical National Conference*. L’Aquila; 11–14 September 2002. p. 579–588 [in Italian].

- [7] Scotto di Santolo A, Evangelista L, Silvestri F, et al. (2015) Investigations on the stability conditions of a tuff cavity: the Cimitero delle Fontanelle in Napoli. *Riv Ital di Geotec.* 2015:28–46.
- [8] Scotto di Santolo A, Evangelista L, Evangelista A. Analysis of the stability of a rock cavern: the Fontanelle cemetery. In: Lollino G, Giordan D, Marunteanu C, Christaras B, Yoshinori I, Margottini C, eds. *Engineering Geology for Society and Territory*. Cham: Springer; 2015.; 8.
- [9] de Silva F., Scotto di Santolo A. (2018) Probabilistic performance-based approaches to the static and seismic assessment of rock cavities. *International Journal of Rock Mechanics and Mining Sciences* 112 (2018) 354–368.
- [10] de Silva F., Scotto di Santolo A. (2020) Post-earthquake resilience of a room and pillar rock cavity in Naples. In: Calvetti F., Cotecchia F., Galli A., Jommi C. (eds) *Geotechnical Research for Land Protection and Development*. CNRIG 2019. *Lecture Notes in Civil Engineering*, vol 40. 229-308. Springer, Cham.
- [11] Vinale F. Caratterizzazione del sottosuolo di un'area campione di Napoli ai fini della microzonazione sismica. *Riv Ital Geotec.* 1988;22(3):77 – 100 [in Italian].
- [12] Fabozzi S., Bilotta E., Russo G. (2016). Numerical interpretation of monitoring data of an instrumented tunnel segmental ring. 1° IMEKO-TC4 International Workshop on Metrology for geotechnics. *MetroGeotechnics 2016* pp. 350-355. Benevento, Italy / March 17-18, 2016.
- [13] Fabozzi S., Licata V., Autuori S., Bilotta E., Russo G., Silvestri F. (2017) Prediction of the seismic behavior of an underground railway station and a tunnel in Napoli (Italy). *Underground Space* 2 (2017) 88–105. <http://dx.doi.org/10.1016/j.undsp.2017.03.05>.
- [14] Kuhlemeyer R.L and Lysmer J. (1973) Finite Element Method Accuracy for Wave Propagation Problems. *Journal of the Soil Mechanics and Foundation Division*, 99(5), 421- 427.
- [15] Fabozzi S., Catalano S., Falcone G., Pagliaroli A., Peronace E., Porchia A., Romagnoli G., Moscatelli M. (2021) Stochastic approach to study the site response in presence of shear wave velocity inversion: application to seismic microzonation studies in Italy. *Engineering Geology* 280 (2021) 105914 <https://doi.org/10.1016/j.enggeo.2020.105914>.

EFFICIENCY OF SEISMIC LIQUEFACTION MITIGATION METHODS FOR EXISTING STRUCTURES

Alexandros I. Valsamis¹, Taxiarchoula G. Limnaiou¹ and Achilleas G. Papadimitriou¹

¹ School of Civil Engineering, National Technical University of Athens
9 Iroon Polytechniou Street, Zographou, 15780, Greece
e-mails: a_valsamis@hotmail.com, tlimnaiou@gmail.com, apapad@civil.ntua.gr

Abstract

This paper investigates numerically the seismic liquefaction-induced "failure" mechanisms of elongated structures founded on the ground surface of a liquefiable sandy layer, which is first considered horizontal and then having a mild inclination angle of 2°. In accordance with the literature, the paper shows that if the layer is horizontal, the structure suffers from accumulation of settlement. It also shows that even such a mild inclination leads to the additional hazard of horizontal displacement and rotation of the structure due to lateral spreading of its foundation soil. The paper continues with an investigation of the beneficial effects of implementing rows of prefabricated drains or diaphragm walls at the perimeter of the foundation soil of these structures. The former mitigation method aims at reducing the developing excess pore pressures, while the latter targets at increasing the equivalent stiffness of the foundation system. The study is performed via non-linear dynamic fully coupled plane strain analyses with the finite-difference method, while the soil response is modeled with NTUA-SAND, a sophisticated bounding surface plasticity model with verified ability of simulating the response of liquefiable granular soils. It shows that diaphragm walls are much more efficient in reducing settlements, horizontal displacements and rotations than prefabricated drains. However, this efficiency is fully attained only if their depth reaches the bottom of the liquefiable layer.

Keywords: Diaphragm Walls, Drains, Earthquakes, Foundation Failure, Ground Improvement, Liquefaction, Numerical Analysis

1 INTRODUCTION

Since 1964 when the Alaska and Niigata earthquakes occurred, liquefaction has been treated as one of the most severe geo-hazards for civil engineering structures. Nowadays, there exists a large number of soil improvement techniques for liquefaction mitigation, which can be easily used prior to construction in many variants (e.g., densification by vibro-flotation or dynamic compaction, grouting/mixing by deep soil mixing or compaction grouting, drainage and stiffening by gravel piles). Yet, at already developed sites, the majority of these techniques cannot be applied due to the inability to perform improvement works under the structure footprint, as well as due to the possibility of severely affecting the infrastructures or neighboring structures during these works (e.g., due to vibrations from densification techniques). More importantly, there is a significant gap of knowledge for the applicability of existing mitigation techniques in cases where lateral spreading of liquefied ground is anticipated, either due to small inclination of the ground surface (angles of 0.5° to 6°), or due to free face proximity.

In this paper, a numerical investigation of the behavior of strip footings founded directly on a liquefiable soil layer is being presented, focusing initially on the differences between having a horizontal and a mildly inclined ground surface (angle of 2°). Then, the effectiveness of two different liquefaction mitigation techniques is being analyzed for horizontal and inclined ground surface conditions. Particularly, the investigation focuses on the application of rows of prefabricated drains or narrow diaphragm walls solely at the perimeter of the foundation. Such configurations may not sound ideal for mitigating the liquefaction hazard since they do not cover the footprint of the structures. However, they are the only configurations that may be readily implemented in existing structures that is our primary concern here. Moreover, there exist limited experimental evidence of the efficiency of such configurations, and this comes from dynamic centrifuge studies for drains [1] and diaphragm walls [2] only for horizontal ground conditions.

2 NUMERICAL METHODOLOGY

The numerical investigation is performed with the finite difference code FLAC [3] and its User-Defined-Model capability. Particularly, the constitutive model NTUA-SAND ([4], [5]) is used for the simulation of the liquefiable soil layer after its implementation in FLAC. It is a well-established bounding surface Critical State plasticity model, which has proven ability to simulate the cyclic behavior of non-cohesive soils (sands and silts), under any (small-medium-large) cyclic shear strain amplitude using a single (sand-specific) set of constants, irrespective of the initial stress and density conditions. It is based on a previously proposed model ([6], [7]), but in its current form it is characterized by a vanished elastic region. In addition, it incorporates three (3) open cone-type surfaces with apex at the origin of stress space: (i) the Critical State surface at which deformation develops for fixed stresses and zero volumetric strain, (ii) the Bounding surface which locates the (ever-current) peak stress ratio states and (iii) the Dilatancy surface which dictates the sign of the plastic volumetric strain rate during loading. The NTUA-SAND model has been extensively validated against centrifuge experiments related to a number of different liquefaction-related problems: lateral spreading ([8]), foundation settlement ([9]), pile response ([10]), use of drains for liquefaction mitigation ([11]). As such it is considered very reliable for the task at hand in this paper.

As shown in Figure 1, the liquefiable soil layer has a thickness $H = 10\text{m}$, while the strip footing width is $B = 5\text{m}$. In order to ensure no effects from the boundaries, the soil layer has a total width of 100m . This soil domain is discretized into 1000 rectangular zones (the “elements” in FLAC terminology). The mesh is denser in the vicinity of the footing (for an ap-

proximate width of $2.0B = 10\text{m}$), reaching a zone thickness equal to 0.5m . The footing is considered massless, rigid and rough, and is simulated by beam elements on the top of the mesh. The same mesh is also used for the analyses that considered improvements at the perimeter of the footing. Specifically, a row of elements (of 0.5m thickness) has either a permeability coefficient 1000 times larger than that of the natural soil (prefabricated drains) or was considered elastic with very increased stiffness (diaphragm walls, made of reinforced concrete). As also shown in Figure 1, this row of elements was considered at a distance of 0.5m from the edge of both sides of the footing, while the effects of the depth of the improvement H_{imp} was studied parametrically as part of this study.

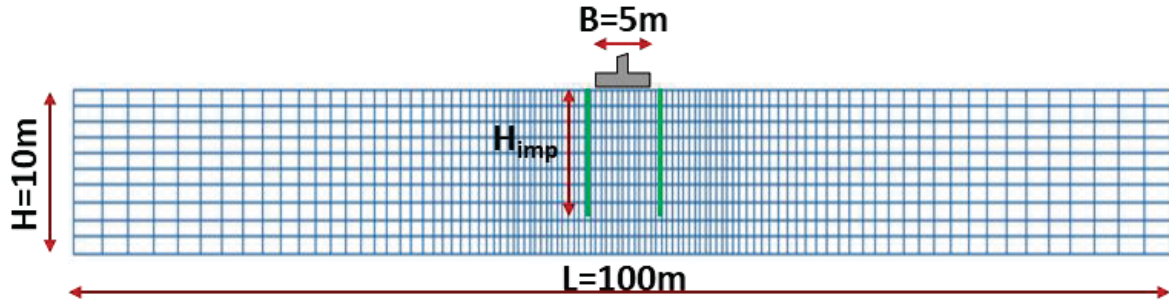


Figure 1: Basic definitions and dimensions of the numerical simulation model (horizontal ground).

The liquefiable soil is (fine) Nevada sand of relative density $D_r=45\%$, dry density 1.53Mgr/m^3 , void ratio 0.718 and permeability $k=6.5 \times 10^{-5}\text{m/s}$. This is considered in the analyses via the values of the NTUA-SAND model constants, as adopted from numerous successful simulations using this sand in the literature (e.g., [3], [4], [8], [9], [10], [11]). A uniform vertical load of 100kPa is applied to the footing in all numerical analyses presented herein. The base excitation is an acceleration time history that is sinusoidal, consisting of ten (10) main cycles with period $T=0.35\text{s}$ and maximum acceleration $a_{\text{max}}=0.20g$. Two (2) additional cycles of variable acceleration have been added to the start and the end of the acceleration time-history to ensure gradual increase and decrease of the acceleration. The lateral boundaries of the model that are at the same altitude are tied to one-another to ensure that they will have the same horizontal displacements throughout the excitation, thus simulating the shaking behavior of a laminar box container, or the free field response insitu.

For the numerical simulation of footings resting on mildly inclined ground (angle $i=2^\circ$), the same grid has been used with the following adjustments:

- the gravity vector has been rotated by 2° to simulate the sloping ground (see [8] for details)
- a minor “excavation” has been modeled at the footing location, to ensure the footing rests on horizontal ground, despite the inclination of the sloping ground

In addition, for reference purposes, the inclined ground response analysis without the existence of footing (lateral spreading of soil at the free-field) is also performed and denoted as free-field (FF) herein.

3 TYPICAL STRUCTURAL RESPONSE ON LIQUEFIABLE SAND

As it was expected, the performed numerical analyses verify the severe problems caused by the existence of a liquefied sand layer of significant thickness underneath existing structures. The developed “failure” mechanism of each footing in the liquefied soil can be deduced from Figure 2, where the accumulated shear strains in the soil underneath the footing at the end of shaking are shown, both for horizontal (subplot 2a) and (mildly) inclined (subplot 2b) ground conditions.

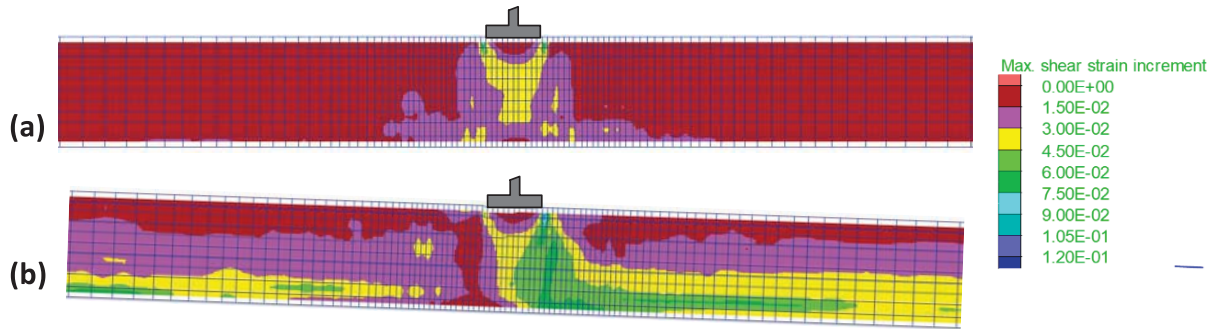


Figure 2: Accumulated shear strains underneath strip footings of width $B=5\text{m}$ (at the end of shaking) resting on liquefied ground of thickness $H=10\text{m}$ that is: (a) horizontal and (b) inclined by 2°

In horizontal ground conditions (Figure 2a) the shear strains concentrate in the area beneath the strip footing, creating a “punching” failure mechanism that reaches the bottom of the liquefied layer (at depth $2.0B$ here) without extending laterally. This “failure” mechanism is narrower and deeper than the well-known bearing capacity mechanism of footings in non-liquefied soils (generalized failure in the shape of a logarithmic spiral), which extends to distances up to $3.5B$ to $5.0B$ laterally and down to $1.5B$ in depth. When the same footing rests on a mildly inclined ground surface, the punching “failure” mechanism reaches again the bottom of the liquefied layer, but is no longer symmetrical (see Figure 2b). Particularly, the zone of intense shearing is more pronounced towards the downslope side and is connected to the shear band that appears at the base of the liquefied layer due to lateral spreading.

In order to gain further insight into the structural response, Figure 3 presents the time-histories of footing displacement (horizontal x and vertical z) and rotation (θ) during the excitation, for both horizontal and inclined ground conditions. Particularly, in Figure 3a the horizontal displacement of the footing resting on inclined ground is being presented (blue line) in comparison with the horizontal displacement of the ground surface of the corresponding free-field laterally spreading layer (dashed green line), under the same excitation. The positive sign depicts downslope displacements. The figure shows that in both cases the horizontal displacements accumulate linearly with time, or with the number of sinusoidal excitation cycles. In quantitative terms, the footing is carried away by the laterally spreading of the liquefied ground, since the footing displacement is practically identical to that of the free field displacement. Hence, despite that the footing increases the vertical stresses in the ground below its footprint, the procuring local increase of shear strength does not suffice for reducing the horizontal drift of the footing. It is believed that this response is the worst-case scenario for a footing and it is due to its relatively small width B in comparison to the thickness H of the liquefied layer, that takes a value of $B/H = 0.5$ here. In other cases where $B/H > 1$, it is expected that the footing drift would be smaller than the horizontal displacement of the ground surface of the corresponding free-field laterally spreading layer.

In addition, Figure 3b presents the accumulated settlement of the (centerline of the) footings in both horizontal (purple line) and inclined (blue line) ground conditions, under the same excitation. It is observed that the settlement of the footing on the inclined layer is of the same magnitude (actually slightly larger) with that of the same footing if the layer is horizontal. This means that the existence of a mild ground inclination does not significantly affect the settlement response. Note also that the final settlement value is in the order of 25-27cm, i.e., much smaller than the 48cm of horizontal displacement of the footing. Finally, Figure 3c presents the rotation of the rigid footing resting on the inclined layer during the excitation, with the negative value of θ depicting downslope rotation, i.e., clockwise rotation for the case of Figure 2b.

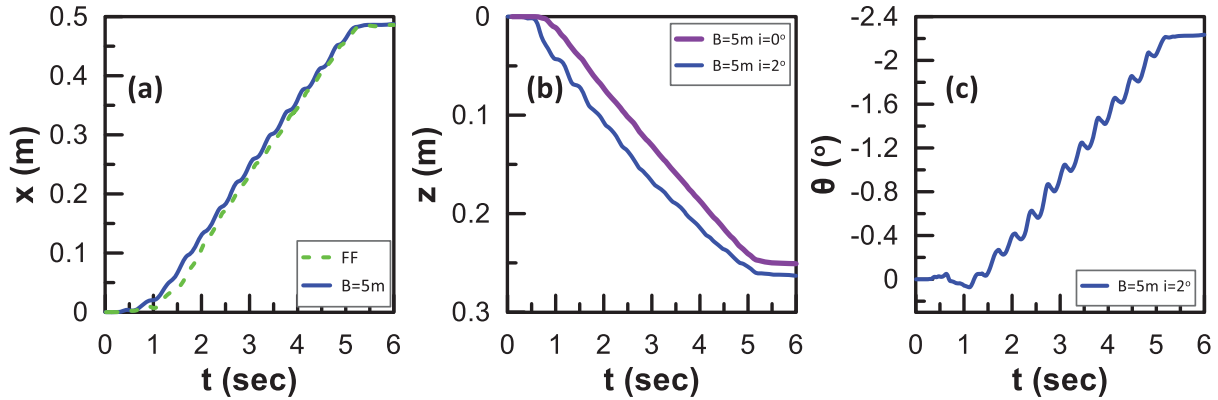


Figure 3: Time-histories of response characteristics of strip footing of width $B = 5\text{m}$ on liquefied ground with $H=10\text{m}$ that is horizontal or inclined, in terms of: (a) horizontal displacement, (b) settlement, and (c) rotation.

There is no other curve in Figure 3c for comparison purposes, since the footing in horizontal ground does not rotate (due to zero static eccentricity). Observe that the rotation also accumulates linearly with time and its final value of $\theta = 2.2^\circ$ is quite significant, i.e., slightly larger than the ground inclination of 2° . As was the case for horizontal displacements, this large value of θ is also due to the small B/H ratio that allows for easier rotations, in comparison to cases with $B/H > 1$ that are expected to rotate less under the same excitation.

Overall, Figure 3 shows that the existence of a mild ground inclination (just 2° in our case) leads to the added hazard of (significant) horizontal displacement and rotation of the structure due to the lateral spreading of the liquefied layer. Hence, such large combined rigid body translations of the structure cannot be safely accommodated by any structural system and the need for soil improvement is more pronounced than for horizontal ground conditions.

4 MITIGATION WITH PERIMETRICAL PREFABRICATED DRAINS

The first improvement technique for existing structures examined here is the application of dense rows of prefabricated drains at the perimeter of an existing footing, which for a strip footing corresponds to the area denoted with green color in Figure 1. This configuration is inspired by pertinent centrifuge tests [1] and aims at reducing the developing excess pore pressures beneath the footing. In our analyses, the drains are considered to extend to the bottom of the liquefied layer, i.e., $H_{\text{imp}}=H=10\text{m}$. For the purpose of the numerical simulation, the permeability of the elements at the improved zone has been considered to be 1000 times higher than that of the natural sand, i.e., it is considered equal to $k=6.5 \times 10^{-2}\text{m/s}$. Note that the improvement area of width 0.5m simulates the effective area of dense series of prefabricated drains (each one of which has a small diameter of a few cm), which as a system offers the foregoing drainage capability to the natural sand. Since the drains are not made of gravel, the response is only affected in terms of drainage. Hence, the constitutive model for the improvement area is still the NTUA-SAND model calibrated identically to the natural sand.

In order to study the effectiveness of this liquefaction mitigation technique, Figure 4 presents the time-histories for the footing displacements x and z and rotations θ with and without the perimetrical prefabricated drains. The results for the cases with drains are different when the liquefiable layer is horizontal (khaki line with spikes) and inclined (green line with crosses). More specifically, Figure 4a presents the comparison in terms of horizontal displacement x of the footing, where only a minor decrease is obtained (approximately 10%) with the installation of the perimetrical drains. Similar conclusions are derived in Figure 4b for the footing settlements, only that the reduction in seismic settlements is approximately 20% for both horizontal and inclined ground surface conditions.

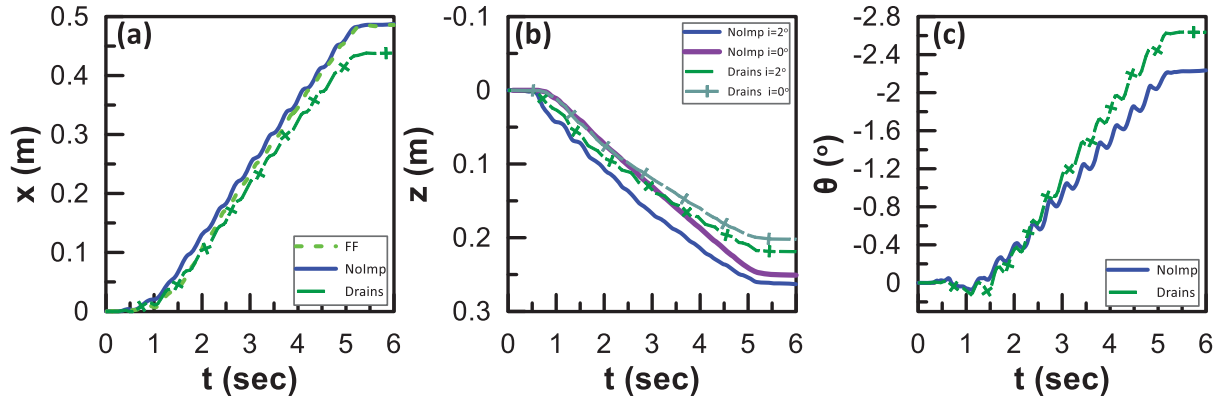


Figure 4: Effect of perimetrical drains on time-histories of response characteristics of strip footing of width $B = 5\text{m}$ on liquefiable ground with $H=10\text{m}$ that is horizontal or inclined, in terms of: (a) horizontal displacement, (b) settlement and (c) rotation.

Unfortunately, these small benefits in reduced footing displacements come at a price of increased footing rotations (in the order of 20%) in the case of laterally spreading inclined sand, as depicted in Figure 4c.

Overall, solely perimetrical drains do not seem to offer any significant benefit in the footing response, while they may even be considered unfavorable if rotations are of primary concern. Either positive or negative, the effects of such drains on the footing response are quantitatively small. This is corroborated by the images of accumulated shear strains in the foundation soil at the end of shaking, that are presented in Figure 5, for both horizontal (in subplot 5a) and inclined (in subplot 5b) ground conditions in the presence of perimetrical drains. Specifically, if one compares these images with the respective plots in Figure 2, a great resemblance is depicted. For example, observe the “punching” failure mechanism when the soil is horizontal in both cases for horizontal ground (subplots 2a and 5a). Also observe that when the soil is mildly inclined, the foregoing failure mechanism becomes asymmetrical and (roughly) connected to the shear band at the base of the liquefied layer due to lateral spreading in the downslope side of the footing, regardless of whether perimetrical drains are implemented (subplot 5b) or not (subplot 2b).

In closing, it is underlined here that this inefficient liquefaction mitigation is a result of the inability of the solely perimetrical drains to effectively reduce the excess pore pressures below the footing. If it was possible to implement drains throughout the area below the footing, the resulting liquefaction mitigation would be more efficient. However, such configuration can only be implemented before the construction of a new footing, and not below existing structures that is the aim of this investigation.

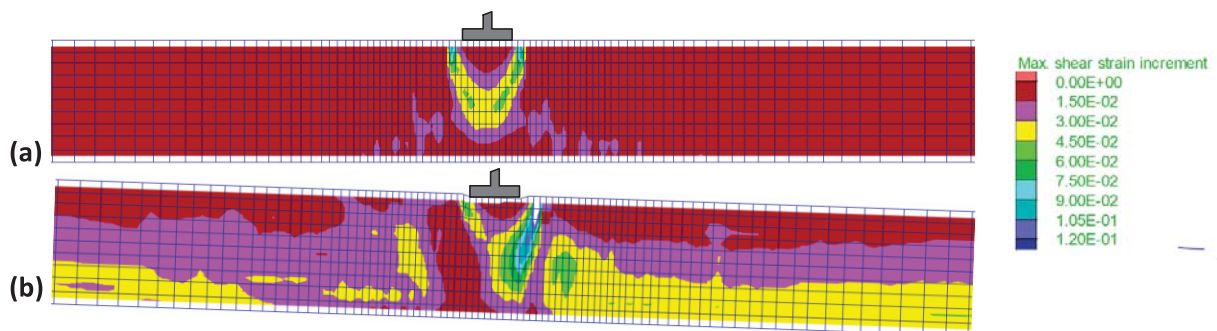


Figure 5: Accumulated shear strains underneath strip footings of width $B=5\text{m}$ with perimetrical drains (at the end of shaking) resting on liquefiable sand of thickness $H=10\text{m}$ that is: (a) horizontal and (b) inclined by 2°

5 MITIGATION WITH PERIMETRICAL DIAPHRAGM WALLS

The second technique investigated for the mitigation of liquefaction underneath an existing structure is the construction a stiff containment wall at its perimeter and within the foundation soil (see concept in Figure 1, as inspired by [2]). This wall retains the soil underneath the structure in place, while increasing the overall stiffness of the foundation system. The construction material of this wall may vary, but in the analyses presented herein it is considered to be reinforced concrete. In this respect, these containment walls are named diaphragm walls. Two different wall lengths are examined, a) full-depth wall, from the ground surface to the bottom of the liquefiable layer ($H_{imp} = H = 10\text{m}$), b) half-depth wall, from the ground surface to the mid-depth of the liquefiable layer ($H_{imp} = H/2 = 5\text{m}$). The full-depth walls are considered pinned to the base of the mesh, thus following the base excitation, while the mid-depth walls are considered floating inside the liquefiable layer. The retaining wall of 0.5m thickness is simulated with an elastic model of bulk modulus equal to 16.7GPa, shear modulus equal to 12.5GPa, mass density 2.50Mgr/m³ and are practically impermeable (in our analyses a permeability of $6.7 \times 10^{-7}\text{m/s}$ is considered, i.e., 100 times lower than that of the surrounding soil).

In order to study the effectiveness of this liquefaction mitigation technique, Figure 6 presents the time-histories for the footing displacements x and z and rotations θ with and without the perimetrical full-depth diaphragm walls. In order to distinguish the results for the cases with these walls, those pertaining to the horizontal liquefiable layer are depicted by a red line with quotations, while those that refer to the inclined layer with a purple line with squares. Interestingly, the construction of the walls seems to offer maximum improvement, since all footing response characteristics (displacements x , z and rotation θ) become essentially zero, regardless of whether the liquefiable layer is horizontal or not.

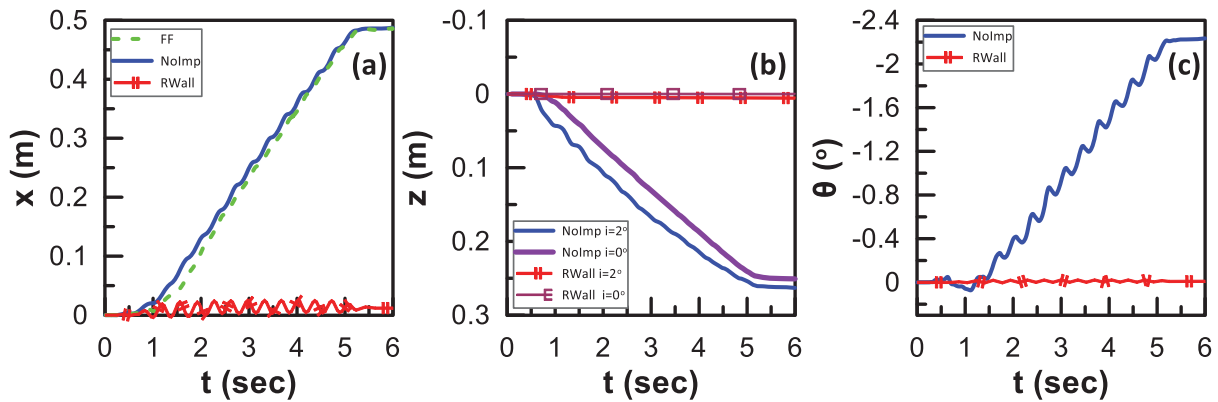


Figure 6: Effect of full-depth ($H_{imp}=10\text{m}$) perimetrical diaphragm walls on time-histories of response characteristics of strip footing of width $B = 5\text{m}$ on liquefiable ground with $H=10\text{m}$ that is horizontal or inclined, in terms of: (a) horizontal displacement, (b) settlement and (c) rotation.

This impressive performance of the full-depth diaphragm walls is corroborated by the images of accumulated shear strains in the foundation soil at the end of shaking, that are presented in Figure 7 for both horizontal (in subplot 7a) and inclined (in subplot 7b) ground conditions in the presence of such walls. Specifically, if one compares these images with the respective plots in Figure 2, a totally different response is depicted. For horizontal ground, there are no shear bands formed underneath the footing, thus explaining the zero footing settlements. On the contrary, shear bands are formed in the inclined ground. Specifically, the uphill shear band is related to the laterally spreading sand layer that drifts towards the footing area. This soil movement is hindered by the uphill rigid wall, thus leading to upward relative movement of the soil against it, which in turn creates a shear band at the interface.

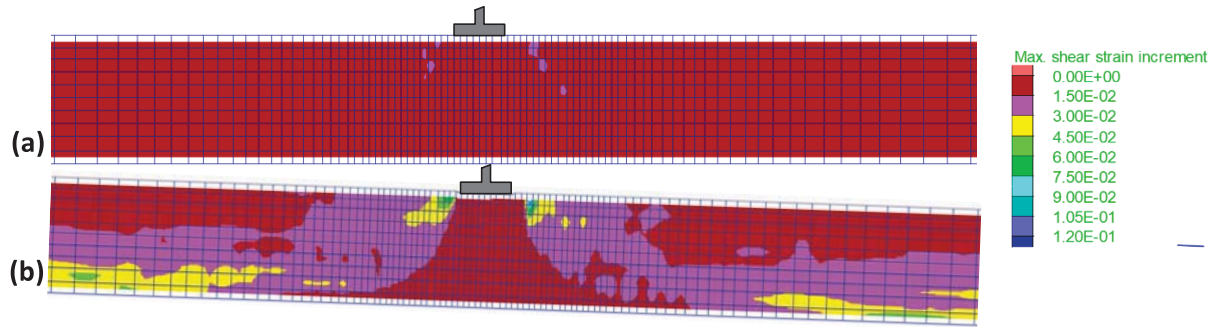


Figure 7: Accumulated shear strains underneath strip footings of width $B=5\text{m}$ with (full-depth $H_{\text{imp}}=10\text{m}$) perimetrical diaphragm walls (at the end of shaking) resting on liquefiable sand of thickness $H=10\text{m}$ that is: (a) horizontal and (b) inclined by 2°

Similarly, the downhill shear band is related to the laterally spreading sand layer that drifts away from the footing area. As this soil mass moves, there is downward relative movement of the soil versus the downhill rigid wall, thus creating the pertinent shear band at their interface. It becomes evident that these shear bands have no effect on the footing response itself since they are formed outside the walls and not underneath the footing. As such, zero displacements and rotation appear in the unaffected footing.

It has to be underlined here that the rigidity of the diaphragm walls is key for this excellent performance. In other words, if these full-depth containment walls are constructed with a less stiff material (e.g., deep soil mixing with cement, or lime), then their performance is not expected to be as excellent, i.e., some settlements or rotations of the footing may persist. Another issue of importance is how the depth of the diaphragm walls affects the footing response. This is the reason that analyses with half-depth perimetrical diaphragm walls are performed herein. Their efficiency is explored in Figure 8 that presents the time-histories for the footing displacements x and z and rotations θ with and without these half-depth walls in the format of Figure 6. Interestingly, the operation of these half-depth walls does not seem as effective as that of its full-depth counterparts. Specifically, these half-depth walls manage to reduce horizontal displacement x (in subplot 8a) by just 10%, settlements z by 20% (in subplot 8b) and downhill rotations by 75% (in subplot 8c). In other words, the half-depth walls seem significantly effective only for the reduction of footing rotations in cases that the sand layer is mildly inclined. For the footing (horizontal and vertical) displacements, these walls appear to offer improvement that is comparable to that of full-depth perimetrical drains.

In order to understand the reasons behind this significantly reduced effectiveness of half-depth diaphragm walls, images of accumulated shear strains in the foundation soil at the end of shaking are presented in Figure 9 for both horizontal (in subplot 9a) and inclined (in subplot 9b) ground conditions. Observe in subplot 9a that the soil mass in between the diaphragm walls and under the footing seems to move downwards as a rigid block (creating shear bands in the inner interfaces of the walls), thus translating the “punching” bearing capacity failure in the lower half of the liquefied layer where the diaphragm walls do not reach. Similarly, in subplot 9b, the shear band at the bottom of the laterally spreading soil layer seems little affected by the existence of the half-depth walls, thus explaining their inability to reduce the horizontal drift of the footing. In addition, the clear asymmetry of the failure mechanism under the footing that appears in the untreated case (see Figure 2b) seems less pronounced in the case of the half-depth walls of subplot 9b, an observation that may explain the smaller (yet non-zero) rotations of the footing when half-depth walls are in place.

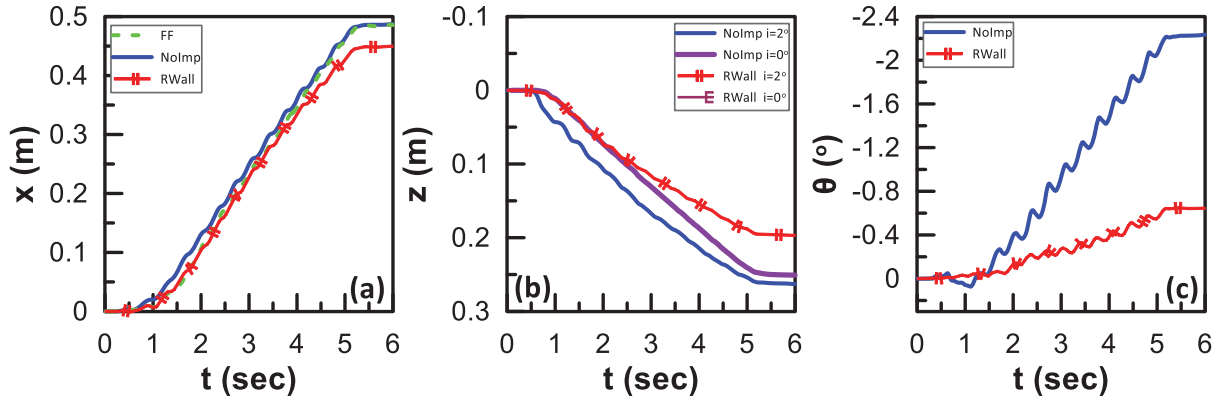


Figure 8: Effect of half-depth ($H_{imp}=5m$) perimetrical diaphragm walls on time-histories of response characteristics of strip footing of width $B = 5m$ on liquefiable ground with $H=10m$ that is horizontal or inclined, in terms of: (a) horizontal displacement, (b) settlement and (c) rotation.

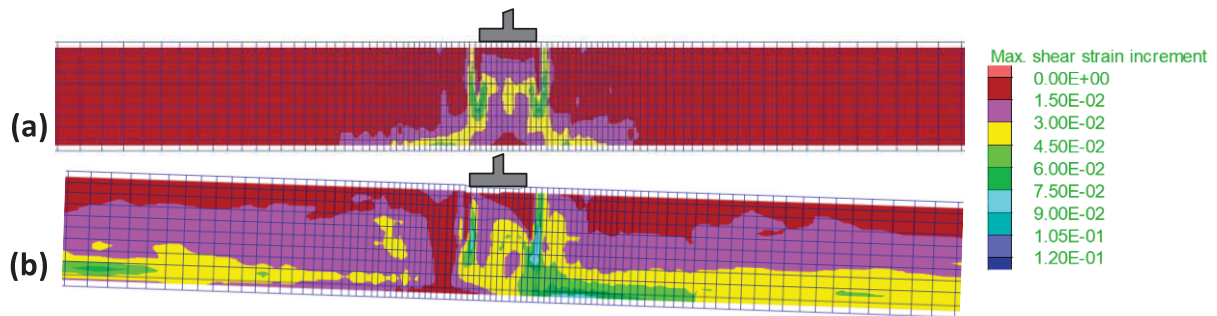


Figure 9: Accumulated shear strains underneath strip footings of width $B=5m$ with (half-depth $H_{imp}=5m$) perimetrical diaphragm walls (at the end of shaking) resting on liquefiable sand of thickness $H=10m$ that is: (a) horizontal and (b) inclined by 2° .

6 CONCLUSIONS

Fully coupled numerical analyses are performed in order to examine the response of shallow-founded structures on horizontal and/or mildly inclined liquefiable layers of relatively significant thickness. The results show that besides significant settlements, even a very mild slope (2° here) creates lateral spreading, which in turn causes the additional hazard of similarly large horizontal displacements and rigid body downhill rotations of the structure.

Then, the efficiency of two liquefaction mitigation methods that can be readily implemented in existing structures resting on the foregoing layers is examined numerically. Specifically, the use of prefabricated drains at the perimeter of the structure does not prove efficient, since it reduces by 10-20% its horizontal displacements and settlements, but may even increase slightly its rotations. On the contrary, the implementation of reinforced concrete perimetrical walls with depth until the bottom of the liquefiable layer proves exceptionally efficient, since all structural displacements and rotations become zero. The investigation also shows that this efficiency disappears if the perimetrical walls are shallower than the bottom of the liquefiable layer. For example, if these walls reach the mid-depth of the liquefiable layer, the perimetrical diaphragm walls become similarly efficient as the perimetrical drains.

7 ACKNOWLEDGMENTS

This research is carried out / funded in the context of the project “Applicability of seismic liquefaction mitigation via nano-material injection under existing infrastructures” (MIS 5049429) under the call for proposals “*Researchers' support with an emphasis on young re-*

searchers- 2nd Cycle”. The project is co-financed by Greece and the European Union (European Social Fund- ESF) by the Operational Programme Human Resources Development, Education and Lifelong Learning 2014-2020.



8 REFERENCES

- [1] B. Paramasivam, S. Dashti, A. Liel, Influence of prefabricated vertical drains on the seismic performance of structures founded on liquefiable soils, *Journal of Geotechnical and Geoenvironmental Engineering, ASCE*, **144**, no. 10, 04018070, 2018
- [2] H. Mitrani, S.P.G. Madabhushi, Rigid containment walls for liquefaction remediation, *Journal of Earthquake and Tsunami*, **6**, No. 2, 1250017, 2012
- [3] Itasca Consulting Group Inc., Fast Lagrangian Analysis of Continua, 2011.
- [4] K.I. Andrianopoulos, A.G. Papadimitriou, G.D. Bouckovalas, Explicit integration of bounding surface model for the analysis of earthquake soil liquefaction, *International Journal for Numerical and Analytical Methods in Geomechanics*, **34**(15): 1586-1614, 2010
- [5] K.I. Andrianopoulos, A.G. Papadimitriou, G.D. Bouckovalas, Bounding surface plasticity model for the seismic liquefaction analysis of geostructures, *Soil Dynamics and Earthquake Engineering*, **30**(10): 895-911, 2010
- [6] A.G. Papadimitriou, G.D. Bouckovalas, Y.F. Dafalias, Plasticity model for sand under small and large cyclic strains, *Journal of Geotechnical and Geoenvironmental Engineering, ASCE*, **127**, no. 11, 973-983, 2001
- [7] A.G. Papadimitriou, G.D. Bouckovalas, Plasticity model for sand under small and large cyclic strains: a multiaxial formulation, *Soil Dynamics and Earthquake Engineering* **22** (3), 191-204, 2002.
- [8] A.I. Valsamis, G.D. Bouckovalas, A.G. Papadimitriou, Parametric investigation of lateral spreading of gently sloping liquefied ground, *Soil Dynamics and Earthquake Engineering* **30** (6), 490-508, 2010.
- [9] D.K. Karamitros, G.D. Bouckovalas, Y.K. Chaloulos, K.I. Andrianopoulos, Numerical analysis of liquefaction-induced bearing capacity degradation of shallow foundations on a two-layered soil profile, *Soil Dynamics and Earthquake Engineering* **44**, 90-101, 2013.
- [10] A.I. Valsamis, G.D. Bouckovalas, Y.K. Chaloulos, Parametric analysis of single pile response in laterally spreading ground *Soil Dynamics and Earthquake Engineering* **34** (1), 99-110, 2012.
- [11] A. G. Papadimitriou, M.-E. Moutsopoulou, G. D. Bouckovalas, A. J. Brennan, Numerical investigation of liquefaction mitigation using gravel drains, *Proceedings, 4th International Conference on Earthquake Geotechnical Engineering*, Thessaloniki, June 25-28, Paper 1548, 2007.

PREDICTING RAILWAY DISPLACEMENTS WITH THE HARDENING SOIL SMALL STRAIN MODEL NEAR CRITICAL SPEED

J. Fernández-Ruiz¹ and P. Alves Costa²

¹ Department of Civil Engineering, University of La Coruña
Campus de Elviña, 15071 La Coruña (Spain)
e-mail: jesus.fernandez.ruiz@udc.es

² CONSTRUCT, Faculty of Engineering, University of Porto, Porto, Portugal
R/ Dr Roberto frias, 4200-465 Porto (Portugal)
pacosta@fe.up.pt

Abstract

The prediction of railway track displacements is a topic of great interest in railway engineering. Different constitutive models of the materials (ballast, sub-ballast and ground) have been applied, from the linear elastic model to non-linear models based on the Equivalent Linear approach. In the technical literature, it is shown how non-linear models enhance the prediction of the displacements of the railway track, especially when the train's running speed approaches the critical speed. In this paper and for the first time to the authors' knowledge, the Hardening Soil Small Strain model is applied and experimentally validated to the study of track displacements near critical speed. Specifically, the well-known case at Ledsgaard (Sweden) has been used for its evaluation, showing numerical results very similar to those measured experimentally. Moreover, the critical speed is calculated, showing values significantly lower than those calculated with the linear elastic model. This is relevant for practical geotechnical engineers, even assuming a certain complexity of the model, because its use is increasingly widespread in commercial finite element codes.

Keywords: Critical speed, Non-linear soil behaviour, Railway geotechnics, Soil dynamics, Numerical modelling

1 INTRODUCTION

The study and conceptualization of the phenomenon of critical speed in railway lines have been developed since the 1990s, after the problems arising from the increase in the speed of train operation following the rehabilitation of the railway line in Ledsgard [1-4]. This increase in speed led to a considerable increase in the track displacements.

From a theoretical point of view, the critical speed is the speed of a non-oscillating moving load that implies the greatest amplification of the dynamic response. It is the properties of wave propagation in the embankment-ground system and the bending wave propagation in the track that completely determine this phenomenon [5-8]. This is associated with a considerable increase in ground deformations, which may even be permanent [9-10], which can be of great importance in high-speed lines [11-12] and be critical in soft soils.

When a train travels at lower speeds and speeds far from those of Rayleigh wave propagation on the ground, the level of strains induced in it is low and may be in the range of small deformations. It is known that here the behavior of the ground is elastic and linear, where G does not undergo any significant degradation. In this sense, when the train runs on stiff soils, the geotechnical safety associated with the behavior of the ground is practically guaranteed and the calculation of the track displacements can be carried out with a simple and numerically highly efficient model such as the linear elastic model. However, when the speed of the train approaches the speed of propagation of Rayleigh waves in the ground, the deformations in the ground increase considerably causing a degradation of the stiffness of the ground that becomes totally relevant and that has an important influence both on the magnitude of the track displacements and on the value of the critical speed. In these cases, the accuracy and suitability of the linear elastic model is lower and non-linear cyclic models with degradations of the value of G are required to satisfy the strain conditions of the ground. In this respect, [13] has shown how the use of an Equivalent Linear approach (ELA) has led to reductions of between 10-20% in the value of the critical speed with respect to that obtained with the linear elastic model. Similar values have been found in the studies presented by [2,14].

The constitutive soil model known as the Hardening Soil Small Strain model (HSsmall) [15] is an advanced ground behavior model which takes into consideration the full degradation curve of G , from the very small strains to the large strains associated with the failure of the soil. It forms part of the package of constitutive software models for commercial use such as Plaxis or Zsoil. Although it is a complex model, it is within the reach of all geotechnical engineers, making it a good tool of analysis for this type of cases. However, to the knowledge of the authors, it has never been experimentally validated in cases of critical speed in railway lines. For this reason and for the advance that this might lead to in the practice of geotechnical railway engineering, this study is presented with the aim of verifying whether the HSsmall model is a reliable tool for the prediction of displacements undergone by the track near critical speed and for the prediction of the critical speed. To do this, a numerical simulation of the famous Ledsgard case[1-4] has been performed, comparing the numerical results (with the HSsmall and Elastic Linear model) with those measured in reality.

2 CASE STUDY OF LEDSGARD

2.1 Generalities

The Ledsgard site is located 25 km to the south of Gothenburg. In the 1990s, excessive vibrations were detected all along the track and this led to an intense investigation on the geotechnical properties of this site [2]. Both the properties of the ground and those of the track have been shown in the many studies made of this case [1-4,16] and the reader is advised to

consult them. In this study, the data proposed by [2] have been used. These are summarized below, thus avoiding a reiterative description of the data found in the technical literature.

2.2 Soil and track properties

The geotechnical profile and a detail of the ballasted track is shown in fig. 1.

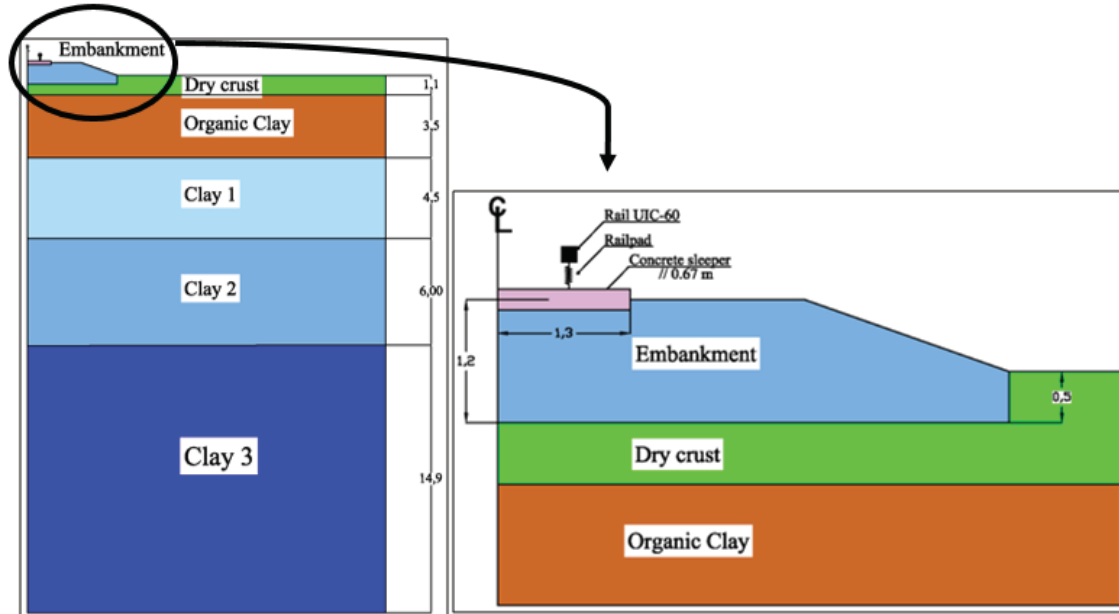


Figure 1: Soil (left) and ballasted track geometry (right)

The elastic properties of the ground are shown in Table 1, taken from the data provided by [2].

Layer	Thickness (m)	Specific weight (kN/m ³)	G ₀ (kN/m ²)	Poisson's ratio
Embankment	1.2	18.00	79.51·10 ³	0.19
Dry crust	1.1	15.00	5.95·10 ³	0.49
Organic Clay	3.5	12.60	2.17·10 ³	0.49
Clay 1	4.5	14.75	5.31·10 ³	0.49
Clay 2	6	14.75	11.18·10 ³	0.49
Clay 3	14.9	14.75	14.75·10 ³	0.49

Table 1: Soil elastic properties

As regards the degradation curves of G and the damping considered in the HSsmall model, these have the following equations [17] and are shown in fig.2:

$$G_s/G_0 = \frac{1}{1 + \frac{0.385 \cdot \gamma}{\gamma_{0.7}}} \quad (1)$$

$$\xi = \frac{E_D}{4\pi E_s} \quad (2)$$

$$E_D = \frac{4 \cdot G_0 \cdot \gamma_{0.7}}{0.385} \left(2 \cdot \gamma - \frac{\gamma}{1 + \gamma_{0.7}/0.385 \cdot \gamma} - \frac{2 \cdot \gamma_{0.7}}{0.385} \cdot \ln \left(1 + \frac{0.385 \cdot \gamma}{\gamma_{0.7}} \right) \right) \quad (3)$$

$$E_s = \frac{G_0 \cdot \gamma^2}{2 + 2 \cdot 0.385 \cdot \gamma / \gamma_{0.7}} \quad (4)$$

where $\gamma_{0.7}$ is the shear strain for $G_s/G_0 = 0.722$

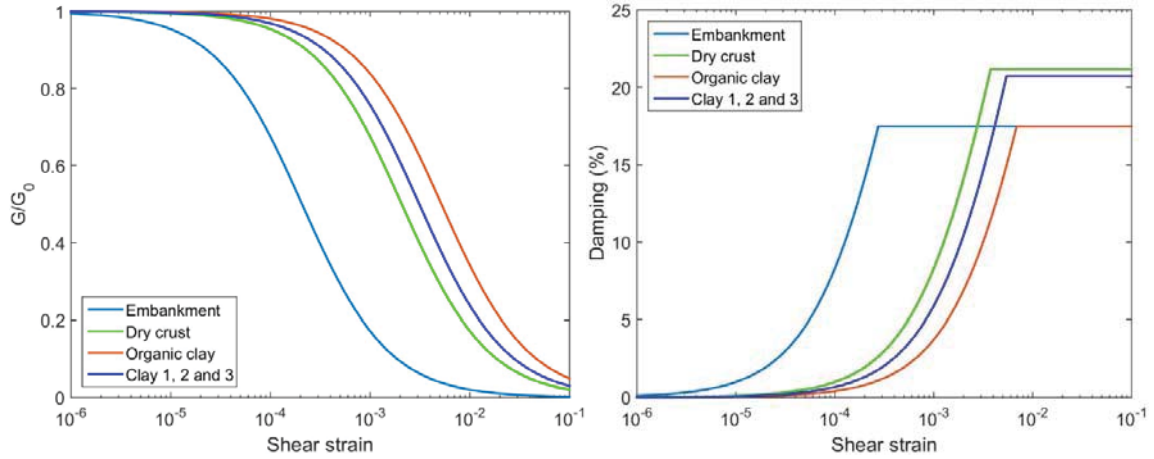


Figure 2: Shear modulus reduction (left) and damping ratio (right) (adapted [2])

Given that numerical simulations have also been made considering a linear elastic behavior of the ground, a Rayleigh damping has been considered. As regards the characteristics of the railway track, this corresponds to a ballasted track, with a rail type UIC60 which is seated on railpads of a stiffness of 250 kN/mm. The sleepers have a length of 2.6 m, a height of 0.2 m and are separated by 0.67m. Their elastic properties are mass density 2,500 kg/m³, Young's modulus 3x10⁷ kN/m² and Poisson's ratio 0.2. The ballast is included in the embankment shown in fig. 1, this being made up both of ballast and of gravels and sands [2]. The measurement of the track response during train passage was made with the X2000 train at different speeds. The geometry and axle load of this train are shown in fig. 3. The tests were performed in both directions, i.e. Northbound and Southbound but in this study only the Southbound direction is considered.

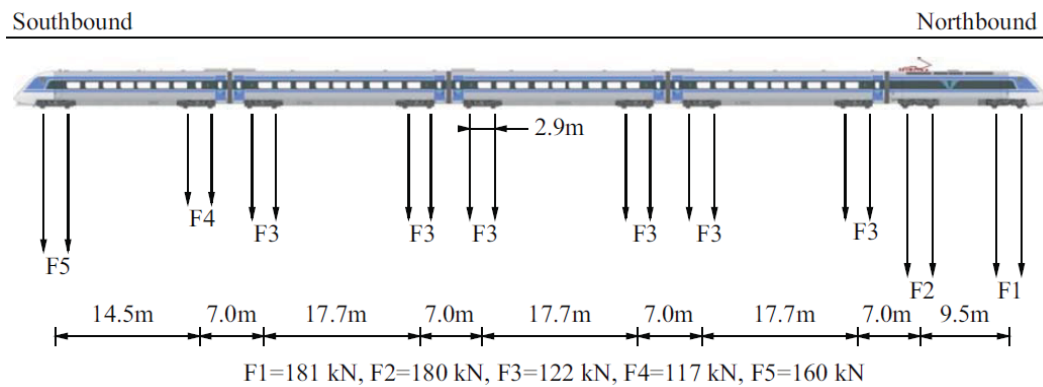


Figure 3: Geometry and axle load of X2000 train

3 EXPERIMENTAL VALIDATION

3.1 Numerical model

To validate the HSsmall model experimentally, a dynamic 3D model formulated in the time domain has been developed in Plaxis software [15]. The geometry of the numerical model is shown in detail in fig. 4 and as can be seen it corresponds to a symmetric case, so that only half of it has been modeled. The dimensions of the model are 70x40x30 m in the longitudinal, horizontal and vertical directions respectively, which are values considered and experimentally validated in 3D models of finite elements formulated in the time domain similar to those used here [16,18-21]. The railpad is modeled as a linear spring, whereas the rail has been simulated as a beam, with the normalized properties of the UIC-60 type. The rest of the track components (sleeper, ballast and subballast) and ground were modeled using 3D solid elements.

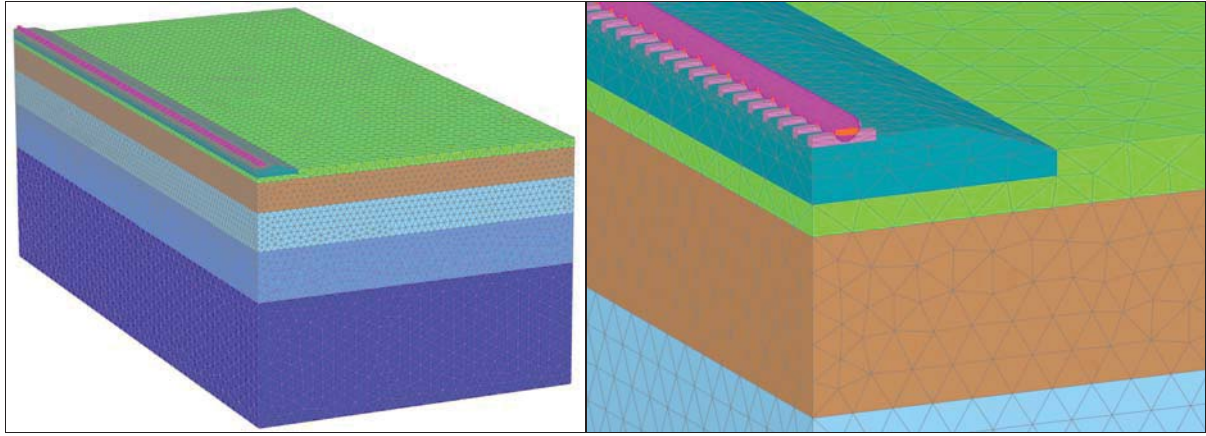


Figure 4: Numerical model: 3D view mode (left) and track detail (right)

The numerical model is made up of 370,181 elements and 523,961 nodes. Quadratic tetrahedral elements (10 node elements) are used for solid elements. The boundary conditions correspond to viscous dampers [15] in all boundaries except the plane of symmetry, where horizontal movements are impeded, and the ground surface, which is a free boundary.

As for the numerical modeling of the moving load, this has been applied using the equivalent nodal force method, in keeping with that described in [22] and the time step has been considered according to the criteria of Courant-Friedrichs-Lewy [16,22], with an implicit Newmark integration scheme, as shown below:

$$C_n = \frac{\Delta t \times C}{L_{min}} < 1 \quad (5)$$

where C_n is the Courant number, Δt is the time step, C is the moving load speed and L_{min} is the distance between two adjacent loading nodes.

3.2 Experimental validation

Fig. 5 shows the experimental validation for four different train speeds: 70, 140, 180 and 204 km/h. As can be seen, the results obtained with the Linear Elastic model show relevant differences from those actually measured for the four speeds, these differences becoming

more evident the higher the speed of the train. The Linear Elastic model tends to underestimate the dynamic response, and in quantitative terms it predicts only half of the actual displacement of the sleeper. These differences are important.

As for the results obtained by the HSsmall model, these are quite close to those actually measured for the four speeds studied. It is worth noting that the adjustment is quite acceptable and that it is more precise when the train speed is higher. In fact, for speeds of 180 and 204 km/h the accuracy of the model is quite good while for the lower speeds (70 and 140 km/h), the results are also very close but with slightly greater differences than for the high speeds.

In this case, the critical speed is approximately 200 km/h. Around these speeds, the results of the HSsmall model are highly accurate, showing that the constitutive model is correctly reproducing the behavior of the different ground layers.

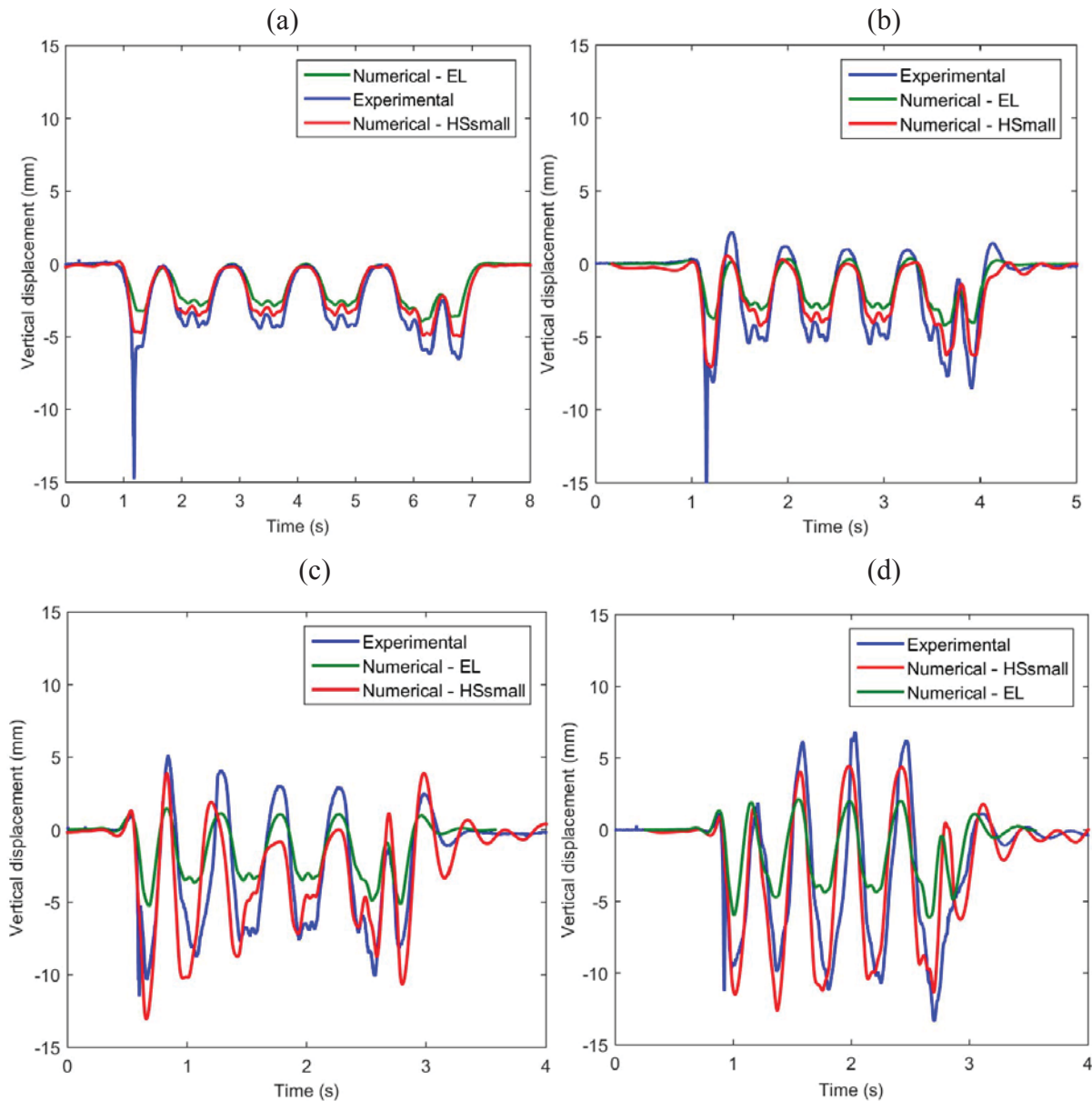


Figure 5: Measured and computed time histories of sleeper displacements for different train speeds (Southbound direction): (a) $V=70$ km/h; (b) $V=140$ km/h; (c) $V=180$ km/h and (d) $V=204$ km/h

Comparing the results between the HSsmall and LE models at low speeds, it can be observed that there is also an appreciable degradation of the stiffness of the ground layers, which the HSsmall model is also correctly simulating but which is obviously not being simulated correctly with the Linear Elastic model. This fact shows that the degradation of the stiffness of the ground is not only substantial near the critical speed, but that for speeds considerably lower than the critical speed there is also a significant degradation of the stiffness. It is likely that at low speeds the degradation of stiffness is more important in the structural layers of the track: ballast and subballast, while at speeds close to the critical speed, the degradation of the stiffness of the underlying ground plays a more important role than at low speeds.

3.3 Critical speed for a single moving point load

It has been considered of interest, once the HSsmall model has been experimentally validated, to calculate the critical speed of the Ledsgard case for a single moving point load. For this, the same numerical model has been considered, but with only one moving load. Two scenarios have been considered: Linear Elastic model and HSsmall model. The displacements of the sleeper and the Dynamic Amplification Factor (DAF) as a function of the speed of the load are shown in figure 6, where it can be seen how the HSsmall model gives a critical speed value of 47 m/s, while for the Linear Elastic model it is 53 m/s. Therefore, the use of the HSsmall model results in a critical speed which is 12% lower than that of the Linear Elastic model. These differences are relevant and demonstrate the suitability of the HSsmall model for predicting the critical speed of the train.

Regarding the displacements and the DAF, the HSsmall model yields higher values than the Linear Elastic model, so for the prediction of the track movements, the HSsmall model is more suitable, both for low speeds and those close to the critical speed, as shown above.

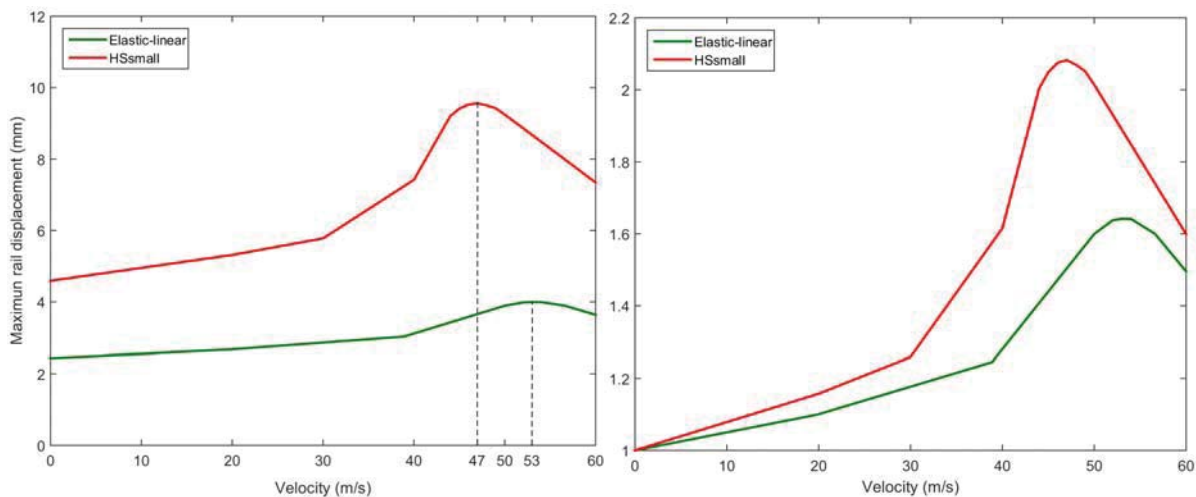


Figure 6: Sleeper displacements vs velocity (left); DAF in sleeper vs velocity (right)

4 CONCLUSIONS

This research has studied the applicability of the HSsmall constitutive model to the prediction of the movements of the track in railway lines. Numerical values have been obtained which are very close to those actually measured in the Ledsgard case, both for speeds close to the critical speed and for low speeds. In this respect, the HSsmall model has proven to be a reliable tool for the prediction of the movements of the track with a very acceptable level of accuracy. Moreover, it has been shown how the critical speed is 12% lower when analyzed

with the HSsmall model with respect to that obtained by the Linear Elastic model. Hence, the use of the HSsmall model may be of greater use when in-depth studies are made of the critical speed.

REFERENCES

- [1] L. Hall, Simulations and analyses of train-induced ground vibrations in finite element models. *Soil Dynamics and Earthquake Engineering*, 23, 403-413, 2003.
- [2] P. Alves Costa, R. Calçada, A. Silva Cardoso, A. Bodare, Influence of soil non-linearity on the dynamic response of high-speed railway tracks. *Soil Dynamics and Earthquake Engineering*, 30(4), 221-235, 2010.
- [3] C. Madshus and M. Kaynia, High-speed railway lines on soft ground: dynamic behaviour at critical train speed. *Journal of Sound and Vibration*, vol. 231(3), 689-701, 2000.
- [4] H. Takemiya, Simulation of track-ground vibrations due to a high-speed train: the case of X-2000 at Ledsgard. *Journal of Sound and Vibration*, 261, 503-526, 2003.
- [5] Alves Costa P, Colaço A, Calçada R, Cardoso AS. Critical speed of railway tracks. Detailed and simplified approaches. *Transportation Geotechnics*, 2, 30-46, 2015.
- [6] Dieterman HA, Metrikine A. The equivalent stiffness of a half-space interacting with a beam. Critical velocities of a moving load along the beam. *European Journal of mechanics a/solids*, 15(1), 67-90, 1996.
- [7] Dieterman HA, Metrikine A. Steady-state displacements of a beam on an elastic half-space due to a uniformly moving constant load. *European Journal of mechanics a/solids*, 16(2), 295-306, 1997.
- [8] Sheng X, Jones C, Thompson D. A theoretical study on the influence of the track on train-induced ground vibration. *Journal of Sound and Vibration*, 272, 909-36, 2004.
- [9] Alves Costa P, Lopes P, Silva Cardoso A. Soil shakedown analysis of slab railway tracks: numerical approach and parametric study. *Transportation Geotechnics*, 16, 85-96, 2018.
- [10] Madshus C, Lacasse S, Kaynia A, Harvik L. Geodynamic challenges in high speed railway projects. In: *GeoTrans 2004 - geotechnical engineering for transportation projects*, ASCE; 192-215. Los Angeles, 2004.
- [11] Kaynia M, Madshus C, Zackrisson P. Ground vibrations from high-speed trains: prediction and countermeasure. *Journal of Geotechnical Geoenvironmental Engineering* 126(6), 531-537, 2000.
- [12] Krylov V. Generation of ground vibrations by superfast trains. *Applied Acoustics*, 44, 149-64, 1995.
- [13] Dong, K., Connolly, D.P., Laghrouche, O., Woodward, P.K., Alves Costa, P. Non-linear soil behaviour on high speed rail lines. *Computers and Geotechnics*, 112, 302-318, 2019.
- [14] TShih, J.Y., Thompson, D.J., Zervos, A. The influence of soil nonlinear properties on the track/ground vibration induced by trains running on soft ground. *Transportation Geotechnics*, 11, 1-16, 2017.

- [15] Brinkgreve, R.B.J., Kumarswamy, S., Swolfs, W.M., Zampich, L., Ragi Manoj, N. 2019. *Plaxis 2019 User Manuals*. Plaxis bv, Delft.
- [16] Abu Sayeed, Md., Shahin, M.A. Three-dimensional numerical modelling of ballasted railway track foundations for high-speed trains with special reference to critical speed. *Transportation Geotechnics*, 6, 55-65, 2016.
- [17] Brinkgreve RBJ, Kappert MH, Bonnier PG. Hysteretic damping in a small-strain stiffness model. *Numerical Models in Geomechanics-NUMOG X- Pande & Pietruszczak (eds)*, 2007 Taylor&Francis Group, London, ISBN 978-0-415-44027-1
- [18] El Kacimi, A., Woodward, P.K., Laghrouche, O., Medero, G. Time domain 3D finite element modelling of train-induced vibration at high speed. *Computers and Structures*, 118, 66-73, 2013.
- [19] Fernández Ruiz, J., Alves Costa, P., Calçada, R., Medina Rodríguez, L.E. and Colaço, A. Study of ground vibrations induced by railway traffic in a 3D FEM model formulated in the time domain: experimental validation. *Structure and Infrastructure Engineering* 13(5), 652-664, 2017.
- [20] Fernández-Ruiz, J., Medina Rodríguez, L.E., Alves Costa, P., Martínez-Díaz, M. Benchmarking of two three-dimensional numerical models in time/space domain to predict railway-induced ground vibrations. *Earthquake Engineering and Engineering Vibration*, 20, 245–256, 2021.
- [21] Fernández-Ruiz J, Medina Rodríguez LE, Costa PA. Use of Tyre-Derived Aggregate as Backfill Material for Wave Barriers to Mitigate Railway-Induced Ground Vibrations. *International Journal of Environmental Research and Public Health*, 17(24), 9191, 2020.
- [22] Galavi V, Brinkgreve RBJ. Finite element modelling of geotechnical structures subjected to moving loads. In: *Hicks et al., editors. VIII ECNUGME – numerical methods in geotechnical engineering*. Delft, Netherlands: Taylor & Francis – Balkema; 235–40, 2014.

NON-DESTRUCTIVE AND DESTRUCTIVE TESTS ON *OPUS INCERTUM* MASONRY PANELS

F. Autiero^{1*}, G. De Martino¹, M. Di Ludovico¹, A. Prota¹

¹ Department of Structures for Engineering and Architecture, University of Naples Federico II, Italy
e-mail: francesca.autiero@unina.it
giuseppina.demartino2@unina.it
diludovi@unina.it
aprota@unina.it

Abstract

The conservation of ancient masonry structures requires knowledge of their structural behavior. At the same time, the possibility to perform standard mechanical tests on heritage structures is limited by the need for the preservation of the cultural heritage.

This paper presents the results of a deep experimental program aimed at the mechanical characterization of masonry panels reproducing the ancient technique opus incertum found at the Pompeii archaeological site. They were built based on the traditional technique by using original rock units and a typical mortar mixture. The experimental program firstly involved sonic pulse velocity tests and diagonal compression tests on three masonry panels, 1.20m x 1.20m x 0.45m. Then, axial compression tests on five masonry specimens extracted from the three panels were carried out.

In the following, the main results of the experimental program are presented and discussed and relevant correlations among the results of non-destructive tests and destructive tests are defined to provide a useful tool for a preliminary assessment of the structural behavior of similar ancient masonries.

Keywords

Pompeii archaeological site; Masonry Panels, Rubble Stone Masonry, Non-destructive tests, Axial Compression Test, Mechanical Properties

1 INTRODUCTION

The conservation of heritage masonry structures set specific issues from a structural point of view concerning the achievement of adequate knowledge of the mechanical parameters of the structural elements and their components [1,2]. Despite different methodologies are available for the investigation of the mechanical properties of existing building materials and masonry assemblages, several limitations may occur in heritage contexts. Indeed, the execution of destructive and minor-destructive tests, DTs and MDTs (e.g. diagonal compression tests, axial compression tests, single or double flat-jack tests), which is required for a direct estimation of fundamental mechanical parameters, is strongly restricted in such a context. This is related to the need for conservation of the heritage structures and technical challenges related to the extraction of undamaged and adequate size test specimens. On the other hand, non-destructive tests, NDTs (e.g. sonic tests, tomography, radar, thermography), can provide only a qualitative evaluation of structures (i.e. homogeneity and consistency of the specimens, presence of voids or material alterations) or indirect estimation of the mechanical parameters based on empirical correlations with DTs results. Moreover, their results are strongly affected by the structural state of conservation and by test conditions. For these reasons, the implementation of appropriate databases containing the results of different types of tests related to specific material and structural typologies can be very useful tools for the definition, by analogy, of the mechanical properties of similar elements.

A possible approach for the structural knowledge of heritage masonry structures is the realization and testing of new masonry panels representing the old typologies. This would allow performing a comprehensive experimental program involving the execution of DTs to obtain essential information on the structural behavior of traditional masonry typologies. Moreover, the execution of NDTs on reproduced panels would allow a comparison with the results obtained on the ancient structures. Stone masonries with irregular arrangements are typical of historical and archaeological contexts. Several studies involving the characterization through DTs of irregular stone masonry panels reproducing old typologies (particularly diagonal compression tests and axial compression tests) are available in the technical literature [3–5]. Few other studies focused on the definition of proper relationships between the results of DTs and NDTs obtained on the same masonry specimens, particularly focusing on the use of sonic pulse velocity tests (STs) [6–9]. Indeed, ST is considered an effective method for a qualitative structural assessment of existing masonry structures, and few applications of STs on the archaeological structures at the Pompeii site are also available [10,11]. However, the available set of data is still limited and robust empirical correlations are still lacking.

This paper presents a wide experimental program aimed at the characterization of rubble stone masonry panels reproducing one of the most common masonry typologies at the archaeological Pompeii site (Italy), the ancient building technique *opus incertum*. The masonry panels were produced based on a deep survey of the ancient technique and using original rock units and new mortar compliant with the ancient one. This latter was produced with precious volcanic sand coming from the same volcanic region where the ancient builders collected their *pulvis puteolanus*, i.e. the Phlegrean area, next to the Bay of Naples. The characterization involved extensive sonic pulse velocity tests, three diagonal compression tests carried out in an open space laboratory equipped at the Pompeii site, and five axial compression tests conducted in the laboratory of the University of Naples.

In the following, the experimental program is presented along with the results provided by tests. Moreover, a discussion and comparison of the results obtained from the different NDTs and DTs performed and a comparison with available data from literature is presented.

2 EXPERIMENTAL PROGRAMME

Given the impossibility of performing DTs or MDTs on archaeological structures, this experimental program involved the realization and characterization through NDTs and DTs of Pompeii-like rubble stone masonry panels compliant with the ancient building technique *opus*

incertum. The panels were built by using original stone units collected within the archaeological excavations started at *Regio V* in 2018 and mortar compatible with the ancient one, i.e. made with lime putty and pozzolan with a binder to aggregate ratio 1:3 by volume. The pozzolan used in the mortar was precious volcanic sand coming from the same volcanic region where the ancient builders collected their *pulvis puteolanus*, i.e. the Phlegrean area, next to the Bay of Naples. The masonry panels were constructed by experienced masons inside a specifically dedicated test area at *Regio V* (Figure 1). Indeed, a first part of the experimental program was carried out in the on-site test area, involving: i) realization and storage of the panels; ii) execution of NDTs, i.e. sonic pulse velocity tests (STs) at different ages; iii) execution of DTs, i.e. diagonal compression tests. After that, the final phase of the experimental program was carried out in the laboratory of the University of Naples, involving the execution of axial compression tests on masonry specimens extracted from the undamaged portions of the panels after the diagonal compression tests. In the following, details of the experimental program are reported.

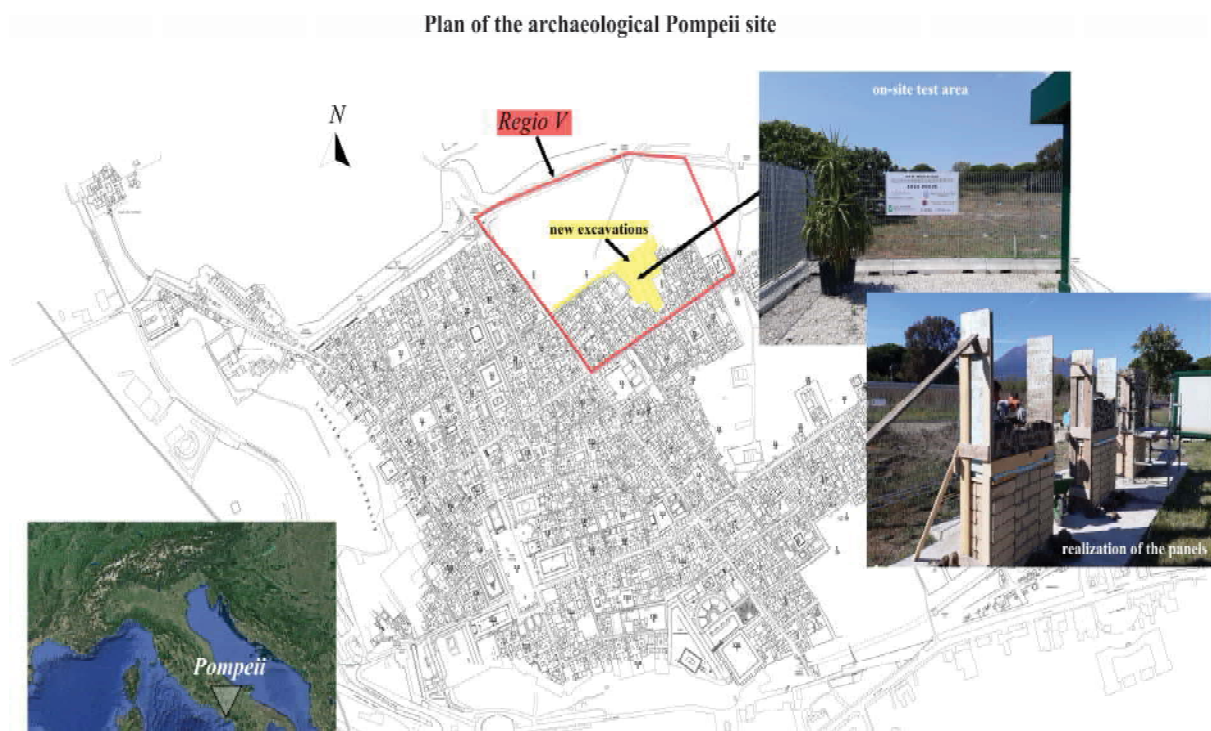


Figure 1: Plan of the archaeological Pompeii site with the indication of the localization of the city of Pompeii in Italy; the borders of the *Regio V*; the area of the new excavations at the *Regio V*; the localization and pictures of the on-site test area.

2.1 Pompeii-like masonry panels

For the production of the panels, detailed geometric and material surveys of archaeological *opus incertum* masonry structures were firstly carried out (Figure 2 (a)), then stone units belonging to collapsed masonry structures found throughout the excavations at *Regio V* were collected (Figure 2 (b)). According to this preliminary study, the panels were realized with two external leaves made of about 30% of mortar and 70% of irregularly shaped units of lava, travertine, and foam lava, with few fragments of other materials. The internal core was made of abundant mortar and stone fragments and smaller units (Figure 2 (c)). The wall thickness was defined as equal to 0.45m, based on the values detected on similar walls, and no transversal connecting elements between the external leaves were inserted. The panels had a size of 1.20m x 1.20m x 0.45m, according to the standard ASTM E 519-02 regarding the execution of diagonal compression tests on masonry wall panels [12]. They were progressively identified as S1, S2, and S3 (Figure 6Figure 2 d) [13]. Mechanical characterization of the stone units and mortar constituting the panels was also performed [14,15]. The tests performed

on the stone units resulted in mean bulk density and compressive strength equal to 2358 kg/m³ and 38 MPa, 1380 kg/m³ and 6 MPa, 859 kg/m³ and 4 MPa, for the lava, travertine and foam lava, respectively. The tests performed on the mortar specimens resulted in mean bulk density and compressive strength equal to 1105 kg/m³ and 3 MPa, at two months of curing.

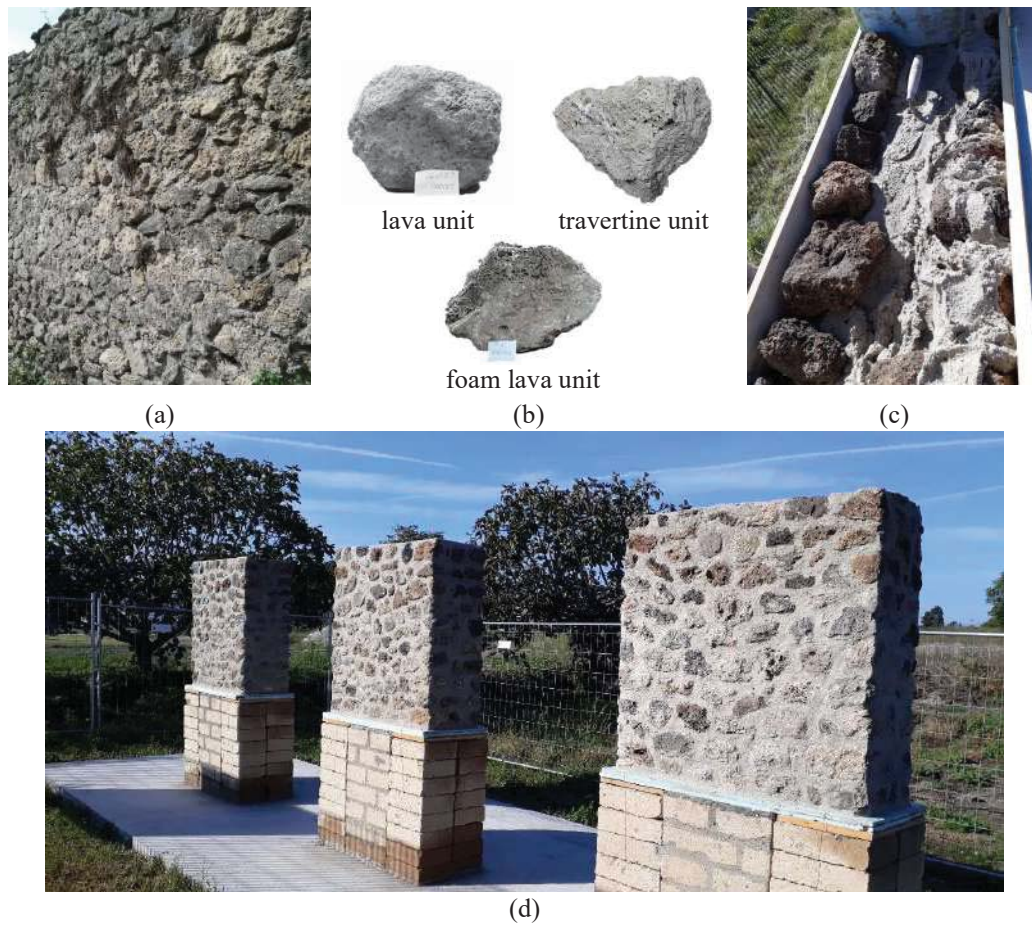


Figure 2: Pompeii-like masonry panels: view of archaeological *opus incertum* masonry structure (a); typologies of the stone units used to make the panels (b); cross-section of a panel during the construction phase (c) and view of the completed panels (from the right S1, S2, and S3) (d).

2.2 Non-destructive testing

An extensive program of STs was carried out on the new masonry panels to provide useful data for comparison with archaeological *opus incertum* at the site, to monitor the hardening process in the panels, and to assess the presence of any correlation with results of DTs. The tests were performed by transparency, employing a piezoelectric hammer transducer and a piezoelectric broadband receiver, with 55 KHz resonance frequency and internal pre-amplification of 20 dB, and a coupling material between the receiver and the masonry surface. The tests were carried out at 12, 44 and 148 days from the realization of the panels; a modular mesh, 0.10m spaced, with 121 acquisition points was investigated on each panel (Figure 3). For each point, the velocity was calculated from the conventional path length, equal to the thickness of the panel, divided by the mean of three recorded values of travel time. Thus, the mean velocity for each panel at each age was calculated as the mean of the points.

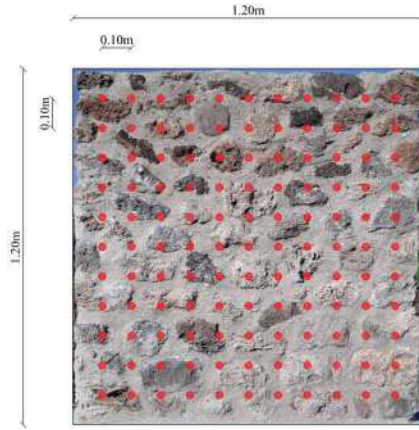


Figure 3: Modular mesh 1.00m x 1.00m, 0.10m spaced, on the masonry panels S1.

2.3 Destructive testing

After the Sts, the experimental program involving DTs started with the in-situ diagonal compression tests (these were carried out after 5 days from the last STs, i.e. 153 days from the production of the panels), to obtain essential information on the shear behavior of the *opus incertum* masonry and to correlate these results with those provided by DTs. The tests were performed with a specific custom-designed set-up for the outdoor tests. According to the standard ASTM E 519-02 [12], the shear stress, τ , the shear strain, γ , and the shear modulus of elasticity, G , were derived from the tests. In this formulation, a uniform shear stress state is assumed and the tensile strength is equal to the shear capacity, τ_{\max} . The tests were carried out with single loading ramps under displacement control with a rate of 0.02mm/s. Devices for the measurement of the in-plane displacements were applied on the two leaves of each panel [13].

Once diagonal tests were completed, five masonry specimens were extracted from the undamaged portion of the panels for the execution of axial compression tests in the laboratory. The masonry specimens were identified as C1, C2, C3, C4 and C5. The first test, performed on C1, was carried out with a single loading ramp to determine the specimen capacity, the following ones involved cyclic testing protocols set between 10% and 50% of the maximum load attained in the first test. This to investigate the elastic behavior of the specimen, according to what is suggested in the standard EN 1052-1 [16]. Note that two cycles were performed with C2, then three cycles were performed with C3, C4 and C5. For each test, the axial compressive strength, f_c , was evaluated as the maximum compressive stress achieved by the panel, σ_{\max} , i.e. the maximum compression load recorded divided by the area of the loaded cross-section. The elastic modulus, E , was evaluated by making a linear least-squares fit the loading ramp of the cycle in the stress-strain curves and calculating the mean of the slopes of the three obtained lines, as shown in Figure 4.

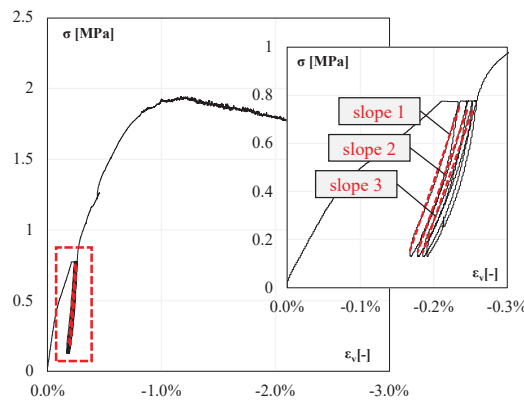


Figure 4: Scheme of determination of the mean elastic modulus of the three loading/unloading cycles of each test.

Considering the anisotropy of masonry specimens, two different Poisson ratios were also calculated for each specimen: in the horizontal, v_h (1), and transversal, v_t (2), direction.

$$v_h = \frac{\varepsilon_h \left(\frac{l}{3} \right)}{\varepsilon_v \left(\frac{l}{3} \right)} \quad (1)$$

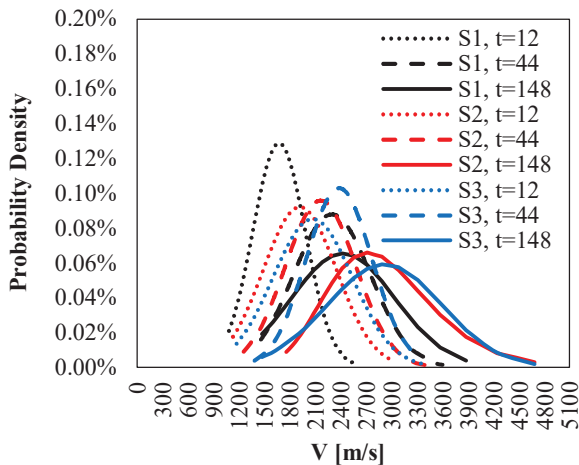
$$v_t = \frac{\varepsilon_t \left(\frac{l}{3} \right)}{\varepsilon_v \left(\frac{l}{3} \right)} \quad (2)$$

where $\varepsilon_v (1/3)$, $\varepsilon_h (1/3)$ and $\varepsilon_t (1/3)$ are the vertical, horizontal and transversal strain corresponding to one-third of the maximum compressive stress, being each of them calculated as the mean of the values recorded on loading ramps of the loading/unloading cycles.

3 EXPERIMENTAL RESULTS

3.1 Sonic pulse velocity tests

Figure 5 summarizes the results of the STs for each panel at 12, 44 and 148 days in terms of probability density distributions of the velocities and mean velocities with their coefficients of variation, CoV. The velocities detected on the panels increased with time, consistently with the evolution of the hardening process in the mortar. The mean velocity at 144 days resulted equal to 2428m/s, 2923m/s and 2767m/s, for S1, S2 and S3 respectively.



Specimen	$V_{t=12}$ [m/s]	$V_{t=44}$ [m/s]	$V_{t=148}$ [m/s]
S1	1673 (CoV = 19%)	2297 (CoV = 20%)	2428 (CoV = 25%)
S2	1919 (CoV = 23%)	2163 (CoV = 19%)	2923 (CoV = 23%)
S3	2070 (CoV = 23%)	2381 (CoV = 16%)	2918 (CoV = 23%)
mean	1890 (CoV = 11%)	2280 (CoV = 5%)	2767 (CoV = 11%)

Figure 5: Probability density distributions of the velocities recorded at 12, 44 and 148 days for each panel and summary of the mean velocities with their coefficients of variation.

3.2 Diagonal compression tests

Table 1 reports the main outcomes of the diagonal compression tests, in terms of maximum shear stress attained, τ_{max} , shear strain corresponding to the maximum shear stress, γ_{tmax} , shear strain corresponding to the conventional failure assumed as strength degradation of 20% of the peak force, γ_u , and the shear modulus of elasticity, G . This latter was not derived for S3 due to inaccurate local recordings. Different values of the shear capacities were detected, with the maximum stress attained by S2 (i.e. 0.27 MPa) and the minimum one attained by S1 (i.e. 0.19 MPa). The values of the shear strain corresponding to the maximum shear stress and of the shear modulus of elasticity were similar among the panels, while a certain variability was again detected in terms of shear strain at the conventional failure. The variability detected in the outcomes was probably related to the different specific arrangements and quantities of the single building materials in each panel.

Table 1: Main outcomes of the on-site diagonal compression tests.

Specimen	τ_{\max} [MPa]	$\gamma_{\tau\max}$ [%]	γ_u [%]	G [MPa]
S1	0.19	0.16	0.90	522
S2	0.27	0.17	2.13	520
S3	0.25	0.16	1.24	-
mean	0.23 (CoV=16%)	0.16 (CoV=3%)	1.42 (CoV=44%)	521

The failure mode was consistent among the panels. It resulted in the development of the main crack along the compressed diagonal dividing each panel into two almost symmetric parts. The crack pattern mainly developed in the mortar, but occasionally involved rock units, particularly travertine and foam lava. Indeed, this latter had a lower compressive strength compared to the lava. Figure 6 shows each panel at the end of the diagonal compression test with the indication of the final crack pattern and the masonry specimens extracted from the undamaged portions for the execution of the axial compression tests.

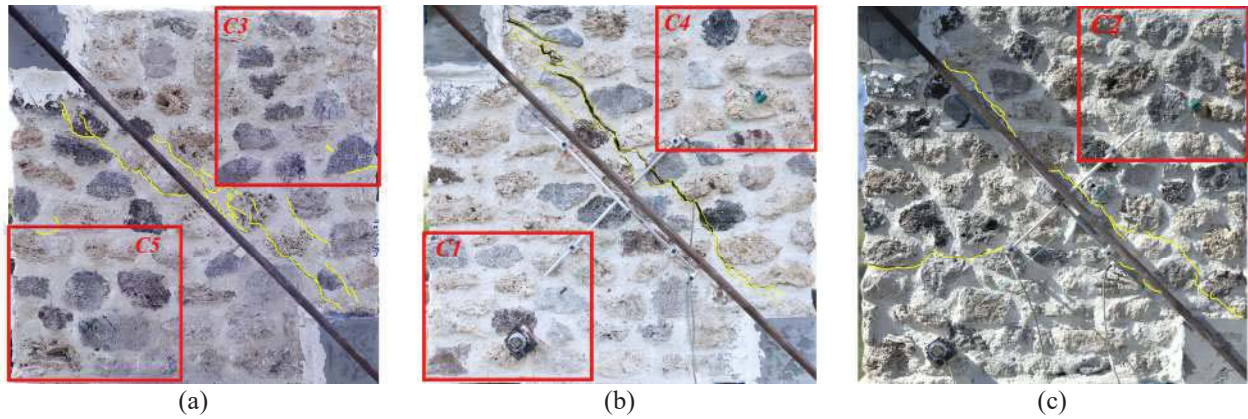


Figure 6: Crack pattern of the masonry panels S1 (a), S2 (b) and S3 (c) with the indication (red boxes) of the masonry specimens extracted for the execution of the axial compression tests.

3.3 Axial compression tests

Table 2 reports the main outcomes of the axial compression tests, in terms of maximum compressive stress attained, σ_{\max} , vertical, horizontal and transversal strain corresponding to the maximum compressive stress, $\varepsilon_{\sigma\max}$, $\varepsilon_{h\sigma\max}$ and $\varepsilon_{t\sigma\max}$, vertical strain corresponding to the conventional failure assumed as a strength degradation of 20% of the peak force, ε_u , modulus of elasticity, E, Poisson ratios in the horizontal, ν_h , and transversal, ν_t , directions. Note missing values of ε_u are related to the fact that the conventional failure was not achieved and missing values of ν_h and ν_t are related to inaccurate local recordings. The outcomes of the axial compression tests are also summarized in Figure 7, which plots the compressive stress-vertical strain relationships for C1, C2, C3, C4 and C5. Specimen C4 showed the highest values of compressive stress and corresponding vertical strain, while C3 showed the lowest ones. C3 also showed the lowest elastic modulus, while the highest value was showed by C2. The highest variability of the results was detected for the Poisson ratios. However, the overall dispersion of these results has been considered acceptable considering the proper inhomogeneity of the masonry typology and consistent with what was found from the sonic tests and diagonal compression tests.

Table 2: Main outcomes of the axial compression tests.

Specimen	σ_{\max} [MPa]	$\varepsilon_{\sigma\max}$ [%]	ε_u [%]	E [MPa]	ν_h [-]	ν_t [-]
C1	1.52	0.59	-	-	0.08	-
C2	1.49	0.52	-	1253	0.24	0.03
C3	0.96	0.40	-	843	-	-
C4	1.95	1.17	2.77	1053	0.07	0.08
C5	1.46	0.89	2.37	862	-	-
mean	1.48	0.71	2.57	1003	0.13	0.05
	(CoV=24%)	(CoV=44%)	(CoV=11%)	(CoV=19%)	(CoV=75%)	(CoV=66%)

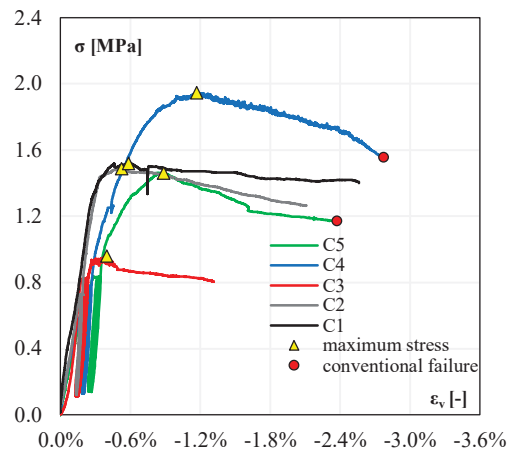


Figure 7. Compressive stress-vertical strain curves.

Figure 8 shows the specimens at failure. For all the specimens, the first cracks were vertical and thin and involved the mortar matrix, finally, the expulsion of material outward occurred and several stone units were also damaged. The units involved in the cracks were travertine and foam lava, consistently with what was found in the diagonal compression tests. In many cases, the first cracks developed in the central part of the cross-section of the specimens. However, clear detachments of the external leaves from the internal core were not detected on the final crack pattern but cracks distributed over the entire cross-section of the wall. Indeed, due to the irregular arrangement of the masonry assemblage along with its thickness, the separation between the core and the leaves was not sharply defined.



(a)

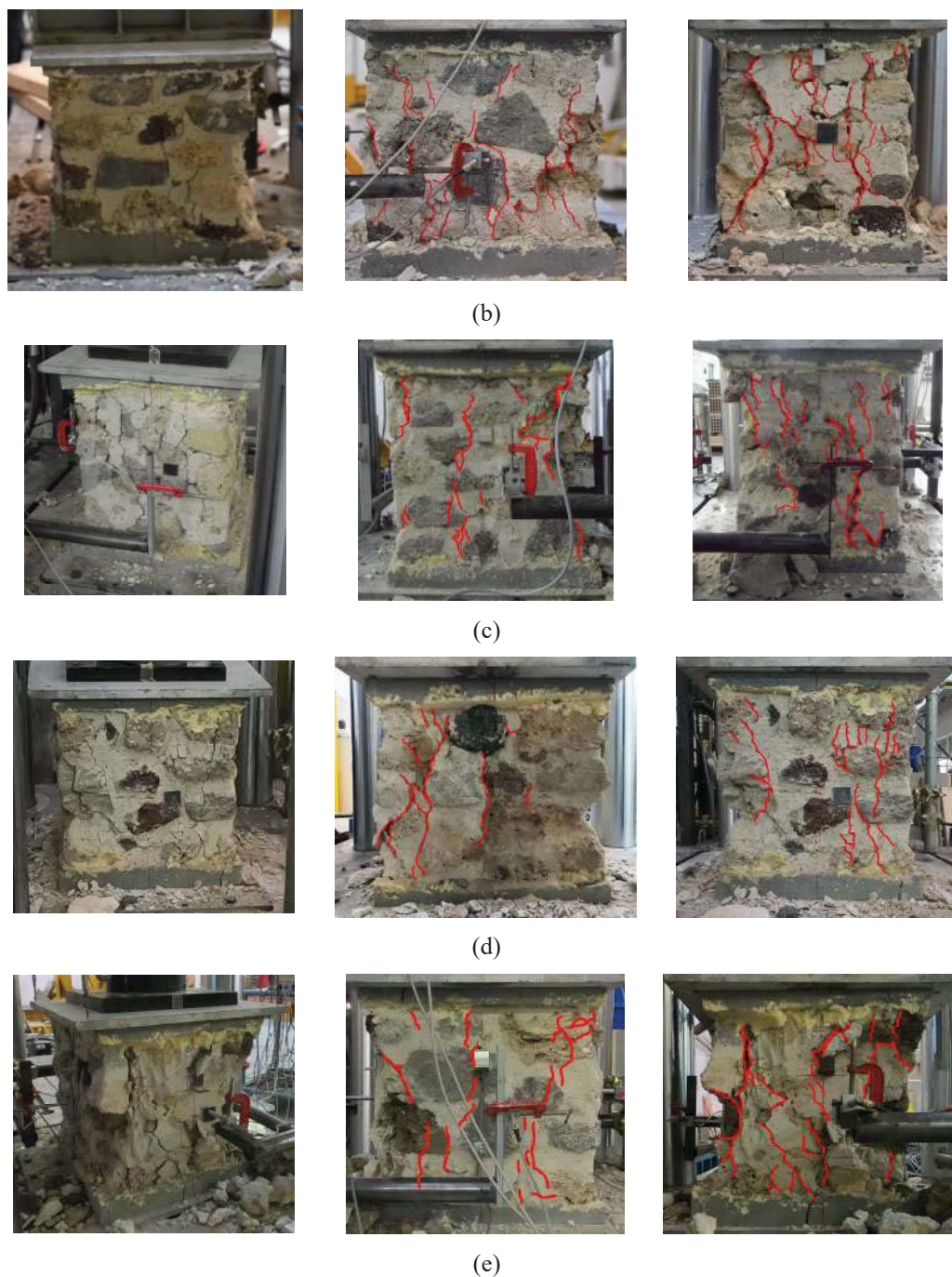


Figure 8. Specimens crack pattern on two orthogonal sides of the panel C1 (a), C2 (b), C3 (c), C4 (d) and C5 (e).

4 DISCUSSION OF THE RESULTS AND COMPARISONS

Table 3 summarizes the main results of the mechanical characterization through NDTs and DTs of the Pompeii-like masonry panels.

Table 3. Main experimental outcomes of sonic pulse velocity tests, diagonal compression tests and axial compression tests.

	V	τ_{\max}	G		σ_{\max}	E	v_h	v_t
3 masonry panels 1.20m x 1.20m x 0.45m	[m/s]	[MPa]	[MPa]	5 masonry specimens 0.45m x 0.45m x 0.45m (average sizes)	[MPa]	[MPa]	[-]	[-]
	2767	0.23	521		1.48	1003	0.13	0.05
	11%	16%	-		24%	19%	75%	-

The final mean velocity achieved by the panels ($V=2767\text{m/s}$, $\text{CoV}=11\%$) can be associated with good-quality stone masonry, according to a common classification found in the literature [17] (Table 4). This result is consistent with what was found in similar experimentations on stone masonry panels reproducing historical typologies, with good compactness [18,19]. Instead, lower values of velocity were found for historical or archaeological masonry structures [6,10,11] or reproduced panels incorporating flaws or inclusions [20]. Indeed, the sonic pulse velocity is greatly affected by differences in the building materials and inner and superficial conditions of the structure.

Table 4. Relations between the masonry overall conditions and the mean sonic pulse velocity value.

	Poor-quality masonry	Medium-quality masonry	Good-quality masonry
Range of velocities [17]	< 1500m/s	1500m/s - 2500m/s	2500m/s <

Table 5 reports a literature review of the main results obtained from diagonal compression tests and axial compression tests on stone masonry panels reproducing traditional typologies. Despite the general scatter, the obtained results are comparable with the available data from the literature. In particular, the obtained shear strength is comparable with the experiments by Milosevic et al., Gattesco et al. and Magenes et al., and lower value of the shear modulus compared to Gattesco et al. and Magenes et al. was probably related to a lower amount of mortar and more regular textures in the specimens investigated in these latter [3–5]. Moreover, as regards the compressive strength and modulus of elasticity lower values found in this study compared to available literature data were probably related to relatively low capacity, deterioration and pre-existing damage of several of the archaeological stone units used in this work.

Table 5. Literature review of experimental outcomes of diagonal compression tests and axial compression tests on reproduced stone masonry panels.

Source	Masonry type	$\tau_{\text{mean, ASTM}}$ [MPa]	$G_{\text{mean, ASTM}}$ [MPa]	σ_{max} [MPa]	E [MPa]	v_h [-]	v_t [-]
Milosevic et al. 2013	Rubble stone masonry, made with hydraulic lime-based mortar and limestone units	0.29	321	8.01	1640	-	-
Gattesco et al. 2015*	Rubble stone masonry, made with two types of lime-based mortar	0.19	1051	-	-	-	-
Magenes et al. 2010	Reproduced rubble stone masonry, made with hydraulic lime based mortar and calcareous sandstone units	0.20	840	3.28	2550	0.19	0.15
Valluzzi 2000	Rubble stone masonry, made with a lime-based mortar and rough-shaped limestone blocks bonded in sub-horizontal courses (original panels)	-	-	1.82	1858	-	-
	(injected panels)	-	-	2.46	2347	-	-
Silva 2012	Rubble stone masonry, made with a hydraulic lime-based mortar and rough-shaped limestone blocks bonded in sub-horizontal courses (original panels)	-	-	2.1-2.9	1837-2335	0.01-0.67	0.03-0.12
	(injected panels)	-	-	3.7-5.4	2565-5205	0.003-0.09	0.02-0.87
<i>*results were adapted to the ASTM formulation for the comparison with the results of the present study</i>							

Despite the number of data collected in this investigation is not enough to define reliable correlations, a preliminary correlation between STs and DTs results can be formulated using the obtained experimental results. Indeed, the results of the last STs were in good agreement with the results of the diagonal compression tests, with the maximum shear stress achieved being higher for

the panels which showed the higher mean sonic velocity (i.e. $V=2923\text{m/s}$ and $\tau_{\max}=0.27$ for S2, $V=2918\text{m/s}$ and $\tau_{\max}=0.25$ for S3, and $V=2428\text{m/s}$ and $\tau_{\max}=0.19$ for S1) (Figure 9).

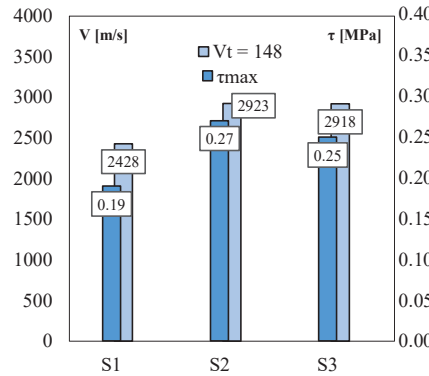


Figure 9: Values of the mean sonic pulse velocity at 148 days and maximum shear stress achieved by the masonry panels 1.20m x 1.20m x 0.45m with diagonal compression tests.

On the contrary, the results obtained from STs in terms of modulus of elasticity of the masonry did not comply with the one obtained from the DTs. Indeed, from the well-known formula defined for homogeneous materials and also applied to concrete [21] (3):

$$E_d = V^2 \frac{\rho(1-2\nu)(1+\nu)}{(1-\nu)} \quad (3)$$

with V equal to the mean sonic velocity of the specimen at 148 days, ν equal to the mean horizontal Poisson ratio resulting from the axial compression tests and ρ equal to the bulk density of the masonry calculated with a simplified homogenization procedure from the bulk density of the single building materials (i.e. equal to 1406 kg/m^3), the resulting dynamic modulus of elasticity, E_d , is equal to 10058 MPa, i.e. ten times higher than the mean value obtained from the axial compression tests. This result shows that eq. (3) is not reliable to predict the elastic modulus of rubble masonry.

5 CONCLUSIONS

This paper presents the results of a wide experimental program aimed at the mechanical characterization of masonry panels reproducing the ancient technique *opus incertum* found at the Pompeii archaeological site. Non-destructive tests (NDTs) and destructive tests (DTs) were carried out on masonry panels built according to the traditional technique by using original rock units and a typical mortar mixture. The experimental program firstly involved sonic pulse velocity tests and diagonal compression tests on three masonry panels, 1.20m x 1.20m x 0.45m. Then, axial compression tests on five masonry specimens extracted from the three panels were carried out.

The following main conclusions may be drawn:

- The panels showed a mean sonic pulse velocity at 148 days after their construction equal to 2767, $\text{CoV} = 11\%$;
- The on-site diagonal compression test resulted in a mean shear strength equal to 0.23 MPa, $\text{CoV} = 16\%$, and a mean shear modulus of elasticity equal to 521 MPa. These results are comparable with what found in similar experiments on other typologies of reproduced stone masonry structures;
- The axial compression tests resulted in a mean compressive strength of 1.48 MPa, $\text{CoV} = 24\%$, and mean modulus of elasticity equal to 1003 MPa, $\text{CoV} = 0.19\%$;

- The Poisson ratios in the horizontal and transversal direction derived from the axial compression tests resulted equal to 0.13, CoV = 75%, and 0.05, respectively. High scattering of these values was also found in other studies;
- The final mean velocity resulting from the sonic tests was consistent with the results of the diagonal compression tests, with the higher velocities showed by the panels that also achieved the maximum shear strength;
- The mean dynamic elastic modulus calculated from the sonic pulse velocity was found to be ten times higher than the one obtained from the axial compression tests.

The information here provided could support the assessment of several archaeological masonry structures in the exceptional context of the Pompeii site and similar archaeological and historical contexts.

ACKNOWLEDGMENTS

The authors acknowledge the former director of *Parco Archeologico di Pompei (PAP)*, Prof. Massimo Osanna; the Lead Project Manager of the new works in *Regio V*, Arch. Annamaria Mauro; the Managers of the *Laboratorio di Ricerche Applicate* of *PAP*, Archt. Bruno De Nigris and Dr. Alberta Martellone; the Director of works in *Regio V*, Archt. Gianluca Vitagliano; the member of the Technical Secretariat of the Great Pompeii Project Eng. Vincenzo Calvanese and the research center *STRESS S.c.a.r.l.* for the support provided to this research.

REFERENCES

- [1] ICOMOS, Recommendations for the analysis, conservation and structural restoration of architectural heritage, (2003) 1–37. https://ancientgeorgia.files.wordpress.com/2012/04/recommendations_icomos-principles-and-guidelines.pdf.
- [2] Italian Ministry of Cultural Heritage and Activities, Linee guida per la valutazione e la riduzione del rischio sismico del patrimonio culturale con riferimento alle Norme tecniche per le costruzioni di cui al decreto del Ministero delle Infrastrutture e dei trasporti del 14 gennaio 2008, (2010).
- [3] G. Magenes, A. Penna, A. Galasco, M. Rota, Experimental characterisation of stone masonry mechanical properties, 8th Int. Mason. Conf. 2010. (2010) 1–10.
- [4] N. Gattesco, I. Boem, A. Dudine, Diagonal compression tests on masonry walls strengthened with a GFRP mesh reinforced mortar coating, Bull. Earthq. Eng. 13 (2015) 1703–1726.
- [5] J. Milosevic, A.S. Gago, M. Lopes, R. Bento, Experimental assessment of shear strength parameters on rubble stone masonry specimens, Constr. Build. Mater. 47 (2013) 1372–1380. <https://doi.org/10.1016/j.conbuildmat.2013.06.036>.
- [6] G. Riva, C. Bettio, C. Modena, The use of sonic wave technique for estimating the efficiency of masonry consolidation by injection, IB2MAC - 11th Int. Brick Block Mason. Conf. Shanghai, China. (1997) 28–39.
- [7] B. Silva, M. Dalla Benetta, F. Da Porto, M.R. Valluzzi, Compression and sonic tests to assess effectiveness of grout injection on three-leaf stone masonry walls, Int. J. Archit. Herit. 8 (2014) 408–435. <https://doi.org/10.1080/15583058.2013.826300>.
- [8] M. Berra, A. Faticcioni, Non destructive evaluation of the efficacy of masonry strengthening by grouting techniques, (1992) 1457–1464.
- [9] L.F. Miranda, J. Rio, J. Miranda Guedes, A. Costa, Sonic Impact Method - A new technique for characterization of stone masonry walls, Constr. Build. Mater. 36 (2012) 27–35. <https://doi.org/10.1016/j.conbuildmat.2012.04.018>.
- [10] H. Dessales, Villa de Diomède. Campagne d'étude 2015, Chronique des activités archéologiques de l'École française de Rome, 2015. <http://cefr.revues.org/1293>.
- [11] M.R. Valluzzi, F. Lorenzoni, R. Deiana, S. Taffarel, C. Modena, Non-destructive

- investigations for structural qualification of the Sarno Baths, Pompeii, *J. Cult. Herit.* 40 (2019) 280–287. <https://doi.org/10.1016/j.culher.2019.04.015>.
- [12] ASTM, E 519-02. Standard Test Method for Diagonal Tension (Shear) in Masonry Assemblages, *Am. Soc. Test. Mater.* (2002) 5. <https://doi.org/10.1520/E0519>.
 - [13] F. Autiero, G. De Martino, M. Di Ludovico, A. Prota, Mechanical performance of full-scale Pompeii-like masonry panels, *Constr. Build. Mater.* 251 (2020) 118964. <https://doi.org/10.1016/j.conbuildmat.2020.118964>.
 - [14] F. Autiero, G. De Martino, M. Di Ludovico, A. Prota, Mechanical properties of rock units from the Pompeii archaeological site, Italy, in: P. De Wilde (Ed.), *Struct. Stud. Repairs Maint. Herit. Archit.* XVI, 2019: pp. 341–350. <https://doi.org/10.2495/STR190291>.
 - [15] F. Autiero, G. De Martino, M. Di Ludovico, A. Prota, Mechanical behavior of ancient mortar specimens from Pompeii site, in: *Proc. 7th Int. Conf. Comput. Methods Struct. Dyn. Earthq. Eng. (COMPDYN 2015)*, Institute of Structural Analysis and Antiseismic Research School of Civil Engineering National Technical University of Athens (NTUA) Greece, Athens, 2019: pp. 1251–1262. <https://doi.org/10.7712/120119.6994.18836>.
 - [16] CEN, EN 1052-1. Methods of test for masonry - Part 1: Determination of compressive strength, *Eur. Comm. Stand.* (1999) 10969.
 - [17] M.C. Forde, K.F. Birjandi, A.J. Batchelor, Fault detection in stone masonry bridges by nondestructive testing, in: *Proc. 2nd Int. Conf. Struct. Faults Repair, Engineering Technics Press*, Edinburgh, 1985: pp. 373–379.
 - [18] B.L. Silva, *Diagnosis and Strengthening of Historical Masonry Structures: Numerical and Experimental Analysis*, 2012.
 - [19] M.R. Valluzzi, *Comportamento meccanico delle murature consolidate con materiali e tecniche a base di calce*, Università degli studi di Trieste, 2000.
 - [20] M.R. Valluzzi, E. Cescatti, G. Cardani, L. Cantini, L. Zanzi, C. Colla, F. Casarin, Calibration of sonic pulse velocity tests for detection of variable conditions in masonry walls, *Constr. Build. Mater.* 192 (2018) 272–286. <https://doi.org/10.1016/j.conbuildmat.2018.10.073>.
 - [21] ASTM, C 597 - 02. Pulse Velocity Through Concrete, *United States Am. Soc. Test. Mater.* 04 (2003) 3–6. <https://doi.org/10.1520/C0597-09>.

PRELIMINARY NONLINEAR STATIC AND DYNAMIC ANALYSIS OF THE MAIN PYRAMID OF HUACA DE LA LUNA, PERU

Selman Tezcan¹, Miguel A. Pando², Rafael Aguilar³, Benjamin Castañeda⁴,

Carol Rojas⁵, Renato Perucchio¹

¹ Department of Mechanical Engineering, University of Rochester, Rochester, New York, USA
email: selmantezcan@rochester.edu, rlp@me.rochester.edu

² Department of Civil, Architectural and Environmental Engineering, Drexel University, Philadelphia,
Pennsylvania, USA
email: map522@drexel.edu

³ Department of Civil Engineering, Pontificia Universidad Católica, del Perú - PUCP, Lima, Peru
email: raguilar@pucp.edu.pe

⁴ Department of Electrical Engineering, Pontificia Universidad Católica, del Perú - PUCP, Lima, Peru
email: castaneda.b@pucp.edu.pe

⁵ Research Division, Arkeos Asesores y Consultores, Lima, Peru
email: carolrojas.vega@gmail.com

Abstract

Huaca de la Luna is a monumental earthen complex located near Trujillo in the North coast of Peru built from 200 AD to 850 AD by the Moche civilization on the slopes of the Cerro Blanco mountain. The principal structure is a massive stepped pyramid built with millions of adobe bricks. The pyramid presents severe structural damage near the NW corner. The static and dynamic response of the pyramid is analyzed using 2D plane strain nonlinear FE models representing the east-west middle section together with the underlying soil profiles. We perform a sensitivity analysis of the static and dynamic response to (a) the pyramid stepped west side profile, (b) the underlying soil and bedrock configuration, and (c) the adobe material tensile strength. Under static conditions the models develop internal fractures but in none of the cases considered these grow to cause the structural collapse of the west side. The west side suffers complete collapse under horizontal accelerations as low as 0.135g.

Keywords: massive earthen construction, archaeological heritage, dynamic analysis, structural failure, non-linear explicit FE analysis, soil-structure interaction.

1 INTRODUCTION AND OBJECTIVES

1.1 Historical introduction

The archaeological site of Huaca de la Luna, or Temple of the Moon, is a monumental earthen complex built by the Moche civilization approximately from 200 AD to 850 AD and located near the modern city of Trujillo in the North coast of Peru. Huaca de la Luna was erected on the lower slopes of the Cerro Blanco as part of a sprawling urban center considered to be the capital of the Moche state. The Moche is one of the most important pre-Inca culture, recognized for its distinctive ceramics and architectural decorations [1]. Huaca de la Luna is considered one of the best examples of the Moche cultural achievements because of its well-preserved mural bas-reliefs particularly on the north façade of its main pyramid [2]. After extinction of the Moche culture, circa 850 A.D., the complex was naturally buried under eolian sand deposits, which reduced exposure to seismic loading demands during possible historical earthquakes in that region of Peru. The sand deposits also protected the extensive bas-relief on the north façade from the erosion caused by El Niño torrential rains. The archaeological works that started in the beginning of the 90s has systematically unearthed and exposed the entire Huaca de la Luna complex [2]. Archeologists working at the site interpret Huaca de la Luna as consisting of three pyramids composed by large platforms at various levels, connected by open spaces as reconstructed in Fig. 1(a). Typical of Moche monumental architecture, the complex was entirely built using millions of adobe bricks connected with mud mortar.

The principal structure is a massive stepped pyramid – shown in its present state in Fig. 1(b) – which served for leading political and religious ceremonial events including human sacrifices and elite burials. This pyramid is the result of a succession of construction stages, each consisting in a taller and larger building erected on top of the previous one, so that the new structure encapsulates in its interior all preceding constructions. Each stage was built by erecting adjacent vertical piers of well textured adobe masonry. The pyramid shows signs of extensive anthropogenic and natural damage, primarily in the north and west façade and in the built-up area unearthed by the archaeological excavations on top of the pyramid [2]. A large excavation, attributed to treasure hunting digging during colonial time, cuts deeply in the north façade – Fig. 1(b), while several tunnels dug by treasure hunters pierce the west façade at different levels – Fig. 2(b). Structural damage is mainly present in the NW sector of the pyramid including the substantial collapse of the NW corner – Fig. 2(a) - and large cracks in the upper areas which penetrate deeply in the structural system.

1.2 Research objectives

The main pyramid is the long term objective of a multidisciplinary study focused on determining the structural behavior of its massive core as well as the built up areas on the top of the pyramid under static and dynamic conditions. Previous work has included a detailed laser-scan survey and 3D reconstruction of the pyramid [3], the mechanical characterization of adobe brick and mud mortar construction through lab testing [4, 5] and the geotechnical and geophysical exploration of the foundation soils along the northern façade [6]. These results have been incorporated into a series of preliminary nonlinear FE models of increasing complexity in order to understand how the soil-structure interaction affects the static and dynamic stability of the pyramid. Taking into account the location of the Huaca on the slope of the Cerro Blanco and the results of the geotechnical and geophysical exploration, the FE models assume that the east side of the pyramid is supported on solid bedrock while the west side is built directly on layers of soft sand, with large adobe blocks serving as the foundation layer. Previous research has investigated the relationship between the observed damage and the soft soil support under static

conditions using a simplified 2D plane strain model derived from the geometry and the ground level of the north façade [7]. In the present research we turn our attention to west side of the pyramid to capture the effect of the original ground level, located 5.5 m below the north side. To this end, we develop a refined 2D geometry which includes all superimposed construction layers down to the original ground level as revealed by the archaeological excavations along the west side of the pyramid. Adopting a plane strain formulation, this geometry is used to model the structural behavior of an EW cross section positioned in the middle of the pyramid. We then perform a sensitivity analysis of the static and dynamic response to variations in (a) the pyramid stepped west side profile, (b) the underlying soil and bedrock configuration, and (c) the adobe material tensile strength. In each case, the dynamic response is evaluated by applying lateral and vertical ground accelerations leading to the structural collapse of the stepped (west) side of the 2D model. Following a macro-modeling strategy [8, 9], the analysis is performed in Abaqus CAE/Explicit using the concrete damaged plasticity formulation to represent a continuum with the mechanical properties of adobe [10]. The soil layers are modelled using the Mohr-Coulomb formulation [11]. The specific material parameters are given below in the modeling section.

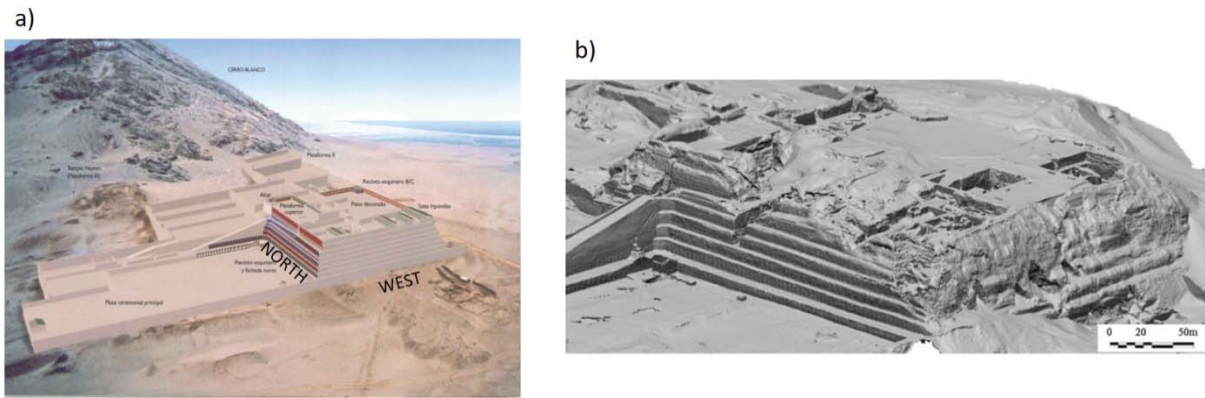


Figure 1: (a) 3D model of Huaca de la Luna [2] and (b) Laser scanning of main pyramid of Huaca de la Luna [3].



Figure 2: (a) Damaged NW corner of the main pyramid, and (b) West façade of the main pyramid (remaining of the buttress system is highlighted) [7].

2 METHODOLOGY

In order to determine the formation of local damage and its evolution into structural failure in the cross-sectional model under static and dynamic conditions, we apply the energy based

approach previously developed for the failure analysis of other concrete damaged plasticity models [12, 13]. In brief, the time-evolution of strain (SE), kinetic (KE), and dissipative energy (PD – due to plastic deformations simulating internal fractures) is used to identify the development of local damage conditions up to structural collapse. Consider a simple vertical wall under lateral acceleration normal to the wall – Fig. 3. After gravitational loading, a uniform monotonically increasing horizontal acceleration is applied to the model using the explicit FE formulation available in Abaqus. The desired quasi-static condition is enforced by adopting long time intervals for the application of both gravitation and lateral accelerations: in the example shown, five seconds for gravitation to increase linearly from 0 to 1 g followed by ten seconds for lateral acceleration to go from 0 to 0.8 g. As long as structural integrity is maintained under increasing lateral acceleration, KE remains negligible during the evolution of quasi-static structural response. Structural failure is associated with the sudden transition from quasi-static to a fully dynamic state and is detected by the accompanying asymptotic growth of KE. PD follows an identical growth pattern, becoming asymptotic at collapse. Notice also that the viscous dissipative energy (VD) produced by the fictitious viscosity parameter used in Abaqus/CAE Explicit to dampen possible oscillatory behavior remains negligible during static conditions and then goes asymptotic at failure.

The examination of the energy plots in Figure 4 suggests complementary ways to associate a specific time interval to failure. KE begins to develop at 7.3 s and becomes asymptotic at 7.9 s, reaching the 10% value of the total internal energy (i.e. SE + PD + KE) at 7.7 s. PD, which can be taken to represent the work necessary to propagate the fractures at the base of the wall, begins to appear at 6.6 s and crosses the SE at 7.85 s. Thus, purely on energy considerations, total failure can be reasonably defined to happen between $t = 7.7$ s (when the loading process cannot anymore be regarded as static) and $t = 7.85$ s (when the PD equals the SE).

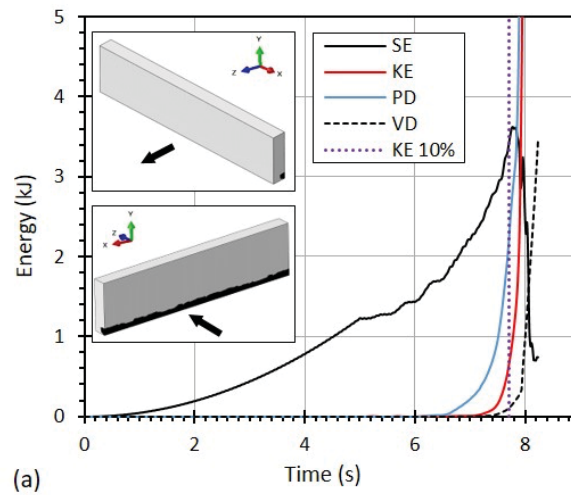


Figure 3: Wall under normal acceleration: energy curves versus analysis time [13].

In the present work, after gravitational loading, lateral accelerations are applied directly to the boundary conditions at bedrock level. In this case, since the entire model is accelerating under inertial forces, KE develops rapidly well before collapse conditions and cannot be used to detect collapse. Under these circumstances, we can still depend on PD to trace the evolution of damage to full collapse, with the latter taken to be the time at which PD equals SE.

The explicit (dynamic) nonlinear FE formulation is preferred over the implicit one because of its capability to sustain large deformations and attendant local material failures, and to capture unequivocally the collapse condition due to lateral accelerations. In fact, in most of the

cases of the present study, it may be not possible to detect the actual failure condition using an implicit nonlinear FE formulation because the analysis terminates due to numerical error (e.g., the stiffness matrix becomes singular) before the actual structural failure occurs. On the negative side, dynamic explicit models are computationally costly. In order to ensure algorithmic convergences, Abaqus Explicit requires the time increments of the order of 10^{-6} second for both gravitation and lateral acceleration.

3 DESIGN OF MODELS

The sensitivity analysis of the static and dynamic response of the EW cross section is based on twenty seven models derived from the combination of three variations of the west side stepped profile, three underlying soil and bedrock configuration, and three adobe material tensile strength.

3.1 West side stepped profile

Based on the archaeological reconstruction, the original platform level on the west side of the pyramid can be located at approximately 25.2 m from the ground [14]. Of relevance for interpreting the geotechnical data, we notice that the ground level on the west side is approximately 5.5 m lower than level of the plaza in front of the north façade. The architecture of the upper west side is well defined in terms of step dimensions. However, due to higher level of damage, less is known with certainty about the original configuration of the lower steps [15, 16]. Thus, working from the archeological cross sections, the upper five steps – extending approximately the 17.1 m in elevation – can be reasonably reconstructed and matched with the identical steps on the north façade. However, the architectural configuration for the remaining 8.1 m is ambiguous and can be interpreted as consisting of either three equally spaced steps, or the combination of two irregular steps (a single higher step replacing the two lowest ones from the previous configuration), or even including a triangular buttress at ground level. The resulting three geometrical configurations – hereafter labelled C1, C2, and C3 – are shown in Fig. 4. Notice that the footprint of the stepped west side changes according to the configuration, with C2 resulting in a substantially smaller footprint than C1 or C3.

3.2 Soil and bedrock configurations

The reconstruction of the foundation soil configuration below the EW cross section is based on the geotechnical data produced during the exploration conducted in front and to the west of the north façade [6, 7]. Figure 5 shows the location where cone penetration tests (CPT) were performed and the resulting EW soil stratigraphy configuration with the ground level set at the base of the north façade, i.e., 5.5 m above the ground level on the west side. Based on additional geological considerations, the stratigraphy illustrated in Fig. 6 is assumed for a NS section taken to the west of the pyramid in correspondence of the CPT02 location (Fig. 5). Starting from these data we construct three alternative bedrock configurations for the EW cross section taken in the middle of the pyramid and referred to the west ground level, see Fig. 6. Configuration B1 assumes the same bedrock position as determined in front of the north façade. For configuration B2, the bedrock layer is shifted uniformly 5 m down. Configuration B3 is derived from B1 by positioning the bedrock 5 m lower only in correspondence of second CPT location. As a result, the amount of soft soil below the pyramid in B2 and B3 is larger than B1, while the contact surface between the pyramid and the soft soil is essentially unchanged between B1 and B3 but increases markedly in B2.

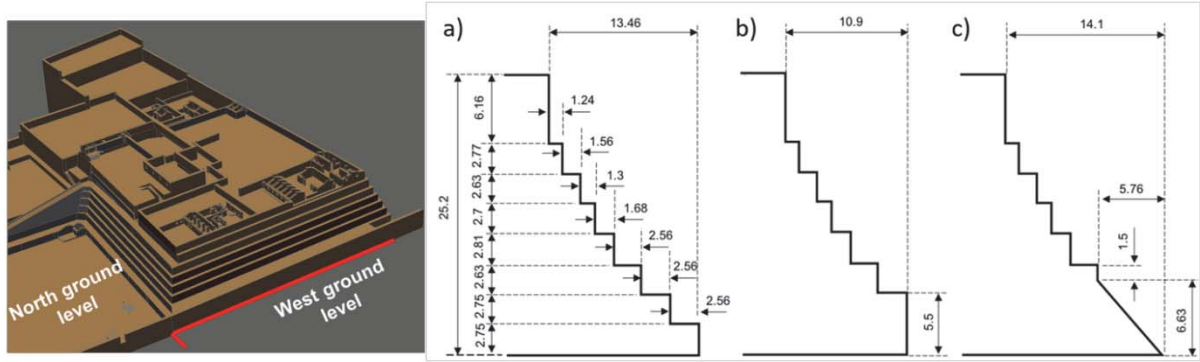


Figure 4: 3D solid model with north and west ground elevation difference on the left, (a) C1 configuration - regular steps, (b) C2 configuration - higher lower step, and (c) C3 configuration - buttress system.

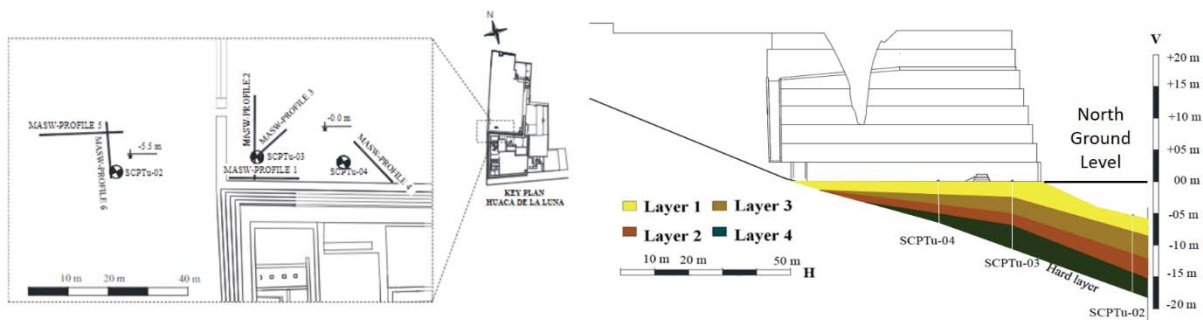


Figure 5: Geotechnical test location (left), bedrock layout and EW soil stratification based on north ground (right) [6, 7].

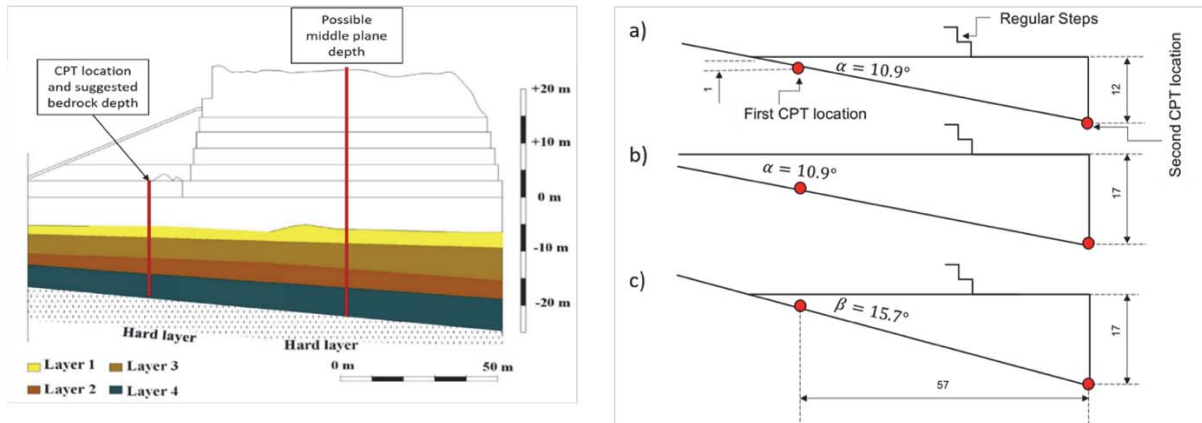


Figure 6: NS bedrock layout and soil stratification (left) [6, 7], and (a) B1 bedrock configuration, (b) B2 bedrock configuration, (c) B3 bedrock configuration.

3.3 Adobe tensile strength

In quasi-brittle materials such as adobe masonry, performing tensile tests are extremely difficult. In this case, tensile properties are derived from the compressive strength σ_c [8, 9]. For the present case we consider three adobe materials characterized by the same compressive behavior but with tensile strength set as $1/10 \sigma_c$ (M1), $1/20 \sigma_c$ (M2), and $1/30 \sigma_c$ (M3). The post-critical tensile stress versus displacement input for the three cases are shown in Fig.7.

4 MATERIAL CHARACTERIZATION

We use the material parameters for the adobe masonry and the soft soil stratification experimentally given in [4, 5] and [6, 7], respectively.

4.1 Concrete damaged plasticity parameters (adobe)

The concrete damaged plasticity in Abaqus/CAE Explicit requires separate characterization for the elastic, plastic, and inelastic behavior. For the elastic part, the density is $\rho = 1735 \text{ kg/m}^3$, the Young's modulus $E = 123 \text{ MPa}$, and the Poisson ratio $\nu = 0.2$. The plastic properties are given in Table 1.

Dilation Angle (°)	Eccentricity	f_b/f_c0	K	Viscosity Parameter
1	0.1	1.16	0.67	1E-8

Table 1: Plastic properties for the adobe material

The inelastic behavior is defined separately for tension and compression. While in [7] the compressive curve is expressed as stress versus total strain, Abaqus requires that the uniaxial compressive response be given in terms of stress versus inelastic strain [10]. The following equation is used to convert the strain data:

$$\varepsilon_i = \varepsilon_t - \sigma/E \quad (1)$$

where ε_i denotes the inelastic strain, ε_t the total strain, E the elastic modulus, and σ the compressive stress. As in [7] the postcritical tensile response is expressed in terms of stress versus crack-opening displacement. The resulting material curves for inelastic compression and tension are given in Fig. 7. The tensile curves for M2 and M3 are derived by scaling the M1 curve by 1/2 and 1/3, respectively.

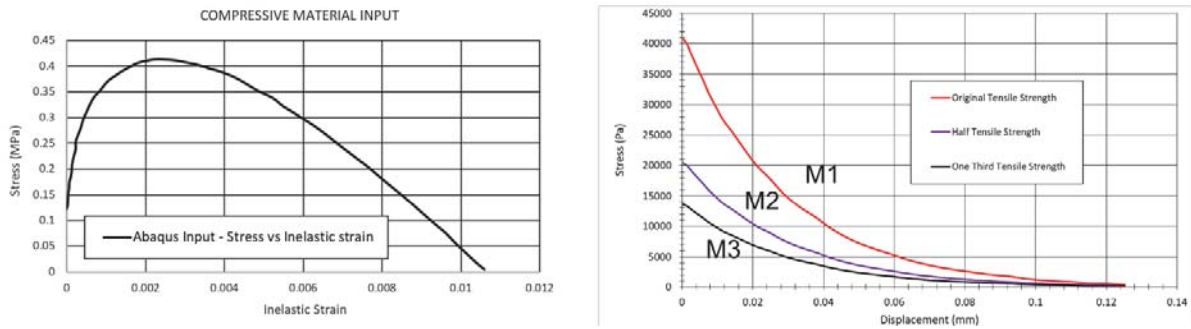


Figure 7: Compressive behavior stress versus inelastic strain (left), material variation on tensile strength as M1, M2 and M3 (right).

4.2 Mohr-Coulomb parameters (soft soils)

For the B1, B2 and B3 soil and bedrock configurations defined above, the soil stratification and related properties follow the CPT data given in [6, 7]. The foundation soils are comprised of layers of eolian sands that range from medium dense near the surface to very dense at deeper depths approaching the bedrock. Each of the four layer shown in Figures 5 and 6 is assumed to behave like a Mohr-Coulomb material with properties given in Table 2. To take into account the marginal cohesion of eolian sand, the cohesion strength of each layer is set to 10 Pa.

Parameter	Layer 1	Layer 2	Layer 3	Layer 4
Mass density (kg/m ³)	1900	2000	2000	2250
Elastic modulus (MPa)	17	43	57	58
Poisson ratio	0.43	0.43	0.42	0.41
Friction angle	40°	42°	43°	43°

Table 2: Material properties of soil layers under Huaca de la Luna [6, 7].

5 RESULTS

Although none of the twenty seven M-B-C pyramid configurations reaches structural failing conditions under static loading, all of them exhibit some level of adobe plasticity at the soil-structure interface in proximity to the west edge. The size and intensity of this damage, the additional development of vertically penetrating fractures originating from the top of the pyramid and of damage along the west steps are all affected by the variation in adobe tensile strength and bedrock configuration, and, in a lesser measure, by the step architecture.

We begin by considering how the variation of underlaying bedrock configurations and adobe tensile strength affect material damage under static conditions. Shown in Fig. 8 is the plastic dissipation energy (PD) measured in the adobe mass at the end of gravitational loading. PD increases with bedrock configurations from B1 to B3 and also, as expected, with the adobe tensile strength decreasing from M1 to M3. It is clear that the bedrock configuration has the highest effect on the plastic dissipation energy. Thus, the combined effect of steeper bedrock angle and deeper soft soil foundation - configuration B3 - produces the highest plastic dissipation on the main pyramid. Considering that, as explained earlier, plastic dissipation is directly proportional to the formation of fracture damage in the adobe material, it can be concluded that the bedrock layout makes the most important contribution to material damage under static conditions. This consideration will be further explored by analyzing the results of the various models built with combination of bedrock layout, step architecture, and material tensile strength.

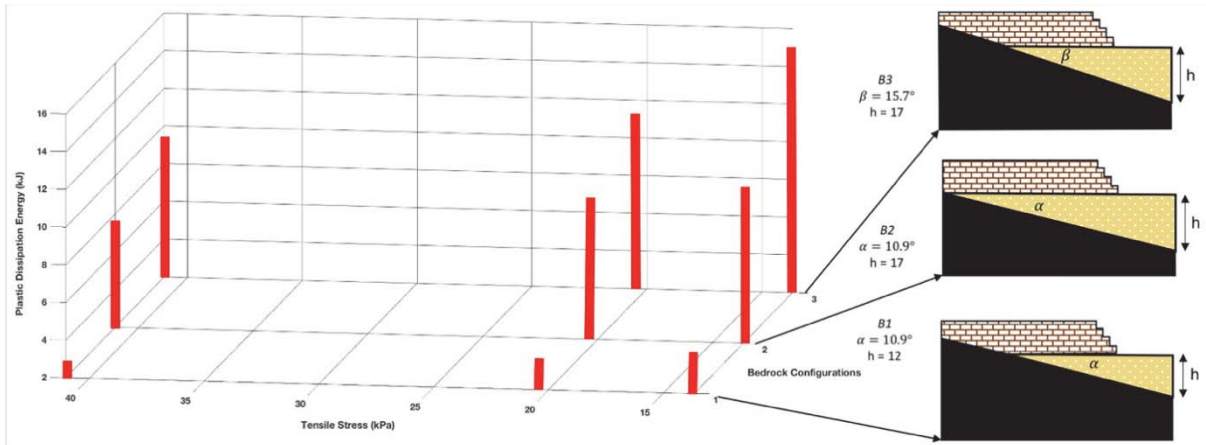


Figure 8: Plastic dissipation energy for material and bedrock variations.

The distribution of maximum principal plastic strains on bedrock configurations B1, B2, and B3 with the highest tensile strength of adobe (M1) are shown in Fig. 9 (a)-(c). These are compared with the results for the same configurations but with the lowest tensile strength (M3), Fig. 9 (d-f). The black zones indicate areas where the strains are above the 10^{-3} threshold, and thus where fracture damage can be predicted. For all the M1 cases, compressive stresses – although remaining below compressive strength – produce a nucleus of low level tensile plastic strains at the base of the pyramid in proximity of the west edge – see B3, Fig. 9(c). For B1 and B2 their

magnitude is below $2.5e^{-4}$ and thus not visible in Fig. 9(a) and (b). While there is no fracture development on the top level of the pyramid for B1, a downward vertical fracture forms at the angle between the top platforms for B2 and B3.

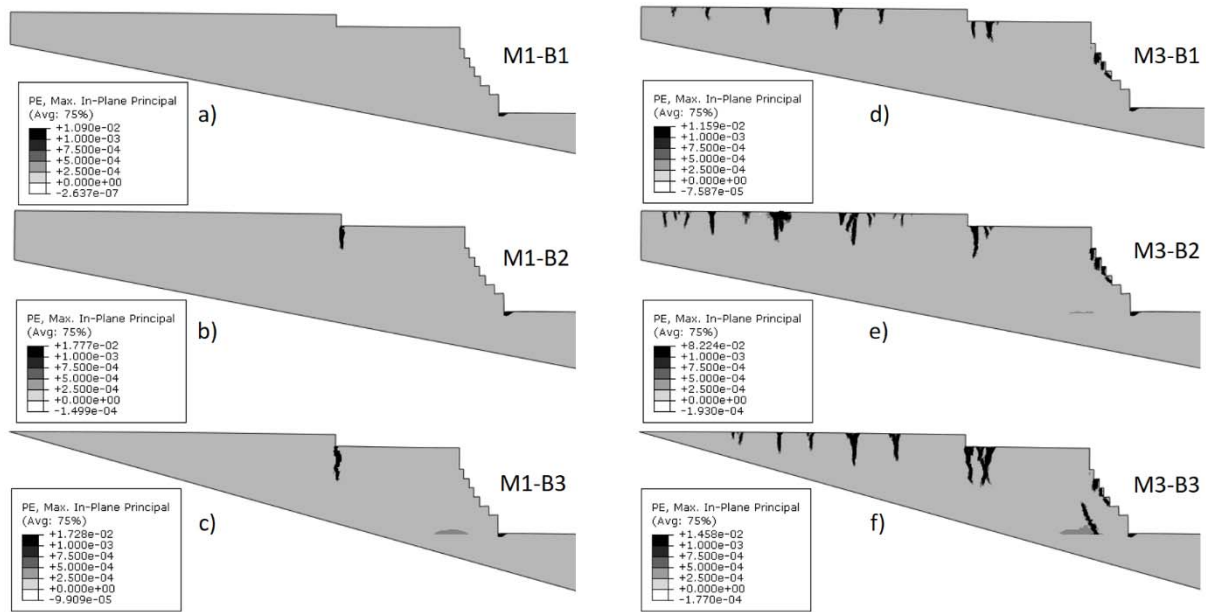


Figure 9: Plastic strain results of bedrock variation for M1 (a-c) and M3 (d-f).

As shown in Fig. 9(d)-(f), the M3 models under static conditions exhibit similar damage patterns at the base of the pyramid. In all three bedrock configurations, however, the downward fractures on the top level increase noticeably in number and in depth and damage appears along the steps on the west side of the pyramid. For M3-B3, a substantial fracture propagates upward from the base near the west corner – Fig. 9(f).

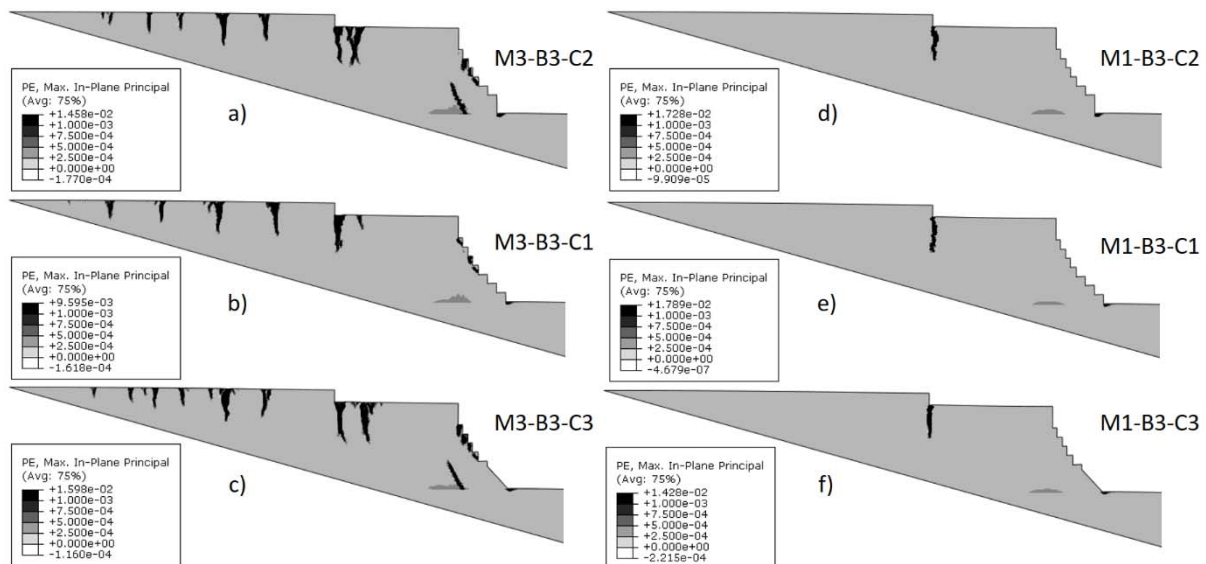


Figure 10: Plastic strain results of step architecture variation for M1-B3 (a-c) and M3-B3 (d-f).

Figure 10 shows the effect of the step architecture on the B3 configurations with material M1 and M3 under static conditions. The regular step architecture (C1) produces the least damaged conditions. For the M3 cases, C1 appears to stabilize the west façade by containing the

expansion of the fracture zone at the base, while for the M1 cases, it produces the least plastic dissipation energy. The downward fractures at the top platforms are consistent with those shown in Fig. 9 for M1 and M3. For the M1 cases, there is a single fracture at top of the pyramid, which is not affected by the step architecture. All M3 cases show several downward penetrating fractures at the same location. In addition, the M3-B3-C2 and M3-B3-C3 cases show more extensive damage along and in the proximity of the west steps.

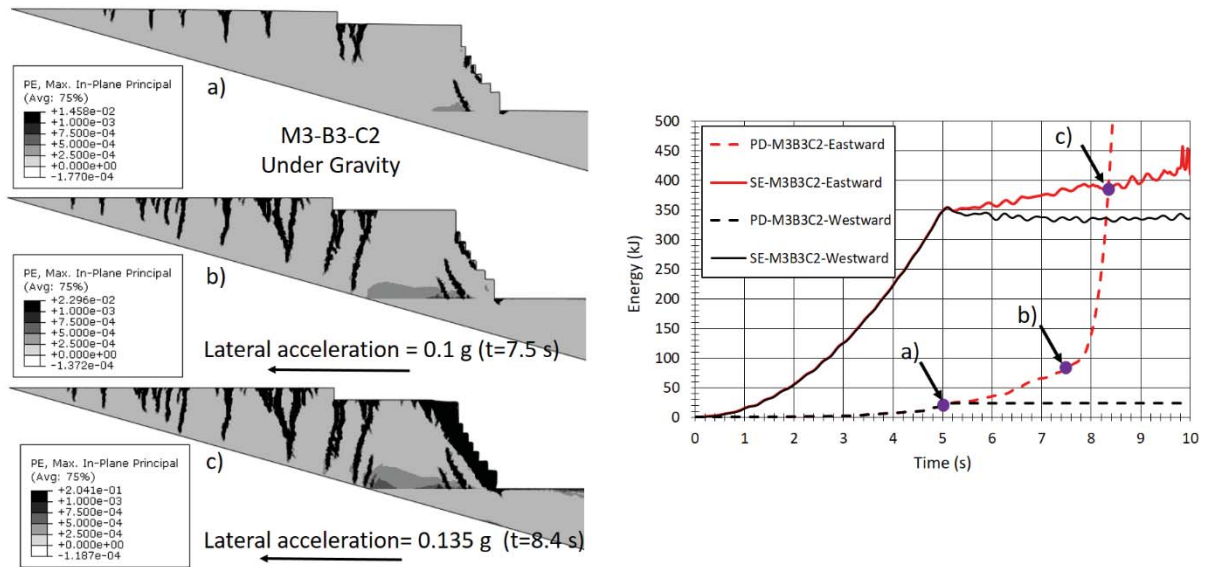


Figure 11: Plastic strain results of M3-B3-C2 configuration under gravity and eastward acceleration (a-c) on the left, energy results of both eastward and westward acceleration cases on the right.

We now examine the effect of horizontal acceleration on the M3-B3-C2 configuration, which exhibits the highest level of structural damage under gravitational loading. The horizontal acceleration is applied at the bedrock level after gravitational loading as a linear function of time, gradually increasing from 0.0 g to 0.2 g over 5 seconds. In order to account for the asymmetry of the model, two separate tests are performed with the acceleration applied eastward in one case and then westward in the other. As expected, the results indicate that the pyramid is critically vulnerable under the eastward acceleration as clearly shown by the difference in PD energy curves for the two cases – Fig. 11. The effect of the eastward acceleration is shown in Fig. 11 in terms of damage progression starting at 5 s (at the end of gravitational loading, Fig 11(a)), at the beginning of collapse at 7.5 s (horizontal acceleration 0.1 g, Fig. 11(b)), and at full collapse at 8.4 s (horizontal acceleration 0.135 g, Fig. 11(c)). The structural collapse involves the separation of the entire west side of the pyramid. In contrast, the energy curves for the westward case reveal that the structural situation remains essentially unchanged from the static condition through the following 5 s of increasing horizontal acceleration.

To explore the effect of horizontal and vertical accelerations applied simultaneously to the M3-B3-C2 model after gravitational loading, a downward acceleration is also added as a ramp increasing from 0.0 g to 0.1 g over the same 5 s. The vertical acceleration is selected as half of the horizontal one in consideration that earthquake vertical peak ground accelerations in this area are generally significantly lower than the horizontal component. As shown in Figure 12, the results demonstrate that the addition of downward acceleration changes the structural failure condition only marginally, with the horizontal acceleration at failure shifting from 0.135 g to 0.139 g.

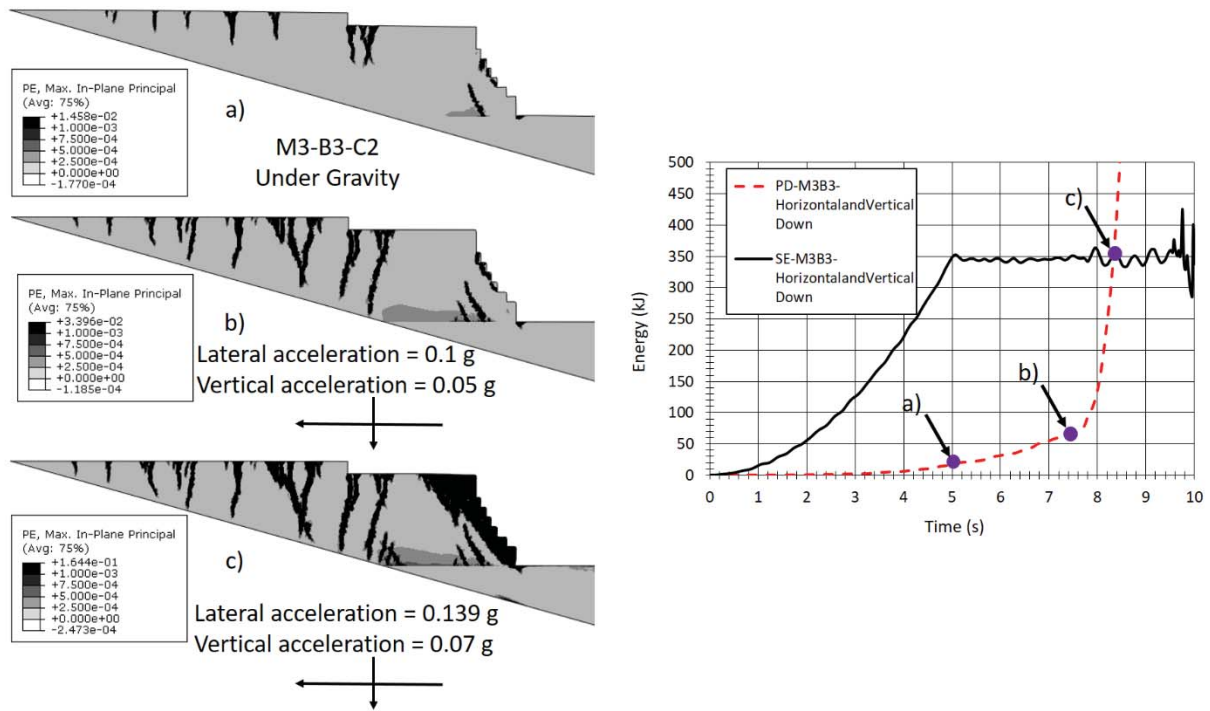


Figure 12: Plastic strain results of M3-B3-C2 configuration under gravity and eastward and downward acceleration (a-c) on the left, energy results on the right.

Figure 13 illustrates the effect of maximum adobe tensile strength as in the M1-B3-C1 case under eastward horizontal accelerations. The lateral capacity of the structure is further increased from 0.135 g to 0.24 g (78% more than M3-B3-C2). Finally, Fig. 14 illustrates the effect of the step configuration on the M3-B3 model under horizontal accelerations. The comparison with Fig. 11 is revealing. The presence at the ground level of a buttress (C3) or an addition step (C1) increases the lateral capacity by 33% and 45%, respectively.

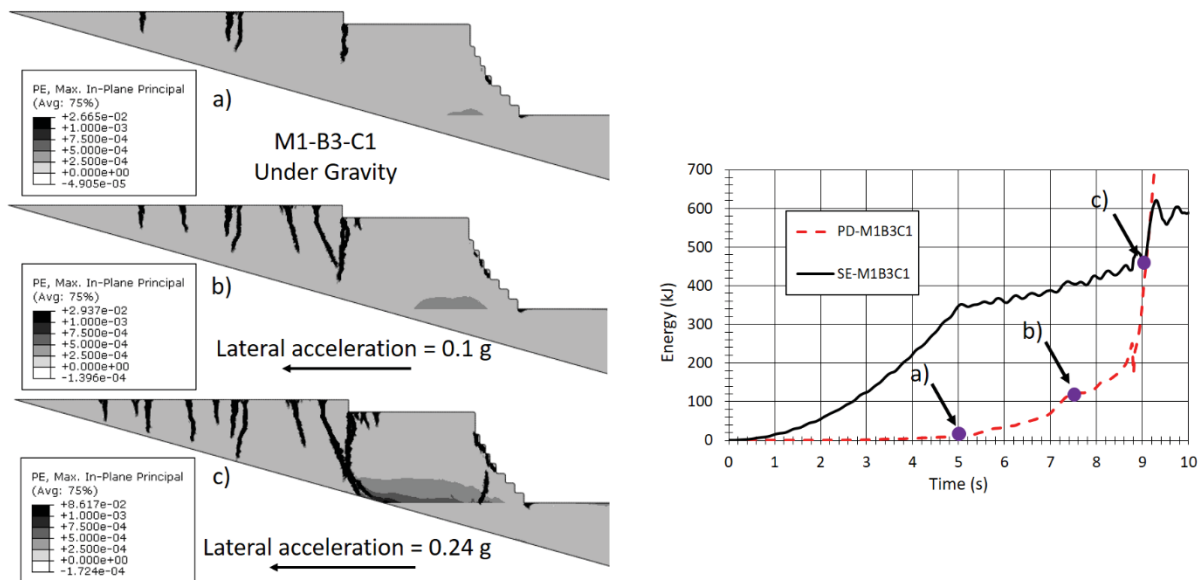


Figure 13: Plastic strain results for M1-B3-C1 configuration under gravity and eastward acceleration (a-c) on the left, energy results on the right.

It is worth noting the similarity in the failure pattern along the west side between all the M3-B3 model and the actual collapse present on the NW corner of the pyramid, Fig. 14.

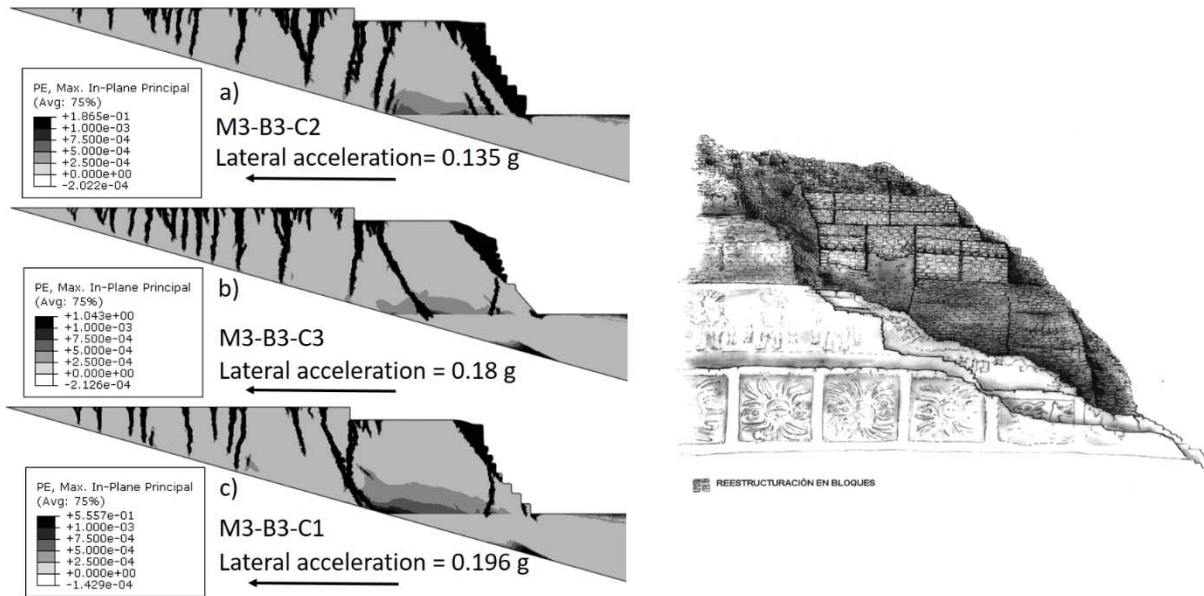


Figure 14: Lateral resistance of M3-B3 cases for step architecture variation (left), damage status of the NW corner of the main pyramid (right) [16].

6 DISCUSSION

Results indicate that under the assumptions made for material properties, bedrock and soil stratification, and architectural configuration, the 2D plane strain model shows localized material damage but does not collapse under gravitational loading. For each adobe tensile strength considered the bedrock configuration produces a major effect on the extension of the damaged areas, while the step architecture affects damage only marginally. Within the bedrock configurations, B2 is characterized by the largest structure-soil contact, thus inducing higher displacements and strain energy for the pyramid, but less damage than the B3 configuration. Although B3 yields less structure-soil contact, it assumes a steeper bedrock angle than B1 and B2, resulting in a deeper amount of soft soil under the west side of the pyramid.

The lateral acceleration tests indicate that the pyramid will reach failure conditions characterized by the extensive collapse of the west side under eastward accelerations ranging from 0.135 g to 0.24 g. The lowest value is due to the combined effect of lowest adobe tensile strength (M3) with steeper bedrock angle (B3) and shorter step footprint on the west side (C2). Although for the M3-B3 set the step architecture appears to contribute marginally to structural stability under gravitation, it affects significantly its lateral capacity. The C3 and C1 configurations increase lateral capacity from 0.135 g under C2 to 0.18 g and 0.196 g for C3 and C1, respectively. As expected in the case of a massive earthen structure, the material tensile strength plays a major – if not dominant – role in determining the lateral capacity. Replacing the lowest tensile strength (M3) adobe in the B3-C2 configuration with the highest tensile strength (M1) increases the lateral capacity from 0.135 g to 0.24 g (a 78% increment).

In conclusion, the results of the present preliminary study can be tentatively extrapolated to the actual pyramid to suggest that the uneven structure/soft soil/ bedrock interaction due to the pyramid location is not likely to cause the west side structural collapse under static conditions. Under this perspective, the extensive structural damage present in the NW corner could be at-

tributed to lateral accelerations produced by seismic actions rather than soft soil support conditions as initially suspected. However, given the inherent limitations of the 2D plane strain formulation, the characteristic features of Moche building techniques ignored in the present continuum model, and, most importantly, the uncertainties of the actual NS soil stratifications, these are still tentative considerations to be used as a point of departure for future in depth studies.

REFERENCES

- [1] L.J. Castillo, S. Uceda, The Mochicas. *Handbook of South American Archaeology*, Springer, New York, 707–729, 2008.
- [2] S. Uceda, R. Morales, *Moche: Pasado y presente*. Patronato del Valle de Moche, Trujillo, Peru, 2010.
- [3] R. Aguilar, G. Zavala, B. Castañeda, S. Lopez, S. Retamozo, M. Montesinos, M.A. Pando, Y. Dong, R. Perucchio, Structural damage assessment of Huaca de la Luna, Perú: Preliminary results from ongoing multidisciplinary study. *10th International conference on Structural Analysis of Historical Constructions: Anamnesis, diagnosis, therapy, controls (SAHC 2016)*, Leuven, Belgium, Sep. 13-15, 465-472, 2016.
- [4] E. Ramírez, M. Montesinos, R. Marques, R. Morales, S. Uceda, P.B. Lourenço, R. Aguilar, Análisis mecánico de albañilería arqueológica de adobe bajo cargas de compresión uniaxial: El caso de Huaca de la Luna. *3rd International Conference on Mechanical Models in Structural Engineering*, Sevilla, Spain, June 24-26, 77–90, 2015.
- [5] R. Aguilar, M. Montesinos, S. Uceda, Mechanical characterization of the structural components of Pre-Columbian earthen monuments: Analysis of bricks and mortar from Huaca de la Luna in Perú. *Case Studies in Construction Material*, **6**, 16-28, 2017.
- [6] G. Zavala, S. López, M. Pando, J. Zegarra, R. Morales, S. Uceda, B. Castañeda, R. Aguilar, Geotechnical and geophysical exploration in archaeological heritage: Initial assessment at Huaca de la Luna. *15th Panamerican Conference on Soil Mechanics and Geotechnical Engineering*, Buenos Aires, Argentina, 557–564, 2015.
- [7] R. Aguilar, M. Pando, C. Briceno, G. Zavala, B. Castañeda, R. Perucchio, S. Uceda, Structural and geotechnical engineering assessment of Huaca de la Luna – A massive earthen Moche culture pyramid in Northern Peru. *Journal of Cultural Heritage*, **34**, 83-94, 2018.
- [8] P. Roca, P. B. Lourenço, Introduction to masonry mechanics and modeling techniques. *Advanced Master in Structural Analysis of Historical Constructions and Monuments Lecture Notes*, Spain, 2008.
- [9] P. B. Lourenço, Recent advances in masonry modelling: micro-modelling and homogenization. U. Galvanetto, M.H. Ferri Alibadi eds. *Multiscale Modelling in Solid Mechanics: Computational Approaches*, Imperial College Press, London, England, 2010.
- [10] Abaqus Analysis Theory Manual Simulia v.6.14.4.5.2 Damage plasticity model for concrete and other quasi-brittle materials. Dassault System Corporation, Providence, RI, 2019.

- [11] Abaqus Analysis Theory Manual Simulia v.6.14.23.3.3 Inelastic behavior, Mohr-Coulomb. Dassault System Corporation, Providence, RI, 2019
- [12] S. Tezcan, N. Tambe, C. Muir, R. Aguilar, R. Perucchio, Nonlinear FE analysis of the response to lateral accelerations of the triumphal arch of the church of Andahuaylillas, Peru. R. Aguilar *et. al.* eds. *11th International Conference of Structural Analysis of Historical Constructions (SAHC 2018)*, Cusco, Peru, Sep. 11-13, 2018.
- [13] J. Sun, S. Tezcan, R. Perucchio, The structural function of the Dutch buttressing of the east curtain wall of Elmina Castle, Elmina, Ghana. P. Roca, L. Pelà and C. Molins eds. *12th International Conference on Structural Analysis of Historical Constructions (SAHC 2021)*, Barcelona, Spain, Sep. 29 – Oct. 1, 2021.
- [14] Proyecto Arqueológico Huaca de Sol y de la Luna, *Planta y Cortes Huaca de la Luna: Secciones y elevaciones cotas actuales*. AutoCAD documents, 2013.
- [15] S. Uceda, E. Mujica, R. Morales, *Proyecto Arqueológico Huaca de Sol y de la Luna: Investigaciones en la Huaca de la Luna 2000*. Facultad de Ciencias Sociales, Universidad Nacionales de Trujillo, 2006.
- [16] S. Uceda, R. Morales, *Proyecto Arqueológico Huaca de Sol y de la Luna: Informe Técnico 2002*, Facultad de Ciencias Sociales, Universidad Nacionales de Trujillo, 2003.

MODELING STRATEGIES FOR NON-LINEAR SEISMIC ANALYSES: COMPARISON AMONG EFM AND FEM RESULTS ON AN EXISTING URM CASE STUDY

M. Pegoraro¹, E. Saler², M. Salvalaggio¹ and M.R. Valluzzi¹

¹ Department of Cultural Heritage, University of Padova
Piazza Capitaniato 7, 35139 Padova, Italy
marco.pegoraro@dicea.unipd.it, matteo.salvalaggio@unipd.it, mariarosa.valluzzi@unipd.it

² Department of Geosciences, University of Padova
via Gradenigo 6, 35131 Padova, Italy
elisa.saler@unipd.it

Abstract

Italian building heritage is widely composed of masonry buildings, whose characteristics largely vary depending on geographical location, construction techniques and materials typology. This type of structures has shown a high vulnerability to horizontal loads that must not be ignored, especially due to the high seismic hazard of Italian territory. Hence, appropriate numerical models are required to assess the complex structural behavior of unreinforced masonry (URM) existing structures, implementing the non-linear behavior of both materials and structure.

In this framework, two different approaches have been widely acknowledged: the Equivalent Frame Model (EFM) and the continuum Finite Element Model (FEM). This paper presents the application and comparison of these modeling strategies to an URM building dating back to XVII century, located in the Italian Alpine region (Roana, Vicenza). Non-linear static analyses were carried out by means of the software 3Muri (EFM), DIANA FEA and Midas FEA-NX (FEM). Results were compared in terms of ultimate resistance, capacity, ductility, and evolution of the damage state. Finally, assessment of the global behavior was carried out according to the Italian seismic code, pointing out the differences of the two approaches. Results showed that the EFM appears to be more conservative than FEM.

Keywords: Masonry buildings, Seismic vulnerability assessment, Non-linear static analysis, Finite Element Model, Equivalent Frame Model.

1 INTRODUCTION

The importance of preserving the Cultural Heritage in Italy has become more and more important, even due to the seismic events, which interested Italian territory [1]. The complexity of masonry structures, which widely compose built heritage, derives from its nature, being an extremely non-homogeneous material, whose properties vary depending on units and binder characteristics, assembling techniques, geometric layout. Computational methods can be helpful for taking into account some uncertainties, which affect the structural behavior and therefore are becoming more and more essential for the seismic assessment of unreinforced masonry (URM) structures.

This paper aims to compare various modelling strategies applied to an existing URM building in north Italy (Veneto region). The models, based on different approaches for the non-linear behavior of both materials and structure, were compared through pushover analyses, which are able to represent the global structural behavior, providing an estimation for the structure's capacity. For this approach to be valid, the assumption of "box behavior" has to be made, thus considering only in-plane resistance for masonry panels and excluding the activation of out-of-plane mechanisms, which could lead to local collapses.

The results were also processed in terms of Near-Collapse PGA capacity, in order to evaluate how the different modelling strategies can affect seismic assessment.

1.1 Numerical modeling of masonry structures

Two of the most acknowledged modeling strategies for masonry structures are the Equivalent Frame Model (EFM) and the Finite Element Model (FEM) approaches [2]. EFM is based on the discretization of masonry walls through three different macro-elements: piers, spandrels, and rigid nodes. This subdivision idealizes a frame structure where piers and spandrels are connected through un-deformable elements (rigid nodes), while non-linear properties are lumped at hinge elements. This method is subject to multiple uncertainties, regarding the frame schematization and non-linear hinges behavior [3]. It is indicated for the in-plane analysis of regular structures [4], since the out-of-plane behavior is not considered [5].

FEM can provide more detailed discretization, yet it presents a higher computational cost. Different approaches can be used in FE masonry modeling [6], depending on the complexity and purposes of the analyses. A relatively simple yet effective approach is the continuum modeling, in which the heterogeneous characteristics of masonry (i.e., resistant units and binder) are merged into a homogeneous one, and non-linearities are uniformly distributed. This method allows creating complex models able to identify out-of-plane mechanisms and more accurate crack patterns [7].

1.2 "La Cattedra" Case Study

The case study is part of "La Cattedra" complex, located in Canove di Roana (province of Vicenza), in the Italian Alpine region, about 1000 m AMSL. It corresponds to the older portion of the complex (Figure 1a), dating back to XVI century and it is characterized by a rectangular layout of about 10 m x 13 m, split in half by a central wall (Figure 1b). The building is adjacent to the remaining complex on the north side. It is a regular three-story building with the arrangement of the windows on three distinct rows. The main entrance is centered on the eastern façade, whereas the inner stairs are placed on the opposite side.

Due to the lack of a particular economic value, the complex underwent numerous renovations, which altered the original layout. For this reason, experimental investigations had to be carried out to identify the structural elements of the building and determine their physical parameters.

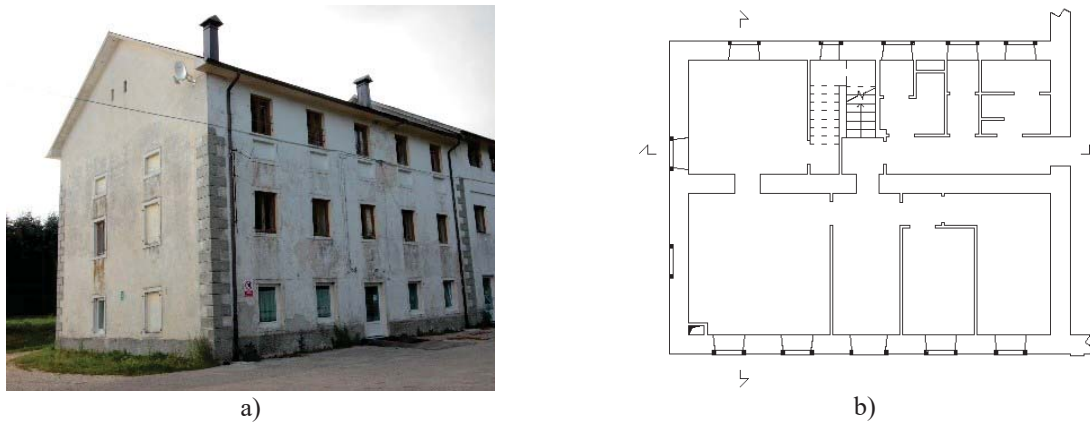


Figure 1: a) Picture of 'La Cattedra' case study, b) plan scheme of the case study.

The experimental investigation campaign was carried out in 2019 implementing semi-destructive and non-destructive tests. Firstly, scarifications were realized on different spots of the main walls, to identify the masonry type, detecting a stratigraphic composition; the lower portion is characterized by a local calcareous stone block (*Biancone*) masonry, whereas the upper section presents a hollow clay block one, due to a superelevation intervention realized on the last century. Walls' thickness varies from about 70 cm on the bottom to 60 cm on top of the building.

Two types of horizontal structures were detected: RC with slab for the first two floors, and RC without slabs for the third floor and the roof.

For the identification of masonry properties, both IQM (masonry quality index) analyses [8] and penetrometer tests on mortar samples were carried out: a very poor mortar was detected, especially for the stone masonry, while the characteristics improve for the block one.

2 MODEL GENERATION

The numerical models were developed via 3MURI (EFM), DIANA FEA and MIDAS FEA NX+ (FEA) (Figure 3), which represent some of the most common tools for EFM and FEM analyses of URM structures.

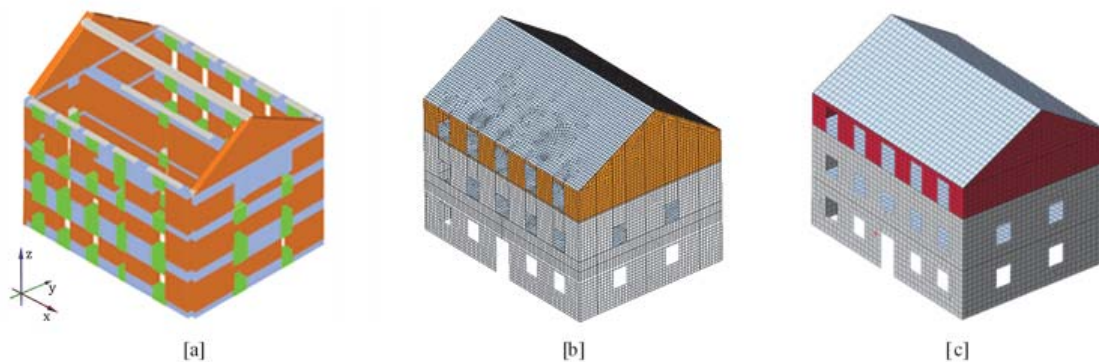


Figure 3: Numerical models: 3MURI (a), DIANA (b) and MIDAS (c)

2.1 EFM model

3MURI software [9] was used for the EFM modeling [10], allowing the automatic mesh generation. Material's properties assigned for masonry elements (Table 1) were defined from the Italian seismic code [11] and the experimental investigations previously described. The non-linear properties, different for piers and spandrels, were described by two collapse criteria, related to a flexural and a shear behavior. The constitutive laws adopted for each criterion presents a bilinear behavior without hardening, followed by progressive resistance softening (Figure 4). A 50% reduced stiffness is generally suggested [11] to simulate the cracked conditions of masonry elements. However, this assumption strongly affects the initial global stiffness, and it's commonly accepted the use of un-reduced values, since adopted parameters are already conservative, deriving from code tables and being already reduced by safety factors [12]. Hence, having to compare different modelling strategies, uncracked stiffness was considered.

Floors were modeled as 4-noded orthotropic plane strain elements, whose elastic properties for both types are listed in Table 2.

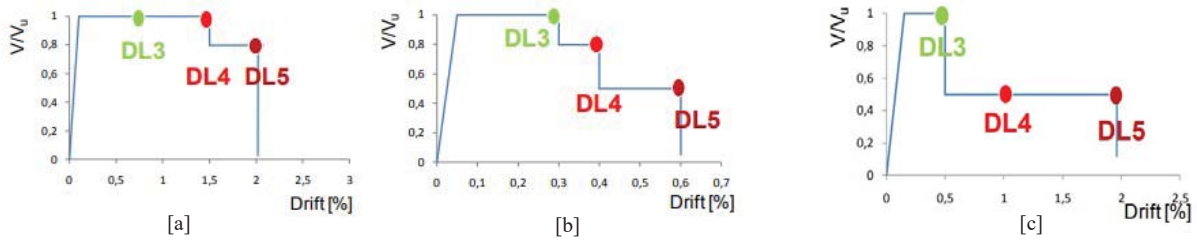


Figure 4: Constitutive laws adopted for EFM in 3MURI: a) flexural and b) shear behavior for piers, c) lintel model for spandrels (DL: Damage Level) [13].

2.2 FEM model

FEM analyses were carried out by means of two software: DIANA FEA [14] and MIDAS FEA NX+ [15], referring to a continuum approach. In both cases, masonry walls were modeled through curved shell elements, considering the material as nonlinear isotropic. For the non-linear behavior of masonry, the smeared crack approach was chosen, originally developed for concrete [16] and later adapted to masonry. The parameters which characterize this model (*Total Strain Based Crack* for DIANA, *Concrete Smeared Crack* for MIDAS) are the tensile (f_t) and compressive (f_c) ultimate stresses and the fracture energy values (G_t and G_c) to define the post-peak of the stress-strain curve. The behavior is described by a linear softening function in tension and a parabolic function in compression. In addition, a shear retention factor (β) was defined. The parameters implemented for each masonry type in the FE model (Table 1), are equal for both FE models. As for the EF model, the reference values derive from Italian seismic code [11], in accordance with the results of experimental tests, while fracture energy values were suggested by scientific literature [17].

Floors were modeled as elastic orthotropic shell element and elastic properties, equal for EF model, are reported in Table 2.

	EFM		FEM	
Parameter	SB Masonry	HCB Masonry	SB Masonry	HCB Masonry
E [MPa]	1740	4550	1740	4550
ν	0.25	0.25	0.25	0.25
w [kN/m ³]	20	14	20	14
Tens. function	-	-	Linear softening	Linear softening
f_t [MPa]	0.018	0.037	0.018	0.037
G_t [N/mm]	-	-	0.00135	0.0045
Comp. function	-	-	Parabolic	Parabolic
f_c [MPa]	1.12	1.85	1.12	1.85
G_c [N/mm]	-	-	4.8	5
β	-	-	0.01	0.01

Table 1: Mechanical parameter for masonry type in EFM and FEM model. SB: stone blocks; HCB: hollow clay blocks.

Parameter	RC floor (with slab)	RC floors (without slab)
E_x [MPa]	39200	36000
E_y [MPa]	20000	0
G_{xy} [MPa]	8300	1000

Table 2: Mechanical parameter for floors types (equal for EFM and FEM)

3 RESULTS

The seismic assessment was carried out through modal and pushover analyses. These last, as stated by the Italian code [11], were performed for both principal directions, following two load profiles: proportional to mass distribution and proportional to mode shape. The results, consisting in four capacity curves for each model, permitted to evaluate the seismic vulnerability for the global structure in terms of peak ground acceleration (PGA).

3.1 Modal analyses

The models were firstly compared through eigenvalue analyses. Table 3 reports the results for the three models in terms of modal frequencies and participant mass percentage for each principal direction. The comparison shows a good correlation for the first modes, especially between the two FE models, whose frequencies are close. For higher modes, differences become more significant, although less important than former ones.

Observing mass participation percentages, the FE models present similar values (about 75%), for the first two modes, corresponding to the main bending modes in Y and X direction, respectively. Major differences can be observed for the EF model, especially on the second and third modes, which both are oriented in X direction, although involving less dynamic mass. Thus, while FE models shows a global dynamic behavior, with participating masses lumped in the first modes, EF model does not.

MODE	3MURI			DIANA FEA			MIDAS FEA NX+		
	f [Hz]	mx [%]	my [%]	f [Hz]	mx [%]	my [%]	f [Hz]	mx [%]	my [%]
1	6.059	0.1%	80.8%	6.286	0.0%	75.6%	6.329	0.0%	77.4%
2	6.851	22.4%	5.4%	8.230	76.2%	0.0%	8.283	73.5%	0.0%
3	7.418	56.1%	1.2%	9.779	2.2%	0.0%	9.430	5.1%	0.0%
4	12.152	10.3%	0.0%	13.220	0.0%	6.0%	11.200	0.0%	0.1%
5	16.367	0.0%	0.4%	15.483	0.0%	0.0%	13.001	0.0%	2.8%
6	17.452	0.2%	9.4%	20.009	0.0%	3.6%	16.047	0.1%	0.0%
7	19.508	4.6%	1.4%	20.119	4.5%	0.0%	16.638	0.0%	1.9%
8	20.509	0.3%	0.2%	20.849	0.1%	0.8%	17.635	0.0%	0.0%
9	21.716	2.2%	0.3%	21.361	0.7%	0.1%	18.728	0.0%	0.7%
10	22.738	0.0%	0.0%	21.870	2.4%	0.0%	19.751	0.1%	0.0%

Table 3: Results of modal analyses

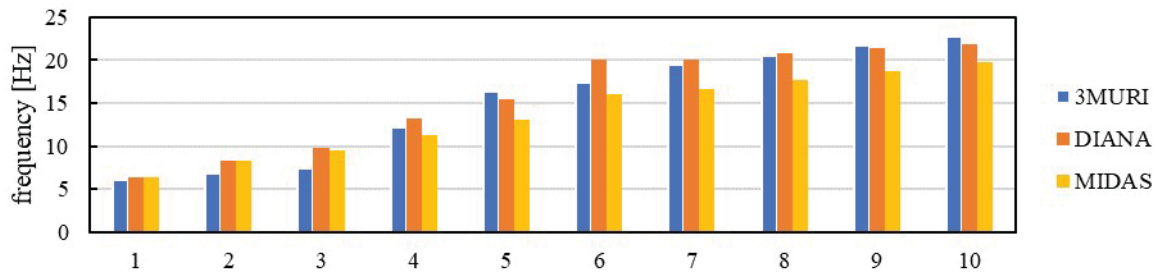


Figure 5: Comparison between modal frequencies

3.2 Pushover analyses

The capacity curves deriving from pushover analyses pointed out significant differences among the three models (Figure 6). The EF curves were characterized by two very distinct sections: the first elastic and the second almost perfectly horizontal. On the FE curves, instead, the transition between elastic and post-elastic behavior was less defined. This difference is due to the nature of non-linearities in the models. On the EF model, the behavior is ruled by few idealized elements (plastic hinges), while on FE model the non-linearities are spread to all the elements; therefore, the transition between the linear and nonlinear phase is much more dilatated, depending on the status of more elements.

Differences can be noticed even in the post-elastic phase, thus inducing major divergencies on displacement capacity, as the FEM analyses provide higher values for ultimate displacement and peak shear capacity, which brings to a brittle failure of the structure. Significant differences can be observed even between the FE models: while the curves coincided in the elastic section due to the equal elastic properties of the materials' model, the post-elastic behavior changed, due to the different non-linear model implemented by the two software: MIDAS curves were characterized by a higher post-elastic stiffness, leading to higher maximum shear values.

The models were also compared on damage evolution (Figure 7). For the EF model, the damage is represented by a color scale legend of the status reached by every element based on the related plastic hinges status, while for FE model, the damage is represented by major principal strain. Firstly, a correspondence between the rigid node elements of EF model and the un-damaged portion of FEM walls can be noticed, thus validating the assumptions of the EF approach. Secondly, all the three models pointed out the major damage located at the piers of the first floor, suggesting the activation of a soft story mechanism, which led to the collapse

of the structure. The main difference can be observed on the damage at upper levels, as the FE model led to the damage located on the piers of the second floor, while the EF on the third one.

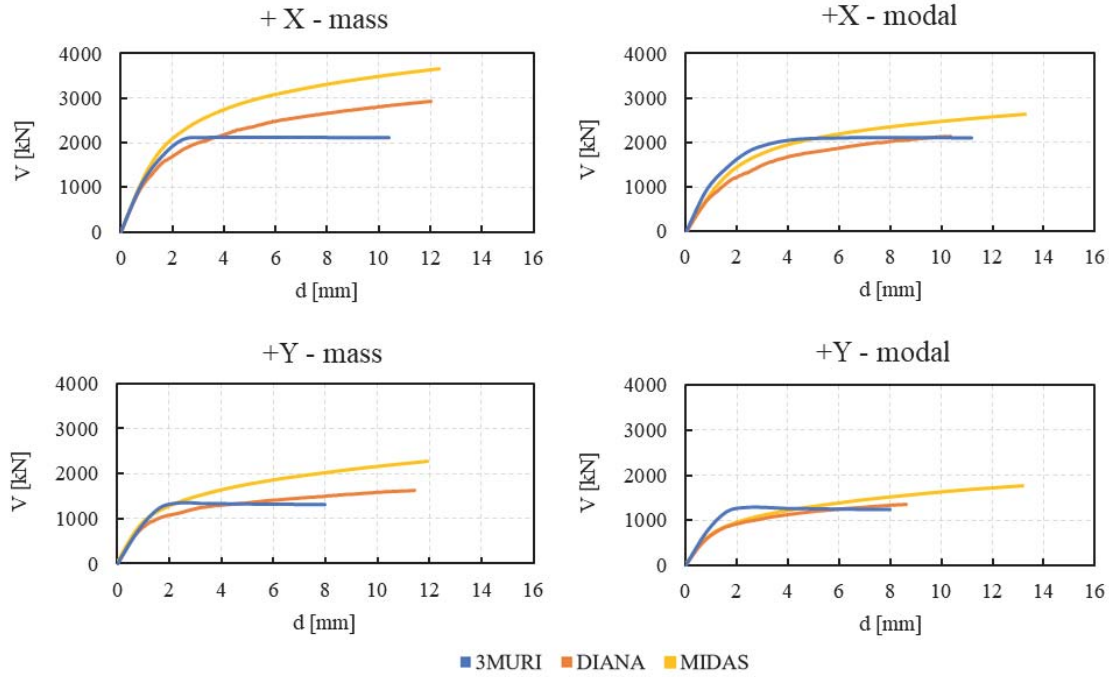


Figure 6: Comparison among pushover curves of different models

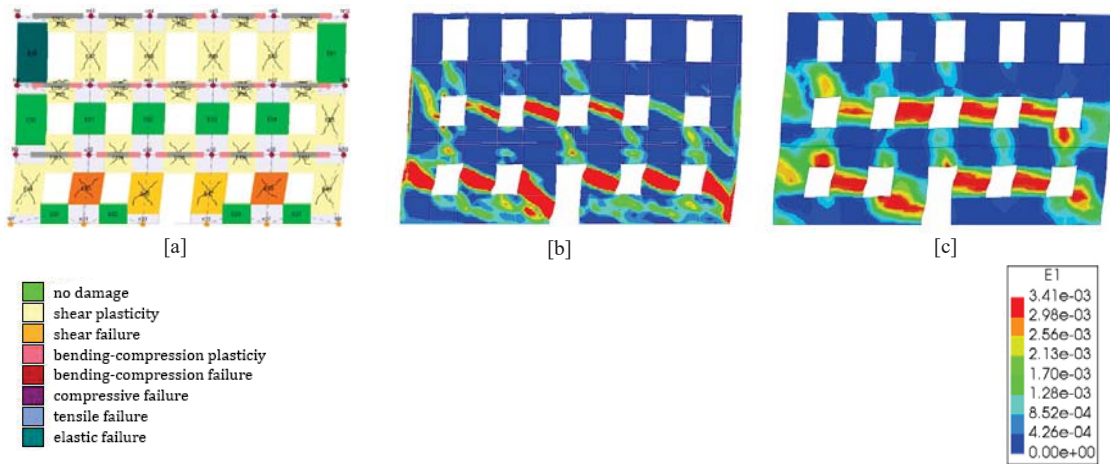


Figure 7: Damage pattern example for each model: 3MURI (a), DIANA (b) and MIDAS (c).
Analysis case: Modal X

3.3 Seismic capacity assessment

Verifications were carried out following the Italian seismic code [10][18], obtaining the capacity in terms of Near-Collapse PGA (PGA_C) for every pushover curve. Resulting PGA capacities of FE models were compared to EF ones (Δ_{PGA}) and reported in Table 4. Results pointed out that the Y direction is the most vulnerable one, providing lower values of Near-Collapse PGA (PGA_C). Comparing the modeling strategies, lower values can be observed for the EF model, especially for the transversal direction analyses, suggesting a more conservative approach. The FE models deliver similar PGA values for Y-direction analyses, while dif-

ferences emerge from X-direction ones, as MIDAS values are significantly higher than DIANA ones.

Analysis	3MURI	DIANA FEA		MIDAS FEA NX+	
	PGA _C [g]	PGA _C [g]	ΔPGA [%]	PGA _C [g]	ΔPGA [%]
X Mass	0.220	0.222	+0.9	0.289	+31.3
Y Mass	0.125	0.187	+49.6	0.189	+51.2
X Modal	0.194	0.174	-10.4	0.200	+3.1
Y Modal	0.104	0.114	+9.6	0.118	+13.5

Table 4: Near-collapse PGA capacities (PGA_C) and percentage variation ΔPGA on EFM model.

4 CONCLUSIONS

In this contribution, different modeling strategies for existing URM buildings have been applied to a representative case study.

The case study was a three-story URM building located in the Italian Alpine region. It has a rectangular plan shape, as well as it is regular in elevation. Lower portion was built using local calcareous stone blocks, while the upper portion was made of hollow clay blocks.

Equivalent Frame (EF) and Finite Element (FE) models were implemented using different software [9,14,15]. The comparison of analyses results showed that:

- differences related to the various approaches can be observed, especially in damage evolution and post elastic behavior;
- both EFM and FEM approaches identified the same soft story mechanism involving the first floor's piers, even if differences can be observed in damage pattern among the strategies;

In this study, EFM approach produced more conservative results than FEM ones, providing lower capacity PGA values. Other examples led to controversial results [2][4][7], suggesting that one or other strategy has to be carefully chosen, depending on case study characteristics and analysis purposes; besides its low computational effort, the EFM approach appears to be suitable for seismic assessment of regular building. FE approach is indicated for more irregular structures, which cannot be easily schematized with EF method. They even provide more detailed results, allowing local damage patterns to be better identified, however they require way more computational time.

ACKNOWLEDGEMENTS

This work was supported by the CORE-WOOD (COmpetitive REpositioning of WOOD sector) Italian project, in the framework of POR-FESR 2014–2020 Line 1 Action 1.1.4 of the Veneto Region.

REFERENCES

- [1] L. Sorrentino, S. Cattari, F. da Porto, G. Magenes, and A. Penna, Seismic behaviour of ordinary masonry buildings during the 2016 central Italy earthquakes, *Bull. Earthq. Eng.*, vol. 17, no. 10, pp. 5583–5607, 2019.
- [2] J. A. Kollerathu, S. Krishnachandran, and A. Menon, Modelling and seismic analysis of existing masonry structures, *Struct. Anal. Hist. Constr. Anamn. diagnosis, Ther. Con-*

- trol. - Proc. 10th Int. Conf. Struct. Anal. Hist. Constr. SAHC 2016*, no. February 2017, pp. 257–264, 2016.
- [3] E. Quagliarini, G. Maracchini, and F. Clementi, Uses and limits of the Equivalent Frame Model on existing unreinforced masonry buildings for assessing their seismic risk: A review, *J. Build. Eng.*, vol. 10, no. December 2016, pp. 166–182, 2017.
 - [4] R. Siano, G. Camata, V. Sepe, E. Spacone, P. Roca Fabregat, and L. Pelà, Finite elements vs. equivalent frame models for URM walls in-plane behaviour, in *16th World Conference on Earthquake Engineering 16WCEE 2017*, 2017, no. December, pp. 1–11.
 - [5] M. R. Valluzzi, M. Salvalaggio, and L. Sbrogio, Repair and conservation of masonry structures, in *Numerical Modeling of Masonry and Historical Structures*, vol. 66, Elsevier, 2019, pp. 201–235.
 - [6] P. B. Lourenço, Structural Masonry Analysis: Recent Developments and Prospects, *J. Chem. Inf. Model.*, vol. 53, no. 2004, p. 160, 2008.
 - [7] F. Clementi, V. Gazzani, M. Poiani, and S. Lenci, Assessment of seismic behaviour of heritage masonry buildings using numerical modelling, *J. Build. Eng.*, vol. 8, pp. 29–47, 2016.
 - [8] A. Borri and A. De Maria, Indice di Qualità Muraria (IQM): correlazione con le caratteristiche meccaniche e livelli di conoscenza, *ReLuis 2015 - Linea Costr. Muratura*, pp. 45–63, 2015. (in Italian)
 - [9] S.T.A. DATA, Manuale d'uso 3Muri ver. 10.9.0.
 - [10] S. Lagomarsino, A. Penna, A. Galasco, and S. Cattari, TREMURI program: An equivalent frame model for the nonlinear seismic analysis of masonry buildings, *Eng. Struct.*, vol. 56, pp. 1787–1799, 2013.
 - [11] Ministero delle Infrastrutture e dei Trasporti, D.M. 17 gennaio 2018, “Aggiornamento delle «Norme tecniche per le Costruzioni»”, 2018. (in Italian)
 - [12] S. Bracchi, M. Rota, A. Penna, and G. Magenes, “Consideration of modelling uncertainties in the seismic assessment of masonry buildings by equivalent-frame approach,” *Bull. Earthq. Eng.*, vol. 13, no. 11, pp. 3423–3448, 2015.
 - [13] CNR-DT 212/2013. Istruzioni per la Valutazione Affidabilistica della Sicurezza Sismica di Edifici Esistenti 2014. (in Italian)
 - [14] TNO Building and Construction Research, “DIANA – Finite Element Analysis User’s Manual - Release 10.4”, 2020
 - [15] MIDAS Engineering, “MIDAS FEA NX User Manual”, 2019
 - [16] M. Petrangeli and J. Ožbolt, “Smeared Crack Approaches—Material Modeling,” *J. Eng. Mech.*, vol. 122, no. 6, pp. 545–554, 1996.

- [17] L. Bejarano-Urrego, E. Verstrynge, G. Giardina, and K. Van Balen, “Crack growth in masonry: Numerical analysis and sensitivity study for discrete and smeared crack modelling,” *Eng. Struct.*, vol. 165, pp. 471–485, 2018.
- [18] C.S.LL.PP, Circolare 21 gennaio 2019, n. 7, “Circolare applicativa delle nuove Norme Tecniche per le Costruzioni approvate con D.M. 17 gennaio 2018”, 2019. (In Italian)

ANALYSIS OF THE DAMAGE STATE OF A MONUMENTAL BUILDING BY CONSIDERING THE VARIATIONS IN SOIL CONDITIONS

Lenticchia E.^{1,2}, Miraglia G.^{1,2}, Coccimiglio S.¹ and Ceravolo R.^{1,2}

¹ Politecnico di Torino, Department of Structural, Geotechnical and Building Engineering (DISEG)
Torino, Italy

² Responsible Risk Resilience interdepartmental Centre (R3C), Politecnico di Torino,
Torino, Italy

erica.lenticchia@polito.it; gaetano.miraglia@polito.it; stefania.coccimiglio@polito.it; rosario.ceravolo@polito.it

Abstract

This paper investigates whether it is possible to identify the influence of soil conditions on the modal parameters of the structure for damage detection and overall structural health monitoring. To do so, the data gathered on a large monumental building damaged by differential settlements are analyzed. In particular, the dynamic response of the case study, a large monumental masonry building, was experimentally investigated within an operational modal analysis (OMA) campaign. Mechanical data obtained from the geophysical tests were in turn employed to build and characterize a numerical model of the soil underlying and surrounding the building. The resulting model was then used to study the sensitivity of the modal characteristics of the building with respect to variations of external environmental factors (e.g., the water table level) which affect the underlying soil.

The results obtained from this numerical study is deemed to represent a starting point for future experimental tests and investigations, whose final aim is relating ambient vibration measurement to the occurrence of differential settlements or subsidence, in order to detect progressive, and possibly pathological, behaviors.

Keywords: soil-structure interaction, degree of saturation, environmental data series, FEM, foundation settlements, Operational Modal Analysis, Structural Health Monitoring, ground-water table.

1 INTRODUCTION

It is well-known that soil conditions may affect the response of a building. This is especially true for monumental buildings in masonry, which are unable to bear strong flexural internal stresses caused by differential settlements or subsidence [1]. Cyclic oscillations of water table levels may alter the soil characteristics and potentially activate or worsen these phenomena, damaging the superimposed structures. Dynamic monitoring systems are a widespread tool for Structural Health Monitoring (SHM) and consist of accelerometers installed on the superstructure [2]. However, alterations occurring at the foundation level are difficult to understand from the outputs of these systems. Moreover, the systems dedicated to dynamic SHM are usually not equipped with sensors dedicated to controlling the effects of the soil, as they are set to capture responses from the superstructure only.

The present paper wants to investigate how the modal behavior of the structure is affected by the variation of the soil characteristics, such as the degree of saturation and the water table evolution. The aim is to study how a dynamic sensing system mounted only on the structure would capture the evolution of these parameters correlated to the structure response. To this aim, the case study of the Chiarugi building in Racconigi (Piedmont, Italy) is presented as a benchmark. The “Chiarugi” pavilion is a monumental three-story masonry structure presenting a double quadrangular plan with two inner courtyards overlooking the walkways loggias at the various floors. The building, which has been used as a psychiatric hospital for over a century, is distributed in various wings, a common design solution adopted at the time for hospice and hospital in general, and it includes a baroque chapel dedicated to the Madonna del Buon Consiglio. The building covers about 4.000 m², with a total usable area of about 17.000 m² distributed between the basement and the various floors and reaches a maximum height of 21 m. The building, whose construction is dated between the end of the 18th century and the beginning of the 19th century, has been in disuse for more than twenty years and has been in a latent danger state. Currently, the building is affected by a condition of widespread degradation and severe damaging phenomena: internal collapse, local deformations, wide cracks scattered on the whole building. These damaging phenomena, documented for over 50 years, are distributed differently in the various wings in which the building is subdivided. The structural problems of the “Chiarugi” pavilion are essentially due to two main causes mentioned in all the static surveys carried out since 1972: the maintenance problems and the soil characteristics [3]. In fact, the structural damage affecting the building is caused by the hydrogeological conditions and the seasonal oscillations of the groundwater layer. Moreover, the maintenance problems had led to the deterioration of the roofs, causing infiltration and percolation of the meteoric waters into the walls, sometimes worsened by the absence or inefficiency of the gutters in the structure [4].



Figure 1: (a-b) some cracks on the various facade of the building (2015); (c) collapse of a portion of the southern façade (2016).

In 2016 a portion of the southern façade suddenly collapsed. The collapse is presumably due to the collapse of the masonry pillars that supported the vaults of the underlying plan. Another collapse followed in 2019.

2 MODELING STRATEGY

The building is located on a plane with a slight slope of about -0.15% to the north, in an area concentric to the city of Racconigi (259 m above sea level in the northern part of the "Pianura Cuneese"), historically influenced by the depositional process of the Maira torrent whose riverbed is currently spaced about 800 m west of the building. The first stratigraphic indications of the soil were obtained from the documentation on the hospital's thermal power plant; however, specific analyses were subsequently carried out, which determined the characteristics of the soils more precisely [3].

Given the complexity of the problem, in a first approach to the study, the superimposed structure has been modeled through a low fidelity approach, essentially using finite shell elements and without considering the opening. Instead, for the soil-foundation system, brick and shell elements with 8 and 4 nodes, respectively (3 Degree of Freedom – DoF and 6 DoF at each node) have been used.

The superimposed structure has been modeled to consider in a simplified way the effect of its mass and stiffness distribution along the foundations. To this aim, the soil-foundation-structure system has been calibrated, going to update the equivalent values of Young's moduli of floors and masonry walls for the different sleeves. The updating was possible thanks to the availability of the experimental modes identified after an intensive experimental campaign carried out in situ by the authors. The results of the calibration, reported in Table 1, demonstrate how the grey-box representation of the updated superimposed structure is able to satisfactorily trace the first two modes of the building, providing a good estimate of the global stiffness/mass distribution of the system, which is the aim of the low-fidelity representation of the superimposed structure.

Identified natural frequencies [Hz]	Numerical frequencies [Hz]	MAC between identified and predicted mode shapes	
2.233	2.195	0.841	0.000
2.464	2.382	0.004	0.741

(a)

(b)

Table 1: Results of the numerical calibration of the superimposed structure: (a) natural frequencies. (b) Modal Assurance Criterion (MAC).

The Finite Element (FE) model of the soil counts 219716 elements and 41754 nodes, with a maximum mesh size of 2 m. The main dimensions of the soil volume in the vertical and horizontal direction have been chosen starting from the geotechnical campaign results carried out by [3]. Starting from these data, the total depth of the volume was fixed to 18 m, while the distance between the soil edge and the foundation was fixed to 5 m in each direction. The total dimensions of the soil volume resulted in being 127 m in the East-West direction (X direction in the FE model), 88 m in the North-South direction (Y direction in the FE model), and 18 m in the vertical direction (Z direction in the FE model). The total number of soil layers follows the experimental findings (see Figure 2 for clarity). Finally, the foundations are laid at a depth of 3 m from the surface. The data of the elastic properties of the soil obtained by the geotechnical investigation are reported in Table 2.

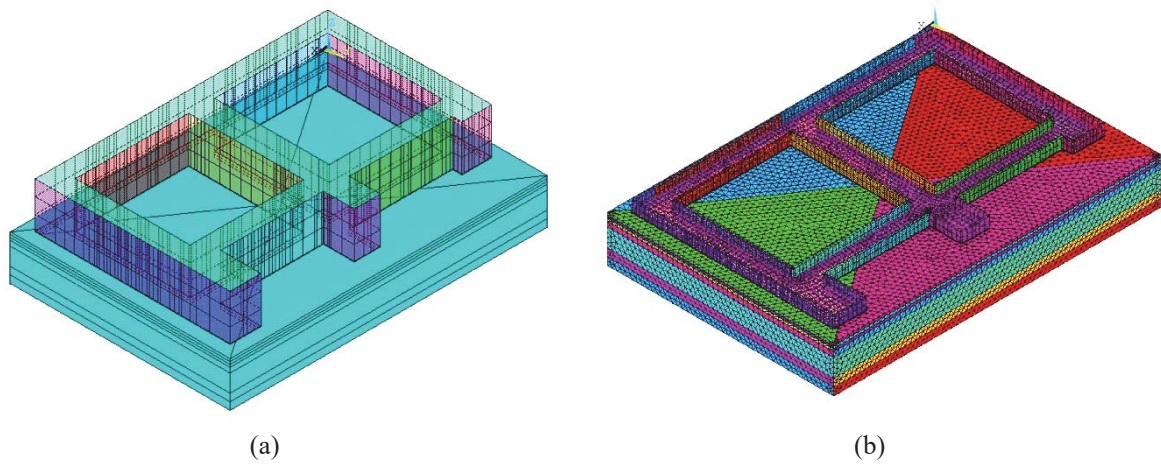


Figure 2: (a) Grey-box model of the superimposed structure and Finite Element (FE) model of the soil-foundation system. (b) FE mesh of the soil-foundation system (each color represents a different constitutive material).

Layer Id.	Depth at the bottom of the layer [m]	Soil type [3]	Density [kg/m ³]	East S-wave speed [m/s]	North S-wave speed [m/s]	South S-wave speed [m/s]	West S-wave speed [m/s]
1	1	- heterogeneous material (peat)	1200	300	250	200	250
2	2	- clayey silts (vegetable rind)	1500	300	250	200	250
3a	3	- fine sands, sandy gravels, and silty sands	1750	300	250	200	250
3b	5	- fine sands, sandy gravels, and silty sands	1750	300	250	200	250
4	12	- medium and coarse gravels and sandy gravels	1850	450	335	500	350
5	15	- medium gravels and silty gravelly sands	1950	450	500	500	350
6	18	- silty gravelly sands and gravels	1850	750	650	250	650

Table 2: Available elastic properties of the soil used to build the FE model.

Layer 3 was divided into 2 sub-layers because of the presence of the water table, which oscillates from a minimum of -5 m up to a maximum of -3 m, where it touches the building's foundations [3], [5]. In the absence of more information, the Poisson ratio was set to uniform in the model and equal to 0.33 at the time of the geotechnical investigations. For the foundations, Young's modulus of 2 GPa and a density of 1800 kg/m³ were then assumed. The vertical faces of the soil volume were then fixed in the horizontal direction, while a total restraint was given to the bottom face (at -18 m).

3 SIMULATIONS AND RESULTS

The simulations are aimed to numerically study the influence of soil conditions on the modal and the static response of the structure for Structural Health Monitoring (SHM) of the building. The structure is known to be affected by the water table oscillation, which affects the elastic

properties of layer 3 of the FE model. The oscillation of the water table affects the saturation of the overlying layers, as demonstrated by several literature studies, e.g. [6], [7], [8], [9]. This is mainly due to the capillary rise of water in the soils (in this case, mainly sands) and obviously to the infiltration properties of the surface layers, which allow the access of meteoric rains to the depth. Thus, the rain contributes not only to the direct modification of the degree of saturation on the surface but also to the modification of the height of the aquifer, and therefore (indirectly) to the modification of the capillary rise and the degree of saturation of the soil above the aquifer. Then, the elastic properties of the soil are affected by the degree of saturation as demonstrated by several studies, e.g. [10], [11], [12], [13], [14]. In this study, the elastic properties of layer 3 are supposed to vary in accordance to the wave speed laws derived and experimentally validated by [10] starting from the Van Genuchten relation [15]:

$$V_p(S_r) = V_p^s + \frac{V_p^d - V_p^s}{[1 + (a_p S_r)^{n_p}]^{m_p}} \quad (1)$$

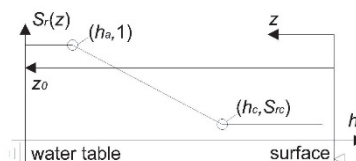
$$V_s(S_r) = V_s^s + \frac{V_s^d - V_s^s}{[1 + (a_s S_r)^{n_s}]^{m_s}} \quad (2)$$

where V_p^s , V_p^d , V_s^s , V_s^d and S_r are the *saturated* and *dry* P-wave and S-wave velocity and degree of saturation respectively, while a_p , n_p , m_p , a_s , n_s , m_s , are empirical model parameters. Starting from the P-wave and S-wave velocity it is possible to evaluate the Poisson ratio, ν , [13] by combining the theoretical formulations for the oedometric modulus M , Young's modulus E and shear modulus G :

$$M = V_p^2 \rho; G = V_s^2 \rho; E = M \frac{(1 + \nu)(1 - 2\nu)}{(1 - \nu)} = 2G(1 + \nu) \quad (3)$$

$$\nu(S_r) = \frac{V_p^2(S_r) - 2V_s^2(S_r)}{2(V_p^2(S_r) - V_s^2(S_r))} \quad (4)$$

where ρ denotes density. From equations (3) and (4), it is possible to conclude that having $V_p(S_r)$, $V_s(S_r)$ and ρ it is possible to derive the elastic properties of the soil as a function of the degree of saturation. In the present paper the laws (1) and (2) are those reported in [10] for sand (see [10] for the model parameters). Then the laws have been normalized to the values obtained from the geotechnical campaign in order to maintain a consistency of the analyses with the case study. Regarding the degree of saturation in the soil layer, it was assumed to be linearly variable between the *air entry height* region h_a , and the *maximum capillary height* region h_c , evaluated starting from the water table depth [6], [9]. For height lower than h_a the soil is known to be saturated (i.e., $S_r=1$), while for height over h_c the degree of saturation tends to be uniform, and in the first approximation it was assumed to be constant and equal to S_{rc} . Thus, the model that describes the variation of S_r along the soil depth z from the surface (positive downwards) is:



$$S_r(z, z_0) = \begin{cases} 1; & \text{for } h(z, z_0) \leq h_a \\ 1 + \frac{1 - S_{rc}}{h_c - h_a} (h_a - h(z, z_0)); & \text{for } h_a < h(z, z_0) < h_c \\ S_{rc}; & \text{for } h(z, z_0) \geq h_c \end{cases} \quad (5)$$

Figure 3: Scheme of the linear model assumed for the degree of saturation S_r along the depth z .

where $h_c > h_a$. In the equation, $h = z_0 - z$ and z_0 represents the depth of the water table (i.e., variable from 5 m to 3 m in the present study), while z varies from 5 m to 2 m in the present application (thickness of the 3rd soil layer). For the study, the average values for sand reported in [9], [16], [17] have been used for the air entry height and the maximum capillary height ($h_a = 0.22$ m and $h_c = 0.59$ m). Figure 3 depicts a schematization of the model defined by equation (5). Finally, to practically cast the results of (5) in the FE model, which is discretized in uniform soil layers, the average degree of saturation $S_{r,avg}$ along the 3 m of thickness of layer 3 has been calculated and used for the evaluation of the elastic properties with equations (3) and (4).

The aforementioned methods have been applied to carrying out a parametric analysis focusing the attention on the effect of soil characteristics on the modal response (in terms of the first two identified natural frequencies) and the static response (in terms of the standard deviation of foundation settlements). In the study, only the elastic characteristics of layer 3 have been changed, maintaining constant the properties of the first two soil layers.

Figure 4 shows the variation of the first two natural frequencies of the model as a function of z_0 and S_{rc} . The figure demonstrates as a sudden decrease in frequency is detected when the soil saturation increases (decrease of water table depth or increase of S_{rc}). Extremely dry condition of the soil, such those one caused by extreme warm seasons, will thus result in an increase of natural frequency. The absolute variations are however very low and without intelligent feature extractions the effect of the alteration of the third soil layer in the "Chiarugi" pavilion could be confused with other Environmental and Operational Variations (EOVs).

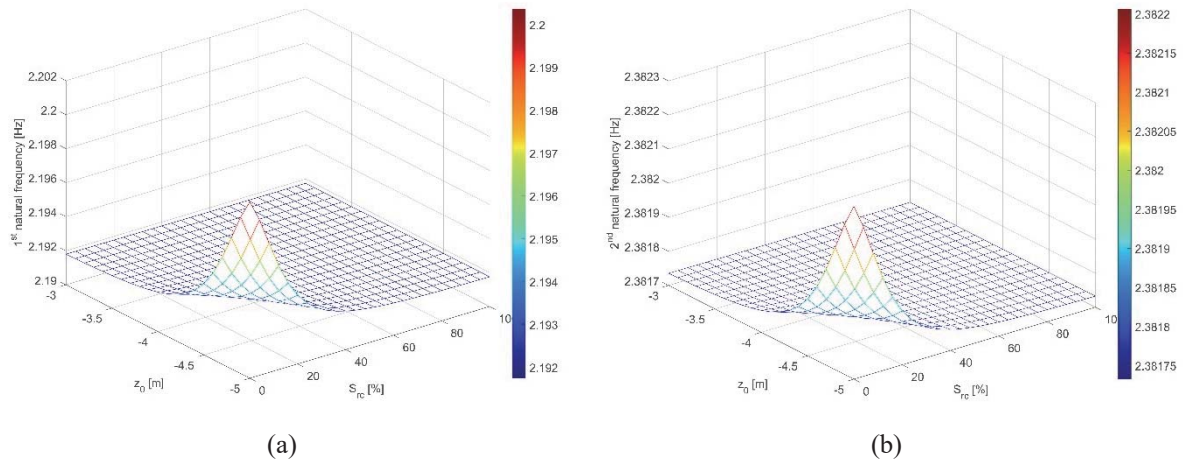


Figure 4: (a) First natural frequency of the calibrated FE model as a function of the degree of saturation of superficial layers S_{rc} and the water table depth z_0 . (b) second natural frequency of the calibrated FE model.

Figure 5 reports the results of the static analysis. In Figure 5a, the standard deviation of the foundation settlements is reported. From the figure, it is also clear that an increase of the saturation in the soil produces an increase of the standard deviation of the settlements. Figure 5b, instead, depicts the settlement profiles at the foundation's depth in case of dry ($z_0=5$ m and $S_{rc}=0$) and saturated ($z_0=3$ m and $S_{rc}=1$) conditions of the third layer. Comparing Figure 5b with Figure 5c (which depicts the actual condition of the building), it is possible to note how the corroboration of the FE model with the experimental data gathered during the geotechnical campaign can positively produce fitting results since the maximum depression zone foreseen by the model coincides with the area below the collapsed portion of the structure.

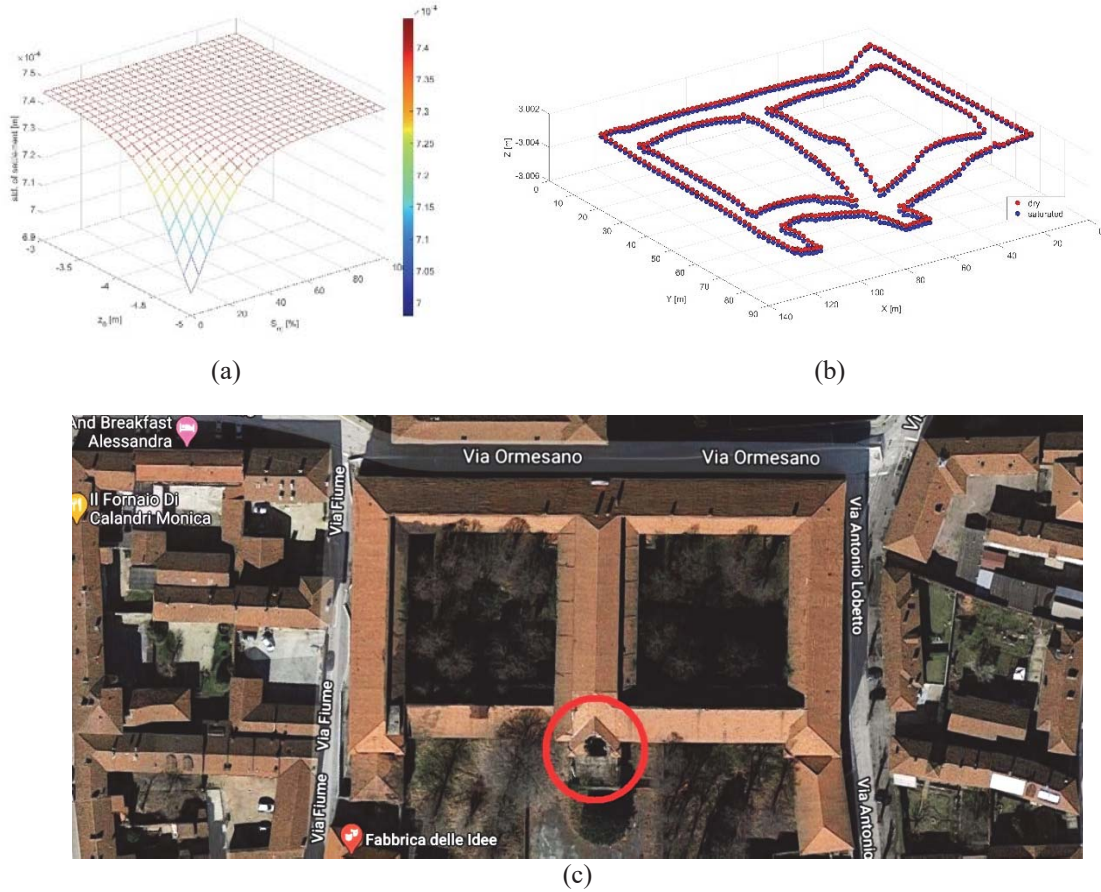


Figure 5: (a) Standard deviation of the foundation settlements as a function of the degree of saturation of superficial layers S_{rc} and the water table depth z_0 . (b) foundation settlements for the dry (red) and saturated (blue) condition of the 3rd soil layer. (c) Google Maps picture of the structure (lat. 44.765470, long. 7.678842) on March 3rd, 2021 with highlighted (see the red circle) the collapsed portion of the building <https://www.google.it/maps>.

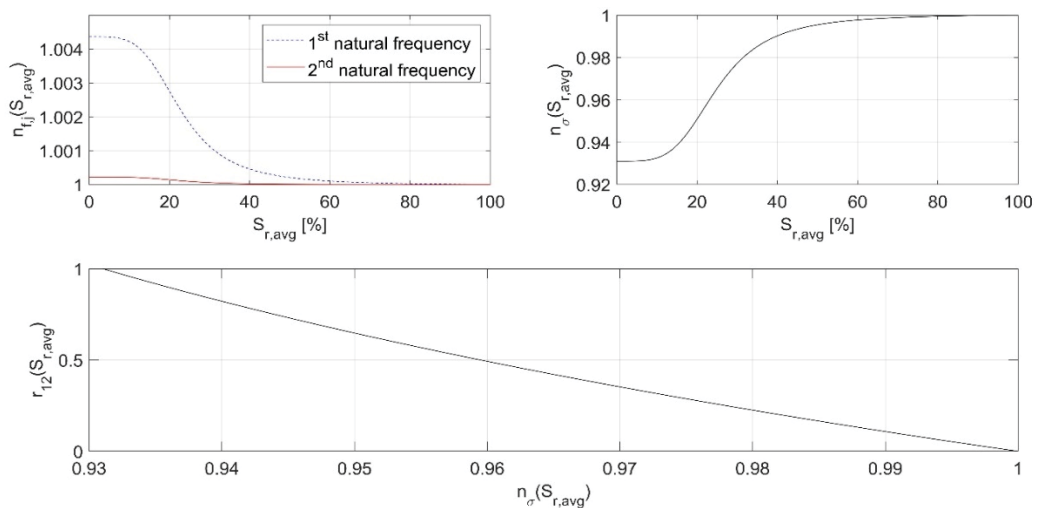


Figure 6: Results in terms of normalized values.

The previous results demonstrate as the modal and the static response of the building are quite correlated. In particular, the standard deviation of the foundation settlements has been considered in this study since it is related to the potential damage of the superimposed structure.

The results of the study are presented in Figure 6 in a normalized scale. In Figure 6, the following quantities are depicted:

$$n_{f,j}(S_{r,avg}) = \frac{f_j(S_{r,avg})}{f_{j,s}} \quad (6)$$

$$n_{\sigma}(S_{r,avg}) = \frac{\sigma_c(S_{r,avg})}{\sigma_{c,s}} \quad (7)$$

$$r_{12}(S_{r,avg}) = \frac{f_1(S_{r,avg})f_{2,s} - f_2(S_{r,avg})f_{1,s}}{f_{1,d}f_{2,s} - f_{2,d}f_{1,s}} \quad (8)$$

with $j=1,2$; f_j j -th natural frequency; $f_{j,s}$ j -th natural frequency at saturation; $f_{1,d}$ and $f_{2,d}$ 1st and 2nd natural frequency in dry conditions; σ_c , standard deviation of the foundation settlements; $\sigma_{c,s}$, standard deviation of the foundation settlements at saturation, while $n_{f,j}$, n_{σ} , and r_{12} are the j -th natural frequency normalized to the saturated value, the standard deviation of the foundation settlements normalized to the saturated values, and the difference between $n_{f,1}$ and $n_{f,2}$ normalized to the difference between the values taken in $S_{r,avg} = 0$. From Figure 6a, the relative variation of the first two natural frequencies demonstrates as the main variations are detected for the first mode and are in the order of 0.4%. On the other hand, Figure 6b depicts a relative variation of the standard deviation of the settlements of about 6%. Despite the fact that these variations are not worrying for the immediate stability of the building, their cyclic nature can determine damage accumulation in the superimposed structure, bringing in time to brittle collapses such as those occurred in the South façade of the "Chiarugi" pavilion. It is worth stressing that data and parameters extracted from real dynamic monitoring systems would be affected by several EOVs (such as the temperature effect) that could hide variations due to soil conditions. Commonly these EOVs, acting on the whole system, do not affect only the first natural frequency. Thus instead of focusing the attention on the variation of single frequencies, intelligent algorithms could be applied to the relative variations of these parameters (see, for example [18]). In these terms, Figure 6c conceptually shows as the normalized difference of the normalized frequencies can provide a correlation to the static response that is more amplified.

4 CONCLUSIONS

The paper investigated the influence of soil conditions, in terms of water table depth and degree of saturation, on the modal parameters of the "Chiarugi" pavilion. The modal response of the soil-foundation-structure system has also been correlated to variables potentially associated with the occurrence of damage in the superstructure (i.e., the standard deviation of the foundation settlements). The results of the study can be summarized in the following points:

- The absolute variations of the natural frequencies with respect to the variation of the degree of saturation of the third soil layer are quite low (maximum variations of about 0.4%);
- A variation in the first natural frequency value is reflected on a variation of the standard deviation of the settlements, which is an order of magnitude higher than that of the frequency (i.e., about 6%);
- Despite the low variations of natural frequency, the cyclic oscillation of the water table and the meteoric phenomena in Racconigi can change the degree of saturation

of the 3rd soil layer between 0.13 to 1 (under the made assumptions), and this results in a slow material deterioration that can lead to the sudden collapse of the masonry structure, as happened for the "Chiarugi" pavilion in 2016 and 2019;

- The low variations in natural frequency can be amplified if relative variations of the modal parameters of the structure are considered instead of absolute ones and if intelligent algorithms are used to separate the effects of other EOVs.

It is worth underlining that the results of this study are valid under the made hypotheses. For example, in a real scenario, the actual behavior of the soil with respect to the water table oscillation could diverge from linearity. Then, due to the infiltration processes also the soil characteristics of the surface soil layers will be affected by the changes in the degree of saturation, and thus the frequency variations could be even higher than those one reported in the study. These and other aspects (such as a full physical representation of the superimposed structure) will be addressed in future works, which might also focus on the prognosis of the "Chiarugi" pavilion thanks to nonlinear representation of the time degradation of the soil-foundation-structure system and the availability of some experimental variables in time, such as the time histories of water table depth and the degree of saturation of surface soil layers.

REFERENCES

- [1] D. F. D'Ayala, "Numerical Modelling of masonry structures," in *Structures and Construction in Historic Building Conservation*, M. Forsyth, Ed. Blackwell, 2007.
- [2] R. Ceravolo, G. De Lucia, E. Lenticchia, and G. Miraglia, "Seismic structural health monitoring of cultural heritage structures," in *Springer Tracts in Civil Engineering*, Springer, 2019, pp. 51–85.
- [3] G. M. Asselle, "Relazione di sintesi dell'indagine geologica, geotecnica e di caratterizzazione sismica, relativa ai terreni sottostanti le fondazioni del ex ospedale psichiatrico padiglione chiarugi," S. di Geologia, Ed. 2015.
- [4] G. Pistone, Ceravolo R., Lenticchia E., "Survival of the historical wing of the former neuropsychiatric hospital of Racconigi (CN)," *IF CRASC '17*, 2017.
- [5] M. V Civita *et al.*, "Le acque sotterranee della pianura e della collina cuneese," *Scribo2011*, 2011.
- [6] R. Hird and M. D. Bolton, "Clarification of capillary rise in dry sand," *Eng. Geol.*, vol. 230, pp. 77–83, 2017.
- [7] M. G. Abdullahi and I. Garba, "Effect of rainfall on groundwater level fluctuation in Terengganu, Malaysia," *J. Geophys. & Remote Sens.*, vol. 4, no. 2, pp. 142–146, 2015.
- [8] N. Lu and W. J. Likos, "Rate of capillary rise in soil," *J. Geotech. Geoenvironmental Eng.*, vol. 130, no. 6, pp. 646–650, 2004.
- [9] Q. Liu, N. Yasufuku, J. Miao, and J. Ren, "An approach for quick estimation of maximum height of capillary rise," *Soils Found.*, vol. 54, no. 6, pp. 1241–1245, 2014.
- [10] O.-D. S. Taylor, A. L. Cunningham, R. E. Walker, M. H. McKenna, K. E. Martin, and P. G. Kinnebrew, "The behaviour of near-surface soils through ultrasonic near-surface inundation testing," *Near Surf. Geophys.*, vol. 17, no. 4, pp. 331–344, 2019.

- [11] Y. Abdi, G.-R. Khanlari, and A. Jamshidi, "Correlation between mechanical properties of sandstones and P-wave velocity in different degrees of saturation," *Geotech. Geol. Eng.*, pp. 1–10, 2018.
- [12] T.-H. Kwon and G.-C. Cho, "Smart geophysical characterization of particulate materials in a laboratory," *Smart Struct. Syst.*, vol. 1, no. 2, pp. 217–233, 2005.
- [13] W. T. Oh and S. K. Vanapalli, "Relationship between Poisson's ratio and soil suction for unsaturated soils," in *Proc., 5th Asia-Pacific Conf. on Unsaturated Soils*, 2011, pp. 239–245.
- [14] W. T. Oh and S. K. Vanapalli, "The relationship between the elastic and shear modulus of unsaturated soils," in *Proceedings of the 5th international conference on unsaturated soils, Barcelona, Spain*, 2010, pp. 341–346.
- [15] M. T. Van Genuchten, "A closed-form equation for predicting the hydraulic conductivity of unsaturated soils," *Soil Sci. Soc. Am. J.*, vol. 44, no. 5, pp. 892–898, 1980.
- [16] R. S. Malik, S. Kumar, and I. S. Dahiya, "An approach to quick determination of some water transmission characteristics of porous media," *Soil Sci.*, vol. 137, no. 6, pp. 395–400, 1984.
- [17] R. S. Malik, S. Kumar, and R. K. Malik, "Maximal capillary rise flux as a function of height from the water table," *Soil Sci.*, vol. 148, no. 5, pp. 322–326, 1989.
- [18] G. Coletta *et al.*, "Use of the cointegration strategies to remove environmental effects from data acquired on historical buildings," *Eng. Struct.*, vol. 183, pp. 1014–1026, 2019.

ADVANCED NUMERICAL PREDICTION OF UNREINFORCED U-SHAPED MASONRY WALLS LOADED OUT-OF-PLANE

Scacco, Jacopo¹; Silva, Luís C.²; Vasconcelos, Graça³; Milani, Gabriele¹ and Lourenço, Paulo B.³

¹Department of Architecture Built Environment and Construction Engineering ABC,
Piazza Leonardo da Vinci 32, 20133 Milan, Italy
jacopo.scacco@polimi.it, gabriele.milani@polimi.it

²ISISE, Faculty of Engineering, University Lusófona de Humanidades e Tecnologias,
Campo Grande, 1749-024 Lisbon, Portugal,
luís.silva@ulusofona.pt

³ISISE, Department of Civil Engineering, University of Minho,
Azurém, 4800-058 Guimarães, Portugal,
graca@civil.uminho.pt, pbl@civil.uminho.pt

Abstract

The seismic vulnerability of unreinforced masonry structures is a relevant topic as they stand for one of the most typical building typologies in the world. Despite the effort carried out by researchers, further experimental campaigns can help to increase the level of knowledge on the most frequent collapse mechanism and to suggest the most adequate reinforcement technique for the specific case. In this context, we address here a study on a mixed construction technique, in particular a type of building with masonry walls and concrete slabs, the so-called “Placa” buildings. Such buildings are typical of the Lisbon region and were mainly erected from 1930 to 1960. In this period, there was low awareness about the effects of adding heavy slabs to the global and local behavior of masonry structures. The seismic vulnerability of such structures is high, which is relevant in a medium-high seismic hazard region such as Lisbon.

An experimental campaign will be performed at the University of Minho. The set-up comprises a U-shaped brick wall tested subjected to an out-of-plane load and three tests are planned to perform: an unreinforced and two (different) reinforced configurations.

In this paper, sensitivity analyses concerning the unreinforced wall are shown. The primary goal is the identification of the correct set-up that would allow the exploitation of the energy at the orthogonal connection without leading to undesirable rocking phenomena of the wall. In such a way, the subsequent application of the reinforcement will have a major role in vulnerability reduction.

Keywords: “Placa” buildings, brick walls, out-of-plane, micro-modeling, concrete damage plasticity.

1 INTRODUCTION

Masonry structures are one of the most typical building typologies all over the world. Despite their great efficacy for sustaining gravity loads, they may suffer severe damage when subjected to horizontal loads coming from destructive events like earthquakes [1][2][3]. In recent years, several efforts were made to reduce the seismic vulnerability of such structures [4][5]. Indeed, not only for historical structures, but also for schools [6], hospitals and palaces that assume strategic importance during possible emergency management. Many of these buildings are relatively recent and can present a mixed technology, in which both masonry brick walls and reinforced concrete slabs are combined. A remarkable example of such construction typology is represented by the so-called “Placa” buildings, typical of the urban expansion of Lisbon in the period from 1930 to 1960.

In the progressive trend of introducing the reinforced concrete as the main structural element, the “Placa” buildings are characterized by brick walls, which stand as structural elements and reinforced concrete (RC) slabs. However, such a combination was realized in a period of insufficient awareness of the consequence of adding heavy concrete slabs (if compared to the timber ones) for the local and overall response of the buildings. Many deficiencies, along with inadequate construction details, can be typically found in “Placa” buildings, namely: i) internal structural irregularities, ii) limited capacity of the vertical elements against shear forces and bending, iii) a low number of vertical elements, iv) interruption between floor slabs and masonry walls affecting the rigid diaphragm behavior. All these aspects, combined with the increase of inertia loads because of concrete slabs, might lead to a marked seismic vulnerability, enhanced by the relevant seismic exposition of Lisbon.

An experimental campaign has been planned to investigate the local structural capacity of such buildings. The primary focus is the investigation of the out-of-plane capacity of the brick masonry walls that rarely have enough resistance against forces acting perpendicular, causing local collapse mechanism. Three U-shaped brick walls will be tested by applying a uniform pressure on the internal side of the wall (as done in [7]). The first configuration (unreinforced wall) will serve as a reference for the two subsequent reinforced configurations. To get a damage pattern that resembles what is observed in “Placa” buildings, particular care has been addressed in the design process of the experimental set-up. Indeed, in order to define the most effective strengthening solution and provide a fair comparison, the damage should spread mainly at the connection with the orthogonal walls. For this reason, it is necessary to avoid, or significantly postpone, any rocking of the U-shaped wall. In such a way, the improvements ensured by the reinforcement technique will be more noticeable. To this end, this paper summarizes distinct hypotheses for the geometry, load and boundary conditions on the unreinforced configuration. Damage patterns and load-displacement curves are presented in order to provide a comparison of the results.

2 EXPERIMENTAL PLAN: AN OVERVIEW

In this section, the experimental plan is exposed in each step. I will include: i) material characterization tests, ii) test on one scaled unreinforced configuration, iii) test on two different scaled reinforced configurations. Regarding the firsts, masonry wallets with an English-bond arrangement (the same as the U-shaped walls) have been built and will be tested according to the recommendations given in EN 1052-1:1998 [8] and EN 1052-2 [9]. In particular, 3 wallets will be tested under compression and 3 wallets under diagonal compression in order to define the in-plane behavior. The out-plane behavior will be investigated by testing 5 wallets under

horizontal flexural tests and 5 wallets under vertical flexural tests. Along with these tests, a mechanical characterization of the mortar will be provided.

The geometric configuration of the walls has been defined to represent a typical façade and corresponding transversal walls of a ‘Placa’ building. As mentioned, bricks are arranged according to an English-bond arrangement with dimensions $250\text{mm} \times 120\text{mm} \times 60\text{mm}$. The initial geometric dimensions of the set-up are: 3.24m of façade wall length, walls’ height of 1.40m, transversal walls’ length of 1.20m and thickness of 0.25m. However, as it will be clearer in the next Sections, such initial assumption resulted to not be sufficient for avoiding a rocking of all systems. So, a slight modification of such configuration is later justified.

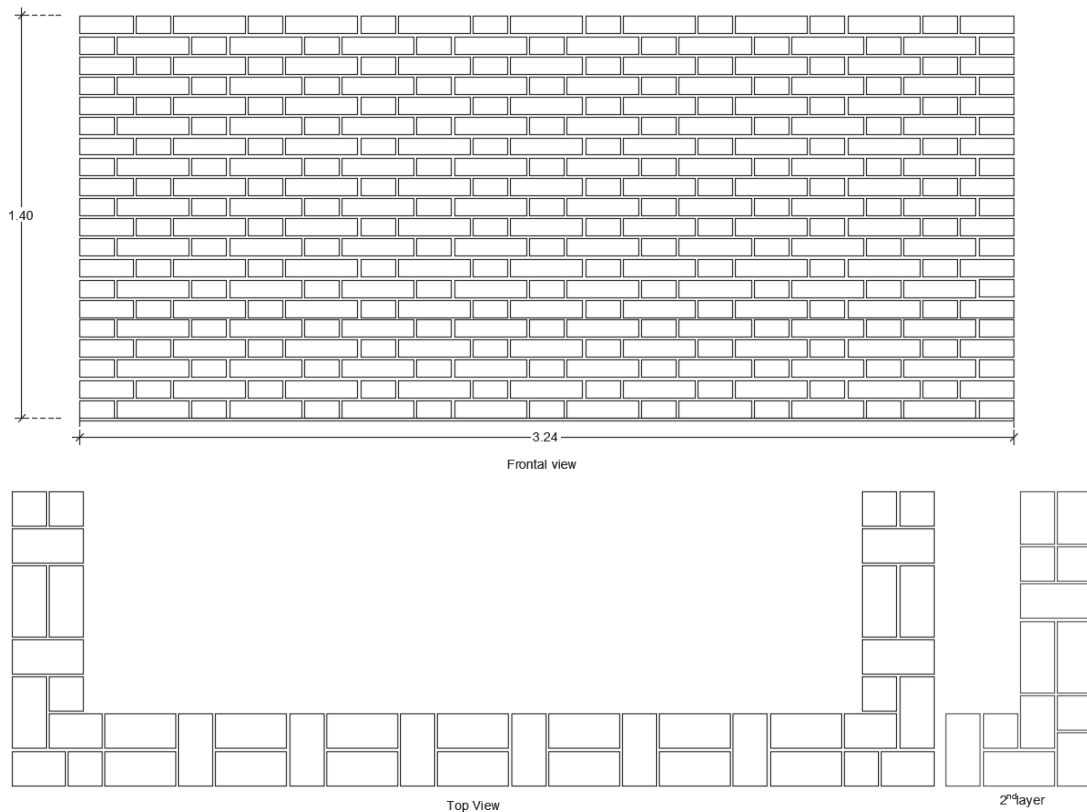


Figure 1 Frontal view (top) and top view (bottom) of the planned configuration.

The plan includes two different strengthening solutions are planned to be carried out: i) an anchored system between façade and transversal walls; ii) a textile reinforced mortar on the outer façade eventually coupled with the anchored system. In order to provide a further reference, the unreinforced wall will be reinforced after the damage and led to the collapse.

3 NUMERICAL STRATEGY: A MICRO-MODELING APPROACH

In the current prediction stage of the experimental campaign, a detailed heterogonous approach has been picked to reproduce accurately the failure modes. In such an approach, the bricks and mortar joints are modeled separately with contiguous 3D elements. No interfaces are interposed between them and the non-linear mechanical properties are exclusively lumped at the joints, addressing only elastic properties to the bricks (as done in [10–12]). Such simplification is reasonable as the good mechanical properties of bricks and the weak capacity of the mortar. Specifically, the mortar intended to be used in the tests is characterized as Mortar5, with a compressive strength equal to 5 MPa. All the analyses are carried out in the FE-based software Abaqus and non-linearities are addressed through the already available constitutive

model Concrete Damage Plasticity. In such a way, it is possible to input a differential behavior in compression and tension and define a specific softening law. In this predictive stage, a tensile strength equal to 0.2 MPa has been addressed to the mortar along with fracture energy of 0.02 N/mm. Regarding the mesh, taking advantage of the symmetry of the setup, a half wall has been modeled. The average size of the 3D brick elements is around 10-20 mm leading to an overall number of nodes around 140000.

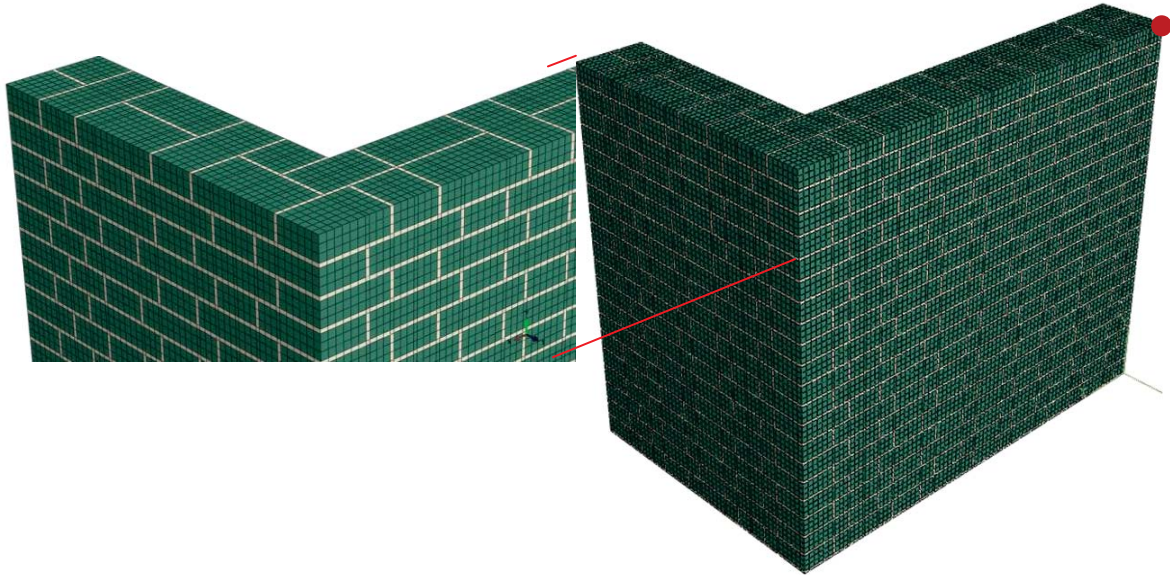


Figure 2 Model in Abaqus of half wall and mesh detail.

The analyses are carried out by applying a perpendicular uniform pressure on the internal side of the main wall in order to simulate the load transferred from the airbag that will be used in the experimentation (same procedure followed in [7]). In this way, the analyses are all performed under load control and the arch-length algorithm is employed for obtaining the softening response of the structure. Fixed boundary conditions are imposed at the bottom of the wall where a mortar layer (with the same mechanical properties used for the joints) is posed.

4 NUMERICAL RESPONSE OF THE U-SHAPED URM WALL: PARAMETRIC ANALYSES

The sensitivity (in terms of geometry, pre-stress level and boundary conditions) numerical analyses that will be shown in the next Sections are applied only at the unreinforced masonry case. Indeed, the main goal of the present work is the definition of the correct set-up with the view of applying different strengthening techniques on the same configuration in a subsequent step.

The first parametric analysis concerns the amount of pre-stress that is necessary to impose on the side walls in order to avoid or postpone any rocking phenomena. In Figure 3a it is provided a comparison of the load-displacement curves related to different values of the imposed pre-stress. The control point is picked exactly at the top middle of the wall (red circle in Figure 1). It is important to highlight that the global loads to which reference is made are related to the half specimen. As it is noticeable, the U-shaped wall tested with no pressure on the top of the side walls is characterized by a marked softening behavior. However, as shown in Figure 3b, such behavior is associated with a rocking phenomenon that is not desirable. The softening branch is strongly reduced at the increase of the pre-stress applied, reaching a plateau when a pre-stress of 100 kPa is considered. In fact, in Figure 3c, it is possible to appreciate the reduction of the damage at the bottom of the wall. However, its extent is still too clear and further sensitivity analyses are required.

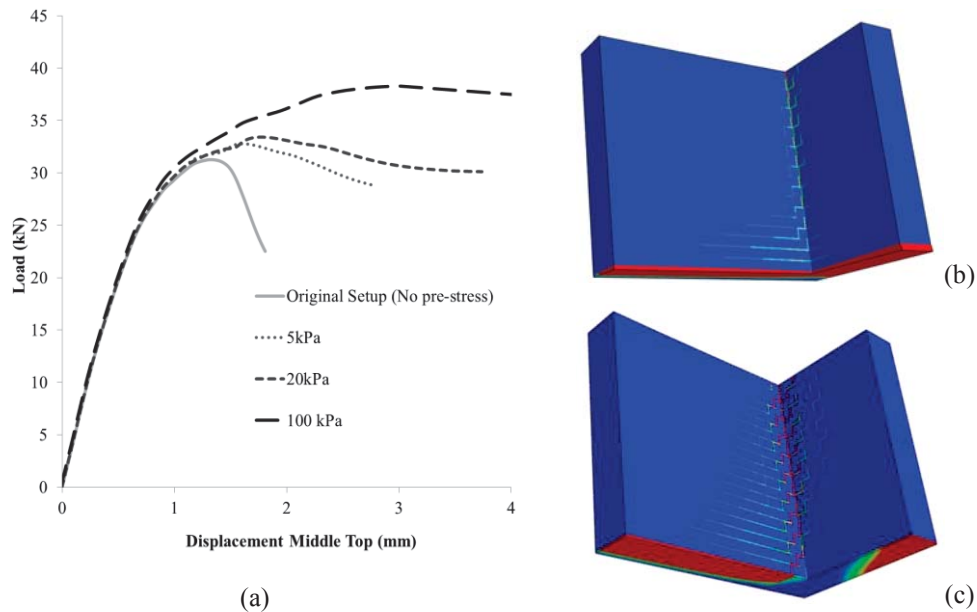
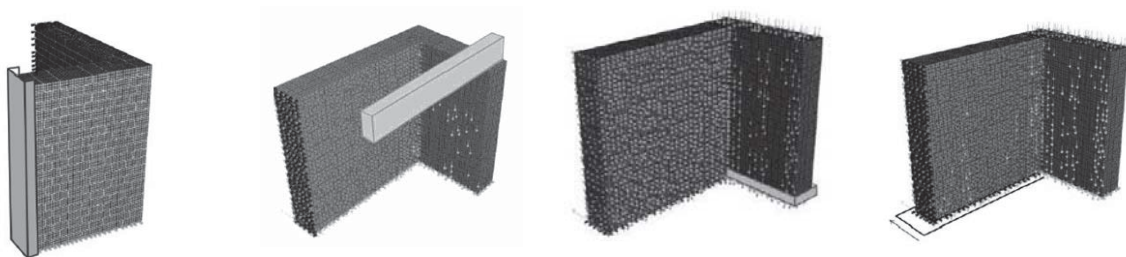


Figure 3 Load-displacement curves related to the wall in its original configuration by applying different values of pressure (a); damage configuration of the wall without pre-stress(b); damage configuration of the wall subjected to a pressure of 100 kPa (c).

The next sensitivity analyses are focused on the possibility to impose further constraints. In Figure 4 it is provided a qualitative overview of the results obtained. In particular, in Figure 4a the back face of the side wall is constrained. This hypothesis can be implemented by embedding the back portion of the lateral wall in U-shaped steel beams (a similar setup can be found in [13]). In such a way, the rotation of the side walls is prevented and the damage spread mostly at the connection as required. A similar result can be achieved by imposing a steel beam above the top back corner of the lateral walls. As it is noticeable in Figure 4b the damage pattern can be superimposed to the previous case. These strategies are highly efficient but, on the other hand, the control of the load attained by such constraints might be complicated.

In Figure 4c-d it is shown an attempt of modifying the boundary conditions at the base of the wall. In Figure 4c, the first layer of brick and mortar is furtherly constrained, but in such a way the rocking trend is only delayed. In Figure 4d, a different hypothesis has been made. In this case, the central wall is considered only supported at the base (a layer of sand can serve the purpose) leading to a single curvature bending moment. However, the damage pattern is concentrated mainly at the connection at the base of the walls



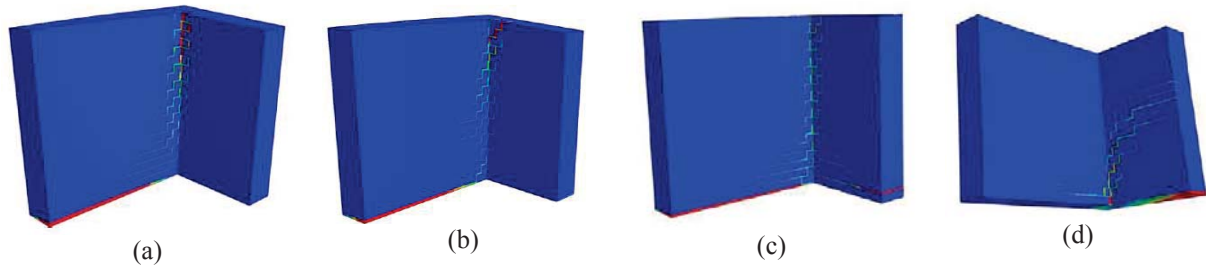


Figure 4 Boundary condition applied at the back face of the side wall and related damage pattern (a); boundary condition applied at the top of the side wall and related damage pattern (b); boundary condition applied at the bottom (fixing two layers of bricks) of the side wall and related damage pattern (c); boundary condition released at the bottom of the main wall and related damage pattern (d).

From the previous analyses, it seems evident the necessity to change the original geometric configuration presented in Section 2. So, a parametric analysis is conducted on the length of the main wall and side walls. These lengths are increased to 25 cm (model “SWL_25cm” that stands for Side Wall Longer of 25 cm) and to 50 cm (model “SWL_50cm”). The main wall is modified by adding 80 cm and 120 cm (model “402_SWO”) that stands for the main wall of 402 cm and the Side Wall Original and model “442_SWO”). Also, a combination of both modifications is provided in the models “402_SWL_25cm” and “442_SWL_25cm”. In all the cases a vertical pre-stress of 20 kPa is imposed.

In Figure 5 the global responses of all the models are reported. It is interesting to notice the strong enhancement that the extension of the side walls can provide (Fig. 5a). From a comparison of the capacity curves, the outcomes are very similar to the one obtained when a vertical pre-stress of 100 kPa is imposed. However, comparing the damage pattern (Fig. 6a-b), the rocking behavior is much less evident. Moreover, no evident differences can be noticed among the curves related to the models SWL_25cm and SWL_50cm but as shown in Figures 6a and 6b the damage at the base of the side wall is almost absent in this case. This might have huge relevance when the reinforced configurations will be treated.

Figure 5b provides the results related to the extension of the main wall (also in combination with an extension of 25 cm of the side walls). It is quite evident how increasing the length of the side walls is much more effective than extending the longitudinal dimension of the main wall. Moreover, this strategy would require much more material for the construction of the walls without leading to further improvements (see the comparison of the damage pattern in Figure 6a and Figure 6c).

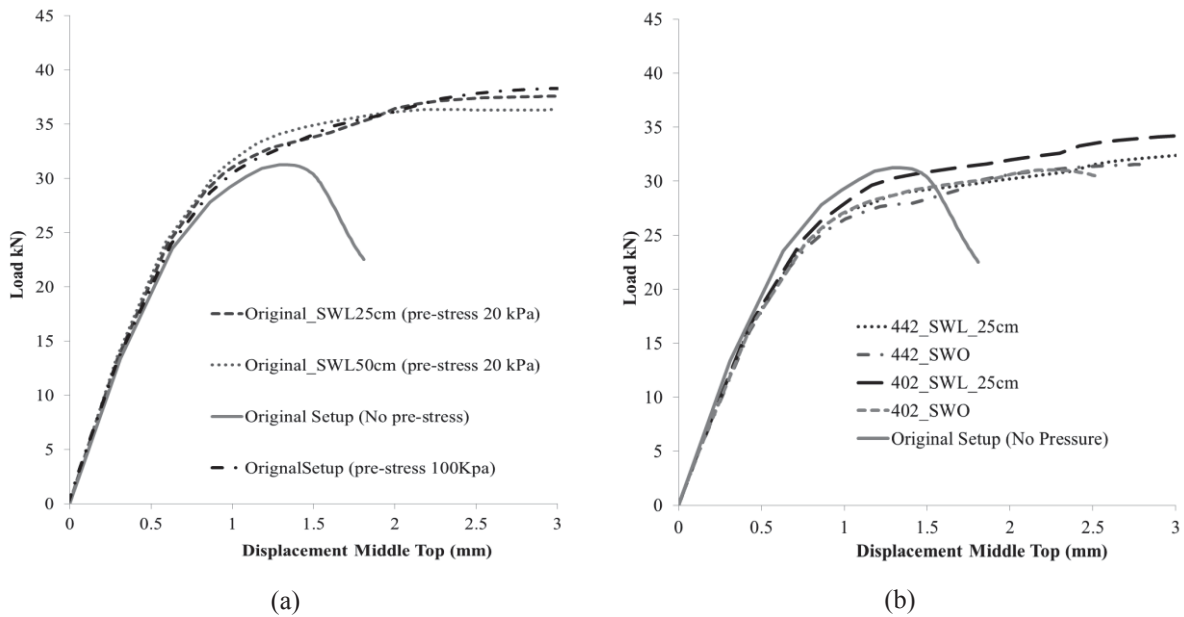


Figure 5 Load-displacement curves related to the original setup by changing the length of the side walls (a); Load-displacement curves of the original setup by changing the length of the main and of the side walls.

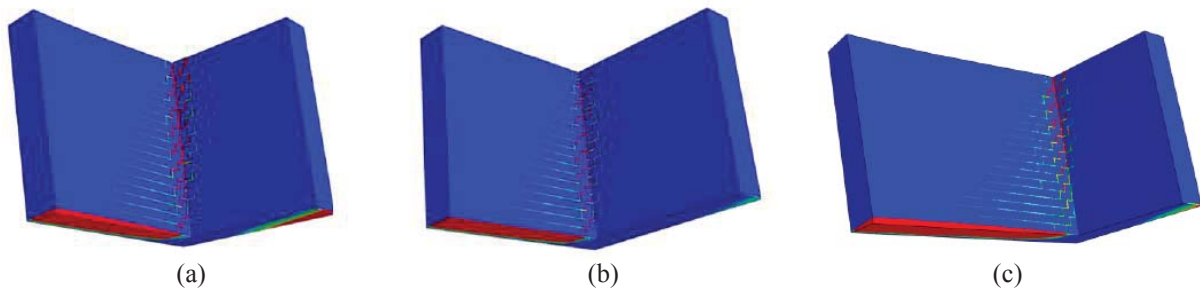


Figure 6 Damage pattern of the model SWL_25cm (a); Damage pattern of the model SWL_50cm (b); Damage pattern of the model 442_SWL_25cm (c).

5 CONCLUSIONS

The paper summarizes preliminary analyses conducted on an unreinforced brick masonry wall. The main scope was the definition of the correct set-up in terms of geometric configuration, the load applied and boundary conditions for upcoming experimental tests that will be performed at the facilities of the University of Minho in Guimarães.

The experimental campaign will focus on the seismic vulnerability and possible strengthening solutions for building realized with a mixed technology: masonry walls and RC slabs. The so-called “Placa” buildings are a typical example of such configuration, and particularly vulnerable as mainly spread in the Lisbon region. In order to resemble this structural typology, a U-shaped brick wall has been conceived. Several parametric analyses have been carried out to highlight the parameters that have more influence on both the global behavior and collapse mechanism. The different proposed scenarios revealed the necessity to adapt the initially planned configuration to prevent any rocking mechanism of the structure that would be undesirable. In fact, the occurrence of such a collapse mechanism would prevent the spread of damage at the connection between transversal walls, which will be the point of more interest when defining the strengthening solutions will be discussed. In the upcoming numerical analyses concerning the reinforced scenarios, the

composite materials might be added using a detailed micro-modeling [10][14] or through a simplified approach [15]. Whereas, the anchors might be introduced explicitly in the model or through truss FEs [7] avoiding an increase in the computational demand.

7 REFERENCES

- [1] Bianchini N, Mendes N, Lourenço PB. Seismic evaluation of Bagan heritage site (Myanmar): The Loka-Hteik-Pan temple. *Structures*, **24**, 905–21 (2020).
- [2] Giordano E, Clementi F, Nespeca A, Lenci S. Damage Assessment by Numerical Modeling of Sant ’ Agostino ’ s Sanctuary in Offida During the Central Italy 2016 – 2017 Seismic Sequence. **4**, 1–17 (2019).
- [3] Micelli F, Cascardi A. Structural assessment and seismic analysis of a 14 th century masonry tower. *Eng. Fail. Anal.*, **107**, (2020).
- [4] Aşıkoğlu A, Avşar Ö, Lourenço PB, Silva LC. Effectiveness of seismic retrofitting of a historical masonry structure: Kütahya Kurşunlu Mosque, Turkey. *Bull. Earthq. Eng.*, **17**, 3365–95 (2019).
- [5] Mosoarca M, Apostol I, Keller A, Formisano A. Consolidation methods of Romanian historical building with composite materials. *Key Eng. Mater.*, **747 KEM**, 406–13 (2017).
- [6] Formisano A, Iaquinandi A, Mazzolani FM. Seismic retrofitting by FRP of a school building damaged by Emilia-Romagna earthquake. *Key Eng. Mater.*, **624**, 106–13 (2015).
- [7] Murano A, Ortega J, Vasconcelos G, Rodrigues H. In fl uence of traditional earthquake-resistant techniques on the out-of-plane behaviour of stone masonry walls : Experimental and numerical assessment. *Eng. Struct.*, **201**, 109815 (2019).
- [8] EN 1052-1. EN 1052-1: Methods of test for masonry, Part 1: Determination of compressive strength, European Committee for Standardization, Bruxelles, Belgium.
- [9] CEN. EN 1052-2, European norm for methods of test for masonry – Part 2: Determination of flexural strength, 2000.
- [10] Scacco J, Ghiassi B, Milani G, Lourenço PB. A fast modeling approach for numerical analysis of unreinforced and FRCM reinforced masonry walls under out-of-plane loading. *Compos. Part B*, **180**, (2020).
- [11] Lourenço PB, Silva LC. Computational applications in masonry structures: from the meso-scale to the super-large/super-complex. *Int. J. Multiscale Comput. Eng.*, **18**, 1–30 (2020).
- [12] Silva LC, Lourenço PB, Milani G. Numerical homogenization-based seismic assessment of an English-bond masonry prototype: Structural level application. *Earthq. Eng. Struct. Dyn.*, **49**, 841–62 (2020).
- [13] Prota A, Marcari G, Fabbrocino G, Manfredi G, Aldea C. Experimental In-Plane Behavior of Tuff Masonry Strengthened with Cementitious Matrix–Grid Composites. *J. Compos. Constr.*, **10**, 223–33 (2006).
- [14] Scacco J, Milani G, Lourenço PB. A micro-modeling approach for the prediction of TRM bond performance on curved masonry substrates. *Compos. Struct.*, **256**, 113065 (2021).
- [15] Bertolesi E, Milani G, Poggi C. Simple holonomic homogenization model for the non-linear static analysis of in-plane loaded masonry walls strengthened with FRCM composites. *Compos. Struct.*, **158**, 291–307 (2016).

LOW-COST BASE ISOLATION SYSTEMS FOR UNREINFORCED MASONRY BUILDINGS IN DEVELOPING COUNTRIES

Nagavinothini Ravichandran¹, Daniele Losanno¹, and Fulvio Parisi^{1,2}

¹ Department of Structures for Engineering and Architecture, University of Naples Federico II, Via Claudio 21, 80125, Napoli, Italy
e-mail: {nagavinothini.ravichandran, danielle.losanno, fulvio.parisi}@unina.it

² Institute for Complex Systems, National Research Council of Italy, Via dei Taurini 19, 00185 Rome, Italy

Abstract

Unreinforced masonry (URM) buildings are one of the most common constructions in developing countries and are usually constructed based on traditional knowledge without engineering intervention. Due to poor seismic performance of URM buildings, the development of seismic protection systems can play a key role in the mitigation of losses in future earthquakes. Despite the availability of different interventions for seismic strengthening of URM buildings, the quest for a cost-effective technique still exists. On the basis of recent outcomes by these authors, this study presents the design of low-cost base isolation systems for a class of URM buildings deemed representative of the building stock of developing countries. The proposed base-isolation system is made by recycled-rubber fibre-reinforced elastomeric isolators (RR-FREIs). Building classes were defined by properly selecting those parameters which are expected to mostly affect the seismic behaviour of the building such as number of storeys, masonry type and in-plan irregularity. Three-dimensional numerical models of URM buildings were developed in SAP2000 using nonlinear layered shell elements and bilinear models for RR-FREIs. Nonlinear time history analyses were carried out for a set of ground motion records to investigate the performance of both fixed-base (FB) and base-isolated (BI) configurations of URM buildings. The comparison of results shows a significant reduction of inter-storey drift ratios for BI configuration, thus demonstrating the effectiveness of RR-FREIs.

Keywords: Unreinforced masonry buildings, base isolation system, recycled rubber, fiber reinforced elastomeric isolators, finite element analysis.

1 INTRODUCTION

Unreinforced masonry (URM) buildings are usually constructed using locally available bricks, based on traditional knowledge without engineering intervention. Such non-engineered constructions (NEC) are highly susceptible to damage when subjected to lateral loads like seismic motion. This is mainly due to the lack of seismic design, low strength construction materials and poor structural detailing [1]. The common URM buildings found in developing nations of the world are constructed using masonry walls with roofs made up of reinforced concrete. Such type of buildings tends to develop deep cracks and undergo significant damage even under moderate earthquakes [2]. The collapse of such non-engineered and semi-engineered buildings during seismic events had resulted in huge losses especially in developing nations like India, Nepal, Philippines, Pakistan, Mexico, and Indonesia. Notable events include the 2006 Yogyakarta earthquake and 2005 Kashmir earthquake in India and Pakistan, respectively [3].

Considering the economic impact, the complete replacement of NECs with earthquake-resistant buildings is unfeasible. Hence, there is a need for a sustainable control strategy with reduced cost. One of the promising solutions is the base isolation technology in which the seismic response of the superstructure is reduced by introducing isolation bearings between the superstructure and the foundation of the building [4,5,6]. However, the cost of the base isolation system being high, the application is usually limited to important structures such as hospitals and historic buildings. The continuous development in this field had led to the development of novel configurations of elastomeric bearings for base isolation. Among these, fibre-reinforced elastomeric isolators (FREIs) have been developed in the recent years as an alternative to conventional laminated rubber bearings [7,8]. The replacement of internal shims with flexible reinforcement makes FREIs less heavy and easier to install in comparison with conventional isolators.

In order to further reduce the cost of FREIs, significant research effort is being dedicated currently to developing a novel elastomeric bearing using recycled rubber. The extremely low cost of recycled-rubber fibre-reinforced elastomeric isolators (RR-FREIs) would make them highly suitable for application in developing nations [9,10,11,12]. However, research on the suitability and effectiveness of the novel RR-FREIs for base isolation of URM buildings is scarce in the literature [13]. A recent study by Losanno et al. investigated the effectiveness of RR-FREIs for a box-type URM building in developing nations [14]. The study assessed the response of fixed-base (FB) and base-isolated (BI) building models developed based on macro-modelling approach using SAP2000 [15]. The use of such simplified macro-modelling approach for nonlinear analysis of base-isolated structures can be widely seen in the literature [16, 17]. Developing a suitable modelling approach with acceptable accuracy is necessary to capture the exact response of the masonry structures [14,18,19,20].

In this context, the present study aims at investigating the effect of low-cost base isolation system on typical URM buildings from the stock of developing nations. Three building types were chosen in order to address the effect of plan variability, wall density and number of storeys on effectiveness of base isolation under a set of earthquake records. Nonlinear time history analyses of the FB and BI-URM buildings were carried out using a simplified three-dimensional numerical model developed in SAP2000.

2 SELECTION OF CASE STUDIES

Three different masonry buildings representing URM buildings in developing nations are considered for the aim of the study. The first building prototype (URM1) is a single-story building reported by Shahzada et al. (2012) with plan dimensions 4.115 m \times 3.505 m, built

with 0.228-m-thick walls as shown in Figure 1a. The experimental and numerical analysis results of URM1 are available in the literature [14,21,22]. The second building prototype (URM2) is selected based on a detailed investigation on the URM building stock in developing nations and the building plan with dimensions 8.0 m \times 6.0 m is shown in Figure 1b. The building plan is framed by also considering the Indian Standards for earthquake design [23]. The third building prototype (URM3) considered in the study is a two-storey building with the same building plan of URM2.

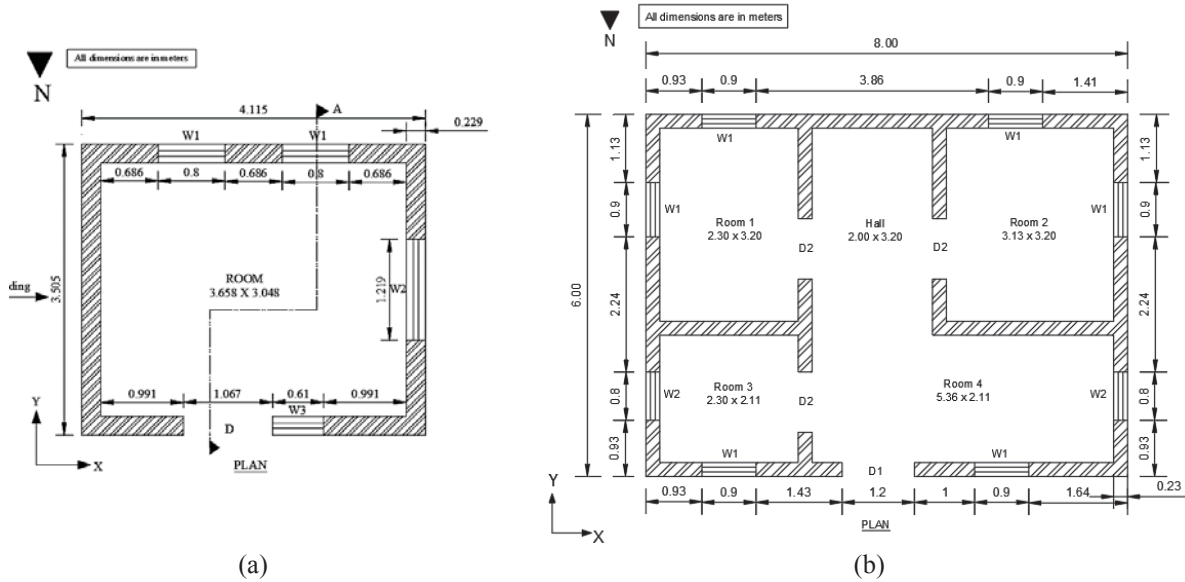


Figure 1: Plan view of URM buildings: (a) URM1; (b) URM2 and URM3.

The wall thickness is constant in plan and elevation, and equal to 0.228 m; the roof of the URM buildings was considered to be made up of 0.152 m reinforced concrete slab. Further, the buildings were also provided with a 0.152 m thick RC lintel above the openings to improve the building resistance to gravity loads. The inter-storey height of the structures was taken equal to 3.3 m. Mohr-Coulomb failure criterion with associated flow rule was used for simulating the inelastic shear behaviour and failure of the masonry. The RC elements were assumed as linear elastic and a rigid diaphragm constraint was assigned to the roof level of the buildings.

In order to consider the variability of mechanical properties, the material properties of the masonry structures considered in the present study were selected from previous studies on URM buildings located in developing nations such as India, Nepal, Pakistan and Iran [21,24,25,26,27]. The statistical distributions, mean value and coefficient of variation (CoV) of the main material properties are listed in Table 1.

Material properties	Distribution	Mean	CoV
Mass density [kg/m^3]	Lognormal	1707.5	0.13
Compressive strength [MPa]		4.2	0.43
Tensile strength [MPa]		0.16	0.56
Shear strength [MPa]		0.24	0.66
Young's modulus [MPa]		1302	0.68

Table 1: Material properties of URM buildings.

3 DESIGN OF BASE ISOLATION SYSTEM

Detailed research on RR-FREIs has been carried out in the recent years both numerically and experimentally. The RR-FREI sample and its experimental shear behaviour obtained from Losanno et al. (2020) is shown in Figure 2 [12]. These bearings are made up of rubber grains from used tires and industrial leftovers that are crumbled and glued together. The devices are installed in unbounded configuration in order to achieve an easier installation and significantly releasing internal stress within the isolator. The cost of this innovative RR-FREIs has been estimated in the order of 10% of the cost of conventional laminated rubber bearings.

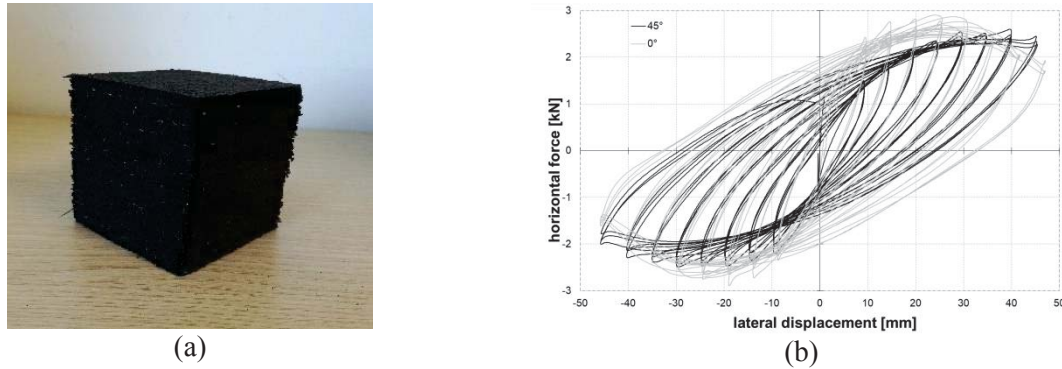


Figure 2: RR-FREI prototype: (a) picture; (b) experimental shear behaviour [12].

The weight of the building plays a major role in the design of rubber-based isolation systems. Considering the low weight of single-story URM buildings, only a smaller number of bearings would be required to achieve a conventional target period in the range of 2.00 to 2.50 s. But the requirement of a deep beam spanning over the whole length of the masonry walls poses a major challenge. In order to maintain the overall lateral stiffness of the system, a suitable trade-off needs to be identified while designing the base isolation systems with a limited number of bearings trying to avoid a deep base-beam. In the present study, the reinforced concrete base beam was designed in accordance with Indian code provisions confirming minimum concrete strength and internal reinforcement for URM buildings. The width of the base bond beam is maintained same as that of the wall thickness. Dead load analysis of finite element model was carried out with varying support locations to identify the most suitable position of the least number of isolators while satisfying the requirements in terms of both stress and deformation limits provided by the code. The number of isolators used in the three BI-URM buildings considered in the present study is equal to 8 (URM1) and 15 (URM2 and URM3), respectively. The layout of the isolation bearings is shown in Figure 3.

The properties of the square RR-FREIs used in the building prototypes are listed in Table 2. Square-shaped devices are considered for the possibility of easy cutting RR-FREIs from larger size rubber pads. The width of the bearing is defined according to stability requirements. The target period of BI-URM buildings is obtained as a trade-off between the longer period range for a more significant mitigation of spectral accelerations and the lower period value corresponding to limited displacement demand of the isolation system.

According to previous studies by the authors, the stability limit and damping capacity of RR-FREIs were set equal to 50% shear strain and 15% of critical damping, respectively [11]. Shear modulus for URM1 was set equal to 0.70 MPa [14]. A lower value of that modulus, i.e. 0.40 MPa, was selected for URM2 and URM3 in order to obtain a more stable geometry of the bearings. A laboratory investigation is being developed in order to reduce the shear modulus to a value which is typical of a softer compound.

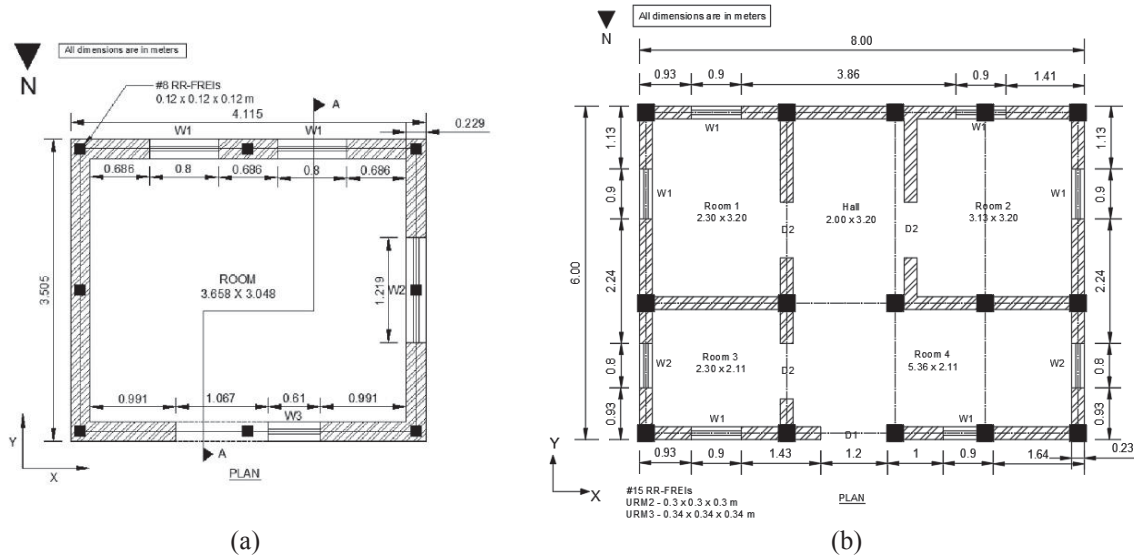


Figure 3: Location of RR-FREIs in URM buildings: (a) URM1; (b) URM2 and URM3.

Building model	FB fundamental period (s)	Target BI	Target displacement (mm)	Equivalent damping (%)	Shear modulus (MPa)	Rubber height (mm)
URM1	0.12	1.30	60	15	0.70	120
URM2	0.10	1.50	150	15	0.40	300
URM3	0.14	1.70	170	15	0.40	340

Table 2: Properties of RR-FREIs used in BI-URM buildings.

Due to increasing weight, a higher target period can be achieved with larger URM buildings, i.e. URM2 and URM3 in comparison with URM1. The variability associated with the properties of the isolators is not considered in the present study.

4 NUMERICAL MODELLING OF URM BUILDINGS

Masonry being a complex material demands extensive computational effort and experienced users in order to model the exact characteristics of the structure. Further, the inclusion of orthotropic properties of masonry requires additional material properties that are not readily available. Thus, a detailed experimental study on the masonry structure under investigation is necessary to reproduce the realistic behaviour of the masonry through numerical modelling. Hence, simplified macro-modelling techniques are preferred when the aim of the research is mainly focussed on the global behaviour of the structure. In macro-modelling techniques, masonry is modelled as a homogeneous material with equivalent mechanical properties.

The numerical model of the buildings was developed using this simplified macro-modelling approach in SAP2000 software package with nonlinear layered shell elements. In this macro-modelling approach, masonry was considered as an isotropic material. The shell layers are defined with different constitutive law in the thickness direction. Two stress-strain curves corresponding to normal and shear stresses were used to represent the nonlinear behaviour of the masonry [1,16]. The uniaxial compressive strength of the masonry was defined based on the analytical model developed by Kaushik et al. [28]. The uniaxial tensile strength of the masonry was defined based on the relationship suggested by Akhaveissy and Milani

[29]. The presented numerical approach had also been proven to be accurate and computationally efficient compared to other micro modelling approaches used in masonry modelling. The comparison of numerical and experimental results of the box-type structure can be seen in Losanno et al. [14]. Furthermore, a detailed research article on the comparison of different macro-modelling approaches for URM buildings highlights the suitability of this method [30]. In case of base-isolated buildings, the RC base beam is modelled using linear elastic frame elements. The RR-FREIs are modelled using a simplified bilinear model to account for non-linear behaviour of the bearings. The initial and post-yielding stiffness values were used in order to provide the effective stiffness and equivalent damping ratio obtained with the base isolation system design according to values listed in Table 2. The numerical models of the base-isolated buildings along with their first mode of vibration are shown in Figure 4. The first mode of BI-URM buildings clearly shows the rigid-body motion in the superstructure.

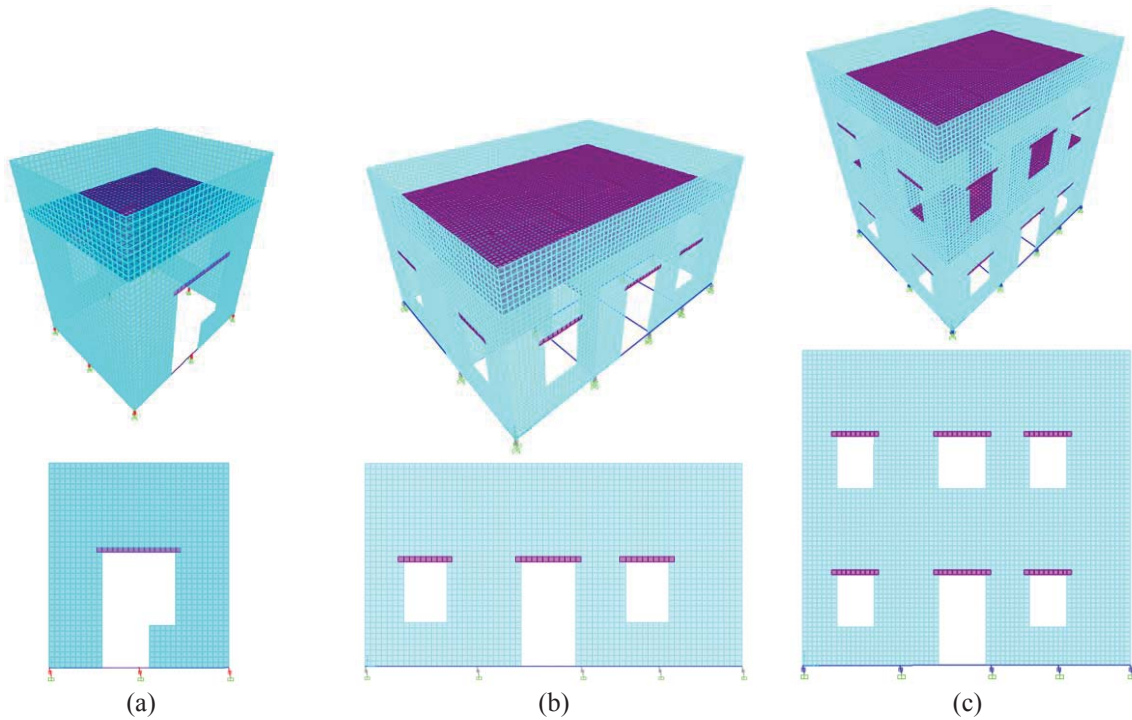


Figure 4: Numerical model (first mode of vibration) of base-isolated buildings using RR-FREIs: (a) URM1; (b) URM2; (c) URM3.

5 SEISMIC ANALYSIS OF URM BUILDINGS

In order to consider the uncertainties associated with earthquake ground motion (i.e. record-to-record variability), the response of the FB- and BI-URM buildings was studied under 20 ground motions recorded in several developing nations all around the world. The peak ground acceleration (PGA) of the selected records ranges from 0.01g to 1.78g. The moment magnitude and epicentral distance of the earthquakes associated with those ground motions range from 5.2 to 7.9 and 2.2 to 190 km, respectively. The variation of PGA with moment magnitude and epicentral distance of the ground motions is shown in Figure 5.

In order to model uncertainties associated both with the ground motions and material properties, Latin hypercube sampling (LHS) technique is used in the present study to select the random variables. Using this technique, 20 sets of random parameters were selected and randomly combined with 20 ground motion records. Then, direct integration nonlinear time-history analysis (NLTHA) of FB- and BI-URM buildings was carried out and the structural

response is obtained. Thus, a total of 120 NLTHAs were carried out over the different cases considered in the study.

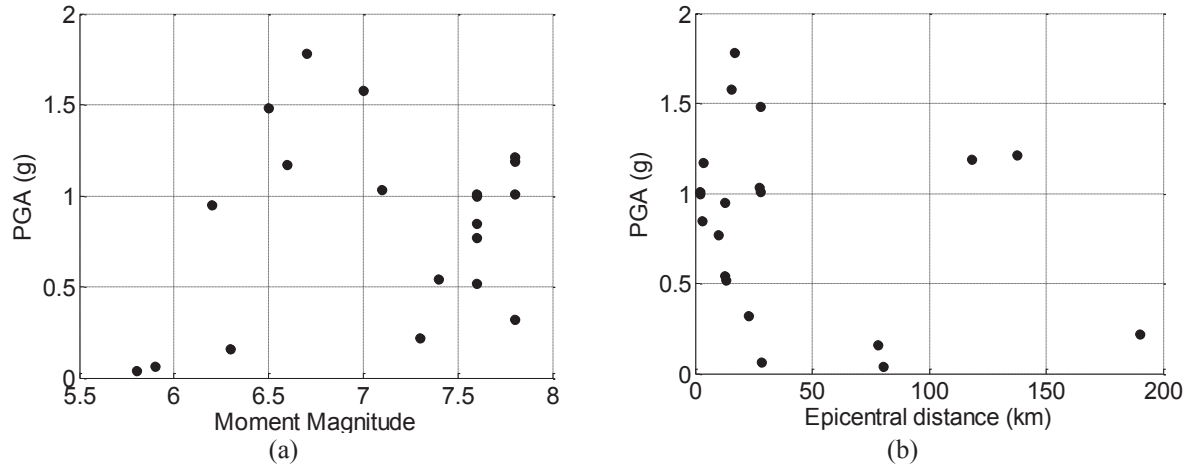


Figure 5: Selected input ground motion records: (a) PGA vs. moment magnitude; (b) PGA vs. epicentral distance.

6 RESULTS AND DISCUSSION

Structural response in terms of inter-storey drift ratio (IDR), which is the ratio between relative lateral displacement measured at the roof level and inter-story height, was computed for all case studies. IDR values were studied due to their direct correlation with the damage of the masonry buildings. The range of IDR corresponding to different damage levels varies in accordance with the building type and material strengths [31]. Previous studies suggest that IDR values greater than 0.2% usually correspond to extensive damage and significant strengthening interventions would be necessary. As far as isolators' displacements are concerned, a maximum response value was not explicitly given since the present study mainly focused on effectiveness of base isolation on seismic response of URM buildings. As a further development of the subject, the authors will study the fragility of the different structural components including base isolators.

6.1 URM1 building

The comparison between FB and BI configurations of URM1 building is shown in Figure 6. The results clearly highlight the effectiveness of base isolation. Under $PGA = 1.78g$, the reduction in IDR in the BI-URM building reaches approximately 91% whereas the reduction corresponding to the lowest PGA level, i.e. $0.04g$, is about 40%. It is also important to note that the IDR values of BI-URM1 building under all the earthquake excitations would be less than 0.2%, which demonstrates the absence of extensive damage. Furthermore, comparatively higher reduction in IDR is observed under seismic excitations with $PGA > 1g$. The percentage reduction of IDR in BI-URM1 in comparison with FB-URM1 building is shown in Figure 7, with average value equal to 63% over all shaking intensities. For ground motion records with $PGA \approx 1g$, a wide variation in the building response is observed due to the combined variation in material properties and record characteristics. It can be noted that a linear regression model would be poorly accurate in providing an estimate of IDR reduction versus PGA due to significant non-linear behaviour in both FB- and BI-URM buildings.

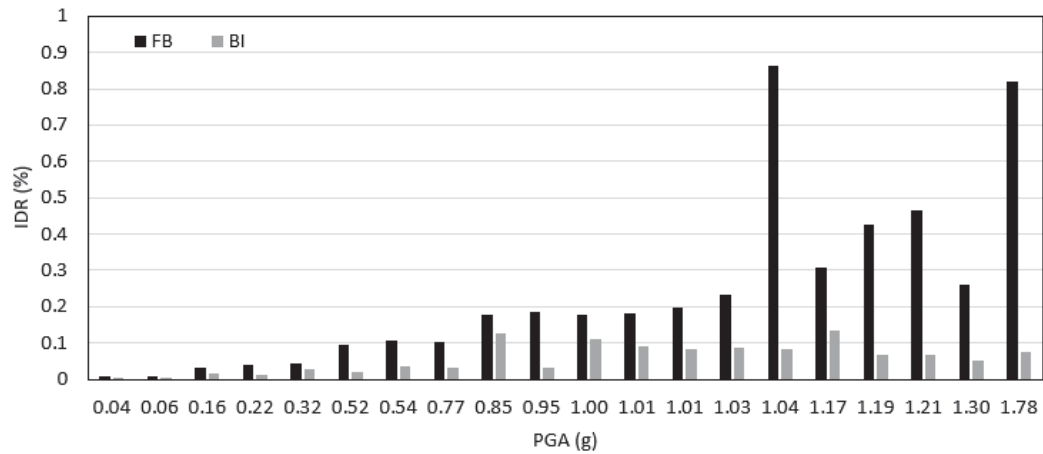


Figure 6: Seismic response of URM1 building.

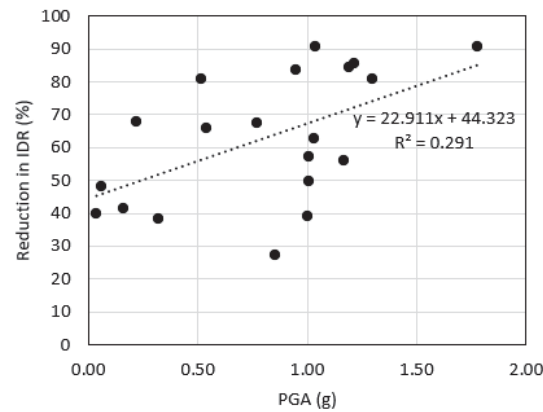


Figure 7: Percentage reduction in IDR of base isolated URM1 building.

6.2 URM2 building

URM2 building prototype is considered to identify the effect of base isolation with the variation in wall density along the direction of excitation (X-axis) and plan area in comparison with URM1 building. The response of URM2 building under earthquake excitations is shown in Figure 8. A significant reduction in IDR is observed in BI-URM2 building.

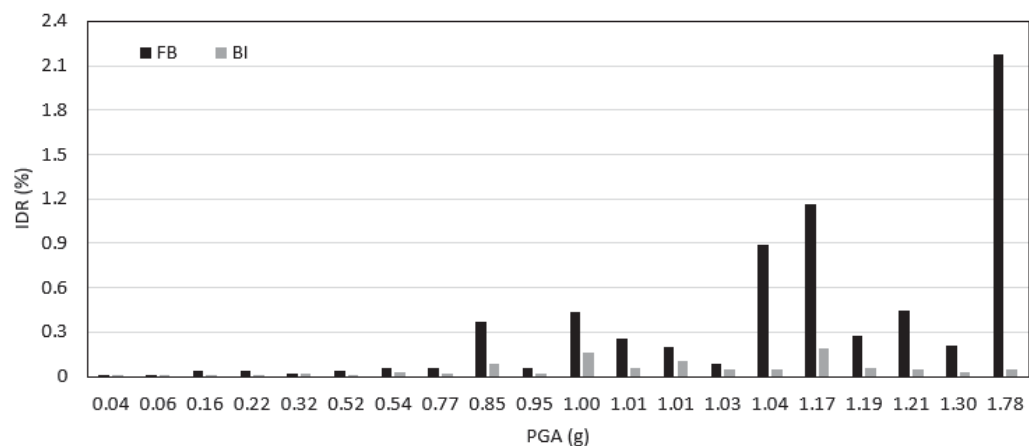


Figure 8: Seismic response of URM2 building.

Similar to URM1 building, the base isolation technique is found to be more effective under seismic excitations with $PGA > 1g$. The reduction in IDR due to base isolation under earthquake ground motion with $PGA = 1.78g$ is around 98% and response reduction in BI-URM2 building under varying PGA is shown in Figure 9. The average percentage reduction in IDR is about 66%, i.e. a higher value in comparison with URM1 building.

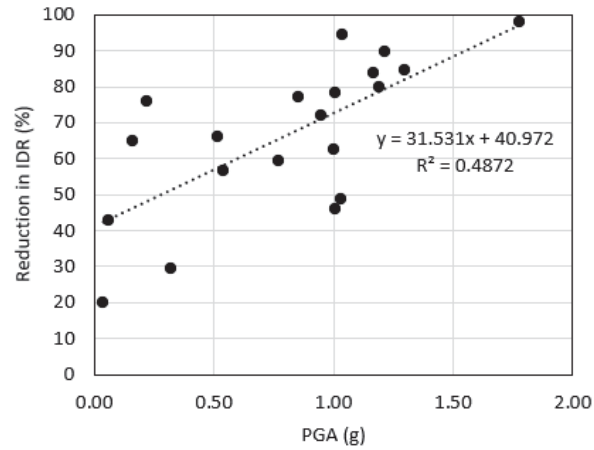


Figure 9: Percentage reduction in IDR of base isolated URM2 building.

6.3 URM3 building

URM3 building is considered in the present study to assess the effect of an increased number of storeys. The two-storey URM building is deemed more representative of a common building type found in developing nations, classified under low-to-medium income socio-economic people. The building response in terms of IDR is shown in Figure 10 and the percentage reduction is given in Figure 11. The properly designed base isolation system offers a great reduction in terms of structural response, thus avoiding severe damage even under higher PGA levels. The average percentage reduction in IDR of URM3 building is about 81%, which is significantly higher than that predicted on others URM buildings due to increased mass of the building. Differently from previous cases, a linear regression model would result more accurate in predicting IDR reduction. These outcomes confirm the effectiveness of RR-FREIs under medium-size URM buildings, laying the basis for a further development of the subject.

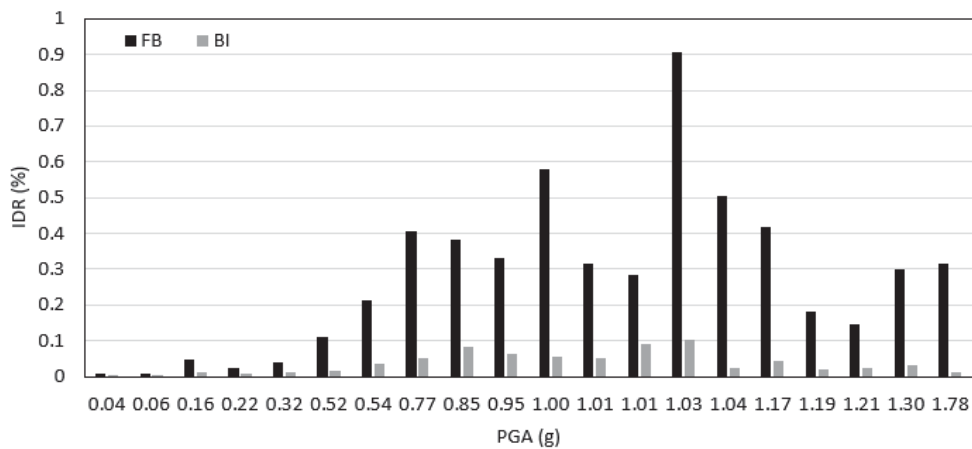


Figure 10: Seismic response of URM3 building.

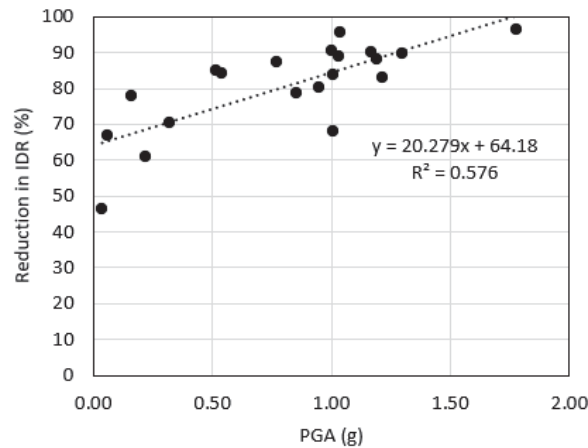


Figure 11: Percentage reduction in IDR of base isolated URM3 building.

7 CONCLUSIONS

In the present study, a low-cost base isolation system using recycled-rubber fibre-reinforced bearings for URM buildings in developing countries is assessed. Three URM buildings are selected as representative of nonengineered constructions and the numerical models are developed in SAP2000 using nonlinear layered shell elements. The base isolation system is designed for all the selected buildings and modelled using a simplified bilinear model. Statistical distributions of material properties were calibrated from previous studies available in the literature. Then, the nonlinear time history analyses of the URM buildings were carried out under both fixed-base and base-isolated configurations. In order to consider the variability associated with both material properties and earthquake excitation, 20 sets of random variables were obtained through Latin hypercube sampling technique and each combined with a different earthquake ground motion recorded in developing countries. The results show a significant reduction in the IDR of the base-isolated URM buildings in comparison with their fixed-base counterparts under all selected ground motions. Furthermore, the reduction in IDR due to base isolation is more effective in URM2 and URM3 buildings in comparison with URM1 building due to their higher mass, i.e. a longer base isolation period is achieved due to a more stable geometry of the isolators. These promising results confirm the suitability of a novel low-cost base isolation concept for URM buildings in developing nations. The lower IDRs of the BI configuration are a major proxy of a significant reduction in the conditional probability of damage to the URM structure under seismic events. In next studies, the authors will thus investigate the seismic fragility of base isolated URM buildings, explicitly accounting for the limited displacement capacity of base isolators as additional critical parameter.

REFERENCES

- [1] M. Valente, G. Milani, Non-linear dynamic and static analyses on eight historical masonry towers in the North-East of Italy. *Engineering Structures*, 114, 241-270, 2016.
- [2] A.S. Arya, T. Boen, Y. Ishiyama, *Guidelines for earthquake resistant non-engineered construction*. UNESCO, 2014.

- [3] A. Naseer, A.N. Khan, Z. Hussain, Q. Ali, Observed seismic behavior of buildings in northern Pakistan during the 2005 Kashmir earthquake. *Earthquake Spectra*, 26(2), 425-449, 2010.
- [4] F. Naeim, J.M. Kelly, *Design of seismic isolated structures: from theory to practice*. John Wiley & Sons, 1999.
- [5] N. Vaiana, S. Sessa, F. Marmo, L. Rosati, An accurate and computationally efficient uniaxial phenomenological model for steel and fiber reinforced elastomeric bearings. *Composite Structures*, 211, 196-212, 2019.
- [6] I.E.M. Sierra, D. Losanno, S. Strano, J. Marulanda, P. Thomson, Development and experimental behavior of HDR seismic isolators for low-rise residential buildings. *Engineering Structures*, 183, 894-906, 2019.
- [7] J.M. Kelly, Analysis of fiber-reinforced elastomeric isolators. *Journal of Seismology and Earthquake Engineering*, 2(1), 19-34, 1999.
- [8] N.C. Van Engelen, Fiber-reinforced elastomeric isolators: A review. *Soil Dynamics and Earthquake Engineering*, 125, 105621, 2019.
- [9] M. Spizzuoco, A. Calabrese, G. Serino, Innovative low-cost recycled rubber–fiber reinforced isolator: experimental tests and finite element analyses. *Engineering Structures*, 76, 99-111, 2014.
- [10] A. Calabrese, M. Spizzuoco, G. Serino, G. Della Corte, G. Maddaloni, Shaking table investigation of a novel, low-cost, base isolation technology using recycled rubber. *Structural Control and Health Monitoring*, 22(1), 107-122, 2015.
- [11] D. Losanno, M. Spizzuoco, A. Calabrese, Bidirectional shaking-table tests of unbonded recycled-rubber fiber-reinforced bearings (RR-FRBs). *Structural Control and Health Monitoring*, 26(9), e2386, 2019.
- [12] D. Losanno, A. Calabrese, I.E. Madera-Sierra, M. Spizzuoco, J. Marulanda, P. Thomson, G. Serino, Recycled versus natural-rubber fiber-reinforced bearings for base isolation: review of the experimental findings. *Journal of Earthquake Engineering*, 1-20, 2020.
- [13] A. Calabrese, D. Losanno, M. Spizzuoco, S. Strano, M. Terzo, Recycled Rubber Fiber Reinforced Bearings (RR-FRBs) as base isolators for residential buildings in developing countries: The demonstration building of Pasir Badak, Indonesia. *Engineering Structures*, 192, 126-144, 2019.
- [14] D. Losanno, N. Ravichandran, F. Parisi, A. Calabrese, G. Serino, Seismic performance of a Low-Cost base isolation system for unreinforced brick Masonry buildings in developing countries. *Soil Dynamics and Earthquake Engineering*, 141, 106501, 2021.
- [15] Computers & Structures, Inc, (CSI), SAP2000-Integrated software for structural analysis and design, *Comput Struct*, 2020.
- [16] V.N. Thuyet, S.K. Deb, A. Dutta, Mitigation of seismic vulnerability of prototype low-rise masonry building using U-FREIs. *Journal of Performance of Constructed Facilities*, 32(2), 04017136, 2018.
- [17] A.B. Habieb, M. Valente, G. Milani, Base seismic isolation of a historical masonry church using fiber reinforced elastomeric isolators. *Soil Dynamics and Earthquake Engineering*, 120, 127-145, 2019.

- [18] N. Ravichandran, A comparative study of phenomenological hysteretic models with application to recycled rubber-fibre reinforced bearings. *Journal of Vibroengineering*, 22(8), 1798-1813, 2020.
- [19] N. Vaiana, M. Spizzuoco, G. Serino, Wire rope isolators for seismically base-isolated lightweight structures: experimental characterization and mathematical modeling. *Engineering Structures*, 140, 498-514, 2017.
- [20] N. Vaiana, S. Sessa, M. Paradiso, L. Rosati, Accurate and efficient modeling of the hysteretic behavior of sliding bearings. In *7th International Conference on Computational Methods in Structural Dynamics and Earthquake Engineering (COMPDYN 2019)*, Crete, Greece, 2019.
- [21] K. Shahzada, A.N. Khan, A.S. Elnashai, M. Ashraf, M. Javed, A. Naseer, B. Alam, Experimental seismic performance evaluation of unreinforced brick masonry buildings. *Earthquake Spectra*, 28(3), 1269-1290, 2012.
- [22] T. Choudhury, G. Milani, H.B. Kaushik, Comprehensive numerical approaches for the design and safety assessment of masonry buildings retrofitted with steel bands in developing countries: The case of India. *Construction and Building Materials*, 85, 227-246, 2015.
- [23] Bureau of Indian Standards (IS:1893-Part 1), Criteria for earthquake resistant design of structures, 2002.
- [24] S.B. Kadam, Y. Singh, L. Bing, Seismic fragility reduction of an unreinforced masonry school building through retrofit using ferrocement overlay. *Earthquake Engineering and Engineering Vibration*, 19, 397-412, 2020.
- [25] A. Bakshi, K. Karimi, Performance evaluation of masonry buildings using a probabilistic approach, *Scientia Iranica*, 15(3), 295-307, 2013.
- [26] Y. Singh, D.H. Lang, J.S.R. Prasad, R. Deoliya, An analytical study on the seismic vulnerability of masonry buildings in India. *Journal of Earthquake Engineering*, 17(3), 399-422, 2013.
- [27] N. Giordano, F. De Luca, A. Sextos, Analytical fragility curves for masonry school building portfolios in Nepal. *Bulletin of Earthquake Engineering*, 19(2), 1121-1150, 2021.
- [28] H.B. Kaushik, D.C. Rai, S.K. Jain, Uniaxial compressive stress-strain model for clay brick masonry. *Current Science*, 497-501, 2007.
- [29] A.H. Akhaveissy, G. Milani, Pushover analysis of large scale unreinforced masonry structures by means of a fully 2D non-linear model. *Construction and Building Materials*, 41, 276-295, 2013.
- [30] N. Ravichandran, D. Losanno, F. Parisi, Comparative assessment of finite element macro-modelling approaches for seismic analysis of non-engineered masonry constructions. *Bulletin of Earthquake engineering*, Under review.
- [31] G.M. Calvi, A displacement-based approach for vulnerability evaluation of classes of buildings. *Journal of earthquake Engineering*, 3(03), 411-438, 1999.

NONLINEAR STATIC ANALYSIS OF MASONRY BUILDINGS THROUGH FIBRE-BASED CAPACITY MODELLING

E. Acconcia, V. Buonocunto, F. Parisi

Department of Structures for Engineering and Architecture, University of Naples Federico II
Via Claudio 21, 80125 Naples, Italy
e-mail: elia.acconcia@unina.it, valentina.b.707@gmail.com, fulvio.parisi@unina.it

Abstract

Seismic performance assessment of masonry buildings requires a nonlinear response analysis to achieve a reliable understanding of the possible effects of future earthquakes in terms of damage and losses. Equivalent frame (EF) modelling combined with nonlinear static procedures has been recognized as an efficient tool, which was validated in several studies through both experimental data and post-earthquake damage inspections.

In this paper, a new macroelement based on a fibre formulation is implemented into a matrix analysis approach to build up a nonlinear EF model and to perform incremental static (push-over) analysis with response control. For each step of the analysis, the stiffness matrix of the structure is updated using the novel macroelement model, accounting for geometric and mechanical nonlinearities both in terms of flexural and shear behaviour. Floor systems are modelled with truss elements, the stiffness of which can be varied in order to consider either rigid or flexible floors. In addition, the capacity model can simulate different degrees of connection at wall intersections and can easily be adapted to consider structural elements made of reinforced concrete, steel, wood, or other materials.

The capacity modelling procedure proposed in this study was first validated by simulating the in-plane lateral behaviour of a full-scale masonry wall with opening, and then, implemented to run pushover analysis of existing masonry buildings representative of those located in the Campania region (southern Italy).

Keywords: Masonry buildings, Macroelement modelling, Fibre formulation, Experimental validation, Nonlinear static analysis, Seismic performance.

1 INTRODUCTION

Post-earthquake reconnaissance missions and experimental programs have shown a significant vulnerability of unreinforced masonry (URM) structures to earthquakes, resulting in huge losses of life and money [1]. Despite the wide use of masonry as the oldest construction technology worldwide, the simulation of the seismic behaviour of URM structures and their retrofitting still need to be further investigated.

Over the years, various approaches have been proposed for simulation of URM structures, simplifying the problem differently according to the type of construction (e.g., modern or historical building, church, castle, bridge), specific purpose of the analysis (e.g., structural performance assessment under gravity loads, seismic actions, settlements), and the expected accuracy level and resolution of mechanical behaviour. Accurate results can be obtained through finite element (FE) simulation based on micro-modelling techniques, where masonry units, mortar joints and, if any, unit-mortar interfaces are distinctly modelled with nonlinear finite elements [2–5]. Several authors have proposed simplified micro-models in which only masonry units and joints are considered [6,7]. Even though micro-modelling techniques allow accurate simulations of masonry structures, they require a detailed knowledge of masonry constituents and have a considerable computational cost. This is a major drawback that makes FE micro-modelling rather difficult to apply in engineering practice and/or in structural assessments based on few data. In this respect, the macro-modelling approach [2] based on the assumption of masonry as equivalent homogeneous material allows a good trade-off between computational accuracy and cost, hence being applicable to real constructions and/or structures with few known properties.

An alternative computational strategy for structural response analysis of URM constructions, particularly in the case of buildings for their global seismic performance assessment, is based on macroelement modelling of walls with openings, i.e., the idealization of each wall as an equivalent frame (EF) with vertical and horizontal elements simulating pier and spandrel panels, respectively [8,9]. Macroelements with different behavioural modes can be used to model such types of masonry panels, which have comparable size with respect to openings. Pier-spandrel joint panels can be implicitly considered within the EF model, making use of macroelements with rigid parts at their ends. Macroelement modelling was validated on several structures, including those having an irregular layout of openings [10].

This paper presents a novel macroelement modelling procedure that permits the seismic analysis of masonry buildings, simulating the in-plane nonlinear response of load-bearing walls. The proposed macroelement, which is based on a fibre formulation, was validated in a previous study against experimental tests on single piers. In this study, the macroelement is implemented into a matrix-based formulation for development of EF models and their seismic performance assessment via nonlinear incremental static (pushover) analysis with response control. The overall approach is then validated at the system scale by comparing numerical results to experimental data of a lateral loading test on a full-scale masonry wall with central opening. The final part of this paper describes the application of the fibre-based macroelement approach to an URM structure representative of real buildings located in Campania (Italy), for their seismic fragility assessment.

2 MACROELEMENT ANALYSIS PROCEDURE

This study builds upon a fibre-based macroelement that was recently developed and experimentally validated by Parisi and Acconcia [11,12]. The aim was to develop a matrix-based procedure for nonlinear incremental static (pushover) analysis of masonry walls and buildings.

The macroelement allows the simulation of flexural, shear and rocking contributions to deformations associated with in-plane lateral loading, considering geometric and mechanical nonlinearity sources as well as the macroscopic constitutive behaviour of masonry.

The pushover analysis procedure is based on a nonlinear incremental algorithm with response control, namely, where the structure is subjected to increasing horizontal displacement of a control point located at the roof level. The macroelement proposed by Parisi and Acconcia [12] is modified to incorporate the presence of possible rigid end parts, simulating the presence of pier-spandrel joint panels. Each macroelement is formulated according to Timoshenko's beam theory and its stiffness matrix is defined by accounting for axial, flexural, shear, and torsional behaviour. The stiffness matrix of the structure is then assembled and updated according to the secant method during pushover analysis. The stiffness matrix coefficients are indeed a function of the displacement components at the two ends of the macroelement. In each analysis step, the secant stiffness matrix is evaluated through an iterative procedure that can be summarized in the following phases:

- linearized solution of the structure under the displacements imposed in the current step;
- evaluation of the displacements experienced by each macroelement and corresponding stresses and strains throughout fibres;
- computation of the secant stiffness for each macroelement;
- linearized solution of the structure based on the updated stiffness matrix;
- convergence check in terms of internal forces for each macroelement;
- iteration of previous steps or termination of stiffness matrix updating.

In the following sections, the EF modelling and analysis algorithm is validated by comparing pushover analysis results to experimental data in the case of a full-scale tuff stone masonry wall [13]. The procedure is then used to build up the EF model of an URM building, the seismic vulnerability of which is evaluated through fragility analysis.

3 EXPERIMENTAL VALIDATION AT SYSTEM SCALE

The EF modelling approach and pushover analysis procedure was validated against a lateral loading test on a full-scale URM wall with central opening [13]. The wall specimen consisted of two piers connected to each other by a spandrel with timber lintel above the opening (Fig. 1). The wall was made of tuff stone masonry with running bond and 10-mm-thick mortar joints. Overall, the wall was 5.10-m-long, 3.62-m-high, and 310-mm-thick. The piers were 1.70-m-long, whereas the spandrel was 1-m-high. The specimen was first subjected to vertical loads on top of the piers and then to horizontal loading with displacement control. Vertical loads had an intensity of 200 kN. The horizontal load consisted of a displacement-controlled force that was applied to the wall at a height of approximately 3.00 m from the base of the piers. The tuff masonry was composed of yellow tuff stones and a pozzolanic mortar, having the mechanical properties listed in Table 1.

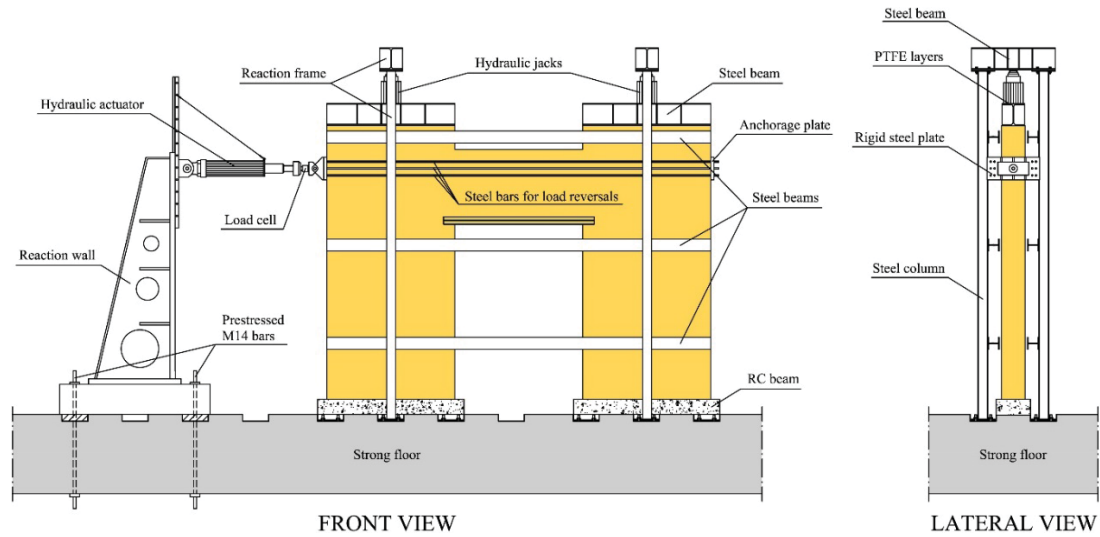


Figure 1: Experimental setup of lateral loading test on full-scale URM wall with opening [13].

Material	Tensile strength f_t [MPa]	Compressive strength f_c [MPa]	Young's modulus E [GPa]	Shear modulus G [GPa]
Tuff masonry under compression parallel to mortar bed joints (case of spandrel)	0.192	3.85	2.07	0.86
Tuff masonry under compression perpendicular to mortar bed joints (case of piers)	0.198	3.96	2.22	0.92

Table 1: Mechanical properties of tuff stone masonry.

Figures 2a and 2b show the EF model of the wall specimen and a numerical-experimental comparison in terms of base shear versus top displacement curves, respectively. The numerical procedure allows a satisfactory reproduction of the initial stiffness, the peak base shear (experimental value of 184.31 kN against numerical value of 182.96 kN), and maximum lateral displacement. The damage observed on the wall specimen at the end of test was also well simulated, indicating a flexural failure of both piers and a diagonal shear cracking in the spandrel.

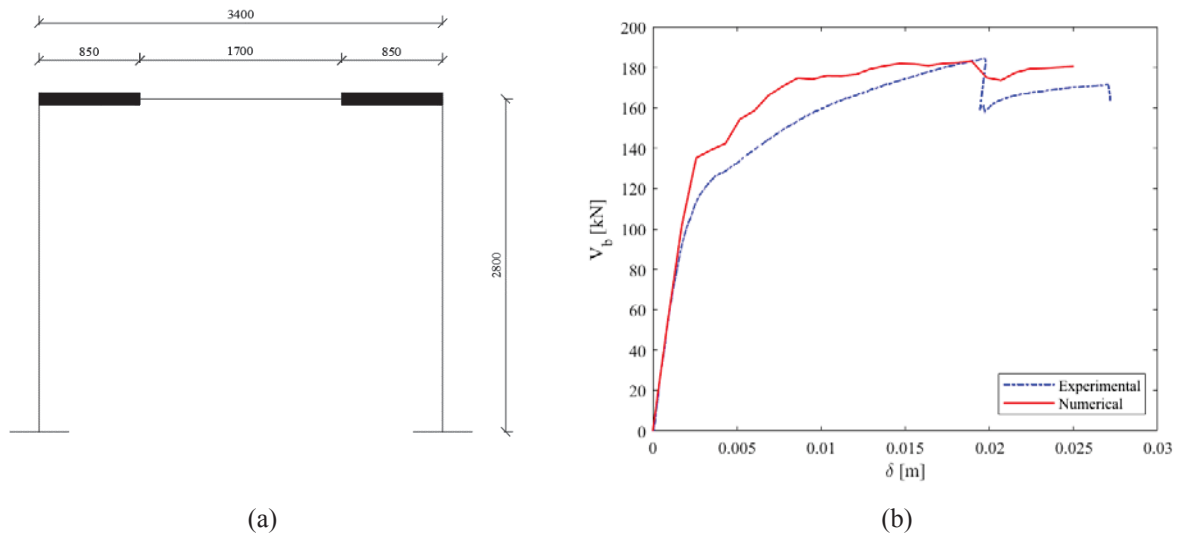


Figure 2: (a) EF model of wall specimen; (b) numerical-experimental comparison in terms of base shear versus top displacement curve.

4 FRAGILITY ANALYSIS OF CASE-STUDY BUILDINGS

The definition of case studies was based upon typological-structural data regarding existing URM buildings in the Campania region (Italy), in order to generate a sample of archetype buildings representative of residential buildings surveyed in that area. In detail, reference was made to real data from the CARTIS database [15], which collects information on typological and geometric characteristics of Italian buildings. Based on the 2011 Italian census data [16], the Campania region is characterized for more than 47% by masonry buildings, 94% of which were built before the first Italian code on masonry structures, namely DM 20/11/1987 [17]. In terms of size distribution, the masonry buildings in the area are composed of single-storey buildings (19%), two-storey buildings (45%), three-storey buildings (22%), and buildings with more than three storeys (14%).

By querying the CARTIS database [15], the pre-code building class in the area under study was characterized in more detail. It was found that 57.9% of existing buildings are made of tuff stone masonry with load-bearing walls having the following distribution of thickness at the ground floor: 700 mm in 32.9% of cases and 800 mm in 39.4%, with remaining values equal to 400, 500 and 600 mm. The mean thickness of load-bearing walls at the ground floor is 660 mm. In plan, the on-centre distance between walls was found to be 4.50 m in 80.2% of cases, 5.0 m in 15.3%, and 4.0 m in 4.5%, with a mean value of 4.64 m. The mean floor area of buildings falls in the interval $[100 \text{ m}^2, 150 \text{ m}^2]$ in 41% of cases, $[60 \text{ m}^2, 100 \text{ m}^2]$ in 24%, $[150 \text{ m}^2, 250 \text{ m}^2]$ in 28%, and $[250 \text{ m}^2, 350 \text{ m}^2]$ in 3%, with the remaining 4% of buildings having an area larger than 350 m^2 . The mean floor area is 159 m^2 . It was also found that 79% of tuff stone masonry buildings have flat floors, whereas the remaining 21% of them is characterized by vaults. Among flat floors, there are 68% of them consisting of steel I-beams and hollow tiles, 14% made of wooden beams, 12% made of concrete and hollow tiles, 5% consisting of wooden beams and tiles, and 1% made of SAP-type prefabricated systems with steel-reinforced tiles. The selected building has a rectangular plan with 3 walls in the X direction and 5 walls in the Y direction and consists of 2 floors (Fig. 3). The geometric characteristics agree with statistics reported above, so the distance between walls is approximately 4.60 m, the thickness of walls

at the ground floor is 660 mm, reducing to 500 mm at the first floor. The floors have an area of 246 m² and consist of steel I-beams and hollow clay tiles.

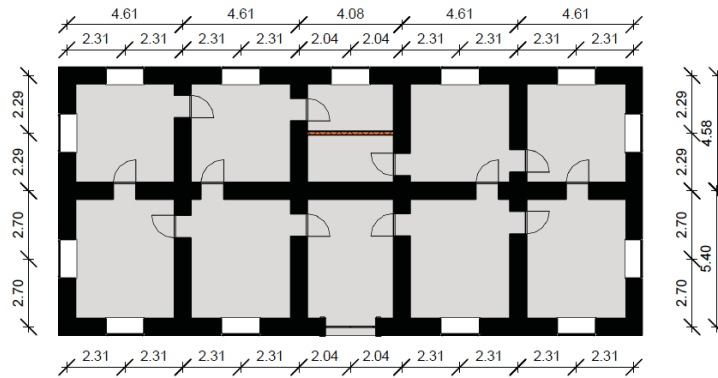


Figure 3: Plan of the building (longitudinal and transverse walls in the X and Y directions, respectively).

As regards the mechanical characteristics, the tuff stone masonry under study was regarded as ‘regular soft stone masonry’ according to the Italian building code NTC 2018 [18]. The mean values of mechanical properties assumed here were set to the average of those provided by the Italian building code commentary CS.LL.PP. 21/01/2019 n.7 [19]. According to CNR-DT 212-2013 guidelines on seismic reliability assessment of existing buildings [20] and previous studies [7,14], uncertainties in material properties were modelled as outlined in Table 2, defining the dispersion of lognormally distributed variables as follows:

$$\beta = \frac{X_{\max} - X_{\min}}{2} \quad (1)$$

where X_{\min} and X_{\max} are the minimum and maximum values of the natural logarithms of the property.

Property	Symbol	Unit	Range		Distribution	μ	β
			min	max			
Compressive strength	f_m	MPa	2.00	3.20	Lognormal	2.60	0.24
Diagonal shear strength	τ_0	MPa	0.04	0.08	Lognormal	0.06	0.35
Sliding shear strength	f_{v0}	MPa	0.10	0.19	Deterministic	0.145	-
Young’s modulus	E	MPa	1200	1620	Lognormal	1410	0.15
Shear modulus	G	MPa	400	500	Lognormal	$0.33E$	-
Tensile strength	f_t	MPa	-	-	Lognormal	$0.05f_m$	-
Tensile fracture energy	G_{ft}	N/mm	-	-	Deterministic	0.0025	-
Specific weight	w	kN/m ³	-	-	Deterministic	16	-

Table 2: Uncertainty modelling of material properties.

As regards the mechanical modelling of masonry, the compressive behaviour was simulated by assigning the constitutive model proposed by Augenti and Parisi [21]. That model is defined by the peak compressive strength f_m and the corresponding axial strain, which was assumed so that the secant modulus of elasticity at $0.3f_m$ was equal to Young’s modulus E provided in [19]. The tensile behaviour of masonry was assumed to be linear elastic up to the peak strength f_t and

followed by an exponential post-peak phase, assuming $f_t = 0.05f_m$ and a deterministic value of tensile fracture energy $G_{ft} = 0.0025$ N/mm.

The selected building was analysed through an equivalent frame model (Fig. 4) in which macro-elements were equipped with rigid offsets suitably sized to take into account the pier-spandrel joint flexibility and interaction according to previous studies [10,22]. Floor systems were modelled through linear truss elements with axial stiffness derived from size and material properties. That modus operandi allowed on one hand the floor flexibility to be considered in the distribution of horizontal actions between walls, and on the other, the axial force in spandrels to be computed. By the way, the flange effect due to wall-to-wall connections was taken into account in the structural model. It is also noted that one-way floors were assumed to span in the Y direction of the building plan, hence transmitting gravity loads to walls oriented in the X direction. Therefore, the gravity loads on walls in the Y direction were barely associated with self-weight of structural elements. Pushover analysis was performed with response control under two lateral load profiles, namely, the ‘modal profile’ with lateral forces proportional to the first vibration mode times inertia masses and the ‘mass profile’ proportional to inertia masses only. The centre of mass at the roof level was assumed as control point for nonlinear seismic analysis.

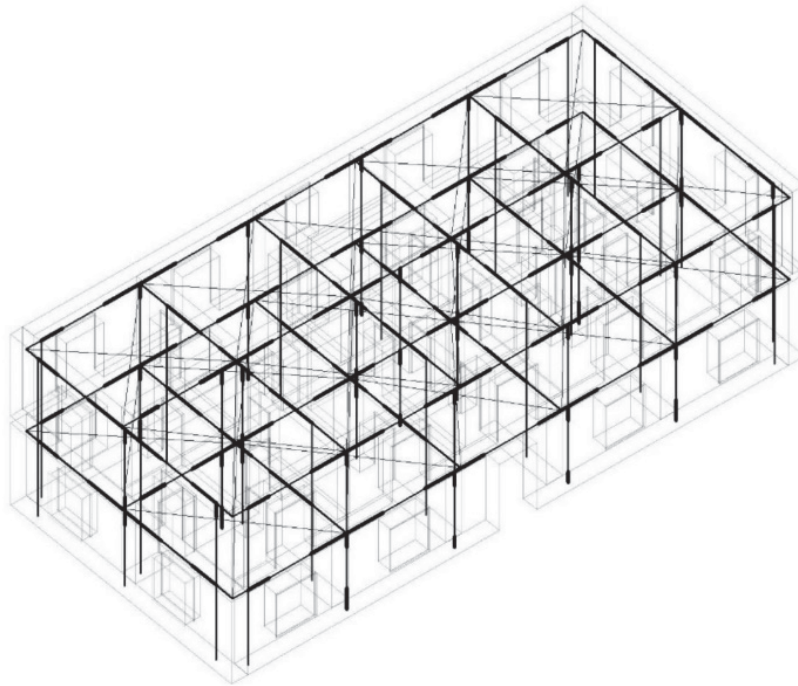


Figure 4: Equivalent frame model of the cases-study building.

Fragility analysis was carried out on 27 structural models of the building, corresponding to as many samples of material properties assumed to be lognormally distributed according to Table 2. More specifically, three possible values equal to μ , $\mu e^{-\beta}$ (16th percentile) and $\mu e^{+\beta}$ (84th percentile) were assigned to f_m , σ and E , resulting in 3^3 combinations of those material properties. Figure 4 shows the capacity curves corresponding to each direction and profile of horizontal forces.

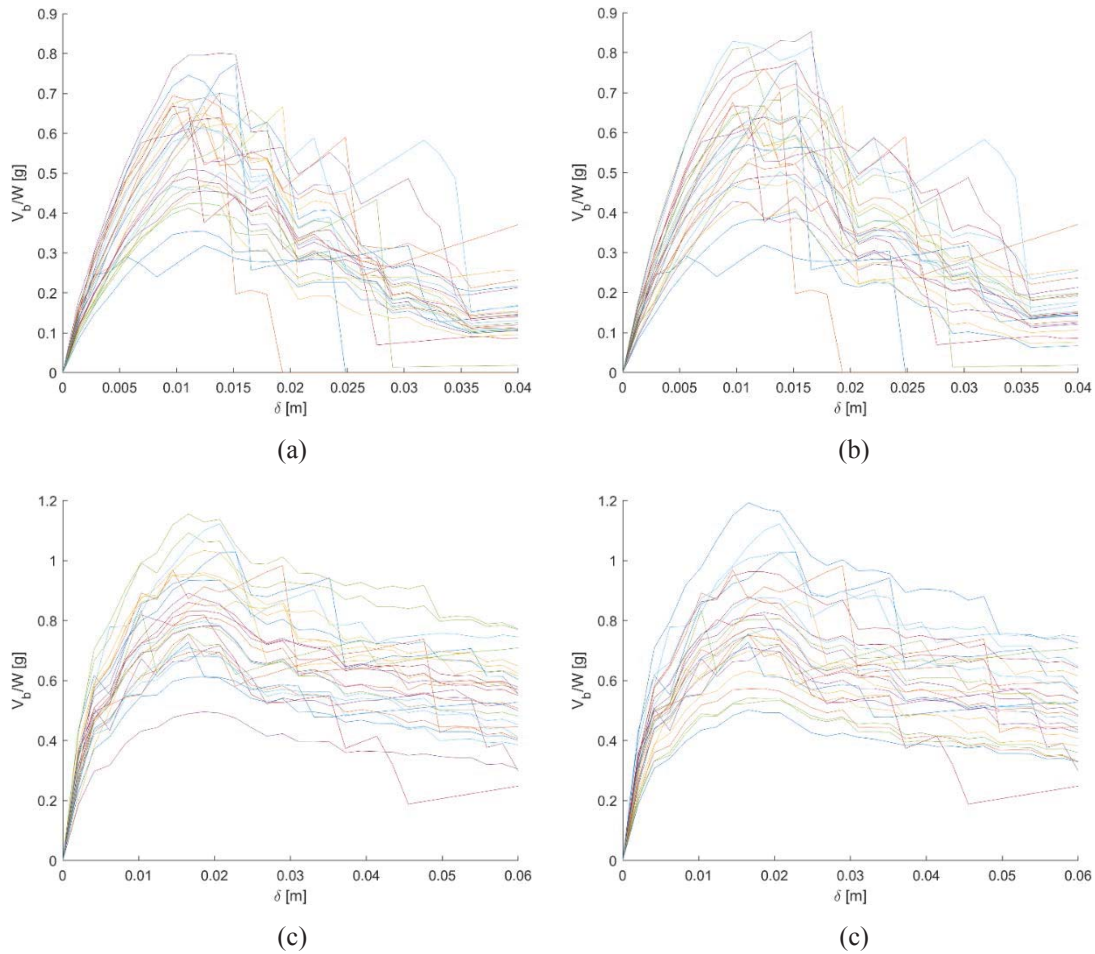


Figure 4: Pushover capacity curves of case-study building: (a) X direction and modal profile; (b) X direction and mass profile; (c) Y direction and modal profile; (d) Y direction and mass profile.

Seismic demand was evaluated in accordance with the N2 method [23], allowing global safety checking in terms of displacement. The building was assumed to be located on ground type A, i.e., rock or rock-like soil. Damage assessment was then performed with respect to four damage states (DSs), allowing seismic fragility associated with each DS to be computed under varying peak ground acceleration (PGA) that was assumed as intensity measure. The following DSs were considered: slight damage (DS1) associated with 60% of the maximum base shear; moderate damage (DS2) associated with the maximum base shear; extensive damage (DS3) associated with 20% post-peak degradation of base shear; collapse (DS4) corresponding to 50% post-peak degradation of base shear.

After that fragility points were individually derived, a lognormal probability distribution was fitted to them. The total dispersion was computed as square root of the sum of squares of dispersion associated with capacity (i.e., dispersion derived via fitting) and dispersion associated with demand, the latter set equal to 0.4.

Figures 5 and 6 show that the seismic fragility of the building was rather insensitive to the lateral load profile, while highlighting a significant sensitivity to the orientation of seismic actions. Indeed, the highest fragility of the structure is related to the Y direction, as expected according to the lowest intensity of gravity loads on walls parallel to one-way floors.

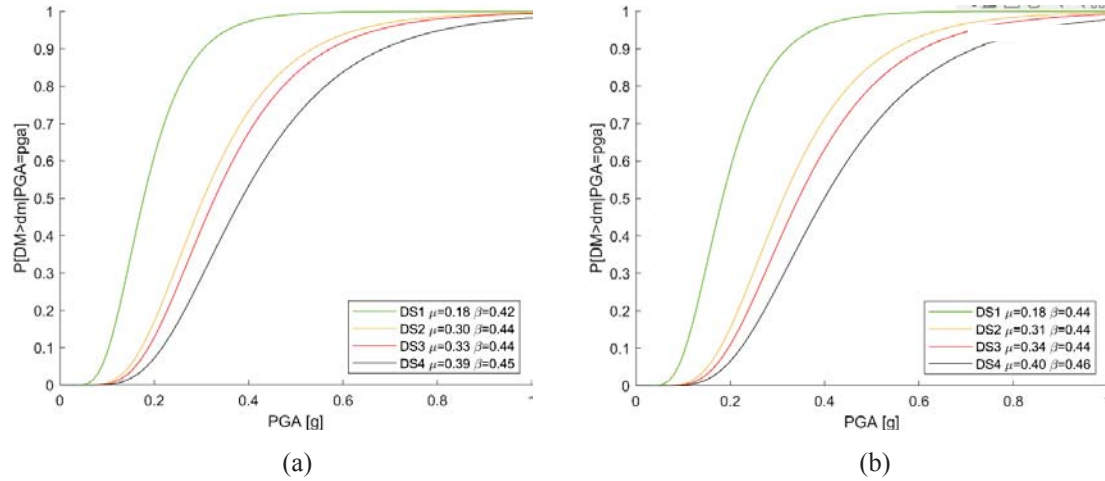


Figure 3: Fragility curves in the X direction: (a) modal profile; (b) mass profile.

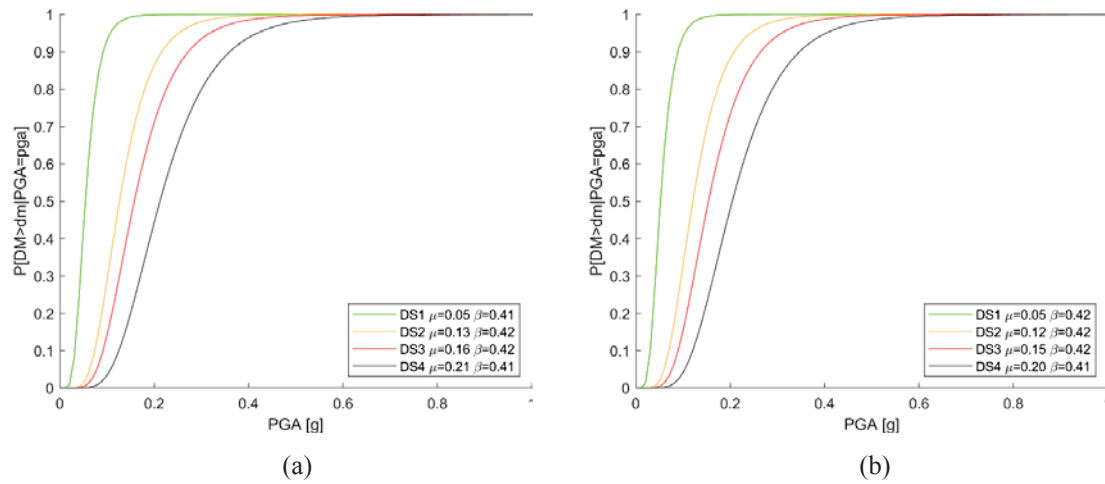


Figure 4: Fragility curves in the Y direction: (a) modal profile; (b) mass profile.

5 CONCLUSIONS

In this paper, a novel macroelement modelling procedure for masonry buildings has been presented and experimentally validated, creating the basis for efficient computation of seismic fragility through pushover analysis with response control. The macroelement modelling procedure is based on the fibre modelling approach and is framed within a matrix analysis approach, allowing consideration of material nonlinearities and real construction features (e.g. wall-to-wall connections, floor flexibility, presence of lintels). The macroelement modelling procedure build upon a macroelement that was originally validated against an experimental test on piers, and then it was extended to the structural system scale. Therefore, the matrix-based analysis procedure was validated against experimental data of a lateral load test on a full-scale masonry wall with central opening, highlighting a satisfactory numerical-experimental agreement.

The final part of this paper has presented the implementation of the proposed procedure in the seismic vulnerability assessment of a masonry building. The building geometry was modelled according to statistical data on existing masonry buildings located in the Campania region, Italy. Uncertainties in material properties were modelled and propagated through pushover

analysis, considering 27 samples of the building. Assuming four damage states corresponding to as many performance levels of the building, fragility curves were obtained to provide the conditional probability of exceeding each damage state given seismic intensity, which was measured in terms of peak ground acceleration.

The output of this study can be of interest for seismic risk assessments at regional scale and can be extended to other geometric configurations, types, and classes of masonry buildings at national scale. The fragility curves presented in this paper will be compared to those derived through Monte Carlo simulation, assessing the influence of the uncertainty in capacity that is usually of paramount importance particularly in the case of existing masonry buildings. Further developments of this study will also include a computationally efficient computation of the uncertainty in seismic demand, using nonlinear time history analysis of equivalent elastic-plastic oscillators associated with the pushover curves of the building samples.

REFERENCES

- [1] F. Parisi, N. Augenti, Earthquake damages to cultural heritage constructions and simplified assessment of artworks. *Engineering Failure Analysis*, **34**, 735-760, 2013.
- [2] P.B. Lourenço, *Computational strategies for masonry structures*. PhD thesis, Delft University Press, 1996.
- [3] A.W. Page, Finite element model for masonry. *Journal of Structural Division*, **104**(8), 1267-1285, 1978.
- [4] P.B. Lourenço, J.G. Rots, Multisurface interface model for the analysis of masonry structures. *Journal of Structural Engineering*, **123**(7), 660-668, 1997.
- [5] F. Parisi, C. Balestrieri, D. Asprone, Nonlinear micromechanical model for tuff stone masonry: Experimental validation and performance limit states. *Construction and Building Materials*, **105**, 165-175, 2016.
- [6] F. Parisi, G.P. Lignola, N. Augenti, A. Prota, G. Manfredi, Rocking response assessment of in-plane laterally-loaded masonry walls with openings. *Engineering Structures*, **56**, 1234-1248, 2013.
- [7] F. Parisi, G.P. Lignola, N. Augenti, A. Prota, G. Manfredi, Nonlinear behavior of a masonry sub-assembly before and after strengthening with inorganic matrix-grid composites. *Journal of Composites for Construction*, **15**(5), 821-832, 2011.
- [8] F. Parisi F., Seismic design of box-type unreinforced masonry buildings through direct displacement-based approach. *The Open Construction & Building Technology Journal*, **10**(Suppl 2: M9), 293-311, 2016.
- [9] N. Augenti, F. Parisi, *Teoria e Tecnica delle Strutture in Muratura*. Hoepli, 2019.
- [10] F. Parisi, N. Augenti, Seismic capacity of irregular unreinforced masonry walls with openings. *Earthquake Engineering and Structural Dynamics*, **42**(1), 101-121, 2013.
- [11] F. Parisi, E. Acconcia, Fibre-based capacity model for URM piers subjected to combined in-plane and out-of-plane actions. *16th European Conference on Earthquake Engineering*, Thessaloniki, Greece, June 18-21, 2018.
- [12] F. Parisi, E. Acconcia, Formulation and experimental validation of distributed plasticity macroelement for unreinforced masonry walls. J. Kubica, A. Kwiecień, Ł. Bednarz, eds.

- Brick and Block Masonry – From Historical to Sustainable Masonry, Proceedings of the 17th International Brick/Block Masonry Conference, Kraków, Poland, July 5-8, 2020.*
- [13] N. Augenti, F. Parisi, A. Prota, G. Manfredi, In-plane lateral response of a full-scale masonry subassemblage with and without an inorganic matrix-grid strengthening system. *Journal of Composites for Construction*, **15**(4), 578-590, 2011.
- [14] F. Parisi, G. Sabella, N. Augenti, Constitutive model selection for URM cross sections based on best-fit analytical moment–curvature diagrams. *Engineering Structures*, **111**, 451-466, 2016.
- [15] G. Zuccaro, M. Dolce, D. De Gregorio, E. Speranza, C. Moroni, La scheda CARTIS per la caratterizzazione tipologico- strutturale dei comparti urbani costituiti da edifici ordinari. Valutazione dell’esposizione in analisi di rischio sismico. *34th National Conference GNGTS*, Trieste, Italy, November 17-19, 2015.
- [16] ISTAT. *15th Italian national census of population*. Italian National Institute of Statistics, 2011.
- [17] D.M. 20/11/1987: *Norme tecniche per la progettazione, esecuzione e collaudo degli edifici in muratura e per il loro consolidamento*. Italian Ministry of Public Works, 1987.
- [18] NTC 2018. D.M. 17/01/2018: *Norme tecniche per le costruzioni*. Ministry of Infrastructure and Transportation, 2018.
- [19] CS.LL.PP. 21/01/2019 n.7: *Istruzioni per l’applicazione dell’«Aggiornamento delle “Norme tecniche per le costruzioni”» di cui al decreto ministeriale 17 gennaio 2018*. Ministry of Infrastructure and Transportation, 2019.
- [20] CNR-DT 212-2013: *Istruzioni per la valutazione affidabilistica della sicurezza sismica di edifici esistenti*. Consiglio Nazionale delle Ricerche, 2014.
- [21] N. Augenti, F. Parisi, Constitutive models for tuff masonry under uniaxial compression. *Journal of Materials in Civil Engineering*, **22**(11), 1102-1111, 2010.
- [22] M. Dolce, Schematizzazione e modellazione degli edifici in muratura soggetti ad azioni sismiche. *L’Industria delle Costruzioni*, **25**(242), 44-57, 1991.
- [23] P. Fajfar, P. Gašperšič, The N2 method for the seismic damage analysis of RC buildings. *Earthquake Engineering and Structural Dynamics*, **25**, 31-46, 1996.

A DISCRETE-MACRO-ELEMENT-MODEL FOR THE IN-PLANE ANALYSIS OF MASONRY STRUCTURES STRENGTHENED BY FRCMS

P. Zampieri¹, R. Piazzon¹, B. Pantò² and C. Pellegrino¹

¹ Department of Civil, Environmental and Architectural Engineering, University of Padua,
Via Marzolo 9, 35131 Padua, Italy
paolo.zampieri@unipd.it – paolo.zampieri@dicea.unipd.it

² Department of Civil and Environmental Engineering, Imperial College London
London SW7 2BU, UK
b.panto@imperial.ac.uk

Abstract

Recent earthquakes demonstrated the vulnerability of existing and historical masonry constructions. Many strengthening techniques for the seismic retrofitting of these structures have been introduced in the literature. Among these, FRCM strategies, based on the application of fibre-reinforced composite materials on the masonry surface through inorganic mortar layers, has become rather popular due to their physic and mechanic compatibility with historical masonries, low invasiveness and capacity to improve both the in-plane and the out of plane masonry behaviour. In this paper, a simplified discrete model, working at the material macroscale, is proposed to simulate the in-plane behaviour of masonry panels strengthened by FRCM systems. The proposed modelling approach is based on the DMEM model, whose calibration is enhanced to encompass the properties of the externally bonded strengthening system. According to the proposed strategy, the masonry support and the FRCM layers are simulated by an equivalent homogeneous material, discretised by a mesh of shear-deformable articulated quadrilaterals interacting along their edges by means of 2D unilateral cohesive-friction links. The model is implemented in OpenSees and validated by simulating experimental shear-diagonal tests, available in literature.

Keywords: FRCM, Composite material, Masonry structures, DMEM, in-plane behaviour, non-linear analysis.

1 INTRODUCTION

The numerical description of the mechanical behavior of masonry elements strengthened with externally bonded systems, such as Fabric Reinforce Polymer (FRP) or Fabric Reinforced Cementitious Matrix (FRCM) systems, represent a current complex task and requires complex mathematical models due to the non-linearity and anisotropy of masonry and the non-linear interaction between the reinforcement and the masonry support [1,2]. An effective modelling approaches to simulate unreinforced and reinforced masonry panels are represented by mesoscale finite element models [3-7] which explicitly simulate masonry, brick-block, units and mortar joints. According to these strategies, nonlinear zero-thickness interfaces describe both the behaviour of mortar joints and the masonry-reinforcement layer. However, these models require high computational costs; especially for external reinforced masonry elements where the matrix, the reinforce and the interfaces are detailed represented [8]. Consequently, these methods are not suitable for engineering applications.

Then the challenging problem of the scientific community is to simulate the complex mechanical behavior of unreinforced/strengthened masonry constructions with a limited computational cost and with sufficient accuracy. Is the case of simplified continuum finite element models where the masonry is represented as an equivalent homogenized continuum material [9,10]. Simplified structural macro-models aiming at drastically reduce the computational effort by describing each structural element through a single computational element (macro-element) or a coarse mesh of them, are largely used both in engineering practice and research [11,12]. Two of the most popular structural macro-models are represented by Equivalent Frame Model (EFM), in which the masonry building is represented by an equivalent nonlinear frame structure constituted by nonlinear beam element and rigid offsets [13,14], and the Macro-Element Model (DMEM), in which masonry panels are represented by shear-deformable 2D macro-elements interacting by discrete nonlinear interfaces [15-18]. The latter model guarantees a geometrically consistent description of masonry panels thanks to its 2D kinematics also allowing a more accurate simulation of the interaction between masonry panels and beam/column elements [19].

In this paper, a new simplified numerical strategy for the simulation of the in-plane FRCM strengthened masonry walls is proposed. This approach is based on the subdivision of a FRCM-strengthened masonry panel in a macro-mesh of shear-deformable elements interacting by discrete interfaces, according to the DMEM modeling strategy. Each interface is composed of a set of 2D links which describe the flexural/axial and shear behavior of masonry and the reinforcement layer. The proposed model is applied to simulate some experimental diagonal-compression tests performed on unreinforced and FRCM-strengthened masonry panels. The comparisons are presented in terms of load-force capacity curves and distribution of damage at the failure of the panel. The results of the analyses confirmed that the proposed model is able to simulate the response of the specimens with a satisfactory level of accuracy.

2 DESCRIPTION OF THE NUMERICAL STRATEGY

According to the proposed strategy, the masonry panel is subdivided in a mesh of shear-deformable panels (*shear panel*) that simulate the shear deformability of masonry portion represented. It is worth pointing out that, contrary to mesoscale approaches, the mesh discretization is not directly related to the brick-masonry arrangement which is taken into account by the calibration procedures of the interfaces. Following the DMEM approach, each shear panel can be described by an articulated

quadrilateral with rigid edges which are used to connect the interface links allowing the interaction between the shear panel and the adjacent elements. . Each interface (horizontal and vertical interfaces in Figure 1) is constituted by m nonlinear 2D links which model the flexural and shear-sliding behaviours of masonry and their coupling.

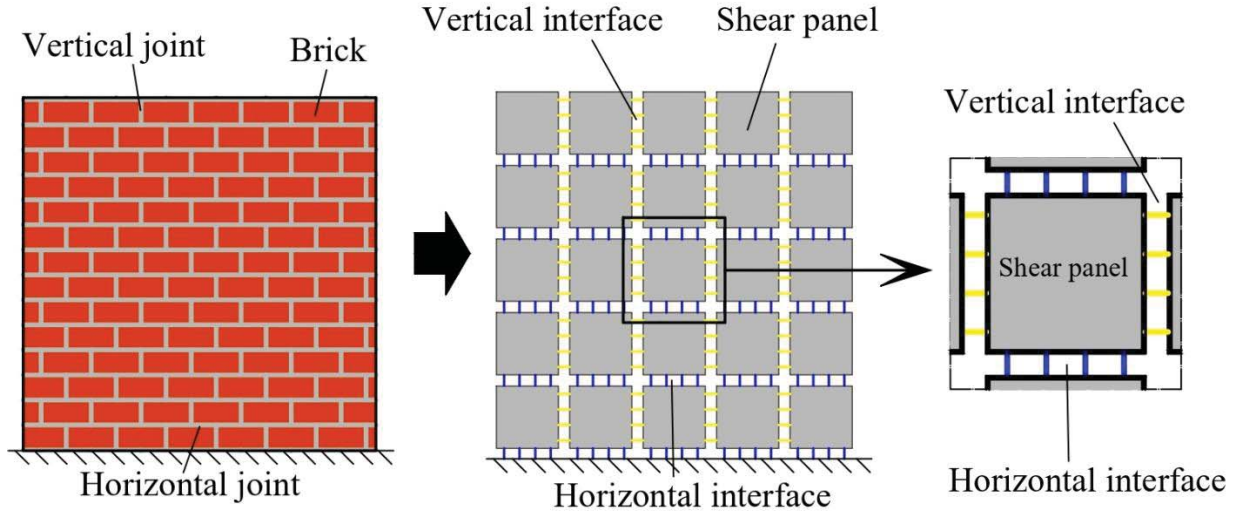


Figure 1 Real masonry wall (left); numerical representation with discrete elements (center); Single discrete element (right)

Each interface link, as depicted in Figure 2, is constituted by two one-dimension springs arranged in-series. One spring is oriented along the direction perpendicular to the connected panel edge (normal spring) and one spring is parallel to the edge (shear spring). The normal spring simulating the masonry axial behaviour is character by the normal displacement U_N and force F_N while the shear spring is characterized by the shear displacement U_T and force F_T . The two springs behaviour is coupled according to the Mohr coulomb failure criterion, based on the friction coefficient (μ) and the cohesive force (F_0). $K_{N,0}$ and $K_{T,0}$ are the initial values of the stiffness respectively in normal and in tangential direction.

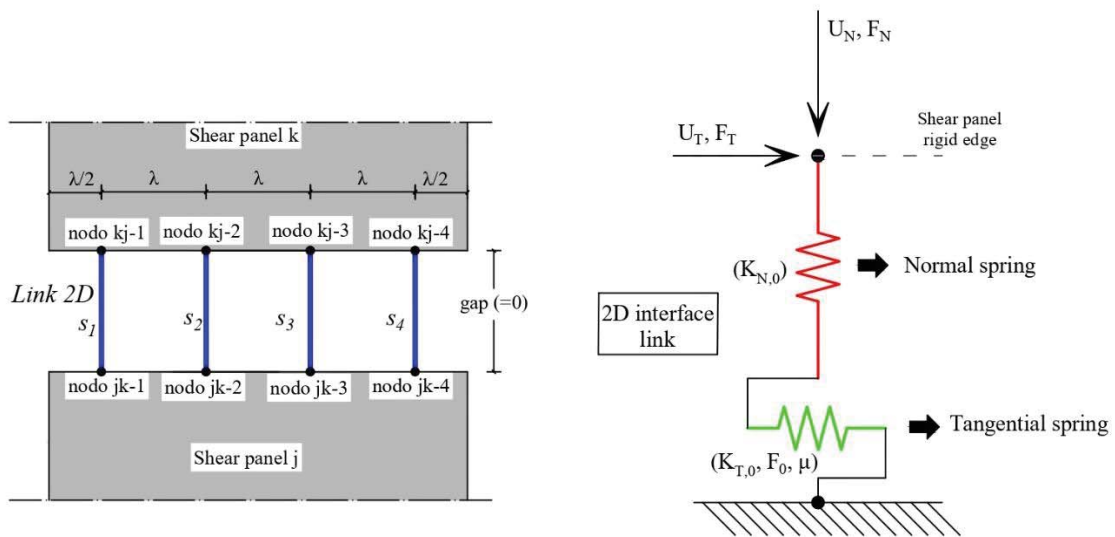


Figure 2 Discrete element interface with representation of all the nodes that are connected with 2D links (left); single 2D link numerical representation (right)

3 MODEL CALIBRATION

3.1 Calibration of the 2D masonry links

The constitutive law of the normal spring in compression is characterized by a parabolic relationship until the peak-strength, followed by a linear-softening and a residual strength (Figure 3a). The tensile behavior is linear elastic until the material strength after a linear softening is considered. When the displacement $U_{N,tu}$ is reached the material is considered cracked and the residual tensile strength is equal to zero. This model considers the masonry material in two conditions: cracked and uncracked considering two different force-displacement curves as shown in Figure 3b and in Figure 3c.

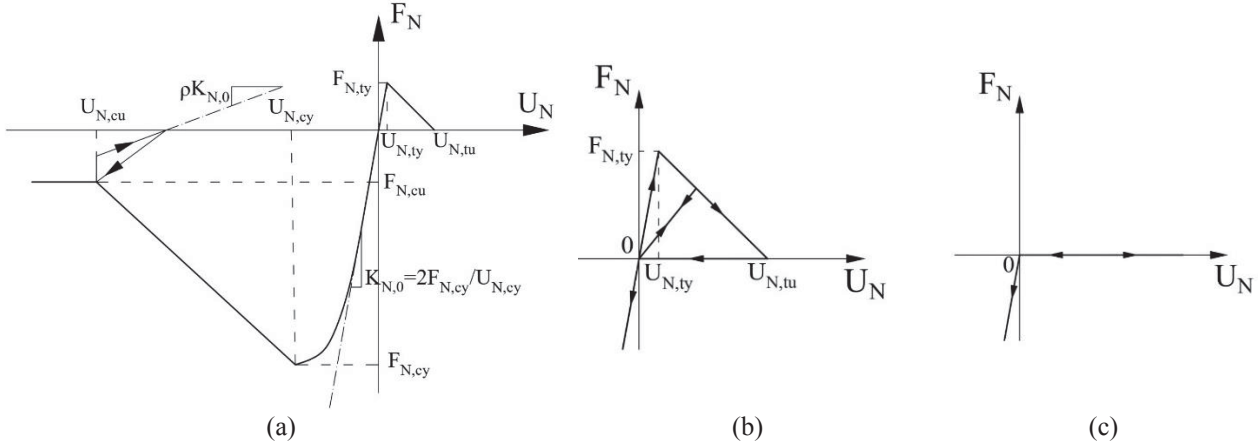


Figure 3 Constitutive law of the normal spring: backbone curve in compression and tension and unload-reload rules in compression; unloading behaviour in tension before cracking (b); behaviour in tension after material cracked (c)

The initial stiffness $K_{N,0}$ calibration is obtained assigning to each link the axial rigidity of the corresponding masonry strip. The same process is applied to assign to the normal material the compression and tensile yielding force $F_{N,cy}$, $F_{N,ty}$. In the case of the calibration of the interface link that connect two shear panels we have:

$$K_{N,0} = \frac{E \cdot \lambda \cdot s}{h_{infl,tot}} \quad (1)$$

$$F_{N,cy} = s \cdot \lambda \cdot \sigma_c \quad (2)$$

$$F_{N,ty} = s \cdot \lambda \cdot \sigma_t \quad (3)$$

Where: E is the Young modulus of the masonry, λ is the distance between two 2D links, s is the thickness of the represented masonry panel, $h_{infl,tot}$ is the sum of the two semi length of the adjacent shear panels, measured in the direction orthogonal to the direction of the interface; σ_c and σ_t are the compressive and tensile yielding stresses. The compressive yielding displacement $U_{N,cy}$ and the tensile yielding displacement $U_{N,ty}$ are calculated considering rigidity, force and the constitutive law.

The shear spring are characterized by an elasto-plastic constitutive law with linear softening (Figure 4), governed by a Mohr Coulomb yielding surface. The sliding occurs when the force in the direction tangential reaches its limit value, F_{lim} , calculated as reported in Eq. (4) in which μ is the friction coefficient, F_N is the force acting in the normal spring of the 2D link and $F_0 = c \cdot \lambda \cdot s$, and c is the cohesive strength of the masonry.

$$F_{T,lim} = \mu \cdot F_N + F_0 \quad (4)$$

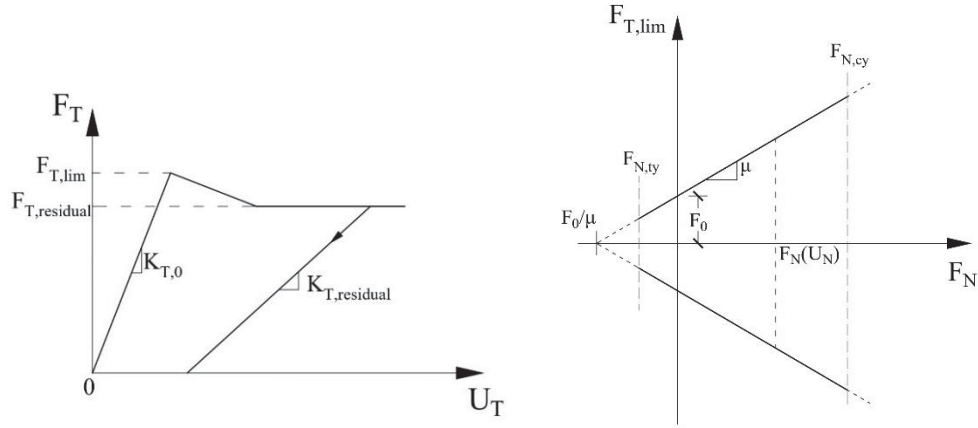


Figure 4 Shear behaviour of the 2D link (left); influence of the normal force agent in the 2D link to the limit shear force $F_{T,lim}$ (right)

3.2 Calibration of FRCM strengthening system

The FRCM matrix is represented by an additional 2D links in parallel with the 2D masonry links and distributed along the panel edge with the same interval. The shear spring of the reinforcement link is characterized by the same constitutive law of the shear spring of the masonry links (figure 3b), calibrated considering the experimental shear strength of the mortar layer or the reinforcement [21-25]. The normal spring is characterized by an arbitrary multi-linear force-slip ($\sigma-U_N$) relationship in tension, calibrated according to the force-slip relationship determined by a shear lap test [21-25] (Figure 5), and zero compression strength.

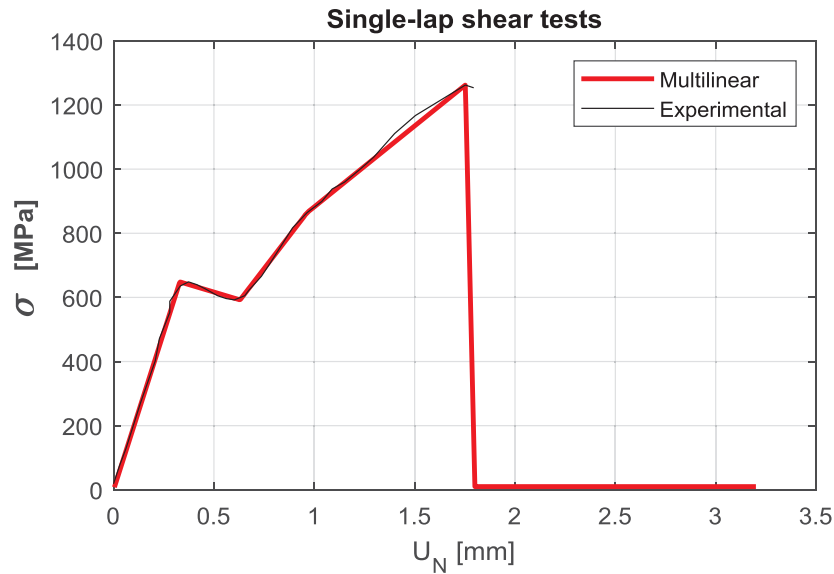


Figure 5 Comparison between the experimental result of the single shear lap test and the behaviour of the multilinear material to assign to the element that represent the fibers. In the graph σ stands for the tension in the fibers area, without the matrix; U_N is the sliding between fibers and matrix.

4 NUMERICAL SIMULATIONS OF DIAGONAL COMPRESSION TESTS FRCM STRENGTHENED MASONRY WALL

This case study considers the results of the diagonal compression test brick masonry walls, executed experimentally [20]. The wall tested in laboratory (129x129x25 cm³) were built using standard clay bricks and hydraulic lime-based mortar for the bed joints.

The tests are executed at displacement control, applying the vertical load along the principal diagonal direction of the square panel. Deformations along the two principal directions were recorded by using linear potentiometric transducers. The results are reported using τ - γ diagrams, considering γ as the sum of the deformations along the principal diagonals ($\varepsilon_c, \varepsilon_t$); τ is the tangential stress calculated as $\tau = P/A_d$, in which P is the load applied and A_d is the section of the wall measured on the principal diagonal of the specimen. These tests are reproduced numerically with a mesh 10x10 of discrete elements (Figure 6).

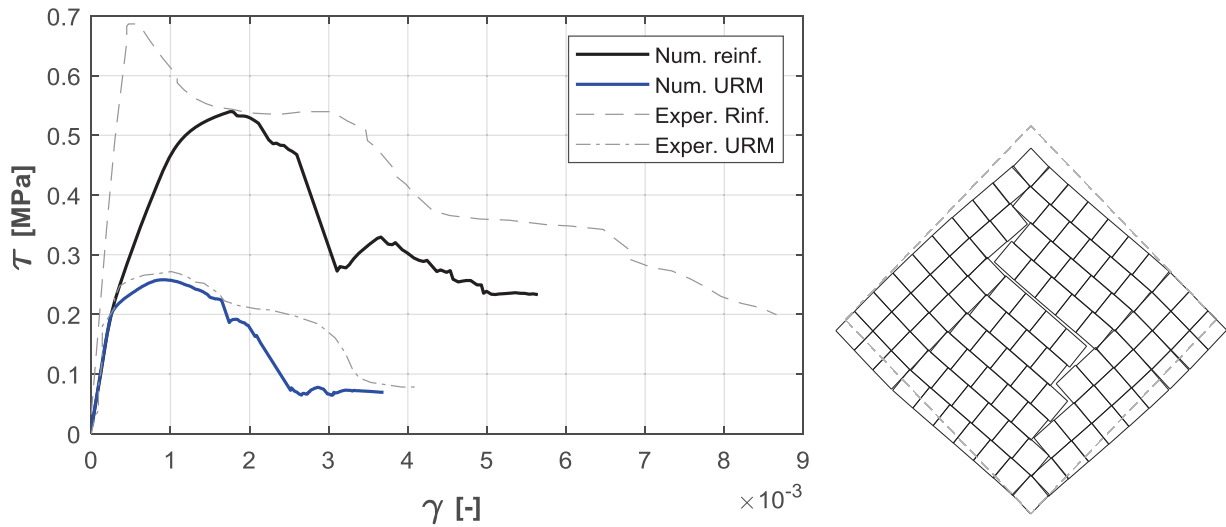


Figure 6 Comparison between the experimental and numerical results (left) and deformed shape registered after the first peak in the numerical strengthened wall, considering an amplification factor of 50 (right)

5 DISCUSSION OF THE RESULTS

The proposed procedure well simulates the nonlinear behavior of the URM wall in terms of initial stiffness, peak load and residual load. Moreover, observing the numerical deformation, is evident the formation of a single diagonal cracking. This collapse mechanism reflects the failure mode experimentally observed.

In the case of the strengthened panel, some differences are observed between the experimental and numerical capacity curves, mainly in the peak-strength phase. However, the global trend of the experimental curve is reproduced with a satisfactory approximation, moreover the failure mechanism is well reproduced (Figure 6). Analyzing the stress and deformations of the Links representing masonry, mortar matrix and fibers, it is possible to determine the failure points of each element, as reported in Figure 7. The first part of the curve corresponds to the linear part, in which masonry and matrix aren't cracked. In this phase the tensile stresses in the fibers are lower than 200 MPa. The first peak corresponds to the cracking of the masonry in the central part of the panel, followed by the cracking of the matrix along the loaded diagonal. After this point, the external force decreases due to opening of the diagonal crack, that can be clearly seen in the deformed shape. The tensile deformations in the cracked interfaces continue to increase, allowing the fibers to increase tensile deformations and stresses, which result much higher than those registered during the uncracked phase. The second increase in strength is due indeed to the contribution of the elements that represents the fibers. The second peak corresponds to the yield of the fibers in the central part of the panel.

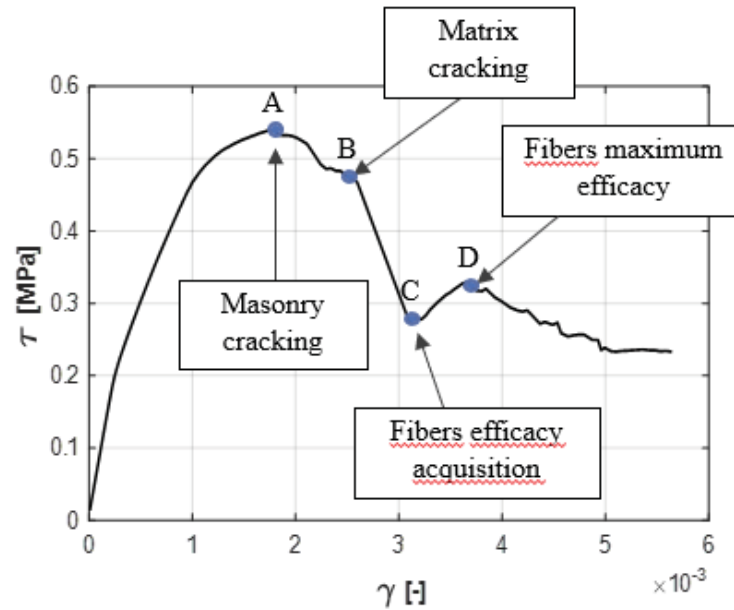


Figure 7 Numerical result with the indication of collapse of every material

6 CONCLUSION

This paper introduces a simplified model for the simulation of the nonlinear in-plane response of masonry panels strengthened by FRCM systems. The masonry is described by a mesh of discrete elements able to simulate the main collapse modes of masonry material. The FRCM reinforcement is simulated by a simple and efficient method. The calibration of the model is immediate and based on the materials parameters. As a numerical case study, a diagonal compression test has been simulated. The comparison between experimental and numerical results highlights the efficiency of the method in reproducing the global collapse modalities of the mixed system constituted by the masonry and the reinforcement. In the numerical simulation, according to the experiments, the matrix contributed to the first peak of the capacity curve while the contribution of the fibers resulted predominant in the post-peak phase where the capacity curve showed a second peak, after a main diagonal crack was developed.

7 REFERENCES

- [1] Nicolò Simoncello, Paolo Zampieri, Jaime Gonzalez-Libreros, Carlo Pellegrino, 2019. Experimental behaviour of damaged masonry arches strengthened with steel fiber reinforced mortar (SFRM), *Composites Part B: Engineering*, Volume 177,.
- [2] Paolo Zampieri, Nicolò Simoncello, Jaime Gonzalez-Libreros, Carlo Pellegrino, 2020. Evaluation of the vertical load capacity of masonry arch bridges strengthened with FRCM or SFRM by limit analysis, *Engineering Structures*, Volume 225.
- [3] Macorini, L. and Izzuddin, B.A., 2011. A non- linear interface element for 3D mesoscale analysis of brick- masonry structures. *International Journal for numerical methods in Engineering*, 85(12), pp.1584-1608.
- [4] Simone Tiberti, Gabriele Milani, 2020. Fast brick-based homogenized limit analysis for in- and out-of-plane loaded periodic masonry panels, *Computers & Structures*, Volume 231.

- [5] R. Gagliardo, F.P.A. Portioli, L. Cascini, R. Landolfo, P.B. Lourenço, 2021. A rigid block model with no-tension elastic contacts for displacement-based assessment of historic masonry structures subjected to settlements, *Engineering Structures*, Volume 229.
- [6] M. Rossi, C. Calderini, B. Di Napoli, L. Cascini, F. Portioli, 2021. Structural analysis of masonry vaulted staircases through rigid block limit analysis, *Structures*, Volume 23.
- [7] Bertolesi E, Milani G, Casolo S, 2018. Homogenization towards a mechanistic rigid body and spring model (HRBSM) for the non-linear dynamic analysis of 3D masonry structures. *Meccanica* 53(7):1819–1855
- [8] G.P. Lignola, A. Bilotta, F. Ceroni, 2019. Assessment of the effect of FRCM materials on the behaviour of masonry walls by means of FE models, *Engineering Structures*, Volume 184, , Pages 145-157.
- [9] Cavalagli, N., Cluni, F., Gusella, V. 2011. Strength domain of non-periodic masonry by homogenization in generalized plane state, *European Journal of Mechanics, A/Solids*
- [10] Jacopo Scacco, Bahman Ghiassi, Gabriele Milani, Paulo B. Lourenço, 2020. A fast modeling approach for numerical analysis of unreinforced and FRCM reinforced masonry walls under out-of-plane loading, *Composites Part B: Engineering*, Volume 180.
- [11] Aşıkoğlu, A., Vasconcelos, G., Lourenço, P.B. and Pantò, B., 2020. Pushover analysis of unreinforced irregular masonry buildings: Lessons from different modeling approaches. *Engineering Structures*, 218, p.110830.
- [12] Maio, R., Ferreira, T.M., Estêvão, J.M., Pantò, B., Calì, I. and Vicente, R., 2020. Seismic performance-based assessment of urban cultural heritage assets through different macroelement approaches. *Journal of Building Engineering*, 29, p.101083.
- [13] Lagomarsino S, Penna A, Galasco A, Cattari S, 2013. Tremuri program: an equivalent frame model for the nonlinear seismic analysis of masonry buildings. *Eng Struct* 56:1787–1799.
- [14] E. Quagliarini, G. Maracchini, F. Clementi, 2017. Uses and limits of the Equivalent Frame Model on existing unreinforced masonry buildings for assessing their seismic risk: A review, *Journal of Building Engineering*, Volume 10.
- [15] Calì, M. Marletta, B. Pantò, 2012. “A new discrete element model for the evaluation of the seismic behaviour of unreinforced masonry buildings”, *Engineering Structures* 40, 327–338.
- [16] Pantò, B., Calì, I. and Lourenço, P.B., 2018. A 3D discrete macro-element for modelling the out-of-plane behaviour of infilled frame structures. *Engineering Structures*, 175, pp.371-385..
- [17] Penna A, Lagomarsino S, Galasco A, 2014. A nonlinear macroelement model for the seismic analysis of masonry buildings. *Earthq Eng Struct Dyn* 43(2):159–179
- [18] Minga, E., Macorini, L., Izzuddin, B.A. and Calio, I., 2020. 3D macroelement approach for nonlinear FE analysis of URM components subjected to in-plane and out-of-plane cyclic loading. *Engineering Structures*, 220, p.110951.
- [19] Marques, R. and Lourenço, P.B., 2014. Unreinforced and confined masonry buildings in seismic regions: Validation of macro-element models and cost analysis. *Engineering Structures*, 64, pp.52-67.
- [20] A. Incerti, A.R. Tilocca & A. Bellini, 2020. “In-plane behaviour of FRCM-strengthened masonry panels”, *Brick and Block Masonry -From Historical to Sustainable Masonry – Kubica, Kwiecień & Bednarz (eds) © Taylor & Francis Group, London, ISBN 978-0-367-56586-2*

- [21] A. Bilotta, F. Ceroni, E. Nigro, M. Pecce, 2017. "Experimental tests on FRCM strengthening systems for tuff masonry elements", *Construction and Building Materials*, Volume 138, Pages 114-133.
- [22] A. Bellini, S. K. Shahreza, C. Mazzotti, 2019. "Cyclic bond behavior of FRCM composites applied on masonry substrate", *Composites Part B: Engineering*, Volume 169, Pages 189-199.
- [23] A. Bellini, M. Bovo, C. Mazzotti, 2019. "Experimental and numerical evaluation of fiber-matrix interface behaviour of different FRCM systems", *Composites Part B: Engineering*, Volume 161, Pages 411-426.
- [24] A. Tilocca, A. Incerti, A. Bellini, M. Savoia, 2019. "Influence of Matrix Properties on FRCM-CRM Strengthening Systems". *Key Engineering Materials*. 817. 478-485. [10.4028/www.scientific.net/KEM.817.478](https://doi.org/10.4028/www.scientific.net/KEM.817.478).
- [25] Luisa Rovero, Stefano Galassi, Giulia Misseri, 2020. Experimental and analytical investigation of bond behavior in glass fiber-reinforced composites based on gypsum and cement matrices, *Composites Part B: Engineering*, Volume 194.

NUMERICAL MODELLING OF DIAGONAL COMPRESSION TESTS ON MASONRY PANELS STRENGTHENED BY FRCM

Francesca Ferretti¹, Francesco S. Murgo², and Claudio Mazzotti²

¹ Department of Civil, Chemical, Environmental and Materials Engineering, University of Bologna,
Viale Risorgimento 2, 40136 Bologna, Italy
{francesca.ferretti10, francesco.murgo2, claudio.mazzotti}@unibo.it

Abstract

Fiber Reinforced Cementitious Matrices (FRCM) are innovative materials currently adopted for the structural strengthening of existing masonry structures. With reference to the in-plane behavior of masonry, FRCM systems are effective in enhancing the shear capacity and in influencing the failure mode of masonry panels, which moves from a very brittle failure, typical of unreinforced masonry walls, to a less brittle failure mode. The main objective of this paper is to study the structural behavior of masonry panels strengthened with a FRCM system through nonlinear numerical analyses of diagonal compression tests performed on an unreinforced and a reinforced panel. With reference to the masonry substrate, a brick-to-brick modelling approach is adopted. According to this approach, the non-linearities are all concentrated in the mortar joints and in correspondence with potential crack surfaces located in the middle of each brick. The FRCM strengthening system is discretized by means of a continuous bi-directional fiber grid constituted by trusses embedded into the mortar matrix, which is bonded to the masonry substrate. A calibrated bond-slip relationship is assigned to the matrix-fiber interface, assuming an idealized bilinear law. The nonlinear analyses allow to capture the typical experimental shear response of a reinforced masonry panel, characterized by a load-displacement curve in which three principal phases can be identified, corresponding with different failure mechanisms: masonry cracking, mortar matrix cracking and ultimate failure of the panel. The numerical results are, indeed, compared with experimental results, showing a good agreement and confirming the suitability of the modelling approach in reproducing the described experimental behavior. Parametric studies on both the material and the geometrical parameters of the FRCM system are also performed.

Keywords: Masonry, FRCM, Diagonal Compression Test, Numerical Modelling, Nonlinear Analysis.

1 INTRODUCTION

The damages caused by the most severe earthquakes in recent decades have drawn attention to the problem of the vulnerability of the built cultural heritage, mostly consisting of masonry buildings [1,2]. In this framework, the use of composite materials, such as Fiber Reinforced Cementitious Matrix (FRCM), to strengthen masonry panels became very popular due to the extremely low weight-to-strength ratio, the ease of application, and the capability of maintaining the original stiffness of the unreinforced element unchanged [3,4]. These materials proved to be very effective for the enhancement of the shear behavior of masonry structural elements, both in terms of load bearing capacity and failure mode [5,6].

Significant research has been also devoted to the numerical simulation of the behavior of FRCM strengthened structural elements, adding to the specific aspects of the masonry modelling, further issues related to the FRCM systems, considering all the possible failure modes [3]. In literature, the FRCM systems are often modeled as homogenized materials, under the assumption of having the mortar matrix layers homogenized with a distributed reinforcement, fully embedded inside the matrix elements [7-10]. Moreover, the hypothesis of a perfect bond between the FRCM systems and the masonry substrate is usually introduced. Some research works have introduced simplified analytical-numerical approaches to model the interaction between the fibers and the mortar matrix to analyze the debonding/delamination phenomena of the FRCM system from the substrate [11,12]. According to these models, the interface behavior between the mortar matrix and the fibers is based on the stress vs slip curves deduced from experimental tests.

The objective of the paper is the numerical investigation of the in-plane behavior of FRCM strengthened masonry panels subject to diagonal compression test by proposing a specific modelling approach. In more detail, the masonry is modelled using a brick-to-brick model, based on the simplified micro-modelling approach developed in the past and also known in literature as meso-scale approach [13,14]. With reference to the FRCM system, each component (i.e. mortar matrix, fiber, matrix-fiber interface) is specifically modelled and the constitutive laws are purposely calibrated on the basis of experimental results to account for several possible failure modes. For the validation of the proposed model, the comparisons between the results of nonlinear numerical simulations and the experimental results of previous experimental campaigns [15,16] are discussed, together with the results of several parametric analyses.

2 NUMERICAL MODEL

In this paper, the in-plane shear behavior of an unreinforced (URM) and a FRCM strengthened panel is simulated by means of nonlinear numerical analyses of diagonal compression tests. The geometry of the panels ($1210 \times 1210 \times 120$ mm³), the setup and the boundary conditions (Figure 1a) are chosen to reproduce the ones used in previous experimental campaigns on masonry panels built with clay bricks and 10-mm thick cementitious mortar layers, then strengthened by a FRCM system composed of a bidirectional carbon fiber grid embedded in a lime-based mortar, having a total thickness of 6 mm per side [15,16]. The bidirectional carbon grid is characterized by a weight density of 170 g/m², a grid spacing of 10 mm, an equivalent thickness of 0.047 mm and a yarn perimeter equal to 4 mm. The masonry components and the FRCM system were subject to experimental tests for the determination of their mechanical properties, which are here used as input parameters in the numerical model, as will be explained in the following.

A 2D numerical description of the problem is considered: this is consistent with the fact that the tested masonry panels are single-wythe walls, characterized by a regular bond pattern.

The numerical analyses are carried out by using the finite element software DIANA FEA 10.1. The quality and refinement of the mesh adopted both for the URM panel and the FRCM strengthened one (Figure 1b,c) is the result of a mesh sensitivity analysis. Numerical analyses are carried out under displacement control, applying the displacement to the top steel cradle.

To include the presence of the FRCM strengthening system over the masonry panel, an improved modelling approach is here proposed. More in detail, the approach consists of modelling masonry with a brick-to-brick model, where the nonlinearities are all concentrated in the zero-thickness interface elements modelling the mortar joints and in correspondence with potential crack surfaces located in the middle of each brick. The mortar matrix presents discrete cracks at the same locations of the masonry substrate and it is considered perfectly bonded to the substrate. Then, the single fiber bundles are individually modelled as embedded in the mortar matrix through a bond-slip law. In more detail, the bond-slip law of the considered carbon FRCM system is calibrated based on experimental bond tests, performed in a Round Robin test of the RILEM 250-CSM Technical Committee [4]. The graphical representation of the adopted modelling approach is shown in Figure 2.

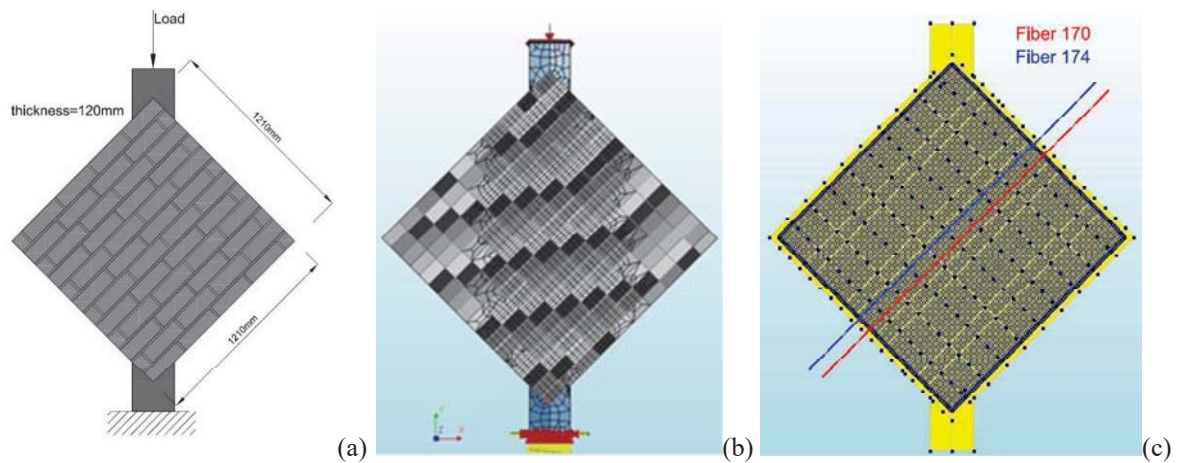


Figure 1: Diagonal compression test: (a) setup, (b) FE model of the URM panel, (c) FE model of the FRCM strengthened panel.

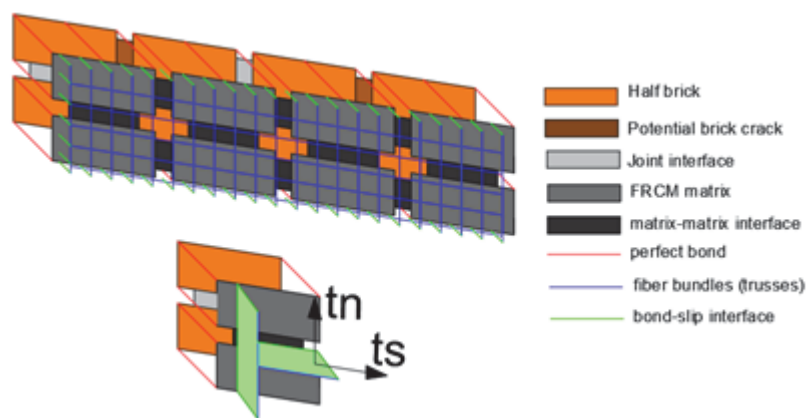


Figure 2: Modelling approach adopted for the FRCM strengthened panel.

2.1 Masonry

According to the brick-to-brick modelling approach, each mortar joint, consisting of mortar and two brick-mortar interfaces, is lumped into a zero-thickness interface element, while the bricks, modelled with continuum elements, are expanded to keep the overall geometry un-

changed. Interface elements are also used in the middle of each brick to model its potential cracking. The bricks are modelled as a linear elastic material and all the nonlinearities of the problem are lumped in the interface elements. The purpose of this approach is to concentrate all the damages in the mortar joints and in the brick interfaces. The adopted mesh includes eight-node quadratic elements for the bricks and six-node quadratic elements for brick-mortar and potential brick crack interfaces.

Large values of normal (k_n) and tangential (k_s) stiffness are adopted for the interfaces located in the middle of the bricks to ensure material continuity and to avoid the interpenetration. An exponential tension softening model was used for these elements without a specified shear or compression failure criteria. The elastic stiffness parameters for the zero-thickness interfaces modelling the mortar joints are determined starting from the elastic properties of brick and mortar, as reported in [14].

The nonlinear behavior of the mortar joint interface elements is introduced by considering the combined cracking-shearing-crushing model available in the software DIANA FEA, which was developed and improved in past research works [13,17]. This model includes the failure mechanisms that characterize masonry: cracking of the joints, sliding along bed or head joints at low values of normal stress, cracking of the bricks in direct tension, brick diagonal tensile cracking and masonry crushing. In more detail, the adopted model is based on multi-surface plasticity and it includes a Coulomb friction model combined with a tension cut-off and an elliptical compression cap.

Equations 1-3 describe the Coulomb friction yielding criterion, the yield value and the coupling between cohesion and friction softening, respectively:

$$f_1(\sigma, \kappa_1) = |\tau| + \sigma \tan \phi(\kappa_1) - \bar{\sigma}_1(\kappa_1) \quad (1)$$

$$\bar{\sigma}_1(\kappa_1) = ce^{-\frac{c}{G_f^{II}} \kappa_1} \quad (2)$$

$$\tan \phi = \tan \phi_0 + (\tan \phi_r - \tan \phi_0) \frac{c - \bar{\sigma}_1(\kappa_1)}{c}, \quad (3)$$

where c is the cohesion of the brick-mortar interface, ϕ_0 and ϕ_r are the initial and the residual friction angles, respectively, G_f^{II} is the mode-II fracture energy and κ_1 is an internal softening parameter that controls the softening behavior. Non constant mode-II fracture energy is considered since the softening of the friction angle is taken proportional to the exponential cohesion softening. The dilatancy effect is also included in the model [17] by using the parameter:

$$u_p = \frac{\Psi_0}{\delta} \left\langle 1 - \frac{\sigma}{\sigma_u} \right\rangle \left(1 - e^{-\delta v_p} \right), \quad (4)$$

where Ψ_0 is the dilatancy at zero confining stress and shear slip, σ_u is the confining stress at which the dilatancy becomes zero, and δ is the dilatancy shear slip degradation coefficient.

For the tension mode, the yield function reads:

$$f_2(\sigma, \kappa_2) = \sigma - \bar{\sigma}_2(\kappa_2) \quad (5)$$

$$\bar{\sigma}_2(\kappa_2) = f_t e^{-\frac{f_t}{G_f^I} \kappa_2},$$

with f_t tensile strength of the brick-mortar interface and G_f^I mode-I fracture energy.

The yield function for the cap model is given by:

$$f_3(\sigma, \kappa_3) = C_{mm}\sigma^2 + C_{ss}\tau_2 + C_n\sigma - (\bar{\sigma}_3(\kappa_3))^2, \quad (6)$$

where C_{mm} , C_{ss} , and C_n are a set of material parameters, controlling the center of the cap and its intersection with the tensile part of the normal stress axis, and $\bar{\sigma}_3$ is the yield value. The cap mode is described by a parabolic hardening rule, until the peak compressive strength of the masonry f_c is reached at the plastic strain κ_p . After the peak, the softening behavior under compression is described by a parabolic/exponential softening rule and depends on the fracture energy $G_{f,c}$, considered according to Eq. 7 [18]:

$$G_{f,c} = 15 + 0.43f_c - 0.0036f_c^2. \quad (7)$$

The introduced geometrical and mechanical properties are reported in Table 1 and Table 2, together with the properties of the FRCM system described in Section 2.2, and they are derived mainly from experimental results or calibrated by considering data found in literature.

The vertical displacement along the compressed diagonal is assigned through two steel cradles placed at two opposite corners of the panels. The contact surfaces between the panel and the cradles are also modelled: the normal stiffness of the interface was high (10^8 N/mm³) to avoid interpenetration while a small tangential stiffness value (450 N/mm³) was calibrated to allow relative displacements and to properly simulate the confinement at the corners.

Property	Brick	Mortar	FRCM matrix	Fiber
E [GPa]	14	7	17	240
f_c [MPa]	44	8	5	-
f_t [MPa]	5	3	3	2400

Table 1: Mechanical parameter directly obtained from experimental tests.

Interface	k_n [$\frac{N}{mm^3}$]	k_t [$\frac{N}{mm^3}$]	f_t [MPa]	G_f^I [$\frac{N}{mm}$]	c [$\frac{N}{mm}$]	ϕ_0 [rad]	ϕ_r [rad]	G_f^{II} [$\frac{N}{mm}$]	Ψ_0 [rad]	σ_u [MPa]	δ [-]	$G_{f,c}$ [$\frac{N}{mm}$]	κ_p [-]
Brick-mortar	1350	550	0.25	0.001	0.40	0.85	0.85	0.05	0.75	-2	5	21	0.0044
FRCM matrix-matrix	2000	800	3.00	0.025	0.55	0.85	0.85	0.10	0.75	-2	9	17	0.0013

Table 2: Mechanical parameter derived from experimental or literature data.

2.2 FRCM

The modelling approach here introduced to describe the FRCM strengthening system behavior allows for relative slips between the fiber bundles and the mortar matrix. The formers are introduced as a grid of 1D elements, connected to the 2D continuum elements, representing the mortar matrix, through bond-slip reinforcement interfaces. In more detail, the fiber bundles are modelled as 2-noded linear trusses connected by line-shell interface elements to the mortar matrix in which they are located (Figure 2). Trusses representing the fibers are considered elastic in tension and not effective in compression. The use of a linear elastic behavior for the truss elements is a simplification verified and supported by experimental evidence [19]. The bond-slip model adopted within the software DIANA FEA sets a nonlinear

relation between the shear stress and the shear slip, while the relation between normal traction and normal relative displacement is maintained linear.

The mortar matrix, composed of 2D elements, is introduced in the model as perfectly bonded to the masonry panel. This hypothesis is consistent with the experimental failure modes [15,16], never characterized by detachment or shear slip between the mortar matrix and the masonry substrate. Accordingly, the mortar matrix is allowed to crack together with the masonry substrate, in correspondence of the same weak locations, i.e. mortar bed joints and in the middle of the bricks. Therefore, the mesh of the mortar matrix is considered coincident with the mesh of the masonry, and the same potential discontinuities are introduced through zero-thickness nonlinear interfaces (Figure 2), modelled by adopting the combined cracking-shearing-crushing material model, already introduced. Only the definition of the normal and the tangential interface stiffness is modified, considering the presence of one material only: $k_n=E/t$ and $k_s=G/t$, being E , G and t the elastic modulus, the shear modulus and the thickness of the mortar matrix, respectively. Since a 2D mesh is used for the mortar matrix, t is introduced as the overall thickness of the mortar, including both the inner and the outer layers.

In FRCM strengthened masonry panels, the interaction between the reinforcement system and the substrate is highly complex and different failure modes are possible. In this work, for reasons of simplicity, all the delamination and slippage phenomena are concentrated at the matrix-fiber interface. This is indeed the most frequent mechanism leading to failure, after the rupture of the fibers, which can be explicitly taken into account by the fiber model.

The potential slippage of the fiber bundles with respect to the mortar matrix is described by zero-thickness interface elements with six-nodes, a quadratic displacement field and a plane stress assumption. Since they connect 1D elements (fiber bundles) to 2D shell elements (mortar matrix layer), two separate interface laws are assigned along the longitudinal direction and along the direction orthogonal to the fiber bundle alignment. The adopted constitutive laws are based on a total deformation theory, which expresses the stresses as a function of the total relative displacements. The relation between the normal traction and the normal relative displacement is assumed to be linear elastic and characterized by the k_n stiffness. The large deformability of fibers along the direction orthogonal to their alignment and the possibility of relative slippage between orthogonal bundles, suggest that a negligible value of the stiffness should be considered. Therefore, a very weak stiffness is given to the bond-slip interface elements along the direction orthogonal to the fiber bundles, to neglect their contribution along that direction. A bilinear shear stress vs slip curve is considered along the longitudinal direction; this is a simple but common choice for FRCM systems [9]. Given the purpose to perform structural analyses with a large number of interface elements and the growing difficulty of calibrating increasingly complex laws, the choice seems appropriate. Shear laws for positive and negative values of slips are equal.

To calibrate the bond-slip interface laws and to verify the simplified assumptions introduced, preliminary numerical simulations of bond tests are carried out using the software DIANA FEA 10.1. In more detail, experimental bond tests [4] performed on the same carbon FRCM system considered for the diagonal compression tests are numerically modelled. The prevalent experimental failure modes were the delamination at the matrix-fiber interface and the slippage of the fibers within the mortar matrix. In the numerical simulations, the brick is considered as a linear elastic material and the FRCM system is modelled as previously described. To simulate the bond tests, the free edges of the fiber bundles (truss elements) were pulled horizontally by imposing a common displacement, while restraining the brick substrate. The numerical results of the bond tests in terms of axial stress vs slip curves are shown in Figure 3a. The axial stress is evaluated as the applied force divided by the cross section of the

dry fibers. The calibration of the bilinear bond-slip law is performed by direct comparison and fitting of the experimental results. Figure 3a shows a good matching between the numerical axial stress *vs* slip curve and the experimental envelope. This finding confirms the suitability of the adopted modelling choices. The parameters describing the bilinear bond-slip law are reported in Figure 3b.

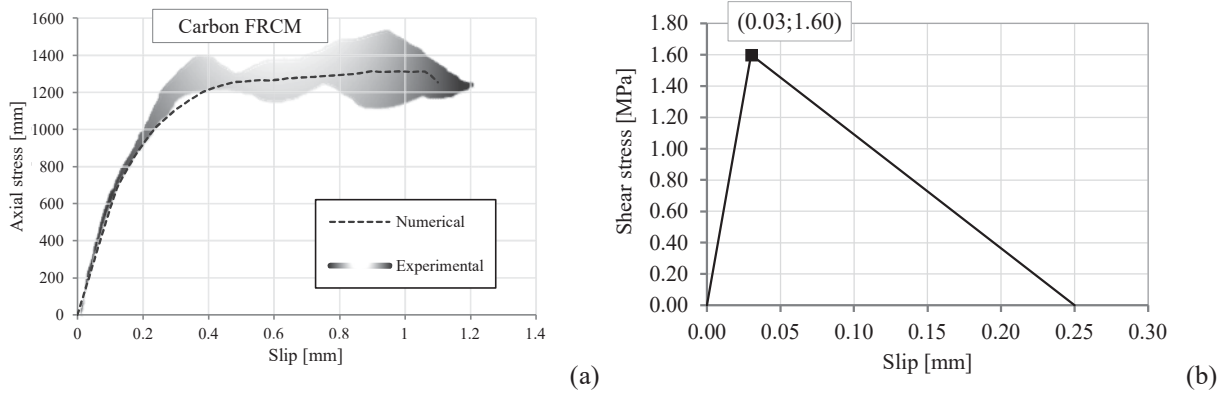


Figure 3: Numerical simulations of bond tests: (a) axial stress *vs* slip curve; (b) bilinear bond-slip law.

3 NUMERICAL RESULTS

The results of the nonlinear numerical analyses are presented in this Section for both the URM and the FRCM strengthened panels. They are compared with the experimental results obtained in a previous experimental campaign [15,16], in which two unreinforced and two FRCM strengthened panels were tested, to validate the proposed approach and understand the capabilities and limitations of the model. In more detail, the load *vs* vertical displacement (δv) curves are shown in Figure 4a.

With regards to the URM panels, a good agreement can be noticed between the numerical curve and the experimental ones, both in terms of peak load and corresponding displacement. The initial stiffness of the system is properly captured as well as the stiffness decrease registered around the 85% of the peak load. The experimental post-peak behavior was not properly registered due to the fragility of the experimental failure.

The experimental behavior of the FRCM strengthened panels is well described by the numerical load *vs* vertical displacement curve: the initial stiffness and the load bearing capacity increment (+30%) with respect to the URM panels are properly captured. In terms of vertical displacements, the prediction is realistic and inside the experimental range.

From the numerical results, the mechanical contribution of each single component of the FRCM strengthened panel (i.e masonry, mortar matrix and fibers) can be observed and described. In more detail, the reference points highlighted in Figure 4b can be identified, corresponding to the following phases of the diagonal compression tests:

- Point A: end of the elastic phase for the masonry panel. The first crack appears locally inside the substrate while the external mortar matrix layer is still uncracked.
- Point B: diffused masonry cracking, while the FRCM layers are still uncracked.
- Point C: presence of macro-cracks within the mortar matrix. Along the cracking lines, the fibers reach the peak shear stress and the onset of local delamination. In this phase, the load reduction between points B and C can be related to the amount and type of mortar matrix and fibers.

- Point D: the crack opening with the fiber slippage determines the significant load drop, until the stress redistribution allows for a proper bonding of fibers, working alone bridging the cracks. Until this condition is stable, the system can recover the load.
- Point E: the peak shear stress is reached for few further fiber alignments.
- Point F: bond failure of a significant number of fibers: the extent of stress redistribution is so diffused that fibers do not have the needed minimum bond length. This phase corresponds to the final failure of the FRCM system (due to delamination).

These findings confirm that the crack pattern and failure mechanism of the FRCM strengthened panels are directly affected by both the fibers and the mortar matrix characteristics. The mortar matrix gives stiffness and peak stress contributions, while the fibers allow to reseal the crack of the masonry panel and then determine a less brittle post-peak behavior and eventual force recovery (if the bond is effective).

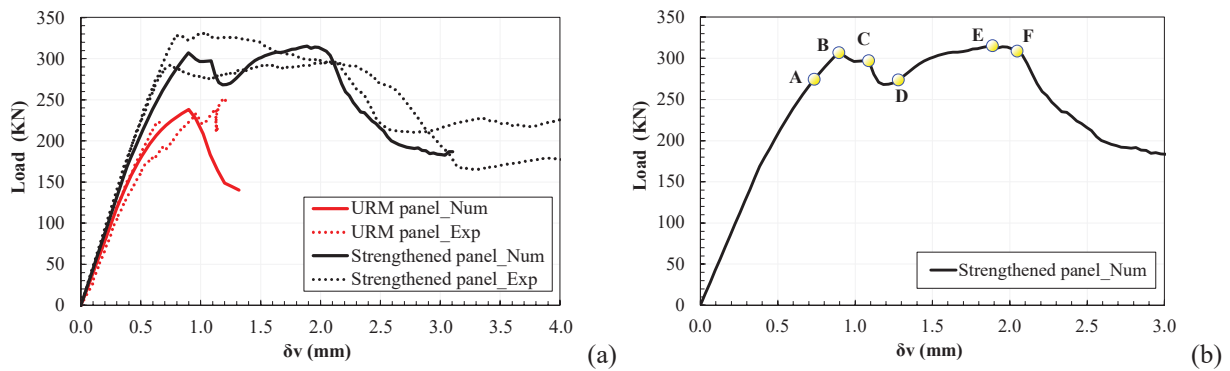


Figure 4: Load vs vertical displacement curves: (a) numerical vs experimental results; (b) strengthened panel.

The vertical stress and the interface normal stress are reported in Figure 5 and Figure 6 for the URM panel at peak and for the FRCM strengthened panel in correspondence with Point C of Figure 4b, respectively. Moreover, to better investigate the delamination process of the fibers within the mortar matrix during the diagonal compression tests, two representative fiber bundles are considered, in the positions denoted in Figure 1c. The shear stress distribution along the two fibers at different vertical displacements (B-F points of Figure 4b) is shown in Figure 7. The potential cracking lines, in correspondence of mortar joint interfaces and of the middle of the bricks are represented with vertical black lines. For the fiber bundle 170 (Figure 7a), an increase in the shear stress, even leading to the reaching of the bond strength, can be observed along some section when the mortar matrix starts to crack (lines B-C). In the following steps, a shift of the peak shear stress can be noticed due to the development of the delamination process. In correspondence with the formation of new cracks (e.g. position at 293.8 mm), a sudden failure (delamination) and a subsequent stress redistribution towards less stressed portions are observed, until the reaching of the minimum bond length, when the bundle fully delaminates. An analogous behavior can be noticed for the fiber bundle 174, even if the trend of the shear stress is influenced by the different position of the bundle within the masonry panel. Indeed, the delamination process starts later with respect to the fiber bundle 170, but the shift of the stress diagram is much larger. Starting from these observations and considering that the fully delamination can be reached at different time instants for the bundles, it can be observed that a stress redistribution is allowed between the bundles (beyond point F of Figure 4b). A FRCM strengthened masonry panel can exploit this important resource in the post-peak phase, depending on the quality of the matrix-fiber bond.

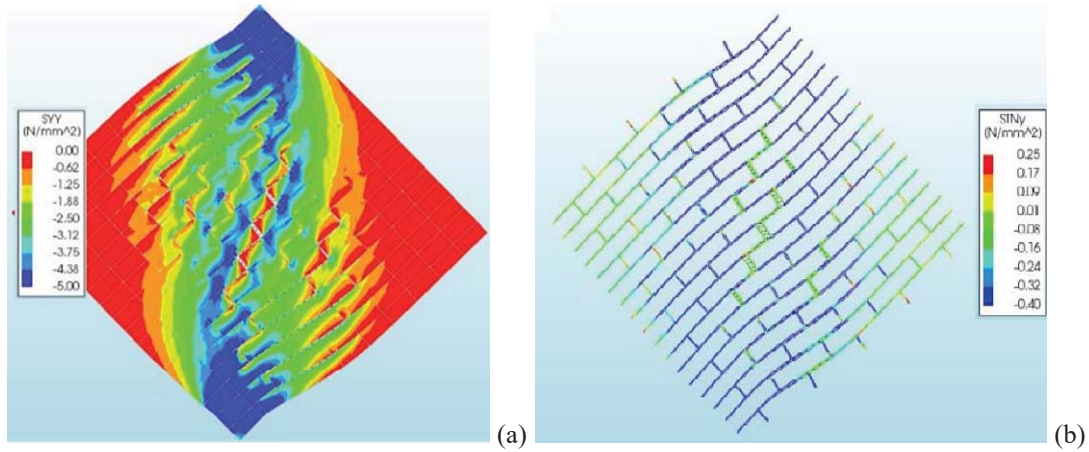


Figure 5: Numerical results for the URM panel at peak: a) vertical stresses on the brick elements, b) interface normal stresses.

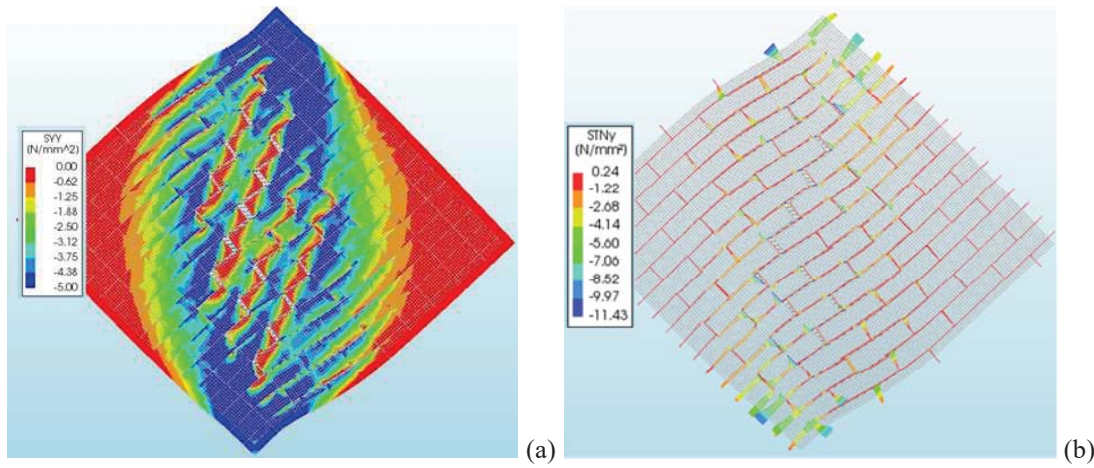


Figure 6: Numerical results for the FRCM strengthened panel: a) vertical stresses on the bricks, b) interface normal stresses.

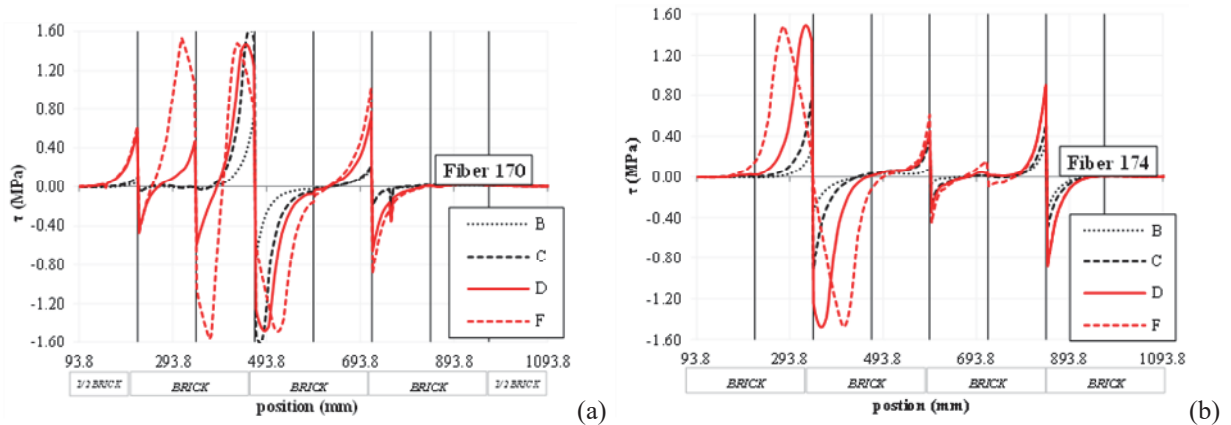


Figure 7: Tangential stress distributions along: a) fiber bundle 170, b) fiber bundle 174.

The numerical and experimental results are also compared in terms of failure mode. For the URM panel, the numerical failure is governed by the formation and development of one main crack along the compressed diagonal, in good accordance with experimental evidence (Figure 8a). For the FRCM strengthened panel, the presence of the composite system improves the failure mechanism, bridging the main crack and allowing for an effective stress

redistribution, which leads to the formation of multiple cracks before failure (Figure 8b). Correspondingly, the sample is allowed to reach much greater deformations before failure, with respect to the URM panel.

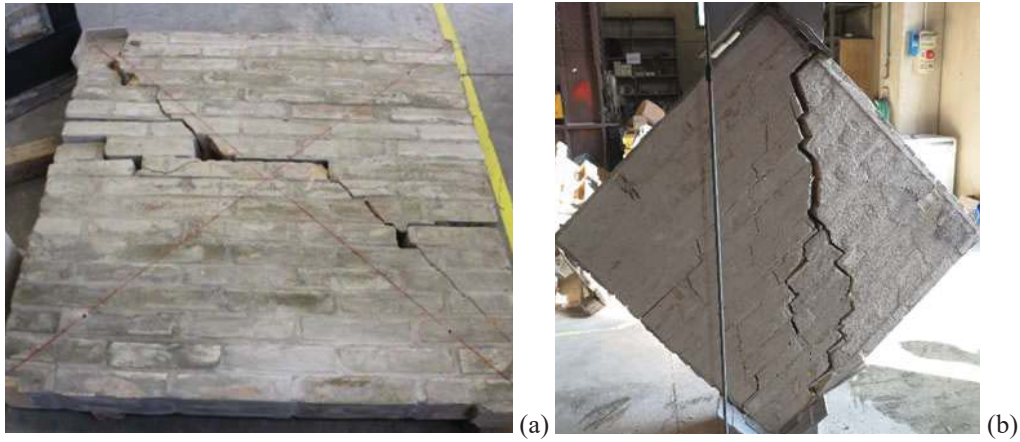


Figure 8: Typical failure modes of (a) URM panel and (b) FRCM strengthened panel.

4 PARAMETRIC ANALYSES

After the validation of the proposed numerical model by comparison with experimental diagonal compression tests, parametric analyses are performed to investigate some of the parameters which could affect the structural response. The variations here considered regards the mortar matrix properties, i.e. elastic modulus and tensile strength, and the amount of fibers embedded within the mortar matrix, according to Table 3. In more detail, the considered range of variability of the elastic modulus of the mortar matrix covers adoption of soft mortars and of thick mortar layers: the cross section of the mortar matrix is indeed kept constant in the model and the membrane stiffness is properly modified through the variation of the elastic modulus only. Concerning the variation of the amount of fibers, different cross sections and perimeters are considered, selecting appropriate ranges according to the products available in the market.

Model	E_{matrix} [MPa]	$f_{t,matrix}$ [MPa]	Area [mm ²]	Perimeter [mm]
Reference	17	3	0.47	4
Soft matrix	5.5	3	0.47	4
Stiff matrix	51	3	0.47	4
Weak matrix	17	1	0.47	4
Strong matrix	17	6	0.47	4
Matrix only	17	3	-	-
Double density	17	3	0.92	5.64
High density	17	3	1.38	6.92
Light density	17	3	0.23	2.83
Double layer	17	3	0.92	4

Table 3: Parametric analyses on mortar matrix properties and amount of fibers.

The results of the parametric analyses are reported in Figure 9 in terms of load vs vertical displacements. In particular, from Figure 9a it can be noticed that the value of the elastic modulus of the mortar matrix affects the stiffness of the initial uncracked branch, as expected.

A large deformability of the mortar matrix (soft curve) leaves the masonry alone in the definition of the first peak, which is then remarkably reduced with respect to other cases (ref., and stiff); on the contrary, a too stiff mortar matrix (stiff) cracks before the masonry, leaving almost unaffected the stress at first peak. After the first peak, the mortar matrix stiffness also affects the possibility of having a force recovery, due to a possible tension stiffening mechanism allowing for an effective distribution of the cracks around the central portion of the panel. Figure 9a shows also the effect of the mortar matrix tensile strength on the shear behavior: a weak mortar matrix cracks before the masonry and it produces a sudden stiffness reduction. Correspondingly, the first peak is significantly lower with respect to the Reference case. On the other side, a high value of tensile strength seems partially not effective without a coherent increase of elastic modulus, since the first peak is shifted towards larger deformations and crack openings, where the larger mortar matrix force contribution is balanced by the smaller masonry counterpart, clearly inside its softening behavior. Moreover, once the tensile strength is locally reached, the post-peak stress behavior is more brittle and, correspondingly, the global force redistribution capability is reduced. Once the mortar matrix is cracked, the second peak is mainly governed by the amount of fibers and their strength. These findings are also confirmed by recent research works [6].

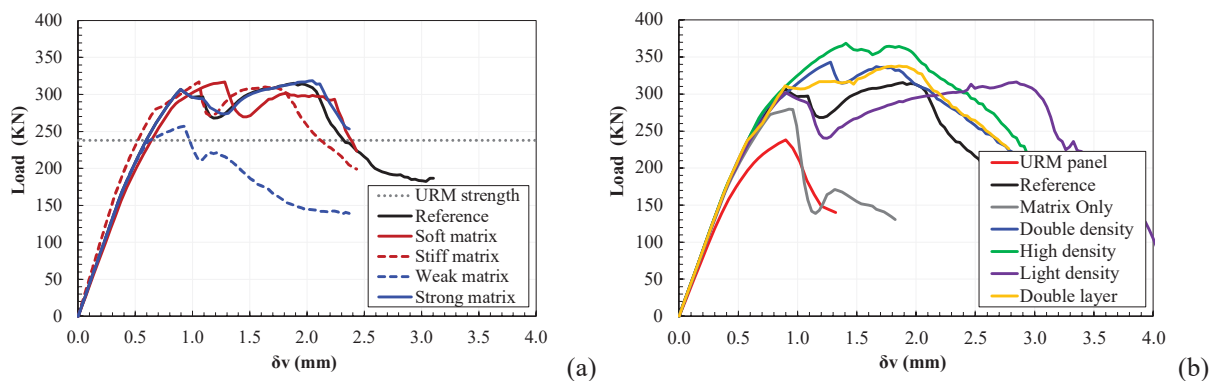


Figure 9: Load vs vertical displacement curves: (a) numerical vs experimental results; (b) strengthened panel.

The effect of the use of different amounts of fibers is presented in Figure 9b. It can be noticed that a growing amount of fibers inside the mortar matrix does not improve the first peak so much, since before cracking mortar matrix is more effective than fibers. Only when the amount of fibers is relevant (double density and high density) and properly bonded, the initial capacity is remarkably enhanced, even because the mortar matrix is thin. In fact, when two layers of strengthening grids are considered (double layer), first peak is not so affected and the effect of fibers can be observed only later, because of the limited bond between mortar matrix and fibers. The force drop after the first peak and the slope of the following force recovery branch (tension stiffening effect) are strongly related to the amount of fibers: the former being inversely dependent and the latter being proportional to it. This can be explained by considering the better stress redistribution which takes place around the main cracks with growing amount of fibers. As a consequence, a stronger reinforcement tends to merge the two peaks into one. Finally, as expected, the application of a layer of mortar matrix only produces an increase of stiffness and shear strength with respect to the URM panel but a very brittle failure occurs.

5 CONCLUSIONS

In the present paper, the in-plane shear behavior of FRCM strengthened masonry panels subject to diagonal compression tests is investigated by means of nonlinear numerical analyses. A novel modelling strategy is proposed to include the contribution of each component of the FRCM system. In more detail, the FRCM system is discretized by using linear trusses embedded into the mortar matrix and a proper bond-slip law is calibrated from experimental bond tests.

The numerical simulations allow to identify the different phases, characterizing the improved shear behavior of a FRCM strengthened panel, highlighting the role of each component, i.e. masonry substrate, mortar matrix and fibers. In particular, it is observed that, in most of the cases, the masonry cracks before the external mortar matrix, without introducing a sudden change of slope of the force vs vertical displacement curve. Then, the presence of the mortar matrix mostly influences the first peak load, while the presence of the fibers has an impact in the post-peak branch and in the determination of a second load peak. Parametric analyses on the mortar matrix properties and on the amount of fiber are performed to better analyze the influence of these parameters on the overall structural response.

It can be concluded that the described modelling approach can determine a satisfactory match between numerical and experimental results both for the unreinforced and the FRCM strengthened masonry panel. It could be extended to different typologies of FRCM systems, with a proper calibration of the mechanical properties of the materials and of the matrix-fiber bond-slip interface laws.

ACKNOWLEDGEMENTS

The authors gratefully acknowledge the financial support of the Italian Department of Civil Protection (ReLUIS 2021 Grant – Innovative Materials).

REFERENCES

- [1] A. Penna, P. Morandi, M. Rota, et al., Performance of masonry buildings during the Emilia 2012 earthquake. *Bulletin of Earthquake Engineering*, **12**, 2255-2273, 2014. <https://doi.org/10.1007/s10518-013-9496-6>
- [2] F. Ferretti, B. Ferracuti, C. Mazzotti, M. Savoia, Destructive and minor destructive tests on masonry buildings: Experimental results and comparison between shear failure criteria. *Construction and Building Materials*, **199**, 12-29, 2019. <https://doi.org/10.1016/j.conbuildmat.2018.11.246>
- [3] L. Ascione, G. de Felice, S. De Santis, A qualification method for externally bonded Fibre Reinforced Cementitious Matrix (FRCM) strengthening systems. *Composites Part B: Engineering*, **78**, 497-506, 2005. <https://doi.org/10.1016/j.compositesb.2015.03.079>
- [4] F.G. Carozzi, A. Bellini, T. D'Antino, Experimental investigation of tensile and bond properties of Carbon-FRCM composites for strengthening masonry elements. *Composites Part B: Engineering*, **128**, 100-119, 2017. <https://doi.org/10.1016/j.compositesb.2017.06.018>
- [5] M. Del Zoppo, M. Di Ludovico, A. Balsamo, A. Prota, Experimental In-Plane Shear Capacity of Clay Brick Masonry Panels Strengthened with FRCM and FRM Compo-

- sites. *Journal of Composites for Construction*, **23**, 04019038, 2019. [https://doi.org/10.1061/\(ASCE\)CC.1943-5614.0000965](https://doi.org/10.1061/(ASCE)CC.1943-5614.0000965)
- [6] F. Ferretti, C. Mazzotti, FRCM/SRG strengthened masonry in diagonal compression: experimental results and analytical approach proposal. *Construction and Building Materials*, **283**, 122766, 2021. <https://doi.org/10.1016/j.conbuildmat.2021.122766>
- [7] A. Garofano, F. Ceroni, M. Pecce, Modelling of the in-plane behaviour of masonry walls strengthened with polymeric grids embedded in cementitious mortar layers. *Composite Part B: Engineering*, **85**, 243–258, 2015. <https://doi.org/10.1016/j.compositesb.2015.09.005>
- [8] M. Basili, G. Marcari, F. Vestroni, Non-linear analysis of masonry panels strengthened with textile reinforced mortar. *Engineering Structures*, **113**, 245–258, 2016. <https://doi.org/10.1016/j.engstruct.2015.12.021>
- [9] E. Bertolesi, G. Milani, C. Poggi, Simple holonomic homogenization model for the non-linear static analysis of in-plane loaded masonry walls strengthened with FRCM composites. *Composite Structures*, **158**, 291–307, 2016. <https://doi.org/10.1016/j.compstruct.2016.09.027>
- [10] X.Wang, B. Ghiassi, D.V. Oliveira, C.C. Lam, Modelling the non-linear behaviour of masonry walls strengthened with textile reinforced mortars. *Engineering Structures*, **134**, 11–24, 2017. <https://doi.org/10.1016/j.engstruct.2016.12.029>
- [11] F.G. Carozzi, G. Milani, C. Poggi, Mechanical properties and numerical modelling of Fabric Reinforced Cementitious Matrix (FRCM) systems for strengthening of masonry structures. *Composite Structures*, **107**, 711–725, 2014. <https://doi.org/10.1016/j.compstruct.2013.08.026>
- [12] E. Bertolesi, F.G. Carozzi, G. Milani, C. Poggi, Numerical modelling of Fabric Reinforce Cementitious Matrix composites (FRCM) in tension. *Construction and Building Materials*, **70**, 531–548, 2014. <https://doi.org/10.1016/j.conbuildmat.2014.08.006>
- [13] P.B. Lourenço, *Computational strategies for masonry structures*. Delft University of Technology, 1996.
- [14] J.G. Rots, *Structural masonry: an experimental/numerical basis for practical design rules*. Balkema, Rotterdam, 1997.
- [15] F. Ferretti, A. Incerti, B. Ferracuti, C. Mazzotti, Diagonal compression tests on masonry panels strengthened by FRP and FRCM. *10th International Conference on Structural Analysis of Historical Constructions (SAHC 2016)*, Leuven, Belgium, 2016.
- [16] F. Ferretti, A. Incerti, B. Ferracuti, C. Mazzotti, FRCM Strengthened Masonry Panels: The Role of Mechanical Anchorages and Symmetric Layouts. *Key Engineering Materials*, **747**, 334–341, 2017. <https://doi.org/10.4028/www.scientific.net/KEM.747.334>
- [17] G.P.A. van Zijl, (2004) Modelling masonry shear-compression: Role of dilatancy highlighted. *Journal of Engineering Mechanics*, **130**, 1289–1296, 2004. [https://doi.org/10.1061/\(ASCE\)0733-9399\(2004\)130:11\(1289\)](https://doi.org/10.1061/(ASCE)0733-9399(2004)130:11(1289))
- [18] Comité Euro-International du Béton, *CEB-FIB Model Code 1990*, 1993.
- [19] E. Grande, G. Milani, Interface modelling approach for the study of the bond behavior of FRCM strengthening systems. *Composites Part B: Engineering*, **141**, 221–233, 2018. <https://doi.org/10.1016/j.compositesb.2017.12.052>

EMPIRICAL AND MECHANICAL ANALYSIS METHODS FOR SEISMIC VULNERABILITY ASSESSMENT OF CLUSTERED BUILDINGS OF HISTORICAL CENTRES: A CASE STUDY

A. Formisano¹, G. Mochi² and N. Chieffo³

¹ Department of Structures for Engineering and Architecture
University of Naples “Federico II”
Piazzale V. Tecchio 80 – 80125 Naples (Italy)
antoform@unina.it

² Department of Civil and Environmental Engineering
University of Perugia
Via. G. Duranti 93 – 06125 Perugia (Italy)
giovanni.mochi@unipg.it

³ Department of Architecture and Urbanism
Politehnica University of Timisoara
Traian Lalescu Street 2/A – 300223 Timisoara (Romania)
nicola.chieffo@student.upt.ro

Abstract

Presently, in historical centres, it is very difficult to analyse buildings as independent structures, since they share the same boundary walls with adjacent structural units. These constructions of the building aggregate interact among themselves under seismic actions, so that their behaviour differs from that of the individual buildings considered as isolated structures. Therefore, it is emerging the need to assess seismic vulnerability of building aggregates. Thus, in this paper both simple empirical and mechanical refined vulnerability evaluation methods of masonry building aggregates are examined in general terms and illustrated in detail through the application on a case study in Mirandola, a district of Modena. On one hand, two empirical assessment methodologies, mainly based on the basic observational data of masonry constructions and properly calibrated on macro-element analysis results on a significant number of clustered buildings, are proposed taking properly into account the interactions among adjacent constructions. On the other hand, a mechanical analysis method at the individual building scale is also applied to evaluate more realistically the seismic behaviour of clustered structural units through the development of appropriate capacity curves.

Keywords: Seismic Vulnerability, Masonry Aggregates, Empirical Methods, Quick evaluation, Mechanical Methods, Capacity curves.

1 INTRODUCTION

The seismic safety of existing masonry buildings represents, as it is known, one of the main priorities for reducing the seismic risk of historical centres and is conditioned from multiple geometrical and mechanical factors that influence their behaviour against earthquakes [1].

Nowadays, in most Italian centres, it is easy to find a building heritage characterized by historic masonry constructions without an adequate structural apparatus to resist the increasingly frequent and disastrous seismic actions. This structural inadequacy generates a drastic increase of the global vulnerability and, therefore, of the seismic risk of entire urbanized sectors.

Buildings erected in aggregate conditions are often made up according to the traditional constructive practice with very variable types of vertical structure (i.e. heterogeneous or multi-leaf masonry walls) and deficient construction details (bad connections between orthogonal walls and between walls and floors, variation in the thickness of the walls along with the building height, etc.), which implicitly involve behavioural deficiencies in terms of stability in areas characterized by considerable seismicity. Furthermore, the interactions among the contiguous structural cells must be appropriately considered in the study of the vulnerability of the whole aggregate, since the dynamic response of each cell is strongly influenced by both the number of aggregate units and the position within the clustered building [2].

Based on these considerations, the present study aims to focus on the seismic response of a masonry aggregate located in the historical Centre of Mirandola, a municipality within the province of Modena. The selected masonry aggregate is made of brick walls with deformable floors, which is a typical structural typology representative of the building classes present in the examined urban area. The main objective of the present research is to study seismic vulnerability through empirical and mechanical procedures in order to provide a judgement on the effectiveness of simple analysis methods in predicting seismic vulnerability of masonry structural units of clustered buildings.

2 CASE STUDY MASONRY AGGREGATE

The case study historical building is a row masonry aggregate (Figure 1) composed of different structural units (SUs), mutually interacting to each other, which occupy different positions (heading or intermediate) within the examined clustered compound.



Figure 1: Case study aggregate placed in the historical centre of Mirandola.

From a structural point of view, the height of the structural units varies from 2 to 4 floors above ground, with an average inter-storey height of 2.80 m. The vertical structures, characterized by solid brick walls, have an average thickness ranging from 0.24 m to 0.50 m.

The horizontal structures are mainly made of wooden beams with double planking. The street views of the study building compound, together with the division of the masonry aggregate in different SUs, are depicted in Figure 2.



Figure 2: Structural layout and identification of the SUs.

Concerning the physical conditions, it has been observed that the main facades along Franciacorta street do not show, globally, a marked deterioration of the materials. Nevertheless, there are evident spots of humidity and partial detachment of the plaster, which, however, do not alter the static behaviour of buildings. Similarly, the façade facing Dei Quartieri street does not display signs of structural decay or cracks.

3 EMPIRICAL VULNERABILITY ASSESSMENT

To estimate the seismic vulnerability of the reference case study aggregate, firstly, it is adopted a specific vulnerability index method (V.I.M.) proposed in [3], which is appropriately conceived for historical buildings aggregates. The proposed survey form takes into account the effects of mutual interaction among SUs under seismic actions with suitable five parameters accurately calibrated on mechanical analyses. So, the vulnerability index of each SU is achieved as the weighted sum of the score of each parameter multiplied by the respective weight. Consequently, the seismic vulnerability of the entire aggregate is estimated as the weighted mean of the vulnerability indices of each SUs, considering the ratio between the cell volume and that of the entire aggregate, as shown in the following Equation 1:

$$V_{I,agg.} = \sum_{i=1}^n \left(V_I^{SU_i} \cdot \frac{Vol_{SU^i}}{Vol_{agg.}} \right) \quad (1)$$

Subsequently, the methodology proposed in [4] is applied. This seismic vulnerability assessment procedure is essentially based on specific vulnerability indices, which describe, according to various constructive and functional parameters (geometric characteristics, construction period, collapse mechanisms, etc.), the seismic criticality degree of each aggregate.

This methodology allows estimating the seismic vulnerability based on a global analytical vulnerability index (V_{GA}) of the aggregate, providing an immediate quantification of the haz-

ard of the single aggregate. Mathematically, the used analytic expression is shown in the following Equation 2:

$$V_{GA} = DM \cdot P_{DM} + RF \cdot P_{RF} + RT \cdot P_{RT} + LP \cdot P_{LP} + VT \cdot P_{VT} + MRC \cdot P_{MRC} + MSS \cdot P_{MSS} \quad (2)$$

where: DM is the masonry disconnection index, RF is the index of façades overturning, RT is the index of the gable overturning, LP is the index of strut-cracks, VT is the shear index, MRC is the R.C. hammering index and MSS is the hammering index due to staggered floor. The above mentioned factors are vulnerability indices identifying the portion of the aggregate, which results to be exposed at seismic damage. Moreover, the coefficients P_i (P_{DM} , P_{RF} , ..., P_{MSS}) are the weights associated to the previously defined indices, whose numerical values are assigned proportionally to the corresponding collapse mechanism activated [4].

The two assessment methods are applied to the case study building aggregate. Figure 3 shows the comparison between the analytical indices assessed using the applied methodologies and the respective typological vulnerability curves [5] of the entire aggregate case study.

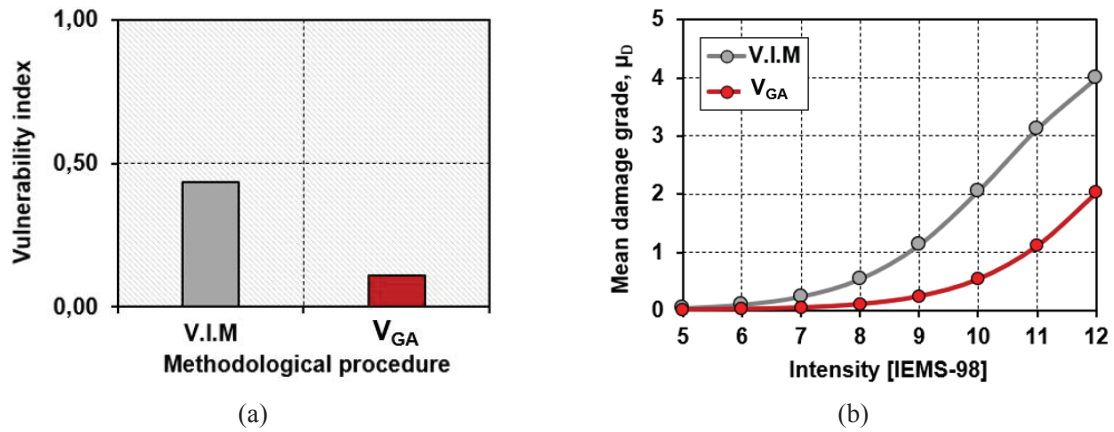


Figure 3: Comparison between the proposed methodologies in terms of vulnerability index (a) and vulnerability curves (b).

From the results acquired, it is shown how the V.I.M shows a significant increase in vulnerability (+ 26%) compared to the V_{GA} method (Figure 3a). This discrepancy is essentially due to the parameters monitored in the two methods used. The V.I.M. establishes its applicability mainly on the interactions of structural units, considering the incidence of the plane-altimetric configuration of the single SUs. On the contrary, the V_{GA} method is based on the definition of a set of indices, that affect the behaviour of the façades of the building examined. The comparison results are also presented in terms of vulnerability curves in Figure 3b, where it is seen that, starting from a macro-seismic intensity of nine, the V_{GA} method tends to underestimate of one level the expected damage compared to that of the other method proposed.

4 MECHANICAL VULNERABILITY ASSESSMENT

The numerical analyses are performed according to the 3Muri software [6] based on the Frame Macro-Elements (FME) theory. In this analysis method, it is assumed that masonry walls are considered as a set of single-dimensional macro-elements suitably interconnected to each other by rigid nodes.

The strength criteria of deformable elements are assumed based on EN 1998-3 provisions [7], which establish as maximum drifts for shear and flexural collapse failures the values of

0.4% and 0.6%, respectively. Furthermore, to consider the confinement effect of the structural units contiguous to the reference one, the SUs are modelled with the 3Muri software considering half part of adjacent structural cells accounting for their contribution in terms of stiffness and mass. In Figure 4, the most representative SUs extrapolated from the whole aggregate, namely head unit (SU1) confined on one side only, intermediate unit (SU7) confined on three sides and intermediate unit (SU13) confined on two sides, are depicted.

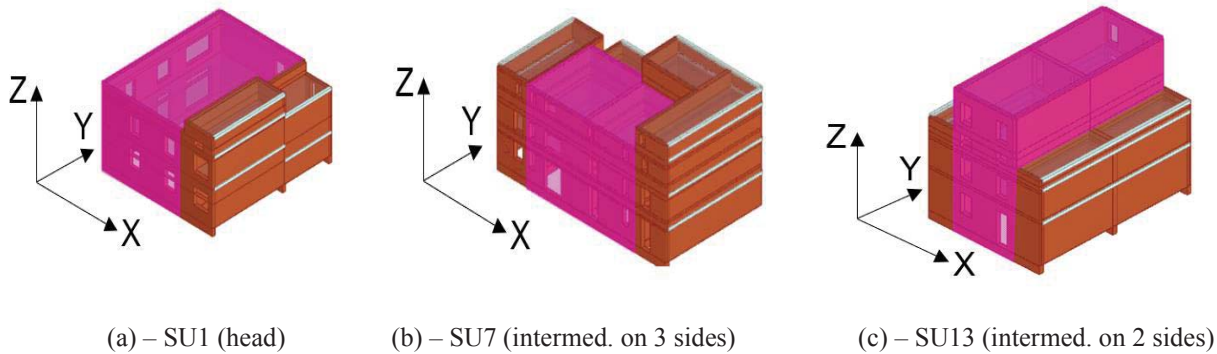


Figure 4: Numerical models of some structural cells: head SU (a) intermediate SU confined on 3 sides (b) and intermediate SU confined on 2 sides (c).

Subsequently, the above-presented structural configurations are compared in terms of capacity curves, as reported in Figure 5.

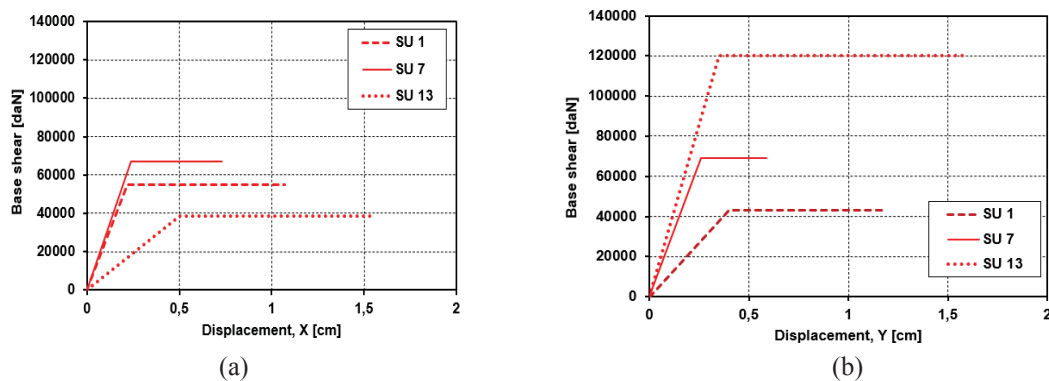


Figure 5: Capacity curves of the inspected SUs in X (a) and Y (b) analysis directions.

From the analysis of the achieved results, it is possible to appreciate how the structural behaviour of the examined SUs in the two analysis directions is very different to each other.

In particular, it is observed that in the transverse direction (X) the SU1 (head) and SU7 (intermediate, confined on three sides) provide an increase of strength about of 42% and 72%, respectively, with respect to the SU13 (intermediate, confined on two sides). Moreover, considering the comparison in terms of the ultimate displacement, d_u , the SU13 exhibits the best performance, with a value from 1.5 to 2.0 times greater than that of the other above-mentioned SUs. Conversely, in the longitudinal direction (Y), the examined structural cells display a different structural behaviour. In fact, as it is seen from the results attained in Figure 5b, the SU13 shows strength of about 3 and 2 times greater than that of SU1 and SU7, respectively. In addition, by comparing the ultimate displacements of the examined clustered units, it is noticed how the SU13 provides a value about 1.5 and 2.5 times greater than those of SU1 and SU7, respectively. Finally, the V.I.M method is applied to each of the SUS of the building compound to highlight the differences detected with the results gotten from the mechani-

cal analyses applied to each of the SUS of the whole buildings aggregate. The comparison of results deriving from the used analysis procedures are shown in Figure 6.

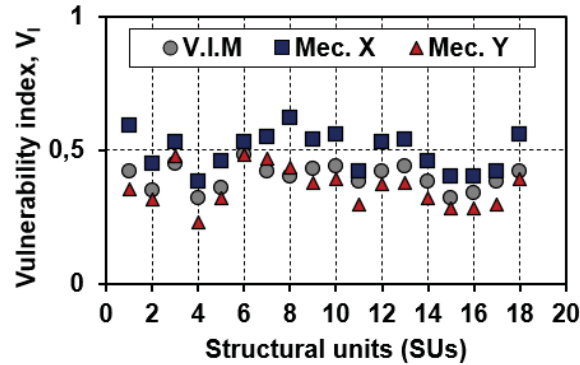


Figure 6: Comparison between V.I.M. results and mechanical method ones.

From the comparison presented, it is clear how, globally, the vulnerability level obtained by the empirical method is not very dissimilar from what is obtained by mechanical analysis. In particular, in the direction X, the mechanical analysis indices differ on average by +25% (estimated dispersion concerning the entire sample of data examined) compared to the mean value of the empirical procedure. On the contrary, in the direction Y, the data obtained by the mechanical approach differ on average by -10% compared to the average empirical one. This circumstance leads to consider that the proposed V.I.M. method is almost effective for the simplified estimation of the seismic vulnerability of SUs of masonry building compounds.

5 CONCLUSIONS

The present research applied different analysis procedures for seismic vulnerability evaluation of historical buildings in aggregate condition. In particular, two different approaches, namely empirical (V.I.M. and A.V.I.) and mechanical, were used to determine the seismic vulnerability of a clustered building located in the municipality of Mirandola. From the application of empirical methods, based on specific and synthetic survey forms, it was found that:

- The V.I.M method, specifically conceived for cluster buildings, allowed to estimate the vulnerability of the whole building aggregate as a weighted average of the indices of the individual structural units (SUs), providing a medium-low vulnerability level equal to 0.43;
- The method proposed by Gulli et al., which was derived as a weighted sum of specific local vulnerability indices, mainly taking into consideration the behaviour of the façade walls, provided a synthetic vulnerability index equal to 0.106 (low vulnerability);
- The comparison between the empirical methodologies showed how the V_{GA} index underestimates, on average, the expected vulnerability by + 26% compared to the V.I.M. one. This discrepancy was reflected in the evaluation of the average damage degree too. In fact, starting from a macroseismic intensity equal to nine, a mean underestimation of the expected damage degree of 33% was found by applying the methodology proposed by Gulli et al.

Subsequently, mechanical analysis was carried out on each of the SUs composing the aggregate to compare the achieved results with the corresponding ones deriving from the empirical V.I.M. method. From comparison, it was noticed that:

- In the two analysis directions, a variation of the seismic capacity was observed for the SUs examined. In particular, in the direction X, the monitored base shear provided by the SU1 and SU7 was 42% and 72% higher than those of the corresponding SU13, respectively.

Moreover, the SU13 exhibited a significant increase of the capacity displacement, with a value from 1.5 to 2.0 times greater than that of the other above-mentioned SUs. On the contrary, in direction Y, it was observed how the SU13 provided a shear strength about 3 and 2 times higher than that of SU1 and SU7, respectively. In addition, by comparing the ultimate displacements of the examined clustered units, it has been noticed how the SU13 provided a value about 1.5 and 2.5 times greater than those of SU1 and SU7, respectively.

- The vulnerability level attained by the empirical V.I.M. method did not result dissimilar from what was obtained by the mechanical approach. In particular, in the direction X, the mechanical simulation overestimated by +25% the mean index of empirical procedure. On the contrary, in the direction Y, the vulnerability index obtained by the mechanical approach underestimated on average by 10% the seismic safety condition deriving from the simple empirical method.
- In conclusion, based on the above-mentioned results, it was found that the V.I.M. method is quite suitable in predicting, through a simple analysis tool, the seismic vulnerability of SUs of clustered buildings.

ACKNOWLEDGEMENTS

The Authors would like to acknowledge the DPC-ReLUIS 2019-2021 research project for the financial support to the development of the research activity presented in the current paper.

REFERENCES

- [1] M. Mosoarca, I. Onescu, E. Onescu, A. Anastasiadis, Seismic vulnerability assessment methodology for historic masonry buildings in the near-field areas. *Engineering Failure Analysis*, **115**, 104662, 2020.
- [2] A. Formisano, Theoretical and Numerical Seismic Analysis of Masonry Building Aggregates: Case Studies in San Pio Delle Camere (L'Aquila, Italy). *Journal of Earthquake Engineering*, **21**, 227-245, 2017.
- [3] A. Formisano, G. Florio, R. Landolfo, and F. M. Mazzolani, Numerical calibration of an easy method for seismic behaviour assessment on large scale of masonry building aggregates. *Advances in Engineering Software*, **80**, 116–138, 2015.
- [4] R. Gulli, G. Mochi, G. Predari, An expeditious methodology for the seismic vulnerability assessment of building aggregates. *Technologies Engineering Materials Architecture*, **4**, 2018.
- [5] N. Chieffo, I. Onescu, A. Formisano, M. Mosoarca, M. Palade, Integrated empirical-mechanical seismic vulnerability analysis method for masonry buildings in timișoara: Validation based on the 2009 italian earthquake. *The Open Civil Engineering Journal*, **14**, 314–333, 2020.
- [6] S.T.A data srl, 3Muri 10.9.0 - User Manual, 2020.
- [7] EN 1998-3 - Eurocode 8: Design of structures for earthquake resistance – Part 3: Assessment and retrofitting of buildings, CEN. (2004) 1–97.

SETTLEMENT-INDUCED DAMAGE ASSESSMENT IN UNILATERAL MASONRY-LIKE STRUCTURES: A PIECEWISE RIGID DISPLACEMENT APPROACH

Ida Mascolo¹, Antonio Fortunato¹

¹ University of Salerno
Department of Civil Engineering
Via Giovanni Paolo II, 132 - 84084 Fisciano (SA)
e-mail: {imascolo, a.fortunato}@unisa.it

Keywords: Masonry, arch bridge, seismic behaviour, Piecewise Rigid Displacement approach.

Abstract. Settlements severely affect historic masonry structures, and in fact, settlement-induced structural failures are common worldwide. This paper describes a rigid block detection and identification procedure of the crack pattern in masonry-like structures subjected to dead loads and finite displacements (e.g., settlements). The procedure is based on the Piecewise Rigid Displacements (PRD) approach. The equilibrium problem is formulated in the framework of Limit Analysis by means of a suitable variational formulation for the Boundary Value Problem (BVP) of Normal Linear Elastic No-Tension material (NENT). The equilibrium states of masonry-like structures are obtained as an optimization of Total Potential Energy (TPE). The application of the proposed method to real case studies highlights its potential in the field of mechanics and the mechanisms of fracture.

1 INTRODUCTION

Masonry arch bridges are susceptible to extensive structural damage, failure, and even collapse when subjected to exceptional loading or massive differential settlements induced by floods, ship-worm infestations of wooden foundations, scouring, and other natural or man-made events. The Scrivia River, Trigno, and Rubianello bridges in Italy (2002, 2003, 2013), the Ballynameen and Bishopsford Road bridges in England (2015, 2019), the Deba bridge in Spain (2018) are just some examples of recent spread world wide masonry bridges failures under scour-induced settlements [1]-[6] are just a few examples of recent worldwide masonry bridges failures under scour-induced settlements. These events are further proof of the urgent need for the analysis and assessment of the load-carrying capacity of masonry bridges. The number of scientific research papers dealing with this topic is impressive. The main methods of structural analysis of masonry construction are:

- FEM-based approaches, which are subdivided into three main categories depending on the representative scale: macro-modeling [7]-[9], discontinuous models [10] and micro-modeling [11]. Moving from the macro- to the micro-scale, the level of accuracy increases, but the modeling and numerical implementation challenges and the computational efforts also significantly increase;
- homogenization approaches [12, 13], in which a structural elementary cell (consisting of different components such as mortar and blocks) is modeled as an equivalent homogeneous medium (i.e., a continuum) with mechanical parameters that are derived from each of its individual components; and
- Limit Analysis-based approaches, modern approaches that support the classical methods employing thrust line theory, graphic statics, and Limit Analysis. Their origins date to the English school in the late 1600s, with the theory of the chain having firstly been proposed by Robert Hooke (1676) and used later by Christopher Wren in Saint Paul's dome (1675), by Giovanni Poleni in St. Peter's dome in Vatican (1743), and, more recently, by Antoni Gaudí i Cornet for the design of the church of Colònia Güell in Barcelona (c. 1900) [14, 15]. Their modern formulation, due to Anthony Kooch, Jacques Heyman and Olgierd Cecil Zienkiewicz [16]-[18], is based on the No-Tension assumption. The material is modeled as a no-tension rigid or elastic material, with unilateral no-friction contact conditions [19]-[22].

Nonetheless, the issue is far from being exhausted because each of these three methods yields results only within its own bounds. There is to date no generally accepted way to assess masonry structures.

This paper focuses on analyzing and predicting crack patterns in masonry arch bridges subjected to dead loads and finite displacements. In the framework of the modern Limit Analysis-based approaches, the equilibrium problem is reformulated with a classical variational inequality form or equivalently as a constrained minimization problem of a non-differentiable functional (i.e., the Total Potential Energy) over the set of admissible displacements [23]-[?]. The main novelty is the consideration of a fictitious elasticity of the material to guarantee the convergence of the proposed method. The solution is then obtained by making the elastic deformation tensor tend to zero. This procedure is based on the Piecewise Rigid Displacements approach [21], which consists of restricting the minimization problem by a finite class of piecewise rigid displacements with support on a

finite partition of the whole structural domain. This reduces the equilibrium problem to a convex optimization problem for which existence and uniqueness are ensured. The case study of the Deba Bridge failure in Spain is also considered to capture the essence of the proposed method and its effectiveness.

The structure of the paper is as follows: Section 2 focuses on the Deba Bridge and its failure occurred in 2018, Section 3 presents the mathematical model and theoretical framework of the proposed numerical approach, Section 4 applies such a procedure to the case study of Deba Bridge. The results show a satisfactory agreement between the numerical-based crack pattern and the observed one, proving to be a powerful and versatile tool for the study of the mechanisms of fracture of No-Tension materials. The proposed method can be usefully exploited for the study of collapse mechanisms and ultimate load capacity of a wide range of masonry-like structures as it is emphasized in the concluding remarks drawn in Section 5.

2 The Deba Bridge

The Deba Bridge is a four-span stone bridge connecting the city of Deba with Mutriku in the Basque Country of Spain. It was built from 1865 and 1866 as part of a larger coastal motorways project that aimed to link the cities of San Sebastián and Bilbao. For its artistic and historic value, the Deba Bridge has special protection within the Monumental Complex of the Camino de Santiago. The underlying geology of the Deba riverbed is mainly composed of alluvial soil mixed with silt, sand, and gravel that constantly experiences landslides, dolines, and rockfalls. This is reflected in many episodes of settlement-induced bridge failures over the years. The latest occurred at the beginning of July 2018, when the central pier experienced a vertical settlement of about 0.80-0.90m, resulting in a great depression in the road, damage and cracking of the two central bridge vaults, and, consequently, closure of the bridge (Figure 1).



Figure 1: Views of the Deba Bridge (Debako Zubia kaltetuta)

3 Mathematical model

Let us consider an elastic body that occupies, in its undeformed state, an open and bounded subset $\Omega \in \mathbb{R}^2$ with a sufficiently smooth boundary (i.e., $\mathcal{C}^{1,1}$ -regular curve $\partial\Omega$), consisting of two open disjoint parts $\partial\Omega = \partial\Omega_D \cup \partial\Omega_N$. They are bound to first-type (i.e., Dirichlet) and second-type (i.e., Neumann) boundary conditions (i.e., here, the displacements and the surface forces are prescribed), respectively:

$$\mathbf{u} = \bar{\mathbf{u}} \quad \text{on } \partial\Omega_D, \quad \mathbf{T}^{(n)} = \mathbf{p}, \mathbf{b} \quad \text{on } \partial\Omega_N. \quad (1)$$

Here, $\bar{\mathbf{u}}$ denotes the vector field of prescribed surface displacements; $\mathbf{p} = \{p_i\}$ and $\mathbf{b} = \{b_i\}$ denote the prescribed forces and the body forces; and $\mathbf{T}^{(n)} = \mathbf{T}\mathbf{n}$, where \mathbf{n} is the outward normal vector on the boundary of Ω . Let $\mathbf{E} = \boldsymbol{\varepsilon} + \boldsymbol{\lambda}$ denote the infinitesimal strain tensor, additively decomposed into an elastic ($\boldsymbol{\varepsilon}$) and an anelastic part ($\boldsymbol{\lambda}$); \mathbf{T} the stress tensor; and \mathbb{C} , the positive-definite elasticity tensor. The constitutive equations for the NENT material we investigate are described by the set of relations:

$$\text{strain-stress relation:} \quad \mathbf{E} = \mathbb{C}^{-1}\mathbf{T} + \boldsymbol{\lambda}, \quad (2)$$

$$\text{internal constraint:} \quad \mathbf{T} \in \text{Sym}^-, \quad (3)$$

$$\text{normality law:} \quad \boldsymbol{\lambda} \in \text{Sym}^+ \wedge \mathbf{T} \cdot \boldsymbol{\lambda} = 0. \quad (4)$$

The Boundary Value Problem (BVP) for a NENT material is given by:

Problem 3.1 Find an admissible state $(\mathbf{u}, \boldsymbol{\lambda}, \mathbf{T})$ (i.e., displacement, anelastic strain and stress fields):

1. equilibrium

$$\text{div}\mathbf{T} + \mathbf{b} = \mathbf{0}, \quad \text{on } \Omega \quad (5)$$

2. stress-strain constitutive law

$$\mathbf{T} = \mathbb{C}(\mathbf{E} - \boldsymbol{\lambda}), \quad (6)$$

3. internal constraint and normality law

$$\mathbf{T} \in \text{Sym}^-, \quad \boldsymbol{\lambda} \in \text{Sym}^+, \quad \mathbf{T} \cdot \boldsymbol{\lambda} = 0, \quad (7)$$

4. boundary conditions

$$\mathbf{T}\mathbf{n} = \mathbf{p}, \quad \mathbf{u} = \bar{\mathbf{u}}|_{\partial\Omega_N}, \quad \text{on } \partial\Omega_N. \quad (8)$$

The resulting weak formulation, i.e., the variational formulation of such a problem, can be formulated as follows:

Problem 3.2

$$\text{minimize}_{\mathbf{u} \in \mathcal{K}, \boldsymbol{\varepsilon}} : \quad \mathcal{E}_p(\boldsymbol{\varepsilon}) = \int_{\Omega} \phi_{\mathbb{E}i}(\boldsymbol{\varepsilon}) da - \int_{\Omega} \mathbf{b} \cdot \mathbf{u} da - \int_{\partial\Omega_N} \mathbf{p} \cdot \mathbf{u} ds, \quad (9)$$

$$\text{subject to :} \quad \mathbf{A}\mathbf{U} \geq 0, \quad \mathbf{B}\mathbf{U} = 0 \quad (10)$$

where \mathcal{K} is a proper finite class of piece-wise rigid displacements obeying material conditions and having support on a finite partition of the whole domain $\Omega = \bigcup_1^m \Omega_i$

$$\mathcal{K} \subset \{\mathbf{u} \in \mathcal{S}(\Omega) : \boldsymbol{\lambda} \in \text{Sym}^+ \text{ and } \mathbf{u} = \bar{\mathbf{u}} \text{ on } \partial\Omega_N\} \quad (11)$$

$\phi_{\mathbb{E}_i}$ denotes the strain energy density, $\mathbf{U} \in \mathbb{R}^{3m}$ is the vector collecting the three Lagrangian parameters of the elementary mesh element Ω_i , and the matrices \mathbf{AU} and \mathbf{BU} collect the no-concentration and no-sliding conditions, respectively (See ... for more details). Note that the resulting optimization problem involves a quadratic functional subjected to linear constraints. By minimizing the TPE with respect to both displacements and elastic deformation, we are forcing the elastic part of the strain tensor to vanish. It is equivalent to coupling the initial rigid structure, characterized by a positive semi-definite stiffness \mathbf{K} , with a fictitious elastic structure, characterized by a positive-definite stiffness \mathbf{K}_s . It can be proven that the problem of finding an admissible state of displacement for the initial structure is equivalent to the same problem formulated for a structure having a positive-definite stiffness, $\mathbf{K}_\delta = \mathbf{K} + \delta\mathbf{K}_s$, because regularization parameter δ tends to zero [30].

4 Numerical analysis

The proposed method is validated by analyzing the case study of the Deba Bridge failure. The convex optimization problem related with the proposed approach was solved here by the Interior Point method [31, 32], which is particularly advantageous when the problem involves a large number of variables ($3 \cdot 1012$ in the case analyzed here). The bridge domain is discretized into 1012 quadrilateral elements and a vertical displacement of 0.9m and a counterclockwise rotation of 1.13 is imposed on the central pier of the bridge. The obtained results, both in terms of displacements and macro-block identification, show good agreement with the failure geometrical survey. On the basis of blocks rigid roto-translations, six macroblocks have been identified. The two on the outside (the light blue blocks in Figure 2) are fixed. Then a four-block isostatic substructure can be identified, the kinematic motion of which is closer to that seen in the bridge failure (Figure 2).

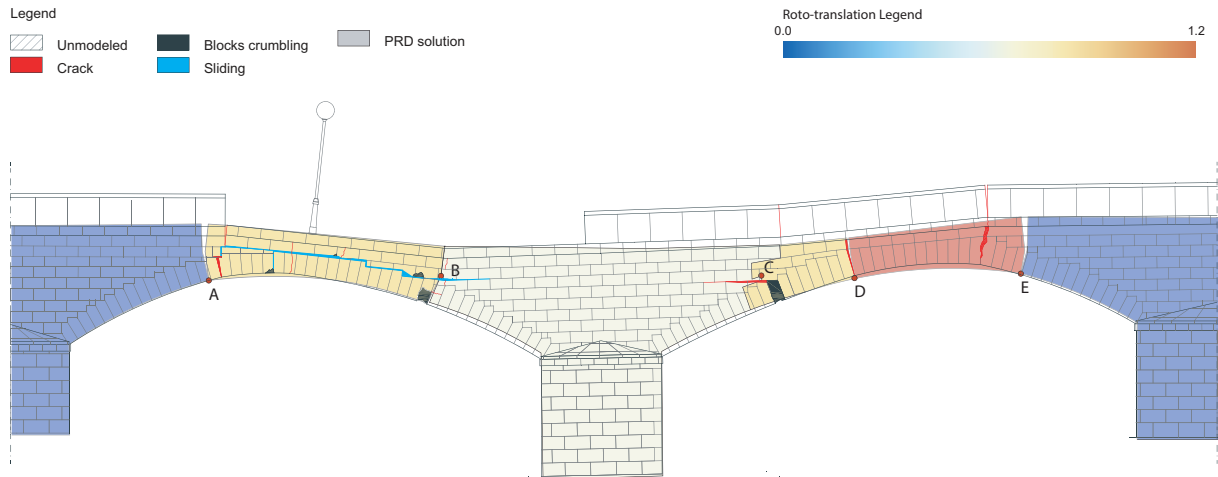


Figure 2: Superposition of PRD numerical results and failure geometrical survey (red dots A, B, C, D, and E mark the hinges location between two adjacent macroblocks).

5 CONCLUSIONS

A preliminary study of the mechanics of fracture mechanisms in unilateral no-tension bridge structures subjected to pier settlements is proposed here. This approach falls into

the so-called block-based Limit Analysis methods. The equilibrium problem is formulated by a convex optimization problem with a quadratic objective function and linear inequality constraints. The main innovation introduced by this approach is consideration of a Normal Linear Elastic No-Tension material in which the elastic part of the strain tensor is considered only fictitious. By minimizing the TPE with respect to both displacements and elastic deformation, we force the elastic part of the strain tensor to vanish. In this way, the problem of finding an admissible state of displacement for the NENT structure became equivalent to the same problem formulated for a No-Tension No Rigid material. The proposed approach is applied to a case study of the Deba Bridge failure (2018). The obtained results indicate very good agreement between the numerical model and the failure survey. The method is simple, effective, and promising. The range of applicability of this method can be broadened to facade and complex NENT structures. It provides a good starting point for the study of the collapse mechanisms and ultimate load capacity of masonry-like structures.

REFERENCES

- [1] Zampieri P., Zanini, M.A. Faleschini, F. Hofer L., Pellegrino C., 'Failure analysis of masonry arch bridges subject to local pier scour', *Eng. Fail Anal.*, Vol. 79, pp. 371–84, 2017.
- [2] Tubaldi E., Macorini L., Izzuddin B.A., 'Three-dimensional mesoscale modelling of multi-span masonry arch bridges subjected to scour', *Eng. Struct.*, Vol. 165, pp. 486–500, 2018.
- [3] S. Galassi, G. Misseri, L. Rovero, G. Tempesta, Failure modes prediction of masonry voussoir arches on moving supports *Engineering Structures* 173 (2018) 706–717
- [4] Scozzese F., Ragni, L. Tubaldi E. and Gara F., Modal properties variation and collapse assessment of masonry arch bridges under scour action, *Engineering Structures*, Vol. 199, 109665, 2019.
- [5] A. Tralli, A. Chiozzi, N. Grillanda, G. Milani, Masonry structures in the presence of foundation settlements and unilateral contact problems. *International Journal of Solids and Structures*, 191-192, 187–201, 2020.
- [6] Malena M., Angelillo M., Fortunato A., de Felice G., Mascolo I., Arch bridges subject to pier settlements: continuous vs. piecewise rigid displacements methods, *Meccanica*, 2021. (Under Review)
- [7] Benedetti A., Pelà L., Aprile A., Masonry properties determination via splitting tests on cores with a rotated mortar layer., A: *International Seminar on Structural Masonry. "8th International seminar on structural masonry: proceedings: 05-07 November 2008"*. Estambul: Istanbul Technical University, 1-8, 2008.
- [8] Mallardo V., Malvezzi R., Milani E., Milani G., Seismic vulnerability of historical masonry buildings: A case study in Ferrara, *Engineering Structures*, 30(8), 2223–2241, 2008.

- [9] Pelà L., Aprile A., Benedetti A., Seismic assessment of masonry arch bridges, *Engineering Structures*, 31(8), 1777–1788, 2009.
- [10] Pegon P., Pinto A.V., Géraudin M., Numerical modelling of stone-block monumental structures, *Computers & Structures*, 79(22–25), 2165–2181, 2013.
- [11] Casolo S., Macroscale modelling of micro-structure evolution damage by a rigid body and spring model, *J. Mech. Mater. Struct.*, 4(3), 551–570, 2009.
- [12] Zucchini A., Lourenco P.B., A micro-mechanical model for the homogenisation of masonry, *International Journal of Solids and Structures*, 39(12), 3233–3255, 2002.
- [13] Milani G., Lourenco P.B., Tralli A., Homogenised limit analysis of masonry walls, Part I: Failure surfaces, *Computers & Structures*, 84(3-4), 166–180, 2006.
- [14] Rafols, J.F., Gaudì 1928, Universitat Politècnica de Catalunya. Iniciativa Digital Politécnica; N.º 1 edición (4 julio 2011), 2021.
- [15] Heyman J., Hooke’s cubico-parabolical conoid, *Notes Rec. R. Soc.*, 52(1), 39–50, 1989.
- [16] Kooharian A., Limit Analysis of voussoir and concrete arches, *J. Amer. Concrete Inst.*, 24, 317–328, 2021.
- [17] Heyman J., Limit Analysis of voussoir and concrete arches, *Int. J. Solids and Structures*, 2, 249–279, 1966.
- [18] Zienkiewicz O.C., Valliappan S., King I.P., Stress analysis of rock as a ‘No Tension’ material, *Géotechnique*, 18(1), 56–66, 1968.
- [19] Lucchesi M., Padovani C., Pasquinelli G. and Zani N., ‘Masonry constructions: mechanical models and numerical applications’, *Lecture Notes in Applied and Computational Mechanics*, 39, Springer, Berlin, 2008.
- [20] Angelillo M., Fortunato A., Gesualdo A., Iannuzzo A., Zuccaro G. ‘Rigid block models for masonry structures’, *International Journal of Masonry Research and Innovation*, 3(4), 349–368, 2018.
- [21] Iannuzzo A., Olivieri C., Fortunato A., Displacement capacity of masonry structures under horizontal actions via prd method. *Journal of Mechanics of Materials and Structures*, 14(5), 703–718, 2019.
- [22] Angelillo M., Olivieri C., DeJong M.J., A new equilibrium solution for masonry spiral stairs. *Engineering Structures*, 238, 112176, 2021. DOI: 10.1016/j.engstruct.2021.112176
- [23] Anzellotti G. A class of convex non-coercive functionals and masonry-like materials, *Ann. Inst. Henri Poincaré*, 2(4), 261–307, 1985.
- [24] Del Piero G., Constitutive equation and compatibility of the external loads for linear elastic masonry-like materials, *Meccanica*, 24(3), 150–162, 1989.

- [25] Giaquinta M., Giusti E., 'Researches on the equilibrium of masonry structures', Arch. Ration. Mech. An., 88(4), 359–392, 1985.
- [26] Mascolo I., Fulgione M., Pasquino M., Lateral torsional buckling of compressed open thin walled beams: experimental confirmations. Int. J. Masonry Research and Innovation, 4(1/2), 150–158, 2019. DOI: 10.1504/IJMRI.2019.096829
- [27] Olivieri C., Angelillo M., Gesualdo A., Iannuzzo A. and Fortunato A., Parametric design of purely compressed shells. Mechanics of Materials, 155, 103782, 2020.
- [28] Fortunato A., Gesualdo A. and Mascolo I. and Monaco M., P-Bézier energy optimization for elastic solutions of masonry-like panels. Int. J. of Masonry Research and Innovation, 2021. (In Press) DOI: 10.1504/IJMRI.2021.10037508
- [29] Mascolo I., Gesualdo A., Olivieri C., Fortunato A., On rigid blocks detection in unilateral masonry-like structures. Int. J. of Masonry Research and Innovation, 2021. (In Print)
- [30] Stavroulakis G.E., Panagiotopoulos P.D., Al-Fahed A.M., On the rigid body displacements and rotations in unilateral contact problems and applications. Computers & Structures, 40(3), 599–614, 1991.
- [31] Boyd S., Vandenberghe L., Convex Optimization. Cambridge University Press, 2004.
- [32] Dantzig G.B., Orden A., Wolfe P., The generalized simplex method for minimizing a linear form under linear inequality constraint. Pacific. J. Math., 5(2), 183–195, 2015.

ON THE USE OF DIGITAL TWINS FOR SEISMIC STRUCTURAL HEALTH MONITORING OF A MONUMENTAL MASONRY TOWER

A. Kita¹, N. Cavalagli¹, I. Venanzi¹ and F. Ubertini¹

¹Department of Civil and Environmental Engineering, University of Perugia
Via G. Duranti 93, 06125 Perugia, Italy
e-mail: {alban.kita, nicola.cavalagli, ilaria.venanzi, filippo.ubertini}@unipg.it

Keywords: Structural Health Monitoring, Digital Twin, Incremental Dynamic Analysis, Surrogate model, Post-earthquake damage assessment, Cultural Heritage.

Abstract. *This paper presents the introduction of Digital Twins in the case of an historic masonry tower for rapidly addressing earthquake-induced damage identification. In the context of the present paper, a digital twin is a model or a suite of models of the considered structure that are updated/modified during time based on monitoring data. In particular, the proposed approach combines Operational Modal Analysis (OMA), Surrogate Modeling (SM) and non-linear Incremental Dynamic Analysis (IDA). On the one hand, OMA-based Structural Health Monitoring (SHM) systems successfully allow the detection of small structural damages occurring during earthquakes, and on the other, SM exploits the correlation between continuous vibration data and structural stiffnesses while IDA is carried out from a tuned model together with in situ recorded seismic data. The San Pietro bell tower has been considered for the validation of the proposed methodology. The tower is a monumental medieval masterpiece, located in Perugia, Italy, and it represents a relevant case study in the scientific literature due to its important experience during the 2016-2017 seismic sequence that occurred in Central Italy. While the OMA-vibration data processing assessed distinct earthquake-induced changes in its global dynamic behavior, the focus of the present work is the results on the use of linear as well as non-linear modeling, i.e. SM and IDA, respectively, aimed for post-earthquake damage localization and quantification.*

1 INTRODUCTION

Vibration-based SHM methods based on unsupervised learning techniques have been recently demonstrated in the literature as eminently efficient for early-stage damage detection [1, 2, 3, 4, 5, 6, 7, 8, 9, 10, 11, 12, 13]. Due to their limitation to detection only, more advanced approaches are required in order to address higher levels of damage identification for Cultural Heritage (CH) masonry structures.

The introduction of Digital Twin (DT) in civil engineering in the case of historic masonry constructions is a recent concept of scientific interest [14]. DT can be defined as a model or a suite of models of the structure that continuously exchanges information with the physical reality through experimental/field data, thus providing evidence of novelties or changes, for instance, related to a faulty or damage conditions.

Surrogate models (SM) have been lately investigated as computationally efficient tools to reproduce the behavior of a numerical model, potentially allowing a continuous model updating procedure for damage identification that is compatible with continuous SHM systems in historic masonry structures [15, 16, 17]. The damage localization task is performed through the inverse calibration problem on a surrogate of the linear FE model where equivalent elastic properties of macrostructural elements are considered as uncertain parameters, and by using long-term vibration data.

Other approaches are adapted given the strong development of computer processing power and advanced structural analysis software packages, aiming at more accurate analysis methods for the assessment of masonry buildings. Noteworthy to mention, non-linear dynamic analysis (NLDA) can provide a reliable assessment of the structural response of masonry constructions [18, 19, 20, 21]. In particular for NLDA, Incremental Dynamic Analysis (IDA) [22] considers the selection of time histories to be scaled at increasing seismic intensities. The application of IDA to CH masonry structures is comparatively less common with respect to RC structures. The recent research carried out in [21] proposed the use of an IDA-based approach for damage localization and quantification in the case of a laboratory masonry structure, but still, further investigations can be carried out in the case of full-scale historic masonry constructions.

The methodology proposed in this paper combines OMA, SM and IDA for earthquake-induced damage identification in historic masonry towers. It is applied to the San Pietro bell tower, an iconic Cultural Heritage masonry building that was hit by the three main shocks of the 2016 Central Italy seismic sequence: (i) Accumoli Mw6.0 earthquake of August 24th and the following shocks, (ii) Ussita Mw5.9 earthquake of October 26th and (iii) Norcia Mw6.5 of October 30th [4, 23, 24]. Fig. 1 illustrates a schematic view of the monitoring system and the FE model constructed in the ABAQUS platform [25]. With concern to the proposed methodology, the tower is ideally subdivided into three distinct structural parts: the shaft, the belfry and the cusp.

The paper is organized as follows. Section 2 describes the proposed methodology, while Section 3 reports the results and its validation. Finally, Section 4 summarizes the main conclusions of the work.

2 METHODOLOGY

This paper investigates a new methodology for rapid damage detection, localization and quantification in long-term monitored historic masonry towers subjected to earthquakes. It merges the data-driven OMA-based approach for a rapid and automated damage detection with two combined Digital Twins for damage localization and quantification: (i) SM-based damage

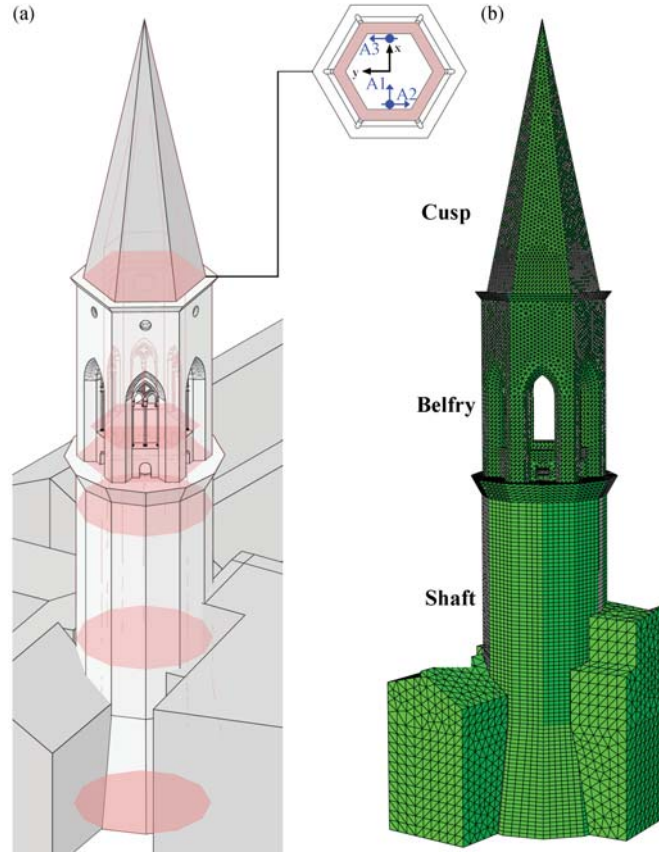


Figure 1: The monitoring system installed on the San Pietro bell tower (a) and view of the calibrated FE model (b).

identification based on linear numerical modeling and long-term vibration monitoring data and (ii) IDA-based damage identification relying on a non-linear model and seismic response to earthquakes.

The OMA is based on a Stochastic Subspace Identification (SSI) technique. Concerning the SM, among different SM models available in the literature, the Response Surface Method (RSM) has been proposed to be used here. Finally, the IDA approach investigates tensile damage (d_t) as a Damage Measure (DM) versus significant uncorrelated Intensity Measures (IMs).

Main theoretical aspects about SM and IDA can be found in [16, 17] and [21], respectively.

3 VALIDATION RESULTS

The OMA-based damage detection has been applied using 5 years of vibration-based monitoring data, from December 2014 onwards. Time series of identified natural frequencies have been used for the novelty analysis. Fig. 2 illustrates the control chart where earthquake-induced damage has been identified in correspondence to the seismic events. It is clear from the plot that it represents anomalous deviations from normal conditions due to small permanent changes of the structural behavior of the bell tower, highlighted right after the Accumoli earthquake, as well as after Ussita and Norcia shocks.

The SM of the San Pietro bell tower has been constructed considering the FEM ideally subdivided into three distinctive macroelements and thus parametrized by means of a set of damage-sensitive features. A training population of $N=2048$ individuals has been uniformly generated by using a Latin Hypercube Sampling (LHS) method. The design variables are represented by the stiffness multipliers k_i of the shaft, belfry and cusp, respectively ($\mathbf{x} = [k_1, k_2, k_3]^T$).

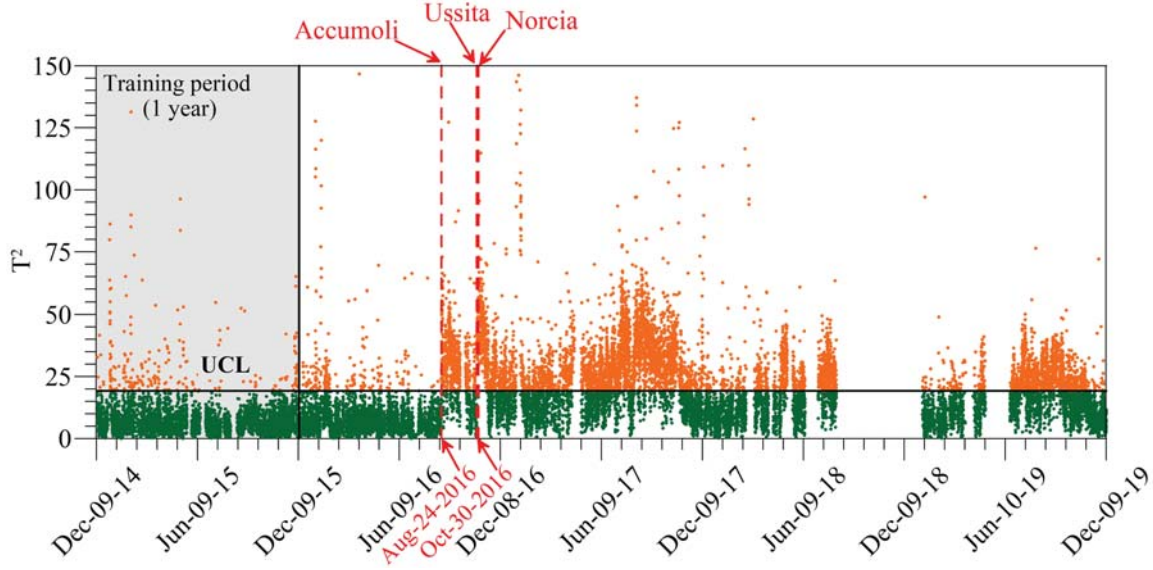


Figure 2: OMA-based damage detection: 5-year control chart with main seismic events highlighted.

Subsequently, the SM-based damage identification approach has been applied before and after the 2016 seismic sequence for localizing and quantifying earthquake-induced damage, whereby time series of cleansed natural frequencies and experimental eigenvector components have been used as input for solving the inverse FE model calibration problem on the RSM-type SM.

A first investigation on the time histories of the stiffness multipliers k_i has been carried out, where instant decays have been quantitatively evaluated for each macroelement by comparing values identified before and after each shock. The k_2 multiplier experiences the highest variation, denoting that damage has occurred in the belfry macroelement, while the shaft and the cusp show insignificant values. Subsequently, the k_i vectors have been independently used to build the statistical models for novelty analysis. The control charts are illustrated in Fig. 3, where the damage can be clearly localized in the belfry macroelement. The relative frequency

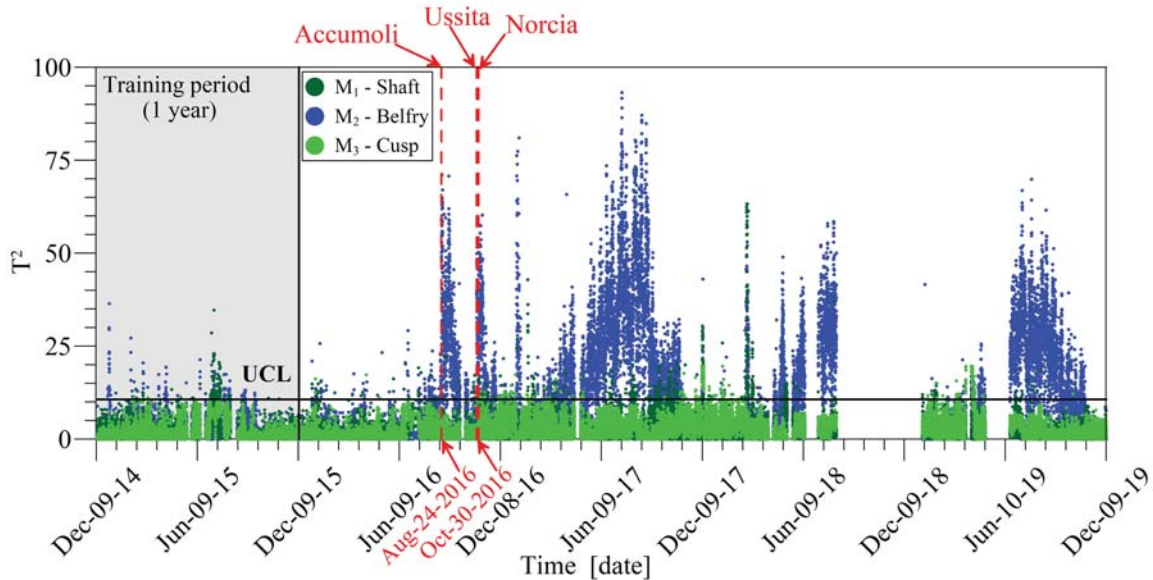


Figure 3: SM-based damage identification: 5-year control charts obtained with stiffness multipliers k_i .

of outliers in the case of the belfry "jumps" from 2.21% before the earthquake sequence to 36.41% after the sequence, while for the shaft and the cusp it remains under 2.5%.

As reported by the statistical correlation analysis carried out in [21], nineteen weakly correlated IMs have been investigated for the construction of the IDA curves, independently from the case study. These IMs have been exploited in the present paper for the San Pietro bell tower, while tensile damage (d_t) has been used as DM (computed as a volume-averaged damage parameter). Local damage conditions have been investigated for the three distinct macroelements: shaft, belfry and cusp. Figs. 4a-b depict IDA curve sets obtained from spectral accelerations $S_a(T1)$ and Peak Ground Velocity (PGV), while other curves can be found in [24]. From the plots, the belfry can be immediately identified as the most vulnerable macroelement where the maximum numerically obtained tensile damage d_t is equal to about 0.85.

The recordings of the main earthquakes of the 2016 Central Italy seismic sequence have been used in the IDA-based damage identification approach. Once all the IDA curve sets have been

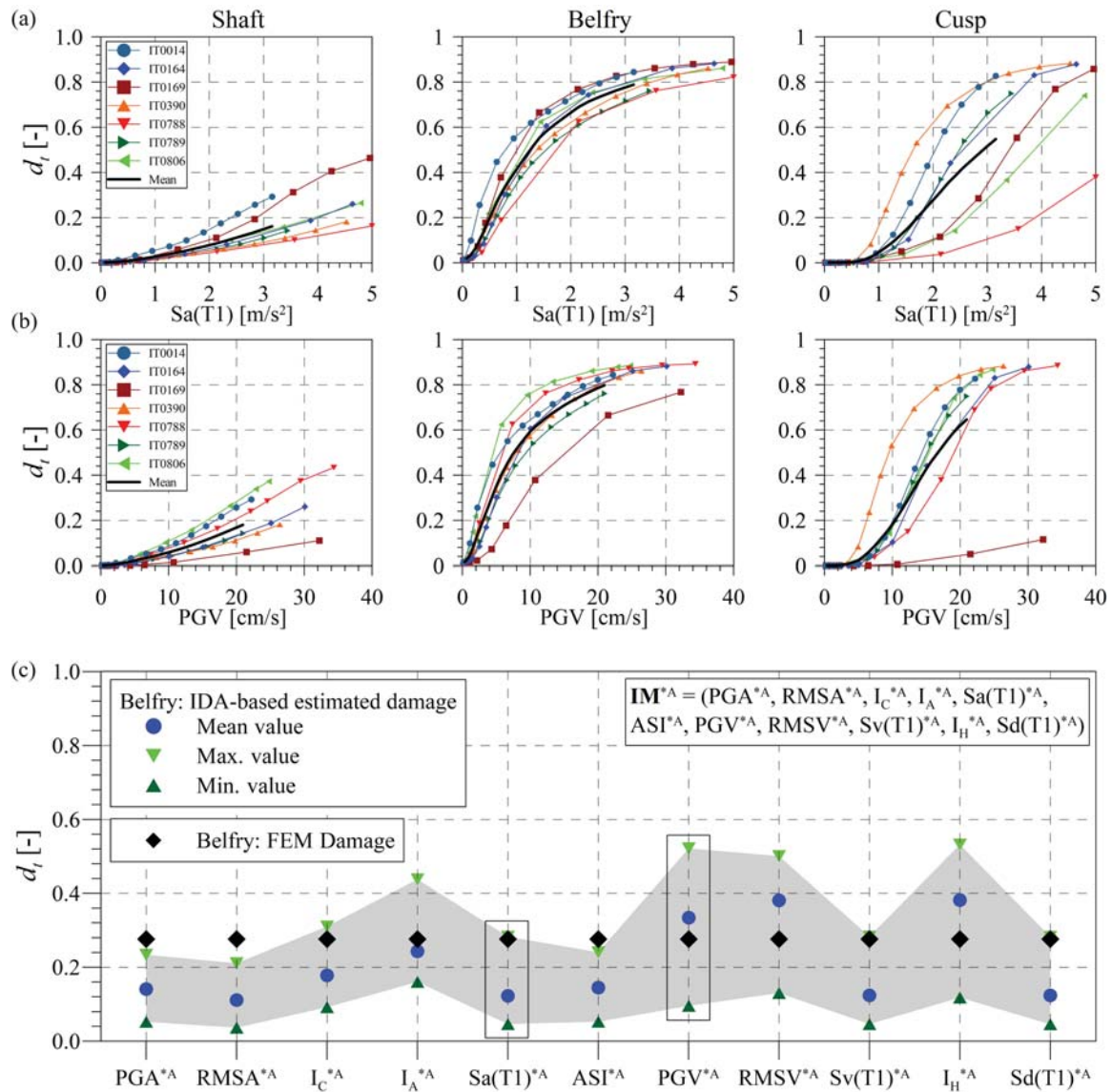


Figure 4: The IDA curve sets obtained with tensile damage, d_t , versus $S_a(T1)$ (a) and PGV (b), and IDA-based tensile damage estimated for the belfry macroelement by means of eleven input IMs calculated from Accumoli earthquake (c).

constructed and their dispersion investigated, local damage conditions have been assessed by using seismic input and response IMs of the real aforementioned seismic events. Eleven seismic input IMs have been computed from the base seismic records and seven seismic response IMs have been calculated from the top seismic records. Fig. 4 illustrates damages estimated in the belfry macroelement by applying all eighteen IMs that are computed from Accumoli, Ussita and Norcia earthquakes, respectively. Besides IDA-based damages that are reported in terms of minimum, maximum and mean values, damage predicted through a direct non-linear FEM simulation is also reported for comparative purposes. It can be seen that there is relatively good consistency, whereby d_t values fall within the corresponding estimated ranges.

4 CONCLUSIONS

The paper presented the validation results of the proposed methodology for earthquake-induced damage identification in historic masonry towers. The San Pietro bell tower (Perugia, Italy) that was hit by the 2016 Central Italy seismic sequence has been considered as the case study.

The main concluding remarks are listed below.

- The OMA-based data-driven method is extended through the introduction and implementation of Digital Twins, in particular SM and IDA, for localization and quantification of earthquake-induced damage.
- Both SM and IDA are comparatively combined for higher accuracy of the method: (i) the former uses a linear model while the latter a non-linear one, (ii) IDA uses the recorded seismic response of an earthquake, whereas OMA and SM are based on long-term vibration monitoring data in operational conditions.
- Five years of continuous monitoring data of the San Pietro bell tower have been used in the SM-based procedure for earthquake-induced damage detection and localization and damage has been localized mainly in the belfry macroelement.
- Non-linear seismic IDA procedure has also identified the belfry as the most significantly vulnerable and damaged macroelement of the bell tower. In addition, top recorded seismic responses during earthquakes have allowed the introduction of seismic response IMs.
- Both Digital Twins have localized and consistently quantified earthquake-induced damage in the belfry macroelement.

The successful validation of the Digital Twins can result potentially useful in more severe future earthquake scenarios due to the precious information provided for needed first inspections, retrofit and strengthening interventions.

ACKNOWLEDGEMENTS

The supports of the Italian Ministry of University and Research (MIUR) and the University of Perugia are acknowledged, within the Program “Dipartimenti di eccellenza 2018-2022”.

REFERENCES

- [1] L.F. Ramos, L. Marques, P.B. Lourenço, G. De Roeck, A. Campos-Costa, J. Roque, Monitoring historical masonry structures with operational modal analysis: Two case studies. *Mechanical Systems and Signal Processing*, **24**, 1291–1305, 2010.
- [2] M.G. Masciotta, L.F. Ramos, P.B. Lourenço, The importance of structural monitoring as a diagnosis and control tool in the restoration process of heritage structures: A case study in Portugal. *Journal of Cultural Heritage*, **27**, 36–47, 2017.
- [3] F. Clementi, A. Pierdicca, A. Formisano, F. Catinari, S. Lenci, Numerical model upgrading of a historical masonry building damaged during the 2016 Italian earthquakes: the case study of the Podesta palace in Montelupone (Italy). *Journal of Civil Structural Health Monitoring*, **7**, 703–717, 2017.
- [4] F. Ubertini, N. Cavalagli, A. Kita, G. Comanducci, Assessment of a monumental masonry bell-tower after 2016 Central Italy seismic sequence by long-term SHM. *Bulletin of Earthquake Engineering*, **16**, 775–801, 2018.
- [5] A. Saisi, C. Gentile, A. Ruccolo, Continuous monitoring of a challenging heritage tower in Monza, Italy. *Journal of Civil Structural Health Monitoring*, **8**, 77–90, 2018.
- [6] D. Pellegrini, M. Girardi, P.B. Lourenço, M.G. Masciotta, N. Mendes, C. Padovani, L.F. Ramos, Modal analysis of historical masonry structures: Linear perturbation and software benchmarking. *Construction and Building Materials*, **189**, 1232–1250, 2018.
- [7] C. Gentile, A. Ruccolo, A. Saisi, Continuous Dynamic Monitoring to Enhance the Knowledge of a Historic Bell-Tower. *International Journal of Architectural Heritage*, **13**, 992–1004, 2019.
- [8] A. Kita, N. Cavalagli, F. Ubertini, Temperature effects on static and dynamic behavior of Consoli Palace in Gubbio, Italy. *Mechanical Systems and Signal Processing*, **120**, 180–202, 2019.
- [9] I. Venanzi, A. Kita, N. Cavalagli, L. Ierimonti, F. Ubertini, Continuous OMA for damage detection and localization in the Sciri Tower in Perugia, Italy. S.D.R. Amador, R. Brincker, E.I. Katsanos, M. L. Aenlle, P. Fernandez eds. *8th International Operational Modal Analysis Conference Proceedings (IOMAC 2019)*, p. 127-136, Copenhagen, Denmark, May 13-15, 2019.
- [10] E. Giordano, N. Mendes, M.G. Masciotta, F. Clementi, N.H. Sadeghi, R.A. Silva, D.V. Oliveira, Expedient damage index for arched structures based on dynamic identification testing. *Construction and Building Materials*, **265**, 120236, 2020.
- [11] A. Formisano, G. Di Lorenzo, L. Krstevska, R. Landolfo, Fem Model Calibration of Experimental Environmental Vibration Tests on Two Churches Hit by L’Aquila Earthquake. *International Journal of Architectural Heritage*, **15**, 113-131, 2021.
- [12] R. Alaggio, A. Aloisio, E. Antonacci, R. Cirella, Two-years static and dynamic monitoring of the Santa Maria di Collemaggio basilica. *Construction and Building Materials*, **268**, 121069, 2021.

- [13] G. Standoli, E. Giordano, G. Milani, F. Clementi, Model Updating of Historical Belfries Based on OMA Identification Techniques. *International Journal of Architectural Heritage*, **15**, 132–156, 2021.
- [14] G. Angjeliu, D. Coronelli, G. Cardani, Development of the simulation model for Digital Twin applications in historical masonry buildings: The integration between numerical and experimental reality. *Computers and Structures*, **238**, 106282, 2020.
- [15] A. Cabboi, C. Gentile, A. Saisi, From continuous vibration monitoring to FEM-based damage assessment: Application on a stone-masonry tower. *Construction and Building Materials*, **156**, 252–265, 2017.
- [16] I. Venanzi, A. Kita, N. Cavalagli, L. Ierimonti, F. Ubertini, Earthquake-induced damage localization in an historic masonry tower through long-term dynamic monitoring and FE model calibration. *Bulletin of Earthquake Engineering*, **18**, 2247–2274, 2020.
- [17] E. Garcia-Macías, I. Venanzi, F. Ubertini, Metamodel-based pattern recognition approach for real-time identification of earthquake-induced damage in historic masonry structures. *Automation in Construction*, **120**, 103389, 2020.
- [18] P. Zampieri, M.A. Zanini, F. Faleschini, L. Hofer, C. Pellegrino, Failure analysis of masonry arch bridges subject to local pier scour. *Engineering Failure Analysis*, **79**, 371–384, 2017.
- [19] C.F. Manzini, G. Magenes, A. Penna, F. da Porto, D. Camilletti, S. Cattari, S. Lagomarsino, Masonry Italian Code-Conforming Buildings. Part 1: Case Studies and Design Methods. *Journal of Earthquake Engineering*, **22**, 54-73, 2018.
- [20] G. Karanikoloudis, P.B. Lourenço, Structural assessment and seismic vulnerability of earthen historic structures. Application of sophisticated numerical and simple analytical models. *Engineering Structures*, **160**, 488–509, 2018.
- [21] A. Kita, N. Cavalagli, M.G. Masciotta, P.B. Lourenço, F. Ubertini, Rapid post-earthquake damage localization and quantification in masonry structures through multidimensional non-linear seismic IDA. *Engineering Structures*, **219**, 110841, 2020.
- [22] D. Vamvatsikos, N.A. Cornell, Incremental dynamic Analysis. *Earthquake Engineering and Structural Dynamics*, **31**, 491-514, 2002.
- [23] P.F. Giordano, F. Ubertini, N. Cavalagli, A. Kita, M.G. Masciotta, Four years of structural health monitoring of the San Pietro bell tower in Perugia, Italy: Two years before the earthquake versus two years after. *International Journal of Masonry Research and Innovation*, **5**, 445-467, 2020.
- [24] A. Kita, N. Cavalagli, I. Venanzi, L. Ierimonti, F. Ubertini, Earthquake-Induced Damage Localization and Quantification in Historic Masonry Towers Using OMA and IDA. *Lecture Notes in Civil Engineering, European Workshop on Structural Health Monitoring Proceedings (EWSHM 2020)*, **127**, 958–967, 2021.
- [25] Simulia, Corp, *Abaqus Analysis User's and theory Manual. Version 6*. Dessault Systemes, USA, 2019.

MICROMECHANICAL ANALYSIS OF UNREINFORCED AND REINFORCED MASONRY ARCHES

Daniela Addessi, Cristina Gatta, Mariacarla Nocera and Domenico Liberatore

Department of Structural and Geotechnical Engineering, Sapienza University of Rome
Via Eudossiana 18, 00184 Rome, Italy
e-mail: {daniela.addessi,cristina.gatta,mariacarla.nocera,domenico.liberatore}@uniroma1.it

Keywords: Micromechanical modeling, Finite element, Masonry arch, Reinforcement.

Abstract. *This work analyzes the in-plane response of unreinforced and reinforced masonry arches by adopting micromechanical finite element (FE) models. These allow to describe onset and evolution of degrading mechanisms until failure, including the accurate characterization of the pre- and post-peak behavior. Two different models are adopted: the first considers each masonry component, brick and mortar, as continuous material discretized with quadrilateral FEs; the second connects properly resized bricks through interfaces representing both mortar and mortar-units interaction. Linear elastic behavior is assumed for bricks, whereas a coupled damage-friction constitutive law is adopted for mortar to account for typical arch collapse mechanisms involving flexural hinges and shear sliding. As concerns the modeling of the reinforcements, these are considered as truss elements with bilinear response in tension. In such a way the debonding and delamination phenomena are accounted in a simplified way.*

Results obtained with the proposed models are validated through comparison with experimental data and solutions obtained from other numerical approaches. It emerges that the response of both the unreinforced and reinforced elements are satisfactorily described, as well as the positive effect of the introduction of the reinforcement on the collapse load and failure mechanism.

1 INTRODUCTION

Most of historical masonry constructions, including monuments, urban buildings and bridges, are based on arch systems. These typically show high carrying capacity under gravity loads, but under point loads or seismic actions the thrust line falls outside the arch central core, inducing tensile stresses with the onset and growth of microcracks which, eventually, lead to the structural collapse. A traditional strengthening technique consists of the insertion of tie-rods which, however, have a strong visual impact and in some cases are not accepted. The scientific community proposed and developed several types of alternative strengthening techniques aimed at improving the arch performance with no visual impact and with negligible added mass. These are based on innovative composite materials consisting of glass fibers, carbon fibers, steel rod or other materials embedded in polymer or mortar matrices. Several experimental campaigns proved the efficiency of such strengthening systems [1], which usually increase the structural capacity in terms of both ductility and maximum strength. Apparently, the type of reinforcement and matrix [2, 3] and the reinforcement location [4, 5] significantly affect the overall response. Moreover, the classical collapse mechanism of unreinforced arches, involving the formation of four flexural hinges, is modified for strengthened structures. The failure modes are, in fact, usually characterized by shear sliding, masonry crushing, reinforcement rupture, debonding and delamination phenomena [1].

The experimental research is developed together with the formulation of efficient numerical models to reproduce and predict the arch structural response. In this framework, limit analysis approach is a consolidated tool for the assessment of the arch safety. Starting from the first applications of Heyman [6], many other enriched models have been proposed, where Heyman's hypotheses are partially or all removed [7, 8, 9]. The success of these models is mainly due to their simplicity and the reduced number of material parameters required in the analysis. The main limit is that no information is given on the pre- and post-peak response as well as the evolution process of the nonlinear mechanisms. To overcome these restrictions, accurate nonlinear finite element (FE) models have been developed [10, 11, 12]. Most of these are typically based on micromechanical, multiscale and macromechanical approaches [13, 14] and introduce nonlinear constitutive laws to describe the onset and evolution of degrading mechanisms. In particular, detailed micromechanical finite element formulations model each masonry constituent, brick and mortar, and their interaction. However, some simplified hypotheses are usually assumed to reduce the computational complexity, still ensuring enough accurate results. Neglecting the explicit modeling of the unit-mortar interfaces, the composite masonry material is regarded as the assembly of bricks/units and mortar joints which simultaneously describe mortar material and interfaces. According to this approach, in this work two strategies are adopted and compared to analyze the in-plane response of masonry arches. The first model, recently presented in [15], considers masonry components, units and mortar, as continuous materials discretized with quadrilateral FEs. Conversely, in the second model, masonry is modeled as the assembly of expanded units and interface elements representing both mortar and unit-mortar interaction. The two models are based on the same constitutive hypotheses, i.e. linear elastic and nonlinear behavior are assumed for bricks and mortar, respectively. The damage-friction law originally proposed in [16] is employed for joints. This allows to capture the typical failure modes of arches due to fracture mode I and II, and has been recently extended to mortar joints modeled as 2D [17] or 3D [18] interfaces. Moreover, when dealing with strengthened arch systems, reinforcements are modeled with truss elements, whose constitutive response is properly identified to also reproduce the debonding and delamination phenomena in a simplified

and conventional way [8, 10, 19].

To prove the capability of the proposed models to reproduce the response of unreinforced and reinforced arches, some numerical applications are performed on properly selected experimental tests. The results, in terms of global response curves and failure mechanisms, are compared with the experimental outcomes, as well as with those obtained by means of different FE numerical approaches.

2 MICROMECHANICAL FINITE ELEMENT MODELS

Two micromechanical FE models are presented to investigate the response of masonry arches. Both adopt isoparametric quadrilater FEs to discretize the bricks, but differ in the way the mortar joints are modeled. The first (Figure 1(a)), named as *continuous model* (CM), also uses isoparametric quadrilater FEs to describe mortar as continuous materials. The second (Figure 1(b)), later called as *interface model* (IM), adopts interface elements to model the mortar joints. Moreover, truss elements are used to introduce in a simple but effective way the strengthening material.

In the following, details about the constitutive assumptions made for brick, mortar and reinforcement are provided. Figure 2 gives a summary of the modeling choices.



Figure 1: Micromechanical models: masonry as the assembly of (a) bricks and mortar joints, (b) interfaces and expanded bricks.

2.1 Constitutive laws of masonry constituent materials and reinforcement

Similar constitutive hypotheses hold for the two micromechanical models CM and IM, as both assume nonlinear mechanisms only occurring in the mortar and linear-elastic response for units. Plane stress conditions are considered. Hence, the linear elastic relation between stresses, $\boldsymbol{\sigma}^b = \{\sigma_1^b \sigma_2^b \tau_{12}^b\}^T$, and strains $\boldsymbol{\varepsilon}^b = \{\varepsilon_1^b \varepsilon_2^b \gamma_{12}^b\}^T$, holds for bricks:

$$\boldsymbol{\sigma}^b = \mathbf{C}^b \boldsymbol{\varepsilon}^b \quad (1)$$

being \mathbf{C}^b the elastic constitutive matrix for 2D plane stress problems, depending on the Young's modulus E^b and Poisson coefficient ν^b .

As for the mortar, the damage-friction law proposed in [16, 17] is assumed. This is properly formulated to analyze the response of arbitrarily curved masonry elements with variable inclination of mortar joints [15]. The constitutive law accounts for the typical flexural and shear degrading mechanisms characterizing masonry nonlinear behavior, that is degradation due to the onset of microcracks, friction effects caused by closure of microcracks in compression and unilateral stiffness recovery.

Herein, the main governing equations are recalled, specializing them on the basis of the modeling approach, CM or IM, adopted for the mortar. Indeed, stresses, $\boldsymbol{\sigma}$, and strains, $\boldsymbol{\varepsilon}$, are the static and kinematic descriptors of the mortar as continuous material, whereas tractions,

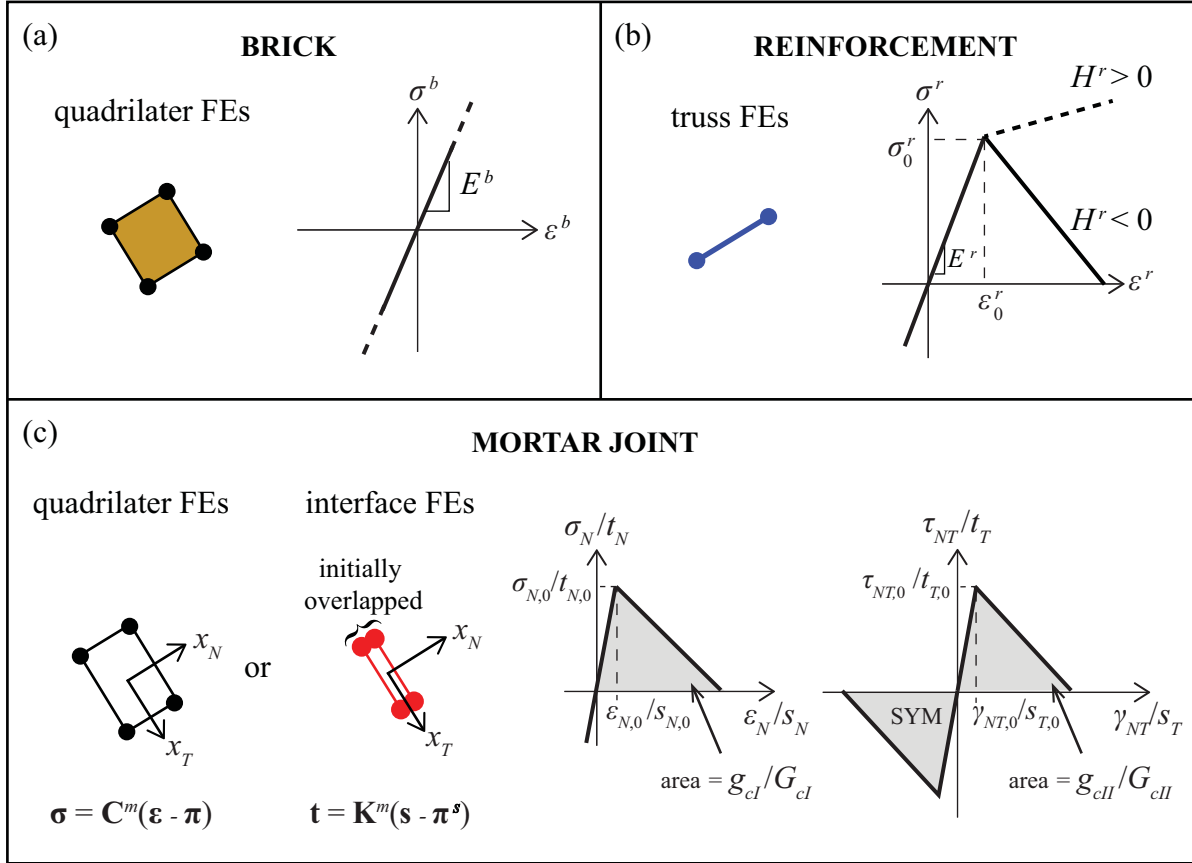


Figure 2: Types of finite elements and constitutive laws adopted for: (a) brick, (b) reinforcement and (c) mortar.

\mathbf{t} , and displacement jumps, \mathbf{s} , are the corresponding quantities in case of interfaces modeling mortar joints.

The constitutive law is firstly defined in the local reference system (x_T, x_N) of each mortar layer, being T and N the directions aligned with mortar joint width and thickness (Figure 1(c)). Then, it is expressed in the global system (x_1, x_2) by using standard transformation rules. The constitutive law for the CM is expressed as:

$$\underbrace{\begin{bmatrix} \sigma_T \\ \sigma_N \\ \tau_{NT} \end{bmatrix}}_{\boldsymbol{\sigma}} = \mathbf{C}^m \left(\underbrace{\begin{bmatrix} \varepsilon_T \\ \varepsilon_N \\ \gamma_{NT} \end{bmatrix}}_{\boldsymbol{\varepsilon}} - D \underbrace{\begin{bmatrix} h(\varepsilon_N)\varepsilon_T \\ h(\varepsilon_N)\varepsilon_N \\ \gamma_{NT}^p \end{bmatrix}}_{\boldsymbol{\pi}} \right) \quad (2)$$

where \mathbf{C}^m is the mortar elastic constitutive matrix for plane stress conditions and $\boldsymbol{\pi}$ is the inelastic strain vector accounting for damage D , unilateral contact and slip γ_{NT}^p .

Similarly, tractions \mathbf{t} at the interfaces are computed as:

$$\underbrace{\begin{bmatrix} t_T \\ t_N \end{bmatrix}}_{\mathbf{t}} = \mathbf{K}^m \left(\underbrace{\begin{bmatrix} s_T \\ s_N \end{bmatrix}}_{\mathbf{s}} - D \underbrace{\begin{bmatrix} s_T^p \\ h(s_N)s_N \end{bmatrix}}_{\boldsymbol{\pi}^s} \right) \quad (3)$$

being \mathbf{K}^m the diagonal matrix collecting the stiffness values, K_T and K_N , along the tangential and normal directions, respectively, to the interface. In Eqs. (2) and (3), $h(\bullet)$ denotes the Heaviside function ($h(\bullet) = 1$, if $\bullet \geq 0$ and $h(\bullet) = 0$ otherwise), describing the unilateral stiffness

recovery due to the re-closure of the tensile cracks in compression.

According to its physical meaning, the damage variable D can range between 0 and 1, representing virgin and fully degraded material states, respectively. Its evolution law is stated as:

$$D = \max_{history} \left\{ 0, \min \left\{ 1, \frac{1}{\eta} \left(\frac{\beta}{1 + \beta} \right) \right\} \right\} \quad (4)$$

where β is the damage associated variable which assumes the following forms for continuous and interface mortar, respectively:

$$\beta = \sqrt{\left(\frac{\langle \varepsilon_N \rangle_+}{\varepsilon_{N,0}} \right)^2 + \left(\frac{\gamma_{NT}}{\gamma_{NT,0}} \right)^2} - 1, \quad \beta = \sqrt{\left(\frac{\langle s_N \rangle_+}{s_{N,0}} \right)^2 + \left(\frac{s_T}{s_{T,0}} \right)^2} - 1 \quad (5)$$

In Eq. (5), the Macaulay's brackets $\langle \bullet \rangle_+$ select the positive part of the quantity; $\varepsilon_{N,0}$ and $\gamma_{NT,0}$ are the first crack strains, while $s_{N,0}$ and $s_{T,0}$ are the displacement jumps at the onset of the damaging mechanism (see Figure 2(c)).

Parameter η introduced in Eq. (4) rules the coupling of mode I and II of fracture, and assumes the following expression for CM:

$$\eta = 1 - \frac{1}{\alpha^2} [\langle \varepsilon_N \rangle_+^2 \eta_N + (\gamma_{NT})^2 \eta_{NT}] \quad \text{with} \quad \alpha = \sqrt{\langle \varepsilon_N \rangle_+^2 + (\gamma_{NT})^2} \quad (6)$$

being η_T and η_{NT} quantities defined on the basis of the peak values of the stresses, $\sigma_{N,0}$ and $\tau_{NT,0}$, and the mode I and II fracture energy densities, g_{cI} and g_{cII} , as:

$$\eta_N = \frac{\sigma_{N,0} \varepsilon_{N,0}}{2 g_{cI}}, \quad \eta_{NT} = \frac{\tau_{NT,0} \gamma_{NT,0}}{2 g_{cII}} \quad (7)$$

As for IM, the expressions corresponding to Eqs. (6) and (7) are obtained simply introducing the peak tractions, $t_{N,0}$ and $t_{T,0}$, the displacement jumps, $s_{N,0}$ and $s_{T,0}$, and the fracture energies for unit area, G_{cI} and G_{cII} .

Finally, the classical Mohr-Coulomb yield function is adopted to govern the evolution of the inelastic slip, γ_{NT}^p , modeling the frictional mechanisms at the interface between mortar and bricks for CM:

$$\varphi(\boldsymbol{\sigma}^d) = \mu \sigma_N^d + |\tau_{NT}^d| \quad (8)$$

or s_T^p for IM,

$$\varphi(\mathbf{t}^d) = \mu t_N^d + |t_T^d| \quad (9)$$

being μ the friction parameter. Then, the following non-associated flow rules are considered:

$$\dot{\gamma}_{NT}^p = \dot{\lambda} \frac{\tau_{NT}^d}{|\tau_{NT}^d|}, \quad \dot{s}_T^p = \dot{\lambda} \frac{t_T^d}{|t_T^d|} \quad (10)$$

together with the Kuhn-Tucker loading-unloading conditions. The resulting constitutive responses for mode I and mode II are schematically depicted in Figure 2(c).

As concerns the constitutive response in tension of the truss element modeling the reinforcement layer, the bilinear elastic-damage law proposed in [20] is adopted:

$$\sigma^r = (1 - D^r) E^r \varepsilon^r \quad (11)$$

where D^r is the damage variable evolving on the basis of the following rule:

$$D^r = \max_{history} \left\{ 0, \frac{|\varepsilon^r - \varepsilon_0^r|}{\varepsilon^r} \left(1 - \frac{H^r}{E^r} \right) \right\} \quad (12)$$

As emerges from Figure 2(b), the resulting stress-strain relationship in compression is linear elastic and in tension is bilinear, with the first elastic branch characterized by stiffness E^r and the second branch described by the reduced stiffness H^r . In case, the constitutive relationship in Eq. (11) and the damage evolution law in Eq. (12) could easily be modified and enriched to describe the typical trilinear responses of composite reinforcement under tensile loads [3, 21].

2.2 Regularization techniques

The constitutive relationships adopted for reinforcements and mortar joints exhibit strain softening branches, as clearly shown in Figure 2(b,c). This means that the typical pathological mesh-dependency would affect the numerical FE response, if no proper regularization techniques are applied in the case of the continuous models adopted for the mortar and the reinforcement. In this work, two different regularization strategies are assumed: the nonlocal integral approach and the fracture energy technique.

The evolution problem of damage in each mortar joint is ruled by nonlocal quantities. In particular, variables β , η and α in Eqs. (5)_a and (6) are evaluated on the basis of the nonlocal strain vector $\bar{\varepsilon}$. At the generic point \mathbf{x} of the k -th mortar joint, $\bar{\varepsilon}$ is defined as:

$$\bar{\varepsilon}(\mathbf{x}) = \frac{1}{\int_{\Omega^k} \psi(\mathbf{x}, \mathbf{y}) d\Omega^k(\mathbf{y})} \int_{\Omega^k} \psi(\mathbf{x}, \mathbf{y}) \varepsilon(\mathbf{y}) d\Omega^k(\mathbf{y}) \quad (13)$$

where Ω^k denotes the area of the mortar joint k . The weight function ψ , measuring the influence of the point placed at \mathbf{y} on the analyzed point located at \mathbf{x} , is assumed as the classical Gaussian function. This latter depends on the nonlocal radius l_c related to the characteristic length of the mortar. No interaction between different joints is accounted for.

The fracture energy approach is employed to regularize the numerical response of the reinforcement. This is a consolidated tool based on the adjustment of the post-peak slope of the stress-strain law depending on the size of the element. To this end, the stress-strain curve is properly modified. The energy dissipated in the finite element is equal to G^r , i.e. the assigned value in tension. A characteristic length l^e is defined for each truss element. The specific fracture energy g^r , defined in Eq. (14), is then scaled so that it results $g^r l^e = G^r$ for each truss element with:

$$g^r = \int_{\varepsilon_0^r}^{\varepsilon^r} \sigma^r(\varepsilon^r) d\varepsilon^r + \frac{1}{2} \sigma_0^r \varepsilon_0^r \quad (14)$$

For each scaled g^r , the corresponding value of the reduced stiffness H^r is defined, with the aim of evaluating the evolution of damage, as described in Eq. (12).

3 CORRELATION STUDIES: EXPERIMENTAL-NUMERICAL COMPARISON

Capability of the presented models in describing mechanical response of arch systems is evaluated with reference to the experimental campaign performed by Oliveira et al. [5]. The

tests investigated the response of twelve segmental half-scaled masonry arches subjected to increasing concentrated load applied at the quarter span up to failure. Two unreinforced arches, called US1 and US2, were tested and their reference response was used to evaluate the efficiency of strengthening techniques. The remaining samples were strengthened with different arrangements of GFRP (Glass Fiber-Reinforced polymer) strips. Continuous and localized strips were located at the intrados and/or extrados, also varying the reinforcement width.

Each arch was built with clay bricks (size $100 \times 50 \times 25 \text{ mm}^3$) assembled with 10 mm thick mortar joints. Figure 3(a) shows the resulting geometry characterized by an internal span and radius equal to 1467 mm and 750 mm, respectively, thickness 50 mm and out-of-plane width 450 mm.

In the following, the mechanical response of the arches is numerically reproduced and the results are compared with the experimental outcomes and those derived by other numerical approaches. Particular attention is devoted to the analysis of the onset and evolution of the degrading mechanisms and the variation of the maximum load and failure mode caused by the presence of the reinforcement.

3.1 Response of unreinforced arches

The response of the unreinforced arches US1 and US2 is analyzed adopting both CM and IM. The first model, CM, discretizes each brick and mortar joint with 5×3 and 5×1 quadrilateral isoparametric FEs, respectively. The last, IM, adopts a similar discretization for the resized units, but 5×1 zero-thickness interface elements for each joint. As for the mechanical parameters of the constituent materials, these are set according to the available experimental data [5] and the numerical analyses performed by Di Re et al. [11]. Tables 1 and 2 contain the mortar mechanical parameters assumed for CM and IM, respectively. In detail, Table 2 shows the same quantities of Table 1 but expressed for the interfaces, and derived assuming that each interface models a mortar joint with a constant thickness equal to $l^m = 10 \text{ mm}$. Consequently, $K_N = E^m/l^m$, $K_T = G^m/l^m$, $G_{cI} = g_{cI} \times l^m$ and $G_{cII} = g_{cII} \times l^m$ are set. Young's modulus $E^b = 5000 \text{ MPa}$ and Poisson ratio $\nu^b = 0.2$ are assumed for bricks when adopting the continuous model. Instead, a scaled value $E^{b*} = 7000 \text{ MPa}$ is considered for IM to account for brick scaling and, consequently, describe the correct initial stiffness of the arches. Considering that resized bricks have length $l = l^b + l^m$, E^{b*} is evaluated as $E^{b*} = \frac{l}{l^b} E^b$.

E^m [MPa]	G^m [MPa]	$\sigma_{N,0}$ [MPa]	$\tau_{NT,0}$ [MPa]	g_{cI} [MPa]	g_{cII} [MPa]	μ
1200	500	0.25	0.25	1.8×10^{-3}	1.25×10^{-3}	0.5774

Table 1: Mechanical properties adopted for the mortar (CM).

K_N [N/mm ³]	K_T [N/mm ³]	$t_{N,0}$ [MPa]	$t_{T,0}$ [MPa]	G_{cI} [N/mm]	G_{cII} [N/mm]	μ
120	50	0.25	0.25	1.8×10^{-2}	1.25×10^{-2}	0.5774

Table 2: Mechanical properties adopted for the mortar joint interfaces (IM).

The numerical simulations are performed assuming for both materials unit weight $\gamma = 17 \text{ kN/m}^3$ and imposing a concentrated monotonically increasing load under displacement control at the nineteenth brick counted from the left impost, mimicking the loading conditions in

Figure 3(a). The global response of the arch is depicted in Figure 3(b) in terms of vertical force F -vertical displacement s . The dashed blue lines correspond to the experimental outcomes, the green curve is that evaluated with the IM and the red line refers to the numerical results derived from the CM, and already presented in [15], assuming the nonlocal radius equal to the mortar characteristic length, that is $l_c = 10$ mm. Finally, for further comparison, the black curve shows the results of the multiscale model proposed by Di Re et al. [11], which adopts the same constitutive modeling assumptions but employs a force-based beam formulation in conjunction with the energy regularization technique. On the overall, a very good agreement is detected between

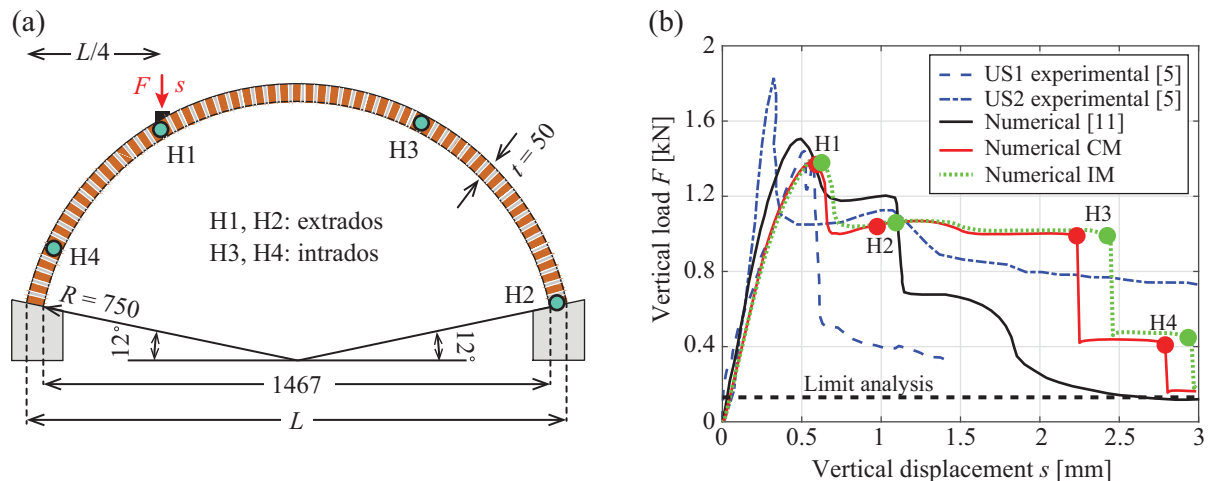


Figure 3: Unreinforced arches tested by Oliveira [5]: (a) geometry (dimensions in mm), loading conditions and experimental hinge (H) location, (b) experimental and numerical load-displacement global curves.

all solutions in terms of initial stiffness, collapse load and ductility. The curves referring to the CM and IM show slight discrepancies caused by the intrinsic differences between the two modeling assumptions. For instance, the mechanical characteristics assigned to each interface FEs are derived assuming, in a simplified manner, a constant mortar thickness of 10 mm, thus failing to describe the small variation of thickness characterizing each mortar joint starting from the intrados to the extrados of the arch. Moreover, unlike IM, CM adopts a nonlocal integral formulation which consistently affects the evolution of degrading mechanisms.

Moreover, in Figure 3(b), the collapse load value evaluated by the classical limit analysis is depicted with dashed black line. This is estimated following the three hypotheses of Heyman [6]: masonry has no tensile strength, masonry has infinite compressive strength and sliding cannot occur between joints. It is noted that both numerical and experimental response curves approach the limit value from above, thus predicting a higher peak load. This interesting aspect is caused by the not negligible tensile strength of the mortar, which moves away from the first Heyman's hypothesis, as more in detail investigated in [8, 15].

As for the failure mechanism, this experimentally involves the formation of the classical four flexural hinges located at the intrados and extrados, alternatively (Figure 3(a)). Same results are obtained with the proposed numerical models, as evident from Figure 4(a) and (b) which contain the arch deformed configurations at the end of the analyses for IM and CM, respectively. The distribution of the damage variable D defined in Eq. (4) is also illustrated in Figure 4(b), showing that damage variable, varying between 0 and 1 according to its physical meaning, is concentrated in the zones where tensile stresses are expected to be higher. The onset of fully

cracked sections, corresponding to the formation of nonlinear hinges, is the cause of the steep load drops characterizing the load-displacement global curve in Figure 3(b), as indicated by the green and red circle markers. Finally, it should be emphasized that the two models provide indistinguishable results in terms of deformed structural configuration and predict location and order of formation of the hinges in accordance with the experimental outcomes.

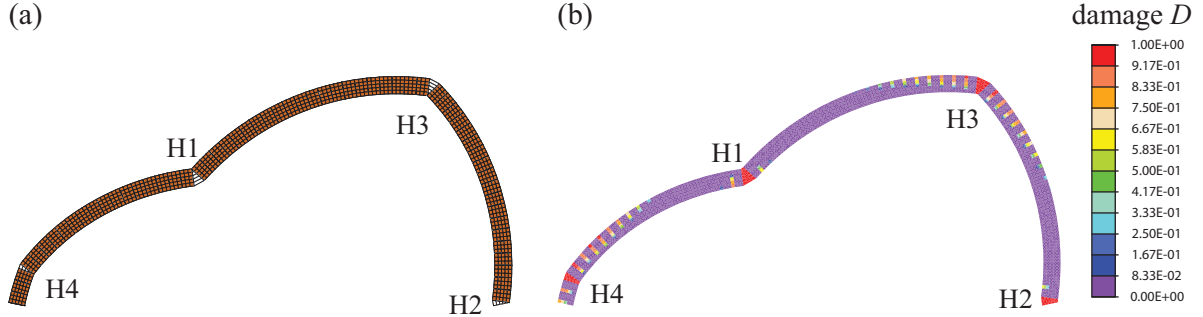


Figure 4: Numerical failure mode of the unreinforced arches tested by Oliveira [5]: (a) deformed shape obtained with IM, (b) deformed shape and distribution of the damage variable D obtained with CM.

3.2 Response of GFRM strengthened arches

The response of the GFRP strengthened arches is analyzed by employing the CM. As mentioned before, three main strengthening approaches were tested in [5]. Here, continuous configuration at the extrados is considered and numerically reproduced. The experimental set was composed of two arches (CSE1 and CSE2) strengthened with two continuous GFRP strips of 50 mm width, and the other two arches (CSE3 and CSE4) with two GFRP strips 80 mm width each. In Figure 5(a), the strengthening arrangement applied over the external substrate is schematically shown.

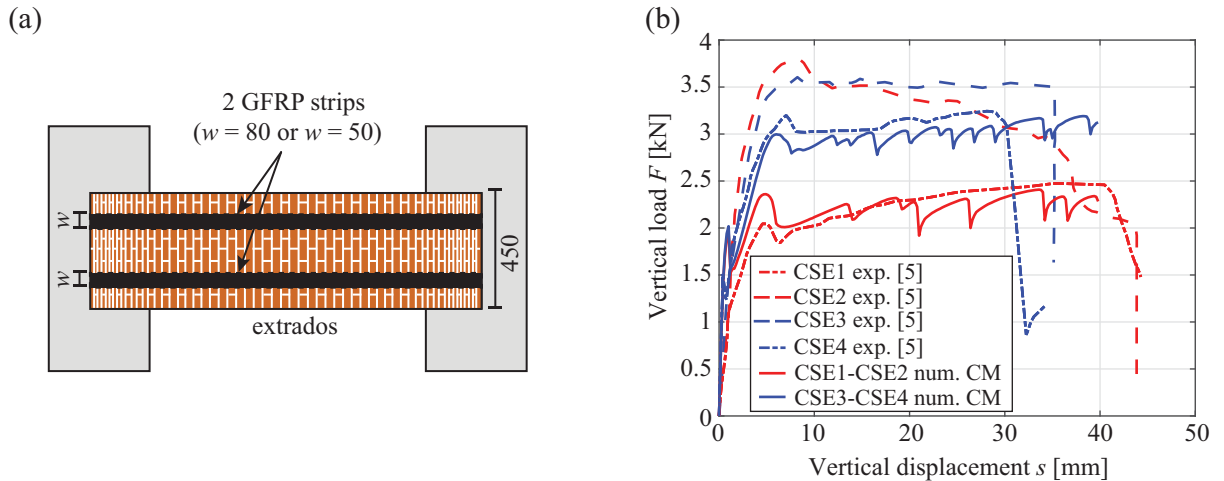


Figure 5: Strengthened arches tested by Oliveira [5]: (a) location of continuous extrados strengthening (dimension in mm), (b) experimental and numerical load-displacement global curves.

Two numerical models are considered to reproduce the different configurations by varying the size of the strips for the reinforcement and assuming the geometrical characteristic provided

in [22]. Young's modulus is set equal to $E^r = 80000$ MPa, according to the experimental results of the tensile tests performed on several GFRP samples [22]. The reduced stiffness, characterizing the second branch of the bilinear stress-strain relationship in tension, is assumed equal to $H^r = 0.01E^r$. The tensile strength, $\sigma_0^r = 200$ MPa, is calibrated to reproduce the experimental response and this is representative of both the reinforcement tensile strength and the reinforcement/masonry interaction behavior.

Figure 5(b) shows the comparison of the vertical load-vertical displacement global curves numerically and experimentally evaluated. Results referring to the configuration with 50 mm GFRP strips are depicted in red color, whereas those related to 80 mm GFRP strips are reported in blue color. Overall, a good agreement emerges between the experimental and numerical responses. The sliding failure characterized all the experimental specimens CSE, almost certainly due to their weak resistance against shear mode. The failure mechanism exhibited during testing is illustrated in Figure 6(a). It involves the formation of three hinges: in particular, a sliding hinge was located close to the right support. In Figure 6(b) the deformed numerical configuration is shown referring to the end of the analysis and to the case of strips 50 mm wide. According to the experimental outcomes, two sliding hinges appear. The first is located underneath the loading point, the second close to the right support. The numerical failure mechanism and the damage distribution shown in Figure 6(b) are representative of both the strengthening configurations. In fact, it is noted that the increase of the GFRP strips size from 50 mm to 80 mm did not produce significant variations in the structural response in terms of failure mechanism. Although this type of strengthening does not permit joint opening at the extrados, a widespread damage distribution seems to appear in the numerical model at the location opposite to the load application.

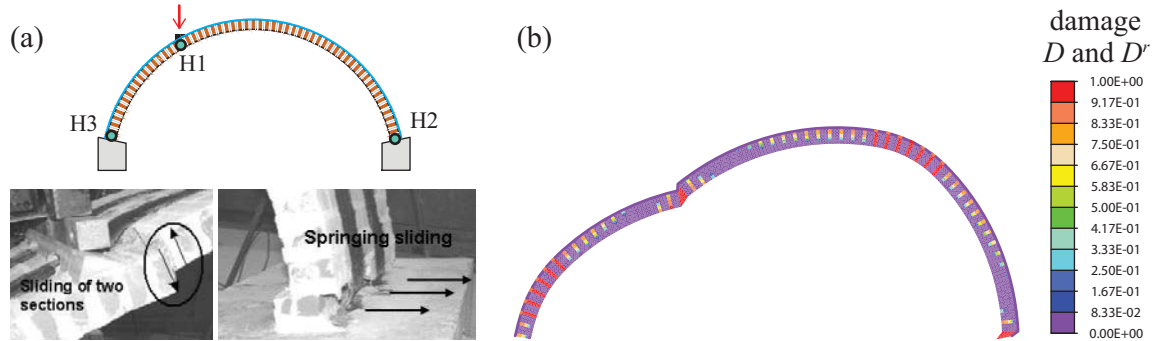


Figure 6: Externally strengthened masonry arches tested by Oliveira [5]: (a) experimental failure mechanism [5, 22], (b) numerical failure mechanism and distribution of the damage variables D and D^r obtained with CM.

4 CONCLUSIONS

- This paper presented two micromechanical FE models for the analysis of the in-plane response of masonry arches. These are based on the same constitutive assumptions, but adopt different strategies to model mortar joints. The CM considers the mortar as a continuous material modeled with 4-node isoparametric FEs, whereas the IM discretizes each mortar joint by means of 2+2 zero thickness interface elements. Linear elastic behavior is assumed for bricks, whereas a coupled damage-friction constitutive law is adopted for mortar to account for flexural and shear failure mechanisms.

- Effectiveness of the models in describing maximum strength and collapse modes of unreinforced and strengthened arches was proved by comparison with experimental outcomes.
- Satisfactory agreement is found between numerical and experimental results as regards the unreinforced case. The numerical load-displacement global curves, as well as the four hinge mechanism, well match the experimental counterpart. Moreover, the two numerical models provided very similar structural responses with only slight discrepancies caused by the different modeling assumptions. Hence, it emerged that the adoption of interface elements to model response of mortar joints is an efficient alternative to the use of continuum finite elements.
- The numerical results referring to strengthened arches with GFRP strips bonded at the extrados are encouraging. Despite the reinforcement was modeled in a simplified way by means of truss elements with mechanical properties representative of both reinforcement itself and its interaction behavior with the substrate, the change of the structural response with respect to the unreinforced case is well reproduced. The presence of the reinforcement prevented the hinge mechanism formation and let the shear sliding mechanism to prevail.
- Further improvements of the model could be performed by introducing the explicit modeling of the reinforcement-substrate interaction in order to distinguish failure mechanisms due to debonding and reinforcement rupture. To this end proper interface elements connecting masonry and reinforcement [23, 24] could be considered. Moreover, the constitutive assumptions could be modified and enriched to account for the nonlinear mechanisms involving the bricks, as masonry crushing is likely to occur in strengthened arches due to the onset of high compressive stresses.

REFERENCES

- [1] P. Zampieri, N. Simoncello, C.D. Tetougueni, C. Pellegrino, A review of methods for strengthening of masonry arches with composite materials. *Engineering Structures*, **171**, 154–169, 2018.
- [2] V. Alecci, F. Focacci, L. Rovero, G. Stipo, M. De Stefano, Intrados strengthening of brick masonry arches with different FRCM composites: Experimental and analytical investigations. *Composite Structures*, **176**, 898–909, 2017.
- [3] F.G. Carozzi, C. Poggi, E. Bertolesi, G. Milani, Ancient masonry arches and vaults strengthened with TRM, SRG and FRP composites: Experimental evaluation. *Composite Structures*, **187**, 466–480, 2018.
- [4] A. Borri, P. Casadei, G. Castori, J. Hammond, Strengthening of brick masonry arches with externally bonded steel reinforced composites. *Journal of Composites for Construction*, **13**(6), 468–475, 2009.
- [5] D.V. Oliveira, I. Basilio, P.B. Lourenço, Experimental behavior of FRP strengthened masonry arches. *Journal of Composites for Construction*, **14**, 312–322, 2010.

- [6] J. Heyman, The stone skeleton. *International Journal of Solids and Structures*, **2**, 249–279, 1966.
- [7] C. Casapulla, L. Cascini, F. Portioli, R. Landolfo, 3D macro and micro-block models for limit analysis of out-of-plane loaded masonry walls with non-associative Coulomb friction. *Meccanica*, **49(7)**, 1653–1678, 2014.
- [8] E. Bertolesi, G. Milani, F.G. Carozzi, C. Poggi, Ancient masonry arches and vaults strengthened with TRM, SRG and FRP composites: Numerical analyses. *Composite Structures*, **187**, 385–402, 2018.
- [9] M. Pepe, M. Pingaro, P. Trovalusci, Limit Analysis approach for the in-plane collapse of masonry arches. *Proceedings of the Institution of Civil Engineers-Engineering and Computational Mechanics*, 1-43, 2021.
- [10] E. Bertolesi, G. Milani, R. Fedele, Fast and reliable non-linear heterogeneous FE approach for the analysis of FRP-reinforced masonry arches. *Composites Part B: Engineering*, **88**, 189–200, 2016.
- [11] P. Di Re, D. Addessi, E. Sacco, A multiscale force-based curved beam element for masonry arches. *Computers & Structures*, **208**, 17–31, 2018.
- [12] C. Gatta, D. Addessi, F. Vestroni, Static and dynamic nonlinear response of masonry walls. *International Journal of Solids and Structures*, **155**, 291–303, 2018.
- [13] E. Sacco, D. Addessi, K. Sab, New trends in mechanics of masonry. *Meccanica*, **53(7)**, 1565–1569, 2018.
- [14] A.M. D’Altri, V. Sarhosis, G. Milani, J. Rots, S. Cattari, S. Lagomarsino, E. Sacco, A. Tralli, G. Castellazzi, S. de Miranda, Modeling strategies for the computational analysis of unreinforced masonry structures: review and classification. *Archives of Computational Methods in Engineering*, 1–33, 2019.
- [15] M. Nocera, C. Gatta, D. Addessi, D. Liberatore, Micromechanical modeling of unreinforced masonry arches accounting for flexural hinges and shear slidings. *Accepted for publication*.
- [16] E. Sacco, A nonlinear homogenization procedure for periodic masonry. *European Journal of Mechanics-A/Solids*, **28**, 209–222, 2009.
- [17] D. Addessi, C. Gatta, S. Marfia, E. Sacco, Multiscale analysis of in-plane masonry walls accounting for degradation and frictional effects. *International Journal for Multiscale Computational Engineering*, **18(2)**, 159–180, 2020.
- [18] D. Addessi, P. Di Re, C. Gatta, E. Sacco, Multiscale analysis of out-of-plane masonry elements using different structural models at macro and microscale. *Computers & Structures*, **247**, 106477, 2021.
- [19] F. Gobbin, G. de Felice, J. Lemos, A Discrete Element Model for Masonry Vaults Strengthened with Externally Bonded Reinforcement. *International Journal of Architectural Heritage*, 1–14, 2020.

- [20] D. Addessi, E. Sacco, P. Di Re, Multi-scale analysis of masonry structures. *Proceedings of the International Masonry Society Conferences*, **0(222279)**, 307–323, 2018.
- [21] C. Carloni, D.A. Bournas, F.G. Carozzi et al., Fiber reinforced composites with cementitious (inorganic) matrix. *Design procedures for the use of composites in strengthening of reinforced concrete structures*, Springer, Dordrecht, 349–392, 2016.
- [22] I. Basilio, Strengthening of arched masonry structures with composite materials, 2007.
- [23] B. Pantò, F. Cannizzaro, S. Caddemi, I. Calì, C. Chàcara, P.B. Lourenço, Nonlinear modelling of curved masonry structures after seismic retrofit through FRP reinforcing. *Buildings*, **7(3)**, 2017.
- [24] C. D’Ambra, G.P. Lignola, A. Prota, F. Fabbrocino, E. Sacco, FRCM strengthening of clay brick walls for out of plane loads. *Composites Part B: Engineering*, **174**, 107050, 2019.

ANALYTICAL AND NUMERICAL ANALYSIS OF S. MARTINO'S DEI GUALDESI CHURCH DAMAGED DURING THE 2016 CENTRAL ITALY SEISMIC SEQUENCE

Elvis Cescatti¹, Michol Rampado¹, Veronica Follador², Francesca da Porto¹, Claudio Modena³

¹ Depart. of Geosciences - University of Padova
Via G. Gradenigo, 6, 35131 Padova (IT)
elvis.cescatti@dicea.unipd.it; michol.rampado@dicea.unipd.it; francesca.daporto@unipd.it

² DICATAM - University of Brescia
Via Branze, 43, 25123, Brescia (IT)
v.follador@unibs.it

³ ITC - CNR
Corso Stati Uniti, 4, 35127, Padova (IT)
claudio.modena@unipd.it

Abstract

The seismic response of churches is peculiar due to the building typology, the structural features and the used materials. During last decades a great work of research on damages occurred on such structures after seismic events was performed and some insight of this behavior have pointed out suggesting different intervention techniques. This lead to apply, during past years, some interventions on churches already damaged. In particular, the Umbria-Marche region, has stroked by three relevant earthquakes: Norcia 1979 (Mw 5.8), Colfiorito-Annifo 1997 (Mw 6.0), Norcia 2016 (Mw 6.5). The last events occurred on structures already damaged in past and strengthened by interventions that aim at improving their seismic behavior. Starting from the conclusions of such extended survey campaign and analyzing the effect of interventions, the Church of S. Martino's dei Gualdesi in Castelsantangelo sul Nera (MC – Italy) was modelled and studied with both linear and non-linear methods. The paper presents the results of such analysis comparing also the observed damages and the effectiveness of some interventions performed in past years on the church.

Keywords: Masonry Churches, Seismic Vulnerability, Numerical Analysis, Limit Analysis.

1 INTRODUCTION

The study of structures damaged from earthquakes is the most interesting benchmark to evaluate the analytical and numerical tools available in the vulnerability analysis and commonly used to design retrofit or refurbishment interventions.

The study herein reported is a preliminary stage of a deeper project carried out on the San Martino's dei Gualdesi Church. The case-study selection derives from a wider observation on a dataset of about 900 churches stricken by the 2016 earthquake swarm [1] that recognize in Castelsantangelo sul Nera, an interesting opportunity to evaluate vulnerability and effect of interventions.

The paper presents a qualitative evaluation of interventions carried out in the municipality and reports the analysis carried out on San Martino. The presented analysis looks at the unreinforced church and aims at evaluating the seismic multiplier. Moreover, a non-linear static analysis has carried out to evaluate its reliability in predicting the damage pattern and to support the kinematic analysis.

2 RESPONSE OF CHURCHES IN CASTELSANTANGELO SUL NERA

The municipality of Castelsantangelo sul Nera, located in the Marche Region, was interested by numerous seismic events in past years and also by the 2016 Central Italy seismic swarm. This last caused severe damage to structures including the churches of the region [2].

In order to evaluate the vulnerability and the seismic response of such structures, a focus on the municipality cluster, composed by 19 cases, was carried out beginning from the enlarge database collected in the Centre of Italy [1]. All the churches in the cluster undergone a PGA between 0.52g and 0.54g evaluated by INGV shake-maps. Therefore, considering similar actions, the damage observed is mainly guided by the vulnerability of each structure.

The Damage Index (i_d) has evaluated by the A-DC form [3, 4] and the Vulnerability Index (i_v) was first defined according to the II level form for the church survey [5]. The i_d have shown an high heterogeneity, ranging from 0.33 to 0.85 (variation of 0.52, average of 0.52 and standard deviation of 0.14) that could be attributed to the vulnerability of the constructions since the seismic actions were quite similar. The analysis of i_v did not show significant variations varying between 0.36 and 0.57 (average of 0.48 and standard deviation of 0.06). This could lead to suggest a small representativeness of the i_v value to describe the different vulnerabilities, suggested also by the fact that the variation of the damage index calculated by formulation available in literature [6] would be 0.09, for the i_v and PGA values ranges herein described.

To better highlight the raised differences, a specific evaluation on each case has performed, also considering the consolidation interventions carried out in past years with the aim of obtaining insight into their effect on the seismic response.

From the observation of all cases, some intervention highlighted always a positive behavior such as tie rods applied for both goals: prevent the out-of-plane mechanisms of the walls and counterbalance the loads of arches and vaults. This intervention pointed out some issues only in case of poor masonry quality with the disaggregation of wall [7]. Another very positive intervention is the introduction of a metallic hopping system on the bell-tower. Indeed, two churches two hundred meters close, very similar in geometry and dimensions, like S. Stefano and San Martino's dei Gualdesi pointed out two emblematic boundaries in behavior (Figure 1) between the total collapse and only a cracking of the bell-tower due to the presence, in the case of St. Martino, of hooping interventions on the belfry that avoid the collapse after the mechanism activation. On the other hand, some interventions show generally worsening effects such as some concrete slab reinforcement of roofs, where due to the increase of loads and stiffnesses, masonry collapse or severe damage occurred. The task of containing the overturning of the

walls and distributing the vertical loads was entrusted to the ring beam. Sometimes, it was observed an overall achievement of the goal, whereas either in the case of reinforced concrete ring beam and in the steel beam sometimes some damage caused by this intervention were observed such as horizontal cracks at the height of the ring beam and the disintegration of the masonry below it. The causes can be associated with poor masonry quality as well as an ineffective or absent connection between the ring beam and the masonry.

The results obtained from this analysis have determined different responses in terms of local and global damages although the earthquake was the same. For these reasons, in order to understand which parameters have the greatest influence on the vulnerability, a seismic behavior analysis of a specific church, that may represent the cluster, has been implemented and herein presented.



Figure 1: S. Stefano's tower (left) and San Martino's bell tower (right) after the 30th of October 2016

3 SAN MARTINO'S DEI GUALDESI CHURCH

San Martino's dei Gualdesi church, in Castelsantangelo sul Nera (MC), was built in the 14th century. The structure is mostly made of local limestone (two leaves masonry 70-120 cm thick) and lime mortar. The structure is 30.60 x 7.40 m in plan and 6.87 m height for the nave with an height of 17 m for the tower and it is of medium size compared to those present in the region [1]. The church consists of a single nave, marked by four pointed arches arranged transversely, covered by a timber gable roof. Externally, the church has the same internal regularity: the longitudinal south-west facade is characterized by two entrance portals and by further secondary openings. The transversal gabled facade, located to the north-west side, is composed by a simple window in the central area.

The structural data were entirely deduced from the information collected during the on-site surveys and through some documentary additions provided by the Superintendence for Cultural Heritage of Ancona. To date, it has not been possible to carry out diagnostic campaigns for the characterization of construction details or materials. For this reason, the materials' mechanical properties were obtained from a critical analysis of masonry arrangements by the study of the masonry quality index (IQM) [8] of some panels and masonry sections. These investigations with its typological and qualitative definition helped in identify two different masonry typologies according to the Italian National Standard [9], whose mechanical properties [10] are summarized in Table 1.

In this case, since the investigations are limited, the confidence factor calculated according the Italian guidelines for cultural heritage [11] is equal to 1.24 and the level of knowledge reached is KL1.

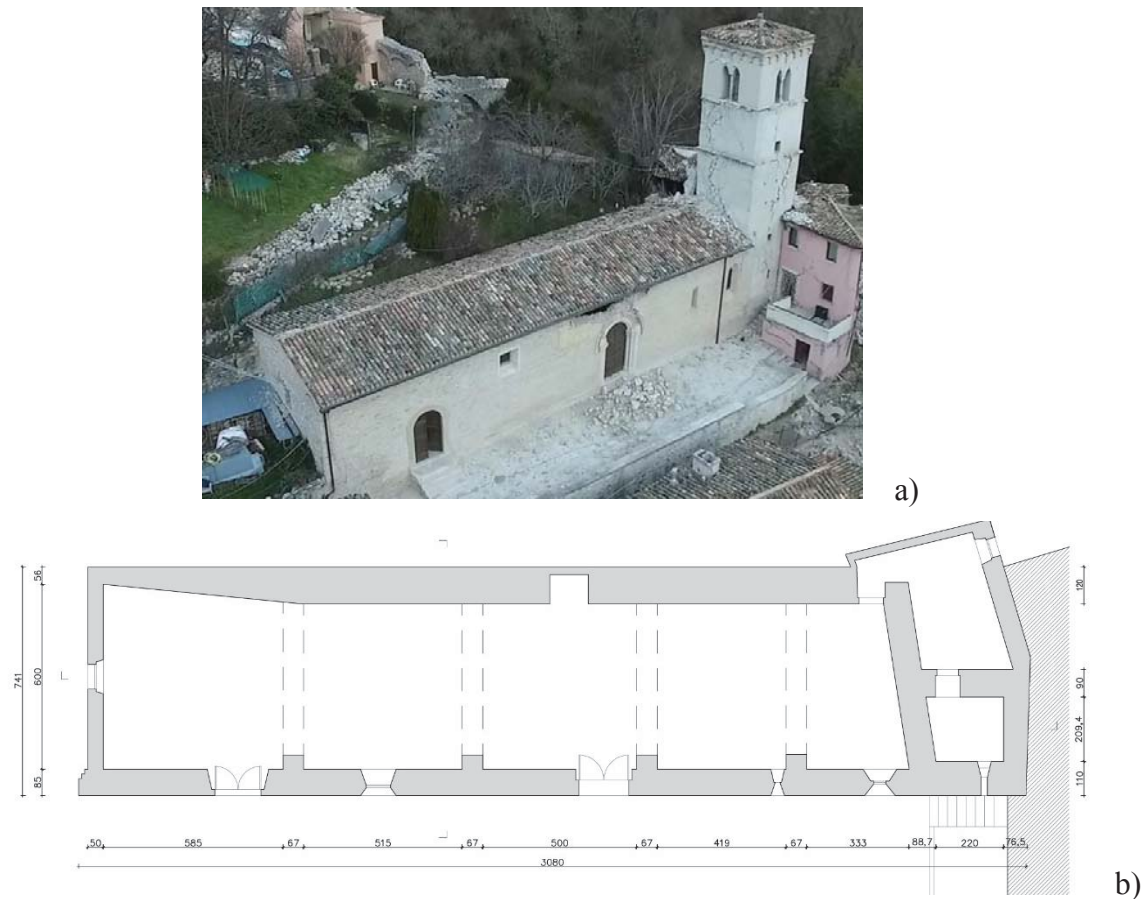


Figure 2: Aerial view (a), and plan (b) of San Martino's dei Gualdesi church.

MASONRY TYPOLOGIES	$f_{m,d}$ (N/mm^2)	$\tau_{0,d}$ (N/mm^2)	E (N/mm^2)	G (N/mm^2)	w (kN/m^3)
Masonry: Roughly cut stone masonry with good texture - III	2.6	0.056	1740	580	21
Arches: Stone blocks squared masonry- V	5.8	0.090	2850	950	22

Table 1: Mechanical properties of the masonries used.

3.1 Interventions related to the past seismic events

The most significant earthquakes for the Castelsantangelo sul Nera area were the earthquakes of Norcia, M_w 5.8 in 1979, and the Umbria-Marche earthquake, M_w 6.0 in 1997. These seismic events had a strong impact with regard to both the identification of seismic damage and the implementation of series of interventions aimed at mitigating its effects (not always with real benefits). The church of San Martino's dei Gualdesi, entering into this context, was subjected to four intervention campaigns (in 1988, 1999, 2000 and in 2014). Some of the older interventions had been replaced in subsequent refurbishments. Therefore, a description of the present configuration of the church with the current interventions is presented below.

In general, two significant phases of intervention can be distinguished: one relating to the 2000 restorations, which mainly involved the bell tower, and a more recent restoration of 2014 regarding the structure of the nave.

In 2014 interventions, a systematic demolition of the top of the wall was carried out with subsequent reconstruction of it for a height of 30-50 cm. In addition, a UPN 220 metal profile

has been inserted and anchored with the underlying wall with a $\phi 16$ bar 85 cm long, every 50 cm. The bars were inserted inside perforations (with a diameter of 24 mm) and subsequently injected with lime mortar (blue line in Figure 3). A further intervention was the injection of a fluid hydraulic lime mortar on the walls. Four holes per square meter with a diameter of 22 mm were injected (red dot fill in Figure 3). A final and significant structural intervention performed on the nave concerns the execution of a series of steel bars reinforcement between the longitudinal walls of the nave and the internal arches. Twelve stainless steel bars with a diameter of 16 mm were inserted and injected with epoxy resin inside drillings of 24 mm of diameter (red strip hatch in Figure 3). Regarding the bell tower, in 2000, two orders of metal hooping beams have been inserted in elevation under the belfry and at the level of the mouldings (blue dashed line in Figure 3). Finally, about 20 perforations per wall were made on the tower's walls with subsequent insertion of steel bars presumably with a diameter of 20 mm (green dot mesh in Figure 3).

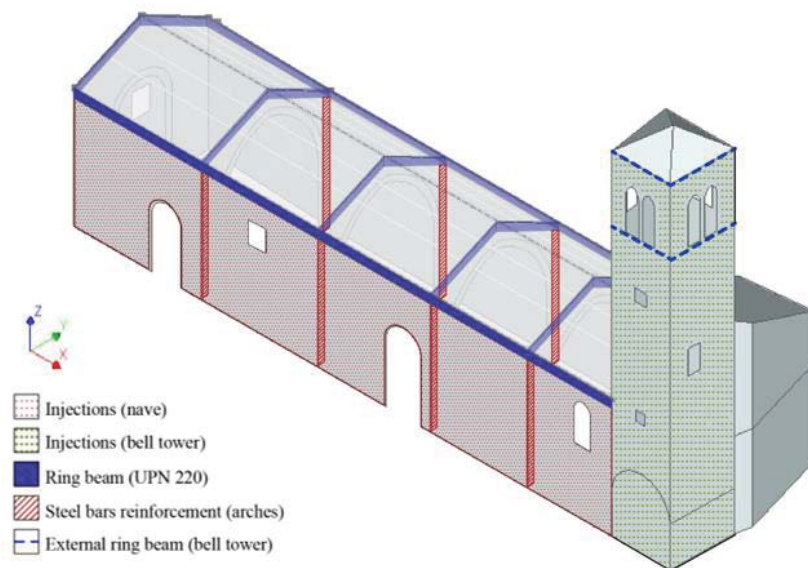


Figure 3: Representation of interventions implemented in 2014 and 2000 to the San Martino's dei Gualdesi church.

3.2 Analysis of damage

The church of San Martino's dei Gualdesi, referring to the A-DC form [3, 4], has an intermediate damage index ($i_d=0.60$). Although the i_d value is slightly higher than the average of the Castelsantangelo's cluster (see § 2), the church showed only a small collapse of the wall above the entrance (Figure 4d) but, any other structural element of the nave and the tower had not collapsed. The main damages are located in the internal part of the church, in particular near the pointed arches, in some parts of the perimeter wall and in the bell tower.

The cracks affecting the internal part of the church are mainly located between the longitudinal walls and the central arches. From the structure of the church, it is clear that the pointed arches, placed transversely to the nave, support the roof and transmit the loads to the side pillars and to the perimeter walls. Figure 4b highlights some cracks between pillars and the longitudinal wall probably due to the weak connection in shear between the two. Moreover, it seems that some interactions in traction are present since some sliding in first voussoirs is present, probably due to the introduction of rebars and a consequent movement of the pillar according to the out-of-plane of the lateral wall.

More cracks are located at the interface between the extrados of the arch and the masonry, due to the absence of connection between the two different materials. In the same pictures (Figure 4b), reduced cracks are observed even at the level of the roof, perhaps due to the insertion of the metallic ring beam that may have limited their opening but also promoted the detachment.

Other cracks were located in the transverse walls of the nave, in particular in the north-west facade, which still has the shape of the original door. The distribution of the cracks follows the intersection between the original wall and the added element showing the typical shear cross shape (Figure 4a).

Lastly, deep cracks were found on the bell tower (Figure 4c). The position of these cracks is related to the presence of windows and small openings. The windows and the little columns of the upper level represent the weakest. However, although characterized by widespread cracks, the bell tower did not show the collapse of masonry parts or other elements. This proves the effectiveness of the past hooping interventions, which have defined a better connection between the orthogonal walls ensuring the box behavior during the seismic events.

Unlike the other facades of the church, the longitudinal wall located to the south shows a loss of the curtain wall with the detachment of the upper portion of the masonry (Figure 4d). The collapse of this masonry portion seems to be promoted by the reinforcement (of the past interventions) at the top. Indeed, if the metallic beam presents excessive stiffness, it can generate damages related to the tangential stresses in the contact area with the masonry and therefore a detachment between the parts. Moreover, the entire wall suffered from an out-of-plane displacement in the order of 15-20 cm. The overall displacement of that seems to be provided by the monolithic behavior probably promoted and enhanced by injections.

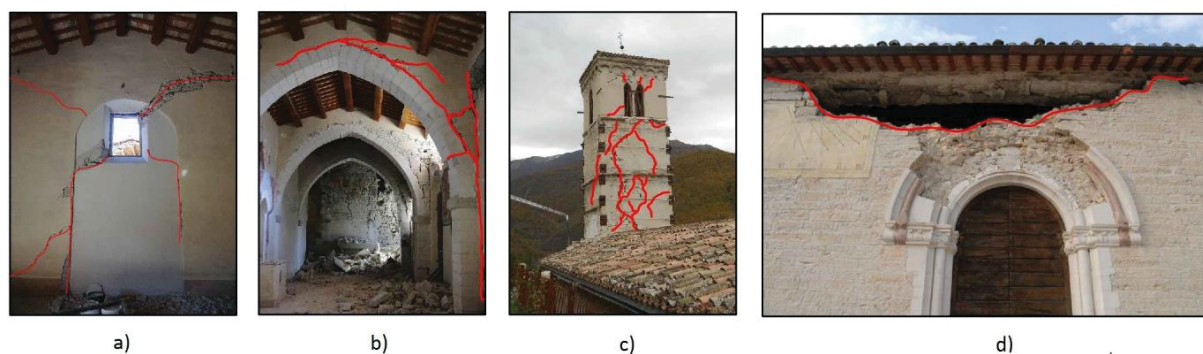


Figure 4: Damages observed on the north-west facade (a), central arch (b), bell tower (c) and on the south-west facade.

4 STRUCTURAL ANALYSIS

The preliminary structural analysis of the church has focused on the pointed arch behavior and on the influence that this has on the overall behavior. With this aim, a kinematic study was performed together with a non-linear static analysis with a Finite Element Model in order to validate the assumptions made.

4.1 Definition of the seismic action

The seismic action used for the assessment of the church is determined by following the indications provided by the Italian Standard [12]. The design parameters used in the analysis are represented in Table 2. The return period, considering the ecclesiastical function, is of 712 years.

Parameters (DLS)				Parameters (ULS)			
a_g	0.120	q	1.00	a_g	0.283	q	2.000
F_0	2.305	S	1.80	F_0	2.400	S	1.554
T_c^*	0.288	η	1.00	T_c^*	0.339	η	1.000
S_S	1.500	T_B	0.15	S_S	1.295	T_B	0.170
C_C	1.584	T_C	0.45	C_C	1.500	T_C	0.510
S_T	1.200	T_D	2.08	S_T	1.200	T_D	2.726

Table 2: Design parameters used in the analysis

4.2 Kinematic analysis

The kinematic analysis is based on the limit analysis and the principle of virtual works and refers to the upper bound solution [13]. This, on one hand, make easier the analysis and, on the other, it requires defining the minimum multiplier to obtain the exact solution. Therefore, the Finite Element Model helps in defining the proper crack pattern and hinges location.

The out-of-plane limit analysis was guided by the actual crack pattern observed, and hence evaluating those mechanisms activated during the earthquake (Figure 5). In detail, the south-west wall of the nave and the north-west corner of the tower were analyzed as out-of-plane mechanisms, while the central arch as in-plane mechanisms.

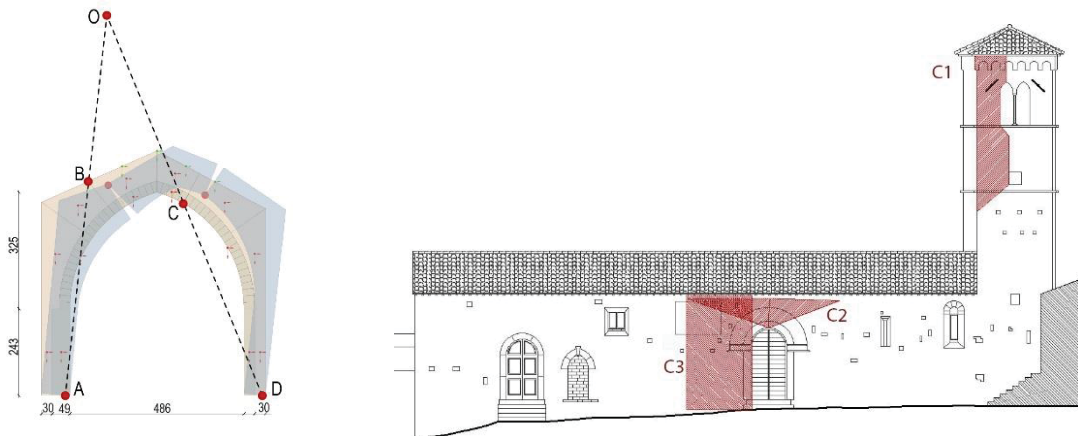


Figure 5: In-plane (left) and out-of-plane (right) analysis of the church.

Table 3 shows the results of the kinematic analysis implementing linear methods. The factor ζ is the safety coefficient defined as the ratio between the seismic capacity and the demand for each macro-element. Values greater than one indicate that the mechanism is verified at the damage limit state (DLS) and at the ultimate limit state (ULS). As regards the out-of-plane kinematic mechanisms, the linear verification is not verified for any mechanisms. The activation multiplier was calculated accounting for the masonry compression hence considering the hinge in the middle of the stress-block. The lower multiplier refers to the wall overturning (C3 Figure 5) and it figures out that the restrain contribution of the roof is not negligible, since that mechanism does not reach the collapse although it has activated with an overall ultimate displacement of about 15-20 cm. The tower mechanism activated also on the real case but it was counteracted by the hooping system that avoided the collapse, as did not happen for the near church of S. Stefano. Lastly, the highest multiplier found (mechanism C2) of 0.535 has activated but not avoided by any interventions resulting in the collapse of the macro-element. That value is similar to the highest PGA recorded in the swarm of 0.541 the 26th of October 2016.

1° Mode			
Kinematics	α (t/2)	ζ (DLS)	ζ (ULS)
C1	0.266	0.38	0.44
C2	0.535	0.68	0.74
C3	0.143	0.58	0.57

Table 3: Results of the kinematic analysis for the out-of-plane mechanisms

Similar to what has been observed for the out-of-plane mechanism, the hypothesis of interaction among macro-elements may lead to significantly different solutions also for in-plane analysis. Due to this, different combinations (Table 4) have been defined.

For the in-plane analysis of the arch, which is placed in the transversal direction of the nave (Y direction), the hinges position was defined by the analysis of the principal traction strains. The latter were obtained by the non-linear static analysis of the church, considering that this comes from static considerations which belong to the lower bound solution. Therefore, the obtained multiplier should be the exact one also for the interaction among longitudinal walls and the arch.

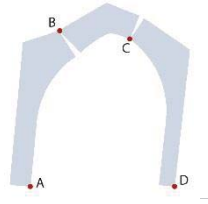
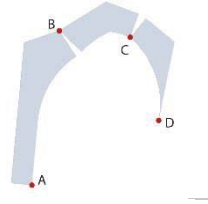
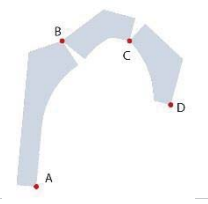
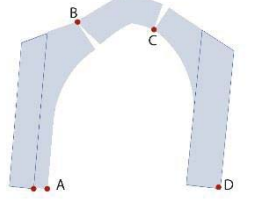
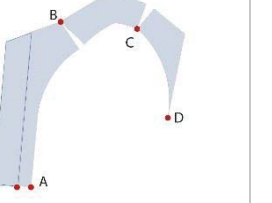
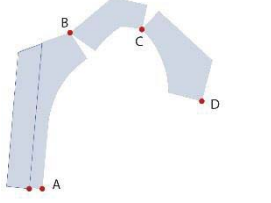
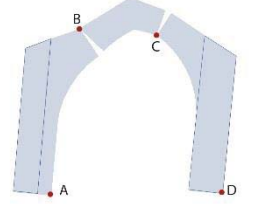
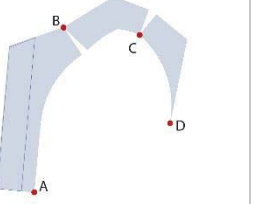
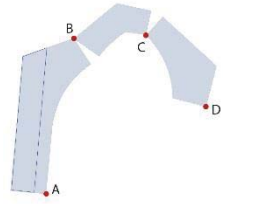
	D1- All hinges as FEM	D2 – Hinge D on the impost	D3 – Hinge D in the wall
Case A Only arch			
Case B Only tension between the arch and the wall			
Case C Shear and tension between the arch and the wall			

Table 4: Type of kinematic analysis implemented

The possible variability may concerns the in-plane and out-of-plane interaction of the longitudinal wall and of the soil on the mountain side. Therefore, looking at Table 4, cases A, B, C considers different interactions among macro-elements whereas cases from D1 to D3 evaluate differently positions of the hinge on the mountain side (hinge D).

Table 5 reports the obtained activation multipliers α , always considering the hinge regression, and the factor ζ that report the structural verification. Due to the not symmetric geometry, the multiplier of both directions is reported.

In case A the arch is alone, neglecting the contributions of lateral walls, whereas in cases B and C walls are considered. In the latter the coupling between the arch and the wall is perfect,

with transmission of normal and shear stresses on the interface, while in case B only the normal action is considered.

2° Mode (+Y) North/mountain dir.					2° Mode (-Y) South/valley dir.				
	case	α (t/2)	ζ (DLS)	ζ (ULS)		case	α (t/2)	ζ (DLS)	ζ (ULS)
D1	A	-0.002	-	-	D1	A	0.079	0.34	0.34
	B	0.188	0.80	0.79		B	0.172	0.73	0.72
	C	0.189	0.80	0.79		C	0.184	0.78	0.77
D2	A	-1.030	-	-	D2	A	0.108	0.45	0.44
	B	0.065	0.28	0.28		B	0.137	0.59	0.59
	C	0.064	0.28	0.27		C	0.159	0.69	0.68
D3	A	-0.550	-	-	D3	A	0.107	0.44	0.44
	B	0.277	1.16	1.14		B	0.161	0.68	0.67
	C	0.306	1.28	1.26		C	0.198	0.83	0.82

Table 5: Results of the kinematics analysis for the in-plane mechanisms

In the case A, in the positive direction of Y, there is a negative multiplier that means that there is no equilibrium in the thrust of the arch without the lateral walls providing a counterbalancing effect even in static conditions. Therefore, the case A is not a reliable hypotheses of the actual behavior. Considering the fact that the FEM model reliably describes the hinge positions, and comparing with the actual observations, also cases D2 and D3 are not suitably describing the real situation because did not appear evident cracks next to the guessed hinge position D.

In conclusion, the cases more similar to the actual situation are B and C in conditions D1. Herein, case B is selected as the most reliable (Table 5 in bold) because even the intervention with rebars performed in 2014 could not guarantee the shear transfer, as pointed out by the crack pattern occurred (Figure 4b). Therefore the final multipliers selected are α 0.188 and 0.172 in the positive and negative Y direction respectively.

4.3 Fem analysis

The numerical analysis of San Martino's dei Gualdesi was performed using the DianaFea software. In detail, a linear and a non-linear static analysis were performed in order to obtain results consistent with the actual damages observed.

The church has modeled using two-dimensional elements. The roof analysis of weight has performed following the information obtained by documents on past interventions. The vertical elements of the model have defined as regular curved shells: quadrilateral elements with eight nodes and a quadratic behavior. The mesh has a size of 0.25 m. The linear elements such as beams have specified as beam elements curved and characterized by three nodes (Class-III 3D). Boundary conditions were defined to constrain all translations and two rotations except the out-of-plane. Finally, the material properties were defined following Table 1 for the linear properties. To account for the non linear behavior a total strain cracked model has been adopted with a parabolic behavior in compression and a exponential one for the softening in tension. The fracture energy has defined following the literature [14].

First, a linear static analysis was performed to evaluate the static conditions of the model. Regarding the reaction forces, the maximum vertical value is 74.9 kN. The vertical deformation (Z direction), due to its own weight, is located on the bell tower and is approximately 1.7 mm. Lastly, as regards the main stresses, the compression stress located at the base of the bell tower is 0.45 MPa.

Subsequently, the static non-linear analysis was implemented to analyze the non-linear behavior of the structure. The analysis concerns both the longitudinal (X) and transverse directions of the church (Y), with more attention to the transversal direction (east-west direction). The own weight of the structure was applied in a single load step, followed by the application of a global acceleration (proportional to the masses) into different load steps.

Results show greater deformations and displacements refer to the analysis with transverse direction of the seismic action (+Y, -Y). In the first case (+Y, mountain dir.), the displacements of the control nodes positioned at the top of the central arch are approximately equal to 0.20 m in agreement with the actual observations. Analyzing the results relating to strains, the main stresses are located on the transversal walls. However, high cracks are also located on the longitudinal facades of the church and on the tower's walls (Figure 6).

In the negative direction of Y (-Y, valley dir.), the greatest displacement is measured at the top of the bell tower (0.12 m) even the control nodes at the top of the central arch reach considerable displacements of 0.10 m.

Regarding the analysis in the longitudinal direction (+X, -X) the main deformations and displacements are located on the upper part of the bell tower.

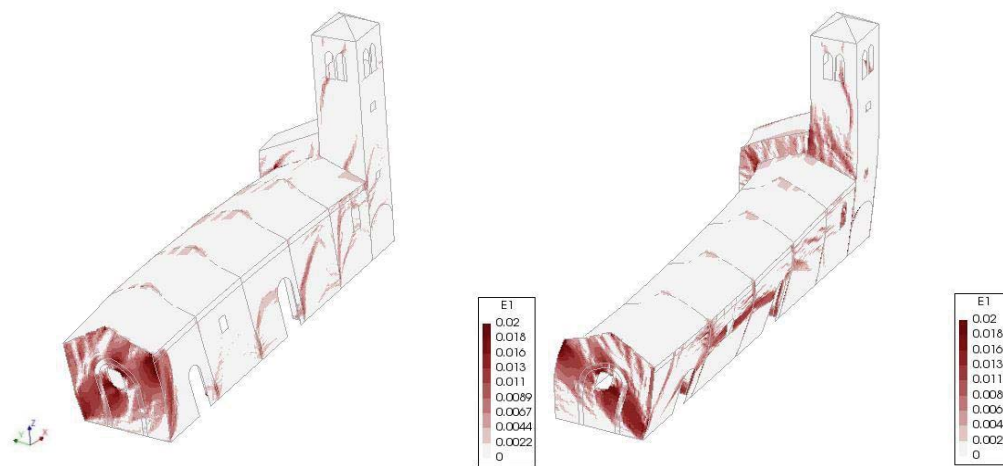


Figure 6: Major principal strain for the analysis in the +Y direction (left) and -Y direction (right).

4.4 Comparison between the damages observed and the numerical analysis

The results obtained from the numerical analysis has been compared with the damages described in the previous paragraph (§3.2). The structural parts investigated are the north-west and the south-west facade of the nave, the walls of the bell tower and finally the internal arches of the nave.

Figure 7a shows that strains, and thus cracks concerning the internal arch, are mainly located between its lateral part and the longitudinal part of the south-western masonry and in the interface between the extrados of the arch and the masonry above. From this crack pattern, the four hinges location for the limit analysis presented above was defined (§4.2). Moreover, damages and cracks coincide with the damages observed in the on-site survey (Figure 4b), confirming the reliability of this type of analysis.

Less deformation and damages occurred in the north-east walls, again corresponding to the actual condition. In this case, the pillars are embedded in the wall itself, ensuring a better connection between them. The greatest displacements are reached in the analysis with transverse direction of the seismic action.

The longitudinal south-west wall showed significant damage due to the longitudinal action. Figure 7b shows cracks on the entire wall and in particular near the transverse arches and openings. More cracks are located in the interface between the wall of the bell tower and in the upper part of the nave facade. These damages coincide also with the current state of the church.

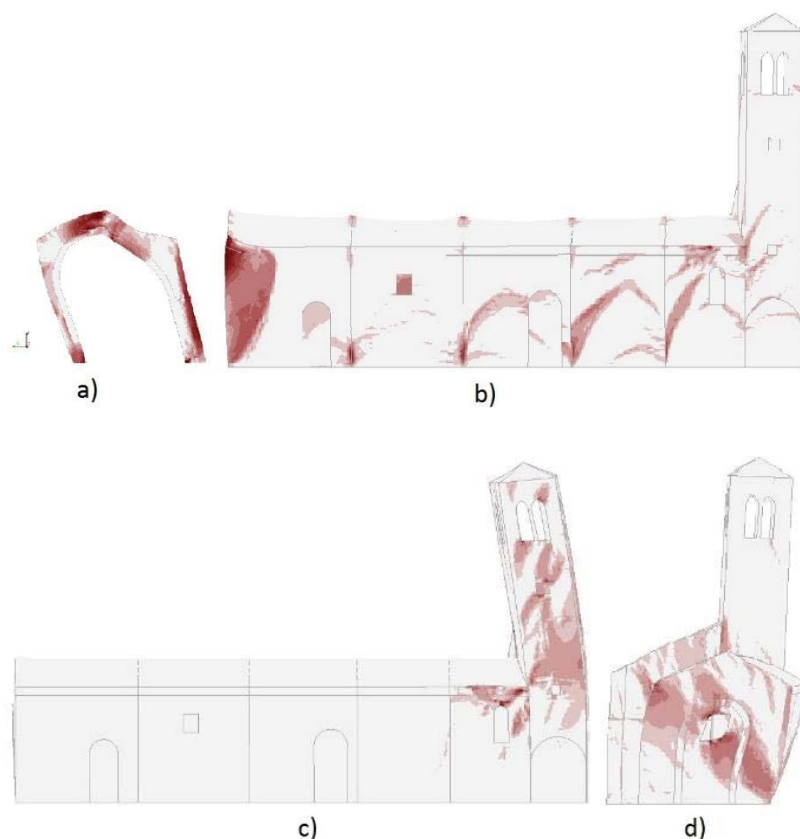


Figure 7: Localized deformations in the central arch (a), south-west wall (b), tower (c) and north-west wall (d).

The north-west facade is characterized by significant damages in the case of transverse seismic action. Cracks obtained from the numerical model provide almost the same pattern observed in the structure. The distribution of cracks follows the intersection between the original wall and the added element.

Lastly, the south-western wall of the bell tower shows significant deformations due to the longitudinal action (-X). The principal strains, obtained from the numerical model, are located near the mullioned windows, in the small openings below and lastly in the contact area between the roof of the church and the belfry. These critical points are also observed on the damage picture (Figure 4c).

5 CONCLUSIONS

- The paper presents the first stage of studies carried out on the San Martino's dei Gualdesi church, confirming that the integrated methodology among different type of analysis (i.e. kinematic and non-linear static analysis) lead to achieve reliable results compared to the real case observations.
- The kinematic analysis, supported by some non-linear analysis in the definition of the mechanisms, proved to be a valuable tool in the definition of the activating accelerations.

The evaluation of the interaction in-plane and out-of-plane may also be detrimental to obtain the correct value.

- The static non-linear analysis confirms to be a reliable method of structural modeling detecting a crack pattern very similar to the real one.
- Future works aim at evaluating through capacity curves the real performances of the structure, even compared with the real occurred earthquake, and furtherly improving analysis by the implementation of interventions.

ACKNOWLEDGMENTS

The authors wants to acknowledge Sara Coppo and Estefania Chaves Moreno to their preliminary contributions on the research. Special thanks are due to the Italian Department of Civil Protection (DPC), which funded this study in the framework of the *ReLUIS-DPC Project 2019-2021 – Work Package 5: Interventi su edifici vincolati monumentali e/o di culto*.

REFERENCES

- [1] E. Cescatti, P. Salzano, C. Casapulla, D. Ceroni, F. da Porto, A. Prota, Damages to masonry churches after 2016–2017 Central Italy seismic sequence and definition of fragility curves. *Bull Earthquake Eng*, **18**, 297–329, 2020.
- [2] A. Penna, C. Calderini, L. Sorrentino, C.F. Carocci, E. Cescatti, R. Sisti, A. Borri, C. Modena, A. Prota, Damage to churches in the 2016 central Italy earthquakes. *Bull Earthquake Eng*, **17**, 5763–5790, 2019.
- [3] DPCM 23/02/2006, Approval of forms for the seismic damage assessment of cultural heritage buildings. G.U. no. 55, 7/03/2006, 2006. (in Italian)
- [4] MiBACT, Direttiva 23 aprile 2015, Aggiornamento della direttiva 12 dicembre 2013, relativa alle “Procedure per la gestione delle attività di messa in sicurezza e salvaguardia del patrimonio culturale in caso di emergenze derivanti da calamità naturali. GU Serie Generale n.169 del 23-7-2015, 2015. (in Italian)
- [5] Italian Ministry of Public Building and Works, G.U. no. 47. 2011, February 26. (suppl. ord. no. 54). Directive of the Prime Minister dated on 9/02/2011, Assessment and mitigation of seismic risk of cultural heritage with reference to the Technical Code for the design of constructions, issued by D.M. 14/1/2008, 2011. (in Italian)
- [6] S. Lagomarsino, S. Podestà, Seismic Vulnerability of ancient churches: II. Statistical analysis of surveyed data and methods for risk analysis. *Earthquake Spectra*, **20**(2), 395–412, 2004b.
- [7] E. Cescatti, M. Secco, F. da Porto, G. Artioli, C. Modena, L. Xu, Characterization of mortar and stone masonry quality in Amatrice historical buildings hit by the 2016 central Italy earthquake. *17th International Brick and Block Masonry conference*. Kraków, Poland, July 5-8, 2020. DOI:10.1201/9781003098508-65
- [8] A. Borri, C. Corradi, G. Castori, A. De Maria, A method for the analysis and classification of historic masonry. *Bulletin of Earthquake Engineering*, **13**(9), 2647-2665, 2015.

- [9] Italian Ministry of Infrastructures, Circolare Esplicativa 21 gennaio 2019, n. 7 C.S.LL.PP. Istruzioni per l'applicazione dell' «Aggiornamento delle “Norme tecniche per le costruzioni”» di cui al decreto ministeriale 17 gennaio 2018, Rome, 2019. (In Italian)
- [10] A. Vignoli, S. Boschi, C. Modena, E. Cescatti, In-situ mechanical characterization of existing masonry typologies: A research project in Italy finalized to update the structural codes. *16th International Brick and Block Masonry conference*, Padova, Italy, 26-30 June, 2016.
- [11] Italian Ministry for Cultural Heritage and Activities, LL.GG.BB.CC. Linee guida per la valutazione e riduzione del rischio sismico del patrimonio culturale. Rome, 2010. (In Italian)
- [12] D.M. 17/01/2018. Norme Tecniche per le Costruzioni (NTC 2018). Gazzetta Ufficiale, n. 42 del 20/02/2018, Supplemento ordinario n.8, Rome, 2018. (In Italian)
- [13] M. Gilbert M, Limit analysis applied to masonry arch bridges: state-of-the-art and recent developments. *5th International Conference on Arch Bridges*, Madeira, Portugal, 12-14 September, 2007.
- [14] P.B. Lourenço, Recent advances in masonry modeling: micromodelling and homogenisation. In: U. A. M. H. Galvanetto, ed. *Multiscale Modeling in Solid Mechanics: Computational Approaches*. London, Imperial College Press, 2009.

A NURBS-BASED NUMERICAL APPROACH FOR THE ASSESSMENT OF MASONRY VAULTS UNDERGOING DIFFERENTIAL SETTLEMENTS

Andrea Chiozzi¹, Nicola Grillanda², Gabriele Milani², Antonio Tralli¹

¹ Department of Engineering, University of Ferrara
Via Saragat 1, 44122 Ferrara (Italy)
e-mail: {andrea.chiozzi, tra}@unife.it

² Department of Architecture, Built Environment and Construction Engineering (A. B. C.), Polytechnic University of Milan
Piazza Leonardo Da Vinci 32, 20133 Milan (Italy)
email: {nicola.grillanda, gabriele.milani}@unife.it

Abstract

In this paper, we propose a NURBS-based adaptive approach to the three-dimensional analysis of masonry vaults undergoing foundation settlements. A given masonry vault of arbitrary geometry is described through its NURBS (Non-Uniform Rational B-Spline) parametric representation in the three-dimensional Euclidean space. The vault surface is then discretized into an initial set of rigid elements. Such discretization is obtained by suitably subdividing the NURBS parameters space. Jumps of displacement are allowed solely at the interfaces. Given a known displacement on the external boundary, which comprises possible settlements, the resulting displacement field is computed by minimizing the total potential energy of the system by means of a linear programming optimization algorithm. Moreover, a mesh adaptation scheme based on a suitable Genetic Algorithm (GA) is used to determine the crack pattern yielding the mechanism actually induced by the settlement. The procedure is here demonstrated through a numerical example.

Keywords: Masonry, Foundation Settlements, NURBS, Genetic Algorithm

1 INTRODUCTION

The interest in studying the crack patterns induced by foundation settlements in masonry structures is quite recent. In fact, differential settlements are one of the most frequent causes of cracks in historical masonry structures. When undergoing foundation settlements, masonry structures deform like mechanisms in order to be able to accommodate such settlements, accompanied by a pattern of cracks. The strong nonlinearities of the masonry material, which have been summarized by Heyman [1] by means of the no-tension material assumption, render masonry constructions quite unsuited to resist differential settlements. In the last decades, the problem of settlements on masonry structures has been studied by means of nonlinear analyses within the Finite Element Method (FEM) [2–4], the Discrete Element Method (DEM) [5], or, rigid blocks analyses under the hypothesis of unilateral contact and simple linear programming techniques [6–9].

The analysis of the response to settlements response using systems of rigid blocks entails procedures similar to the ones typical of limit analysis. Under the action of settlements, the above structure reaches a new configuration of equilibrium exhibiting small deformation [10]. However, since masonry cannot withstand deformations of any kind, cracks appear and propagate within the structure, transforming the initially continuous construction into an assembly of relatively big and approximately rigid blocks. The new configuration of equilibrium can be described through a discontinuous displacement field. As a result, the structure behaves like a mechanism and can be studied by using limit analysis techniques. The analogy between limit analysis and analysis of settlements for rigid blocks structures has been analyzed in detail in a recent publication [11]. Here, it is shown that the discontinuous displacement field can be obtained by solving a unilateral contact problem. The discrete formulation can be written in terms of a linear programming problem, in which the external work is maximized. The formulation by rigid blocks and linear programming allows a quick assessment of crack patterns with a sensibly reduced computational effort with respect to standard finite element nonlinear techniques and iterative procedures.

In this contribution, we present the study of masonry vaults undergoing differential settlements through a new adaptive GA-NURBS based approach. A masonry vault is modeled through NURBS rigid shell elements, which allow accurate reproduction of the actual geometry even with a small number of elements is used. Given an initial mesh of NURBS rigid element, the displacement field is found by maximizing the work of external loads. A Genetic Algorithm mesh adaptation search scheme is devised in order to find the actual displacement field induced by a given settlement. The procedure is illustrated by solving the historical vault previously analyzed in [13–14].

2 DISCRETE VARIATIONAL FORMULATION

The behavior of a masonry structures undergoing foundation settlements can be studied by idealizing it as an assembly of rigid blocks and applying unilateral contact conditions at the interfaces [11]. The solution \mathbf{u} of the variational contact problem, at the continuum level, is given by

$$\mathbf{u} = \arg \inf_{\mathbf{v} \in M^m} \Pi_r(\mathbf{v}), \quad (1)$$

where

$$\Pi_r(\mathbf{v}) = - \sum_{i=1}^{N_b} \ell_i(\mathbf{v}) \quad (2)$$

is the potential energy of external loads acting on each block and, M^{*m} is the convex set of rigid motions and $\ell(\cdot)$ is the linear form:

$$\ell(\mathbf{v}) = \int_{\Gamma_q} \mathbf{q}\mathbf{v} d\gamma. \quad (3)$$

In other words, a displacement field solution of the boundary value problem at hand, can be found by minimizing the potential energy of the external loads in the set M^{*m} of all the mechanisms satisfying the unilateral constraints in the normal direction and the no-sliding condition.

At the discrete level, a generic piecewise two-dimensional rigid displacement $\mathbf{v} \in M^{*m}$ is represented by a vector \mathbf{d} composed by $3N_b$ elements being the three barycentric components of rigid body motion (two translations and a rotation) for each block. Obviously, it is possible to define the potential energy associated to the rigid body motion \mathbf{v} represented by the vector \mathbf{d} as a linear function of \mathbf{d} :

$$\Pi_r(\mathbf{v}) = -\hat{\mathbf{q}}^T \mathbf{d}, \quad (4)$$

where $\hat{\mathbf{q}} \in \mathbb{R}^{3N_b}$ is a vector containing, for each body \mathcal{B}_i , the resultants – in terms of two translational forces and one moment – of the external load distribution $\mathbf{q}(\mathbf{x})$ on Γ_q . Therefore, the discrete linear programming problem associated to (1) can be written as follows:

$$\text{find } \mathbf{d} \text{ s.t. } \{\hat{\mathbf{q}}^T \mathbf{d}\} \text{ is maximum,} \quad (5)$$

under the following linear constraints:

$$\mathbf{A}\mathbf{d} \leq \mathbf{0} \quad (6)$$

$$\mathbf{B}\mathbf{d} = \mathbf{0} \quad (7)$$

$$\mathbf{C}\mathbf{d} = \hat{\mathbf{u}}_0, \quad (8)$$

where $\mathbf{A}, \mathbf{B} \in \mathbb{R}^{N_{col,p} \times 3N_b}$, $\mathbf{C} \in \mathbb{R}^{N_{col,r} \times 3N_b}$ and $\hat{\mathbf{u}}_0$ is a vector whose elements are the values of the function $\mathbf{u}_0(\mathbf{x})$, representing the non-homogeneous essential boundary conditions, evaluated at collocation points on Γ . Constraints (6) and (7) represent the requirement that $v_n \leq 0$ on Γ_c and $v_t = 0$ on Γ_c respectively, Γ_c being the union of all the possible contact curves among the blocks. On the other hand, constraint (8) represents the non-homogeneous essential boundary conditions (i.e. foundation settlements) on Γ_u . It should be noticed that the objective function in (5) is the work of the assigned external loads.

3 ADAPTIVE GA-NURBS SCHEME

The structural response is described by roto-translations of the rigid blocks and jumps of displacement on the contact points. The overall displacement field can be obtained by solving problem (5), in which the external work is maximized under the constraints imposed by unilateral contact conditions, by means of an efficient linear programming.

In this work, a discretization through few NURBS shell rigid elements is adopted. The NURBS geometry description of the mesh allows to preserve the actual geometry of the structure even when using a small number of elements, avoiding the need for fine discretizations which would be otherwise required for masonry vaults. Thus, in place of modeling every single brick composing the structure, NURBS elements reproduce the curved macro-blocks

which determine the mechanism induced by the applied settlement, provided that the crack pattern is suitably adjusted by means of a suitable meta-heuristic optimization algorithm. On each interface, the unilateral contact conditions are applied. In case a rigid plastic behavior is to be accounted for, an associative flow rule can be adopted. As already discussed, the overall disposition of interfaces, i.e. the mesh adopted, represents only a possible crack pattern but, since the real crack pattern is not a-priori known, mesh adaptation is required. For this reason, in order to find the absolute maximum of the external work, we allow a Genetic Algorithm (GA) to adjust the initial mesh until a good approximation of the actual crack pattern is obtained. The procedure is very similar to the one used in the GA-NURBS limit analysis of masonry vaults proposed in [12], which was proven to be effective in the study of several typologies of masonry constructions [15–22].

4 NUMERICAL EXAMPLE

As an example, we study a reproduction of the historical barrel vault which constituting the roofing of the central nave of the Bothwell Parish Church (Glasgow, United Kingdom, see Fig. 1(a)). An in-depth geometrical survey revealed that the vault is slightly skewed, with cracks that has opened over the years due to settlement across the less braced South edge. In [14], this response of this vault under foundation settlements has been investigated by means of finite element analyses and several experimental test (also carried out in [13]) on a 1/12 scaled model (Fig. 1(b)). The actual vault geometry features an interior span of 6.1 m, a rise of 3.8 m, and a length of 16.8 m, and an average thickness of 36 cm. We assume a 520 kg/m³ density for masonry material. Finally, in order to better reproduce sliding deformations observed in the experimental test performed in [14], a 3D Mohr-Coulomb failure surface with tension cut-off and compression linear cap is assumed, with ultimate tensile and compression stresses equal to 0.03 MPa and 2.6 MPa respectively. Shear failures are controlled by a cohesion of 0.02 MPa and a tangent of the friction angle of 0.5. To replicate the experimental test, in the first numerical simulation, a vertical linear settlement has been applied (see Fig. 2), with a 1 cm maximum drop along the external edge.



Figure 1: (a) Bothwell Parish Church (Glasgow, UK) barrel vault [14] and (b) crack pattern observed in the experimental test [13].

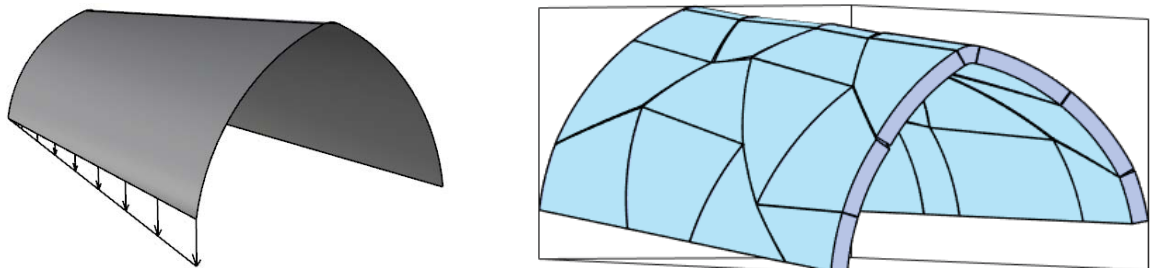


Figure 2: Analysis of the displacement field under the action of non-uniform vertical settlement.

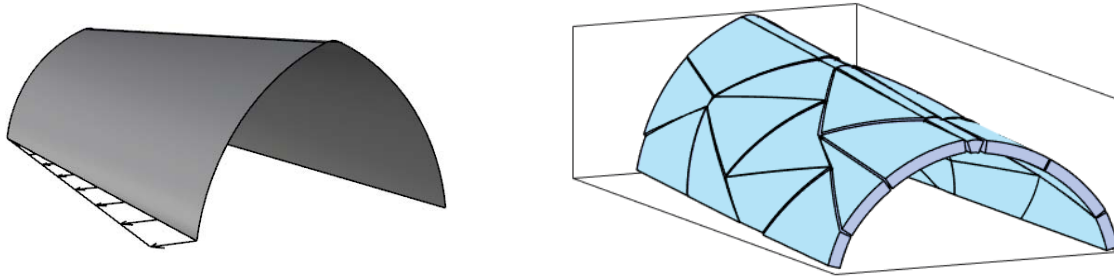


Figure 3: Analysis of the displacement field under the action of non-uniform horizontal settlement.

Each of the two NURBS surfaces describing half of the vault is discretized with 3×4 shell elements. Fig. 2 depicts the obtained displacement field. It can be noted that the crack pattern close to the external arch reproduces the typical hinges of the masonry arch undergoing a vertical differential settlement [11]. The shape of the crack pattern long the longitudinal direction of the vault is mainly due to settlements inducing torsional effects. The crack obtained with the proposed procedure is in good agreement with the results previously obtained both experimentally and numerically [13].

This barrel vault has been also studied under a horizontal linear settlement. Differential horizontal settlements are common in vaults used as roof elements in historical constructions, in which collapse during seismic events often occurs because of the differential movement of their supports, rather than because of the horizontal seismic actions applied to the vault. Fig. 3, represents the applied settlements and the obtained results. As in the previous case, it can be noted that the extremal part of the vault behaves like an arch. Also in this configuration, the proposed adaptive GA-NURBS scheme allows to accurately predict the 3D behavior of the vault.

5 CONCLUSIONS

In this paper, a NURBS-based adaptive approach to the three-dimensional analysis of masonry vaults undergoing foundation settlements is presented. A given masonry vault of arbitrary geometry is described through its NURBS parametric representation in the three-dimensional Euclidean space. The vault surface is then discretized into an initial set of rigid elements. Such discretization is obtained by suitably subdividing the NURBS parameters space. Jumps of displacement are allowed at the interfaces only. Given a known displacement on the external boundary, which comprises possible settlements, the resulting displacement field is computed by minimizing the total potential energy of the system by means of a linear programming optimization algorithm. Moreover, a GA-based mesh adaptation scheme is used to determine the crack pattern yielding the mechanism actually induced by the settlement. The example

ACKNOWLEDGEMENTS

Andrea Chiozzi gratefully acknowledges the grant “Bando per il finanziamento della ricerca scientifica - Fondo per l’Incentivazione alla Ricerca (FIR) – Anno 2020”, issued by the University of Ferrara.

REFERENCES

- [1] J. Heyman, The stone skeleton, *International Journal of Solids and Structures*, **2**, 249-

- 256, 1966.
- [2] G. Giardina, A.V. van de Graaf, M.A.N. Hendriks, J.G. Rots, A. Marini, Numerical analysis of a masonry façade subject to tunnelling-induced settlements, *Engineering Structures*, **54**, 234-247, 2013.
- [3] P. Zampieri, M.A. Zanini, F. Faleschini, L. Hofer, C. Pellegrino, Failure analysis of masonry arch bridges subject to local pier scour, *Engineering Failure Analysis*, **79**, 371-384, 2017.
- [4] E. Reccia, G. Milani, A. Cecchi, A. Tralli, Full 3D homogenization approach to investigate the behavior of masonry arch bridges: The Venice trans-lagoon railway bridge, *Construction and Building Materials*, **66**, 567-586, 2014.
- [5] T.T. Bui, A. Limam, V. Sarhosis, M. Hjiar, Discrete element modelling of the in-plane and out-of-plane behaviour of dry-joint masonry wall constructions, *Engineering Structures*, **136**, 277-294, 2017.
- [6] G. Milani, M. Rossi, C. Calderini, S. Lagomarsino, Tilting plane tests on a small-scale masonry cross vault: Experimental results and numerical simulations through a heterogeneous approach, *Engineering Structures*, **123**, 300-312, 2016.
- [7] F. Portioli, L. Cascini, Assessment of masonry structures subjected to foundation settlements using rigid block limit analysis, *Engineering Structures*, **113**, 347-361, 2016.
- [8] F. Portioli, L. Cascini, Large displacement analysis of dry-jointed masonry structures subjected to settlements using rigid block modelling, *Engineering Structures*, **148**, 485-496, 2017.
- [9] A. Iannuzzo, M. Angelillo, E. De Chiara, F. De Guglielmo, F. De Serio, F. Ribera, A. Gesualdo, Modelling the cracks produced by settlements in masonry structures, *Mechanica*, **53**, 1857-1873, 2018.
- [10] M. Como, *Statics of historic masonry constructions*. Berlin: Heidelberg, 2013.
- [11] A. Tralli, A. Chiozzi, N. Grillanda, G. Milani, Masonry structures in the presence of foundation settlements and unilateral contact problems, *International Journal of Solids and Structures*, **191-192**, 187-201, 2020.
- [12] A. Chiozzi, G. Milani, A. Tralli, A Genetic Algorithm NURBS-based new approach for fast kinematic limit analysis of masonry vaults, *Computers & Structures*, **182**, 187-204, 2017.
- [13] J. Hudson, D. Theodossopoulos, Gothic barrel vaults under differential settlement: The effects of boundary conditions and FRP on structural behaviour, *Key Engineering Materials*, **747**, 496-503, 2017.
- [14] A.M. D'Altri, S. De Miranda, G. Castellazzi, V. Sarhosis, J. Hudson, D. Theodossopoulos, Historic Barrel Vaults Undergoing Differential Settlements, *International Journal of Architectural Heritage*, 1-14, 2019.
- [15] A. Chiozzi, G. Milani, A. Tralli, Fast kinematic limit analysis of FRP reinforced masonry vaults through a new genetic algorithm nurbs-based approach, *Proceedings of the 7th European Congress of Computational Methods in Applied Science and Engineering (ECCOMAS 2016)*, **3**, 5326-39, 2016.
- [16] A. Chiozzi, G. Milani, N. Grillanda, A. Tralli, Fast and reliable limit analysis approach for the structural assessment of FRP-reinforced masonry arches, *Key Engineering Materials*, **747**, 196-203, 2017.
- [17] N. Grillanda, A. Chiozzi, F. Bondi, A. Tralli, F. Manconi, F. Stochino, A. Cazzani, Numerical insights on the structural assessment of historical masonry stellar vaults: the case of Santa Maria del Monte in Cagliari, *Continuum Mechanics and Thermodynamics*, **33**, 1-24, 2021.
- [18] N. Grillanda, A. Chiozzi, G. Milani, A. Tralli, Collapse behavior of masonry domes

- under seismic loads: an adaptive NURBS kinematic limit analysis approach, *Engineering Structures*, **200**, 109517, 2019.
- [19] N. Grillanda, M. Valente, G. Milani, A. Chiozzi, A. Tralli, Advanced numerical strategies for seismic assessment of historical masonry aggregates, *Engineering Structures*, **212**, 110441, 2020.
- [20] N. Grillanda, A. Chiozzi, G. Milani, A. Tralli, Efficient meta-heuristic mesh adaptation strategies for NURBS upper-bound limit analysis of curved three-dimensional masonry structures, *Computers & Structures*, **236**, 106271, 2020.
- [21] S. Tiberti, N. Grillanda, V. Mallardo, G. Milani, A Genetic Algorithm adaptive homogeneous approach for evaluating settlement-induced cracks in masonry walls, *Engineering Structures*, **221**, 111073, 2020.
- [22] N. Grillanda, A. Chiozzi, G. Milani, A. Tralli, Tilting plane tests for the ultimate shear capacity evaluation of perforated dry joint masonry panels. Part II: Numerical analyses, *Engineering Structures*, **228**, 111460, 2021.

NUMERICAL MODELLING OF BONDED BRICKWORK UNDER CYCLIC COMPRESSION LOADING

Mohammad Asad¹, Tatheer Zahra¹, and Julian Thamboo²

¹ School of Civil and Environmental Engineering, Queensland University of Technology,
4000, Brisbane, Australia

m.asad@qut.edu.au, t.zahra@qut.edu.au

² Department of Civil Engineering, South Eastern University of Sri Lanka,
32360 Oluvil, Sri Lanka

jathamboo@seu.ac.lk

Abstract

Bonded brickwork as loadbearing walls is widely found in the heritage structures worldwide. The bonded brickwork consists of two or more bricks in the thickness direction which causes them to behave differently to single leaf walls which are the basis of masonry design guidelines. The evaluation of bonded masonry structures under dynamic seismic actions therefore requires appropriate numerical modelling techniques accounting for the cyclic loading. Subsequently, a simplified 3D mesoscale numerical model has been developed in this paper to analysis different thicknesses of bonded brickwork under cyclic compression. Each masonry brick was defined using 3D solid elements with 8 nodes and 24 degree of freedom (DOF) representing an enlarged brick consists of a full-scale brick enveloped by half thickness of the mortar bedding layer all around. These masonry bricks were arranged in multiple layers using zero thickness cohesive interface elements to simulate the bond behaviour under shear, tension, and compression actions. A plasticity-based damage constitutive model to represent the damage in the masonry bricks under cyclic compression loading was employed. A threshold strain level was used to enact the element deletion technique for initiating the brittle crack opening in the masonry units. Whereas the joint interface failure between the masonry units was defined using a cohesive model represented by a simple bi-linear traction-separation constitutive law exhibiting an initial linear elastic behaviour at the interface followed by the initiation of the damage and evolution until the surface bonding degradation. The robustness of the developed model under cyclic compression loading has been proven by validating the test data presented for the clay brick selected to construct 9 masonry wallettes of single, double and triple brick thicknesses. The failure modes, cyclic stress-strain curves and stiffness degradation have been studied.

Keywords: *Brickwork; Clay brick; Cyclic Compression; Numerical Modelling; Element deletion; Damage model; Cohesive Zone model*

1 INTRODUCTION

Bonded masonry is invariably used as loadbearing elements in structures and the compressive strength characteristics of this masonry are of prime importance in the design of new and assessment of existing masonry structures. Subsequently, plenty of research efforts have been put in place to comprehend the compressive strength characteristics of various masonry assemblies in the past [1-4]. However, most of the studies in the past were dedicated to determining the monotonic compressive strength properties of masonry, where only limited studies were dedicated to understand the cyclic compression characteristics of masonry, which are needed to assess the performance of masonry elements against seismic or dynamic actions. Moreover, the non-loadbearing masonry infill walls in reinforced concrete or steel frames are also considered to act as diagonal compression struts under in-plane actions [5-6], thus analysing such infill frames under dynamic actions need cyclic compression properties of masonry.

The limited experimental studies on the cyclic compression behaviour of bonded masonry revealed that the characteristics of masonry under cyclic compression are different to monotonic compression in terms of the attainment of strength and deformation characteristics [7-9], where relatively low compressive strength and considerably larger deformation were depicted under cyclic compression than the monotonic loading. As a result of lack of cyclic compression experimental data on various assemblies, the development of constitutive models for masonry under cyclic compression was generally derived from the studies on concrete under cyclic compression [10-12]. While there are some similarities on the general characteristics between the masonry and concrete under cyclic compression, the damage evolution under cyclic compression is greatly different to concrete due to the anisotropic nature and interfacial incompatibility between unit and mortar in masonry. Recently, Thamboo et al. [13] compared the predictability of cyclic compression behaviour of the existing masonry models with the available experimental data and highlighted that most of the models were not able to predict one or other cyclic compression characteristics such as envelop response, plastic strain, unloading and reloading paths accurately. Nonetheless, experimental studies are not always viable to develop constitutive models for masonry under cyclic compression, owing to the diversity of masonry assemblies exist and difficulty in carrying out the cyclic testing. Therefore, numerical assessment of masonry under cyclic compression is a prudent solution.

Although plenty of progresses have been made to develop numerical methods to assess the masonry at different scales (micro, meso and macro) under various loading conditions [14-16], no systematic methodologies were developed to evaluate the cyclic compression behaviour of masonry in the past. Obviously, micro modelling technique is the most appropriate approach to assess the various assemblies of masonry under a localised loading situation. As an alternative to complex micro-modelling, simplified micro modelling of bonded masonry can save computational effort and avoid complexity of modelling additional mortar joints in the thickness of bonded brickwork. In this technique, mortar thickness is omitted by expanding the bricks into an equivalent masonry material which are joined to make assemblies of various patterns through zero thickness interfaces. Simplified micro-modelling based numerical assessment under cyclic compression could predict the characteristics of masonry reasonably,

especially in terms of damage evolution and localised stress-strain responses as it has been used earlier for the monotonic loading conditions [17-19].

This paper provides the details of a simplified 3D micro-scale modelling technique to assess the characteristics of bonded masonry under cyclic compression. The rationality of the developed modelling technique and outcome under cyclic compression loading simulation have been validated against the results from the experimental campaign carried out previously to assess the cyclic characteristics of bonded brickworks by the third author. Subsequently, Section 2 explains the simplified micro-modelling based numerical procedures established to simulate the cyclic compression behaviour of masonry. The validation of the numerical method against the experimental data is described in Section 3. Finally, the key conclusions derived from the study are mentioned in Section 4.

2 NUMERICAL MODELLING TECHNIQUE

An explicit finite element modelling method was developed to simulate the bonded brickwork response under cyclic compression loading. A simplified 3D mesoscale homogenised material model was adopted to analyse different thicknesses of bonded brickwork under cyclic compression. The material and contact non-linearities were incorporated in this model, and the parameters were calibrated using the datasets of the single brick thick wallette test specimens. Figure 1 shows the developed FE model of the brickwork constructed of single, double and triple bricks in their thickness.

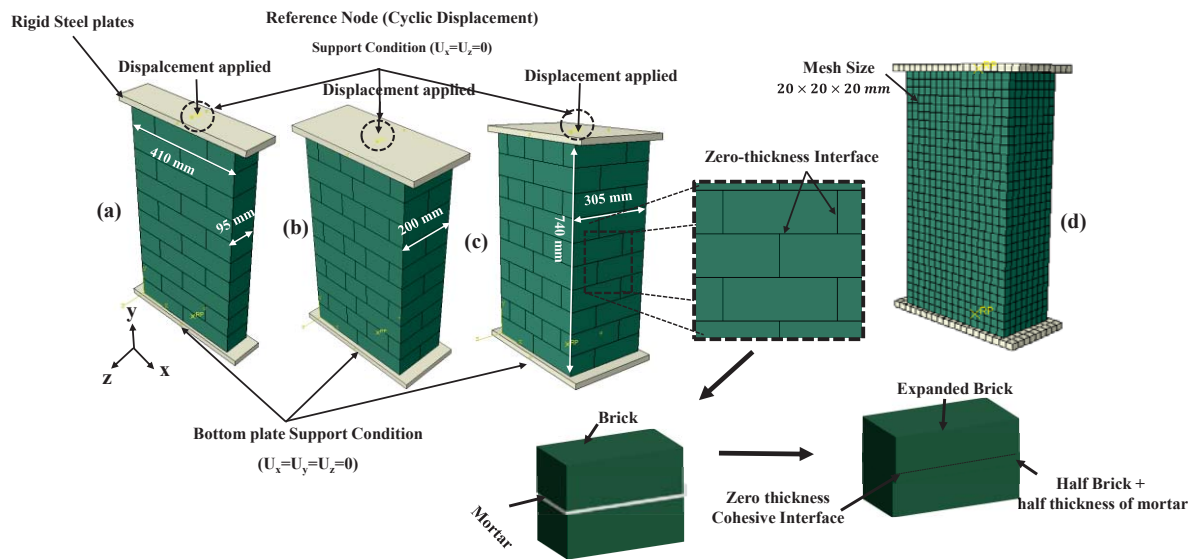


Figure 1: Wallettes model details (a) Single brick (b) Double brick (c) Triple brick with detail of expanded bricks and (d) Mesh size

2.1 Geometry Details

In the simplified 3D mesoscale homogenised numerical modelling method, the homogenised units were modelled using 3D solid elements (C3D8R) with 8 nodes and 24 degrees of freedom. The selected mesh size (shown in Figure 1(d)) was 20 mm \times 20mm \times 20mm based on the mesh sensitivity analysis performed in [17]. The brick size representing an enlarged brick consists of full-scale brick enveloped by half-thickness of the mortar bedding layer all around,

was modelled as shown in Figure 1. These masonry bricks were arranged in multiple layers using zero thickness cohesive interface elements to simulate the bond behaviour under shear, tension, and compression actions. The sizes of single, double and triple brick thick brickwork samples were 410 (L) \times 740 (H) \times 95 (T) mm, 410 (L) \times 740 (H) \times 200 (T) mm, and 410 (L) \times 740 (H) \times 305 (T) mm, respectively. Loading plates were also modelled to distribute the compressive load uniformly over the specimens and to restrain the specimens against displacement from the bottom.

2.2 Material properties and constitutive model of expanded bricks

A plasticity-based damage constitutive model to represent the damage in the masonry bricks under cyclic compression loading was employed. The concrete damage plasticity (CDP) model in-built in ABAQUS was used to simulate homogenised brick and mortar behaviour. This model can predict two main failure modes: tensile cracking and compression crushing. Beyond the failure limit, the formation of minor and major cracks were represented with a softening stress-strain response, as shown in Figure 2. The stress-strain and other material data were taken from the experimental results of Thamboo & Dhanasekar [20], which were used in the calibration and validation of model results. A threshold strain level was used to enact the element deletion technique for initiating the brittle crack opening in the masonry units. The elastic modulus of the expanded clay bricks was input as 200 MPa. The Poisson's ratio was kept as 0.18 as was observed from the experiments [20]. In addition, the CDP model requires five main parameters: dilation angle (ψ) to account for the volume change caused by the inelastic behaviour of bricks, flow potential eccentricity (e) that defines the rate at which the hyperbolic flow potential approaches its asymptote, the ratio of the biaxial compressive strength of the material to its uniaxial compressive strength ratio (f_{b0}/f_{c0}), shape factor (K_c) which is the ratio of the tensile to the compressive meridian for describing the shape of the yield surface and viscosity (μ) that represents the relaxation time of the visco-plastic system, and is used for the visco-plastic regularisation. More details of these parameters can be found in [21]. The assigned CDP parameters are given in Table 1.

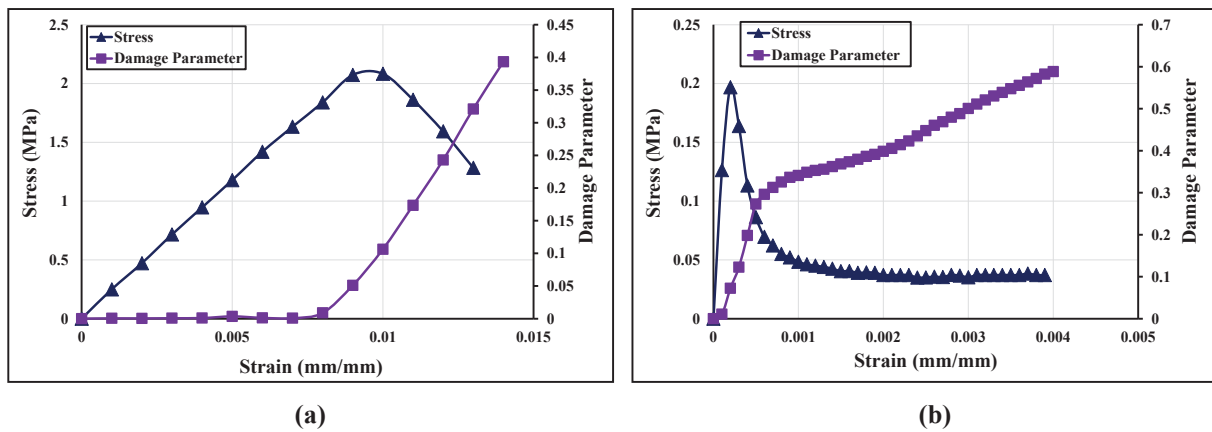


Figure 2: Stress-strain curve with damage properties of clay brick for CDP material model (a) Compression and (b) Tension

Parameter	Magnitude
Dilation angle (ψ)	30^0
Eccentricity (e)	0.1
Strength ratio (f_{b0}/f_{c0})	1.16
Shape factor (K_c)	0.66
Viscosity (μ)	0.001

Table 1: CDP model parameters for expanded bricks

2.3 Zero thickness interface: cohesive zone model

The zero-thickness interface between the homogenised expanded bricks was simulated using the cohesive zone model as shown in Figure 3(a). The interaction between the bricks was modelled using the simple bi-linear separation constitutive law, as shown in Figure 3 (b). The traction law is graphically represented using the traction force (τ) resulted in the opening displacement (δ). The interface allowed a damage initiation based on the threshold value which is followed by damage evolution until complete degradation of the surface bonding. The interface's elastic behaviour relates the normal and the shear (tractions) to the normal and shear displacements (separation) across the interface.

The normal stiffness matrix (K_n) is directly related to the thickness of the adhesive (cement) properties and the stiffness of the mortar (bedding layer). To evaluate the normal stiffness at the interface, a mathematical expression used for this relation is given in Equation (1).

$$K_n = \left(\frac{1}{\frac{t_{\text{mortar}}}{E_{\text{mortar}}} + \frac{t_{\text{ad}}}{E_{\text{ad}}}} \right) \quad (1)$$

Where t_{ad} represents the thickness of the adhesive found in the cement [22], t_{mortar} is the thickness of the mortar bedding layer and the E_{mortar} [20] and E_{ad} [22] are the young modulus of the mortar and the adhesive, respectively.

Similarly, the shear stiffness matrix (K_{ss} and K_{tt}) at the interface is mathematically expressed as shown in Equation (2).

$$K_0 = K_{ss} = K_{tt} = \left(\frac{1}{\frac{t_{\text{mortar}}}{G_{\text{mortar}}} + \frac{t_{\text{ad}}}{G_{\text{ad}}}} \right) \quad (2)$$

Where, G_{ad} and G_{mortar} are defined as the shear moduli of adhesion and mortar, respectively. The input values for the interface modelling are provided in Table 2.

The damage initiation in the interface was assumed to occur when a quadratic traction factors involving the combined normal stress and shear stress ratio reached to the value of 1 as shown in Equation (3). These criteria can be represented as

$$\left\{ \frac{\langle \sigma_n \rangle}{\sigma_n^0} \right\}^2 + \left\{ \frac{\langle \tau_s \rangle}{\tau_s^0} \right\}^2 + \left\{ \frac{\langle \tau_t \rangle}{\tau_t^0} \right\}^2 = 1 \quad (3)$$

Where σ_n is the cohesive tensile and the τ_s and τ_t are the shear stresses of the interfaces and n,s and t refers to the direction of the stress component as shown in Figure 3(c).

However, the interface damage evolution was expressed in terms of fracture energy release as shown in Equation (4).

$$G_n^c + (G_s^c - G_t^c) \left(\frac{G_s + G_t}{G_n + G_s + G_t} \right)^\eta = G^c \quad (4)$$

Where, G is the fracture energy; the superscript c represents the critical fracture energy and the dependency of the fracture energy η is a material parameter (Benzeggagah & Kenane [23]). The Benzeggagah- Kenane fracture criterion defines the critical fracture energies when the deformation along the first and the second shear directions are same. The properties of the zero-thickness interface to account for cohesion, traction separation law and friction are listed in Table 2.

Parameter	Magnitude
Normal stiffness, K_n (N/mm ³)	28
Shear stiffness, K_{ss} and K_{tt} (N/mm ³)	32
Friction coefficient	0.6
Maximum tensile stress, σ_n^0 (MPa)	0.68
Maximum shear stress, τ_s^0 and τ_t^0 (MPa)	0.82

Table 2: Mechanical properties of cohesive interfaces

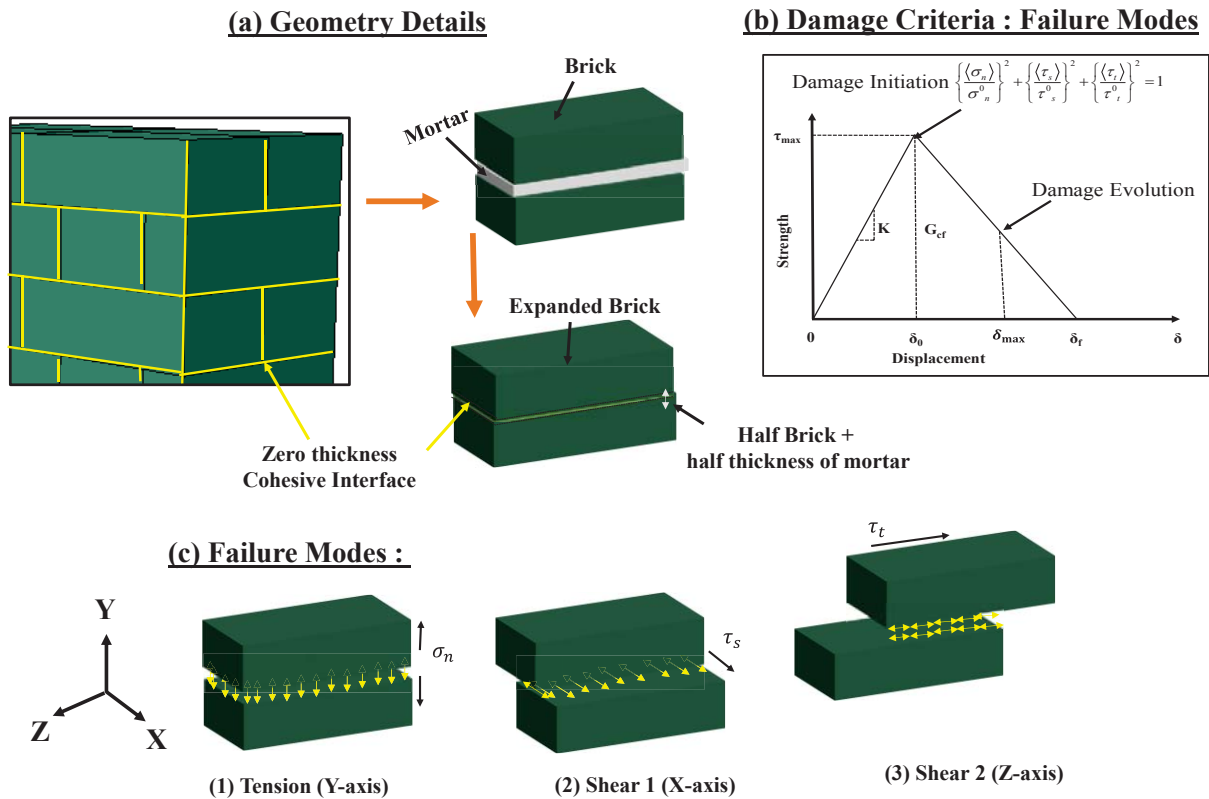


Figure 3: Zero thickness Cohesive Interface model details (a) geometry details of zero-thickness interface (b) damage criteria at the interface (c) failure modes at the interface

3 VALIDATION RESULTS

This section presents the validation of the FE model using the experimental results of single, double and triple brick thick wallettes under cyclic compression loading presented in [20]. The validation includes the failure modes of bonded brickwork wallettes, stress-strain curves comparison with the experimental results and the strain variation in the region of damage.

3.1 Details of experimental programme

The experimental investigation on the cyclic response of the masonry wallettes was studied by the authors in the previous study [20]. The tested bonded brickwork samples in this experimental programme were constructed using clay bricks. The material properties and geometrical descriptions of types of bonded brickworks are presented in Figures 1 and 2. The properties of clay bricks varied mainly due to the manufacturing process depending on the controlled and uncontrolled firing in the kiln. However, the bricks used in this study with low strength and modulus of rupture are very common in practice in many developing countries. These bricks also have resemblance to the brick types mainly found in the historical masonry structures. In total, nine bonded brickwork wallettes were constructed with three different thickness (single, double, and triple) to assess their cyclic compression behaviour. The wallettes were built and tested according to BS EN 1052-1 provisions and loaded under the cyclic displacement-controlled protocol. The thickness of the mortar was restricted to 10 mm with the help of an experienced mason. The constructed masonry wallettes were air cured for 28 days under an ambient temperature of 34°C.

The wallettes were tested in a 1000 kN capacity servo-controlled Universal Testing Machine (UTM). A 5 mm thick plywood was used between the top and bottom platens of the UTM to uniformly distribute the compression loading on the surfaces. In total eight displacement transducers were attached to record the axial and lateral deformation in each wallette. Four transducers were attached vertically on both faces (two on each face) of the wallette to record the axial deformation. Similarly, four remaining transducers (two on each face) were placed horizontally to record lateral deformation on each face of the wallette. A typical cyclic loading protocol applied to the specimens is shown in Figure 4. The cyclic displacement procedure was taken from the load-displacement responses of the similar wallettes under monotonic testing [20]. The elastic, hardening and peak limits were identified from the load displacement response presented in [20]. The elastic limit point was observed at the one third of the peak load and the hardening limit was considered as 0.8 times the peak load. The number of cycles within each limit are reported in the Table 3.

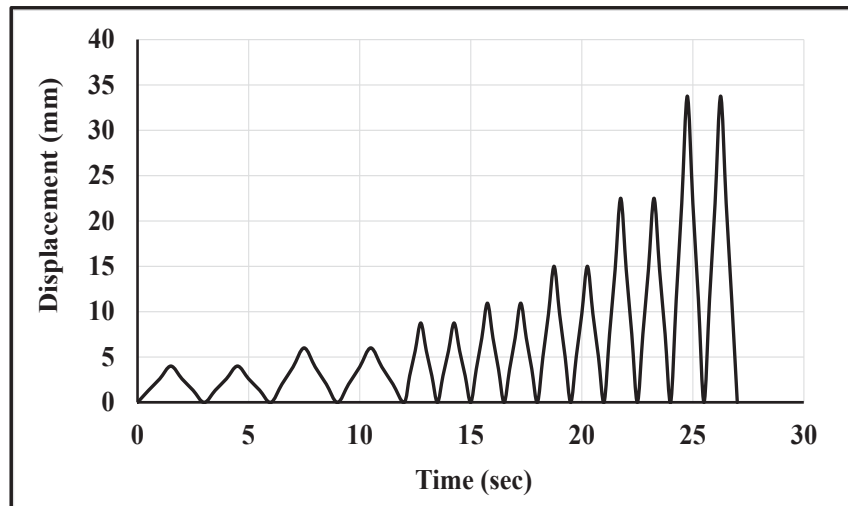


Figure 4: Loading input for the cyclic test of the wallettes

Monotonic Loading	Cyclic Loading	
Load-Displacement Response	Number of Steps	Number of Cycles
Elastic Limit (one third of peak load)	4 steps	2 cycles at each step
Hardening Limit (0.8 times the peak load)	4 Steps	2 cycles at each step
Peak Limit	3 Steps	2 cycles at each step

Table 3: Typical Cyclic loading protocol

3.2 Failure modes

The failure modes of single, double and triple brick thick bonded brickwork models are shown in Figure 5 in terms of principal strain. The failure pattern observed in the numerical model for all wallettes was in close agreement with the experimental failure modes as shown in Figure 5. For single brickwork wallette, vertical cracks developed in the bricks, mainly on the central area and near the edges of the faces at about 50 to 70% of the peak force. After the peak load, these cracks propagated diagonally and opened leading to the spalling from the edges of the wallettes. However, for the double and triple brick wallettes, a single splitting crack through the thickness of the wallettes and the parallel tensile cracks were observed along the width of the wallettes. During the post-peak stage, the cyclic loading resulted in the wider crack propagation within small span of time associated with the spalling of brick-and-mortar pieces.

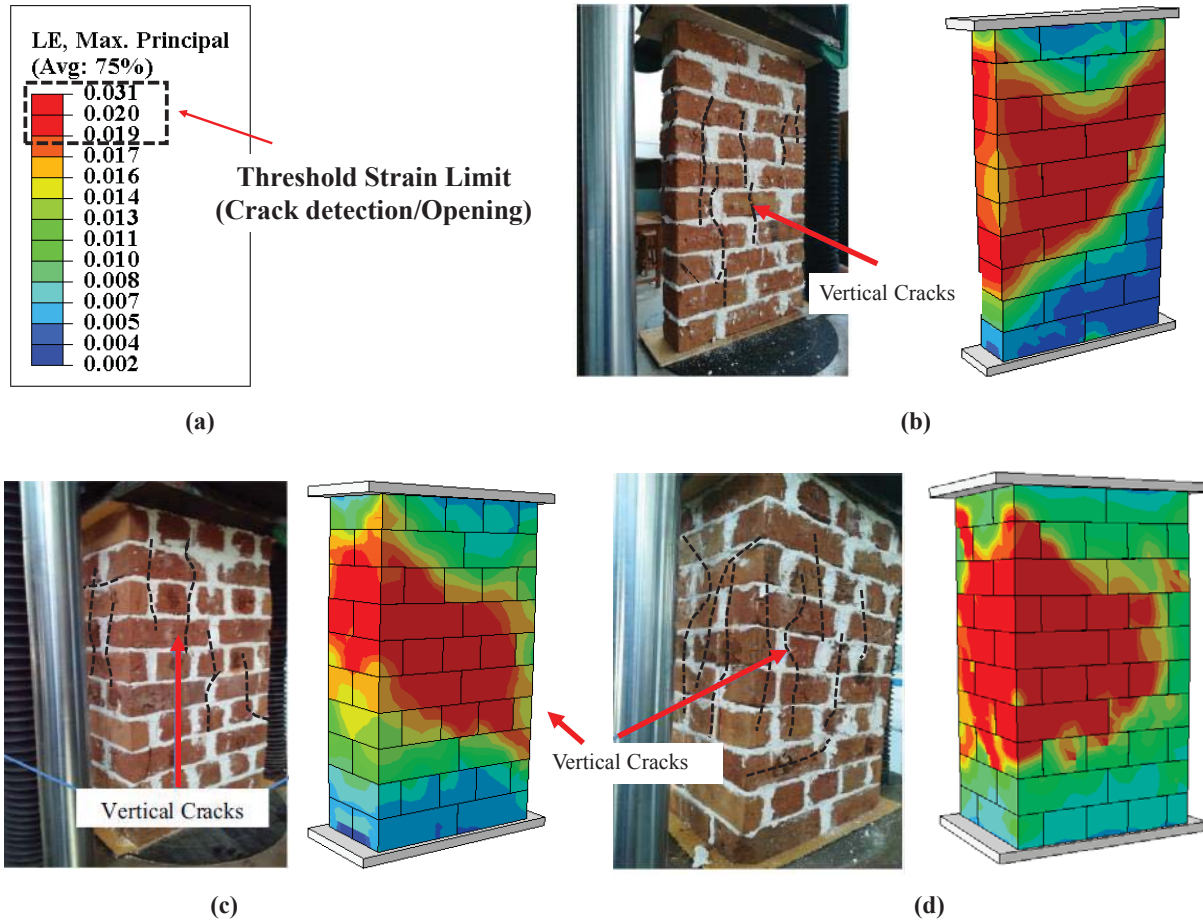


Figure 5: Numerical Failure modes of the brick wallettes: (a) Maximum Strain contour (b) Single brick (c) Double brick and (d) Triple brick

3.3 Stress-strain relationship

Figure 6 shows the compressive strength of single, double and triple brick thick bonded brickwork models under cyclic compression loading. The compressive strength predicted by the FE model of all three brickwork specimens matched well with the experimental data with only 5~10% approx. deviation. The experimental and numerical results show a 10% increase in the compressive strength of the double brick thick brickwork compared to the single- brick wallette. The marginal increase in the compressive strength can be attributed to the reduction in the slenderness ratio (height-to-thickness ratio). However, no significant enhancement in the compressive strength observed when compared double brick to triple brick wallettes. The reason for not increasing the compressive strength is the increase in the number of weak joints (more perpendicular joint) with the increase in the thickness of the wallettes.

Additionally, it was also observed that the compressive strength for the cyclic loading was lower than for the monotonic loading [20]. The compressive strength reduction observed in the cyclically loaded wallettes was mainly because of the accumulating lateral tractions and inelastic strains in the bonded brickwork. Hence, the accumulation of the strain over time history is significant for the compressive strength of the bonded brickworks as well as for defining the mitigating strategies under cyclic loading.

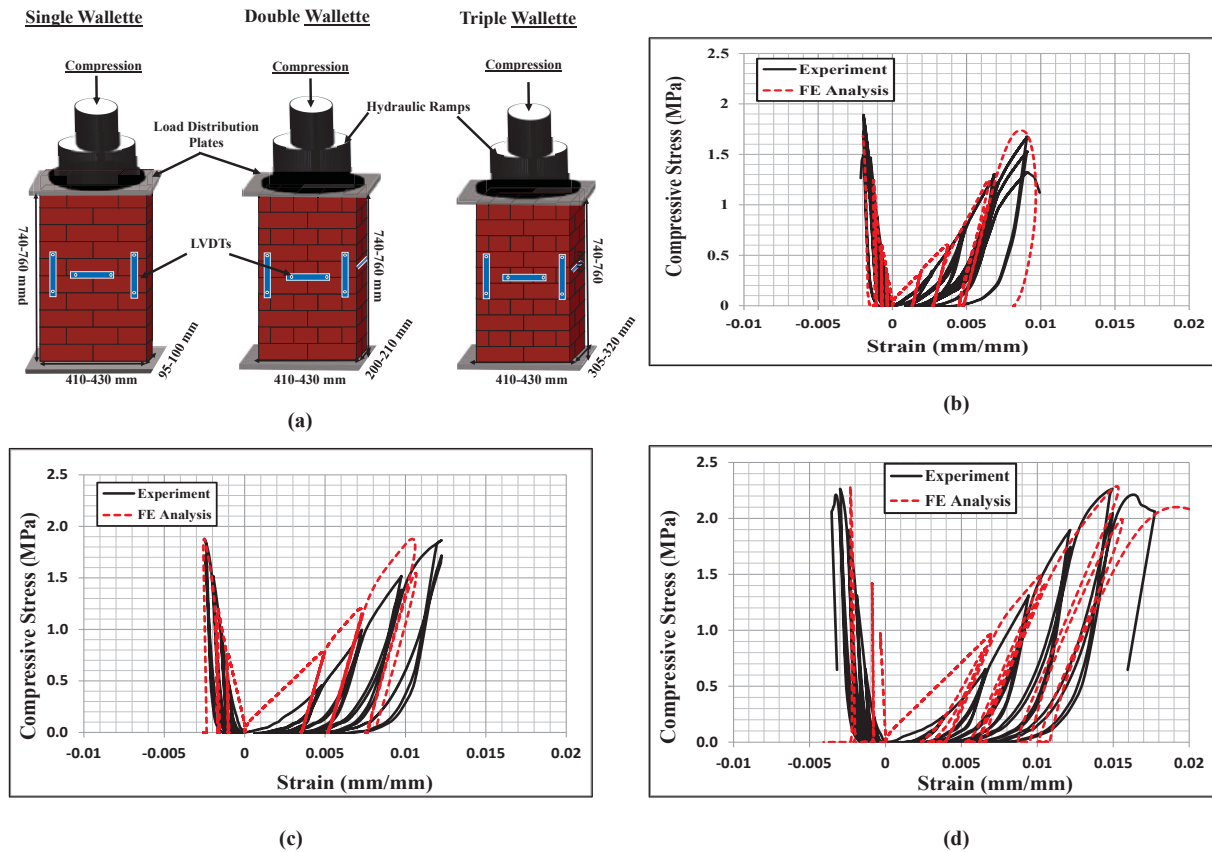


Figure 6: Stress-strain variation of the bonded brick wallettes (a) Experimental setup (b) Single brick (c) Double brick and (d) Triple brick

4 CONCLUSION

A simplified 3D finite element model incorporating expanded bricks with zero thickness cohesive interfaces, representing brick – mortar joints, has been developed for predicting the cyclic compression behaviour of different thicknesses of bonded brick masonry wallettes. The experimental results of bonded brickwork constructed with single, double and triple brick thickness were used for validating the developed model. The FE prediction of the failure modes and cyclic stress-strain curves under the cyclic loading matched well with the experimental results. The change in the thickness of the brickwork samples did not significantly alter the failure pattern of the bonded brickwork confirming the experimental findings that the effect of increase in the thickness of the bonded brickwork (or decrease in the slenderness) was insignificant on the compressive strength of the bonded brickwork.

5 REFERENCES

- [1] Sassoni E, Mazzotti C, Pagliai G. Comparison between experimental methods for evaluating the compressive strength of existing masonry buildings. *Construction and Building Materials*. 2014;68:206-19.
- [2] Drougkas A, Roca P, Molins C. Numerical prediction of the behavior, strength and elasticity of masonry in compression. *Engineering Structures*. 2015;90:15-28.
- [3] Zahra T, Dhanasekar M. Prediction of masonry compressive behaviour using a damage mechanics inspired modelling method. *Construction and Building Materials*. 2016;109:128-38.

- [4] Ferretti D. Dimensional analysis and calibration of a power model for compressive strength of solid-clay-brick masonry. *Engineering Structures*. 2020;205:110064.
- [5] Celarec D, Ricci P, Dolšek M. The sensitivity of seismic response parameters to the uncertain modelling variables of masonry-infilled reinforced concrete frames. *Engineering Structures*. 2012;35:165-77.
- [6] Cavaleri L, Di Trapani F. Cyclic response of masonry infilled RC frames: Experimental results and simplified modeling. *Soil Dynamics and Earthquake Engineering*. 2014;65:224-42.
- [7] AlShebani MM, Sinha S. Stress-strain characteristics of brick masonry under uniaxial cyclic loading. *Journal of Structural Engineering*. 1999;125:600-4.
- [8] Oliveira DV, Lourenço PB, Roca P. Cyclic behaviour of stone and brick masonry under uniaxial compressive loading. *Materials and structures*. 2006;39:247-57.
- [9] Facconi L, Minelli F, Vecchio FJ. Predicting uniaxial cyclic compressive behavior of brick masonry: New analytical model. *Journal of Structural Engineering*. 2018;144:04017213.
- [10] Crisafulli FJ. Seismic behaviour of reinforced concrete structures with masonry infills. 1997.
- [11] La Mendola L, Papia M. General stress-strain model for concrete or masonry response under uniaxial cyclic compression. *Structural engineering and mechanics: An international journal*. 2002;14:435-54.
- [12] Sima JF, Roca P, Molins C. Nonlinear response of masonry wall structures subjected to cyclic and dynamic loading. *Engineering Structures*. 2011;33:1955-65.
- [13] Thamboo J, Bandara J, Perera S, Navaratnam S, Poologanathan K, Corradi M. Experimental and Analytical Study of Masonry Subjected to Uniaxial Cyclic Compression. *Materials*. 2020;13:4505.
- [14] Zucchini A, Lourenço PB. A micro-mechanical model for the homogenisation of masonry. *International Journal of solids and structures*. 2002;39:3233-55.
- [15] Milani G, Lourenço PB, Tralli A. Homogenised limit analysis of masonry walls, Part II: Structural examples. *Computers & Structures*. 2006;84:181-95.
- [16] Zahra T, Jelvehpour A, Thamboo JA, Dhanasekar M. Interfacial transition zone modelling for characterisation of masonry under biaxial stresses. *Construction and Building Materials*. 2020;249:118735.
- [17] Zahra T, Asad M, Thamboo J. Effect of geometry on the compression characteristics of bonded brickwork. *Structures*. 2021.
- [18] Abasi A, Hassanli R, Vincent T, Manalo A. Influence of prism geometry on the compressive strength of concrete masonry. *Construction and Building Materials*. 2020;264:120182.
- [19] Bolhassani M, Hamid AA, Lau AC, Moon F. Simplified micro modeling of partially grouted masonry assemblages. *Construction and Building Materials*. 2015;83:159-73.
- [20] Thamboo J, Dhanasekar M. Assessment of the characteristics of lime mortar bonded brickwork wallettes under monotonic and cyclic compression. *Construction and Building Materials*. 2020;261:120003.
- [21] Jankowiak T, Lodygowski T. Identification of parameters of concrete damage plasticity constitutive model. *Foundations of civil and environmental engineering*. 2005;6:53-69.
- [22] Asad M, Dhanasekar M, Zahra T, Thambiratnam D. Characterisation of polymer cement mortar composites containing carbon fibre or auxetic fabric overlays and inserts under flexure. *Construction and Building Materials*. 2019;224:863-79.
- [23] Benzeggagh ML, Kenane M. Measurement of mixed-mode delamination fracture toughness of unidirectional glass/epoxy composites with mixed-mode bending apparatus. *Composites Science and Technology*. 1996;56:439-49.

FULL 3D CAD PROCEDURE FOR THE LIMIT ANALYSIS OF LONGHU PAGODA IN CHINA

Peixuan Wang¹, Alessandro De Iasio², Jacopo Scacco¹, Gabriele Milani¹, and Shengcai Li³

¹ Politecnico di Milano, Department of Architecture Built Environment and Construction Engineering,
Piazza Leonardo da Vinci, 32, 20133, Milan, Italy
peixuan.wang@polimi.it, gabriele.milani@polimi.it, jacopo.scacco@polimi.it

² University of Nottingham, Faculty of Engineering, Centre for Structural Engineering and Informatics
alessandro.deiasio@nottingham.ac.uk

³ Yangzhou University, College of Civil Science and Engineering, Huayang Avenue, 198, Yangzhou,
Jiangsu, China
lisc@yzu.edu.cn

Abstract

This paper adopts a very convenient 3D CAD method to quickly assess the seismic vulnerability of existing masonry towers. The study selected five typical collapse mechanisms, vertical splitting, base rocking, overturning with diagonal cracks (Heyman 1992), a combination of splitting and diagonal overturning and base sliding. The Longhu pagoda in China is selected as the research case. Based on the principle of virtual works, assuming that the masonry material is a no-tension material, and the collapse acceleration under loads G1 and G2 is calculated from the four main directions. The research results show that vertical splitting of collapse mechanism is the easiest to appear, which is in full compliance with the results of the on-site survey after the Longhu pagoda earthquake, further demonstrating the reliability of this method. This method does not require complex mathematical foundations, can be easily mastered by non-professionals, and at the same time greatly reduces the amount of simulation calculation, which is helpful for the promotion of seismic research of masonry structures.

Keywords: Masonry pagoda; limit analysis; Collapse mechanism, Collapse acceleration.

1 INTRODUCTION

As one of the four ancient civilizations, Chinese ancient buildings are a precious heritage left over from history. The ancient masonry pagoda is a typical representative, which combines the crystallization of the world's wisdom and the essence of architectural art. With the development and changes of the times, most of the ancient pagodas left behind have become historical sites, which not only brighten the city's scenery, but also promote Chinese culture and enrich tourism resources. The ancient pagoda is mainly located in the north and south of China, with many styles and characteristics. After going through the changes of the times, the existing masonry pagodas have extremely high historical and cultural, aesthetic art and scientific research value. Therefore, trying to protect and repair the ancient masonry pagoda has become an important mission for contemporary people.

Masonry pagoda has the advantages of high compressive strength, low cost, convenient construction, fire resistance, and good heat and sound insulation performance. It is a brittle material with relatively high tensile and shear strength. These pagodas have undergone a century of historical vicissitudes and changes, and have withstood countless baptisms of nature, with more or less damage to a certain degree. However, according to investigations and studies, most of the damage or collapse of ancient masonry pagodas structures are mainly caused by earthquakes. Once an earthquake occurs, it will cause great harm to human society [1]. China is located in the middle of the Eurasian seismic belt and the Pacific Rim seismic belt. There are many and strong earthquakes. The area of seismic belts is also very wide and scattered. It is one of the countries that suffer the most from earthquake disasters in the world [2]. In view of this, it is of extraordinary significance to understand and master the structural form and construction technology of ancient masonry towers, study its dynamic characteristics under earthquake action, find out the weak links of the structure, and reduce the losses caused by earthquake disasters.

After subjected to earthquakes, the accumulation of damage will lead to collapse of pagoda that is major threat of structural safety. The main damage characteristics of pagodas which were made by earthquake are following (Figure 1): 1) the tilt and collapse of pagoda spire, 2) the tilt and bend of pagoda body, 3) the break in the middle part of the pagoda, 4) the split of pagoda body along the central axis, 5) overall collapse [3].

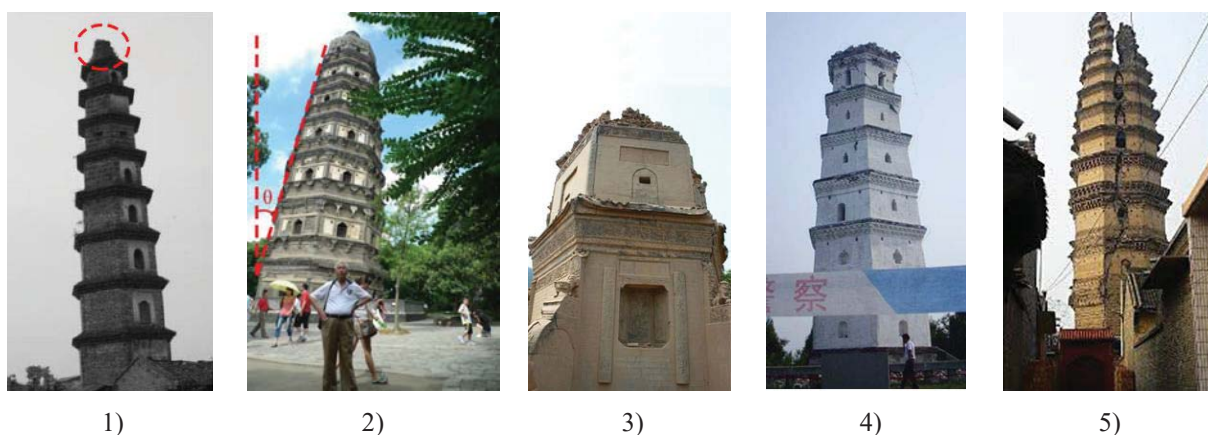


Figure 1. Damage characteristics of pagodas [3].

Studying masonry towers seismic vulnerability is not a trivial task. The current research work of Chinese scholars on the ancient pagoda is mainly carried out in the three aspects of classical theory, test data and numerical simulation [4]. Among the others, a "cantilever rod model" has been proposed, combining different tools to simplify the structural analysis model,

and apply these theories to the study of real cases such as Quanzhou pagoda, Fawang pagoda, Wenfeng pagoda, etc. [5,6]. For example, Y. Shen et al. analyzed the dynamic characteristics and the seismic capacity of the ancient masonry Xiaoyan pagoda based on the historical survey and reinforcement data. They discussed its seismic performance [7]. F. Zhu et al. conducted a seismic simulation shaking table test of the China Dinosaur pagoda model structure to observe the weak links and failure mechanism of the model structure under the action of earthquakes. They conducted a comprehensive technical evaluation of the seismic capacity and the technical feasibility of the construction of the pagoda [8]. Seoul National University in Korea has cleverly built a five-story full-scale model to study the seismic performance of the masonry pagoda, conducted destructive tests on it. Through the actual test results, the earthquake effect of the prototype tower body was reversed [9].

Western scholars deeply studied the seismic vulnerability of ancient masonry towers in the past years applying even more sophisticated methods. Non-linear static and dynamic analyses have been widely used to apply the earthquake loads [10-13]. University of Minho, Portugal conducted material mechanical performance tests and ingenious static tests on 24 masonry walls, evaluated the earthquake resistance level of the masonry structure, and summarized the relevant non-destructive testing methods, which provided information for the improvement of its seismic resistance level [14]. A. Carpinteri, S. Invernizzi, G. Lacidogna et al. conducted non-disturbing non-destructive testing of two ancient masonry pagodas in Italy in the 13th century, and they also did preliminary linear analysis, which basically coincided with the measured stress level. Non-linear cracking and damage analysis was also carried out, the evolution of principal stress damage and damage distribution are predicted. It was found that the damage is mainly distributed in the local high strain area. The results of the numerical analysis provide meaningful guidance to the monitored parts and evaluate the seismic performance analysis [15]. S.T. Sperbeck et al. conducted on-site investigation and testing of ancient masonry pagodas, comprehensively analyzed the influencing factors, established an H-dimensional solid model, applied loads of different levels and directions, and changed boundary conditions [16]. The dynamic characteristics are evaluated, and the influence of the parameters on the test results was discussed in detail.

To sum up, based on meticulous field exploration and experimental research, it is possible to conduct dynamic characteristic testing and numerical calculation analysis on ancient masonry pagodas. In this way, the structural damage of the ancient masonry pagoda can be identified, and the seismic performance of the structure can be effectively evaluated, which provides a reference for the seismic resistance of the project.

However, all the above-mentioned researchers are based on strong mathematics, dynamics, and computer engineering. In the society where the seismic research of masonry buildings has become the common demand and desire of many people, such a professional research method is not conducive to the widespread dissemination of knowledge of ancient architectural heritage protection.

In order to overcome this drawback, Researchers have recently proposed a kinematic limit analysis where vulnerability can be estimated assuming that a tower fails for the formation of five possible different pre-assigned failure mechanisms, namely vertical splitting, base rocking, overturning with diagonal cracks (Heyman 1992), a combination of splitting and diagonal overturning and base sliding (Figure 2). G. Milani et al. has also used this method in the vulnerability assessment of a large number of Italian masonry buildings, which greatly proved the practical significance of this method [17,18].

This paper aims to apply a fast full 3D CAD limit analysis method to the seismic performance evaluation of Longhu pagoda. The research is based on the principle of virtual works, assuming that the masonry material is a no-tension material, and quickly assesses the

horizontal acceleration when the building collapses. The research only needs a detailed 3d model, basic mechanics knowledge and calculation ability, simple and easy to learn, can well adapt to the diversified requirements of research and protection of masonry structure buildings. At the same time, the amount of calculation for simulation research can be greatly reduced.

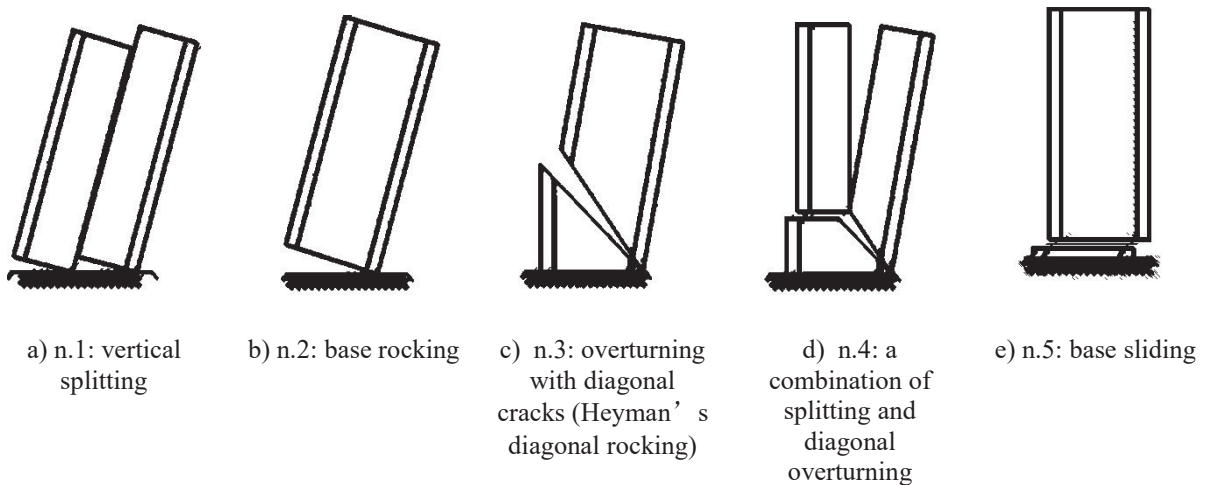


Figure 2. Collapse mechanism for masonry towers selected in [17] (images adapted from [17]).

2 INFORMATION ABOUT LONGHU PAGODA

Longhu pagoda (Figure 3) which was built in 1342 A.D. is located in Xiaoquan, Deyang, Sichuan province (East longitude $104^{\circ} 17'$, North latitude $31^{\circ} 15'$) and is the only preserved masonry pagoda made in Yuan dynasty [19,20]. It has a square plan with 13 layers of eaves outside it, and it is roughly 33 meters tall which contains 2 meters of stylobate and 31 meters of body.



Figure 3. Longhu pagoda.

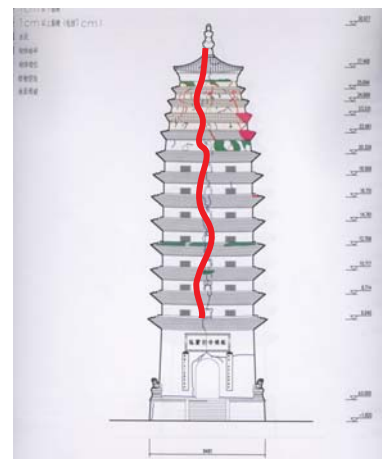


Figure 4. Damage of longhu pagoda

On May 12, 2008, a 8.0 magnitude Richter earthquake occurred in Wenchuan, Sichuan province, China, and the epicenter was in a small town whose name is Yingxiu. Wenchuan earthquake is destructive and has a strong impact, its maximum acceleration peak value which appeared after the start of the crustal movement (65 s - 82 s) is nearly 424 cm/s^2 . According to incomplete statistics, the earthquake killed around 69227 people, injured 376443 people, and

17,923 people were missing. Large numbers of architectures were collapsed and cultural relics were severely damaged, which resulted immeasurable losses.

The position of Longhu pagoda is not very far away from the epicenter (about 100 km), and it was influenced by the east-west seismic wave. The post-earthquake disaster investigation showed that the Longhu pagoda had a north-south through crack from the bottom to the top of the body. The cracks developed along the height, and the higher the position, the larger its width. The pagoda body was shaken into two parts, east and west, and its integrity was severely damaged (Figure 4).

3 LIMIT ANALYSIS

In the previous literature, the kinematic theorem of limit analysis has been widely used to calculate the collapsed ground acceleration of a masonry structure, especially some masonry pagodas [21,22]. Compared with complex finite element simulation calculations, this method can predict the collapse mechanism and collapse acceleration of masonry pagodas more easily and conveniently. The calculation results are quite reliable and can be quickly grasped by non-professionals. At the same time, when conducting a more detailed and in-depth study of masonry structures, the results of limit analysis can be compared with pushover and nonlinear dynamic analysis to improve the accuracy of simulation calculations.

According to Figure 2, this paper applied the same research method in the limit analysis of Longhu pagoda. The collapse accelerations related to the five collapse mechanisms of Figure 1 have been computed on the real 3D geometric model, applying the kinematic theorem of limit analysis, and considering the masonry as a no-tension material with infinite compressive strength. It has been decided to do not optimize the position of the vertical cutting planes (as done in [22]) but to roughly position them as passing through the middle points of the base edges. The inclined planes of mechanisms n.3 and n.4 (Figure 2) have been posed with an inclination of 30° , 45° or 60° to the horizontal plane. Each collapse mechanism is simulated from four main directions (X^+ , X^- , Z^+ , Z^-). It is worth noting that a Mohr-Coulomb failure criterion has been used in mechanism n.5 calculation; and the friction angle has been taken equal to 30° following what stated in [23]. The analysis in load control, and the considered loading conditions are G1 and G2. G1: principal distribution of forces proportional to the mass and linearly proportional to the height of the structure (the so-called “inverted triangle”). G2: secondary distribution of forces proportional to the mass and constant along the height of the structure.

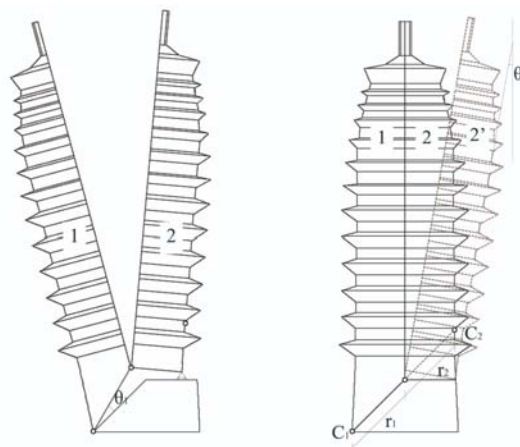


Figure 5. Collapse mechanism n.4 that considering the negative work done by the block n.2.

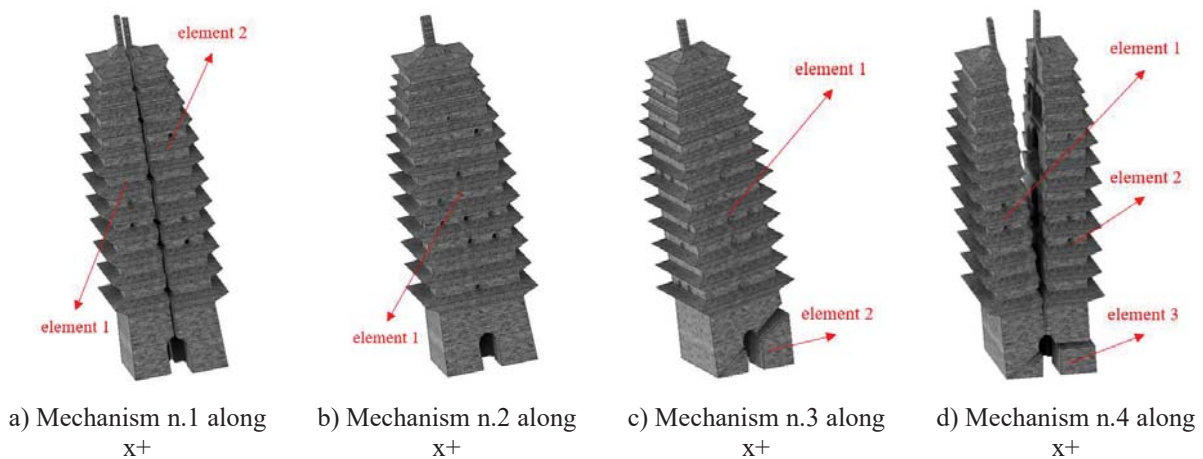


Figure 6. Some of the studied collapse mechanisms.

The mathematical basis of this method is very simple: only a first-order equation and basic geometry consideration are needed, and the collapse multiplier is easily computed for each mechanism. The kinematic theorem is applied through the equating of the work done by external forces (inertia forces) and internal forces (self-weight). However, some changes have been introduced in this paper with respect to reference [21,22] and they are here explained: the tensile strength has been considered as null (it was not in the reference research) and the mechanism n.4 (Figure 2) has been slightly modified by considering the negative work done by the block n.2 (Figure 5)

The collapse accelerations values for each mechanism are reported in Table 1, and Figure 6 represents some of the collapse mechanisms applied to the 3D model of the pagoda. The results have shown that the vertical splitting (mech. n.1) is always the most likely to occur.

Direction	Mechanism	Inclination Angle [°]	Collapse Acceleration G2 [g]	Collapse Acceleration G1 [g]
x	#1	/	0.155	0.124
x	#2	/	0.310	0.249
x-	#3	30	0.276	0.226
		45	0.252	0.215
		60	0.214	0.195
	#4	30	0.165	0.127
		45	0.180	0.138
		60	0.219	0.168
x+	#3	30	0.278	0.226
		45	0.255	0.216
		60	0.215	0.195
	#4	30	0.165	0.127
		45	0.181	0.138
		60	0.224	0.169
x	#5	/	0.577	0.577
z	#1	/	0.155	0.125
z	#2	/	0.310	0.249
z-	#3	30	0.280	0.228
		45	0.255	0.217
		60	0.215	0.196
	#4	30	0.167	0.128
		45	0.184	0.140
		60	0.225	0.171

z ⁺	#3	30	0.274	0.226
		45	0.251	0.215
		60	0.216	0.195
	#4	30	0.166	0.128
		45	0.180	0.139
		60	0.222	0.169
z	#5	/	0.577	0.577

Table 1. Limit analysis results. The minimum of each direction is formatted in bold.

4 CONCLUSIONS

This paper uses a 3D CAD method to perform a quick limit analysis of the Longhu pagoda. It mainly calculated the collapse accelerations along the four main directions for four different collapse mechanisms under G1 and G2 loads. Under G1 load, a_g/g along the X direction is 0.155, and a_g/g along the Z direction is 0.124. Under G2 load, a_g/g along the X direction is 0.155, and a_g/g along the Z direction is 0.125. The research results show that collapse mechanism n.1 which is vertical splitting is the most likely occurrence. This is also consistent with the on-site survey of Longhu pagoda earthquake damage after the Wenchuan earthquake.

ACKNOWLEDGEMENTS

The author Peixuan Wang who is studying in Politecnico di Milano was funded by China Scholarship Council. Thanks to the support from Politecnico di Milano, Department of Architecture Built Environment and Construction Engineering.

REFERENCES

- [1] A. Guo. Research on seismic design method and reliability of passive energy dissipation structur. *Doctoral Dissertation of Harbin Institute of Technology*, 1992.
- [2] Y. Hu. Earthquake Engineerin. *Beijing: Seismological Press*, 2006.
- [3] Q. Xie, J. Xue , H. Zhao. Investigation and Enlightenment of Ancient Buildings in Wenchuan Earthquake, *Journal of Architectural Structures*, **31(S2)**, 18-23, 2010.
- [4] J. Yuan, S. Li, Q. Lu. Research on Modeling Method of Dynamic Characteristics of Ancient Brick Tower. *Engineering Seismic*, **1**, 22-25, 1998.
- [5] L. Wen, S. Wang, H. Liu. Analysis of Seismic Reliability of Masonry Structure and Countermeasures. *Engineering Seismic*, **1**, 21-23, 1996.
- [6] L. Wen, S. Wang, H. Liu. Analysis of Anti-seismic Performance of Ancient Pagoda. *Engineering Seismic*, **4**, 19-30, 1995.
- [7] Y. Shen. Analysis of Anti-seismic Performance of Xiaoyan Pagoda and Research on Foundation Structur. *Xi'an University of Architecture and Technology*, 2010.
- [8] F. Zhu. Experimental study on seismic performance of China Dinosaur Pagoda. *Harbin Institute of Technology*, 2011.
- [9] J. Kim, H. Ryu. Seismic Test of A Full-Scale Model of A Five-Storey Stone Pagoda. *Earthquake Engineering and Structural Dynamics*, **32**, 731-750, 2003.

- [10] A. D’Ambrisi , V. Mariani , M. Mezzi. Seismic assessment of a historical masonry tower with nonlinear static and dynamic analyses tuned on ambient vibration tests. *Engineering Structure*, **36**, 210–219, 2012.
- [11] F. Peña, P. Lourenço, N. Mendes, D. Oliveira. Numerical models for the seismic assessment of an old masonry tower. *Engineering Structure*, **32**, 1466–1478, 2010.
- [12] S. Casolo, G. Milani, G. Uva, C. Alessandri. Comparative seismic vulnerability analysis on ten masonry towers in the coastal Po Valley in Italy. *Engineering Structure*, **49**, 465–490, 2013.
- [13] M. Valente, G. Milani. Non-linear dynamic and static analyses on eight historical masonry towers in the North-East of Italy. *Engineering Structure*, **114**, 241–270, 2016.
- [14] A. Carpinteri, S. Invernizzi, G. Lacidogna. In situ damage assessment and nonlinear modelling of a historical masonry tower. *Engineering Structure*, **27**, 387–395, 2005.
- [15] A. Carpinteri, S. Invernizzi, G. Lacidogna. Numerical evaluation of cracking and crushing in ancient masonry towers. *11th International Conference on Fracture*, ICF11, **5**:3223-3228, 2005.
- [16] S. Sperbeck, H. Budelmann. Prestressing of masonry as strengthening measure against earthquake loading-Experimental and numerical investigations and influences on simulation results. *Structural Analysis of Historic Construction Conference on Structural Analysis of Historic Construction*, SAHC08, **2**, 1043-1051.
- [17] G. Milani, S. Casolo, A. Naliato, A. Tralli, “Seismic assessment of a medieval masonry tower in northern Italy by limit, nonlinear static, and full dynamic analyses”. *International Journal of Architectural Heritage*, **6(5)**, 37–41, 2012.
- [18] G. Milani, R. Shehu, M. Valente, “Role of inclination in the seismic vulnerability of bell towers: FE models and simplified approaches”. *Bulletin of Earthquake Engineering*, **15**, 1707–1737, 2017.
- [19] Y. Liu. Study on the Damage Characteristics of the Longhu Pagoda in the Wenchuan Earthquake, *Yangzhou University*, 2012.
- [20] D. Ren, Experimental Study on the Impact of Earthquake Damage on the Dynamic Characteristics of Masonry Pagoda, *Yangzhou University*, 2016.
- [21] V. Sarhosis, G. Milani, A. Formisano, F. Fabbrocino. Evaluation of different approaches for the estimation of the seismic vulnerability of masonry towers, *16, Springer Netherlands*, 2018.
- [22] G. Milani. Fast Vulnerability Evaluation of Masonry Towers by Means of an Interactive and Adaptive 3D Kinematic Limit Analysis with Pre-assigned Failure Mechanisms. *International journal of Architectural Heritage*, **13**, 941–962, 2019.
- [23] M. Acito, C. Chesi, G. Milani, S. Torri. Collapse analysis of the Clock and Fortified towers of Finale Emilia, Italy, after the 2012 Emilia Romagna seismic sequence: Lesson learned and reconstruction hypotheses. *Construction Build Material*, **115**, 193–213, 2016.

ROLE OF REPEATED SEISMIC EVENTS ON THE COLLAPSE OF TWO CALIDARIA IN ROME DATING BACK TO THE IMPERIAL AGE

Francesca Faleri¹, Nicola Grillanda¹, Selman Tezcan², Renato Perucchio², Gabriele Milani¹

¹Department of Architecture, Built Environment and Construction Engineering (ABCE), Polytechnic University of Milan

Piazza Leonardo Da Vinci 32, 20133 Milan (Italy)

email: francescafaleri2@gmail.com, nicola.grillanda@polimi.it, gabriele.milani@polimi.it

²Department of Mechanical Engineering, University of Rochester, Rochester, NY, USA

email: stezcan@ur.rochester.edu, rlp@me.rochester.edu

Abstract

The seismic assessment of two vaulted monuments made of Roman concrete is here presented. Both their structural forms and constituent materials are here explored, whose combination enabled to build such largescale structures, and whose knowledge is essential for assessing and maintaining the safety of the portions of such structures that still exist.

Specifically, two different monuments dating back to the Imperial age are analyzed: the Calidarium of the Baths of Caracalla and the Calidarium of the Diocletian's Baths. The two structures were built at a distance of less than one century one each other and both were erected with the same construction technique. Nowadays both Calidarium structures no longer exist: the first one still presents two not collapsed monumental pillars, whilst the ruins of the second were demolished in the Sixteenth Century. Therefore, the present work aims at investigating the causes behind their collapse and how their collapse occurred by performing advanced numerical simulations.

Keywords: seismic assessment, vaulted monuments, roman concrete, monuments, Imperial age, structural analyses.

1 INTRODUCTION

Roman vaulted structures belonging to the imperial age represent one of the most important contributions to the artistic, architectural and engineering heritage of the entire world and their extraordinary durability is an aspect that should make the whole scientific community reflect and inspire. These large spans and curvilinear forms are still visible in buildings such as the Pantheon, the thermal baths of Caracalla and Diocletian, the Trajan's Markets and the Basilica of Maxentius, but these are just some of the many monuments still preserved in an impressive way. The secret of the majesty of these monuments and their longevity lies in the combination of the use of monumental vaulted forms and Roman concrete [1].

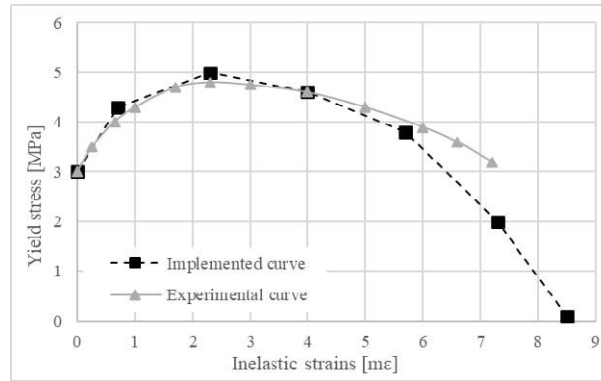
Caracalla's and Diocletian's Calidaria were two of the largest vaulted structures built with unreinforced pozzolanic Roman concrete. The high complexity of such constructions requires advanced numerical techniques to be analyzed. The characteristics of the Roman concrete, poor tensile resistance compared with high compressive strength, provide it a quasi no-tension behavior [2] allowing to follow the numerical strategies proposed for vaulted masonry structures [3]. Among the methods currently available from the technical literature, we can mention the modern limit analysis tools based on the static [4–6] and the kinematic theorem [7–12] but also the recent numerical techniques relying on the Finite Element (FE) method [13–16].

In this paper, a numerical investigation behind the causes of the collapse of these vaulted structures is conducted. The seismic vulnerability is studied through non-linear dynamic simulations carried out on FE models in the software Abaqus/CAE, where the behavior of the pozzolanic concrete (*opus caementicium*) is represented by means of the concrete damage plasticity model [17] available within Abaqus. Finally, non-linear time-history analyses are carried out on both structures by applying an accelerogram compatible with the response spectrum of Rome.

2 ABOUT ROMAN CONCRETE “OPUS CAEMENTICIUM”

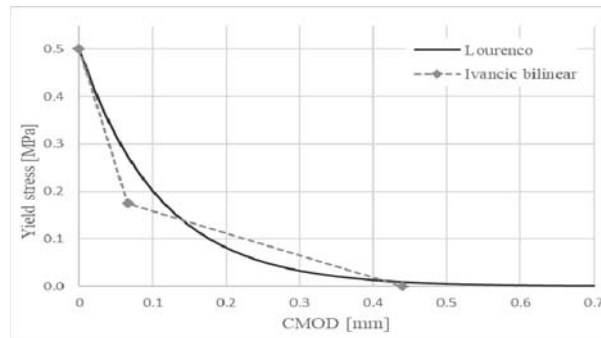
The material used in vaulted monuments such as Caracalla and Diocletian Baths consists in a composite masonry structure, called *opus latericium*, made of two external brick walls with a triangular shape and a concrete core composed by a pozzolanic lime mortar containing large pieces of stone, brick, marble and tufa (*opus caementicium*). The distribution of materials with decreasing density are observed: a distinct gradation of brick in the lower third (1800 kg/m^3), tufo lionato in the middle third (1600 kg/m^3), and Vesuvian scoria in the upper third (1400 kg/m^3).

The mechanical characterization of the Roman concrete was possible thanks to the analysis of the results obtained from a consistent test campaign carried out at the University of Rome “La Sapienza” (1996) and conducted by A. Samuelli Ferretti [18]. According to the experimental results, the elastic parameters adopted in the structural analyses are: elastic modulus $E = 3000 \text{ MPa}$, Poisson modulus $\nu = 0.5$, compression strength $f_c = 5 \text{ MPa}$ and tensile strength $f_t = 0.5 \text{ MPa}$. Post elastic non-linear behavior is taken into account through the Concrete Damaged Plasticity Model. Damage plasticity is a continuum macro-model for concrete, originally developed by Lubliner et al. [17] and modified by Lee and Fenves [19], which incorporates tensile cracking and compressive crushing as the primary failure mechanisms. Moreover, it assumes the fracture energy formulation for concrete developed in [20]. Regarding the post-elastic behavior on the Roman concrete, an innovative study was performed at the University of Rochester by Ivancic, Brune and Perucchio [21] which allowed to construct a nonlinear damage plasticity formulation for both compressive and tensile response of the *opus caementicium* suitable for 3D implementation in Abaqus (see Figure 1).



Yield stress [MPa]	3	4.3	5	4.6	3.8	2	0.1
Inelastic strains [10^{-3}]	0	0.7	2.3	4	5.7	7.3	8.5
Damage Variable	0	0.2	0.25	0.4	0.5	0.7	0.98

(a)



Yield stress [MPa]	0.500	0.398	0.317	0.253	0.202	0.160	0.128	0.081	0.052	0.033	0.021	0.008	0.005	0.003	0.002	0.001
CMOD [mm]	0	0.025	0.050	0.075	0.125	0.150	0.200	0.250	0.300	0.350	0.400	0.450	0.500	0.550	0.600	0.7
Damage Variable	0	0.1	0.2	0.3	0.4	0.45	0.5	0.55	0.6	0.65	0.7	0.75	0.8	0.85	0.9	0.98

(b)

Figure 1: Non-linear (a) compression and (b) tension damage-plasticity model implemented in Abaqus for the Roman concrete (where CMOD stands for Crack Mouth Opening Displacement).

3 NON-LINEAR DYNAMIC ANALYSIS OF TWO CALIDARIA IN ROME

The dynamic non-linear analysis of the Calidaria of the Baths of Caracalla (216 A.D.) and the Baths of Diocletian (306 A.D.) are here presented.

The Calidarium of the Caracalla's baths (see Figure 2) was a circular room paved in marble and roofed with a dome of almost 36 m diameter, very similar to the dimension of the Pantheon. The weight of the dome was carried by eight pillars made in Roman concrete. The plan view shows a structure composed of an internal diameter of 36 m and pillars with a thickness of 6 m (1/6 of the external radius). Two levels of vaults can be observed from the cross-sections. The first one consists of vaults whose springers are located at a height of 11 m from the ground; conversely, those at the upper level have a particular shape that maximizes the light entering the structure. The thickness of the dome at the crown is assumed to be equal to 1.5 m, as in the dome of the Pantheon.

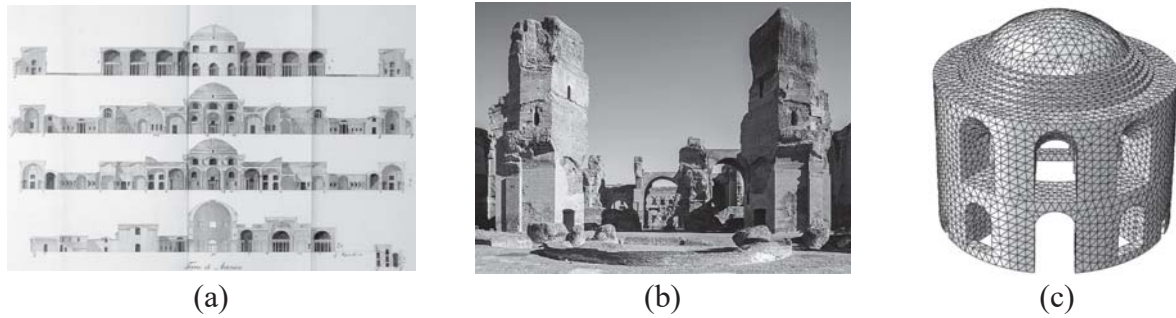


Figure 2: Baths of Caracalla: (a) drawings made by Palladio, (b) current state of the Calidarium, and (c) FE model.

By following the prescriptions given by the regional authority (Regione Lazio), an appropriate accelerogram compatible with the response spectrum was adopted and applied in both directions (x and y). The shape and the duration of the seismic input can be observed in Figure 3. Three meaningful instants indicated through the points A, B, and C, are defined in the accelerogram and highlighted in the results.

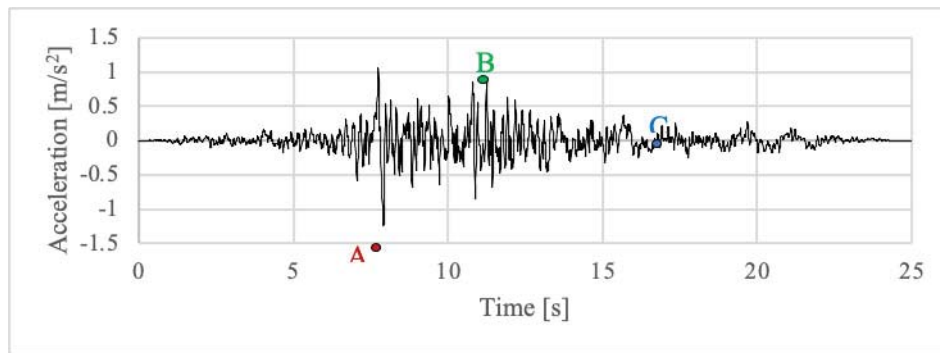


Figure 3: Accelerogram adopted in the dynamic non-linear analyses (points A: $t = 7.9$ s, B: $t = 11.3$ s, C: $t = 17$ s).

The level of damage suffered by the *Calidarium* is represented in terms of plastic strains in the different time instants, see Figure 4. The dark areas indicate the presence of plastic strains generated by traction, therefore they correspond to the areas where tensile cracks develop.

As it can be observed from Figure 4, after the first peaks of the accelerogram (point A), high plastic strains develop within the structure: fracture lines propagate from the vaults up to the top of the dome.

Figure 5 shows the trend of the strain energy and plastic dissipation energy during the analysis. It can be observed that point A (i.e. peak value of the accelerogram) coincides with the instant in which the plastic dissipation energy begins to increase, while in point C it has already assumed its final value. At the end of the analysis, the plastic dissipation energy and the strain energy have almost the same value. The energy plastically dissipated at the end of the strongest part of the accelerogram reaches a sort of plateau and its value remains stable until the end of the analysis. Therefore, it can be supposed that an accumulation of damage has been generated in the *Calidarium* but that the seismic action is not sufficient to cause the failure of the dome. Therefore, it can be stated that the collapse of the *Calidarium* is not associated with a single seismic event, but probably is due to the repetition of multiple earthquakes.

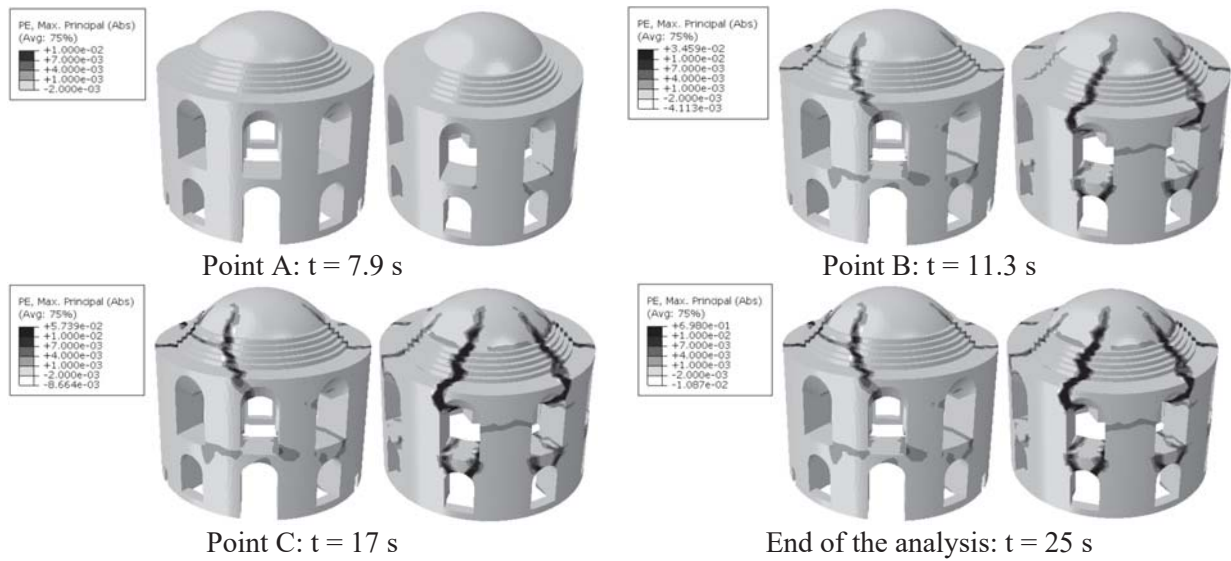


Figure 4: Plastic-strain maps for the Calidarium of the Bath of Caracalla.

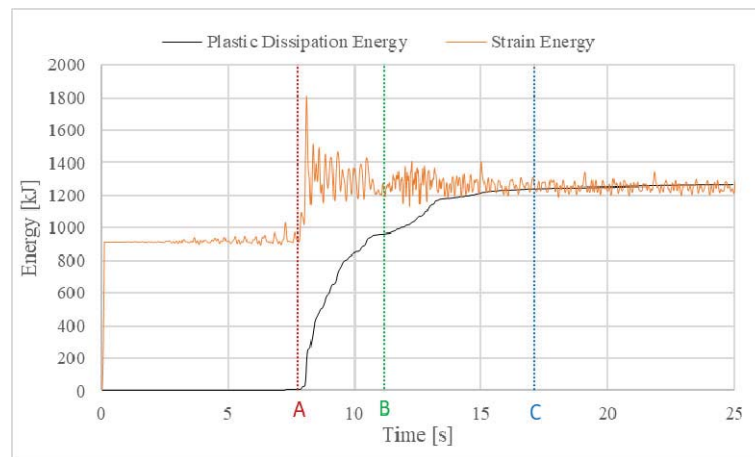


Figure 5: Internal energy-time diagrams (accelerogram applied along both directions).

The Baths of Diocletian, see Figure 6, represent the largest thermal complex ever built in ancient Rome. Its Calidarium was a rectangular room paved in marble and roofed by a system of three cross vaults. The entire structure was made in Roman concrete with the exception of the entablature blocks and granite columns on which the cross vaults rested. Moreover, there were three lateral apses, also supported by granite columns. Nowadays only a small portion of the north-eastern side of the *Calidarium* is still standing (Figure 6b).



Figure 6: Baths of Diocletian: (a) transversal cross-section of the Calidarium (E. Paulin, 1880), (b) current state, and (c) FE model

The results of the non-linear dynamic analysis here presented are obtained by considering the same accelerogram used for the *Calidarium* of Caracalla (Figure 3) and applying it in both x and y directions. The analysis stops before the ending of the duration time of the accelerogram due to the collapse of the front apse that provoked the excessive distortion of the elements of the mesh. By observing the derived crack patterns depicted in Figure 7, the Calidarium appears totally intact, except for the front apse that at the time instant C presents a high level of plastic strains.

The trend of the internal energies evaluated in the roof of the *Calidarium* and in its central apse are reported in Figure 8. While the energy plastically dissipated in the roof is very low, in the apse it reaches very high values (Figure 8b). This result demonstrates that the collapse of the apse occurs before the roof suffers high damages. Deduction that is completely in accordance with the ruins of the structure represented in the drawing made by Dosio (1533-1611).

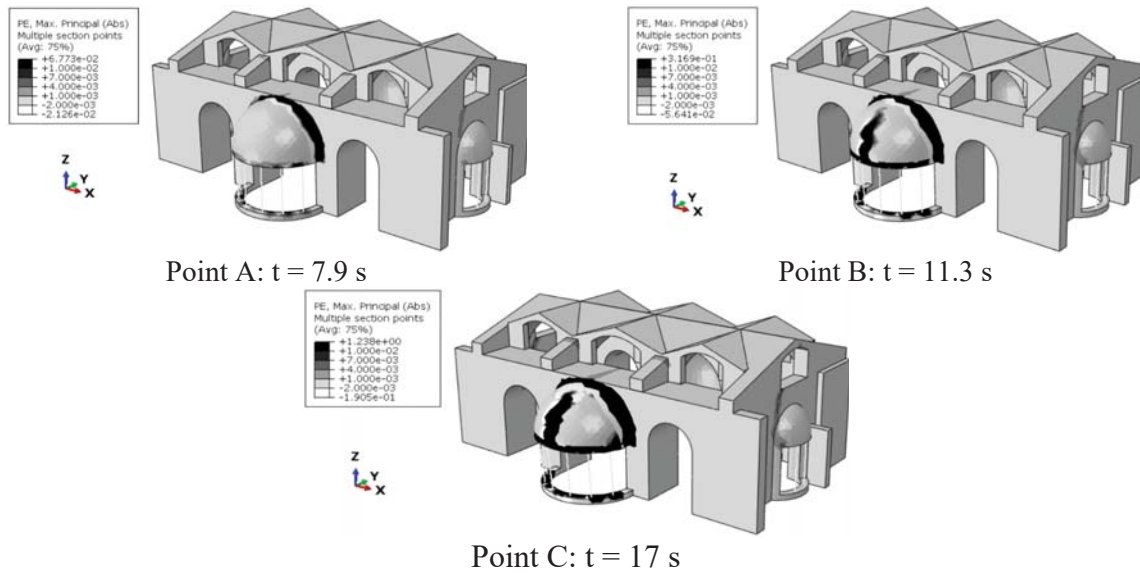


Figure 7: Plastic strain maps for the Calidarium of Diocletian.

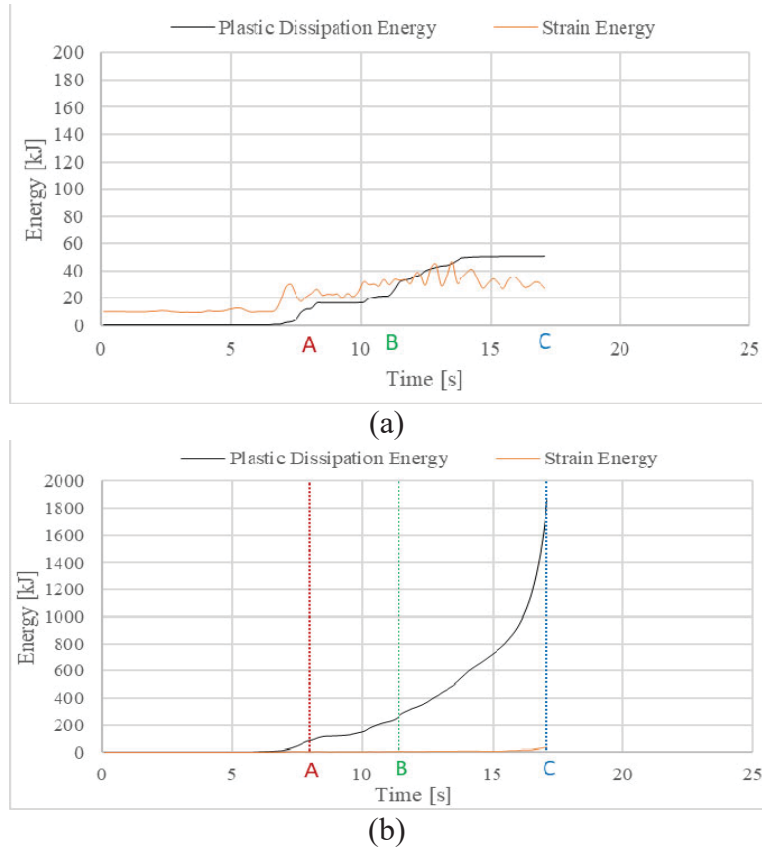


Figure 8: Internal energy-time diagrams: (a) roof and (b) apse.

4 CONCLUSIONS

In this paper, the collapse of two Roman concrete Calidaria in Rome has been investigated by means of advanced non-linear dynamic analyses performed in Abaqus. The behavior of the Roman concrete, the so-called *opus caementicium*, is represented by means of the concrete damage plasticity model. A non-linear damage plasticity law for both compressive and tensile response of the *opus caementicium* has been implemented in Abaqus to correctly reproduce the post-elastic behavior.

As far as the Calidarium of the Caracalla's Baths is concerned, the application of a single accelerogram is not sufficient to generate its collapse condition. However, at the end of the dynamic analysis, high plastic strains develop within the structure, indicating that the application of a further accelerogram may cause the collapse of its dome. Therefore, it can be argued that the seismic events occurring in Rome over the course of its post-Imperial history generated damages that had accumulated within the structure, greatly reducing its resistance. Consequently, the collapse may have occurred during or after one of those seismic events, just when the structure itself was already damaged.

The analyses carried out on the Calidarium of the Diocletian's Baths show that the front apse is the first structural part to have collapsed. Despite how reported by Dosio in its drawings, in which the Calidarium is represented without its front apse and its roof, at the end of the dynamic analysis the upper cross vaults appear poorly damaged.

Eventually, for both Calidaria it has been discovered that their collapse is not associated with a single seismic event, but with the repetition of multiple earthquakes.

REFERENCES

- [1] L.C. Lancaster, Concrete Vaulted Constructions in Imperial Rome: Innovations in Context, New York: Cambridge University Press, 2005.
- [2] J. Heyman, The stone skeleton. *International Journal of Solids and Structures*, **2**, 249-56, 1966.
- [3] A. Tralli, C. Alessandri and G. Milani, Computational methods for masonry vaults: A review of recent results. *Open Civil Engineering Journal*, **8**, 272-87, 2014.
- [4] P. Block P and J. Ochsendorf, Thrust network analysis: A new methodology for three-dimensional equilibrium. *Journal of the International Association for shell and spatial structures*, **48**, 1-7, 2007.
- [5] F. Marmo and L. Rosati, Reformulation and extension of the thrust network analysis. *Computers & Structures*, **182**, 104-18, 2017.
- [6] N.A. Nodargi and P. Bisegna, Thrust line analysis revisited and applied to optimization of masonry arches. *International Journal of Mechanical Sciences*, **179**(105690), 2020.
- [7] E. Milani, G. Milani and A. Tralli, Limit analysis of masonry vaults by means of curved shell finite elements and homogenization. *International Journal of Solids and Structures*, **45**, 5258-88, 2008.
- [8] M. Pavlovic, E. Reccia and A. Cecchi, A Procedure to Investigate the Collapse Behavior of Masonry Domes: Some Meaningful Cases. *International Journal of Architectural Heritage*, **10**, 67-83, 2016.
- [9] A. Chiozzi, G. Milani and A. Tralli, A Genetic Algorithm NURBS-based new approach for fast kinematic limit analysis of masonry vaults. *Computers & Structures* **182**, 187-204, 2017.
- [10] N., Grillanda, A. Chiozzi, G. Milani and A. Tralli, Collapse behavior of masonry domes under seismic loads: an adaptive NURBS kinematic limit analysis approach. *Engineering Structures*, **200**(109517), 2019.
- [11] N. Grillanda, M. Valente, G. Milani, A. Chiozzi and A. Tralli, Advanced numerical strategies for seismic assessment of historical masonry aggregates. *Engineering Structures*, **212**(110441) 2020.
- [12] N. Grillanda, M. Valente and G. Milani, ANUB-Aggregates: a fully automatic NURBS-based software for advanced local failure analyses of historical masonry aggregates. *Bulletin Earthquake Engineering*, **18**, 3965-61, 2020.
- [13] J. Scacco, G. Milani and P.B. Lourenço, Automatic mesh generator for the non-linear homogenized analysis of double curvature masonry structures. *Advanced Engineering Software*, **150**(102919), 2020.
- [14] J. Scacco, B. Ghiassi, G. Milani and P.B. Lourenço, A fast modeling approach for numerical analysis of unreinforced and FRCM reinforced masonry walls under out-of-plane loading. *Composites Part B: Engineering*, **180**(107553), 2020.
- [15] J. Scacco, G. Milani and P.B. Lourenço, A micro-modeling approach for the prediction of TRM bond performance on curved masonry substrates. *Composites Structures*, **256**(113065), 2021.
- [16] M. Valente, G. Milani, E. Grande and A. Formisano, Historical masonry building

- aggregates: advanced numerical insight for an effective seismic assessment on two row housing compounds. *Engineering Structures*, **190**, 360-79, 2019;190:360–79.
- [17] J. Lubliner, J. Oliver, S. Olle and E. Onate, A Plastic-Damage Model for Concrete. *International Journal of Solids and Structures*, **25**, 299-326, 1989.
- [18] A. Saumelli Ferretti, Materiali da costruzione e tecnologie costruttive del patrimonio archeologico e monumentale romano *Unpublished research conducted at Università degli Studi di Roma "La Sapienza"*, 1996.
- [19] J. Lee and G. L. Fenves, Plastic-Damage Model for Cyclic Loading of Concrete Structures. *Journal of Engineering Mechanics*, **124**, 892-900, 1998.
- [20] M. Modéer, P. Petersson and A. Hillerborg, Analysis of crack formation and crack growth in concrete by means of fracture mechanics and finite elements. *Cement and Concrete Research*, **6**(6), 773-82, 1976.
- [21] P. Brune, R. Perucchio and S. Ivancic, A Concrete Damage Plasticity Model fo Ancient Roman Pozzolan Concrete. *9th International Masonry Conference*, Guimarães, Portugal, 7-9 July 2014.

3D ADVANCED NUMERICAL MODELLING OF A CATALAN-LAYERED MASONRY VAULT UNREINFORCED AND REINFORCED WITH GLASS-TRM MATERIALS AND SUBJECTED TO VERTICAL SUPPORT MOVEMENTS

E. Bertolesi¹, G. Milani², J. Adam³ and P. Calderón³

¹Brunel University London, UB8 3PH Uxbridge, UK
e-mail: elisa.bertolesi@brunel.ac.uk

²Politecnico di Milano, Piazza Leonardo da Vinci 32, 20133 Milan, Italy
gabriele.milani@polimi.it

³Universitat Politècnica de València, Camino de Vera s/n, 46022 Valencia, Spain
{joadmar, pcaldero}@upv.es

Abstract

This paper presents the numerical results obtained simulating a 4x4mq masonry vault (unreinforced and reinforced with glass-TRM) tested at the Universitat Politècnica de Valencia (Spain). The vault was built using a traditional Catalan layered-construction technique and its structural behavior was analyzed when subjected to monotonic vertical displacements in one of its supports. The geometry and construction technique of the vault resembled those in a church on the outskirts of Valencia, which collapsed probably due to soil settlements. Indeed, due to their peculiar geometric and mechanical features, these structures are especially prone to damage from support movements produced by ground settlements or earthquakes.

Two advanced 3D numerical models were developed using the commercial software Abaqus to study the vault response with and without the application of an extrados layer of lime based TRM strengthening material. The FE software allowed the adoption of a concrete damage plasticity (CDP) material model which was employed to both masonry support and TRM strengthening material, after a preliminary tuning of the compressive and tensile mechanical properties of the constituent materials.

The outputs obtained with the FE models coupled with the results of the tests, provided valuable information to the scientific community on the available modelling strategies to be used to evaluate the behavior of ancient masonry double-curvature structures pre-damaged by vertical movements of the vault supports and repaired with TRM materials.

Keywords: Masonry vaults, Textile Reinforced Mortar (TRM) materials, Vertical Settlements.

1 INTRODUCTION

Textile Reinforced Mortar (TRM) materials represent a valid alternative to Fiber Reinforced Polymers (FRP) [1]-[7] for the reinforcement of ancient structures [8]-[12]. The advantages offered by TRM materials are mainly related to their compatibility with weak ancient substrates and their permeability. In addition, TRM materials offer some of the advantages of FRP composites, as their ease of installation and adaptability to complex geometries. Until now, TRM materials have been studied to characterize their mechanical properties which in turn have helped define guidelines and guide professionals during their design [10]. One of the most important features of this strengthening material, is represented by the mortar matrix, which is generally characterized by a low tensile strength. The adoption of TRM materials has been encouraged in the case of ancient masonries by leveraging their high compatibility and reversibility with respect to ancient supports. An obvious development therefore was the promotion of lime matrices instead of cementitious ones. Unfortunately, the adoption of low tensile strength matrices decreases the global performance of the strengthening solutions themselves which thus needed to be engineered by mixing them with reinforcing fibers. Unlike FRPs, engineered TRM materials usually fail due to slippage phenomena between the reinforcing textile and the mortar matrix [8][10].

Several research groups focused on this aspect, while few research works were developed to study their actual applicability to full-scale structures [13]-[16]. This aspect is particularly important when the support on which the reinforcement is applied is a weak material characterized by negligible tensile strength as in the case of old masonries. In fact, the suitability of a reinforcing solution needs to be evaluated taking into account possible adverse failure mechanisms that the reinforcing material could trigger. Several researches highlighted this aspect especially on isolated masonry panels subjected to diagonal compression or arches reinforced with different strengthening solutions [15]. Furthermore, advanced computational models and analytical approaches were developed mainly on a local scale to study the bonding performance of TRM materials, completely disregarding the effects these reinforcement solutions have on full-scale structures [17]-[22]. One of the first examples of a comprehensive study on the adoption of TRM materials is represented by [23][24]. This work shows the positive and negative effects of TRM solutions when applied on full-scale structures. The results obtained by the lab investigation were used in the present work to propose a 3D macro-modelling strategy to study the structural response of masonry layered vaults. The models were used to deduce important outcomes on the limitations of TRM strengthening materials.

2 EXPERIMENTAL CAMPAIGN

This section is devoted to the discussion of the results obtained by a unique laboratory investigation developed at the *Universitat Politècnica de Valencia* (Valencia, Spain) on one masonry timbered vault damaged by vertical settlements and repaired by an extrados radial TRM strengthening configuration. The vault had a square 4x4 m² shape and it was constructed on four concrete supports interconnected by a steel bracing frame. The vault was subjected to different settlements during two laboratory tests: a downward settlement up to 40 mm was applied to one support (I test), then the vault was repaired by applying an extrados layer of TRM materials and it was re-tested by imposing a total downward settlement up to 120 mm (II test). The vault geometry and displacement history are depicted in Figure 1 -a and -b respectively. The reader is referred to [23][24] for further details. The strengthening material was composed of a 10-15 mm thick fibre reinforced natural hydraulic lime and eco-pozzolan based mortar reinforced with a glass textile.

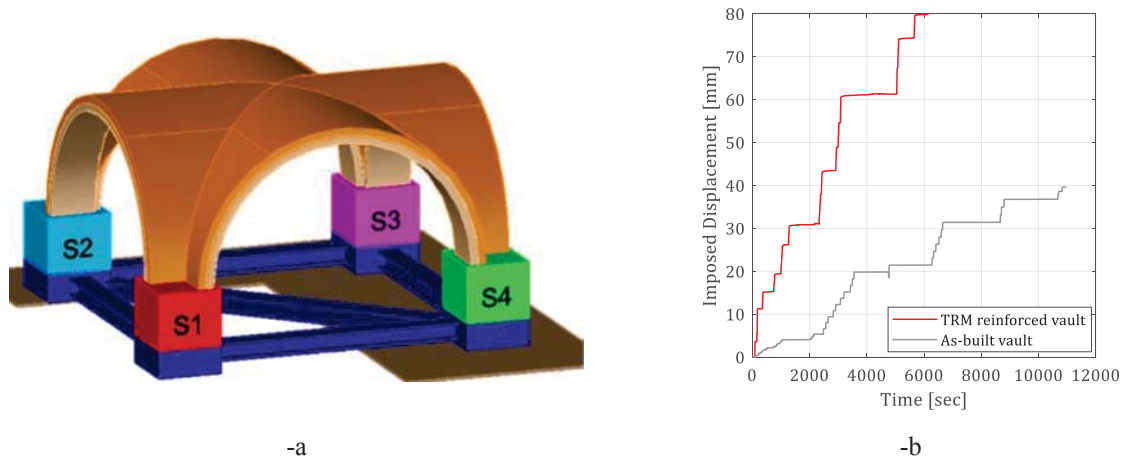


Figure 1: Geometry of the tested vault (-a) and downward settlement applied to one support (-b).

The vault was rested on four supports: the vertical settlement was applied in S1, the opposite counterpart (S3) was completely fixed while, the remaining two supports (S2 and S4) were only allowed to slide horizontally. The vertical downward displacement was applied by means of two mechanical jacks placed below S1. Similarly to S2 and S4, S1 was designed to slide horizontally. The vault behavior was monitored by means of different sensors, namely: Linear Variable Displacement Transducers and Fiber Optic sensors. In particular, Figure 2 -a and -b depicts the results obtained at the end of the experimental investigation in terms of reaction force vs. imposed settlement curves and damage patterns, respectively (test II).

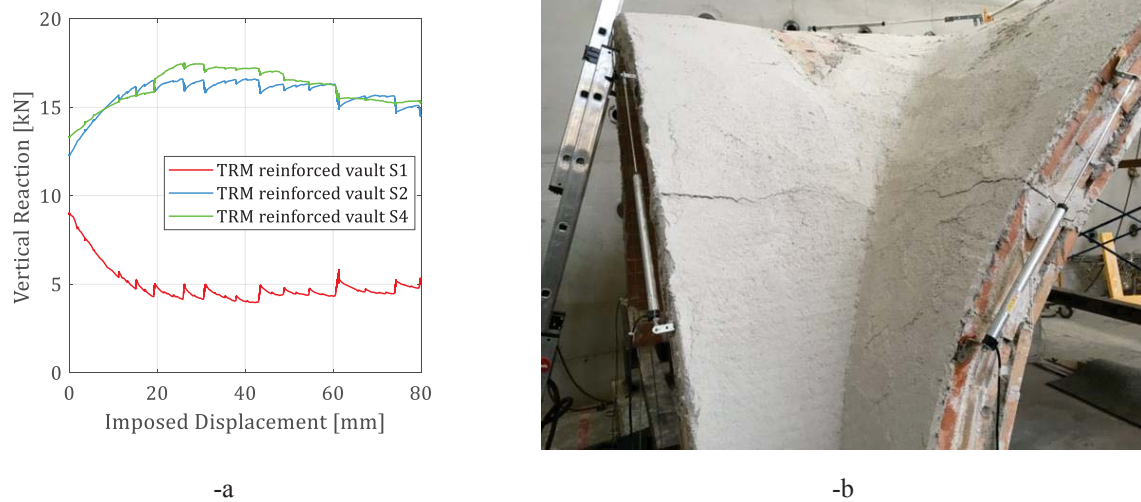


Figure 2: Experimental reaction force vs vertical settlement curves (-a) and crack patterns at the end of the investigation (-b).

As visible in Figure 2, the vault reinforced with TRM composites, experienced the formation of various cracks, namely an extrados diagonal crack connecting the two lateral supports S2-S4 and traditional hinged mechanisms in the lateral arches (S1-S2 and S1-S4). The application of TRM materials was able to restore the continuity of the masonry structure severely damaged by previous settlements. Also, the damage patterns showed that for extrados

reinforcements, the strengthening material experienced some mortar cracking without textile slippages or tensile failures.

3 NUMERICAL MODELLING

This section is provided to discuss the assumptions made during the FE analysis. The following hypotheses lie at the basis of the models developed in Abaqus:

- The masonry support was modeled as a homogeneous material. This simplification, not normally available for traditional masonry, is adopted here due to the peculiar characteristics of layered masonry structures. The layered support was in fact composed of a stacked sequence of tiles and joints arranged along two perpendicular directions.
- The longitudinal axis of symmetry was considered to reduce the computational cost of the simulations. In fact, the masonry structure should have behaved symmetrically during the entire experimental campaign. During the laboratory investigations some torsional effects were observed, due to geometric and material heterogeneity. These effects do not invalidate the initial hypothesis since they could hardly be considered in standard simulations.
- The vault behavior during the two-stage lab campaign was decoupled allowing the adoption of two models: one considering the unreinforced masonry and the other considering the TRM strengthening material applied on an undamaged support. This assumption holds considering that the masonry support was subjected to repointing and injections before applying the TRM material. Also, the reaction force-settlement curves showed that the initial stiffness of the vault was completely restored after the strengthening interventions.

3.1 Unreinforced and TRM Reinforced structure

The vault behavior was modeled using a 3D macro-modelling strategy using 4-noded shell elements representing the masonry support and strengthening material. The final models are depicted in Figure 3 -a and -b, respectively considering the unreinforced and TRM reinforced vaults.



Figure 3: 3D models of the timbrel vault: unreinforced structure (-a) and TRM reinforced structure (-b).

In details, the thickness of the masonry supports was considered equal to 70.5 mm for the vault and 159.5 mm in the lateral arches while, the TRM thickness was set to 10 mm. In order to realistically study the effect of vertical settlements, the masonry support and TRM materials were simulated using a Concrete Damage Plasticity (CDP) model available in Abaqus. The elastic modulus of the masonry support was set to 1700 MPa, with tensile and compressive strengths equal to 0.23 MPa and 10 MPa, respectively. The TRM mechanical properties were deduced according to the data provided by the manufacturer when available. In details, the authors assumed an elastic modulus equal to 3179 MPa and compressive strength equal to 17 MPa.

4 NUMERICAL RESULTS

4.1 Unreinforced Structure

This section discusses the results obtained using the Abaqus FE model and considering only the unreinforced vault. For the sake of brevity, the damage maps are briefly discussed in this section (see Figure 4). Figure 4-a and -b depicts the tensile damage maps (red stands for 90% damage whereas blue stands for 0% of damage) obtained at the end of the simulation and at the end of the first lab test, respectively.

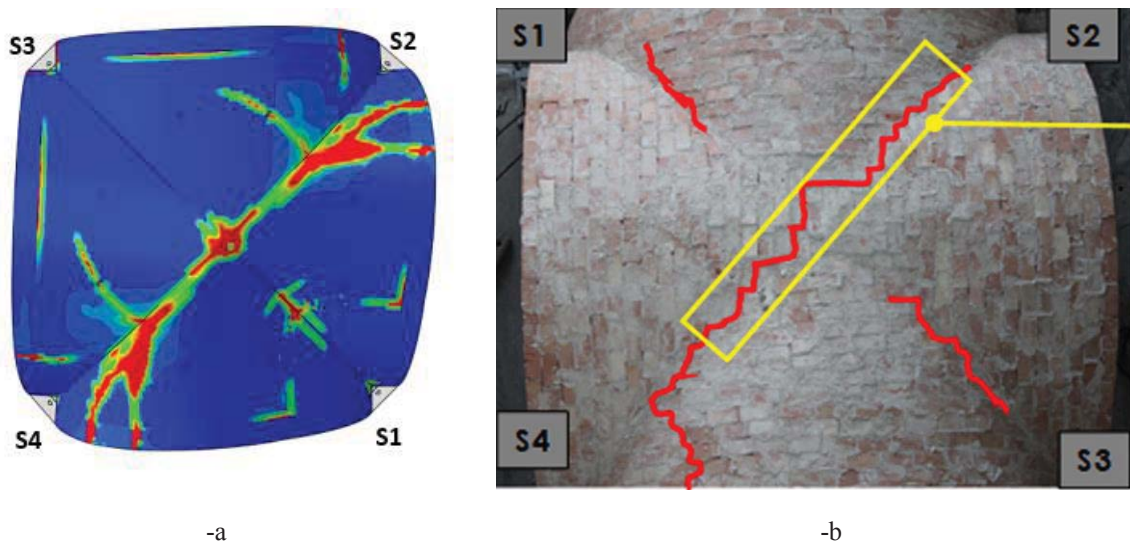


Figure 4: Tensile damage maps at the vault extrados: FE modelling (-a) and lab test (-b).

As visible comparing Figure 4-a and -b, the model was able to describe accurately the development of the failure mechanism found experimentally. The most important damage was observed along the diagonal connecting supports S2-S4 and along the lateral arches S1-S2 and S1-S4.

4.2 TRM Reinforced Structure

The TRM reinforced vault was modelled using the same approach discussed in the previous sections. In this section the most important numerical results are presented and discussed with respect to the experimental outcomes. Figure 5 -a depicts the numerical tensile damage maps plotted at the vault extrados at the end of the simulation while, Figure 5-b proposes a

comparison between the reaction forces-settlement curves obtained experimentally and numerically.

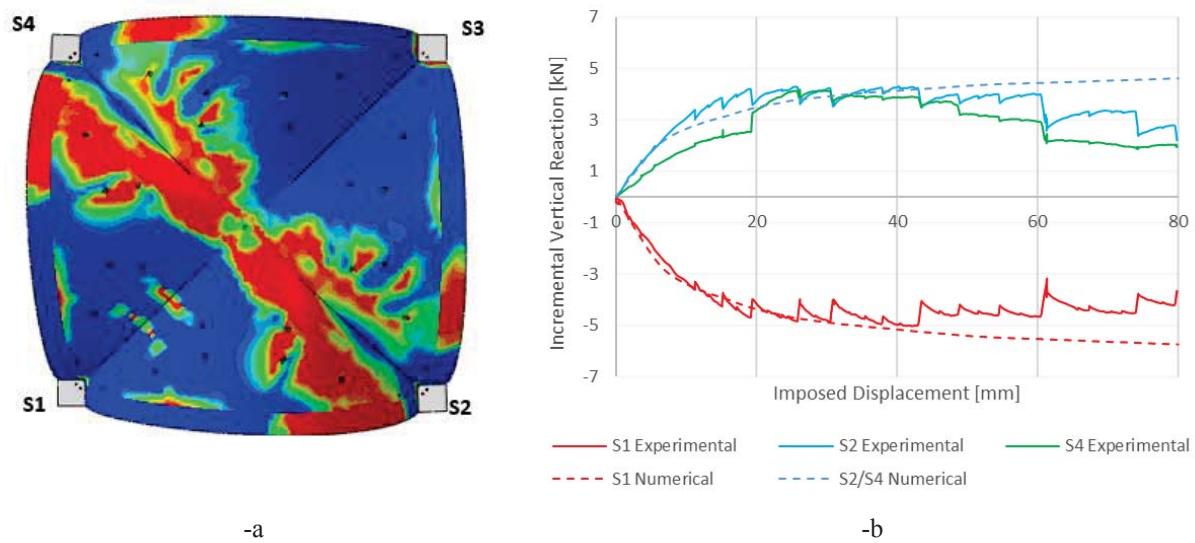


Figure 5: Experimental reaction force vs vertical settlement curves (-a) and crack patterns at the end of the investigation (-b).

As visible in Figure 5-b the model is able to capture the global structural response of the vault in terms of initial stiffness, peak reaction load and post peak behavior. Similarly, the adopted FE approach successfully described the failure mechanism which was characterized by spreading tensile damages on the masonry substrate in correspondence of the S2-S4 diagonal and mostly in the lateral arches S1-S4 and S1-S2.

5 CONCLUSIONS

The article discusses a series of numerical simulations developed using the commercial software Abaqus to study the structural response of masonry vaults damaged by vertical settlements. Based on the results obtained, the following conclusions could be drawn:

- A macro-modelling approach was successfully adopted to study the behavior of unreinforced and TRM reinforced masonry vaults.
- The model, although simplified, was able to capture the global structural response of the structure and the development of the failure mechanism.
- The TRM strengthening was successfully applied to restore the continuity of the vault also, extending the displacement capacity of the structure. Conversely, increasing the displacement capacity increases spreading the damages on the masonry support before failure of the strengthening material. This is particularly evident comparing Figure 4-a with Figure 5-a.
- This latter finding is particularly interesting as it suggests using the TRM materials cautiously especially for historic structures where the focus is on preserving the structural integrity. The results suggest to couple FE models to monitoring strategies in order to verify the behavior of the structure and implement soil improvement interventions before reaching a critical state of the masonry.

REFERENCES

- [1] T. Rotunno, M. Fagone, E. Bertolesi, E. Grande, G. Milani, Single lap shear tests of masonry curved pillars externally strengthened by CFRP strips, *Composite Structures*, **200**, 434-448, 2018.
- [2] E. Bertolesi, G. Milani, M. Fagone, T. Rotunno, E. Grande, Micro-mechanical FE numerical model for masonry curved pillars reinforced with FRP strips subjected to single lap shear tests, *Composite Structures*, **201**, 916-931, 2018.
- [3] G. Milani, M. Fagone, T. Rotunno, E. Grande, E. Bertolesi, Development of an interface numerical model for C-FRPs applied on flat and curved masonry pillars, *Composite Structures*, **241**, 2020.
- [4] E. Grande, M. Fagone, T. Rotunno, E. Bertolesi, G. Milani, Modelling of the bond behaviour of curved masonry specimens strengthened by CFRP with anchor spikes, *Composites Part B: Engineering*, **171**, 235-245, 2019.
- [5] T. Rotunno, M. Fagone, E. Bertolesi, E. Grande, G. Milani, Curved masonry pillars reinforced with anchored CFRP sheets: An experimental analysis, *Composites Part B: Engineering*, **174**, 2019.
- [6] M. Fagone, T. Rotunno, E. Grande, E. Bertolesi, G. Milani, The influence of the joint thickness on the adhesion between CFRP reinforcements and masonry arches, *Procedia Structural Integrity*, **11**, 258-265, 2018.
- [7] E. Grande, M. Fagone, T. Rotunno, E. Bertolesi, G. Milani, Coupled interface-based modelling approach for the numerical analysis of curved masonry specimens strengthened by CFRP, *Composite Structures*, **200**, 498-506, 2018.
- [8] L. Alexandros, S.K. Thanasis, C. Triantafyllou, State-of-the-art on strengthening of masonry structures with textile reinforced mortar (TRM), *Constr Build Mater*, **188**, 1221-1233, 2018.
- [9] E. Bertolesi, M. Buitrago, E. Giordano, P. A. Calderón, J. J. Moragues, F. Clementi, J. M. Adam, Effectiveness of textile reinforced mortar (TRM) materials in preventing seismic-induced damage in a U-shaped masonry structure submitted to pseudo-dynamic excitations, *Constr Build Mater*, **248**, 2020.
- [10] E. Bertolesi, F. G. Carozzi, G. Milani, C. Poggi, Numerical modeling of Fabric Reinforce Cementitious Matrix composites (FRCM) in tension, *Constr Build Mater*, **70**, 531-548, 2014.
- [11] F. G. Carozzi, C. Poggi, E. Bertolesi, G. Milani, Ancient masonry arches and vaults strengthened with TRM, SRG and FRP composites: Experimental evaluation, *Composite Structures*, **187**, 466-480, 2018.
- [12] E. Bertolesi, G. Milani, F. G. Carozzi, C. Poggi, Ancient masonry arches and vaults strengthened with TRM, SRG and FRP composites: Numerical analyses, *Composite Structures*, **187**, 385-402, 2018.
- [13] B. Torres, S. Ivorra, F. J. Baeza, L. E. B. Varona, Textile reinforced mortars (TRM) for repairing and retrofitting masonry walls subjected to in-plane cyclic loads. An experimental approach, *Engineering Structures*, **231**, 2021.
- [14] B. Torres, F.B. Varona, F.J. Baeza, D. Bru, S. Ivorra, Study on retrofitted masonry elements under shear using digital image correlation, *Sensors*, **20**, 2020.

- [15] X. Wang, C.C. Lam, V. Panlu, Comparison of different types of TRM composites for strengthening masonry panels, *Constr Build Mater*, **219**, 184-194, 2019.
- [16] F.A. Kariou, S.P. Triantafyllou, D.A. Bournas, L.N. Koutasc, Out-of-plane response of masonry walls strengthened using textile-mortar system, *Constr Build Mater*, **165**, 769-781, 2018.
- [17] E. Grande, G. Milani, Procedure for the numerical characterization of the local bond behavior of FRCM, *Composite Structures*, **258**, 2021.
- [18] E. Grande, M. Imbimbo, S. Marfia, E. Sacco, Numerical simulation of the de-bonding phenomenon of FRCM strengthening systems, *Frat Ed Integrita Strutt*, **13**, 321-333, 2019.
- [19] E. Grande, B. Ghiassi, M. Imbimbo, Theoretical and FE models for the study of the bond behavior of FRCM systems, *Numer Model Mason Hist Struct*, 685-712, 2019.
- [20] E. Grande, G. Milani, Interface modeling approach for the study of the bond behavior of FRCM strengthening systems, *Compos B Eng*, **141**, 221-233, 2018.
- [21] E. Bertolesi, G. Milani, C. Poggi, Simple holonomic homogenization model for the non-linear static analysis of in-plane loaded masonry walls strengthened with FRCM composites, *Composite Structures*, **158**, 291-307, 2016.
- [22] E. Bertolesi, J. M. Adam, P. Rinaudo, P. A. Calderón, Research and practice on masonry cross vaults – A review, *Engineering Structures*, **180**, 67-88, 2019.
- [23] B. Torres, E. Bertolesi, J.J. Moragues, P.A. Calderón, J.M. Adam, Experimental investigation of a full-scale timbrel masonry cross vault subjected to vertical settlement, *Constr Build Mater*, **221**, 421-432, 2019.
- [24] E. Bertolesi, B. Torres, J. M. Adam, P. A. Calderón, J. J. Moragues, Effectiveness of Textile Reinforced Mortar (TRM) materials for the repair of full-scale timbrel masonry cross vaults. *Engineering Structures*, **220**, 110978, 2020.

DYNAMIC ANALYSIS OF MASONRY CHIMNEYS BY MEANS OF A SIMPLE RIGID BEAM MODEL

Daniele Baraldi¹, Gabriele Milani², and Vasilis Sarhosis²

¹ Department of Architecture, Università Iuav di Venezia
Terese, Dorsoduro 2206, 30123, Venezia, Italy
e-mail: danielebaraldi@iuav.it

² Department of Architecture, Built Environment and Construction Engineering, Technical University
of Milan
Piazza Leonardo Da Vinci 32, 20133, Milano, Italy
e-mail: gabriele.milani@polimi.it

³ School of Civil Engineering, University of Leeds
LS2 9JT, Leeds, UK
e-mail: v.sarhosis@leeds.ac.uk

Abstract

In this contribution, a simple and effective Rigid Beam Model, recently introduced for simulating the dynamic behavior of slender freestanding masonry columns and walls, is adopted and improved for studying masonry chimneys. These structures represent a particular masonry building typology, characterized by a conical shape with a very large slenderness, they are prone to collapse in case of seismic actions due to poor material mechanical characteristics and poor state of conservation. The original model is improved by considering the chimney subdivided into several portions along its height, and each portion is modelled as a rigid beam element with an annular cross-section. Small displacements and no-sliding at the interfaces between the beam elements are the main adopted hypotheses, following the typical assumptions taken by Housner. Material nonlinearity is considered by means of a moment-rotation constitutive law at interface level, also accounting for masonry stiffness and tensile strength. Several numerical tests are performed by considering an existing case study and comparing the modal analysis results of the Rigid Beam Model with respect to those obtained with traditional FE models; then, harmonic tests with varying acceleration and frequency are performed.

Keywords: Masonry, chimneys, Rigid Beam Model, harmonic excitation.

1 INTRODUCTION

Unreinforced masonry chimneys are a particular building typology [1], characterized by a truncated-conical shape with a considerable height and a consequent large slenderness. Masonry chimneys were built in most of the industrial countries around the middle of the 19th century, for releasing combustion gases from the industrial plants. Due to the industrial technological improvements, masonry chimneys started to be dismissed in the middle of the 20th century and became part of the huge and various masonry-built environment. However, these structures turned out to be prone to earthquake effects because of their slenderness and their poor state of conservation, mostly motivated by atmospheric agents and due to the limited interest on their restoration. For these reasons, the seismic analysis of unreinforced masonry chimneys is an important challenge in the field of Earthquake Engineering, especially because of the non-standard shape and size of the structure with respect to ordinary monumental and minor masonry buildings.

In this contribution, the original rigid beam model, introduced by authors for modelling the dynamic behavior of monolithic and multi-drum freestanding columns [2] and recently extended for studying cantilever walls [3], is further improved for modelling the dynamic behavior of masonry chimneys. The updated model assumes the chimney subdivided into distinct portions, which are modelled as rigid beam elements with annular cross-section. The model keeps the hypotheses of small displacements and no sliding at interfaces, but it considers masonry mechanical properties for defining interface stiffness and strength into a moment-rotation constitutive law.

An existing case study, represented by a tall masonry chimney located in Ferrara (Italy), is taken into consideration for evaluating the effectiveness of the updated rigid beam model (Figure 1a). This chimney was hit by the Emilia earthquake in May 2012 and after the seismic sequence [4] it was shortened (Figure 1b) by removing an upper damaged portion for safety reasons, since the building is located into the Scientific Campus of University of Ferrara. Several numerical tests have been already performed by adopting accurate three-dimensional models [4,5]; in particular, modal analysis results are here taken as reference for setting the stiffness parameters of the rigid beam model of the chimney. Then, a set of dynamic analyses are performed for determining the safe-unsafe domains of both full and shortened case studies.

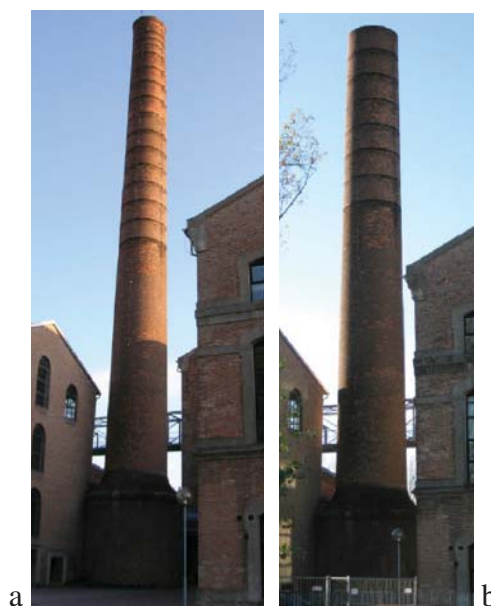


Figure 1: Masonry chimney in Ferrara before (a) and after (b) shortening [5].

2 RIGID BEAM MODEL FOR MASONRY CHIMNEYS

This work considers a generic masonry chimney with a simplified geometry, having overall height H , and characterized by varying outer diameter D and thickness t along the height (Figure 2a,b). The structure is subdivided into n portions having height h_i . The rigid beam model is then generated by considering n rigid beam elements and $n+1$ nodes as shown in Figure 2c. Each beam element represents a portion of the chimney and each node represents an interface between the portions. In particular, the first node/interface represents the contact between the foundation and the first portion of the chimney, whereas the last node represents the top of the chimney. Chimney diameter and thickness are defined at each interface level. Nodal horizontal translational degrees of freedom are considered, namely u_i , \dot{u}_i , and \ddot{u}_i represent, respectively, nodal horizontal translation, velocity, and acceleration (Figure 2c). Each i -th beam element is characterized by a mass m_i , which depends on material density γ and on the volume of the corresponding portion, which is considered for simplicity as the difference between the volumes of outer and inner cylinders (Figure 2d), assuming an average diameter \tilde{D}_i and an average thickness \tilde{t}_i with respect to upper and lower ones. Due to the rigid beam hypothesis, each element is subjected to a rigid rotation depending on the horizontal translations at beam ends and beam height, h_i (Figure 2e):

$$\theta_i = (u_{i+1} - u_i) / h_i \quad (1)$$

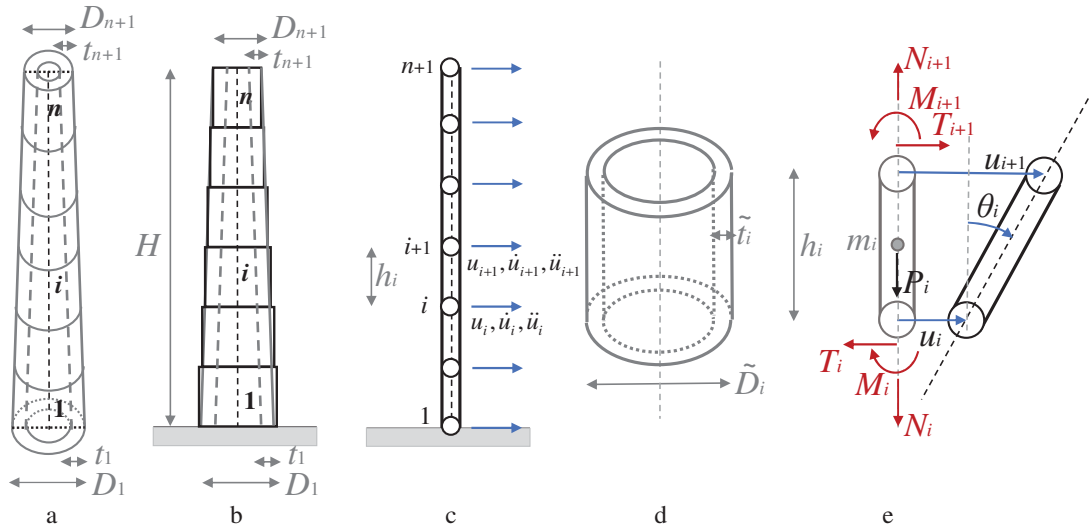


Figure 2: Masonry chimney subdivided into n portions (a), corresponding vertical section (b), corresponding rigid beam model (c), generic chimney portion with average diameter and thickness (d), corresponding rigid beam element (e).

Internal forces of the beam element are given by a normal force N_i , a shear force T_i , and a bending moment M_i , acting at each beam end (Figure 3d).

The translational and rotational equations of motion can be defined with the approach already adopted for multi-drum freestanding columns [2]. If a horizontal ground acceleration $a_g(t)$ acts at the base of the chimney and the top of the chimney is assumed free to move, equations of motion can be written for the entire structure by obtaining the following system of differential equations to be solved:

$$\mathbf{M}(\theta) = \mathbf{G}\mathbf{M}_a\ddot{\mathbf{u}} - \mathbf{G}\mathbf{A}_g + \mathbf{I}_G\ddot{\mathbf{u}} - \mathbf{B}_g \quad (2)$$

Where each bending moment M_i in \mathbf{M} depends on the rotation θ_i of the corresponding i -th drum (Eq. 1). Matrices \mathbf{M}_a , \mathbf{G} , and \mathbf{I}_G can be called, respectively, mass coefficient matrix, geometric coefficient matrix, and polar inertia coefficient matrix. Details of such matrices and vectors \mathbf{A}_g and \mathbf{B}_g can be found in [3].

The system of differential equations in (2) is solved by means of a Runge-Kutta ODE solver. At this stage, the nonlinear behavior that can affect the chimney is the bending failure at each interface between the portions, whereas, following Housner's hypothesis, shear failure cannot occur [6]. The bending moment M_i at each interface follows a bi- or tri-linear moment-rotation relationship, which represents the maximum stabilizing moment for varying block rotation (Figure 3), and it is slightly modified with respect to Housner's law by means of an initial elastic stiffness $K_{M,i}$ and a smoothing parameter $\xi \leq 1$.

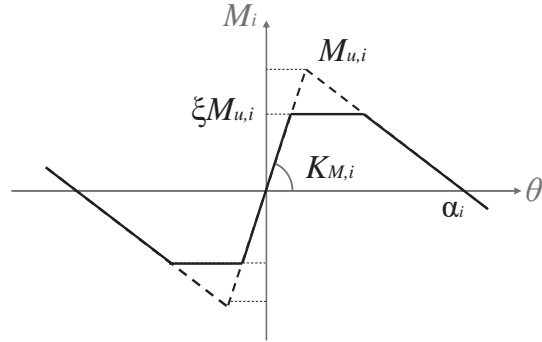


Figure 3: Moment-rotation relationship.

The maximum stabilizing moment in Figure 3 on one hand accounts for the maximum eccentricity of the normal force acting at the i -th interface; on the other hand, it also accounts for the tensile strength F_t of the i -th interface, depending on masonry tensile strength f_t and chimney cross-section A_i :

$$M_{u,i} = \frac{d_i}{2} (N_i + F_{t,i}) = \frac{d_i}{2} \left(\sum_{j=i}^n P_j + A_i f_t \right) \quad (3)$$

At the moment, an infinite compressive strength for masonry is assumed, as it was done in the original rigid beam model [2]. Eq. 3 is also adopted into an existing rigid block model for evaluating the bending strength of masonry panel interfaces [7]. However, it can be demonstrated that in case of dead loads close to the 10% of masonry compressive strength, the stabilizing moment evaluated with Eq. 3 is overestimated of about 11% with respect to that accounting for masonry compressive strength.

In the original rigid block model defined for masonry columns or walls, the interface bending stiffness $K_{m,i}$ depends on the elastic modulus of the material E_m , on the interface thickness e_i and on the moment of inertia of interface cross-section J_i : $K_{m,i} = E_m e_i J_i$. In case of a masonry chimney, an interface does not actually represent a joint between masonry blocks or drums, hence an interface normal stiffness is introduced: $K_{m,i} = k_m J_i$.

3 NUMERICAL TESTS

As stated into introduction, the slender masonry chimney located in the old industrial facility that houses the Scientific-Technological Campus of the University of Ferrara, Italy (Figure 1), is taken into consideration for the numerical tests. The full chimney, 50 m high, suffered severe damages during the 2012 Emilia seismic sequence. Afterward, for security reasons, the upper damaged portion, 12.40 m high, was disassembled, leading to a shortened chimney 37.60 m high. Geometric characteristics of the structure are taken from [5] and resumed in

Figure 4a. It is worth noting that the data at only 4 and 3 levels for the full and shortened chimney, respectively, are adopted for the rigid beam model. Mechanical characteristics of masonry for the rigid beam model are material density $\gamma = 1800 \text{ kg/m}^3$, tensile strength $f_t = 0.1 \text{ MPa}$.

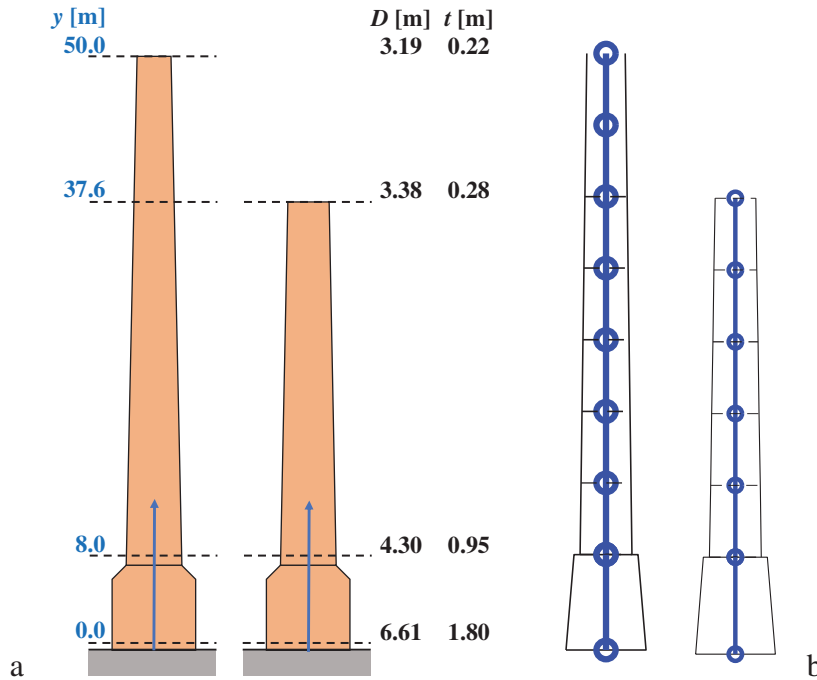


Figure 4: Masonry chimney in Ferrara before and after shortening [5], geometric characteristics (a) and corresponding rigid beam models (b).

Since the chimney is characterized by a thick base from 0 to 8 m, having a larger diameter with respect to the entire chimney, such a base portion is modelled by one rigid beam element. Then, the full chimney from 8 to 50 m is subdivided into 7 equal portions, whereas the shortened chimney from 8 to 37.60 m is subdivided into 5 equal portions, hence by removing the two upper beam elements from the full chimney (Figure 4b). The rotation at the base node of both models is fixed, whereas the stiffness of the interfaces is calibrated by means of a modal analysis of full and shortened chimneys, assuming as reference existing numerical results obtained with an accurate three-dimensional FE model [5].

3.1 Modal analysis

chimney	model	frequency	
		1st	2nd
full	rigid beam model	0.43 Hz	2.03 Hz
	FEM [5]	0.46 Hz	2.16 Hz
shortened	rigid beam model	0.93 Hz	-
	FEM [5]	0.85 Hz	-

Table 1: Comparison between frequencies of the full and shortened chimneys obtained with the proposed rigid beam model and with an accurate 3D FE model [5].

Considering the full chimney, assuming $k_m = 800 \text{ MPa/mm}$ for all the interfaces of the model, the first and second frequencies obtained with the rigid beam model turn out to be in excellent agreement with existing numerical results obtained with accurate 3D models [5]. Furthermore, the same stiffness parameter applied to the rigid beam model of the shortened chimney allows

to obtain at least the first frequency in good agreement with existing numerical results (Table 1).

3.2 Dynamic analysis, harmonic excitations

In order to evaluate the dynamic behavior of the full and shortened masonry chimney, with particular attention to their level of safety and to the potential collapse mechanisms that can be activated by dynamic excitations, a set of harmonic tests is performed by varying input frequency and acceleration amplitude at the base of the rigid beam models introduced and calibrated in the previous sub-section.

Starting with the full chimney, Figure 5 shows the deformed configurations obtained at the end of the harmonic tests by assuming several values of base acceleration and input frequency. The corresponding horizontal displacements versus time, evaluated at the top of the full chimney and at the 2nd node (after the thick base) of the rigid beam model are collected in Figure 6. Collapse mechanisms close to the top of the chimney, involving the last or the last two beam elements, are obtained several times: with 0.25g and 0.5 Hz, 0.5g and 1.0 Hz, 0.5g and 2 Hz. In some cases (0.25g with 0.5 Hz and 1.0 Hz) the deformed configurations are also characterized by a significant rigid rotation of a huge portion of the chimney over the thick base.

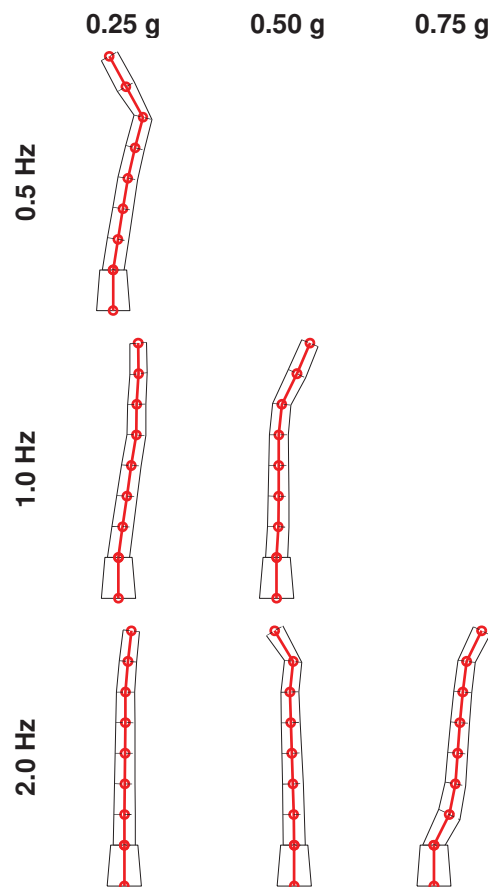


Figure 5: Deformed configurations of the full masonry chimney close to the end of several harmonic excitations.

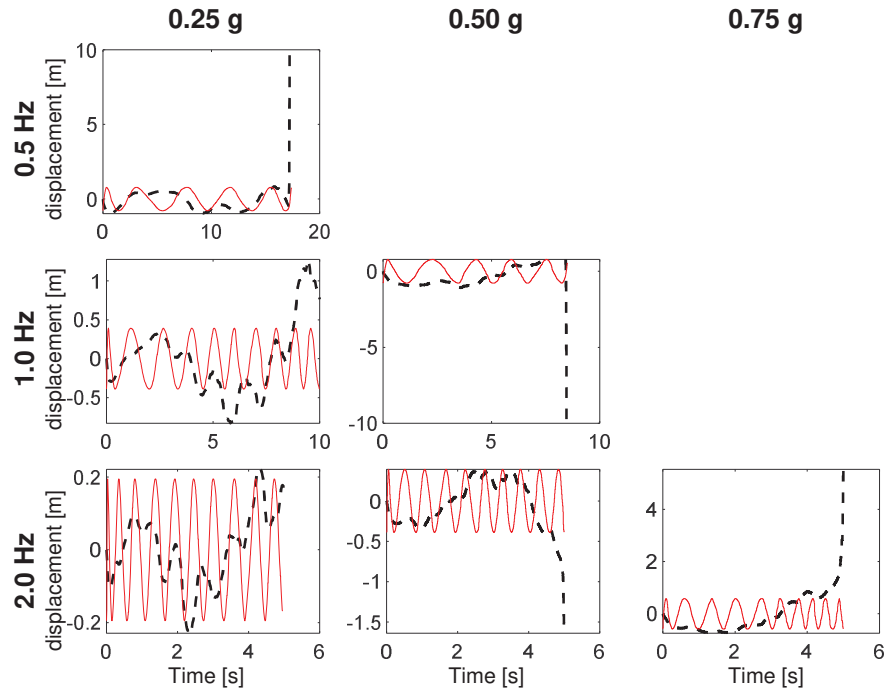


Figure 6: Base (red continuous line) and top (black dashed line) displacements for a of the full masonry chimney subjected to several harmonic excitations.

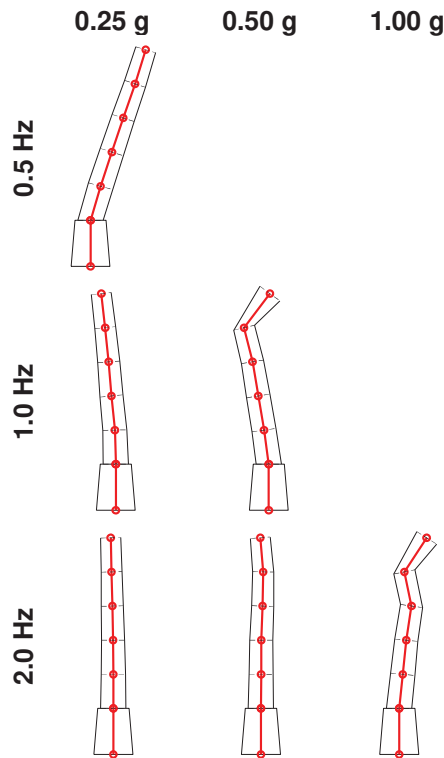


Figure 7: Deformed configurations of the shortened masonry chimney close to the end of several harmonic excitations.

Focusing on the shortened chimney, Figure 7 shows the deformed configurations obtained at the end of the harmonic tests by assuming several values of base acceleration and input frequency. The corresponding horizontal displacements versus time, evaluated at the top of the

full chimney and at the 2nd node (after the thick base) of the rigid beam model are collected in Figure 8.

Collapse mechanisms close to the top of the chimney, involving the last beam element, are obtained several times, with larger acceleration amplitudes and frequencies with respect to the full chimney: 0.5g and 1.0 Hz, 1g and 2 Hz. Similarly to the full chimney, in some cases (0.5g with 1.0 Hz) the deformed configurations are also characterized by a significant rigid rotation of a huge portion of the chimney over the thick base. However, with 0.25g and 0.5 Hz, the rigid rotation of the chimney with respect to the thick base involves the entire shortened chimney.

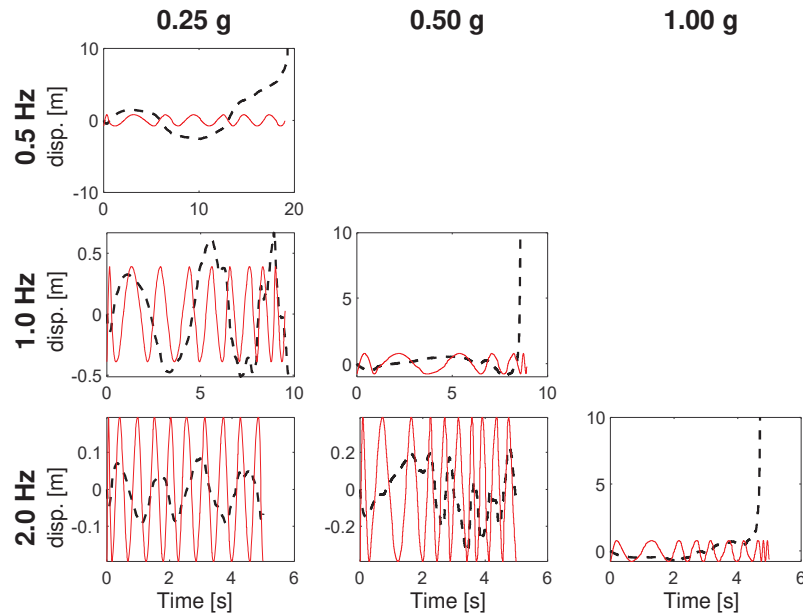


Figure 8: Base (red continuous line) and top (black dashed line) displacements for a of the shortened masonry chimney subjected to several harmonic excitations.

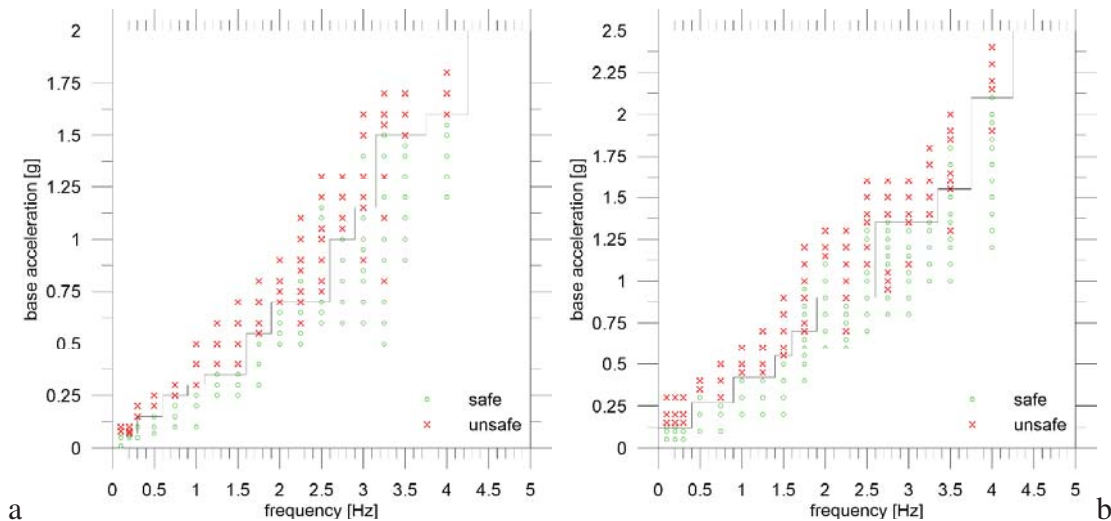


Figure 9: Safe-unsafe domain for the full (a) and shortened (b) chimneys subjected to harmonic excitations.

Figure 9a and b shows the final results of the campaign of numerical simulations on the full and shortened masonry chimneys, by highlighting safe and unsafe conditions at the end of the harmonic tests; a comparison between the two domains is presented in Figure 10. As ex-

pected, the shortened chimney is characterized by a larger safe domain with respect to the full one.

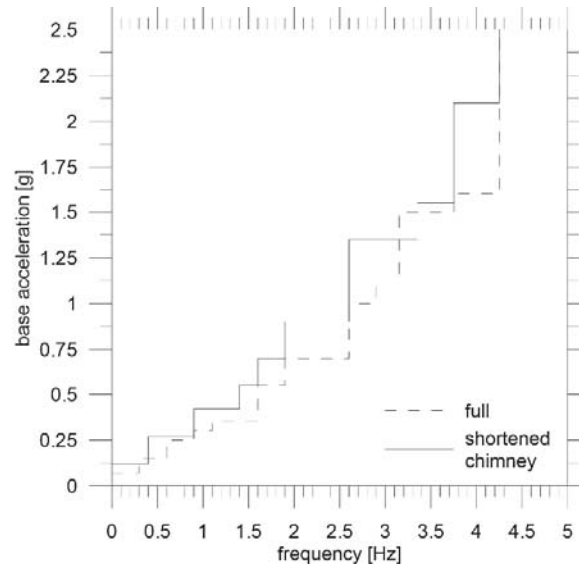


Figure 10: Comparison between the safe-unsafe domains of the full and shortened chimneys subjected to harmonic excitations.

4 CONCLUSIONS

This paper presents a simple and effective rigid beam model for studying the dynamic behavior of tall and slender chimneys. The model applied to a real case study i.e. the chimney located in the Scientific Campus of the University of Ferrara which was hit by the Emilia earthquake in May 2012. During the earthquake, the upper part of the chimney was severely damaged. For safety reasons, the chimney shortened (from 50 m which was originally to 37.5 m) by removing its upper damaged portion. In the proposed rigid model, both the original and shortened chimneys investigated. The chimney subdivided into several portions along its height, and each portion was modelled as a rigid beam element with an annular cross-section. In each model, material non-linearity allowed by means of a moment-rotation constitutive law at interfaces, which accounts for masonry stiffness and tensile strength. Initially, modal analysis results were used to obtain the stiffness parameters of the rigid beam model of the chimney. Later, a set of dynamic analysis were performed and the safe-unsafe domains of both full and shorten chimneys obtained. From the results analysis, it is shown:

- A comparison between frequencies of the full and shortened chimneys obtained from the proposed rigid beam model found to be in excellent agreement with existing numerical results obtained from 3D models.
- With respect to the dynamic behaviour of the full height chimney, harmonic excitations with low amplitude (i.e., 0.25g) resulted in rotations and collapse of the upper part of the chimney. On the other hand, harmonic excitations greater or equal to 0.75g caused collapse mechanism of the entire chimney.
- With respect to the dynamic behaviour of the shortened chimney, harmonic excitations with low amplitude (i.e., 0.25g) resulted in rotations and collapse of the upper part of the chimney. The harmonic excitation characterized by 0.75g causes a collapse mechanism involving the entire chimney.
- A comparison between the safe-unsafe domains of the full and shortened undertaken. As expected, the shortened chimney is characterized by a larger safe domain with respect to the full one.

REFERENCES

- [1] F. J. Pallarés, S. Ivorra, L. Pallarés, J. M. Adam, State of the art of industrial masonry chimneys: A review from construction to strengthening, *Construction and Building Materials*, **25**(12), 4351-4361, 2011.
- [2] D. Baraldi, G. Milani, V. Sarhosis, Numerical models for simulating the dynamic behaviour of freestanding ancient columns, *COMPDYN2019 Proceedings*, 1526-1536, 2019.
- [3] D. Baraldi, V. Sarhosis, G. Milani, A Rigid-Beam-Model for studying the dynamic behaviour of cantilever masonry walls, *Structures*, submitted.
- [4] F. Minghini, G. Milani, A. Tralli, Modal Seismic risk assessment of a 50 m high masonry chimney using advanced analysis techniques, *Engineering Structures*, **69**, 255-270, 2014.
- [5] F. Minghini, E. Bertolesi, A. Del Grosso, G. Milani, A. Tralli, Modal pushover and response history analyses of a masonry chimney before and after shortening, *Engineering Structures*, **110**, 307-324, 2016.
- [6] G.W. Housner, The behavior of inverted pendulum structures during earthquakes, *Bulletin of Seismological Society of America*, 53(1), 403-417, 1963.
- [7] D. Baraldi, A. Cecchi, Discrete approaches for the nonlinear analysis of in plane loaded masonry walls: molecular dynamic and static algorithm solutions, *European Journal of Mechanics A/Solids*, **57**, 165-177, 2016.

COMPARATIVE ANALYSIS AMONG DIFFERENT ANALYSIS PROGRAMS FOR SEISMIC VULNERABILITY EVALUATION OF A MASONRY BUILDING COMPOUND IN THE DISTRICT OF NAPLES

Generoso Vaiano¹ and Antonio Formisano²

¹ Dept. of Structures for Engineering and Architecture, University of Naples Federico II
Piazzale Tecchio 80, 80125 Naples (Italy)
generoso.vaiano@inwind.it

² Dept. of Structures for Engineering and Architecture, University of Naples Federico II
Piazzale Tecchio 80, 80125 Naples (Italy)
antoform@unina.it

Abstract

Masonry building compounds are sets of structural units having at least one common wall. The numerical analysis of the structural units grouped in aggregate, which are very diffused in Italian historical centres, is needed for identifying the structural interactions among them. Starting from these premises, in the current paper a masonry building aggregate built in the early twentieth century in the municipality of Cercola (district of Naples, Italy) and made of four structural units has been investigated as a case study. The structural behaviour under seismic forces has been investigated through non-linear static analyses. In particular, both the whole aggregate and the individual structural units have been modelled. Moreover, the single structural units have been considered both in the grouped and isolated conditions in order to assess either the beneficial or detrimental effect of the aggregated condition. The numerical models have been carried out with three different FEM software, namely 3MURI, CDS Win and Edilus, which schematise masonry buildings in different way. The analysis purpose has been to highlight the different results obtained with the three programs and to assess the most reliable seismic behaviour of investigated structural units. Finally, the susceptibility at damage of the case study aggregate has been evaluated through empirical fragility curves and mechanical vulnerability curves, which have been compared to each other and can be considered as preliminary tools to setup effective rehabilitation interventions.

Keywords: Seismic vulnerability, Building compounds, FEM analysis programs, Macro-element approach, Equivalent frame model.

1 INTRODUCTION

The structural heritage facing the most part of Italian historical centres is made of masonry buildings without adequate structural performance level against seismic actions. Therefore, these types of buildings have high seismic vulnerability [1,2]. For this reason, the seismic safety assessment of existing masonry buildings is needed by many researchers working in the field of Seismic Engineering [3,4].

Seismic vulnerability is the tendency of buildings to suffer a certain degree of damage during a seismic event. The vulnerability assessment methods proposed in current standards are often based on the knowledge of construction features, i.e. connections between orthogonal walls, floor types and presence of tie beams, which are difficult to detect in old urban centres. The existing masonry buildings in historic centres are often grouped in aggregates. So, clustered buildings are sets of independent structural units (SUs) which interact to each other under seismic actions. Since SUs are often characterized by masonry walls with poor mechanical properties, as well as by poor connections between orthogonal walls and between walls and floors, their seismic behaviour is no easy to be determined [5, 6].

However, the performance of clustered buildings is influenced by several factors, that mainly depend on the interactions between the individual SUs. Moreover, the presence of effective interconnections between SUs prevents the occurrence of local collapse mechanisms. Instead, the presence of geometrical irregularities in height and/or the lack of an effective connection between orthogonal walls can cause the activation of out-of-plane collapse mechanisms [1,7,8].

The bearing capacity of individual SUs may differ significantly from the whole aggregate one. A SU inside of a building aggregate has a highly non-linear and complex behaviour, which can lead to evaluation errors in the evaluation of its seismic behaviour. Therefore, it is essential to consider simplified, but reliable, structural models, which should foresee as well as possible the vulnerability level of the aggregated constructions [9-13].

The main vulnerability factors are the elevation discontinuities between adjacent units, the presence of staggered floors and the structural heterogeneity usually leading to disconnections of walls. All of these factors must be taken into account when studying the global seismic capacity of buildings, because they significantly affect the dynamic response of the structures. In this framework, in various studies many mechanical models accounting for uncertainties associated to the vulnerability factors have been developed to quantify the seismic response of the whole aggregate [14-16].

Based on these considerations, the present study focuses on the seismic response of a masonry aggregate located in Cercola, a municipality near the city of Naples, in the South of Italy. The selected aggregate consists of four SUs (two head units and two intermediate ones) arranged in line, which interact to each other under earthquake. These clustered buildings date back to the 19th century and they are representative of the most common building classes present in the Campania Region. In this study the influence of structural units on the global response of the whole aggregate is investigated. For this reason, non-linear static analyses are carried out to simulate the response of structural units in both isolated and aggregate conditions and their seismic responses are compared with those of the whole aggregate. Finally, by selecting the most unfavourable analysis conditions, the fragility curves proposed in [17] are developed and illustrated for all examined cases in order to estimate their propensity at seismic damage.

2 THE CASE STUDY

The case study is a masonry building aggregate located in the municipality of Cercola (Figure 1), an urban district located near Naples. This agglomerate of constructions was built at the end of the 19th century as one of the most representative example of the classic typology of clustered buildings of the Campania Region historical centres. From a structural point of view, it consists of 4 structural units, two in the head position and two in intermediate one. The head SUs have 3 floors, while the intermediate SUs develop on 4 floors. Buildings have commercial use at ground floor and residential use at other floors. Figure 2a shows the external view of the aggregate main façade, while the geometrical plan layouts of the clustered buildings are shown in Figures 2b, 2c and 2d. The head SUs have the first floor characterized by masonry vaults, while the remaining floors are made of wooden beams. The intermediate SUs have steel floors or RC ones at the first level. As the head SUs, the remaining floors are made of wooden beams. The masonry walls are characterised by Neapolitan yellow tuff stones and have an average thickness of 0.80 m at the first floor and 0.50 m at the other floors. Due to the absence of accurate on-site test procedures, wall mechanical properties are assumed according to the indications provided by the Italian Standard [18] by applying a confidence factor (FC) equal to 1.35, which corresponds to a knowledge level LC1 (limited knowledge) [18,19]. So, the wall mechanical features are as follows: average compressive strength (f_m)= 2.00 MPa; average shear strength (f_{v0})= 0.10 MPa; Young modulus (E)= 1410 MPa; Shear modulus (G) 450 MPa and dead weight (w)=16 kN/m³.

In order to estimate the aggregate seismic influence on single SUs, two different cases are studied: (i) the whole aggregate (Figure 2b) and the head structural unit (acronym HSU), both in aggregated (Figure 2e) and isolated (Figure 2f) configurations.



Figure 1: Identification of the case study.

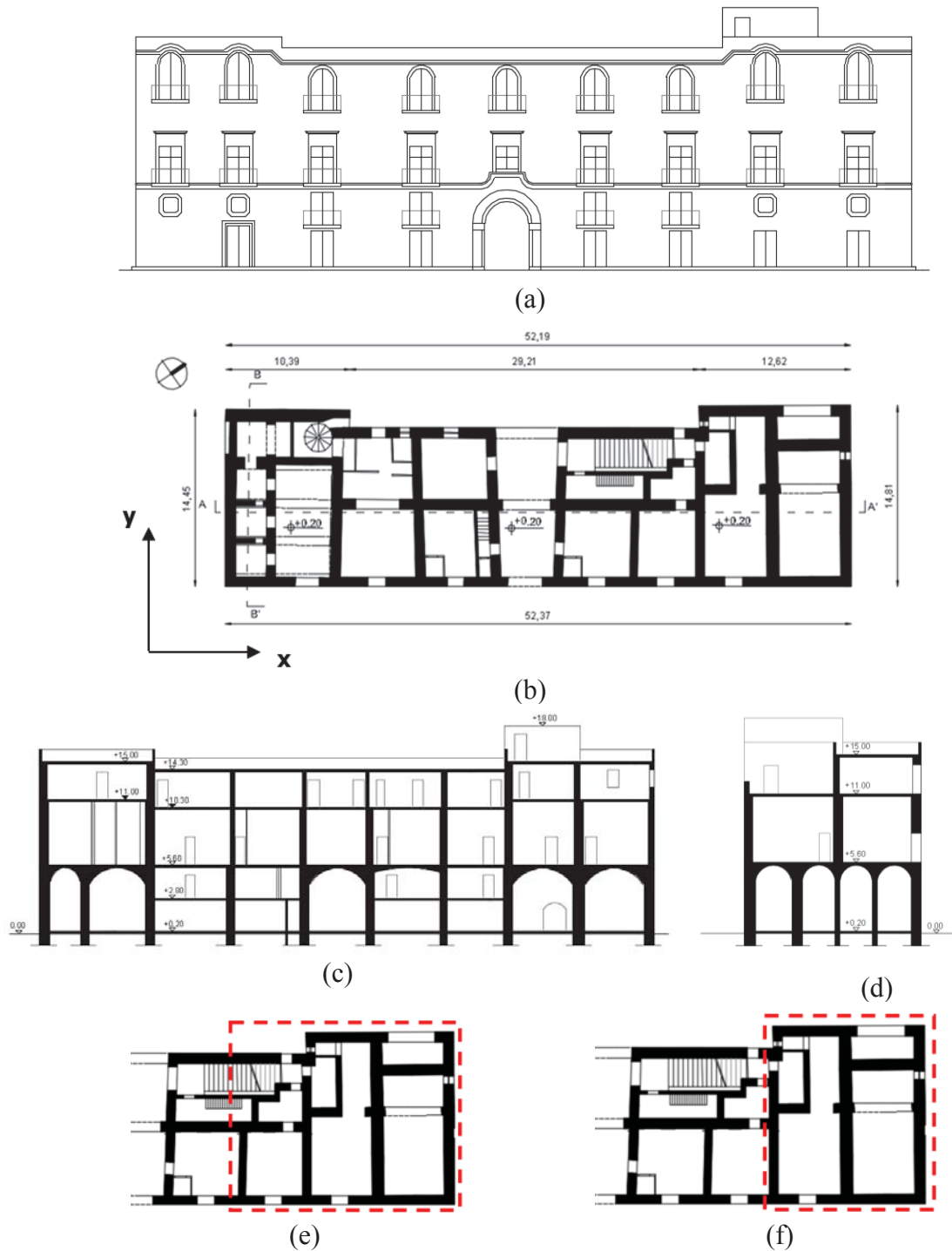


Figure 2: Graphic representation of the case study: main view (a), plan layout (b) and sections (c, d) of the building aggregate; aggregated (e) and isolated (f) HUS plan layouts.

3 NUMERICAL MODELS

The numerical models are carried out using three different FE analysis programs based on 2 different modelling approaches: from one side, the equivalent frame adopted by 3MURI and CDS win and, on the other side, the shell model adopted by Edilus. Figures 3,4 and 5 shows

numerical models developed by the three employed software packages. The basic modelling concepts of the implemented FEM models are shown in the following sections.

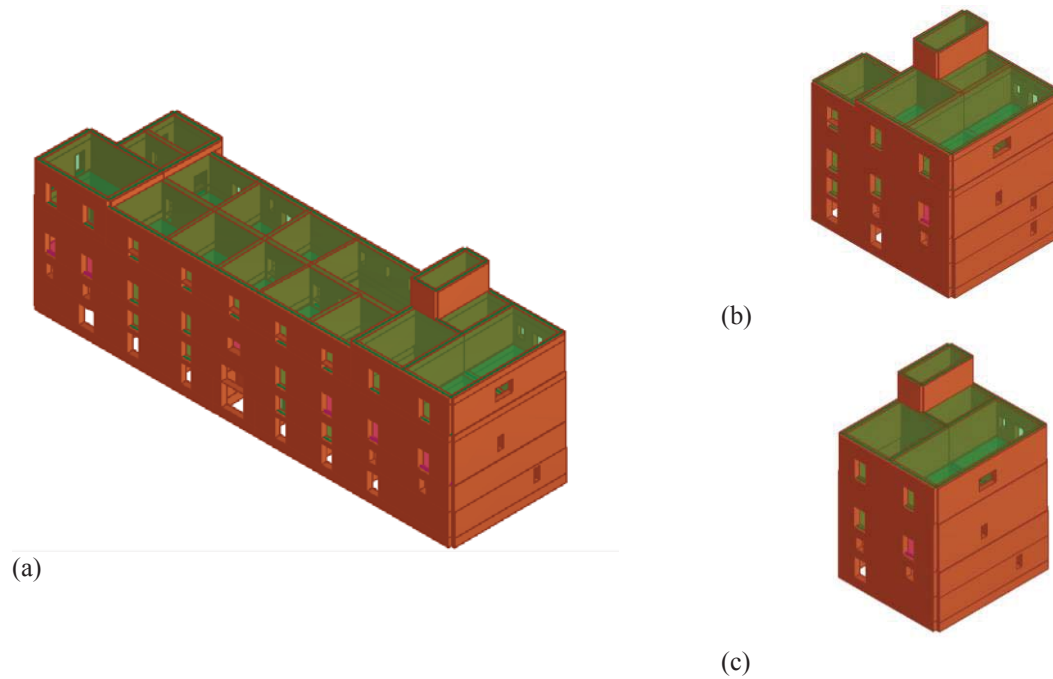


Figure 3: The 3MURI software numerical models: whole aggregate (a) and HSU in aggregated (b) and isolated (c) conditions.

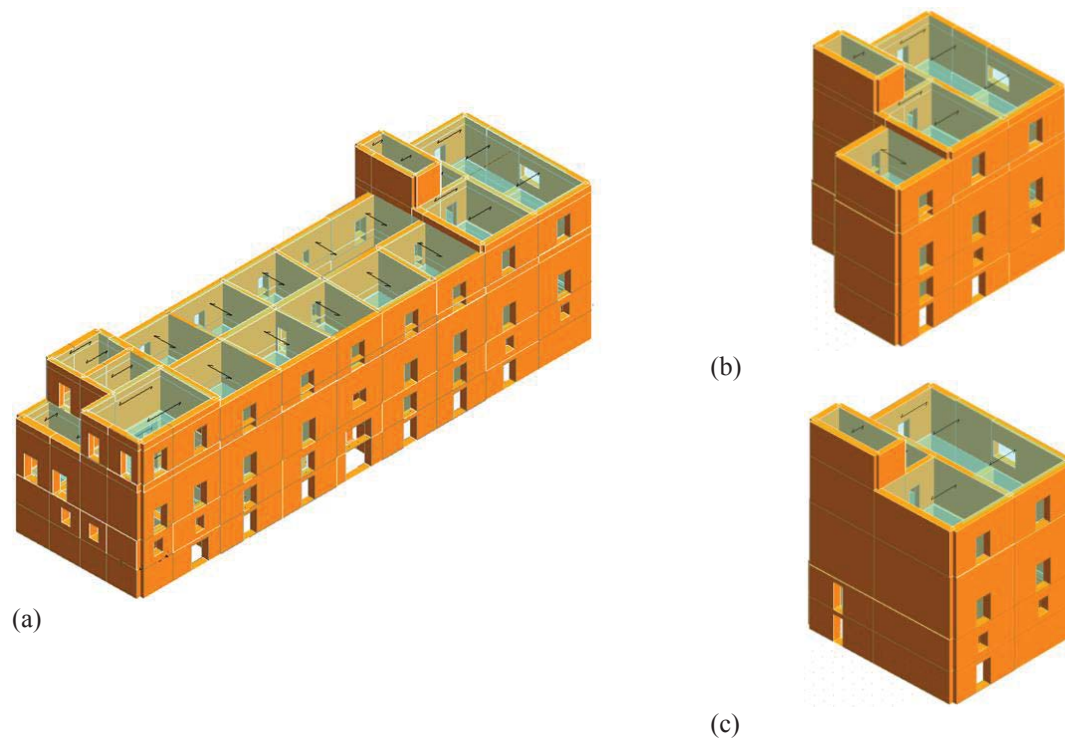


Figure 4: The CDS Win software numerical models: whole aggregate (a) and HSU in aggregated (b) and isolated (c) conditions.

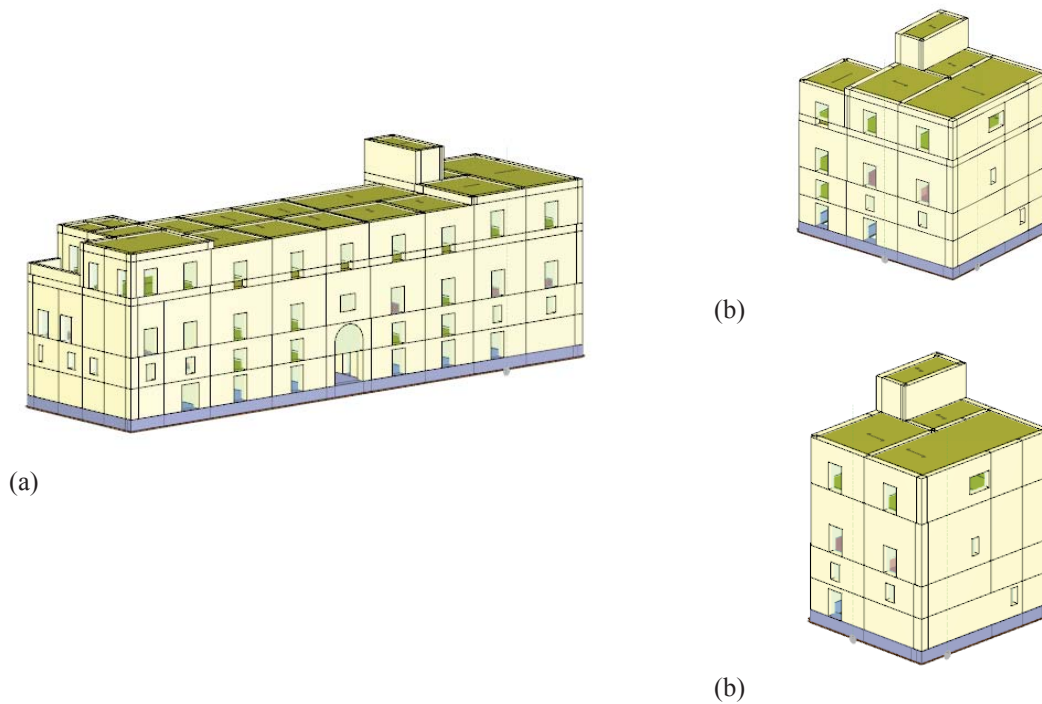


Figure 5: The Edilus software numerical models: whole aggregate (a) and HSU in aggregated (b) and isolated (c) conditions.

3.1 Equivalent frame model

3MURI and CDS analysis programs adopt a mathematical model based on Frame by Macro-Elements (FME) theory, which implements the Equivalent Frame Model approach (Figure 6). The reference model is a three-dimensional equivalent frame, where the walls represent the vertical elements able to resist both vertical and horizontal loads. The horizontal elements, namely the floors, transfer the horizontal forces to the walls according to the stiffness they have in their own plane. Therefore, the numerical modelling of a building is carried out by inserting walls, which are discretized into macro-elements representative of deformable components (piers and spandrels), while nodes (rigid links) are masonry portions typically less subjected at seismic damage. Usually, rigid links connect piers and spandrels which are contiguous to the openings. The numerical analyses allow to foresee the expected damage mechanism into masonry buildings, which can occur in deformable elements by either shear or compression-bending. So, each pier is composed by three parts: one deformable in the element central part, having a certain strength value, and other two placed at the element ends, having infinite strength and stiffness. Instead, spandrels are represented with frame elements having horizontal axis. It is assumed that the deformable part corresponds to the opening length, while the element remaining part is modelled with infinitely rigid beams. Floors are modelled as finite elements with 3-node orthotropic membrane, having 2 degrees of freedom per node and connected to the three-dimensional nodes of the building model.

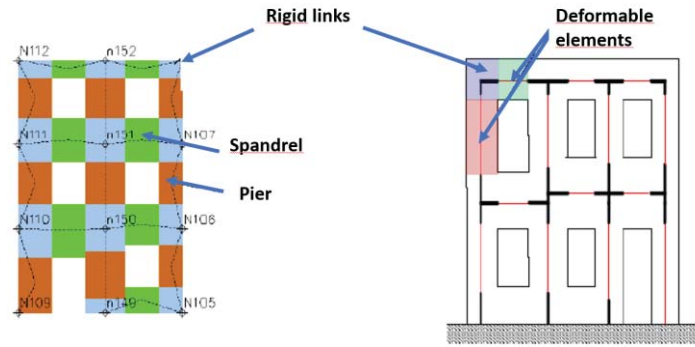


Figure 6: Schematic representation of the Equivalent Frame Model.

3.2 Shell model

Edilus software adopts the *Shell60* model, which consists of high-performance shell elements composed of a membrane part and a flexural one, whose effects can be coupled in order to have plates having large thickness and different layers, which can be anyway oriented. The membrane element has stiffness to normal rotation, which allows for a more faithful schematization of shell structures not completely connected to a plane and linked with beam elements. The implemented elements have triangular or quadrangular shape with three and four nodes, respectively. The quadrangular elements are obtained by automatically assembling several triangular elements. The triangular elements are High Performance Elements (HPE). However, the use of only triangular elements has undoubted advantages. In fact, the triangular elements allow for a faster analysis execution. The subdivision of any surface is also easier and more accurate.

The *Shell60* element (Figure 7) has a formulation that makes it rather insensitive to distortion. This feature is particularly useful in a pre-processing phase, which generate the mesh automatically. The formulation of the HPE *Shell60* element is based on the composition of an *AnDeS* triangular membrane element with drilling degree of freedom with the *DKT* (Discrete Kirchhoff Triangle) element. The degree of freedom towards rotation (drilling DoF) is added by describing the deformation of each side.

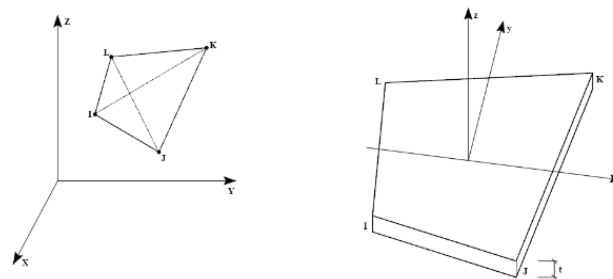


Figure 7: Linear shell model definition.

4 PUSHOVER ANALYSES

The seismic behaviour of the buildings facing the case study is investigated through pushover analyses. Based on the provisions of the Italian standard [19], these analyses are performed along the two main directions “X” and “Y” of the building aggregate (see Figure 2b). For each direction, the positive and negative accidental eccentricities are considered. Furthermore, 4 different verses of the seismic forces ($\pm X$, $\pm Y$) and 2 dissimilar force distributions (proportional either to masses or to the first vibration mode of the building) are considered.

So, 24 pushover analyses are performed. Figures 8, 9 and 10 show the pushover analysis curves in the 'X' and 'Y' directions performed with 3MURI, CDS Win and Edilus programs, respectively. In particular, for the sake of representation, among the 24 combinations, the worst one, that is the analysis minimizing the capacity acceleration of the aggregate, is considered.

The analysis results show that the most deformable direction is the "Y" one for the whole aggregate and the "X" one for HSU, both in aggregated and isolated conditions. In general, strength and stiffness increase switching from the HSU isolated, passing through the HSU (aggregated), to the whole aggregate. With respect to ductility, an opposite behaviour occurs.

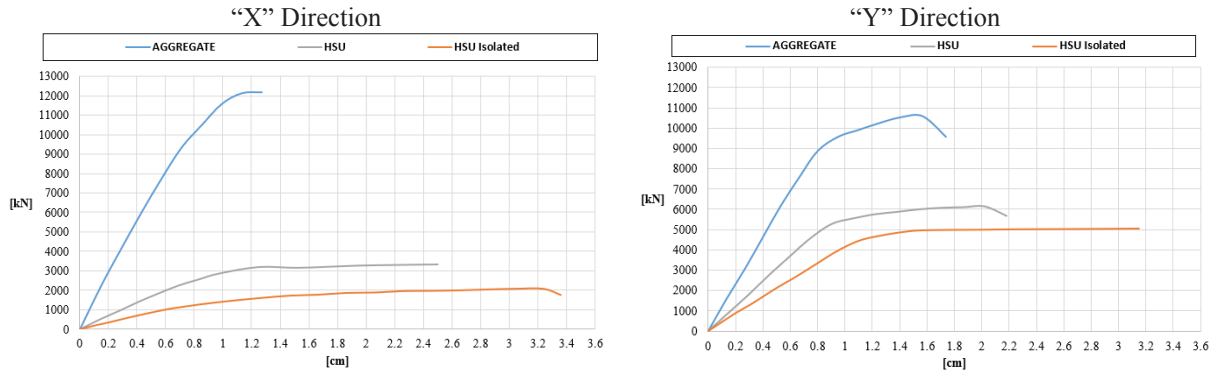


Figure 8: Pushover curves along X and Y directions carried out by the 3MURI software.

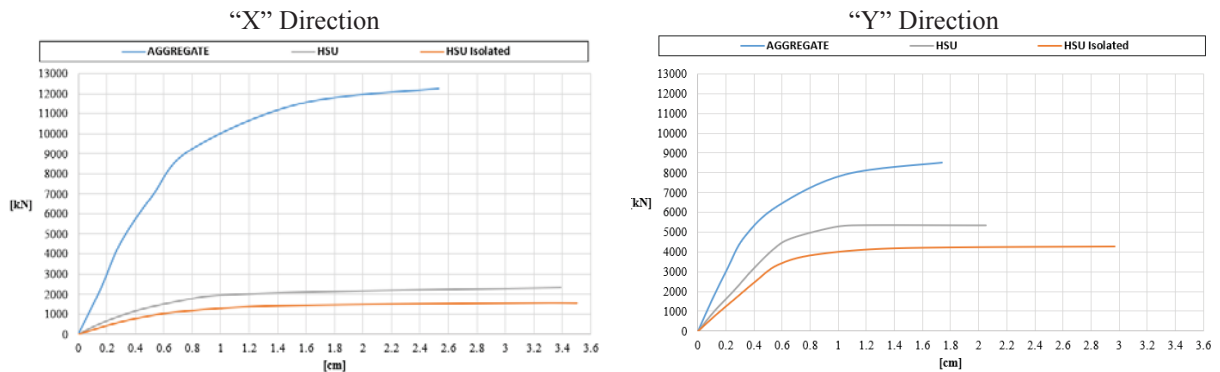


Figure 9: Pushover curves along X and Y directions carried out by the CDS Win software.

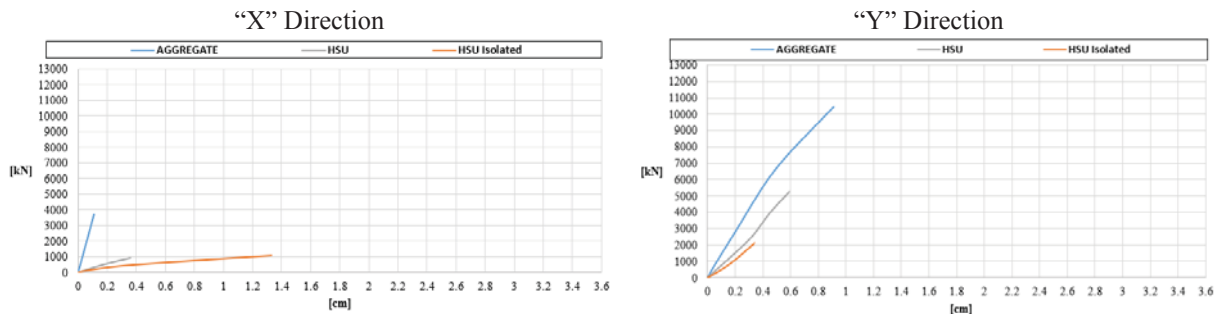


Figure 10: Pushover curves along X and Y directions carried out by the Edilus software.

The three models use different calculation solvers and the solutions obtained are not always like each other. Therefore, a comparison in terms of pushover curves is made. In this

case, only one curve for each software is taken into account. In particular, among the worst analyses performed with each analysis program, only the pushover curve proving the lowest resistance value of the aggregate is chosen. This curve is then compared with the corresponding curves of the other 2 programs, as shown in Figure 11.

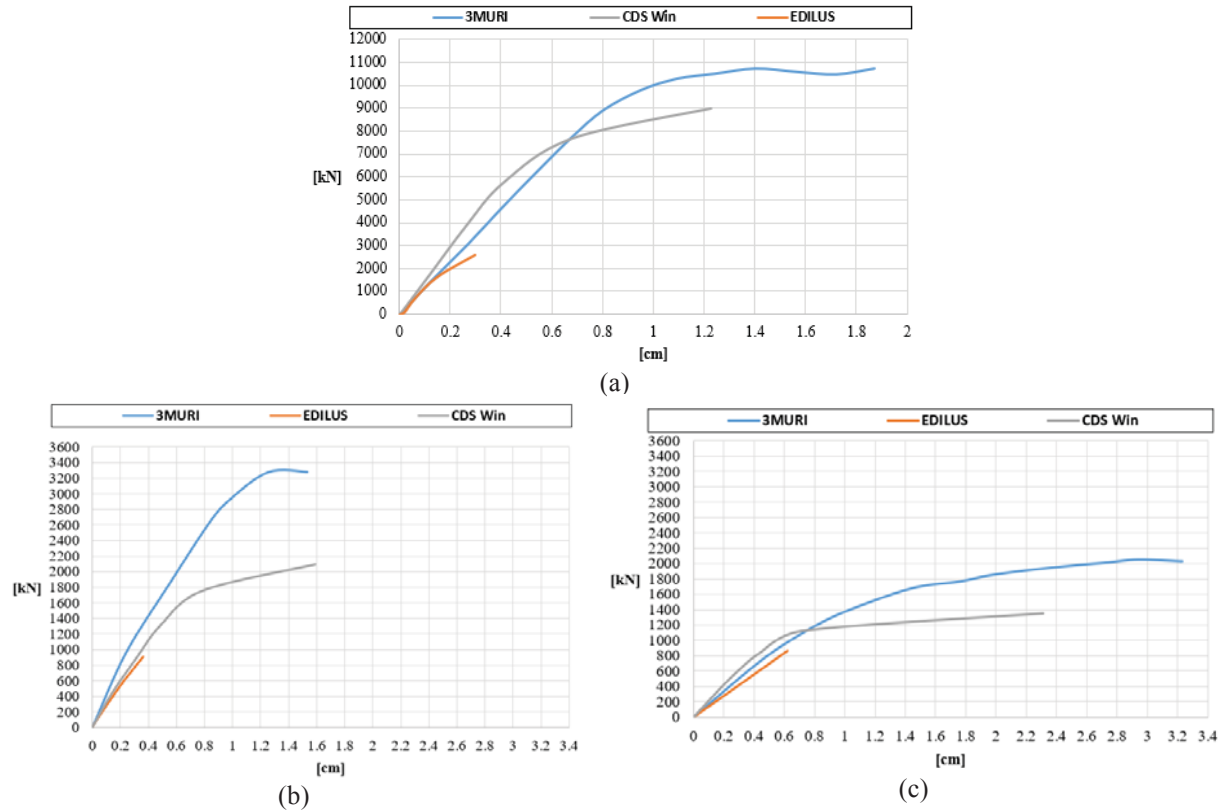


Figure 11: Comparison between analysis programs in terms of pushover curves: results for aggregate (a) and head structural unit in aggregated (b) and isolated (c) conditions.

From the analysis results presented in Figures from 8 to 11 it can be observed that the curves provided by the Edilus software have a different trend compared to the other ones. In fact, these pushover curves have an almost linear behaviour. This is because the software does not adopt a multi-collapse analysis procedure, but, when the first collapse mechanism occurs in the structure, the software stops the pushover curve. Conversely, 3MURI and CDS Win programs work with a multi-collapse analysis, where the analysis is not blocked when some elements attain the ultimate displacement, but the structure is pushed until collapse. This type of analysis is allowed by the Italian Standard [19] for existing masonry structures.

5 FRAGILITY ANALYSIS

In the last part of the study, the fragility curves of investigated buildings are derived. These curves represent the probability of exceeding a certain damage state varying the intensity measurement, generally represented by either the PGA or the spectral displacement. The evaluation of the fragility curves is carried out according to the methodology proposed in [17]. In particular, four damage levels, namely D1 (slight), D2 (moderate), D3 (near collapse), and D4 (collapse), are considered (Table 1). These damage states are defined starting from the yielding displacement (d_y) and ultimate displacement (d_u) of the SDoF system associated to the MDoF structural system. The fragility curves are analytically defined as follows:

$$P[DS|PGA]=\Phi\cdot\left[\frac{1}{\beta}\cdot\ln\left(\frac{PGA}{PGA_{DS}}\right)\right] \quad (1)$$

where Φ is the cumulative distribution function, PGA_{DS} is the median acceleration value associated to each damage threshold and β is the standard deviation of the log-normal distribution.

Damage thresholds, DS_i		
D1	$0.7 \cdot d_y$	Slight
D2	$1.5 \cdot d_y$	Moderate
D3	$0.5 \cdot (d_y + d_u)$	Near-collapse
D4-D5	d_u	Collapse

Table 1: Evaluated damage thresholds D_i [19]

Based on these above considerations, the fragility functions are plotted considering the most unfavourable structural analysis conditions both for the whole aggregate (Figure 12) and the head structural unit in aggregated (Figure 13) and isolated (Figure 14) conditions.

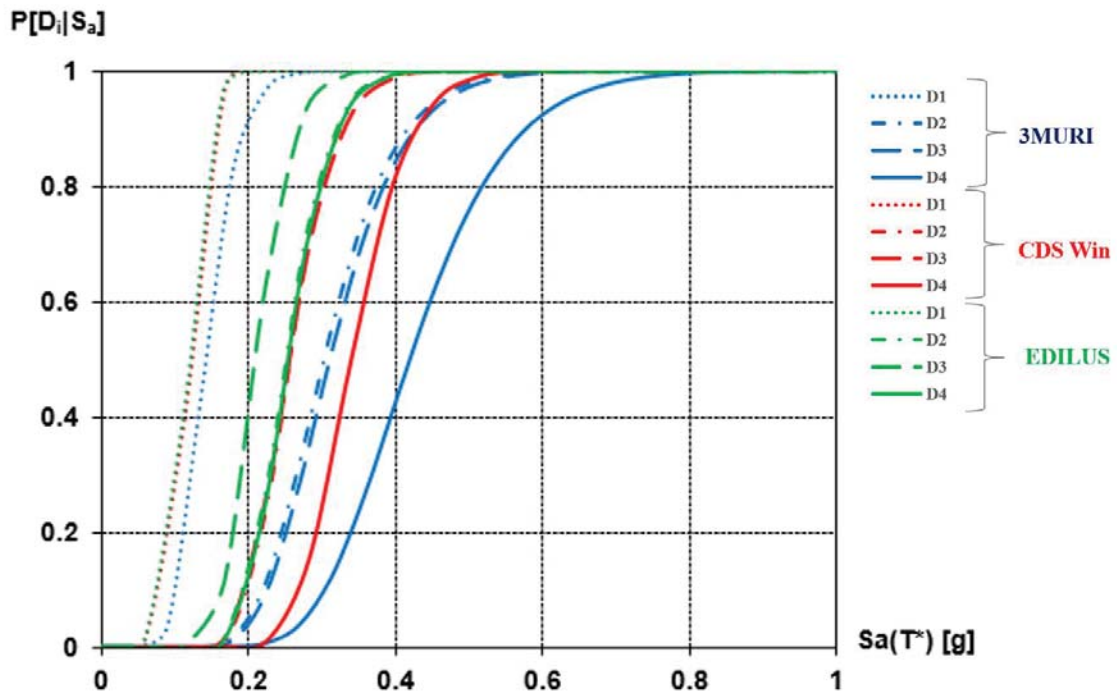


Figure 12: Comparison among fragility curves of the whole aggregate in “Y” direction based on the pushover curves deriving from the three used programs.

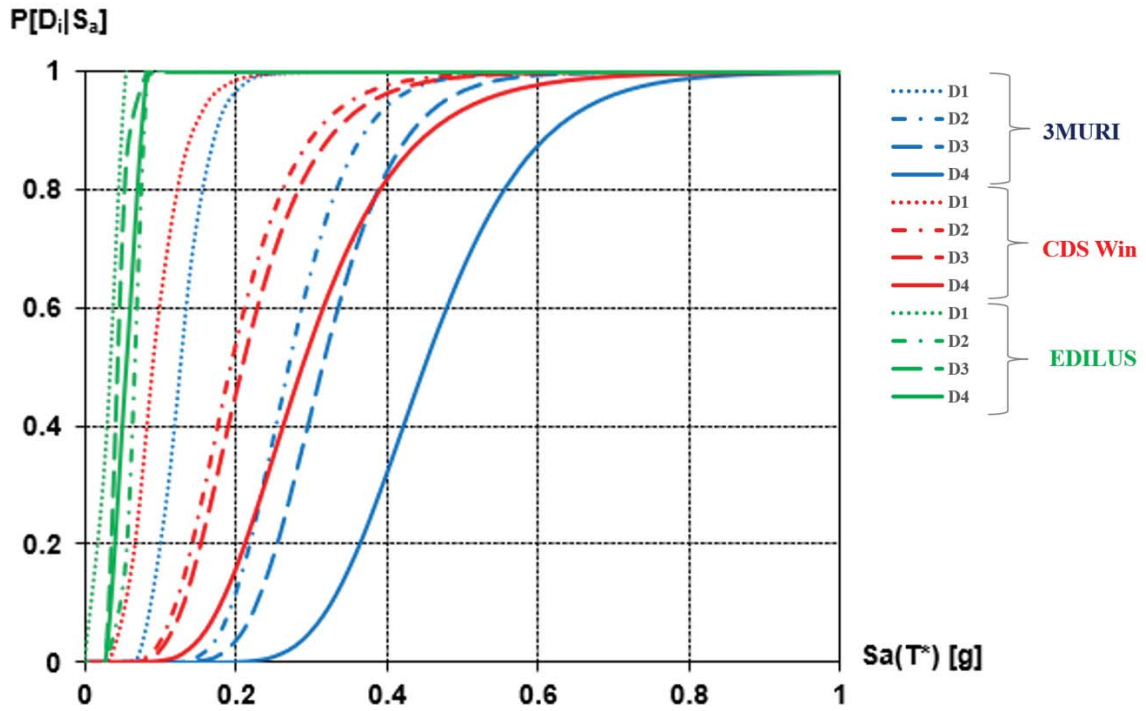


Figure 13: Comparison among fragility curves of the aggregated HSU in “X” direction based on the pushover curves deriving from the three used programs.

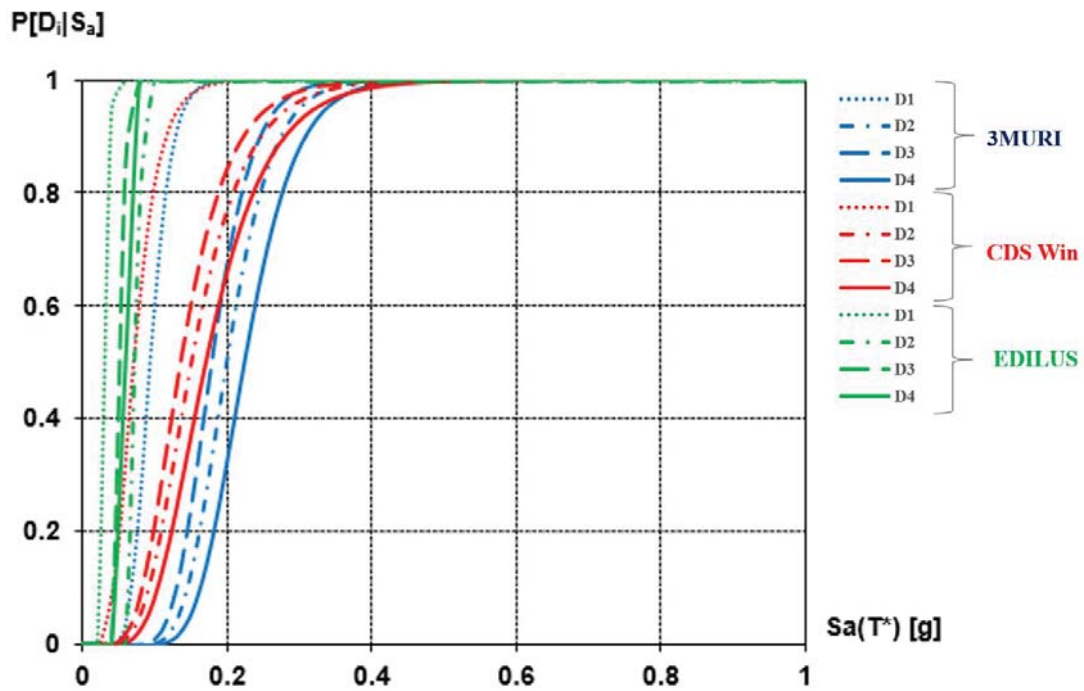


Figure 14: Comparison among fragility curves of the isolated HSU in “X” direction based on the pushover curves deriving from the three used programs.

From the acquired results it is observed that for all cases the probability of exceeding a certain threshold of damage D_i ($i = 1, \dots, 4$) is greater for the HSU in isolated condition. Fur-

thermore, the probability increases passing from the whole aggregate to the HSU in aggregated condition.

Finally, it is possible to make some considerations on the results achieved from different programs used. In particular, it is found that the Edilus software shows the most conservative results, while the CDS Win exhibits safety thresholds higher than those of the 3MURI Software. Considering that the PGA of Cercola at Collapse Limit State (CLS) is 0.263g [18], in Tables 2,3 and 4 the expected damages evaluated with the different programs for the whole aggregate, the aggregated HSU and the isolated HSU are respectively shown.

Whole aggregate				
Software	D₁	D₂	D₃	D₃
3MURI	99.35%	28.18%	25.07%	2.03%
CDS Win	99.95%	55.55%	55.55%	8.50%
Edilus	100%	86.85%	60%	56.88%

Table 2: Expected damages for the whole aggregate.

Aggregated HSU				
Software	D₁	D₂	D₃	D₃
3MURI	99.54%	64.76%	23.60%	3.36%
CDS Win	100%	80%	74.15%	40.16%
Edilus	100%	100%	100%	100%

Table 3: Expected damages for the aggregated HSU.

Isolated HSU				
Software	D₁	D₂	D₃	D₃
3MURI	100%	94.18%	86.75%	74.84%
CDS Win	100%	96.04%	92.55%	86.81%
Edilus	100%	100%	100%	100%

Table 4: Expected damages for the isolated HSU.

6 CONCLUSIONS

In this paper the seismic response of a masonry building aggregate located in Cercola, a municipality near the city of Naples, was investigated. The aggregate is made of four SUs, namely two in heading position and two in intermediate one. Both the whole aggregate and the single SUs, both in isolated and aggregate conditions, were analysed to estimate the influence of the mutual interaction among adjacent structural units. Non-linear static analyses were carried out according to the Italian standards using three Italian popular programs, namely 3MURI, CDS Win and EDILUS, which work with different modelling approaches to schematise the seismic behaviour of existing masonry buildings. From the non-linear analysis results it was observed that in most cases the maximum strength and stiffness are offered by the whole aggregate and they reduced with the aggregated SU and much more with the isolated SU. On the contrary, the structural ductility offered by the US in isolated condition is more pronounced than the one of the aggregated US, which exhibited greater ductility than that of the aggregate. Finally, the fragility curves of the buildings under study were plotted to estimate expected damages as a function of different PGA levels. The results achieved showed

that the Edilus software provides the most conservative results, while CDS Win exhibits safety thresholds higher than those of the 3MURI Software.

ACKNOWLEDGEMENTS

The Authors would like to acknowledge the DPC-ReLUIIS 2019-2021 research project for the financial support to the development of the research activity presented in the current paper.

REFERENCES

- [1] A. Formisano, Theoretical and Numerical Seismic Analysis of Masonry Building Aggregates: Case Studies in San Pio Delle Camere (L'Aquila, Italy). *Journal of Earthquake Engineering*, **2017**, 21, 227-245, 10.1080/13632469.2016.1172376.
- [2] N. Chieffo, A. Formisano, Geo-hazard-based approach for the estimation of seismic vulnerability and damage scenarios of the old city of Senerchia (Avellino, Italy), *Geosciences* (Switzerland). **2019**, 9, doi:10.3390/geosciences9020059.
- [3] A.H. Barbat, M.L. Carreño, L.G. Pujades, N. Lantada, O.D. Cardona, Marulanda, M.C. Seismic vulnerability and risk evaluation methods for urban areas. A review with application to a pilot area. *Structure and Infrastructure Engineering*, **2010**, 6, 17-38, 10.1080/15732470802663763.
- [4] G. Marghella, A. Marzo, B. Carpani, M. Indirli, A. Formisano, Comparison between in situ experimental data and Italian code standard values, in Brick and Bloc Masonry: trends, Innovations and Challenges. In Proceedings of the 16th International Brick and Block Masonry Conference, IBMAC (Padua), **2016**, 1707–1714.
- [5] N. Chieffo, I. Onescu, A. Formisano, M. Mosoarca, M. Palade, Integrated empirical-mechanical seismic vulnerability analysis method for masonry buildings in timișoara: Validation based on the 2009 Italian earthquake. *The Open Civil Engineering Journal*, **2020**, 14, 314–333, doi: 10.2174/1874149502014010314.
- [6] A. Formisano, G. Vaiano, F. Fabbrocino, G. Milani, Seismic vulnerability of Italian masonry churches: The case of the Nativity of Blessed Virgin Mary in Stellata of Bondeno. *Journal of Building Engineering*, **2018**, 20, pp. 179-200.
- [7] A. Formisano, N. Chieffo, B. Milo, F. Fabbrocino, The influence of local mechanisms on large scale seismic vulnerability estimation of masonry building aggregates, *AIP Conference Proceedings 1790*, **2016**, art. no. 130010, DOI: 10.1063/1.4968728.
- [8] P. B. Lourenço, J.A. Roque, Simplified indexes for the seismic vulnerability of ancient masonry buildings, *Construction and Building Materials*, **2006**, 20, pp. 200–208.
- [9] P. B. Lourenço, D.V. Oliveira, J.C. Leite, J.M. Ingham, C. Modena, F. Da Porto, Simplified indexes for the seismic assessment of masonry buildings: International database and validation, *Engineering Failure Analysis*, **2013**, 34:585–605.
- [10] P.A. Mezzapelle, F. Clementi, S. Lenci, The seismic vulnerability of historic masonry buildings: from knowledge to structural consolidation, *Cultural capital: Studies on the Value of Cultural Heritage* (in Italian), n. 16, **2017**.

- [11] D. Rapone, G. Brando, E. Spacone, G. De Matteis, Seismic vulnerability assessment of historic centers: description of a predictive method and application to the case study of scanno (Abruzzi, Italy). *International Journal of Architectural Heritage*. **2018**, 12, 1171–1195, doi:10.1080/15583058.2018.1503373.
- [12] F. Clementi, V. Gazzani, M. Poiani, S. Lenci, Assessment of seismic behaviour of heritage masonry buildings using numerical modelling. *Journal of Building Engineering*, **2016**, 8, 29-47, 10.1016/j.jobbe.2016.09.005.
- [13] A. Formisano, A. Marzo, Simplified and refined methods for seismic vulnerability assessment and retrofitting of an Italian cultural heritage masonry building. *Computers and Structures*, **2017**, 180, 13-26, 10.1016/j.compstruc.2016.07.005.
- [14] M. Mosoarca, I. Onescu, E. Onescu, Anastiasadis, A. Seismic vulnerability assessment methodology for historic masonry buildings in the near-field areas. *Engineering Failure Analysis*, **2020**, 115, <https://doi.org/10.1016/j.engfailanal.2020.104662>, 2020.
- [15] M. Mosoarca, I. Onescu, E. Onescu, B. Azap, N. Chieffo, M. Szitar-Sirbu, Seismic vulnerability assessment for the historical areas of the Timisoara city, Romania. *Engineering Failure Analysis*, **2019**, 101, 86-112.
- [16] D. D'Ayala, A. Ansal, Non linear push over assessment of heritage buildings in Istanbul to define seismic risk. *Bulletin of Earthquake Engineering*, **2012**, 10, 285-306, 10.1007/s10518-011-9311-1.
- [17] S. Cattari, E. Curti, S. Giovinazzi, S. Lagomarsino, S. Parodi, A. Penna, *Un modello meccanico per l'analisi del costruito in muratura a scala urbana*. In Proceedings of the XI Congresso Nazionale “L’ingegneria Sismica in Italia”, ANIDIS (Genova), 2004, (in Italian).
- [18] Ministry of Infrastructure and Transport. *Instructions for the application of the new technical code for constructions* (in Italian), Official Gazette (nr. 35 of 11-02-2019), Rome, 2019.
- [19] Ministry of Infrastructure and Transport. *Technical standards for construction* (in Italian), Official Gazette (nr. 42 of 20-2-2018), Rome, 2018.

TERRITORIAL ANALYSIS OF SEISMIC PERFORMANCE OF ANCIENT CHURCHES: METHODS AND APPLICATION TO CASE STUDIES

D'Amato M.¹, Laguardia R.², Gigliotti R.,² Formisano A.³

¹ DICEM – Dept. of European and Mediterranean Cultures: Architecture, Environment, Cultural Heritages, University of Basilicata, Via Lanera, 75100 Matera, Italy
michele.damato@unibas.it

² DISG – Dept. of Structural Engineering, “Sapienza” University of Rome,
Via Eudossiana 18, 00184 Rome, Italy
e-mail: {raffaele.laguardia, rosario.gigliotti}@uniroma1.it

³ Dept. of Structures for Engineering and Architecture, University of Naples “Federico II”,
Piazzale Tecchio 80, 80125 Naples, Italy
antoform@unina.it

Abstract

In this paper two simplified methods are presented in order to assess the seismic performance of a set of Italian ancient churches. The methods applied are characterized by an increasing refinement level, requiring only some qualitative information in order to evaluate representative indexes of global seismic response. The methods considered may be applied for screening and identifying the current priorities at a territorial level and for planning, where necessary, more refined analysis for evaluating seismic response and required interventions (if necessary). Finally, applications to case studies are illustrated and compared with the aim of highlighting the limitations of the methods considered.

Keywords: Ancient masonry churches, cultural heritage, monuments, seismic risk, seismic vulnerability

1 INTRODUCTION

Recent earthquakes have revealed, due to significant damage encountered, high vulnerability of cultural heritage [1]-[2]. Therefore, to date several works have been proposed in the published literature in order to evaluate the actual seismic risk of existing structures, considering different cultural heritage assets, such as palaces, old buildings, churches, monuments, etc. [3]-[7].

Among these works, also fast appraisal methods for preliminary screening the seismic vulnerability at a territorial level have been proposed, too. They have the advantage of requiring, with limited costs, few and not quantitative information for estimating a global index (also indicated as score) useful, in relative terms, for comparing seismic performance of an entire territorial asset. At the end of this preliminary screening, more refined methods have to be applied for specific and more precise evaluations, and also for designing the interventions required [8]-[15].

Recently a multilevel approach is indicated by Italian Directive [16], where three Levels of Valuation (LV) are considered for seismic assessment. These levels, indicated as *LV1*, *LV2* and *LV3* have a different refinement level requiring an increasing information amount. Specifically, the first two levels (*LV1* and *LV2*) are established on simplified analyses for seismic assessment, while FEM analyses are possible through the *LV3* level. In addition, with particular reference to ancient churches, recently in accordance with the approach indicated by the Italian Directive, also a simplified method has been proposed in [14, 15] indicated as *Level of Evaluation 0 (LV0)*. This method is very simple to apply and, coherently with the multilevel approach indicated in [16], is simpler to use representing a fast appraisal method useful at a territorial scale as decision-making tool, and applicable with only qualitative and historical information.

This paper deals with a territorial analysis of seismic performance of an ancient churches set located in the historic centre of Matera (Italy), recognized as UNESCO site since 1993. In particular, the main results obtained are illustrated and commented by applying the *LV0* method proposed in [14, 15], and the *LV1* method proposed by the Italian Directive [16]. More details on the churches considered and on the obtained results are reported elsewhere [9, 14].

2 LV0 METHOD [14, 15]

This method, proposed and validated in [14, 15], is particularly devoted to territorial seismic analyses of ancient churches. It provides, for each church examined, *seismic risk score R*, by applying the symbolic risk equation [17, 18]:

$$R = H \times V \times E \quad (1)$$

where *H*, *V*, and *E* are, respectively, the scores assigned to hazard, vulnerability and exposed elements or assets at risk. The score for each factor is calculated by means of a specific tool, as specified in the following:

Tool 1 allows of rating the exposition *E*, through information gathered from classifications of investigated cultural heritage and any conservation document;

Tool 2 provides a scoring related to the seismic hazard considering many threats with the related hazard maps;

Tool 3 is referred to the seismic vulnerability assessment. It assigns a score starting from the available information provided in the other seismic vulnerability forms and any other historic documents archives.

This method may be also implemented for assessing the seismic vulnerability provided that, unless the exposition factor E , the higher the seismic risk the higher the seismic vulnerability. Therefore, under this assumption the *seismic risk score* R , may be calculated as:

$$R = [H + 1] \times V \quad (2)$$

where the score R , in accordance with the simplified method, may be calculated through the scores H and V , obtained with the *Tool 2* and *Tool 3*, respectively. Moreover, as proposed in this method the score is added to unity for obtaining the resulting score R greater than one. In the following *Tool 2* and *Tool 3* are briefly described since applied in this study. More details about the *Tool 1* may be found in [14, 15].

2.1 Tool 2

Tool 2 is addressed to provide a score regarding several threats including the seismic action. Threats are divided, according to the occurrence frequency, in “*sporadic events*” and “*continuous processes*”. The intensity assessment may be conducted by referring to existing documents where events occurred into past are reported. If no information is available, therefore a possible intensity estimation may be done considering also data available within the scientific literature. In the following sporadic and continuous processes considered are listed.

Sporadic events. This group considers:

- i. *earthquake*, expressed through the maximum Mercalli Intensity;
- ii. *landslide or rock fracture* as a consequence of an earthquake.

Continuous processes. The following processes are considered:

- iii. *rainfall erosion*, due to the precipitations amount depending on coastal distance, relative humidity, direction and speed of prevailing winds;
- iv. *physical stress*, to assess the material damage provoked by temperature oscillations as, for instance, particles water icing with a consequent disintegration or cracking of materials;
- v. *air pollution*, associated to traffic of vehicles, airplanes and boats, producing dissolution by acid rainfalls;
- vi. the *socio-organizational, threat* analysing the overload or damage on the monuments for the presence of intensive tourism and possible vandalism;
- vii. *demographic decline*, provoking monuments abandonment and maintenance lack.

The damage score $h_{k,i}$, assigned to the k -th threat, is reported in the Table 1 for three different intensities: *no hazard*, *low or gradual*, *catastrophic*.

The resulting *seismic hazard score*, that is a dimensionless parameter ranging between 0 and 1, is given by the expression:

$$H = \sum_{k=1}^7 h_{k,i} \quad (3)$$

Table 1–Seismic hazard scoring [14, 15].

Threats		Severity of damage $h_{k,i}$		
		No damage/ No hazard	Low or gradual	Catastrophic
<i>Sporadic events</i>	Seismic action	0	0.20	0.40
	Landslide or rock fracture	0	0.15	0.25
<i>Continuous processes</i>	Erosion	0	0.05	0.10
	Physical stress	0	0.05	0.10
	Air pollution	0	0.01	0.05
	Socio - organizational	0	0.01	0.05
	Demographic decline	0	0.01	0.05

2.2 Tool 3

Tool 3 provides a score related to the seismic vulnerability assessment. In order to provide a fast vulnerability estimation several factors are considered, including:

- foundation system and building position*, in order to consider potential weaknesses or deficiencies of foundations;
- plan and elevation irregularity*, that may increase, as known, the vulnerability of the building against earthquakes;
- distance between walls*, by considering wall slenderness, out of plumb, excessive length in plan between two transversal walls and other potential weaknesses;
- non-structural elements*, by considering potential failures of hanged elements or other accessories;
- roof configuration*, by evaluating the roof deformability, its connection to the walls and the effects of thrusts on the walls;
- conservation status*, by considering eventual existing damages and the global and local conservation situations;
- fire vulnerability*.

Four different vulnerability levels are considered for each parameter that are *A*, *B*, *C*, *D*, where *A* is assigned in the case of absent (or very low) vulnerability, while level *D* corresponds to the case of high vulnerability. The resulting *vulnerability score* V , may be calculated as weighted sum of the vulnerability scores assigned to each parameter considered:

$$V = \sum_{k=1}^{13} \rho_k v_{k,i} \quad (4)$$

where $v_{k,i}$ is the vulnerability score of the k -th parameter and ρ_k the associated weight (Table 2).

Table 2 – Parameters scores and weights for seismic vulnerability evaluation [14, 15].

Parameter		Vulnerability $v_{k,i}$				Weight ρ_k
		A	B	C	D	
1	Position of the building and foundations	0	1.35	6.73	12.12	0.75
2	Floor plan configuration or geometry	0	1.35	6.73	12.12	0.5
3	Elevation configuration	0	1.35	6.73	12.12	1.0
4	Distance between walls	0	1.35	6.73	12.12	0.25
5	Non-structural elements	0	1.35	6.73	12.12	0.25
6	Type and organization of the resistant system	0	1.35	6.73	12.12	1.5
7	Quality of the resistant system	0	1.35	6.73	12.12	0.25
8	Horizontal structures	0	1.35	6.73	12.12	1.0
9	Roof configuration	0	1.35	6.73	12.12	1.0
10	Conservation status	0	1.35	6.73	12.12	1.0
11	Environmental alterations	0	1.35	6.73	12.12	0.25
12	Construction system alterations	0	1.35	6.73	12.12	0.25
13	Fire Vulnerability	0	1.35	6.73	12.12	0.25

3 LV1 METHOD [16]

The Italian Directive [16] proposes a multilevel approach for evaluating the seismic performance of a cultural heritage. As introduced, this approach consists of three different Levels of Evaluation, namely *LV1*, *LV2* and *LV3* having an increasing refinement level.

In particular, this study focuses on the *LV1* related to the ancient masonry churches proposed in [16], indicated for preliminary evaluation at a territorial scale. This method is particularly simple to use since only qualitative information gathered with a visual inspection are

required. The method assigns a *vulnerability index* i_v , and then estimates the ground acceleration corresponding to the achievement of a certain limit state. This procedure does not allow of designing any structural intervention.

As for the i_v , it may be comprised between 0 and 1, and estimated through the expression:

$$i_v = \frac{1}{6} \frac{\sum_{k=1}^{28} \rho_k (v_{ki} - v_{kp})}{\sum_{k=1}^{28} \rho_k} + \frac{1}{2} \quad (5)$$

In the previous equation ρ_k is the k -th collapse mechanism weight, equal to: 0 if the mechanism is not present or not active, or else between 0.5 and 1 in the other cases. v_{ki} and v_{kp} are scores assigned to the k -th mechanism measuring, according to this method, vulnerability and to any seismic-resistant device, respectively. The weights are equal to 1 for the most important macro-elements regarding the seismic behaviour of a church (such as façade overturning, nave longitudinal transversal response, triumphal arch transversal response, etc.), while secondary mechanisms (such as prothyrum – narthex response, mechanisms of transepts and chapels) may have a weight varying between 0.5 and 1 [16].

Once the *vulnerability index* i_v is calculated, ground acceleration corresponding to achievement of *Damage Limit State (DLS)* and *Life-Safety Limit State (LSLS)* may be estimated with the equations reported in the following, established on a statistical basis:

$$a_{DLS}S = 0.025 \cdot 1.8^{2.75-3.44i_v} [g] \quad (6)$$

$$a_{LSLS}S = 0.025 \cdot 1.8^{5.1-3.44i_v} [g] \quad (7)$$

4 APPLICATION TO CASE STUDIES

4.1 Description of case studies chosen

The *LV0 method* [14, 15] and the *LV1 method* [16] are applied in order to perform a territorial scale evaluation regarding five ancient masonry churches. They fall within the historic centre of Matera (Italy), recognized UNESCO site since 1993. The case studies chosen are illustrated in Figure 1 where, for brevity, only a plan of each church considered is reported. The churches considered in this study are: *SS Maria della Bruna*, *San Giovanni Battista*, *San Pietro Caveoso*, *San Rocco*, *San Francesco d'Assisi*. They have in common the fact that they were constructed with the same masonry, composed by calcarenite units of sedimentary rock, improperly named ‘tufo’ (tuff) due to its apparent similarity to the volcanic rock properly denominated tuff, and lime mortar joints. This rock has the main property of being a very porous rock, very soft and characterized by low-compressive strength. This masonry is present with an extraordinary continuity for realizing walls and vaulted structures, and quite often is present in recurrent dimensions. Usually, mortar joints have a thickness varying from 0.5 cm up to 1.5 cm, while blocks have the following dimensions: 45-60 cm length, 25-27 cm height, 20-25 cm width. All the churches have a one-floor elevation configuration and, in some case, they have also more than one nave; the roof structures are made with vaulted structures in masonry, or with wood elements in the case *San Pietro Caveoso* and *San Francesco d'Assisi*. In none of the considered churches interventions are present for reducing seismic vulnerability. A detailed description of the churches considered may be found in [9, 14].

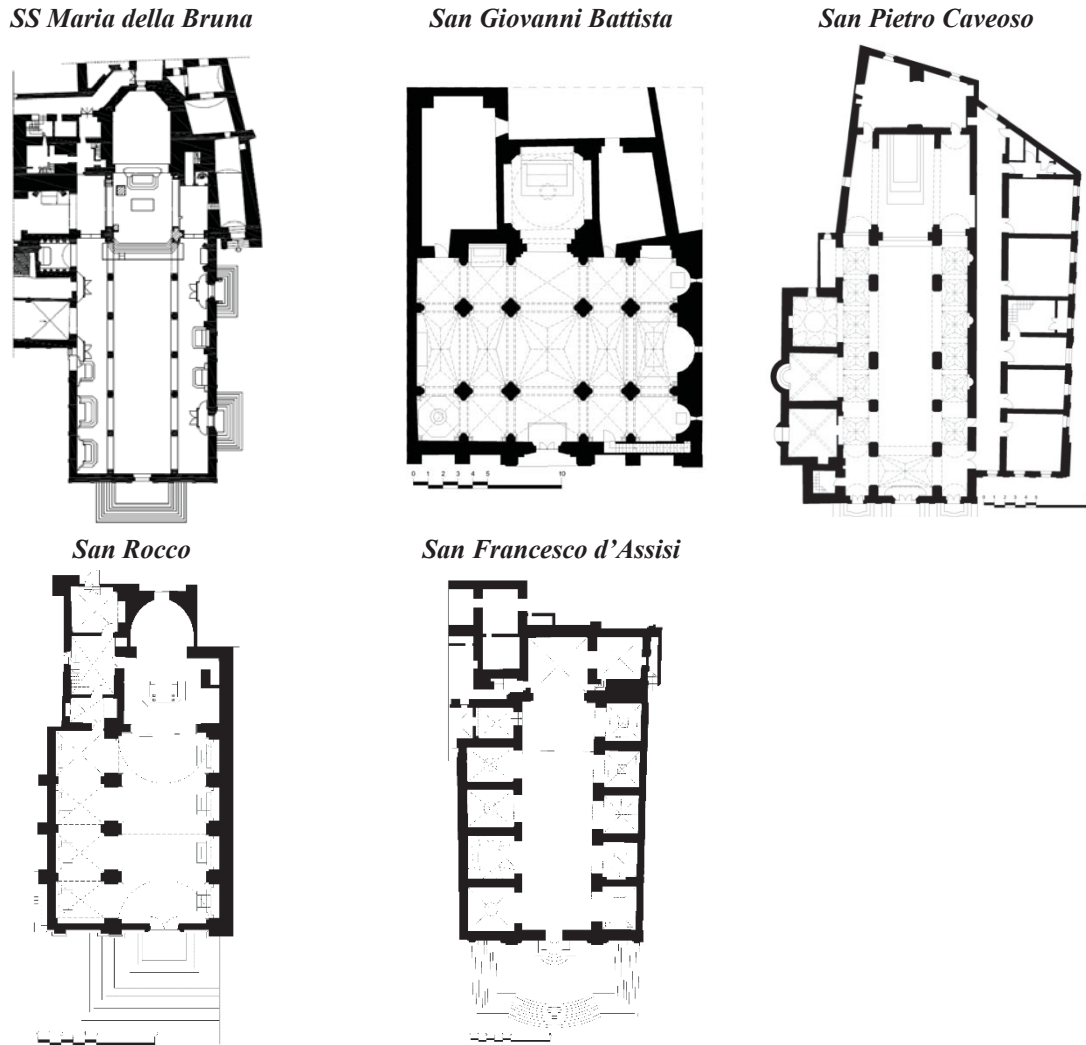


Figure 1 – Floor plan of the considered case studies

4.2 Application to case studies

The results of the application of the *LV0 method* are illustrated in the form of histogram in Figure 1. In particular: Figure 1a) reports the hazard assessment according to the Table 1 for obtaining the *seismic hazard score* H ; Figure 1b) illustrates the vulnerability assessment according to the Table 2 for obtaining the *vulnerability score* V ; and Figure 1c) summarizes the resulting *seismic risk score* R calculated with the Eq. (2). As one may see the lowest R score is obtained in the case of *SS Maria della Bruna* ($R=22.15$), while the highest one is obtained for *San Francesco church* (i.e. $R=30.46$). In the case of other churches (*San Giovanni Battista*, *San Pietro Caveoso*, *San Rocco*) similar R scores are found (25.00, 25.25, 25.39, respectively). The results of the seismic risk score reported in ascending order in the Figure 1c) are reported also into Figure 3, in terms of ratio R_i/R_{min} . R_i is the seismic risk score of each church, and R_{min} is the minimum score found, corresponding in this case to the *SS Maria della Bruna* score ($R=22.15$). The same figure also reports the results of the *LV1 method* as proposed by the Italian Directive [16]. As for the *LV1 method* results, the dimensionless return period $T_{i,LSLS}/T_{LSLSmin}$ and the dimensionless ground acceleration capacity $a_{i,LSLS}/a_{LSLSmin}$ for the *Life Safety Limit State (LSLS)* are reported. Details on these obtained results are reported in [9, 14]. Both these ratios express a measure of the seismic vulnerability resulting that the seismic vulnerability decreases as these ratios increase (in terms of acceleration or return period). By

comparing the results obtained with the *LV0* and *LV1 method*, it can be noted that both methods are in good agreement. Therefore, the *LV0 method* may be also used for ranking the seismic vulnerability of a certain sample at a territorial scale. It provides a seismic risk assessment having the same trend of the vulnerability assessment conducted with the *LV1 method*, resulting simpler to use since requires less information than the *LV1 method*.

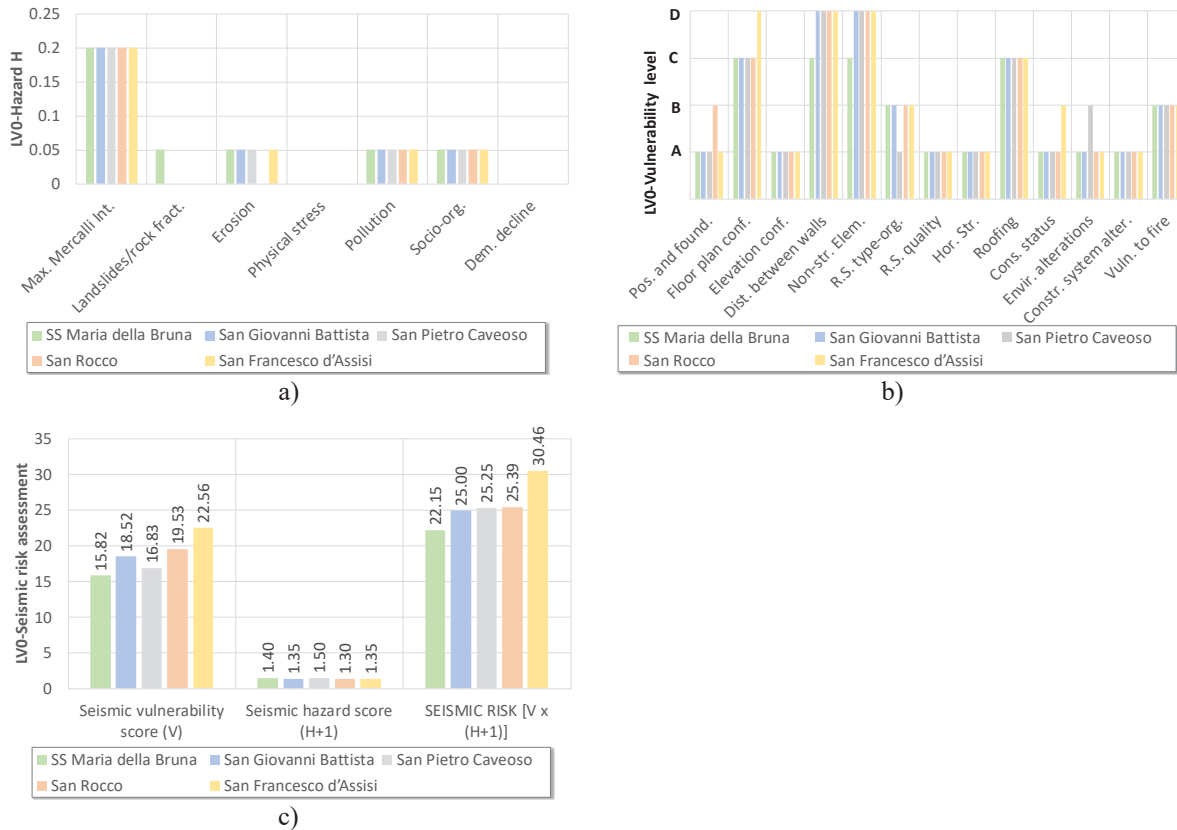


Figure 2 – Results of the LV0 method: a) Hazard assessment, b) vulnerability level assessment and c) resulting seismic risk

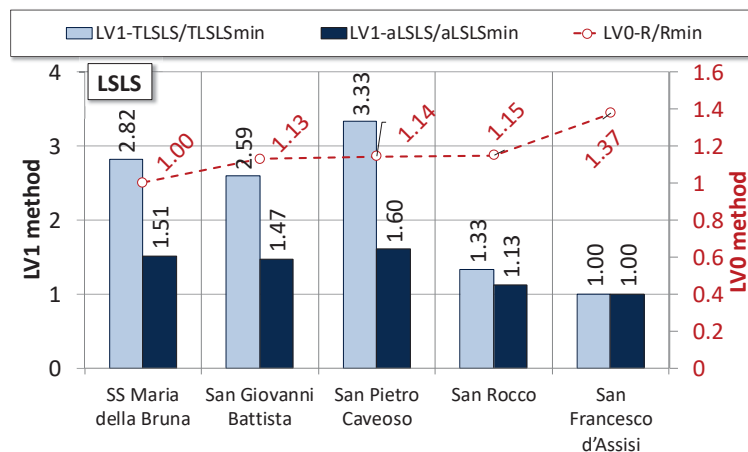


Figure 3 - Comparison of results obtained with the LV0 and LV1 method.

5 CONCLUSIONS

In this paper two simplified methods have been applied in order to assess the seismic performance of a sample of ancient churches. These methods are implemented within a multi-level approach, and result very simple to be applied since they require only qualitative information for obtaining a score to be applied within a territorial evaluation.

As shown, the *LV0 method* is a fast tool for ranking within a certain area the priorities needing to be investigated with more refined methods. While, the *LV1 method* provides in quantitative terms a first estimation of the seismic performance starting from few qualitative information that may be gathered with an in-situ survey. Both methods, are not capable of designing any intervention. To this aim, within the multi-level approach indicated in the Italian Directive [16], the *LV2* and *LV3 methods* may be applied. However, they require geometrical and mechanical information on structures and materials rarely available and, therefore, known only after specific survey campaigns.

REFERENCES

- [1] D. C. Alexander, *Natural disasters*. Springer, 2017
- [2] B. M. Feilden, J. Jokilehto, *Management guidelines for world cultural heritage sites*. ICCROM, 1998
- [3] D'Amato, M., Laguardia, R., Di Trocchio, G., Coltellacci, M., Gigliotti, R., 2020. Seismic Risk Assessment for Masonry Buildings Typologies from L ' Aquila 2009 Earthquake Damage Data. *Journal of Earthquake Engineering*. <https://doi.org/10.1080/13632469.2020.1835750>
- [4] Laterza, M., D'Amato, M., Casamassima, V.M., 2017. Seismic performance evaluation of multi-span existing masonry arch bridge. AIP Conference Proceedings, 1863, art. no. 450010. International Conference of Numerical Analysis and Applied Mathematics 2016, ICNAAM 2016; Rodos Palace Hotel Rhodes; Greece; 19 September 2016 through 25 September 2016
- [5] D'Amato, M., Laterza, M., Casamassima, V.M., 2017. Seismic performance evaluation of a multi-span existing masonry arch bridge. *Open Civil Engineering Journal*, 11 (11), pp. 1191-1207
- [6] Sarhosis, V., Milani, G., Formisano, A., Fabbrocino, F., 2018. Evaluation of different approaches for the estimation of the seismic vulnerability of masonry towers, *Bulletin of Earthquake Engineering*, 16 (3), pp. 1511-1545. DOI: 10.1007/s10518-017-0258-8
- [7] Krstevska, L., Tashkov, L., Naumovski, N., Florio, G., Formisano, A., Fornaro, A., Landolfo, R., 2010. In-situ experimental testing of four historical buildings damaged during the 2009 L'Aquila earthquake, COST ACTION C26: Urban Habitat Constructions under Catastrophic Events - Proceedings of the Final Conference, pp. 427-432.

- [8] Luchin, G., Ramos, L. F., D'Amato, M., 2020. Sonic Tomography for Masonry Walls Characterization. *International Journal of Architectural Heritage*, 14(4), 589–604. <https://doi.org/10.1080/15583058.2018.1554723>
- [9] D'Amato, M., Gigliotti, R., Laguardia, R., 2019. Comparative seismic assessment of ancient masonry churches. *Frontiers in Built Environment*, 5:56. <https://doi.org/10.3389/fbuil.2019.00056>
- [10] Fabbrocino, F., Vaiano, G., Formisano, A., D'Amato, M., 2019. Large-scale seismic vulnerability and risk of masonry churches in seismic-prone areas: two territorial case studies. *Frontiers in built environment*, 5:102. <https://doi.org/10.3389/fbuil.2019.00102>
- [11] Lopez, S., D'Amato, M., Ramos, L., Laterza, M., Lourenco, P., 2019. Simplified formulations for estimating the main frequencies of ancient churches. *Frontiers Built Environment*, 5:18. <https://doi.org/10.3389/fbuil.2019.00018>
- [12] Fuentes, D. D., D'Amato, M., Laterza, M., 2019. *Seismic Vulnerability and Risk Assessment of Historic Constructions: The Case of Masonry and Adobe Churches in Italy and Chile. SAHC 2018, 11th International Conference on Structural Analysis of Historical Constructions*. 18, pp. 1127-1137. Cusco, Perú, 11-13 September 2018: RILEM Bookseries
- [13] Ramirez, E., Lourenco, P. B., D'Amato, M., 2019. Seismic assessment of the Matera Cathedral. *SAHC 2018, 11th International Conference on Structural Analysis of Historical Constructions* (pp. 1346-1354). Cusco, Perú, 11-13 September 2018: RILEM Bookseries
- [14] D'Amato, M., Laterza, M., Diaz Fuentes, D., 2020. Simplified Seismic Analyses of Ancient Churches in Matera's Landscape. *International Journal of Architectural Heritage*, 14(1), 119–138. <https://doi.org/10.1080/15583058.2018.1511000>
- [15] D. Díaz Fuentes, 2016. *Diseño de herramientas de evaluación del riesgo para la conservación del patrimonio cultural inmueble. Aplicación en dos casos de estudio del norte andino chileno*. México, Escuela Nacional de Conservación, Restauración y Museología
- [16] G.U. n. 47. (February 26, 2011). Directive of the Prime Minister dated on 09/02/2011. Assessment and mitigation of seismic risk of cultural heritage with reference to the technical code for the design of constructions, issued by D. M. 14/ 01/2008 (in Italian)
- [17] UNDRO. 1979. Natural disasters vulnerability analysis. New York, NY: United Nations Disaster Relief Organisation
- [18] FEMA. 2004. Primer for design professionals (FEMA 389). Washington, D.C: Department of Homeland Security Emergency Preparedness and Response Directorate

FE MODELING OF A SEISMIC ISOLATOR MADE OF HDR AND REGENERATED EPDM

Gaetano Pianese¹, Gabriele Milani¹, Antonio Formisano²

¹ Politecnico di Milano
Piazza Leonardo da Vinci 32, 20133 Milano, Italy
e-mail: gaetano.pianese@polimi.it, gabriele.milani@polimi.it

² School of Polytechnic and Basic Sciences “Federico II”
Piazzale Tecchio 80, 80125 Napoli, Italy
antonio.formisano@unina.it

Abstract

Losses and damages induced by strong earthquakes are a dramatic reality worldwide. As a consequence, the implementation of innovative protection strategies for both existing and new constructions is of key societal importance. Elastomeric isolators are special devices for seismic isolation of structures. Typically, they are made of alternate layers of steel or fiber reinforced laminas and rubber and they are interposed between the ground and the foundation in order to increase the natural period of the structure and reduce the inertia forces to apply in case of an earthquake. This study proposes a detailed 3D FE modelling of isolators conceived for low-rise masonry buildings in developing countries, carried out through the FE software code Abaqus. The isolator under study consists of an energy dissipation core made by relatively High Damping Rubber and an external EPDM ring. In addition, in order to reduce the production cost and allow its applicability in developing countries, it presents unbonded boundary conditions. In fact, the upper and lower edges do not exhibit any bond with the supports. The main feature of such a device is the large deformability thanks to the rollover deformation and the favorably lower lateral stiffness compared to the bonded isolator.

Keywords: Base Isolation, Fiber Reinforced Elastomeric Isolator, High Damping Rubber, Regenerated EPDM, FE Analysis.

1 INTRODUCTION

Some commercial base elastomeric isolators have been introduced in the last four decades to protect buildings from vibration and earthquake. Typically, they are constituted by several alternating layers of rubber pads and steel, interposed by two continuous pads that limit vertical deformability (Steel Reinforced Elastomeric Isolator, SREI). This system reduces the seismic demand and isolates the energy transmission of the earthquakes to the structure. A very effective seismic isolator shall satisfy the following functions: good performance under all service loads (vertical and horizontal); provide enough horizontal flexibility to reach the natural target period for the isolated structure; recentering capability after the ground motion, so that no residual horizontal displacement can downgrade the serviceability of the structure; provide an adequate level of energy dissipation (damping) to control the displacement that could damage other structural members. Fiber-reinforced elastomeric isolator (FREI) is a new type of elastomeric isolator. Instead of steel lamina, it's constituted by thin fiber layers for the vertical reinforcement. Compared with SREIs, FREIs have considerably lower weight and can be manufactured through cold vulcanization. Furthermore, FREIs can be applied to the structure in unbonded conditions without steel supports [1, 2, 3, 4, 5]. So, the isolators can be installed between the upper structure and foundation without any bonding or fastening. The advantage is related to the low production cost, that makes the device suitable for the application in developing countries. The reduced quality of the rubber material used and the unbonded condition allow their utilization only for low-rise residential masonry buildings, which are however quite widespread in developing countries. From a technical point of view, the unbonded condition results in a stable rollover lateral deformation, which reduces the horizontal stiffness and increases the efficiency of the devices. Comparing to the identical specimen but in bonded conditions, the unbonded FREIs exhibit an interesting superior performance concerning the damping [6]. This paper proposes a novel typology of base seismic isolator, Unbonded Fiber Elastomeric Isolator (UFREI), made with a core made by a relatively High Damping Rubber and reactivated Ethylene Propylene Diene Monomer (EPDM) used as ring of each pad. In this way the ageing of the device is strongly reduced. Preliminary FE results of a non-linear 3D numerical analysis carried out on a single isolator subjected to cyclic tests are presented.

2 RUBBER MECHANICAL PROPERTIES

Two rubber compounds have been considered for the design of the unbonded fiber elastomeric isolator. The first one is a relatively high damping rubber [7], and it constitutes the damping core of the isolator. This type of rubber compound, made of natural rubber (NR), guarantees a good performance in terms of energy dissipation (Figure 1), but at the same time, it is vulnerable to quick aging.

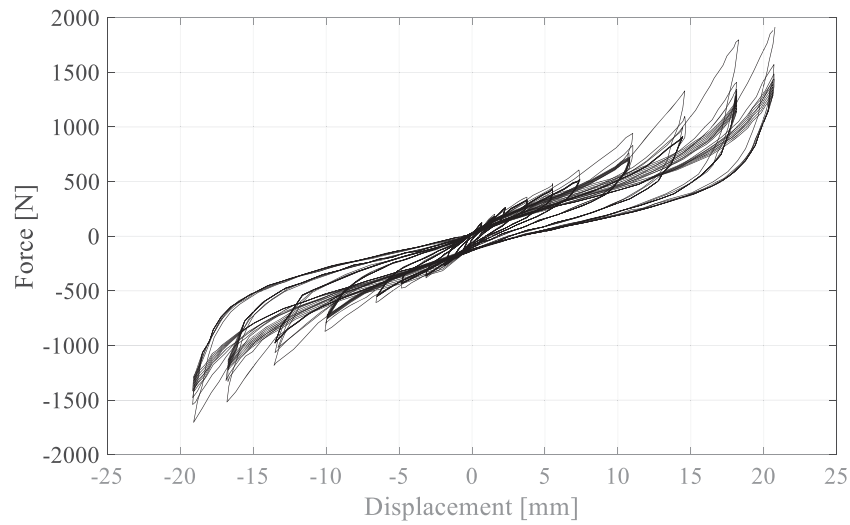


Figure 1: Hysteretic curves for different deformation levels of High Damping Rubber [7]

To protect the HDR, it has been considered a second rubber compound used as ring for each pad, namely a reactivated EPDM made with 2/3 of regenerated rubber and 1/3 of virgin rubber [8, 9, 10] which shows good performances even under aging effects (Figure 2). In Figure 3 it's possible to see the single rubber pad, made of an EPDM frame (Green) with a thickness of 5 mm, and the core ($65 \times 65 \text{ mm}^2$) of HDR (Red).

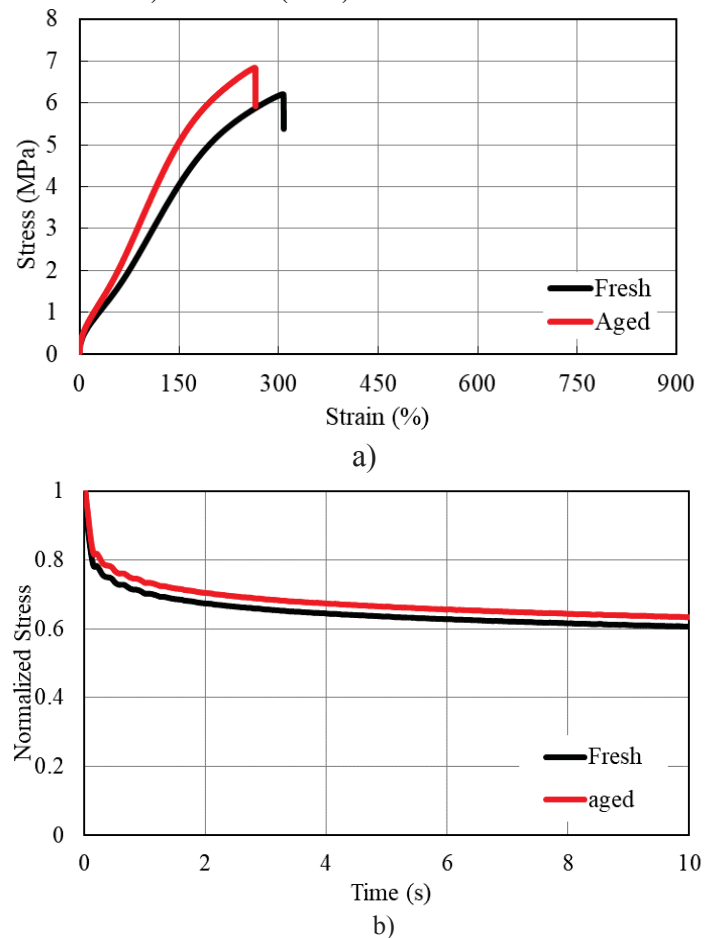


Figure 2: Stretch-stress (a) and relaxation curves (b) of reactivated EPDM, before and after aging [9]

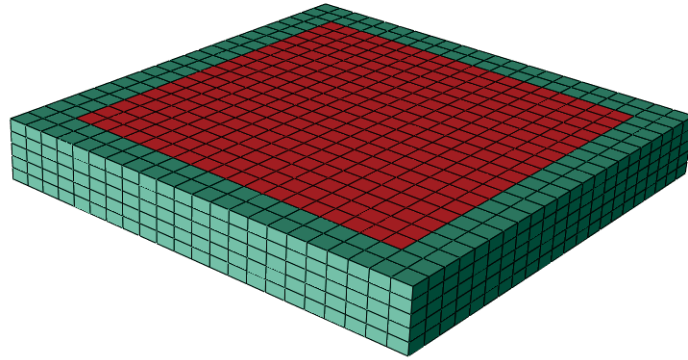


Figure 3: Rubber pad made of HDR and reactivated EPDM

3 HIGH DAMPING RUBBER BEARING

The device object of the study (Figure 4) is constituted by five pads of HDR and reactivated EPDM (10 mm thick), and four GFRP laminas (0.5 mm thick) with a square section of 75x75 mm². On the top and on the bottom, there are two pads of EPDM (3 mm thick) in direct contact with the superstructure and the foundation.

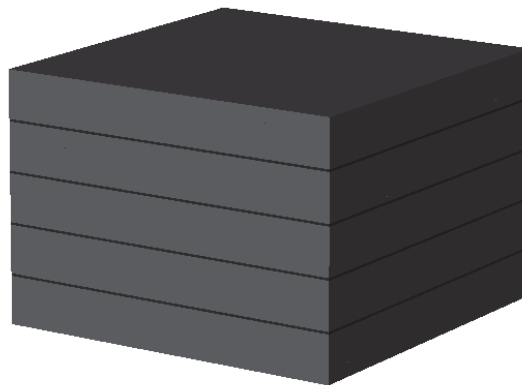


Figure 4: Design of Unbonded Fiber Elastomeric Isolator made of HDR and EPDM

4 3D FE MODEL - CYCLIC SHEAR ANALYSIS

In this section, detailed 3D FE analyses are performed on a single UFREI. In particular, the device is subjected to a 0.5 Hz cyclic horizontal displacement up to 60 mm applied at the top under a constant vertical pressure of 1 MPa.

4.1 3D FE Model

The isolator has been modeled using almost 18000 eight-node brick (C3D8RH) elements with dimensions 3.5 x 3.5 x 2 mm³. The final mesh is shown in Figure 2. Unbonded condition has been simulated. No bonding is present between the supports and the rubber pad. So, a penalty surface-interaction model has been introduced between the two surfaces and a friction coefficient of $\mu=1$ has been applied. On the contrary, a perfect bond using the surface-to-surface tie constraint between HDR, EPDM and GFRP has been adopted.

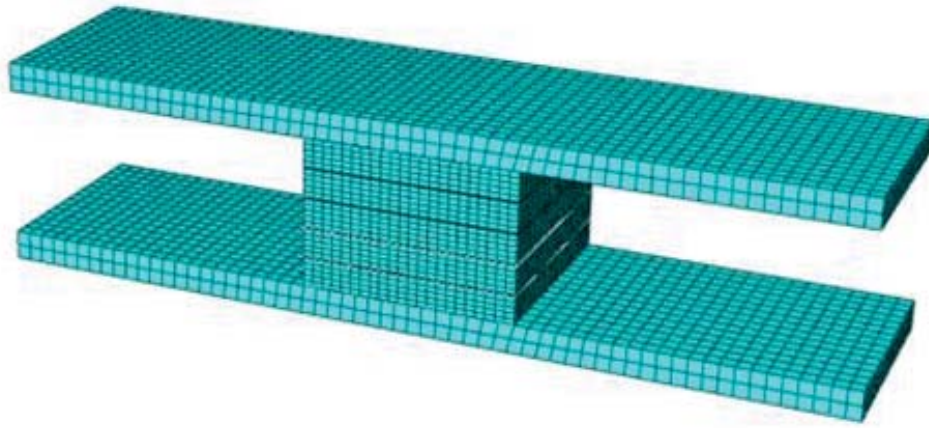


Figure 5: FE model of Unbonded Fiber Reinforce Elastomeric Isolator

4.2 Results

Effective horizontal stiffness $K_{H,eff}$ and damping ratio ξ have been evaluated on four cycles with maximum displacement equal to 15 mm, 30 mm, 50 mm, and 60 mm respectively. The computations are based on the equations (1)-(4):

$$K_{H,eff} = (F_{max} - F_{min}) / (\Delta_{max} - \Delta_{min}) \quad (1)$$

$$\xi = W_d / (4\pi W_s) \quad (2)$$

$$W_s = (1/2) * K_{H,eff} * \Delta_{max,ave}^2 \quad (3)$$

$$\Delta_{max,ave} = (\Delta_{max} + \Delta_{min}) / 2 \quad (4)$$

Cycle	Effective horizontal stiffness $K_{H,eff}$ [N/mm]	Damping ratio ξ [%]
Device cured at 130° for 40 minutes		
1°	39.69	5.60
2°	31.91	8.22
3°	22.48	11.65
4°	19.46	14.42

Table 1: Damping ratio and Effective horizontal stiffness for each cycle on the device.

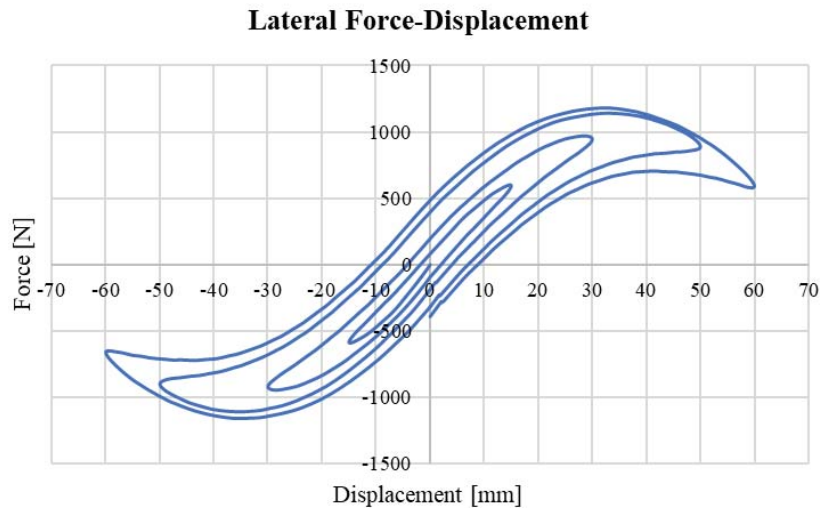


Figure 6: Lateral force-displacement curve for the unbonded FREI.

In Figure 6, the lateral force-displacement curves of the device are shown. The effective horizontal stiffness decreases from the first to the last cycle, up to the final displacement equal to 60 mm (Table 1). This is a typical characteristic of unbonded application, rollover (Figure 7), which causes a nonlinear behavior, resulting in a softening behavior.

5 CONCLUSIONS

In this paper, preliminary FE analyses on a novel typology of Unbonded Fiber Reinforced Elastomeric Isolator have been presented.

Each pad of the isolator is constituted by two rubber compounds, HDR as core and EPDM as external layer; the aim is to obtain -at low cost- a base seismic isolator with good performance in terms of damping and good durability. Subsequently, a detailed 3D FE model of the isolator has been considered, carrying out the analyses through the FE software code Abaqus; in particular, cyclic shear tests with a maximum displacement of 60 mm have been performed. The preliminary numerical results obtained seem promising to consider this new device suitable to isolate low-rise masonry buildings in developing countries, where the low cost and the promotion of circular economy will be crucial in the future decades.

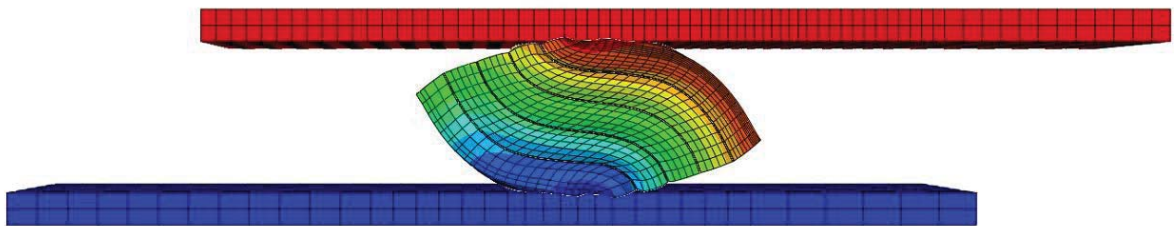


Figure 7: Typical rollover deformation due to unbonding, which causes a softening behavior

REFERENCES

- [1] A. B. Habieb, M. Valente, G. Milani, Hybrid seismic base isolation of a historical masonry church using unbonded fiber reinforced elastomeric isolators and shape memory alloy wires. *Engineering Structures*, 196, #109281, 2019

- [2] A. B. Habieb, G. Milani, T. Tavio, Two-step advanced numerical approach for the design of low-cost unbonded fiber reinforced elastomeric seismic isolation systems in new masonry buildings. *Engineering Failure Analysis*, 90, 380-396, 2018.
- [3] H. Toopchi-Nezhad, J. Tait M., G. Drysdale R., Lateral response evaluation of fiber-reinforced neoprene seismic utilized in an unbonded application. *Journal of Structural Engineering*, Vol. 134(10), 1627-1637, 2008.
- [4] G. Russo, M. Pauletta, Sliding instability of fiber-reinforced elastomeric isolators in unbonded applications. *Engineering Structures*, Vol. 48, 70-80, 2013.
- [5] N. C. Van Engelen, P. M. Osgooei, M. J. Tait, D. Konstantinidis, Partially bonded fiber-reinforced elastomeric isolators (PB-FREIs). *Structural Control and Health Monitoring*, Vol. 22(3), 417-432, 2015.
- [6] A. B. Habieb, M. Valente and G. Milani, Base seismic isolation of a historical church using fiber reinforced elastomeric isolators. *Soil Dynamics and Earthquake Engineering*, Vol. 120, 127-145, 2019.
- [7] I. E. Madera Sierra, D. Losanno, S. Strano, J. Marulanda, P. Thomson, Development and experimental behavior of HDR seismic isolators for low-rise residential buildings, *Engineering Structures*, 183, 894–906, 2019.
- [8] A. B. Habieb, G. Milani, F. Milani, R. Cerchiaro, Rubber compounds made of reactivated EPDM for fiber-reinforced elastomeric isolators: an experimental study. *Iranian Polymer Journal*, 2020.
- [9] A. B. Habieb, G. Milani, R. Cerchiaro, V. Quaglini, F. Milani, Numerical study on rubber compounds made of reactivated ethylene propylene diene monomer for fiber reinforced elastomeric isolators, *Polymer Engineering and Science*, 2020.
- [10] A. B. Habieb, G. Milani, V. Quaglini, F. Milani, Experimentation and numerical modeling of recycled rubber pads for seismic isolation under accelerated ageing. *AIP Conference Proceedings*, 2116, # 420006, 2019.

INFLUENCE OF CROSSLINKING ON THE SEISMIC PERFORMANCE OF UNBONDED FIBER REINFORCED ELASTOMERIC ISOLATORS (UFREI) MADE OF REGENERATED RUBBER

Gaetano Pianese¹, Davide Torrini¹, Gabriele Milani¹, Antonio Formisano²

¹ Politecnico di Milano
Piazza Leonardo da Vinci 32, 20133 Milano, Italy
e-mail: gaetano.pianese@polimi.it, davide.torrini@mail.polimi.it, gabriele.milani@polimi.it

² School of Polytechnic and Basic Sciences "Federico II"
Piazzale Tecchio 80, 80125 Napoli, Italy
antonio.formisano@unina.it

Abstract

Recent earthquakes have highlighted the high seismic vulnerability of the structures and the need of retrofitting interventions. Different seismic protection strategies and techniques can be used to increase the seismic capacity of existing masonry constructions. Common retrofitting techniques are generally based on a strengthening approach. Instead, innovative retrofitting strategies can be used to mitigate the effect of earthquakes, with the aim of decreasing the seismic demand on the structure or increasing its energy dissipation capacity. One of the most innovative devices is the Unbonded Fiber Reinforced Elastomeric Isolators. UFREIs are made of alternate layers of fiber and rubber and they are interposed between the ground and the foundation, with the particularity that no bonding or fastening is provided between the bearing and top-bottom supports. In this paper, through the FE software code Abaqus, a series of nonlinear dynamic analysis are performed to investigate the influence of crosslinking on the seismic performance of UFREI made of regenerated rubber. Numerical results show that the devices vulcanized at 130°C for 40 minutes, although having suboptimal crosslinking density, are suitable to properly isolate low-rise buildings.

Keywords: Base Isolation, Fiber Reinforced Elastomeric Isolator, Vulcanization, Regenerated Rubber, FE Analysis.

1 INTRODUCTION

The elastomeric isolators are the most used devices to seismically isolate the buildings. Applying the elastomeric isolators can restore the horizontal seismic force and does not cause residual displacements of the isolated building after an earthquake. Usually, they are constituted by several alternating layers of rubber pads and steel interposed by two continuous pads, having the role of limiting vertical deformability. At the same time, they exhibit good deformation capacity in the horizontal direction when subjected to a seismic load. This system isolates the energy transmission of the earthquake from the foundation to the upper structure. Fiber-reinforced elastomeric isolator (FREI) is a new type of elastomeric isolator. Instead of using steel lamina, thin fiber layers are utilized for the vertical reinforcement. FREIs can be applied to the structure in several methods: bonded [1], unbonded [2, 3, 4, 5], partially bonded [6], and friction (no-bonding between rubber and fiber layers). Without steel supports, the isolators can be simply installed between the upper structure and foundation without any bonding or fastening. So, the shear load is transferred through the friction generated between the isolator and the structure surfaces.

A fundamental part of the manufactory process is vulcanization. During this stage, rubber is heated with sulfur or peroxides, accelerators, and activators at around 140-160 °C. This process triggers the formation of crosslinks between long rubber molecules, creating the so called polymer network. Thanks to crosslinks, the chains are prevented from sliding along each other and the rubber becomes elastic. The final mechanical properties of rubber (such as elastic modulus, tensile strength, hardness, etc.) are strongly affected by the degree of curing [7]. Curing temperature and the exposition time are critical parameters to establish to obtain optimal and homogenously distributed mechanical properties of rubber items. This paper investigates the influence of vulcanization on the seismic performance of Unbonded Fiber Reinforced Elastomeric Isolator made of regenerated rubber [8, 9, 10], considering two types of vulcanization, one at 130°C for 40 minutes and one at 150°C for 40 minutes.

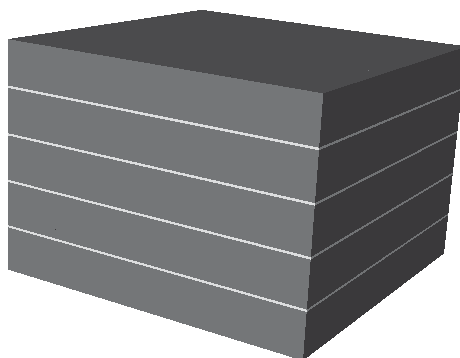


Figure 1: Design of the device object of the study

2 BASE SEISMIC ISOLATOR

The device object of the study is constituted by five pads (10 mm thick) of reactivated EPDM made with 2/3 of regenerated rubber and 1/3 of virgin rubber, and four GFRP lamina (0.5 mm thick) with a square section of 75x75 mm² (Figure 1). The results obtained in [11] show that the device cured with a temperature of 130° for 40 minutes exhibits a non-uniform curing level. So, rubber mechanical properties are non-homogenous within the isolator. On the other hand, the curing temperature of 150° leads to homogenous curing, with a homogenous distribution of mechanical properties. To investigate the distribution of curing level for the under-vulcanized device, knife-cuts on the middle vertical and diagonal sections (Figure 2)

have been done, and the Shore A hardness has been measured with a digital Shore A durometer. As expected, the hardness varies from inner to outer points from values of 48 ± 2 Shore A to 60 ± 2 Shore A (Figure 2).

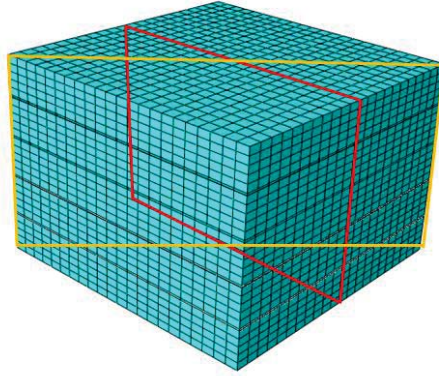


Figure 2: Middle vertical (Red) and diagonal (Yellow) sections for the measurements of the Shore A hardness

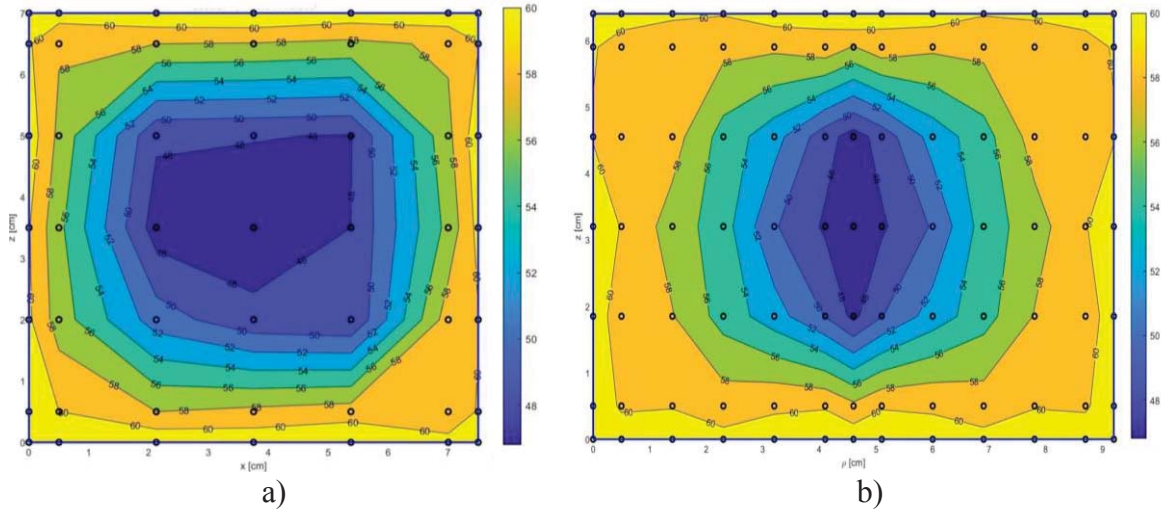


Figure 3: Shore A hardness measured on the middle vertical section (a) and along the diagonal (b) of a device cured at $T=130^\circ$ for 40 minutes

3 3D FE MODEL - CYCLIC SHEAR ANALYSIS

In this section, detailed 3D FE analyses are performed on a single UFREI. In particular, the device is subjected to a 0.5 Hz cyclic horizontal displacement up to 50 mm (Total rubber height) applied at the top under constant vertical pressure of 2 MPa.

Two devices are analyzed. The first one cured at 150°C for 40 minutes, with the rubber mechanical properties uniformly distributed, and the second cured at 130°C for 40 minutes, with a non-homogeneous distribution of rubber mechanical properties, which vary almost linearly within the isolator in accordance with the results shown in Section 2.

3.1 3D FE Model

The isolator has been modeled using almost 18000 eight-node brick (C3D8RH) elements with dimensions $3.5 \times 3.5 \times 2$ mm. The final mesh is shown in Figure 4. In this study, an unbonded condition has been simulated. There is no bonding between the supports and the rubber pad. For this purpose, a penalty surface-interaction model has been introduced between

the two surfaces, and a friction coefficient of $\mu=1$ has been applied. On the contrary, a perfect bond using the surface-to-surface tie constraint between rubber and GFRP has been adopted. As visible in Figure 3, rubber mechanical properties on the device cured at 130°C linearly changes within the isolator. So, in order to assign different mechanical properties to the model, the EPDM pad has been partitioned into several cubes (Figure 5).

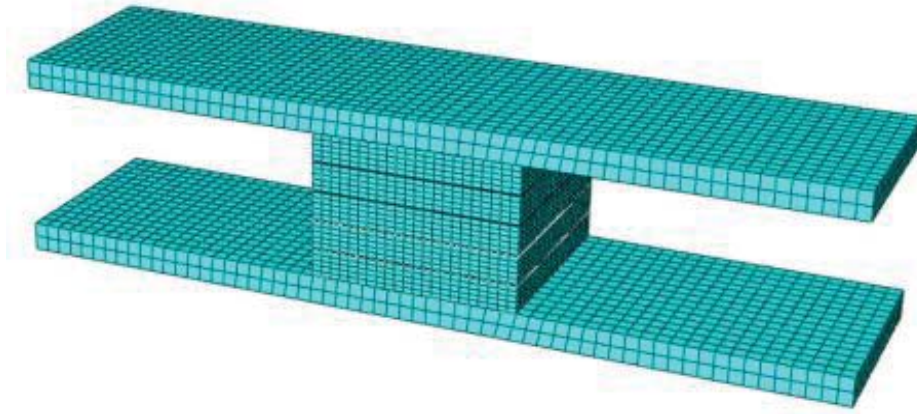


Figure 4: FE model of UFREI75

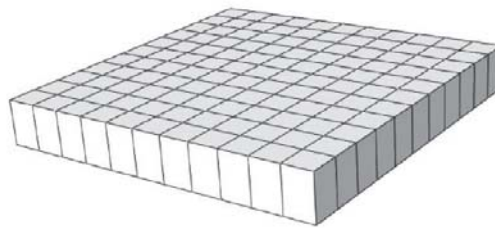


Figure 5: EPDM pad subdivided into several cubes on ABAQUS

Then, three different pads have been considered: middle pad, intermediate pad, and external pad. On each pad, a different distribution of mechanical properties has been assigned as visible in Figure 6 and Figure 7, where the red part is linked to 50 Shore A rubber properties, the orange one to 54 Shore A, and the green one to 60 Shore A.

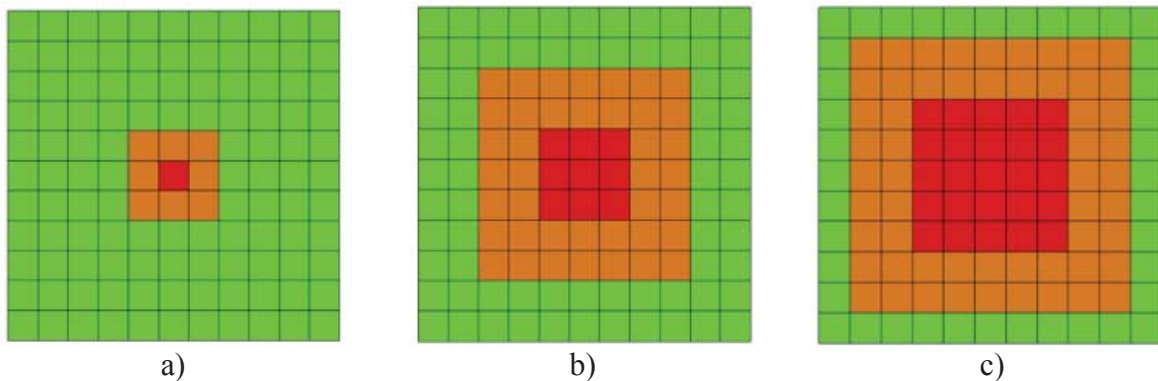


Figure 6: a) external pad section, b) intermediate pad section, c) middle pad section.

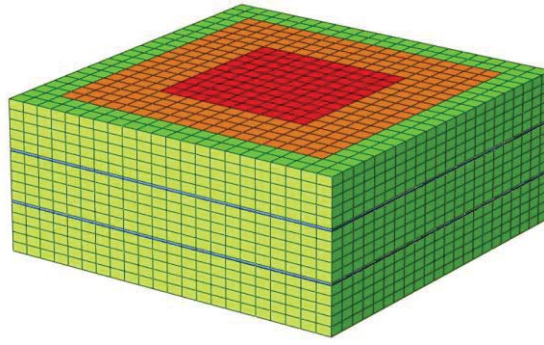


Figure 7: Middle horizontal section of FREI cured at T=130°.

3.2 Results

To compare devices' structural responses, effective horizontal stiffness $K_{H,eff}$ and damping ratio ξ have been evaluated on four cycles with maximum displacement equal to 5 mm, 15 mm, 30 mm and 50 mm respectively. The computations are based on the equations (1)-(4):

$$K_{H,eff} = (F_{max} - F_{min}) / (\Delta_{max} - \Delta_{min}) \quad (1)$$

$$\xi = W_d / (4\pi W_s) \quad (2)$$

$$W_s = (1/2) * K_{H,eff} * \Delta_{max,ave}^2 \quad (3)$$

$$\Delta_{max,ave} = (\Delta_{max} + \Delta_{min}) / 2 \quad (4)$$

Cycle	Effective horizontal stiffness $K_{H,eff}$ [N mm]	Damping ratio ξ [%]	Effective horizontal stiffness $K_{H,eff}$ [N mm]	Damping ratio ξ [%]
	Device cured at 130° for 40 minutes		Device cured at 150° for 40 minutes	
1°	67.59	6.38	87.65	7.86
2°	64.86	5.67	82.41	7.68
3°	50.30	7.73	65.34	10.01
4°	35.08	11.20	46.20	13.92

Table 1: Damping ratio and Effective horizontal stiffness for each cycle on the device cured at 130° for 40 minutes and at 150° for 40 minutes.

In Figure 8, the lateral force-displacement curves for the device cured at 130° and at 150° for 40 minutes are compared. In both cases, the effective horizontal stiffness decreases, passing from first to last cycle. This is a typical feature of unbonded application: the device experiences a rollover (Figure 9) which causes a nonlinear behavior, resulting in a softening behavior. Another remarkable feature appreciable in both the devices is the variation of damping ratio with the increase of lateral displacement.

The results summarized in Table 1 show how the device cured at 130° is characterized by lower effective horizontal stiffness compared to the one cured at 150°. The same holds for the damping ratio.

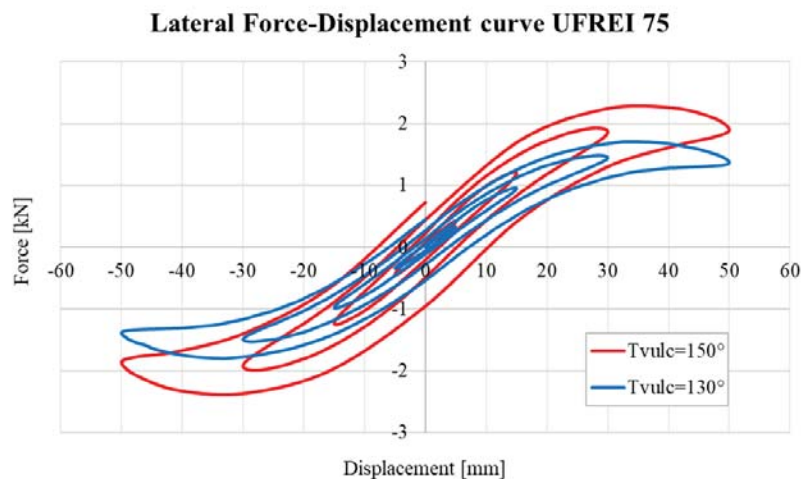


Figure 8: Lateral force-displacement curve for the unbonded FREI cured at 130° for 40 minutes (blue curve) and cured at 150° for 40 minutes (red curve).

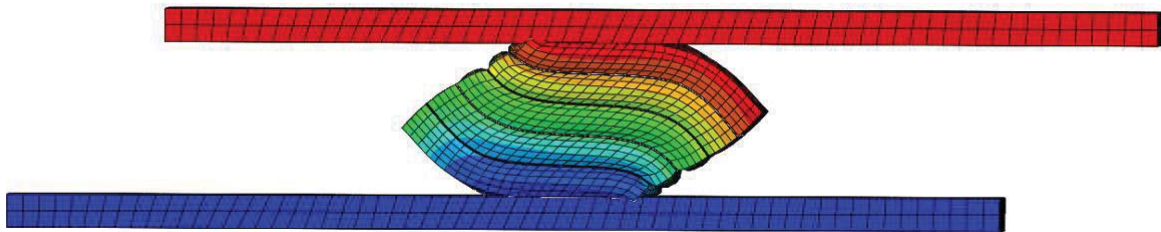


Figure 9: Typical rollover deformation due to unbonding, which causes a softening behavior

4 CONCLUSIONS

In this paper, the seismic performance of under-vulcanized Unbonded Fiber Reinforced Elastomeric Isolators has been studied, and it has been compared with a well-vulcanized one.

Firstly, to investigate the distribution of curing level of the under-vulcanized device, the Shore A hardness has been measured with a digital Shore A durometer along two sections. Results have shown the non-homogeneous hardness distribution and the non-homogeneous rubber mechanical properties within the base isolator.

Subsequently, the device has been modeled through the FE software code Abaqus and cyclic shear tests have been performed, with a maximum displacement of 50 mm. Two different seismic performances of the under-vulcanized UFREI and the well-vulcanized one have been obtained. The device cured at 130° is characterized by lower effective horizontal stiffness and lower damping ratio than the one cured at 150°.

In conclusion, although the devices show different behavior in these cyclic shear tests, both are suitable to isolate low-rise buildings properly.

REFERENCES

- [1] A. B. Habieb, M. Valente, G. Milani, Base seismic isolation of a historical church using fiber reinforced elastomeric isolators. *Soil Dynamics and Earthquake Engineering*, Vol. 120, 127-145, 2019.

- [2] A. B. Habieb, M. Valente, G. Milani, Hybrid seismic base isolation of a historical masonry church using unbonded fiber reinforced elastomeric isolators and shape memory alloy wires. *Engineering Structures*, 196, #109281, 2019
- [3] A. B. Habieb, G. Milani, T. Tavio, Two-step advanced numerical approach for the design of low-cost unbonded fiber reinforced elastomeric seismic isolation systems in new masonry buildings. *Engineering Failure Analysis*, 90, 380-396, 2018.
- [4] H. Toopchi-Nezhad, J. Tait M., G. Drysdale R., Lateral response evaluation of fiber-reinforced neoprene seismic utilized in an unbonded application. *Journal of Structural Engineering*, Vol. 134(10), 1627-1637, 2008.
- [5] G. Russo, M. Pauletta, Sliding instability of fiber-reinforced elastomeric isolators in unbonded applications. *Engineering Structures*, Vol. 48, 70-80, 2013.
- [6] N. C. Van Engelen, P. M. Osgooei, M. J. Tait, D. Konstantinidis, Partially bonded fiber-reinforced elastomeric isolators (PB-FREIs). *Structural Control and Health Monitoring*, Vol. 22(3), 417-432, 2015.
- [7] G. Milani, F. Milani, Optimal vulcanization of tires: Experimentation on idealized NR-PB natural and poly-butadiene rubber blends, phenomenological smoothed numerical kinetic model and FE implementation, *Polymer Testing*, 72, 63-85, 2018.
- [8] A. B. Habieb, G. Milani, F. Milani, R. Cerchiaro, Rubber compounds made of reactivated EPDM for fiber-reinforced elastomeric isolators: an experimental study. *Iranian Polymer Journal*, 2020.
- [9] A. B. Habieb, G. Milani, R. Cerchiaro, V. Quaglini, F. Milani, Numerical study on rubber compounds made of reactivated ethylene propylene diene monomer for fiber reinforced elastomeric isolators, *Polymer Engineering and Science*, 2020.
- [10] A. B. Habieb, G. Milani, V. Quaglini, F. Milani, Experimentation and numerical modeling of recycled rubber pads for seismic isolation under accelerated ageing. *AIP Conference Proceedings*, 2116, # 420006, 2019.
- [11] G. Pianese, G. Milani, R. Cerchiaro, F. Milani, Optimal Vulcanization of Unbonded Fiber Reinforced Elastomeric Isolator Devices, *Chemical Engineering Transactions*, Vol. 86, 2021.

COMBINING OPERATIONAL MODAL ANALYSIS AND GENETIC ALGORITHMS TO UNDERSTAND THE ACTUAL STRUCTURAL BEHAVIOR OF HISTORICAL CONSTRUCTIONS

G. Standoli¹, G. P. Salachoris¹, M. G. Masciotta² and F. Clementi¹

¹ Dept. ICEA, Università Politecnica delle Marche, Via Brecce Bianche, 60131 Ancona, Italy
e-mail: {g.standoli, g.p.salachoris}@pm.univpm.it, francesco.clementi@univpm.it

² Dept. of Engineering and Geology, University “G. d’Annunzio” of Chieti-Pescara, Viale Pindaro 42,
65127 Pescara, Italy
e-mail: g.masciotta@unich.it

Abstract

Evolution of technologies both in the fields of in situ investigations and Finite Element (FE) modeling strongly enhanced the possibility to understand the structural dynamic behavior of masonry historical constructions, allowing a periodic or continuous analysis of their response to environmental, anthropic, and exceptional actions and the formulation of accurate hypotheses about their future behavior, which is fundamental for Cultural Heritage preservation. In order to improve the assessment of the health status of historical buildings, inverse methods re-sorting to dynamic identification techniques are often used to provide experimentally verified data for the accurate calibration of FE models representative of the investigated structures.

In this paper, vibration-based identification methods are coupled with an automatic FE model updating procedure to study the dynamic behavior of the Civic Tower of Ostra, Italy, and obtain baseline information for future comparative analyses. The experimental data obtained from two different campaigns of ambient vibration tests are used to update the mechanical characteristics of the detailed FE model of the tower. The updating process, unsolvable via common calibration procedures, is automatically managed through a powerful bio-inspired tool, i.e. the Genetic Algorithm (GA), allowing to closely reproduce the actual behavior of the tower.

Keywords: Masonry Towers, Cultural Heritage, Structural Health Monitoring, Operational Modal Analysis, Automated Model Updating, Genetic Algorithms.

1 INTRODUCTION

Masonry towers are one of the most widespread structural typologies among the various Italian Cultural Heritage (CH) buildings. The intrinsic characteristics and peculiarities of these artefacts make them unique objects but, at the same time, render these structures particularly vulnerable against seismic events [1–6], sometimes in irreparable way. Due to the historical, social and economic importance that CH plays in many countries of the world, it is crucial to guarantee appropriate maintenance plans and to undertake regular preventive actions in order to avoid irreversible damages to these iconic structures, and to historical buildings in general.

Early damage detection should be one of the primary tasks to ensure the integrity of ancient buildings and the safety of their users. To this end, several non-destructive techniques relying on the observation of the dynamic behavior of these structures, commonly known under the expression “Structural Health Monitoring (SHM)”, have been developed in the last decades [7–11]. Among these techniques, those exploiting vibration-based monitoring tools can be of great help in terms of dynamic characterization of heritage towers, allowing to improve the knowledge of the global behavior of these structures without resorting to any invasive method, which is necessary when the historical value of the construction must be respected. To this end, a grid of sensors, each one communicating with a central processing unit through wires or wirelessly, can be deployed across the structure and used to collect the vibration response of the system to ambient excitations. Such data are then post-processed to determine the modal parameters of the structure in operational conditions, applying the methodologies of Operational Modal Analysis (OMA). As widely known, modal features, if tracked on a regular basis, can provide useful information for the evaluation of the health status of the structures over time, also allowing the detection of possible changes associated to their dynamic behavior in case of exceptional events [12] as well as the estimation of future structural scenarios.

With the aim of providing reliable experimental data for the calibration of realistic numerical models (NMs), closely representative of the investigated buildings, ambient vibration testing (AVT) is often coupled with another essential tool in the dynamic assessment of historical structures: the Finite Element (FE) modeling. Various examples of synergy between these two techniques can be found in the literature [8,13,14], where the results obtained from OMA are employed in the process of FE model updating so that the unknown parameters of the structure (such as material properties, boundary conditions, quality of connections between elements, etc.) are iteratively updated until the difference between experimental and numerical modal results is minimized. This operation, if performed manually [15], as it often happens, can result unwieldy and onerous from a computational standpoint, making difficult to attain a precise calibration of the model in case of large and multi-dimensional problems. In order to overcome this limitation, a methodology for the automatic modal-based updating of Finite Element (FE) models is proposed hereafter making use of genetic algorithms.

The genetic algorithm (GA) is one of the oldest and most known metaheuristics used for optimization purposes [16–18]. The search for the solution space mimics, in a sense, the Darwinian theory of species evolution. In the present work, a GA provided by the open-source FE solver Code_Aster is properly exploited to automatically calibrate the elastic properties of the materials assigned to the model of the Clock Tower of Ostra, an emblematic historical tower located in Central Italy. To analyze in depth the GA potential, different mesh refinements of the tower’s geometry are examined along with the adoption of an isotropic constitutive law for the materials [19–24].

2 DESCRIPTION OF THE CASE STUDY: OSTRA CIVIC TOWER

The Civic Tower of Ostra (Figure 1), also known as “Clock Tower”, is the most characteristic historical structure located in the homonymous village of the Marche region, Central Italy.

Originally built in 1552 to serve as bell tower the adjacent church of San Giovanni (no longer existing today) and severely damaged during the aerial bombardments of 1944, in the second half of the XX century the Civic Tower underwent a profound intervention aimed at reinstating its sound condition. The works included the strengthening of the uncovered foundation and of the base walls as well as the restoration of some parts of the external walls and of the battlement, damaged by the bursts of artillery bullets.



Figure 1: Ostra Civic Tower: localization and external view.

2.1 Geometrical and material survey

The Ostra tower is a 30 m high masonry structure featuring four main parts: basement, central body or shaft, belfry, and top roof (Figure 2).

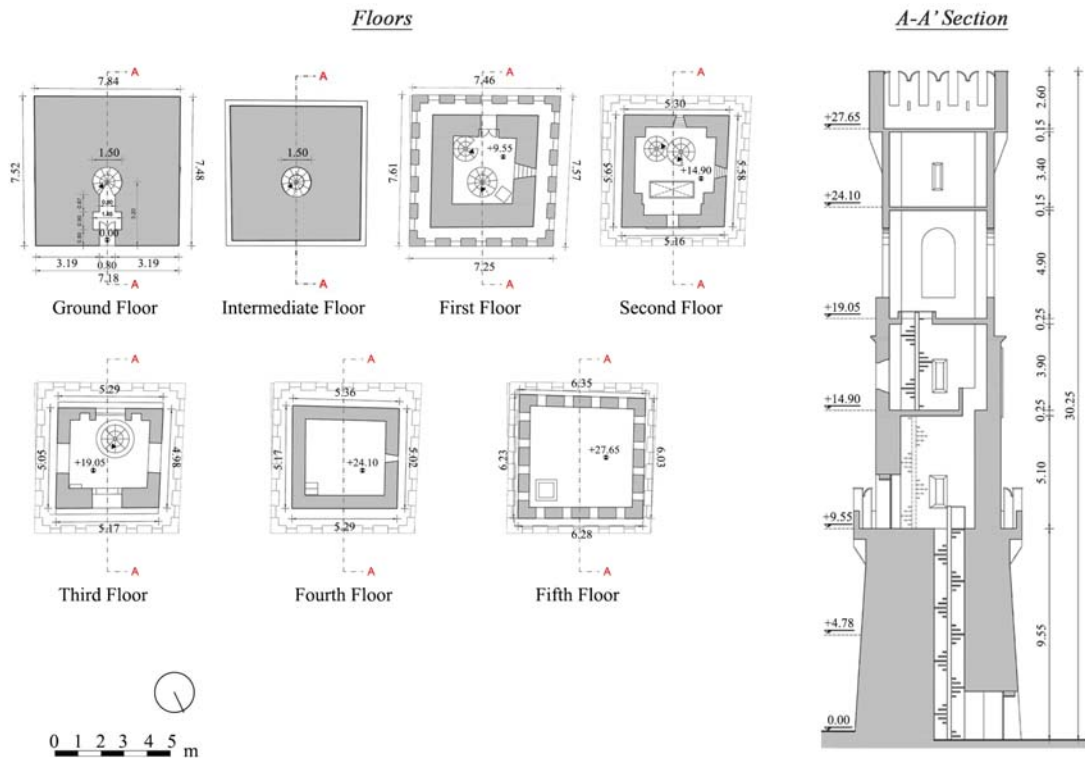


Figure 2: Geometrical survey of the investigated tower.

The basement resembles a truncated pyramid with a lower base of approximately 7.30 x 7.50 m² and an upper base of 5.30 x 5.60 m². This part is characterized by massive walls with outer brick wythes and develops upwards for a height of 9.95 m, ending with an embattled balcony. The shaft, partially reconstructed, starts from this height and keeps the same quadrilateral cross-section for additional 9.50 m. Then, at the level of the belfry, the tower's cross-section dimensions slightly reduce and remain unchanged till the top enlargement of the battlement. Likewise, the thickness of the brick masonry walls of both shaft and belfry progressively decreases upwards, passing from 1.1 m of the first floor to 0.6 m of the last floor.

The entrance door is located at the ground level, in correspondence of the main façade which overlooks Piazza dei Martiri. Five additional floors can be distinguished along the tower height: the first three are connected through spiral staircases, whereas the fourth (rebuilt in reinforced concrete during the intervention) and the last floor are accessible by means of an iron ladder. The clock mechanism is located on the second floor, while the bell is placed at the third level, being visible through the arch openings of the perimetral walls.

3 AMBIENT VIBRATION TESTING

Ambient vibration testing (AVT) has become a common technique in the world of non-destructive experimental characterization of the global behavior of historical constructions [13,25]: indeed, studying the full-scale response of structures to environmental and anthropic actions in real operational conditions, namely without interrupting the normal use of the building and based on its true boundary conditions, results extremely advantageous for many reasons, which go far beyond the economic aspects [11]. Moreover, the non-invasive character of the experiment makes AVTs particularly suited for CH buildings, as proven by the numerous works that in the last years have shown the potentialities of vibration-based monitoring through accelerometric sensors in the study of the dynamic behavior of historical buildings, both in the short-term and in the long-term [26,27].

3.1 Instrumentation, sensor layout and acquisition parameters

Two AVT campaigns were conducted on the Civic Tower of Ostra to assess its dynamic behavior: the first one on 29th June 2018 and the second one on 22nd February 2019.

The sensor network which was used to acquire the structural vibration response in eight specific points defined beforehand consisted of four triaxial MEMS-based piezoelectric accelerometers (model MonoDAQ-E-gMeter) embedded into a data acquisition device simply connected to the PC by a network cable using EtherCAT protocol. One of the major advantages of this sensing system is that analog to digital conversion is performed inside the device itself, thus eliminating any noise pickup in analog cabling. Sensors were placed across four levels (Figure 4), namely at the height of 9.55 m, 14.90 m, 19.05 m, and 27.65 m. At each level, two MEMS accelerometers were deployed at opposite corners, thereby allowing to catch also the expected torsional modes.

To comply with the time-window length requirements [28] and in order to avoid any possible influence from non-stochastic excitations, the duration set for the signal acquisition was far greater than 2000 times the structure's fundamental period: for each setup the registration lasted around 40 minutes and the nodal processes were recorded with a sampling rate of 1024 Hz, resulting in nearly two and a half million data points per channel.

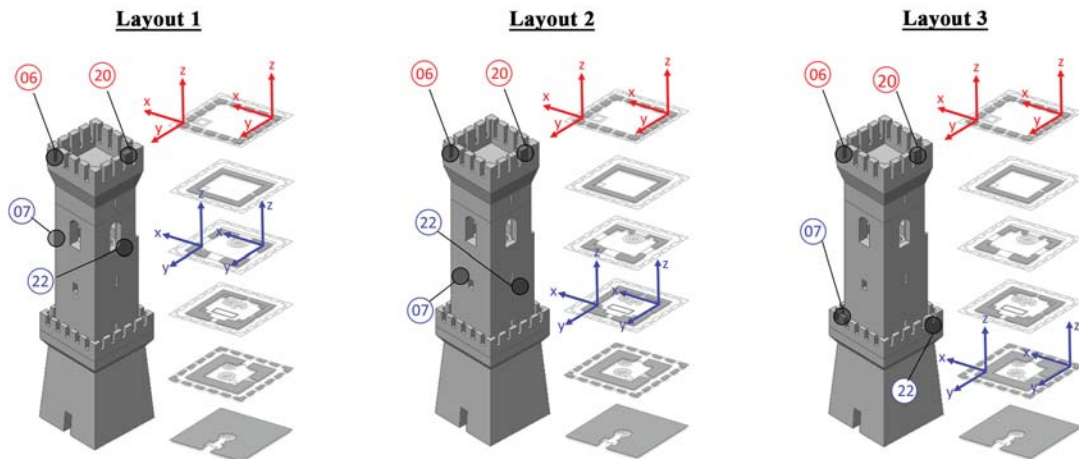


Figure 3: Sensor layouts and corresponding acceleration time series for 2018 and 2019 dynamic testing campaigns.

3.2 Operational modal analysis: method and results

The elaboration of the acquired vibration data allowed the construction of an Experimental Model (EM) of the structure, whose estimated dynamic parameters were subsequently employed to calibrate the Numerical Model (NM) of the tower in order to realistically reproduce its structural behavior, as better discussed in the next Section. The dynamic feature extraction process was carried out and cross-validated through the application of two OMA techniques: the Enhanced Frequency Domain Decomposition (EFDD) [29] and the Stochastic Subspace Identification – Principal Components (SSI-PC) [30], both available in the commercial software ARTEMIS [31].

Modal frequencies (f), damping ratios (ξ) and mode shapes of the five vibration modes identified in each AVT campaign are reported and compared in Table 1 and Figure 4, respectively.

Mode	f_{EM18} [Hz]	ξ_{EM18} [%]	f_{EM19} [Hz]	ξ_{EM19} [%]	Δf [%]	$\Delta \xi$ [%]	MAC [%]
$\phi 1$	2.082	0.817	2.092	0.762	0.478	-7.218	99.2
$\phi 2$	2.156	0.893	2.165	0.787	0.416	-13.469	99.5
$\phi 3$	6.293	0.578	6.302	0.666	0.143	13.213	98.1
$\phi 4$	6.442	2.423	6.449	3.397	0.109	28.672	99.0
$\phi 5$	6.941	2.463	6.872	2.739	-1.004	10.077	97.1

Table 1: Modal frequencies and damping ratios estimated for EM2018 and EM2019 along with their corresponding percentage variation.

As expected, the first two identified frequency values correspond to the translational modes of the tower in x and y directions, respectively, thus resulting quite closely spaced (with a difference of just 3.43% in 2018 and 3.37% in 2019). The other three frequency values fall in the range 6-7 Hz and correspond to the torsion and double bending modes of the tower. The frequency results, sensibly higher if compared to commonly studied masonry towers, are not only affected by the low aspect ratio of the structure ($\lambda = 4$) but also highlight an elevated stiffness of the system which is likely imputable to past restoring interventions. No substantial variation in the dynamic behavior of the structure is recorded during the period elapsed between the dynamic campaigns.

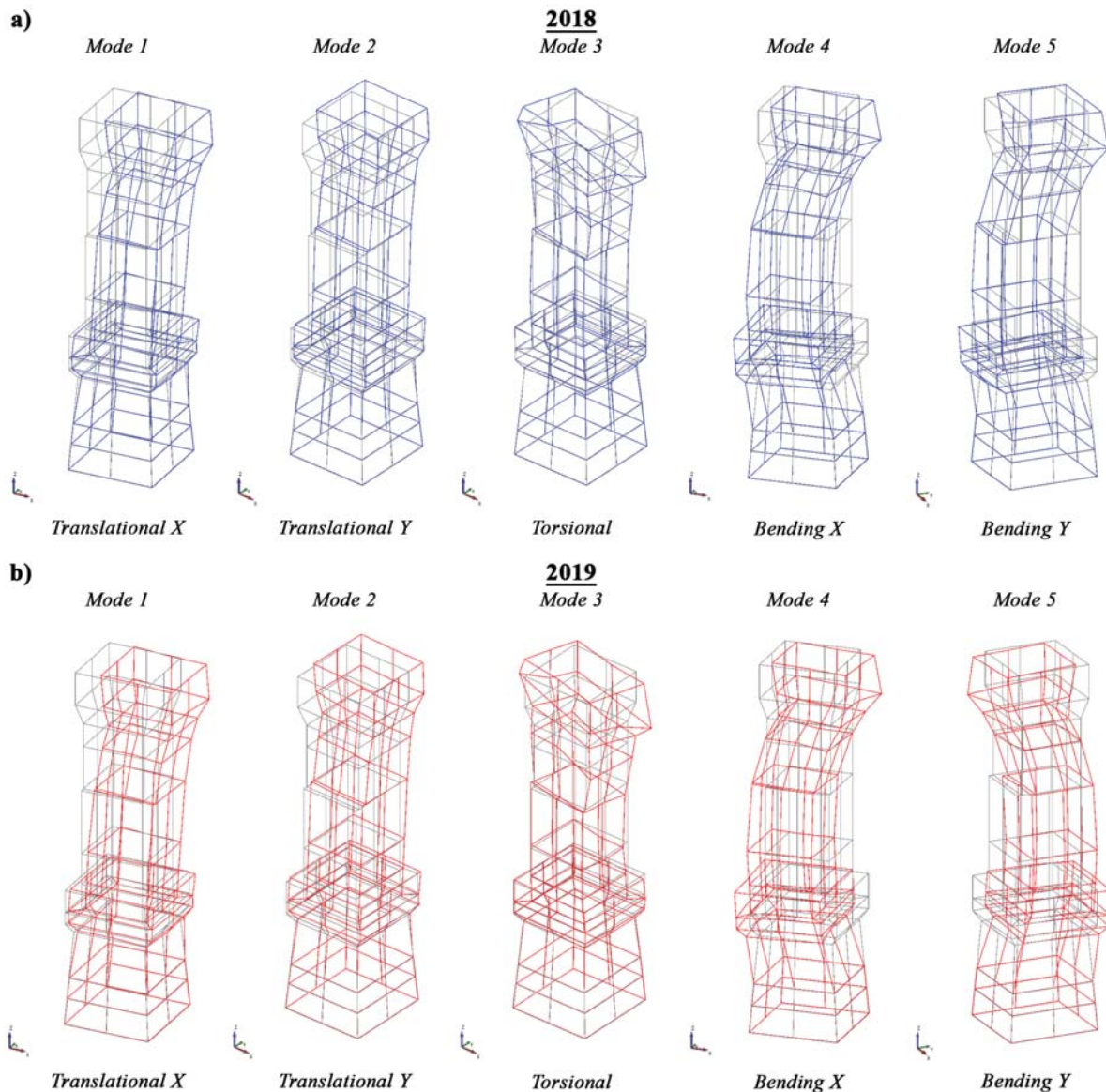


Figure 4: Comparison between the mode shapes of EM 2018 (a) and the corresponding ones of EM 2019 (b).

4 AUTOMATIC MODEL UPDATING WITH GENETIC ALGORITHM

4.1 Preliminary FE model and modal analysis results

A FE model of the tower was realized using MidasFea©. This NM was needed in the first stage to preliminary assess the dynamic characteristics of the tower and drive the setting of the acquisition parameters for the field-testing campaign.

Particular attention was paid to the geometrical features of the tower as well as to the modeling of the masonry infill walls present in the first two levels, given the nonnegligible influence of both aspects in the modal response of the structure. The reinforced concrete floors were considered as rigid in their plane, while secondary elements, like stairs, deformable wooden floors, clock mechanism and towers, were not explicitly modelled, but their presence was taken into account in the form of added masses.

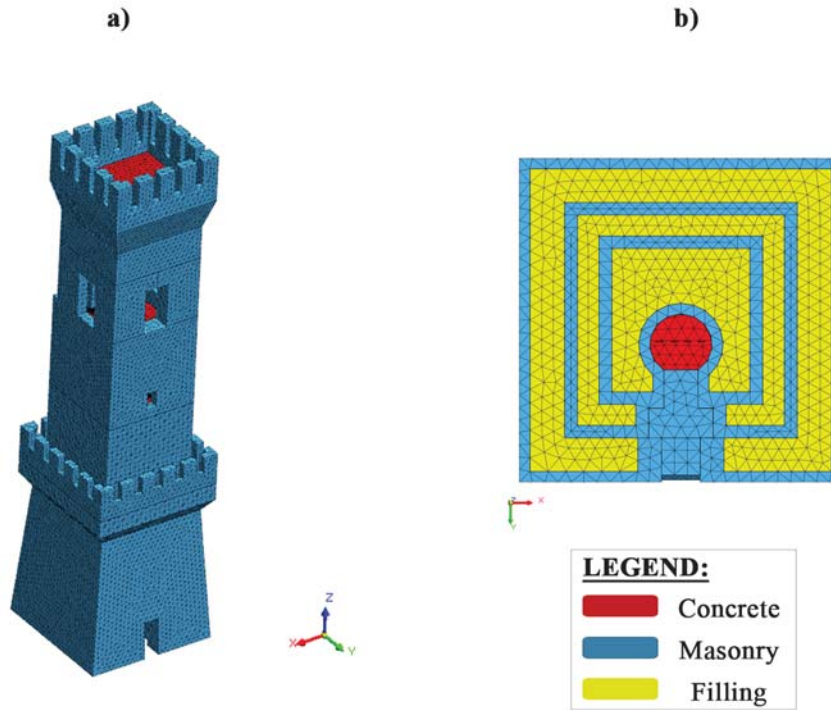


Figure 5: FE modeling of the Civic Tower of Ostra: (a) Assonometric view, (b) Bottom view at foundation level.

The FE model, shown in Figure 5, consisted of 78926 4-nodes tetrahedral elements and 21726 nodes. The mesh size was established equal to 0.3 m. The tower was assumed to be clamped at the base and constituted by three groups of homogeneous and isotropic materials (three-group discretization) whose initial mechanical properties, chosen in accordance to the Italian Technical Standards for Structures [32], are reported in Table 2.

Material	E [MPa]	ν [-]	γ [kN/m ³]
Masonry	1800	0.20	18
Concrete	18000	0.20	25
Filling	1100	0.20	18

Table 2: Mechanical properties of the initial FE model: Young's Modulus (E), Poisson's ratio (ν) and mass density (γ).

The results of the preliminary modal analysis, implemented through the Lanczos method [17,21,33,34], are resumed in Table 3 and Figure 6. A remarkable difference is found among the frequencies of the EM and those of the NM, being the latter not yet calibrated on the basis of the experimental outcome.

Mode	f_{NM0} [Hz]	Eff. Mass X dir [%]	Eff. Mass Y dir [%]	f_{EM18} [Hz]	f_{EM19} [Hz]	$ \Delta f_{EM18-NM0} $ [%]	$MAC_{EM18-NM0}$ [%]	$ \Delta f_{EM19-NM0} $ [%]	$MAC_{EM19-NM0}$ [%]
$\phi 1$	1.509	35.80	0.00	2.082	2.092	27.52	77.6	27.87	82.5
$\phi 2$	1.536	0.00	35.72	2.156	2.165	28.76	81.5	29.05	67.2
$\phi 3$	5.012	0.00	0.00	6.293	6.302	20.36	22.1	20.47	2.6

φ_4	5.821	21.21	0.00	6.442	6.449	9.64	52.2	9.74	47.6
φ_5	5.883	0.00	29.38	6.941	6.872	15.24	1.1	14.39	44.7

Table 3: Preliminary numerical results (NM0) and percentage error with the experimental frequencies (EM)

Analogous considerations can be drawn about the mode shapes (Figure 6), whose main displacement components are visually correlated with their experimental counterpart – being the first two modes translational in x and y direction, the third torsional, and the last two double bending modes in x and y direction – but a low degree of consistency is found between them when MAC values are computed (Table 3).

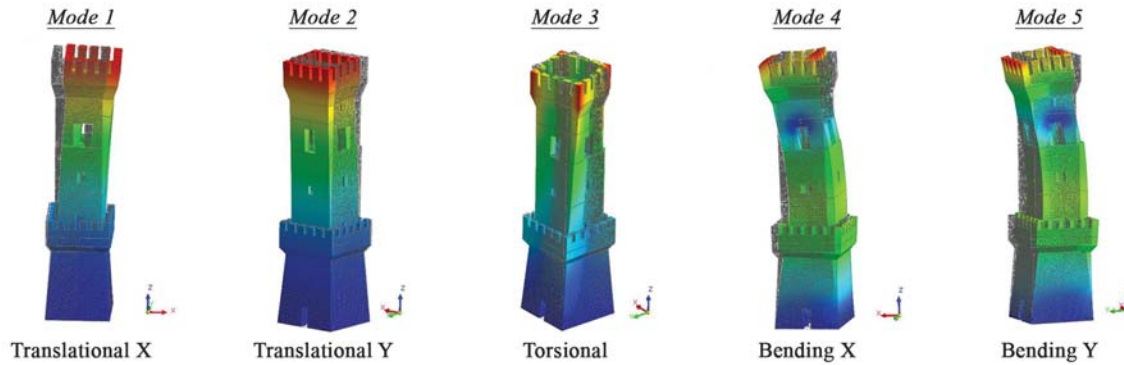


Figure 6: Mode shapes of the preliminary FE model.

4.2 Genetic Algorithms

The genetic algorithms (GAs) are heuristic techniques inspired by Darwin's theory and are based on the imitation of the natural selection process. These algorithms allow to solve optimization problems through an automatic procedure where the final set of optimal solutions is iteratively selected from an initial set of candidate solutions, based on their fitness score [35–38]. As for the present case, the initial population of solutions was represented by all the plausible values of material properties falling within pre-defined upper and lower bounds [17,18]. A two-term objective function considering both frequencies and mode shapes residuals between EM and NM was employed for the selection of the optimal values.

In order to avoid the limitations imposed by a manual calibration approach, the iterative process was implemented into Code_Aster© software environment. The procedure, summarized in Figure 7, started with the creation of a condensed model, carrying all the dynamic characteristics of the EM, and with its projection onto the NM. This operation allows scaling the EM DOFs up to those of the NM and, consequently, the creation of dependencies for calculating the gaps between their nodal displacements.

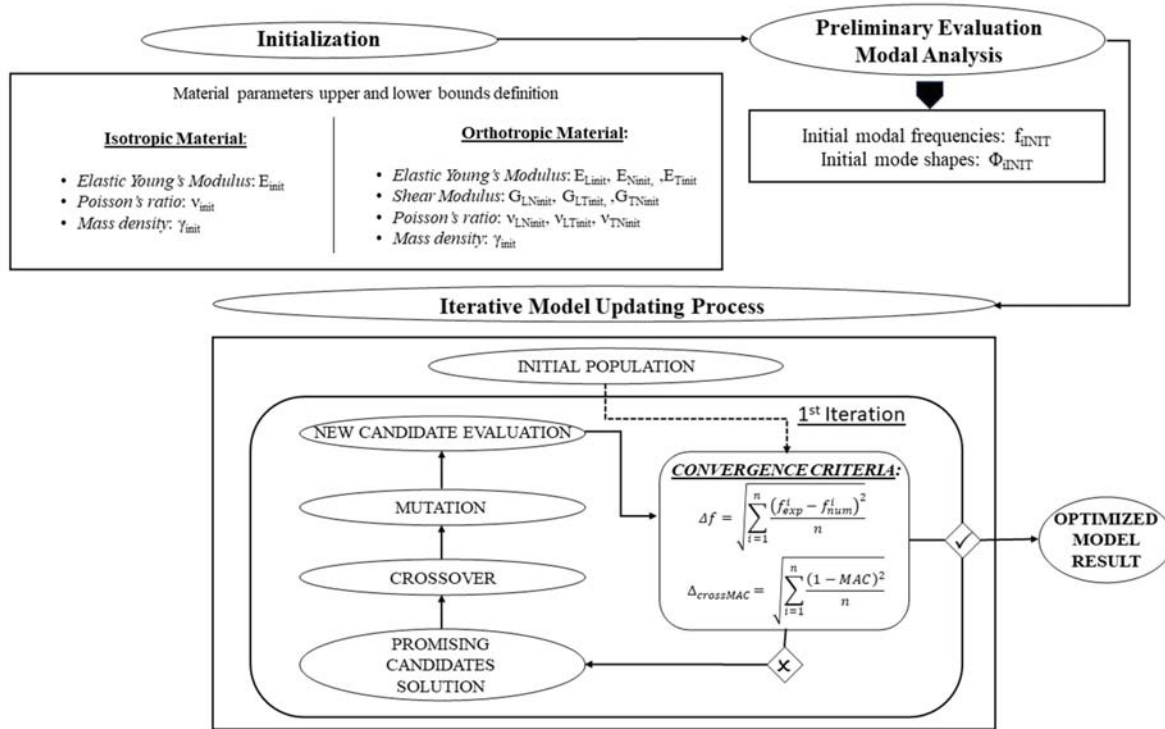


Figure 7: GA-based model updating flowchart.

The model updating process consisted of four phases (objective function, selection, crossover, mutation) and stopped only when the global optimum was located. Indeed, one of the main advantages of GA is the possibility to explore diverse regions of interest by running the same search problem on different conditions and finally locate the global optimum without getting trapped in local minima [16,17,39,40]. In the present work, these conditions are checked by resorting to the following objective function (1):

$$\Delta f = \sqrt{\sum_{i=1}^n \frac{(f_{exp}^i - f_{num}^i)^2}{n}} \quad (1)$$

$$\Delta_{crossMAC} = \sqrt{\sum_{i=1}^n \frac{(1 - MAC)^2}{n}}$$

Convergence criteria were satisfied when the residual tolerance of two consecutive steps reached $1e-4$ or after 1000 evaluations.

5 CALIBRATION PROCESS AND RESULTS

In order to improve control over the model dynamic response and to achieve a better tuning with the experimental data, the calibration process was performed operating a further discretization of the preliminary NM in terms of material properties distribution, while the mesh size remained unchanged. This operation was driven by the careful observation of the masonry appearance and morphology across the tower, which ultimately led to a twelve-group discretization of the updating variables (Figure 8).

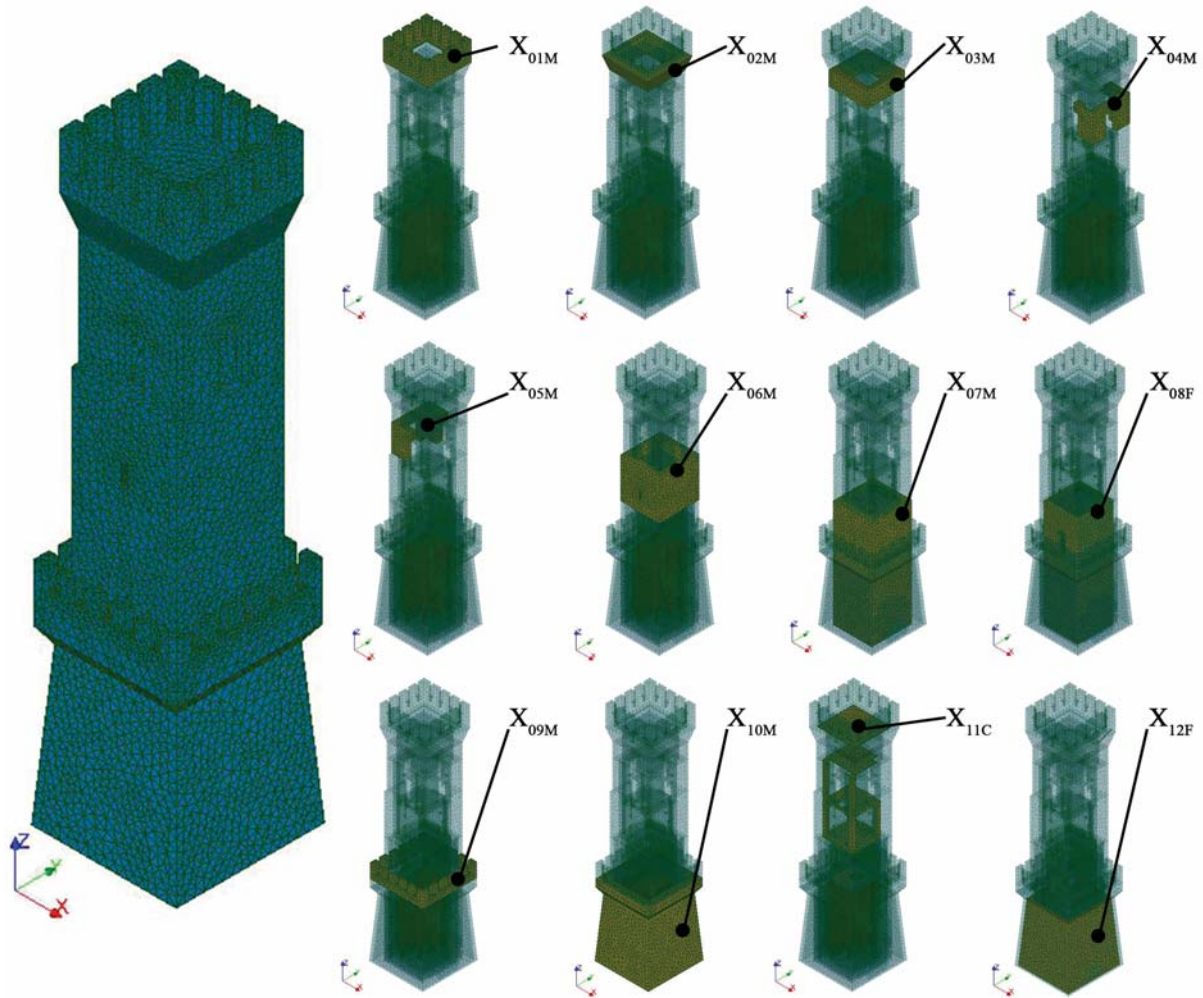


Figure 8: Updating variables for the twelve-group discretization of the FE model. Each material group is named as “X” followed by a subscript composed by a number (00 to 12), which stands for the group, and a letter indicating the material (“M”: masonry, “C”: concrete, “F”: masonry infill).

For each group, properties were attributed considering an isotropic constitutive law for the materials, thus leading to a total number of 36 updating variables. The pre-defined ranges of variability for the material parameters, presented in Table 4, were again assigned in accordance with the Italian Technical Standards for Structures [32].

Material	E [MPa]	ν [-]	γ [kN/m ³]
	Min - Max	Min - Max	Min - Max
Masonry	600 - 3300	0.01 - 0.45	15 - 20
Filling	600 - 2400	0.01 - 0.45	15 - 20
Concrete	27000 - 32000	0.01 - 0.45	23 - 26

Table 4: Lower and upper bounds for isotropic elastic properties

The optimal mechanical properties resulting from the model updating are summarized in Table 5. It is worth noting that the obtained values, especially the Young’s Moduli, consistently reflect the masonry changes produced by the strengthening interventions that the

Tower underwent in the past: indeed, E first tends to decrease moving from the basement (restored during the 1950s) to the central body (partially restored) and the belfry, and then increases towards the top part of the tower (added afterwards).

Updating Parameter	NM 2018			NM 2019		
	E [MPa]	ν [-]	γ [kN/m ³]	E [MPa]	ν [-]	γ [kN/m ³]
X _{01M}	1909	0.11	15	1616	0.28	15
X _{02M}	2783	0.10	15	1886	0.15	15
X _{03M}	851	0.16	15	618	0.21	15
X _{04M}	1118	0.18	16	1500	0.14	18
X _{05M}	1202	0.15	15	1417	0.22	15
X _{06M}	3152	0.17	18	3194	0.18	18
X _{07M}	3113	0.21	20	3154	0.16	20
X _{08F}	2368	0.16	20	2344	0.14	20
X _{09M}	2623	0.17	18	2491	0.17	18
X _{10M}	3290	0.23	20	2724	0.27	19
X _{11C}	27096	0.15	24	28833	0.33	24
X _{12F}	1662	0.19	17	1951	0.27	20

Table 5: Optimal values for the material parameters of the isotropic FE model after calibration

The results of the modal analyses run over 2018 and 2019 NMs, both calibrated through the automatic GA-based procedure previously described, are exposed in Table 6 and Table 7. The comparison between EM and NM frequency values is satisfactory, being the relative error less than 3% in all cases, with the sole exception of the 4th mode that shows a slightly higher error for the pair EM18-NM18.

Mode	f_{EM18} [Hz]	f_{NM18} [Hz]	Eff. Mass X dir [%]	Eff. Mass Y dir [%]	$ \Delta f_{EM18-NM18} $ [%]	$MAC_{EM18-NM18}$ [%]
ϕ_1	2.082	2.087	34.14	0.01	0.24	97.9
ϕ_2	2.156	2.130	0.01	33.53	1.21	97.3
ϕ_3	6.293	6.274	0.26	0.00	0.30	97.2
ϕ_4	6.442	6.654	29.89	0.11	3.29	95.7
ϕ_5	6.941	6.799	0.12	29.25	2.05	95.3

Table 6: Comparison between 2018 experimental (EM) and numerical (NM) frequencies

Mode	f_{EM19} [Hz]	f_{NM19} [Hz]	Eff. Mass Direc- tion X [%]	Eff. Mass Direc- tion Y [%]	$ \Delta f_{EM19-NM19} $ [%]	$MAC_{EM19-NM19}$ [%]
ϕ_1	2.092	2.097	33.94	0.00	0.24	96.5
ϕ_2	2.165	2.141	0.00	33.41	1.11	96.6
ϕ_3	6.302	6.275	0.41	0.06	0.43	95.7

$\varphi 4$	6.449	6.629	29.22	0.03	2.79	95.8
$\varphi 5$	6.872	6.761	0.02	28.48	1.62	95.8

Table 7: Comparison between 2019 experimental (EM) and numerical (NM) frequencies

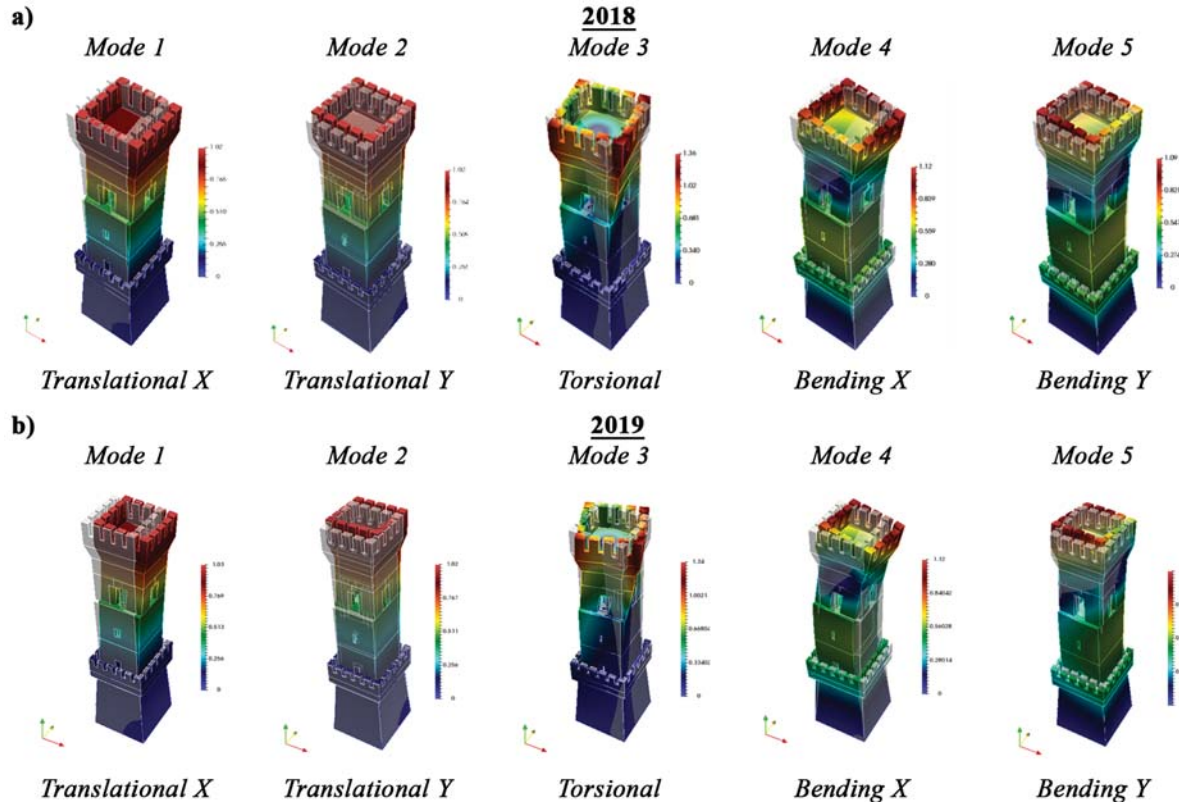


Figure 9: Numerical mode shapes after calibration of 2018 NM and 2019 NM.

Very good results are also achieved in terms of mode shapes (Figure 9), as confirmed by the optimal levels of correlation ($MAC > 95\%$) obtained from the comparison between experimental and calibrated modal vectors, proving the validity and robustness of the GA-based model updating when tackling optimization problems otherwise ungovernable with conventional approaches.

6 CONCLUSIONS

The paper showed and discussed the results obtained by combining AVT-based dynamic identification methodologies and FE model updating techniques, through the application of an automatic procedure based on GA for the assessment of the dynamic behavior of the Ostra Civic Tower (Italy).

After an initial geometrical and material survey to define the main morphological and structural characteristics necessary for the creation of a preliminary NM (over which more advanced non-linear analyses will be implemented in order to estimate the structural response against future scenarios), two modal testing campaigns were carried out to acquire the vibration response of the tower to ambient noise. Innovative sensing solutions based on MEMS were adopted for this purpose.

After extracting the main dynamic parameters of the tower (i.e. modal frequencies, modal damping and mode shapes) through well-known OMA techniques, the EM of the structure was implemented into Code_Aster© and used as a target reference for the calibration of the afore-mentioned finite element NM. In both campaigns, the same five vibration modes were identified, meaning that no changes in the structural condition of the tower occurred between 2018 and 2019.

All the eigenfrequencies and eigenvectors associated to these five modes were exploited for the subsequent automated calibration process, which consisted in a perturbation of the mass and stiffness matrices of the NM in order to find optimal yet physically meaningful values of the unknown material properties of the tower, so that the difference between estimated (OMA) and calculated (FEM) eigen-parameters was minimized. The search problem was solved by applying a metaheuristic inspired by the process of natural selection, namely the GA, to the OMA eigen-data projected onto the equivalent NM. The employment of such an algo-rithm was pivotal given the population of candidate solutions taken into account for the mod-al-based FE updating.

The results, obtained assuming an isotropic behavior for the materials, were satisfactory. Future developments will take into consideration orthotropic constitutive laws for the masonry in the attempt to further minimize the discrepancies between numerical and experimental models.

7 REFERENCES

- [1] M. Acito, M. Bocciarelli, C. Chesi, G. Milani, Collapse of the clock tower in Finale Emilia after the May 2012 Emilia Romagna earthquake sequence: Numerical insight, *Eng. Struct.* 72 (2014) 70–91. <https://doi.org/10.1016/j.engstruct.2014.04.026>.
- [2] M. Betti, A. Vignoli, Numerical assessment of the static and seismic behaviour of the basilica of Santa Maria all’Impruneta (Italy), *Constr. Build. Mater.* 25 (2011) 4308–4324. <https://doi.org/10.1016/j.conbuildmat.2010.12.028>.
- [3] G. Brandonisio, G. Lucibello, E. Mele, A. De Luca, Damage and performance evaluation of masonry churches in the 2009 L’Aquila earthquake, *Eng. Fail. Anal.* 34 (2013) 693–714. <https://doi.org/10.1016/j.engfailanal.2013.01.021>.
- [4] G. Milani, Lesson learned after the Emilia-Romagna, Italy, 20–29 May 2012 earthquakes: A limit analysis insight on three masonry churches, *Eng. Fail. Anal.* 34 (2013) 761–778. <https://doi.org/10.1016/j.engfailanal.2013.01.001>.
- [5] S. Lagomarsino, S. Podestà, Damage and Vulnerability Assessment of Churches after the 2002 Molise, Italy, Earthquake, *Earthq. Spectra.* 20 (2004) 271–283. <https://doi.org/10.1193/1.1767161>.
- [6] A. Ferrante, F. Clementi, G. Milani, Dynamic Behavior of an Inclined Existing Masonry Tower in Italy, *Front. Built Environ.* 5 (2019). <https://doi.org/10.3389/fbuil.2019.00033>.
- [7] F. Magalhães, A. Cunha, E. Caetano, Vibration based structural health monitoring of an arch bridge: From automated OMA to damage detection, *Mech. Syst. Signal Process.* 28 (2012) 212–228. <https://doi.org/10.1016/j.ymssp.2011.06.011>.
- [8] M. Pieraccini, D. Dei, M. Betti, G. Bartoli, G. Tucci, N. Guardini, Dynamic identification of historic masonry towers through an expeditious and no-contact approach: Appli-

- cation to the “Torre del Mangia” in Siena (Italy), *J. Cult. Herit.* 15 (2014) 275–282. <https://doi.org/10.1016/j.culher.2013.07.006>.
- [9] N. Cavalagli, G. Comanducci, C. Gentile, M. Guidobaldi, A. Saisi, F. Ubertini, Detecting earthquake-induced damage in historic masonry towers using continuously monitored dynamic response-only data, *Procedia Eng.* 199 (2017) 3416–3421. <https://doi.org/10.1016/j.proeng.2017.09.581>.
- [10] A. Saisi, C. Gentile, A. Ruccolo, Static and dynamic monitoring of a Cultural Heritage bell-tower in Monza, Italy, *Procedia Eng.* 199 (2017) 3356–3361. <https://doi.org/10.1016/j.proeng.2017.09.563>.
- [11] M.G. Masciotta, L.F. Ramos, Dynamic identification of historic masonry structures, in: P.B. Ghiassi, Bahman; Lourenco (Ed.), *Long-Term Perform. Durab. Mason. Struct.*, Woodhead, Publishing Series in Civil and Structural Engineering, Woodhead Publishing (2019), 2019: pp. 241–264. <https://doi.org/10.1016/B978-0-08-102110-1.00008-X>.
- [12] P.F. Giordano, F. Ubertini, N. Cavalagli, A. Kita, M.G. Masciotta, Four years of structural health monitoring of the San Pietro bell tower in Perugia, Italy: two years before the earthquake versus two years after, *Int. J. Mason. Res. Innov.* 5 (2020) 445–467. <https://doi.org/10.1504/IJMRI.2020.111797>.
- [13] F. Clementi, A. Pierdicca, A. Formisano, F. Catinari, S. Lenci, Numerical model upgrading of a historical masonry building damaged during the 2016 Italian earthquakes: the case study of the Podestà palace in Montelupone (Italy), *J. Civ. Struct. Heal. Monit.* 7 (2017) 703–717. <https://doi.org/10.1007/s13349-017-0253-4>.
- [14] C. Gentile, A. Saisi, P. Borlenghi, FE modelling for seismic assessment of an ancient tower from ambient vibration survey, in: *8th IOMAC - Int. Oper. Modal Anal. Conf.*, Copenhagen, 2019: pp. 295–305. <http://hdl.handle.net/11311/1124063>.
- [15] G. Standoli, E. Giordano, G. Milani, F. Clementi, Model Updating of Historical Belfries Based on Oma Identification Techniques, *Int. J. Archit. Herit.* (2020) 1–25. <https://doi.org/10.1080/15583058.2020.1723735>.
- [16] T. Bartz-Beielstein, J. Branke, J. Mehnen, O. Mersmann, *Evolutionary Algorithms*, Wiley Interdiscip. Rev. Data Min. Knowl. Discov. 4 (2014) 178–195. <https://doi.org/10.1002/widm.1124>.
- [17] M. Girardi, C. Padovani, D. Pellegrini, L. Robol, A finite element model updating method based on global optimization, *Mech. Syst. Signal Process.* (2020) 107372. <https://doi.org/10.1016/j.ymssp.2020.107372>.
- [18] D. Pellegrini, M. Girardi, P.B. Lourenço, M.G. Masciotta, N. Mendes, C. Padovani, L.F. Ramos, Modal analysis of historical masonry structures: Linear perturbation and software benchmarking, *Constr. Build. Mater.* 189 (2018) 1232–1250. <https://doi.org/10.1016/j.conbuildmat.2018.09.034>.
- [19] M.. Betti, G.. Bartoli, R.. Corazzi, V.. Kovacevic, Strumenti Open Source per l’ingegneria strutturale. Modellazione meccanica non lineare di edifici in muratura, *Boll. Ing.* 60 (2013) 3–15.
- [20] G. Bartoli, M. Betti, A.M. Marra, S. Monchetti, A Bayesian model updating framework for robust seismic fragility analysis of non-isolated historic masonry towers, *Philos. Trans. R. Soc. A Math. Phys. Eng. Sci.* 377 (2019) 20190024. <https://doi.org/10.1098/rsta.2019.0024>.

- [21] A. Garcia-Gonzalez, A. Gonzalez-Herrera, A. Garcia-Cerezo, Damage Localization based on Modal Parameters using the Finite Element Method and Neural Networks, in: n.d. <https://doi.org/10.4203/ccp.93.48>.
- [22] K. Smarsly, K. Dragos, J. Wiggenbrock, Machine learning techniques for structural health monitoring, 8th Eur. Work. Struct. Heal. Monit. EWSHM 2016. 2 (2016) 1522–1531.
- [23] Y. Ying, J.H. Garrett, I.J. Oppenheim, L. Soibelman, J.B. Harley, J. Shi, Y. Jin, Toward Data-Driven Structural Health Monitoring: Application of Machine Learning and Signal Processing to Damage Detection, *J. Comput. Civ. Eng.* 27 (2013) 667–680. [https://doi.org/10.1061/\(ASCE\)CP.1943-5487.0000258](https://doi.org/10.1061/(ASCE)CP.1943-5487.0000258).
- [24] M. Sanayei, E.S. Bell, C.N. Javdekar, J.L. Edelmann, E. Slavsky, Damage Localization and Finite-Element Model Updating Using Multiresponse NDT Data, *J. Bridg. Eng.* 11 (2006) 688–698. [https://doi.org/10.1061/\(ASCE\)1084-0702\(2006\)11:6\(688\)](https://doi.org/10.1061/(ASCE)1084-0702(2006)11:6(688)).
- [25] C. Gentile, A. Saisi, Ambient vibration testing of historic masonry towers for structural identification and damage assessment, *Constr. Build. Mater.* 21 (2007) 1311–1321. <https://doi.org/10.1016/j.conbuildmat.2006.01.007>.
- [26] I. Venanzi, A. Kita, N. Cavalagli, L. Ierimonti, F. Ubertini, Continuous OMA for damage detection and localization in the Sciri Tower in Perugia, Italy, in: 8th IOMAC - Int. Oper. Modal Anal. Conf. Proc., 2019: pp. 127–136.
- [27] C. Gentile, M. Guidobaldi, A. Saisi, One-year dynamic monitoring of a historic tower: damage detection under changing environment, *Meccanica*. 51 (2016) 2873–2889. <https://doi.org/10.1007/s11012-016-0482-3>.
- [28] J. Rodriguez, Identificação Modal Estocástica: Métodos de Análise e Aplicações em Estruturas de Engenharia Civil, 2004.
- [29] A.P. Brincker R, Zhang L, Modal identification from ambient responses using frequency domain decomposition, in: Proc. 18th Int. Modal Anal. Conf. San Antonio, TX, Febr., San Antonio, Texas, 2000: pp. 625–630.
- [30] B. Peeters, G. De Roeck, Reference-Based Stochastic Subspace Identification for Output-Only Modal Analysis, *Mech. Syst. Signal Process.* 13 (1999) 855–878. <https://doi.org/10.1006/mssp.1999.1249>.
- [31] ARTeMIS Modal, (2018).
- [32] Ministero delle Infrastrutture e dei Trasporti, D.M 17 gennaio 2018 “Aggiornamento delle Norme tecniche per le Costruzioni,” Suppl. Ordin. Alla “Gazzetta Uff. n. 42 Del 20 Febbraio 2018- Ser. Gen. (2018) 1–198.
- [33] R.S. Olivito, S. Porzio, A new multi-control-point pushover methodology for the seismic assessment of historic masonry buildings, *J. Build. Eng.* 26 (2019) 100926. <https://doi.org/10.1016/j.jobbe.2019.100926>.
- [34] S. Bagchi, T.B. Roy, A. Bagchi, Multiple damage localization of gravity dam: Strain energy based approach using random data, *Proceedings, Annu. Conf. - Can. Soc. Civ. Eng.* 2019-June (2019).
- [35] Á. Bautista-De Castro, L.J. Sánchez-Aparicio, P. Carrasco-García, L.F. Ramos, D. González-Aguilera, A multidisciplinary approach to calibrating advanced numerical

- simulations of masonry arch bridges, *Mech. Syst. Signal Process.* 129 (2019) 337–365. <https://doi.org/10.1016/j.ymssp.2019.04.043>.
- [36] A. Aloisio, I. Capanna, R. Cirella, R. Alaggio, F. Di Fabio, M. Fragiaco, Identification and Model Update of the Dynamic Properties of the San Silvestro Belfry in L'Aquila and Estimation of Bell's Dynamic Actions, *Appl. Sci.* 10 (2020). <https://doi.org/10.3390/app10124289>.
- [37] C. Leyder, E. Chatzi, A. Frangi, Vibration-based model updating of a timber frame structure, *Procedia Eng.* 199 (2017) 2132–2139. <https://doi.org/10.1016/j.proeng.2017.09.141>.
- [38] T. Zordan, B. Briseghella, T. Liu, Finite element model updating of a tied-arch bridge using Douglas-Reid method and Rosenbrock optimization algorithm, *J. Traffic Transp. Eng. (English Ed. 1)* (2014) 280–292. [https://doi.org/10.1016/S2095-7564\(15\)30273-7](https://doi.org/10.1016/S2095-7564(15)30273-7).
- [39] J.P. Escallón, C. Wendeler, E. Chatzi, P. Bartelt, Parameter identification of rockfall protection barrier components through an inverse formulation, *Eng. Struct.* 77 (2014) 1–16. <https://doi.org/10.1016/j.engstruct.2014.07.019>.
- [40] S. Kokot, Z. Zembaty, Damage reconstruction of 3D frames using genetic algorithms with Levenberg--Marquardt local search, *Soil Dyn. Earthq. Eng.* 29 (2009) 311–323. <https://doi.org/10.1016/j.soildyn.2008.03.001>.

SEISMIC ASSESSMENT OF MASONRY CROSS VAULTS THROUGH NON-LINEAR STATIC ANALYSES

M. Alforno¹, A. Monaco¹, F. Venuti¹ and C. Calderini²

¹ Politecnico di Torino, Dept. of Architecture and Design
Viale Mattioli 39, 10125 Torino - Italy
M. Alforno: marco.alforno@polito.it
A. Monaco: alessia.monaco@polito.it
F. Venuti: fiammetta.venuti@polito.it

² University of Genoa, Dept. of Civil, Chemical and Environmental Engineering
Via Montallegro 1, 16145, Genoa, Italy
C. Calderini: chiara.calderini@unige.it

Abstract

Masonry cross vaults are common structural elements in historical buildings. They are largely diffused in all European countries, including those characterized by higher levels of seismicity. Although they have been constructed for centuries, they represent some of the most vulnerable elements of traditional architecture, especially with reference to horizontal loads. The understanding of their behaviour under seismic loading and the definition of their safety are crucial aspects for the accurate assessment of the global health conditions of historical buildings. In the present work, masonry cross vaults are analysed through the Finite Element Method (FEM) and static non-linear analyses are performed considering the effect of different brick pattern.

A simplified micro-modelling approach is adopted for the generation of the FEM models and two different brick arrangements are considered, i.e., radial bricks and diagonal bricks, which are the most widespread in European cross vaults. Static non-linear analyses are performed by monotonically incrementing a lateral acceleration until collapse. Results are analysed in terms of maximum load factor, crack pattern and damage mechanisms. The analysis of the results shows that the masonry apparatus strongly influences the vault seismic response both in terms of stiffness and ductility as well as in terms of global capacity.

Keywords: Cross vaults; Masonry apparatus; FEM model; Push-over analysis, Seismic behaviour.

1 INTRODUCTION

European historical masonry buildings are often characterized by the presence of vaulted structures of complex geometry and cross masonry vaults are among the most widespread types. They are largely diffused in all European countries, including those characterized by higher levels of seismicity. Although they have been constructed for centuries, they represent some of the most vulnerable elements of traditional architecture, especially with reference to horizontal loads when the construction site is characterized by high levels of seismicity. For this reason, the assessment of their behaviour under seismic loading, and consequently the definition of a safety level, is a crucial precondition for the accurate assessment of the global safety of historical buildings.

Compared to simple masonry walls, numerical modelling of masonry vaulted structures is particularly complex due to their three-dimensional curved geometry and articulated masonry pattern. As a matter of facts, vaults can be built according to different brick patterns, which, in historical building practices, were generally chosen for technical reasons.

In the present work, cross vaults of ideal geometry are modelled through the simplified micro-modelling approach in the framework of Finite Element Method (FEM) [1]. This modelling approach has already been used by the authors and successfully validated with physical in-scale models [2]. The use of micro-mechanical models allows to simulate block-to-block interactions and therefore the real interlocking of bricks. In this work, two different brick arrangements are considered, i.e., radial bricks and diagonal bricks, which are most found in European cross vaults. Static non-linear analyses are performed by monotonically incrementing a lateral acceleration until collapse. Results are analysed in terms of maximum load factor, crack pattern and damage mechanisms.

2 DESCRIPTION OF THE MODEL

In this section the main features of the FEM model are described in terms of geometry, mechanical parameters of materials and interface properties. Moreover, the load cases and the boundary conditions are illustrated.

2.1 Geometry and mechanical features

The geometry of the vault is obtained as intersection of two semi-circular barrel vaults. The base is squared with a net span of approximately 3.1 m and rise of 1.175 m. The volume is discretized into bricks of size 6x12x24 cm. The shape of the interlocked bricks along the diagonal arches is idealized and simplified. Four rigid corner supports are modelled at the base of the vault. Two different masonry apparatus are modelled, namely those which follow radial (R) and diagonal (D) path. More in detail, in the case of radial pattern, the longitudinal courses between bricks are disposed normal to the ring arches; conversely, in the case of diagonal pattern, the bed joints are oriented at a 45° angle. Figure 1 shows the details of the geometry and the discretization into bricks; as an example the vault with radial brick pattern is reported.

The discretization of the solid volume of the vault is conducted by means of a simplified micro-modelling approach which allows for the detailed definition of the brick pattern [1]. Such a method consists in the assemblage of a series of blocks connected with zero-thickness interfaces endowed with proper tangential and normal mechanical properties.

The mechanical properties of the blocks are defined through simple elastic behaviour, adopting the values suggested by [3] for historic brick-masonry. In particular, the density of the material ρ is assumed equal to 1800 kg/m³ while the elastic modulus E and the Poisson's ratio ν are equal to 1200 MPa and 0.2, respectively. The behaviour of the mortar joints is sim-

ulated through the insertion of an interaction property between all masonry surfaces into contact. The Authors have already validated this modelling approach in some previous research [2,4,5]. In the local tangential direction, the response is ruled by frictional behaviour in which the contribution of cohesion is neglected as suggested in [6]. In particular, a static friction coefficient μ equal to 0.5 is assumed. In the normal direction, detachment is allowed with zero stiffness while an almost infinite stiffness k_n is assumed in compression to simulate a rigid normal contact. Tangential and normal behaviour are assumed uncoupled. The mechanical parameters adopted in the model are reported in Table 1.

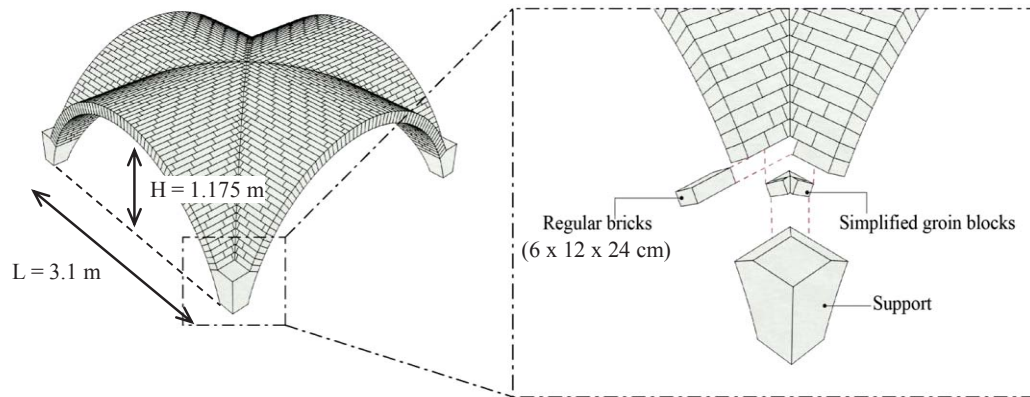


Figure 1: Geometry and discretization of the vault.

Blocks			Joints	
ρ [kg/m ³]	E [MPa]	ν [-]	μ [-]	k_n [N/m ³]
1800	1200	0.2	0.5	$5 \cdot 10^9$

Table 1: Mechanical parameters.

2.2 Load conditions

The seismic performance of the cross vault is analysed through pushover analyses, by applying a monotonic lateral load to the structure. The analysis is divided in two steps: first the gravitational acceleration is applied, then the horizontal acceleration is applied. Two different inclinations of the horizontal acceleration are considered, i.e., $\theta = 0^\circ$ and $\theta = 45^\circ$, the angle θ being defined in Figure 2. It is noted that, because of the symmetry of the model, there is no need to study both positive and negative directions.

The vault is confined by lateral Deformable Arches (DA) on three sides and by a rigid wall on one side (Figure 3). The boundary arches are 27 cm thick (i.e., about twice the vault thickness) and 50 cm depth. The mechanical properties adopted for the DAs are the same adopted for the masonry of the vault. Figure 3 also shows the fictitious plane which is introduced in the model to simulate the unilateral constraint of a rigid wall: the head arch of the vault in contact with the fictitious plane can detach from the plane, while it is prevented to compenetrare inside it. Similarly, contact between blocks of head arches and boundary structures is defined using the same interface behaviour adopted in the block-to-block contact definition. This means that normal compressive forces can arise, while no tension forces can develop.

Shear forces along the planes of the boundary structures can be generated, depending on the normal forces, according to the Mohr-Coulomb criterion.

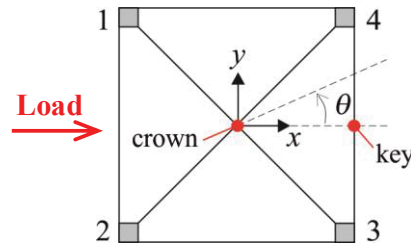


Figure 2: Push-over analysis: lateral load direction and control nodes.

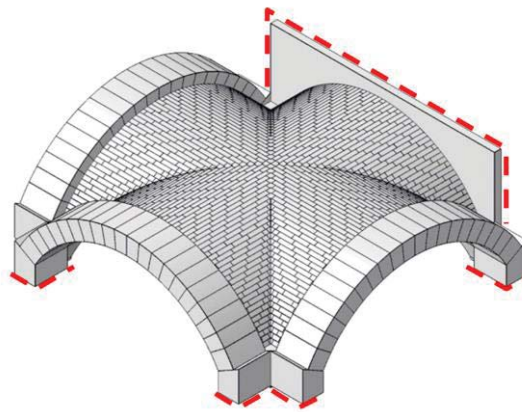


Figure 3: Boundary conditions. Pinned supports in red.

3 PARAMETRIC ANALYSIS

A parametric numerical study is conducted with the aim of highlighting the effect of the masonry apparatus. Table 2 reports the list of the performed simulations. The results will be commented in the following sections.

ID	Pattern	Confinement	Angle [°]
1	R	DA	0
2	D	DA	0
3	R	DA	45
4	D	DA	45

Table 2: Parametric analysis.

4 RESULTS

By looking at the deformed shapes in Figure 4, it is possible to notice that the two vaults behave quite differently. Note that the deformed shapes are plotted without boundary arches, with the exception of plan and axonometric views, to better highlight the collapse mechanism of the vaults. When $\theta=0^\circ$, the radial vault collapses due to the formation of a global mechanism characterized by four parallel hinges normal to the direction of the seismic action. On the contrary, the diagonal vault does not experience a global collapse, but only one cap under-

goes instability. When the angle of the seismic action is $\theta=45^\circ$, the deformed shapes show an almost symmetric collapse mechanism on both radial and diagonal vaults, with respect to groins, as visible in Figure 5. In particular, the radial vault shows the formation of parallel hinges along the bed joints, once again denoting a global collapse mechanism. However, a local failure occurs in the region along the groins, where the sliding and detachment of few bricks take place. The diagonal vault shows a quite different crack pattern in comparison to the radial vault and a local failure occurs at the head arches of two opposite caps.

Figure 6 plots the load-displacement curves in the case of horizontal acceleration along the x -axis direction ($\theta=0^\circ$), for both considered masonry patterns. Two different control nodes have been chosen, in order to monitor the horizontal displacement in the x -direction: one node at the crown of the vault and one node at the key of the head arch of one cap, as shown in Figure 2. The load factor is obtained by normalizing the sum of the horizontal forces at the abutments to the vault's weight W , including the weight of the lateral confinement structures. The markers in Figure 6 and Figure 7 are referred to the values of imposed displacement $u_{c,Crown}$ and $u_{c,Key}$ that correspond to the activation of a failure mechanism.

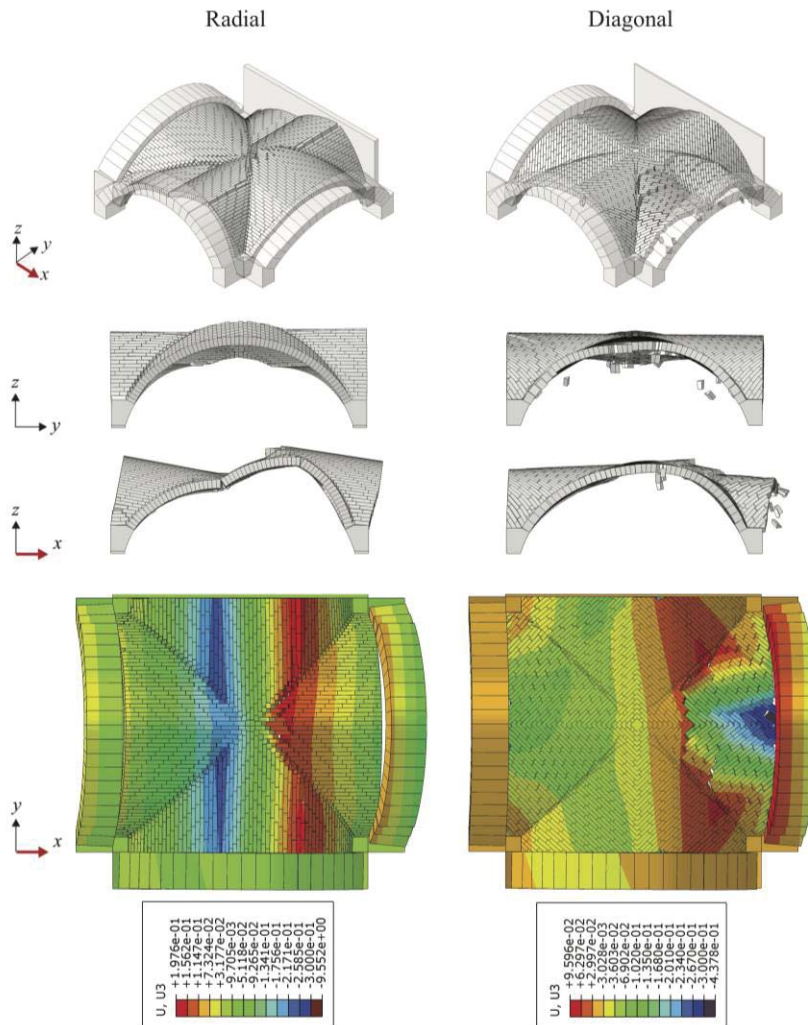


Figure 4: Collapse shapes in Pushover analysis for $\theta = 0^\circ$: axonometric view (first row), x - z plane view (second row), y - z plane view (third row), planar view with contour plot of u_z displacement [m] (fourth row).

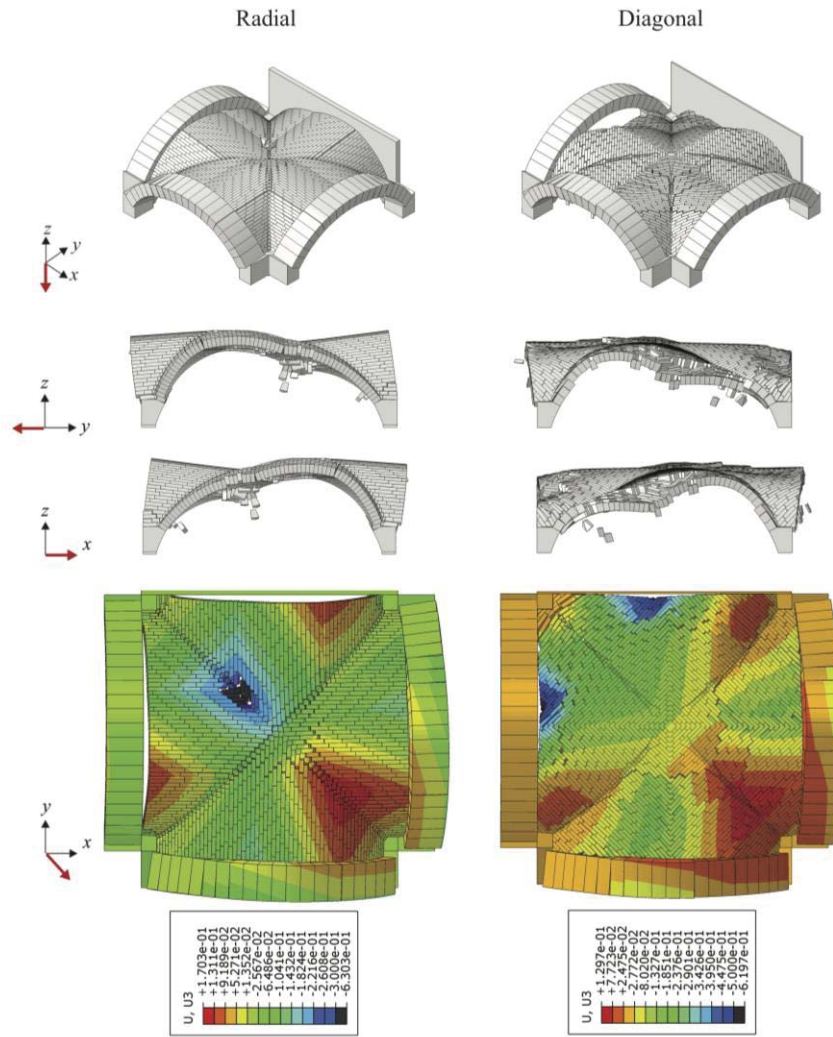


Figure 5: Collapse shapes in Pushover analysis for $\theta=45^\circ$: axonometric view (first row), y-z plane view (second row), x-z plane view (third row), planar view with contour plot of u_z displacement [m] (fourth row).

They have been identified by monitoring the reaction forces at each support, referring to a sudden decrease of force on the load-displacement curves, as visible in Figure 8.

In order to compare the capacity curves, the following quantities have been identified:

- R_{\max} , peak value of the load factor;
- $u_{c,Crown}$, maximum horizontal displacement at the crown of the vault before the activation of a collapse mechanism;
- $u_{c,Key}$, maximum horizontal displacement at the key of one head arch before the activation of a collapse mechanism;
- K_{el} , elastic stiffness, calculated as the ratio R_{60}/u_{60} between the 60% of R_{\max} and the corresponding settlement;
- u_{80}/u_{60} , ductility parameter where u_{80} is the settlement corresponding to R_{80} , i.e., to a post-peak 20% reduction of R_{\max} .

Table 3 reports the values of the above-defined quantities, while Table 4 reports their variation with respect to the radial pattern case for $\theta=0^\circ$. In particular, the table reports the variations in terms of $\Delta Q = (Q_{\text{pattern}} - Q_{\text{radial}})/Q_{\text{radial}} \cdot 100$, where Q is the generic quantity.

It can be observed that the two vaults have quite similar capacity, with variations below 20% with respect to the radial configuration for $\theta=0^\circ$. Also their behaviour in terms of elastic stiffness is similar, whereas the values of ductility differs greatly, depending on the considered pattern and value of θ . Specifically, when $\theta=0^\circ$ the diagonal vault is the one characterized by the lowest elastic stiffness (14.52% lower than the radial vault) and by the highest reduction of ductility with respect to the radial pattern (-53.08%). This last aspect is also visible in the load displacement curves in Figure 6, by looking at the values of displacement of the control nodes. As a matter of fact, in the radial vault, the horizontal displacement of the head arch is only 1.16 times greater than the horizontal displacement of the crown of the vault, whereas in the diagonal vault it is 2.65 times greater.

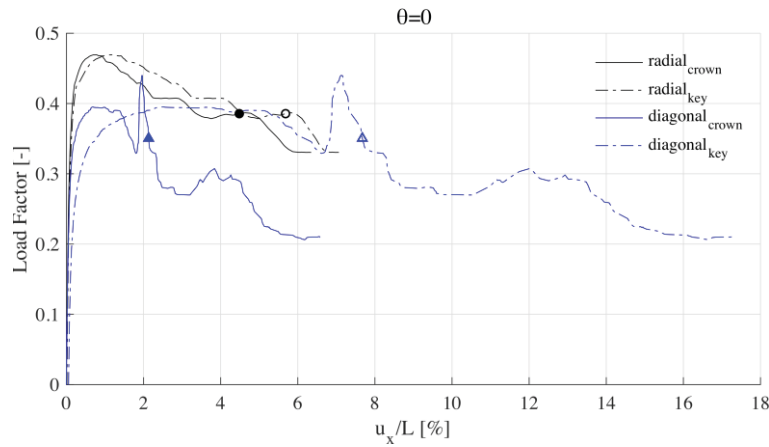


Figure 6: Capacity curves of confined radial and diagonal cross vaults for $\theta=0^\circ$.

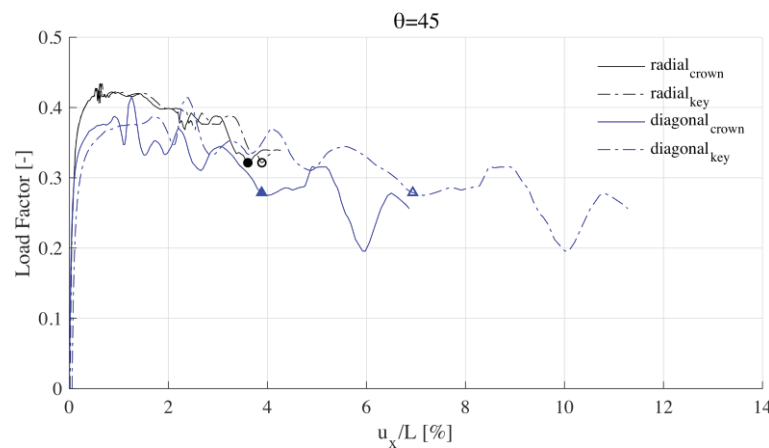
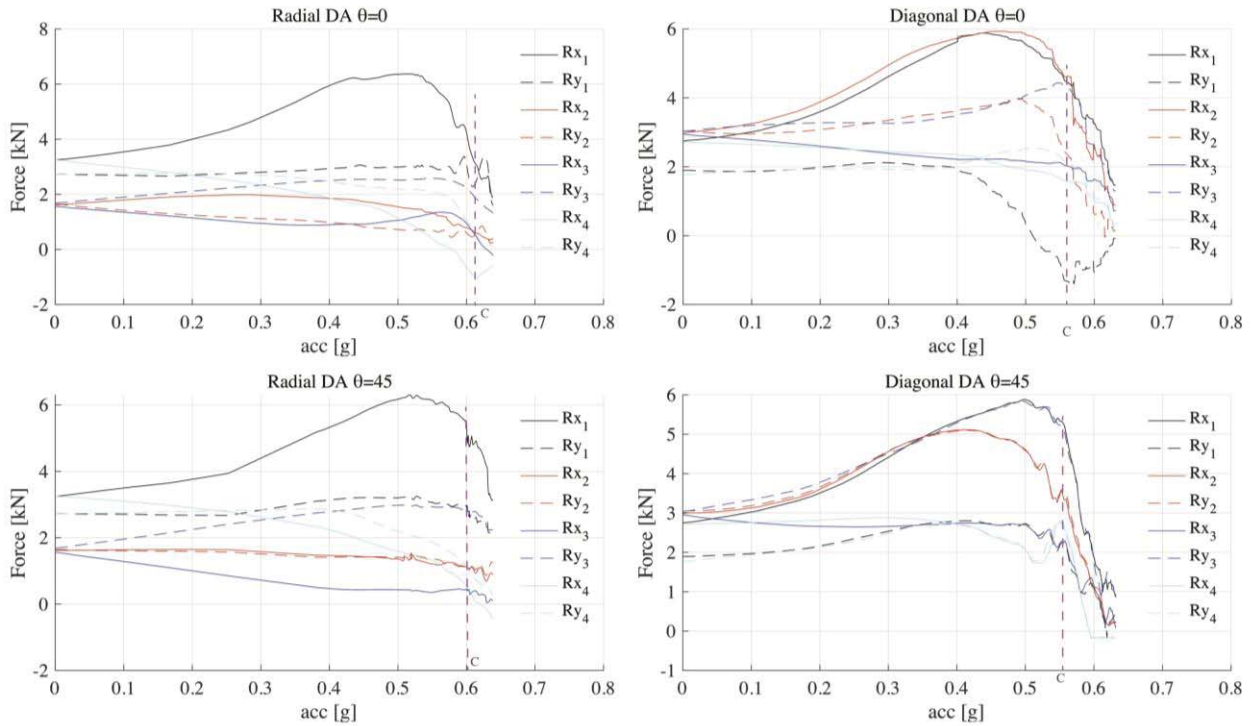


Figure 7: Capacity curves of confined radial and diagonal cross vaults for $\theta=45^\circ$.

Figure 8: Reaction forces R_x and R_y at the abutments vs. horizontal acceleration.

This means that the diagonal vault undergoes a partial collapse of one cap, but the crown of the vault is still stable. The different deformation mechanism induced by the two brick laying techniques is also highlighted by the vertical displacement field of the vaults, plotted before the activation of a collapse mechanism. In the case of the diagonal vault it is clearly visible how the damage is concentrated mostly in one cap, while the rest of the structure results almost undamaged.

When the direction of the seismic action is parallel to the groins, hence for $\theta=45^\circ$, the vault arranged with the diagonal pattern provides the greatest increase of ductility (+31.67%), while the radial vault suffers a decrease of ductility of about 8.84% if compared to the same vault with $\theta=0^\circ$. The radial vault also experiences the greatest increase of elastic stiffness, being 20.61% greater than the loading condition with $\theta=0^\circ$.

Pattern	R_{\max} [-]	$u_{c,Crown}$ [m]	$u_{c,Key}$ [m]	R_{60} [-]	$u_{60,Crown}$ [m]	K_{el} [N/m]·10 ⁶	$u_{80,Crown}$ [m]	u_{80} / u_{60} [-]
Radial $\theta=0^\circ$	0.469	0.131	0.169	0.282	0.0020	10.05	0.158	78.9
Diagonal $\theta=0^\circ$	0.394	0.064	0.233	0.236	0.0019	8.59	0.072	37.02
Radial $\theta=45^\circ$	0.419	0.109	0.118	0.251	0.0015	12.12	0.107	71.94
Diagonal $\theta=45^\circ$	0.374	0.118	0.211	0.225	0.0014	11.07	0.150	68.45

Table 3: Critical quantities used for comparison between brick patterns.

Pattern	ΔR_{\max} [%]	ΔK_{el} [%]	$\Delta(u_{80} / u_{60})$ [%]
Diagonal $\theta = 0^\circ$	-16.07	-14.52	-53.08
Radial $\theta = 45^\circ$	-10.68	20.61	-8.84
Diagonal $\theta = 45^\circ$	-20.22	10.21	31.67

Table 4: Variation of peak reaction force, elastic stiffness and ductility compared to the radial vault with $\theta = 0^\circ$.

5 CONCLUSIONS

- In this paper the results of a parametric analysis on the seismic response of cross masonry vaults are presented.
- The geometry of an ideal vault is considered taking into account its detailed brick pattern.
- The FEM simplified micro-modelling approach is adopted for the discretization of the volume of the structure, endowing the interfaces with tangential frictional behaviour and normal rigid compressive contact. Free detachment is allowed under traction. Linear elastic behaviour is assumed for the masonry blocks.
- Two different brick patterns are considered, i.e., radial and diagonal. Static non-linear analyses are performed, assuming two different directions of the seismic input in the horizontal plane, namely 0° and 45° .
- The results show that the influence of the brick pattern on the seismic response is limited in terms of seismic load capacity and elastic stiffness, while it highly affects the ductility. In particular, diagonal bed joints are able to provide the vault with almost twice displacement capacity.

REFERENCES

- [1] P.B. Lourenco, J.G. Rots, J. Blaauwendraad, Two approaches for the analysis of masonry structures - micro and macro-modeling. *HERON*, **40**(4), 313-340, 1995.
- [2] M. Alforno, A. Monaco, F. Venuti, C. Calderini. Validation of simplified micro-models for the static analysis of masonry arches and vaults. *International Journal of Architectural Heritage*, 1-17, 2020.
- [3] M. Rossi, C. Calderini, S. Lagomarsino. Experimental testing of the seismic in-plane displacement capacity of masonry cross vaults through a scale model. *Bulletin of Earthquake Engineering*, **14**, 261-281, 2016.
- [4] M. Alforno, F. Venuti, A. Monaco. The structural effects of micro-geometry on masonry vaults. *Nexus Network Journal*, **22**, 1237–1258, 2020.
- [5] M. Alforno, C. Calderini, A. Monaco, F. Venuti, Numerical modelling of masonry vaults with different brick pattern. *IASS Annual Symposium 2019 – Structural Membranes 2019 – Form and Force*, Barcelona, Spain, October 7-10, 2019.

- [6] A.M. D’Altri, V. Sarhosis, G. Milani, J. Rots, S. Cattari, S. Lagomarsino, E. Sacco, A. Tralli, G. Castellazzi, S. de Miranda. Modeling Strategies for the Computational Analysis of Unreinforced Masonry Structures: Review and Classification. *Archives of Computational Methods in Engineering*, **27**, 1153–1185, 2020.

“SCAGLIA ROSSA” EXPERIMENTAL CAMPAIGN AND MODEL UPDATING FOR NUMERICAL DAMAGE EVALUATION

G.P. Salachoris¹, E. Magagnini², and F. Clementi²

¹ Department of Civil and Building Engineering, and Architecture
Via Breccie Bianche n.12, 60131 Ancona, Italy
e-mail: g.p.salachoris@pm.univpm.it; e.magagnini@staff.univpm.it; francesco.clementi@univpm.it

Abstract

This paper outlines the characterization of masonry walls composed of “Scaglia Rossa”, a typical stone of the Apennine area between the Umbria and Marche Regions in Central Italy. The study focuses the assessment of the mechanical behavior by means of an experimental campaign carried out in the laboratory of the Polytechnic University of Marche, where the samples of “Scaglia Rossa” masonry, obtained from the controlled demolition of three school buildings, were reconstructed with the same techniques of the 1950s-‘60s, and then tested in order to identify both the constituent materials, stone and mortar, and the composite masonry. The experimental tests were prior to a numerical analysis implemented by the adoption of a nonlinear model capturing the cracking behavior. The main mechanical parameters were then calibrated by means of an optimization algorithm of Levenberg-Marquardt, considering a continuous approach in macro-modelling techniques and obtaining resistance parameters not deriving directly from the experimental tests. The comparison between the results obtained from the Levenberg - Marquardt algorithm by changing the parameters of the damage model based on data given by the experimental campaign allowed to confirm the validity of the approach used.

Keywords: Central Italy Earthquake, Masonry, Experimental Tests, FE Modeling, Levenberg Marquardt Optimization Algorithm, Scaglia Rossa.

1 INTRODUCTION

In the recent years all over the world an elevated number of seismic events was seen, especially in the southern subregion of Europe [1]–[4]. These events caused important damages to the architectural heritage and lead to the need of in-depth investigation on the quality of materials and buildings. The features that complement a construction are, in fact, of fundamental importance in order to acquire a complete comprehension of how historical building heritage behaves under both static and dynamic loads. Italy, has been affected by diverse earthquakes (Friuli (1976), Irpinia (1980), Umbria-Marche (1996-1997), Molise (2002), L’Aquila (2009), Emilia-Romagna (2012), and Central Italy (2016-2017)) and the need to evaluate damage before a restoration project commenced was outlined. The occurred events characterized the damage and collapse of a great number of buildings demonstrating how fundamental is to assess adequately restoration works since the common ground between the various cases is made by poor quality mechanical characteristics of masonry, together with absence of connection between vertical and horizontal elements components that define the structures. The quality of masonry is determined by the features of both mortar and stone and presents in many cases the starting point of the investigation for the diagnosis, since the processes of rehabilitation and restoration are accomplished if the actual state is known. The behavior of masonry’s components (mortars and stones), becomes important since masonry is a composite material that is obtained by joining artificial or natural bricks by means of mortar layers. Due to this above-mentioned reason, stiffness and resistance have great variability but can still characterize masonry materials by means of average values that are not only provided through means of codes or manuals but also experimental campaigns. In most of the Italian Regions it was seen that the seismic activity was intense through the centuries and especially in the area that defines the Apennine region between Umbria and Marche where the heritage is characterized by rural, vernacular masonry [5]. The material mostly used to define the construction techniques of the area is called “Scaglia Rossa” and is the focus of the experimental campaign and numerical non-linear modelling approach of the present paper [6], [7]. In Section 2, the methodology for the experimental campaign is presented and it is explained also the numerical approach used to identify the results of the campaign numerically. Section 3 dwells in more detail on the construction technique utilized for the components that were used during the experiments and Section 4 gives more detail on the numerical approach and damage evaluation results that were defined. In Section 5 the summarized discussion and conclusions are found.

2 METHODOLOGY

The methodology that was followed for the present work is divided in three parts. The first part contains the research done in bibliography for the identification of the construction schemes that used the “Scaglia Rossa” material in the Apennine area and the in-situ campaign that was done in order to identify visually the constructions and select the sample materials that are to be used later in the laboratory experimental tests. The second part englobes the tests that followed to identify the mechanical properties of the samples were done in the the “*Laboratorio Prove Materiali e Strutture*” of the Polytechnic University of Marche (Ancona, Italy). The test considered were divided in two categories, the first for the mortar and the second for the stone samples. In summary, these tests consisted of three-point bending tests, load bearing tests for the mortar and “Scaglia Rossa” samples individually and shear - compression tests for matrices that were constructed in the laboratory, following the double leaves technique. The third part was initiated once the results of the experimental campaign were known. It was then that the numerical modelling began and was done in order to calibrate with the Levenberg-Marquardt algorithm present in the open source software Code_Aster, the non-

linear Mazars damage model parameters onto the experimental results, [8]–[12]. This was done to see if the algorithm can calibrate the parameters and to confirm numerically with a macro-model approach the evolution of the damage seen in the experimental campaign.

3 CASE STUDY

In the Apennine area, after the II World war, the zones between Marche and Umbria were built with a relatively new, compared to the older techniques, local material that was easily available and abundant called “Scaglia Rossa”. This material monopolized the market in the years between the 50’s and 60’s instead of bricks, tuff and concrete blocks that were also later introduced. Coming into more recent years and specifically concentrating attention on the 2016-2017 seismic sequence and the damages it caused in Central Italy, the examinations of engineers reported that the structures consisting of this limestone were considerably damaged. The damage reports consider at the end of the seismic sequence cases of disintegration of the masonry, and out-of-plane mechanisms were rare compared to frequent cracks encountered on the examined panel planes.

The experimental campaign was carried out in the “*Laboratorio Prove Materiali e Struttura*” of the Polytechnic University of Marche (Ancona, Italy), where the samples of “Scaglia Rossa” masonry were accumulated. The samples derived from three school buildings [13]–[15], where controlled demolitions were done. The samples then were assembled using the construction technique of 1950’s – 60’s and were tested in order to identify the mechanical properties of the constituent materials, stone and mortar, and the composite masonry. Initially, load bearing tests were carried out for the selected “Scaglia Rossa” specimens and tested to measure the compressive resistance of the limestones. Afterwards, four matrices were assembled with a cement mortar mixture with percentages that were found in literature to near the construction technique of the initial period (1950’s – 60’s). Mortar samples were extracted and tested with three-point bearing and load bearing tests (on the remaining portions), after 28 days of curing.

Diverse FE models were developed to reproduce the data acquired by the experimental campaign and a calibration process was executed with the Levenberg – Marquardt algorithm present in open source software Code Aster, developed by EDF (Electricité de France), in order to obtain the parameters that characterize the non-linear evolution and could not be directly measured from the experimental tests.

4 SPECIMENS SETUP AND MECHANICAL CHARACTERIZATION

The constructed walls for the masonry mechanical parameters evaluation are four in number and are made with samples of different sizes and shapes utilizing a double leaves technique (Figure 1). Two different kind of tests were performed: a load bearing test in order to establish the behavior under vertical static loads on one wall and load-bearing tests in order to establish the resistance to horizontal loads acting in the plane for all three walls. The dimensions of the four constructed walls are reported in Table 1.

Wall N.	Base (mm)	Length (mm)	Height (mm)
Wall matrix n.1	760	846	500
Wall matrix n.2	750	862	500
Wall matrix n.3	720	860	500
Wall matrix n.4	740	857	500

Table 1: Wall specimens’ geometrical properties



Figure 1: Construction process followed for the wall specimens with "Scaglia Rossa" limestone applying the double leaves technique.

The load bearing test for the wall matrix follows the Italian legislation and is provided by UNI EN 1052-1:2001. This experiment aimed to understand the level of axial force that can be supported by the composite specimen and to provide indications in presence of only vertical forces. The force-displacement curve was obtained by using two LVDT between the frame and the steel plate in the top of the specimen to gain the displacement (Figure 2).

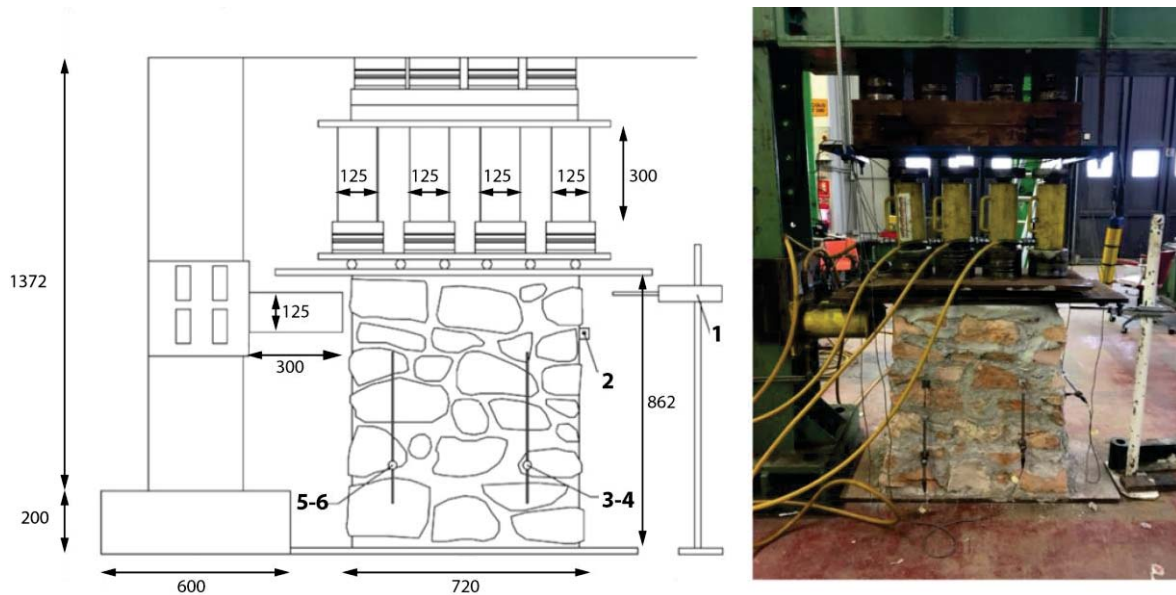


Figure 2: Load-bearing - shear apparatus with example of one matrix specimen. The numbers indicate the dimensions of the apparatus and the positioning of the strain gauges used to measure displacements (measures in mm).

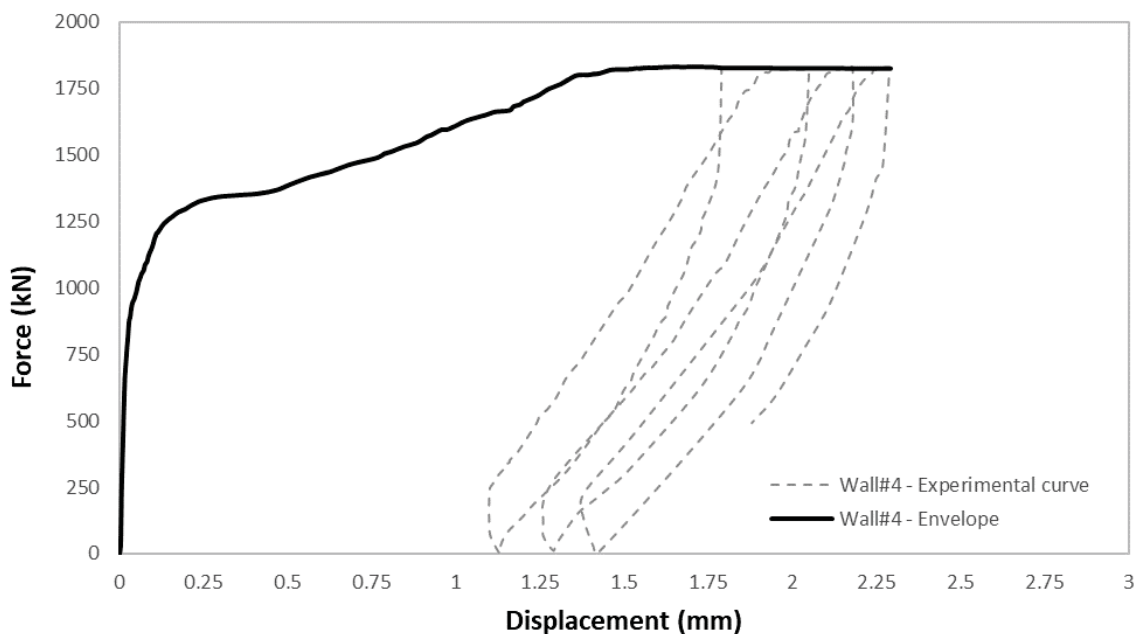


Figure 3: Force - Displacement (kN - mm) evolution curve with the enveloped curve of the Wall#4 that was subjected to load-bearing test.

The results indicate that the range between 0 – 800 kN the displacement values are almost null, while the in the range between 900 – 1200 kN there is augmented displacement. The peak of the curves is found in the 1800 kN range where a clear plateau is visible (Figure 3). Once the horizontal evolution was observed, three ulterior cycles were applied to evaluate residual displacements and possible accumulated damage. The wall had reached its ultimate limit and is able to withstand numbers of cycles without a decrease in stiffness (Figure 4).

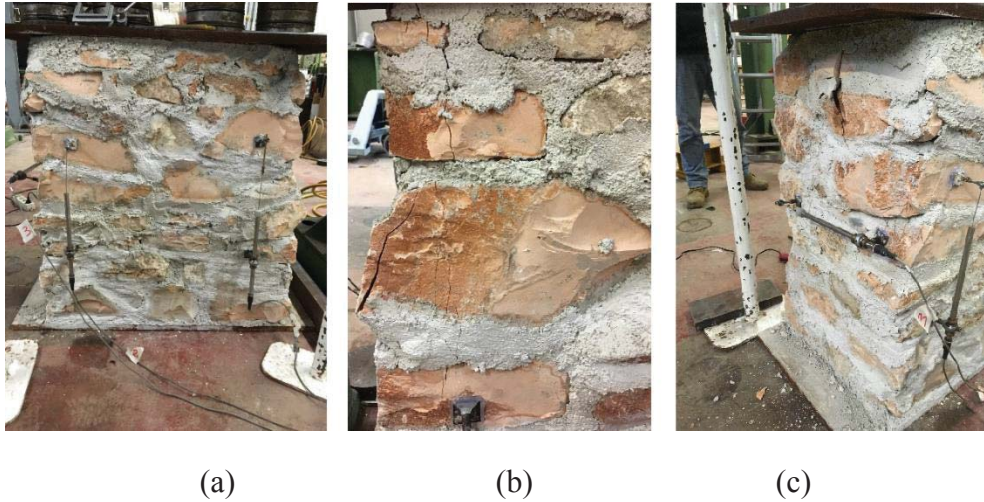


Figure 4: (a) Installed displacement transducers on the wall matrix, (b, c) damage on the specimen caused by the load - bearing test.

For the shear-compression tests a constant precompression load of 400 kN was applied and kept constant during the entirety of the procedure. Afterwards, the hydraulic actuators are activated once the stabilization of the vertical force has occurred. The resulting shear force-displacement curves of the three specimens are shown in Figure 5.

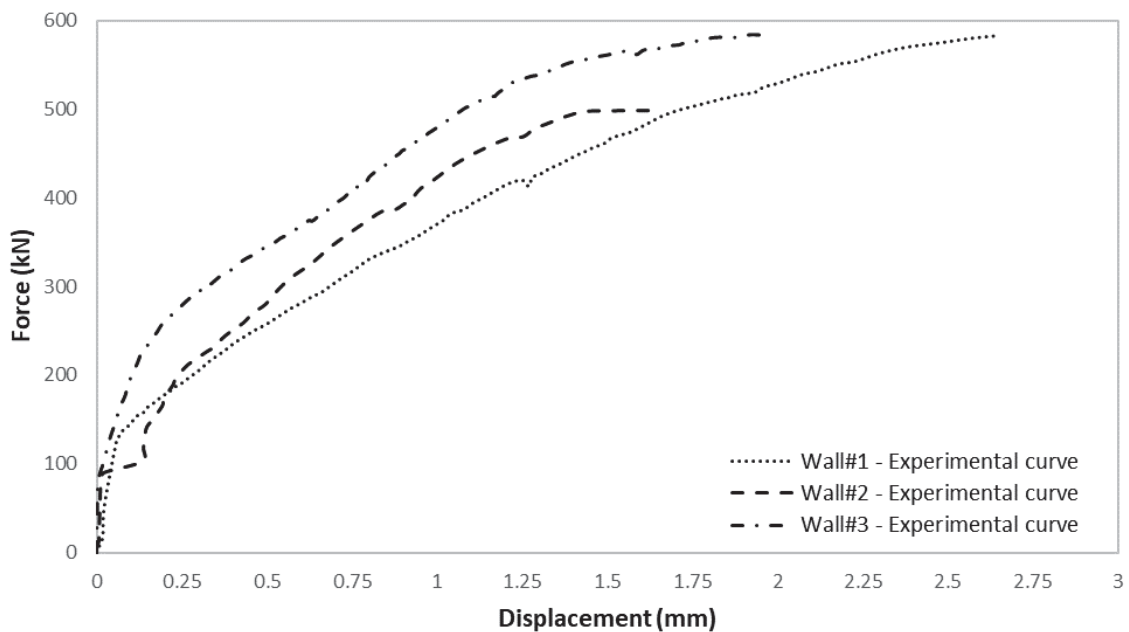


Figure 5: Summary of the horizontal force (kN -mm) curves of the specimens subjected to load-bearing-shear tests

All the performed tests showed homogeneity in their behavior, with a maximum resistance standing above 500 kN except for local criticalities. In more detail, Wall#1 retains the maximum force applied at 580 kN with the displacement arriving at 2.6 mm or the drift is 0.31%. For Wall#2, the maximum force stands at 500kN for a drift of 0.18% and Wall#3 a maximum force of 580kN is observed for a drift of 0.22%. The drift values are comparable with values encountered in National Standards for nonlinear analysis of masonry's walls. The absence of plateau is given to the highly fragile behavior of the specimens once the maximum force is reached. The damage observed indicates in all the specimens a diagonal rupture due to compression and shearing and in some cases panel disintegration when the maximum force applied was reached (Figure 6).



Figure 6: Damaged specimens at the end of the load-bearing-shear test for Wall#1, Wall#2 and Wall#3.

The non-monolithic behavior of such matrix is well represented and does confirm the behavior found commonly in stone walls made by substantially joined faces with diatones providing connections transversally.

5 NUMERICAL METHODOLOGICAL ANALYSIS AND RESULTS

Once the experimental campaign was concluded, with the geometrical information received, diverse Finite Element models were developed for each test of the campaign. To consider the material non linearities, Mazars damage model was considered, and a calibrations process was followed. The process had as its objective the calibration of Mazars damage model parameters (Isotropic scalar damage model), with the Levenberg – Marquardt algorithm,[16], in order to capture the force – displacement curves course and to visualize and evaluate the resulting damage coming of the specimens at the end of the experimental campaign on macro – models, [17]–[21].

The model for the analysis and calibration of Mazars damage model was constituted by 3887 nodes and 16930 tetrahedral elements. For the load-bearing model, the nodes number arrives at 4231 while the tetrahedral elements are 16445. The left side panel substitutes the place of the two hydraulic heads with an equivalent plate. The decision to model this part was to reduce possible errors of the calculation by mesh incompatibilities. The loading was given at the top and left face of the equivalent steel plates of the model while the bottom side is fixed (Figure 7).

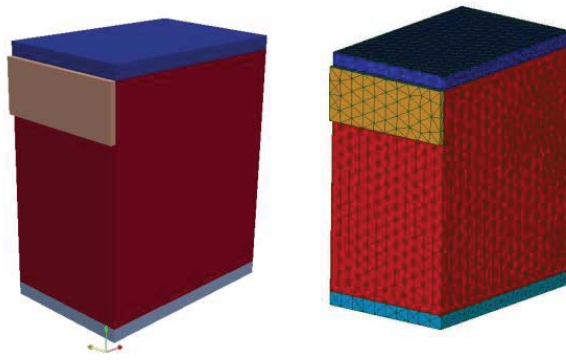


Figure 7: Macromodel geometry and mesh representation

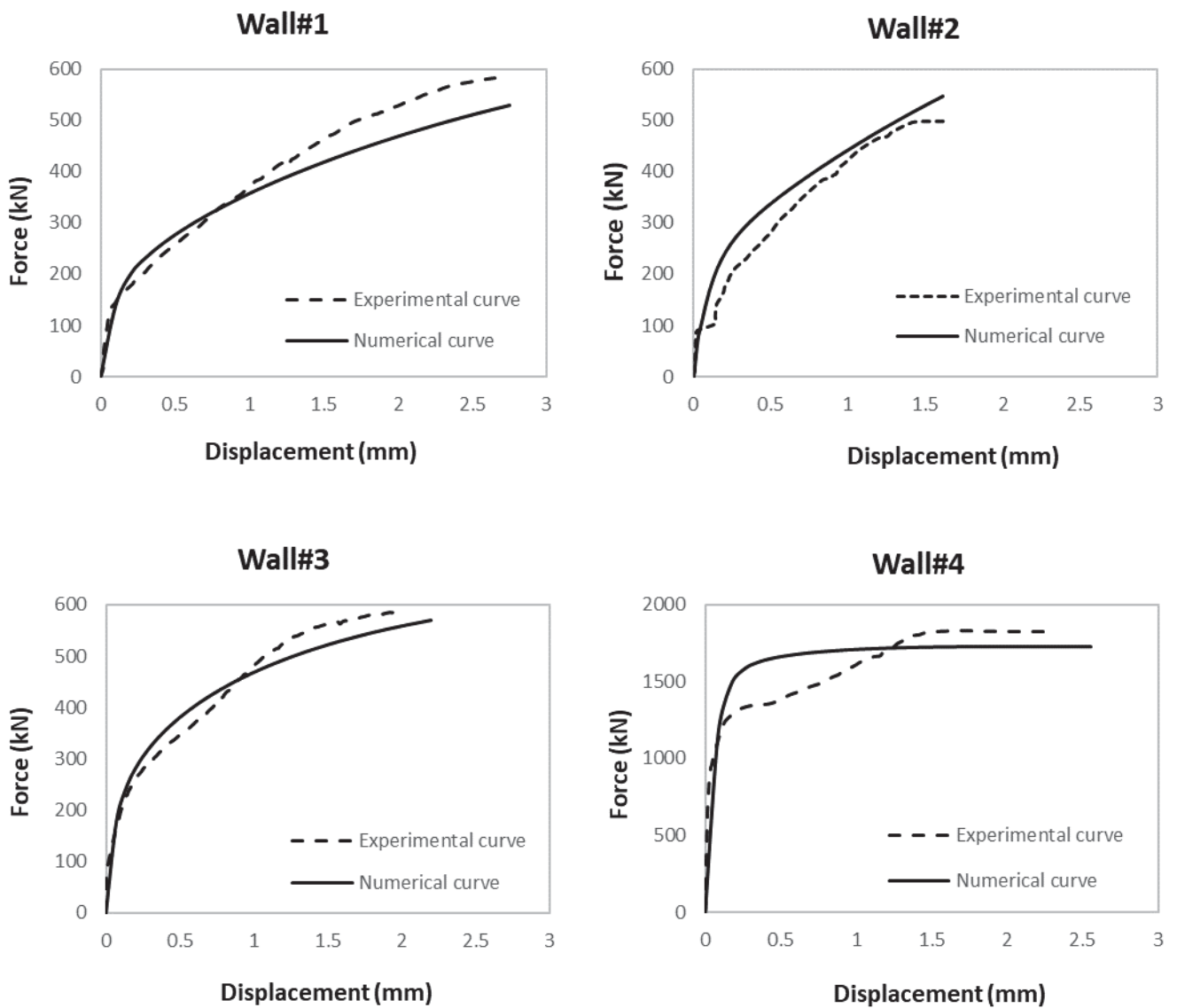


Figure 7: Comparison between the experimental and numerical force - displacement curves (kN - mm), results of the macro-modelling approach.

The results of the calibration by the Levenberg – Marquardt algorithm, obtained under the form of force – displacement curves and the fit with the experimental curves is shown in Figure 8 and the values product of the optimization process in Table 2. In all cases, it was possible to capture the progress of the compression – shearing with discrepancies shown for Wall#2 and Wall#3 that was caused by progressive disaggregation of the materials during the experimental tests.

Wall #	E (MPa)	ν	A_t	A_c	B_t	B_c	k	E_0 (10^{-5})	Error (%)
(1)	4049.3	0.243	1.120	0.158	5020	99.3	0.808	5.66	1.56
(2)	3000.0	0.400	1.170	0.843	6800	0.10	1.090	0.108	3.69
(3)	4843.8	0.150	0.460	0.223	7260	104.0	0.700	0.0276	3.94
(4)	8000.0	0.400	0.191	0.017	14000	136.0	0.258	40.40	13.21

Table 2: Calibration results of Mazars damage model parameters

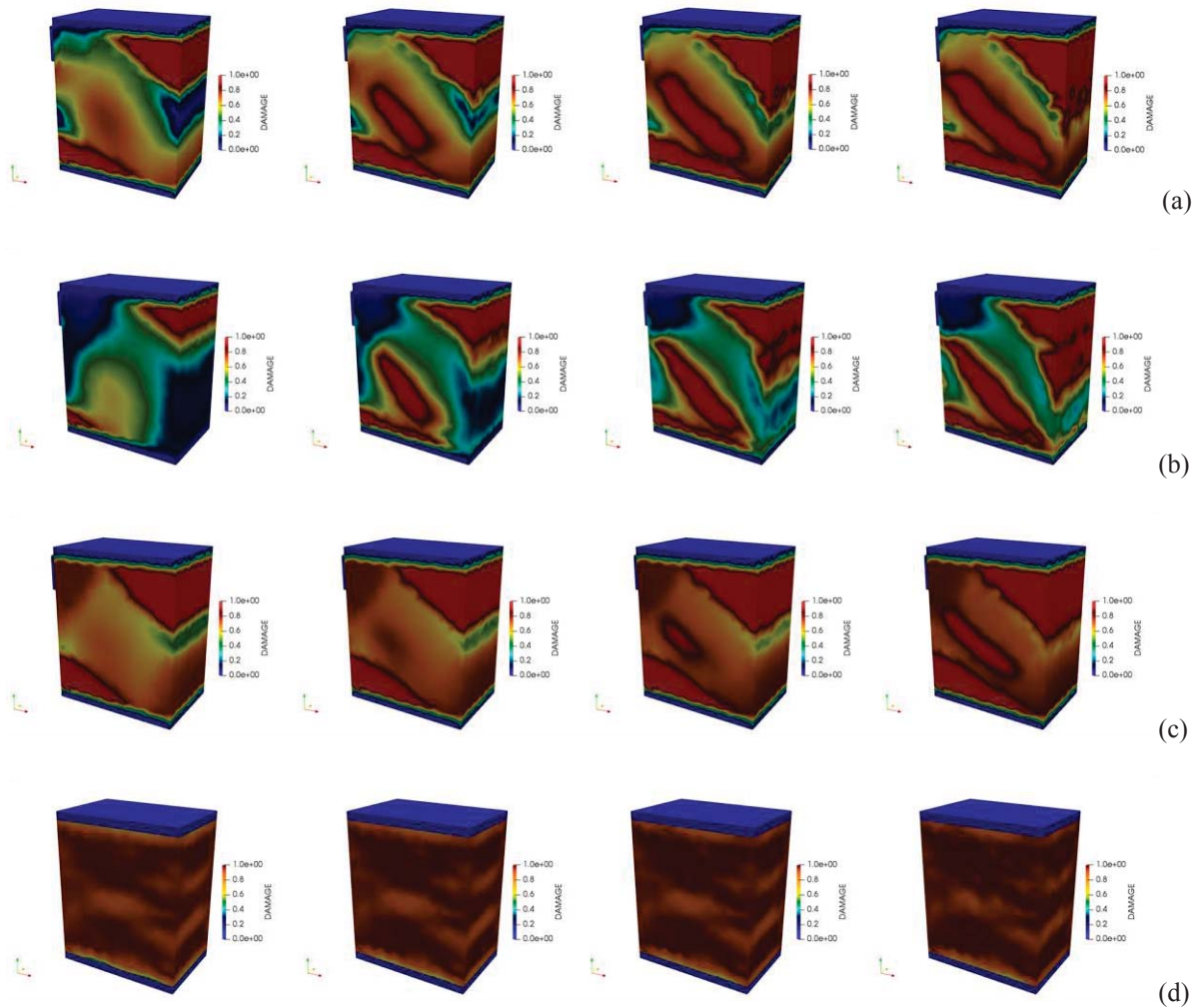


Figure 8: Numerical damage evolution for (a) Wall#1, (b) Wall#2, (c) Wall#3, (d) Wall#4.

The damage of the numerical models is concentrated to the upper-right and lower-left sides of the specimens and evolves later in the middle part of the specimens where the diagonal

damage is evident. In comparison to the actual damaged state of the specimens, visually the damage is found to evolve diagonally and at the base of the specimen, so the numerical propagation in this point seems to be visually in good correspondence as can be seen in Figure 8. The damage evolution is initially concentrated in the inverse diagonal in respect to the experimental schemes. While the shearing process continues so does the damage in the correct diagonal direction and it is at that point that it corresponds to the results of the campaign.

6 CONCLUSIONS

The studies of the present work are carried out to assess the mechanical behavior of masonry walls build utilizing the “Scaglia Rossa” stone, a material typical of the area that encircles the Apennine regions between Umbria and Marche in Central Italy. Diverse experimental tests and numerical analyses by finite element method were performed with the aim to provide quantitative indications for the professionals that are involved in the reconstruction and rehabilitation works in the area affected by the renowned earthquake of Central Italy in 1997. The experimental campaign involved several tests on the constructed masonry composite that was reconstructed using techniques adopted in 1950’s and 1960’s. The specimens, in presence of shear loading, demonstrated an evident fragile behavior connected with the diagonal failure due to compression and shearing deformations. This characteristic mechanism was observed in all investigated cases. Also, several finite element models were developed aiming to reproduce the resulting data of the experimental campaign. This work was assisted by a calibration process by the Levenberg – Marquardt algorithm to fit the numerical process on the experimental results and validate if Mazars damage model can reproduce the specimen’s evolution of damage. The results obtain under the form of force – displacement curves on a macro – modelling approach and reproduced the experimental behavior visually. The summary of both experimental and numerical approaches appear to be of importance in order to define the non-linear and numerical behavior of the material “Scaglia Rossa” masonry, in order to be utilized under design orders for specific restoration projects whose focus is based on structural fragilities featuring the recent seismic activities.

REFERENCES

- [1] J. M. Jara, E. J. Hernández, B. A. Olmos, and G. Martínez, “Building damages during the September 19, 2017 earthquake in Mexico City and seismic retrofitting of existing first soft-story buildings,” *Eng. Struct.*, p. 109977, Dec. 2019.
- [2] K. Sharma, L. Deng, and C. C. Noguez, “Field investigation on the performance of building structures during the April 25, 2015, Gorkha earthquake in Nepal,” *Eng. Struct.*, vol. 121, pp. 61–74, Aug. 2016.
- [3] M. Corradi, A. Borri, and A. Vignoli, “Strengthening techniques tested on masonry structures struck by the Umbria–Marche earthquake of 1997–1998,” *Constr. Build. Mater.*, vol. 16, no. 4, pp. 229–239, Jun. 2002.
- [4] D. Domínguez, F. López-Almansa, and A. Benavent-Climent, “Would RC wide-beam buildings in Spain have survived Lorca earthquake (11-05-2011)?,” *Eng. Struct.*, vol. 108, pp. 134–154, Feb. 2016.
- [5] M. Corradi, A. Borri, and A. Vignoli, “Experimental study on the determination of strength of masonry walls,” *Constr. Build. Mater.*, vol. 17, no. 5, pp. 325–337, Jul. 2003.
- [6] L. Binda, A. Saisi, and C. Tiraboschi, “Investigation procedures for the diagnosis of

- historic masonries,” *Constr. Build. Mater.*, vol. 14, no. 4, pp. 199–233, Jun. 2000.
- [7] J. M. Pereira, A. A. Correia, and P. B. Lourenço, “In-plane behaviour of rubble stone masonry walls: Experimental, numerical and analytical approach,” *Constr. Build. Mater.*, p. 121548, Nov. 2020.
- [8] L. Berto, A. Saetta, R. Scotta, and R. Vitaliani, “An orthotropic damage model for masonry structures,” *Int. J. Numer. Methods Eng.*, vol. 55, no. 2, pp. 127–157, Sep. 2002.
- [9] D. Liberatore and D. Addessi, “Strength domains and return algorithm for the lumped plasticity equivalent frame model of masonry structures,” *Eng. Struct.*, vol. 91, pp. 167–181, 2015.
- [10] D. Addessi, E. Sacco, and A. Paolone, “Cosserat model for periodic masonry deduced by nonlinear homogenization,” *Eur. J. Mech. A/Solids*, vol. 29, no. 4, pp. 724–737, 2010.
- [11] L. Gambarotta and S. Lagomarsino, “Damage models for the seismic response of brick masonry shear walls. Part I: the mortar joint model and its applications,” *Earthq. Eng. Struct. Dyn.*, vol. 26, no. 4, pp. 423–439, Apr. 1997.
- [12] L. Gambarotta and S. Lagomarsino, “Damage models for the seismic response of brick masonry shear walls. Part II: the continuum model and its applications,” *Earthq. Eng. Struct. Dyn.*, vol. 26, no. 4, pp. 441–462, Apr. 1997.
- [13] F. Clementi, A. Ferrante, E. Giordano, F. Dubois, and S. Lenci, “Damage assessment of ancient masonry churches stroked by the Central Italy earthquakes of 2016 by the non-smooth contact dynamics method,” *Bull. Earthq. Eng.*, vol. 18, no. 2, pp. 455–486, Jan. 2020.
- [14] L. Sorrentino, S. Cattari, F. da Porto, G. Magenes, and A. Penna, “Seismic behaviour of ordinary masonry buildings during the 2016 central Italy earthquakes,” *Bull. Earthq. Eng.*, vol. 17, no. 10, pp. 5583–5607, Oct. 2019.
- [15] C. Clementi, F. Clementi, and S. Lenci, “Nonlinear analyses and failure patterns of typical masonry school buildings in the epicentral zone of the 2016 Italian earthquakes,” in *AIP Conference Proceedings*, 2017, vol. 1906, p. 090005.
- [16] E. Sassine, Y. Cherif, and E. Antczak, “Parametric identification of thermophysical properties in masonry walls of buildings,” *J. Build. Eng.*, vol. 25, no. May, p. 100801, 2019.
- [17] P. B. Lourenço, “Computational strategies for masonry structures : multi-scale modeling, dynamics, engineering applications and other challenges,” *Congr. Métodos Numéricos en Ing.*, pp. 1–17, 2013.
- [18] R. Morbiducci, “Nonlinear parameter identification of models for masonry,” *Int. J. Solids Struct.*, vol. 40, no. 15, pp. 4071–4090, 2003.
- [19] F. Khosravikia, J. Kurkowski, and P. Clayton, “Fragility of masonry veneers to human-induced Central U.S. earthquakes using neural network models,” *J. Build. Eng.*, vol. 28, no. June 2019, p. 101100, 2020.
- [20] M. Betti, G. Bartoli, R. Corazzi, V. Kovačević, and V. Kovacevic, “Strumenti Open Source per l’ingegneria strutturale. Modellazione meccanica non lineare di edifici in muratura,” *Bolletino Ing.*, vol. 60, no. 12, pp. 3–15, 2012.
- [21] L. Facchini, M. Betti, R. Corazzi, and V. C. Kovacevic, “Nonlinear seismic behavior of historical masonry towers by means of different numerical models,” *Procedia Eng.*, vol. 199, pp. 601–606, 2017.

BEHAVIOUR FACTOR ASSESSMENT OF ANCIENT MASONRY TOWERS THROUGH AN INNOVATIVE SIMPLIFIED PUSHOVER METHOD

De Iasio, Alessandro¹, Wang, Peixuan², Milani, Gabriele² and Ghiassi, Bahman¹

¹ University of Nottingham, Faculty of Engineering, Centre for Structural Engineering and Informatics
University Park, Nottingham, United Kingdom
{alessandro.deiasio, bahman.ghiassi}@nottingham.ac.uk

² Politecnico di Milano
Department of Architecture Built Environment and Construction Engineering ABC, Piazza Leonardo
da Vinci, 32, 20144, Milan, Italy
{gabriele.milani, peixuan.wang}@polimi.it

Abstract

The seismic vulnerability of masonry towers is a critical research field and it has an important role in the preservation of worldwide conservation of such kind of masonry building. Indeed, masonry towers have a very high seismic vulnerability and are often located in high seismic hazard zones. Researches about this topic have become even more frequent in the last decades. However, the results about the seismic behaviour of the masonry towers are still limited and further researches are needed. This paper aims to study the value of the behaviour factor (usually called q -factor or R -factor) of ancient masonry tower-like structures. This parameter provides quantitative information about the ductility of the tower and it can be computed by the capacity curve of the structure. In particular, the pushover curve can be bilinearized, and the q -factor can be computed according to the equal displacement or equal energy rule. The bilinearization of the capacity curve implies the knowledge of the ultimate displacement, whose computation is not a trivial task for this kind of structures because the capacity curves usually computed for such structures are apparently infinite ductility curves and the ultimate displacement cannot be directly computed. Therefore, an innovative pushover method (called “manual” pushover) has been formulated and implemented in a Matlab® code to achieve the q -factor computation goal. The tower is modelled by a vertical cantilever beam with lumped plasticity and it is loaded by self-weight and a user-defined horizontal distributed load profile. The non-linearities are modelled by the Moment-Curvature diagram of the cross-section where the plasticity is lumped. These cross-sections are positioned along the height of the tower splitting it into parts as uniform as possible in material and geometry characteristics. It allows considering the influence of openings and irregularities. The capacity curve is built by curvature control; it is similar to a displacement control and it allows to

capture the softening branch and, consequently, to compute the ultimate displacement. This method is quick, computationally light and it has been properly benchmarked with FEM results. The obtained capacity curve fits the request of the q -factor computation method presented above. It is worth noting that the Moment-Curvature diagrams have been computed by a Matlab code based on digital image processing. In particular, it can read the geometry of a generic cross-section through its digital image representation and it automatically computes the diagram according to equilibrium, compatibility and energy considerations. Finally, the q -factor value has been computed for various real case-studies highlighting its strong variability on the tower geometry (e.g. slenderness and shear area). The results have been compared with the suggested behaviour factor given by the Italian Guidelines for Built Heritage (2011) and it has been found that the code suggestions overestimate the tower ductility and they are too limited.

Keywords: masonry towers; earthquake; simplified models; pushover; Matlab; behaviour factor.

1 INTRODUCTION

The seismic vulnerability of masonry towers is a critical research field and it has an important role in the preservation of worldwide conservation of such kind of masonry building. Indeed, masonry towers have a very high seismic vulnerability and are often located in high seismic hazard zones. Researches about this topic have become even more frequent in the last decades. However, the results about the seismic behaviour of the masonry towers are still limited and further researches are needed.

Masonry towers have usually shown high seismic vulnerability [1–6] and their seismic response is complex and depends on various parameters, both mechanical and geometrical. In [7,8], the authors have demonstrated that five collapse mechanisms (Figure 1) are the most likely to occur and they depend on both slenderness and shear area.

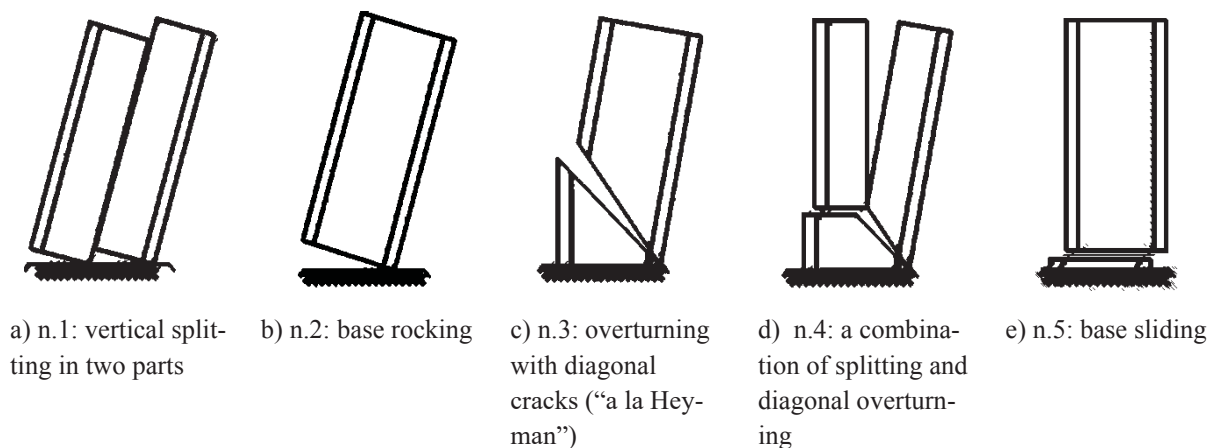


Figure 1 Collapse mechanism for masonry towers selected in [7] (images adapted from [7]).

Various analysis methods have been usually applied. Non-linear static and dynamic analysis are the most diffused analysis tools and they have been fully and successfully used in [1,2,9–12]. Also, simplified methods have been introduced, like the kinematic limit analysis has shown its accuracy and efficiency in various studies (e.g. in [7,8,13,14]). More sophisticated methods have been recently discovered, like the DEM modelling [7,15] or the Non-Smooth Contact Dynamic method [16].

Towers specific features have been analysed too. In [17–19] it has been demonstrated the importance of the tower inclination in their seismic assessment, while the influence of the surrounding buildings has been studied in [20].

This paper aims to study the value of the behaviour factor (usually called q -factor or R -factor) of ancient masonry tower-like structures. This parameter provides quantitative information about the ductility of the tower and it can be computed by the capacity curve of the structure. The capacity curve can be bi-linearized, and the behaviour factor may be computed according to the equal displacement rule or equal energy rule.

The bilinearization of the capacity curve implies the knowledge of the ultimate displacement, whose computation is not a trivial task for this kind of structures because the capacity curves usually computed by FE simulations for such structures are apparently infinite ductility curves and the ultimate displacement cannot be directly computed.

To achieve this goal, an innovative pushover method has been developed by the authors and it has been called "manual" pushover analysis. It is based on the modelling of the tower as a cantilever beam with lumped plasticity and it is loaded by self-weight and a user-defined horizontal distributed load profile.

The non-linearities are modelled by the Moment-Curvature diagram of the cross-section where the plasticity is lumped. These cross-sections are positioned along the height of the tower splitting it into parts as uniform as possible in material and geometry characteristics. It allows considering the influence of openings and irregularities.

The capacity curve is built by *curvature* control; it is similar to a displacement control and it allows to capture the softening branch and, consequently, to compute the ultimate displacement. This method is quick, computationally light and it has been properly benchmarked with FEM results. The obtained capacity curve fits the request of the q-factor computation method presented above. The Moment-Curvature diagrams have been computed by a Matlab code based on digital image processing. In particular, it can read the geometry of a generic cross-section through its digital image representation and it automatically computes the diagram according to equilibrium, compatibility and energy considerations.

Finally, the q-factor value has been computed for various real case-studies highlighting its strong variability on the tower geometry (e.g. slenderness and shear area). The results have been compared with the suggested behaviour factor given by the Italian Guidelines for Built Heritage (2011) and it has been found that the code suggestions overestimate the tower ductility and they are too limited. In particular, the suggestion made by the Italian Guidelines provides a double choice for the behaviour factor value: equal to 3.6 for regular towers and 2.8 for irregular ones. This value is used in the LV1 procedure proposed by guidelines, which is a method to quickly study the seismic vulnerability of such structures. The behaviour factor value is inversely proportional to the applied inertia horizontal forces; therefore its overestimation may lead to unsafe results. Similar final considerations have been produced also in [21].

A real case-study will be considered: a Chinese masonry pagoda (the *Longhu Pagoda*). It is the case study presented in [22], in which several FE pushover analyses have been carried out. These data will be used in this paper.

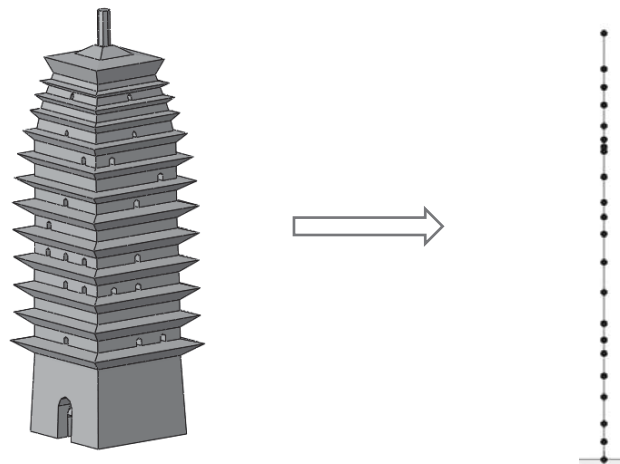


Figure 2 Lumped plasticity model for the "manual" PO applied to the Longhu Pagoda.

The structure of this paper is as follow. Section 2 will briefly present the “manual” pushover method and its validation. Finally, in Section 3 the assessment of the behaviour factor value is reported. Discussions and conclusions are drawn in Section 4.

2 THE “MANUAL” PUSHOVER ANALYSIS

Unfortunately, pushover analysis often needs sophisticated FE tools. Thus, a simplified pushover method is presented for masonry towers seismic assessment. The computational cost

is lower, and no FE software are needed. A similar method but with different algorithms and analysis tools has been proposed in [23].

The tower is modelled as a cantilever beam with lumped plasticity. The plastic properties are considered through the Moment-Curvature ($M-\chi$) diagram where the plasticity is lumped. The tower body is split into n parts, posing the horizontal cutting, particularly at openings and irregularities. Each part has to be as uniform as possible in geometry and materials, similarly to what is suggested by Italian guidelines [24] to apply the LV1 analysis. An example is represented in Figure 2.

The $M-\chi$ diagram has been computed by a Matlab subroutine the author has created that can compute specific cross-sections properties based on a digital image processing of cross-section itself and equilibrium equations (a specific study will be published on this algorithm by the authors, an example is shown in Figure 3). The diagram is computed by considering a compressive axial force equal to the weight of the tower above the cross-section itself. The material model is implemented through a non-linear stress-strain relationship with softening both in tension and compression. Figure 4 shows the implemented stress-strain relationship, while Table 1 reports the main mechanical parameters. The material properties have been supposed according to the usual values of masonry models.

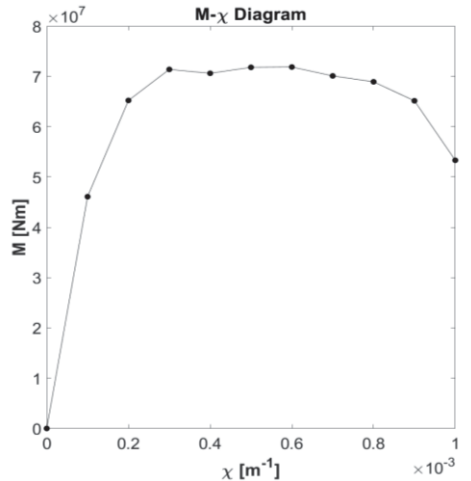


Figure 3 Example of the implemented $M-\chi$ diagrams.

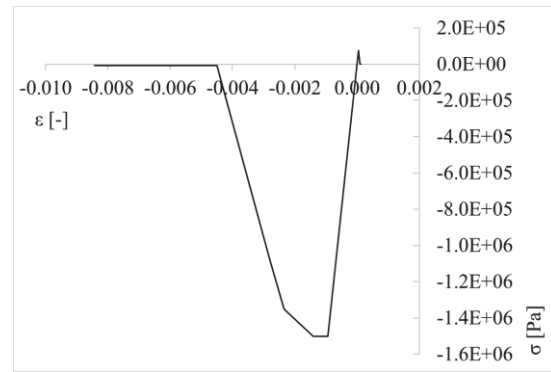


Figure 4 The implemented stress-strain relationship.

Density ρ [kg/m ³]	Young's Modulus E [MPa]	Poisson's Coeff. ν [-]	σ_c [MPa]	σ_t [MPa]
2000	1600	0.2	1.5	0.075

Table 1 Main mechanical parameters.

The proposed “Manual” pushover analysis is performed in *curvature* control. It is a sort of *displacement* control method that allows capturing the softening branch. The curvature is progressively increased in a chooses cross-section (i.e. the first one that would fail, named *controlled* cross-section). Both G1 and G2 (Figure 5) load distributions have been used. The structure is statically determined, thus the bending moment diagram depends only on equilibrium considerations and its expression will never lose its validity during the whole analysis procedure. The usual formulas used to compute the bending moment distribution on a cantilever beam have been used. The external horizontal load is progressively incremented

and the equilibrium at each step is achieved. Through the bending moment at each cross-section and the related $M-\chi$ diagrams, the curvature distribution is computed along the height and, subsequently the top displacement. Finally, the capacity curve is obtained by the base shear and the top displacement at each step.

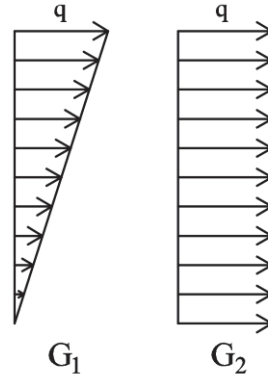


Figure 5 G1 and G2 load distributions.

The horizontal load value decrease after that the structure strength reaches its pick and the same happen to the bending moment distribution. However, while in the *controlled* cross-section the *curvature* is continuously increased, the other cross-sections experience a decreasing in bending moment and the same happens to the curvature: linear unloading is implemented for them.

The method has been applied to real case-studies and its results have been compared to capacity curves obtained by FE simulations. It is the *Longhu Pagoda* which is a Chinese masonry pagoda and it is the case study presented in [22]. The data collected in this latter study are presented here to show the validity of the “manual” pushover method.

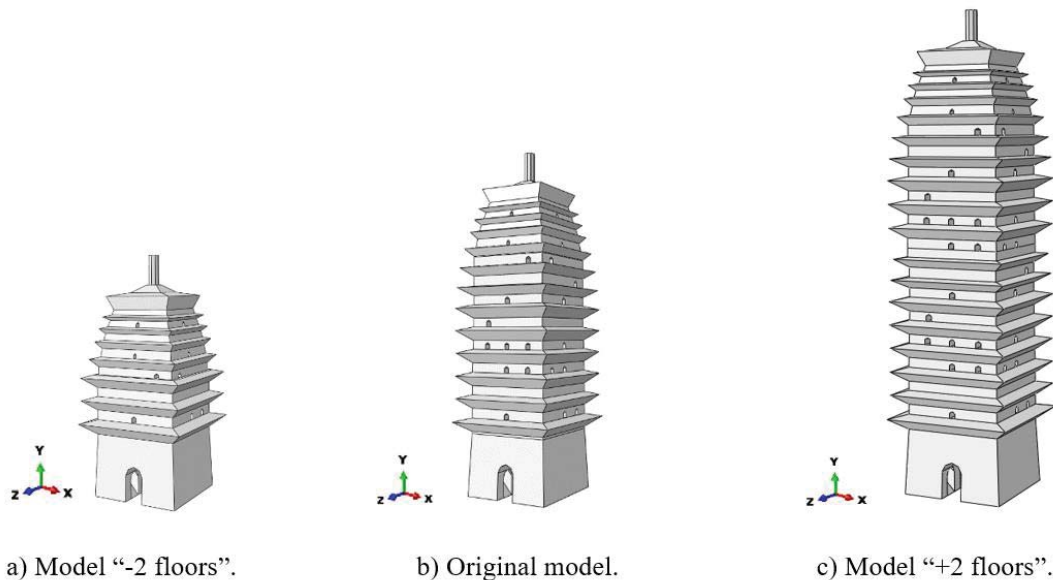


Figure 6 The pagoda models.

In [22] peculiar considerations have been made on the slenderness influence by building two fictitious models of the pagoda adding and removing two floors. In this way, the interiors

and mass distribution are still plausible. The three models are shown in Figure 6 and the interested reader is remanded to [22] for further details about them. Therefore, three case-studies will be presented in the following. The material model is reported in Figure 4 and Table 1. Both G1 and G2 load cases have been considered and the pushovers have been carried out along the z^+ direction only (Figure 6).

The “manual” pushover results have been compared with the FEM pushover capacity curves presented in [22] and carried in the Abaqus environment. The material models are similar in terms of a stress-strain relationship. Figures 7-9 shows the comparison between the capacity curves for the three models. The “Load Factor” is the ratio between the total base shear and the total weight of the structure. A new phenomenon is here present: the *snap-back* of the top displacement in the last phases of the analysis. This novelty has been possible to be caught only thanks to the special pushover control parameter used (i.e. the *curvature* control in the worst cross-section). Apart from the “+2 Model”, in which the predictions of the two methods differ, in the other cases good agreement is achieved. These results will be used to compute the behaviour factor of the pagoda.

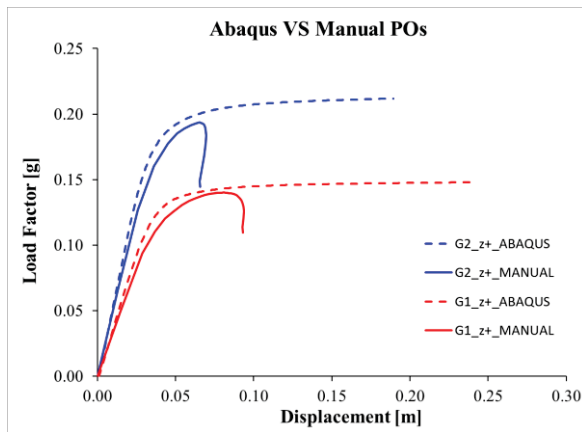


Figure 7 Abaqus vs Manual POs: original model.

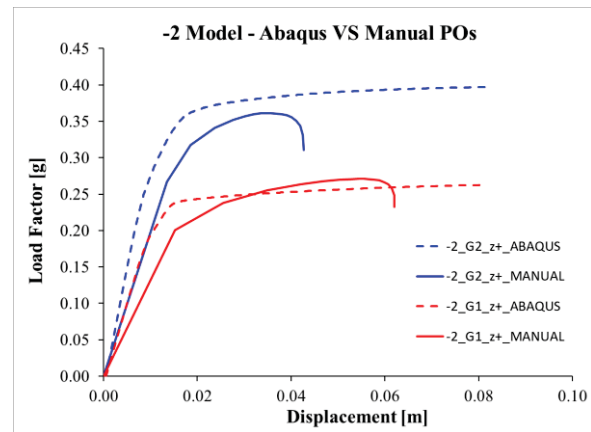


Figure 8 Abaqus vs Manual POs: “-2 Model”.

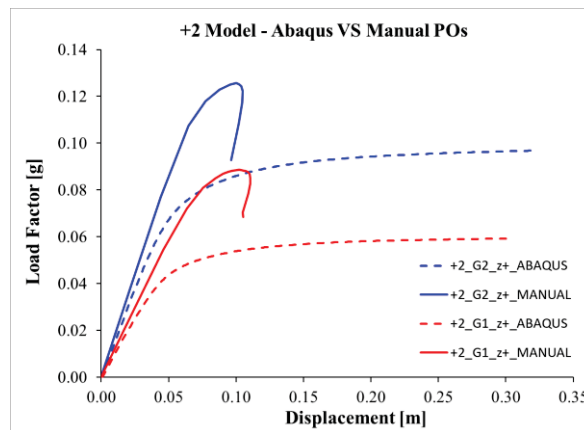


Figure 9 Abaqus vs Manual POs: “+2 Model”.

3 THE BEHAVIOUR FACTOR OF THE TOWER

To estimate the q -factor it has been decided to use the bi-linearization of the capacity curve and then to apply the equal displacement rule or the equal energy rule. The bi-linearization

procedure is taken from the Italian building code [25] and its schematization is shown in Figure 10. It is a function of the frequency content of the seismic action (its elastic-response spectrum) and the natural period of the structure.

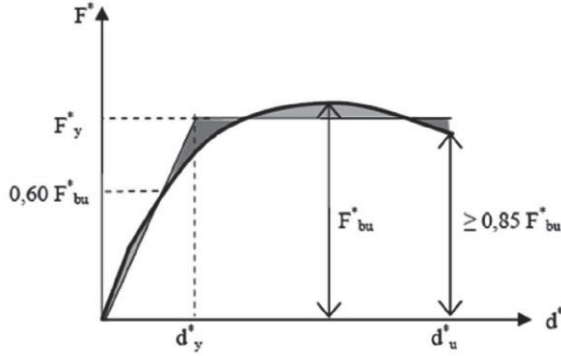


Figure 10 Equivalent bi-linear curve (adapted from [25]).

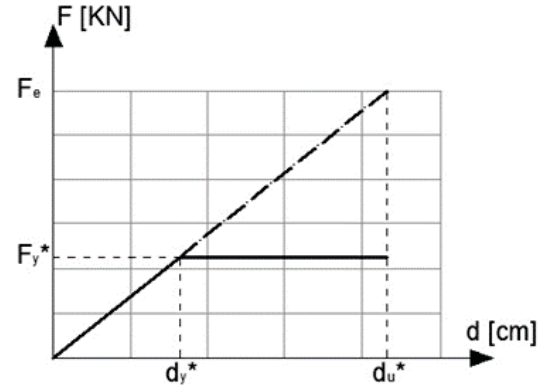


Figure 11 Equal displacement criterion (adapted from [26]).

In particular, considering the elastic system and the elastic-plastic system (Figure 11), they are related between each other according to the value of the natural period of the structure and the period T_c , which is the upper limit of the period of the constant spectral acceleration branch in the elastic response spectrum that represents the seismic demand (as defined in the Eurocode 8 [27]). In this case $T_c = 0.4 \text{ s}$ (according to the spectrum defined by the Chinese Building Code [28] for the site of the pagoda and presented in [22]). Two cases can be defined:

- $T \geq T_c$: the ultimate displacement is the same between the elastic and the elastic-plastic system (Figure 11) (“equal displacement” criterion).
- $T < T_c$: the deformation energy is the same between the elastic and the elastic-plastic system (“equal energy” criterion).

The q-factor can be computed by Eq. (1).

$$\begin{aligned} q &= \mu & T &\geq T_c \\ q &= 1 + (\mu - 1) \frac{T}{T_c} & T &< T_c \end{aligned} \quad (1)$$

where $\mu = \frac{d_u^*}{d_y^*}$. Note that $\frac{F_e}{F_y^*} = \frac{d_u^*}{d_y^*}$ if $T \geq T_c$.

This method has been applied to the capacity curves obtained from the “manual” pushovers. As an example, the computations made on the capacity curve related to the “manual” pushover performed on the original model along the z+ direction with a G1 load distribution is shown in detail (Table 2 and Figure 12). Table 3 report the behaviour factors computed for each case. It is worth noting that the behaviour factor changes as the applied load and the height change. Moreover, the value computed for the “+2 Model” might be furtherly studied due to the discrepancy between the “manual” pushover and the FE capacity curves.

It is noticeable that the behaviour factor values presented in Table 3 are lower than the values proposed by the Italian guidelines [24] and they are different from each other. This means that what is suggested in [24] may lead to unsafe and unrealistic results in terms of seismic vulnerability. Indeed, the Italian guidelines [24] propose two values of the behaviour factor:

3.6 for regular towers and 2.8 for irregular ones and these suggestions are not confirmed by this research.

F_{MAX}	F_Y	d_Y	d_U	T	T_C	μ	q
[g]	[g]	[m]	[m]	[s]	[s]	[-]	[-]
0.14	0.131	0.039	0.09	0.6537	0.4	2.398	2.398

Table 2 q-factor assessment for the original model case (G1 load).

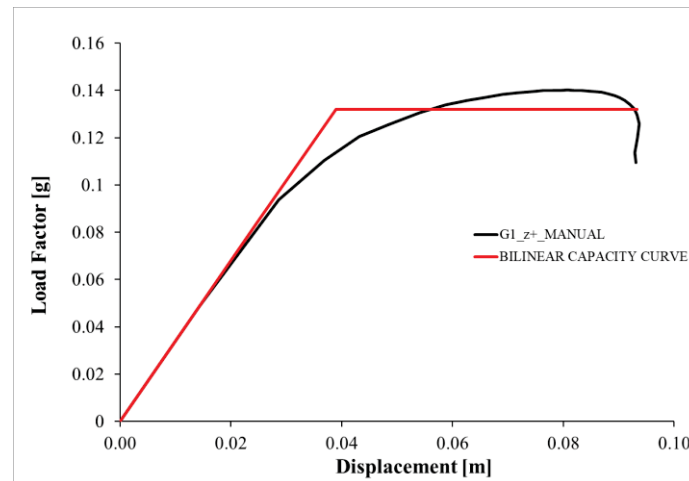


Figure 12 Capacity curve and the relative equivalent bilinear curve for the original model case (G1 load).

Model	Load Case	q [-]
original	G1	2.398
original	G2	1.883
-2	G1	2.578
-2	G2	2.095
+2	G1	1.503
+2	G2	1.485

Table 3 Behaviour factor's values

4 CONCLUSIONS

This paper has studied the value of the behaviour factor of masonry towers through an innovative pushover method that allows to capture the softening branch and thus, to apply the bi-linearization procedure to the capacity curve to compute the behaviour factor.

The behaviour factor values have been computed for some case-studies: three Chinese masonry pagodas with different slenderness. The behaviour factor has been computed by the capacity curves of these structures obtained from the application of the “manual” pushover method using both a G1 and G2 load distribution.

The computed values of the behaviour factors show that the suggestions of the Italian guidelines may underestimate it. Indeed, the Italian guidelines [24] propose two values of the

behaviour factor: 3.6 for regular towers and 2.8 for irregular ones and these suggestions are not confirmed by this research.

Therefore, further analysis of this topic may be useful to better quantify the behaviour factor of masonry towers and to propose new guidelines. Indeed, the simple and reliable formula may be very useful for practitioners for the safety assessment of the masonry towers. However, this study has shown that the behaviour factor may depend on several factors, among them the geometry of the structures. To assess these dependencies, further researches will be needed.

REFERENCES

- [1] D'Ambrisi A, Mariani V, Mezzi M. Seismic assessment of a historical masonry tower with nonlinear static and dynamic analyses tuned on ambient vibration tests. *Eng Struct* 2012;36:210–9. <https://doi.org/10.1016/j.engstruct.2011.12.009>.
- [2] Milani G, Casolo S, Naliato A, Tralli A. Seismic assessment of a medieval masonry tower in Northern Italy by limit, nonlinear static, and full dynamic analyses. *Int J Archit Herit* 2012;6:489–524. <https://doi.org/10.1080/15583058.2011.588987>.
- [3] Ge, C. MZT. Research on the Safety Evaluation of Ancient Stone Pagodas in the Earthquake: a Case Study of Qingjing Pagoda. *Chinese Cult Reli Res* 2013;(02):46-50.
- [4] Jianli Y, Shengcai L. Study of the seismic damage regularity of ancient masonry pagodas in the 2008 Wenchuan Earthquake. *WIT Trans Built Environ* 2013;132:421–32. <https://doi.org/10.2495/ERES130341>.
- [5] Bertolesi E, DelGrosso A, Milani G, Minghini F, Tralli A. 3D FE pushover and non-linear dynamic analyses of a masonry chimney before and after shortening. *COMPdyn 2015 - 5th ECCOMAS Themat Conf Comput Methods Struct Dyn Earthq Eng* 2015:2158–66. <https://doi.org/10.7712/120115.3529.722>.
- [6] Formisano A, Milani G. Seismic vulnerability analysis and retrofitting of the SS. Rosario church bell tower in finale emilia (Modena, Italy). *Front Built Environ* 2019;5. <https://doi.org/10.3389/fbuil.2019.00070>.
- [7] Sarhosis V, Milani G, Formisano A, Fabbrocino F. Evaluation of different approaches for the estimation of the seismic vulnerability of masonry towers. vol. 16. Springer Netherlands; 2018. <https://doi.org/10.1007/s10518-017-0258-8>.
- [8] Milani G. Fast Vulnerability Evaluation of Masonry Towers by Means of an Interactive and Adaptive 3D Kinematic Limit Analysis with Pre-assigned Failure Mechanisms. *Int J Archit Herit* 2019;13:941–62. <https://doi.org/10.1080/15583058.2019.1645241>.
- [9] Peña F, Lourenço PB, Mendes N, Oliveira D V. Numerical models for the seismic assessment of an old masonry tower. *Eng Struct* 2010;32:1466–78. <https://doi.org/10.1016/j.engstruct.2010.01.027>.
- [10] Casolo S, Milani G, Uva G, Alessandri C. Comparative seismic vulnerability analysis on ten masonry towers in the coastal Po Valley in Italy. *Eng Struct* 2013;49:465–90. <https://doi.org/10.1016/j.engstruct.2012.11.033>.
- [11] Valente M, Milani G. Non-linear dynamic and static analyses on eight historical masonry towers in the North-East of Italy. *Eng Struct* 2016;114:241–70. <https://doi.org/10.1016/j.engstruct.2016.02.004>.
- [12] Poiani M, Gazzani V, Clementi F, Milani G, Valente M, Lenci S. Iconic crumbling of the clock tower in Amatrice after 2016 central Italy seismic sequence: Advanced numerical insight. *Procedia Struct Integr* 2018;11:314–21. <https://doi.org/10.1016/j.prostr.2018.11.041>.

- [13] Milani G, Shehu R, Valente M. A kinematic limit analysis approach for seismic retrofitting of masonry towers through steel tie-rods. *Eng Struct* 2018;160:212–28. <https://doi.org/10.1016/j.engstruct.2018.01.033>.
- [14] Grillanda N, Valente M, Milani G. ANUB-Aggregates: a fully automatic NURBS-based software for advanced local failure analyses of historical masonry aggregates. *Bull Earthq Eng* 2020;18:3935–61. <https://doi.org/10.1007/s10518-020-00848-6>.
- [15] Tavafi E, Mohebbkhah A, Sarhosis V. Seismic Behavior of the Cube of Zoroaster Tower Using the Discrete Element Method. *Int J Archit Herit* 2019;0:1–16. <https://doi.org/10.1080/15583058.2019.1650135>.
- [16] Ferrante A, Loverdos D, Clementi F, Milani G, Formisano A, Lenci S, et al. Discontinuous approaches for nonlinear dynamic analyses of an ancient masonry tower. *Eng Struct* 2021;230:111626. <https://doi.org/10.1016/j.engstruct.2020.111626>.
- [17] Ferrante A, Clementi F, Milani G. Dynamic behavior of an inclined existing masonry tower in Italy. *Front Built Environ* 2019;5:1–16. <https://doi.org/10.3389/fbuil.2019.00033>.
- [18] D’Altri AM, Milani G, de Miranda S, Castellazzi G, Sarhosis V. Stability analysis of leaning historic masonry structures. *Autom Constr* 2018;92:199–213. <https://doi.org/10.1016/j.autcon.2018.04.003>.
- [19] Prizeman OEC, Sarhosis V, D’Altri AM, Whitman CJ, Muratore G. MODELLING from the PAST: The LEANING SOUTWEST TOWER of CAERPHILLY CASTLE 1539-2015. *ISPRS Ann Photogramm Remote Sens Spat Inf Sci* 2017;4:221–7. <https://doi.org/10.5194/isprs-annals-IV-2-W2-221-2017>.
- [20] Vaiano G, Venanzi I, Formisano A, Ubertini F. Seismic behaviour of isolate and aggregate masonry towers: The case study of the sciri tower in Perugia. *COMPDYN Proc* 2019;1:1441–59. <https://doi.org/10.7712/120119.7010.19301>.
- [21] Bocciarelli M. On the behavior factor of masonry towers. *Soil Dyn Earthq Eng* 2017;101:81–9. <https://doi.org/10.1016/j.soildyn.2017.05.027>.
- [22] De Iasio A, Wang P, Scacco J, Milani G. Longhu pagoda : Advanced numerical investigations for assessing performance at failure under horizontal loads (in press). *Eng Struct* 2021.
- [23] Bocciarelli M, Barbieri G. A numerical procedure for the pushover analysis of masonry towers. *Soil Dyn Earthq Eng* 2017;93:162–71. <https://doi.org/10.1016/j.soildyn.2016.07.022>.
- [24] Italian Ministry for Cultural Heritage. Assessment and mitigation of seismic risk of cultural heritage with reference to the Italian Building Code (NTC2008). Directive of the Prime Minister, 9/02/2011. G.U. no. 47, 26/02/2011 (suppl. ord. no. 54) (in Italian) 2011.
- [25] Italian Ministry for Transports and Infrastructures. CIRCOLARE 21 gennaio 2019, n. 7 C.S.LL.PP. Istruzioni per l’applicazione dell’«Aggiornamento tecniche per le costruzioni» di cui al decreto gennaio 2018. (19A00855) (in Italian) 2019:1–14.
- [26] Pisano B. Alla scoperta del “fattore di comportamento n.d.
- [27] European Commission. EN 1998-1 (2004) (English): Eurocode 8: Design of structures for earthquake resistance – Part 1: General rules, seismic actions and rules for buildings. n.d.
- [28] GB 50011(2016): GB 50011 Code for Seismic Design of Buildings, PRC. n.d.

FE PUSHOVER ANALYSES OF A 20TH-CENTURY MASONRY CHIMNEY IN SPAIN: COLLAPSE BEHAVIOUR AND NUMERICAL UNCERTAINTIES

Alessandro De Iasio¹, Gabriele Milani² and Jose M Adam³

¹ University of Nottingham, Faculty of Engineering, Centre for Structural Engineering and Informatics
University Park, Nottingham, United Kingdom
alessandro.deiasio@nottingham.ac.uk

² Politecnico di Milano
Department of Architecture Built Environment and Construction Engineering ABC, Piazza Leonardo
da Vinci, 32, 20144, Milan, Italy
gabriele.milani@polimi.it

³ ICITECH, Universitat Politècnica de València, Camino de Vera s/n, 46022 Valencia, Spain
joadmar@upv.es

Abstract

The seismic vulnerability of masonry chimneys is a critical research topic, and it has an important role in the preservation of such kind of structural type. Indeed, masonry chimneys have a very high seismic vulnerability and are sometimes located in high seismic hazard zones. Researches about this topic have become even more frequent in the last decades. However, the results are still limited, and further studies are needed. This paper aims to study the seismic behaviour of a 20th-century masonry chimney located in Spain, focusing on its ultimate behaviour. In particular, various FE pushover analyses have been carried out in Abaqus/CAE using a quite accurate 3D model of the chimney. The pushover analyses have been made along the four principal directions, and both G1 and G2 load distributions have been applied. The material properties have been chosen according to previous studies carried out on similar structures because no specific experimental data were available. The obtained capacity curves have been compared with each other, and the main weak points of the chimney have been pointed out. Finally, a sensitivity analysis has been done to better understand the influence of the viscosity parameter on the pushover results in terms of ultimate capacity and computational effort. The latter one is an input value of the Concrete Damage Plasticity model, an Abaqus built-in material model, widely used to represent the non-linear behaviour of masonry structures.

Keywords: masonry chimneys; earthquake; pushover; Finite Element Method; CDP; viscosity parameter; computational effort

1 INTRODUCTION

The seismic vulnerability of masonry chimneys is a critical research topic, and it has an important role in the worldwide conservation of such kind of masonry structures. Indeed, masonry chimneys have a very high seismic vulnerability and are often located in high seismic hazard zones. Researches about this topic have become even more frequent in the last decades. However, the results about the seismic behaviour of the chimneys are still limited, and further research is needed.

Generally, masonry tower-like structures have usually shown high seismic vulnerability [1–6]; their seismic response is complex and depends on various parameters, both mechanical and geometrical. Different analysis methods have been usually applied. Non-linear static and dynamic analysis are the most used analysis tools, and they have been fully and successfully used in [1,2,7–10]. Also, simplified methods have been introduced, like the kinematic limit analysis has shown its accuracy and efficiency in various studies (e.g. in [11–14]). [15–17] have demonstrated the importance of the tower inclination in their seismic assessment, while the influence of the surrounding buildings has been studied in [18].

Chimneys are usually brickwork structures, and their typical high slenderness makes them very vulnerable when subjected to horizontal actions: it has been highlighted in [19] that such structures may be affected by several actions, and among them, earthquakes play a significant role. Therefore, their ductility against horizontal loads is crucial. Specific studies on these structures have been presented in [5,19–25].

This paper aims to study the ultimate behaviour of such structures by using some pushover analysis carried out with Abaqus/CAE and applied to a real case-study: a 20th-century masonry chimneys located in Villar del Arzobispo (Spain) (Figure 1). It is almost 28m high, and the base edge is 2.4m long. The base cross-section is a square and became octagonal after almost 5m from the ground. A small opening is present on one of the base facades, and it is directly connected with the flue, which runs from the base to the top of the chimney with the same shape as the exteriors. Figure 2 shows the 2D technical drawing of the chimney.



Figure 1: The chimney located in Villar del Arzobispo (Spain) used as a case-study of this research.

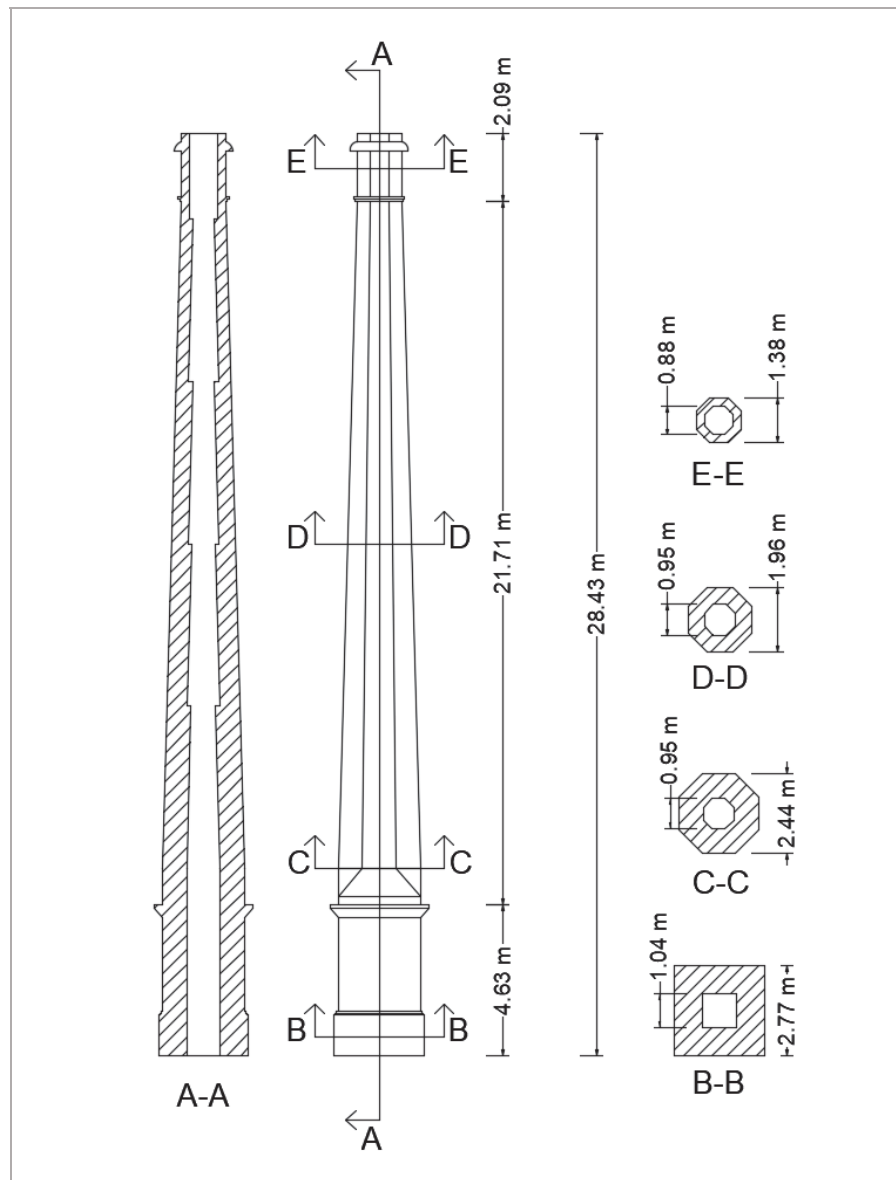


Figure 2: Technical drawing of the Villar del Arzobispo's chimney.

Different POs analyses have been produced, loading the chimney along the four principal directions and using both the G1 and G2 load distributions (Figure 3). The material properties have been chosen according to previous studies carried out on similar structures because no specific experimental data were available. The plastic properties have been considered through the Concrete Damage Plasticity (CDP) model, an Abaqus built-in material model, widely used to represent the non-linear behaviour of masonry structures. The results have been used to compare the capacity curves between each other and point out the chimney's main weak points. Finally, a sensitivity analysis has been done on the viscosity parameter. The latter one is a numerical input value of the CDP, and it helps the analysis's steps to converge by smoothing the yield surface. It has been often highlighted that the viscosity parameter increment tends to overestimate the ultimate capacity (e.g. in [26]). On the other hand, the decreasing of the viscosity parameter increase the computational effort; therefore, a sensitivity

analysis on this parameter may be helpful to better understand the influence of this parameter on the pushover results.

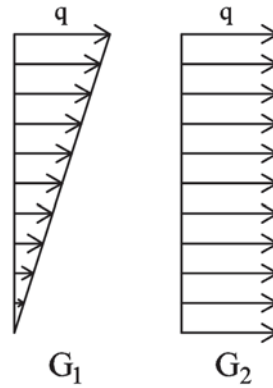


Figure 3: G1 and G2 load distributions.

The structure of this paper is as follow. Section 2 will briefly present the pushover results related to the analyses carried out on the four principal directions with fixed model properties, while, in Section 3, the influence of some numerical parameters has been presented. Discussions and conclusions are drawn in Section 4.

2 THE FE PUSHOVER RESULTS

The pushover analyses have been carried out on a 3D Finite Element model in Abaqus/CAE [27]. The FE model uses a 3D representation of the actual chimney geometry (Figure 4), which has been built in the Autodesk Inventor environment starting from the available 2D drawings.

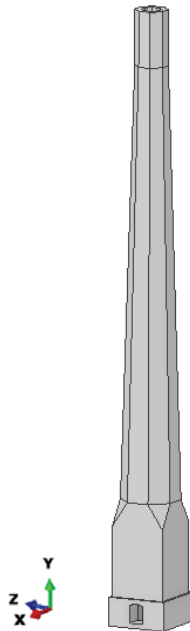


Figure 4: 3D model of the chimney case-study.

It has been decided to adopt a macro-modelling approach, and, in light of this latter choice, solid, homogeneous, and isotropic properties have been applied to the whole chimney body. The material properties have been chosen following the study presented in [20], and the main

mechanical parameters are shown in Table 1. The material non-linearities have been modelled employing the Concrete Damage Plasticity (CDP) model, whose main parameters are reported in Table 1 Main mechanical parameters.

. The compressive behaviour has been modelled by a brickwork feasible stress-strain relationship (Figure 5), while the fracture energy approach has been used for the tensile behaviour (Figure 6). The fracture energy has been computed by Eq. (1) as suggested in [28], and it is equal to 8.1 N/m.

$$G=0.025 (2\sigma_t)^{0.7} \quad (1)$$

Density ρ [kg/m ³]	Young's Modulus E [MPa]	Poisson's ratio ν [-]	σ_c [MPa]	σ_t [MPa]
1800	1500	0.15	3.5	0.1

Table 1 Main mechanical parameters.

Dilatation Angle	Eccentricity	f_{b0}/f_{c0}	K_c	Viscosity parameter
10°	0.1	1.16	0.667	0.0005

Table 2 Main parameters for the CDP

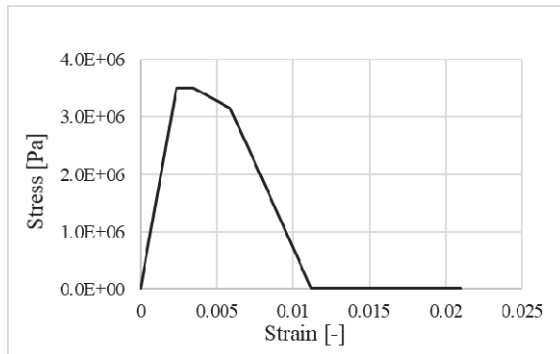


Figure 5: Compressive stress-strain branch to define the compressive CDP part in Abaqus.

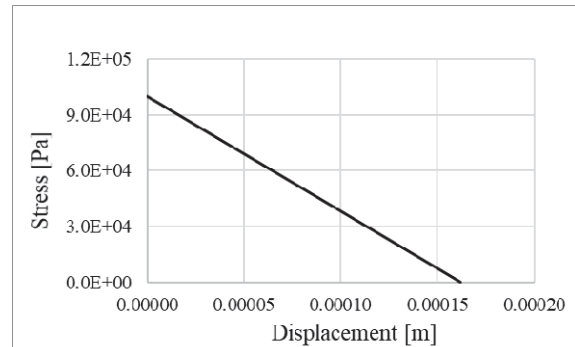


Figure 6: The post-failure tensile stress-fracture energy curve used to define the tensile CDP part in Abaqus.

The chimney body has been meshed through the Abaqus's automesh command. A seed dimension equal to 0.2m has been input, and linear tetrahedral elements of type C3D4 has been chosen. The model has a total number of 17289 nodes and 79666 elements. Figure 7 shows the meshed body, being possible to see that the discretisation is very refined. The element dimension may be considered adequate since the elements are linear.

The pushover analyses have been carried out along the four principal directions applying a G1 load distribution and along the z+ direction involving a G2 load distribution. The capacity curves have been built using the Load Factor (which is the ratio between the base shear and the total weight of the structure) and the horizontal displacement of a control point located at the top of the chimney. Both the latter quantities are related to the pushover direction. Furthermore, the tensile damage maps have been analysed.

Figure 8 shows the pushover analyses' capacity curves along the four principal directions using a G1 load distribution. It is worth noting that the four curves almost coincide; therefore, the singularities of the chimney body, i.e. the small opening at the base, doesn't play a crucial

role in the seismic response (differently from [26], in which it has been shown that the opening at the base of the case-study pagoda constitutes a weak point for the overall dynamic response). Figure 9, instead, presents a comparison between the G1 and the G2 loads' application along the z^+ direction. As expected, the ultimate capacity in the latter case is higher.



Figure 7: The meshed model .with 3D elements

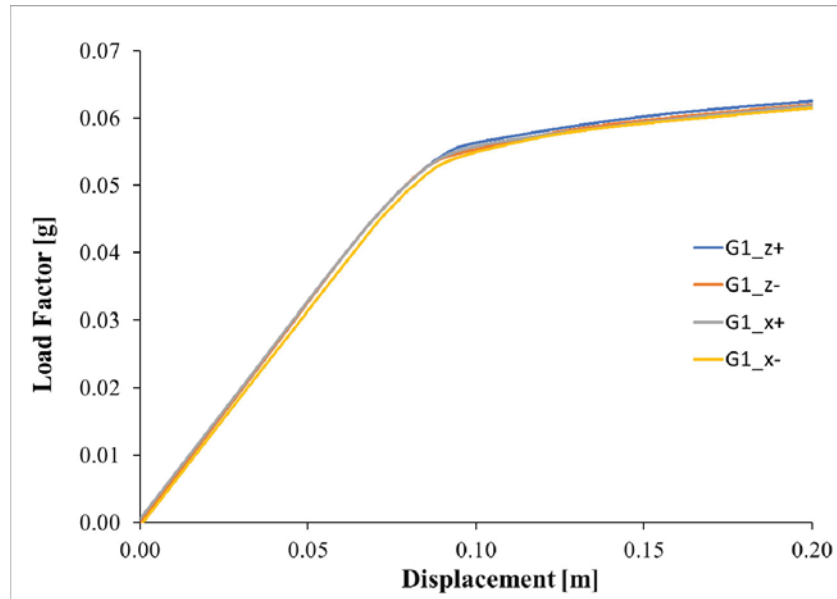


Figure 8: Capacity curves of the pushovers along the four principal directions.

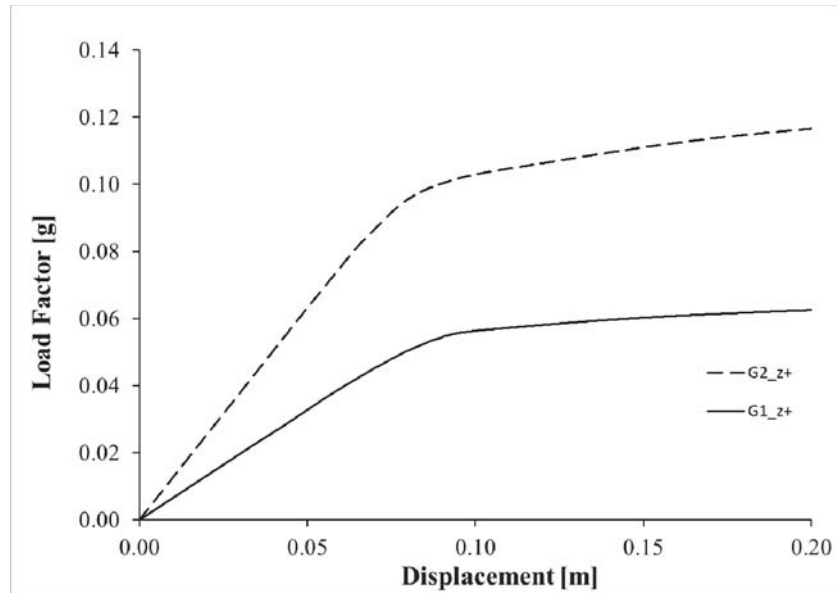


Figure 9: Comparison between the G1 and G2 loads' application along the z+ direction.

It could be interesting to highlight the phases of the damage spread. All the cases behave qualitatively similar due to the approximative axial symmetry of the structure; thus, the damage evolution of the z+ case is taken as an example and presented in Figure 10. It is shown how the loss of linearity is due to some horizontal cracks born on the tended fibres at a height between 5m and 9m; then, an additional horizontal crack born at the base. The plateau is approached when the aforementioned cracks spread and propagate as inclined along the faces parallel to the pushover load until collapse. Moreover, it is worth noting that the most critical sections are those at a quota between 5m and 9m. The damage maps suggest that a collapse mechanism based on a plastic hinge mechanism is activated. Based on [11], it is one of the most probable collapse mechanisms in tower-like structures under seismic actions when the structural slenderness is considerable.

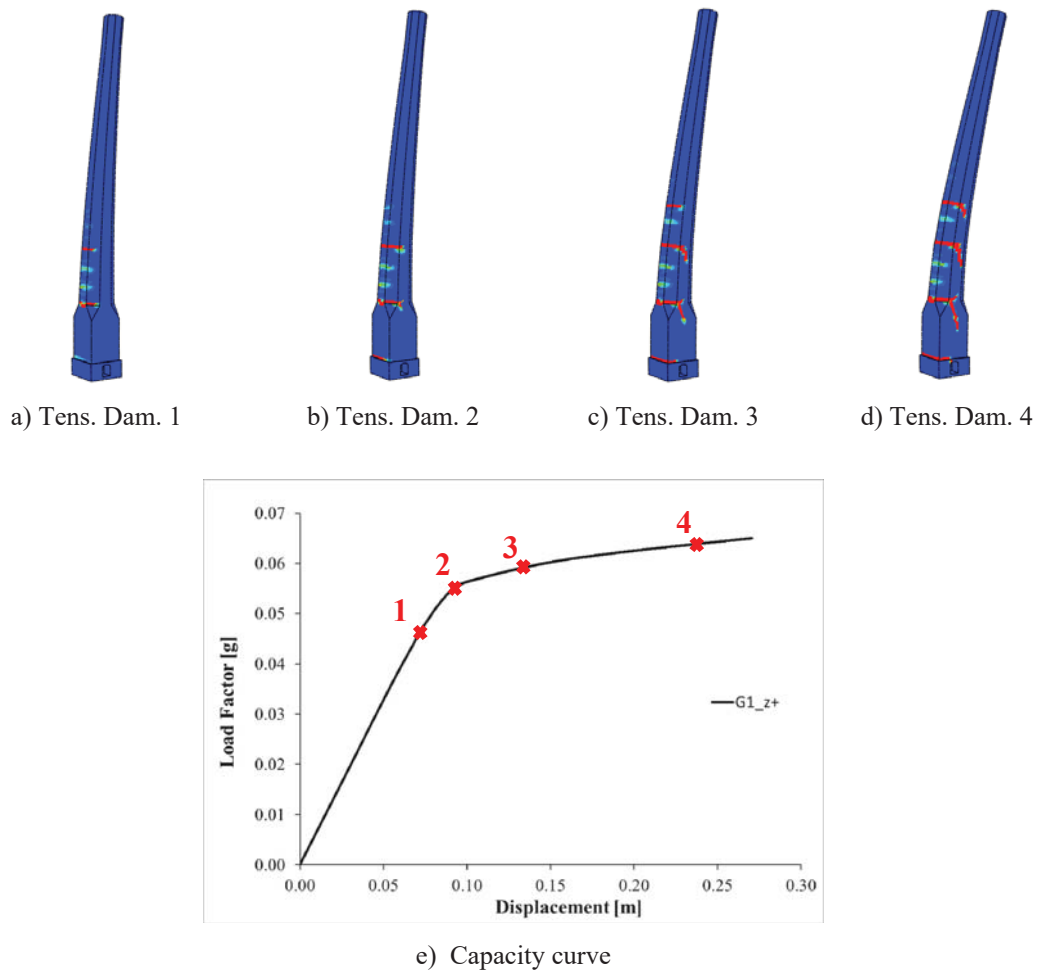


Figure 10: Damage evolution in z+ pushover.

3 SENSITIVITY ANALYSES ON THE VISCOSITY PARAMETER

A sensitivity analysis is proposed to highlight how the viscosity parameter value influences the analysis's results. The authors decided to select the G1 load and the z+ direction and varying the viscosity parameter only (the used values are shown in Table 3).

Viscosity parameter
0.001
0.0005
0.0001
0.00005

Table 3: Viscosity parameter's values used for the sensitivity analysis

Figure 11 shows the results of the sensitivity analysis. It is noticeable that the ultimate capacity significantly increases when the viscosity parameter is incremented. Moreover, the capacity curve's length is directly proportional to the viscosity parameter's value (the total load

increments number is fixed to 1200). The authors expected both the latter facts since the viscosity parameter smooth the yield surface and helps the steps' convergence and speed up. Increasing the viscosity parameter also increases the efficiency of the analysis by allowing larger load increments at each step but overestimate the ultimate capacity. Therefore, those who use the Concrete Damage Plasticity model in their studies must be aware of that and critically analyse the analyses' results also in light of the selected viscosity parameter's value.

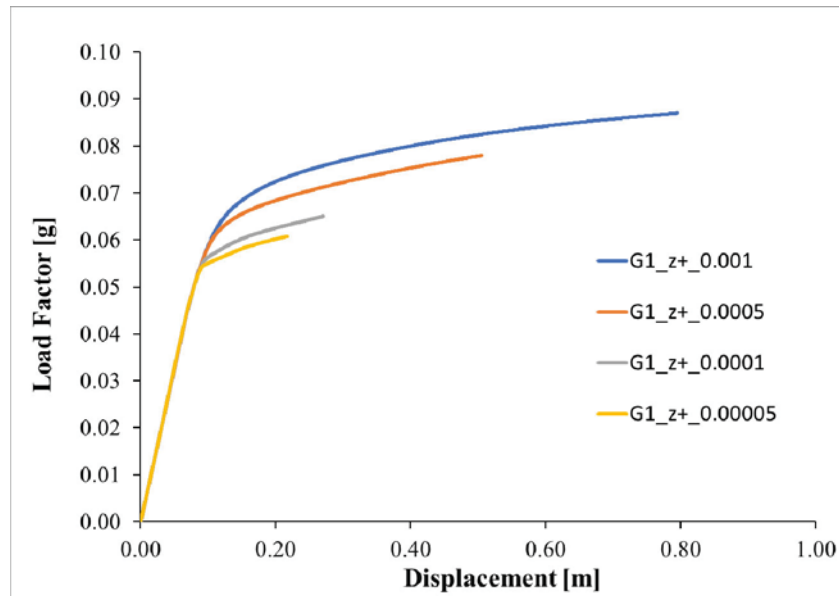


Figure 11: Sensitivity analysis on the viscosity parameter value.

4 CONCLUSIONS

This study has presented some FE simulations carried out on a real 20th-century masonry chimney located in Villar del Arzobispo (Spain). Pushover analyses have been carried out using the FE software Abaqus/CAE on a quite accurate 3D model of the case-study. Different simulations have been presented: various pushover analyses along the chimney along the four principal directions, using both G1 and G2 load distributions. The material properties have been chosen according to previous studies carried out on similar structures because no specific experimental data were available, and the plastic properties have been represented through the Concrete Damage Plasticity (CDP) model, which is an Abaqus built-in material model, widely used to represent the non-linear behaviour of masonry structures.

The results have been used to compare the capacity curves between each other and point out that the main weak points of the chimney are the cross-sections at a quota between 5m and 9m. Finally, a sensitivity analysis has been done on the viscosity parameter. The latter one is a numerical input value of the CDP, and it helps the analysis's steps to converge by smoothing the yield surface. It has been often highlighted that the viscosity parameter increment tends to overestimate the ultimate capacity. On the other hand, the decreasing of the viscosity parameter increase the computational cost; therefore, a sensitivity analysis on this parameter may be helpful to better understand the influence of this parameter on the pushover results. Results confirmed that the viscosity parameter significantly affects the ultimate capacity.

This paper aims to present an overview of the seismic vulnerability of the selected case-study. These results allowed to estimate the order of magnitude of the collapse acceleration and the main weak points of the structure. Moreover, the results have shown the importance of the modelling choices in terms of numerical parameters of the material model. However,

different windows remain open, and the authors intend to continue the research work carrying out non-linear dynamic analyses with both real and artificial accelerogram and testing innovative and simplified methods that would allow fast analyses (which might be useful in case of scale campaigns) or the calculation of the ultimate displacements needed to carry out eventual Displacement Based Design procedures. In this framework, simplified beam models or kinematic limit analysis procedures might be applied.

REFERENCES

- [1] D'Ambrisi A, Mariani V, Mezzi M. Seismic assessment of a historical masonry tower with non-linear static and dynamic analyses tuned on ambient vibration tests. *Eng Struct* 2012;36:210–9. <https://doi.org/10.1016/j.engstruct.2011.12.009>.
- [2] Milani G, Casolo S, Naliato A, Tralli A. Seismic assessment of a medieval masonry tower in Northern Italy by limit, nonlinear static, and full dynamic analyses. *Int J Archit Herit* 2012;6:489–524. <https://doi.org/10.1080/15583058.2011.588987>.
- [3] Ge, C. MZT. Research on the Safety Evaluation of Ancient Stone Pagodas in the Earthquake: a Case Study of Qingjing Pagoda. *Chinese Cult Reli Res* 2013;(02):46-50.
- [4] Jianli Y, Shengcai L. Study of the seismic damage regularity of ancient masonry pagodas in the 2008 Wenchuan Earthquake. *WIT Trans Built Environ* 2013;132:421–32. <https://doi.org/10.2495/ERES130341>.
- [5] Bertolesi E, DelGrosso A, Milani G, Minghini F, Tralli A. 3D FE pushover and non-linear dynamic analyses of a masonry chimney before and after shortening. *COMPdyn 2015 - 5th ECCOMAS Thematis Conf Comput Methods Struct Dyn Earthq Eng* 2015:2158–66. <https://doi.org/10.7712/120115.3529.722>.
- [6] Formisano A, Milani G. Seismic vulnerability analysis and retrofitting of the SS. Rosario church bell tower in finale emilia (Modena, Italy). *Front Built Environ* 2019;5. <https://doi.org/10.3389/fbuil.2019.00070>.
- [7] Peña F, Lourenço PB, Mendes N, Oliveira D V. Numerical models for the seismic assessment of an old masonry tower. *Eng Struct* 2010;32:1466–78. <https://doi.org/10.1016/j.engstruct.2010.01.027>.
- [8] Casolo S, Milani G, Uva G, Alessandri C. Comparative seismic vulnerability analysis on ten masonry towers in the coastal Po Valley in Italy. *Eng Struct* 2013;49:465–90. <https://doi.org/10.1016/j.engstruct.2012.11.033>.
- [9] Valente M, Milani G. Non-linear dynamic and static analyses on eight historical masonry towers in the North-East of Italy. *Eng Struct* 2016;114:241–70. <https://doi.org/10.1016/j.engstruct.2016.02.004>.
- [10] Poiani M, Gazzani V, Clementi F, Milani G, Valente M, Lenci S. Iconic crumbling of the clock tower in Amatrice after 2016 central Italy seismic sequence: Advanced numerical insight. *Procedia Struct Integr* 2018;11:314–21. <https://doi.org/10.1016/j.prostr.2018.11.041>.
- [11] Sarhosis V, Milani G, Formisano A, Fabbrocino F. Evaluation of different approaches for the estimation of the seismic vulnerability of masonry towers. vol. 16. Springer Netherlands; 2018. <https://doi.org/10.1007/s10518-017-0258-8>.
- [12] Milani G. Fast Vulnerability Evaluation of Masonry Towers by Means of an Interactive and Adaptive 3D Kinematic Limit Analysis with Pre-assigned Failure Mechanisms. *Int J Archit Herit* 2019;13:941–62. <https://doi.org/10.1080/15583058.2019.1645241>.
- [13] Milani G, Shehu R, Valente M. A kinematic limit analysis approach for seismic retrofitting of masonry towers through steel tie-rods. *Eng Struct* 2018;160:212–28.

- <https://doi.org/10.1016/j.engstruct.2018.01.033>.
- [14] Grillanda N, Valente M, Milani G. ANUB-Aggregates: a fully automatic NURBS-based software for advanced local failure analyses of historical masonry aggregates. *Bull Earthq Eng* 2020;18:3935–61. <https://doi.org/10.1007/s10518-020-00848-6>.
 - [15] Ferrante A, Clementi F, Milani G. Dynamic behavior of an inclined existing masonry tower in Italy. *Front Built Environ* 2019;5:1–16. <https://doi.org/10.3389/fbuil.2019.00033>.
 - [16] D’Altri AM, Milani G, de Miranda S, Castellazzi G, Sarhosis V. Stability analysis of leaning historic masonry structures. *Autom Constr* 2018;92:199–213. <https://doi.org/10.1016/j.autcon.2018.04.003>.
 - [17] Prizeman OEC, Sarhosis V, D’Altri AM, Whitman CJ, Muratore G. MODELLING from the PAST: The LEANING SOUTWEST TOWER of CAERPHILLY CASTLE 1539-2015. *ISPRS Ann Photogramm Remote Sens Spat Inf Sci* 2017;4:221–7. <https://doi.org/10.5194/isprs-annals-IV-2-W2-221-2017>.
 - [18] Vaiano G, Venanzi I, Formisano A, Ubertini F. Seismic behaviour of isolate and aggregate masonry towers: The case study of the sciri tower in Perugia. *COMPdyn Proc* 2019;1:1441–59. <https://doi.org/10.7712/120119.7010.19301>.
 - [19] López-Patiño G, Adam JM, Verdejo Gimeno P, Milani G. Causes of damage to industrial brick masonry chimneys. *Eng Fail Anal* 2017;74:188–201. <https://doi.org/10.1016/j.engfailanal.2017.01.014>.
 - [20] Minghini F, Bertolesi E, Del Grosso A, Milani G, Tralli A. Modal pushover and response history analyses of a masonry chimney before and after shortening. *Eng Struct* 2016;110:307–24. <https://doi.org/10.1016/j.engstruct.2015.11.016>.
 - [21] Bamonte P, Cardani G, Condoleo P, Talierecio A. Crack patterns in double-wall industrial masonry chimneys: Possible causes and numerical modelling. *J Cult Herit* 2021;47:133–42. <https://doi.org/10.1016/j.culher.2020.09.001>.
 - [22] Lopes V, Guedes JM, Paupério E, Arde A, Costa A. Ambient vibration testing and seismic analysis of a masonry chimney. *J Build Apprais* 2009;5:101–21. <https://doi.org/10.1057/jba.2009.24>.
 - [23] Lourenço PB. Recommendations for restoration of ancient buildings and the survival of a masonry chimney. *Constr Build Mater* 2006;20:239–51. <https://doi.org/10.1016/j.conbuildmat.2005.08.026>.
 - [24] Anzani A., Baila A., Bamonte P, Condoleo P, Togliani C. Structural survey of a chimney between XIX and XX century 2012.
 - [25] Bamonte P, Talierecio A. Understanding crack patterns in masonry chimneys. *Procedia Struct Integr* 2018;11:322–30. <https://doi.org/10.1016/j.prostr.2018.11.042>.
 - [26] De Iasio A, Wang P, Scacco J, Milani G. Longhu pagoda : Advanced numerical investigations for assessing performance at failure under horizontal loads (under review). *Eng Struct* 2021.
 - [27] Smith M. ABAQUS/Standard User’s Manual, Version 6.9. United States: Dassault Systèmes Simulia Corp; 2009.
 - [28] Magenes G, Morandi P, Penna A. Test results on the behaviour of masonry under static cyclic in plane lateral loads, 2008. Deliverable Project No. Coll – Ct - 2003 - 500291 ESECMaSE Enhanced Safety and Efficient Construction of Masonry Structures in Europe

FINITE ELEMENT ANALYSIS OF JUMA MOSQUE IN UZBEKISTAN BASED ON LASER SCANNING AND AMBIENT STUDIES

Shakhzod M. Takhirov¹ and Bakhodir S. Rakhmonov²

¹ Structures Laboratory, Civil and Environmental Engineering Department, University of California,
Berkeley
337 Davis Hall, Berkeley, CA 94720, USA
takhirov@berkeley.edu

² Construction and Architecture Department, Urgench State University
14, Khamid Olimjon Str., Urgench, 220100, Uzbekistan
rah-bahodir@yandex.com

Abstract

This paper highlights the main objectives and some of the results of an extensive structural health monitoring (SHM) project recently started in Khiva, Uzbekistan. The research team consisted of experts from the University of California, Berkeley (Berkeley, USA) and Urgench State University (Urgench, Uzbekistan). The paper presents results for the Juma Mosque in Itchan Kala. The structural health monitoring project was planned as a comprehensive study consisting of three major phases. In Phase 1, a terrestrial laser scanner was deployed to capture 3D geometry and identify anomalies in the monument's geometry. In this phase, the monument's geometry was captured as a collection of points, the so-called "point clouds". In Phase 2, a finite-element (FE) model based on the as-found geometry of the point clouds was generated. This model was generated to optimize placement of the conventional instruments to be used in Phase 3. A number of structural anomalies were discovered during Phase 1 and all of them are incorporated into the FE model. In Phase 3, there is a plan to monitor the monument by means of conventional instruments (accelerometers, displacement transducers, temperature gages and others). Accelerometers will be used to measure the resonant frequencies due to ambient vibrations. Displacement transducers will be used along with temperature gages to monitor the opening and closing of cracks under different thermal conditions and to measure the long-term growth trends of the cracks. The FE model will be updated based on the results of Phase 3. Preservation and restoration strategies will be developed based on the performance of the FE model under static and dynamic loads.

Keywords: Heritage Building Preservation, Laser Scanning, Finite Element Modelling, Structural Dynamics.

1 INTRODUCTION

This paper presents some of the results of the ongoing structural health monitoring program being conducted in Khiva, Uzbekistan. This paper focuses on the finite element (FE) modelling of the Juma Mosque in Itchan Kala, the inner city of Khiva. The main objective of the modelling is to develop an accurate representation of the actual monument so it can be investigated for seismic loading. The geometry of the FE model is based on the 3D point cloud collected during Phase 1 of the project. The main objective of Phase 2 is to generate a FE model with some assumptions about material properties. The next phase (Phase 3) will include field studies by means of conventional instruments: accelerometers, displacement transducers and thermocouples, to name a few. Since the number of instruments is limited and the access duration to the site is tight, the locations of the instruments need to be optimized to collect valuable information with the limited resources and within a reasonable timeframe. The results of this portion of the work are discussed herein. The model will be updated later based on the results of Phase 3.

2 GEOMETRY BASED ON POINT CLOUDS

The results of Phase 1 were published earlier [1]. As presented in Figure 1, the heritage structure consists of a courtyard surrounded by walls and a minaret incorporated into its north wall. The courtyard is covered by a roof that is supported by numerous timber columns. The heritage structure was scanned by ScanStation C10 from Leica Geosystems [2] and the so-called registration of the point clouds was conducted in Cyclone [3], also from Leica Geosystems.

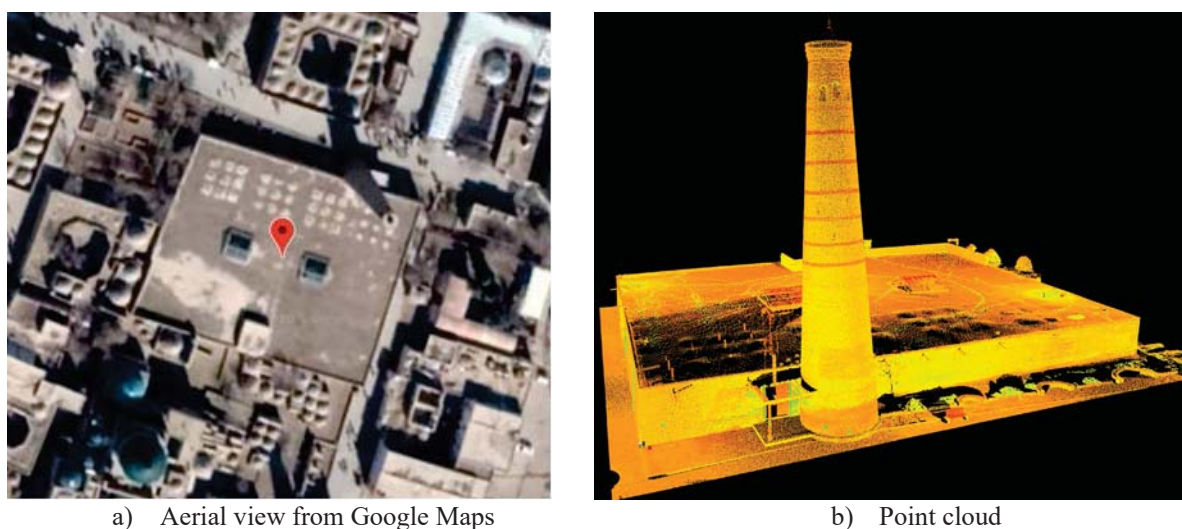


Figure 1: Juma Mosque [1].

3 MODELLING OF MINARET

The minaret was modelled in SAP2000 [4] by utilizing solid 3D elements and some results were published earlier [5]. In this study of the minaret the interaction of the minaret with the walls was not considered and as such, the monument was studied as a stand-alone structure as presented in Figure 2. In this paper, the minaret's model is integrated into the walls of the heritage structure. From the analysis of the point clouds, it was observed that the minaret's axis is inclined in respect to the vertical gravitational axis. This imperfection is included into the model discussed herein.

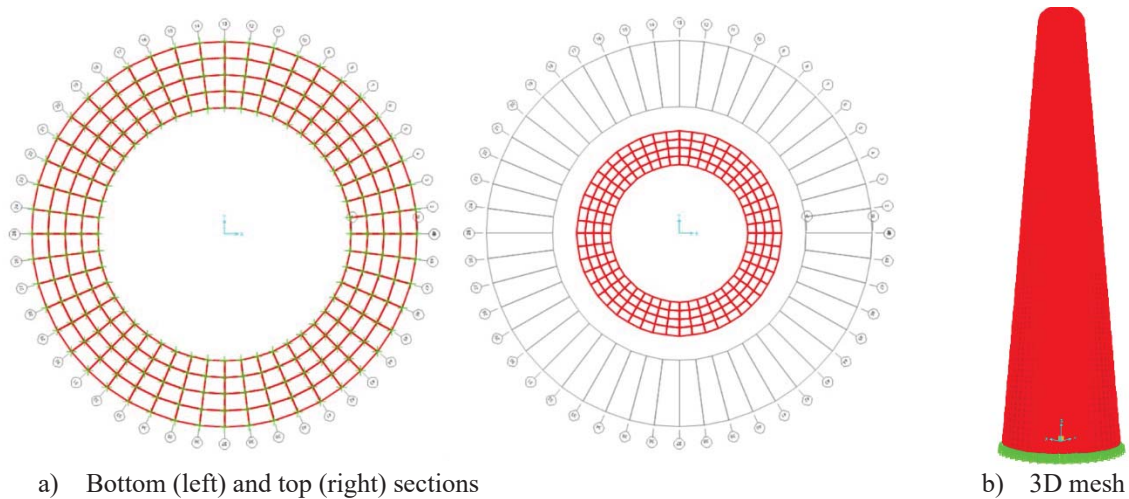


Figure 2: Model of minaret [5].

4 MODELLING OF WALLS

The walls of the heritage structure were also modelled in SAP2000 [4] by utilizing solid 3D elements. A global view of the heritage structure with a vertical reference plane crossing the wall is presented in Figure 3a. A plane view of the typical cross section of the wall's point cloud is presented in Figure 3b. In this image, a spacing between the grid lines is 0.25 m and one of the vertical grid lines is selected to be parallel to the inner wall. Based on the image, the following was concluded. First, the overall height of the wall is about 5 m and the roof starts at about 4 m. Second, the wall thickness at the very bottom is about 1.0 m and about 0.75 m at the roof level. Third, the outer surface of the wall has a slope in respect to a vertical line. Fourth, the inner surface of the wall is very close to vertical.

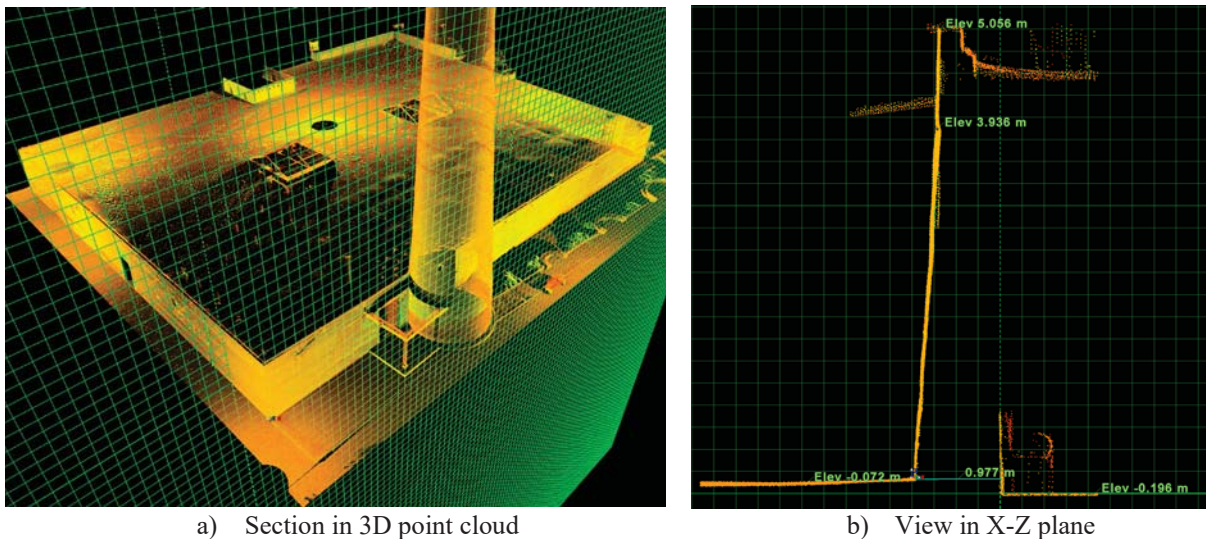


Figure 3: Typical geometry of wall's cross section.

The overall length of the north wall is presented in Figure 4. A length of each wall was published earlier [1] and the corner locations are shown in Figure 5. All of this information was used in the generation of the FE model.

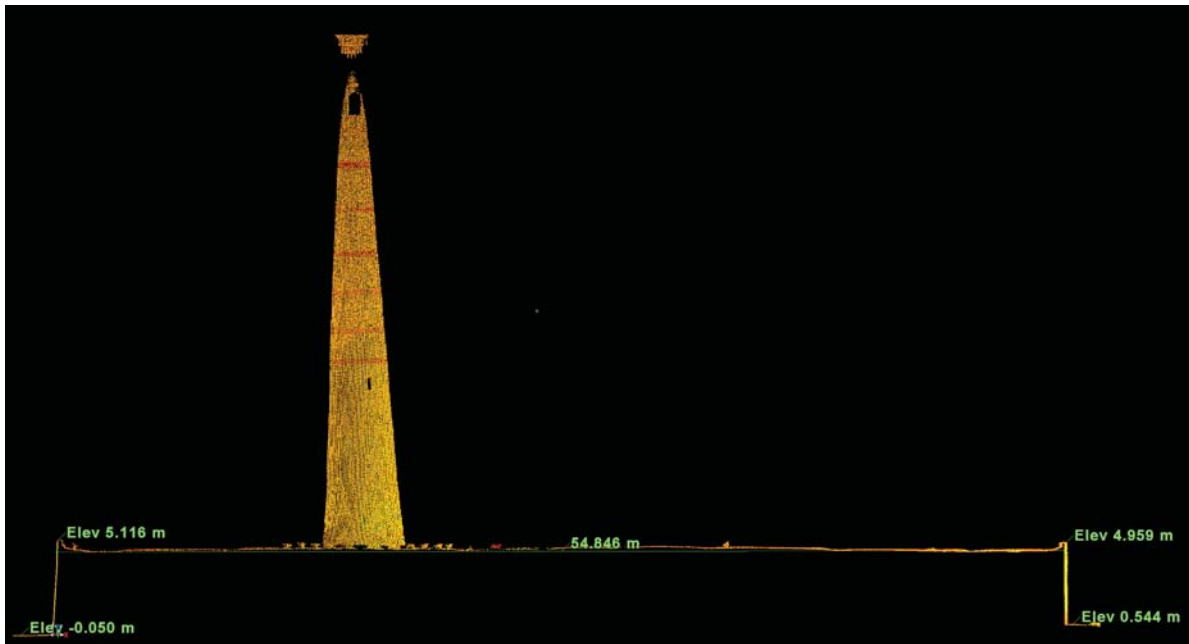


Figure 4: Overall length of north wall.

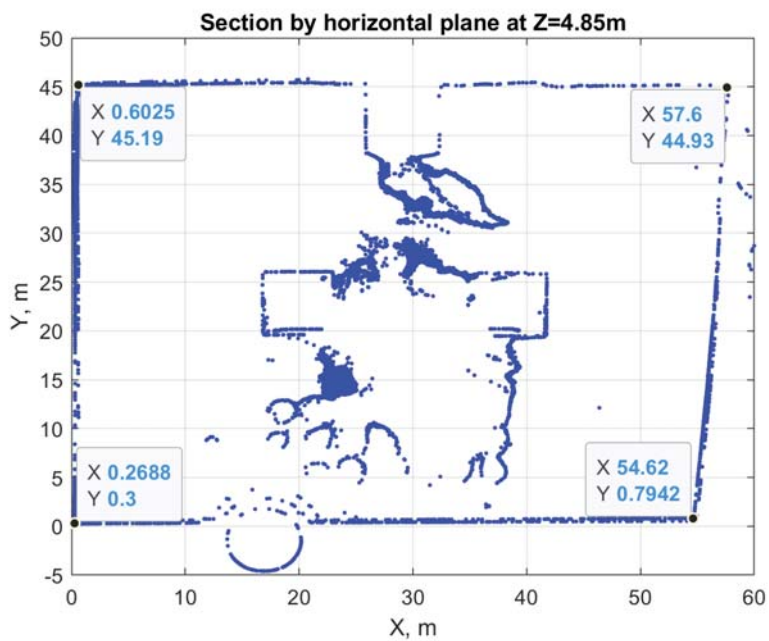
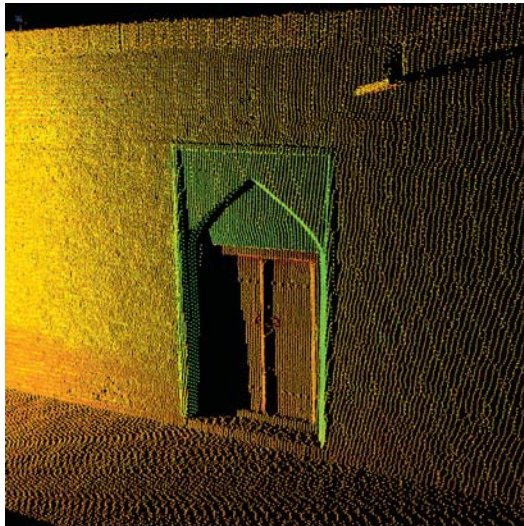
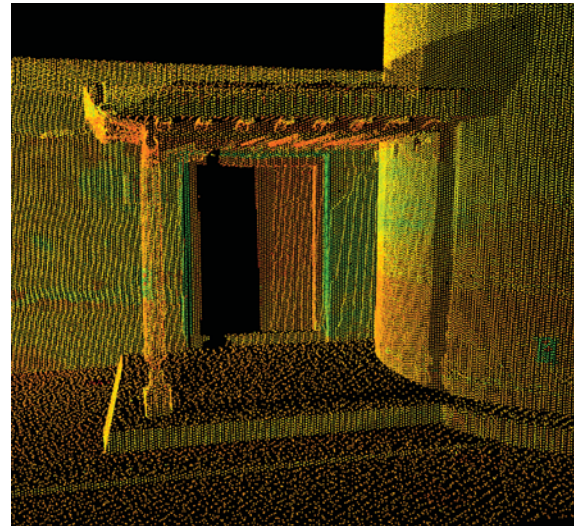


Figure 5: Plan view at Z=4.85 m: corner locations.

The openings in the north and east walls shown in Figure 6 were also taken into account. The opening in the north wall right next to the minaret serves as the main entrance into the heritage structure.



a) East wall

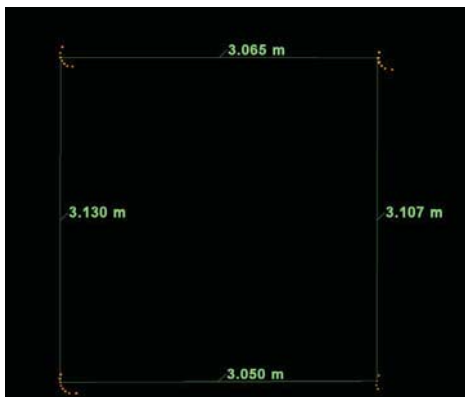


b) North wall

Figure 6: Wall openings.

5 MODELLING OF ROOF DIAPHRAGM

The roof diaphragm was modelled by shell elements in SAP2000. Based on the measurements of the point clouds, the spacing between the columns was very close to 3 m as presented in Figure 7a. A typical view inside of the courtyard is presented in Figure 7b. A proper selection of the boundary conditions closely replicating the support columns is very important to ensure that the model closely represents the heritage structure. In the majority of cases the column has a narrow end at its bottom, which is installed into a stone or concrete footing as presented in Figure 8a. The interface between the narrow end and the concrete or stone is packed with a soft material as presented in Figure 8b. Therefore, it was assumed that the columns are free to rock and as such, roller type boundary conditions were assumed under the roof diaphragm at the locations of the columns.



a) Spacing between columns



b) Typical inside view in the courtyard

Figure 7: Support columns.



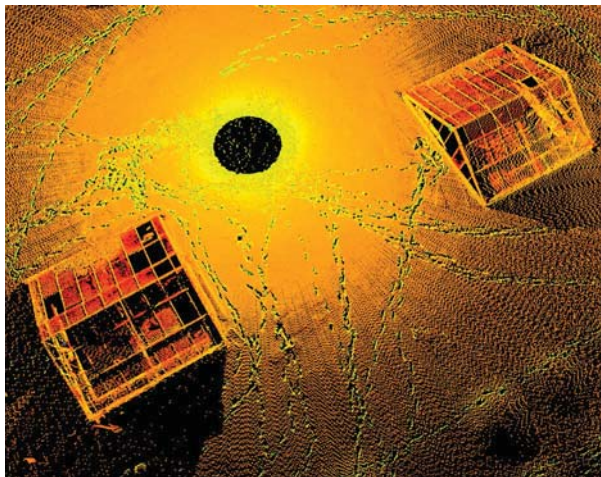
a) Typical layout of columns



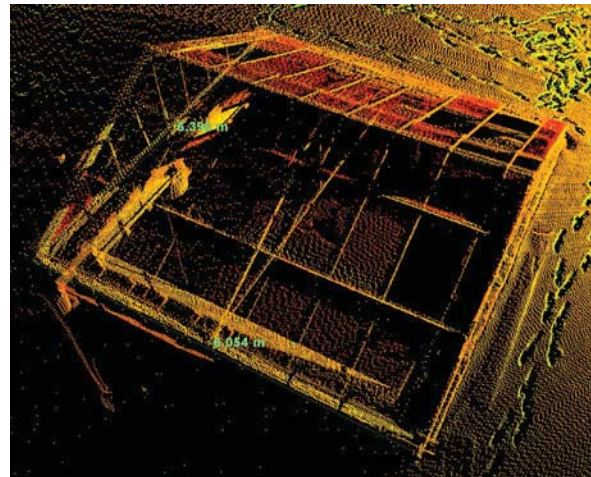
b) Boundary conditions at bottom of columns

Figure 8: Support columns: details.

There are two skylights in the roof as presented in Figure 9. They were also introduced into the roof model as openings in the diaphragm.



a) Two skylights



b) Typical dimensions

Figure 9: Skylights in roof diaphragm.

6 FINITE ELEMENT MODEL

A final model of the heritage structure that consists of the walls, minaret and roof diaphragm is presented in Figure 10a. It was assumed that there is a rigid connection between these major components of the model. A modal analysis was performed. A typical result showing the first modal shape is presented in Figure 10b. The first modal shape is associated with the first flexural vibration mode of the minaret.

The second mode was also associated with the first flexural mode of the conical body in a horizontal plane orthogonal to the one of the first mode as presented in Figure 11a. The third mode was also associated with the minaret's vibrational mode and corresponded to a second mode of the conical body as presented in Figure 11b.

The fifth modal shape was associated with the minaret and represented the torsional mode of the vibrations of the conical body. The modal shapes 6, 7, and 8 corresponded to the higher modes of the minaret. Only starting from mode 9 a vibration mode of the walls was observed

as presented in Figure 12a. The modal shape of the east and west walls are shown in Figure 12b.

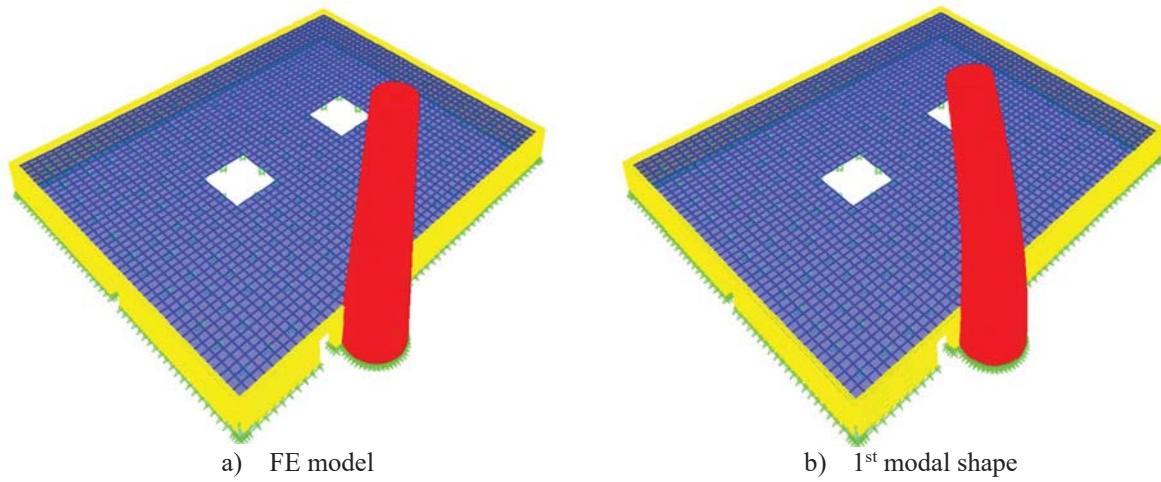


Figure 10: FE model and 1st modal shape.

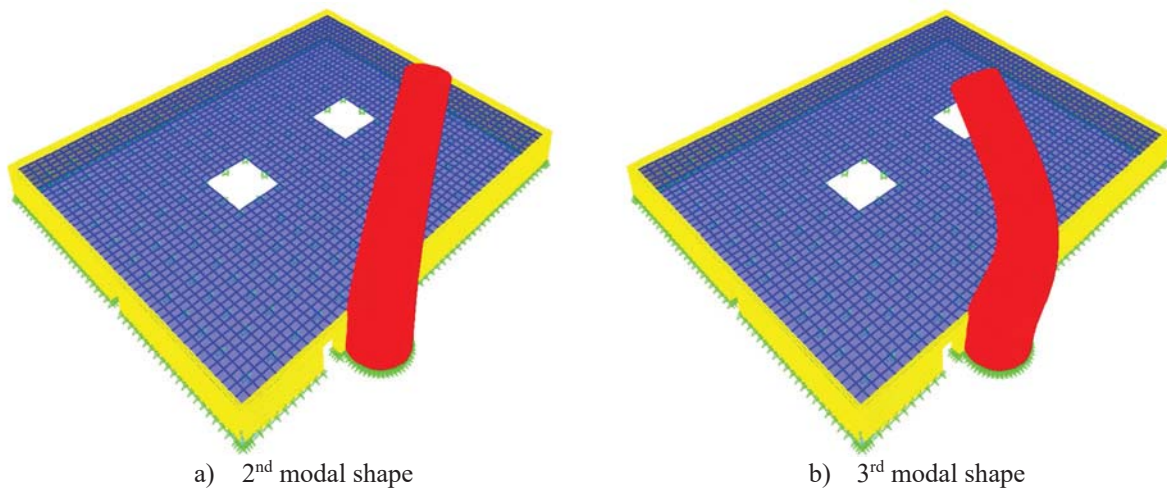


Figure 11: Typical results of modal analysis: minaret modes.

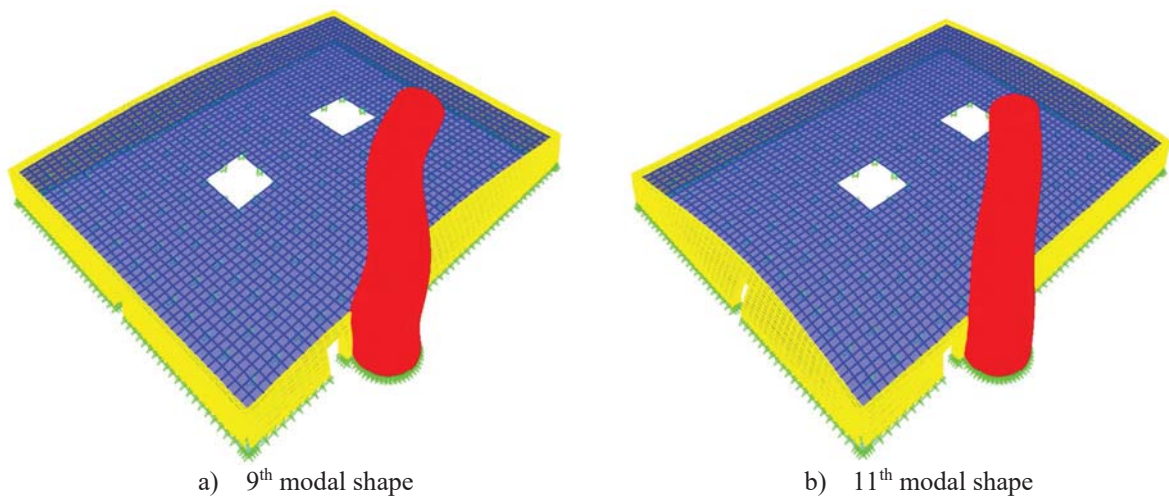


Figure 12: Typical results of modal analysis: wall modes.

Estimates of the following frequencies were obtained for the assumed material properties. The first resonant frequency of the minaret is about 2.2 Hz. The estimates of the resonant frequencies of the walls were greater than 20 Hz. The resonant frequency of the roof is greater than 27 Hz. To capture the first three modes of the minaret the accelerometers in Phase 3 will be installed at the elevations shown in Figure 13.

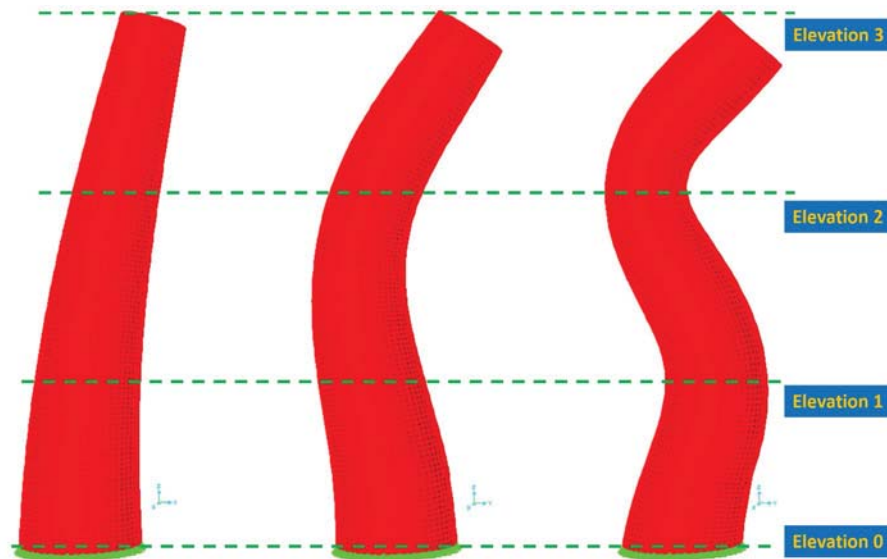


Figure 11: Typical results of modal analysis: wall modes.

To capture the torsional mode of the minaret the accelerometers will be installed at diametrically opposite locations of Elevation 0 and Elevation 3.

7 CONCLUSIONS

A detailed finite element model of the Juma Mosque in Uzbekistan was generated. The geometry of the heritage structure was obtained from the point clouds captured by a laser scanner. Typical material properties for brick masonry and timber were assumed. The modal analysis of the FE revealed the following.

- The first eight resonant frequencies of the heritage structure are associated with various flexural modes of the minaret.
- The wall frequencies are greater than 20 Hz.
- The roof frequency is greater than 27 Hz.
- A placement of accelerometers in the upcoming Phase 3 of the project was optimized based on the analysis of modal shapes. The FE model will be updated after ambient vibration studies of the heritage structure which is the main objective of Phase 3.

8 ACKNOWLEDGMENTS

The project would not be possible without funding provided by the Central Asia University Partnerships Program (UniCEN). UniCEN is sponsored by the U.S. Embassy in Tashkent, Uzbekistan and administered by the American Councils for International Education. Special thanks are due to Mr. Brian Quigley of BNZ, Uzbekistan for providing access to a terrestrial laser scanner. The authors would like to acknowledge the Delta Group Max, Uzbekistan for logistical and technical support provided for the laser scanning project. The authors also

would like to acknowledge a large group of faculty and students of Urgench State University, Uzbekistan for active participation in this multi-phase project. Special thanks are due to Holly Halligan of UC Berkeley for editing the paper.

REFERENCES

- [1] Shakhzod Takhirov, Bakhodir Rakhmonov, Ravshanbek Nafasov, Abbos Samandarov, Sevara Sultanova, Javlon Musurmanov, Bakhtiyor Takhirov (2021). Structural Health Monitoring of Juma Mosque in Itchan Kala, Uzbekistan by Laser Scanning. 10th International Conference on Structural Health Monitoring of Intelligent Infrastructure. 30 June - 2 July, 2021, Porto, Portugal.
- [2] Leica Geosystems AG (2011). Leica ScanStation C10. https://w3.leica-geosystems.com/downloads123/hds/hds/ScanStation%20C10/brochures-datasheet/Leica_ScanStation_C10_DS_en.pdf.
- [3] Leica Geosystems (2018). Cyclone Version 9.2.1.
- [4] Computers and Structures, Inc., CSI (2014): SAP2000 Ultimate Version 16.1.1. Structural Analysis Program.
- [5] Shakhzod M. Takhirov and Bakhodir Rakhmonov (2020). Structural Health Monitoring of the Juma Mosque in Itchan Kala in Khiva (Uzbekistan): Laser Scanning Combined with Numerical Modelling. 12th International Conference on Structural Analysis of Historical Constructions, SAHC 2020, P. Roca, L. Pelà and C. Molins (Eds.)

CONTINUOUS AND DISCONTINUOUS DESCRIPTIONS OF BLOCKED STRUCTURES: THE CASE STUDY OF SANTISSIMO CROCIFISSO CHURCH IN PRETARE (ITALY)

F. Clementi¹, A. Ferrante², E. Giordano² and S. Lenci¹

¹ Department of Civil and Building Engineering, and Architecture, Polytechnic University of Marche,
via Brece Bianche, 60131, Ancona, Italy
e-mail: {francesco.clementi, s.lenci}@univpm.it

² Department of Civil and Building Engineering, and Architecture, Polytechnic University of Marche,
via Brece Bianche, 60131, Ancona, Italy
e-mail: {a.ferrante, e.giordano}@pm.univpm.it

Abstract

Advanced numerical modelling of the masonry “Apennine Church” of Santissimo Crocifisso in Pretare, Arquata del Tronto (AP), was here utilized to have an insight into the dynamic properties and behavior of the structure under strong nonlinear dynamic excitations. The objectives were achieved by comparing nonlinear dynamic analyses through discontinuous and continuous approaches. In the discrete element approach, the Non-Smooth Contact Dynamics method, implemented in LMGC90©, was applied, adopting a full 3D detailed discretization. The Church was schematized as an arrangement of discrete rigid blocks, subjected to sliding by friction and perfect plastic collisions, governed by Signorini’s impenetrability condition and dry-friction Coulomb’s law, with a null restitution coefficient. In the finite element approach, the Concrete Damaged Plasticity model available in Midas FEA NX© was involved. This model allows reproducing the tensile cracking, the compressive crushing, and the degradation of the material under cyclic loads. At the end, the structure exhibited a complex dynamic behavior, because of the geometrical nonlinearity and the non-smooth nature of the contact laws. Finally, the numerical analyses provided a valuable picture of the actual behavior of the church, which is mandatory for future strengthening interventions.

Keywords: Masonry, Dynamics, Nonlinear Dynamic Analysis, Non-Smooth Contact Dynamics Method, Concrete Damaged Plasticity.

1 INTRODUCTION

Over the years Italy has seen a succession of strong and frequent seismic events. This predisposition is because the peninsula is located on two tectonic plates, the Eurasian and the African, which by pushing themselves accumulate energy that causes earthquakes when released. The boundary line of these tectonic plates covers all the Apennines and the Alps, which are precisely the places where strong seismic events have developed most frequently. The most recent sequence took place between 2016 and 2017 and hit the mountain area of four regions of Central Italy: Abruzzo, Lazio, Marche, and Umbria. As visible in Figure 1, the first strong shock of magnitude 6.0 was recorded on 24th August 2016 with epicenter between the municipalities of Accumoli, Amatrice and Arquata del Tronto. This was the shock that caused most of the damage to the town of Arquata del Tronto, in fact there was a level of damage of the X degree of the European Macroseismic Scale (EMC). In the following days and months, nine thousand tremors were recorded, of which nine with a magnitude equal to or greater than 5 [1]. Relevant were those of 26th October 2016 with magnitude 5.4 and epicenter between Castelsantangelo sul Nera, Visso, Ussita and Preci and that of October 30th 2016 of magnitude 6.5 with epicenter between Norcia, Castelsantangelo sul Nera and Preci.

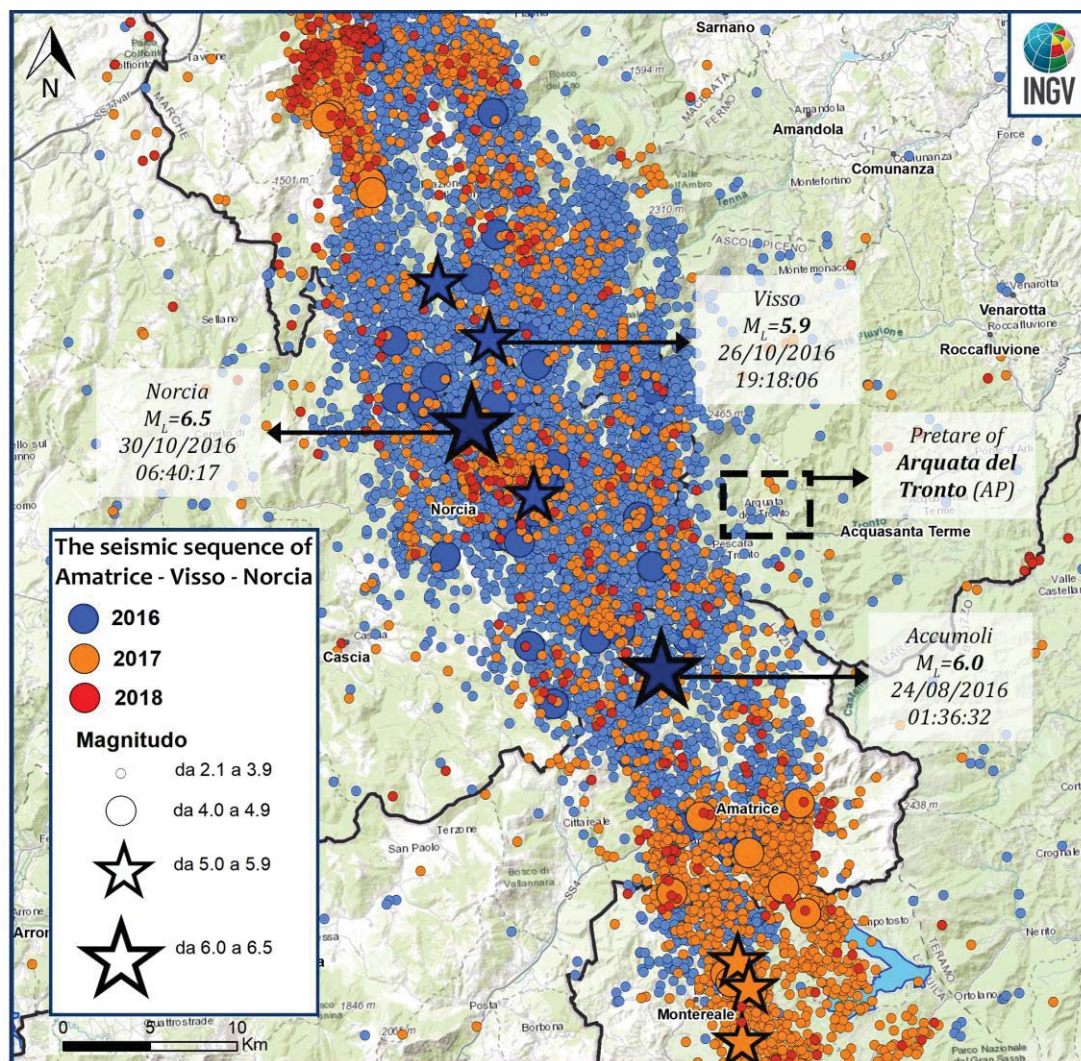


Figure 1: The Central Italy seismic sequence of 2016 (source: <http://itaca.mi.ingv.it>) and the geographic location of Pretare in the municipality of Arquata del Tronto (AP).

The case study analyzed in this research work is the Santissimo Crocifisso Church located in Pretare, municipality of Arquata del Tronto in the province of Ascoli Piceno (AP) (Marche region, Central Italy). For its position near the epicenters of the main strong motions, the structure suffered severe damages during the 2016 seismic sequence. To investigate in depth the nonlinear behavior of the structure, comparative work was carried out on continuous and discontinuous approaches applying the Concrete Damaged Plasticity (CDP) model and the Non-Smooth Contact Dynamics (NSCD) method, respectively. Other applications on towers [2–5] and churches [6–8] are introduced in the literature, but a comparison of these methods has not yet been developed.

2 HISTORICAL AND GEOMETRIC DESCRIPTION OF THE CHURCH

The origins of the Santissimo Crocifisso Church are not known and the first information showing its existence dates to the 15th century, when it was dedicated to Santa Maria della Cecca. During these years, the church was used sporadically and left in a state of neglect. The first restoration interventions were executed between 1910 and 1911. In these years, the church was almost completely rebuilt, the interior paintings were realized and the two niches on the lateral walls were created. After this restoration, the church was dedicated to the Santissimo Crocifisso in honor of an ancient wooden crucifix recovered from the old parish. In 1950 the church was deconsecrated and used as a parish theater. After the works of 1970 (reconstruction of the roof, reconstruction of the floor, and construction of the steeple in reinforced concrete (RC)) the church was reopened for worship. After the 1997 Umbria-Marche earthquake, the church presented extended damages. In the years 2014-2015 a new restoration was carried out, including interventions to improve the structural response. The masonry was reinforced with interventions of “scuci e cuci” and injection of mortar. A steel curb was inserted at the top main façade and the wooden roof was completely rebuilt. Finally, the church suffered severe damages following the 2016 Central Italy earthquakes, until its closure for safeguard reasons. Indeed, after these events, the church exhibited deep cracks and masonry disaggregation damages on the upper part of the main façade and extended cracks at the connections of the nave walls (see Figure 2). All of the masonry walls introduce the activation of overturning mechanisms.

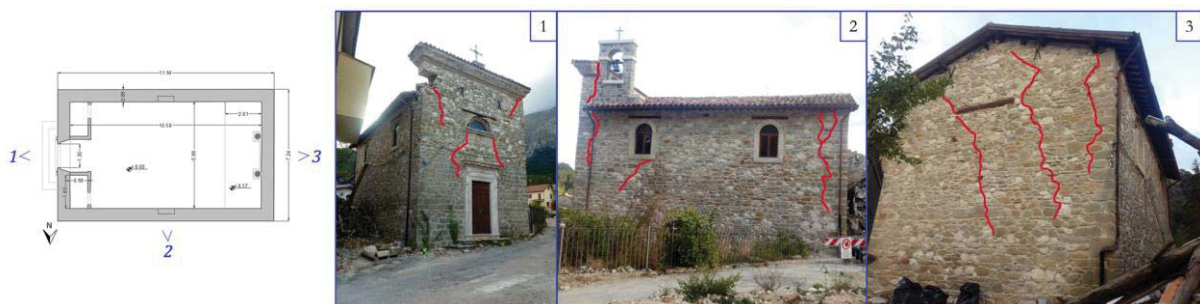


Figure 2: Crack pattern of the Santissimo Crocifisso Church in Pretare (Arquata del Tronto, AP) after the earthquakes of 2016 on 1) the main façade and the 2) North and 3) West facades.

From a geometric point of view, the structure introduces a rectangular plan measuring 11.94 m x 7.24 m and it is covered by light vaults in camorcanna, as visible in **Errore. L'origine riferimento non è stata trovata.** The structure reaches a maximum height of 10.59 m in correspondence with the steeple. Two single arched openings are on the lateral sides of the nave and a semicircular opening is located above the portal of the main facade. The bearing masonry structure is characterized by local stone and travertine. The steeple and the curb at

the top of the main facade are built with reinforced concrete. Finally, the roof is made of chestnut wood.

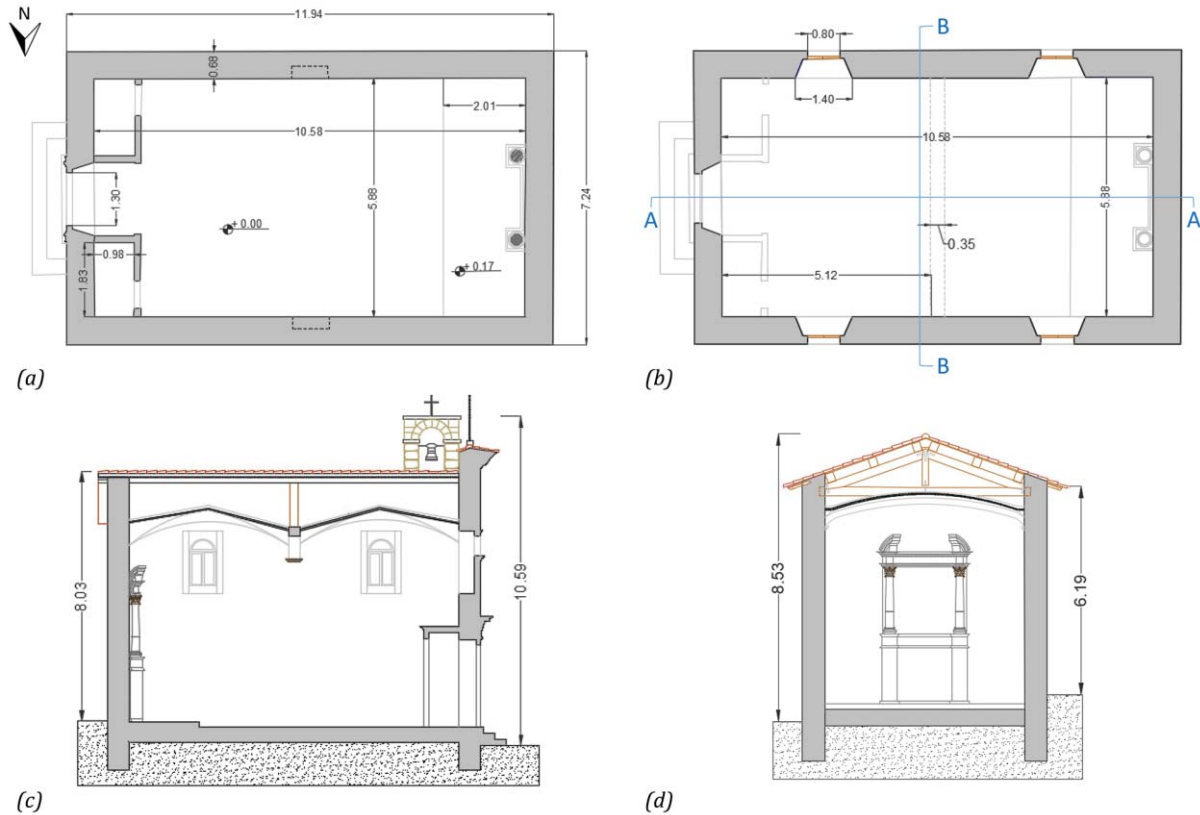


Figure 3: Geometric configuration of the Santissimo Crocifisso Church in Pretare (Arquata del Tronto, AP).

3 COMPARISON OF THE FINITE AND DISCRETE ELEMENT

In this comparative work, the FEM and DEM modeling are used to analyze the case study. Both models were subjected to nonlinear dynamic analyses considering the three main shocks of the 2016 Central Italy sequence: 24th August 2016, 26th October 2016, and 30th October 2016. The events recorded in the surrounding area of the church and in the epicenters were applied at the base of the FE and DE models in Figure 4. Strong motions of 10 seconds were considered in sequence, with 5 seconds of rest among them.

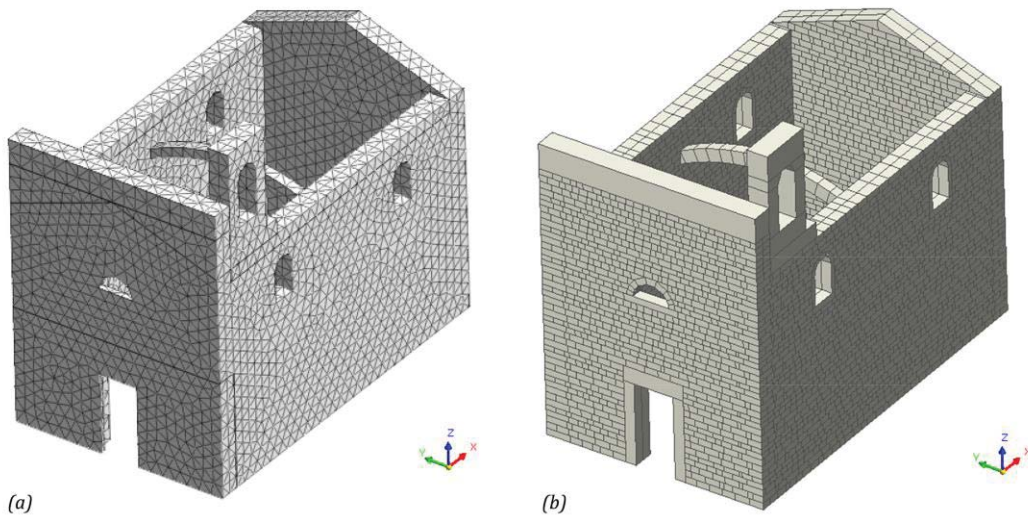


Figure 4: a) FE and b) DE models of the Santissimo Crocifisso Church in Pretare (Arquata del Tronto, AP).

3.1 Finite Element model

The continuous model was accurately reproduced using tetrahedral 3D elements of average size 0.4 m. In total the model is composed of 23020 elements, 6283 nodes and 19782 degrees of freedom (see Figure 4a). The foundations were simulated by preventing both the displacements and the translations of the base nodes, while the presence of the camorcanna vaults was taken into consideration as an additional mass on the lateral walls of the nave.

To simulate the nonlinear behavior of the masonry, the Concrete Damage Plasticity Method (CDP) implemented in the Midas FEA NX© software was used. This type of modeling developed by Lubliner [9] and implemented by Lee & Fenves [10] was initially used for the study of reinforced concrete but subsequently proved to be optimal also for simulating fragile materials such as masonry [11,12].

Starting from the indications in the literature [13], it has been assumed that the masonry obeys a Drucker-Prager resistance criterion with an unassociated flow rule. The surface of this criterion was deformed through a coefficient K_c , to resemble that of Mohr-Coulomb, while the tip of the cone was beveled to avoid numerical convergence problems through an eccentricity parameter. To consider, the ratio between biaxial and mono axial ultimate compressive strength, it was considered with an appropriate ratio between f_{bo} and f_{co} . In addition, the dilatancy angle and the viscosity parameter were defined. The mechanical parameters applied in the CDP model are reported in Table 1. The nonlinear behavior of the masonry was defined assigning suitable inelastic mono-axial stress-strain curves in traction and compression.

Parameter	Value
Dilatancy angle (°)	10
Eccentricity	0.1
f_{bo}/f_{co}	1.16
K_c	0.667
Viscosity Parameter	0

Table 1: Mechanical parameters of CDP model

3.2 Discrete Element model

The discontinuous model reproduces the masonry structure through an assembly of 3D blocks modeled similarly to the existing masonry texture. The complex model is composed by a total of 7636 blocks (see Figure 4b).

The NSCD method belongs to the family of DE models, distinguishing from the classical Distinct Element Method (DEM) for three differences: (i) it integrates the non-smooth contact laws directly, (ii) it uses an implicit integration scheme, and (iii) it does not account for any structural damping. It is important to stress the fact that the NSCD method is based on some modelling simplifications. The main assumption is that bodies are rigid. Since the contact between blocks is governed by the Signorini's impenetrability condition and the dry-friction Coulomb's law, the churches exhibit discontinuous dynamics. Regarding the contacts between bodies, the above-mentioned relations imply perfectly plastic impact, i.e., the Newton law with restitution coefficient equal to zero, which does not account for bounces after impact. This presents two main advantages: (i) the contribution of impacts to the computational complexity is modest since they are modelled in a very basic and simple way; (ii) since the impact is perfectly plastic, it dissipates energy, and, from a mechanical viewpoint, this is a way to account for material damages and micro-cracks, which form in the stones at impact, and, from

a computational point of view, dissipation contributes to the stability of the numerical integration. In addition, the friction contributes to dissipation, but damping, a fundamental ingredient of continuum models, is not considered here.

3.3 Critical discussion

For brevity of the paper, the main results of the nonlinear dynamic analyses under the seismic actions recorded near the church location and performed with the CDP model and NSCD method are plotted Figure 5a and Figure 5b, respectively. A good match between the numerical damages and the existing crack pattern (see Figure 2) is reached. The resultant behaviors explain the relevant applicability of these methods in order to obtain similar failures despite the different laws that govern the two approaches.

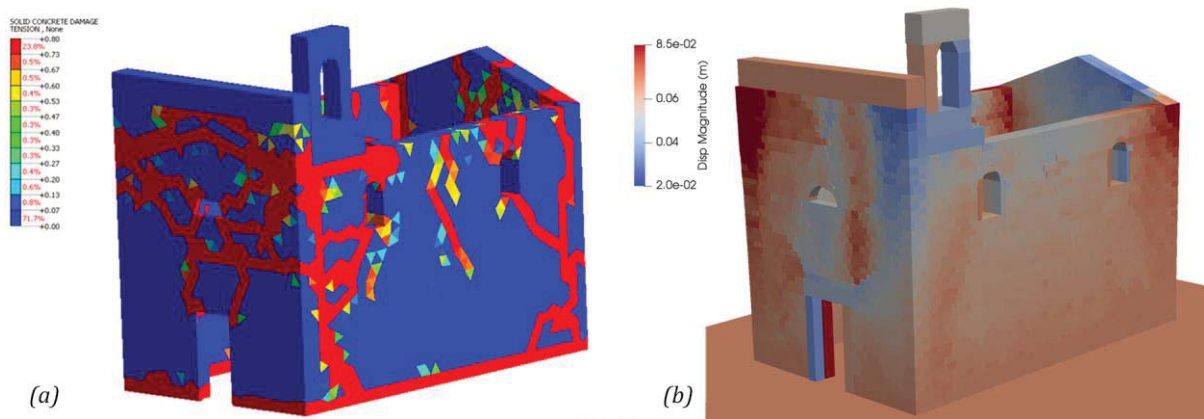


Figure 5: Comparison of the numerical damages of the Santissimo Crocifisso Church in Pretare (Arquata del Tronto, AP) resulting from the nonlinear dynamic analyses with 1) the CDP model and 2) the NSCD method.

4 CONCLUSIONS

The numerical modeling of the Santissimo Crocifisso Church in Pretare, Arquata del Tronto (AP), was carried out by means of advanced FE and DE models. The relevance of the findings is related to the deep investigation of the masonry nonlinear response. The seismic actions registered near the church leads to the validation of both continuous and discontinuous methods through a good match with real cracks of the structure. The application of the epicentral seismic actions allows to obtain a development of the failure mechanisms with the amplification of the damages. All these numerical results appear to be interesting in light of design the retrofiting works. Indeed, the complex nonlinear behavior of the church is clearly pointed out with CDP model. Moreover, the NSCD method allows to investigate the local failure mechanisms, as the masonry disaggregation which is neglected in FEM.

REFERENCES

- [1] Dipartimento di Protezione Civile, I numeri del sisma del Centro Italia, 2018.
- [2] A. Ferrante, F. Clementi, G. Milani, Advanced numerical analyses by the Non-Smooth Contact Dynamics method of an ancient masonry bell tower, *Math. Methods Appl. Sci.* (2020). <https://doi.org/10.1002/mma.6113>.
- [3] A. Ferrante, D. Loverdos, F. Clementi, G. Milani, A. Formisano, S. Lenci, V. Sarhosis,

- Discontinuous approaches for nonlinear dynamic analyses of an ancient masonry tower, *Eng. Struct.* 230 (2021) 111626. <https://doi.org/10.1016/j.engstruct.2020.111626>.
- [4] A. Ferrante, F. Clementi, G. Milani, Dynamic Behavior of an Inclined Existing Masonry Tower in Italy, *Front. Built Environ.* 5 (2019). <https://doi.org/10.3389/fbuil.2019.00033>.
- [5] G. Standoli, E. Giordano, G. Milani, F. Clementi, Model Updating of Historical Belfries Based on Oma Identification Techniques, *Int. J. Archit. Herit.* (2020) 1–25. <https://doi.org/10.1080/15583058.2020.1723735>.
- [6] F. Clementi, A. Ferrante, E. Giordano, F. Dubois, S. Lenci, Damage assessment of ancient masonry churches stroked by the Central Italy earthquakes of 2016 by the non-smooth contact dynamics method, *Bull. Earthq. Eng.* (2019). <https://doi.org/10.1007/s10518-019-00613-4>.
- [7] E. Giordano, F. Clementi, A. Nespeca, S. Lenci, Damage Assessment by Numerical Modeling of Sant’Agostino’s Sanctuary in Offida During the Central Italy 2016–2017 Seismic Sequence, *Front. Built Environ.* 4 (2019). <https://doi.org/10.3389/fbuil.2018.00087>.
- [8] G. Milani, M. Valente, Failure analysis of seven masonry churches severely damaged during the 2012 Emilia-Romagna (Italy) earthquake: Non-linear dynamic analyses vs conventional static approaches, *Eng. Fail. Anal.* 54 (2015) 13–56. <https://doi.org/10.1016/j.engfailanal.2015.03.016>.
- [9] J. Lubliner, J. Oliver, S. Oller, E. Oñate, A plastic-damage model for concrete, *Int. J. Solids Struct.* 25 (1989) 299–326. [https://doi.org/10.1016/0020-7683\(89\)90050-4](https://doi.org/10.1016/0020-7683(89)90050-4).
- [10] J. Lee, G.L. Fenves, Plastic-Damage Model for Cyclic Loading of Concrete Structures, *J. Eng. Mech.* 124 (1998) 892–900. [https://doi.org/10.1061/\(ASCE\)0733-9399\(1998\)124:8\(892\)](https://doi.org/10.1061/(ASCE)0733-9399(1998)124:8(892)).
- [11] G. Milani, M. Valente, Comparative pushover and limit analyses on seven masonry churches damaged by the 2012 Emilia-Romagna (Italy) seismic events: Possibilities of non-linear finite elements compared with pre-assigned failure mechanisms, *Eng. Fail. Anal.* 47 (2015) 129–161. <https://doi.org/10.1016/j.engfailanal.2014.09.016>.
- [12] R. Illampas, I. Ioannou, P.B. Lourenço, Seismic appraisal of heritage ruins: The case study of the St. Mary of Carmel church in Cyprus, *Eng. Struct.* 224 (2020) 111209. <https://doi.org/10.1016/j.engstruct.2020.111209>.
- [13] G. Milani, M. Valente, C. Alessandri, The narthex of the Church of the Nativity in Bethlehem: A non-linear finite element approach to predict the structural damage, *Comput. Struct.* 207 (2018) 3–18. <https://doi.org/10.1016/j.compstruc.2017.03.010>.

LATTICE DISCRETE MODELING OF OUT-OF-PLANE BEHAVIOR OF IRREGULAR MASONRY

Micaela Mercuri¹, Madura Pathirage², Amedeo Gregori¹ and Gianluca Cusatis²

¹University of L'Aquila
Department of Civil, Building and Environmental Engineering, L'Aquila, Italy
e-mails: micaela.mercuri@graduate.univaq.it, amedeo.gregori@ing.univaq.it

²Northwestern University
Department of Civil and Environmental Engineering, Evanston, IL, USA
e-mails: madura.pathirage@u.northwestern.edu, g-cusatis@northwestern.edu

Keywords: Out-of-Plane Behavior, Earthquake, Lattice Discrete Particle Model, Stone Irregular Masonry, Local Collapse Mechanisms, Global Collapse Mechanisms

Abstract. *Stone masonry buildings are known to be highly vulnerable to seismic actions. In this context, the analysis of the out-of-plane response of unreinforced masonry structures is crucial. For this purpose, the Lattice Discrete Particle Model (LDPM) was employed to simulate the mechanical behavior of stone masonries up to their failure. Unlike commonly used continuum-based methods or simplified analytical models, that are often limited in modeling correctly complex failure mechanisms, LDPM is able to capture accurately crack distributions and failure patterns. LDPM describes the masonry at the scale of stones and takes into account their interactions through tailored constitutive equations for tensile, compressive, shear, and frictional behaviors. First, LDPM was validated against experimental results on masonry panels subjected to out-of-plane loading. Next, the vertical bending mechanism was studied in the cases of one- and two-story walls with and without openings. Finally, more complex mechanisms were considered where the damage evolution and the fracture propagation were analyzed for a set of panels assumed to be placed within the continuity of a facade. The overall results presented in this paper show that LDPM can realistically predict the collapse mechanisms associated with out-of-plane loading for different structural configurations and geometries.*

1 INTRODUCTION

Unreinforced masonry structures often constitute a large part of the cultural and architectural heritage of historical cities, and they are known to be highly vulnerable to earthquakes. Commonly, masonry structures are made of multiple load-bearing walls placed in orthogonal planes and with flexible floor diaphragms [1]. When an earthquake occurs, masonry structures dissipate kinetic energy both at the structural and at the material levels [2, 3]. At the structural scale, several factors affect the global response: the slenderness of the load-bearing walls [4, 5], the connections between the walls and the horizontal members, which allows for the box behavior [6, 7, 8, 9], and the presence of specific rigid floor diaphragms [10, 11, 12, 13, 14, 15, 16]. At the material scale, the mechanical properties of the masonry constituents (mortar and stones) [17, 18, 19, 20] and the quality of the construction work [21, 22] greatly affect the overall response. During a seismic event, masonry walls are typically subjected to in-plane and out-of-plane motions. Whereas in-plane behavior is the topic of a large number of studies available in the literature, the out-of-plane behavior is often neglected. This paper focuses on the latter behavior, as one of the most common damage reported in post-seismic surveys is the failure of peripheral masonry walls. Indeed, the earthquake intensity required to obtain out-of-plane collapse of walls is lower than the one required for in-plane collapse [3].

Several analytical methods exist to analyze the out-of-plane behavior of masonry walls, namely force-equilibrium and displacement-based methods. The first type of formulation is based on the static equilibrium analysis of rigid body mechanisms and limit theorem of plasticity [23, 24, 25, 26, 27, 28, 29, 30, 31, 32]. Force-equilibrium methods are generally adopted for large scale analysis and are known to lead to rather conservative limit states [8]. On the other hand, displacement-based methods [33, 34, 35, 36, 37, 38, 39, 40, 41, 42, 43, 44] appear to better estimate the limit values of masonry walls in out-of-plane loading. The rigid-block assumptions are often adopted within the postulates of limit theorem analysis (no-tensile strength, infinite compressive strength and absence of sliding between blocks) [23]. A capacity curve describing the horizontal multiplier α (limit equilibrium of the system) as a function of displacement d can then be obtained. When the displacement is zero, the value $\alpha(0) = \alpha_0$ represents the activation of the overturning. The loss of equilibrium is attained when $d = d_u$ where by definition $\alpha(d_u) = 0$. This curve can also be expressed in terms of spectral acceleration versus spectral displacement curve [45] or in terms of force-displacement curve. The rigid-block method within the displacement-based formulation is chosen in this paper for one part of the analysis of the out-of-plane behavior of masonry walls.

More advanced descriptions of the out-of-plane behavior of masonry walls and in general of the mechanical behavior of stone masonry require numerical models. Different methods are available and correspond to different levels of modeling resolution and computational costs [46, 47]. The finite element method is often used and allows micro-, meso-, or macro-modeling and the reader is referred to [48], [49], and [50], respectively. Although successful for regular masonry, the meshing complexity and the lack of accurate constitutive equations limit this method. Discrete element methods have also been employed [51, 52, 53, 54]. Multiple structures such as one or two-story buildings were modeled using 2D and 3D discrete element method [55], but limitations were found especially in capturing realistic out-of-plane responses. Moreover, these simulations were unable to correctly describe the fracture initiation and propagation. Indeed, in quasi-brittle materials such as masonry, understanding the development of the fracture process zone is crucial. An accurate model must also be able to capture the effect of stress parallel to cracks on the size of the fractured zone as shown recently in [56, 57], which

might be important in large masonry structures often under multiaxial state of stresses. To overcome these limitations, the Lattice Discrete Particle Model (LDPM) [58, 59] is here adopted for the numerical modeling. This model was originally conceived to simulate the behavior of concrete and other granular materials at the meso-scale level by modeling the interaction between coarse aggregate pieces. It was recently applied successfully for the modeling of stone masonry structures [60, 61]. LDPM is able to simulate accurately the fracturing behavior from crack trigger to localization, propagation, and to global failure, by taking into account the material heterogeneity. The interaction between stone aggregates embedded in the irregular matrix of lime or clay mortar is explicitly considered through dedicated constitutive equations, defined in a vectorial form to account for the correct state of stresses in the material.

In this study, the numerical model is first explained and validated against a set of experimental data relevant to masonry panels subjected to out-of-plane loading conditions. Next, the numerical model is used to assess its capability to simulate local collapse mechanisms, more specifically the bending mechanism. Finally, more complex mechanisms are analyzed with multiple structural configurations to simulate masonry walls within the continuity of the facade and to study the effect of transversal walls, floors and roofs on the overall behavior.

For a thorough investigation of the topic presented in this paper, the reader is referred to recent work of Mercuri and coworkers [61].

2 NUMERICAL MODEL AND VALIDATION

2.1 The Lattice Discrete Particle Model

The Lattice Discrete Particle Model (LDPM) was proposed by Cusatis and coworkers [58, 59] to simulate concrete at the coarse aggregate level. This model has a unique capability in capturing crack distribution and damage in granular quasi-brittle materials. It has been adopted to simulate the mechanical behavior of concrete [59, 62], mortar [63, 64], fiber reinforced concrete [65, 66], or to reproduce multi-physics phenomena such as hygro-thermo-chemical processes, alkali-silica reaction, and aging [63, 67, 68]. This lattice discrete model was also used to simulate the mechanical behavior of reinforced and unreinforced stone masonry [60, 61].

In the LDPM formulation, the masonry stones are simulated as spherical particles (see Fig. 1a and b). They are placed randomly from the largest to the smallest size in a given volume of material. The particle size distribution follows a Fuller sieve curve defined from a set of mix-design parameters: cement-mortar content c , water-to-mortar ratio w/c , maximum and minimum stone size d_a and d_0 , respectively, and Fuller coefficient n_f . Fig. 1e shows on an example the particle placement inside a dog-bone specimen. The geometry of the interaction between stone-particles is described as follows. First, a Delaunay tetrahedralization is performed with the centers of the particles to generate a lattice system (see Fig. 1c). Next, a domain tessellation is performed to identify the possible failure locations between adjacent stone-particles (see Fig. 1d). These two steps result in the generation of a system of polyhedral cells enclosing the particles (see Fig. 1f). These irregular cells idealize real textures and shapes of typical masonry stones and their surrounding mortar layer. The surface of each polyhedral cell is composed of triangular facets (see Fig. 1g) where the LDPM constitutive equations, facet stresses and strains are formulated in a vectorial form. The constitutive equations take into account the softening behavior for pure tension and shear-tension and the plastic hardening behavior for pure compression and shear-compression. For the complete set of constitutive equations, as well as the compatibility and equilibrium equations, and the numerical implementation, the reader is referred to the work of Cusatis and coworkers [58], and the recent work of Mercuri and coworkers [61].

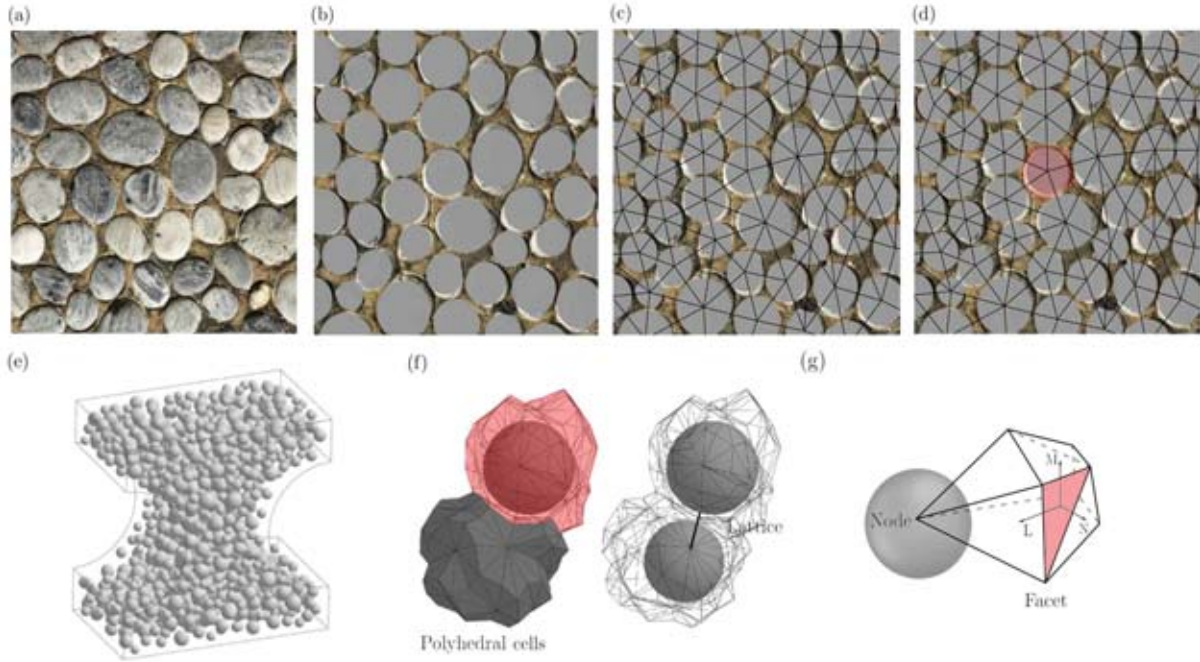


Figure 1: (a) 2D representation of irregular stone masonry; (b) approximation with spherical particles; (c) Delaunay tetrahedralization; (d) Domain tessellation and generation of a system of polyhedral cells; (e) particle distribution in a dogbone specimen; (f) two adjacent LDPM polyhedral cells enclosing two stones; (g) tetrahedron portion associated with a stone-particle and one triangular facet.

2.2 Validation with experimental data

2.2.1 Description of experiments and numerical modeling

The Lattice Discrete Particle Model is here validated against experimental data reported in Degli Abbati and coworkers [69]. The experiments consisted in loading in out-of-plane direction three masonry panels of different dimensions. The sizes of the specimens and their slenderness ratios are shown in Table 1. Lime mortar was used as binder in the preparation of the specimens. The stones were irregular with an average block size of $180 \times 120 \times 120$ mm. All the panels were built on top of a masonry base with a larger thickness. For the testing setup, a steel cable was fixed at $2/3$ of the panel height at the center of the transverse section on one end and attached to a restraint frame on the other end. The cable was equipped with a load cell to measure the applied force along the cable. The displacement was measured at the location where the cable was fixed. The test was carried out in three phases. In Phase 1, the cable was pulled horizontally in order to form a cracked surface at the bottom of the specimen. In Phase 2, the cable was released to obtain a standing panel as in the initial configuration. Finally, in Phase 3, the cable was pulled horizontally and statically in displacement controlled conditions.

The LDPM parameters used in this study were calibrated in [60] on diagonal compression performed on a similar stone masonry mix composition. All the model parameters and the parameters related to the geometrical characterization can be found in details [60] and in [61], and are therefore not reported here for the sake of brevity. Fig. 2 shows the random stone-particle placement inside the three panels. One can note that the base of the specimen and the panel were modeled using one LDPM mesh. At the bottom of the base, the particles were fixed in translations and rotations. A velocity was applied directly to a set of particles at $2/3$ of the

Panel number	Width B [mm]	Height H [mm]	Thickness D [mm]	Slenderness λ [-]
P1	900	900	300	3
P2	900	1100	220	5
P3	900	1500	300	5

Table 1: Dimensions of the panels for model validation.

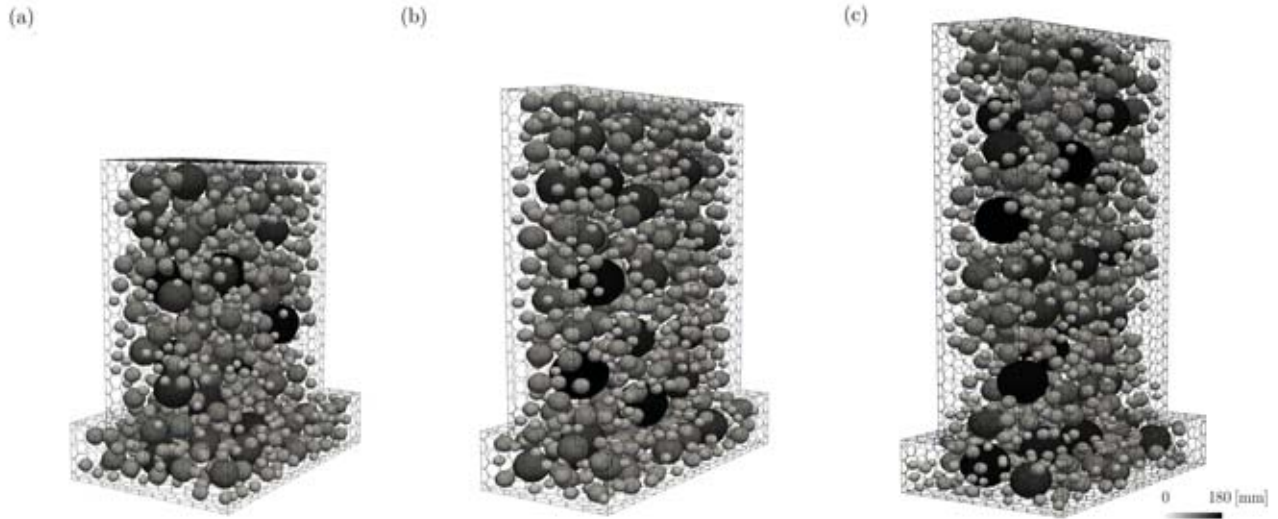


Figure 2: Spatial distribution of stone-particles in the three panels: (a) panel 1, (b) panel 2, (c) panel 3.

panel height to reproduce the experimental setup. Its magnitude was chosen low enough to obtain a quasi-static simulation. Two sets of simulations were performed. The first strategy was to reproduce the same testing procedure as in the experiments, i.e. in three phases. The second strategy, less computationally expensive, was to apply the static load directly to the uncracked specimen, from the beginning of the test, up to cracking and overturning of the panel. Finally, for all the simulations, three different stone distributions within the volume of the panels were used to capture the experimental scatter due to the spatial variability of stone size and distribution. Thus, the results shown afterwards are the average of the three individual results.

2.2.2 Numerical results and discussion

Fig. 3 refers to panel 2 and it shows the results of the two modeling strategies previously stated. One can see that replicating the experimental procedure (see Fig. 3a) and loading directly the sample from the initial uncracked configuration (see Fig. 3b) provide identical results. Fig. 3b shows clearly the fracturing part of the test followed by the overturning or rocking phenomenon once the fracture is formed. In order to save computational time, the second strategy was used to generate the results presented next.

Fig. 4 shows the load-displacement curves of for the three panels. One can see that the numerical results well predict the experimental data, especially for panels 1 and 2. In terms of fracture, all the three specimens failed at the base (see Fig. 5) as expected and observed in the experimental tests of panels 1 and 2. For panel 3, experimentally, the fracture formed at a height of 300 mm from the base, where the stones were not well interlocked. This unexpected failure

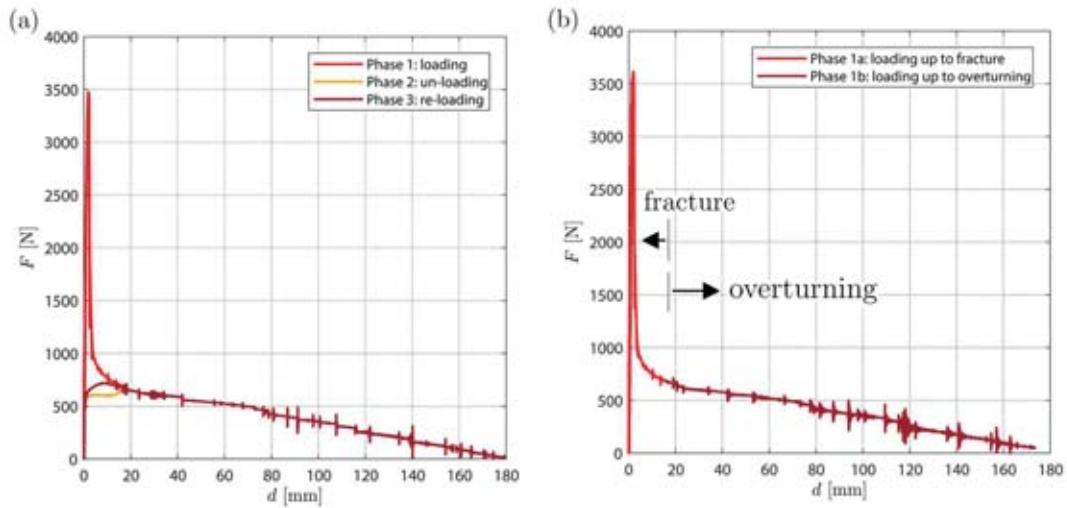


Figure 3: Force versus displacement curves for Panel 2: (a) Three phases loading; (b) Loading directly from the initial uncracked configuration

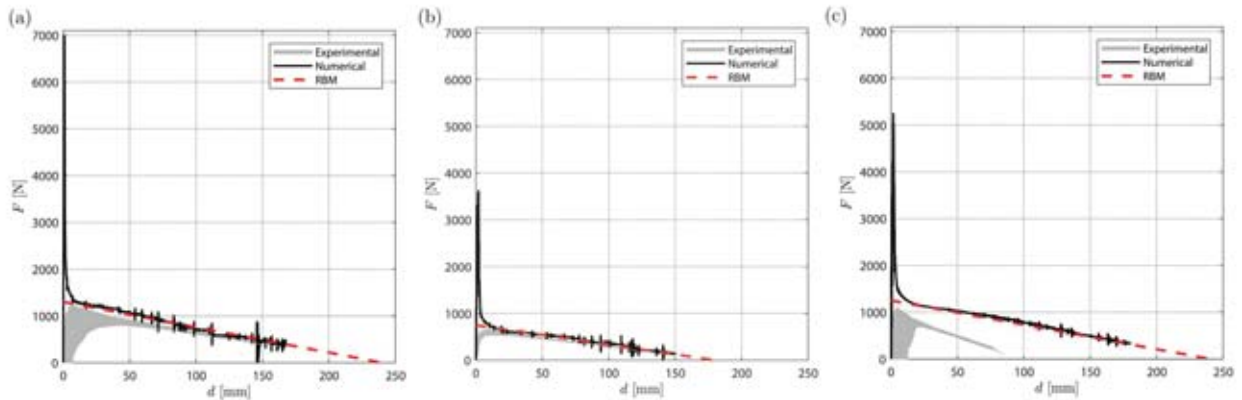


Figure 4: Force versus displacement curves in: (a) panel 1; (b) panel 2; (c) panel 3.

could be due to the preparation of the panels. The numerical response for panel 3 therefore overestimates the experimental results as the predicted failure occurred at the base.

For all the panels, the load-displacement trend is identical. First, the load increases linearly which represents the initial elastic phase. Next, a non-linear phase is reached while the load keeps increases which relates to the crack formation. In the post-peak regime, a softening behavior is observed and corresponds to the fracture propagation. Finally, a decreasing linear trend is observed for the load as the displacement increases. This phase characterizes the overturning process. One can analyze the latter phase using non-linear kinematic analysis, and more specifically the rigid-block displacement-based method.

Fig. 4 shows the results from the analytical method obtained from the kinematic analysis. The parameters used to perform the linear and non linear kinematic analyses are reported in Table 2. One can see that there is an excellent agreement with the numerical results. It is interesting to note that the horizontal force associated with the activation of the overturning F_0 are close to the kink point predicted by LDPM.

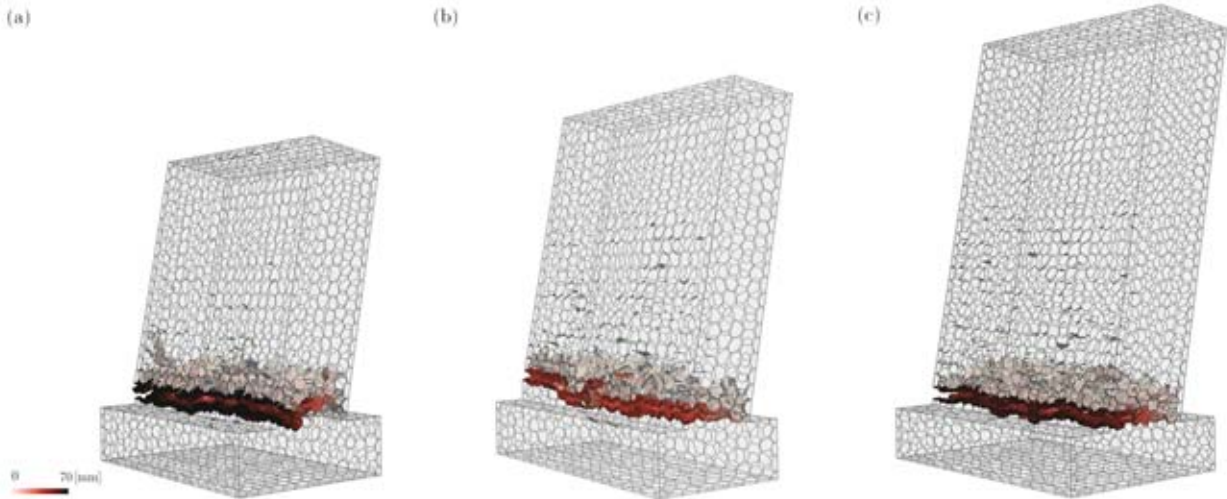


Figure 5: Total crack opening in: (a) panel 1; (b) panel 2; (c) panel 3.

Table 2: Parameters used to perform the linear and non linear kinematic analyses: initial horizontal multiplier α_0 , ultimate displacement d_u , participant mass fraction e^* , initial spectral acceleration a_0^* , initial horizontal force F_0 . The initial condition is referred to the activation of the overturning and the ultimate condition is associated with the loss of the overall equilibrium.

Panel Number	α_0 [-]	d_u [mm]	e^* [-]	a_0^* [m/s ²]	F_0 [N]
P1	0.333	240	1.0	1.962	1252
P2	0.200	180	1.0	1.962	673
P3	0.200	240	1.0	3.270	1252

3 APPLICATION TO COMPLEX STRUCTURES

3.1 Local bending mechanism

3.1.1 Vertical bending mechanism

Design codes usually require the analysis of local collapse mechanism in unreinforced masonry walls for the assessment of seismic vulnerability [70]. Vertical bending mechanism was here considered as a first application of the numerical model and can be viewed as an alternative to kinematic analysis. The vertical bending mechanism is characterized by the fracture and the out-of-plane simultaneous rotation of two blocks of a facade with respect to the horizontal axis (often located at mid-height of the panel). This bending mechanism is observed for single or multi-story walls and the mechanical response depends on the effectiveness of the connection system with floors and the presence of openings or discontinuities.

For the simulation of vertical bending, two wall geometries were considered to be representative of real masonry walls. The first wall geometry was a one-story wall. It had a height of 3,000 mm, a thickness of 500 mm and a width 4,000 mm. Using this geometry, two cases were considered: case 1B-NO without openings and case 1B-O with openings. The dimensions of the openings were chosen to replicate the presence of windows (of 1,200 mm height, 500 mm thickness, 800 mm width) and doors (of 2,400 mm height, 50 mm thickness and 800 mm width). The second wall geometry was a two-story wall. It had a height of 6,000 mm, a thickness of 500 mm and a width 4,000 mm. Again, two cases were considered: case 2B-NO without openings and case 2B-O with openings. For all the walls, the translation and rotation of the stone-particles

were fixed on the bottom and the top sides. The load was applied in quasi-static conditions as a velocity prescribed to the surface particles at mid-height of the walls. Finally in order to consider self-weight, gravity load was applied prior to testing.

3.1.2 Results and discussion

Fig. 6 and Fig. 7 show the results of the simulations, for one-story and two-story walls, respectively.

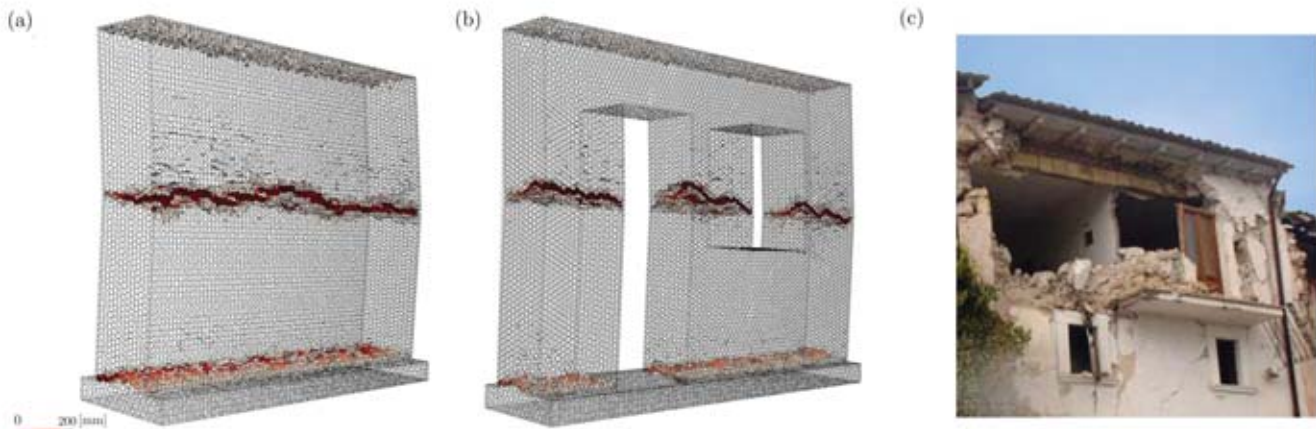


Figure 6: Total crack opening: (a) one-story wall with no openings (1B-NO); (b) one-story wall with openings (1B-O); (c) Example of one-story bending mechanisms caused by the 2009 L'Aquila earthquake (Arch. Fot. Vice Comm. Del. Beni Culturali - Sisma Abruzzo 2009).

One can see that the main failure occurs at mid-height for the no-opening cases, with a secondary damage along the base (see Fig. 6a and Fig. 7a). In the cases with openings, one can notice that the crack occurs at about mid-height for the one-story wall (see Fig. 6b). For the two-story panel, the presence of windows affects the position of the main fracture, which is located close to the bottom of the windows and follows the discontinuity due to their inclusion (see Fig. 7b). Fig. 7d shows the load-displacement curves for the four cases. The trend is the same for all the walls. The load increases in an elastic phase and reaches a peak value. Next, a softening behavior is observed. As expected, the peak loads for the smaller walls are higher than the two-story panels. A reduction of the stiffness and the bearing capacity is observed when openings are considered. In particular, for the one-story bending mechanism, the stiffness and the bearing capacity decrease by 3.5% and 37.1%, respectively. For the two-story bending mechanism, the stiffness and the bearing capacity decrease of 6.9% and 16.4%, respectively.

3.2 Combined and Complex Mechanisms

3.2.1 Numerical modeling

In the analysis of local collapse mechanisms, all the possible failure mechanisms need first to be identified before being analyzed, for example using kinematic analysis. In more complex cases, such a process is impossible and simplified analytical methods are no longer satisfactory for an accurate study. In real structures, masonry walls are always in interaction with other structural elements. For example, the walls might be located within the continuity of a facade. There might also be transversal walls, floors and roofs attached to the main panel subjected

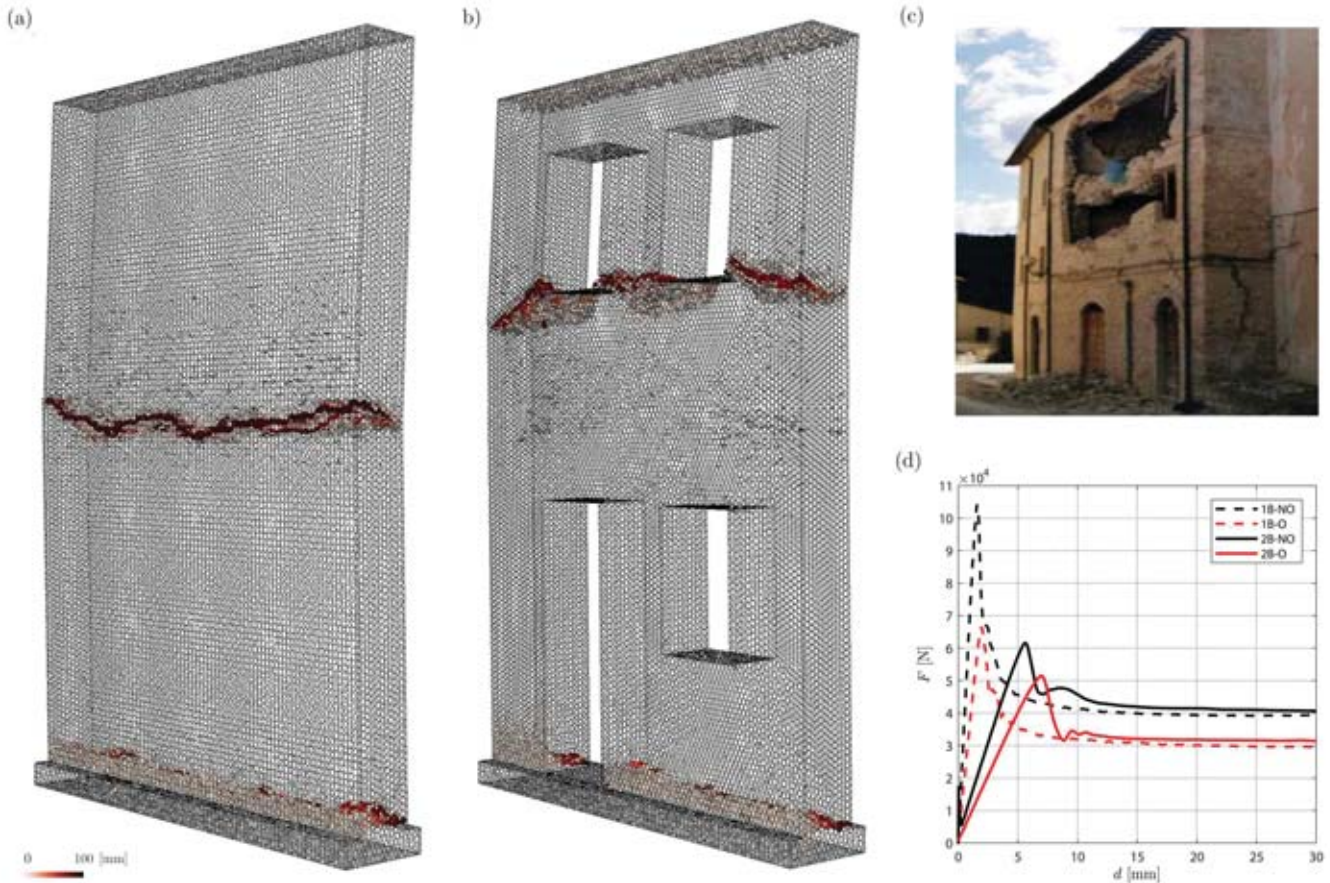


Figure 7: Total crack opening: (a) two-story wall with no openings (2B-NO); (b) two-story wall with openings (2B-O); (c) Example of two-story bending mechanisms caused by the 2009 L'Aquila earthquake (Arch. Fot. Vice Comm. Del. Beni Culturali - Sisma Abruzzo 2009); (d) force versus displacement curves for Cases 1B-NO, 1B-O, 2B-NO and 2B-O.

to out-of-plane loading. Moreover, masonry walls are usually the result of different stratification phases occurred over the course of many centuries. Here, three modeling strategies were adopted to reproduce different structural and time relations between the panels: (i) relation of contemporaneity (STRC), (ii) relation of anteriority (STRA) and (iii) relation of posteriority (STRP). In total, seven different cases were considered and they were based on the two-story bending wall with openings presented earlier.

STRC panels were modeled to replicate walls belonging to the same historical period. A single LDPM mesh was used and three sets of boundary conditions were considered to model different degrees of tothing between the walls. Fig. 8a, b, c show the models ordered by increasing level of constraint. The first model assumed the particles at the bottom surface to be fixed (see Fig. 8a). The second model assumed the particles at the bottom surface and the back surfaces of the transversal walls to be fixed (see Fig. 8b). The third model assumed the particles at the bottom surface, the back surfaces of the transversal walls and the lateral surfaces of the lateral walls to be fixed (see Fig. 8c).

STRP panels were modeled to replicate walls built after the adjacent structures. The main wall and the lateral-transversal walls were modeled using three separate LDPM meshes. All the particles at the bottom surface, the back surfaces of the transversal walls, and the lateral surfaces of the lateral walls were assumed to be fixed. A sliding with friction constraint model [59] was used at the interface between the panels. In order to simulate different levels of tothing

between the walls, two different friction conditions were adopted. High friction conditions were simulated using a static friction factor $s_{ff} = 0.13$ and a dynamic friction factor $d_{ff} = 0.015$ (see Fig. 8d), whereas low friction conditions were simulated with $s_{ff} = 0.03$ and a $d_{ff} = 0.0084$ (see Fig. 8e).

STRA panels were modeled to replicate walls built before the adjacent structures. The central-transversal walls and the lateral walls were modeled using three separate LDPM meshes. The structure composed by the main central panel and the transversal walls was assumed to belong to a previous historical period with respect to the lateral walls. The particles belonging to the bottom surface, to the back surfaces of the transversal walls and the lateral surfaces of the lateral walls were fixed. In order to simulate different levels of tothing between walls, the same sliding with friction algorithm was used and applied to the discontinuity surfaces between the panels. The same parameters for the friction mode were assumed, i.e. high friction (see Fig. 8f) and low friction (see Fig. 8g).

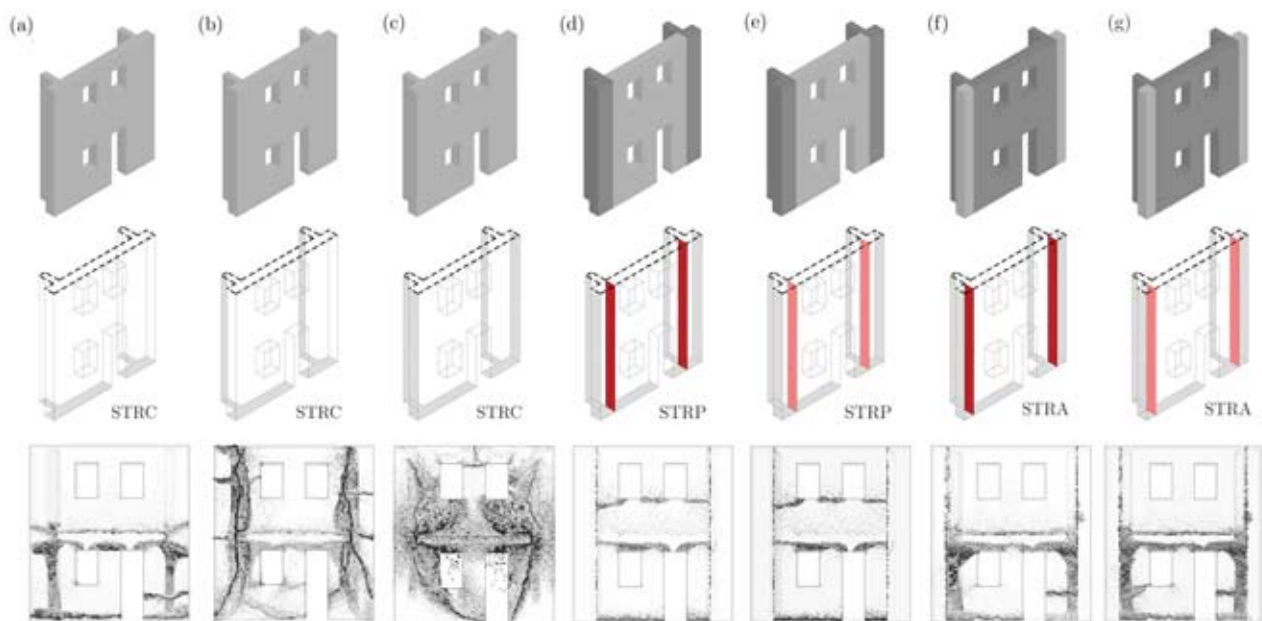


Figure 8: Geometry (top), boundary conditions (middle) and crack contours (bottom). In the middle row, the gray areas represent surfaces with all constrained displacements, the areas included within the black dotted lines represent the surfaces with horizontal displacements constrained in the out-of-plane direction and the red areas represent frictional interfaces (dark red for high friction and light red for low friction).

For all the simulated walls, the load was applied in quasi-static conditions by prescribing a velocity to particles of 300 mm height, between 2,700 mm and 3,000 mm, to reproduce the horizontal load of a floor activated by the seismic action. On top of the wall (at the second floor), the translations of the particles were constrained horizontally in the out-of-plane direction. The remaining boundary conditions and geometrical features of the structure are identical to the ones reported for the local bending mechanism case with opening case 2B-O.

3.2.2 Results and discussion

Fig. 8 and Fig. 9a, b, c, d, e, f show the damage distribution in the structures for the different configurations. Little similarities could be found with the local bending mechanism analyzed earlier. The fracture obviously depend on the boundary conditions and the connections between

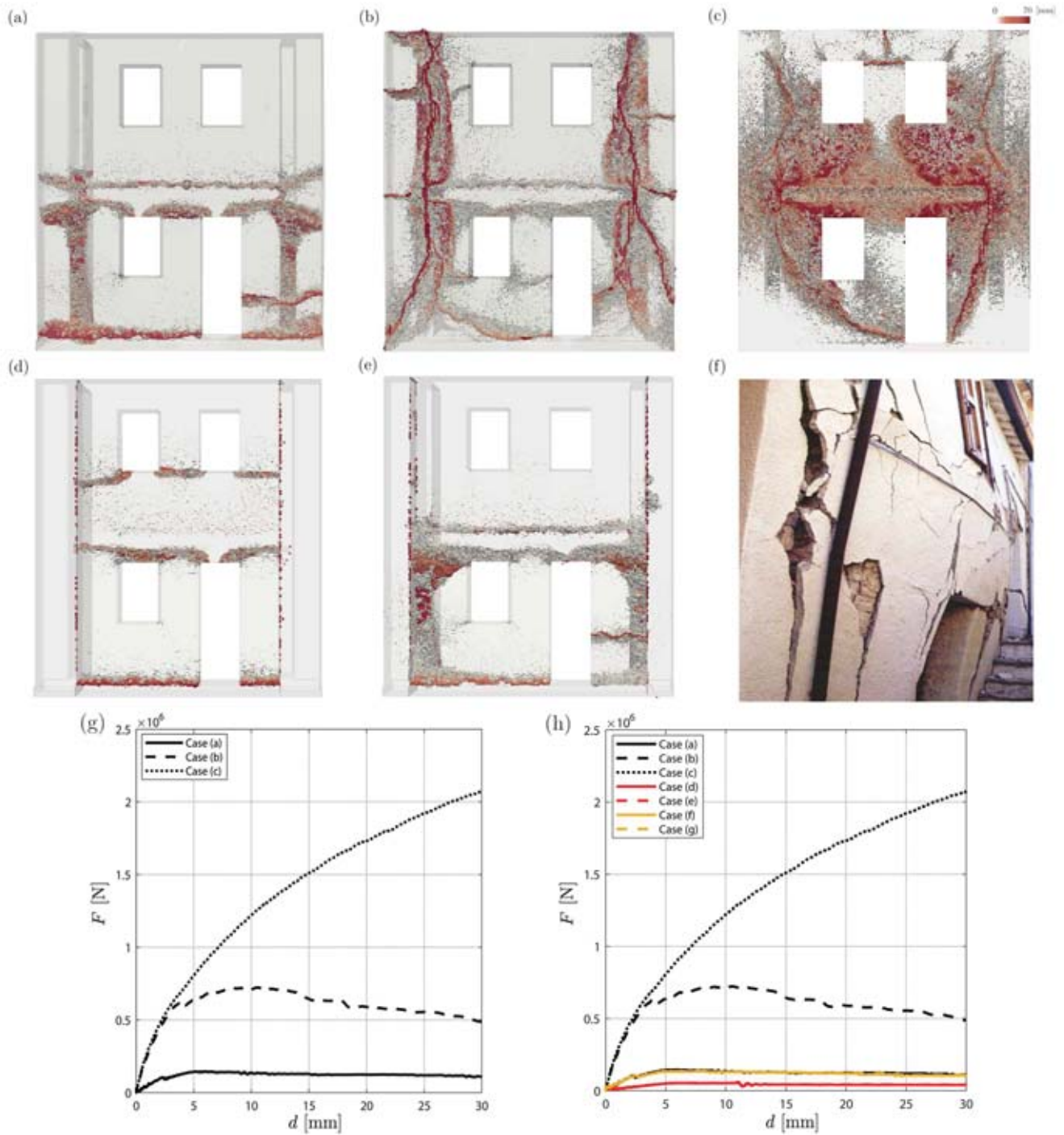


Figure 9: Total crack opening: (a), (b) and (c) STRC; (d) STRP; (e) STRA; (f) example of a complex mechanism (Arch. Fot. Vice Comm. Del. Beni Culturali - Sisma Abruzzo 2009). Force versus displacement curve: (g) for the cases (a), (b), (c); (h) for all the cases.

the central panel and the lateral and back walls. The damage in the case depicted in Fig. 8f, Fig. 8g and Fig. 9e is similar to the damage in the case shown in Fig. 8a and Fig. 9a. The reason might be that the continuity between the central and the transversal walls generates cracks in the lower floor as well as in the upper part. The main cracks in the cases depicted in Fig. 8b and Fig. 9b are vertical. On the contrary, the damage is distributed through the entire wall and are slightly concentrated in the central area (see Fig. 8c and Fig. 9c). In terms of quantitative analysis, Fig. 9g shows the load-displacement curves for the cases depicted in Fig. 8a, b, c. Fig. 9h shows all the curves. The more constrained case (see Fig. 8c) and the least constrained one (see Fig. 8d) define the upper and lower bound curves, respectively. One can deduce from these results that the choice of the correct boundary conditions in the analysis of such structures is complex and only a good estimation might be made. It also underlines the importance of performing accurate surveys to understand the architectural configuration and the historical evolution of the building.

4 CONCLUSIONS

The proposed Lattice Discrete Particle Model (LDPM) is presented, validated and used in the prediction of the mechanical behavior of unreinforced masonry structures in out-of-plane loading conditions. The model was first validated against experimental data and compared with nonlinear kinematic analysis (rigid-block displacement-based method). LDPM was then used to analyze more complex structures. Local bending mechanism was studied on walls with and without openings. The interaction between adjacent walls were also taken into account. The proposed numerical model is able to predict realistic fracture pattern in complex structures. On the basis of the results discussed in this paper, the following conclusions can be drawn.

- The damage distribution resulting from the collapse of masonry walls is well captured by LDPM.
- LDPM results were verified experimentally and with kinematic analysis. This suggests the use of this model to perform limit analysis for the assessment of local collapse mechanisms.
- Unlike typical kinematic analysis, LDPM does not require to identify a priori local collapse mechanisms. More complex configurations impossible to investigate analytically can also be considered.
- The presence of openings within walls and the application of adequate boundary conditions greatly affect the stiffness and bearing capacities of the walls.
- The results of this paper underlines the necessity to perform accurate in-field surveys in order to correctly model real masonry walls under out-of-plane loading.

REFERENCES

- [1] G. Magenes, G. M. Calvi, In-plane seismic response of brick masonry walls, *Earthquake engineering & structural dynamics* 26 (11) (1997) 1091–1112.
- [2] A. Menon, G. Magenes, Out-of-plane seismic response of unreinforced masonry: definition of seismic input, Rose School, IUSS Press, 2008.

- [3] T. M. Ferreira, A. A. Costa, A. Costa, Analysis of the out-of-plane seismic behavior of unreinforced masonry: A literature review, *International Journal of Architectural Heritage* 9 (8) (2015) 949–972.
- [4] K. Lang, H. Bachmann, On the seismic vulnerability of existing unreinforced masonry buildings, *Journal of Earthquake Engineering* 7 (03) (2003) 407–426.
- [5] P. Morandi, G. Magenes, Second order effects in out-of-plane strength of urm walls subjected to bending and compression, *ROSE Report* (2006).
- [6] A. A. Costa, A. Arêde, A. Costa, C. S. Oliveira, In situ cyclic tests on existing stone masonry walls and strengthening solutions, *Earthquake Engineering & Structural Dynamics* 40 (4) (2011) 449–471.
- [7] A. A. Costa, A. Arêde, A. Costa, C. S. Oliveira, Out-of-plane behaviour of existing stone masonry buildings: experimental evaluation, *Bulletin of Earthquake Engineering* 10 (1) (2012) 93–111.
- [8] D. D’Ayala, E. Speranza, Definition of collapse mechanisms and seismic vulnerability of historic masonry buildings, *Earthquake Spectra* 19 (3) (2003) 479–509.
- [9] M. R. Valluzzi, On the vulnerability of historical masonry structures: analysis and mitigation, *Materials and structures* 40 (7) (2007) 723–743.
- [10] R. Gabellieri, P. Diotalleivi, L. Landi, Effect of diaphragm flexibility on the dynamic behaviour of unreinforced masonry walls in out-of-plane bending, in: *Proceedings of the 15th World Conference on Earthquake Engineering*, 2012, pp. 24–28.
- [11] M. Gallonelli, Dynamic response of masonry buildings with rigid or flexible floors, Ph.D. thesis, Master Thesis, Rose School (2007).
- [12] S. K. Jain, P. C. Jennings, Analytical models for low-rise buildings with flexible floor diaphragms, *Earthquake engineering & structural dynamics* 13 (2) (1985) 225–241.
- [13] O. Penner, K. J. Elwood, Out-of-plane dynamic stability of unreinforced masonry walls in one-way bending: shake table testing, *Earthquake Spectra* 32 (3) (2016) 1675–1697.
- [14] D. F. Peralta, J. M. Bracci, M. B. D. Hueste, Seismic behavior of wood diaphragms in pre-1950s unreinforced masonry buildings, *Journal of Structural Engineering* 130 (12) (2004) 2040–2050.
- [15] C. C. Simsir, Influence of diaphragm flexibility on the out-of-plane dynamic response of unreinforced masonry walls, *University of Illinois at Urbana-Champaign*, 2004.
- [16] A. Tena-Colunga, D. P. Abrams, Seismic behavior of structures with flexible diaphragms, *Journal of Structural Engineering* 122 (4) (1996) 439–445.
- [17] S. Casolo, G. Uva, Nonlinear analysis of out-of-plane masonry façades: full dynamic versus pushover methods by rigid body and spring model, *Earthquake Engineering & Structural Dynamics* 42 (4) (2013) 499–521.

- [18] G. D. Felice, R. Giannini, Out-of-plane seismic resistance of masonry walls, *Journal of earthquake engineering* 5 (02) (2001) 253–271.
- [19] G. de Felice, Out-of-plane seismic capacity of masonry depending on wall section morphology, *International Journal of Architectural Heritage* 5 (4-5) (2011) 466–482.
- [20] A. Giuffrè, A mechanical model for statics and dynamics of historical masonry buildings, in: *Protection of the architectural heritage against earthquakes*, Springer, 1996, pp. 71–152.
- [21] P. B. Lourenço, J. G. Rots, Multisurface interface model for analysis of masonry structures, *Journal of engineering mechanics* 123 (7) (1997) 660–668.
- [22] V. Giamundo, V. Sarhosis, G. Lignola, Y. Sheng, G. Manfredi, Evaluation of different computational modelling strategies for the analysis of low strength masonry structures, *Engineering Structures* 73 (2014) 160–169.
- [23] J. Heyman, The stone skeleton, *International Journal of solids and structures* 2 (2) (1966) 249–279.
- [24] J. Heyman, *The Masonry Arch*, 1982.
- [25] A. Giuffrè, *Lecture sulla meccanica delle murature storiche*. (1991).
- [26] L. Restrepo-Vélez, A simplified mechanics-based procedure for the seismic risk assessment of unreinforced masonry buildings, *Individual Study* (2003).
- [27] C. Casapulla, Resistenze attrittive in una parete muraria soggetta ad azioni normali al suo piano medio, in: *L’Ingegneria Sismica in Italia; Proc. 9th nat. conf.*, Torino, 20-23 September 1999, 1999.
- [28] L. Picchi, *Risposta sismica per azioni fuori dal piano di pareti murarie*, Graduation Thesis, University of Pavia (2002).
- [29] G. A. Cundari, G. Milani, Homogenized and heterogeneous limit analysis model for pushover analysis of ancient masonry walls with irregular texture, *International Journal of Architectural Heritage* 7 (3) (2013) 303–338.
- [30] S. Tiberti, G. Milani, 2d pixel homogenized limit analysis of non-periodic masonry walls, *Computers & Structures* 219 (2019) 16–57.
- [31] S. Tiberti, G. Milani, 3d voxel homogenized limit analysis of single-leaf non-periodic masonry, *Computers & Structures* 229 (2020) 106186.
- [32] S. Tiberti, G. Milani, 3d homogenized limit analysis of non-periodic multi-leaf masonry walls, *Computers & Structures* 234 (2020) 106253.
- [33] K. T. Doherty, *An investigation of the weak links in the seismic load path of unreinforced masonry buildings*, Ph.D. thesis (2000).
- [34] M. Tomaževič, *Seismic resistance verification of masonry buildings: Following the new trends*, 1997.

- [35] G. W. Housner, The behavior of inverted pendulum structures during earthquakes, *Bulletin of the seismological society of America* 53 (2) (1963) 403–417.
- [36] M. Priestley, R. Evison, A. Carr, Seismic response of structures free to rock on their foundations, *Bulletin of the New Zealand National Society for Earthquake Engineering* 11 (3) (1978) 141–150.
- [37] D. Liberatore, G. Spera, Response of slender blocks subjected to seismic motion of the base: description of the experimental investigation, in: *5th International Symposium on Computer Methods in Structural Masonry*, Rome, 2001, pp. 117–124.
- [38] J. Zhang, N. Makris, Rocking response of free-standing blocks under cycloidal pulses, *Journal of Engineering Mechanics* 127 (5) (2001) 473–483.
- [39] L. Sorrentino, S. Kunnath, G. Monti, G. Scalora, Seismically induced one-sided rocking response of unreinforced masonry façades, *Engineering structures* 30 (8) (2008) 2140–2153.
- [40] O. A. Shawa, G. de Felice, A. Mauro, L. Sorrentino, Out-of-plane seismic behaviour of rocking masonry walls, *Earthquake Engineering & Structural Dynamics* 41 (5) (2012) 949–968.
- [41] I. N. Psycharis, Dynamic behaviour of rocking two-block assemblies, *Earthquake Engineering & Structural Dynamics* 19 (4) (1990) 555–575.
- [42] P. D. Spanos, P. C. Roussis, N. P. Politis, Dynamic analysis of stacked rigid blocks, *Soil Dynamics and Earthquake Engineering* 21 (7) (2001) 559–578.
- [43] R. Gabellieri, L. Landi, P. Diotallevi, A 2-dof model for the dynamic analysis of unreinforced masonry walls in out-of-plane bending, in: *Proc. of the 4th ECCOMAS Thematic Conference on Computational Methods in Structural Dynamics and Earthquake Engineering*, 2013.
- [44] H. Derakhshan, M. C. Griffith, J. M. Ingham, Out-of-plane behavior of one-way spanning unreinforced masonry walls, *Journal of Engineering Mechanics* 139 (4) (2011) 409–417.
- [45] S. Lagomarsino, Seismic assessment of rocking masonry structures, *Bulletin of earthquake engineering* 13 (1) (2015) 97–128.
- [46] S. Casolo, G. Milani, A simplified homogenization-discrete element model for the non-linear static analysis of masonry walls out-of-plane loaded, *Engineering Structures* 32 (8) (2010) 2352–2366.
- [47] P. Lourenço, Computational strategy for masonry structures, Delft University of Technology and DIANA Research (1996).
- [48] A. W. Page, Finite element model for masonry, *Journal of the Structural Division* 104 (8) (1978) 1267–1285.
- [49] G. Milani, P. Lourenço, A. Tralli, Homogenization approach for the limit analysis of out-of-plane loaded masonry walls, *Journal of structural engineering* 132 (10) (2006) 1650–1663.

- [50] P. B. Lourenço, Computations on historic masonry structures, *Progress in Structural Engineering and Materials* 4 (3) (2002) 301–319.
- [51] J. Lemos, Discrete element modelling of the seismic behaviour of stone masonry arches, *Computer methods in structural masonry* 4 (1998) 220–227.
- [52] G. Sincraian, J. Lemos, C. Oliveira, Assessment of the seismic behavior of stone masonry aqueduct using the discrete element method, in: *Proc. 11th European Conf. on Earthquake Engineering*, 1998.
- [53] A. Drei, C. S. Oliveira, P. Lourenço, P. Roca, The seismic behaviour of the “aqueduto da amoreira” in elvas using distinct element modelling, in: *Proceedings of the 3rd International Seminar on Historical Constructions*, Guimarães Portugal November 7–9, 2001, 2001, pp. 7–9.
- [54] C. Oliveira, J. V. Lemos, G. Sincraian, Modelling large displacements of structures damaged by earthquake motions, *European Earthquake Engineering* 16 (3) (2002) 56–71.
- [55] A. Alexandris, E. Protopapa, I. Psycharis, Collapse mechanisms of masonry buildings derived by the distinct element method, in: *Proceedings of the 13th world conference on earthquake engineering*, Vol. 59, 2004, p. 60.
- [56] H. Nguyen, M. Pathirage, M. Rezaei, M. Issa, G. Cusatis, Z. P. Bažant, New perspective of fracture mechanics inspired by gap test with crack-parallel compression, *Proceedings of the National Academy of Sciences* (2020).
- [57] H. T. Nguyen, M. Pathirage, G. Cusatis, Z. P. Bažant, Gap test of crack-parallel stress effect on quasibrittle fracture and its consequences, *Journal of Applied Mechanics* 87 (7) (2020).
- [58] G. Cusatis, D. Pelessone, A. Mencarelli, Lattice discrete particle model (ldpm) for failure behavior of concrete. i: Theory, *Cement and Concrete Composites* 33 (9) (2011) 881–890.
- [59] G. Cusatis, A. Mencarelli, D. Pelessone, J. Baylot, Lattice discrete particle model (ldpm) for failure behavior of concrete. ii: Calibration and validation, *Cement and Concrete composites* 33 (9) (2011) 891–905.
- [60] M. Angiolilli, A. Gregori, M. Pathirage, G. Cusatis, Fiber Reinforced Cementitious Matrix (FRCM) for strengthening historical stone masonry structures: Experiments and computations, *Engineering Structures* 224 (2020): 111102.
- [61] M. Mercuri, M. Pathirage, A. Gregori, G. Cusatis, Computational modeling of the out-of-plane behavior of unreinforced irregular masonry, *Engineering Structures* 223 (2020): 111181.
- [62] C. Ceccato, M. Salviato, C. Pellegrino, G. Cusatis, Simulation of concrete failure and fiber reinforced polymer fracture in confined columns with different cross sectional shape, *International Journal of Solids and Structures* 108 (2017) 216–229.
- [63] M. Pathirage, F. Bousikhane, M. D’Ambrosia, M. Alnaggar, G. Cusatis, Effect of alkali silica reaction on the mechanical properties of aging mortar bars: Experiments and numerical modeling, *International Journal of Damage Mechanics* 28 (2) (2019) 291–322.

- [64] L. Han, M. Pathirage, A-T. Akono, G. Cusatis, Lattice Discrete Particle Modeling of Size Effect in Slab Scratch Tests, *Journal of Applied Mechanics* 88, no. 2 (2021).
- [65] E. A. Schaufert, G. Cusatis, Lattice discrete particle model for fiber-reinforced concrete. i: Theory, *Journal of Engineering Mechanics* 138 (7) (2011) 826–833.
- [66] J. Smith, G. Cusatis, D. Pelessone, E. Landis, J. O’Daniel, J. Baylot, Discrete modeling of ultra-high-performance concrete with application to projectile penetration, *International Journal of Impact Engineering* 65 (2014) 13–32.
- [67] M. Alnaggar, G. Cusatis, G. Di Luzio, Lattice discrete particle modeling (ldpm) of alkali silica reaction (asr) deterioration of concrete structures, *Cement and Concrete Composites* 41 (2013) 45–59.
- [68] M. Pathirage, D. Bentz, G. Di Luzio, E. Masoero, G. Cusatis, The onix model: a parameter-free multiscale framework for the prediction of self-desiccation in concrete, *Cement and Concrete Composites* 103 (2019) 36–48.
- [69] S. Degli Abbati, M. Rossi, S. Lagomarsino, Out-of-plane experimental tests on masonry panels, in: *Proceedings of the 2nd European Conference on Earthquake Engineering and Seismology*, 2014, pp. 25–29.
- [70] Decreto del ministro delle infrastrutture 17 gennaio 2018. aggiornamento delle “norme tecniche per le costruzioni”, *Gazzetta Ufficiale della Repubblica Italiana*.

NUMERICAL STUDY ON SEISMIC RETROFIT OF URM WALLS USING TIMBER PANELS

D. Cassol¹, I. Giongo¹, and M. Piazza¹

¹ University of Trento, Department of Civil, Environmental and Mechanical Engineering
via Mesiano 77, 38123, Trento, Italy
e-mail: {davide.cassol-1, ivan.giongo, maurizio.piazza}@unitn.it

Abstract

Unreinforced masonry (URM) buildings are characterized by high vulnerability to lateral loading, which is often manifested when an earthquake occurs. The present study investigates the effectiveness of a timber-based retrofit solution aimed at reducing the seismic vulnerability of existing URM structures. The retrofit technique consists of connecting timber-based panels, to the interior surface of the walls of a building using mechanical or adhesive point-to-point connections. The application of those panels allows to considerably increase both the in-plane and the out-of-plane capacity of the URM walls, while preserving the original external facades of the retrofitted building. This solution resulted to be relatively fast and easy to install and the reversible nature of the system allows to reduce the impact of the retrofit intervention.

In this work the in-plane behaviour of the retrofitted walls was investigated numerically, building on previous preliminary analyses and in the lights of the results of experimental evidence collected by the authors' research team. The effectiveness of this retrofit solution was analysed on several masonry types, considering different masonry properties and geometries. The influence of various parameters (such as masonry-to panel connection typology, connectors number and position) on the increase of lateral capacity of the retrofitted walls was studied by means of a series of non-linear quasi-static simulations.

Keywords: Unreinforced masonry, Seismic retrofit, Seismic rehabilitation, Timber panels.

1 INTRODUCTION

The retrofit solution studied herein aims at reducing the seismic vulnerability of existing masonry buildings while preserving the external facades. The retrofit consists of timber-based panels connected to the interior surfaces of the masonry walls of a building using mechanical or adhesive point to point connections. The use of the timber guarantees fast execution and reversibility of the system. A detailed description of this retrofit solution and the outcomes of numerical simulations were provided by Giongo et al. [1] while the effectiveness of this retrofit technique was experimentally investigated by Giongo et al. [2] via onsite testing of masonry shear walls strengthened with timber panels. Further experimental evidence on walls retrofitted with timber panels and timber-to-masonry connections can be found in Borri et al. [3], Pozza et al. [4], Riccadonna et al. [5] and Rizzi et al. [6].

Other examples of timber based retrofit techniques for masonry structures include the timber *strong-backs* retrofit solution and the timber *frames and sheathing* retrofit solution. The timber strong-backs retrofit solution aims to increase the out-of-plane capacity of the URM walls by connecting vertical timber elements to the masonry with mechanical screws or bolts. The effectiveness of this solution was investigated experimentally by Giaretton et al. [7], Dizhur et al. [8] and by Cassol et al. [9]. The timber *frames and sheathing* retrofit technique is instead a hybrid solution between the *strong-backs* and the *timber panels* retrofit techniques with the goal of increasing both the in-plane and the out-of-plane capacity of the URM walls. The effectiveness of this retrofit solution was recently tested by Guerrini et al. [10]. The use of timber panels as retrofit components was also studied for the seismic strengthening of reinforced concrete structures by Sustersic and Dujic [11] [12] and by Smiroldo et al. [13].

In this work the in-plane behaviour of walls retrofitted with cross-laminated timber (CLT) panels was investigated through non-linear quasi-static analysis. Starting from previous numerical analyses reported in [1], different modelling approach and type of analysis were adopted so as to improve the convergence and reach larger deformations. The properties of the connections (panel-to-masonry connections, panel-to-panel connections and anchoring system) were properly calibrated based the results of the aforementioned experimental testing campaigns carried out by the authors. The influence of different parameters on the effectiveness of the retrofit solution was investigated considering the behaviour of single piers, walls with openings and multi-storey walls. An example of retrofitted masonry wall is reported in Figure 1.

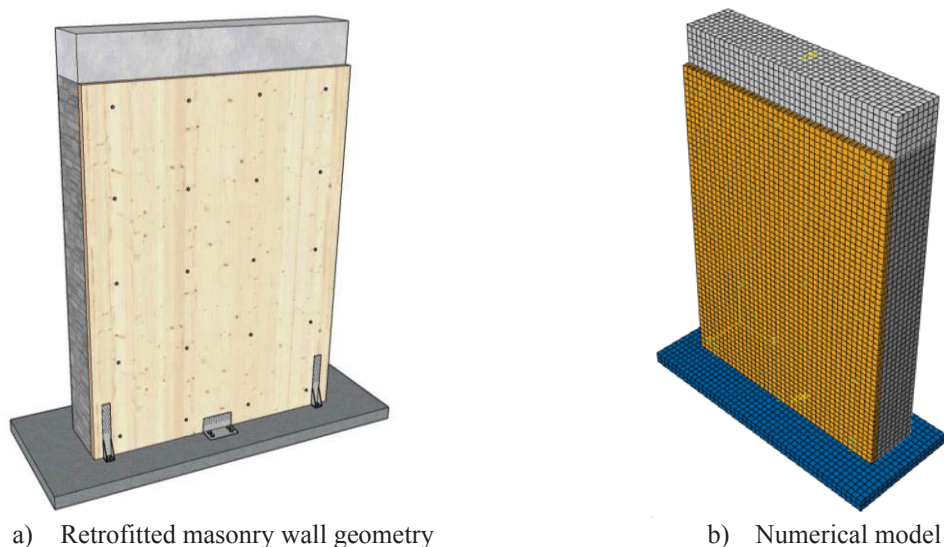


Figure 1: Retrofitted masonry wall.

2 NUMERICAL MODEL

The numerical models were realized using the finite element software Abaqus/Explicit [14]. The masonry was modelled as an equivalent, homogeneous and isotropic material. The post cracked behaviour was described with the Concrete Damage Plasticity (CDP) constitutive model. Such model was developed by Lubliner et al. [15] and improved with the modifications proposed by Lee and Fenves [16] and it is suitable to represent the behaviour of quasi-brittle materials such as masonry. The adopted yield surface function is a modified version of the Drucker-Prager model, which is governed by a parameter K_c . This parameter represents the ratio of the second stress invariant on the tensile meridian to that on the compressive meridian and it was assumed equal to 0.667. The dilatation angle, the flow potential eccentricity and the ratio of initial equibiaxial compressive yield stress to initial uniaxial compressive yield stress were assumed equal to 40° , 0.1 and 1.16 respectively, while visco-plastic phenomena were neglected. Parabolic and bilinear stress-strain relations were adopted to describe the compressive and tensile behaviours of the material under axial loading. The maximum values of the stress strain curves correspond to the compressive and tensile strengths while the post cracked behaviours are determined considering the fracture energy in tension and in compression. Such energy values were calculated as recommended by Lourenço [17].

The CLT panel was modelled as a three-layer solid, where the two external layers were defined with the principal direction oriented vertically while the inner layer was oriented horizontally. The timber was implemented as an orthotropic material where inelastic phenomena (such as local crushing at the panel's toe) were approximated using a plastic constitutive model. In this study the timber properties were selected considering timber grade C24 [18]. The point-to-point connections between the CLT panel and the masonry were modelled using one-dimensional connector elements. The properties of such elements were carefully calibrated on the experimental outcomes of different experimental campaigns. Cartesian and Radial thrust connectors were used and the connection between fastener extremities and masonry or timber was ensured by coupling constraints, considering adequate influence radii. Similar approach was adopted also for simulating the presence of anchoring devices such hold-downs (for tension forces) and angle-brackets (for shear forces). A concrete beam and a concrete base were also modelled using an indefinitely elastic and isotropic material with the aim of improving the transfer of the horizontal and the vertical loads to the masonry, and consistently with the load configuration of the experimental tests used as reference for the model validation. The surface-to-surface connections between the masonry and the concrete beam and the base were modelled using the tie constraint (no displacement allowed between coinciding nodes), while the interaction between the other elements was modelled with a hard contact constrain to avoid overlapping of materials.

A regular mesh pattern with eight nodes three dimensional elements (C3D8R) was used. The selected mesh size (i.e. 50 mm) is the maximum size that allowed to describe the material response close to the fasteners with adequate accuracy. Dynamic quasi-static analyses were performed to reduce the computational cost of simulations and to improve the convergence. The geometric nonlinearities were considered. The horizontal load was applied in the form of an imposed displacement while the vertical load was simulated as a uniform pressure. The loads were applied slowly (ranging between 0.05 and 0.2 mm/s) and the ratio between the kinetic and the internal energies of the system was monitored to verify the reliability of the analysis.

The model reproducing unreinforced masonry (URM) conditions was validated on the results from cyclic shear-compression testing of double-leaf rubble limestone masonry performed by Gattesco et al [19]. Figure 2 presents the comparison between the experimental

outcomes [19] and the numerical model employed in this work. It can be observed that the numerical results are consistent with the experimental data in terms of both *lateral load vs. displacement* curve and failure mechanism.

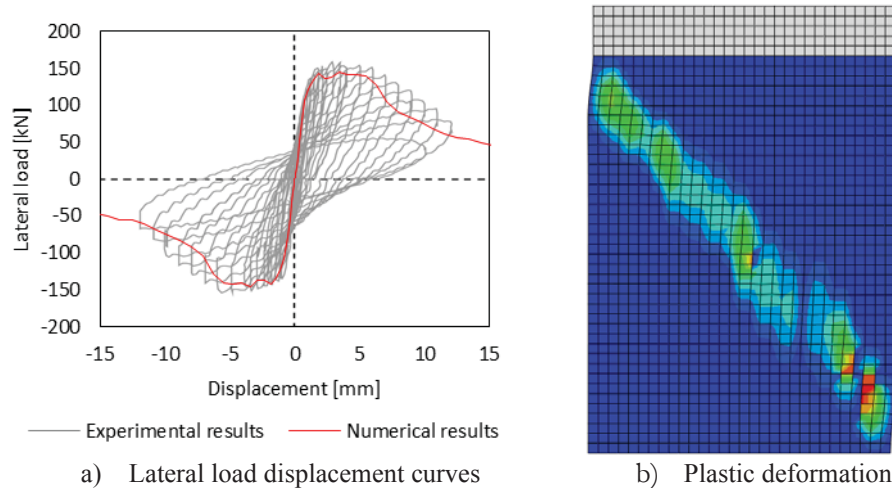


Figure 2: Model validation by means of a comparison between numerical and experimental results [19].

3 NUMERICAL ANALYSES

The effectiveness of the CLT panel retrofit solution was numerically investigated considering masonry piers retrofitted with one or more timber panels, walls with openings and multi-storey walls. The behaviour of the retrofitted walls was compared with the response of URM walls and parametric analyses were conducted.

3.1 Behaviour of retrofitted masonry piers

The first analyses were developed with the aim of testing the influence of different parameters on the response of the retrofitted walls. Different retrofit configurations were considered by changing the following parameters:

- Masonry properties (M1-M2-M3)
- Masonry thickness (T1-T2-T3)
- Masonry length (L1-L2-L3-L4-L5)
- Masonry overburden (Q1-Q2-Q3-Q4)
- Fastener configuration (C1-C2-C3-C4-C5-C6-C7)
- Connection properties (K1-K2-K3-KR)
- Hold-down properties (HD1-HD2-HD3-HDR)
- Angle bracket properties (AB1-AB2-AB3-ABR)

The mechanical properties of masonry vary widely and are greatly dependent on the properties of its components. Three masonry types were chosen to represent the masonry typologies that can be encountered when retrofitting existing masonry buildings. Table 1 reports the values of the adopted masonry properties. Three different thicknesses were selected with the aim of representing thin, medium and thick walls, see Table 2. All of the tested walls were characterized by the same height (2700 mm masonry + 300 mm concrete beam) while three different lengths were considered, see Table 3. The analysis was developed in displacement

control with the vertical load applied uniformly over the concrete beam. Four values of overburden were applied, see Table 4. Two boundary conditions were studied, assuming the wall's ends as either fixed-free (i.e. vertical cantilever) or double fixed. The real behaviour of the top constraint depends on several factors, such as the presence of the bond beam, the features of the lintels and the type of floor-diaphragm. The two selected boundary conditions represent the limit cases of weak and strong spandrels [20]. The combination of the previous properties (masonry properties, masonry thickness, overburden and boundary conditions) resulted in wall models characterized by different failure modes (e.g. rocking and diagonal cracking).

Masonry ID	M01	M02	M03
Elastic modulus E [MPa]	600	1200	1800
Compression strength f_c [MPa]	1.50	3.00	4.50
Compression fracture energy G_c [N/mm]	3.98	7.50	10.58
Tension strength f_t [MPa]	0.050	0.075	0.100
Tension fracture energy G_t [N/mm]	0.02	0.02	0.02

Note: for all the masonry types the density is 18 kN/m^3 and the Poisson ratio is 0.25.

Table 1: Masonry properties.

Thickness ID	T1	T2	T3
Thickness [mm]	250	400	600

Table 2: Masonry thicknesses.

Length ID	L1	L2	L3	L4	L5
Length [mm]	1500	2000	3000	4500	6000
Length to height ratio [-]	0.50	0.67	1.00	1.50	2.00

Table 3: Masonry lengths.

Overburden ID	Q1	Q2	Q3	Q4
Overburden [MPa]	0.10	0.15	0.20	0.25

Table 4: Overburdens.

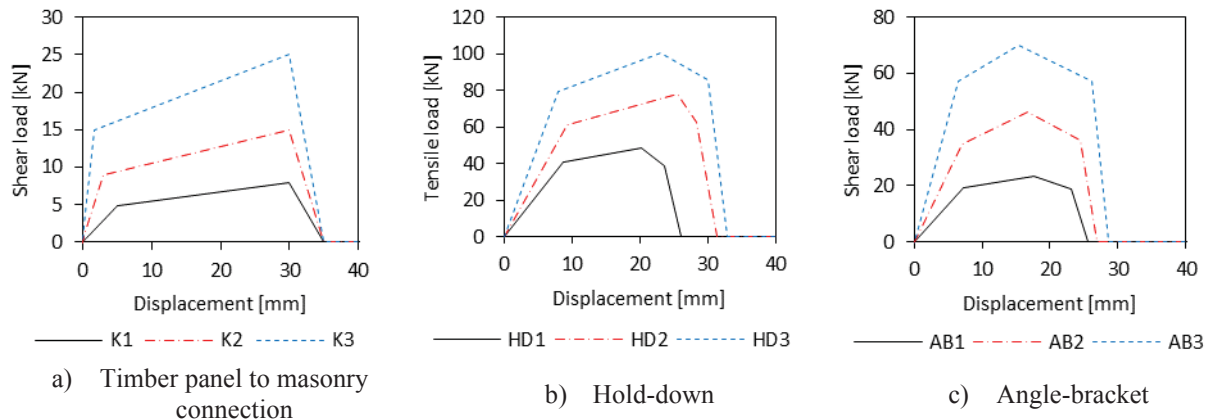
The retrofit solution proposed herein consists of fixing a 60 mm CLT panel on the surface of the masonry wall. The point-to-point connection between the masonry wall and the timber panel is provided by mechanical or adhesive connections. Different retrofit configurations were analysed by changing the number and the position of the fasteners, see Table 5. The values of the connection stiffness and shear capacity were selected in accordance with the experimental results obtained in [5] and [6], where experimental testing of dry and adhesive connections under monotonic and cyclic shear loading was performed. The implemented load-displacement curves of the timber to masonry connections are reported in Figure 3a. The connection K1 represents a typical dry connection realised with screw-fasteners [5] and which was used to connect the timber elements (panels or strong-backs) to the wall in the experimental campaigns reported in [2] and [9]. Two adhesive connection types were also considered through K2 and K3 curves [6]. Additionally, a rigid connection (KR) was modelled to represent the limit case.

The timber panel was constrained to the ground by two hold-down devices positioned on either side of the timber panel at 100 mm from the lateral edge and by an angle bracket positioned at the middle of the base of the panel, see Figure 1. Three tensile and shear load dis-

placement curves were chosen to model the hold-down and the angle bracket connections based on the experimental outcomes presented in [21] and [22], see Figure 3b,c. The cases of rigid tensile and shear connections were also studied (HDR and ABR) to simulate the properties of high-stiffness connections such as the one presented in [23].

Configuration ID	C1	C2	C3	C4	C5	C6	C7
Connectors number [-]	12	15	16	20	24	28	35
Horizontal spacing [mm]	800	800	533	533	533	533	400
Vertical spacing [mm]	800	600	800	600	480	400	400
Connectors/m ² [-/m ²]	2.22	2.78	2.96	3.70	4.44	5.19	6.48

Table 5: Connector's configurations.



Note: It was also studied the case of rigid connections (KR, HDR, ABR).

Figure 3: Connection properties.

A base configuration was defined considering the retrofitted masonry wall reported in Figure 1 with the properties M1, T2, L2, Q1, C4, K1, HD2, AB3. Figure 4 presents the results obtained for this configuration in the unreinforced (URM) and retrofitted (R) states for two boundary conditions (fixed-free and double-fixed). It can be observed that in case of shear cracking behaviour (SB) the application of the retrofit allows to increase the lateral and the displacement capacities of the masonry wall considerably. The crack pattern of this model (R-SB) is characterized by the formation of a diagonal crack (point 1) followed by a further increase of load bearing capacity. The maximum capacity increase (56%) corresponds to the condition where the fasteners' shear capacity is reached. In case of rocking behaviour (RB), the application of the retrofit provides an increase in lateral capacity of 67%. The crack pattern is characterized by the formation of a first horizontal crack (point 2) next to the wall base, typical of the rocking behaviour, followed by the formation of second horizontal crack at mid-height of the tension side (point 3) and then, when the maximum lateral capacity is reached, a third crack developed (point 4). The second and the third cracks' formation is due to the tensile stress induced in the masonry by the fasteners. The URM-RB model exhibits a displacement capacity larger than 60 mm due to the properties of the URM wall. The displacement capacity limit imposed by the Italian code standard [24] is 30 mm for the URM-RB failure (1% wall's height) and 15 mm (0.5% wall's height) for the URM-SB failure, therefore in this work the behaviour of the masonry walls was studied within the displacement interval from 0 to 60 mm.

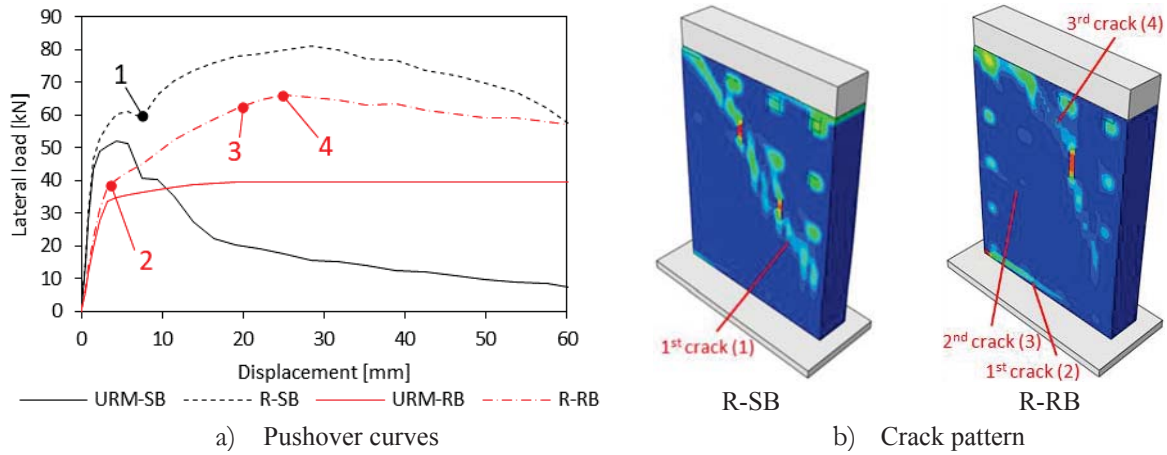


Figure 4: Standard configuration results (M1, T2, L2, Q1, C4, K1, HD2, AB3) (unreinforced masonry URM, retrofitted R, shear behaviour SB, rocking behaviour RB).

3.1.1. Timber panel anchoring connection

Four retrofit configurations were analysed considering different CLT panel anchoring connections: 1) a retrofit solution with no anchoring system to fix the panel to the foundation (CLT); 2) a solution with the connection provided by the sole hold-downs (HD); 3) a solution with just the angle bracket (AB) and 4) a solution with both the hold-downs and the angle bracket (HD+AB). Figure 5 presents the results for the two boundary conditions. It can be observed that in the first case (double-fixed condition and shear cracking behaviour), the application of the timber panel considerably increases the displacement capacity. As expected, the application of the hold-downs does not affect the performance of the retrofit while the constraint provided by the angle bracket produces a notable increase in the lateral capacity of the URM wall (AB and HD+AB). In the second case (cantilever and rocking behaviour), on the contrary, the hold-downs are of paramount importance in determining the effectiveness of the retrofit.

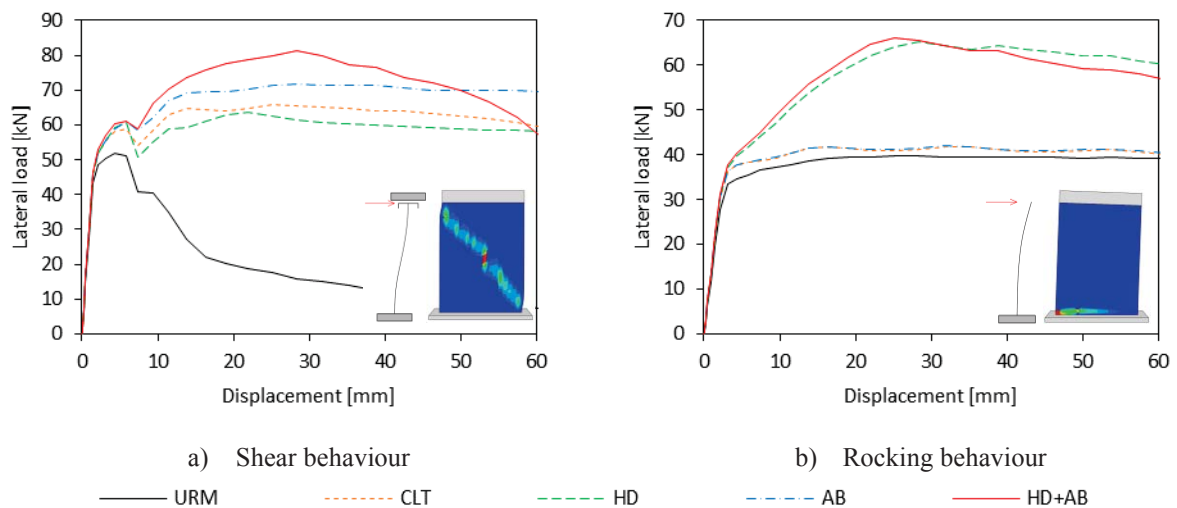


Figure 5: Effectiveness of the CLT panel to ground connection on the response of the retrofitted wall (base configuration M1, T2, L2, Q1, C4, K1, HD2, AB3).

Additional analyses were performed considering different hold-down and angle bracket properties, see Figure 6. The effect of the angle bracket properties was investigated considering the shear cracking behaviour (Figure 6a) and it was shown that the adoption of stiffer and

stronger angle brackets (AB3) appreciably increases the maximum capacity. Figure 6b shows the effect of different hold-downs on the response of the retrofitted wall in the case of rocking behaviour. The hold-down properties affect the stiffness of the second part of the response curves, when the first horizontal crack is already developed, while the lateral capacity of the retrofitted walls does not change. The shear load on the angle bracket was between 20 and 40 kN while the tensile load on the hold-downs ranged from 40 to 60 kN.

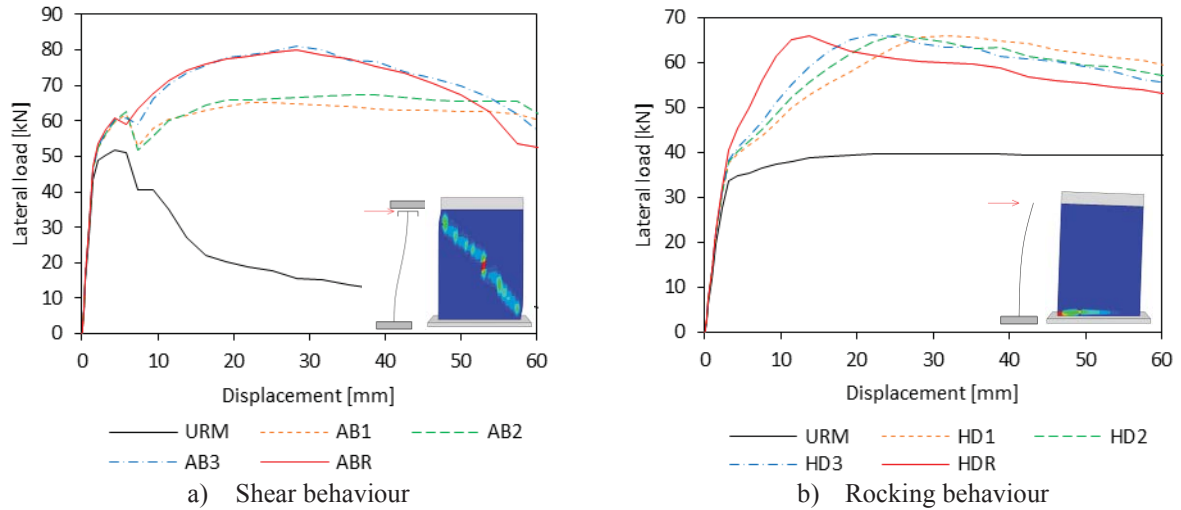


Figure 6: Effectiveness of angle bracket (SCB) and the hold-down (RB) properties on the response of the retrofitted wall (base configuration M1, T2, L2, Q1, C1, K1, HD2, AB3).

3.1.2. Timber panel to masonry wall connection

Figure 7 reports the behaviour of masonry walls retrofitted considering different types of CLT panel to masonry connections (see Figure 3a). The increase of connection stiffness slightly increases the effectiveness of the retrofit intervention for both failure modes. It can be noticed that in the shear cracking behaviour case, the response of the dry connection K1 presents a small decrease in the load bearing capacity as soon as the wall starts cracking followed then by a strength regain and a further increase. This phenomenon is due to the reduced stiffness of the connection, which requires the wall to displace 10 mm prior to engaging sufficient fasteners' shear to further increase the global lateral capacity.

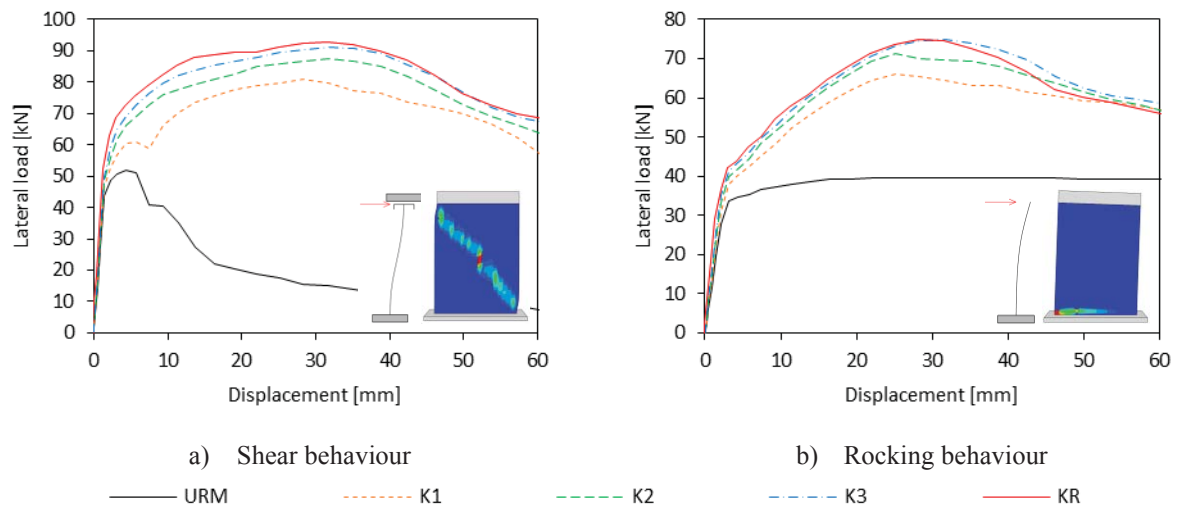


Figure 7: Effectiveness of the CLT panel to masonry connection on the response of the retrofitted wall (base configuration M1, T2, L2, Q1, C1, HD2, AB3).

The influence of the timber-to-masonry connection layout was analysed by varying the number and the position of the point-to-point fasteners, see Figure 8. Not surprisingly, the effectiveness of the retrofit solution grows when increasing the number of connectors, especially for the shear cracking behaviour. It can be observed that the pushover curves obtained from increasing the number of connectors are compatible with those obtained from increasing the fastener stiffness (Figure 7). The inevitable local stress-concentration associated with the stiffer fasteners appeared therefore not to be detrimental to the overall wall performance. As a result, the adoption of fewer fasteners of larger diameter seems a viable option to reduce costs, especially when adhesive fasteners are used.

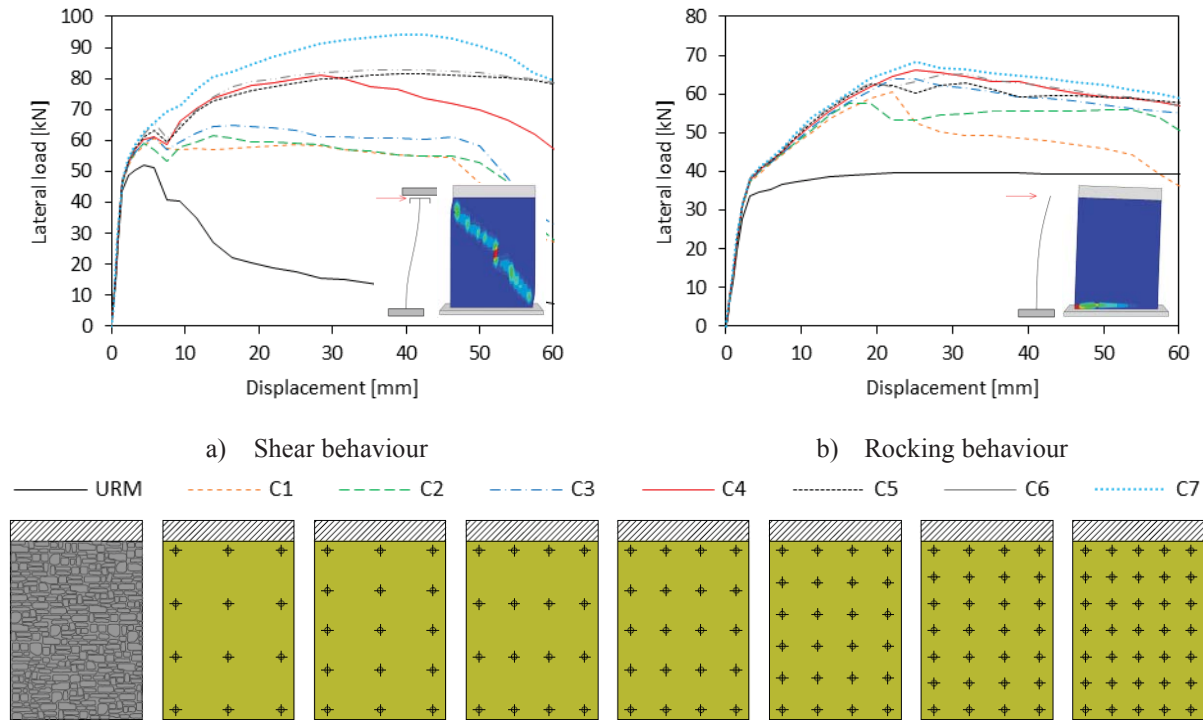


Figure 8: Effectiveness of the connector's configuration on the response of the retrofitted wall (base configuration M1, T2, L2, Q1, K1, HD2, AB3).

3.1.3. Overburden

Figure 9 reports the behaviour of retrofitted masonry walls for different overburden levels (see Table 4). As expected, the increase in overburden improves the load bearing capacity of both URM walls and retrofitted walls. Regarding the displacement capacity, when the wall response was governed by rocking (i.e. fixed-free walls), an increase in the vertical loading produced a reduction in the URM wall capacity due to toe crushing (URM-Q3 and URM-Q4). Conversely, when the walls responded in shear (i.e. double fixed-end walls) the displacement capacity was not appreciably affected by the overburden level. As concerns the retrofitted walls, the response appeared not to be influenced by variations in the vertical load independently from the boundary conditions.

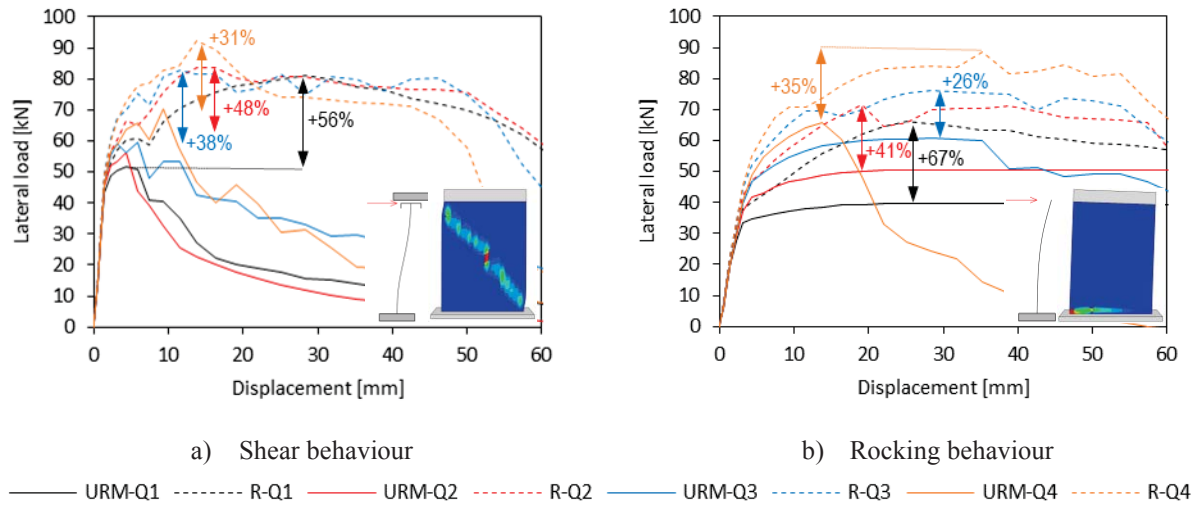
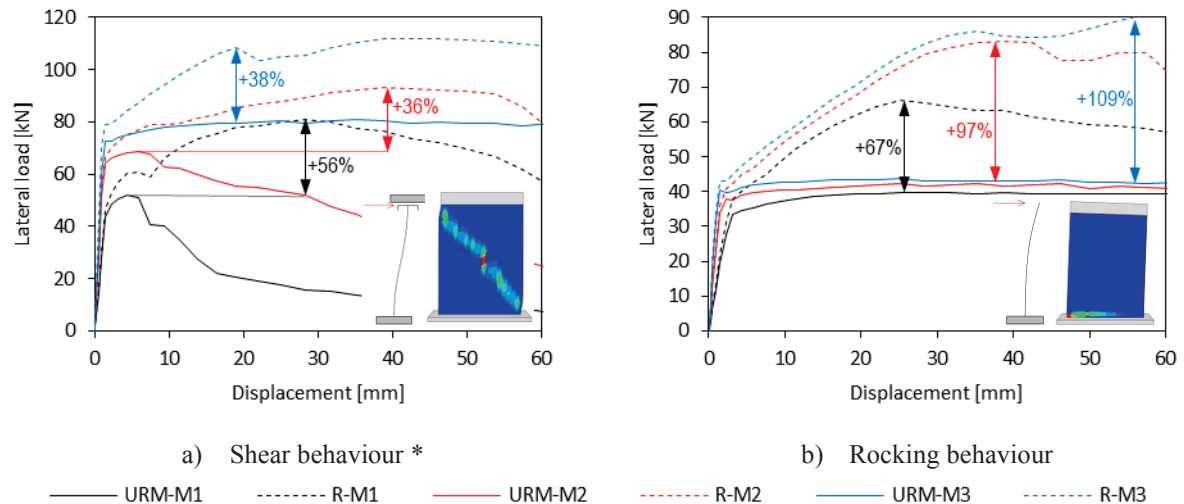


Figure 9: Effectiveness of the CLT panel retrofit on URM walls characterized by overburdens (base configuration M1, T2, L2, C1, K1, HD2, AB3).

3.1.4. Masonry wall characteristics

Figure 10 reports the behaviour of retrofitted masonry walls characterized by different masonry properties (see Table 1). It can be noticed that the application of the retrofit solution is effective for all the investigated configurations. Predictably, an increase in the elastic modulus affects the initial slope of the response curves while the improvement of tensile and compressive strength values impacts the behaviour of both the URM and retrofitted walls. The walls URM-M3 and R-M3 are characterized by rocking even in the case of double-fixed conditions. Such response is characterized by the formation of two horizontal cracks, one at the bottom and one at the top of the wall, and the retrofit solution resulted to be effective also in this case. For the RB cases, the effectiveness of the retrofit solution grows when improving the masonry properties. This phenomenon is mainly due to the increase of tensile strength which allows to transfer more load on the masonry wall before that the third diagonal crack occurs (Figure 4).



Note: * walls URM-M3 and R-M3 are characterized by a rocking behaviour for both boundary conditions.

Figure 10: Effectiveness of the CLT panel retrofit solution on URM walls characterized by different masonry properties (base configuration T2, L2, Q1, C1, K1, HD2, AB3).

Figure 11 reports the behaviour of retrofitted masonry walls characterized by different masonry thicknesses (see Table 2). It can be observed that the application of the retrofit solution considerably increases the shear and the displacement capacities of all the investigated configurations, except for case R-T3 (600 mm thickness) with double-fixed conditions, where the retrofit has an appreciable impact only over the displacement capacity that increases tenfold.

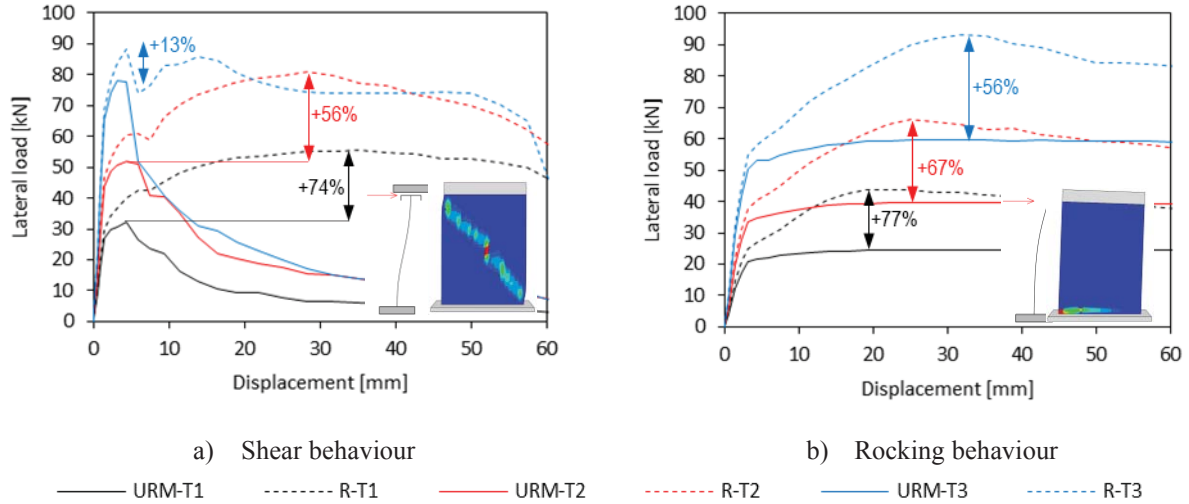
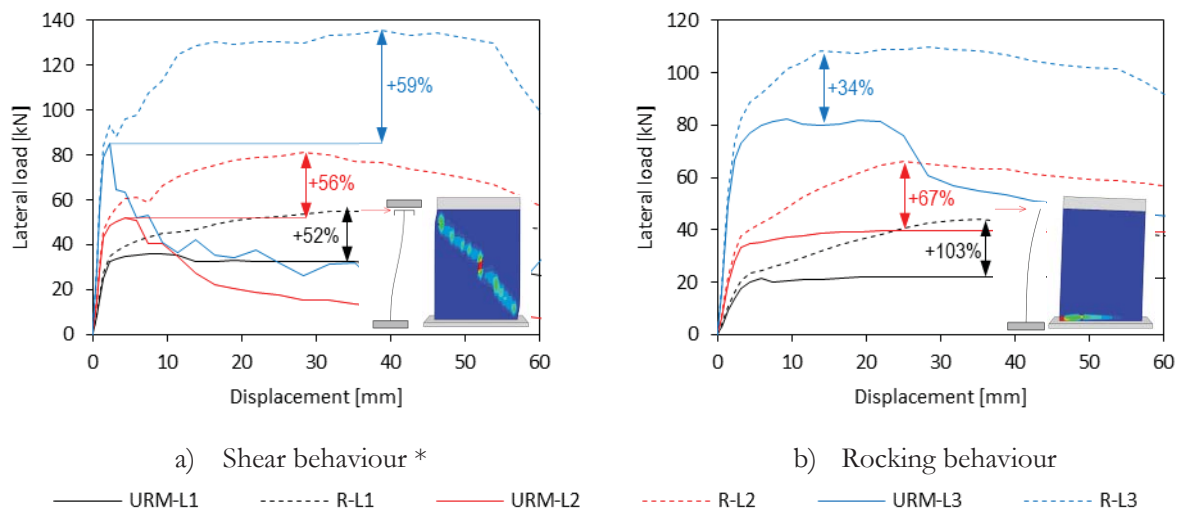


Figure 11: Effectiveness of the CLT panel retrofit solution on URM walls characterized by different thicknesses (base configuration M1, L2, Q1, C1, K1, HD2, AB3).

Figure 12 shows the behaviour of retrofitted masonry walls characterized by different masonry height to length ratios (see Table 3). The retrofit solution resulted to be effective for all the investigated configurations. As expected, the increase of the length to height ratio reduces displacement capacity of the URM walls in the cantilever condition, but it does not affect the displacement capacity of the retrofitted walls. The shorter walls URM-L1 and R-L1 are characterized by rocking failure independently from the boundary conditions adopted, with the retrofit proving to be effective for both wall configurations. The cases L4 and L5 are described in the following section when considering a multi-panel retrofit.



Note: * walls URM-L1 and R-L1 are characterized by a rocking behaviour for both boundary conditions.

Figure 12: Effectiveness of the CLT panel retrofit on URM walls characterized by different aspect-ratios (base configuration M1, T2, Q1, C1, K1, HD2, AB3).

3.2 Behaviour of URM walls retrofitted with multiple timber sub-panels

The dimensions of the CLT panels employed for the wall-retrofit are often subjected to limitation due to transport issue inside the buildings and, consequently, the strengthening of a single wall can be obtained by using two or more “sub-panels” shorter than the wall. In such case, the panel-to-panel connection and the anchoring connections are key aspects in determining the effectiveness of the retrofit solution. The panel-to-panel connection could be achieved by inserting fully threaded timber screws at an angle of 45° to the joint line (e.g. 8 mm diameter screws spaced at 200 mm). This connection was modelled using one-dimensional connector elements calibrated on the experimental outcomes obtained by Hossain et al. [25]. Two panel behaviours were analysed considering different anchoring conditions: the “single panel behaviour” (SPB) (Figure 13a) and the “multi-panel behaviour” (MPB) (Figure 13b). The SPB is characterized by the presence of a hold-down positioned at the two corners of the wall. In such case, the CLT sub-panels behave as a single panel with some interface slip at the panel-to-panel joint due to the screw connection deformability. In the second case (MPB), instead, each sub-panel is anchored at its base with two hold-downs and the CLT panels’ response is more similar to that of independent single panels.

Figure 14 and Figure 15 report the pushover curves of a 3000 mm long URM wall retrofitted with two panels 1500 mm wide, for the SPB and the MPB. Three panel-to-panel connections were studied: no panel-to-panel connection (J0), panel-to-panel screwed connection [25] (shear stiffness 3000 N/mm, tension stiffness 3000 N/mm, shear capacity 6000 N) and rigid connection (JR). As visible from the graphs, the adoption of connection J1 resulted in a higher peak capacity if compared to the case with J0, comparable to the performance obtained with the rigid connection JR. In previous analyses reported in [1], the influence of the panel-to-panel connection was found to be less pronounced. It is worth noting that the analyses in the preliminary study reached drift ratios (≈ 0.2 - 0.3%) smaller than those at which the impact of the panel-to-panel connection observed herein became appreciable. The multi-panel solution was then applied to two squat walls, with length to height ratios of 1.5 and 2.0 (L4 and L5), using respectively 3 and 4 CLT panels 1500 mm wide. The panel retrofit was modelled assuming a SPB which resulted in improvements of the walls’ maximum load-bearing capacities larger than 30%. As expected, the squat walls responded mainly in shear with formation of diagonal cracks. As a consequence, rocking was a secondary mechanism, with the tension forces in the “SPB hold-downs” being smaller than 35 kN for all three configurations L3, L4 and L5. The maximum shear force measured in the angle-brackets was also small (< 30 kN) because of the increased number of angle-brackets (one for each CLT panel).

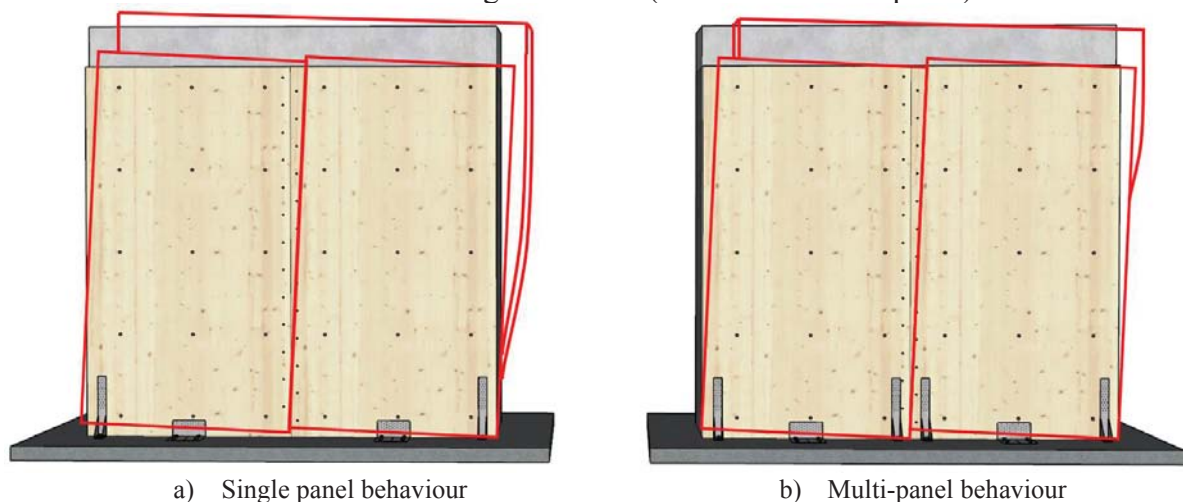


Figure 13: Multi-panel retrofit solutions.

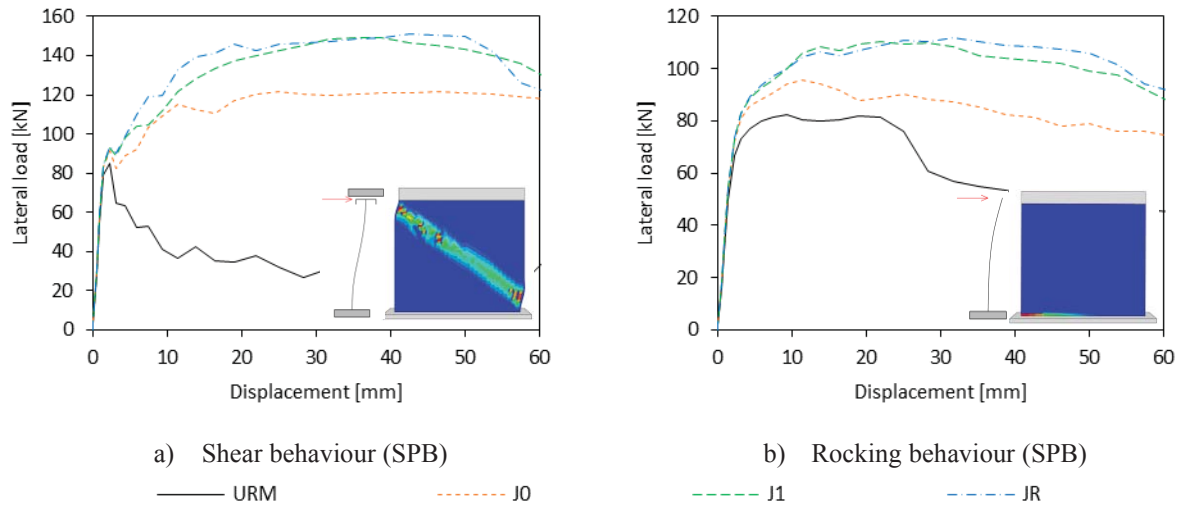


Figure 14: Effectiveness of the CLT panel retrofit solution on URM walls, single panel behaviour (SPB) (base configuration M1, T2, L3, Q1, C1, K1, HD2, AB3).

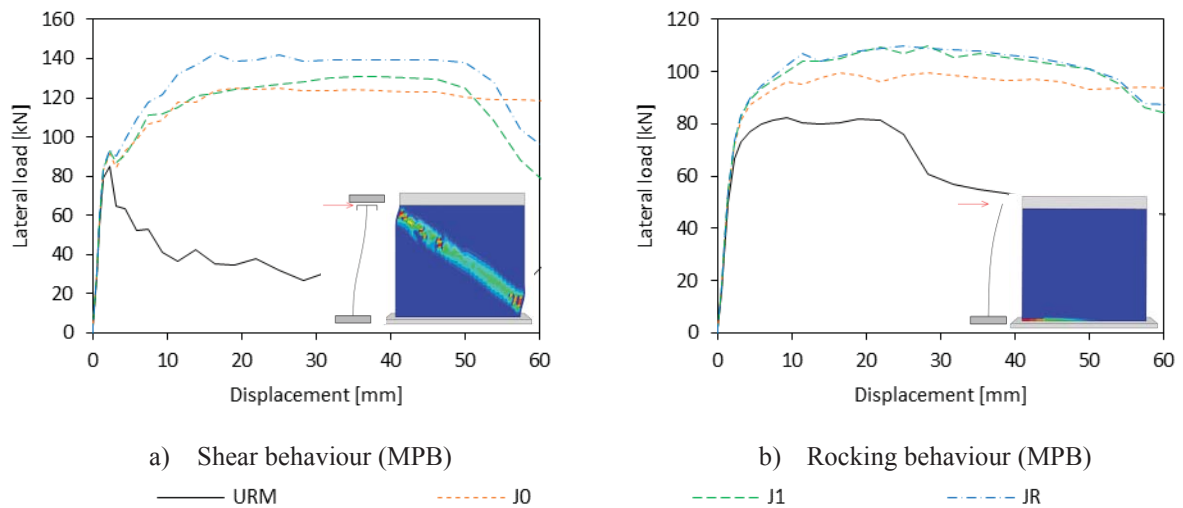


Figure 15: Effectiveness of the CLT panel retrofit solution on URM walls, multi panel behaviour (MPB) (base configuration M1, T2, L3, Q1, C1, K1, HD2, AB3).

3.3 Behaviour of retrofitted masonry walls with openings

The effectiveness of the retrofit when applied to masonry walls with openings was also studied. Two cases were modelled, consisting of two-pier walls with a door opening ($900 \times 2100 \text{ mm}^2$) or a window opening ($900 \times 1000 \text{ mm}^2$, sill height 1100 mm). The piers had the same characteristics of those described previously (M1, T2, L2, Q1, C1, K1, HD2, AB3). The spandrel was modelled without any additional tension-resisting element (no lintel nor concrete ring-beam). Figure 16 gives the response curves of the retrofitted walls. Three retrofit conditions were modelled: 1) R1, where the reinforcement was applied only to the masonry piers; 2) R2 that sees also the reinforcements of the spandrels, but without any connection between the CLT panels, and 3) R3, where the connection between the CLT panels strengthening the piers and the ones fixed to the spandrels was ensured by inclined timber screws, similarly to what reported in the previous section for the panel-to-panel connection. All three

retrofit solutions produced a remarkable increase in the shear capacity of the masonry walls (increase $> 30\%$) with the contribution of the spandrel retrofit being more effective, expectedly, when the panel-to-panel connection is present.

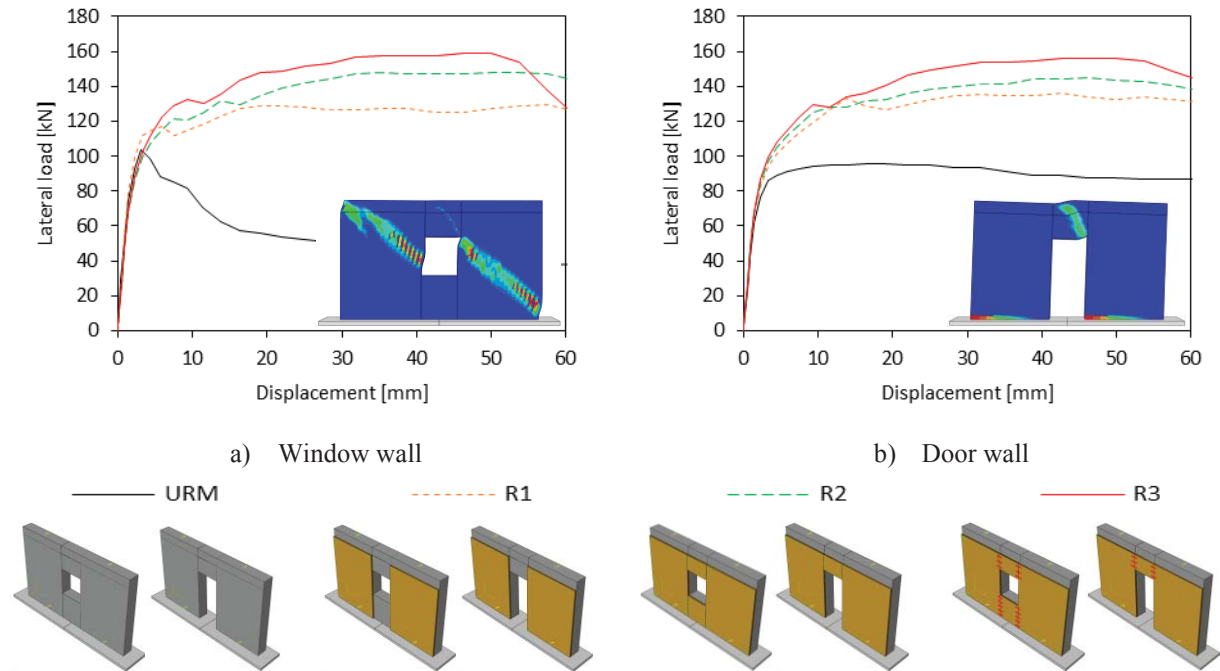


Figure 16: Effectiveness of the CLT panel retrofit solution on URM walls with openings (base configuration M1, T2, Q1, C1, K1, HD2, AB3).

3.4 Behaviour of two-storey retrofitted masonry walls with openings

Figure 17 shows the behaviour of two-storey retrofitted masonry walls. The geometry of such walls was derived from the “Door wall” and the “Window wall” analysed in the previous section, respectively for the first and the second level. The horizontal loading was applied at the diaphragm levels assuming a uniform distribution. The three retrofit configurations R1, R2 and R3 previously introduced for the one-storey walls were evaluated also for the two-storey walls. Three inter-storey force transfer mechanisms were analysed: 1) compression only (IS1); 2) compression and tension (IS2); and 3) compression, tension and shear (IS3). The condition IS1 can be obtained by creating slots in the bottom portion of the CLT panels at the second level, so that direct panel-to-panel contact is possible despite the presence of the diaphragm joists (see Figure 17), while the conditions IS2 and IS3 can be achieved by adding steel plates to transfer the tensile and shear forces. The tension and the shear inter-storey anchors were modelled adopting the force displacement curves of HD2 and AB3. The retrofit solution R3-IS3 resulted to be the most effective (increase of lateral load bearing capacity $> 70\%$) while the response curves of the other cases provided an increase of lateral capacity larger than 25%. All the retrofit solutions also guaranteed a noticeable increase in the displacement capacity.

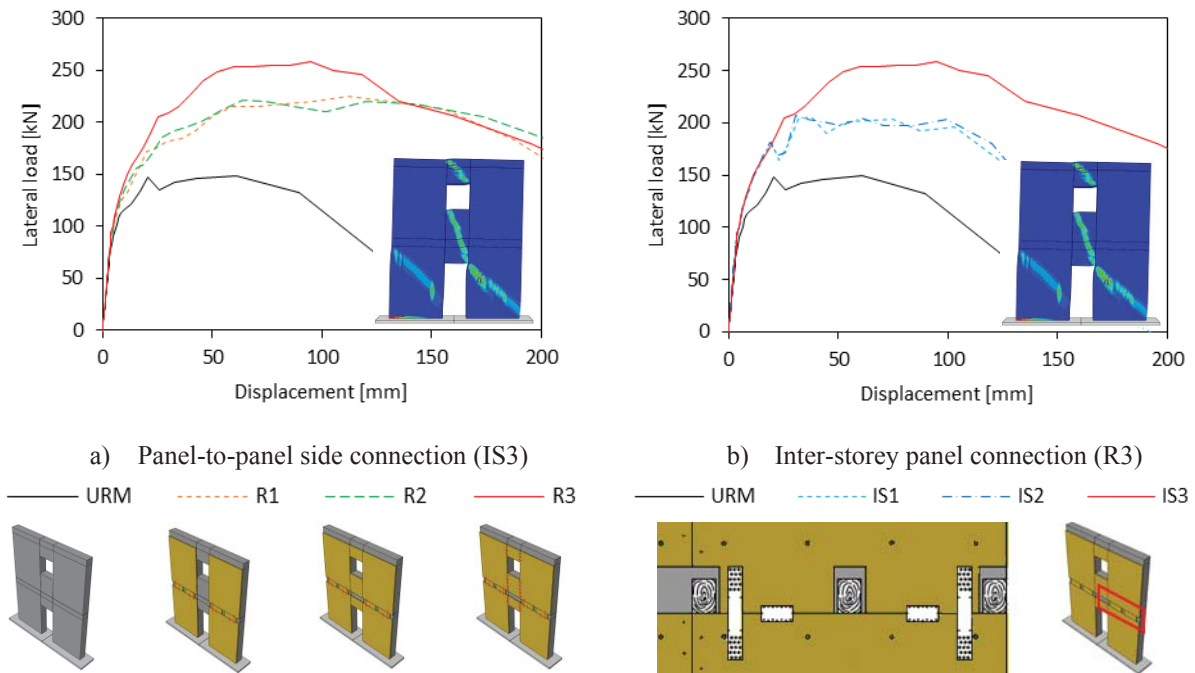


Figure 17: Effectiveness of the CLT panel retrofit solution on two-storey URM walls with openings (base configuration M1, T2, Q1, C1, K1, HD2, AB3).

4 CONCLUSIONS

The effectiveness of a timber based retrofit solution where timber panels are connected to the masonry walls through distributed point-to-point connection was numerically investigated. The parametric study addressed several aspects including masonry properties, wall geometry and boundary conditions, and various retrofit configurations. The results obtained herein confirmed and extended the outcomes of a preliminary numerical study previously reported by the authors. The adoption of a quasi-static approach allowed to investigate the behaviour of the retrofitted walls for a wider deformation range and to obtain further information about the lateral load and displacement capacity. The models described herein, benefitted from the outcomes of recent experimental campaigns that were relied to for the calibration of the properties of the connections and that enabled to obtain more refined results. The following conclusions can be drawn:

- The application of the retrofit technique under study can produce a considerable increase in the in-plane strength and displacement capacity of the masonry walls. The timber panel retrofit resulted to be effective for all the studied URM wall configurations characterized by different masonry properties, geometries, stress levels and boundary conditions. The increase in load bearing capacity of masonry walls up to 40 cm thick, ranged from $\approx 25\%$ to $\approx 100\%$. Regarding the displacement capacity, all wall-configurations reached drift values (top displacement/wall height) larger than 1.5%.
- The connection system to anchor the panels to the foundation or to transfer inter-storey forces was confirmed to play a major role in determining the retrofit effectiveness. The best performance was achieved in those configurations where the anchoring/interstorey connection system allowed transferring of compressive, tensile and shear loads (increase of wall shear capacity up to 90%). Expectedly, the properties of the hold-downs (tension anchors) were most influential when the walls showed a rocking behaviour, while the

properties of the angle brackets (shear anchors) were most relevant for squat walls with marked shear behaviour. In the case of walls exhibiting diagonal cracking, the timber panel strengthening generated a noticeable increase in the wall displacement capacity even in the absence of any anchoring device.

- An effective *timber panel-to-masonry* connection can be achieved by installing both dry and adhesive point-to-point fasteners. Fasteners with higher stiffness were found to produce minor yet visible improvements to the intervention effectiveness independently from the wall failure mode. However, the choice of the type of fastener should not prescind from considerations on the masonry type, with adhesive connections being recommended for irregular masonry with thick mortar joints. The parametric study on the fastener numbers and layout showed that 4 connectors per square meter of wall-surface can be considered as sufficient.
- In case of long walls, the application of the timber-based strengthening can be facilitated by installing multiple sub-panels shorter than the wall, without any detriment to the overall effectiveness. In fact, when screwed panel-to-panel connection was provided and when the “timber coating” was anchored at its base by two hold-downs and by an angle-bracket for every timber sub-panel the result was consistent with that obtained employing a single CLT panel as long as the masonry wall.
- Predictably, the strengthening of the spandrels can further increase the performance of the retrofit solution (+50-70% in wall strength with reference to the configuration where only the piers are strengthened) especially when a *spandrel-panel to wall-panel* connection is ensured, and when the number of storeys increases and accentuates the spandrel role in coupling the piers.

ACKNOWLEDGEMENTS

The research work was carried out within the framework of the 2019-2021 ReLUIS-DPC network (Italian University Network of Seismic Engineering Laboratories and Italian Civil Protection Agency).

REFERENCES

- [1] I. Giongo, G. Schiro, M. Piazza, On the use of timber-based panels for the seismic retrofit of masonry structures. F. M. Mazzolani, A. Lamas, L. Calado, J. M. Proenca, B. Faggiano eds. *In Proceedings of the 3rd International Conference on Protection of Historical Constructions*, Lisbon, Portugal, 2017.
- [2] I. Giongo, E. Rizzi, D. Riccadonna, M. Piazza Onsite testing of masonry shear walls strengthened with timber panels. *Structure and buildings*, 2021.
- [3] A. Borri, R. Sisti, M. Corradi, Combined Reinforcement of Rubble Stone Walls with CLT Panels and Steel Cords, *Structures and Buildings*, 2021.
- [4] L. Pozza, L. Marchi, D. Trutalli, R. Scotta, In-plane strengthening of masonry buildings with timber panels. *Structures and Buildings*, 2021.

- [5] D. Riccadonna, I. Giongo, G. Schiro, E. Rizzi, M. A. Parisi, Experimental shear testing of timber-masonry dry connections for the seismic retrofit of unreinforced masonry shear walls. *Construction and Building Materials*, 52-72, 2019.
- [6] E. Rizzi, I. Giongo, D. Riccadonna, M. Piazza, Testing of irregular stone masonry strengthened with cross-laminated timber. *Prohitech 2020, 4th International Conference on Protection of Historical Constructions*. Athens ,2021.
- [7] M. Giaretton, D. Dizhur, J. M. Ingham, Shaking table testing of as-built and retrofitted clay brick urm cavity-walls. *Engineering Structures*, 70-79, 2016.
- [8] D. Dizhur, M. Giaretton, I. Giongo, J. Ingham, Seismic retrofit of masonry walls using timber strong-backs, *SESOC Journal*, vol. 30, No.2, 2017.
- [9] D. Cassol, I. Giongo, J. Ingham, D. Dizhur, Seismic out-of-plane retrofit of URM walls using timber strong-backs. *Construction and Building Materials*, 2021.
- [10] G. Guerrini, N. Damiani, M. Miglietta, F. Graziotti, Cyclic response of masonry piers retrofitted with timber frames and boards. *Structures and Buildings*, 2021.
- [11] I. Sustersic, B. Dujic, Seismic Strengthening of Existing Buildings with Cross Laminated Timber Panels, *WCTE*, Auckland, New Zealand, 2012.
- [12] I. Sustersic, B. Dujic, Seismic shaking table testing of a reinforced concrete frame with masonry infill strengthened with cross laminated timber panels, *WCTE*, Quebec City, Canada, 2014.
- [13] F. Smirollo, I. Giongo, M. Piazza, Seismic retrofit of masonry infilled frames by using timber panels, *In 17th word conference on Earthquake engineering, 17WCEE*, Sendai, Japan, 2020.
- [14] ABAQUS Computer Software (v.9.12) and user's manual. *Simulia*, Dassault Systemes.
- [15] J. Lubliner, J. Oliver, S. Oller, E. Oñate, A plastic-damage model for concrete. *International Journal of Solid and Structures*, vol 25, 299-326, 1989.
- [16] J. Lee, G. L. Fenves, Plastic-damage model for cyclic loading of concrete structures. *Journal of Engineering Mechanics*, vol 124, no. 8, 892-900, 1998.
- [17] P. Lourenco, Structural masonry analysis: recent developments and prospects, *Proceedings of the 15th International brick & brick masonry conference*, Sydney, Australia, 1341-1356, 17-20 February 2008.
- [18] UNI EN 338, Structural timber – Strength classes, *European Committee for Standardization*, Brussels, 2016.
- [19] N. Gattesco, C. Amadio, C. Bedon, Experimental and numerical study on the shear behavior of stone masonry walls strengthened with GFRP reinforced mortar coating and steel-cord reinforced repointing, *Engineering and Structures*, 143-157, 2015.
- [20] Applied Technology Council, FEMA 306 Evaluation of earthquake damaged concrete and masonry wall buildings, *Federal Emergency Management Agency*, 1998.
- [21] M. Piazza, T. Sartori, Caratterizzazione meccanica attraverso prove monotone e cicliche dei principali dispositivi di connessione utilizzati negli edifici multipiano in legno. *ReLUI5 2015-PR4_Allegato_01-UR_UNITN*, 2015.

- [22] I. Gavric, A. Ceccotti, M. Fragicomo, Experimental cyclic tests on cross-laminated timber panels and typical connections, *ANIDIS*, Bari, 2011.
- [23] Smioldo F., Gaspari A., Viel D., Piazza M., Giongo I.: High performance connections to mitigate seismic damage in cross laminated timber (CLT) structures. *In 17th World Conference on Earthquake Engineering, 17WCEE*, Sendai, Japan, 2020.
- [24] DM 17/01/18. (2008). Norme Tecniche per le Costruzioni – NTC 2008. *Ministero delle infrastrutture*, Italy, 2018.
- [25] A. Hossain; I. Danzig, T. Tannert, Cross-Laminated Timber Shear Connections with Double-Angled Self-Tapping Screw Assemblies, *J. Struct. Eng.*, 2016.

OPTIMIZATION OF EMPIRICAL SEISMIC VULNERABILITY ASSESSMENT FOR MASONRY BUILDINGS FOLLOWING NONLINEAR ANALYSIS

E. Onescu¹, I. Onescu², and M. Mosoarca²

¹ Faculty of Architecture and Urban Planning, Polytechnic University of Timisoara, Romania
Piata Victoriei nr. 2
e-mail: eugen.eugen@student.upt.ro

² Urban Planning and Architecture Research Center, Polytechnic University of Timisoara, Romania
Traian Lalescu 2A
e-mail: iasmina.onescu@upt.ro, marius.mosoarca@upt.ro

Abstract

Timisoara is the most important city located in Banat seismic area, characterized by shallow earthquakes of crustal type and was selected to be European Capital of Culture 2021. The majority of the historical buildings are made in masonry, with masonry vaults and wooden floors.

First part of the paper presents a quick and simplified empirical methodology based on European studies. The second part presents a detailed mechanical nonlinear analysis obtained for some of the most important historical buildings in Timisoara, based on complete survey and site inspection. Moreover, the authors present a direct correlation between the empirical and the mechanical seismic vulnerabilities. In the end, based on the correlation results, there is presented the proposed empirical seismic vulnerability assessment methodology for the near-field events. The methodology considers the specific failure mechanism for buildings with same characteristics and the particularities of Banat seismic area.

The proposed methodology aims to adapt the quick and simplified empirical methodology to the near-field earthquakes effects. This could serve for quick and simplified assessment of seismic vulnerability for any building with similar mechanical, geometrical, architectural and urbanistic characteristics as the case study buildings, in areas with earthquakes similar to those specific to Banat seismic area. This kind of study could provide a better knowledge for the local authorities, helping them to develop or improve earthquake mitigation plan and to define new earthquake engineering design recommendations.

Keywords: masonry, earthquake, vulnerability assessment, history, nonlinear analysis

1 INTRODUCTION

1.1 Case study area

Seismic vulnerability assessment represents an interdisciplinary task than can offer valuable tools for the risk reduction policies at a municipal level. The lack of seismic design rules at the moment of design or the lack of proper consolidation work during the lifetime of the buildings has led to an increase in the seismic risk of historic urban centers. The seismic risk can be divided into the sum of three elements, such as hazard, vulnerability, and exposure [1]. This paper aims to evaluate the seismic vulnerability of some historical masonry building and adapt an existing European vulnerability assessment methodology to the particularities of the site.

The Banat region represents an important area located in the western part of Romania. The biggest city in the Banat region is Timisoara, that was first recognized in 1177 as the “Fortress of Timis,” after the main nearby river [2]. After several administrations, such as Ottoman, Habsburgic, and Austro-Hungarian, the city developed into an important commercial and defensive pole, presenting a bastionary fortification system in Vauban architectural style, as shown in Figure 1 [2].



Figure 1: The bastionary fortification system for Timisoara city [2]

The most important historical area of the town is the Cetate district, located in the interior contour of the fortification, followed by two other districts, Iosefin and Fabric, which appeared outside the defensive walls, as presented in Figure 2 [3].

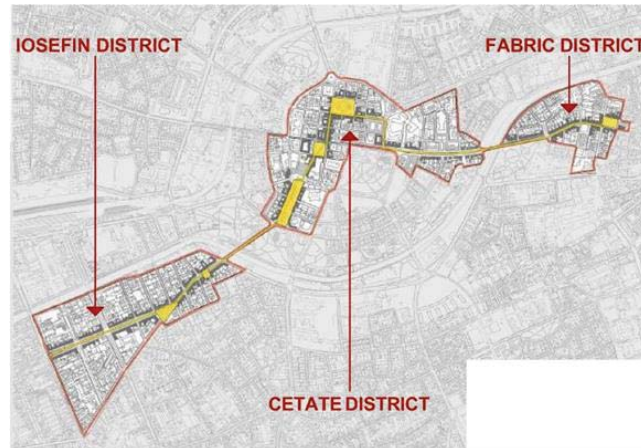


Figure 2: The three historic districts of Timisoara city [3]

The case study area in this paper is Fabric historic district, which appeared at first as a residential area for the craftsman. The streets are both rectangular and organic, with widths between 10 and 16 meters, and the buildings are made in masonry. Despite the industrial aspect of the area, the existing succession of public squares increases the quality of life in the area. An image from 1901 with the character of the district is illustrated in Figure 3 [2].



Figure 3: The spirit of Fabric district in 1901 [2]

1.2 Seismicity of the area

The determination of the seismic hazard for a specific area represents a difficult task, than can be achieved through both probabilistic and deterministic methods. At a global level, there was made a seismic hazard map, as presented in Figure 4 [4].

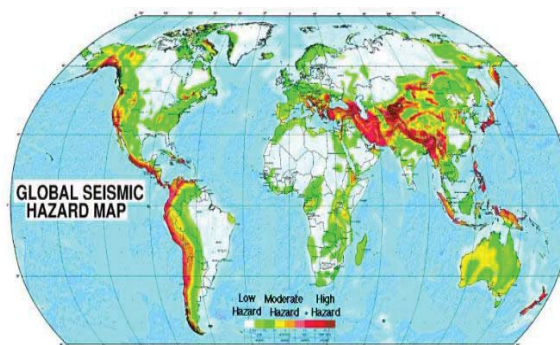


Figure 4: Seismic hazard map at a global level [4]

In Romania, there are two seismic areas, Vrancea and Banat. Vrancea is the most important seismic region, characterized by strong earthquakes with magnitudes around $M_w = 7.0$ of intermediate depth. Less dangerous earthquakes characterize the Banat region, with magnitudes around $M_w = 5.6$ of crustal type, with focal depths between 1 and 35 km [5]. The general seismicity of Romania, faults, and past seismic events is presented in Figure 5 [6].

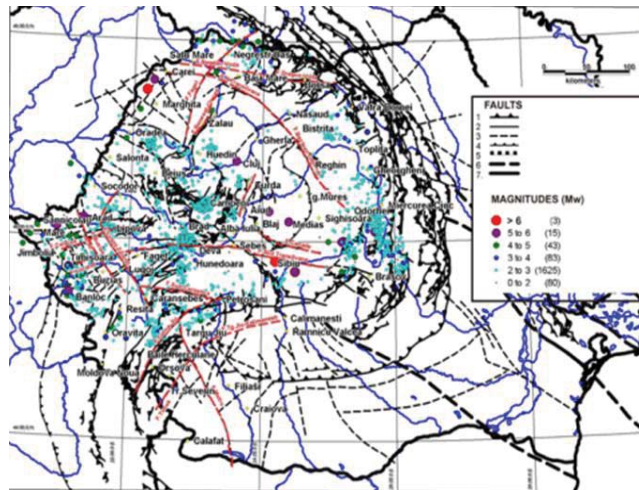


Figure 5: The location of the seismic faults and past earthquakes in Romania [6]

In Timisoara city, there are two active seismic faults located at less than 10 km from the city center, as shown in Figure 6 [3].

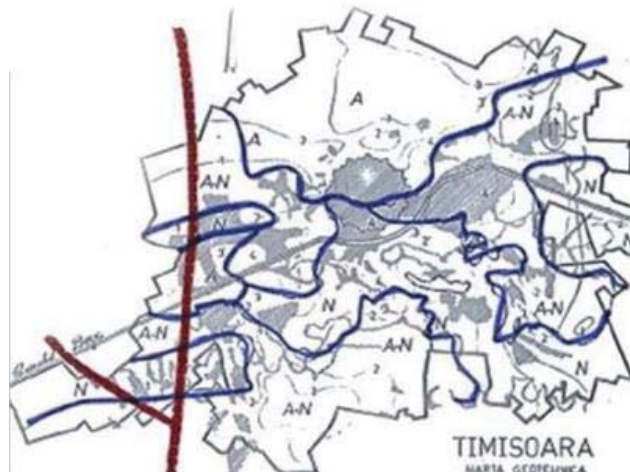


Figure 6: The location of the two active seismic faults in Timisoara [3]

The strongest seismic event registered in Banat area was the earthquake from 1991, in Banloc city, at less than 40 km from Timisoara, with a magnitude $M_w = 5.5$ and a focal depth of 11 km, followed by a strong aftershock of a magnitude $M_w = 5.3$ and a focal depth of 5 km [7]. After the event, there were registered damages, especially to attics, arches, lintels, and chimneys, as presented in Figure 7 [3],[8].



Figure 7: Damages to masonry buildings in the epicenter after Banloc earthquake, 1991 [3], [8]

There were observed both in-plane and out-of-plane failure mechanisms. The in-plane mechanism that can be noticed is mostly the diagonal shear cracking, especially in the façade masonry walls. Also, the vertical cracks can be seen due to the presence of strong vertical forces and L and R surface waves. Following the on-site observation, there was defined a specific failure mechanism for historic masonry buildings located in the near-field areas, after earthquakes of crustal type, as illustrated in Figure 8 [9].

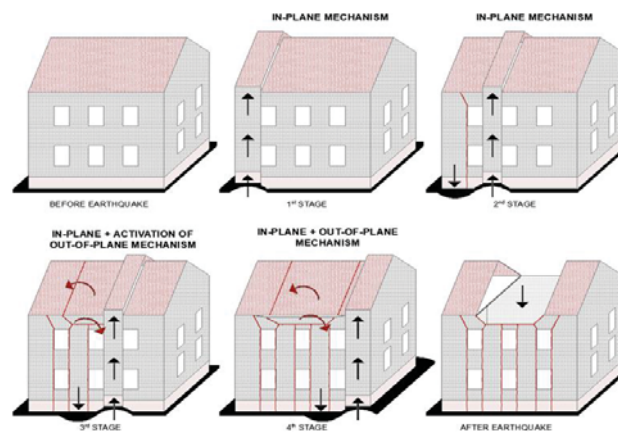


Figure 8: The specific failure mechanism for historic masonry buildings in the near-field areas similar to Banloc seismic region [9]

When the real observed damages were compared with the EMS-98 damage scale for masonry buildings [10], there was noticed the fact that the real damage was around damage state D2-D3, as shown in Figure 9 [9].

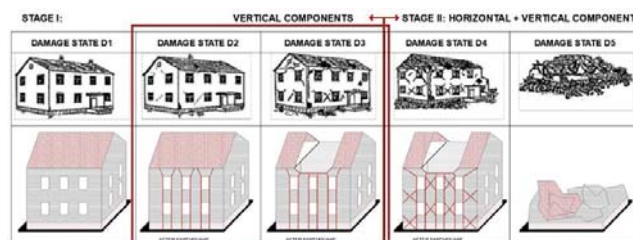


Figure 9: Correlation between EMS-98 damage scale and real damage observed after Banloc earthquake, 1991 [9]

For Timisoara city, there can be generated an expected damage scenario, similar to the one that occurred in Banloc area. The peak ground acceleration for Timisoara is considered to be 0.20g after the Romanian design code [11]. Following a simplified correlation law presented in Equation (1), there was determined that the most probable macroseismic intensity for the area is IX EMS-98, as shown in Figure 10 [12].

$$\ln(\text{PGA}) = 0.24 \times I_{\text{EMS-98}} - 3.9 \quad (1)$$

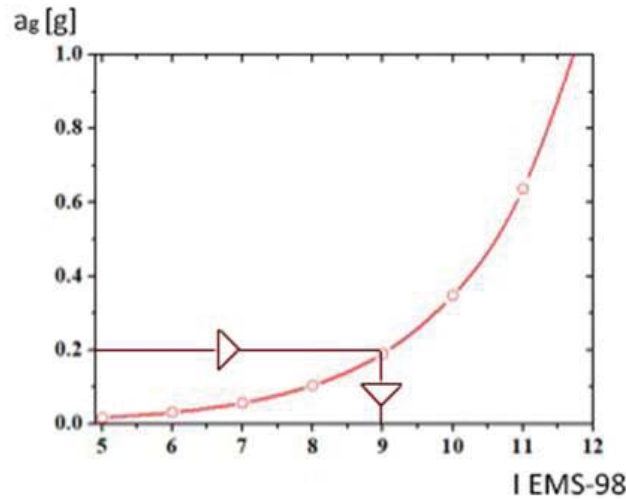


Figure 10: Correlation between EMS-98 damage scale and real damage observed after Banloc earthquake, 1991 [12]

1.3 Case study buildings

The investigated buildings are considered to be representative of the area, from all existing height regimes. Their location is presented in Figure 11 [13].



Figure 11: Location of the case study buildings [13]

In the area, there can be noticed that almost all buildings present the basement, while the minimum height regime is basement and ground floor, and the biggest is a basement, ground floor and two levels. The structural system of all investigated buildings is the masonry of burnt clay brick and lime. The buildings are located with the longest dimension along the main street, presenting massive façade and intermediate walls with thicknesses from 80 centimeters in the basement and 40 centimeters on the last floor. The transversal walls are not connected with the façade walls in most of the cases and are much thinner, around 15 centimeters [3], [14].

The horizontal structural systems are masonry vaults above the basement and sometimes ground floor and wooden floors for the other levels. There can be noticed, in many cases, a very tall complex wooden framework for the roof structure [3], [14].

The six selected buildings for investigation are presented in Figure 12 [13].



Figure 12: The six selected buildings for further investigation [13]

2 EMPIRICAL SEISMIC VULNERABILITY ASSESSMENT

2.1 Description of the existing methodology

The empirical methodologies represent a useful tool for a quick and simplified seismic vulnerability assessment that can also be applied at an urban scale [15].

The existing methodology that is used in this paper was proposed at first by Benedetti and Petrini [16] and was later developed by Mazzolani and Formisano [17].

The procedure is simple, based on visual inspection that leads to the fulfillment of an investigation form (Fig. 13), in which for several parameters, there is assigned a score for each possible situation. The parameters are in a number of 10 when the building is considered as isolated structural unit and 15 when there is also considered the influence of the adjacent buildings from the aggregate. For each parameter, there is also assigned a weight that illustrates its importance. All parameters and their associated weight are used following the existing Italian methodology [17]. The vulnerability index represents the sum of each parameter, whit the class score and weight assigned, following Equation (2) [9].

$$I_v = \sum s_i \times w_i \quad (2)$$

No	Factor	Class				Weight
		A	B	C	D	
1	Organization of vertical structures	0	5	20	45	1
2	Nature of vertical structures	0	5	25	45	0.25
3	Location of the building and type of foundation	0	5	25	45	0.75
4	Distribution of plan resisting elements	0	5	25	45	1.5
5	Plain regularity	0	5	25	45	0.5
6	Vertical regularity	0	5	25	45	1
7	Type of floors	0	5	15	45	1
8	Roofing	0	15	25	45	0.75
9	Details	0	0	25	45	0.25
10	Physical conditions	0	5	25	45	1
11	Presence of adjacent buildings with different height	-20	0	15	45	1
12	Position of the buildings in the aggregate	-45	-25	-15	0	1.5
13	Presence and number of staggered floors	0	15	25	45	0.5
14	Effect of either structural or typological heterogeneity among adjacent structural unit	-15	-10	0	45	1.2
15	Percentage difference of opening area among adjacent façade	-20	0	25	45	1

Figure 13: Empirical vulnerability form [9]

After the determination of the vulnerability index, the index is normalized in the range of 0÷1, following Equation (3) [9].

$$V = (I_V - I_{V \text{ MIN}}) / (I_{V \text{ MAX}} - I_{V \text{ MIN}}) \quad (3)$$

The last step in the process of determination of the empirical seismic vulnerability is the damage estimation, where following the normalized vulnerability index, there can be estimated the mean damage grade and the expected damage state, following Equation (4). The correlation between the mean damage grade and expected damage level is illustrated in Figure 14 [18].

$$\mu_D = 2.5 \{1 + \tanh[(I + 6.25V - 13.1)/\Phi]\} \quad (4),$$

where I represents the macroseismic intensity, V is the normalized vulnerability index and Φ is the factor that modifies the vulnerability curve slope and is considered equal to 2.3 for residential buildings [19].

μ_D	Damage state	Most probable degradation level
0.0-1.5	D1	Slight (no structural damage, slight non-structural damage)
1.5-2.5	D2	Moderate (slight structural damage, moderate non-structural damage)
2.5-3.5	D3	Substantial to heavy (moderate structural damage, heavy non-structural damage)
3.5-4.5	D4	Very heavy (heavy structural damage, very heavy non-structural damage)
4.5-5.0	D5	Destruction (very heavy structural damage)

Figure 14: Correlation between mean damage grade and expected level of damage [18]

2.2 Results of the applied existing methodology

The application of the empirical seismic vulnerability has led to a series of vulnerability indexes for ten and 15 parameters, as presented in Table 1.

Building	I_{V10}	I_{V15}
1	68.75	98.75
2	108.75	110.25
3	98.75	61.25
4	93.75	118.75
5	113.75	66.75
6	130	160

Table 1. Vulnerability indexes for the six investigated buildings

Following the determined vulnerability indexes, there were also designed the vulnerability curves, as presented in Figure 15 for buildings considered as isolated and in Figure 16 for buildings considered in aggregate. The comparison between the mean vulnerability curves for both situations is illustrated in Figure 17.

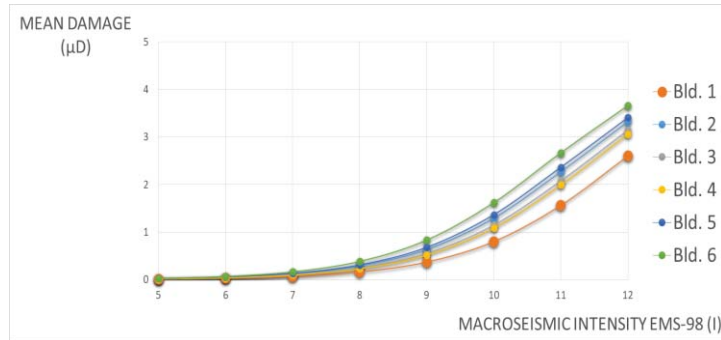


Figure 15: Empirical vulnerability curve for the six investigated buildings considered as isolated structural units

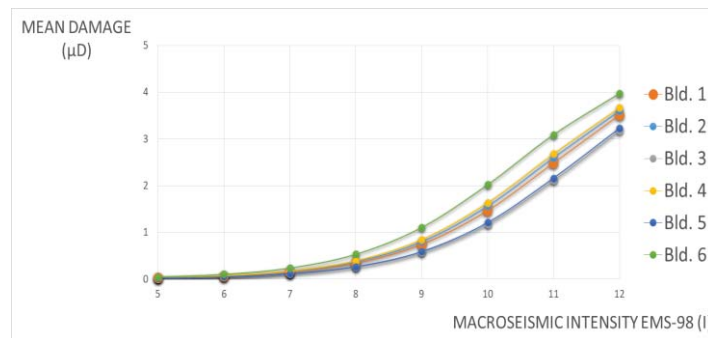


Figure 16: Empirical vulnerability curve for the six investigated buildings considered in aggregate

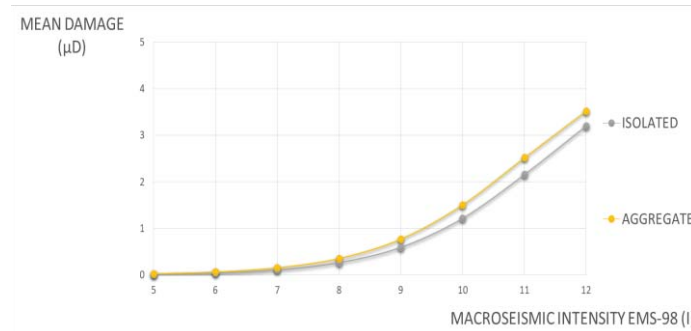


Figure 17: Comparison between mean vulnerability curves for both isolated and aggregate situations

The results illustrate a low vulnerability for a macroseismic intensity IX EMS-98, according to the most probable seismic scenario, in the range of damage state D1 for both situations, which means no expected damages.

Considering the real damages observed in Banloc in a similar situation, in the ranges of D2-D3, there is highlighted the need for performing nonlinear analysis to adapt the empirical methodology for near-field effect.

3 MECHANICAL SEISMIC VULNERABILITY ASSESSMENT

3.1 Nonlinear analysis

The numerical analysis represents a more precise tool in the process of seismic vulnerability assessment, indicating the weakest points of the structure [20].

The pushover analysis was obtained with Tremuri software and investigated the in-plane failure mechanism for the six investigated buildings, considered as isolated structural units. There was used the local seismic spectrum for Banat region, as illustrated in Figure 18 [21] while the mechanical proprieties for the masonry structures were determined following experimental tests and other technical expertise for similar buildings, as illustrated in Table 2 [3].

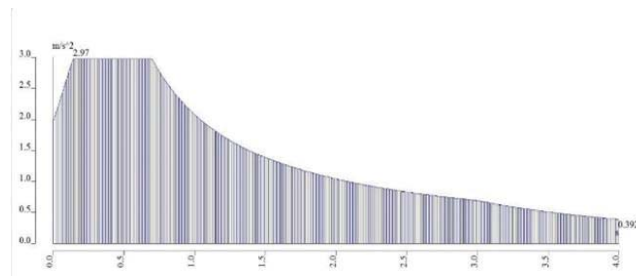


Figure 18: The local spectrum for Banat seismic region [21]

	f_k [N/mm ²]	f_{vk0} [N/mm ²]	E [N/mm ²]	G [N/mm ²]	Density [kg/m ³]
URM	2.35	0.06	2350	940	1800

Table 2. Mechanical proprieties for the masonry structures

The analysis made with Tremuri is a simplified analysis, appropriate for the investigation of more than one building, and can be used for historical masonry buildings. It has revealed the expected cracks damage distribution, as presented in Figure 19 [13].

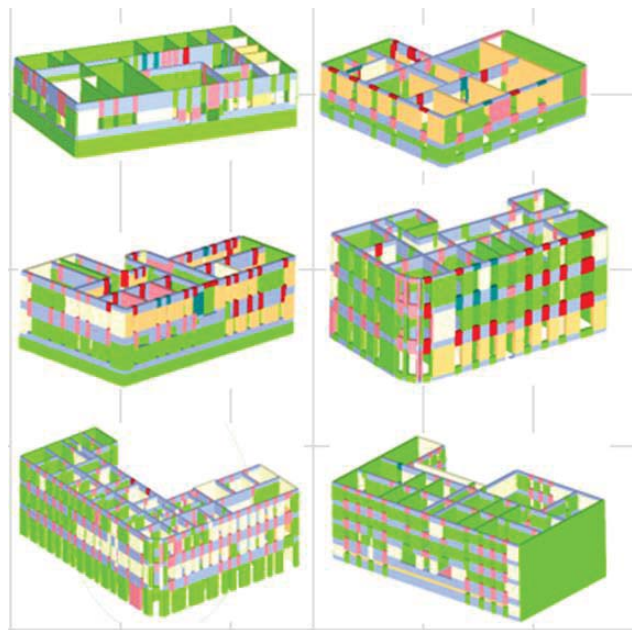


Figure 19: Cracks and failures to the six investigated buildings after pushover analysis [13]

The pushover analysis has revealed that the buildings would suffer both nonstructural and structural damages for the considered seismic scenario, around damage states D2-D3. In Table 3, there are presented the yielding and ultimate displacement and also the maximum shear forces [13].

Bld. No.	Yielding displacement Δ_y [cm]	Maximum shear force V [kN]	Ultimate displacement Δ_u [cm]	Interstorey drift [%]
1	0.08	3482	0.28	0.040
2	0.14	966	0.62	0.107
3	0.04	4006	0.12	0.113
4	0.79	2735	2.84	0.318
5	0.60	5309	1.74	0.160
6	0.54	15096	1.74	0.220

Table 3. Displacements, shear forces and interstorey drift for the six investigated buildings [13]

According to the interstorey drift values, there can also be estimated the most probable damage state for each investigated building, following Table 4 [13].

URM	Damage state D2	Damage state D3	Damage state D4	Damage state D5
	$ID < 0.1\%$	$0.1\% < ID < 0.3\%$	$0.3\% < ID < 0.6\%$	$0.6\% < ID$

Table 4. Correlation between interstorey drift values and most probable damage state [13]

3.2 Conclusion of the numerical analysis

The results indicated by the pushover analysis highlight the possibility of an appearance of cracks and failures due to bending forces, especially to the lintels at the upper part of the buildings. Also, there can be noticed, in some cases, cracks and failures due to shear forces at the spandrels also located on the top floors. These aspects indicate a general damage state of D2-D3 for all six investigated buildings.

Also, the investigation of the interstorey drift values indicates the same damage states D2-D3 for all six investigated buildings.

The two aspects previously presented suggest that the existing empirical seismic vulnerability assessment methodology tends to underestimate the real vulnerability of historic masonry buildings located in the near-field areas.

In this case, an adaptation is necessary to be able to provide precise and quick results at an urban scale for similar buildings located in seismic regions with characteristics similar to Banloc region.

Because the existing methodology is well-used at the European scale, there is proposed to keep it in the original form and modify only the damage estimation formula.

4 NEW PROPOSED EMPIRICAL METHDOLOGY FOLLOWING NONLINEAR ANALYSIS

4.1 New proposed damage estimation formula

The investigation of real damages after past earthquakes in similar areas and on similar buildings have illustrated considerable damages to structural elements, without affecting the bearing capacity of the structure, so a damage state of D2-D3.

The same probable damage state was indicated by the nonlinear analysis obtained with Tremuri software and also, by the investigation of the interstorey drift values obtained following the pushover analysis.

Both visual and numerical investigation revealed the fact that, for a macroseismic intensity of IX EMS-98, there is the need to adapt the damage estimation formula.

This adaptation could provide the necessary tools for correctly assessing the seismic vulnerability of historic masonry buildings in the near-field areas, similar to Banloc region, in a quick and simplified way.

The first part of the methodology, regarding the fulfillment of the vulnerability form and determination of the vulnerability index and implicitly the normalized vulnerability index, are proposed to remain precisely in the original structure. There is recommended to modify just one parameter from the damage distribution formula (Equation 4), the parameter that influences the slope of the vulnerability curve. The new proposed damage estimation formula is presented in Equation (5) [13].

$$\mu_D = 2.5 \{1 + \tanh[(I + 12.5V - 13.1)/\Phi]\} \quad (5),$$

where I represents the macroseismic intensity, V is the normalized vulnerability index and Φ represents the parameter of the curve's slope, equal with 2.3 for residential buildings.

4.2 New vulnerability curves following the proposed damage estimation formula

Following the new proposed damage estimation formula, there were redesigned the vulnerability curves for the six investigated buildings, as illustrated in Figure 20 and Figure 21.

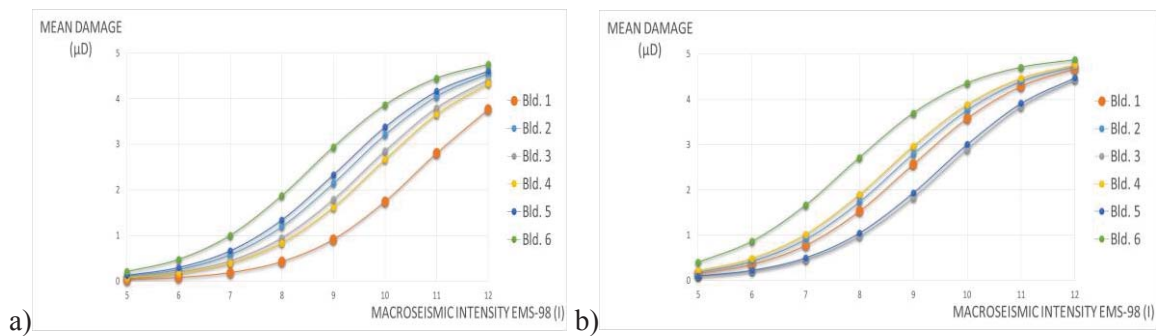


Figure 20: New empirical vulnerability curve for the six investigated buildings after proposed damage estimation formula considered: a) as isolated structural units; b) in aggregate condition

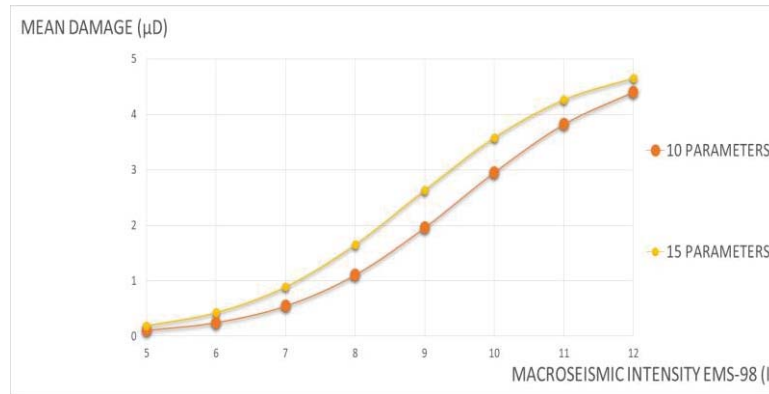


Figure 21: New comparison between mean vulnerability curves for both isolated and aggregate situations, following proposed damage estimation formula

5 CONCLUSION

The new results are in accordance with the real damages observed after the Banloc earthquake from 1991 and also with the results of the numerical analysis.

This aspect indicates the fact that the proposed damage estimation formula is appropriate for assessing the seismic vulnerability for historic masonry buildings located in the near-field areas similar to Banloc seismic region.

The most probable damage states of D2-D3 indicates a medium vulnerability for the investigated buildings that can be dangerous for the historic areas of Timisoara city. There is a high possibility of having significant damages to nonstructural elements and moderate damages to structural ones, but without affecting the bearing capacity of the structures. Because all the buildings are in protected areas, there is highlighted the possibility of losing irreplaceable cultural, architectural-artistic and urbanistic valuable elements.

The new proposed damage estimation formula could help provide quick and accurate vulnerability curves for historic masonry building with similar characteristics to the ones in Timisoara city, that are located in seismic regions with the same proprieties with Banloc area.

REFERENCES

- [1] A. Formisano, *Expected Seismic Risk in a District of the Sant'antimo's Historical Centre*, Trends in Civil Engineering and its Architecture, vol. 2, no. 1, 2018.
- [2] M. Opris, *Timisoara - mica monografie urbanistica*, In Romania. Bucuresti: Editura Tehnica, 1987.
- [3] M. Mosoarca, I. Onescu, E. Onescu, B. Azap, N. Chieffo, and M. Szitar-Sirbu, *Seismic vulnerability assessment for the historical areas of the Timisoara city, Romania*, Engineering Failure Analysis, vol. 101, pp. 86–112, Jul. 2019.
- [4] J. Oluwatobi et al., *Review of world earthquakes*, International Journal of Civil Engineering and technology, vol. 9, issue 9, pp. 440-464, 2018.
- [5] E. Oros and M. Diaconescu, *Recent vs. historical seismicity analysis for Banat seismic region (western part of Romania)*, Mathematical Modelling in Civil Engineering, vol. 11, no. 1, pp. 1–10, 2015.
- [6] A. Bala and V. Raileanu, *Crustal seismicity and active fault systems in Romania*, International Multidisciplinary Scientific GeoConference Surveying Geology and Mining Ecology Management, SGEM, vol. 3, no. 1, pp. 799–806, 2015.

- [7] E. Oros, *Macroseismic and instrumental seismicity of the Banat Region and its significance on the local seismic hazard and risk*, in Proc. and CD-Rom of the “Thirty Years from the Romania Earthquake of March 4, 1977” Symposium, 2007.
- [8] IPROTIM, *Banloc earthquake report*, unpublished, 1992.
- [9] M. Mosoarca, I. Onescu, E. Onescu, and A. Anastasiadis, *Seismic vulnerability assessment methodology for historic masonry buildings in the near-field areas*, Engineering Failure Analysis, 2020.
- [10] R. P. Borg, M. Indirli, T. Rossetto, and L. A. Kouris, *L’Aquila earthquake April 6th, 2009: the damage assessment methodologies*, in COST Action C26 “Urban Habitat Constructions Under Catastrophic Events,” 2010.
- [11] Ministry of regional development public administration and european funds, *Romanian Design Code P100-1/2013*, in Romanian, 2013.
- [12] N. Chieffo and A. Formisano, *The Influence of Geo-Hazard Effects on the Physical Vulnerability Assessment of the Built Heritage: An Application in a District of Naples*, Buildings, vol. 9, no. 1, p. 26, 2019.
- [13] I. Apostol, *Seismic vulnerability of historical centers*, Ph.D. Thesis, Polytechnic University of Timisoara, 2020, unpublished
- [14] I. Apostol et al., *Solutions for improving seismic vulnerability of historic masonry buildings*, in Modern Technologies for the 3rd Millennium, 2018, pp. 131–136.
- [15] G. Calvi, R. Pinho, G. Magenes, J. Bommer, L. Restrepo, and H. Crowley, *Development of Seismic Vulnerability Assessment Methodologies over the Past 30 Years*, ISET Journal of Earthquake Technology, vol. 43, no. 472, pp. 75–104, 2006.
- [16] D. Benedetti and V. Petrini, *On the seismic vulnerability of masonry buildings: an evaluation method* (in Italian), L’Industria delle Costruzioni, vol. 149, pp. 66–74, 1984.
- [17] A. Formisano, R. Landolfo, F. Mazzolani, and G. Florio, *A quick methodology for seismic vulnerability assessment of historical masonry aggregates*, COST Action C26: Urban Habitat Constructions under Catastrophic Events, no. September, 2010.
- [18] B. Azap, I. Apostol, M. Mosoarca, N. Chieffo, and A. Formisano, *Seismic vulnerability scenarios for historical areas of Timisoara*, in Modern Technologies for the 3rd Millennium, 2018, pp. 149–154.
- [19] R. Vicente, S. Parodi, S. Lagomarsino, H. Varum, J. A. R. Mendes, and D. Silva, *Seismic vulnerability assessment, damage scenarios and loss estimation. Case study of the old city centre of Coimbra, Portugal*, in The 14th World Conference on Earthquake Engineering, 2008.
- [20] R. Maio, *Seismic Vulnerability Assessment of Old Building Aggregates*, Universidade de Aveiro, 2013.
- [21] A. I. Keller, *Complex assessment of historical wooden framework*, Ph.D. Thesis, Polytechnic University of Timisoara, 2020, unpublished.

NONLINEAR SIMULATION OF MASONRY VAULTS UNDER EARTHQUAKE LOADING

A. Plavsic¹, B. Pantó¹, C. Chisari², L. Macorini¹, B. A. Izzuddin¹, I. Boem³, N. Gattesco³

¹Department of Civil and Environmental Engineering Imperial College London
South Kensington Campus, London SW7 2AZ, UK
e-mail: {adam.plavsic, b.panto, l.macorini, b.Izzuddin}@imperial.ac.uk

²Department of Architecture and Industrial Design, Università della Campania “Luigi Vanvitelli”
via San Lorenzo – Abazia di San Lorenzo, Aversa (CE), Italy
e-mail: corrado.chisari@unicampania.it

³Department of Engineering and Architecture, University of Trieste
Piazzale Europa, Trieste, Italy
e-mail: boem@dicar.units.it gattesco@units.it

Abstract

Masonry vaults are present in a large number of historical structures and often used as flooring and roofing systems in monumental palaces and religious buildings, typically incorporating no backfill. Many of these structures are located in seismic regions and have been shown to be particularly vulnerable during recent earthquakes, with a need for accurate modelling to avoid future losses. Masonry vaults are often analysed using limit analysis procedures under the hypotheses of no-tension material and absence of sliding along the masonry joints. However, this method can be inaccurate for barrel vaults found in buildings, which are typically slender with no backfill. In this case, the masonry tensile strength and the progressive damage propagation play an important role in the nonlinear behaviour and ultimate strength of the vault. In this study, a detailed mesoscale finite element mesoscale approach is used to model slender unreinforced barrel vaults subjected to cyclic quasi-static and dynamic loading. According to this approach, 3D solid elements connected by 2D damage-plasticity interfaces are used to represent the arrangement of bricks and mortar present in the masonry. The proposed numerical description is first validated against the results from physical tests on a barrel vault under quasi-static cyclic loading. Subsequently, the shear response of a prototype vault is analysed by performing nonlinear simulations under prescribed horizontal displacements at the supports, considering also the influence of previous damage induced by earthquakes with different magnitudes.

Keywords: Seismic risk, Historical masonry structures, Cyclic analyses, Nonlinear time-history analyses, Discrete FEM approach, Mesoscale models.

1 INTRODUCTION

Several existing buildings worldwide of historical, cultural and architectural significance incorporate vaulted masonry components. A high percentage of these buildings is located in high-seismic regions, and masonry vaults and domes have been observed to be particularly vulnerable under lateral loading imposed by earthquakes [1]. Hence, to prevent the potential loss of cultural heritage assets, there is a need to model both unreinforced masonry vaults and potential strengthening measures accurately to ensure protection of vaulted structures against future seismic events.

Masonry vaults are usually analysed using limit analysis procedures [2][3]. However, this approach provides only ultimate load predictions but no description of the behaviour of the structure up to failure. Furthermore, the assumptions of no-tension material and no-sliding along the mortar joints [4], often made in these methods, may lead to unrealistic results in the case of barrel vaults in buildings, which are typically slender, with high span to thickness ratios, and which do not include backfill thus sustaining very low compressive stresses [5].

To achieve accurate response predictions at different loading levels up to collapse, detailed finite element (FE) models based on mesoscale or macroscale masonry models can be used. The first strategy allows for the specific masonry bond utilising nonlinear zero-thickness interface elements [6] to predict the development of cracks at the mortar joints within brick units. This accurate modelling strategy has been previously adopted in [7] to investigate the cyclic behaviour of masonry structures under cyclic loading. Detailed work using the mesoscale approach has been carried out on masonry arched structures by Zhang et al. [8] and on multi-span masonry arch bridges by Tubaldi et al. [9].

The alternative is a macroscale smeared crack approach [10] in which masonry is assumed as a homogeneous isotropic material, and specific nonlinear material models based on damage and plasticity frameworks are typically utilised to represent the development and propagation of damage in the brickwork. An example of the latter is the use of a damage model proposed in [11], which uses homogenised mechanical parameters. Smeared crack models have also been used by Stablon et al. [12] and by Gattesco et al. [13, 14] to model masonry vaults also in presence of strengthening systems.

A modelling approach, alternative to FE analysis, has been proposed in [15] and applied to simulate unreinforced and reinforced arches and vaults [15, 16]. The model is composed of shear deformable macro-elements, interacting by means of non-linear zero-thickness interface elements which simulate the masonry flexural behaviour and potential shear sliding.

This study proposes a detailed FE mesoscale approach to model typical barrel vaults of religious buildings. The model allows for the inhomogeneity of masonry and the damage accumulated in reverse cycles of loading. The numerical results are validated against experimental results obtained through a new testing layout in which the vault is subjected to horizontal forces proportional to the structural self-mass [17]. Further numerical simulations have been conducted to investigate the ability of a representative barrel vault to transfer shear forces acting as a floor diaphragm in a building structure subjected to earthquake loading.

2 THE MESOSCALE MODELING APPROACH

The mesoscale approach used here has been developed at Imperial College [6] and applied to different extreme loading conditions [7-9]. According to this approach, the masonry is discretised into 3D solid brick elements separated by 2D zero thickness non-linear interface elements representing the mortar joints. As the thickness of the mortar joints is generally much smaller than the scale of the bricks, the collapsing of the mortar joints into interfaces is a suit-

able simplification, but still captures the inherently nonlinear character of masonry as a material. This restricts the cracking to the predefined interfaces, which again is realistic in the context of masonry, where the joints act as preferential fracture planes. The interfaces are hence positioned to coincide with the mortar joints. Additional interfaces are placed in the midplane of each brick, in line with the head joints of adjacent bricks, to allow the propagation of cracks through the brick units themselves as observed in real masonry structures. This results in a regular, structured mesh, where the properties of the interfaces allow a physical representation of the 3D bond arrangement. This is important especially where 3D behaviour is of interest, in which case plane stress or plane strain assumptions can be unrepresentative of the true structure.

Specifically, for the vaults considered in this study, the bricks are modelled as 20-noded quadratic solid elements which for which the constitutive material response is linear elastic. All the material nonlinearity is captured by the 16-noded interface elements described by [6], hence the material model for these becomes of prime importance. Figure 1 shows the placement of joints to represent bed joints, head joints and brick failure surfaces. This allows the simulation of hinge formation, shear sliding and ring separation which are typical failure mechanisms for vaults and arches. A damage-plasticity constitutive law, proposed in [7], is employed for the interface elements. The plastic yield surface consists of three yield functions: two planar surfaces for mode I (tensile) and mode III (crushing) fracture which cap the ends of a conical Coulomb surface for mode II (shear) fracture. The level of damage in each mode is a function of the ratios the plastic work in tension ($W_{pl,t}$), shear ($W_{pl,s}$) and compression ($W_{pl,c}$). Based on physical observations, the damage in tension is influenced by the plastic work in both tension and shear, the damage in shear is influenced by plastic work in all three modes, while damage in compression is only related to the plastic work in compression. Numerical results obtained by this model were found to be close to those of experimental data, with the main drawback of the approach being its high computational cost. This was eased by using a partitioning approach which allowed parallel computing to reduce run time [8, 18].

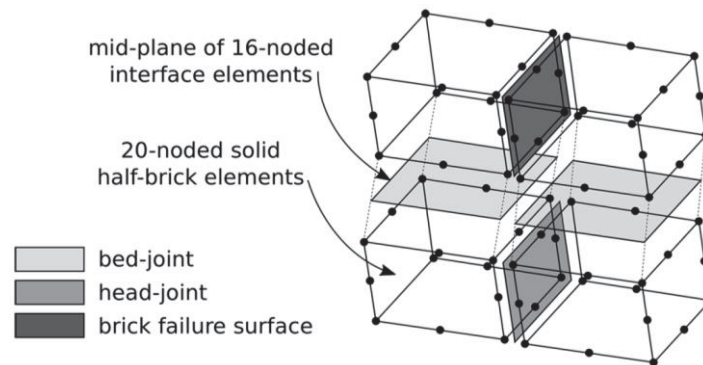


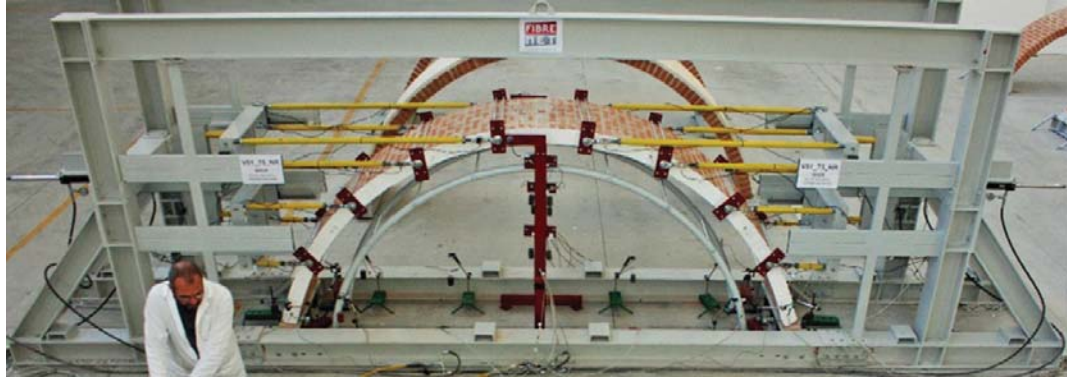
Figure 1: Brick and interface elements used in the mesoscale model [6,7]

3 THE EXPERIMENTAL TESTS

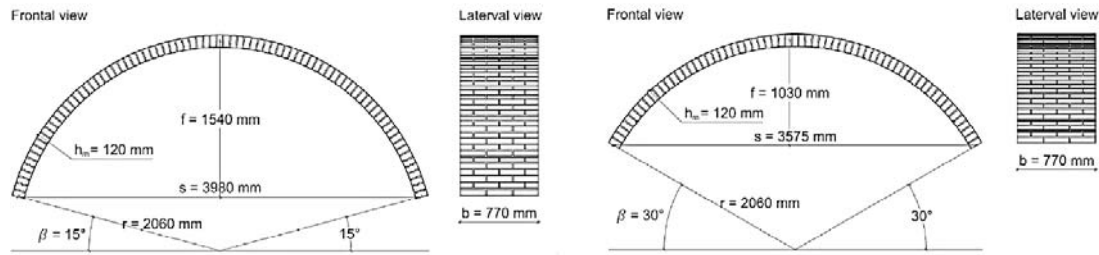
The numerical model applied in this study is validated against experimental results from [17] which used a novel bench setup to apply cyclic horizontal forces proportional to the mass of the arch. To elaborate, a quasi-static cyclic load was applied as a prescribed displacement by a hydraulic actuator and distributed evenly to 8 points either side of the vault by the frame shown in Figure 2a. The load was increased each cycle up to the failure of the vault.

The abutments were fixed during the test allowing no relative displacement. Two geometric layouts have been tested (Figure 2b): V75-NR (rise 1540mm, rise/span 0.75) and V50-NR (rise 1030mm, rise/span 0.5). Both were 120mm thick and 770mm wide, with a common ra-

dius of 2060mm. The mortar joints were 10mm thick on average. Differing lime mortars were used for each vault, with Young's Module tested as 9632 MPa and 11790 MPa for the V75-NR and V50-NR tests, respectively. Flexural tests on masonry samples resulted in strengths of 0.42 MPa (V75-NR) and 0.84 MPa (V50-NR). Solid brick units with self-weight 15.64kN/m^3 were used for both vaults. The main results of interest were that collapse occurred via the formation of a hinge mechanism in all cases, with most specimens forming four hinges at failure [17].



(a)



(b)

Figure 2: Test layout (a) and geometry of vaults (b) used in the experimental study [17].

4 MODEL VALIDATION

The full arrangement of bricks around the circumference is modelled using 20-noded solid brick elements for each brick, connected by 16-noded interface elements representing the mortar bed joints, following the modelling approach described in Section 2. As displacement perpendicular to the span was prevented in the test, the arrangement of head joints through the width of the arch is not modelled. Instead, a strip model is assumed, comprised of a single solid brick element for the width of strip. The reactions obtained are then scaled up accordingly by the ratio of the vault width to the strip thickness. The final brick at each skewback is not explicitly included in the numerical model, rather interface elements are placed at the end of each vault and fully fixed to represent the mortar joint to this fixed brick.

The experiment employed devices to prevent the inward or outward slip of the vault at the skewbacks and this is simulated by giving the interfaces at each skewback arbitrarily high shear strength and stiffness values, preventing shear sliding. In the experiment a device was used to oppose the uplift at each skewback. It is modelled by a linear spring with normal stiffness of 1.1 N/mm arranged in parallel with the skewback interfaces. This value was obtained with reference to a subsequent numerical study performed in [17]. The model mesh is shown in Figure 3, with the zero-thickness interfaces shown as the full thickness of the mortar joints

for clarity. To simulate the experimental loading arrangement, 3D dynamic analyses are performed employing spreader elements available in ADAPTIC [19] which allow an acceleration time history to be applied at a ‘master’ node and the resulting forces to be distributed according to predefined ratios at a number of ‘slave’ nodes. In the analyses, according to the experimental findings, the same ratio is applied to all “slave” nodes.

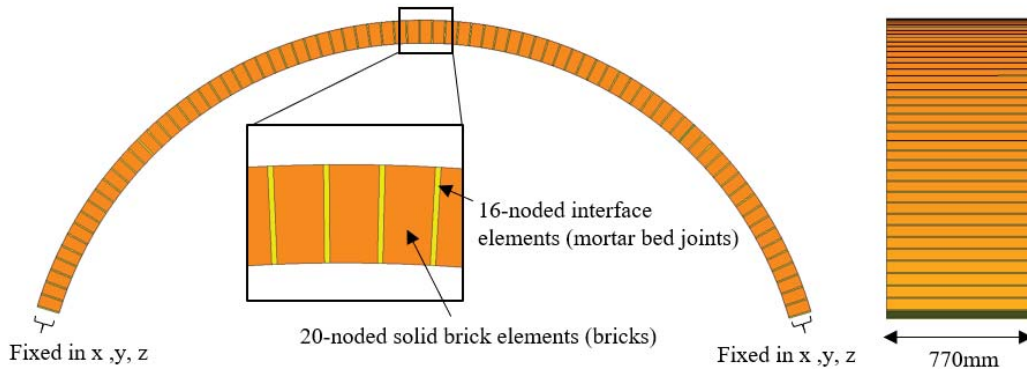


Figure 3: Mesh used for the vault V75-NR

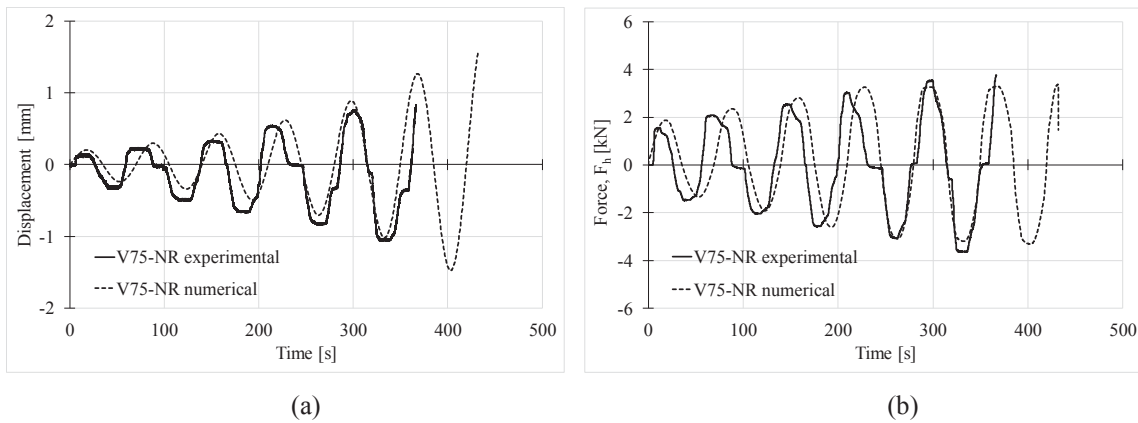


Figure 4: Displacement (a) and force (b) time-histories of the hydraulic actuator in the test and at the master node of the model.

Figure 4 shows the displacement history registered by the hydraulic actuator and those considered in the numerical analysis. Each analysis is performed in two separated phases: the self-weight of the vault is applied first as an initial load, then the lateral loads are applied by means of a displacement-control procedure. No viscous damping is considered in the analyses since it is expected negligible when compared to the hysteretic energy dissipation.

For both vaults, the interface tensile strength is calculated from the masonry tensile strength at the macroscopic scale according to [20]. The Young’s modulus of the bricks is estimated applying a simple homogenization procedure and fixing arbitrary high values for the tangential and normal stiffness (k_t and k_n) according to [21]. The resulting Young’s moduli are 4260MPa and 5280MPa for the V75-NR and V50-NR specimens, respectively. Finally, Poisson’s ratio 0.2 and specific weight 1664kN/m³ are considered for both the two tests.

The parameters for the Coulomb model are taken from values obtained with reference a numerical study performed on the same experimental results [14], resulting a friction coefficient of 0.58 for both vaults and cohesion of 0.19MPa and 0.38MPa for vaults V75 and V50, respectively. The fracture energy for modes I and II are assumed in line with values from previous studies [21,22] where it was found that values for mode I (tensile) were typically in the

range 0.01 to 0.08 N/mm and for mode II (shear) from 0.1 to 0.2 N/mm. The fracture energy in mode I is assumed at a low value to reflect the brittle response observed experimentally. The set of parameters adopted for each vault are summarised in Tables 1, where k_n and k_t are the normal and tangential elastic stiffness; f_t , f_c and c are the tensile strength, compression strength and cohesion; $\tan(\phi)$ and $\tan(\phi_g)$ are the friction and dilatancy coefficients; $G_{f,t}$, $G_{f,s}$ and $G_{f,c}$ are the fracture energy in tension, shear and compression, respectively.

Test	k_n [N/mm ³]	K_t	f_t	F_c [MPa]	c	$G_{f,t}$	$G_{f,s}$ [N/mm]	$G_{f,c}$	$\tan(\phi)$	$\tan(\phi_g)$ [-]	μ
V75-NR	1000	1000	0.14	5.00	0.19	0.01	0.125	1.0	0.58	0.00	0.1
V50-NR	1000	1000	0.28	6.20	0.38	0.05	0.125	1.0	0.58	0.00	0.1

Table 1: Mechanical parameters of the mortar joint interfaces.

5 CYCLIC QUASI-STATIC ANALYSIS

All analyses are performed using the general nonlinear Finite Element software ADAPTIC [19]. The total horizontal force applied (F_h) plotted against the horizontal displacement at the crown section (δ_h) is shown in Figure 5 and compared to the experimental hysteresis loops for both tests. The experiment on vault V75-NR exhibited an early hinge forming at one haunch in one loading direction, which is attributed to an imperfection in the mortar bond. This resulted in one skewback not cracking and led to an asymmetric response. To simulate this aspect, one artificially weakened skewback is introduced in the model considering a reduced tensile strength ($f_{t,skewl}=0.01\text{MPa}$). Moreover, it is noted that for both vaults the experimental results recorded a very high initial stiffness and very high unloading stiffnesses during cycles. This was a by-product of the testing rig arrangement and not representative of the physical behaviour of the vault. The numerical collapse mechanisms are shown in Figure 6, where the normal stress along the span (s_{xx} MPa) is represented. For the vault V75-NR, the model captured the formation of the 2 hinges at both skewbacks and then the third at the haunch. After this point, convergence was lost (Figure 6a). For the vault V50-NR, the first hinge occurred at the right skewback. Subsequently, the second and third hinges formed near simultaneously at the left skewback and right mid-span, then the 4th hinge opened at the remaining haunch (Figure 6b). After 4 hinges are formed, a rocking motion involving the three uncracked spans sustained a residual load which increased to around 5 kN, at which point additional damage occurred near the skewbacks and the blocks lost shear strength, with the final sliding failure occurring at approximately 24 mm. This mechanism was also observed experimentally, confirming the reliability and robustness of the interface model. Table 2 summarises the behaviour of each vault alongside the experimental results.

Test	F_{max} [kN]	$F_{max,exp}$ [kN]	$(F_{max} - F_{max,exp})/F_{max,exp}$ [kN]
V75-NR	3.37	3.76	-10%
V50-NR	12.23	13.01	-6%

Table 2: Numerical (F_{max}) and experimental ($F_{max,exp}$) horizontal peak loads.

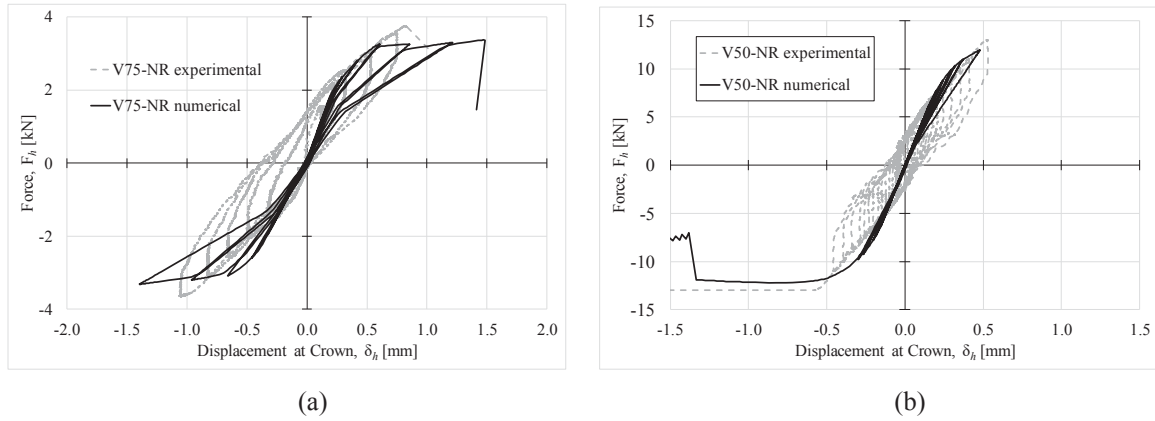


Figure 5: Experimental and numerical cyclic responses of vault specimens V75-NR (a) and V50-NR (b).

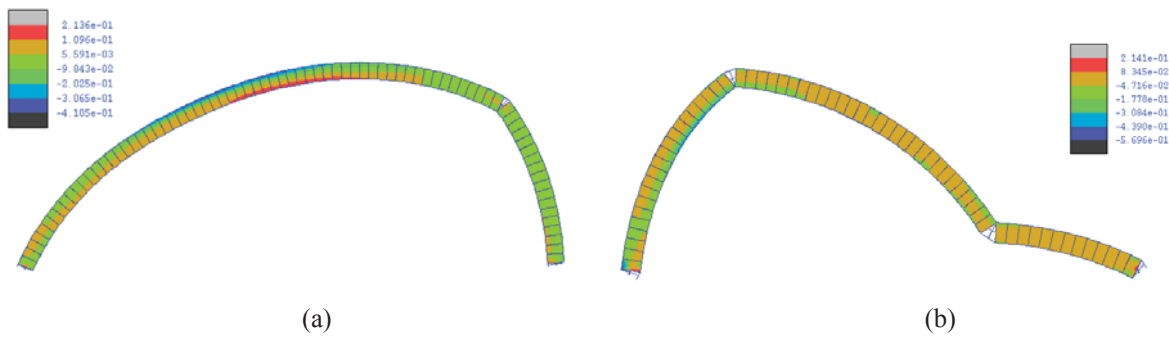


Figure 6: (a) Deformed shape of the V75-NR model at the activation of the 3rd hinge; (b) deformed shape of the V55-NR model at the formation of the 4th hinge (displacements scale: 100).

6 NUMERICAL SIMULATIONS UNDER EARTHQUAKE LOADING

In this section, the behaviour of the V75-NR prototype, subjected to a time-history acceleration, applied at each skewback, is investigated. The full mortar bond arrangement is modelled using two different types of interfaces to represent the mortar-brick head joints and the brick-brick joints. The later allowing cracks to form through the centre of each brick. By alternating the placement of these interfaces in the y direction, the realistic arrangement of bricks and mortar can be simulated. The brick-brick joint interfaces are calibrated, according to specific literature referring to similar masonry units [6], as no direct information was available experimentally on the specific brick properties required. These are presented in Table 3.

The earthquake record from Southern Italy Irpina earthquake (1980), Sturmo station, is selected from the European Strong-Motion Database (ISESD) [23] with the linear baseline of the acceleration time history corrected. Two horizontal components (Figure 7) are simultaneously applied to the vault to observe the full 3D behaviour. The direction with the higher peak ground acceleration of 0.32g is applied parallel to the span of the vault (x direction), while the record with PGA 0.22g is applied perpendicular to the span (y direction). The original record is scaled up and down by 50%. The resulting acceleration time histories scale the original record by factors of 0.5 (EQ0.5), 1.0 (EQ1.0) and 1.5 (EQ1.5), and the peak ground accelerations for each simulation are shown in the first two rows of Table 4. A further test used the unscaled record with peak ground acceleration 0.32g applied only in the x-direction (EQ1.0x) to explore the influence of the shaking in the y direction.

The numerical response under EQ1.0, in terms of horizontal displacement at the crown section versus the horizontal base shear, is plotted in Figure 8a, superposed onto the experimental

results. Collapse is evidenced for cases EQ1.0 and EQ1.5, while the structure remains almost elastic for case of EQ0.5. These collapses correspond to the activation of four hinges.

k_n	K_t	f_t	F_c	c	$G_{f,t}$	$G_{f,s}$	$G_{f,c}$	$\tan(\phi)$	$\tan(\phi_g)$	μ
[N/mm ³]			[MPa]			[N/mm]			[-]	
1E+5	1E+5	1.67	20.77	2.8	0.05	0.125	1.0	1.0	1.0	0.1

Table 3: Mechanical parameters of the brick-to-brick interfaces

In the three simulations EQ1.0, EQ1.5 and EQ1.0x, a four-hinge mechanism forms in the x-direction, with two hinges at each skewback forming first, followed by hinges at the two haunches of each vault. In terms of the failure mechanism, the x-direction was dominant, with cracks forming along the full width of the bed joints. This is partially explained by the peak acceleration in the x direction being approximately 1.5 times that in the y-direction and considering the limited width of the vault.

Hinge locations are close to those obtained from the cyclic simulations. For the vaults accelerated in both directions, up until the formation of four hinges little deformation in the y-direction is observed, but once forms the vault lost shear stiffness along the cracked bed joints. Typically, a fifth hinge forms near the crown, and rotation of the uncracked blocks is observed, as shown in Figure 8b for simulation EQ1.5.

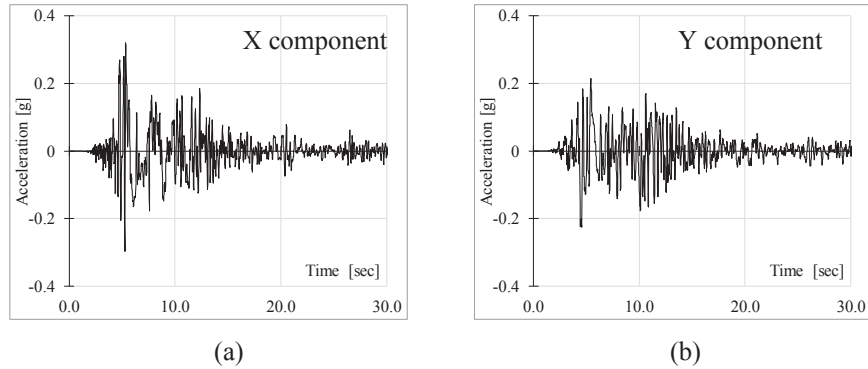
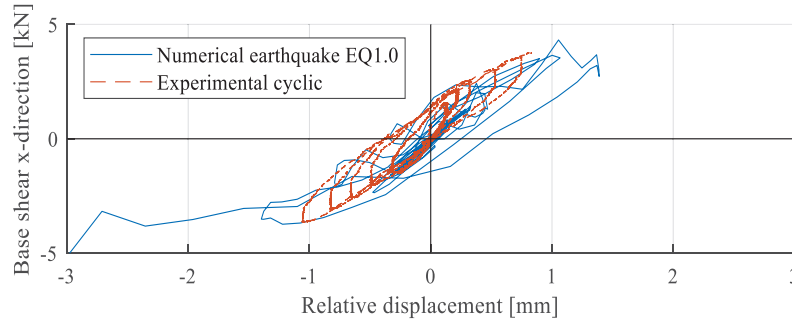


Figure 7: Earthquake signals applied along the longitudinal (a) and transversal (b) directions of the arch.

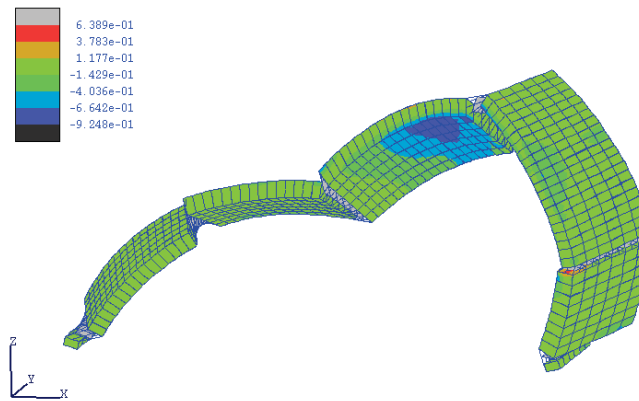
The study shows damage tending to be uniform along each bed joint, with damage being of a smaller magnitude along the head joints. Generally, up to the point of collapse, the behaviour under earthquake acceleration can be observed to be similar to that of cyclic loading, with the 3rd hinge tending to form at a similar load and displacement as that experimentally. As the fourth hinge begins to form, and collapse begins, the base shear varies sharply and at times is observed to be larger than at the formation of the hinges. This is in part due to the collapsing vault imparting large forces on its supports as the mechanism was formed. The main results of the analyses are summarised in Table 4. Comparing the results from the two simulations EQ1.0 and EQ1.0x, it can be seen that there is minimal difference in the load capacities obtained, with the vault accelerated in both directions (EQ1.0) actually reaching a slightly higher load at collapse of 4.32kN compared with 4.23kN for EQ1.0x. This demonstrates that the acceleration in the y-direction does not contribute significantly to the collapse load in x or to the failure mechanism observed. As discussed above, past the formation of 4 hinges, the rotation of blocks due to the y acceleration becomes noticeable. This indicates testing in only one directing and using a strip model in the previous section is justified for this type of barrel vault. The load at the formation of 4 hinges tended to be slightly higher than that obtained experimentally, which could be related to the dynamic effects of base acceleration.

Parameter		EQ0.5	EQ1.0	EQ1.5	EQ1.0x	Experiments
PGA x direction	[g]	0.16	0.32	0.48	0.32	-
PGA y direction	[g]	0.11	0.22	0.33	0.00	-
Peak base shear x	[kN]	1.78	4.32	4.78 (3.89)	4.23	3.76
Peak base shear y	[kN]	1.15	2.67	4.29	0.00	-
Max displacement x	[mm]	0.28	1.96	7.29 (2.31)	3.57	0.84
Max displacement y	[mm]	0.10	0.43	1.26 (0.73)	0.00	-

Table 4: Maximum peak ground accelerations leading to the formation of a four-hinge mechanism in the vault.



(a)



(b)

Figure 8: (a) Total shear-crown horizontal displacement under base acceleration EQ1.0; (b) Failure mechanism under base acceleration EQ1.5 (displacements scaled by 100).

6.1 The shear stiffness of barrel vaults

Masonry barrel vaults represent the floor diaphragms of numerous historical buildings. Their shear behaviour influences the local and global response of the structure and its seismic performance. In this section, the performance of a barrel vault specimen under shear loading is numerically investigated considering the effects of accumulated damage caused by earthquake motions.

The same geometrical layout of the barrel vault investigated in Section 5 but with a width equal to the arch span (3980mm) is considered. The nonlinear model is first subjected to the X and Z component of the Irpinia earthquake. At the end the motion, a quasi-static shear drift is applied at the base of the two skewbacks. Four amplification factors, 50% and 75%, 85% and 100% are chosen to scale the original signal in order to cause plastic damage but no structural collapse.

In Figure 9, the relative displacement between the two skewbacks is plotted for each model versus the external shear load. In the graph, the curve of the undamaged vault is also plotted for the comparison. The damaged models show a brittle behaviour with a lower displacement capacity when compared to the undamaged vault. The ultimate shear displacement of the vault decreases as the PGA of the seismic input increases.

The failure mechanisms of the undamaged vault and the damaged vault (75% of signal) are reported in Figure 10a and Figure 10b, respectively. The undamaged model shows a failure mechanism characterised by the formation of 4 significant cracks along the mortar joints developing from the lateral faces of vaults. The cracks propagate towards the middle of the vault following a diagonal path (Figure 10a). The damaged vaults show a different failure mechanism, characterised by the sliding at the skewbacks leading to a rigid rotation of the vault (Figure 10b).

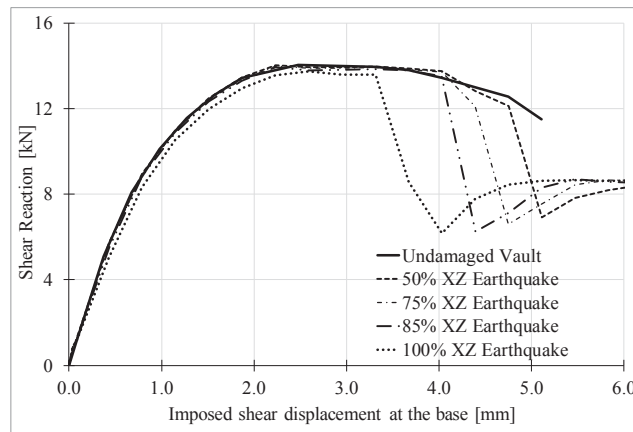


Figure 9: Shear reaction – deformation curves for different earthquake intensities.

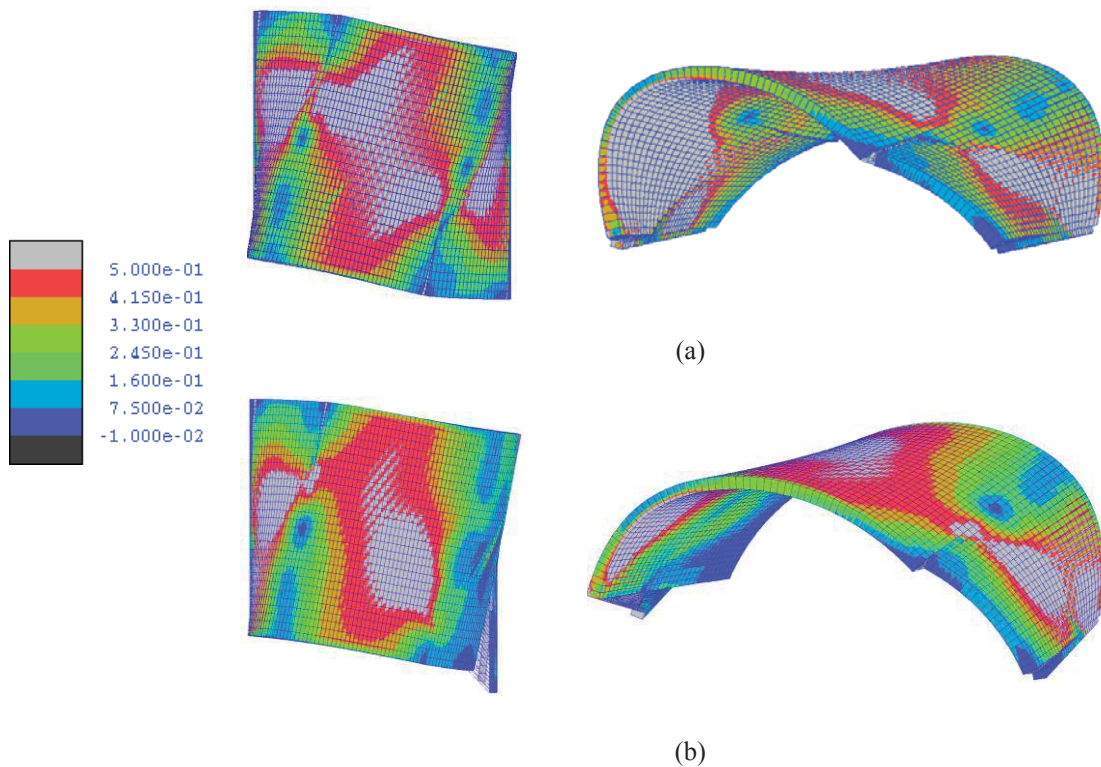


Figure 10: Shear failure and Von Mises stress (in MPa): (a) undamaged vault, (b) damaged vault.

7 CONCLUSIONS

This study applies a detailed meso-scale model to simulate unreinforced masonry vaults subjected to earthquake loading. Both quasi-static cyclic loads and base accelerations are considered. The model simulates each brick by means of 20-noded elastic solid brick elements interacting by means of 16-noded interface elements. The effective mortar bond is modelled using two different types of interfaces to represent either the mortar bed joints or to simulate the cracks passing the bricks. The numerical results are compared to experimental findings obtained by means of a novel test setup to apply cyclic horizontal forces proportional to the mass of the vault. The meso-scale model is found to be effective in capturing the complex failure modes and predicting crack locations in unreinforced vaults. In the last part of the paper, the influence of different magnitudes of earthquake, including the resulting damage, on the shear deformability and shear strength of the investigated vault specimen is evaluated. The results show that previous damage can reduce significantly the shear displacement capacity of the vault potentially hindering its ability to act as an effective floor/roof diaphragm.

REFERENCES

- [1] Parisi, F. and Augenti, N. Earthquake damages to cultural heritage constructions and simplified assessment of artworks. *Engineering Failure Analysis* (2013) **34**:735-760.
- [2] Milani, E., Milani, G., and Tralli, A. Limit analysis of masonry vaults by means of curved shell finite elements and homogenization. *International Journal of Solids and Structures* (2008) **45**(20): 5258-5288.
- [3] Casapulla, C., and D'Ayala, D. Lower bound approach to the limit analysis of 3D vaulted block masonry structures. *Computer Methods in Structural Masonry* (2001) **5**: 177-183.
- [4] Heyman, J. *The Stone Skeleton: Structural Engineering of Masonry Architecture*. Cambridge, Cambridge University Press (1995).
- [5] Ramaglia, G., Lignola, G. P. and Prota, A. Collapse analysis of slender masonry barrel vaults. *Engineering Structures* (2016) **117**:86-100.
- [6] Macorini, L. and Izzuddin, B.A. A non-linear interface element for 3D mesoscale analysis of brick-masonry structures. *International Journal for numerical methods in Engineering* (2011) **85**(12):1584-1608.
- [7] Minga, E., Macorini, L. and Izzuddin, B. A. A 3D mesoscale damage-plasticity approach for masonry structures under cyclic loading. *Meccanica* (2018) **53**(7): 1591-611.
- [8] Zhang, Y., Macorini, L. and Izzuddin, B. A. Mesoscale partitioned analysis of brick-masonry arches. *Engineering Structures* (2016) **124**: 142-166.
- [9] Tubaldi, E., Macorini, L. and Izzuddin B. A. Three-dimensional mesoscale modelling of multi-span masonry arch bridges subjected to scour. *Engineering Structures* (2018) **165**: 486-500.
- [10] Minga, E., Macorini, L., Izzuddin, B.A. and Calio', I. Macromodeling, In: B. Ghiassi and G. Milani (Eds.): Numerical Modeling of Masonry and Historical Structures, from Theory to Application, Woodhead Publishing Series in Civil and Structural Engineering (2019) pp. 263-294.
- [11] Chisari, C., Macorini, L. and Izzuddin, B.A. Multiscale model calibration by inverse analysis for nonlinear simulation of masonry structures under earthquake loading. *International Journal for Multiscale Computational Engineering* (2020) **18**(2).
- [12] Stablon, T., Sellier, A., Domede, N., Plu, B. and Dieleman, L. Influence of building process on stiffness: numerical analysis of a masonry vault including mortar joint shrinkage

- and crack re-closure effect. *Materials and Structures* (2012) **45**(6): 881-898.
- [13] Gattesco, N., Amadio, C. and Bedon, C. Experimental and numerical study on the shear behavior of stone masonry walls strengthened with GFRP reinforced mortar coating and steel-cord reinforced repointing. *Engineering Structures* (2015) **90**: 143-157.
- [14] Gattesco, N., Boem, I. Review of experimental tests and numerical study on masonry vaults reinforced through fiber-reinforced mortar coating. *Bulletin of Earthquake Engineering* (2019) **17**(7): 4027-4048
- [15] Cannizzaro, F., Pantò, B., Caddemi, S., and Calì, I. A Discrete Macro-Element Method (DMEM) for the nonlinear structural assessment of masonry arches. *Engineering Structures* (2018) **168**: 243-256.
- [16] Pantò, B., Cannizzaro, F., Caddemi, S., Calì, I., Chácará, C., and Lourenço, P. B. Non-linear modelling of curved masonry structures after seismic retrofit through FRP reinforcing. *Buildings* (2017) **7**(3): 79.
- [17] Gattesco, N., Boem, I. and Andretta, V. Experimental behaviour of non-structural masonry vaults reinforced through fibre-reinforced mortar coating and subjected to cyclic horizontal loads. *Engineering Structures* (2018) **172**: 419-431.
- [18] Jokhio, G.A. and Izzuddin, B.A. A dual super-element domain decomposition approach for parallel nonlinear finite element analysis. *International Journal for Computational Methods in Engineering Science and Mechanics* 2015 **16**(3): 188-212.
- [19] Izzuddin, B.A. Nonlinear dynamic analysis of framed structures, Imperial College London (University of London) (1991).
- [20] Milani, G. 3D upper bound limit analysis of multi-leaf masonry walls. *International Journal of Mechanical Sciences* (2008) **50**(4): 817-36.
- [21] Chisari, C., Macorini, L., Amadio, C. and Izzuddin, B. A. Identification of mesoscale model parameters for brick-masonry. *International Journal of Solids and Structures* (2018) **146**: 224-240.
- [22] Chisari, C., Macorini, L., Izzuddin, B. A. and Amadio, C. Experimental-numerical strategies for the calibration of detailed masonry models. *10th International Masonry Conference, IMC* (2018) July 9, 2018 - July 11, 2018, Milan, Italy, International Masonry Society. pp.1732-1745.
- [23] Ambraseys, N., Smit P., Sigbjörnsson R., Suhadolc P., and Margaritis. B. Internet-Site for European Strong-Motion Data (2001), <http://www.isesd.cv.ic.ac.uk>.

LOW-COST RUBBER COMPOUNDS FOR FIBER-REINFORCED ELASTOMERIC ISOLATORS: RECOVERED POWDERS AND WASTE OILS FROM RUBBER MANUFACTURING PROCESSES

Gaetano Pianese¹, Gabriele Milani¹, Federico Milani², Ahmad Basshofi Habieb³

¹ Politecnico di Milano
Piazza Leonardo da Vinci 32, 20133 Milano, Italy
e-mail: gaetano.pianese@polimi.it, gabriele.milani@polimi.it

² Chem.Co. Consultant
Via Kennedy 2, 45030 Occhiobello, Rovigo, Italy
federico-milani@libero.it

³ Institut Teknologi Sepuluh Nopember
Keputih, Sukolilo, Surabaya City, East Java 60117, Indonesia
ahmad.basshofi@its.ac.id

Abstract

In recent years the concept of recycling and reuse is a popular issue faced in many fields. During manufacturing processes a huge amount of materials is recovered to minimize waste. In particular, this study investigates the possibility of reuse materials recovered during the production of rubber in standard industrial practice, for the realization of low-cost rubber compounds for fiber-reinforced elastomeric isolators. To cope with this task, a new composition is developed basing on the past experience of the research group and in particular with reference to a previous study by A. B. Habieb et al, where a part of virgin rubber was replaced by regenerated one. Subsequently, a comparison between the two compositions in terms of rheometer curves, uniaxial tensile curves, hardness and compression sets, before and after the process of aging is provided. It is found that the new composition exhibits attractive performances with economic advantages and environmental benefits.

Keywords: Rubber compounds, Regenerated rubber, Elastomeric isolator.

1 INTRODUCTION

The rubber material is widely used either for household or industrial needs. Since the pre-historic era, rubber has been involved in human life by exploiting the latex from specific trees. The first use of rubber in the industrial sector occurred at the beginning of the 18th century [1]. Nowadays, rubber is commonly used for tires, vibration or seismic isolators, impermeable layers, and sports equipment. It can be in the natural or synthetic form of material. Some popular synthetic rubber types include Hypalon, Ethylene Propylene Diene Monomer (EPDM), Nitrile-Butadiene Rubber (NBR), Viton, Neoprene, Silicone rubber (SiR), and Styrene-Butadiene Rubber (SBR).

For elastomeric isolators, rubber pads have a main role. Damping performance is a prerequisite for isolation bearing materials. Besides, the materials must have an excellent overall performance, such as high strength to resist damage [2, 3]. Natural Rubber (NR) exhibits desirable physical and mechanical properties, good processing properties, and excellent flexibility, and it is an indispensable material for industrial applications. However, NR has a quite poor damping performance, which greatly limits its application in the field of anti-seismic materials [4] [5]. Artificial rubber seems promising for the fabrication of isolators since NR is vulnerable to quick aging and its industrial production capability is limited. Less frequently it is EPDM or an NBR-EPDM blend vulcanized with an increasing amount in weight of carbon black [6]. To be ready for application, rubber should be processed through several stages; mixing or milling, and vulcanization [7, 8]. In the mixing process, some additives are added to obtain the expected behavior of the rubber compound. In the vulcanization process, the rubber is heated with sulfur, accelerator, and activator at around 140-160 °C. The process triggers the formation of cross-links between long rubber molecules, thus improving tensile strength, hardness, and weather resistance.

Rubber waste recycling is one of the most critical emergencies in terms of sustainability, considering that massive rubber waste has polluted the environment. According to the literature, regenerative rubber and powdered rubber are important forms of recycled rubber used to combat the rubber industry's expanding demand for raw material. Studies proposed by A. B. Habieb et al. [9, 10, 11] validate the possibility of use regenerated EPDM compounds for the production of unbonded Fiber Reinforced Elastomeric Isolators. The utilization of regenerated EPDM appears very interesting because the EPDM backbone is essentially the same as the starting material.

The present study investigates the possibility of using recovered powder and oils from rubber manufacturing to fabricate rubber pads for low-cost seismic isolation systems. A new composition is developed basing on the past experience of the re-search group and in particular with reference to a previous study by A. B. Habieb et al. [12, 13].

In addition to the environmental benefits, the research wants to reveal remarkable ones of using recycled rubber waste from industries to drop down the cost of the isolation system. Such a consideration is particularly essential when dealing with seismic protection in developing countries (Indonesia, The Philippines, Thailand, for instance) where the cost of the commercial isolation system is considered too expensive for massive applications.

2 REGENERATED EPDM COMPOUND

The reference regenerated EPDM compound is the Batch 4 developed by A. B. Habieb et al. [14]. Commercial virgin rubber is blended with regenerated EPDM. Final rubber specimens are composed for 2/3 of regenerated EPDM and 1/3 of virgin rubber. In the following figures and tables are shown the mechanical properties of the recycled rubber.

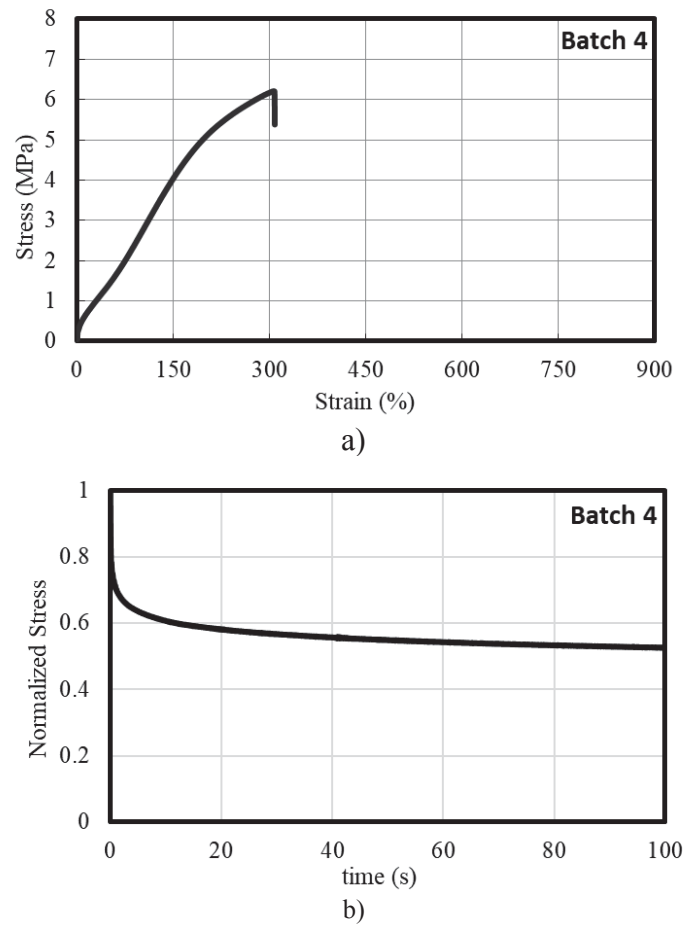


Figure 1: Stretch-stress (a) and relaxation curves (b) of reactivated EPDM [9]

Time test mm:ss	T °C	M _L kg-m	T _{s1} mm:ss	T _{s2}	T ₁₀	T ₅₀	T ₉₀	M _H kg-m	Final kg-m
36:00	150	0.062	1:46	2:03	2:10	7:37	1:35	0.352	0.352
24:00	160	0.057	1:16	1:27	1:32	4:56	15:55	0.342	0.342
12:00	170	0.054	1:05	1:13	1:17	2:34	7:25	0.352	0.352
6:00	180	0.052	0:42	0:48	0:48	1:52	4:40	0.272	0.272

Table 1: Several parameters obtained in the rheometer test on specimens at different temperatures.

Density g/cm ³	Shore A Hardness	Compression set %
1.089	66	25

Table 2: Density, Shore A Hardness and Compression Set of reactivated EPDM

3 RUBBER COMPOUND WITH RECOVERED POWDERS AND OILS

Respect the original composition of the rubber compound, carbon black and paraffinic oil have been totally replaced by recovered powders and oils (Table 3). Both replacements are obtained by recovering materials during the rubber manufacturing process, in particular, during the mixing process. In the following figures and tables are shown the mechanical properties of the new rubber compound.

Batch 4		Recovered	
Ingredient	gr.	Ingredient	gr.
Virgin EPDM	100.00	Virgin EPDM	100.00
Regenerated EPDM	300.00	Regenerated EPDM	300.00
ZnO Zinc Oxide	4.00	ZnO Zinc Oxide	4.00
Stearic acid	1.00	Stearic acid	1.00
Calcium Carbonate	40.00	Calcium Carbonate	40.00
Carbon black N550 FEF II	185.00	Recovered powder	208.00
Paraffinic oil	95.00	Recovered oil	88.00
-	-	Kezadol GR	12.00
MBT Premix	1.50	MBT Premix	1.52
Sulfur Premix	2.50	Sulfur Premix	2.52
TMTD Premix	2.00	TMTD Premix	2.00
Total	731.00	Total	759.04

Table 3: Composition for the two rubber compounds analyzed: “Batch 4” and “Recovered”

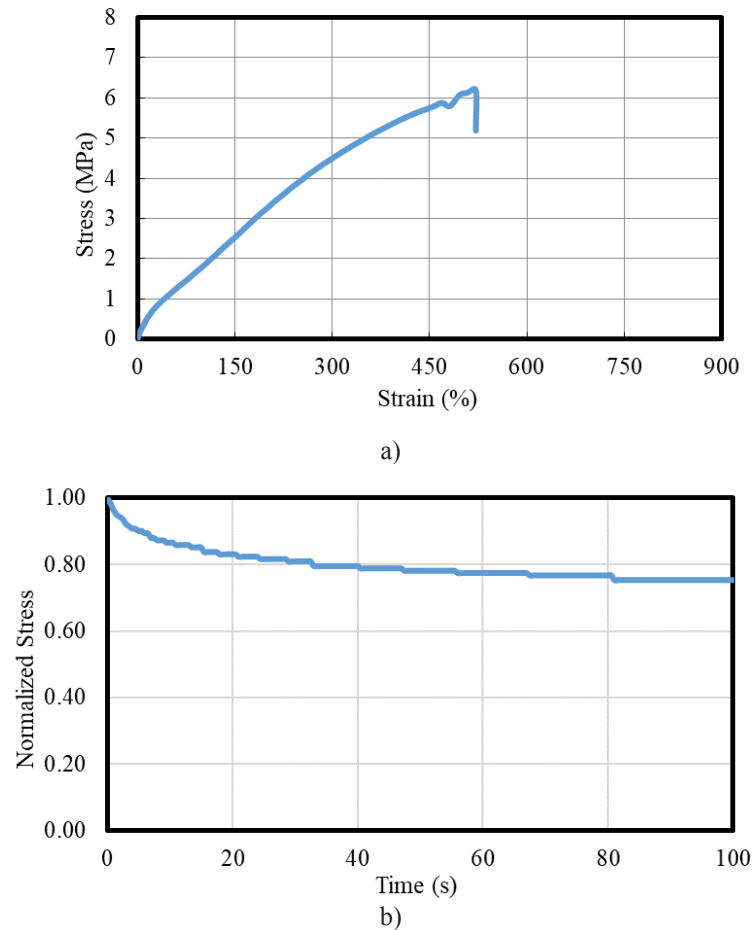


Figure 3: Stretch-stress (a) and relaxation curves (b) of rubber compound with recovered powder and waste oil

Time test mm:ss	T °C	M _L kg-m	T _{s1} mm:ss	T _{s2} mm:ss	T ₁₀ mm:ss	T ₅₀ mm:ss	T ₉₀ mm:ss	M _H kg-m	Final kg-m
36:00	150	0.081	2:50	3:22	3:25	6:46	19:47	0.327	0.327
24:00	160	0.077	1:52	2:09	2:11	4:16	12:20	0.323	0.323
12:00	170	0.074	1:15	1:26	1:26	2:39	6:51	0.311	0.311
6:00	180	0.072	0:53	1:00	1:00	1:45	3:52	0.293	0.293

Table 4: Several parameters obtained in the rheometer test on specimens at different temperatures.

Density g/cm ³	Shore A Hardness	Compression set %
1.279	61	70.74

Table 5: Density, Shore A Hardness and Compression Set of reactivated EPDM

4 COMPARISON BETWEEN THE RUBBER COMPOUNDS

The new rubber compound exhibits similar behavior to the original one. In figure 3 and in tables 1 and 4, it's possible to appreciate the same characteristic rheometer curves (Table 1, Table 4).

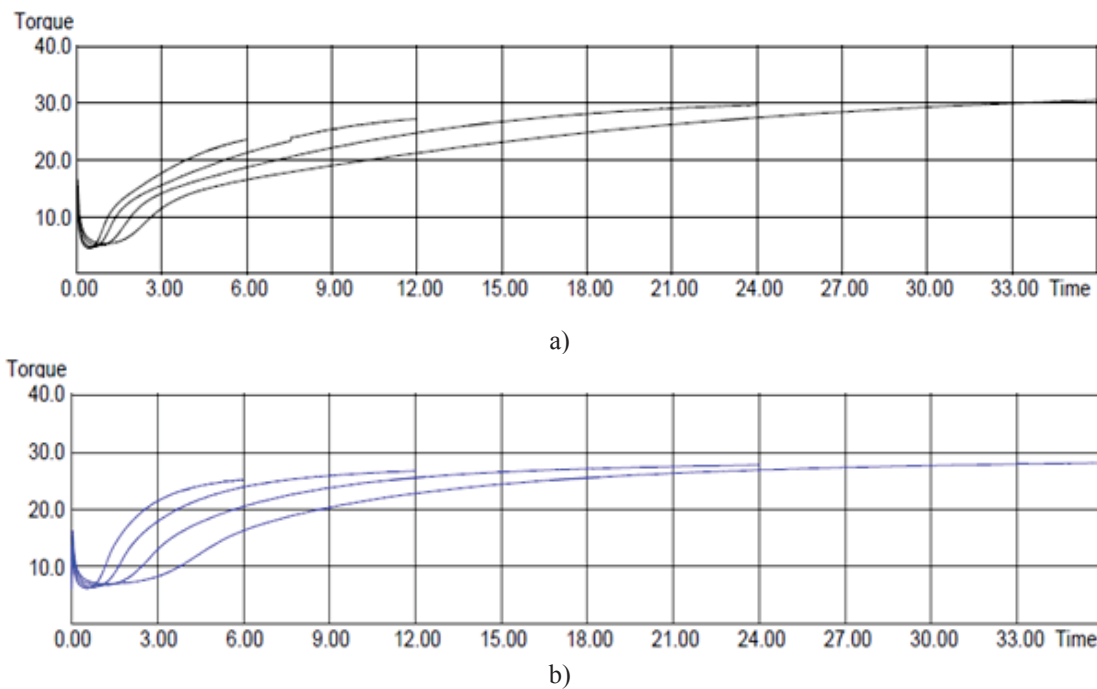


Figure 3: Rheometer curves of "Batch 4" (a) and "Recovered" (b) at different temperatures

For the stretch-strain test, the results obtained have shown that the new rubber compound presents a higher elongation at break and almost the same breaking stress of the original composition (Figure 4a). For the relaxation curves, the original rubber compound reaches a plateau at a value of normalized stress, of 0.57, while the new one reaches a plateau at a value of 0.79.

Furthermore, a comparison of densities, Shore A Hardnesses and Compression Sets has been made. As it is possible to see in Table 6, only the compression set exhibits a different behavior, with a difference percentage of 177.04% lower than the original one.

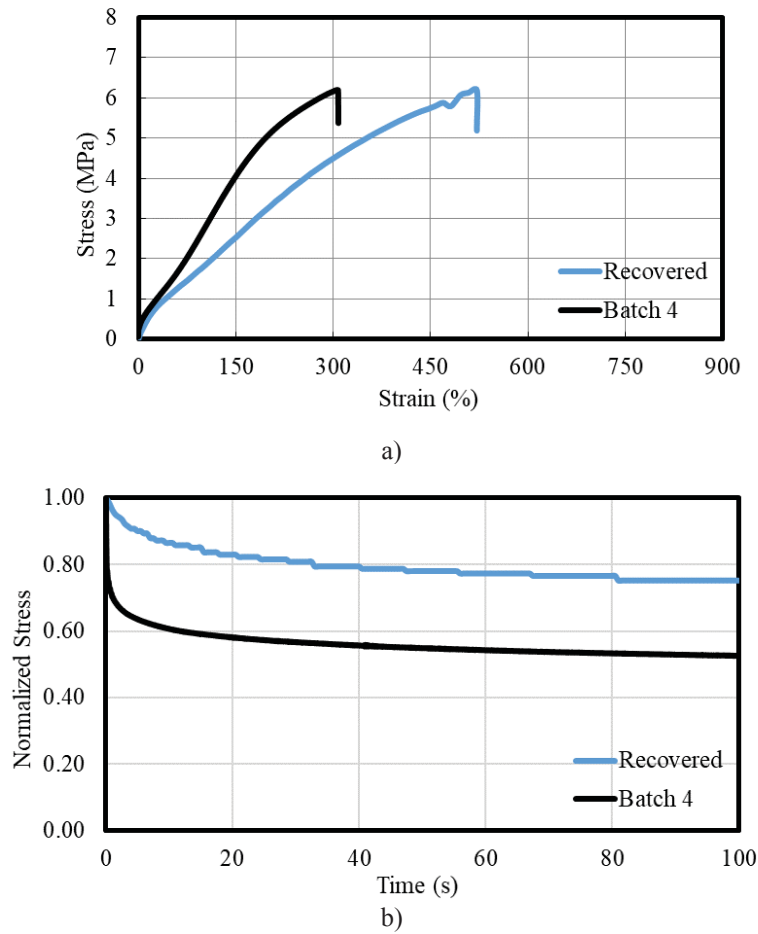


Figure 4: Comparison of stretch-stress (a) and relaxation curves (b) of the two rubber compounds

Rubber compound	Density g/cm^3	Shore A Hardness	Compression set %
Batch 4	1.089	66	25
Recovered	1.279	58	70.74
Δ (%)	0.017	12.12	177.04

Table 6: Comparison and percentage difference of densities, Shore A Hardnesses and Compression Sets

5 CONCLUSIONS

This paper has investigated the possibility of reuse materials recovered during the production of rubber in standard industrial practice to realize low-cost rubber compounds for fiber-reinforced elastomeric isolators.

Firstly, from a previous study of A.B. Habieb et al., a rubber compound made of reactivated EPDM has been considered. From the original composition, carbon black and paraffinic oils have been totally replaced by recovered powder and oils. A comparison between the new rubber compound and the original one in terms of rheometer curves, uniaxial tensile curves, relaxation curves, hardness, and compression set has been done. The new rubber compound exhibits a good overall performance, except for the compression set. In fact, it has shown a percentage difference of 177.04% lower than the original one.

So, for the production of rubber compounds for the low-cost elastomeric isolator, the recovered materials can't be used in total replacement of ingredients. Still, the results of rheometer curves, uniaxial tensile curves, relaxation curves, and hardness seem promising for future developments of this research where new compositions with partial replacements of recovered powder and waste oils will be proposed.

REFERENCES

- [1] A. Coates, *The commerce in rubber: the first 250 years*. 2015.
- [2] W. Wang, et al. Novel slide-ring material/natural rubber composites with high damping property. *Scientific Report*, Vol. 6, 22810/1–22810/13, 2016.
- [3] Y-S. Choun, J. Park, I-K. Choi, Effects of mechanical property variability in lead rubber bearings on the response of seismic isolation system for different ground motions. *Nuclear Engineering and Technology*, Vol. 46, 605-618, 2014.
- [4] R. Qin, R. Huang, X. Lu, Use of gradient laminating to prepare NR/ENR composites with excellent damping performance. *Materials and Design*. 2018, Vol. 149, 43–50.
- [5] L. Burtcher S., A., Dorfmann, Compression and shear tests of anisotropic high damping rubber bearings. *Engineering Structures*, Vol. 26, 1979–1991, 2004.
- [6] G. Milani, F. Milani, Stretch-stress behavior of elastomeric seismic isolators with different rubber materials: numerical insight. *Journal of engineering mechanics*, Vol. 138(5), 416-429, 2012.
- [7] C. Guise-Richardson, Redefining vulcanization: Charles goodyear, patents, and industrial control, 1834-1865. *Technol Cult*, 51:357-387, 2010.
- [8] G. Pianese, G. Milani, R. Cerchiario, F. Milani, Optimal Vulcanization of Unbonded Fiber Reinforced Elastomeric Isolator Devices, *Chemical Engineering Transactions*, Vol. 86, 2021.
- [9] A. B. Habieb, G. Milani, V. Quaglini, F. Milani, Experimentation and numerical modeling of recycled rubber pads for seismic isolation under accelerated ageing. *AIP Conference Proceedings*, 2116, # 420006, 2019.
- [10] A. B. Habieb, G. Milani, T. Tavio, Two-step advanced numerical approach for the design of low-cost unbonded fiber reinforced elastomeric seismic isolation systems in new masonry buildings. *Engineering Failure Analysis*, 90, 380-396, 2018.
- [11] A. B. Habieb, M. Valente, G. Milani, Base seismic isolation of a historical church using fiber reinforced elastomeric isolators. *Soil Dynamics and Earthquake Engineering*, Vol. 120, 127-145, 2019.
- [12] A. B. Habieb, G. Milani, F. Milani, R. Cerchiario, Rubber compounds made of reactivated EPDM for fiber-reinforced elastomeric isolators: an experimental study. *Iranian Polymer Journal*, 2020.
- [13] A. B. Habieb, G. Milani, V. Quaglini, F. Milani, Experimentation and numerical modeling of recycled rubber pads for seismic isolation under accelerated ageing. *AIP Conference Proceedings*, 2116, # 420006, 2019.
- [14] A. B. Habieb, G. Milani, R. Cerchiario, V. Quaglini, F. Milani, Numerical study on rubber compounds made of reactivated ethylene propylene diene monomer for fiber reinforced elastomeric isolators, *Polymer Engineering and Science*, 2020.

HORIZONTAL FORCE CAPACITY OF A HEMI-SPHERICAL DOME

Carlo Olivieri¹, Anna Castellano², Isabella Elia², Antonio Fortunato¹, Ida Mascolo¹

¹University of Salerno,
Department of Civil Engineering,
Fisciano (SA), Italy e-mail: colivieri,a.fortunato,i.mascolo}@unisa.it

² Polytechnic University of Bari,
Department of Civil Engineering Sciences and Architecture,
Bari, Italy
e-mail: {anna.castellano, isabella.elia}@poliba.it

Keywords: Masonry, No-Tension materials, Membrane Equilibrium Analysis, Domes, Horizontal loads, parametric analysis, compressed shells.

Abstract. The assessment of the ultimate load capacity of masonry domes and vaults is a complex open issue of both professional and research concern. 3D curved geometry of such structures entails biaxial stress states and highly nonlinear mechanical behaviors which require advanced computational strategies to be rigorously dealt with.

This study focuses on the assessment of the capacity of masonry hemispherical domes subjected to horizontal forces (such as those produced by wind and earthquake). In the framework of Limit Analysis (LA), a parametric Membrane Equilibrium Analysis (MEA) is proposed based on No-Tension (NT) material assumptions in the sense of Heyman: the unilateral membrane must lay inside the boundary surfaces of the dome and the membrane stress must have a non-positive concave potential. The membrane equilibrium problem for the dome is then formulated in Pucher form and controlled by a few parameters to be optimized. Two elementary examples are also provided to illustrate the method.

1 INTRODUCTION

The assessment of the structural capacity under horizontal forces (e.g., wind, inertial forces induced by earthquake etc.) of masonry domes or vaults is a challenging issue of structural engineering of relevant practical importance [1]-[9]. This is a very complicated problem, due to the interaction between biaxial stress on curved geometries and the highly non-linear mechanical behavior of masonry material. A number of researchers over the years have tried to develop complex Finite or Discrete Element (FEM, DEM) numerical strategies, often with very sophisticated material models mimicking the actual properties of masonry (such as anisotropy, plasticity, viscosity, damage and degradation processes, non-linear behavior etc.) in some detail. The precision and the accuracy of these models depend on the amount and quality of geometric and mechanical data used for the simulations [10]-[17]. However, the number of uncertainties and randomness related to the definition of such geometric and mechanical parameters make it arduous, not to say impossible, to draw definite and correct masonry models. This observation opened the way to a number of experimental approaches based, for example, on tilting tests on scale models [18]-[21].

Many papers have appeared in recent years setting a new promising approach in the framework of Limit Analysis, based on the application of the static and kinematic theorems to admissible stress and strain fields [22]-[31]. They exploit the unilateral masonry-like material model, also known as No-Tension (NT) model, dating back to the pioneering works of Heyman [32] and Zienkiewicz [33]. The key advantage of such approach is that no mechanical properties are required.

Inspired by the pioneering works of Angelillo and Fortunato and Angelillo et al. [34]-[36], the present paper proposes an innovative and promising parametric approach based on the Membrane Equilibrium Analysis (MEA) [37, 40]. The key idea is to extend the Thrust Line Analysis (TLA), widely used for 2D equilibrium problems concerning arches, to 3D dome or vault equilibrium problems. Equilibrium states of masonry domes can be thought of as carried by an ideal membrane that due to Heyman's assumptions, must be compressed (i.e. the generalized stress is negative semi-definite) and entirely contained within the dome volume. The membrane equilibrium is formulated in Pucher form [41] in terms of two unknown scalar functions, namely the stress potential and the elevation of the membrane. Then, the equilibrium equations are reduced to the transverse equilibrium only by introducing the Airy stress potential function. On adopting a form-finding strategy, the shape on which the membrane stress acts is assumed as unknown in the Pucher equation and tuned by a number of geometric parameters to be optimized. The constrained optimization procedure consists in maximizing the value of the load factor under the unilateral constraints related to the NT material assumption. The lines along which the membrane surface approaches or crosses the limit surfaces of the dome (i.e. the intrados or extrados surfaces) provide candidate lines of hinging at collapse. Such a prediction can be easily cross checked with predictions obtained with experimental results.

The paper is organized as follows: Section 2 provides the mathematical preliminaries on the membrane equilibrium problem and its formulation in terms of Pucher stress, Section 3 presents the proposed parametric procedure and the adopted form-finding strategy, Section 4 gives two trivial application of the proposed method to a hemi-spherical dome with the sole aim of illustrating the method, finally concluding remarks and future prospects are summarized in Section 5.

2 MEMBRANE EQUILIBRIUM OF A DOME

2.1 Geometry: "a la Monge" description

Let us consider a masonry dome subjected to its own weight and to the action of horizontal body forces controlled by a load factor $\lambda = (\lambda_1, \lambda_2)$ (Fig.1). With respect to a right-hand orthogonal coordinate system $O(x_1, x_2, x_3)$, the geometry of membrane surfaces can be conveniently represented by a Monge patch:

$$\{\mathbf{x} = (x_1, x_2, f(x_1, x_2)), (x_1, x_2) \in \Omega\} \quad (1)$$

where $f(x_1, x_2)$ is, in general, an arbitrary continuous function of its arguments (x_1, x_2) and Ω is the so-called planform of the membrane, namely a connected plane region obtained as projection of the inner or outer membrane surfaces (i.e. S_i and S_e) on the x_1x_2 -transverse plane.

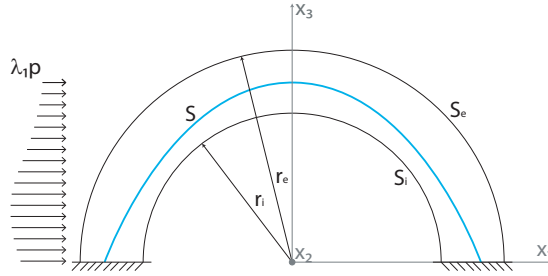


Figure 1: Section of a typical hemispherical dome in the x_1x_3 -coronal plane.

The surface forces per unit projected membrane area, applied to the dome are

$$\mathbf{p} = \{\lambda_1 p, \lambda_2 p, -p\} \quad (2)$$

where $p = btJ^*$ is the dome self-load per unit projected area; t is the dome thickness and J^* is the area ratio between the loading surface and the planform. For the sake of simplicity, we suppose that such forces are lumped to a conveniently chosen loading surface S_p all contained in the dome thickness.

When the body force p is given, by tuning the load factor λ we search for a thrust surface S (i.e. a membrane surface) which carries the applied loads and lays entirely within the limit surfaces S_i , S_e of the masonry dome and capable of sustaining the applied loads through purely compressive stresses.

2.2 Equilibrium

The equilibrium problem of the membrane S subjected to the surface force per unit platform area p can be described through a Differential Geometry (DG) approach [34] based on the Pucher formulation [41] as follow

$$\begin{cases} S_{11,1} + S_{12,2} + \lambda_1 p = 0 \\ S_{21,1} + S_{22,2} + \lambda_2 p = 0 \\ S_{11}f_{,11} + S_{22}f_{,22} + 2S_{12}f_{,12} - f_{,1}\lambda_1 p - f_{,2}\lambda_2 p + p = 0 \end{cases} \quad (3)$$

where S_{ij} is the ij Pucher stress component. Hereafter, we use the subscript notation $(*)_{,i}$ to describe the partial differentiation of $(*)$ with respect to x_i , and the subscript notation $(*)_{,ij}$ to describe the second derivative of $(*)$ with respect to x_i and x_j ($i, j = 1, 2$).

The equilibrium of the Pucher stress in the planform can be solved on introducing a stress potential, in the following way

$$\begin{cases} \tilde{S}_{11} = S_{11} + \int \lambda_1 p dx_1 = F_{,22} \\ \tilde{S}_{12} = S_{21} = -F_{,12} \\ \tilde{S}_{22} = S_{22} + \int \lambda_2 p dx_2 = F_{,11} \end{cases} \quad (4)$$

were $F(x_1, x_2)$ is the so called Airy stress function, which here is assumed to be only continuous (more detailed information with regard to the underlying assumptions can be found in [34]). Based on the Airy solution (4) and setting $h_i(\lambda_i) = \int \lambda_i p dx_i$ ($i = 1, 2$), the equilibrium equations (3) reduce to a single linear equation in the unknown stress potential function $F(x_1, x_2)$

$$(F_{,22} - h_1(\lambda_1))f_{,11} + (F_{,11} - h_2(\lambda_2))f_{,22} - 2F_{,12}f_{,12} - f_{,1}\lambda_1 p - f_{,2}\lambda_2 p + p = 0 \quad (5)$$

This is a second order Partial Differential Equation (PDE) in which the components of the second fundamental form of the surface $f(x_1, x_2)$ represent non-constant coefficients. Depending on the definiteness of the Hessian of the shape function f the equation (5) can be elliptic, hyperbolic or parabolic.

2.3 Constitutive restrictions

By assuming a Normal Rigid No-Tension (NRNT) material, the membrane stress tensor $\tilde{\mathbf{S}}$ must be negative semi-definite ($\tilde{\mathbf{S}} \in \text{Sym}^-$) (see [34]), namely, in 3D Euclidian space

$$\text{tr} \tilde{\mathbf{S}} \leq 0 \wedge \det \tilde{\mathbf{S}} \geq 0 \quad (6)$$

These conditions, in terms of the stress function $F(x_1, x_2)$ read

$$F_{,11} + F_{,22} \leq 0 \wedge F_{,11}F_{,22} - F_{,12}^2 \geq 0 \quad (7)$$

which means that the stress surface described by $F(x_1, x_2)$ has to be concave.

3 METHODOLOGY: FORM-FINDING PROBLEM

By assuming that the shape $f(x_1, x_2)$ of the membrane is known, the Boundary Value Problem (BVP) for the unilateral membrane S consists in finding an admissible (i.e. concave) stress function $F(x_1, x_2)$ (i.e. compressive membrane stresses) satisfying the equation (5) and either Dirichlet or Neumann boundary conditions:

$$F|_{\partial\Omega} = g \vee \left. \frac{dF}{dn} \right|_{\partial\Omega} = h \quad (8)$$

where, $\partial\Omega$ is the projected boundary, i.e. the closed boundary of the platform Ω ; $g(x_1, x_2)$ and $h(x_1, x_2)$ are the moment and the shear forces generated by applying the projected tractions on a 1D beam with the same form as $\partial\Omega$. In other words, since the PDE (5) is a second-order equation (rather than a fourth-order equation as happens in plane linear

elasticity) we can choose to prescribe the normal or the tangential component (i.e. F or $\frac{dF}{dn}$) of the stress or even any combination of the two at the projected boundary, in a quite equivalent manner.

At any fixed value of the load factor λ , the BVP problem formulated in these terms admits a unique solution which, however, disregards the constitutive restrictions (7). Then the equilibrium problem of the unilateral membrane S governed by Pucher's equation (5) can be reduced to a form-finding problem. We search in an assigned n -parameter family of shape functions $f(x_1, x_2, \alpha_1, \alpha_2, \dots, \alpha_n)$, constrained to be entirely contained within the dome volume and such that the Hessian is definite (i.e. a convex polynomial function), the only one that provides a solution of the transverse equilibrium equation (5) which fulfills the BVP as well as the concavity conditions (7). The parameters α_i can represent, for example, the size, the position or the asymmetry of the stress membrane S . The restriction on the Hessian ensures that transverse equilibrium equation (5) is elliptic and then easy to solve by a FEM-like numerical strategy. Then, to assess the ultimate load capacity of the dome, i.e. the load factor λ , we can search for the maximum value of $\|\lambda\|$ within the feasible region such that a concave solution of the BVP so defined exists (i.e. $F \in Sym^-$).

4 Numerical applications

The goal of this section is to illustrate how the method works through two trivial examples. All examples consider a hemispherical dome with thickness-radius ratio (t/L) equal to 0.2. It is also assumed that, without loss of generality, the horizontal load \mathbf{p} is settled to be constant per projected area and equal to $\{\lambda p, 0, -p\}$ defining the loading surface S_p as

$$S_p = \{(x_1, x_2, f_p(x_1, x_2)), (x_1, x_2) \in \Omega\}; \quad (9)$$

where $f_p(x_1, x_2)$ is the paraboloid (Fig. 2)

$$f_p(x_1, x_2) = L \left(1 - \frac{x_1^2 + x_2^2}{t^2} \right); \quad (10)$$

L is the middle radius of the dome. Note that, for convenience purposes, all the geometrical dimensions are adimensionalized with respect to the reference length L .

Figure 2: Loading surface S_p

The Pucher's equation governing the equilibrium problem (5) is parametrically solved for the shape $f(x_1, x_2, \alpha_1, \alpha_2, \dots)$ by using the PDEs tool implemented in Mathematica© (Version 12) [42] and based on a triangular Finite Element discretization (Please refer to [27] for more details).

4.1 Example 1

In the first example we choose an initial membrane shape corresponding to the paraboloid (10). This shape is fully contained within the dome thickness but it is not dependent on the geometrical parameters α_i . The maximum value of λ at which the stress ceases to be a negative semi-definite concave surface is $\lambda = 0.35$. Fig. 3 shows the principal stresses

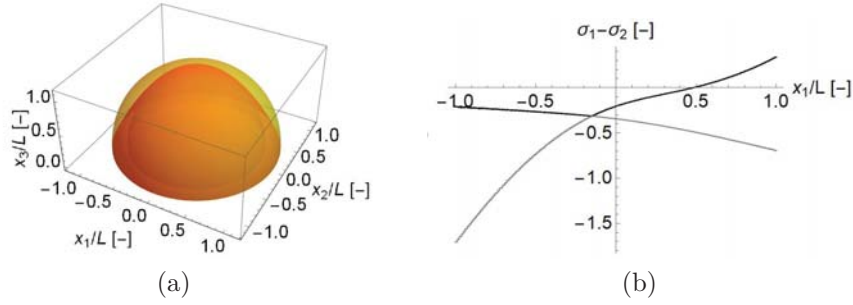


Figure 3: Thrust surface S_p inside the dome (a) and principal stresses profile in the sagittal plane for $\lambda = 0.38$ (b)

profile in the x_2x_3 -sagittal plane for a value of $\lambda = 0.38$ that leads to tensile stresses upwind with respect to the direction of the horizontal force.

In order to optimize the membrane shape $f(x_1, x_2) = S_p$, we have added to f_p a convenient shape function $\Delta f(x_1, x_2, \alpha_1, \alpha_2, \dots, \alpha_n)$, that is a cubic interpolating spline function with an appropriate set of control points $\alpha_1, \alpha_2, \dots, \alpha_n$ (i.e. maximum height, middle radius and inflexion point of membrane shape). By numerically solving the parametric equilibrium equation 5 we obtain a class of membrane forms depending on the load factor λ . By regarding the load factor λ as the objective function, the parameters $\alpha_1, \alpha_2, \dots, \alpha_n$ are finally optimized by maximizing $\lambda(\alpha_1, \alpha_2, \dots, \alpha_n)$.

The so optimized membrane shape $f(x_1, x_2, \alpha_1, \alpha_2, \dots, \alpha_n)$ enables a significant increase in the maximum value of λ at which the thrust surface is contained entirely inside the dome and conditions (7) hold, namely $\lambda = 0.42$.

Fig. 4 shows the corresponding profile of the principal stresses corresponding to the optimized solution in the x_1x_3 -coronal and in the x_2x_3 -sagittal planes. The contour plot of the principal (minimum and maximum) projected stress values and the corresponding isostatic lines are also reported.

4.2 Example 2

In this example we analyze a dome which displays a certain pattern of crack, due to horizontal actions which exceed the limit value. In such a case the stress membrane is not contained entirely in the dome (Figs. 5). Therefore, we allow for a small enlargement of the extrados surface and look for the intersection of the membrane surface with the original extrados surface S_e . In this case, the maximum load factor such that the stress is negative semi-definite is $\lambda = 0.45$. The contour plot of the minimum and maximum principal stresses and the corresponding isostatic lines are reported in Figs. 5, in particular the maximum principal stress almost vanish for $x_1 \in (-17, -5)$, leeward with respect to the horizontal action. Notice that the isostatic lines corresponding to zero principal stresses, are almost straight, meaning that the surface profile in such directions consists of funicular lines. In Fig. 5b the profile of the curve of intersection of the optimized membrane surface with the original extrados surface S_i is shown (black lines).

5 CONCLUDING REMARKS

This paper presents a new parametric approach, based on the Membrane Equilibrium Analysis, to the assessment of the load carrying capacity of masonry domes or vaults under horizontal body forces. By using the MEA the load applied to a dome composed of

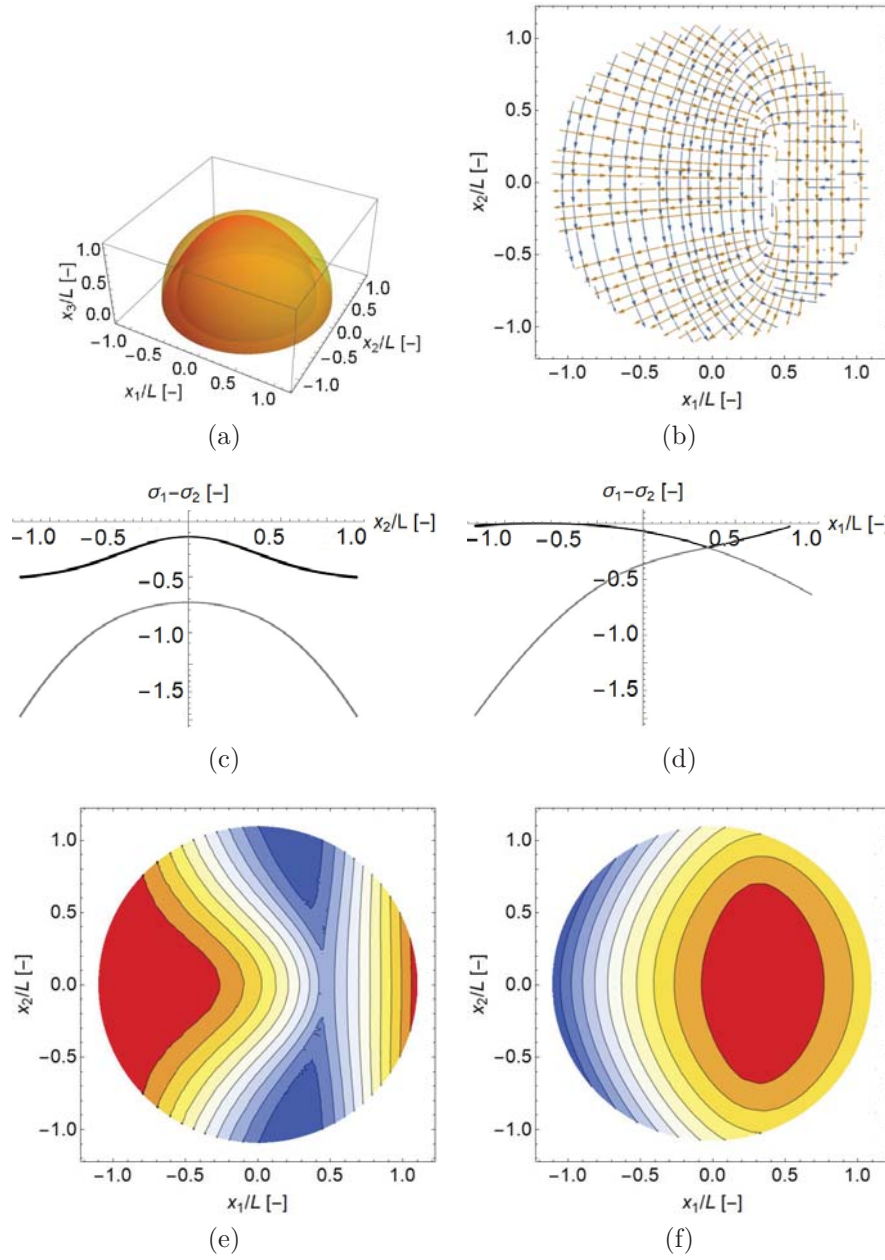


Figure 4: Optimized thrust surface S corresponding to the optimal value of λ (a); principal lines of curvature (b); principal stress profile in the coronal plane (c); principal stress profile in the sagittal plane (d); contour plot of minimum and maximum principal projected stress values (e,f)

unilateral Heyman material is lumped to a loading surface S_p and is carried by a thrust surface S contained inside the masonry. By changing its shape f through the tuning of a finite number of geometric parameters, the generalized membrane stress balancing the loads as well as its projection on the planform change. The optimal value of the geometric parameters, i.e. the optimal shape function of the stress membrane, is obtained by maximizing the horizontal load multiplier λ , with the constraints that the generalized stress is non-positive definite, the surface S is fully contained inside the dome volume and the Hessian of the shape function f is positive definite (i.e. f belongs to a n -parameter

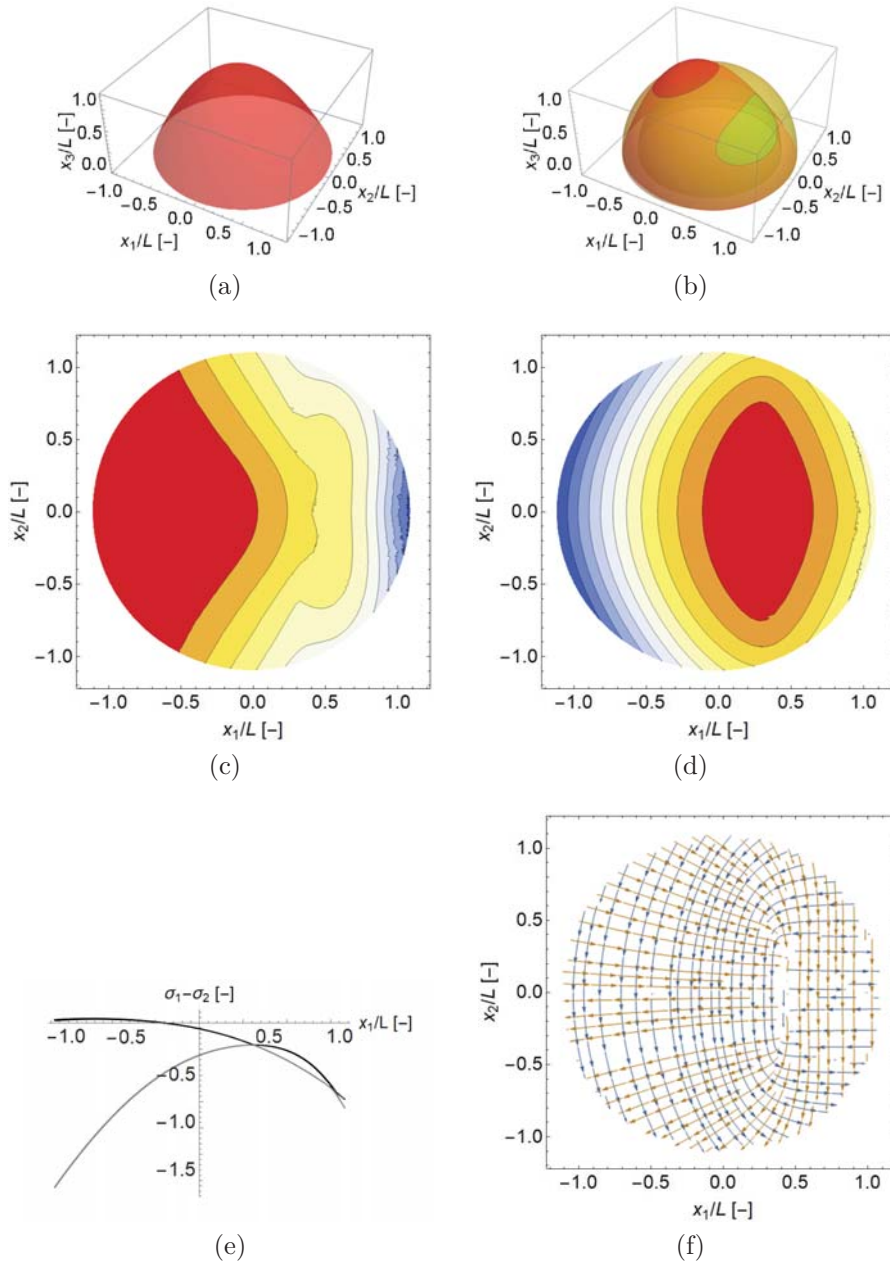


Figure 5: Optimized thrust surface S (a); thrust surface S partially inside the dome (b); contour plots minimum and maximum principal projected stress values contour plot (c,d); principal stress profile in the sagittal plane (e); isostatic lines corresponding to projected principal stress values (f).

function family of convex polinomia). The latter condition guarantees that the Pucher's equilibrium equation is elliptic and then easy to solve though a FEM-like numerical strategy. The proposed approach can be applied to either design or assessment of ultimate load capacity and can be easily extended to more complex geometries (i.e. thin-thick, flatted or pointed domes and semi-circular, cross, Rib or Fan vaults) even though it needs a substantial effort in terms of implementation.

FUNDING

This work was supported by the Italian Ministry of Education, University and Research (MIUR) under the "Departments of Excellence" grant L.232/2016.

REFERENCES

- [1] O'Dwyer, D.W. Funicular analysis of masonry vaults. *Computers and Structures*, 73(1-5), 187–197, 1999.
- [2] Block P., Ciblac T., Ochsendorf J., Real-time limit analysis of vaulted masonry buildings. *Computers and Structures*, 84(29), 1841–1852, 2006.
- [3] De Lorenzis, L., DeJong, M.J. and Ochsendorf, J. Failure of masonry arches under impulse base motion. *Earthquake Engineering and Structural Dynamics*, 36(14), 2119–2136, 2007.
- [4] Mallardo, V., Malvezzi, R., Milani, E., and Milani, G. Seismic vulnerability of historical masonry buildings: A case study in Ferrara. *Engineering Structures*, 30, 2223–2241, 2008.
- [5] DeJong, M.J. Seismic Assessment Strategies for Masonry Structures, PhD dissertation Building Technology at the Massachusetts institute of technology, 2009.
- [6] Foraboschi, P. Resisting system and failure modes of masonry domes. *Engineering Failure Analysis*, 44, 315–337, 2014. DOI: 10.1016/j.engfailanal.2014.05.005
- [7] Khan M.A., Paul D.K. Seismic Performance of Masonry Arches and Vaults. In: Rodrigues H., Elnashai A., Calvi G. (eds) *Facing the Challenges in Structural Engineering. GeoMEast 2017. Sustainable Civil Infrastructures*, Springer, Cham, 2018. DOI: 10.1007/978-3-319-61914-9_3
- [8] Iannuzzo, A., Olivieri, C., and Fortunato, A. Displacement capacity of masonry structures under horizontal actions via prd method. *Journal of Mechanics of Materials and Structures*, 14(5), 703–718, 2019. DOI:10.2140/jomms.2019.14.703
- [9] Mascolo, I., Fulgione, M., Pasquino M. Lateral torsional buckling of compressed open thin walled beams: experimental confirmations. *Int. J. Masonry Research and Innovation*, 4(1/2), 150–158, 2019. DOI: 10.1504/IJMRI.2019.096829
- [10] Chetouane, B., Dubois, F., Vinches M. and Bohatier, C. NSCD discrete element method for modeling masonry structures. *International Journal for Numerical Methods in Engineering*, 64, 65–94, 2005.
- [11] Lemos, J.V. Numerical issues in the representation of masonry structural dynamics with discrete elements. In M. Papadrakakis, D.C. Charmpis, N.D. Lagaros, Y. Tsompanakis (Eds.), *ECCOMAS Thematic Conference on Computational Methods in Structural Dynamics and Earthquake Engineering*. Crete, Greece, 2007.
- [12] Malena, M. and Casciaro, R. Finite element shakedown analysis of reinforced concrete 3D frames. *Computers and Structures*, 86, 1176–1188, 2008.

- [13] Lucchesi, M., Padovani, C., Pasquinelli, G. and Zani, N. Masonry constructions: mechanical models and numerical applications. *Lecture Notes in Applied and Computational Mechanics*, 39, Springer, Berlin, 2008.
- [14] de Felice, G., Amorosi, A. and Malena M. Elasto-plastic analysis of block structures through a homogenization method. *J. Numer. Anal. Meth. Geomech.*, 34, 221–247, 2010.
- [15] de Felice, G., and Malena M. Failure pattern prediction in masonry. *J. Mech. Mater. Struct.*, 14, 663–682, 2019.
- [16] Gobbin, F., de Felice G. and Lemos, J.V. A discrete element model for masonry vaults strengthened with externally bonded reinforcement. *Int. J. Archit. Herit.*, 1–14, 2020. DOI: 10.1080/15583058.2020.1743792
- [17] Paris, V., Pizzigoni, A. and Adriaenssens, S. Statics of self-balancing masonry domes constructed with a cross-herringbone spiraling pattern. *Engineering Structures*, 215, 110440, 2020. DOI: 10.1016/j.engstruct.2020.110440
- [18] Rossi, M., Calderini, C., Lagomarsino, S. and Milani, G. Seismic response of masonry vaulted structures: experimental and numerical modelling. in Lourenço, P. B., Haseltine, B. A., and Vasconcelos, G. (eds) 9th International Masonry Conference. Guimarães: Universidade do Minho, 2014.
- [19] Rossi, M., Calderini, C. and Lagomarsino, S. Experimental testing of the seismic in-plane displacement capacity of masonry cross vaults through a scale model. *Engineering Structures*, 123, 300–312, 2016.
- [20] Milani, G., Rossi, M., Calderini, C. and Lagomarsino, S. Tilting plane tests on a small-scale masonry cross vault: Experimental results and numerical simulations through a heterogeneous approach. *Bulletin of Earthquake Engineering*, 14(1), 261–281, 2016. DOI: 10.1007/s10518-015-9815-1
- [21] Barsotti, R., Bennati, S., Ochsendorf, J.A. and Tirabasso C. Scale models for the experimental analysis of the collapse mechanisms of masonry bay windows under horizontal actions. in *COMPDYN 2017. Proceedings of the 6th ECCOMAS Thematic Conference on Computational Methods in Structural Dynamics and Earthquake Engineering*, 15 June 2017 through 17 June 2017, Rhodes Island, Greece, 2017.
- [22] Huerta, S. Arcos bóvedas y cúpulas. Geometría y equilibrio en el cálculo tradicional de estructuras de fábrica. Madrid : Instituto Juan de Herrero, 2016.
- [23] Angelillo, M. Practical applications of unilateral models of masonry equilibrium. in Angelillo M. (ed.) *Mechanics of masonry structures*, Springer, Vienna, 109–210, 2014.
- [24] De Chiara E., Cennamo C., Gesualdo A., Montanino A., Olivieri C., Fortunato A. Automatic generation of statically admissible stress fields in masonry vaults. *Journal of Mechanics of Materials and Structures*, 14(5), 719–737, 2019.
- [25] Fraddosio A., Lepore N., Piccioni M.D. Lower Bound Limit Analysis of Masonry Vaults Under General Load Conditions. *RILEM Bookseries*, 2019. DOI:10.1007/978-3-319-99441-3_118.

- [26] Gesualdo A., Brandonisio G., De Luca A., Iannuzzo A., Montanino A. and Olivieri C. Limit analysis of cloister vaults: the case study of Palazzo Caracciolo di Avellino. *Journal of Mechanics of Materials and Structures*, 14(5), 739–750, 2019.
- [27] Olivieri C., Angelillo M., Gesualdo A., Iannuzzo A. and Fortunato A. Parametric design of purely compressed shells, *Mechanics of Materials*, 155, 103782, 2020 DOI: 10.1016/j.mechmat.2021.103782
- [28] Olivieri C., Fortunato A., DeJong M. A new equilibrium solution for masonry railway bridges: the case study of Marsh Lane Bridge. *Int. J. of Masonry Research and Innovation*, 2021. (In press) DOI: 10.1504/IJMRI.2021.10037557
- [29] Mascolo I., Gesualdo, A., Olivieri C., Fortunato A. On rigid blocks detection in unilateral masonry-like structures: a continuous displacement fields approach. *Int. J. of Masonry Research and Innovation*, 2021. (In Print)
- [30] Malena M., Angelillo M., Fortunato A., de Felice G., Mascolo I., Arch bridges subject to pier settlements: continuous vs. piecewise rigid displacements methods. *Meccanica*, 2021. (Under Review)
- [31] Fortunato, A., Gesualdo, A., Mascolo I. and Monaco, M. P-Bézier energy optimization for elastic solutions of masonry-like panels. *Int. J. of Masonry Research and Innovation*, 2021. (In Press) DOI: 10.1504/IJMRI.2021.10037508
- [32] Heyman, J. The stone skeleton. Cambridge University Press.
- [33] Zienkiewicz, O.C., Valliappan S., King I.P., Stress analysis of rock as a 'No Tension' material. *Géotechnique*, 18(1), 56–66, 1968.
- [34] Angelillo M., Fortunato A. Equilibrium of masonry vaults. in *Lecture notes in applied and computational mechanics, novel approaches in civil engineering*, Berlin: Springer, 14, (Fremond M, Maceri F Eds), 2004.
- [35] Angelillo, M., Babilio, E., and Fortunato, A. Singular stress fields for masonry-like vaults. *Continuum Mechanics and Thermodynamics*, 25, 423–441, 2013.
- [36] Angelillo, M., Babilio, E., Fortunato, A., Lippiello, M., Montanino, A. Analytic solutions for the stress field in static sandpiles. *Mechanics of Materials*, 95, 192–203, 2016
- [37] ABlock P., Ochsendorf J. Thrust network analysis: a new methodology for three-dimensional equilibrium. *Shell. Spat. Struct.*, 48(155), 167–173, 2007
- [38] Briccola D., Bruggi M., Analysis of 3D lineelastic masonry-like structures through the API of a finite element software. *Adv. Eng. Softw.*, 133, 60–75, 2019
- [39] Liew A., Avelino R. , Moosavi V., Van Mele T., Block P., Optimising the load path of compression-only thrust networks through independent sets. *Structural and Multidisciplinary Optimization*, 60, 231–44, 2019
- [40] Bruggi M., A constrained force density method for the funicular analysis and design of arches, domes and vaults. *Int. J. Solids Struct.*, 193-194, 251–69, 2020

- [41] Pucher, A. Über der spannungzustand in gekrumnten flachen. Beton u Eisen, 33, 298–304, 1934.
- [42] Wolfram S. The Mathematica Book, 5th ed., Wolfram Media, 2003.

SEISMIC RETROFITTING TECHNIQUES FOR EXISTING MASONRY BUILDINGS

Ida Mascolo¹, Antonio Fortunato¹, Carlo Olivieri¹ and Antonio Gesualdo²

¹ University of Salerno
Department of Civil Engineering
Via Giovanni Paolo II, 132 - 84084 Fisciano (SA)
e-mail: {imascolo, colivieri, a.fortunato}@unisa.it

² University of Naples “Federico II”
Department of Structural Engineering
Naples 80125, Italy
e-mail: antonio.gesualdo@unina.it

Keywords: Masonry, homogenization, seismic behaviour, retrofitting techniques.

Abstract. In many seismically active regions of the world there are large numbers of masonry buildings. Most of these buildings have not been designed for seismic loads. Recent earthquakes have shown that many of these buildings are seismically vulnerable and should be considered for retrofitting. Different conventional and unconventional retrofitting techniques are available to increase the strength and/or ductility of unreinforced masonry (URM) walls. This paper reviews and discusses seismic retrofitting of masonry walls with emphasis on the conventional techniques. Retrofitting procedures are discussed with regard to a case study: a stone masonry building in Irpinia region, damaged by the 1980 earthquake. The interventions are evaluated by means of finite elements with a macroelement obtained with an homogenization technique. Linear and nonlinear procedures are compared, and peculiarities of each procedure are shown.

1 INTRODUCTION

Masonry structures are prone to extensive damage followed by failure and collapse when subjected to loads resulting from wind, earthquake and other natural or man-made events. Recent earthquakes and terrorist acts have clearly demonstrated that the development of effective and affordable strategies for the analysis and strengthening of masonry is urgently needed. Many older masonry structures currently in use were in fact designed and constructed with little or no consideration of these aggressive factors. In addition, recent changes in seismic requirements have left many URM buildings in need of strengthening. In many cases, these natural effects were not considered in ancient time [1]. Very few masonry buildings have been built in modern times, and knowledge of the related design methods is no longer part of a civil engineer's training [2]. Despite a growing need for rehabilitation and conservation of these structures, understanding of their behavior has been declining in the first decades of last century, and the available methods for assessing them are of questionable reliability. In recent times the strong need of rehabilitation, together with the development of numerical tools, has improved knowledge about assessment methods for masonry buildings [3]-[12]. As a response to the challenges offered by the assessment of URM, several intervention methods have been proposed [13]. Nevertheless the first step toward a complete assessment of an intervention method is the understanding of constitutive behaviour of both URM and reinforcement [15]-[26].

One of the reliable tools developed in the last years are the homogenization techniques. The development of these techniques in the field of composite materials has induced a similar approach in the field of masonry structures, in which the masonry material is the result of two different elements, spacially arranged in different geometries [27]. Since it is a key point in the bulk behaviour of masonry, careful attention must be posed on the behaviour of block-masonry interface [28, 29] and in the spatial arrangement of the blocks. Differently from fiber reinforced materials, in which a periodic structure can be often recognized, homogenization of non-periodic structures is a complex process [30]. Based on classical homogenization methods [31, 32], this paper presents an analysis of a stone masonry building performed before and after the reinforcement with grout injections. The basic cell of the homogenized medium is a non-standard one, with stone elements irregularly arranged in the representative Volume Element (RVE). Elementary load cases were developed in order to obtain the constitutive bulk parameters of the homogenized medium [33, 34]. According to the above considerations, the model has been developed by means of finite element analysis, since a closed form for the homogenization problem in this case is not available. A numerical finite element analysis was performed on this existing building taking into account the bulk parameters derived in the homogenization procedure. The case study is a stone masonry building with simple and irregular shape in Irpinia (a seismic region of Southern Italy), severely damaged by the 1980 earthquake.

2 THE STRUCTURAL MODEL

2.1 Homogenization

It is well known that the mechanical characteristics of masonry should be detected in order to define the constitutive laws of the material for the mathematical model assumptions. Nevertheless all the parameters defining these characteristics cannot be measured on site. The only parameters that can be measured at the moment on site are the modulus of elasticity, the Poisson ratio in the direction parallel to the bed joints, the value of

the stress at onset of cracking on the external face of a wall. A masonry wall has in fact different properties along different axes according to the units texture and the directions and geometry of the mortar joints. To evaluate the different properties according the directions, an homogenization procedure has been performed to describe masonry as a composite medium in terms of macro or average properties so that it can be assumed to be an homogeneous material. The first problem to solve was the choice of RVE, i.e. the minimum material to evaluate the macro-parameters of masonry. In the case of periodic structure of masonry it is in general a simple problem to consider the basic cell as RVE. In Southern Italy irregular stone masonry is widely diffused, so that basic cells are not simple to recognize. In this paper an iterative method, based on test windows, was taken into account [35, 36] considering a linear elastic behaviour for both mortar and stone units. A 3D model was built for the RVE (Figure 1a), performig linear and non linear analyses and considering two different types of bonding between the mortar and the stone unit:

1. perfect bonding: in this case a bulk linear elastic behaviour for masonry was obtained as a result;
2. unperfect bonding: in this case an unilateral frictional contact with Mohr-Coulomb constitutive law for the interface mortar-stone unit was taken into account. A nonlinear elastic bulk behaviour was obtained for masonry.

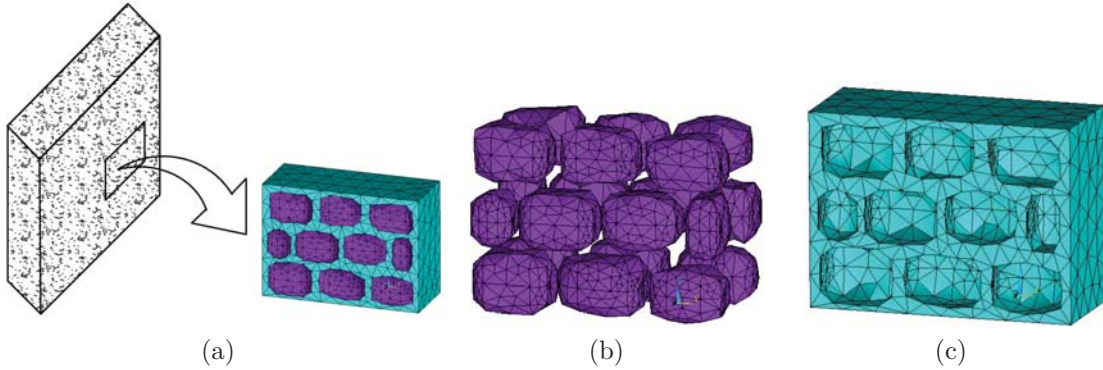


Figure 1: Representative volume element (a), discretized stone units (b) and mortar matrix (c).

In Figures 1 the discretized model of the basic cell is shown: it is a $110 \times 150 \times 60$ cm block in which 20 irregular stone units are embedded in a mortar matrix. The spatial distribution of the stones is irregular too. A finite element analysis was performed on the block, in order to evaluate the mechanical bulk properties to be employed in the numerical analysis of the entire building. Both the constituents were considered isotropic elastic [37]. Their mechanical properties are reported in Table 1.

A picture of the discretized basic cell is represented in Figure 2a. Numerical analyses have shown that negligible changes in the mechanical homogenized parameters were observed in masonry panels with larger dimensions with respect to the chosen one, so that the above block can be considered as a representative volume element.

Several sensitive analyses were carried out on different, more chaotic spatial distributions of stones in a masonry panel having the same bulk dimensions, as that reported in

Material	Elasticity Modulus	Poisson coefficient	Friction coefficient
Stone	6000 MPa	0.23	0.60
Mortar	2500 MPa	0.20	

Table 1: Values of mechanical parameters.

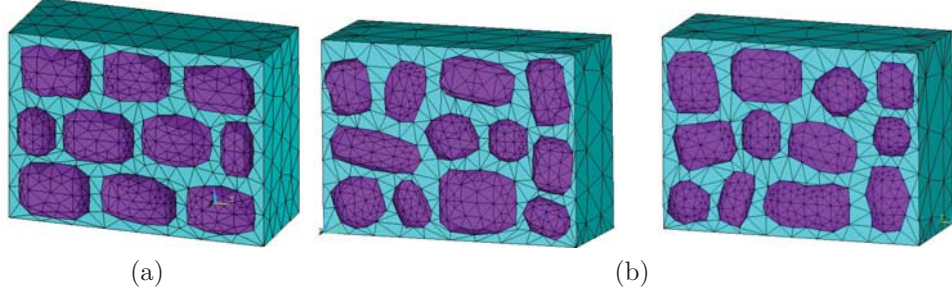


Figure 2: Discretized masonry block: basic cell (a) and tentative discretized cells (b).

Figure 2b. The analyses have shown that a transversal isotropic behaviour can be recognized in these last cases. The symmetry axis is that one orthogonal to the medium plane of the masonry panel. The anisotropic case has been chosen for the case study, both for the similarity of the stone arrangement with the real case and for the generality of the constitutive behaviour.

2.2 Numerical analysis

The results of the analysis performed by means of the ANSYS program [38] on the masonry block are shown in the following. Standard CONTA173 and TARGE170 were used to model the unperfect bonding, while elements SOLID45 were used to discretize both mortar and stone units.

Different load conditions were analyzed in order to obtain the compliance tensor for the homogenized medium. The stiffness tensor was obtained as the inverse matrix of the compliance one. As a synthesis of the results, the stiffness tensor for the homogenized medium is given in the two analyzed cases, with or without frictional contact. The stiffness tensor in the elastic case without frictional contact is reported in Tables 2a. As it can be seen, the stiffness matrix of the material modelled without frictional contact corresponds, as expected, to that of an orthotropic material, so that the symmetry of the matrix is preserved.

No interventions (MPa)						Grout injections (MPa)					
10928	1826	1790	0	0	0	18043	2256	2213	0	0	0
1826	6812	1321	0	0	0	2256	10584	1514	0	0	0
1790	1321	5492	0	0	0	2213	1514	8875	0	0	0
0	0	0	2045	0	0	0	0	0	3802	0	0
0	0	0	0	1938	0	0	0	0	0	2780	0
0	0	0	0	0	1488	0	0	0	0	0	2570

(a)

(b)

Table 2: Stiffness elastic tensor (no frictional contact).

In this case, in fact, the existence of an elastic potential can be demonstrated. Table 2 refers to the constitutive model of the block without interventions, while Table 2b reports the same data in case of grout interventions.

The case in which frictional contact is taken into account is different: an unsymmetric constitutive matrix is the result of the dissipative behaviour due to the unilateral frictional contact. In this case, in fact, the dissipation cannot assure the existence of an elastic potential function for the material behaviour, which corresponds to a symmetric constitutive matrix.

The above symmetry cannot be observed in fact in the case of frictional contact, shown in Tables 3a. In this case too Table 3a refers to the constitutive model of the block without interventions, while Table 3b reports the same data in case of grout interventions.

As it can be seen, the homogenized material shows more deformability in the case of frictional contact with respect to the perfect bonding.

No interventions (MPa)						Grout injections (MPa)					
7672	17146	9367	2525	8983	-4854	14142	8850	8506	4406	1390	-9051
5878	5702	6188	2216	4771	-4891	5787	8842	5505	2761	2247	-4273
2478	5783	3875	3464	3464	-181	4415	4274	6642	1632	1052	-4991
-128	-208	-146	-1091	-1091	181	-109	-101	-207	566	-5	1806
53	73	50	617	617	-53	35	52	37	21	653	-105
-11	2	-12	58	58	711	-4	10	-1	12	47	6908

(a)
(b)

Table 3: Stiffness elastic tensor (frictional contact).

This can be explained with the possibility of relative displacement between mortar and stones, due to chosen model of friction, which involves unilateral contact. To complete the set of data obtained by the homogenized procedure performed, the elastic bulk parameters in the two cases analyzed are reported in the following Tables 4a and 4b.

No interventions			Grout injections			No interventions			Grout injections		
E_x [MPa]	10 928.07		18 043.00			E_x [MPa]	7453.99		14 067.99		
E_y [MPa]	6812.06		10 584.03			E_y [MPa]	5091.56		8753.76		
E_z [MPa]	5492.05		8875.00			E_z [MPa]	3629.77		6695.40		
ν_{yx}	0.21		0.18			ν_{yx}	0.41		0.39		
ν_{xy}	0.13		0.11			ν_{xy}	0.47		0.43		
ν_{zx}	0.27		0.22			ν_{zx}	0.41		0.39		
ν_{xz}	0.14		0.11			ν_{xz}	0.46		0.43		
ν_{zy}	0.19		0.14			ν_{zy}	0.42		0.38		
ν_{yz}	0.16		0.12			ν_{yz}	0.44		0.40		
G_{xy} [MPa]	2045.57		3802.74			G_{xy} [MPa]	800.19		1204.02		
G_{yz} [MPa]	138.68		2782.28			G_{yz} [MPa]	661.33		1277.46		
G_{zx} [MPa]	1488.61		2574.19			G_{zx} [MPa]	697.49		1387.34		

(a) No frictional contact
(b) Frictional contact

Table 4: Mechanical parameters.

In the two cases examined the elastic modulus increase is significant, while a less significant decrease can be observed in the Poisson coefficients. The expected overall increase of stiffness in the injected homogenized medium with respect to that without interventions is confirmed.

2.3 Structural analysis

A stone masonry building in Irpinia was chosen as a case study. It was built in 1930, with a planar L shape, and sort of regularity in the z -direction, being x and y the directions of the two external walls of the building (Figure 3a) and z the vertical one.

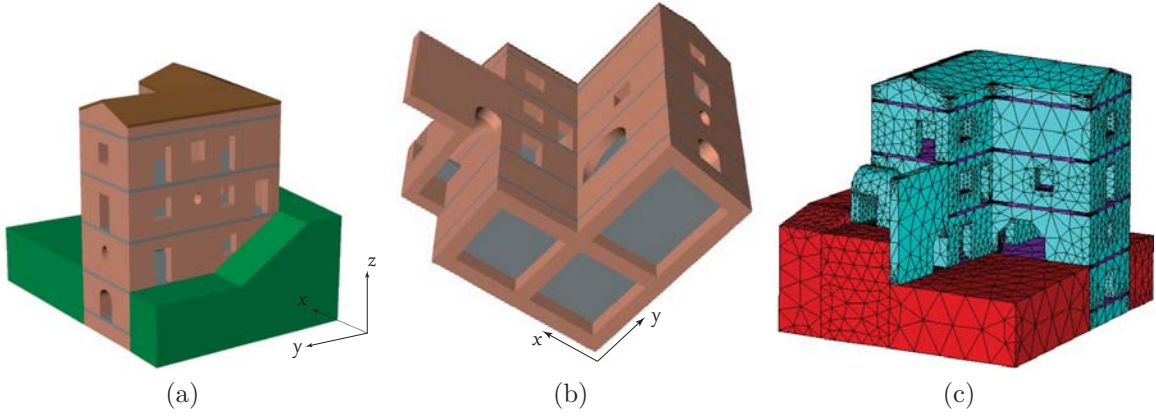


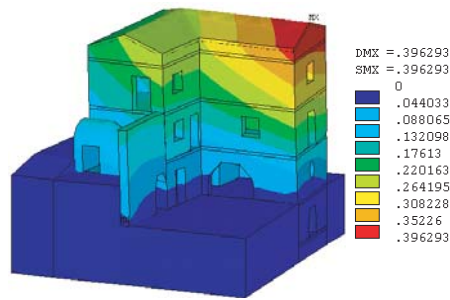
Figure 3: Pictures of the building with reference axes (a)-(b). Discretized model of the building (c).

The stiffness in the y -direction is higher to that in the x -direction as it can be seen in Figure 3b. The masonry walls were modelled with the bulk properties examined above, while floors and roofs were considered as plate elements with high in-plane stiffness (Figure 3c). The homogenized properties evaluated in the previous sections have been considered as the properties of the building masonry walls. The numerical analysis was performed by means of the numerical code ANSYS, with tetrahedral four-node solid elements SOLID45.

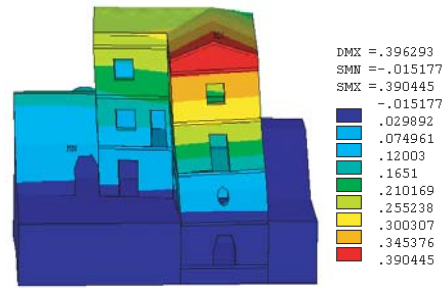
In the following a discussion about the displacements results is provided, in order to assess the reliability of the method proposed. Figure 4a presents the distribution of displacements for an earthquake loading along x -direction in the case of orthotropic behaviour. The constitutive model without frictional contact was taken into account. As it can be seen, the displacement evaluated at the top of the building is about 0.4 cm, better represented in Figure 4b. If the seismic loading is directed along the y -direction, the maximum displacement at the top of the building is about 0% of the previous, as expected according to the building geometry (Figure 4c).

The reduction of the displacement amount due to the contribute of grout injections in the case of orthotropic behaviour is represented in Figure 4d and 4e. As it can be seen, there is a similarity of overall behaviour of the structure, with increased stiffness due to the injections. The analysis performed and shown above involves orthotropic behaviour with a stiffness matrix in which the non-zero terms are derived from the stiffness matrix developed in the case of frictional contact. The isotropic model could not represent the behaviour of the real case study, as it can be seen in the following table, in which the results of a finite element analysis, involving both isotropic and orthotropic behaviour, has been reported.

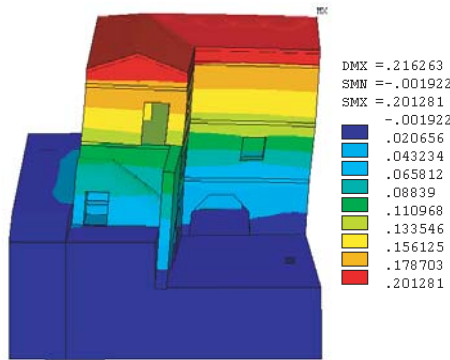
Tables 5 and 6 show that an elevate stiffness can be recognized in the isotropic case, so that the maximum displacements in the four load cases examined for the isotropic behaviour are about 15% of the displacements obtained in the corresponding orthotropic



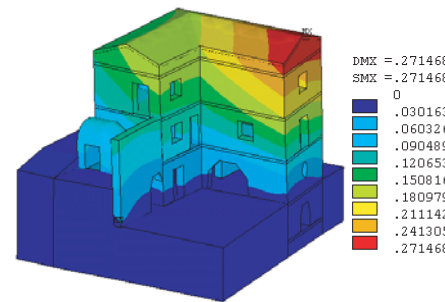
(a) Total displacements for earthquake x-loading (no interventions, orthotropic behaviour)



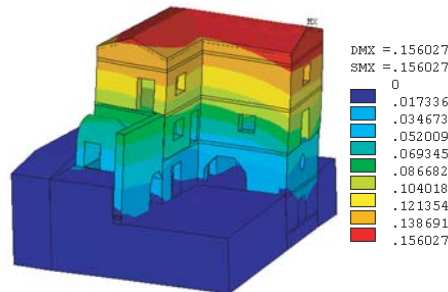
(b) Displacement x-direction for earthquake x-loading (no interventions, orthotropic behaviour)



(c) Displacement y-direction for earthquake y-loading (no interventions, orthotropic behaviour)



(d) Displacements x-direction for earthquake x-loading (with grout injections, orthotropic behaviour)



(e) Displacements y-direction for earthquake y-loading (with grout injections, orthotropic behaviour)

Figure 4: Results.

ones. Usually the isotropic models represent the different behaviour according the load directions only with reference to structural geometry, without considering the influence of the material geometry.

A similar finite element analysis has been performed and the displacements in the same four load cases for the orthotropic behaviour have been compared in three different cases: no interventions, grout injections and connections between the two wythes. This last case has been considered to evaluate the influence of transversal connections in masonry. In general, a good quality masonry presents different leaves with transversal connections, made in general by overlapped stones or long regular stones transversally placed. In the

	Isotropic case	Orthotropic case
x-direction-x-loading	0.057	0.390
y-direction-y-loading	0.035	0.201
Absolute x-loading	0.058	0.396
Absolute y-loading	0.037	0.216

Table 5: Maximum displacements in the elastic cases, no interventions (cm).

	No interventions	Grout injections	Steel connections
x-direction-x-loading	0.390	0.267	0.280
y-direction-y-loading	0.201	0.146	0.147
Absolute x-loading	0.396	0.271	0.284
Absolute y-loading	0.216	0.156	0.157

Table 6: Maximum displacements in the intervention cases, orthotropic behaviour (cm).

cases in which the leafs that constitute the wall are not connected, a retrofitting connection is needed. Traditional interventions involve the placement of transversal stones. Recently local interventions by means of steel bars have been considered. Due both to the cost and to the difficulties connected with the insertion of the bars, usually these last interventions are taken into account if the portion of the masonry wall requiring a retrofit intervention is limited. The analyses show that the performance of the building subjected to a retrofitting intervention made with grout injections is comparable with that of a good quality masonry building.

3 CONCLUSIONS

The geometric and physical-mechanical characterization of the masonry texture is a key point in the homogenization of historical buildings. The numerical homogenization analysis can be focused as a standard procedure to identify the fundamental parameter to correctly model a masonry structure. The outcomes of the proposed approach point out that the anisotropic analysis is accurately formulated and are strongly influenced by the modeling parameters. It has also been shown that isotropic analysis provides different results from the anisotropic one.

REFERENCES

- [1] N. Domède, G. Pons, A. Sellier, Y. Fritih. Mechanical behaviour of ancient masonry. *Materials and Structures*, 42, 2008.
- [2] D.C. Rai. A generalized method for seismic evaluation of existing buildings. *Current Science*, 94(3), 2008.
- [3] D.E. Allen, J.H. Rainer. Guidelines for the seismic evaluation of existing buildings. *International Journal of Rock Mechanics and Mining Sciences and Geomechanics Abstracts*, 33(2):91A-91-A(1), 1996.

- [4] A. Iannuzzo, C. Olivieri, A. Fortunato. Displacement capacity of masonry structures under horizontal actions via prd method. *Journal of Mechanics of Materials and Structures*, 14(5), 703–718, 2019.
- [5] C. Olivieri, M. Angelillo, A. Gesualdo, A. Iannuzzo, A. Fortunato. Parametric design of purely compressed shells. *Mechanics of Materials*, 155, 103782, 2020.
- [6] M. Angelillo, C. Olivieri, M.J. DeJong. A new equilibrium solution for masonry spiral stairs. *Engineering Structures*, 238, 112176, 2021. DOI: 10.1016/j.engstruct.2021.112176
- [7] D.B. Hom, J.H. Rainer. Seismic evaluation of existing buildings. ASCE, American Society of Civil Engineers, USA, 31(3), 2003.
- [8] A. Gesualdo, M. Monaco. Seismic retrofitting techniques for existing masonry buildings. *Journal of Civil Engineering and Architecture*, 5(11), 1011–1018, 2011.
- [9] M. Monaco, I. Bergamasco, M. Betti. A no-tension analysis for a brick masonry vault with lunette. *Journal of Mechanics of Materials and Structures*, 13(5), 703–714, 2018.
- [10] A. Gesualdo, B. Calderoni, A. Sandoli, M. Monaco. Minimum energy approach for the in-plane shear resistance of masonry panels. *Ingegneria Sismica*, 36(1), 42–53, 2019.
- [11] A. Gesualdo, B. Calderoni, A. Iannuzzo, A. Fortunato, M. Monaco. Minimum energy strategies for the in-plane behaviour of masonry. *Frattura ed Integrità Strutturale*, 14(51), 376–385, 2020.
- [12] A. Iannuzzo, A. De Luca, A. Fortunato, A. Gesualdo, M. Angelillo. Fractures detection in masonry constructions under horizontal seismic forces. *Ingegneria Sismica*, 35(3), 87–103, 2018.
- [13] A.S. Arya. Guidelines for repair, restoration, condition assessment and seismic strengthening of masonry buildings. 13th International Brick and Block Masonry Conference, Amsterdam, 2006.
- [14] M. Fraldi, A. Gesualdo, F. Guarracino. Influence of actual plastic hinge placement on the behavior of ductile frames. *Journal of Zhejiang University-SCIENCE A*, 15(7), 482–495, 2014.
- [15] I. Mascolo, M. Fulgione, M. Pasquino. Lateral torsional buckling of compressed open thin walled beams: experimental confirmations. *Int. J. Masonry Research and Innovation*, 4(1/2), 150–158, 2019. DOI: 10.1504/IJMRI.2019.096829
- [16] M. Monaco, M. Aurilio, A. Tafuro, M. Guadagnuolo. Sustainable Mortars for Application in the Cultural Heritage Field. *Materials*, 14(3), 598, 2021.
- [17] M. Monaco, G. Faella, M. Guadagnuolo. Analysis of pozzolanic mortars for restoration. *International Journal of Conservation Science*, 12(1), 41–50, 2021.

- [18] G. Buonocore, A. Gesualdo, M. Monaco, M.T. Savino. Improvement of Seismic Performance of Unreinforced Masonry Buildings using Steel Frames. in: *Civil-Comp Proceedings*: 106, B.H.V. Topping and P. Iványi eds., Civil Comp Press, Kippen, Stirlingshire, U.K., 2014. ISBN 978-1-905088-61-4
- [19] A. Gesualdo, M. Monaco. Seismic vulnerability reduction of existing masonry buildings. Modelling of retrofitting techniques. *Urban Habitat Construction Under Catastrophic Events*. Vol. 1, 853–858, London, New York: CRC Press, Taylor & Francis Group, 2010. ISBN: 9780415606851
- [20] A. Fortunato and A. Gesualdo and I. Mascolo and M. Monaco. P-Bézier energy optimization for elastic solutions of masonry-like panels. *Int. J. of Masonry Research and Innovation*, 2021. (In Press) DOI: 10.1504/IJMRI.2021.10037508
- [21] M. Malena, M. Angelillo, A. Fortunato, G. de Felice, I. Mascolo. Arch bridges subject to pier settlements: continuous vs. piecewise rigid displacements methods *Meccanica*, 2021. (Under Review)
- [22] I. Mascolo, A. Gesualdo, C. Olivieri, A. Fortunato. On rigid blocks detection in unilateral masonry-like structures. *Int. J. of Masonry Research and Innovation*, 2021. (In Print)
- [23] M. ElGawady, P. Lestuzzi, M. Badoux. A review of conventional seismic retrofitting techniques for URM. Draft Second Revision of IS 13935, 2004.
- [24] J. Macabuag. Dissemination of seismic retrofitting techniques to rural communities. EWB-UK National Research Conference 2010 ‘From Small Steps to Giant Leaps...putting research into practice’ Royal Academy of Engineering, 19th February 2010, 2010.
- [25] A. Smith, T. Redman. A Critical Review of Retrofitting Methods for Unreinforced Masonry Structures. EWB-UK Research Conference 2009 Hosted by The Royal Academy of Engineering, University of Bristol, 2009.
- [26] M.R. Valluzzi, M. Munari, C. Modena, L. Binda, G. Cardani, A. Saisi. Multilevel approach to the vulnerability analysis of historic buildings in seismic areas, Part 2. *Restoration of Buildings and Monuments*, 13(6), 2009.
- [27] A. Zucchini, P.B. Lourenco. MA micro-mechanical model for the homogenization of masonry. *International Journal of Solids and Structures*, 39, 2002.
- [28] B. Luccioni, V.C. Rougier. Shear behaviour of brick–mortar interface in CFRP retrofitted or repaired masonry. *International Journal of Mechanical Sciences*, 52(4), 2010.
- [29] P. Wriggers. *Computational contact mechanics*. Springer, Berlin, Heidelberg, New York., 2006.
- [30] F. Cluni, V. Gusella. Homogenization of non-periodic masonry structures. *International Journal of Solids and Structures*, 41, 2004.

- [31] S.G. Lekhnitskii. Theory of elasticity of an anisotropic elastic body, J.J. Brandstatter, San Francisco, 1963.
- [32] S. Nemat-Nasser. Micromechanics: overall properties of heterogeneous materials, North-Holland, 1993.
- [33] S. Pietruszczak, Z. Mroz. Formulation of anisotropic failure criteria incorporating a microstructure tensor. Computers & Geotechnics, 26, 2000.
- [34] S. Pietruszczak, R. Ushaksaraei. Description of inelastic behaviour of structural masonry. International Journal of Solids and Structures, 40, 2003.
- [35] A. Gesualdo, L. Nunziante. Omogeneizzazione di murature storiche (In Italian). Proceedings XVII National Congress AIMETA, Florence, ISBN: 88-8453-313-9, 2005.
- [36] M. Modano, F. Fabbrocino, A. Gesualdo, G. Matrone, I. Farina, F. Fraternali. On the forced vibration test by vibrodyne. In: COMPDYN 2015, 5th ECCOMAS Thematic Conference on Computational Methods in Structural Dynamics and Earthquake Engineering Crete Island, Greece, 25–27 May 2015 Crete Island, 209-2J, 2015.
- [37] S.C. Cowin. The relationship between the elasticity tensor and the fabric tensor. Mechanics of Materials, 4, 1985.
- [38] ANSYS. User's Manual, Version 8.0, Swanson Analysis Systems Inc. (SASI), Houston, PA, 2004.

PRELIMINARY DESIGN METHOD FOR ROCKING AND NEGATIVE STIFFNESS SYSTEMS

Natalia Reggiani Manzo¹, and Michalis F. Vassiliou¹

¹ ETH Zürich
Institute of Structural Engineering
Stefano-Franscini-Platz 5, 8093 Zürich, Switzerland
{reggianimanzo,vassiliou}@ibk.baug.ethz.ch

Abstract

This paper proposes a simple analytical system that can be used to describe the dynamics of Negative Stiffness Bilinear Elastic (NSBE) systems, and consequently design them in a simpler manner. The NSBE oscillator is a mathematical idealization, which can be used to describe rocking structures with or without flexible restraining systems or curved extension at their bases. The paper defines the characteristic quantities to make the bilinear system and actual rocking structures equivalent.

A simpler “equivalent” system to describe the behavior of NSBE systems is proposed: The equivalent system is the Zero Stiffness Bilinear Elastic (ZSBE) system, which is a bilinear system with zero stiffness in the second branch. The ZSBE system is useful and simpler because it needs one parameter less than the NSBE to be defined. The paper proceeds by defining the “Equal Displacement” and “Equal Energy” rules that provide estimates of the maximum displacement of the NSBE based on the response of the ZSBE. Using a simpler system to predict the response of a more complicated one, is a concept similar to the $R_{\mu}T$ relations that provide estimates of the response of bilinear yielding systems based on the response of an equivalent linear elastic system. However, the method should not be confused with the approach of FEMA 356: it does not resort to a linear elastic system but to the ZSBE.

Finally, the preliminary design of a real rocking structure is presented, as a case of study. The paper compares the response predicted by the proposed methodology to the one predicted by a more accurate numerical analysis.

Keywords: negative stiffness systems, dimensional analysis, non-linear dynamics, bilinear systems

1 INTRODUCTION

Rocking has been proposed as a seismic isolation method for both bridges [1-20] and buildings [21–23], because uplift works as a mechanical fuse and limits the design forces of both the superstructure and the foundation. Unlike structures designed to yield, the free rocking rigid block exhibits negative post-uplift stiffness [24]. In particular, this paper focuses on negative stiffness systems that are designed to sustain rocking motion without sliding [25–32], and do not exhibit hysteretic damping. Thus, it loads and unloads on the same branch. These systems do not accumulate displacements as negative stiffness hysteretic systems would. To avoid confusion, note that this paper uses the term “elastic” to describe not only linear elastic systems but all systems that unload on the same branch, linear or nonlinear. Therefore, an unrestrained rocking system is a negative stiffness elastic system.

Plastic design has found its way to practice, partially because a simplified design methodology that is based on the linear elastic response spectrum has been developed. For most structures designed to yield, a time history analysis is not required and an approach based on linear elastic spectra is allowed. This convenient design approach was originally developed for elastoplastic systems, including the ones exhibiting post-yield hardening. It has been extended to include recentering (rocking) systems exhibiting positive post-uplift stiffness [33, 34]. However, it is not applicable to negative stiffness rocking systems, because there is no “equivalent linear elastic system” for them [35]. Therefore, time-consuming time history analysis is required and the linear elastic response spectra that are defined by codes become useless for such structures.

This paper suggests that there can be a simplified design method for Negative Stiffness Bilinear Elastic (NSBE) systems (Fig.1a), based not on an equivalent linear elastic system, but on an equivalent bilinear elastic system of constant restoring force (i.e., zero post-uplift stiffness)—a Zero Stiffness Bilinear Elastic (ZSBE) system (Fig.1b). Even though the equivalent ZSBE system does not present the convenience of a linear elastic system where the response scales proportionally to the excitation, it is useful because it reduces the dimensionality of the problem and it allows the development of design spectra (not linear elastic) for negative stiffness systems.

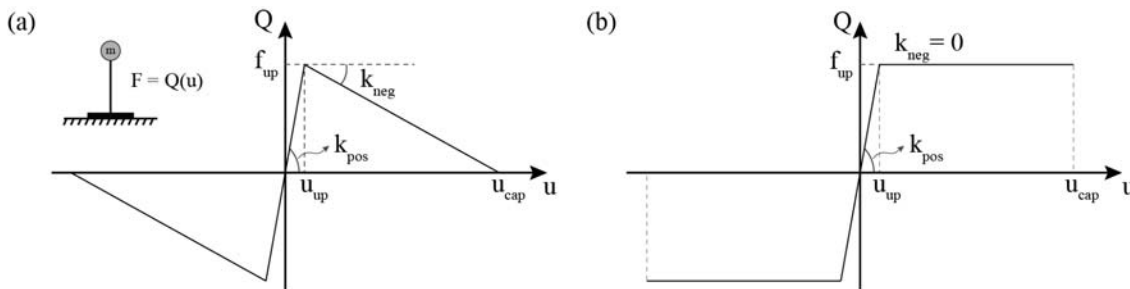


Figure 1: a) Characteristic pushover curve of the Negative Stiffness Bilinear Elastic (NSBE) system; b) Proposed bilinear elastic system of constant restoring force (Zero Stiffness Bilinear Elastic [ZSBE]) system.

It should be noted that the results of this study are not directly applicable to design procedures. However, they suggest approaches that might be used to develop a rational design procedure for earthquake resistance of rocking structures.

2 EQUIVALENT DESCRIPTION OF ROCKING SYSTEMS WITH NSBE SYSTEMS

One of the challenges in designing a rocking structure is that for a given height of a flat-based unrestrained rocking structure, usually defined by architectural considerations, its displacement capacity (i.e., the displacement that would cause overturn) is coupled to its uplifting force, because they both depend on its slenderness α (or, equivalently, on its base width $2b$). Therefore, extending the base to increase the displacement capacity of the structure causes an increase in the design forces of both the superstructure and the foundation.

In an effort to isolate buildings via a rocking story, Soviet engineers [36] were the first to suggest a way to decouple the displacement capacity from the uplift acceleration: They extended the base of the block by a curved part. This increases the displacement capacity while keeping the uplifting acceleration constant [8]. The post-uplift stiffness can be positive or negative depending on the curvature of the extension. A similar behavior can be obtained by using a flexible restraining system [14, 16].

The idealized systems presented above assume that the structure is rigid – a questionable assumption as the size of the blocks increase. Fig.1a shows the force-deformation curve of a rocking structure, when its deformability is considered [37–44]. In this case, the pre-uplift displacement is not zero but takes a finite value u_{up} . Therefore, all systems cited above can be described by an elastic bilinear system, up to a linear approximation.

The SDOF NSBE studied here is shown in Fig.1a. It has a mass m and a restoring force described by Fig.1a. The initial positive stiffness (k_{pos}) branch represents any pre-uplift deformability. The second branch has negative stiffness (k_{neg}), and it starts at the uplift displacement (u_{up}). The system displacement capacity (u_{cap}) is defined as the displacement that results to zero restoring force, even though there are rare cases where a system can dynamically exceed this displacement without collapsing.

Based on its characteristic pushover curve, the oscillator's equation of motion is:

$$m \cdot \ddot{u}(t) + f_{up} \cdot \frac{u(t)}{u_{up}} = -m \cdot \ddot{u}_g(t), \quad |u(t)| \leq u_{up} \quad (1)$$

$$m \cdot \ddot{u}(t) + f_{up} \cdot \left(\frac{u_{cap} - u(t)}{u_{cap} - u_{up}} \right) = -m \cdot \ddot{u}_g(t), \quad |u(t)| > u_{up} \quad (2)$$

The upper sign in Eq. 2 corresponds to a positive displacement and the lower to a negative displacement.

The main source of energy dissipation in rocking structures with protected ends is impact damping—unless extra damping is provided. For this reason, this paper assumes that the proposed NSBE model dissipates energy instantaneously. When the displacement is equal to the uplift displacement (i.e., when there is impact in the case of rocking structures), the integration is halted, and the post impact velocity is computed by a coefficient of restitution:

$$r_c = \frac{\dot{u}_{postimpact}}{\dot{u}_{preimpact}} \quad (3)$$

Herein, the ratio of the preimpact to postimpact velocities will be assumed equal to 0.95. Notably, the system unloads on the same branch and does not dissipate energy while unloading (apart from the instantaneous energy loss when it reaches the yielding displacement).

For the case of rigid systems, the parameters of the system of Fig.1a that make it mathematically equivalent to a variety of rocking systems are given in Table 1 and named \tilde{m} , \tilde{f}_{up} ,

and \tilde{u}_{cap} . Note that in order for the system of Fig.1a to be equivalent to these rocking systems, the excitation used for the equivalent bilinear system needs to be multiplied by a factor Γ , also given in Table 1. Then, the equation for the equivalent bilinear system becomes:

$$\tilde{m} \cdot \ddot{u}(t) + \tilde{f}_{up} \cdot \left(1 - \frac{u(t)}{\tilde{u}_{cap}}\right) = -\Gamma \tilde{m} \cdot \ddot{u}_g(t) \quad (4)$$

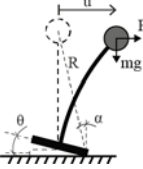
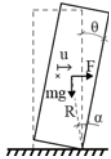
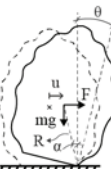
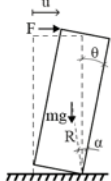
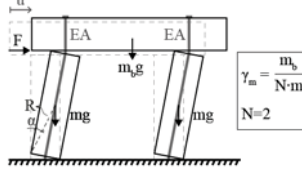
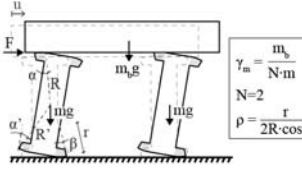
#		\tilde{m}	\tilde{f}_{up}	\tilde{u}_{cap}	Γ
1		m	$mg\alpha$	$R\sin\alpha$	1
2		$\frac{4}{3}m$	$mg\alpha$	$R\sin\alpha$	$\frac{3}{4}$
3		$\frac{I_o}{R^2}$	$mg\alpha$	$R\sin\alpha$	$\frac{mR^2}{I_o}$
4		$\frac{m}{3}$	$\frac{mg\alpha}{2}$	$2R\sin\alpha$	$\frac{3}{2}$
5		$\frac{(1+3\gamma_m)Nm}{3}$	$\frac{Nmg}{2}(1+2\gamma_m)\alpha$	$\frac{\left(\frac{1}{2}+\gamma_m\right)}{\left(\frac{1}{2}+\gamma_m\right)-\frac{EA}{mg}\alpha^2}2b$	$\frac{3(1+2\gamma_m)}{2(1+3\gamma_m)}$
6		$\frac{(1+3\gamma_m)m}{3}$	Rolling: $\frac{mg}{2}(1+2\gamma_m)\alpha$	$\frac{2R\sin\alpha}{(1-2\rho)} \leq 2R'\sin\alpha'$	$\frac{3(1+2\gamma_m)}{2(1+3\gamma_m)}$

Table 1: Parameters of the bilinear elastic system for different rocking systems

3 EQUAL DISPLACEMENT AND EQUAL ENERGY RULE

Using the elastic spectrum for the analysis of negative stiffness structures would have been very convenient as engineers are used to it and as elastic spectra for design already exist and are included in codes. However, this is not feasible for NSBE systems, because their response has been proven to be uncorrelated to any “equivalent” elastic system [35].

Therefore, this section defines Equal Displacement and Equal Energy rules that are applied not on an equivalent elastic system but on an equivalent ZSBE system (Fig.1b). We refer to it as “equivalent,” but this does not imply that it is *linear* elastic. It is a *bilinear* elastic system with finite pre-uplift displacement and zero post-uplift stiffness system.

To correlate the responses of the NSBE and of the ZSBE, the quantity of interest is the ratio:

$$\gamma = \frac{u_{dem,NS}}{u_{dem,ZS}} \quad (5)$$

where $u_{dem,NS}$ and $u_{dem,ZS}$ are the maximum displacements of the NSBE and ZSBE systems, respectively.

The Equal Displacement rule assumes that the NSBE and the equivalent ZSBE system will experience the same maximum displacement (Fig.2a):

$$u_{dem,NS} = u_{dem,ZS} \rightarrow \gamma_{ED} = 1 \quad (6)$$

The Equal Energy rule assumes that the monotonic loading curves of the NSBE and the ZSBE system will produce the same work, that is, the two shaded areas in Fig.2b are equal. Based on Fig.2b, one can compute that the Equal Energy rule gives:

$$\gamma_{EE} = \frac{u_{dem,NS}}{u_{dem,ZS}} = \frac{u_{cap}}{u_{dem,ZS}} - \sqrt{\frac{(u_{cap} - u_{up})}{u_{dem,ZS}} \cdot \frac{(u_{cap} - 2 \cdot u_{dem,ZS} + u_{up})}{u_{dem,ZS}}} \quad (7)$$

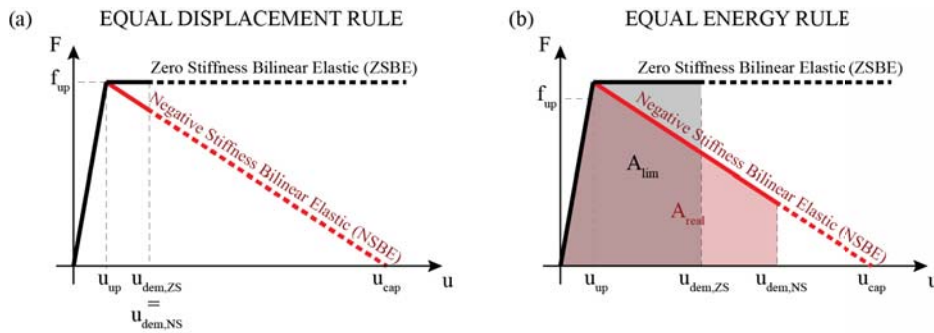


Figure 2: a) Equal Displacement, and b) Equal Energy rules for NSBE systems

4 RESPONSE OF RIGID-NEGATIVE STIFFNESSES SYSTEMS TO RECORDED GROUND MOTIONS

This section explores the accuracy of the rules defined in the section above, when applied to NSBE systems that present minimal pre-uplift displacement, i.e. systems with small u_{up} .

4.1 FEMA P695 Ground Motions

There is no consensus in the engineering community on what ground motions should be used in time history analysis. This paper focuses on the far-field set of ground motions proposed by FEMA P695 [45].

4.2 Median displacement spectra

Seismic design does not involve a single excitation, but a set of excitations that characterize the seismic hazard at a given site. Thus, this paper compares NSBE and ZSBE not by comparing their responses to individual ground motions, but by comparing the statistics of the responses to ensembles of ground motions [46]. The Equal Displacement and Equal Energy rules are assessed by focusing on the median displacement spectra for three variations of the set: scaled so that their PGV is equal to $0.5 \overline{\text{PGV}}$, or $1.0 \overline{\text{PGV}}$, or $2.0 \overline{\text{PGV}}$. $\overline{\text{PGV}}$ is defined as:

$$\overline{\text{PGV}} = \text{median}_{i=1 \dots N} \left(\sqrt{\text{PGV}_{i_x} \cdot \text{PGV}_{i_y}} \right) \quad (8)$$

where N is the number of ground motions and x and y are their two components.

4.3 Equal Displacement Rule for NSBE systems

Fig.3a plots the median of the maximum displacement of the NSBE stiffness system as a function of its strength normalized by the system's self-weight (f_{up}/mg) for several values of the displacement capacity. The uplift displacement is set to $u_{up}=5 \times 10^{-4}$ m to study quasi-rigid systems. For reasons of plot clarity, each line is plotted only for $f_{up}/mg > (f_{up}/mg)_{crit}$, where $(f_{up}/mg)_{crit}$ is the maximum uplift strength for which there is failure. The figure shows that:

- As long as the system is not close to failure, the displacement only loosely depends on the displacement capacity. So, when the system is not close to failure, instead of computing a different spectrum for each displacement capacity, one can compute the spectrum for the ZSBE system (i.e. for an NSBE with $u_{cap} \rightarrow \infty$) and use it to calculate the displacement demand on any NSBE of the same strength.
- As the system gets closer to collapse, the "Equal Displacement rule" does not apply and is unconservative: Systems with smaller displacement capacity exhibit larger displacements than the ones with larger displacement capacity. Moreover, close to failure the slope of the spectrum increases dramatically, i.e. a small decrease of the system strength would lead to a tremendous increase of the maximum displacement. This is not in agreement with a rational design, in which it would be required that this steep part is avoided.

4.4 Equal Energy rule for NSBE systems

Fig.3a show that the Equal Displacement rule is on the unconservative side, especially as the displacement demand approaches the capacity. To examine the performance of the Equal Energy rule, Fig.3b presents the median of the maximum displacement u_{max} divided by the factor γ_{EE} (Eq.7) as a function of the system normalized strength f_{up}/mg . The plots are constructed for several values of displacement capacity u_{cap} and for uplift displacement $u_{up}=5 \times 10^{-4}$ m.

The curves almost collapse to a unique curve, the one that represents the ZSBE system. Notably, this happens for all 3 different scalings of the ground motions. Hence, the Equal Energy rule gives a good estimate of the maximum displacement of NSBE systems with a finite displacement capacity. Comparing the Equal Displacement to the Equal Energy rule, the

former is simpler, but the latter is overall more conservative, especially for larger displacements. Therefore, unless there is a reason to opt for simplicity, the use of the Equal Energy rule is proposed.

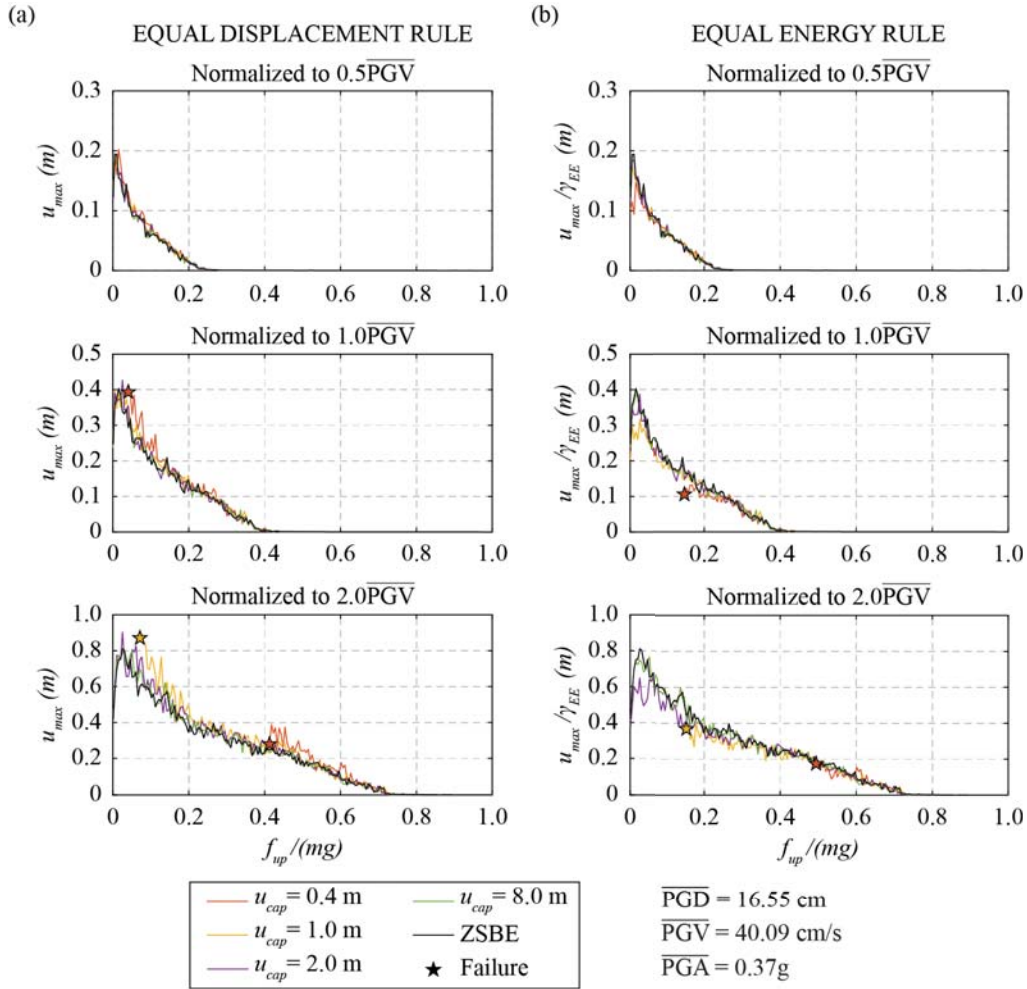


Figure 3: a) Median displacement spectra; b) Median displacement spectra normalized by γ_{EE}

The above conclusions also hold for the near-field pulse-like and near-field no pulse-like FEMA ground motion sets [47].

4.5 Design Example

Next, a case study is used to illustrate a design method based on the Equal Displacement and Equal Energy rules. The method is applied for the design of a rocking bridge equipped with a restraining system that increases the displacement capacity, while keeping the post-uplift stiffness negative.

The geometry of the bridge is typical of overpass bridges. The columns have a height of 9.6 m and a diameter of 1.6 m, whereas the deck is much heavier than the columns ($\gamma_m \rightarrow \infty$). Planar rocking (i.e., one directional excitation) is assumed as a first approximation (even though this has been proven unconservative [3, 20]). Then, the proposed design steps are:

1. Calculate the normalized yielding strength of the system ($f_{up}/(mg)$). If the restraining tendon is not prestressed, this depends solely on the column geometry, and is equal to α .
2. Obtain the displacement demand for the infinite capacity curve ($u_{dem,ZS}$) using the ZSBE curves. The ZSBE curves are the median response of the system subjected to ensembles of ground motions.
3. Calculate the design displacement capacity of the system, as:

$$u_{cap} = FS \cdot u_{dem,NS} = FS \cdot \gamma \cdot u_{dem,ZS} \quad (9)$$

in which FS is a safety factor and γ is defined by Eq. 9. Two alternative approaches were evaluated: One based on the Equal Displacement ($\gamma = 1$) and one on the Equal Energy ($\gamma = \gamma_{EE}$, Eq.7) rule.

Table 2 presents the design values when the two rules are applied on the set of ground motions under the three different scalings. u_{cap} is the capacity required for a $FS=2.5$ (Eq.9). For a system with a displacement capacity u_{cap} , $u_{dem,TH}$ is the median displacement demand of each set computed with time history analysis. $u_{dem,ED}$ and $u_{dem,EE}$ are equal to $\gamma_{ED} \cdot u_{dem,ZS}$ and $\gamma_{EE} \cdot u_{dem,ZS}$, respectively. $u_{dem,ZS}$ is the median response of the ZSBE system. The error is defined as $error = (u_{dem,ED/EE} - u_{dem,TH})/u_{dem,TH}$.

	Equal Displacement			Equal Energy		
	0.5 PGV	1.0 PGV	2.0 PGV	0.5 PGV	1.0 PGV	2.0 PGV
u_{cap} (m)	1.60	1.60	1.60	1.60	1.60	1.60
$u_{dem,TH}$ (m)	0.031	0.169	0.447	0.031	0.169	0.447
$u_{dem,ED}$ (m)	0.030	0.152	0.449	0.030	0.159	0.540
Error (%)	-2.65	-10.56	0.41	-8.61	-5.87	20.78

Table 2: Design Values for the Equal Displacement ($\gamma=1$) and Equal Energy rule ($\gamma = \gamma_{EE}$)

The Equal Displacement rule, in general, underpredicts the result, with a maximum under-prediction error of 10%. The Equal Energy rule is conservative in 1 out of 3 cases. None of the rules led to collapse, because of the safety factor $FS = 2.5$.

5 CONCLUSIONS

Rocking systems (free, restrained, or with curved extensions) that exhibit negative post-uplift stiffness can be described as elastic bilinear oscillators with a negative stiffness second branch, herein denoted as NSBE. This description can also take into account their pre-uplift deformability.

In this paper, it was proposed that these systems can be described by an equivalent bilinear elastic system that has the same strength, zero post-uplift stiffness, and zero uplift displacement, i.e. a one-parameter system, a ZSBE system with zero uplift displacement. Based on this equivalent system, the response of the original negative stiffness oscillator can be obtained by either an “Equal Displacement rule” or an “Equal Energy rule”, the former being simpler, the latter being more accurate. The above methodology is similar to the “ $R\mu T$ ” concept for elastoplastic structures with one fundamental difference: The equivalent system is not linear elastic, but a bilinear elastic system with zero stiffness of the second branch (ZSBE).

This equivalence suggests that the ZSBE oscillator should be extensively studied under a larger database of recorded ground motions to derive non-linear spectra describing its behavior. This will provide the engineering community with a tool to easily design rocking (or any other negative stiffness bilinear elastic) structures, without having to perform time consuming time history analysis.

6 ACKNOWLEDGEMENT

This work was supported by the ETH Zurich under grant ETH-10 18-1.

REFERENCES

- [1] N. Makris, M.F. Vassiliou, Planar rocking response and stability analysis of an array of free-standing columns capped with a freely supported rigid beam. *Earthq. Eng. Struct. Dyn.*, **42**, 431–449, 2012.
- [2] P. Sideris, A. J. Aref, and A. Filiatrault, Quasi-Static Cyclic Testing of a Large-Scale Hybrid Sliding-Rocking Segmental Column with Slip-Dominant Joints. *J. Bridg. Eng.*, **19** (10), 04014036, 2014.
- [3] M. F. Vassiliou, Seismic response of a wobbling 3D frame. *Earthq. Eng. Struct. Dyn.*, **47** (5), 1212–1228, 2018.
- [4] J. A. Bachmann, M. Strand, M. F. Vassiliou, M. Broccardo, and B. Stojadinović, Is rocking motion predictable?. *Earthq. Eng. Struct. Dyn.*, **47** (2), 535–552, 2018.
- [5] A. Dar, D. Konstantinidis, and W. El-Dakhakhni, Seismic response of rocking frames with top support eccentricity. *Earthq. Eng. Struct. Dyn.*, **47** (12), 2496–2518, 2018.
- [6] M. M. Kashani, A. Gonzalez-Buelga, R. P. Thayalan, A. R. Thomas, and N. A. Alexander, Experimental investigation of a novel class of self-centring spinal rocking column. *J. Sound Vib.*, **437**, 308–324, 2018.
- [7] Y. Xie, J. Zhang, R. DesRoches, and J. E. Padgett, Seismic fragilities of single-column highway bridges with rocking column-footing. *Earthq. Eng. Struct. Dyn.*, **48** (7), 843–864, 2019.
- [8] J. A. Bachmann, M. F. Vassiliou, and B. Stojadinovic, Rolling and rocking of rigid uplifting structures. *Earthq. Eng. Struct. Dyn.*, **48** (14), 1556–1574, 2019.
- [9] R. Thiers-Moggia and C. Málaga-Chuquitaype, Seismic protection of rocking structures with inerters. *Earthq. Eng. Struct. Dyn.*, **48** (5), 528–547, 2019.
- [10] A. I. Giouvanidis and Y. Dong, Seismic loss and resilience assessment of single-column rocking bridges. *Bull. Earthq. Eng.*, **18** (9), 4481–4513, 2020.
- [11] M. Sieber, S. Klar, M. F. Vassiliou, and I. Anastasopoulos, Robustness of simplified analysis methods for rocking structures on compliant soil. *Earthq. Eng. Struct. Dyn.*, **49** (14), 1388–1405, 2020.
- [12] I. M. Thomaïdis, A. J. Kappos, and A. Camara, Dynamics and seismic performance of rocking bridges accounting for the abutment-backfill contribution. *Earthq. Eng. Struct. Dyn.*, **49** (12), 1161–1179, 2020.
- [13] N. Makris and M. F. Vassiliou, Are Some Top-Heavy Structures More Stable?. *J.*

- Struct. Eng.*, **140** (5), 06014001, 2014.
- [14] N. Makris and M. F. Vassiliou, Dynamics of the Rocking Frame with Vertical Restrainers. *J. Struct. Eng.*, **141** (10), 04014245, 2015.
 - [15] E. G. Dimitrakopoulos and A. I. Giouvanidis, Seismic Response Analysis of the Planar Rocking Frame. *J. Eng. Mech.*, **141** (7), 04015003, 2015.
 - [16] M. F. Vassiliou and N. Makris, Dynamics of the Vertically Restrained Rocking Column. *J. Eng. Mech.*, **141** (12), 04015049, 2015.
 - [17] A. Agalianos, A. Psychari, M. F. Vassiliou, B. Stojadinovic, and I. Anastasopoulos, Comparative assessment of two rocking isolation techniques for a motorway overpass bridge. *Front. Built Environ.*, **3**, 1–19, 2017.
 - [18] A. I. Giouvanidis and E. G. Dimitrakopoulos, Seismic Performance of Rocking Frames with Flag-Shaped Hysteretic Behavior. *J. Eng. Mech.*, **143** (5), 04017008, 2017.
 - [19] M. F. Vassiliou, K. R. Mackie, and B. Stojadinovic, A finite element model for seismic response analysis of deformable rocking frames. *Earthq. Eng. Struct. Dyn.*, **46** (3), 447–466, 2016.
 - [20] M. F. Vassiliou, S. Burger, M. Egger, J. A. Bachmann, M. Broccardo, and B. Stojadinovic, The three-dimensional behavior of inverted pendulum cylindrical structures during earthquakes. *Earthq. Eng. Struct. Dyn.*, **46** (14), 2261–2280, 2017.
 - [21] J. A. Bachmann, M. F. Vassiliou, and B. Stojadinovic, Dynamics of rocking podium structures. *Earthq. Eng. Struct. Dyn.*, **46** (14), 2499–2517, 2017.
 - [22] M. Aghagholizadeh and N. Makris, Earthquake response analysis of yielding structures coupled with vertically restrained rocking walls. *Earthq. Eng. Struct. Dyn.*, **47** (15), 2965–2984, 2018.
 - [23] G. Ríos-García and A. Benavent-Climent, New rocking column with control of negative stiffness displacement range and its application to RC frames. *Eng. Struct.*, **206**, 110133, 2020.
 - [24] G. W. Housner, The behavior of inverted pendulum structures during earthquakes. *Bull. Seismol. Soc. Am.*, **53** (2), 403–417, 1963.
 - [25] A. Dar, D. Konstantinidis, and W. W. El-Dakhakhni, Evaluation of ASCE 43-05 Seismic Design Criteria for Rocking Objects in Nuclear Facilities. *J. Struct. Eng.*, **142** (11), 04016110, 2016.
 - [26] D. Kalliontzis, S. Sritharan, and A. Schultz, Improved Coefficient of Restitution Estimation for Free Rocking Members. *J. Struct. Eng.*, **142** (12), 06016002, 2016.
 - [27] M. N. Chatzis, M. G. Espinosa, and A. W. Smyth, Examining the Energy Loss in the Inverted Pendulum Model for Rocking Bodies. *J. Eng. Mech.*, **143** (5), 04017013, 2017.
 - [28] A. G. Sextos, G. D. Manolis, N. Ioannidis, and A. Athanasiou, Seismically induced uplift effects on nuclear power plants. Part 2: Demand on internal equipment. *Nucl. Eng. Des.*, **318**, 288–296, 2017.
 - [29] A. I. Giouvanidis and E. G. Dimitrakopoulos, Nonsmooth dynamic analysis of sticking impacts in rocking structures. *Bull. Earthq. Eng.*, **15** (5), 2273–2304, 2017.
 - [30] E. Voyagaki, P. Kloukinas, M. Dietz, L. Dihoru, T. Horseman, O. Oddbjornsson, A.J.

- Crewe, C. A. Taylor, A. Steer, Earthquake response of a multiblock nuclear reactor graphite core: Experimental model vs simulations. *Earthq. Eng. Struct. Dyn.*, **47** (13), 2601–2626, 2018.
- [31] L. Di Sarno, G. Magliulo, D. D’Angela, and E. Cosenza, Experimental assessment of the seismic performance of hospital cabinets using shake table testing. *Earthq. Eng. Struct. Dyn.*, **48** (1), 103–123, 2019.
- [32] Y. Bao and D. Konstantinidis, Dynamics of a sliding-rocking block considering impact with an adjacent wall. *Earthq. Eng. Struct. Dyn.*, **49** (5), 498–523, 2020.
- [33] C. Christopoulos, A. Filiatrault, and B. Folz, Seismic response of self-centring hysteretic SDOF systems. *Earthq. Eng. Struct. Dyn.*, **31** (5), 1131–1150, 2002.
- [34] A. Palermo, S. Pampanin, and G. M. Calvi, Concept and development of hybrid solutions for seismic resistant bridge systems. *J. Earthq. Eng.*, **9** (6), 899–921, 2005.
- [35] N. Makris and D. Konstantinidis, The rocking spectrum and the limitations of practical design methodologies. *Earthq. Eng. Struct. Dyn.*, **32** (2), 265–289, 2003.
- [36] S. Polyakov, *Design of Earthquake Resistant Structures*. Mir. Publishers., 1974.
- [37] A. K. Chopra and S. C. -S. Yim, Simplified Earthquake Analysis of Structures with Foundation Uplift. *J. Struct. Eng.*, **111** (4), 906–930, 1985.
- [38] I. N. Psycharis, Effect of base uplift on dynamic response of SDOF structures. *J. Struct. Eng.*, **117** (3), 733–754, 1991.
- [39] I. Anastasopoulos, R. Kourkoulis, F. Gelagoti, and E. Papadopoulos, Rocking response of SDOF systems on shallow improved sand: An experimental study. *Soil Dyn. Earthq. Eng.*, **40**, 15–33, 2012.
- [40] S. Acikgoz and M. J. DeJong, The interaction of elasticity and rocking in flexible structures allowed to uplift. *Earthq. Eng. Struct. Dyn.*, **41** (15), 2177–2194, 2012.
- [41] M. F. Vassiliou, K. R. Mackie, and B. Stojadinovic, Dynamic response analysis of solitary flexible rocking bodies: modeling and behavior under pulse-like ground excitation. *Earthq. Eng. Struct. Dyn.*, **43** (10), 1462–1481, 2014.
- [42] M. F. Vassiliou, R. Truniger, and B. Stojadinovic, An analytical model of a deformable cantilever structure rocking on a rigid surface: development and verification. *Earthq. Eng. Struct. Dyn.*, **44** (15), 2775–2794, 2015.
- [43] R. Truniger, M. F. Vassiliou, and B. Stojadinovic, An analytical model of a deformable cantilever structure rocking on a rigid surface: experimental validation. *Earthq. Eng. Struct. Dyn.*, **44** (15), 2795–2815, 2015.
- [44] E. Avgenakis and I. N. Psycharis, Modeling of Inelastic Rocking Bodies under Cyclic Loading. *J. Eng. Mech.*, **146** (4), 04020020, 2020.
- [45] FEMA P695, Quantification of Building Seismic Performance Factors, Federal Emergency Management Agency, *Rep. FEMA P695*, Washington, DC, 2009.
- [46] M. F. Vassiliou, M. Broccardo, C. Cengiz, M. Dietz, L. Dihoru, S. Gunay, K. M. Mosalam, G. Mylonakis, A. Sextos, B. Stojadinovic, Shake table testing of a rocking podium: Results of a blind prediction contest. *Earthq. Eng. Struct. Dyn.*, **50** (4), 1043–1062, 2021.
- [47] N. Reggiani Manzo and M. F. Vassiliou, Simplified analysis of bilinear elastic systems

exhibiting negative stiffness behavior. *Earthq. Eng. Struct. Dyn.*, 50 (2), 580–600, 2021.

PREFABRICATED REINFORCED CONCRETE CLADDING PANELS SUPPORTS: DESIGN AND NUMERICAL MODELLING

Flavio Stochino^{1,*}, Fausto Mistretta¹, Mario Lucio Puppio¹, Mauro Sassu¹,

¹ Department of Civil, Environmental Engineering and Architecture, University of Cagliari, Cagliari,
09123, Italy fmistret@unica.it, mariol.puppio@unica.it; msassu@unica.it, fstochino@unica.it

* Corresponding author

Abstract

Prefabricated Reinforced Concrete (RC) cladding panels are often adopted in industrial facilities. While they are usually characterized by high strength and easiness of construction, their supports can represent a weak point. Indeed, the connections between the panel and the structure play a key role for the cladding safety. Without an appropriate design the connection can presents a brittle behaviour. High stress concentration, aging and exposure to aggressive environmental conditions that can accelerate the materials degradation represent some of the critical aspects in the connection design. This work, starting from a real case study describing the collapse of a RC cladding panel of a cooling tower, presents new simple design approaches for the supports. An accurate numerical analysis of the mechanical behaviour is also performed with a nonlinear Finite Element model developed in ANSYS environment.

Keywords: reinforced concrete, supports, durability, connections, fragility

1 INTRODUCTION

Prefabricated Reinforced Concrete (PRC) elements exhibit in some cases a brittle failure. The technology of precast concrete elements has become wide-spread particular from the 70s. Its main advantages are the reduced costs, the high quality of construction products and the speed of the entire construction process. Prefabricated buildings have been widely used in industrial/production plants. Their modular solutions, with shorter execution times and the possibility to use a reduced number of components have been adopted in several cases. The technology of extrusion consent to furnish low-cost panels with the same cross sections and different length. The designer of PRC elements preferred in time the application of quasi-isostatic structure with punctual connection. The reasons must be found in the possibility to absorb the viscous deformation. So, the joints between the various components are often represented by punctual elements (bars, plugs etc.) and so the support areas are reduced to the possible minimum value to better exploit the materials and to reduce the overall dimensions and costs of the connections and of the structure.

Recent earthquakes and, in particular, those that recently hit Italy (Abruzzo in 2009 and Emilia 2012 [1–3]), have highlighted the high vulnerability of the connections: numerous collapses or disasters occurred because of their fragility and inadequate capacity. The consequence, in Italy, was the development of specific guidelines and research activities for structural retrofitting of the joints [4–7]. Another relevant point are the ongoing changes in climate that produces significant effects, sometimes unexpected, on environmental actions [8–10]

However, the seismic event is not the only trigger for collapses or instability in such structures: in many cases the degradation of the material accompanied by a reduced maintenance activity non exhaustive code indication and improper structural design has produced situations of instability even in the presence of service loads only [11]. This is due to the reduced redundancy with which the support was conceived. This elements, joined to degradation due to aging [12–14], uncertain mechanical property of materials [15, 16] and poor cure of structural details [17, 18] produce dangerous static and seismic vulnerability. Indeed, without a conservative approach, there is an high sensitive to construction, material, installation or maintenance imperfections that can lead to failure [19–21]. From this the strategic relevance of specific survey and on site investigation to detect signals [22, 23].

This work reports on fall of RC cladding of a cooling tower located in an Italian industrial plant built in the early 2000s. This case is representative of the brittle behavior worsen by micro-climate conditions (marine salt vapors) reducing the durability of the elements, due to inadequate structural design. Indeed, in the original design the possibility of imperfections in the supports has not been considered, nor any strength or residual bearing capacity have been attributed to the connection [24, 25].

The examined collapse happened on the north-western Italian coast which, for reasons of privacy, are not explained here. The examination of the deficit conditions put in lights some elements of weakens in the conception of the structure, which is the result of the culture of “allowable stress”, the precedent design criteria that provide a limitation in the stress. Indeed, this approach do not paying attention to aspects of redundancy and sensitivity to imperfection.

Consolidation strategies are presented together with a proposal of a simple design criteria. In addition, a numerical model, in view to extend the results of the example in other similar situations, is developed with Ansys rel 18.1.

2 COOLING TOWER CLADDING PANEL COLLAPSE

A collapse of some cladding panels (Figure 1) is happened in a cooling tower of an energy production facility (47 x 32 m plant dimensions and 15.7 m height) built in the early 2000s. This event was triggered by the failure of the edge of one of the support cantilevers of the panels, on the south-west corner of the building. The damaged condition of the corner appears in a visible defect in the panels support (Figure 2). The small dimension of collapsed support is the main cause of the collapse. The microclimatic condition of nebulized sea water, percolating into the cooling tower, had a not negligible influence. This sea water, insinuated in the porosities of the concrete, has accelerated the structural degradation in a detail in which the sensitivity to imperfection plays a significant role.

A survey was carried to obtain proper information about the:

- mechanical characterization of the concrete of the various components (panels, columns, support);
- reinforcements emerging from the collapsed panels and cantilever;
- cracks on the lower edge panels still in position.

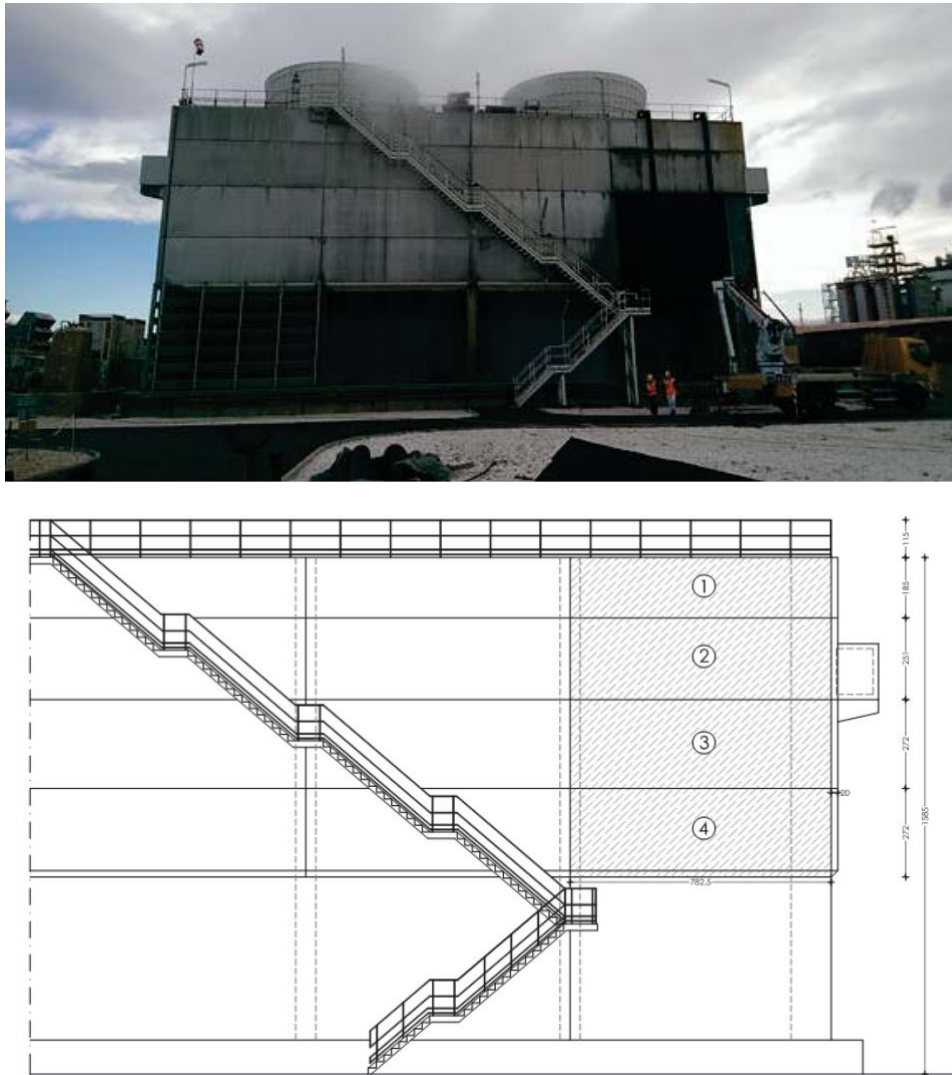


Figure 1: Cooling tower view with collapsed panels (top), drawing with highlighted collapsed panels (bottom).

The concrete of panels, cantilever and columns is characterized by cubic compressive strength equal to 50 MPa. This has been assessed using rebound hammer, pull out tests and destructive compressive strength tests on cores. The analysis of the reinforcements emerging from the concrete cantilever confirms that the collapse was triggered by the failure of concrete cover and of a 16 mm diameter steel threaded bar designed just to enable an accurate assembly of the panels but without structural role. The analysis of the cracks on the other corner panels (Figure 3) showed how all the corners not yet affected by collapses present visible cracks (up to almost 1.0 mm wide). This highlights that the conditions of the other panels support are not safe. In addition, the support zone of all the panels is very small.

A simple explanation of the collapse can be obtained with elementary equilibrium evaluation. On the concrete cover of the RC cantilever there is a permanent load of about $P=106.35$ kN. Indeed, the density of concrete is 25 kN/m^3 while the volume of the collapsed panel is 8.51 m^3 .

The reinforcements of the cantilever could not offer any resistance to shear. Indeed, Figure 4 show that the collapse crack developed quite far from the reinforcement. Thus, the 16 mm diameter threaded bar, designed just to place the cladding panel, was hugely deformed and cannot bear the panel load. Indeed, its cross section A_{res} is too small to bear the load. The force P , representing the panel load, induces an average shear stress τ equal to:

$$\tau = P/A_{res} = 106350/154 = 705 \text{ MPa} \quad (1)$$

This stress is beyond the material limit (360 MPa) even without considering any additional bending. To further adjust and make more uniform the stress between panel and cantilever a polymeric foam, based on polyurethane, was applied. However, this produced an imperfect contact between the panel and the cantilever.



Figure 2: South-West corner before (left) and after (right) the collapse.



Figure 3: Cracks on the remaining panels.

2.1 Retrofitting

To improve the safety of the other RC panels several additional connectors, realized with AISI 316 L steel ($\phi 27$ mm, $L=500$ mm), were applied throughout an injection with epoxy resins. These elements can guarantee structural integrity over time even in aggressive microclimatic conditions (Figure 4). Their external position (Figure 5) allows to carry out periodic maintenance inspections and to keep the support condition under control. The philosophy of intervention is to introduce redundancy in the system. Instead, the original detail did not have structural robustness, and, in case of material degradation, the failure is incipient.

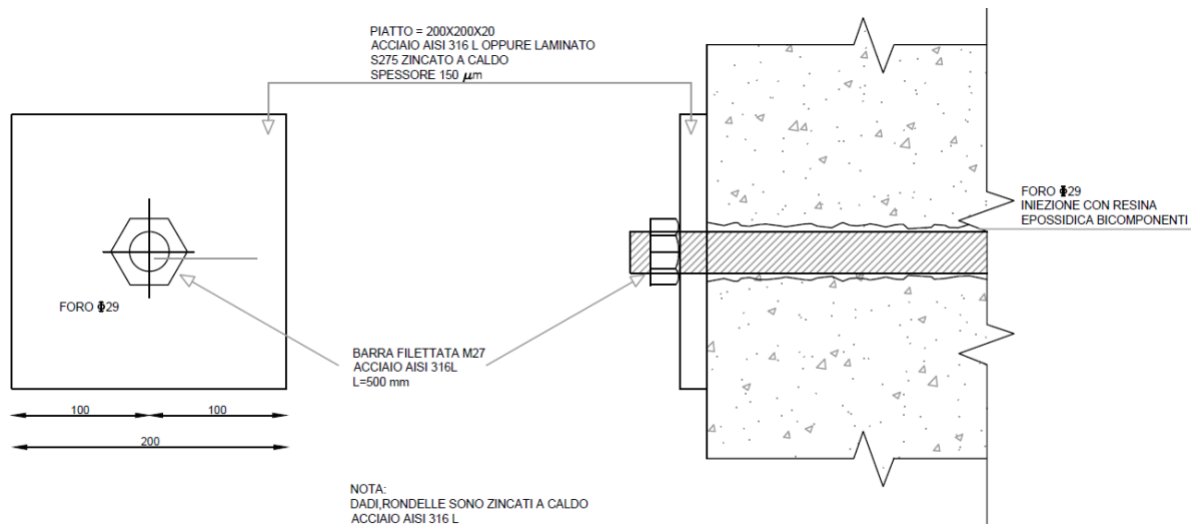


Figure 4: Details of additional steel connectors



Figure 5: Details of on-site installation of the connectors.

3 DESIGN CRITERIA PROPOSAL

To reduce this kind of fragile collapse new design approach should be introduced in a stochastic framework [26]. In the following two of them are described.

3.1 Effective trace

The effective trace of the support surface a_{ef} should be evaluated as:

$$a_{ef} = a - (s + \sum d_i) \quad (2)$$

Where s is the horizontal gap between the panel and the column, while d_i are the distances presented in Figure 6.

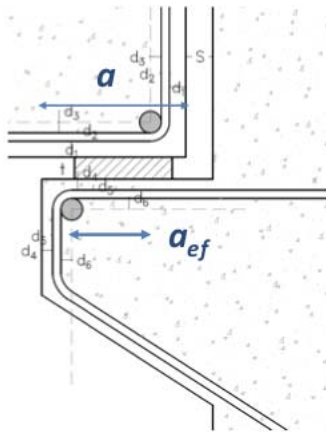


Figure 6: Details of effective trace approach.

Considering that a can be measured in a deterministic way, the uncertainties are in $(s + \sum d_i)$. The latter expression can be described with a stochastic approach. Indeed, it is possible to assume that this term it is defined by a log-normal probability distribution. For example,

considering the case described in Section 2 $s_k = 1.3$ cm, $d_{i,k} = 1.3$ cm the following characteristic value of the effective trace is obtained:

$$a_{ef,k} = a - 1.3(s + \sum d_i) \quad (3)$$

Now it is interesting to point out that for the previous case $a = 15$ cm, while $a_{ef} = 2$ cm and $a_{ef,k} < 0$.

Equation (3) allows to develop a probabilistic reliability analysis of this structural detail.

3.2 Sliding surface

Considering the common “sliding surface” approach a simple geometric safety criterion. The fracture line is here characterized by an inclination of 45° with respect to the horizontal plane. Then it is overlapped on the reinforcement details of the support cantilever. If this line crosses the horizontal distance between the reinforcement, (Figure 7), it is possible sustain the load. Vice versa if it cannot cross this horizontal line the collapse is expected.

Clearly this graphical criterion can be expressed through a mathematical formulation, see equation (4) and Figure 7 for the symbols meaning.

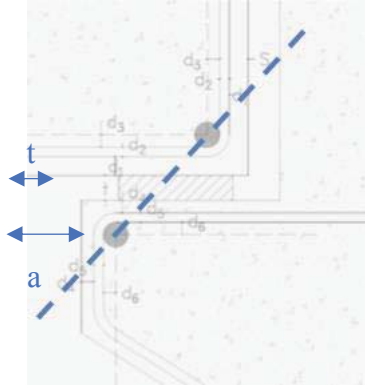


Figure 7: Details of sliding surface approach.

$$a > t + \sum d_i \quad (4)$$

Considering a log-normal probability distribution is assumed for each geometrical variable it is possible to obtain also in this case a stochastic value of the safety coefficient.

4 NUMERICAL MODEL

A fem model of the structural detail is carried out with Ansys (rel 18.1). Three different conditions with different values of the horizontal distance between the bar in the cantilever and the bar in the panel (a_{ef} see equation (2)) have been analyzed. The geometrical description with loads and boundary conditions is reported in Figure 8. The cantilever is fixed in the back and in the bottom surface while the load is applied on the top of a panel section. The whole model is constrained in the z direction (transversal to the cantilever plane) to consider a plain problem. In any case a 3D modelling strategy has been developed to model the transversal rebars inside the concrete mesh.

The numerical model has been developed in ANSYS environment using SOLID65 elements for concrete and LINK180 for rebars. Concrete class is C20/25 while steel for rebars is B450C, see NTC18 [27]. The nonlinear behaviour of concrete and its progressive failure has been modelled with the Willam e Warnke

criterion [28] while the steel rebars behavior is always linear elastic. Two transversal rebars ($\phi 10$ mm) have been modelled following the scheme presented in Figure 6: one in the bottom right corner of the panel and one in the top left corner of the cantilever.

A nonlinear quasi-static analysis has been performed with a progressive load applied as a uniform pressure on the panel top surface. This load has been varied to test what is the ultimate capacity for the three different geometrical configurations (denoted Left, Central and Right) characterized by different a_{ef} parameter values, see Figure 6 and Table 1.

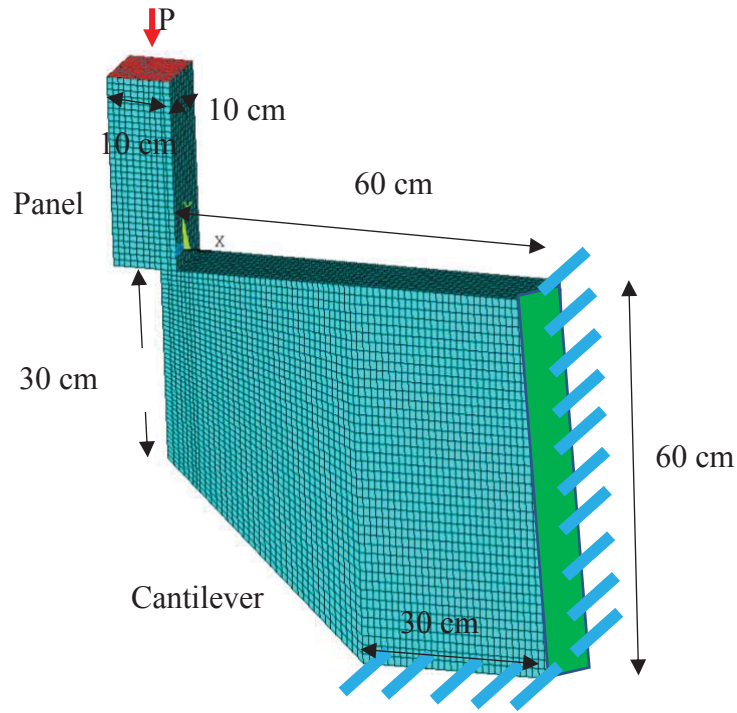


Figure 8: Model mesh, loading and boundary conditions.

	Left	Central	Right
a_{ef} (cm)	0	2.4	4.4
P_u/P_{MAX}	0.05	0.60	1.00

Table 1: Geometrical parameter a and relative ultimate load for different configurations.

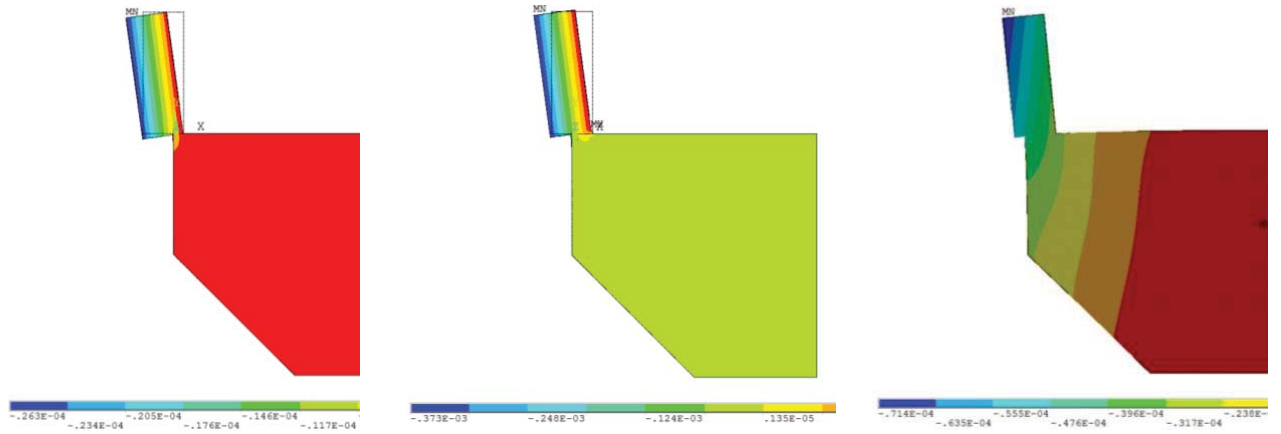


Figure 9: Displacement Contour vertical direction, measures are in m.

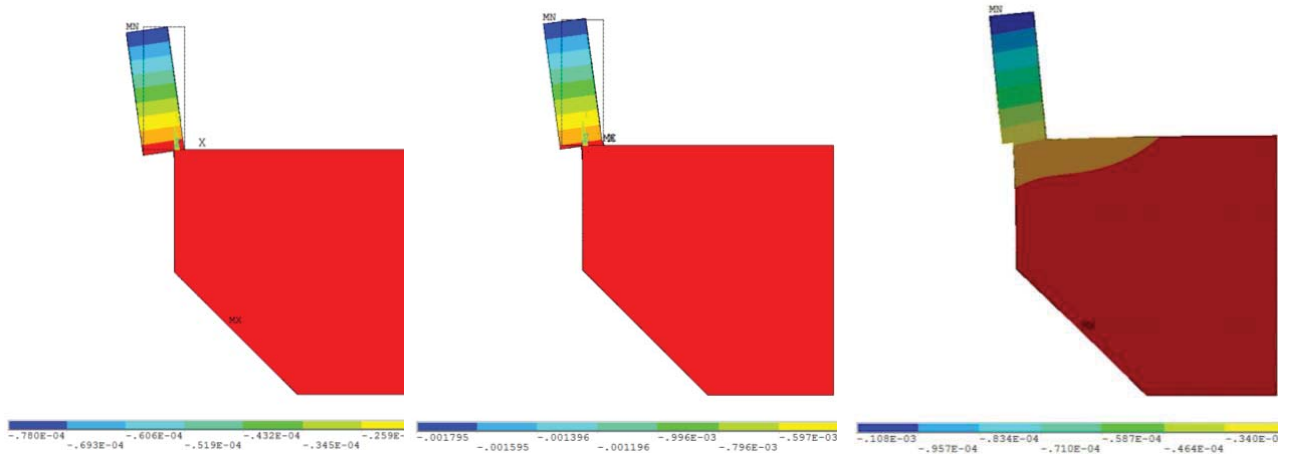


Figure 10: Displacement Contour horizontal direction, measures are in m.

Both displacement and convergence criteria has been enforced with a Newton-Raphson approach to solve the nonlinear problem. When is not possible to find an equilibrium configuration the simulation is stopped and the maximum load is measured P_u . Its relative values are reported in Table 1. As expected, the configuration with the maximum a_{ef} (denoted as Right) presents the maximum load P_{MAX} , the left and central configuration instead produced a reduced ultimate load respectively equal to the 5% and 60% of the P_{MAX} .

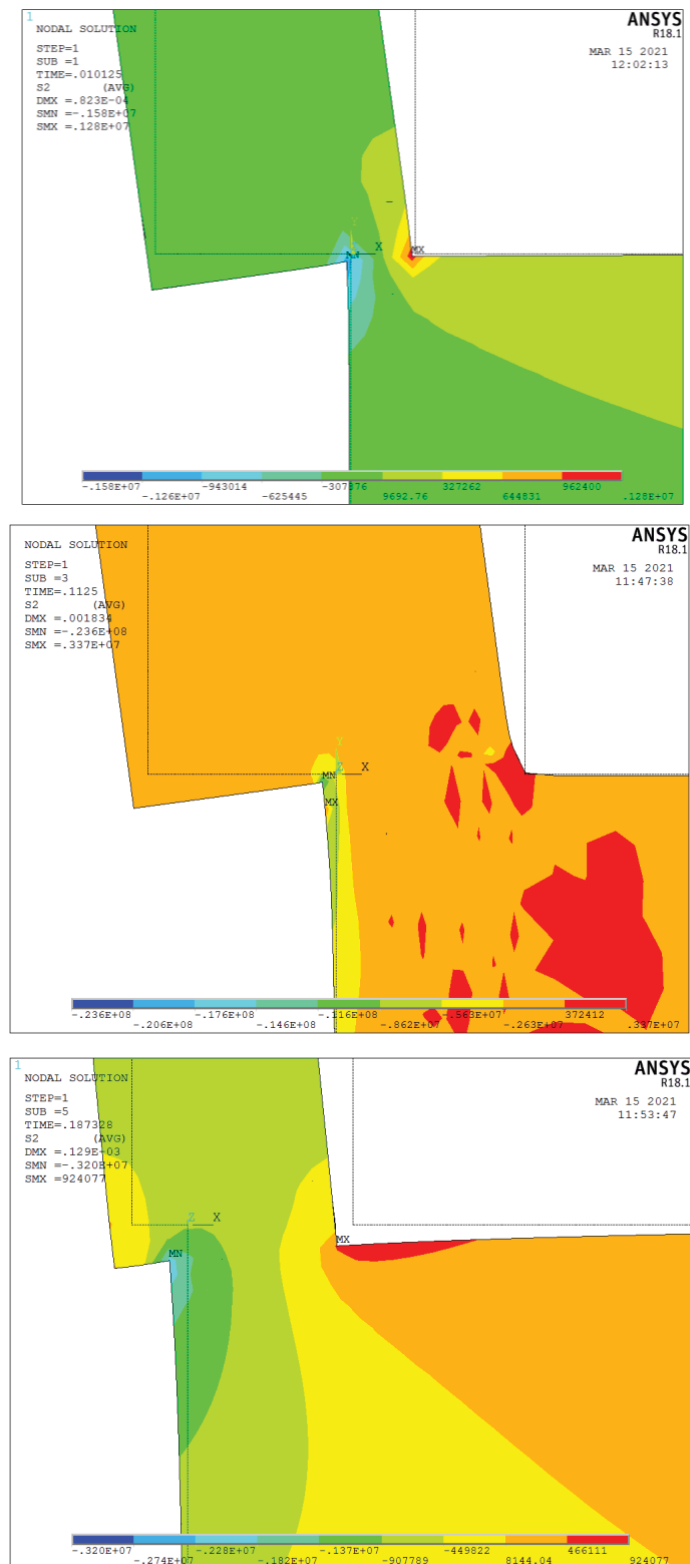


Figure 11: 2nd principal stress contour.

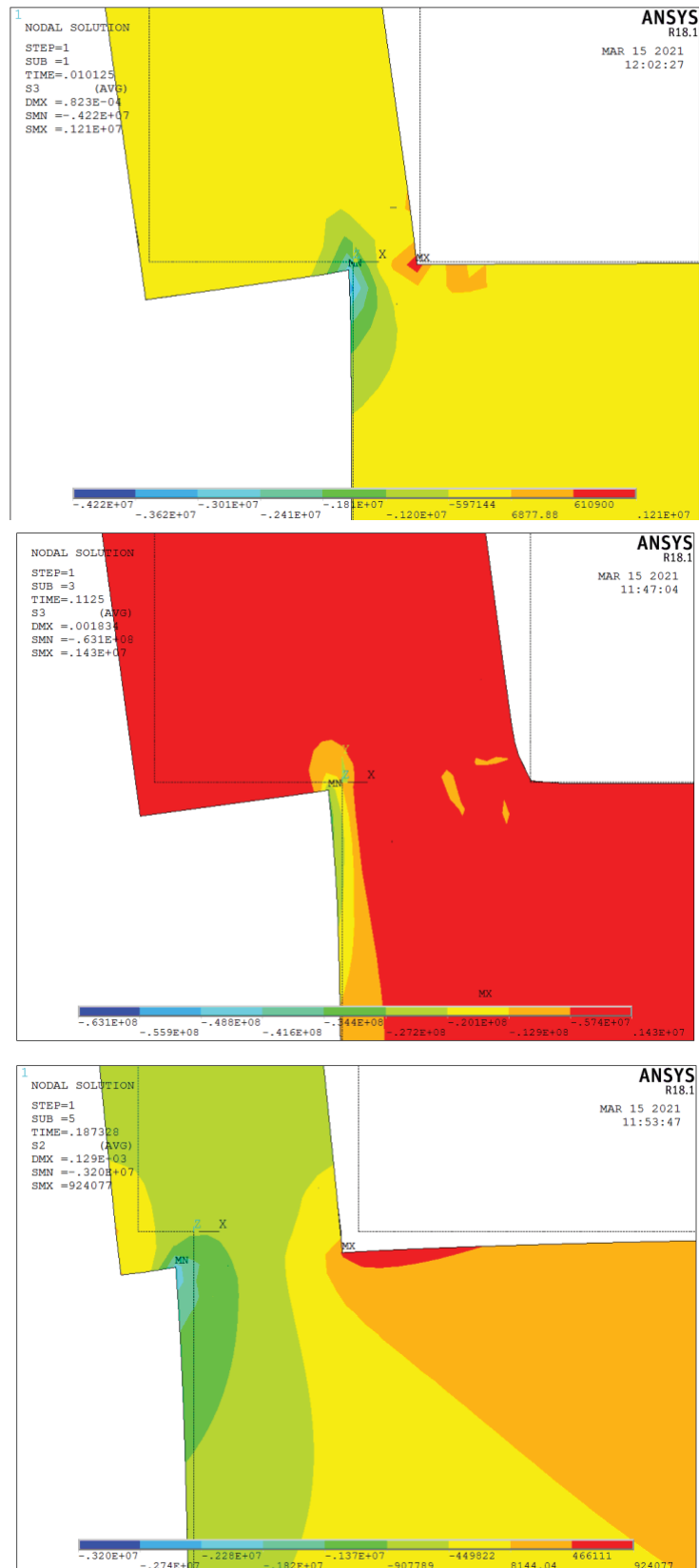


Figure 12: 3rd principal stress contour.

The vertical and horizontal displacement contours in the ultimate load step are reported in Figure 8 and 9 for the three configurations. It is clear that the left configuration ($a_{ef}=0$ cm) arrive at collapse with most of the deformation concentrated in the panel while the cantilever is still almost undeformed. Instead, the right configuration ($a_{ef}=4.4$ cm) requires that also the cantilever is deformed to reach the collapse condition.

Figures 10 and 11 presents the contours of 2nd and 3rd principal stress highlighting that the edge of the contact surfaces between the panel and the cantilever are the most stressed part of the element. Maximum compression is generally reached on the left part while maximum tension can be found on the right part.

The failure mechanism is almost the same for the three cases: the tensile crack appears in the top part of the cantilever on the right side of the contact edge between panel and cantilever. A representative picture of the crack propagation can be found in Figure 13 that points with red marks the tensile cracks. Clearly the crack pattern starts on the right and it develops toward left till the structure is not capable of finding an equilibrium condition.

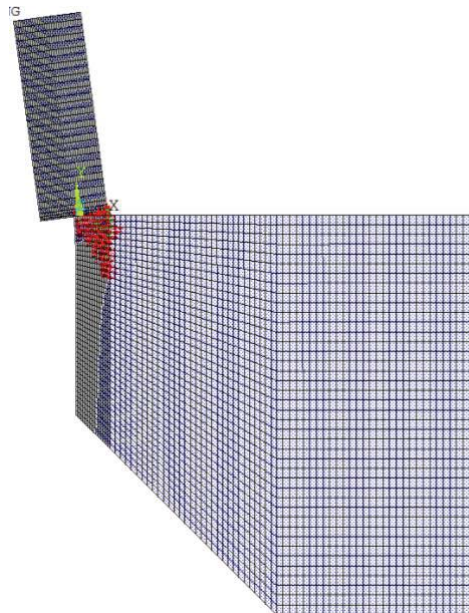


Figure 13: Typical Crack pattern.

5 CONCLUSIONS

This paper reports on recurrent situations typical of a poor concept of the prefabricated elements supports. In the modern performance-based design ductility, robustness hierarchy of structural element importance are key aspects. The possibility that a local collapse can trigger macroscopic collapses must be considered in existing PRC Structure. A structural retrofitting as well as proper sealing strategy of the existing joints must be taken into account [29].

The numerical model showed how a bigger contact surface and a bigger distance between the transversal rebars a_{ef} yield to high load capacity. In addition, the failure mechanism highlights how it is critical the left end of the contact between the panel and the cantilever suggesting improving the resistance of this mechanism using appropriate reinforcements.

A modern trend is nowadays to evaluate also minor details in a resilience perspective. Thus, also the design of constructive details [30] should take into account the needs of inspection, the

possible faults or malfunctions warning signs, and should avoid that any local collapse does spread in an uncontrolled global collapse.

Further developments of this research are expected for a stochastic evolution of the proposed design criteria or considering the effect of material irregularities.

REFERENCES

- [1] Giresini, L. (2017). Design strategy for the rocking stability of horizontally restrained masonry walls, M. F. M. Papadrakakis (Ed.), *COMPADYN 2017 - Proceedings of the 6th International Conference on Computational Methods in Structural Dynamics and Earthquake Engineering* (Vol. 2), Rhodes Island, Greece, 2963–2979. doi:10.7712/120117.5620.18188
- [2] Stochino, F.; Fadda, M. L.; Mistretta, F. (2018). Low cost condition assessment method for existing RC bridges, *Engineering Failure Analysis*, Vol. 86, 56–71. doi:10.1016/j.engfailanal.2017.12.021
- [3] Bontempi, F. (2017). ELEMENTI DI INGEGNERIA FORENSE IN CAMPO STRUTTURALE ACADEMIC YEAR 2017 Advanced Professional Training. doi:10.13140/RG.2.2.28844.46721
- [4] Manfredi, G.; Prota, A.; Verderame, G. M.; De Luca, F.; Ricci, P. (2014). 2012 Emilia earthquake, Italy: reinforced concrete buildings response, *Bulletin of Earthquake Engineering*, Vol. 12, No. 5, 2275–2298. doi:10.1007/s10518-013-9512-x
- [5] Toniolo, G.; Colombo, A. (2012). Precast concrete structures: The lessons learned from the L'Aquila earthquake, *Structural Concrete*, Vol. 13. doi:10.1002/suco.201100052
- [6] Andreini, M.; De Falco, A.; Giresini, L.; Sassu, M. (2014). Mechanical characterization of masonry walls with chaotic texture: procedures and results of in-situ tests, *International Journal of Architectural Heritage: Conservation, Analysis, and Restoration*, Vol. 8, No. 3, 376–407. doi:10.1080/15583058.2013.826302
- [7] Giresini, L.; Casapulla, C.; Denysiuk, R.; Matos, J.; Sassu, M. (2018). Fragility curves for free and restrained rocking masonry façades in one-sided motion, *Engineering Structures*, Vol. 164, 195–213. doi:10.1016/j.engstruct.2018.03.003
- [8] Croce, P.; Formichi, P.; Landi, F.; Marsili, F. (2019). Evaluating the effect of climate change on thermal actions on structures, *Life-Cycle Analysis and Assessment in Civil Engineering: Towards an Integrated Vision - Proceedings of the 6th International Symposium on Life-Cycle Civil Engineering, IALCCE 2018*, 1751–1758
- [9] Puppino, M. L.; Novelli, S.; Sassu, M. (2018). Failure evidences of reduced span bridges in case of extreme rainfalls the case of Livorno, *Frattura Ed Integrità Strutturale*, Vol. 12, No. 46, 190–202. doi:10.3221/IGF-ESIS.46.18
- [10] Forzieri, G., Cescatti, A., e Silva, F. B., & Feyen, L. (2017). Resilience of large investments and critical infrastructures in Europe to climate change., *The Lancet Planetary Health*, No. 1(5), e200–e208
- [11] Porcu, M. C.; Pittau, F. (2015). Excessive pedestrian-induced swaying in code-compliant walkways, *Structural Engineering International: Journal of the*

- International Association for Bridge and Structural Engineering (IABSE)*, Vol. 25, No. 4, 450–459. doi:10.2749/101686615X14355644771298
- [12] Marsili, F.; Croce, P.; Friedman, N.; Formichi, P.; Landi, F. (2017). Seismic reliability assessment of a concrete water tank based on the Bayesian updating of the finite element model, *ASCE-ASME Journal of Risk and Uncertainty in Engineering Systems, Part B: Mechanical Engineering*, Vol. 3, No. 2. doi:10.1115/1.4035737
 - [13] Frangopol, D. M.; Biondini, F. (2014). Bridge design , maintenance and management, *Structure and Infrastructure Engineering*, Vol. 10, No. 4, 419
 - [14] Biondini, F.; Camnasio, E.; Titi, A. (2015). Seismic resilience of concrete structures under corrosion, *Earthquake Engineering and Structural Dynamics*, Vol. 44, No. 14, 2445–2466. doi:10.1002/eqe.2591
 - [15] Puppio, M.; Pellegrino, M.; Giresini, L.; Sassu, M. (2017). Effect of Material Variability and Mechanical Eccentricity on the Seismic Vulnerability Assessment of Reinforced Concrete Buildings, *Buildings*, Vol. 7, No. 4, 66. doi:10.3390/buildings7030066
 - [16] Puppio, M. L.; Giresini, L.; Doveri, F.; Sassu, M. (2019). Structural irregularity: The analysis of two reinforced concrete (r.c.) buildings, *Engineering Solid Mechanics*, Vol. 7, No. 1. doi:10.5267/j.esm.2018.12.002
 - [17] Stochino, F.; Mistretta, F.; Mancini, G.; Pani, L. (2019). Structural assessment and retrofitting of damaged reinforced concrete water bridge, *20th Congress of IABSE, New York City 2019: The Evolving Metropolis - Report*, 1477–1485
 - [18] Stochino, F.; Fadda, M. L.; Mistretta, F. (2018). Assessment of RC Bridges integrity by means of low-cost investigations”, *Fracture and Structural Integrity*, Vol. 12, 216225. doi:10.3221/IGF-ESIS.46.20.
 - [19] Tattoni, S.; Stochino, F. (2013). Collapse of prestressed reinforced concrete jetties: durability and faults analysis, *Case Studies in Engineering Failure Analysis*, Vol. 1, 131–138
 - [20] Sassu, M.; Giresini, L.; Puppio, M. L. (2017). Failure scenarios of small bridges in case of extreme rainstorms, *Sustainable and Resilient Infrastructure*, Vol. 2, No. 3, 108–116. doi:10.1080/23789689.2017.1301696
 - [21] Croce, P.; Landi, F.; Formichi, P. (2019). Probabilistic Seismic Assessment of Existing Masonry Buildings, *Buildings*, Vol. 9, No. 12. doi:10.3390/buildings9120237
 - [22] Mistretta, F.; Piras, M. V.; Deias, L. (2010). Fuzzy logic application to the vulnerability assessment of concrete structures affected by degradation, *Proceedings of the 12th International Conference on Inspection, Appraisal, Repairs and Maintenance of Structures* (Vol. 1), 65–74
 - [23] Pucci, A.; Sousa, H. S.; Puppio, M. L.; Giresini, L.; Matos, J. C.; Sassu, M. (2019). Method for sustainable large-scale bridge survey.pdf, *Towards a Resilient Built Environment Risk and Asset Management*, IABSE, Zurich, 1034–1041
 - [24] Puppio, M. L.; Giresini, L. (2019). Estimation of tensile mechanical parameters of existing masonry through the analysis of the collapse of Volterra’s urban walls, *Frattura Ed Integrita Strutturale*, Vol. 13, No. 49. doi:10.3221/IGF-ESIS.49.65
 - [25] Giresini, L.; Puppio, M. L.; Taddei, F. (2020). Experimental pull-out tests and design

- indications for strength anchors installed in masonry walls, *Materials and Structures*, Vol. 53, No. 4, 103. doi:10.1617/s11527-020-01536-2
- [26] Croce, P.; Marsili, F.; Klawonn, F.; Formichi, P.; Landi, F. (2018). Evaluation of statistical parameters of concrete strength from secondary experimental test data, *Construction and Building Materials*, Vol. 163, 343–359. doi:10.1016/j.conbuildmat.2017.11.001
- [27] Decreto Ministeriale 17/01/2018. (2018). Italian Technical Standards for buildings (Nuove Norme Tecniche per le Costruzioni, in italian)
- [28] Willam, K. J.; Warnke, E. D. (1975). Constitutive Model for the Triaxial Behavior of Concrete, *Proceedings of International Association for Bridge and Structural Engineering*, vol. 19, 1-30.
- [29] Coni, M.; Portas, S.; Maltinti, F.; Pinna, F. (2018). Sealing Of Paving Stone Joints, Elsevier (Ed.), *IJPRT - International Journal of Pavement Research and Technology - Volume 11, Issue 8*, Chinese Society of Pavement Engineering, 813–818
- [30] Arangio, S.; Crosti, C.; Bontempi, F. (2013). Causal models for the forensic investigation of structural failures, *Research and Applications in Structural Engineering, Mechanics and Computation - Proceedings of the 5th International Conference on Structural Engineering, Mechanics and Computation, SEMC 2013*, No. September, 2353–2358. doi:10.1201/b15963-424

INFLUENCE OF THE ELASTO-PLASTIC BEHAVIOR OF TIE-RODS IN THE RESPONSE OF ROCKING MASONRY WALLS THROUGH SEISMIC DEMAND HAZARD CURVES

F. Solarino¹, L. Giresini^{2*}, and P. Croce³

¹ Department of Energy, Systems, Territory and Constructions Engineering
University of Pisa
Largo L. Lazzarino, 1, 56126 Pisa
e-mail: f.solarino1@studenti.unipi.it

² *corresponding author. Department of Civil and Industrial Engineering
University of Pisa
Largo L. Lazzarino, 1, 56126 Pisa
email: linda.giresini@unipi.it

³ Department of Civil and Industrial Engineering
University of Pisa
Largo L. Lazzarino, 1, 56126 Pisa
email: p.croce@ing.unipi.it

Abstract

Rocking analysis is a powerful tool to assess the seismic vulnerability assessment of masonry walls subjected to out-of-plane modes, especially when in view of checking the efficiency of traditional retrofitting solutions, such as steel tie-rods restraining rocking blocks. The study focuses on a probabilistic approach for the seismic assessment of the out-of-plane behavior of masonry walls, mainly aiming to reliably predict fragility and seismic demand hazard curves in case steel tie rods are used as anti-seismic device. To identify the most appropriate steel tie-rod device, more than thousand multistripe analyses have been performed considering the Italian site with highest seismic hazard (Carlentini, Sicily), duly modifying ductility and strength of the tie rods themselves. The resulting fragility curves and seismic demand hazard curves are critically discussed, so allowing the definition of the most efficient and proficient intensity measures referring to five relevant limit states. As expected, remarkable changes in the response are recorded by passing from a brittle to a ductile tie-rod, but when the ultimate strain is bigger than 2%, an increased tie-rod ductility does not sensitively improve the response even for high-intensity earthquakes. The probabilistic approaches show that even low-ductility tie-rods can sensibly reduce the probability of exceedance of limited and moderate rocking limit states, up to an order of magnitude. As for the influence of the tie-rod strength, even low-medium values produce a remarkable reduction of annual exceedance rate. For instance, a severe rocking limit state occurs for the unrestrained monumental wall every 450 years and every 2000 years for the wall restrained by a tie rod of strength just fitting the minimum required design value.

Keywords: rocking, brittle tie-rod, ductile tie-rod, historic masonry, annual exceedance rate, restrained walls, out-of-plane.

1 INTRODUCTION

Masonry structures can be seen as an assembly of macro-elements. Independently on the masonry type [1] and mechanical properties [2], these macro-elements that can be considered as a rigid system, provided that the masonry is monolithic. The rocking analysis of rigid blocks is a non-linear dynamic analysis capable of simulating the behavior of masonry walls rocking out-of-plane. The out-of-plane behavior is undesired for masonry buildings but unfortunately very common for the lack of proper connections between walls and between walls and horizontal diaphragms. Owing the fact that many types of such connections were developed over the centuries, ad hoc detailed studies are necessary to understand their effectiveness [3].

Nowadays, a wide literature is available on rocking analyses of free-standing walls as well as vertically/horizontally restrained walls, including analytical formulations [4]–[9], experimental outcomes [10]–[13] and numerical approaches [5], [14]–[18]. All these contributions are aimed at reliably representing the dynamic behavior of a masonry wall rocking out-of-plane during an earthquake.

Horizontal restraints are often provided by steel tie-rods, traditionally used in historic masonry buildings [19]–[21]. The response of free-standing blocks is strongly influenced by the size and slenderness ratio of the wall, besides the frequency content and numerous intensity measures associated to the seismic input. In addition to these parameters, the dynamic response of blocks restrained by horizontal tie-rods depends on the position and on the mechanical properties of the tie-rods themselves, as discussed in [22]. In [22] it was demonstrated on one hand that, as expected, tie-rods reduce the maxima amplitude rotations, but on the other hand that tied walls behavior is not significantly dependent on the aspect ratio of two walls of comparable size. The latter remark is still valid for walls restrained by tie-rods at different heights; more generally, it can be observed that the influence of tie-rod length as well as of normalized pre-stress is very limited. As for the influence of the mechanical properties, the role of the axial stiffness appears to be negligible. The yield strength was the most relevant parameter that influences the response, besides the brittle or ductile behavior of the tie-rod.

This contribution takes inspiration from the cited work but it considers different geometries and assumptions for the tie-rods. Moreover, this paper adopts a full stochastic approach for the seismic vulnerability assessment [23]–[26], whereas in [22] a semi-probabilistic approach is considered. After the presentation of the analytical formulation (Section 2) and the assumptions (Section 3) taken into account in the analysis, the work discusses the results in terms of fragility curves (Section 4) and seismic hazard curves (Section 5), which is a new frontier in the probabilistic assessment of seismic vulnerability [27].

2 ANALYTICAL FORMULATION

2.1 Mechanical model and equation of motion

The out-of-plane behavior of existing masonry structures can be investigated through non-linear dynamic analyses also called rocking analyses. This section describes the model considered for analyzing the one-sided motion of masonry walls restrained by steel tie-rods, displayed in Figure 1. In it, the wall is assumed as single degree of freedom rigid block of mass m and of perpendicular shape. Its size and slenderness are respectively given by R and $\alpha = \arctan\left(\frac{h}{b}\right)$. The equation of motion, found in previous works of the Authors [14], [15], [17], is the following:

$$I_0 \ddot{\vartheta} + \text{sgn}(\vartheta) m g R \sin A_\vartheta + T_t + T_L = m \ddot{u}_g R \cos A_\vartheta \quad (1)$$

The right hand side contains the seismic input term as acceleration time history $\ddot{u}_g(t)$ of the earthquake. The terms on the left hand side are related to the inertia forces, the self-weight stabilizing the response up to a rotation threshold equal to α , the tie-rod of stiffness K (T_t) and the transverse walls simulated by a spring bed of unitary stiffness K'_c (T_L). As for the symbols, I_0 is the polar inertia moment with respect to the pivot point O or O' equal to $\frac{4}{3}mR^2$, whereas $A_\vartheta = \alpha - \text{sgn}(\vartheta)\vartheta$.

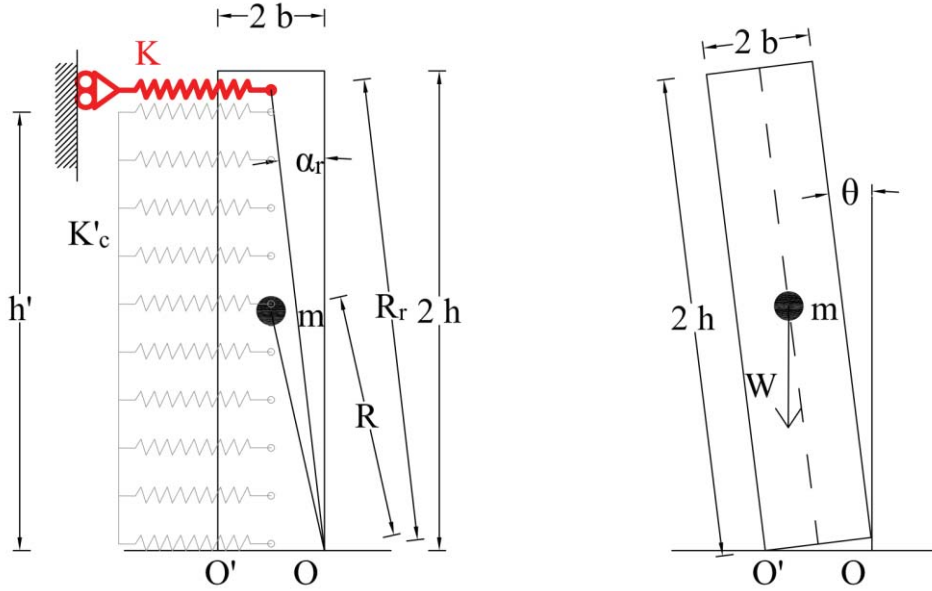


Figure 1: schematics of the model considered in the rocking analyses.

The term T_t assumes the form:

$$T_t = \text{sgn}(\vartheta) K \beta^2 R^2 \cos A_{r,\vartheta} [\sin \alpha_r - \sin A_{r,\vartheta}] \quad (2)$$

in which $A_{r,\vartheta} = \alpha_r - \text{sgn}(\vartheta)\vartheta$ where α_r is a position angle dependent on the position coefficient $\beta = R_r/R$ (Figure 1). The tie-rod can behave either as elastic or as plasticized. If the tie-rod is in the elastic field, the corresponding term can be simply calculated from the external work made by it, obtaining:

$$T_{t,e} = [\text{sgn}(\vartheta) K R_r (\sin \alpha_r - \sin A_{r,\vartheta}) + F_0] R_r \cos A_{r,\vartheta} \quad (3)$$

$T_{t,e}$ is considered in the equation of motion if the tie-rod displacement d_t is in the range of $0 \leq d_t \leq d_y$ (the sub-index y stands for yielding) or $d_r \leq d_t \leq d_{max}$ (the sub-index max stands for ultimate displacement). The tie-rod can be subjected to a prestress F_0 . Once yielding is attained, $d_t > d_{max}$ or equivalently $d_t > d_{max}$, the spring exerts the constant yielding force F_y . The term related to the plastic tie-rod contribution is then:

$$T_{t,p} = \text{sgn}(\vartheta) F_y R_r \cos A_{r,\vartheta} \quad (4)$$

As usual, a compressed tie-rod is considered inactive. In case of unloading, the constitutive law follows the elastic branch. Anyway, the constitutive model is fully described in [28]. The tie-rod influence can be controlled through the following parameters: stiffness, yielding, ductility and strength associated to it.

T_L is different from zero only for counterclockwise rotations (spring bed in compression, Figure 1). In that case it is expressed by[29]:

$$T_L = \operatorname{sgn}(\vartheta) K'_c h' \left(A + \frac{Bh'}{2} + \frac{Ch'^2}{3} \right), \quad (5)$$

where:

$$A = \operatorname{sgn}(\vartheta) 4b^2 \sin \vartheta \cos \vartheta (1 - \cos \vartheta); \quad (6)$$

$$B = 2b (\sin^2 \vartheta \cos \vartheta - \cos^3 \vartheta + \cos^2 \vartheta);$$

$$C = \operatorname{sgn}(\vartheta) \sin \vartheta \cos^2 \vartheta.$$

h' is the extension of the spring bed, $2b$ is the wall thickness and K'_c is the stiffness of the spring bed. K'_c can be calculated as function of the horizontal elastic modulus of masonry E_x , actual transverse wall length $L_{L,eff}$ and transverse wall thickness t_t according to the multi-struts model presented in [29].

The solution of the equation of motion (Eq. (1)) gives the rotation time history $\vartheta(t)$ of the block and all the other parameters (acceleration, velocity, displacement) related to the center of mass and to the other significant points of the wall. The solution of the differential equation is performed by means of the ODE45 solver available in MATLAB [30], which uses a 4th-5th order Runge-Kutta integration technique.

2.2 Probabilistic model for the determination of fragility curves and seismic hazard curves

The probabilistic model employed for calculating the fragility curves is extensively described in [31] and that for obtaining the seismic hazard curves is illustrated in [23]. To be concise, only a general description of them is given in the following. The fragility curves are plotted by calculating the conditional probability of exceedance of specific limit states defined by the engineering demand parameter EDP ϑ/α . The EDPs, taken as maximum normalized rotation of each response time-history, clearly depend on the seismic input, in turn defined by specific intensity measures IMs. The conditional probability $P(EDP > C|IM)$ that the EDP overcomes a capacity threshold C conditioned to an IM is expressed by:

$$P_{ex}(EDP > C|IM) = \Phi \left(\frac{\ln D - \ln C}{\beta_{D|IM}} \right). \quad (7)$$

The capacity thresholds C considered for the corresponding limit states are:

1. LS0, rocking initiation, $EDP > 0.0$;
2. LS1, limited rocking, $EDP = 0.1$;
3. LS2, moderate rocking, $EDP = 0.4$;
4. LS3, severe rocking, $EDP = 1.0$.
5. LS4, near-collapse rocking, $EDP = 1.5$.

Φ is the standard cumulative distribution function Φ , $\beta_{D|IM}$ is the logarithmic standard deviation, or dispersion, of the demand conditioned on the IM level. D is the median structural demand which for univariate fragility curves is equal to:

$$D = a IM^b. \quad (8)$$

D coincides with the EDP coming from the rocking analyses, while a and b are the two correlation coefficients which derive from the post-processing of the results expressing D in logarithmic terms.

Preliminarily, the results of a set of rocking analyses with variable seismic inputs should be obtained. Each output of the rocking analysis, for a fixed geometry and fixed boundary conditions (mechanical properties of the tie-rods) is a single realization. These realizations are then elaborated to obtain the correlation coefficients. The larger is the correlation coefficient b , the more practical is the correlation with the intensity measure. The lower the dispersion coefficient $\beta_{D|IM}$, the more efficient is the correlation. A third correlation coefficient is $\zeta = \beta_{D|IM}/b$ to assess proficiency. The realizations are then used for calculating the fragility as conditional probability of failure [32], where the demand D is represented by the EDPs calculated from the rocking analyses and the capacity C is defined by the five limit states also expressed in [31], [33]. Different fragility curves can be plotted, depending on the fact that the case is categorical (rocking-non rocking) or a specific limit state is exceeded. In this paper the so-called “final probability” P_f is plotted combining the probability of exceedance P_{ex} to the probability of overturning P_{RO} . The complete procedure is described in [34].

3 ASSUMPTIONS OF THE ANALYSIS

This section illustrates the assumptions of the analysis in terms of choice of geometries, seismic inputs and mechanical properties of tie-rods. Indeed, all these parameters have an impact on the dynamic response.

3.1 Wall geometries

Two wall geometries are selected to give a first glimpse of their influence on the response. A medium-high slenderness ratio of $\alpha = 0.1$ is chosen, corresponding to a ratio of wall height/thickness (conventional slenderness) equal to 10. Upper limit values of conventional slenderness are fixed to 12 for unreinforced brick masonry (10 for stone masonry). These limit values are valid for earthquake resistant walls [35]. For what concerns the wall size, two thickness values are considered: 30 cm and 60 cm. Consequently, being $\alpha = 0.1$, the two respective heights are 300 cm and 600 cm. The walls have unit width and specific weight of 19 kN/m³. For the sake of clarity, one can define the first wall as ordinary wall, and the second one as monumental wall, since its greater size is similar to that of the main façades of historic or monumental buildings.

3.2 Mechanical properties of the tie-rods and transverse walls

This paper is mainly aimed at assessing the influence of the tie-rods in the dynamic response. The variability of mechanical properties is taken into account in terms of:

- Yield stress f_y (which assumes the values 142-235-294 MPa);
- Area A (calculated according to the procedures of kinematic linear analyses [35] assuming $PGA=0.278g$);
- Yielding force $F_y = f_y \cdot A$;
- Ultimate strain ϵ_u (which assumes the values 0-2-10%).

The yielding strength is that typical of existing tie-rods in unreinforced masonry structures, also historical [36]. The last parameter is related to the ductility of the tie-rod. This investigation has the purpose of analyzing its effect on the response depending on the level of ductility of the

tie-rod material. It is physically expectable that a brittle tie-rod behaves differently from a ductile tie-rod, but the quantitative difference can be assessed only through a comparison of non-linear dynamic analyses. Moreover, deterministic analyses are not fully reliable due to the fact that the response is input-dependent.

The response is reported in terms of a dimensionless parameter called *restraining efficiency coefficient* $\rho_{M,e}$. This parameter reads as ratio of a resisting moment M_r to a seismic demand moment M_d . In particular, the resisting moment can be expressed as:

$$M_r = F_y \cdot h_r \quad (9)$$

where h_r is the lever arm of the tie-rod, that is the distance of the tie-rod from the rocking hinge on the wall foundation. The seismic demand moment is calculated assuming an acceleration variable with the block height based on its first modal shape, whose maximum acceleration a_d is assumed to be equal to the gravity acceleration:

$$a_d = \ddot{\theta}(z = 2h) \cdot z = \frac{g}{2h} z \quad (10)$$

Considering the distance z of the mass per unit of length μ from the rocking base hinge, the corresponding force is:

$$dF_d = \mu \cdot a_d dz \quad (11)$$

The seismic demand moment reads, considering Eq. (11) and Eq. (12):

$$M_d = \int_0^{2h} dF_d \cdot z = \int_0^{2h} \mu \frac{g}{2h} \cdot z^2 dz. \quad (12)$$

In the present case, being μ constant, it results:

$$M_d = \frac{4}{3} Wh \quad (13)$$

where W is the wall weight. Finally, when the tie is installed at the top of the wall, namely $h_r = 2h$, the restraining efficiency coefficient $\rho_{M,e}$ assumes the following expression:

$$\rho_{M,e} = \frac{M_r}{M_d} = \frac{3 F_y}{2 W} \quad (14)$$

In the present case, since the diameter of the tie-rod is calculated from the design criterion of the kinematic linear analysis [35], $\rho_{M,e}$ is constant for both cases (Table 1). By contrast, the consequent tie-rod diameter φ varies as reported in Table 2, because the yielding strength changes.

	W [kN]	F_y [kN]	$\rho_{M,e}$ [-]
ordinary wall	17.1	5.7	0.5
monumental wall	68.4	22.9	0.5

Table 1: Weight of the analyzed walls, yielding force and restraining efficiency coefficient of the tied configuration.

f_y [MPa]	142	235	294
ordinary wall	7.2	5.6	5
monumental wall	14	11	10

Table 2: Variation of tie-rod diameter (in mm) with the yielding strength.

As for the transverse walls, the following parameters are considered: extension of the spring bed $h' = 2h$, horizontal elastic modulus of masonry $E_x = 690 \text{ MPa}$, actual transverse wall length $L_{L,eff} = 1.2 \text{ m}$ and transverse wall thickness $t_t = 2b$. By substituting the values for the two wall cases, one has $K'_c = 172.5 \text{ MN/m}^2$ and $K'_c = 345.0 \text{ MN/m}^2$ respectively for the ordinary wall and for the monumental wall.

3.3 Seismic inputs

A number of 48+48 seismic records, taken from the ESM database [37], has been considered for the stochastic analyses. The number is doubled because each of the 48 seismic records has been also changed in sign and used as second set of inputs. Among the 48 accelerograms, 24 were registered in Central Italy, whereas 24 were taken from [31]. Several significant intensity measures (IMs) can be associated to each accelerogram. It is important to point out that numerous IMs - acceleration, velocity and energy based - can be calculated for each of them. Nevertheless, in this contribution the focus is on peak ground acceleration (PGA), on Arias intensity (I_a) and on peak ground velocity (PGV), the most common IMs referred to in seismic vulnerability analysis. PGV is in particular an IM very significant for rocking blocks. The seismic inputs considered in the analysis are listed in Table 3.

n.	waveform ID [yyyymmdd-hhmm-SSS ¹ -DD ²]	site -	M_L [-]	PGA [g]	PGV [cm/s]
1	20160824-0136-AMT-WE	Accumoli	6.0	0.87	43.55
2	20160824-0136-NRC-NS	Accumoli	6.0	0.37	29.75
3	20160824-0233-FOC-WE	Norcia	5.4	0.18	2.79
4	20160824-0233-NRC-NS	Norcia	5.4	0.19	9.80
5	20160826-0428-AMT-NS	Amatrice	4.7	0.34	11.00
6	20160826-0428-PCB-NS	Amatrice	4.7	0.31	5.50
7	20161026-1710-CMI-WE	C.S.A. sul Nera	5.4	0.72	55.70
8	20161026-1710-CNE-WE	C.S.A. sul Nera	5.4	0.56	17.34
9	20161026-1918-CMI-WE	Visso	5.9	0.65	43.76
10	20161026-1918-FOC-WE	Visso	5.9	0.62	20.00
11	20161030-0640-MZ24-WE	Norcia	6.1	1.02	73.60
12	20161030-0640-MZ51-NS	Norcia	6.1	0.96	74.98
13	20161101-0756-MMO-NS	Visso	4.7	0.19	7.58
14	20161101-0756-RQT-WE	Visso	4.7	0.13	2.80
15	20161103-0035-PBN-NS	P. Torina	4.8	0.31	8.47
16	20161103-0035-T1219-WE	P. Torina	4.8	0.34	7.88
17	20170118-0925-AMT-NS	Capitignano	5.4	0.35	13.15
18	20170118-0925-PCB-NS	Capitignano	5.4	0.18	3.79
19	20170118-1014-AMT-NS	Capitignano	5.4	0.32	16.10
20	20170118-1014-PCB-NS	Capitignano	5.4	0.60	21.02
21	20170118-1025-MSCT-NS	Monteale	5.3	0.28	17.03
22	20170118-1025-PCB-NS	Monteale	5.3	0.56	19.35
23	20170118-1333-MSCT-NS	C. Amiterno	5.1	0.16	6.27
24	20170118-1333-PCB-NS	C. Amiterno	5.1	0.29	5.55
25 - 48	records [51 - 74], Table 5, in Giresini et al. 2018		> 5.5	var	> 45

¹SSS: station code.

²DD: earthquake direction (North-South, NS; West-East, WE).

Table 3: Seismic inputs used in the analysis.

3.4 Single realizations of the non-linear dynamic analyses and correlation coefficients

The single realizations coming from the rocking analyses are performed for both geometries and for the ten cases (free-standing and nine types of tie-rods as described in 3.2). A multistripe analysis [23] is carried out considering six values of PGA (hazard site: Carlentini, Italy [38], [39]). For each PGA value 1920 analyses have been performed, so that 11520 runs resulted in total. An extract of the graphs for the free-standing and tied case of the monumental façade ($f_y = 235$, $\varphi = 11$ mm, $\varepsilon_u = 10\%$) is reported in Figure 2. In the vertical axis of the graphs the maximum engineering demand parameter is reported for each rocking analysis with fixed seismic input. Each circle represents the maximum response of single realization obtained from each seismic input. Each accelerogram has a corresponding pair of PGA and PGV displayed in the abscissa axes; each one is scaled for six values of PGA corresponding to specific return periods of the selected construction site. It is evident that when the wall is not restrained by any tie-rod the normalized rotation is greater, and overturning frequently attained (Figure 2a). In case the wall is horizontally restrained by a ductile tie-rod of medium strength ($\varepsilon_u = 10\%$, $f_y = 235$ MPa, $\varphi = 11$ mm), the non-rocking cases are more numerous and the number of overturning cases is only three. Analyzing the results, the correlations coefficients can be easily calculated.

The best correlation is always obtained considering the PGA, with the exception of the monumental unrestrained wall, for which the best IM is the Arias Intensity I_a .

For the same cases displayed in Figure 2, Figure 3 reports the estimated curve with the correlation coefficients:

- b -coefficient (Eq. (8)), for the practicality;
- dispersion coefficient $\beta_{D|IM}$, for the efficiency;
- $\zeta = \beta_{D|IM}/b$, for the proficiency;
- Coefficient of determination R^2 , defined as $1 - \frac{\sum(\ln D - \ln S_D)^2}{\sum(\ln D - \text{mean}(\ln D))^2}$;

The correlation is made only for the cases of safe rocking, namely for $1e-4 < \vartheta/\alpha < 1.5$. That is the reason why Figure 3b shows only two values of PGA for multistripe analysis (see also for comparison the blue circles in Figure 2b). Therefore, the probability of exceedance of a specific limit state is calculated only for the safe-rocking cases.

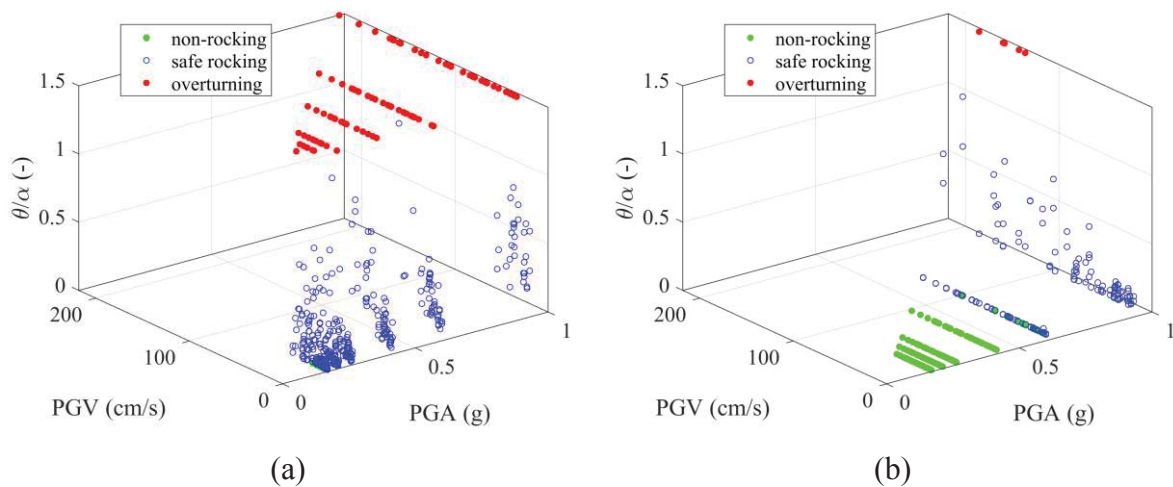


Figure 2: Realizations of the rocking analysis for specific values of PGA and PGV for unrestrained (a) and tied (b) monumental wall.

Looking at the results, it is possible to observe that, when the correlation is made towards the PGA (Figure 3a, b), the unrestrained case is worse correlated than the tied case in terms of efficiency and proficiency. As for practicality, the unrestrained case is better correlated. The results in terms of Arias Intensity, for which the correlation is the most efficient for the unrestrained case, are scattered because this intensity measure is calculated after that the PGA of each accelerogram is scaled according to the formula given in [31]. the unrestrained case is worse correlated than the tied case in terms of efficiency and proficiency (Figure 3c, d). Concerning practicality – and also proficiency – the unrestrained case is again better correlated than the restrained case. Since the dispersion coefficient for the unrestrained case is slightly greater than that for the tied case, the correlation of the first one is more efficient. The maximum coefficient of determination is observed for the correlation of PGA (restrained case) and of I_a (unrestrained case) and is equal to 0.57 for both scenarios (Figure 3b, c).

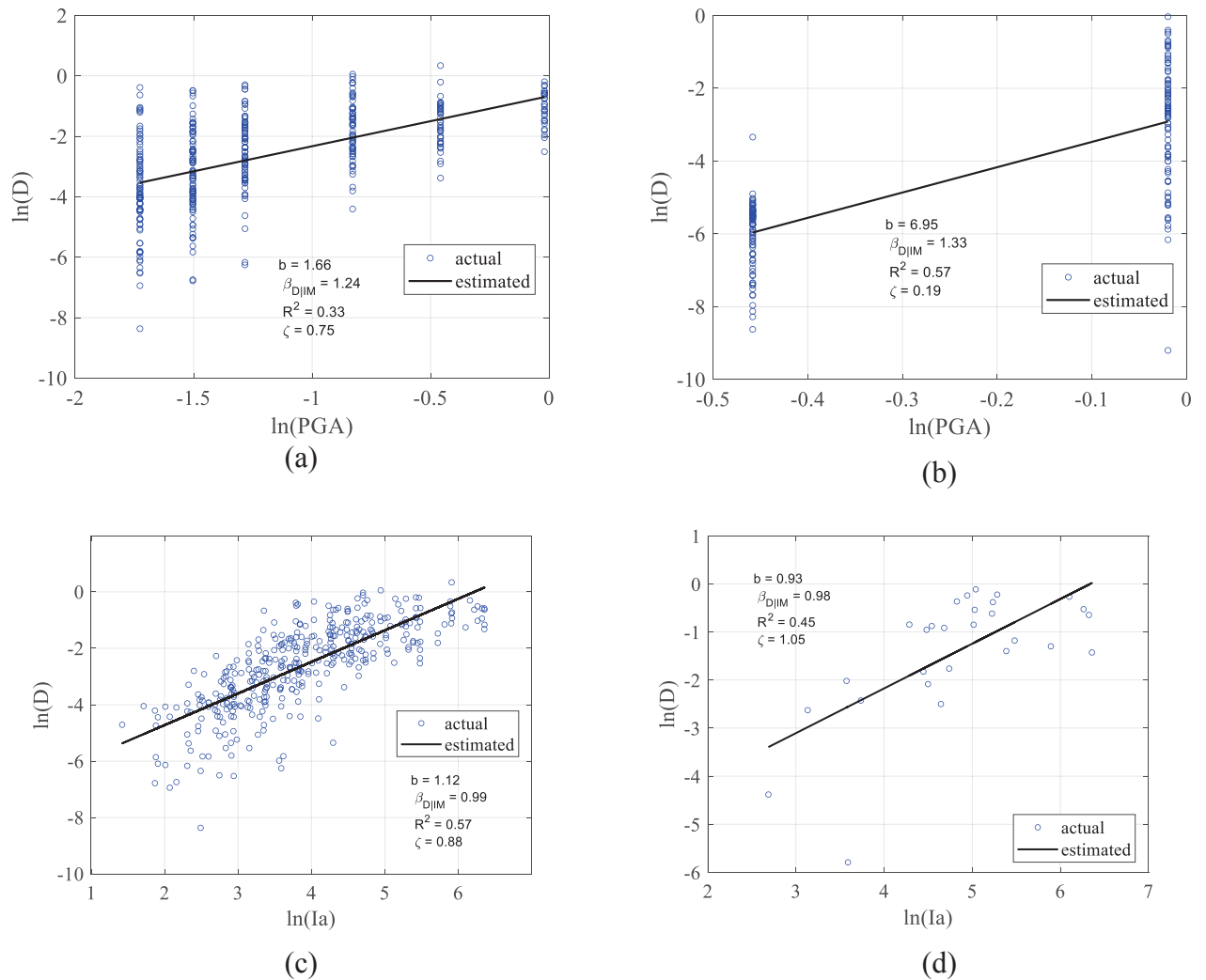


Figure 3: Structural demand and correlation coefficients for unrestrained (a, c) and tied (b,d) monumental wall.

4 FRAGILITY CURVES

This section discusses the fragility curves obtained for all the cases with the calculation process described in section 2.2. A first comparison can be made between the ordinary and the monumental wall. Their slenderness value is the same (height to thickness = 10) but the size of

the ordinary wall is half of that monumental. The fragility curves representing the conditional probability of the EDP conditioned to PGA are reported in Figure 4 for all the five limit states. The probability of occurrence of the rocking initiation state is much less for the ordinary wall rather than that of the monumental wall. For the ordinary wall, of small size, there is a narrower difference between probability of occurrence of the limit states, from the rocking initiation to the near-collapse. The ordinary wall appears more stable than the monumental wall, although the slenderness values are the same. In this case, therefore, the common scale effect usually exhibited by free rocking blocks is not observed.

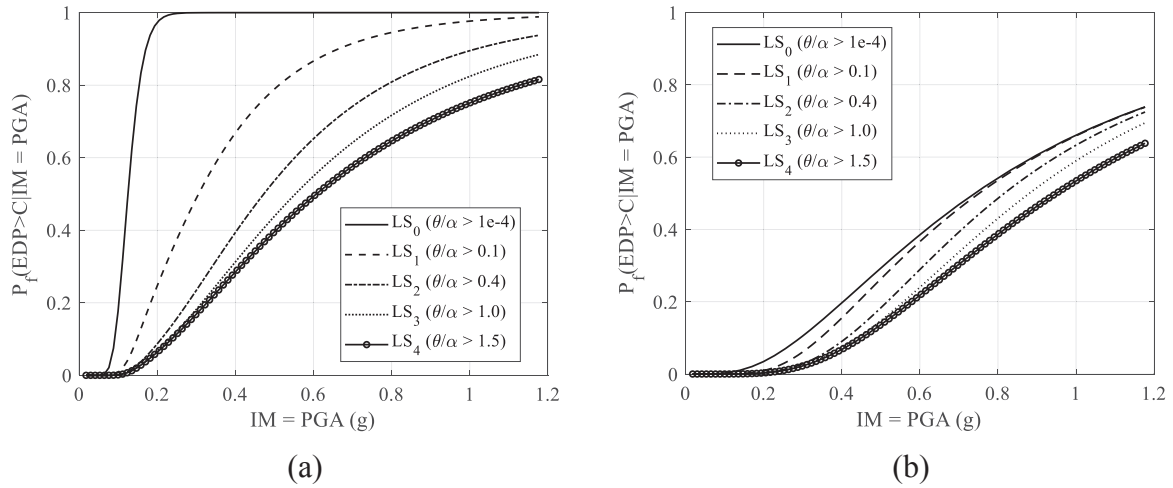


Figure 4: Fragility curves for the unrestrained monumental (a) and ordinary (b) wall.

Considering the monumental wall, the fragility curves considering again the five limit states but with different values of ductility capacity of the tie-rod are displayed in Figure 5. The sub-figures respectively indicate the response for the unrestrained wall (a), the wall restrained by a brittle tie-rod with $\varepsilon_u=0\%$ (b), by a low ductility tie-rod with $\varepsilon_u=2\%$ (c), by a high ductility tie-rod with $\varepsilon_u=10\%$ (d). It is evident that a more ductile tie-rod reduces the probability of overcoming the attainment of an EDP threshold. The case with the most ductile tie-rod results in flatter fragility curves which lose their typical s-shape, which indicate greater uncertainty.

For the medium steel axial strength (235 MPa, $\varphi = 11$ mm), the probability of exceedance for the limited rocking state (LS₁) is reported in Figure 6a: the most dangerous case is the brittle tie-rod, as expected. The probability of exceedance of the limited rocking state is respectively by 85%, 30%, 8% and 3% for unrestrained wall, wall restrained by brittle, ductile and low-ductile tie rod for PGA=0.8 g. PGA values lower than it, no remarkable difference is observed in terms of probability of exceedance, since the tie-rod impedes a considerable wall rocking. The trend of reduction of probability of exceedance above mentioned, not fully expected for ductile and low-ductile tie-rod, depends on the higher uncertainty that affects the probability of exceedance of a ductile tie-rod. So, even though the curve related to the ductile tie-rod is not considered, the reduction of probability of exceedance is sensitively strong being an order of magnitude lower for the low-ductile tie-rod (Figure 6a). Therefore, it is extremely beneficial to restrain the wall even with a low-ductile (but also a brittle) tie-rod. The choice will depend on the assumed probability of exceedance depending on the return periods established by the standards.

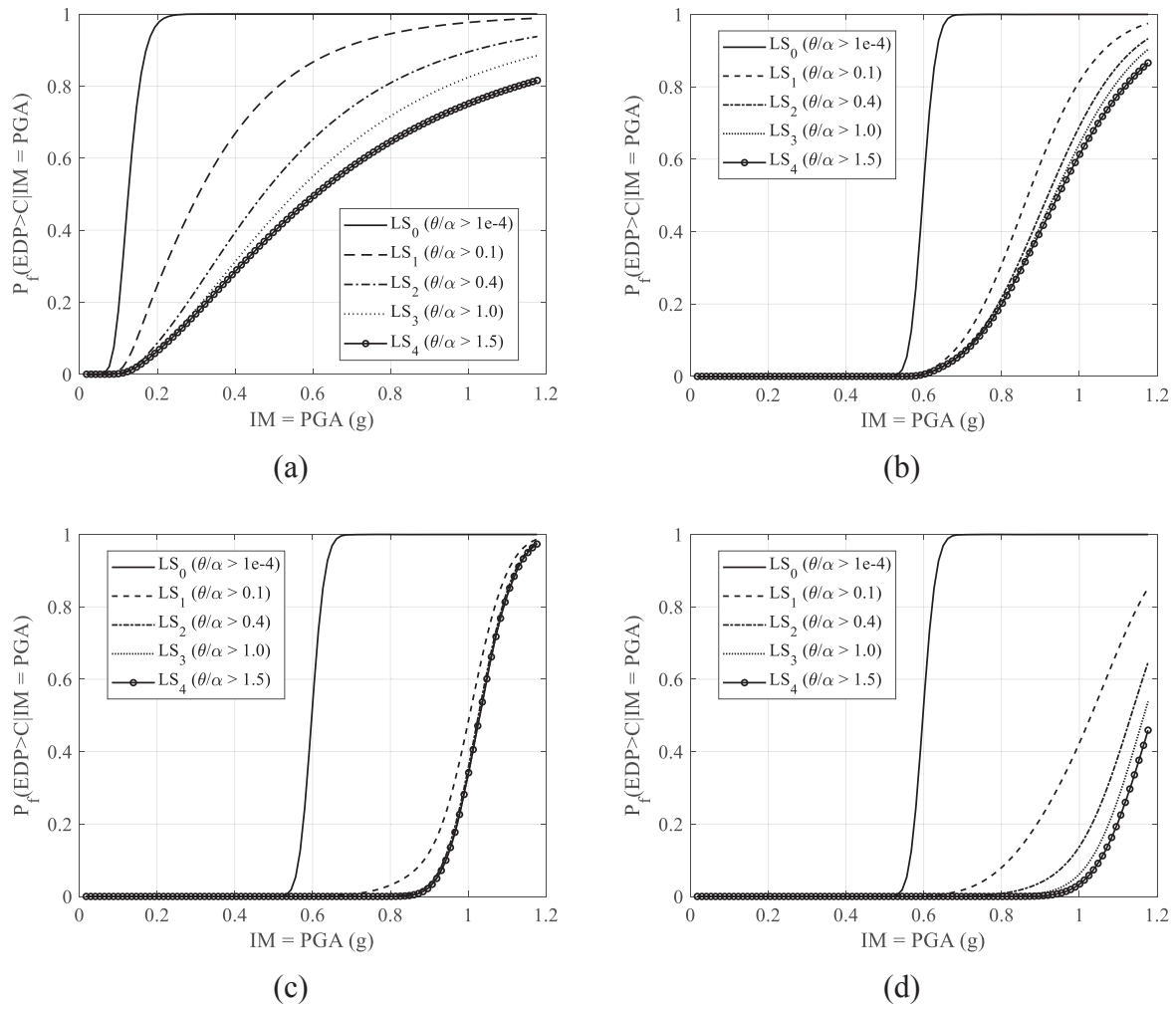


Figure 5: Fragility curves for the monumental wall: unrestrained (a); brittle (b); low ductility (c) and ductile (d) tie-rod.

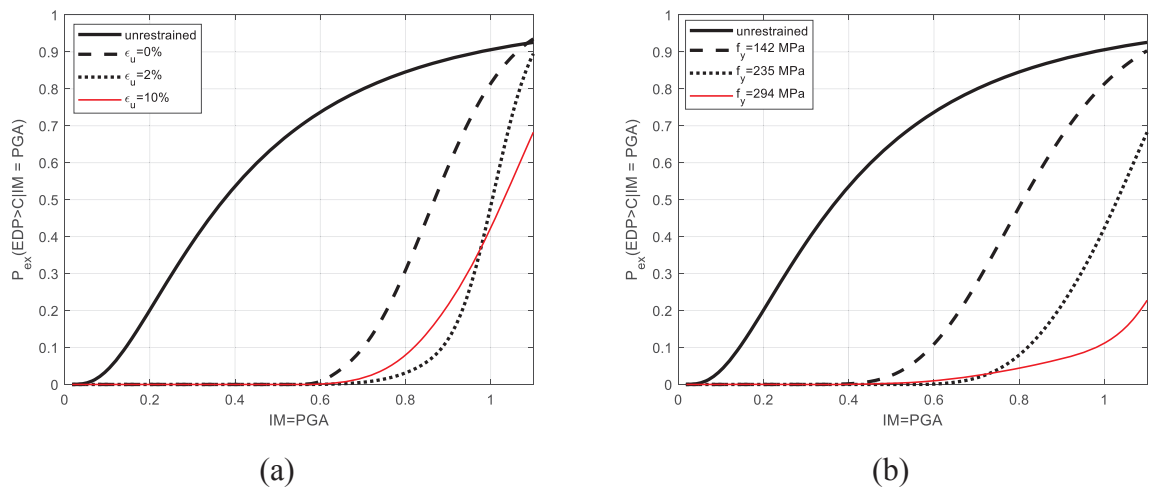


Figure 6: Fragility curves for monumental wall: parametric analyses in terms of (a) steel ductility and (b) axial strength for the limited rocking state (LS1).

As for the variation of steel strength, keeping constant the tie-rod ultimate strain to 10%, the weaker material has an increased probability of exceedance that anyway remains low (about 10% for $\text{PGA}=0.6\text{ g}$) even for medium-high intensity earthquakes. As a consequence, in many cases even a weak tie steel can be really beneficial for the reduction of the probability of exceedance of the limited rocking state. The cases of medium-high strength ties (235 MPa, $\varphi = 11\text{ mm}$ and 294 MPa, $\varphi = 10\text{ mm}$) give coincident fragility curves since the stress of 235 MPa is never overcome.

5 SEISMIC DEMAND HAZARD CURVES

The seismic demand hazard curves are obtained by following the procedure described in [23]. The output is readable as annual exceedance rate $\lambda_{EDP}(edp)$ for the five limit states indicated in the abscissa axis ($\vartheta/\alpha = 1\text{E-}4, 0.1, 0.4, 1.0, 1.5$). This information is more complete than the mere fragility curves, as the demand hazard is considered in the probabilistic assessment. The seismic demand hazard curve is much more conservative in case of restrained condition than for the unrestrained monumental wall (Figure 7a). Considering the same steel strength (235 MPa, $\varphi = 11\text{ mm}$) and varying the ultimate strain of the tie-rod (Figure 7b), it is clear that the annual exceedance rate is the lowest in case of low ductile tie-rod behavior than in case of brittle behavior. Moreover, a brittle behavior of the tie-rod could lead to unexpected performance of the tie-rod especially in case of historical ties, where localized failures can occur [36]. Thus, it is recommended to prefer even a low-ductile behavior that strongly reduces the seismic demand hazard curves. Indeed, for instance considering the moderate rocking limit state ($\vartheta/\alpha = 0.4$), the annual exceedance rate decreases by over 60% passing from a brittle to a low-ductile tie rod. Again the red curve, related to a highly ductile tie-rod, for same ranges of EDP exhibits unexpected performance. In any case, such a behavior can be neglected being the corresponding fragility curves characterized by greater uncertainties.

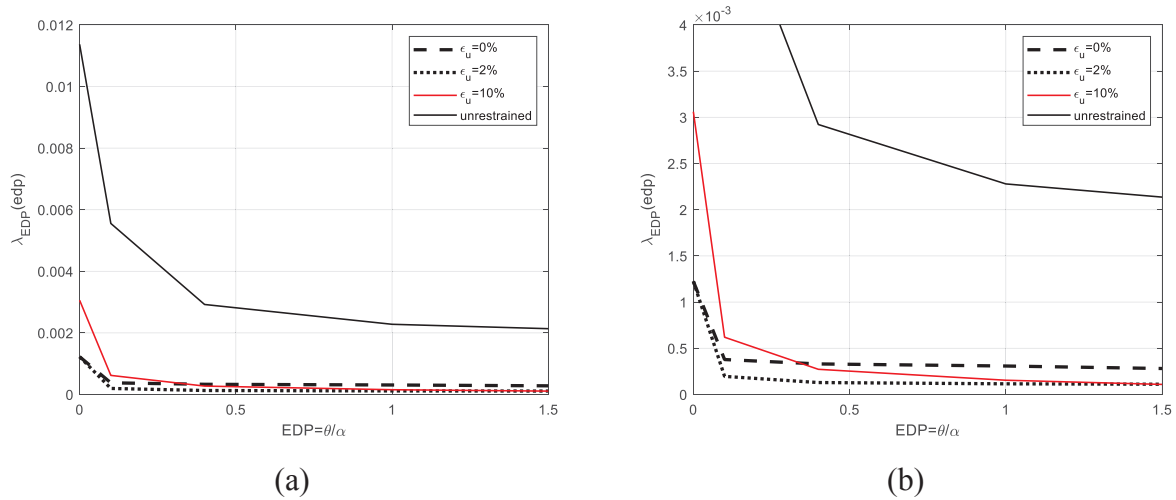


Figure 7: Seismic hazard curves for the monumental wall: parametric analyses in terms of steel ductility (a) with a detail for the restrained case (b).

Discussing how the tie-rod strength influences the seismic risk, it is evident that, as observed for the fragility curves, there is not a sensitive change in the annual rate of exceedance whether a high-strength tie-rod is assumed or a medium strength is considered (Figure 8).

Referring to the moderate rocking limit state ($\vartheta/\alpha = 0.4$), the annual exceedance rates are:

- $1.8\text{e-}5$ for the strength values of 294 MPa, $\varphi = 10\text{ mm}$;

- $7.7 \cdot 10^{-5}$ for 235 MPa;
- $2.7 \cdot 10^{-4}$ for 142 MPa;
- $2.9 \cdot 10^{-3}$ for the unrestrained case.

They respectively correspond to the fact that this limit state is exceeded once every 56000 years (high tie-rod strength) 13000 (medium), 3700 (low) and 345 years. Therefore, even with a low-strength tie-rod, the rate of occurrence is reduced.

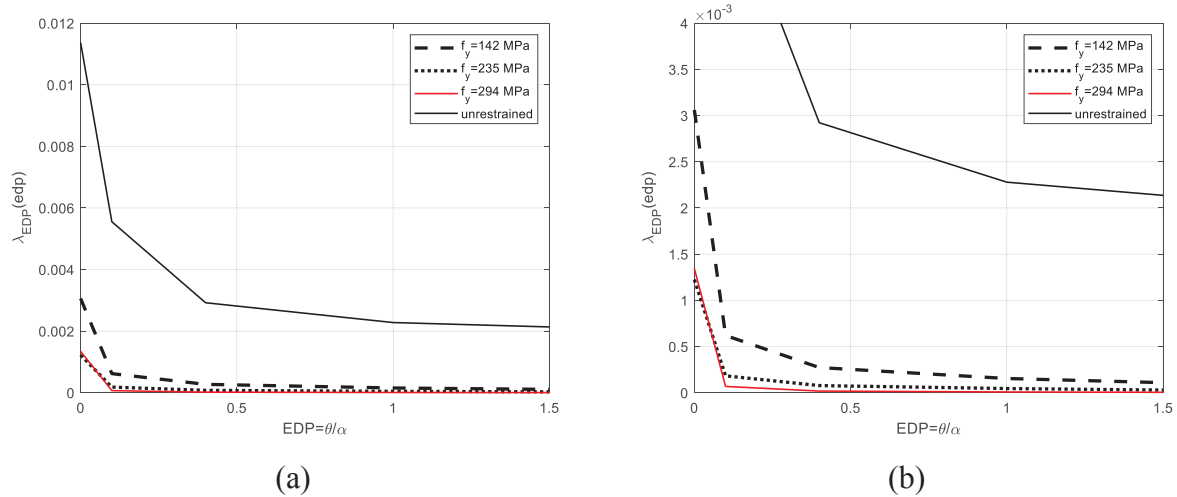


Figure 8: Seismic hazard curves for the monumental wall: parametric analyses in terms of steel strength (a) with a detail for the restrained case (b).

Taking into account the severe rocking ($\theta/\alpha = 1.0$), the annual exceedance rates are:

- $8 \cdot 10^{-6}$ for the strength value of 294 MPa, $\varphi = 10$ mm (one occurrence every 125000 years);
- $4.5 \cdot 10^{-5}$ for 235 MPa (22000 years);
- $1.5 \cdot 10^{-4}$ for 142 MPa (2000 years);
- $2.2 \cdot 10^{-3}$ for the unrestrained case (450 years).

Obviously, the two latter cases are over-conservative considering the life cycle of a masonry building, therefore even small strength values are sufficient to guarantee a remarkable increase of safety. For the severe rocking limit state, the reduction of annual exceedance rate is less evident than that for the moderate rocking limit state.

6 CONCLUSIONS

This paper discussed the role of tie-rods in the dynamic response of restrained masonry walls subjected to earthquakes. The analysis was performed by following a fully probabilistic approach with a multi-stripe analysis obtaining seismic fragility and hazard curves. Two typical masonry wall, one ordinary and the other of monumental type, were taken into account as unrestrained and restrained by tie-rods of different mechanical properties. Considering the results of over 11500 analyses, the best correlated intensity measures were observed to be peak ground acceleration and Arias Intensity.

Observing the fragility curves, the most dangerous case is the brittle tie-rod, as expected. The probability of exceedance of the limited rocking state is respectively by 85%, 30%, 8% and 3% for unrestrained wall, wall restrained by brittle, ductile and low-ductile tie rod for $PGA=0.8$

g. The reduction of probability of exceedance is significant being an order of magnitude lower for the case of low-ductile tie-rod with respect to the case of brittle tie-rod. Therefore, it is extremely beneficial to restrain the wall even with a low-ductile (but also a brittle, in comparison with an unrestrained wall) tie-rod. The choice of a specific tie-rod will depend on the admissible probability of exceedance depending on the return periods established by the standards.

As for the variation of steel strength, keeping constant the tie rod ultimate strain to 10%, the weaker material has an increased probability of exceedance that anyway keeps low (about 10% for $PGA=0.6$ g) even for medium-high intensity earthquakes. As a consequence, in many cases even a weak steel can be really beneficial for the reduction of the probability of exceedance of the limited rocking state.

For what concerns the seismic hazard demand curves, it is preferable for the tie-rod a low-ductile rather than a brittle behavior that strongly reduces the seismic demand hazard curves. A highly ductile performance could cause more uncertainties in the results. Considering the moderate rocking limit state, the annual exceedance rate decreases by over 60% passing from a brittle to a low-ductile tie rod. As for the influence of the tie-rod strength, even a low-medium values produce a remarkable reduction of annual exceedance rate. For instance, a sever rocking limit state occurs for the unrestrained monumental wall every 450 years and every 2000 years for the wall restrained by a tie rod of strength 142 MPa and a diameter of 14 mm. The return period of the same event increases to 22000 years for a strength of 235 MPa (and diameter 11 mm) and to 125000 years for 292 MPa (diameter 10 mm). Obviously, the two latter cases are over-conservative considering the life cycle of a masonry building, therefore even small strength values are sufficient to guarantee a remarkable increase of safety.

Finally, the probabilistic approach described here for the seismic assessment of the out-of-plane of masonry walls is able to reliably predict the seismic demand hazard curves to define the most appropriate type of steel tie rod to use as anti-seismic device.

REFERENCES

- [1] M. Sassu, L. Giresini, E. Bonannini, and M. L. Puppio, On the Use of Vibro-Compressed Units with Bio-Natural Aggregate. *Buildings*, **6**, 2016.
- [2] M. L. Puppio and L. Giresini, Estimation of tensile mechanical parameters of existing masonry through the analysis of the collapse of Volterra's urban walls. *Frattura ed Integrità Strutturale*, **13**, 2019.
- [3] F. Solarino, D. Oliveira, and L. Giresini, Wall-to-horizontal diaphragm connections in historical buildings: A state-of-the-art review. *Engineering Structures*, **199**, 2019.
- [4] L. Giresini and M. Sassu, Horizontally restrained rocking blocks: evaluation of the role of boundary conditions with static and dynamic approaches. *Bulletin of Earthquake Engineering*, **15**, 385–410, 2017.
- [5] L. Giresini, Design strategy for the rocking stability of horizontally restrained masonry walls. , in *COMPDYN 2017 6th ECCOMAS Thematic Conference on Computational Methods in Structural Dynamics and Earthquake Engineering, Rhodes Island, Greece, 15–17 June 2017.*, 2017.
- [6] N. Makris and M. F. Vassiliou, Dynamics of the Rocking Frame with Vertical Restrainers. *Journal of Structural Engineering*, **141**, 2015.
- [7] C. Casapulla, P. Jossa, and A. Maione, Rocking motion of a masonry rigid block under seismic actions: A new strategy based on the progressive correction of the resonance

- response | Il moto sotto sisma del blocco murario: Analisi per progressiva correzione della risposta in risonanza. *Ingegneria Sismica*, **27**, 35–48, 2010.
- [8] C. Casapulla and A. Maione, Critical Response of Free-Standing Rocking Blocks to the Intense Phase of an Earthquake. *International Review of Civil Engineering*, **8**, 1–10, 2017.
 - [9] C. Casapulla and A. Maione, Free Damped Vibrations of Rocking Rigid Blocks as Uniformly Accelerated Motions. *International Journal of Structural Stability and Dynamics*, **17**, 1–19, 2016.
 - [10] L. Giresini, M. Sassu, and L. Sorrentino, In situ free-vibration tests on unrestrained and restrained rocking masonry walls. *Earthquake Engineering & Structural Dynamics*, **47**, 3006–3025, 2018.
 - [11] L. Giresini, M. L. Puppio, and F. Taddei, Experimental pull-out tests and design indications for strength anchors installed in masonry walls. *Materials and Structures*, 2020.
 - [12] H. Derakhshan, M. C. Griffith, and J. M. Ingham, Out-of-plane seismic response of vertically spanning URM walls connected to flexible diaphragms. *Earthquake Engineering & Structural Dynamics*, **45**, 563–580, 2016.
 - [13] C. Casapulla and F. Portioli, Experimental tests on the limit states of dry-jointed tuff blocks. *Materials and Structures/Materiaux et Constructions*, **49**, 751–767, 2016.
 - [14] L. Giresini, F. Solarino, O. Paganelli, D. V. Oliveira, and M. Froli, One-sided rocking analysis of corner mechanisms in masonry structures: influence of geometry, energy dissipation, boundary conditions. *Soil Dynamics and Earthquake Engineering*, **123**, 357–370, 2019.
 - [15] C. Casapulla, L. Giresini, L. U. Argiento, and A. Maione, Nonlinear Static and Dynamic Analysis of Rocking Masonry Corners Using Rigid Macro-Block Modeling. *International Journal of Structural Stability and Dynamics*, **19**, 1950137, 2019.
 - [16] L. U. Argiento, A. Maione, and L. Giresini, The corner failure in a masonry building damaged by the 2016-2017 central Italy earthquake sequence. , in *COMPDYN 2019 7th ECCOMAS Thematic Conference on Computational Methods in Structural Dynamics and Earthquake Engineering*, 2019, 633–650, .
 - [17] L. Giresini, B. Pantò, S. Caddemi, and I. Calì, Out-of-plane seismic response of masonry façades using discrete macro-element and rigid block models. , in *COMPDYN 2019 7th ECCOMAS Thematic Conference on Computational Methods in Structural Dynamics and Earthquake Engineering*, 2019, 702–717, .
 - [18] C. Casapulla, A. Maione, L. U. Argiento, and E. Speranza, Corner failure in masonry buildings: An updated macro-modeling approach with frictional resistances. *European Journal of Mechanics, A/Solids*, **70**, 2018.
 - [19] A. De Falco, L. Giresini, and M. Sassu, Temporary preventive seismic reinforcements on historic churches: numerical modeling of San Frediano in Pisa. *Applied Mechanics and Materials*, **351**, 1393–1396, 2013.
 - [20] L. Giresini and C. Butenweg, Earthquake Resistant Design of Structures According to Eurocode 8. , in *Structural Dynamics with Applications in Earthquake and Wind Engineering*, 2019, 197–358, .

- [21] M. Andreini, A. De Falco, L. Giresini, and M. Sassu, Collapse of the historic city walls of Pistoia (Italy): causes and possible interventions. *Applied Mechanics and Materials*, **351–352**, 2013.
- [22] O. AlShawa, D. Liberatore, and L. Sorrentino, Dynamic One-Sided Out-Of-Plane Behavior of Unreinforced-Masonry Wall Restrained by Elasto-Plastic Tie-Rods. *International Journal of Architectural Heritage*, **13**, 340–357, 2019.
- [23] B. A. Bradley, The seismic demand hazard and importance of the conditioning intensity measure. *Earthquake Engineering & Structural Dynamics*, **41**, 1417–1437, 2012.
- [24] P. Croce, F. Landi, and P. Formichi, Probabilistic Seismic Assessment of Existing Masonry Buildings. *Buildings*, **9**, 2019.
- [25] P. Croce, M. L. Beconcini, P. Formichi, F. Landi, B. Puccini, and V. Zotti, Bayesian Methodology for Probabilistic Description of Mechanical Parameters of Masonry Walls. *ASCE-ASME Journal of Risk and Uncertainty in Engineering Systems, Part A: Civil Engineering*, **7**, 4021008, 2021.
- [26] M. L. Beconcini, P. Croce, F. Marsili, M. Muzzi, and E. Rosso, Probabilistic reliability assessment of a heritage structure under horizontal loads. *Probabilistic Engineering Mechanics*, **45**, 198–211, 2016.
- [27] P. Croce, M. L. Beconcini, P. Formichi, F. Landi, B. Puccini, and V. Zotti, Seismic risk evaluation of existing masonry buildings: Methods and uncertainties. , in *20th Congress of IABSE, New York City 2019: The Evolving Metropolis – Report 2019*, 2019, 2510–2515, .
- [28] L. Giresini, F. Solarino, F. Taddei, G. Mueller, and P. Croce, Influence of stiffness and damping parameters of seismic passive control devices in one-sided rocking of masonry walls. *submitted to Journal of Structural Engineering*, 2021.
- [29] Giresini L., Sassu M., Horizontally restrained rocking blocks: evaluation of the role of boundary conditions with static and dynamic approaches. *Bulletin of Earthquake Engineering*, **15**, 385–410, 2017.
- [30] MATLAB. version 9.4.0.813654 (R2018a). The MathWorks Inc., Natick, Massachusetts, 2018. . .
- [31] L. Giresini, C. Casapulla, R. Denysiuk, J. Matos, and M. Sassu, Fragility curves for free and restrained rocking masonry façades in one-sided motion. *Engineering Structures*, **164**, 195–213, 2018.
- [32] J. E. Padgett, B. G. Nielson, and R. DesRoches, Selection of optimal intensity measures in probabilistic seismic demand models of highway bridge portfolios. *Earthquake Engineering & Structural Dynamics*, **37**, 711–725, 2008.
- [33] L. Giresini, F. Taddei, C. Casapulla, and G. Mueller, Stochastic assessment of rocking masonry façades under real seismic records. , in *COMPDYN 2019 7th ECCOMAS Thematic Conference on Computational Methods in Structural Dynamics and Earthquake Engineering*, 2019, 673–689, .
- [34] F. Solarino and L. Giresini, Fragility curves and seismic demand hazard analysis of rocking walls restrained elasto-plastic ties. *Earthquake Eng. Struct. Dyn. (submitted to)*, 2021.
- [35] Ministero delle infrastrutture e dei trasporti, *Circolare applicativa 21 gennaio 2019, n.*

- 7, *Istruzioni per l'applicazione dell'«Aggiornamento delle “Norme tecniche per le costruzioni”»*. In Italian. 2019.
- [36] C. Calderini, R. Vecchiattini, C. Battini, and P. Piccardo, Mechanical and metallographic characterization of iron tie-rods in masonry buildings: An experimental study. , in *Proceedings of the 10th International Conference on Structural Analysis of Historical Constructions, SAHC, Leuven, Belgium, September 13–15 2016*, 2016, 1293–300, .
- [37] L. Luzi, R. Puglia, E. Russo, and O. WG5, Engineering Strong Motion Database, version 1.0, Istituto Nazionale di Geofisica e Vulcanologia, Observatories & Research Facilities for European Seismology. . 2016.
- [38] General Assembly of the Superior Council of Public, *Circolare attuativa del D.M. 17/01/2018 (NTC 2018)*. 2019.
- [39] Decreto Ministeriale 17/01/2018, Italian Technical Standards for buildings (Nuove Norme Tecniche per le Costruzioni, in italian). . 2018.

GRAPHICAL METHODS, KINEMATIC AND FINITE ELEMENT ANALYSIS OF THE PREMILCUORE MASONRY BRIDGE

Linda Giresini¹, Daniela De Paola², Mario Lucio Puppio^{3,*} and Giovanni Buratti¹

¹ Department of Civil and Industrial Engineering
Largo Lucio Lazzarino, 1, 56100 Pisa (Italy)
linda.giresini@unipi.it, giovanni.buratti.2707@gmail.com

² Project Engineer
Pisa (Italy)
depaola.daniela@gmail.com

³ Department of Civil, Environmental Engineering and Architecture
Via Marengo, 2, 09123 Cagliari (Italy)
mariol.puppio@unica.it

*corresponding Author

Abstract

This paper presents the results of static and seismic vulnerability analyses performed on a single-span masonry bridge located in Northern Italy. The structure, dated back to the 17th century, is a bridge with single-span of about 16 meters and height of 8 meters, built with rubble and irregular masonry. A preliminary static analysis was performed on the bridge through traditional graphic approaches such as the Méry's rule and the Durand-Claye's method. Afterwards, a kinematic non-linear analysis was executed once the collapse mechanism under horizontal earthquake-type actions was identified. Finally, a static finite element analysis with brick elements was performed to state the seismic vulnerability of the bridge, by changing its mechanical properties to evaluate their influence on the structural response. Collapse load factors have been also computed considering non-uniform gravitational loads and horizontal settlements at the bridge foundations.

Keywords: masonry bridge, graphical methods, plastic hinge, arch bridge, seismic vulnerability; pushover analysis.

1 INTRODUCTION

Masonry Arch Bridges (MAB) represent a considerable portion of the ancient road infrastructures. The main characteristics of this artwork is a massive structure with significant stiffness and resistance. This aspect allows these infrastructures being less prone to vibration and deformation with respect to the modern structures. Furthermore, masonry bridges, as other historical structures, are characterized by a significant durability that permits their survival over the centuries.

MAB have an ancient origin. The first application of masonry in river overpasses are probably abutments and architraves of elementary bridges, made by simply supported wooden decks. The diffusion of arches in Mesopotamia and in Egypt gave a significant impulse to their use. The first stone arch can be dated back to the 4th millennium BC. Here the substitution of a previous slab made of intertwined reeds with dry stones and sun-dried bricks created the first documented arch of the history.

The first MAB was probably built in China, in the 3rd millennium BC. Later the Romans, famous road builders, massively used arches for the construction of bridges and aqueducts, some of which still survive nowadays [1].

For what concerns the computational modelling of MAB, from simplified methods to complex nonlinear finite element or discrete elements, interesting contributions can be found in [2–4]. For a proper computational modelling, the definition of geometry and mechanical properties of MAB is essential. In [5], the significant role of geometrical and mechanical parameters like arch thickness and filling is highlighted. In the same paper, a geometrical survey of 59 segmental MABs located in Portugal and Spain is reported. Thus, an accurate geometrical and mechanical survey is crucial in the safety evaluation; modern techniques can be very precious in this sense [6], especially when the internal core is not accessible. Specific techniques can be applied to limit the uncertainties in the composition of internal cores [7, 8]. When performing a structural assessment, it is important to vary the masonry and soil mechanical properties in case of uncertainties in their definition [9]. Sensitivity analyses are then often proposed to investigate the impact of the most important parameters such as the tensile strength of masonry [10–12]. Moreover, when dealing with uncertainties, it could be relevant to perform probabilistic analysis. For example, Casas [13] proposes a probabilistic assessment of MAB at the Serviceability and Ultimate Limit States. This work also illustrates recurring failure modes: four-hinge mechanism, the ring separation in multi-ring arches and the slip-page at the foundations. In [14] a simplified approach is proposed for the evaluation of fragility curves of MAB in case of seismic action. The study is carried out on numerous structures and broadened to a stock of roadway and railway bridge networks in dangerous condition to provide stakeholders a management tool.

There are diverse methodologies to study the static and the dynamic behavior of MAB. Very interesting graphical and numerical methods were developed in the past (from the 18th century) to study the static behavior of arch, in particular from the French Engineering Grand Écoles. This paper has the aim of performing all the possible analysis methods usually performed for MAB and of proposing qualitative comparisons.

In Section 2 a review of traditional and modern techniques is presented and applied to a representative case of study. The MAB selected for the investigation, reported in Section 3, is the *Premilcuore bridge* located in the District of Forlì-Cesena, Central Italy. The graphical methods and the numerical analyses are illustrated in Section 4.

2 BACKGROUND

2.1 Traditional graphical methods

In order to carry out a first simplified study of the stability of the vault, two different traditional methods have been employed: the so-called Mèry's Rule and Durand-Claye's Method.

Mèry's Rule, to which the credit for formalising the concept of thrust line is attributed, has risen to fame in the technical field particularly thanks to its ease of application. Indeed, it is interesting to observe how it is the only method still quoted in today's textbooks. Even though it was based on arbitrary assumptions [15], this method was applied for over a century for the design of arches and vaults. The foundation of this procedure is the personal criterium according to which the ideal condition for the arch can be identified by a thrust line that is entirely contained in the area defined by the middle third of the sections, intending to guarantee that the latter are completely reactive and the arch is not subjected to failure.

In accordance with Méry's studies, among the infinite curves of this type, which are able to ensure the arch equilibrium, the definition of the design line relies on the hypothesis that this thrust line passes through three pre-defined points: the lower middle third of the two sections in close proximity to the springers and the upper middle third in the keystone, where the direction of normal force is horizontal, according to the premise of symmetry of the applied load.

The second method, which is a more refined form from the theoretical point of view, is the one studied by Durand-Claye. It was conceived as a method to assess the stability of a symmetrical arch, symmetrically loaded by vertical forces under the condition that the material has finite value of the compressive strength and that it has a negligible tensile resistance.

This method essentially consists in defining the set of all the possible values of the internal forces in the keystone, the normal force N and the bending moment M , or, alternatively, the normal force and its eccentricity in relation to the axis curve, which ensure equilibrium and are compatible with the material strength. According to the assumptions, through each cross-section, possibly partialized, the compressive stresses vary with a linear law. The result of this procedure gives the graphical representation of the envelope of the aforementioned forces.

This method, unlike the previous one, allows to identify all the possible thrust lines capable of ensuring the balance in compliance with the limits of the material strength. Its value resides in checking the existence of admissible solutions without requiring to find the true one, which could be reached only by bringing into play the elastic properties of the material and the compatibility conditions. Assuming that the true solution exists, it is definitely included among these ones.

The Durand-Claye's method does not require either special hypotheses regarding the shape of the thrust line or regarding a predefined position of rupture joints, allowing to obtain several advantages. In particular, it allows to evaluate the degree of safety of the arch, the possible trend of the thrust line and the identification of the most stressed sections of the structure. This method is well suited to various types of arches, having different geometries and made with different materials.

2.2 Rigid block and arch models for kinematic analyses

A more modern approach to investigate the structural behavior of masonry buildings and bridges refers to limit analysis and non-linear dynamic analysis of rigid block models. Often, masonry structures - and especially historic constructions - can be regarded as composed by structurally independent parts or rigid blocks connected by ideal hinges. This occurs particularly when the connections between vertical members and between horizontal dia-

phragms/roof and walls are not effective [16]. In order to avoid such an undesirable behavior, tie-rods [17, 18], fiber composite stripes [19, 20] and strength anchors [21, 22] of suitable characteristics can be used. An extensive review on kinematic and rocking approaches for monolithic masonry walls, specifically regarded as rigid blocks on rigid foundations is reported in [23]. Among the methodologies based on limit analysis, recently many contributions were proposed considering the frictional forces [24–29] playing a crucial role in the assessment of the mechanism evolution. Evidently, these frictional forces should be determined through proper experimental testing [30]. Among the methods based on non-linear dynamic MAB (rocking) analysis, there exist models of walls connected with different types of horizontal diaphragms [31], but also of the corner mechanism as typical out-of-plane mode of masonry buildings [32]. A comparative study between the kinematic and non-linear dynamic methods investigating the 3D corner failure mechanism, also considering the thrusting roof and the stabilizing contribution of frictional resistances exerted within interlocked walls, is reported in [33]. One of the main issues arisen in these analyses is the output variability observed when input and boundary conditions change. Thus, probabilistic approaches suitable to describe the behavior of rocking structures have been defined [34, 35]. Moreover, rocking can be also seen as seismic dissipation technique for slender structures [36] and masonry walls [37]. Referring to arch-type structures, the rocking arch model assumes rigid blocks and rigid supports and is therefore only dependent on geometric properties similarly to the rocking block model. The susceptibility of masonry arches to earthquake loading is analytically and experimentally evaluated in [38] where the rocking arch model is a four-hinge mechanism. However, the approach currently most used in the professional practice for rigid block models is the kinematic analysis based on the displacement-based method. In it, the capacity in terms of both forces and displacements is compared with the seismic demand through the construction of acceleration-displacement response spectra. The standards from different countries (e.g. New Zealand [22] and Italy [39]) give specific indications about the way of calculating the collapse multipliers for each collapse mechanism and the methods to assess the seismic vulnerability through the acceleration-displacement curves. The *Premilcuore* bridge is here analyzed considering different single degree of freedom four-hinge mechanisms originated by different positions of the ideal hinges along the arch. The first aim of the kinematic analysis is to identify the most probable collapse mechanism, which corresponds to the lowest collapse multiplier according to the kinematic theorem of the limit analysis. Afterwards, the capacity curve is computed by following the Italian standards [40] and the safety verification is made through a kinematic non-linear analysis, namely by comparing the displacement demand with the displacement capacity.

2.3 Finite element and discrete element models

More refined approaches model masonry structures using micro and macro-modelling techniques. The formers separately consider the mechanical properties of the single components (bricks/blocks and mortar joints); the latter use simplified elements with homogenized properties. A consolidated model is represented by discrete macro-elements able to reproduce typical failures of masonry walls [41, 42]. A comparison between discrete macro-element and rigid block models used to assess the seismic vulnerability of a church façade is presented in [43]. An alternative method to discrete macro-element models regards the well-known finite element models, where masonry is modelled by means of planar (shell-plate type) or tridimensional (brick) elements with homogenized mechanical properties. A crucial issue of this modelling strategy consists in the correct selection of the masonry non-linear constitutive law and of the domain failure. These models offer a wide range of output, in terms of stress, strain, displacement, forces and energy [44], which have to be properly treated. Recently, some au-

thors developed discrete element models for the structural analysis of bridges [45, 46], whereas refined finite element models of multi-span masonry bridges were proposed in [47] performing nonlinear static, nonlinear dynamic, and incremental dynamic analyses under 14 earthquake records. This paper proposes the modeling of the *Premilcuore* bridge through a finite element model made of brick elements, whose features are illustrated in Section 3.2. The different modelling and analysis procedures, including the graphical methods and the kinematic analyses, are then discussed analogously to what is done in [48] in Section 5.

3 CASE OF STUDY

3.1 Geometry and masonry type

The *Ponte Nuovo (New Bridge)* of *Premilcuore* is named from the rebuilding (in 1650-1656) of a previous roman bridge, probably dated to the 2nd century AD [49]. The reconstruction of the New Bridge (Figure 1) was made after the collapse of the previous one, whose right abutment was kept (Figure 2a). The infrastructure is placed along the historical Florentine roads, which connected the two Italian regions Tuscany and Emilia Romagna across the *Rabbi* stream.



Figure 1: Aerial view of the bridge

The structure is characterized by a segmental arch with a length of 15.90 m and a maximum rise of 4.35 m. The deck is built with a “donkey back” shape with a slope of the ramp of about 22 degrees according to the canons of the medieval period.

The masonry of the abutments, of the wing walls and of the parapets is made of irregular stones except for the ring stone and the lower part of the abutment, which is built with regular stone. The river-bed appears irregular and the lithotype of the foundation has a predominant rock component. A large cracking under the bridge highlights a hypogea cavity that collects the runoff water.

The three metallic ties that appear under the arch (Figure 2b) are installed in the 1930's, after some seismic events that affected the area producing damages in the adjacent building (1818-1819).



(a) (b)
Figure 2: Details of the bridge: wing wall (a) and intrados (b)

3.2 Assumptions of the analysis

A detailed survey of the geometry is carried out according to [50]. A literary review allowed to define a part of the geometry that was not directly measured on site, by means of the design criteria used when the reconstruction took place [15, 51, 52]. The extension of the abutment and the thickness of the arch are in line with the 17th century design rules.

At the time of the construction of *Premilcuore bridge* there was no technical distinction between the part of the backfill that had or not a static rule in the bridge conception, so all the filling placed over the masonry vault is considered as non-structural [1, 53].

An identification of the mechanical properties of the bridge is carried out according to [54, 55]. The material variability, in existing buildings, is considered to be one of the most significant causes of uncertainties particularly affecting the structural response [56–58]. To consider the uncertainties in masonry properties a sensitivity analysis is carried out considering a variation of the mechanical properties in the range $\pm 40\%$ with respect to the average values reported in Table 1. The tensile strength is assumed to be 1/10 of the compressive strength.

The Max Stress criterion, also known as *Galileo-Rankine's criterion*, was assumed in the analysis.

Material	Elements	c [MPa]	ϕ [Deg]	E [MPa]
1	Vaults, spandrel walls	0.253	54.9	975
2	Arch ring, abutment	0.411	54.9	1320
3	Backfill	0.05	21.8	500

Table 1: Mechanical properties of the bridge components.

For all the elements a uniform specific weight of 18 kN/m^3 is assumed. The live load assumed is a distributed load of 5 kN/m^2 ; this value is indicated in [59] and in CNR Guidelines [60] for the masonry carter bridges of the 19th and 20th century and represents the same value that is currently used for the design of a pedestrian footbridge.

3.3 Finite element model

A tridimensional model of the central segment of the bridges is implemented in the software Straus 7 (r2.3.3). The model is composed by 8242 nodes, 7908 brick and 288 beam elements (Figure 3). The beam properties are *cut-off bars* with no tensile strength to model the interface with the soil foundation. The parapets are modelled as *non-structural masses*.

The material properties of Table 1 are assigned to the different parts of the bridge. In Magenta the material 1, in Yellow the material 2 and in Cyan the material 3 (Figure 3).

The lateral portions of the abutments adjacent to the soil of the access ramp (parallel to plane y-z) are restrained only in x-direction. The nodes under the foundations (parallel to plane x-y) are completely fixed.

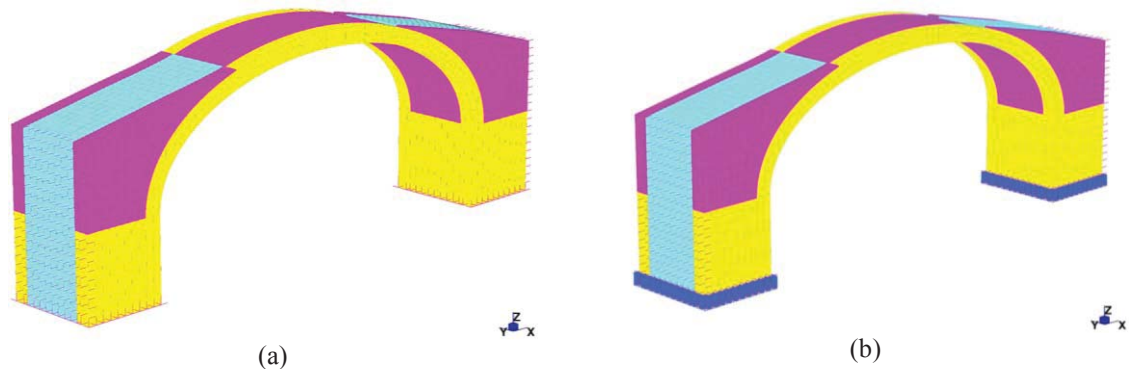


Figure 3: Three-dim model, for Static (a) and Seismic (b) analysis.

4 ANALYSIS OF THE PREMILCUORE BRIDGE

4.1 Traditional / Graphical methods

In order to assess the stability of the arch, the Mery's Rule has been firstly applied. Preliminarily, the arch between the springer and the keystone has been divided into ten voussoirs with the same length, Δs . Then, the study has been focused on the section of the arch between the intermediate rupture joint and the keystone. In accordance with well-established assumptions [51], the lower section can be located halfway, in terms of height, between the springing line and the highest point of the intrados, meaning between the voussoirs 7 and 8.

Self-weight and traffic loads have been considered, and the latter has been schematized as a uniform load acting longitudinally along the entire bridge. Its intensity was set equal to 5 kN/m². The different loads acting on each element of the structure are shown in Table 2.

Voussoirs	Specific weight $\gamma = 18 \text{ kN/m}^3$				Equivalent Traffic Load $q_k = 5 \text{ kN/m}^2$		Resultant Force
	Voussoirs Self-Weight Load	Filling Load	Parapet of the bridge Load	Resultant Load	Length of the voussoirs	Traffic load	R
	[kN]	[kN]	[kN]	[kN]	[kN]	[kN]	[kN]
1	45.4	0.0	12.8	58.2	106.3	15.4	73.6

2	45.4	0.0	11.0	56.4	105.4	15.3	71.7
3	45.4	0.0	10.6	56.0	104.3	15.1	71.1
4	45.4	1.8	10.9	58.1	102.8	14.9	73.0
5	45.4	9.8	11.1	66.4	100.1	14.5	80.9
6	45.4	24.0	11.1	80.5	95.9	13.9	94.4
7	45.4	43.5	10.7	99.6	89.2	12.9	112.5
8	45.4	64.7	9.7	119.9	77.6	11.3	131.1
9	45.4	74.7	7.4	127.5	56.9	8.3	135.7
10	45.4	41.0	2.9	89.4	20.9	3.0	92.4
Total							936.4

Table 2 – Discretization of the Arch.

Applying the loads on each segment, the funicular polygon passing through the upper middle third of the keystone and the lower middle third of the previously mentioned section has been drawn. Thus, the thrust line of the arch has been graphically obtained, together with the magnitude of the forces at the extremities, H and S (Figure 4).

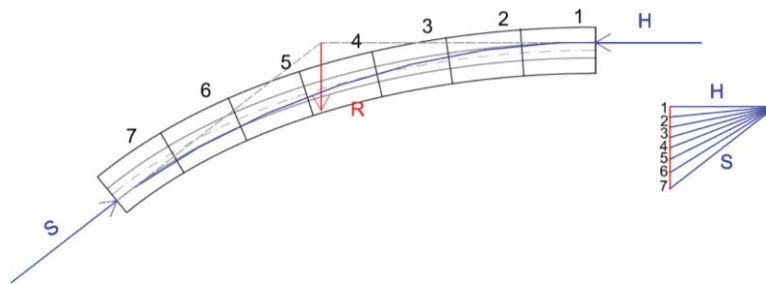


Figure 4: Thrust line according to Mery's Rule.

Subsequently, with the purpose of assessing in a different way the stability property of the vault, the Durand-Claye's method has been applied. The arch has been schematized in the same way, with ten voussoirs between the springer section and the keystone. The same loads have also been considered (Figure 5).

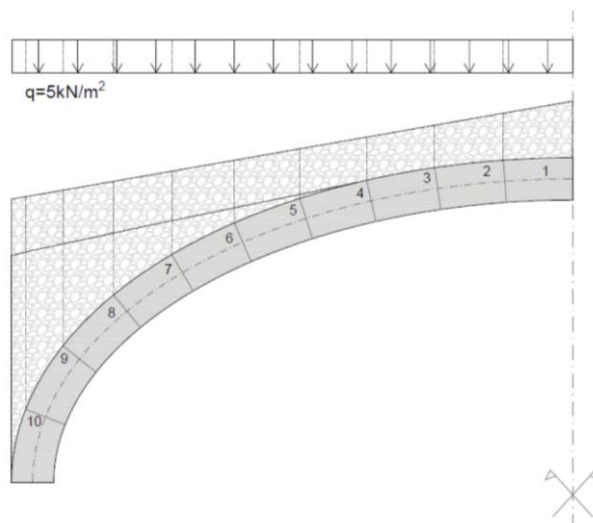


Figure 5: Mechanical model for the arch – Durand-Claye's method.

The rectangular cross section has a width of 3.65 m and a height of 0.65 m. The resistance of the material was evaluated considering the average value referred to the various parts of the structure; it has been assumed equal to $f_c=2.10$ MPa.

By applying the Durand-Claye's method for three different control sections, the same number of areas of stability at the keystone have been identified (Figure 6), hence, their intersection has been found (Figure 7).

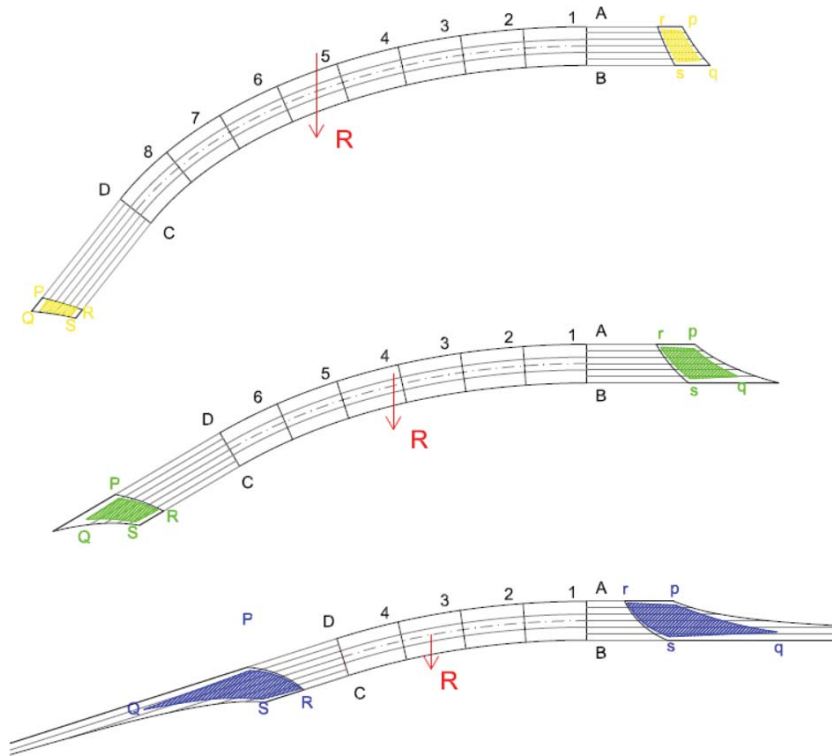


Figure 6: Durand-Claye's stability areas

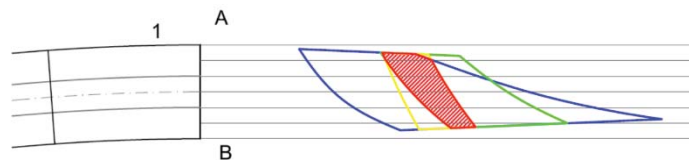


Figure 7: Intersection among the stability areas

The thrust lines corresponding to the four vertices of the stability curve identify the area within which the actual pressure thrust will be included. The latter satisfies the conditions of balance and strength of the material. Each line can be associated with the value of the force acting on the arch (Figure 8). The arch is more vulnerable where the area containing the pressure curve is outside the middle third of the section.

Having identified the solutions related to the two simplified methods, Mery and Durand-Claye, their comparison shows that the values obtained using the Mery's rule fall within the range identified with the Durand-Claye's method, as expected (Figure 9).

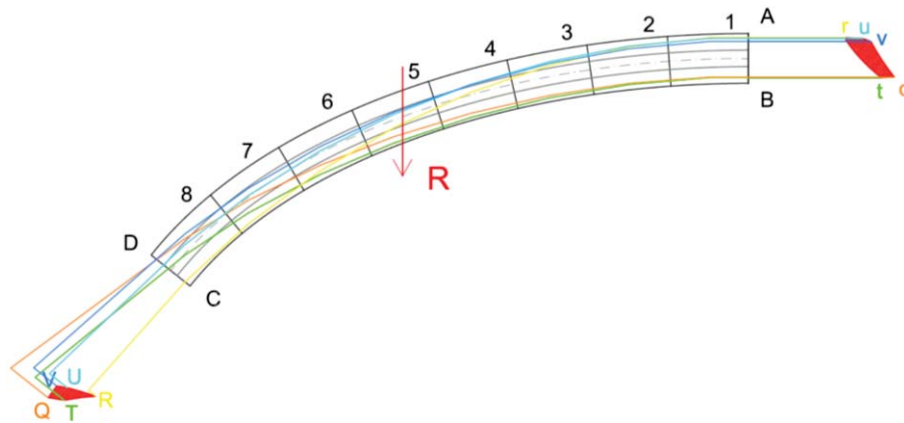


Figure 8: Thrust line according to Durand-Claye's Method.

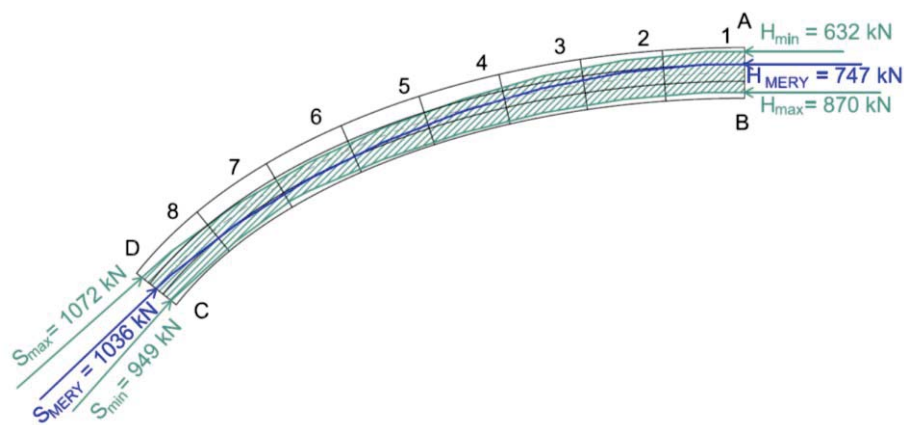


Figure 9: Comparison between Méry's and Durand-Claye's graphical solution

4.2 Identification of the collapse mechanism and non-linear kinematic analysis

Let us assume that the single span bridge is made of rigid blocks whose contact surfaces have null tensile strength, infinite compressive strength and sliding impeded. These three conditions are the well-known Heyman's hypotheses [53]. From a static point of view, the bridge is subjected to its self-weight and to the permanent loads of backfill and bridge deck with parapets. According to the Heyman's safe theorem, "if a line of thrust can be found which is in equilibrium with the external loads and which lies wholly within the masonry, then the structure is safe". The rigid block analysis is aimed at assessing the seismic vulnerability of the bridge arch and consists in two steps:

- 1) identification of the more likely failure (four-hinge) mechanism;
- 2) non-linear kinematic analysis in which the displacement capacity is compared to the displacement demand.

When the seismic action is considered, the arch is subjected to inertial forces which modify the line of thrust. The distribution of inertial forces q_i is not unique as the interaction between arch and backfill is complex. Four possible models, schematically displayed in Figure 10 considering a horizontal ground acceleration from right to left, are considered [61]:

- (M1): only the sub-blocks of the left semi-arch are subjected to the inertial force q_i , equal to the horizontal acceleration multiplied by the mass of the block itself and that

of the tributary individual horizontal strip of the backfill included between the extrados and the vertical line passing from the corresponding arch springer. The semi-arch on the right is not interested by inertial forces as here the backfill is supposed to be detached from the extrados.

- (M2): analogous to (M1), but with the sub-blocks of the semi-arch on the right subjected to the inertial force q_i ;
- (M3): each sub-block is subjected to a horizontal force equal to the gravitational load that it is bearing;
- (M4): the inertial forces applied as uniform horizontal load only act on the semi-arch on the right. The resulting force of q_h is equal to the total vertical load (self-weight and backfill weight).

Considering all four models, the process to identify the four-hinge mechanism is iterative. Firstly, an attempt position of the four hinge is assumed considering only the arch since the bridge piles are stocky (Figure 10). The principle of virtual work allows calculating the collapse multiplier α by dividing the external work made by the vertical forces with that made by the horizontal forces. Once α is calculated, the reaction and internal forces between each sub-block are computed and the line of thrust, passing through the assumed hinges, can be drawn. If this line of thrust lies wholly within the masonry, α is also a statically admissible multiplier according to the limit analysis theorem and therefore the actual collapse multiplier. Otherwise, the procedure should be repeated by moving the hinges where the eccentricity (given by the ratio of bending moment to normal force on each block) is maximum, up to the condition for which the line of thrust lies wholly within the masonry. M4-m2-m3-m1

Comparing the results obtained by applying this procedure, (M1) and (M4) provide the highest and lowest estimation of the collapse multiplier respectively. (M3) corresponds to a collapse multiplier between that of (M1) and (M2). The most conservative model is therefore (M4) but the assumption of a constant horizontal load (Figure 10) is not fully realistic. On the contrary, (M3) is the simplest model and, as already illustrated in [61], can be accepted for a reliable estimation of the collapse multiplier.

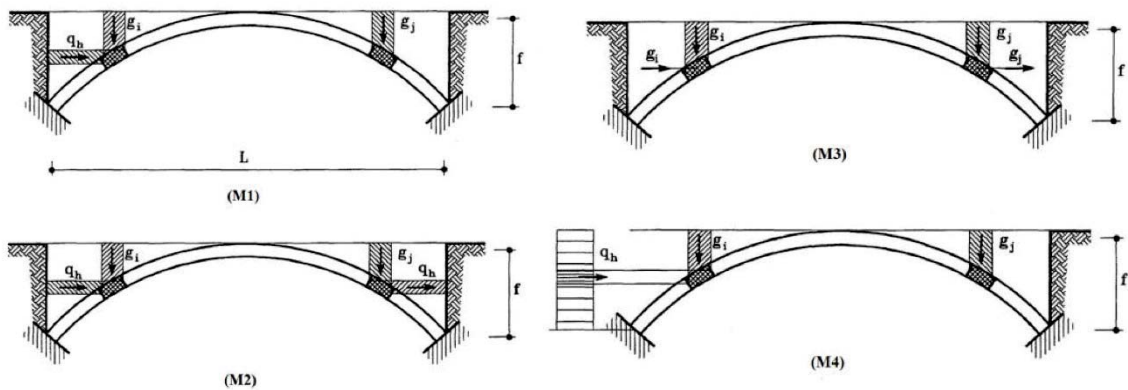


Figure 10: Models with different distribution of inertial forces (from [61]).

Its collapse multiplier is close to that of M1 and therefore such a different assumption does not markedly change the final result. For these reasons, model (M3) is considered in the following calculations. By performing the described iterative procedure, the eccentricity trend

shown in Figure 11.a is obtained at the third attempt and the corresponding deformed shape is displayed in Figure 11.b.

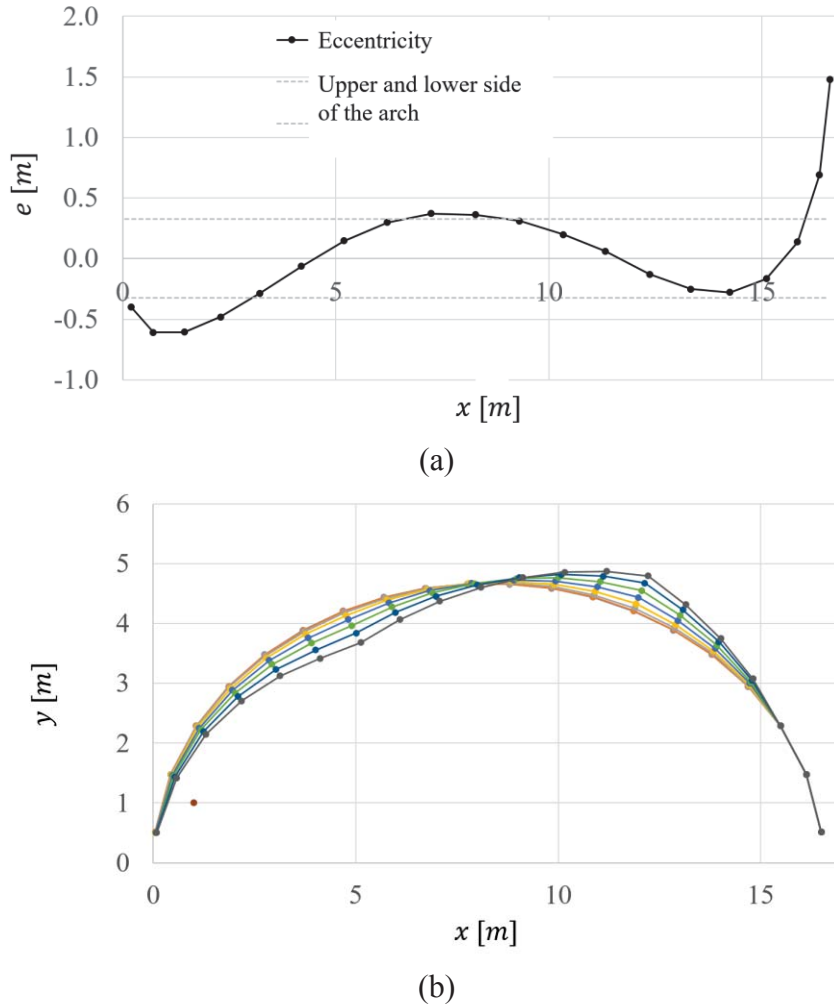


Figure 11: Eccentricity of the line of thrust obtained with the third attempt of hinge position change (a); evolution of deformed shape in the construction of the acceleration-displacement curve (b).

For this collapse mechanism, the capacity curve is firstly drawn by monotonically increasing the rotational angles between the rigid blocks constituting the arch. The displacements in x and y directions can be calculated through trivial geometric considerations from these rotational angles. This results in a progressive change of the deformed shape visible in Figure 11.b. The capacity curve is obtained by calculating through the principle of virtual work the acceleration corresponding to each imposed displacement (black curve of Figure 12).

The control point is selected as the center of mass of the key-stone and the confidence factor required to compute the acceleration is $CF = 1.35$ [40]. The ultimate displacement, corresponding to the zero acceleration capacity, is (Figure 12):

$$d_0 = S_{d,0} = 8.90 \text{ cm} \quad (1)$$

And the corresponding displacement capacity d_{ULS} is, for the ultimate limit state ULS [40]:

$$d_{ULS} = 0.4 \times S_{d,0} = 3.56 \text{ cm} \quad (2)$$

The displacement demand has to be computed by considering the secant period T_{SL} corresponding to the ultimate limit state from the expression found in the Italian standards [40]:

$$T_{SL} = 1.68\pi \sqrt{\frac{d_{ULS}}{a(d_{ULS})}} = 0.62 \text{ s} \quad (3)$$

The intersection between the dotted line of Figure 3 identified by T_{SL} and the elastic acceleration demand response spectrum (ADRS) gives the displacement demand:

$$S_d(T_{SL}) = 2.01 \text{ cm} \quad (4)$$

to compare with the displacement capacity. The verification is satisfied, being the capacity higher than the demand:

$$d_{ULS} = 3.56 \text{ cm} > S_d(T_{SL}) = 2.01 \text{ cm} \quad (5)$$

Resulting in a safety factor SF of:

$$SF = \frac{d_{ULS}}{S_d(T_{SLV})} = \frac{3.56}{2.01} = 1.77 > 1. \quad (6)$$

The bridge therefore results in a safe condition, which results even safer by considering a design ADRS with a behavior factor q [39]. This aspect confirms that these arches are rarely vulnerable to such mechanism, as already discussed in [61].

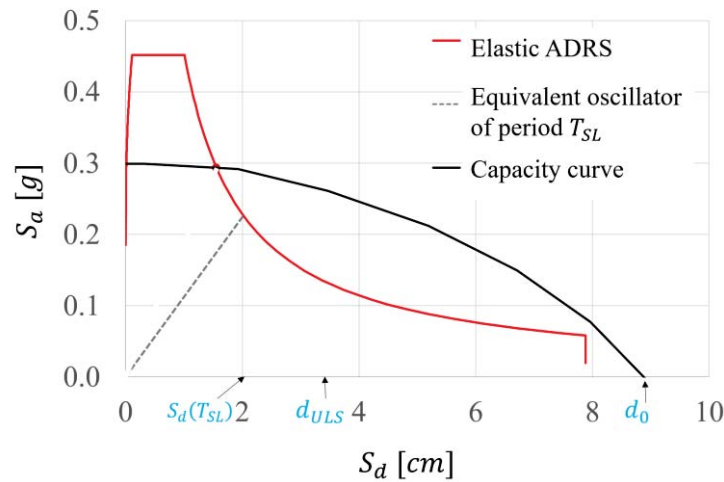
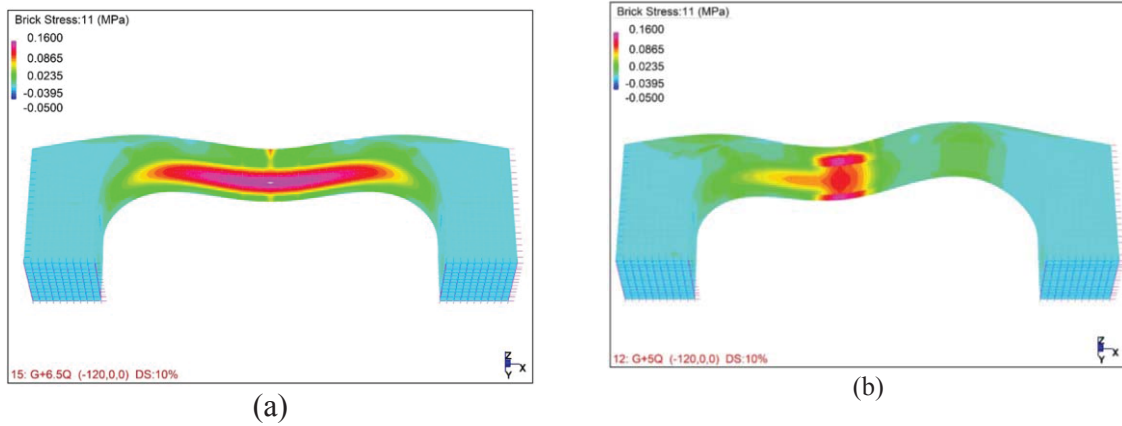
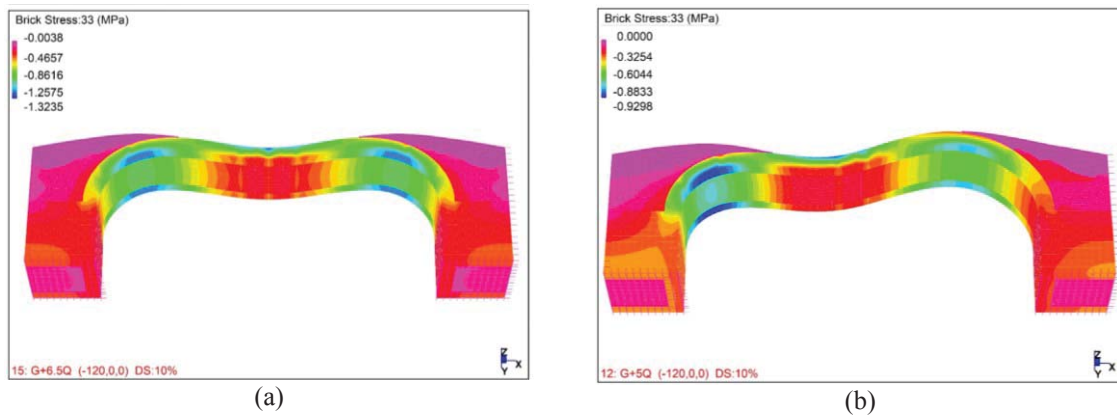


Figure 12: Seismic vulnerability assessment through non-linear kinematic analysis.

4.3 FEM analysis

4.3.1. Nonlinear static analysis (gravitational loads)

Nonlinear static analysis is carried out considering both symmetric and asymmetric incremental live loads. The gravitational load is applied into the two first steps. After that, an increasing live load is applied to identify the collapse multiplier (λ) with respect to 5 kN/m². The collapse is identified considering the numerical divergencies of the model. In Figure 13 and in Figure 14 the maximum principal stresses are displayed. The collapse multipliers λ are illustrated in Table 3. The bridge is safe with respect to the static live load, also considering a non-uniform distribution, and the worse resistance for masonry.

Figure 13: Contour of σ_{11} in case of symmetric (a) and asymmetric live load (b).Figure 14: Contour of σ_{33} in case of symmetric (a) and asymmetric live load (b).

Material	$\lambda_{uniform}$	$\lambda_{non-uniform}$
Average – 40%	4.0	4.5
Average	6.5	5.0
Average + 40%	9.0	6.0

Table 3: Collapse multiplier for static analysis.

4.3.1. Nonlinear static analysis (seismic actions)

A seismic push-over analysis is performed on the model of Figure 3 (b). The analysis is set applying first the gravitational load and after introducing the seismic action in transverse direction (Y-direction in Figure 3). The transverse direction is chosen since kinematic analyses are performed in the longitudinal section of the arch. The effect of transverse ties is neglected for the sake of safety.

The pushover curves are shown in Figure 15, considering the control displacement of a node in the middle of the arch (node 716). In these curves, the ultimate displacement depends on the material quality. It is interesting to highlight that all the curves end up at $V_b=1585$ kN that corresponds to a shear value of about the 90 % of the design seismic action. The overturning (joined to a crushing of masonry at the foundation) is the cause of this behavior. The hypothesis of smooth constraints (without friction) on the lateral face of the bridge consents the global

overturning. The analysis, made this prudential assumption, shows a good performance of the structure with respect to transverse action. This result is in line with the main indication in literature, which considers the kinematic approach as the most interesting for MAB.

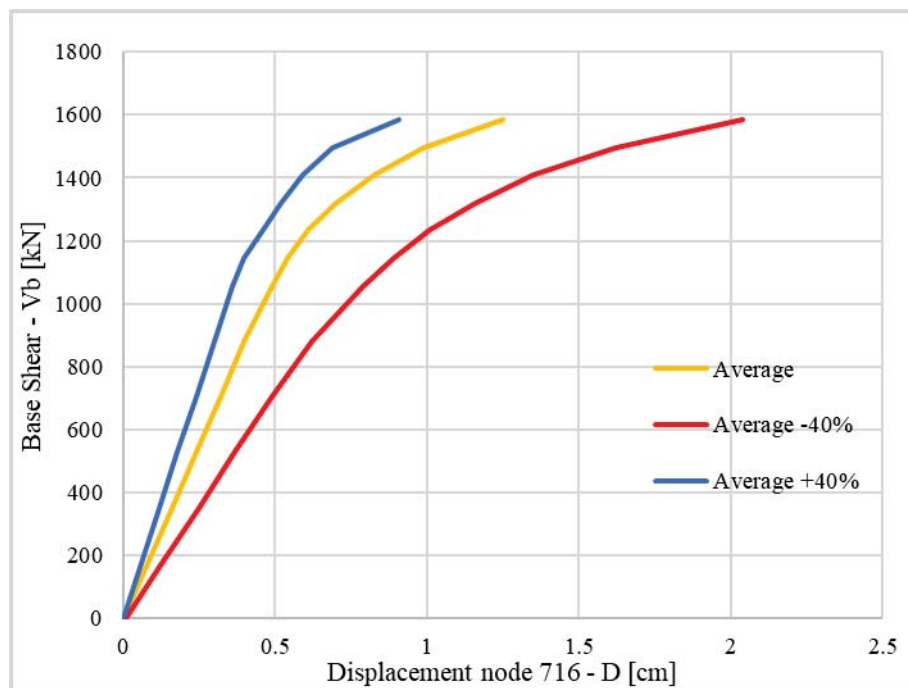


Figure 15 – Capacity curves.

5 CONCLUSIONS

The present work dealt with the static and seismic analyses of an historical masonry bridge placed in *Premilcuore*, a small village in Central Italy. The vulnerability analysis was tackled with several methods, considering both the traditional static approaches and the modern types of seismic analysis.

Considering the hypotheses, which are based on different structural aspects, it is very difficult to carry out a rational comparison of the numerical results. The different approach moreover produced different results that is hard to merge to a common factor.

However, the following conclusions can be drawn. As for the graphical methods, their graphical comparison shows that the values obtained using the Mèry's rule fall within the range identified with the Durand-Claye's method.

These methods show how the shape of the arch and the mechanical properties of the material are able to ensure the stability of the structure for the vertical loads considered above. In the analysis, the shear actions have been neglected. Therefore, the structure resulted to be safe under vertical gravitational loads.

With the purpose of analysing the bridge through other numerical methods, the non-linear kinematic analysis, based on rigid block model and limit analysis, the estimation of the collapse multiplier of the arch considered as set of rigid blocks was made. The analysis shows that the bridge arch, assumed subjected to inertial forces computed by the gravitational loads, is safe even with an elastic acceleration demand response spectrum. This aspect confirms the low vulnerability of these types of arch mechanisms to horizontal seismic actions, confirming

literature results. Finally, the *Premilcuore bridge* was subjected to a FEM sensitivity analysis considering three materials and two different models, for static and seismic actions.

The static analysis, with an incremental live load, allowed to evaluate the collapse factors. Both the load scenarios investigated are safe also considering precautionary hypotheses on the bridge material.

The seismic analysis identified the collapse loads and the most likely failure modes in presence of transverse seismic actions. The transverse direction is chosen here as complementary of the natural direction of kinematic analysis of the arch, in the transverse direction of the bridge. The more severe scenarios, approximately obtained in correspondence of the 80-90% of the design seismic actions, highlights a failure mode with a crushing on the foot of the foundation, with a mechanism that recalls to an incipient overturning of the bridge.

Summarizing, a comparison of the different methods, highlights that the bridge is structurally safe from a static point of view, as confirmed by FE analysis and graphical methods, whereas it presents some critical vulnerabilities in case of seismic actions acting along the river direction when FE models are adopted.

6 ACKNOWLEDGEMENTS

The financial support is also given by Region Sardinia (RICRAS-CTC/2018 and RAS L.R. 7/2007) and by the project “Monitoring of the structural and energy behavior of the existing constructions” that is acknowledged by Mario Lucio Puppio.

7 REFERENCES

- [1] Page, J. (1993). *Masonry Arch Bridges*, London
- [2] Bićanić, N.; Stirling, C.; Pearce, C. J. (2003). Discontinuous modelling of masonry bridges, *Computational Mechanics*, Vol. 31, No. 1, 60–68. doi:10.1007/s00466-002-0393-0
- [3] Thavalingam, A.; Bicanic, N.; Robinson, J. I.; Ponniah, D. A. (2001). Computational framework for discontinuous modelling of masonry arch bridges, *Computers & Structures*, Vol. 79, No. 19, 1821–1830. doi:10.1016/S0045-7949(01)00102-X
- [4] Stochino, F.; Fadda, M. L.; Mistretta, F. (2018). Low cost condition assessment method for existing RC bridges, *Engineering Failure Analysis*, Vol. 86, 56–71. doi:10.1016/j.engfailanal.2017.12.021
- [5] Oliveira, D. V.; Lourenço, P. B.; Lemos, C. (2010). Geometric issues and ultimate load capacity of masonry arch bridges from the northwest Iberian Peninsula, *Engineering Structures*, Vol. 32, No. 12, 3955–3965. doi:https://doi.org/10.1016/j.engstruct.2010.09.006
- [6] Mistretta, F.; Sanna, G.; Stochino, F.; Vacca, G. (2019). Structure from motion point clouds for structural monitoring, *Remote Sensing*, Vol. 11, No. 16. doi:10.3390/rs11161940
- [7] Solla, M.; Lorenzo, H.; Riveiro, B.; Rial, F. I. (2011). Non-destructive methodologies in the assessment of the masonry arch bridge of Traba, Spain, *Engineering Failure Analysis*, Vol. 18, No. 3, 828–835. doi:https://doi.org/10.1016/j.engfailanal.2010.12.009
- [8] Puppio, M. L.; Giresini, L. (2019). Estimation of tensile mechanical parameters of

- existing masonry through the analysis of the collapse of Volterra's urban walls, *Frattura Ed Integrità Strutturale*, Vol. 13, No. 49, 725–738. doi:10.3221/IGF-ESIS.49.65
- [9] Croce, P.; Landi, F.; Formichi, P. (2019). Probabilistic Seismic Assessment of Existing Masonry Buildings, *Buildings*, Vol. 9, No. 12. doi:10.3390/buildings9120237
- [10] Lubowiecka, I.; Arias, P.; Riveiro, B.; Solla, M. (2011). Multidisciplinary approach to the assessment of historic structures based on the case of a masonry bridge in Galicia (Spain), *Computers & Structures*, Vol. 89, No. 17, 1615–1627. doi:https://doi.org/10.1016/j.compstruc.2011.04.016
- [11] Beconcini, M. L.; Cioni, P.; Croce, P.; Formichi, P.; Landi, F.; Mochi, C. (2018). Non-linear static analysis of masonry buildings under seismic actions, *IMSCI 2018 - 12th International Multi-Conference on Society, Cybernetics and Informatics, Proceedings* (Vol. 1), 126–131
- [12] Conde, B.; Ramos, L. F.; Oliveira, D. V.; Riveiro, B.; Solla, M. (2017). Structural assessment of masonry arch bridges by combination of non-destructive testing techniques and three-dimensional numerical modelling: Application to Vilanova bridge, *Engineering Structures*, Vol. 148, 621–638. doi:https://doi.org/10.1016/j.engstruct.2017.07.011
- [13] Casas, J. R. (2011). Reliability-based assessment of masonry arch bridges, *Construction and Building Materials*, Vol. 25, No. 4, 1621–1631. doi:https://doi.org/10.1016/j.conbuildmat.2010.10.011
- [14] Zampieri, P.; Zanini, M. A.; Faleschini, F. (2016). Derivation of analytical seismic fragility functions for common masonry bridge types: methodology and application to real cases, *Engineering Failure Analysis*, Vol. 68, 275–291. doi:https://doi.org/10.1016/j.engfailanal.2016.05.031
- [15] Foce, F.; Aita, D. (2003). The masonry arch between «limit» and «elastic» analysis. A critical re-examination of Durand-Claye's method, F. D. S. Huert, Madrid: I. Juan de Herrera, SEdHC, ETSAM, A.E. Benvenuto, COAM (Ed.), *First International Congress on Construction History (Madrid, 20th-24th January 2003)*, Madrid, Spain
- [16] Solarino, F.; Oliveira, D.; Giresini, L. (2019). Wall-to-horizontal diaphragm connections in historical buildings: A state-of-the-art review, *Engineering Structures*, Vol. 199
- [17] De Falco, A.; Giresini, L.; Sassu, M. (2013). Temporary preventive seismic reinforcements on historic churches: numerical modeling of San Frediano in Pisa, *Applied Mechanics and Materials*, Vol. 352
- [18] Andreini, M.; De Falco, A.; Giresini, L.; Sassu, M. (2013). Collapse of the historic city walls of Pistoia (Italy): Causes and possible interventions, *Applied Mechanics and Materials*, Vols 351–352
- [19] Alecci, V.; Barducci, S.; D'Ambrisi, A.; Stefano, M. De; Focacci, F.; Luciano, R.; Penna, R. (2019). Shear capacity of masonry panels repaired with composite materials: Experimental and analytical investigations, *Composites Part B: Engineering*, Vol. 171, 61–69. doi:https://doi.org/10.1016/j.compositesb.2019.04.013
- [20] Sara, B.; Valerio, A.; Mario, D. S.; Giulia, M.; Luisa, R.; Gianfranco, S. (2020). Experimental and Analytical Investigations on Bond Behavior of Basalt-FRCM

- Systems, *Journal of Composites for Construction*, Vol. 24, No. 1, 4019055. doi:10.1061/(ASCE)CC.1943-5614.0000985
- [21] Giresini, L.; Puppio, M. L.; Taddei, F. (2020). Experimental pull-out tests and design indications for strength anchors installed in masonry walls, *Materials and Structures*, Vol. 53, No. 4, 103. doi:10.1617/s11527-020-01536-2
 - [22] NZSEE. (2017). New Zealand Society for Earthquake Engineering, Section C8: Unreinforced masonry buildings Part C – Detailed Seismic Assessment
 - [23] Casapulla, C.; Giresini, L.; Lourenço, P. B. (2017). Rocking and kinematic approaches for rigid block analysis of masonry walls: State of the art and recent developments, *Buildings*, Vol. 7, No. 3. doi:10.3390/buildings7030069
 - [24] Casapulla, C. (2008). Lower and upper bounds in closed form for out-of-plane strength of masonry structures with frictional resistances, F. E. D'Ayala D. (Ed.), *SAHC08-Structural Analysis of Historic Constructions*, Bath, 1191–1198
 - [25] Casapulla, C.; Argiento, L. U.; Maione, A.; Speranza, E. (2021). Upgraded formulations for the onset of local mechanisms in multi-storey masonry buildings using limit analysis, *Structures*
 - [26] Casapulla, C.; Maione, A.; Argiento, L. U.; Speranza, E. (2018). Corner failure in masonry buildings: An updated macro-modeling approach with frictional resistances, *European Journal of Mechanics, A/Solids*, Vol. 70, 213–225. doi:10.1016/j.euromechsol.2018.03.003
 - [27] Casapulla, C.; Maione, A.; Argiento, L. U. (2017). Seismic analysis of an existing masonry building according to the multi-level approach of the italian guidelines on cultural heritage, *Ingegneria Sismica*, Vol. 34, No. 1, 40–59
 - [28] Casapulla, C.; Argiento, L. U.; Maione, A. (2018). Seismic safety assessment of a masonry building according to Italian Guidelines on Cultural Heritage: simplified mechanical-based approach and pushover analysis, *Bulletin of Earthquake Engineering*, Vol. 16, No. 7, 2809–2837
 - [29] Casapulla, C.; Portioli, F.; Maione, A.; Landolfo, R. (2013). A macro-block model for in-plane loaded masonry walls with non-associative Coulomb friction, *Meccanica*, Vol. 48, No. 9, 2107–2126. doi:10.1007/s11012-013-9728-5
 - [30] Casapulla, C.; Portioli, F. (2016). Experimental tests on the limit states of dry-jointed tuff blocks, *Materials and Structures/Materiaux et Constructions*, Vol. 49, No. 3, 751–767. doi:10.1617/s11527-015-0536-3
 - [31] Giresini, L. (2017). Design strategy for the rocking stability of horizontally restrained masonry walls, M. F. M. Papadrakakis (Ed.), *COMPDYN 2017 - Proceedings of the 6th International Conference on Computational Methods in Structural Dynamics and Earthquake Engineering* (Vol. 2), Rhodes Island, Greece, 2963–2979. doi:10.7712/120117.5620.18188
 - [32] Giresini, L.; Solarino, F.; Paganelli, O.; Oliveira, D. V.; Froli, M. (2019). One-sided rocking analysis of corner mechanisms in masonry structures: influence of geometry, energy dissipation, boundary conditions, *Soil Dynamics and Earthquake Engineering*, in press
 - [33] Casapulla, C.; Giresini, L.; Argiento, L. U.; Maione, A. (2019). Nonlinear Static and

- Dynamic Analysis of Rocking Masonry Corners Using Rigid Macro-Block Modeling, *International Journal of Structural Stability and Dynamics*, Vol. 19, No. 11, 1950137. doi:10.1142/S0219455419501372
- [34] Giresini, L.; Taddei, F.; Casapulla, C.; Mueller, G. (2019). Stochastic assessment of rocking masonry façades under real seismic records, *COMPADYN 2019 7th ECCOMAS Thematic Conference on Computational Methods in Structural Dynamics and Earthquake Engineering*, Crete; Greece; 24th-26th June 2019, 673–689
- [35] Solarino, F.; Giresini, L. (2021). Seismic vulnerability of rocking walls restrained with elasto-plastic ties, *Earthquake Eng. Struct. Dyn. (Submitted To)*
- [36] Froli, M.; Giresini, L.; Laccone, F. (2019). Dynamics of a new seismic isolation device based on tribological smooth rocking (TROCKSISD), *Engineering Structures*, Vol. 193, 154–169
- [37] Giresini, L.; Solarino, F.; Taddei, F.; Mueller, G. (2021). Experimental estimation of energy dissipation in rocking masonry walls restrained by an innovative seismic dissipator (LICORD), *Bulletin of Earthquake Engineering*. doi:10.1007/s10518-021-01056-6
- [38] DeJong, M. J.; De Lorenzis, L.; Adams, S.; Ochsendorf, J. A. (2008). Rocking Stability of Masonry Arches in Seismic Regions, *Earthquake Spectra*, Vol. 24, No. 4, 847–865. doi:10.1193/1.2985763
- [39] Decreto Ministeriale 17/01/2018. (2018). Italian Technical Standards for buildings (Nuove Norme Tecniche per le Costruzioni, in italian)
- [40] Ministero delle infrastrutture e dei trasporti. Circolare 21 gennaio 2019, n. 7 Istruzioni per l'applicazione dell'«Aggiornamento delle “Norme tecniche per le costruzioni”», , 35 Gazzetta Ufficiale della Repubblica Italiana 1–337 (2019), 1–337
- [41] Chácará, C.; Cannizzaro, F.; Pantò, B.; Calì, I.; Lourenço, P. B. (2019). Seismic vulnerability of URM structures based on a Discrete Macro-Element Modeling (DMEM) approach, *Engineering Structures*, Vol. 201, 109715. doi:https://doi.org/10.1016/j.engstruct.2019.109715
- [42] Caddemi, S.; Calì, I.; Cannizzaro, F.; Pantò, B. (2017). New Frontiers on Seismic Modeling of Masonry Structures, *Frontiers in Built Environment*, Vol. 3, 39. doi:10.3389/fbuil.2017.00039
- [43] Giresini, L.; Pantò, B.; Caddemi, S.; Calì, I. (2019). Out-of-plane seismic response of masonry façades using discrete macro-element and rigid block models, *COMPADYN 2019 7th ECCOMAS Thematic Conference on Computational Methods in Structural Dynamics and Earthquake Engineering*, Crete; Greece; 24th-26th June 2019, 702–717
- [44] Giresini, L. (2016). Energy-based method for identifying vulnerable macro-elements in historic masonry churches, *Bulletin of Earthquake Engineering*, Vol. 14, No. 3, 919–942. doi:10.1007/s10518-015-9854-7
- [45] Caddemi, S.; Calì, I.; Cannizzaro, F.; D'Urso, D.; Occhipinti, G.; Pantò, B.; Zurlo, R. (2018). A 'parsimonious' 3D Discrete Macro-Element Method for masonry arch bridges, *10th International Masonry Conference, G. Milani, A. Taliercio and S. Garrity (Eds.), Milan, Italy*
- [46] Caddemi, S.; Calì, I.; Cannizzaro, F.; D'Urso, D.; Pantò, B.; Rapicavoli, D.;

- Occhipinti, G. (2019). 3D discrete macro-modelling approach for masonry arch bridges, *IABSE Symposium*
- [47] Gönen, S.; Soyöz, S. (2021). Seismic analysis of a masonry arch bridge using multiple methodologies, *Engineering Structures*, Vol. 226, 111354. doi:<https://doi.org/10.1016/j.engstruct.2020.111354>
- [48] Zampieri, P.; Perboni, S.; Tetougueni, C. D.; Pellegrino, C. (2020). Different Approaches to Assess the Seismic Capacity of Masonry Bridges by Non-linear Static Analysis, *Frontiers in Built Environment*, Vol. 6, 47. doi:10.3389/fbuil.2020.00047
- [49] Pavan, M. (2012). *Ponti Della Romagna. Un Tesoro Nascosto*, Il Ponte Vecchio
- [50] Pucci, A.; Sousa, H. S.; Puppio, M. L.; Giresini, L.; Matos, J. C.; Sassu, M. (2019). Method for sustainable large-scale bridge survey.pdf, *Towards a Resilient Built Environment Risk and Asset Management*, IABSE, Zurich, 1034–1041
- [51] Campanella, G. (1928). *Trattato Generale Teorico Pratico Dell'arte Dell'ingegnere Civile, Industriale Ed Architetto: Ponti in Muratura*, Vallardi, Milano
- [52] Campanella, G. (n.d.). *Masonry Bridges for Engineers*, Biblioteca Tecnica Internazionale, Milano
- [53] Heyman, J. (1966). The stone skeleton, *International Journal of Solids and Structures*, Vol. 2, No. 2, 249–279. doi:10.1016/0020-7683(66)90018-7
- [54] Borri, A.; De Maria, A. (2019). Il metodo IQM per la stima delle caratteristiche meccaniche delle murature : allineamento alla circolare n. 7/2019, ANIDIS (Ed.), *XVIII Congresso Nazionale "L'ingegneria Sismica in Italia"*, Ascoli Piceno 15-19 Settembre 2019, Ascoli Piceno, 3–21
- [55] D.M. 17/01/2018. (2018). Aggiornamento delle 'Norme Tecniche per le Costruzioni' (in italian)
- [56] Puppio, M. L.; Giresini, L.; Doveri, F.; Sassu, M. (2019). Structural irregularity: The analysis of two reinforced concrete (r.c.) buildings, Vol. 7. doi:10.5267/j.esm.2018.12.002
- [57] Parisi, F.; Augenti, N. (2012). Uncertainty in Seismic Capacity of Masonry Buildings, *Buildings*, Vol. 2, No. 3, 218–230. doi:10.3390/buildings2030218
- [58] Puppio, M. L.; Pellegrino, M.; Giresini, L.; Sassu, M. (2017). Effect of material variability and mechanical eccentricity on the seismic vulnerability assessment of reinforced concrete buildings, *Buildings*, Vol. 7, No. 3. doi:10.3390/buildings7030066
- [59] Torre, C. (2003). *Ponti in Muratura. Dizionario Storico-Tecnologico*, Alinea Editrice, Firenze
- [60] CNR - Commissione di studio per la predisposizione e l'analisi di norme tecniche relative alle costruzioni. (2015). CNR-DT 213/2015 - Istruzioni per la Valutazione della Sicurezza Strutturale di Ponti Stradali in Muratura, Roma
- [61] Clemente, P. (1997). *La Verifica Degli Archi a Conci Lapidiei*, ENEA, Unità comunicazione e informazione

REDUCTION OF HOUSNER'S COEFFICIENT OF RESTITUTION FOR MASONRY WALLS UNDER ONE-SIDED ROCKING

L. Giresini^{1*} and P. Croce²

^{1*}Department of Civil and Industrial Engineering
University of Pisa
Largo L. Lazzarino, 1, 56126 Pisa
email: linda.giresini@unipi.it

² Department of Civil and Industrial Engineering
University of Pisa
Largo L. Lazzarino, 1, 56126 Pisa
email: p.croce@ing.unipi.it

Abstract

The out-of-plane dynamics of masonry walls is strongly influenced by seismic input, mass, wall geometry and boundary conditions. Nevertheless, the parameter that mostly affects the dynamic response of a rocking wall is the coefficient of restitution, defined by Housner as ratio of angular velocity after and before an impact on the ground. Such a parameter defines the amount of energy dissipated over motion and is of paramount importance in assessing the seismic vulnerability of a rocking wall, due to the sensitivity of the dynamic response to small changes of it. This paper critically illustrates the preliminary results of an experimental campaign performed on a masonry wall subjected to one-sided rocking. These results are presented in terms of experimental ratios of coefficients of restitution. Two methods for calculating the experimental ratios of coefficients of restitution are described according to whether rocking is one-sided or two-sided. In addition, the paper compares these ratios with those of other experimental tests on two sided rocking and horizontally restrained masonry walls available in the literature. A numerical example is provided by showing that the assumption of a correct coefficient of restitution is crucial for a realistic and correct seismic vulnerability assessment.

Keywords: rocking, one-sided, two-sided, coefficient of restitution, masonry, out-of-plane.

1 INTRODUCTION

The appropriate types of analysis that can be carried out on masonry buildings under earthquakes depend on the degree of connection between walls and between walls and horizontal diaphragms, including arches, vaults and roofs [1]–[3]. Seismic retrofitting interventions are generally needed to ensure the box-type behavior; nowadays, seismic consolidation techniques are coupled with low-impact solutions also from an environmental point of view [4], [5]. Nevertheless, when the connection is poor, only local analyses are meaningful for a proper seismic vulnerability assessment. In that case, the most common approach consists in computing collapse loads of local rigid block mechanisms [6]–[10], properly considering floor spectra [11]. An alternative approach, which can be seen as complementary to the mentioned kinematic non-linear analysis, is the non-linear dynamic analysis or rocking analysis. This investigates the dynamic behavior of the rigid block according to the Housner's equation [12], duly considering the energy dissipated over motion. A synthetic parameter describing this energy dissipation is the coefficient of restitution [13], [14]. The coefficient of restitution can be defined in several ways [8], but they are equivalent only in case of frictionless impact [9].

The coefficient of restitution has a relevant influence on the free damped vibration of a rigid block [15] as well as on its resonance conditions [16], [17]. In the present paper, the coefficient of restitution proposed by Housner is considered, which is defined as ratio of the square root of kinetic energies after and before each impact [12]. Yet, the values of the coefficient of restitution analytically found by Housner [12] as a function of the block slenderness generally overestimate experimental values.

Actually, tests executed on blocks of different materials (e.g. stone, masonry, concrete, etc.) showed scattered values of the coefficient of restitution. For example, tests on rectangular concrete blocks with aluminum base reported [18] were in satisfactory agreement with the Housner predictions ratio: in fact, ratio between experimental and analytical value of coefficient of restitution e_{Exp}/e_H was respectively 101% and 98%. But similar tests performed on non-rectangular blocks [19] and prismatic steel blocks [20] exhibited not recognizable trends. By contrast, at least a qualitative trend of coefficient of restitution with respect to the analytical one can be appreciated when dealing with masonry blocks. Indeed, in general rocking masonry/stone elements dissipate more energy than that is predicted by the Housner's formulation. Literature values refer to ratios of experimental to analytical coefficient of restitution percentage of 85% – 95% for free walls [21], [22] and of about 80% for horizontally restrained walls [22].

This paper analyzes the preliminary experimental results of free-vibration tests executed on an unrestrained masonry wall made of clay brick and cementitious mortar. The dynamics of one sided rocking can be analytically and numerically studied through a modified equation of motion (Section 2). Section 3 illustrates the general features of the experimental campaign and the results in terms of coefficients of restitution, whilst Section 4 compares the so-obtained results with literature values valid for walls of the same typology in two-sided rocking.

2 ANALYTICAL FORMULATION

The mechanical model considered for a classical non-linear dynamic analysis is displayed in Figure 1. The wall is assimilated to a perpendicular rigid block of mass m , size R , polar inertia moment I_0 rocking around its base. The rigid block is subjected to an acceleration time history $\ddot{u}_g(t)$ which can be registered or artificial (spectrum compatible). The rocking wall might be connected to transverse walls of unitary stiffness K'_c (acting only in compression for

the sake of simplicity) and to horizontal tie-rods of stiffness K . Using the Euler-Lagrange formulation, it is simple to obtain the corresponding terms of the equation of motion (T_L and T_t respectively) as described in detail in [23].

The equation of motion reads:

$$I_0 \ddot{\vartheta} + \text{sgn}(\vartheta) mgR \sin A_\vartheta + T_t + T_L = m \ddot{u}_g R \cos A_\vartheta \quad (1)$$

$$A_\vartheta = \alpha - \text{sgn}(\vartheta) \vartheta$$

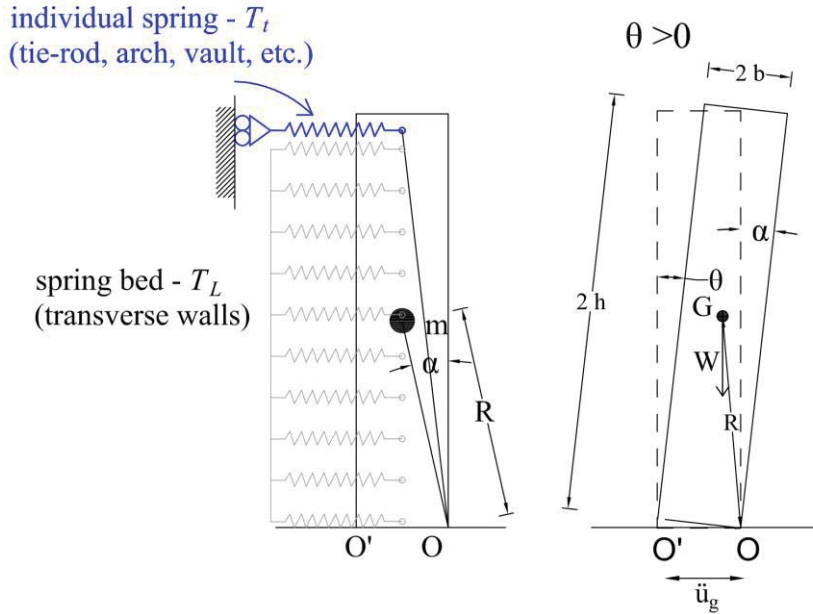


Figure 1: Mechanical model assumed for a rigid block masonry wall.

The energy dissipation is not directly visible in Eq. (1) since it is introduced during the resolution of the equation of motion as change of boundary condition when the block rotation passes from zero to a negative/positive value. Generally, in the dynamics of slender and rectangular rigid blocks the coefficient of restitution as defined by Housner [12] is considered:

$$e_H = 1 - \frac{3}{2} \sin^2 \alpha \quad (2)$$

Where $\alpha = \text{atan}\left(\frac{h}{b}\right)$ (Figure 1). This expression is obtained by equating the moment of momentum about O' immediately before impact to that immediately after impact on the ground. The coefficient of restitution is expressed as ratio of the square root of the two kinetic energies after and before each impact. As it will be illustrated in Section 3.2, there are different manners to express the coefficient of restitution, depending on whether the rocking is symmetric or not.

3 EXPERIMENTAL CAMPAIGN ON A MASONRY WALL IN ONE-SIDED ROCKING

3.1 Features of the rocking wall and testing set-up

This section illustrates the tests executed on a clay brick and cementitious mortar wall. The wall, tested in free-vibration, has the following dimensions: height 2.70 m, thickness 0.36 m and width 1.68 m. Its weight is 29.4 kN and its slenderness ratio, given by the arctangent of

thickness to height, is 0.133. The wall is pulled out-of-plane through a tie-rod up to attain a specific displacement (50 mm, 100 mm and 150 mm) of the wall at 2.56 m from the base. A detailed description of the experimental tests and of the mechanical features of the wall can be found in [24], [25]. The only difference with the tests already performed is that the hinge is in this case formed at 0.23 m above the wall base, and not at the wall foundation. This makes the wall stockier as its height diminishes.

Once the wall attains the specified displacement, a quick release system frees it making it rocking. The motion is one-sided, namely the wall impacts against two transverse walls (Figure 2) of length 1.50 m and thickness 0.12 m each. The transverse walls have the same mechanical properties as the rocking wall. The displacement and acceleration time-histories are recorded by potentiometric displacement transducers and accelerometers respectively, positioned on the tested wall as shown in [25]. An example of the experimental outputs is reported in Figure 3, where also the velocity time histories, obtained by derivation of the displacement time-histories, are plotted.

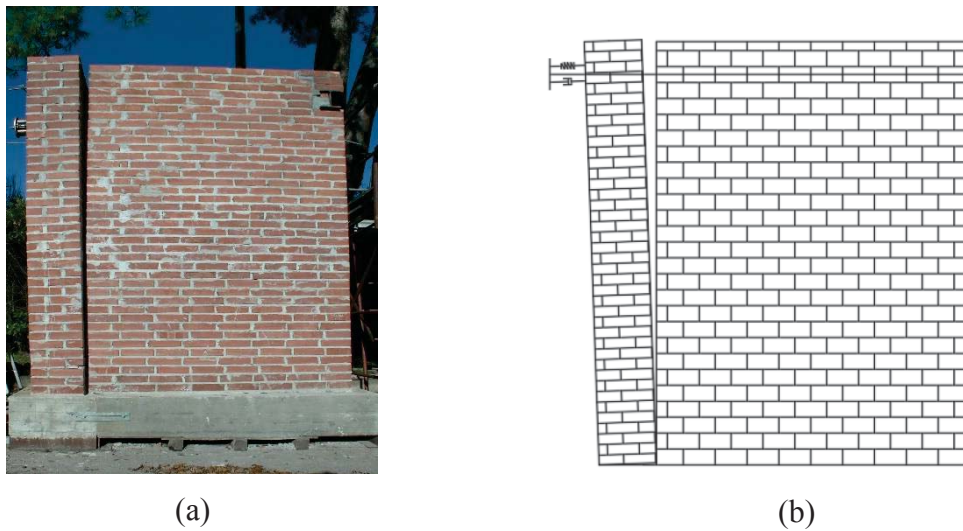


Figure 2: Masonry wall tested in one-sided rocking.

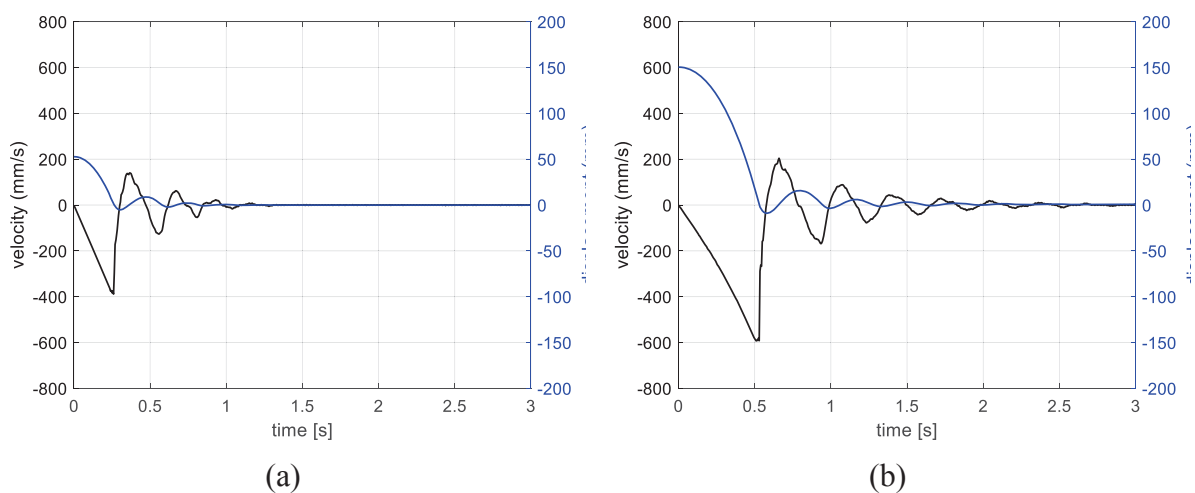


Figure 3: Selection of experimental results: displacement and velocity time-histories of a point located at 2.56 m from the wall base: imposed displacement of 50 mm (a) and of 150 mm (b).

3.2 Computation of coefficient of restitution from experimental results

These outputs are furtherly elaborated to obtain the experimental coefficients of restitution by two alternative approaches:

1. The traditional one, which computes the experimental coefficient of restitution considering consecutive peaks of velocity. Referring to Figure 4, the coefficient of restitution is calculated as mere ratio of velocity at peak (i+1)-th to velocity at peak i-th:

$$e_{exp} = \left| \frac{v_{i+1}}{v_i} \right| < 1 \quad (3)$$

regardless of the rotation sign.

2. A more refined one, where two coefficients of restitution are calculated, considering the asymmetric behavior due to the one-sided rocking caused by the impact on transverse walls:

$$e_{exp}^+ = \sqrt{\frac{v_{i+3}^+}{v_{i+1}^+}}; \quad e_{exp}^- = \sqrt{\frac{v_{i+2}^-}{v_i^-}} \quad (4)$$

The need of shifting from Eqn. (3) to Eqn. (4) is due to the fact that, for one-sided rocking, the consecutive negative and positive peaks of velocity are strongly different and the behavior depends on the rotation. Therefore, the calculation of the coefficient of restitution, function of the velocity peaks, should consider such a relevant aspect. This issue was already highlighted for diverse properties of horizontal restraints in [25] and for non-homogeneous walls in [22].

We call “experimental ratio of coefficient of restitution” the term:

$$r = \frac{e_{exp}}{e_H} \quad (5)$$

in which e_{exp} is the experimental value of the coefficient of restitution and e_H the analytical value as defined by Housner [12] and recalled in Eq. (2). Three ratios can be therefore defined to calculate the coefficient of restitution:

$$r = \frac{e_{exp}}{e_H} \text{ (method 1); } r^+ = \frac{e_{exp}^+}{e_H} \text{ and } r^- = \frac{e_{exp}^-}{e_H} \text{ (method 2)} \quad (6)$$

The wall under examination has a slenderness ratio $\alpha = 0.133$, therefore according to Eq. (2) the analytical Housner's coefficient of restitution is $e_H = 0.974$.

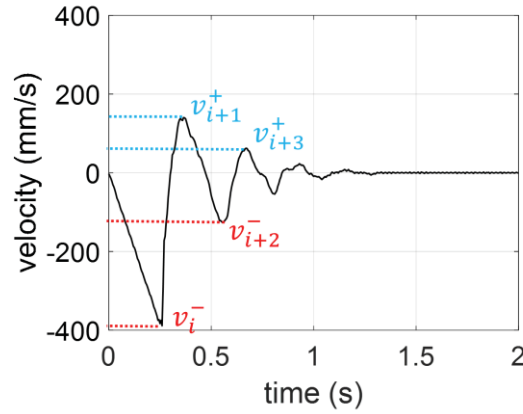


Figure 4: Labels of velocity peaks.

3.3 Experimental values of coefficients of restitution

The results in terms of ratios of coefficient of restitution (Eqns. (5)-(6)) are reported in Table 1. Each value is labelled with the imposed displacement and the progressive number of the test. So, for example, test # 150_2 indicates the second consecutive test where an initial imposed displacement of 150 mm at the top of the wall has been released. These values are calculated as mean considering the first six impacts, since after them the motion amplitude is negligible. Thus, the two ratios r^+ and r^- are computed as average of two values, whereas r is computed by considering five values. It is worthy to observe that the average values of r do not sensitively differ from r^+ or r^- only because the differences between experimental coefficients of restitution are smoothed when the overall average is considered. This aspect is shown in Figure 5: this diagram evidently shows that the average for test #50_1 is very close to $r^+ = 62\%$ or $r^- = 59\%$ (Table 1), although each individual coefficient of restitution markedly change (from 35% to 88%) considering the actual ratios. The difference between r^+ and r^- is by about 10%. This means that, when the wall impacts against the transverse walls (inward rotation), there is a dissipation of energy by 10% greater than what occurs in the condition of out-of-plane rocking (outward rotation).

It should be noticed that is not a huge difference, because the length of the transverse walls (2.0 m) is not enough to produce a rebound effect. Indeed, the oscillations are bilateral as visible in Figure 3 and not unilateral as it should be in actual rocking walls, where the transverse walls are much longer and therefore more rigid. On the contrary, the difference between r^+ and r^- is only by 3% for the test #50_1, owing the fact that the initial displacement amplitude is only 50 mm and therefore the condition of bilateral oscillations is more pronounced. This difference is then not considered as representative, due to the small initial displacement. Consequently, excluding test #50_1, from Table 1 an average value of 59% can be estimated for r_1^- , which is a reduction by about 40% with respect to $r = 95\%$, evaluated for one-sided rocking walls.

test#	r^+	r^-	r
150_1	67%	59%	57%
150_2	65%	57%	59%
150_3	71%	61%	66%
100_1	68%	58%	63%
50_1	62%	59%	59%

Table 1: Mean experimental ratios of coefficients of restitution for the unrestrained wall in one-sided rocking (r^+ = outward rotation, r^- = inward rotation).

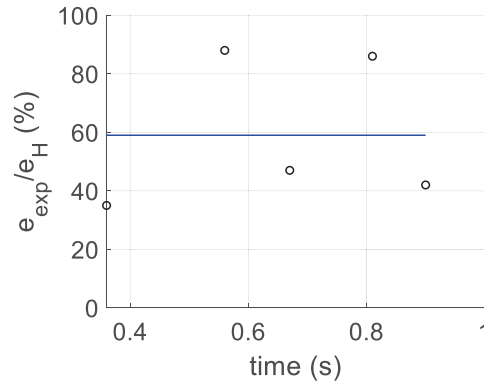


Figure 5: Local values of experimental ratios and average (blue line) for test #50_1.

4 COMPARISON BETWEEN ONE-SIDED AND TWO-SIDED ROCKING WALLS

This section illustrates a comparison in terms of experimental ratios of coefficient of restitution found for:

- (i) unrestrained walls, in bilateral (two-sided) rocking;
- (ii) unrestrained walls, in unilateral (one-sided) rocking;
- (iii) walls restrained by dissipative and non-dissipative horizontal restraints.

The first and third condition refer to the experimental tests described in [22], [25], whereas the second condition regards the experimental tests illustrated here.

4.1 Unrestrained walls in one- and two-sided rocking

As for the unrestrained walls in two-sided rocking, the mean coefficients of restitution do not vary considering either consecutive peaks or consecutive peaks of the same sign (second and third column of Table 2. In the first test (A_T0_1), there is a greater dissipation of energy, probably because the first impacts, breaking small parts of the mortar joints on the wall base, “smoothen” the rocking surface. For the tested wall, the values of coefficient of restitution range from 88% to 98%. In [25] the tests were executed also for a slenderer wall of equal characteristics: for it, the results were less scattered, being the minimum r 95% and the maximum r 96%. A reference value of 95% can be then assumed for the unrestrained walls in two-sided rocking. This ratio is different to that found for *in-situ* tests performed on historic rubble masonry [22]. This aspect can be explained considering that the *in-situ* conditions, such as imperfect foundation surface and interference of the rocking wall with the adjacent walls, undoubtedly imply an increase of energy dissipation. The results found in [25] are instead in agreement with the literature results of solid clay brick walls tested in two sided rocking [21], for which an average ratio of 95% was found.

test#	r^+	r^-	r	r (2 impacts)
A_T0_1	93%	93%	92%	97%
A_T0_2	97%	97%	94%	94%
A_T0_3	97%	97%	94%	99%

A_T0_4	97%	98%	95%	99%
A_T0_5	91%	92%	90%	88%

Table 2: Mean experimental ratios of coefficients of restitution obtained from experimental tests on the unrestrained wall in two-sided rocking illustrated in [25].

Comparing the results reported in Table 2 and in Table 1, it is clear that the one-sided motion presents much more scattered value of the experimental coefficients of restitution, while their difference increases by 10% passing from outward rotation to inward rotation (section 3.3). Obviously, in the two-sided rocking the coefficient of restitution does not change significantly when the rotation sign changes.

As described in section 3.3, the average value of r_1^- is 59%, corresponding to a reduction by about 40% from the value, $r = 95\%$, calculated for two-sided rocking walls. It is therefore of interest to distinguish the amount of energy dissipated by the impact at the ground from that originated by the impact on transverse walls.

Moreover, the presence of transverse walls introduces a non-linearity in the coefficient of restitution as it immediately influences the value of the coefficient of restitution itself. This aspect can be observed by considering the ratios pertaining the first impact only (r_1), or the first two impacts (r_1^+ and r_1^-). Indeed, the so calculated coefficients of restitution in the inward rotation (r_1^- in Table 3) are about 55%, that is almost 50% of the corresponding coefficients of restitution for the two-sided rocking wall (Table 2).

test#	r_1^+	r_1^-	r_1
150_1	65%	52%	32%
150_2	66%	53%	34%
150_3	69%	59%	37%
100_1	60%	52%	34%
50_1	64%	56%	35%

Table 3: Experimental ratios of coefficients of restitution for the first impact of the unrestrained wall in one-sided rocking (r_1^+ = outward rotation, r_1^- = inward rotation).

4.2 Restrained walls in one-sided and two-sided rocking

For what concerns the same wall restrained by a damped and stiff horizontal device, a reduction by 5% of the coefficient of restitution in unrestrained rocking was found in [25]. Therefore, the coefficient of restitution to assume for rocking analysis should be equal (on average) to 90%. The same reduction by 5% was computed in [22] passing from an unrestrained rubble masonry wall to the same wall restrained by an undamped elastic element. It must be stressed that such a reduction mainly depends on the horizontal restraint type and position, while the influence of masonry texture, material or age, seems negligible.

5 CASE STUDY: FAÇADE OF A THREE-NAVE CHURCH

Numerical analyses are performed in this Section to investigate the relevance of the coefficient of restitution in one-sided rocking motion. The selected case study is the façade of the San Filippo church (Figure 6a) located in Central Italy and struck by the 2016-2017 Central Italy earthquake. During the seismic swarm, a horizontal hinge formed at about 14 meters from the ground, causing the façade to rock and, finally, to overturn and collapse (Figure 6b).

5.1 Geometric and mechanical properties

The façade is made of clay brick and cementitious mortar masonry, having a specific weight around 18 kN/m^3 . The façade is assimilated to a rocking rectangular block of equivalent height 7.64 m (obtained considering the equivalence with center of mass and inertia moment of the original geometry), thickness 0.80 m and width 12.00 m (Table 4).

The parameters necessary to perform the rocking analysis are the radius vector R , the slenderness ratio α , the inertia moment I_0 and the compression spring bed stiffness K'_c reported in Table 4.



Figure 6: Case of study: San Filippo Neri's church in Camerino (Macerata): main façade before (a) and after (b) collapse.

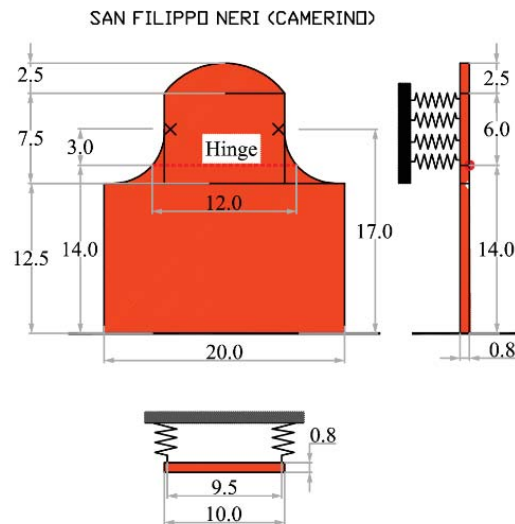


Figure 7: Geometrical dimensions of the case of study (from [26]).

Equivalent height [m]	Thickness [m]	Width [m]	R [m]	α [rad]	I_0	K'_c [MN/m ²]
					[m ⁴]	
7.64	0.80	12.00	3.84	0.10	$2.36 \cdot 10^6$	750

Table 4: Geometric characteristics of the rocking façade.

5.2 Analysis method

As already said, the main façade of the church is assumed as rigid block with a compression spring bed simulating the transverse walls. The 40 seismic excitations considered in the study were selected among the most intense ground motions of the 2016-2017 Central Italy earthquake: these earthquakes, belonging to the entire seismic swarm, occurred between August 2016 and January 2017 [26]. Among them, the four that caused the highest rotation amplitudes of the masonry façade – and also its overturning – are here considered.

Their features in terms of Peak Ground Acceleration (PGA) and Peak Ground Velocity (PGV), obtained from the Engineering Strong Motion Database [27], are summarized in Table 5.

Seismic record	PGA	PGV
(date and station)	(g)	(cm/s)
20160824_AMT	1.10	55.31
20160824_NRC	0.46	37.79
20161030_CLO	0.54	66.33
20161030_NRC	0.62	61.33

Table 5: Peak Ground Acceleration and Peak Ground Velocity of the considered seismic records [27].

The equation of motion (Eqn. (1)), described in detail in [23], is solved with a MATLAB code to analyze the dynamic behavior of the façade. Since the rocking hinge is not formed at the wall base, the seismic records should be applied after a filtering process, duly taking into account the vibration effects of the substructure. Here, considering the wall geometry, a magnification factor of 1.27 is adopted, as explained in [26], [28].

Two values of coefficients of restitution are considered in the analyses:

- 1) The Housner's analytical value, labelled with $e_H = 0.980$ and calculated with Eq. (2).
- 2) The experimental value of coefficient of restitution, evaluated, as said before, considering the average of the values reported in Table 1, and excluding the test #50_1. This process results in considering, for the inward rotation, an average coefficient of restitution $e_e = 0.59$, whereas for the outward rotation the coefficient of restitution is $e_e = 0.68$.

5.3 Discussion of results

Firstly, the strongest records in terms of normalized rotation (θ/α) amplitude are considered. They occurred in 2016, October 30th and, as visible in Table 5, are associated to the highest PGV values. This aspect confirms the seismic vulnerability of rocking walls to high PGVs [29].

Figure 8 displays the time-histories of the normalized rotational response together with the ground acceleration (scaled by the magnification factor of 1.27). At first sight, the adoption of the experimental values of the coefficients of restitution instead of the analytical ones suggested by Housner, leads to generally unsafe-sided results. But it should be considered that an additional dissipation of energy takes undoubtedly place when transverse walls are present and that disregarding it would lead to over conservative results. Seismic vulnerability assessment executed by neglecting the transverse walls could suggest retrofitting interventions that are actually not needed. This aspect is particularly relevant in case of historic buildings, where it is recommended to avoid unnecessary interventions for the preservation of the cultural heritage. In any case, under the 20161030_NRC, which is not characterized by the highest PGA and PGV, in both cases the overturning is delayed, but not prevented if the reduced experimental value of the coefficient of restitution (e_e) is considered. By contrast, under the 20161030_CLO, adopting e_e the façade survives, although its normalized rotation is quite high ($\theta/\alpha > 0.5$).

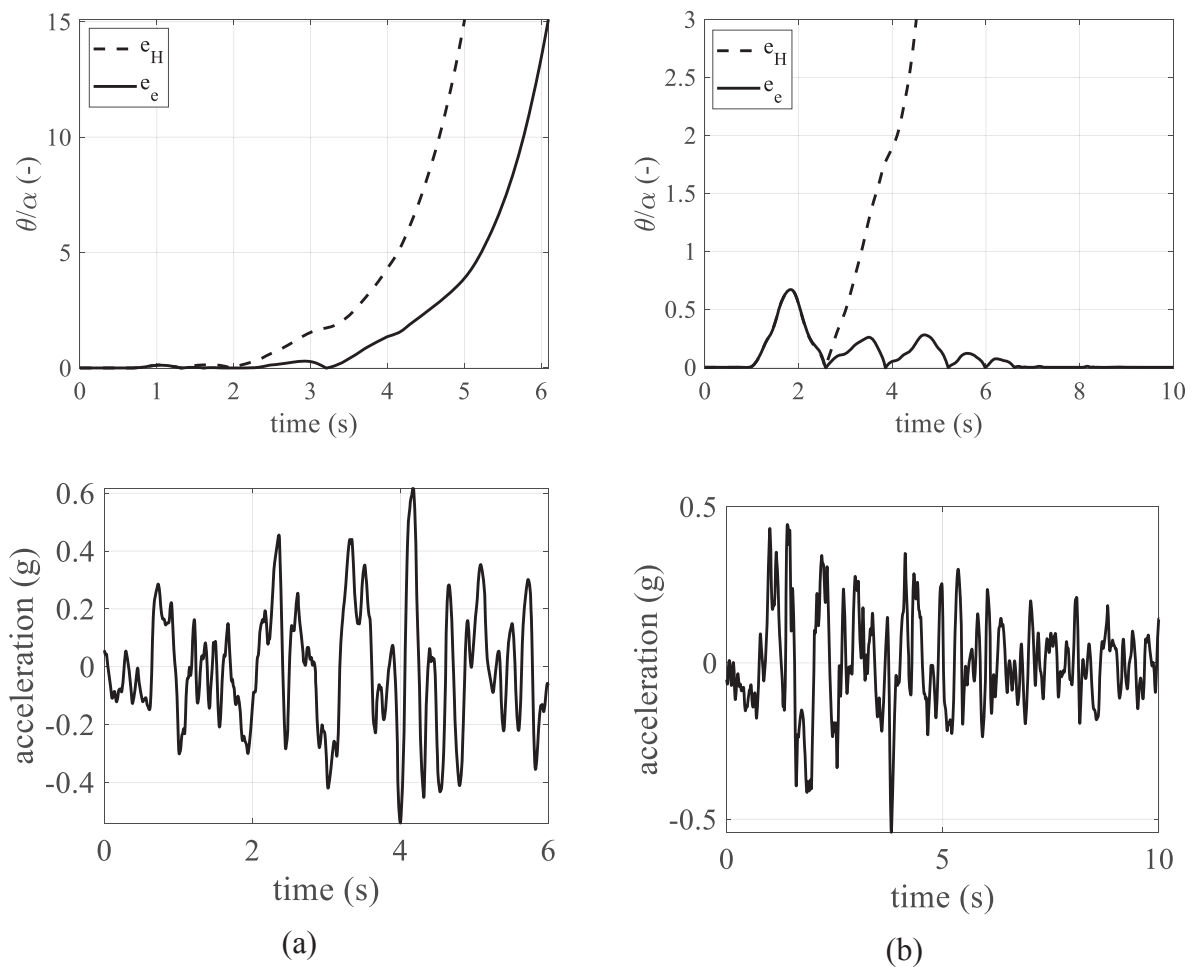


Figure 8: Rocking response to 20161030_NRC (a) and to 20161030_CLO (b).

Considering the less intense earthquake occurred in 2016, August 24th, the passage from the analytical to the experimental value of coefficient of restitution implies a reduction of the amplitude peaks, as evident from Figure 9. In particular, under the earthquake with highest PGA and PGV, the rocking wall experiences a maximum normalized rotation about 60% that of the maximum rotation computed with the analytical coefficient of restitution.

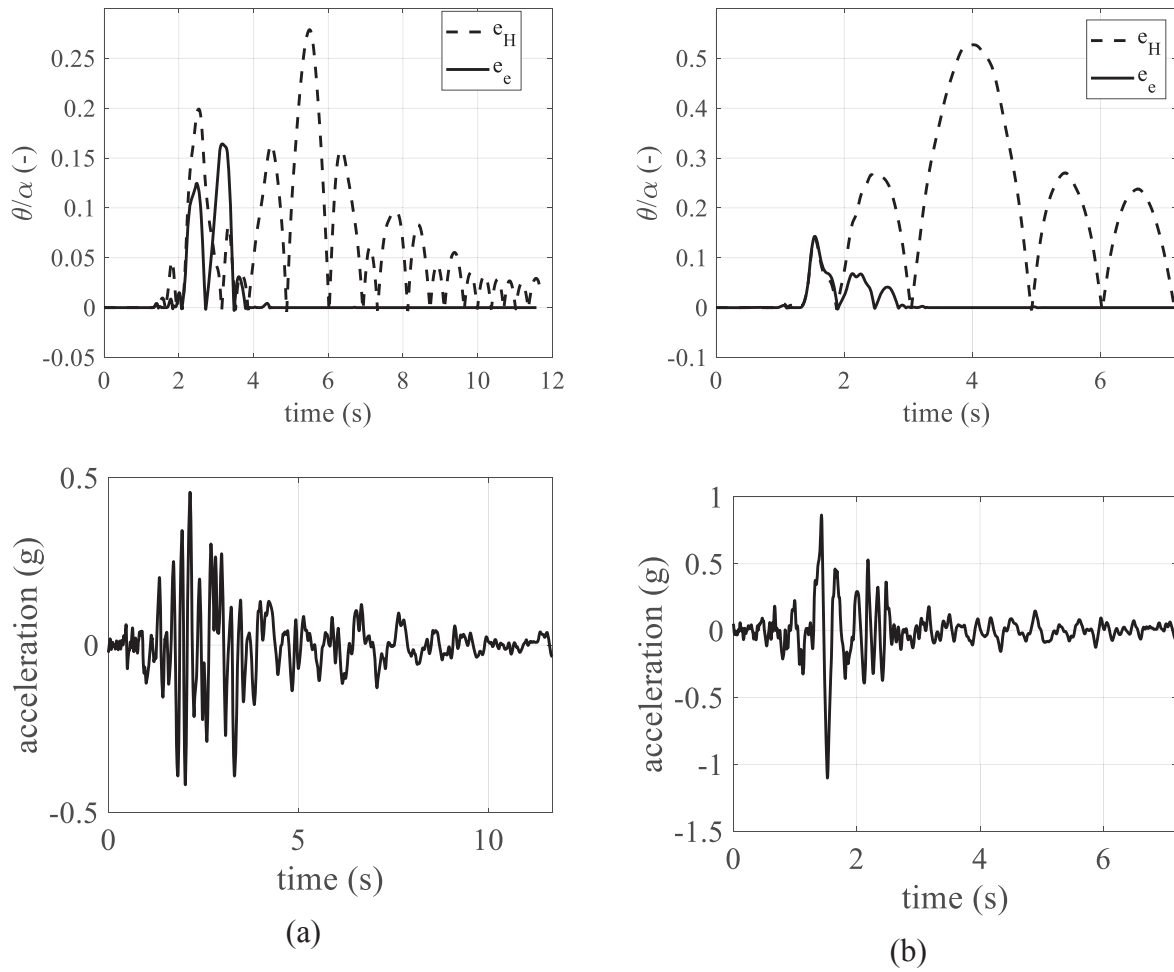


Figure 9: Rocking response to 20160824_NRC (a) and to 20160824_AMT (b).

Moreover, the maximum response is strongly reduced when the experimental coefficient of restitution is used, indeed it is about 25% of the maximum rotation computed with its analytical expression. In both cases, the peaks do not occur at the same time, but with the analytical coefficient of restitution the peak is delayed.

6 CONCLUSIONS

This paper discussed the experimental results of a set of rocking tests performed on a clay brick and cementitious mortar masonry wall tested in free vibration. The ratios of experimental to analytical coefficients of restitution were computed by the peaks of velocity time histories. Afterwards, their average values were used to perform numerical analyses on a church façade struck by the 2016-2017 Central Italy earthquake. The experimental results of the one-sided rocking wall were compared with those obtained on similar unrestrained and restrained walls in the two-sided rocking condition. The comparison shows that relevant parameters are more scattered in the one-sided rocking condition. Regarding the coefficient of restitution, it can be remarked that it is nearly independent on the rotation sign in the two-sided rocking condition; on the contrary, in the one-sided rocking condition it decreases by about 15% passing from the outward rotation to the inward rotation.

The outcomes of the numerical analyses demonstrate that, since the actual experimental values of the coefficient of restitution are generally sensibly lower than the ones estimated according to Housner expression, indirectly considering the influence of transverse walls, their adoption leads to less demanding responses. Consequently, assumption of the Housner coefficients can result too much safe-sided, so implying needs of interventions not always justified. Moreover, the substitution of the Housner coefficients of restitution with more realistic ones, on the one hand, delays but not prevents overturning under the stronger earthquakes, on the other hand maximizes the differences between the stable responses under earthquakes characterized by lower PGAs and PGVs.

In conclusion, since a realistic and critical evaluation of the coefficient of restitution is a key topic in order to avoid unnecessary and expensive retrofitting interventions especially regarding heritage structures, further studies are ongoing.

REFERENCES

- [1] F. Solarino, D. Oliveira, and L. Giresini, Wall-to-horizontal diaphragm connections in historical buildings: A state-of-the-art review. *Engineering Structures*, **199**, 2019.
- [2] M. Sassu, L. Giresini, E. Bonannini, and M. L. Puppio, On the Use of Vibro-Compressed Units with Bio-Natural Aggregate. *Buildings*, **6**, 2016.
- [3] A. De Falco, L. Giresini, and M. Sassu, Temporary preventive seismic reinforcements on historic churches: numerical modeling of San Frediano in Pisa. *Applied Mechanics and Materials*, **351**, 1393–1396, 2013.
- [4] L. Giresini, S. Paone, and M. Sassu, Integrated Cost-Analysis Approach for Seismic and Thermal Improvement of Masonry Building Façades. *Buildings*, **10**, 2020.
- [5] L. Giresini, F. Stochino, and M. Sassu, Economic vs environmental isocost and isoperformance curves for the seismic and energy improvement of buildings considering Life Cycle Assessment. *Engineering Structures*, **233**, 111923, 2021.
- [6] C. Casapulla, A. Maione, L. U. Argiento, and E. Speranza, Corner failure in masonry buildings: An updated macro-modeling approach with frictional resistances. *European Journal of Mechanics, A/Solids*, **70**, 2018.
- [7] C. Casapulla, L. U. Argiento, A. Maione, and E. Speranza, Upgraded formulations for the onset of local mechanisms in multi-storey masonry buildings using limit analysis. *Structures*, 2021.
- [8] C. Casapulla, A. Maione, and L. U. Argiento, Performance-based seismic analysis of rocking masonry façades using non-linear kinematics with frictional resistances: a case study. *International Journal of Architectural Heritage*, 2019.
- [9] C. Casapulla, L. Giresini, L. U. Argiento, and A. Maione, Nonlinear Static and Dynamic Analysis of Rocking Masonry Corners Using Rigid Macro-Block Modeling. *International Journal of Structural Stability and Dynamics*, **19**, 1950137, 2019.
- [10] L. Giresini and C. Butenweg, Earthquake Resistant Design of Structures According to Eurocode 8. , in *Structural Dynamics with Applications in Earthquake and Wind Engineering*, 2019, 197–358, .
- [11] S. Degli Abbatì, S. Cattari, and S. Lagomarsino, Theoretically-based and practice-oriented formulations for the floor spectra evaluation. *Earthquake and Structures*, **15**,

- 2018.
- [12] G. W. Housner, The behavior of inverted pendulum structures during earthquakes. *Bulletin of the Seismological Society of America*, **53**, 403–417, 1963.
 - [13] W. J. Stronge, Smooth dynamics of oblique impact with friction. *Int. J. Impact Eng.*, **51**, 36–49, 2013.
 - [14] P. Croce, Nonlinear Dynamics of Swinging Clapper Bells under Arbitrary or Resonant Forcing Functions. *Appl.Sci.*, **10**, 2020.
 - [15] C. Casapulla and A. Maione, Free Damped Vibrations of Rocking Rigid Blocks as Uniformly Accelerated Motions. *International Journal of Structural Stability and Dynamics*, **17**, 1–19, 2016.
 - [16] C. Casapulla, P. Jossa, and A. Maione, Rocking motion of a masonry rigid block under seismic actions: A new strategy based on the progressive correction of the resonance response | Il moto sotto sisma del blocco murario: Analisi per progressiva correzione della risposta in risonanza. *Ingegneria Sismica*, **27**, 35–48, 2010.
 - [17] C. Casapulla and A. Maione, Critical Response of Free-Standing Rocking Blocks to the Intense Phase of an Earthquake. *International Review of Civil Engineering*, **8**, 1–10, 2017.
 - [18] M. Aslam, W. G. Godden, and D. T. Scalise, Earthquake Rocking Response of Rigid Bodies. *Journal of the Structural Division*, **106**, 377–392, 1980.
 - [19] M. J. N. Priestley, R. J. Evison, and A. J. Carr, Seismic response of structures free to rock on their foundations. *Bulletin of the New Zealand National Society for Earthquake Engineering*, **11**, 141–150, 1978.
 - [20] P. R. Lipscombe and S. Pellegrino, Free rocking of prismatic blocks. *Journal of Structural Engineering*, **119**, 1387–1410, 1993.
 - [21] L. Sorrentino, O. AlShawa, and L. D. Decanini, The relevance of energy damping in unreinforced masonry rocking mechanisms. Experimental and analytic investigations. *Bulletin of Earthquake Engineering*, **9**, 1617–1642, 2011.
 - [22] L. Giresini, M. Sassu, and L. Sorrentino, In situ free-vibration tests on unrestrained and restrained rocking masonry walls. *Earthquake Engineering & Structural Dynamics*, **47**, 3006–3025, 2018.
 - [23] F. Solarino, L. Giresini, and P. Croce, Influence of the elasto-plastic behavior of tie-rods in the response of rocking masonry walls through seismic demand hazard curves. , in *COMPDYN 2021 8th ECCOMAS Thematic Conference on Computational Methods in Structural Dynamics and Earthquake Engineering M. Papadrakakis, M. Fragiadakis (eds.) Streamed from Athens, Greece, 27–30 June 2021*, 2021.
 - [24] L. Giresini, M. L. Puppio, and F. Taddei, Experimental pull-out tests and design indications for strength anchors installed in masonry walls. *Materials and Structures*, 2020.
 - [25] L. Giresini, F. Solarino, F. Taddei, and G. Mueller, Experimental estimation of energy dissipation in rocking masonry walls restrained by an innovative seismic dissipator (LICORD). *Bulletin of Earthquake Engineering*, 2021.
 - [26] L. Giresini, C. Casapulla, R. Denysiuk, J. Matos, and M. Sassu, Fragility curves for free

- and restrained rocking masonry façades in one-sided motion. *Engineering Structures*, **164**, 195–213, 2018.
- [27] L. Luzi, R. Puglia, E. Russo, and O. WG5, Engineering Strong Motion Database, version 1.0, Istituto Nazionale di Geofisica e Vulcanologia, Observatories & Research Facilities for European Seismology. . 2016.
- [28] Ministero delle infrastrutture e dei trasporti, *Circolare applicativa 21 gennaio 2019, n. 7, Istruzioni per l'applicazione dell'«Aggiornamento delle “Norme tecniche per le costruzioni”»*. In Italian. 2019.
- [29] L. Giresini, F. Solarino, O. Paganelli, D. V. Oliveira, and M. Froli, One-sided rocking analysis of corner mechanisms in masonry structures: influence of geometry, energy dissipation, boundary conditions. *Soil Dynamics and Earthquake Engineering*, **123**, 357–370, 2019.

AN EQUIVALENT VISCOUS DAMPING PROPOSAL FOR BLOCK-BASED ROCKING MODELS

Georgios Vlachakis¹, Carla Colombo¹, Anastasios I. Giouvanidis¹, Anjali Mehrotra¹,
Nathanael Savalle¹, and Paulo B. Lourenço¹

¹ University of Minho, ISISE, Department of Civil Engineering,
4800-058, Guimarães, Portugal

e-mail: giorgovlachaki@gmail.com, carla.colombo95@gmail.com, agiouvanidis@civil.uminho.pt,
a.a.mehrotra@tudelft.nl, n.savalle@civil.uminho.pt, pbl@civil.uminho.pt

Abstract

Masonry structures have been observed to display a high vulnerability to failure under seismic action. This stems from the fact that their structural configurations usually lack adequate connections among the distinct elements, resulting in the formation of local mechanisms experiencing Out-Of-Plane (OOP) collapse. In this context, rocking dynamics has proven to be a valuable methodology for the analysis of masonry walls. Classical rocking theory can provide a fast solution to the dynamic phenomena taking place if simple configurations are examined. Nevertheless, as the degrees of freedom and the boundary conditions increase, the complexity increases, and thus the classical rocking theory becomes impractical. In the meantime, recent developments in computational modelling of masonry structures are gaining significant attraction. This includes block-based models which inherently consider the complexity of the problem and enable the solution to be obtained easily in the discretised spatial and time domains. However, despite their widespread use, applications of such models usually lack a reliable treatment of damping.

The present work attempts to bridge the gap between the well-established energy loss of the classical rocking theory and the treatment of damping of block-based computational models. To do so, the dynamics of the problem are reviewed and an equivalent viscous damping model is proposed. A unilateral dashpot formulation allows the replication of the impulsive nature of the energy loss at impact. Afterwards, a calibration methodology is adopted for the practical range of the problem's parameters and a ready-to-use equation is provided, which respects energy equivalence. The performance of the proposed damping model is also evaluated through comparisons with experimental results.

Keywords: rocking, coefficient of restitution, viscous damping, numerical modelling, out-of-plane.

1 INTRODUCTION

Masonry structures constitute a significant part of our built heritage, with earthquakes representing a severe threat to their integrity [1]. During seismic events, such structures tend to fail via specific collapse mechanisms, with out-of-plane (OOP) collapse recognised to be the most frequent and destructive – especially in the case of façade walls inadequately connected with the rest of the structural elements [2]. Static approaches have been widely used to assess the collapse of the OOP mechanisms, resorting either to limit analysis methods [3], or to advanced numerical techniques [4]. However, static approaches display inherent limitations, since the inertial effects are neglected and the dynamic reserve of stability is disregarded. Therefore, over-conservatism characterises the static approaches [5], while dynamic techniques suggest a more reliable modelling solution [6].

In this context, rocking dynamics has been proposed to simulate the response of OOP mechanisms [7]. In the classical work of Housner [8], the equations of motion of a rigid body rocking over its base have been developed. Since then, extensive research has evaluated the influence on the rocking response of both seismological characteristics [9], and structural features, such as the presence of transverse walls [10, 11], horizontal elements [12–14] and restraints [13, 15–17]. Rocking dynamics assumes that energy is lost at every impact, and is captured by the Coefficient of Restitution (CoR) which correlates the angular velocity of the structure before and after impact. The CoR may be computed analytically by assuming conservation of angular momentum [8]. Despite small discrepancies, experimental campaigns have confirmed the validity of the analytical approach [18–20], particularly from a statistical perspective [21]. Nevertheless, as the Degrees-Of-Freedom (DOFs) and the Boundary-Conditions (BCs) of the problem increase, the complexity introduced transforms the method to one of impractical interest [22, 23].

In the meanwhile, recent developments in numerical simulation methods with block-based models are gaining momentum, especially due to the ease in representing complex masonry textures, BCs, interactions between the contacting bodies, and material nonlinearities. Among them, the most commonly used are the Finite Element Method (FEM) [24], the Discrete Element Method (DEM) [25], and the multi-body dynamics [26, 27]. However, despite their widespread use, block-based numerical modelling techniques lack a reliable method of replicating energy loss at impact [28, 29]. Usually, viscous damping models are employed [30–32], yet, without confidence about their equivalence with the overall more consistent rocking theory.

The present work aims to bridge the gap between the treatment of energy loss of the statistically-accurate classical rocking theory and the widely used numerical block-based modelling. This is achieved by “tuning” a viscous damping model to replicate both the manner and extent of energy loss indicated by the rocking theory based on the CoR. To this end, the main dynamic and modelling characteristics of both the theoretical and numerical modelling techniques are described in Section 2. Subsequently, Section 3 presents the calibration methodology, resulting in the proposal of a pertinent ready-to-use equation which respects energy loss equivalence between the examined methods. Finally, the performance of the numerical viscous damping model is assessed in Section 4, where an experimental campaign from the literature is employed as a reference.

2 STRATEGIES FOR MODELLING ROCKING STRUCTURES

2.1 Analytical modelling

Consider a rigid block exhibiting planar rocking motion over its rigid base, as shown in Figure 1 (a). In this case, the equation of motion can be written as [8]:

$$\ddot{\theta} = -p^2 \left[\sin(\pm\alpha - \theta) + \frac{\ddot{u}_g}{g} \cos(\pm\alpha - \theta) \right] \quad (1)$$

where α is the slenderness of the block, θ describes the rocking response and \ddot{u}_g denotes the seismic ground acceleration. The positive and negative signs in Eq. (1) depend on the sign of θ , while p is defined as $p = \sqrt{mgR / I_0}$, with m referring to the mass of the block, and I_0 the rotational moment of inertia with respect to the pivot points. The moment-rotation diagram of the rigid system is indicated by the solid line in Figure 1 (c).

The equation of motion (Eq. (1)) describes the smooth part of the rocking motion, i.e. when pivoting, while nonsmooth impacts interrupt the response. Impacts are treated as instantaneous events that lead to energy loss in the form of radiation damping. Assuming no bouncing or sliding, the CoR e sufficiently describes the contact event, by connecting the pre-impact and post-impact angular velocities. Then, conservation of angular momentum yields [8]:

$$e = 1 - \frac{3}{2} \sin^2 \alpha \quad (2)$$

Clearly, the energy loss, in this case, relies solely upon the slenderness of the block and not its material characteristics.

The solution of the analytical problem herein is obtained by solving the differential Eq. (1) interrupted by event-based impacts, using mathematical programming in MATLAB.

2.2 Numerical modelling

Numerical block-based models introduce an interface stiffness to describe the interaction of the contact bodies (in this case, the block and the base, see Figure 1 (b)), working on the normal (k_n) and tangential (k_s) directions of contact. Importantly, the interface stiffness might be used to replicate actual stiffness properties of contacting bodies [33], simulate macro characteristics such as mortar flexibility [19] and degradation [34], or foundation flexibility

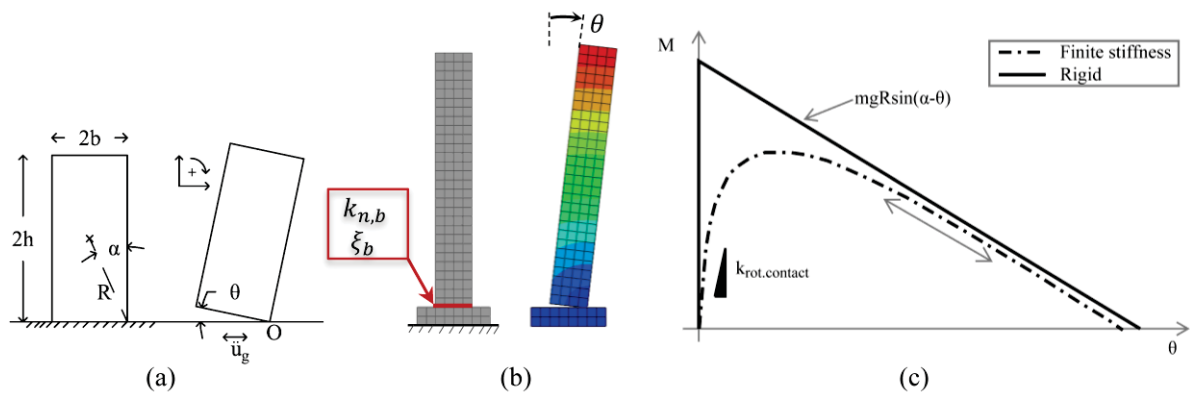


Figure 1: (a) Scheme of the classical rocking rigid block; (b) Numerical modelling of the rocking block with finite stiffness; and (c) Moment-rotation diagram of rigid and finite stiffness modelling techniques.

[35]. Consequently, the finite stiffness of the system ($k_{rot.contact}$, the moment-rotation curve for which is also shown also in Figure 1 (c)), results in impacts that occur over finite displacement and time, in contrast with the instantaneous behaviour of the analytical model.

Concerning energy loss, numerical block-based models commonly adopt viscous damping formulations, which are mathematical “artifices” used to simulate dissipative phenomena not considered explicitly [36]. Note that viscous damping models have a continuous nature, seemingly in contrast with the event-based CoR theory. A variety of viscous damping formulations are available depending on: i) the degrees of freedom used, ii) the response of the model during the time-history, and iii) the methods used to calibrate them [37]. Among them, a stiffness-proportional dashpot definition acting at the contact interfaces seems the most appropriate for simulation of the instantaneous features of the rocking impacts [38].

In the present work, the finite element environment of ABAQUS CAE [39] is used, where the solution is obtained using an explicit time-stepping integration. The rocking block is set to interact with its base through the normal k_n and tangential k_s interface stiffnesses. Moreover, a unilateral dashpot viscous damping model governs the interacting bodies, with a damping ratio ξ . It is worth noting that the validity of the adopted modelling technique has been confirmed also in other block-based simulation software [38], including implicit FEM and explicit DEM methods. This indicates universal applicability of the proposed numerical viscous damping model.

3 A VISCOUS DAMPING MODEL PROPOSAL

3.1 Calibration methodology

Since all viscous damping models need to be “tuned” to reproduce the desired energy dissipation, a phenomenological calibration methodology is adopted. More specifically, the energy loss of the classic rocking dynamics is considered as a reference, and the numerical viscous damping model is adjusted to mimic the former. In essence, the objective is to find a correlation among the CoR e and the damping ratio ξ . Evidently, the free-rocking problem is examined, where dissipation phenomena have a major impact on the response.

To this end, both modelling techniques are used to solve the rocking problem and pairs of $\xi - e$ are generated based on which response-histories match the best. This is done after comparing the rocking response of the two modelling techniques and minimising their root mean square difference. During the calibration process, all parameters possibly affecting the response are examined, i.e. i) the scale R , ii) the slenderness H/B , iii) the rocking amplitude θ_0/α , and iv) the normal interface stiffness k_n . In addition, the influence of the CoR e is also varied, independently of the slenderness of the block, i.e. Eq. (2) is disregarded. This choice allows the viscous damping proposal to be adaptable to any CoR correction suggestions, based either on experimental [10, 19], or theoretical basis [40, 41]. The ranges of the independent parameters that are varied during the calibration process are shown in Table 1. Among them, the scale has been found not to affect the viscous damping model, while non-significant influence is caused by the variations of the rocking amplitude (for more details, see [38]). Therefore, only the slenderness and the normal interface stiffness are essential to be included in the viscous damping model proposal.

Parameter	Range	Reference value
Scale: R [m]	1.4 – 2.8	2.1
Slenderness: h/b [-]	4.0 – 15.0	7.0
Amplitude: θ_0/α [-]	0.3 – 0.8	0.5
Normal interface stiffness: k_n [N/m^3]	$0.5 \cdot 10^8$ – $30 \cdot 10^8$	$5 \cdot 10^8$

Table 1: Independent parameters considered for calibration.

3.2 Proposed viscous damping model

The generated $\xi - e$ pairs of all the previously mentioned variations, 245 in total, are fitted through a multivariable nonlinear regression analysis. As a result, the following predictive equation is proposed which correlates the CoR e with the damping ratio of the viscous model ξ :

$$\xi_b = -0.000292 \cdot \left(\frac{H}{B} \right)^{0.935} \cdot k_n^{0.343} \cdot \ln e \quad (3)$$

Note that Eq. (3) is characterised by a coefficient of determination of $R^2 = 0.978$ over the 245 data $\xi - e$ pairs, showing a noteworthy estimation capability.

To illustrate the phenomenological calibration, one exemplary case of the predictive performance of Eq. (3) is shown in Figure 2. The comparison examines a rocking block with dimensions $2h = 4.2$ m and $2b = 0.6$ m, CoR $e = 0.97$, normal interface stiffness $k_n = 5 \cdot 10^8$ [N/m^3] and damping ratio $\xi = 5.9$ % according to Eq. (3). More specifically, Figure 2 (a) shows the rocking response of both the numerical viscous model and the analytical CoR based model, while Figure 2 (b) illustrates the corresponding energy content of both models. Clearly, a very good agreement is observed between the two methods. Importantly, the numerical viscous model presents a step-like response similar to that of the analytical CoR-based model: significant energy is lost only at impacts, gradually dissipating the free-rocking response. A small divergence is noticed only at smaller rocking amplitudes, i.e. $\theta_0/\alpha \leq 0.1$, which, however, are not expected to be decisive for the rocking stability of the structure, and thus assumed acceptable. Overall, the numerical viscous damping model shows a similar dissipative nature with that of the analytical CoR-based model, and the fitted relationship Eq. (3) a good predictive capability.

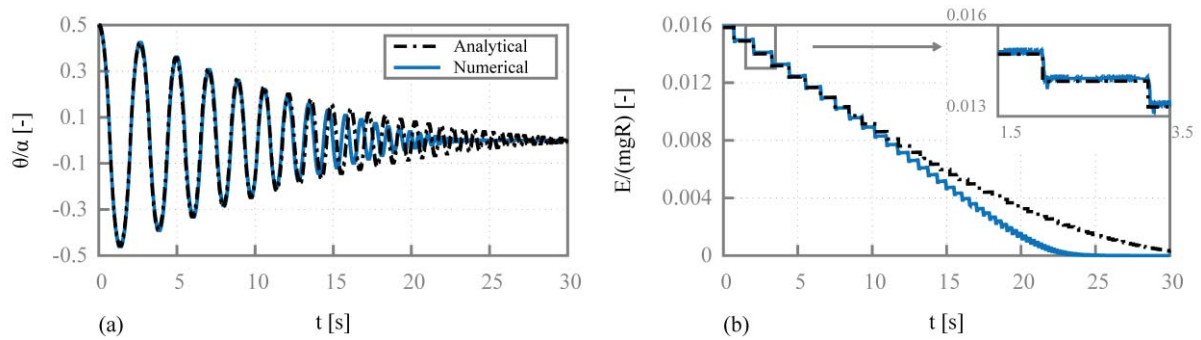


Figure 2: Behaviour of the viscous damping model. Comparison with the analytical model, in terms of variation of the (a) rocking angle and (b) total energy content over time. Details of the examined structure: $2h = 4.2$ [m],

$2b = 0.6$ m, $e = 0.97$, $k_n = 5 \cdot 10^8$ [N/m^3] and $\xi = 5.9$ %.

4 EVALUATION OF THE PROPOSED VISCOUS MODEL

Finally, the performance of the proposed numerical viscous damping model is assessed. While its calibration has been based on the analytical rocking model, its robustness is tested using actual experimental results. To this end, the experimental campaign reported by Peña [42] is used, where granite rocking blocks were tested under free- and forced-rocking vibrations. Details regarding the specimens' and excitation characteristics can be found in Table 2 and [42]. Given the fact that the proposed model has been calibrated independently of Eq. (2), the experimentally measured CoRs can be inserted in Eq. (3) to get the damping ratio ξ of the viscous damping model.

Specimen	$2h$ [m]	$2b$ [m]	e_{exp} [-]	Tests examined
1	1.0	0.25	0.936	i) Free rocking, ii) Hanning sine with $f = 3.3$ Hz and $a_p = 7$ mm
2	1.0	0.17	0.973	i) Free rocking
3	1.0	0.12	0.978	i) Synthetic ground excitation record 18, load factor 0.5, [42] for details

Table 2: Details of the specimens and examined tests [42].

4.1 Free rocking

Figure 3 (a) compares the free-rocking response of Specimen 1, while Figure 3 (b) the free-rocking response of Specimen 2, respectively. The results of the numerical simulations show a very good match with the experimental response both in terms of rocking phase and amplitude. Slight differences appear after several cycles, yet, given the experimental uncertainties and the simplicity of the problem, the overall dissipative phenomena are very well captured.

4.2 Forced rocking

To further evaluate the numerical viscous damping model, results of forced-rocking tests are compared in Figure 4. More specifically, Figure 4 (a) shows Specimen 1 under a hanning-sine excitation, while Figure 4 (b) illustrates Specimen 3 under a synthetic ground motion excitation [42]. For both cases, the numerical viscous damping model presents a rather good estimation of the experimental response. Slight differences are also observed, most notably the earlier collapse of the numerical model of Specimen 3. Nevertheless, considering the non-deterministic and bifurcating behaviour of the rocking problem, the performance of the nu-

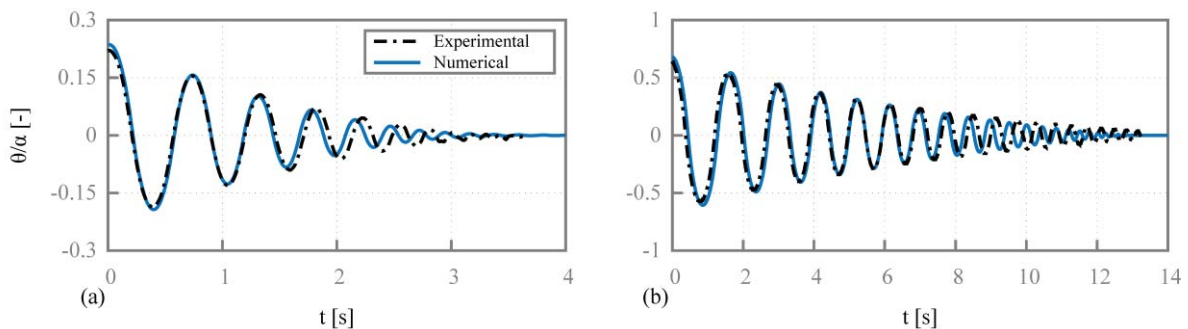


Figure 3: Free-rocking response of the proposed numerical viscous damping model compared to the experimental response reported in [42] of (a) Specimen 1 and (b) Specimen 2.

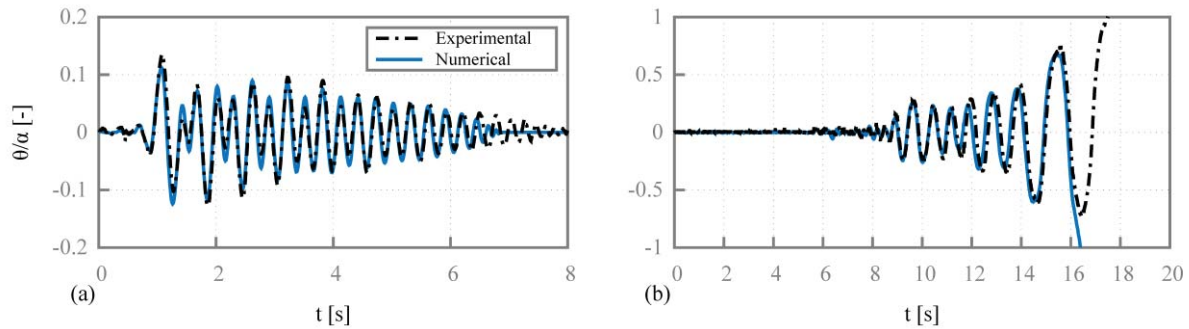


Figure 4: Forced-rocking response of the proposed numerical viscous damping model compared to the experimental response reported in [42] of (a) Specimen 1 under hanning-sine excitation and (b) Specimen 3 under synthetic ground excitation (Table 2).

merical viscous damping model is regarded as satisfactory.

5 CONCLUSIONS

This work proposes a numerical viscous damping model, aimed at simulation of the energy losses of the rocking problem using numerical block-based modelling techniques. This is achieved by following a phenomenological calibration methodology, where the analytical CoR-based rocking model is assumed as a reference and the viscous damping model is tuned accordingly. It is noteworthy that the suggestion of using a stiffness-proportional unilateral dashpot model results in impulsive energy losses, similarly to that of the CoR method. The performance of the proposed viscous damping model has been evaluated against experimental results from the literature, both under free- and forced-rocking vibrations, where its adequacy is highlighted.

In conclusion, the present paper suggests a reliable and consistent way to model energy losses when using numerical block-based models. This offers the possibility of modelling the rocking phenomena of more complex structures, with many DOFs or varying BCs, while additional material nonlinearities can be also easily included. Moreover, the proposed viscous damping model is universal and adaptable, as it can be used with any block-based numerical method and with any experimental or theoretical corrections on the used CoR.

REFERENCES

- [1] N. Augenti and F. Parisi, “Learning from construction failures due to the 2009 L’Aquila, Italy, earthquake,” *J. Perform. Constr. Facil.*, vol. 24, no. 6, pp. 536–555, 2010.
- [2] G. Vlachakis, E. Vlachaki, and P. B. Lourenço, “Learning from failure: Damage and Failure of Masonry Structures, after the 2017 Lesvos Earthquake (Greece),” *Eng. Fail. Anal.*, vol. 117, 2020.
- [3] J. Vaculik, M. C. Griffith, and G. Magenes, “Dry stone masonry walls in bending-Part II: Analysis,” *Int. J. Archit. Herit.*, vol. 8, no. 1, pp. 29–48, 2014.
- [4] G. Vlachakis, M. Cervera, G. B. Barbat, and S. Saloustros, “Out-of-plane seismic response and failure mechanism of masonry structures using finite elements with enhanced strain accuracy,” *Eng. Fail. Anal.*, vol. 97, pp. 534–555, 2019.
- [5] M. Godio and K. Beyer, “Evaluation of force-based and displacement-based out-of-plane seismic assessment methods for unreinforced masonry walls through refined

- model simulations,” *Earthq. Eng. Struct. Dyn.*, vol. 48, no. 4, pp. 454–475, 2019.
- [6] L. Sorrentino, D. D’Ayala, G. de Felice, M. C. Griffith, S. Lagomarsino, and G. Magenes, “Review of Out-of-Plane Seismic Assessment Techniques Applied To Existing Masonry Buildings,” *Int. J. Archit. Herit.*, vol. 11, no. 1, pp. 2–21, 2017.
 - [7] C. Casapulla, L. Giresini, and P. B. Lourenço, “Rocking and kinematic approaches for rigid block analysis of masonry walls: State of the art and recent developments,” *Buildings*, vol. 7, no. 3, 2017.
 - [8] G. Housner, “The behavior of inverted pendulum structures during earthquakes,” *Bull. Seismol. Soc. Am.*, vol. 53, no. 2, pp. 403–417, 1963.
 - [9] A. I. Giouvanidis and E. G. Dimitrakopoulos, “Rocking amplification and strong-motion duration,” *Earthq. Eng. Struct. Dyn.*, vol. 47, no. 10, pp. 2094–2116, 2018.
 - [10] L. Sorrentino, O. AlShawa, and L. D. Decanini, “The relevance of energy damping in unreinforced masonry rocking mechanisms. Experimental and analytic investigations,” *Bull. Earthq. Eng.*, vol. 9, no. 5, pp. 1617–1642, 2011.
 - [11] O. Al Shawa, G. De Felice, A. Mauro, and L. Sorrentino, “Out-of-plane seismic behaviour of rocking masonry walls,” *Earthq. Eng. Struct. Dyn.*, vol. 41, no. 5, pp. 949–968, 2012.
 - [12] L. Giresini, M. Fragiaco, and P. B. Lourenço, “Comparison between rocking analysis and kinematic analysis for the dynamic out-of-plane behavior of masonry walls,” *Earthq. Eng. Struct. Dyn.*, vol. 44, no. 13, pp. 2359–2376, 2015.
 - [13] A. Mauro, G. de Felice, and M. J. DeJong, “The relative dynamic resilience of masonry collapse mechanisms,” *Eng. Struct.*, vol. 85, pp. 182–194, 2015.
 - [14] O. AlShawa, D. Liberatore, and L. Sorrentino, “Dynamic One-Sided Out-Of-Plane Behavior of Unreinforced-Masonry Wall Restrained by Elasto-Plastic Tie-Rods,” *Int. J. Archit. Herit.*, vol. 13, no. 3, pp. 340–357, 2019.
 - [15] A. I. Giouvanidis and E. G. Dimitrakopoulos, “Seismic Performance of Rocking Frames with Flag-Shaped Hysteretic Behavior,” *J. Eng. Mech.*, vol. 143, no. 5, 2017.
 - [16] M. F. Vassiliou and N. Makris, “Dynamics of the Vertically Restrained Rocking Column,” *J. Eng. Mech.*, vol. 141, no. 12, 2015.
 - [17] E. G. Dimitrakopoulos and A. I. Giouvanidis, “Seismic response analysis of the planar rocking frame,” *J. Eng. Mech.*, vol. 141, no. 7, p. 04015003, 2015.
 - [18] P. R. Lipscombe and S. Pellegrino, “Free Rocking of Prismatic Blocks,” *J. Eng. Mech.*, vol. 119, no. 7, pp. 1387–1410, 1993.
 - [19] A. A. Costa, A. Arêde, A. Penna, and A. Costa, “Free rocking response of a regular stone masonry wall with equivalent block approach: experimental and analytical evaluation,” *Earthq. Eng. Struct. Dyn.*, vol. 42, no. 15, pp. 2297–2319, 2013.
 - [20] D. Kalliontzis and S. Sritharan, “Characterizing dynamic decay of motion of free-standing rocking members,” *Earthq. Spectra*, vol. 34, no. 2, pp. 843–866, 2018.
 - [21] J. A. Bachmann, M. Strand, M. F. Vassiliou, M. Broccardo, and B. Stojadinović, “Is rocking motion predictable?,” *Earthq. Eng. Struct. Dyn.*, vol. 47, no. 2, pp. 535–552, 2018.

- [22] A. I. Giouvanidis and Y. Dong, “Seismic loss and resilience assessment of single - column rocking bridges,” *Bull. Earthq. Eng.*, 2020.
- [23] A. Mehrotra and M. J. Dejong, “A methodology to account for interface flexibility and crushing effects in multi-block masonry collapse mechanisms,” *Meccanica*, 2020.
- [24] A. M. D’Altri *et al.*, “Modeling Strategies for the Computational Analysis of Unreinforced Masonry Structures: Review and Classification,” *Arch. Comput. Methods Eng.*, vol. 27, pp. 1153–1185, 2019.
- [25] J. V Lemos, “Discrete Element Modeling of the Seismic Behavior,” *Buildings*, vol. 9, no. 2, 2019.
- [26] A. I. Giouvanidis and E. G. Dimitrakopoulos, “Nonsmooth dynamic analysis of sticking impacts in rocking structures,” *Bull. Earthq. Eng.*, vol. 15, no. 5, pp. 2273–2304, 2017.
- [27] F. Portioli and L. Cascini, “Contact Dynamics of Masonry Block Structures Using Mathematical Programming,” *J. Earthq. Eng.*, vol. 22, no. 1, 2018.
- [28] G. de Felice, S. De Santis, P. B. Lourenço, and N. Mendes, “Methods and Challenges for the Seismic Assessment of Historic Masonry Structures,” *Int. J. Archit. Herit.*, vol. 11, no. 1, pp. 143–160, 2017.
- [29] M. F. Vassiliou *et al.*, “Shake table testing of a rocking podium : Results of a blind prediction contest,” *Earthq. Eng. Struct. Dyn.*, 2020.
- [30] O. AlShawa, L. Sorrentino, and D. Liberatore, “Simulation Of Shake Table Tests on Out-of-Plane Masonry Buildings. Part (II): Combined Finite-Discrete Elements,” *Int. J. Archit. Herit.*, vol. 11, no. 1, pp. 79–93, 2017.
- [31] J. V. Lemos and A. Campos Costa, “Simulation of Shake Table Tests on Out-of-Plane Masonry Buildings. Part (V): Discrete Element Approach,” *Int. J. Archit. Herit.*, vol. 11, no. 1, pp. 117–124, 2017.
- [32] D. Malomo, A. Mehrotra, and M. J. Dejong, “Distinct element modeling of the dynamic response of a rocking podium tested on a shake table,” *Earthq. Eng. Struct. Dyn.*, no. December, pp. 1–7, 2020.
- [33] C. Campaña, B. N. J. Persson, and M. H. Muser, “Transverse and normal interfacial stiffness of solids with randomly rough surfaces,” *J. Phys. Condens. Matter*, vol. 23, 2011.
- [34] M. C. Griffith, N. Lam, J. L. Wilson, and K. Doherty, “Experimental Investigation of Unreinforced Brick Masonry Walls in Flexure,” *J. Struct. Eng.*, vol. 130, no. 3, 2004.
- [35] P. D. Spanos, A. Di Matteo, A. Pirrotta, and M. Di Paola, “Rocking of rigid block on nonlinear flexible foundation,” *Int. J. Non. Linear. Mech.*, vol. 94, pp. 362–374, 2017.
- [36] F. A. Charney, “Unintended consequences of modeling damping in structures,” *J. Struct. Eng.*, vol. 134, no. 4, pp. 581–592, 2008.
- [37] J. F. Hall, “Problems encountered from the use (or misuse) of Rayleigh damping,” *Earthq. Eng. Struct. Dyn.*, vol. 35, no. 5, pp. 525–545, 2006.
- [38] G. Vlachakis, A. I. Giouvanidis, A. Mehrotra, and P. B. Lourenço, “Numerical block-based simulation of rocking structures using a novel universal viscous damping model,” *J. Eng. Mech.*, 2021, (under review).

- [39] Simulia, *Abaqus 6.12 documentation*. Rhode Island, US: Dassault Systèmes Simulia, 2012.
- [40] D. Kalliontzis, S. Sritharan, and A. Schultz, “Improved Coefficient of Restitution Estimation for Free Rocking Members,” *J. Struct. Eng.*, pp. 1–7, 2016.
- [41] T. Ther and L. P. Kollar, “Refinement of Housner’s model on rocking blocks,” *Bull. Earthq. Eng.*, vol. 15, pp. 2305–2319, 2017.
- [42] F. Peña, P. B. Lourenço, and A. Campos-Costa, “Experimental dynamic behavior of free-standing multi-block structures under seismic loadings,” *J. Earthq. Eng.*, vol. 12, no. 6, pp. 953–979, 2008.

PROBABILISTIC SEISMIC FRAGILITY FOR ROCKING MASONRY FAÇADES USING CLOUD ANALYSIS

Armando Benenato¹, Stefania Imperatore¹, Gian Piero Lignola², Barbara Ferracuti¹

¹ Niccolò Cusano University, Via don Carlo Gnocchi 3, 00166, Rome Italy
{armando.benenato, stefania.imperatore, barbara.ferracuti}@unicusano.it

² Department of Structures for Engineering and Architecture,
University of Naples “Federico II”, Via Claudio 21, I-80125 Napoli, Italy
gignola@unina.it

Abstract

The seismic performance of masonry churches is mainly governed by the out-of-plane mechanisms. Among them, the greater seismic vulnerability can be associated to the out-of-plane mechanism of the façade. If the masonry quality ensures a monolithic out-of-plane behaviour, the dynamic analysis of a rigid rocking block allows a reliable estimation of the seismic capacity of the façade, provided that the element boundary conditions are well assessed. In the present paper, the literature rocking models are adopted for a vulnerability assessment of churches' masonry façades characterized by different geometries. At this aim, fragility curves are defined by means of the Cloud Analysis approach considering earthquakes recorded in the Central Italy area to account for the record-to-record variability.

Keywords: Rocking; masonry façades; cloud analysis; fragility curves.

1 INTRODUCTION

The seismic performance of historic masonry churches is governed by the local out-of-plane response of the single structural components (i.e., façades, transverse walls, etc.). Among all the macro-elements, the post-earthquake surveys highlight the greatest vulnerability of the façade [1]-[6], which dynamic performance is typically characterized by a rigid-body behaviour.

A common methodology for the dynamic simulation of simple overturning mechanisms is based on rocking motion models where the impacts occurring at the base of the block or against elements preventing inward rotation (i.e. transverse walls or roofings) are accounted for by means of a kinetic energy dampening. The dynamic analysis of the “two-sided rocking” –occurring in the case of isolated elements– was firstly studied by Housner [7]. Subsequently, Yim et al. [8] observed a great sensitivity by the dimensional characteristics of the block or by the

ground motion shapes, whilst Makris & Roussos [9] found a dependence of the block overturning on both the earthquake intensity and the pulse length. The first studies on the “*one-sided rocking*” –developing if the inward rotations are prevented– were performed by Hogan [10], lately the issue was more extensively addressed: the energy dissipation phenomena were experimentally and theoretically investigated by Sorrentino et al. [11]-[12], while a different mechanical model to study the unilateral rocking motion was proposed by Giresini et al. [13]-[14]. All the theoretical models proposed in the scientific literature were applied to investigate the vulnerability of different masonry macro-elements, among which the church façades [15]-[16].

In this paper, the classic rocking models are employed to define fragility curves for five geometries of masonry church façades subjected to unscaled ground motions recorded in the Central Italy area. Aim of the work is the application of a non-linear dynamic procedure, known as Cloud Analysis [17], in which a structural response parameter (i.e. the maximum rotation of the rocking block) and the intensity measures of an as-recorded ground motion are fitted in the logarithmic scale to obtain a linear regression model. The approach was employed for its simplicity and the limited number of required analyses. In the paper, both the two-sided and the one-sided rocking motion are considered. The obtained fragility curves are finally compared to evaluate the influence of the geometrical features of the blocks and of the kinematic mechanism (one-sided or two-sided) on the seismic vulnerability of masonry churches’ façades.

2 MODEL FOR THE ROCKING MOTION OF A MASONRY FAÇADE

If the masonry can be regarded as a no-tension monolithic material characterized by an infinite compressive strength, a masonry church façade can be studied as a rigid block involved into a rocking motion as a consequence of an earthquake over a certain magnitude.

The analytical model of the rocking mechanism starts from the Lagrange equation and reaches the formulation proposed by Housner in 1963 [7], if the body deformability is neglected and the occurrence of rotations without sliding is assumed:

$$\ddot{\theta} = -p^2 \cdot [\operatorname{sgn}\theta \cdot \sin(\alpha - |\theta|) + a_g(t) \cdot \cos(\alpha - |\theta|)] \quad (1)$$

where θ is the rotation of the block, $p^2 = (m \cdot g \cdot R) / I_0$ is the dynamic coefficient of the block, $I_0 = I_G + m \cdot R^2$ is the moment of inertia about the two centres of rotation (points O and O' in Fig. 1), I_G is the moment of inertia about the centre of gravity, m and R are the mass and the half-diagonal of the block respectively, α is the inverse of the block slenderness and $a_g(t)$ is the ground motion acceleration.

The rocking motion starts if the seismic acceleration exceeds the kinematic acceleration a_{RM} :

$$a_{RM} = g \tan \alpha \quad (2)$$

and the overturning condition defines the failure when a rotation of the block under the seismic motion higher than the angle α is attained. This statement may be overcome in the case of forced oscillatory motion: consecutive contrary pulses can in fact bring the system again in an equilibrium condition even if the rotation of the block exceeds the angle α .

Eq. (1) can be employed for any simple out-of-plane mechanism, on the condition to properly account for the dissipative phenomena taking place at each impact. Therefore, at the theoretical level, the difference between the one-sided and two-sided rocking behaviour is related only to the kinetic energy damped due to the different boundary conditions. The issue can be assessed considering the velocity reduction experienced by the element after each impact during the two-sided or the one-sided rocking motion.

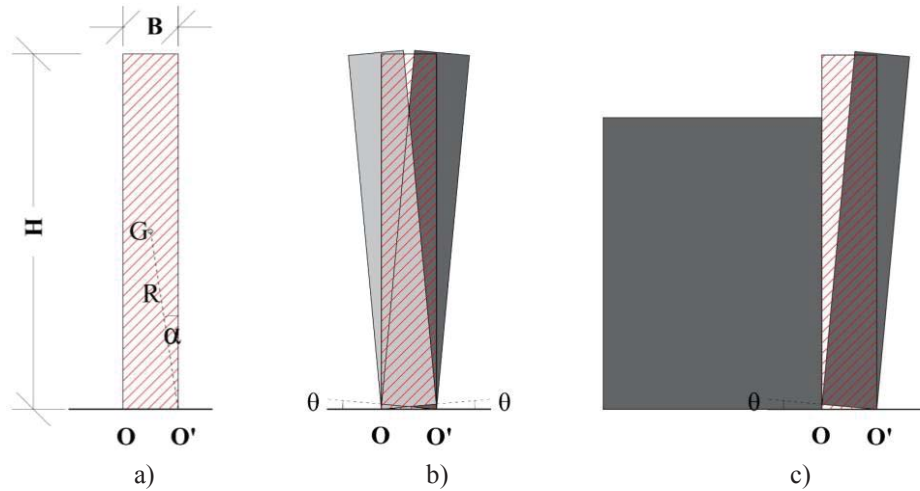


FIGURE 1. Models of the rocking block (the geometrical features are expressed by the base B , the height H , the radius vector R , the angle α , the center of gravity G): a) initial position; b) two sided model; c) one sided model.

In the case of two-sided motion (Fig. 1), the behaviour is governed by the rotation θ around the two corners O and O' , those alternatively become the centers of block rotation. After each oscillation, the element comes back into the vertical position and an impact on the base occurs. Such rebound effect implies a reduction of the kinetic energy after the impact, with a consequent energy damping. According to the model proposed by Housner in 1963 [7], the reduction in angular velocity due to an impact of infinitesimal duration can be evaluated by means of the velocity reduction factor $e_{an,2s}$, given by the ratio between the velocities experienced by the block after and before the impact. By imposing the conservation of the angular momentum about the center of rotation before and after the impact, the velocity reduction factor can be evaluated for a rectangular block as:

$$e_{an,2s} = 1 - \frac{3}{2} \sin^2 \alpha \quad (5)$$

With Eq. (5) the initial conditions after each impact can be evaluated and the amplitude of the oscillation during the rocking motion can be still estimated by using Eq. (1). The higher the velocity reduction factor, the smaller is the energy loss due to impact and consequently the damping of the rocking motion of the element.

When the rocking motion is admitted only in one direction, as shown in the Figure 1, the block will oscillate around the corner O , and after reaching the maximum rotation it comes back again to its initial position and will impact to the restraint, which prevents the rotation around the opposite corner. In this case the motion is defined *one-sided rocking*. The influence of the sidewalls on the rocking motion can be studied according to Sorrentino et al. 2011 [12]. In this model the transverse wall is modelled as a fixed restraint. Admitting that there is a little gap between façade and transverse walls, after the first impact against the base, the block experiences an infinitesimal counter-clockwise rotation and a subsequent impact against the upper corner. The latter condition involves an initial change in the rocking hinge and a rotation reversal of the element: the clockwise rotation around O will cause a third impact, against the base, after which the block has returned to vertical position. According to this approach [12], the analytic transversal velocity reduction factor for the one-sided rocking motion $e_{an,1s}$, is:

$$e_{an,1s} = \left(1 - \frac{3}{2} \sin^2 \alpha\right)^2 \left(1 - \frac{3}{2} \cos^2 \alpha\right) \quad (6)$$

Of course, in the case of one-sided rocking the velocity reduction factor is smaller than the two-sided ones, due to the higher dissipation occurring at each impact.

3 DYNAMIC ANALYSES

The seismic performance of typical Italian masonry churches' façades or portion of them have been investigated by means of rocking dynamic analysis. The overturning conditions of masonry churches' façades, involved in earthquake events, is here evaluated with reference to five rigid blocks. In table 1 are reported the principal features of the investigated elements: typology, height (H), base (B), slenderness $\lambda = H/B$, kinematic accelerations a_{rm} (minimum acceleration that causes rocking). With the first set of geometries (1, 2 and 3), the incidence of the variation in slenderness is investigated. For the second set (1, 4 and 5), it is analyzed the influence of the base dimension fixed the slenderness. The selected geometries are subjected to the unscaled natural ground motions described in the following.

<i>Geometry</i>	<i>Typology</i>	<i>Height</i>	<i>Base</i>	λ	a_{rm}
[-]	[-]	[m]	[m]	[-]	[m/s ²]
F1	Façade of small church	6	0.6	10	0.98
F2	Intermediate façade between 1 and 3	4.5	0.6	7.5	1.31
F3	Façade of uppermost story	3	0.6	5	1.98
F4	Façade of big church	12	1.2	10	0.98
F5	Plane belfry	3	0.3	10	0.98

TABLE 1. Principal features of the walls: typology, height, base, slenderness and kinematic acceleration.

With the aim to simulate the performance of the Apennine Churches stricken by the Central Italy seismic sequence, 89 natural accelerograms recorded during the last twenty years in the Central Italy area are considered to account for the record-to-record variability.

89 time-histories characterized by magnitude between 4 and 6.5 has been collected into a database; according to [18], moment magnitude M_L lower than 3.5 are excluded. The adopted database covers intervals of peak ground acceleration (PGA) up to 1g, peak ground velocity (PGV) up to 0.85 m/s, Housner Intensity (H_I) up to 2.8 cm and Arias Intensity (I_A) up to 7 m/s.

ID	Station	Date	Time	Epicentral Distance	PGA	PGV	I_A	H_I
				[km]	[g]	[m/s]	[m/s]	[cm]
MZ30 ₂	Amatrice	30/10/2016	06:40:18	27.2	0.48	0.48	1.54	1.22
T1201 ₂	Domo	30/10/2016	06:40:18	22.6	0.48	0.87	2.24	2.12

Table 2. Seismic Characteristics of the Selected Natural Ground Motion.

In order to analyze the sensitivity of the selected masonry churches' façades on the shape of the natural ground motion, two records with the same peak ground acceleration were selected. Consequently, the other seismic intensity measures (Peak Ground Velocity, PGV, Arias Intensity, I_A ; Housner Intensity, H_I) differ as reported in Table 2. In Figure 5 the time-histories of the selected ground-motions are shown.

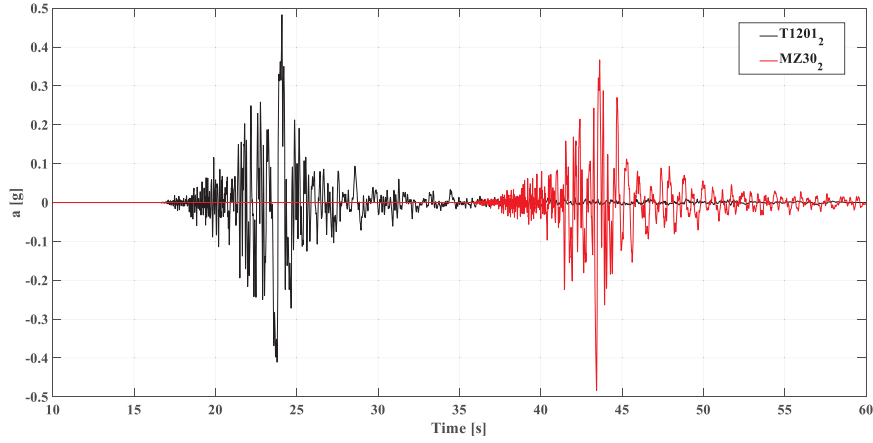


FIGURE 2: Selected ground-motions (the second one is shifted by 35 seconds).

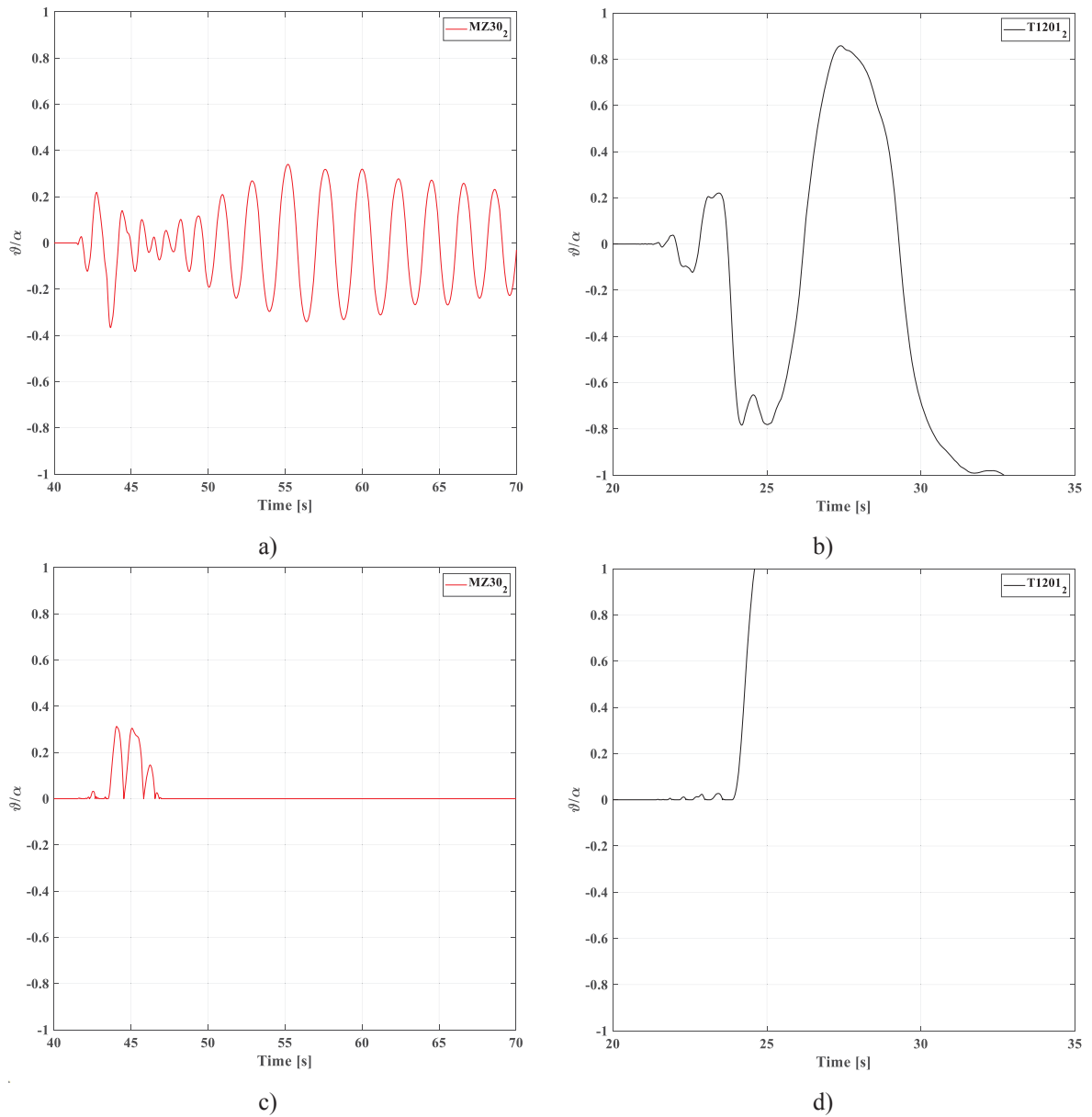


FIGURE 3: Seismic response of faades GEO1 involved in the two-sided rocking motion: a) MZ30₂ earthquake rocking-inducing; b) T1201₂ earthquake overturning-inducing; c) MZ30₂ earthquake rocking-inducing; d) T1201₂ earthquake overturning-inducing.

The seismic response of the façades in two-sided rocking motion characterized by slenderness $\lambda=10$ (F1) subjected to the MZ30₂ (Fig.3a) or to the T1201₂ (Fig.3b) earthquakes is firstly investigated. It is important to observe the different response of the façades to the earthquakes: the MZ30₂ time-history induces the rocking motion, while the T1201₂ ground motion –characterized by higher PGV, Arias Intensity and Housner intensity– causes the failure of the element, i.e. the block overturning. Similarly, the one-sided seismic response of the façades with $\lambda=10$ (GEO1) to the MZ30₂ (Fig.3c) or to the T1201₂ (Fig.3d) ground-motions shows the dependence of the façade performance by the earthquake's shape.

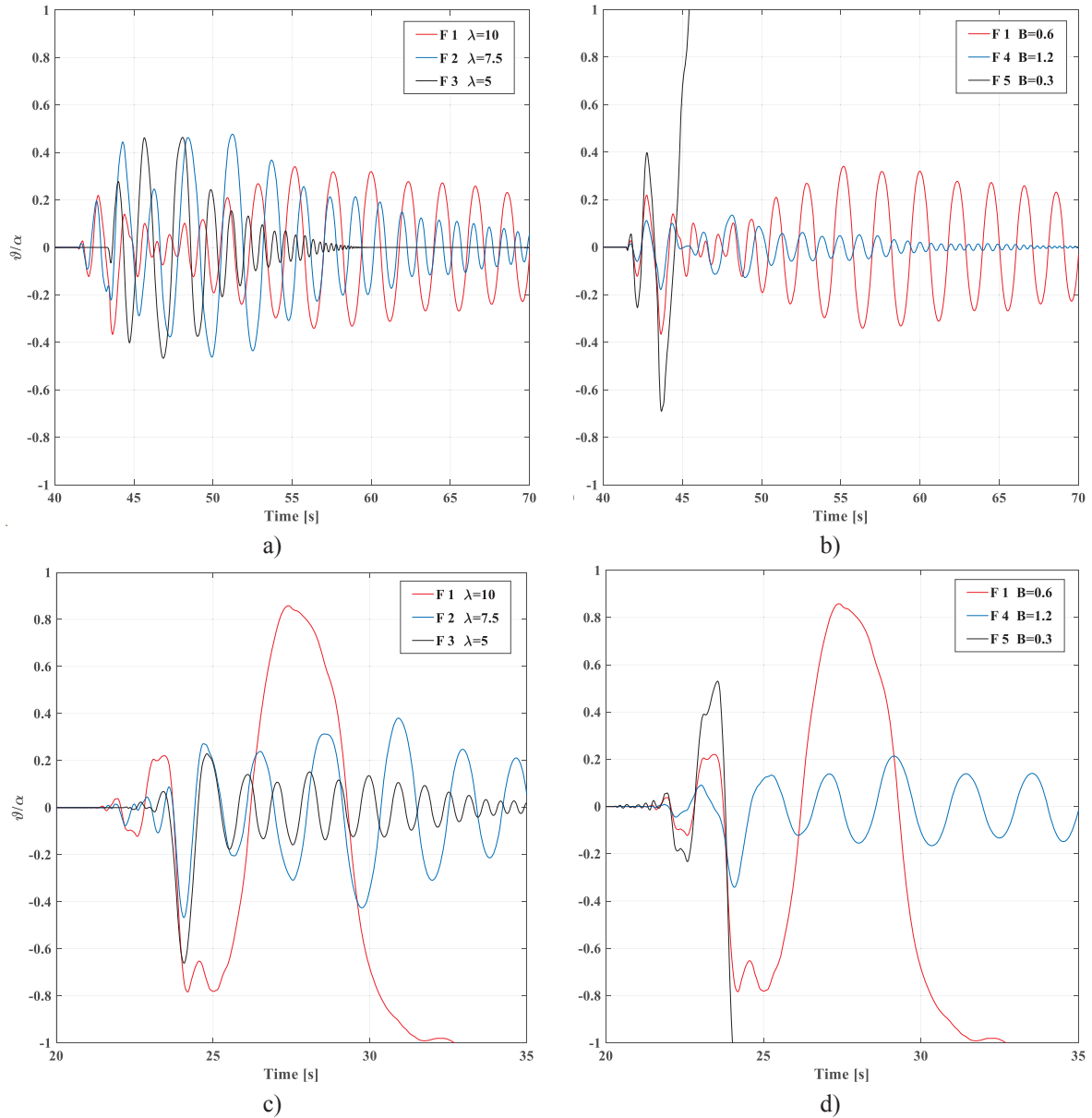


FIGURE 4: Two-sided seismic response of all façades subjected to MZ30₂: a) influence of the slenderness λ for $b=0.6$; b) influence of the base b for $\lambda=10$, and subjected to T1201₂: c) influence of the slenderness λ ; d) influence of the base b .

Finally, the results obtained by the parametric analysis are represented. In Figure 4 the influence of both the façade slenderness and thickness on the dynamic response in two-sided motion is represented. It can be noted that increasing the slenderness (Fig.4a and Fig.4c) the

rocking motion is delayed, due to the different value of the kinematic acceleration a_{RM} . Additionally, once the rocking motion begins, stockier blocks with similar slenderness (F2 and F3) are characterized by similar responses, while the slender block collapses under the heavier earthquake (T1201₂). With equal slenderness (Fig.4b and Fig.4d) the stabilizing effect due to the base dimension is clear: smaller the base, higher is the block rotations. Therefore, the block with the smaller base (F5) can collapse also under the lighter earthquake (MZ30₂).

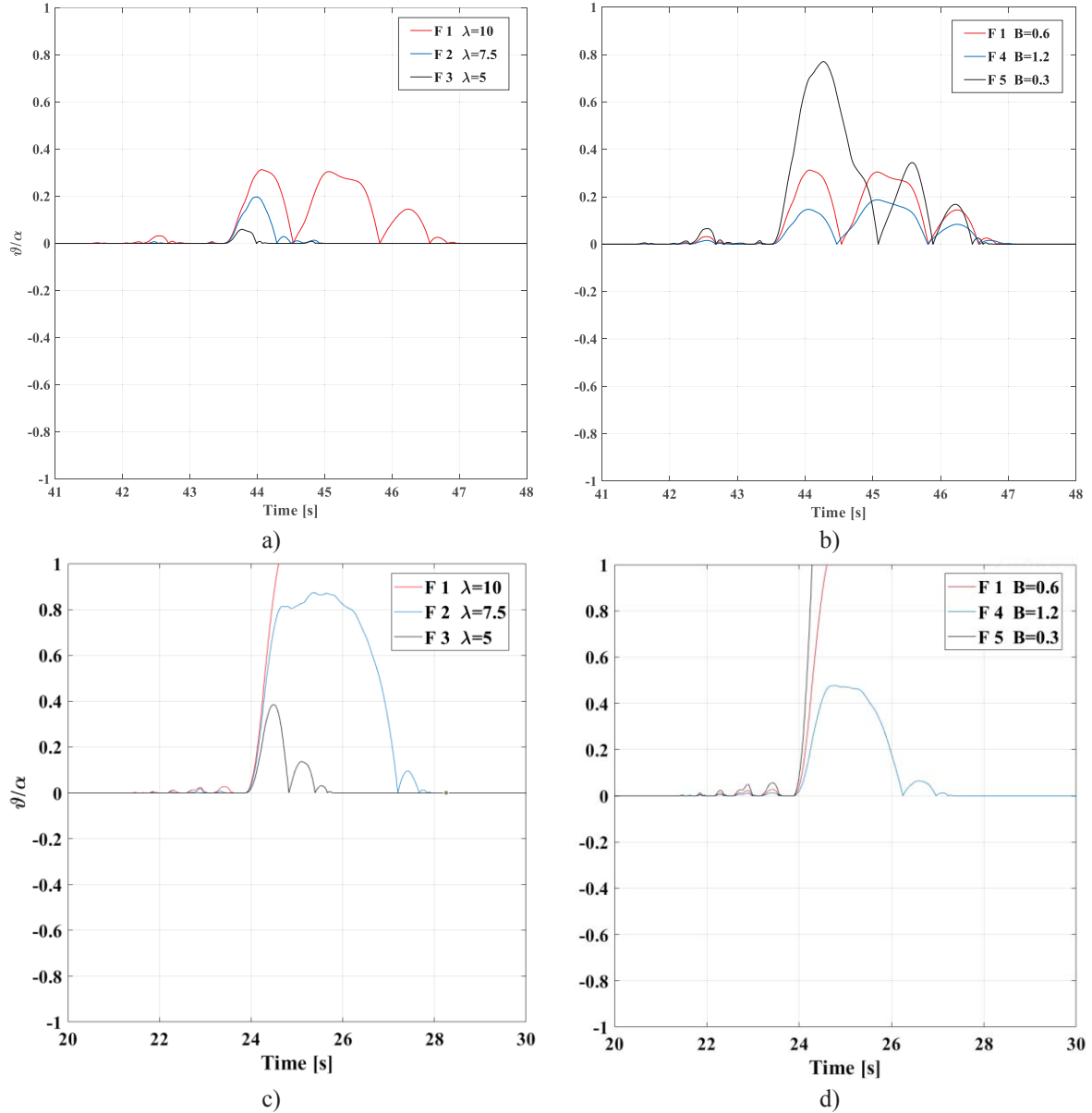


FIGURE 5: One-sided seismic response of all façades subjected to MZ30₂: a) influence of the slenderness λ for $b=0.6$; b) influence of the base b for $\lambda=10$, and subjected to T1201₂; c) influence of the slenderness; d) influence of the base.

Concerning the one-sided rocking response, a similar trend can be observed (Fig. 5). Nevertheless, the dynamic response in the one-sided can be more dampened than the two-sided rocking, depending on the ground motion shape as well as for the dissipative effect of the impacts against the sidewalls. In detail, the rocking motion is delayed increasing the slenderness (Fig.5a and Fig.5c), and the slender block collapses under the heavier earthquake (T1201₂) once the

rocking motion begins. Moreover, with equal slenderness (Fig.5b and Fig.5d) the dimension of the base has a stabilizing effect on the dynamic response: smaller the base, higher the rotations.

4 PROBABILISTIC SEISMIC ANALYSIS

The vulnerability of the selected masonry churches' façades is assessed by estimating the conditional probability P that the seismic demand D (measured with a specific engineering demand parameter, EDP) is higher than its capacity C for a given value of a seismic intensity (IM). Conventionally, the capacity C is derived by the results of incremental dynamic analysis (IDA) or multi stripe analysis (MSA). In the present work, instead, the Modified Cloud Analysis [17], an innovative and at the same time simple approach, is employed. The effectiveness of the proposed approach has been already established in other structural applications [19].

The structural fragility obtained by a modified cloud analysis in order to include the "collapse cases" [17] can be expressed as the probability that D exceeding the unity for a given IM :

$$P(EPD > 1|IM) = \Phi\left(\frac{\ln\eta_{D|IM}}{\beta_{\ln D|IM}}\right) \cdot \frac{e^{-(\alpha_0 + \alpha_1 \ln(IM))}}{1 + e^{-(\alpha_0 + \alpha_1 \ln(IM))}} + \frac{1}{1 + e^{-(\alpha_0 + \alpha_1 \ln(IM))}} \quad (9)$$

where Φ is the standardized Gaussian cumulative distribution function (CDF), and $\eta_{D|IM}$ and $\beta_{D|IM}$ are the conditional median and logarithmic standard deviation (dispersion) of the natural logarithm of D given IM for the No Collapse data. Based on the Cloud Analysis, these two parameters are obtained by performing a logarithmic linear regression on the No-Collapse data.

The parameter α_0 and α_1 have been instead evaluated through the logistic regression model applied to all records, distinguishing 1 or 0 depending on the collapse attainment or not [17].

The EPD assumed for the rigid block is the maximum normalized rotation, i.e. the ratio of the maximum rotation θ_{max} attained during the dynamic rocking analysis for each ground motion and the overturning limit condition $\alpha = \tan(B/H)$, corresponding to the loss of equilibrium.

Therefore, the EDP can assume the following values: the element is stationary (non-rocking), $|\theta_{max}|/\alpha = 0$; the rocking motion is enabled, $0 < |\theta_{max}|/\alpha < 1$; the element fails (rocking overturning), $|\theta_{max}|/\alpha > 1$. A percentage of the rocking blocks overturn, in such a case the EPD attains an arbitrarily large value $|\theta_{max}|/\alpha \rightarrow \infty$. The remaining dynamic analyses terminate without overturning, and finite (nonzero) values of $|\theta_{max}|/\alpha$ are observed.

In this study, the fragility curves at limit state corresponding to the rocking overturn, is developed. The Figure 6a illustrates the obtained fragility curves at collapse for the façades with different slenderness given $IM=PGA$. As already observed by the outcomes of dynamic analyses, slender façades are more vulnerable with respect to the squatter one. The Figure 6b illustrates the probability of overturning for the façades with different value of B . Although the slenderness of the façades is the same, the fragility curve shows an increment in collapse probability decreasing the base dimension. It is worth to note that the fragility curves obtained with the Cloud Analysis for the façades F1, F4 and F5 are comparable to those obtained by Lagomarsino et al. [20] performing the conventional IDA; therefore, the Cloud Fragility approach is reliable for the fragility assessment of elements involved in the two-sided rocking motion.

Concerning the one-sided rocking motion, the fragility curves given $IM=PGA$ are evaluated considering a set of 178 ground motion, 89 in positive direction and 89 in negative direction. In detail, Figure 6c illustrates the probability of overturning for the façades with different slenderness λ . It is worth to note that the obtained fragility curve for F1 (slenderness $\lambda=10$), is similar to that obtained by Giresini et al. [15] by adopting the conventional IDA approach, therefore the Cloud Fragility is feasible also for the one-sided rocking.

As already observed for the two-sided case, the façade vulnerability increases with increasing the slenderness. Considering the façades with the same slenderness and different base (Fig. 6d), the greater vulnerability decreasing the base can be observed, as for the two-sided motion. Comparing the fragility curves for one-sided and two-sided case, in the case of the one-sided rocking motion the fragility curves show higher mean and standard deviation with respect to the two-sided oscillation.

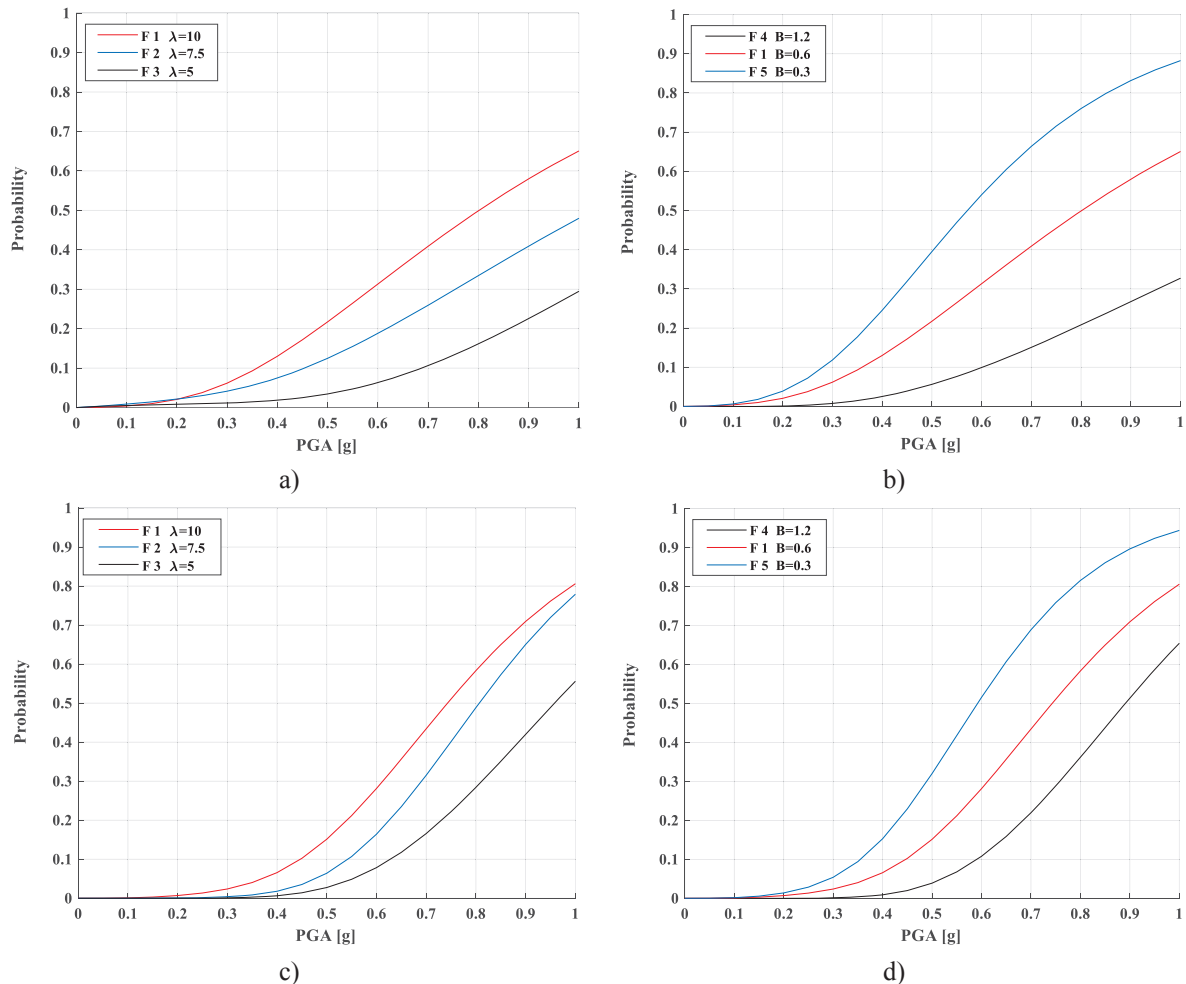


FIGURE 6. Cloud fragility in the two-sided motion: a) influence of the slenderness; b) influence of the base, and Cloud fragility in the one-sided motion: c) influence of the slenderness; d) influence of the base.

The presented fragility curves are developed adopting the PGA as *IM*, because it is in general the most used *IM* for various structural typologies. Nevertheless, the PGA is not always the most efficient *IM* for the analyzed structural typologies [14][21][22][23]. In particular, the most efficient *IM* can be different for the case of two-sided oscillation with respect to the one-side oscillation as already observed in previous studies. Further developing will be devoted in evaluating the fragility curves for the most efficient *IM* for each rocking motion.

5 CONCLUSIONS

The goal of this study is the estimation of the fragility curves at collapse for masonry church façades through a Cloud Analysis. At this aim, numerical nonlinear dynamic analyses, performed according to classical literature models, has been performed by applying more than

89 unscaled records of past earthquakes occurred in the area stricken by the 2016 Central Italy Earthquake. Therefore, the effects of record-to-record variability on the dynamic response was considered. Five different façade geometries were considered, defined observing the masonry churches' façades recurrent in the Central Italy. The obtained fragility curves, that are in line with those derived by other authors adopting different numerical approaches, clearly highlight the influence of the geometry on the seismic vulnerability of façades. Even if it is not meaningful to simply compare the fragility curves for the two-sided and the one-sided rocking motion, since the most efficient seismic intensity measure parameter differ for the two kinematic mechanisms, it should be noted the higher vulnerability for the one-sided compared to the two-sided rocking motion for higher values of PGA. This aspect, already observed by other authors in the past, requires a deeper investigation.

ACKNOWLEDGEMENTS

The authors would like to acknowledge the financial contribution provided by the Italian Network of Seismic Engineering University Laboratories (ReLUIS-DPC 2019-2021 project).

REFERENCES

- [1] F. da Porto, B. Silva, C. Costa, C. Modena "Macro-scale analysis of damage to churches after earthquake in Abruzzo (Italy) on April 6, 2009." *Journal of Earthquake Engineering*, 16(6), 739-758 (2012).
- [2] Colonna, S., Imperatore, S., Ferracuti, B. 2018. The 2016 central Italy earthquake: Damage and vulnerability assessment of churches. *Proceedings of the International Masonry Society Conferences Volume 0, Issue 222279*, 2018, Pages 2425-2440 10th International Masonry Conference, IMC 2018; Milan; Italy; 9 - 11 July 2018.
- [3] L. Sorrentino, L. Liberatore, L. D. Decanini, D. Liberatore "The performance of churches in the 2012 Emilia earthquakes." *Bulletin of Earthquake Engineering*, 12(5), 2299-2331 (2014).
- [4] A. Penna, C. Calderini, L. Sorrentino, C. F. Carocci, E. Cescatti, R. Sisti, A. Borri, C. Modena, A. Prota "Damage to churches in the 2016 central Italy earthquakes." *Bulletin of earthquake engineering*, 17(10), 5763-5790 (2019).
- [5] E. Cescatti, P. Salzano, C. Casapulla, F. Ceroni, F. da Porto, A. Prota "Damages to masonry churches after 2016–2017 Central Italy seismic sequence and definition of fragility curves." *Bulletin of Earthquake Engineering*, 1-33 (2019).
- [6] P. Salzano, C. Casapulla, F. Ceroni, A. Prota "Seismic vulnerability and simplified safety assessments of masonry churches in the Ischia Island (Italy) after the 2017 earthquake." *International Journal of Architectural Heritage*, 1-27 (2020).
- [7] G.W. Housner "The Behaviour of Inverted Pendulum Structures during Earthquakes." *Bull Seism Soc Am*, 53 (2), 403–17 (1963).
- [8] C.S. Yim, A.K. Chopra, J. Penzien "Rocking response of rigid blocks to earthquakes." *Earthquake Engineering & Structural Dynamics*, 8(6), 565-587 (1980).

- [9] N. Makris, Y. S. Roussos “Rocking response of rigid blocks under near-source ground motions”. *Geotechnique*, 50(3), 243-262 (2000).
- [10] S.J. Hogan “On the motion of a rigid block, tethered at one corner, under harmonic forcing.” *Proceedings of the Royal Society, Mathematical and Physical Sciences*, 439(1905), 35-45 (1992).
- [11] L. Sorrentino, S. Kunnath, G. Monti and G. Scalora, “Seismically induced one-sided rocking response of unreinforced masonry façades”. *Eng Struct*, 30(8), 2140-2153 (2008).
- [12] L. Sorrentino, O. AlShawa and L.D. Decanini “The Relevance of Energy Damping in Unreinforced Masonry Rocking Mechanisms. Experimental and Analytic Investigations.” *Bull Earth Eng*, 9 (5), 1617–42 (2011).
- [13] L. Giresini, M. Fragiocomo and M. Sassu “Rocking analysis of masonry walls interacting with roofs.” *Eng Struct*, 116, 107-120 (2016).
- [14] L. Giresini and M. Sassu “Horizontally restrained rocking blocks: evaluation of the role of boundary conditions with static and dynamic approaches”. *Bull Earth Eng*, 15(1), 385-410 (2017).
- [15] L. Giresini, C. Casapulla, R. Denysiuk, J. Matos and M. Sassu “Fragility Curves for Free and Restrained Rocking Masonry Façades in One-Sided Motion.” *Eng Struct*, 164, 195–213 (2018).
- [16] S. Colonna, S. Imperatore and B. Ferracuti “Fragility curves of masonry churches façades”. *COMPdyn 2019-7th ECCOMAS Thematic Conference on Computational Methods in Structural Dynamics and Earthquake Engineering*, M. Papadrakakis, M. Fragiadakis (eds.) Crete, Greece, 24–26 June (2019).
- [17] Jalayer, F., Ebrahimian, H., Miano, A., Manfredi, G., & Sezen, H. (2017). Analytical fragility assessment using unscaled ground motion records. *Earthquake Engineering & Structural Dynamics*, 46(15), 2639-2663.
- [18] Cornell C. A., Jalayer F., Hamburger R. O and Foutch D. A. “Probabilistic basis for 2000 SAC federal emergency management agency steel moment frame guidelines”. *J Struct Eng*, 128(4), 526-533 (2002).
- [19] Miano, A., Sezen, H., Jalayer, F., & Prota, A. (2019). Performance-based assessment methodology for retrofit of buildings. *Journal of Structural Engineering*, 145(12), 04019144.
- [20] Lagomarsino, S. (2015). Seismic assessment of rocking masonry structures. *Bulletin of earthquake engineering*, 13(1), 97-128.
- [21] S. Belliazzi, G.P. Lignola and E. Cosenza (2021). Dynamic response of asymmetric bodies assuming a rocking behavior”. *Proceedings of the Institution of Civil Engineers – Structures and Buildings*. DOI: 10.1680/jstbu.20.00151
- [22] L. Sorrentino, R. Masiani and L.D. Decanini “Overturning of rocking rigid bodies under transient ground motions”. *Struct Eng Mech*, 22(3), 293-310 (2006).
- [23] Benenato A., Imperatore S., Ferracuti B. and Lignola G. P. “Evaluation of the most efficient IM for the vulnerability assessment of masonry façades”. In *AIP Conference Proceedings* (Vol. 2293, No. 1, p. 240007). AIP Publishing LLC. (2020, November).

MODELLING OF THE OUT-OF-PLANE BEHAVIOUR OF UNREINFORCED MASONRY PANELS USING THE DISCRETE MACRO-ELEMENT METHOD (DMEM)

Valeria Cusmano¹, Bartolomeo Pantò², Ivo Calì¹ and Paulo B. Lourenço³

¹ Department of Civil Engineering and Architecture (DICAR), University of Catania
Piazza Università 2, 95131 Catania, Italy
e-mail: valeria.cusmano@phd.unict.it, ivo.calio@unict.it

² Faculty of Engineering, Department of Civil and Environmental Engineering, Imperial College
London, UK
e-mail: b.panto@imperial.ac.uk

³ Institute for sustainability and Innovation in Structural Engineering (ISISE), University of Minho
Campus Azurém, 4000-058 Guimarães, Portugal
e-mail: pbl@civil.uminho.pt

Abstract

Existing unreinforced masonry (URM) buildings, including historical and monumental structures, represent an important architectural and cultural heritage for several countries worldwide. The response of URM, subjected to earthquake excitations, is strongly governed by the out-of-plane (OOP) response of masonry walls, which can lead to local failure mechanisms, even at low levels of seismic loading. The OOP failure conditions are mainly controlled by the geometry of the structure and the masonry quality. Different strategies are used for modelling the OOP response of URM structures including limit analysis and nonlinear FEM. A further recently proposed strategy is based on the discrete macro-element method (DMEM) which allows the simulation of the in-plane and the OOP response of masonry walls with a reduced computational cost compared to the other numerical strategies. In this paper, the DMEM is applied to simulate a masonry wall rocking experimental campaign for which other numerical strategies have already been applied. The dissipation effects, related to the rocking motion and the repetitive impacts, are taken into account according to an equivalent viscous damping approach. Furthermore, the role of masonry deformability is investigated by comparing the results obtained by the DMEM model, for different value of masonry elastic modulus, with those obtained by typical rigid-block based models. The results clearly demonstrate that the DMEM can be efficiently adopted to accurately predict the dynamic response of monumental structures.

Keywords: URM structure, OOP failure mechanism, Modelling strategies, DMEM approach, Rigid-block models, FEM analysis.

1 INTRODUCTION

The existing buildings stock in several seismic area world around includes historical and monumental unreinforced masonry buildings (URM) which possess, in some cases, an important architectural and cultural value. The dynamic response of URM subjected to earthquake excitations is governed by the in-plane (IP) and out-of-plane (OOP) response of masonry walls. When the connections between vertical and horizontal structural elements do not guarantee a box-type behavior, the OOP failure mechanisms are the main source of seismic vulnerability of the building and the failure conditions are mainly controlled by the geometry and gravity loads directly applied to the wall. Due to the low tensile strength, cylindrical hinges tend to separate macro-portion of masonry leading to relative rotations between the different parts. If the number of hinges is such that a kinematic mechanism is allowed the corresponding equilibrium limit condition can be evaluated and a limit value of load multiplier leading to the incipient collapse condition can be determined. Due to the negligible tensile strength of masonry and the slenderness that generally characterise masonry walls, masonry walls can lose the equilibrium and overturn even under low values of seismic loadings. However, damage observation after strong earthquakes have proved that dynamic equilibrium can take place even after the rocking mechanism has been activated [1].

The simplified macro-block limit analysis approach is commonly adopted to assess the rocking behavior of masonry walls, according to the original Heyman's hypotheses [2]: no-tension material, rigid behavior in compression and absence of sliding. Consistently with these assumptions, a number of selected potential local mechanisms are selected whose ultimate load-multipliers correspond to upper-bound prediction of the effective load-multiplier, according to the limit analysis static theorem. Hence the lower load-multiplier represents the best prediction of the actual collapse mechanism within the investigated ones.

Upon the results of the limit analysis, the rocking capacity is evaluated by following the force-based or displacement-based approaches [3]. The force-based approach, consisting in comparing the load multiplier to the attendend in-situ PGA, represents the easiest tool to assess the seismic capacity of rocking blocks [4]. The displacement-based approach aims at comparing the displacement capacity of the assumed OOP mechanism with the corresponding displacement demand evaluated on an equivalent bi-linear or tri-linear single degree of freedom system [5]. Another simplified analysis method to assess the OOP response of masonry walls is based upon the hypothesis of tilting rigid block [6] according to which non-linear dynamic analyses are performed on a rigid block scheme assumed representative of the rocking behavior of the masonry wall. The dissipations sources involved in the OOP behavior of the wall are considered by means of a *coefficient of restitution* ruling the velocity of the rocking system after each impact. An extensive review on rigid block dynamics, when applied to URM structures, can be found in [7].

The main sources of approximation of limit analysis and rigid block models are related to the fact that they totally neglect the effects of masonry deformability and do not properly take into account the interaction between the portion of structure subjected to the overturning motion and the remaining part of the structure that is also subjected to the earthquake loadings and represents the source of loading and the constraint at the same time.

More recently, refined advanced discrete models have been applied to assess OOP rocking mechanisms such as the Distinct Element Methods (DEM) according to which masonry units are explicitly modelled by rigid irregular blocks while joints are modelled as a contact unilateral-friction links [8]. It is worth noting that these methods, difficult to calibrate, are quite computational expensive in the case of large structures and for these reasons although promising are currently limited to academic researches.

An alternative strategy of analysis to assess the OOP rocking mechanisms [CompDyn2017] is based on the discrete macro-element method (DMEM) which allows the simulation of the in-plane and the OOP response of masonry walls [Pantò et al 2017]. This innovative method has been firstly proposed and validated in the non-linear static field ([9] [10]), and more recently has been extended in dynamic field and validated through the comparison with experimental tests and refined FE simulation [11], [12]. According to DMEM, masonry walls are discretized as a mesh of shear deformable spatial macro-elements interacting through zero-thickness interfaces whose discretization follows a straightforward fiber calibration strategy. The single macro-element has a shear deformability governed by a single degree of freedom. The capability of the proposed DMEM to account for the IP and OOP behavior of masonry structure has been already numerical and experimental investigated [13], [14].

In this paper, the DMEM methods is applied to simulate the experimental response of masonry walls obtained by free-vibration and shake table tests already presented in the literature. Some parametric analyses are also performed to evaluate the influence of energy dissipation and the masonry deformability, comparing the results obtained by the DMEM model to the closed form solution of the classical rocking theory developed by Housner [6].

2 ANALYSIS METHODOLOGY AND OBJECTIVES

In this paper the rocking behavior of isolated walls exhibiting a cantilever mechanism, parapet wall (PW), or a simple supported wall (SSW) mechanism, is numerically investigated by using the DMEM approach and the classical rocking theory developed by Housner in 1963 [6]. The static schemes of the two considered mechanisms are reported in Figure 1. The main research goal of the present study is to identify and investigate critical issues related to the use of the DMEM model to describe the rocking motion of masonry walls. To reach this objective, the paper aim at:

- validating an equivalent viscous damping model for the DMEM, consistent to the contact-damping of the rigid model and experimental observations.
- estimating the effects on the rocking response of the masonry deformability, neglected in all the rigid-block-based approaches.

A brief description of the two methodologies of analysis is reported in the following subsection showing the main hypotheses according to which they are based on and highlighting their differences.

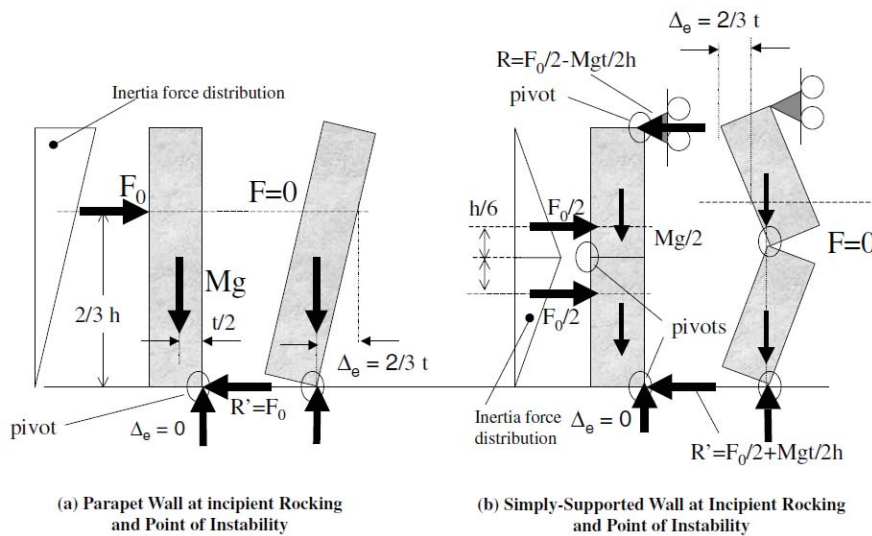


Figure 1: Rocking motion of isolated wall exhibiting a cantilever mechanism (a) and a simply supported mechanism (b) (from Doherty et al. 2002).

2.1 Classical Theoretical Model of Housner and the main Geometric Parameters influencing rocking

The dynamic behavior of a single rigid rectangular block, $2h$ height and $2b$ width, standing on a rigid base, with the assumption that friction between the block and the base is high enough to prevent sliding and neglecting bouncing, was first described by Housner in [6], hereinafter referred as the classical theory. When the rocking is activated, the rigid block can pivot on one of the two base vertexes. The main geometric features influencing the rocking response are the slenderness ratio $\alpha = \tan^{-1}(b/h)$ and the radius vector R connecting the pivot point to the center of mass of the block. A relevant finding of the classical theory is that, between two rigid rectangular blocks of the same slenderness, the block with the higher radius vector is more stable [15]. The equation governing the rocking motion under horizontal, $\ddot{u}_g(t)$, and vertical, $\ddot{v}_g(t)$, ground acceleration is reported in (1) where the rotation θ is the rotation angle of the block, assumed as the Lagrangian parameter, I_0 the moment of inertia of the block about an axis perpendicular to the plane of the wall and passing through its barycenter and g is the gravity acceleration.

$$(mR^2 + I_0)\ddot{\theta} + m(h \cdot \cos(\theta) + \operatorname{sgn}(\theta)b \cdot \sin(\theta))\ddot{u}_g + m(\operatorname{sgn}(\theta)b \cdot \cos(\theta) - h \cdot \sin(\theta))(g + \ddot{v}_g) = 0 \quad (1)$$

The rocking motion of the block $\theta(t)$, can be evaluated by integrating equation (1), within each time interval between two consecutive impacts, considering as initial conditions $\theta(t_i) = 0$; $\dot{\theta}(t_i) = \dot{\theta}_i$, where t_i is the time of the last impact and $\dot{\theta}_i$ the rotational velocity of the block after the impact. Considering a free-vibration motion of the block with maximum amplitude θ_0 , the periods of oscillation of the block (under the assumptions of parapet wall, Figure 1a, and simply supported wall, Figure 1b) are given by:

$$T_{PW} = \frac{4}{p} \cosh^{-1} \left(\frac{1}{1 - \frac{\theta_0}{\alpha}} \right) \quad (2)$$

$$T_{SSP} = 1 - 2\sin^2(\alpha_1) \quad (3)$$

Where $p = \sqrt{3g/4R}$ is a *frequency parameter* of the block referring to the pendulum frequency of the block assumed hanging from its pivot point and α_1 is the slenderness ratio of simple supported wall. Observing Eqs. (2) and (3), it is worth mentioning that the natural periods of the rigid body motion depend on the rocking amplitude in addition of the geometry of the system.

Several studies have been conducted to investigate the response of a rocking rigid block, subjected to a free-vibration motion ([6], [16], [17]), harmonic oscillations ([17], [18]) and earthquake loadings ([19], [15]). One of the main purpose of these studies was the representation of the energy dissipated during the rocking motion.

According to the classic theory, the dissipation is only concentrated at the impacts, when the rotation is switched from one base vertex to the another. It is generally assumed that the impact induces an instantaneous reduction of the velocity controlled by the introduction of a restitution coefficient (e) ranging from 0 to 1. A value of $e = 0$ corresponds to a totally inelastic impact, while $e = 1$ indicates a perfectly elastic impact. By imposing the conservation of the angular moment about the centre of rotation, just before and after each impact, the classical

theory provides analytical expressions of the restitution coefficient for parapet walls, e_{PW} in Eq. (4), and simple supported walls, e_{SSW} in Eq. (5).

$$e_{PW} = 1 - \frac{3}{2} \sin^2 \alpha \quad (4)$$

$$e_{SSW} = 1 - 2 \sin^2 \alpha_1 \quad (5)$$

Some experimental observations showed different values of the restitution coefficient than those predicted by the classic theory [20] suggesting that continuum energy dissipations due to flexural masonry deformation and plastic deformations at the rocking interfaces contribute significantly to the energy dissipation process. In a recent work, Graziotti et Al. [21] found values of the coefficient of restitution ranging from 0.84 to 0.91.

In view of to this observations, continuous viscous damping models alternative to the impact dissipation have been adopted, with constant or variable damping ratios, also considering the ease mathematical formulation and software implementation of the viscous damping model [22] [23] [24].

Continuous viscous damping models are generally implemented removing the hypothesis of rigid block dynamics and describing the rocking behavior assuming a single degree of freedom (SDOF) system characterized by a one-dimensional bi-linear [25] or tri-linear [5] [26] force-displacement relationship, as depicted in Figure 2, where the backbone curve of the ideal rigid block equilibrium path is characterized by the ultimate load multiplier (F_0) and the ultimate displacement (Δ_u) while the SDOF system is characterized by the initial elastic stiffness (k_L), the yield force ($F_y = \beta F_0$) and the yield displacement ($\Delta_y = F_y/k_L$).

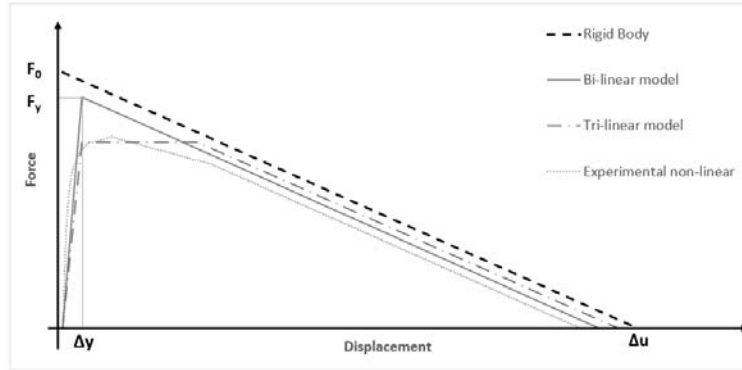


Figure 2: Force-displacement relationship models

Several studies have been performed to find a correlation relation between the equivalent viscous damping ratio, ξ , and the dissipation related to impacts controlled by coefficient of restitution [16] [20] [27] [28]. More recently, Tomasetti et Al. [21] proposed an energy equivalence between restitution coefficient and SDOF analytical formulation for different viscous damping models, constant damping coefficient (CDC), constant damping ratio (CDR) and stiffness-proportional damping ratio (SDR), proposing the empirical expression reported in Eq. (5) to evaluate the damping ratio ξ_{eq} to associate to the initial elastic frequency of the system ($\omega_L = \sqrt{K_L/m_{eff}}$), where m_{eff} is the effective mass of associated to the system [21]. They found $x_{CDC} = 0.667$, $x_{CDR} = 0.350$, $x_{SDR} = 0.218$ and $y_{CDC} = 0.450$, $y_{CDR} = 0.074$, $y_{SDR} = 0.195$.

$$\xi_{eq} = -x (\Delta_y/\Delta_u)^y \ln(e) \quad (6)$$

2.2 The Discrete Macro-Element Model

According to Discrete Macro-Element (DMEM) approach, the masonry is modelled through an equivalent mechanical scheme constituted by a hinged quadrilateral, whose in-plane deformability is governed by a single Lagrangian parameter, to rule the diagonal shear behavior. Each macro-element interacts with contiguous elements or constraints along its four edges by means of a discrete distribution of nonlinear springs, denoted as interfaces which govern the flexional and the sliding behavior. This approach was originally introduced for modelling the in-plane behavior of Unreinforced Masonry Structures [9], Figure 3a. The plane element possesses four degrees of freedom, a single row of transversal links and a single in-plane sliding link and is able to model the main failure mechanisms of the masonry in its own plane. Two subsequent upgrades were achieved to expand the potentialities of the approach. First, the out of plane (spatial) behavior, typical of historical constructions, was added [10] by considering additional rows of transversal links and two additional out-of-plane sliding links (able to govern the out of plane shear behavior and the torsion), thus enabling the out of plane degrees of freedom, Figure 3b. Subsequently, a further upgrade was introduced considering a shell macro-element characterized by an irregular geometry, variable thickness along the element and skew interfaces [29] to deal with curved structures, such as vaults and domes, Figure 3c.

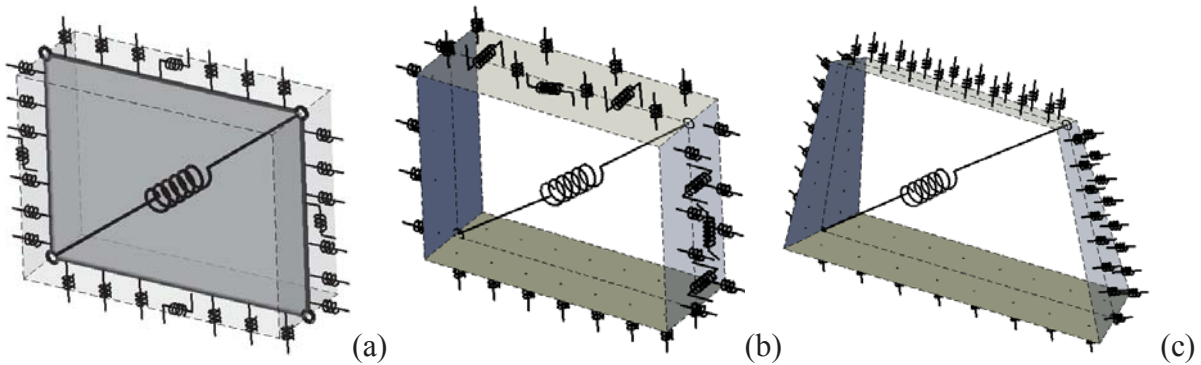


Figure 3: Layout of the macro-element adopted for masonry at its three stages: (a) plane element, (b) spatial regular element and (c) three-dimensional element for curved structures.

The flexural (rocking) response of macro-elements is governed by the interface transversal links which are calibrated following a fibre-discretization approach of the panel cross section [10]. According to this strategy, the initial stiffness of the links is related to the axial stiffness of the corresponding masonry strips, evaluated in Eq. (8) where E_m , is the masonry Young's modulus and L_n , A_{sn} , the length and cross-section area of the masonry strip. The yielding forces in tension (F_{ytn}) and in compression (F_{ycn}) are related to the influence area and to the tensile and compressive strength respectively. Finally, the tensile and compressive yielding displacement (u_{yt} and u_{yc}) are associated with the yielding forces and the initial stiffness, Table 1.

The DMEM has been employed to simulate the seismic behavior of monumental masonry constructions by means of non-linear static (pushover) analysis. A more recent upgrade extended the DMEM approach to the dynamic field allowing the simulation of the non-linear dynamic behavior under seismic load. The mass of each macro-element is concentrated at its barycenter. According to this hypothesis, a diagonal mass matrix with, along the diagonal, the three translational inertia components and the three rotational inertia components of the volume represented by the macro-element [13]. More details on the DMEM are reported in the

referenced papers.

K_n	F_{ytn}	F_{ycn}	u_{yt}	u_{yc}
$2 \frac{E_m A_{Sn}}{L_n}$	$A_{Sn} \cdot f_{tn}$	$A_{Sn} \cdot f_{cn}$	$\frac{F_{yt}}{K_n}$	$\frac{F_{yc}}{K_n}$

Table 1: Calibration of the interface transversal links.

3 NUMERICAL SIMULATIONS

The numerical simulations are performed considering rectangular blocks subjected to two-side rocking motion. Free vibration motion is considered in Section 3.1 whilst earthquake excitations are considered in Section 3.2.

Three models are considered. Namely, the ideal rigid block (RB) model, Figure 3a, a simplified DMEM model with the interfaces located at the base rocking section, Figure 2b, and a refined DMEM model in which the wall height is discretized by a mesh of macro-elements with height equal to the wall thickness, Figure 2c. The response of the RB model is evaluated considering the analytical solution of Eq. (1) while, the analyses on the DMEM models are performed using the software HISTRA [30] through the Newmark method considering the Newmark's parameters $\alpha=0.9$, $\beta=0.25$ and $\gamma=0.5$ and a time step of 0.005 s.

At each step, the dynamic equilibrium is imposed with reference to the initial configuration while the effects of the geometric nonlinearities are considered by updating the load vector position (P - δ effects). The wall thickness is divided in ten rows of links and characterized by the distribution of normal stiffness $k_n = K_n/\lambda$ where K_n already defined in Table 1 and λ the distance between the links along the wall thickness. Although different constitutive laws can be adopted in the DMEM, aiming at performing a consistent comparison a linear behavior in compression and zero tensile strength have been assumed. Furthermore, a viscous damping, proportional to the global stiffness matrix, has been calibrated according to Eq. (6) evaluating the ratio Δ_y/Δ_u through a pushover analysis.

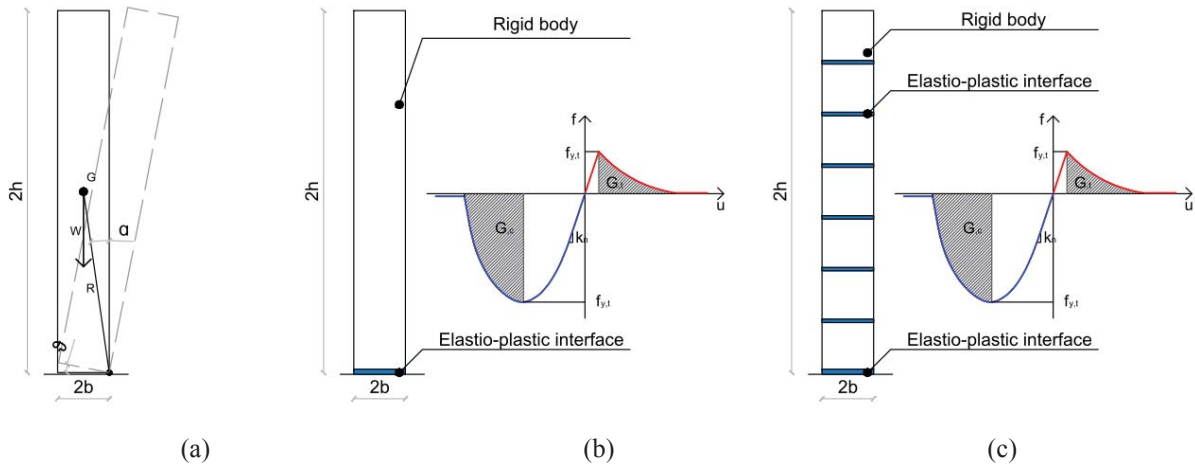


Figure 4: a) Rigid block model (RB), b) DMEM simplified model, c) DMEM refined model.

3.1 Free-vibration analyses

In this section, rectangular blocks subjected to two-side free-vibration rocking motions, activated imposing an initial displacement of the wall top section equal to the wall half-width ($b/2$), are analysed by the rigid block (RB), Figure 4a, and the DMEM model, Figure 4b and

Figure 4c. The analytical response of the RB is obtained by integrating Eq. (1) considering $\theta(0) = b/4$; $\dot{\theta}(0) = 0$. Two different parapet walls (PWs), characterized by different geometries and slenderness ratios (λ_w) and already numerically investigated in the literature [21], are considered.

For simplified DMEM models, two different values of coefficient of restitution are considered in the analyses, namely the analytical value (e_{an}) calculated by Eq. (4) and a reduced value of ($e=0.85$) consistent with experimental observations [31]. The normal stiffness of the DMEM interfaces (k_n) is evaluated by considering a reference value of masonry Young modulus $E_m=800$ MPa. The effective mass (m_{eff}) used to evaluate the lateral frequency (ω_L) is assumed equal to $4/3m$ in the case of the DMEM and equal to the mass activated at the first mode of vibration in the case of the DMEM refined model. The complete set of parameters characterising the DMEM simplified model is reported in Table 2 while, the characterisation of the DMEM refined model is reported in Table 3 where both the stiffness of the base interface ($k_{n,base}$) and inner interfaces connecting two contiguous macro-elements ($k_{n,base}$) are reported.

The time history of the top section of PW₁ and PW₂, obtained by the DMEM simplified model, are reported in Figure 5 and Figure 6, respectively. The results are compared with those obtained by RB solution. A satisfactory agreement is observed between the two models, in all the cases investigated, although the DMEM model tends to underestimate the peaks when compared to the RB model.

Wall	2h [m]	2b [m]	λ_w [-]	e_{an} [-]	k_n [N/m ³]	K_L [N/m]	ω_L [1/s]	Δ_y/Δ_u [-]	$\xi_{SDR}(e_{an})$ [-]	$\xi_{SDR}(e)$ [-]
PW1	4.2	0.6	0.143	0.97	3.8E+08	4.6E+06	14.98	0.086	0.011	0.057
					9.5E+08	1.1E+07	23.69	0.034	0.013	0.068
PW2	3.0	0.3	0.100	0.98	5.3E+08	1.6E+06	14.69	0.12	0.0048	0.053
					13.3E+08	3.9E+06	23.22	0.05	0.0058	0.063

Table 2: Details of the walls analysed by the simplified DMEM model.

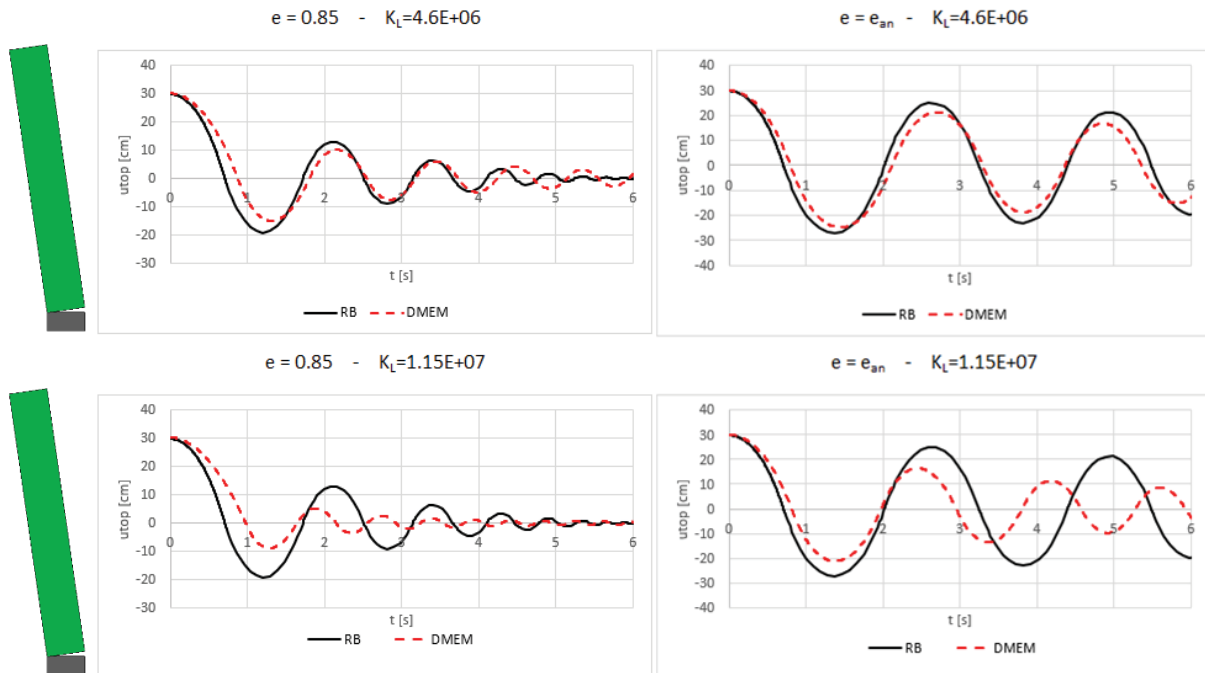


Figure 5: Free vibrations of the PW1 sample evaluated by the RB and simplified DMEM models.

Wall	2h [m]	2b [m]	λ_w [-]	m_{eff} [Ns ² /m]	$k_{n,base}$ [N/m ³]	$k_{n,inner}$ [N/m ³]	K_L [N/m]	ω_L [1/s]	Δ_y/Δ_u [-]	$\xi_{SDR}(e)$ [-]
PW1	4.2	0.6	0.143	20550.5 9850.5	5.3E+09	2.7E+09	1.2E+07	24.24 35.55	0.049	0.063
PW2	3.0	0.3	0.100	7339.45 3398.2	1.1E+10	5.3E+09	3.7E+06	22.67 33.32	0.063	0.060

Table 3: Details of the walls analysed by the refined DMEM model.

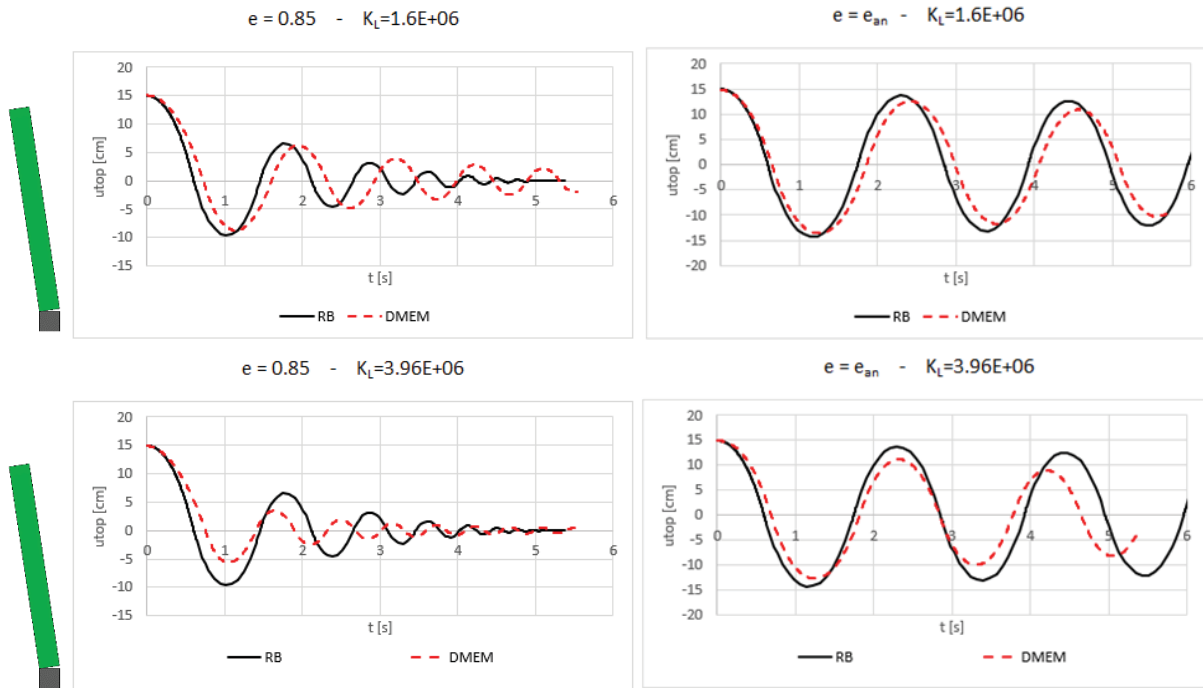


Figure 6: Free vibrations of the PW2 sample evaluated by the RB and simplified DMEM models.

The time history responses and the maximum deformation obtained by the DMEM refined model are reported in Figure 7 compared to the analytical solution of the rigid block model. The two models provide comparable results demonstrating that the equivalent viscous damping model adopted in the DMEM model is energetic consistent to the impact dissipation mechanism characterising the RB model. Finally, Figure 8 shows the hysteretic cycles of the DMEM models, expressed in terms of top displacement versus the wall base shear, superposed to the corresponding push-over curve. It can be observed that the dynamic responses show a significant deviation from the static curve due to the presence of the inertia and damping forces.

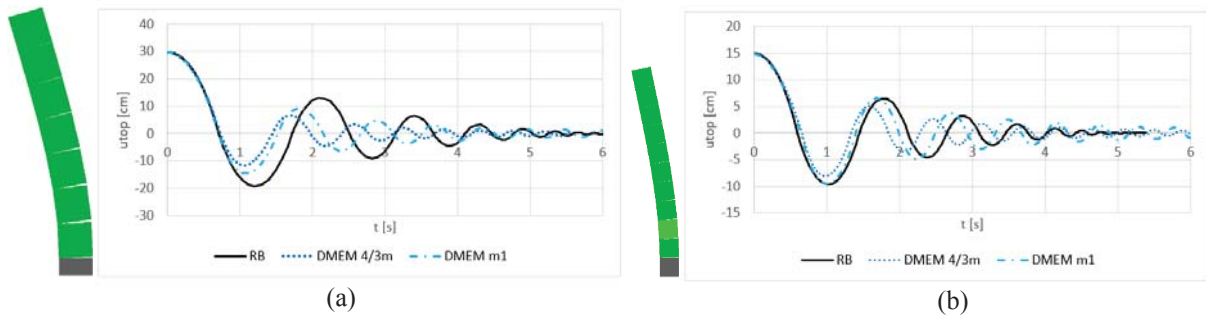


Figure 7: a) PW1 Refined DMEM, b) PW2 Refined DMEM.

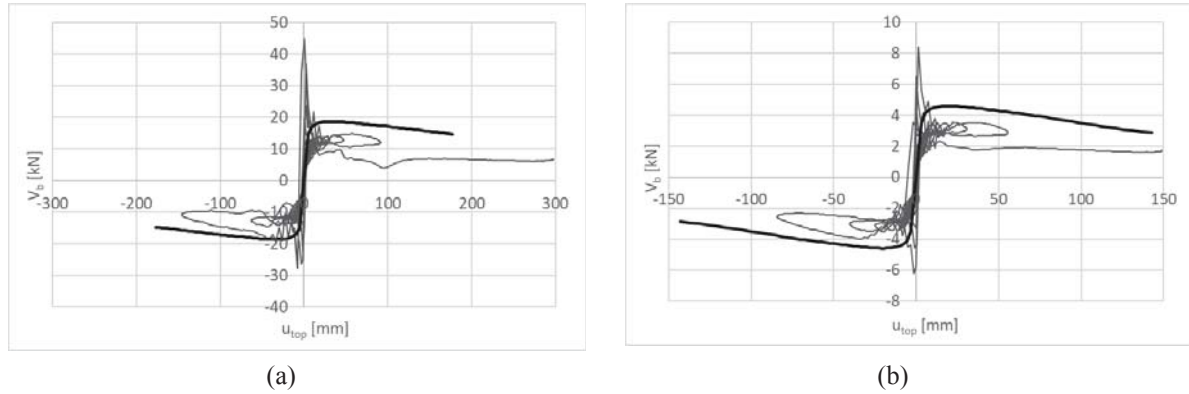


Figure 8: Pushover and dynamic hysteresis cycles a) PW1, b) PW2

3.2 Earthquake analyses

In this section, non-linear dynamic analysis under earthquake excitations are performed on a Vertical Spanning Walls (SPW) already experimentally and numerically investigated in the literature [32] [33]. The tested specimen was composed of regular tuff blocks, with self-weight 12.3 kN/m^3 , and lime-cementitious mortar. The wall was 3.48m height, 1.53m width and 0.25m thick. On the top section of the wall it was located a reinforced brick-work beam 0.27m height and 0.25m thick, characterised by a self-weight of 18 kN/m^3 . The beam was connected to the underlying masonry with 600 mm long connectors in steel reinforced grout (SRG). The horizontal displacements of the beam were constrained by a steel IPE200 beams, placed on top of lateral stiffened steel frames. Rubber cylinders were placed between the IPE200 and the specimen to permit the upward displacement and rotations of the top section of the wall.

The test layout comprised an additional load of 6 kN placed on the top of the reinforced-brick beam. The characteristics of the input signals are reported in Table 4. The specimen was numerical investigated by means of a 2D DEM model using the software UDEC (Itasca 2010) using different scale factors for the signals [32].

Earthquake information			Horizontal component			Vertical component		
Event	Record station	Or.	PGA [g]	PGV [mm/s]	PGD [mm]	PGA [g]	PGV [mm/s]	PGD [mm]
Irpinia 1980	BGI	E-W	0.18	344	117	0.10	154	74

Table 4: Input signal

The DMEM model is developed using 78 macro-elements corresponding to 546 DoFs. The boundary conditions on the top of the wall are simulated by inserting elastic stiff macro-elements whose mass density is evaluated to simulate the mass of the brick-wall beam plus the external load and restrained against the horizontal displacements. The analysis is performed in two stages, first a static analysis is conducted applying the gravity loads, then the dynamic analysis is performed assuming as initial condition the final configuration of the vertical analysis. The complete set of parameters characterising the DMEM models are reported in Table 5.

h [m]	b [m]	e_{an} [-]	k_n [N/mm ³]	K_L [N/m]	E [N/mm ²]	σ_t [N/mm ²]	G_t [N/mm]	m_{eff} [Ns ² /m]	ω_L [1/s]	Δ_y/Δ_u [-]	$\xi_{SDR}(e)$ [-]
3.48	1.53	0.85	4.9E+08	1.05E+06	294	0.001	0.01	1112.64	30.69	0.064	0.060

Table 5: Parameters characterizing the DMEM model

The results of the analyses are reported in Figure 9 in terms of time history of the point subject to maximum displacement which is located approximately at a height of 2.15m. The Different amplification factors are considered to scale the signal ($SF=1.25$; 1.5; 2.0). In Figure 9a the response of the wall to the signal scaled by 1.25 scale factor is shown. In the graph, the maximum displacement registered during the test are also reported. A very good agreement can be observed between the peak displacement predicted by the DMEM model and that observed experimentally. In Figure 9b the numerical responses to the different levels of amplification of the signal are reported. It is evident how the DMEM model is able to catch the period elongation of the system due to the opening of the tensile cracks and the activation of the rocking mechanism.

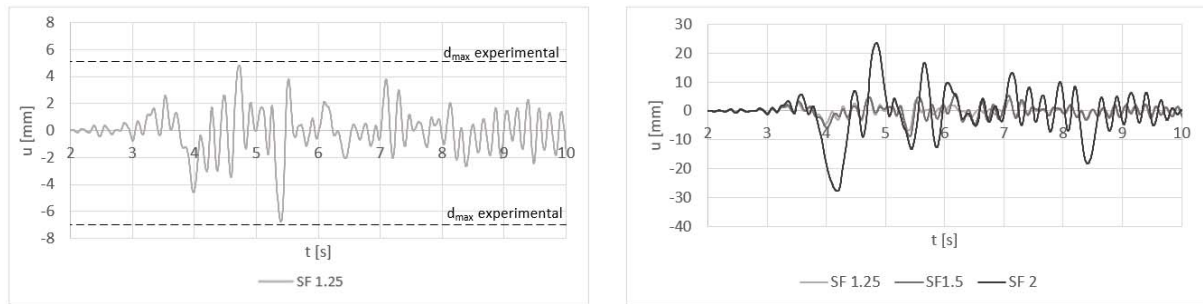


Figure 9: Time history DMEM model

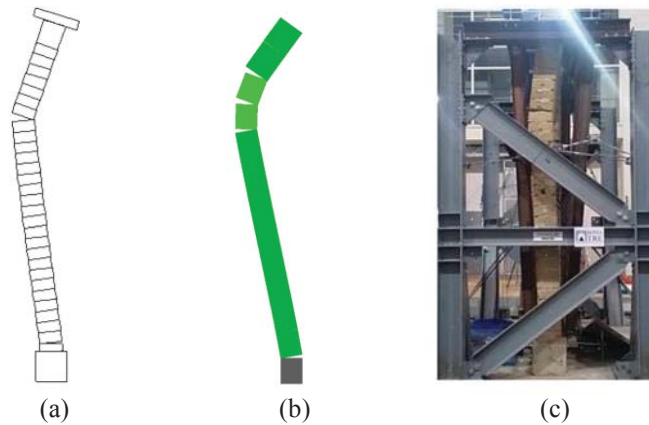


Figure 10: Failure mechanism estimated by: a) DEM model [32], b) DMEM model, c) experimental [32]

4 CONCLUSIONS

This paper applies the DMEM model to simulate the rocking behaviour of unreinforced masonry walls. The results of the DMEM model are compared with the exact solution consistent to the rigid block theory as well as to an experimental campaign for which other numerical strategies have already been applied. The effects of the energy dissipation and masonry deformability are investigated in the analysis. A stiffness-proportional viscous damping model to be employed in the DMEM analyses has been calibrated and validated. The results demonstrate that the DMEM can be adopted to accurately predict the dynamic response of monumental structures with a limited computational burden showing the capability of the method to be employed for the simulation of large historical masonry monumental structures, being able to simulate both the in-plane and out-of-plane response of masonry walls.

REFERENCES

- [1] M. Aslam, A. M. ASCE, W. G. Godden, M. ASCE and T. Scalise, Earthquake rocking response of rigid bodies, 1980.
- [2] J. Heyman, "The stone Skeleton," *International Journal of Solids and Structures*, vol. 2(2), pp. 249-256, 1966.
- [3] D. D. d. F. G. M. L. S. M. G. Sorrentino L., "Review of Out-of-Plane Seismic Assessment Techniques Applied To Existing Masonry Buildings," *International Journal of Architectural Heritage*, vol. 11, pp. 2-21, 2016.
- [4] M. Andreini, A. De Falco, L. Giresini and M. Sassu, "Collapse of the historic city walls of Pistoia (Italy): causes and possible interventions.," *Adv. in Civil Structures*, no. 352, pp. 1389-1392.
- [5] K. Doherty, M. C. Griffith, N. Lam and J. Wilson, "Displacement-based seismic analysis for out-of-plane bending of unreinforced masonry walls," *Earthquake Engineering and Structural Dynamics*, vol. 31, pp. 833-850, 2002.
- [6] G. W. Housner, "The behavior of inverted pendulum structures during earthquakes," *Bulletin of the Seismological Society of America*, vol. 53, no. 2, pp. 403-401, 1963.
- [7] T. M. Ferreira, A. A. Costa and A. Costa, "Analysis of the Out-of-Plane Seismic Behaviour of Unreinforced Masonry: A Literature Review," *International Journal of Architectural Heritage*, vol. 9, pp. 949-972, 2015.
- [8] S. Caddemi, I. Calì, F. Cannizzaro and B. Pantò, "New Frontiers on seismic Modeling of masonry Structures," *Frontiers in Built Environment*, pp. 3-39, 2017.
- [9] I. Calì, M. Marletta and B. Pantò, "A new discrete element model for the evaluation of the seismic behavior of unreinforced masonry buildings," *Engineering Structures*, vol. 40, pp. 237-338, 2012.
- [10] B. Pantò, F. Cannizzaro, I. Calì and P. B. Lourenço, "Numerical and experimental validation of a 3D macro-model for the in-plane and the out-of-plane behavior of unreinforced masonry walls," *International Journal of Architectural Heritage*, 2017.
- [11] C. Chàcara, P. B. Lourenço, B. Pantò, F. Cannizzaro and I. Calì, "Parametric numerical studies on the dynamic response of unreinforced masonry structures," in *Structural Analysis of Historical Constructions: Anamnesis, Diagnosis, Therapy, Controls*, Leuven, Belgium, 2016, 13-15 Settembre.
- [12] C. J. C. Espinoza, *Macro-Element Nonlinear Dynamic Analysis for the Assessment of the Seismic Vulnerability of Masonry Structures*, PhD Thesis, Universidade do Minho, Escola de Engenharia, 2018.
- [13] C. Chàcara, F. Cannizzaro, B. Pantò, I. Calì and P. B. Lourenço, "Assessment of the dynamic response of unreinforced masonry structures using a macro-element modelling approach," *Earthquake Engineering and Structural Dynamics*, vol. 47, pp. 2426-2446, 2018.
- [14] F. Cannizzaro and P. B. Lourenço, "Simulation of shake table tests on out-of-plane masonry buildings," *International Journal of Architectural Heritage*, vol. 11(1), pp. 125-142, 2017.
- [15] A. N. Kounadis, "New findings in the rocking instability of one and two rigid block system under ground motion," *Meccanica*, vol. 50, pp. 2219-2238, 2015.

- [16] M. Priestley, R. Evison and A. Carr, "Seismic Response of Structures free to rock on their foundation," *Bulletin of New Zealand Society of Earthquake Engineering*, vol. 11, pp. 141-150, 1978.
- [17] A. K. C. J. P. C. Y. Yim, *Rocking response over Rigid blocks to earthquakes*, Berkley, California: University of California, 1980.
- [18] A. N. Kounadis, "Parametric study in rocking instability of a rigid block under harmonic ground pulse: A unified approach," *Soil Dynamics and Earthquake Engineering*, pp. 125-143, 2013.
- [19] Y. Ishiyama, "Motions of rigid bodies and criteria for overturning by earthquake excitations," in *3rd South Pacific Regional Conference on Earthquake Engineering*, Wellington, 1983.
- [20] N. Makris and D. Konstantinidis, "The rocking spectrum and the limitations of practical design methodologies," *Earthquake Engineering and structural dynamics*, vol. 32, pp. 265-289, 2003.
- [21] U. Tomasetti, F. Graziotti, L. Sorrentino and A. Penna, "Modelling rocking response via equivalent viscous damping," *Earthquake Engineering and Structural Dynamics*, vol. 48, pp. 1277-1296, 2019.
- [22] M. C. Griffith, G. Magenes, G. Melis and L. Picchi, "Evaluation of Out-of-Plane Stability of Unreinforced Masonry Walls Subjected to Seismic Excitation," *Journal of Earthquake Engineering*, vol. 7, pp. 141-169, 2003.
- [23] N. Lam, M. Griffith, J. Wilson and K. Doherty, "Time-history analysis of URM walls in out-of-plane flexure," *Eng Struct.*, vol. 25, no. 6, pp. 743-754, 2003.
- [24] U. Tomasetti, F. Graziotti, A. Penna and G. Magenes, "Modelling one-way out-of-plane response of single-leaf and cavity walls," *Eng Struct.*, vol. 167, pp. 241-255, 2018.
- [25] S. Lagomarsino, "Seismic assessment of rocking masonry structures," *Bull Earthquake Engineering*, vol. 13, pp. 97-128, 2015.
- [26] O. Al Shawa, G. de Felice, A. Mauro and L. Sorrentino, "Out-of-plane seismic behavior of rocking masonry walls," *Earthquake Engineering and Structural dynamics*, vol. 41, pp. 949-968, 2012.
- [27] R. Giannini and R. Masiani, "Risposta in frequenza del blocco rigido: stabilità delle soluzioni," in *Proceedings of the 10th Italian National Conference of Theoretical & Applied Mechanics*, Pisa, Italy, 1990.
- [28] M. J. DeJong and E. G. Dimitrakopoulos, "Dynamically equivalent rocking structures," *Earthquake Engineering and Structural Dynamics*, vol. 43, pp. 1543-1563, 2014.
- [29] I. Calì, F. Cannizzaro and M. Marletta, "A discrete element for modelling masonry vaults," *Adv. Mater. Res.*, pp. 133-134;447-452, 2010.
- [30] G. S. s.r.l., "*HiStrA (Historical Structure Analysis)*", Catania, Italy, 2015.
- [31] A. A. Costa, A. Arede, A. Penna and A. Costa, "Experimental Evaluation of the coefficient of restitution of rocking stone masonry facades," in *15th International Brick and Block masonry conference*, Florianopolis, Brasil, 2012.
- [32] P. Meriggi, S. De Santis, G. de Felice and F. Gobbin, "Distinct Element Modelling of Masonry Walls under Out of Plane Seismic Loading," *International Journal of Architextural Heritage*, 2019.

- [33] D. C. G. d. G. F. D. F. E. R. I. De Santis S., "Seismic out-of-plane vertical bending behavior of masonry walls reinforced with textile reinforced mortar," in *10th International Masonry Conference*, Milano, Italy, 2018.
- [34] M. Tomazevic, The computer program POR, Ljubljana, Slovenia, 1978.
- [35] T. M., *Earthquake-Resistant Design of Masonry Buildings*, 1st ed., vol. 1, IMPERIAL COLLEGE PRESS, 1999.
- [36] G. Magenes and G. S. Calvi, "In-plane seismic response of brick masonry walls," *Earthquake Engineering and Structural Dynamics*, vol. 26, pp. 1091-112, 1997.
- [37] G. Magenes and A. Della Fontana, "Simplified non-linear seismic analysis of masonry buildings," 1998.
- [38] S. Lagomarsino, A. Penna, A. Galasco and S. Cattari, "TREMURI program: An equivalent frame model for the nonlinear seismic analysis of masonry buildings," *Engineering structure*, vol. 56, pp. 1787-99, 2013.
- [39] A. Tzmatzis and P. Asteris, "Finite Element analysis of masonry structures: Part I-Review of previous work," 2003.
- [40] P. Roca, M. Cervera, G. Gariup and L. Pelà, "Structural analysis of masonry historical constructions. Classical and advanced approaches," *Arch Comput Methods Eng*, 2010.
- [41] P. A. Cundall, "Formulation of a three dimensional distinct element model - Part I: A scheme to detect and represent contacts in a system composed of many polyhedral blocks," *International Journal of Rock Mechanism and Mining Sciences*, vol. 25, pp. 107-116, 1988.
- [42] J. V. Lemos, "Discrete Element Modelling of Masonry Structures," *International Journal of Architectural Heritage*, vol. 1, pp. 190-213, 2007.
- [43] C. Casapulla, L. Giresini, M. Sassu and P. B. Lourenço, "Rocking and kinematics approaches for masonry walls: state of art and recent developments," *Buildings*, 2017.
- [44] R. D. Hart, P. A. Cundall and J. V. Lemos, "Formulation of a three-dimensional distinct element model - Part II: Mechanical calculations," *International Journal of Rock Mechanism and Mining Sciences*, vol. 25, pp. 117-125, 1988.
- [45] C.-S. Yim, A. K. Chopra and J. Penzien, "Rocking response of rigid blocks to earthquakes," National technical information service, Berkeley, California, 1980.
- [46] M. Giaretton, J. Ingham and D. Dizhur, "Dynamic testing of as-built clay brick unreinforced masonry parapets," *Engineering Structures*, vol. 127, pp. 676-685, 2016.

VISUAL PROGRAMMING FOR MACRO-BLOCK ANALYSIS OF MULTI-STOREY MASONRY BUILDINGS

Elham Mousavian*, Luca U. Argiento, Claudia Casapulla

University of Napoli Federico II, Department of Structures for Engineering and Architecture,
Via Forno vecchio, 36, 80134, Napoli, Italy
 {elham.mousavian,lucaumberto.argiento,casapulla}@unina.it

Abstract

This paper presents a Grasshopper (GH) plugin to evaluate the admissible out-of-plane mechanisms in multi-storey masonry buildings and visually display the possible locations for each admissible mechanism at which the failure can happen. Adopting the macro-block modelling approach, GH components are developed considering a limited number of geometric and construction parameters as inputs that allow the possible mechanisms. These include the quality of the connections between the building walls, applied strengthening devices, and the examined building location within an urban block. Modelling the building, all the potential mechanisms and their possible locations are demonstrated in a user-friendly and readable way. The plugin can finally compute the actual mechanism and its optimised geometry as well as the actual building out-of-plane capacity adopting the limit analysis method.

Keywords: 3D Macro-Block Model, Out-of-Plane Behaviour, Limit Analysis, Visual Programming, Grasshopper Plugin.

1. INTRODUCTION

Out-of-plane (OOP) mechanisms can take place in masonry buildings without a box-type behaviour, especially in the peripheral walls of existing buildings, even when they are under low intensities of ground motion [1]. The most recurrent ones are related to simple and complex rocking mechanisms, as well as to flexure mechanisms, as identified and classified by systematic surveys of the typical seismic damages and crack patterns in masonry buildings [2-5]. Post-seismic surveys [2, 6] and experimental tests [7] have also identified particular conditions governing the classified OOP mechanisms, including: the quality of the connections between the orthogonal walls as well as the walls and horizontal diaphragms, the roof typology, the positions of the openings and of the building within an urban block. The seismic assessment of historical masonry buildings with respect to OOP mechanisms cannot disregard these aspects, especially when non-linear static and dynamic analysis are employed [8-10] and strengthening interventions [11-13] or dissipative devices are to be designed [14].

Within the simplified approaches to investigate the OOP failure modes in masonry buildings, the kinematic method of limit analysis is one of the most popular and reliable in the literature [15, 16]. According to it, local mechanisms can be considered as kinematic chains of masonry portions, regarded as rigid macro or micro-block assemblages, interacting through interface elements. In particular, the macro-block model assumes that the general failure involves a number of cracks, which separate the structure into a few rigid macro-blocks, and all the possible relative motions among units (rocking and/or sliding) are concentrated along these cracks [5, 17].

However, despite several advantages of the macro-block modelling approach, like being computationally efficient, it normally faces a considerable level of uncertainties, since the given input data for the analysis are simplified into a limited number of parameters. These aspects are well addressed in [2], where the FaMIVE (Failure Mechanism Identification and Vulnerability Evaluation) procedure is introduced to evaluate the most recurrent failure modes in aggregate buildings and to find the optimal option among them. When the advanced macro-block model developed in [5] is adopted, the admissibility of possible mechanisms in aggregate buildings also depends on the involved portions of walls at each storey and on the height ratios between the main building and the adjacent ones, in addition to the position of strengthening devices and the wall connections quality considered by FaMIVE.

Determining the admissible and inadmissible mechanisms for each storey/side of a building is though not very handy and readable using the text-based representations proposed in [2] and [5]. Instead, their graphical visualization would help the evaluator to better assess the reliability of the final solution as well as the other possible alternatives.

To this aim, taking advantage of the 3D visualization [18, 19], this paper presents a novel graphical approach based on the development of a Rhino Grasshopper (GH) plugin. This allows to parametrically model multi-storey masonry buildings and visually check all the potential OOP failure modes and their positions in real time, evaluated according to the work of Casapulla et al. [5]. Using the powerful optimization toolbox, the plugin can also compute the collapse load factors related to each possible mechanism at each storey and visualize the crack pattern of the related OOP mechanism and specifically performs the most likely collapse mechanism configuration and its related (optimal) load factor.

Adopting the concept of visual programming, the developed plugin provides a fast and user-friendly tool for: 1) parametric modelling; 2) visual analysis of all the possible mechanisms in a multi-storey masonry building; 3) computing the minimum load factor among all the possible mechanisms and visualize the related crack pattern; 4) easily linking the modelled building and mechanisms to other analytical software implementations, e.g.,

macro or micro-model finite element [20] and discrete element [21] approaches for further analyses.

In the following, an overview on the typical OOP failure mechanisms and the evaluation process to find the admissible mechanisms at each storey of a building is presented, with an application to the corner failure as an example. Then, the computational implementation of the GH plugin is presented to visually check the admissible and optimized mechanisms in real time.

2. MODELLING THE OOP FAILURE MODES

The adopted macro-block model [5] is a 3D portion of walls in a multi-storey masonry building that remains undamaged under the seismic motion and is based on the assumption that the constituent micro-blocks (units) have infinite compressive, tensile and shear strengths. Walls are considered to be single-leaf with the modular masonry units at each storey arranged with the running bond pattern. The contact interfaces between the units have no tensile and finite frictional resistance governed by the Coulomb failure criterion. A horizontal static action as a percentage of dead loads (by means of a load factor) is applied to the centre of mass of each moving macro-block, in addition to all the other external loadings.

Figure 1 shows some of the most recurrent OOP mechanisms for a façade wall of a multi-storey building, that are the rocking (M_A , M_B and M_C) and flexural (M_D and M_E) failures. The onset of each mechanism is represented by advanced formulations considering frictional resistances, which are obtained by the linear kinematic approach of limit analysis, as elaborated in [5].

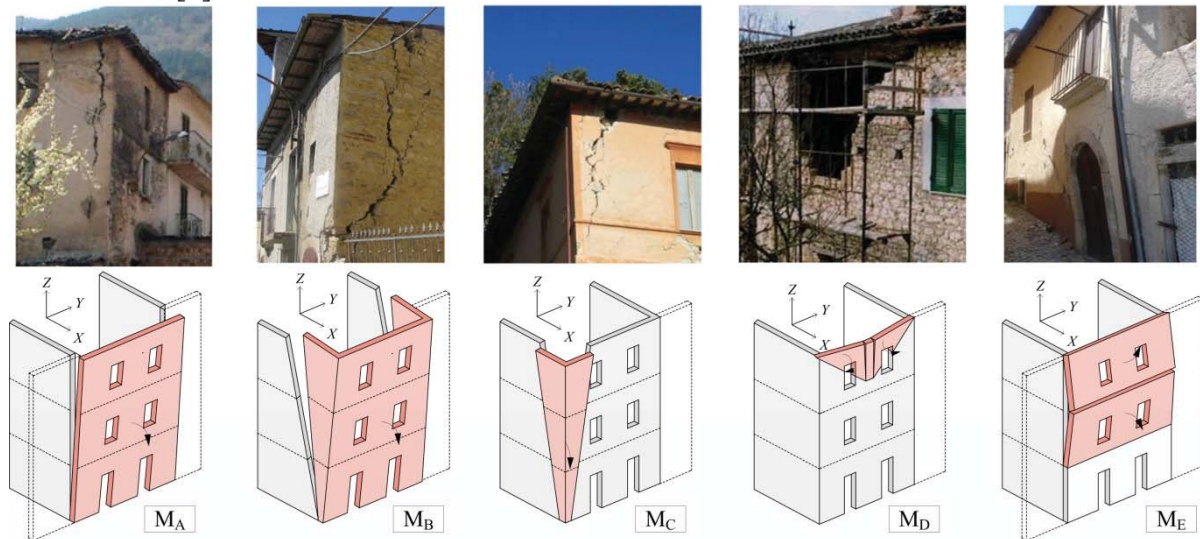


Figure 1: Simple (M_A) and compound (M_B) rocking walls, rocking corner (M_C). Horizontal (M_D) and vertical (M_E) flexural OOP mechanisms.

2.1 Parameters governing the admissibility of OOP failure mechanisms

The admissibility of the failure mechanisms shown in Figure 1 is strictly related to the specific features of the aggregate buildings under study, as highlighted by previous works [2, 3]. The main geometric and construction parameters herein considered are the following ones:

1. Quality of the connection between the façade and sidewalls: this structural feature strongly affects the mechanical integrity of the main building. Poor connection quality between these orthogonal walls usually results in generating the failure modes M_A and

M_E . On the other hand, mechanisms M_B and M_C can occur in the presence of strong connections, while failure mode M_D is not affected by this feature.

2. Position of the building within the urban block (Figure 2): it is herein assumed that the position of the building can influence the failure mechanisms M_C and M_D . Besides, the height of the main building with respect to the adjacent buildings is another important aspect, which has not been taken into account in [2] and [3]. In fact, when, e.g., the building is located in a middle position (P_M and P_S cases), mechanism M_C can only occur if the main building is higher than the adjacent ones, while the horizontal arch failure (mechanism M_D) cannot be triggered because the lateral restraints exerted by the adjacent buildings would prevent any lateral displacements.
3. Strengthening devices: Figure 3 shows six configurations of strengthening devices including ring beams and tie-rods. The presence of strengthening devices influences the feasibility of all the mechanisms considered in Figure 1. In fact, all mechanisms can occur in the absence of strengthening devices, except the failure mode M_E that requires their presence to onset. Since the corner failure in the walls below the tie-rods locations are usually prevented, in the cases of implementing S_{RB} , S_{T3} , and S_{T2} , no mechanism is possible beneath them.

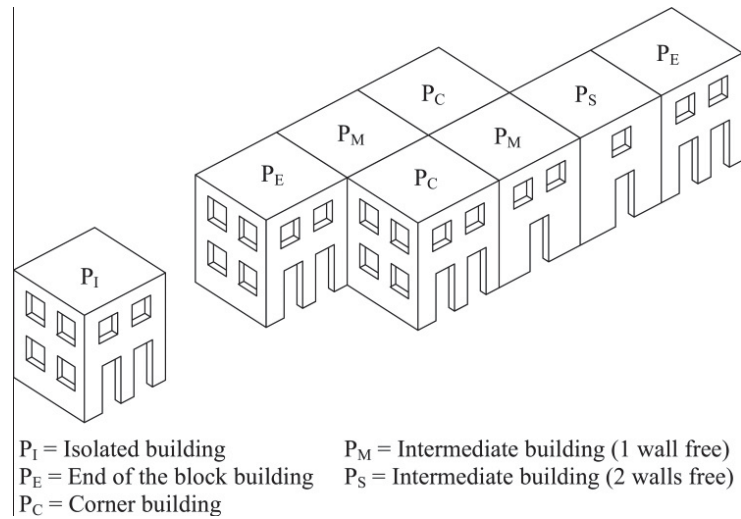


Figure 2: Position of the building within an urban block.

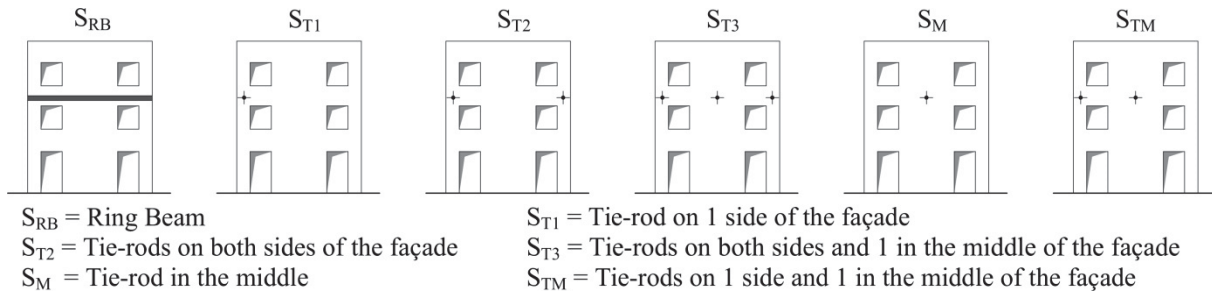


Figure 3: Simple layouts of different configurations of strengthening devices.

Each of these three parameters is linked to each mechanism that may occur at a generic storey of a multi-storey building, as displayed in Table 1. If a mechanism is feasible, it will be identified as an admissible mechanism (A), while inadmissible (I) in the opposite case. In some cases, the admissibility of a mechanism depends on the conditions that vary from storey

to storey, e.g., in the case of different heights of the adjacent buildings it is related to the number of free storeys (D1), while in the presence of strengthening devices (D2) it depends on the highest storey where they are placed.

Obviously, for a given building, the table should be made explicit for each storey, with the admissibility of each possible mechanism depending on the storey properties. Also, to have a more comprehensive evaluation, the table must be extended to each side of the façade wall when, e.g., the storeys number of the adjacent buildings on the right and left sides are different or in the case of having asymmetric strengthening devices (S_{T1} and S_{TM}) applications. These aspects would make the table relatively complex and reduce its readability.

To shed more light on this evaluation process, mechanism M_C (corner failure) is herein chosen as a reference example and how its admissibility is evaluated for a given building is elaborated in the next section.

Mechanism	Connection with sidewalls		Position of the building within the urban block		Strengthening devices			
	Strong	Weak/Absent	$P_I - P_E - P_C$	$P_M - P_S$	NO	$S_{RB} - S_{T3} - S_{TM}$	$S_{T1} - S_{T2}$	S_M
M_A	I	A	A	A	A	D2	D2	D2
M_B	A	I	A	A	A	D2	D2	D2
M_C	A	I	A	D1	A	D2	D2	A
M_D	A	A	A	D1	A	D2	A	D2
M_E	I	A	A	A	I	D2	D2	D2

A: admissible possible mechanism

D1: mechanism occurrence depending on the number of stories of the adjacent buildings

D2: mechanism occurrence depending on the highest storey with the strengthening devices

Table 1: Relation between the construction parameters of a building and the feasibility of the mechanisms.

2.2 Conditions governing the corner failure

The failure mechanism of a free corner (Mechanism M_C in Figure 1) is quite common in masonry buildings isolated, positioned at the end of an urban block, or in their free higher storeys. It is characterised by the rocking-sliding of a rigid wedge-shaped macro-block around a hinge point. The corner failure in a masonry building generally involves well-connected masonry walls under orthogonal forces, whose geometry is not known a priori.

Figure 4 shows a 4-storey façade between two adjacent buildings (case P_S) with two and one stories on the left and right sides, respectively, having the S_{T1} configuration of strengthening devices at the first floor (Storey no. 4 on the right side of the building). Table 2 shows the possibility of occurrence of mechanism M_C at the top-most (Storey no. 1) to the lowest level (Storey no. 4).

As shown in the table, the admissibility of each mechanism is checked (A for being admissible and I for being inadmissible) regarding the connection quality, building position, and the applied strengthening devices separately and, finally, the overall admissibility check is executed for each storey. First of all, according to the first column of the table, mechanism M_C is a possible failure mode for all storeys since the connections are considered strong enough in both right and left sides of the façade wall. On the other hand, since the adjacent buildings on both sides are shorter than the main building, the corner failure is possible on both sides, at the free storeys only. However, since the adjacent buildings have different heights, the corner failure may have different configurations in either the left or right sides of the building. Similar conditions can occur regarding the applied strengthening device, which

is also asymmetric. The last column of the table shows the overall admissibility check for the corner failures at each storey of the building.

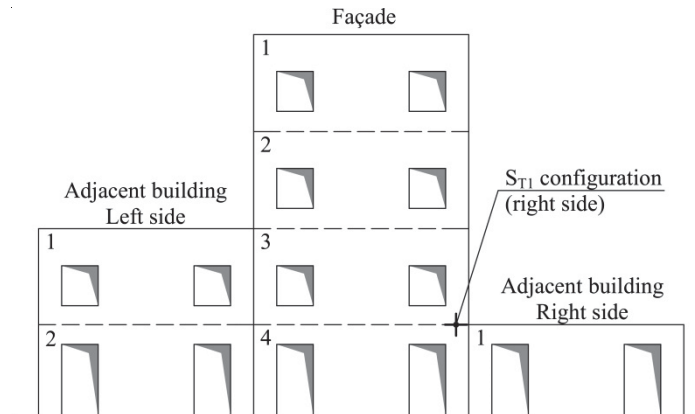


Figure 4: Example of the main building position within an urban block.

Storey	Connection with sidewalls = Strong		Position of the building within the block = P_S		Strengthening devices Devices = S_{T1} (right side-storey 1)		Final assessment	
	Left side	Right side	Left side	Right side	Left side	Right side	Left side	Right side
1	A	A	A	A	A	A	A	A
2	A	A	A	A	A	A	A	A
3	A	A	I	A	A	A	I	A
4	A	A	I	I	A	I	I	I

A: admissible mechanism
I: inadmissible mechanism

Table 2: The possibility of occurrence of mechanism M_C for the 4-storey building.

To achieve a comprehensive admissibility evaluation, the same procedure should be developed for all the other mechanisms and the admissibility results gathered all together, which would provide very large tables, even difficult to read. Adding a visual approach would, instead, overcome these difficulties and allow a more user-friendly evaluation.

The following section presents the GH plugin that has been developed to firstly visualise all the possible OOP mechanisms and their locations for a multi-storey building and then to find the actual load factor and the related geometry of the corner failure, used as the reference example.

3. COMPUTATIONAL IMPLEMENTATION

A GH plugin has been developed to visually and parametrically demonstrate the potential mechanisms by which a multi-storey masonry building surrounded by adjacent buildings might fail and to compute the actual (optimal) failure mechanism for the building.

The GH plugin has three main functions:

- It enables the user to model the main and adjacent buildings by assigning the number of storeys and the related height. The main building is modelled assigning the length, height, and thickness of the façade and sidewalls, as well as choosing the configuration

and position of the strengthening devices. The user can parametrically change the input values and observe the updated model in real time.

- Given these geometric inputs, the plugin displays all the potential failure modes (among the selected six mechanisms) that are possible for the model and demonstrates all the possible locations at which the model might fail.
- Given a set of mechanical and external load information, the plugin computes and demonstrates the optimal geometry of the actual failure mechanism and the related load factor.

In the following, these three functionalities are described in detail.

3.1 Modelling

The plugin extends the GH environment, a visual programming add-on for Rhinoceros 3D. To develop the plugin, C# language has been used. The first developed component of the plugin enables the user to visualize the examined buildings and, through parametric change of the inputs, simply observe the updated model in real time. Figure 5 demonstrates all the inputs necessary to construct the main and adjacent buildings. The inputs can be parametrically changed by the user.

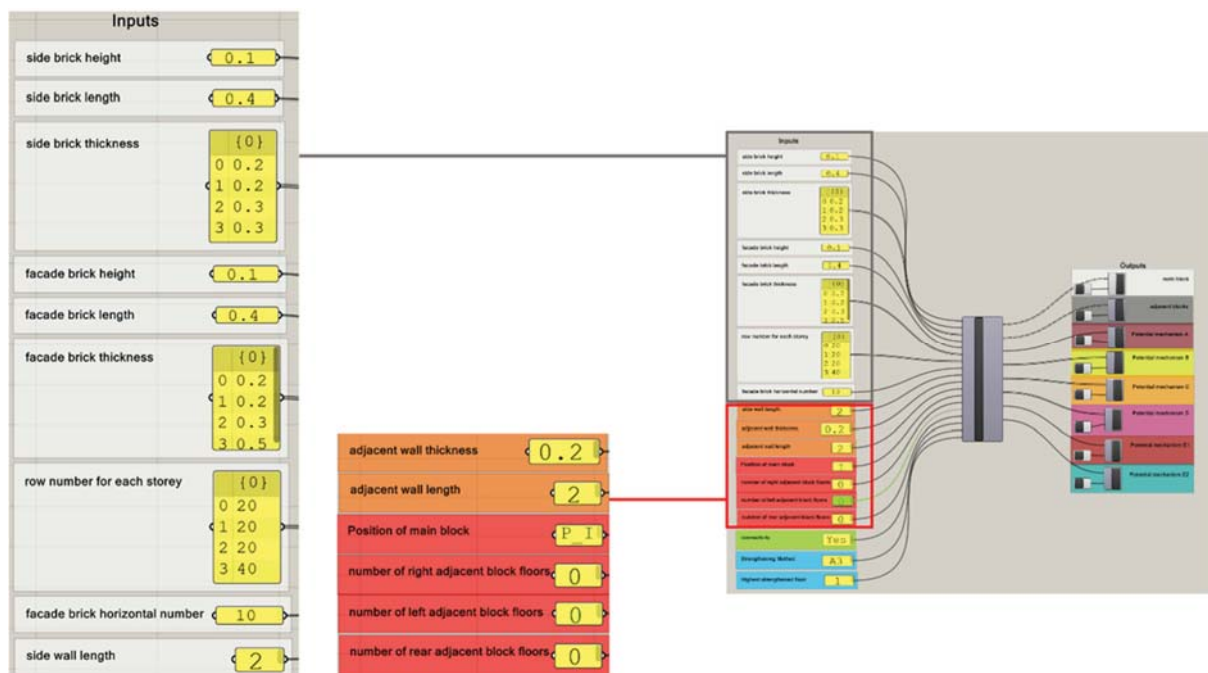


Figure 5. Masonry building modelling component and its inputs.

As examples, Figure 6 illustrates different models developed by different inputs, regarding different storey numbers and heights for the main building as well as different façades, sidewalls lengths and thicknesses. Besides, Figure 7 displays different storey numbers and lengths of the adjacent buildings.

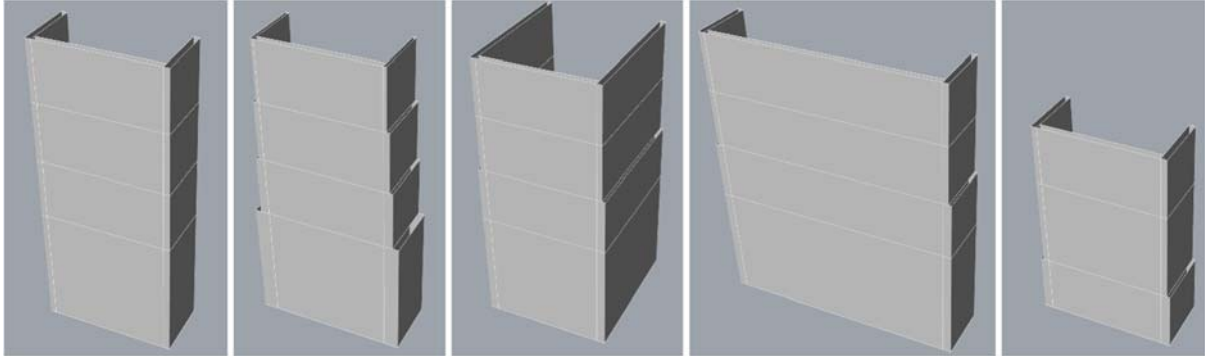


Figure 6. Parametric change of the geometric inputs of the main building.

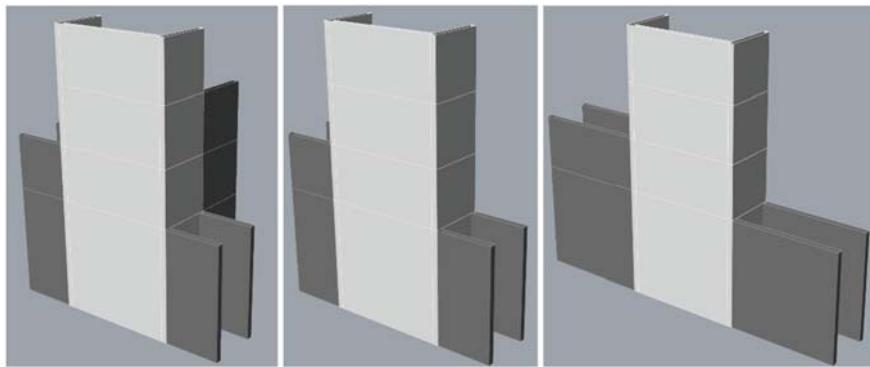


Figure 7. Parametric change of the geometric inputs of the adjacent buildings.

3.2 Potential mechanism visualization

Taking advantage of the 3D visualization in GH, the approach elaborated in Section 2 has been adopted to develop a GH component to demonstrate all the possible mechanisms and the locations at which a specific potential failure can occur. Figure 8 shows all the feasible mechanisms and locations among those gathered in Figure 1 and related to the example in Figure 4.

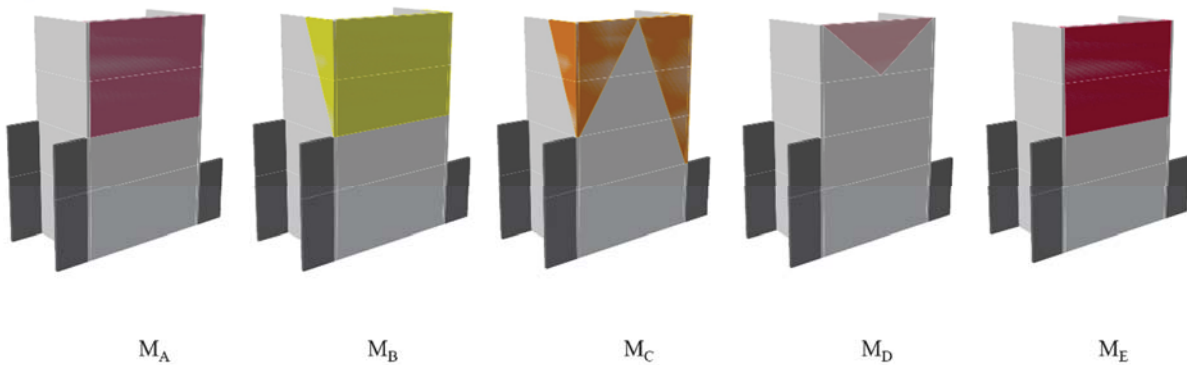


Figure 8. Different types of potential mechanisms along with all the locations at which the failure is possible.

In particular for the corner failure, Figure 9 visually represents the data reported in Table 2, i.e., all the potential mechanisms that can occur for the main façade presented in Figure 4 and all the possible locations to form a hinge (blue dots) as well as all the possible crack inclinations are visually presented. It is worth highlighting that the crack lines in dry-joint masonry walls have the maximum inclination given by the staggering ratio of the masonry

units [9]. As can be observed, the readability of the potential failure mechanisms is considerably improved if compared to the data in Table 2.

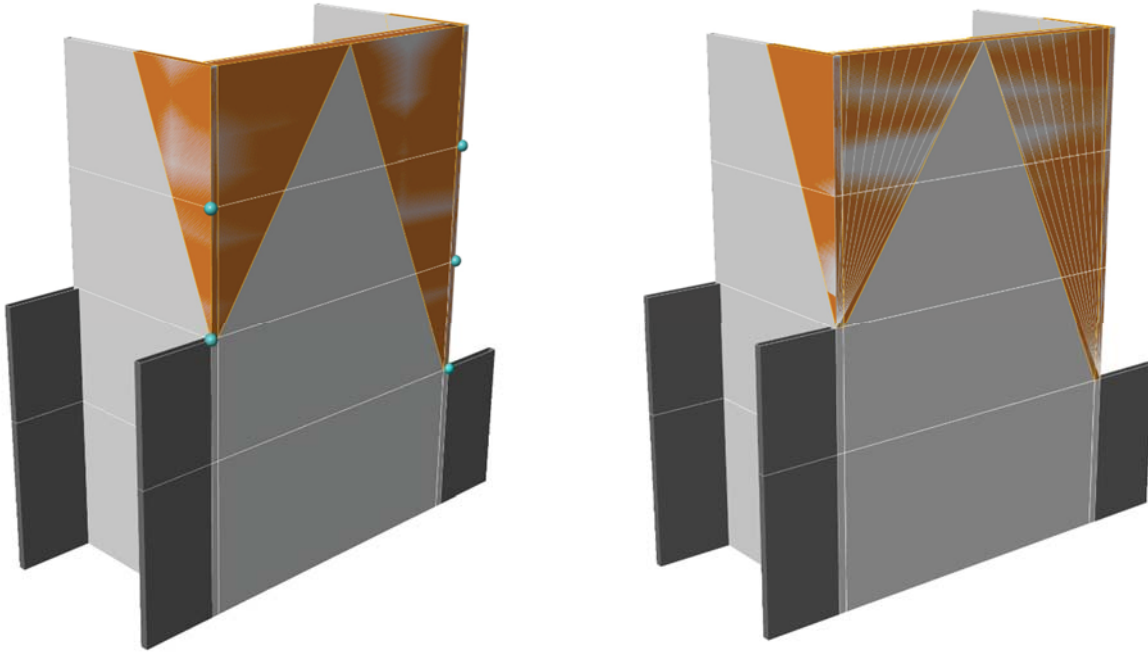


Figure 9. Visualizing all the possible locations for the hinges (blue dots) and crack inclination of mechanism M_C .

3.3. Actual mechanism visualization

The plugin can also compute the actual load factor and find the related mechanism shape through managing specific geometric parameters by which the mechanism can be modelled. For example, mechanism M_C can simply be modelled only by finding the hinge position and the crack inclinations on the façade and sidewalls. The optimization formulations, developed in [5] using Eqs. (10) and (11) of that paper, have been adopted in this work for the assessment of the corner failure. In particular, the geometric variables of the mechanism are the inclinations of the two crack lines for the façade and sidewalls, defining the wedge at each storey where the hinge is placed.

The optimization is executed using MATLAB as the back end. Given the geometric inputs as well as the external loads and the mechanical properties, the developed GH component computes the actual load factor and demonstrates the optimised failure mechanism. For example, Figure 10 demonstrates the actual mechanism M_C for the building of Figure 4 with its detailed dimensions. As shown in the figure, the expected load factors for the left and right sides of the wall are 0.295 and 0.282, respectively, while the hinges are formed respectively at the second and first storeys (from the bottom to the top). However, the crack inclinations on the façade wall in both mechanisms are both equal to 26° and similarly the crack inclinations on both sidewalls are 25° .

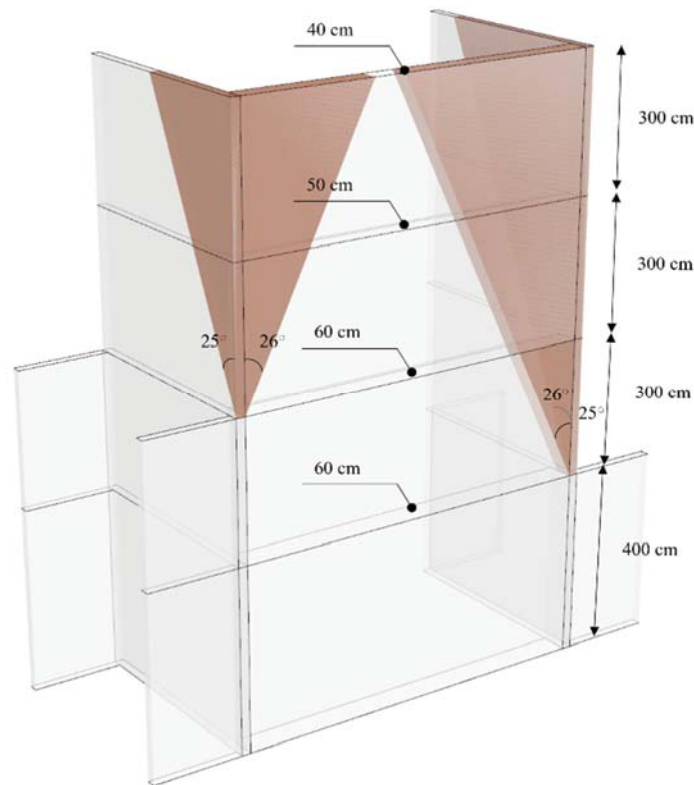


Figure 10. Crack pattern of the corner failures on both sides of the main building.


4. CONCLUSIONS

This work deals with the graphic visualization of the seismic vulnerability of historical masonry buildings, isolated or in aggregate, with respect to local failure mechanisms. The mechanical model is based on the kinematic approach of limit analysis developed in [5]. A GH plugin has been developed to parametrically model the main building and visualise all the possible OOP mechanisms and their potential locations, based on the adopted macro-block modelling approach. The plugin has been developed using C# language.

The visual output data for the potential mechanisms have been compared to similar tables existing in the literature, showing the readability improvements of the visual outcomes comparing to the tables. The plugin can also compute the optimised mechanism and visualize its actual geometry. MATLAB has been used to perform the optimization tasks.

In future works other types of collapse mechanisms will be introduced together with strengthening devices, whether made of traditional or innovative materials. The final goal is to develop a digital framework able to forecast and verify the seismic capacity of the most recurrent local mechanisms, both on the urban scale and building scale.

ACKNOWLEDGMENTS

 This project has received funding from the European Union's Horizon 2020 research and innovation programme under the Marie Skłodowska-Curie Grant Agreement No. 791235.

REFERENCES

- [1] M.C. Griffith, G. Magenes, G. Melis, L. Picchi, Evaluation of out-of-plane stability of unreinforced masonry walls subjected to seismic excitation. *Journal of Earthquake Engineering*, **7**, 141-169, 2003.
- [2] E. Speranza, *An integrated method for the assessment of the seismic vulnerability of historic buildings*. Ph.D. Thesis, University of Bath (UK), 2003.
- [3] D. D'Ayala, E. Speranza, Definition of collapse mechanisms and seismic vulnerability of historic masonry buildings. *Earthquake Spectra*, **19**, 479-509, 2003.
- [4] L. Sorrentino, D. D'Ayala, G. de Felice, M.C. Griffith, S. Lagomarsino, G. Magenes, Review of out-of-plane seismic assessment techniques applied to existing masonry buildings. *International Journal of Architectural Heritage*, **11(1)**, 2-21, 2016.
- [5] C. Casapulla, L.U. Argiento, A. Maione, E. Speranza, Upgraded formulations for the onset of local mechanisms in multi-storey masonry buildings using limit analysis. *Structures*, **31**, 380-394, 2021.
- [6] M.L. Puppio, L. Giresini, Estimation of tensile mechanical parameters of existing masonry through the analysis of the collapse of Volterra's urban walls. *Frattura ed Integrità Strutturale*, **13(49)**, 725-738, 2019.
- [7] P.X. Candeias, A. Campos Costa, N. Mendes, A.A. Costa, P.B. Lourenço, Experimental assessment of the out-of-plane performance of masonry buildings through shaking table tests. *International Journal of Architectural Heritage*, **11(1)**, 31-58, 2017.
- [8] S. Lagomarsino, S. Cattari, PERPETUATE guidelines for seismic performance-based assessment of cultural heritage masonry structures. *Bulletin of Earthquake Engineering*, **13(1)**, 13-47, 2015.
- [9] C. Casapulla, L. Giresini, L.U. Argiento, A. Maione, Nonlinear static and dynamic analysis of rocking masonry corners using rigid macro-block modelling. *International Journal of Structural Stability and Dynamics*, **19(11)**, (1950137) 1-32, 2019.
- [10] L. Giresini, F. Solarino, O. Paganelli, D.V. Oliveira, M. Froli, One-sided rocking analysis of corner mechanisms in masonry structures: influence of geometry, energy dissipation, boundary conditions. *Soil Dynamics and Earthquake Engineering*, **123**, 357-370, 2019.
- [11] L. Giresini, Design strategy for the rocking stability of horizontally restrained masonry walls. *6th ECCOMAS Thematic Conference on Computational Methods in Structural Dynamics and Earthquake Engineering (COMPDYN 2017)*, Rhodes Island, Greece, June 15-17, 2017.
- [12] A. Maione, C. Casapulla, F. Ceroni, M. Di Ludovico, A. Prota, Efficiency of injected anchors in connecting T-shaped masonry walls: a modelling approach. *Construction and Building Materials*, under review, 2021.
- [13] A. De Falco, L. Giresini, M. Sassu, Temporary preventive seismic reinforcements on historic churches: numerical modeling of San Frediano in Pisa. *Applied Mechanics and Materials*, **352**, 1393-1396, Trans Tech Publication, 2013.
- [14] L. Giresini, F. Solarino, F. Taddei, G. Mueller, Experimental estimation of energy dissipation in rocking masonry walls restrained by an innovative seismic dissipator (LICORD). *Bulletin of Earthquake Engineering*, **19**, 2265-2289, 2021.

- [15] J. Heyman, The stone skeleton. *International Journal of Solids and Structures*, **2(2)**, 249-279, 1966.
- [16] R.K. Livesley, Limit analysis of structures formed from rigid blocks. *International Journal for Numerical Methods in Engineering*, **12(12)**, 1853-1871, 1978.
- [17] A. Orduña, P.B. Lourenço, Three-dimensional limit analysis of rigid blocks assemblages. Part I: Torsion failure on frictional interfaces and limit analysis formulation. *International Journal of Solids and Structures*, **42(18-19)**, 5140-5160, 2005.
- [18] M.F. Funari, S. Spadea, P. Lonetti, F. Fabbrocino, R. Luciano, Visual programming for structural assessment of out-of-plane mechanisms in historic masonry structures. *Journal of Building Engineering*, **31**, 101425, 2020.
- [19] E. Mousavian, C. Casapulla, Quantifiable feasibility check of masonry assemblages composed of interlocking blocks. *Advances in Engineering Software*, **149**, art. no. 102898, 2020.
- [20] P.B. Lourenço, J.G. Rots, J. Blaauwendraad, Two approaches for the analysis of masonry structures: micro and macro-modeling. *Heron*, **40(4)**, 1-28, 1995.
- [21] V. Sarhosis, J.V. Lemos, K. Bagi, *Discrete element modelling*, B. Ghiassi, G. Milani eds. Numerical Modeling of Masonry and Historical Structures: From Theory to Application. Elsevier, Woodhead Publishing Series in Civil and Structural Engineering, 469-501, 2019.

OUT-OF-PLANE RESPONSE OF T-SHAPED MASONRY WALLS STRENGTHENED WITH CFRP INJECTED ANCHORS: MODELLING AND DESIGN PROVISIONS

Alessandra Maione^{1*}, Claudia Casapulla¹, Francesca Ceroni², Marco Di Ludovico¹,
Andrea Prota¹

¹ University of Naples Federico II, Department of Structures for Engineering and Architecture
Via Forno Vecchio 36, 80134, Naples, Italy
[alessandra.maione, casacla, diludovi, aprota}@unina.it](mailto:{alessandra.maione, casacla, diludovi, aprota}@unina.it)

² University of Naples Parthenope, Engineering Department
Centro Direzionale, is. C4, 80143, Naples, Italy
francesca.ceroni@uniparthenope.it

Abstract

The assessment of the effectiveness of strengthening interventions against the out-of-plane failure mechanisms of masonry walls requires developing a proper modelling approach. In this paper, the attention is focused on strengthening systems based on injected anchors made of carbon fibre reinforced polymer (CFRP) tubes. The resistance to corrosion and the possibility of using traditional grouts make such systems a promising alternative to steel bars in interventions on masonry structures aimed at improving poor connections between orthogonal walls. The paper introduces a modelling approach to assess the anchors contribution in the out-of-plane response of T-shaped masonry walls under horizontal actions. The approach adopts a rigid macro-block model of masonry based on the kinematic method of limit analysis. The contribution of the anchors is evaluated at the onset of the out-of-plane response of the strengthened system, defining its horizontal capacity and the crack inclination of the expected mechanism. The results obtained with the proposed model are firstly validated through the comparison with literature experimental findings. Then, parametric analyses are developed accounting for geometric and loading parameters characterizing T-shaped wall connections, and the performance of different layouts of anchors is assessed. Preliminary design indications are also provided to address the optimal balance between effectiveness, low invasiveness, and costs of such strengthening interventions.

Keywords: Masonry T-shaped walls, injected anchors, CFRP, macro-block model, limit analysis, out-of-plane mechanisms.

1 INTRODUCTION

Poor connections between orthogonal walls represent one of the primary sources of vulnerability for existing masonry buildings under seismic actions [1], together with weak connections between walls and horizontal diaphragms [2]. Indeed, they frequently cause the onset of out-of-plane failure mechanisms involving entire walls or portions of them, which can collapse for loss of equilibrium. Strengthening interventions based on injected anchors have been used since the first decades of the last century in buildings with masonry made of traditional and innovative aggregates [3]. Traditional injected anchors consist of tensile steel elements grouted in boreholes, crossing the wall connection; they can provide horizontal resistance either by bond or anchor plates, improving masonry wall connections [4].

Despite the widespread use of such a typology of anchors, their long-term durability has proved unsatisfactory due to corrosion phenomena and grout powdering. Such an aspect implies high economic and environmental impact during the building life cycle [5]. Thus, innovative typologies have recently been used in masonry structures as an alternative to steel devices [6]. They deal with anchors made of stainless steel or fibre reinforced polymer (FRP) materials, like glass or carbon fibres; they overcome the critical issues mentioned above and achieve better compatibility with the masonry substrate when used together with traditional no-cement grouts.

Many research works have investigated the behaviour of injected anchors: typical local failure modes have been identified, involving both the bond failure at the interface grout-masonry or grout-anchors, and the cone masonry detachment [7-9]; experimental campaigns have investigated the influence of geometrical and mechanical parameters on the pull-out strength [10-12], and analytical formulations have been proposed to evaluate the pull-out strength based on experimental data [13]. However, the definition of a proper modelling approach to assess the effectiveness of injected anchors on the out-of-plane response of masonry walls is still an open issue together with the formulation of design provisions [9] to achieve the best balance of effectiveness, low invasiveness and costs.

The present paper aims to address these issues, providing a modelling strategy to assess the horizontal load capacity and the expected failure mechanism of T-shaped walls, strengthened with CFRP injected anchors. An extended rigid macro-block model is first developed and applied to a literature case study [14] to verify its reliability against experimental results. Then, parametric analyses are carried out to investigate the influence of geometric and loading parameters on the performance of two different layouts of the strengthening system. The results of these analyses are used to derive preliminary design indications.

2 A MODELLING STRATEGY FOR ROCKING-SLIDING MECHANISMS IN T-SHAPED MASONRY WALLS STRENGTHENED WITH CFRP INJECTED ANCHORS

2.1 The rigid macro-block model

This section presents a modelling approach to assess the horizontal load capacity of T-shaped masonry walls strengthened with CFRP injected anchors. The approach is developed as an extension of the rigid macro-block model proposed by Casapulla et al. [15, 16] to assess the out-of-plane behaviour of unreinforced stone masonry structures. It is based on the non-linear kinematic method of limit analysis and accounts for frictional resistances. Both force and displacement-based assessments are possible.

The adopted model assumes that the relative displacements among the masonry units involved in out-of-plane failure mechanisms are concentrated along a few main cracks, separating

the structure into a number of rigid macro-blocks. Moreover, the macro-blocks and the constituent units have infinite strength in compression, tension and shear, while no-tension and frictional behaviour characterise the contact interfaces along the cracks (Coulomb failure criterion).

When the onset of a failure mechanism is investigated, the horizontal capacity of unreinforced stone masonry structures can be found as the minimum horizontal force verifying the limit equilibrium condition of the involved macro-blocks. The equilibrium refers to the rest position of the macro-blocks since their rotation is null at the onset of the mechanism. In particular, for a T-shaped wall (Figure 1a), the geometry of the macro-block involved in a rocking-sliding is defined by two parameters: the height, H_o , of the rotational hinge from the base, and the inclination angle of the main crack, α_c , affecting the spine wall (Figure 1b,c). Such parameters represent the geometric variables used in the minimization procedure and characterise the possible failure modes (Figure 1b-d).

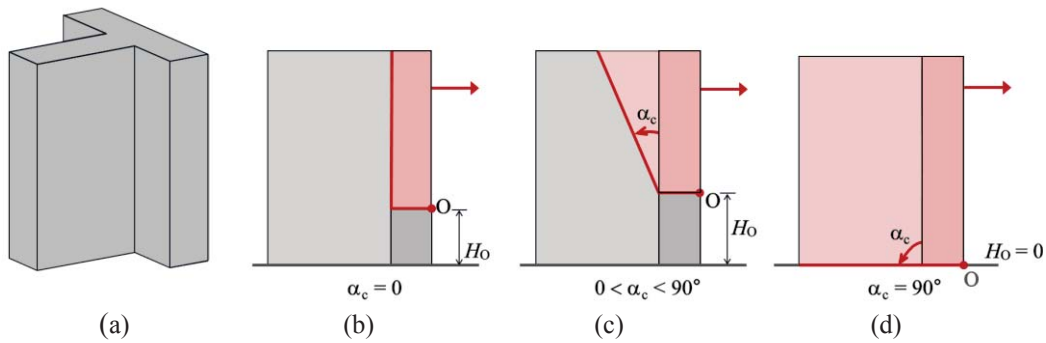


Figure 1. Rocking-sliding failure modes of a T-shaped wall: (a) geometrical configuration, (b) simple and (c) compound rocking of part of the front wall, (d) rocking of the whole T-shaped wall.

Once identified the geometry of the macro-block at the onset, a displacement-based approach allows following the evolution of the mechanism up to collapse. To this aim, the equilibrium of the macro-block defines the horizontal capacity related to each value of the rotation angle θ , representing the kinematic configuration of the system.

The macro-block model also accounts for the frictional resistance; in particular, for combined rocking-sliding mechanisms, the criterion proposed and validated by Casapulla et al. [15] evaluates the actual frictional force F_i acting on the i^{th} bed joint as a rate of the maximum value \bar{F}_i through a coefficient ω , which depends on α_c . Hence, it can be expressed as:

$$F_i = \omega \bar{F}_i = \left(1 - \frac{\alpha_c}{\alpha_b}\right) \bar{F}_i \quad (1)$$

where α_b is the inclination angle corresponding to the units staggering ratio, i.e., $\alpha_b = \tan^{-1}(v/h)$ (Figure 2a). It is worth noting that, according to the proposed criterion, the frictional forces are taken into account only if $\alpha_c < \alpha_b$; otherwise, a simple rocking mechanism occurs without frictional resistances.

The frictional forces achieve the maximum value, \bar{F}_i when the bed joints along the crack are involved in a simple sliding mechanism, i.e., in the case of a vertical crack with inclination angle $\alpha_c = 0$ (Figure 2b). \bar{F}_i can, indeed, be expressed as the sum of two components due to the self-weight and the overload affecting the spine wall (see Figure 2a):

$$\bar{F}_i = [i \cdot (\gamma \cdot t_s \cdot h \cdot v) + q_s \cdot v] \cdot f \quad (i = 1, \dots, n_c) \quad (2)$$

being γ the unit weight of masonry, t_s the thickness of the spine wall, h the height of the units, v their overlapping length, q_s the overload per unit length, uniformly distributed on the spine

wall, f the friction coefficient, n_c the number of involved courses ($n_c \leq n$, being n the total number of courses along with the height). It is worth noting that Eqs. (1) and (2) refer to single leaf walls arranged in a running bond pattern; such an idealised regular arrangement of unit blocks assures the monolithic behaviour of the transversal section of the wall. Non-regular bond patterns can also be implemented if an average size of the unit blocks can be identified, as in [16].

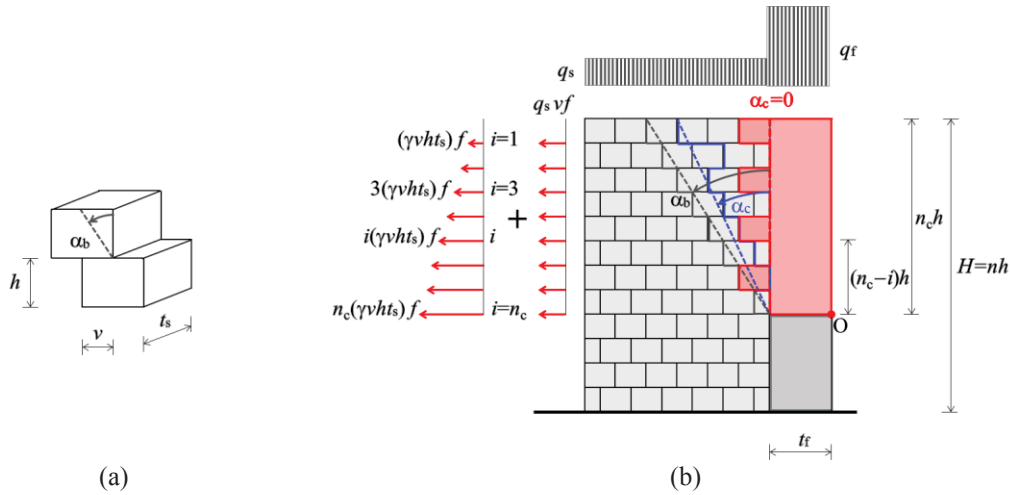


Figure 2. (a) Stone masonry unit dimensions; (b) maximum frictional forces, acting on each bed joint.

2.2 A modelling approach for strengthened T-shaped walls

The macro-block modelling approach is herein extended to the analysis of T-shaped masonry walls strengthened with CFRP injected anchors. The contribution of such a strengthening system can be taken into account on the basis of some assumptions described in the following.

First of all, it is assumed that the tensile behaviour of CFRP injected anchors can be described in a simplified way through a bi-linear load-slip relationship, T - s , as:

$$T = K_1 s \quad \text{if } s \leq s_1 \quad T = T^* - K_2 (s - s_1) \quad \text{if } s > s_1 \quad (3)$$

As an example, Figure 3a represents a bi-linear curve overlaid on experimental curves derived from literature pull-out tests [13]. It refers to CFRP tubes wrapped with a stainless-steel fabric (Figure 3b, c) and will be used in the numerical analyses developed in the following.

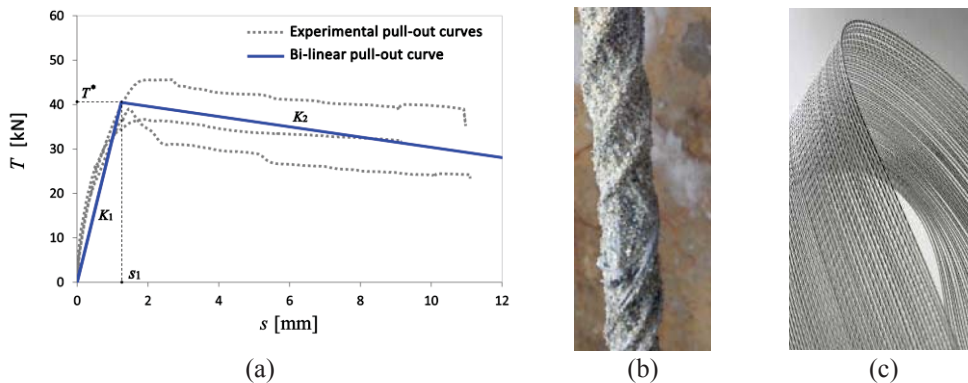


Figure 3. (a) Simplified bi-linear curve overlaid on experimental pull-out curves related to wrapped CFRP tubes [13]; (b) wrapped CRFP tubes; (c) stainless steel fabric.

The parameters defining such a bi-linear curve can be derived from the experimental data as average values; they are $K_1 = 32.4$ kN/mm, $K_2 = -1.2$ kN/mm, $T^* = 40.5$ kN, $s_1 = 1.25$ mm.

It is also assumed that the anchors are only tensioned by the relative horizontal displacements occurring along the crack line; thus, a generic row of anchors contributes to the global resistance if it crosses the main crack, and the embedded length in the resting portion of the wall is higher than that required to achieve the maximum strength. For the wrapped CFRP tubes considered in this paper, the minimum embedded length l_0 is 250 mm, based on literature pull-out tests [13]. Such a value allows exploiting the maximum strength T^* (Figure 3a).

Lastly, the resultant contribution of the active anchors at the onset of a failure mechanism is not calculated on the initial position ($\theta = 0$) of the macro-block but on the kinematic configuration ($\theta > 0$) that provides the maximum value of such contribution. The approximation can reasonably be accepted considering that CFRP anchors have very high elastic modulus and achieve the maximum tensile strength T^* for very small displacements, as fully verified in [17]. However, it is pointed out that the maximum contribution of the whole system of active anchors does not imply that they all achieve the maximum strength, T^* . This, because the forces provided by the anchors depend on the horizontal displacements that, in the rigid model, increase with the distance from the rotational hinge; consequently, the lowest rows of anchors may not reach T^* .

Based on these assumptions, it is possible to consider the limit equilibrium condition of the strengthened macro-block involved in a rocking-sliding failure mechanism. The related forces (Figure 4a) are the horizontal force F_h applied to the control point C, the resultant W of all the gravitational loads (self-weight of the macro-block and overloads), the tensile forces T_{Aj} provided by m rows of injected anchors ($j = 1, \dots, m$ from the top) and the frictional forces F_i acting on the bed joint i ($i = 1, 2, \dots, n$, from the top). It is easy to verify that the values of W and F_i strictly depend on the unknown crack inclination angle, α_c , as well as on H_0 (see Eq. (1)).

In a generic varied kinematic configuration, identified by the finite rotation angle θ (Figure 4b), the position of the forces is defined by their polar coordinates with respect to the hinge O, i.e., by their position radius R and its inclination angle, $\alpha + \theta$, on the horizontal axis.

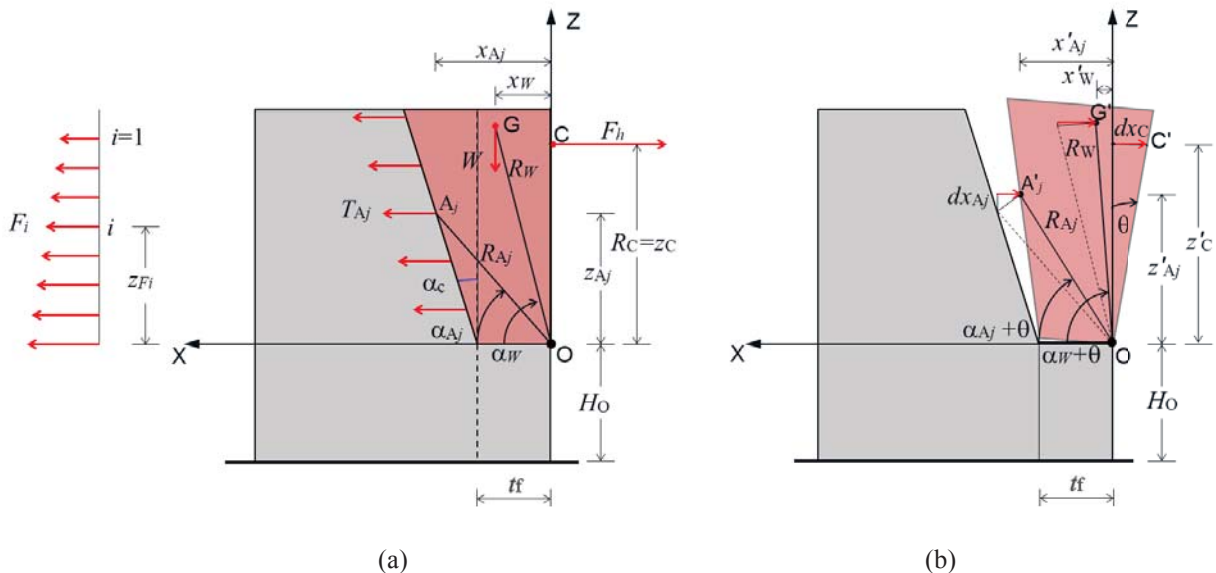


Figure 4. (a) Forces acting on the rocking-sliding macro-block with (b) their polar coordinates related to a generic rotation angle θ .

Hence, the horizontal force F_h related to the generic rotation angle θ can be obtained as the sum of the contributions $F_{h,m}$ and $F_{h,T}$ due to masonry and injected anchors, respectively:

$$F_h = F_{h,m} + F_{h,T} = \frac{Wx'_G + \sum_{i=1}^n F_i z'_{Fi}}{z'_G} + \frac{\sum_{j=1}^m T_{Aj} z'_{Aj}}{z'_G} \quad (4)$$

where the parameters with the superscript are the lever arms of the forces in the varied configurations [16, 17]:

Assuming $\theta = 0$, Eq. (4) provides the lever arms of the forces at the onset of the mechanism. Under such an assumption, for the as-built configuration ($T_{Aj} = 0$), the expected geometry of the moving macro-block is obtained by minimising the horizontal force F_h in Eq. (4), with respect to the position of the hinge, H_0 , and the inclination of the crack, $\tan\alpha_c$, assuming $H_0 \leq H$.

For the reinforced configuration, on the other hand, F_h in Eq. (4) is not a continuous function of $\tan\alpha_c$, since the contribution T_{Aj} of the j^{th} row of anchors at the height h_j becomes null for the angle:

$$\alpha_{cj} = \tan^{-1}(L_s - l_0)/h_j \quad (5)$$

being L_s the length of the spine wall crossed by the anchors and l_0 the minimum embedded length (Figure 5); note that α_{cj} depends on the length l_0 , which is a function of both the axial stiffness of the anchors and the mechanical properties of masonry and grout [10].

Hence, the pursuit of the crack inclination providing the minimum value of F_h has to be carried out in a discrete form by comparing a set of values, F_{hj} , representing the minimum related to all the possible configurations of active rows of anchors. As an example, for the strengthening system with three rows of anchors in Figure 5, the values F_{hj} have to be calculated in the following ranges of α_c :

$$0 \leq \alpha_c < \alpha_{c1}, \quad \alpha_{c1} \leq \alpha_c < \alpha_{c2}, \quad \alpha_{c2} \leq \alpha_c < \alpha_{c3}, \quad \alpha_{c3} \leq \alpha_c < 90^\circ \quad (6)$$

Indeed, the values F_{hj} correspond to a progressive reduction of the rows of active anchors starting from the upper one.

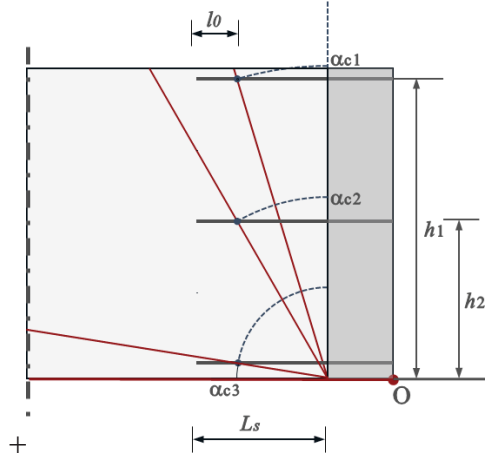


Figure 5. Crack inclination angle α_{cj} excluding the j^{th} row of anchors.

3 EXPERIMENTAL VALIDATION OF THE ANALYTICAL APPROACH

In this section, the proposed modelling approach is applied to a literature case study to illustrate the methodology and verify its reliability. The case study deals with the full-scale T-shaped wall experimentally investigated by Maddaloni et al. [14]; it was strengthened with anchors made of CFRP tubes wrapped with a stainless-steel fabric (Figure 3b) and injected with pozzolana-based grout. The geometric features of the T-shaped wall are represented in Figure 6, together with the layout of the strengthening system. The anchors had a length of 1200 mm and were placed in 30 mm diameter holes, alternatively along two vertical lines at a distance of

250 mm. Since the experimental pull-out curves in Figure 3a refer to the same typology of anchors, the bi-linear schematization represented in the same figure has been used in the numerical analyses.

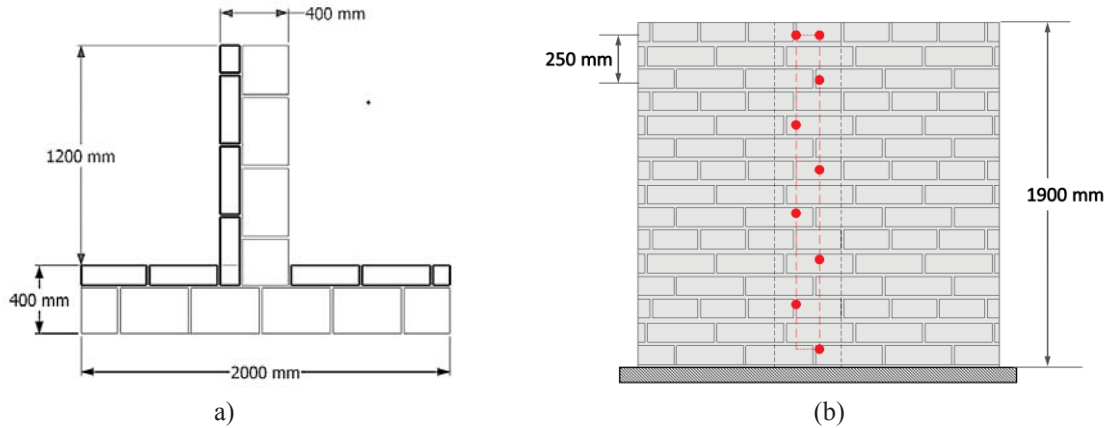


Figure 6. T-shaped wall tested by Maddaloni et al. [14]: (a) overall dimensions and arrangement of the unit blocks (b) layout of the strengthening system made of CFRP injected anchors.

3.1 Assessing the case study with the proposed approach

In applying the frictional macro-block model to the case study, a schematization of the arrangement of the stone masonry units is introduced, considering average values for both the overlapping length v and the height h of the units (Figure 2a), based on the actual ones. The friction coefficient is taken as $f = 0.6$, based on experimental data for dry-jointed tuff blocks [15]. The adopted values are reported in Table 3, with the related ones, i.e., n and $\tan\alpha_b$.

v	h [mm]	$n = H/h$	$\tan\alpha_b = v/h$	f
100	158	12	0.63	0.6

Table 2. Values of the parameters used to schematize the arrangement of the unit blocks.

The validation of the proposed approach concerns the pursuit of the crack inclination angle α_c^* providing the expected failure mechanism for the strengthened system and the minimum value F_h^* of the horizontal capacity F_h . To this aim, F_h and its components, $F_{h,m}$ and $F_{h,CFRP}$, are displayed in Figure 7a as functions of the crack inclination angle, α_c . For each α_c , the maximum values of both components are reported, assuming they occur at the onset, as previously explained. It is worth noting that F_h is applied at the control point used in the experimental test, placed at 1600 mm from the base (point C in Figure 4).

Figure 7a first shows that $F_{h,m}$ increases with α_c , with different trends due to the contribution of the frictional forces, which become null for $\alpha_c = \alpha_b = 32^\circ$ (see Eq. (1)). Its minimum value (about 49 kN) corresponds to the activation of the most likely mechanism for the unreinforced wall system, which occurs for $\alpha_{c0} = 5^\circ$, in good agreement with the experimental results related to the as-built specimen [14]. On the other hand, $F_{h,CFRP}$ exhibits a stepwise decreasing trend, where the shift from a step to the next one represents the progressive reduction of the active rows of anchors, starting from the top. For each step, the sum of the two contributions $F_{h,m}$ and $F_{h,CFRP}$ achieves a minimum value F_{hj} , which is highlighted on the red curve by a star marker. It represents the horizontal load capacity related to the failure mechanism with the crack inclination α_{cj} ($j = 0, \dots, m$, being m the rows of anchors), which excludes the first j rows of anchors, starting from the top. The crack inclinations α_{cj} associated with the possible failure mechanisms

are summarised in Figure 7b.

Thus, the horizontal load capacity of the strengthened T-shaped wall coincides with the minimum among the values F_{hj} , i.e., $F_h^* = F_{h8} = 71$ kN. Such a value corresponds to the crack inclination $\alpha_c^* = \alpha_{c8} = 82^\circ$ that excludes all the eight rows of anchors and identifies the expected failure mechanism for the strengthened T-shaped wall.

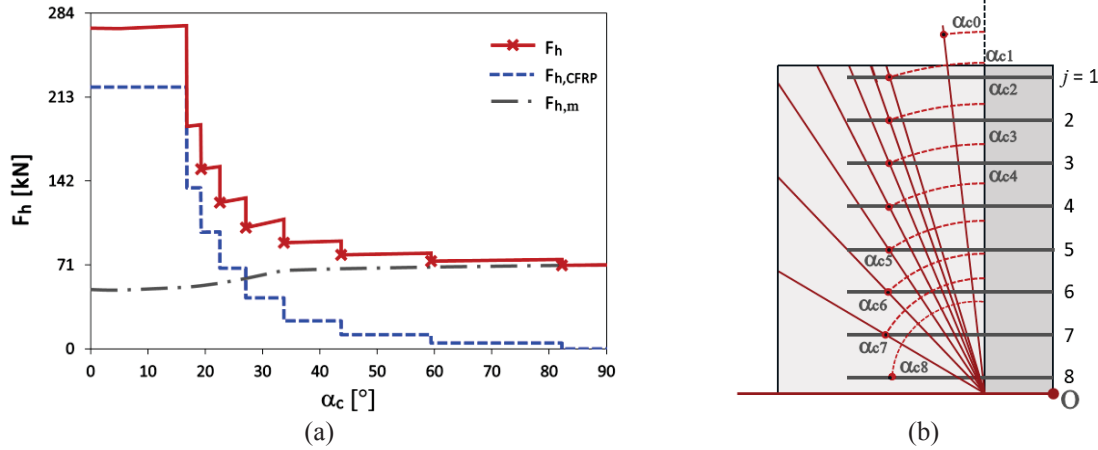


Figure 7. (a) Horizontal load capacity as the sum of masonry and CFRP anchors contributions vs. crack inclination angle; (b) crack inclination angles characterizing the possible failure mechanisms.

By concluding, it can be asserted that the proposed approach allows defining with good approximation both the failure mechanism and the horizontal load capacity of the experimental case study; this latter, in fact, after the strengthening intervention, exhibited a failure mechanism of global rocking with a cylindrical hinge at the base ($\alpha_c = 90^\circ$), with a triggering horizontal load of about 71 kN.

4 PARAMETRIC ANALYSES

This section analyses the influence of geometric and loading parameters on the horizontal load capacity of a T-shaped wall. The system is strengthened with injected anchors made of wrapped CFRP tubes, as the case study previously presented. Two layouts of the reinforcement are taken into account: Layout A, with eight rows of anchors as the experimental case study, and Layout B, with only three rows (Figure 8). For both of them, the length of the anchors is 1200 mm and the bi-linear relation presented in Figure 3a is used to describe their tensile behaviour.

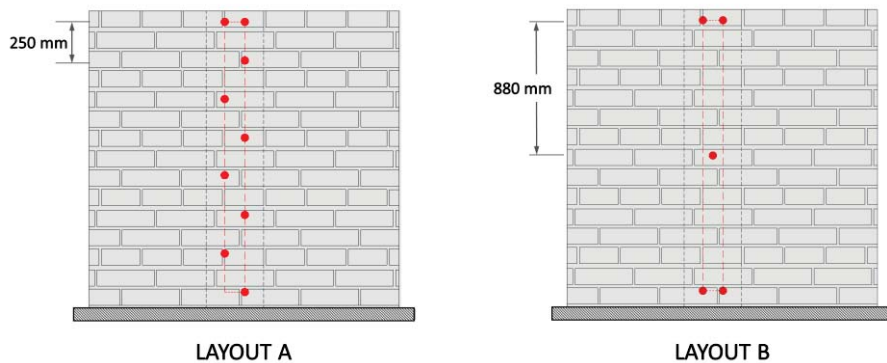


Figure 8. Layouts of CFRP injected anchors adopted in the parametric analyses.

The analyses account for the independent non-dimensional parameters reported in Table 3

with their reference and limit values; in the same table, the dependent dimensional parameters and the fixed ones are also reported. Most of them are displayed in Figure 2.

The reference values of the parameters and the global dimensions of the analysed T-shaped wall are similar to those of the case study, but a non-limited length is assumed for the spine wall to exclude the failure mechanism of global rotation, which actually does not occur in a real T-shaped wall connection. Moreover, to generalize the procedure, the horizontal force F_h is applied to the gravity centre of the moving macro-block.

It is worth noting that the variable parameter ρ refers to the overload due to upper masonry levels and affects both the façade and the spine wall; the parameter η , instead, refers to the overload due to floor slabs and is fixed. In the first set of parametric analyses, η only affects the façade wall, with $\eta = \eta_f$ in the expression of q_f (Table 3); then, in a further set of parametric analyses, it affects the overload on the spine wall, with $\eta = \eta_s$. In the latter case, the expressions of the overloads reported in Table 3 change as follows: $q_f = \rho \gamma_m H$ (with $0.05 \leq q_f \leq 0.15 \text{ N/mm}^2$) and $q_s = \eta_s \rho \gamma_m H$ (with $0.15 \leq q_s \leq 0.45 \text{ N/mm}^2$).

According to the proposed approach, the horizontal capacity, F_h^* , of a strengthened T-shaped wall, at the onset of the failure mechanism, coincides with the minimum among the horizontal forces F_{hj} related to the possible failure mechanisms with crack inclination angles α_{cj} ($j = 0, \dots, m$, being m the rows of anchors). On the other hand, among the angles α_{cj} , α_c^* provides the minimum F_{hj} , i.e. F_h^* , and identifies the expected failure mechanism.

Hence, F_{hj} and the related α_{cj} are evaluated for different values of the accounted parameter and each layout. Figure 9 reports the results related to $\eta = \eta_f$, for all the investigated parameters ($\tan\alpha_b$, ρ , f , n). The results related to $\eta = \eta_s$ are reported in Figure 10 only for the most significant parameters, i.e., ρ and $\tan\alpha_b$. In both figures, the values of the horizontal capacity (i.e., the minimum F_{hj}) are highlighted by red circles, and the values of the related inclination angle α_c^* are reported.

The analyses show that the parameters ρ and $\tan\alpha_b$ are the most relevant ones for both layouts. Their increasing values imply increasing horizontal capacity of T-shaped walls. Moreover, such a trend is enhanced when the spine wall is loaded more than the façade, i.e., in the case of $\eta = \eta_s$ (Figure 10). As an example, for $\tan\alpha_b = 1.5$, Table 4 compares the values of the horizontal capacity F_h^* provided by Layouts A and B for $\eta = \eta_f$ (Figure 9a,b) and $\eta = \eta_s$ (Figure 10a,b).

	Parameters	ID	Reference values	Range of variation
Variable, independent non-dimensional parameters	Staggering ratio	$\tan\alpha_b$	0.63	0.5 - 1.5
	Size ratio	n	12	8 - 19
	Overload parameter	ρ	3.63	1.67 - 5
	Friction coefficient	f	0.6	0.35 - 0.75
Variable, dependent dimensional parameters	Overlapping	$v = h \tan\alpha_b$	100 mm	
	Height of masonry units	$h = H/n$	158 mm	100 - 238 N/mm ²
	Façade wall overload	$q_f = \eta_f \rho \gamma_m H$	0.3 N/mm ²	0.15 - 0.45 N/mm ²
	Spine wall overload	$q_s = \rho \gamma_m H$	0.1 N/mm ²	0.05 - 0.15
Fixed parameters	Masonry unit weight	γ_m	14.5 kN/m ³	
	T-wall height	$H = n h$	1900 mm	
	Compressive stress	$\sigma = \gamma_m H$	0.03 N/mm ²	
	Overload	η	3	

Table 3: Ranges of variation of parameters considered in the analyses.

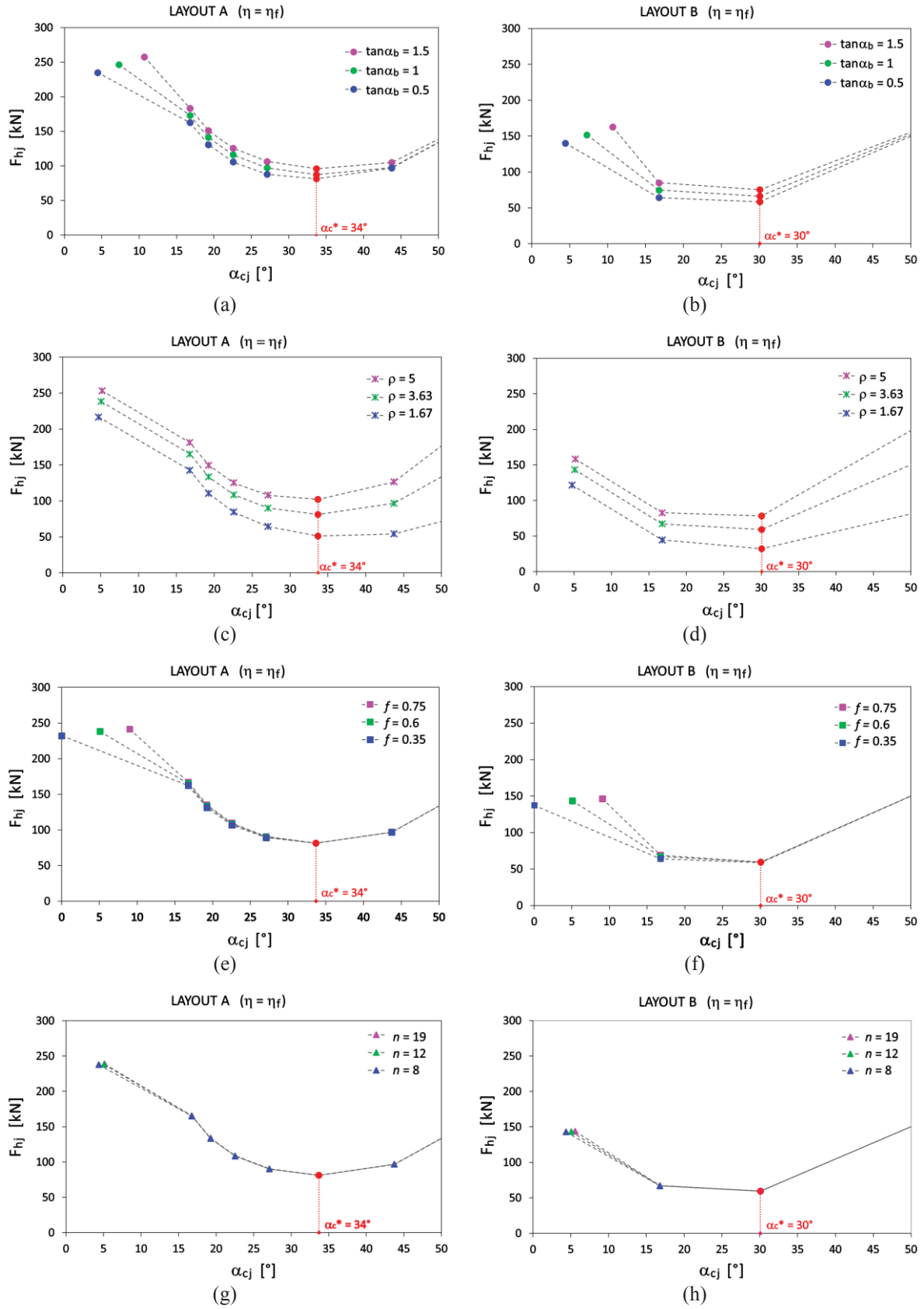


Figure 9. Results of the parametric analyses based on $\eta = \eta_f$, for (a, c, e, g) Layout A and (b, d, f, h) Layout B.

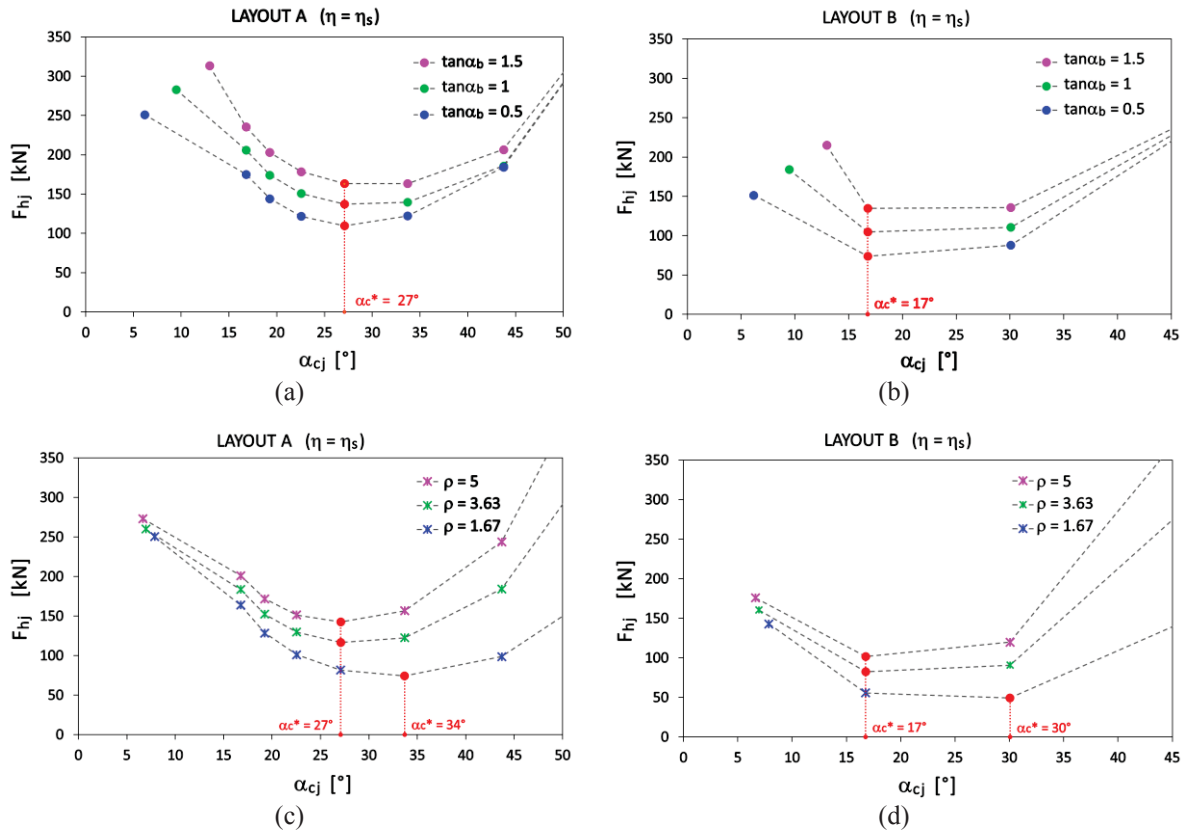


Figure 10. Results of the parametric analyses based on $\eta = \eta_s$, for (a, c) Layout A and (b, d) Layout B.

Layout	F_h^*		ΔF_h^*	%
	$\eta = \eta_f$	$\eta = \eta_s$		
A	96 kN	163 kN	67 kN	70%
B	75 kN	135 kN	60 kN	80%

Table 4. Comparison of the horizontal capacities provided by Layouts A and B related the cases $\eta = \eta_f$ and $\eta = \eta_s$, being $\tan \alpha_b = 1.5$, $\rho = 3.63$, $f = 0.6$, $n = 12$.

Figure 9e-h, related to $\eta = \eta_f$, also shows that the friction coefficient, f , and the size ratio, n , are not very significant. On the other hand, the crack inclination angle α_c^* characterizing the expected failure mechanisms ranges in 30° - 34° , being quite close to $\alpha_b = 32^\circ$, which implies that the frictional forces are close to zero according to Eq. (1). The influence of the parameter η also concerns the crack inclination angle α_c^* . In particular, when $\eta = \eta_f$ (Figure 9), α_c^* keeps constant with all the variable parameters ($\tan \alpha_b$, ρ , f , n), being $\alpha_c^* = \alpha_{c,j=5} = 34^\circ$ for Layout A and $\alpha_c^* = \alpha_{c,j=2} = 30^\circ$ for Layout B. It means that the number of active rows of anchors (five for Layout A and two for Layout B) and their contribution to the resistance do not vary with the accounted parameters. Consequently, the increase of the horizontal capacity is only due to masonry, whose contribution instead increases with such parameters.

When $\eta = \eta_s$, α_c^* is still constant with $\tan \alpha_b$ (Figure 10a,b), being $\alpha_c^* = 27^\circ$ for Layout A and $\alpha_c^* = 17^\circ$ for Layout B. Both values, however, are lower than those related to $\eta = \eta_f$ (Figure 9a,b), implying a higher number of active rows of anchors and consequently an improved contribution of the strengthening system. On the other hand, α_c^* can vary with the parameter ρ (Figure 10c,d). In particular, for both layouts, the lowest values of α_c^* occur when $\rho \geq 3.36$; it

confirms that when the overload on the spine wall is higher enough, the strengthened system exhibits a better performance. The parameters f and n when $\eta = \eta_s$ still have a negligible effect on the horizontal capacity as in the case $\eta = \eta_f$, although lower values of the angle α_c^* have been obtained; thus, the related analyses are not represented in Figure 10.

Finally, it is interesting to note that the values of α_c^* provided by all the parametric analyses are always lower than 90° , highlighting that the global rocking mechanism obtained both experimentally and analytically for the T-shaped wall case study never occurs. This result can be explained considering that in the parametric analyses, the length of the spine wall is not limited to 1600 mm, as for the case study, but has a realistic value; thus, for $\alpha_{cj} > \alpha_c^*$, the sewing action of the active anchors allows increasing the involved portion of the spine wall, preventing from the potential failure mechanisms with the crack inclination angles higher than α_c^* . It is worth noting that a length of only two meters is required to obtain such a result with all the accounted parameters.

5 DESIGN INDICATIONS

The performance of Layouts A and B resulting from the previous parametric analyses is herein discussed to derive preliminary design indications. For this purpose, only the most significant parameters are considered, i.e., $\tan\alpha_b$ and ρ , for both cases of $\eta = \eta_f$ and $\eta = \eta_s$.

Firstly, Table 5 summarises the better performance of the accounted layouts in terms of the percentage increase of the horizontal capacity against the as-built configuration. Such a performance is achieved for the lowest considered values of $\tan\alpha_b$ and ρ , i.e., $\tan\alpha_b = 0.5$ and $\rho = 1.67$, keeping fixed the other parameters to their reference values (Table 3).

Layout	$\tan\alpha_b = 0.5$; $\rho = 3.63$		$\rho = 1.67$; $\tan\alpha_b = 0.63$	
	$\eta = \eta_f$	$\eta = \eta_s$	$\eta = \eta_f$	$\eta = \eta_s$
A	101%	136%	133%	148%
B	44%	59%	46%	64%

Table 5. Percentage increase of the horizontal capacity against the as-built configuration.

Then, the performances of the two layouts are compared with reference to a fixed value of the required capacity, F_{hD} . It might represent the seismic demand related to a definite limit state, and for only illustration purpose, it is assumed $F_{hD} = 70$ kN, which is close to the horizontal capacity of the case study at the onset of the global rocking mechanism. The comparison capacity-demand is displayed in Figure 11, where the horizontal line representing F_{hD} is overlaid on the curves representing the horizontal load capacity of Layout A and B versus $\tan\alpha_b$ and ρ , for $\eta = \eta_f$ and $\eta = \eta_s$. The capacity related to the as-built configuration is also represented as a reference.

Hence, Figure 11a shows that, for $\eta = \eta_f$, Layout B is not adequate for the seismic demand of 70 kN until $\tan\alpha_b < 1.25$, while for $\tan\alpha_b > 1.25$, it is suitable and preferable to A for the lower number of anchors. On the other hand, for $\eta = \eta_s$ (Figure 11c), the strengthening intervention is not required until $\tan\alpha_b > 0.85$, while, when $\tan\alpha_b < 0.85$, Layout B is satisfactory. Similar considerations can be done when the parameter ρ is taken into account in Figure 11b and 11d, identifying the preferable layout.

Moreover, when the non-dimensional parameters assume the reference values ($\tan\alpha_b = 0.63$ and $\rho = 3.63$) identified in Figure 11 by a dotted vertical line, Layout B is not adequate for the seismic demand of 70 kN if $\eta = \eta_f$, while it is satisfactory if $\eta = \eta_s$.

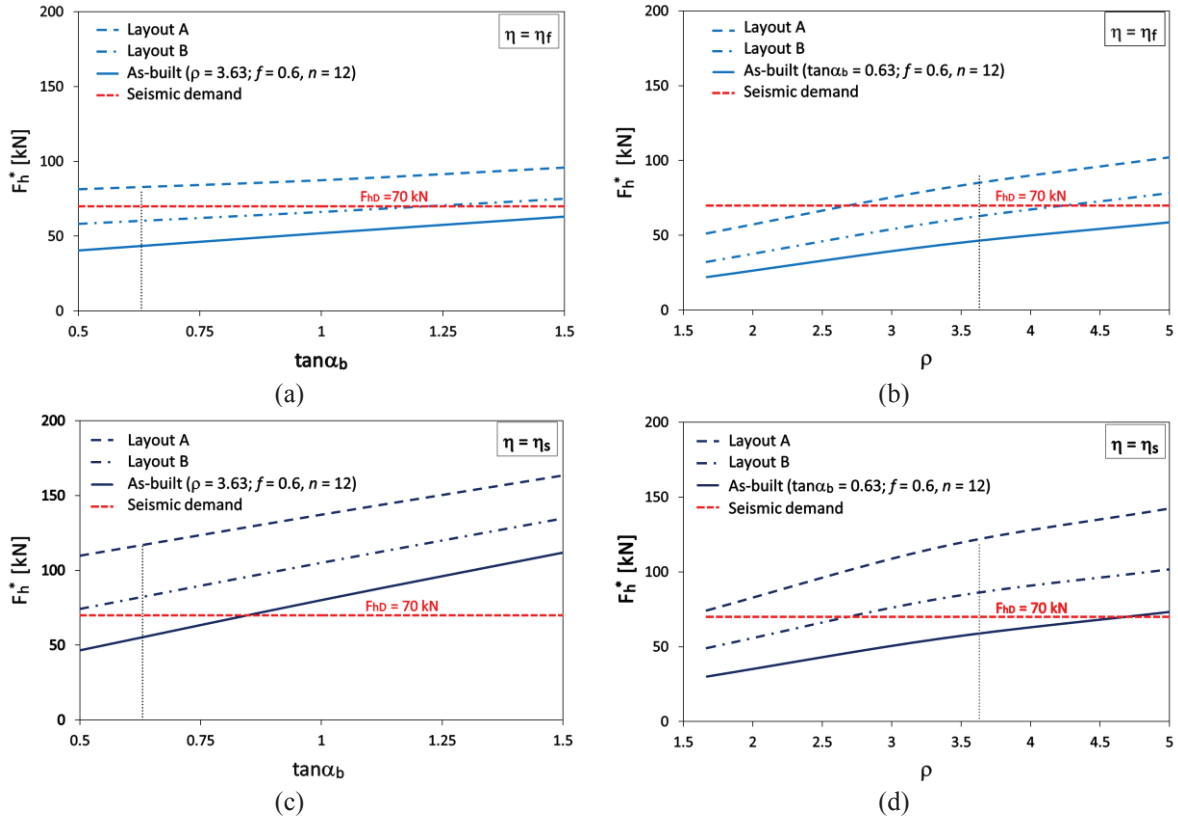


Figure 11. Performance of Layouts A and B and as-built specimen depending on $\tan \alpha_b$ and ρ , for (a, b) $\eta = \eta_f$ and (c, d) $\eta = \eta_s$.

Finally, a higher length of the anchors could be adopted to improve the performance of Layout B, especially when $\eta = \eta_f$. Thus, to generalise the issue, the effect of the variable length of the anchors, L_a , is analysed in Figure 12 for $\eta = \eta_f$ and $\eta = \eta_s$ and for both the layouts, A and B. The values of the parameters characterising the T-shaped connection are the reference ones listed in Table 3 (i.e., $\tan \alpha_b = 0.63$, $\rho = 3.63$, $f = 0.6$, $n = 12$).

Figure 12 shows that the horizontal load capacity of the strengthened system increases with the length of the anchors, as expected. However, a threshold length can be recognised, after which a further increase is irrelevant since the horizontal load capacity keeps constant. Such a threshold length is the same for Layouts A and B, i.e., 3000 mm when $\eta = \eta_f$ and 2200 mm when $\eta = \eta_s$. The horizontal load capacity of Layout A is clearly always higher than Layout B because of the higher number of anchors, but, when $\eta = \eta_f$, an increased length of 1500 mm makes Layout B adequate to sustain the seismic demand $F_{hD} = 70$ kN. Generalising, from Figure 12, it is possible to identify the length of the anchors required for a given performance and compare the different layouts.

Such considerations represent a first approach to the design issues that will be addressed comprehensively in the ongoing research.

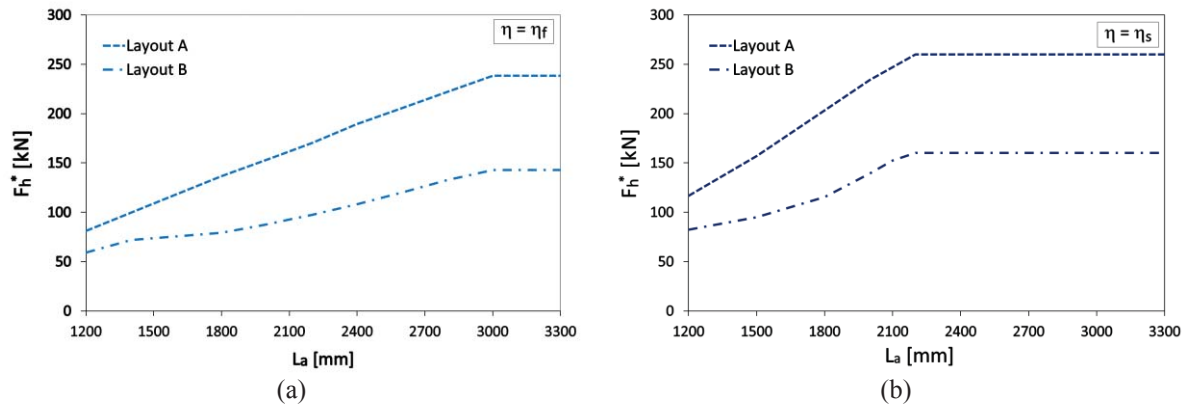


Figure 12. Horizontal load capacity vs. length of the anchors for $\eta = \eta_f$ and $\eta = \eta_s$ provided by (a) Layout A and (b) Layout B, being $\tan\alpha_b = 0.63$, $\rho = 3.63$, $f = 0.6$, $n = 12$.

6 CONCLUSIONS

In this paper, a modelling approach has been presented to assess the onset of the out-of-plane response of T-shaped masonry walls, strengthened with CFRP injected anchors. The approach has been developed using a rigid macro-block model already validated for unreinforced stone masonry structures; it is based on the kinematic method of limit analysis and accounts for the frictional resistances. The attention has been focused on identifying the horizontal load capacity corresponding to the onset of the expected failure mechanism for the strengthened T-wall.

Assumptions have been made to account for the contribution of CFRP anchors in the rigid model adopted for masonry. These assumptions have been validated by applying the model to a literature experimental case study, and a good match has been found between experimental outcomes and analytical predictions in terms of both horizontal load capacity and expected failure mechanism.

After validating the model, parametric analyses have been carried out, based on some geometric and loading parameters affecting T-shaped masonry walls, and the most significant ones influencing the horizontal capacity have been identified. Moreover, the performance of two strengthening layouts, characterised by a different number of injected anchors with a fixed length, has been compared. The results of the parametric analyses have been used to derive preliminary design indications aimed at identifying the adequate layout for a given value of the seismic demand. Finally, the effect of a variable length of the anchors on the horizontal capacity has also been investigated, and a threshold length has been recognised, after which a further increment is irrelevant since the horizontal load capacity keeps constant.

The results of the proposed modelling approach allow deriving preliminary indications to optimise the design of strengthening interventions with injected anchors. Such a crucial topic, however, will more comprehensively be addressed in the ongoing research.

Acknowledgements

The study presented in this paper has been carried out in the framework of PRIN research project “Innovative Systems for the UpgRade of MasOnry structUres and Non sTructural elements (SURMOUNT)”

REFERENCES

- [1] P.B. Lourenço, N. Mendes, L.F. Ramos, D.V. Oliveira, Analysis of masonry structures without box behavior. *International Journal of Architectural Heritage*, **5(4-5)**, 369-382, 2011.

- [2] F. Solarino, D.V. Oliveira, L. Giresini, Wall-to-horizontal diaphragm connections in historical buildings: A state-of-the-art review. *Engineering Structures*, **199**, art. no. 109559, 2019.
- [3] M. Sassu, L. Giresini, E. Bonannini, M.L. Puppio, On the use of vibro-compressed units with bio-natural aggregate, *Buildings*, **6(3)**, art. no. 40, 2016.
- [4] B. Gigla, Bond strength of injection anchors as supplementary reinforcement inside historic masonry. *13th International Brick and Block Masonry Conference*, Amsterdam, Netherlands, July 4-7, 2004.
- [5] L. Giresini, F. Stochino, M. Sassu, Economic vs environmental isocost and isoperformance curves for the seismic and energy improvement of buildings considering Life Cycle Assessment. *Engineering Structures*, **233**, art. no. 111923, 2021
- [6] F. Ceroni, A. Prota, Case study: seismic upgrade of a masonry bell tower using glass fiber-reinforced polymer ties, *Journal of Composites for Construction*, **13(3)**, 188-197, 2009.
- [7] F. Ceroni, R. Cuzzilla, M. R. Pecce, In situ pull-out tests of steel and GFRP injected anchors in masonry walls. C. Modena, F. da Porto, M.R. Valluzzi eds. *16th International Brick and Block Masonry Conference*, Padova, Italy, June 26-30, 2016.
- [8] F. Ceroni, H. Darban, R. Luciano, Analysis of bond behavior of injected anchors in masonry elements by means of Finite Element Modeling. *Composite Structures*, 241, art. no. 112099, 2020.
- [9] S. Paganoni, D. D'Ayala, Testing and design procedure for corner connections of masonry heritage buildings strengthened by metallic grouted anchors. *Engineering Structures*, **70**, 278-293, 2014.
- [10] L. Giresini, M.L. Puppio, F. Taddei, Experimental pull-out tests and design indications for strength anchors installed in masonry walls. *Materials and Structures/Materiaux et Constructions*, **53**, art. no. 103, 2020.
- [11] F. Silveri, P. Riva, G. Profeta, E. Poverello, C. Algeri, Experimental study on injected anchors for the seismic retrofit of historical masonry buildings. *International Journal of Architectural Heritage*, **10(2-3)**, 2016.
- [12] M. Panizza, P. Girardello, E. Garbin, M.R. Valluzzi, G. Cardani, M. Dalla Benetta, P. Casadei, On-site pull-out tests of steel anchor spikes applied to brickwork masonry. *Key Engineering Materials*, **624**, 266-274, 2015.
- [13] F. Ceroni, M. Di Ludovico, Traditional and innovative systems for injected anchors in masonry elements: Experimental behavior and theoretical formulations. *Construction and Building Materials*, **254**, art. no. 119178, 2020.
- [14] G. Maddaloni, M. Di Ludovico, A. Balsamo, A. Prota, Out-of-plane experimental behaviour of T-shaped full scale masonry wall strengthened with composite connections. *Composites Part B: Engineering*, **93**, 328-343, 2016.
- [15] C. Casapulla, L.U. Argiento, In-plane frictional resistances in dry block masonry walls and rocking-sliding failure modes revisited and experimentally validated. *Composites Part B: Engineering*, **132**, 197-213, 2018.
- [16] C. Casapulla, A. Maione, L.U. Argiento, Performance-based seismic analysis of rocking masonry façades using non-linear kinematics with frictional resistances: A case study," *International Journal of Architectural Heritage*, 2019, doi: 10.1080/15583058.2019.1674944.
- [17] A. Maione, C. Casapulla, F. Ceroni, A. Prota, Efficiency of injected anchors in connecting t shaped masonry walls: a modelling approach. *Construction and Building Materials*, under review.

NUMERICAL MESO-MODEL FOR REINFORCED CONCRETE FRAMES WITH RETROFITTED MASONRY INFILL

Gianni Blasi¹, Daniele Perrone^{1,2}, Maria Antonietta Aiello¹.

¹University of Salento, Italy, {[gianni.blasi](mailto:gianni.blasi@unisalento.it), [daniele.perrone](mailto:daniele.perrone@unisalento.it), [antonietta.aiello](mailto:antonietta.aiello@unisalento.it)}@unisalento.it

²University School for Advanced Studies, Italy, daniele.perrone@iusspavia.it

Abstract

Several research outcomes have ascertained the need of considering the infill walls in the dynamic response evaluation of reinforced concrete framed buildings. In the case of buildings designed prior the introduction of modern seismic codes, the presence of strong infill might highly influence the failure mode in case of earthquake. Furthermore, considering the increasingly adoption of retrofit techniques aimed at enhancing the in-plane and out-of-plane capacity of the infill walls, its influence on the seismic performance of the structure should be investigated at global and local level. In this study, a numerical model to simulate the response to lateral loads of reinforced concrete frames with retrofitted masonry infill walls is developed. Particularly, since the use of composites is widespread due to the well-known benefits of these materials, the work is focused on the in-plane infill retrofit by fibre-reinforced polymer (FRP). The proposed model for the retrofitted infill is validated by numerical simulation of diagonal compression tests on masonry panels previously conducted at university of Salento. Aiming to analyse the influence of the retrofit on the seismic performance of the frame, the retrofitted infill and unreinforced infill performances are compared. Depending on the infill type considered, the failure modes of the frame members, the energy dissipated under lateral loading and the displacement capacity are analysed.

Keywords: Meso-modelling, Infilled frames, retrofitted infill, seismic vulnerability, RC frames.

1 INTRODUCTION

The in-plane or out-of-plane collapse of infill walls caused by earthquakes can represent a major threat for life safety, particularly during seismic emergency. Moreover, the seismic damage on infills might cause in-direct losses which affect the serviceability of the building, such as failure of piping lines or electrical wiring embedded in the walls. The severe damage on masonry infill walls, documented in several post-seismic on-site recognitions [1–3], led to recent investigations through laboratory tests [4–6] and numerical studies [7,8], with the scope of characterizing their seismic response. Aiming to avoid infill's damage due to earthquake, state-of-art retrofit solutions are increasingly employed on existing buildings. Textile-Reinforced Mortar (TRM), Composite-Reinforced-Mortar (CRM) or Steel-Reinforced-Grout (SRG) jacketing significantly increase the lateral load capacity of masonry panels [9–11], even though such techniques are not always applicable due to the mass and thickness increase. On the other hand, the use of fibre-reinforced polymers (FRP) retrofit prevents out-of-plane failure and increases the in-plane tensile strength of the wall without majorly modifying its thickness [12,13].

The increasingly number of studies on strengthened masonry walls allowed to comprehensively define their in-plane and out-of-plane response, as well as the failure modes in case of lateral loading. Several analytical models were calibrated based on experimental findings, contributing to the development of guidelines for retrofit techniques [14,15], which provide instruction for their design, installation and maintenance. Most of the studies on strengthened panels are addressed to load-bearing walls in masonry structures, which are widespread in Mediterranean regions and represent a building category with high seismic vulnerability. On the other hand, the research outcome also applies to non-structural masonry panels in RC framed structures. To this regard, despite the strengthening techniques adopted for infill walls are generally identical to those used in masonry structures, additional considerations are required in the former case to account for the frame-infill interaction.

The influence of the infills on the dynamic performance of RC framed structures is well-known in earthquake engineering. Several studies provided simplified formulations to simulate the lateral behaviour of infilled frames and to predict the seismic demand depending on the properties of the masonry walls [16,17]. Additionally, the analysis of the effect of the infills on the seismic behaviour of RC frames is addressed in recent building codes [18–20]. In the case of buildings built before the introduction of modern seismic design codes, the presence of strong infill walls not only provides a significant contribution to the lateral stiffness, but can also influence the failure mode of the frame members [21–23]. The additional shear demand in columns with poor shear reinforcement caused by the infill-frame interaction can lead to early brittle failure and, consequently, reduce the displacement and ductility capacity of the RC structures [24].

Since the retrofit techniques currently used to prevent non-structural walls collapse significantly increase their lateral strength, an accurate evaluation of the consequences of the retrofit on the structural performance is strictly required when dealing with gravity load designed RC frames. In fact, a shear strengthening of the columns might be also required, in order to avoid brittle failure caused by the interaction with the retrofitted infill walls [25]. Recent studies have shown the reliability of the available numerical models in predicting the shear demand in frame members caused by the interaction with the infill, both employing macro or micro modelling approaches [26–29]. On the other hand, the complex behaviour of retrofitted infill walls might require more advanced numerical modelling approaches, which allow to account for all the possible failure modes. For instance, the simulation of the interface interaction between masonry substrate and retrofit layer is required to account for cohesive failure, which is a common failure mode in case of FRP retrofit [30].

A numerical model for the simulation of the in-plane response to lateral loads of an infilled RC portal frame is developed in this study. Two infill types are considered, namely an unreinforced masonry wall and a masonry wall retrofitted with fibre-reinforced-polymer layers. The cross section and the reinforcement of

the RC frame members were defined according to a simulated gravity load design, assuming the considered frame as part of the first floor in a four-storey building. This approach allowed to reproduce the configuration of existing buildings, characterized by low performance under seismic actions. Aiming to accurately simulate the failure modes of the analysed frames, a meso-modelling approach is adopted, explicitly defining the brick units in the wall, as well as the interface interaction with the RC frame and the retrofit. The model developed for the masonry wall is firstly validated by simulating diagonal compression tests previously performed at university of Salento [31]. The lateral behaviour of the case study RC portal frames was investigated by mean of non-linear static analyses, to evaluate the failure modes, the energy dissipation and the displacement capacity depending on the infill properties.

2 DESCRIPTION OF THE CASE STUDY PORTAL FRAMES

The portal frame considered in this study replicates the first floor in a 4-storey and 4-bay RC building designed for gravity loads, with bay length, L , equal to 5.4 m in both directions and floor height, h , equal to 3 m. The dead and live loads on the slab were assumed equal to 5.8 kN/m² and to 2.0 kN/m², respectively. The cross section of the columns was designed computing the axial load through to the tributary area method, while the beam's cross-section was assumed equal to $L/10$. The longitudinal and transverse reinforcement was defined according to the gravity load design provisions of the Italian building code [32]. The mechanical properties assumed for concrete and reinforcing steel are provided in **Table 1**.

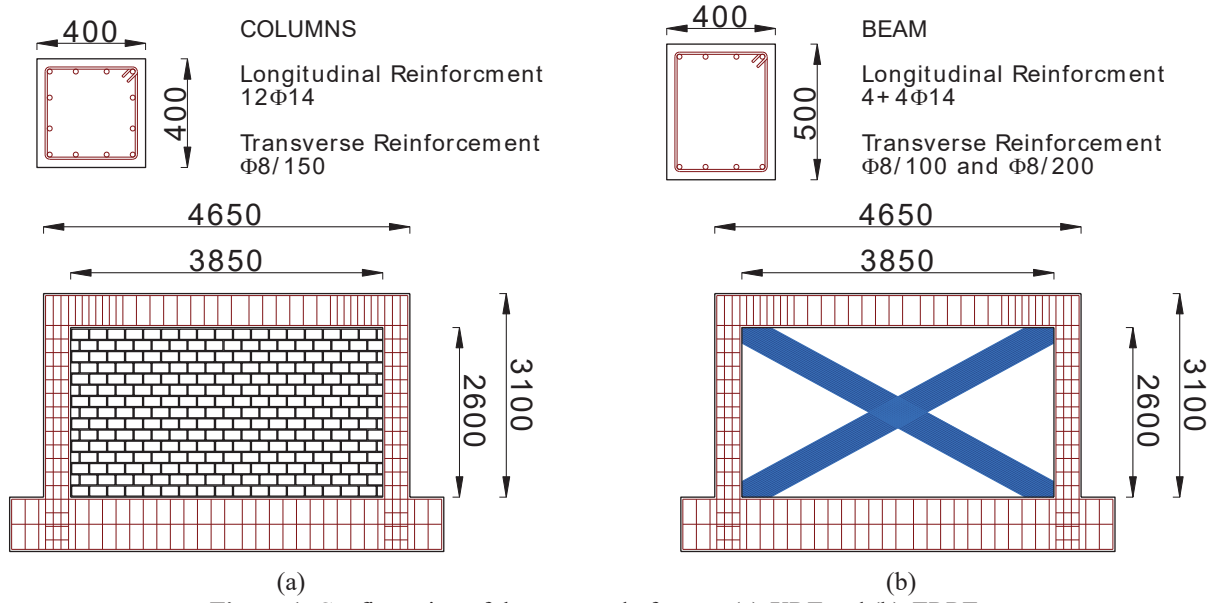
Concrete	
Compressive strength f_c [MPa]	27.0
Young's modulus E_c [MPa]	32306.0
Tensile strength f_{ct} [MPa]	2.7
Reinforcing steel	
Yielding strength f_{ys} [MPa]	450.0
Young's modulus E_s [MPa]	210000.0

Table 1. Mechanical properties of concrete and steel rebars assumed for the numerical model.

In **Table 2**, a description of the analyzed frames is provided. An identification code is assigned to each frame depending on the considered configuration (URF = Frame with UnReinforced infill; FRPF = Frame with Fiber-Reinforced-Polymer infill). The portal frame in its two configurations considered in this study is illustrated in **Figure 1**. The infill wall was composed of tuff stone bricks typical of southern Italy, whose properties were defined based on laboratory tests previously conducted at University of Salento [31]. The compressive strength, f_{cw} , and the elastic modulus, E_w , were equal to 13.9 MPa and 7796 MPa, respectively. The bed joints were characterized by cementitious mortar with low mechanical properties, to simulate the behaviour of infill walls in existing old buildings.

ID	Column cross section [mm]	Beam cross section [mm]	Infill thickness [mm]	Infill retrofit type
URF	400x400	400x500	200	none
FRPF	400x400	400x500	200	FRP Layer

Table 2. ID of the case study frames.

Figure 1. Configuration of the case study frames: (a) *URF* and (b) *FRPF*.

2.1 Simulated design of the retrofit

The FRP retrofit of the infill wall is composed of diagonal basalt-fibre composite sheets with thickness, t_{FRP} , and width, b_{FRP} , equal to 0.14 mm and 650 mm, respectively. The tensile strength, f_{FRP} , and the elastic modulus, E_{FRP} , were equal to 2326 MPa and 75.98 GPa, respectively. The wall retrofit was designed by replicating a realistic scenario in which a lateral strengthening of the infill is required to avoid severe in-plane cracking in case of earthquake. A target lateral shear strength of the wall, F_{hw} , was computed based on the seismic base shear demand, F_h , defined according to the equivalent static approach described in the Italian building code [32]:

$$F_h = \frac{S_a(T_1) \cdot \lambda \cdot W_b}{q_b} \quad (1)$$

In equation (1), W_b is the total weight of the building, q_b is the behaviour factor, λ is the participating mass coefficient and $S_a(T_1)$ is the spectral acceleration corresponding to the first period of the structure.

The behaviour factor was assumed equal to 1.5 to assume a low ductility of the frame, in consistency with the gravity load design. The value of $S_a(T_1)$ was defined based on a high seismic hazard zone in Italy and considering a design return period equal to 475 years, as prescribed in the Italian building code for residential buildings [32].

The value of F_{hw} was calculated as $F_{hw} = \alpha_w \cdot F_h / [n_w \cdot (\alpha_w + 1)]$, being α_w the infill-to-frame relative elastic stiffness (equation (2)) and n_w the number of infill walls in the considered direction. This approach assumes that the total base shear in the building is distributed among the RC columns and the infill walls along the perimeter, proportionally to the lateral stiffness of each element.

$$\alpha_w = \frac{n_w G_w t_w l_w h_c^3}{n_c 12 E_c I_c h_w} \quad (2)$$

In equation (2), l_w and h_w are the length and the height of the infill wall, respectively; E_c , I_c and h_c are the elastic modulus of the concrete (computed according to Italian building design code [32]), the moment of inertia of the cross section and the height of the columns, while n_c is the number of columns oriented in the considered direction. It is worth mentioning that the approach adopted for the evaluation of F_{hw} assumes the masonry infill walls as part of the lateral loads resisting system.

Based on the target shear strength, the retrofit was designed adopting simplified formulations provided in the literature. The shear strength of the retrofitted infill, F_{FRP} , was computed according to CNR-DT 200/2013 [14]:

$$F_{hw} \leq F_{FRP} = \tau_w \cdot A_w + F_{f,FRP} \quad (3)$$

In equation (3), τ_w and A_w are the shear strength and the cross sectional area of the infill wall, respectively, $F_{f,FRP}$ is the shear strength contribution provided by the composite, defined through equation (4), depending on the elastic modulus (E_f) the thickness (t_f) and the fracture energy (Γ_f) of the FRP layer.

$$F_{f,FRP} = 0.48 \cdot l_w \cdot 2t_f \cdot \sqrt{\frac{2 \cdot E_f \cdot \Gamma_f}{t_f}} \quad (4)$$

3 NUMERICAL MODEL DESCRIPTION

A three-dimensional model was developed in ABAQUS [33] for the simulation of the lateral behaviour of the infilled portal frames (**Figure 2**). The RC frame members were modelled using eight-node linear elements (C3D8R) with embedded trusses (T3D2), representing concrete and reinforcement rebars, respectively. A simplified elastic-perfectly plastic behaviour in compression was assumed for concrete, where the elastic stress limit was equal to the compressive strength, f_c , and the ultimate strain, ϵ_{cu} , was computed according to Italian building code [32]. The tensile behaviour featured a linear elastic branch up to the tensile strength, f_{ct} , followed by tension stiffening. Referring to reinforcing steel, an elastic-perfectly plastic behaviour was assumed both in compression and tension, assuming strain at failure, ϵ_{su} , equal to 0.075.

A discrete meso-modelling approach was adopted for the masonry infill wall, explicitly defining the brick units in the geometry. The mesh of the bricks was characterized by eight-node linear elements

(C3D8R), with linear elastic mechanical behaviour, since their high compressive strength suggested the unlikely occurrence of crushing failure. To validate this statement, the maximum stress in the brick was checked at the end of each simulation performed.

A cohesive law was adopted at the brick-to-brick interface, to simulate the presence of mortar joints (**Figure 2**). The interface behaviour in tension and in the two shear directions was characterized by a linear elastic response up to maximum strength, followed by linear softening, simulating cracking evolution. The damage initiation is ruled by the maximum stress criterion provided in equation (5):

$$\max \left\{ \frac{t_n}{t_{nL}}, \frac{t_{s1}}{t_{s1L}}, \frac{t_{s2}}{t_{s2L}} \right\} = 1 \quad (5)$$

where t_n , t_{s1} and t_{s2} are the stress values in the three principal directions and t_{nL} , t_{s1L} and t_{s2L} are the limit values when the separation is either purely normal to the interface or purely in the first or the second shear direction, respectively. The tensile limit, t_{nL} , was assumed equal to 0.26 MPa, based on the results of three-point-bending tests on mortar specimens. The values of t_{s1L} and t_{s2L} correspond to the shear strength of mortar joints, τ_w , which was calibrated based on diagonal compression tests performed at university of Salento, as described in the following section. The elastic slope of the cohesive behaviour in pure tension and pure shear are equal to $k_{ss} = G_{mj}/h_{mj}$ and $k_{nn} = E_{mj}/h_{mj}$, respectively, being E_{mj} and G_{mj} the Young's and shear modulus of mortar and h_{mj} the mortar joints thickness.

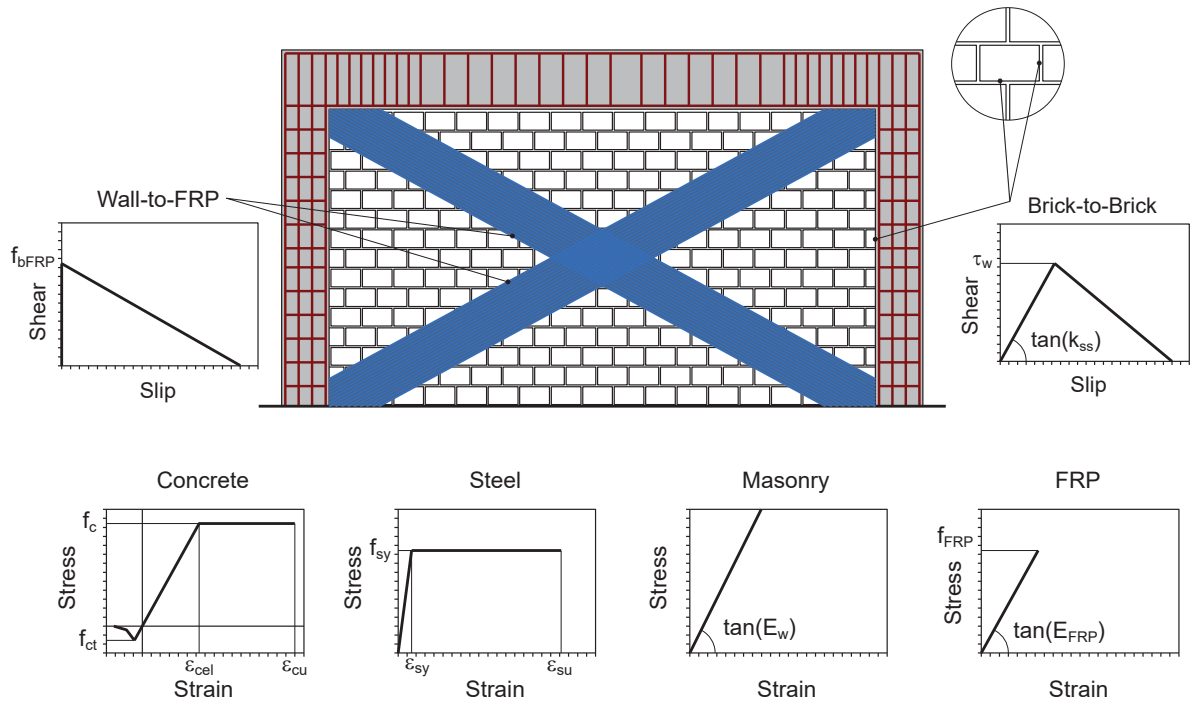


Figure 2. Description of the numerical model.

The damage evolution was defined based on the mixed-mode criterion, representing cohesive failure by equation (6):

$$\frac{G_n}{G_{nL}} + \frac{G_{s1}}{G_{s1L}} + \frac{G_{s2}}{G_{s2L}} = 1 \quad (6)$$

where G_n , G_{s1} and G_{s2} are the energy values in the three principal directions and G_{nL} , G_{s1L} and G_{s2L} are fracture energy values when the separation is either purely normal to the interface or purely in the first or the second shear direction, respectively. As for the shear strength of mortar joints, the fracture energy values were calibrated based on the results of diagonal compression tests described in the following section. In **Figure 2**, the curve representing the cohesive response in pure shear is provided. The same cohesive law was used to simulate the interaction at the wall-frame interface.

The FRP retrofit was modelled through plane surfaces meshed using three-node shell elements (S3). The mechanical stress-strain behaviour of the FRP sheets was composed of a linear elastic branch up to the attainment of the tensile strength, f_{FRP} , followed by tensile failure. Aiming to simulate debonding, a cohesive law was defined at the wall-FRP interface (**Figure 2**). A rigid response was assumed up to failure, followed by linear softening. Since lateral loading mainly produces in-plane internal forces at the interface, no tensile damage was assumed. The shear stress limit, $f_{b,FRP}$, and the fracture energy value were defined based on provisions in CNR-DT 200 R1/2013 [14].

3.1 Calibration of the model adopted for the infill

The model used for the unreinforced and the retrofitted infill was firstly calibrated by simulating diagonal compression tests on masonry specimens. Two tests previously performed at university of Salento on tuff stone masonry walls were selected [31]. The tests setup and the details of the specimens are provided in **Figure 3** and **Table 3**, respectively.

ID	Dimensions [mm]	Masonry type	f_{cw} [MPa]	E_w [MPa]	t_{FRP} [mm]	b_{FRP} [mm]	f_{FRP} [MPa]	E_{FRP} [MPa]
URW	650x650	Tuff stone	13.9	7796.0	-	-	-	-
FRPW	650x650	Tuff stone	13.9	7796.0	0.14	90.0	2326.0	75980.0

Table 3. Specimens' details in diagonal compression tests.

The tests were conducted according to the ASTM E 519-02 standard [34] and were aimed at characterizing the in-plane strength of tuff stone masonry walls typical of Southern Italy. The specimens were composed of 11 layers of masonry bricks with dimensions equal to 100x50x100 mm and cementitious mortar joints of about 10 mm thickness. It is worth noting that the mechanical properties of the masonry wall and the FRP retrofit are the same described in section 2.1.

A monotonic force-controlled loading protocol was applied along the diagonal direction of the specimens through a manually-operated hydraulic jack. The restrained corners of the wall were cut to uniformly distribute the applied load on a plane surface. The diagonal deformations of the specimens were monitored

through linear variable displacement transducers (LVDT), placed at both sides along the two diagonals of the walls. An additional LVDT was also placed at each side to detect possible out-of-plane displacements.

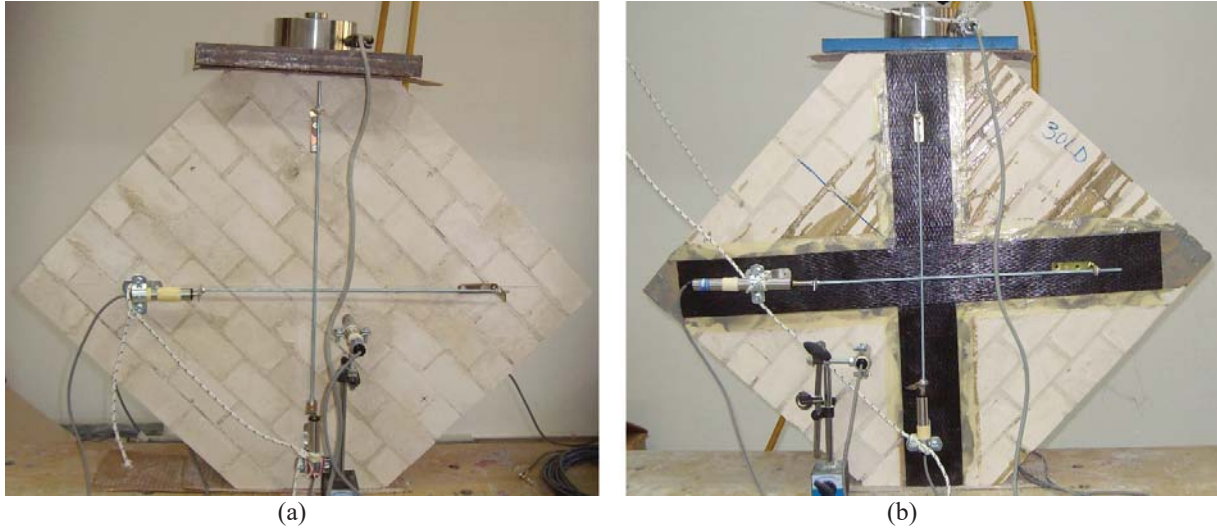


Figure 3. Test setup for (a) *URW* and (b) *FRPW*.

The response of *URW* specimen to diagonal compression was characterized by a brittle failure caused by shear cracking of mortar joints. An off-diagonal cracking path was observed (**Figure 4a**), starting from the corner of the loaded surface. Additionally, geometry imperfections in the specimen caused a minor out-of-plane failure mode. This aspect is evidenced by the significant difference between the displacement measurements provided the vertical LVDTs at the two sides of the wall (LVDT s_x and LVDT d_x , respectively). The Load-displacement curve is provided in **Figure 5a**. The maximum strength, $F_{m,test}$, and the corresponding displacement, $D_{m,test}$, were equal to 21.5 kN and 0.32 mm, respectively.

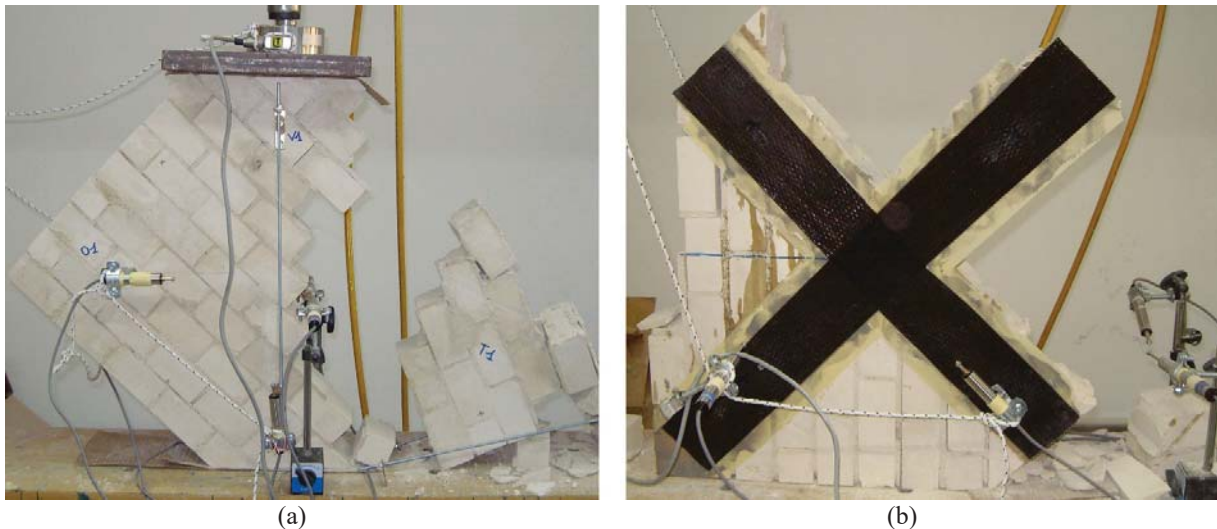


Figure 4. Failure in case of (a) *URW* and (b) *FRPW*.

In the case of *FRPW* specimen, the failure mode was characterized by cohesive debonding of the FRP layer at both sides of the wall, followed by collapse (**Figure 4b**). The presence of retrofit significantly enhanced both the maximum strength and the displacement capacity with respect to the unreinforced

configuration. The values of $F_{m,test}$ and $D_{m,test}$ were equal to 53.1 kN (+146% with respect to *URW*) and 0.71 mm (+ 296% with respect to *URW*), respectively. Consequently, a significant increase of the cumulative energy dissipated, ED , was obtained in the case of retrofitted wall, as shown in **Table 4**.

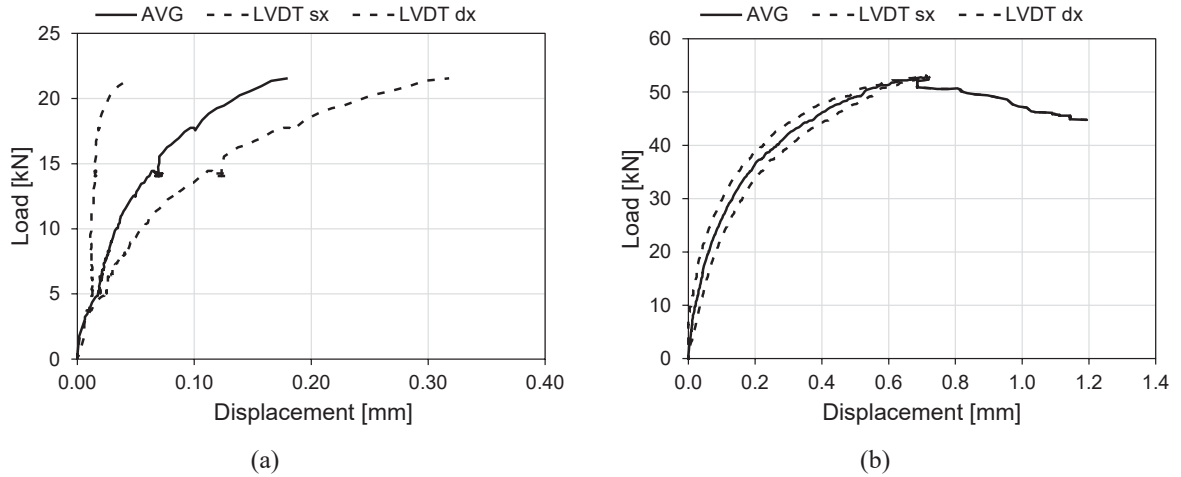


Figure 5. Load-displacement curves obtained for (a) *URW* and (b) *FRPW*.

In the numerical model, the boundary conditions were simulated by including translational restraints in the three-principal directions and a displacement-controlled vertical load at the bottom and the top surface of the wall, respectively (**Figure 6**). The fracture energy and the shear limit values in the cohesive laws employed for the brick-to-brick and the wall-to-FRP interaction were adjusted to obtain a satisfactory matching of the experimental Load-displacement curves. The comparison between the numerical and the experimental results is provided in **Figure 7**, while the failure modes obtained in the numerical simulations are shown in **Figure 8**. In the case of *URW*, a satisfactory matching of the linear elastic slope of the experimental curve was obtained, up to a load value equal to 12 kN. Nevertheless, the progressive slope reduction observed in the test, caused by out-of-plane failure, was not simulated by the numerical model. It is worth reminding the unsymmetric vertical displacement measurements provided by the LVDTs placed at opposite sides of the wall, which suggest a significant influence of the specimen's imperfections on the test results. Being this feature not replicated in the numerical model, an accurate match of the post-elastic phase of the curve was not possible.

ID	$F_{m,test}$ [kN]	$D_{m,test}$ [mm]	ED_{test} [kNmm]
URW	21.5	0.18	2.76
FRPW	53.1	0.71	51.93

Table 4. Diagonal compression tests results.

On the other hand, a satisfactory agreement was obtained in terms of maximum strength, displacement capacity and, consequently, cumulative energy dissipated. The difference between the experimental and numerical maximum strength ($F_{m,test}$ and $F_{m,FEM}$, respectively) was equal to 4.8%. The displacement corresponding to the maximum strength in the numerical simulation ($D_{m,FEM}$) was equal to 0.17 mm, that is 5.5% lower compared to $D_{m,test}$. The failure mode in numerical simulation was characterized by minor diagonal cracking followed by bed joint sliding (**Figure 8a**). The difference between numerical and experimental results can be related to the specimen imperfections. Furthermore, it is worth evidencing that

the actual mortar joint thickness was not explicitly included in the numerical model, possibly causing a different path of internal forces comparing to the test.

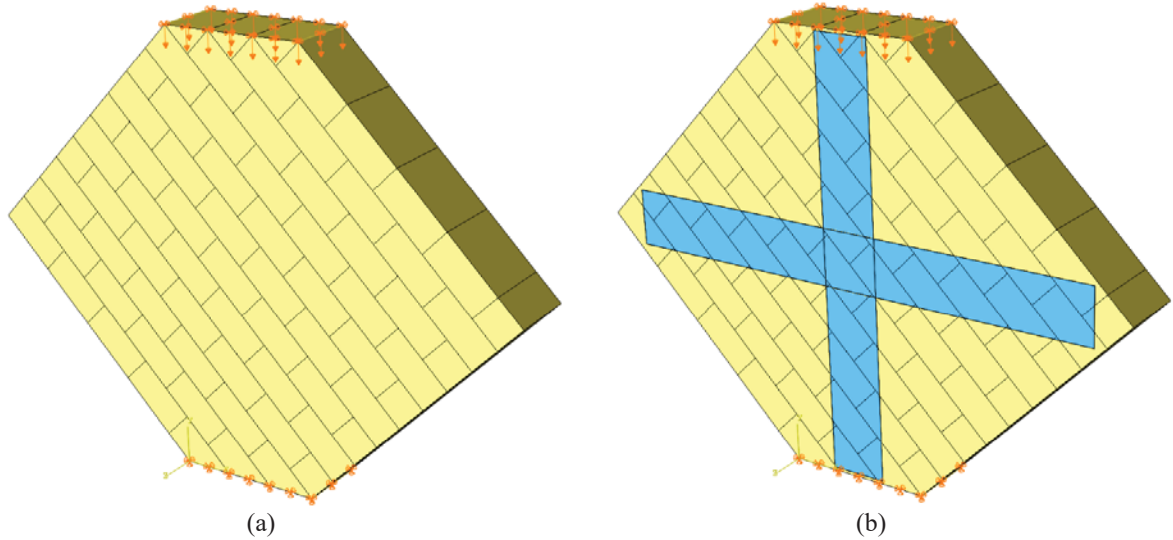


Figure 6. Numerical model for the simulation of the diagonal compression tests: (a) *URW* and (b) *FRPW*.

In the case of *FRPW*, both elastic and post-cracking response were precisely simulated by the numerical model, resulting in a satisfactory matching of the energy dissipation capacity up to the maximum strength. The curve obtained from the numerical simulation is characterized by a first, minor debonding of the FRP layer, followed by a redistribution of the internal forces at the wall-FRP interface and stiffness restoration up to failure (**Figure 8b**). Despite the neglectable difference between the numerical and the experimental value of F_m (+1.0%), the numerical model was unable to simulate the post-peak response and the displacement capacity of the specimen. The value of $D_{m,FEM}$ was 23.7% higher than $D_{m,test}$, while the difference between numerical and experimental ED at failure was equal to 23.65%. This result is probably due to the high complexity of the failure mode of FRP-retrofitted wall, which can be highly influenced by imperfections, such as uneven adhesion of the FRP layer on the wall surface.

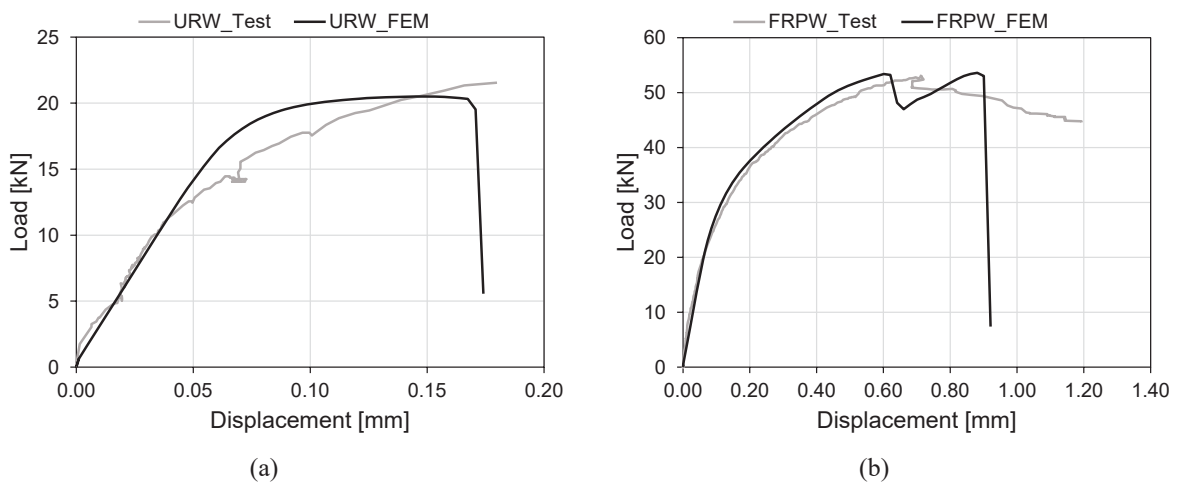


Figure 7. Comparison between numerical and experimental Load-displacement curves for (a) *URW* and (b) *FRPW*.

The calibrated values of the fracture energy and the shear limit in the cohesive laws employed for the brick-to-brick and the wall-to-FRP interaction were used in the finite element model developed for the simulation of the lateral behaviour of the infilled frames. The same properties as the diagonal compression tests specimens were assumed for masonry brick units and FRP retrofit. The wall thickness was modified from 100 mm to 200 mm, in order to reproduce the configuration of infill walls in full-scaled portals.

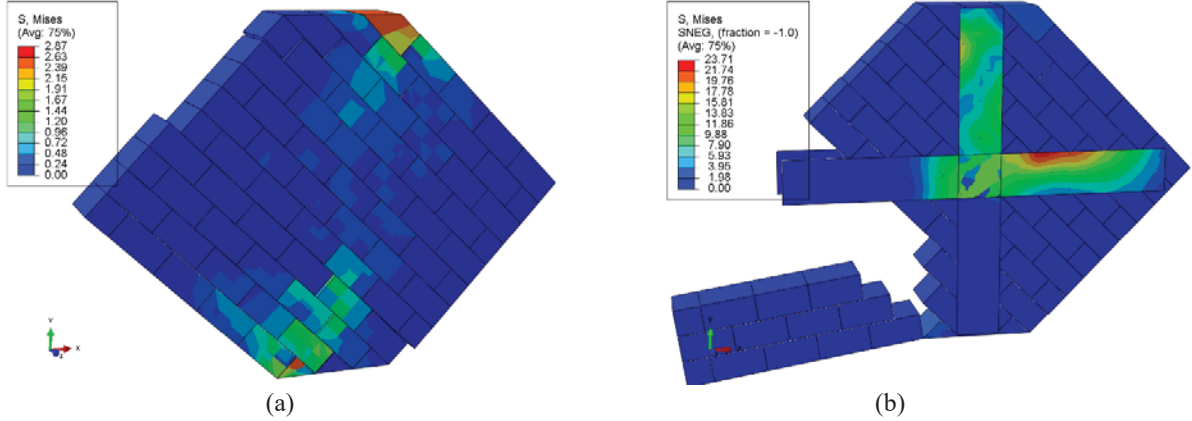


Figure 8. Failure modes in numerical simulation for (a) *URW* and (b) *FRPW*.

4 PUSHOVER ANALYSIS OF THE FRAMES

The pushover analysis of the frames was performed considering a horizontal displacement-controlled loading protocol, applied to the top of the portal frame. The displacement amplitude was increased up to the achievement of the maximum value Δ_{max} , assumed equal to $\theta_{u,c} \cdot h_c$, being $\theta_{u,c}$ the expected ultimate chord rotation of the columns, computed using equation (7) provided in Eurocode 8 [35].

$$\theta_{u,c} = 0.825 \cdot 0.016 \cdot h_c \cdot (0.3^v) \left[\frac{\max(0.01; \omega') f_c}{\max(0.01; \omega)} \right]^{0.225} \left(\frac{L_v}{h_c} \right)^{0.35} 25^{\left(\alpha \rho_{sx} \frac{f_{yw}}{f_c} \right)} \quad (7)$$

In the equation (7), v is the axial load ratio, ω and ω' are the reinforcement index for tensile and compressive longitudinal rebars, f_c is the cylindrical compressive strength of the concrete, L_v is the shear span, α is the confinement coefficient, ρ_{sx} and f_{yw} are the transverse reinforcement ratio and tensile strength, respectively. The value of Δ_{max} can be reasonably assumed as an upper displacement limit, since the presence of the masonry infill walls generally reduces the displacement capacity of RC frames with respect to a bare configuration.

The lateral load-displacement response and the failure modes of the analysed frames is reported in **Figure 9** and **Figure 10**, respectively. It is worth mentioning that the shear failure of the RC frame members was not detectable by the modelling approach developed, since the mechanical model used for concrete does not account for material degradation under shear. Therefore, the occurrence of the shear failure was assessed by comparing, for each column, the maximum of shear obtained from the analysis to the analytical shear strength, V_{Rc} . The value of V_{Rc} was computed according to the variable inclination strut model [36].

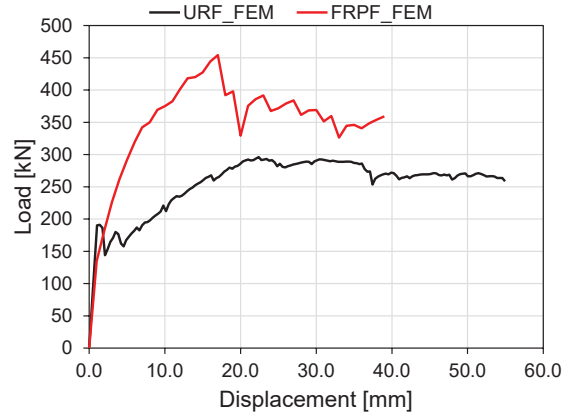


Figure 9. Lateral response of the analysed portal frames.

As shown in **Figure 9**, the maximum lateral strength, F_m , was 53.4% higher in case of **FRPF** compared to **URF**. On the other hand, the contribution of the FRP layer to the elastic stiffness is neglectable. In the case of **FRPF**, retrofit debonding was observed after the attainment of F_m , at a displacement amplitude equal 17 mm. Referring to **URF**, the onset of damage in the infill wall was characterized by mortar joints cracking, followed by the generation of a strut mechanism. The maximum strength was attained for a displacement amplitude equal to 22.4 mm, while the post-peak behaviour featured mortar bed joints sliding. The strut mechanism generation, representing the compression field in the wall, leads to an uneven shear distribution among the two columns. This phenomenon is more noticeable in the case of **FRPF**, since the presence of the retrofit delays the cracking generation in mortar joints, as shown in **Figure 11**.

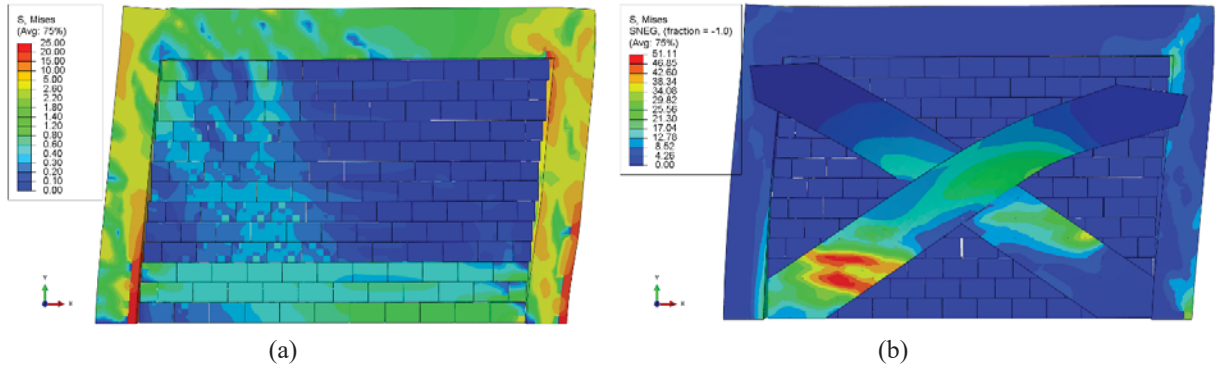


Figure 10. Failure modes in numerical simulation for (a) **URF** and (b) **FRPF**.

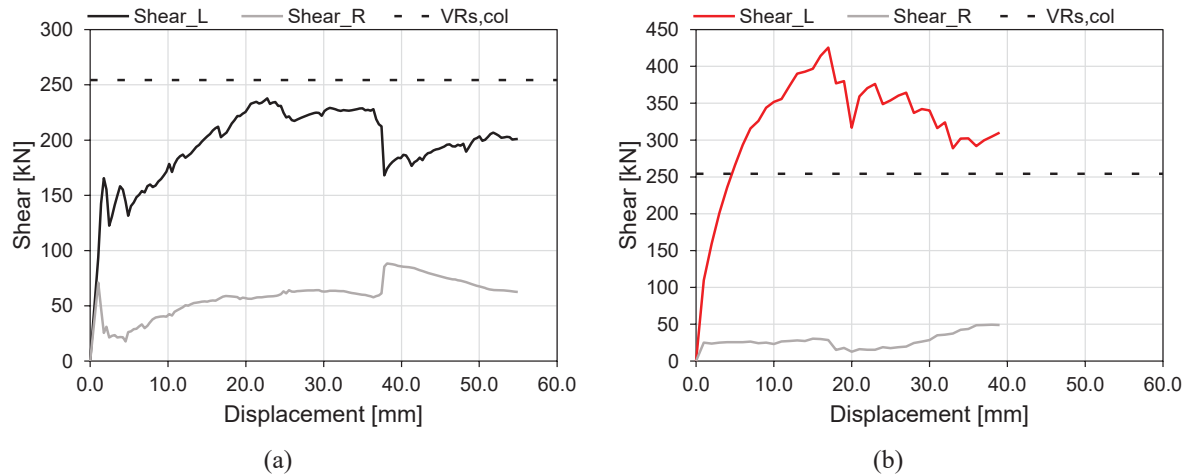


Figure 11. Shear-displacement response obtained for both columns (Shear_L and Shear_R) in case of (a) *URF* and (b) *FRPF*.

The maximum shear in the column in case of retrofitted infill was 67% higher than the shear strength of the column, suggesting early shear failure (**Figure 11b**). Additionally, the displacement amplitude corresponding to the attainment of the shear strength of the column was equal to 4.5 mm, namely 73% lower compared to the debonding displacement. In the case of *URF*, the value of V_{Rc} was higher than the maximum shear (**Figure 11a**), suggesting a ductile failure mode of the frame and, consequently, higher displacement and energy dissipation capacity compared to *FRPF*. The comparison of the cumulative energy dissipated up to failure (ED_{SF}), provided in **Figure 12**, evidences the high influence of the retrofit on the performance of the infilled frames analysed. The value of ED_{SF} decreases by 93.2% comparing *URF* to *FRPF* results.

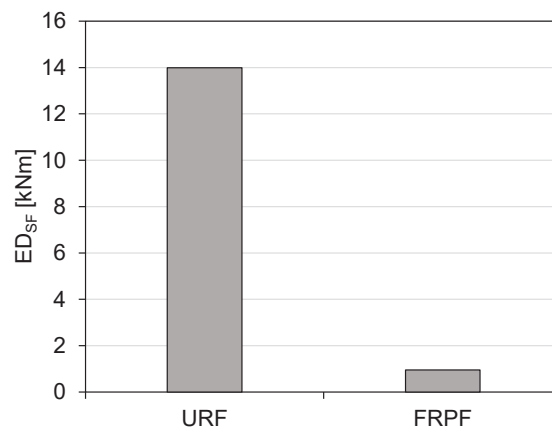


Figure 12. Energy dissipation capacity up to failure of the analysed portal frames.

5 CONCLUSIONS

The influence of infill walls on the seismic performance of RC buildings has been widely demonstrated in the literature. The presence of infill walls characterized by high shear strength can significantly increase the shear demand in the columns, leading to possible premature shear failure in RC frames without adequate structural detailing. The use of FRP to avoid the out-of-plane failure of masonry infills, as well as to improve

their in-plane capacity is commonly adopted nowadays. However, this retrofit intervention is often not designed accounting for the interaction between the infill wall and the surrounding RC frame.

In this study, the response of a masonry infilled RC portal frames designed for gravity load was analysed. Two configurations were considered. The first one was characterized by unreinforced masonry infill, while in the second configuration, FRP retrofit of the of the infill was assumed. A non-linear static analysis was performed on the considered frames, aiming to assess the influence of the infill retrofit on the maximum strength, the displacement and the energy dissipation capacity.

A three-dimensional numerical model was developed, including interface interaction laws between the brick units, at the frame-infill and at the infill-retrofit interface. The interaction laws were calibrated based on diagonal compression tests on tuff stone specimens previously performed at University of Salento. The scope of the modelling approach was the accurate evaluation of the internal forces' distribution, as well as the simulation of the main mechanisms characterizing the lateral response of the analysed infilled frames.

The comparison between numerical and experimental results, referred to the diagonal compression tests, showed a high reliability of the developed finite-element models in simulating the shear response of unreinforced and retrofitted masonry walls. A satisfactory agreement was obtained in terms of maximum shear strength, elastic stiffness and failure modes. The numerical model accurately reproduced the mortar bed joints sliding and the debonding of the FRP retrofit from the wall surface.

The results of the non-linear static analyses carried out on the RC portal frames showed a significant difference in the lateral response of the considered configurations. A ductile failure mode was observed in the case of unreinforced infill, featuring flexural failure of the columns, while the introduction of the FRP reinforcement led to a severe reduction of the ductility capacity of the structure. Despite the increase of the maximum lateral strength caused by the retrofit, early brittle failure of the columns was observed.

The results of this study pointed out the importance of accounting for the interaction between RC frame and infill walls when retrofit techniques, which increase the capacity of the masonry infills, are adopted. Further studies are still required to define design prescriptions which regulate the seismic retrofit of infill walls with composite materials in existing RC buildings.

ACKNOWLEDGEMENTS

This work was supported by “The Laboratories University Network of Seismic Engineering” (RELUIS) under Grant DPC-RELUIS 2019-2021.

REFERENCES

- [1] Dhakal RP (2010): Damage to non-structural components and contents in 2010 Darfield earthquake. *Bulletin of the New Zealand Society for Earthquake Engineering*, **43** (4), 404–11.
- [2] Perrone D, Calvi PM, Nascimbene R, Fischer EC, Magliulo G (2018): Seismic performance of non-structural elements during the 2016 Central Italy earthquake. *Bulletin of Earthquake Engineering*, 1–23.
- [3] Verderame GM, Ricci P, De Luca F, Del Gaudio C, De Risi MT (2014): Damage scenarios for RC buildings during the 2012 Emilia (Italy) earthquake. *Soil Dynamics and Earthquake Engineering*, **66**, 385–400.
- [4] Messali F, Ravenshorst G, Esposito R, Rots J (2017): Large-scale testing program for the seismic characterization of Dutch masonry walls. *16th World Conference on Earthquake*, Santiago Chile, p. Paper N° 4753.

- [5] Pujol S, Fick D (2010): The test of a full-scale three-story RC structure with masonry infill walls. *Engineering Structures*, **32** (10), 3112–21.
- [6] Butenweg C, Marinković M, Salatić R (2019): Experimental results of reinforced concrete frames with masonry infills under combined quasi-static in-plane and out-of-plane seismic loading. *Bulletin of Earthquake Engineering*, **17**, 3397–422.
- [7] Celarec D, Ricci P, Dolšek M (2012): The sensitivity of seismic response parameters to the uncertain modelling variables of masonry-infilled reinforced concrete frames. *Engineering Structures*, **35**, 165–77.
- [8] Di Trapani F, Bertagnoli G, Ferrotto MF, Gino D (2018): Empirical Equations for the Direct Definition of Stress–Strain Laws for Fiber-Section-Based Macromodeling of Infilled Frames. *Journal of Engineering Mechanics*, **144** (11), 04018101.
- [9] Facconi L, Minelli F, Giuriani E (2018): Response of infilled RC frames retrofitted with a cementitious fiber-mesh reinforced coating in moderate seismicity areas. *Construction and Building Materials*, **160**, 574–87.
- [10] Koutas L, Bousias SN, Triantafillou TC (2015): Seismic Strengthening of Masonry-Infilled RC Frames with TRM: Experimental Study. *Journal of Composites for Construction*, **19** (2), 04014048.
- [11] Altin S, Anil Ö, Kopraman Y, Belgin Ç (2010): Strengthening masonry infill walls with reinforced plaster. *Proceedings of the Institution of Civil Engineers: Structures and Buildings*, **163** (5), 331–42.
- [12] Corradi M, Borri A, Castori G, Sisti R (2014): Shear strengthening of wall panels through jacketing with cement mortar reinforced by GFRP grids. *Composites: Part B*, **64**, 33–42.
- [13] Erol G, Taskin K, Yuksel E, Karadogan HF (2005): Strengthening of infilled RC frames by CFRP. *WIT Transactions on the Built Environment*, **81**, 591–600.
- [14] Consiglio Nazionale delle Ricerche (2013): *Istruzioni per la Progettazione, l'Esecuzione ed il Controllo di Interventi di Consolidamento Statico mediante l'utilizzo di Compositi Fibrorinforzati*. Italy.
- [15] Consiglio Superiore dei Lavori Pubblici (2018): *Linea Guida per la identificazione, la qualificazione ed il controllo di accettazione di compositi fibrorinforzati a matrice inorganica (FRCM) da utilizzarsi per il consolidamento strutturale di costruzioni esistenti*. Italy.
- [16] Perrone D, Leone M, Aiello MA (2016): Evaluation of the infill influence on the elastic period of existing RC frames. *Engineering Structures*, **123**, 419–33.
- [17] Huang H, Burton H V., Sattar S (2020): Development and Utilization of a Database of Infilled Frame Experiments for Numerical Modeling. *Journal of Structural Engineering*, **146** (6), 04020079.
- [18] FEMA 356 (2000): *FEMA 356 Prestandard and Commentary for the Seismic Rehabilitation of Building*. Federal Emergency Management Agency.
- [19] Jeon J-S, Park J-H, DesRoches R (2015): Seismic fragility of lightly reinforced concrete frames with masonry infill. *Earthquake Engineering and Structural Dynamics*, **44**, 1783–803.
- [20] Burton H, Deierlein G (2013): Simulation of Seismic Collapse in Non-Ductile Reinforced Concrete Frame Buildings with Masonry Infills. *Journal of Structural Engineering*, **140** (8), A4014016.
- [21] Blasi G, Perrone D, Aiello MA (2020): Influence of the modelling approach on the failure modes of RC Infilled frames under seismic actions. *Lecture Notes in Civil Engineering - Proceedings of Italian Concrete Days 2018*, vol. 42, Springer.

- [22] Blasi G, Perrone D, Aiello MA (2018): Fragility functions and floor spectra of RC masonry infilled frames: influence of mechanical properties of masonry infills. *Bulletin of Earthquake Engineering*, **16**, 6105–6130.
- [23] Madan A, Reinhorn AM, Mander JB, Valles RE (1997): Modeling of Masonry Infill Panels for Structural Analysis. *Journal of Structural Engineering*, **123** (10), 1295–302.
- [24] Blasi G, De Luca F, Aiello MA (2018): Brittle failure in RC masonry infilled frames: The role of infill overstrength. *Engineering Structures*, **177**, 506–18.
- [25] Blasi G, Perrone D, Aiello MA, Fleischman R (2020): Retrofit of masonry infills: local interaction with RC frames. *Proceedings of the 17th world conference on Earthquake Engineering*, p. Paper N 3e-0019.
- [26] Cavaleri L, Di Trapani F (2015): Prediction of the additional shear action on frame members due to infills. *Bulletin of Earthquake Engineering*, **13** (5), 1425–54.
- [27] Redmond L, Stavridis A, Kahn L, DesRoches R (2018): Finite-Element Modeling of Hybrid Concrete-Masonry Frames Subjected to In-Plane Loads. *Journal of Structural Engineering*, **144** (1), 04017178.
- [28] Akhoundi F, Lourenço PB, Vasconcelos G (2014): Numerical Modelling of Masonry-Infilled Reinforced Concrete Frames: Model Calibration and Parametric Study. *9th International Masonry Conference (9IMC2014)*.
- [29] Pantò B, Calì I, Lourenço PB (2017): Seismic safety evaluation of reinforced concrete masonry infilled frames using macro modelling approach. *Bulletin of Earthquake Engineering*, **15** (9), 3871–95.
- [30] Marcari G, Manfredi G, Prota A, Pecce M (2007): In-plane shear performance of masonry panels strengthened with FRP. *Composites Part B: Engineering*, **38** (7–8), 887–901.
- [31] Leone M, Sciolti MS, Aiello MA (2012): In-plane shear behavior of BFRP reinforced masonry panels. *Proceeding of the New boundaries in the application of FRP composites in Civil Engineering - 6th International Conference on FRP composites in civil engineering*, Rome (IT).
- [32] NTC-2018 (2018): *Aggiornamento delle «Norme tecniche per le costruzioni»*. D.M. 17 Gennaio 2018, Italy.
- [33] Dassault Systemes (2016): *Abaqus Theory Manual*.
- [34] ASTM E 519-02 (2002): *Standard Test Method for Diagonal Tension (Shear) in Masonry Assemblages*. American National Standard.
- [35] EN 1998-3 (2005): *Eurocode 8 - Design of structures for earthquake resistance - Part 3: Assessment and retrofitting of buildings*. European Standard.
- [36] Fardis MN (2009): *Seismic design, assessment and retrofitting of concrete buildings*. Springer.

ASSESSMENT OF OUT-OF-PLANE STRENGTH OF MASONRY INFILLS ACCORDING TO EC6

L. Liberatore¹

¹ Department of Structural and Geotechnical Engineering, Sapienza University of Rome
Via Gramsci, 53 - 00197 Rome, Italy
e-mail: laura.liberatore@uniroma1.it

Abstract

In the last decades the attention to the out-of-plane response of infills has been increasingly growing due to their influence on the global seismic behaviour of frame structures. In order to assess their out-of-plane capacity, different approaches have been proposed, such as those based on the arching effect and on the yield-line theory. Both methods are implemented in Eurocode 6 for masonry structures. The first approach is based on the observation that an arching effect develops in a wall provided that surrounding elements are able to resist thrust. The second approach consists in defining a kinematically admissible mechanism (yield-line mechanism) and calculating the limit load by equating the internal and external works. This method was implemented in Eurocode 6 (EC6) as well as in other codes by means of coefficients, which depend on the orthogonal ratio of the masonry flexural strengths, the degree of fixity at the edges of the wall and the wall aspect ratio. The suitability of the methods proposed in EC6 is investigated herein for masonry infills through comparison with experimental tests. It is found that, considering the second approach, the results are, on the average, conservative, contrary to the assumption that the method should provide an upper bound of the resistance.

Keywords: Infilled frames, Out-Of-Plane Collapse, Arching Effect, Yield-line Theory, Compressive Strength, Flexural Strength.

1 INTRODUCTION

The influence of masonry infills to the structural response of frame buildings is widely recognized. The presence of regularly distributed infills is usually beneficial, due to their capacity to reduce the displacement demand and to dissipate energy [1–5]. On the other hand, irregular distributions due to the lack of one or more panels may lead to the increase of internal forces and displacements as well as to brittle failures [6–9]. In addition, the collapse of infills, especially in the out-of-plane (OOP) direction, occurs also for moderate intensity of the ground motion [10–13], causing casualty risks and economic losses. This explains the fact that in the last years the OOP response of infills and the interaction between in-plane (IP) and OOP actions have become issues of major concern [14–19]. Different methods have been put forward for their assessment, like those based on rigid body mechanisms or on numerical and iterative solutions [20,21]. The first category includes methods derived from the yield-line theory as well as methods which take into account the arching effect.

The first approach, based on the yield-line theory, was initially proposed to determine the collapse load of reinforced concrete slab [22,23] and was subsequently applied to masonry walls [24,25]. The method allows taking into account different strengths in two orthogonal directions and the bending resistance along supports. It consists in defining a kinematically admissible mechanism in which all deformations (rotations) take place along yield lines and edges, and the single portions of the wall rotate as rigid bodies (Figure 1a). The limit load is estimated by equating the internal work, which is given by the energy dissipated along the yield lines, to the external work, i.e. the work done by the applied loads. Among the infinite number of mechanisms, the collapse mechanism is the one that occurs under the smallest load. Considering the upper bound theorem of the limit analyses, it is possible to recognise that the yield-line method provides an upper bound of the wall strength. This method was implemented in Eurocode 6 [26] (EC6 hereinafter) as well as in other codes [27] by means of coefficients, which depend on the degree of fixity at the edges of the wall, the wall aspect ratio and the orthogonal ratio of the masonry flexural strengths.

The second approach is based on the observation that the arching effect develops in a wall provided that surrounding elements are able to resist thrust. In the one-way arching model, the collapse is associated to a three-hinge mechanism (Figure 1b), which is usually activated along the shorter dimension, and the collapse load depends on the masonry compressive strength and on the wall slenderness [28]. When the infill is restrained at four edges, a two-way arching action may develop, thus increasing the OOP strength [29,30]. The one-way arching method is included in EC6 which provides an equation of the limit load that can be used when lateral deflections are small.

The suitability of the methods proposed in EC6 for masonry structures and described in § 2, is investigated herein for masonry infills through comparison with experimental tests. Specifically, a dataset of 71 experimental tests on one-storey one-bay infilled frames is compiled (§ 3) and the related experimental OOP strengths are compared with those predicted by the EC6 formulations in § 4.

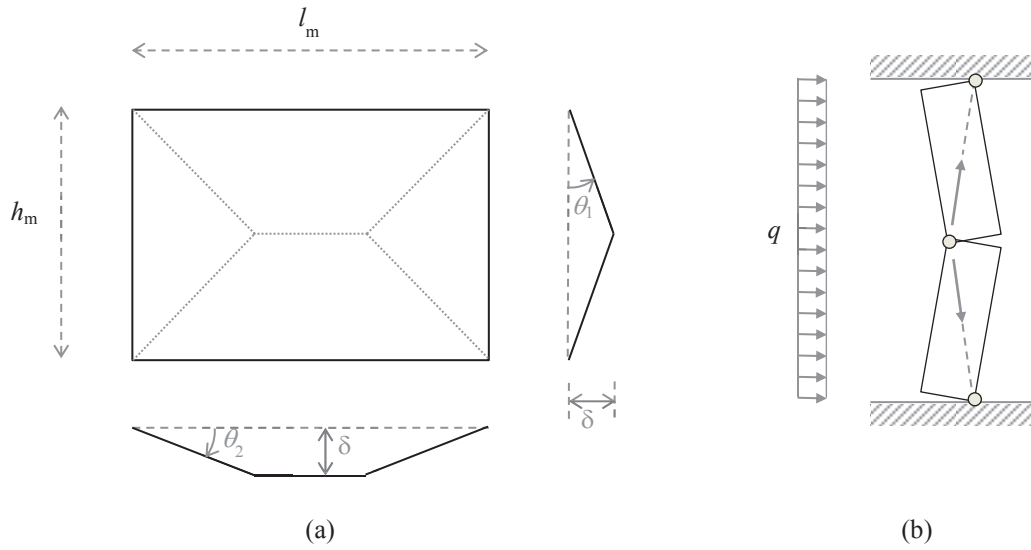


Figure 1: a) example of a kinematically admissible mechanism for an infill supported on four edges for use in the yield-line method; b) one-way arching model, the collapse is associated to a three-hinge mechanism.

2 EC6 PREDICTIVE MODELS

As mentioned above, the yield-line method was included in EC6 in form of tabulated coefficients. The procedure consists in verifying that the design value of the moments applied to a masonry wall does not exceed the corresponding moments of resistance. The design moments per unit length in two orthogonal directions, M_{Ed1} and M_{Ed2} , acting on a wall subjected to the design lateral uniform pressure q_d can be calculated as:

$$M_{Ed1} = \alpha_1 q_d l_m^2 \quad (1)$$

$$M_{Ed2} = \alpha_2 q_d l_m^2 \quad (2)$$

while the moments of resistance as:

$$M_{Rd1} = f_{xd1} Z \quad (3)$$

$$M_{Rd2} = f_{xd2} Z \quad (4)$$

where: α_2 is a coefficient provided in Annex E of EC6; $\alpha_1 = \mu \alpha_2$; μ is the orthogonal ratio, i.e. the ratio between the flexural strength in the horizontal direction, f_{x1} , and in the vertical direction, f_{x2} (Figure 2); l_m is the length of the wall; Z is the elastic section modulus of unit length of the wall:

$$Z = t^2/6 \quad (5)$$

and t is the panel thickness.

The inequality between the design value of the applied moment and the design value of the moment of resistance gives:

$$\alpha_1 q_d l_m^2 \leq f_{xd1} Z \quad (6)$$

$$\alpha_2 q_d l_m^2 \leq f_{xd2} Z \quad (7)$$

thus:

$$q_d \leq \frac{f_{xd2} Z}{\alpha_2 l_m^2} \quad (8)$$

Values of α_2 , which are provided in Annex E for different boundary conditions, orthogonal ratios and aspect ratios, are given by the following equation:

$$\alpha_2 = \frac{f_{xd2} Z}{q l_m^2} \quad (9)$$

where q is the uniform load which leads to collapse, calculated through the yield-line theory. An example of calculations is reported in [31].

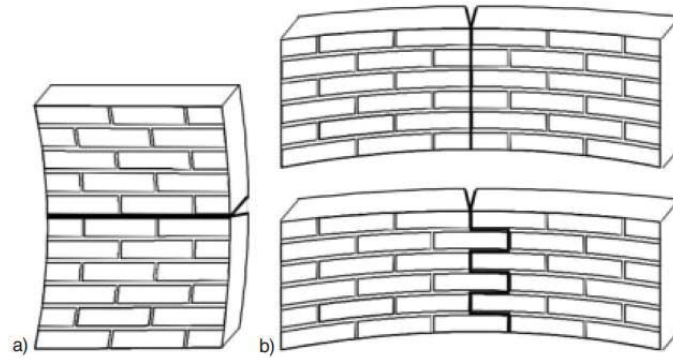


Figure 2: Plane of failure of masonry in bending: a) parallel to bed joints, flexural strength f_{x1} ; b) perpendicular to bed joints, flexural strength f_{x2} [26].

The other approach encompassed in EC6 is based on the assumption that an arching effect develops in unreinforced masonry walls having slenderness ratio not greater than 20 and design value of the vertical stress not less than 0.1 MPa. In these cases, a wall subjected to lateral loading may be designed by employing the following equation:

$$q_d = f_d \left(\frac{t}{l_a} \right)^2 \quad (10)$$

where: q_d is the design lateral strength per unit area; f_d is the design compressive strength of the masonry in the direction of the arch thrust; l_a is the length or the height of the wall depending on the direction along which the arching effect develops and t is the wall thickness.

Finally, it is worthwhile to mention that Eurocode 8 [32] suggests measures to avoid the OOP collapse of slender masonry panels with specific reference to panels with slenderness ratio greater than 15. Examples of measures for the improvement of both IP and OOP response include the use light wire meshes, wall ties fixed to the columns, wind-posts and concrete belts.

3 EXPERIMENTAL TESTS

Seventy-one experimental tests are employed in this study (Table 1). Both infilled reinforced concrete and steel frames are considered as well as confined masonries. The slenderness ratio, $sr = l_a/t$, and the aspect ratio, $ar = h_m/l_m$, vary in the range 7–34 and 0.5–1.0, respectively (Table 2).

The walls were made up of clay bricks having horizontal or vertical hollows, solid clay bricks and concrete blocks having vertical hollows, as specified in Table 2. The masonry

compressive strength varies between 0.5 and 28.1 MPa. However, in 80% of the cases it not greater than 15.0 MPa, higher values are related to concrete block infills.

In 39 tests the infill were loaded in the OOP direction only. Generally, the OOP loads were applied monotonically by means of airbags, in some cases they were applied at four points or at mid-height.

The interaction between IP and OOP actions was considered in 32 tests, where an IP horizontal displacement was applied at the beam level prior to the OOP load. Maximum IP interstorey drift ratios (*IDR*) are specified in Table 1.

Reference	OOP ⁽¹⁾	IP-OOP ⁽²⁾	Frame ⁽³⁾	Supported edges ⁽⁴⁾	<i>IDR</i> ⁽⁵⁾ (%)	OOP load type
Dawe and Seah (1989) [29]	6	-	Steel	3 (1 test), 4 (5 tests)	-	airbag
Angel <i>et al.</i> (1994) [33]	1	5	RC	4	0.22, 0.25, 0.34	airbag
Flanagan (1994) [34]	3	2	Steel	4	0.42, 0.84	airbag
Flanagan and Bennett (1999) [35]	3	2	Steel	4	0.42, 0.84	airbag
Calvi and Bolognini (2001) [36]	1	2	RC	4	0.4, 1.2	four points
Pereira <i>et al.</i> (2011, 2014) [37,38]	-	4	RC	4	0.5	airbag
Varela-Rivera <i>et al.</i> (2011) [39]	6	-	CM	3 (3 tests) 4 (3 tests)	-	airbag
Varela-Rivera <i>et al.</i> (2012) [40]	6	-	CM	4	-	airbag
Da Porto <i>et al.</i> (2013) [41]	-	3	RC	4	0.5, 0.19	four points
Hak <i>et al.</i> (2014) [42]	-	3	RC	4	1.0, 1.5, 2.5	mid-height
Furtado <i>et al.</i> (2016) [43]	2	1	RC	4	0.5	airbag
Akhoundi <i>et al.</i> (2016) [44]	1	-	RC	4	-	airbag
Wang (2017) [45]	3	1	RC (3 tests) Steel (1 test)	3 (1 test) 4 (3 tests)	1.34	airbag
Sepasdar (2017) [46]	2	2	RC	4	0.65, 1.7	airbag
Ricci <i>et al.</i> (2018) [47]	1	3	RC	4	0.16, 0.37, 0.58	four points
De Risi <i>et al.</i> (2019) [48]	1	3	RC	4	0.15, 0.28, 0.51	four points
Di Domenico <i>et al.</i> (2019) [49]	3	-	RC	3 (2 tests) 4 (1 test)	-	four points
Akhoundi <i>et al.</i> (2020) [50]	3	3	RC	4	0.3, 0.5, 1.0	airbag

⁽¹⁾ number of tests subjected to OOP loads only;

⁽²⁾ number of tests subjected to IP drift and OOP load;

⁽³⁾ Frame material: RC = Reinforced Concrete, CM = Confined Masonry;

⁽⁴⁾ number of supported edges;

⁽⁵⁾ Interstorey Drift Ratio.

Table 1: Experimental tests on infilled frames.

Reference	Masonry units ⁽¹⁾	$f_m^{(2)}$ (MPa)	$sr^{(3)}$	$ar^{(4)}$
Dawe and Seah (1989) [29]	concrete blocks, vh	20.20 – 28.10	15 – 31	0.78
Angel <i>et al.</i> (1994) [33]	solid clay bricks	4.6 – 11.5	17 – 34	0.67
Flanagan (1994) [34]	clay bricks, hh	2.29 – 5.59	7 – 24	1.00
Flanagan and Bennett (1999) [35]	clay bricks, hh	1.1	20	0.66
Calvi and Bolognini (2001) [36]	clay bricks, hh	1.26 – 1.34	11 – 19	0.51
Pereira <i>et al.</i> (2011, 2014) [37,38]	clay bricks, hh	3.0	12 – 24	0.49
Varela-Rivera <i>et al.</i> (2011) [39]	concrete blocks, vh	2.45 – 2.84	18 – 24	0.74 – 0.95
Varela-Rivera <i>et al.</i> (2012) [40]	concrete blocks, vh	2.0 – 6.0	9 – 22	0.64
Da Porto <i>et al.</i> (2013) [41]	clay bricks, hh (1 test) and vh (2 tests)	4.64	8	0.70
Hak <i>et al.</i> (2014) [42]	clay bricks, vh	0.53	15	0.55
Furtado <i>et al.</i> (2016) [43]	clay bricks, hh	1.59	20	0.68
Akhoundi <i>et al.</i> (2016) [44]	clay bricks, hh	7.9 – 9.0	11–15	0.73
Wang (2017) [45]	concrete blocks, vh	9.4 – 9.7	11	0.73
Sepasdar (2017) [46]	concrete blocks, vh	1.80	23	0.78
Ricci <i>et al.</i> (2018) [47]	clay bricks, hh	2.37	23	1.00
De Risi <i>et al.</i> (2019) [48]	clay bricks, hh	1.65 – 2.44	15 – 29	0.78
Di Domenico <i>et al.</i> (2019) [49]	clay bricks, hh	1.17	20	0.68
Akhoundi <i>et al.</i> (2020) [50]	clay bricks, hh			

⁽¹⁾ hh = horizontal hollows, vh = vertical hollows;
⁽²⁾ masonry compressive strength;
⁽³⁾ slenderness ratio;
⁽⁴⁾ aspect ratio.

Table 2: Experimental tests on infilled frames, mechanical and geometrical data.

4 ASSESSMENT OF EC6 MODELS

In order to compare the OOP strength predicted by the formulations reported in EC6 (Eq. 8 and Eq. 10) with the strength obtained in experimental test, the following assumption are made.

- The experimental flexural strength, f_{x2} , is employed in Eq. 8 instead of the design flexural strength, f_{xd2} . When the former value was not available, the flexural strength provided by EC6 for different masonry types was adopted. Such value was multiplied by 1.5 to obtain a mean value from the characteristic one.
- Similarly, when the orthogonal ratio was not available from experimental campaigns, it was derived from EC6.
- The experimental compressive strength of masonry, f_m , is used in Eq. 10 in the place of the design strength, f_d , for a consistent comparison with experimental tests.
- Eq. 10 is applied also in case of walls having slenderness ratio greater than 20 in order to investigate the influence of such parameter.

Therefore, the predicted OOP strength, q_{pred} , is determined as

$$q_{pred} = \frac{f_{x2} Z}{\alpha_2 l_m^2} \quad (11)$$

and

$$q_{pred} = f_m \left(\frac{t}{l_a} \right)^2 \quad (12)$$

according to whether the method is based on the yield-line theory (Eq. 11) or on the arching effect (Eq. 12). As mentioned in § 2, l_a is the dimension of the wall in the direction along

which the arching effect develops. Therefore, in case of infills having a top gap l_a is the wall length, whereas for infills supported along four edges, it is the height, since aspect ratios are not greater than 1.0.

The experimental strength, q_{exp} , is the maximum OOP pressure recorded during the tests. In cases where the OOP load was applied in concentrated points, an equivalent uniform pressure was estimated so as to provide the same maximum bending moment as the concentrated forces.

4.1 Results

The comparison between predicted (q_{pred}) and experimental (q_{exp}) OOP strength is shown in Figure 3 to 5, where the ratio q_{pred}/q_{exp} is plotted against the masonry compressive strength, the slenderness ratio, the aspect ratio and the IDR . The mean and the mean \pm one standard deviation of q_{pred}/q_{exp} are also shown. The expressions “yield line” and “arching action” used in the figures refer to the application of Eq. 11 and Eq. 12, which are based on the two approaches, respectively.

In Figures 3 and 4 only pure OOP tests are reported. First of all, it is noticed that the application of the arching action approach leads to a considerable overestimation of the strength when the masonry compressive strength f_m is greater than 20 MPa, while it underestimates the strength when f_m is less than 2 MPa (Figure 2a). This outcome implies that q and f_m are not linearly proportional to one another and that Eq. 12 should not be used for strong masonries. In the following comparisons, such cases (6 tests) are disregarded.

On the average, both methods underestimate the strength, being the mean ratio between predicted and experimental values equal to 0.51 and 0.86 in case of predictions obtained through the yield-line theory (Eq. 11) and the one-way arching effect method (Eq.12), respectively. However, the application of Eq. 12 leads to a significant scatter due also to the fact that it does not take into account the effect of the aspect ratio. The yield-line method gives more conservative results and a smaller scatter.

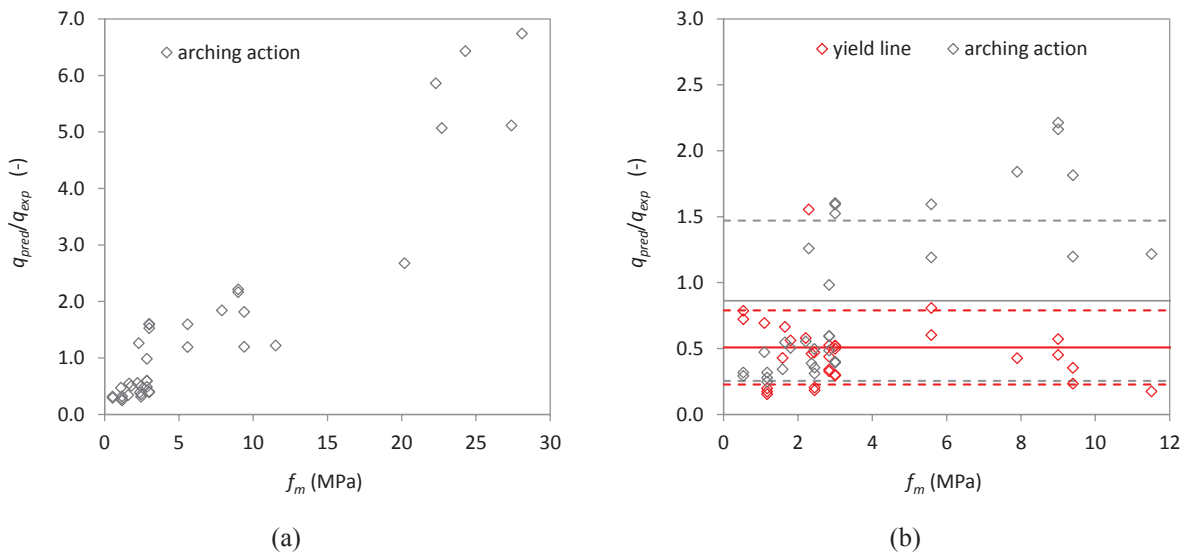


Figure 3: Ratio between predicted and experimental values of the OOP strength (for tests loaded OOP only) plotted against the masonry compressive strength. Continuous lines represent the mean values, dotted lines represent the mean \pm one standard deviation: red = yield line, grey = arching effect.

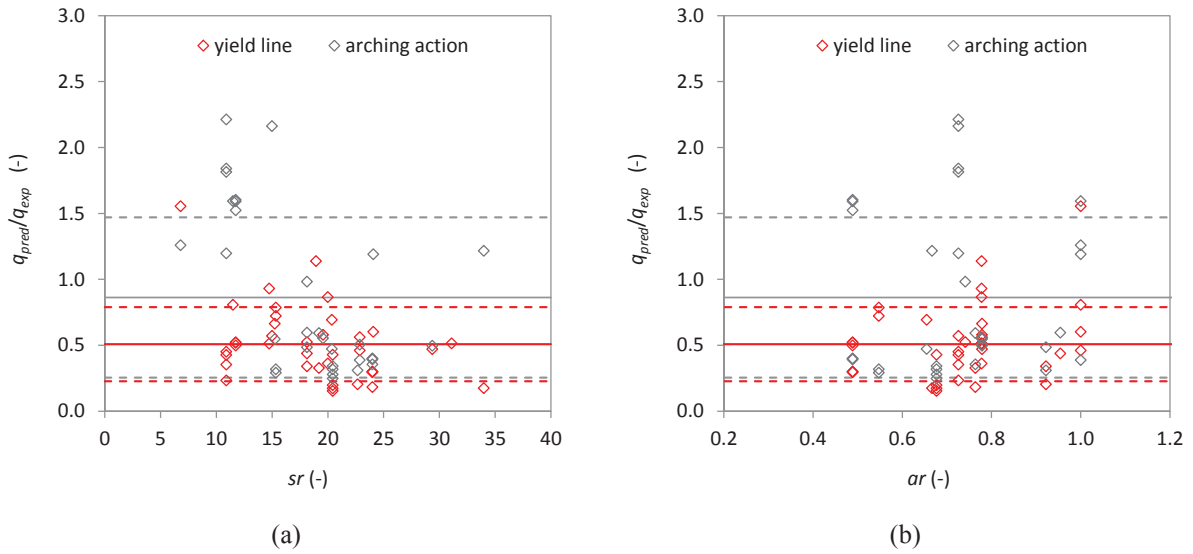


Figure 4: Ratio between predicted and experimental values of the OOP strength (for tests loaded OOP only) plotted against the slenderness ratio (a) and the aspect ratio (b). Continuous lines represent the mean values, dotted lines represent the mean \pm one standard deviation: red = yield line, grey = arching effect.

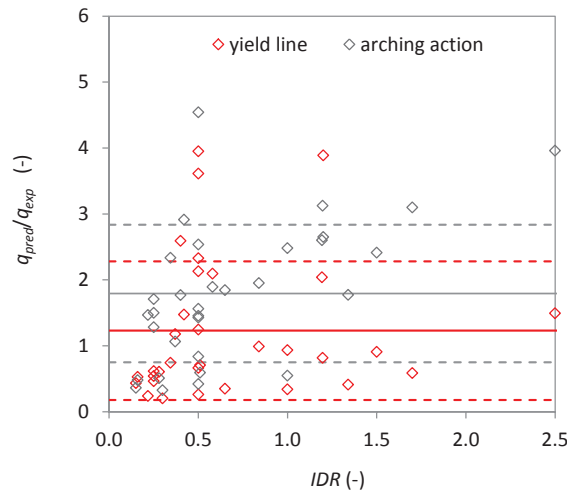


Figure 5: Ratio between predicted and experimental values of the OOP strength (for tests loaded to IP drift + OOP load) plotted against the IP interstory drift ratio (IDR). Continuous lines represent the mean values, dotted lines represent the mean \pm one standard deviation: red = yield line, grey = arching effect.

Figure 4 shows that, contrary to what expected, the predictive capacity of Eq. 12 does not worsen for slenderness ratios greater than 20. In general, the ability of the two methods in predicting the strength does not show a clear trend with varying aspect and slenderness ratios.

The predictions in case of previous IP damage are reported in Figure 5. Obviously, in this case both models overestimate, on the average, the experimental values. In fact, they do not account for previous IP damage. Also in this case, Eq. 11 gives more conservative results.

Finally, the yield-line equations provide the collapse mechanisms related to the minimum collapse pressure [31]. In Figure 6 the occurrences of predicted mechanisms is reported as a function of the infill aspect ratio. “Type 1” mechanisms (Figure 6a) refer to those cases which are most frequently observed in experimental campaigns: for infills supported along four edges the collapse mechanism is related to a first horizontal crack followed by inclined cracks

running to the corners of the panel; for infills with no support along the top, a vertical crack develops at the centre of the panel followed by inclined cracks running to the bottom corners. In “type 2” mechanisms, the first crack is vertical for panels supported along four edges, whereas in panel with a top gap only inclined cracks develop (Figure 6b). Figure 6c indicates that “type 1” mechanisms develop when ar is in the range 0.49–0.78, whereas “type 2” mechanisms occur when ar ranges between 0.64 and 1.00. The yield-line method predicts the “type 2” mechanism more frequently than “type 1”, in contrast to what observed experimentally. In fact, the method is not always able to predict the experimental collapse mechanisms, which are often a combination of different failure modes.

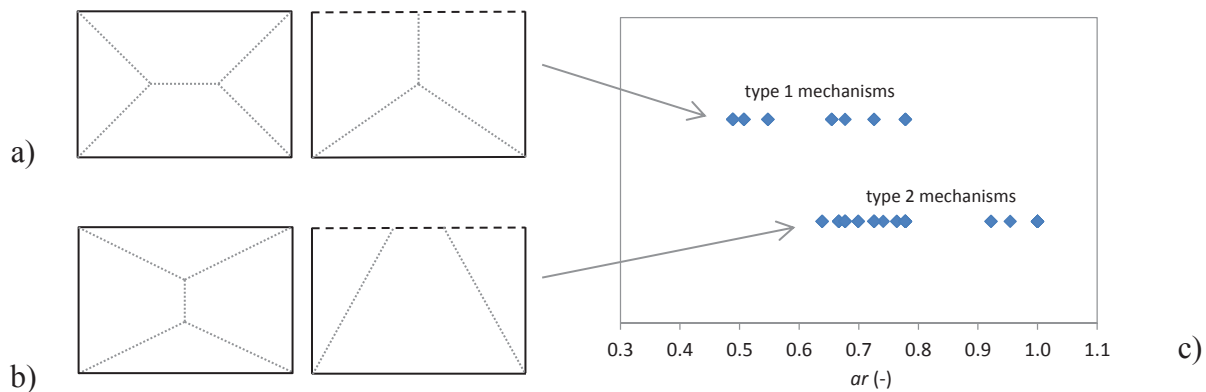


Figure 6: a) crack patterns of type 1 collapse mechanisms; b) crack patterns of type 2 collapse mechanisms; c) occurrences of predicted collapse mechanisms.

5 CONCLUSIONS

In this study the methods encompassed in EC6 to determine the OOP strength of masonry walls are investigated to evaluate their possible suitability for infills. To this aim, a dataset of 71 experimental tests available in the literature is employed. The following conclusions are inferred:

- Eq. 11, based on the yield-line theory, is, on the average, conservative. In this case, the mean value of the ratio between predicted and experimental values is equal to 0.51. This is probably due to the fact that the masonry flexural strength used to estimate the OOP resistance is derived from tests on simply supported specimen and therefore does not account for the confining effect of the frame.
- On the average, Eq. 12, which is based on the one-way arching effect, is slightly conservative, being the mean value of the ratio between predicted and experimental values equal to 0.86. However, the scatter of data is noticeable, also because the two-way arching action and the influence of the aspect ratio are not taken into account by the model.
- The effect of previous IP damage is not considered in the examined formulations and therefore, as expected, the predictions are unconservative when previous *IDR* was applied to the infilled frame. The mean value of the ratio between predicted and experimental strength is equal to 1.23 and 1.79 when using Eq. 11 and Eq. 12, respectively.
- The yield-line method is not always able to predict the experimental crack patterns related to the collapse mechanisms observed experimentally.

REFERENCES

- [1] Dolšek M, Fajfar P. The effect of masonry infills on the seismic response of a four storey reinforced concrete frame-a probabilistic assessment. *Eng Struct* 2008;30:3186–92. doi:10.1016/j.engstruct.2008.04.031.
- [2] Cavaleri L, Di Trapani F. Cyclic response of masonry infilled RC frames: Experimental results and simplified modeling. *Soil Dyn Earthq Eng* 2014;65:224–42. doi:10.1016/j.soildyn.2014.06.016.
- [3] Liberatore L, Mollaioli F. Influence of Masonry Infill Modelling on the Seismic Response of Reinforced Concrete Frames. *Proc. Fifteenth Int. Conf. Civil, Struct. Environ. Eng. Comput.*, 2015. doi:10.4203/ccp.108.87.
- [4] Liberatore L, Noto F, Mollaioli F, Franchin P. Comparative assessment of strut models for the modelling of in-plane seismic response of infill walls. *COMPADYN 2017, 6th Int. Conf. Comput. Methods Struct. Dyn. Earthq. Eng.*, 2017. doi:10.7712/120117.5643.17476.
- [5] Liberatore L, Noto F, Mollaioli F, Franchin P. In-plane response of masonry infill walls: Comprehensive experimentally-based equivalent strut model for deterministic and probabilistic analysis. *Eng Struct* 2018;167:533–48. doi:10.1016/j.engstruct.2018.04.057.
- [6] Verderame GM, De Luca F, Ricci P, Manfredi G. Preliminary analysis of a soft-storey mechanism after the 2009 L'Aquila earthquake. *Earthq Eng Struct Dyn* 2011;40:925–44. doi:10.1002/eqe.1069.
- [7] Liberatore L, Decanini LD. Effect of infills on the seismic response of high-rise RC buildings designed as bare according to Eurocode 8. *Ing Sismica* 2011;28:7–23.
- [8] Tanganelli M, Viti S, de Stefano M, Reinhorn AM. Influence of infill panels on the seismic response of existing RC buildings: A case study. *Geotech Geol Earthq Eng* 2013;24:119–33. doi:10.1007/978-94-007-5377-8__9.
- [9] Blasi G, De Luca F, Aiello MA. Brittle failure in RC masonry infilled frames: The role of infill overstrength. *Eng Struct* 2018. doi:10.1016/j.engstruct.2018.09.079.
- [10] Decanini LD, Liberatore L, Mollaioli F. Damage potential of the 2009 L'Aquila, Italy, earthquake. *J Earthq Tsunami* 2012;6. doi:10.1142/S1793431112500327.
- [11] Inel M, Ozmen HB, Akyol E. Observations on the building damages after 19 May 2011 Simav (Turkey) earthquake. *Bull Earthq Eng* 2013;11:255–83. doi:10.1007/s10518-012-9414-3.
- [12] Masi A, Chiauzzi L, Santarsiero G, Manfredi V, Biondi S, Spacone E, et al. Seismic response of RC buildings during the Mw 6.0 August 24, 2016 Central Italy earthquake: the Amatrice case study. *Bull Earthq Eng* 2017:1–24. doi:10.1007/s10518-017-0277-5.
- [13] Mollaioli F, AlShawa O, Liberatore L, Liberatore D, Sorrentino L. Seismic demand of the 2016–2017 Central Italy earthquakes. *Bull Earthq Eng* 2018. doi:10.1007/s10518-018-0449-y.
- [14] Mosalam KM, Günay S. Progressive collapse analysis of reinforced concrete frames with unreinforced masonry infill walls considering in-plane/out-of-plane interaction. *Earthq Spectra* 2015;31:921–43. doi:10.1193/062113EQS165M.

-
- [15] Ricci P, Di Domenico M, Verderame GM. Empirical-based out-of-plane URM infill wall model accounting for the interaction with in-plane demand. *Earthq Eng Struct Dyn* 2018. doi:10.1002/eqe.2992.
- [16] Liberatore L, Pasca M. Assessment of the Out-of-Plane Resistance of Masonry Infill Walls. *Proc. Fifteenth Int. Conf. Civil, Struct. Environ. Eng. Comput.*, 2015. doi:10.4203/ccp.108.173.
- [17] Liberatore L, Marson C, AlShawa O, Pasca M, Sorrentino L. Failure of masonry infill walls under out-of-plane loads. *Proc Int Mason Soc Conf* 2018:78–88.
- [18] Zizzo M, Cavaleri L, Di Trapani F. Out of Plane Capacity of Infills After in Plane Loading : a Prediction Analytical Model. *COMPdyn 2019, 7th ECCOMAS Themat. Conf. Comput. Methods Struct. Dyn. Earthq. Eng.*, Crete, Greece, 24–26 June: 2019.
- [19] Liberatore L, AlShawa O, Marson C, Pasca M, Sorrentino L. Out-of-plane capacity equations for masonry infill walls accounting for openings and boundary conditions. *Eng Struct* 2020. doi:10.1016/j.engstruct.2020.110198.
- [20] Pasca M, Liberatore L, Masiani R. Reliability of analytical models for the prediction of out-of-plane capacity of masonry infills. *Struct Eng Mech* 2017;64:765–81. doi:10.12989/sem.2017.64.6.765.
- [21] Liberatore L, Bruno M, Al Shawa O, Pasca M, Sorrentino L. Finite-discrete element modelling of masonry infill walls subjected to out-of-plane loads. *ECCOMAS Congr. 2016 - Proc. 7th Eur. Congr. Comput. Methods Appl. Sci. Eng.*, vol. 3, 2016. doi:10.7712/100016.2175.8924.
- [22] Johansen K. *Yield-Line Theory*. Copenhagen: Cement and Concrete Association, London; 1962.
- [23] Johansen K. *Yield-Line Formulae for Slabs*. London: Cement and Concrete Association; 1972.
- [24] Hendry A. The lateral strength of unreinforced brickwork. *Struct Eng* 1973;51:43–50.
- [25] Haseltine B, West H, Tutt J. Design of walls to resist lateral loads. *Struct Eng* 1977;55:422–30.
- [26] Eurocode 6. *Design of Structures for Earthquake Resistance, Part 1: General rules, seismic actions and rules for buildings* Masonry Structures, European Committee for Standardization; Brussels, Belgium. 2005.
- [27] Bakeer T. Theoretical Verification of Existing Solutions on Lateral Loading of Masonry Infill Walls. *Mauerwerk* 2011;15:35–42. doi:10.1002/dama.201100487.
- [28] McDowell EL, McKee KE, Sevin E. Arching theory of masonry walls. *J Struct Div* 1956;82:915–1–915–8.
- [29] Dawe JL, Seah CK. Out-of-plane resistance of concrete masonry infilled panels. *Can J Civ Eng* 1989;16:854–64. doi:10.1139/l89-128.
- [30] Bashandy T, Rubiano N, Klingner R. *Evaluation and Analytical Verification of Infilled Frame Test Data*. 1995.
- [31] Liberatore L, AlShawa O. On The Application Of The Yield-Line Method To Masonry Infills Subjected To Combined In-Plane And Out-Of-Plane Loads. *Structures* 2021;32:1287–301.

-
- [32] EC8-1. Eurocode 8: Design of structures for earthquake resistance—Part 1: General rules, seismic actions and rules for buildings. Brussels: European Committee for Standardization; 2004.
- [33] Angel R, Abrams D, Shapiro D, Uzarski J, Webster M. Behavior of Reinforced Concrete Frames with Masonry Infills, University of Illinois Engineering Experiment Station. College of Engineering. University of Illinois at Urbana-Champaign. ISSN: 0069-4274. vol. SRS-589. 1994.
- [34] Flanagan RD. Behavior of structural clay tile infilled frames. University of Tennessee, Knoxville, 1994.
- [35] Flanagan R, Bennett R. Bidirectional behavior of structural clay tile infilled frames. *J Struct Eng* 1999;125:236–44. doi:10.1061/(ASCE)0733-9445(1999)125:3(236).
- [36] Calvi GM, Bolognini D. Seismic response of reinforced concrete frames infilled with weakly reinforced masonry panels. *J Earthq Eng* 2001;5:153–85. doi:10.1080/13632460109350390.
- [37] Pereira MFP, Pereira MFN, Ferreira JED, Lourenço PB. Behavior of masonry infill panels in RC frames subjected to in plane and out of plane loads. *Amcm2011 - 7th Int Conf Anal Model New Concepts Concr Mason Struct* 2011.
- [38] Pereira MFP, Pereira MFN, Ferreira JE, Lourenço PB. Infill Masonry : Simple Analytical Methods for Seismic Design. *9th Int Mason Conf* 2014:1–12.
- [39] Varela-Rivera JL, Navarrete-Macias D, Fernandez-Baqueiro LE, Moreno EI. Out-of-plane behaviour of confined masonry walls. *Eng Struct* 2011;33:1734–41. doi:10.1016/j.engstruct.2011.02.012.
- [40] Varela-Rivera J, Moreno-Herrera J, Lopez-Gutierrez I, Fernandez-Baqueiro L. Out of Plane Strength of Confined Masonry Walls. *J Struct Eng* 2012;138:1331–41. doi:10.1061/(ASCE)ST.1943-541X.0000578.
- [41] da Porto F, Guidi G, Dalla Benetta M, Verlato N. Combined In-Plane/Out-of-Plane Experimental Behaviour of Reinforced and Strengthened Infill Masonry Walls. *12th Can Mason Symp* 2013:1–11.
- [42] Hak S, Morandi P, Magenes G. Out-of-Plane Experimental Response of Strong Masonry Infills. *Second Eur. Conf. Earthq. Eng. Seismol.*, Istanbul: 2014, p. 1–12.
- [43] Furtado A, Rodrigues H, Arêde A, Varum H. Experimental evaluation of out-of-plane capacity of masonry infill walls. *Eng Struct* 2016;111:48–63. doi:10.1016/j.engstruct.2015.12.013.
- [44] Akhoundi F, Vasconcelos G, Lourenço PB, Silva LM. Out-of-plane response of masonry infilled RC frames: Effect of workmanship and opening. *16th Int. Brick Block Mason. Conf.*, 2016, p. 1147–54.
- [45] Wang C. Experimental Investigation on the Out-Of-Plane behaviour of concrete masonry infilled frame. Dalhousie University Halifax, Nova Scotia, 2017.
- [46] Sepasdar R. Experimental investigation on the out-of-plane behaviour of concrete masonry infilled RC frames. Dalhousie University Halifax, Nova Scotia, 2017.
- [47] Ricci P, Di Domenico M, Verderame GM. Experimental assessment of the in-plane/out-of-plane interaction in unreinforced masonry infill walls. *Eng Struct* 2018.

doi:10.1016/j.engstruct.2018.07.033.

- [48] De Risi MT, Di Domenico M, Ricci P, Verderame GM, Manfredi G. Experimental investigation on the influence of the aspect ratio on the in-plane/out-of-plane interaction for masonry infills in RC frames. *Eng Struct* 2019;189:523–40. doi:10.1016/j.engstruct.2019.03.111.
- [49] Di Domenico M, Ricci P, Verderame GM. Experimental assessment of the out-of-plane strength of URM infill walls with different slenderness and boundary conditions. *Bull Earthq Eng* 2019. doi:10.1007/s10518-019-00604-5.
- [50] Akhoundi F, Vasconcelos G, Lourenço P. Experimental Out-Of-Plane Behavior of Brick Masonry Infilled Frames. *Int J Archit Herit* 2020. doi:10.1080/15583058.2018.1529207.

INFLUENCE OF PRIOR IN-PLANE DAMAGE ON THE OUT-OF-PLANE RESPONSE OF NON-LOAD BEARING UNREINFORCED MASONRY WALLS UNDER SEISMIC LOAD

**Bogdan Šakić¹, Aleksa Milijaš¹, Marko Marinković², Christoph Butenweg³,
Sven Klinkel¹**

¹ Lehrstuhl für Baustatik und Baudynamik, RWTH Aachen University, Mies-Van-der-Rohe- Straße 1, 52074 Aachen, Germany.

e-mail: sakic@lbb-rwth-aachen.de, milijas@lbb-rwth-aachen.de, klinkel@lbb-rwth-aachen.de

² Department of Engineering Mechanics and Theory of Structures, Faculty of Civil Engineering, University of Belgrade, Bulevar kralja Aleksandra 73, 11000 Belgrade, Serbia.

e-mail: mmarinkovic@grf.bg.ac.rs

³ CWE – Center for Wind and Earthquake Engineering, RWTH Aachen University, Mies-van-der Rohe-Straße 1, 52074 Aachen, Germany.

e-mail: butenweg@lbb-rwth-aachen.de

Abstract

Reinforced concrete frames with masonry infill walls are popular form of construction all over the world as well in seismic regions. While severe earthquakes can cause high level of damage of both reinforced concrete and masonry infills, earthquakes of lower to medium intensity sometimes can cause significant level of damage of masonry infill walls. Especially important is the level of damage of face loaded infill masonry walls (out-of-plane direction) as out-of-plane load cannot only bring high level of damage to the wall, it can also be life-threatening for the people near the wall. The response in out-of-plane direction directly depends on the prior in-plane damage, as previous investigation shown that it decreases resistance capacity of the infills. Behaviour of infill masonry walls with and without prior in-plane load is investigated in the experimental campaign and the results are presented in this paper. These results are later compared with analytical approaches for the out-of-plane resistance from the literature. Conclusions based on the experimental campaign on the influence of prior in-plane damage on the out-of-plane response of infill walls are compared with the conclusions from other authors who investigated the same problematic.

Keywords: Earthquake Engineering, Unreinforced masonry walls, Out-of-plane load, In-plane damage, Out-of-plane failure.

1 INTRODUCTION

Reinforced concrete frames with masonry infill walls and partition walls are popular form of construction all over the world. As infill and partition walls are not included into load-bearing system of a building, they are called *Non-structural elements*. Nevertheless, they are not included into load-bearing system of a building, they can be loaded with huge portion of in-plane or out-of-plane forces during earthquakes. They are not designed to withstand seismic forces and they depend on their own characteristics to resist these forces [1]. As a consequence, damage of non-structural elements often represents primary source of losses in seismic events [2]. Also, damage of non-structural elements during earthquakes can cause not only unacceptable economic losses, but also some serious safety concerns if the non-structural components and their supports are not properly designed for the expected seismic force [3]. Some examples of the damage of non-load bearing masonry walls during earthquakes are presented on Figure 1.



Figure 1: Left : Damage due to L'Aquila 2009 earthquake in a residential building [4,5] ; Right: Masonry wall damage of a 6-story office building in downtown area of Jiangyou City during Wenchuan earthquake in 2008 [6]

Non-structural elements can be classified either as deformation or acceleration sensitive. Deformation sensitive elements are the ones vulnerable to inter story drifts, while acceleration sensitive are the ones sensitive to the acceleration of the floors [1,7–10]. Masonry infill walls are non-structural elements which are both, deformation and acceleration sensitive elements.

Due to rigid connection of masonry infill to the surrounding concrete, as a consequence of horizontal load, compressive force is activated in the masonry wall. The paths of compressive forces in the wall mainly follow diagonal path [11–14]. Above mentioned in-plane forces can cause different failure modes of masonry infill walls, such as infill sliding shear failure, diagonal cracking failure, diagonal compression failure and corner crushing failure [12,14].

Masonry infill walls are also acceleration sensitive elements. Face load or out-of-plane loading on the masonry walls is proportional to the acceleration and the mass of the wall. Before affecting walls loaded in out-of-plane direction, ground motion is modified and filtered by two actions: by the response of in-plane loaded walls and by the response of floor diaphragm [15,16]. Furthermore, out-of-plane behaviour of masonry infill walls is highly influenced by arching effect, which introduces membrane forces into the masonry wall and increases its out-of-plane strength [17–19]. However, arching effect, as well as out-of-plane behaviour of masonry walls, is highly dependent on boundary conditions [20]. In the case of good beam-to-wall or floor-to-wall connections, and if beams / diaphragms are rigid relative to the wall, one-way bending (arching effect) can occur. This will significantly increase walls out-of-plane strength. In the case of stiff frames, properly connected on all four sides to masonry walls, those frames can guarantee two-way bending (arching effect) and in that case, walls with low tensile

strength can withstand high out-of-plane forces without losing its stability [17,20]. However, if in-plane forces are also imposed, connections of the infill wall to the surrounding frame can be damaged, and thus, it can decrease out-of-plane capacity. Out-of-plane deformation mechanism for two-sided and four-sided walls are presented on Figure 2.

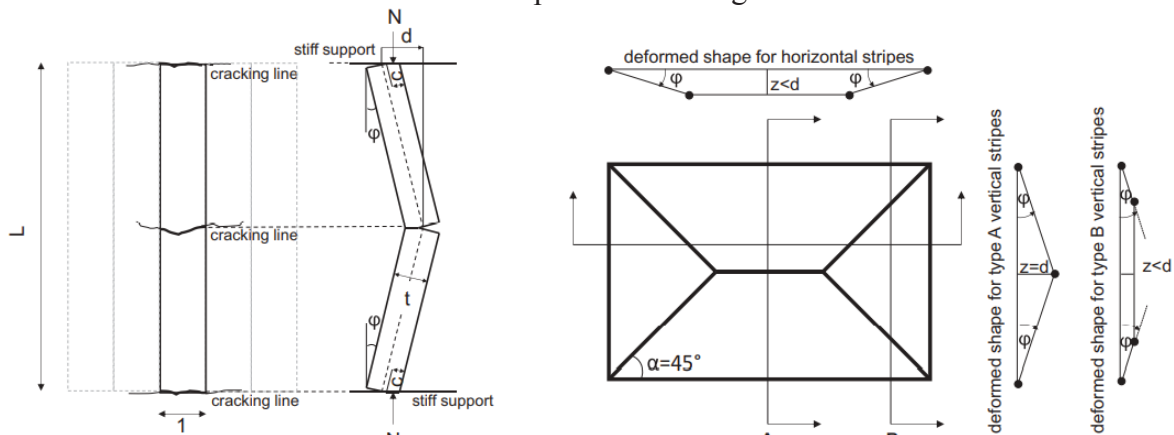


Figure 2: Crack pattern of two – sided (left) and four – sided (right) masonry infill walls subjected to out-of-plane loading [19,21]

Even though highest accelerations in buildings occur at highest floors, out-of-plane failure of masonry infills often occurs at intermediate floors. The reason for this is the interaction of in-plane and out-of-plane forces during earthquakes. Effect of in-plane and out-of-plane interaction is nicely presented in the paper of Ricci et al. [22], and it is shown on Figure 3. There it can be seen, that as a consequence of in-plane damage on masonry infills at intermediate building stories, out-of-plane capacity is reduced and can be smaller than out-of-plane strength demand.

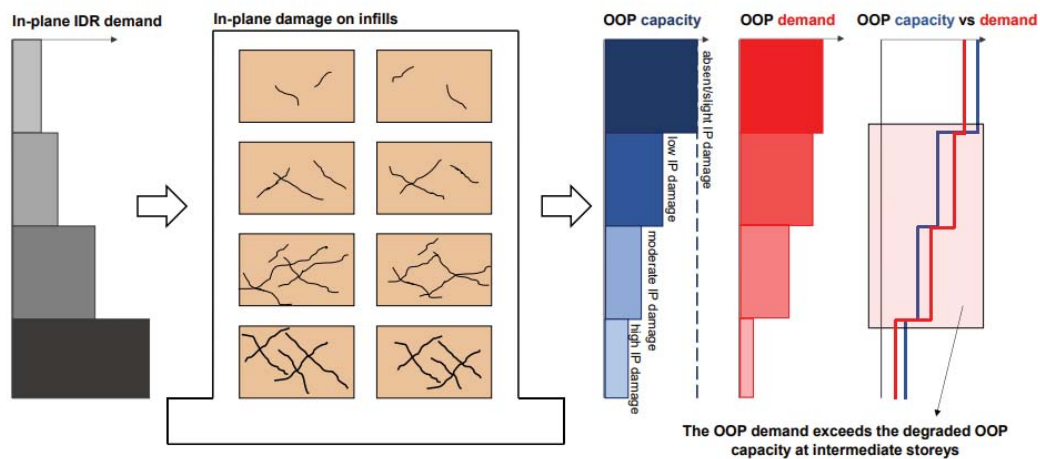


Figure 3: Influence of in-plane and out-of-plane interaction on the out-of-plane capacity at different floor levels[22]

Influence of prior in-plane damage on the out-of-plane load-capacity of masonry walls has been highlighted in few experimental campaigns. Angel and Abrams [23] stated that the slenderness (h/t) of infill wall has the highest effect on the decrease of out-of-plane capacity after prior in-plane damage. Flanagan and Bennett [24] investigated the behaviour of prior in-plane damage on the out-of-plane capacity of masonry walls made of clay bricks connected to steel frames. They stated that prior in-plane damage had minor effect on the out-of-plane capacity of the walls, but that it has induced higher out-of-plane displacements and reduction of out-of-plane stiffness.

In the experimental campaign conducted by Calvi and Bolognini [25] walls previously exposed to 0.4 % of in-plane drift had decrease of out-of-plane capacity for around 50 percent and for prior in-plane drift of 1.2 %, out-of-plane capacity decreased for the factor of 5.62. Investigating different thicknesses and in-plane drift level influence on out-of-plane capacity, Da Porto et al. [26] pointed out that in-plane drift limit of 0,5 % percent given by Italian Building Code is appropriate for thick walls, but not for the thin masonry walls. Hak et al. [27] pointed out that the specimens with prior in-plane drift of 1.0 and 1.5% for fully infilled walls had similar out-of-plane residual capacity, but that the significant stiffness degradation of approximately 40 % occurred. Specimen subjected to prior in-plane drift of 2,5% had decrease of out-of-plane capacity around 60 %, followed with stiffness degradation of 75 %. Furtado et al. [28] came to the conclusion that the walls without prior in-plane damage had 4 times higher out-of-plane capacity compared to the specimen with prior in-plane drift of 0,5 %. It was also pointed out that prior in-plane damage significantly decreased out-of-plane wall stiffness. DiDomenico [19] and Ricci et al. [29,30] stated after their experimental campaign on two different slenderness ratios of masonry infills, 15.2 and 22.9, that slenderness ratio affects in-plane and out-of-plane interaction if it is lower than 20.4 and that higher values of slenderness ratio have similar influence on the interaction as the slenderness ratio of 20.4. They pointed out the importance of “critical” in-plane drift, after which, further increase of in-plane displacement will decrease out-of-plane capacity of the wall. Akhoundi et al. [31] concluded that prior in-plane damage reduces out-of-plane stiffness and strength. They also stated the importance of the workmanship, as bad constructed top joints can significantly decrease out-of-plane strength of the wall. In their experimental campaign, Butenweg and Marinković [32] pointed out that prior in-plane drift of 1.25 % led to the 8-10 times smaller out-of-plane capacity compared with the wall without prior damage. De Risi et al. [33] investigated different length-to-height (w/h) ratios of masonry infills with the same slenderness ratios of 22.9. They stated that specimens with higher w/h ratios (1.26) showed higher level of damage after cycles of in-plane loading and higher reduction of out-of-plane strength compared to the square walls. Xie et al. [34] investigated 7 full-scaled masonry infilled one-span reinforced concrete frames for a typical classroom building in China. The investigation showed that prior in-plane drift significantly decreases out-of-plane wall capacity, when certain value of prior in-plane drift is reached. According to the authors, this limit value is between 0.1–0.3 % of in-plane drift. Da Porto et al. [35] conducted experimental campaign on thick masonry infill walls with and without openings and stated that after different levels of in-plane drifts, out-of-plane capacity of thick infills walls is satisfactory. In the experimental campaign of Di Domenico et al. [36] it was concluded that square panels are less prone to the interaction of in-plane and out-of-plane compared to the rectangular ones.

2 EXPERIMENTAL CAMPAIGN AND TEST SETUP

In order to investigate the influence of prior in-plane damage on out-of-plane behaviour of unreinforced masonry infill walls, experimental campaign was conducted on 2 wall specimens. This experimental campaign was carried out in the scope of the project “Development of an innovative approach for decoupling infills and non load-bearing masonry walls from the main structure” [37]. Walls were made of clay bricks, and the dimension of the bricks were 247 x 249 x 300 mm³. Dimensions of wall specimens and surrounding concrete frame are shown on Figure 4.

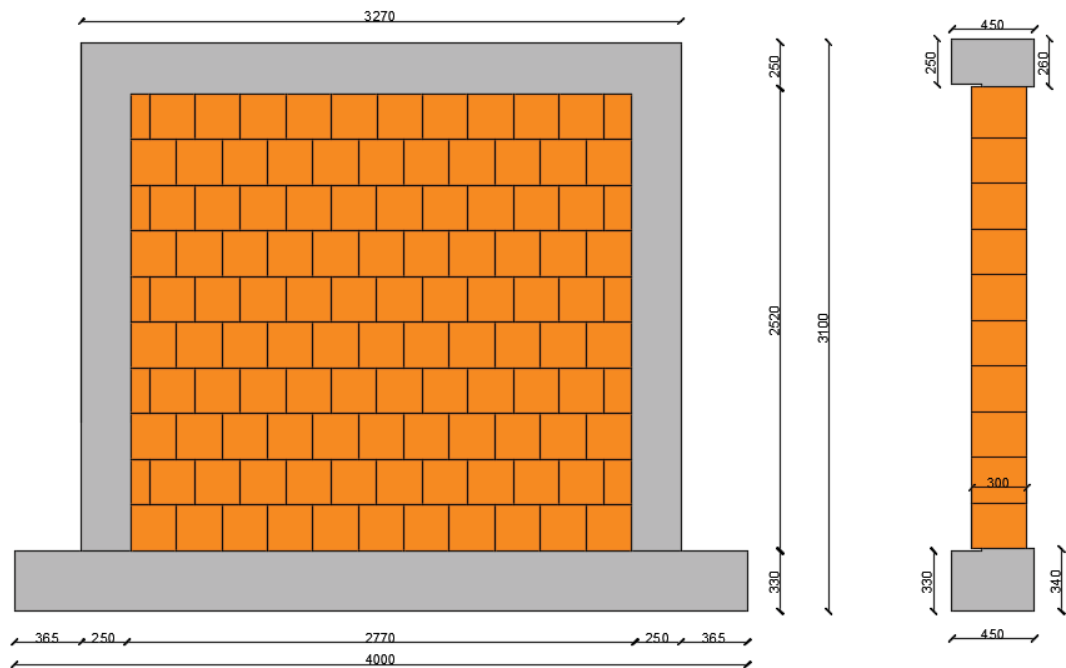



Figure 4: Front and side view of frame and wall specimens for tests T1 and T2

Characteristic values of used materials are presented in Table 1. Only bed joints were mortared, using thin layer mortar Maxit D900.

Table 1: Material property values for the materials used in experimental campaign

Tests T1 and T2					
Mortar MAXIT	Mortar type	Compressive strength f_m (N/mm ²)		Flexural tensile strength $f_{m,flex}$ (N/mm ²)	
	Thin layer mortar	12.8		2.4	
	General purpose mortar	16		2.4	
Brick Thermo plan SX10	Dimensions L/T/H (mm)	Compressive strength f_{ck} (N/mm ²)		Voids (%)	Gross dry density (kg/m ³)
	247/300/249	Vertical	Longitudi- nal	56	600
		9.57	1.67		
Masonry	Compressive strength f_k (N/mm ²)			Modulus of elasticity E_m (N/mm ²)	
	2.68			2680	

Masonry infill walls were connected on all 4 sides to the surrounding concrete frame. Axial force of 200 kN per column was introduced by hydraulic actuator, and it was kept constant during both experiments. In-plane displacement was imposed by steel frame and hydraulic

actuators. Steel bars and plates were placed to keep self-equilibrium and to keep the force in the system. Out-of-plane loading was imposed using 4 airbags. Velocity of the applied load for the out-of-plane direction was 50 N/sec. Reaction plate was made at the back side of the wall, to keep airbags in the contact with the wall. Test setup is presented on Figure 5.

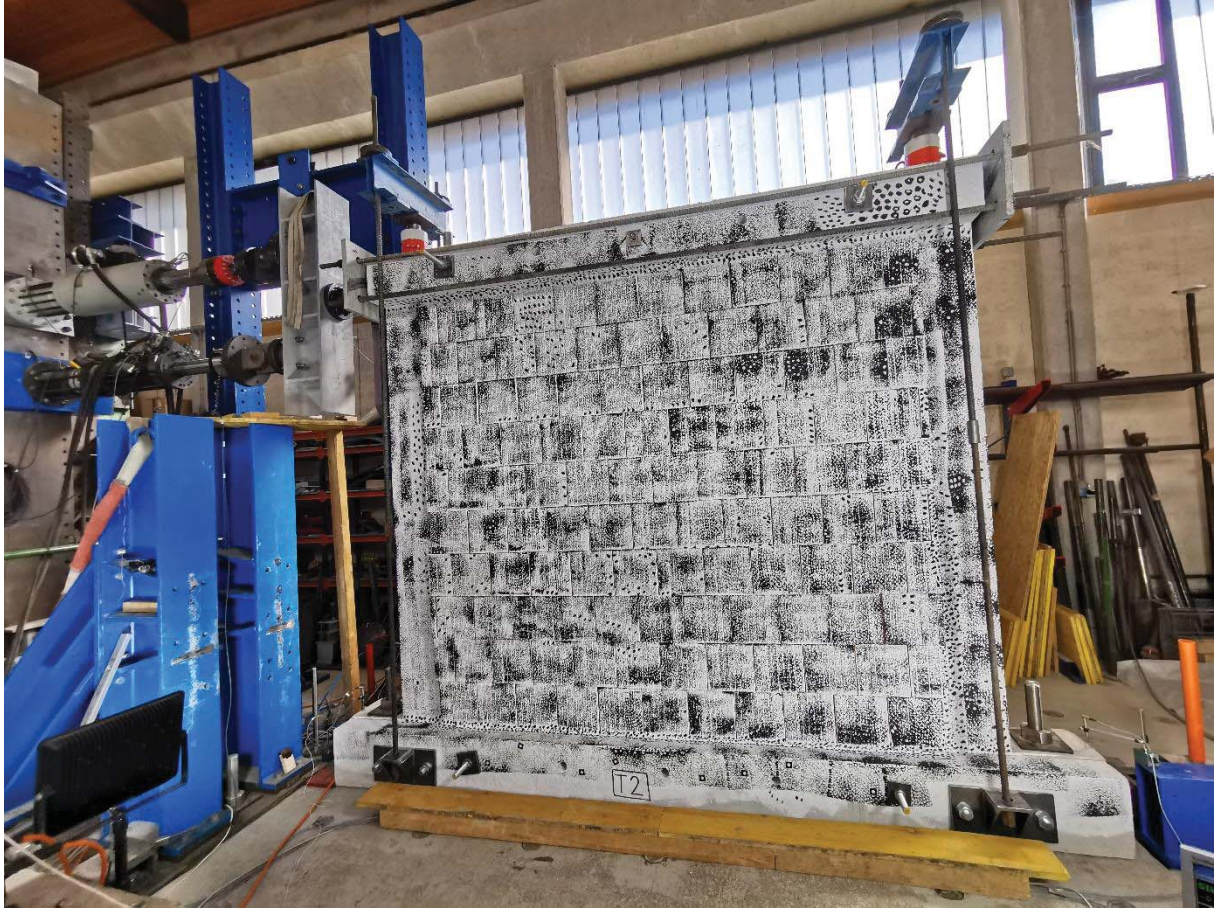


Figure 5: Test specimen with test setup for in-plane movement of the specimen

2.1 Test T1

Test T1 was pure out-of-plane test, without any prior in-plane drift imposed. Velocity of the load applied in out-of-plane direction was 50 N/sec, and it was introduced by 4 airbags, in load cycles of 90 kN. At the end of the first cycle, highest displacement of 1.6 mm was measured at the center of the wall, as it is shown on Figure 6. Wall didn't exhibit any kind of visible damage at that moment. As it can be seen from the Figure 6, based on out-of-plane displacements, two-way arching was activated.

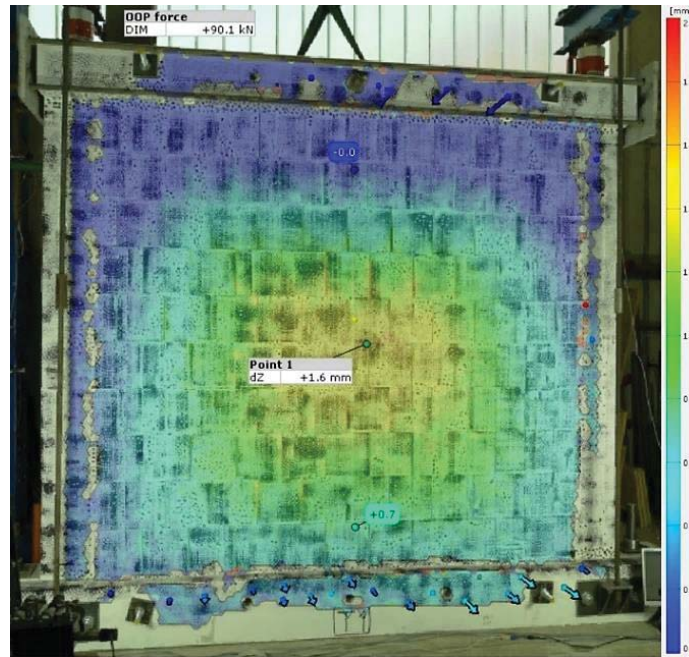


Figure 6: Out-of-plane displacement of infill wall at the end of first cycle of test T1

At the end of the first cycle, residual displacement in out-of-plane direction was minimal and it was near 0. During the second cycle, when the force of around 136 kN was reached, first small cracks in the mortar joints occurred. Future increase of the load led to the first cracks in the bricks in the upper right part of the wall, which occurred at 154 kN. When force reached 170 kN, high intensity crack of the bricks occurred, which was followed by fast increase of out-of-plane displacement with small increase of out-of-plane force. At the force of 176 kN, brittle failure of the wall occurred. It was governed by failure of bricks in the upper right part of the wall. Rotation of the wall due to arching effect occurred through the cracked cross section of the brick, which led to brittle and fast failure of the wall in out-of-plane direction. At the moment of failure, displacement at the center of the wall was 9.86 mm. Complete force – displacement curve of the test T1 is shown on Figure 7. Outlook of the test specimen after the brittle collapse can be seen on Figure 7.

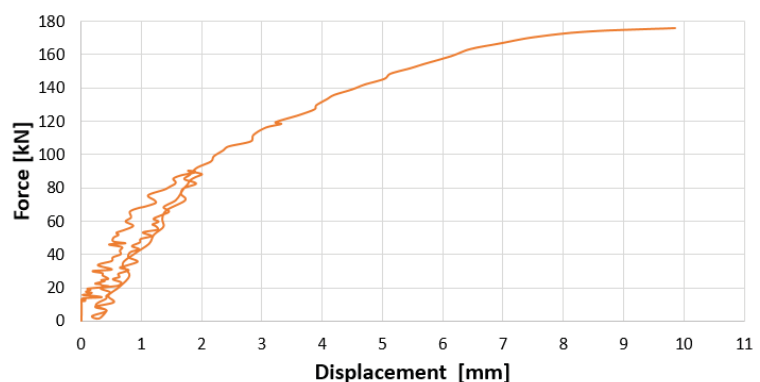


Figure 7: Look of test specimen T1 at the end of the test (left) and force – displacement curve for the out-of-plane behaviour of test specimen T1 (right)

Top rotation point for the arching effect was moved from the connection of the top beam and infill wall, to the cracked section of the bricks in the last row. This is shown on Figure 8, where it can be seen that cracks initiate through the thickness of the wall, breaking thin webs of the brick and making this weakened cross section as a plane around which the wall rotates. This type of the behaviour can be explained with yield line theory, presented for the out-of-plane behaviour of masonry infills by Dawe and Seah [21]. In their approach, mortar joints at the wall middle and at the top and bottom connection of masonry infill to surrounding concrete represent cracked cross sections. When the test specimen T1 was bricked up, mortar connection of the wall and top beam was made of high quality thin bed layer mortar, which was inserted using the pump under high pressure. Nevertheless, it is important to point out that this high quality of mortar joint connections to the surrounding concrete is difficult to have on a construction site, and it is not expected to be done in that manner, as it is time-consuming.



Figure 8: Look of test specimen T1 at the end of the test and cracks penetrating through the thickness of the wall in the plane of the rotation, cause collapse of thin brick webs

2.2 Test T2

Test specimen T2 was subjected to 1.2 % of in-plane drift prior to the out-of-plane loading. Complete hysteresis curves of force–displacement and force–drift for both directions of in-plane load are shown on Figure 9.

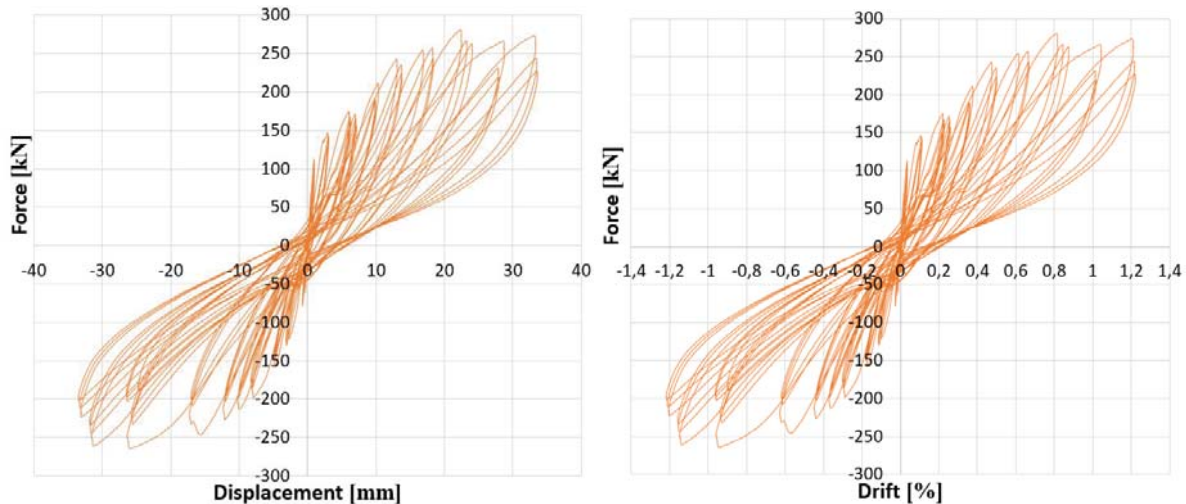


Figure 9: Force – displacement (left) and force – drift (right) hysteresis curve for the in – plane phase of loading of test specimen T2

For each cycle of in – plane drift, three amplitudes were reached. Time period for reaching prescribed displacement for each of the amplitudes was 15 seconds. First change of the stiffness was noticed in the fourth cycle, when in–plane drift of 0.022 % was reached. Reason for the first dropdown of the stiffness were initiations of the cracks in mortar bed joints, mainly at right part of the wall. Force that was reached at that moment was 60 kN. Surface plot of the strains is shown on Figure 10a.

Highly pronounced compressive struts, characteristic for the masonry infill walls, occurred in sixth cycle, with prescribed drift of 0.11 %. At this point, bricks were still undamaged. Only visible damages were a bit cracked mortar joints at the connection of the infill wall to the concrete columns and top beam. Surface plots of the strains are shown on Figures 10b and 10c.

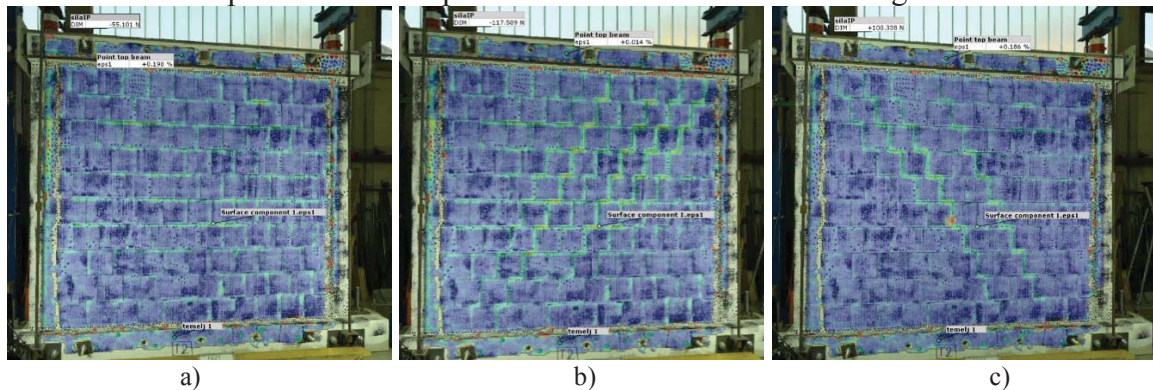


Figure 10: Surface plot of the wall strains of specimen T2 at drift levels of 0.012 % (a); 0.11% when moving the wall from right to left (b); and 0.11% when moving the wall from left to right (c)

Peak force of the in–plane hysteresis curve for both directions of in–plane loading was reached at 11th cycle. Corresponding force of 280 kN was reached when the frame was pushed from left to the right. Drift reached at this cycle was 0.8 %. Surface plot of the tensile strains at drift level of 0.8 %, while moving the wall from left to right, is presented on Figure 11a. At the end of 15th cycle, last for in–plane phase of the test, drifts of 1.2 % were reached, and the forces were 225 and 196 kN, respectively. Surface plot of the tensile strains at drift level of 1.2 %, while moving the wall from left to right and right to left, are presented on Figures 11b and 11c.

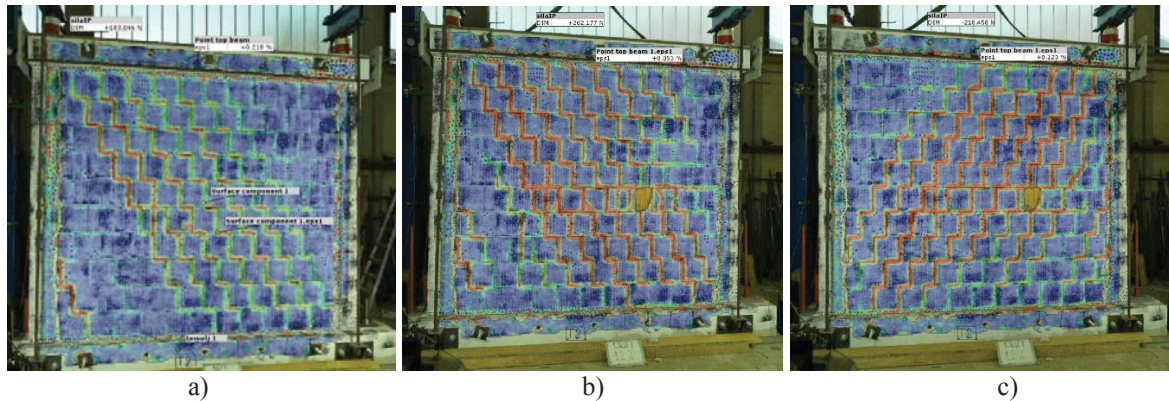


Figure 11: Surface plot of the wall strains of specimen T2 at drift levels of 0.8 % (a) ; 1.2% when moving the wall from left to right (b); and 1.2 % when moving the wall from right to left (c)

At this level of in-plane drift, significant amount of the damage on infill wall was noticed. At the back side of the wall, almost along whole length of the wall, outer brick shells were cracked in rows 5 and 6. Cracks were also pronounced on the bricks at top right and left corner, and they also went through concrete columns. On the front side of the wall, outer shells of the bricks felt off from 2 bricks in the 5th row. Minor diagonal cracks were seen on the bricks close to the columns on the front side off the wall, which were following the trajectory of compressive struts.

In the second phase of the test, investigation of the out-of-plane capacity of the wall with prior in-plane damage was conducted. Out-of-plane loading was carried out in 11 cycles. In the last cycle, while reaching out-of-plane force of 87 kN, high increase of out-of-plane displacement occurred, followed by dropdown of out-of-plane force. In order to prevent brittle failure, test was stopped. Out-of-plane displacement at the end of the test was 18.42 mm, as it is shown on Figure 12. Furthermore, from the Figure 12, where the surface plot of out-of-plane displacement is shown, it can be seen that two-way arching was exhibited, as in test T1. It can be concluded that even though mortar joint at the connection of infill wall and top beam had cracks, they were insufficient to jeopardize two-way arching. Out-of-plane displacement of the wall from the laboratory is shown on Figure 13, as well as force–displacement curve for the second phase of test T2.

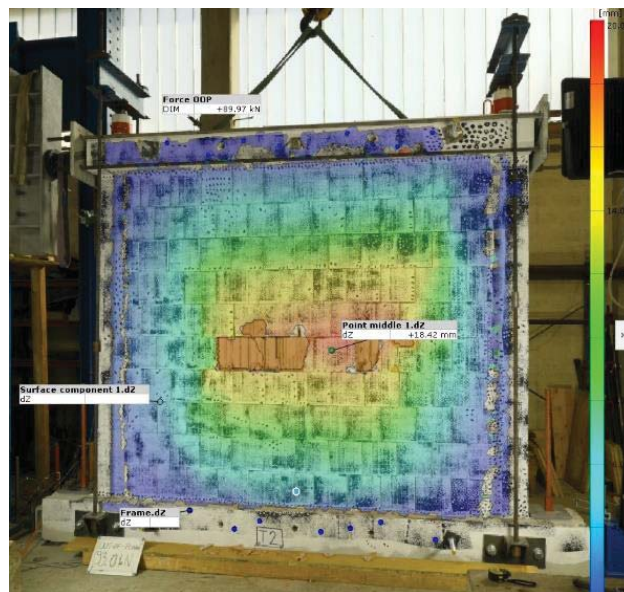


Figure 12: Surface plot of out-of-plane displacement at the end of the test on test specimen T2

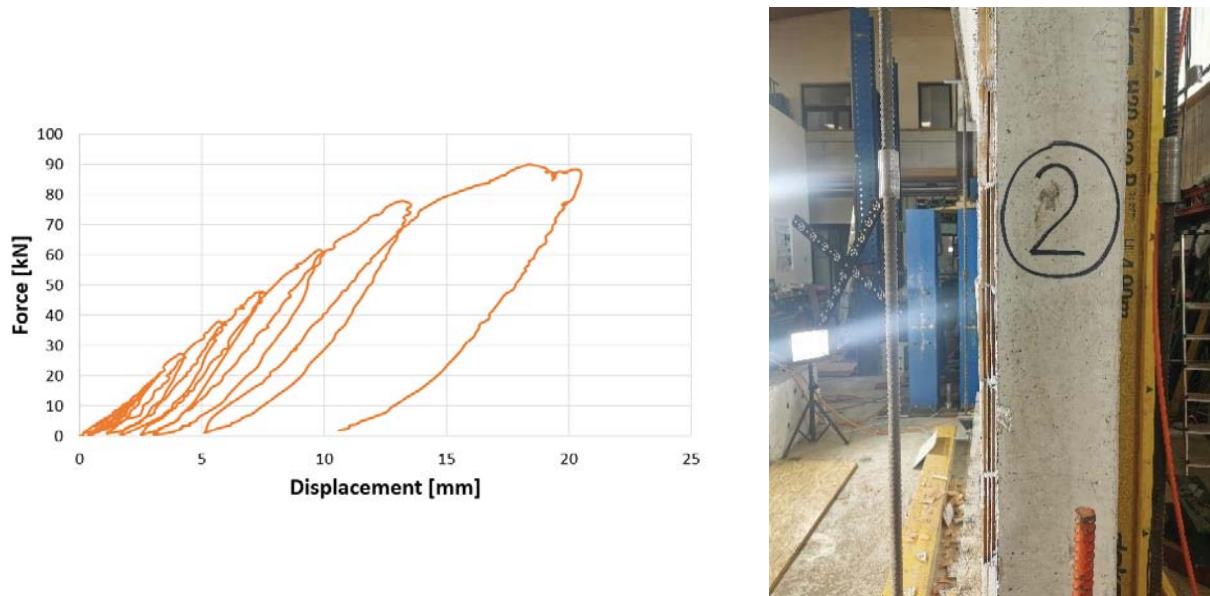


Figure 13: Force – displacement curve of the out-of-plane loading phase of test specimen T2 (left) and lateral look of the out-of-plane displacement at the end of the test (right)

3 COMPARISON OF THE OUT-OF-PLANE BEHAVIOUR OF TEST SPECIMENS T1 AND T2

As it can be seen from Figures 6 and 12, and surface plots of out-of-plane displacements of the walls T1 and T2, both walls remained in full contact on all 4 sides to the surrounding concrete. This implicates that the walls exhibited two-way bending and arching effect. Such fact goes on contrary with the conclusions of some of the authors stated in the literature review, as it is often the case that due to prior in-plane drift, connection of the masonry infill and concrete frame is partially or completely lost. Full connection of the masonry infill and concrete frame on all 4 sides during all the phases of in-plane and out-of-plane loading in tests T1 and T2 is a consequence of unrealistically high bond strength of the mortar joints. The reason for that high bond strength of connection joints was, as it was already explained in Chapter 2, the use of high-pressure pump for placing the mortar. This construction procedure highly increased bond strength of mortar joints. Use of the pump in that manner is inapplicable in practice due to time-consuming reasons and construction difficulties on the construction site, so it can be said that this full connection of infill walls to surrounding concrete after in-plane loading cannot truly represent real behaviour in practice.

Comparison of the out-of-plane force-displacement curves for tests T1 and T2 is shown on Figure 14. It can be seen that reduction of the out-of-plane capacity was 51 %.

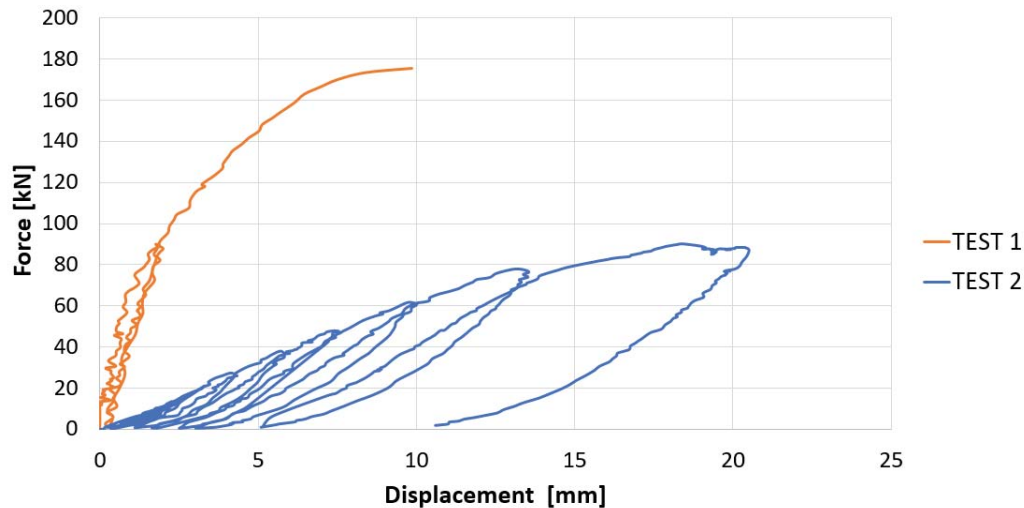


Figure 14: Force – displacement curves of the out-of-plane loading phase for test specimens T1 and T2

Also, it can be seen that prior in-plane damage triggered significant decrease of stiffness in out-of-plane direction. This goes in the line with the conclusions of all previous experimental campaigns from the literature, where the authors pointed out the importance of prior in-plane damage on the stiffness degradation in out-of-plane direction.

It is important to mention brittle behaviour of test specimen T1. Even though this specimen showed high level of out-of-plane capacity compared to the test specimen T2, wall T1 had small out-of-plane displacements at the failure, compared to the ones reached in test T2. Comparing the values of displacement at failure and wall thickness, out-of-plane displacement at failure of wall T1 was equal to 3.29 % of the wall thickness. This represents quite a small value for pure out-of-plane tests, as according to some theoretical approaches for out-of-plane capacity, displacement at the failure can reach around 50 % of wall thickness [18]. The reason for small out-of-plane displacement at failure for test specimen T1 can also be explained with perfect boundary conditions and connection of the infill wall with surrounding frame. This fact decreased the possibility for the rotation of the wall through the cross sections in the mortar plane. On contrary, rotation cross sections and “hinges” occurred at the first and last row of the bricks, at the moment when the bricks started to crack through the thickness of the wall. Also, this was the reason for the fast and brittle failure after appearance of the cracks. As it is already mentioned, test specimen T2, subjected to prior in-plane loading, kept the connection to the surrounding concrete for the entire duration of the test. Nevertheless, the main reason for the increase of the displacement at failure in out-of-plane direction during the second phase of test 2 was the influence of prior in-plane loading on mortar joints within the wall and next to the surrounding concrete. This prior in-plane loading decreased the level of rigidity of mortar connections and also it changed the boundary conditions at the connection of top beam and the wall. For the test T1, this connection was almost clamped and for test T2 it showed more hinged-like connection due to prior in-plane loading.

4 COMPARISON OF TEST RESULTS WITH ANALYTICAL APPROACHES

Results from the test specimens described in experimental campaign were compared with the existing analytical approaches which take into account influence of prior in – plane damage on out-of-plane capacity of masonry infill walls. The interaction of in-plane and out-of-plane loading is usually taken into account with factor R , which represents the decrease of out-of-plane capacity due to prior in-plane damage. Factor R is related to the level of in-plane drift to

which the wall had been previously exposed, so it is a kind of displacement – based and not strength – based factor. First one to propose reduction factor which takes into account prior in-plane damage to the out-of-plane capacity was Angel [23], and the reduction factor is shown in Equation 1. Reduction factor can be used if in-plane drift is higher than “critical” in-plane drift at which first brick cracking occurs. Else, $R=1$. Interstory drift ratio is denoted as IDR.

$$R = \left(1,08 - 0,015 \left(\frac{h}{t} \right) - 0,00049 \left(\frac{h}{t} \right)^2 + 0,000013 \left(\frac{h}{t} \right)^3 \right)^{\frac{IDR}{2IDR_{cr}}} \quad (1)$$

New Zealand standard NZSEE 2017 [38] proposes reduction factor which takes into account slenderness ratio of the wall. This reduction factor is shown in Equation 2.

$$R = \min \left(1,1 \left(1 - \frac{h/t}{55} \right); 1 \right) \quad (2)$$

FEMA 274 [39], FEMA 356 [40], ASCE/SEI 41-06 [41] and ASCE 41-13 [42] proposed reduction factor R equal to 0.76 for all situations of the interaction of prior in-plane damage on out-of-plane capacity.

FEMA 306 [43] suggests to use Equation 1 for the calculation of reduction factor, with further description that for moderate in-plane damage it should be taken into account that $IDR=IDR_{cr}$ and that for severe damage $IDR=2IDR_{cr}$.

ASCE/SEI 41-17 [44] suggest that reduction factor R should be equal to 0.6. It is calculated using Equation 1, for the situation when $IDR=2IDR_{cr}$ and slenderness ratios is equal to 25.

Morandi et al. [45] proposed reduction factor to be calculated using Equation 3. Their reduction factor is fitted and calibrated for slender infills.

$$R = \begin{array}{ll} 1 - 2.67IDR & IDR \leq 0.30\% \\ 0.2 & 0.30\% < IDR \leq 1.00\% \\ 0 & IDR > 1.00\% \end{array} \quad (3)$$

Based on the experimental results, Verlato et al. [46] proposed Equation 4 for the reduction factor.

$$R = \begin{array}{ll} 1 - 0.86IDR & IDR \leq 0.70\% \\ 0.4 & 0.70\% < IDR \leq 1.20\% \\ 0 & IDR > 1.20\% \end{array} \quad (4)$$

Cavaleri et al. [47] reduction factor R reported in Equation 5, has been proposed based on the experimental database.

$$R = \min(0.26IDR^{-0.37}; 1) \quad (5)$$

Ricci et al. [29] proposed reduction coefficient R using statistical regression, based on the some results from the literature. This reduction coefficient is shown in Equation 6.

$$R = \min(0.14IDR^{-1.12}; 1) \quad (6)$$

Later, Ricci et al. [30] also proposed another reduction coefficient R , after conducting experimental campaign. This reduction coefficient is based on statistical regression and it is shown in Equation 7, and it is calibrated according to Authors for thin walls ($h/t > 15.2$). For walls with lower slenderness ratio, Equation 8 is proposed. Equation 8 is calibrated based on two wall specimens from the literature with slenderness ratio equal to 8.8.

$$R = \min \left\{ 1; \left(0.98 - 0.04 * \left(\min \left(\frac{h}{t}; 20.4 \right) \right) * IDR^{-0.97} \right) \right\} \quad (7)$$

$$R = \min \left\{ 1; \left(1.21 - 0.05 * \left(\min \left(\frac{h}{t}; 20.4 \right) \right) * IDR^{-0.89} \right) \right\} \quad (8)$$

Based on their experimental campaign, Akhoundi et al. [31] proposed that reduction of out-of-plane capacity due to prior in-plane damage should be taken into account using Equation 8.

$$R = \frac{2 - IDR}{2} \quad (9)$$

Da Porto et al. [35] used data from their experimental campaign on thick infill walls to proposed reduction coefficient R , shown in Equation 9.

$$R = \frac{1}{2.1} * (1.1 * e^{-(2.6*IDR)^2} + 1) \quad (10)$$

Using statistical regression and data available from the literature, Di Domenico et al. [36] proposed reduction factor R for thin and thick walls, presented in Equations 10 and 11, respectively. Equation 10 can be used if $h/t > 15$, while Equation 11 can be used for walls with $h/t > 8$.

$$R = \min \left\{ 1; \left(1.438 - 0.245 \left(\frac{w}{h} \right) - 0.042 * \left(\min \left(\frac{h}{t}; 20.4 \right) \right) * IDR^{-0.719} \right) \right\} \quad (11)$$

$$R = \min \left\{ 1; \left(1.510 - 0.190 \left(\frac{w}{h} \right) - 0.050 * \left(\min \left(\frac{h}{t}; 20.4 \right) \right) * IDR^{-0.730} \right) \right\} \quad (12)$$

In order to use some of the above mentioned Equations for the calculation of reduction coefficient R , input data should be IDR_{cr} which represents in-plane drift at which first crack in the wall occurs. For test T2, described in this paper, drift of 0.027 % is taken as IDR_{cr} . At that drift level, first stepwise cracks through the wall occurs, as it is shown on Figure 15.

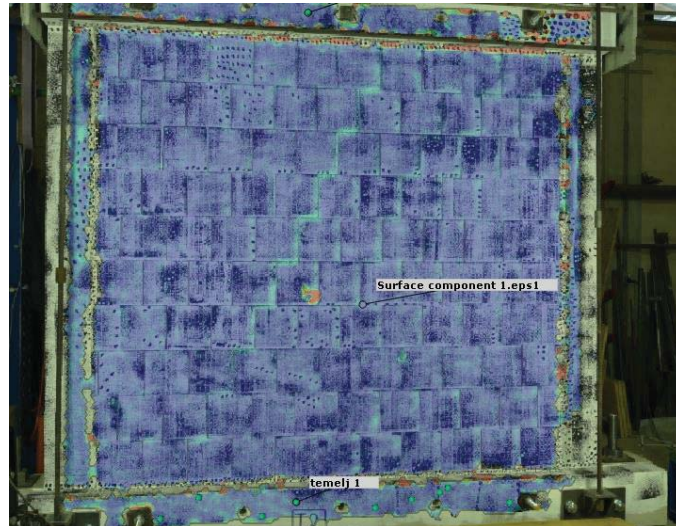


Figure 15: Surface plot of crack pattern of the specimen T2 under in – plane drift of 0.027 %

Above mentioned analytical approaches for the calculation of out-of-plane capacity due to prior in-plane damaged are compared with measured values for test specimen T2. Values of the parameters necessary for the use of Equations 1-12 are the following: $h/t= 8.4$; $w/h= 1.1$; $IDR= 1.2\%$ and $IDR_{cr}= 0.027\%$. In experimental campaign, with above mentioned values, test specimen T2 exhibited reduction of the out-of-plane capacity due to prior in-plane damage for a factor $R= 0.49$. Comparison of the experimental result with existing analytical approaches is shown on Figure 16. Values of the predicted reduction coefficients are shown in Table 2.

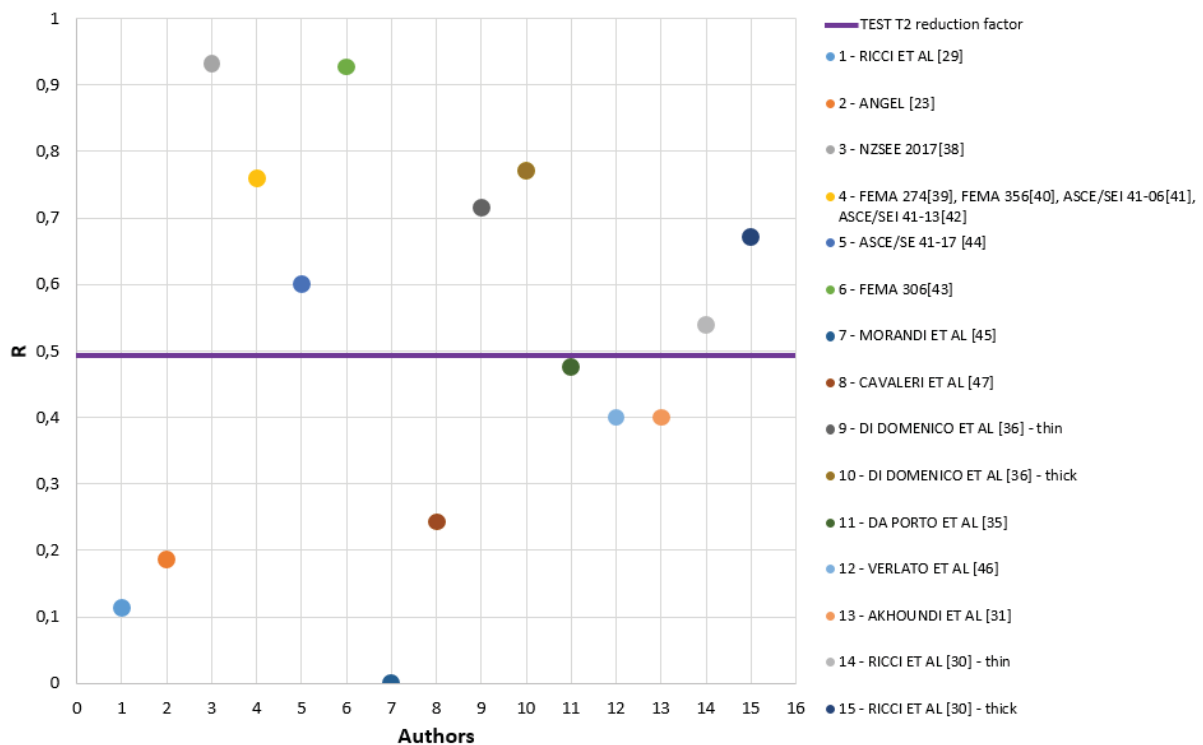


Figure 16: Comparison of predicted and measured reduction factor for test specimen T2 using existing analytical approaches

Table 2: Comparison between predicted and experimental reduction factor for different analytical approaches

Author	R_{pred}	R_{pred} / R_{exp}
Ricci et al. [29]	0.114	0.231
Angel [23]	0.186	0.376
NZSEE 2017 [38]	0.932	1.885
FEMA 274 [39]	0.760	1.538
FEMA 356 [40]	0.760	1.538
ASCE/SEI 41-06 [41]	0.760	1.538
ASCE/SEI 41-13 [42]	0.760	1.538
ASCE/SEI 41-17 [44]	0.600	1.213
FEMA 306 [43]	0.927	1.875
Morandi et al. [45]	0	0
Cavaleri et al. [47]	0.243	0.492
Di Domenico et al. (thin walls) [36]	0.716	1.449
Di Domenico et al. (thick walls) [36]	0.771	1.560
da Porto et al. [35]	0.476	0.963
Verlato et al. [46]	0.400	0.809
Akhoundi et al. [31]	0.400	0.809
Ricci et al. (thin walls) [30]	0.540	1.092
Ricci et al. (thick walls) [30]	0.672	1.359

As it can be seen from the Figure 16 and Table 2, the closest prediction of the reduction factor for the test specimen T2 was obtained using Equation 10, proposed by da Porto et al. [35]. Reduction factor calculated using above mentioned Equation 10 is 0.476, while reduction factor calculated from the experimental campaign was 0.494. The reason for this good match is probably in the fact that Equation 9 is fitted for the walls which had same thickness as wall T2, and similar h/t ratio. Also, reduction coefficient proposed by Ricci et al. [30] showed good match with the experimental one, as it slightly overestimates walls out-of-plane capacity. This reduction coefficient is calculated using Equation 7. Among all other Equations, only the Equation 12 is fitted for the walls with smaller slenderness ratios than 15, but this Equation 12 also doesn't give satisfying match, as it is calibrated only on one experimental campaign from the literature, using statistical regression. Regarding the level of in-plane drift, presented Equations are valid for drift values until 1.2 %, which was the drift level imposed in the experimental campaign. However, it is important to mention that reduction factor of 0.494 for wall specimen T2 should be taken with reserve, having in mind that connection of masonry infill to the concrete frame is not constructed in usual manner. Regarding that, this high quality connection could potentially increase residual out-of-plane capacity and overestimate reduction factor, compared with the situation when connection joints are constructed as in practice. Nevertheless, it can be concluded that, even though there is certain amount of existing equations which take into account reduction of out-of-plane capacity due to prior in-plane loading, they are empirical – based and fitted only for some results available from the literature, or only for one existing experimental campaign. Regarding that, conclusion is that they can be used for calculation of the reduction factor if wall parameters are very similar to the ones for which these equations are calibrated, but there is a need for developing new equations which can take into account reduction of out-of-plane capacity due to in-plane damage for more general application.

5 CONCLUSIONS

In this paper, influence of prior in-plane damage on the out-of-plane capacity of masonry infills has been investigated. First, literature review of previous experimental campaigns dealing with this topic has been conducted. It has been pointed out that all the studies concluded that prior in-plane damage of masonry infill walls decreases stiffness of the wall and initiates higher displacements in out-of-plane direction.

Since experimental test on full scale specimens, investigating influence of in-plane loading on out-of-plane capacity, are rare, experimental campaign on two different wall specimens made of clay brick masonry, was conducted. Wall specimen denoted as T1 was subjected to cyclic out-of-plane loading until failure. Failure occurred at the load of 176 kN. Wall denoted as T2 was loaded in two phases. In the first phase, in-plane load was imposed on the system in 15 cycles, each containing 3 amplitudes. Highest drift level that was reached was 1.2 %, and the wall peak force occurred at drift level of 0.8 %. Afterwards, specimen was unloaded in in-plane direction, and out-of-plane cyclic load was imposed in 11 cycles. At the load of 87 kN, high increase of out-of-plane displacement followed by the decrease of the force occurred, and the test was stopped.

Analyzing the results from conducted experimental campaign it can be concluded that in-plane drift significantly decreases out-of-plane strength capacity and stiffness of masonry infills. Also, it changes the behaviour of the wall in a way that walls exhibit more ductile behaviour due to the higher deformability of mortar joints, if previously, in-plane force is introduced. Out-of-plane displacements at failure in test T1 were low due to different type of the behaviour of the wall than expected. The reason for that were boundary conditions at the connection of masonry infill to the surrounding concrete. Reason for that lies in the fact that, for the placing of mortar, high-pressure pump was used. This pump is not used so far in practice, so it can be said that above mentioned conclusions represent the situation with perfect boundary conditions and very high mortar bond strength, which is not the case in the practice. Due to this construction procedure and mortar bond strength, crack planes for the out-of-plane rotation of infill walls were moved from the top and bottom connection of masonry infills to the first and last row of the bricks. This led to fast and brittle failure of the specimen T1, when the tensile cracks penetrated through the thickness of the wall, destroying thin webs of the brick.

Wall denoted as T2 had reduction of out-of-plane capacity of 51 % compared to the wall specimen denoted as T1, as a consequence of prior in-plane damage. In-plane drift of 1.2 % damaged the wall, which had some minor and some moderate damages. Most common damage of the bricks was falling out of the outer shells of the bricks in the middle two rows of the wall. From the investigation at the site, it can be pointed out that these bricks probably had to be replaced, if the same situation happened in the building. This implies that repair would not be an option. Also, due to high compressive forces, some bricks near the columns exhibit diagonal cracks, which were also visible in the concrete columns. Mortar joints at the connection of masonry infill and concrete were cracked. This cracks in mortar joints didn't jeopardize two-way arching of the masonry infill wall, which stayed in contact with surrounding concrete until the end of the test. Also, it is important to point out that even though in-plane damage decreased out-of-plane capacity of the wall, the wall still had significant amount of out-of-plane capacity.

It can be concluded that prior in-plane damage has to be taken into account when out-of-plane capacity of the wall is discussed, and that this interaction poses an important factor and safety hazard for masonry infill walls during seismic events.

Results from test campaign for the out-of-plane capacity with prior in-plane damage were compared with analytical approaches for reduction of out-of-plane capacity from the literature. Best match was noticed with the approach proposed by da Porto et al. [35], due to similar wall parameters. Nevertheless, it has been concluded that reduction factor equations from the literature are empirical - based and that results from those equations need to be taken with reserve. Further investigations are needed and they are planned as the part of comprehensive experimental campaign within the AIF project “Development of innovative approach for decoupling infills and non-load bearing masonry walls from the main structure” [37].

ACKNOWLEDGEMENTS

The authors would like to acknowledge the support from the “Institut für Ziegelforschung Essen e.V” and express their special thanks to Dr. Matija Gams from the University of Ljubljana for the support and fruitful discussions during the execution of experimental campaign within “Development of innovative approach for decoupling infills and non-load bearing masonry walls from the main structure” project.

REFERENCES

- [1] R. Villaverde, Seismic design of secondary structures : State of the art, J. Struct. Eng. (1997) 1011–1019.
- [2] N.I. of S. and Technology, Seismic Analysis , Design , and Installation of Nonstructural Components and Systems – Background and Recommendations for Future Work, 2017.
- [3] H. Sucuoğlu, Implications of masonry infill and partition damage in performance perception in residential buildings after a moderate earthquake, Earthq. Spectra. 29 (2013) 661–667.
- [4] F. Braga, V. Mandredi, A. Masi, A. Salvatori, M. Vona, Performance of non-structural elements in RC buildings during the L ’ Aquila , 2009 earthquake, Bull. Earthq. Eng. (2010) 307–324.
- [5] V. Manfredi, A. Masi, Combining in-plane and out-of-plane behaviour of masonry infills in the seismic analysis of RC buildings, Earthq. Struct. 6 (2014) 515–537.
- [6] B. Zhao, F. Taucer, T. Rossetto, Field investigation on the performance of building structures during the 12 May 2008 Wenchuan earthquake in China, Eng. Struct. 31 (2009) 1707–1723.
- [7] FEMA74, FEMA E-74 6: Seismic Protection of Nonstructural Components, (2011) 106–117.
- [8] N. Fardis, Seismic design, assessment and retrofitting of concrete buildings based on EN-Eurocode 8, 2009.
- [9] R.S. Vicente, H. Rodrigues, H. Varum, A. Costa, J.A.R.M. da Silva, Performance of masonry enclosure walls: Lessons learned from recent earthquakes, Earthq. Eng. Eng.

- Vib. 11 (2012) 23–34.
- [10] S. Taghavi, E. Miranda, Response assessment of nonstructural building elements, 2003.
 - [11] P.G. Asteris, S.T. Antoniou, D.S. Sophianopoulos, C.Z. Chrysostomou, Mathematical macromodeling of infilled frames: State of the art, *J. Struct. Eng.* 137 (2011) 1508–1517.
 - [12] C.Z. Chrysostomou, P.G. Asteris, On the in-plane properties and capacities of infilled frames, *Eng. Struct.* 41 (2012) 385–402.
 - [13] L. Liberatore, F. Mollaioli, Influence of masonry infill modelling on the seismic response of reinforced concrete frames, *Civil-Comp Proc.* (2015).
 - [14] T. Nicola, C. Leandro, C. Guido, S. Enrico, Masonry infilled frame structures: State-of-the-art review of numerical modelling, *Earthq. Struct.* 8 (2015) 225–251.
 - [15] A. Menon, G. Magenes, Definition of seismic input for out-of-plane response of masonry walls: I. parametric study, *J. Earthq. Eng.* 15 (2011) 165–194.
 - [16] M.J.. Priestley, Seismic behaviour of unreinforced masonry walls, *Bull. New Zeal. Natl. Soc. Earthq. Eng.* 18 (1985).
 - [17] T. Paulay, M.J.. Priestley, *Seismic Design of Reinforced Concrete and Masonry Building*, 1992.
 - [18] M.C. Griffith, G. Magenes, G. Melis, L. Picchi, Evaluation of out-of-plane stability of unreinforced masonry walls subjected to seismic excitation, *J. Earthq. Eng.* 7 (2003) 141–169.
 - [19] M. Di Domenico, Out-of-plane seismic response and modelling of unreinforced masonry infill walls, University of Naples Federico II, 2018.
 - [20] D. Abrams, O. Alshawa, P.B. Lourenco, L. Sorrentino, Out-of-Plane Seismic Response of Unreinforced Masonry Walls : Conceptual Discussion , Research Needs , and Modeling Issues, *Int. J. Archit. Herit.* (2017).
 - [21] J.L. Dawe, C.K. Seah, Out-of-plane resistance of concrete masonry infilled panels, *Can. J. Civ. Eng.* 16 (1989) 854–864.
 - [22] P. Ricci, M. Di Domenico, G.M. Verderame, Effects of the In-Plane/Out-of-Plane Interaction in URM Infills on the Seismic Performance of RC Buildings Designed to Eurocodes, *J. Earthq. Eng.* (2020).
 - [23] R. Angel, D. Abrams, *Behaviour of Reinforced Concrete Frames with Masonry Infills*, 1994.
 - [24] R.D. Flanagan, R. Bennett, Biderctional Behaviour of Structural Clay Tile Infilled Frames, *J. Struct. Eng.* 125 (1999) 236–244.
 - [25] G.M. Calvi, D. Bolognini, Seismic response of reinforced concrete frames infilled with weakly reinforced masonry panels, *J. Earthq. Eng.* 5 (2001) 153–185.
 - [26] F. da Porto, G. Guidi, M. Dalla Benetta, N. Verlato, Combined In-Plane/Out-of-Plane Experimental Behaviour of Reinforced and Strengthened Infill Masonry Walls, 12th *Can. Mason. Symp.* (2013) 1–11.
 - [27] P. Morandi, S. Hak, G. Magenes, Out-of-plane experimental response of strong masonry infills, 9th *Int. Mason. Conf.* July 7, 8, 9; 2014; Guimarães. (2014) 1–12.

- [28] A. Furtado, A. Arêde, H. Varum, H. Rodrigues, Experimental study of the out-of-plane behaviour of masonry infill walls with and without previous in-plane damage, *Brick Block Mason. Trends, Innov. Challenges - Proc. 16th Int. Brick Block Mason. Conf. IBMAC 2016*. (2016) 1201–1208.
- [29] P. Ricci, M. Di Domenico, G.M. Verderame, Experimental assessment of the in-plane/out-of-plane interaction in unreinforced masonry infill walls, *Eng. Struct.* 173 (2018) 960–978.
- [30] P. Ricci, M. Di Domenico, G.M. Verderame, Experimental investigation of the influence of slenderness ratio and of the in-plane/out-of-plane interaction on the out-of-plane strength of URM infill walls, *Constr. Build. Mater.* 191 (2018) 507–522.
- [31] F. Akhoundi, G. Vasconcelos, P. Lourenço, Experimental Out-Of-Plane Behavior of Brick Masonry Infilled Frames, *Int. J. Archit. Herit.* 14 (2018) 221–237.
- [32] C. Butenweg, M. Marinković, R. Salatić, Experimental results of reinforced concrete frames with masonry infills under combined quasi - static in - plane and out - of - plane seismic loading, *Bull. Earthq. Eng.* 17 (2019) 3397–3422.
- [33] M.T. De Risi, M. Di Domenico, P. Ricci, G.M. Verderame, G. Manfredi, Experimental investigation on the influence of the aspect ratio on the in-plane/out-of-plane interaction for masonry infills in RC frames, *Eng. Struct.* 189 (2019) 523–540.
- [34] X. Xie, Z. Qu, H. Fu, L. Zhang, Effect of prior in-plane damage on the out-of-plane behavior of masonry infill walls, *Eng. Struct.* 226 (2021) 111380.
- [35] F. da Porto, M. Donà, N. Verlato, G. Guidi, Experimental Testing and Numerical Modeling of Robust Unreinforced and Reinforced Clay Masonry Infill Walls, With and Without Openings, *Front. Built Environ.* 6 (2020).
- [36] M. Di Domenico, M.T. De Risi, P. Ricci, G.M. Verderame, G. Manfredi, Empirical prediction of the in-plane/out-of-plane interaction effects in clay brick unreinforced masonry infill walls, *Eng. Struct.* 227 (2021)
- [37] Development of an innovative approach for decoupling masonry infills and non load-bearing masonry walls from the main structure, <https://www.cwe.rwth-aachen.de/earthquake-engineering-projects/development-of-an-innovative-approach-for-decoupling-infills-and-non-load-bearing-masonry-walls-from-the-main-structure/>
- [38] New Zealand Society for Earthquake Engineering (NZSEE), The Seismic Assessment of Existing Buildings (the Guidelines), Part C - Detailed Seismic Assessment, 2017.
- [39] FEMA 274. NEHPR Commentary on the Guidelines for the Seismic Rehabilitation of Buildings, published by the Federal Emergency Management Agency, Washington, DC, 1997.
- [40] FEMA 356. Prestandard and comentary for the seismic rehabilitation of buildings. Washington, DC. 2000.
- [41] ASCE/SEI 41-06. Seismic rehabilitation of existing buildings. American Society of Civil Engineers, 2006.
- [42] ASCE/SEI 41-13. Seismic rehabilitation of existing buildings. American Society of Civil Engineers, 2013.
- [43] FEMA 306. Evaluation of earthquake damaged concrete and masonry wall buildings,

- basic procedures manual, published by the Federal Emergency Management Agency, Washington, DC., (n.d.).
- [44] ASCE/SEI 41-17. Seismic rehabilitation of existing buildings. American Society of Civil Engineers, 2017..
 - [45] P. Morandi, S. Hak, G. Magenes, Simplified Out-of-plane Resistance Verification for Slender Clay Masonry Infills in RC Frames, (2013).
 - [46] N. Verlato, G. Guidi, F. da Porto, Experimental testing and numerical modelling of infill masonry walls subjected to in-plane damage, Proc. Second Eur. Conf. Earth Eng. Seismol. 25-29 August 2014, Istanbul, Turkey.
 - [47] L. Cavaleri, M. Zizzo, P.G. Asteris, Residual out-of-plane capacity of infills damaged by in-plane cyclic loads, Eng. Struct. 209 (2020) 109957.

EXPERIMENTAL INVESTIGATION OF BEHAVIOUR OF MASONRY INFILLED RC FRAMES UNDER OUT-OF-PLANE LOADING

Aleksa Milijaš^{1*}, Bogdan Šakić¹, Marko Marinković², Christoph Butenweg³,
Sven Klinkel¹

¹ Chair of Structural Analysis and Dynamics, RWTH Aachen University
Mies-van-der-Rohe-Straße 1, 52074 Aachen, Germany

milijas@lbb.rwth-aachen.de, sakic@lbb.rwth-aachen.de, klinkel@lbb.rwth-aachen.de

² Department of Engineering Mechanics and Theory of Structures, Faculty of Civil Engineering,
University of Belgrade

Bulevar kralja Aleksandra 73, 11000 Belgrade, Serbia

mmarinkovic@grf.bgd.ac.rs

³ Center for Wind and Earthquake Engineering, RWTH Aachen University
Mies-van-der-Rohe-Straße 1, 52074 Aachen, Germany

butenweg@lbb.rwth-aachen.de

Abstract

Masonry infills are commonly used as exterior or interior walls in reinforced concrete (RC) frame structures and they can be encountered all over the world, including earthquake prone regions. Since the middle of the 20th century the behaviour of these non-structural elements under seismic loading has been studied in numerous experimental campaigns. However, most of the studies were carried out by means of in-plane tests, while there is a lack of out-of-plane experimental investigations. In this paper, the out-of-plane tests carried out on full scale masonry infilled frames are described. The results of the out-of-plane tests are presented in terms of force-displacement curves and measured out-of-plane displacements. Finally, the reliability of existing analytical approaches developed to estimate the out-of-plane strength of masonry infills is examined on presented experimental results.

Keywords: Seismic loading, Masonry infill, Out-of-plane load, Out-of-plane strength.

1 INTRODUCTION

The influence of infills on the seismic response of frame structures has long been recognised [1]. However, the issue of how the infills affect the seismic performance of an RC building is intricate as well as their exact role during an earthquake is complex and not yet clearly understood [2]. Regularly distributed infills may significantly contribute to withstand the seismic actions, as also proved during moderate and strong earthquakes, reducing the deformation demand and improving the energy dissipation capacity of the system [3,4]. However, regular infill distribution is not easy to be accomplished in practice. Furthermore, as the deflection of RC frame activates much stiffer infill walls that have a low drift capacity of 0.2–0.3% [5] and rather stiff and brittle in-plane response, infill panels achieve its maximum load capacity very fast which is followed by a sudden decrease of strength. Therefore, it can be concluded that infill wall increases the strength of infilled frame, but it highly decreases its ductility, which conflicts with ductile seismic design [5]. Increase of the stiffness of the overall system due to the infills leads to an increase of the natural frequencies and thus to an increase of the horizontal earthquake loads with a significantly different global vibration behaviour of the overall structure [6]. In addition to this, if the infills are irregularly arranged in plan and elevation, torsional effects can lead to additional loads with unfavourable load distributions which accelerate a failure of the infills [7,8,9]. Moreover, additional critical torsional effects may also occur over the course of the successive failure of overloaded infill elements, even if the infills are arranged in a regular manner [6]. If taking these shortcomings into account, it is not surprising that in almost every moderate to high intensity earthquake event RC frames with masonry infill walls suffered damage, in some cases even a total collapse [10]. In order to provide better understanding of the complex frame-infill interaction and its influence on overall seismic performance of structures, most experimental campaigns focused on behaviour of infilled frames under in-plane component of seismic loading.

On the other side, the performance of infilled frames under out-of-plane seismic loading component was the subject of significantly smaller number of experimental researches. In one of the first experimental investigations on out-of-plane behaviour of URM walls conducted by McDowell et al. (1956a,b) [11,12], the important arching action or arching effect was discovered. Further experimental studies on out-of-plane response of masonry infills were carried out by Dawe and Seah (1989b) [13], Angel et al. (1994) [14], Flanagan and Bennett (1999b) [15] and Di Domenico (2018) [16], among others. In the work of these authors, the parameters affecting arching action were investigated and it was concluded that infill wall built in a traditional way with a full contact to surrounding frame can achieve a several times larger out-of-plane capacity than its expected flexural capacity. In addition to this, the results showed that arching effect is mostly governed by a compressive strength of the wall, panel dimensions (slenderness), boundary conditions between the infill and the frame and stiffness of the surrounding frame. Furthermore, the development of arching or rigid body mechanism can be distinguished depending on the condition of infill-frame connections [17]. The ineffective frame-infill connections can be caused by poor quality execution as pointed out in [18] or mortar shrinkage. In more recent studies, the influence of workmanship was therefore investigated in the work of Akhoundi et al. (2020) [19]. The further investigations of out-of-plane behaviour of masonry infills appear to be inevitable after observations of damages after recent earthquake events. For instance, in the L'Aquila 2009 earthquake in Italy, out-of-plane mechanisms led to the lowest capacity of the infills, thus representing the condition of highest risk for human safety [20]. To make the matters worse, not only can the out-of-plane failure occur on upper storeys of buildings due to higher amplification of ground acceleration, but masonry infills can also suffer substantial damage due to interaction of in-plane and out-of-

plane actions in the lower storeys of buildings. The detrimental combination of in-plane and out-of-plane loading was pronounced in recent earthquakes in L'Aquila 2009, Central Italy 2016, Lorca 2011, and Albania 2019.

The available experimental results have served as a useful basis for many researchers to propose simple analytical equations based on arching theory that can be applied in engineering practice for the estimation of out-of-plane capacity of masonry infill walls. Despite the fact that most theories agree in recognizing the aforementioned out-of-plane behaviour for the infilled frames, their results are often conflicting. In most cases this may be justified by substantially different choices in the reference experimental programs [21]. In this paper results of two experimental tests carried out on masonry infills with different boundary conditions are presented. Furthermore, analytical approaches based on arching theory are summarized and their accuracy in estimation of out-of-plane capacity is examined on test results.

2 EXPERIMENTAL TESTS

For the purpose of investigating the correctness of analytical expressions for out-of-plane strength of infill walls, two out-of-plane experimental tests will be used. The first test was conducted within the experimental campaign of the European research project INSYSME (Innovative systems for earthquake resistant masonry in reinforced concrete buildings) [22], whereas the second one was carried out in the scope of the project "Development of an innovative approach for decoupling infills and non load-bearing masonry walls from the main structure" [23] and represents the continuation of the research work done within the INSYSME project [22]. In this paper, only out-of-plane tests on two masonry infills are described. Test BO was carried out in the former and test T1 in the latter experimental campaign.

2.1 Test specimens

Both infill walls were constructed in a usual way of bricklaying. Bed joints were filled with thin layer mortar while head joints were made as dry joint connection without mortar. However, it has to be pointed out that in the specimen BO, the general purpose mortar was used to fill the remaining gap at the top, while in specimen T1 the execution of the top joint was carried out by a special pump in order to completely and perfectly fill the top gap with thin layer mortar. In both specimens bottom and side connections of masonry infill to the surrounding frame were made by general purpose mortar, but in the specimen BO a gap of 5 cm between infill and RC column was left in order to consider the case of wall having door opening along its whole height. In that sense, BO specimen presents three-sided and T1 specimen four-sided wall. The dimensions and mechanical characteristics of bricks, thin layer and general purpose mortar used in specimens are summarized in Table 1 and 2.

The surrounding reinforced concrete frames were designed according to DIN EN 1992-1-1 (2011) [24] and DIN EN 1998-1 (2010) [25] considering the German national annexes for ductility class L. Columns have 25/25 cm quadratic cross section with the 1.48 % of longitudinal reinforcement. The percentage of transverse reinforcement in middle column section is 0.42 %, while there is 0.63% of transverse reinforcement in column corners. Beam was designed to have a width of 45 cm and height of 25 cm with the 1.05% of longitudinal reinforcement and 0.23% and 0.35% of transverse reinforcement in middle and corner sections, respectively. Dimensions of the frame and arrangement of reinforcement can be found in [6, 17].


Test BO					
Mortar ZP99	Mortar type	Compressive strength f_m (N/mm ²)		Flexural tensile strength $f_{m,flex}$ (N/mm ²)	
	Thin layer mortar	15.7		3.67	
	General purpose mortar	8.9		2.47	
Brick MZ70	Dimensions L/T/H (mm)	Compressive strength f_{ck} (N/mm ²)		Voids (%)	Gross dry density (kg/m ³)
	250/365/249	Vertical	Longitudinal	62.3	553
		6.3	4.8		
Masonry	Compressive strength f_k (N/mm ²)			Modulus of elasticity E_m (N/mm ²)	
	3.1			4870	

Table 1. Mean values of the material properties and strengths (Test BO, INSYSME [22])


Test T1					
Mortar MAXIT	Mortar type	Compressive strength f_m (N/mm ²)		Flexural tensile strength $f_{m,flex}$ (N/mm ²)	
	Thin layer mortar	12.8		2.4	
	General purpose mortar	16		2.4	
Brick Thermo plan SX10	Dimensions L/T/H (mm)	Compressive strength f_{ck} (N/mm ²)		Voids (%)	Gross dry density (kg/m ³)
	247/300/249	Vertical	Longitudinal	56	600
		9.57	1.67		
Masonry	Compressive strength f_k (N/mm ²)			Modulus of elasticity E_m (N/mm ²)	
	2.68*			2680*	

Table 2. Mean values of the material properties and strengths (Test T1, Development of an innovative approach for decoupling infills and non load-bearing masonry walls from the main structure [23])

*Values calculated according to Eurocode 6 [37]

2.2 Test setup and loading protocols

The test setup for specimen BO was specifically constructed for the experimental tests within the INSYSME project [22]. Vertical force of 200 kN per column was applied with the vertical hydraulic jacks before the application of out-of-plane load and kept constant during the whole test. Air bags for out-of-plane loading were placed between the stiff supporting panel and infill wall thus allowing only the deformation of infill wall. Detailed description of the test setup for specimen BO can be found in [6, 17].

The test setup for specimen T1 was purposely designed for the experimental tests within the project “Development of an innovative approach for decoupling infills and non load-bearing masonry walls from the main structure” [23]. Vertical force of 200 kN per column was applied by one-way hydraulic actuators connected to a pressure accumulator to ensure near constant pressure during the test. A special harness is used for these actuators, which consists of two rods per column, a steel beam at the top and specially designed steel angles connected to the frame at the foundation beam. After the application of vertical load, the out-of-plane load is imposed to the infill by four airbags. The airbags are placed between the infill and a wooden reaction wall at the back of the wall.

2.3 Experimental results

2.3.1. Test BO

In test BO masonry infill wall supported on three sides with one free vertical edge was subjected to out-of-plane loading applied in four cycles. On Figure 1 load-displacement curve is presented. It shows that the specimen achieved maximum resistance of about 170 kN which corresponds to a uniformly distributed load of about 24 kN/m². In first two loading cycles the out-of-plane displacements were relatively small due to stable arching action. However, in the third load cycle at the load level of about 24 kN/m² sudden friction failure occurred in the top joint between infill and the upper beam of the frame which triggered the tilting of the wall. In addition to this, splitting and overloading of the bricks in the uppermost infill row caused the loss of boundary condition at the top. The substantial increase of displacements was observed at the infill free edge, especially at the top (Figure 2).

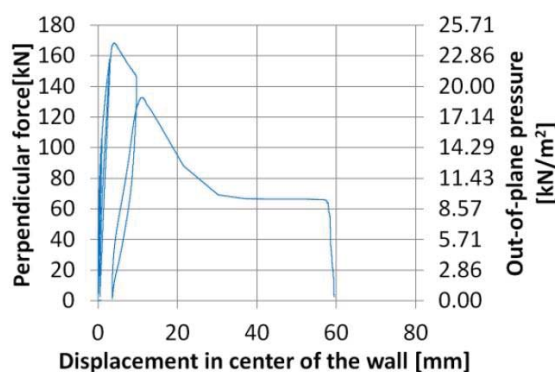


Figure 1. Force-displacement curve for out-of-plane loading of the test BO (Marinković, 2018) [17]

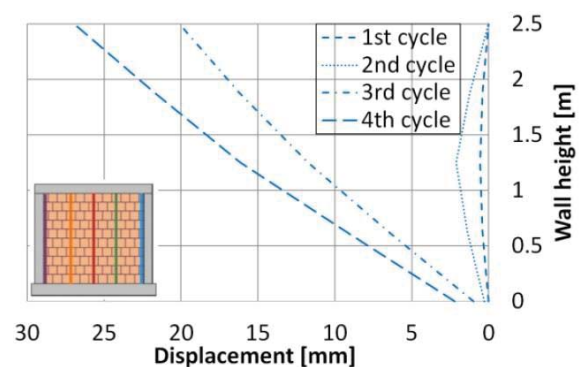


Figure 2. Side view of the out-of-plane displacements of the vertical section at the free edge of the wall in test BO (Marinković, 2018) [17]

In the final load cycle the splitting of the bricks at the wall base occurred too and thus destroyed the bottom boundary condition. As a consequence, the formation of arching effect was prevented. Right side of the wall moved as a rigid body until the occurrence of cracking through head joints in the central part of infill (Figure 3). The measured out-of-plane displacements at the end of the fourth cycle are presented in Figure 4.

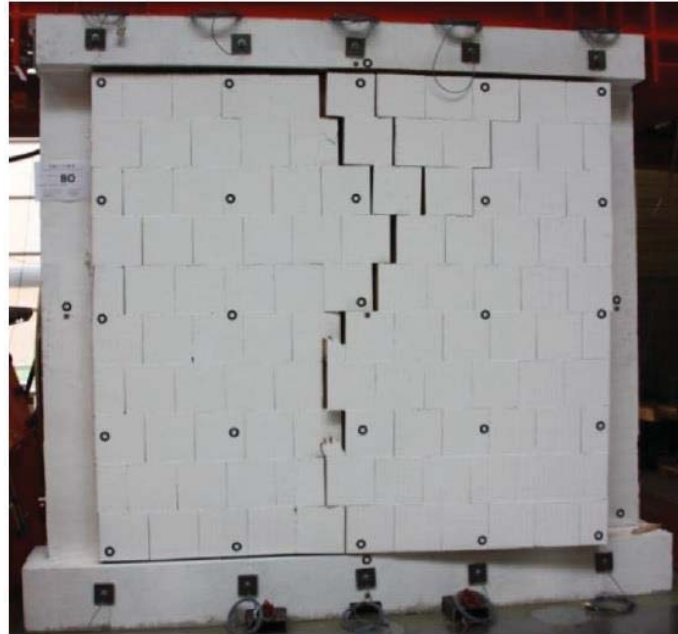


Figure 3. Damage to the wall at the end of the test BO (Butenweg et al. 2019) [6]

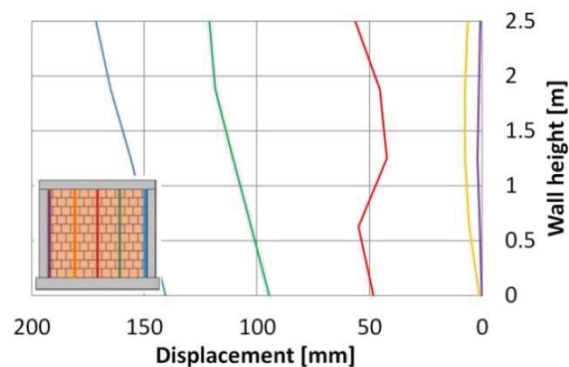


Figure 4. Side view of the out-of-plane displacements at the end of the fourth loading cycle of the test BO (Butenweg, et al. 2019) [6]

2.3.2. Test T1

In test T1 four side supported masonry infill wall was subjected to out-of-plane loading applied in two cycles. On Figure 5 load-displacement curve is presented. The specimen was able to withstand the total out-of-plane force of 175.6 kN which corresponds to 25.2 kN/m² of uniform load. The wall deflection in the first load cycle indicated the formation of two-way arching mechanism (Figures 6 and 7). The out-of-plane displacements in this loading phase were quite small, not exceeding 2 mm. With the further application of the out-of-plane loading in the second cycle, the out-of-plane displacements increased. Central vertical and horizontal strips deflected more than the outer strips (Figure 8) thus confirming the presence of strong two-way arching action. Although there were no visible signs of any substantial

damage to the masonry infill, at the load level of about 25 kN/m^2 the part of the infill abruptly fell out. Due to strong and undamaged connections at the top and bottom of the infill wall, the rotation between topmost row of bricks and upper beam and lowermost row of bricks and bottom beam was limited at higher load levels. Due to this, compressive stresses increased faster in the compressive thrust near the arc supports. The thin and brittle webs of bricks in compression zones of arc supports crushed under excessive compressive stresses which led to the expulsion of the part of the wall and complete failure of specimen (Figure 9).

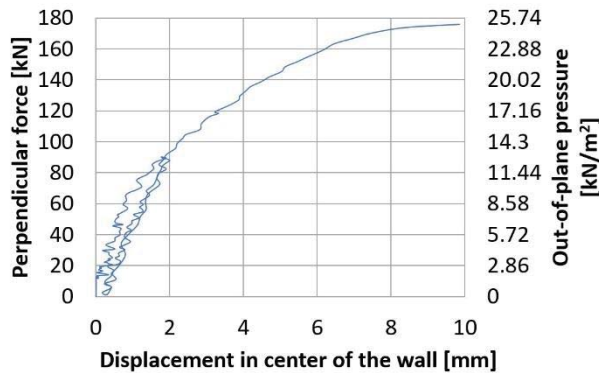


Figure 5. Force – displacement curve for out-of-plane loading of the test T1

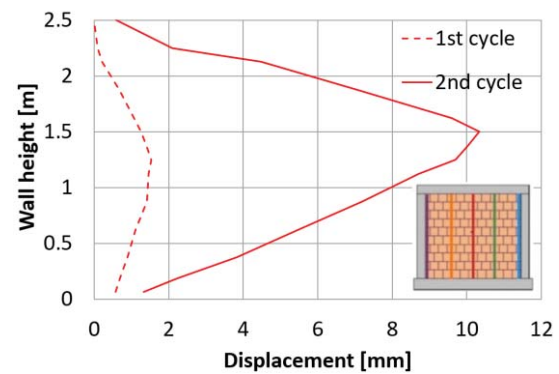


Figure 6. Side view of the out-of-plane displacements of the central vertical section of the test T1

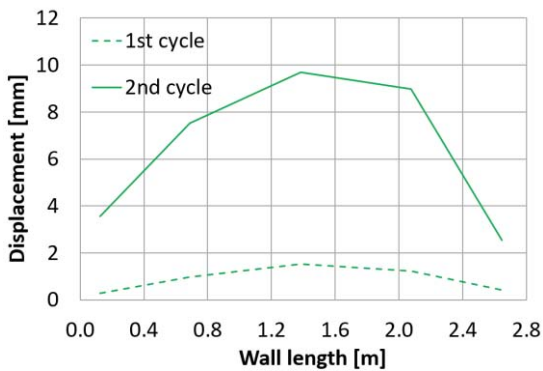


Figure 7. Top view of the out-of-plane displacements of the central horizontal section of the test T1

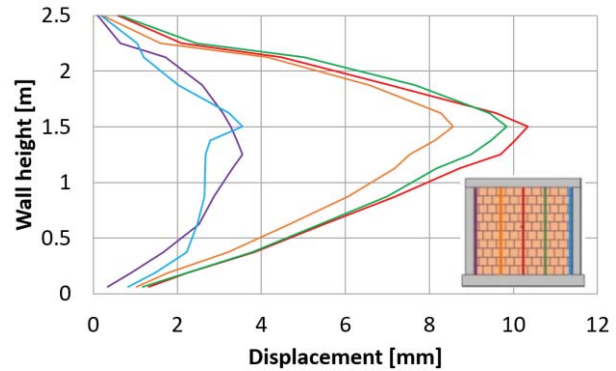


Figure 8. Deflection of vertical strips in the end of second loading cycle of test T1

Even after the collapse of the infill, thin layer mortar at the top remained intact and strongly connected to the top beam and rest of the bricks in the uppermost row of the infill. Namely, during the inspection of specimen after the test, it was noticed that vertical holes of bricks were filled with a huge amount of thin layer mortar since it had been falling into narrow voids during its application by a special pump.



Figure 9. Infill wall after the collapse (test T1)

3 SUMMARY OF ANALYTICAL APPROACHES ESTIMATING OUT-OF-PLANE CAPACITY

In the case of earthquake loading, masonry infills are subjected to out-of-plane loads due to the mass and inertia of the wall. Since the out-of-plane loads can be approximated as uniformly distributed, out-of-plane capacity of masonry infills is usually defined as the uniform lateral pressure causing the collapse of the wall. Some of the first approaches used for estimation of out-of-plane capacity were derived from Timoshenko theory (Timoshenko and Woinowsky-Krieger, 1959) [26]:

$$q = \frac{f_{mt}}{6\beta_1 \left(\frac{h}{t}\right)^2} \quad (1)$$

The governing parameter is a tensile strength f_{mt} of linearly elastic, homogeneous and isotropic material, while β_1 is a coefficient depending on the aspect ratio of the panel and its restraint conditions. In the other methods two-way action was taken into account by using yield line analysis (Hendry, 1973; Hendry and Kheir, 1976) [27,28]. In the approach proposed by Haseltine (Haseltine, 1976; Haseltine et al. 1977) [29,30] the governing parameter is flexural tensile strength f_{xk2} orthogonal to the bed joints:

$$q = \frac{f_{xk2}}{6a \left(\frac{h}{t}\right)^2 \gamma_m \gamma_f} \quad (2)$$

Panel shape and restraint conditions are taken into account by bending coefficient a , γ_m is safety coefficient related to the materials and γ_f is an importance factor.

These approaches that considered tensile or flexural strength as the governing parameter appeared to be limited in the prediction of ultimate out-of-plane capacity and only capable of estimation of masonry cracking. However, experiments [13-16] showed that membrane forces appear in the wall due to deformation of the wall after cracking, thus proving that the arching action is a predominant resisting mechanism.

McDowell et al. (1956a,b) [11,12] were the first to propose calculation of out-of-plane capacity of masonry walls considering one-way arching action. Instead of flexural or tensile strengths which were used in preceding approaches, they incorporated compressive strength of masonry into their formulation. In the researches that followed this one, two-way arching action was also considered in analytical models.

After verification of their postcracking analysis program on the results of out-of-plane tests on concrete masonry infills surrounded by steel frames, Dawe and Seah (1989b) [13] conducted an extensive parametric study in order to determine the most important parameters affecting out-of-plane capacity of masonry infills. Based on the results of this study they developed empirical relationship for the calculation of out-of-plane capacity of masonry infills:

$$q = 0.8f_m'^{0.75}t^2 \left(\frac{\alpha}{l^{2.5}} + \frac{\beta}{h^{2.5}} \right) \quad (3)$$

where f_m' is masonry compressive strength (MPa), t is the infill thickness (mm), h is the infill height (mm), l is the infill length (mm). Parameter α takes into account the relative stiffness of the bounding column, while parameter β takes into account the relative stiffness of the bounding beam. The parameters should be calculated according to the equations below, distinguishing the case of four-sided wall (eq. 4 and 5) or three-sided wall with the gap at the top (eq. 6 and 7):

$$\alpha = \frac{1}{h} (EI_c h^2 + G_c J_c t h)^{0.25} \leq 50 \quad (4)$$

$$\beta = \frac{1}{l} (EI_b l^2 + G_b J_b t l)^{0.25} \leq 50 \quad (5)$$

$$\alpha = \frac{1}{h} (EI_c h^2 + G_c J_c t h)^{0.25} \leq 75 \quad (6)$$

$$\beta = 0 \quad (7)$$

In the equations (4-7), E is the modulus of elasticity of frame material (MPa), I_c is the moment of inertia in the plane of the infill of the column (mm^4), I_b is the moment of inertia in the plane of the infill of the beam (mm^4), G is shear modulus (MPa), J_c is torsional constant of the column (mm^4), J_b is torsional constant of the beam (mm^4).

Angel et al. (1994) [14] developed analytical model based on arching action of an infill strip spanning between two rigid supports. The authors distinguished two failure modes depending on the slenderness ratio; for the infills with h/t values lower than determined critical slenderness ratio crushing at arc boundaries is expected to occur, otherwise the snap through the panel may appear. In addition to this, they considered the effects of previous in-plane damage, flexibility of the confining frame and panel slenderness ratio on the out-of-plane behaviour. Therefore, the ultimate out-of-plane strength could be estimated by the following equation:

$$q = R_1 R_2 \frac{2f_m' \lambda}{h/t} \quad (8)$$

where t is the thickness of the wall (mm), h is the height of the wall (mm), l is the length of the wall (mm), f'_m is the compressive strength of masonry infill (MPa) and λ is the dimensionless parameter that can be calculated according to equation (9) proposed by Flanagan and Bennett (1999c) [31]. Coefficient R_1 is the reduction factor that considers previous in-plane damage and coefficient R_2 accounts for the flexibility of the confining frames in the case of edge location of the infill, meaning that the panel is located in the exterior bay or the uppermost story. Coefficients R_1 and R_2 can be calculated by using the equations (10-12).

$$\lambda = 0.154 \exp\left(-0.0985 \frac{h}{t}\right) \quad (9)$$

$$R_1 = (1.08 - 0.015 \frac{h}{t} - 0.00049 \left(\frac{h}{t}\right)^2 - 0.000013 \left(\frac{h}{t}\right)^3)^{\frac{\Delta}{2\Delta_{cr}}} \quad (10)$$

for $\frac{\Delta}{2\Delta_{cr}} \geq 0.5$

$$R_2 = 0.357 + 2.49 EI \cdot 10^{-14} \text{ for } EI < 25.83 \cdot 10^{12} \quad (11)$$

$$R_2 = 1 \text{ for } EI \geq 25.83 \cdot 10^{12} \quad (12)$$

$$EI = E \min\{I_b; I_c\} \quad (13)$$

where Δ represents the maximum in-plane inter-story drift that panel has experienced and Δ_{cr} is the cracking drift, EI is the flexural stiffness corresponding to the smallest member of the confining frame at the panel edge with no continuity.

In the thorough study of Flanagan and Bennett (1999c) [31], the performance of analytical methods proposed by Dawe and Seah (1989b) [13] and Angel et al. (1994) [14] in estimating the out-of-plane strength of masonry infills was examined on 36 experimental tests carried out by Thomas (1953) [32], Anderson and Bright (1976) [33], Dawe and Seah (1989b) [13], Fricke et al. (1992) [34], Frederiksen (1992) [35], Angel et al. (1994) [14] and Flanagan and Bennett (1999b) [15]. The empirical method proposed by Dawe and Seah (1989b) [13] provided the best prediction of out-of-plane capacity, but with consistent overestimation. Therefore, Flanagan and Bennett (1999c) [31] modified the constant in (3) from 0.8 to 0.73 and proposed the following equation for the calculation of out-of-plane capacity of masonry infills:

$$q = 0.73 f'_m{}^{0.75} t^2 \left(\frac{\alpha}{l^{2.5}} + \frac{\beta}{h^{2.5}} \right) \quad (14)$$

where f'_m is masonry compressive strength (MPa), h is the height of the wall (mm), l is the length of the wall (mm). The authors recommend the application of the modified thickness of the wall $t_2 = h/8$ if the infill walls slenderness ratio is less than 8 ($h/t < 8$). Parameters α and β can be calculated according to the following equations:

$$\alpha = \frac{1}{h} (EI_c h^2)^{0.25} \leq 50 \quad (15)$$

$$\beta = \frac{1}{l} (EI_b l^2)^{0.25} \leq 50 \quad (16)$$

In the equations (15-16), E is the modulus of elasticity of frame material (MPa), I_c is the moment of inertia in the plane of the infill of the column (mm^4), I_b is the moment of inertia in the plane of the infill of the beam (mm^4). The authors neglected the influence of torsional stiffness on the out-of-plane capacity of masonry infills which was considered in the method of Dawe and Seah (1989b) [13].

In Eurocode 8 (2004) [36] it is stated that particular attention should be paid to masonry panels with a slenderness ratio greater than 15, but there are no specific design recommendations for the calculation of out-of-plane strength of masonry infills. However, in Eurocode 6 (2005) [37] one-way arching action is assumed as lateral loads resisting mechanism of URM wall and the out-of-plane capacity of URM walls can be calculated according to the equations:

$$q = f'_m (t/a)^2 \text{ for } t/a < 20 \quad (17)$$

where f'_m is compressive strength of masonry infill (MPa), t is the thickness of the wall (mm), h is the height of the wall (mm), l is the length of the wall (mm) and a is taken as:

$$a = \max\{h; l\} \quad (18)$$

Based on analytical investigation of the behaviour of masonry infills supported on two sides under transverse loading, Moghaddam and Goudarzi (2010) [38] developed semi-empirical relationship between out-of-plane capacity of masonry infills and rigidity of the bounding frame, properties of the masonry material and slenderness ratio. Two failure modes are distinguished: boundary crushing (q_{cr}), when the crushing takes place at the supports of the infill and transverse instability (q_{max}), which occurs due to the large transverse deflection of the infill. The out-of-plane capacity corresponds to the smaller of two values:

$$q = \min\{q_{cr}; q_{max}\} \quad (19)$$

$$q_{cr} = \left(\frac{0.85 f'_m}{(h/t)^2} - \left(0.12 + \frac{0.045}{\alpha} \right) \frac{f_m'^2}{E_m} \right) \quad (20)$$

$$q_{max} = \left(\frac{0.18 E_m}{\left(0.12 + \frac{0.045}{\alpha} \right) \left(\frac{h}{t} \right)^4} \right) \quad (21)$$

$$\alpha = 384 \frac{EI_b h}{E_m t l^4} \quad (22)$$

where f'_m is compressive strength of masonry infill (MPa), E is Young's modulus of frame material (MPa), E_m is Young's modulus of masonry infill wall (MPa), t is the thickness of the wall (mm), h is the height of the wall (mm), l is the length of the wall (mm).

Morandi et al. (2013) [39] proposed the equation for the calculation of ultimate out-of-plane capacity of the masonry infill based on the recommendations from Eurocode 6 (2005)

[37]. Besides the contribution of the arching mechanism to out-of-plane capacity of the infill, the presence of vertical reinforcement in the masonry infill may also be taken into account:

$$q = 0.72 \left(\frac{t}{h} \right)^2 f'_m + 7.2 \frac{t}{lh^2} A_s f_y \quad (23)$$

where, f'_m is the compressive strength of masonry infill (MPa), t is the thickness of the wall (mm), h is the height of the wall (mm), l is the length of the wall (mm), A_s is the total cross sectional area of the vertical reinforcement in tension (mm²) and f_y is the reinforcement yield strength (MPa). However, the authors stated that the equation refers to the masonry infills which did not suffer any previous in-plane damage.

Unsatisfied with the reliability of existing formulations for prediction of out-of-plane strength, first cracking load and displacement at the collapse of masonry infills, Ricci et al. (2018) [40] proposed semi-empirical approach that defines the characteristic points of a trilinear out-of-plane force-displacement curve based on geometric and mechanical properties of infills. They applied a linear least square regression in their work and defined the cracking and peak out-of-plane uniformly distributed loads q_{crack} and q_{max} , respectively:

$$q_{crack} = 0.31 f_m'^{0.05} \frac{t}{h^{2.66}} \quad (24)$$

$$q_{max} = 1.95 f_m'^{0.35} \frac{t^{1.59}}{h^{2.96}} \quad (25)$$

where t is the thickness of the wall (m), h is the height of the wall (m) and f'_m is the compressive strength of masonry infill (MPa).

4 ESTIMATION OF OUT-OF-PLANE CAPACITY

Results of described experimental tests are used to examine the precision of predicting out-of-plane capacity of masonry infills by means of simple analytical equations summarized in Chapter 3 of this paper. It has to be pointed out that only methods based on arching theory were considered. Figure 10 and Table 3 show the comparison of predicted and experimental values from test BO, whereas the comparison of analytical and experimental results for test T1 is presented in Figure 11 and Table 4.

From Figure 10 and Table 3, it could be concluded that only estimation by method of Flanagan and Bennett (1999c) [31] is in good agreement with experimental result of test BO. This could be explained with the fact that this semi-empirical analytical approach could be applied to walls with a gap at one side by setting parameter α that accounts for stiffness of columns to 0. The similar semi-empirical equation proposed by Dawe and Seah (1989b) [13] overestimates the actual capacity 34 %, although it also considers case of three-sided BO wall by neglecting columns stiffness. However, it is surprising that predictions calculated according to Angel et al. (1994) [14], Eurocode 6 (2005) [37], Moghaddam and Goudrazi (2010) [38], Morandi et al. (2013) [39] substantially overestimate the actual capacity of BO specimen as their theories are based on one-way arching which was the major resisting mechanism in test BO until the occurrence of tilting. Such a significant discrepancy between experimental result and out-of-plane strengths predicted by these analytical approaches might be due to the loss of boundary conditions at the top and bottom of the BO wall which led to the inhibition of the arching action and therefore moving of the infill out of RC frame plane. The reason for overestimation of actual capacity of specimen BO by semi-empirical approach

of Ricci et al. (2018) [40] could be that it was based on regression that produces satisfactory ratio of predicted to experimental values of masonry infills supported on four sides.

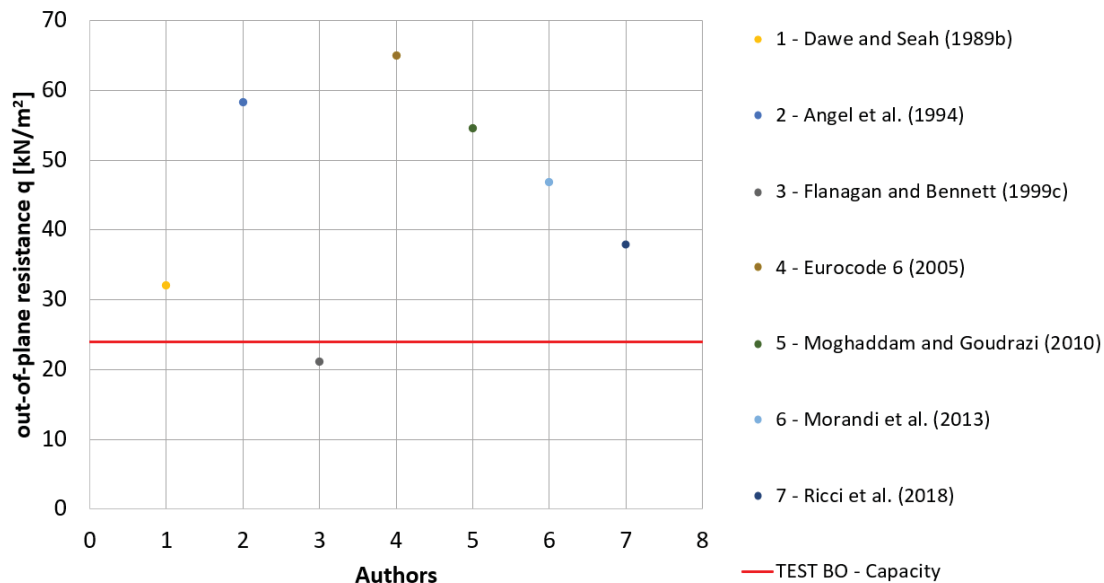


Figure 10. Comparison of calculated out-of-plane capacities with actual capacity in test BO

Author	q_{pred} [kN/m ²]	q_{pred} / q_{exp}
Dawe and Seah (1989b) [13]	32.06	1.34
Angel et al. (1994) [14]	58.29	2.43
Flanagan and Bennett (1999c) [31]	21.08	0.88
Eurocode 6 (2005) [37]	65.03	2.71
Moghaddam and Goudrazi (2010) [38]	54.54	2.27
Morandi et al. (2013) [39]	46.83	1.95
Ricci et al. (2018) [40]	37.84	1.58

Table 3. Comparison of calculated out-of-plane capacities with actual capacity in test BO

On the other side, perhaps due to the same reason explained above, in the case of masonry infill restrained on four sides analyzed in test T1 the best estimation of out-of-plane capacity is achieved by semi-empirical approach proposed by Ricci et al. (2018) [40]. Among two formulations that take into account two-way arching effects, Flanagan and Bennett (1999c) [31] appeared to be closer to actual out-of-plane strength of specimen T1 due to the lower numerical constant in their equation (14) than in the equation (3) of Dawe and Seah (1989b) [13]. The small discrepancy between out-of-plane capacities predicted by Angel et al. (1994) [14] and Morandi et al. (2013) [39] and experimentally measured out-of-plane resistance of four-sided specimen in test T1 needs to be interpreted cautiously since the contribution of horizontal arching was not considered in the approaches of these two authors, but it is pronounced in specimen in test T1. Other two approaches developed assuming one-way arching (Eurocode 6 (2005) [37] and Moghaddam and Goudrazi (2010) [38]) overestimated the actual out-of-plane strength of T1 specimen with an error of about 25 %.

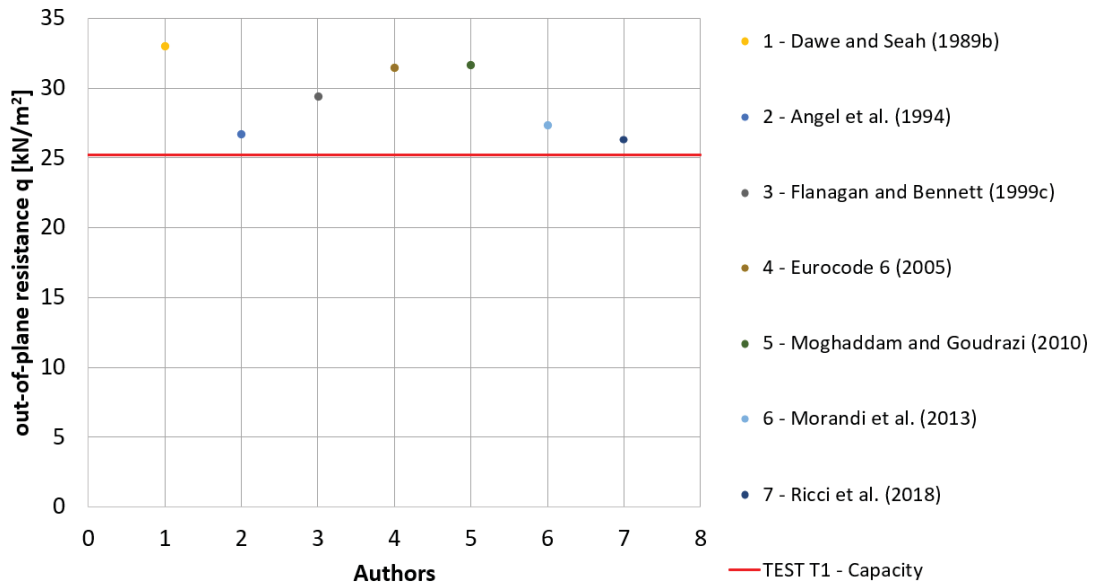


Figure 11. Comparison of calculated out-of-plane capacities with actual capacity in test T1

Author	q_{pred} [kN/m ²]	q_{pred} / q_{exp}
Dawe and Seah (1989b) [13]	33.01	1.31
Angel et al. (1994) [14]	26.67	1.06
Flanagan and Bennett (1999c) [31]	29.39	1.17
Eurocode 6 (2005) [37]	31.44	1.25
Moghaddam and Goudrazi (2010) [38]	31.65	1.26
Morandi et al. (2013) [39]	27.35	1.09
Ricci et al. (2018) [40]	26.32	1.04

Table 4. Comparison of calculated out-of-plane capacities with actual capacity in test T1

This short study shows that Flanagan and Bennett (1999c) [31] can quite accurately predict the out-of-plane capacity of three-sided masonry infill in test BO since ratio of predicted to experimental value is 0.88. As expected, estimation of Dawe and Seah (1989b) [13] is less conservative than Flanagan and Bennett (1999c) [31] as predicted to experimental ratio is 1.34. The other approaches overestimate the actual strength of specimen BO more than 1.5 times. The lowest ratio of predicted to experimental out-of-plane capacity ($q_{pred}/q_{exp} = 1.04$) of four-sided masonry infill in test T1 is achieved by application of semi-empirical approach by Ricci et al. (2018) [40], while calculation according to Dawe and Seah (1989) [13] leads to the largest ratio of 1.31.

5 CONCLUSIONS

This paper deals with investigation of out-of-plane behaviour of masonry infills. Firstly, full scale out-of-plane experimental tests carried out in the scope of two related experimental campaigns are described. The out-of-plane response of masonry infills with different boundary conditions was investigated in the tests. Three side supported wall resisted the imposed out-of-plane loading by stable vertical arching action. However, due to loss of boundary conditions at the top and bottom whole wall started to move out of RC frame plane, with largest deflections at the free edge. The out-of-plane displacements of infill were relatively small until the sudden loss of top joint connection which prevented the arching action and triggered the wall tilting. On the other side, in the four side supported infill wall

pronounced two-way arching action was established. The out-of-plane displacements were relatively small until the explosion-like collapse of the wall. Unlike the first test, frame-infill connections did not suffer any damage and remained in good condition thanks to perfectly executed, but difficult and time demanding filling of the gap at the top with thin layer mortar by pump. Due to this, the rotation was shifted from top connection one joint lower. Additionally, thin brick webs crushed under high compressive stresses induced by arching action. As a consequence, part of the infill defined by head joints and crushed bricks fell out of wall plane.

It has to be pointed out that achieved out-of-plane capacities of both infills represent a significant level of seismic safety in terms of out-of-plane failure. This can be explained by favourable slenderness ratios ($h/t = 6.9$ in test BO; $h/t = 8.4$ in test T1) and relatively low weight of hollow clay bricks resulting in low mass of the considered walls (about 1.5 t in test BO; 1.3 t in test T1). However, the results show a clear dependency of out-of-plane response on the quality of execution of frame-infill joints, especially at the top.

Furthermore, the existing analytical approaches for prediction of out-of-plane strength are summarized. The importance of discovery and consideration of arching effect in the evaluation of out-of-plane strength of masonry infills is explained and various parameters affecting arching mechanism are discussed.

In the end a short study was conducted with the aim to test the reliability of analytical equations proposed in the literature on presented experimental results. The out-of-plane capacity of three-sided panel investigated in test BO was fairly well predicted by analytical equation of Flanagan and Bennett (1999c) [31], while Dawe and Seah (1989b) [13] overestimated the experimental value, but with smaller error in comparison to predictions of other approaches. The recommendation from Ricci et al. (2018) [40] was the most precise in the estimation of out-of-plane strength of four-sided panel in test T1. Out-of-plane capacities of specimen T1 calculated according to equations proposed by Angel et al. (1994) [14] and Morandi et al. (2013) [39] are also in good agreement with the experimental value, but the results need to be studied with special attention as these two approaches were not developed under consideration of two-way arching action which is pronounced in test T1. If taking average value of predicted to experimental ratio from both experimental tests into account, the method proposed by Flanagan and Bennett (1999c) [31] seems to be applicable in prediction of out-of-plane strengths of both three-sided and four-sided infills. However, the larger experimental database should be considered in order to determine the analytical equation with best fitting to experimental results. In addition to this, the important aspect of the interaction between in-plane and out-of-plane seismic actions should be investigated in the future experimental studies in order to provide more realistic evaluation of out-of-plane capacity of masonry infills. As most of the analytical approaches do not consider the influence of in-plane loading on the out-of-plane strength and thus considerably overestimate the out-of-plane resistance of masonry infills, more work on the formulation that accounts for reduction of out-of-plane capacity due to in-plane damage should be carried out.

ACKNOWLEDGEMENTS

The authors would like to acknowledge the support from the “Institut für Ziegelforschung Essen e.V” and express their special thanks to Dr. Matija Gams from the University of Ljubljana for the support and fruitful discussions during the execution of experimental campaign within “Development of an innovative approach for decoupling infills and non load-bearing masonry walls from the main structure” project.

REFERENCES

- [1] Liberatore, L., and Mollaioli, F. (2015). Influence of masonry infill modelling on the seismic response of reinforced concrete frames. *Civil-Comp Proceedings*, 108.
- [2] Stavridis, A. (2009). Analytical and experimental study of seismic performance of reinforced concrete frames infilled with masonry walls. University of California, San Diego.
- [3] L.D. Decanini, A. De Sortis, L. Liberatore, F. Mollaioli, “Estimation of near source ground motion and seismic behaviour of RC framed structures damaged by the 1999 Athens earthquake”, *Journal of Earthquake Engineering*, 9(5), 609-635, 2005.
- [4] Decanini, L. D., Liberatore, L., & Mollaioli, F. (2012). Damage potential of the 2009 L'Aquila, Italy, earthquake. *Journal of Earthquake and Tsunami*, 6(03), 1250032.
- [5] Tasligedik, A. S., & Pampanin, S. (2017). Rocking cantilever clay brick infill wall panels: a novel low damage infill wall system. *Journal of Earthquake Engineering*, 21(7), 1023-1049.
- [6] Butenweg, C., Marinković, M., & Salatić, R. (2019). Experimental results of reinforced concrete frames with masonry infills under combined quasi-static in-plane and out-of-plane seismic loading. *Bulletin of Earthquake Engineering*, 17(6), 3397-3422.
- [7] Fardis MN, Panagiotakos TB (1997) Seismic design and response of bare and masonry-infilled reinforced concrete buildings part II: infilled structures. *J Earthq Eng* 1(03):475–503
- [8] Masi A (2003) Seismic vulnerability assessment of gravity load designed R/C frames. *Bull Earthq Eng* 1(3):371–395
- [9] Verderame GM, De Luca F, Ricci P, Manfredi G (2011) Preliminary analysis of a soft-storey mechanism after the 2009 L'Aquila earthquake. *Earthq Eng Struct Dyn* 40:925–944
- [10] Marinković, M., & Butenweg, C. (2020). Out-of-plane behavior of decoupled masonry infills under seismic loading. In *17th World Conference on Earthquake Engineering*.
- [11] McDowell, E. L., McKee, K. E., and Sevin, E. (1956a). —Arching action theory of masonry walls. *J. Struct. Div.*, 82(ST2), 915/1–915/18.
- [12] McDowell, E. L., McKee, K. E., and Sevin, E. (1956b). —Discussion of arching action theory of masonry walls. *J. Struct. Div.*, 1067, 27–40.
- [13] Dawe J. L. and Seah C. K. (1989b). Out-of-plane resistance of concrete masonry infilled panels. *Journal of the Canadian Society of Civil Engineering*, Vol. 16, pp. 854-864.
- [14] Angel R., Abrams D., Shapiro D., Uzarski J. and Webster M. (1994). Behavior of Reinforced Concrete Frames with Masonry Infills. *Civil Engrg. Studies, Structural Re-search Series No. 589, UILU-ENG-94-2005*, Dept. of Civil Engineering, University of Illinois at Urbana Champaign.
- [15] Flanagan, R. D., and Bennett, R. M. (1999b). Bidirectional behavior of structural clay tile infilled frames. *Journal of structural engineering*, 125(3), 236-244.

- [16] Di Domenico, M. (2018). *Out-of-plane seismic response and modelling of unreinforced masonry infill walls* (Doctoral dissertation, PhD Dissertation. University of Naples Federico II).
- [17] Marinković M., Innovative system for seismic resistant masonry infills in reinforced concrete frame structures (PhD Thesis), University of Belgrade – Faculty of Civil Engineering, 2018.
- [18] Manfredi, V. and Masi, A. (2014). Combining in-plane and out-of-plane behaviour of masonry infills in the seismic analysis of RC buildings. *Earthquakes and Structures*, 6(5), 515-537.
- [19] Akhoundi, F., Vasconcelos, G., & Lourenço, P. (2020). Experimental out-of-plane behavior of brick masonry infilled frames. *International Journal of Architectural Heritage*, 14(2), 221-237.
- [20] Braga, F., Manfredi, V., Masi, A., Salvatori, A., & Vona, M. (2011). Performance of non-structural elements in RC buildings during the L'Aquila, 2009 earthquake. *Bulletin of Earthquake Engineering*, 9(1), 307-324.
- [21] Asteris, P. G., Cavaleri, L., Di Trapani, F., & Tsaris, A. K. (2017). Numerical modelling of out-of-plane response of infilled frames: State of the art and future challenges for the equivalent strut macromodels. *Engineering Structures*, 132, 110-122.
- [22] INSYSME (2016). Innovative systems for earthquake resistant masonry in reinforced concrete buildings, <http://www.insysme.eu>.
- [23] Development of an innovative approach for decoupling masonry infills and non load-bearing masonry walls from the main structure, <https://www.cwe.rwth-aachen.de/earthquake-engineering-projects/development-of-an-innovative-approach-for-decoupling-infills-and-non-load-bearing-masonry-walls-from-the-main-structure/>
- [24] DIN EN 1992-1-1 (2011) Eurocode 2: Bemessung und Konstruktion von Stahlbeton- und Spannbetontragwerken – Teil 1-1: Allgemeine Bemessungsregeln und Regeln für den Hochbau; Deutsche Fassung EN 1992-1-1:2004 + AC:2010
- [25] DIN EN 1998-1 (2010) Eurocode 8: Auslegung von Bauwerken gegen Erdbeben – Teil 1: Grundlagen, Erdbebeneinwirkungen und Regeln für Hochbauten; Deutsche Fassung EN 1998-1:2004 + AC:2009
- [26] Timoshenko, S. P., and Woinowsky-Krieger, S. (1959). *Theory of plates and shells*. McGraw-hill.
- [27] Hendry AW. (1973). The lateral strength of unreinforced brickwork. *Struct Eng*;51(2):43–50.
- [28] Hendry AW, Kheir AMA. (1976) The lateral strength of certain brickwork panels. In: *Proceedings of the fourth international brick masonry conference*, Brugge, Belgium.
- [29] Haseltine, B.A. (1976) Design of laterally loaded wall panels. *Proceedings of the British Ceramic Society*, vol. 5(24). UK: Load Bearing Brickwork. Stoke-on-Trent; p. 115–26.
- [30] Haseltine, B. A., West, H. W. H. and Tutt, J. N. (1977). Design of walls to resist lateral loads. *Struct Eng*;55(10):422–30.

- [31] Flanagan, R. D., and Bennett, R. M. (1999c). Arching of masonry infilled frames: Comparison of analytical methods. *Practice Periodical on Structural Design and Construction*, 4(3), 105-110.
- [32] Thomas, F. G. (1953). The Strength of Brickwork. *The Structural Engineer*, Part 2, Vol. 36, pp. 35-41.
- [33] Anderson, C., and Bright, N. J. (1976). Behaviour of non-loadbearing block walls under wind loading. *Concrete*, 10(9), 27–30.
- [34] Fricke, K. E., Jones, W. D., and Huff, T. E. (1992). In situ lateral load testing of an unreinforced masonry hollow clay tile wall. *Proc., 6th Can. Masonry Symp., University of Saskatchewan, Saskatoon, Saskatchewan*, 519–530.
- [35] Frederiksen, V. T. (1992, June). Membrane effect in laterally loaded masonry walls: a second order phenomenon. In *Proceedings of the 6th Canadian Masonry Symposium, University of Saskatchewan, Saskatoon, Saskatchewan* (pp. 537-547).
- [36] EN 1998-1 (2004). Eurocode 8: Design of structures for earthquake resistance. Part 1: General rules, seismic actions and rules for buildings (EN 1998-1). CEN, Brussels, Belgium.
- [37] EN 1996-1-1 (2005). Eurocode 6: Design of masonry structures. Part 1-1: General rules for reinforced and unreinforced masonry structures (EN 1996-1). CEN, Brussels, Belgium.
- [38] Moghaddam, H., & Goudarzi, N. (2010). Transverse resistance of masonry infills. *ACI Structural Journal*, 107(4), 461-467.
- [39] Morandi, P., Hak, S., & Magenes, G. (2013). Simplified out-of-plane resistance verification for slender clay masonry infills in RC frames. *Proceedings of the XV ANIDIS, L'Ingegneria Sismica in Italia, Padua, Italy*, 30.
- [40] Ricci, P., Di Domenico, M., & Verderame, G. M. (2018). Empirical-based out-of-plane URM infill wall model accounting for the interaction with in-plane demand. *Earthquake Engineering & Structural Dynamics*, 47(3), 802-827.

STRUCTURAL CONCEPTS IN THE DESIGN OF MASONRY-INFILLED STEEL FRAMES

D. Šokić¹, D. Markulak¹, T. Dokšanović¹, I. Radić¹

¹ Josip Juraj Strossmayer University of Osijek, Faculty of Civil Engineering and Architecture,
Vladimira Preloga 3, HR – 31000 Osijek, Croatia.
e-mail: (dsokic, markulak, tdoksanovic, radic)@gfos.hr

Abstract

Despite numerous research studies conducted in the field of masonry-infilled steel (and concrete) frames, there is still no adequate codified design method. There is, however, a consensus that masonry-infilled frames should be treated as potentially hazardous earthquake context structural solutions. While masonry infill has positive effects on steel frames, which are often neglected in design, adverse effects cannot be overlooked. Over the last decade, several structural solutions aimed to improve the overall structural behavior of these interactive composite systems were proposed and tested in laboratory conditions. It is not rare that these approaches are opposite to each other, which additionally stresses the fact that there is a need for recognition and validation of the key structural directions. Among various proposed design options, the authors are very interested in those which tend to include the beneficial effect of masonry infill, but at the same time preserve desired ductile behavior of steel frames, all by using simpler and easy to apply structural solutions. Some of them are already proposed by the authors, which are discussed in the paper, along with a summary and comparison of contemporary structural solutions in steel masonry-infilled frames, as an important step towards codification.

Keywords: steel-masonry, composite structure, earthquake design, structural solutions

1 INTRODUCTION

Masonry blocks, due to easy production, installation and accessibility are the most widespread infill type in frame structures, especially in Europe. It is known that the presence of masonry infill can significantly increase stiffness and strength, but it can also limit the ductile behavior of frames in case of higher lateral load such as an earthquake. Consequently, researchers evaluate the contribution of the masonry infill and their influence on the frame, and through this process started to develop innovative structural concepts to mitigate the negative effects of

masonry infill. Based on this, numerous structural concepts in the design of infilled frames can be found, aimed to improve the overall interaction between infill and frame. The typical solutions are application of various infill types (i.e. using soft or strong materials for infill), modification of the failure mechanisms, reinforcing of the infill etc. These methods can be generally categorized into two groups [1]:

- Strengthening of the masonry infill through which the composite structure frame+infill behaves as a monolithic construction.
- Limiting frame-infill interaction through which both monolithic and separate behavior of the frame and the infill may be observed.

The strengthening methods are mainly characteristic for concrete frames, while the limited interaction is characteristic for steel frames, although some deviations can be found in the literature review that follows.

One of the most natural types of strengthening infill was covered in the study done by Pul and Arslan [2]. They used and compared plastered, non-plastered, and wire-plastered masonry walls made from hollow clay brick. Results show that plaster and wire plaster enhance load-carrying capacity and ductility, which is good since most of the masonry application includes a plaster surface layer. Jebadurai et al. [3] focused their research on enhancing the bond strength between masonry units in RC frames by adding a different percentage of styrene-butadiene rubber latex in the mortar. Experiments showed that using modified mortar with a certain percentage of latex increased ductility by 12.90%. Binici et al. [4] investigated a well-known infill type, autoclaved aerated concrete, but with an improvement regarding infill execution - metal slider connectors in AAC blocks. Due to this slider connector, the interaction between the RC frame and infill is limited. As a result, the in-plane damage is postponed at higher drift ratios and the out-of-plane damage is limited. Ruey-Shyang Ju et al. [5] studied separation of RC infill walls from steel moment frames by making vertical slits and leaving a horizontal gap between the upper steel beam and the infill RC wall. Results of this study showed that proper design and arrangement of slits can absorb the relative deformation between the column and infill wall and it can isolate the separated wall from damage. Innovative isolation of masonry infill from steel frames is presented by Tsantilis and Triantfillou [6], as they use a cellular material (foamed polyethylene) placed in the frame-infill interface. The cellular material has high deformation capabilities which mitigate interaction between the steel frame and masonry infill in the initial phase of loading. As loads get higher the cellular material gets fully compressed and the diagonal compression strut is activated. M. Mohammadi et al. [7] investigated three different techniques to improve steel frame ductility: (i) cornerless infill, (ii) column fuse, and (iii) infill fuse (applied metal sheets in infill layer to provide horizontal sliding). The infill fuse method has shown a significant increase of ductility with no significant cracks or corner crushing up to 7.1% drift. Preti and Bolis [8], and Morandi et. al. [9], tested the steel frame by dividing infill into more subpanels with wooden boards placed in the horizontal and vertical direction. Each of those configurations has shown a serious reduction of infill stiffness and strength in comparison to the reference masonry infill. Marinkovic and Butenweg [10] developed a system named INODIS, in which an elastomeric cellular material is used around the infill frame surface. Besides reduced interaction between the frame and infill, it reduced stress and infill damage. Moreover, the INODIS system allowed higher interstory drifts (more than 3%). Silva et. al [11] developed new units with an interlocking tongue and groove configuration, with vertical reinforcement. Due to reinforcement, an increase of lateral resistance up to 40% in relation to the bare frame was observed. Aliaari and Memari [12] introduced an idea of seismic isolator subframes attached to the structural frame, which they named SIWIS - a system made of one horizontal and two vertical sandwiched light-gauge steel members with a brittle element inside. They aimed to reduce the story drift at low and moderate lateral loads through the beneficial

effect of infill (higher stiffness and strength), while at higher lateral loads the brittle element acts as a „fuse“ in which they attempt to separate infill-frame interaction. Misir et al. [13] researched a new potential infill type without layers of mortar between them - locked brick. Besides the cracks in plaster, locked bricks stay intact and are less damaged in comparison to standard infill. Markulak et. al [14] presented a newly developed masonry unit for infill with lower initial stiffness and strength with a tendency to achieve minimal detrimental influences on the frame, while at the same time acknowledging environmental aspects.

Through a brief overview of structural concepts, it can be observed that there are numerous efforts of researchers to provide adequate solutions to undesired structural behavior of masonry infilled frames. Although some of them are challenging in terms of the execution (e.g. complexity, extra work hours, overall economic costs), provided experimental results and conclusions are of significant importance. The authors of this paper also conducted various experiments on infilled-steel frames in the mentioned direction, some of them accompanied with corresponding numerical models. The main intention being to keep favorable properties of the masonry while maintaining the steel frame ductile behavior at higher lateral loads. For calibration of experimental results various numerical models are used, with more details given in [15, 16]: (i) single equivalent strut (SSM), (ii) three equivalent struts (MSM), (iii) infill panel element (SPM), (iv) micro-model (AMM).

This paper presents findings regarding the influence of the different types of infill on steel frames. This is done through a short literature overview, to correlate the purpose of different experiments. Conducted experiments will be presented along with calibrated numerical results and grouped based on infill type - hollow clay brick (strong infill), autoclave aerated block (weak infill), the combination of those two (innovative solution proposed by authors), and newly developed RBA-EP unit (new structural concept proposed by authors).

2 STEEL FRAMES INFILLED WITH CLAY HOLLOW AND SOLID UNITS

Masonry units are the most used infill in conducted experiments [6, 17, 18, 19, 20, 21]. The masonry infill can be grouped depending on the unit configuration, i.e. as hollow clay block (HC) and solid clay block (SC). Despite different configurations, both types of blocks considerably increase initial stiffness and lateral bearing capacity. In most of the infilled frames, a diagonal compression strut mechanism is developed, accompanied with horizontal sliding along the bed joints. Horizontal shear sliding is the predominant mode of cracking in most of the experiments where the mortar is of insufficient strength. Most of the cracks are developed through the bed and head joints. Diagonal cracking or corner crushing is observed as an ultimate failure mechanism. Besides corner crushing, spalling of blocks is also observed.

The experimental setup that the authors executed consisted of three specimens of a one-bay, one-story rigid steel frame infilled with hollow clay units, designated as RF-C-i, with frame dimensions of 2176x1613 mm [1, 15]. Hollow clay units' average vertical and horizontal compressive strengths were 13.10 MPa and 2.10 MPa, respectively. Cement-lime mortar was utilized, with an average compressive strength of 5.02 MPa. The average value of compressive strength and modulus of elasticity of masonry wallets made from hollow clay units was 2.0 MPa and 4613 MPa, respectively. The steel frame is constructed using HE 120 A profiles for columns and beam with steel grade S275. All the properties of the steel frame were identical for all three specimens. The loading protocol of each specimen consists of two types of loading. At the initial stage up to yielding, quasi-static and cyclic loads were applied stepwise in a series of increments of 10 kN. After yielding, the load was applied as a displacement control in which displacements were increased by increments of 1 mm until a drift of 1.0-2.0% was reached.

Table 1 presents the key parameters that were tested - initial stiffness (S_0), the load at the start of yielding (F_y), ultimate load (F_u), and corresponding maximum displacement (d_{max}) in

which (F_y) represents the onset of the first significant crack. The mean initial stiffness was determined as 31.3 kN/mm and the first significant crack was observed at loads of 59 kN, 70 kN, and 51 kN. For all three specimens, the first crack occurred in the middle of the infill with cracks through the mortar. The average maximum achieved load was 135 kN, while the average maximum displacement at a corresponding drift ratio of 1.39% was 22.46 mm. It should be noted that the steel frame on tested specimens did not exhibit significant plastic deformations. By exceeding the compression strength of infill diagonal cracking occurred with the appearance of shattering and spalling of hollow clay units. Alongside aforesaid failure, bed joint sliding shear failure was also observed. Those types of failure mechanisms are also noticed for the same infill type but with less pronounced corner crushing in [6]. An identical failure mechanism is observed with solid clay units in [19], but with permanent plastic deformation at the bottom of columns.

Experimental results					Numerical results		
Labels	S_0 (kN/mm)	F_y (kN)	F_u (kN)	d_{max} (mm)	Model	S_0 (kN/mm)	F_u (kN)
RF-C-1	32.07	59	139	21.33	SSM	31	134
RF-C-2	27.89	70	139	21.87	MSM	29	124
RF-C-3	34.00	51	128	24.20	SPM	37	140
RF-C _{av}	31.30	60	135	22.46	AMM	31	130

Table 1: Experimental and numerical results of specimens with strong infill

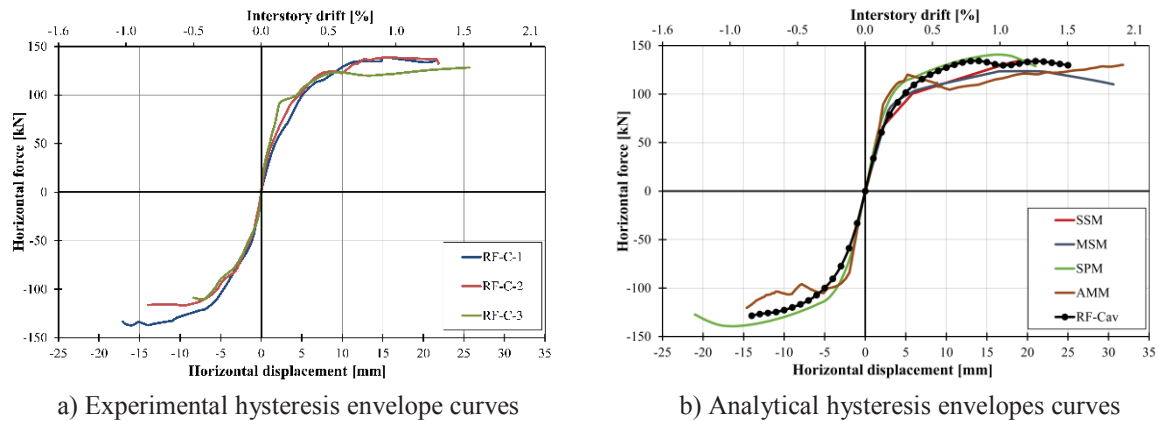


Figure 1: Comparison of experimental hysteresis envelopes (a) and analytical results for C-i series (b)

Regarding numerical models, Table 1 shows a good agreement with experimental results in terms of initial stiffness. SSM and AMM models provide the best agreement, while the SPM method overestimates the initial stiffness (19%). Considering the ultimate lateral load, SSM again provides the best agreement with only a 1% difference. MSM and AMM models underestimated the ultimate lateral load by 8% and 4%, respectively. Figure 1 presents hysteresis envelope curves for each calibrated numerical model, along with experimental results. SSM and MSM models predict a bilinear behavior, although the MSM model provides a smoother envelope. The envelope curve obtained from the AAM model matches very well with experimental initial stiffness, although lateral loads are somewhat lower. The envelope curve obtained from SPM shows a good fit for experimental results overall. It can be concluded that all calibrated models provide a good fit regarding infill made of HC units.

3 STEEL FRAMES INFILLED WITH AUTOCLAVED AERATED UNITS

Autoclaved aerated concrete block (AAC) is a light-weight unit with a significantly lower compressive strength compared to HC and SC units. Due to their small weight, they are favorable units to use as an infill, especially in terms of seismic design. Experiments based on AAC units as infill in steel frames are presented in [22-24], where it is confirmed that they increase initial stiffness and ultimate load capacity. They have lower compressive strength and infill tends to crack at very low loads, as shown in [24] where cracks developed diagonally passing through AAC units and mortar. All of the mentioned three studies report yielding of the steel frame and in [22, 23] local buckling of the flange in the base of the column was reported. Furthermore, in [23] AAC panels crushed and began to spall at similar displacement when the top flange of the column buckled. Contrary to that, in [24] AAC blocks did not fail even at the drift of 1.4% when the test was stopped due to the yielding of the steel frame, but without out-of-plane instability.

The experimental setup that the authors executed consisted of three specimens with the same experimental arrangement as described for RF-C-i specimens (Section 2), with samples designated as RF-A-i [1, 15]. Detailed results of testing individual AAC units and wallets are available in [15] - units vertical compression strength was 2.11 MPa, mortar glue compression strength 9.13 MPa, wallets vertical compressive strength and modulus of elasticity 1.21 MPa and 1174 MPa, respectively.

The experimental results are given in Table 2, from which it can be observed that RF-A-i specimens have lower initial stiffness than RF-C-i specimens (60%). The mean initial stiffness was 19.83 kN/mm. Sample RF-A-1 stands out in regards to initial stiffness (Fig 2.), which can be attributed to inaccuracies during erection [15]. Despite an earlier onset of cracking (average of 51 kN) in relation to RF-C-i specimens, the infill remained compact. The maximum achieved load is 146 kN, with a maximum displacement of 28.01 mm at a corresponding drift ratio of 1.74%. It can be noticed that maximum loads are higher than for RF-C specimens, despite lower mechanical characteristics of AAC blocks. This could be due to the higher compressive strength of bonded glue. Attained ultimate drift ratio of 1.74% signifies that there is plastic deformation at the steel column base.

Experimental results					Numerical results		
Labels	S_0 (kN/mm)	F_y (kN)	F_u (kN)	d_{max} (mm)	Model	S_0 (kN/mm)	F_u (kN)
RF-A-1	26.23	54	152	26.83	SSM	13	152
RF-A-2	15.07	51	139	30.73	MSM	15	123
RF-A-3	17.50	49	146	26.47	SPM	19	134
RF-A _{av}	19.83	51	146	28.01	AMM	23	141

Table 2: Experimental and numerical results of the specimen with weak infill

The failure mode of the RF-A-i specimens is similar to RF-C-i specimens, but with less intensity of diagonal cracking, i.e. infill was compact with more minor cracks and without extensive crushing and separation from the steel frame with horizontal sliding along the bed joints.

Initial stiffness obtained by the SSM model does not coincide with experimental results and the SPM method provides the best agreement in this regards (deviation of 10%). The AAM model slightly overestimates the value of the initial stiffness. In terms of ultimate lateral load MSM, SPM and AMM models underestimate values regarding all three specimens, while the SSM model overestimates the ultimate lateral load concerning all specimens. For a detailed

comparison of behavior between experimental and numerical results Figure 2 presents hysteresis envelope curves for each numerical model.

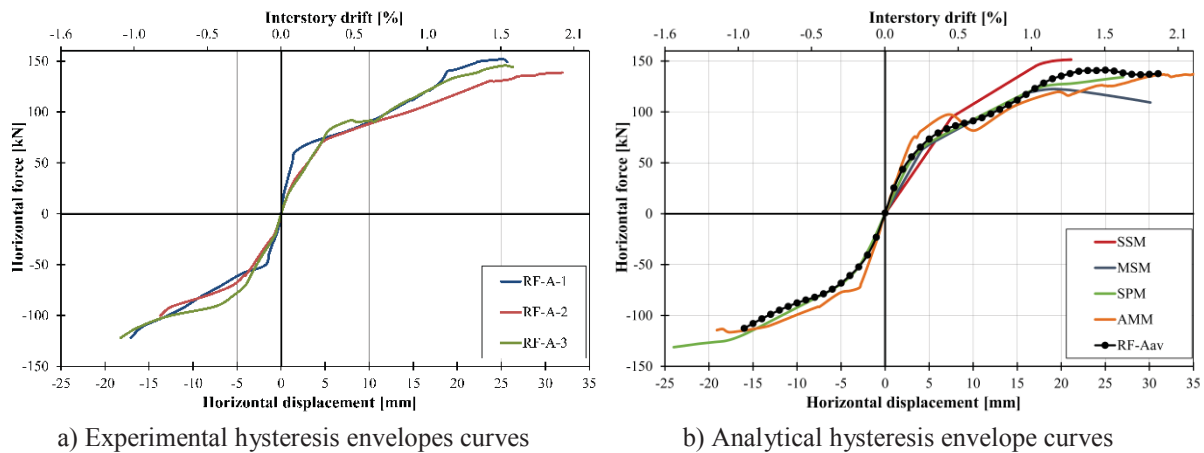


Figure 2: Comparison of experimental hysteresis envelopes (a) and analytical results for A-i series (b)

4 STEEL FRAMES WITH COMBINATION OF CLAY AND AAC UNITS INFILL

This innovative structural concept, presented in [15], is based on limiting (reducing) the interaction between the masonry infill and the steel frame. It is based on the solution of using a combination of AAC and HC units in an infill, to utilize the lower and higher compressive strengths in areas where needed. Weak infill is placed near the column-masonry interaction area are to act as a fuse. Since the AAC units have significantly lower compressive strength, the assumption was that those units will fail first and the steel frames will be preserved from further negative impacts of infill. This solution is distinct by two types of behavior: the monolithic at the initial stage of loading (higher initial stiffness and bearing capacity) and after the separation happens a steel frame dominated behavior. A similar solution can be found in [5, 6, 10, 12] where there are also two stages of behavior, but the initial stage is designed to be dominated by the steel frame, and at higher loads, the steel frame starts to interact with the masonry infill.

The executed experimental programme consisted of three specimens of steel frames infilled with combined HC and AAC units. The AAC units were additionally weakened with drilled holes of different diameters ($\varnothing 54$, $\varnothing 74$, $\varnothing 84$) to alter their compressive strength - vertical compressive strength of 2.11 MPa (for AAC= $\varnothing 54$), 2.03 MPa (for AAC= $\varnothing 74$) and 1.6 MPa (for AAC= $\varnothing 84$) are determined. The experimental setup and loading protocol were the same as for RF-C-i and RF-A-i testing (Section 2 and 3). The influence of holes is significant and it should be emphasized that three specimens of this type of infill represent three different systems.

Experimental results presented in Table 3 show that specimens RF-CA-i, in general, provide higher initial stiffness than RF-A samples, which can be attributed to the higher influence of clay blocks. Despite the higher initial stiffness, cracks were observed much earlier in all three specimens and mostly in AAC blocks. RF-CA-1 achieved the desirable behavior (higher initial stiffness and bearing capacity in the initial loading stage regarding bare frame) whereas the weakening of AAC blocks for other samples was excessive with premature separation occurring. The main difference between RF-A and RF-CA-1 was that the steel frame did not exhibit plastic deformations and the central part of masonry infill was practically undamaged in RF-CA-1. Despite the undamaged infill, proper attention should be paid to the out-of-plane restraint, which can be prevented from falling out-of-plane by construction provisions [1,15]. The maximum obtained load of RF-CA-1 was 106 kN, while the maximum measured displacement was

15.27, which corresponds to a drift ratio of 0.95%. Table 3 presents the numerical results. Concerning the initial stiffness, SSM provides the poorest fit to experimental results (deviation of 38%) and the closest fit is provided with the SPM model. Figure 3 illustrates experimental and numerically predicted behavior, from which the desired effect of pronounced bilinear behavior can be seen. The AAM calibrated envelope curve almost perfectly matches with results for RF-CA-1, which is also true regarding cracks forming in the infill [1, 15].

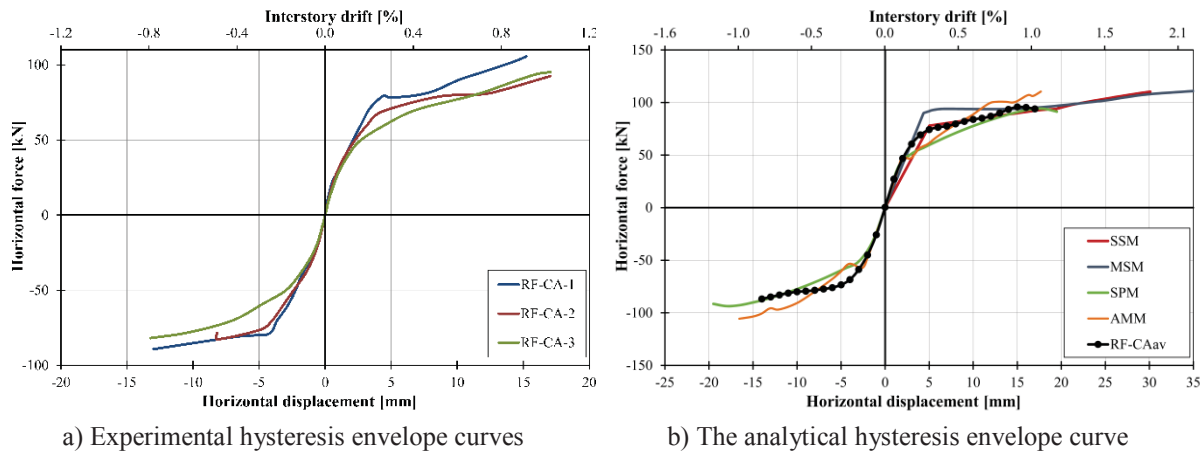


Figure 3: Comparison of experimental hysteresis envelopes (a) and analytical results for CA-i series (b)

Experimental results					Numerical results		
Labels	S_0 (kN/mm)	F_y (kN)	F_u (kN)	d_{max} (mm)	Model	S_0 (kN/mm)	F_u (kN)
RF-CA-1	23.93	39	106	15.27	SSM	15	94
RF-CA-2	23.26	40	93	17.15	MSM	21	94
RF-CA-3	19.49	50	95	17.16	SPM	22	92
					AMM	25	106

Table 3: Experimental and numerical results of the specimen with strong-weak infill

5 STEEL FRAMES WITH NEWLY DEVELOPED UNITS INFILL

Previous experiments indicate that achieving higher compressive strength and modulus of elasticity of the masonry units is not of great importance to improve the behavior between infill and steel frame, especially in terms of achieving higher ultimate load. Hence, the lower stiffness and strength of the masonry unit can also benefit a steel-masonry infill system. Having this in mind, a new structural solution to this composite structure is proposed by developing a masonry unit that will mitigate negative effects on the steel frame, while preserving positive aspects of an infilled system. Consequently, masonry units from self-compacting concrete (SCC) were developed at the Faculty of Civil Engineering and Architecture in Osijek.

The newly developed masonry block is presented in previous research [25], with the main idea being to manipulate the composition of the developed block. For that purpose, self-compact concrete (SCC) was selected and to reduce stiffness and strength, replacement of natural aggregate was done with recycled crushed brick (RB) and ground expanded polystyrene (GEP) – RBA-EP. The mean value of compressive strength of RBA-EP is 4.04 MPa, which is in comparison with the hollow clay bricks 70% lower and 48% higher compared with AAC block. The modulus of elasticity obtained from wallets made of RBA-EP is 2746 MPa, which is in comparison to wallets made of hollow clay brick and AAC 60% lower and 57% higher, respectively. When considering the weight, the masonry panel made of RBA-EP, AAC, and hollow clay

brick was 293.2 kg, 140.0 kg, and 264.0 kg respectively. For the testing in frames, two types of RBA-EP units are made (Figure 4) - RBA-EP-Type A as a standard unit and RBA-EP-Type B as a weakened unit without one vertical wall along the sidewall.

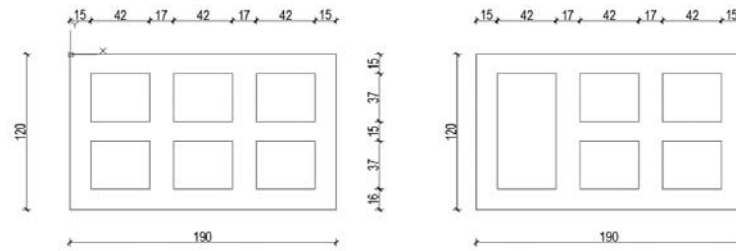


Figure 4: Configuration of Type A (left) and Type B (right)

Experimental testing of steel frames infilled with newly developed masonry units was done in two series, in a one-bay, one-story rigid steel frame and a pinned steel designated as RF and PF, respectively (dimensions 2332x1683 mm as in previous cases). The rigid steel frame was constructed of HE 120 A profile for columns and beam, while the pinned frame was constructed of HE 280 A profiles. Besides one bare rigid frame (RF) as a control specimen, the rest of the specimens were done as two samples per series. RF-M was infilled with RBA-EP-Type A units only whereas RF-MF was infilled with both RBA-EP-Type A and Type B units. RBA-EP-Type B units were placed at the column-masonry contact, which attempted to be used as a fuse. PF-MF was infilled with RBA-EP-Type A units in the pinned steel frame. All specimens were bonded with M5 class mortar. The loading protocol consists of a horizontal load applied by displacement control with increasing displacement by 0,5mm in each consecutive stage.

Experimental results reported in Table 4 present key parameters that were tested - initial stiffness (S_0), load at start of yielding (F_y), ultimate load (F_u), and corresponding maximum pushover displacement (d_{max}). RF-M and RF-MF have the highest initial stiffness of the tested specimens. Average values of initial stiffness for RF, RF-M, RF-MF, and PF are, respectively, 3.1 kN, 14.4 kN, 14.3 kN, and 7.6 kN. According to the highest initial stiffness, the highest ultimate loads are obtained for RF-M and RF-MF specimens, while the lowest is for PF specimen. The similarity of RF configuration is observed in the value of the horizontal load at start of yielding (the average F_y for RF, RF-M, and RF-MF was respectively, 69.4 kN, 64.9 kN, and 68.4 kN [14]). Although those values are close, the achieved horizontal displacements at the corresponding F_y were significantly different. Average horizontal displacement d_y for RF, RF-M, and RF-MF were, respectively, 23.8 mm, 7.4 mm, and 6.2 mm. Horizontal load F_y of PF-M configuration deviates from the other specimens and it is significantly lower (average F_y 21.0 kN). Average values of F_y and d_y in the comparison of RF-M and RF-MF specimens are very alike, which exposes the fact that the activation of Type B units as a fuse was not achieved. Consequently, the desired separation of infill and frame was not realized. The average ultimate drift of RF-M and RF-M is 2.5%.

Specimen label	Infill type	S_0 (kN/m)	F_y (kN)	F_u (kN)	d_{max} (mm)
RF	-	3.1	69.4	81.5	69.0
RF-M	RBA-EP Type A	14.4	64.9	128.0	48.7
RF-MF	RBA-EP Types A and B	14.3	68.3	132.3	59.9
PF-M	RBA-EP Type A	7.6	21.1	52.8	46.8

Table 4: Experimental results of the specimen with newly developed units

Figure 5 presents an even more detailed behavior of all specimens with RBA-EP units [14]. All tested specimens provide a much higher initial stiffness than the bare frame. Despite the higher initial stiffness of the pinned steel frame, the ultimate lateral load is much lower than for RF. From the PF-M envelope curve, it can be observed (especially on the positive side of the envelope) that there are frequent changes in behavior, which can illustrate the consequent redistribution of the loads in the masonry infill. Furthermore, it is obvious that the contribution of the infill in the pinned frame cannot be simply added to the bare frame to achieve the structural behavior of the infilled frames. As for rigid frame specimens (RF-M and RF-MF), the envelope is smoother and there is symmetry in the negative and positive sides of envelopes. It can be also observed that RF-M and RF-MF specimens have high ductility (maximum drift ratio 2.1%-3.7%).

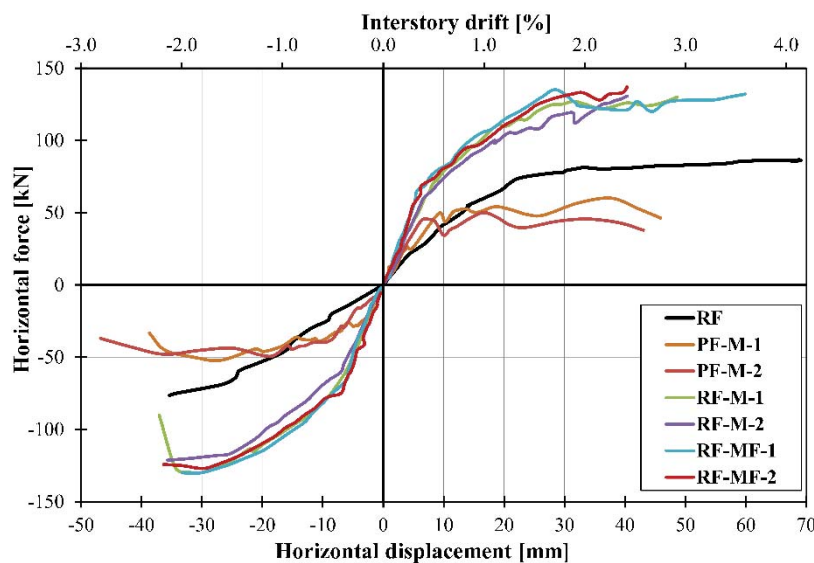


Figure 5: Hysteresis envelope curves of specimens

Regarding the fracture mechanism, RF-M and RF-MF again showed similarities. Dominated fracture mechanism on the change of initial stiffness is the diagonal formation of concentrated strain, and it is in line with mortar head and bed joints. Moreover, the configuration of RF-M and RF-MF ensures the composite system behavior in the quasi-elastic area, but without significant damage to the frame [14]. The highest concentration of strain in PF-M is also observed at the diagonals, but it is also spread over the whole panel. In terms of out-of-plane stability during in-plane loading, it is noticed that perforated units are more prone to out-of-plane stability issues (e.g., hollow clay brick). Despite that, the RBA-EP unit did not present that issue. This can be associated with their low elastic modulus and thick sidewalls [25].

6 COMPARISON OF RESULTS

The experimentally obtained average values of initial stiffness, load at the start of yielding, ultimate load, and maximum drift ratio are summarized in Table 5. It can be noticed that the average values of RF-C specimens, RF-C, provides the highest initial stiffness among all tested specimens, which was expected based on the highest compression strength of the masonry units and the modulus of elasticity of the masonry wallet. The lowest initial stiffness was achieved in the specimen with RBA-EP units, as was planned, but the ultimate load does not deviate from other specimens. Consequently, the authors successfully manipulated the properties of RBA-EP in which ultimate lateral bearing capacity is not significantly reduced. This similar behavior

is presented in the values of RF-A which had the highest ultimate load. Through the ultimate drift ratio, as a measure of ductility, it can be observed that specimens with RBA-EP units are more ductile than the rest of the specimens. The average value of the ultimate drift ratio for RF-M and RF-MF is 2.5%, while for RF-A and RF-C is 1.7% and 1.39% respectively. The lowest drift ratio is observed in RF-C_{av} specimens which had the highest initial stiffness. At the cost of ductility, higher initial stiffness is not a favorable property of infill. RF-M and RF-MF specimens additionally show similarity to the RF-A values in terms of compactness of the infill panel (e.g., no falling out of blocks, redistribution of stress through the infill). Besides numerous similarities, the difference is observed in the onset cracking. in the value of RF-A indicates that it happens earlier, while in RF-M and RF-MF the value of F_y is similar to the bare frame, but with different values of displacement. This confirms that the configuration of the specimens with RBA-EP preserved the steel frame from higher detrimental effects.

Specimen label	S_0 (kN/m)	F_y (kN)	F_u (kN)	$D_{r,max}$ (%)
BF	3.1	69.4	81.5	3.25
RF-C _{av}	31.3	60.0	135	1.39
RF-A _{av}	19.83	51.3	146	1.74
RF-M	14.4	64.9	128.0	2.50
RF-MF	14.3	68.3	132.3	2.65
PF-M	7.6	21.1	52.8	2.70

Table 5: Comparison of initial stiffness and ultimate load

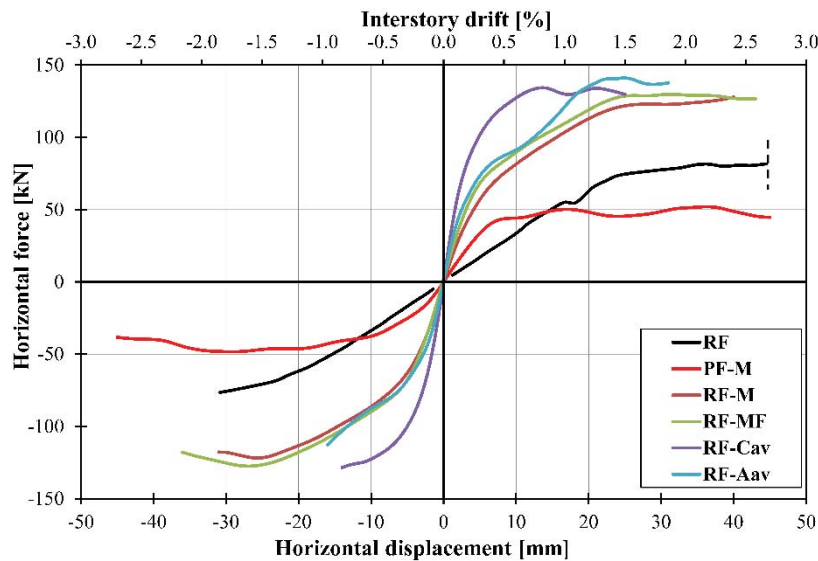


Figure 6: Hysteresis envelope curves of all tested specimens

Figure 6 [14] presents the hysteresis envelope curves of all tested specimens with different type of infills. It confirms a higher ultimate load in the presence of infill but with very different drifts. It can be noticed that RF-C value quickly attains the ultimate load which leads to an earlier onset of the failure mechanism. The hysteresis curve offers one more similarity between RF-M, RF-MF, and RF-A – trilinear behavior which ensures gradual redistribution of stress.

Through the experiments, it is once again confirmed that an infill panel plays an important role in the behavior of an infilled frame concerning the seismic design and that there is no adequate codified design method.

7 CONCLUSIONS OF CONDUCTED EXPERIMENTAL TESTS

A comparison of experimental programmes from previous studies is shown in this paper – rigid steel infilled frames with various types of infill, pinned steel frame, and a bare steel frame. The infill was made of hollow clay blocks, AAC blocks, and newly developed RBA-EP blocks. The experimental results show that simple construction provisions can lead to better behavior. Results can be summarized into the following conclusions:

- Infill provides a higher stiffness to the frame. Among all tested specimens, the highest initial stiffness was obtained in the RF-C configuration, which was expected because of the significantly higher compressive strength of hollow clay blocks. Despite higher initial stiffness, the ductility of these frames was lower. Lower initial stiffness did not negatively influence the ultimate strength of RF-A, RF-M, and RF-MF specimens. Consequently, the behavior of RF-A, RF-M, and RF-MF specimens is favorable.
- In terms of ductility, frames with RBA-EP units achieve higher ductility than RF-A specimens, which is manifested through ultimate drift. The average ultimate drift of RF-M and RF-MF specimens is 2.5%, which is 30% higher than RF-A.
- RBA-EP units are heavier in comparison to the AAC and hollow clay blocks, but they are environmentally favorable because they use waste products (recycled crush brick and polystyrene) in their production.
- Regarding the PF-M configuration, the results deviate in comparison to the rigid configurations, especially in terms of the ultimate load and the change of initial stiffness. Beyond that, the observed concentration of strain is spread over the whole panel and the stress state does not coincide with the infill in a rigid frame. Through this configuration, it is concluded that the bearing capacity of an infilled frame also depends on the rotation capacity of joints.
- Regarding the numerical models, it can be concluded that SSM and MSM can give good predictions in the case of C units, with a lack of accuracy for AAC units. Despite that, they still represent an acceptable method based on simplicity regarding the rest of the methods (fast calculation, the capability of producing hysteresis behavior). AMM and SPM models predict behavior much better with the included various types of failure mechanisms. Although the obtained results are better, the required time and complexity are important setbacks.

In future work, experimental tests of specimens with RBA-EP should be accompanied by numerical models to compare with C and AAC units. Furthermore, probabilistic methods should be conducted to evaluate the reliability of this type of structural concept.

REFERENCES

- [1] D. Markulak, I. Radić, V. Sigmund, Cyclic testing of single bay steel frames with various types of masonry infill, *Engineering Structures*, **51**, 267–277 (2013).
- [2] S. Pul, M.E. Arslan, Cyclic behaviors of different type of hollow brick infill walls: A hinged rigid frame approach, *Construction and Building Materials*, **211**, 899–908 (2019).

- [3] S.V.S. Jebadurai, D. Tensing, P.M. Pradhan, G. Hemalatha, Enhancing performance of infill masonry with latex modified mortar subjected to cyclic load, *Structures*, **23**, 551–557 (2020).
- [4] B. Binici, *et al.* Seismic behavior and improvement of autoclaved aerated concrete infill walls, *Engineering Structures*, **193**, 68–81 (2019).
- [5] R.S. Ju, H.J Lee, C.C. Chen, C.C. Tao, Experimental study on separating reinforced concrete infill walls from steel moment frames, *Journal of Construction Steel Research*, **71**, 119–128 (2012).
- [6] A.V. Tsantilis, T.C. Triantafillou, Innovative Seismic Isolation of Masonry Infills in Steel Frames using Cellular Materials at the Frame-Infill Interface, *Journal of Earthquake Engineering*, **24**, 1729–1746 (2020).
- [7] M. Mohammadi, V. Akrami, R. Mohammadi-Ghazi, Methods to Improve Infilled Frame Ductility, *Journal of Structural Engineering*, **137**, 646–653 (2011).
- [8] M. Preti, V. Bolis, A. Stavridis, Design of masonry infill walls with sliding joints for earthquake structural damage control, *Brick and Block Masononry: Trends, Innovations and Challenges - Proceedings of the 16th International Brick Block Masononry Conference, IBMAC 2016* 1317–1324 (2016).
- [9] P. Morandi, R.R. Milanesi, C.F. Manzini, G. Magenes, Experimental tests of an engineered seismic solution of masonry infills with sliding joints, *16th World Conference on Eearthquake*, **4442**, (2017).
- [10] M. Marinković, C. Butenweg, Innovative decoupling system for the seismic protection of masonry infill walls in reinforced concrete frames, *Engineering. Structures*, **197**, 109435 (2019).
- [11] L. Silva, G. Vasconcelos, P. Lourenço, F. Akhoundi, Experimental evaluation of a constructive system for earthquake resisting masonry enclosure walls, *Brick and Block Masononry: Trends, Innovations and Challenges - Proceedings of the 16th International Brick Block Masononry Conference. IBMAC 2016* **2003**, 1333–1340 (2016).
- [12] M. Aliaari, A.M. Memari, Analysis of masonry infilled steel frames with seismic isolator subframes, *Engineering. Structures*, **27**, 487–500 (2005).
- [13] I.S. Misir, Potential Use of Locked Brick Infill Walls to Decrease Soft-Story Formation in Frame Buildings, *Journal of Performance of Constructed Facilitie*, **29**, 04014133 (2015).
- [14] D. Markulak, T. Dokšanović, I. Radić, J. Zovkić, Behaviour of steel frames infilled with environmentally and structurally favourable masonry units, *Engineering. Structures*, **204**, (2020).
- [15] I. Radić, Ponašanje čeličnih okvirnih građevina sa zidanim ispunom pri djelovanju potresa. *PhD Thesis*. Osijek: Josip Juraj Strossmayer University of Osijek; 2012 [in Croatian].
- [16] I. Radić, D. Markulak, V. Sigmund, Analitičko modeliranje čeličnih okvira sa zidanom ispunom, *Tehnički. Vjesnik*, **23**, 115–127 (2016).
- [17] M.Y. Kaltakci, A. Koken, H.H. Korkomaz, An experimental study on the behaviour of infilled steel frames under reversed-cycling loading, *Iranin Journal of Sciece & Technol-*
ogy, **32**, 157-160 (2008)

- [18] H. A. Moghaddam, Lateral load behavior of Masonry infilled steel frames with repair and retrofit, *Journal of Structural Engineering*, **130**, 56-63 (2004)
- [19] A.A. Tasnimi, A. Mohebkah, Investigation on the behavior of brick-infilled steel frames with openings , experimental and analytical approaches, *Engineering Structures*, **33**, 968–980 (2011).
- [20] R.D. Flanagan, R.M. Bennett, In-plane behavior of structural clay tile infilled frames, *Journal of Structural Engineering*, **125**, 590-599 (1999)
- [21] M. Mohammadi, S.M.M Emami, Multi-bay and pinned connection steel infilled frames; an experimental and numerical study, *Engineering structures*, **188**, 43-59 (2019)
- [22] Y. Liu, G. Li, Behavior of steel frames with and without AAC infilled walls subjected to static and cyclic horizontal loads, *13th World Conference on Eartquake Engineering*, **1112**, (2004)
- [23] C. Zhenggang, P. Du, F. Feng, F. Ming, Cyclic testing and parametric analyses of the fabricated steel frames infilles with autoclaved aerated concrete panels, *Advance in Structural Engineering*, **20**, 473-490 (2016)
- [24] S. Ravichandran, Design provisions for autoclaved aerated concrete (AAC) infilled steel moment frams, *Ph.D Dissertation*. Austin, Texas: The University of Texas at Austin
- [25] D. Markulak, T. Dokšanović, I. Radić, I. Miličević, Structurally and environmentally favorable masonry units for infilled frames, *Engineering Structures*, **175**, 753–764 (2018).

A SIMPLE METHODOLOGY FOR THE INFILL MASONRY WALL STIFFNESS ESTIMATION

Vanni Nicoletti¹, Davide Arezzo¹, Sandro Carbonari¹, and Fabrizio Gara¹

¹ Dept. ICEA, Università Politecnica delle Marche
Via Brece Bianche, 60131, Ancona, Italy
e-mail: v.nicoletti@pm.univpm.it, d.arezzo@pm.univpm.it, s.carbonari@univpm.it, f.gara@univpm.it

Abstract

The importance of assessing the overall dynamic behavior of buildings considering the contribution of infills is nowadays widely recognized considering that they play an important role in the verifications at damageability limit states and, at ultimate limit states, they can trigger fragile mechanisms of structural members preventing the evolution of dissipative ones. In addition, in case of strategic structures, for which often high performance levels are required such as the full operativity condition (i.e. absence of damage to both structural and non-structural components) after severe earthquake, the contribution of non-structural members should be necessarily included in the seismic assessment.

The paper proposes a simplified procedure for estimating the stiffness of masonry infill walls through expeditious dynamic impact tests. Stiffness can be adopted to model infills into conventional 3-D finite element models of buildings. The procedure is validated by means of an experimental campaign carried out on a laboratory real-scale mock-up and then applied to a real infilled reinforced concrete frame building. Experimental results are compared with those obtained from refined finite element models including infills, proving the methodology reliability.

Keywords: Infill masonry wall stiffness, impact load tests, experimental modal analysis, ambient vibration tests, building finite element modelling.

1 INTRODUCTION

Infill masonry walls are very common components used worldwide in r.c. frame buildings and nowadays it is well known that the stiffness and strength, together with the mass, provided by these non-structural elements may significantly affect the global behavior of buildings, especially in earthquake prone regions [1-4]. The common practice of modelling infills within building f.e. models only in terms of masses is recognized to be not correct, particularly when the f.e. models must be representative of the real building behavior. As an example, the prediction of the real building behavior subjected to earthquake becomes crucial in case of strategic buildings (e.g. hospital, fire and police stations) that must remain in operational condition to guarantee the post-earthquake emergency management [5-6]. Moreover, reliable f.e. models of buildings, i.e. capable to represent the building operational conditions, could be very useful to develop Structural Health Monitoring (SHM) systems [7-9] and to interpret data collected during the monitoring period, in order to assess the building conditions and to detect possible damage to the structural and non-structural members.

From above considerations it is evident the importance of modelling these non-structural components in a reliable manner. Many works in the technical and scientific literature deals with infill modelling strategies, from the simple adoption of a single diagonal strut [10-11] to refined linear and non-linear models [12-13]. Anyway, modelling uncertainties always exist and could affect the modelling correctness. Many researchers investigated the infill behavior with the aim of reducing these uncertainties: most of them studied infills subjected to static lateral loads [14-15], other adopted out of plane loads, and very few used dynamic tests on infills, as, for instance, Ambient Vibration Tests (AVTs) [16-17]. It clearly emerges that a standardization of the infill properties is almost impossible to achieve, considering they are built with different construction materials and typologies all around the world.

This paper proposes a procedure to estimate the stiffness of infill masonry walls that can be used to model these non-structural components within f.e. models of buildings. The proposed approach is based on a combined experimental and numerical procedure: the former foresees the development of dynamic tests on infills through which the modal parameters of the non-structural components are identified; the latter consists in the development of a f.e. model of the structures in which the infills are modelled and investigated with the aim of estimating their stiffness, expressed in terms of elastic modulus. The proposed procedure is preliminary well described, then it is validated through the support of a real-scale laboratory mock-up, used as a case study. Finally, the methodology is applied to a real building to verify its applicability to real structures.

2 THE PROPOSED METHODOLOGY

The proposed methodology is a combined experimental and numerical procedure that foresees dynamic tests on infills and their numerical investigation through the support of f.e. models. In the sequel a summary of the methodology, is reported; for further details the reader can refer to [18].

The dynamic tests performed on infill masonry walls are Impact Load Tests (ILTs) that allow the determination of the Out Of Plane (OOP) dynamic behavior of the non-structural components. ILTs consist in exciting the wall with hammer blows and in recording input and output in the horizontal direction, orthogonal to the wall plane. The output are the time histories of the accelerations produced by the impacts. To perform tests, an instrumented hammer and one or more accelerometers can be used: the accelerometer is fixed on a specified position on the wall, while hammer blows are applied in several points, with the target to identify the panel vibration modes, possibly considering also superior modes. The use of more than one sensor (or moving

the sensor in different positions) may be useful to identify modes that present null value of modal displacement in proximity of the sensor position. The wall can be suitably divided with a regular grid whose spatial resolution depends on the accuracy and on the number of modes that have to be identified. The accelerometer is fixed in one grid point, while hammer blows are provided in all points, applying more than one impact for each of them, allowing to obtain a reliable data set. The impulse-acceleration data recorded are adopted to identify the OOP modal parameter of the panel, performing Single-Input Single-Output modal analyses. In the sequel, the Line-Fit algorithm [19] (a simple degree of freedom identification methodology working in the frequency domain) is adopted to identify the infill modal parameters.

The numerical step of the methodology consists in performing an iterative procedure with the aim of estimating the infill stiffness and, particularly, its elastic modulus. Indeed, despite masonry infills are generally characterized by an orthotropic behavior, the adopted strategy is based on the idea that the dynamics of infills subjected to low input excitations (like hammer blows) can be well captured through homogenous isotropic elastic thin plate elements. So, the stiffness of these non-structural components is mainly governed by the elastic modulus, assuming a constant Poisson's coefficient (e.g. 0.25 as suggested in [20]). At first, the investigated infill is modelled as bidimensional shell elements into the f.e. model of the bare frame structure, adopting its real thickness and with mass estimated based on the adopted construction materials, which are known in most cases. The first tentative elastic modulus E_0 of the infill can be calculated based on closed-form expressions available in the literature for clamped rectangular plates. Considering the formulation proposed in [21], the tentative elastic modulus is calculated as follows:

$$E_0 = \frac{48\rho(1-\nu^2)}{\pi^2 t^2} f_{1,exp}^2 \left[\left(\frac{1+\Delta_m}{l} \right)^2 + \left(\frac{1+\Delta_n}{h} \right)^2 \right]^{-2} \quad (1)$$

where ρ is the mass per unit area, t is the wall thickness, ν is the Poisson's coefficient, l and h are the length and height of the wall, $f_{1,exp}$ is the first OOP vibration mode frequency experimentally identified and Δ_m and Δ_n are the edge effect factors, that can be calculated as:

$$\Delta_m = \left[\left(\frac{l}{h} \right)^2 + 2 \right]^{-1} + 0.017 \quad (2a)$$

$$\Delta_n = \left[\left(\frac{h}{l} \right)^2 + 2 \right]^{-1} + 0.017 \quad (2b)$$

Then, eigenvalue analyses are performed and the numerical modal parameters relevant to the infill OOP dynamic behavior are determined. This procedure is performed several times, varying at each step the infill elastic modulus, until the numerical modal parameters fit well the experimental ones. In order to quantify the goodness of the estimated moduli, two convergence criteria are introduced, based on the comparisons of the experimental and numerical natural frequencies and mode shapes, respectively. When criteria satisfy the conditions reported in Eqs. 3a and b, the estimating procedure stops and the elastic modulus is considered as representative for the wall at hand.

$$\frac{\sum_{i=1}^N \frac{1}{i} \left| \frac{f_{i,exp} - f_{i,num}}{f_{i,exp}} \right|}{\sum_{i=1}^N 1/i} \leq \delta_f \quad (3a)$$

$$1 - \frac{\sum_{i=1}^N \frac{MAC_i}{i}}{\sum_{i=1}^N 1/i} \leq \delta_s \quad (3b)$$

In Eq.s 3a and b $f_{i,exp}$ and $f_{i,num}$ represent the i -th experimental and numerical frequency value of the total N identified OOP vibration modes, while MAC_i is the i -th Modal Assurance Criterion index [22] used to compare two mode shapes. δ_f and δ_s represent the admissible errors in the comparison between frequencies and mode shapes, respectively; in this work, values of $\delta_f = 0.05$ and $\delta_s = 0.25$ are proposed and considered in the successive case studies.

As common in practice, r.c. frame structures are usually modelled with frame elements, so the area of modelled infills is greater than the real one since physical dimensions of columns and beams are neglected. Thus, when infills are modelled with shell elements within frame structure f.e. models, their dimensions (length and height) are greater than the real ones; consequently, to consider this approximation, the mass and stiffness of the modelled panel must be suitably modified. In detail, the mass density (ρ_m) and the elastic modulus (E_m) of the modelled infill are reduced by a factor λ that represents the mean percentage increment of the panel dimensions for both sides:

$$\rho_m = \rho / \lambda^2 \quad (4a)$$

$$E_m = E / \lambda^2 \quad (4b)$$

The estimation of infill elastic modulus, assuming the geometry and mass to be known, permits the reduction of the uncertainties and the updating of parameters in sophisticated f.e. models of infilled frame structures. Obviously, the elastic modulus estimated with this procedure permits to predict the infill behavior under low level of excitation and, consequently, it is useful when building behavior under low level of excitation needs to be interpreted. Indeed, as shown in the sequel, refined f.e. models of structures, obtained modelling the infill with the proposed approach, reveal to be able to well predict the structural responses under ambient vibration excitations.

3 METHODOLOGY VALIDATION THROUGH A LABORATORY CASE STUDY

The proposed methodology is applied on a laboratory mock-up considered as case study, experimentally tested, and then numerically investigated. The aim is to validate the proposed approach through an application to a simple structure under controlled laboratory conditions with limited uncertainties. The mock-up is a steel-concrete composite structure consisting of a pair of one-story two-bay moment-resisting frames with height of 3.00 m and span length of around 4 m (Fig. 1). Columns and beams are realized with steel profiles and the composite slab is obtained with a 12 cm thick concrete layer casted on a collaborating steel sheet. Some concrete blocks are placed over the composite floor to simulate permanent and live loads on the structure. Two infill walls (W1 and W2) are built with hollow clay bricks (dimension of 25 x 25 x 6 cm) and mortar joints, filling only one of the two longitudinal bays. Successively, both sides of both walls are covered with a thin gypsum plaster layer (less than 1 cm). This infill typology can be considered representative for the light infills adopted very often to realize interior partitions in common buildings.

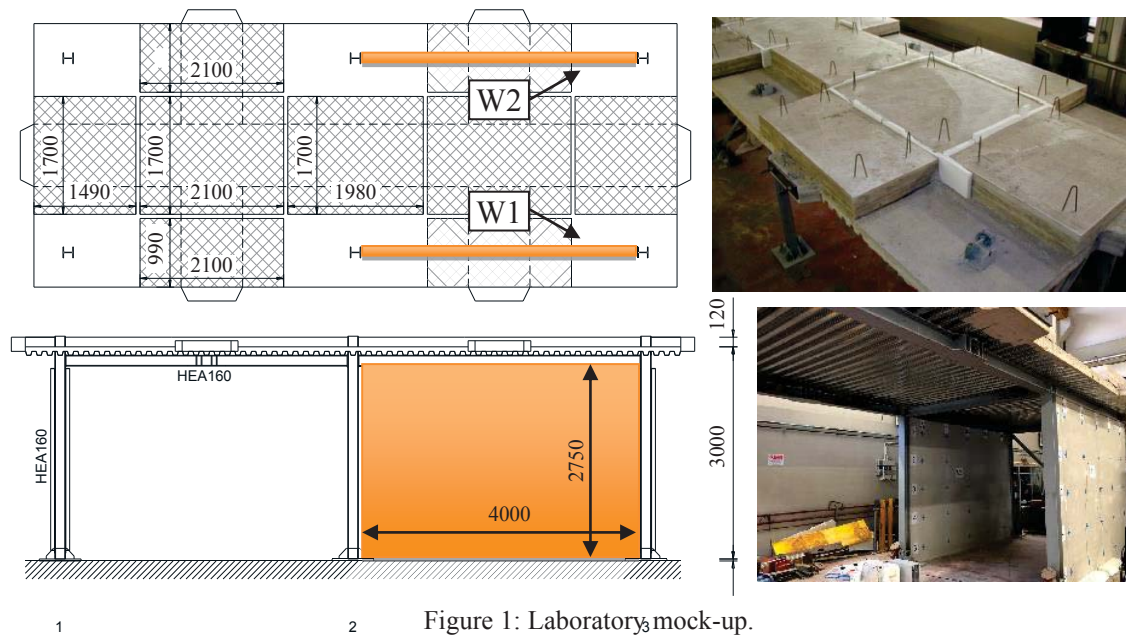


Figure 1: Laboratory mock-up.

Both infills are dynamically tested through ILTs; for each of them, a regular grid of twenty-five points is drawn on a panel face and two accelerometers are fixed on the wall in two grid points with the target to identify as many vibration modes as possible. Then, hammer blows are provided at each grid point, recording both impulses and accelerations, for a time length of 10 s per impact, considered adequate to capture the entire oscillation. It is worth noting that both panels are tested twice, before and after the plastering. Based on acceleration and impact records, the OOP modal parameters of each infill are identified; in detail, many vibration modes are found, as can be observed from Tab. 1 and Fig. 2. Each mode is named with a couple of number that represent the number of semi waves present in the mode shape along the horizontal and vertical directions. Identified natural frequencies, listed in Tab. 1, show that both walls are characterized by almost the same frequency values, even if those relevant to W2 are slightly higher than those of W1. Moreover, after the plaster, all frequency values increase, as expected. Fig. 2 provides an example of the mode shapes of W1 with plaster. Those relevant to W2 are not reported, being very similar to W1.

To validate the proposed procedure, a 3-D full-shell element f.e. model of the bare mock-up is created (Fig. 3a). Moreover, this preliminary model is calibrated with the support of the global 3-D mock-up experimental modal parameters determined through AVTs performed on the bare structure. After that, the two infills are added in the calibrated f.e. model (Fig. 3b), both with shell elements having thickness equal to the real ones. Based on the experimental fundamental frequency of each wall, a first tentative elastic modulus E_0 is calculated. Values of 2445 and 2775 MPa are calculated for W1, before and after plastering, respectively, while 2210 and 2420 MPa are calculated for W2. At this point, iterative procedures are performed by varying the elastic modulus of each wall one by one, until the convergence criteria (calculated considering all the identified OOP modal parameters) are satisfied. The obtained elastic moduli at the end of the procedures are listed in Tab. 2; it is interesting to observe that the Young's moduli of the two walls are quite similar but not equal. After the plastering, the infill elastic moduli increase, mostly for W1.

Table 1: Experimental natural frequencies for both infills without and with plaster.

Mode	Frequency [Hz]			
	W1		W2	
	No plaster	Yes plaster	No plaster	Yes plaster
<i>1,1</i>	16.80	17.30	17.90	18.10
<i>2,1</i>	27.47	31.60	29.53	32.15
<i>1,2</i>	40.10	49.00	48.00	49.97
<i>3,1</i>	46.55	49.40	45.35	50.50
<i>2,2</i>	57.54	63.88	59.20	64.50
<i>4,1</i>	63.07	66.50	66.85	68.10
<i>5,1</i>	76.85	120.71	78.93	119.90
<i>3,2</i>	79.79	85.98	76.10	82.67
<i>2,3</i>	/	105.30	/	107.13
<i>4,2</i>	104.98	113.75	104.40	127.30
<i>3,3</i>	117.77	131.19	119.40	133.20
<i>5,2</i>	132.28	143.93	139.10	155.90
<i>5,3</i>	177.60	198.85	175.24	212.50

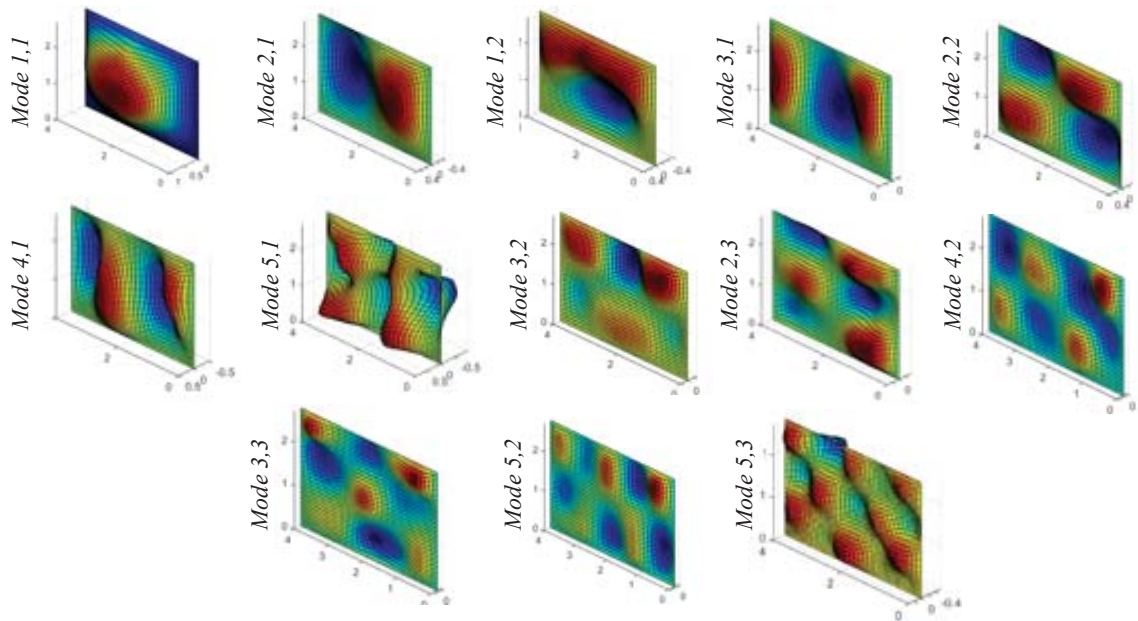


Figure 2: Experimental mode shapes for W1 with plaster.

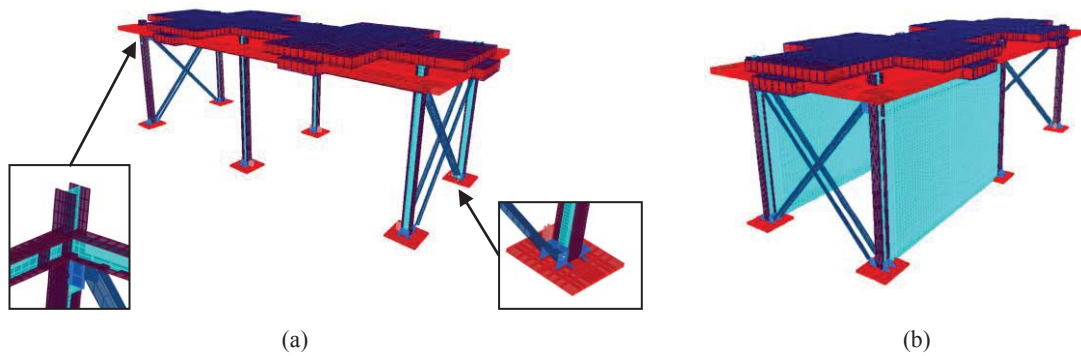


Figure 3: 3-D global f.e. model of the mock-up: a) bare structure, b) infilled structure.

To assess the reliability of the estimated elastic moduli, the numerical modal parameters of the whole infilled mock-up (using the infill elastic moduli reported in Tab. 2) are compared with those obtained from AVTs performed on the whole infilled structure before and after the plastering. Comparisons, in terms of natural frequencies and mode shapes (the latter obtained through the MAC indexes), are reported in Tab. 3. As can be observed, the numerical modal parameters (NUM) are in very good agreement with the experimental ones (EXP), proving the reliability of the elastic moduli estimation. It is worth noting that, in this case, the mass densities and the elastic moduli used in the global f.e. model are not reduced since the modelled infill dimensions are the same of the real ones.

Table 2: Estimated elastic moduli E for both infills without and with plaster.

Wall	Elastic modulus [MPa]	
	No plaster	Yes plaster
W1	4700	4900
W2	5340	5360

Table 3: Comparison between experimental and numerical infilled mock-up modal parameters.

Mock-up mode	Mode typology	Before plaster			After plaster		
		Frequency [Hz]		MAC	Frequency [Hz]		MAC
		EXP	NUM		EXP	NUM	
1 st	Transverse	8.40	8.40	1.00	8.37	8.38	1.00
2 nd	Rotational	12.72	12.94	0.93	13.39	13.08	0.97
3 rd	Longitudinal	16.32	16.38	0.81	17.69	17.71	0.99

4 APPLICATION TO A REAL BUILDING CASE STUDY

The proposed methodology is applied to a real building in order to prove its usefulness and applicability to real structures. The considered case study is a r.c. frame building (Fig. 4a) with plan dimensions of around 16.50 x 11.70 m composed by two stories, for a total height of about 8.00 m. The underground level is mainly realized by r.c. retaining walls, while the upper one is realized with spatial r.c. frames. The infill masonry walls are built both along the building perimeter and inside the building, and they can be divided into three main typologies, as reported in Fig. 4b: E1 is adopted for all external infills, I1 is adopted to separate the housing units within the building at the underground and ground levels, while I2 is adopted to realize all the interior partitions. The building was investigated and tested during its construction process; in detail, AVTs were performed on the bare and on the infilled structure, whereas ILTs on infills were performed only in the phase without plaster.

As for tests on infills, three infills representative for all the infills typologies are tested (W-E1, W-I1 and W-I2). All walls are located at the ground floor and have no openings. The geometry of the tested infills is illustrated in Fig. 5. ILTs on the three infills are performed with the same instrumentation and test protocols adopted for tests on laboratory mock-up infills, and the infill OOP modal parameters are identified again using the Line-Fit algorithm. The experimental OOP modal parameters of the walls are reported in Fig. 6, both in terms of frequencies and mode shapes. As can be observed, four vibration modes are identified for each infill.

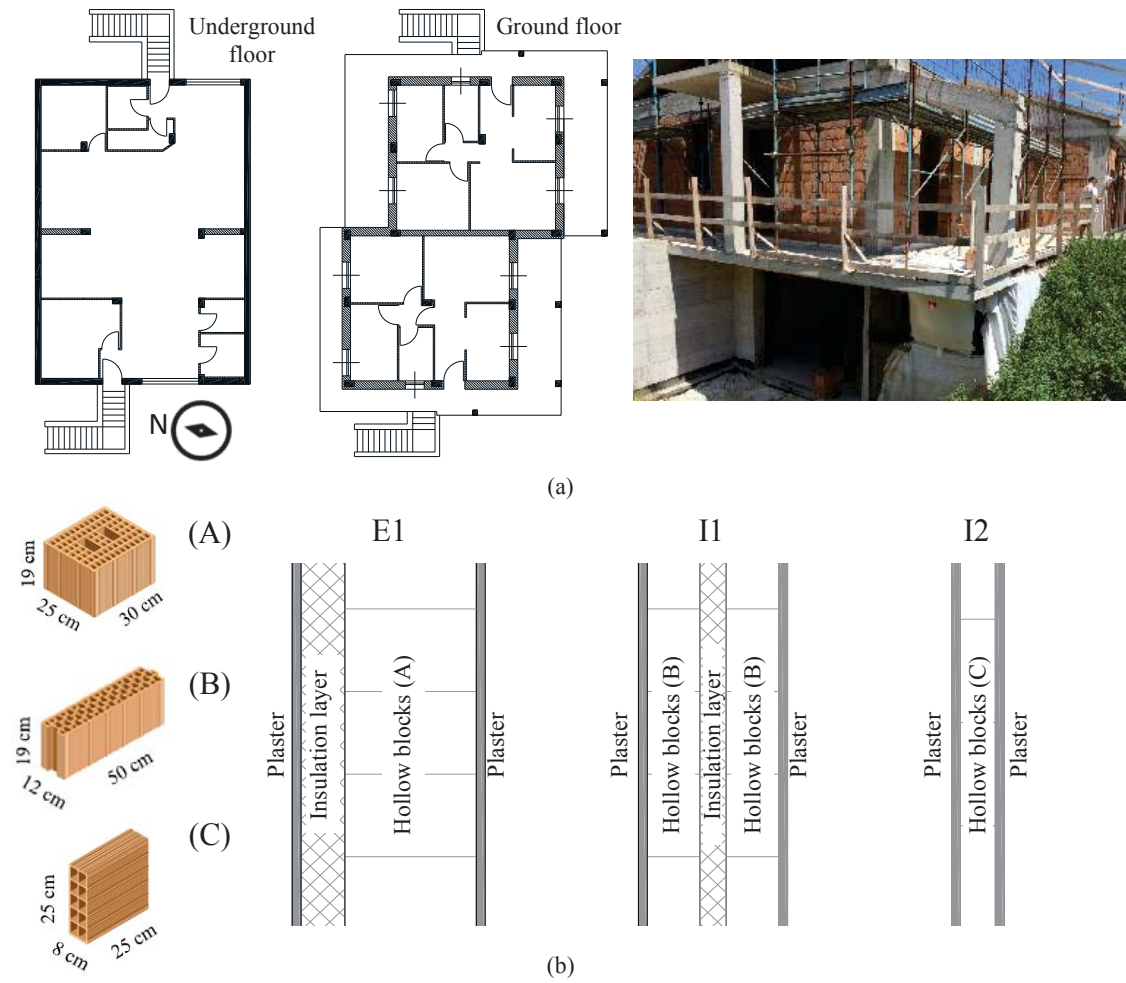


Figure 4: Real case study: a) building floor plans and picture during construction, b) infill masonry wall typologies.

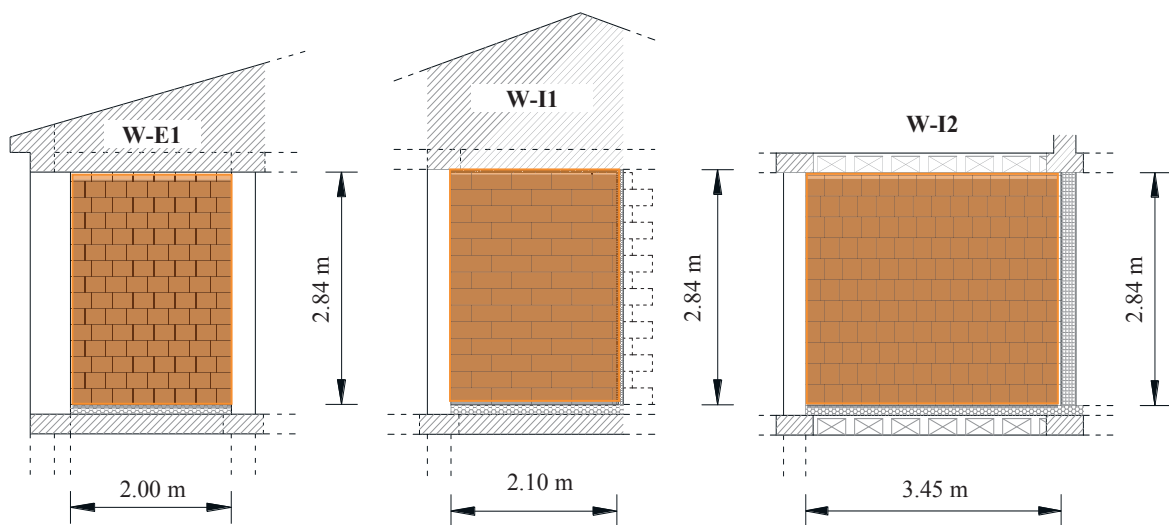


Figure 5: Geometry of tested infill masonry walls of the building.

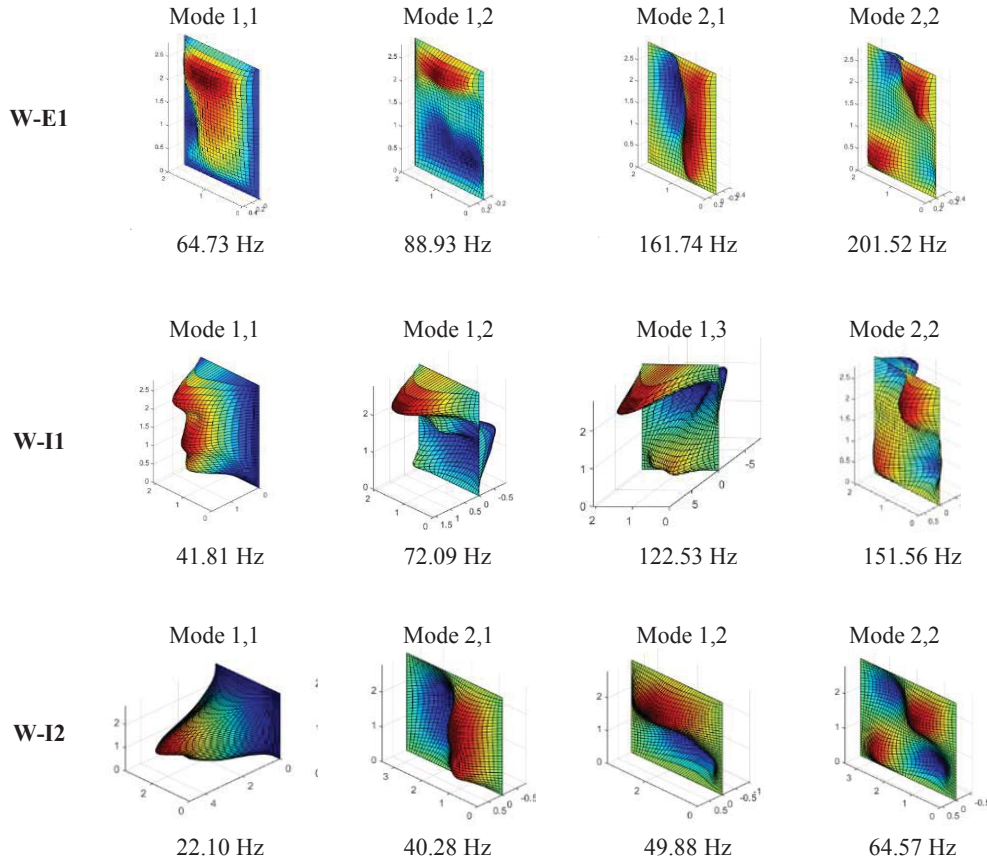


Figure 6: Experimental OOP modal parameters of tested infills.

The numerical investigation of infills is performed to estimate their elastic moduli. The f.e. model of the bare building is developed, modelling the r.c. frame with frame elements, while floors, slabs and retaining walls with shell elements. This model is preliminary calibrated based on experimental modal parameters of the whole building obtained from AVTs on the bare structure, with the aim to accurately predict the building dynamic behavior. Then, the investigated infills and the adjacent ones (to consider accurately the infill boundary conditions) are modelled with shell elements. Thus, three separated iterative procedures are performed, one for each investigated wall, and the elastic moduli are estimated once the convergence criteria (the same adopted before for the laboratory mock-up) are satisfied. In this case, four OOP modal parameters for each infill are considered in the iterative procedures to calculate the convergence criteria. Differently from the laboratory mock-up, the r.c. frame elements are modelled with beam elements, so the modelled infills have greater dimensions with respect to the real ones. Hence, the mass and elastic modulus of each infill is reduced, considering, for the sake of simplicity and with good approximation the mean percentage increment λ of the infill dimensions of each panel. The estimated elastic moduli are 3000 MPa for wall W-E1, 2550 MPa for W-I1 and 3150 MPa for wall W-I2. As before, to assess the reliability of these elastic moduli estimation, all infills are modelled within the global f.e. model of the building, considering their typology, openings and adopting the estimated elastic modulus for each infill typology. The numerical modal parameters of this infilled f.e. model are compared with the experimental ones obtained from AVTs measurements on the infilled structure, and the results are reported in Tab. 4. As can be noted, both frequencies and mode shapes are in very good agreement, proving the reliability of the proposed approach also when applied to real buildings.

Table 4: Comparison between experimental and numerical modal parameters of the infilled building.

Building mode	Frequency [Hz]		MAC
	EXP	NUM	
1 st	10.71	10.74	0.78
2 nd	13.04	13.09	0.83
3 rd	15.75	14.94	0.96

5 CONCLUSIONS

A procedure to estimate the stiffness of infill masonry walls through a combined experimental and numerical procedure has been proposed in this paper. The procedure is firstly validated through investigations on a real-scale laboratory mock-up and then applied to a real infilled r.c. frame building. In both cases, the methodology reveals capable to furnish a reliable and realistic infill stiffness estimation, leading to obtain trustworthy f.e. models of the infilled structures. The proposed approach furnishes a practical and expeditious tool that can be suitably used to reduce uncertainties in the f.e. modelling of framed buildings when infills must be included. This should be fundamental when results of ambient vibration measurements need to be interpreted with refined f.e. models of structures or when results of structural health monitoring systems must be analyzed. The procedure has the great advantage of requiring fast and non-invasive dynamic tests on infills, thus it can be executed in new or in existing buildings.

REFERENCES

- [1] L. Cavaleri, M. Fossetti, M. Papia, Infilled frames: developments in the evaluation of cyclic behavior under lateral loads. *Structural Engineering and Mechanics*, **21**, 469-494, 2005.
- [2] D. Perrone, M. Leone, M. A. Aiello, Non-linear behaviour of masonry infilled rc frames: influence of masonry mechanical properties. *Engineering Structures*, **150**, 875-891, 2017.
- [3] G. Gabbianelli, D. Perrone, E. Brunesi, R. Monteiro, Seismic acceleration and displacement demand profiles of non-structural elements in hospital buildings. *Buildings*, **10**(12), 1-19, 2020.
- [4] J. Cheng, A. A. Koutras, P. B. Shing, Evaluation of collapse resistance of reinforced masonry wall systems by shake-table tests. *Earthquake Engineering and Structural Dynamics*, **50**(2), 475-494, 2021.
- [5] F. Gara, S. Carbonari, D. Roia, A. Balducci, L. Dezi, Seismic retrofit assessment of a school building through operational modal analysis and f.e. modelling. *Journal of Structural Engineering*, **147**(1), article number 04020302, 2021.
- [6] F. Gara, D. Arezzo, V. Nicoletti, S. Carbonari, Monitoring of the modal properties of a RC school building during the Central Italy seismic swarm. *Journal of Structural Engineering (ASCE)*, DOI: 10.1061/(ASCE)ST.1943-541X.0003025, forthcoming.
- [7] R. Astroza, H. Ebrahimian, J. P. Conte, J. I. Restrepo, T. C. Hutchinson, Influence of the construction process and nonstructural components on the modal properties of a five-story building. *Earthquake Engineering and Structural Dynamics*, **45**(7), 1063-1084, 2016.

- [8] K. Erazo, B. Moaveni, S. Nagarajaiah, Bayesian seismic strong-motion response and damage estimation with application to a full-scale seven story shear wall structure. *Engineering Structures*, **186**, 146-160, 2019.
- [9] M. Regni, D. Arezzo, S. Carbonari, F. Gara, D. Zonta, Effect of environmental conditions on the modal response of a 10-story reinforced concrete tower. *Shock and Vibrations*, ID 9476146, 2018.
- [10] R. Vicente, H. Rodrigues, A. Arede, H. Varum, Simplified macro-model for infill masonry walls considering the out-of-plane behaviour. *Earthquake Engineering and Structural Dynamics*, **45**(4), 507-524, 2016.
- [11] F. Di Trapani, P. B. Shing, L. Cavaleri, Macroelement model for in-plane and out-of-plane responses of masonry infills in frame structures. *Journal of Structural Engineering*, **144**(2), 1-13, 2018.
- [12] A. B. Mehrabi, P. B. Shing, Finite element modelling of masonry-infilled RC frames, *Journal of Structural Engineering*, **123**(5), 604-613, 1997.
- [13] I. Koutromanos, A. Stavridis, P. B. Shing, K. Willam, Numerical modelling of masonry-infilled RC frames subjected to seismic loads. *Composite Structures*, **89**(11-12), 1026-1037, 2011.
- [14] G. Magenes, G. M. Calvi, In-plane seismic response of brick masonry walls. *Earthquake Engineering and Structural Dynamics*, **26**(11), 1091-1112, 1997.
- [15] J. Yacila, G. Camata, J. Salsavilca, N. Tarque, Pushover analysis of confined masonry walls using a 3-D macro-modelling approach. *Engineering Structures*, **201**, article number 109731, 2019.
- [16] A. Furtado, H. Rodrigues, A. Arede, H. Varum, Modal identification of infill masonry walls with different characteristics. *Engineering Structures*, **145**, 118-134, 2017.
- [17] A. De Angelis, M. R. Pecce, Out-of-plane structural identification of a masonry infill wall inside beam-column RC frame. *Engineering Structures*, **173**, 546-558, 2018.
- [18] V. Nicoletti, D. Arezzo, S. Carbonari, F. Gara, Expeditious methodology for the estimation of infill masonry wall stiffness through in-situ dynamic tests. *Construction and Building Materials*, **262**, article number 120807, 2020.
- [19] D. J. Ewins, *Modal testing: theory, practice and application*. John Wiley and Sons, 2009.
- [20] EN1996-2. Eurocode 6: Design of masonry structures – Part 2: Design considerations, selection of materials and execution of masonry. European Community for Standardization, Brussels, 2006.
- [21] A. K. Mitchell, C. R. Hazel, A simple frequency formula for clamped rectangular plates. *Journal of Sound and Vibrations*, **118**(2), 271-281, 1986.
- [22] R. J. Allemang, D. L. Brown, A correlation coefficient for modal vector analysis. *1st Int. Modal Analysis Conference*, Bethel, CT, USA, 1982.

ASSESSMENT OF DAMAGE TO MODERN REINFORCED CONCRETE BUILDINGS – ENGINEERING ANALYSIS OF THE M6.4 ALBANIA EARTHQUAKE, 26th OF NOV. 2019

**Lars Abrahamczyk¹, Davorin Penava², Melad Haweyou¹, Filip Anić², Arturo E.
Schultz³, Jeff Rautenberg⁴**

¹ Bauhaus-University Weimar
Chair of Advanced Structures
Marienstr. 13D, 99423 Weimar, Germany
{lars.abrahamczyk, melad.haweyou}@uni-weimar.de

² Josip Juraj Strossmayer University of Osijek
Faculty of Civil Engineering and Architecture Osijek
Vladimir Prelog Str., HR-31000 Osijek, Republic of Croatia
{davorin.penava, fanic}@gfos.hr

³ The University of Texas at San Antonio
Department of Civil and Environmental Engineering
San Antonio, TX, United States
arturo.schultz@utsa.edu

⁴ Wiss Janney Elstner and Assoc.
Minneapolis, MN, United States
JRautenberg@wje.com

Abstract

On November 26, 2019, a magnitude $M_w = 6.4$ earthquake struck Northwestern Albania. It was the strongest to hit Albania in more than 40 years. Cities such as Thumanë, Tirana, and Durrës suffered damage, but Durrës was the hardest hit with several buildings collapsed [1,2].

A reconnaissance team under the auspices of American Concrete Institute (ACI) visited Durrës, Albania to assess the extent of damage to modern reinforced concrete (RC) buildings (i.e. built after 1990). The team^{*1} surveyed buildings during the week of January 12, 2020, with a focus on RC buildings that were infilled with clay block masonry. Over the course of seven days the team documented 55 buildings that had RC frames as their main lateral resisting system. All of the surveyed buildings had unreinforced masonry infills (hollow clay blocks). Most of the buildings had ribbed or waffle slabs. Typical damage observed in these buildings was in-

^{*1} Researchers from University of Nebraska-Lincoln, Wiss, Janney, and Elstner Associates, Inc., University of Minnesota-Twin Cities, Epoka University (Tirana, Albania), Josip Juraj Strossmayer University of Osijek (Osijek, Croatia), and Bauhaus-Universität Weimar (Weimar, Germany)

plane or out-of-plane failure (dominant) of masonry infill walls throughout the building height. More damage was observed when these masonry walls were not confined well within the RC frame i.e. acting as partitions. In many cases, these masonry walls were not connected to the RC frame at all, having only bed-joints filled with mortar.

This report focuses on the performance of masonry components (infill walls, partitions, etc.) in the buildings in Durrës that were affected by the earthquake. Examples of the damage to the masonry infill, structural details that affected the damage, and its impact on building performance are described.

The paper provides an overview of the earthquake-induced damages in several building types and their variation within different structural systems focusing on RC frames with unreinforced masonry infills in Durrës. Reasons for significant differences in observed damage will be discussed in close relation to the building code development and the preferred design concepts. Besides response phenomena and typical damage patterns which have been observed after other earthquakes worldwide, an attempt is made to investigate parameters with high damage potential according to [3].

1 INTRODUCTION

The field reconnaissance missions following natural disasters provide valuable information on the performance of buildings during such events. As part of the American Concrete Institute disaster reconnaissance committee (ACI 133) mission, a team of researchers from the US, Croatia, Albania and Germany surveyed 55 buildings affected by the M_w 6.4 earthquake in Durrës, Albania on November 26, 2019.

The earthquake struck Northwestern parts of Albania, with an epicentral distance of 17 km from Durrës and about 35 km away from the northwest of the capital city of Tirana. Fifty-one people died because of the earthquake and 100,000 were affected. The earthquake caused serious damage to more than 1,400 buildings in Tirana, and about 900 buildings in the city of Durrës and the town of Thumanë with reported cases of collapsed buildings. Besides partial to complete failure due to shaking, a few buildings in the Durrës area were tilted due to liquefaction [4,5].

Events in Albania with a magnitude ($5.0 < M < 7.0$) are considered to be rare [6]. The last large event in the region was the earthquake in Montenegro on April 15, 1979 [7]. It was suggested that the region is going to be at a low seismicity rate interval from the event in Montenegro until the end of the second decade of the 21st century based on the seismic energy release for Albanian earthquakes [8].

The most affected buildings by the earthquake damage were reinforced concrete (RC) frame buildings with infill walls in Durrës. The poor performance of unreinforced masonry infill walls dominated the damage pattern, mostly due to simultaneous in- and out-of-plane dynamic excitation [9]. Thus, the global damage grade is mostly governed by the behavior of the partition/infill walls. Further, up to two or three grades, larger damages to the infill walls could be observed which makes the assignment of the damage grade according to EMS-98 [11] difficult.

Infill/partition walls are usually treated as non-structural/secondary elements (see Eurocode 8, and EMS-98), whereas past earthquakes have shown that they mainly contribute to the horizontal stiffness and seismic resistance. The herein presented field observation highlight again the need for a proper design to avoid brittle behavior and out-of-plane failure (Eurocode 8).

In this study, the damaged buildings surveyed in Durrës are assessed and key observations are highlighted. Besides, quantitative measurements are used to assign the seismic vulnerability of buildings using the Hassan and Sozen index [10].

2 EARTHQUAKE CHARACTERISTICS AND CONSTRUCTION PRACTICE IN ALBANIA

2.1 Parameters of the earthquake

The earthquake of Nov. 26, was recorded at seven accelerometric stations of the Albanian network, in the range of epicentral distances from 15 km to 130 km as shown in Figure 1.

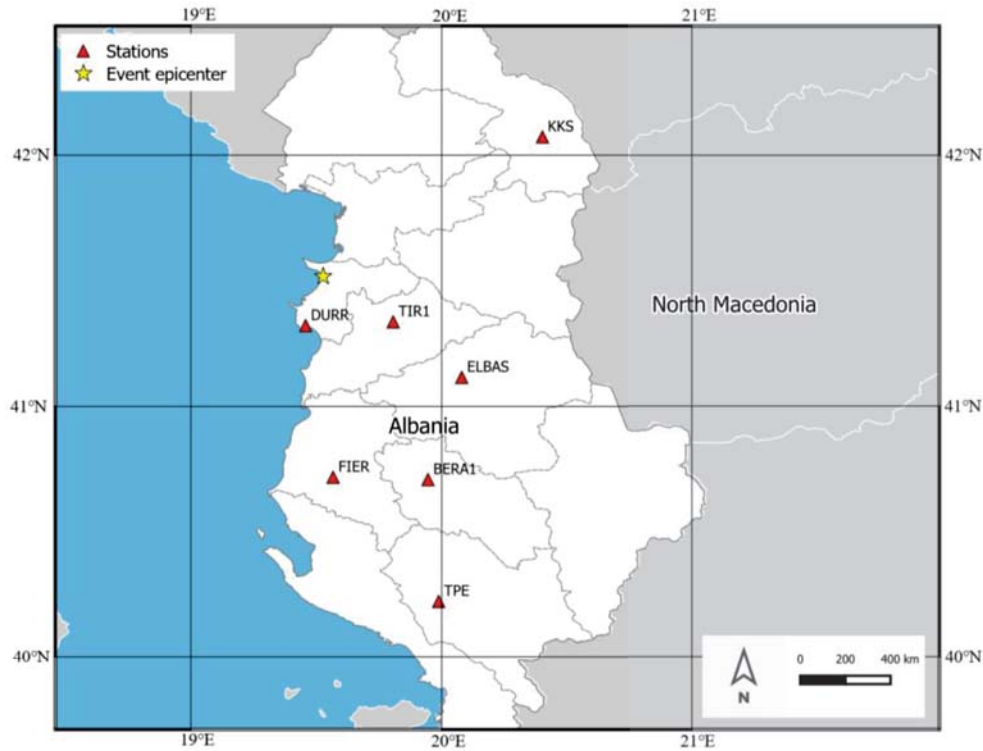


Figure 1: Strong motion stations in Albania that recorded the Nov. 26, 2019 earthquake and its epicenter [2].

The mainshock was followed by multiple aftershocks, two of which have a magnitude $M_w > 5.0$ as shown in Table 1. Figure 2 shows the shakemap of the mainshock calculated using surveyed macroseismic dataset collected through felt reports by the EMSC [11] and combined with expected intensities derived from strong-motion records using the correlation function of Faenza and Michelini, 2010 [12]. Up to intensity $I_{EMS} = VIII$ on the EMS-98 intensity scale [13] was estimated.

DURR station in Durrës, which lays on soft soil recorded only 15 s of the mainshock due to electricity pause [2]. This record has a horizontal peak ground acceleration (PGA) of 0.196g and spectral acceleration of more than 0.5g for 5% damping in a period range of 0.25s to 1s, as shown in Figure 4. This period range could be related to the fundamental period of buildings with five or more stories according to Eurocode 8 (EC8), which lays in the height range of observed damaged and collapsed buildings in the area.

Date	Time (UTC)	Lat. (°)	Long. (°)	M_w	Depth (km)	Reference name
26/11/2019	02:54:12	41.514	19.526	6.4	22	Mainshock
26/11/2019	06:08:21	41.571	19.424	5.5	10	Aftershock (1)
27/11/2019	14:45:23	41.550	19.479	5.3	10	Aftershock (2)

Table 1: Focal parameters of the Nov. 26, 2019 mainshock and following moderate aftershocks (USGS).

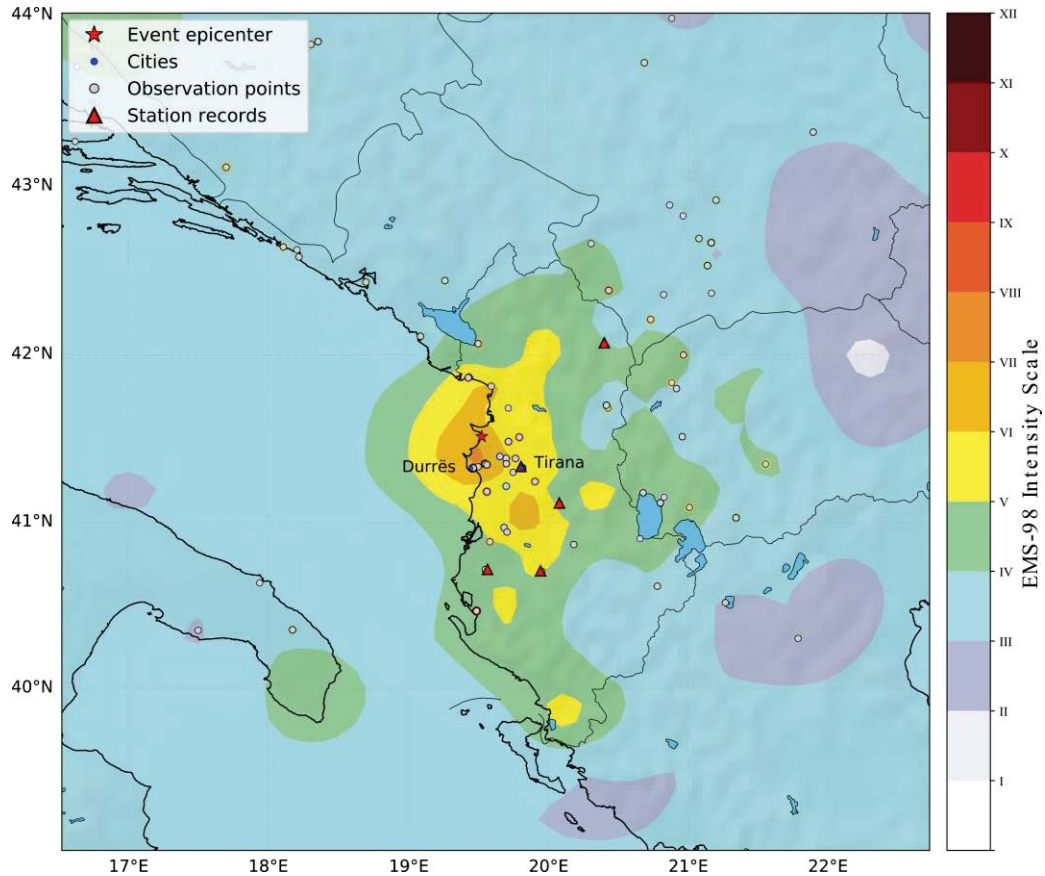


Figure 2: Macroseismic shakemap with EMS-98 intensity for the mainshock.

To evaluate the spectral acceleration obtained from the mainshock, response spectra from EC8 and the Albanian code (KTP-89) are calculated as shown in Figure 3. EC8 spectra are calculated with a PGA of 0.24g obtained from a probabilistic seismic hazard map with a 475-year return period proposed by [6] for Albania. The KTP-89 spectra are calculated based on the seismic code map with intensity $I_{MSK-64} = VIII$ for Durrës. By comparing the code spectra with the recorded mainshock spectra, the mainshock spectrum from the DURR station exceeded the KTP-89 spectra for periods higher than 0.2s for all soil types. However, the EC8 spectrum with soil type D (soft-soil) covered the recorded spectra. The aftershock records showed similar period ranges to the mainshock (0.2 to 1s) as shown in Figure 4.

It can be concluded that buildings designed according to the KTP-89 spectra were affected by higher ground motion, whereas the design forces according to EC8 and a PGA equal or greater than 0.2g covered the ground motion of the 2019 Albania EQ.

2.2 Design and construction standards

The current officially enforced earthquake design code in Albania is the 1989 KTP-89 code [14]. This code uses the seismic zoning map with expected intensities based on MSK-64 scale for the next 100 years and zones from $I_{MSK-64} = VI$ to IX developed by [15]. Multiple studies highlighted the need for increasing the seismic coefficients used in the code as they show a low return period when compared with the probabilistic assessment of seismic hazard studies [6,16]. In particular, the city of Tirana, assigned to $I_{MSK-64} = VII$ with of 0.08g seismic coefficient according to KTP-89, has a return period of approximately 50 years for a rock soil (category I) [16].

There were recent efforts to translate and implement the Eurocodes in Albania. Drafts of national annexes were prepared with updated seismic hazard maps [17]. However, the Albanian legislation still requires following the KTP-89 code and allow using Eurocodes voluntarily [18].

In addition, local engineers reported that building regulations were not properly enforced during the 1990s and early 2000s. That resulted in problems as buildings without a permit and improper addition of stories to existing buildings, which were reported in some of the collapsed buildings in Durrës [19].

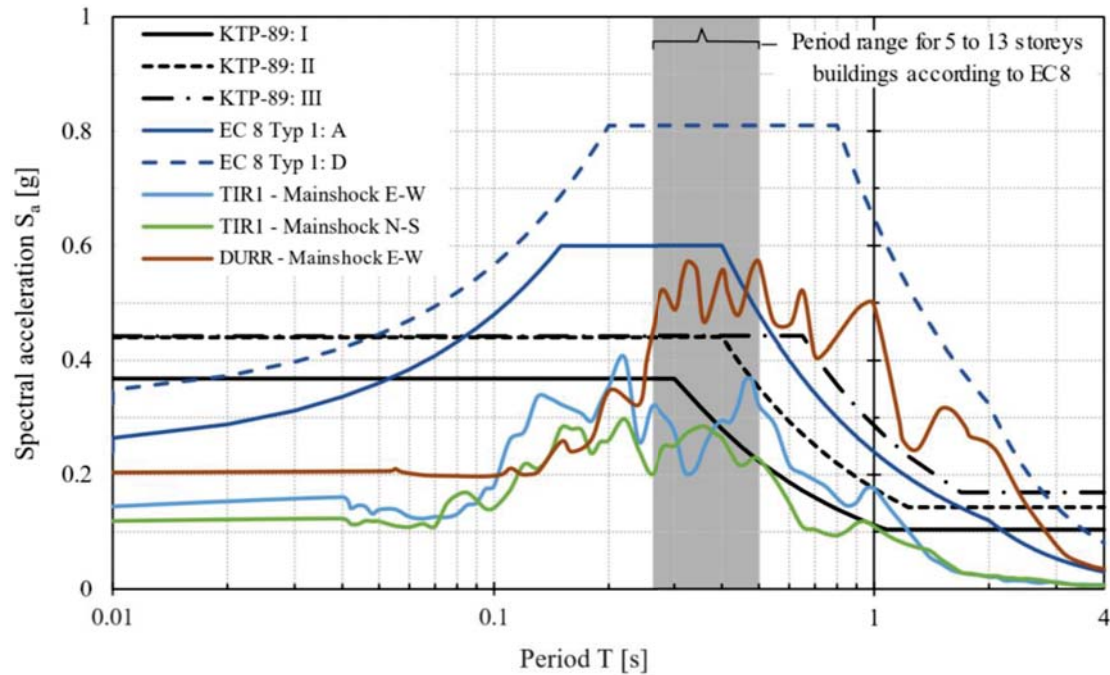


Figure 3: Response spectra of mainshock (5% damping) with KTP-89 and EC8 spectra.

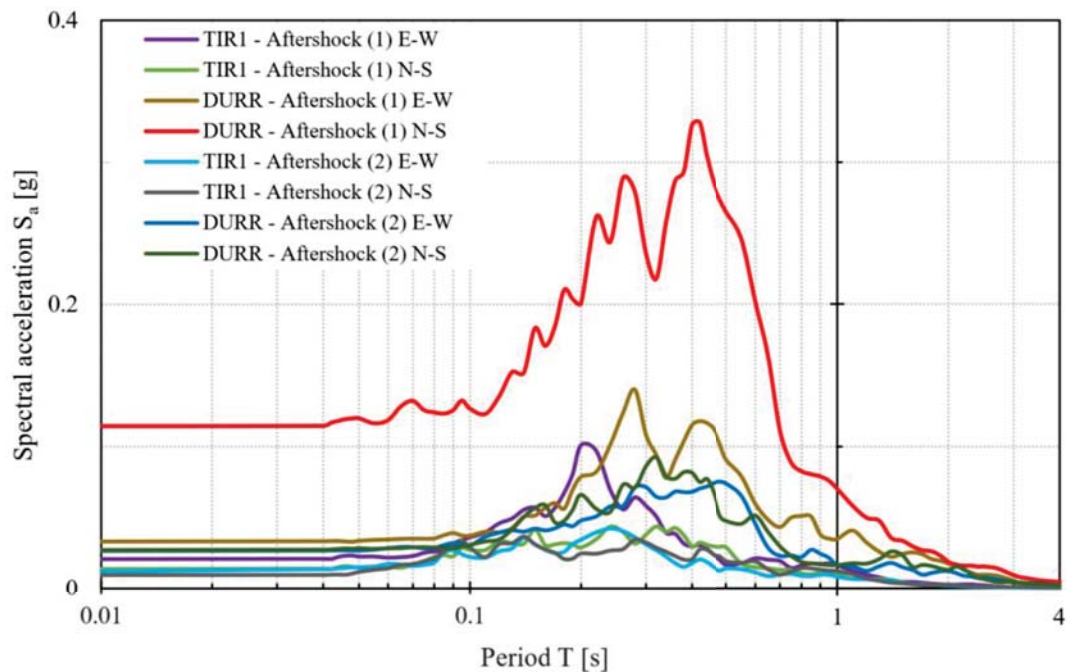


Figure 4: Response spectra of aftershocks (5% damping).

3 PERFORMANCE OF THE MAJOR BUILDING TYPES

3.1 Surveyed buildings

During the reconnaissance mission in Durrës city, totally 55 buildings were surveyed with a focus on modern multi-story RC buildings (i.e. built after 1990). Figure 5 shows the location of the surveyed buildings (all in the area of $I_{EMS} = VII$), in addition to 4 out of 7 reported collapsed buildings in Durrës [19]. Data was collected from the surveyed buildings in the form of building type, dimensions, structural characteristics, and damage observations if exist. Table 2 shows the damage levels description used in the survey for RC elements and masonry infill walls. The damage level is linked to the EMS-98 damage classification [13].

The team focused on mid to high-rise buildings (see Figure 6 for sampled surveyed buildings). Figure 7 (a) and (b) shows the height distribution and damage levels for the infills and structural elements respectively in the surveyed buildings.

Material	Damage level	EMS-98 damage classification	Definition
RC (Structural)	Light	Grade 2	Hairline inclined cracks and/or flexural cracks
	Moderate	Grade 3	Spalling of concrete cover
	Severe	Grade 4	Local structural failures
Masonry (Non-structural)	Light	Grade 1	Hairline cracks. Flaking of plaster
	Moderate	Grade 2	Cracks in walls and joints between panels. Flaking of large pieces of plaster
	Severe	Grade 3	Wide and through cracks in walls and joints between panels

Table 2: Definition of damage levels used in the survey forms and in compliance with [20]

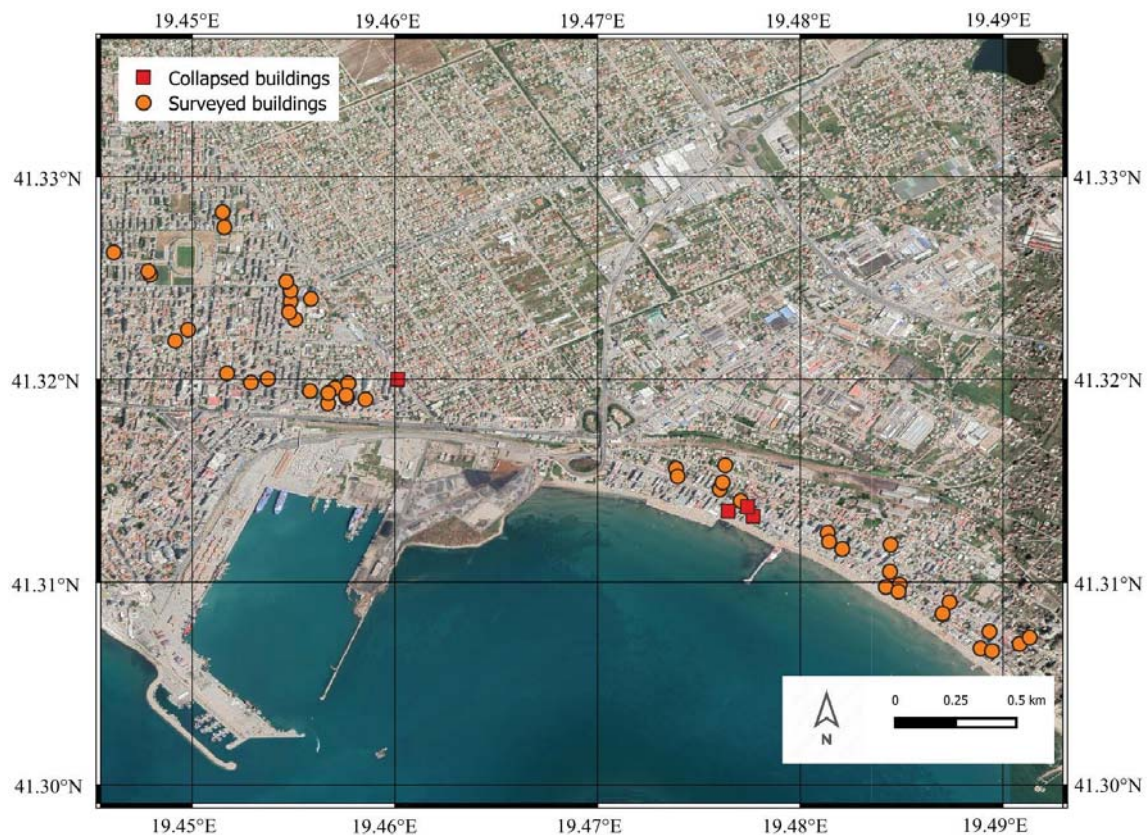


Figure 5: Locations of surveyed and collapsed buildings (Basemap: [21]).

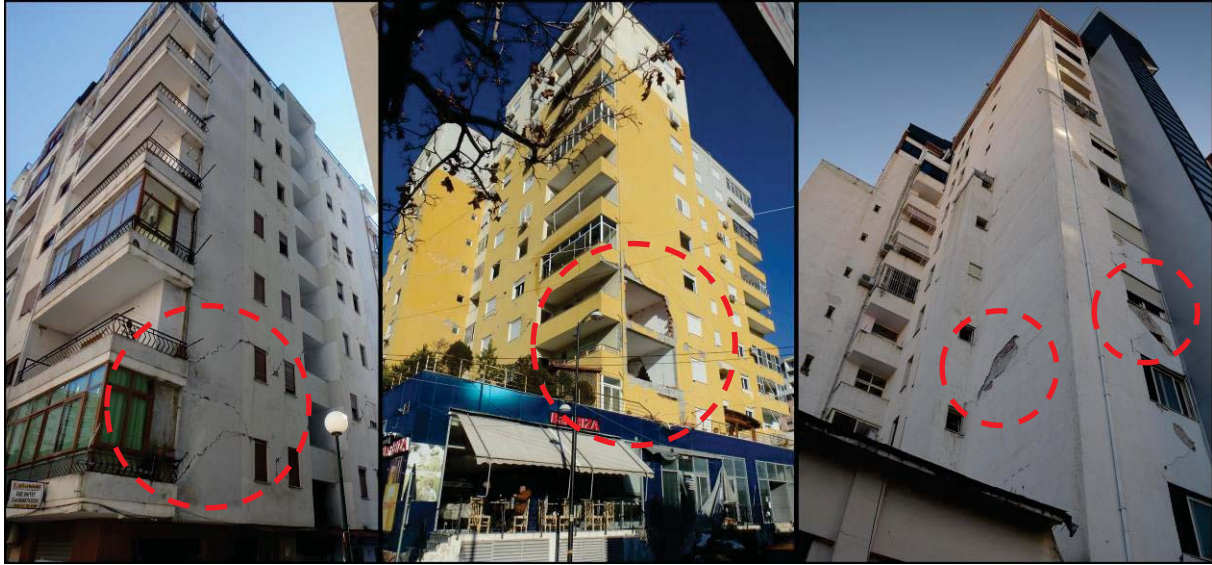


Figure 6: Samples of the surveyed building with 8, 12, and 13 stories.

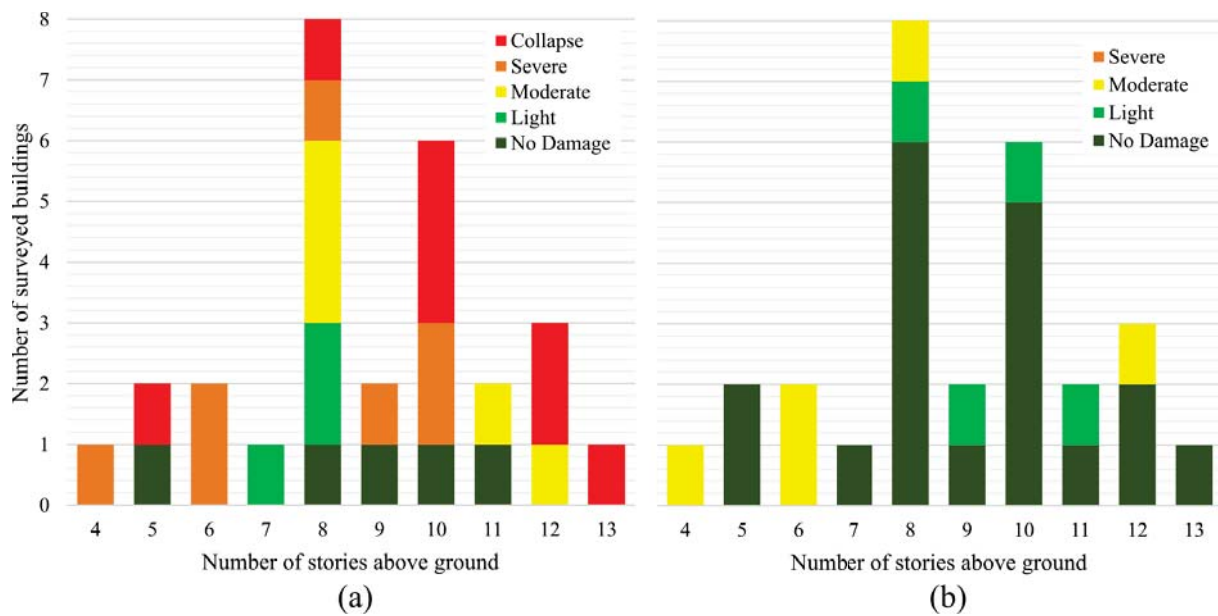


Figure 7: Distribution of the number of stories for surveyed buildings with (a) masonry infill damage levels, (b) RC element damage levels.



Figure 8: Undamaged multi-story masonry structures in Durrës.

It is worth mentioning that no significant structural damage to low-rise multi-story unreinforced masonry structures was observed in the surveyed city areas during the reconnaissance mission (see Figure 8).

3.2 Observed damage to RC buildings

The inspected buildings were scattered among the two most affected areas of the earthquake; the inner part of the city and the coastal (beach) area (see Figure 5). Those buildings were mostly built after the year 2000. Based on the field observations, the RC frame with infill walls was the dominant structural system in the inspected area. The presence of a dual system (RC frame + shear wall) was less common. Shear walls, if present, were mainly used for elevator core shafts.

The structural plans of the buildings were diverse. Buildings with soft-story and vertical irregularity were observed. Nevertheless, in most buildings, light or no structural damage was observed in the load-bearing RC elements, as it seems that the structural systems dissipated the seismic shock properly.

3.2.1 Damages on infill walls

Even though the structural safety in many of the observed buildings was met, the serviceability conditions of the observed buildings were poor. Considerable damage was observed in the infill walls, (see Figure 9 for in-plane failure samples). Usually, the damage was proportional to the number of stories. As expected, the ground floors were the most heavily damaged. The damage level was reduced with increased height. One of the most dominant characteristics of the damaged infill walls was observed to be poor workmanship and the lack of a proper connection between the masonry units. In all the cases, standard clay blocks with high volume horizontal voids were used (Group 4 in compliance with EC6).

It was observed that there was a lack of head joints in some of the inspected buildings. The brick-laying practice mainly consisted of the application of a bed joint and leaving the bricks unconnected with mortar vertically as shown in Figure 10 (a). Lack of vertical confinement at walls intersections was also observed, as in Figure 10 (b and c).

Another problem was the arrangement of the hollow bricks. In some of the observed buildings, the hollow bricks (even though horizontally perforated) were purely placed with voids horizontally (perpendicular to the direction of gravity). There is a lack of interlocking force of the bricks that is achieved through alternating their positions.

Extensively damaged infill walls are also considered to be a consequence of a ductile design of the buildings. The absence of the shear walls and RC cores has made the structure more flexible and was more susceptible to drifts. The path of load transfer of the lateral seismic loads through columns goes through the infills in the form of compression struts (only not in case of dominant bed joint sliding). The shear-force induced inside the infills (which seem to not have been designed to carry any shear load) has caused the damage of the infills. The extent of cracking is closely related to the workmanship quality, area of the infill, and opening presence. There were cases where the outer walls showed slight cracks only, but the interior walls were heavily damaged.

Another important observation related to the infill walls, was the improper connection of the wall to the frame, as well as in many cases, the lack of that connection. This phenomenon caused large pieces of the walls (sometimes the whole infill panels) to be dislocated and fall out of the plane (Figure 11). Lack of confining beams that are cast inside the infill walls was observed.



Figure 9: Infill in-plane failure.



Figure 10: Poor workmanship for infill walls (a) Lack of head-joints (b) and (c) Lack of vertical confinement at walls intersection.

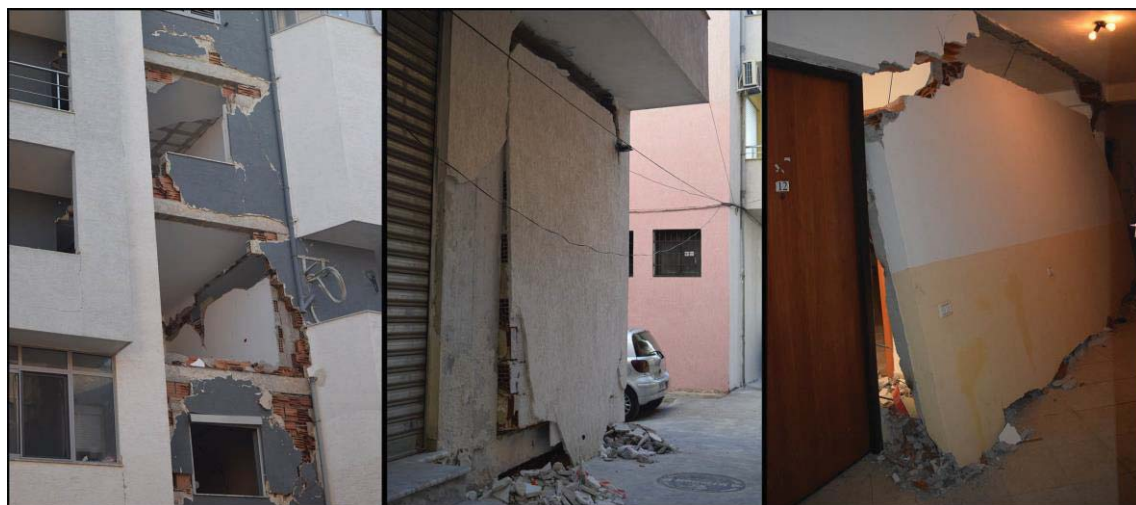


Figure 11: Infill out-of-plane failure.

The summarized damage observations show the challenges in making vulnerability and damage grade assignments according to EMS-98 [13], especially with respect to the relation between structural and non-structural damage. From Figure 12, it can be observed that moderate and severe structural (RC frame) damage co-existed with severely damaged and collapsed infill walls. However, non-structurally damaged buildings experienced different levels of infill damage. Thus, the behavior of non-structural components can heavily influence the global damage grade. Therefore, the vulnerability affecting factors like the number of stories and the properties of non-structural elements should be considered as important attributes of a building typology and the corresponding vulnerability table/matrix [22]. The damage observations lead to the conclusion and confirm that the quality of construction and material of the infill walls may have a strong influence on the interaction with the primary (structural) load-bearing system [23,24].

At the same time, many out-of-plane damages could also be observed on the upper and lower floors (see also [25,26]), caused by the influence of bi-directional loading and IP damage, where the two components of a floor movement are of similar importance. The magnitude of the loads in-plane decreases at the upper floors, while the forces acting perpendicular to the plane increase due to the increase in acceleration over the height of the building.

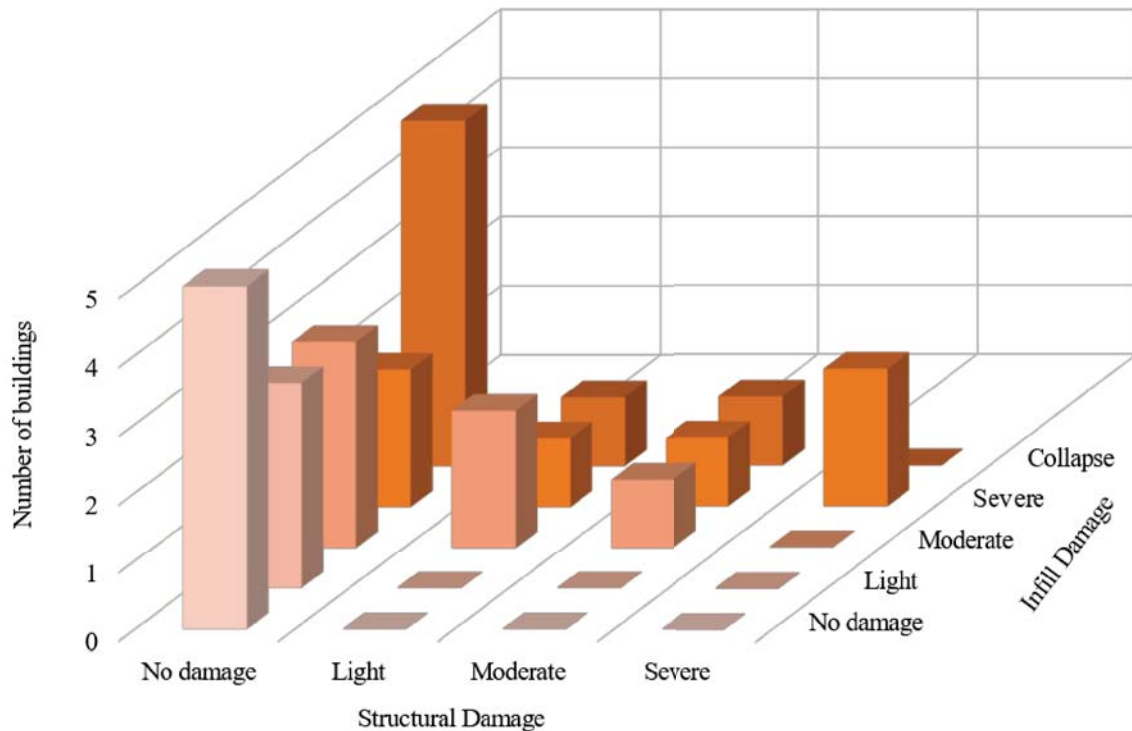


Figure 12: Observed infill damage level linked to observed structural damage level.

3.2.2 Damaged RC frame elements

Besides the surveyed buildings, it was reported that 7 buildings collapsed in Durrës due to the earthquake [19]. Figure 13 and Figure 14 show collapsed 4-story and soft-story buildings respectively. The collapse of these buildings could be attributed to the high shaking effects, poor construction practice, and the insufficient respect of the building code requirements.



Figure 13: 4-story collapsed building in Durrës (Left photo: [27], Right photo: courtesy of C. McKenney [28]).



Figure 14: Collapsed Lubjana Hotel in Durrës (Left photo: [29], Right photo: courtesy of C. McKenney [28]).



Figure 15: Soil settlement in buildings.

3.2.3 Damage due to the ground conditions

The ground conditions in the near coastal part were susceptible to liquefaction, which was observed during the survey in few buildings as shown in Figure 15. It was reported that extensive soil liquefaction was observed along the coastal side of Durrës city [30]. This settlement caused tilting of buildings, which could be visually observed.

4 ASSESSMENT OF SURVEYED BUILDINGS

To evaluate the surveyed buildings quantitatively, the two indices method proposed by Hassan and Sozen [10] is used. This method is based on wall index (WI) and column index (CI), calculated as follows:

$$WI = (\Sigma A_w + 0.1 \Sigma A_m) / \Sigma A_f \quad (1)$$

$$CI = (0.5 \Sigma A_c) / \Sigma A_f \quad (2)$$

where ΣA_w , ΣA_m , ΣA_c and ΣA_f are the sum of: RC walls area at ground floor in the direction of smallest RC wall area, masonry walls at ground floor in the direction of smallest RC wall area, columns area at ground floor, and total floor area above the ground floor respectively. Figure 16 shows the column and wall indices for the surveyed buildings, where floor plans were sketched or obtained.

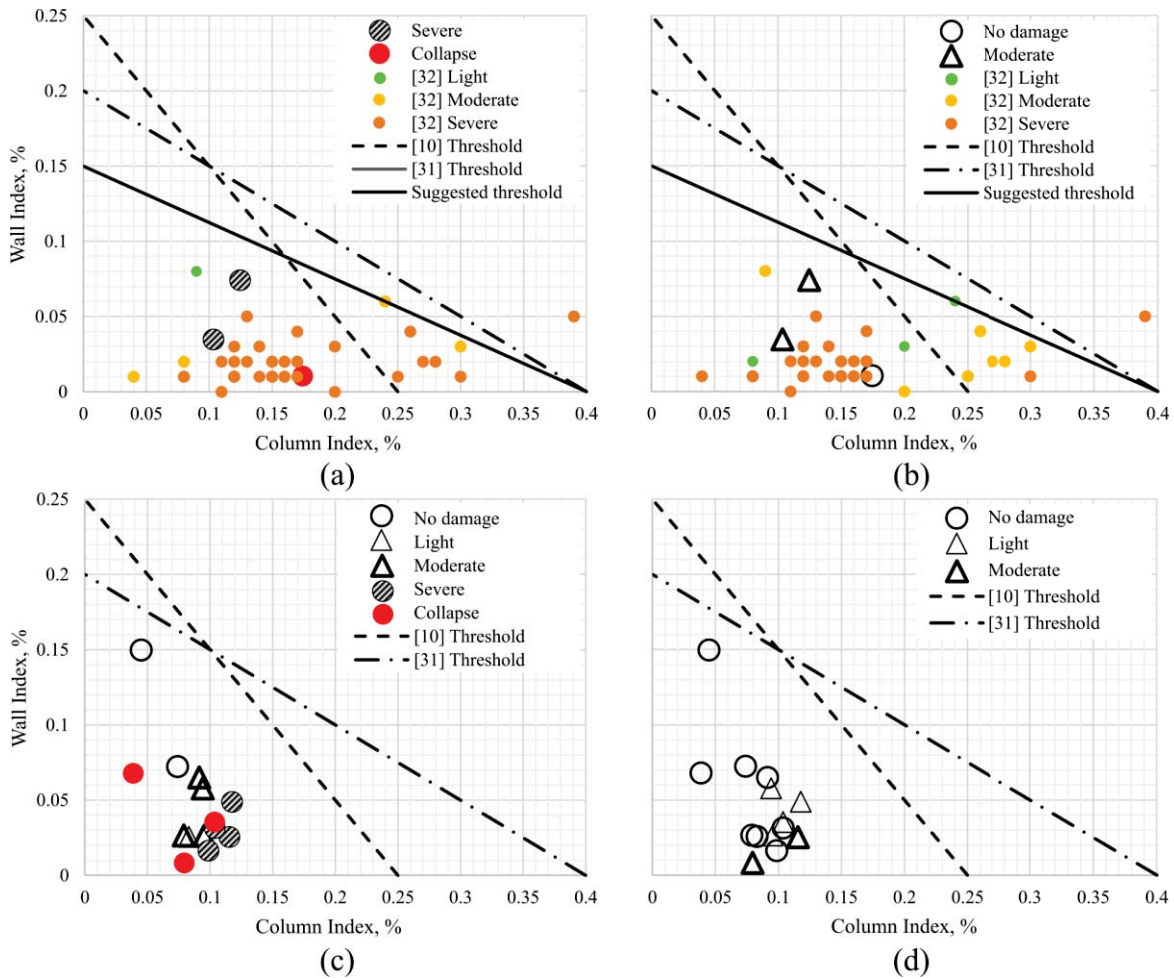


Figure 16: Calculated wall and column indices for surveyed buildings (a) Infill damage (4-6 stories) (b) Structural damage (4-6 stories) (c) Infill damage (≥ 7 stories) (d) Structural damage (≥ 7 stories).

Since more damage was observed in the infill walls, the indices are separately related to infill damage and structural damage states. In addition, the buildings were separated into two groups (mid-rise: 4-6 stories and high-rise: ≥ 7 stories). Especially, to consider that the originally proposed relation is not valid for buildings with more than 7 stories.

Figure 16 (b) and (d) show that all buildings lay beyond the thresholds suggested by [10,31]. These thresholds are suggested for low-rise [10] and low to mid-rise [31] structures to identify the most vulnerable to damage and may not be suitable for medium and high-rise buildings. A reduction in the limits by reducing the wall index limit is suggested to better fit the data with $(WI + 0.375CI = 0.15\%)$ for midrise structures similar to [31]. In addition it is suggested to further adapt the wall and column indices for high-rise structures, because of the rather large margin/distance between the derived data points and the thresholds by [10,31]. This decrease in the wall index and might be also in the column index could be related to the “nonlinear” ratio of the wall area at the ground floor and the total floor area above the ground floor. Whereas, more data need to be elaborated towards structural and non-structural damage to define an appropriate threshold for high-rise buildings.

Figure 16 (a) and (c) show the infill wall damage grades related to the wall and column indices of each building, separately. The data sets are extended by the field study of the 2016 earthquake in Ecuador [32] for further justification of the very limited Albania data set for mid-rise buildings. It highlights the need for column indices larger than 0.4 to also limit infill wall damages. Whereas, it is clear that further data need to be elaborated for justification.

5 CONCLUSION

A reconnaissance mission was conducted after the $M_w = 6.4$ earthquake that struck Albania on November 26, 2019. The damage to RC frame buildings with masonry infill walls built in compliance with contemporary building codes, i.e. after 1990's, was assessed by surveying 55 buildings. The observed performance of RC buildings in Durrës to the earthquake – less damage to RC elements (except in case of highly irregular construction); heavy in- and out-of-plane damage to the unreinforced masonry infill/partition walls – is the result of one or more of these aspects:

- 1) Improper construction practice, as the building code is not appropriately updated and enforced, especially towards the infill/partition walls.
- 2) Lack of proper shear walls in mid to high rise building to increase the stiffness and reduce drifts.
- 3) Poor workmanship of masonry infills, as they were built without head joints and confining elements, and not restrained against out-of-plane failure.

The seismic wall and column indices were calculated using the collected data and related to RC frame (or wall) and masonry infill wall damage. Thresholds for mid to high-rise RC buildings are suggested.

The survey and observation confirm that non-structurally damaged buildings (un- or slight-damaged RC elements) may experience different levels – up to grade 4 and 5 – of infill damage. Thus, the behavior of non-structural components can heavily influence the global damage grade and therefore need to be properly designed or build.

The gained experience and damage observations confirm the principle results of recent analytical and experimental studies [3,33,34]. As a next step, the previously experimentally validated models will be applied to the detailed surveyed Albanian buildings for further real-world validation by the comparison of a damage prognosis with the observation. A number of useful data sets could be collected as part of the reconnaissance mission for further analytical studies.

6 ACKNOWLEDGMENT

The writers express their appreciation to the American Concrete Institute (ACI) for supporting the reconnaissance mission. Efforts from Prof. Santiago Pujol to coordinate the mission and from Prof. Chungwook Sim to both coordinate and carry the field survey are gratefully acknowledged. The efforts from Dr. Enea Mustafaraj, Andi Gjoci, and Jurgen Mema from Epoka University in Albania in the field survey are greatly appreciated.

The kind help of Peshawa Luqman Hasan from Bauhaus-University Weimar to prepare the shakemap is highly appreciated.

7 REFERENCES

- [1] A. Ganas, P. Elias, P. Briole, F. Cannavo, S. Valkaniotis, V. Tsironi, and E. I. Partheniou, “Ground deformation and seismic fault model of the M6.4 Durres (Albania) nov. 26, 2019 earthquake, based on GNSS/INSAR observations”, *Geosciences (Switzerland)*, vol. **10**(6), pp. 1–16, 2020.
- [2] L. Duni and N. Theodoulidis, “Short Note on the November 26, 2019, Durres (Albania) M6.4 Earthquake: Strong Ground Motion with Emphasis in Durres City: EMSC online report”, 2020, http://www.itsak.gr/uploads/news/earthquake_reports/EQ_Albania_2019-11-26_M6.4.pdf.
- [3] I. Guljaš, D. Penava, L. Laughery, and S. Pujol, “Dynamic Tests of a Large-Scale Three-Story RC Structure with Masonry Infill Walls”, *Journal of Earthquake Engineering*, vol. **24** (11), pp. 1675–1703, 2020.
- [4] E. Lekkas, S. Mavroulis, D. Papa, and P. Carydsi, “The November 26, 2019 Mw 6.4 Durres (Albania) earthquake”, *Newsletter of Environmental Disaster and Crises Management Strategies*, vol. **15**, 2019.
- [5] R. Ormeni, I. Hoxha, P. Naco, and D. Gego, *The strong earthquake of 26 November 2019 (MW6.4) and its associate active tectonic of Durres Region in Albania*, Tirana, Albania, 2020.
- [6] A. Fundo, L. Duni, S. Kuka, E. Begu, and N. Kuka, “Probabilistic seismic hazard assessment of Albania”, *Acta Geodaetica et Geophysica Hungarica*, vol. **47**, 2012.
- [7] E. Peterschmitt, “The destructive earthquake of 15 April 1979, Extension of the seismic activity, in The Earthquake of 15 April 1979 and the Elimination of Its Consequences”, 1980.
- [8] B. Muço and L. Puka, “Periodic Features of Seismic Activity in Albania”, *Pure and Applied Geophysics*, vol. **141**(1), pp. 59–69, 1993.
- [9] M.H. Al Hanoun, L. Abrahamczyk, and J. Schwarz, “Macromodeling of in- and out-of-plane behavior of unreinforced masonry infill walls”, *Bulletin of Earthquake Engineering*, vol. **17**(1), pp. 519–535, 2019.
- [10] A.F. Hassan and M.A. Sozen, “Seismic vulnerability assessment of low-rise buildings in regions with infrequent earthquakes”, *ACI Structural Journal*, vol. **94**(1), pp. 31–39, 1997.
- [11] European-Mediterranean Seismological Centre, “M6.4 ALBANIA on November 26th 2019 at 02:54 UTC”, 3/1/2021, <https://www.emsc-csem.org/Earthquake/262/M6-4-ALBANIA-on-November-26th-2019-at-02-54-UTC>.
- [12] L. Faenza and A. Michelini, “Regression analysis of MCS intensity and ground motion parameters in Italy and its application in ShakeMap”, *Geophysical Journal International*, vol. **180**(3), pp. 1138–1152, 2010.
- [13] G. Grünthal, R. Musson, J. Schwarz, and M. Stucchi, *European Macroseismic Scale 1998*, Cahiers du Centre Européen de Géodynamique et de Séismologie, Luxembourg, 1998.
- [14] KTP-N.2-89, “Earthquake resistant design provisions (in Albanian)”, Publication of Academy of Sciences and Ministry of Constructions, 1989.
- [15] E. Sulstarova, S. Koçiu, and S. Aliaj, “Seismic zonation of Albania”, 1980.
- [16] E. Dunin and N. Kuka, “Seismic hazard assessment and site-dependent response spectra parameters of the current seismic design code in Albania”, *Acta Geodaetica Et Geophysica Hungarica - ACTA GEOD GEOPHYS HUNG*, vol. **39**, pp. 161–176, 2004.

- [17] R. Hasanaj and K. Dedja, *Status and Further Development of Eurocodes in Albania (Presentation): Support of Capacities of the Institute for Standardisation of Bosnia and Herzegovina in the Area of Implementation of Eurocodes*, 2018.
- [18] R. Luka, *Present status of Eurocodes in Albania (Presentation): The way forward for the Eurocodes implementation in the Balkans*, Tirana, 2018.
- [19] Shqiptarja, “Historiku i 10 pallateve të mallkuara që u shembën dhe zunë nën rrënoja banorët në Durrës dhe Thumanë (In Albanian)”, <https://shqiptarja.com/lajm/historiku-i-pallateve-qe-u-shemb-ben-dhe-zune-nen-rrenoja-banoret-ne-durres-dhe-thumane>.
- [20] G. Ozcebe, M.S. Yucemen, V. Aydogan, and A. Yakut, “Preliminary Seismic Vulnerability Assessment of Existing Reinforced Concrete Buildings in Turkey”, In *Seismic Assessment and Rehabilitation of Existing Buildings*, S. T. Wasti and G. Ozcebe, Eds., pp. 29–42, Springer Netherlands, Dordrecht, 2003.
- [21] Google Maps, “Durrës city, Imagery Date: 8/3/2020”, <https://goo.gl/maps/vSzwYeB8vYv7EU5c9>.
- [22] L. Abrahamczyk, S. Brzev, López Menjivar M.A., V. Silva, D.H. Lang, J. Schwarz, “WHE Housing reports - A review with respect to past and current earthquake damage observations”, *17th World Conference on Earthquake Engineering*, Sendai, Japan, paper-no. 1396, 2021.
- [23] T. Wenk, C. Lacave, and K. Peter, “The Adana-Ceyhan earthquake of June 27, 1998: report on the reconnaissance mission from July 6-12, 1998 of the Swiss Society of Earthquake Engineering and Structural Dynamics (SGEB)”, Swiss Society of Earthquake Engineering and Structural Dynamics, 1998.
- [24] L. Abrahamczyk, H. Maiwald, J. Schwarz, and D. Lobos, “Das Magnitude 8.8 Maule (Chile)-Erdbeben vom 27. Februar 2010 - Ingenieuranalyse der Erdbebenschäden, Teil 1”, *Bautechnik*, vol. **87**(8), pp. 462–473.
- [25] A. Charleson, N. Vesho, and A. Marku, eds., *Structural engineering observations from the 26 November 2019 M6.4 Albanian earthquake*, 2020.
- [26] F. Anić, D. Penava, I. Guljaš, V. Sarhosis, and L. Abrahamczyk, “Out-of-plane cyclic response of masonry infilled RC frames: An experimental study”, *Engineering Structures*, vol. **238**, 2021.
- [27] Google street view, “Durrës city, Imagery Date: 6/2016”, <https://www.google.com/maps/@41.3134605,19.4777315,3a,75y,205.95h,100.85t/data=!3m6!1e1!3m4!1sLk8f8Hui4u08YVjO3m4JCQ!2e0!7i13312!8i6656>.
- [28] McKenney C., “Albania M6.4 Earthquake (Nov-26) - Durrës Survey (Nov-27, Nov-28) [Online Google Photos Album]”, <https://photos.app.goo.gl/ENgE4GrEW6pqScoN9>.
- [29] Transit Navitime, “Lubjana Hotel”, 3/1/2021, <https://transit.navitime.com/en/al/hotel/TR003-4333978>.
- [30] G. Papadopoulos, A. Agalos, P. Carydis, E. Lekkas, S. Mavroulis, and I. Triantafyllou, “The 26 November 2019 Mw 6.4 Albania Destructive Earthquake”, *Seismological Research Letters*, pp. 1–10, 2020.
- [31] P. Shah, S. Pujol, M. Kreger, and A. Irfanoglu, “2015 Nepal Earthquake”, *Concrete International*, vol. **39**(3), 2017.
- [32] E. Villalobos, C. Sim, J. P. Smith-Pardo, P. Rojas, S. Pujol, and M. E. Kreger, “The 16 April 2016 Ecuador Earthquake Damage Assessment Survey”, *Earthquake Spectra*, vol. **34**(3), pp. 1201–1217, 2018.
- [33] F. Anić, D. Penava, L. Abrahamczyk, and V. Sarhosis, “A review of experimental and analytical studies on the out-of-plane behaviour of masonry infilled frames”, *Bulletin of Earthquake Engineering*, vol. **18**(5), pp. 2191–2246, 2020.
- [34] V. Sigmund et al., “FRAMed–MAsonry Composites for Modeling and Standardization, FRAMA, International Benchmark within Research Project,” Josip Juraj Strossmayer University of Osijek, Croatia, 2014.

INFLUENCE OF THE INFILL TYPOLOGY IN THE EVALUATION OF THE ANNUAL LOSSES OF RC STRUCTURES THROUGH THE APPLICATION OF A NEW METHOD

Andrea Rossi¹, Paolo Morandi², Riccardo R. Milanesi³ and Guido Magenes³

¹ IUSS Pavia and Cairepro
via Ruini, Reggio nell'Emilia (RE), Italy
andrea.rossi@iusspavia.it , andrea.rossi@cairepro.it

²Eucentre
via Ferrata 1, Pavia (PV), Italy
paolo.morandi@eucentre.it

³ Dept. of Civil Engineering and Architecture, University of Pavia
via Ferrata 3, Pavia (PV), Italy
riccardo.milanesi@unipv.it , guido.magenes@unipv.it

Abstract

The comparison of the seismic performance of different typologies of masonry infills is usually related to the technical response according to post-seismic inspection, experimental outcomes, and numerical studies. Although the economic losses due to the achievement of some limit states could represent one of the main aspects that should be taken into account in the selection of the masonry typology to be adopted for the masonry infills, few studies have been addressed to this topic ([1]). Moreover, the economic losses related to the seismic response of masonry infills are usually dealt without a specific procedure that differentiates the masonry of the infill, the infill typology (e.g., traditional vs innovative infill systems), and other aspects which may modify the seismic performance of non-structural element. In this paper, a comparison in terms of the economic losses between different “traditional” masonry infills and an innovative solution with sliding joints [2] is presented through the adoption of a new approach ([8]) that computes the expected annual losses based on the PERR's PBEE procedure.

Keywords: Expected annual losses, infill seismic performances, innovative infill, sliding joints, performance based earthquake engineering.

1 INTRODUCTION

The seismic performance of buildings is usually evaluated through their structural response that is typically referred to their capacity to withstand earthquake action without threaten human-life and/or exceed specific levels of damage. Although it is widely recognized that the safety of the inhabitants must always be guaranteed, the need to limit the damage, also in case of minor earthquakes, and to reduce the costs of repairing or of the downtime of the activities conducted within the structure, is becoming more and more important.

Focusing the attention on reinforced concrete (RC) frame buildings with masonry infill walls, field observations after major earthquake events have highlighted the vulnerability of these structure, if specific seismic-details are not adopted (*i.e.*, [3],[4],[5]). Moreover, also in case of recently designed buildings or with low seismic actions, where the collapse of the structural members is avoided, the damage could occur in the infill walls due to their high vulnerability and the associated monetary losses could be quite relevant.

In order to improve the seismic response of the infills and to reduce the detrimental effects of the interaction between RC frame and masonry panels, typical for traditional masonry walls built in-place with no specific seismic details, the researchers of the University of Pavia have conceived an innovative infill typology, characterized by the presence of deformable mortar at the frame/infill interface and sliding joints within the masonry panel. Further information regarding the system is provided by Morandi *et al.* ([2]).

This technology proved to be promising, ensuring good seismic performance of the infill-frame system based on an extended experimental campaign, as fully described by Morandi *et al.* ([2]) about the in-plane seismic behaviour, by Milanesi *et al.* ([6]) regarding the out-of-plane seismic response and by Manzini *et al.* ([7]) for the overall building performance.

The recent studies conducted ([1],[8]), mainly developed in numerical researches on this topic (*i.e.* [9],[10]), have also demonstrated that the adoption of such an innovative infill typology could lead to a significant reduction of the costs of reparation of the building and of the elements after significant seismic events, despite an initial higher cost of construction, compared to the same RC structure with traditional infill walls.

This paper aims at presenting the results by applying a novel methodology proposed by Rossi *et al.* ([8]) and evaluate the influence of the choice of a specific infill typology in the computation of the expected annual losses for a typical RC frame building in Italy, built in compliance with current seismic codes. Moreover, the structural and monetary advantages given by the adoption of the innovative infill solution are discussed.

2 NEW METHODOLOGY FOR THE EVALUATION OF THE LOSSES IN INFILLED RC FRAMES

A novel procedure to evaluate the expected annual losses (EAL), tailored specifically for RC infilled frame, was conceived by Rossi *et al.* ([8]) within the well-known PEER's PBEE framework ([11],[12],[13],[14],[15]).

The EAL is the expected loss that should be paid every year in order to repair or even replace a specific reference structure. The novel procedure considered to evaluate the EAL of infilled frame structures has been partially adopted in early studies carried by Rossi *et al.* ([16] and [17]). Recently, Di Trapani *et al.* ([1]) presented a similar study, also based on PBEE framework, including an innovative infill solution with sliding joints studied by Preti *et al.* ([18]).

In the present work, the definition of damage in all the considered infills was inferred directly by laboratory tests and by numerical simulations on the same infill panels adopted in the analyses and the computation of losses is referred to updated official costs of repair and

replacement actually adopted in Italy. Finally, the evaluation of the seismic performance in terms of EAL of a building with specific indications on infill typologies allows a consistent comparison on the effective contribution of different infill solutions and an estimation of the economic benefits that the use of innovative infill systems could provide as respect to traditional infills.

According to Baker and Cornell ([13]), EAL is computed as a discrete summation:

$$EAL = \sum E[DV|IM=im] \cdot \Delta \lambda_{IM}(im) \quad (1)$$

where, DV is decision variable, IM is the intensity measure, im is a specific value of the IM , $E[DV|im]$ is the expected total repair/replacement cost conditioned on $IM = im$, $\lambda_{IM}(im)$ is the conventional hazard curve, being equal to the mean annual frequency (MAF) of IM exceeding a certain value of IM .

The decision variable, DV , is the metric necessary to evaluate the performance of the building and used by the stakeholders to justify their decisions.

Therefore, according to Equation (1) the EAL is the area under the curve, depicted in Figure 1.

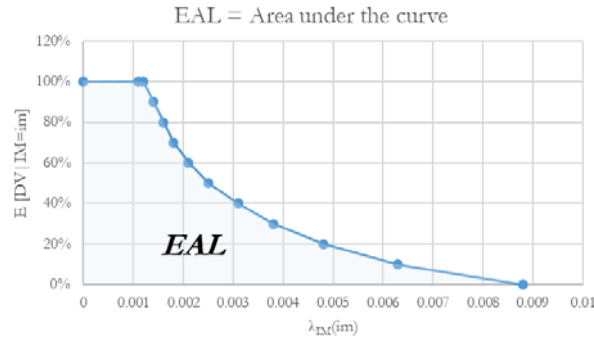


Figure 1. Graphical representation of a generic EAL.

The methodology, in accordance with Cornell and Krawinkler ([11]), could be subdivided in four steps: facility definition, structural analysis, damage analysis and loss analysis.

The aspects of novelty introduced in the methodology proposed stay in the fact that the attention is mainly focused on the influence of infill walls in the evaluation of the structural and economic performance of the overall building. In particular, the definition of damage in all the considered infills was inferred directly by laboratory tests and by numerical simulations on the same infill panels adopted in the analyses; moreover, the computation of the losses was referred to updated official costs of repair and replacement actually adopted in Italy. The evaluation of the seismic performance in terms of EAL of a building with specific indications on infill typologies has allowed a consistent comparison on the effective contribution of different infill solutions and an estimation of the economic benefits that the use of an innovative infill system could provide as respect to traditional infills.

3 APPLICATION TO CASE STUDY

3.1 Facility definition

In order to evaluate the influence on infill walls in the seismic performance of a common newly designed 6-storeys high RC frame building in Italy, a reference model was assumed. The structure aimed to represent a typical residential building designed in high ductility class in compliance with the Italian standards ([19]) and Eurocodes ([20],[21]), therefore in accord-

ance with the “capacity design” principles. The building is regular both in plan and elevation and located on a flat ground, with soil type C, in L’Aquila (Italy). Further details on the reference structure are fully described in Hak *et al.* ([22]).

The numerical model is a 2D frame of the entire building, being representative of all the structure, as shown in Figure 2. The analyses have been conducted using Ruaumoko finite element program ([23]) and a macro-model approach was deemed to be the best compromise between reliable results and reasonable computational burden.

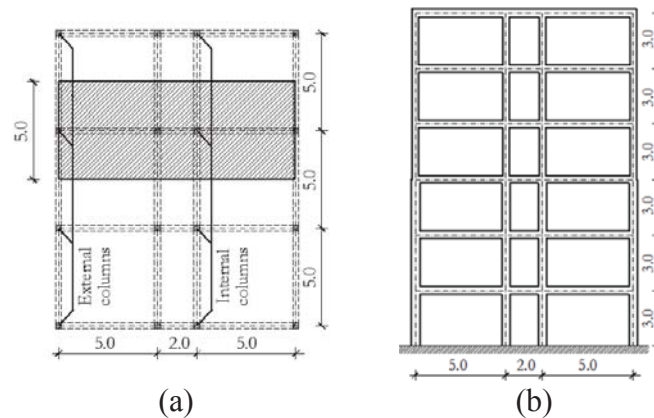


Figure 2. Geometry of the reference building: (a) plan view; (b) elevation view.

In the numerical model, only the structural elements (RC beams and columns) and the infills walls have been modelled, whereas the other non-structural components, assumed to be irrelevant to the structural response of the system, although they could be damaged, have been accounted only *a-posteriori*.

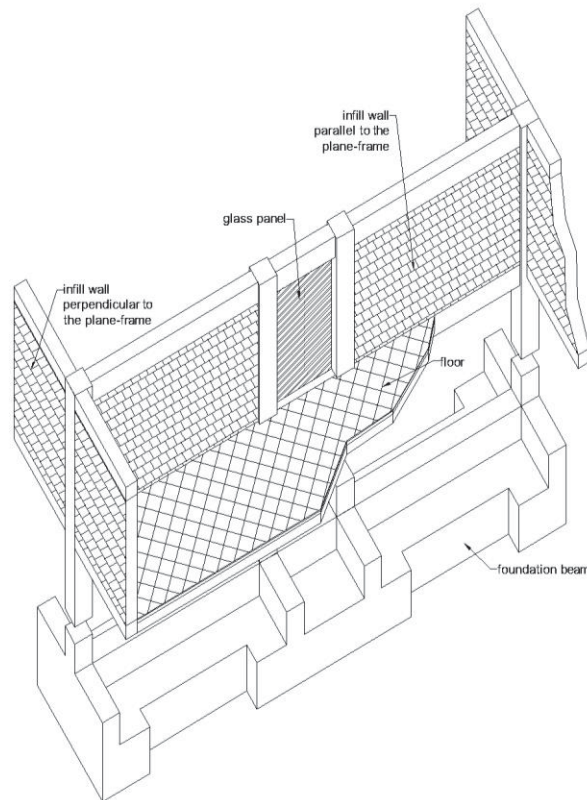


Figure 3. Portion of the structure analyzed.

The additional shear demand on the columns of the frame due to the in-plane thrust of the infill and the out-of-plane verification on the panels have been considered as reported according to Rossi *et al.* ([8]); the local interaction method is based on the specific studies ([24],[25]), meanwhile the out-of-plane verifications are referred to researches based on experimental results (*i.e.* [26],[27],[28],[29],[6]).

The foundation beam is considered to behave perfectly elastically and not damageable, except in case of global collapse of the building. In that case, also the costs of demolition and rebuilding of the foundation beam is accounted. In the central bay of the in-plane frame, a glass panel representing a door is assumed to be placed.

The arrangement of infills and of all the elements is shown in Figure 3, and a list of all damageable elements accounted in the case-study is reported in Table 1.

Typology	Element	Dimension	Quantity
Structural elements	Foundation beam	Height: 1.7 m; Width _{top} : 0.45 m; Width _{bottom} : 2.0 m; Length: 23 m	53.25 m ³ in total
	Columns	Section of elements at the 1 st , 2 nd and 3 rd floor: 45x45cm; otherwise: 35x35cm	11.70 m ³ in total
	Beams	Section: 30x45cm	23.65 m ³ in total
Non structural elements	Infill panels – in-plane, 1 st floor	2.775x4.55m each	25.25 m ² per floor
	Infill panels – in-plane, 2 nd & 3 rd floor	2.55x4.55m each	23.21 m ² per floor
	Infill panels – in-plane, 4 th , 5 th , & 6 th floor	2.55x4.65m each	23.72 m ² per floor
	Infill panels – out-of-plane, 1 st floor	2.775x4.55m each	25.25 m ² per floor
	Infill panels – out-of-plane, 2 nd & 3 rd floor	2.55x4.55m each	23.21 m ² per floor
	Infill panels – out-of-plane, 4 th , 5 th , & 6 th floor	2.55x4.65m each	23.72 m ² per floor
	Ground floor slab	60 m ² (per floor)	60.0 m ²
	Floor slab, from 1 st to 5 th floor	60 m ² (per floor)	60.0 m ² per floor
	Roof	60 m ² (per floor)	60.0
	Ceilings	60 m ² (per floor)	60.0 m ² per floor
	Piping (hot and cold water) and electrical, hydraulic and heating systems	Small diameter threaded steel pipes ($\leq 60\text{mm}$)	60.0 m per floor
	Internal glass door, 1 st floor	2.775x1.55m each	5.33 m ² per floor
	Internal glass door, 2 nd & 3 rd floor	2.55x1.55m each	5.10 m ² per floor
	Internal glass door, 4 th , 5 th , & 6 th floor	2.55x1.65m each	5.20 m ² per floor
	Sanitary, boilers and machines	Engineering judgement: 140 € / m ²	
	Partition wall	Gypsum walls, 18mm thick	25 m ² per floor
	Frames	4 windows and 4 doors	10.24 m ² per floor

Table 1. List of the damageable elements.

With the aim to represent common traditional masonry infill typologies, three different “non-ductile” solutions have been studied. The masonry panels were made of clay units and considered as built in full contact with the surrounding RC frame. Their characteristics are resumed herein and sketched in Figure 4:

- 1) Typology T2 (“medium strength/stiffness infill solution”). It is represented by double-leaf 12 cm thick walls with horizontally perforated “weak” units, with 60% void percentage. The panel has 1 cm of plaster on each external side of the leaf.
- 2) Typology T3 (“strong infill solution”). It is made of vertically perforated (50% of void) robust 30 cm thick blocks. The panel has 1 cm of plaster on each side of the wall.
- 3) Typology TA (“strong infill solution”). Similar to T3 solution, but the vertically perforated blocks are thicker (35 cm) and the tested masonry infills has provided higher deformation capacity than T3. The panel has 1 cm of plaster on each side of the wall.

The strength and stiffness of the infills adopted are different in order to account for a quite wide range of typologies.

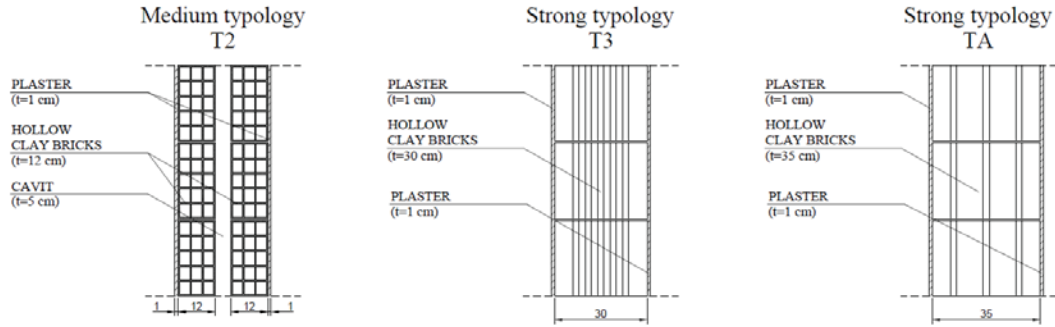


Figure 4. Masonry infill typologies [22].

Besides the non-ductile “traditional” infills, the innovative ductile infill solution with sliding joints (“TSJ1”, [2]) was considered, with the goal to estimate if this solution improves the performance as respect to rigidly attached typologies, also terms of economic benefits. The innovative system was conceived to improve the seismic response of the infills and to control the damage and the stability of the panels, being characterized by the presence of sliding joints that divide the infill into horizontal stripes and that are designed specifically to allow the relative in-plane movement of these stripes ([2]). Moreover, at the wall-frame interface, flexible joints limit the detrimental interaction of the infill with the surrounding RC frame (Figure 5). The unreinforced masonry of the infill is constructed with 25 cm thick vertically perforated lightweight clay units and 1 cm thick general-purpose mortar bed- and head-joints. The overall thickness was equal to 29 cm due to the plaster layer of 2.0 cm which is placed on both sides of the panel. The out-of-plane stability of the infill is ensured by properly designed steel “shear keys” attached to the column and by “C-shaped” clay units placed at the edges of the masonry panel. Further details on this innovative system are described in Morandi *et al.* ([2]) and Milanesi *et al.* ([6]).

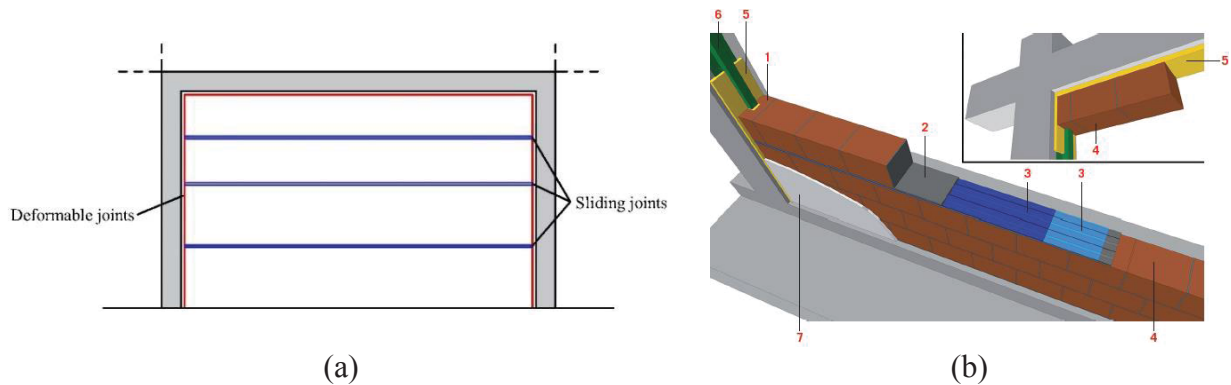


Figure 5. (a) Innovative masonry infill with sliding joints and deformable joints at the panel/frame interface; (b) Details of the innovative masonry infill with sliding joints: 1.C-shape units; 2. mortar bed-joints; 3. Sliding joints; 4. clay units; 5. interface joints; 6. shear keys; 7. plaster [2].

3.2 Seismic Hazard

In order to apply the same (scaled) ground motions to all the building models with different infill walls, there was the need to adopt an intensity measure metric capable to ensure consistency. For the purpose of the present work, the average spectral acceleration, $AvgSa$, introduced in Kohrangi *et al.* ([30],[31]), was assumed to be a good metric, defined as the mean of the log spectral accelerations (Sa) at a set of n periods of interest (Equation 2 from [31]):

$$AvgSa = [\prod_{i=1}^n Sa(T_i)]^{1/n} \quad (2)$$

This metric is considered a good predictor for both inter-story drift ratio and peak floor acceleration; moreover, its hazard can be evaluated using existing ground motion prediction equations.

Twenty ground acceleration time histories, for each of the ten levels of intensity-measure, were supposed to be sufficient for the purposes of the present study, giving sufficiently good estimation of the most probable response of the structure. Each ground motion, *GM*, had two perpendicular components (North-South and East-West); the one adopted in the analyses was the one with the highest value of spectral acceleration at $T=1$ second. Further information is reported in Rossi *et al.* ([8]).

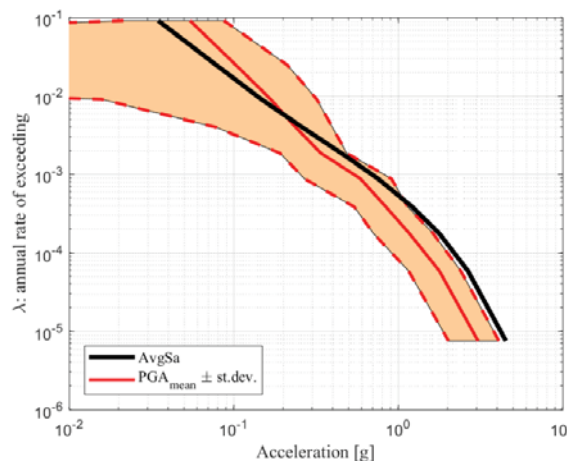


Figure 6. Seismic hazard curve.

4 STRUCTURAL PERFORMANCE

In order to evaluate the infill influence in the overall performance of the building, both nonlinear static and nonlinear dynamics analyses have been performed. The discrete selection of *IM* level, introduced previously, was adopted to perform a MSA (Multiple Stripe Analysis) ([32]). As aforementioned, the numerical models were considering only columns, beams and infill walls. The other non-structural elements were assumed to do not influence the structural behavior of the frame also in the case of the nonlinear time-history analyses.

The overall results reported in Figure 7 have demonstrated that the structural performance of the RC frames is strictly related to the structural performance of the typology of infill walls adopted. In particular, Figure 7a, shows the force-drift envelopes of the infill contribution only to the in-plane horizontal response. The dots indicate the thresholds of the three limit states of infill walls in terms of inter-storey drift, as defined by Morandi *et al.* ([33],[2]): operational limit state (OLS), damage limitation limit state (DLS) and life safety/ultimate limit state (LSS/ULS). In Figure 7b, the pushover curves of the buildings characterized by the presence of the four same infill typologies are shown. Also in this case, the dots show when the performance-level thresholds are exceeded by the infill walls.

The main results of the MSA are represented by the fragility curves of the infilled RC frames, which are reported in Figure 8.

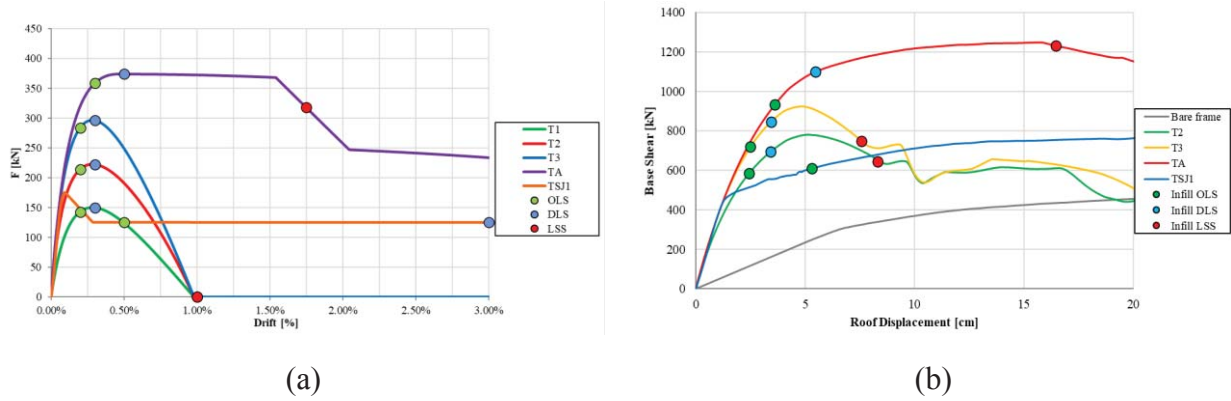


Figure 7. (a) Envelopes of the infill contributions; (b) Pushover curves.

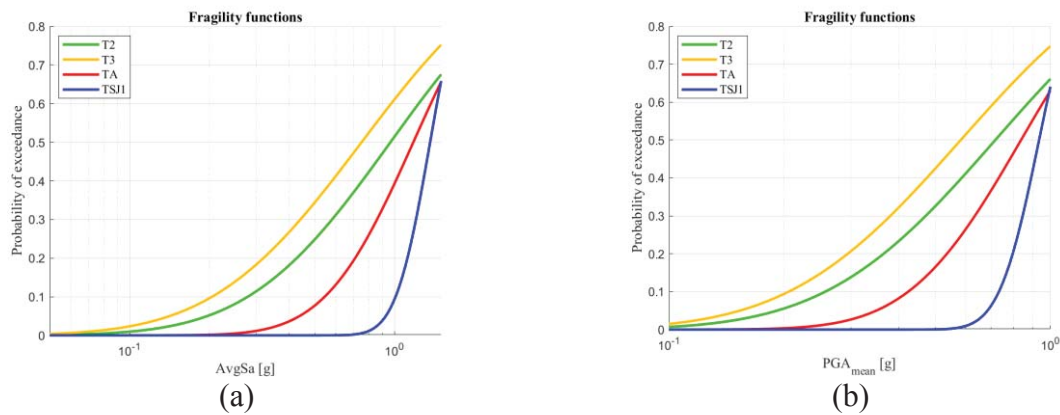


Figure 8. Global fragility function related to the collapse of the infilled frames, (a) nonlinear dynamic analyses; (b) nonlinear static analyses.

The fragility function related to the plane-frame with the innovative ductile infill system shows very small values of probability of exceedance till a value of $AvgSa$ of about $1g$, where the slope of the curve rapidly increases. In the range of ground motions with PGA similar to the design PGA , the adoption of the innovative infill solution leads to have a probability of collapse almost equal to zero. This result is quite encouraging, because it demonstrates that the adoption of this innovative infill, conceived with the purpose of limiting the damage in the infill, has also a beneficial influence on the overall in-plane seismic response of the structure.

A peculiarity of this work is the fact that the correlation between the level of damage in the infill walls and the inter-story drift (*i.e.*, the *EDP*: engineering demand parameter) was deterministic. Actually, this fact does not represent a limitation, because the *EDP*-damage relationship was inferred from full-scale in-plane cyclic tests on the same infill panels adopted in the analysis, with the same mechanical characteristics and aspect ratio.

5 MONETARY LOSSES

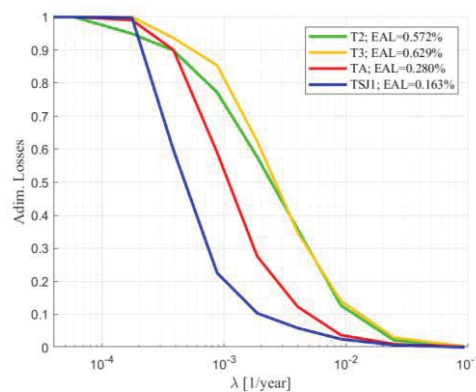
The results of the structural analyses have allowed the identification of specific values of damage, which can be therefore correlated with costs of repair/reconstruction. The consequence function specifically created for each vulnerable element ([8]), both structural and non-structural, have permitted to define the costs in accordance with the Public Works Price-list of 2020 ([34]) along with an engineering judgement. Table 2 resumes all the cost of construction and demolition for each of the aforementioned elements.

		T2	T3	TA	TSJ1
Structural elements	Foundation beam	21'008 €	21'008 €	21'008 €	21'008 €
	Columns & beams	31'111 €	31'111 €	31'111 €	31'111 €
Non structural elements	Infill panels IN PLANE	16'765 €	19'620 €	21'316 €	23'309 €
	Infill panels OOP (with thermal insulation)	20'366 €	23'222 €	24'917 €	26'910 €
	Floor slabs (roof included)	89'143 €	89'143 €	89'143 €	89'143 €
	Ceilings	17'833 €	17'833 €	17'833 €	17'833 €
	Pipings (hot and cold water)	73'109 €	73'109 €	73'109 €	73'109 €
	Internal glass door	6'915 €	6'915 €	6'915 €	6'915 €
	Sanitary, boilers and machines	50'000 €	50'000 €	50'000 €	50'000 €
	Partition walls	11'982 €	11'982 €	11'982 €	11'982 €
	Windows and doors	35'741 €	35'741 €	35'741 €	35'741 €
	Complete demolition	17'463 €	17'463 €	17'463 €	17'463 €
	Demolition + Building cost	391'437 €	397'148 €	400'539 €	404'525 €
	Building cost only	373'974 €	379'685 €	383'075 €	387'062 €
	Building cost / m ²	1'039 €	1'055 €	1'064 €	1'075 €

Table 2. Costs of demolition and complete reconstruction of all damageable elements.

Furthermore, the global vulnerability functions, related to each building with the four infill typologies, are shown in Figure 9. The costs have been evaluated through consequence functions specifically defined for each element. Further information is reported in Rossi *et al.* ([8]). The expected annual loss (EAL) of one building is the area under its vulnerability curve. In agreement with the previous results, the smallest value of EAL is the one of the RC frame with the innovative infill system (EAL=0.16%). This value is more than about 2 and 4 times smaller than the one of buildings with the TA (EAL=0.28%) and the T2-T3 (EAL=0.57%-0.63%) traditional infills, respectively. The return period of the investment has been found to be always less than 10 years (9 years for TA, 8 years for T2, and 4 years for T3). This period of time has been estimated without considering the risk of injuring and losing the life of people and without considering all the indirect costs and the downtime of the building, which would have furtherly decrease such time.

Finally, according to the Italian law DM 58 ([35]) which defines a method for a simplified classification of the seismic risk for constructions, the building with infill typologies T2 and T3 would lie in risk class A_{EAL}, whilst the building with infill typologies TA and TSJ1 in class A⁺_{EAL} (*i.e.*, the class with best performance).

Figure 9. Global vulnerability function relative to the frame structure (Rossi *et al.* ([8])).

6 CONCLUSIONS

Within the present work, a novel method to compute the annual losses has been adopted to compare the seismic performance of three different non-ductile rigidly attached masonry infills and an innovative ductile system with sliding joints [2]. The economic comparison, which has been conducted through nonlinear analyses on code-compliant RC frame structure, has demonstrated the influence of the infill typology in the computation of the expected annual loss (EAL). The choice of a particular infill typology, in a common RC frame structure, could strongly influence both the structural and economic performance of the building, despite the fact that they are assumed to be non-structural elements. The EAL has been calculated through a novel methodology presented by Rossi *et al.* ([8]) in accordance with PERR's PBEE procedure ([11],[12],[13],[14],[15]). In the computation, the influence of the non-structural elements that do not interfere with the seismic structural response has been considered *a-posteriori*.

The monetary losses relative to each building were compared. The loss analyses confirm that the adoption of an infill system conceived with the explicit intent to reduce the damage in the masonry panel, as the innovative solution proposed by researchers of Pavia ([2],[6]), should be preferred as respect to traditional infill solutions without any seismic detail. The initial investment, due to the higher cost of construction of a structure with the innovative infill solution, is paid back by the lower costs of repair in the case of seismic events.

Although the present work shows an updated picture of the situation, the ongoing research on ductile masonry infills with sliding joints (*e.g.*, about the local structure-panel interaction effects [36]), and the continuous development of new typologies of masonry infills (*e.g.*, [37],[38]), represent some of the future upgrades of the presented study.

ACKNOWLEDGEMENTS

The present study was carried out by the researchers of University of Pavia, Eucentre and IUSS, thanks to the project INSYSME "Innovative Systems for earthquake resistant Masonry Enclosures in rc buildings", grant FP7-SME-2013-2-GA606229, 2013-2016 and the Executive Project DPC-RELUIS 2013-2019. The financial support received is gratefully acknowledged. A particular acknowledgement is due to Prof. Paolo Bazzurro, who gave us precious suggestions and indicates possible future developments of this work.

REFERENCES

- [1] Di Trapani, F., Bolis, V., Basone, F., Preti, M., Seismic reliability and loss assessment of RC frame structures with traditional and innovative masonry infills. *Engineering Structures*, **208**, 110306, 2020.
- [2] Morandi, P., Milanesi, R.R., Magenes, G., Innovative solution for seismic-resistant masonry infills with sliding joints: in-plane experimental performance. *Engineering Structures*, **176**, 719-733, 2018.
- [3] Decanini, L. D., De Sortis, A., Goretti, A., Liberatore, L., Mollaioli, F., Bazzurro P., Performance of reinforced concrete buildings during the 2002 Molise, Italy, Earthquake, *Earthquake Spectra*, **20**(S1), S221-S255, 2004.
- [4] Pinto, A. V., Tsionis, G., Mola, E., Taucer, F., Preliminary Investigation of the Molise (Italy) Earthquakes of 31 October and 1 November 2002, *Bulletin of Earthquake Engineering*, **1**, 349-370, 2004.

- [5] Maffei, J., Bazzurro, P., The 2002 Molise, Italy, Earthquake, *Earthquake Spectra*, **20**(S1), S1-S22, 2004.
- [6] Milanesi R.R., Morandi P., Manzini C.F., Albanesi L., Magenes G., Out-of-plane response of an Innovative Masonry Infill with Sliding Joints from shaking table tests, *Journal of Earthquake Engineering*, doi: 10.1080/11632469.2020.1739173, 2020.
- [7] Manzini, C.F., Morandi, P., Milanesi, R.R., Magenes, G., Shaking-table test on a two-storey RC framed structured with innovative infills with sliding joints, *Proc. 16th ECEE*, Thessaloniki, Greece, 18-21 June 2018.
- [8] Rossi, A., Morandi, P., Magenes, G., A novel approach for the evaluation of the economical losses to seismic actions on RC buildings with masonry infills, *Soil Dynamics and Earthquake Engineering*, 145, 106722, doi 10.1016/j.soildyn.2021.106722, 2021.
- [9] Milanesi, R.R., Hemmat, M., Morandi, P., Totoev, Y., Rossi, A., Magenes, G., Modeling strategies of ductile masonry infills for the reduction of the seismic vulnerability of RC frames, *Frontiers in Built Environment*, **6**, doi: 10.3389/fbuil.2020.601215, 2020.
- [10] Bolis, V., Stavridis, A., Preti, M., Numerical Investigation of the In-Plane Performance of Masonry-Infilled RC Frames with Sliding Subpanels, *Journal of Structural Engineering*, **143**(2), 04016168. doi: 10.1061/(ASCE)ST.1943-541X.0001651, 2017.
- [11] Cornell, C.A., Krawinkler, H., Progress and challenges in seismic performance assessment, *PEER Cent News*, **3**, apps.peer.berkeley.edu/news/2000spring/performance.html, 2000.
- [12] Porter, K. A., An Overview of PEER's Performance-Based Earthquake Engineering Methodology, *Proc. 9th International Conference on Applications of Statistics and Probability in Civil Engineering*, San Francisco, California, USA, 2003.
- [13] Baker, J. W., Cornell, C. A., Uncertainty Specification and Propagation for Loss Estimation Using FOSM Methods, *PEER Report 2003/07*, Pacific Earthquake Engineering Research Center, College of Engineering, University of California, Berkeley, USA, 2003.
- [14] Krawinkler, H., Zareian, F., Medina, R. A., Ibarra, L. F., Decision support for conceptual performance-based design, *Earthquake Engineering and Structural Dynamics*, **35**, 115-133, DOI: 10.1002/eqe.536, 2006.
- [15] Haselton, C. B., Goulet, C. A., Mitrani-Reiser, J., Beck, J. L., Deierlein, G. G., Porter, K. A., Stewart, J. P., Taciroglu, E., An Assessment to Benchmark the Seismic Performance of a Code-Conforming Reinforced Concrete Moment-Frame Building, *PEER Report 2007/12*, Pacific Earthquake Engineering Research Center, College of Engineering, University of California, Berkeley, USA, 2008.
- [16] Rossi, A., Structural and Economic Performance of RC Buildings with Different Types and Configurations of Masonry Infills, *Doctoral Dissertation*, Scuola Universitaria Superiore IUSS Pavia, Italy, 2018.
- [17] Rossi A., Morandi P., Milanesi R.R., Magenes G., Economic and technical advantages of an innovative infill solution in the seismic response of RC buildings, *4th International Workshop on the Seismic Performance of Non-Structural Elements (SPONSE)*, Pavia, Italy, May 2019.

- [18] Preti, M., Bettini, N., Plizzari, G., Infill Walls with Sliding Joints to Limit Infill-Frame Seismic Interaction: Large-Scale Experimental Test, *Journal of Earthquake Engineering*, **16**(1), 125–141, 2012.
- [19] MIT, D.M. 14/01/2008 *Norme Tecniche per le Costruzioni (NTC08)* (in Italian), G.U., n. 29 14/02/2008 – Supplemento ordinario n.30, Roma, Italy, 2008.
- [20] CEN, *Eurocode 2 - Design of concrete structures, Part 1-1: General rules and rules for buildings*, ECS, EN 1992-1-1, Brussels, Belgium, 2004.
- [21] CEN, *Eurocode 8 - Design of structures for earthquake resistance - Part 1: General rules, seismic actions and rules for buildings*, ECS, EN 1998-1: 2004. Brussels, Belgium, 2004.
- [22] Hak S., Morandi P., Magenes G., Sullivan T. J., Damage Control for Clay Masonry Infills in the Design of RC Frame Structures, *Journal of Earthquake Engineering*, **16**(1), 1-35, doi:10.1080/13632469.2012.670575, 2012.
- [23] Carr, A.J., *Ruaumoko Manual*, University of Canterbury, Cristchurch, New Zealand, 2007.
- [24] Hak, S., Morandi, P., Magenes, G., Evaluation of infill strut properties based on in-plane cyclic tests, *Gravedinar*, **65**(6), 509-521, 2013.
- [25] Milanesi, R.R., Morandi, P., Magenes, G., Local effects on RC frames induced by AAC masonry infills through FEM simulation of in-plane tests, *Bulletin of Earthquake Engineering*, **16**, 4053-4080, 2018.
- [26] Morandi, P., Hak, S., Magenes, G., Simplified Out-of-plane Resistance Verification for Slender Clay Masonry Infills in RC Frames, *Proc. of XV ANIDIS Conference*, Padova, Italy, 30/06-4/07 2013.
- [27] Ricci, P., Di Domenico, M., Verderame, G.M., Experimental assessment of the in-plane/out-of-plane interaction in unreinforced masonry infill walls, *Engineering Structures*, **173**, 960-978, 2018.
- [28] Morandi, P., Hak, S., Milanesi, R.R., Magenes, G., In-plane/out-of-plane interaction of strong masonry infills: from cyclic tests to out-of-plane verifications. *Earthquake Engineering and Structural Dynamics*, under review, 2021.
- [29] da Porto, F., Donà, M., Verlato, N., Guidi, G., Experimental Testing and Numerical Modeling of Robust Unreinforced and Reinforced Clay Masonry Infill Walls, With and Without Openings, *Frontiers in Built Environment*, **6**, 591985, doi: 10.3389/fbuil.2020.591985, 2020.
- [30] Kohrangi, M., Bazzurro, P., Vamvatsilos, D., Conditional spectrum-based ground motion record selection using average spectral acceleration, *Earthquake Spectra*, **32**(3), 1507-1524, 2016.
- [31] Kohrangi, M., Bazzurro, P., Vamvatsilos, D., Spillatura, A., Vector and Scalar IMs in Structural Response Estimation, Part I: Hazard Analysis, *Earthquake Engineering and Structural Dynamics*, 2017.
- [32] Baker, J. W., Efficient Analytical Fragility Function Fitting Using Dynamic Structural Analysis, *Earthquake Spectra*, **31**(1), 579-599, 2015.

- [33] Morandi, P., Hak, S., Magenes, G., Performance-based interpretation of in-plane cyclic tests on RC frames with strong masonry infills, *Engineering Structures*, **156**, 503–521, <https://doi.org/10.1016/j.engstruct.2017.11.058>, 2018.
- [34] Public Works Pricelist, [2020] *Prezzario regionale delle opere pubbliche* (in Italian), Municipality of Milan and with the concert of the Interregional Provveditorato to Public Works of Lombardy and Emilia Romagna, Volumes 1.1, 1.2 and 2.1, 2020.
- [35] DM 58: *Decreto Ministeriale numero 58 del 28/02/2017* (in Italian): <http://www.mit.gov.it/normativa/decreto-ministeriale-numero-58-del-28022017>, 2017.
- [36] Milanesi, R.R., Bolis, V., Pelucco, S., Morandi, P., Magenes, G., Preti, M., Local effects due to the seismic interaction between innovative ductile masonry infills and RC elements, *Proc. COMPDYN 2021*, Athens, Greece, 27-30 June 2021.
- [37] Valluzzi, M.R., da Porto, F., Garbin, E., Panizza, M., Out-of-plane behaviour of infill masonry panels strengthened with composite materials, *Materials and structures*, **47**(12), 2131-2145, 2014.
- [38] Furtado, A., Rodrigues, H., Arêde, A., Melo, J., Varum, H., The use of textile reinforced mortar as a strengthening technique for the infill walls out-of-plane behaviour, *Composite Structures*, doi: <https://doi.org/10.1016/j.compstruct.2020.113029>, 2020.

LOCAL EFFECTS DUE TO THE SEISMIC INTERACTION BETWEEN INNOVATIVE DUCTILE MASONRY INFILLS AND RC ELEMENTS

Riccardo R. Milanesi¹, Valentino Bolis², Simone Pelucco², Paolo Morandi³,
Guido Magenes¹, Marco Preti²

¹ University of Pavia, D.I.C.Ar.
via Ferrata 3, 27100, Pavia (PV), Italy
riccardo.milanesi@unipv.it, guido.magenes@unipv.it

² University of Brescia, D.I.C.A.T.A.M.
via Branze 43, 25123, Brescia (BS), Italy
valentino.bolis@unibs.it, s.pelucco@unibs.it, marco.preti@unibs.it

³ Eucentre
via Ferrata 1, 27100, Pavia (PV), Italy
paolo.morandi@eucentre.it

Abstract

The seismic vulnerability of rigidly attached masonry infills has been repeatedly highlighted through post-event surveys, experimental and numerical studies. Although many innovative solutions have been proposed, especially in the last decades, many aspects of these systems are object of ongoing or future studies. The ductile infills with sliding joints have been currently investigated by different researchers starting from experimental tests and using the test outcomes to calibrate and create finite element models with the aim to perform parametric analysis and define the local and global interaction with the structure. Moreover, the innovative infills with sliding joints have shown a completely different in-plane behavior with respect to the non-ductile ones. Since the creation of the diagonal strut is avoided and the shear sliding mechanisms fostered in predefined sliding joints, the interaction between the masonry panel and the RC members represents novelty with respect to the “traditional” rigidly attached masonry solutions. Within the present paper the results of a numerical model calibrated according to in-plane experimental tests are presented and the local interaction between the RC structural member and the innovative ductile infill with sliding joints is discussed. The study adopts a validated finite element model approach to an experimental campaign that has never been simulated through detailed FEMs and compares the numerical results with the experimental results related to the local effects.

Keywords: Local effects, infill-frame interaction, innovative infills, ductile infills, sliding joints, fem modeling of infills.

1 INTRODUCTION

The seismic vulnerability of rigidly attached masonry infills, also called non-ductile infills, has been repeatedly highlighted through recent post-event surveys (*i.e.*, [1],[2],[3],[4]). Several problems have been observed such as the in-plane/out-of-plane interaction in the seismic response of these non-structural elements (Figure 1a), the global influence in the overall seismic behaviour of the structure and the structural damages caused by local interaction between the masonry panels and the structural members (Figure 1b). The seismic behaviour of non-ductile masonry infills has been studied also experimentally and numerically into many researches that had different goals such as, the infill/structural global interaction ([5],[6],[7]), the in-plane behaviour ([8],[9]), the out-of-plane response ([10],[11],[12]). The in-plane/out-of-plane interaction ([13],[14],[15]), the economic evaluation of the expected annual losses ([16],[17]) and the local interaction between the infill and the structural members ([18],[19],[20]) as, for example, shown in Figure 2, were investigated as well.



Figure 1: (a) Infill damage and collapse due to in-plane and out-of-plane behaviour during the Central Italy earthquake 2016 ([3]), (b) Focus on the local damages on RC members due to the infill-structure local interaction ([2]).

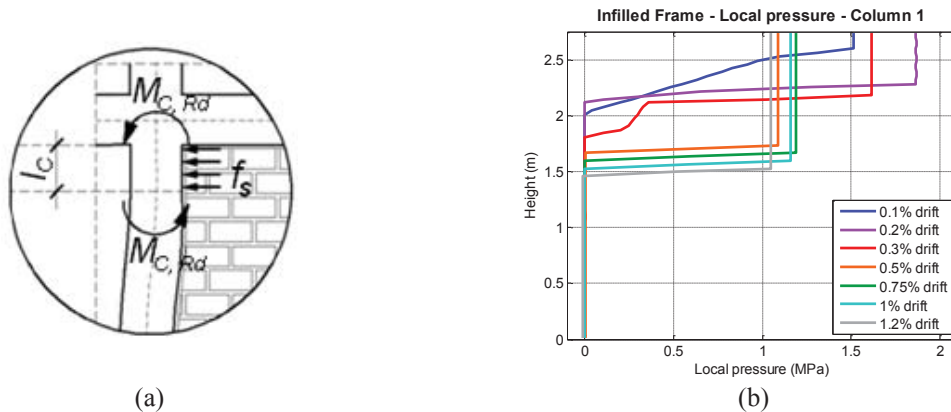


Figure 2: (a) Local effects on a non-ductile infill to the adjacent column ([20]); (b) Example of local pressure at different drift on the RC columns due to the presence of a non-ductile infill made of AAC units ([20]).

The aforementioned issues have recently encouraged the research and the industry in developing innovative infills that can be generally classified into three categories: the enhanced infills ([21],[22],[23],[24]), the panels uncoupled from the frame ([25],[26]) and the ductile infills ([27],[28],[29],[30],[31]). The latter innovative infill typology, that has been recently proposed and studied both experimentally and numerically, is object of ongoing and future studies. The infill with sliding joints, which are investigated in this work, are classified as ductile infills. The innovative infills with sliding joints have shown a completely different in-plane behaviour with

respect to the non-ductile ones [32]. Since the creation of the diagonal strut is avoided and the shear sliding mechanisms fostered in predefined sliding joints, the interaction between the masonry panel and the RC members represents a novelty with respect to the “traditional” rigidly attached masonry solutions.

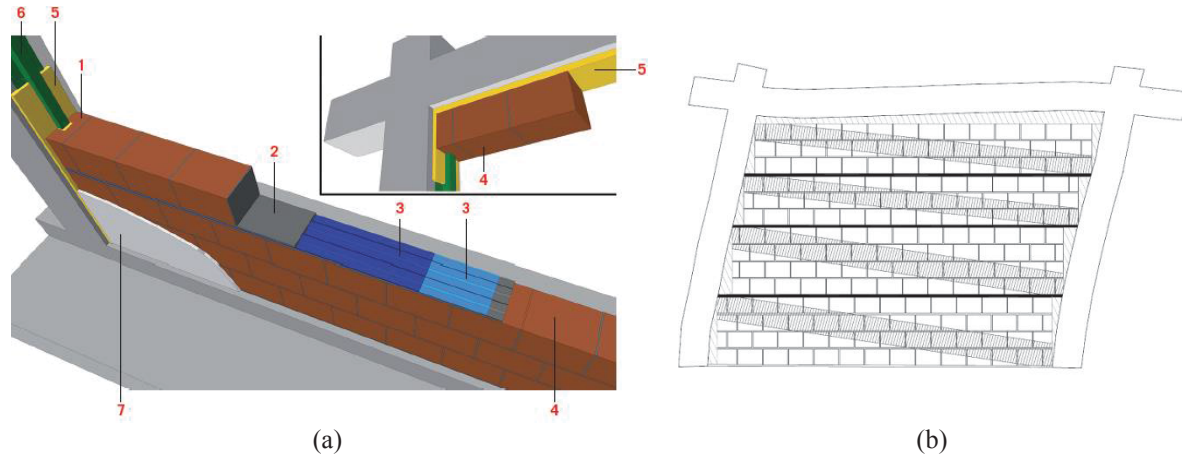


Figure 3: (a) Details of the innovative masonry infill with sliding joints: 1. C-shape units; 2. mortar bed-joints; 3. sliding joints; 4. clay units; 5. interface joints; 6. shear keys; 7. plaster ([28],[29]); (b) Idealization of the compressed strut in the case of ductile infill with sliding joints ([28]).

Within the present paper the results of a numerical model calibrated according to in-plane experimental tests are presented and the local interaction between the reinforced concrete structural member and the innovative ductile infill with sliding joints is discussed. The study adopts a validated finite element model approach ([33]) extended to an experimental campaign ([28]) that has never been simulated through detailed FEMs and compares the numerical results with the experimental ones related to the local effects.

2 SPECIMEN DESCRIPTION AND INSTRUMENTATION

At the Department of Civil Engineering and Architecture and at the Eucentre Foundation, within the European FP7 “INSYSME” project, a ductile seismic resistant masonry infill with sliding-joints ([28] and [29]) with original details has been conceived, based on the conceptual design proposed in Preti *et al.* [34]. The engineered system reduces the interaction between the structure and the infill in the in-plane direction by facilitating the shear-sliding damage in specific previously designed elements corresponding to the sliding joints. The infill is subdivided into four horizontal subpanels that can mutually slide through properly conformed sliding joints. Moreover, the interface between the masonry subpanels and the reinforced concrete is filled with a deformable mortar to decrease the stress concentration. The unreinforced masonry used in the subpanels of the infill is realized with vertically perforated lightweight clay units and general-purpose 1 cm thick mortar bed- and head-joints.

The reference experimental campaign has included test on characterization on every material (concrete, reinforcement, mortar, clay units and masonry), in-plane pseudo-static cyclic tests (called IPL) on fully and partially infilled (with a central opening) full scale one-storey one-bay reinforced concrete frames. The infill without opening has been tested also at “high-velocity” (called IPH) to study the behaviour of the sliding joints subjected to dynamic actions. Subsequently, the same specimens have been tested dynamically out-of-plane on a shaking table to investigate the out-of-plane response. Finally, a dynamic test on a shaking table on a prototype 2-storeys 5-bays building has been carried out. The in-plane response is presented by Morandi

et al. [28], the out-of-plane experimental behaviour is discussed in Milanesi *et al.* [29], whereas the building test is presented in Manzini *et al.* [35].

The full infill, named TSJ1, had a length of 4.22 m and a height of 2.95 m, and the reinforced concrete members have a square section with base/height of 35 cm (Figure 4). The specimen design, that aimed to represent a part of a realistic full-scale reinforced frame structure, is detailed in other works ([9] and [28]).

The experimental displacements and deformations occurred during the in-plane tests have been measured through 45 displacement transducers (linear potentiometers) (Figure 5a). The ones numerated between 30 and 44 are located at the panel/column interface to measure the compression of the deformable mortar joint or the detachment of the subpanel with the reinforced concrete column (Figure 5b). Each subpanel has 2 potentiometers for each masonry/column interface, being one at the top and the other at the bottom of the subpanel.

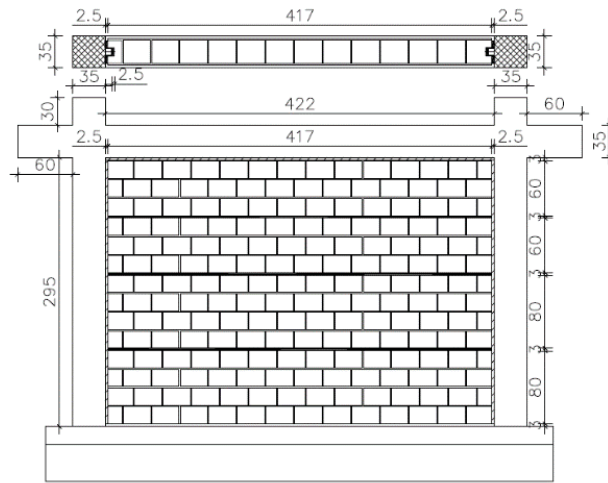


Figure 4: Layout of the fully infilled specimen represented without plaster ([28]).

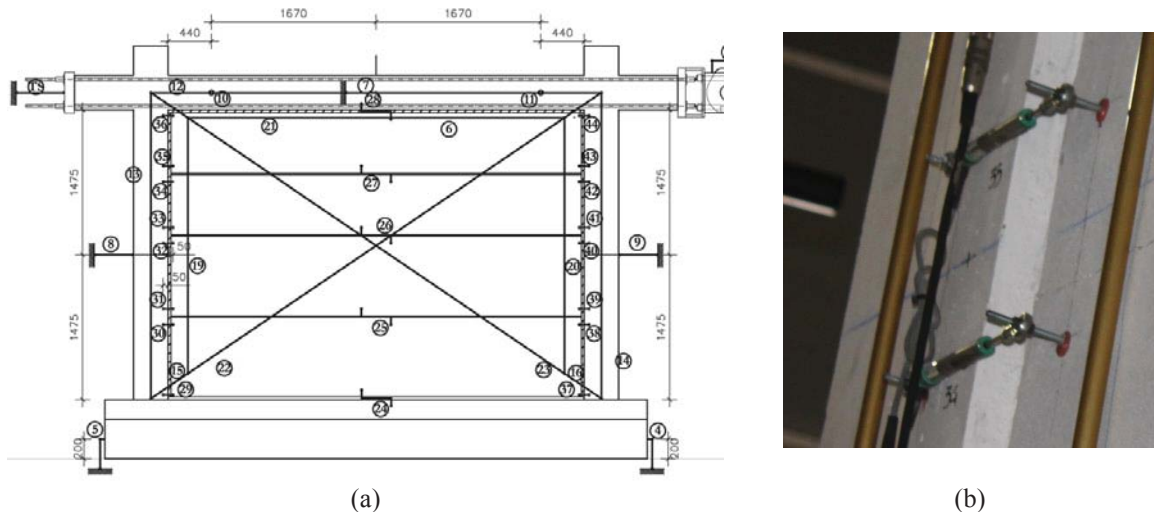


Figure 5: (a) Sketch of the linear potentiometer installed in the specimen during the in-plane cyclic test; (b) Detail of the potentiometer 34 and 35 installed to monitor the subpanel/column local interaction.

3 EXPERIMENTAL RESULTS

The force-displacement hysteretic curves and the corresponding envelopes for each cycle of the fully infilled configuration (TSJ1) are reported in Figure 6a, whereas the results of the bare frame specimen (called TNT) are shown in Figure 6b. The TNT specimen has been taken as

reference for a proper evaluation of the infill contribution and it has been tested in a previous experimental campaign ([9]).

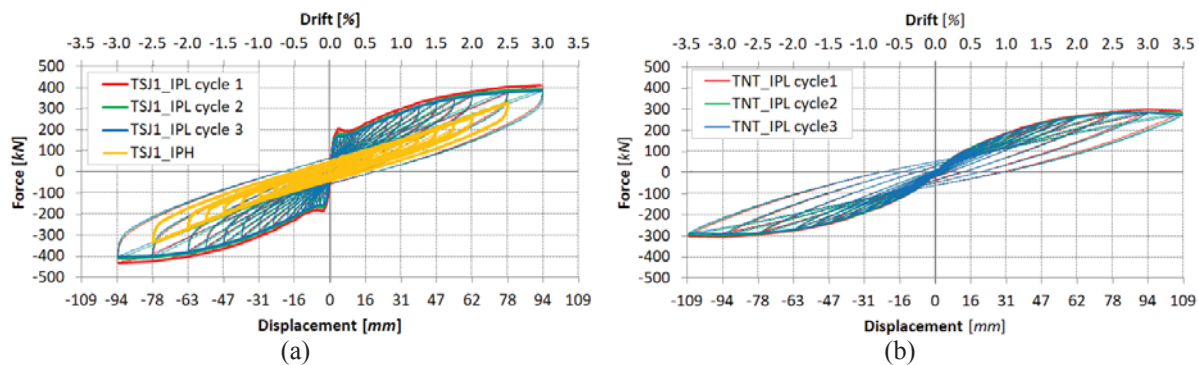


Figure 6: Experimental force-displacement cyclic and envelopes curves of (a) specimen TSJ1, fully infilled and (b) bare frame.

The damage related to the in-plane tests, which is detailed in Morandi *et al.* [28], can be summarized to horizontal cracks corresponding to the sliding mechanism of the sliding joints starting from low levels of drift (from 0.20%), sub-horizontal flexural and light diagonal cracks in the upper and bottom part of the reinforced concrete columns due to the in-plane deformation of the structural frame (at about 1.00-1.25%), detachment of small area of plaster in corner of the subpanels (2.00%) and spalling of the concrete cover at the bottom of the columns (3.00%). At the subpanel/column interface, the occurrence of the sliding mechanism in the engineered sliding joints has created a contact area and a detached portion for every subpanel due to the deformation of the reinforced concrete frame respect to the infill (Figure 7).

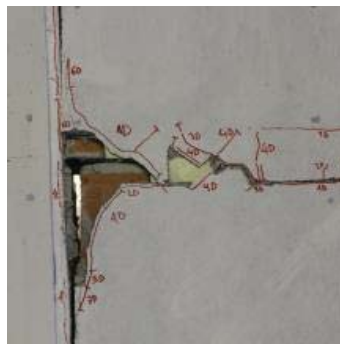


Figure 7: Focus of the masonry/column interface joint at the max imposed in-plane drift of 3.00%.

As aforementioned, the experimental campaign has included also a comprehensive mechanical characterization of the materials. The masonry has been therefore characterized through vertical, horizontal, and diagonal compressive strength tests, flexural pure bending tests, and tests on triplets to determine the initial shear resistance and the friction coefficient of the mortar bed-joints and the sliding joints. All tests of characterization on masonry have been conducted on specimens with and without plaster in order to evaluate its influence for each resistance. In the present work only the horizontal compressive resistance of the masonry (Figure 8a) and the shear tests on masonry triplets to characterize the cohesion and the friction coefficient of the mortar bed-joints and the sliding joints (Figure 8b) have been considered.

Figure 8c reports the results of the triplet tests on masonry for the sliding joints, for the mortar bed-joint with and without plaster. The stress-strain curve obtained from the horizontal compressive tests is reported in Figure 12b.

Furthermore, the deformable interface mortar (called “deformable mortar” in the following) placed between the masonry subpanels and the structural member has been characterized in several ways: by testing mortar prisms in compression (Figure 9a), mortar pads (Figure 9b) to investigate the influence of the dimension and by replicating the whole interface region also including the steel omega element and the C-shape clay unit (Figure 9c). The results, that are reported in Figure 13a, highlight the lack of a common curve and the necessity to make some assumption regarding the compressive behaviour of this material.

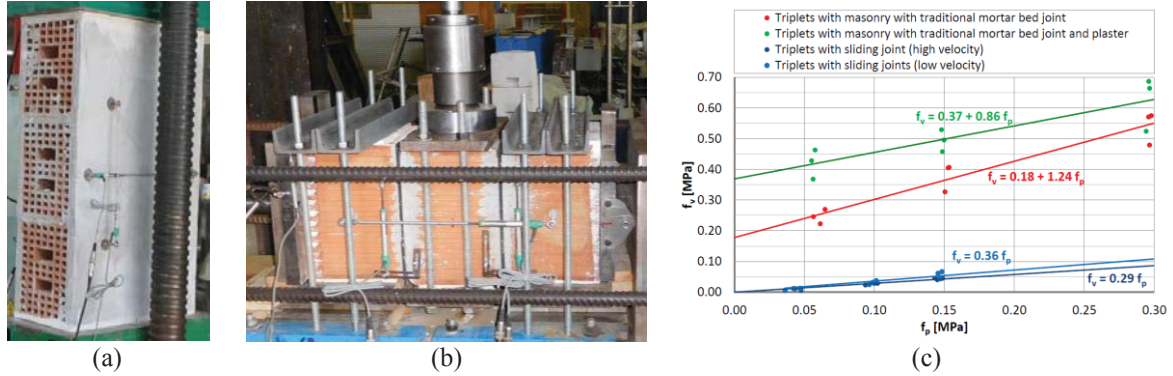


Figure 8: Picture of the tests of characterization to determine the (a) horizontal resistance of the masonry, (b) friction coefficient of the sliding joints. (c) Results of the initial shear resistance of the masonry triplets.

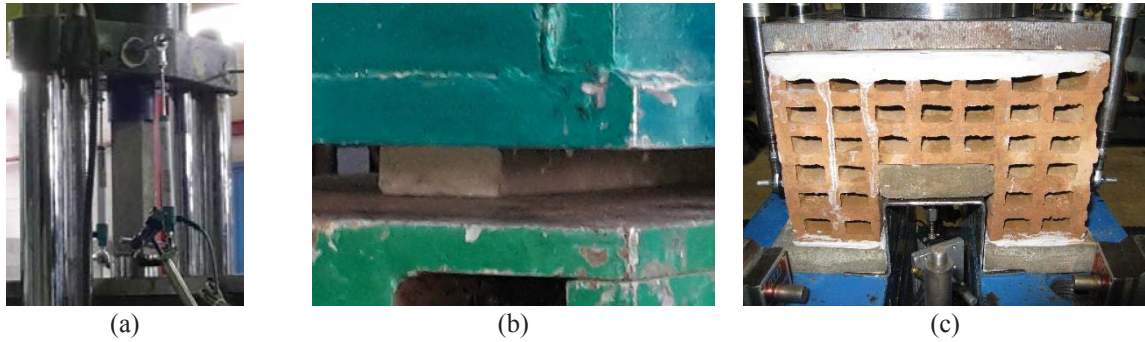


Figure 9: Picture of the tests of characterization for the deformable mortar at the panel/frame interface (a) test on mortar prism; (b) test on mortar pad; (c) replication of the whole contact system.

4 MODELING DESCRIPTION

The modelling technique here adopted to interpret the test response is based on the approach proposed in several studies ([36][37],[38]) and specified for sliding joint infill in Bolis *et al.* ([33]). The specific configuration of the infill with sliding joints and the layer of deformable mortar interposed at the frame to masonry interface, is modelled with interface and smeared-crack elements, respectively. For the specific specimen under consideration here, the deformable mortar is modelled assuming a simplified linear response calibrated on the mechanical characterization tests.

The model is a two-dimensional plane-stress finite element model implemented using the FEAP ([39]) environment.

The modelling scheme of reinforced concrete columns, beam members and masonry infill ([38]) are reported in Figure 10. The sliding joints are modelled using interface elements; the lateral deformable mortar joints are simulated using a smeared-crack element directly connected to the nearest reinforced concrete member on one side and through an interface element to the adjoining masonry subpanel. Unlike the model proposed in Bolis *et al.* ([33]) the base

joint is modelled like the horizontal mortar joints and the top deformable mortar joint between the masonry infill and the beam is modelled like the lateral vertical joints (Figure 11).

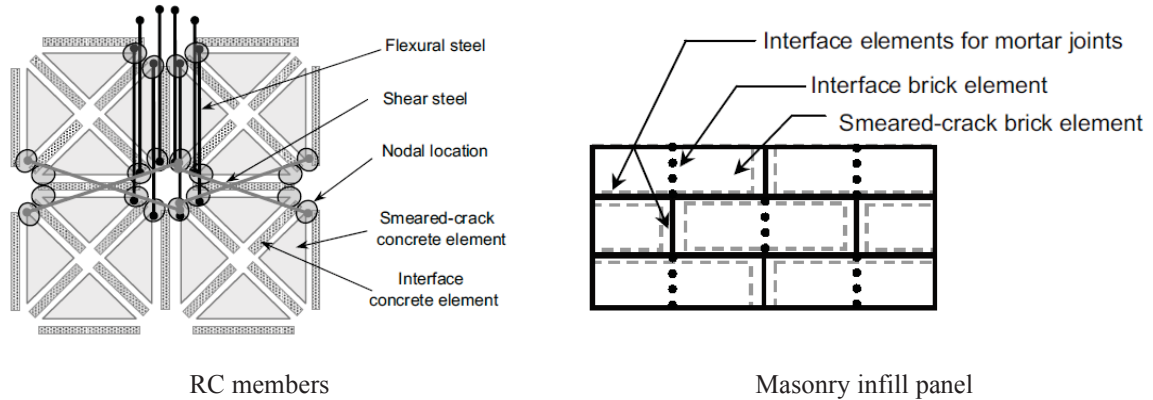


Figure 10: Finite element discretization reprinted from Stavridis and Shing ([38]).

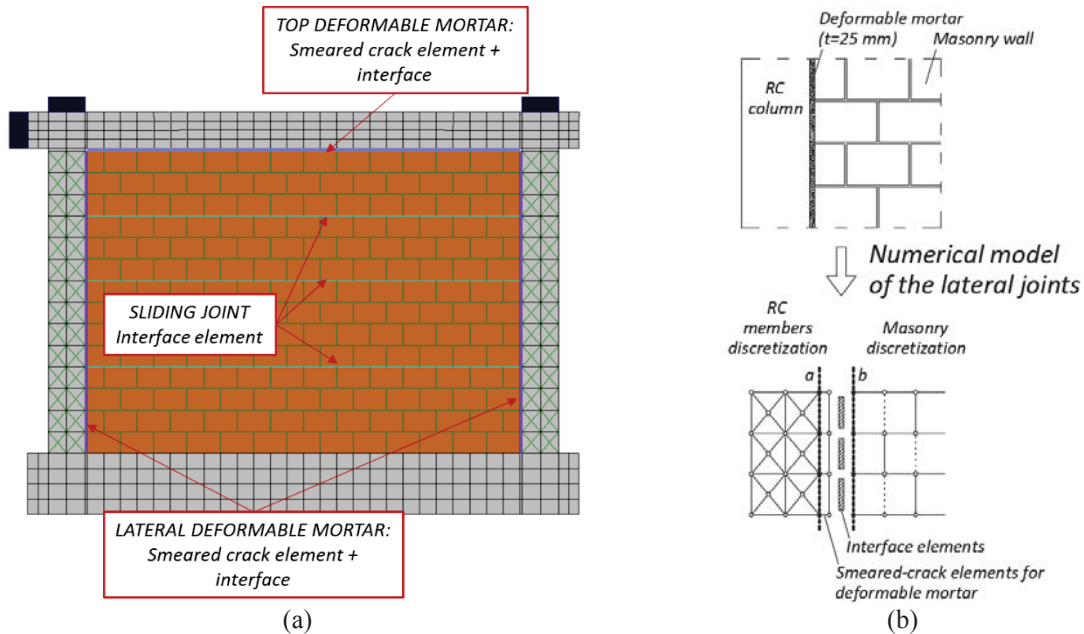


Figure 11: (a) Infill frame mesh and detail of the sliding and contact joints; (b) detail of the contact joint modeling

4.1 Parameter calibration

The model parameters are calibrated as proposed in Stavridis and Shing ([38]) and Bolis *et al.* ([33]), referring to experimental tests performed on subassembly and to literature references. The main parameters are reported in Table 1 and Table 2.

Material	SMEARED-CRACK ELEMENTS					
	E [MPa]	G [MPa]	ν [-]	t [mm]	f_c [MPa]	f_t [MPa]
Concrete	25000	10417	0.20	350	37	1
Masonry	2600	1150	0.13	250	2.9	0.6
Deformable Mortar top	5	2	0.38	100	10.0	2.0
Deformable Mortar lateral	8	2.9	0.38	250	10.0	2.0

Table 1: Main parameters adopted for the smeared-crack elements.

The comparison between the numerical and experimental results of the main calibration tests are reported in the following Figure 12 and Figure 13.

Lateral and top deformable mortar joints are modelled using smeared-crack elements calibrated to have an elastic behaviour in the range of deformation of interest. The elastic modulus of the lateral deformable mortar is calibrated to obtain a stress strain curve secant to the experimental one in the range of strain of 15-20%, which corresponds to the peak strain level measured in the experiment on the infilled frame structure at drift level of about 2.0%. In Figure 13a is reported the comparison between the assumed elastic curve and the experimental stress-strain ones obtained in the characterization tests. A similar approach is adopted for the top deformable mortar, accounting for a lower strain demand during the test.

The interface elements representing the sliding joints are calibrated fitting the residual yield surface to the experimental results. The initial yield surface is obtained by shifting upward the residual one calibrated to the test of the only sliding joint to consider the effect of the reduced plaster thickness at the sliding joint location.

Material	INTERFACE ELEMENTS					
	s_0 [MPa]	μ_0 [-]	μ_r [-]	r_0 [MPa]	r_r [MPa]	t [mm]
Bed joints	0.45	0.88	0.75	0.005	0.005	250
Brick head joints	0.70	1.00	0.80	0.28	0.21	250
Mortar vertical joints	0.90	0.862	0.75	0.005	0.005	250
Concrete joints	1.00	0.90	0.70	0.25	0.20	350
Lateral joints	0.05	0.50	0.45	0.10	0.10	250
Top joint	0.05	0.25	0.20	0.10	0.10	250
Sliding joints	0.15	0.361	0.361	0.02	0.02	250

Table 2: Main parameters adopted for the interface elements.

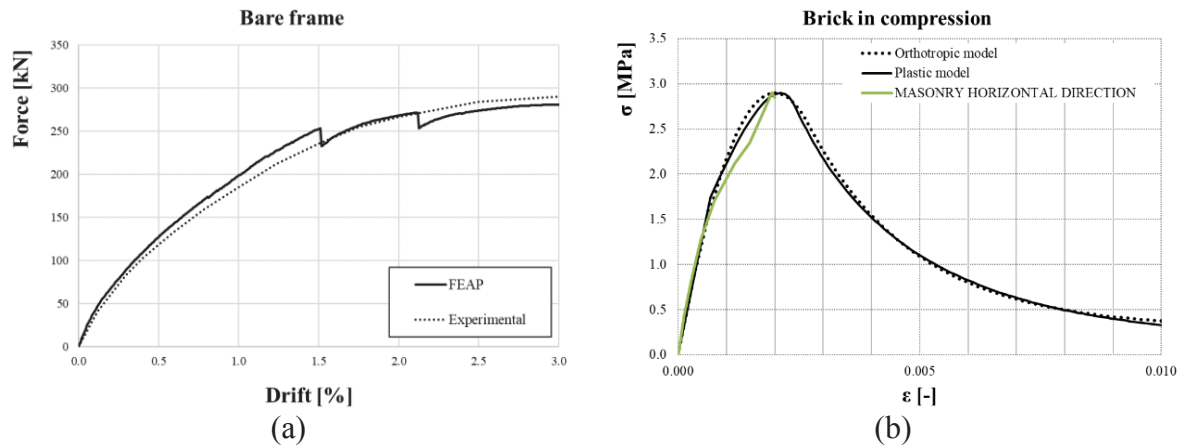


Figure 12: (a) Numerical and experimental results for bare frame; (b) Comparison of experimental test of characterization and numerical simulation of the stress-strain response of the masonry in the horizontal direction.

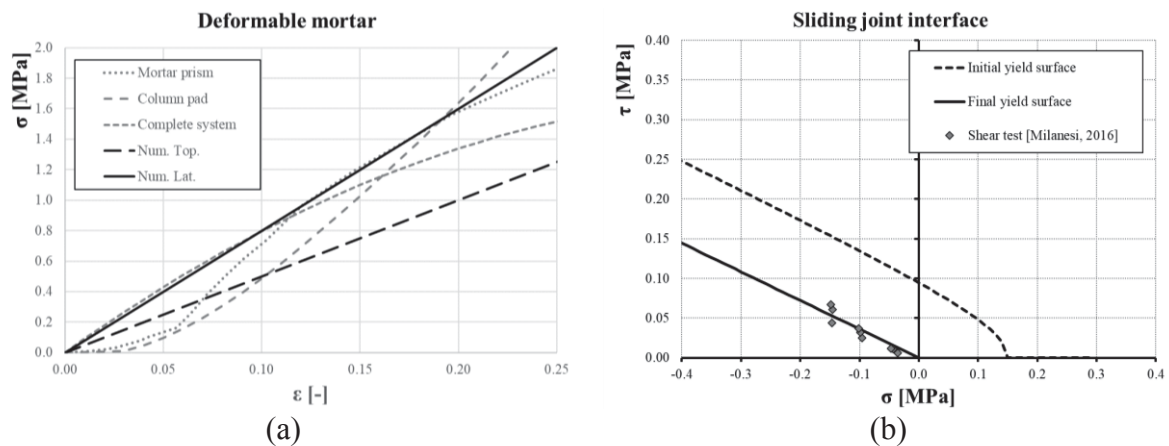


Figure 13: (a) Comparison of the stress-strain experimental response of deformable mortar test and the elastic model adopted in the numerical model; (b) Comparison of the shear stress–compressive stress experimental response and the numerical model adopted.

5 NUMERICAL AND EXPERIMENTAL RESULTS COMPARISON

5.1 Global behavior

In Figure 14 the monotonical hysteresis is reported in terms of force applied at the top of the frame versus the displacement for both positive and negative in-plane loading, for experimental and numerical results. The experimental curve considered is the envelope of positive (push) and negative (pull) displacements of the cyclic tests conducted. Given the symmetry of the model the same numerical behaviour is considered for each load direction.

In both direction of loading the initial stiffness is well captured, whereas the initial peak of resistance is slightly underestimated, probably due to the uncertainties in the evaluation of the reduced thickness of the plaster over the sliding joints. As the drift increases, the horizontal joints start sliding and the behaviour exhibits a stiffness decay. The peak resistance reached in the simulation is slightly higher than the experimental ones, with an overestimation lower than 10% and more evident in the positive direction.

The quality of the numerical simulation can be better evaluated by focusing on the local response of the masonry/column deformable mortar joints shown in Figure 15.

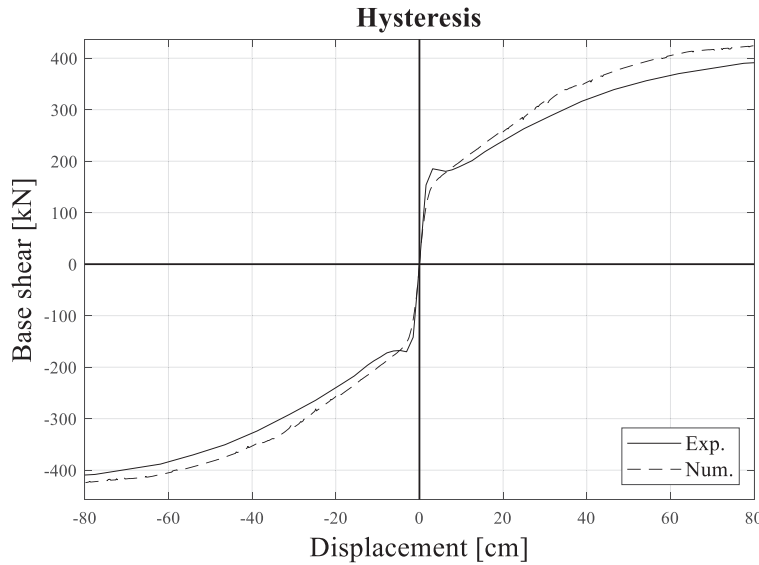


Figure 14: Experimental and numerical hysteresis.

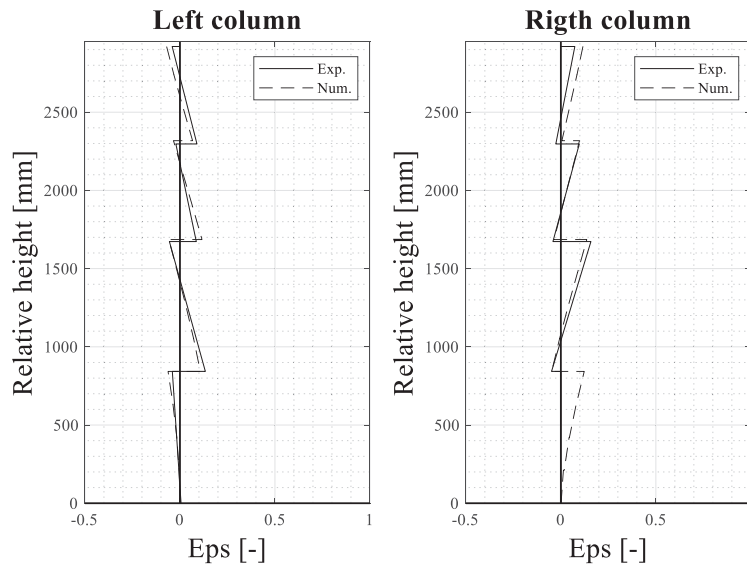
5.2 Local behavior

The comparison between experimental and numerical local deformation of the lateral joints along the frame height is herein presented. Given that the masonry is two order of magnitude stiffer than the deformable mortar, therefore, the local experimental deformations are estimated assuming that the displacement read by the potentiometer is localized in the deformable mortar joint only. The ratio between the displacement output and the thickness of the interface mortar joint, equal to 25 mm, has been assumed as the experimental strain of the deformable material. Since there are two potentiometers for each subpanel, the deformation profile of each of them is obtained considering the line interpolating the two values.

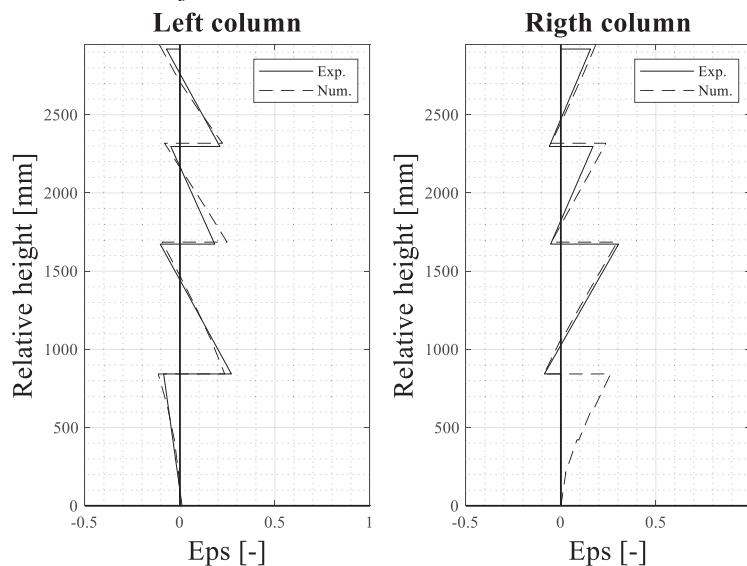
Numerically, the deformation profile is obtained directly from the difference of displacement between the masonry node and the concrete node near the lateral joints (alignment “a” and “b” in Figure 11).

It is important noting that the profile given represents the average strain in the lateral joint and it is not the specific deformation of the mortar. However, it can be assumed as an acceptable estimation of the compression strain level.

For all drift level the compression area is well captured. At 2.00% of drift the maximum compressive strain is approximately equal to 20‰, confirming the strain level considered for the deformable mortar elastic modulus calibration.



Lateral joints deformation for each column at 0.5% Drift



Lateral joints deformation for each column at 1.0% Drift

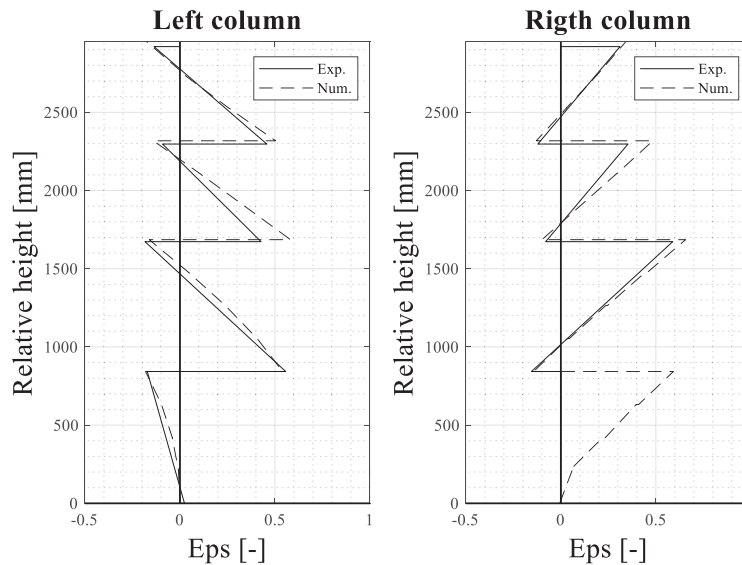


Figure 15: Lateral joint deformation for each column at different levels of drifts.

6 CONCLUSIONS

The recent outcomes from different post-seismic inspections and experimental and numerical studies on infills have identified many issues on non-ductile rigidly attached masonry infills. Three categories of innovative solutions have been proposed to improve the seismic response of these non-structural elements, being the ductile infills with sliding or deformable joints the latest respect to the others that aim to enhance the masonry and to uncouple the panel from the structure. The innovative ductile infill system with sliding joints is object of ongoing and future investigation to improve the knowledge about this new infill typology.

The experimental tests summarized in the present work ([28]) have been integrated with a detailed finite element model that has been previously adopted for a similar infill ([27],[33]). The model is a two-dimensional plane-stress finite element model implemented using the FEAP ([39]) environment. The results of the numerical simulation of the experimental in-plane test on the fully infilled solution has shown the capability of the model to capture both the overall behaviour and the local deformation located in the deformable mortar at the masonry/column interface. Moreover, one future development of the present study will be the computation of the local forces that occur in every subpanel/column contact area starting from the strain plots of the interface deformable mortar discussed herein.

Finally, the experimental evidence and the numerical results highlight the different in-plane behaviour of the infill typology and their new local interaction with the structure respect to non-ductile “traditional” systems, therefore new design provisions for the shear verification of the structural members could represent another future development of the present study.

ACKNOWLEDGEMENT

The experimental campaign presented in this work has been conducted thanks to the financial support of the European Commission within the project INSYSME “INnovative SYStems for earthquake resistant Masonry Enclosures in rc buildings”, grant FP7-SME-2013-2-GA606229, 2013-2016 is acknowledged. ANDIL and its associated companies, and RUREDIL spa are gratefully acknowledged as industrial partners of the INSYSME project, where the University of Pavia has also been partner. The contribution of Capaccioli srl for the supply of the sliding joints is acknowledged. The numerical part and the study of the local effects have been

whereas conducted within the framework of DPC/ReLUIS project 2019-2021, WP10, where both the University of Pavia and the University of Brescia are involved.

REFERENCES

- [1] Manzini, C.F., Morandi, P., 2012. Rapporto preliminare sulle prestazioni ed i danneggiamenti agli edifici in muratura portante moderni a seguito degli eventi sismici emiliani del 2012 (in Italian), Eucentre, www.eqclearinghouse.org/2012-05-20-italy/.
- [2] Parisi F., De Luca F., Petruzzelli F., De Risi R., Chioccarelli E., Iervolino I., 2012. *Field inspection after the May 20th and 29th 2012 Emilia-Romagna earthquakes*, available at <http://www.reluis.it>.
- [3] Fragomeli, A., Galasco, A., Graziotti, F., Guerrini, G., Kallioras, S., Magenes, G., Malomo, D., Mandirola, M., Manzini, C.F., Marchesi, B., Milanesi, R.R., Morandi, P., Penna, A., Rossi, A., Rosti, A., Rota, M., Senaldi, I., Tomassetti, U., Cattari, S., da Porto, F., Sorrentino, L., 2017. Comportamento degli edifici in muratura nella sequenza sismica dell'Italia centrale del 2016 – Parte 1: Quadro generale (in Italian), *Progettazione sismica*, **8**(2), 49-77.
- [4] Fikri, R., Dizhur, D., Walsh, K., Ingham, J., 2019. Seismic performance of Reinforced Concrete Frame with Masonry Infill buildings in the 2010/2011 Canterbury, New Zealand earthquake, *Bulletin of Earthquake Engineering*, **17**, 737-757.
- [5] Fiore, A., Netti, A., Monaco, P., 2012. The influence of masonry infill on the seismic behaviour of RC frame buildings. *Engineering Structures*, **44**, 133-145.
- [6] Ricci, P., De Risi, M.T., Verderame, G.M., Manfredi G., 2013. Influence of infill distribution and design typology on seismic performance of low- and mid-rise RC buildings, *Bulletin of Earthquake Engineering*, **11**, 1585-1616
- [7] Pantò, B., Calì, I., Lourenço, P.B., 2017. Seismic safety evaluation of reinforced concrete masonry infilled frames using macro modelling approach, *Bulletin of Earthquake Engineering*, **15**, 3871-3895.
- [8] Mehrabi, A.b., Shing, P.B., 1997. Finite element modeling of masonry-infilled RC frames, *Journal of Structural Engineering*, **123**(5), 604-613.
- [9] Morandi, P., Hak, S., Magenes, G., 2018. Performance-based interpretation of in-plane cyclic tests on RC frames with strong masonry infills, *Engineering Structures*, **155**, 503-521.
- [10] Abrams, D.P., Angel, R., Uzarski, J., 1996. Out-of-plane strength of unreinforced masonry infill panels, *Earthquake Spectra*, **12**(4): 825-844.
- [11] Palieraki, V., Zeri, C., Vintzileou, E., Adami, C.E., 2018. In-plane and out-of-plane response of currently constructed masonry infills, *Engineering Structures*, **177**, 103-116.
- [12] Milanesi, R.R., Morandi, P., Hak, S., Magenes, G., 2021. A new prospective towards out-of-plane verifications of URM infills, *Proc. 14th Canadian Masonry Symposium*, 16-19 May 2021, Montreal, Canada.
- [13] Calvi, G.M., Bolognini, D., 2001. Seismic response of RC frames infilled with weakly reinforced masonry panels, *Journal of Earthquake Engineering*, **5**(2), 153-185.

- [14] Di Trapani, F., Shing, P.B., Cavaleri, L., 2017. Macroelement model for in-plane and out-of-plane responses of masonry infills in frame structures, *Journal of Structural Engineering*, **144**(2):04017198.
- [15] Ricci, P., Di Domenico, M., Verderame, G.M., 2020. Effects of the in-plane/out-of-plane interaction in URM infills on the seismic performance of RC buildings designed to Eurocodes, *Journal of Earthquake Engineering*, DOI: 10.1080/13632469.2020.1733137
- [16] Di Trapani, F., Bolis, V., Basone, F., Preti, M., 2020. Seismic reliability and loss assessment of RC frame structures with traditional and innovative masonry infills. *Engineering Structures*, **208**, 110306, 2020.
- [17] Rossi, A., Morandi, P., R.R., Magenes, G., 2021. A novel approach for the evaluation of the economical losses to seismic actions on RC buildings with masonry infills, *Soil Dynamics and Earthquake Engineering*, 145, 106722, doi 10.1016/j.soildyn.2021.106722.
- [18] Crisafulli, F.J., Carr, A.J., Park, R., 2000. Analytical Modeling of Infilled Frame Structures - A General Review, *Bulletin of the New Zealand Society for Earthquake Engineering*, **33**.
- [19] Cavaleri, L., Di Trapani, G., 2015. Prediction of the additional shear action on frame members due to infills. *Bulletin of Earthquake Engineering*, **13**, 1425-1454.
- [20] Milanesi, R.R., Morandi, P., Magenes, G., 2018. Local effects on RC frames induced by AAC masonry infills through FEM simulation of in-plane tests, *Bulletin of Earthquake Engineering*, **16**, 4053-4080.
- [21] Valluzzi, M.R., da Porto, F., Garbin, E., Panizza, M., 2014. Out-of-plane behaviour of infill masonry panels strengthened with composite materials, *Materials and structures*, **47**(12), 2131-2145.
- [22] Verderame, G.M., Balsamo, A., Ricci, P., Di Domenico, M., Maddaloni, G., 2019. Experimental assessment of the out-of-plane response of strengthened one-way spanning masonry infill walls, *Composite Structures*, **230**, 111503.
- [23] Pohoryles, D.A., Bournas, D.A., 2020. Seismic retrofit of infilled Rc frames with textile reinforced mortars: state-of-the-art review and analytical modelling, *Composites Part B*, **183**, 107702.
- [24] Furtado, A., Rodrigues, H., Arêde, A., Melo, J., Varum, H., 2020, The use of textile reinforced mortar as a strengthening technique for the infill walls out-of-plane behaviour, *Composite Structures*, doi: <https://doi.org/10.1016/j.compstruct.2020.113029>
- [25] Marinkovic, M., Butenweg, C., 2019. Innovative decoupling system for the seismic protection of masonry infill walls in reinforced concrete frames, *Engineering Structures*, **197**, 109435.
- [26] Binici, B., Canbay, E., Aldermir, A., Demirel, I.O., Uzgan, U., Eryurtlu, Z., Bulbul, K., Yakut, A., 2019. Seismic behaviour and improvement of autoclaved aerated concrete infill walls, *Engineering Structures*, **193**, 68-81.
- [27] Preti, M., Bettini, N., Plizzari, G., 2012. Infill Walls with Sliding Joints to Limit Infill-Frame Seismic Interaction: Large-Scale Experimental Test, *Journal of Earthquake Engineering*, **16**(1), 125–141.

- [28] Morandi, P., Milanesi, R.R., Magenes, G., 2018. Innovative solution for seismic-resistant masonry infills with sliding joints: in-plane experimental performance, *Engineering Structures*, **176**, 719-733.
- [29] Milanesi, R.R., Morandi, P., Manzini, C.F., Albanesi, L., Magenes, G., 2020. Out-of-plane response of an innovative masonry infill with sliding joints from shaking table tests. *Journal of Earthquake Engineering*. DOI: 10.1080/11632469.2020.1739173.
- [30] Cheng, X., Zou, Z., Zhu, Z., Zhai, S., Yuan, S., Mo, Y., Chen, W., He, J., 2020. A new construction technology suitable for frame partitioned infill walls with sliding nodes and large openings: test results, *Construction and Building Materials*, **258**, 119644.
- [31] Totoev, Y.Z., Al Harthy, A., 2016. Semi interlocking masonry as infill wall system for earthquake resistant buildings: a review. *The Journal of Engineering Research (TJER)*, **13**, 33-41.
- [32] Preti, M., Bolis, V., Stavridis, A., 2017. Seismic infill-frame interaction of masonry walls partitioned with horizontal sliding joints: analysis and simplified modelling, *Journal of Earthquake Engineering*, DOI: 10.1080/13632469.2017.1387195.
- [33] Bolis, V., Stavridis, A., Preti, M., 2017. Numerical Investigation of the In-Plane Performance of Masonry-Infilled RC Frames with Sliding Subpanels, *Journal of Structural Engineering*, **143**(2), 04016168. doi: 10.1061/(ASCE)ST.1943-541X.0001651
- [34] Preti, M., Migliorati, L., Giuriani, E., 2015. Experimental testing of engineered masonry infill walls for post-earthquake structural damage control, *Bulletin of Earthquake Engineering*, **13**(7), 2029–2049.
- [35] Manzini, C.F., Morandi, P., Milanesi, R.R., Magenes, G., 2018. Shaking-table test on a two-storey RC framed structure with innovative infills with sliding joints, *Proc. 16th ECEE*, 18-21 June 2018, Thessaloniki, Greece.
- [36] Lotfi, H.R., Shing, P.B., 1991. An appraisal of smeared crack models for masonry shear wall analysis, *Computers & Structures*, **41**(3), 413–425, doi: 10.1016/0045-7949(91)90134-8.
- [37] Lotfi, H.R., Shing, P.B., 1994. Interface Model Applied to Fracture of Masonry Structures, *Journal of Structural Engineering*, **120**(1), 63–80, doi: 10.1061/(ASCE)0733-9445(1994)120:1(63).
- [38] Stavridis, A., Shing, P.B., 2010. Finite-Element Modeling of Nonlinear Behavior of Masonry-Infilled RC Frames, *J. Struct. Eng.*, **136**(3), 285–296, doi: 10.1061/(ASCE)ST.1943-541X.116.
- [39] Taylor, R.L., Govindjee, S., *FEAP - A Finite Element Analysis Program*, p. 705.

A DEGRADING BOUC-WEN DATA-DRIVEN MODEL FOR THE CYCLIC BEHAVIOR OF MASONRY INFILLED RC FRAMES

Matteo Pellicciari^{1,2}, Stefano Sirotti^{1,2}, Fabio Di Trapani³, Bruno Briseghella¹, Giuseppe Carlo Marano³, Camillo Nuti⁴, and Angelo Marcello Tarantino²

¹College of Civil Engineering, Fuzhou University, 350108 Fuzhou, PR China
e-mail: bruno@fzu.edu.cn

² Dipartimento di Ingegneria “Enzo Ferrari”, Università degli Studi di Modena e Reggio Emilia,
41125 Modena, Italy
e-mail: {matteo.pellicciari,stefano.sirotti,angelomarcello.tarantino}@unimore.it

³ Dipartimento di Ingegneria Strutturale, Edile e Geotecnica, Politecnico di Torino, 10121
Torino, Italy
e-mail: {fabio.ditrapani,giuseppe.marano}@polito.it

⁴ Dipartimento di Architettura, Università degli Studi Roma Tre, 00153 Roma, Italy
e-mail: {camillo.nuti}@uniroma3.it

Keywords: Infilled RC frames, Hysteresis, Macro-model, Bouc-Wen, OpenSees.

Abstract. *Mechanics-based macro-models are often used to simulate the cyclic response of infilled reinforced concrete (RC) frames. However, these approaches are affected by uncertainties regarding damage and failure mechanisms. Therefore, this contribution proposes a new smooth data-driven model for the hysteresis of infilled RC frames. The infill panel is modeled through a damage-based Bouc-Wen element, which accounts for both pinching and deterioration of the mechanical characteristics. The parameters of the model are calibrated from an experimental data set of cyclic responses of RC infilled frames. Analytical correlations between parameters and geometric and mechanical characteristics of the infilled frame are derived. Blind validation tests are carried out in order to demonstrate the effectiveness of the proposed model.*

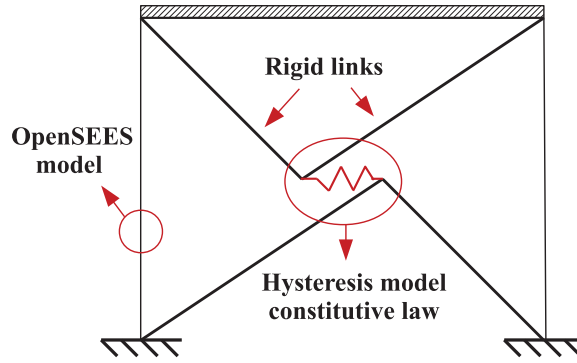


Figure 1: Scheme of the macro-model for the infilled frame: the bare frame is modeled with the software OpenSees, while the infill panel is simulated as a spring whose constitutive law is given by the Bouc-Wen model.

1 INTRODUCTION

The cyclic behavior of infilled frames has been widely investigated from both theoretical and experimental points of view [1–5]. However, the mechanical modeling of such structural systems is still an open challenge [6]. This mainly because the response of an infilled frame depends on many geometric and mechanical factors, which influence the damage mechanisms.

Many authors developed equivalent strut macro-models to predict the in-plane behavior of infilled frames [7–10]. However, predictions from different models lead to results that are often conflicting. Moreover, these modeling strategies are often complex and involve a large number of parameters that are very difficult to predict a priori. For the above reasons, recently many mechanics-based data-driven models have been developed [9, 11, 12]. In this case, the parameters governing the mechanical behavior of the structural system are estimated using regression formulas based on large data-sets. This modeling strategy has been proven to be reliable for many typologies of infilled frames.

This contribution proposes a new hysteresis data-driven macro-model based on the Bouc-Wen equation [13–15]. Deterioration of both stiffness and strength are taken into account through degrading functions for cyclic damage [16]. Pinching is introduced by adding in series a slip-lock element [17] to simulate the effect of masonry cracking. The model is governed by 11 parameters that have clear physical meanings. The regression formulas of these parameters were obtained with a data-driven approach, based on calibrations performed with experimental data of real infilled frames. The validation of the model was performed through additional blind prediction tests. The model proposed in this work is an effective tool for nonlinear dynamic analyses and probabilistic assessments [18, 19].

2 MACRO-MODELING OF THE INFILLED FRAME

The infill panel was replaced by a spring connected to the bare frame through rigid links, as shown in Figure 1. The constitutive behavior of the spring was defined by the hysteresis model proposed in this work. The bare frame was modeled on the OpenSees 2.5 software platform by using fiber-section beam-column elements with distributed plasticity.

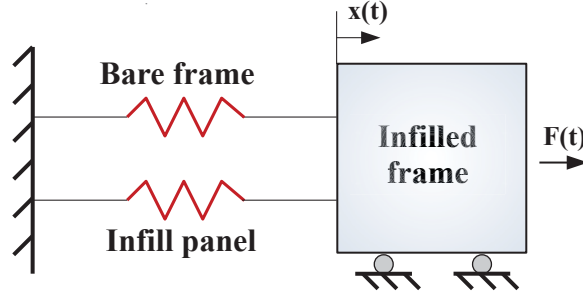


Figure 2: The infilled frame is regarded as a simple oscillator composed of two springs in parallel, one representing the bare frame and one representing the infill panel.

As depicted in Figure 1, the rigid links constrain the frame and the spring to undergo the same horizontal displacement. Thus the infilled frame was regarded as a simple oscillator whose stiffness is given by two contributions. One is provided by the bare frame, the other by the spring representing the panel. The sum of these two contributions gives the response of the entire infilled frame (Figure 2).

In the following section, the analytical formulation of the hysteresis model for the spring (infill panel) is presented.

3 ANALYTICAL DESCRIPTION OF THE PROPOSED HYSTERESIS MODEL

The proposed hysteresis model consists in a degrading Bouc-Wen element [13, 14] integrated with a slip-lock element [17, 20]. The latter was specifically introduced to simulate the typical pinching of masonry due to cracks opening and closure.

The equation of motion for a single-degree-of-freedom system is

$$m\ddot{x} + c\dot{x} + F_s[x(t), z(t), t] = F(t) \quad (1)$$

where x is the relative displacement of the mass of the system m with respect to the ground, c is the linear viscous damping coefficient, $F_s[x(t), z(t), t]$ is the non-damping restoring force, $z(t)$ is the hysteresis displacement and $F(t)$ is the external excitation. The overdots indicate the derivative with respect to the time, thus \dot{x} and \ddot{x} represent velocity and acceleration, respectively.

The Bouc-Wen model gives the following expression for the restoring force:

$$F_s[x(t), z(t), t] = \alpha kx(t) + (1 - \alpha)kz(t) \quad (2)$$

where k is the elastic stiffness of the system and α is the ratio between the final tangent stiffness k_f and the elastic stiffness ($0 \leq \alpha \leq 1$). Eq. (2) is composed of two contributions: the linear elastic component $\alpha kx(t)$ and the hysteresis component $(1 - \alpha)kz(t)$, which depends on the past history of stresses and strains. The hysteresis displacement $z(t)$ is given by the differential equation

$$\dot{z}(t) = A\dot{x}(t) - [\beta|\dot{x}(t)||z(t)|^{n-1}z(t) + \gamma\dot{x}(t)|z(t)|^n] \quad (3)$$

with the initial condition $z(0) = 0$. The parameters β , γ , and n control the shape of the hysteresis cycles. The parameter A determines the tangent stiffness but it is set to unity to avoid redundancy [21, 22]. The hysteresis energy dissipated by the system is defined as the area under the hysteresis restoring force $F^h[z(t), t] = (1 - \alpha)kz(t)$ along the total

displacement $x(t)$. The hysteresis energy can be normalized with respect to the mass, as follows [23, 24]:

$$\varepsilon(t) = \int_{x(0)}^{x(t)} \frac{F^h[z(t), t]}{m} dx = (1 - \alpha)\omega_0^2 \int_0^t z(\tau)\dot{x}(\tau)d\tau. \quad (4)$$

According to some results in literature [25–27] a linear proportionality between β and γ was introduced

$$\gamma = \eta_0\beta. \quad (5)$$

A dimensionless damage index, involving both energy dissipated and maximum displacement reached, was considered

$$d_i(t) = \frac{\varepsilon(t)}{kx_y^2/m} + \frac{|x_{max}(t)|}{x_y} \quad (6)$$

where x_y is the yielding displacement and $x_{max}(t)$ is the maximum displacement of the system until time t . Since the degrading Bouc-Wen model is a smooth hysteresis model, there is not a standard way to compute the yielding displacement x_y . Hence, this is an unknown parameter that must be identified along with the other model parameters.

The damage index $d_i(t)$ allows to define the following stiffness and strength degrading functions [16]:

$$\begin{aligned} A(d_i) &= e^{-\delta_k d_i(t)p_k(d_i)} \\ \beta(d_i) &= \beta_0 e^{[\delta_k p_k(d_i) - n\delta_f]d_i(t)} \end{aligned} \quad (7)$$

where δ_k and δ_f are two parameters that control respectively the amount of stiffness and strength degradation. The function $p_k(t)$ controls the stiffness degradation rate

$$p_k(t) = e^{-\psi d_i(t)} \quad (8)$$

where ψ is a parameter that controls the rising of stiffness degradation.

With the introduction of the degrading functions, the differential equation defining $z(t)$ assumes the following expression:

$$\begin{aligned} \dot{z}(t) &= A(d_i)\dot{x}(t) - \beta(d_i)(|\dot{x}(t)||z(t)|^{n-1}z(t) + \eta_0\dot{x}(t)|z(t)|^n) = \\ &= e^{-\delta_k d_i(t)p_k(d_i)}\dot{x}(t) - \beta_0 e^{[\delta_k p_k(d_i) - n\delta_f]d_i(t)}(|\dot{x}(t)||z(t)|^{n-1}z(t) + \eta_0\dot{x}(t)|z(t)|^n). \end{aligned} \quad (9)$$

A slip-lock element [17] was introduced in order to properly simulate the opening and closure of cracks in the infill panel. The slip-lock element was linked in series with the Bouc-Wen element (see Figure 3). Therefore, the relationship between the two elements is the following:

$$x(t) = x_1(t) + x_2(t) \quad (10)$$

where x is the total displacement of the system. The term x_1 is the contribution of the degrading Bouc-Wen differential equation, expressed by Eq. (9). The term x_2 is the contribution of the slip-lock element, which is given by the following relation:

$$\dot{x}_2(t) = a(t)f(z)\dot{z}(t). \quad (11)$$

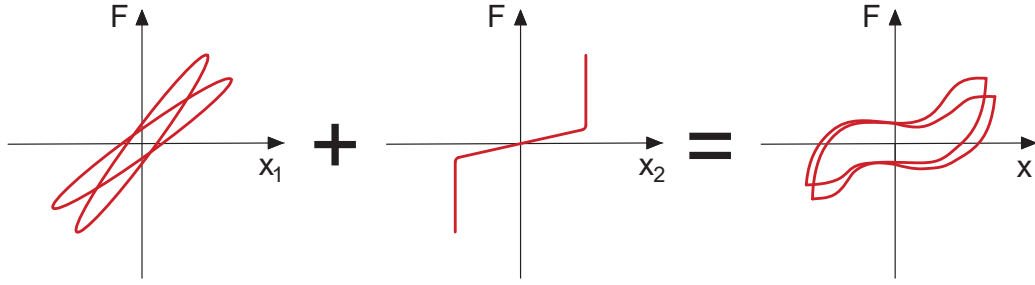


Figure 3: Schematization of the proposed hysteresis model, which is obtained as composition of degrading and slip-lock elements.

The function $f(z)$ defines the shape of the slip-lock phenomenon and is defined as

$$f(z) = e^{-z^2/Z_s^2} \quad (12)$$

where Z_s is the range of z in which the slip lock occurs. Parameter a is a function of the attained ductility

$$a(t) = A_s \frac{|x_{max}(t)|}{x_y} \quad (13)$$

where A_s is a parameter that controls the slip length, x_{max} is the maximum displacement reached at the prior cycle and x_y is the yielding displacement.

Combining Eqs. (9), (10) and (11), the following differential equation for the hysteresis displacement is obtained:

$$\dot{z}(t) = \dot{x}(t) \frac{A(d_i) - \beta(d_i)[\text{sgn}(\dot{x})|z(t)|^{n-1}z(t) + \eta_0|z(t)|^n]}{\{1 + a(t)f(z)[A(d_i) - \beta(d_i)(\text{sgn}(\dot{x})|z(t)|^{n-1}z(t) + \eta_0|z(t)|^n)]\}}. \quad (14)$$

4 CALIBRATION OF THE PROPOSED MODEL USING EXPERIMENTAL DATA

The model parameters were calibrated according to experimental data. The data involve 10 real specimens and were collected from the experimental campaigns by Cavaleri and Di Trapani [6], Mehrabi et al. [2], Colangelo [28], Kakaletsis and Karayannis [29] and Mansouri et al. [30]. For each specimen, the force-displacement hysteresis curve was acquired. All the campaigns considered performed displacement control tests in quasi-static loading.

For each specimen, the contribution of the infill panel was represented by the difference between the entire response of the infilled frame and the response of the bare frame modelled on OpenSees. The parameters of the proposed model for the infill panel were calibrated on the basis of this contribution. For each specimen, the calibration of the parameters was performed through a genetic algorithm implemented in a MATLAB® code. The genetic algorithm finds the set of parameters that minimizes the following objective function

$$OF(\boldsymbol{\theta}) = \frac{\int_{x_0}^{x_f} |[F_e(x) - F_s(\boldsymbol{\theta}, x)]| dx}{\int_{x_0}^{x_f} |F_e(x)| dx} \quad (15)$$

where $\boldsymbol{\theta}$ is the parameter vector, x_i and x_f are the initial and final displacement records, $F_e(x)$ is the force derived from the experimental data and $F_s(\boldsymbol{\theta}, x)$ is the one simulated by

Table 1: Calibrated values of the hysteresis model parameters for the reference specimens.

Reference	Spec.	α	β_0	η_0	n	k	x_y	δ_k	δ_f	ψ	Z_s	A_s
Cavaleri and Di Trapani [6]	S1A	0.003	0.35	0.2	1.5	76	1.45	0.017	0.003	0.001	0.16	5.91
Mehrabi et al. [2]	4	0.003	0.41	0.2	1.5	84	1.23	0.035	0.013	0.001	0.16	4.55

The values of k and x_y are given respectively in kN/mm and mm.

Table 2: Predicted values of the hysteresis model parameters for the reference specimen for validation.

Reference	Spec.	α	β_0	η_0	n	k	x_y	δ_k	δ_f	ψ	Z_s	A_s
Cavaleri and Di Trapani [6]	S1C	0.003	0.32	0.2	1.5	79	1.70	0.022	0.006	0.001	0.18	4.86

The values of k and x_y are given respectively in kN/mm and mm.

the proposed model. Parameters α , η_0 , n and ψ assumed very similar values for different specimens. Thus their values were fixed for simplicity, since small variations did not affect the results significantly.

The calibration was performed for 10 specimens, but in this work only 2 of them are shown for the sake of brevity. The two specimens considered are S1A from [6] and specimen 4 from [2]. The parameters identified in the calibration are listed in Table 1 and the results are shown in Figure 4.

5 EMPIRICAL CORRELATION LAWS AND BLIND VALIDATION TEST

The dependence of the parameters k , x_y , β_0 , δ_k , δ_f , Z_s , A_s on the geometrical and mechanical properties of infilled frames was investigated. The most representative quantities like the elastic modulus of masonry, the compression strength of masonry or the compression strength of concrete were gathered in a functional. Considering all the specimens, the values assumed by each model parameters were put in relation with the values assumed by the functional. In this way, the correlation laws defined are able to predict the values of the model parameters in function of the geometrical and mechanical properties of a generic infilled frame.

The proposed correlation laws were validated on the basis of experimental data related to a specimen different from the one used for calibration. The specimen used for validation is specimen S1C from the experimental campaign in [6]. The geometrical and mechanical properties of specimen S1C are different from those of the specimens used for in the calibration. Therefore, this specimen was considered eligible for the blind validation test. Table 2 collects the parameters predicted by the correlation laws and Figure 5 shows the result of the validation test.

6 CONCLUSIONS

The data-driven macro-model proposed in the present contribution is able to predict the hysteresis response of infilled frames. The combination of degrading Bouc-Wen element and slip-lock element provides a model that captures hysteresis and damage of such structural systems.

The model involves 11 parameters with clear physical meanings. Four of them have less impact on the final behavior, so they were fixed. The 7 remaining parameters were

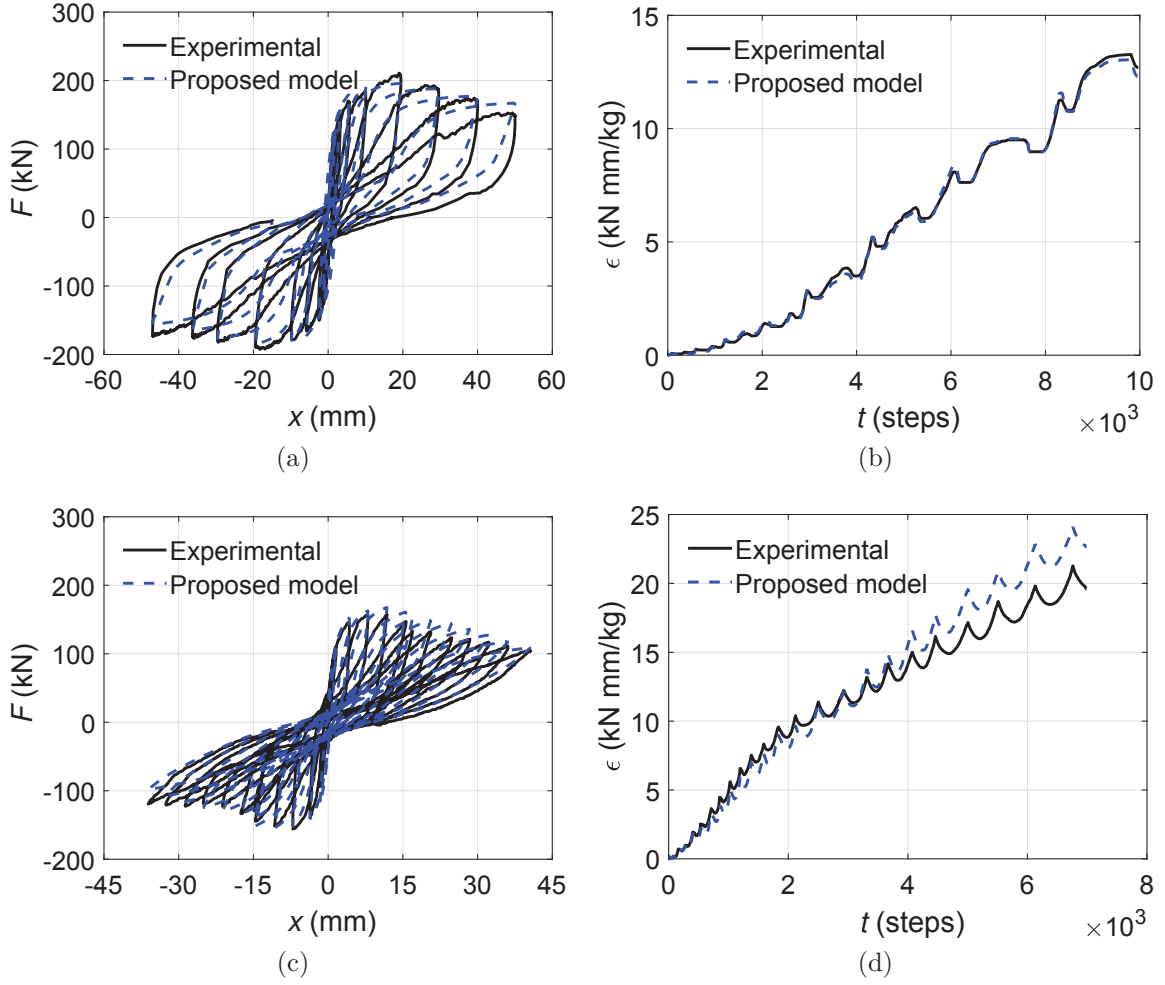


Figure 4: Results of the calibration for specimen S1A from Cavaleri and Di Trapani [6] and specimen 4 from Mehrabi et al. [2]: (a) S1A hysteresis cycles; (b) S1A dissipated energy; (c) Mehrabi 4 hysteresis cycles; (d) Mehrabi 4 dissipated energy.

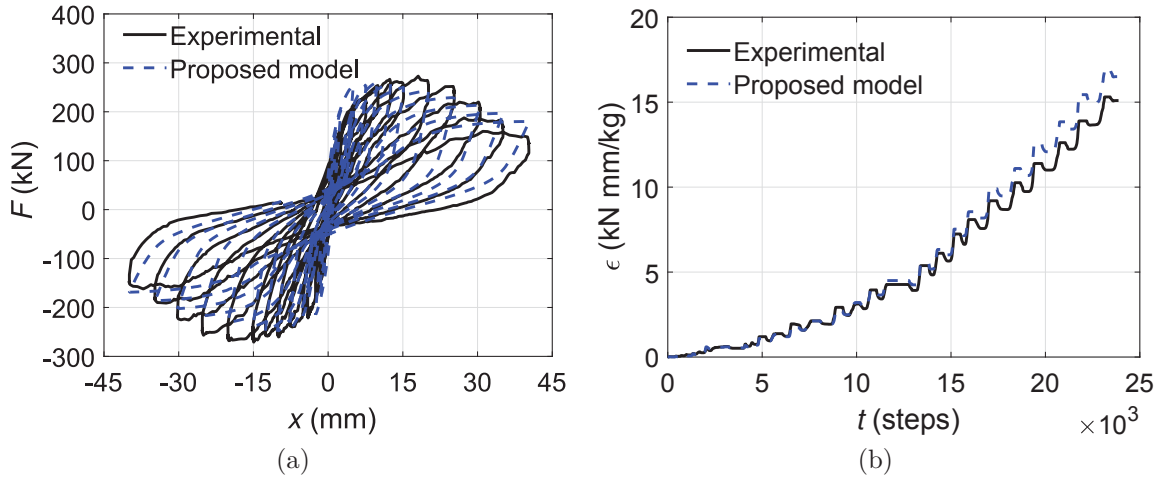


Figure 5: Blind validation test on specimen S1C from Cavaleri and Di Trapani [6]: (a) hysteresis cycles; (b) dissipated energy.

calibrated on the basis of experimental data of real infilled frames. Regression laws were estimated and final blind validation tests were performed. The results demonstrated that the model is accurate.

The simplicity and the smooth nature of the governing equations make the proposed model suitable for numerical simulations, such as nonlinear time-history and stochastic analyses.

REFERENCES

- [1] F. Pires and E. C. Carvalho. The behaviour of infilled reinforced concrete frames under horizontal cyclic loading. In *Proceedings of the 10th World Conference on Earthquake Engineering*, volume 6, pages 3419–33422, 1992.
- [2] A. B. Mehrabi, P. Benson Shing, M. P. Schuller, and J. L. Noland. Experimental evaluation of masonry-infilled RC frames. *Journal of Structural Engineering*, 122(3):228–237, 1996.
- [3] G. M. Calvi and D. Bolognini. Seismic response of reinforced concrete frames infilled with weakly reinforced masonry panels. *Journal of Earthquake Engineering*, 5(02):153–185, 2001.
- [4] D. J. Kakaletsis and C. G. Karayannis. Experimental investigation of infilled reinforced concrete frames with openings. *ACI Structural Journal*, 106(2), 2009.
- [5] G. Verderame, P. Ricci, C. Del Gaudio, and M. De Risi. Experimental tests on masonry infilled gravity-and seismic-load designed RC frames. In *Brick and Block Masonry*, pages 1349–1358. CRC Press, 2016.
- [6] L. Cavaleri and F. Di Trapani. Cyclic response of masonry infilled RC frames: Experimental results and simplified modeling. *Soil Dynamics and Earthquake Engineering*, 65:224–242, 2014.
- [7] T. Paulay and M. N. Priestley. *Seismic design of reinforced concrete and masonry buildings*. Wiley New York, 1992.
- [8] L. Cavaleri, M. Fossetti, and M. Papia. Infilled frames: developments in the evaluation of cyclic behaviour under lateral loads. *Structural Engineering and Mechanics*, 21(4):469–494, 2005.
- [9] L. Liberatore, F. Noto, F. Mollaioli, and P. Franchin. In-plane response of masonry infill walls: Comprehensive experimentally-based equivalent strut model for deterministic and probabilistic analysis. *Engineering Structures*, 167:533–548, 2018.
- [10] M. T. De Risi, C. Del Gaudio, P. Ricci, and G. M. Verderame. In-plane behaviour and damage assessment of masonry infills with hollow clay bricks in RC frames. *Engineering Structures*, 168:257–275, 2018.
- [11] F. Di Trapani, G. Bertagnoli, M. F. Ferrotto, and D. Gino. Empirical equations for the direct definition of stress–strain laws for fiber-section-based macromodeling of infilled frames. *Journal of Engineering Mechanics*, 144(11):04018101, 2018.

- [12] H. Huang, H. V. Burton, and S. Sattar. Development and utilization of a database of infilled frame experiments for numerical modeling. *Journal of Structural Engineering*, 146(6):04020079, 2020.
- [13] R. Bouc. A mathematical model for hysteresis. *Acta Acustica united with Acustica*, 24(1):16–25, 1971.
- [14] Y. K. Wen. Method for random vibration of hysteretic systems. *Journal of Engineering Mechanics*, 102(2):249–263, 1976.
- [15] M. Pellicciari, G. C. Marano, T. Cuoghi, B. Briseghella, D. Lavorato, and A. M. Tarantino. Parameter identification of degrading and pinched hysteretic systems using a modified Bouc–Wen model. *Structure and Infrastructure Engineering*, 14(12):1573–1585, 2018.
- [16] M. Pellicciari, B. Briseghella, F. Tondolo, L. Veneziano, C. Nuti, R. Greco, D. Lavorato, and A. M. Tarantino. A degrading Bouc–Wen model for the hysteresis of reinforced concrete structural elements. *Structure and Infrastructure Engineering*, 16(7):917–930, 2020.
- [17] A. Madan, A. M. Reinhorn, J. B. Mander, and R. E. Valles. Modeling of masonry infill panels for structural analysis. *Journal of Structural Engineering (ASCE)*, 123:1295–1302, 1997.
- [18] F. Di Trapani and M. Malavisi. Seismic fragility assessment of infilled frames subject to mainshock/aftershock sequences using a double incremental dynamic analysis approach. *Bulletin of Earthquake Engineering*, 17(1):211–235, 2019.
- [19] F. Di Trapani, V. Bolis, F. Basone, and M. Preti. Seismic reliability and loss assessment of RC frame structures with traditional and innovative masonry infills. *Engineering Structures*, 208:110306, 2020.
- [20] T. T. Baber and M. N. Noori. Random vibration of degrading, pinching systems. *Journal of Engineering Mechanics*, 111(8):1010–1026, 1985.
- [21] F. Ma, H. Zhang, A. Bockstedte, G. C. Foliente, and P. Paevere. Parameter analysis of the differential model of hysteresis. *Journal of Applied Mechanics*, 71(3):342–349, 2004.
- [22] A. E. Charalampakis and V. K. Koumousis. On the response and dissipated energy of Bouc-Wen hysteretic model. *Journal of Sound and Vibration*, 309(3–5):887–895, 2008.
- [23] G. C. Foliente. Hysteresis modeling of wood joints and structural systems. *Journal of Structural Engineering*, 121(6):1013–1022, 1995.
- [24] G. A. Ortiz, D. A. Alvarez, and D. Bedoya-RuíZ. Identification of Bouc-Wen type models using multi-objective optimization algorithms. *Computers & Structures*, 114:121–132, 2013.
- [25] R. H. Sues, S. T. Mau, and Y. K. Wen. Systems identification of degrading hysteretic restoring forces. *Journal of Engineering Mechanics*, 114(5):833–846, 1988.

- [26] P. Sengupta and B. Li. Modified Bouc-Wen model for hysteresis behavior of RC beam-column joints with limited transverse reinforcement. *Engineering Structures*, 46:392–406, 2013.
- [27] M. Ye and X. Wang. Parameter estimation of the Bouc-Wen hysteresis model using particle swarm optimization. *Smart Materials and Structures*, 16(6):2341, 2007.
- [28] F. Colangelo. Pseudo-dynamic seismic response of reinforced concrete frames infilled with non-structural brick masonry. *Earthquake Engineering & Structural Dynamics*, 34(10):1219–1241, 2005.
- [29] D. Kakaletsis and C. Karayannis. Influence of masonry strength and openings on infilled R/C frames under cycling loading. *Journal of Earthquake Engineering*, 12(2):197–221, 2008.
- [30] A. Mansouri, M. S. Marefat, and M. Khanmohammadi. Experimental evaluation of seismic performance of low-shear strength masonry infills with openings in reinforced concrete frames with deficient seismic details. *The Structural Design of Tall and Special Buildings*, 23(15):1190–1210, 2014.

SEISMIC PERFORMANCE OF PAKISTANI-TECHNIQUE INFILLED REINFORCED CONCRETE FRAMES

Nisar Ali Khan^{1*}, Alessandro Vittorio Bergami², Camillo Nuti³, Giorgio Monti⁴,
Marco Vailati⁵ and Bruno Briseghella⁶

^{1,2,3} Department of Architecture, University Roma Tre, Rome, Italy

E-mail: {[nisarali.khan](mailto:nisarali.khan@uniroma3.it); [alessandro.bergami](mailto:alessandro.bergami@uniroma3.it); [camillo.nuti](mailto:camillo.nuti@uniroma3.it) }@uniroma3.it,

⁴ Department of Structural and Geotechnical Engineering, Sapienza University of Rome, Italy,

E-mail: giorgio.monti@uniroma1.it

⁵ Department of Civil, Construction-Architectural
and Environmental Engineering, University of L'Aquila, Italy

E-mail: marco.vailati@univaq.it

⁶ College of Civil Engineering, Fuzhou University, China,

E-mail: bruno@fzu.edu.cn

* Corresponding author: nisarali.khan@uniroma3.it

Abstract

Infilled reinforced concrete (IRC) frames are commonly built across the world. Modern building codes address the influence of infill walls in seismic design and assessment of existing structures. Other building codes commonly consider infill walls as non-structural elements and do not require any explicit verification. One of such codes is the Pakistan Building Code (PBC), which does not foresee recommendations and guidelines for IRC frame structures, despite being a common construction typology in the Country. Records of past earthquakes show that infill types and material properties strongly affect the seismic response of buildings thus highlighting the importance of such parameters and making the topic worth investigating in detail.

This paper introduces a numerical model for infill walls, which predicts different features of the nonlinear response, such as cracking, peak force, failure and residual force. Such features are expressed as function of infill friction coefficient between mortar and brick surface and mortar strength, whose effects are commonly neglected in available numerical models. The model is applied to a comprehensive case study of a three-story IRC frame factory building, located in the city of Mirpur, Pakistan, hit by an earthquake of magnitude 5.9 on 24 September 2019. The results obtained the model show good agreement with the observed in-situ damage patterns, thus revealing the importance of correctly modeling the infill walls when seismically designing and assessing Pakistani IRC buildings.

Keywords: Masonry infill wall, Nonlinear analysis, Diagonal strut model, Non-structural element, Infilled Reinforced Concrete (IRC) frame structures.

1 INTRODUCTION

The construction typology of infilled reinforced concrete (IRC) frames is not only common in Pakistan but across the globe. The typology became more common in Pakistan especially after October 2005 Kashmir earthquake [1], [2], [3], [4], [5]. With the increasing demand for IRC frame constructions in the country, the local research community and practitioners started developing an increasing interest towards several important issues, such as, frame-infill interaction models, role of brick types, and optimal material properties of the infill wall constituents [6]. While the use of IRC frames has been growing in the Country, the Pakistan building code (PBC) has not developed any recommendation or guideline for their design and construction [1], [7]. This is also the case of many building codes around the world [8], [9], whereas some more advanced building codes, including Eurocode, already include some essential yet incomplete considerations about the role of infill walls in both design and assessment of IRC frame structures. As a matter of fact, many practitioners still consider infill walls as non-structural elements, despite being aware of their strong influence on the seismic response of IRC frame structures [10], [11]. This is also due to the fact that, although extensive studies have been dealing with the topic in the past 50 years, sound and reliable design and assessment methods including the effects of infills seem still far from being used in practice [12]. Besides, there is a lack of basic understanding regarding the infill walls contribution to the IRC frame response, whether it is beneficial or detrimental and under which circumstances. This depends on various parameters, such as: infills-frame interaction, infills-frame relative strength and stiffness, type of materials used for bricks, mortar and concrete [13][14][9]. Assessment of seismic performance of IRC frames requires proper modeling techniques and reliable analytical equations to correctly predict their response [15]. Many existing IRC frames are more vulnerable to seismic actions as a result of improper and poor understanding of such features [16].

Some usually neglected parameters, such as friction coefficient between mortar and brick surface, mortar strength, and their effects on the seismic performance of IRC frames are not reported in the literature, despite their strong influence on the failure mode of infill walls [17]. Recent earthquakes show that also newly built IRC frames designed with seismic detailing are equally vulnerable as older ones, due to the detrimental interaction with infills [18]. Moreover, IRC frames are not only vulnerable during natural seismic events, but also due to human-made hazardous events, such as blast and terrorism acts, which makes the topic worth investigating [19].

In case infill walls are uniformly distributed in plane and elevation of the building, IRC frames under seismic action are less vulnerable than the equivalent bare frames, because the infill walls interact directly with the surrounding RC frame [20]. However, brittle failures may occur in columns, beams and joints, due to local interaction. These issues should be dealt with when modeling an existing building [21].

The infill walls can be modeled by different numerical approaches, such as micro, meso, and macro modeling [22]. The former two require detailed computational efforts and are commonly used for detailed research purposes, while the latter makes use of one or more diagonal struts, which require less computational effort and are preferred in practical applications [23].

Usually, in Pakistan, common practice with IRC frames only accounts for infill walls through their dead load [2], [7]. As a consequence of such design practice, the same types of infill walls made of fire burnt clay bricks are used across the northern part, including Punjab, Khyber Pakhtunkhwa, Pakistan-administrated Kashmir, Baluchistan, capital territory Islamabad, and other seismic prone regions of the country, without the necessary variations in size and properties required by the local seismic hazard [24]. Besides, there are no variations in thickness or infill

types related to the occupancy/types of the building, i.e., hospital, school, industrial, or residential, which is not a reasonable strategy for the seismic safety of those buildings [2], [1].

2 NUMERICAL MODELLING

Satisfactory advancements in modeling infill walls have been recently achieved in terms of simplified macro modeling, in which the infill panel is replaced by equivalent diagonal single or multiple struts. The laying of bricks and the materials mechanical characteristics affect the ability of such models to predict the local response and the damage pattern. In terms of global response, it has been widely recognized that the modeling choices of infill walls affect the overall seismic performance of IRC frame structures and bring to largely different outcomes.

Generally, seismic forces affect infill walls both in-plane and out-of-plane. In-plane interaction has been the object of several experimental researches, which concluded that infill panels behave as a monolithic resisting system, until partially detached from the surrounding frame and start behaving as a compression strut, which claims for adequate modeling. The proposed model focusses on this aspect.

Considering the construction typology of IRC frames in Pakistan, the materials used, and the common design practice, is the objective of the proposed numerical model, which is a modified version of Combescure (1996) [25] model expressed as function of friction coefficient between mortar and brick surface and mortar strength. It considers a compression diagonal strut representing the infill wall in the in-plane, with a simple yet effective constitutive law shown in figure 1.

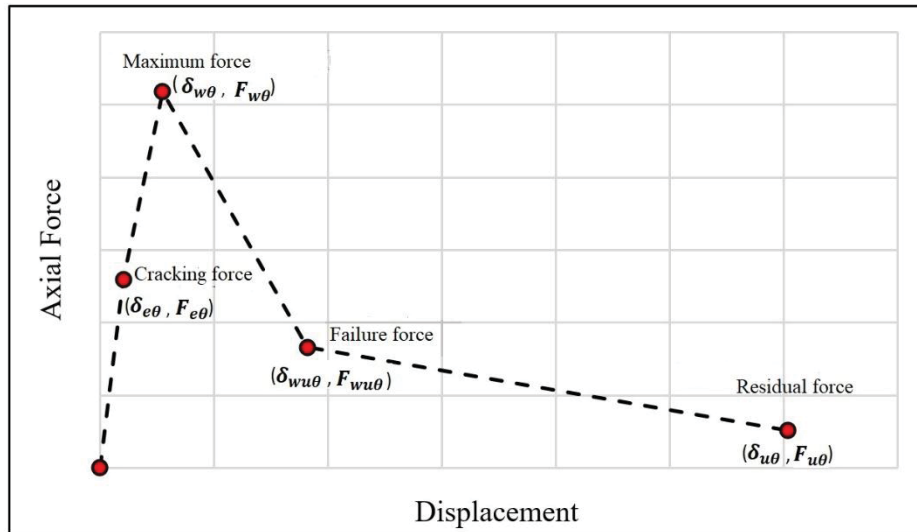


Figure 1. Adopted model for infill walls showing the main features of the response

The proposed model aims at better capturing such response at different stages, i.e., elastic, cracking, maximum force, failure, and residual force.

The relative stiffness between infill wall and column can be calculated by the dimensionless parameter first proposed by Stafford Smith (1967).

$$\lambda_h = h_c \left[\frac{E_m t_w \sin 2\theta}{4 E_c I_c h_w} \right]^{1/4} \quad (1)$$

where h_c is the height of the RC frame to the centerline of the beam, E_m , E_c are the moduli of elasticity of masonry and concrete respectively, t_w , h_w are the thickness and height of the infill wall, respectively, I_c is the moment of inertia of the column, θ is the angle of the diagonal panel strut.

Many authors proposed different formulations for the diagonal panel strut width[22]. According to Mainstone (1974), it can be calculated by the following equation:

$$\frac{w_w}{d_w} = 0.17 \lambda_h^{-0.4} \quad (2)$$

Where w_w , d_w are width and inclined length of the diagonal strut.

The four branches, i.e., cracking, maximum force, failure, and residual force shown in figure 1, are described sequentially by the following equations.

It is expedient to start from the maximum force and the corresponding displacement:

$$F_{w\theta} = f_w \cdot t_w \cdot w_w \quad (3)$$

$$\delta_{w\theta} = \frac{f_w}{E_{w\theta}} d_w \quad (4)$$

where, f_w , t_w and w_w are the compression strength of the wall along the diagonal direction, the wall thickness, and the strut width, respectively, and $E_{w\theta}$ is the elastic modulus along the diagonal direction at angle θ , given by the following equation [26]:

$$E_{w\theta} = \left[\frac{\cos^4 \theta}{E_{mh}} + \frac{\sin^4 \theta}{E_{mv}} + \cos^2 \theta \sin^2 \theta \left(\frac{1}{G} - 2 \frac{\nu}{E_{mh}} \right) \right]^{-1} \quad (5)$$

Where E_{mh} , E_{mv} are the horizontal and vertical elastic moduli of masonry walls, respectively, G is the masonry shear modulus, and ν is the Poisson ratio.

The cracking force of the infill and the corresponding displacement at the onset of the first branch of figure 1, can be found as:

$$F_{e\theta} = \frac{F_{w\theta}}{2} \quad (6)$$

$$\delta_{e\theta} = \frac{F_{e\theta}}{2K_{w\theta}} \quad (7)$$

Where $K_{w\theta}$ is the diagonal strut axial stiffness, calculated as:

$$K_{w\theta} = \frac{E_{w\theta} t_w w_w}{d_w} \cos^2 \theta \quad (8)$$

Where θ is the strut angle.

The failure force and the corresponding displacement at the end of the third branch of figure 1 can be found as:

$$F_{wu\theta} = \mu (f_m t_w w_w) \quad (9)$$

$$\delta_{wu\theta} = 0.005 \frac{h_w}{\cos \theta} \quad (10)$$

Where, μ , f_m , t_w , and w_w are friction coefficient between mortar and brick surface, mortar compressive strength, wall thickness, strut width, respectively, and h_w is the infill wall height.

Finally, the last point of residual force is proposed as:

$$F_{u\theta} = \frac{F_{w\theta}}{10} \quad (11)$$

$$\delta_{u\theta} = 18 \delta_{w\theta} \quad (12)$$

Having calibrated the strut model, in the following section it is applied in the comprehensive modeling of an infilled frame reinforced concrete building, selected as a case study.

3 CASE STUDY

The selected case study considers an IRC three-story factory building situated in Mirpur city, Pakistan, which was severely hit by the earthquake on 24 September 2019. The factory building is 17.7 km away from the epicenter. The model of the building and a satellite image are shown in figure 2. According to the acquired information, the building was designed in 1986, when the code did not enforce any seismic provisions. As per common practice in the country, infill walls were considered as non-structural components.



Figure 2. Model of the selected factory building (left) and satellite image location of the building from the epicenter (right)

According to the detailed site visits and survey reports of the building, some cracks were observed in the beams, columns and their joints whereas the infill walls are badly damaged, as shown in figures 3-6.

The overall in-plane dimensions of the building are 94.91 m \times 24.38 m and the typical inter-storey height is 3.66 m. It consists of three blocks, i.e., storage, manufacturing, and office at the back, center, and front, respectively. The infill walls are 228 mm (9 inches) thick made of solid fire burnt clay bricks. The geometry of beams and columns are rectangular with variable sizes depending on their location and ranging from 228 mm \times 457 mm to 228 mm \times 2438 mm and 305 mm \times 305 mm to a maximum of 381 mm \times 381 mm.



Figure 3. Cracks observed in beam (left), and column (right)



Figure 4. Cracks observed in column and infill (left), and joints (right)



Figure 5. Cracks and damages observed in the infill walls in different parts of the building



Figure 6. Cracks in column due to the presence of opening in infill (right) severe cracks in infill on the frame selected for analysis (left)

4 NUMERICAL MODELS

A 2-D frame is considered, pertaining to the office block where maximum damages in the infill walls were observed. Nonlinear static pushover analysis was performed considering two configurations: bare frame (BF) as reference, and infilled frame (IF). The foundation plan, the elevation of the selected frame having five equal bays of length 4.88m, equal inter-story height of 3.66m and the geometry of beams and columns are shown in figures 7-9.

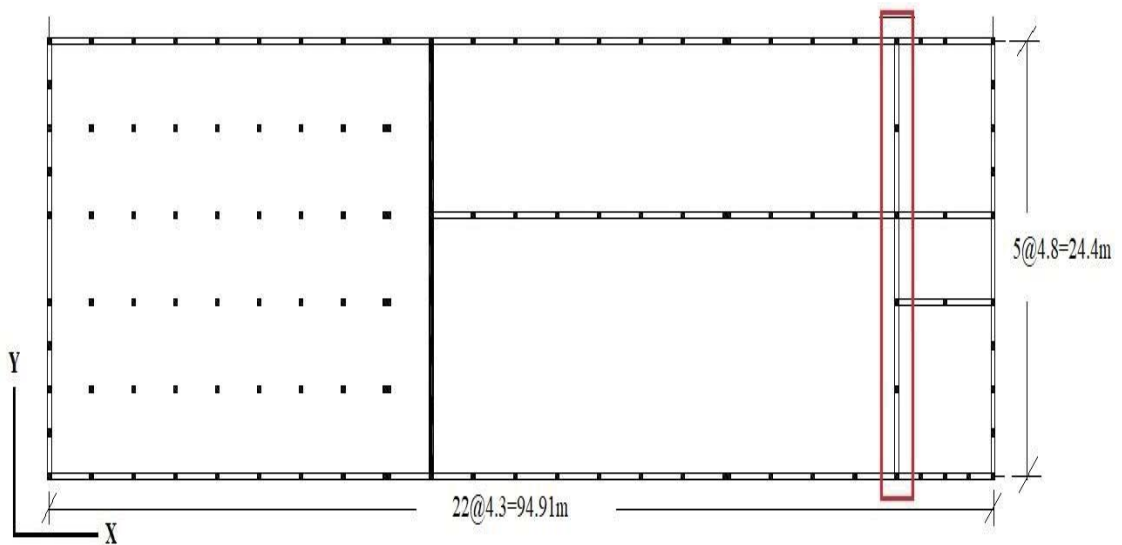


Figure 7. Foundation plan of the building and, highlighted, the frame selected for analysis

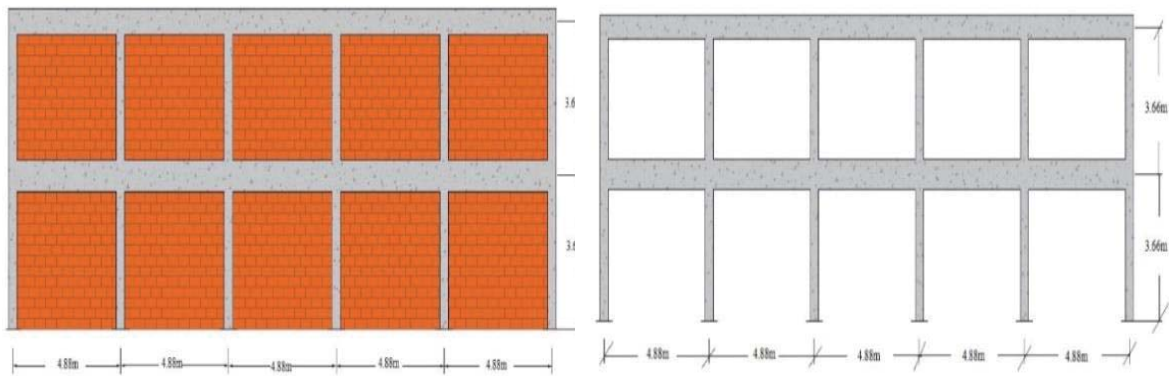


Figure 8. Frame selected for analyzing the infills (left), bare frame (right)

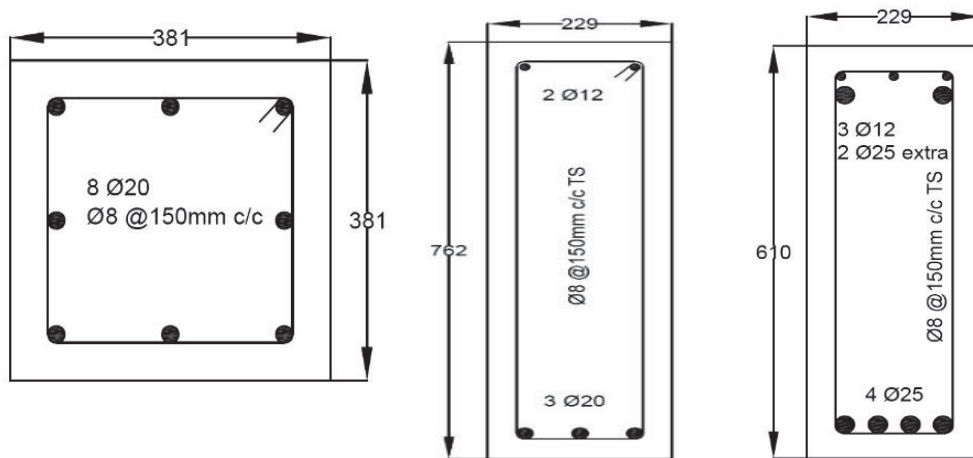


Figure 9. Section of columns (left), first-floor beam (center), second-floor beam (right)

The frame was modeled in SAP2000 where frame elements were used for beam-column elements and nonlinear multilinear elastic link with the proposed model properties were used for the infills. Mander (1988) [27] model was used for confined and unconfined concrete within the cross sections of the structural elements. From the available drawings and design specifications of the building, the characteristic values of compressive strength of the brick unit, brick masonry, mortar, concrete, and yield strength of steel are set as 8 MPa, 4.3 MPa, 5 MPa, 20 MPa, and 400 MPa, respectively, which are commonly used properties in the country [2], [1], [24], [28], [29]. Other materials properties, such as friction coefficient between mortar and brick surface, and Poisson ratio are considered as 0.3 and 0.14, respectively. The models of IF and BF are shown in figure 10.

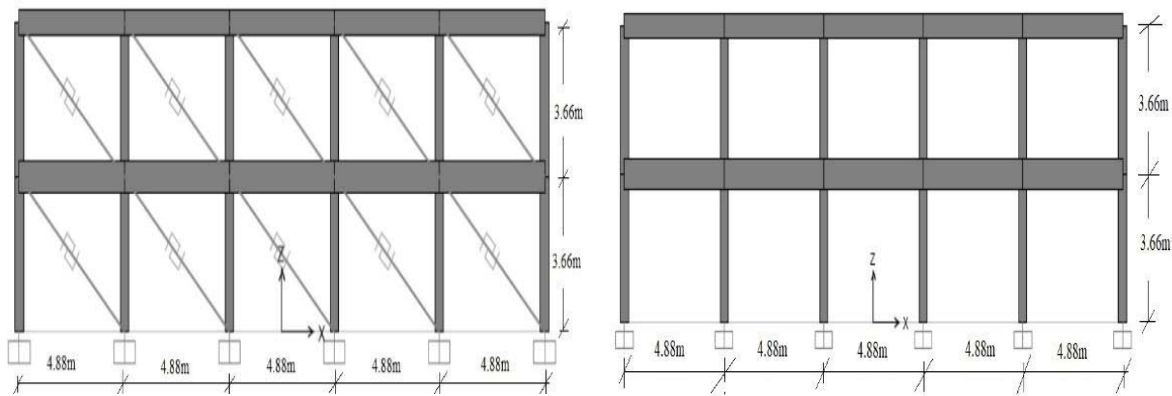


Figure 10. Models considering different configurations: infilled frame (left) bare frame (right)

5 RESULTS AND COMPARISON WITH IN-SITU OBSERVED DAMAGE

Detail surveys and site inspections of the building after the earthquake showed that the RC elements were not significantly damaged by the earthquake action. As shown in the figures 3-6, some beams and columns were partially damaged, however, most of the damages were observed in the infill walls. In fact, they sustained a large portion of the horizontal forces and, consequently, increased significantly the stiffness and strength of the building, thus preventing the structural components from failing. In this case, the presence of the infills was beneficial to the overall performance of the structural elements. The BF model predicted much higher damage in the structural elements, while the IF model, thanks to the inclusion of the proposed struts, showed good agreement with the observed damage in the structure.

From the quantitative standpoint, the resulting capacity curves of IF and BF can be appreciated in figure 11. It is noticed that IF has an almost 3 times larger strength than BF, provided by the presence of the infills. Also, the initial stiffness increased 11 times, which resulted in a 70% decrease of the fundamental vibration period. It was also observed that drift ratio, top story drift, and ductility of IF compared to BF decreased by 60%, 7%, and 40% respectively. Using the ATC-40 capacity spectrum method, it was possible to ascertain that the presence of the infills allowed the IF performance to increase up to 130% with respect to BF.

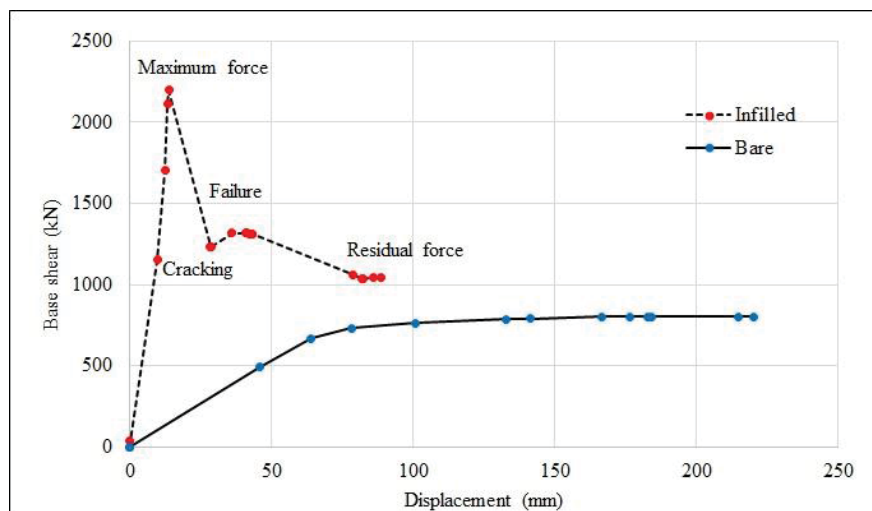


Figure 11. Capacity curves of the bare frame (solid line) and of the infilled RC frame (dashed line)

The IF model allowed to correctly detect the presence of the most relevant in-plane failure mechanisms in the infill walls, such as, diagonal cracking, corner crushing, bed sliding/shear failure (figures 5-6). This was highlighted by the behavior of the strut elements, which got damaged in the same locations observed in the building. It was also confirmed that the infill walls stiffen the frame and thus reduce the damage in the reinforced concrete elements. Finally, as a last remark, it was confirmed that if the infill walls are made with bricks having strength higher than the mortar strength, an additional friction-related energy dissipation develops during cyclic loading, thus reducing the overall response of the structure and thus avoiding brittle failures in the bricks. This important phenomenon, which has two-fold beneficial consequences, is naturally accounted for in the proposed model through the use of the basic parameters of friction coefficient between mortar and brick surface and mortar strength

6 CONCLUSIONS

The following conclusions can be drawn from the study presented in this paper:

- The analysis results obtained from numerical model show good agreement with the observed in-situ failure pattern on the case study building.
- The analysis results show that the seismic performance of the selected building is correctly predicted by including an appropriate model of the infilled frame.
- In-situ observation and analysis results confirm that infill walls have strong influence on the seismic performance of building. Therefore, types of infill walls, material used and mechanical characteristics of materials are important to consider when deal with IRC frame structures, especially in Pakistan where this practice is not commonly applies.
- Strength and stiffness of the selected IRC building considerably increased with infill walls while less ductile failure is observed. Therefore, effect of infill walls should be carefully accounted for in appropriate models, both in designing new structures and in assessing existing structures.
- The proposed numerical model considers the effects of commonly ignored yet important parameters such as friction coefficient between mortar and brick surface and mortar strength, which is simple to apply and requires less computation efforts as compare to more detail models, thus, helping practitioners and structural engineer to deal with IRC structures.

7 ACKNOWLEDGMENT

The author acknowledged the financial supports of the Italian Agency for development co-operation (AICS) partnership for knowledge (PfK) 4 Project, the Italian ministry of foreign affairs for providing an opportunity to present the contribution reported here. The present work has been partially carried out in the framework of DPC/ReLUIS project 2019/2021.

8 REFERENCES

- [1] N. A. Khan, C. Nuti, B. Briseghella, G. Monti, and A. V. Bergami, "State of the art and practice of masonry infilled RC frame structures subjected to in plane loading, in Pakistan, China and Europe," in *First South Asia Conference on Earthquake Engineering*, 2019, no. 21-22 February 2019.
- [2] S. A. A. Shah, K. Shahzada, and Q. Samiullah, "Influence of Brick Masonry Infilled Wall on Seismic Performance of Reinforced Concrete Frame," *NED Univ. J. Res.*, vol. XVII, no. 3, pp. 15–29, 2020, doi: 10.35453/nedjr-stmech-2018-0013.
- [3] J. Akbar, N. Ahmad, B. Alam, and M. Ashraf, "Seismic performance of RC frames

- retrofitted with haunch technique,” *Struct. Eng. Mech.*, vol. 67, no. 1, pp. 1–8, 2018, doi: 10.12989/sem.2018.67.1.001.
- [4] M. Ahmed, S. H. Lodi, S. S. Ali, and N. Alam, “Seismic Risk Assessment of Built Environment in Pakistan,” 2014, vol. Second Eur, no. Aug. 25-29, 2014.
- [5] W. H. Encyclopedia, “Brick masonry construction in Pakistan,” 2013.
- [6] A. V. Bergami and C. Nuti, “Experimental tests and global modeling of masonry infilled frames,” *Earthq. Struct.*, vol. 9, no. 2, pp. 281–303, 2015, doi: 10.12989/eas.2015.9.2.281.
- [7] B. C. of P. [2007] Seismic, “Building Code of Pakistan [2007] Seismic Provisions, Ministry of Housing and Works, Islamabad, Pakistan.”
- [8] A. Furtado, H. Rodrigues, A. Arêde, H. Varum, M. Grubišić, and T. K. Šipoš, “Prediction of the earthquake response of a three-storey infilled RC structure,” *Eng. Struct.*, vol. 171, no. May, pp. 214–235, 2018, doi: 10.1016/j.engstruct.2018.05.054.
- [9] A. Furtado and M. Teresa De Risi, “Recent Findings and Open Issues concerning the Seismic Behaviour of Masonry Infill Walls in RC Buildings,” *Adv. Civ. Eng.*, vol. 2020, 2020, doi: 10.1155/2020/9261716.
- [10] H. Rodrigues, H. Varum, and A. Costa, “Simplified macro-model for infill masonry panels,” *J. Earthq. Eng.*, vol. 14, no. 3, pp. 390–416, 2010, doi: 10.1080/13632460903086044.
- [11] N. A. Khan, M. F. Tahir, C. Nuti, B. Briseghella, and A. V. Bergami, “Influence of Brick Masonry Infill Walls on Seismic Response of RC Structures,” *Tech. Journal, UET Taxila*, vol. 24, no. 3, pp. 15–23, 2019.
- [12] H. Huang and H. V. Burton, “A database of test results from steel and reinforced concrete infilled frame experiments,” *Earthq. Spectra*, vol. 36, no. 3, pp. 1525–1548, 2020, doi: 10.1177/8755293019899950.
- [13] D. Addessi, P. Di, C. Gatta, and E. Sacco, “Multiscale analysis of out-of-plane masonry elements using different structural models at macro and microscale,” vol. 247, 2021.
- [14] B. Behera and R. P. Nanda, “In-plane shear strengthening of brick masonry panel with geogrid reinforcement embedded in bed and bed-head joints mortar,” vol. 227, no. February 2020, 2021.
- [15] H. Huang, H. V. Burton, and S. Sattar, “Development and Utilization of a Database of Infilled Frame Experiments for Numerical Modeling,” *J. Struct. Eng.*, vol. 146, no. 6, p. 04020079, 2020, doi: 10.1061/(asce)st.1943-541x.0002608.
- [16] L. Facconi and F. Minelli, “Retrofitting RC infills by a glass fiber mesh reinforced overlay and steel dowels: experimental and numerical study,” *Constr. Build. Mater.*, vol. 231, 2020, doi: 10.1016/j.conbuildmat.2019.117133.
- [17] H. Huang and H. V. Burton, “Classification of in-plane failure modes for reinforced concrete frames with infills using machine learning,” *J. Build. Eng.*, vol. 25, 2019, doi: 10.1016/j.jobbe.2019.100767.
- [18] C. Butenweg, M. Marinković, and R. Salatić, “Experimental results of reinforced concrete frames with masonry infills under combined quasi - static in - plane and out - of - plane seismic loading,” *Bull. Earthq. Eng.*, no. 0123456789, 2019, doi: 10.1007/s10518-019-00602-7.
- [19] L. N. Koutas and D. A. Bournas, “Out-of-Plane Strengthening of Masonry-Infilled RC Frames with Textile-Reinforced Mortar Jackets,” *J. Compos. Constr.*, vol. 23, no. 1, p. 04018079, 2019, doi: 10.1061/(asce)cc.1943-5614.0000911.
- [20] A. Furtado, H. Rodrigues, A. Arêde, and H. Varum, “Double-Leaf Infill Masonry Walls Cyclic In-Plane Behaviour: Experimental and Numerical Investigation,” *Open Constr. Build. Technol. J.*, vol. 12, no. 1, pp. 35–48, 2018, doi: 10.2174/1874836801812010035.

- [21] M. G. d'Aragona, M. Polese, M. Di Ludovico, and A. Prota, "Seismic vulnerability for RC infilled frames: Simplified evaluation for As-built and retrofitted building typologies," *Buildings*, vol. 8, no. 10, 2018, doi: 10.3390/buildings8100137.
- [22] N. Tarque, L. Candido, G. Camata, and E. Spacone, "Masonry infilled frame structures: State-of-the-art review of numerical modelling," *Earthq. Struct.*, vol. 8, no. 1, pp. 225–251, 2015, doi: 10.12989/eas.2015.8.1.225.
- [23] F. Di Trapani, L. Cavaleri, G. Bertagnoli, G. Mancini, D. Gino, and M. Malavisi, "Definition of a fiber macro-model for nonlinear analysis of infilled frames," *COMPdyn 2017 - Proc. 6th Int. Conf. Comput. Methods Struct. Dyn. Earthq. Eng.*, vol. 2, pp. 3281–3296, 2017, doi: 10.7712/120117.5645.18525.
- [24] N. Ahmad, Y. I. Badrashi, Q. Ali, H. Crowley, and R. Pinho, "Development of Displacement-Based Method for Seismic Risk Assessment of RC Building Stock of Pakistan," *Proc Int. Conf. Earthq. Eng. Seismol.*, no. Icees, 2011.
- [25] D. Combesure, F. Pires, P. Cerqueira, and P. Pegon, "Tests on masonry infilled r/c frames and its numerical interpretation," *11th World Conference on Earthquake Engineering, Acapulco*. 1996.
- [26] Sacchi, M.G., and Riccioni, R., "Comportamento Statico e Sismico Delle Strutture Murarie," *CLUP Ed. Milano, Italy*, 1982.
- [27] J. B. Mander, M. J. N. Priestley, and R. Park, "Theoretical stress-strain model for confined concrete," *Struct. Eng.*, vol. 114, no. 8, pp. 1804–1826, 1988.
- [28] A. Ahmed and K. Shahzada, "Seismic vulnerability assessment of con fi ned masonry structures by macro- modeling approach," vol. 27, no. June, pp. 639–649, 2020.
- [29] M. Javed, "Seismic Risk Assessment of Unreinforced Brick Masonry Buildings System of Northern Pakistan," *Engineering*, p. 230, 2009.

GENERATION OF OUT-OF-PLANE FRAGILITY FUNCTIONS FOR IN-PLANE DAMAGED UNREINFORCED MASONRY INFILLS

Bharat Pradhan¹, Liborio Cavaleri¹, Vasilis Sarhosis², Marco Filippo Ferrotto^{1*}

¹ University of Palermo
Viale delle Scienze, Palermo
{bharat.pradhan, liborio.cavaleri, marcofilippo.ferrotto}@unipa.it

² University of Leeds
LS2 9JT, Leeds, United Kingdom
V.Sarhosis@leeds.ac.uk

Abstract

Fragility assessment of unreinforced masonry (URM) infill walls under seismic loads is a current research topic for large scale risk analysis of reinforced concrete frame structures. In this paper, Out-of-Plane (OoP) fragility functions are developed by probabilistic approach based on Monte Carlo simulations employing a numerical macro-element model for the evaluation of the OoP capacity of infills. Uncertainties in the capacity were considered depending on the level of In-Plane (IP) damage and the variability in the geometrical and mechanical properties of the masonry infills. The fragility functions are therefore obtained considering the variability in the capacity instead of the seismic input as for other studies, considering also their sensitivity to the position in low rise buildings.

Keywords: Fragility, Macro-element model, URM infill, Out-of-plane, IP-OOP interaction.

1 INTRODUCTION

Seismic risk mitigation for reinforced concrete (RC) structures requires the use of reliable strategies for the evaluation of the seismic capacity in view of performing large scale analysis [1]. RC structures exhibit often significant structural and non-structural damage when subjected to medium-to-strong ground shakings. Retrofitting strategies as well as energy dissipation and isolation can be considered effective strategies for the improvement of the seismic behavior of load bearing frame elements such as beams or columns [2-12]. However, non-structural damage related to elements such as infill walls is often neglected in the evaluation of the overall structural behavior.

Damages in infills result in huge economic loss due to a significant downtime and repair cost [13]. Particularly, out-of-plane (OoP) failure can be a big threat to human life. Such infill walls resulted to be highly vulnerable to in-plane (IP) and out-of-plane (OoP) actions caused by seismic loads in past and recent earthquakes [14, 15] and it has been confirmed by a number of experimental studies that OoP capacity of the infills reduce as the IP damage increases [16-20].

Fragility functions are important tools to estimate the probability of OoP collapse of infill walls. But very few works have been done in this direction, often limited because of the computational effort in analyzing a huge number of cases due to variations in infills' properties as well as the IP-OoP interaction [21-23]. Some of the available fragility curves were developed by using macro-element models considering the IP-OOP interaction in determining the OoP strength of infill walls [24-31].

Another important aspect is that the most of the available fragility functions were derived considering the variability in the ground motions (uncertainties in the demand) without taking into account uncertainties in the capacity due to the variability of infill mechanical and geometrical properties and, at the same time, the IP-OoP interaction: this is the main aim of this study for the case of low-rise buildings.

The novel contribution of this work is therefore to consider the variability of the capacity of infills by employing a probabilistic approach based on Monte Carlo simulations including the uncertainties in the mechanical and geometrical properties instead of the variability in the seismic input. The macro-element model proposed by Pradhan and Cavaleri [28] has been used for numerical analysis. The probabilistic approach allowed to consider the uncertainty in the infills' strength and geometric features as well as the uncertainty in the IP drift (inter-storey drift ratio) during an earthquake. Fragility curves have been derived for infill walls built with two types of masonry units (hollow and solid) and interested by three different levels of IP damage: low, medium and high corresponding to three ranges of IP-drift. The fragility curves proposed in this study refer to infills positioned at different floors of low-rise RC frame buildings.

2 PROCEDURE PROPOSAL TO DERIVE FRAGILITY CURVES

2.1 Theoretical framework

For the derivation of OoP fragility curves of masonry infill walls, a probabilistic approach employing a specific range of variability for the input parameter has been implemented by using Monte Carlo simulation. The outputs are therefore affected by random assumption over a range of representative input cases.

To reproduce the physical process using a probabilistic approach, first, a cycle of IP demand randomly assigned is applied to an infilled frame with random geometrical and mechanical characteristics, and then the infill is pushed in OoP direction to determine the capacity

and consequently the Peak Ground acceleration (PGA). Monte Carlo methodology includes the following steps:

- 1) Random generation of variables such as the thickness and strength of masonry, IP displacement demand, etc.;
- 2) Calculation of OoP capacity by a macro-element model in OpenSees [32];
- 3) Determination of the equivalent OoP pseudo (spectral) acceleration;
- 4) Derivation of the PGA associated to the pseudo acceleration;
- 5) Determination of the probability of exceedance of OoP collapse and obtaining of the fragility for a given case study.

The above procedure was implemented first in Matlab code for the generation of a random input variables' matrix characterized by a certain number of cases; then, the random matrix was linked to OpenSees [32] to perform numerical analyses, getting the matrix of the results corresponding to each case of analysis. The results obtained by OpenSees were the maximum OoP forces and the corresponding displacements. Additionally, the value of forces, corresponding to one-third of the maximum ones, and the associated OoP displacements, were extracted for each analysis to derive OoP stiffness of the infills.

2.2 Range of parameters and base assumptions

Two fragility groups have been defined for URM infill walls: a) infill with solid masonry units (isotropic property), and b) infill with hollow masonry units (orthotropic property). Additionally, the fragility has been sub-grouped according to the level of IP damage as: low, medium and high (0-0.7%, 0.7-1.4% and 1.4-2% respectively) and the aspect ratios of infills (1.0, 1.25, 1.50 and 1.75). Only one damage state has been considered in the OoP direction i.e. the damage state of collapse. The masonry infill collapse in OoP direction is immediately identified by the OoP pseudo acceleration equal to the ratio between the OoP strength and mass. However, as before-mentioned, the Peak ground acceleration (PGA) has been taken as an Engineering Demand Parameter for the fragility assessment.

Infill walls are bounded by square columns of size 300 mm×300 mm and 300 mm×400 mm beams at top and bottom. Columns are provided with 8 @18 mm longitudinal rebars while the beams have 3 @16 mm rebars at top and bottom. The concrete in the frame members is confined by rectangular stirrups (@ 8 mm) kept at a spacing of 75 mm. The effect of confinement, - provided by the steel reinforcement, as suggested in [33, 34], has been taken in to account according to Mander's model [35]. The yield strength of reinforcement steel is taken as 500 MPa.

For the solid masonry, minimum thickness of infill has been kept as 100 mm while the maximum thickness is assumed to be 200 mm and for the hollow masonry, the thickness was varied from 100 mm to 300 mm. For sake of simplicity, for infill walls built with solid masonry units, the mechanical properties of masonry are assumed as isotropic. In case of masonry with hollow masonry units, orthotropic properties are considered. Elastic modulus of masonry material is assumed as 1000 times the value of compressive strength in both isotropic and orthotropic cases. The main characteristics of the random variables are shown in Table 1. An example of distribution of the compressive strength of masonry for orthotropic and isotropic masonry cases is shown in Fig. 1 a-b.

For each case of low, medium and high IP damage and for each different case of aspect ratio of infill wall, 400 different random samples were generated. Inter-storey drift ratio (IDR) imposed on the infill wall is taken as a measure of IP damage. In Fig. 2a, a sample distribution of IDR to consider three different levels of IP damage is shown while in Fig. 2b, the distribution of the masonry thickness for the case of solid and hollow unit masonry is shown.

Variable	Property	Distribution features
Strength of concrete	Uniform distribution	
	Min (MPa)	20
	Max (MPa)	30
IP damage	Uniform distribution	
	Low level (%)	IDR 0 to 0.7
	Medium level (%)	IDR 0.7 to 1.4
Thickness of solid masonry	Uniform distribution	
	Min (mm)	100
	Max (mm)	200
Thickness of hollow masonry	Uniform distribution	
	Min (mm)	100
	Max (mm)	300
Strength of solid masonry (Isotropic behavior)	Gaussian distribution	
	Min (MPa)	3.0
	Max (MPa)	7.0
	Mean (μ)	5.0
Strength of hollow masonry (Orthotropic behavior)	Gaussian distribution	
	Min (MPa)	1
	Max (MPa)	6
	Mean (μ)	3.5
	Standard deviation (σ)	1.0

Table 1: Distribution of the input parameters.

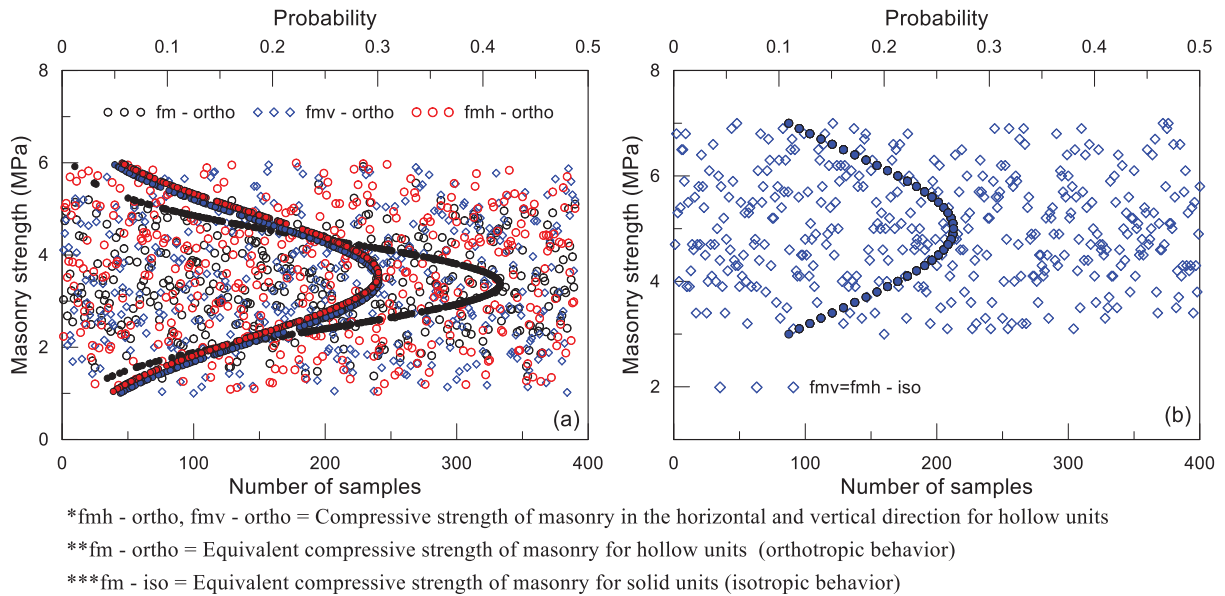


Figure 1: Distribution of the compressive strength of the masonry: a) orthotropic case (hollow units), b) isotropic case (solid units)

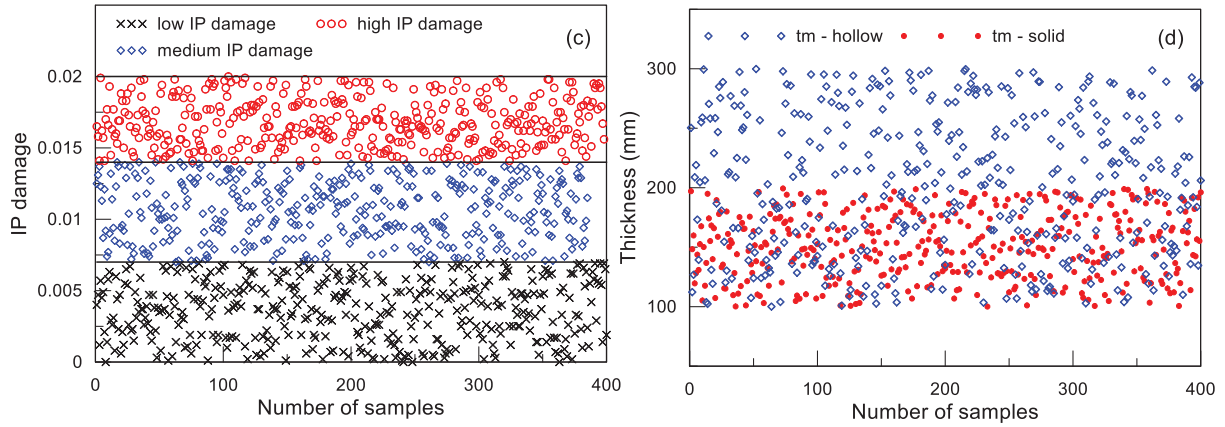


Figure 2: IP damage (a), OOP collapse (b)

2.3 Macro-element modeling of the URM infill walls

The capacity of the panels has been calculated by using macro-element model by Pradhan and Cavaleri [28]. The model consists of four struts (two diagonals, one horizontal and one vertical). The model was validated with results of different experiments [16-18, 29, 36] covering the range of infills' geometrical and mechanical characteristics. Each strut in the model is represented by two fiber-section beam-column elements connected by a node at the mid-span (Fig. 3).

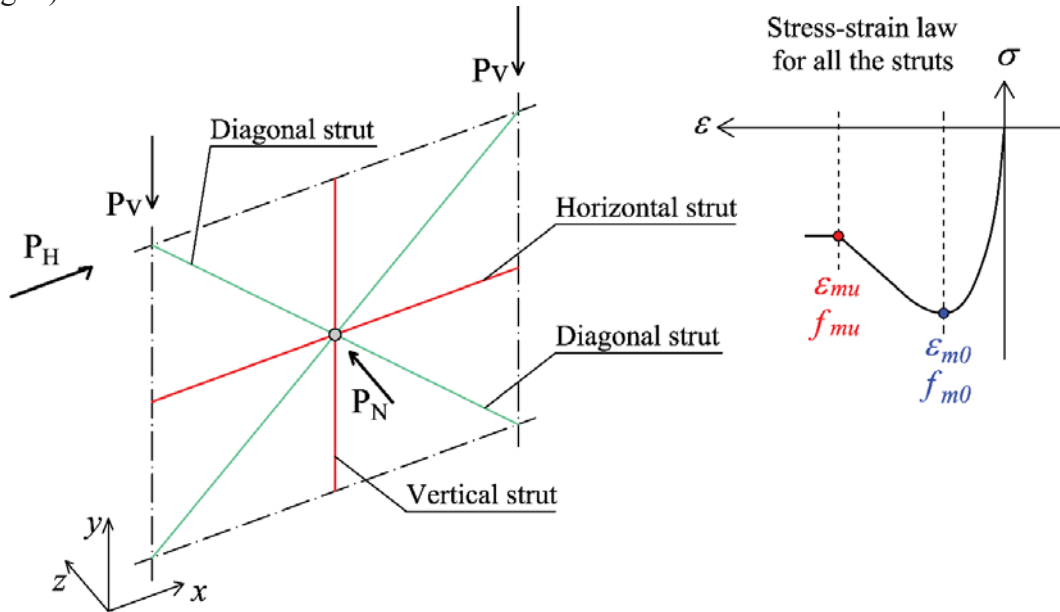


Figure 3: Macro-element model (Pradhan and Cavaleri 2020)

In the model, the width of the diagonal struts w_d is defined as one-third of the diagonal length d while the widths of the horizontal strut w_h and vertical struts w_v are calculated as a function of w_d in the following ways:

$$w_d = d/3 \quad (1)$$

$$d = \sqrt{l^2 + h^2} \quad (2)$$

$$w_h = h - w_d / \cos \theta \quad (3)$$

$$w_v = l - w_d / \sin \theta \quad (4)$$

where l and h are the length and height of the infill wall respectively, while l' indicates centre to centre distance between the columns and h' indicates the height of infill plus half the height of top beam and θ is the angle defining the slope of the diagonal struts. In the model, to represent both IP and OoP resistances of the infill wall more accurately, the width and thickness of the diagonal, vertical and horizontal struts were replaced by the surrogated values. For any of the struts with width w and thickness t , surrogated width \bar{w} and surrogate thickness \bar{t} are derived in the following ways:

$$\bar{w} = \frac{f_{mo}}{f_m} \times w \quad (5)$$

$$\bar{t} = \frac{f_m}{f_{mo}} \times t \quad (6)$$

The mechanical properties of the strut fibres in compression are defined by using four stress strain parameters, namely, f_{mo} , f_{mu} , ε_{mo} and ε_{mu} as shown in Fig. 3. These numerical parameters can be calculated based on two different mechanical properties of masonry i.e. the equivalent compressive strength f_m and equivalent elastic modulus E_m , according to the equations provided in Pradhan and Cavaleri [28].

The equivalent properties of masonry, namely f_m and E_m , are derived by taking into account the directional properties following the Eqs. 7-8.

$$f_m = \sqrt{f_{mv} \times f_{mh}} \quad (7)$$

$$E_m = \sqrt{E_{mv} \times E_{mh}} \quad (8)$$

where f_{mv} and f_{mh} represent the masonry's compressive strength in vertical and horizontal directions and E_{mv} and E_{mh} indicate the masonry's elastic modulus respectively in two directions respectively. This provision facilitates the model to consider the orthotropic nature of masonry. The definition of f_m and E_m is purely conventional and this technique relates well with the equivalent strut stress-strain parameters to be used in the model.

For the current study, in case of solid masonry units, the equivalent properties of masonry are derived considering itself as isotropic ($f_{mv} = f_{mh}$ and $E_{mv} = E_{mh}$) and for the case of hollow units as orthotropic. The numerical modelling was performed in OpenSees platform. The concrete and infill materials were modelled by using Concrete02 material, while the steel reinforcement was simulated by using Steel02 material available in OpenSees. The numerical model of any infilled frame was prepared by interfacing Matlab to OpenSees, the former allowed the generation of each set of random parameters. To consider the effect of IP damage in the OoP capacity, IP load was applied to achieve randomly generated IDR demands before the application of OoP load. IP displacement demand was imposed at the top of the infilled frame while OoP load was applied to the centre of the equivalent struts. The OoP capacity of infill walls considering the effect of IP-OoP interaction was thus estimated for all cases investigated.

2.4 Evaluation of PGA from the response spectrum

For a given case, in evaluating the approximate capacity in terms of pseudo (spectral) acceleration, the OoP strength is divided by the mass of the infill wall. In calculating the mass of the infill, density of solid masonry is assumed to be 1900 kg/m^3 in average while for hollow masonry it is assumed as 900 kg/m^3 . Each pseudo (spectral) acceleration can be associated to a PGA by the demand spectra.

Demand spectra for non-structural elements like infills depend upon their position along the height of a building, the fundamental period of the infill and the fundamental period of the building [37, 38]. According to the Italian Building Code 2018 [37], the expression of the demand spectrum $S_a(T_a, T_1, Z/H)$ is given as:

$$S_a = \begin{cases} \left[PGA \left(1 + \frac{Z}{H} \right) \frac{a_p}{1 + (a_p - 1) \left(1 - \frac{T_a}{aT_1} \right)^2} \right] \geq PGA & \text{for } T_a \leq aT_1 \\ PGA \left(1 + \frac{Z}{H} \right) a_p & \text{for } aT_1 \leq T_a < bT_1 \\ \left[PGA \left(1 + \frac{Z}{H} \right) \frac{a_p}{1 + (a_p - 1) \left(1 - \frac{T_a}{bT_1} \right)^2} \right] \geq PGA & \text{for } T_a \geq bT_1 \end{cases} \quad (9)$$

In the above expression, T_a is the fundamental vibration period of the infill wall, T_1 is the fundamental vibration period of the building, H is the height of the building, and Z is the level at which the infill is located. In Eq. 9, PGA is expressed in g (gravity acceleration). In the present work, the fundamental period of the building is evaluated by means of a simplified equation as follows:

$$T_1 = c \cdot H^{3/4} \quad (10)$$

c being a coefficient depending on the type on the material (0.075 for RC structures). In Eq. 9, the parameters a , b and a_p define the interaction between the infill and the structure depending on the fundamental period T_1 according to Table 2 [39].

	a	b	a_p
$T_1 < 0.5 \text{ s}$	0.8	1.4	5.0
$0.5 \text{ s} < T_1 < 1.0 \text{ s}$	0.3	1.2	4.0
$T_1 > 1.0 \text{ s}$	0.3	1.0	2.5

Table 2: Parameters for the response spectrum interaction.

Once the period of the panel T_a and the fundamental period of the structure T_1 are obtained, by imposing the equivalence between the spectral acceleration $S_a(T_a, T_1, Z/H)$ and the pseu-

do-acceleration obtained numerically (that is the infill OoP capacity), it is possible to use Eq. (9) to derive the PGA associated to the infill OoP capacity.

2.5 Evaluation of the fundamental period of the panel

Two different approaches were made in view of calculating the fundamental period of the panel in the OOP direction:

1. By analytical approach proposed by the Italian Building Code 2018 suggestions [37]
2. From the numerical model based on the results of the analyses in terms of stiffness.

Regarding the analytical approach, the fundamental period T_a of the masonry infill in the out-of-plane direction is calculated by the expression given in Eq. (11), where m_w is the mass of the infill per unit height h , E_w is the vertical modulus of elasticity of masonry and I_w is the moment of inertia of the infill horizontal cross section with respect the line obtained as intersection of the middle plane of the infill and the horizontal cross section. Eq. (11) is:

$$T_a = \frac{2h^2}{\pi} \sqrt{\frac{m_w}{K_{red} \cdot E_w \cdot I_w}} \quad (11)$$

It is to be noted that, in evaluating the period of the panel, the reduction in the flexural stiffness due to the IP damage has been considered to obtain a more realistic prediction. To do so, the coefficient K_{red} for the OOP stiffness reduction proposed by Cavaleri et al. [40] was used, that is:

$$K_{red} = [\min(1; 0.17 IDR^{-0.67})] \quad (12)$$

being IDR the inter-storey drift in percentage experienced/assigned by/to the panel in IP direction. The above equation was validated by the authors against a range of experimental and numerical cases.

The second approach is based on the results provided by the numerical analysis depending on the effective stiffness evaluated at one-third of the OoP maximum force and the corresponding displacement. In detail, the numerical period is calculated by using the well-known formula for one degree of freedom system (the equivalent one dof system is that described by the OoP displacement in the center of an infill and the corresponding restoring force) as follows:

$$T_a^* = 2\pi \sqrt{\frac{M^*}{K_{num}}}, \quad K_{num} = \frac{F_{\max, OOP/3}}{\delta(F_{\max, OOP/3})} \quad (13)$$

In calculating the vibration period, the participating mass M^* corresponding to the first OoP mode of vibration of the infill has been taken as 50% of the total mass of the infill wall. As regard to this choice, different values have been adopted in the literature [21, 22, 23, 29, 31]. The affinity of currently used model with the study of Di Trapani et al [23] oriented such choice of assuming 50% first mode mass in this study.

2.6 Determination of the probability of exceedance of OOP collapse, and obtaining of the fragility for a given case study

Fragility curves are cumulative distribution functions that represent the probability of exceedance of a certain damage state (DS) for a given type of building/structural element over a range of an intensity measure IM (in the context of the present work, the Peak Ground Acceleration “PGA”). A log-normal distribution function can be and is here assumed for the fragility associated to the collapse state according to the following expression:

$$P[DS / IM] = \phi \left(\frac{\ln(IM) - \ln(\overline{IM})}{\beta} \right) \quad (14)$$

where ϕ is the standard normal cumulative distribution function, \overline{IM} refers to a median value and β is the log-standard deviation that accounts for the uncertainties in the capacity of the building/structural element fragilities for the collapse damage state.

In the present study, the uncertainties were assigned for i) the strength of concrete of the reinforced concrete frame surrounding an infill, ii) level of IP damage, iii) thickness of infill, and iv) compressive strength of masonry, employing different distributions of variables. It allowed the evaluation of the median and the log-standard deviation in the results.

3 RESULTS

The fragility curves were obtained in this work assuming low-rise reinforced concrete buildings i.e. 3-storey moment resisting RC frame structure with an inter-storey height of 3 m (total height of the building is 9 m) for which the fundamental period resulted 0.39 sec (Eq. 10). In this context, the fragility was evaluated considering also the influence of the position of the panel with respect to the floors of the structure, evaluating the PGA at collapse state for infill walls placed at the ground storey (first floor) and at the top storey (third floor) of the reference structure.

In the following description of the results, the analyses were labelled depending on the type of masonry (i.e. iso and ortho for solid and hollow masonry respectively), the level of IP damage (i.e. ld, md, hd for low, medium, and high IP damage respectively), the aspect ratio in terms of length-to-height (1.0, 1.25, 1.5, 1.75) and the positioning of the panel with respect to the structure (I and III for the first and the third floor respectively). As an example, the fragility curve iso_ld_1.0_I indicates the fragility for an infilled wall made with solid masonry units, with low IP damage for a panel with aspect ratio 1.0, placed at the first floor, while, the fragility curve ortho_hd_1.5_III indicates the fragility for an infilled wall made with hollow masonry units, with high IP damage for a panel with aspect ratio 1.5, placed at the third floor.. In addition, I or I* and III or III* it is used respectively to give distinction between results calculated by using the period calculated by Eq. (11) (analytical evaluation) or Eq. (13) (by numerical results).

3.1 Influence of the fundamental period in the evaluation of the PGA

The PGAs obtained by using the two different approaches before mentioned for the evaluation of the vibration period of infills in the OoP direction were compared highlighting the sensitivity to the interaction with the response spectrum. In this comparison, the infills placed at the third floor of the low rise reference structure were considered.

First, it has to be noticed that, as expected, the OoP pseudo acceleration as well as the PGA decrease with the increasing level of IP damage and the increasing of the aspect ratio. For a given level of IP damage, infill panels with aspect ratio 1.0 provided higher OoP capacity than panels with aspect ratio 1.25, 1.5 or 1.75. At the same time, for a given value of aspect ratio, infill panels experiencing low levels of IP damage (0.0-0.7%) showed higher capacity compared to that obtained by increasing the level of IP damage (medium and high – drift in the ranges 0.7-1.4% and 1.4-2.0% respectively).

Another consideration has to be done regarding the different responses obtained depending on the type of masonry walls. Overall, it was noticed that hollow masonry showed PGA values higher than solid masonry. This is due to the higher thickness coupled with a low mass of the panels that provided higher pseudo-accelerations and lower vibration periods. Table 3

shows the results for each case of analysis in terms of median values of the PGA and mean values for the vibration period for the two approaches. It is reminded that T_a and T_a^* refer to vibration period calculated by Eq. (11) and Eq. (13) respectively.

At the same time, the vibration period of the panels is affected by the IP damage and aspect ratio. The increasing of the vibration period leads to a different positioning in the response spectrum. It was noticed that with the increasing of the level of IP damage and the increasing of the aspect ratio, the vibration period of the panel increases too and in some cases, it changes from the first branch of the response spectrum ($T < aT_I$) to the second ($aT_I < T < bT_I$). This requires to use a different equation in evaluating the PGA as shown in Eq. (9). This was observed in most of the analysis cases. Having said this, by using Eq. (11), the period of vibration is not much affected by the aspect ratio but only by the level of IP damage. Conversely, by using Eq. (13), the vibration period is significantly influenced both by aspect ratio and IP damage level because the numerical model takes into account the change in stiffness directly. This causes high scatter between T_a and T_a^* that can make the former up to two times the latter. These variations are clearly highlighted in Fig. 4 and Fig. 5 for hollow and solid masonry units respectively. For the above-described reasons, in the subsequent results regarding the evaluation of the fragility curves, it was assumed to evaluate the PGA by using the vibration period calculated from the numerical data to obtain more reliable results.

Solid masonry – iso (isotropic)												
low IP damage				medium IP damage				high IP damage				
Analytical		Numerical		Analytical		Numerical		Analytical		Numerical		
Aspect ratio	PGA (g)	Ta (sec)	PGA (g)	Ta* (sec)	PGA (g)	Ta (sec)	PGA (g)	Ta* (sec)	PGA (g)	Ta (sec)	PGA (g)	Ta* (sec)
1	2.32	0.11	2.70	0.06	1.11	0.16	1.68	0.09	0.67	0.19	0.92	0.12
1.25	1.78	0.11	2.29	0.08	0.96	0.15	1.25	0.11	0.48	0.19	0.59	0.13
1.5	1.59	0.10	1.57	0.09	0.69	0.16	0.67	0.13	0.43	0.19	0.45	0.15
1.75	1.25	0.10	1.11	0.10	0.51	0.16	0.46	0.15	0.32	0.19	0.32	0.19
Hollow masonry - ortho (orthotropic)												
1	3.96	0.08	4.78	0.04	1.96	0.11	2.49	0.07	1.22	0.13	1.56	0.09
1.25	3.59	0.07	3.98	0.05	1.50	0.11	1.79	0.08	1.03	0.12	1.14	0.10
1.5	2.64	0.07	2.79	0.06	1.22	0.11	1.29	0.10	0.80	0.13	0.81	0.13
1.75	2.37	0.07	2.30	0.08	1.00	0.11	1.03	0.12	0.63	0.13	0.55	0.15

Table 3: Results of the Monte Carlo simulations for infill walls placed at the third floor of the reference structure.

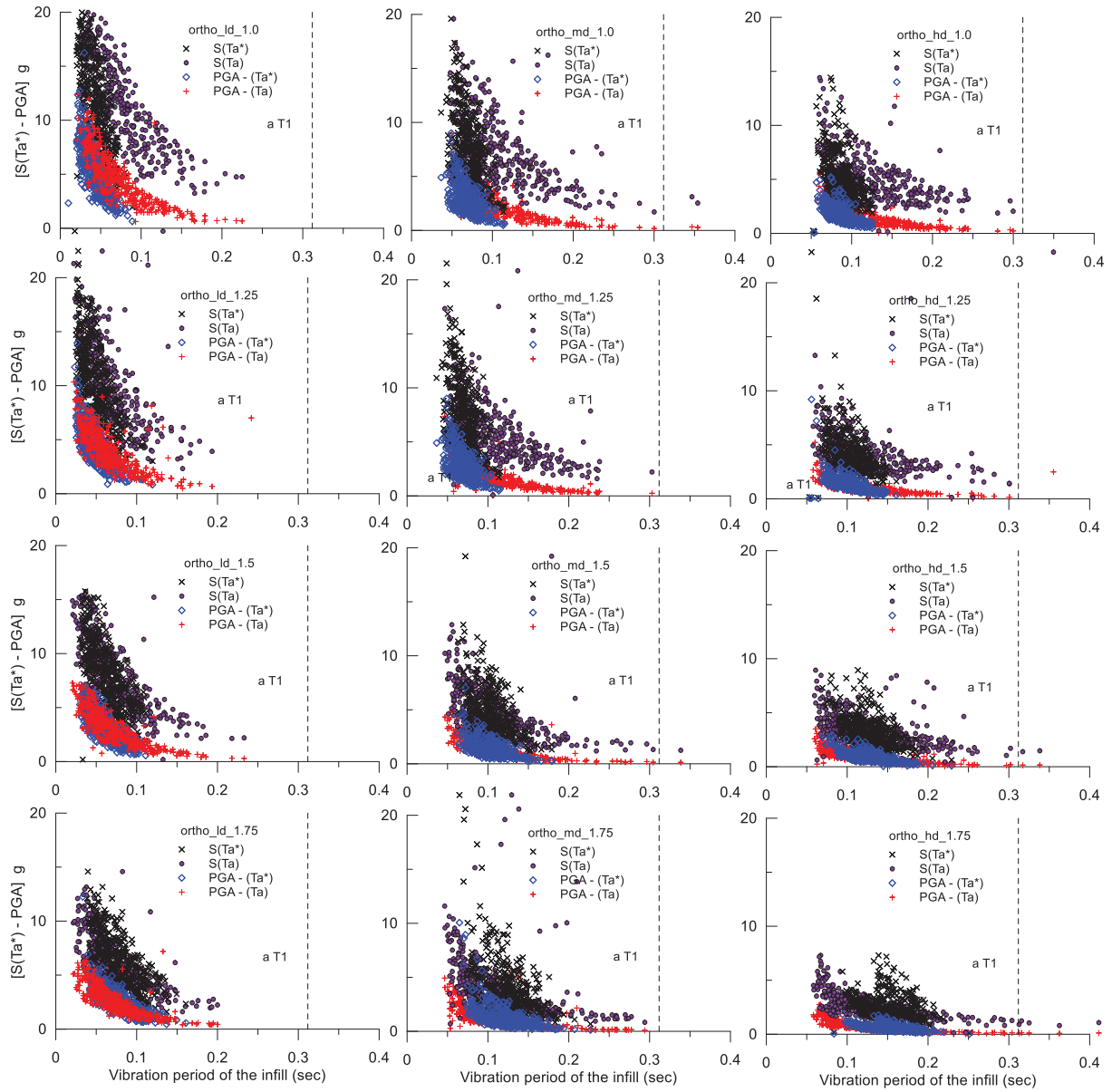


Figure 4: Results of the Monte Carlo simulations: pseudo-acceleration and PGA depending on the vibration period of the infilled walls for the case of orthotropic masonry

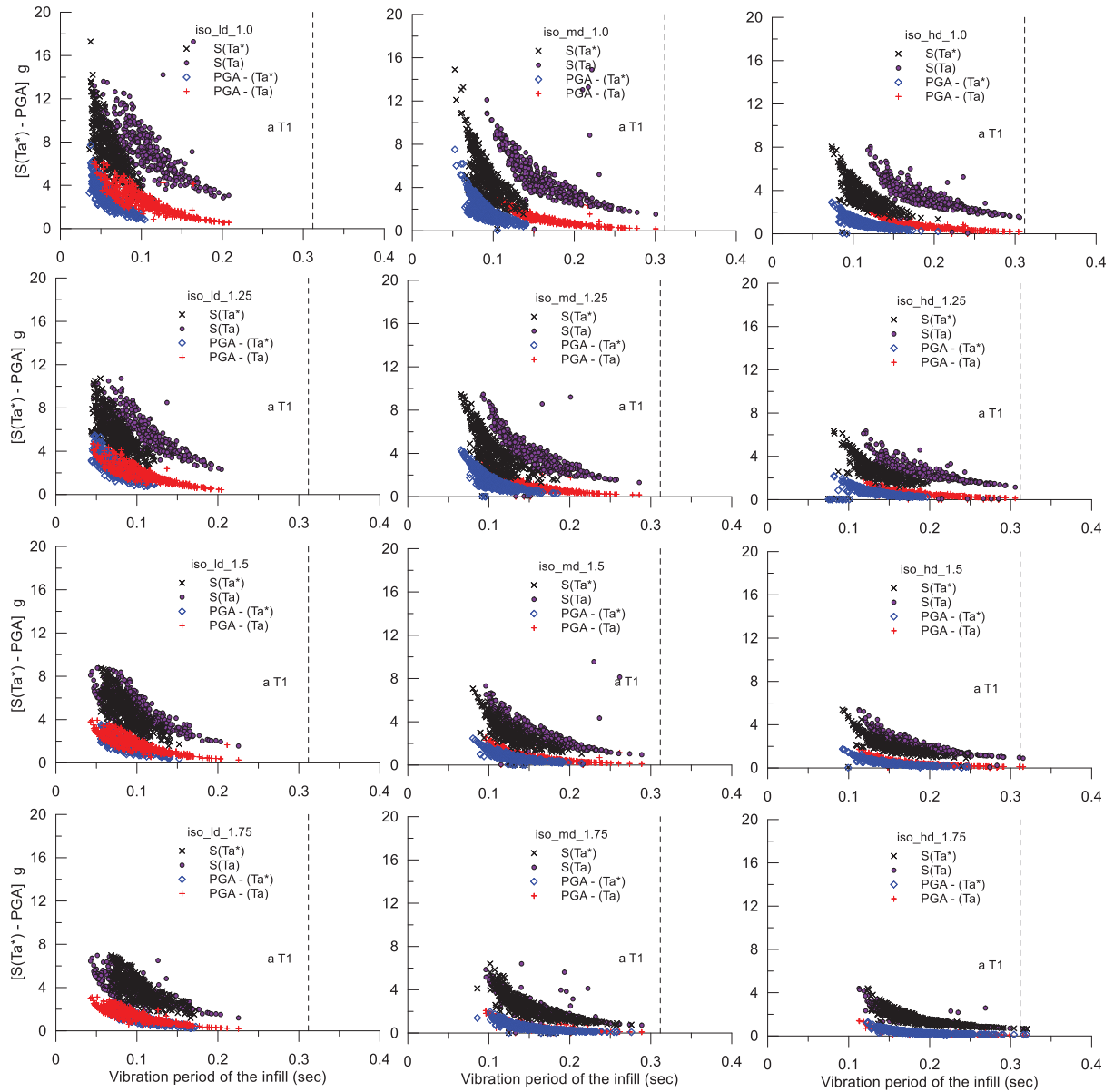


Figure 5: Results of the Monte Carlo simulations: pseudo-acceleration and PGA depending on the vibration period of the infilled walls for the case of isotropic masonry

3.2 OoP fragility curves

The OoP fragility curves obtained by means of the proposed procedure are shown focusing on the influence of the different assumptions during the investigation, which are:

- aspect ratio;
- level of IP damage;
- positioning of the infill panel with respect to the structure;
- type of masonry (solid and hollow units).

The results in terms of fragility curves obtained for solid and hollow units are shown for panels placed at both the first floor and the third floor, considering all the three levels of IP damage (low, medium, high), depending on the aspect ratio of the infill walls. In detail, Figs. 6-7 show the comparisons for given aspect ratio, while Figs. 8-9 show the comparisons for

given range of IP damage. The median and standard deviation values obtained for each case of analysis are shown in Table 4.

The fragility for the panels placed at the top of the reference structure (third floor) resulted to be higher compared to that at the base (first floor) for the same level of IP damage. At the same time, the fragility appeared higher when the level of IP damage and the aspect ratio increased. Overall, what above described was observed for both types of infills made with hollow and solid masonry units. In detail, for aspect ratio 1.0, the PGA (median) values at the first and the third floor resulted of 4.24 g and 2.70 g for the infills with solid units, while for the case of hollow masonry units, the PGA resulted in 7.52 g and 4.78 g respectively. By increasing the aspect ratio from 1.0 to 1.75 and by increasing the level of IP damage from low to high, it was observed that the PGA values dropped to 0.40 g and 0.32 g for the solid masonry units and 0.86 g and 0.55 g for the hollow units. This resulted to be very important in view of showing the high variability in the results depending upon different assumptions.

Based on the results, it can be stated that, in the absence of previous IP damage, the infilled frames provide a high strength and high PGA in the out-of-plane direction. Consequently, lower vulnerability is obtained. On the other hand, in the presence of previous IP damage, regardless of whether it is medium or high, the strength in the OoP direction drops to critical values, providing to the infilled frames very high vulnerability for low values of PGA especially at higher floors and for high values of aspect ratio. To clarify better what above described, the fragility curves for infilled frames with different aspect ratio at high level of IP damage, placed at the top of the reference 3-storey RC structure, are shown in Fig. 10 for both type of masonry walls (solid and hollow units).

	ld I			ld III			md I			md III			hd I			hd III		
Aspect ratio	median			std dev			median			std dev			median			std dev		
PGA iso (g)																		
1	4.24	2.70	1.49	2.13	1.68	1.72	1.44	0.92	1.70									
1.25	2.90	2.29	1.50	1.59	1.25	2.00	0.92	0.59	2.01									
1.5	2.46	1.57	1.53	1.06	0.67	2.15	0.71	0.45	1.81									
1.75	1.74	1.11	1.58	0.73	0.46	2.24	0.40	0.32	1.65									
PGA ortho (g)																		
1	7.52	4.78	1.63	3.92	2.49	1.66	2.45	1.56	1.63									
1.25	6.25	3.98	1.64	2.81	1.79	1.73	1.79	1.14	1.77									
1.5	4.38	2.79	1.67	2.02	1.29	1.73	1.27	0.81	1.73									
1.75	3.48	2.30	1.67	1.31	1.03	1.97	0.86	0.55	1.70									

Table 4: Results of the Monte Carlo simulations for infill walls placed at the third floor of the reference structure.

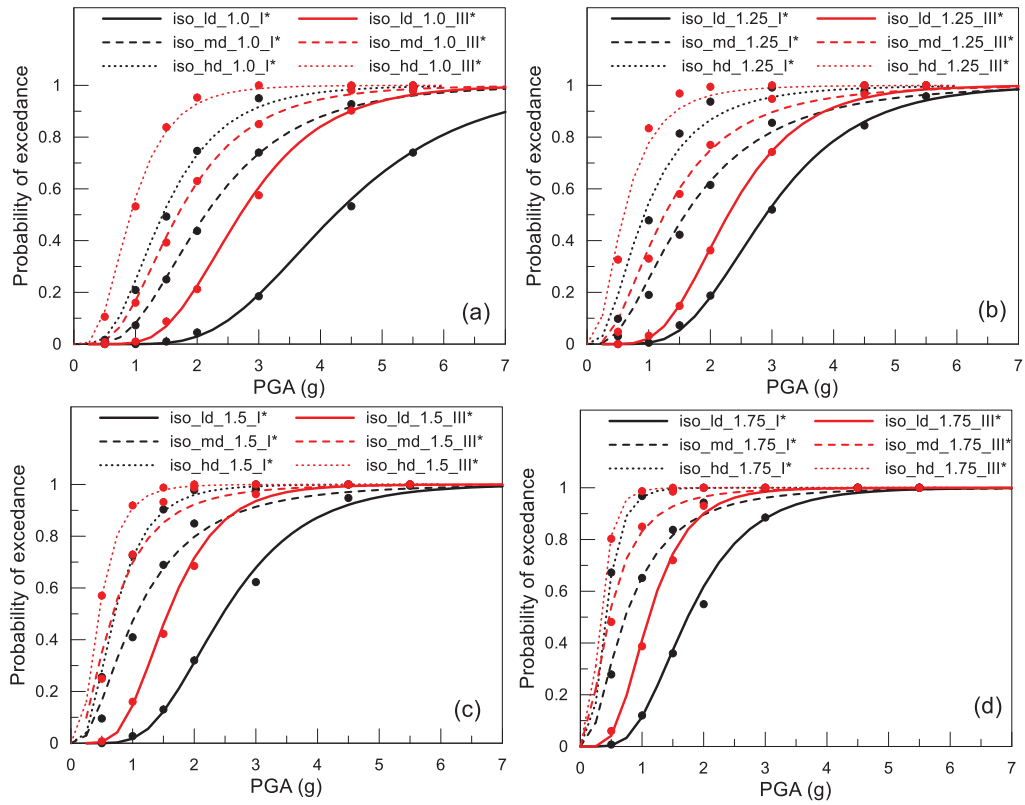


Figure 6: Fragility curves for solid masonry including low, medium and high IP damage for different aspect ratio: a) 1.0, b) 1.25, c) 1.5, d) 1.75.

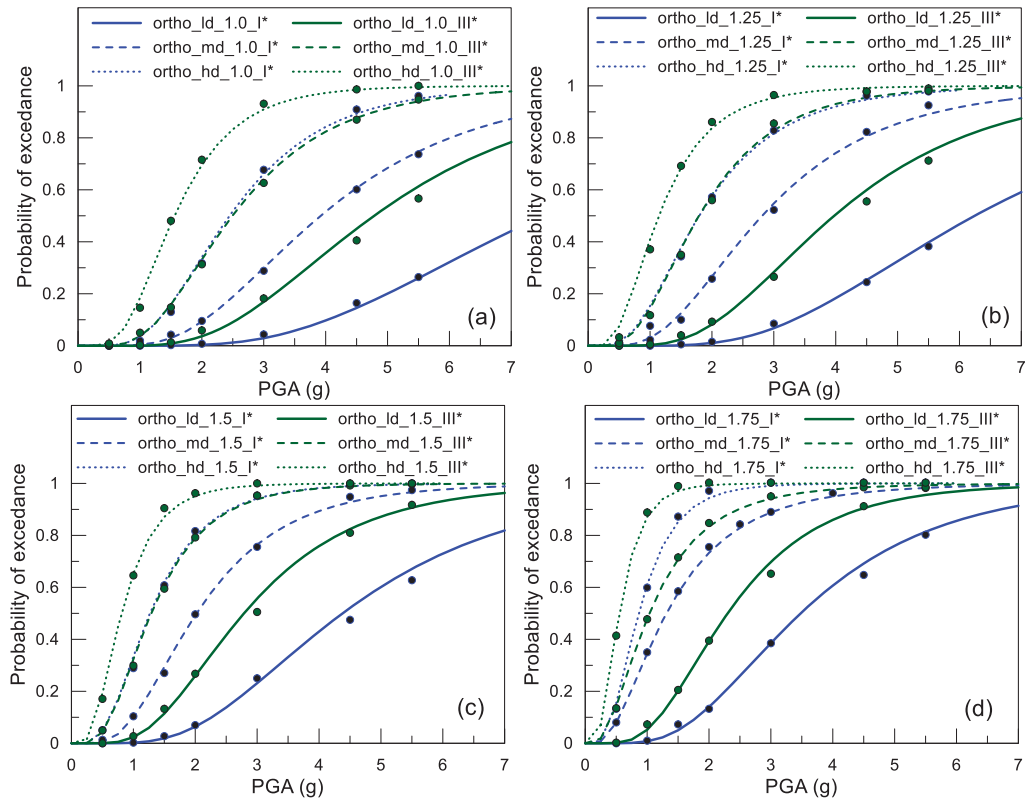


Figure 7: Fragility curves for hollow masonry including low, medium and high IP damage for different aspect ratio: a) 1.0, b) 1.25, c) 1.5, d) 1.75.

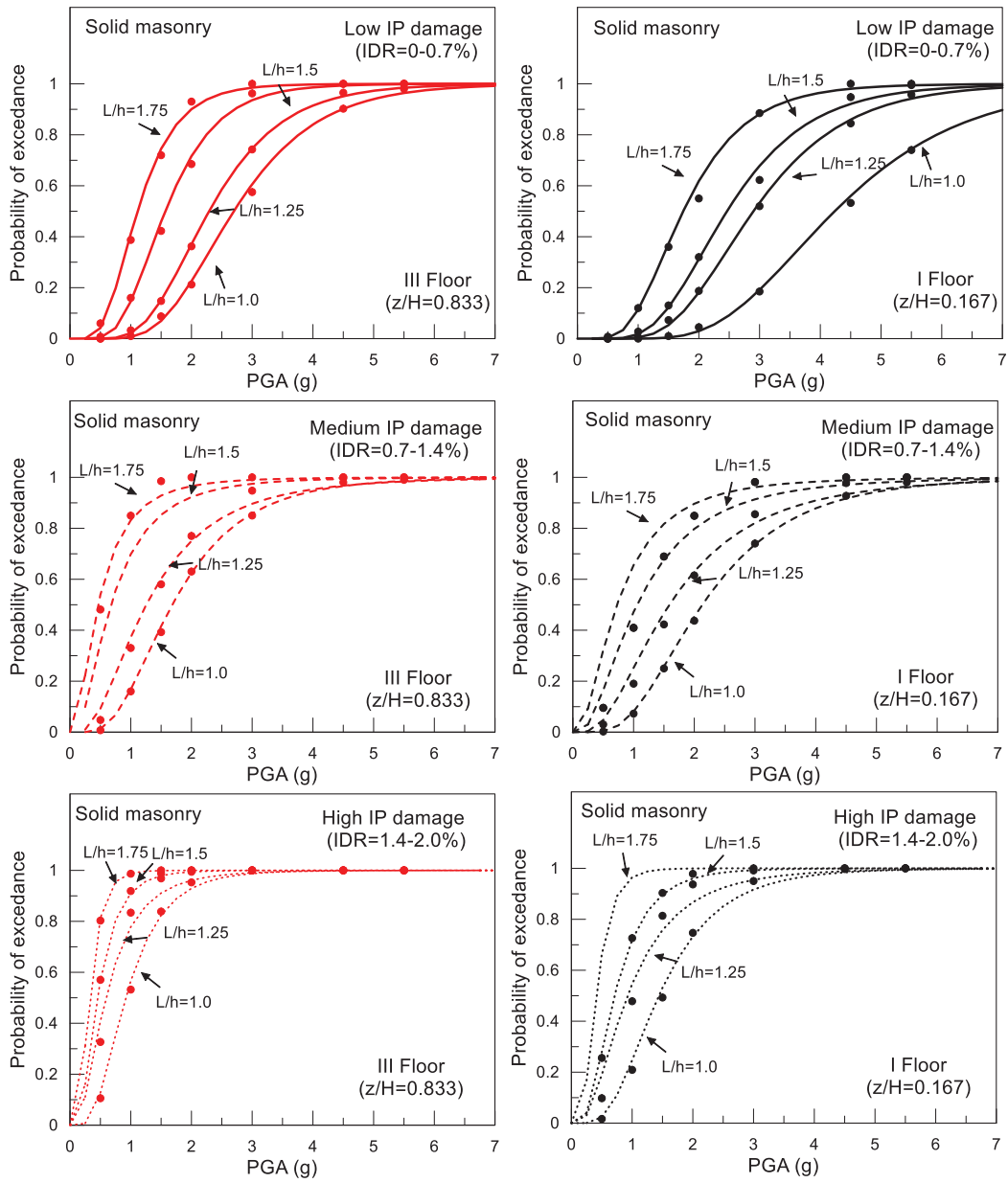


Figure 8: Fragility curves for solid masonry: influence of the aspect ratio for a given level of IP damage.

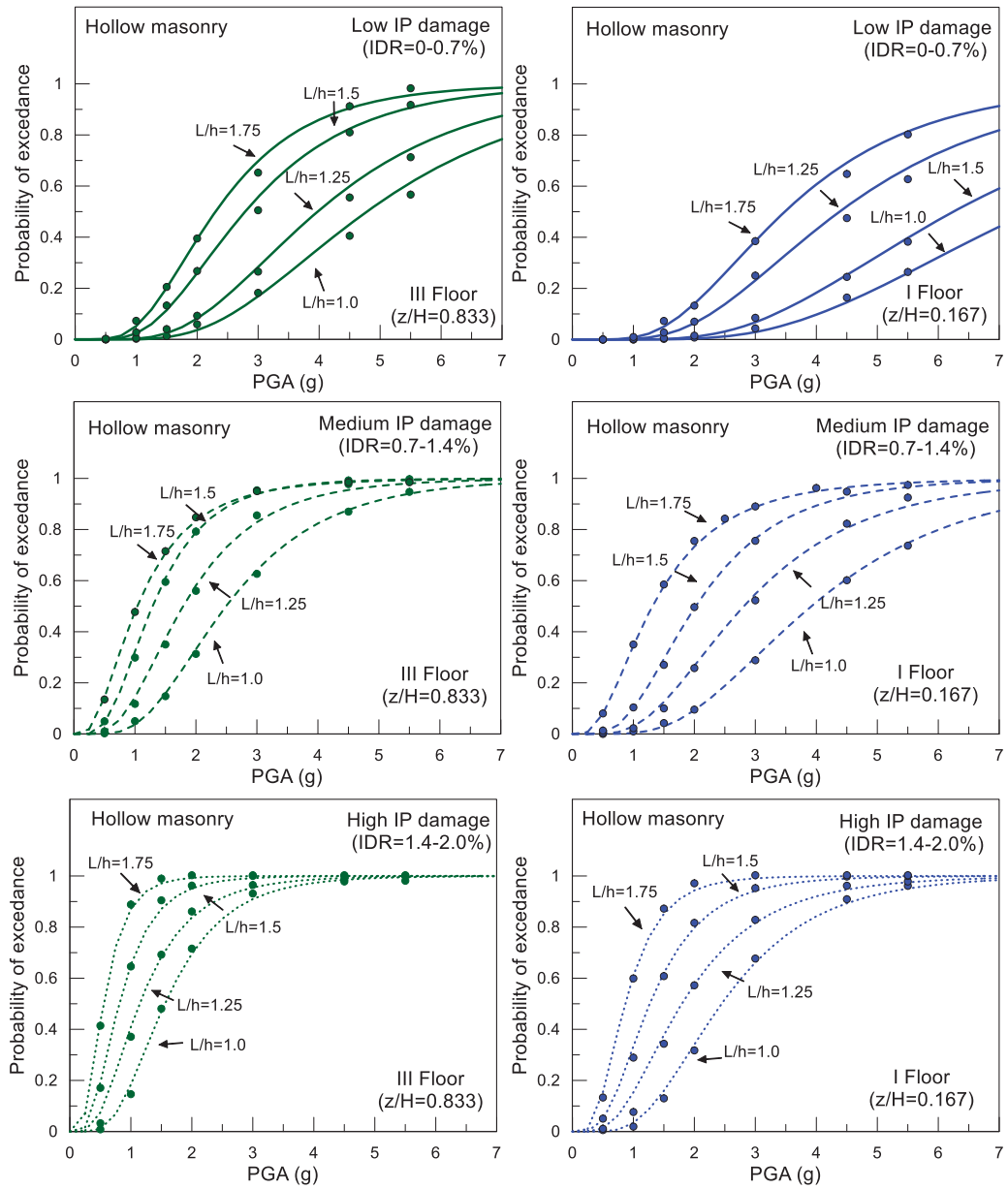


Figure 9: Fragility curves for hollow masonry: influence of the aspect ratio for a given level of IP damage.

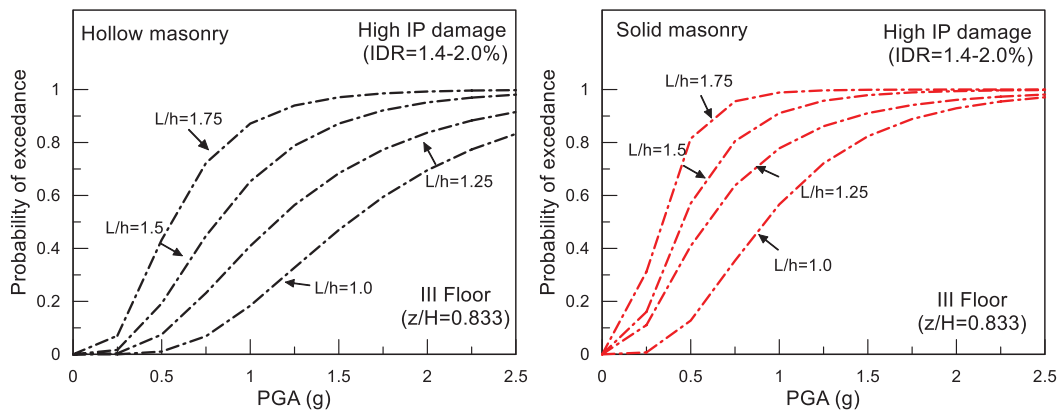


Figure 10: Page layout. Fragility for infilled frames with high IP damage placed at the top of the three-storey reference RC structure.

4 CONCLUSIONS

This paper presented a procedure for the derivation of infill walls out-of-plane fragility functions for low rise RC buildings with respect to the Peak Ground Acceleration (PGA) at collapse. A probabilistic procedure was employed based on Monte Carlo simulations, generating random input variables such as geometrical and mechanical characteristics of the panels and in-plane damage, assuming significant variations. Differently from available studies dealing with infill walls OoP fragility, the novel contribution of the present work was to take into account the uncertainties the capacity instead of in the demand. In evaluating the results, different aspects were investigated such as the influence of the aspect ratio, the influence of the level of IP damage, the influence of the positioning of the infill panel with respect to the structure and the influence of the type of masonry (solid and hollow units).

The results indicated that the OoP fragility of the infill walls increases as the level of IP damage increases as well as for the increasing of the aspect ratio. In the presence of previous IP damage, regardless of whether it is medium or high, the strength in the OOP direction drops to critical values, providing very high fragility for low values of PGA. In addition, for a given level of IP damage and aspect ratio at all floor levels from bottom to the top, the probability of collapse resulted to be higher for panels placed at the top of the structure than those placed at the base of the structure, where the pseudo acceleration of the structure is higher too.

Moreover, for the ranges assumed in this study, high PGA at collapse i.e. lower fragility was observed for infill walls made with hollow masonry units in comparison to infills made with solid masonry units.

REFERENCES

- [1] P. Ricci, F. De Luca, G.M. Verderame. 6th April 2009 L'Aquila earthquake, Italy: reinforced concrete building performance. *Bulletin of Earthquake Engineering*, **9**(1), 285–305, 2011.
- [2] M.F. Ferrotto, L. Cavaleri, F. Di Trapani, FE modeling of Partially Steel-Jacketed (PSJ) RC columns using CDP model, *Computers and Concrete*, **22**,143-152 2018.

- [3] M.F. Ferrotto, O. Fischer, L. Cavaleri. A strategy for the finite element modeling of FRP-confined concrete columns subjected to preload, *Engineering Structures*, **173** (2018), 1054-1067.
- [4] M.F. Ferrotto, L. Cavaleri, M. Papia. Compressive response of substandard steel jacketed RC columns strengthened under sustained loads: from the local to the global behavior. *Construction and Building Materials*, **179** (2018), 500-511.
- [5] G. Campione, F. Cannella, M.F. Ferrotto, M. Gianquinto. Compressive behavior of FRP externally wrapped R.C. column with buckling effects of longitudinal bars. *Engineering Structures*, **168**, 809–818, 2018.
- [6] M.F. Ferrotto, O. Fischer, L. Cavaleri. Analysis-oriented stress–strain model of CRFP-confined circular concrete columns with applied preload. *Materials and Structures*, 51:44, 2018. <https://doi.org/10.1617/s11527-018-1169-0>.
- [7] G. Campione, L. Cavaleri, F. Di Trapani, M.F. Ferrotto. Frictional effects on structural behavior of no-end-connected steel-jacketed RC columns: Experimental results and new approaches to model numerical and analytical response, *Journal of Structural Engineering ASCE*, **143**,04017070, 2017. DOI: 10.1061/(ASCE)ST.1943-541X.0001796.
- [8] M.F. Ferrotto, O. Fischer, R. Niedermeier. Experimental Investigation on the Compressive Behavior of Short Term Preloaded CFRP-Confined Concrete Columns. *Structural Concrete*,1-14, 2017. DOI:10.1002/suco.201700072.
- [9] G. Alotta, L. Cavaleri, M. Di Paola, M.F. Ferrotto. Solution for the Design and Increasing of Efficiency of Viscous Dampers, *The Open Construction and Building Technology Journal*, 10, (Suppl 1: M6) 106-121, 2016.
- [10] L. Cavaleri, F. Di Trapani, M.F. Ferrotto. Experimental determination of viscous dampers parameters in low velocity ranges. *Ingegneria Sismica*, **34**(2), 64-74, 2017.
- [11] M.F. Ferrotto, P.G. Asteris, L. Cavaleri. Strategies of Identification of a Base-Isolated Hospital Building by Coupled Quasi-Static and Snap-Back Tests, *Journal of Earthquake Engineering*, 2020. DOI: 10.1080/13632469.2020.1824877;
- [12] M.F. Ferrotto, L. Cavaleri, F. Di Trapani, P. Castaldo. Full scale tests of the base-isolation system for an emergency hospital. In *COMPADYN 2019 7th International Conference on Computational Methods in Structural Dynamics and Earthquake Engineering - vol.1* (pp. 2012-2025), 2019. M. Papadrakakis, M. Fragiadakis (eds.). Crete, Greece, 24–26 June 2019.
- [13] C. Del Vecchio, M. Di Ludovico, S. Pampanin, A. Prota, A. Repair Costs of Existing RC Buildings Damaged by the L’Aquila Earthquake and Comparison with FEMA P-58 Predictions. *Earthquake Spectra*, **34**(1), 237–263, 2018.
- [14] F. Braga, V. Manfredi, A. Masi, A. Salvatori, M. Vona. Performance of non-structural elements in RC buildings during the L’Aquila, 2009 earthquake.” *Bulletin of Earthquake Engineering*, **9**(1), 307–324, 2011.
- [15] H. Varum, A. Furtado, H. Rodrigues, L. Dias-Oliveira, N. Vila-Pouca, A. Arêde. “Seismic performance of the infill masonry walls and ambient vibration tests after the Ghorka 2015, Nepal earthquake. *Bulletin of Earthquake Engineering*, **15**(3), 1185–1212, 2017.

- [16] R. Angel, D. Abrams, D. Shapiro, J. Uzarski, M. Webster. *Behavior of reinforced concrete frames with masonry infills*. ISSN: 0069-4274, University of Illinois at Urbana-Champaign, Illinois, 1994.
- [17] F. Da Porto, G. Guidi, M.D. Benetta, N. Verlato. Combined in-plane/out-of-plane experimental behavior of reinforced and strengthened infill masonry walls. *12th Canadian masonry symposium*, **12**, 2013.
- [18] M.T. De Risi, M. Di Domenico, P. Ricci, G.M. Verderame, G. Manfredi. Experimental investigation on the influence of the aspect ratio on the in-plane/out-of-plane interaction for masonry infills in RC frames. *Engineering Structures*, **189**, 523–540, 2019.
- [19] S. Hak, P. Morandi, G. Magenes. Out-of-plane experimental response of strong masonry infills. In: *2nd European conference on earthquake engineering and seismology*, 12, 2014.
- [20] P. Ricci, M. Di Domenico, G.M. Verderame. Experimental investigation of the influence of slenderness ratio and of the in-plane/out-of-plane interaction on the out-of-plane strength of URM infill walls. *Construction and Building Materials*, **191**, 507–522, 2018.
- [21] M. Di Domenico, P. Ricci, G.M. Verderame. Empirical unreinforced masonry infill macro-model accounting for in-plane/out-of-plane interaction. In: *Proceedings of the 6th International Conference on Computational Methods in Structural Dynamics and Earthquake Engineering (COMPDYN 2017)*, Institute of Structural Analysis and Anti-seismic Research School of Civil Engineering National Technical University of Athens (NTUA) Greece, Rhodes Island, Greece, 1606–1624, 2017.
- [22] G. Gesualdi, L.R.S. Viggiani, D. Cardone, D. Seismic performance of RC frame buildings accounting for the out-of-plane behavior of masonry infills. *Bulletin of Earthquake Engineering*, **18**(11), 5343–5381, 2020.
- [23] F. Di Trapani, M. Malavisi, P.B. Shing, L. Cavaleri. Definition of out-of-plane fragility curves for masonry infills subject to combined in-plane and out-of-plane damage. *Brick and Block Masonry - From Historical to Sustainable Masonry*, J. Kubica, A. Kwiecień, and Ł. Bednarz, eds., CRC Press, 943–951, 2020.
- [24] S. Kadysiewski, K.M. Mosalam. Modeling of Unreinforced Masonry Infill Walls Considering In-Plane and Out-of-Plane Interaction. PEER 2008/102, University of California, Berkeley, **144**, 2009.
- [25] K.M. Mosalam, S. Günay. Progressive Collapse Analysis of RC Frames with URM Infill Walls Considering In-Plane/Out-of-Plane Interaction. *Earthquake Spectra*, **26**, 2015.
- [26] A. Furtado, H. Rodrigues, A. Arêde, H. Varum. Simplified macro-model for infill masonry walls considering the out-of-plane behaviour: Macro-model for Infill Walls Considering the Out-of-plane Behaviour.” *Earthquake Engineering & Structural Dynamics*, 45(4), 507–524, 2016.
- [27] F. Di Trapani, P.B. Shing, L. Cavaleri. Macroelement Model for In-Plane and Out-of-Plane Responses of Masonry Infills in Frame Structures. *Journal of Structural Engineering*, **144**(2), 04017198, 2018.
- [28] B. Pradhan, L. Cavaleri. IP-OOP interaction in URM infilled frame structures: A new macro-modelling proposal. *Engineering Structures*, **224**, 111211, 2020.

- [29] P. Ricci, M. Di Domenico, G.M. Verderame. Empirical-based out-of-plane URM infill wall model accounting for the interaction with in-plane demand. *Earthquake Engineering & Structural Dynamics*, **47**(3), 802–827, 2018.
- [30] P. Ricci, M. Di Domenico, G.M. Verderame. Nonlinear dynamic assessment of the out-of-plane response and behaviour factor of unreinforced masonry infills in reinforced concrete buildings. Proceedings of the 7th International Conference on Computational Methods in Structural Dynamics and Earthquake Engineering (COMPDYN 2019), Institute of Structural Analysis and Antiseismic Research School of Civil Engineering National Technical University of Athens (NTUA) Greece, Crete, Greece, 2103–2115, 2019.
- [31] P. Ricci, M. Di Domenico, G.M. Verderame. Effects of the In-Plane/Out-of-Plane Interaction in URM Infills on the Seismic Performance of RC Buildings Designed to Eurocodes. *Journal of Earthquake Engineering*, 1–35, 2020.
- [32] F. McKenna, G.L. Fenves, M.H. Scott. Open system for earthquake engineering simulation. University of California, Berkeley, CA. 2000.
- [33] G. Campione, L. Cavaleri, M.F. Ferrotto, G. Macaluso, M. Papia. Efficiency of Stress-Strain Models of Confined Concrete With and Without Steel Jacketing to Reproduce Experimental Results. *The Open Construction and Building Technology Journal*, **10**, (Suppl 1: M4) 65-86, 2016.
- [34] L. Cavaleri, F. Di Trapani, M.F. Ferrotto, L. Davì. Stress-Strain Models for Normal and High Strength Confined Concrete: Test and Comparisons of Literature Models Reliability in Reproducing Experimental Results. *Ingegneria Sismica*, **34**, Special Issue B, 114-137, 2017.
- [35] J.B. Mander, M.J.N. Priestley, R. Park. Theoretical Stress - Strain Model for Confined Concrete. *Journal of Structural Engineering*, **114**(8), 1804 – 1826, 1988.
- [36] G.M. Calvi, D. Bolognini, D. Seismic response of reinforced concrete frames infilled with weakly reinforced masonry panels. *Journal of Earthquake Engineering*, **5**(2), 153–185, 2001.
- [37] NTC 2018. Decreto Ministeriale delle Infrastrutture e dei Trasporti 17 gennaio 2018, Aggiornamento delle «Norme tecniche per le costruzioni»
- [38] EN 1998-1. 2004. Eurocode 8: Design of Structures for Earthquake Resistance - Part 1: General Rules, Seismic Actions and Rules for Buildings. European Committee for Standardization, Brussels.
- [39] Circolare 21 gennaio 2019, n. 7 C.S.LL.PP. Istruzioni per l'applicazione dell'«Aggiornamento delle “Norme tecniche per le costruzioni”» di cui al decreto ministeriale 17 gennaio 2018
- [40] L. Cavaleri, M. Zizzo, P.G. Asteris. Residual out-of-plane capacity of infills damaged by in-plane cyclic loads. *Engineering Structures*, 109957, 2019.

EMPIRICAL FORMULATION OF THE OUT-OF-PLANE RESISTANCE OF INFILLED FRAMES

Fabio Di Trapani^{1*}, Alessandro Vizzino¹, Giovanni Tomaselli¹, P. B. Shing²

¹ Politecnico di Torino
Dipartimento di Ingegneria Strutturale Edile e Geotecnica
Corso Duca degli Abruzzi 24
{fabio.ditrapani, giovanni.tomaselli, alessandro.vizzino}@polito.it

² University of California San Diego
Dept of structural Engineering
La Jolla, CA 92093
pshing@ucsd.edu

Abstract

The assessment of out-of-plane resistance of infilled frames is an issue of primary importance, in fact, post-earthquake damage observations have shown that infills subject to combined in-plane and out-of-plane inertial forces may fail out-of-plane. This collapse mode results particularly dangerous for the safety of people in the proximity area of a building subject to earthquake loads. Therefore, the possibility to perform accurate safety evaluations is fundamental to prevent this kind of failures. Available expressions for the evaluation of out-of-plane resistance of infilled frames are based on too restricted or too large datasets of experimental investigations. Because of this, such expressions are many times conflicting, showing good reliability in some cases and less in others. In order to fill this gap, this paper proposes a new data-driven empirical expression estimating OOP resistance of infilled frames. This expression is based on hybrid data-set, merging experimental data with data from numerical simulations obtained from a refined FE micro-model. The new expression has the advantage to take into account both the aspect ratio of the infilled frame, the influence of vertical loads and the mode of application of the OOP load. Validation tests are finally carried out against experimental and numerical specimens.

Keywords: ABAQUS, empirical, FEM, Masonry, Infilled Frames, Reinforced concrete, Data-driven

1 INTRODUCTION

The evaluation of out-of-plane (OOP) resistance of infilled frames is an issue of primary importance in the assessment of seismic risk of frame structures. In fact, even if infills are not primary structural elements, they strongly interact with primary structures undergoing in-plane (IP) damage and therefore becoming more vulnerable against out-of-plane forces. OOP failure of infills is quite dangerous to the safety of people who are around a building during an earthquake. Simple and at the same time reliable verification methods are therefore necessary to engineers to perform safety checks of OOP resistance of masonry infills.

Experimental and numerical studies have been carried out in recent years to investigate the behaviour of infilled frames subjected to combined in-plane and out-of-plane (IP + OOP) actions [1-8]. These studies converged in claiming that, following a seismic event, infill panels are weakened due to in-plane actions and combined IP and OOP cracks lead to different potential damage, ranging from the loss of functionality of the infill to its complete collapse. It should be also observed that infills with moderate-to-low slenderness and well restrained at the sides, can develop significant resistance and displacement capacity because of the arching mechanism and two-way bending effect which develops under out-of-plane actions. Several studies addressed specifically out-of-plane resisting mechanism [1,4,5,7,9-18], developing different formulations estimating OOP resistance to perform safety checks [1,18-24]. Although starting from similar theoretical consideration, results provided by these models are often conflicting [24], giving the impression that some of them are more reliable in some cases and less in others. The recognized difficulty of analytical models to achieve a general validity is due to three major aspects: a) large heterogeneity masonry constitutive materials and different potential combination with the boundary frames in terms of aspect ratio, slenderness, relative strength and stiffness; b) limited experimental background (e.g. with respect to in-plane tests); c) different OOP test loading condition (e.g. 4-point OOP test or airbag uniform pressure test). Because of these uncertainties, the definition of a generalized relationship providing a good estimation of the OOP resistance of masonry infill is still a needed.

Considering the aforementioned aspects, this paper proposes a new empirical expression estimating OOP resistance of infilled frames. The formulation of the new predictive model is based on a hybrid data-set collecting data from real experimental tests and numerical tests from a refined FE model realized in Abaqus environment which has been experimentally calibrated and validated. Parametric analyses on the FE model were carried out to generate additional reference numerical tests investigating the effect of the variation of mechanical, geometric and load conditions on the ultimate OOP resistance. A reliability comparison with available literature model is finally presented.

2 CONSIDERATIONS ON LITERATURE DESIGN MODELS FOR THE EVALUATION OF OUT-OF-PLANE RESISTANCE OF MASONRY INFILLS

For the sake of space a selection of only four literature models is presented. To make the different formulations comparable, they are expressed in terms of OOP force, by multiplying the ultimate pressure by the area of the infill ($w \times h$). One of the most popular expressions for the estimation of the ultimate OOP load capacity of an infilled frames (F_{OOP}) was proposed by Angel, 1994 [1] and Abrams et al., 1996 [9].

Those studies evaluated the out-of-plane resistance of masonry infills as a function of the degree of in plane damage. Results brought a formulation able to take in consideration the effect of previous in-plane damage and the effect of frame stiffness according to the following formulation:

$$F_{OOP} = \frac{2f_m}{(h/t)} \cdot \lambda \cdot R_1 \cdot R_2 \cdot w \cdot h \quad (1)$$

where f_m is the vertical compressive strength of the masonry expressed in [MPa] and h , w and t are the infill height, width and thickness respectively. The lengths are expressed in [mm]. Coefficients R_1 , R_2 and λ , are related to the degree of in-plane damage (Eq. 2), to the frame members flexural stiffness (Eq. 3) and to the infill slenderness (Eq. 4) respectively, so that:

$$R_1 = \left(1.08 + \left(\frac{h}{t} \right) \left\{ -0.015 + \left(\frac{h}{t} \right) \left[-0.00049 + 0.000013 \left(\frac{h}{t} \right) \right] \right\} \right)^{\Delta/2\Delta_{cr}} \quad (2)$$

$$R_2 = 0.357 + 2.49 \times 10^{-14} EI \leq 1.0 \quad (3)$$

$$\lambda = 0.154e^{-0.0985(h/t)} \quad (4)$$

in which Δ is the current previous in-plane relative displacement, Δ_{cr} is the same displacement associated with the formation of the first crack in the panel, EI is the flexural rigidity of the smallest element composing the concrete frame.

In the Eurocode 6 [22], the following formulation, based on the one-way arching mechanism, is provided:

$$F_{OOP} = f_m \left(\frac{t}{h} \right)^2 \cdot w \cdot h \quad (5)$$

Symbols appearing in Eq. (5) have the same meaning of those previously described. In this formula the out-of-plane resistance has inverse proportionality with the square of the infill slenderness ratio. An adjustment of the prediction models in Eq. (5) has been provided by Ricci et al. 2017 [23], who corrected the expression with the introduction of empirical coefficients. The experimental dataset included the tests by Angel 1994 [1], Flanagan e Bennet 1999 [10,11], Calvi and Bolognini 2001 [12], Hak et al. 2014 [13] and Furtado et al. 2016 [14]. The obtained final formulation was:

$$F_{OOP} = 1.95 f_m^{0.35} \frac{t^{1.59}}{h^{2.96}} \cdot w \cdot h \quad (6)$$

where the lengths are expressed in mm.

More recently, Liberatore et al. 2020 [24] provided a further updated considering also the influence of the aspect ratio (h/l) on the infill with the following expression:

$$F_{OOP} = 0.26 f_m^{0.9} \frac{h}{l} \left(\frac{h}{t} \right)^{-1.23} \cdot w \cdot h \quad (7)$$

Previous studies (e.g. Liberatore et. al 2020 [24]) have shown significant scattering of predictive results from these expressions, but two major considerations have to be done. The first is that some of these expression (e.g. Angel et al. 1994 [1]) were based on a limited experimental dataset. The second is that is it not realistic thinking that these expressions can be reliable in predicting the OOP resistance even of infills with RC of steel frames and also of

confined masonry. Considering single categories would be more proper but, of course, this would reduce the experimental database. The strategy adopted in the following of the paper aims to consider only infills with reinforced concrete frames. A selected number of very complete experimental tests was considered to form the database. The latter is expanded through the definition of a numerical database that is generated based on refined FE model of infilled RC frame, experimentally validated. Details of the model definition are provided in the following section.

3 REFINED FE MICRO-MODEL

The refined FE micro-model was realized with the Abaqus [25] software platform. Masonry blocks constituting the infill were modelled individually as well as frame and reinforcement elements. Mortar joint between blocks and between blocks and columns were modelled by frictional interface elements. The reference experimental test used for the model definition and calibration is specimen 80_OOP_4E by Ricci et al. 2018 [5]. The reference test considers a hollow clay masonry infilled RC frame infill restrained at the four sides having dimensions 2350mm x 1830 mm and thickness 80 mm (Fig. 1a). The out-of-plane load was applied by imposing an out-of-plane displacement with an actuator equipped with four point-load devices (Fig. 1b). Mechanical properties of specimen materials are shown in shown in Table 1.

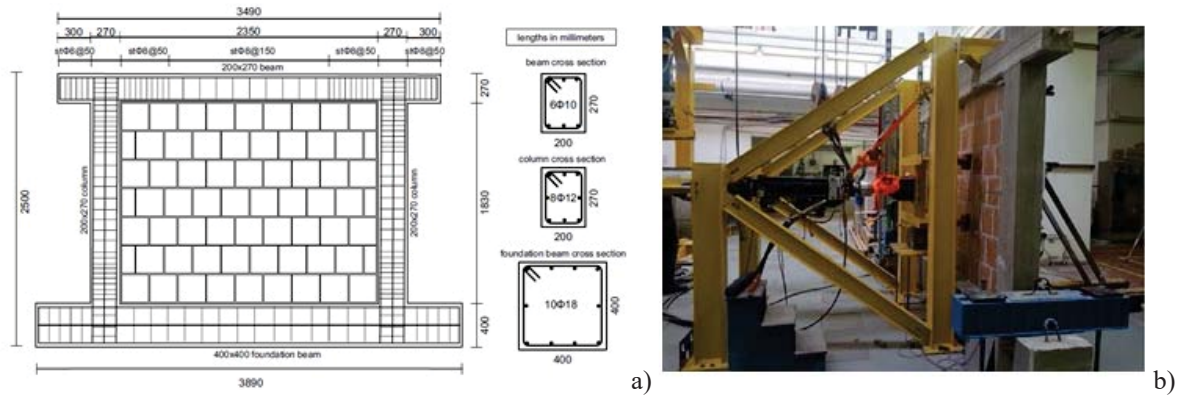


Figure 1: Specimen 80_OOP_4E by Ricci et al. 2018 [5]: a) Design details of the specimen; b) Test setup.

Mechanical properties	Symbol	Mean value (MPa)
Concrete compressive strength	f_{cm}	36.00
Steel rebars' yielding stress	f_{ym}	552
Masonry tensile strength	f_t	0.23
Bricks' compressive strength (parallel to holes)	f_{bh}	5.00
Bricks' compressive strength (perpendicular to holes)	f_{bv}	2.00
Mortar compressive strength	f_j	8.29

Table 1: Mechanical properties of the materials used in test 80_OOP_4E, Ricci et al. 2018 [5]

The concrete damaged plasticity model was used model the behaviour of brittle materials, namely concrete frame members and masonry blocks. The blocks were modelled as solid isotropic brick elements. To take into consideration the orthotropic behaviour due to the presence of hollows, a quadratic mean between the two compressive resistance in horizontal and verti-

cal direction of the block was used to define a unique reference conventional resistance value (\tilde{f}_b), so that:

$$\tilde{f}_b = \sqrt{f_{bh} \cdot f_{bv}} \quad (7)$$

where f_{bh} is the experimental horizontal compressive resistance of the unit and f_{bv} is the vertical one. The conventional elastic modulus of the blocks was estimated as a function of \tilde{f}_b , in analogy of what suggested in Eurocode 6 [22] for masonries, as:

$$\tilde{E}_b = 1000 \cdot \tilde{f}_b \quad (8)$$

The constitutive law used to define the compression behaviour of the block is of the parabolic type with a linear softening branch up to the ultimate strain ε_{cu} [26]. The model proposed by Hsu & Mo 2010 [27] was used to describe the tensile behaviour of the blocks. In Fig. 2 the constitutive laws adopted for the masonry units are shown.

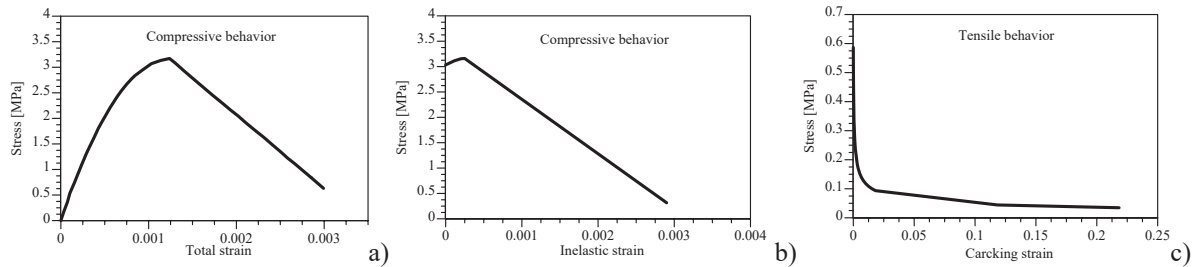


Figure 2: Constitutive laws adopted for masonry blocks: a) Compressive stress- total strain response; b) Compressive stress-inelastic strain response; c) Tensile stress- cracking strain response.

The elastic and plastic parameters in Table 2 are used for the materials definition. As regards the angle of dilatancy for the concrete a value of 37° was assumed as suggested in [25], while for masonry an angle of 10° was adopted as suggested by Van der Pluijm et al. 2000 [28]. Plastic parameters regulating the eccentricity (ε), biaxial resistance domain f_{b0}/f_{co} , and viscosity were assumed as suggested in [25].

Material	Mass density ton/m ³	Elasticity parameters			Plasticity parameters			
		Young's modulus (MPa)	Poisson's ratio ν	Dilatation Angle ψ	Eccentricity ε	f_{b0}/f_{co}	K_c	Viscosity
Concrete	2.5E-09	32308	0.3	37	0.1	1.16	0.667	0.0003
Masonry bricks	1.10E-09	3160	0.2	10	0.1	1.16	0.667	0.0003

Table 2: Material properties of concrete and masonry blocks used in ABAQUS

Steel reinforcement was modelled using 1D truss elements whose mechanical response is simulated by a simple elasto-plastic with strain hardening material model. Steel rebars were modelled as embedded elements within the concrete, so that relative sliding between steel bars and concrete could not occur.

Mortar joints behaviour was modelled using elasto-plastic interfaces with friction and cohesion. The interface normal (k_{nn}) and transverse (k_{ss} , and k_{tt}) stiffnesses were obtained following a calibration process of the model. Obtained values are reported in Table 3.

Tangential	Normal	Stiffnesses (MPa)		
Friction coefficient	Hard contact	K_{nn}	K_{ss}	K_{tt}
0.6		200	88	88

Table 3: Interfaces mechanical properties.

All the model elements were modelled by solid 3D elements with 8 nodes (C3D8R) with a sufficiently refined mesh. Fig. 3 shows the scheme of the model assembly (Fig. 3a) and the mesh of the elements (Fig. 3b). A non-linear quasi-static analysis was performed to simulate the test. Out-of-plane displacements were imposed at the four loading plates.

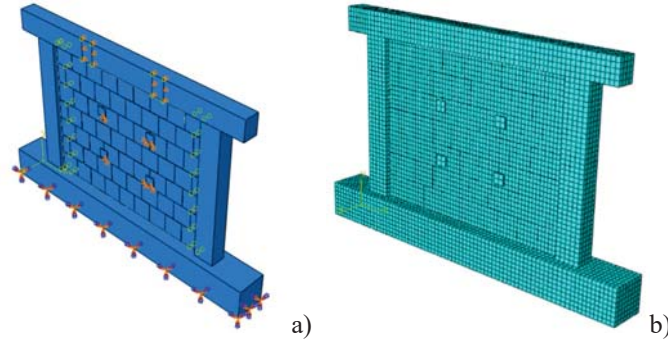


Figure 3: Definition of the micromodel: a) Scheme of the model assembly; b) Mesh of the model,

Results of the numerical simulation of the OOP test are shown in Fig. 4 and compared with the experimental response. It can be observed that the model is able to effectively reproduce the experimental behaviour in terms of initial stiffness, peak resistance, and the post peak behaviour. The deformed shape of the model in correspondence of the peak load is also shown in Fig. 5.

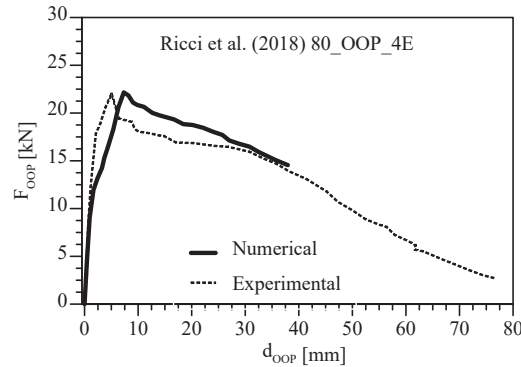


Figure 4: Comparison between numerical simulation and experimental response of the OOP test 4E by Ricci et al. 2018 [5]

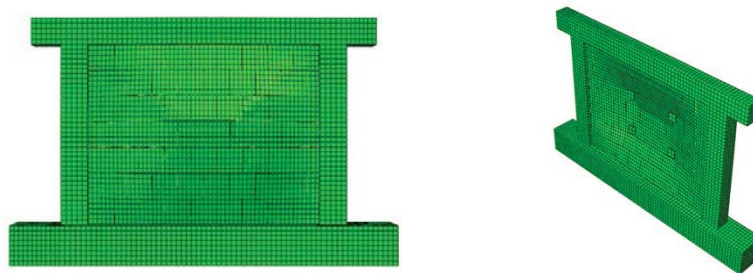


Figure 5: Deformed shape of the infilled frame micro-model in correspondence of the peak-load

The analysis allowed also an investigation in terms of stress distribution and damage localization. Figs. 6-7 show the compressive and tensile principal stresses on the windward and leeward sides of the specimen in correspondence of the peak load. The analysis of the stress field confirms that the model effectively reproduced the horizontal and vertical arching action and the 2-way bending response. A further comparison between tensile damage pattern resulting by the FE model at the ultimate displacement and real cracking pattern in shown in Fig. 8, confirming a certain consistency.

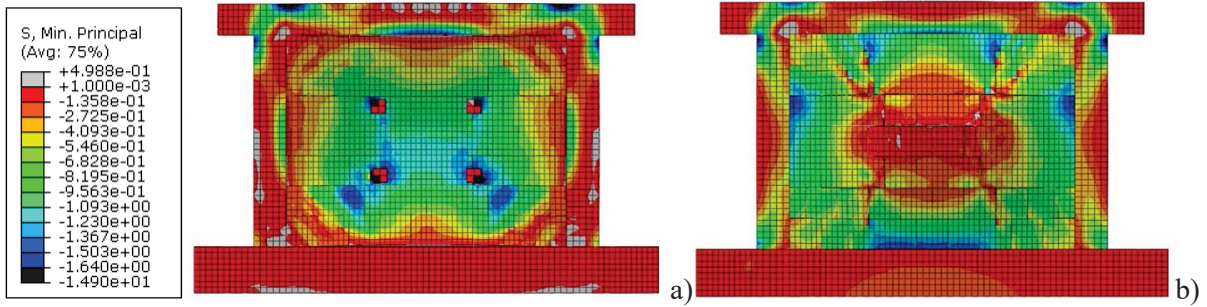


Figure 6: Compressive stress field at the peak load: a) windward side; b) leeward side.

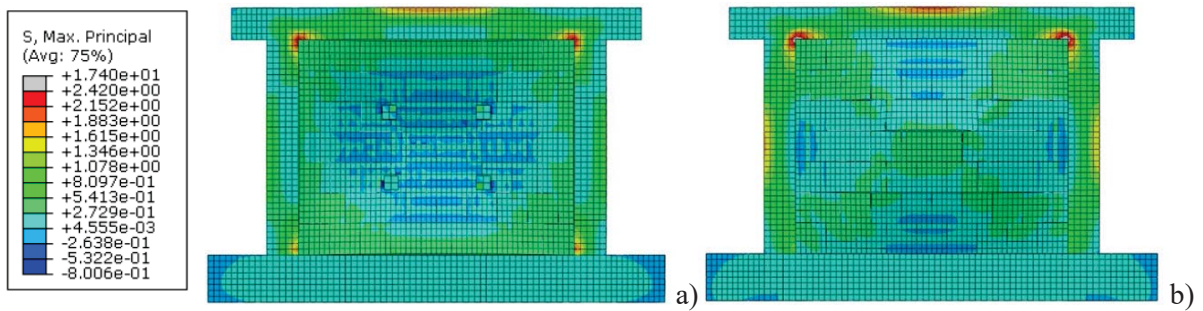


Figure 7: Tensile stress field at the peak load: a) windward side; b) leeward side.

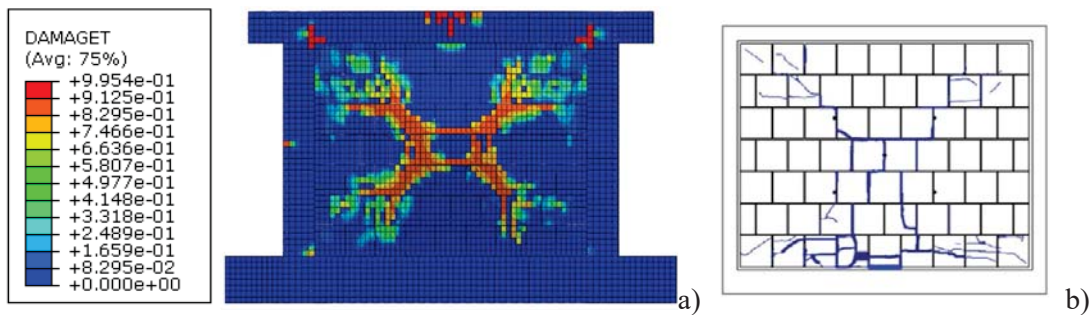


Figure 8: Ultimate displacement damage at: a) model tensile damage pattern; b) experimental cracking pattern by Ricci et. al 2018 [5].

After the calibration, the model predictive capacity has been blind-tested against two further experimental tests. These were specimens 120_OOP_4E by Ricci et al. 2018 [5] and De Risi et al. 2019 [7]. These two specimens were modelled according to the above described procedure. Experimental / numerical comparisons are shown in Fig. 9. The latter, besides validating the model, confirmed its suitability to be used as a reliable predictive tool to generate reliable simulated tests.

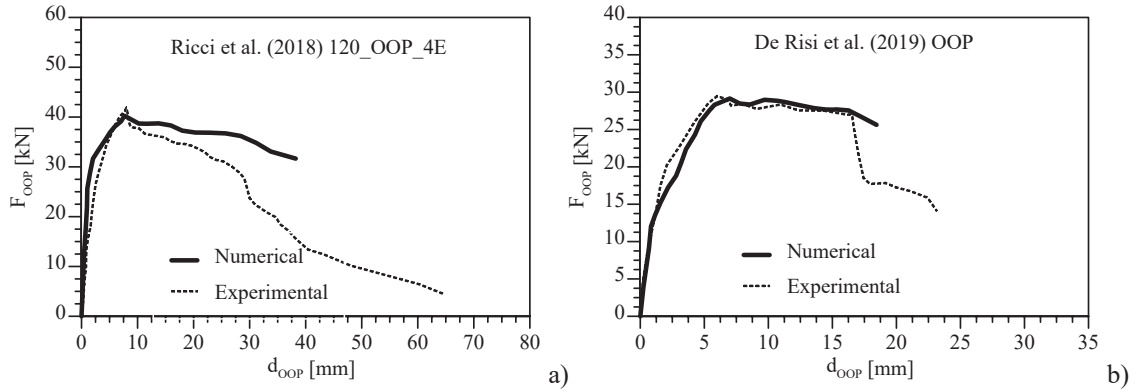


Figure 9: Comparison of numerical and experimental OOP response: a) Specimen 120_OOP_4E by Ricci et al. 2018 [5]; (b) Specimen by De Risi et al. 2019 [7] OOP

4 PARAMETRIC INVESTIGATION

The additional FE tests were generated starting from the reference models and individually varying single parameters. In this way, the influence of each variation to the overall resistance was analysed. Varied parameters were the infill slenderness (h/t), the blocks conventional resistance (\tilde{f}_b), the entity of the distributed load applied on the upper beam (q).

The variation of the slenderness ratio was performed on two different models, characterized by a different aspect ratio ($w/h=1-1.28$). The slenderness was varied between 9.15 and 22.87, to cover a sufficiently wide range. Results confirmed inverse proportionality between OOP ultimate load and slenderness (Figs. 10-11).

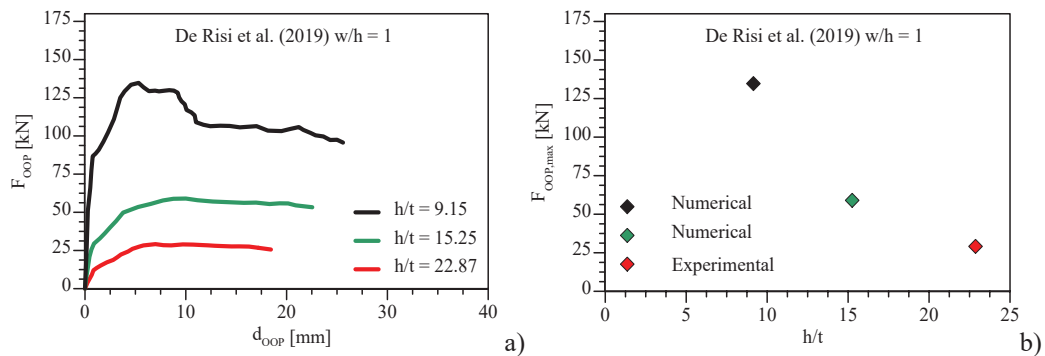


Figure 10: Effect of slenderness variation ($w/h = 1.00$): a) OOP force-displacement curves; b) Maximum OOP force vs. slenderness.

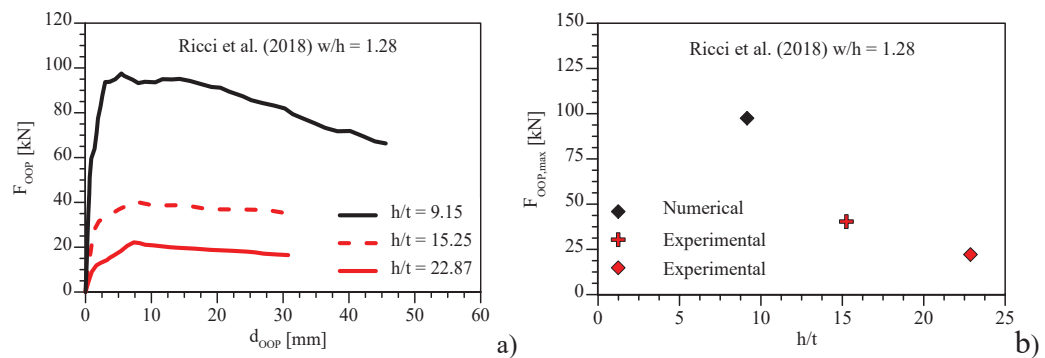


Figure 11: Effect of slenderness variation ($w/h = 1.28$): a) OOP force-displacement curves; b) Maximum OOP force vs. slenderness.

The effect of units resistance variation was evaluated on three different models, Ricci et al. 2018 [5] (infill thickness 80 and 120 mm) and De Risi et al. 2019 [7]. The latter was varied in the range 0.5-2.0 $\tilde{f}_{b,ref}$, where $\tilde{f}_{b,ref}$ is the conventional resistance originally used in the calibration and validation phases. Results show that an increment of the unit strength involves an increase of the out-of-plane resistance of the infilled frame (Figs. 12-14). This behaviour seems to be characterized by a limit, beyond which further increases of the unit strength do significantly affect the OOP resistance.

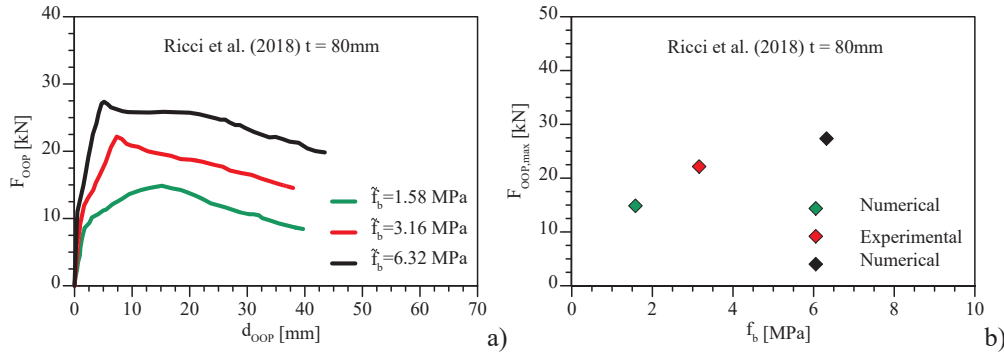


Figure 12: Effect of unit's compressive strength on the ultimate OOP capacity: a) OOP force-displacement curves; b) Maximum OOP force vs. \tilde{f}_b . Reference specimen by Ricci et al. 2018 ($t=80$ mm) [5]

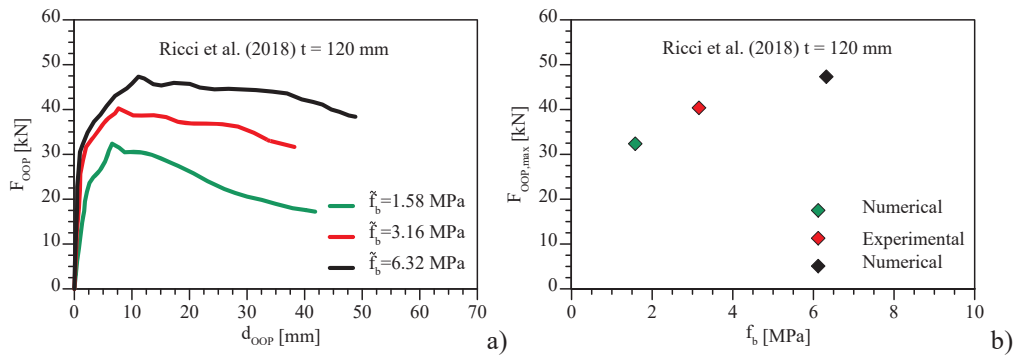


Figure 13: Effect of unit's compressive strength on the ultimate OOP capacity. a) OOP force-displacement curves; b) Maximum OOP force vs. \tilde{f}_b . Reference specimen in Ricci et al. 2018($t=120$ mm) [5]

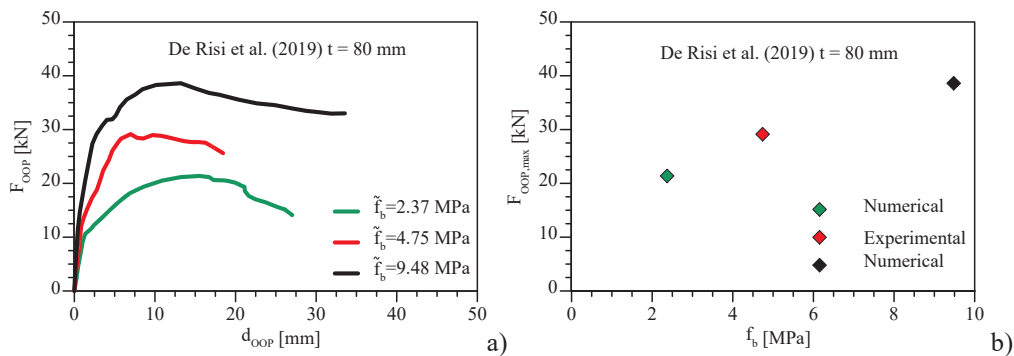


Figure 14: Effect of unit's compressive strength on the ultimate OOP capacity. a) OOP force-displacement curves; b) Maximum OOP force vs. \tilde{f}_b . Reference specimen in De Risi et al. 2019 ($t=80$ mm) [7]

The influence of a distributed load acting on the top beam was finally investigated using specimen 80_OOP_4E [5] as reference. The load was varied in the range 0-30 kN/m.

A linear increment of the OOP resistance was observed as a function of the extent of the vertical load (Fig. 15). This trend is justified by the pre-stressing action exerted on the infill by the compression load, which makes the arching mechanism more effective.

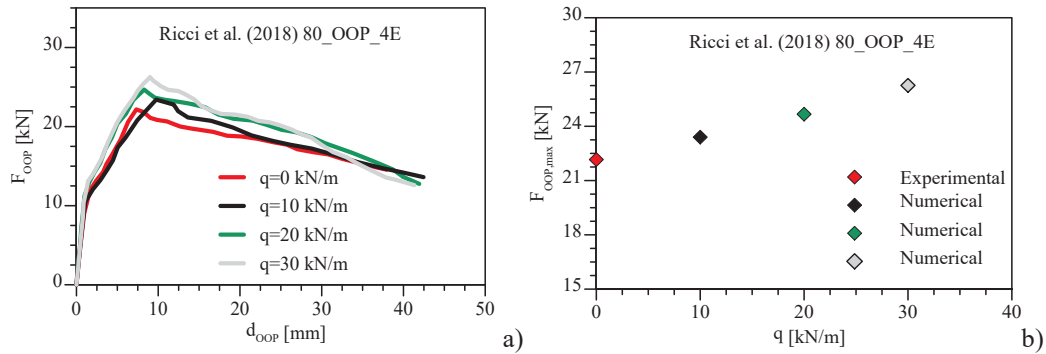


Figure 15: Effect of vertical load (q) on the ultimate OOP capacity. a) OOP force-displacement curves; b) Maximum OOP force vs. q . Reference specimen in Ricci et al. 2018 ($t=80$ mm) [5]

5 DEFINITION OF THE EMPIRICAL FORMULATION

An hybrid database composed of 9 experimental tests [1,4,5,7,12,15-17] and the 13 numerical simulations presented before was assembled to put in relation test results with the geometric and mechanical properties of the infilled frames. Data processing was performed to derive an empirical analytical relationship between the out-of-plane resistance the most relevant geometric and mechanical features of a generic infilled RC frame. The reference experimental tests and the numerical simulations are collected in Tab. 4 together with the specification of the parameters varied for each test/simulation and the modality of application of the vertical load. This latter parameter has been specifically investigated to evaluate its influence in conditioning the out-of-plane resistance. To highlight this aspect a specific test was carried out using the reference FE model 8_OOP_4E [8] and simulating its OOP response by applying a uniform load (instead of the original 4-point loading), which is more similar to the actual trend of inertial forces. Results evidenced a double OOP resistance if the infill is uniformly loaded (Fig. 16).

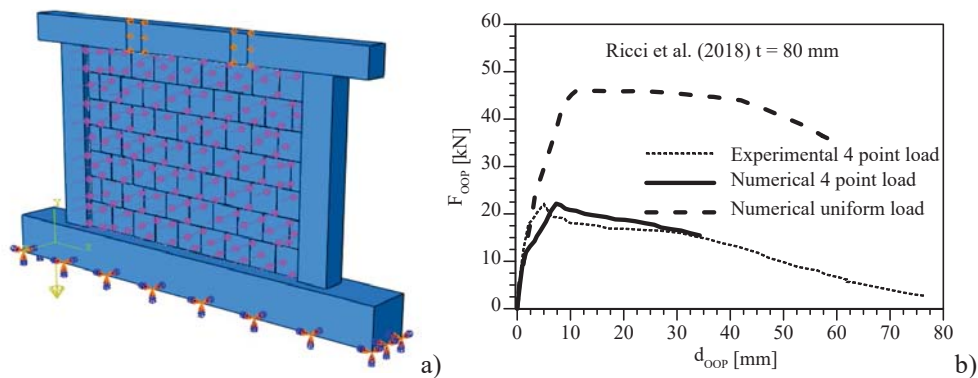


Figure 16: Effect of the way of application of the OOP load on the ultimate capacity: a) Simulation of the application of the uniform load on the FE model; b) OOP response of the FE model with 4-point and uniform load.

In consideration of results of previous numerical tests and past experimental evidence the search for a new empirical formulation considered the following major parameters: aspect ratio of the infill (w/h), slenderness of the infill (h/t), conventional resistance of the units (\tilde{f}_b),

resulting vertical load acting on the upper beam ($Q = q \cdot w$) and mode of application of the OOP load (α). The latter coefficient allows uniformizing OOP test results obtained by 4-point load tests and airbag tests (uniform loading). The proposed predictive relationships allows direct evaluation of the undamaged OOP resistance of an infilled frame. The latter has the following expression:

$$F_{OOP} = \alpha \cdot \left[\left(\frac{w \cdot h}{100} \right)^\beta \left(\frac{w}{h} \right)^{-0.41} \tilde{f}_b^{0.43} \left(\frac{h}{t} \right)^{-1.67} + 0.058 \cdot Q \right] \quad (9)$$

where β is an aspect-ratio related coefficient defined as:

$$\beta = -0.372 \cdot \left(\frac{w}{h} \right)^2 + 0.787 \frac{w}{h} + 0.3455 \quad (10)$$

and α is the conversion factor used to make experimental 4-point load test and uniform load tests comparable and assuming the following values:

$$\begin{cases} \alpha = 1 & \text{4-point load} \\ \alpha = 1.557 \left(\frac{w}{h} \right)^{1.138} & \text{uniform load} \end{cases} \quad (11)$$

A comparison between experimental and numerical OOP resistance values with the predictions by Eq. (9) is shown in Fig. 17, demonstrating very low dispersion of results by the proposed empirical model.

Test reference	Specimen	h (mm)	w (-)	w/h (mm)	t (mm)	h/t (-)	\tilde{f}_b (N/mm ²)	Q (kN)	Load appl.	F_{OOP} (kN)
Ricci et al. [5]	80_OOP_4E	1830	2350	1.28	80	22.9	3.16	0	4-point	22.16
	120_OOP_4E	1830	2350	1.28	120	15.3	3.16	0	4-point	41.90
De Risi et al. [7]	OOP	1830	1830	1.00	80	22.9	4.74	0	4-point	29.14
Calvi & Bolognini [12]	10	2750	4200	1.53	135	20.4	6.57	0	4-point	33.70
Koutas & Bournas [16]	S_CON	1250	1700	1.36	65	19.2	21.00	0	4-point	29.00
Angel et al. [1]	1	1625	2438	1.50	48	33.9	23.90	0	Airbag	33.90
Sepasdar [4]	IF-ND	980	1350	1.38	90	10.9	12.80	0	Airbag	87.71
Akhoundi et al. [15]	SIF-B	1635	2415	1.48	80	20.4	4.29	0	Airbag	39.70
Nasiri & Liu [17]	IFNG	980	1350	1.38	90	10.9	25.00	0	Airbag	140.00
FEM – Analyses	FEM-R-L1	1830	2350	1.28	80	22.9	3.16	0	Airbag	45.43
	FEM-DR-G1	1830	1830	1.00	120	15.3	4.74	0	4-point	56.98
	FEM-R-G2	1830	2350	1.28	200	9.2	3.16	0	4-point	101.39
	FEM-DR-G2	1830	1830	1.00	200	9.2	4.74	0	4-point	133.72
	FEM-R-M1	1830	2350	1.28	80	22.9	1.58	0	4-point	16.29
	FEM-R-M2	1830	2350	1.28	80	22.9	6.32	0	4-point	29.57
	FEM-DR-M1	1830	1830	1.00	80	22.9	2.37	0	4-point	21.49
	FEM-DR-M2	1830	1830	1.00	80	22.9	9.48	0	4-point	39.00
	FEM-R-M3	1830	2350	1.28	120	15.3	1.58	0	4-point	32.07
	FEM-R-M4	1830	2350	1.28	120	15.3	6.32	0	4-point	58.20
	FEM-R-Q1	1830	2350	1.28	80	22.9	3.16	23.5	4-point	23.31
	FEM-R-Q2	1830	2350	1.28	80	22.9	3.16	47.0	4-point	24.68
	FEM-R-Q3	1830	2350	1.28	80	22.9	3.16	70.5	4-point	26.04

Table 4: Hybrid experimental/numerical database

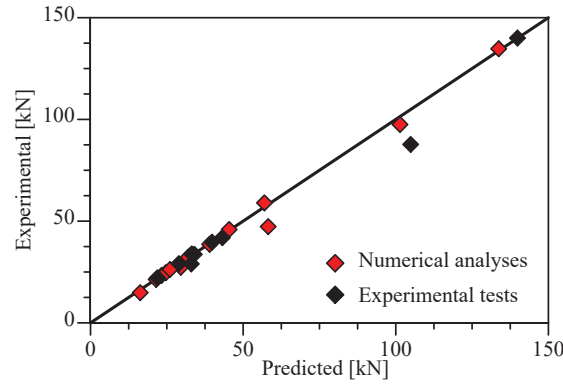


Figure 17: Comparison between experimental and predicted OOP resistance values by the proposed formulation.

6 COMPARISONS WITH THE EXISTING PREDICTIVE MODELS

A comparative analysis of the proposed relationship with respect to the predictive models available in the literature is finally carried. For this comparison only experimental test results were considered. The reference experimental tests and the respective experimental and predicted OOP resistance values are shown Table 5. Results are graphically represented in Fig. 18. It can be observed how the proposed model is able to fit better than the other predictive models. The models proposed by Ricci et al. 2017 [23] and Liberatore et al. 2020 [24] provided also an adequate reliability although they seem having an overestimation tendency. On the contrary, the model by Angel 1994 [1] significantly underestimated the experimental results. The improved predictive capacity shown by the proposed model with respect to the previous ones is justified by the fact that this model enriches the formulation taking into account additional information such as the influence of vertical loads and the mode of application of the out-of-plane load. Moreover, the model is specifically calibrated using only OOP tests of in-filled RC frames, therefore it results more accurate than the other formulations base on a more heterogeneous database.

Experimental study	Specimen	$F_{OOP,exp}$ [kN]	$F_{OOP,pred}$ [kN]				Proposed model
			Angel [1]	EC6 [22]	Ricci [23]	Liberatore [24]	
Ricci et al. [5]	80_OOP_4E	22.16	6.84	14.88	31.10	52.58	21.95
	120_OOP_4E	41.90	19.81	30.51	57.37	31.61	43.20
De Risi et al. [7]	OOP	29.14	7.13	15.17	26.62	47.88	28.95
Calvi & Bolognini [12]	10	33.70	21.79	30.62	48.30	82.71	33.99
Koutas & Bournas [16]	S_CON	29.00	20.95	55.74	61.44	40.28	33.03
Angel et al. [1]	1	33.90	10.32	39.12	34.07	16.99	33.15
Sepasdar [4]	IF-ND	87.71	47.40	104.89	130.44	170.46	104.88
Akhoundi et al. [15]	SIF-B	39.70	3.20	9.45	32.39	80.52	39.80
Nasiri & Liu [17]	IFNG	140.00	91.42	190.80	160.83	99.48	139.87
<i>Mean exp/pred</i>			3.49	1.45	0.83	0.86	0.97
<i>Std. Dev.</i>			3.47	1.12	0.24	0.58	0.07

Table 5: Experimental OOP resistance values and their analytical prediction.

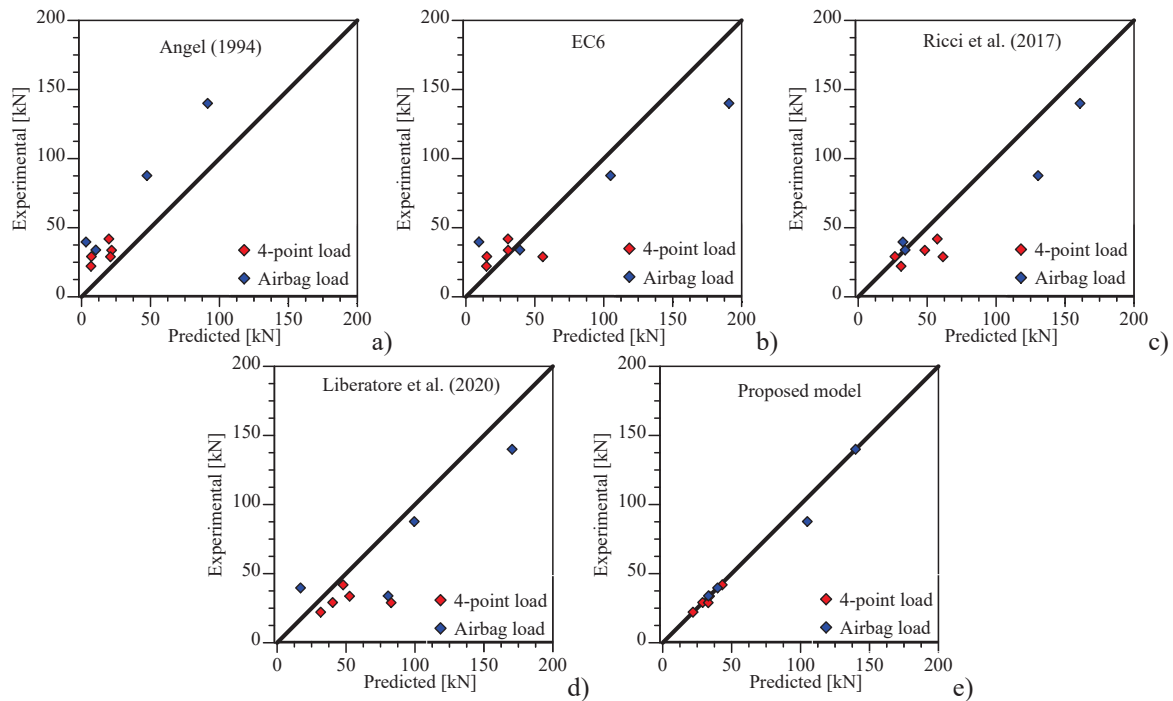


Figure 18: Reliability comparison of models for the prediction of OOP resistance: a) Angel 1994 [1]; b) Euro-code 6 [22]; c) Ricci et al. 2017 [23]; d) Liberatore et al. 2020 [24]; e) proposed model.

7 CONCLUSIONS

Assessment of out-of-plane capacity of infilled frames is not straightforward. Available literature models for the prediction of the out-of-plane resistance are often conflicting, being in general too conservative or, on the contrary, overestimating the capacity. The reasons of this inconsistencies are different. First of all, some of the available models (e.g. Angel et al. [1]) are calibrated based on a limited investigation. Conversely, other literature models have been defined using a too wide dataset, including also steel infilled frames or confined masonries. Finally, the way of application of the OOP load influences on the OOP capacity, therefore some formulations can result unsuitable in match experimental results of specimens loaded with different modalities (e.g. 4-point load or uniform load). In consideration of this, a hybrid database, composed of 9 experimental tests and 13 numerical simulations by a refined FE micro-model was specifically defined. FE models allowed increasing the extent of the dataset and to investigate on the influence of some parameters not taken into account by previous experimental investigations (e.g. the influence of distributed load on the upper beams or the influence of the modality of application of the OOP load).

Postprocessing of the collected data allowed defining a new empirical relationship for the direct estimation of the OOP resistance of a generic infilled frame. The proposed model showed matching better the other the experimental results. The reasons of its better capability in estimating experimental results is justified by the following major considerations:

- The model takes into account the way of application of the OOP load, which greatly influences the OOP resistance.
- The model considers the influence of vertical loads which increase the effectiveness of the arching mechanism.

- The model proposes the use of the conventional unit compressive strength (\tilde{f}_b) instead of the vertical strength of the masonry as parameter having major correlation with the OOP resistance of the infill.

REFERENCES

- [1] Angel R. Behavior of reinforced concrete frames with masonry infill walls. *University of Illinois at Urbana-Champaign*, Illinois; 1994.
- [2] Calvi G.M., Bolognini D. Seismic response of reinforced concrete frames infilled with weakly reinforced masonry panels. *Journal of Earthquake Engineering*, 5, 153-185; 2001.
- [3] Morandi P., Hak S., Magenes G. 2011. Report of the experimental campaign on robust clay masonry infills. *Fondazione Eucentre*, Pavia; 2011.
- [4] Sepasdar R. Experimental investigation on the out-of-plane behaviour of concrete masonry infilled frames. *Master's Thesis, Dalhousie University*; 2017.
- [5] Ricci P., Di Domenico M., Verderame G.M. Experimental assessment of the in-plane/out-of-plane interaction in unreinforced masonry infill walls. *Engineering Structures*, 173, 960–978; 2018.
- [6] Wang C. Experimental investigation on the out-of-plane behaviour of concrete masonry infilled frames. *Master's Thesis, Dalhousie University*; 2019.
- [7] De Risi M.T., Di Domenico M., Ricci P., Verderame G.M., Manfredi G. Experimental investigation on the influence of the aspect ratio on the in-plane/out-of-plane interaction for masonry infills in RC frames. *Engineering Structures*, 189, 523-540; 2019.
- [8] Di Domenico M., De Risi M.T., Ricci P., Verderame G.M., Manfredi G. Empirical prediction of the in-plane/out-of-plane interaction effects in clay brick unreinforced masonry infill walls. *Engineering Structures*, 227, 111438; 2021.
- [9] Abrams D.P., Angel R., Uzarski J. Out-of-plane strength of unreinforced masonry infill panels. *Earthquake Spectra*, 12(4), 825–844; 1996.
- [10] Flanagan R.D., Bennett R.M. Arching of masonry infilled frames: Comparison of analytical methods. *Practice Periodical on Structural Design and Construction*, 4(3), 105-110; 1999a.
- [11] Flanagan R.D., Bennett R.M. Bidirectional behavior of structural clay tile infilled frames. *ASCE Journal of Structural Engineering*, 125(3), 236-244; 1999b.
- [12] Calvi G.M., Bolognini D. Seismic Response of Reinforced Concrete Frames Infilled with Weakly Reinforced Masonry Panels. *Journal of Earthquake Engineering*, 5, 153-185; 2001.
- [13] Hak S., Morandi P., Magenes G. Out-of-plane experimental response of strong masonry infills. *2nd European conference on earthquake engineering and seismology*; 2014.
- [14] Furtado A., Rodrigues H., Arede A., Varum H. Experimental evaluation of out-of-plane capacity of masonry infill walls. *Engineering Structures*, 111, 48-63; 2016.

- [15] Akhoundi F., Vasconcelos G., Lourenço P. Experimental out-of-plane behavior of brick masonry infilled frames. *International Journal of Architectural Heritage*, 18, 1-7; 2018.
- [16] Koutas L.N., Bournas D.A. Out-of-plane strengthening of masonry-infilled RC frames with textile-reinforced mortar jackets. *Journal of Composites for Construction*, 23 (1); 2019.
- [17] Nasiri E., Liu Y. Effect of prior in-plane damage on the out-of-plane performance of concrete masonry infills. *Engineering Structures*, 222, 111-149; 2020.
- [18] McDowell E.L., Mckee K.E., Sevin E. Arching action theory of masonry walls. *Journal of the Structural Division*, 82, 915/1-18; 1956a.
- [19] Dawe J.L., Seah C.K. Out-of-plane resistance of concrete masonry infilled panels. *Canadian Journal of Civil Engineering*, 16(6), 854-864; 1989.
- [20] Bashandy T., Rubiano N., Klingner R. Evaluation and analytical verification of infilled frame test data. P.M. Ferguson Structural Engineering Laboratory, *Report No.95-1, Department of Civil Engineering University of Texas at Austin*, Austin, Tx; 1995.
- [21] FEMA 356 (Federal Emergency Management Agency). Prestandard and commentary for the seismic rehabilitation of buildings. *Washington DC: FEMA*; 1997.
- [22] CEN (European Committee for Standardisation). Eurocode 6 – Design of masonry structures, Part 1-1: Common rules for reinforced and unreinforced masonry structures. *EN 1996-1-1*, Brussel, Belgium: CEN; 2005.
- [23] Ricci P., Di Domenico M., Verderame G.M. Empirical based out of plane URM infill wall model accounting for the interaction with in plane demand. *Earthquake Engng Struct Dyn*;1–26; 2017.
- [24] Liberatore L., AlShawa O., Marson C., Pasca M., Sorrentino L. Out-of-plane capacity equations for masonry infill walls accounting for openings and boundary conditions. *Engineering Structures*, 207, 110198; 2020.
- [25] Simulia. ABAQUS/CAE *User Manual, version 6.13*; 2013.
- [26] Kent D.C., Park R. Flexural Members with Confined Concrete. *Journal of Structural Division*, 97, 1969-1990; 1971.
- [27] Hsu T.T.C, Mo Y.L. Unified Theory of Concrete Structures. *John Wiley&Sons, Ltd*; 2010.
- [28] Van der Pluijm R., Rutten H., Ceelen M. Shear behaviour of bed joints. *12th international brick/block masonry conference*, 1849-1862; 2000.

MECHANICAL VS EMPIRICAL MODELS FOR MODELS IN-PLANE RESPONSE OF INFILLED FRAMES: RELIABILITY COMPARISON AND VALIDATION OF A NEW DATA-DRIVEN MODEL

Fabio Di Trapani^{1*}, Giovanni Tomaselli¹, and Gabriele Bertagnoli¹

¹ Politecnico di Torino
Dipartimento di Ingegneria Strutturale Edile e Geotecnica
Corso Duca degli Abruzzi 24
{ fabio.ditrapani, giovanni.tomaselli, gabriele.bertagnoli }@polito.it

Abstract

The paper proposes a new quadri-linear empirical force-displacement relationship to model the inelastic response of infill equivalent struts. The definition of the model is based on a data-driven approach rather than a mechanical one, therefore parameters defining the force-displacement curve are analytically evaluable by means of empirical correlations. The latter link the force-displacement parameters regulating the axial response to the geometrical and mechanical features of an infilled frame. The analytical correlations are obtained from an experimental data-set enlarged with data from refined finite element simulations. Blind validation tests of the proposed modelling procedure are carried out against experimental results different from those used to build the data-set. A reliability comparison between mechanics-based models and empirical models is finally presented and discussed.

Keywords: OpenSees, empirical, FEM, Masonry, Infilled Frames, Reinforced concrete, Data-driven

1 INTRODUCTION

Infill-frame interaction has been largely investigated during last 60 years by researchers from all over the world. Despite this, the interest devoted to this topic is still noticeable. This can be easily observed, for example, by the experimental activity, which continues nowadays. In fact, besides the availability of a number of in-plane experimental tests (e.g. [1- 7]), several new ones have been performed out only recently (e.g. [8-14]). In the same period, thanks to the improvements in the efficiency of computational capacity of computers and software, in-depth numerical studies were also addressed to assess the global influence of infills in seismic response of building frames [15-23] or local interaction issues [24-28].

Comparing an overview of past and recent literature on in-plane equivalent strut modelling of infilled frames, it results that predictions from different models lead to results which are many times conflicting [16,29-32], raising doubts on the reliability of the different models. One of the possible reasons is the fact that most of the force-displacement relationships used to model the response of the equivalent struts, are based on mechanical approaches, which are typically a consequence of supposing limit equilibrium conditions. Unfortunately, this way of approaching this problem may fail in accuracy if the actual collapse mechanism is different from the one assumed. Another reason is that most of past design equations were calibrated on the experimental knowledge available in a previous period or for a specific typology of infills. Based on these premises, this paper first presents a new equivalent strut macro-model, which is defined using an empirical data-driven approach. A typical quadri-linear axial-force/axial-displacement relationship is proposed for the axial response of the struts. The force-displacement model is simply ruled by four parameters modulating the cracking strength, the post-cracking stiffness, the softening branch, and the residual strength peak strength. Analytical expressions for these parameters are derived in the paper making use of a hybrid experimental/numerical data-set, built after an iterative calibration process of the equivalent strut models on real experimental tests and additional finite element simulations. The four analytical correlation laws directly link geometrical and mechanical properties of an infilled frame to four parameters (called force-displacement parameter) regulating the force-displacement relationship. Blind validation tests of the model are carried out against eight different experimental test data, not belonging to those used to build the data-set used to derive the correlation laws. The proposed model predictive capacity is also compared to that of other six literature models making consideration about the different reliability of mechanics based and empirical based formulations.

2 PROPOSED EQUIVALENT STRUT MODEL

2.1 Computational model and formulation

The computational scheme of the proposed model refers to the classical configuration of a pair of compression-only concentric equivalent struts (**Fig. 1a**). Beam and column elements are modelled using distributed plasticity fiber-section elements. The equivalent strut elements are modelled as trusses with inelastic force-displacement behaviour, characterized by the axial force – axial displacement behaviour illustrated in **Fig. 1b**. In the current study, the *OpenSees* software platform [34] is used to perform modeling and simulations. The *Pinching 4* material is used to model the axial response of the struts. However, this modelling strategy can be easily reproduced with any structural software handling nonlinear analysis of frame structures, using multilinear plastic links as shown by [11].

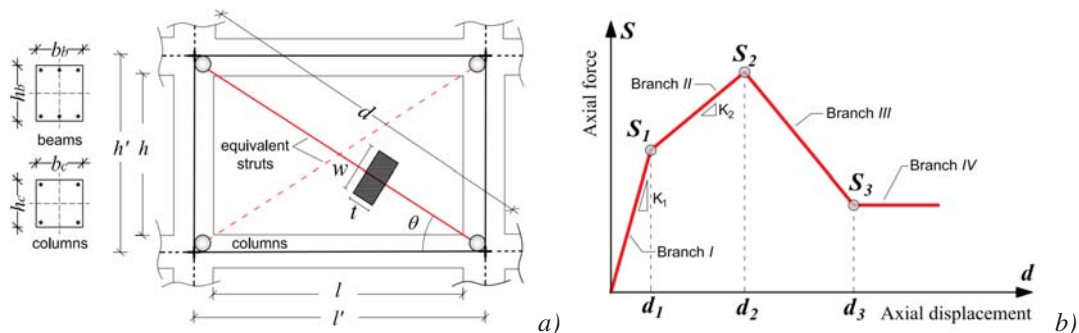


Figure 1. Equivalent strut modelling of the frame-infill system: a) Geometric configuration; b) Proposed axial force – axial displacement model for the struts.

The shape of the inelastic relationship for the strut is the same as the one proposed by other authors (e.g. [35,36]). The latter provides an initial uncracked branch up to the point S_1-d_1 , characterized by the stiffness K_1 , a second cracked stiffness branch up to the peak point S_2-d_2 , having stiffness K_2 , a third softening branch and a fourth residual strength branch starting in correspondence of the point S_2-d_3 . The latter branch can be considered having unlimited or specified deformation threshold. The force-displacement is defined as follows.

Branches 1 and 2, are evaluated similarly to what provided by [11] and [37], therefore, the initial stiffness (branch I) is defined as:

$$K_1 = \frac{\tilde{E}_m t w}{d} \quad (1)$$

where t , w and d are the thickness, the width and the length of the diagonal strut and \tilde{E}_m is the conventional elastic modulus, defined as [33]:

$$\tilde{E}_m = \sqrt{E_{m1} \cdot E_{m2}} \quad (2)$$

in which E_{m1} and E_{m2} are the Young moduli of masonry along the horizontal and vertical direction respectively. As regards the identification of the equivalent strut cross-section width (w), this is performed by following the procedure proposed by [33]. The stiffness of branch II is related to the stiffness K_1 by the parameter β (≤ 1) as:

$$K_2 = \beta K_1 \quad (3)$$

The peak strength S_2 can be considering S_2 as the product of the diagonal peak resistance of the strut (f_{md0}) and the area of its cross section, namely:

$$S_2 = f_{md0} t w \quad (4)$$

where f_{md0} can be analytically evaluated as provided by [33]. Once evaluated S_2 , the peak strength S_1 is defined through the parameter α (≤ 1) as:

$$S_1 = \alpha S_2 \quad (5)$$

The cracking and peak displacements are then defined as:

$$d_1 = \frac{S_1}{K_1}; \quad d_2 = d_1 + \frac{S_2 - S_1}{K_2} \quad (6)$$

The softening branch is obtained as a linearization of the exponential softening branch proposed by [37]. This is done connecting the point S_2-d_2 and the auxiliary point $S_3^*-d_3^*$ (**Fig. 2a**), where for S_3^* it is conventionally set $S_3^*=0.7S_2$, and d_3^* is obtained through the expression [11] (**Fig. 2b**):

$$d_3^* = \frac{1}{\zeta} \ln \left[\frac{S_2}{S_3^*} \exp(\zeta d_2) \right] \quad (7)$$

in which ζ is one of the empirical parameters to be calibrated.

Finally, the residual strength (S_3) is related to the peak strength by the parameter η (≤ 1) as:

$$S_3 = \eta S_2 \quad (8)$$

The displacement at which the constant branch starts is obtained as interception of the lines identifying the branches II and IV, which results from the following equation:

$$d_3 = d_2 + (\eta - 1) \left(\frac{d_3^* - d_2}{S_3^* - S_2} \right) S_2 \quad (9)$$

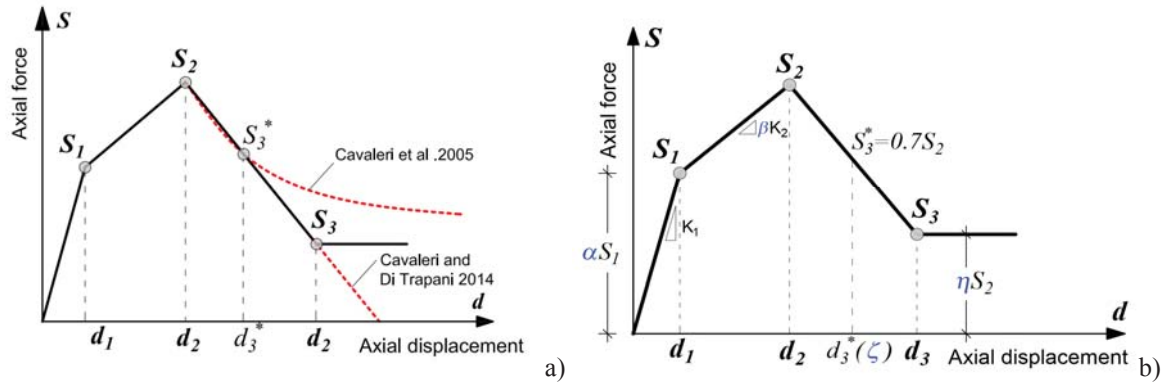


Figure 2. Force-displacement relationship for the equivalent strut: a) Comparison with **Cavaleri et al.** [38] and **Cavaleri and Di Trapani** [11] relationships; b) Calibrations parameters.

According to previous equations the force-displacement response is defined once the four parameters α , β , ζ , and η (called “force-displacement parameters”) are defined. These parameters have a strict dependence on masonry mechanical properties, but, more in general, their values depend on geometrical and mechanical features of the whole infilled frame. Their determination is possible by the empirical analytical correlations derived in the following sections.

3 CALIBRATION OF FORCE-DISPLACEMENT PARAMETERS FROM EXPERIMENTAL TESTS

The reference specimens are selected from the experimental tests by [2,5,6,7,11]. Geometric and typological details of specimens are reported in **Table 1**, while the other mechanical properties are shown in **Table 2**, together with the equivalent strut cross-section widths and the other parameters evaluated for the identification of the struts.

The simulation of the tests was carried out in OpenSees by conducting simple pushover analyses of the equivalent strut model of each specimen. The calibration process was performed by comparing the obtained monotonic force-displacement curves with the backbone curves of the cyclic experimental responses. Results are shown in **Figures 3-7**, where numerical pushover curves at the end of the calibration process, and the experimental results (positive and negative backbone curves) are overlapped.

The experimental values of masonry shear strength (f_{vm}) and compressive strength along orthogonal directions (f_{m1} and f_{m2}) are reported in **Table 3** together with the conventional compressive strength (\tilde{f}_m) defined as [33]:

$$\tilde{f}_m = \sqrt{f_{m1} \cdot f_{m2}} \quad (10)$$

and the diagonal compressive strength (f_{md0}) of the equivalent struts.

References	Spec. #	Masonry units type	t (mm)	h (mm)	h' (mm)	l (mm)	l' (mm)	l/h -	d (mm)	b_c (mm)	h_c (mm)	b_b (mm)	h_b (mm)
Cavaleri & Di Trapani [11]	S1A	Calcarenite	200	1600	1800	1600	1800	1.00	2545.6	200	200	200	400
Cavaleri & Di Trapani [11]	S1B	Clay / hollow	150	1600	1800	1600	1800	1.00	2545.6	200	200	200	400
Mehrabi et al. [2]	4	Brick / hollow	92	1422	1536	2032	2210	1.43	2691.5	178	178	152.4	228.6
Mehrabi et al. [2]	5	Brick / solid	92	1422	1536	2032	2210	1.43	2691.5	178	178	152.4	228.6
Mehrabi et al. [2]	11	Brick / solid	92	1422	1536	2948	3126	2.07	3483.1	178	178	152.4	228.6
Mehrabi et al. [2]	6	Brick / hollow	92	1422	1536	2032	2235	1.43	2712.3	203.2	203.2	152.4	228.6
Kakaletsis & Karayannis [7]	S	Brick	60	800	900	1200	1350	1.50	1622.5	150	150	100	200
Papia et al. [5]	S2A	Calcarenite	200	1600	1800	1600	1800	1.00	2545.6	200	200	200	400
Papia et al. [5]	S2B	Clay / hollow	150	1600	1800	1600	1800	1.00	2545.6	200	200	200	400
Colangelo [6]	C1	Clay / hollow	120	1300	1425	1700	1900	1.31	2375.0	200	200	200	250
Colangelo [6]	L2	Clay / hollow	120	1300	1425	2300	2500	1.77	2877.6	200	200	200	250
Colangelo [6]	N1	Clay / hollow	160	1300	1425	2300	2500	1.77	2877.6	200	200	200	250

Table 1. Geometric and typological details of reference specimens.

References	Spec. #	F_v (kN)	E_{m2} (MPa)	E_{m1} (MPa)	\tilde{E}_m (MPa)	E_c (MPa)	ν -	c -	β -	ε_v (%)	κ -	γ -	λ^* -	w (mm)
Cavaleri & Di Trapani [11]	S1A	400	3933	7408	5397	25000	0.150	0.260	0.150	0.20	1.048	1.50	2.186	631.4
Cavaleri & Di Trapani [11]	S1B	400	6040	5070	5697	25000	0.100	0.254	0.148	0.20	1.046	1.50	1.730	636.8
Mehrabi et al. [2]	4	294	4600	4600	4600	17000	0.150	0.260	0.150	0.27	1.059	3.08	0.978	587.1
Mehrabi et al. [2]	5	294	8949	8949	8949	18064	0.150	0.260	0.150	0.26	1.060	3.08	1.791	536.6
Mehrabi et al. [2]	11	294	9604	9604	9604	18133	0.150	0.260	0.150	0.26	1.059	10.24	1.664	726.7
Mehrabi et al. [2]	6	294	4198	4198	4198	19856	0.150	0.260	0.150	0.18	1.038	3.08	0.654	590.1
Kakaletsis & Karayannis [7]	S	100	670.3	660.7	665.5	29961	0.150	0.260	0.150	0.07	1.015	3.53	0.046	470.5
Papia et al. [5]	S2A	400	7106	9528	8228	23000	0.090	0.253	0.148	0.22	1.058	1.50	3.622	578.2
Papia et al. [5]	S2B	400	6040	5070	5697	23000	0.100	0.254	0.148	0.22	1.051	1.50	1.881	633.1
Colangelo [6]	C1	400	4230	1688	2672	34200	0.100	0.254	0.148	0.15	1.030	2.46	0.277	598.8
Colangelo [6]	L2	400	4230	1688	2672	35417	0.100	0.254	0.148	0.14	1.029	5.90	0.218	610.8
Colangelo [6]	N1	400	1212	2623	1782	34429	0.100	0.254	0.148	0.15	1.030	5.90	0.199	621.6

Table 2. Equivalent strut widths and associate ed mechanical data.

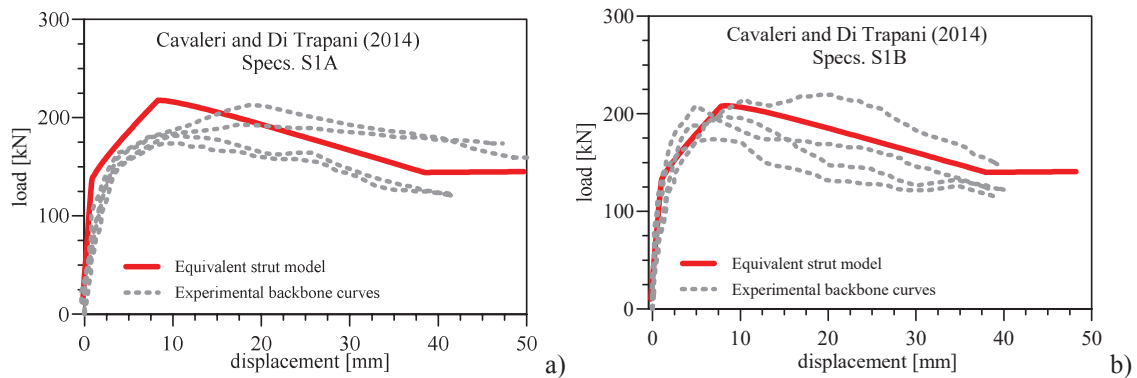


Figure 3. Experimental backbone curves by Cavaleri and Di Trapani [11] and pushover curves of the equivalent strut infilled frame model after the calibration: a) Specimens S1A; b) Specimens S1B.

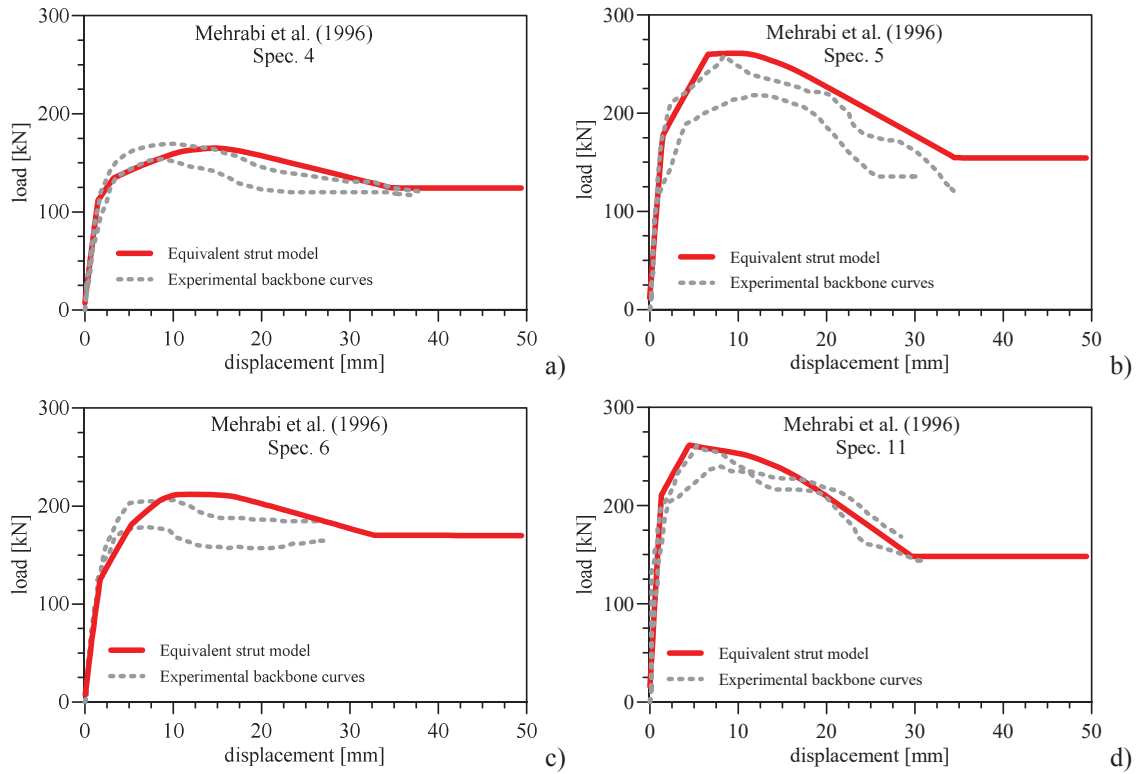


Figure 4. Experimental backbone curves by **Mehrabi et al. [2]** and pushover curves of the equivalent strut infilled frame model after the calibration: a) Specimen 4; b) Specimen 5; c) Specimen 6; d) Specimen 11.

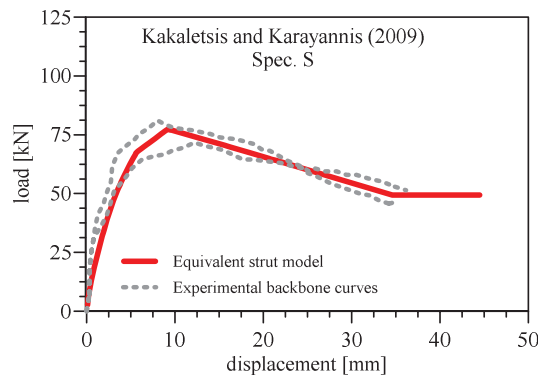


Figure 5. Experimental backbone curves by **Kakaletsis et al. [7]** and pushover curves of the equivalent strut infilled frame model after the calibration.

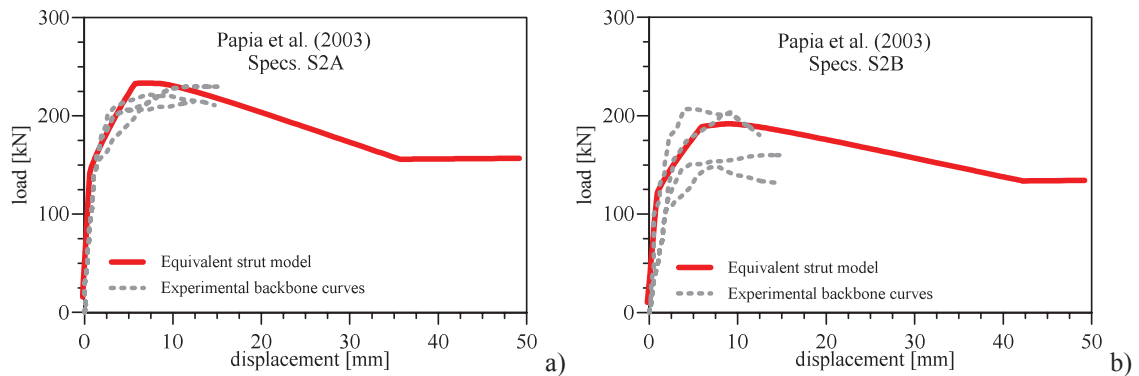


Figure 6. Experimental backbone curves of specimens by **Papia et al. [5]** and pushover curves of the equivalent strut infilled frame model after the calibration: a) Specimens S2A; b) Specimens S2B.

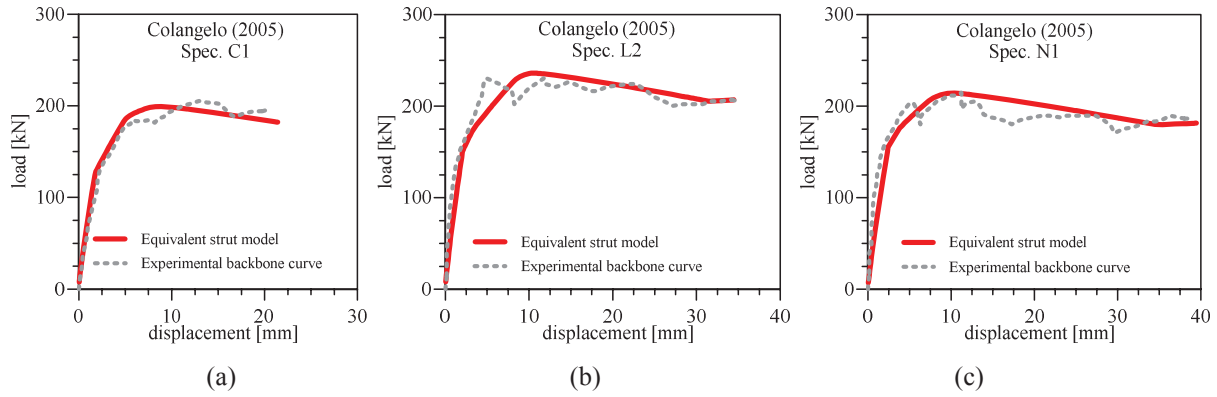


Figure 7. Experimental backbone curves by Colangelo [6] and pushover curves of the equivalent strut infilled frame model after the calibration: a) Specimen C1; b) Specimen L2; c) Specimen N1.

The optimal force-displacement parameters (α , β , ζ and η) obtained after the calibration are finally reported in **Table 4** together with the resulting force-displacement values for the struts.

References	Spec. #	f_{vm} (MPa)	f_{m2} (MPa)	f_{m1} (MPa)	\tilde{f}_m (MPa)	f_{md0} (MPa)
Cavaleri & Di Trapani [11]	S1A	0.73	2.67	3.08	2.86	2.0
Cavaleri & Di Trapani [11]	S1B	1.07	8.70	4.18	6.00	2.5
Mehrabi et al. [2]	4	0.93	5.09	2.75	3.74	2.4
Mehrabi et al. [2]	5	1.15	13.84	13.84	13.84	5.3
Mehrabi et al. [2]	11	1.03	11.44	11.44	11.44	3.8
Mehrabi et al. [2]	6	0.7	4.86	2.62	3.57	2.6
Kakaletsis & Karayannis [7]	S	0.08	5.11	2.63	3.66	2.3
Papia et al. [5]	S2A	0.89	4.57	3.92	4.23	2.5
Papia et al. [5]	S2B	1.07	8.70	4.18	6.00	2.3
Colangelo [6]	C1	0.87	5.10	3.39	4.15	2.05
Colangelo [6]	L2	0.87	5.10	3.39	4.15	1.8
Colangelo [6]	N1	0.58	2.74	3.90	3.24	1.4

Table 3. Experimental mechanical data of masonry and resulting conventional and diagonal strengths.

References	Spec. #	α	β	ζ	η	S_1 (kN)	d_1 (mm)	S_2 (kN)	d_2 (mm)	S_3 (kN)	d_3 (mm)
Cavaleri & Di Trapani [11]	S1A	0.7	0.06	0.030	0.50	176.8	0.66	252.6	5.38	176.8	25.2
Cavaleri & Di Trapani [11]	S1B	0.7	0.08	0.030	0.50	167.2	0.78	238.8	4.97	167.2	24.8
Mehrabi et al. [2]	4	0.9	0.10	0.033	0.30	116.7	1.26	129.6	2.67	90.7	27.9
Mehrabi et al. [2]	5	0.75	0.10	0.037	0.30	196.2	1.20	261.6	5.18	183.2	27.7
Mehrabi et al. [2]	11	0.85	0.075	0.040	0.25	215.9	1.17	254.0	3.93	177.8	26.2
Mehrabi et al. [2]	6	0.85	0.09	0.035	0.35	119.9	1.43	141.1	4.23	98.8	26.3
Kakaletsis & Karayannis [7]	S	0.8	0.70	0.035	0.40	519.4	4.52	64.9	6.14	45.4	26.5
Papia et al. [5]	S2A	0.65	0.09	0.030	0.50	187.9	0.50	289.1	3.51	202.4	23.3
Papia et al. [5]	S2B	0.7	0.10	0.025	0.50	152.9	0.72	218.4	3.80	152.9	27.6
Colangelo [6]	C1	0.8	0.15	0.030	0.50	117.8	1.46	147.3	3.89	103.1	23.7
Colangelo [6]	L2	0.95	0.10	0.030	0.40	125.3	1.84	131.9	2.81	92.3	26.6
Colangelo [6]	N1	0.95	0.10	0.025	0.45	132.3	2.15	139.2	3.28	97.5	29.4

Table 4. Parameters α , β , ζ and η after the calibration and resulting force and displacement values for the struts.

4 FORCE-DISPLACEMENT PARAMETERS CALIBRATION FROM FE MODELS

In order to enlarge the data-set, additional numerical tests were considered by taking those provided by [33]. The latter are obtained through a refined FE model experimentally validated and implemented in the ATENA 2D software platform. A view of the reference FE model is illustrated in **Fig. 8a**. The comparison between the FE model prediction and the reference experimental tests used for the validation (Specs. S1B by [11]) is also shown in **Fig. 8b**.

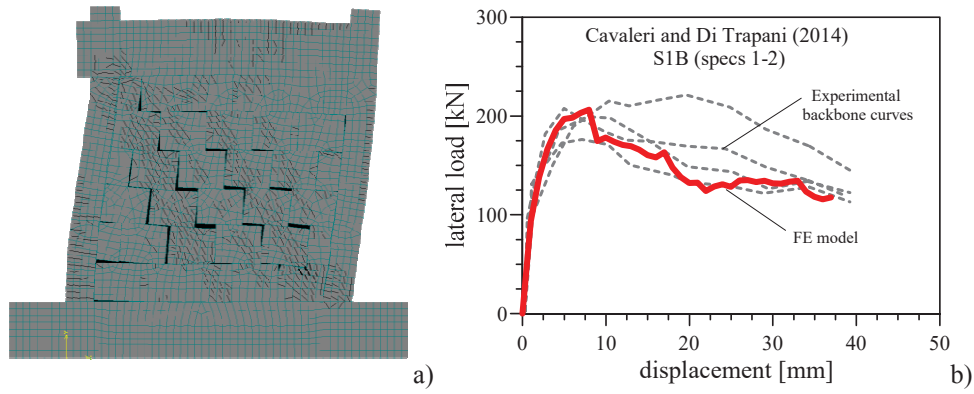


Figure 8. Reference FE model: a) View of the model during a typical pushover test; b) Comparison between FE model prediction and experimental backbone curves of specimens S1B (Cavaleri and Di Trapani [11]).

Numerical tests specimens extrapolated by the reference FE model were obtained by varying compressive and tensile strength of masonry (f_m and f_{vm}), infill thickness (t) and masonry elastic Young's modulus (E_m). The interface and concrete parameters were instead maintained fixed, as well as the geometry of the frame (spec. S1B by [11]). The geometrical and mechanical parameters which were varied to generate the numerical models are reported in **Table 5**, highlighting those each time varied. The infilled frame equivalent strut models associated with the generated FE models were then built and calibrated to derive force-displacement parameters as shown in the previous section. Force-displacement curves at the end of the calibration are depicted **Fig. 9** together with the respective force-displacement curves of the FE model simulations. Parameters evaluated at the end of the calibration and related force-displacement parameters obtained are finally reported in **Table 6** together with the resulting force-displacement values for the struts.

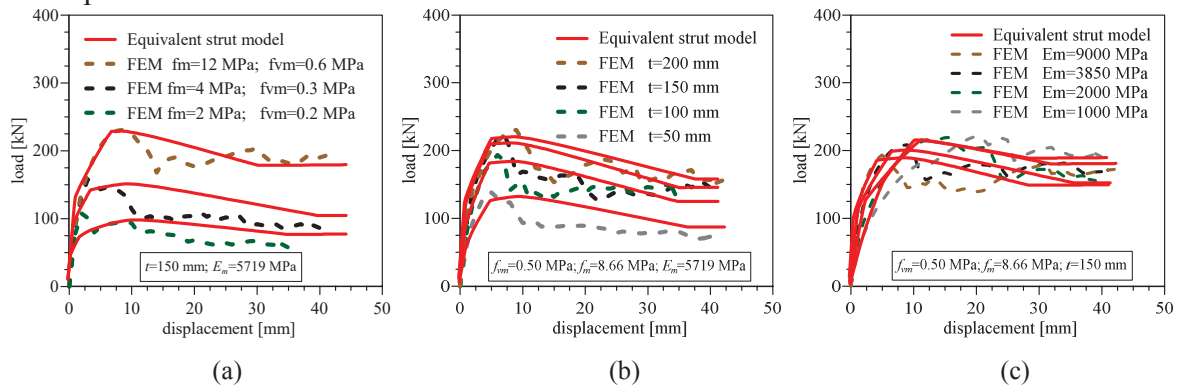


Figure 9. Force-displacement curves from FE models and equivalent strut models after the calibration: a) variation of masonry strength; b) variation of infill thickness; c) variation of elastic modulus.

Spec. #	f_{vm} (MPa)	$f_m = \tilde{f}_m$ (MPa)	t (mm)	$E_m = \tilde{E}_m$ (N/mm ²)
FEM-1S	0.60	12.00	150	5719
FEM-2S	0.40	4.00	150	5719
FEM-3S	0.20	2.00	150	5719
FEM-1T	0.50	8.66	50	5719
FEM-1T	0.50	8.66	100	5719
FEM-1T	0.50	8.66	150	5719
FEM-1T	0.50	8.66	200	5719
FEM-1E	0.50	8.66	150	1200
FEM-2E	0.50	8.66	150	2000
FEM-3E	0.50	8.66	150	3850
FEM-4E	0.50	8.66	150	9000

Table 5. Geometric and mechanical data of numerical models generated from the S1B specimen model.

Spec.	λ^*	w	f_{md0}	α	β	ζ	η	S_1	d_1	S_2	d_2	S_3	d_3
-	-	(mm)	(MPa)	-	-	-	-	(kN)	(mm)	(kN)	(mm)	(kN)	(mm)
FEM-1S	1.737	636.4	1.70	0.7	0.12	0.03	0.40	113.6	0.7	162.3	2.42	113.6	2.42
FEM-2S	1.737	636.4	2.90	0.6	0.15	0.027	0.60	166.1	0.6	276.8	4.22	193.8	4.22
FEM-3S	1.737	636.4	0.80	0.8	0.07	0.038	0.30	61.1	0.8	76.4	1.30	53.5	1.30
FEM-1T	0.579	744.3	3.50	0.5	0.3	0.040	0.30	65.1	0.5	130.3	3.38	91.2	3.38
FEM-1T	1.158	673.8	3.20	0.5	0.25	0.033	0.45	107.8	0.5	215.6	3.56	150.9	3.56
FEM-1T	1.737	636.4	2.70	0.6	0.16	0.030	0.50	154.7	0.6	257.8	3.73	180.4	3.73
FEM-1T	2.316	611.7	2.20	0.6	0.15	0.025	0.55	161.5	0.6	269.2	3.20	188.4	3.20
FEM-1E	0.608	739.2	2.20	0.6	0.18	0.022	0.75	146.4	0.6	243.9	7.90	170.7	7.90
FEM-2E	1.169	672.8	2.30	0.6	0.16	0.025	0.60	139.3	0.6	232.1	4.71	162.5	4.71
FEM-3E	0.304	817.7	2.00	0.7	0.4	0.02	0.80	171.7	0.7	245.3	7.38	171.7	7.38
FEM-4E	2.734	598.2	2.50	0.6	0.12	0.025	0.60	134.6	0.6	224.3	2.78	157.0	2.78

Table 6. Identification parameters of equivalent strut, parameters α , β , ζ and η after the calibration and resulting force and displacement values for the struts.

5 DEFINITION OF THE EMPIRICAL CORRELATION LAWS

The experimental and numerical data-sets containing the calibrated parameters α , β , ζ and η together with the associated geometrical and mechanical features of the respective infilled frames were merged in to a unique hybrid data-set. Results were then analysed in order to understand the dependence of α , β , ζ and η on the parameters involved in the identification process of each model. In detail parameters λ^* , \tilde{E}_m , (l/h) , t , \tilde{f}_m , f_{md0} , f_{vm} where individuated as the most meaningful to the inelastic response of an infill frame, as these take into account the aspect ratio, the stiffness ratio and the strengths of the masonry and of the strut. The relationships with α , β , ζ and η have been found by defining four correlation parameters (A , B , Z and Y) to get the maximum determination coefficients (R^2) of the analytical interpolating functions relating α , β , ζ and η as $f(A)$, $f(B)$, $f(Z)$ and $f(Y)$. Results provided the following expressions for the correlation parameters:

$$A = \lambda^{*0.1} \left(\frac{l}{h} \right)^{-3} \left(\frac{f_{md0}}{f_{vm}^{0.4}} \right) \quad (11)$$

$$B = \lambda^{*0.7} \left(\frac{l}{h} \right)^{1.8} \left(\frac{f_{md0}^{-1.7}}{f_{vm}^{-0.7}} \right) \frac{1}{t^{0.5}} \quad (12)$$

$$Z = \left(\frac{\tilde{E}_m}{\tilde{f}_m} \right)^{0.7} \left(\frac{l}{h} \right)^{0.7} \left(\frac{f_{md0}^{0.7}}{f_{vm}^{0.35}} \right) \frac{1}{t} \quad (13)$$

$$Y = \left(\frac{\tilde{E}_m^{0.7}}{t} \right) \left(\frac{l}{h} \right)^{1.2} \left(\frac{\tilde{f}_m^{-0.5}}{f_{vm}^{0.1}} \right) \quad (14)$$

The relationships between parameters α , β , ζ and η and correlation parameters A , B , Z and Y are illustrated in **Fig. 10**, together with the obtained optimal analytical correlation laws.

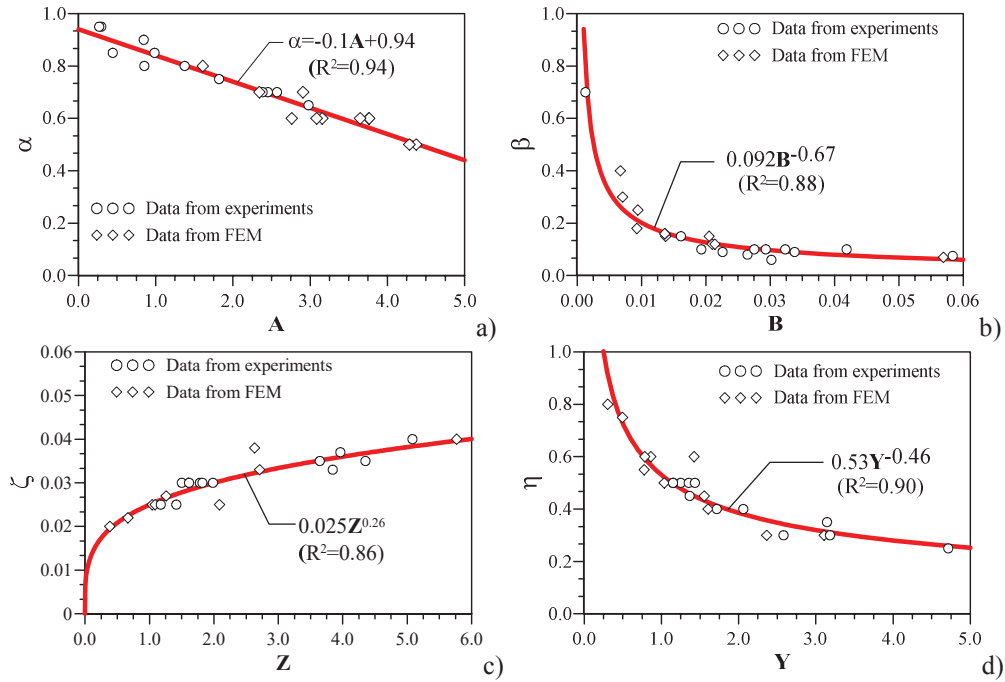


Figure 10. Relationships between parameters α , β , ζ and η and correlation parameters A , B , Z and Y and proposed analytical correlation laws.

Based on the obtained equations, the procedure for the complete identification of the equivalent strut follows the below reported steps:

1. Evaluation of the equivalent strut width w [33];
2. Evaluation of the peak strength of the strut S_2 (Eq. 4);
3. Evaluation of correlation parameters A , B , Z , Y (Eqs. 12-15);
4. Evaluation of force-displacement parameters α , β , ζ , η (Fig.10);
5. Determination of the force-displacement relationship for the strut (Eqs. 1, 3 and 5-9);

6 BLIND VALIDATION TESTS AND RELIABILITY COMPARISONS

The proposed empirical correlations have been validated with the experimental test results of eight specimens, not belonging to the set of specimens used to derive the correlations. The considered specimens were those by [14] (Spec. TA-2), [10] (Spec. URM-U), [6] (Spec. V21), [12] (Spec. FT-2), [13] (Specs. GLD and SLD), [9] (Spec Unr), [11] (Spec S1C). With regards to the experimental campaign by [6], of which some specimens have been used to build the data-set, it should be specified that experimental results used for the validation are those of Specimen V21, which has not been previously considered and presents substantially different mechanical properties of the masonry infill with respect to those included in the data-set. The same considerations may be taken for the specimen S1C of the experimental campaign by [11]. The other six specimens belong to other experimental campaigns not considered at all in the calibration phase. It should be also specified that specimens GLD and SLD by Verderame et al. [13] have the same geometric and mechanical characteristics for what concerns the frame and the infill. The differences are instead in the arrangement of the longitudinal and transverse reinforcement that is made considering gravity loads only (GLD) or seismic loads (SLD). Geometric details of the specimens are listed in Table 7. Equivalent strut models have been defined according to the procedural steps described in the previous section. Tables 7-9 collect all the fundamental geometric and mechanical data of the models and the associated parameters used for the definition of struts. The correlation and force-displacement param-

eters evaluated by means of **Eqs. (12-15)** and equation if **Fig. 10** are shown in **Tables 10-11**, together with the obtained values for the axial-force / axial-displacement relationship of the struts. The comparison between experimental force-displacement curves and numerical predictions are depicted in **Fig. 11**. It can be observed that for all the considered cases, numerical predictions resulted in a very good matching with experimental data, providing sufficient reliability despite the large heterogeneity of the blind test specimens and in consideration of the uncertainty degree affecting masonry mechanics in general and infilled frames in particular.

In order to compare the reliability of the proposed model predictive capacity with respect to that of other existing ones, the simulation of the blind tests has been conducted also implementing other six equivalent strut models available in the literature and applying them on the blind tests. The equivalent strut models are the models by Di Trapani et al.[33], Panagiotakos and Fardis [35], Dolsek and Fajfar [38], Bertoldi et al. [36], De Risi et al. [32], Sassun et al. [39]. The comparisons between the experimental test responses and those by the seven equivalent strut models are illustrated in **Fig. 11**.

References	Spec. #	Masonry units type	t (mm)	h (mm)	h' (mm)	l (mm)	l' (mm)	l/h (-)	d (mm)	b_c (mm)	h_c (mm)	b_b (mm)	h_b (mm)
Morandi et al. [14]	TA2	Clay Holl.	350	2950	3125	4220	4570	1.43	5536	350	350	350	350
Da Porto et al. [10]	URM-U	Clay Holl.	300	2650	2775	4150	4450	1.56	5244	300	300	300	250
Colangelo [6]	V21	Clay	160	1300	1425	2300	2500	1.76	2878	200	200	200	250
Bergami & Nuti [12]	-	Clay Holl.	120	1300	1425	2300	2500	1.76	2878	200	200	200	250
Verderame et al. [13]	GLD-SLD	Clay Holl.	80	1350	1475	2100	2300	1.55	2732	200	200	200	250
Sigmund & Penava [9]	Unr	Clay	120	1300	1400	1800	2000	1.38	2441	200	200	120	200
Cavaleri & Di Trapani [11]	S1C	Concrete	150	1600	1800	1600	1900	1.00	2617	300	300	300	400

Table 7. Geometric and typological details of the specimens used for the validation.

References	E_{m2} (MPa)	E_{m1} (MPa)	\tilde{E}_{b1} (MPa)	G (MPa)	E_c (MPa)	f_{m2} (MPa)	f_{m1} (MPa)	\tilde{f}_{m1} (MPa)	f_{vm} (MPa)	f_{md0} (MPa)
Morandi et al. [14]	5299	494	1618	2119.6*	30000	4.64	1.08	2.24	0.36	0.94
Da Porto et al. [10]	4312	1767	2760	1713	30000	6.00	1.19	2.67	0.2	1.15
Colangelo [6]	3188	3188	3188	1574	33900	2.24	2.56	2.39	0.35	1.58
Bergami & Nuti [12]	7228	4031	5398	4031	31475	6.19	2.91	4.24	1.26	2.41
Verderame et al. [13]	3940	3940	3940	1724.8*	27870	4.88	3.19	3.94	0.36	2.27
Sigmund & Penava [9]	3900	638**	1577	1560*	36283	2.7	0.44***	1.092	0.7	1.11
Cavaleri & Di Trapani [11]	4565	1944	2979	2042	25000	1.74	0.3	0.722	0.29	0.75

(*estimated as $0.4E_{m2}$; **estimated as $R_{b1}/R_{b2}E_{m2}$; ***estimated as $R_{b1}/R_{b2}f_{m2}$; R_{bi} =block resistance in direction 1-2)

Table 8. Experimental mechanical data of the specimens and evaluated mechanical properties.

References	F_v (kN)	ν -	c -	β -	κ -	γ -	λ^* -	w (mm)
Morandi et al. [14]	800	0.1	0.254	0.148	1.023	3.094	0.401	1203.34
Da Porto et al. [10]	800	0.17	0.263	0.151	1.032	4.007	0.740	1045.62
Colangelo [6]	400	0.10	0.254	0.148	1.030	5.899	0.362	571.98
Bergami & Nuti [12]	318	0.10	0.254	0.148	1.026	5.899	0.495	533.46
Verderame et al. [13]	200	0.10	0.254	0.148	1.018	3.928	0.302	571.26
Sigmund & Penava [9]	730	0.10	0.254	0.148	1.051	2.838	0.198	654.44
Cavaleri & Di Trapani [11]	400	0.10	0.254	0.148	1.018	1.500	0.392	783.39

Table 9. Equivalent strut widths and associated mechanical identification parameters.

References	A	B	Z	Y	α	β	ζ	η
	-	-	-	-	-	-	-	-
Morandi et al. [14]	0.440	0.029	0.503	0.573	0.899	0.097	0.021	0.685
Da Porto et al. [10]	0.553	0.027	1.139	1.052	0.888	0.103	0.026	0.518
Colangelo [6]	0.392	0.024	2.856	2.524	0.904	0.112	0.033	0.346
Bergami & Nuti [12]	0.371	0.041	3.166	3.214	0.906	0.078	0.034	0.310
Verderame et al. [13]	0.805	0.013	5.442	3.896	0.863	0.167	0.039	0.284
Sigmund & Penava [9]	0.411	0.034	2.080	2.115	0.902	0.087	0.030	0.376
Cavaleri & Di Trapani [11]	1.119	0.029	2.850	2.399	0.831	0.098	0.033	0.354

Table 10. Correlation parameters and force-displacement parameters

References	S_1	d_1	S_2	d_2	S_3	d_3
	(kN)	(mm)	(kN)	(mm)	(kN)	(mm)
Morandi et al. [14]	355	2.882	395	6.211	270	24.173
Da Porto et al. [10]	320	1.940	361	4.315	187	26.475
Colangelo [6]	131	1.290	145	2.520	50	26.112
Bergami & Nuti [12]	140	1.166	155	2.722	48	26.960
Verderame et al. [13]	89	1.358	104	2.650	29	24.469
Sigmund & Penava [9]	79	1.553	87	3.482	33	27.975
Cavaleri & Di Trapani [11]	73	0.547	88	1.684	31	24.994

Table 11. Final axial force- axial displacement data calculated for the blind test specimen equivalent struts.

It can be firstly observed that the accuracy of each model in reproducing the experimental responses is different for the different cases. For example, while for the test by da Porto et al. [10] (**Fig. 11b**), Colangelo [6] (**Fig. 11c**) and Verderame [13] (**Figs. 11e-f**), all the models performed with similar reliability, very significant differences in the predictions are recognized for the test by Morandi et al. [14] (**Fig. 11a**). However, it should be also recognized that data-driven empirical models as the proposed one and the one by Di Trapani et al. [33], performed with noticeable reliability for all the considered tests. On the other hand, the models by Panagiotakos and Fardis [35], Dolsek and Fajfar [38] and De Risi et al. [32] have shown good predictive capacity in 5 out of 8 tests, while they led to significant strength overestimation in the tests by Morandi et al. [14] (**Fig. 11a**), Bergami and Nuti [12] (**Fig. 11d**) and Sigmund & Penava [9] (**Fig. 11g**). For the model by Panagiotakos and Fardis [35] and Dolsek and Fajfar [38] this is justified by the fact that the estimation of the strength capacity by these models is obtained considering a single collapse mode, leading to incorrect evaluations in all the cases in which a different mechanism develops. A confirmation of this comes observing the performance of the model by Bertoldi et al. [36] and Sassun et al. [39], which instead, based on their mechanism-sensitive formulation, resulted more effective in general with respect to the peak-strength estimation, although they still give a peak strength overestimation in 2 out of 8 cases. Another noteworthy issue is related to the softening branch, which is in general more accentuated by Panagiotakos and Fardis [35] and Dolsek and Fajfar [38] models. But while for the former this can be calibrated by a stiffness coefficient, the assumption by Dolsek and Fajfar [38] of an ultimate displacement of 5 times the peak one is generally not acceptable for more ductile infilled frames. The forced prediction of a brittle behaviour is accentuated by the low or null residual strength provided by these models, which instead it has been found to range between 0.25 and 0.8 the peak strength, as it can be deduced from the η coefficients reported in **Tables 4, 6 and 10**. In conclusion it can be observed that data-driven empirical models, including the proposed one, resulted more reliable with respect to the mechanics-based in predicting the lateral response of an infilled frame. This can be reasonably justified by two main factors. The first is that their calibration is analytically updated in consideration of a large number of parameters characterizing both the frame and the infill. More-

over, the analytical equations used to calibrate the model are based on robust correlations considering a significant number of experimental and numerical tests. The second aspect to take into account, is that the mechanics-based models here considered, despite largely employed in the practice, have been validated on a reduced number of experimental tests with respect to those available currently, and therefore they can only reflect well the behaviour of infilled frames having similar characteristics to those at the base of their validation.

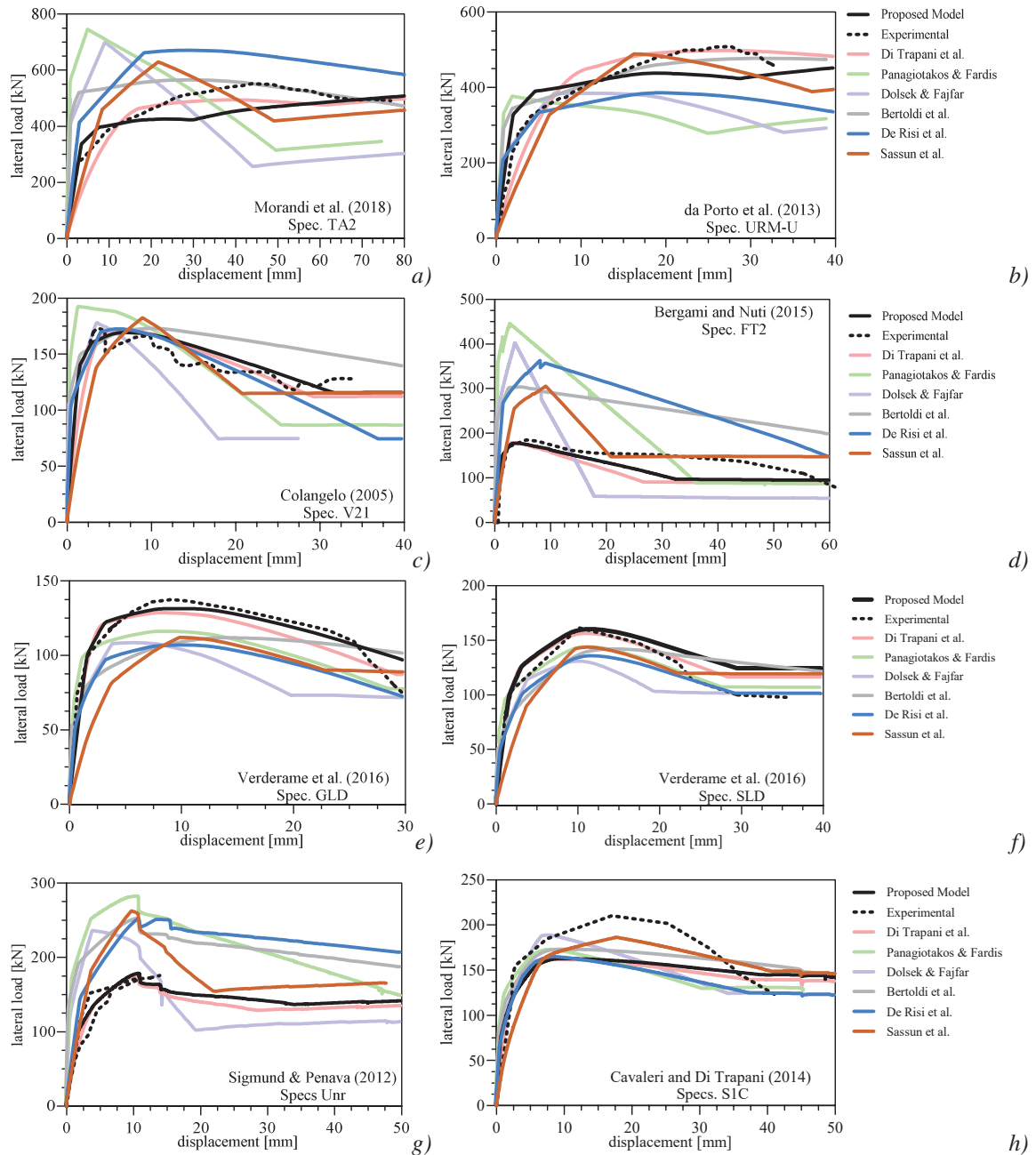


Figure 11. Blind validation tests of the proposed model with experimental test results: a) Morandi et al. (TA-2) [14]; b) da Porto et al. (URM-U)[10]; c) Colangelo (V21)[6]; d) Bergami and Nuti (FT-2)[12]; e-f) Verderame et al. (GLD-SLD)[13]; g) Sigmund & Penava [9] (Spec Unr); h) Cavaleri and Di Trapani [11] (Spec SIC)

7 CONCLUSIONS

Assessment of inelastic response of infilled frames is not straightforward. Phenomenological models have to summarize a large number of variables into a relatively simple model. The flexibility of available strut models to update their force-displacement (or stress-strain) response, as a function of the different potential failure damage mechanisms occurring for infilled frame, is fundamental to get reliable predictions. The uncertainty in predicting the collapse mode, which depends on a large amount of geometric and mechanical parameters, propagates in the reliability of estimations.

In consideration of this, the paper has shown a proposal for a new single equivalent strut model based on axial-force/axial-displacement relationship of the strut. The model can be easily implemented in most of the finite element codes handling nonlinear analysis of frame structures. The major advantage of the proposed model is that the force-displacement relationship is modulated by four analytical correlation equations linking the geometrical and mechanical features of an infilled frame to the force-displacement parameters. The correlation equations are derived from a robust data-set realized including experimental data and refined numerical simulations.

Validation tests have been carried out against eight experimental test data different from those used to define the empirical data-set. Results have demonstrated the predictive reliability of the proposed model and of the empirical relationships used to define it. This suggests the proposed approach as an effective methodology when performing nonlinear static analyses for the assessment of seismic performance, and also highlights the potential use of correlation equations as design tools for the performance-based design of the infilled frames. The same tests are used to carry out a comparison with six additional equivalent-strut models available in the literature besides the proposed one. Results have shown a major reliability of data-driven models because of the flexibility of the case-by-case calibration provided. On the other hand, the lower reliability of mechanics-based model is justified by the reduced number of experimental tests available when they were validated.

ACKNOWLEDGEMENTS

This paper was supported by DPC-ReLuis 2019-2021, WP10, Subtask 10.1.2 Non-structural masonry (infills and partitions).

REFERENCES

- [1] Pires F., Carvalho E.C. The behaviour of infilled reinforced concrete frames under horizontal cyclic loading. *Proceedings of the 10th world conference on earthquake engineering*, Madrid; 1992.
- [2] Mehrabi A.B., Shing P.B. Finite element modelling of masonry-infilled RC frames. *Journal of Structural Engineering*, 123(5), 604-13; 1996.
- [3] Calvi G.M., Bolognini D. Seismic response of reinforced concrete frames infilled with weakly reinforced masonry panels. *J Earthq Eng*;5(02):153–85; 2001.
- [4] Al-Chaar G., Issa M., Sweeney S. Behavior of Masonry-Infilled Nonductile Reinforced Concrete Frames. *J. Struct. Eng.*, 128:1055-1063; 2002.

- [5] Papia M., Cavaleri L., Fossetti M. Infilled frames: developments in the evaluation of the stiffening effect of infills. *Structural engineering and mechanics*, 16(6), 675-93; 2003.
- [6] Colangelo F. Pseudo-dynamic seismic response of reinforced concrete frames infilled with non-structural brick masonry. *Earthq Eng Struct Dyn*, 34, 1219-1241; 2005.
- [7] Kakaletsis D.J., Karayannis C.G. Experimental investigation of infilled reinforced concrete frames with openings. *ACI Structural Journal*, 102(2), 132-141; 2009.
- [8] Stylianidis K.C. Experimental investigation of masonry infilled R/C frames. *Open Constr Build Technol J*; 6(Suppl. 1-M13):194-212; 2012.
- [9] Sigmund V., Penava D. Experimental study of masonry infilled R/C frames with opening. *Proceedings of the 15WCEE, Lisbon, Portugal*; 2012
- [10] da Porto F., Guidi M., Dalla Benetta N., Verlato F. Combined in-plane/out-of-plane experimental behaviour of reinforced and strengthened infill masonry walls. *12th Canadian Masonry Symposium, June 2-5, Vancouver, Canada*; 2013.
- [11] Cavaleri L., Di Trapani F. Cyclic response of masonry infilled RC frames: Experimental results and simplified modeling. *Soil Dynamics and Earthquake Engineering*, 65, 224-242; 2014.
- [12] Bergami A. V., Nuti C. Experimental tests and global modeling of masonry infilled frames. *Earthquakes and Structures*, April, 1-24; 2015.
- [13] Verderame G.M., Ricci P., Del Gaudio C., De Risi M.T. Experimental tests on masonry infilled gravity- and seismic-load designed RC frames. *16th international brick and block masonry conference, IBMAC 2016*; p. 1349-58; 2016.
- [14] Morandi P., Hak S., Magenes G. In-plane Experimental Response of Strong Masonry Infills. *Engineering Structures*, 156, 503-521; 2018.
- [15] Celarec D., Ricci P., Dolšek M. The sensitivity of seismic response parameters to the uncertain modelling variables of masonry-infilled reinforced concrete frames. *Eng Struct*, 35: 165-177; 2012.
- [16] Uva G., Raffaele D., Porco F., Fiore A. On the role of equivalent strut models in the seismic assessment of infilled RC buildings. *Engineering Structures*, 42, 83-94; 2012.
- [17] Fiore A., Porco F., Raffaele D., Uva G. About the influence of the infill panels over the collapse mechanisms active under pushover analyses: Two case studies. *Soil Dynamics and Earthquake Engineering*, 39, 11-22; 2012.
- [18] Asteris P.G., Repapis C.C., Tsaris A.K., Di Trapani F., Cavalieri L. Parameters affecting the fundamental period of infilled RC frame structures. *Earthquake and Structures*, 9(5), 999-1028; 2015.
- [19] Asteris P.G., Cavaleri L., Di Trapani F., Sarhosis V. A macro-modelling approach for the analysis of infilled frame structures considering the effects of openings and vertical loads. *Structure and Infrastructure Engineering*, 12(5), 551-566; 2016.
- [20] Martinelli E., Lima C., De Stefano G. A simplified procedure for Nonlinear Static Analysis of masonry infilled RC frames. *Engineering Structures*, 101, 591-608; 2015.
- [21] Cavaleri L., Di Trapani F., Asteris P.G., Sarhosis V. Influence of column shear failure on pushover-based assessment of masonry infilled reinforced concrete framed structures: A case study. *Soil Dynamics and Earthquake Engineering*, 100, 98-112; 2017.

- [22] Di Trapani F., Malavisi M. Seismic fragility assessment of infilled frames subject to mainshock/aftershock sequences using a double incremental dynamic analysis approach. *Bull Earthq Eng*; 17(1):211–35; 2019.
- [23] Di Trapani F., Bolis V., Basone F., Preti M.G. Seismic reliability and loss assessment of RC frame structures with traditional and innovative masonry infills. *Eng Struct*, 208:110306; 2020a.
- [24] Koutromanos I., Stavridis A., Shing P.B., Willam K. Numerical modelling of masonry-infilled RC frames subjected to seismic loads. *Computers and Structures*, 89, 1026-1037; 2011.
- [25] Cavaleri L., Di Trapani F. Prediction of the additional shear action on frame members due to infills. *Bulletin of Earthquake Engineering*, 13(5), 1425-1454; 2015.
- [26] Calì I., Pantò B. A macro-element modelling approach of Infilled Frame Structures. *Computers and Structures*, 143, 91-107; 2014.
- [27] Milanese R.R., Morandi P., Magenes G. Local effects on RC frames induced by AAC masonry infills through FEM simulation of in-plane tests. *Bull of Earthq Eng*, 16(1): 4053-4080; 2018.
- [28] Pantò B., Rossi P.P. A new macromodel for the assessment of the seismic response of infilled RC frames. *Earthq Eng and Struct Dyn*, 48: 792-817; 2019.
- [29] Di Trapani F., Macaluso G., Cavaleri L., Papia M. Masonry infills and RC frames interaction: literature overview and state of the art of macromodeling approach. *European Journal of Environmental and Civil Engineering*, 19(9), 1059-1095; 2015.
- [30] Pasca, M., Liberatore, L., Masiani, R. Reliability of analytical models for the prediction of out-of-plane capacity of masonry infills. *Structural Engineering and Mechanics*, 64(6):765-781; 2017.
- [31] Liberatore L., Noto F., Mollaioli F., Franchin P. In-plane response of masonry infill walls: Comprehensive experimentally based equivalent strut model for deterministic and probabilistic analysis. *Eng Struct*, 167: 533–548; 2018.
- [32] De Risi M.T., Del Gaudio C., Ricci P., Verderame G.M. In-plane behaviour and damage assessment of masonry infills with hollow clay bricks in RC frames. *Eng Struct*, 168: 257–275; 2018.
- [33] Di Trapani F., Bertagnoli G., Ferrotto M.F., Gino D. Empirical equations for the direct definition of stress-strain laws for fiber-section based macro-modeling of infilled frames. *J Eng Mech*, 144(11):04018101; 2018b.
- [34] McKenna F., Fenves G.L., Scott M.H. *Open system for earthquake engineering simulation*. University of California, Berkeley, CA; 2000.
- [35] Panagiotakos, T.B., Fardis, M.N. Seismic response of infilled RC frames structures. *XXI WCEE, Acapulco, Mexico*; 1996.
- [36] Bertoldi S. H., Decanini L.D., Gavarini C. Telai tamponati soggetti ad azioni sismiche, un modello semplificato: confronto sperimentale e numerico. *Atti del 6 Convegno Nazionale ANIDIS*, 2, Perugia; 1993.

- [37] Cavaleri, L., Fossetti, M., & Papia, M. Infilled frames: Developments in the evaluation of cyclic behaviour under lateral loads. *Structural Engineering and Mechanics*, 21, 469–494; 2005.
- [38] Dolšek, M., Fajfar, P. The effect of masonry infills on the seismic response of four storey reinforced concrete frame - a deterministic assessment. *Engineering Structures*, 30(7), 1991–2001; 2008.
- [39] Sassun, K., Sullivan, T.J., Morandi, P., Cardone, D. Characterising the In-Plane Seismic Performance of Infill Masonry. *Bull. N. Z. Soc. Earthq. Eng.*, 49, 98–115; 2015.
- [40] Di Trapani, F., Bolis, V., Basone, F., Preti M. Seismic reliability and loss assessment of RC frame structures with traditional and innovative masonry infills. *Engineering Structures*, 208, 110306; 2020.
- [41] Cavaleri L., F. Di Trapani F., Ferrotto M.F. A new hybrid procedure for the definition of seismic vulnerability in Mediterranean cross-border urban areas. *Natural Hazards*, 86, no. S2, 517–541; 2017.
- [42] Cavaleri, L., Di Trapani, F., Ferrotto, M.F., Davì, L. Stress-strain models for normal and high strength confined concrete: Test and comparison of literature models reliability in reproducing experimental results. *Ingegneria Sismica*, 34(3-4), 114-137; 2017.

EARTHQUAKE EARLY WARNING AND RAPID RESPONSE SYSTEM BASED ON SMART SEISMIC AND MONITORING SENSORS EMBEDDED IN A COMMUNICATION PLATFORM AND COUPLED WITH BIM MODELS

Georgios Balaskas¹, Benno Hoffmeister¹, Christoph Butenweg², Marco Pilz³, Anna Bauer⁴

¹ Institute of Steel Construction, RWTH Aachen University
{g.balaskas, hoff}@stb.rwth-aachen.de

² Institute of Structural Analysis and Dynamics, RWTH Aachen University
butenweg@lbb.rwth-aachen.de

³ Seismic Hazard and Risk Dynamics, GFZ German Research Center for Geosciences
pilz@gfz-potsdam.de

⁴ Wölfel Engineering & Co: GmbH
anna.bauer@woelfel.de

Abstract

This paper describes the concept of an innovative, interdisciplinary, user-oriented earthquake warning and rapid response system coupled with a structural health monitoring system (SHM), capable to detect structural damages in real time. The novel system is based on interconnected decentralized seismic and structural health monitoring sensors. It is developed and will be exemplarily applied on critical infrastructures in Lower Rhine Region, in particular on a road bridge and within a chemical industrial facility. A communication network is responsible to exchange information between sensors and forward warnings and status reports about infrastructures' health condition to the concerned recipients (e.g., facility operators, local authorities). Safety measures such as emergency shutdowns are activated to mitigate structural damages and damage propagation. Local monitoring systems of the infrastructures are integrated in BIM models. The visualization of sensor data and the graphic representation of the detected damages provide spatial content to sensors data and serve as a useful and effective tool for the decision-making processes after an earthquake in the region under consideration.

Keywords: early warning and response system, interconnected sensor systems, seismic structural damage detection via SHM, integration SHM in BIM

1 INTRODUCTION

Germany's seismicity in general is characterized as low or moderate. However, there are seismic events of moderate to strong ground motions with damage potential (Tailfingen 1978 $M_w = 5.7$, Roermond 1992 $M_w = 5.9$). These events arouse attention because the exposed regions are densely populated, highly industrialized and have an extended network of critical infrastructures. These infrastructures were mainly designed according to currently outdated or none seismic provisions. The early warning and rapid response system combined with local health monitoring systems can act supplementary as an additional arrow in the quiver of earthquake engineering to reduce the seismic risk, especially for critical infrastructures.

This contribution describes the conception and the progress of the works, that had been performed in the framework of the German nationally funded research project "ROBUST". Fundamental element of the novel system is the automated interaction of smart seismic or structural sensors and sensor systems, which are capable not only to record motions or strains, but also to process the recordings decentral and to forward the results of the assessment. In the past decades, the breakthrough in software and hardware development of sensors and techniques for data processing enabled the extended and low-cost use of a remarkable number of seismic and monitoring sensors [1]. Reliable earthquake early warning systems (EWS) were developed all over the world and especially in seismic prone areas as Japan, California and Mexico [2]. Simultaneously, engineering diagnostics is an emerging field concerning health assessment of civil engineer's structures. Post-earthquake damage detection through sensor systems is a research topic of increasing interest. Acknowledging the developments in both directions (SHM and EWS), the examined system tries to incorporate and extend their advantages and provide a useful tool for the protection of critical infrastructures [3]. The examined system is going to be applied in Lower Rhine Region. A road bridge and a chemical industrial facility are selected as benchmark structures. The innovative system consists of four basic components: (i) the seismic sensors network, (ii) the local monitoring systems for the critical infrastructures, (iii) the communication infrastructure and (iv) the integration of the sensor data in BIM models of the monitored critical infrastructure.

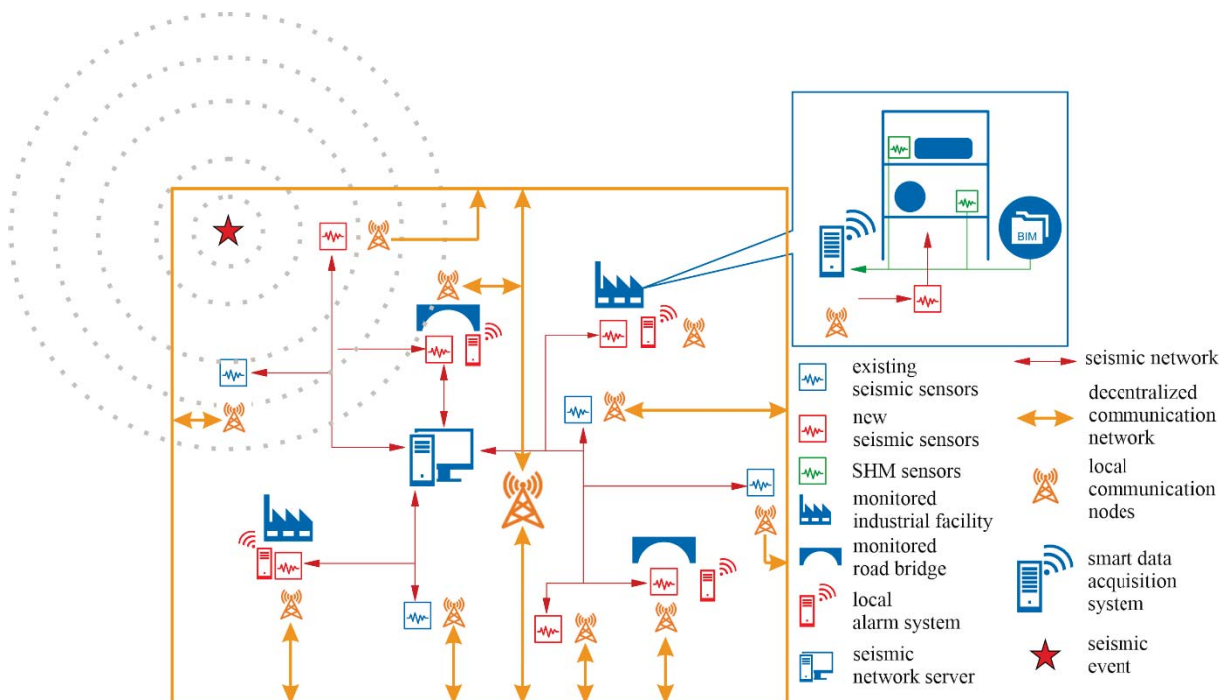
Regarding the first component, namely the seismic network, the existing sparse regional network is being extended by new smart seismic sensors. To this end, an algorithm has been developed, aiming at the optimization of the location of the new sensors such, that while accounting for the geophysical conditions, reliable information on earthquakes relevant for the infrastructures can be obtained and communicated to maximize the lead time while, at the same time, to minimize the risk of false alarms. The novel sensors, developed by the German Research Center for Geosciences (GFZ), are capable to evaluate the intensity of the ground motion in real time and to send out messages via the developed communication network to the operators of critical infrastructures or local authorities (civil protection), before the arrival of the destructive seismic waves to the structures of interest. The information on a detected earthquake triggers also the local monitoring systems.

The flow of the seismic incidence information takes place through a communication network, which consists of several decentralized nodes. Every seismic sensor and every monitored infrastructure correspond to a communication node, which is responsible to send and receive the appropriate information. Synchronously, the same communication infrastructure, under development by Fraunhofer Institute for Open Communication (FOKUS), will provide warnings regarding the expected damages to the concerned parties (local authorities, operators of critical infrastructures). This allows the recipients to trigger safety measures. The kind and the intensity of the measures depend on the expected damages of the detected ground motion and can be

updated relying on the most current measured data. After the assessment of the seismic performance of the monitored structures, health reports will be sent to interested actors.

The local health monitoring systems consist of a number of sensors (accelerators, velocity recorders, displacement transducers, strain gauges, thermometers etc.) and data acquisition devices. The sensors are placed in appropriate positions to record effectively the response of the structure or components and to detect particular damage indicators. The definition of the damage indicators depends on the geometry, dynamic properties and seismic risk of the various components of the monitored infrastructures. In “almost” real time, the measurements from the monitoring sensors are evaluated either decentral and locally by smart data acquisition systems or remotely at a central site by linked computers. The results of the damage identification are integrated in two steps in the communication platform. Right after the earthquake, very basic information is forwarded (e.g., whether a bridge is accessible or not or if parts of the facility are severely damaged). Gradually, more detailed information based on a refined interpretation of the sensors’ recordings will be communicated to the clients, including a graphical representation of the damages.

One of the fundamental objectives and an innovative part of the project is the graphic representation of the damage distribution of the monitored infrastructures right after an earthquake. This is possible because of the integration of the SHM system in 3D BIM models. Necessary precondition is the coupling of the sensor data with the graphic objects representing the real sensors in BIM models. For this purpose, the Desite MD software was selected. It provides the opportunity to link databases containing sensor measurements with an imported BIM model. Responsible for the development of the monitoring systems, the damage detection techniques and the integration of the sensor data in BIM models are the Center for Wind and Earthquake Engineering (CWE) of RWTH Aachen University and Wölfel Engineering GmbH.



2 EARTHQUAKE EARLY WARNING AND RAPID RESPONSE SYSTEM

2.1 General Information

The Lower Rhine Embayment in Western Germany is one of the most important areas of earthquake recurrence north of the Alps, facing a moderate level of seismic hazard in European context, but a significant level of risk due to a high population density and a large number of critical industrial infrastructures. As the seismic faults are directly crossing the study area, the lead time, i.e. the time between the onset of an earthquake and the arrival of the destructive seismic waves is in the order of a few seconds at most for events in the Lower Rhine Embayment. In this context, the project aims at designing a user-oriented hybrid earthquake early warning (EEW) and rapid response system where regional seismic monitoring is combined with smart, on-site sensors, resulting in the implementation of decentralized early warning procedures.

2.2 Seismic scenarios for the area of interest

One of the tasks of this project deals with finding an optimal regional seismic network arrangement given the known seismicity in the area. The optimization approach used here requires a representative sample of relevant seismic recordings. In the design of an EEW network, it is critical that all potential and known earthquake sources in the area are considered. Due to the sparsity of significant earthquake recordings in the region, stochastic simulations of scenario earthquakes were performed using the finite-source ground motion simulation code EXSIM [4] and the known seismicity in the area [5]. Overall, over 700 realistic scenario earthquakes were considered (for their location see Figure 2). This approach is ideally suited for the purposes of our study, as our emphasis is not on the simulation of the complete wavefield for given scenario earthquakes, but rather on the generation of a large set of spectra for hypothetical sources located according to a seismic catalog.

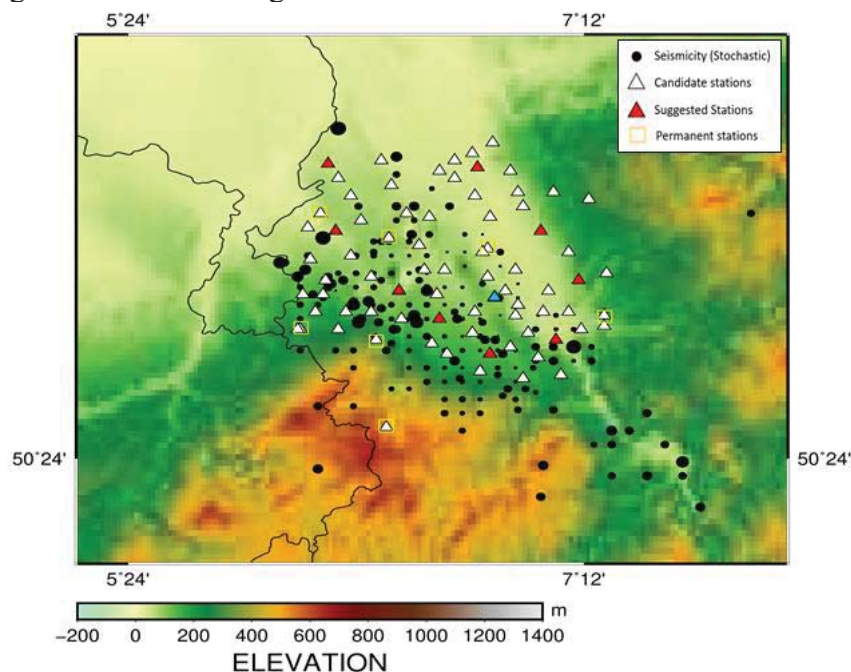


Figure 2: The Lower Rhine Embayment, Germany. The potential network is represented by candidate stations (white triangles) and suggested installations sites (red triangles) together with the existing permanent stations (yellow squares). The blue triangle represents the target site. The simulated scenario earthquakes are represented by black dots with diameter proportional to earthquake magnitude.

2.3 Optimal densification for real time assessment and early warning

The possible station locations were considered by public buildings (municipalities, schools etc) in the Lower Rhine Embayment. For each location, stochastic seismograms were computed for all scenario earthquakes resulting in a database consisting of more than 30,000 traces representing ground acceleration. An important aspect of an EEW system's performance is its ability to give not only timely, but also reliable warnings with respect to the shaking that needs to be expected at the target site. For our study site, a threshold of 0.02 g was selected, as such events can be considered as potentially damaging. The optimal network is the one that can give the correct level warning (i.e., correct level of expected ground motion at the target site) at a sufficiently long lead time for the highest number of scenario earthquakes.

To quantify this network quality, we use the cost function developed by Oth et al [6]. For finding the optimal station locations, a microgenetic algorithm was used. Such algorithms are a specific subset of genetic algorithms (GAs), which are guided search techniques based on evolutionary principles to find optimal models with respect to a given objective function (i.e., cost function). By minimizing the cost function, a comparison of the best earthquake early warning system design can be performed and the potential usefulness of existing and additional stations in the region is considered (see Figure 1). As indicated by the red triangles, by adding nine stations to the existing network, such optimal design will allow strong ground-motions with respect to the target site to be detected most quickly and most reliably.

2.4 Rapid response system

An earthquake early warning system can reduce the seismic risk on critical infrastructure more effectively, if combined with a response system. The term response system includes all automated measures that can be taken immediately after the detection of the first earthquake waves within the lead time. Structural damages are not the only threat especially for critical infrastructures. Accidents or side effects due to a seismic event such as fire or more rarely explosions or dispersion of toxic substances can have even more harmful consequences than the mechanical damages directly induced by the ground motion [7]. Possible countermeasures to limit damages and prevent domino effects that can be performed in range of seconds are emergency shutdown of gas lines, activating backups, safe stop of lifts or other equipment, interruption of medical operations, access prevention in road bridges or tunnels [7]. Within the ROBUST project, the production process of the chosen industrial facility is not interrupted automatically. The warning for a coming seismic incidence and the damage prediction is forwarded to the facility operators, who are responsible to trigger appropriate measures. Regarding the bridge, the access can be interrupted by a traffic light, in case an earthquake with damage potential is detected. Depending on “almost” real time assessment from the local monitoring system of the bridge, the access restriction will be recalled or it will remain for all or some kind of vehicles.

3 COMMUNICATION NETWORK

Essential part of the developed system is the decentralized communication network. It enables the interaction between seismic sensors and local monitoring sensor systems and is responsible to forward warning messages and structural health status reports to subscribed recipients (user oriented). Each user has access to different level and kind of information depending on his involvement. As users can be considered facility managers, local authorities, civil protection or rescue teams. From the communication infrastructure point of view, all the participants are divided into two categories: (i) sensors and (ii) actors. Sensors “produce” information and actors “consume” information. The nodes are spatially distributed and one node corresponds to

each seismic sensor. At the monitored infrastructures one node is responsible for the seismic sensor and for the controller of the local monitoring system. Predefined subscriptions specify the flow of information between the nodes. At the idle period, the platform is responsible to control, which devices are connected, their health status and the plausibility of the measurements of the sensors. The administrators of each subsystem are informed through automated messages about the health status of the whole sensor infrastructure.

When a ground motion, which exceeds a predefined threshold of acceleration, is detected by the seismic network, the communication node of the corresponding seismic sensor forwards the information to the subscribed recipients to trigger the monitoring system to measure with a higher sampling ratio, in order to obtain detailed information for the response of the structures during the seismic event. If a seismic event with damage potential is detected by the seismic network, messages, graded indicative lamp systems or smart traffic lights will inform the corresponding users about the upcoming event. No emergency shutdowns or other measures are triggered directly by the communication platform. During the seismic event, the sensor signals are continuously evaluated with regard to exceedance of values indicating damages. Right after the earthquake, the health status of the infrastructures, is evaluated based on the recording of the monitoring system and sent via the communication infrastructure to the concerned subscribers. The first report includes a rapid assessment of the performance of the structure (e.g. partial or total collapse of the infrastructure, risk for fire or explosion, operational status of a bridge). After a few minutes, a second more precise health status report is delivered. It contains information about the detection of damages and their spatial distribution. The second health status report includes information about the operability of the infrastructure and a graphic 3D representation of the structural damages.

4 STRUCTURAL HEALTH MONITORING OF CRITICAL FACILITIES

4.1 Critical Infrastructures

Critical infrastructures, according to German Federal Office for Civil Protection and Disaster Assistance, are organizations and facilities with crucial significance for the state community, the failure or impairment of which would result in lasting difficulties in supply chain, significant threats for the public security or other dramatic consequences [8]. Although buildings are considered to be the most vulnerable component of the urban built environment to seismic hazard, the resilience of complex systems like transport and utility networks, gas and electric network systems, health care system, power plants and selected industrial facilities is even more critical, as they have an extreme socio-economic impact and can affect the regional prosperity [9]. Although the seismic code provisions in Germany are constantly improving [10] and seismicity of the Lower Rhine Embayment was investigated in detail the recent years [11], an important part of the critical infrastructure was designed with lower seismic actions or without any seismic code provisions. According to [11], in this region there are 51 electricity supply substations, 108 hospitals, about 1500 industrial facilities, 4 industrial chemical parks and 8 road and railway bridges over Rhine.

Interdependencies between complex systems may result in rapid damage propagation. Therefore, there is a demand for interconnected monitoring systems, that can detect damages and provide this information to crisis management centers. Appropriate safety measures to prevent or mitigate damages can be triggered effectively, only if sufficient information is available within a short time. Awareness of the structural health status of critical nodes of the transport network, such as bridges, is beneficial for the definition the optimal routes for rescue teams and ambulances (interaction health care system – transport network). Chemical industries are an important component of the infrastructure in Lower Rhine. The main threat after an earthquake

in chemical industries with hazardous processes is the risk of accidental scenarios such as fire, explosion or dispersion of toxic substances due to loss of containment. Immediate countermeasures must be triggered to limit the consequences of such events in terms of fatalities, environment pollution and repair cost [12].

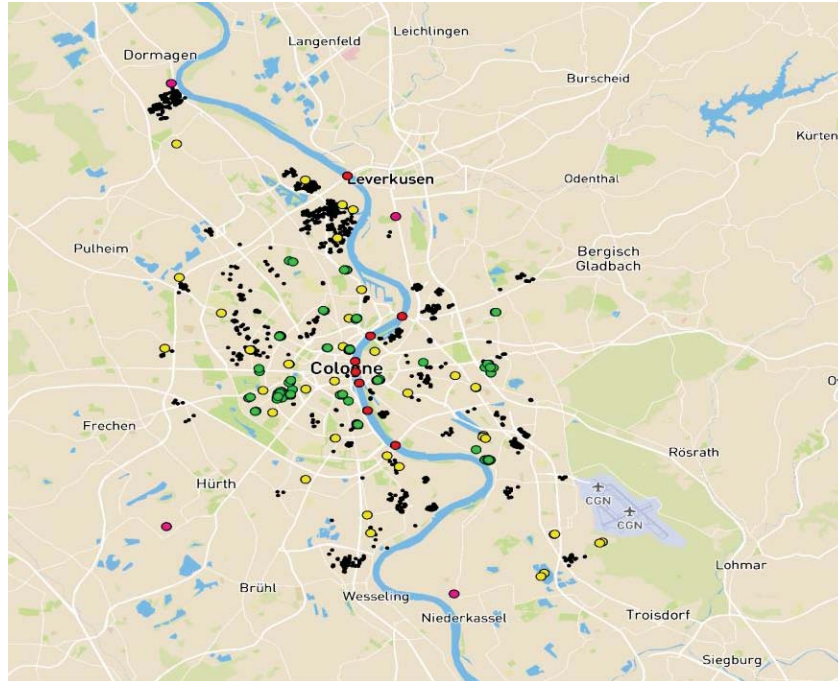


Figure 3: Distribution of critical infrastructures in Lower Rhine Region: electricity substations (yellow circles), hospitals (green circles), road & railway bridges over Rhine (red circles), industrial facilities (black circles), chemical industry parks (purple circles) [11]

4.2 Implementation of health structural monitoring system on demonstration facilities

Taking into consideration the distribution of critical infrastructures in Lower Rhine Region, an industrial facility (chemical industry) and a road bridge are selected as case studies for the installation of the local SHM systems. For both infrastructures, a probabilistic earthquake risk analysis is carried out, to define the seismic hazard. The vulnerability curves of different elements and components are defined based on the corresponding literature [13][26][27][28]. The most susceptible components are prioritized, their possible failure modes and the position of the expected damages is investigated in detail. Especially for the industrial facilities, the influence of non-structural components should be taken into account. Storage tanks, vertical and horizontal vessels, processing equipment, pumps and piping systems are connected with each other and structural damages on one process unit can generate a multiplicity of accident chains due to mutual interactions [14]. After the basic identification of the facilities, suggestions for further damage prevention or damage limitation will be provided and discussed with the facility operators [12]. The damage scenarios determined by simulations will be communicated to the operators and may be used for improving emergency actions and prevention of cascade effects. For this purpose, appropriate damage indicators and assessment methods, providing necessary information about the global performance of the structure or local failures of critical component will be implemented. Structural damages can result in a loss of stiffness, indicated by changes in natural frequency, mode shapes or modal shape curvature. For the monitored bridge, the critical indicators are aiming at the condition of the superstructure (global response, local damages) and at the bearings (critical movement of the superstructure) [29][30]. Regarding the industrial facilities, peak floor acceleration (PFA), interstorey drift ratio (SDR), residual SDR,

response of connections or strains in critical locations, for example elbow or tee connections of pipelines can be used as damage indicators [15] [16]. The number and the kind of the selected sensors (accelerators, velocity and displacement transducers, strain gauges etc.) depends on the chosen indicators and are structure specific.

Immediate damage detection and quantification, especially for critical infrastructures, is essential to minimize their operation interruption due to shut down time. Traditionally, engineering inspections and nonlinear analyses are necessary to evaluate the capacity of the structures after seismic events. This may last weeks or months, accompanied with an important economic cost due to shut down. Modern structural health systems can provide real time damage detection based on changes in dynamic properties of the monitored structures [16]. There is a variety of methods both in time and frequency domain such as autoregressive methods, stochastic subspace identification, frequency domain decomposition method, which can assess the seismic performance and health condition through different indicators [17]. The comparison of measurement data and simulation data allows a more precise prediction of damage stage and distribution within the infrastructures. Moreover, the existence of a geotechnical seismic sensor close to the monitored facilities, allows the application of either output only or input/output methods [18]. For different structural types, different types of damage indicators may be more effective [16]. The functionality of the measurement chain, selected damage indicators and assessment methods will be verified in scaled benchmark structures and substructures in laboratory in advance. In the aftermath of an earthquake, the fundamental information that should be extracted from the monitoring system concern the operational ability of the corresponding infrastructure depending on the distribution of damages. The smart data acquisition devices, which are capable to process data in real time and forward the crucial information to the communication network [19] play an important role in the integration of local monitoring system to the whole early warning and response system.

4.3 Integration health monitoring system in BIM modelling

The integration of the local monitoring systems of critical infrastructures in 3D BIM models is one of the objectives of the research project. BIM is an intelligent 3D model - based process, which promotes the interdisciplinary cooperation of different architects, engineers, constructors and facility operators [20]. The integration of SHM systems in BIM offers geospatial content to the measured and processed data and provides better control and management of the infrastructure [21]. In case of an earthquake with damage potential, the visualization of damages provides a fast and structured overview for operators of critical infrastructure and supports the decision-making processes. Another asset concerns mainly the rescue teams for whom a comprehensive graphic overview of the damages before entering a facility is important. Finally, the knowledge of the updated health status of infrastructures is a useful tool for the effective management and decision making at regional level.

The implementation is divided in two main parts: (i) the generation of a BIM Model including sensors and (ii) the coupling of the graphic objects with sensor data. For the creation of a 3D BIM model, Revit Structure 2020 [31] is selected. The principle is presented using the example of a simple steel frame structure. At first, the steel frame is designed according to the Eurocodes. The next step is the implementation of accelerometers as separate family component by means of an IFC class for the graphical representation of the sensors. The accelerometer created as a family component is imported in the main model. The IFC class names *IfcSensor* and *IfcSensorType* in Revit are classified as specialty equipment object [22]. Therefore, a subcategory "accelerometer" is manually defined in the file "exportlayers-ifc-IAI.txt". Alternatively, it is possible to use an existing object from the Revit library, such as fire alarm. However,

this may result in misunderstanding between different users. Revit gives the opportunity to provide static information like position, Id/name, manufacturer, type, cost etc. to each sensor [23].

However, the key challenge is the development of a “dynamic” BIM Model with continuous connection to the actual sensor data. For this purpose, Desite MD (Manage Data) is chosen [24]. Desite MD provides the opportunity to import BIM Models as IFC files and to interact with them through a Javascript API. The interaction is possible via an internal customized web browser, which allows the development of user-oriented applications [25]. Two main tasks have to be implemented: (i) the coupling of the IFC objects representing sensors with the corresponding measurements on the database and (ii) the representation of seismic damages in a 3D model. Concerning the first target, through the API, when a graphic sensor is selected by the user, its ID is identified and can be linked with data available in the database. The data are requested by the API from the corresponding table of the database. In general, it is possible to request either raw data or post-processed data. The sensor values are updated in time intervals appropriate for the specific application. The measurements can either be represented in tabulated views or in diagrams. The color of the sensor objects can be adapted considering the sensors operation status and the corresponding measurements. For example, an accelerometer can be: (i) grey: for sensor out of function, (ii) green: for sensor in function and maximum recorded acceleration during the last 30 sec. lower than m_1 , (iii) orange: for sensor in function and maximum measurement during the last 30 sec. between m_1 and m_2 and (iv) red: for sensor in function and maximum measurement during the last 30 sec. higher than m_2 . Threshold values (m_1 , m_2) depend on the requirements of each structure. Moreover, through the web form module, a graphical interface will be developed, where the user can request various data from sensors – namely from the database (raw or evaluated values, maximum/minimum values within a time period etc.).

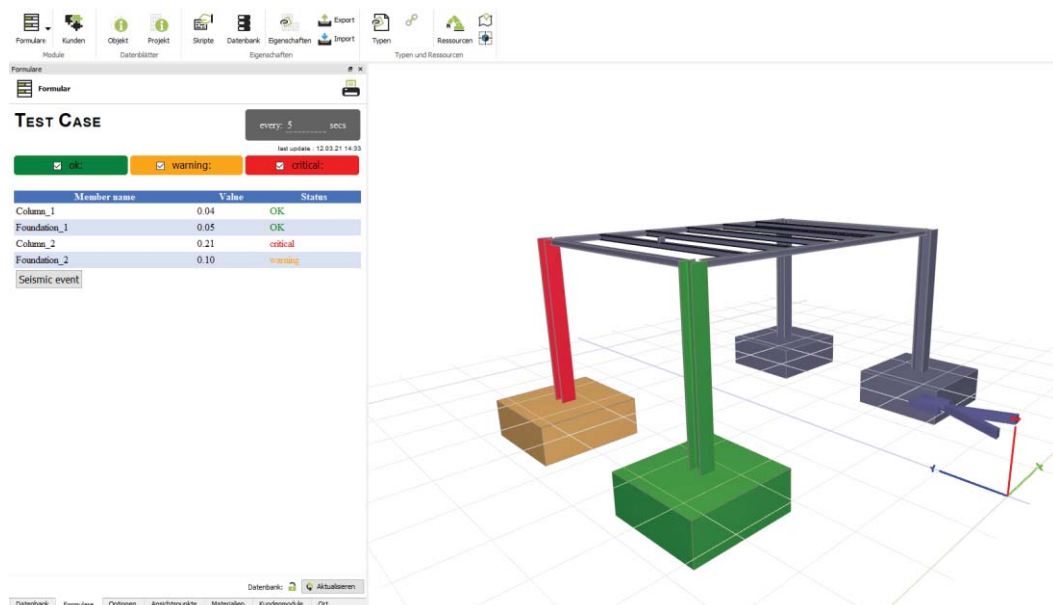


Figure 4: Visualization of damage detection after a seismic event

Regarding the damage detection, the color of monitored members/components is adapted depending on defined damage threshold values (Figure 4). The predefined threshold values (for instance interstorey drift ratio limits) are compared with post-processed sensor data, which result from one or more sensors. The updated model with the adapted colors of critical members/components and sensors is saved and compressed in a packed model after every update. After a seismic event, members and sensors maintain the most unfavorable health status-color,

even if measurements return to values below thresholds after the seismic event. The compressed file of the model including the visual distribution of damages is forwarded to the interested subscribers. Civil protection and rescue teams equipped with a BIM-Viewer will be able to open on tablets or smartphones the adapted compressed 3D model, in which the identified damages are indicated e.g., by colors and descriptive labels.

5 CONCLUSION

The presented paper describes the concept of a user-oriented earthquake early warning and rapid response system based on interconnected decentralized smart sensors and sensor systems integrated in BIM models. Aim of the project is to contribute to the mitigation of seismic risk, especially with respect to critical infrastructures. The investigated system is prototypically applied in Lower Rhine Region, which is one of the most important seismic areas north of the Alps. Although its seismicity can be categorized as moderate in European context, the seismic risk due to the population and infrastructure density is high. Exemplarily, a road bridge and a chemical industrial facility will be monitored and investigated in a holistic approach, considering their interactions with other infrastructures and networks. The essential relay between the seismic network (responsible for the early warning), the local monitoring systems (responsible for the evaluation of the seismic performance and detection of damages of critical infrastructure) and the interested parties, namely the facility operators and the local authorities, is the decentralized communication network, which enables the transfer of warning, health status and other critical information. The integration of SHM system in BIM models is a step forward in the management of infrastructures. The opportunity to visualize the detected damages in 3D models will improve the understanding and the decision-making processes for facility managers and will increase the resilience by reducing production interruptions and related economic losses. Furthermore, it is a useful tool to support rescue teams.

6 ACKNOWLEDGEMENTS

The authors are grateful for the financial support by BMWI, which funded the ROBUST research project in the thematic program “Geo-Research for Sustainability (GEO:N)” in the framework program “Research for Sustainable Development (FONA 3) under the call “Natural Risks – Early Detection of Earthquakes and their Consequences”.

REFERENCES

- [1] C. Ranieri, G. Fabbrocino, and E. Cosenza, “Structural health monitoring systems as a tool for seismic protection,” 14th World Conference on Earthquake Engineering, October 12-17, 2008 Beijing China.
- [2] R. M. Allen, P. Gasparini, O. Kamigaichi, and M. Bose, “The Status of Earthquake Early Warning around the World: An Introductory Overview,” *Seismological Research Letters*, vol. 80, no. 5, pp. 682–693, 2009, doi: 10.1785/gssrl.80.5.682.
- [3] W. Stephen and B. James, “Synergistic combination of systems for structural health monitoring and earthquake early warning for structural health prognosis and diagnosis,”
- [4] D. M. Boore, “Comparing Stochastic Point-Source and Finite-Source Ground-Motion Simulations: SMSIM and EXSIM,” *Bulletin of the Seismological Society of America*, vol. 99, no. 6, pp. 3202–3216, 2009, doi: 10.1785/0120090056.

- [5] G. Grünthal, D. Stromeyer, C. Bosse, F. Cotton, and D. Bindi, “The probabilistic seismic hazard assessment of Germany—version 2016, considering the range of epistemic uncertainties and aleatory variability,” *Bull Earthquake Eng*, vol. 16, no. 10, pp. 4339–4395, 2018, doi: 10.1007/s10518-018-0315-y.
- [6] A. Oth, M. Böse, F. Wenzel, N. Köhler, and M. Erdik, “Evaluation and optimization of seismic networks and algorithms for earthquake early warning – the case of Istanbul (Turkey),” *J. Geophys. Res.*, vol. 115, B10, p. 321, 2010, doi: 10.1029/2010JB007447.
- [7] E. Salzano, A. Garcia Agreda, A. Di Carluccio, and G. Fabbrocino, “Risk assessment and early warning systems for industrial facilities in seismic zones,” *Reliability Engineering & System Safety*, vol. 94, no. 10, pp. 1577–1584, 2009, doi: 10.1016/j.res.2009.02.023.
- [8] Bundesamt für Bevölkerungsschutz und Katastrophenhilfe, https://www.bbk.bund.de/DE/AufgabenundAusstattung/KritischeInfrastrukturen/kritischeinfrastrukturen_node.html.
- [9] K. Pitilakis, *SYNER-G: typology definition and fragility functions for physical elements at seismic risk: Buildings, lifelines, transportation networks and critical facilities*. Dordrecht: Springer, 2014.
- [10] DIN-Normenausschuss Bauwesen (NABau), “Draft DIN EN 1998-1/NA, National Annex – Nationally determined parameters – Eurocode 8: Design of structures for earthquake resistance - Part 1: Basic principles, seismic actions and rules for buildings, 2020.
- [11] M. Pilz et al., “Seismic risk analysis in Germany: an example from the Lower Rhine Embayment. Final report,” 2020.
- [12] F. Paolacci, R. Giannini, and M. De, “Analysis of the Seismic Risk of Major-Hazard Industrial Plants and Applicability of Innovative Seismic Protection Systems,” in *Petrochemicals*, V. Patel, Ed.: InTech, 2012.
- [13] Component fragility evaluation, seismic safety assessment and design of petrochemical plants under design-basis accident conditions (INDUSE-2-SAFETY): Final report. Luxembourg: Publications Office of the European Union, 2019.
- [14] K. Nasseradesi and G.-A. Mohsen, “Major contributing factors to seismic risk of industrial facilities,” 2008.
- [15] G. Varelis, A. M. Gresnigt, and S. Karamanos, “Steel elbow response under strong cyclic loading,” *Proceedings of the International Offshore and Polar Engineering Conference*, pp. 487–496, 2012.
- [16] S.-H. Hwang and D. G. Lignos, “Assessment of structural damage detection methods for steel structures using full-scale experimental data and nonlinear analysis,” *Bull Earthquake Eng*, vol. 16, no. 7, pp. 2971–2999, 2018, doi: 10.1007/s10518-017-0288-2.
- [17] R. Brincker and C. E. H. Ventura, *Introduction to operational modal analysis*. Chichester, West Sussex: John Wiley and Sons Inc, 2015. [Online]. Available: <http://search.ebscohost.com/login.aspx?direct=true&scope=site&db=nlebk&AN=1017454>
- [18] P. Avitabile, *Modal Testing: A practitioner's guide*. Hoboken: Wiley, 2018. [Online]. Available: <http://onlinelibrary.wiley.com/book/10.1002/9781119222989>
- [19] National Instruments, *Specifications cRIO-9045*.

- [20] R. Sacks, C. M. Eastman, G. Lee, and P. M. Teicholz, BIM handbook: A guide to building information modeling for owners, designers, engineers, contractors, and facility managers. Hoboken, New Jersey: Wiley, 2018. [Online]. Available: <https://onlinelibrary.wiley.com/doi/book/10.1002/9781119287568>
- [21] Chen Jianli, Bulbul Tanyel, Taylor John E., and Olgun Guney, A Case Study of Embedding Real-time Infrastructure Sensor Data to BIM.
- [22] ISO 16739-1:2018 Industry Foundation Classes (IFC) for data sharing in the construction and facility management industries — Part 1: Data schema.
- [23] M. Valinejadshoubi, A. Bagschi, and O. Moselhi, “Managing Structural Health Monitoring Data Using Building Information Modelling,” Smar 2017 - Fourth Conference on Smart Monitoring, Assessment and Rehabilitation of Civil Structures.
- [24] Thinkproject Deutschland GmbH, Manage your 3D building model interactively. Right from the start.
- [25] Ceapoint, Manage your 3D building model interactively. Right from the start: API - Web Forms.
- [26] FEMA-NIBS, Multi-Hazard Loss Estimation Methodology – HAZUS – MH MR4: Earthquake Model Technical Manual, Federal Emergency Management Agency, Washington, D.C., 2003
- [27] I. Moschonas, A. Kappos and A. Sextos, “Generalised fragility curves for straight bridges, for arbitrary angle of incidence of the seismic action, including soil-bridge interaction”, IBSBI 2011, October 13-15, 2011, Athens, Greece
- [28] I. Kilanitis and A. Sextos, “Integrated seismic risk and resilience assessment of roadway networks in earthquake prone areas,” Bull Earthquake Eng, vol. 17, no. 1, pp. 181–210, 2019, doi: 10.1007/s10518-018-0457-y.
- [29] Z. H. Li and F. T. K. Au, “Damage Detection of a Continuous Bridge from Response of a Moving Vehicle,” *Shock and Vibration*, vol. 2014, no. 2, pp. 1–7, 2014, doi: 10.1155/2014/146802.
- [30] V. Alves, A. Meixedo, D. Ribeiro, R. Calcada, and A. Cury, “Evaluation of the performance of different damage indicators in railway bridges,” *Procedia Engineering* 114 (2015) 746 - 753.
- [31] S. Tickoo, Exploring Autodesk Revit 2020 for structure: Includes application of robot structural analysis professional 2020. Schererville, Indiana: CADCIM Technologies, 2019

MONITORING OF A PRESTRESSED BRIDGE MODEL BY ULTRASONIC MEASUREMENT AND VIBRATION RECORDINGS

Chun-Man Liao, Falk Hille, Daniel Fontoura Barroso and Ernst Niederleithinger

Bundesanstalt für Materialforschung und -prüfung (BAM), Unter den Eichen 87, 12205 Berlin,
GERMANY

{Chun-Man.Liao, Falk.Hille, Daniel.Barroso, Ernst.Niederleithinger}@bam.de

Abstract

The aim of this work is to improve the current structural health monitoring (SHM) methods for civil structures. A field experiment was carried out on a two-span bridge with a built-in unbonded prestressing system. The bridge is a 24-metre long concrete beam resting on three bearings. Cracks were formed subsequently when a prestressing force of 350 kN was changed to 200 kN, so that different structural states could be demonstrated. The structural assessment of this reference bridge was accomplished by the non-destructive testing using ultrasonic devices and vibration measurements. The ultrasonic velocity variations were investigated by using the coda wave interferometry method. The seismic interferometry technique was applied to the vibration recordings to reconstruct the wave propagation field in the bridge. This investigation shows that the wave velocity is sensitive to the current structural state and can be considered as the damage indicator. Overall, the implementation of coda wave interferometry and seismic interferometry technique facilitates structural health monitoring (SHM) in civil engineering.

Keywords: structural health monitoring, non-destructive testing, coda wave interferometry, seismic interferometry, ultrasonic measurement, prestress.

1 INTRODUCTION

The application of prestressing and post-tensioning techniques to civil infrastructures such as long span bridges improves the structural performance in their lifetime. Since the prestress loss can occur while the structure is in service, it is important to monitor the prestressed civil structures. However, a lot of studies lack the reference condition of large-scale test objects for comparison in the evaluation.

In our study, a large-scale concrete bridge model containing a built-in unbonded prestressing system was monitored. The variable prestressing force was a benefit to our investigation on the bridge. As the structural capacity was enhanced by the high prestressing force, the structural condition was considered as the baseline for damage detection. Thus, we could explore damage indicators of the prestressed bridge.

To achieve the research aim, both active and passive procedures were applied in the field experiment. Since damage leads to changes in the dynamic properties of the structure, vibration monitoring is useful as a non-destructive evaluation tool. However, the measured eigenfrequencies are also sensitive to environmental influences [1]. Referring to the advantage of the wave-based method, two kinds of wave propagation were considered in our study: ultrasonic wave propagation, which is widely used for non-destructive testing (NDT), and the resultant of seismic interferometry of noise recordings.

Ultrasonic waves are sensitive to variations of several parameters (stress, temperature, moisture) and to any kind of damage. Different mechanical wave propagation regimes have been investigated for concrete so far [2]. In the attenuation phenomenon, the waves scatter and induce the onset of late arrival, constituting the so-called ultrasonic coda. In seismology, the coda waves are known for its high sensitivity to small perturbations of the medium. Coda waves are defined as the part of the signal that occurs directly after the arriving phases. In a heterogeneous medium, the small change has less influence on the waves arriving first than on the diffusion waves arriving later. As coda waves travel longer distances, the sampling repeats and the influence of the small change is amplified [3]. Hence, the coda energy change is more detectable than the direct ones.

Recently, coda wave interferometry (CWI) has been used to ultrasonic coda and noise recordings in civil structures. The implementation of CWI enabled the detection of early subtle changes in reinforced concrete structures until crack formation [4]. In an earlier study [5] using ultrasound to monitor stress distribution and cracking in concrete beams, they were loaded until failure to detect cracks before visual signs appear on the surface. The application of CWI to the waveform of the cross-correlation function of two vibration records was presented in another study [6] to analyse the wave velocity variation.

This contribution introduces the background of CWI and the application of CWI to our measurement data. We studied the effect of the post-tensioning force change based on the coda wave velocity variation. The experiment result confirms the applicability of the monitoring method using CWI. This research shows the progress towards the development of a cost-effective and reliable technique for real-time monitoring in large-scale structures.

2 CODA WAVE INTERFEROMETRY

We studied the effect of the post-tensioning force change based on the coda wave velocity variation. For this, the same waveform in two different bridge states was compared using coda wave interferometry (CWI). The principle of CWI is to compare the waveform consistency of coda waves recorded in two different states. Figure 1 shows two signals recorded before and after perturbation. The first arrivals of the signals are almost the same, while the coda wave

(later arrivals) shows significant wave propagation time lags. The relative time lag ($\frac{\delta t}{t}$) between the two signals before and after the perturbation indicates the relative wave velocity change ($\frac{\delta v}{v}$). Since the prestress has a homogeneous effect on the wave propagation velocity, the linear relation is applied

$$\frac{\delta v}{v} = -\frac{\delta t}{t}. \quad (1)$$

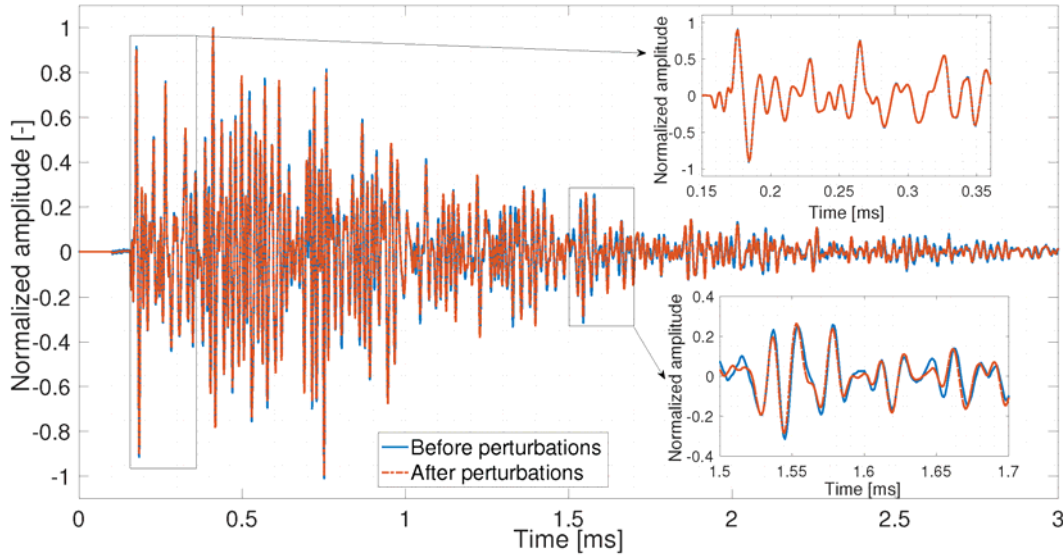


Figure 1: Repeated ultrasonic signals with difference just visible in the coda [7].

The following explains how to estimate the wave velocity variation by applying the stretching method to CWI.

2.1 The stretching method

As the relative velocity decrease is defined as the stretch factor α

$$\alpha = \frac{\delta v}{v}, \quad (2)$$

the shift time in wave propagation is represented by $t(1 + \alpha)$.

Hence:

$$u_s = u_o(t(1 + \alpha)), \quad (3)$$

where the original waveform u_o is stretched and turned into u_s .

According to this formulation, the sign of α is negative if the waveform is compressed.

The cross-correlation between the stretched and the original waveform is then shown as follows

$$CC(\alpha) = \frac{\int_{t-T}^{t+T} u_o(t')u_s(t')dt'}{\sqrt{\int_{t-T}^{t+T} u_o^2(t')dt' \int_{t-T}^{t+T} u_s^2(t')dt'}} \quad (4)$$

The cross-correlation coefficient (CC) is considered as a quality indicator. If two waveforms are identical, the cross-correlation coefficient is equal to 1. Vice versa, the cross-correlation coefficient between -1 and less than 1 indicates the difference depending on the dilation level.

2.2 Application

We investigated the impulse response in the different prestressed states using coda wave interferometry. One waveform was considered as a reference and the other was stretched by the factor α in a range $[-dv, dv]$. The best α was determined by comparing CWI in the reference waveform and the stretched waveform. Such an α maximizes the cross-correlation of two compared waveforms. At the same time, the wave velocity change is obtained in the best fit condition. As a result, we could study the relationship between the prestressing force variations, temperature change and wave propagation velocity in the concrete bridge model.

3 EXPERIMENT

3.1 Test structure BLEIB

The test structure was a prestressed concrete bridge model exposed to the nature environment at the BAM test site [8]. No traffic vibrations were induced as background noise on the bridge. The bridge model has been used for various loading and vibration tests. Thereby, vertical cracks had developed near the two midspans (Fig. 2). For our study, no additional external load was applied to the bridge, thus no significant post-cracking behavior occurred. This reduced the confusion of the external interferon.



Figure 2: The damage condition after vibration and loading tests (photographed in 2018).

We induced the natural damage by opening the already existing cracks. Initially, we increased the prestressing force up to 550 kN (level 1 in Tab. 1) and then adjusted the magnitude of the prestressing force (level 2-9 in Tab. 1) to obtain the different event extensions of the already existing cracks.

Level	Prestressing force [kN]
1	553
2	457
3	403
4	353
5	300
6	255

7	200
8	353
9	455

Table 1: Prestressing force level.

3.2 Vibration measurements

We implemented passive monitoring by vibration measurement. Geophones (Fig. 3 left) were used and the sampling rate was 600 Hz. The blue markers in Fig. 4 indicate the geophones' position. The distance between every two adjacent geophones is 3 m.



Figure 3: Sensors. Left: geophones. Right: ultrasonic transducers SO807 [9].

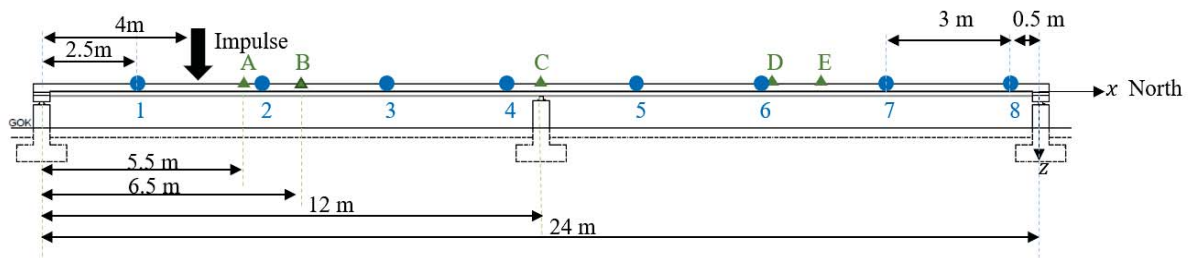


Figure 4: Side view of the bridge and sensor positions.

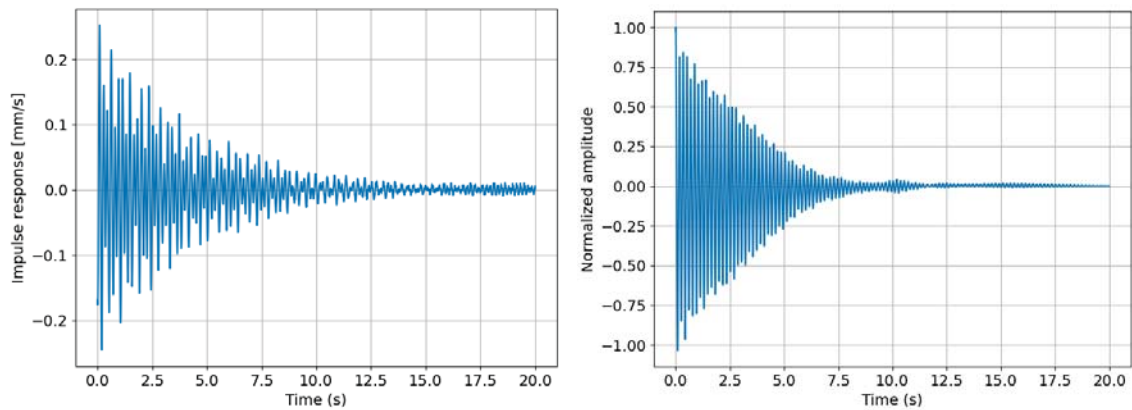


Figure 5: Impulse response in Level 2. Left: hammer impact received at the position 2. Right: seismic interferometry of the ambient noise at the position 1 and 2.

We directly obtained the real impulse response caused by the impulse source excited by the hammer impact (the position reference to the black arrow in Fig. 4). The measured impulse response lasted 20 sec. Fig. 5 on the left shows the impulse response received at the position 2. We also performed the ambient vibration measurement for 3 min. for each prestressing level. To extract the virtual impulse response, the seismic interferometry technique (the cross-

correlation method) dealing with the reconstruction of Green's functions between two receivers was used. One of these two receivers was turned into a virtual source. Finally, two virtual impulse responses extracted from 3-minute measurement data were stacked and normalized. Fig. 5 on the right shows the impulse waveform with the window size of 20 sec. between position 1 and position 2.

3.3 Ultrasonic measurements

For active monitoring, we performed the ultrasonic transmission measurement. 14 ultrasonic transducers “SO807” ([9], Fig. 3 right) were mounted inside the bridge during its construction before casting (position reference to the green markers in Fig. 4 and Fig. 6). This sensor can operate as both a transmitter and a receiver. The ultrasonic wave was generated with a central frequency of 60 kHz. The sampling rate is 1MHz. In the measurement, 10000 samples were taken.

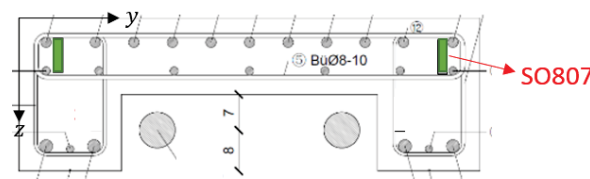


Figure 6: The embedded SO807 sensors in a cross section.

4 RESULTS

First, we show the modal analysis results of the bridge finite element model and the evaluation of the influence of the prestressing force on the natural frequency. Then the results of the ultrasonic impulse response, the real impulse response and the virtual impulse response are presented. The influence of temperature and prestressing on the coda waves is finally discussed.

4.1 Natural frequency and structural stiffness

The opening/close of the already existing cracks caused the overall stiffness change. Consequently, the structural dynamic behaviour changed due to the superposition of two effects from the prestressing force and the cracks. The comparison of the first natural frequency in the simulation of the intact bridge model (Fig. 7) with the measured result in the Level 1 state (Fig. 8 left) showed that the current bridge condition is damaged.

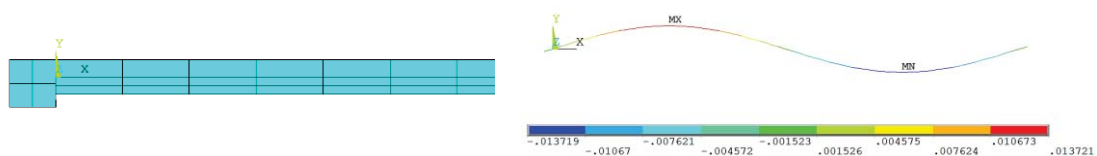


Figure 7: Half span of the finite element (FE) model (left). The first mode shape corresponds to 3.9 Hz (right).

Furthermore, Fig. 8 shows the first two modal frequencies in the Level 1 and 7 states. The decrease of natural frequencies depends on the prestress loss and the event extension of the already existing cracks in the bridge. Based on this, we were able to demonstrate different structural states by adjusting the prestressing force.

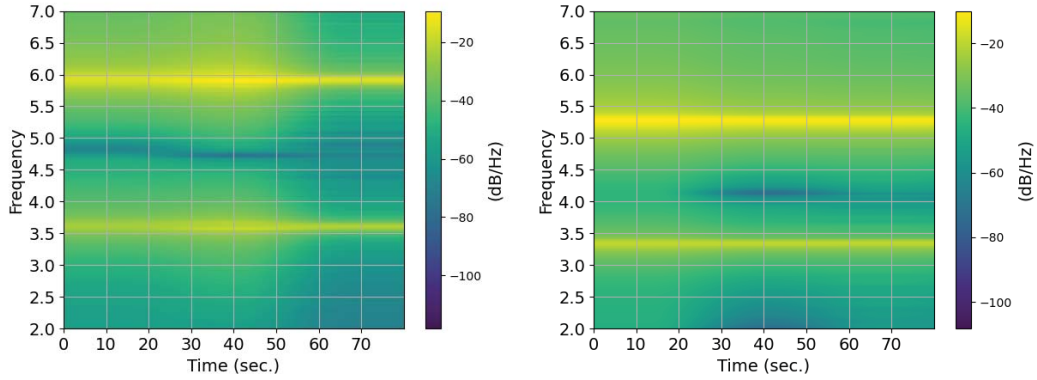


Figure 8: Natural frequency spectrum. Left: Level 1. Right: Level 7.

4.2 Influence of temperature and prestress change

On the measurement day, the ambient temperature increased from 28 °C to 30 °C during the prestressing adjustment from Level 1 to Level 9. Therefore, the high prestress level coincides with the high measured concrete temperature. The increasement in concrete temperature was higher than that of the ambient temperature. The results (Fig. 9 and 10) show that in our case the velocity variation is independent from the temperature change.

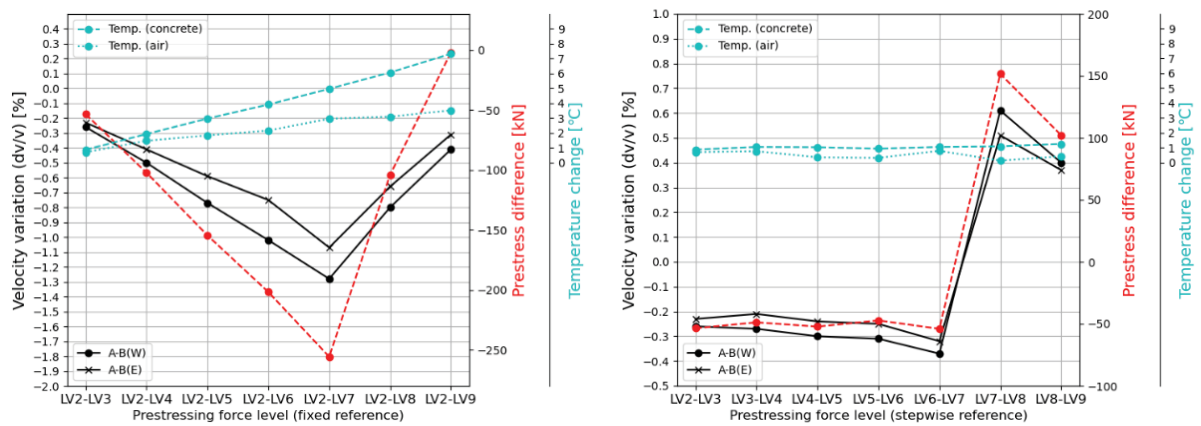


Figure 9: Ultrasonic coda velocity variation. Left: the fixed reference (Level 2). Right: the stepwise reference.

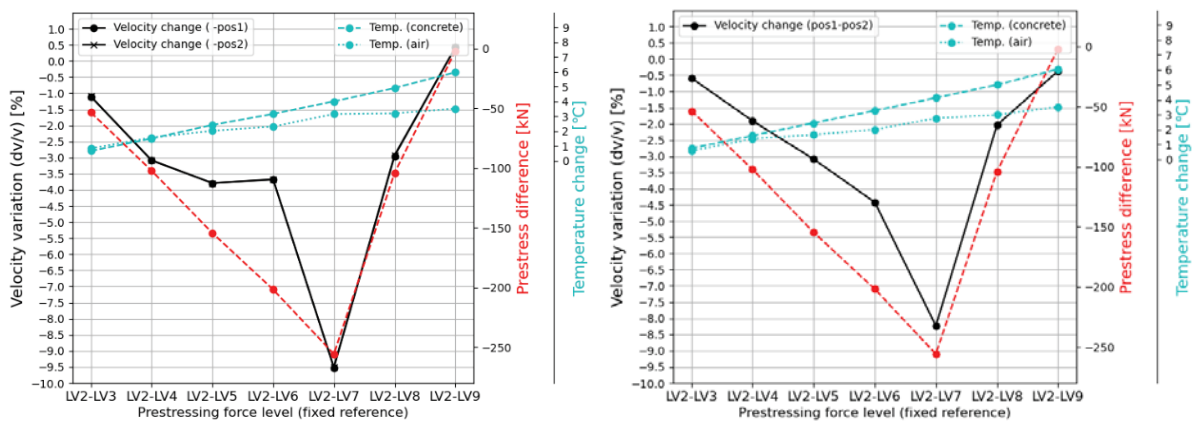


Figure 10: Impulse wave velocity variation (fixed reference: Level 2). Left: obtained from the real impulse response. Right: obtained from the virtual impulse response.

4.3 Discussion

Although Fig. 8 shows the natural frequency change due to the overall stiffness change, it is difficult to quantify the real damage condition and even more difficult to detect the structural property alteration with smaller prestress changes. Moreover, the natural frequency as a global dynamic characteristic is not sensitive to the damage location.

Fig. 9 and 10 show that the variation in velocity for both the ultrasonic coda and the impulse response coda corresponds very well with the prestress change. Particularly the velocity variation of the ultrasonic coda was greater in the west side than in the east sides (Fig. 9 left). The high sensitivity of the ultrasonic coda came as a benefit in the detection of the local damage condition. The wave velocity variations in the impulse response received at the position 1 and 2 were the same (Fig. 10 left). Thus, the hammer impact had the same influence on both receiver positions. Comparing the results shown in Fig. 10, the velocity variation in the virtual impulse response fits the prestress change better than the real impulse response. The applicability of seismic interferometry used to extract the virtual impulse response for CWI is approved. In addition, a significant drop in velocity variation was observed between Level 6 and 7. We state that this result is caused by the open cracks. This revealed the influence of the post-tensioning force on the already existing cracks.

5 SUMMARY AND OUTLOOK

Contrary to many researchers who have focused on the assessment of ultrasonic waves in concrete specimens in the laboratory, our study explored the applicability of ultrasound on a large-scale bridge model in a field experiment. The damage condition and the experiment setting made this bridge an ideal test structure to perform not only active, but also passive monitoring. Coda wave interferometry was applied to the ultrasonic coda and the vibration recordings. We investigated the effect of the prestressing force change based on the coda wave velocity variation. The monitoring schemes were verified by the good match of the coda wave velocity variation and the prestress alteration.

One drawback of our experiment is that the ultrasonic measurement duration at different prestress levels is too short to obtain the relationship between the temperature and the wave velocity. Performing a long-term measurement without prestress change will be our next step to investigate the dependence of the coda wave velocity variation on temperature.

ACKNOWLEDGEMENTS

Thanks to Eva Viefhues, Fred Ziegler and René Seefeld from BAM division 7.2 for their support of our experiment.

This study is part of the GIOTTO project, funded by Bundesministerium für Bildung und Forschung (BMBF) in the frame of “Früherkennung von Erdbeben und ihren Folgen” program (Grant No: 03G0885D).

REFERENCES

- [1] Maeck, J.; Abdel Wahab, M.; De Roeck, G.: Damage Detection in Reinforced Concrete Structures by Dynamic System Identification. In: *Proceedings of the International Seminar on Modal Analysis*, (2)1999, 939-946.

- [2] Planès, T.; Larose, E.: A Review of Ultrasonic Coda Wave Interferometry in Concrete. In: *Cem. Concr*, **53 (11)**2013, 248-255.
- [3] Grêt, A.; Snieder, R.; Scales, J.: Time-lapse Monitoring of Rock Properties with Coda Wave Interferometry. In: *Journal of Geophysical Research: Solid Earth*, **111(B3)**2006.
- [4] Bassil, A.; Wang, X.; Chapeleau, X.; Niederleithinger, E.; Abraham, O.; Leduc, D.: Distributed Fiber Optics Sensing and Coda Wave Interferometry Techniques for Damage Monitoring in Concrete Structures. In: *Sensors*, **19(2)**2019, 356.
- [5] Niederleithinger, E.; Wang, X.; Herbrand, M.; Müller, M.: Processing Ultrasonic Data by Coda Wave Interferometry to Monitor Load Tests of Concrete Beams. In: *Sensors*, **18(6)**2018, 1971.
- [6] Salvermoser, J.; Hadziioannou, C.; Stähler, S. C.: Structural Monitoring of a Highway Bridge Using Passive Noise Recordings from Street Traffic. In: *The Journal of the Acoustical Society of America*, **138(6)**2015, 3864-3872.
- [7] Wang, X.; Chakraborty, J.; Bassil, A.; Niederleithinger, E.: Detection of Multiple Cracks in Four-Point Bending Tests Using the Coda Wave Interferometry Method. In: *Sensors*, **20(7)**2020, 1986. <https://doi.org/10.3390/s20071986>
- [8] Unger, J. F., Gründer, K.-P., Hille, F., Liehr, S., Maack, S., Niederleithinger, E., Pirskawetz, S., Rogge, A., Said, S., Viefhues, E. et al.: Innovative Messsysteme zum Brückenmonitoring am Beispiel einer Versuchsbrücke – vom Sensor bis zur Zustandsprognose. In: *Messen im Bauwesen*, **2017**, 7–19.
- [9] Niederleithinger, E. ; Wolf, J.; Mielentz, F.; Wiggienhauser, H.; Pirskawetz, S.: Embedded Ultrasonic Transducers for Active and Passive Concrete Monitoring. In: *Sensors*, **15(5)**2015, 9756-9772. <https://doi.org/10.3390/s150509756>.

COMPARATIVE NON-STRUCTURAL VULNERABILITY ASSESSMENT METHODS FOR HISTORICAL RESIDENTIAL MASONRY BUILDINGS

Filippos Alogdianakis¹, Konstantinos G. Megalooikonomou², and Georgios S. Papavasileiou³

¹ University of Cyprus
75 Kallipoleos Str., P.O. Box 20537, 1678 Nicosia, Cyprus
e-mail: alogdianakis.filippos@ucy.ac.cy

² GFZ German Research Centre for Geosciences
Telegrafenberg, 14473 Potsdam, Germany
e-mail: kmegal@gfz-potsdam.de

³ University of Wolverhampton
Springfield Campus, Grimstone Street, Wolverhampton, WV10 0JP, United Kingdom
e-mail: G.Papavasileiou@wlv.ac.uk

Abstract

The determination of seismic risk is the foundation for risk mitigation decision-making and a key step in risk management. Large corporations and other enterprises (e.g., local governments) analyze their 'portfolio' of properties, to determine how to best allocate limited funds for structural strengthening of buildings, or other risk reduction measures such as emergency planning. When assessing the seismic vulnerability of buildings, it is essential to first establish the project objectives, before subsequently choosing the most appropriate strategy and tools necessary for building assessment and fulfillment of these objectives. It is also extremely important to understand the difference between the detailed approaches used for individual building assessment and those methods most efficient for larger scale analysis, pursued for city center assessment. While the latter results can be used as a general measure of seismic risk for different types of buildings, the actual seismic risk for any individual building may vary considerably and will depend upon its exact configuration and condition. In this study, some historical masonry buildings located in Alsace France are considered and the dynamic characteristics of these structures were estimated by the analysis of seismic noise recordings by sensors installed at each floor of the buildings under study. The estimated dynamic properties for small amplitude vibrations of these historical structures were used to derive fragility curves through vulnerability models with different level of complexity and accuracy. These fragility curves have been calculated using incremental dynamic analysis for the seismic demands generally imposed upon linear and slightly nonlinear models of single and multiple degrees of freedom, which is the case for the effects of induced seismicity. Considering the latter case of induced seismicity, the vulnerability assessment requires the expected damage to refer to non-structural components. The conclusions through comparison of the results of this study in terms of refinement of the verified structural models will prove useful for both local end-users and industrial stakeholders, with a clear perspective for a better understanding of the risk related to induced and triggered seismicity and its sound management.

Keywords: fragility curves, non-structural components, masonry, induced seismicity.

1 INTRODUCTION

The determination of seismic risk is the foundation for risk mitigation decision-making, a key step in risk management. Large corporations and other enterprises (e.g., local governments) analyze their 'portfolio' of properties to best allocate limited funds for structural strengthening of buildings or other risk reduction measures such as emergency planning. When assessing the seismic vulnerability of buildings, it is essential to first establish the project objectives before choosing the most appropriate strategy and tools necessary for building the assessment and fulfilment of these objectives. It is also extremely important to understand the difference between the detailed approaches used for individual building assessment and those methods most efficient for larger-scale analysis, pursued for city center assessment. While the latter results can be used as a general measure of seismic risk for different types of buildings, the actual seismic risk for any individual building may vary considerably and will depend upon its exact configuration and condition.

In this study, some historical masonry buildings located in Alsace France, are considered, and the dynamic characteristics of these structures were estimated by the analysis of seismic noise recordings by sensors installed at each floor of the buildings under study [1],[2].

In the considered test site, the analysis of the collected exposure information indicates that traditional or historical masonry structures occur in large numbers near to the mostly rural areas close to the geothermal platforms in Alsace region in France [3]. Two general classes of structures, namely unreinforced masonry (URM) and timber-framed masonry (TFM) buildings, have been considered, and the simple performance assessment models [1],[2] have been adopted in order to carry out a preliminary vulnerability assessment for these classes of structures. The objective is to rapidly identify buildings and their non-structural components that are at greater risk in the event of an induced earthquake, and to model their non-structural fragility.

The vulnerability modelling focused on buildings constructed of masonry, which may be more susceptible to the range of ground motion expected in the event of induced seismicity in the area. The measurements have been carried out using the MPwise (Multi-Parameter Wireless Sensing System) smart device [4], which has been designed to carry out rapid measurement activities by exploiting the computing and advanced networking capacities embedded in individual units. Based on environmental, seismic noise measurements, the fundamental frequency of vibration of the inspected buildings has been estimated and used to calibrate the respective fragility curves.

In collaboration with GFZ and ES-Géothermie a three-day acquisition campaign was organized, which involved installing four sets of sensors in private houses located in villages located around the Soultz and Rittershoffen geothermal sites. The fundamental period of these structures was verified by analyzing the ambient noise measured using the MPwise sensors [4], with one sensor installed outside of the buildings and the three others installed on each floor of the houses (basement, ground floor and first floor). The sensors were installed to record the ambient noise and to draw a vulnerability mode that allows the issuing of damage forecasts (Table 1, [1],[2]). Finally, the main geometry required as input for the simplified vulnerability models was taken through field inspection of these buildings.

No	Building Type	Building Latitude	Building Longitude	Fundamental ESDOF Model Period (s)	Fundamental Frequency Sensor (Hz)
1	URM	48.964946	7.881095	0.17	5.5
2	URM	48.902075	7.874917	0.37	2.7
3	URM	48.905270	7.950266	0.11	9
4	TFM	48.914307	7.882233	0.15	6.7
5	URM	48.932865	7.874377	0.32	3.1

Table 1: Real URM and TFM buildings located near the geothermal platforms in Alsace region in France [1],[2].

2 INCREMENTAL DYNAMIC ANALYSIS OF EQUIVALENT SINGLE DEGREE OF FREEDOM SYSTEM (ESDOF)

The estimated dynamic properties for small-amplitude vibrations of these historical structures were used to derive simplified vulnerability models. While steel or concrete frames are mostly lumped systems with stiff diaphragms, URM buildings have distributed mass and stiffness commonly in combination with flexible diaphragms. This fact obstructs the adoption of the established methodologies to URM buildings. Specifically, the latter buildings' fundamental mode shape involves a low percentage of the total mass of the building below the 75% limit required for the good performance of ESDOF-based methods. In order to solve this issue, the simplified procedure of Vamvatsikos and Pantazopoulou (2015) [5] was adopted. In their procedure, the dynamic URM building response is represented. Global response indices are transformed to local deformation measures in closed-form seismic assessment solution both for demand and supply in the critical structural locations. The solution involves the definition of the fundamental vibration mode, approximated by 3D shape function consistent with the building's boundary conditions. Strength and deformation indices are adopted for the evaluation of the acceptance criteria. Typical local failures are estimated through a local shape of deformation while the model captures the global dynamic characteristics. The adopted method allows the automation of the necessary calculations through closed-form expressions.

In the case of TFM the walls are reinforced with timber elements, both horizontal and vertical, but also X-type diagonal braces. It is evident historically, since the Bronze Age, that the timber reinforcement into masonry walls is strongly related to seismic resistance in earthquake-prone areas. In TFM walls, there is also recent experimental and numerical evidence [6] that the diagonal braces' contribution is vital for walls' lateral behaviour in the nonlinear range due to early detachment of the masonry infill from the surrounding timber frame in the event of an earthquake. It is also observed that the diagonals in tension detach from the surrounding frame for very low horizontal displacement. Therefore, it is suggested [6] that the diagonals should contribute to the lateral behaviour only in compression and, moreover, the infill masonry walls of the timber frame should not be considered in the analytical model. Based on these considerations, a macro-model was proposed [6],[7] where its input can be easily determined since it involves only the key geometric characteristics of the timber panels and the timber strength. The latter model facilitates the seismic assessment of TFM walls resulting in a valuable tool for simplified seismic vulnerability and risk analyses [8]. Based on the resulting pushover curves produced by pushover analysis [9] of the TFM walls' macro-model, a shape-function is defined for the derivation of the ESDOF properties which is similar to the methodology already described for URM buildings [5].

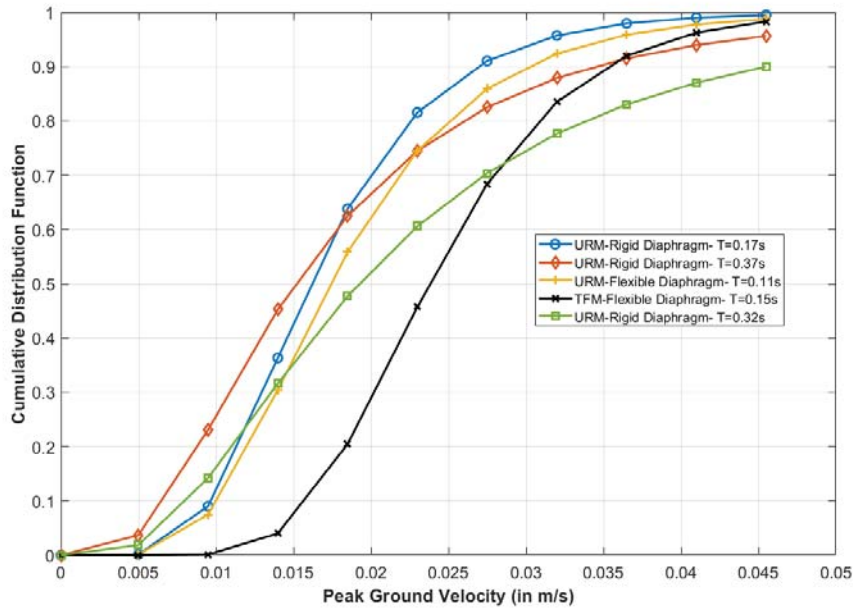


Figure 1: Proposed analytical fragility curves for first damage state (pre-yielding damage state –DS1-0.1% drift limit for non-structural damage [14]) for Unreinforced Masonry Buildings (URM) and Timber-Framed Masonry Buildings (TFM). The buildings are located near the geothermal platforms in Alsace France and are loaded in the weak/short plan view direction of shaking. The fundamental period of these structures was verified with ambient noise measurements through applied sensors [1].

Considering these real TFM and URM building cases in Alsace France (Table 1) the corresponding fragility curves are derived in terms of Peak Ground Acceleration (PGA) with the aid of structural analysis for a gradually increasing intensity (Incremental Dynamic Analysis - IDA) [10]. The latter analysis of ESDOF of the building cases under study was performed with the MATLAB [11] toolbox FEDEAS Lab [12]. The PGA values of the recordings used in the IDA with the corresponding PGV values follow the rule that for very flexible structures (structures with very high fundamental periods) the relative velocity response spectrum of the used record tends to the peak ground velocity (PGV). The induced ground motions obtained from the PEER database were employed and applied in the transverse/short/weak building plan direction [13]. As already mentioned, the fundamental periods of these structures were verified with ambient noise vibration measurements using sensors [4] located at each floor of the buildings under study (Table 1). Moreover, the main geometry required as input for the simplified vulnerability models was taken through field inspection of these buildings. The results are shown in Fig. 1. Comparing the fragility curves for URM and TFM buildings, it can be noticed that URM buildings have approximately the same range of probability of damage while the more earthquake-resistant TFM building is less fragile for low and medium intensities.

3 INCREMENTAL DYNAMIC ANALYSIS OF THREE-DIMENSIONAL MODEL

The above fragility curves (Fig. 1) have been developed using IDA for the seismic demands generally imposed upon linear and slightly nonlinear (serviceability limit state) models of single and multiple degrees of freedom, which is the case for the effects of induced seismicity. If considering the latter case of induced seismicity, the vulnerability assessment requires the expected damage to refer to non-structural components [14]. In this section, a comparison is provided of the results of this study in terms of refinement of the verified structural model for the No.1 building in Table 1 that will prove helpful for both local end-users

and industrial stakeholders, with a clear perspective for a better understanding of the risk related to induced and triggered seismicity and its sound management.

3.1 Structural modelling process

In this work, the production of analytical fragility curves for URM buildings is demonstrated on a box-shaped unreinforced masonry structure, presented in Figure 2. Namely, this building comprises the town hall of Keffenach (URM building No.1 of Table 1) in the Alsace region in France. It can be observed in Figure 2 that the building has one storey, a roof attic and one basement. In the same Figure, the respective views of the structural model are presented.

The structural model was assessed using thick-shell elements for modelling the URM walls, thin-shell elements for the reinforced concrete floor slab, while wooden elastic frame elements with rectangular section were used for modelling the roof members. As far as it concerns material properties and the structure's dimensions, they can be found in the previous work of Megalooikonomou (2020) [2], where ESDOF analysis was performed. The ESDOF model of the URM building did not include an analytical roof model. However, it was found that the roof's bearing structure affected the period of the eigenmodes. Thus, for the analytical 3D model (Fig. 2), the roof was designed to resemble the actual building and obtain the fundamental period corresponding to 0.17 s (Table 1) obtained from the installed sensors.

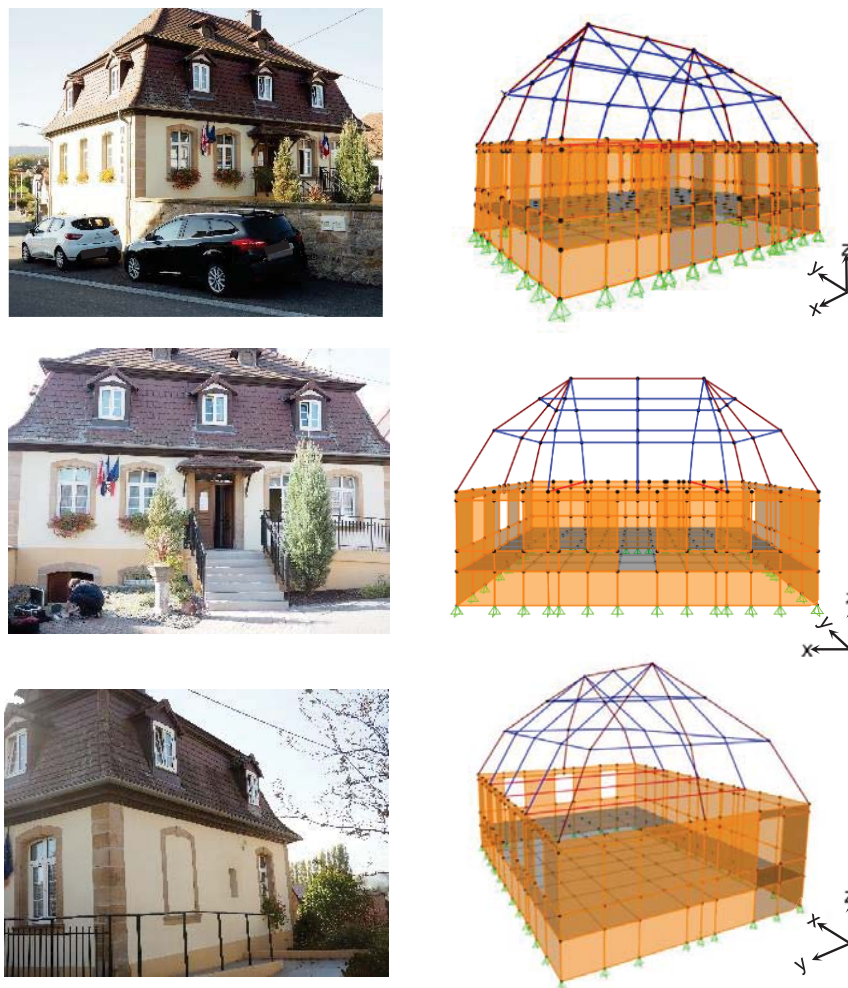


Figure 2: URM building's actual views and the generated model's respective views

3.2 Time history analysis

Producing the analytical fragility curves of the 3D model requires a number of actual induced ground motion recordings, which after scaling, were used in elastic time history analysis of the 3D model. In this work, ground motion data of 9 induced earthquakes was used [13]; more information can be found in Megalooikonomou *et al.* (2018) [1]. The ground motion data was incrementally scaled based on its Peak Ground Acceleration to obtain different shaking levels. The levels of ground acceleration used for scaling were 10 and ranged from 0.1g (9.81 m/s²) to 1g (with increments of 0.1g). Regarding the application of the scaled ground motions, 100% of the motion was applied in the primary (weak) direction (*i.e.* parallel to the y-axis in Figure 2), while 30% of the same ground motion was applied simultaneously in the secondary-strong direction (*i.e.* parallel to the x-axis in Figure 2).

After performing all 200 (20 recorded ground motions x 10 scale factors) elastic time history analyses, the ground motion that produced the largest displacements of the URM building is demonstrated for completeness of the present paper's results. This ground motion was recorded at the Luther Middle School station (Sparks, Oklahoma, USA) in 2011, and the earthquake had a moment magnitude of 5.68 at an epicentre distance of 54 km and generated a peak ground motion of 0.27g [13]. Figure 3a depicts the scaled ground motion of the earthquake rendering the largest displacements of the 3D model. Moreover, the same Figure presents the time-dependent displacements for the node of the URM walls where the maximum displacement was observed for the weak building direction of applied ground motion (Figure 3b) and the same in the strong building direction (Figure 3c).

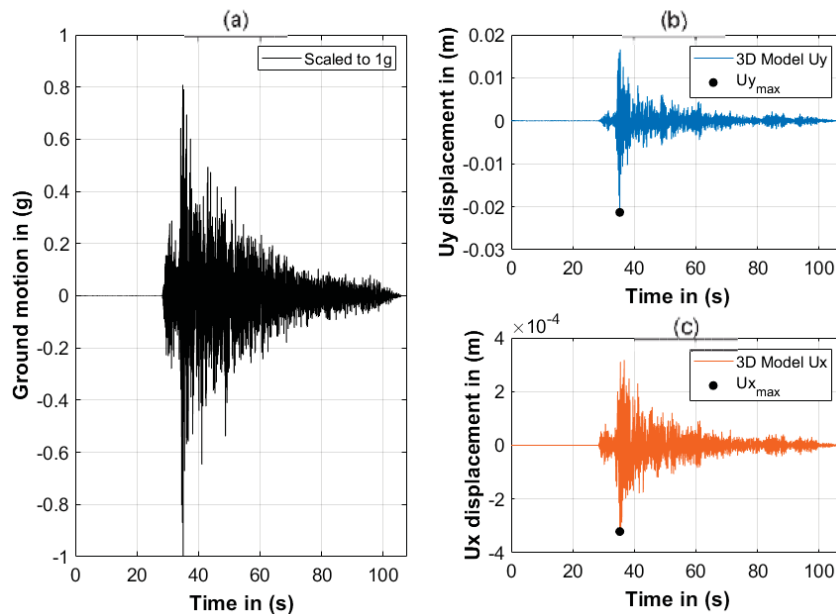


Figure 3: (a) Ground motion of earthquake producing maximum displacements; (b) node displacement for weak building direction (y-direction in Figure 2) and (c) node displacement for strong building direction (x-direction in Figure 2).

3.3 Analysis results

The results of the elastic time history analyses of the 20 ground motions and the considered scale factors for the 3D and ESDOF models were used to fit log-normal distributions for each model. Figure 4a presents the probability density functions of the 3D model and ESDOF. His-

tograms of the natural logarithm of maximum drift comprise the analysis actual results that allowed normal distributions to be fitted for both 3D and ESDOF models (Figure 4a). The fits were used to estimate the fragility curves for the different levels of Peak Ground Velocity (PGV) depicted in Figure 4b [see also Figure 1 (URM, $T=0.17s$)]. It is evident from Figure 4b that the 3D detailed analytical model results to a more vulnerable to non-structural damage historical masonry building.

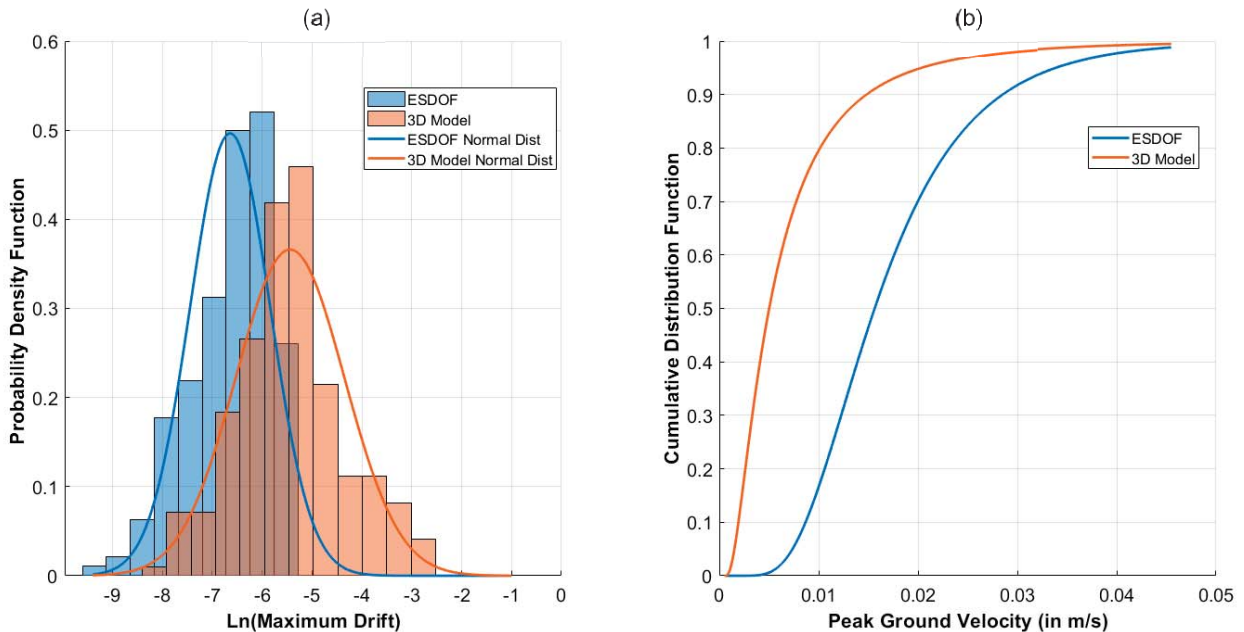


Figure 4: Analysis results for ESDOF and 3D model: (a) Relative frequency and probability density function of the natural logarithm of the maximum drift at height 3.81m and (b) Fragility curves – PGV in (m/s).

4 CONCLUSIONS

- The estimated dynamic properties for small amplitude vibrations of the historical structures near the geothermal platforms in Alsace, France considered in this work were used to derive simplified vulnerability models that were compared with a detailed 3D model for one of these masonry buildings under study.
- Moreover, Eurocode 8 defines the interstorey drift limit of a building for non-structural damage by looking at its displacement-sensitive non-structural components at the serviceability limit state. Adopting these limits and the developed vulnerability models, new non-structural fragility curves for typical historical masonry building types dominant in the region under study are proposed.
- The fragility curves have been calculated using incremental dynamic analysis for the seismic demands generally imposed upon linear and slightly nonlinear models of single and multiple degrees of freedom, which is the case for the effects of induced seismicity.
- A comparison is provided of the results of this study in terms of refinement of the verified structural model. It is evident that using simplified vulnerability models compared to detailed 3D structural models may lead to a considerable error regarding the probability of non-structural damage due to induced seismic events.
- These results will prove useful for both local end-users and industrial stakeholders, with a clear perspective for a better understanding of the risk related to induced and triggered seismicity and its sound management.

REFERENCES

- [1] Megalooikonomou KG, Parolai S, Pittore M. (2018) Toward performance-driven seismic risk monitoring for geothermal platforms: development of ad hoc fragility curves, *Geothermal Energy*, 6(1):8 , doi: 10.1186/s40517-018-0094-3
- [2] Megalooikonomou KG. (2020) Contribution of seismic noise recordings to the non-structural vulnerability assessment. In Proceedings of EURODYN 2020 XI International Conference on Structural Dynamics. Athens Greece 22-24 July 2020 <https://doi.org/10.47964/1120.9395.18340>
- [3] Pittore M, Haas M and Megalooikonomou KG (2018) Risk-Oriented, Bottom-Up Modeling of Building Portfolios with Faceted Taxonomies. *Front. Built Environ.* 4:41. doi: 10.3389/fbuil.2018.00041
- [4] Boxberger T, Fleming K, Pittore M, Parolai S, Pilz M, Mikulla S (2017) The Multi-Parameter Wireless Sensing System (MPwise): its description and application to earthquake risk mitigation. *Sensors* 17(10):2400. doi:10.3390/s17102400
- [5] Vamvatsikos D., Pantazopoulou S. J. (2015) Development of a simplified mechanical model to estimate the seismic vulnerability of heritage unreinforced masonry buildings. *Journal of Earthquake Engineering*, Taylor & Fran, 20(2): 298-325. doi:10.1080/13632469.2015.1060583.
- [6] Kouris LAS., Kappos AJ (2014) A practice – oriented model for pushover analysis of a class of timber-framed masonry buildings, *Engineering Structures Journal*, Elsevier, 75: 489-506. doi: 10.1016/j.engstruct.2014.06.012.
- [7] Kouris LAS., Kappos AJ (2012) Detailed and simplified nonlinear models for timber-framed masonry structures, *Journal of Cultural Heritage*, Elsevier, 13 (1): 47-58. doi: 10.1016/j.culher.2011.05.009.
- [8] Kouris L.A.S., Kappos A.J. (2015) Fragility Curves and Loss Estimation for Traditional Timber-Framed Masonry Buildings in Lefkas, Greece. In: Psycharis I., Pantazopoulou S., Papadrakakis M. (eds) Seismic Assessment, Behavior and Retrofit of Heritage Buildings and Monuments. *Computational Methods in Applied Sciences*, vol 37. Springer, Cham. doi: 10.1007/978-3-319-16130-3_8.
- [9] Antoniou, S, Pinho, R (2004) Development and verification of a displacement-based adaptive pushover procedure, *Journal of Earthquake Engineering* 8(5), 643–661. doi: 10.1080/13632460409350504.
- [10] Vamvatsikos D., Cornell C.A. (2002). Incremental Dynamic Analysis. *Earthquake Engineering and Structural Dynamics*, 31(3): 491-514. doi: 10.1002/eqe.141.
- [11] Mathworks. (2017). MATLAB: User's Guide (r2017a).
- [12] Filippou F.C., Constantinides M., (2004) FEDEAS Lab – Getting Started Guide and Simulation Examples, *NEESgrid Report 2004-22* and *SEMM Report 2004-05*.
- [13] PEER-NGA-East Database (2017). Pacific Earthquake Engineering Research Center, University of California, Berkeley, CA, (<http://peer.berkeley.edu/ngaeast/>).
- [14] CEN (2004) *Eurocode 8: design of structures for earthquake resistance - Part I: general rules, seismic actions and rules for buildings*. European Committee for Standardization (CEN). Brussels, Belgium.

STUDY OF BIAXIAL SHEAR FAILURE ENVELOPE OF REINFORCED CONCRETE COLUMNS

Beatrice Belletti¹, Simone Ravasini¹ and Andrea Alberici¹

¹ Department of Engineering and Architecture
University of Parma, Italy
Parco Area delle Scienze 181/A

beatrice.belletti@unipr.it, andrea.alberici1@studenti.unipr.it, simone.ravasini@unipr.it

Abstract

Several scenarios can trigger bi-axial shear in reinforced concrete (RC) vertical members such as wind actions, earthquake, column loss induced by explosions and/or impacts. The majority of standard codes impose uniaxial shear verification of vertical members and neglect the interaction between shear forces and bending moments acting along the two principal directions of inertia of the transversal cross section. Moreover, bi-axial shear interaction curves proposed by codes are based on the fitting of experimental data conducted on heavily reinforced specimens. In this paper, the bi-axial shear failure envelope of existing RC columns, is investigated. A database previously published by Authors on experimental data on beams and columns tested under bi-axial loading is updated. Afterwards, the experimental shear resistances of the database's members subjected to both monotonic and cyclic loading are compared with analytical predictions. Three different formulations are adopted for the analytical calculation of the uniaxial shear resistance: (i) Model Code 2010, (ii) Eurocode 8 and (iii) the cyclic shear resistance recently proposed by Biskinis and Fardis. Such resistances are adopted to create the bi-axial shear failure envelope. Finally, the shape of the bi-axial shear failure envelope is critically analysed in order to select the formulation that provides the best fitting between experimental and analytical bi-axial shear resistances.

Keywords: Reinforced Concrete columns, Bi-axial shear, Analytical prediction.

1 INTRODUCTION

Seismic as well as wind actions can trigger bi-axial shear in reinforced column members [1]. Moreover, in the robustness assessment of structures, the bi-axial shear demand in beams and columns - associated to vertical element loss scenarios - was also highlighted, even if international codes and guidelines such as Unified Facilities Criteria [2] and Eurocodes [3], [4], are considering only the verifications in the case of uniaxial shear scenarios. Hence, even if the bi-axial shear demand covers almost all the fields of structural engineering, the bi-axial shear resistance is almost neglected in European Codes. Several experimental campaigns were carried out during years to investigate the bi-axial monotonic or cyclic shear behaviour of reinforced concrete columns. Usually, square or rectangular sections were investigated. An early study was conducted by Maruyama et al. [5] in 1979. They observed that the applied lateral loads did not significantly affect the column shear strength until the maximum lateral drift was greater than that corresponding to the maximum monotonic shear strength. Woodward et al. [6] in 1980 conducted several experimental tests on squat reinforced concrete columns with the aim to investigate the effects of both longitudinal and transversal reinforcement ratios. They did not observe a significant increase of the lateral strength with reducing the stirrups spacing. Umehara et al. [7] in 1982 investigated 20 columns with square and rectangular sections subject to unilateral and diagonal loadings. They observed that the shear capacity of squat columns under diagonal loadings could be evaluated based on the response in the two principal directions using interaction domains. In particular, for square section a circumference function can be used to represent the bi-axial shear domain, while an elliptical curve can be used for rectangular sections. In the experimental program by Joh and Shibata [8] in 1984, columns square and rectangular cross-sections were tested under lateral bi-axial loading until achievement of shear failure, using a normalized interaction domain respect to the shear strength along principal directions. Mizoguchi et al. [9] in 1990 investigated the effects of varying axial load on bi-axial loading response of squat columns, observing that columns diagonally loaded had a 5-6% lower resistance compared with counterparts loaded along principal directions. In more recent studies by Pham et al. [10] and Dang et al. [11] the shear strength mechanisms were associated to the lack of transversal reinforcement and vulnerability of low-rise structures characterized by in-plane and elevation irregularities. The mentioned experimental tests were collected from the authors in a Database [12] and used for comparisons with analytical provisions [13].

Actually, the majority of international normative and guidelines such as Model Code 2010 [14] and Eurocode 8 [15] neglect the interaction between shear and bending acting along the two principal directions of cross section. Conversely, the Japan Society of Civil Engineers (JSCE) guidelines [16] can consider bi-axial loading capacity using an interaction domain.

In this paper, three analytical formulations are considered in order to calculate the uniaxial shear resistance; in particular the formulation proposed by Eurocode 8 [15], Model code 2010 [14] and Biskinis and Fardis [17].

Afterwards, according to Japanese Code [16], the bi-axial failure criterion is evaluated. Finally, the bi-axial shear resistances are compared with the experimental results collected by Authors in their database.

2 EXPERIMENTAL DATABASE

In the following, the experimental database collected by Authors is reported in terms of member geometry, reinforcement ratios, mechanical properties and loading conditions. Columns have square or rectangular cross section. The boundary conditions are mostly fixed at the base and allow the lateral displacement at the top according to the so called “shear type” scheme,

see Figure 1a. Only in the experimental campaign conducted by Dang et al. [11], the boundary conditions allow lateral displacement and rotation at the top of the column. The loading is applied at the top of columns by applying monotonic or cyclic forces, Figure 1b. The axial load can be varied to study its influence of shear resistance and lateral drift capacity.

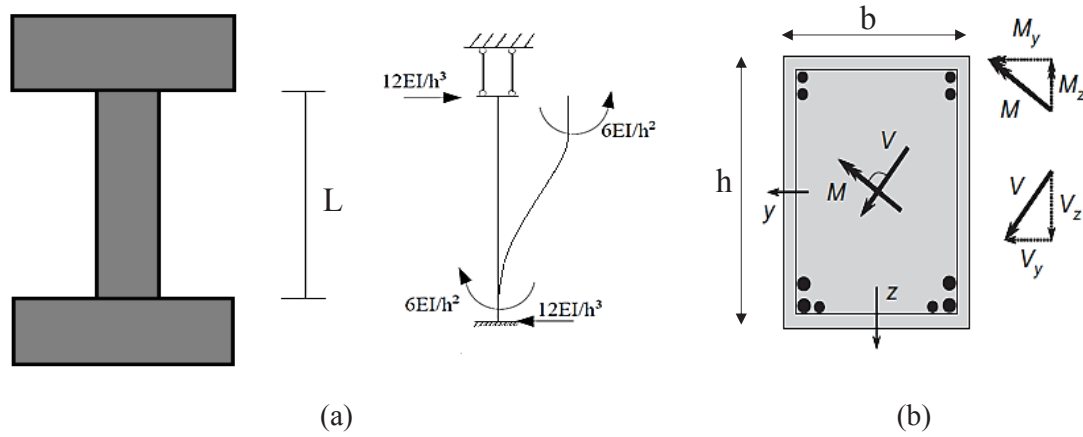


Figure 1 Test setup: (a) specimen geometry and static scheme; (b) cross-section shear/bending decomposition.

Maruyama et al. (1979)	Section properties		Loading condition				Longitudinal reinforcement				Stirrups				Concrete strength
Specimen	b [mm]	h [mm]	v	α [°]	a/d	Loading History	d [mm]	Φ [mm]	ρ [-]	f_{sy} [MPa]	Φ_w [mm]	s_w [mm]	ρ_w [-]	f_{yw} [MPa]	f_c [MPa]
00-V-0-I Uni	305	305	0	0	2.1	Cyclic	219	19	2.44%	448	6	65	0.29%	469	35
00-V-V-S-Diag	305	305	0	45	-	Cyclic	-	19	2.44%	448	6	65	0.29%	469	35

Table 1 Experimental setup and specimen features, by Maruyama et al. [5].

Woodward et al. (1980)	Section properties		Loading condition				Longitudinal reinforcement				Stirrups				Concrete strength
Specimen	b [mm]	h [mm]	v	α [°]	a/d	Loading History	d [mm]	Φ [mm]	ρ [-]	f_{sy} [MPa]	Φ_w [mm]	s_w [mm]	ρ_w [-]	f_{yw} [MPa]	f_c [MPa]
0-86-14-DM	305	305	0	45	-	Cyclic	-	19	2.44%	503	6	65	0.29%	503	41
C-86-14-DM	305	305	0.16	45	-	Cyclic	-	19	2.44%	503	6	65	0.29%	503	36

Table 2 Experimental setup and specimen features, by Woodward et al. [6].

Umehara H. et al. (1982)	Section properties		Loading condition				Longitudinal reinforcement				Stirrups				Concrete strength
Specimen	b [mm]	h [mm]	v	α [°]	a/d	Loading History	d [mm]	Φ [mm]	ρ [-]	f_{sy} [MPa]	Φ_w [mm]	s_w [mm]	ρ_w [-]	f_{yw} [MPa]	f_c [MPa]
OUS	230	410	0	0	1.6	Cyclic	284	19	3.01%	441	6	89	0.28%	413	40
OUW	410	230	0	0	2.4	Cyclic	188	19	3.01%	441	6	89	0.31%	413	40
CUS	230	410	0.162	0	1.6	Cyclic	284	19	3.01%	441	6	89	0.28%	413	35
CUW	410	230	0.162	0	2.4	Cyclic	188	19	3.01%	441	6	89	0.31%	413	35
2CUS	230	410	0.270	0	1.6	Cyclic	284	19	3.01%	441	6	89	0.28%	413	42
CDS30	230	410	0.132	30	-	Cyclic	-	19	3.01%	441	6	89	0.28%	413	43
CDW30	230	410	0.135	60	-	Cyclic	-	19	3.01%	441	6	89	0.55%	413	42

Table 3 Experimental setup and specimen features, by Humehara et al. [7].

Joh, O., Shibata, T. (1984)	Section properties		Loading condition				Longitudinal reinforcement				Stirrups				Concrete strength
Specimen	b	h	v	α	a/d	Loading History	d	Φ	ρ	f_{sv}	Φ_w	s_w	ρ_w	f_{yw}	f_c
	[mm]	[mm]		[°]	[-]		[mm]	[mm]	[-]	[MPa]	[mm]	[mm]	[-]	[MPa]	[MPa]
SS-0-N0 (+)	300	300	0	0	1.7	Cyclic	265	19.1	2.25%	390.3	6	63	0.30%	306.9	22.95
SS-0-N0 (-)	300	300	0	0	1.7	Cyclic	265	19.1	2.25%	390.3	6	63	0.30%	306.9	22.95
SS-0-N1 (+)	300	300	0.17	0	1.7	Cyclic	265	19.1	2.25%	390.3	6	63	0.30%	306.9	23.34
SS-0-N1 (-)	300	300	0.17	0	1.7	Cyclic	265	19.1	2.25%	390.3	6	63	0.30%	306.9	23.34
SS-0-N2 (+)	300	300	0.33	0	1.7	Cyclic	265	19.1	2.25%	390.3	6	63	0.30%	306.9	23.24
SS-0-N2 (-)	300	300	0.33	0	1.7	Cyclic	265	19.1	2.25%	390.3	6	63	0.30%	306.9	23.24
SS-22.5-N0 (+)	300	300	0	23	-	Cyclic	-	19.1	2.25%	390.3	6	63	0.30%	306.9	22.36
SS-22.5-N0 (-)	300	300	0	23	-	Cyclic	-	19.1	2.25%	390.3	6	63	0.30%	306.9	22.36
SS-22.5-N1 (+)	300	300	0.17	23	-	Cyclic	-	19.1	2.25%	390.3	6	63	0.30%	306.9	21.87
SS-22.5-N1 (-)	300	300	0.17	23	-	Cyclic	-	19.1	2.25%	390.3	6	63	0.30%	306.9	21.87
SS-22.5-N2 (+)	300	300	0.33	23	-	Cyclic	-	19.1	2.25%	390.3	6	63	0.30%	306.9	24.71
SS-22.5-N2 (-)	300	300	0.33	23	-	Cyclic	-	19.1	2.25%	390.3	6	63	0.30%	306.9	24.71
SS-45-N0 (+)	300	300	0	45	-	Cyclic	-	19.1	2.25%	390.3	6	63	0.30%	306.9	26.87
SS-45-N0 (-)	300	300	0	45	-	Cyclic	-	19.1	2.25%	390.3	6	63	0.30%	306.9	26.87
SS-45-N1 (+)	300	300	0.17	45	-	Cyclic	-	19.1	2.25%	390.3	6	63	0.30%	306.9	23.73
SS-45-N1 (-)	300	300	0.17	45	-	Cyclic	-	19.1	2.25%	390.3	6	63	0.30%	306.9	23.73
SS-45-N2 (+)	300	300	0.33	45	-	Cyclic	-	19.1	2.25%	390.3	6	63	0.30%	306.9	25.89
SS-45-N2 (-)	300	300	0.33	45	-	Cyclic	-	19.1	2.25%	390.3	6	63	0.30%	306.9	25.89
SR-0-N1 (+)	225	400	0	0	1.2	Cyclic	365	19.1	2.25%	390.3	5.85	71	0.34%	306.9	23.63
SR-0-N1 (-)	225	400	0	0	1.2	Cyclic	365	19.1	2.25%	390.3	5.85	71	0.34%	306.9	23.63
SR-30-N1 (+)	225	400	0.17	30	-	Cyclic	-	19.1	2.25%	390.3	5.85	71	0.34%	306.9	25.10
SR-30-N1 (-)	225	400	0.17	30	-	Cyclic	-	19.1	2.25%	390.3	5.85	71	0.34%	306.9	25.10
SR-60-N1 (+)	225	400	0.17	60	-	Cyclic	-	19.1	2.25%	390.3	5.85	71	0.50%	306.9	26.28
SR-60-N1 (-)	225	400	0.17	60	-	Cyclic	-	19.1	2.25%	390.3	5.85	71	0.50%	306.9	26.28
SR-90-N1 (+)	400	225	0.17	90	2.4	Cyclic	190	19.1	2.25%	390.3	5.85	71	0.28%	306.9	24.81
SR-90-N1 (-)	400	225	0.17	90	2.4	Cyclic	190	19.1	2.25%	390.3	5.85	71	0.28%	306.9	24.81

Table 4 Experimental setup and specimen features, by Joh & Shibata [8].

Pham et al. (2013)	Section properties		Loading condition				Longitudinal reinforcement				Stirrups				Concrete strength
Specimen	b	h	v	α	a/d	Loading History	d	Φ	ρ	f_{sv}	Φ_w	s_w	ρ_w	f_{yw}	f_c
	[mm]	[mm]		[°]	[-]		[mm]	[mm]	[-]	[MPa]	[mm]	[mm]	[-]	[MPa]	[MPa]
S.C-2.4-0.20	350	350	0.2	0	3.3	Cyclic	255	20	2.05%	545	6	125	0.13%	393	23
SC-1.7-0.2	350	350	0.2	0	2.4	Cyclic	255	20	2.05%	545	6	125	0.13%	393	28
S2.4-30	350	350	0.2	30	-	Cyclic	-	20	2.05%	545	6	125	0.13%	511	31
S2.4-45	350	350	0.2	45	-	Cyclic	-	20	2.05%	545	6	125	0.13%	511	29
S1.7-30	350	350	0.2	30	-	Cyclic	-	20	2.05%	545	6	125	0.13%	511	30
S1.7-45	350	350	0.2	45	-	Cyclic	-	20	2.05%	545	6	125	0.13%	511	29
R.C-1.7-0.35-S	250	490	0.35	0	1.6	Cyclic	379	20	2.05%	545	6	125	0.18%	393	27
R.C-1.7-30	250	490	0.35	30	-	Cyclic	-	20	2.05%	545	6	125	0.18%	511	31
R.C-1.7-45	250	490	0.35	45	-	Cyclic	-	20	2.05%	545	6	125	0.18%	511	30
R.C-1.7-60	250	490	0.35	60	-	Cyclic	-	20	2.05%	545	6	125	0.18%	511	29

Table 5 Experimental setup and specimen features, by Pham et al. [10].

Mizoguchi et al.(1990)	Section properties		Loading condition				Longitudinal reinforcement				Stirrups				Concrete strength
Specimen	b [mm]	h [mm]	v	α [°]	a/d [-]	Loading History	d [mm]	Φ [mm]	ρ [-]	f_{sv} [MPa]	Φ_w [mm]	s_w [mm]	ρ_w [-]	f_{vw} [MPa]	f_c [MPa]
0V04+	180	180	0.44	0	1.7	Cyclic	132	12.7	3.13%	342.3	4	41	0.51%	273	26
0V04-	180	180	0	0	1.7	Cyclic	132	12.7	3.13%	342.3	4	41	0.51%	273	26
0V15+	180	180	0.57	0	1.7	Cyclic	132	12.7	3.13%	342.3	4	41	0.51%	273	26
0V15-	180	180	-0.1	0	1.7	Cyclic	132	12.7	3.13%	342.3	4	41	0.51%	273	26
0VA04+	180	180	0.44	0	1.7	Cyclic	132	12.7	3.13%	342.3	4	41	0.51%	273	27
0VA04-	180	180	0	0	1.7	Cyclic	132	12.7	3.13%	342.3	4	41	0.51%	273	27
0VA15+	180	180	0.54	0	1.7	Cyclic	132	12.7	3.13%	342.3	4	41	0.51%	273	27
0VA15-	180	180	-0.1	0	1.7	Cyclic	132	12.7	3.13%	342.3	4	41	0.51%	273	27
2V04+	180	180	0.39	23	-	Cyclic	-	12.7	3.13%	342.3	4	41	0.51%	273	31
2V04-	180	180	0	23	-	Cyclic	-	12.7	3.13%	342.3	4	41	0.51%	273	31
2VA04+	180	180	0.38	23	-	Cyclic	-	12.7	3.13%	342.3	4	41	0.51%	273	31
2VA04-	180	180	0	23	-	Cyclic	-	12.7	3.13%	342.3	4	41	0.51%	273	31
4V04+	180	180	0.4	45	-	Cyclic	-	12.7	3.13%	342.3	4	41	0.51%	273	29
4V04-	180	180	0	45	-	Cyclic	-	12.7	3.13%	342.3	4	41	0.51%	273	29
4V15+	180	180	0.52	45	-	Cyclic	-	12.7	3.13%	342.3	4	41	0.51%	273	29
4V15-	180	180	-0.1	45	-	Cyclic	-	12.7	3.13%	342.3	4	41	0.51%	273	29
4VA04+	180	180	0.4	45	-	Cyclic	-	12.7	3.13%	342.3	4	41	0.51%	273	29
4VA04-	180	180	0	45	-	Cyclic	-	12.7	3.13%	342.3	4	41	0.51%	273	29
4VA15+	180	180	0.5	45	-	Cyclic	-	12.7	3.13%	342.3	4	41	0.51%	273	30
4VA15-	180	180	-0.1	45	-	Cyclic	-	12.7	3.13%	342.3	4	41	0.51%	273	30

Table 6 Experimental setup and specimen features, by Mizoguchi et al. [9].

Dang et al. (2018)	Section properties		Loading condition				Longitudinal reinforcement				Stirrups				Concrete strength
Specimen	b [mm]	h [mm]	v	α [°]	a/d [-]	Loading History	d [mm]	Φ [mm]	ρ [-]	f_{sv} [MPa]	Φ_w [mm]	s_w [mm]	ρ_w [-]	f_{vw} [MPa]	f_c [MPa]
FS 10 U (+)	300	300	0.1	0	3	Cyclic	254	19	2.52%	400	10	200	0.26%	400	27
FS 10 U (-)	300	300	0.1	0	3	Cyclic	254	19	2.52%	400	10	200	0.26%	400	27
FS 10 B (+)	300	300	0.1	17	-	Cyclic	-	19	2.52%	400	10	200	0.26%	400	27
FS 10 B (-)	300	300	0.1	17	-	Cyclic	-	19	2.52%	400	10	200	0.26%	400	27
SC 10 U (+)	300	300	0.1	0	3	Cyclic	254	19	2.52%	400	10	300	0.17%	400	27
SC 10 U (-)	300	300	0.1	0	3	Cyclic	254	19	2.52%	400	10	300	0.17%	400	27
SC 10 B (+)	300	300	0.1	17	-	Cyclic	-	19	2.52%	400	10	300	0.17%	400	27
SC 10 B (-)	300	300	0.1	17	-	Cyclic	-	19	2.52%	400	10	300	0.17%	400	27

Table 7 Experimental setup and specimen features, by Dang et al. [11].

3 ANALYTICAL FORMULATIONS

In this paragraph, the analytical formulations provided by Eurocode 8 [15], MC 2010 [14] and Biskinis & Fardis [17] model are briefly reported.

3.1 Eurocode 8

Firstly, the formulation provided by Eurocode 8 [15] is reported. The yield chord rotation capacity is evaluated for beams and columns, Eq. (1):

$$\theta_y = \phi_y \frac{L_v}{3} + 0.0013 \left(1 + 1.5 \frac{h}{L_v} \right) + 0.13 \phi_y \frac{d_b f_y}{\sqrt{f_c}} \quad (1)$$

The ultimate chord rotation capacity is evaluated through, Eq. (2):

$$\theta_u = \frac{1}{\gamma_{el}} 0.016 \cdot (0.3^v) \left[\frac{\max(0.01; \omega')}{\max(0.01; \omega)} f_c \right]^{0.225} \left(\frac{L_v}{h} \right)^{0.35} 25^{\left(\frac{a p_s}{f_c} \right)} (1.25^{100 \rho_s}) \quad (2)$$

The strength degradation due to cyclic loading is calculated as a function of the ductility $\mu_{\Delta pl}$ which is calculated by the ratio between the plastic and the yield chord rotation, Eq. (3):

$$\mu_{\Delta pl} = \frac{\theta_u}{\theta_y} - 1 \quad (3)$$

The value of $\mu_{\Delta pl}$ may vary between 0 and 5, corresponding to null and maximum degradation, respectively. The resisting shear strength V_r under cyclic conditions can be determined using Eq. (4):

$$V_r = \frac{1}{\gamma_{el}} \left\{ \frac{h-x}{2L_v} \min(N; 0.55 A_c f_c) + [1 - 0.005 \min(5; \mu_{\Delta pl})] \left\{ 0.16 \max[0.5; 100 \rho_{tot}] \left[1 - 0.16 \min\left(5; \frac{L_v}{h}\right) \right] \sqrt{f_c} A_c \right\} + V_w \right\} \quad (4)$$

Three contributions are considered: the axial load magnitude N , steel reinforcement ratio ρ_{tot} and the plastic ductility $\mu_{\Delta pl}$.

3.2 Model Code 2010

The Model Code 2010 [14] formulation is based on in the Level of Approximation (LoA) framework for the evaluation of the shear resistance. LoA I and II are used for both members with and without transverse reinforcement while LoA III can be used only for members with shear reinforcement. Since stirrups are provided in all the analysed members, in this paper the LoA III is used for the calculation of the shear resistance. The longitudinal strain ε_x is evaluated in correspondence of the mid-depth of the effective shear depth as follows, Eq. (5):

$$\varepsilon_x = \frac{1}{2 \cdot E_s \cdot A_s} \left[\frac{M_{Ed}}{z} + V_{Ed} + N_{Ed} \left(\frac{1}{2} \mp \frac{\Delta e}{z} \right) \right] \quad (5)$$

The shear resistance V_{Rd} for elements with stirrups is calculated through Eq. (6):

$$V_{Rd} = V_{Rd,c} + V_{Rd,s} \leq V_{Rd,max}(\theta_{min}) \quad (6)$$

To consider the cyclic degradation effects, Model Code 2010 imposes the use of the following strut inclination angles (linear interpolation is allowed):

- wherever the plastic part of the chord rotation demand is more than twice the elastic part θ_y , set $\cotg(\theta) = 1$.
- for elastic flexural response, with zero plastic chord rotation, set $\cotg(\theta) = 2.5$.

3.3 New proposal by Biskinis and Fardis

The new proposal by Biskinis and Fardis [17] for the assessment of the cyclic shear resistance is based on the monotonic shear resistance of Model Code 2010. The new model allows to consider the degradation effect associated to cyclic loading, by applying the following modifications to the shear resistance formulation proposed in Model Code 2010:

- The longitudinal strain ε_x is firstly evaluated in correspondence of the section mid-depth:

$$\varepsilon_x = \frac{1}{2A_s E_s} \left(\mu \frac{M_{Ed}}{z} + \frac{N_{Ed}}{2} + V_{Ed} \right) \leq \min \left(0.02; \frac{1}{2A_s E_s} \left(\mu \frac{\max M}{z} + \frac{N}{2} \right) \right) \quad (7)$$

- The contribution due to the axial load N in columns is considered by adding the term $V_{R,N}$ given in Eq.(8) :

$$V_{R,N} = N \frac{h-x}{2L_s} \quad (8)$$

Where x is the neutral axis and L_s is the shear span.

- The contribution of transverse steel to shear resistance is:

$$V_{R,S} = (\rho_w b_w z f_{yw}) \cot(\theta) \quad (9)$$

Where the upper limit on the yield stress of shear reinforcement is set equal to $f_{yw} = \min(f_{yw}; 6 / \rho_w)$.

- The contribution of concrete to shear resistance is:

$$\begin{cases} k_V = \frac{0.4}{1 + 1500\varepsilon_x} \left(1 - \frac{V_{Ed}}{V_{Rd,max}(\theta_{min})} \right) \\ V_{Rd,c} = k_V \frac{\sqrt{f_{ck}}}{\gamma_c} z \cdot b_w \end{cases} \quad (10)$$

The shear resistance is calculated based on the selected Level of Approximation as follows:

- For LoA II: $V_R = V_{R,N} + V_{R,S} \leq V_{R,max}$
- For LoA III: $V_R = V_{R,N} + V_{R,S} + V_{R,c} \leq V_{R,max}$

In this study, the Level of Approximation III is used. Note average mechanical properties and partial safety factors equal to 1 are used to compare analytical and experimental shear resistances. The comparisons of the shear capacity in terms of resistance and ductility obtained by using the three formulations are reported in Figure 2.

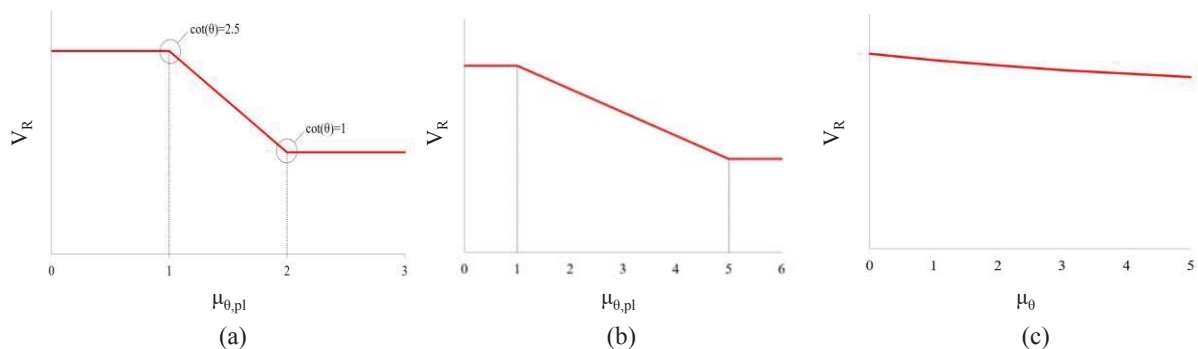


Figure 2 Capacity curves for: (a) Model Code 2010 [14]; (b) Eurocode 8 [15]; (c) Biskinis and Fardis [17].

The previously explained formulations are adopted to calculate the shear resistance under monotonic or cyclic loading along the two principal directions of the transversal cross section of the column. Afterward, to account for bi-axial shear resistance, the interaction domain proposed by JSCE [16] is used, according to Eq. (11):

$$\left(\gamma_i \frac{V_{Ed,x}}{V_{Rd,x}} \right)^2 + \left(\gamma_i \frac{V_{Ed,y}}{V_{Rd,y}} \right)^2 = 1 \quad (11)$$

In Figure 3 are reported possible failure modes of RC columns, based on the intersection between bilinear flexural and shear (based on EC8 [15] approach) capacities curves. Indeed, three failure modes are possible based on the intersection between simplified bilinear flexural capacity and shear resistance provided: (i) flexural failure, without intersection with shear capacity, (ii) mixed flexural-shear failure after achievement of flexural yielding, (iii) shear failure before flexural yielding. In this study, shear and mixed flexural-shear failure modes are considered.

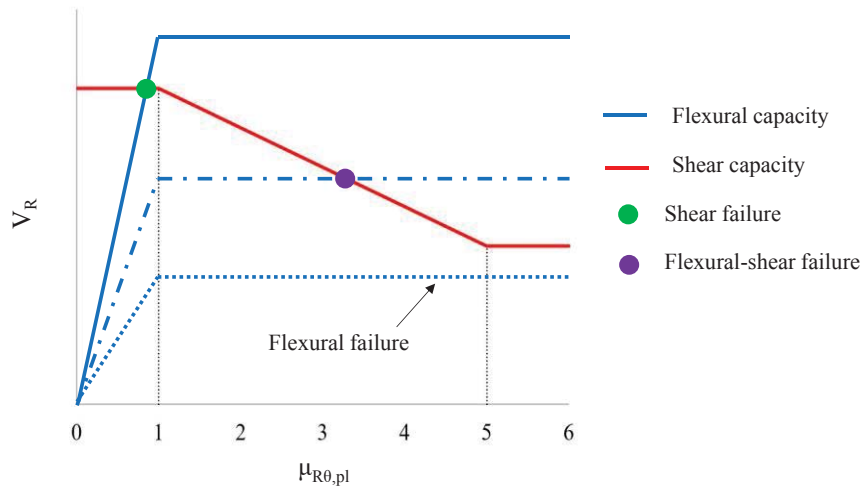


Figure 3 Exemplificative flexural vs shear (EC8 [15] approach) capacities and failure modes.

4 RESULTS AND DISCUSSION

In this paragraph the bi-axial domains obtained from experimental results and analytical formulations are plotted and compared. Average mechanical properties and partial safety factors equal to 1 are used for calculations. Figure 4 and Figure 5 are related to specimens without and with compressive axial load, respectively.

Figure 4 shows that the analytical provision by Biskinis & Fardis [17] tends to underestimate the shear resistance compared to Model Code 2010 and Eurocode 8 provisions. This is attributed to the reduction coefficient equal to 1.8 introduced in the k_ε formulation by Biskinis & Fardis [17] which accounts for cyclic loading. Indeed, this coefficient affects the magnitude of $V_{Rd,max}$ calculated at θ_{min} equal to 21.8° as provided for LoA III, see Eq. (12):

$$\left\{ \begin{array}{l} k_\varepsilon = \frac{1}{1.8(1.2 + 55\varepsilon_1)} \\ V_{Rd,max}(\theta_{min}) = k_\varepsilon \cdot \eta_{fc} \cdot \frac{f_{ck}}{\gamma_c} \cdot b_w \cdot z \cdot \sin(\theta_{min}) \cdot \cos(\theta_{min}) \end{array} \right. \quad (12)$$

As consequence, the coefficient k_V and the corresponding concrete shear resistance contribution $V_{Rd,c}$ reported in Eq. (10) are relatively small.

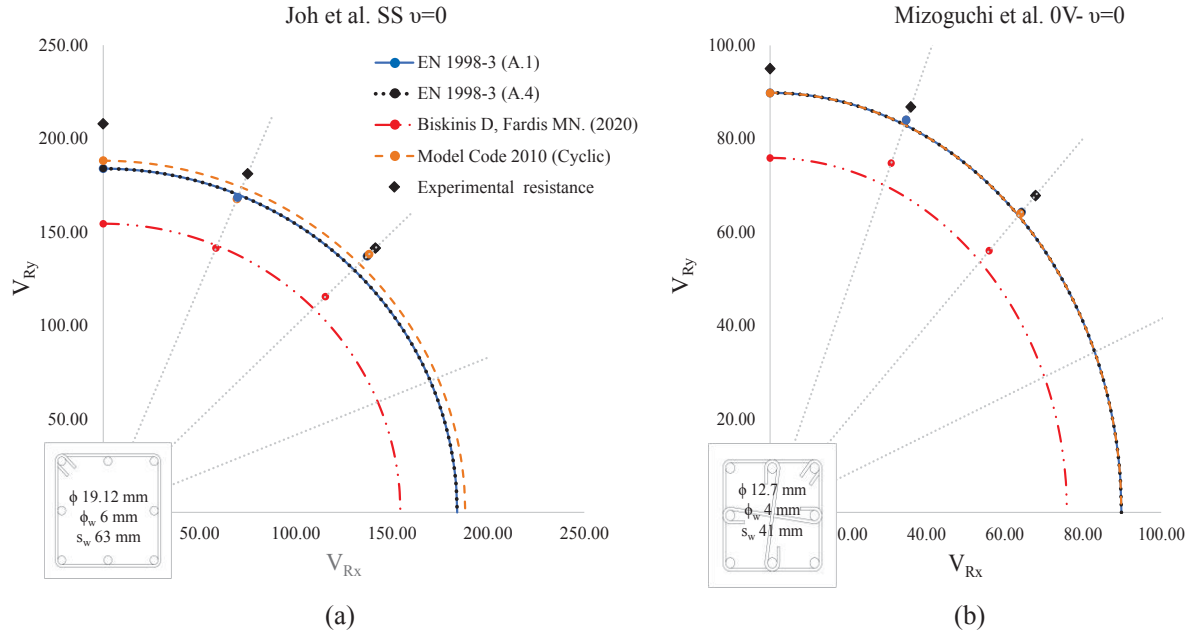
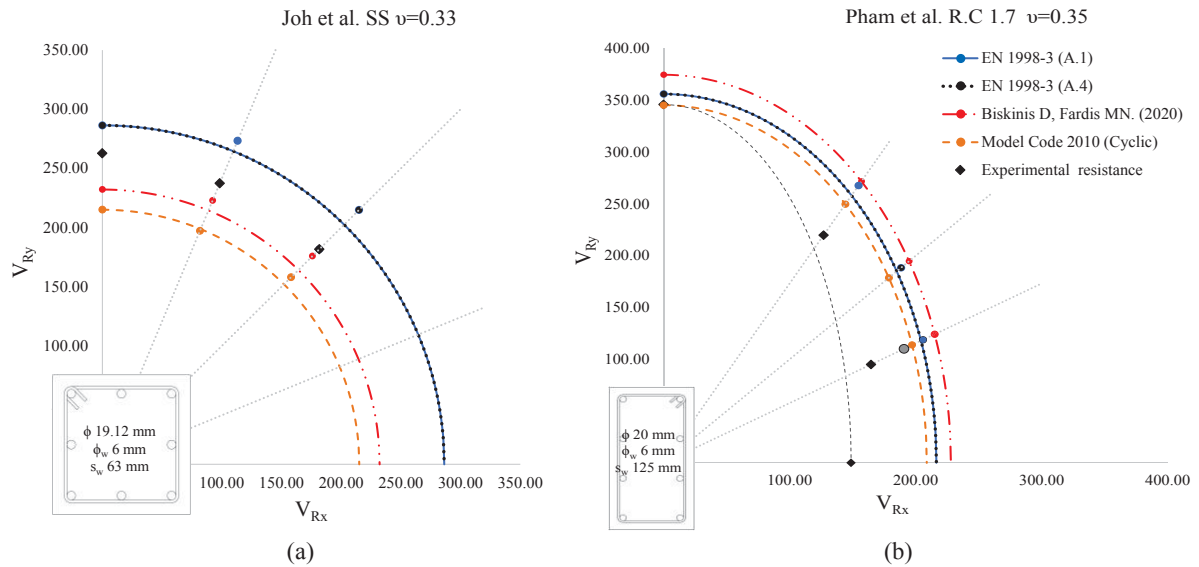

 Figure 4 Interaction domains $N = 0$: (a) Joh & Shibata specimen SSN0-; (b) Mizoguchi et al. specimen 0V-.

Figure 5 shows that in the case of compressive axial force applied to columns, the analytical approaches proposed in Eurocode 8 and by Biskinis & Fardis provide a better fitting of the experimental results. Indeed, the former approaches consider the additional beneficial term related to the compressive axial load contribution, which for Eurocode 8 is defined by Eq. (13), while for Biskinis & Fardis [17], is defined by Eq. (8):

$$V_{R,N} = \frac{h-x}{2L_s} \min(N; 0.55A_c f_c) \quad (13)$$

Conversely to the mentioned approaches, the Model Code 2010 consider the effect of the axial force only in the strains' calculation of the longitudinal reinforcement, according Eq. (5).


 Figure 5 Interaction domains $N < 0$: (a) Joh & Shibata specimen SSN2+; (b) Pham et al. specimen R.C1.7.

Moreover, by analysing the formulations in Eq. (8) and (13), it is evident the dependency on the cross-section height h , the shear span L_s and neutral axis depth x . This latter term is fundamental and can be calculated using different assumptions based in the cross-section deformability level: (i) at ultimate limit state considering tensile rebars at yield and concrete at a compressive strain of 3.5 ‰, (ii) at the elastic state, where compressive concrete strain is below 2 ‰, thus the hypothesis of linear stresses is valid. Therefore, the assumption adopted to calculate the neutral axis should be coherent with the assumed ductility level.

5 CONCLUSIONS

This paper treats the calculation of the bi-axial shear resistance of reinforced concrete columns under cyclic loading. Such shear capacity is calculated by adopting the interaction domains provided by JSCE, starting from the uniaxial resistances of columns calculated along the principal axes of the transversal cross section. Moreover, three different analytical approaches from Eurocode 8, Model Code 2010 and the new proposal by Biskinis & Fardis are compared with available experimental tests collected in a Database created by Authors. The results show that:

- In absence of axial force, the interaction domains calculated from Model Code 2010 (LoA III) provide higher resistances than Eurocode 8 and Biskinis & Fardis approaches and a better fitting of experimental evidences. This is attributed to the fact that in the new formulation by Biskinis & Fardis, a reduction coefficient equal to 1.8 - which accounts for cyclic loading - is applied to the concrete compressive strut resistance. This leads to a considerable reduction of concrete contribution to shear resistance.
- In presence of compressive axial force, the interactions domains calculated from Model Code 2010 (LoA III) provide lower resistances compared to Eurocode 8 and Biskinis & Fardis approaches. This is attributed to the additional term accounting for the beneficial contribution of compressive axial load. The new proposal from Biskinis & Fardis provide a better fitting of experimental evidences compared to the other analytical provisions considered in this paper.

REFERENCES

- [1] Biskinis, D. & Fardis, M. N., “Report No. SEE 2009-01 - Deformations of concrete members at yielding and ultimate under monotonic or cyclic loading (including repaired and retrofitted members),” 2009.
- [2] DoD, *Unified Facilities Criteria (UFC 4-023-03): Design of Buildings To Resist Progressive Collapse*. Department of Defense, Washington DC, 2009.
- [3] CEN-EC1, *EN 1991-1-7: Eurocode 1 – actions on structures: general actions – accidental actions*. Brussels: European Committee for Standardization, 2006.
- [4] CEN-EC2, *EN 1992: Eurocode 2: Design of concrete structures - Part 1-1: General rules and rules for buildings*. Brussels: European Committee for Standardization, 2004.
- [5] Maruyama, K. & Jirsa, J. O., “CESRL Report No. 79-1 - Shear Behavior of Reinforced Concrete Members under Bidirectional Reversed Lateral Loading,” 1979.
- [6] Woodward, K. A. & Jirsa, J. O., “Behavior classification of short Reinforced Concrete columns subject to cyclic deformations,” 1980.
- [7] Umehara, H. & Jirsa, J., “PMFSEL Report No. 82-3 - Shear strength and deterioration

- of short reinforced concrete columns under cyclic deformations,” 1982.
- [8] Joh, O. & Shibata, T., “Shear failure of reinforced concrete columns due to biaxial lateral forces,” in *Proceedings of the 8th World Conference on Earthquake Engineering San Francisco*, 1984, pp. 577–584.
 - [9] Mizoguchi, M., Arakawa, T., Arai, Y. & Yoshida, M., “Shear resisting behavior of short Reinforced Concrete columns under biaxial bending-shear and varying axial load,” *Trans. Japan Concr. Inst.*, vol. 12, pp. 347–354, 1990.
 - [10] Pham, T. P. & Li, B., “Seismic behavior of reinforced concrete columns with light transverse reinforcement under different lateral loading directions,” *ACI Struct. J.*, vol. 110, no. 5, pp. 833–843, 2013, doi: 10.14359/51685836.
 - [11] Dang, H. V., Lee, K., Han, S. W. & Kim, S. J., “Experimental assessment of the effects of biaxial bending moment and axial force on reinforced concrete corner columns,” *Struct. Concr.*, vol. 19, no. 4, pp. 1063–1078, 2018, doi: 10.1002/suco.201700211.
 - [12] Tinini, A., Minelli, F., Belletti, B. & Scolari, M., “Biaxial shear in RC square beams: Experimental, numerical and analytical program,” *Eng. Struct.*, vol. 126, pp. 469–480, 2016, doi: 10.1016/j.engstruct.2016.07.056.
 - [13] Minelli, F., Tinini, A., Belletti, B. & Scolari, M., “Studio sperimentale sul taglio biassiale in travi a sezione quadrata,” in *20° Congresso CTE. Milano, Italia; 6 – 8 Novembre: 77-87*, 2014, p. 8.
 - [14] Ceb-Fip, *fib Model Code for Concrete Structures 2010*. 2013.
 - [15] CEN-EC8, *EN 1998: Eurocode 8: Design of structures for earthquake resistance - Part 1: General rules, seismic actions and rules for buildings*. Brussels: European Committee for Standardization, 2004.
 - [16] JSCE, *Standard Specifications for Concrete Structures*. Japan Society of Civil Engineers, 2007.
 - [17] Biskinis, D. & Fardis, M. N., “Cyclic shear resistance for seismic design, based on monotonic shear models in fib Model Code 2010 and in the 2018 draft of Eurocode 2,” *Struct. Concr.*, vol. 21, no. 1, pp. 129–150, 2020, doi: 10.1002/suco.201900037.

EVALUATION OF THE SEISMIC VULNERABILITY OF EXISTING PRE-CODE RC CORE STRUCTURAL SYSTEMS THROUGH NON-LINEAR PUSHOVER ANALYSES

B. Belletti¹, E. Martinelli², E. Michelini¹ and F. Vecchi¹

¹ Department of Engineering and Architecture, University of Parma
Parco Area delle Scienze 181/A, 43123, Parma, Italy
e-mail: beatrice.belletti@unipr.it, elena.michelini@unipr.it, francesca.vecchi@unipr.it

² Department of Civil Engineering, University of Salerno
via Giovanni Paolo II 132, 84084, Fisciano (SA), Italy
e-mail: enzo.martinelli@unisa.it

Abstract

In the last years, a growing attention has been devoted to the seismic vulnerability assessment of existing Reinforced Concrete (RC) framed buildings designed only for gravitational loads. The seismic behavior of existing framed buildings with an inner RC stairwell core has been investigated much less so far, even if this structural typology has known a certain spread from the Seventies onwards, especially in the Italian largest urban areas. In this work, the seismic behavior a relevant and representative example of existing pre-code RC core medium rise building is evaluated by performing nonlinear pushover analyses. The effect of different modelling assumptions regarding the degree of collaboration between frames and RC walls on the structural response is discussed. The influence of masonry infills on the global structural response is also evaluated by running the analyses both on the bare structure and on a structural model considering a distribution of masonry panels not regular in elevation: the latter distribution corresponds to a typical situation for the considered typology.

Keywords: reinforced concrete, core systems, non-linear analysis, existing structures, infills.

1 INTRODUCTION

A significant share of the existing Italian Reinforced Concrete (RC) building stock was designed for gravity loads only (so-called pre-code buildings), or according to now outdated seismic standards. Consequently, those buildings are generally vulnerable to seismic actions, often showing a non-ductile behavior, due to the non-optimal in-plan distribution of the structural elements (with frames only in one direction and stair cores often placed in an asymmetric position), poor structural details and material properties, deterioration phenomena due to environmental exposure conditions and to a limited maintenance over time.

During the past years, a lot of efforts were devoted to assessing vulnerability of existing RC framed buildings, which represent the most widespread structural typology within the RC building stock, not only in Italy, but also in several other seismic-prone countries in the Mediterranean area. The vulnerability of these structures is typically represented in terms of fragility curves, which express the probability of exceeding a predefined damage level for a wide range of ground motion intensities [1,2]. However, from the Seventies onwards, the presence of multi-story RC frames with shear walls realizing the elevator or stairwell core, has become increasingly common, especially in larger urban areas. It is well known that a correct in-plane disposition of the walls, together with an adequate choice of their dimensions and reinforcement, guarantees a good seismic response of modern RC structural wall buildings, reducing the inter-storey drift at damage limit state and providing enough ductility and strength at collapse. Nevertheless, in pre-code RC core structural systems, the position of elevator or stairwell core often creates structural irregularities and torsional actions, whose effects, together with the poor detailing of reinforcement (both in the walls and in the frame elements) should be carefully taken into account in vulnerability assessment studies. The specific features of existing core buildings, together with the high stiffness of the walls, make their seismic response quite different from that of framed structures, and consequently a different definition of the damage states used for the construction of fragility curves, as well as of the corresponding engineering demand parameters, may be required [3].

A further complication in the vulnerability assessment of these buildings is related to the presence of masonry infills. It is well known that infills significantly alter the seismic response of RC framed buildings, by producing a remarkable increase of lateral stiffness and base shear, as well as a reduction of the period of vibration. Moreover, their spatial arrangement within the framed structure can cause irregularities in the distribution of masses and stiffnesses, both in-plan and/or in elevation, with possible detrimental effects on the seismic response, as proved by observed damage data collected in post-earthquake surveys (i.e., among others, [4-8]). If almost uniformly distributed, infills can instead reduce the dissipation energy demands in frame elements, as well as the maximum displacements of the structure. For this reason, even if infills are traditionally treated as “non-structural” elements, it would be better to include their presence in numerical analyses, to allow a more realistic representation of the global behavior of the structure. Masonry panels are commonly schematized through equivalent nonlinear inclined struts, which represent a good compromise between accuracy and simplicity (i.e. [9-12]). The most of the studies available on this topic in the literature are however mainly focused on infilled RC frames, while the effect of masonry panels in case of framed buildings with an inner RC core has been less investigated so far. In this case, an irregular distribution of infills may alter the expected damage state sequence, due to the interaction between the infills themselves and the RC walls.

In this study analyzes the seismic response of a prototype pre-code RC 6-storey building with frames aligned in the longitudinal direction and RC walls realizing an internal asymmetric stair core. Pushover analyses are performed on the finite element model of the structure, by

simulating frame components with beam elements and the shear walls with shell elements. The nonlinear behavior of RC walls is taken into account through PARC_CL_2.1 constitutive model [13], implemented into the finite element code ABAQUS [14]. The influence of different modelling choices on the global response of the building is explored, by considering the two alternative assumptions of linear elastic pendulum frames and non-linear collaborating frames. Moreover, the influence of infills and of their progressive damage on the global response is investigated, by highlighting their effects in terms of displacement capacity, global stiffness and strength.

2 CASE STUDY

The case study analyzed in this paper is a representative a typical pre-code RC 6-storey building, with frames aligned in the longitudinal direction and RC walls realizing an internal asymmetric stair core. The building has a rectangular plan, with dimensions equal to 11.7 m x 24.4 m, and a total height of 19.04 m. An interstorey height of 3.06 m is assumed, except for the ground floor, where it is set equal to 3.74 m. This lower level is partially underground. The framed structure consists of six bays in the longitudinal direction, with spans ranging between 2.8 m and 5.2 m, and two bays with the same span (equal to 5.7 m) in the transverse direction. As can be seen from the floorplan depicted in Figure 1, in transverse direction beams are present only in the external frames. The stairwell core, which is realized with 200 mm thick RC walls, has an asymmetric position in plan.

Slabs are composed with parallel RC joists, running through the transverse direction, and interposed hollow clay blocks, with a 400 mm thick RC topping. Over the last floor, an inclined roof is realized by means of masonry walls with variable height and ceramic flooring blocks. For intermediate floors, a dead load equal to 6.2 kN/m^2 is assumed, and an additional permanent load of 2.0 kN/m^2 is also applied to account for the presence of internal partitions; the live load is set equal to 2.0 kN/m^2 . For the last storey, a dead load of 7.2 kN/m^2 and a live load of 1.2 kN/m^2 (snow) are instead considered.

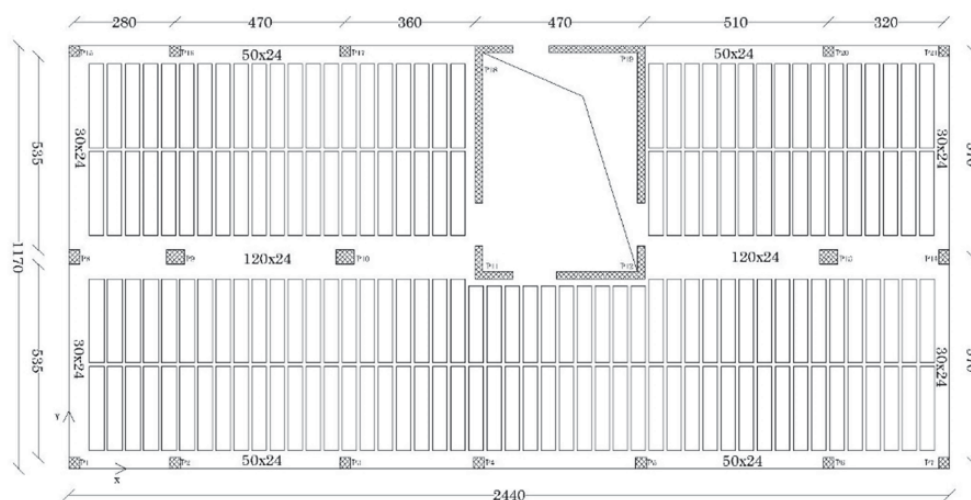


Figure 1: Typical floorplan of the examined case study building (dimensions in cm).

The considered case study represents a typical Gravity Load Designed (GLD) building, without specific provisions for earthquake resistance. RC elements forming the frame are designed to sustain vertical loads only. Beams are realized within the thickness of the slab forming the floor (240 mm), and have a variable width, ranging from 300 to 500 mm for the

external frames, and equal to 1200 mm for the internal one. Columns dimensions are typically equal to 300 x 300mm or 300 x 400 mm, except those belonging to the inner frame, which have a variable cross-section, ranging from 500 mm x 400 mm at the lower storey, to 300 mm x 400 mm at the top storey. The walls around the stairwell are conceived as a core system with high stiffness and are designed to sustain the wind load and a conventional horizontal action equal to 0.5% of the weights. As regards material properties, C25/30 concrete (with $f_{cd} = 14.2$ MPa) and B450 steel (with $f_y = 391$ MPa) are assumed. Further details on the considered case study structure can be found in [15, 16], to which reference is made.

Vertical closures of the buildings are realized by means of double layer brick infills, with a total masonry thickness of (120 + 60) mm. Opening distribution within infills is depicted in Figure 2. Opening dimensions are assumed equal to 1.2 x 1.3 m. As can be seen, infills are assumed to be completely missing only in the rear side of the building (both on the right-hand and left-hand sides of the RC wall belonging to the core) at the lower level, so to allow the entry to garages. This not-regular infill distribution has been chosen since it is quite common for this type of buildings.

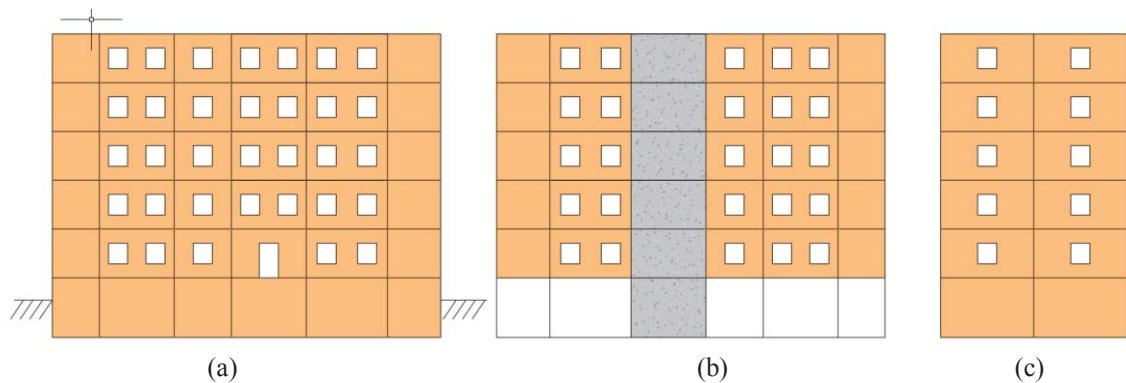


Figure 2: Sketch of the opening distribution within infill panels: (a) main façade; (b) rear side; (c) lateral side of the case study building.

3 MODELLING ASSUMPTIONS

The seismic behavior of the case study structure is studied by performing nonlinear pushover analyses, with the commercial Finite Element (FE) software ABAQUS [14].

As already highlighted, the considered building can be treated as a wall-equivalent dual system, since the elements belonging to the frame are designed for vertical loads only, while possible horizontal loads are mainly absorbed by the walls of the inner core. Taking in mind this aspect, two different models are realized, which are characterized by different complexity and different degree of interaction between the frame and the core during the earthquake. In Model#1, the collaboration of the frame in sustaining horizontal actions is completely disregarded, and all the sources of nonlinearity are simply assigned to the walls forming the core, while beams and columns are assumed as linear elastic. Regarding FE choices, pendulum frame components are modelled by using three-node beam elements with 2 integration points for columns, and 2-node truss elements with one integration point for beams.

In Model#2, the possible interaction between the frame and the core walls is explicitly taken into account (collaborating frame). In this case, beam elements are adopted for the modeling of all the frame component, with 3 nodes and 2 integration points for columns, and 2 nodes and 1 integration point for beams. The nonlinear response of beams and columns is dealt with a concentrated plasticity approach, and consequently they are modelled through elastic elements with rotational hinges at the ends. The assigned moment-curvature relation is

calculated by adopting Saenz law with ultimate strain equal to $3.5 \cdot 10^{-3}$ for concrete and an elastic-perfectly plastic law for steel.

As concerns the presence of infills, the analyses are repeated twice, by considering two different configurations (Figure 3): the limit case of the bare structure (no infills present) and the “real” distribution of infills depicted in Figure 2.

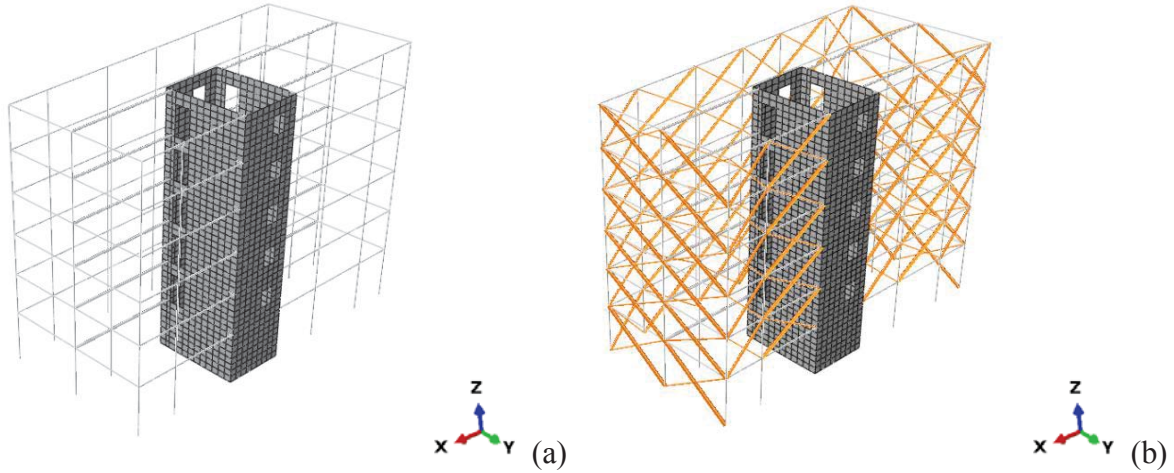


Figure 3: FE model: (a) bare structure; (b) structure with infills, according to the distribution depicted in Figure 2.

In this second case, the effect of infills on the global behaviour of the case study structure is assumed as equivalent to diagonal bracing, by adopting the single-strut model proposed in [12]. Each panel is replaced in the FE model by an equivalent pin-jointed diagonal strut, working only in compression, made with the same material of the infill and characterized by the trilinear lateral force-displacement relation shown in Figure 4a. The first branch of the curve represents the linear elastic response of the infill up to cracking, and its slope can be evaluated as:

$$K_i = \frac{G_w L_{in} t_w}{H_{in}} \quad (1)$$

as a function of the geometric dimensions of the infill (respectively being L_{in} , H_{in} and t_w the length, the clear height, and the thickness of the panel), and of the shear modulus of the masonry G_w .

The cracking force F_c is assumed equal to 0.6 the maximum strength of the infill F_m , which is in turn expressed as:

$$F_m = 0.818 \frac{L_{in} t_w f_{tp}}{C_I} \left(1 + \sqrt{C_I^2 + 1} \right) \quad (2)$$

with:

$$C_I = 1.925 \frac{L_{in}}{H_{in}} \quad (3)$$

and being f_{tp} the cracking strength of the infill (which can be determined from diagonal compression tests). It is assumed that the strength F_m is reached at a storey drift equal to 0.2% and 0.15% respectively in case of infills without and with openings. It should be noted that Equations (1-2) are referred to the horizontal direction, and consequently it is necessary to transform them in the inclined direction θ to obtain the force-displacement envelope of the

diagonal strut. The displacement at collapse is assumed equal to $5 D_m$, being D_m the displacement corresponding to the maximum force (Figure 4a, [12]).

A further reducing coefficient is introduced to represent the presence of openings within the infills and to account for their effect on the initial stiffness and strength of the struts, having the following expression:

$$\lambda_0 = 1 - \frac{1.5 L_0}{L_{in}} \geq 0 \quad (4)$$

being L_0 the horizontal length of the opening. In this work, the following values are assumed for masonry properties: $G_w = 1080$ MPa and $f_{tp} = 0.3$ MPa for the external layer; $G_w = 400$ MPa and $f_{tp} = 0.1$ MPa for the internal one.

In order to reduce computational efforts, even if the infill panels are formed by a double masonry layer, only a single strut (instead of two superimposed struts) is considered, and its force-displacement relation is evaluated as the envelope of those of the two layers. Moreover, in order to insert this relation within the adopted FE code, it is further reworked and expressed in terms of stress vs. strain curve (an example is reported in Figure 4b).

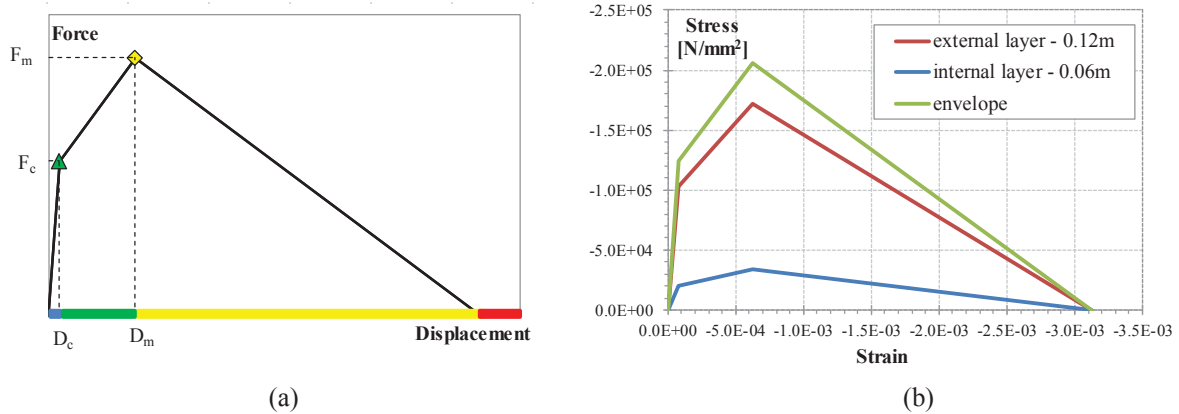


Figure 4: (a) Force-displacement relation for the diagonal struts representing the masonry infills (adapted from [12]; (b) implemented stress-strain law (referred to a strut of unit area), evaluated as the envelope of the two masonry layers.

In both Model #1 and Model #2, the RC walls of the core are modelled with 8-node, one-layered shell elements, with 4 Gauss integration point in the shell plane and 5 Simpson integration points in the thickness (element type S4R5). The nonlinear behavior of the walls under cyclic loads is considered by means of a user-defined constitutive law, named PARC_CL 2.1 [13], which is written in the form of a Fortran subroutine and implemented as a User Material (UMAT) in ABAQUS. PARC_CL 2.1 can be included in the framework of fixed smeared crack models, and it is based on a total strain formulation. The reinforcement is assumed to be smeared within the hosting concrete element through the reinforcement ratio ρ_s . PARC_CL 2.1 was developed starting from a well-validated constitutive model for membrane elements subjected to general plane stresses, named PARC [17], which was previously conceived at the University of Parma for the analysis of RC structures under static loads. For static loads only, an alternative model based on a strain decomposition approach and named 2D-PARC model is also available at the same University [18, 19].

PARC_CL 2.1 can be applied for the prediction of the cyclic and dynamic response of RC structures since it includes the effects of plastic and irreversible deformations in the unloading-reloading phase [20]. The model also allows to correctly catch other aspects which can be

very important in the analysis of existing RC structures, such as the buckling of longitudinal reinforcement [21], time-dependent effects and the corrosion of reinforcement [22], which however lie outside of the scope of this work.

Finally, the presence of rigid diaphragms is included in the FE model by applying a kinematic coupling condition, which constrains the displacements of the nodes at each floor level to those of a reference “master” node. The master node is herein assumed coincident with the bottom-left corner of the RC core.

4 NLFEA: PROCEDURE, RESULTS AND DISCUSSION

The behavior of the case study building under seismic actions is investigated by performing pushover analyses on the different FE models described in Section 3. To this aim, two lateral force distributions are considered: a uniform pattern (uniform response acceleration) and a triangular pattern (or modal pattern) proportional to the displacement shape of the first mode [23, 24]. To take into account the effect of the accidental eccentricity of loads, by limiting at the same time the number of performed analyses, the center of mass is shifted away from its original position, so to maximize its distance from the center of stiffness. This new position of the center of mass is determined by combining the two accidental eccentricities in X and Y directions, calculated according to [24]. The lateral response is described in terms of base shear vs. top displacement relationship. The top displacement is set equal to the average of the values registered at two nodes, placed at the opposite corners of the roof floorplan, i.e. the upper-right and at the lower-left ones (Figure 1).

The results obtained from pushover analyses for Model #1 and Model #2 without infills are shown in Figure 5, with reference to lateral force distributions acting along the negative X and Y directions. As can be seen, Model #2 is characterized by a higher bearing capacity with respect to Model #1 when considering lateral forces acting in $-X$ direction, thanks to the additional resisting contribution offered by the three longitudinal frames. On the contrary, the lack of internal beams connecting the columns in the transverse direction makes almost negligible the bearing contribution of frame elements for seismic loads acting along $-Y$, and the global behavior is consequently governed by the walls belonging to the core. In both models, the asymmetric position of the internal core gives rise to torsional effects, as demonstrated by the deformed shape plotted in Figure 6, which is referred to Model #2 without infills, for a uniform lateral load distribution respectively acting along $+X$ and $+Y$ direction.

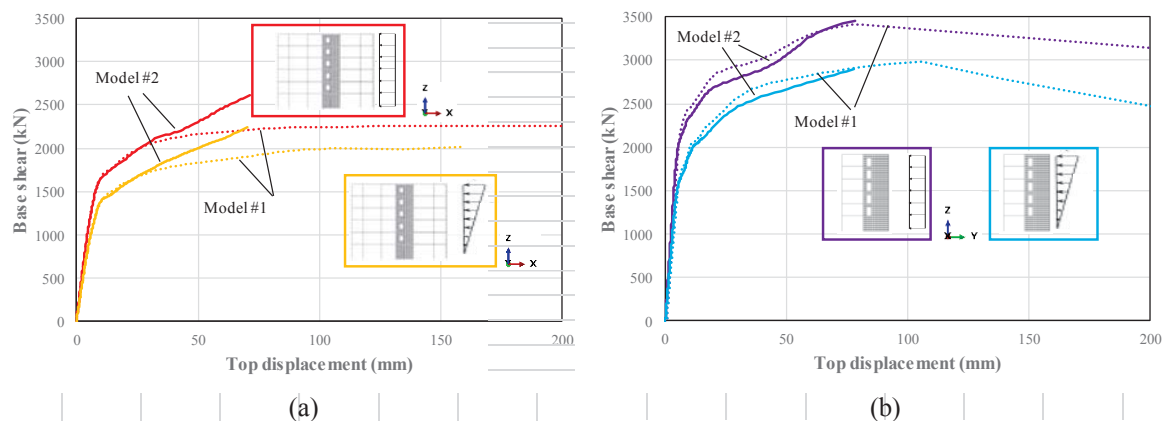


Figure 5: Base shear- top displacement curves obtained for Model #1 and Model #2 without infills from pushover analyses: (a) forces acting along $-X$ direction; (b) forces acting along $-Y$ direction.

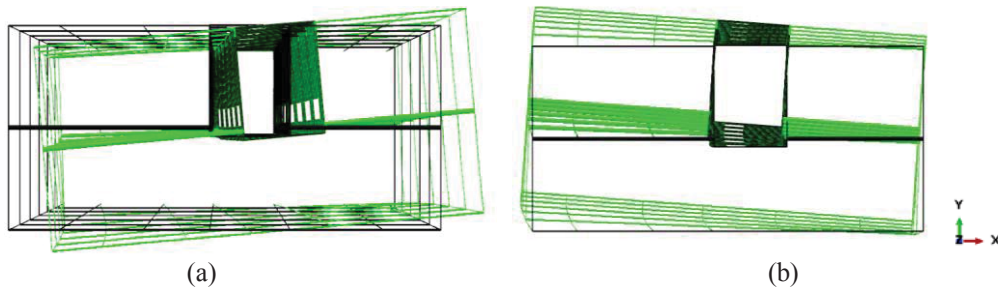


Figure 6: Deformed shape of the case study building obtained from Model #2 without infills subjected to a uniform lateral load distribution acting along direction (a) +X and (b) +Y.

The influence of infills on the global behavior of the structure is shown in Figure 7. For the sake of brevity, only the comparisons based on Model #2 (with collaborating frames) are proposed in the case of uniform lateral load distribution acting in the $-X$ direction. To take into account the progressive damage of infills on the seismic response, the following procedure is proposed. At first, the analysis is carried out by considering the presence of infills according to the distribution depicted in Figure 2 (“Model #2 with infills” in Figure 7). The results of the model are then elaborated so to detect the progressive degradation of infills panels. More in detail, the time increment corresponding to the achievement of the degrading branch of the force-displacement curve in some of the masonry panels is found, and the analysis is restarted from that increment, by removing the damaged infills through the ABAQUS option *MODEL CHANGE, REMOVE, and re-applying the horizontal load distribution. This operation is then repeated until almost all the infills are collapsed, so obtaining a sort of “envelope” curve (“Model #2 with infills – progressive infill damage” in Figure 7). For comparison, an additional “lower-limit” curve is also plotted (“Model #2 with infills – complete infill removal” in Figure 7), which is obtained by removing all the infills together, at the time increment corresponding to the first appearance of damage in some of them. It can be seen that the presence of infills greatly increase the lateral stiffness and strength of the structure; however, with the progressive damage of the panels, the base shear-top displacement curve obviously tends to superimpose that of the bare structure.

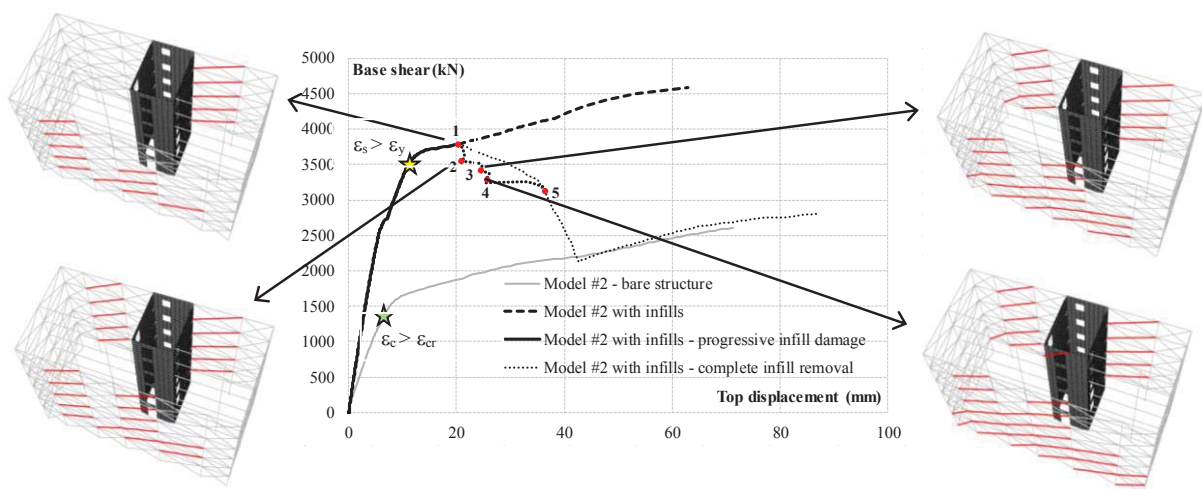


Figure 7: Base shear-top displacement curve for Model #2 with and without infills, with indication of the progressive damage of masonry panels.

The sequence followed for the removal of damaged infills (which are marked in red) is also sketched in Figure 7. It can be observed that the damage distribution within masonry panels is strictly related to the torsional deformation of the building under seismic loads (Figure 8), with a consequent stress concentration localized in some bays of the structure. Furthermore, it can be seen that the degrading branch of the force-displacement curve is reached before in those masonry panels characterized by a greater length L_{in} , where a higher number of openings is assumed according to Figure 2.

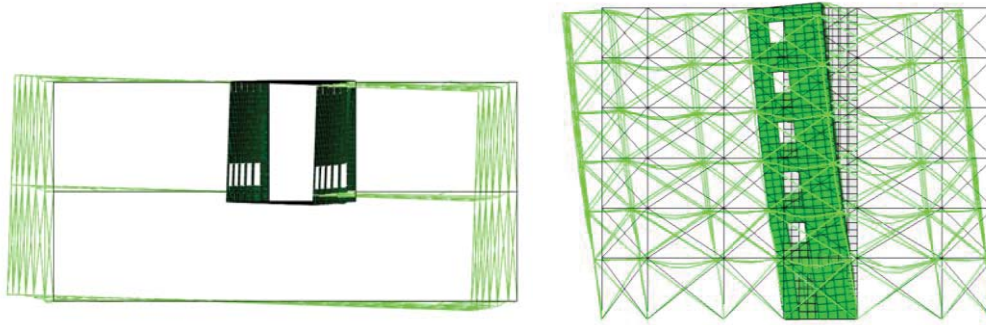


Figure 8: Deformed shape for Model #2 with infills, corresponding to point 1 of the base shear-top displacement curve reported in Figure 7, when the first panels start to damage.

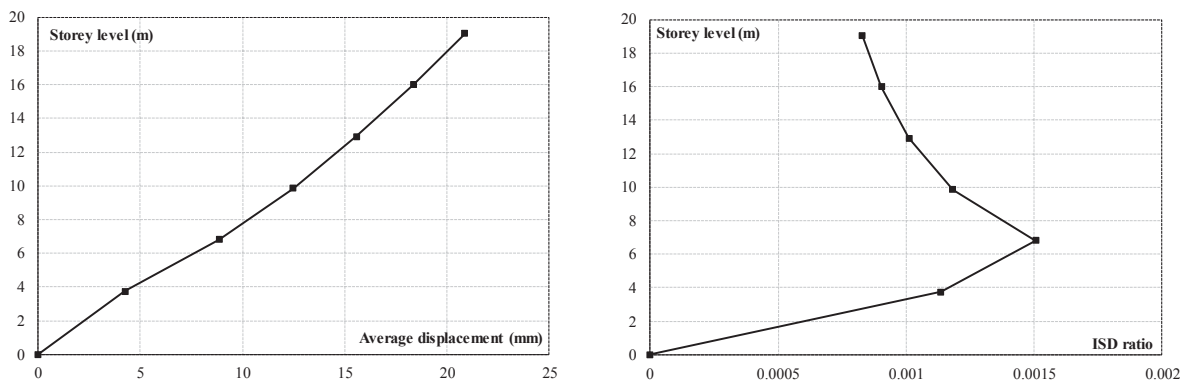


Figure 9: Displacement and inter-story drift profiles corresponding to point 1 in Figure 7.

In correspondence of point 1 in Figure 7, over 33% (almost 45% if referring only to the X-direction) of the infill panels at the second storey have reached they maximum resistance and start to degrade. It can then be assumed that this point corresponds to the reaching of the so-called “Damage Limitation” state (DL LS, see, i.e., [4]), which is defined as a first limit state characterized by quite limited damage almost localized in non-structural elements, that should be easily and economically repaired (also known as slight damage state, LS1). The average values of lateral displacement profile corresponding to point 1 in Figure 7 are shown in Figure 9. The same Figure also reports the inter-story drift ratio, evaluated as the average lateral displacement difference between two consecutive floors (inter-story drift), divided by the height of the storey. The maximum obtained ISD ratio is comparable with the threshold values (typically ranging between 0.1 and 0.25%) suggested in the literature to define the limit state corresponding to slight damage in numerical analyses on framed structures; these values are conventionally adopted when infills are not explicitly included in the FE model.

A further check on the model results reveals that when the first infills start to damage, yielding in RC elements of the frame has not been reached yet, and also the spreading of cracks in the RC walls of the core is very limited. On the contrary, yielding strain of longitudi-

dinal reinforcement is already registered in some portions of the walls (see Figure 10a; it should be noted that the condition $\varepsilon_{s, \text{long}} > \varepsilon_y$ is already reached for an average top displacement of 11 mm, corresponding to the yellow star in Figure 7). This behavior can be explained in the light of the particular distribution considered for infills, which is not-regular in elevation on the rear side of the building, so producing a stress concentration in the RC walls. Moreover, the modelling technique adopted for infills (though diagonal struts) is probably not optimal in case of RC walls, since it may lead to concentrated loads on the shell elements connected to the nodes of the strut. In this specific case study, the not-uniform infill distribution is then responsible for a change in the expected damage sequence, since the yielding of the reinforcement of the walls (which corresponds to a moderate damage, LS2) is reached before the damage of masonry infills (corresponding to slight damage LS1). However, further analyses with different infill distributions are required to draw more general observations.

In a previous work [3] focused on the same structural typology (frame + inner core) investigated herein, the Authors have suggested as a possible criterion for the definition of slight damage limit state LS1 when infills are not explicitly included in the model, the reaching of the cracking strain in the RC elements of the shear walls, by following an approach conceptually similar to that described in FEMA 356 [25]. With reference to the pushover curve reported in Figure 7 (“Model #2 – bare structure”), this criterion leads to the reaching of LS1 for an average top displacement value equal to 6.75 mm (green star in Figure 7). The ISD ratio profile corresponding to that situation is reported in Figure 10b, together with a contour showing the crack pattern in the core walls, as obtained from Model #2 without infills. As can be seen, these values are lower than those commonly associated to infill damage in framed structures.

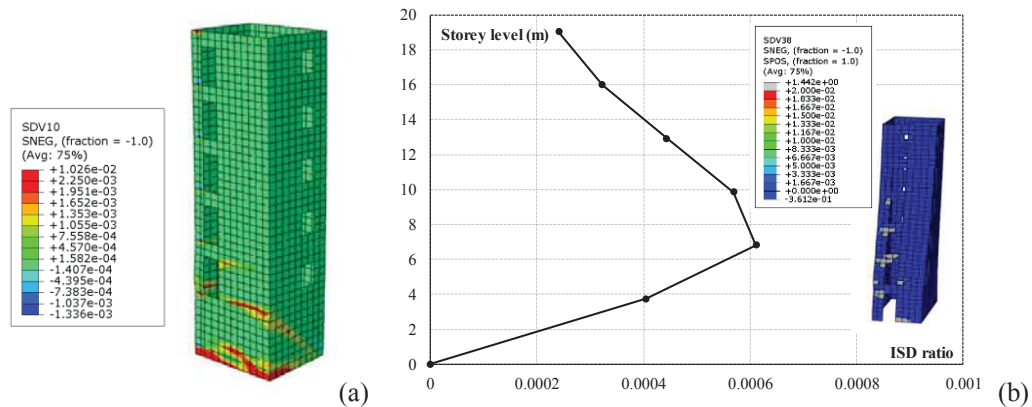


Figure 10: (a) Strain field in the longitudinal reinforcement of the walls corresponding to point 1 in Figure 7; (b) ISD ratio and crack pattern obtained from Model #2 without infills, in correspondence of the green star of Fig. 7.

5 CONCLUSIONS

The results proposed in this paper confirm that presence of an asymmetric core, which is quite typical of pre-code RC buildings realized in large urban centers in the last 40 years, significantly affects the seismic response of the structure, giving raise to torsional effects. Specifically, the following main observations can be highlighted:

- The walls belonging to the core absorb the larger part of the lateral loads; however, the resistant contribution offered by frames (which are usually aligned in one direction only) is not negligible.
- The presence of infills modifies the global response of the structure, providing a remarkable increase the lateral stiffness and strength of the structure, as observed in framed

structures. The reaching of the limit state corresponding to slight damage is often evaluated on the basis of the progressive appearance of damage in infills; when they are not explicitly included in numerical analyses, a conventional value of inter-story drift is often assumed. In case of framed structures with a RC core, alternative approaches, based on a material-level approach, can be also followed.

- Infill distribution has a great influence on the structural response and on the damage sequence taking place in structural and non-structural elements under seismic loads; further studies are required to draw general indications for the individuation of the damage states to be considered in derivation of fragility curves.

REFERENCES

- [1] R. Maio, G. Tsionis, M. L. Sousa, S. Dimova, Review of fragility curves for seismic risk assessment of buildings in Europe. *Proceedings of the 16th World Conference on Earthquake Engineering*, Santiago, Chile, January 9-13, 2017.
- [2] R. Maio, G. Tsionis, *Seismic fragility curves for the European building stock*. Brussels JRC Technical Report, European Commission, 2015.
- [3] B. Belletti, E. Martinelli, E. Michelini, M. Tavano, F. Vecchi, Seismic Risk Assessment of Existing RC Frame Buildings with Shear Walls. *Proceedings of the 9th European Workshop on the seismic behaviour of Irregular and Complex Structures (9EWICS)*, streamed from Lisbon, Portugal, December 15-16, 2020.
- [4] P. Ricci, M. T. De Risi, G. M. Verderame, G. Manfredi, Influence of infill distribution and design typology on seismic performance of low- and mid-rise RC buildings. *Bulletin of Earthquake Engineering*, **11**, 1585–1616, 2013.
- [5] D. Celarec, P. Ricci, M. Dolšek, The sensitivity of seismic response parameters to the uncertain modelling variables of masonry-infilled reinforced concrete frames. *Engineering Structures*, **35**, 165–177, 2012.
- [6] H. B. Kaushik, D. C. Rai, S. K. Jain, Code Approaches to seismic Design of Masonry-Infilled Reinforced Concrete Frames: A State of the Art. *Earthquake Spectra*, **22**(4), 961–983, 2006.
- [7] P. G. Asteris, C. Z. Chrysostomou, I. P. Giannopoulos, E. Smyrou, Masonry infilled reinforced concrete frames with openings. *Proceedings of 3rd ECCOMAS Thematic Conference on Computational Methods in Structural Dynamics and Earthquake Engineering (COMPDYN 2011)*, Corfu, Greece, May 26-28, 2011.
- [8] F. De Luca, G. M. Verderame, F. Gómez-Martínez, A. Pérez-García, The structural role played by masonry infills on RC building performances after the 2011 Lorca, Spain, earthquake, *Bulletin of Earthquake Engineering*, **12**, 1999–2026, 2014.
- [9] N. D. Lagaros, I. A. Naziris, M. Papadrakakis, The influence of masonry infill walls in the framework of the performance-based design. *Journal of Earthquake Engineering*, **14**(1), 57–79, 2010.
- [10] L. Decanini, F. Mollaioli, A. Mura, R. Saragoni. Seismic performance of masonry infilled R/C frame. *Proceedings of 13th World Conference on Earthquake Engineering*, Vancouver, Canada, August 1-6, 2004.

- [11] C. Lima, G. De Stefano, E. Martinelli, Seismic Response of Masonry Infilled RC Frames: Practice-oriented models and open issues. *Earthquakes and Structures*, **6**(4), 409–436, 2014.
- [12] M. Dolšek, P. Fajfar, The effect of masonry infills on the seismic response of a four-storey reinforced concrete frame – a deterministic assessment. *Engineering Structures*, **30**, 1991–2001, 2008.
- [13] F. Vecchi, *PARC_CL 2.1 crack model for the capacity assessment of new and existing reinforced concrete structures using non-linear finite element analysis*. Ph.D. Thesis, Department of Engineering and Architecture, University of Parma, Italy, 2019.
- [14] *ABAQUS User's Manual*. Dassault Systèmes Simulia Corp, Providence, RI, USA.
- [15] AICAP Eds, *Seismic design of RC buildings - Guide to the application of Eurocode 2, with reference to the Italian Code DM 14.1.2008 (in Italian)*. Pubblicamento, 2008.
- [16] G. Toniolo, M. Di Prisco, *Design of structures Vol. 2B - Reinforced concrete. Design for limit states (in Italian), 3rd Edition*. Zanichelli, 2009.
- [17] B. Belletti, R. Cerioni, I. Iori, Physical Approach for Reinforced-Concrete (PARC) Membrane Elements. *ASCE Journal of Structural Engineering*, **127**, 1412–1426, 2001.
- [18] R. Cerioni, I. Iori, E. Michelini, P. Bernardi, Multi-directional modeling of crack pattern in 2D R/C members. *Engineering Fracture Mechanics*, **75**, 615–628, 2008.
- [19] P. Bernardi, R. Cerioni, E. Michelini, A. Sirico, Numerical modeling of the cracking behavior of RC and SFRC shear-critical beams. *Engineering Fracture Mechanics*, **167**, 151–166, 2016.
- [20] B. Belletti, M. Scolari, F. Vecchi, PARC_CL 2.0 crack model for NLFEA of RC structures under cyclic loadings. *Computers and Structures*, **191**, 165–179, 2017.
- [21] B. Belletti, F. Vecchi, Implementation of steel constitutive model including buckling in PARC_CL 2.1 crack model. *Proc. of the 5th fib Congress (fib 2018)*, Melbourne Australia, October 7-11, 2018.
- [22] B. Belletti, F. Vecchi F, C. Bandini, C. Andrade, J.S. Montero, Numerical evaluation of the corrosion effects in PC beams without shear reinforcement. *Structural Concrete*, 2020.
- [23] P. Fajfar, A nonlinear analysis method for performance-based seismic design. *Earthquake Spectra*, **16**, 573–592, 2000.
- [24] UNI EN 1998-1:2013. *Eurocode 8 - Design of structures for earthquake resistance*, CEN: Brussels, 2013.
- [25] FEMA 356, *Prestandard and commentary for the seismic rehabilitation of buildings*. Washington DC, USA, 2000.

CALIBRATION AND VALIDATION OF AN OVERDAMPED DISPLACEMENT ADAPTIVE PROCEDURE FOR SEISMIC ASSESSMENT OF INFILLED RC FRAMES

F. Barbagallo¹, M. Bosco¹, A. Gherzi¹, E. M. Marino¹, P.P. Rossi¹,

¹ 1Department of Civil Engineering and Architecture, University of Catania, via S. Sofia 64, 95125
Catania, Italy

e-mail: {fbarbaga, mbosco, aghersi, emarino, prossi}@dica.unict.it

Abstract

The main part of the existing buildings in the Mediterranean area is extremely vulnerable to seismic actions. Since a complete renewal of the building heritage is not possible, the seismic assessment of existing structures has gained importance to identify the structural deficiencies and design the most appropriate retrofit interventions. Nonlinear dynamic analysis is widely recognised as the most accurate tool to predict the seismic behaviour of structures. However, it has high computational cost and is not suitable for professional purposes. To provide a tool that reliably assesses the seismic behaviour of structures, with an acceptable computational burden, nonlinear static methods of analysis have been developed.

This paper proposes a multimodal adaptive procedure named overDamped Displacement Adaptive Procedure (D-DAP) for seismic assessment of RC frames. The D-DAP is ruled by two main parameters: the value of top displacement adopted as step size and the number of modes of vibrations deemed significant for the determination of the load vector. Furthermore, the D-DAP is equipped with an equivalent damping law to consider the increase of the energy dissipation due to the cumulated damage in both structural and non-structural members.

The goal of this paper is to determine the values of the displacement step size and the number of modes of vibration necessary to achieve a suitable accuracy by means of the D-DAP. In addition, a new equivalent damping law is calibrated considering also infilled frames. In fact, nonlinear static analysis provided in literature are not optimised to estimate the nonlinear behaviour of infilled frames, despite the well known influence of infill panels on the structural response. A parametrical investigation that includes frames with and without infills is conducted. A set of 54 RC frames have been designed to be representative of existing buildings with various levels of seismic deficiencies and analysed. The adopted research methodology assumed the response obtained by Incremental nonlinear Dynamic Analysis (IDA) as target.

Keywords: nonlinear static analysis, infill walls, RC frames, seismic assessment.

1 INTRODUCTION

Recently, increasing efforts have been devoted by the scientific research to develop methods of analysis to predict the seismic behaviour of existing structures. Since real structures cannot keep an elastic behaviour under strong earthquakes, an accurate estimation of the seismic performance of existing structures requires the determination of the inelastic deformation experienced by structural members during earthquakes. To this end, the nonlinear dynamic analysis is considered the most reliable tool. However, due to its complexity and high computational cost, this type of analysis is still considered accessible only for experts in seismic engineering and is not suitable for daily professional use.

From the need of a tool that estimates the inelastic deformations of structures subjected to earthquake with relative low computational burden, the scientific research has developed the nonlinear static methods of analysis. Among the approaches available in scientific literature, the Capacity Spectrum Method (CS), proposed by Freeman [1], and the N2 Method, proposed by Fajfar [2], are the most popular. Although the results obtained by these analyses are generally deemed adequate for low-rise plane frames, common nonlinear static analyses do not take into account the contribution of higher modes of vibration to the seismic response, and do not consider the progressive reduction of the structural stiffness due to the nonlinear behaviour of the structure. To improve the level of accuracy, advanced nonlinear static methods of analysis were developed. Among others, innovative approaches are the DAP proposed by Pinho et al. [3, 4], and the Advanced N1 method proposed by Lenza et al. [5, 6]. Despite the innovative character of these two latter methods, they still suffer from some approximations: the DAP still requires the use of an equivalent SDOF system for the evaluation of the displacement demand, whilst the Advanced N1 method neglects the effect of the energy dissipation due to the inelastic behaviour of the structure.

An additional important aspect is that existing structures are generally endowed with infill panels. Usually, infills are considered nonstructural elements, and their contribution to the seismic response is “conservatively” neglected. However, frames with infill panels have a significantly larger stiffness, and their dissipative capacities and collapse mechanisms are deeply influenced by the presence and mechanical properties of infills. Despite this, neither the nonlinear static methods of analysis suggested by codes, nor the advanced nonlinear static methods were conceived to estimate accurately the nonlinear behaviour of infilled frames, which may be “unconservatively” predicted.

To overcome these issues, in a previous paper [7] the authors proposed a multimodal adaptive nonlinear static procedure named overDamped Displacement Adaptive Procedure (D-DAP). This method was developed by combining the approach by Antoniou and Pinho [3] and Pinho et al. [4] to update the load vector, with the procedure by Lenza et al. [5, 6] to associate the peak ground acceleration to the displacement demand. The D-DAP explicitly considered the increase of the energy dissipation due to the cumulated damage in the structure and, to this end, the equivalent viscous damping ratio was updated at each step of the pushover analysis. The goal of this paper is to calibrate the value of the parameters ruling the method, i.e. number of modes to be enveloped and size of the incremental step. In addition, an equivalent damping law is calibrated here on RC framed structures, with and without infills. Then, the efficiency of the calibrated method in predicting the seismic response of RC frames is investigated. To this end, a set of 54 RC frames has been designed to be representative of existing RC buildings, suffering from various types and levels of seismic deficiency. The set of case studies includes frames endowed with infill panels with negligible, medium and large stiffness and strength. The adopted research methodology assumed the response obtained by Incremental nonlinear Dynamic Analysis (IDA) as target.

2 THE OVERDAMPED DISPLACEMENT ADAPTIVE PROCEDURE

The proposed D-DAP is structured in three main steps: (1) definition, application and scaling of the load pattern, (2) association of the displacement demand to the corresponding PGA, (3) overdamping correction. The three steps are repeated until the structural collapse (or a target displacement) is achieved. Figure 1 shows the flowchart of the procedure.

The D-DAP applies a displacement load pattern, that is updated at every step of the analysis according to the modal shapes of the structure at the current step. For this reason, at the beginning of every step of D-DAP a modal response spectrum analysis is run. The modal response spectrum analysis is carried out assuming an elastic spectrum having a reference peak ground acceleration $a_{g,ref}$ and 5% equivalent viscous damping ratio. The contributions of n modes of vibration to the seismic response are considered. The displacement D_i of the load pattern (at the i -th storey) is calculated as the sum of the interstorey drifts Δ_k from storey 1 to the i -th storey, following the interstorey displacement-based scaling approach suggested in [3, 4]:

$$D_i = \sum_{k=1}^i \Delta_k \quad (1)$$

The interstorey drift Δ_k is determined at every storey as the SRSS combination of the considered modal shapes. The displacements obtained by Equation 1 are normalised to keep the maximum displacement equal to 1. Hence, the normalised modal scaling vector D' defines the shape, not the magnitude, of the load (or increment of load) vector.

At each step of the analysis, a fixed increase of the top displacement ΔD_t is imposed. The displacement load pattern obtained from the modal response spectrum analysis is scaled so that the displacement at the top storey corresponds to ΔD_t . The final load pattern $D_{i,s}$ applied at the current step s at each i -th storey is given by the summation of the displacement vector cumulated up to the previous step $D_{i,s-1}$ and the increase of the loading vector at the current step $\Delta D_{i,s}$.

In order to associate the displacement demand to the corresponding PGA, the following observation is made: as long as the increase of the load pattern is assumed small enough, it can be reasonably assumed that the structure has a linear response within the step [5, 6].

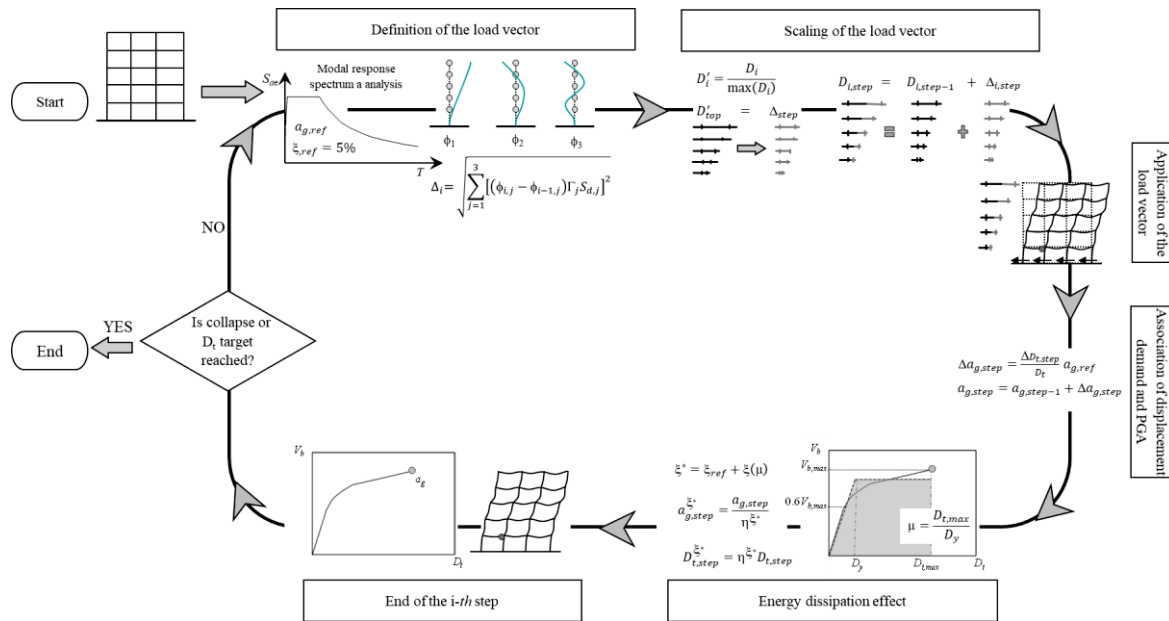


Figure 1 – Flowchart of the D-DAP procedure

Hence, the increase of PGA ($\Delta a_{g,s}$) that has caused the increase of load pattern $\Delta D_{t,s}$ at the step s is evaluated by linear interpolation (note that the increase of load pattern corresponds to the increase of the top displacement of the structure):

$$\Delta a_{g,s} = \frac{\Delta D_{t,s}}{D_t} a_{g,ref} \quad (2)$$

where D_t is the displacement at the top of the structure provided by the modal response spectrum analysis with response spectrum characterised by the reference acceleration $a_{g,ref}$. The acceleration $a_{g,s}$ corresponding to the top displacement at the end of step s is:

$$a_{g,s} = a_{g,s-1} + \Delta a_{g,s} \quad (3)$$

So far, the increase of acceleration Δa_g (Eq. 2) has been evaluated with reference to a fix value of the equivalent viscous damping ratio ξ_{ref} . However, it should be noted that, the equivalent viscous damping ratio increases at every step of the analysis along with the spread of the yielding in the structure. The value of ξ_{ref} is included in the factor η , which appears in the equation proposed by EC8 for the determination of the spectral displacement S_{de} . As ξ_{ref} is assumed equal to 5% in both Equations 5 and 6, the energy dissipated by the structure through yielding is not taken into account yet. To account for this, the PGA evaluated by Equation 6 is corrected considering higher values of ξ_{ref} . Regardless of the fundamental period T_1 or the type of soil, the ratio of a spectral displacement $S_{d,e}^{5\%}$ obtained from the response spectra scaled with 5% damping and the spectral displacement $S_{d,e}^{\xi^*}$ obtained from the response spectra scaled with a larger damping ratio $\xi_{eq} = \xi^*$ is equal to the ratio of the corresponding parameters η :

$$\frac{S_{d,e}^{5\%}}{S_{d,e}^{\xi^*}} = \frac{\eta^{5\%}}{\eta^{\xi^*}} \quad (4)$$

Since η is equal to 1 when the damping ratio is 5% [7] it follows that:

$$S_{d,e}^{\xi^*} = \eta^{\xi^*} S_{d,e}^{5\%} \quad (5)$$

Since the effect of the equivalent viscous damping is the result of the entire damage cumulated by the structure, from the beginning of the analysis until the considered step, the correction that accounts for the increase of the equivalent damping can be applied straightforwardly to the total PGA at the end of each step of the D-DAP:

$$a_{g,s} = \frac{a_{g,s}^{5\%}}{\eta(\xi^*)} \quad (6)$$

3 DESIGN OF CASE STUDIES

Two sets of RC frames have been created to simulate existing buildings with different features. The first set is composed of frames (named GL) that are drawn from buildings designed to sustain gravity loads only and are representative of typical Italian residential buildings of the seventies. The frames of the second set (named SR) are extracted from RC buildings designed for earthquake resistance in low seismicity areas according to the Italian standards for constructions and seismic resistance [10] in force in the nineties. Two different plan layouts have been considered (Figure 3): in the first plan layout, the unidirectional slab is characterised by reinforcements orientated along the y-direction (Figure 2(a) and (c)), while in the second arrangement the unidirectional slab is parallel to the x-direction (Figure 2 (b) and (d)). All the analysed frames lay along the x-direction. Each set of frames includes three types of frames: frame type 1 and 2 are the central and the outermost frames, respectively, extracted from the buildings where the slab is parallel to y-direction. In consequence of the orientation

of the deck, frame type 1 supports larger gravity loads than frame type 2. Frame type 3 is drawn from the building with the slab orientated along the x-direction and supports only the self-weight of beams, columns, infills and the weight of an additional 50 cm wide stripe of deck. Both the SR frames and the GL frames were designed with five 5.5 m wide bays and with a number of storeys equal to 3, 6 and 9. The interstorey height is equal to 3.2 m. To investigate the influence of infill panels on the seismic response of buildings, the RC case study frames have been endowed with infill panels, supposing the distribution of the infills uniform along the height of the frame. Particularly, two kinds of infill panels are considered: one with high stiffness and strength, and another having lower stiffness and strength. Furthermore, the case study frames have been considered in the bare configuration as well. These cases represent the limit case of frames having very weak infill panels. In total, 54 RC frames are analysed.

Hereinafter, each frame is identified by a label. The first two letters indicate which set the frame belongs to, the first number indicates the number of storeys and the last number the amount of gravity load. Frames with the largest gravity loads are indicated with 1, frames with the lowest gravity loads are indicated with 3 and the intermediate loaded frames are indicated with 2. The second part of the label is required in the case of infilled frames. Here, the letter I indicates the presence of infill panels and the number indicates the cracking strength of infills in MPa.

The design internal forces of structural members belonging to GL frames are evaluated considering gravity loads only [8]. The internal axial forces N on columns and the distributed loads on beams are evaluated based on the tributary area concept. The dimensions of the cross sections and the size of steel reinforcements are determined by the allowable stress method [9].

To design the seismic-resistant frames, the regulations for building structures and seismic resistance enforced in Italy in the nineties [10] are followed. The effect of the seismic forces is determined by the lateral force method of analysis supposing that, at the time of construction, the location of the building was classified as low seismicity area.

Details on the design of frames can be found in [7].

4 CALIBRATION OF PARAMETERS

In this section, first, an analysis is conducted to calibrate (1) the number of modes to be enveloped and (2) the value of the displacement step size. The goal is to select the values of the optimal ruling parameters that ensure the best accuracy together with the best efficiency of the D-DAP for the case study frames. Hence, once these optimal parameters have been determined, a new equation of the equivalent viscous damping ratio as a function of the period of the first mode of vibration is proposed. The numerical analyses are performed by OpenSees [11].

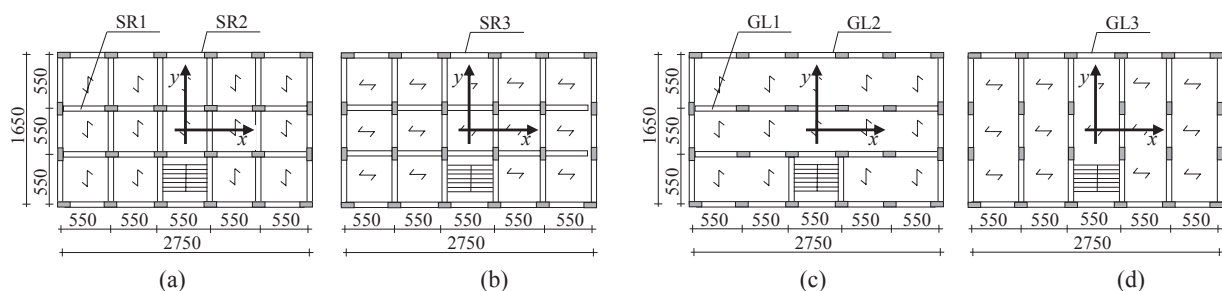


Figure 2 – Plan layout of buildings (units in cm): (a) GL building and (c) SR building with slab perpendicular to longitudinal frames; (b) GL building and (d) SR building with slab parallel to longitudinal frames

4.1 Numerical model and seismic input

The nonlinear response of the case study frames has been investigated by a 2D numerical model with masses concentrated at floor levels. The slab at each level is assumed rigid in its own plane and is simulated by a rigid diaphragm. A leaning column is added to the numerical model to account for $P-\Delta$ effects. For nonlinear dynamic analysis, a Rayleigh viscous damping is used and set at 5% for the first and the third mode of vibration.

The gravity loads assigned to beams and columns are those specified in EC8 for the seismic design situation. The floor masses are determined as a percentage of the total mass of the deck and are equal to 99.3 t for frames GL1 and GL2, 198.6 for frame GL3 and 106.1 t for frames SR. The gravity load at each level of the leaning column is equal to the seismic weight of the storey of the frame (i.e. the floor mass assigned to frame times 9.81).

Beams and columns of the RC frame are modelled as members constituted by an elastic element with plastic hinges at their ends (Beam With Hinges Element in OpenSees). The length of the plastic hinge is equal to the depth of the cross section and a fibre cross section is assigned to each plastic hinge. The concrete part of the cross section is subdivided into fibres having 5 mm depth and width equal to the width of the cross section. Single fibres enclosed in the cross section are used to model rebars.

The Mander constitutive law (“Concrete04” uniaxial material) is assigned to concrete fibres [12]. The parameters used for concrete material are summarized in Table 1. Since frames SR are expected to be endowed with dense and well detailed stirrups, the concrete compression strength of the core of the member cross sections is supposed to increase due to the confinement effect of the stirrups. The confinement effect on the core of member cross sections is neglected for frames GL, because RC structures designed without seismic provisions generally have very few stirrups. An elasto-plastic with strain kinematic hardening constitutive law (“Steel01” uniaxial material) is assigned to steel fibres and the values of the mechanical parameters are reported in Table 2.

A “ZeroLength Element” is added at one end of each beam. This element connects the end of the beam to the corresponding node restrained by the rigid deck and is characterized by a low axial stiffness and very large shear and flexural stiffnesses. This expedient allows the beams to deform axially, so as to prevent arising of axial force, which leads fibre modelled

Table 1 Characterization of concrete for nonlinear analysis of frames

Frame GL		f_{cm} (MPa)	ϵ_{c0}	ϵ_{cu}	E_{cm} (MPa)	f_{im} (MPa)	ϵ_t
3 and 6 storeys	Core	28	0.002	0.0500	29961	0	0
	Cover	28	0.002	0.0035	29961	0	0
9 storeys	Core	33	0.002	0.0500	31477	0	0
	Cover	33	0.002	0.0035	31477	0	0
Frame SR		f_{cm} (MPa)	ϵ_{c0}	ϵ_{cu}	E_{cm} (MPa)	f_{im} (MPa)	ϵ_t
3 and 6 storeys	Core (columns)	37	0.0054	0.0500	29961	0	0
	Cover (columns)	28	0.0020	0.0035	29961	0	0
	Core (beams)	33	0.0039	0.0500	29961	0	0
	Cover (beams)	28	0.0020	0.0035	29961	0	0
9 storeys	Core (columns)	44	0.0055	0.0500	31477	0	0
	Cover (columns)	33	0.0020	0.0035	31477	0	0
	Core (beams)	41	0.0045	0.0500	31477	0	0
	Cover (beams)	33	0.0020	0.0035	31477	0	0

Table 2 Characterization of steel for nonlinear analysis of frames

	f_{ym} (MPa)	E_{sm} (MPa)	b
Frame GL	400	210000	0.0044
Frame SR	450	210000	0.0049

RC beams to an artificial stiffening and strengthening [13]. In the meantime, it ensures the transfer of shear force and bending moment from the beam to the frame node.

Infill panels are modelled as a pair of diagonal trusses without tension resistance. The force-displacement relationship of the diagonal truss is calibrated to replicate the shear force-drift relationship proposed by Panagiotakos and Fardis [14] and Celarec et al. [15]. This relationship consists of four branches and the stiffness and the value of the maximum force of each branch are determined according to the equations proposed in [15]. Two types of infill panels have been considered here and both of them were supposed to be realized by ceramic bricks, with thickness equal to 20 cm, Young modulus and shear modulus equal to 4130 and 1240 MPa, respectively. The so called “strong” infills were characterized by stiffness and cracking strength (0.28 MPa) that were twice the stiffness and strength (0.14 MPa) of the “weak” type of infills. The mechanical properties were taken from the data provided in [15] according to the experimental tests conducted at the University of Pavia [16]. Further details on the adopted infill modelling may be found in [7].

4.2 Calibration of the number of modes of vibration

The load vector applied in the D-DAP is evaluated from the envelope of the modal drifts at each storey. In this regard, it is well recognized that the higher the mode of vibration, the least its contribution to the total seismic response. In order to select the number of modes actually significant for the analysed frames, the seismic response of the case study frames has been evaluated by the D-DAP including an increasing number of modes. For each frame, the number of modes of vibration ranged from 1 to the total number of participating modes, equal to the number of storeys. The final step of each analysis has been set at a target top displacement equal to the 5% of the total height of the frame.

For the sake of simplicity, Figure 3 shows the results of the analysis conducted on frame type GL-1 and SR-1, with 3 and 9 storeys, with and without infills. The seismic responses of

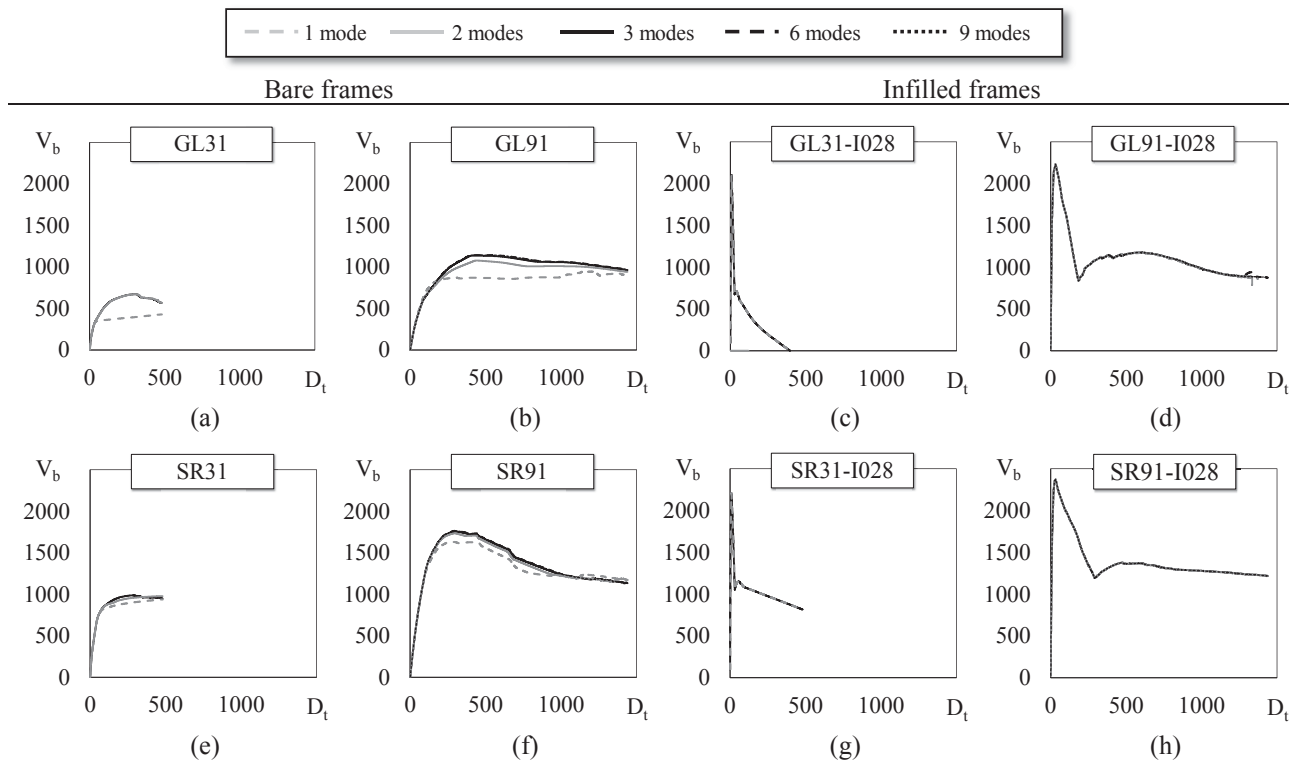


Figure 3 –Analysis of significant modes of vibration for frame (a) GL31, (b) GL91, (c) GL31-I028, (d) GL91-I028 (e) SR31, (f) SR91, (g) SR31-I028, (h) SR91-I028

the considered bare frames (Figures (a), (b), (e) and (f)) show that for a fixed value of the top displacement the influence of the higher modes of vibration leads to a larger base shear. In particular, this tendency becomes more significant when the number of storeys increases. Indeed, when the structure yields, the first mode of vibration becomes very flexible and its period increases. As a consequence, the contribution of the first mode to displacements becomes progressively more significant, while its contribution to the internal forces reduces and tends to be negligible. On the contrary, higher modes of vibration are less influenced by yielding of the structure. Thus, although the structure has already yielded, higher modes still contribute to the internal forces of the structure. This means that when the contribution of higher modes of vibration is taken into account, the base shear of the structure keeps increasing even after yielding of the structure. In particular, for the considered bare frames, the contribution of the second and third modes of vibration is actually significant, while higher modes of vibration become negligible. If infill panels are included in the frame (Figures (c), (d), (g), (h)), the first mode of vibration is predominant regardless of the number of storeys, and the contribution of higher modes of vibration becomes negligible. Based on the previous considerations, it is sufficient to include three modes of vibration when the D-DAP is applied to RC framed structures with or without infill panels

4.3 Calibration of the displacement step size

Another crucial choice is the value of the increment of displacement within the loading step Δ_{step} . In order to select the most appropriate step size, the frames have been analysed by the D-DAP with gradually reduced displacement step sizes. Three values of displacement step size have been considered: 10, 1 and 0.1 mm. Figure 4 shows the results of the analysis conducted for frames GL-1 and SR-1, with 3 and 9 storeys, with and without infill panels. When the step size is 10 mm, sometimes the analysis stops before the target displacement (5% of the total height of the frame) is reached, or fails at the very beginning. A value of $\Delta_{step} = 1$ mm

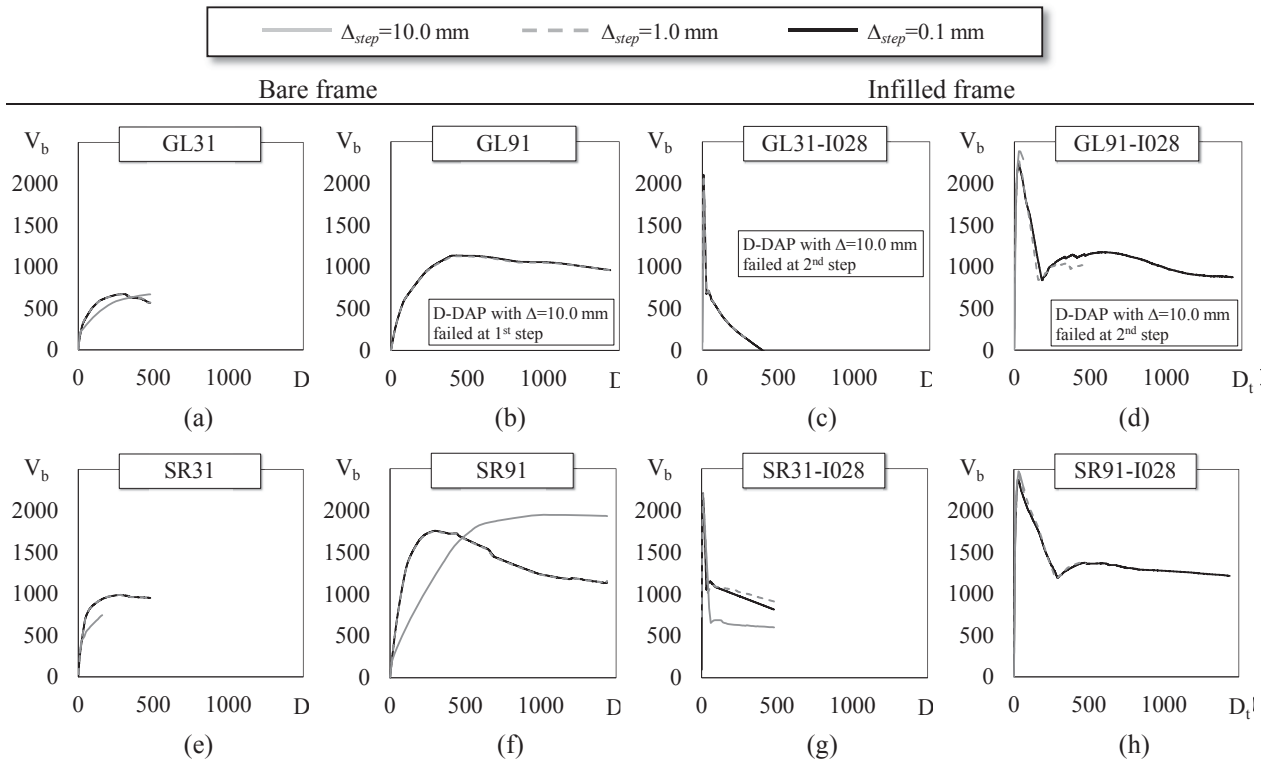


Figure 4 –Analysis of incremental step size for frame (a) GL31, (b) GL91, (c) GL31-I028, (d) GL91-I028 (e) SR31, (f) SR91, (g) SR31-I028, (h) SR91-I028

avoids the untimely failure of the analysis, especially in the case of infilled frames (Figure (c), (d), (g), (h)) whereby the analysis with larger Δ_{step} stopped right after the attainment of the maximum strength of infills. Furthermore, the prediction of the seismic response provided by the D-DAP with $\Delta_{step} = 1$ mm is significantly different from that obtained with $\Delta_{step} = 10$ mm, as showed in Figure 5 (a), (d), (e), (f), (g). No significant changes in the prediction of the seismic response were observed when the step size has been further reduced to 0.1 mm. Since the tendency noted in the shown frames has been essentially observed in all other analysed frames, a value of $\Delta_{step} = 1$ mm could be considered appropriate. However, since the D-DAP with $\Delta_{step} = 1$ mm in very few cases failed slightly before the target displacement was reached, for the sake of accuracy the displacement step size has been assumed equal to 0.1 mm.

4.4 Calibration of the equivalent damping law

The total equivalent viscous damping ratio is the summation of the inherent viscous damping in the elastic range ξ_0 , and the viscous damping ξ_{hyst} due to the hysteretic behavior [17, 18]. The damping ratio due to the hysteretic behaviour ξ_{hyst} (hysteretic damping) is generally assumed as a function of the ductility demand μ , according to the following form:

$$\xi_{hyst} = \xi_{\infty} \left(1 - \frac{1}{\mu^{\alpha_1}} \right) \quad (7)$$

whereby ξ_{∞} represents the asymptotic value that the hysteretic damping reaches for infinite values of ductility demand, and α_1 is a constant usually assumed equal to 0.5 or 1. Here α_1 is taken equal to 1.

The goal of the numerical calibration is the determination of the asymptotic damping ξ_{∞} that is appropriate for the structural types under investigation. To this end, the average drift Δ_m , defined as the summation of drifts at all storeys divided by the total number of storeys, is assumed as the reference parameter of the numerical calibration. Incremental Dynamic Analyses (IDA) are conducted for every case study frame, for PGAs increasing from 0.02 g to 2 g, in steps of 0.02 g. A set of ten artificial ground motions (EC8-Part 1 [19]), compatible with the EC8 elastic spectrum for soil type C and characterized by 5% damping ratio and reference PGA for soil type A equal to 0.35 g, is adopted as reference seismic input. The accelerograms were generated by SIMQKE computer program [20] so that the mean spectrum in terms of acceleration is compatible with the response spectrum proposed by EC8 in Appendix A. For every level of seismic excitation and for each of the 10 ground motions, the maximum value during the time history of the average drift Δ_m is calculated. Then, the mean value of the average drift Δ_m over the 10 ground motions is calculated for each PGA. The value of Δ_m is calculated also at each step of the D-DAP analysis. Thus, every average drift Δ_m corresponds to a value of peak ground acceleration PGA determined by the D-DAP with an elastic response spectrum with fixed 5% damping. Generally, for a fixed Δ_m , the D-DAP with 5% damping underestimates the values of PGA provided by the IDA. Hence, the PGA evaluated by the D-DAP has to be corrected with an appropriate damping ratio. Thus, for every relevant frame, the optimal hysteretic damping ξ_{∞} is calculated as the value that minimizes the summation of the squares of the differences between the PGAs by D-DAP and that by IDA. For every case study frame, the optimization process led to a different value of optimal ξ_{∞} .

In the second part of the calibration, the optimal values of ξ_{∞} obtained for every frame were plotted as a function of different parameters. Out of the considered parameters, the fundamental period T_1 showed the most significant influence on the value of ξ_{∞} . In particular, in the case of very stiff structures the values of ξ_{∞} tend to increase with T_1 (Figure 5a). This ten-

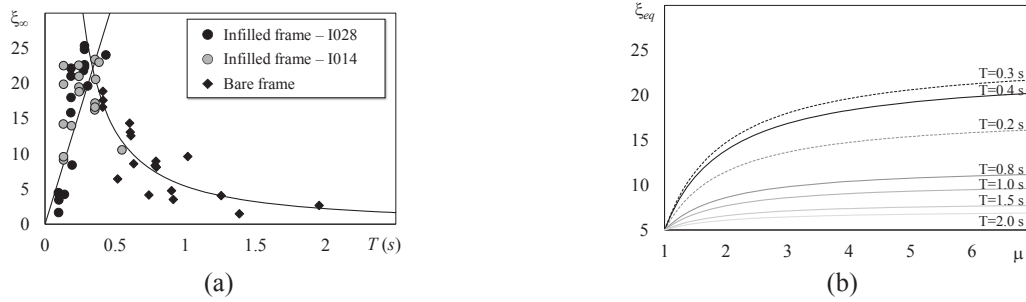


Figure 5 – (a) Relation between the optimized ξ_∞ and the fundamental period T for every case study frame; (b) Equivalent damping evaluated by the proposed law plotted for fixed value of T_1

endency is demonstrated by almost all the infilled case study frames, whose fundamental periods is smaller than 0.4 s (grey and black dots). This tendency is inverted for larger T_1 , and the values of ξ_∞ tend to decrease. This trend is exhibited by all the analysed bare frames (black diamonds). In fact, the lack of infill panels strongly reduces the stiffness of bare structures, which have fundamental periods ranging from 0.40 to 1.95 s. Only two infilled frames fall in this region, and they are frame GL91-I028 and GL91-I014 with T_1 equal to 0.433 and 0.548 s, respectively. Based on these results, the asymptotic damping ratio ξ_∞ can be reasonably expressed as a function of the fundamental period of the structure.

To propose an equation for the evaluation of the asymptotic damping ξ_∞ , the domain $\xi_\infty - T_1$ has been divided into two regions. For low fundamental periods, the relation between ξ_∞ and T_1 could be approximated by a linear function, whilst for larger fundamental periods it could be approximated by a hyperbolic function. The linear equation has been calibrated by minimizing the sum of the square deviations of values of ξ_∞ determined by numerical analyses and by the proposed equation for frames whose fundamental period was lower than 0.40 s. Instead, the hyperbolic function has been calibrated by minimizing the sum of the square deviations of values of ξ_∞ in the case of frames with fundamental period higher than 0.40 s. Hence, given a period T_1 , the value of ξ_∞ to be assumed is the minimum between the values provided by the linear and the hyperbolic equation, as expressed in the following function:

$$\xi_\infty = \min \left(65T_1; \frac{5.4}{T_1^{1.3}} \right) \quad (8)$$

The intersection between the two functions occurs for a period of vibration equal to 0.34 s. In Figure 5(a) Equation 8 is plotted with the continuous black line. It can be seen that the calibrated function approximates with a good accuracy the tendency of the values of ξ_∞ . Finally, the equation of the proposed equivalent viscous damping ratio is:

$$\xi_{eq} = \xi_0 + \min \left(65T_1; \frac{5.4}{T_1^{1.3}} \right) \left(1 - \frac{1}{\mu} \right) \quad (9)$$

Figure 5 (b) plots the proposed equation of ξ_{eq} as function of the ductility demand μ . Each curve displays the results obtained for a different value of T_1 . Regardless of T_1 , the equivalent viscous damping ratio increases with the ductility demand μ . However, when the ductility demand becomes larger, the rate of increase of ξ_{eq} becomes smaller, and the equivalent viscous damping tends towards the asymptotic value $\xi_0 + \xi_\infty(T_1)$.

5 ANALYSIS OF THE RESULTS

To validate the calibrated D-DAP, IDA was run to assess the seismic response of each case

study frame. To this end, the numerical model described in Section 4.1 was subjected to the set of 10 ground motions introduced in Section 4.4. The PGA in IDA was increased in step of 0.02 g until the 5% of storey drift is attained at one of the storeys. For every PGA and for each ground motions, the maximum values during the time history of the following Engineering Demand Parameters (EDP) are evaluated: maximum top displacement D_t , maximum base shear V_b , maximum drift at each i -th storey Δ_i and the maximum average drift Δ_m . The mean over the values of the 10 ground motions is calculated for each EDP and are assumed as the benchmark to evaluate the accuracy of the calibrated D-DAP.

For the evaluation of the seismic response at local level, three limit states were considered in the IDA, i.e. the attainment of a maximum storey drift equal to 1%, 2% and 4%, which correspond to the attainment of the Immediate Occupancy (IO) limit state, the Life Safety (LS)

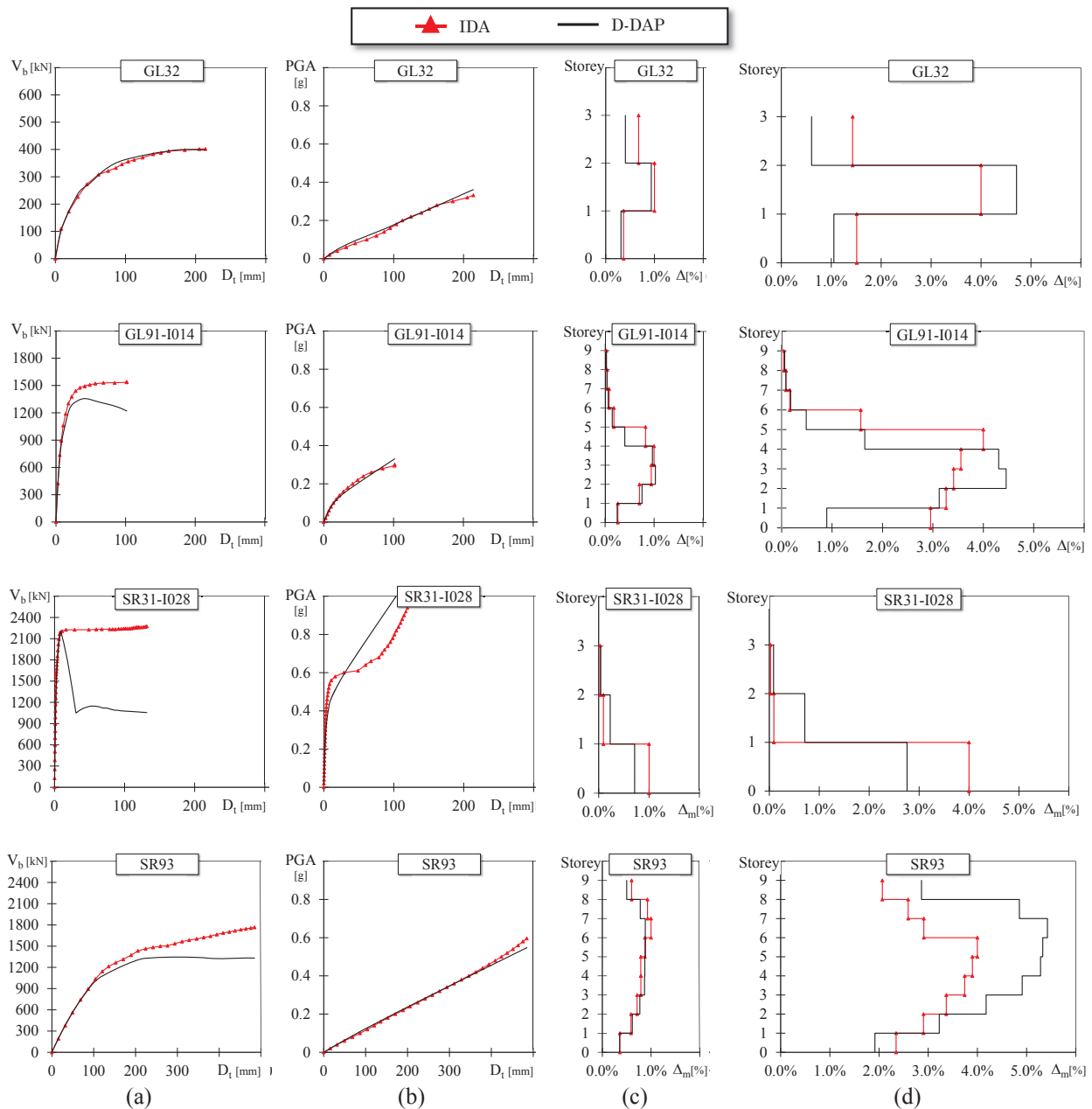


Figure 6 – Seismic performance of frames GL32, GL91-I014, SR31-I028 and SR93 in terms of (a) V_b - D_t , (b) PGA- D_t , (c) distribution of drifts corresponding to the PGA leading to 1% maximum drift in the ID, (d) distribution of drifts corresponding to the PGA leading to 4% maximum drift in the IDA.

limit state and the Near Collapse (NC) limit state, respectively. Given the PGA corresponding to the attainment of the considered limit state in the IDA, the corresponding distribution of storey drift has been evaluated by the D-DAP. For the sake of simplicity, the results are here presented for four significant frames. To cover the widest possible range of behaviour, the four selected frames included frames with 3 and 9 storeys, with large, medium and low gravity loads resting on beams, with and without infills. The frames thus picked are: GL32, GL91-014, SR31-028 and SR91.

The first column of Figure 6 shows the seismic response of the considered frames in terms of V_b-D_t . It can be observed that the D-DAP provides an accurate estimate of the seismic behaviour of the considered bare frames (plots in first and last row of Figure 6). In those cases, the maximum base shear increases with the top displacement, and the D-DAP follows the trend of the IDA, with an error lower than the 18%. In the case of infilled frames, an almost constant branch is observed in the V_b-D_t curve determined by the IDA. This upper value of the base shear is due to the fact that for every PGA the maximum base shear is recorded in the IDA. Thus, once the infills have cracked, the displacement keeps increasing while the maximum base shear maintains almost the same value. This constant branch represents an upper limit for the base shear and is here interpreted as the ultimate lateral strength of the frame. The D-DAP estimates accurately the elastic behaviour predicted by the IDA and provides an abrupt reduction of the base shear force right after the cracking of the infills. Indeed, for such degrading structures, the D-DAP evaluates the maximum resistance with an error lower than 15%. In the second columns of Figure 6, the PGAs associated to the displacement demands by the D-DAP are compared to the values predicted by the IDA. It can be observed that the D-DAP leads to an accurate prediction of the displacement demand regardless of the presence of infill panels.

Eventually, Figure 6 shows the distribution of storey drifts along the height for two of the considered limit cases, i.e. 1% storey drift (column c) and 4% storey drift (column d), respectively. At 1% limit state, the D-DAP estimates the maximum storey drift with an error lower than 5% for GL91-I014 and 35% for SR31-I028. For medium and large storey drifts (i.e. 2% and 4% limit state), the prediction of storey drifts of the IDA obtained by the proposed D-DAP still has an acceptable level of accuracy for the bare frames. Particularly, in the case of infilled frames, the error committed by the D-DAP in evaluating the maximum drift is lower than 12% and 31% for frame GL91-I014 and SR31-I028, respectively.

Even though it is not shown in figure, given the PGA corresponding to the 4% limit state in the IDA, the D-DAP predicted the average drift Δ_m with less than 10% of error for frame GL32. For frame SR93 the error reached a value around 35%. In the case of infilled frames, the error committed by the D-DAP is lower than 14% and 20% for frame SR31-I028 and GL91-I014, respectively. The tendency showed by those cases study can be found generally in all the other case study frames.

6 CONCLUSIONS

The research developed in three steps. First, the parameters ruling the operations of the D-DAP, i.e. The number of modes to be enveloped in the loading vector and the size of the displacement increment, were calibrated. To this end, two analyses were conducted and for the considered frames it was found that (i) the contribution of the modes of vibration higher than the third one is negligible and (ii) a displacement increment of 0.1 mm has to be assigned at each step to get accurate results for all the considered frames at reasonable computational cost. Afterwards, a new damping law was formulated by an optimization process that minimizes the differences between the results provided by the D-DAP and those obtained by the IDA.

The new equivalent damping law is a function of both the ductility demand and the fundamental period of vibration. According to the proposed equation, for very stiff structures, the value of ξ_{eq}

is linearly dependent from T_1 . Instead, for more flexible structures, the relation between ξ_{eq} and T_1 is hyperbolic. The effectiveness of the proposed D-DAP with the proposed damping law is investigated and the following conclusions can be drawn:

- As for the seismic response in terms of V_b-D_t , the D-DAP with the proposed damping law predicted the maximum base shear with an error on average equal to 20% for bare frames, and 15% for infilled frames. The seismic response in terms of a_g-D_t was predicted accurately by proposed D-DAP, as well.
- The proposed D-DAP predicted the average drift at 4% limit state of infilled frames with an error lower than 20%.

REFERENCES

- [1] S.A. Freeman, J.P. Nicoletti, J.V. Tyrell, Evaluations of existing buildings for seismic risk – A case study of Puget Sound Naval Shipyard, Bremerton, Washington, in proceedings of *1st U.S. National Conf. on Earthquake Engineering*, Earthquake Engineering Research Institute, Berkeley, 13-122, 1975.
- [2] P. Fajfar, Capacity spectrum method based on inelastic demand spectra, *Earthquake Engineering and Structural Dynamics*, **28**: 979-993, 1999.
- [3] S. Antoniou, R. Pinho, Development and verification of a displacement – based adaptive pushover procedures, *Journal of Earthquake Engineering*, **8**: 643-661, 2004.
- [4] R. Monteiro R, C. Casarotti, Using the adaptive capacity spectrum method for seismic assessment of irregular frames, In proceedings of the *5th European workshop on the seismic behaviour of irregular and complex structures*, Catania, Italy, 2008.
- [5] A. Gherzi, P. Lenza, M. Pellicchia, Uno sviluppo Multimodale ed adattivo del metodo N1 per la verifica ed il progetto delle strutture intelaiate in c.a. *15th ANIDIS Conference*, Padova, Italy. (in Italian) 2013
- [6] P. Lenza, A. Gherzi, E. M. Marino, M. Pellicchia, A multimodal adaptive evolution of the N1 method for assessment and design of RC framed structures, *Earthquake and Structures*, **12**, 2017.
- [7] F. Barbagallo, M. Bosco, A. Gherzi, E. M. Marino, An overdamped multimodal adaptive nonlinear static procedure for seismic assessment of infilled r.c. buildings. *Engineering Structures*, **229**, 2021.
- [8] Italian Ministry of Public Works: Ministry Decree, 30/05/1974, Technical regulations for constructions with reinforced concrete, prestressed concrete and steel structure, Gazzetta Ufficiale Serie generale, 29/07/1974, Rome. (in Italian)
- [9] Royal Decree n. 2229, 16/11/1939, Regulations for constructions of concrete and reinforced concrete. Supplemento Gazzetta Ufficiale n. 92, 18/04/1940, Rome. (in Italian)
- [10] Italian Ministry of Public Works: Ministry Decree, 16/01/1996, Regulations for constructions in seismic areas, Gazzetta Ufficiale Serie generale, 5/02/1996, Rome. (in Italian)
- [11] S. Mazzoni, F. McKenna, M. H. Scott, G. L. Fenves, B. Jeremic, OpenSees command Language Manual, *Pacific Earthquake Engineering Research Center*, University of California at Berkeley, USA, 2003.
- [12] J.B. Mander, M.J.N. Priestley, R. Park, Theoretical stress strain model for confined concrete Journal of Structural Engineering ASCE, **114**:1804-1825, 1988
- [13] F. Barbagallo, M. Bosco, E. M. Marino, P.P. Rossi, On the fibre modelling of beams in RC framed buildings with rigid diaphragm, *Bulletin of earthquake engineering*, **18**:189–210, 2020
- [14] T. B. Panagiotakos, M.N. Fardis, Seismic response of infilled RC frame structures, in proceedings of the *11th world conference on earthquake engineering*, 1996.
- [15] D. Celarec, P. Ricci, M. Dolšek, The sensitivity of seismic response parameters to the uncertain modelling variables of masonry-infilled reinforced concrete frames, *Engineering Structures*, **35**, 165-177, 2012

- [16] M. Calvi, S. Santini, Preliminary tests in infill masonry, PREC8 Progress Report, University of Pavia, Department of structural mechanics, Pavia, 1994
- [17] C.A. Blandon, M.J.N. Priestley, Equivalent viscous damping equations for direct displacement based design, *Journal of earthquake engineering*, **9**: 257-278, 2005
- [18] M.J.N. Priestley, 2003, Myths and fallacies in earthquake engineering, *The Mallet Milne Lecture*, IUSS Press, Pavia, Italy.
- [19] CEN. Eurocode 8: Design of structures for earthquake resistance - Part 1: Design of seismic resisting buildings, EN 1998-1. European Committee for Standardization: Bruxelles, Belgium, 2005.
- [20] SIMQKE. A program for artificial motion generation, User's manual and documentation, Department of Civil Engineering MIT, 1976.

CYCLIC TESTING OF 1:40 SCALE CANTILEVER RC ELEMENTS WITH DIGITALLY MANUFACTURED REINFORCEMENT

Lorenzo Del Giudice¹, Rafal Wrobel², Antonios Katsamakas¹, Christian Leinenbach²,
and Michalis Vassiliou²

¹ ETH Zurich, Swiss Federal Institute of Technology
Institute of Structural Engineering (IBK)
Stefano-Franscini-Platz 5, CH-8093 Zurich
{delgiudice, katsamakas, vassiliou}@ibk.baug.ethz.ch

² EMPA, Swiss Laboratories for Material Science and Technology
Überlandstrasse 129, CH-8600 Dübendorf
{rafal.wrobel, christian.leinenbach}@empa.ch

Abstract

Time history analysis is considered as the state-of-the-art in modeling of the seismic response of RC structures. Its validation involves predicting the response of an RC structure tested on a shaking table. However, blind prediction contests show that most contestants fail to predict the seismic response of the tested specimens. Given that numerical models are able to accurately capture the behavior of RC members at a component level, we can conclude that a large part of the error sources from the assumptions made to pass from component level to system level, i.e. assumptions related to damping formulation, component interaction, boundary conditions etc. In parallel, the prediction of the response of a structure subjected to a single ground motion has been proven to be too strict of a validation procedure. Oftentimes, a statistical approach involving many specimens and ground motions is necessary. Such an approach is clearly only feasible at a very small scale. At such scales, the reinforcement fabrication and positioning become major issues. We propose to use additive manufacturing technology to digitally fabricate the reinforcement cage necessary for the micro RC element.

This paper presents the results from cyclic tests on 1:40 scale RC cantilever columns. The reinforcing cages were manufactured using a Selective Laser Melting 3D printer that was able to print rebars with submillimeter diameter and yield strength 378MPa. Two different micro-concrete mixtures were used based on cement and gypsum. Each sample was reinforced with 18 longitudinal rebars of 0.6mm diameter, and 0.35mm stirrups with 2.5mm of spacing. The cyclic behavior of the columns closely resembles the behavior of full-scale columns indicating that such small-scale specimens can be used of the statistical validation of global level assumptions that numerical models make.

Keywords: 3D Printing, Physical Modeling, Earthquake Engineering, Cyclic Test, Micro Reinforced Concrete.

1 INTRODUCTION

Non-linear time history analysis is considered to be the state-of-the-art of structural modeling in earthquake engineering. Its most widespread validation procedure consists of predicting the response of an RC structure tested on a shaking table. However, blind prediction contests show that the contestants fail to predict the response of the tested specimens with reasonable accuracy, even for structures much simpler than the ones constructed in practice, and even when the structural properties and measured excitation are given to the contestants [1-4].

In order to better understand where the error sources from, one can break down the problem into 3 levels: Material, Component, and System Level. In fact, given the behavior at each level, the engineer makes certain assumptions to level-up. For instance, for given material properties the engineer uses a set of assumption, such as beam theory, the interaction of rebars, concrete etc., to reach the component level cyclic behavior. Then, using another set of assumptions (boundary conditions, interaction of components, damping model, numerical integration scheme) we reach system-level dynamic behavior. Blind prediction contests on component level cyclic behavior prove that structural models perform relatively well at this level [5, 6]. It is the system level behavior that they fail to predict. Therefore, it is reasonable to assume that one main source of error in the structural models at system-level lies in the assumptions made to scale up from component-level cyclic to system-level dynamic behavior. Hence, these need to be improved and, to this end, more system-level tests are needed.

In parallel, it has been claimed that the appropriate way to validate models in earthquake engineering is to perform multiple tests of virgin specimens under the different ground motions that represent the hazard in a given site and to demand that the structural models predict the Cumulative Distribution Function (CDF) of the maxima of the response quantity of interest. This approach has been investigated by Bachmann et al. [7, 8] who have used this statistical validation procedure on the 1963 Housner dynamic response model of an uplifting structure. They performed 600 shaking table tests as well as 600 numerical simulations and they compared both individual test responses and the statistical aggregates of these responses (empirical CDF of the maximum tilt angle). They showed that the 1963 Housner passed the statistical validation test even though it failed the one-to-one validation test. This statistical approach, is not a “good to have”, but often a necessity given the often not discussed non-repeatability of many tests.

Extending the statistical validation to validate the system-level assumptions of RC structures is not trivial since it would require multiple virgin specimens to be tested on a shaking table. This is cost- and time- wise not viable in full scale. To address this problem we suggest performing the statistical validation carrying out multiple tests with small-scale (1:40) specimens in a geotechnical centrifuge. The validation concerns only the system-level assumptions for given and experimentally determined component level behavior. We have also suggested the same method for masonry structures [9].

Reduced scale models of piles and walls are often used in geotechnical engineering to study soil structure interaction, although using different materials. Knappett et al. 2011 [10] and Loli et al. 2014 [11] developed a micro reinforced concrete to study a rocking isolated RC bridge pier at 1:40 scale. Although their results are encouraging, the manufacturing of the RC elements showed three limitations: the construction time, the accuracy in positioning the reinforcement, and the size limitation of the steel rebars and stirrups. These limitations can be overcome by using a metal 3D printer to manufacture the reinforcement [12]. The use of a metal 3D printer allows manufacturing of the entire reinforcement cage (longitudinal and horizontal reinforcement) with the desired layout. Moreover, these machines can print rebars as small as 200 μ m, which in scale 1:40 correspond to 8mm.

This paper aims at characterizing the flexural behavior of 1:40 scale RC columns by means of full-reversed quasi-static cyclic tests. Two cantilever specimens were constructed using two different types of micro-concrete. One sample was manufactured with cement-based micro-concrete (named HSC), and another with a gypsum based micro-concrete (HSG). The tests were designed according to FEMA-461 [13] and a 3D digital image correlation system was used to analyze the strain field during the tests.

2 MATERIALS AND METHODS

The flexural behavior of micro RC components is investigated performing quasi-static cyclic tests on two small-scale (1:40) micro RC columns. The specimens consist of 2 cantilever elements of 15x15mm cross section and 52.5mm span, with a 65x65x20mm base that functions as a footing (Figure 1). Both samples have the same reinforcement, i.e. 18 rebars of 0.6mm diameter with 0.35mm stirrups with 2.5mm spacing, and a concrete cover of 1.64mm. They differ from each other in terms of the type of micro-concrete used. The HSC Sample (“C” stands for cement) was manufactured using cement based micro-concrete, whereas sample HSG (“G” stands for gypsum) was manufactured with gypsum based micro-concrete. The experiments were performed with a setup that was installed in a Universal Testing Machine (UTM). The measurement system consisted of LVDTs and a 3D-DIC (Digital Image Correlation) system. The latter allowed for the analysis of the displacement and the strain field during the tests.

2.1 Experimental Setup

A fully reversed cyclic loading was applied at the top of the samples. The elements were placed horizontally and fixed on a steel support designed to fit in the UTM and to align the samples to the center of the machine (Figure 2).

The base of specimens was fixed to the lateral support with 4 M6 bolts. A 2mm steel plate was placed between the bolts and the face of the base to avoid local crushing of the concrete due to compressive force applied by the screws. The load is applied at the centerline of the element by two loading pins, which are connected to the double-hinged fork (Figure 2). The latter transfers the vertical load applied by the UTM. The measuring devices consist of 2 LVTD and a 3D-DIC system. The first LVDT measures the vertical displacement at the application point of the load, namely the loading pins shown in Figure 2, the second LVDT measures the vertical displacement of the base of the element (to measure any possible sliding of the base). The DIC was used to measure the displacements and the strain field at the surface. By measuring the strain distribution, we are able to identify any cracks and micro-cracks formed during the tests as well as to locate the plastic hinges that formed at the base on the element.

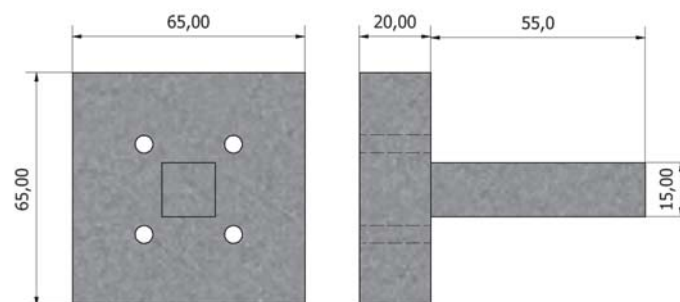


Figure 1. Specimen geometry and dimensions.

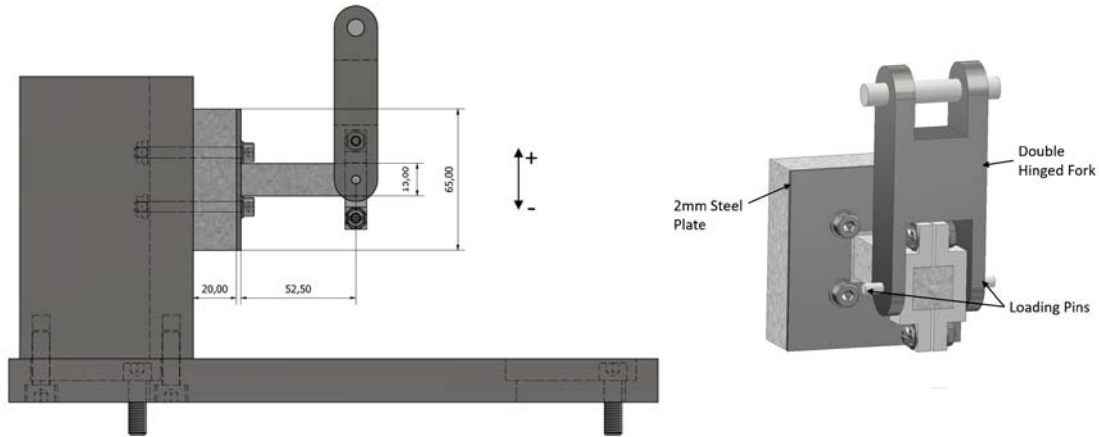


Figure 2. Experimental setup and detail of the loading apparatus.

2.2 Loading Protocol

The load is applied by displacement control, applying a displacement Δ at the top of the elements. Nonetheless, the kinematic parameter that is used to define the loading protocol is the drift ratio φ , which is defined as the ratio between the top displacement and the element length $l_v = 52.5\text{mm}$ (in this case it also represents the shear length).

The test program is defined based on FEMA-461, in which the amplitude increase is defined as $\varphi_{n+1} = 1.4 * \varphi_n$. However, to capture the behavior of the element in the elastic range, the first amplitude was set equal to $0.5 * \varphi_y$ and the second one was set to the yield drift, φ_y (Figure 3). The yield drift was calculated for specimen HSC and HSG using a fiber model in Opensees [14]. The micro-concrete was modelled with a Concrete02 constitutive model whereas the 3D printed steel was modeled using Steel02 model. Both material models were calibrated on uniaxial test results that we performed.

The velocity of application of the load was selected considering two principles. First, the displacement needs to be as slow as possible to neglect any inertia effect and to minimize any strain rate effect. Second, the loading rate needs to be reasonably fast to avoid creep and to make the test feasible time-wise. On these premises we started by defining a strain-rate range $\dot{\epsilon} = 10^{-5} - 10^{-4} \text{sec}^{-1}$. This strain refers to the outermost fiber of the cross section of the column that lies closer to the foundation. The lower end of the strain-rate range corresponds to a displacement rate of the top of the column equal to 0.075mm/min , which was used for the first three amplitudes of the loading protocol. For the subsequent four amplitudes, the displacement rate was set to 0.413mm/min , which corresponds to a strain rate of $5.6 \times 10^{-5} \text{sec}^{-1}$. Finally, the last cycles were applied with a displacement rate of 0.75mm/min , corresponding to the upper limit of the aforementioned strain rate range.

2.3 3D Printed Reinforcement

The use of a 3D printer allows manufacturing of the entire reinforcement cage, namely the longitudinal and shear reinforcement, with the designed layout. The rebars size is not constrained by the manufacturing method. Depending on the 3D printer, we can print rebars as small as 0.20mm ($200\mu\text{m}$), which in the prototype scale (1:40) represent $\Phi 8$ rebars.

In our study, we used a ConceptLaser M2 Laser Powder Bed Fusion (LPBF) printer. It is able to manufacture various types of metal. For our study, we used gas-atomized stainless steel 316L powder with a grain size $15-45 \mu\text{m}$.

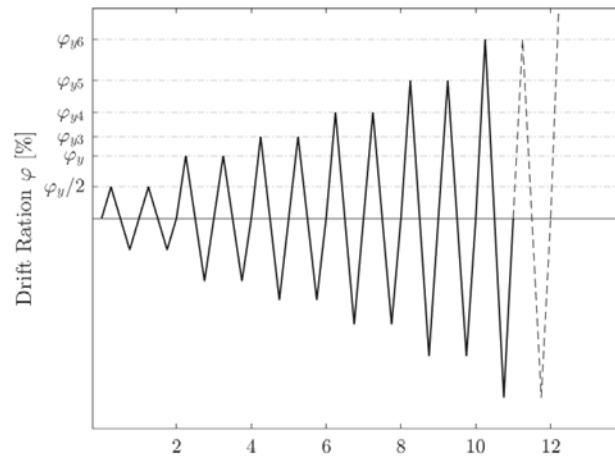


Figure 3. Loading protocol in terms of drift ratio φ .

We tested specimens with a longitudinal reinforcement ratio $\rho_l = 3.7\%$ and a shear reinforcement ratio $\rho_w = 0.9\%$. The reinforcement layout consists of 18 bars of 0.6mm, and 0.35mm diameter stirrups with a 2.5mm of spacing. In addition, the longitudinal bars were linked with shear ties as shown in Figure 4.

All rebars were printed with ribs on the surface to increase bonding with concrete. In addition, the 3D printed steel has a roughness R_a value of 15-20 μm , hence it has an inherent roughness that is beneficial for the steel-concrete bonding.

The mechanical properties of the 3D printed steel were characterized with a series on uniaxial tension tests performed on 0.6mm diameter bars identical to the ones used as reinforcement in the micro RC samples. Due to the small cross-section, we used a sensor arm extensometer, instead of strain gauges, with a gauge length on 30mm to measure the strains during the tests. The resulting average yield strength f_y was 378MPa, the average maximum strength $f_{s,max}$ was 430MPa, and the average Young's Modulus E_s was equal to 180GPa. These values are in line with those reported by Casati et al. 2018 [15] for 3D printed Stainless steel 316L.

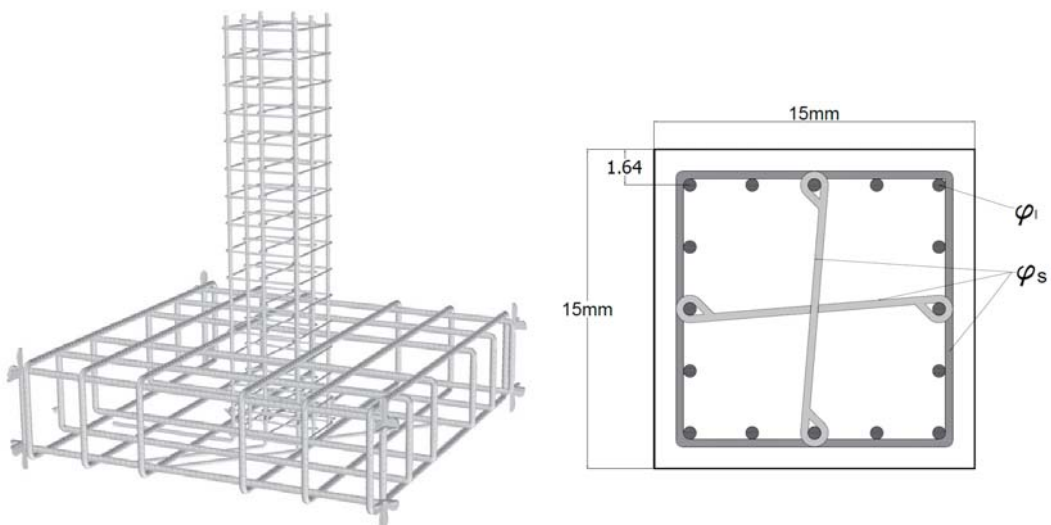


Figure 4. Left: 3D model of the 3D printed reinforcement. Right: Cross section and reinforcement layout.

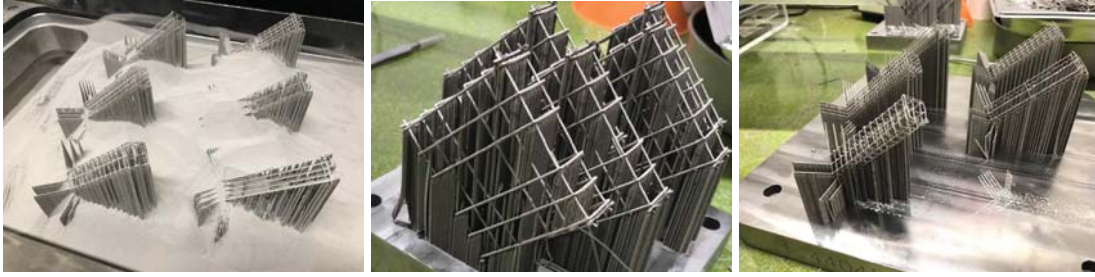


Figure 5. Left: 3D printer Jobbox. Center: Reinforcement cage after the printing process. Right: Footing reinforcement after the printing process.

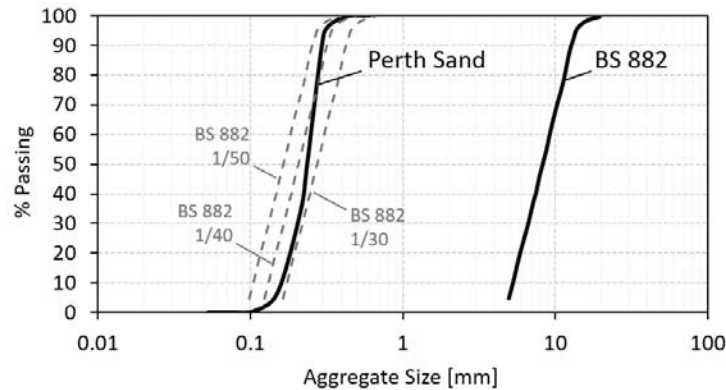


Figure 6. Passing distribution of the sand used for the micro-concrete.

2.4 Micro Concrete

Due to the small scale of the specimens, it is necessary to scale the inert component of the concrete so that the ratio inert size / rebars / cross section is about the same as in the real scale. We used Perth silica sand with a $d_{50} = 0.23\text{mm}$. Its grain distribution compares very well to the typical aggregate size when scaled 40 times (see Figure 6). Moreover, a different binding agent was studied, alongside the more common cement, i.e. gypsum. The use of gypsum to manufacture micro concrete models is not new, in fact, both Knappett et al. 2011 [10], and Harris et al. 1999 [16] suggest using gypsum to accelerate the curing time and consequently speeding up the specimen manufacturing. Gypsum takes around 48 hours to reach the full strength compared to the usual 28 days for concrete, hence the manufacturing of several specimens for the statistical validation would become considerably faster.

The concrete based micro-concrete used in sample HSC comprises a mixture of cement Normo52.5R, Perth sand, and water. The other mixture, i.e. gypsum based micro-concrete used in HSG, was made of alpha-formed gypsum based plaster (Saint-Gobain Hartform 1) instead on cement. The ratio binding component / sand / water was $1 / 1 / 0.5$ and $1 / 1 / 0.6$ for cement and gypsum based mix respectively. The mix designs were chosen to minimize the water percentage while preserving a good workability and flowability of mixture.

The mechanical properties of both types of micro-concrete were investigated through a series of uniaxial compression tests on cylindrical specimens of 20mm diameter and 50 mm height, and several 4 point bending tests performed on prisms specimens with cross section 15 by 15mm and length of 80mm. Table 1 presents the mean values of the compressive strength f_c , the strain at the maximum load ε_1 , the Young's modulus E_c , and the modulus of rupture f_{ct} .

Micro Concrete	f_c [MPa]	ε_1 [%]	f_{ct} [MPa]	E_c [MPa]
Cement	34.5	1.2	3.40	2089.0
Gypsum	18.5	0.9	7.20	1109.9

Table 1. Mechanical properties of micro-concrete.

3 RESULTS

3.1 Cyclic Tests

The lateral force-displacement loops (P- Δ) for specimens HSC and HSG are shown in Figures 7 and 8, respectively. The failure load is conventionally defined as a strength degradation up to 85% of the peak load.

Specimen HSC exhibits a maximum shear load $F_{max} = 172.80\text{N}$ at a drift ratio $\varphi_{F_{max}} = 1.47\%$ and an ultimate strength $F_{0.85} = 146.80\text{N}$ at a drift ratio $\varphi_{0.85} = 3.0\%$. Yielding occurred at a shear load $F_y = 115.60\text{N}$ at a yield drift ratio $\varphi_y = 0.82\%$. Visual inspection of the sample did not show diffuse cracking on any of the surfaces. Nonetheless, the horizontal strain distribution at peak load, measured with 3D-DIC system, shows tensile strains along the span of the elements HSC (Figure 7, right) that suggest that micro cracks formed during the tests. Regardless of the micro cracks, a localized crack at the base of the element followed by the fracture of the outer longitudinal rebars are to be considered as the causes of failure; no other failure mechanisms could be observed, i.e. concrete spalling.

Specimen HSG reached a maximum load $F_{max} = 184.20\text{N}$ at a drift $\varphi_{F_{max}} = 4.76\%$ and ultimate strength $F_{0.85} = 156.57\text{N}$ at a drift ratio $\varphi_{0.85} = 7.65\%$. The load at yielding F_y was equal to 157.40N at a yield drift ratio φ_y of 1.58% . The hysteresis loop in Figure 8 shows a clear pinching behavior, unlike the loop of the HSG sample. The strain distribution at peak load did not show concentrated tensile strains anywhere along the specimen unlike what was observed in specimen HSC. The tensile strains concentrated at the base of the element. This confirms what was observed visually, namely that the failure was caused by a localized crack at the base. Similarly to HSC, in specimen HSG no concrete spalling was observed. Comparing the two results, the sample with cement based micro-concrete resulted in a stiffer and less ductile behavior than the sample with gypsum based micro-concrete. Moreover, cracks are more diffused in the HSC micro RC specimen.

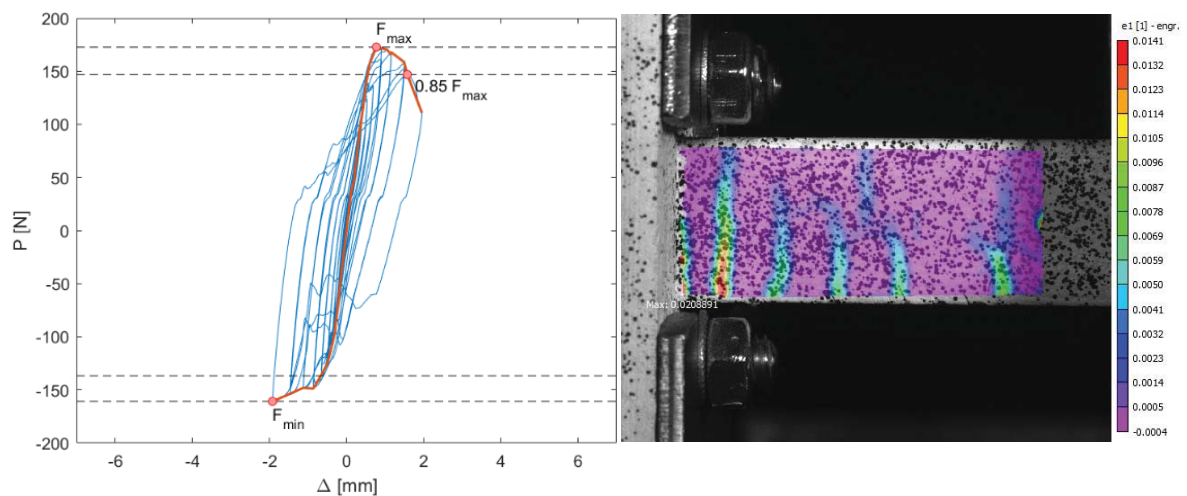


Figure 7. Left: HSC Hysteresis loop and backbone curve. Right: Horizontal strain field at maximum load.

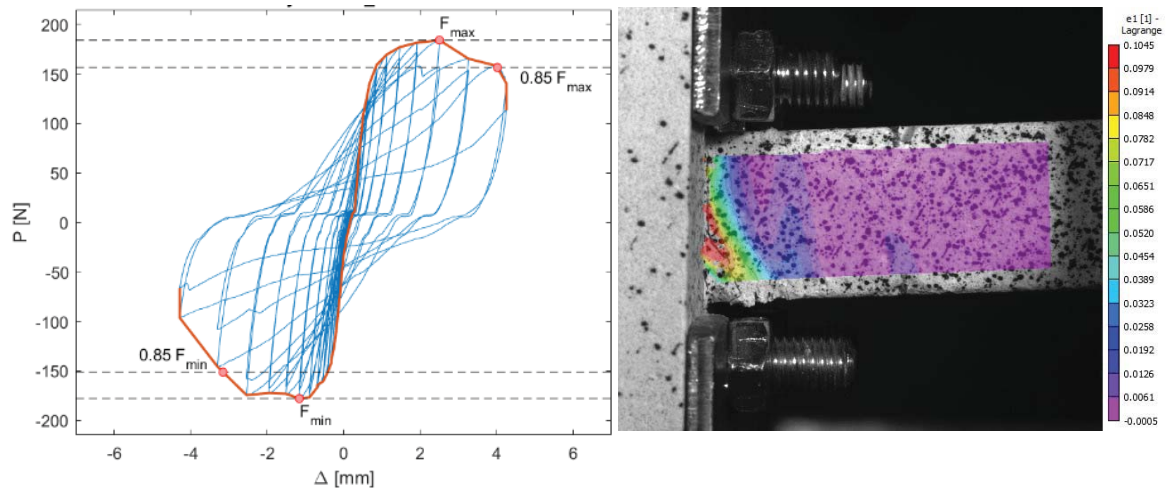


Figure 8. Left: HSG Hysteresis loop and backbone curve. Right: Horizontal strain field at maximum load.

Parameter	Value
f_y	378 [MPa]
E_s	180 [GPa]
b_s	0.004
ϵ_{lim}	0.09

Table 2. Steel02 parameters used in the Opensees model.

Specimen	f_c [MPa]	ϵ_1	f_{cc} [MPa]	ϵ_{cc}	f_{ccu} [MPa]
HSC	34.5	0.012	43.16	0.027	42.64
HSG	185	0.009	26.81	0.029	21.24

Table 3. Concrete02 parameters used in the Opensees model. The properties f_{cc} , ϵ_{cc} , and f_{ccu} refer to the confined concrete of the section core.

3.2 Numerical Model

Numerical models of the cyclic tests were implemented in Opensees, and the results were compared against the experimental curves. The specimens were modelled as cantilever beams with a fixed support. This assumption was confirmed by the DIC measurements that showed no rotation at the connection of the elements with their footings. The reinforcement was modeled using the OpenseesnSteel02 model, and the strain at failure ϵ_{lim} was modeled using the MinMax model. The parameters used are summarized in Table 2.

The Opensees model used for concrete is Concrete 02 with different parameter values for the core and the cover material. The latter was calibrated based on the material level tests on the small-scale specimens, whereas the core concrete properties were calculated using Mander's model [16]. The model parameters are summarized in Table 3.

Figure 9 (left) shows the comparison between the experimental and numerical results of the HSC specimen. The numerical simulation is able to capture the maximum load measured during the test, as well as the strength degradation of the post elastic behavior. The stiffness degradation in the numerical curve is also remarkably similar to the experimental curve. On the other end, the numerical simulation of specimen HSG (see Figure 9, right) fails to capture key values, such as the peak load, the strength degradation, and most of all the stiffness degradation. In fact, the simulation does not show any pinching behavior unlike the experimental curve of HSG.

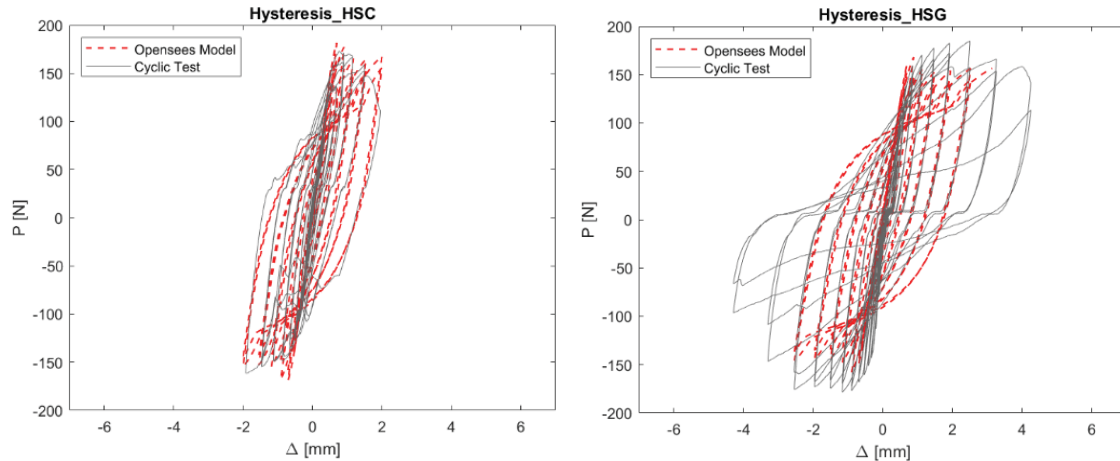


Figure 9. Comparison between experimental curves and Opensees models.

4 CONCLUSION

Additively manufactured reinforcement allows the production on multiple small-scale reinforced concrete specimens. The tested elements show a flexural behavior, which is similar to full size prototype RC structural members. Cement based micro-concrete has a compressive and tensile strength similar to concrete, unlike gypsum based micro-concrete that has a tensile strength substantially higher than concrete. Moreover, the numerical simulations in the case of specimen HSC (cement base micro-concrete) are able to accurately capture the experimental behavior. The numerical model of specimen HSG does not match the behavior observed experimentally, as it could not capture neither the peak strength nor the pinching behavior of the tested specimen. Further component level tests are required to fully characterize the flexural behavior of micro RC specimens. Nonetheless, it seems feasible to produce small-scale models of a full structure to perform dynamic tests in a geotechnical centrifuge. The shake table tests could provide a dataset to statistically validate the assumptions that are usually made to scale up from component-level cyclic to system-level dynamic behavior.

REFERENCES

- [1] M. Schoettler, J. Restrepo, G. Guerrini, D. E. Duck, A full-scale, single-column bridge bent tested by shake-table excitation, 2012.
- [2] V. Terzic, M. J. Schoettler, J. I. Restrepo, S. A. Mahin, Concrete column blind prediction contest 2010: outcomes and observations, *PEER Report*, **1**, 1–145, 2015.
- [3] M. Panagiotou and J. I. Restrepo, Displacement-based method of analysis for regular reinforced-concrete wall buildings: Application to a full-scale 7-story building slice tested at UC–San Diego, *Journal of Structural Engineering*, **137**, no. 6, 677–690, 2011.
- [4] M. Panagiotou, J. I. Restrepo, and J. P. Conte, Shake-table test of a full-scale 7-story building slice. Phase I: Rectangular wall, *Journal of Structural Engineering*, **137**, no. 6, 691–704, 2011.
- [5] M. Trüb, Numerical modeling of high performance fiber reinforced cementitious composites, *IBK Bericht*, vol. 333, 2011.
- [6] X. Lin and X. Lu, Numerical Models to Predict the Collapse Behavior of RC Columns and Frames, *The Open Civil Engineering Journal*, **11**, no. 1, 2017.

- [7] J. A. Bachmann, M. Strand, M. F. Vassiliou, M. Broccardo, and B. Stojadinović, Is rocking motion predictable?, *Earthquake Engineering & Structural Dynamics*, **47**, no. 2, 535–552, 2018, doi:10.1002/eqe.2978.
- [8] J. Bachmann, M. Strand, M. F. Vassiliou, M. Broccardo, B. Stojadinovic, Modelling of rocking structures: Are our models good enough? *2nd International Conference on Natural Hazards & Infrastructure (ICONHIC 2019)*, Chania, Crete, Greece, June 23-26, 2019.
- [9] Del Giudice, L., Vassiliou, M. F. Mechanical properties of 3D printed material with binder jet technology and potential applications of additive manufacturing in seismic testing of structures. *Additive Manufacturing*, **36**, 101714, 2020.
- [10] J. A. Knappett, C. Reid, S. Kinmond, K. O'Reilly, Small-scale modeling of reinforced concrete structural elements for use in a geotechnical centrifuge, *Journal of Structural Engineering*, **137**, no. 11, 1263–1271, 2011.
- [11] M. Loli, J. A. Knappett, M. J. Brown, I. Anastasopoulos, G. Gazetas, Centrifuge modeling of rocking-isolated inelastic RC bridge piers, *Earthquake engineering & structural dynamics*, **43**, no. 15, 2341–2359, 2014.
- [12] Del Giudice, L., Wrobel, R., Leinenbach, C., and Vassiliou, M. F. Static testing of additively manufactured microreinforced concrete specimens for statistical structural model validation at a small scale. *8th International Conference on Advances in Experimental Structural Engineering (8AESE)*, Christchurch, New Zealand, February 3-5. 2020.
- [13] FEMA, A. 461/Interim Testing Protocols for Determining the Seismic Performance Characteristics of Structural and Nonstructural Components. Applied Technology Council, Redwood City, CA, 113. 2007
- [14] Mazzoni, S., McKenna, F., Scott, M. H., Fenves, G. L. OpenSees command language manual. *Pacific Earthquake Engineering Research (PEER) Center*, **264**, 2006.
- [15] R. Casati, J. Lemke, M. Vedani, Microstructure and fracture behavior of 316L austenitic stainless steel produced by selective laser melting, *Journal of Materials Science & Technology*, **32**, no. 8, 738–744, 2016.
- [16] Harris, H. G., Sabnis, G. *Structural modeling and experimental techniques*. CRC press, 1999.
- [17] J. B. Mander, M. J. N. Priestley, R. Park, Theoretical stress-strain model for confined concrete, *Journal of structural engineering*, **114**, no. 8, 1804–1826, 1988.

R/C COLUMN MODELING USING ANSYS AND LOADING RATE AND MESH METHOD INFLUENCE STUDIES

Theodora P. Mitkou¹, Theodoros A. Chrysanidis¹

¹ International Hellenic University
P.O. Box 141, P.C. 57400, Sindos, Thessaloniki, Greece
cie20140082@cie.teithe.gr, theodoros_gr@yahoo.com

Abstract

Many times, either the research engineer or the design engineer needs to model reinforced concrete (R/C) structural elements in order to study their behavior. In the present research work, an attempt is made to study the correct way of modeling a reinforced concrete column using the finite element ANSYS software. Three-dimensional finite elements are used to model the column. The results of the column modeling and analysis using ANSYS software are compared with the corresponding experimental results of a column with the same geometric characteristics and the same material and load properties as those of the analytical modeling. The only difference between the analytical column modeling and the experimental specimen is the difference in the loading rate. The analytical and experimental results are compared with each other. The influence of the loading rate as well as the mesh method is examined. Useful conclusions are drawn regarding the influence of the loading rate and the mesh method on the behavior and results of reinforced concrete components.

Keywords: Column, Reinforced Concrete, Ansys, FEM, Loading Rate, Mesh Methods

1 INTRODUCTION

The rapid growth of technology and the development of the computer, favored the development of theories and computational methods adapted to the capabilities of the computer, in order to solve, yet, unsolved problems in the field of engineering. The most common arithmetic method developed is the Finite Element Method, a numerical approximation method that has the ability to solve complex problems, expressed in the form of differential equations [1]. The basic concept of the Finite Element Method is the ability to represent an area as a set of distinct subareas [2].

As mentioned by Daryl [3], the idea of the Finite Element Method was first presented in the publications of Turner, Clough, Martin and Topp (1956), taking data from research by Courant (1943) [4], Hrenikoff (1941) [5] and McHenry (1943) [6], however, due to the complexity of the arithmetic operations they contained and the lack of computational power of the time, they did not prosper. The official presentation of the Finite Element Method with its current form, took place in the period 1954-60 in the publication of J. Argiris et.al. [7, 8], while the term "Finite Element" was used for the first time in the late 1960s by Clough [9].

In recent years, with the rise of supercomputers and the creation of finite element software run in Windows OS environment, the method has become widely known and accessible, even to the average user, enabling the numerical solution of complex problems while minimizing the need for extensive experimental testing, due to the increased reliability of the method. The most important advantage of the method is that it allows the engineer to see how the product will behave and to point out any mistakes that have been made so far, before proceeding to time-consuming and expensive processes of manufacturing and testing physical prototypes, achieving the early optimization of the product and at the same time, reducing both the time and the cost of studying the experimental process [3].

ANSYS is a general-purpose finite element software, which from the beginning of its creation, has been a pioneering program, with its use in various fields of Engineering [10]. Its analysis process includes the construction of the simplified simulation model, the generation of the finite element grid, the imposition of loads on the model and the solution process using differential equations [10]. The results are exported from the program in a legible way through graphs, tables and / or animations [10].

To investigate the reliability of ANSYS finite element software, the study and comparison of the behavior of a reinforced concrete column, which is subjected to uniaxial compressive load, in relation to the column of the experimental process conducted by Chrysanidis [11]. Chrysanidis in his experiment [11], deals with the study of parameters that affect the stability of seismic reinforced concrete walls, when they are subjected to cyclic loading. For the purposes of the experiment, 10 identical specimens were constructed, on a scale of 1:3, which simulated the edges of a wall, the only difference between the specimens being the increasing degree of elongation and the ratio of longitudinal reinforcement. The fabricated specimens are subjected to two loading cycles, with the first cycle subjecting the specimens to uniaxial tensile loading, with a low loading rate of 4 mm / min, and then, in the second loading cycle, the specimens being gradually subjected to uniaxial compressive loading with a low loading rate of 1 mm / min, until their failure. Based on the experimental process, useful conclusions were drawn about the factors that affect the lateral buckling of the specimens. It has to be noted the fact that other experiments have taken place in the international bibliography concerning the behavior of reinforced concrete columns from various researchers [12]–[23].

In the present research work, a comparison is made between the experimental results of the specimen L-0 and the results of the specimens L-0-A and L-0-B, which are obtained through simulations using ANSYS software. It must be noted that the specimen L-0 characterized as a

‘virgin specimen’ having a degree of elongation equal to 0‰ and a longitudinal reinforcement ratio equal to 1.79%. Also, the experimental specimen has the same geometric characteristics, material and load properties as those of the analytical simulation. It is important to note that the experimental specimen was subjected to uniaxial compressive load with a low loading rate of 1 mm / min. The influence of the soil and its parameters have been neglected [24]–[31].

2 SIMULATION DESCRIPTION IN ANSYS

2.1 Specimens’ characteristics

Therefore, in order to compare the analytical with the experimental results of the L-0 test, as mentioned above, the simulation behavior of two specimens, which are called L-0-A and L-0-B, were studied. The noticeable difference between the two specimens is that the specimen L-0-A, consists only of the active region of the experimental specimen L-0. The active area of the specimen L-0 is the area of the specimen between the two steel blades (Figure 1). As a result, the dimensions of the specimen L-0-A were equal to 15 x 7.5 x 64 cm. Inside the specimen L-0-A are placed the transverse and longitudinal reinforcement, with the longitudinal reinforcement containing 4 reinforcing bars with a diameter of 8.0 mm and, at the same time, the transverse reinforcement contained ties with a diameter of 4.2 mm, which are placed with the distance between them being equal to 33 mm.

The specimen L-0-B consists of the integrated specimen L-0 with dimensions 15 x 7.5 x 76 cm, which at its ends has steel blades. It must be noted that the steel blades penetrate inside of the, so-called, “Shoe”. The “Shoe” is solid, in the form of a cube, in which the dimension of each side is equal to 20 cm and inside of it is placed a spiral with a diameter of 5.0 mm. Specifically, the total height of column of the specimen L-0-B is equal to 90 cm, although, its net height is equal to 76 cm, which is equal to the distance between the two cubes which are called as “Shoes”. Inside the specimen L-0-B are placed the transverse and longitudinal reinforcement, with the longitudinal reinforcement containing 4 reinforcing bars with a diameter of 8.0 mm and, at the same time, the transverse reinforcement contained ties with a diameter of 4.2 mm which are placed at distances equal to 33 mm.

Figure 1 shows the geometry of the experimental specimen L-0 [11] which forms the base of the simulations of specimens L-0-A and L-0-B. Table 1 shows the specimens’ characteristics which are required for the construction of the geometry of the specimens L-0-A and L-0-B. The geometry of the steel blades is not contained at Table 1, due to its complexity and as a result is presented in Figure 2. Table 2 shows the material properties for concrete which is used to make the “Shoe” and the column. Also, Table 3 shows the measured material properties for steel which is used for the longitudinal and transverse reinforcement, the spiral reinforcement and the steel blades [11].

2.1.1. Loading of specimens

The specimens L-0-A and L-0-B were strained under a uniaxial compressive load applied on the upper “Shoe” of each specimen vertically. The load application took place gradually till the resistance of each specimen reduced and the specimens failed. Despite of the experimental procedure, during which the specimen L-0 was strained at a low monotonic loading rate of 1 mm / min, at the analytical simulation, the compressive stress of the specimens is carried out at a high loading rate of 1 mm / sec. Based on that fact, conclusions are drawn, concerning the significant influence of the loading rate on the behavior of reinforced concrete structures. Table 4 shows the load values per time until the resistance of each specimen is greatly reduced and the specimen becomes unstable.

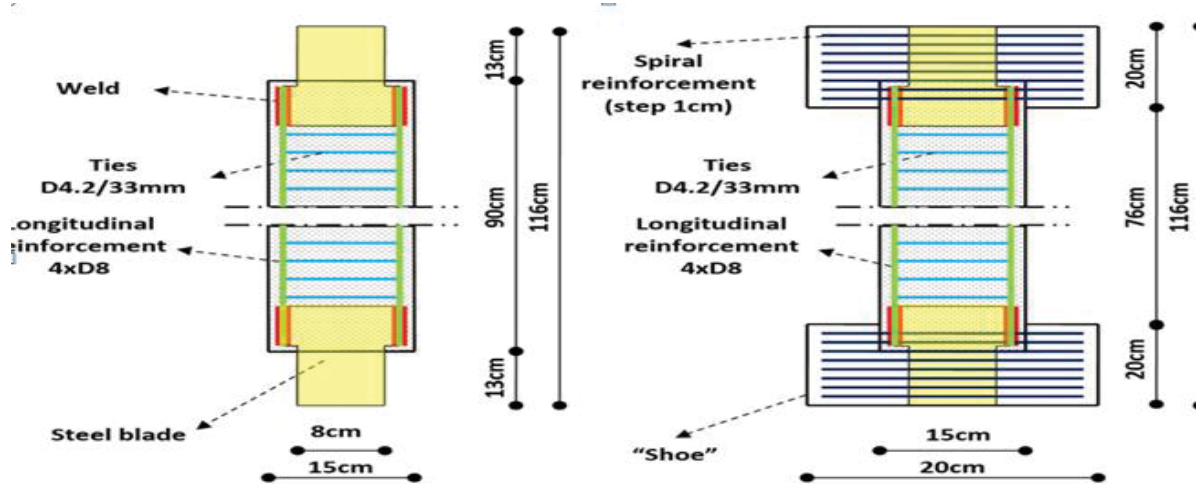
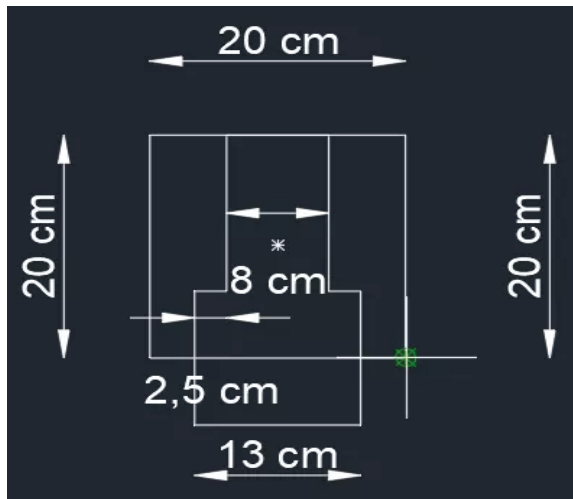
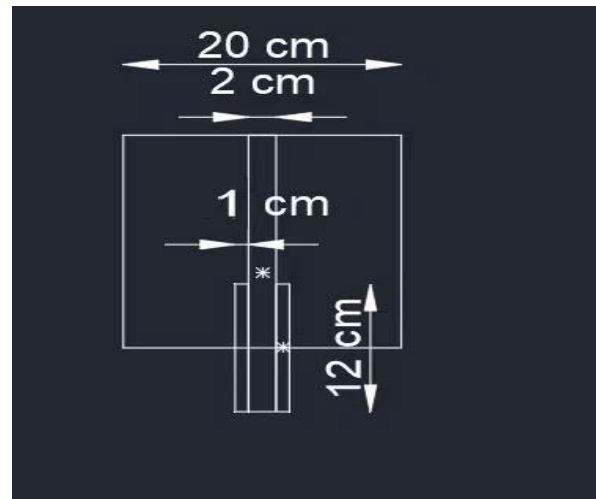


Figure 1: The geometry of the experimental specimen L-0.



(a)



(b)

Figure 2: (a) Face and (b) Side view of steel blade.

SPECIMEN	COLUMN (cm)	LONGITUDINAL REINFORCEMENT	TRANSVERSE REINFORCEMENT	SPIRAL	"SHOE" (cm)
L-0-A	15 x 7.5 x 64	4 x D8	D4.2@33 mm	-	-
L-0-B	15 x 7.5 x 76	4 x D8	D4.2@33 mm	D5/10 mm	20x20x20

Table 1: Specimens' characteristics.

PART	YOUNG'S MODULUS	POISSON'S RATIO	f_{ck}	DENSITY
COLUMN	29.84 GPa	$\nu = 0.20$	23.00 MPa	2306 kgr/m ³
“SHOE”	30.00 GPa	$\nu = 0.20$	54.02 MPa	-

Table 2: Concrete mechanical properties.

MATERIAL	YOUNG'S MODULUS	POISSON'S RATIO	ULTIMATE STRENGTH	YIELD STRESS
LONGITUDINAL REINFORCEMENT	200 GPa	$\nu = 0.30$	743.10 MPa	603.77 MPa
TRANSVERSE REINFORCEMENT	200 GPa	$\nu = 0.30$	674.01 MPa	674.01 MPa
SPIRAL REINFORCEMENT	200 GPa	$\nu = 0.30$	749.04 MPa	742.25 MPa
STEEL BLADE	200 GPa	$\nu = 0.30$	582.92 MPa	404.17 MPa

Table 3: Steel mechanical properties.

STEP (sec)	FORCE (kN)	STEP (sec)	FORCE (kN)
1	0	17	320
2	20	18	340
3	40	19	360
4	60	20	380
5	80	21	400
6	100	22	420
7	120	23	430
8	140	24	350
9	160	25	300
10	180	26	250
11	200	27	200
12	220	28	150
13	240	29	100
14	260	30	50
15	280	31	0
16	300		

Table 4: Compressive load values per step for analytical simulation.

2.2 Simulation of specimens

2.2.1. General

The analytical simulation took place in the educational version of the finite element software ANSYS 20.0. It is important to note that the educational version of ANSYS 20.0 is subject to restrictions. Firstly, the discretization of the specimens requires reducing the numerical number of finite elements until the numerical limit being equal to 32,000, even if the constructed grid is not considered appropriate by the general rules of technical metrics [32]. Furthermore, in the solution stage, the loading time is in seconds versus minutes of the experiment and, as a result, the loading being carried out at a high rate on the specimen. Finally, at the design stage is required to reduce the complexity of the specimen's geometry, which is achieved by making use of the symmetry of the specimen. It is noteworthy that the final restriction took place only during the simulation of the specimen L-0-B.

2.2.2. Specimen L-0-A

The specimen L-0-A is simulated via ANSYS 20.0 software and the Workbench subroutine. The first stage of the simulation was the construction of the geometry of the specimen L-0-A which is designed into the software via the SpaceClaim tab. The design process is started from the inside to the outside part of the geometry of the specimen L-0-A. The definition of materials and their properties are defined through the software library. It is noteworthy that the default library values for each of the materials used are modified only when they have been redefined, as shown in Tables 2 and 3, otherwise they remain the same. Figure 3 shows the specimen L-0-A.

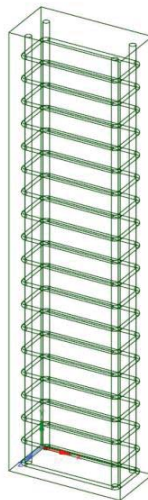


Figure 3: The specimen L-0-A.

The model is discretized via the Multizone Mesh Method by using a set of hexagonal finite elements to construct the grid, with the size of the finite elements being 14 mm. The suitability of the mesh is studied in terms of orthogonal quality, skewness, aspect ratio and element quality parameter, which according to the basic general guidelines for the construction of the mesh [32], the orthogonal quality and skewness parameter provided values within the desired limits even though the aspect ratio parameter did not. In particular, for the skewness parameter, its maximum value is equal to 0.39, while at the same time, the minimum value of the or-

thogonal quality parameter is maintained above 0.72. Nevertheless, the maximum value of the aspect ratio parameter is equal to 4.67.

Regarding the element quality parameter, all possible mesh methods are investigated for the specimen L-0-A, with the Multizone Mesh Method being preferred, which provided for the element quality parameter a minimum value equal to 0.32. On the other hand, the mesh, which is made via Automatic mesh method comprises a combination of hexahedral and tetrahedral elements, with the lowest value for the element quality parameter being 0.01. Moreover, the mesh, which is made via Tetrahedron Mesh Method using a set of tetrahedral elements provides for element quality parameter a minimum value equal to 0.02. It is recalled that, according to the general guidelines for the constructions of the mesh, the element quality parameter has a value range of 0-1, with the value 1 being the best [32].

Figure 4 shows the discretization of the specimen L-0-A via Multizone mesh method. Figure 5 shows the element quality parameter for the possible mesh methods. It is noteworthy that the Sweep and Hex Dominant mesh methods could not model the specimen L-0-A. As a result, the software exported the messages shown in Table 5. For simulation of the loads which the specimen L-0-A is subjected to, the categories of Support and Load are used. Therefore, the Fixed Support command is used by the Support category to define that the specimen is connected at the bottom to a rigid body [10]. At the same time, the loading of the specimen is defined using the Force command via the Load category. Thus, the force was applied vertically at the top of the specimen.

The current research work investigates the results of the stress, the deformation and the strain of the specimen L-0-A. It is noteworthy that for the investigation of the deformation is studied either the total deformation of the specimen L-0-A or the deformation to the horizontal and vertical axis.

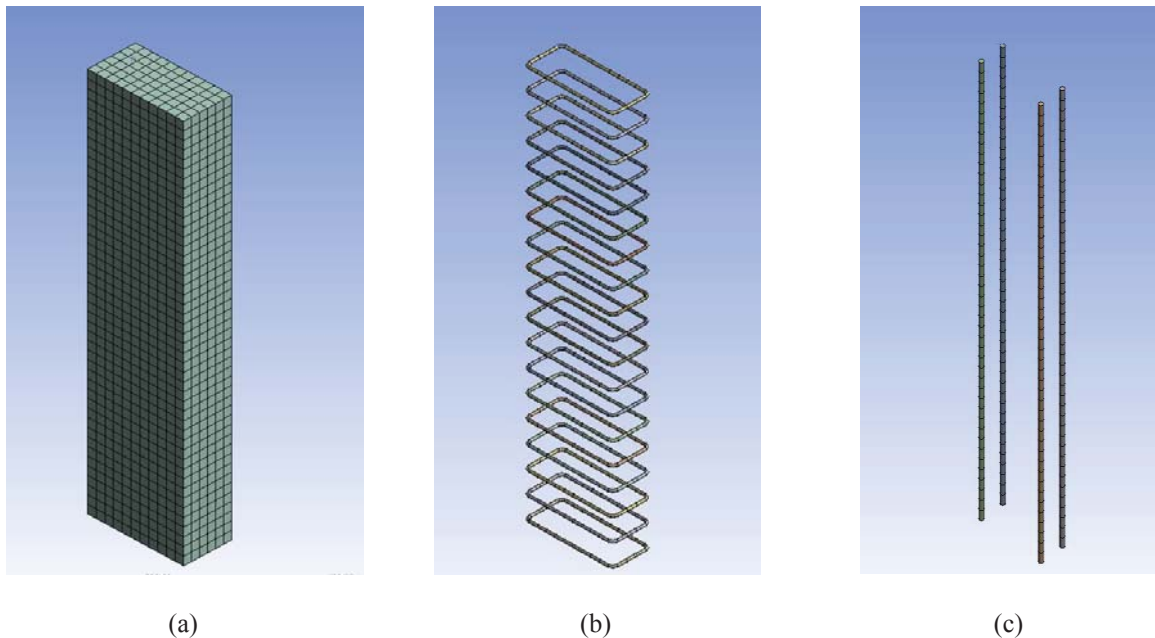


Figure 4: The mesh of the: (a) Concrete, (b) tie, (c) rebar.

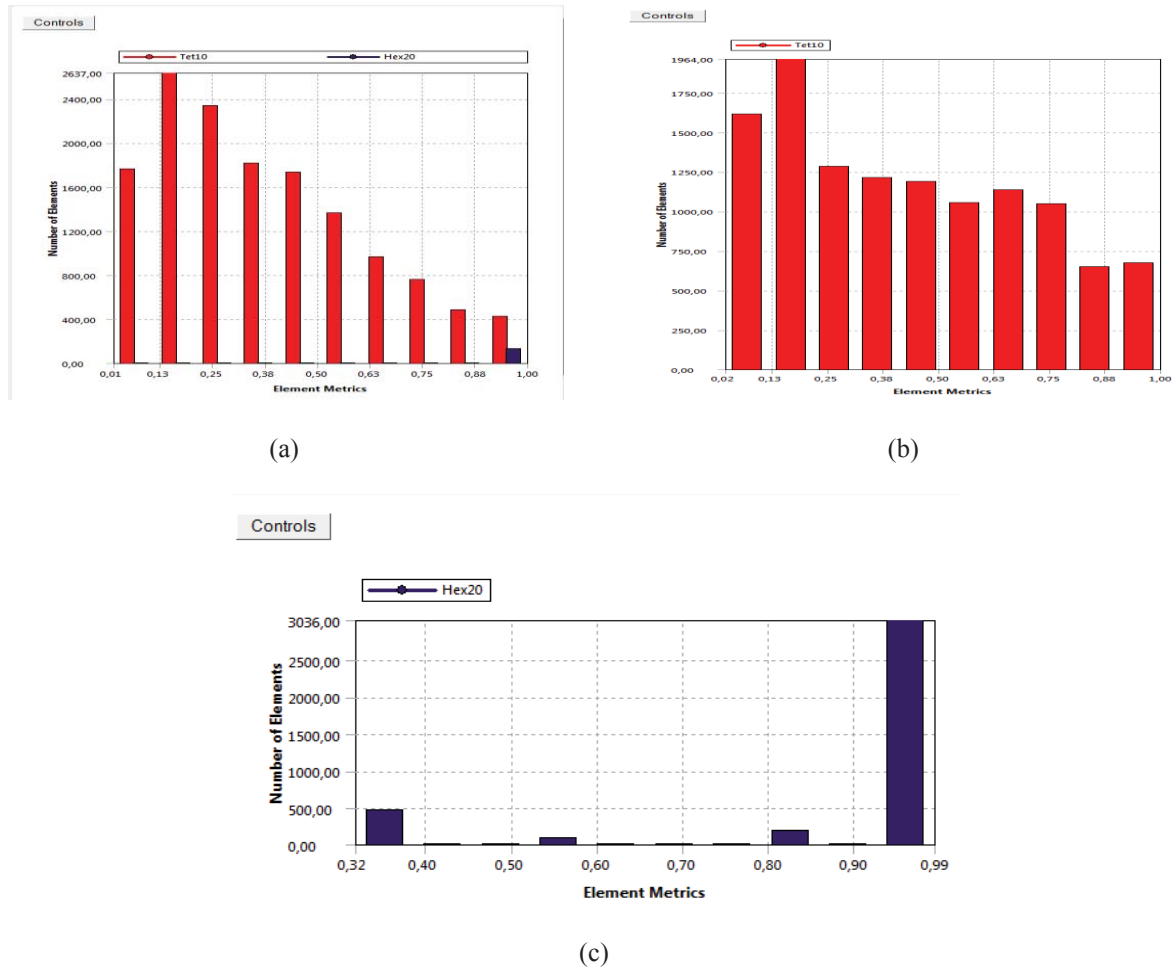


Figure 5: The element quality parameter for: (a) Automatic, (b) Tetrahedron, (c) Multizone Mesh Method.

Mesh Method	Simulation's messages of the specimen L-0-A
Sweep	1. Mesher failed to initialize.
	2. One or more non-sweepable bodies have sweep method controls and cannot be swept.
	3. The mesh generation did not complete due to poor quality elements or incorrect input. Please try meshing with another mesh method or different mesh options.
Hex Dominant	1. Mesher has failed to generate hex dominant mesh for one or more bodies. Try using a different mesh method.
	2. A mesh could not be generated using the current meshing options and settings.
	3. At least one body selected for hex dominant meshing has a small normalized volume to surface area ratio. The result may be a low percentage of hexs or poorly shaped elements.

Table 5: Non-completion messages about simulation of the specimen L-0-A.

2.2.3. Specimen L-0-B

The specimen L-0-B is simulated using ANSYS 20.0 finite element software and the Workbench subroutine. The first stage of modeling was the construction of the geometry of the specimen L-0-A like before, which is designed into the software through four stages via the SpaceClaim tab. The first stage involves the design of the geometry of the column, with the design process being similar to that of the specimen L-0-A, starting from the inside to the outside part of the geometry of the specimen L-0-B.

The second stage is the design process of the geometry of the “Shoe”, which is the same design sequence followed as in the first stage, including the design from the inside to the outside part of the geometry of the “Shoe”. Specifically, first of all, the geometry of the spiral reinforcement is designed, which is placed inside the “Shoe” and then, the “Shoe” cube that surrounds it. The third design stage includes the creation of the steel blades. As a fourth and final design step, the above steps are assembled to produce the specimen L-0-B.

It is noteworthy that due to the limitations of the educational version of ANSYS, which concern the complexity of the geometry of the specimen L-0-B, it is necessary to use the symmetry of the specimen L-0-B. Otherwise, the ties would probably have to be removed, which would not correspond to the geometric features of the specimen L-0. Figure 6 shows the specimen L-0-B.

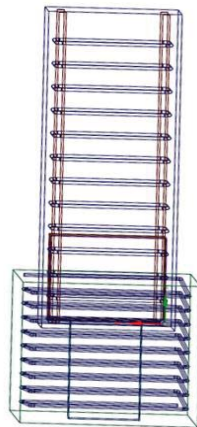


Figure 6: The specimen L-0-B.

The definition of L-0-B test materials and their properties are defined through the software library. It is noteworthy that the default library values for each of the materials used are modified only when redefined, as shown in Tables 2 and 3, otherwise they remain the same. The model is discretized using the Multizone Mesh Method, using a set of hexagonal finite elements to construct the mesh with the finite element size being equal to 18 mm.

The suitability of the mesh is studied in terms of orthogonal quality, skewness, aspect ratio and element quality parameters, which according to the basic general guidelines for the construction of the mesh [32], the orthogonal quality and skewness parameters provided values within the desired limits, even though the aspect ratio parameter did not. In particular, for the skewness parameter, its maximum value is equal to 0.39, while at the same time, the minimum value of the orthogonal quality parameter is maintained above 0.70. However, the maximum value of the aspect ratio parameter is equal to 5.60.

As far as the element quality category is concerned, all possible mesh methods for the L-0-B specimen are being investigated, with the Multizone method being deemed necessary, as no

other mesh method was possible due to the complexity of the model geometry and the small numerical limit on the number of finite elements of the mesh. Therefore, for the Multizone Mesh Method, the minimum value in the element quality parameter is 0.17. It is recalled that, according to the general guidelines for the creation of the grid, the element quality parameter has a value range from 0-1, with the value 1 indicating the perfect quality [32].

Figure 7 shows the discretization of the specimen L-0-B using Multizone mesh method. Figure 8 shows the element quality parameter for the Multizone mesh method. Table 6 shows the messages exported of the impossible discretization with the other mesh methods. Even if, for the Tetrahedron Mesh Method the software does not output any message, however, the specimen L-0-B could not be discretized according to the constraints, even when the finite element size is equal to 200 mm. For simulation of the forces which the specimen L-0-B is subjected to, the categories of Support and Load are used. Therefore, the Fixed Support command is used by the Support category to define that the specimen is connected at the bottom to a rigid body [10]. At the same time, the loading of the specimen is defined using the Force command via the Load category, thus, the force was applied vertically at the top of the specimen.

The current research work investigates also the results of the stress, the deformation and the strain of the specimen L-0-B. It is noteworthy that for the investigation of the deformation is studied either the total deformation of the specimen L-0-B or the deformation to the horizontal and vertical axis.

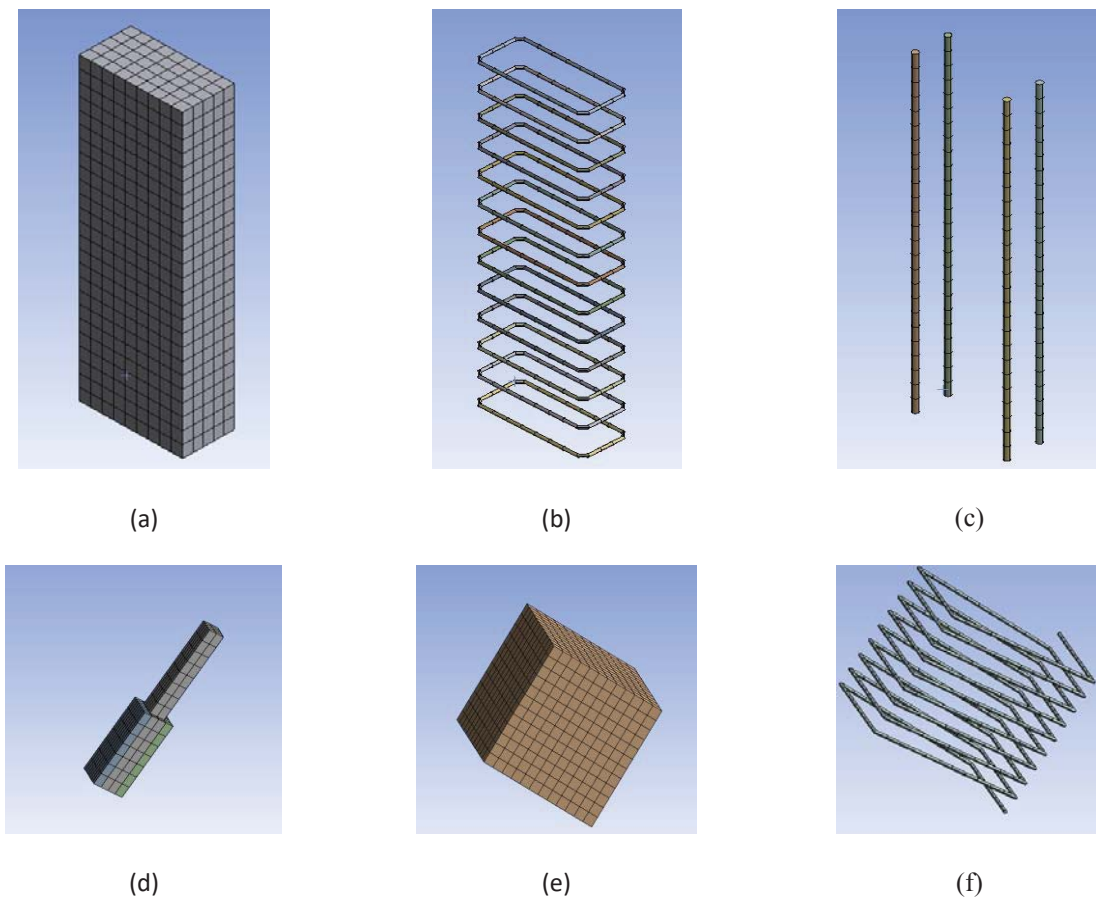


Figure 7: The mesh of specimen L-0-B: (a) Column, (b) Tie, (c) Rebar, (d) Steel Blade, (e) Stub, (f) Spiral.

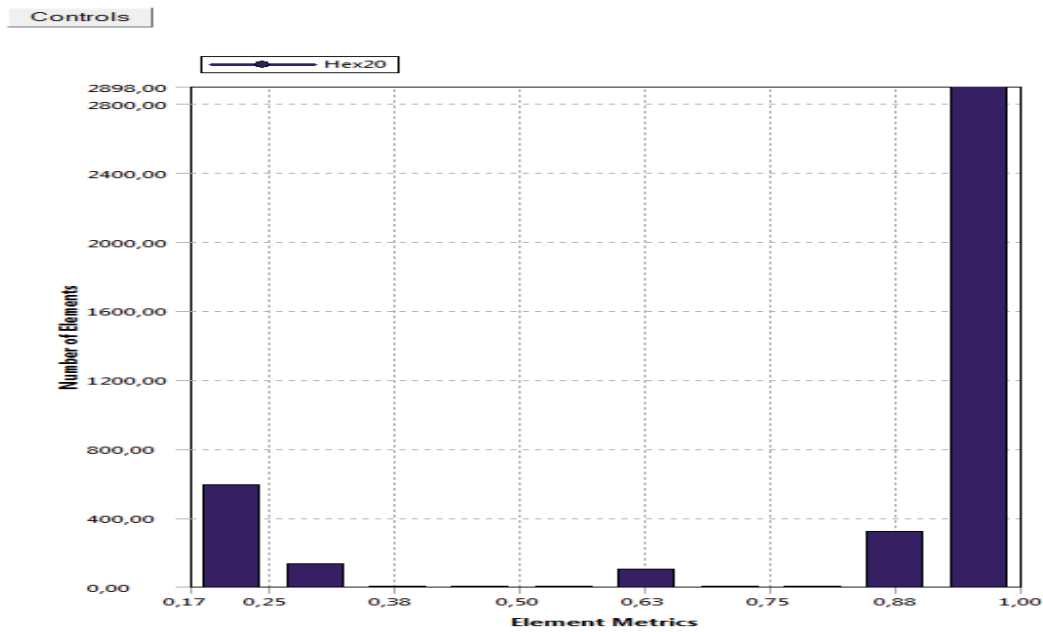


Figure 8: The technical measurement of element quality with the Multizone method for the L-0-B specimen.

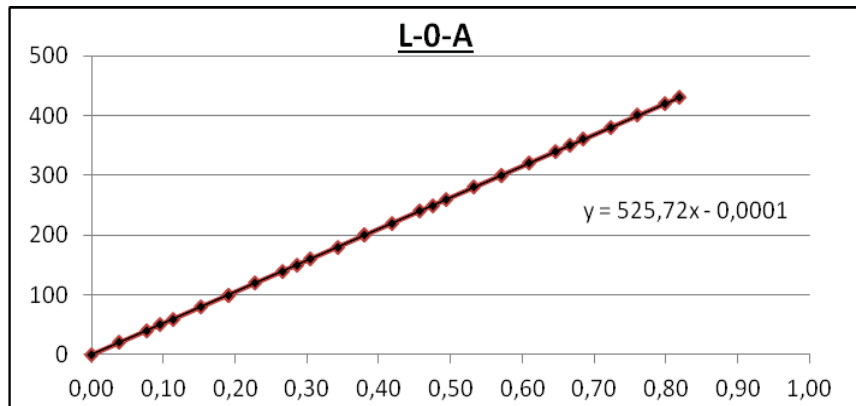
Mesh method	Simulation's messages for the specimen L-0-B
Automatic	<ol style="list-style-type: none"> 1. The source mesh cannot be correctly copied to the target surface. This might be because the surface is a closed surface with degenerate points. Splitting the surface might help.
Sweep	<ol style="list-style-type: none"> 1. An error occurred during sweeping meshing a face. Changing element sizing parameters might help. 2. The meshing failed due to quality checks. The mesh does not meet the specified Shape Checking constraints specified. Please look at the mesh quality and adjust meshing options or mesh sizes to obtain a better-quality mesh, or relax the shape check. 3. A mesh could not be generated using the current meshing options and settings.
Hex Dominant	<ol style="list-style-type: none"> 1. Mesher has failed to generate hex dominant mesh for one or more bodies. Try using a different mesh method. 2. A mesh could not be generated using the current meshing options and settings. 3. At least one body selected for hex dominant meshing has a small normalized volume to surface area ratio. The result may be a low percentage of hexs or poorly shaped elements.

Table 6: Non-completion messages for the modeling of specimen L-0-B.

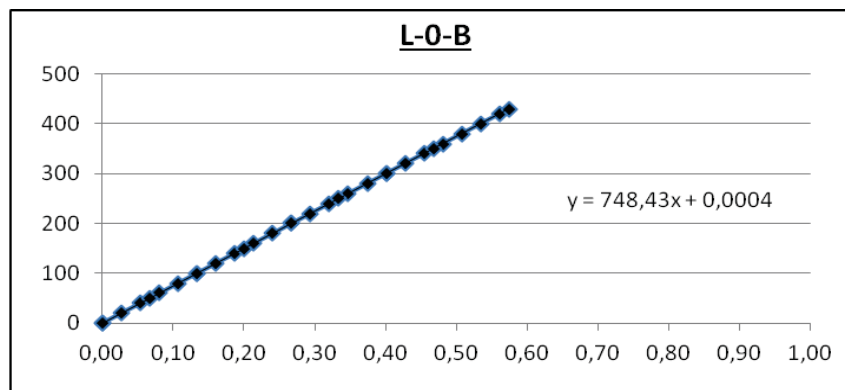
3 RESULTS

3.1 Analytical results

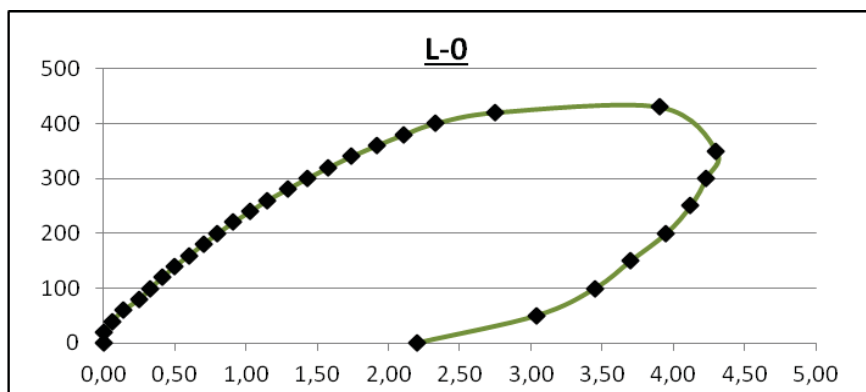
Figure 9 shows the Force-Deformation diagrams for the L-0-A, L-0-B and L-0 specimens. The deformation values were the deformation values of the specimens along the vertical axis.



(a)



(b)



(c)

Figure 9: Load-deformation diagrams for: (a) L-0-A specimen, (b) L-0-B specimen, (c) L-0 specimen.

Table 7 shows the analytical and experimental deformation results for the specimen L-0.

STEP (sec)	FORCE (kN)	L-0-A			L-0-B			L-0
		Total	y'y	x'x	Total	y'y	x'x	
1	0	0.00	0.00	0.00	0.00	0.00	0.00	0.00
2	20	0.00	0.04	0.00	0.00	0.03	0.00	0.00
3	40	0.00	0.08	0.00	0.00	0.05	0.00	0.06
4	60	0.00	0.11	0.00	0.00	0.08	0.00	0.14
5	80	0.00	0.15	0.00	0.00	0.11	0.00	0.25
6	100	0.00	0.19	0.01	0.00	0.13	0.01	0.33
7	120	0.00	0.23	0.01	0.00	0.16	0.01	0.41
8	140	0.00	0.27	0.01	0.00	0.19	0.01	0.50
9	160	0.00	0.30	0.01	0.00	0.21	0.01	0.60
10	180	0.00	0.34	0.01	0.00	0.24	0.01	0.70
11	200	0.00	0.38	0.01	0.00	0.27	0.01	0.80
12	220	0.00	0.42	0.01	0.00	0.29	0.01	0.91
13	240	0.00	0.46	0.01	0.00	0.32	0.01	1.03
14	260	0.00	0.49	0.01	0.00	0.35	0.01	1.15
15	280	0.00	0.53	0.01	0.00	0.37	0.01	1.29
16	300	0.00	0.57	0.01	0.00	0.40	0.01	1.43
17	320	0.00	0.61	0.01	0.00	0.43	0.01	1.58
18	340	0.00	0.65	0.02	0.00	0.45	0.02	1.74
19	360	0.00	0.68	0.02	0.00	0.48	0.02	1.92
20	380	0.00	0.72	0.02	0.00	0.51	0.02	2.11
21	400	0.00	0.76	0.02	0.00	0.53	0.02	2.33
22	420	0.00	0.80	0.02	0.00	0.56	0.02	2.75
23	430	0.00	0.82	0.02	0.00	0.57	0.02	3.90
24	350	0.00	0.67	0.02	0.00	0.47	0.02	4.30
25	300	0.00	0.57	0.01	0.00	0.40	0.01	4.23
26	250	0.00	0.48	0.01	0.00	0.33	0.01	4.12
27	200	0.00	0.38	0.01	0.00	0.27	0.01	3.95
28	150	0.00	0.29	0.01	0.00	0.20	0.01	3.70
29	100	0.00	0.19	0.01	0.00	0.13	0.01	3.45
30	50	0.00	0.10	0.00	0.00	0.07	0.00	3.04
31	0	0.00	0.00	0.00	0.00	0.00	0.00	2.20

Table 7: Analytical and experimental deformation results for specimen L-0.

Table 8 shows the stress results for all three specimens L-0-A, L-0-B and L-0.

STEP (sec)	FORCE (kN)	L-0-A	L-0-B	L-0
		STRESS (MPa)	STRESS (MPa)	STRESS (MPa)
1	0	0.00	0.00	0.00
2	20	2.67	2.51	1.78
3	40	5.34	5.02	3.56
4	60	8.01	7.53	5.33
5	80	10.68	10.04	7.11
6	100	13.35	12.55	8.89
7	120	16.02	15.06	10.67
8	140	18.68	17.57	12.44
9	160	21.35	20.08	14.22
10	180	24.02	22.58	16.00
11	200	26.69	25.09	17.78
12	220	29.36	27.60	19.56
13	240	32.03	30.11	21.33
14	260	34.70	32.62	23.11
15	280	37.37	35.13	24.89
16	300	40.04	37.64	26.67
17	320	42.71	40.15	28.44
18	340	45.38	42.66	30.22
19	360	48.05	45.17	32.00
20	380	50.71	47.68	33.78
21	400	53.38	50.19	35.56
22	420	56.05	52.70	37.33
23	430	57.39	53.95	38.22
24	350	46.71	43.91	31.11
25	300	40.04	37.64	26.67
26	250	33.37	31.37	22.22
27	200	26.69	25.09	17.78
28	150	20.02	18.82	13.33
29	100	13.35	12.55	8.89
30	50	6.67	6.27	4.44
31	0	0.00	0.00	0.00

Table 8: Stress results for specimens L-0.

Table 9 shows the analytical results of strain for specimens L-0-A and L-0-B compared with the experimental results of strain for specimen L-0.

STEP (sec)	FORCE (kN)	L-0-A	L-0-B	L-0
		STRAIN (mm/mm)	STRAIN (mm/mm)	STRAIN (mm/mm)
		‰	‰	‰
1	0	0.000	0.000	0.000
2	20	0.089	0.084	0.000
3	40	0.179	0.168	0.067
4	60	0.268	0.252	0.156
5	80	0.358	0.336	0.278
6	100	0.447	0.420	0.367
7	120	0.537	0.505	0.456
8	140	0.626	0.589	0.556
9	160	0.716	0.673	0.667
10	180	0.805	0.757	0.778
11	200	0.894	0.841	0.889
12	220	0.984	0.925	1.011
13	240	1.073	1.009	1.144
14	260	1.163	1.093	1.278
15	280	1.252	1.177	1.433
16	300	1.342	1.261	1.589
17	320	1.431	1.346	1.756
18	340	1.521	1.430	1.933
19	360	1.610	1.514	2.133
20	380	1.700	1.598	2.344
21	400	1.789	1.682	2.589
22	420	1.878	1.766	3.056
23	430	1.923	1.808	4.333
24	350	1.565	1.472	4.778
25	300	1.342	1.261	4.700
26	250	1.118	1.051	4.578
27	200	0.894	0.841	4.389
28	150	0.671	0.631	4.111
29	100	0.447	0.420	3.833
30	50	0.224	0.210	3.378
31	0	0.000	0.000	2.440

Table 9: Strain results for specimens L-0-A, L-0-B and L-0.

3.2 Analytical results of mesh methods

For investigation of the influence of mesh methods on the reliability of the analytical results, the specimens L-0-A and L-0-B are discretized using all the available mesh methods of

the ANSYS software. It is noteworthy that the geometrical characteristics, the properties of the materials and the loading rate remained the same for each simulation, as mentioned earlier. Table 10 shows the stress results according to the mesh method and Table 11 shows the strain results according to the mesh method.

STEP (sec)	FORCE (kN)	L-0-A			L-0-B
		STRESS (MPa)			STRESS (MPa)
		Automatic	Tetrahedron	Multizone	Multizone
1	0	0.00	0.00	0.00	0.00
2	20	1.99	1.90	2.67	2.52
3	40	3.98	3.81	5.34	5.03
4	60	5.97	5.71	8.01	7.55
5	80	7.96	7.62	10.68	10.07
6	100	9.95	9.52	13.35	12.59
7	120	11.94	11.42	16.02	15.10
8	140	13.93	13.33	18.68	17.62
9	160	15.92	15.23	21.35	20.14
10	180	17.91	17.14	24.02	22.65
11	200	19.90	19.04	26.69	25.17
12	220	21.89	20.94	29.36	27.69
13	240	23.88	22.85	32.03	30.20
14	260	25.87	24.75	34.70	32.72
15	280	27.86	26.66	37.37	35.24
16	300	29.85	28.56	40.04	37.76
17	320	31.84	30.46	42.71	40.27
18	340	33.82	32.37	45.38	42.79
19	360	35.81	34.27	48.05	45.31
20	380	37.80	36.18	50.71	47.82
21	400	39.79	38.08	53.38	50.34
22	420	41.78	39.98	56.05	52.86
23	430	42.78	40.94	57.39	54.12
24	350	34.82	33.32	46.71	44.05
25	300	29.85	28.56	40.04	37.76
26	250	24.87	23.80	33.37	31.46
27	200	19.90	19.04	26.69	25.17
28	150	14.92	14.28	20.02	18.88
29	100	9.95	9.52	13.35	12.59
30	50	4.97	4.76	6.67	6.29
31	0	0.00	0.00	0.00	0.00

Table 10: Stress results according to the mesh method.

STEP (sec)	FORCE (kN)	L-0-A			L-0-B
		STRAIN (mm/mm) ‰			STRAIN (mm/mm) ‰
		Automatic	Tetrahedron	Multizone	Multizone
1	0	0.00	0.00	0.00	0.00
2	20	0.07	0.06	0.09	0.07
3	40	0.13	0.13	0.18	0.13
4	60	0.20	0.19	0.27	0.20
5	80	0.27	0.26	0.36	0.27
6	100	0.33	0.32	0.45	0.33
7	120	0.40	0.38	0.54	0.40
8	140	0.47	0.45	0.63	0.47
9	160	0.53	0.51	0.72	0.53
10	180	0.60	0.57	0.81	0.60
11	200	0.67	0.64	0.89	0.67
12	220	0.73	0.70	0.98	0.73
13	240	0.80	0.77	1.07	0.80
14	260	0.87	0.83	1.16	0.87
15	280	0.93	0.89	1.25	0.93
16	300	1.00	0.96	1.34	1.00
17	320	1.07	1.02	1.43	1.07
18	340	1.13	1.08	1.52	1.13
19	360	1.20	1.15	1.61	1.20
20	380	1.27	1.21	1.70	1.27
21	400	1.33	1.28	1.79	1.33
22	420	1.40	1.34	1.88	1.40
23	430	1.43	1.37	1.92	1.43
24	350	1.17	1.12	1.57	1.17
25	300	1.00	0.96	1.34	1.00
26	250	0.83	0.80	1.12	0.83
27	200	0.67	0.64	0.89	0.67
28	150	0.50	0.48	0.67	0.50
29	100	0.33	0.32	0.45	0.33
30	50	0.17	0.16	0.22	0.17
31	0	0.00	0.00	0.00	0.00

Table 11: Strain results according to the mesh method.

4 ANALYTICAL INVESTIGATION

4.1 Investigation of analytical results

Therefore, the analytical research of the two simulations in the present research has led to the following common results to between the two simulations:

- The rate of loading, in the case of reinforced concrete structures, affects the deformation results, by increasing the resistance of the specimen.

- The rate of loading of vertical and horizontal deformation remains completely constant throughout the load, which is not observed in the experimental results.
- The rate of loading of stress remains perfectly constant throughout the loading duration, just as in the experimental results.
- The values of the transverse deformation remain below zero throughout the loading duration, without observing the behavior of the two stages of deformation, which are described in the research of Chrysanidis [11].
- Increase of the resistance of the specimen L-0-A and L-0-B in relation to the resistance of the experimental specimen L-0.
- The average value of the percentage error for the simulation of specimen L-0-A is of the order of 395.2%, while for the simulation of specimen L-0-B is of the order of 598.8%.

With the percentage error values far from the permissible limits, it becomes obvious that neither the analytical results of the specimen L-0-A nor of the specimen L-0-B converge with the experimental results of Chrysanidis [11] and as a result the two simulations cannot be characterized as reliable in terms of the coherence of the results.

4.2 Investigation of mesh method's results

Based on the element quality diagrams and the tables of the mesh method results, it appears that:

A. For the simulation of specimen L-0-A

- The rate of loading, in the case of reinforced concrete structures, affects the deformation results, increasing the strength of the specimen.
- The mesh is performed only by Automatic, Tetrahedron and the Multizone mesh methods, due to the geometry of the simulation which contained bodies that Sweep and Hex Dominant mesh methods could not mesh.
- Due to the limitation of the educational version for the number of finite elements used, the mesh of the Automatic, Tetrahedron and Multizone mesh methods do not meet the requirements of a suitable grid, according to the general rules for the element quality measurement technique. However, from the above methods, the Multizone mesh method is preferred.
- A mesh made only of hexahedron finite elements provides more reliable results than a mesh made of tetrahedron finite elements.
- The type and the number of finite elements do not affect the behavior of the specimen during the loading period.

B. For the simulation of specimen L-0-B

- The mesh is generated using only the Multizone mesh method.
- Due to the complexity of the geometry, the method of the Automatic and Patch Confirming Tet, cannot distinguish the model with a number of finite elements less than 32,000.

- The Sweep method and the Hex Dominant method do not produce a mesh, due to the geometry of the specimen containing bodies, in which the methods cannot work.
- Due to the limitation of the educational version for the number of finite elements used, the mesh of the Multizone method does not meet the requirements of a suitable grid, according to the general rules for the technique of measurement of the element quality category. However, the choice of mesh made with the Multizone mesh method is considered necessary.
- The type and the number of finite elements do not affect the behavior of the specimen during the loading period.

5 INFLUENCE OF LOADING RATE

According to the detailed results, there are two stages during the duration of the loading. The first stage includes the time from the imposition of the load at 0 kN to the loading with a load equal to 430 kN. Then, the second stage includes the unloading process of the model. In particular, in the first stage there is an increase in the deformation and stress at a constant rate, until the stress reaches its maximum value, in contrast to the experimental results where the rate of deformation follows a different flow. Then, in the second stage, the deformation and the stress are reduced at a constant rate until the values are 0, returning the specimen to its original state. It is noteworthy that during the experimental procedure, there is a deformation with the higher value being calculated at 10% of the height of the L-0 specimen, measured by its base. In addition, it is observed that the number and type of finite elements do not affect the behavior of the specimen during the loading process, despite of the mesh method used.

Therefore, it turns out that the universal load in the behavior of the specimen L-0-A and L-0-B in relation to the experiment by Chrysanidis [11], is due solely to the high loading rate of the two simulations, with which concludes that, in reinforced concrete structures, the loading rate affects the results of deformation increasing the strength of the structure.

6 INFLUENCE OF MESH METHOD

The type and number of finite elements used greatly influence the reliability of the results. In particular, the influence of the type of finite elements on the suitability of the mesh and consequently on the reliability of the results is observed. More specifically, a grid made of hexadecimal elements, such as the mesh of Multizone mesh method, is more suitable, according to the general technical metrics rules, and at the same time more reliable than a grid made of tetrahedral elements, such as the mesh of Tetrahedron mesh method. On the other hand, the number of finite elements depends on the complexity of the geometry of the model that it is called upon to mesh. A grid with a small number of elements in a complex geometry, is quite difficult to be characterized as suitable and at the same time, its results cannot be considered as being reliable.

The large numerical differences between the simulation results are due to both the chosen mesh method and the size of the finite elements of the grid. However, it is impossible to create a more appropriate grid than that in section 2, due to the limitations of the ANSYS educational version.

7 CONCLUSIONS

By comparing the analytical results of the L-0-A and L-0-B specimens with the experimental results of the L-0 specimen [7], the reliability of the ANSYS software and the factors

which might influence it are investigated. The resulting conclusions can be summarized as follows:

- The rate of loading, in the case of reinforced concrete structures, affects the deformation results, increasing the strength of the specimen.
- The number and the size of the finite elements of a simulation affect the accuracy and reliability of the results.
- The number and type of finite elements do not affect the behavior of the model during loading period.
- The number and type of finite elements of a simulation affect the accuracy and reliability of the results, whether or not the grid is suitable.
- The number of finite elements depends on the complexity of the model geometry.
- The type of finite elements affects the reliability of the simulation results, with hexahedron elements providing more accurate results.

REFERENCES

- [1] Bathe, K. J., 2006, *Finite Element Procedures*, Watertown: Prentice Hall, Pearson Education, Inc.
- [2] Madenci, E., Guven, I., 2015, *The Finite Element Method and Applications in Engineering Using ANSYS*, New York: Springer.
- [3] Daryl, L. L., 2007, *A First Course in the Finite Element Method*, Toronto, Ontario: Thomson Canada Limited.
- [4] Courant, R., 1943, "Variational Methods for the Solution of Problems of Equilibrium and Vibrations", *Bulletin of the American Mathematical Society*, Vol. 49, pp. 1–23.
- [5] Hrennikoff, A., 1941, "Solution of Problems in Elasticity by the Frame Work Method", *Journal of Applied Mechanics*, Vol. 8, No. 4, pp. 169–175.
- [6] McHenry, D., 1943, "A Lattice Analogy for the Solution of Plane Stress Problems", *Journal of Institution of Civil Engineers*, Vol. 21, pp. 59–82.
- [7] Argyris, J. H., 1954-1955, "Energy Theorems and Structural Analysis", *Aircraft Engineering*.
- [8] Argyris, J. H., and Kelsey, S., 1960, *Energy Theorems and Structural Analysis*, Butterworths, London, (collection of papers published in *Aircraft Engineering* in 1954 and 1955).
- [9] Clough, R. W., 1960, "The Finite Element Method in Plane Stress Analysis", *Proceedings, American Society of Civil Engineers, 2nd Conference on Electronic Computation*, Pittsburgh, PA, pp. 345–378.
- [10] Lee, H. H., 2010, *Finite Element Simulations with Ansys Workbench 12*, Taiwan: Schoff Development Corporation
- [11] Chrysanidis, T., 2019, "Influence of elongation degree on transverse buckling of confined boundary regions of R/C seismic walls", *Construction and Building Materials*, pp.703-720.

- [12] Y. Chai and D. Elayer, "Lateral stability of reinforced concrete columns under axial reversed cyclic tension and compression," *ACI Structural Journal*, vol. 96, no. 5, pp. 780–789, 1999.
- [13] P. Smaś, "Design of clamped columns for maximizing the axial displacement at buckling," *Structural and Multidisciplinary Optimization*, vol. 33, no. 3, pp. 229–241, 2007, doi: 10.1007/s00158-006-0056-4.
- [14] T. Chrysanidis, "Influence of elongation degree on transverse buckling of confined boundary regions of R/C seismic walls," *Construction and Building Materials*, vol. 211, pp. 703–720, Jun. 2019, doi: 10.1016/J.CONBUILDMAT.2019.03.271.
- [15] T. Chrysanidis, "Low Reinforced Shear Walls: Displacements and Failure Modes Due to Lateral Buckling," *International Journal of Science and Engineering Investigations*, vol. 5, no. 55, pp. 143–148, 2016.
- [16] M. Moyer and M. Kowalsky, "Influence of tension strain on buckling of reinforcement in concrete columns," *ACI Structural Journal*, vol. 100, no. 1, pp. 75–85, 2003.
- [17] H. S. Essa, "Stability of Columns in Unbraced Frames," *Journal of Structural Engineering*, vol. 123, no. 7, pp. 952–957, 2002, doi: 10.1061/(asce)0733-9445(1997)123:7(952).
- [18] J. Aristizabal-Ochoa, "Stability of columns under uniform axial load with semirigid connections," *Journal of Structural Engineering*, vol. 120, no. 11, pp. 3212–3222, 1994.
- [19] T. Chrysanidis and I. Tegos, "Size of seismic tensile strain and its influence on the displacements due to transverse buckling of ultra-highly reinforced structural walls," *ARP Journal of Engineering and Applied Sciences*, vol. 11, no. 23, pp. 13884–13890, 2016.
- [20] T. Chrysanidis, "Size of seismic tensile strain and its influence on the lateral buckling of highly reinforced concrete walls," *IOSR Journal of Mechanical and Civil Engineering*, vol. 11, no. 1, pp. 18–22, 2014, doi: 10.9790/1684-11121822.
- [21] T. Chrysanidis, "Evaluation of Out-of-Plane Response of R/C Structural Wall Boundary Edges Detailed with Maximum Code-Prescribed Longitudinal Reinforcement Ratio," *International Journal of Concrete Structures and Materials*, vol. 14, no. 1, 2020, doi: 10.1186/s40069-019-0378-4.
- [22] T. Chrysanidis and I. Tegos, "Influence of elongation degree on out-of-plane buckling of R/C structural walls with a medium high reinforcement ratio," *International Journal of Civil Engineering and Technology*, vol. 7, no. 4, pp. 358–364, 2016.
- [23] T. Chrysanidis and I. Tegos, "Out-of-plane buckling of highly reinforced seismic walls: Displacements and mode of failure," *International Journal of Civil Engineering and Technology*, vol. 5, no. 6, pp. 101–107, 2014.
- [24] N. Alamanis, "Uncertainties and optimization in geotechnical engineering," *American Scientific Research Journal for Engineering, Technology, and Sciences*, vol. 38, no. 1, pp. 92–111, 2017.
- [25] N. Alamanis and P. Dakoulas, "Effect of the spatial variability of soil properties on the seismic vulnerability of slopes with embedded oil and natural gas pipelines," in *6th*

- International Conference on “Energy, Sustainability and Climate Change” (ESCC 2019)*, 2019.
- [26] N. Alamanis and P. Dakoulas, “Simulation of random soil properties by the Local Average Subdivision method and engineering applications,” *Energy Systems*, pp. 1–21, 2019, doi: 10.1007/s12667-019-00362-y.
- [27] N. Alamanis and P. Dakoulas, “Effect of spatial variability of soil properties on the stability and permanent seismic displacements of highway slopes,” in *The 17th European Conference on Soil Mechanics and Geotechnical Engineering*, 2019.
- [28] G. Papageorgiou, N. Alamanis, I. Chouliaras, and P. Kapsali, “Decision making for designing infrastructure projects: The case of the city of Larissa, Greece,” *Journal of Engineering and Architecture*, vol. 7, no. 1, pp. 115–125, 2019, doi: 10.15640/jea.v7n1a13.
- [29] N. Alamanis, G. Papageorgiou, P. Chantzopoulou, and I. Chouliaras, “Investigation on the influence of permeability coefficient k of the soil mass on construction settlements. Cases of infrastructure settlements in Greece,” *Wseas Transactions on Environment and Development*, vol. 15, pp. 95–105, 2019.
- [30] A. Mouratidis and G. Papageorgiou, “A Rational Approach for Optimization of Road Upgrading,” *Canadian Journal of Civil Engineering*, vol. 37, no. 11, pp. 1462–1470, 2010.
- [31] G. Papageorgiou, N. Alamanis, and N. Xafoulis, “Methodology for optimization of road works schedule according to local climatic data,” *International Journal of Recent Technology and Engineering*, vol. 8, no. 4, pp. 1470–1476, 2019.
- [32] ANSYS, Inc, 2010, *Ansys Meshing User’s Guide*, Canonsburg: ANSYS Inc.

CALIBRATION AND NUMERICAL MODELING OF RC BEAM-COLUMN JOINTS DESIGNED FOR GRAVITY LOADS

Marcello Sabene¹, Maria Zucconi¹, Stefano Pampanin², and Barbara Ferracuti¹

¹ Niccolò Cusano University
Via Don Carlo Gnocchi 3, 00166, Rome, Italy
e-mail: {marcello.sabene, maria.zucconi, barbara.ferracuti}@unicusano.it

² Department of Structural and Geotechnical Engineering, Sapienza University of Rome
Via Eudossiana 18, 00184, Rome, Italy
stefano.pampanin@uniroma1.it

ABSTRACT

Damage reports after recent earthquakes prove that the structural deficiencies of non-ductile Reinforced Concrete (RC) buildings often lead to structural element local damage and collapse of the entire structure. The structural weakness of the Beam-Column joints, due to the absence of seismic detailing and capacity design principles, plays a key role in the seismic vulnerability of European building stock designed before the 1970's, thus before the introduction of modern seismic codes. In RC buildings subjected to reversed cyclic earthquake loads, high stress concentration occurs at the Beam-Column joints, making these regions prone to the occurrence of severe damage and brittle mechanisms. Yet, a common engineering practice consists in modeling the Beam-Column joints as rigid elements in concrete frames, neglecting the joint's deformability and, more importantly, their actual local mechanism. Consequently, the predicted stiffness and the collapse mechanisms of the structure can, unconservatively, change significantly from the actual one. Starting from the experimental results available in literature, this work aims at calibrating the key parameters that characterize the equivalent joint moment-rotation hysteresis behavior of existing substandard Beam-Column joints, by using a simple while reliable lumped plasticity modeling approach. The numerical model was developed in OpenSees and validated on many experimental results collected from the literature. The global joints response relationships under cyclic loads, defined as a function of the joint structural detailing and the axial load, satisfactorily reproduce the experimental findings in terms of first cracking point, yielding point, overall hysteretic behavior, pinching effect, and strength degradation. Moreover, the initial and post-yielding stiffness values of the joint's backbone curve were further improved when compared to those recently proposed by the NZSEE2017 Seismic Assessment Guidelines.

Keywords: Earthquake Engineering, Existing Buildings, Beam-Column Joints, Numerical Calibration, Cyclic Analysis.

1 INTRODUCTION

Several studies on the seismic behavior of reinforced concrete joints within existing frames in seismic areas have been carried out in the last few decades. The brittle failure of joint panels has been recorded more frequently, following the most recent seismic events [1], which, in addition to extensive structural damages, have caused great economic losses [2-5] and highlighted the strong vulnerability of pre-70's buildings [6-9].

In RC frame structures stressed only by gravity loads, joint panel regions are rarely subjected to significant stresses, but the situation is rather different when considering seismic actions. Therefore, a very high stress state is generated in the joint region, where specific transverse/shear reinforcement should be adopted to reduce the stress variation. Instead, older frame buildings are typically characterized by poor reinforcement detailing, poor bond properties, inadequate confinement, and more importantly, lack of capacity design principles.

As shown in many experimental programs, the joint panels of pre-70's were characterized by insufficient tensile strength due to the absence or lack of horizontal and vertical reinforcement. This weakness appears clearly with the joint failure induced usually by shear or bond flaws [9-11]. The flexural and shear forces, generated into the joint panel by the cyclic tests, create a stress distribution transferred through the joint, producing a wide diagonal crack pattern along the principal compressive directions. This pattern leads to either a tensile failure or to a compression/crushing failure of the diagonal strut, and thus to a strength and stiffness deterioration within the joint. In other cases, the joint failure occurred with the instability of the vertical column bars, devoid of horizontal reinforcements, i.e., stirrups or wall beam bars.

Therefore, growing attention in the literature has been focused on the analytical/numerical modeling of gravity load designed RC beam-column, considering the joint panel zone's deformability and capacity [12-14]. In the last decades, many numerical models have been developed and proposed either based on Finite Elements (FE) modeling, or on simplified macro-models or lumped plasticity (e.g. [15-19]) and analytical approaches (e.g. [20]).

The present work analyzes experimental tests conducted on the external joints with the aim to verify the accuracy of the proposed constitutive laws. In particular, the response prediction obtained by a simple moment-rotation backbone, whose parameters are defined a priori based on current knowledge on the topic, with respect to a more complex backbone calibrated ad-hoc from the experimental results. Taking one of these nodes as a case study, a numerical model was built in OpenSees based on a lumped plasticity approach and relying upon a joint rotational spring. Two different relations have been defined: a bi-linear relationship based on the NZSEE2017 Seismic Assessment Guidelines and associated literature [15, 21] and a more refined tri-linear relationship that better approximates the first cracking point, the elastic and softening branches. The hysteresis behavior was modeled through the use of a "uniaxial hysteretic material" already present in OpenSees library. Regarding the other tests analyzed, only the parameters useful for defining their backbone curve are reported.

2 EXPERIMENTAL STUDIES ON RC JOINT SUBSYSTEMS

In literature, several experimental studies on beam-column joints with non-ductile detailing have been carried out to understand the as-built parameters that would influence the seismic performance of these structural connections.

In the last decades many exterior beam-column joints, representatives of pre-1970s construction and/or gravity-only design buildings, characterized by inadequate joint shear reinforcements, inadequate bond resistance, and non-ductile beam anchorage details by modern standards, were tested with the aim to assess the seismic behavior of these connections (e.g. [9-11]), several

design methodologies were developed (e.g. [15-19]) and nowadays suitable types of reinforcement interventions were investigated (e.g. [22-27]). In general terms, depending on the structural detailing adopted and on the axial load variation assumed, the failure modes of beam-column connections can be significantly different, so they need to be checked on a case-by-case basis. To this aim, the moment – axial load performance domain and the hierarchy of strength approach can be used to evaluate the sequence of the collapse events between beam, column, and joint panel zone [28].

Considering the typical structural weaknesses of existing RC buildings, in the late 1990s and early 2000s, Pampanin et al. carried out quasi-static tests on existing RC beam-column joint subsystems considering plain-round reinforcements with end-hook anchorages, under quasi-static cyclic loading and varying column axial load according to the European construction practice of the 1950-1970s period [7-9]. Further comprehensive experimental and numerical testing campaigns on beam-column joint subassemblies have been carried out at the University of Canterbury (2002-2010) [29-31]. Test results [30] and numerical simulations [32] revealed extensive shear damage in the joint panel zone, which would lead to a severe and critical reduction of lateral and gravity load capacity of the overall frame system. The implication of joint damage and collapse within the frame system collapse mechanism become up a crucial issue in recent days.

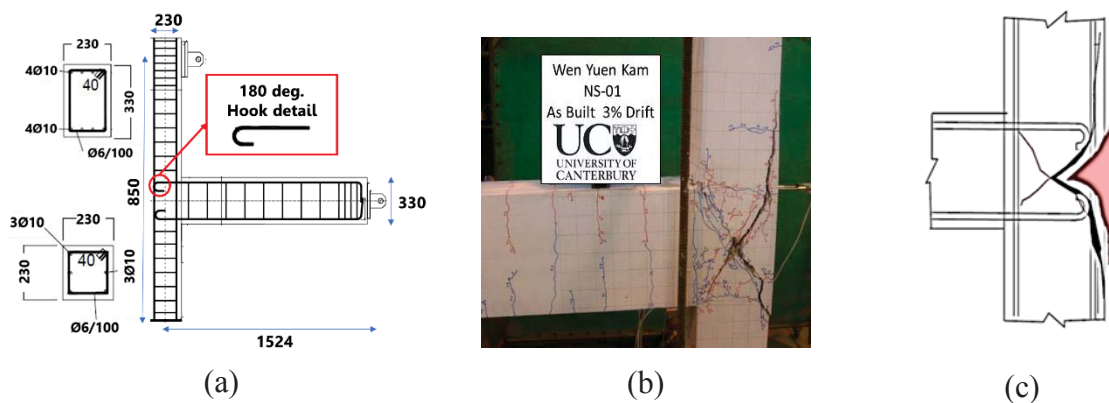


Figure 1: (a) Reinforcing and geometry details for test unit NS-O1 [30], (b) cracks pattern at top drift equal to 3% [30], (c) “concrete wedge” mechanism formation [15].

In this paper, the 2/3-scaled exterior beam-column joint unit NS-01, belonging to the experimental tests carried out by University of Canterbury UC research team [31], shown in Figure 1, was selected to begin the direct calibration of the moment–rotation relationship key parameters, starting from the values suggested by NZSEE Seismic Assessment Guidelines and associated literature [15, 21]. The chosen specimen is characterized by plain-round reinforcements with end-hook anchorages and tested under a unidirectional quasi-static cyclic lateral loading. The geometry of the trial specimen was chosen to be close to the pre-1970s non-ductile RC beam-column joint benchmark, see Figure 1 (a). Deformed mild steel reinforcements and commercial pre-mix concrete compression strength of 30MPa were used. The lateral loading protocol used in this test consisted of two displacement-controlled cycles at increasing amplitudes: 0.1%, 0.2%, 0.5%, 1.0%, 1.5%, 2.0%, 2.5%, 3.0% and 4.0% inter-story drift. The lateral load was coupled with a varying axial loading, N , as suggested since [9], to simulate the actual frame sway action, as per the experimental test, considering N as a function of the lateral load F_C : $N = 110kN \pm 4.63F_C$. Most previous literature experiments on beam-column joint subassemblies (for both existing capacity and retrofit solution evaluations) have used either constant or

zero column axial loads, so the chosen test represent an interesting case- study. The specimen NS-01 showed a crack pattern that develops along the main principal compressive direction at a top drift value equal to 3% (end of the test), as represented in Figure 1 (b). In addition, the punching action from the smooth bars with end up develops the so called “concrete wedge” mechanism [9, 7, 15], due to the development of stresses in the only portion of the joint panel unconfined (no stirrups, no convergent beam), see Figure 1 (c).

In the next sections, the numerical lumped plastic model approach used to evaluate the global force-top drift curve of the proposed experimental test is described along with the various parameters used for evaluating pinching behavior, unloading, and reloading stiffness degradation, strength degradation, and energy dissipation.

3 NUMERICAL MODELING APPROACH

The numerical model adopted to reproduce the experimental test was implemented in OpenSees. For the overall system, a finite element lumped plasticity approach was used, considering for the converging elements a linear-elastic region in the middle and the inelasticity concentrated at the ends. The plastic hinge length was evaluated by using the Priestley formulation [12]. Regarding the joint panel strength-deformation capacity and its non-linear behavior, a simplified macro-model approach was adopted [7, 9, 15]. Thus, joints behavior both in linear and non-linear range was considered through a single rotational spring placed in its core region.

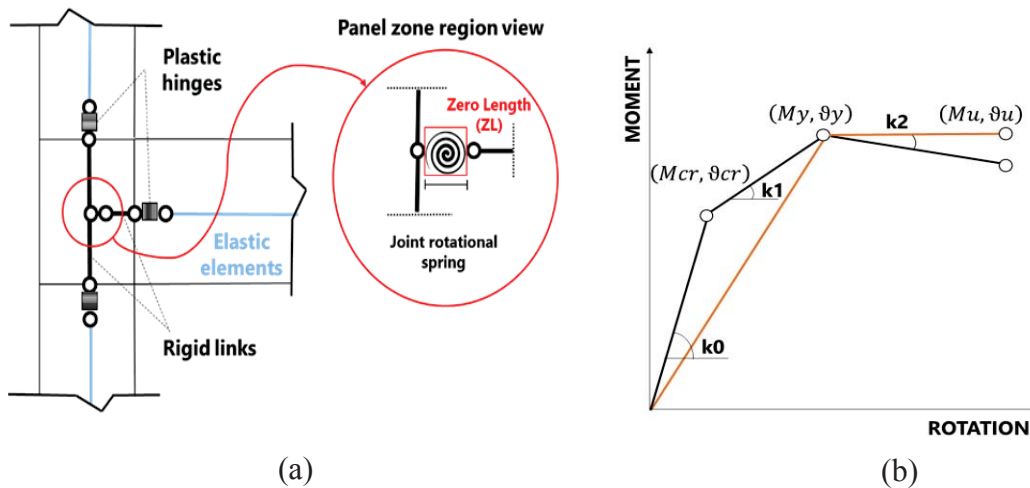


Figure 2: (a) Numerical model performed in OpenSees, (b) bi-linear and tri-linear Backbones.

The rotational spring was linked to beam and column interfaces with rigid links. All plastic hinges non-linearities were included through Zero Length (ZL) elements at the end of the members and in the joint panel, see Figure 2 (a). Once the numerical model has been defined, two backbone types have been used to reproduce the experimental test. The simplest envelope curve, orange line of Figure 2 (b), represents a bi-linear constitutive relationship defined according to the parameters from the NZSEE2017 Seismic Assessment Guidelines [21]; while a more refined version, black line of Figure 2 (b), considers, through a trilinear constitutive relationship, the pre-cracking stage and the softening behavior after the peak. In both curves, the pairs of points (M, ϑ) with the subscript “y” and “u” define the yielding condition and the ultimate condition, respectively. Notably, while the yielding point is the same for both curves, the ultimate points are different. Only for the tri-linear backbone curve, the first cracking condition has been defined and indicated with the subscript “cr” in the black curves of Figure 2 (b), thus forming a knee that anticipates the yielding point. The next section will discuss the parameters

governing the capacity and the hysteretic uniaxial material used for both the bi/tri-linear backbone.

3.1 JOINT MOMENT-ROTATION HYSTERESIS BACKBONE

The joint spring capacity in terms of bending moment can be derived from the principal tensile or compressive stresses, where they consider the axial load acting on the top of the column.

For a joint with no horizontal confinement provided by the stirrups ($\sigma_h = 0$), its capacity, expresses in terms of moment resistance M_{joint} , both in pull and push directions, has been determined by using the following equations:

$$M_{joint} = \frac{v_{jh}/A_c}{\phi} = \frac{V_{jh}}{\phi} \quad (1)$$

$$v_{jh} = \sqrt{p_{t,c}^2 \pm p_{t,c} \left(\frac{N_v}{A_c} \right)} \quad (2)$$

$$\phi = \frac{2L'_b L_c - 1.8dL_b}{L_b 0.9dA_c(L_c - L_b)} \quad (3)$$

In (1) v_{jh} is the horizontal shear stress, A_c represents the column cross section area, and V_{jh} is the horizontal shear force acting at the mid-depth of the joint core. In (2) $p_{t,c}$ are the principal tensile or compressive stresses, evaluated by using the Mohr circle while N_v represents the axial load acting on the top of the column. In (3) ϕ is a geometric term which depends on the joint subsystem dimensions and on the lever arm d . All the terms reported in Equations (1), (2), (3) are represented in Figure 3, while push direction implicates beams upper fibers in compression state and pull direction the tension one. For the complete procedure, refer to NZSEE2017 Seismic Assessment Guidelines and associated literature [15, 21, 23]. For the analyzed test, the bending moment capacity results equal to 35.5 kNm in push-direction and 27.5 kNm in pull direction. Concerning the rotation corresponding to the maximum bending moment, actually no formulations are available and the proposed value by the NZSEE2017 Seismic Assessment Guidelines [21] are independent from the construction details and geometry parameters.

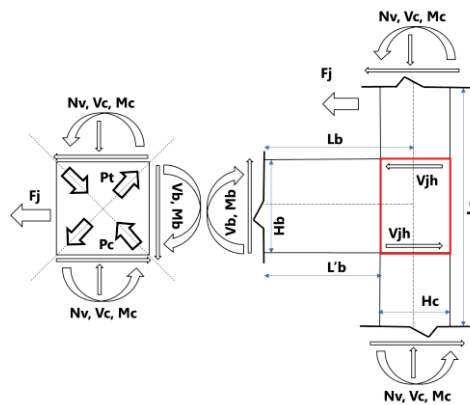


Figure 3: Moment, shear, and stresses at joint region and, Free-body diagram of a beam-column joint subassembly (push direction).

Moreover, no indication on the pre-cracking stage is available, because on the safe side the NZSEE2017 neglects the pre-cracking stage.

Therefore, in the present work a preliminary calibration of the parameters governing the pre-cracking stage is performed based on the analyzed experimental test.

To model the cyclic behavior of the joint panel (e.g. [15, 33]), a hysteretic uniaxial material was adopted in OpenSees library. In addition to the envelope parameters, the initial elastic stiffness K_0 and the pairs of points of the envelope (M, ϑ) , the cyclic model, represented in Figure 4, requires the definition of several inputs parameters such as Pinch- x/y pinching factor for rotation/moment during the reloading branches, Damage 1 due to ductility (μ), Damage 2 due to energy dissipation, and finally the power unloading stiffness (β), which governs the cycles stiffness degradation; they are all schematized in Tab. 1. The calibrated parameters used in the numerical model are: $Pinch_x = 0.3$, $Pinch_y = 0.05$, $Damage_1 = 0.02$, $Damage_2 = 0$, $\beta = 0.5$.

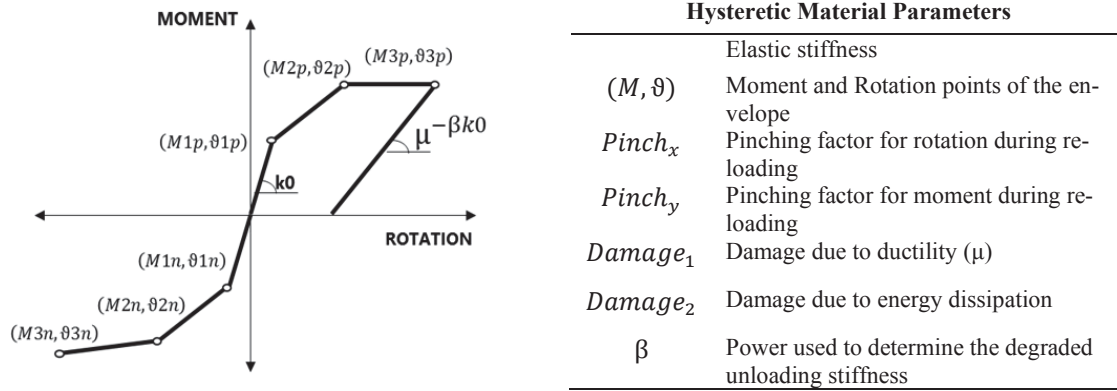


Figure 4: (a) Hysteretic material backbone, (b) Hysteretic material input parameters

The adopted hysteretic model shows the advantage to manage independently the positives (first quadrant) and negatives (third quadrant) notable points of the envelope, with subscripts “p” and “n” in Figure 4. This opportunity allows to account the non-symmetric response of the subsystem in the two directions, push and pull directions, of the seismic action as shown by many experimental tests

4 EXTERIOR JOINT MODEL CALIBRATION AND RESULTS

The bi-linear backbone (BB) and tri-linear backbone (TB) are both adopted to reproduce the experimental response of NS-O1 joint panel. The first simplest backbone is an elastic perfect plastic one and its parameters are defined thanks to the actual guidelines (blind prediction), instead the parameters of the second one is calibrated ad-hoc to match the experimental response on the basis of the analyzed experimental test. As will be shown, both the models capture the experimental test with a slight, and expected difference in the level of accuracy.

In Table 1, all the parameters that characterize the envelope curves are reported, both for bi-linear backbone (BB) and tri-linear backbone (TB). For both the backbones, the parameters governing loading and reloading branches are set equal to $Pinch_x=0.3$, $Pinch_y=0.05$, $D_1=0.02$, $\beta=0.5$, and the maximum bending moment M_y was calculated according to eq. (1) for push

direction, while it was reduced of about 22% in pull direction. Concerning the rotations at yielding and ultimate condition, for the elastic perfectly plastic backbone they are set equal to those proposed by NZSEE2017 Seismic Assessment Guidelines [21] in both directions, while for the trilinear backbone based on the experimental test, they result slightly higher in both the directions.

Proposed envelope curves for specimen NS-01

Model	M_{cr} (kNm)	M_y (kNm)	M_u (kNm)	K_0 (kN/m)	K_1 (kN/m)	K_2 (kN/m)	ϑ_{cr} (rad)	ϑ_y (rad)	ϑ_u (rad)
BB	-	+27.5 -35.5	+27.5 -35.5	+1364 - 1618	-	0	-	± 0.005	± 0.01
TB	+16 -20.5	+27.5 -35.5	+22 -28.4	+3142 +2150	+474 +658	-19 -106	+0.00085 -0.001	± 0.0075	+0.015 -0.012

Table 1: Backbone values used in NS-O1 numerical model.

The axial load protocol used in the numerical analysis was back calculated from the experimental data, where the axial load was imposed during the test. The cyclic analyses in terms of lateral force vs top drift results for NS-O1 are compared with the test results, as shown in Figure 5 (a), (b).

Figure 5 (a) shows the comparison between the experimental test and numerical model with elasto-plastic backbone, while Figure 5 (b) shows the same comparison using a tri-linear backbone curve. Looking at the numerical bi-linear backbone of Figure 5 (a), the stiffness K_0 is equal to 1364 kN/m for the pull and 1618 kN/m for push loading, respectively. This value was 50% and 16% lower than the experimental one equal to 2730 kN/m in the pull direction and 1926 kN/m in the push direction, respectively. The stiffness K_0 under-estimation observed in the cyclic analyses is due to the fact that the elastic perfectly plastic backbone neglecting the pre-cracking stage.

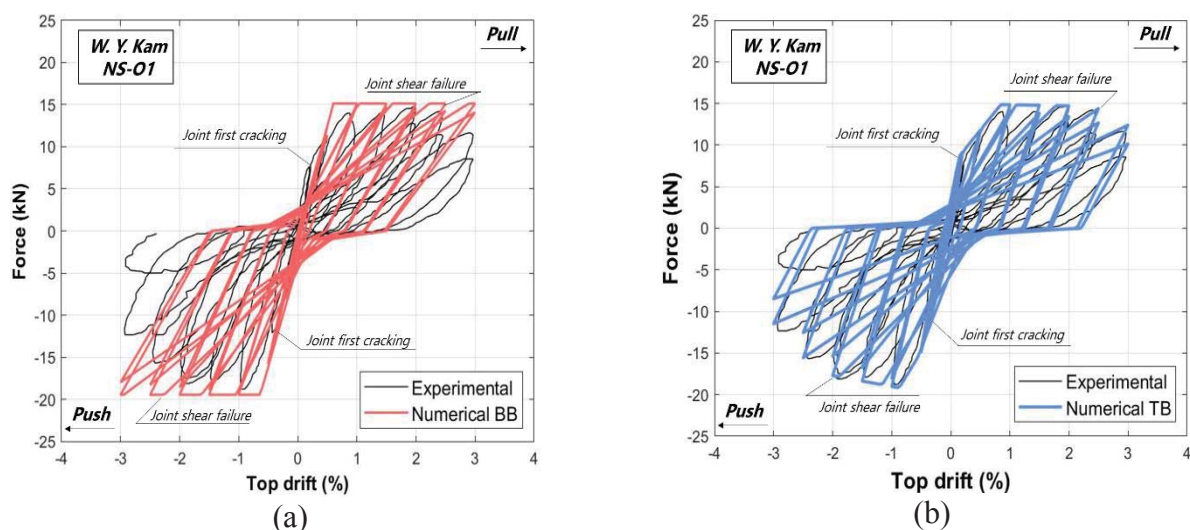


Figure 5: Horizontal Force – Top drift for specimen NS-O1, comparison between experimental and numerical results. (a) bi-linear backbone, (b) tri-linear backbone.

The bi-linear backbone could not fully reproduce the post-peak behavior of the force-top drift hysteresis, especially in the pull direction, where the higher axial loads were both beneficial

(confining the cracked joint core) and harmful (additional compressive force that accelerates bar buckling and concrete spalling) to the joint post-cracking behavior. On the other hand, the monotonic envelope matched well in capturing the peak point as maximum of resistance achieved, in the push direction.

The proposed trilinear backbone model, reported in Figure 5 (b), simulates the response of specimen NS-O1 successfully. However, it slightly overestimates the initial branch slope where the K_0 initial stiffness intends to capture joints first cracking peak.

The tri-linear hysteresis curve is capable, when compared to the simplified bilinear curve, one in capturing the strength degradation, especially the rapid degradation due to the joint concrete spalled occurred for cumulative damage. In the cyclic analysis, the damage accumulation improved the prediction of the post-peak behavior and was computed by using factors damage 1 and β , to govern the strength and stiffness degradation reached at the same displacement-imposed level and the progressive stiffness degradation as the displacement itself increases. These aspects related to the decay system evaluation were considered in both numerical simulations from the pinching re-loading curve after one complete pull-push loading cycle.

Indeed, the bi-linear backbone, given its simplicity, can still remain a valuable tool, yet rather advanced, for professional practice, where there is the need to consider the joint deformability. Furthermore, the experienced practitioner can consider for simplicity, a symmetrical resistance peak in the push-pull directions, taking as a reference one the lower of them, being in safety condition. As further developments, for more detailed studies, a trilinear curve might offer a more accurate representation of the initial stiffness and cracking point.

Worth noting that the strength degradation part of the post-peak region can either be modeled as an additional relationship to the bilinear curve model (e.g., Ruaumoko [33]) or be directly integrated in the trilinear curve as herein demonstrated. In both cases, issues associated with the numerical convergence of a pinched and strength degrading hysteresis loop, particularly when running fully dynamic non-linear time-history analysis can be anticipated and should be carefully considered.

5 PROPOSED BACKBONE VALUES FOR EXTERIOR JOINTS MODEL

Following the numerical calibration of the backbone curve on the experimental results of specimen NS-O1, similar approach was extended to various experimental tests on external joints specimens available in the literature (e.g. [9-11] and [29-32]).

The intent is to report in a simple way the main parameters that allow the user (be it a researcher or an experienced practitioner) to effectively describe the external joints backbone, selecting the appropriate level of targeted accuracy. It is worth noting that, when evaluating the equivalent joint moment capacity, expressed in terms of: M_{cr} , M_y , M_u , as previously described, it is preferable to evaluate the peak moment M_y following Equations (1), (2), (3) as it closely depends on joints geometry, structural details, and axial load variation.

As it can be noted from the calibrations carried out on the proposed experimental tests, the ratio M_{cr}/M_y varies in the range 0.4-0.7 while the ratio M_u/M_y varies between 0.7-1.

As for the rotations, building on the values suggested by NZSEE2017 Seismic Assessment Guidelines and associated literature [15, 21], calibrated values are herein proposed on the basis of the tests shown in Table 2.

Based on these calibrations, it is possible to define ranges for ϑ_{cr} , ϑ_y , ϑ_u to be used as simple and practical references for the joints rotations to be adopted in the numerical models, without going through the full p_t - γ formulation, see Table 3.

Calibrated values for the proposed numerical models

# Reference	ID	M_{cr} (kNm)	M_y (kNm)	M_u (kNm)	K_0 (kN/m)	K_1 (kN/m)	K_2 (kN/m)	ϑ_{cr} (rad)	ϑ_y (rad)	ϑ_u (rad)	M_{cr}/M_y -	M_u/M_y -
1 Pampanin et al 2003. [15]	T1	+9	+18	+18	+599	0	0	+0.0015	± 0.005	± 0.01	0.50	1
		-13	-22	-22	+667			-0.002			0.59	
2 Pampanin et al. 2003 [15]	L1	+7	+11	+11	+1050	0	0	+0.002	± 0.005	± 0.01	0.64	1
		-9	-14	-14	+1408			-0.003			0.79	
3 W. Y. Kam 2010 [30]	NSO1	+15	+28	+22	+3142	+474	-19	+0.00085	± 0.0075	+0.015	0.55	
		-21	-36	-29	+2150	+658	-106	-0.001		-0.012	0.58	0.80
	TDP1	+16	+35	+28	+2481	-	-258	+0.003	+0.0065	+0.015	0.46	0.80
		-19	-21	-15	+3225		-156	-0.0007	-0.0045	-0.018	0.90	0.71
	TDP2	+12	± 30	± 24	+2513	0	-430	+0.0006	± 0.0075	± 0.015	0.40	0.80
		-18			+1843		-390	-0.00075			0.60	
4 E. Hertanto [29]	TDD1	+35	+35	+35	+1142	-	0	+0.0015	+0.0075	+0.018	1	1
		-23	-23	-23	+1804			-0.00065	-0.004	-0.01		
	TDD2	+42	+50	+38	± 1514	-	-329	+0.0004	+0.007	+0.020	0.84	0.76
		-20	-28	-17			-251	-0.00025	-0.0035	-0.018	0.71	0.61
	TSP	+15	+25	+25	+410	-	0	+0.00090	+0.006	+0.015	0.60	1
		-9	-14	-14	-557			-0.0015	-0.003	-0.01	0.64	
5 U. Akguzel 2011 [31]	2D1	+16	+22	+22	+1267	0	-85	+0.00090	+0.0055	+0.018	0.73	1
		-11	-16	-16	-1857		-70	-0.0015	-0.0042	-0.015	0.69	
		+15	+27	+19	+1890	0	-358	+0.0009	± 0.003	± 0.015	0.56	0.70
		-10	-38	-30	+2252		-667	-0.00018			0.26	0.79

Table 2: Backbone values used in numerical models' calibration.

Joint rotations ranges			
Joint's type	ϑ_{cr} (rad)	ϑ_y (rad)	ϑ_u (rad)
External	$0.0006 \leq \vartheta \leq 0.0015$	$0.003 \leq \vartheta \leq 0.0075$	$0.01 \leq \vartheta \leq 0.02$

Table 3: Proposed ranges for external joints rotations.

Figure 6 shows the envelopes obtained for the experimental tests on external joints analyzed in terms of joint rotation (ϑ) vs normalized moment (M/M_y). By observing the shape of the proposed curves, it can be seen that on the basis of the case study, the most appropriate backbone was chosen to describe the joints behavior (bi-linear or tri-linear).

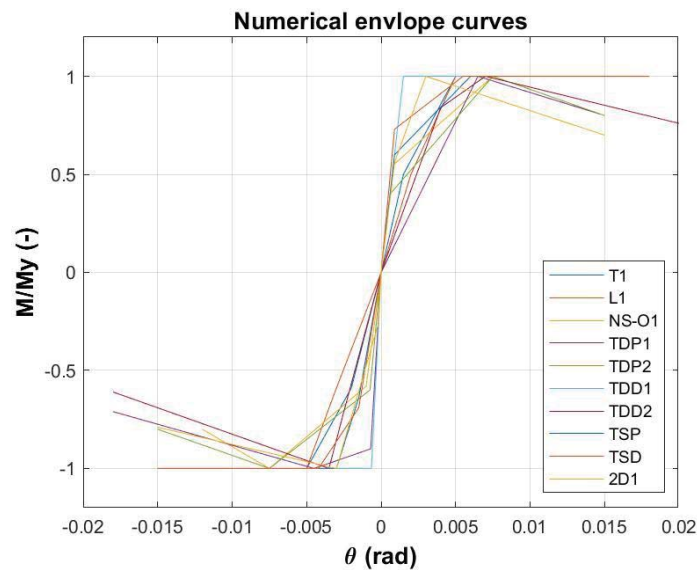


Figure 6: Envelope curves of numerical tests on literature specimens reported in Table 2.

6 CONCLUSIONS

In this paper, an experimental test on an exterior beam-column joint designed for gravity loads has been numerically modelled by a lumped plasticity approach. The joint non-linear deformation capacity represented through a single non-linear rotational spring placed at beam-column intersection. For what concerns the numerical settings, it was necessary to define an efficient moment-rotation relationship allowing to obtain a reliable prediction of the selected exterior joint specimen NS-O1. Moreover, the parameters to be defined were the elastic stiffness, pre- and post-cracking slopes, as well as the pinching behavior, as a function of the type of joints (exterior), joint dimensions, axial load ratio, longitudinal reinforcement type, anchorage details.

Finally, two different backbones were chosen to simulate the experimental test in terms of top force-global drift response. The first one consists of a simple bi-linear relationship, useful for the experienced practitioner, which should adopt the most convenient approach to consider joint deformation capacity, according to NZSEE2017 Seismic Assessment Guidelines [21].

The second one consists of a tri-linear relationship, useful in the research field when the goal is to capture detailed aspects of the experimental test to be reproduced, or in general of the overall joint behavior, depending on the required degree of accuracy and scope of work. In this case, the tri-linear backbone can capture and better model the point of first cracking, the elastic and softening branches.

All the parameters that characterize the backbone curves and their hysteretic behavior are reported, highlighting how the values provided by NZSEE2017 Seismic Assessment Guidelines [21] are intentionally and reasonably providing average behavior, while, for a case-by-case specific analysis, more appropriate parameters can be identified to better describe the joints performances. This work represents a small part of a more extensive numerical simulation campaign on existing joints currently under development.

ACKNOWLEDGEMENTS

The authors wish to acknowledge the financial support received by the Italian Department of Civil Protection (ReLUI 2019-2021 Grant – Inventory of existing structural and building types- CARTIS).

REFERENCES

- [1] M. Di Ludovico, A. Digrisolo, F. Graziotti, C. Moroni, A. Belleri, S. Caprili, C. Carocci, A. Dall'Asta, G. De Martino, S. De Santis, B. Ferracuti, D.K Ferretti, G. Fiorentino, A. Mannella, A. Marini, C. Mazzotti, A. Sandoli, A. Santoro, S.M Silvestri, L. Sorrentino, G. Magenes, A. Masi, A. Prota, M. Dolce, G. Manfredi, 2017. The contribution of ReLUI to the usability assessment of school buildings following the 2016 central Italy earthquake. *Bollettino di Geofisica Teorica ed Applicata*, 58(4), 353-376.
- [2] H. Crowley, R. Pinho, J.J. Bommer, A Probabilistic Displacement-based Vulnerability Assessment Procedure for Earthquake Loss Estimation. *Bulletin of Earthquake Engineering* 2004; 2(2): 173–219.
- [3] J.W. Baker, C.A. Cornell, Uncertainty propagation in probabilistic seismic loss estimation. *Structural Safety* 2008; 30(3): 236–252.

- [4] F. Romano, M. Faggella, R. Gigliotti, M. Zucconi, B. Ferracuti, Comparative seismic loss analysis of an existing infilled RC building based on element fragility functions proposals. *Eng. Struct.* 2018; 177: 707–723.
- [5] F. Romano, M.S. Alam, M. Zucconi, M. Faggella, A.R. Barbosa, B. Ferracuti, Seismic demand model class uncertainty in seismic loss analysis for a code designed URM infilled RC frame building. *Bull. Earthq. Eng.* 2021; 19(1): 429–462.
- [6] M. Zucconi, M. Sabene, S. Pampanin, B. Ferracuti, Seismic assessment of a RC frame building designed for gravity loads including joint deformation capacity model, *Proceedings of Phdsymp 2021*.
- [7] G. Calvi, G. Magenes, S. Pampanin, Relevance of beam-column joint damage and collapse in rc frame assessment. *J. Earthq. Eng.*, 2002, 6, 75-100.
- [8] S. Pampanin, D. Bolognini, A. Pavese, Performance-Based Seismic Retrofit Strategy for Existing Reinforced Concrete Frame Systems Using Fiber-Reinforced Polymer Composites, 2007, *J. Compos. Constr.*, Vol. 11(2), 211-226.
- [9] S. Pampanin, G. M. Calvi, M. Moratti, Seismic behaviour of R.C. beam-column joints designed for gravity loads, *12nd European Conf. on Earthquake Engineering*, 2002.
- [10] A. Masi., G. Santarsiero, D. Nigro, Cyclic tests on external RC beam–column joints: role of seismic design level and axial load value on the ultimate capacity. *J Earthquake Eng.* 2013;17(1):110–36.
- [11] A. Masi., G. Santarsiero, G. P. Lignola, G. M. Verderame, Study of the seismic behavior of external RC beam-column joints through experimental tests and numerical simulations, *Eng. Struct.*, vol. 52, 207–219, 2013.
- [12] M. J. N. Priestley, Displacement-based seismic assessment of reinforced concrete buildings, *J. Earthq. Eng.*, 1(1), 1997, 157–192.
- [13] C.P. Pantelides, C. Clyde, L.D. Reaveley, Performance-based evaluation of reinforced concrete building exterior joints for seismic excitation. *Earthquake Spectra*, 2002.
- [14] M. Sabene, M. Zucconi, B. Ferracuti, S. Pampanin, Open Issues on Testing and Modeling Existing RC Beam-Column Joints, *AIP Conference Proceedings* 2293, 240002 (2020).
- [15] S. Pampanin, G. Magenes, A. Carr, Modelling of shear hinge mechanism in poorly detailed RC beam-column joints, *fib Symposium Concrete Structures in Seismic Regions*, 2003, 171.
- [16] J. Hegger , A. Sherif, W. Roeser, Nonlinear finite element analysis of reinforced concrete beam–column connections. *ACI Struct J*, 2004;101(5):604–14.
- [17] A.C. Birely, L.N. Lowes, E. Lehman, A model for the practical nonlinear analysis of reinforced-concrete frames including joint flexibility. *Eng Struct* 2012;34(1):455–65.
- [18] M. T. De Risi, P. Ricci, G. M. Verderame, Modelling exterior unreinforced beam-column joints in seismic analysis of non-ductile RC frames, *Earthq. Eng. Struct. Dyn.*, 46, no. 6, pp. 899–923, May 2017.
- [19] G. J. O'Reilly, T. J. Sullivan, Modeling Techniques for the Seismic Assessment of the Existing Italian RC Frame Structures, *J. Earthq. Eng.*, 2469, 1–35, 2017.
- [20] J. Shayanfar, H. A. Bengar, A. Parvin, Analytical prediction of seismic behavior of RC joints and columns under varying axial load, *Eng. Struct.* 174 (2018) 792-813.

- [21] NZSEE (2017). New Zealand Society for Earthquake Engineering, Wellington, New Zealand.
- [22] S. Pampanin, Alternative Performance-Based Retrofit Strategies and Solutions for Existing RC Buildings, Chapter 13 (267-295) in *Seismic Risk Assessment and Retrofitting, Geotechnical, Geological, and Earthquake Engineering 10* (Editors A. Ilki et al.), 2009.
- [23] U. Akguzel, S. Pampanin, Assessment and design procedure for the seismic retrofit of reinforced concrete beam-column joints using FRP composite materials. *J Compos Constr*, 2012.
- [24] C. Del Vecchio, M. Di Ludovico, A. Balsamo, A. Prota, Seismic Retrofit of Real Beam-Column Joints using Fiber-Reinforced Cement (FRC) Composites, *J. Struct. Eng.*, 2018,10.1061.
- [25] S. Pampanin, Towards the practical implementation of performance-based assessment and retrofit strategies for RC buildings: challenges and solutions”, *SMAR2017- 4th Conf. on Smart Monitoring, Assessment and Rehabilitation of Structures*, 2017.
- [26] B. Ferracuti, M. Savoia, M. Zucconi, RC frame structures retrofitted by FRP-wrapping: A model for columns under axial loading and cyclic bending. *Eng. Struct.*, 2020; 207: 110243.
- [27] M. Zucconi, M. Sabene, M. Kioumars, B. Ferracuti, Pre-code RC Bare Frame: seismic retrofit with alternative strategies, *AIP Conference Proceedings* 2293, 240004 (2020).
- [28] C. Del Vecchio, R. Gentile, M. Di Ludovico, M. Uva, S. Pampanin, Implementation and Validation of the Simple Lateral Mechanism Analysis (SLaMA) for the Seismic Performance Assessment of a Damaged Case Study Building, *J. Earthq. Eng.*, 2020, 24(11), 1771-1802.
- [29] E. Hertanto, Seismic assessment of pre-1970s reinforced concrete structures, Department of Civil and Natural Resources Engineering, University of Canterbury, 2005
- [30] W. Y. Kam, Selective weakening, and post-tensioning fro the seismic retrofit of non-ductile RC frames, Department of Civil and Natural Resources Engineering, University of Canterbury, 2010.
- [31] U. Akguzel, Seismic performance of FRP retrofitted exterior RC beam-column joints under varying axial and bidirectional loading, Department of Civil and Natural Resources Engineering, University of Canterbury, 2011.
- [32] G. Genesio, Seismic assessment od rc exterior beam-column joints and retrofit with haunches using post-installed anchors, Institute for Materials in Construction at the University of Stuttgart, 2011
- [33] A. Carr, RUAUMOKO – Inelastic Dynamic Analysis, Department of Civil Engineering, University of Canterbury, 2004.

ASSESSMENT OF THE RESPONSE ENVELOPE OF REINFORCED CONCRETE MEMBERS WITH DIFFERENT FAILURE MODES

Mariano Di Domenico¹, Paolo Ricci¹, and Gerardo M. Verderame¹

¹ Department of Structures for Engineering and Architecture, University of Naples Federico II
Via Claudio 21 – 80125 – Naples, Italy
e-mail: {mariano.didomenico, paolo.ricci, verderam}@unina.it

Abstract

The expected lateral response of reinforced concrete (RC) elements strongly depends on their failure mode. Code-conforming RC members are supposed to exhibit a flexural (F) ductile failure, with complete exploitation of their post-peak displacement/deformation capacity. However, substandard RC elements, which are typical of existing structures, may undergo a shear failure after yielding (FS) or even before yielding (S) of longitudinal reinforcement. In this case, the element is classified as “shear-sensitive” and may be characterized by an abrupt collapse after the attainment of the peak load-capacity, with a fast loss of lateral load-bearing capacity up to the onset of the progressive reduction of the axial load-bearing capacity. This condition may trigger structural collapse, as also shown from surveys of damages due to strong earthquakes in past and recent times. So, the determination of the failure mode of RC members is paramount for a reliable assessment of the seismic safety of structures.

In general, static criteria are applied to pre-classify the expected failure mode of RC members and their response backbone is defined dependently on the determined failure mode. However, a comprehensive approach for modelling, with a unique set of predictive equations, the response envelope of RC members without pre-determining with a deterministic approach their failure mode is missing.

In this paper membership functions are defined to determine for RC columns the possibility that they exhibit an F, an FS, or an S failure. A set of basic predictive equations are defined, based on experimental data, to define a multilinear response envelope. The proposed equations may be combined with membership functions to use a unique set of equation able to reproduce the behaviour of RC columns with different expected failure modes.

Keywords: RC element, existing, seismic assessment, failure mode, response envelope, model.

1 INTRODUCTION

In the last decades, one of the trends of research in the structural engineering field is aimed at providing robust and reliable tools for nonlinear modelling of structural members. This is an essential step towards a complete implementation of a performance-based approach for the seismic design and assessment of structures in technical codes and current practice.

In Reinforced Concrete (RC) structures, primary elements may have a different lateral nonlinear response dependently on their failure mode. If, under lateral loads, the element can first yield and then exploit its entire ductility capacity (as shown in Figure 1), its failure mode is ductile and flexure-controlled. Such a kind of element is defined flexure-critical, the name of its failure mode is usually abbreviated with an “F”, the element itself can be defined as an “F element”. If, under lateral loads, the element cannot exploit its entire ductility capacity (as shown in Fig. 1), the element is defined shear-critical, since the ductile response of the element is prematurely interrupted by the occurrence of a shear failure. Two conditions may occur: if the element is anyhow able to yield, the failure mode is defined “FS”, since it is first governed by flexure (the element can yield), then by shear (the element cannot attain its ductility capacity since a shear failure occurs first); if the element is not able even to yield, since the shear failure occurs before yielding, the failure mode is defined “S”, since it is governed by shear. Also in this case, elements experiencing an FS failure mode are called “FS elements”, while elements experiencing an S failure mode are called “S elements”.

Also from Figure 1, it is clear that RC members with different failure modes have different lateral response. For this reason, the assessment of the expected failure mode (or “classification of the failure mode”) is essential to correctly model the nonlinear response of each member and, so, to obtain a reliable prediction of the structural performance. This is of paramount importance especially when dealing with nonlinear modelling and seismic capacity assessment of existing RC buildings.

In the literature, different approaches have been proposed for the classification of the failure mode of structural members. Some of them have been also introduced in building codes. The first approach to the classification of failure mode was described by Priestley et al. [1] based on ATC-6 [2] provisions. First, it is stated that the shear strength of a RC structural members is maximum when the element is in the elastic field; such a strength decreases at increasing ductility demand due to the damage of the element, up to a minimum (or “residual”) value. Similarly to what is represented in Figure 1, the failure mode is F if the shear force corresponding to flexural strength is less than the residual shear strength; the failure mode is S if the shear force corresponding to flexural strength is more than the initial shear strength; otherwise, the expected failure mode is FS. This approach for the classification of structural members’ failure mode, with consistent nonlinear modelling of the lateral response of these structural members, has been adopted for nonlinear time-history analyses on case-study existing RC buildings in [3]. However, different authors, based on experimental evidences, highlighted that the ratio between the shear strength of a member and the shear demand in equilibrium with its flexural strength cannot completely explain the observed failure mode of RC elements.

For example, Zhu et al. [4] proposed, based on experimental data, a classification method distinguishing F and S elements; FS elements are mostly included among S elements. According to this method, first the transverse reinforcement ratio should be calculated. If this ratio is lower than 0.002, the element is classified as S. Otherwise, the shear span-to-dept of the cross section ratio and the ratio between the plastic shear demand and the shear strength by Sezen and Moehle [5] are calculated. If the first ratio is lower than 2 or the second ratio is higher than 1.05, the element is classified as S. Otherwise, it is classified as F.

Ghannoum and Matamoros [6] and Ghannoum [7] proposed a modification to the method of classification of the failure modes of columns due to splice deficiency reported in ASCE/SEI 41-13 [8]. The proposal has been implemented in ASCE/SEI 41-17 [9] together with a proposal for the definition of the significant points of the lateral response of RC columns depending on the potential failure due to splice deficiency.

Based on experimental data, Hua et al. [10] proposed a classification method of the failure mode of RC members based on the concept of likelihood of shear failure. The probability of shear failure is calculated based on a demand-to-capacity ratio in which the capacity is evaluated through a proposed shear strength model.

Based on experimental data, Ma and Gong [11] proposed the calculation of a factor ω depending on geometric and mechanical characteristics of the RC columns. Based on the value assumed by the factor ω , it is possible to establish the expected failure mode of the element. One of the most significant advantages of this approach is that, differently from other methods, the prediction of the failure mode is independent on the specific shear strength model adopted. A similar approach will be introduced also in this study.

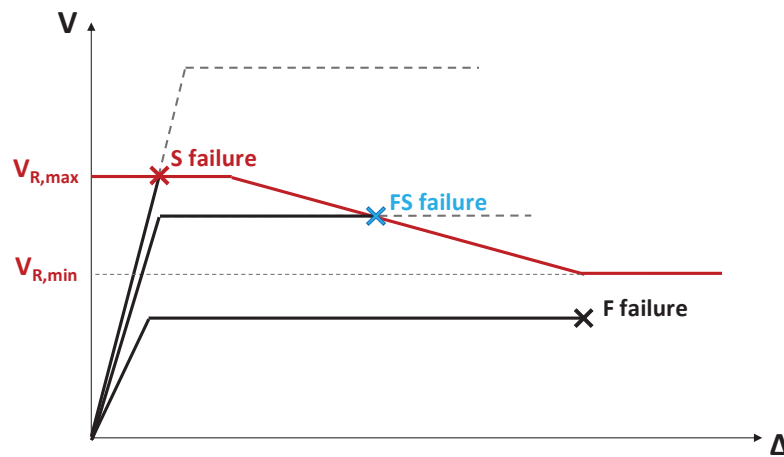


Figure 1: Illustrative sketch of the expected lateral response of F, FS, and S members.

One of the shortcomings of most of these approaches is their deterministic outcome. In this work, an empirical approach based on fuzzy theory is proposed for the assessment of the failure mode of RC members. In other words, the proposed approach aims at assigning to each generic RC structural element the “possibility” (expressed through a scalar between 0 and 1) of being “member” of the sets of F, of FS and of S elements. This scalar is calculated via membership functions which are defined for each of the three sets/failure modes. The definition of a “continuous” classification of the failure mode of structural elements is a preliminary step towards the assessment of the lateral response of RC members without an explicit pre-classification, but by means of an implicit modification of the expected ductile response backbone of the element by using the proposed membership functions. Based on the same experimental database, empirical equations are proposed for the assessment of the expected response envelope of ductile elements.

2 EXPERIMENTAL DATABASE

The definition of the proposed approach for the direct assessment of RC elements’ failure mode is based on the experimental data collected in the ACI 369 Rectangular Column Database [12], which will be briefly named “ACI database” in the following.

The ACI database is constituted by 326 cyclic tests of rectangular RC columns. In this work, only cyclic tests of rectangular-reinforced columns are considered. All specimens are characterized by the presence of deformed (i.e., ribbed) longitudinal rebars, while transverse reinforcement may be realized with deformed or plain bars. For each specimen, the following data are reported:

- Material properties (for concrete, longitudinal and transverse reinforcement);
- Column geometry (for the overall column, longitudinal and transverse reinforcement);
- Confinement details (i.e., the configuration of transverse reinforcement);
- Test configuration details (i.e., how the lateral load was applied on the specimen);
- Test results in terms of observed failure mode, significant values of force and displacement, force-displacement loops (if available).

Since the assessment of the failure mode is the core issue of this work, it is worth mentioning how the definition of the failure mode was performed by the Authors of the database. Two approaches are considered for failure mode classification: the first one is consistent with the approach adopted by PEER in [13] and is more based on the “observed” response of the specimens; the second, which is more “practice-oriented”, is based on the assessment of transverse reinforcement detailing and on the ratio between the plastic shear demand and the expected shear capacity. The discussion presented in this paper is based on the first classification approach, i.e., the one consistent with PEER [13], since it is independent of the assessment of shear strength by means of a specific shear capacity model. In fact, consistently with the PEER approach, a first distinction is made between shear-sensitive and non-shear-sensitive members. If the Authors of each experimental test reports the occurrence of shear damage for a certain specimen, the element is classified as “shear critical”. Otherwise, it is classified as “flexure critical” and the assigned failure mode is F.

Among Shear Critical elements, a mixed analytical/empirical approach is adopted to distinguish FS and S elements. First, for each specimen, the maximum lateral force attained (F_{eff}) is evaluated. Then, the theoretical maximum force corresponding to the attainment of a maximum strain in concrete equal to 0.4% ($F_{0.004}$) is calculated. In addition, based on the experimental response of the specimen, the ductility capacity μ_{fail} is calculated by assuming as failure displacement the one associated with a force capacity equal to 0.80 times F_{eff} on the softening branch of the force-displacement response. If F_{eff} is lower than 0.95 times $F_{0.004}$ or μ_{fail} is equal or lower than 2, the Shear Critical element is classified as S. Otherwise, it is classified as FS.

Among the 326 tests collected in the database, only those for which all the significant geometric, mechanical and response parameters were available have been used for this study. In addition, only “completely cyclic” tests were considered: in other words, test with monotonic loading before and/or after yielding were excluded. In addition, columns with spliced reinforcement were excluded since they can undergo a premature failure due to insufficient anchorage length, as shown, for example, for the specimens by Melek and Wallace [14] that are included in the original ACI dataset but are not considered for this study. Hence, a subset of the ACI database constituted by 260 tests is considered in this work. In this reference subset, hereinafter named “collected database”, 156 tests are classified as F (60% of the database), 69 tests are classified as FS (26% of the database), 35 tests are classified as S (14% of the database). Despite other databases considering shear-sensitive RC members have been collected including a larger amount of S tests (e.g., [15, 16, 17]), it was preferred to adopt ACI database since it includes also F elements, which is fundamental for the scope of this study; on the other hand, “merging” F elements from ACI and FS/S elements from other databases was excluded, in order to use

data associated with RC columns whose failure mode has been classified with a unique and consistent approach.

The tests collected in the reference subset are characterized by $0 \leq v$ (axial load ratio) ≤ 0.90 , $13 \leq f_c$ (compressive strength of concrete) ≤ 118 MPa, $318 \leq f_{yl}$ (yielding stress of longitudinal rebars) ≤ 587 MPa, $249 \leq f_{yw}$ (yielding stress of transverse rebars) ≤ 1424 MPa, $0.0068 \leq \rho_l$ (longitudinal reinforcement ratio) ≤ 0.0694 , $0.0006 \leq \rho_w$ (transverse reinforcement ratio) ≤ 0.0321 , $0.11 \leq h/L_s$ (cross section height-to-shear span aspect ratio) ≤ 0.87 , $0.11 \leq s/d$ (transverse reinforcement spacing-to-effective depth of the cross section ratio) ≤ 1.27 . In addition, the experimental response loops of specimens were corrected, if necessary, in order to remove the spurious effect given by geometric non-linearity (i.e., P- Δ effects) and, so, consider only mechanical sources triggering the post-peak softening. The correction has been performed in order to lead back the experimental response of the selected specimens to “Case I” according to [13].

The database is described more in details in [12].

3 ASSESSMENT OF FAILURE MODE VIA MEMBERSHIP FUNCTIONS

In this work, the collected database is considered as the union of fuzzy sets [18]. A fuzzy set is a collection of objects with a certain membership. More specifically, each specimen can be member of the “F elements” fuzzy set, of the “FS elements” fuzzy set and of the “S elements” fuzzy set. In other words, it is possible to define, for each specimen, if it is certainly F, certainly FS or certainly S.

However, when dealing with a generic structural member belonging to a structure, it is not always possible to define with certainty if it will behave as an F element, or as an FS element or as an S element. In this case, a membership function allows expressing the possibility [19] of that element of behaving as an F element, as an FS element and as an S element. In other words, the membership function for F elements, μ_F , expresses with a number ranging from 0 to 1, the possibility that a certain structural member belongs to the set of F elements; the same applies for the membership function for FS elements, μ_{FS} , and for the membership function for S elements, μ_S . Of course, it is certain that a member will be part of one of the three sets. So, the sum of the values assumed by the three membership functions for a certain structural element should always be equal to 1.

The membership function can express the possibility of a certain structural member of being part of a certain set as a function of a predictive parameter (or of more predictive parameters) that represents the structural member characteristics. Of course, the significant characteristics of the structural member (i.e., those that can define a potential domain – also called support – for the membership function) depend on the nature of the membership function itself. For example, since the membership functions that are defined in this work are related to the concept of failure mode, it is expected that parameters like the axial load ratio or the amount of longitudinal and transverse reinforcement may be appropriate as predictors. Section 3.2 is dedicated to the definition of the most appropriate predictive parameter(s).

Consider now to have defined a certain predictive parameter x . Hence, the membership functions are expressed as $\mu_F(x)$, $\mu_{FS}(x)$, $\mu_S(x)$. The values assumed by the membership functions are set based on the experimental data reported in the collected database. The procedure adopted to define the shape of the membership functions is reported below, with reference to the illustrative sketch reported in Figure 2.

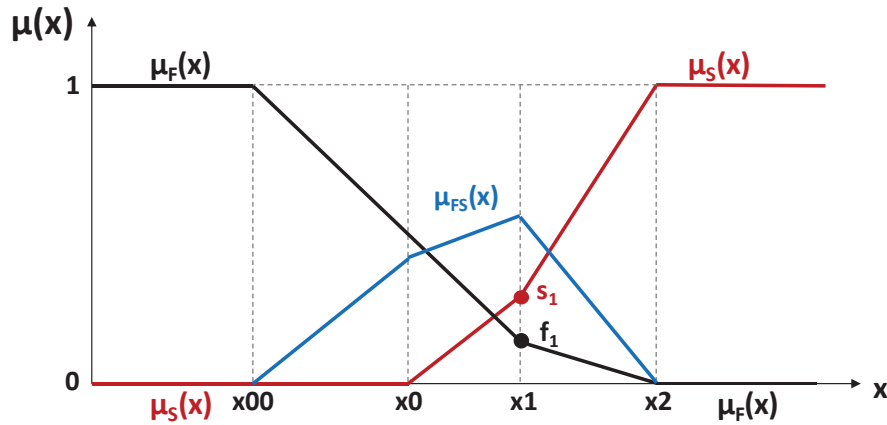


Figure 2: Illustrative sketch of the adopted membership functions.

1. Membership functions are assumed as piecewise linear;
2. The value x_{00} of the predictor parameter is set. It is defined in order to have $\mu_F(x \leq x_{00}) = 1$. In other words, if the predictor x is lower than or equal to x_{00} , it is assumed that certainly the structural member will exhibit an F failure mode. The value of x_{00} is obtained from the collected database as the maximum value of x below which no FS or S failure is observed;
3. The value x_0 of the predictor parameter is set. It is defined in order to have $\mu_S(x \leq x_0) = 0$. In other words, if the predictor x is lower than or equal to x_0 , it is assumed that certainly the structural member will not exhibit an S failure mode. The value of x_0 is obtained from the collected database as the maximum value of x below which no S failure is observed;
4. The value x_2 of the predictor parameter is set. It is defined in order to have $\mu_S(x \geq x_2) = 1$. In other words, if the predictor x is higher than or equal to x_2 , it is assumed that certainly the structural member will exhibit an S failure mode. The value of x_2 is obtained from the collected database as the maximum value of x above which no F or FS failure is observed;
5. The membership function for FS failure mode $\mu_{FS}(x)$ is assumed equal to $1 - \mu_F(x) - \mu_S(x)$;
6. Being $f_1 = \mu_F(x_1)$ and $s_1 = \mu_S(x_1)$, the values of x_1 (which is between x_0 and x_2), f_1 and s_1 are set after an iterative procedure aimed at obtaining the “best performance” for the membership functions, i.e., the set of x_1 , f_1 , and s_1 values for which the adopted membership functions are able to correctly predict the failure mode of the specimens of the collected database in the highest number of cases.

In a previous work [20], different potential predictors were already evaluated, namely the axial load ratio, the aspect ratio and the ratio between the mechanical ratio of longitudinal and transverse reinforcement. In general, as also reported in section 1, the distinction between shear critical and flexural critical structural members can be performed via a “static” approach by comparing shear demand at yielding V_y (i.e., the one in equilibrium with the yielding moment acting at the base of column) and the shear demand at maximum V_{max} (i.e., the one in equilibrium with the maximum moment acting at the base of column), with the shear resistance of the column, V_R . A member is flexure critical if V_{max} is lower than the minimum value of V_R ; otherwise, it is shear-critical. It should be considered that at increasing axial load ratio, both the maximum moment (i.e., V_{max}) and the shear resistance V_R , first increase and then decrease. So,

a specific trend for the frequency of each failure mode at increasing v is not expected. In fact, in [20], it was observed that the axial load ratio alone is not a good predictor of the failure mode. A better performance is obtained by considering as predictor the aspect ratio and the ratio between longitudinal and transverse reinforcement mechanical ratios. However, it was observed that the best performance was obtained by adopting as predictor a combination of these two parameters, as shown in Equation 1.

$$x = \frac{h}{L_s} \frac{\omega_l}{\omega_w} = \frac{h}{L_s} \frac{s}{d} \frac{A_{sl} f_{yl}}{A_{sw} f_{yw}} \quad (1)$$

Since the predictive parameter x has been chosen, it is possible to define the membership functions. Based on the collected database, it is observed that:

1. For x lower than or equal to 0.75, only F failures are observed. Hence, x_{00} (see Figure 2) is assumed equal to 1;
2. No S failure is observed for x lower than or equal to 1.50. Hence, x_0 (see Figure 2) is assumed equal to 1.50;
3. Only S failures are observed for x higher than or equal to 13. Hence, x_2 (see Fig. 2) is assumed equal to 13.

The best performance set of membership functions is obtained if x_1 (see Figure 2) is assumed equal to 3.1, if f_1 (see Figure 2) is assumed equal to 0.07 and if s_1 (see Figure 2) is assumed equal to 0.09. With these assumptions, in fact, a correct prediction of the failure mode (i.e., the more possible failure mode corresponds with the actual failure mode) is obtained in 84% of cases. Note that the values of x_{00} , x_0 , x_2 , x_1 , f_1 , and s_1 are different with respect to those shown in [20] since they were evaluated with respect to a smaller database.

The obtained membership functions are shown in Figure 3 and compared with the experimental failure modes. Experimental failure modes are reported as filled circles if they are predicted as the most possible failure mode by the adopted membership functions; otherwise, they are reported as blank circles.

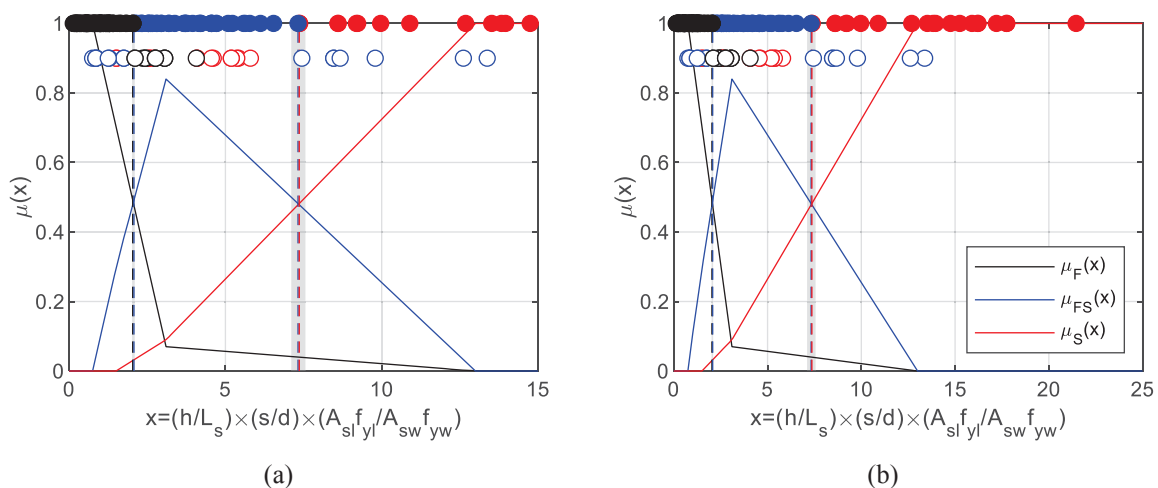


Figure 3: Adopted membership functions. Graph with x between 0 and 15 (a) and graph with x between 0 and 25 (b).

It is possible to observe that for x lower than 2 the most possible failure mode is F; for x between 2 and 7.3 the most possible failure mode is FS; for x higher than 7.3, the most possible failure mode is S. It is worth recalling that for x lower than 0.75 the only possible failure mode is F, while for x higher than 13 the only possible failure mode is S. It is also worth mentioning that for x between 2 and 2.1 and for x between 7.1 and 7.6 there is no failure mode with possibility of occurrence higher than 50%: special caution should be adopted when dealing with structural members belonging to these “transition zones” (grey-filled areas in Figure 3).

4 BASIC RESPONSE ENVELOPE

In this section, the basic bending moment M – chord rotation θ response envelope is determined for ductile members, i.e., for RC columns with x lower than or equal to 0.75.

4.1 Response envelope and methodology

Based on the response envelope of the experimental response of ductile members included in the database, the following characteristic points/conditions were defined.

- The first point of the proposed envelope is yielding point. First, a theoretical prediction of M_y was obtained by means of a fibre section analysis and indicated as $M_{y,fiber}$. Then, the experimental maximum moment M_{max} was determined. If M_{max} resulted higher than $1.07M_{y,fiber}$, the yielding point was identified on the experimental envelope at the attainment of M equal to $M_{y,fiber}$; otherwise, according to [21], the yielding point was identified on the experimental envelope at the attainment of M equal to $0.80M_{max}$;
- The second point of the envelope is the peak load point. It was simply determined at the attainment of a moment equal to the maximum moment M_{max} .
- The third point of the envelope was determined on the descending branch of the experimental response envelope at the attainment of a moment equal to $0.80M_{max}$. This point corresponds to the attainment of a conventional “ultimate” condition.
- The fourth and last point of the envelope is the one corresponding to the complete loss of lateral load capacity of the column. It was determined, on the experimental envelope, by linear extrapolation up to zero moment resistance of the extreme points of the imposed displacement cycles defining the descending branch of the experimental envelope beginning from the experimental point at conventional “ultimate”, as defined at the previous point. Note that, to limit the use of unreliable extrapolated data, only tests for which at least a 50% strength decrease after peak load point attainment were considered for the assessment of this point.

A consistent approach was adopted to define an equivalent set of predictive equations for the assessment of the response envelope of rectangular RC column with plain bars in [22].

The following parameters were adopted to identify the abovementioned characteristic points of the response envelope, as shown in Figure 4.

- The ratio between the flexural secant stiffness at yielding of the member cross-section (also called “effective stiffness”), EI_y , and the flexural stiffness of the gross section EI_g . This ratio allows defining, together with the yielding moment M_y previously defined, the chord rotation at yielding, θ_y ;
- The maximum moment M_{max} together with the corresponding post-yielding plastic chord rotation, θ_{max}^{pl} ;

- The post-capping plastic chord rotation at conventional “ultimate” condition, θ_{ult}^{pc} ;
- The post-ultimate plastic chord rotation at the attainment of zero lateral load capacity, θ_0^{pu} , together with the softening stiffness toward zero lateral load capacity, K_θ .

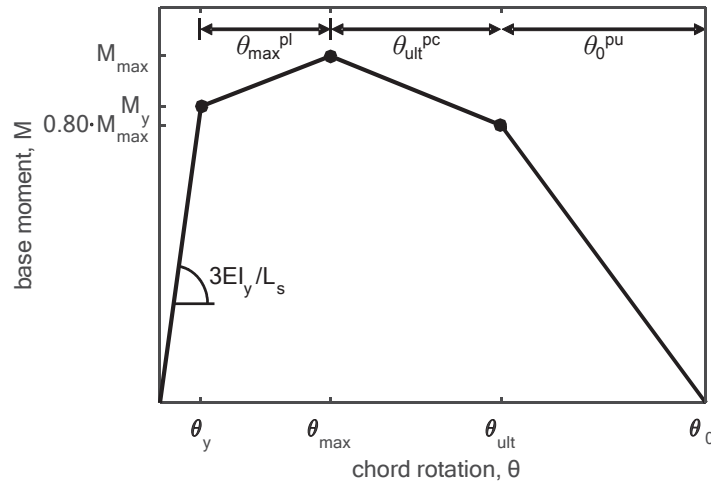


Figure 4: Characteristic points and assumed parameters of the base moment (M) - chord rotation (θ) response envelope.

In order to define empirical formulations for the prediction of the abovementioned response parameters, some potential predictors were selected. The candidate predictors were chosen by considering the outcomes of past studies (e.g., [23]), as well as their expected mechanical influence. In addition to those listed for the description of the experimental database (see section 2), some combinations of them were assumed as potential predictive parameters, namely:

- the ratio between the spacing of transverse reinforcement, s , and the cross-section depth, d ;
- the ratio between the spacing of transverse reinforcement, s , and the diameter of longitudinal rebars, d_b ;
- a factor related to the proneness to buckling of longitudinal bars, $s_b = (s/d_b) \cdot (f_y/100)^{0.5}$;
- the area/mechanical ratio of longitudinal rebars ρ_l and ω_l ;
- the area/mechanical ratio of transverse reinforcement ρ_w and ω_w ;
- the longitudinal reinforcement area/mechanical ratio calculated by separating the contribution of reinforcement in compression (ρ_2 and ω_2 , respectively) from the contribution of reinforcement in tension + web reinforcement (ρ_1 and ω_1 , respectively);
- the ratio between the area/mechanical longitudinal reinforcement ratio for rebars in compression and the mechanical longitudinal reinforcement ratio for rebars in tension.

The statistical procedure adopted for defining the predictive equations below listed is described in detail in [24]. More specifically, linear least squares regressions were performed relating the output variables (expressed in terms of natural logarithm) and the potential predictors (expressed in their natural form, in terms of natural logarithm, or absent). The final equations proposed were selected among the ones with the minimum number of input variables but deemed as “statistically equivalent” – based on F-tests – to the basic predictive equations including all the potential predictors. For the assessment of predictive equations, T-tests were performed to remove outliers from the experimental database [25].

4.2 Predictive equations

The equations derived to define the response envelope of ductile rectangular RC columns with deformed bars are reported below, together with, for each proposed equation, the statistics – mean, median and Coefficient of Variation (CoV) – associated with the set of the observed value-to-predicted value ratios for the entire experimental database. In the proposed equations, forces must be expressed in Newtons and lengths in millimetres.

The ratio between secant-to-yielding and gross section stiffness, EI_y/EI_g can be calculated as reported in Equation 2 (observed-to-predicted ratio: mean=1.09, median=1.00, CoV=0.42).

$$EI_y/EI_g = 0.0318 \cdot 6.11^\nu \cdot (L_s/d)^{1.21} \quad (2)$$

Alternatively, the ratio between secant-to-40% of yielding moment and gross section stiffness, EI_{40}/EI_g can be calculated as reported in Equation 3 (observed-to-predicted ratio: mean=1.13, median=0.99, CoV=0.49).

$$EI_{40}/EI_g = 0.100 \cdot 3.20^\nu \cdot (L_s/d)^{0.871} \quad (3)$$

Note that both Equations 2 and 3 were obtained by considering not only F, but also FS specimens included in the database.

The post-yielding plastic chord rotation, θ_{\max}^{pl} can be calculated as reported in Equation 4 (observed-to-predicted ratio: mean=1.15, median=0.97, CoV=0.54). Note that for the assessment of θ_{\max}^{pl} some tests were not considered since their response envelope was provided with a branch at pseudo-constant moment demand roughly equal to the maximum moment. In these cases, the value of the chord rotation at peak load was not determinable in a unique and not ambiguous way.

$$\theta_{\max}^{pl} = 0.0073 \cdot 0.436^\nu \cdot (s/d)^{-0.261} \cdot 1.05^{100\omega_2} \quad (4)$$

For the calculation of the peak resistance, M_{\max} , a simple mean value is proposed attempting to predict the M_{\max}/M_y ratio, i.e., $M_{\max}/M_y = 1.31$ (observed-to-predicted ratio: CoV=0.15), with M_y calculated by means of a section fibre analysis.

The post-capping “ultimate” plastic chord rotation, θ_{ult}^{pc} can be calculated as reported in Equation 5 (observed-to-predicted ratio: mean=1.16, median=0.99, CoV=0.58).

$$\theta_{ult}^{pc} = 0.0126 \cdot 0.161^\nu \cdot 5.66^{\omega_l} \cdot 1.88^{100\rho_w} \quad (5)$$

The post-ultimate plastic chord rotation towards zero resistance, θ_0^{pu} can be calculated as reported in Equation 6 (observed-to-predicted ratio: mean=1.11, median=1.16, CoV=0.42). It is limited to the maximum value of θ_0^{pu} observed in the database.

$$\theta_0^{pu} = \min(0.065; 0.0193 \cdot 0.061^\nu \cdot 1.19^{100\omega_w}) \quad (6)$$

To avoid modelling issues, namely to avoid that the bilinear softening branch of the response envelope is characterized by decreasing (in absolute value) softening stiffness, the post-ultimate plastic chord rotation resulting from Equation 6 must be further limited according to Equation 7.

$$\theta_0^{pu} \leq 4\theta_{ult}^{pc} \quad (7)$$

4.3 Application

The comparison of the outcomes of proposed model for ductile RC members with six experimental responses included in the experimental database (the three specimens with the “best” performance of the proposed model and the three specimens with the “worst” performance of

the proposed model) is shown in Figure 5, together with the cyclic envelope calculated by applying the model by [23]. The best performance of the proposed model is obtained for specimens C5-00N tested in [26], C1-1 tested in [27] and Test1 tested in [28] while the worst performance is observed for specimens No.7 tested in [29], 214-08 tested in [30], and HC4-8L19-T10-0.1P tested in [31].

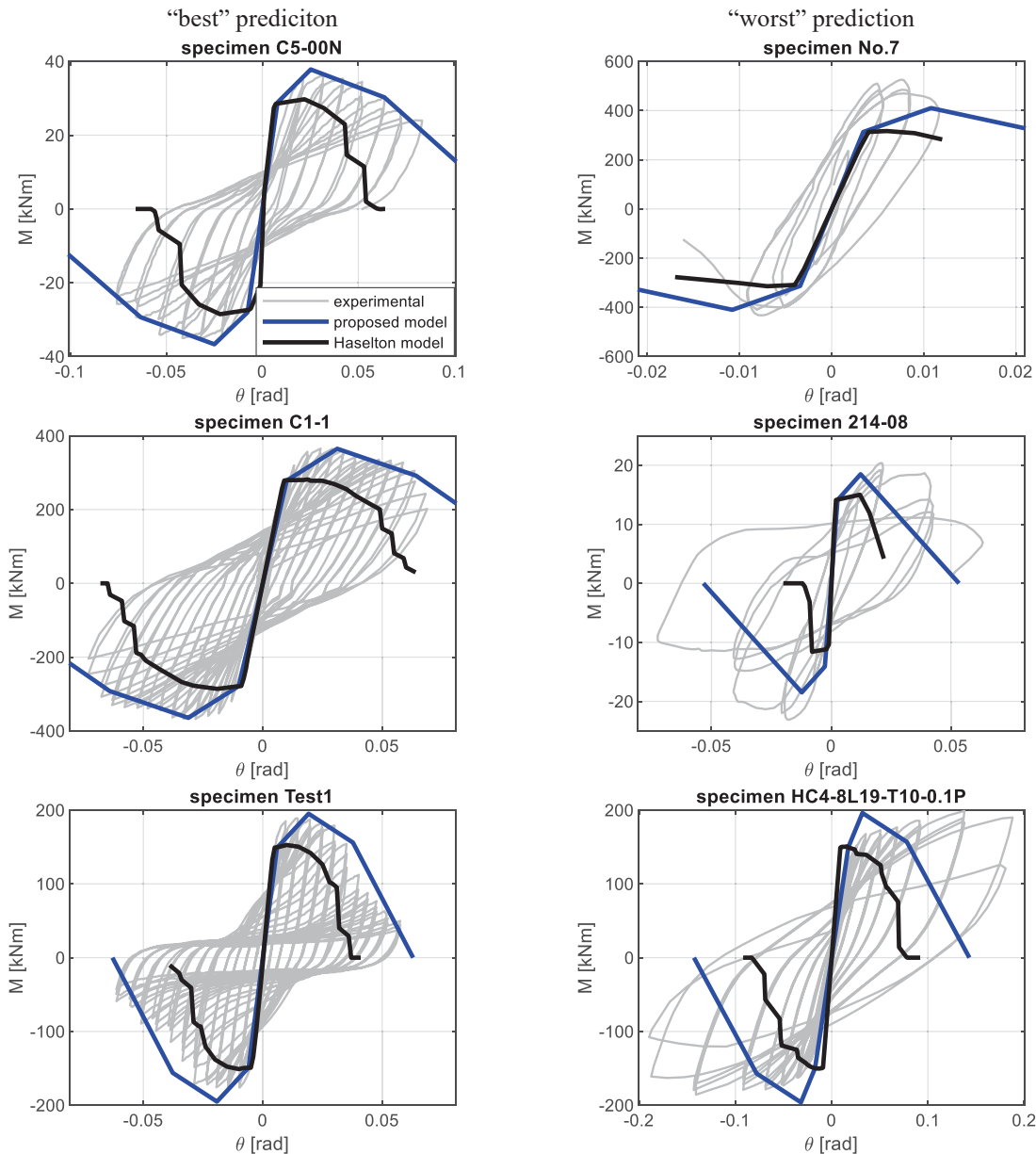


Figure 5: “Best” (left column) and “worst” (right column) predictions of the proposed model compared with the experimental response of the selected specimens and with the cyclic envelope predicted by applying the model proposed by Haselton et al. [23].

Since it was determined based only on cyclic tests, the proposed model already includes in its envelope the sources of strength degradation typical of members under cyclic (such as seismic) loading. On the contrary, the response envelope proposed by Haselton et al. [23] is monotonic, as it is based on the results of monotonic tests and on the expected monotonic envelope derived from a back-analysis of the results of cyclic tests. The cyclic envelope shown in Figure 5 as a

result of the application of the model by Haselton et al. is obtained by modelling the specimen in OpenSees [32] by adopting ModIMKPeakOriented Material model and by applying to it the real imposed displacement path. In general, it was observed that the model by Haselton et al. can show a fast decay of strength capacity, both in terms of maximum moment capacity and in terms of steepness of the softening branch when the imposed displacement path is characterized by a significant number of loading-unloading cycles. On the other hand, the proposed model seems to not predict well the cyclic response envelope when the maximum moment capacity is significantly higher than yielding moment and, in tune, the chord rotation at maximum is significantly higher than the chord rotation at yielding.

5 CONCLUSIONS AND FUTURE DEVELOPMENTS

- A subset of ACI 369 database of experimental tests on rectangular RC columns with deformed longitudinal rebars [12] has been selected. The selected tests were cyclic and realized on columns without lap-sliced anchorage of longitudinal rebars. In addition, they are characterized by different failure modes assessed independently on a specific shear strength model: namely, 156 tests are classified as F (60% of the database), 69 tests are classified as FS (26% of the database), 35 tests are classified as S (14% of the database).
- Based on the experimental database collected, a “continuous” approach for the assessment of the expected failure mode has been proposed. In fact, a single predictor parameter has been identified depending only on geometric and mechanical properties of the RC element. Based on this predictor, named x , membership functions are proposed to calculate the possibility (a number between 0 and 1) that the considered member exhibits an F, and FS or an S failure. RC members with x lower than or equal to 0.75 are expected to exhibit only an F failure mode, while members with x greater than 13 are expected to exhibit only an S failure mode. The proposed approach can correctly predict as most possible the actual failure mode of the specimens included in the database in 84% of cases.
- For RC members with x lower than or equal to 0.75, i.e., for expected ductile RC members, a set of predictive equations have been proposed to assess their cyclic moment – chord rotation response envelope up to the complete loss of lateral load resistance. This set of equations can be useful for modelling RC members, within a lumped plasticity approach, for collapse risk assessment of RC structures via nonlinear analyses.
- In the literature, a similar model with the same aims was already proposed by Haselton et al. [23]. However, it was observed that the cyclic response envelope predicted by applying this model may be affected by premature decay of strength capacity when the RC element is subjected by a significant number of loading-unloading cycles. In addition, the equations proposed by Haselton et al. [23] can predict only the expected monotonic envelope of the RC element, while the cyclic envelope including strength and stiffness degradation effects typical of seismic action can be determined only by applying to the RC member the real imposed displacement path. This makes the model by Haselton et al. [23] unfit for the assessment of RC structures via nonlinear static analysis, which is still a useful tool adopted by practitioners and researchers, especially for the assessment of existing buildings.
- In future works, the proposed equations for the assessment of the cyclic response envelope will be combined with the proposed membership functions in order to make them applicable for the evaluation of the expected response envelope for RC members with whichever

failure mode and, above all, without the necessity of pre-determining the expected failure mode. In addition, the parameters for modelling the cyclic degradation of unloading and reloading stiffness, as well as the so-called “pinching” effect will be calibrated.

ACKNOWLEDGMENTS

This work was developed under the financial support of ReLUIS-DPC 2019-2021 funded by the Italian Department of Civil Protection (DPC). This support is gratefully acknowledged.

REFERENCES

- [1] M.J.N. Priestley, R. Verma, Y. Xiao, Seismic shear strength of reinforced concrete columns. *Journal of Structural Engineering*, **120**(8), 2310-239, 1994.
- [2] Applied Technology Council (ATC), *Seismic design guidelines for highway bridges (ATC-6)*. Berkeley, California, United States of America, 1981.
- [3] P. Ricci, V. Manfredi, F. Noto, M. Terrenzi, M.T. De Risi, M. Di Domenico, G. Camata, P. Franchin, A. Masi, F. Mollaioli, E. Spacone, G.M. Verderame GM, RINTC-e: Towards seismic risk assessment of existing residential reinforced concrete buildings in Italy. *7th ECCOMAS Thematic Conference on Computational Methods in Structural Dynamics and Earthquake Engineering*. June 24-26, Crete, Greece, 2019.
- [4] L. Zhu, K.J. Elwood, T. Haukaas T, Classification and seismic safety evaluation of existing reinforced concrete columns. *Journal of Structural Engineering*, **133** (9), 1316-1330, 2007.
- [5] H. Sezen, J.P. Moehle, Shear strength model for lightly reinforced concrete columns. *Journal of Structural Engineering*, **130** (11), 1692-1703, 2004.
- [6] W.M. Ghannoum, A.B. Matamoros, Nonlinear modelling parameters and acceptance criteria for concrete columns. *ACI Special Publication*, **297**, 1-24, 2014.
- [7] W.M. Ghannoum, Re-evaluation of modeling parameters and acceptance criteria for non-ductile and splice-deficient concrete columns. *16th World Conference on Earthquake Engineering*. January 9-13, Santiago, Chile, 2017.
- [8] American Society of Civil Engineers/Structural Engineering Institute (ASCE/SEI) Committee 41 (2014): Seismic evaluation and retrofit of existing buildings (ASCE/SEI 41-13). Reston, Virginia, United States of America.
- [9] American Society of Civil Engineers/Structural Engineering Institute (ASCE/SEI) Committee 41 (2017): Seismic evaluation and retrofit of existing buildings (ASCE/SEI 41-17). Reston, Virginia, United States of America.
- [10] J. Hua, M.O. Erberhard, L.N. Lowes, X. Gu, Modes, mechanisms, and likelihood of seismic shear failure in rectangular reinforced concrete columns. *Journal of Structural Engineering*, **145** (10), 2019.
- [11] Y. Ma, J.X. Gong, Probability identification of seismic failure modes of reinforced concrete columns based on experimental observations. *Journal of Earthquake Engineering*, **22** (10), 1881-1899, 2018.

- [12] B. Sivaramakrishnan, Non-linear modeling parameters for reinforced concrete columns subjected to seismic loads. The University of Texas at Austin. PhD Dissertation, 2010.
- [13] M. Berry, M. Parrish, M. Eberhard, PEER Structural Performance Database: User's Manual, Version 1.0. Pacific Earthquake Engineering Research Center, University of California, Berkeley, CA, USA, 2004.
- [14] M. Melek, J.W. Wallace, Cyclic Behavior of Columns with Short Lap Splices. *ACI Structural Journal*, **101**(6), 802-811, 2004.
- [15] D.E. Biskinis, G.K. Roupakias, M.N. Fardis, Degradation of shear strength of reinforced concrete members with inelastic cyclic displacement. *ACI Structural Journal*, **101**(6), 773-83, 2004.
- [16] C. Del Vecchio, M. Del Zoppo, M. Di Ludovico, G.M. Verderame, A. Prota, Comparison of available shear strength models for non-conforming reinforced concrete columns. *Engineering Structures*, **148**, 312-327, 2017.
- [17] D.K. Zimos, P.E. Mergos, A.J. Kappos, Modelling of R/C members accounting for shear failure localisation: Hysteretic shear model. *Earthquake Engineering and Structural Dynamics*, **47**, 1722-1741, 2018.
- [18] L.A. Zadeh, Fuzzy sets. *Information and Control*, **8**(3), 338-353, 1965.
- [19] L.A. Zadeh, Fuzzy sets as a basis for a theory of possibility. *Fuzzy Sets and Systems*, **1**, 3-28, 1978.
- [20] M. Di Domenico, P. Ricci, G.M. Verderame GM, Towards a deformation capacity assessment of flexure- and shear-sensitive RC members with a unified approach. *17th World Conference on Earthquake Engineering*. September 13-18, Sendai, Japan, 2020.
- [21] K.J. Elwood, M. Eberhard, Effective stiffness of reinforced concrete columns. *ACI Structural Journal*, **106**(4), 476-484, 2009.
- [22] M. Di Domenico, P. Ricci, G.M. Verderame, Empirical calibration of hysteretic parameters for modeling the seismic response of reinforced concrete columns with plain bars. *Engineering Structures*, **XX**, 2021.
- [23] C.B. Haselton, A.B. Liel, S. Taylor-Lange, G.G. Deierlein, *Beam-column element model calibrated for predicting flexural response leading to global collapse of RC frame buildings*. PEER Report No. 2007/03. Pacific Earthquake Engineering Research Center, University of California, Berkeley, CA, USA, 2008.
- [24] G.M. Verderame, P. Ricci, An empirical approach for nonlinear modeling and deformation capacity assessment of RC columns with plain bars. *Engineering Structures*, **176**, 539-554, 2018.
- [25] B. Rosner, Percentage Points for a Generalized ESD Many-Outlier Procedure, *Technometrics*, **25**(2), 165-172, 1983.
- [26] A.B. Matamoros, *Study of Drift Limits for High-Strength Concrete Columns*. Department of Civil Engineering. Urbana (Illinois); University of Illinois at Urbana-Champaign. Doctor of Philosophy: 484, 1999.
- [27] Y.L. Mo, S.J. Wand, Seismic Behavior of RC Columns with Various Tie Configurations. *Journal of Structural Engineering*, **126**(10), 1122-1130, 2000.

- [28] H.K. Takemura, K. Kawashima, Effect of Loading Hysteresis on Ductility Capacity of Reinforced Concrete Bridge Piers. *Proceedings of Structural Engineering (Japan Society of Civil Engineers)*, **43**(A), 849-858, 1997.
- [29] S. Watson, *Design of Reinforced Concrete Frames of Limited Ductility*. Department of Civil Engineering. Christchurch; New Zealand; University of Canterbury. Doctor of Philosophy: 248, 1989.
- [30] X. Zhou, T. Satoh, W. Jiang, A. Ono, Y. Shimizu, Behavior of Reinforced Concrete Short Column Under High Axial Load. *Transactions of the Japan Concrete Institute*, 9, 541-548, 1987.
- [31] Y. Xiao, A. Martirosyan A, Seismic Performance of High-Strength Concrete Columns. *Journal of Structural Engineering*, **124**(3): 241-251, 1998.
- [32] F. McKenna, G.L. Fenves, M.H. Scott, OpenSees: *Open System for Earthquake Engineering Simulation*. Pacific Earthquake Engineering Research Center. University of California, Berkeley, CA, USA, 2004.

SEISMIC ASSESSMENT OF AN EXISTING RC BUILDING AFFECTED BY SLOW-MOVING LANDSLIDES INDUCED DISPLACEMENTS MONITORED BY REMOTE SENSING TECHNIQUE

Annalisa Mele¹, Andrea Miano¹, Diego di Martire^{2,3}, Donato Infante³, Andrea Prota¹ and Massimo Ramondini^{3,4}

¹ Department of Structures for Engineering and Architecture, University of Naples Federico II
80125, Naples, Italy
{annalisa.mele; andrea.miano; aprota@unina.it}

² Department of Earth, Environment and Resources Sciences, University of Naples Federico II
80126, Naples, Italy
diego.dimartire@unina.it

³ SINTEMA Engineering srl, Spin-Off University of Naples Federico II
80134, Naples, Italy
sintemasrl@gmail.com

⁴ Department of Civil, Architectural and Environmental Engineering, University of Naples Federico II
80125, Naples, Italy
ramondin@unina.it

Abstract

The seismic assessment of reinforced concrete (RC) structures is commonly carried out neglecting previous damage, eventually induced by other phenomena, although different forms of hazard can affect a structure during its existence. The coexistence of many hazard sources is very common, i.e., in countries affected by landslides, also characterized by high seismicity, like Italy. The aim of this work is both to demonstrate the potential utility of satellite data derived from the Differential Synthetic Aperture Radar Interferometry (DInSAR) to support the structural health monitoring of a RC infilled building within a landslide-affected area and to assess its safety conditions after experiencing two different hazards, that are landslide and earthquake. A 3D model of the case study building, including also infills, is created based on the information available from a geometrical survey, obtaining the missing parameters from literature. The seismic assessment of the building structural elements, caused by the design seismic action, is initially shown. Then, the seismic assessment is repeated, considering the building to be in a state of known landslide-induced stress-strain condition. Finally, an interesting comparison is proposed between the safety condition of the building expected in both cases, with or without the consideration of the precedent landslide-induced displacements.

Keywords: Multi-Hazard Assessment, Existing RC Buildings, Remote sensing, Earthquake, Landslide, Damage Assessment

1 INTRODUCTION

Different forms of hazard can affect structures throughout their existence; this is very common, for example, in countries affected both by landslides and high seismicity.

The effects of the single hazard source on existing reinforced concrete (RC) buildings have been a widely discussed research topic worldwide, in the last decades. For the seismic assessment, the international literature includes many methodologies and applications related to specific investigation issues [1-4]. Many studies can also be found regarding the evaluation of the structural damage as consequence of phenomena inducing slow displacements, monitored through satellite data for consistent periods [5-7], in particular for landslides [8-12]. The research in terms of landslide-earthquake multi-risk analysis, indeed, is very limited [13].

In this work, a RC infilled building, constructed in the 60s, located in Moio della Civitella, South of Italy, having typical structural deficiencies of pre-seismic designed structures, is used as case study. A structural 3D model of the building, including infills, is created based on the information available from original documents and an in-situ survey, while the missing parameters are obtained from literature. A modeling approach specifically elaborated for RC members with plain bars [14] is implemented for the non-linear flexural behavior of RC members, concentrating it at the ends of the beams and columns. Couples of diagonal struts are used for infills modeling, which behavior is defined as illustrated by Panagiotakos and Fardis [15].

The effect of the landslide phenomenon on the structure is monitored through the Differential Synthetic Aperture Radar Interferometry (DInSAR) technique [16]. The processing of ascending and descending COSMO-SkyMed images allows to obtain DInSAR deformation data, as a result of detected displacements of targets on the ground (buildings, rocks, infrastructures, etc.), with accuracy of the millimeter, carrying out maps of mean displacement rates and time series of deformations [17-19]. The surface ground movements, detected in the period 2012-2019, and extended to the 2020, have been applied to building foundations.

Then, non-linear static (pushover) analysis procedure is implemented twice: the first time in a condition of integer structure (earthquake [EQ] scenario) and the second time considering the structure already affected by the monitored slow-moving landslide (landslide plus earthquake [LAN+EQ] scenario). In both situations, the analysis results allow to carry out code-based [20, 21] seismic safety assessments, and the calculation of the “seismic safety index” (called for brevity “safety index”) [22, 23] with reference to the Italian Life-Safety (LS) *limit state* (*ls*) [20].

This paper aims to demonstrate the potential utility of DInSAR technique at a small scale, to support the structural health monitoring of an RC building, and to demonstrate the importance of a multi-risk seismic safety assessment, cumulating the actions coming from the two different hazards, that are landslide and earthquake.

2 METHODOLOGY

The fundamental input for the multi-risk analysis, in this work, is the landslide advanced monitoring, for a quite wide period of time, obtained from the DInSAR technique. Then, the aims of the work is pursued by performing pushover analysis and, therefore, the seismic safety local checks for RC members and the global safety index assessment for the whole structure. The theoretical basis of the previous approaches are explained, respectively, in Section 2.1 and Section 2.2. The territorial frame of the case study, its information and the modeling aspects are reported in Section 3. Moreover, Section 4.1 and Section 4.2 present the DInSAR analysis and displacements application, and the seismic structural assessment for the case

study building, in the EQ and LAN+EQ scenario. In conclusion, the results obtained by the multi-risk analysis are compared with the results of the traditional one.

2.1 Differential SAR Interferometry technique

DInSAR approach is based on time series of radar images [24] acquired by sensors installed on satellite platforms, travelling along semi-polar orbits. The acquisition is ensured when the observation of radar targets, namely Permanent Scatterers (PS) [25], is possible. PSs are typically parts of buildings, metallic structures, rocks or other elements already present on the ground, with electromagnetic characteristics more or less constant over time. Having a stack of images on the same area, in which specific PSs can be identified, DInSAR approach allows to create maps of mean displacement rates and time series of the deformations measured along the LoS, with an accuracy of the millimeter. The mentioned type of maps can also be obtained for more significative directions with respect to the phenomena developing on Earth surface. This is possible considering that, because of the Earth rotational movement, an area can be enlightened by a Synthetic Aperture Radar (SAR) sensor, either from East or from West, along descending (from North to South) or ascending orbits (from South to North), respectively. Descending and Ascending acquisitions can be combined, after the definition of a x, y, z Cartesian coordinate system, in which the three directions coincide with the horizontal E-W and N-S and vertical, respectively, thus obtaining the displacement vector. It is important to underline that, due to the geometrical characteristics of the acquisition system the N-S direction is considered negligible [17]. This is a DInSAR technique limit, that, consequently, furnishes deformation components only in the horizontal E-W and vertical directions.

2.2 Seismic assessment framework

The pushover analysis is implemented, through a step-by-step procedure, by subjecting the structure to two monotonically increasing pattern of lateral forces, as recommended in NTC (2018) [20]. The lateral forces, one proportional to the fundamental mode of vibration (Mode X and Mode Y), one proportional to the mass distribution (Mass X and Mass Y), are applied in the model at the centers of floor mass (X and Y directions are assumed accordingly to Fig. 2 (a)). Then, the so-called “inelastic demand point”, D_{inel} is determined, through method A of the standard [26], based on [27], in the Acceleration Displacement Response Spectrum space (ADRS, [28, 29]).

Once the results of the pushover analysis are obtained, the seismic safety checks are reported in this work for the LS- ls [20], equivalent to the Limit State of Significant Damage (SD) defined in EC8-3 [21]. The structural checks in the inelastic demand point D_{inel} at LS- ls are performed with regards to ductile and brittle mechanisms. The structural capacity of beams and columns in ductile terms, θ_u , is evaluated according to the capacity model suggested by [26] and [21], in terms of chord rotation capacity. The brittle failures for beams, columns and beam-column joints are checked according to capacity models suggested by the codes [21, 26, 30].

The seismic structural assessment allows the determination of the inelastic “performance point” of the structure, C_{inel} , at the considered ls , as that point in which the very first structural element experiences a failure mechanism. From C_{inel} it is possible to individuate its elastic correspondent point, C_{el} , necessary to find the “capacity spectrum” of the structure, in the ADRS space. The latter, defined as the elastic spectrum that pushes the structure in crisis, is a fundamental element to quantify the structural safety condition. In fact, the safety index, ζ_E [22, 23], is defined as the ratio between the demand PGA, based on the design seismic action prescribed by the code for the LS- ls , and the capacity PGA of the building, represented by the

anchor acceleration of the capacity spectrum. The structure can be considered safety against seismic actions when ζ_E assumes values greater than one.

3 CASE STUDY AND MODEL DESCRIPTION

3.1 Case study description

The case study RC building is located in the town of Moio della Civitella (Campania Region, Southern Italy), composed of two urban centres, Moio and Pellare. According to the Hydro-geomorphological Setting Plan of Hydrographic District of the Southern Apennines (HDSA)[32], building is affected by significant foundation displacements as a consequence of an intermittent landslide phenomenon with slow kinematics, (*Fig. 1*), as also presented in [33-35].

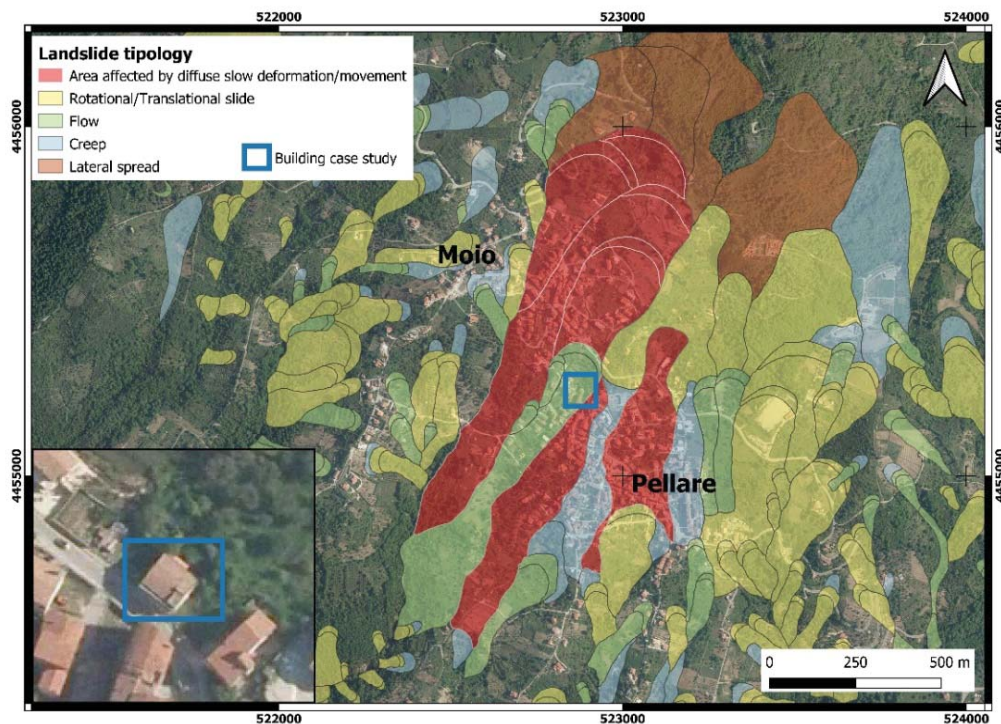


Fig. 1. Landslide inventory map (2012) with location of considered building.

The RC building was constructed in 1960s, and designed for gravitational loads only, with a plane parallel frames structural system; it is independent, with a rectangular plan of 11,90 m by 11,95 m, terraces excluded, built on three levels, with a pitched roof (*Fig. 2(a-c)*).

The most recent of many visual surveys conducted in the last decade, refers to December 2020. From the in situ-inspections, it has been possible to determine the following information. Columns have rectangular cross sections of dimensions 40x55 cm or 40x40 cm, except the stair columns, that are 55x50 cm, 60x35 cm and 55x40 cm. They are reinforced with smooth bars, 4 longitudinal ones, $\phi 16$, and stirrups $\phi 6/20$ " *Fig. 2(d)*. The primary beams, belonging to plane frames, and the secondary beams, that orthogonally link the four frames at the ends, have 35x60 cm and 20x50 cm rectangular cross sections, respectively.

The missing information about the beams reinforcement have been obtained by a simulated design, following the Italian standard R.D.L. [36], according to which the structure has been designed, then combining its results with evidence of local engineers about the construction procedures of the building period. Therefore, longitudinal bars $\phi 16$ have been adopted: 9+3

for the primary beams, while 3+2 for the secondary beams. Moreover, a transversal reinforcement of $\phi 6/15''$ has been utilized.

Regarding the mechanical materials properties, literature references have been employed. For the reinforcement bars, it is assumed the presence of Aq.42 steel, with an average yield strength f_{ym} of 328,6 Mpa, from the work of Verderame et al. [37], and an elastic modulus E of 200000 MPa. For the concrete, a cylindric mean compressive strength f_{cm} , of 21,3 MPa, according to Verderame et al. [38], and an elastic modulus, E , of 27607 MPa have been used.

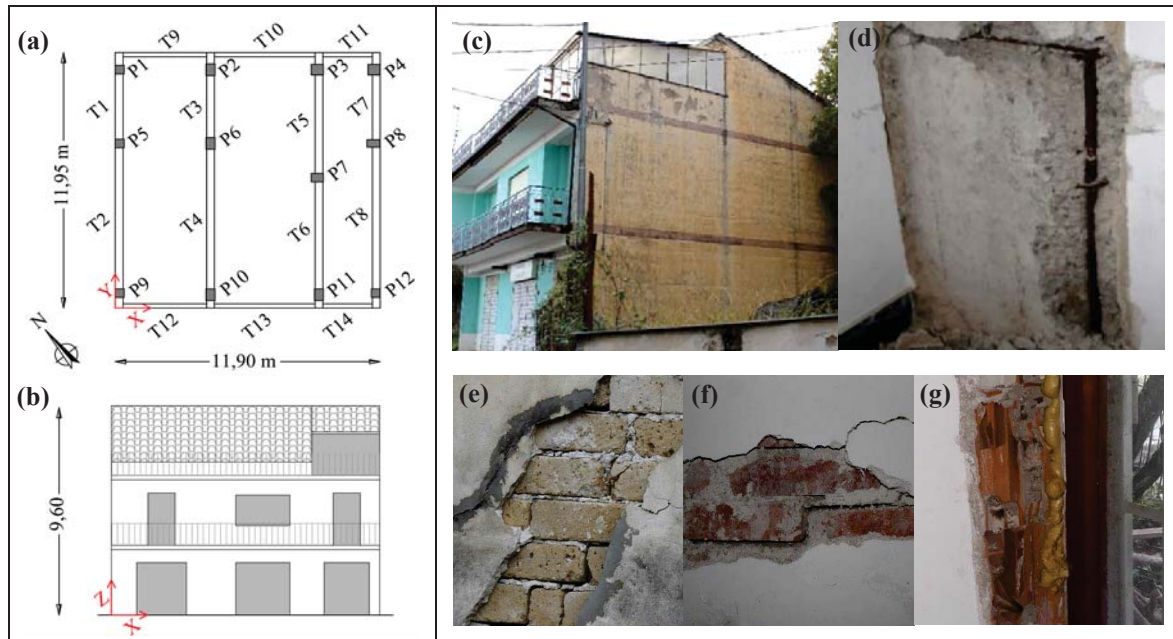


Fig. 2. Schematic geometrical plan (a) and front view of the S-W façade (b). In situ survey (December 2020): external picture (c); vertical smooth bars found at the column base (d); infills details – tuff (e); solid clay bricks (f); hollow clay bricks (g).

Different types of infills have been found during the in-situ inspection, as shown in *Fig. 2* (e-g): double-leaf vertical hollow clay bricks with a thickness of 8+12 cm, then 12+12 cm solid clay bricks and finally regular tuff with a thickness of 25 cm. A clear schematization of the different infills types distribution, with a labelling of the building fields, can be found in *Fig. 3*. In particular, hollow clay bricks, solid clay bricks and tuff are indicated with blue, orange and green lines, respectively. Moreover, it can be noted that AB, BC, A'B' and B'C' are the fields including only infills without openings (solid lines), while CD, DE, EF, C'D', D'E' and E'F' are the fields including also infills with openings (dashed lines).

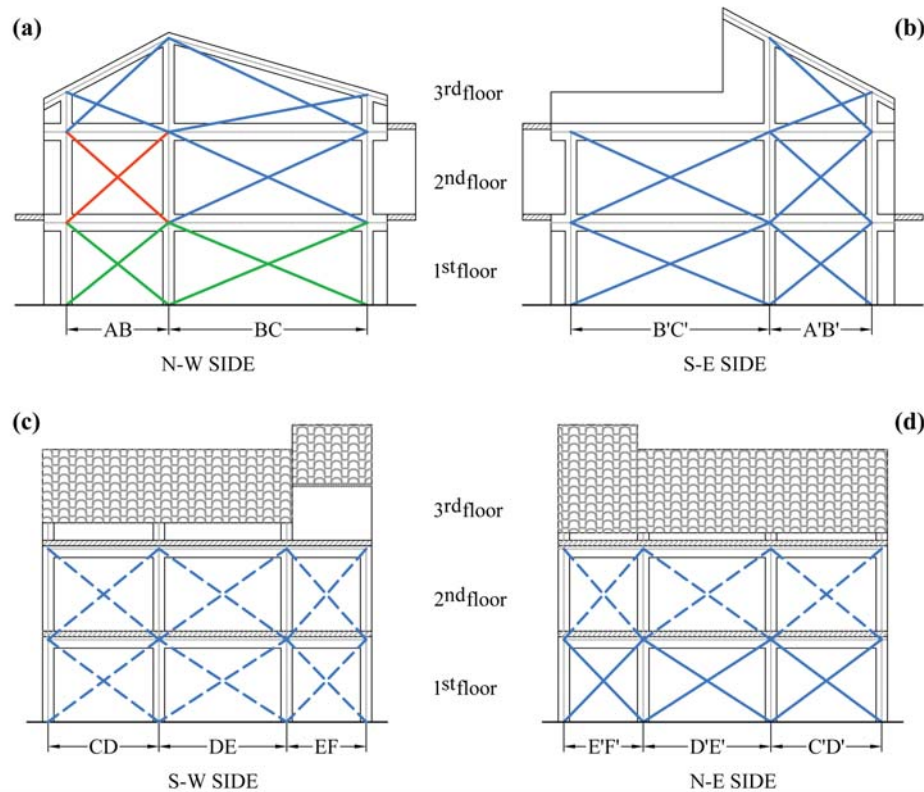


Fig. 3. Building prospects with identification of the different infills types of the building (hollow clay bricks, blue lines; solid clay bricks, orange lines; tuff bricks, green lines) differentiated in: without openings (continuous lines, (a-b)) and with openings (dashed line, (c- d)).

Mechanical properties for tuff and solid clay bricks have been derived from Italian NTC (2018) [20]; for hollow clay bricks, they have been assumed from [39] (see *Tab. 1*).

Mechanical Property	Tuff	Hollow clay bricks	Solid clay bricks
Elastic modulus E_{mh} [N/mm ²]	1410	1255	1500
Shear modulus G_{mh} [N/mm ²]	450	315	500
Tensile strength τ_0 [N/mm ²]	0,060	0,215	0,09

Tab. 1. Mean values of infills mechanical properties.

3.2 Modeling description

As regards the non-linear flexural behavior of RC members, a fourth-linear moment-chord rotation modeling approach, specifically elaborated for plain bars [14], has been adopted. The non-linear flexural behavior has been assigned as a plastic hinge at each end cross section of beams and columns. It has been verified that bending failures precede the shear for the RC members. However, these elements have been verified with respect to shear mechanisms in post processing, using code formulations as suggested in Section 2.2. Moreover, each infill has been modeled with a couple of equivalent diagonal struts resistant to compression, according to Al-Chaar [40] and Fardis [41], with a lateral response modeled following the equivalent single strut model proposed by Panagiotakos and Fardis [15]. The three-linear moment-chord rotation bond has been assigned at the middle cross section of each diagonal strut as axial hinges. More details about the evaluation of the geometric characteristics of these infills can be found in [12].

Based on the acquired geometrical and mechanical information, a 3D FEM structural model has been created using SAP2000 (v. 21.0.2, [42]). 2-D elements have been used for modeling beams, columns and the couple of diagonal struts representing the infills. The base columns have been fixed to consider the presence of foundations. The last floor has been modeled such that its height creates an equivalence of areas of the infills between the second and third order beams. The infills of the third floor, with openings, have been considered only as line masses and as line loads, because of the significant difference in shape from the panels used in the model proposed by Panagiotakos and Fardis [15]. The ones in the fields AB, BC and A'B' have been modelled; finally, there is a parapet in the B'C' field, and in the EF field there is no infill because of the presence of a veranda.

The elastic vibration periods of the 3D model, for the first two vibration modes, are $T_1=0,47$ s and $T_2=0,39$ s, in the direction with and without openings, respectively.

4 SEISMIC ASSESSMENT WITHOUT AND WITH CONSIDERATION OF THE PRECEDENT LANDSLIDE-INDUCED DISPLACEMENTS

4.1 DInSAR analysis and displacements application for the case study building

Cosmo-SkyMed images, obtained in the framework of MapItaly Project [43], were processed by means of DInSAR technique. In detail, X-band stripmap in ascending and descending mode images, characterized by a ground resolution of 3 x 3 m, were processed using SUBSIDENCE software. Coherent Pixel Technique–Temporal Phase Coherence (CPT-TPC) approach [44, 45] has been used to obtain ground displacements from satellite radar images. A detailed description of the whole algorithm can be consulted in [44, 45]. A phase quality value equal to 0,7 has been set in order to obtain an acceptable displacement error, lower than 1,5 mm, and to select an adequate number of points. *Fig. 4 (a, b)* shows mean displacement rates maps for ascending and descending acquisitions.

Starting from the discrete maps, vertical and horizontal E–W displacement components, with millimeter accuracy, have been obtained at the end of each year in the period 2012–2018 and for the first three months of 2019, by a combination process. In this way, the profiles of cumulated vertical and horizontal (in the direction parallel to the building sides) displacements, occurred to building foundations, have been provided. Moreover, to obtain the cumulated displacement components at the end of 2019 and 2020, an extrapolation has been done, based on the hypothesis that the landslide phenomenon keeps evolving linearly in time, as observed in the monitored period. The cumulate displacement profiles are shown in *Fig. 4 (c, d)*. The monitoring of the landslide that caused ever-increasing displacements of the foundation soil over the years can be also considered as base to carefully hypothesize the condition of the future years in order to program typical retrofit operation on the RC building [46] or to make prediction loss assessment evaluation for structures/infrastructures portfolio [47].

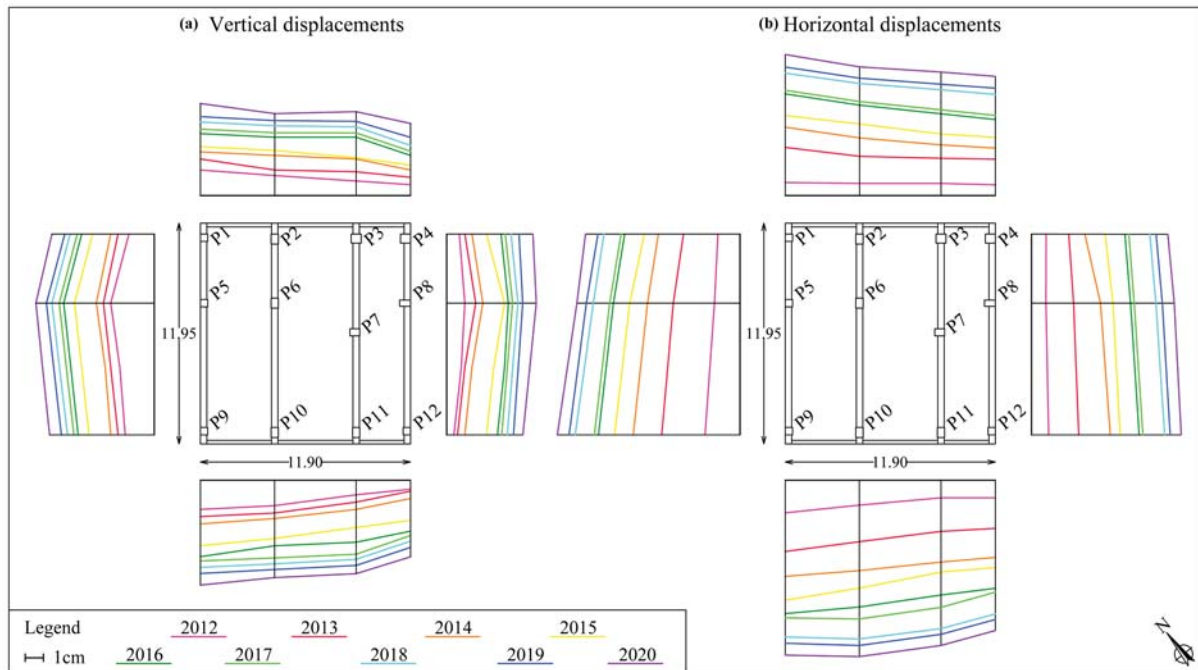


Fig. 4. Foundation displacement profiles the end of each year in the period 2012–2020: vertical (a) and horizontal (b).

4.2 EQ and LAN+EQ results and comparisons

As mentioned in Section 2.2 as first step of the proposed methodology, the seismic capacity of the RC elements at the LS-*ls* has been evaluated, after the definition of the seismic action according to Italian NTC (2018) [20].

The first case investigated is the EQ scenario, in which the building is in a deformed condition only for gravity loads before the application of the seismic action. Then, in the LAN+EQ scenario, the seismic assessment procedure is implemented on the structure, already deformed because of the differential slow-moving landslide-induced displacements, applied at the base of the first-floor columns.

Following what illustrated in Section 2.2, pushover analysis has been implemented, by applying two monotonically increasing pattern of lateral forces to the structure, as recommended in NTC (2018) [20]. The resultant pushover curves are represented in Fig. 5. It can be observed that LAN+EQ scenario's curves (black dotted lines) start from a significant displacement value of the control point induced by the landslide effect, while EQ scenario's curves (grey continuous lines) start from quite null values of roof displacement.

The seismic verifications in terms of ductile and fragile mechanisms in the step corresponding to the inelastic demand point D_{inel} , for the LS-*ls*, have been carried out once obtained the results of the pushover analysis. In Fig. 5, also the evolutions of the failure sequences found for both scenarios are compared. In both cases, the first failure mechanism attained is the tensile-shear failure in beam-columns unconfined joints (represented with red triangles), followed by brittle shear failures in the beams (orange squares) and in the columns (yellow circles). For each load case, ductile failures are never achieved at LS-*ls*, up to D_{inel} (indicated with a green pentagram).

The application of the differential landslide-induced displacements provokes an aggravation of the stress state in the structural elements. In fact, they enter in crisis for lower steps with respect to those attained in the EQ scenario; moreover, the number of elements in crisis at the LS-*ls*, until the corresponding D_{inel} , increases. In particular, in the LAN+EQ scenario,

the first joint failures happen at the step zero of the pushover, meaning that they are caused by the action of the landslide, before the application of the seismic action.

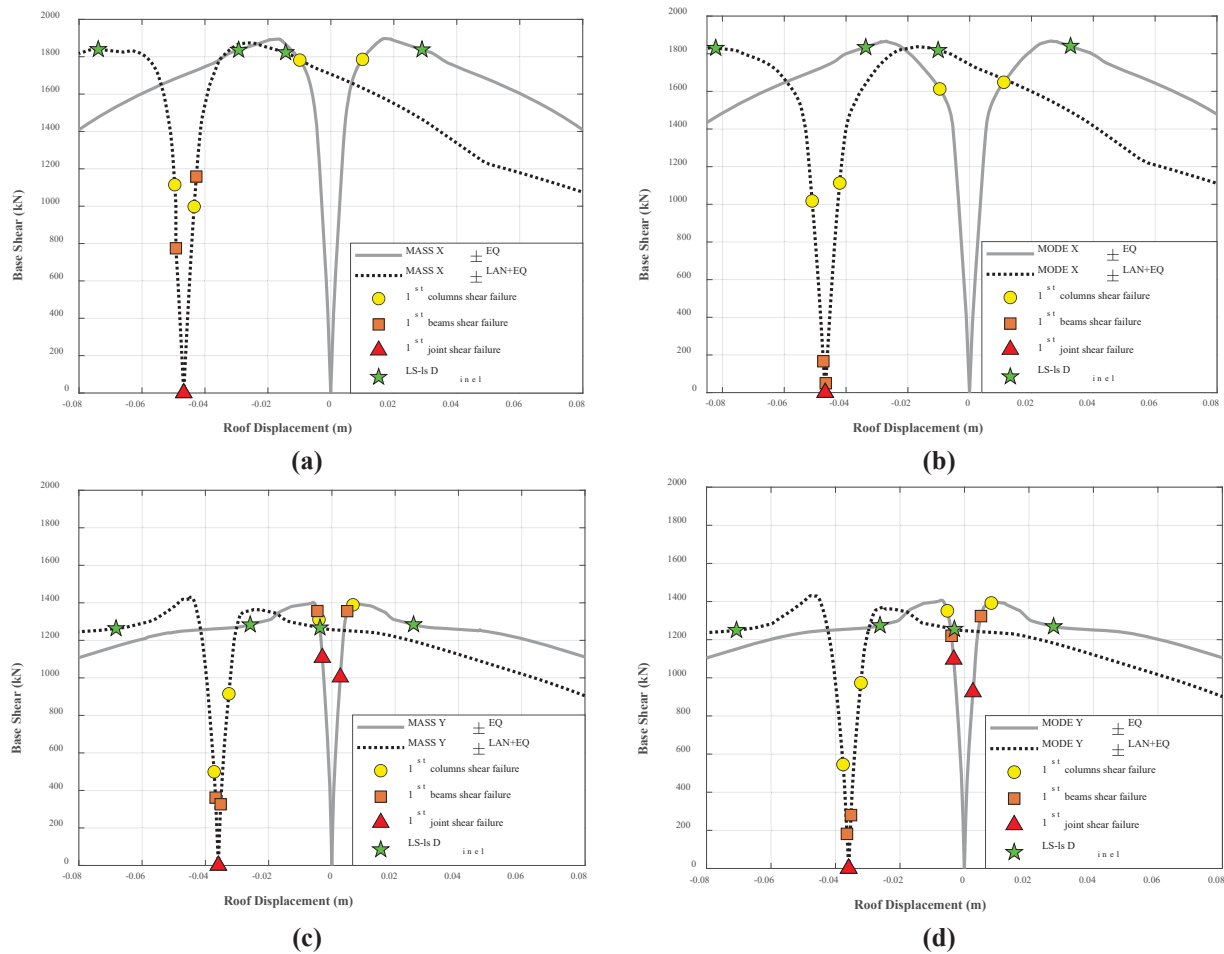


Fig. 5. Comparison of the pushover curves and relative failure mechanism progress of structural elements, until the demand point, in the EQ and LAN+EQ scenarios: Mass X (a), Mode X (b), Mass Y (c) and Mode Y (d).

It can be observed that, from EQ scenario to LAN+EQ scenario, the number of elements experiencing brittle crises at LS-*ls* passes from 11 to 19 for joints, from 7 to 17 for columns and from 2 to 8 for beams. This increase of the number of elements exceeding the *ls* can be attributed to the action of the landslide, which is active independently from the earthquake.

Moreover, an overall comparison of the global structural condition between the two scenarios has been done in terms of safety index, ζ_E as suggested in Section 2.2. In the EQ scenario, the safety index at LS-*ls* is equal to 0,27. Taking into account the previous landslide phenomenon with the first failure at the step zero of the curves, according to Sisma-Bonus Guidelines [48], the spectrum referred to the Beginning of Damage-*ls* (10 years return period) has been considered as a lower limit for the determination of $PGA_{capacity}$. The result is that in LAN+EQ scenario, a ζ_E of 0,11 has been obtained. In both cases the structure shows a lack of seismic capacity, meaning that it is able to withstand only a little percentage of the total design seismic action.

5 CONCLUSIONS

This study presented the seismic safety assessments of an existing RC infilled building, constructed in the 60s, located in a landslide-affected area. The work has a dual purpose.

From one side, it shows how the DInSAR satellite data can be used to support the structural health monitoring of RC buildings affected by slow-moving landslides. In general, the presented methodology can be applied also to phenomena with a different origin, if slowly evolving in time. On the other side, the aim is to highlight the importance of the seismic safety assessment in a multi-risk analysis, cumulating the action coming from the two different hazards, that in the specific case are the landslide and the seismic action.

The DinSAR remote sensing technique has been used for the detection of the landslide-induced displacements, confirming to be an extremely effective tool not only for the monitoring of phenomena at a territorial scale, but also with refers to the detail scale. A structural 3D model of the building, considering infills, has been implemented, to carry out the seismic assessment in two phases. Initially, a traditional seismic assessment, based on non-linear static analysis, has been done. Then, the landslide-induced displacements obtained by DInSAR monitoring technique, affecting the base of the structure, have been applied to the model, allowing to carry out a new pushover analysis in a multi-risk perspective.

In the two cases, the evolution of the stress-strain condition in the members has a different evolution. Since the landslide-induced displacements vary among all the columns bases, the phenomenon causes the born of a heterogeneous stresses path in the structural elements, that becomes the starting condition for the application of the design seismic action. For this reason, in the LAN+EQ scenario, the number of elements exceeding the $LS-ls$ increases.

Moreover, the illustrated results remark that by neglecting the effects of the existing differential displacements landslide-induced, the safety index overestimates the threshold of the seismic safety. It is important to underline that an overestimation of ζ_E can conduct to an underestimation in the definition of the structural retrofit procedures and of their costs.

Acknowledgements

The authors would like to acknowledge Eng. Giuseppe Comella who has contributed to the development of presented work.

REFERENCES

- [1] A. B. Liel, C.B. Haselton, G. G. Deierlein, Seismic collapse safety of reinforced concrete buildings. II: Comparative assessment of nonductile and ductile moment frames. *Journal of Structural Engineering*, **137(4)**, 492-502, 2011.
- [2] M. Fragiadakis, D. Vamvatsikos, M. Aschheim, Application of nonlinear static procedures for seismic assessment of regular RC moment frame buildings. *Earthquake Spectra*, **30(2)**, 767–794, 2013.
- [3] A. Miano, H. Sezen, F. Jalayer, A. Prota, Performance based comparison of different retrofit methods for reinforced concrete structures. *6th ECCOMAS Thematic Conference on Computational Methods in Structural Dynamics and Earthquake Engineering (COMPDYN 2017)*, Rhodes Island, Greece, June 15-17, 2017.
- [4] F. Jalayer, F., H. Ebrahimian, A. Miano, Intensity-based demand and capacity factor design: A visual format for safety checking. *Earthquake Spectra*, **36(4)**, 1952-1975, 2020.
- [5] S. Arangio, F. Calò, M. Di Mauro, M. Bonano, M. Marsella, M. Manunta, An application of the SBAS-DInSAR technique for the assessment of structural damage in the city of Rome. *Structure and Infrastructure Engineering*, **10(11)**, 1469-1483, 2014.

- [6] N. Cavalagli, A. Kita, S. Falco, F. Trillo, M. Costantini, F. Ubertini, Satellite radar interferometry and in-situ measurements for static monitoring of historical monuments: The case of Gubbio, Italy. *Remote Sensing of Environment*, **235**, 111452, 2019.
- [7] A. Drougkas, E. Verstrynghe, K. Van Balen, M. Shimoni, T. Croonenborghs, R. Hayen, P.Y. Declercq, Country-scale InSAR monitoring for settlement and uplift damage calculation in architectural heritage structures. *Structural Health Monitoring*, 1475921720942120, 2020.
- [8] D. Peduto, G. Pisciotta, G. Nicodemo, L. Arena, S. Ferlisi, G. Gullà, ... , D. Reale, A procedure for the analysis of building vulnerability to slow-moving landslides. *1st IMEKO International Workshop on Metrology for Geotechnics*, Benevento, Italy, March 17-18, 2016.
- [9] D. Infante, P. Confuorto, D. Di Martire, M. Ramondini, D. Calcaterra, Use of DInSAR data for multi-level vulnerability assessment of urban settings affected by slow-moving and intermittent landslides. *Procedia Engineering*, **158**, 470–475, 2016.
- [10] D. Infante, D. Di Martire, P. Confuorto, S. Tessitore, R. Tòmas R, D. Calcaterra, M. Ramondini, Assessment of building behavior in slow-moving landslide-affected areas through DInSAR data and structural analysis. *Engineering Structures*, **199**, 109638, 2019.
- [11] M. Del Soldato, L. Solari, F. Poggi, F. Raspini, R. Tomás, R. Fanti, N. Casagli, Landslide-Induced Damage Probability Estimation Coupling InSAR and Field Survey Data by Fragility Curves. *Remote Sensing*, **11(12)**, 1486, 2019.
- [12] A. Miano, A. Mele, D. Calcaterra, D. Di Martire, D. Infante, A. Prota, M. Ramondini, The use of satellite data to support the structural health monitoring in areas affected by slow-moving landslides: a potential application to reinforced concrete buildings. *Structural Health Monitoring*, 1475921720983232, 2021
- [13] C. Negulescu, T. Ulrich, A. Baills, D. M. Seyedi, Fragility curves for masonry structures submitted to permanent ground displacements and earthquakes. *Natural hazards*, **74(3)**, 1461-1474 2014.
- [14] M. Di Domenico, P. Ricci, G. M. Verderame, Empirical calibration of hysteretic parameters for modelling the seismic response of reinforced concrete columns with plain bars. *Engineering Structures*, 112120, 2021.
- [15] T. B. Panagiotakos, M. N. Fardis, Seismic response of infilled RC frames structures, *11th world conference on earthquake engineering*, Acapulco, México, June 23-28, 1996.
- [16] A. K. Gabriel, R. M. Goldstein, H. A. Zebker, Mapping small elevation changes over large areas: Differential interferometry. *Journal of Geophysical Research*, **94**, 9183-9191, 1989.
- [17] C. Colesanti, J. Wasowski, Investigating landslides with space-borne Synthetic Aperture Radar (SAR) interferometry. *Engineering Geology*, **88**, 173-199, 2006.
- [18] M. Costantini, A. Ferretti, F. Minati, S. Falco, F. Trillo, D. Colombo, ... ,S. Costabile, Analysis of surface deformations over the whole Italian territory by interferometric processing of ERS, Envisat and COSMO-SkyMed radar data. *Remote Sensing of Environment*, **202**, 250-275, 2017.
- [19] P. Ezquerro, M. Del Soldato, L. Solari, R. Tomás, F. Raspini, M. Ceccatelli, J. A. Fenandez-Merodo, N. Casagli, G. Herrera, G. Vulnerability assessment of buildings due to land subsidence using InSAR data in the ancient historical city of Pistoia (Italy). *Sensors*, **20(10)**, 2749, 2020.
- [20] DM 17/01/18 (2018) Norme tecniche per le costruzioni, Ministerial Decree, 2018. (in italian)
- [21] Eurocode 8, EN1998-3, Design of structures for earthquake resistance, Part 3: Assessment and retrofitting of buildings, CEN, Brussels, 2005.
- [22] E. Cosenza, C. Del Vecchio, M. Di Ludovico, M. Dolce, C. Moroni, A. Prota, E. Renzi, The Italian guidelines for seismic risk classification of constructions: technical principles and validation. *Bulletin of Earthquake Engineering*, **16(12)**, 5905-5935, 2018.

- [23] R. Frascadore, M. Di Ludovico, A. Prota, G. M. Verderame, G. Manfredi, M. Dolce, E. Cosenza, Local strengthening of reinforced concrete structures as a strategy for seismic risk mitigation at regional scale. *Earthquake Spectra*, **31(2)**, 1083-1102, 2015.
- [24] G. Franceschetti, M. Migliaccio, D. Riccio, G. Schirinzi, SARAS: a synthetic aperture radar (SAR) raw signal simulator. *IEEE Transactions on Geoscience and Remote Sensing*, **30(1)** 110-123, 1992.
- [25] A. Ferretti, C. Prati, F. Rocca, Permanent scatterers in SAR interferometry. *IEEE Transactions on Geoscience and Remote Sensing*. **39(1)**, 8-20, 2001.
- [26] Circolare n. 7 C.S.LL.PP. 21 gennaio 2019 (2019), Commentary to NTC 2018 (in Italian).
- [27] T. Vidic, P. Fajfar, M. Fischinger, Consistent inelastic design spectra: strength and displacement. *Earthquake Engineering & Structural Dynamics*, **23(5)**, 507-521, 1994.
- [28] P. Fajfar, Capacity spectrum method based on inelastic demand spectra, *Earthquake Engineering & Structural Dynamics*, **28(9)**, 979-993, 1999.
- [29] P. Fajfar, A nonlinear analysis method for performance-based seismic design, *Earthquake Spectra*, **16(3)**, 573-592, 2000.
- [30] Eurocode 2, EN 1992-1-1, Design of concrete structures, Part 1-1: General rules and rules for buildings, CEN, Brussels, 2004.
- [31] Eurocode 8, EN 1998-1, Design of structures for earthquake resistance, Part 1: General rules, seismic actions and rules for buildings, CEN, Brussels, 2003.
- [32] Hydro-geomorphological Setting Plan of South Campania River Basin Authority, Via De Gasperi 28, 80133, Naples, Italy, 2012.
- [33] F. Calò, D. Calcaterr, A. Iodice, M. Parise, M. Ramondini, Assessing the activity of a large landslide in southern Italy by ground-monitoring and SAR interferometric techniques. *International Journal of Remote Sensing*, **33(11)**, 3512-3530, 2012.
- [34] D. Di Martire, M. Ramondini, D. Calcaterra, Integrated monitoring network for the hazard assessment of slowmoving landslides at Moio della Civitella (Italy). *Rendiconti Online Società Geologica Italiana*, **35**, 109-112, 2015.
- [35] D. Infante, P. Confuorto, D. Di Martire D, et al, L'utilizzo di dati DInSAR per la valutazione delle conseguenze indotte sugli edifici da frane intermittenti a cinematica lenta. *XXVI Convegno Nazionale Di Geotecnica*. Rome, Italy, June 20-22, 2017.
- [36] R.D.L. 16 novembre 1939 n°2229 (Suppl. Ord. alla Gazz. Uff. del 18 aprile 1940 n°92) Norme per l'esecuzione delle opere in conglomerato cementizio semplice od armato, 1939.
- [37] G. M. Verderame, A. Stella, E. Cosenza, Le proprietà meccaniche degli acciai impiegati nelle strutture in ca realizzate negli anni '60. *X Convegno nazionale "L'Ingegneria Sismica in Italia"*, Potenza, Matera, September 9-13, 2001.
- [38] G. M. Verderame, G. Manfredi, G. Frunzio, Le proprietà meccaniche dei calcestruzzi impiegati nelle strutture in cemento armato realizzate negli anni '60. *X Convegno nazionale "L'Ingegneria Sismica in Italia"*, Potenza, Matera, September 9-13, 2001.
- [39] P. Ricci, M. Di Domenico, G. M. Verderame, Experimental assessment of the in-plane/out-of-plane interaction in unreinforced masonry infill walls. *Engineering Structures*, **173**, 960-978, 2018.
- [40] G. K. Al-Chaar, *Evaluating Strength and Stiffness of Unreinforced Masonry Infill Structures*. ERDC/CERL TR-02-1, 2002.
- [41] M. N. Fardis, *Seismic Design, Assessment and Retrofitting of Concrete Buildings: based on EN-Eurocode 8, Vol.8*. Springer Science & Business Media, 2009.

- [42] SAP2000 v21.0.2, Computers and Structures, Inc., 2019.
- [43] P. Sacco, M. L. Battagliere, M. G. Daraio, A. Coletta, The COSMO-SkyMed constellation monitoring of the Italian territory: the Map Italy project. 66th International Astronautical Congress (IAC 2015), Jerusalem, Israel, October 12-16, 2015.
- [44] O. Mora, J. J. Mallorquí, A. Broquetas, Linear and non-linear terrain deformation maps from a reduced set of interferometric SAR images. *IEEE Transactions on Geoscience and Remote Sensing*, **41**, 2243-53, 2003.
- [45] R. Iglesias, J. J. Mallorqui, D. Monells, C. Lopez-Martinez, X. Fabregas, A. Aguasca, J. A. Gili, J. Corominas, PSI Deformation Map Retrieval by means of Temporal Sublook Coherence on Reduced Sets of SAR Images, *Remote Sensing*, **7**, 530-563, 2015.
- [46] A. Miano, H. Sezen, F. Jalayer, A. Prota, Performance Based Assessment and Retrofit of Non ductile Existing Reinforced Concrete Structures. *Structures Conference 2018*, April 19-21, Fort Worth, Texas, 2018.
- [47] A. Miano, F. Jalayer, R. De Risi, A. Prota, G. Manfredi G., A case-study on scenario-based probabilistic seismic loss assessment for a portfolio of bridges. *12th international conference on applications of statistics and probability in civil engineering (ICASP)*, Vancouver, Canada, July 12-15, 2015.
- [48] Ministerial Decree n. 24, 09/01/2020, Sisma Bonus - Linee guida per la classificazione del rischio sismico delle costruzioni nonché le modalità per l'attestazione, da parte di professionisti abilitati, dell'efficacia degli interventi effettuati, 2020.

VULNERABILITY OF ART WORKS TO BLAST HAZARD: THE FOUNTAIN OF NEPTUNE IN FLORENCE

Marco Domaneschi¹, Marco Tanganelli², Stefania Viti² and Gian Paolo Cimellaro¹

¹ Department of Structural, Geotechnical and Building Engineering (DISEG), Politecnico di Torino,
Corso Duca degli Abruzzi 24, 10129 Torino
e-mail: {marco.domaneschi,gianpaolo.cimellaro}@polito.it

² Department of Architecture (DIDA), University of Florence,
via della Mattonaia 14, 50121 Firenze
{marco.tanganelli,stefania.viti}@unifi.it

Abstract

Conservation and protection of art works is a primary goal of each community, since artifacts represent a fundamental cultural and economic asset. In most cases, art goods are exhibited in Museums, which are appointed for their protection. Some of them, however, are exhibited outdoor, since they are conceived and made to enrich the public areas. In these cases, the art goods result to be even more vulnerable, since they are subjected both to natural hazard (i.e. earthquakes and floods) and to vandalic attacks. Art works have an intrinsic vulnerability, due to their irregular shape, slenderness, fragility and to their oldness. This paper is focused on the dynamic response of statues to blast explosion; a valuable case-study, i.e. the Fountain of Neptune, located in “Piazza della Signoria”, in Florence. The Fountain of Neptune is a marble and bronze opus made by Bartolomeo Ammannati between 1560 and 1565. The main character of the Fountain, Neptune, is a marble statue 5.7 meters tall, with a weight equal to 11.5 ton. A preliminary laser scanner survey has been made to achieve the geometrical representation of the statue. The geometrical model has been arranged, in order to be used for structural analyses. A numerical analysis has been performed to find the dynamic response of the statue to the loading resulting from a blast explosion. Such response has been found by assuming the explosion of assigned amounts of TNT. Some different cases have been considered, and a limit loading condition has been found for the blast, as a function of its amount.

Keywords: Blast loading; artifacts preservation; art works reliability; seismic vulnerability; multi-hazard analysis

1 INTRODUCTION

Artifacts are the focus of the artistic and cultural identity of a country. Despite their fundamental importance, their safety, usually, is not adequately pursued. Different hazard, both natural and human-induced, can threaten the art goods [1]. Furthermore, they are usually very vulnerable, due to their geometrical features (in-plan and in-elevation irregularity, slenderness) their age, and the possible fragility of their material.

Marble sculptures result to be very vulnerable to overturning, due to their high mass and the fragility of the material. Furthermore, the marble sculptures can be very tall, to take advantage of the strength of the material, with a consequent high slenderness. For this reason, many studies have been made on their vulnerability to overturning, with a special attention to the seismic excitations [2-4].

The analysis has been performed on a case-study, i.e. the main sculpture of the Fountain of Neptune, in Florence. It is a marble and bronze opus made by *Bartolomeo Ammannati* between 1560 and 1565 [5]. The main sculpture of the Fountain, Neptune, is 5.7 meters tall, and it has a weight equal to 11.5 ton.

The explosion has been assumed to be caused by the blast of fixed amounts of TNT, compatible to a vandalic or terroristic attack. The response of the statue to the assumed blast has been checked through Finite Element analysis.

The FE methods have been largely developed in these last years [6,7], even thanks to the outstanding developments occurred in the digital survey, with the consequent improvement of the artifact modelling [8,9], and the increasing availability of computational resources.

In this study, the FE model used for the analysis has been arranged on the basis of a very detailed geometrical model defined after a laser-scanner survey, which provided a points-cloud of the Fountain. The geometrical model described the lateral surface of the manufact; it has been arranged in order to represent the volume of the manufact, and simplified, in order to limit the number of tetragons constituting the model, and the main geometrical irregularities.

The analysis has been performed along the “weakest” direction of the sculpture, i.e. the direction with its lowest lateral stiffness. Different amounts of TNT have been considered to find the limit capacity of the sculpture to blast attacks.

2 THE CASE-STUDY

2.1 The Neptune Fountain

The Fountain of Neptune, placed in Florence in *Piazza della Signoria*, was made by *Bartolomeo Ammannati* between 1560 and 1565 [5,10] after the commitment of *Cosimo I de' Medici*.

The Fountain, shown in Figure 1a, consists of many different parts, made in marble and bronze; the main sculpture, representing Neptune, is placed on a central pedestal representing a horse-drawn cart placed in an octagonal basin, a space further decorated with statues of Scylla and Charybdis; all around, some minor marble and bronze sculptures were added, representing river gods, satyrs and sea-horses. Some of the sculptures currently constituting the Fountain are copies made the XIX century, to preserve the original artifacts from vandalism. Indeed, from its construction, the Fountain experienced many vandalic actions. The first documented damage dates back to 1580, and many other damaged were made along the centuries; the last event occurred in 2005, when three vandals climbed Neptune, damaging one hand and the trident of the sculpture.

a. The Fountain of Neptune



b. Neptune



Figure 1. The Fountain of Neptune

2.2 The statue of Neptune

The main character of the Fountain, Neptune, is a marble statue 5.7 meters tall (see Figure 1b), with a weight equal to 11.5 ton. The marble used for the sculpture has been taken by a Carrara quarry. The mechanical properties assumed in the work, listed in Table 1, have been found through an experimental survey made on samples of marble similar to the one used for the statue [11,12]. A special attention has been paid to the value to assume for the friction coefficient [13,14], which plays an important role in the prediction of the collapse mode of the sculptures under horizontal excitations.

Table 1. Mechanical properties of the marble

Density	[kg/m ³]	2700
Young Modulus	[MPa]	50000
Poisson coefficient	[MPa]	0.2
Compressive strength	[MPa]	50
Tensile strength	[MPa]	5
Friction coefficient	-	0.8

2.3 The structural model

The structural model of Neptune has been made on the basis of a geometrical survey made on the Fountain of Neptune, made through laser-scanner. The geometrical survey provided a points-cloud, which has been used to find the geometrical model consisting of a detailed lateral surface described through 1234492 polygons [15]. Such geometrical model has been deeply simplified to obtain the structural model to use for the dynamic analysis, made of a lower number of polygons. Besides being simplified (the number of polygons of the lateral surface of the model has been reduced to 29000), the model has been changed by a “surface”

to a solid one; finally, a model made of 152000 tetragons has been obtained. Figure 2 shows the various steps of the modeling procedure.




a. Points-cloud	b. Geometrical model	c. Structural model	d. Main information
			<p>Height 5.68 m</p> <p>Volume 4.27 mc</p> <p>Weight 11.5 ton</p> <p>Footprint 100 x 134 cm</p>

Figure 2. Geometrical and structural models.

3 THE BLAST ACTION

The loading acting to the sculpture as an effect of the blast has been assumed equal to the reflecting pressure, which has been determined according to the empirical approach [16,17] based on the Kingery and Bulmash [18] contribution.

The pressure applied to the statue surface has been quantified as a function of the normal reflected pressure peak, P_{r0} , defined as a function of the Hopkinson-Cranz scaled distance Z , as provided by Karlos and Solomos [19]:

$$Z = \frac{R}{W^{1/3}} \quad (1)$$

where W is the assumed charge mass (expressed in metric tons) and R is the distance (expressed in meters) of the target surface from the center of the blast. The quantity has been found through the equation (2), according to [16].

$$P_{r0}(Z) = \left(1 + \frac{1}{2e^{10Z}}\right) \exp[2.0304 - 1.8036 \ln Z - 0.09293 \ln^2 Z - 0.8779 \sin(\ln Z) - 0.3603 \sin^2(\ln Z)] \quad (2)$$

After the peak, the pressure wave presents a degrading wave phase [16] of duration t_0 , which ends with the zeroing of the pressure (positive phase), and a further phase characterized by the negative sign of the overpressure (negative phase). There are various expressions to describe the reflected pressure, such as has the *modified Friendlander equation* [20], based on the Heaviside function. In this work, however, a simplified approach has been adopted, and the trend of the pressure in the positive phase has been assumed as triangular, with an effective positive duration, t_0 , quantified through the expressions proposed by Vannucci *et al.* [21]:

$$t_0(Z) = t_{0w} W^{1/3} \quad (3)$$

as a function of the scaled positive duration, t_{0w} , quantified through the equation (4).

$$t_{0w}(Z, W) = \exp\{0.592 + 2.913\ln Z - 1.287\ln^2 Z - 1.788\ln^3 Z + 1.151\ln^4 Z + 0.325\ln^5 Z - 0.383\ln^6 Z + 0.090\ln^7 Z - 0.004\ln^8 Z - 0.0004\ln^9 Z + 0.537\cos^7[1.032(\ln Z - 0.059)] \sin[1.088(\ln Z - 2.023)]\} \quad (4)$$

In this work, two different cases of analysis have been made, differing from each other for the assumed amount of TNT, respectively equal to 10 kg and to 50 kg; both cases are compatible to the quantities compatible to vandalism actions [22]. The placement of the explosive has been assumed equal to 8.8m from the statue, i.e. along the external fence. In Table 2 the main data describing the blast loading have been listed.

Table 2. Main data regarding the blast loading.

Quantity	[unit]	case #1	case #2
Mass of TNT, W	[kg]	10	50
Distance, R	[m]	8.8	8.8
Scaled distance, Z	[m][kg ^{-1/3}]	4.08	2.39
normal reflected pressure peak, P_{r0} ,	[MPa]	0.1676	0.6029
Scaled positive duration (t_0)	[ms][kg ^{-1/3}]	3.53	2.25
Effective positive duration (t_{0w})	[ms]	7.62	8.30

4 THE ANALYSIS

4.1 The preliminary investigations

Some preliminary investigations have been made before performing the dynamic analysis. The analyses have been made by assuming the TNT placed along the direction with the minimum inertia of the statue, as shown in Figure 3; furthermore, the pedestal of the statue has not been included in the analysis. Indeed, due the position of the statue within the Fountain, the pedestal is not fully involved by the pressure wave induced by the explosion (see Figure 4).

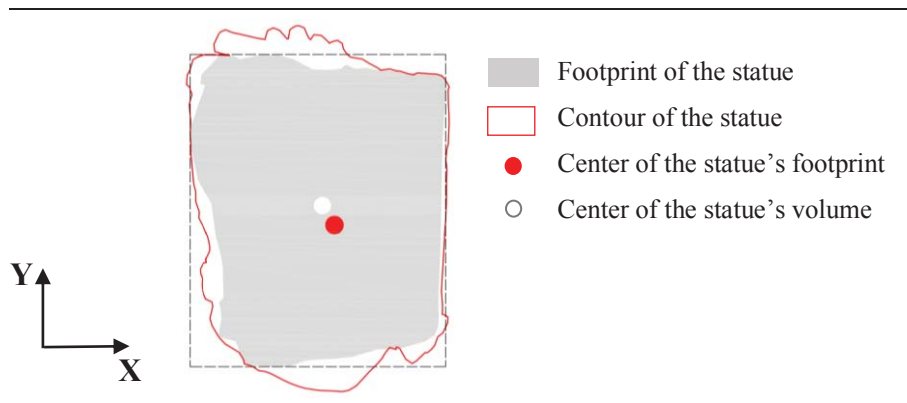


Figure 3. Direction of analysis of the sculpture

First of all, a modal analysis has been made through the software Marc & Mentat [23] to check the dynamic properties of the statue. The results of the modal analysis, in terms of frequencies and correspondent shapes, have been shown in Figure 5. The Fundamental period found for the sculpture is equal to 0.081 sec, compatibly to the ones found for similar statues [3]. As can be seen, the first mode is mostly translational, along the X direction, whilst the following ones have a relevant rotational response.

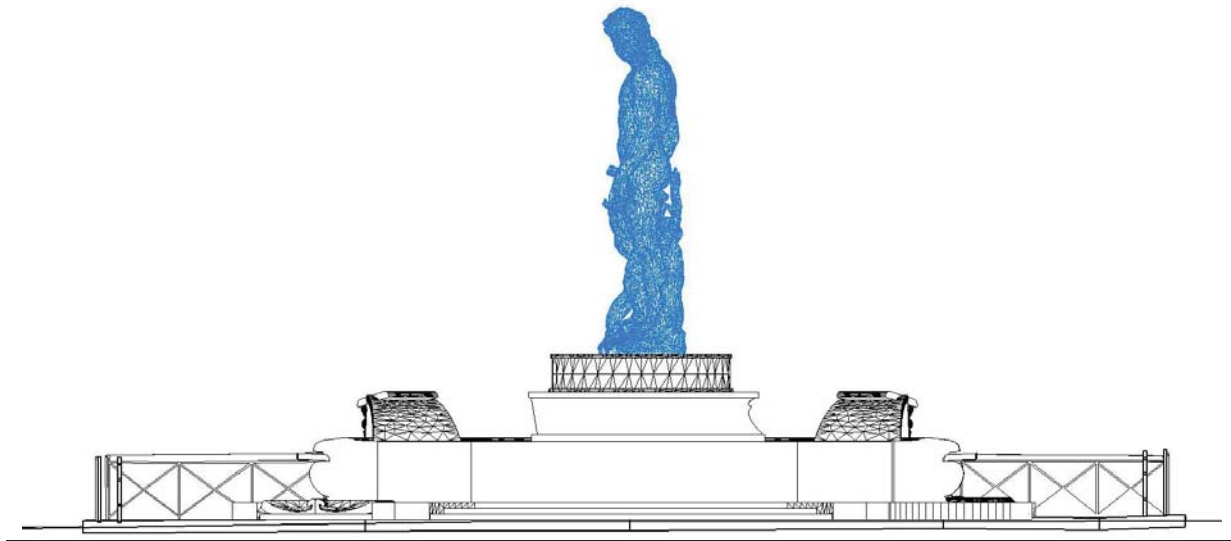


Figure 4. Position of the sculpture within the Fountain

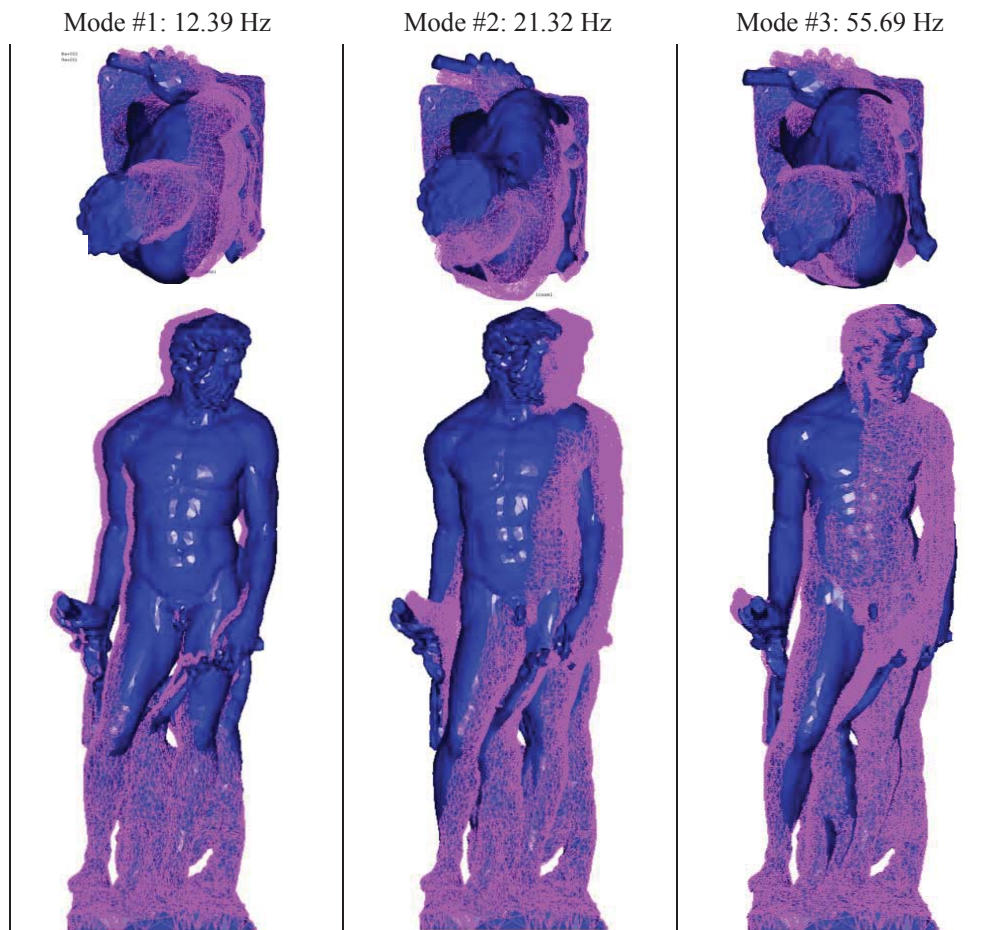


Figure 5. Modal shapes of Neptune.

The level of stress in the material as an effect of the gravitational loads has been checked by performing a linear elastic analysis; the maximum stress achieved in the sculpture at its base (see Figure 6) is equal to about 1.35 MPa, well below the limit value of the material.

Furthermore, the limit conditions in terms of top displacement ($d_{lim} = 1.38$ m) for the overturning (see Figure 7) have been found. The limit top displacement has been found by imposing the gravitational load of the sculpture center at the limit of the inertial core of the sculpture print.

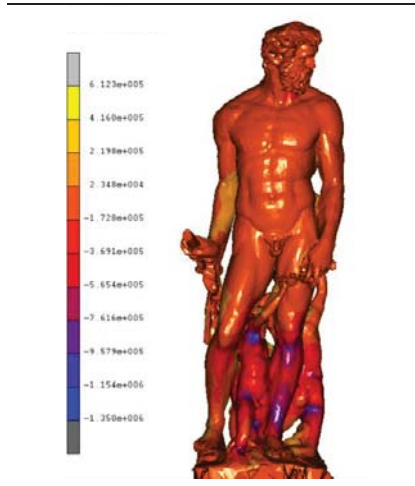


Figure 6. Maximum stress (Pa) under gravitational loads

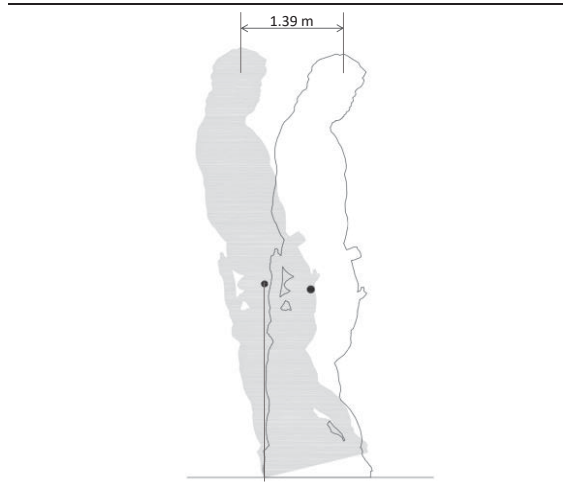


Figure 7. Top displacement at the overturning

The horizontal force corresponding to the overturning, instead, has been found by equalizing the capacity moment to the moment of demand. The moment of capacity is defined as the product of the gravitational load, supposed to be applied to the centroid of the volume and the distance between the centroid and the turning point of the basement; the moment of demand, instead, is defined as the product of the horizontal force - supposed to be applied to the statue centroid - and its distance to the turning point, i.e. the height of the statue centroid, h . This simplified analysis has been made by representing the sculpture as a rigid body simply supported on the pedestal.

4.2 The dynamic analysis

The response of the case-study to the considered blast excitation has been found by performing a dynamic analysis through the Finite Element model described in § 2.3 through the software Marc & Mentat [23]. The duration of the positive pressure wave is very short, so that the blast can be assumed as instantaneous loading. In the numerical simulation, the blast occurs at the time $t = 1$ sec, after the application of the static (gravitational) load. The response of the system to the blast loading has been checked for further 9 seconds, as shown in Figure 8.

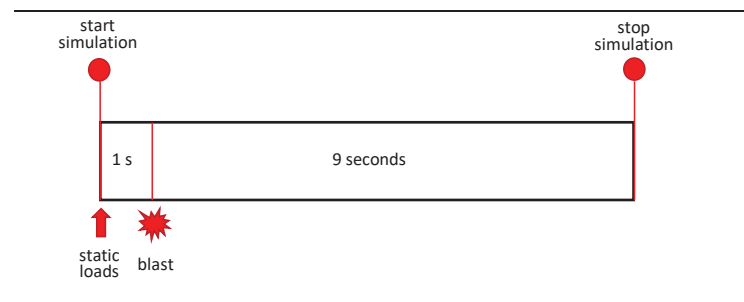


Figure 8. Duration of the analysis and loads timing.

The base restraint has been assumed to be as a simple support, with a friction coefficient between the contact surfaces equal to 0.8, to account for probable roughness of the surfaces and the presence of mortar. The top displacement of the sculpture, i.e. the displacement at the top of the head of the sculpture, has been compared to the displacement experienced by the two extremes (front and back) of its base. Figures 9 and 10 show the displacement histories found for the two assumed quantities of explosive.

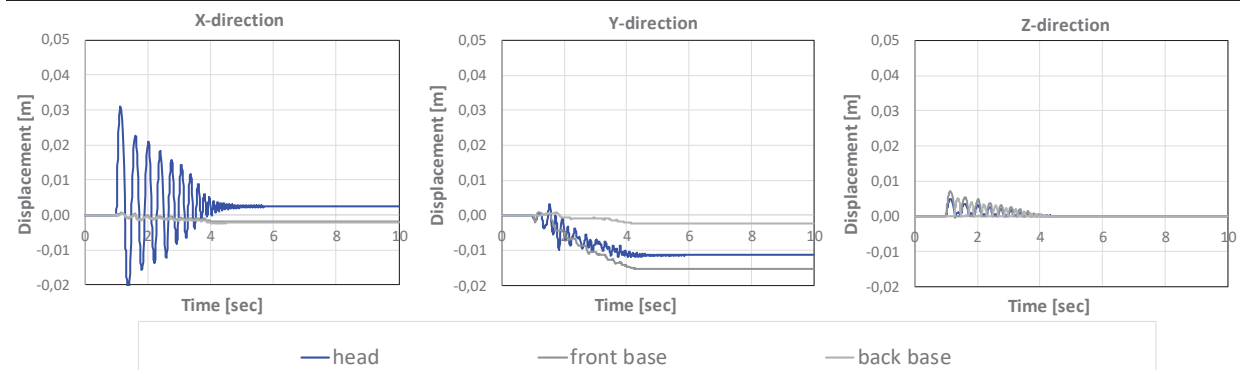


Figure 9. Displacements histories for the case # 1 ($W = 10$ kg)

As can be noted, for the blast induced by 10 kg of TNT (Figure 9), the maximum top displacement, recorded along the X -direction, is around 3 cm, much lower than the overturning limit of the statue. The sculpture exhibits a rocking response, with a different period in the two directions. The dynamic response sculpture of the sculpture is almost symmetric in the X -direction, whilst it is strongly non-symmetric along the Y -direction. In both cases, after the rocking the sculpture settles in a different equilibrium asset.

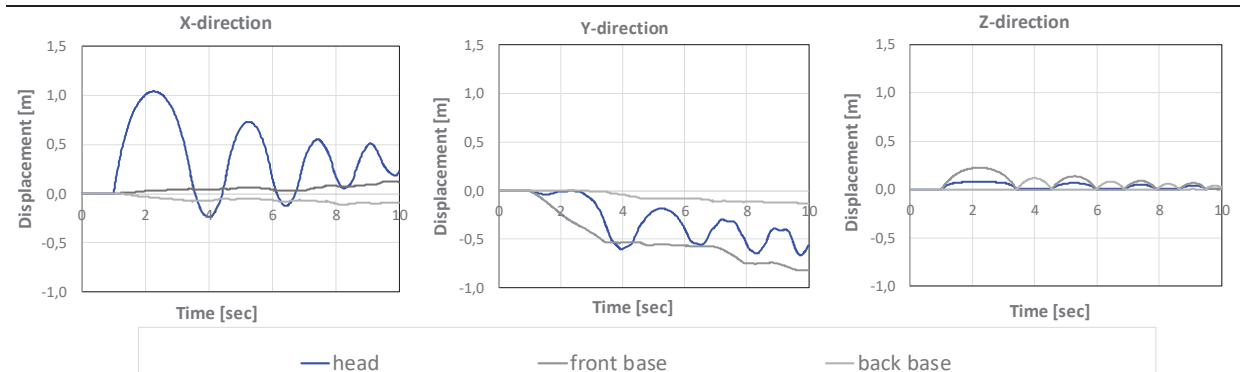


Figure 10. Displacements histories for the case # 2 ($W = 50$ kg)

When the higher loading condition is considered (Figure 10), the maximum displacement achieved by the sculpture head overcomes 1 meter, resulting close to the overturning limit found according to the simplified static analysis. Even in this case, the sculpture exhibits a symmetric response along the X -direction, differently from the Y -direction. The rocking has a period much larger than in the other cases (around 2 seconds), similar for the two directions.

In this case, the system does not achieve a different equilibrium within the duration of the analysis; it should be underlined, however, that no damping has been introduced in the analysis.

5 CONCLUSIONS

In this paper the capacity of the main sculpture of the Fountain of Neptune in Florence has been checked with reference to an explosion due different amounts of TNT, respectively equal to 10 kg and to 50 kg. Before performing the dynamic analysis of the statue under the assumed blast conditions, some preliminary analyses have been carried, to check the dynamic properties of the sculpture, its limit condition to overturning and the static response under gravitational loads only.

The dynamic response of the statue under the assumed blast cases has been found by performing a nonlinear dynamic analysis on a very detailed FE model. The structural model has been set on the basis of a detailed laser-scanner survey, by arranging the geometrical model, starting from the points-cloud.

The analysis evidenced a rocking response of the statue along the *X*-direction, accordantly to results provided by the modal analysis. The dynamic response of the statue shows even a torsional behavior, which can be noted by observing the displacement histories of its base points along the *Y*-direction. The torsional response of the system becomes even more evident at the increasing of the assumed loading intensity. The blast due to the higher amount (50 kg) induces on the system a dynamic response close to its capacity; the maximum top displacement overcomes 1 meter along the *X*-direction, whilst along the *Y*-direction the system does not find a new static equilibrium within the analysis duration.

Further analyses should be made to check the role of the blast position on the statue response, and to assess the best possible restraint condition to minimize the vulnerability of the sculpture.

REFERENCES

- [1] Reinhorn AM, Viti S (2020). Monumental buildings used as museums: Protection or danger for the artifacts? *Procedia Structural Integrity* Vol. 29: pp. 40–47.
- [2] Berto L, Favaretto T, Saetta A, Antonelli F, Lazzarini L (2012). Assessment of seismic vulnerability of art objects: The “*Galleria dei Prigioni*” sculptures at the Accademia Gallery in Florence, *JCH*, 13, 7–21.
- [3] Viti S, Pintucchi B, Rotunno T, Tanganelli M (2020). The seismic analysis of Cerere at the Museum of Bargello. *Bulletin of Earthquake Engineering*, <https://doi.org/10.1007/s10518-020-00802-6>.
- [4] Pintucchi B, Rotunno T, Tanganelli M, Viti S (2019). Bartolomeo Ammannati’s Fountain: comparisons between different numerical models. *RILEM Bookseries – Structural Analysis of Historical Constructions*. Aguilar, R., Torrealva, D., Moreira, S., Pando, M., Ramos, L.F. (Eds.) Springer International Publishing, p. 1201-1209.
- [5] Carlo Cresti (1982). *Le fontane di Firenze*, Firenze, Bonechi, pp. 26-37.
- [6] Pascale G, Lolli A. (2015) Crack assessment in marble sculptures using ultrasonic measurements: Laboratory tests and application on the statue of David by Michelangelo. *JCH* vol. 16 (6), 813–821.
- [7] Sorace S, Terenzi G. (2015) Seismic performance assessment and base-isolated floor protection of statues exhibited in museum halls, *Bull Earthquake Eng*, 13, 1873–1892.
- [8] Bagn  ris M, Cherblanc F, Bromblet P, Gattet E, G  gi L, Nony N, Mercurio V, Pamart A (2017). A complete methodology for the mechanical diagnosis of statue provided by innovative uses of 3D model. Application to the imperial marble statue of Alba-la-Romaine (France). *Journal of Cultural Heritage*, 28:109-116.

- [9] Forcellini D, Giardi F, Tanganelli M (2019). Seismic assessment of the historical third tower in San Marino based on a 3D laser scanner survey (3D-LSS). *Innovative Infrastructure Solutions*, 4 (1), art. no. 20.
- [10] Cristina Acidini Luchinat (1995). Bartolomeo Ammannati artefice di fontane, in “Bartolomeo Ammannati scultore e architetto, 1511-1592”, a cura di Niccolò Rosselli del Turco e Federica Salvi, *Atti del Convegno di Studi* (Firenze-Lucca, 17-19 marzo 1994), Firenze, Alinea, pp. 31-40.
- [11] Tanganelli M, Coli M, Cimellaro GP, Marasco S, Cardoni A, Noori AZ, Viti S (2019). Dynamic analysis of artifacts: experimental tests for the validation of numerical models. In: National Technical University of Athens (NTUA), *Proceedings of the 7th International Conference on Computational Methods on Structural Dynamics and Earthquake Engineering*. vol. 2, p. 2865-2877, M. Papadrakakis, M. Fragiadakis, ISBN: 978-618-82844-7-0, Crete, Greece, 24-26/6/2019.
- [12] Viti S, Tanganelli M (2019). Resimus: A research project on the seismic vulnerability of museums' collections. In: (a cura di): M. Papadrakakis M. Fragiadakis, *COMPdyn Proceedings*. vol. 2, p. 2819-2829, National Technical University of Athens, ISBN: 978-618-82844-7-0, grc, 2019.
- [13] Monaco M, Guadagnuolo M, Gesualdo A. (2014). The role of friction in the seismic risk mitigation of freestanding art objects. *Nat Hazards*, 73:389–402.
- [14] Domaneschi M, Tanganelli M, Viti S, Cimellaro GP (2020). Developing a laboratory facility to assess friction coefficients of standing samples. *PROCEDIA STRUCTURAL INTEGRITY*, vol. 29, p. 142-148, ISSN: 2452-3216, doi: 10.1016/j.prostr.2020.11.150
- [15] Domaneschi M, Tanganelli M, Viti S, Cimellaro GP (2020). Damage risk assessment of historical asset using laser scan and finite element. *PROCEDIA STRUCTURAL INTEGRITY*, vol. 29, p. 183-191, ISSN: 2452-3216, doi: 10.1016/j.prostr.2020.11.155
- [16] Masi F, Stefanou I, Vannucci P, Maffi-Berthier V (2020). Resistance of Museum artefacts against blast loading. *Journal of Cultural Heritage* 44: 163-173.
- [17] Larcher M, Casadei F (2010). Explosions in complex geometries: a comparison of several approaches. *International Journal Protective Structures* 1 (2): 169-195.
- [18] Kingery CN, Bulmash G (1984). Technical Report Arbrl-tr-02555: Air Blast Parameters from Tnt Spherical Air Burst and Hemispherical Burst, U.S. Army Ballistic Research Laboratory, Technical Report.
- [19] Karlos V, Solomos G (2013). JRC - European Commission, “Calculation of Blast Loads for Application to Structural Components. Administrative Arrangement No JRC 32253-2011 with DG-HOME Activity A5 - Blast Simulation Technology Development.
- [20] Friedlander FG (1946). The diffraction of sound pulses. I. Diffraction by a semi-infinite plate. *Proc. R. Soc. Lond. A* (186): 322-344
- [21] Vannucci P, Masi F, Stefanou I (2017). A study on the simulation of blast actions on a monumental structure, hal-01447783v3.
- [22] *Crime Prevention and Security Management in Museum*, De Luca Editori D'Arte.
- [23] MARC & MENTAT (2014). Release 2014.2.0, MSC Software Corporation, Santa Ana, California, USA

SIMPLIFIED ANALYSES FOR THE MODEL SETTING OF SCULPTURES: THE “OCEANO” BY GIAMBOLOGNA

Marco Tanganelli¹, Stefano Galassi¹ and Stefania Viti¹

¹ Department of Architecture (DIDA), University of Florence,
via della Mattonaia 14, 50121 Firenze
{stefano.galassi,marco.tanganelli,stefania.viti}@unifi.it

Abstract

The historical art works represent a priceless asset of communities. Despite their importance, such artifacts are often subjected to many hazards; in Italy, the seismic risk represents one of the most serious dangers which affect the art works, especially those more exposed to overturning. In these years, many studies have been made on the seismic response of artifacts, which evidenced the possible vulnerability of statues to seismic excitations. This paper is focused on the safety assessment of one of the masterpieces of the XVI century art: the marble statue “Oceanus”, made by Giambologna in 1570. The sculpture, currently exhibited at the courtyard of the Museo del Bargello in Florence, has a mass of almost 2 tons, and a height of over three meters, and it is the only giant statue made by Giambologna. In the work, a simplified assessment of the seismic response of the sculpture, and of the consequent seismic safety, has been made, by performing a non-linear static analysis. The role played by the base restraint and by the pedestal of the sculpture have been checked and discussed. The assessment proposed in the paper is aimed at providing a general comprehension of the dynamic response of the case-study under seismic excitations, and to suggest a proper criterion to set a more detailed model for further analyses.

Keywords: Seismic performance of artifacts; artifacts preservation; art works reliability; seismic vulnerability; marble sculptures.

1 INTRODUCTION

Artifacts, at each scale, represent the core of the artistic and cultural identity of communities, and they must be protected against all hazard sources [1-3]. Within artifacts, human-form statues result to be even more vulnerable than others. Beside being subjected to time injuries, they are slender, with an irregular shape and usually made by brittle materials [4]; therefore, they can easily overturn due to horizontal actions. For this reason, the statues result to be very sensitive to the seismic actions, and their capacity to contrast seismic accelerations before overturning has to be carefully checked.

In these last years, many studies have been devoted to the assessment of the vulnerability of statues to horizontal actions. The first contribution to this issue was made by Housner in 1963 [5], with its rigid block analysis, which has been widely developed [6-9]. With the development of the modern techniques of geometrical survey and the consequent possibility to set proper 3D structural models, even the Finite Elements (FE) analysis has been largely adopted for investigating the dynamic response of sculpture to horizontal loading [10-13].

The most suitable method to adopt for predicting the structural behavior of sculptures depends on the contact behavior between them and their supports, and on the expected collapse mechanism. In most cases, marble masterpieces of the Renaissance stand over their pedestal without any specific fixing devices, and therefore their response to horizontal actions are a function of the friction coefficient of the material [14-16]. The proper description of the effective friction at the base of the sculptures requires to adopt proper models and software, able to describe the interface behavior of the object. Furthermore, the effective connection between the artifact and its support is not always known; in many cases, a preliminary study of the quality of the response of the artifact, i.e. the assessment of the most probable collapse mechanism, is essential to correctly drive the choice of the analysis to perform.

In this work, a simplified analysis has been performed to make a quick assessment of the seismic safety of an artifact. Such simplified approach leads to understand if the assessment of the artifact safety is reliable enough; if more comprehensive investigations are needed, it can provide useful information about the choice of the model to use and its setting.

The proposed simplified analysis has been performed on two different models, both defined on the basis of a detailed laser scanner survey. The first model represents the statue as a rigid block, and it leads to investigate its capacity at the overturning. The horizontal action at the overturning has been related to the expected seismic hazard, described through the Technical Code provisions for the area and the foundation soil of the Museum of Bargello, where the statue is placed.

The second model, instead, consists of a FE representation, and provides the amount of stress arising in the case-study under the same assumed seismic excitation. The results provided by the performed analyses have been used to find the Safety Index (SI) of the statue, which has been expressed in term of acceleration, displacement and stress. The SI has been referred to the dynamic response of the sole statue, and of the system made of the statue and its pedestal. The comparison of the obtained results led to have a first assessment of the safety level of the case-study under the expected seismic excitation, and to have useful information to perform further analyses.

2 THE CASE-STUDY

Oceanus is a giant statue made by *Giambologna* between 1572 and 1576 for a Fountain placed in the “Boboli Gardens”, next to *Palazzo Pitti*. The Fountain represented the myth of controlling the waters, as an allegory for good government, and it comprehended even a huge granite basin, roughed out by sculptor and architect *Niccolò Tribolo*. The Fountain was

moved in another position within the Boboli Garden, where it is still now; the sculpture of Oceanus was moved to the National Museum of Bargello in 1911, and it was replaced it in the original location by a copy. At the current time, therefore, Oceanus is placed in the Courtyard of the Museum of Bargello, as can be seen in Figure 1.

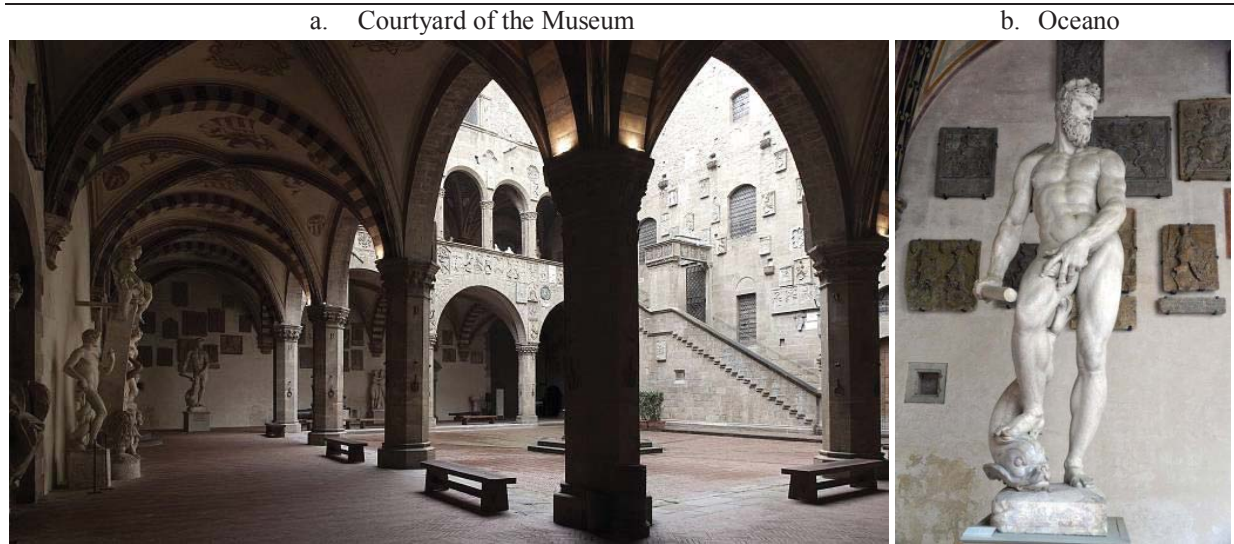
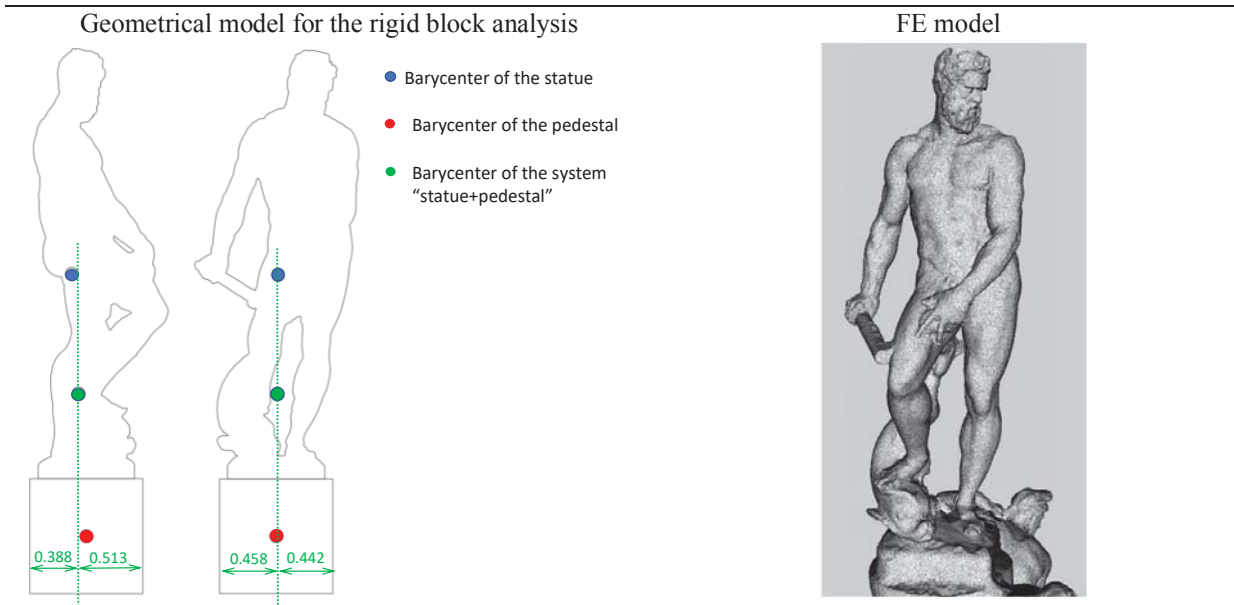


Figure 1. The statue of *Oceanus* at the Museum of Bargello in Florence

Oceanus (see Figure 2) has an height equal to 3.31 m, and a weight of about 2 tons, and it is made of Carrara's marble.



Main data assumed for the analysis

Geometrical model		Mechanical properties of the marble	
Mass of the statue (kg)	1966	Module of Young	50000 MPa
Height of the statue (cm)	331	Compressive strength	50 MPa
Pedestal sides (cmxcmxcm)	90 x 90 x 91	Tensile strength	5 MPa
Pedestal material	concrete	Coefficient of friction	0.8

Figure 2. The statue of *Oceanus*: geometrical and structural models and main data.

The geometry of the statue has been defined after a detailed laser-scanner survey, which led to define both the equivalent rigid block and the FE model. This latter model has been found from the geometric one through some proper arrangements. The first change consisted in a reduction of the polygons from 2000000 to 103259, in order to obtain a simpler model, suitable to be used for the structural analysis. Successively, the “surface” model has been changed in “solid” one, by including the area inscribed in its lateral surface. Figure 2 shows the geometry of the sculpture, together with the main information on the geometry. The barycenter has been found with reference to the statue only and to the system made of the statue and the pedestal together. In the same figure, some information regarding the mechanical properties assumed for the material has been shown. Oceanus is made of Carrara’s marble; the mechanical properties of the marble have been found after proper experimental investigation [17,18] made on marble samples taken from the Carrara’s quarries. A special attention has been paid to the assessment of the friction coefficient (CF). The pedestal of the statue is made of concrete; there is not information regarding the fixing between the statue and the pedestal. In this work, therefore, a CF equal to 0.8 has been assumed, in the hypothesis of lack of specific fixing devices, but assuming a layer of mortar between the statue and the pedestal.

3 THE SAFETY ASSESSMENT

3.1 The preliminary analyses

Two preliminary analyses have been performed to check the dynamic properties of the statue and the amount of stress arising under gravitational loads only. In both cases, a FE model has been adopted, and a fixed base restraint has been assumed. In Figure 3 the first five Periods of the case-study have been listed, together with the corresponding participating mass and modal shape, and the first two modal shapes are shown.

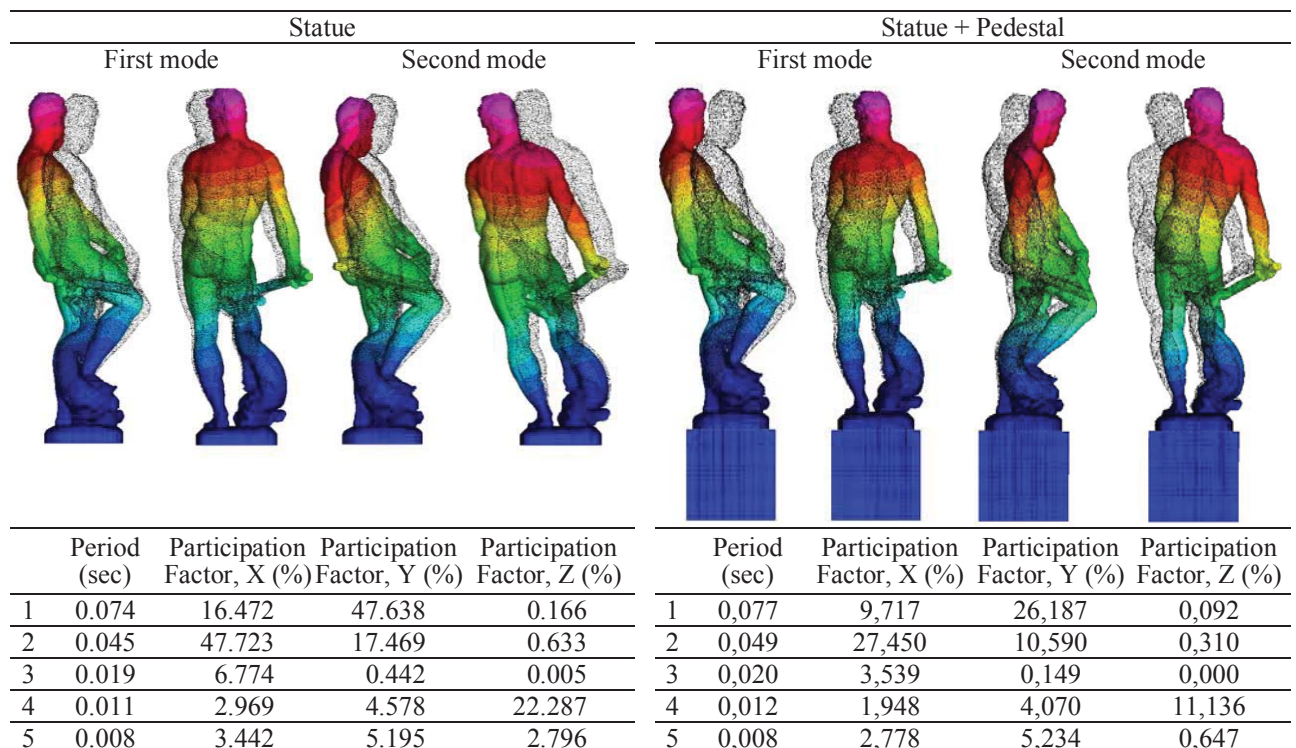


Figure 3. Main vibrational periods and modal shapes of the case-study.

As can be noted, the first mode refers to the Y (front-back of the statue) direction, while the second mode refers to the X (left-right) one. The statue evidences a torsional response even in the first modes. When the pedestal is included in the analysis, the quality of the vibrational modes does not change, but the participation mass of the first modes decreases a lot.

In Figure 4 the distribution of stress experienced by the material under gravitational loads only is shown. As can be observed, the highest stress is gathered in the ankles of Oceanus, which are the narrowest cross sections of the statue. The amount of stress, however, is about 20 times below the elastic limit of the material.

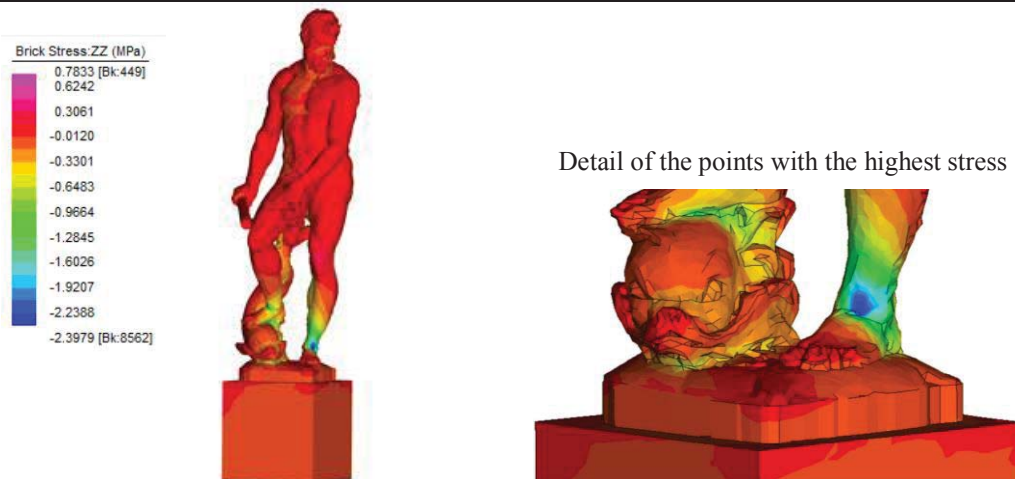


Figure 4. Stress distribution under gravitational loads only.

3.2 The seismic assessment

The assessment of the seismic safety of a statue is related to its collapse mechanism. Previous studies made on similar artifacts [13,19,20] found out the overturning to be the most probable collapse mechanism; such prediction, however, cannot be made regardless of the assumed base restraint and of the mass distribution.

When the base-restraint is a simple support, the amount of stress in the material is quite low, and the collapse is related to the displacement experienced by the object. About Oceanus, the type of the base restraint is not known; the simply supported restraint, however, is the most likely to have been adopted. In this work the simplified seismic safety assessment has been made with reference to both the possible base-restraint hypotheses. In both cases, the seismic response of the case-study has been studied both by considering the statue by itself, and integral with its pedestal.

The limit values of the displacement at the overturning have been determined by imposing the equilibrium of the rigid body. The simplified approach proposed by Parisi and Augenti [21] has been applied, and the overturning of the statue has been represented by equalizing the moment demand, defined as the product of the horizontal force applied to the statue centroid and its distance to the turning point, and the corresponding capacity, defined as the product of the sculpture weight and the distance between its centroid the basement side.

Figure 5 shows the top displacement (TD) at the overturning found for the case-study in the two directions, respectively neglecting the pedestal or taking it into account.

The limit horizontal accelerations corresponding to the system overturning have been found by considering the seismic hazard of the area. A soil class B has been assumed for the foundation, according to previous investigations made on the Museum of Bargello [22].

The seismic ground acceleration, A_g , has been assumed equal to $0.1659g$, corresponding to the *Life Safety* limit state for a class of use $c_u=2$, a nominal life equal to 50 years and a Return Period equal to 949 years (Probability of Occurrence of 10%). The Fundamental Period of the system has been assumed equal to 0 sec, i.e. the sculpture has been assumed as perfectly rigid. The amplification factor (f_a), has been found according to the current Code (NTC 2018, [23]):

$$f_a = \frac{a_0 \times q_a}{A_g \times S \times CF} \quad (1)$$

where a_0 is the acceleration corresponding to the overturning mechanism, q_a is the behavior factor, assumed equal to 2, CF is the confidence factor, assumed equal to 1, and S , assumed as 1.2, is the product of the stratigraphic amplification factor and the topographic amplification factor.

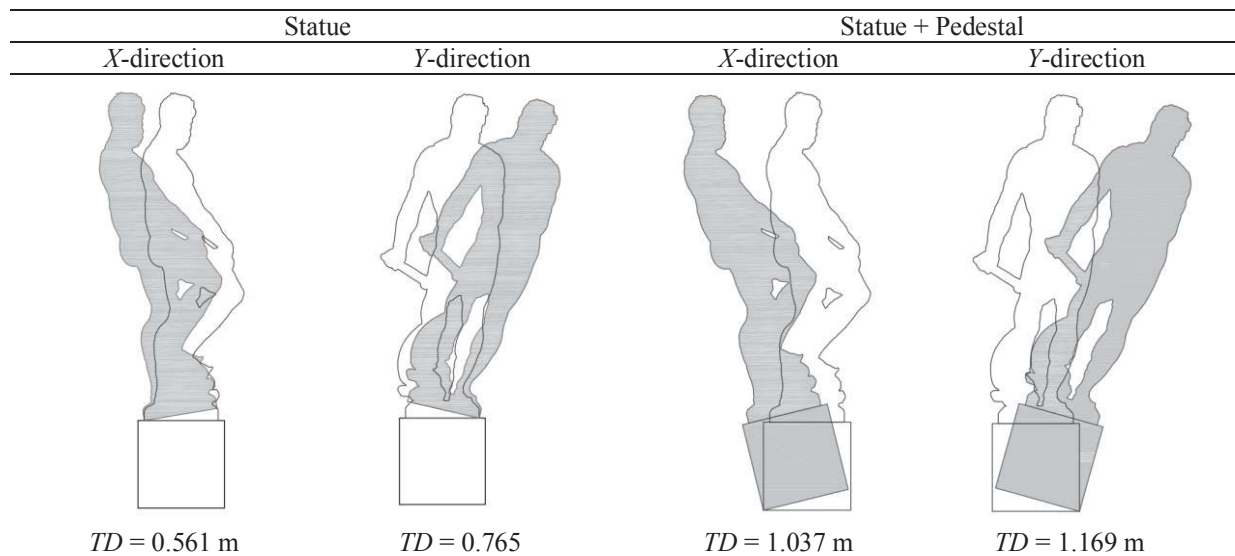


Figure 5. Overturning rotations and Tod Displacements of the case-study.

In Table 1 the values of the overturning acceleration and the amplification factor are listed for the two directions, together with the corresponding Acceleration Safety Index, SI_ACC , defined as $1/f_a$. It is worth noting that the system is safe for SI_ACC values below the unity, and that the safety factor of the system is the highest of those provided by the considered cases of analysis.

Table 1. Parameters assumed for defining the seismic demand.

	Statue		Statue + Pedestal	
	X-direction	Y-direction	X-direction	Y-direction
Overturning acceleration, a_0	0,229	0,166	0,279	0,245
Amplification Factor, f_a	2.30	1.67	2.80	2.46
Safety Index, SI_ACC	0.43	0.60	0.36	0.41

The safety of the case-study has been assessed even in terms of displacements. Figure 6 shows the main quantities involved in the spectral assessment of the Safety Index expressed in terms of displacement, SI_DISPL , which is defined as the ratio between the displacement demand, of the center of mass, D_d , and the corresponding ultimate displacement, D_u^* .

The quantity D_u^* , in turn, is defined as the 40% of D_{max}^* , that is the value of the displacement of the barycenter at the overturning. The displacement demand is found as the intersection of the spectral seismic demand (line in green in Figure 6) and the secant Period of the

system, T^*_S , which has been determined according to the expression provided by the current Technical Code (Circ. n. 7, Section C8.7.1.2.1.8, [24]).

As can be noted, the values found for the spectral demand respectively accounting and not for the statue's pedestal are almost coincident; the corresponding ultimate displacements, though, differ significantly from each other; when the performance of the statue is considered without the contribution of its pedestal, its ultimate displacement reduces a lot. In Table 2 the values found for the SI_DISPL have been listed together with the main quantities found for their determination.

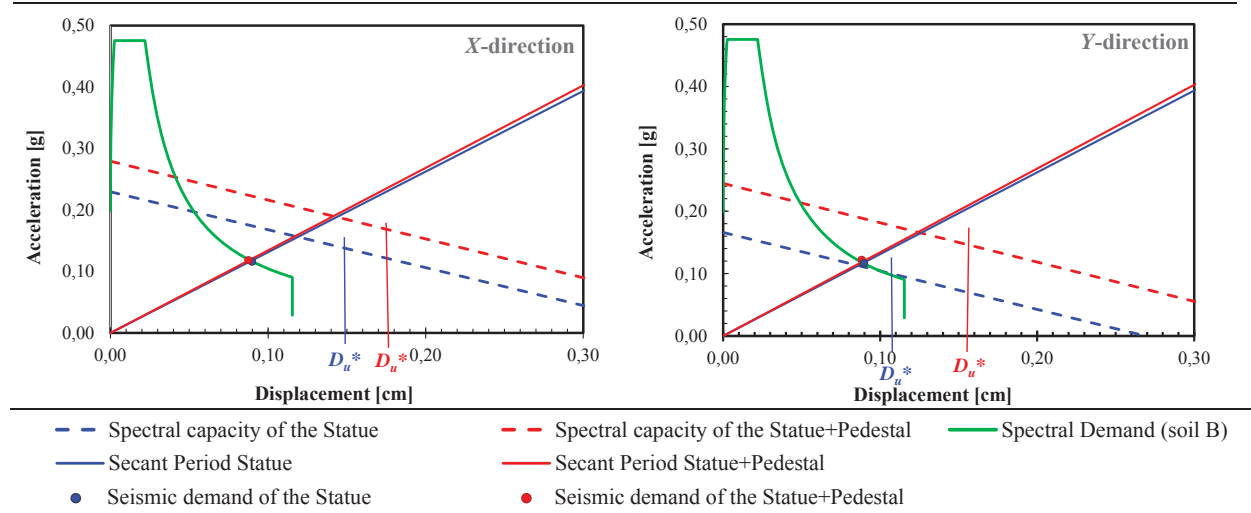


Figure 6. Capacity domains of the case-study along the two main directions.

Table 2. Main quantities used for the safety assessment.

	D_{max}^* (cm)	D_u^* (cm)	T^*_S (sec)	D_d (cm)	SI_DISPL
Statue, X-direction	37.2	14.8	1.73	8.91	0.599
Statue, Y-direction	26.9	10.8	1.73	8.91	0.828
Statue + pedestal, X direction	44.2	17.7	1.75	8.80	0.498
Statue + pedestal, Y direction	38.8	15.5	1.75	8.80	0.567

Finally, the seismic safety has been assessed in terms of stress amount. In this case the statue has been assumed to be fixed at the base, since the amount of stress is larger in fixed, i.e. stiffer, systems. Figure 7 shows the stress distribution within the statue found by performing a modal analysis based on the Code spectrum, by using the same seismic input already described in this Session. As can be observed, the larger tensile stress is placed in the back side of the ankles and at the top of the dolphin. The maximum amount of tensile stress is equal to 2.57 MPa and 3.63 MPa, respectively, for the sole statue and the statue with the pedestal; since the maximum tensile stress of the marble has been assumed equal to 5 MPa, the Safety Index can be expressed in terms of stress (SI_STRESS) as the ratio of the tensile peak and the corresponding capacity.

It is interesting to note that when the pedestal is considered as integral part of the system, the maximum tensile stress is achieved in the front part of the ankles, whilst, when the sole statue is considered, the most tensile points are in the ankles front.

The values of the Safety Index found in terms of acceleration, displacement and stress respectively, have been compared. Figure 8 shows obtained values of SI ; as can be observed, all the SI are well below the unit, even if they differ very much from each other.

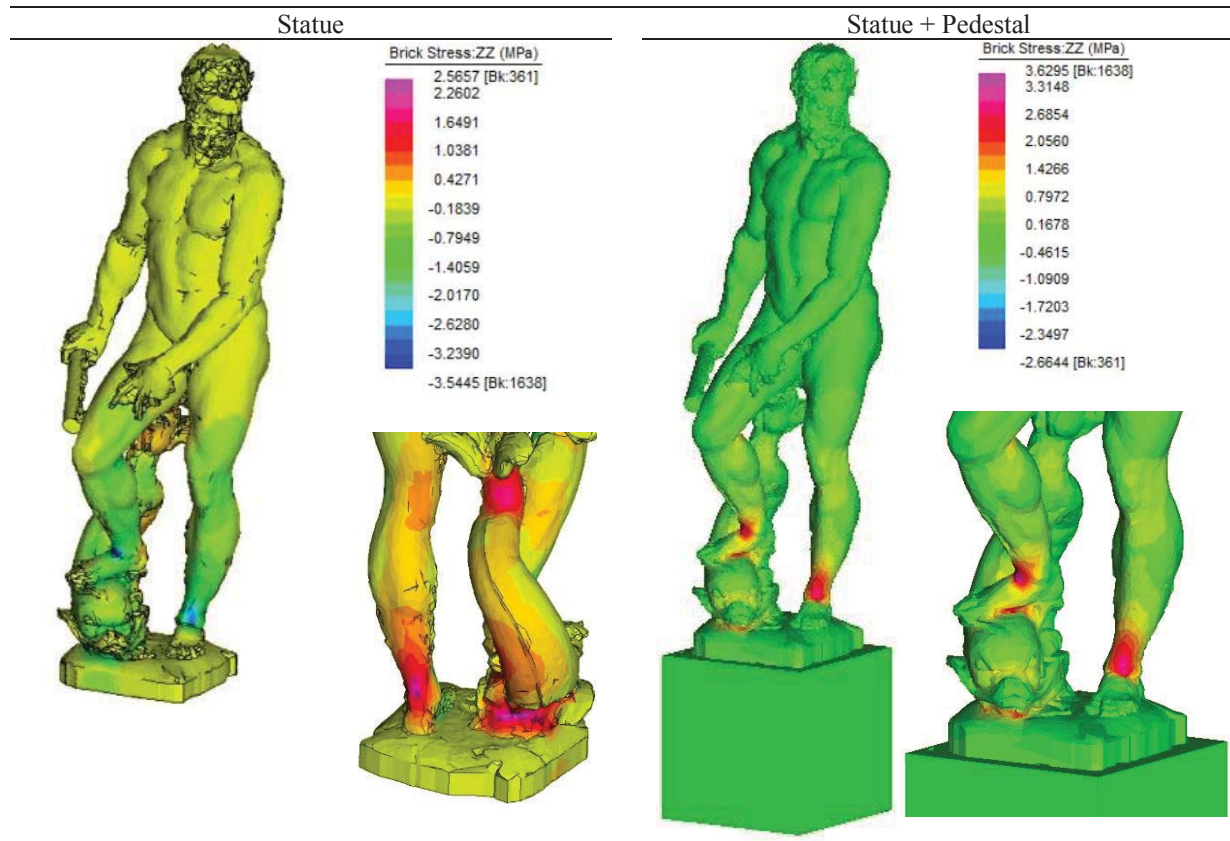


Figure 7. Stress distribution found by performing the modal analysis.

By comparing the values found for the Safety Index, some considerations can be made. First of all, the parameter which is closer to the safety threshold is the displacement; the collapse mechanism to assume for a more comprehensive analysis, therefore, should be the overturning, associated to a simply supported base restraint and a proper mechanical description of the interaction between statue and pedestal. As regards the overturning, when the pedestal is considered as integral to the statue, its contribution improves the performance of the system. The SI_DISPL found for the statue only, however, could not represent the most dangerous seismic response of the system, since it neglects the contribution of the pedestal in the transmission of the seismic action, and/or in the contribution to the total displacement experienced by the statue.

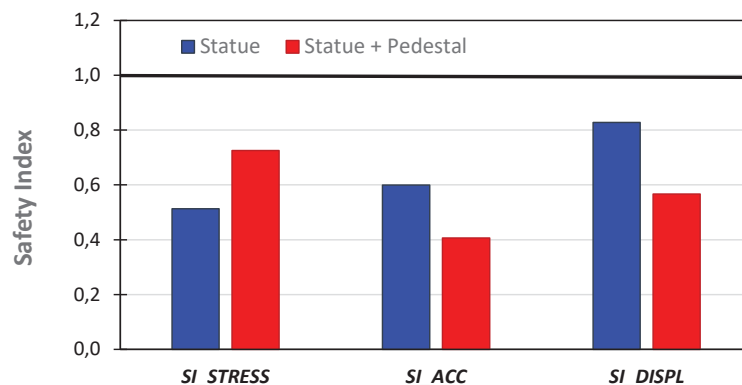


Figure 8. SI values obtained from acceleration, displacement and stress.

4 CONCLUSIONS

In this paper a simplified assessment of the seismic safety of Oceanus, the Renaissance masterpiece made by Giambologna, has been made, applying the simple spectral nonlinear static method. The analyses have been performed by using both a rigid block and a Finite Element models; a special attention has been paid to the role of the pedestal on the seismic response of the case-study and on the restraint condition to assume at the base of the sculpture with reference to the assumed collapse mechanism. Three different Safety Indexes have been found, expressed, respectively, in terms of acceleration, displacement and stress. The analysis states a satisfactory safety level of the statue; however, the differences found between the various Safety Indexes, and the higher value of the *SI* expressed in terms of displacement comparing to the others, suggest to perform further analyses, checking the nonlinear dynamic response of the statue to seismic excitations, and accounting for the contact behavior between the statue and the pedestal, and between the pedestal and the soil.

REFERENCES

- [1] Lowry MK, Farrar BJ, Armendariz D., and Podany J. (2007). Protecting Collections in the J. Paul Getty Museum from Earthquake Damage. *WAAC Newsletter* Volume 29.
- [2] Spyrakos CC, Maniatakis CA, Taflampas IM (2017). Application of predictive models to assess failure of museum artifacts under seismic loads. *Journal of Cultural Heritage* 23, 11–21.
- [3] Reinhorn AM, Viti S (2020). Monumental buildings used as museums: Protection or danger for the artifacts? *Procedia Structural Integrity* Vol. 29: pp. 40–47.
- [4] Wittich CE, Hutchinson TC, Wood RL, Seracini M, Kuester F (2016). Characterization of Full-Scale, Human-Form, Culturally Important Statues: Case Study J. *Comput. Civ. Eng.*, **30**(3).
- [5] Housner GW (1963). The behavior of inverted pendulum structures during earthquakes. *Bulletin of the Seismological Society of America* 53(2)
- [6] Monaco M, Guadagnuolo M, Gesualdo A. (2014). The role of friction in the seismic risk mitigation of freestanding art objects. *Nat Hazards*, 73:389–402.
- [7] Kounadis AN. (2015). New findings in the rocking instability of one and two rigid block systems under ground motion. *Meccanica*, 50:2219–2238.
- [8] Bakhtary E, Gardoni P. (2016). Probabilistic seismic demand model and fragility estimates for rocking symmetric blocks. *Engineering Structures* 114, 25–34.
- [9] Ther T and Kollár, LP (2018). Model for multiblock columns subjected to base excitation. *Journal for the International Association for Earthquake Engineering*, Edited By: Masayoshi Nakashima, Michael Fardis, and Michael C. Constantinou. Volume47, Issue2: 418-437
- [10] Sorace S, Terenzi G. (2015) Seismic performance assessment and base-isolated floor protection of statues exhibited in museum halls, *Bull Earthquake Eng*, 13, 1873–1892.
- [11] Bagn  ris M, Cherblanc F, Bromblet P, Gattet E, G  gi L, Nony N, Mercurio V, Pamart A (2017). A complete methodology for the mechanical diagnosis of statue provided by innovative uses of 3D model. Application to the imperial marble statue of Alba-la-Romaine (France). *Journal of Cultural Heritage*, 28:109-116.

- [12]Forcellini D, Giardi F, Tanganelli M (2019). Seismic assessment of the historical third tower in San Marino based on a 3D laser scanner survey (3D-LSS). *Innovative Infrastructure Solutions*, 4 (1), art. no. 20
- [13]Viti S, Pintucchi B, Rotunno T, Tanganelli M (2020). The seismic analysis of Cerere at the Museum of Bargello. *Bulletin of Earthquake Engineering*, 18(6), pp. 2635-2656, doi: 10.1007/s10518-020-00802-6
- [14]Domaneschi M, Tanganelli M, Viti S, Cimellaro GP (2020). Developing a laboratory facility to assess friction coefficients of standing samples. *PROCEDIA STRUCTURAL INTEGRITY*, vol. 29, p. 142-148, ISSN: 2452-3216, doi: 10.1016/j.prostr.2020.11.150
- [15]Tanganelli M, Coli M, Cimellaro GP, Marasco S, Cardoni A, Noori AZ, Viti S (2019). Dynamic analysis of artifacts: experimental tests for the validation of numerical models. In: National Technical University of Athens (NTUA), *Proceedings of the 7th International Conference on Computational Methods on Structural Dynamics and Earthquake Engineering*. vol. 2, p. 2865-2877, M. Papadrakakis, M. Fragiadakis, ISBN: 978-618-82844-7-0, Crete, Greece, 24-26/6/2019
- [16]Monaco M, Guadagnuolo M, Gesualdo A (2014). The role of friction in the seismic risk mitigation of freestanding art objects. *Natural Hazards* (2014) 73: 389–402. DOI: org/10.1007/s11069-014-1076-9.
- [17]Viti S, Tanganelli M (2019). Resimus: A research project on the seismic vulnerability of museums' collections. In: (a cura di): M. Papadrakakis M. Fragiadakis, *COMPDYN Proceedings*. vol. 2, p. 2819-2829, National Technical University of Athens, ISBN: 978-618-82844-7-0, grc, 2019.
- [18]Tanganelli M Viti S, Cimellaro, GP Domaneschi M (2020). Developing a laboratory facility to assess friction coefficients of standing samples. *PROCEDIA STRUCTURAL INTEGRITY*, vol. 29, p. 142-148, ISSN: 2452-3216, doi: 10.1016/j.prostr.2020.11.150.
- [19]Domaneschi M, Tanganelli M, Viti S, Cimellaro GP (2021). Vulnerability of art works to blast hazard: the Fountain of Neptune in Florence. *COMPDYN 2018*, Papadrakakis and Fragiadakis Eds.
- [20]Domaneschi M, Tanganelli M, Viti S, Cimellaro GP (2021). Protection of art works to blast hazard: the Fountain of Neptune in Florence. *International Journal of Masonry Research and Innovation, ArCo2020 New Approaches in Diagnostic and Safety Evaluation of Cultural Heritage*.
- [21]Parisi F, Augenti N (2013). Earthquake damages to cultural heritage constructions and simplified assessment of artworks. *Engineering Failure Analysis* **34**, 735–760.
- [22]Sapia V, Materni V, Giannattasio F, Marchetti M (2018). Esplorazione geofisica del sottosuolo: primi risultati nel centro storico di Firenze. In: *RESIMUS: Un progetto rivolto alla vulnerabilità sismica delle opere museale*, DIDAPRESS.
- [23]NTC 2018 [2018]. *Decreto del Ministro delle Infrastrutture 17 gennaio 2018. Aggiornamento delle «Norme tecniche per le costruzioni»*. Gazzetta Ufficiale della Repubblica Italiana, n. 42 del 20 febbraio 2018, Supplemento Ordinario n. 8.
- [24]C.S.LL.PP. 21 gennaio 2019. CIRCOLARE, n. 7: Istruzioni per l'applicazione dell'«Aggiornamento delle "Norme tecniche per le costruzioni"» di cui al decreto ministeriale 17 gennaio 2018. (in Italian).

VULNERABILITY ASSESSMENT OF MONUMENTAL ARTWORKS USING CONTACT TIME-HISTORY ANALYSIS

**Raffaele Gagliardo¹, Michele Godio², Lucrezia Cascini¹, Francesco Portioli¹ and
Raffaele Landolfo¹**

¹ Department of Structures for Engineering and Architecture, University of Naples “Federico II”, Italy
via Forno Vecchio 36, 80134 Naples, Italy
raffaele.gagliardo@unina.it, fportioli@unina.it, lucrezia.cascini@unina.it, landolfo@unina.it

² RISE Research Institutes of Sweden
Brinellgatan 4, 504 62 Borås, Sweden
michele.godio@ri.se

Abstract

Strategies for the protection of the Cultural Heritage priceless value are highly demanded, being both earthquake and support movement (and a combination of the two of them) severe threats for their safety and integrity. To this scope, computer-based numerical formulations have been representing a powerful tool for the simulation of expected loss in terms of pieces of art damages, with the scope to save them as much as possible. In this framework, the conference paper is devoted to the vulnerability assessment of monumental artworks using dynamic analysis in a rigid block modelling environment.

The numerical formulation adopts a discrete rigid block-based model, where the mortar joints contribution is accounted for by frictional, no-tension interfaces between the masonry units. The procedure adopted to solve the formulation is based on a dual variational problem where equilibrium, kinematic and failure conditions equations are involved at the same time, and which is solved via mathematical programming.

An application to a system of two blocks vertically stacked, one representing the support and one representing the artefact, subjected to free rocking motion will be proposed in the paper. The main scope is to investigate the seismic response of such a system, which is typical for most of museum's collections (e.g., statues). The computational efficiency and accuracy of the proposed numerical strategy will be discussed.

Keywords: Masonry block structures; Non-linear time history analysis, Free rocking motion, Mathematical programming.

1 INTRODUCTION

The possibility to develop computational strategy for the investigation of museum collections behaviour against seismic-induced dynamic actions represents a challenging task, playing a crucial role in the artworks integrity protection. The response of blocky structures, such as monumental statues made of stone blocks, against lateral forces is typically characterized by rocking behaviour [1–3].

The development and use of analytical and numerical tools for the investigation of blocky structures and historical masonry monuments subjected to different loading conditions by using both static and dynamic approaches is a widespread topic in literature [4–33]. Various numerical approaches are available in literature for the investigation of the dynamic response of multi-block structures and types undergoing rocking. Among those, the interest in the use of Non-Smooth Contact Dynamics (NSCD) methods has been growing in the recent years, essentially due to the advantageous possibility to account for the blocks interactions through a system made of both equilibrium and complementary conditions. In this framework, NSCD approach represent a valid alternative to common modeling approaches such as finite element method (FEM) and discrete element method (DEM) [34–37].

The use of NSCD technique has been increasing especially in the analysis of the structural response of masonry structures [38]–[40], where fast and accurate algorithms are available in the literature for the numerical solution of the formulations proposed for the mathematical programming problem arising from the conditions governing the contact dynamics [41–44].

In this paper we adopt a simple formulation for dynamic analysis of blocky structures aiming to investigate the rocking behaviour of a system of two blocks, comparable to the configuration of a monumental statue typical of museum's collections standing on its base. The aim of this research is to assess the computational efficiency of the in-house numerical procedure and to investigate to which extent it can be properly adopted in the prediction of the rocking behaviour of museum's artefacts to save them against any possible loss or damage. It is worth noting that the modelling approach for contact interfaces can be regarded as the extension to the dynamic field of a contact point formulation developed for limit analysis of collections of polyhedral rigid blocks.

The paper is organized as follows: the dynamic formulation is described in section 2 in terms of static and kinematic variables as well as the problem formulated to govern the behaviour of the rigid block model. Section 3 deals with the numerical application of the adopted procedure to the case study of a two blocks system subjected to free rocking motion already considered in literature.

2 THE RIGID BLOCK DYNAMIC MODEL

The proposed numerical model is composed by a collection of quadrangular rigid blocks i interacting by means of contact points k located at the vertexes of contact surfaces j (Figure 1a). The behaviour of contact interfaces is governed by a no-tension and associative frictional model under the assumption of infinite compressive strength. The dynamic model is formulated according to the approach proposed in [45, 46] for granular materials.

The contact variables are represented by the internal forces located at contact point k , which are essentially the shear and normal force (Figure 1b), collected in the vector \mathbf{c}_k .

The relative displacement rates, both tangential Δu_{tk} and normal Δu_{nk} , represent the kinematic variables associated to the contact forces in a virtual work sense. They are finally collected in the vector $\Delta \mathbf{u}$ (Figure 1c).

The centroid of the rigid block i is attached by the external loads and the position of the block centroid is collected in the vector \mathbf{x}_i as described in equation (1) and Figure 1b.

$$\mathbf{x}_i = [x_i \quad z_i \quad \omega_i]^T \quad (1)$$

θ -method is used to discretize the equations of motions, as described in equations (2) and (3) with regard to time $t = t_0 + \Delta t$.

$$\alpha(t) = \frac{v - v_0}{\Delta t} \quad (2)$$

$$v(t) = \frac{1}{\theta} \left[\frac{\Delta \mathbf{x}}{\Delta t} - (1 - \theta)v_0 \right] \quad (3)$$

being $\Delta \mathbf{x} = \mathbf{x} - \mathbf{x}_0$ the displacement vector, x_0 the known position and v_0 the known velocity at t_0 and $0.5 < \theta \leq 0.5$.

The incremental equation (2) allows to formulate the equation of motion of the collection of rigid blocks using a contact point model as described in the next equation (4):

$$\bar{\mathbf{M}}\Delta \mathbf{x} + \mathbf{A}_0 \mathbf{c} = \bar{\mathbf{f}}_0 \quad (4)$$

where \mathbf{A}_0 is the contact equilibrium matrix, $\bar{\mathbf{M}} = \frac{1}{\theta \Delta t^2} \mathbf{M}$ is related to the mass matrix \mathbf{M} which collects the mass and the inertia moment of each block and $\bar{\mathbf{f}}_0 = \mathbf{f} + \bar{\mathbf{M}}v_0\Delta t$.

Ad-hoc expression are formulated to account for non-penetration condition at potential contact point, by using the so-called Signorini unilateral contact condition.

Finally, sliding failure condition at contact interfaces is governed by a Coulomb friction law, expressed by the following equation (5).

$$\pm t_k - \mu n_k \leq 0 \quad (5)$$

being μ the value of friction coefficient.

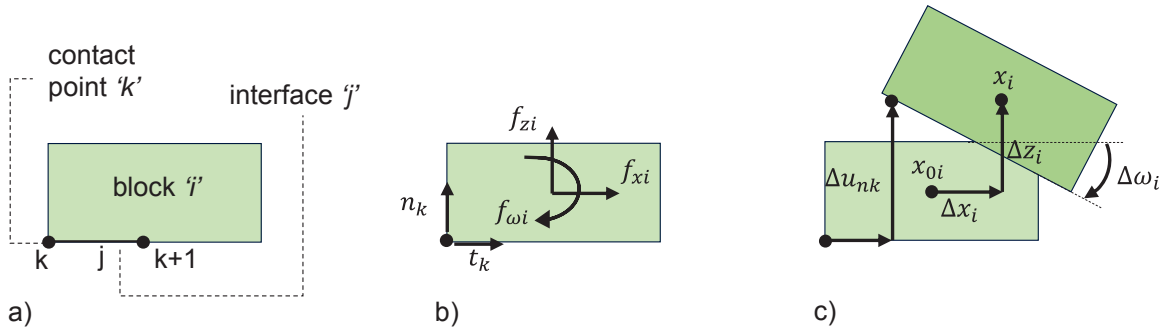


Figure 1. Rigid block dynamic model: (a) Rigid block i , interface j and contact point k ; (b) contact forces and (c) kinematic variables at block centroid i , and contact point k .

2.1 Formulation of the mathematical programming problem

The dynamic problem can be expressed by an equations system which collect the equilibrium equations, the kinematic and the failure conditions in a typical linear complementarity problem (LCP). In this framework, the contact dynamics problem can be posed as described in equation (6), where \mathbf{Y}^T is the matrix of failure condition, λ is the vector of flow multipliers and \mathbf{g}_0 is the vector collecting initial gaps at each contact point.

The problem expressed in equation (6) is uncoupled in two dual quadratic programming problems, a force-based and a displacement-based problem, respectively. In this way, the

computational costs significantly decrease thanks to the possibility to use efficient solution algorithms.

$$\begin{bmatrix} \bar{\mathbf{M}} & \cdot & \mathbf{A}_0 \\ \cdot & \cdot & -\mathbf{Y}^T \\ -\mathbf{A}_0^T & \mathbf{Y} & \cdot \end{bmatrix}_{n \times n} \begin{bmatrix} \Delta \mathbf{x} \\ \lambda \\ \mathbf{c} \end{bmatrix}_{n \times 1} + \begin{bmatrix} \cdot \\ \cdot \\ \cdot \end{bmatrix} \mathbf{y} = \begin{bmatrix} \bar{\mathbf{f}}_0 \\ \cdot \\ -\mathbf{g}_0 \end{bmatrix} \quad (6)$$

$$s.t. \quad -\mathbf{y} \geq 0 \quad \lambda \geq 0 \quad \mathbf{y}^T \lambda = 0$$

It is worth noting that the dynamic problem formulated in the equation (6) is formally equivalent to a classic limit equilibrium problem when the dynamic forces and contact gaps tend to zero. An incremental procedure was implemented to solve the optimization problem assuming kinematic variables derived by Lagrange multipliers and updating the block position and gaps values per each step.

The analyses were carried out a 3.50 GHz Intel Xeon Processor E5-1650 with 16.0 GB of RAM. The value of algorithm parameter θ for time discretization was set equal to 0.7 and time increment was set in the range 0.001-0.002 s.

3 NUMERICAL APPLICATION TO A TWO-BLOCK SYSTEM SUBJECTED TO FREE ROCKING MOTION

The dynamic numerical procedure described in the previous section is here applied to the case study of a two-block system undergoing to free rocking. This case study was previously investigated in [47]. The geometrical properties of the two blocks are showed in Figure 2a, being equivalent to the example performed in [47]. The first block has a slenderness ratio H_1/B_1 equal to 1 whereas the second one has a slenderness ratio H_2/B_2 equal to 2.5. The base widths are $B_1 = 1.25$ m and $B_2 = 1.0$ m respectively. As for the material properties, the two blocks are considered homogeneous, with a weight for unit volume $\rho_1 = \rho_2 = 2500$ kg/m³. The investigated case study is characterized by a value of the starting rotation angles $\theta_1 = \theta_2 = 0.15$ rad and zero starting angular velocities for both the considered blocks.

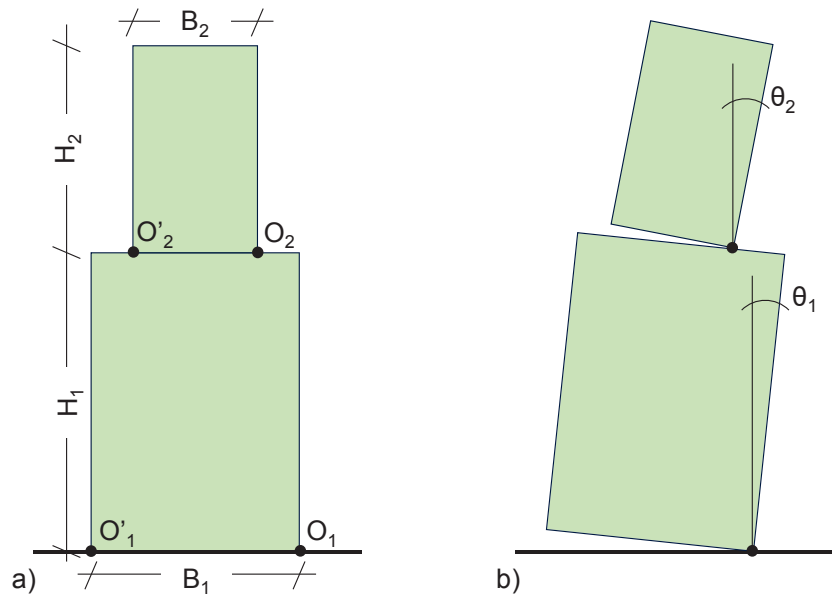


Figure 2. Two-block system: (a) geometrical properties and (b) example of configuration during free rocking motion.

The outcomes of the simulation are reported in Figure 3. According to [47], starting from the initial configuration, the angles of rotation of the two blocks, θ_1 and θ_2 , tend to decrease due to the oscillation movement, and this occurs with a faster rate for the block at the base. In the first part of the motion, the two blocks move as one-single block rocking about the point O_1 , until the occurrence of an impact at the foundation. After the impact, the two blocks start to independently rock and other impacts occur up to the rest. As for the outcomes obtained with the proposed rigid block dynamic model, the curve showed in Figure 3 deals with the rotation angle θ_2 of the upper block around the point O_2 . The results are in a very good agreement with those obtained in [47] until the first impact of the upper block. After this initial stage, the second rotation is somewhat different with respect to the rotation predicted in [47]. Nevertheless, the two curves are very close, and so are the maximum oscillations obtained by the two models. The comparison is, therefore, very satisfying. With regard to the final stage, i.e. after the second impact of the upper block, the results obtained with the proposed rigid block dynamic model tends to predict a faster rocking performance compared with the results obtained in [47]: a higher number of impacts (i.e. change of rotation) is exhibited by the upper blocks. Finally, the two models come to a rest step at about 3.5 seconds analysis.

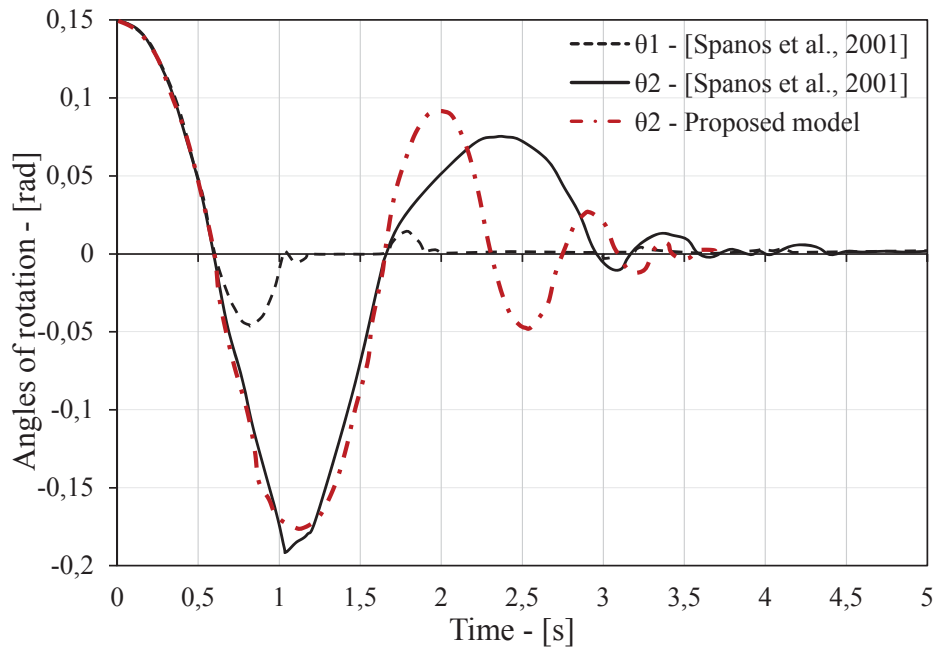


Figure 3. Free vibration response of a two-block system. Comparison with the results obtained in [47].

4 CONCLUSIONS

In this paper an in-house rigid block model for contact time-history analysis was described. The computational strategy is particularly suitable to investigate the response of stacked-blocks objects subjected to ground excitation. From this point of view, the dynamic model could represent a useful numerical tool for the vulnerability assessment of museum's collections affected by seismic-induced action, aiming to the protection of such artworks against earthquakes events. The capabilities of the proposed formulation were tested on a case study of a two-block system experiencing free rocking motion, already investigated in literature. The outcomes showed high potentialities of the adopted strategy in the prediction of the rocking behaviour of blocky objects.

REFERENCES

- [1] O. A. Shawa, G. de Felice, A. Mauro, and L. Sorrentino, "Out-of-plane seismic behaviour of rocking masonry walls," *Earthq. Eng. Struct. Dyn.*, vol. 41, no. 5, pp. 949–968, 2012.
- [2] S. Lagomarsino, "Seismic assessment of rocking masonry structures," *Bull. Earthq. Eng.*, vol. 13, no. 1, pp. 97–128, 2015.
- [3] M. J. DeJong and E. G. Dimitrakopoulos, "Dynamically equivalent rocking structures," *Earthq. Eng. Struct. Dyn.*, vol. 43, no. 10, pp. 1543–1563, 2014.
- [4] C. Casapulla, L. Giresini, and P. B. Lourenço, "Rocking and kinematic approaches for rigid block analysis of masonry walls: State of the art and recent developments," *Buildings*, vol. 7, no. 3, 2017.
- [5] G. De-Felice and M. Malena, "Failure pattern prediction in masonry," *J. Mech. Mater. Struct.*, vol. 14, no. 5, pp. 663–682, 2019.
- [6] M. F. Funari, A. Mehrotra, and P. B. Lourenço, "A tool for the rapid seismic assessment of historic masonry structures based on limit analysis optimisation and rocking dynamics," *Appl. Sci.*, vol. 11, no. 3, pp. 1–22, 2021.
- [7] M. F. Funari, S. Spadea, P. Lonetti, F. Fabbrocino, and R. Luciano, "Visual programming for structural assessment of out-of-plane mechanisms in historic masonry structures," *J. Build. Eng.*, vol. 31, 2020.
- [8] S. Galassi, N. Ruggieri, and G. Tempesta, "A Novel Numerical Tool for Seismic Vulnerability Analysis of Ruins in Archaeological Sites," *Int. J. Archit. Herit.*, vol. 14, no. 1, pp. 1–22, 2020.
- [9] S. Galassi, M. L. Satta, N. Ruggieri, and G. Tempesta, "In-plane and out-of-plane seismic vulnerability assessment of an ancient colonnade in the archaeological site of Pompeii (Italy)," in *Procedia Structural Integrity*, 2020, vol. 29, pp. 126–133.
- [10] S. Galassi and G. Tempesta, "The Matlab code of the method based on the Full Range Factor for assessing the safety of masonry arches," *MethodsX*, vol. 6, pp. 1521–1542, 2019.
- [11] S. Galassi and G. Tempesta, "Porta San Giorgio in Florence. Rigid block model analysis for the crack pattern interpretation," in *COMPdyn Proceedings*, 2019, vol. 1, pp. 651–662.
- [12] A. I. Giouvanidis and E. G. Dimitrakopoulos, "Rocking amplification and strong-motion duration," *Earthq. Eng. Struct. Dyn.*, vol. 47, no. 10, pp. 2094–2116, 2018.
- [13] A. I. Giouvanidis and Y. Dong, "Seismic loss and resilience assessment of single-column rocking bridges," *Bull. Earthq. Eng.*, vol. 18, no. 9, pp. 4481–4513, 2020.
- [14] L. Giresini, M. Fragiocomo, and P. B. Lourenço, "Comparison between rocking analysis and kinematic analysis for the dynamic out-of-plane behavior of masonry walls," *Earthq. Eng. Struct. Dyn.*, vol. 44, no. 13, pp. 2359–2376, 2015.
- [15] L. Giresini, F. Solarino, O. Paganelli, D. V. Oliveira, and M. Froli, "ONE-SIDED rocking analysis of corner mechanisms in masonry structures: Influence of geometry, energy dissipation, boundary conditions," *Soil Dyn. Earthq. Eng.*, vol. 123, pp. 357–370, 2019.
- [16] L. Giresini, F. Solarino, F. Taddei, and G. Mueller, "Experimental estimation of energy dissipation in rocking masonry walls restrained by an innovative seismic dissipator (LICORD)," *Bull. Earthq. Eng.*, vol. 19, no. 5, pp. 2265–2289, 2021.
- [17] N. Grillanda, A. Chiozzi, G. Milani, and A. Tralli, "Tilting plane tests for the ultimate shear capacity evaluation of perforated dry joint masonry panels. Part II: Numerical analyses," *Eng. Struct.*, vol. 228, 2021.

- [18] N. Grillanda, G. Milani, S. Ghosh, B. Halani, and M. Varma, "SHM of a severely cracked masonry arch bridge in India: Experimental campaign and adaptive NURBS limit analysis numerical investigation," *Constr. Build. Mater.*, vol. 280, 2021.
- [19] W. G. Lasciarrea, A. Amorosi, D. Boldini, G. de Felice, and M. Malena, "Jointed Masonry Model: A constitutive law for 3D soil-structure interaction analysis," *Eng. Struct.*, vol. 201, 2019.
- [20] D. Malomo and M. J. DeJong, "A Macro-Distinct Element Model (M-DEM) for simulating the in-plane cyclic behavior of URM structures," *Eng. Struct.*, vol. 227, 2021.
- [21] D. Malomo, A. Mehrotra, and M. J. DeJong, "Distinct element modeling of the dynamic response of a rocking podium tested on a shake table," *Earthq. Eng. Struct. Dyn.*, vol. 50, no. 5, pp. 1469–1475, 2021.
- [22] D. Malomo, R. Pinho, and A. Penna, "Applied Element Modelling of the Dynamic Response of a Full-Scale Clay Brick Masonry Building Specimen with Flexible Diaphragms," *Int. J. Archit. Herit.*, vol. 14, no. 10, pp. 1484–1501, 2020.
- [23] A. Mehrotra and M. J. DeJong, "A methodology to account for interface flexibility and crushing effects in multi-block masonry collapse mechanisms," *Meccanica*, vol. 55, no. 6, pp. 1237–1261, 2020.
- [24] A. Mehrotra and M. J. DeJong, "A CAD-interfaced dynamics-based tool for analysis of masonry collapse mechanisms," *Eng. Struct.*, vol. 172, pp. 833–849, 2018.
- [25] N. A. Nodargi and P. Bisegna, "A unifying computational approach for the lower-bound limit analysis of systems of masonry arches and buttresses," *Eng. Struct.*, vol. 221, 2020.
- [26] N. A. Nodargi and P. Bisegna, "A new computational framework for the minimum thrust analysis of axisymmetric masonry domes," *Eng. Struct.*, vol. 234, 2021.
- [27] A. Orduña and A. G. Ayala, "Non-linear dynamic analysis of ancient masonry structures by 3D rigid block models," in *AIP Conference Proceedings*, 2015, vol. 1702.
- [28] G. Pancani, S. Galassi, L. Rovero, L. Dipasquale, E. Fazzi, and G. Tempesta, "Seismic vulnerability assessment of the triumphal arch of caracalla in volubilis (Morocco): Past events and provisions for the future," in *International Archives of the Photogrammetry, Remote Sensing and Spatial Information Sciences - ISPRS Archives*, 2020, vol. 54, no. M-1, pp. 435–442.
- [29] F. Solarino, L. Giresini, and D. V. Oliveira, "Mitigation of amplified response of restrained rocking walls through horizontal dampers," in *Proceedings of the International Conference on Structural Dynamic , EURODYN*, 2020, vol. 2, pp. 4292–4303.
- [30] G. Tempesta and S. Galassi, "Safety evaluation of masonry arches. A numerical procedure based on the thrust line closest to the geometrical axis," *Int. J. Mech. Sci.*, vol. 155, pp. 206–221, 2019.
- [31] P. Zampieri, M. Amoroso, and C. Pellegrino, "The masonry buttressed arch on spreading support," *Structures*, vol. 20, pp. 226–236, 2019.
- [32] P. Zampieri, N. Simoncello, and C. Pellegrino, "Structural behaviour of masonry arch with no-horizontal springing settlement," *Frat. ed Integrita Strutt.*, vol. 12, no. 43, pp. 182–190, 2018.
- [33] P. Zampieri, N. Simoncello, and C. Pellegrino, "Seismic capacity of masonry arches with irregular abutments and arch thickness," *Constr. Build. Mater.*, vol. 201, pp. 786–806, 2019.
- [34] V. Acary and B. Brogliato, *Numerical methods for nonsmooth dynamical systems*. Berlin: Springer, 2008.

- [35] M. Jean, “The non-smooth contact dynamics method,” *Comput. Methods Appl. Mech. Eng.*, vol. 177, no. 3–4, pp. 235–257, 1999.
- [36] J. V. Lemos, “Discrete element modeling of masonry structures,” *Int. J. Archit. Herit.*, vol. 1, no. 2, pp. 190–213, 2007.
- [37] P. Lotstedt, “MECHANICAL SYSTEMS OF RIGID BODIES SUBJECT TO UNILATERAL CONSTRAINTS,” *SIAM J. Appl. Math.*, vol. 42, no. 2, pp. 281–296, 1982.
- [38] B. Chetouane, F. Dubois, M. Vinches, and C. Bohatier, “NSCD discrete element method for modelling masonry structures,” *Int. J. Numer. Methods Eng.*, vol. 64, no. 1, pp. 65–94, 2005.
- [39] A. Rafiee, M. Vinches, and C. Bohatier, “Modelling and analysis of the Nîmes arena and the Arles aqueduct subjected to a seismic loading, using the Non-Smooth Contact Dynamics method,” *Eng. Struct.*, vol. 30, no. 12, pp. 3457–3467, 2008.
- [40] G. Lancioni, S. Lenci, Q. Piattoni, and E. Quagliarini, “Dynamics and failure mechanisms of ancient masonry churches subjected to seismic actions by using the NSCD method: The case of the medieval church of S. Maria in Portuno,” *Eng. Struct.*, vol. 56, pp. 1527–1546, 2013.
- [41] E. D. Andersen, C. Roos, and T. Terlaky, “On implementing a primal-dual interior-point method for conic quadratic optimization,” *Math. Program. Ser. B*, vol. 95, no. 2, pp. 249–277, 2003.
- [42] A. Tasora and M. Anitescu, “A matrix-free cone complementarity approach for solving large-scale, nonsmooth, rigid body dynamics,” *Comput. Methods Appl. Mech. Eng.*, vol. 200, no. 5–8, pp. 439–453, 2011.
- [43] D. E. Stewart and J. C. Trinkle, “An implicit time-stepping scheme for rigid body dynamics with inelastic collisions and coulomb friction,” *Int. J. Numer. Methods Eng.*, vol. 39, no. 15, pp. 2673–2691, 1996.
- [44] M. Anitescu and F. A. Potra, “A time-stepping method for stiff multibody dynamics with contact and friction,” *Int. J. Numer. Methods Eng.*, vol. 55, no. 7, pp. 753–784, 2002.
- [45] K.-W. Lim, K. Krabbenhoft, and J. E. Andrade, “A contact dynamics approach to the Granular Element Method,” *Comput. Methods Appl. Mech. Eng.*, vol. 268, pp. 557–573, 2014.
- [46] K. Krabbenhoft, J. Huang, M. V. Da Silva, and A. V. Lyamin, “Granular contact dynamics with particle elasticity,” *Granul. Matter*, vol. 14, no. 5, pp. 607–619, 2012.
- [47] P. D. Spanos, P. C. Roussis, and N. P. A. Politis, “Dynamic analysis of stacked rigid blocks,” *Soil Dyn. Earthq. Eng.*, vol. 21, no. 7, pp. 559–578, 2001.

THE TARANTOLA ETRUSCAN PEDIMENT: NDT AND 3D MODEL CONTENT

A. L. Ciuffreda ¹, M. Coli ¹, T. Donigaglia ¹, P. I. Mariotti ², T. Salvatici ¹ and G. Simoni ²

¹ Department of Earth Sciences, University of Florence
Via G. La Pira 4, 50121 Firenze, Italy
annalivia.ciuffreda@unifi.it; coli@unifi.it; tessa.donigaglia@unifi.it; teresa.salvatici@unifi.it

² Opificio delle Pietre Dure
Via degli Alfani 78, 50122 Firenze, Italy
mariotti.p@gmail.com; gabriela.simoni01@gmail.com

Abstract

The Tarantola Etruscan pediment comes from a single-chamber tomb located in the Tarquinia area, dating back to 520-530 B.C.; it was found in 1904, during some agricultural works, close to Villa la Tarantola, from where the name. It consists of a trapezoidal tympanum 3.5 m long and 1 m high with a painting banquet with four diners (men) recumbent on a mattress placed at ground level. Fabrizio Lucarini detached it on behalf of the Royal Archaeological Museum of Florence, now National Archaeological Museum, where it is still conserved. The Tarquinia tombs were carved into the local Quaternary calcarenite named "Macco". The pictorial decoration was removed as solid-wall that was reinforced at the back with a layer of concrete. In the last years, the Tarantola pediment had been restored by the Opificio delle Pietre Dure (OPD). In the frame of a cooperation agreement between OPD and the Department of Earth Science (DST), it has been the subject of NDT analysis and survey for the reconstruction of a 3D model content. According to the MIBACT guideline (2011), the NDT surveys consisted into georadar, sonic and thermographic investigations. The location of the NDT data in their real space in the 3D model allowed their correct interpretation for a multi-disciplinary evaluation about the structures of the pediment. The NDT survey also allowed identifying and locating minor and micro fissures and gypsum integrations below previous painting restorations. In conclusion, the 3D modelling and NDT brought positive improvements for the structural and conservation knowledge of the Tarantola Etruscan pediment allowing better well-addressed restoration works.

Keywords: HBIM, 3D model, NDT investigations, Etruscan tomb, Cultural Heritage.

1. INTRODUCTION

This paper investigates the potential of BIM (Building Information Modelling) methodology applied to cultural heritage. The methodology, used in architecture and engineering, allows to create a three-dimensional model of a project, inserting also the properties and information of any single object. This makes BIM a good way to manage cultural heritage projects, from historic buildings to artworks, in all phase of the restoration work.

The management of a cultural heritage object through an "informative model" presents difficulties related for example, to the modeling of non-standard forms and this is truer in the case of unique and particularly complex objects such as artworks.

The Tarantola pediment is an example of a mural painting detached as a solid-wall from its architectural context and therefore today it can be classified as a mobile artwork exhibited in a museum. Therefore, the pediment represents a case study halfway between wall paintings and artworks, and constitutes an opportunity for experimenting the application of the BIM methodology to objects such as artworks that are particular both for their uniqueness and for the complexity of the shapes.

This paper provides how this tool can be suitable for reconstructing the complex shapes of the cultural asset and at the same time constituting a repository of all the data for a correct 3D placing of all the information supporting the conservation and restoration activities.

A modeling based on a photogrammetric survey and the results of extensive NDT surveying campaigns formed the starting point for the case study represented by the Etruscan pediment of the Tarantola at the National Archaeological Museum of Florence (Italy).

The research has allowed a better address for the restoration of this mural painting that took place in 2019-2020 by the Opificio delle Pietre Dure.

To achieve this objective, the investigations followed the 2011 MIBACT Guidelines (point 4.1.6) [1] and were conducted by DST (Department of Earth Science), in full collaboration with the Museum and the Opificio delle Pietre Dure. The investigations carried out concerned the type and characteristics of the substrate for the Tarantola mural painting. The history of the pediment and its current assembly was studied and a series of non-destructive tests (NDT): GPR, sonic and ultrasonic and thermography.

2. BIM APPLIED TO HISTORIC BUILDINGS AND ARTWORKS

The preservation of the Italian historical and artistic heritage requires an in-depth diagnostic knowledge that is preparatory for every type of intervention and that expresses into non-destructive or slightly destructive investigations campaigns.

The MIBACT 2011 Guidelines [1], dedicated to historical-monumental buildings, draw attention to the historical and constructive knowledge of the asset.

This knowledge can be achieved by means of surveys and investigations that allow the acquisition of often hidden information (under plaster, behind false ceilings, etc.).

In this sense, the Guidelines consents for indirect non-destructive investigation techniques (thermography, georadar, sonic tomography, etc.) or weakly destructive direct inspections (endoscopies, peeling of plaster, essays, small burglaries, etc.).

The management of the knowledge deriving from the diagnostic campaign is always quite complex: there is a lack of coordination between the different disciplines, the multimedia supports are different with the risk of losing information and making difficult for future users to consult them.

In this section will be exposed a brief state of the art of BIM applied to cultural heritage.

2.1 State of art and normative references

The use of digital models in restoration is a topic already investigated by several researchers in order to create a model as a single "container" (2D or 3D) to store geometric information and information relating to the intervention and maintenance phases on the artefact.

In this sense, we can cite examples of 2D Gis models such as Sicar (Information System developed by Liberologico and by the Superintendence of Fine Arts and Landscape for the provinces of Pisa and Livorno, in a working group that involved the National Research Council (CNR), Ministry for Cultural Heritage and Activities (MIBACT) and Small and Medium Enterprises), created to manage documents and analyzes collected during the restoration, or the applications of 3D-GIS by Barattin et al. [2].

In recent years, international studies have multiplied for the application of the BIM process to the historical architecture, the aim being a tool for classification, management and analysis of information. This process is called HBIM.

The first use of BIM applied to existing buildings is represented by the researches of Arayici [3] and Murphy et al. [4,5] who develop Historic Building Information Modeling (HBIM) by experimenting with libraries of parametric objects built from historical data with intelligent data integration and a system to map the parametric object on a point cloud.

Despite the difficulties encountered by these early authors, especially in the modeling phase, contributions on HBIM have multiplied to solve problems by simplifying the workflow of the restoration project and opening new ways for experimentation.

Among the topics covered are the modeling of objects starting from a point cloud [6,7], the enrichment of the model through the insertion of information or the reconstruction of the evolutionary phases of the building with the contributions of Apollonio et al., [8] and Brumana, et al., [9], the integration between BIM and GIS in the research of Dore and Murphy [10].

The methods of consulting the database through web platforms and augmented reality were also studied [11] and the construction of databases for building maintenance [12].

As part of the research activity carried out by the DST, various types of diagnostic investigations are performed on historical buildings and artworks: georadar investigations, sonic and ultrasonic investigations, video inspections, laboratory investigations on stones and mortars, micro-perforations, thermographic investigations, etc.

In order to organize the data collected during the research, 3D models of the cases studies are realized to highlight the geometric characteristics, as well as the location of the surveys in their real 3D location and the results in a unified framework.

This workflow was applied to case studies such as the Resurrection Christ by Piero della Francesca in Sansepolcro [13], the Garden of the Camelie and the Bona Hall in Palazzo Pitti [14].

Finally, a brief mention of the BIM legislation in Europe which has as its reference the "Directive on public procurement of the European Union" 2014/24 of 26 February 2014 [15] that invites EU Member States to encourage the use of BIM for projects, while Italy has adopted UNI 11337 [16] (divided into 10 parts), opening the discussion on the use of the BIM methodology to cultural heritage.

3. THE ETRUSCAN PEDIMENT OF THE TARANTOLA

The Tarantola pediment is a mural painting taken away as a solid-wall from a tomb in the necropolis of Tarquinia. The necropolis was excavated in the local soft calcarenite, called "Macco", which represents the support of the mural paintings that decorate the walls.

Since October 2018 the Pediment of the Tarantola is being restored at the Opificio delle Pietre Dure, as subject of a thesis by SAFS/PFP1 [17].

3.1 Finding and conservative history

The work, known in scientific literature as “Frontone della Tarantola” (Figure 1), was part of the mural decoration of an Etruscan tomb with a single chamber, it was originally located in the Tarquinia area within a property called the Tarantola fund, belonging to the Etruscan necropolis of Monterozzi. Dated around 520-530 B.C., it was found in 1904, during some agricultural works. The pictorial decoration located in the tympanum of the back wall inside the tomb was detached by Fabrizio Lucarini (a well-known restorer), on behalf of the Royal Archaeological Museum of Florence who bought the work from the owner of the land [18].



Figure 1: The pediment before the restoration.

The painting represents a banquet with four diners [19] (all men) recumbent on a mattress placed at ground level and a fair probably a lion, a panther or a particular species of dog. Below there are a continuous frieze of 13 bands in alternating colors, red, white, black and gray.

There are many reasons of interest: from the historical/artistic point of view, as a testimony of high value of Etruscan painting of the Archaic period (end of the 6th century B.C.) [20]; from the point of view of the history of the restoration, it represents a rare testimony of solid-wall detachment framed in wood for strength and transport [21] and, very important, the wooden elements used to detach it still contribute to the conservation of the property, as the diagnostic investigations have confirmed. For the detachment of the painting from the buried tomb at a depth of 4.5 meters, a solid transport was carried out which involved the removal of both the pictorial decoration and the support: in fact, together with the pictorial surface, about 15-18 cm of stone were removed. In order to strength the removed Macco slab, Lucarini applied on the back first a layer of mortar (Malta Lucarini, made with Macco sand) and then a thin layer of concrete. Lucarini enclosed the fragment within a cusped wooden frame. For this reason, it can be assimilated to a pediment.

Since then, with the name of “pediment” (Frontone), due to its triangular shape, it has become part of the exhibition of the National Archaeological Museum of Florence [22]. After the flood of 1966, when it had suffered no particular damage [23], it was first transferred to the warehouses and then to the premises of the archaeological restoration laboratories and exhibited only during exhibitions, often abroad.

4. THE INVESTIGATIONS CAMPAING FOR THE DEFINITION OF THE COGNITIVE FRAMEWORK

The following section describes the research and analysis carried out to understand the materials and the state of conservation of the pediment. In the next paragraphs will analyze the types of NDT investigations carried out and will be showed the results obtained.

The information deriving from the cognitive framework out-lined has been included in the BIM model as described in section 5.

4.1 GPR survey

The Ground Penetrating Radar (GPR) is a Non-Destructive investigation technique that was developed for investigating subsoil objects [24]; subsequently it was used for defining lithological contacts [25, 26], faults [27] and fractures in rock-mass [28, 29] and for defining soil units [30, 31] and the water table level too [32, 33, 34].

GPR has been also applied in investigating the competence of concrete in bridges and tunnels and for the bond durability. Recently GPR has been used for investigate masonry structure and assemblage [35, 36, 37].

The GPR principle uses the two-way travel time between a high-frequency electromagnetic input in the radar range 100 MHz-100 GHz and its return (Figure 2). The radar input travels in the material at a velocity mainly related to the magnetic conductivity and permeability of the medium [38, 39].



Figure 2: GPR operating on Tarantola pediment and principle: an antenna inputs a radar signal in the medium, the boundary between materials with different electromagnetic properties backscatters the signal to the receiver determining the two-way travel time.

The boundary between materials with different electromagnetic properties partially backscatter the signal to the antenna. The entity of penetration of the signal into the material is a function of the material properties and the signal frequency: lower is the frequency and higher is the penetration, but less are the details of the investigation because they are function of the wavelength.

The knowledge of the wave velocity in the medium or that of a distance of a sure signal are compulsory for fixing the scale of the investigation and therefore for correctly placed in the surveyed body the material interfaces, voids included.

In investigating a manifold, a good practice is measuring the thickness of the wall plus placing a still/iron plate as reference to the opposite side of investigation for having a sure end-signal of the masonry, in order to fix the scale of resulting radargram.

The Georadar campaign was carried out on the Tarantola pediment in collaboration with IDS Georadar S.R.L. (Hexagon Group), under the supervision of Dr. David Morandi, using the IDS C-Thru system, with a 2GHz antenna (Figure 2). The acquisition campaign consisted into 4 horizontal scan-lines, spaced of 7-10 cm, all along the entire length of the painted surface. Tomography analysis was made for having information relating to the material setting inside the pediment.

In order to avoid damaging the painting with the wheels of the instrument, the surface was temporarily consolidated in the most delicate areas. The GPR surveys, both the single horizontal surveys and the tomographic survey, were implemented in the 3D model (Figures 3 and 4).

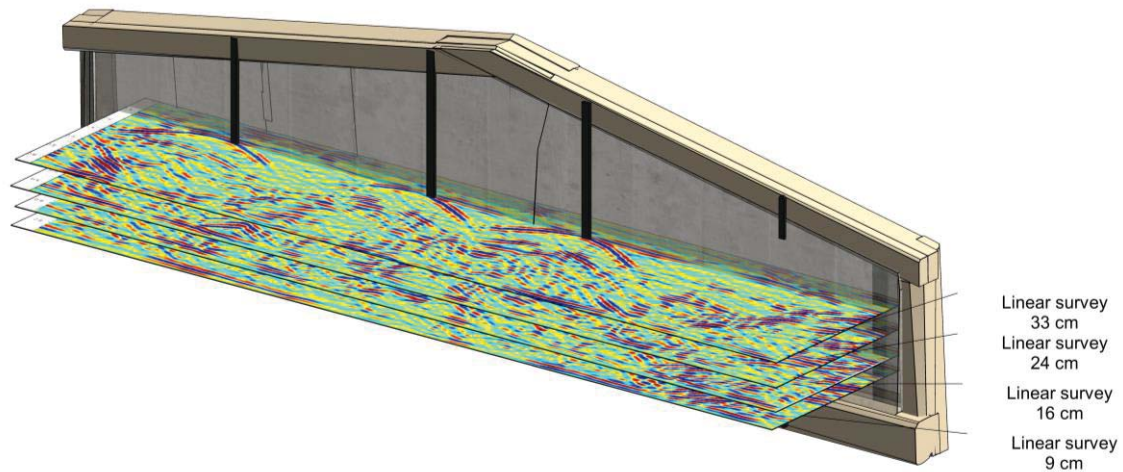


Figure 3: 3D mounting of GPR linear survey on the 3D model

The tomography results outline the Macco be affected by several discontinuities. On the right side of the pediment of concave shape up to a depth of approximately 5 cm is clearly visible, that is referred to a previous integration made by gypsum.

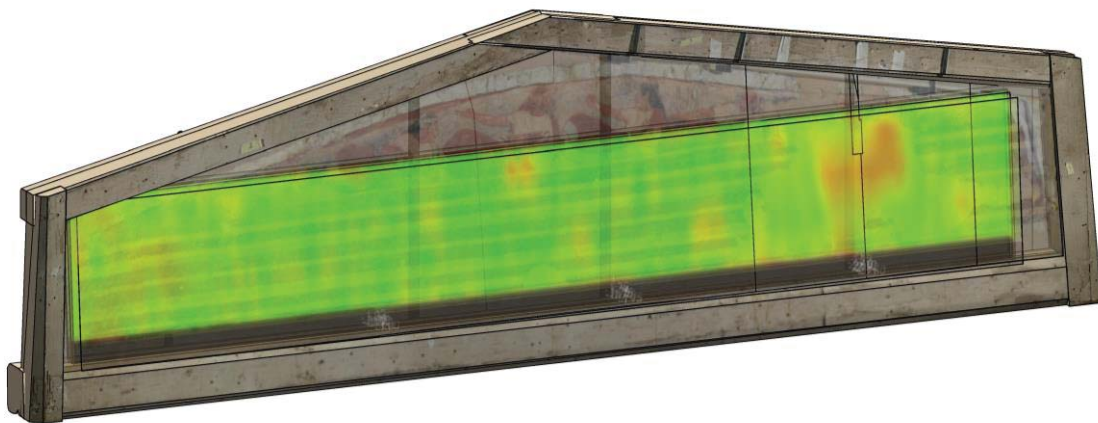


Figure 4: Georadar tomography in a section at 0.5 cm from the front surface, mounted on the 3D model.

Georadar analysis does not recognize the interface between Macco and Lucarini mortar because the composition of the mortar is very similar to that of the Macco, but well defines the interface with the concrete at the back.

4.2 Sonic test

The sonic test is based on the generation of elastic waves in the frequency range of sound (20 Hz - 20 kHz), by means of mechanical impulses generate by a hammer and recorded by a receiver.

The data acquisition system used was a Novasonic U5200 CSD module of IMG. The processing signal consisted of measuring waves travel times, a specific software allows the visualization of the transmitted and received signals on time domain [40]. The first arrival of the wave is obtained using an automatic algorithm that may be checked and corrected by the operator through visual access and manual operation.

Sonic pulse velocity tests were carried out on the Tarantola pediment following two configurations: direct and indirect [41] (Figure 5).

In the first hammer and accelerometer are placed on opposite faces and the longitudinal waves are measured, in the second hammer and accelerometer are placed on the same face this method is more used to access to surface waves.

The pulse velocity represents the qualitative characteristics of the investigated object, influenced by composition, the contact between different materials, as well as by the presence of inhomogeneities, voids, cracks presence and deteriorated areas [42, 43, 44].

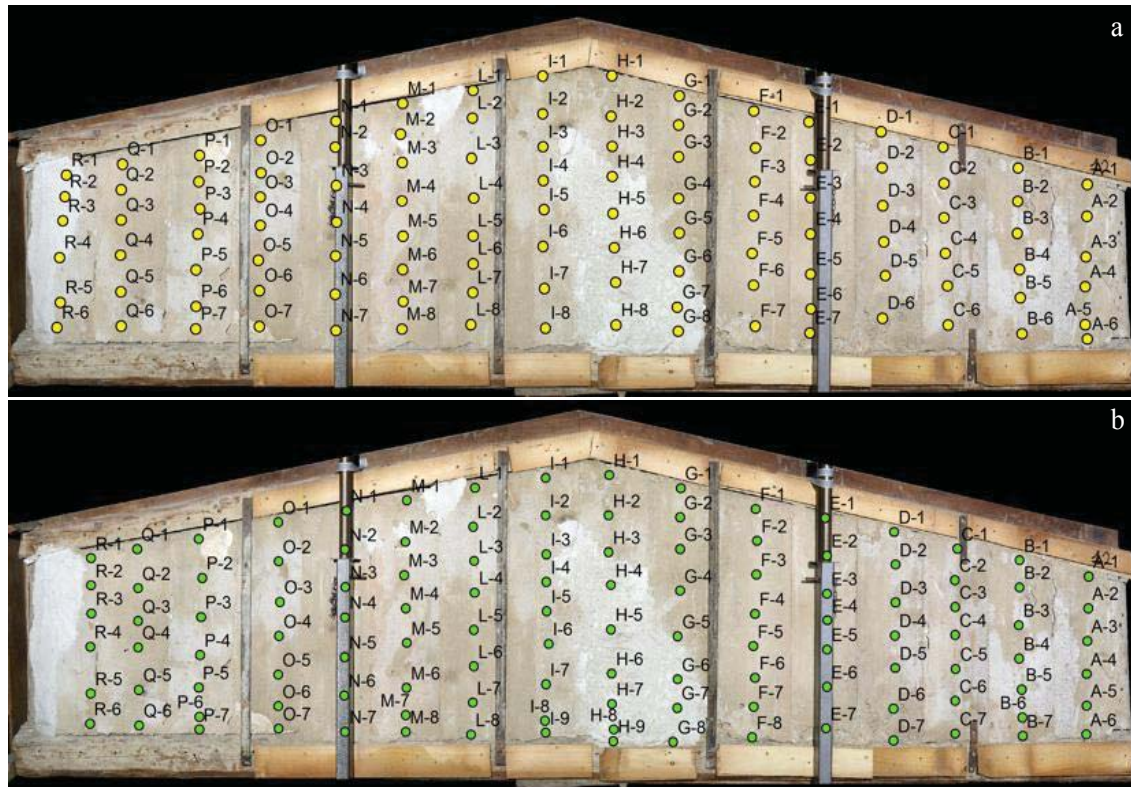


Figure 5: Sonic velocity test configurations, a) direct and b) indirect.

The direct acquisition was carried out considering 111 impact positions located on the back of Tarantola pediment along vertical alignments, while the receive was located in the front (Figure 5a). For each point, 3 travel times were recorded, and considering the thickness of Tarantola pediment as distance between the hammer and the receiver, the sound velocity was computed.

The indirect acquisition was carried out considering 16 impactions on the highest points of the vertical alignments and 100 receptions. For each point, 3 travel times were recorded, and considering the progressive distance between the hammer and the accelerometer, the sound velocity was computed (Figure 5b).

The punctual measurements were elaborated using ESRI® ArcGIS software, in particular the Natural Neighbor interpolation tool [45], to compute a sonic velocity distribution map, the results, both direct and indirect, were reported on the 3D model (Figures 6 and 7) of the Tarantola pediment.

The average velocity of the two configurations is the same of about 600 m/s, this can be explained with the fact that the Tarantola pediment is constituted by a calcarenite (Macco) with a high porosity (20-30%), in addition some restoration supports as mortars and concrete in the back side and gypsum in front right side are present.

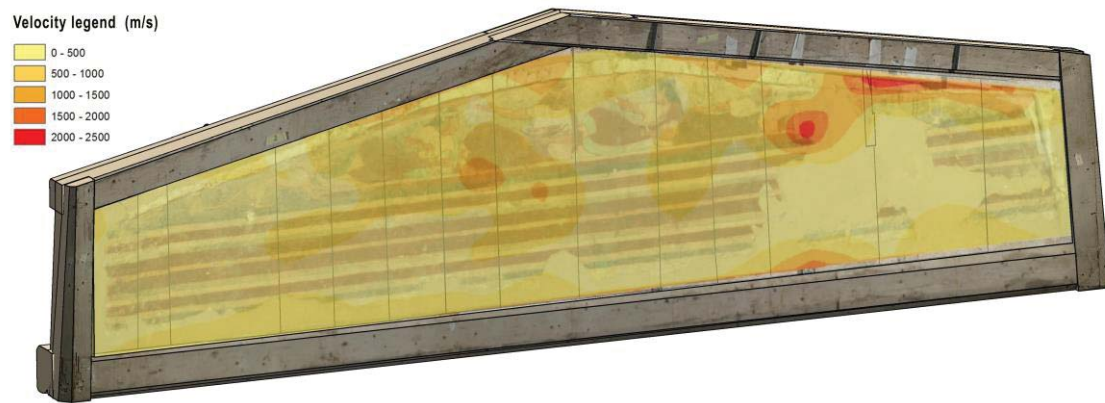


Figure 6: Sonic velocity from indirect acquisition mounted on the 3D model.

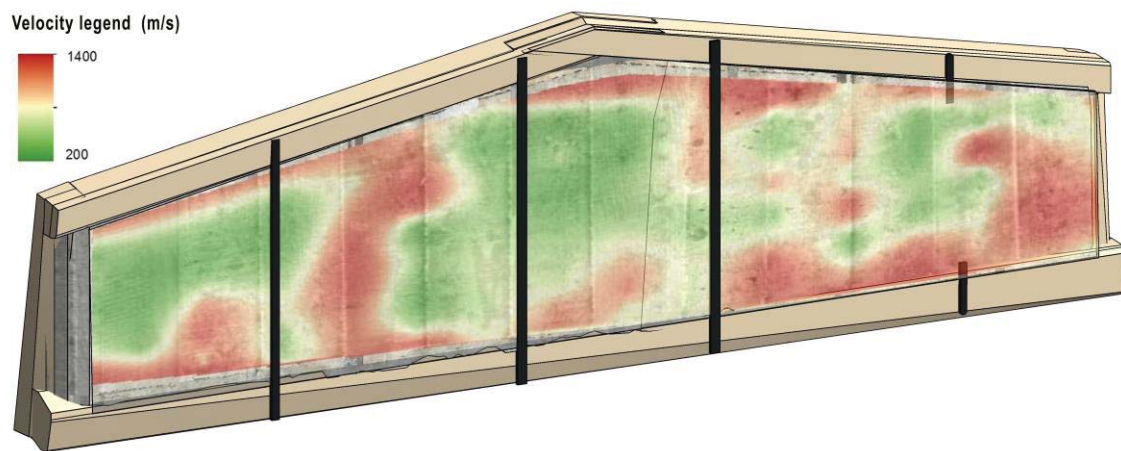


Figure 7: Sonic velocity from direct acquisition mounted on the 3D model.

All these materials lead to a general slowing down of the sound waves, indeed the indirect test shows an average velocity distribution on whole surface, this is the result of superficial velocity on the backside concrete and mortar layers, which is well distributed over the entire pediment.

Of particular interest are the result of direct test, on the back left side a higher speed area is present, this corresponds in the front of an area with the gypsum integration. The gypsum, in this case, is more homogeneous and compact and here the Macco is thinner and two different porous materials such as mortar and gypsum are in contact.

4.3 Thermography campaign

The use of thermography on the cultural heritage on masonry buildings allows, with specific conditions, the view of the internal layers hidden by the plaster; in particular, its use is still helpful to detect the structural part in the slabs and to check the texture of vaults and masonry walls.

Thermography on mural or panel paintings has some examples of use to detect various types of defects in the painting layer [46] or sublayer composition evaluation with the help of adapted image and signal processing algorithms to detect small discontinuities inside structures or extract material characteristic information [47].

Thermography is a no-contact test and can cover large areas. Thermography sums on the external surface the response from the whole masonry, therefore it is difficult to detect the in-

ternal anomalies in the artifact and results can be influenced by conditions and by non-homogeneous heating.

In the case of the pediment, the experimental campaign has been made using a FLIR T460 thermal camera and was carried out in both passive and active conditions, heating the room evenly. The results of the thermographic campaign were subsequently inserted on the 3D model (Figure 8).

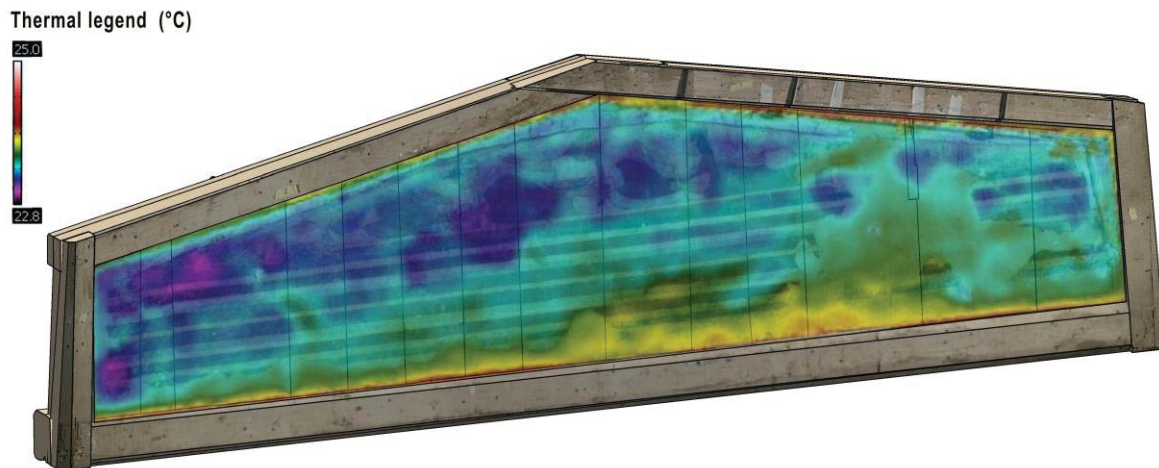


Figure 8: Visualization of the thermographic map inside the model.

In both cases, differences in temperature were detected due to the presence of different materials such as plaster repairs on the front, while no interesting anomalies were found on the back.

5. THE DEFINITION OF THE INFORMATIVE MODEL

In order to organize the data collected during the campaigns, a 3D model of the pediment was realized to highlight the structure, as well as the location of the surveys and their results in a unified framework.

In section 5.1 will describe the phase of the metric survey of the pediment by means of photogrammetry.

In sections 5.2 and 5.3 will describe the operational phase consisting of modeling the pediment and creating customized families for entering the data of the surveys carried out. It will also be presented how to enter data and query the database using specific methods.

5.1 The photogrammetric survey

The starting data for the geometry reconstruction of the pediment come from a photogrammetric survey. It was decided to use photogrammetry due to the speed of data collection and obtaining the results.

Photogrammetry is a technology that allows, starting from the acquisition of high-definition images, the reconstruction of a textured 3D model.

It is already used for architectural, cartographic, topographical survey, and now it is also applied to artistic artefacts. It allows arriving at a detailed knowledge of the surfaces of the artwork in order to obtain information for conservation and valorization.

Using a 24 Mpx camera, 1000 photographic shots were taken, taking care to maintain an adequate overlap between different frames and keeping the machine settings unchanged. The

images were aligned and processed using photogrammetric software in order to obtain a point cloud (Figure 9) and a textured model (Figure 10).

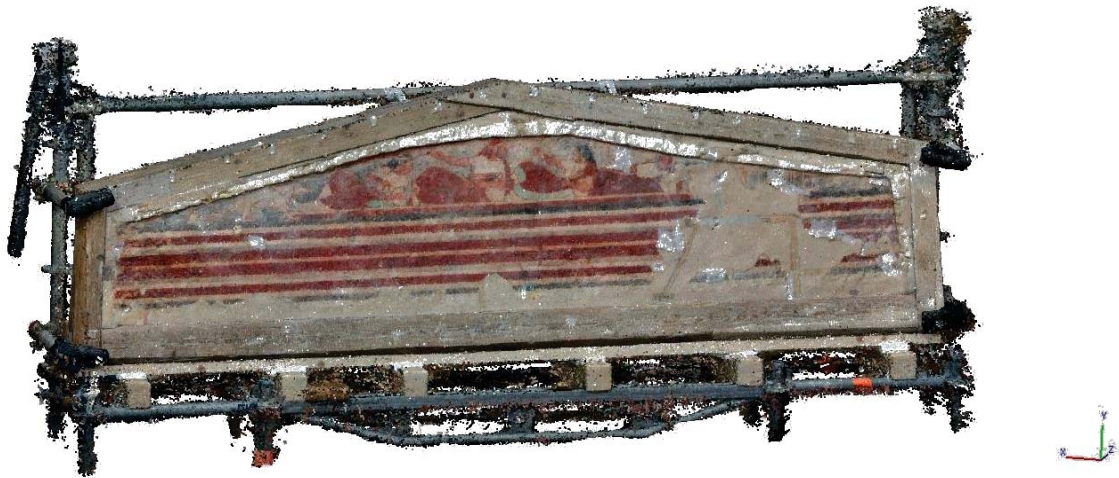


Figure 9: The point cloud deriving from the photogrammetric survey.

The point cloud of the pediment was imported into Autodesk Revit (®Autodesk academic license) for modeling in the BIM environment, while the orthophoto and textures for mapping the BIM model were obtained from the textured model.

The dense point cloud obtained consists of approximately 49.700.000 points, which, during the processing of the mesh, give rise to approximately 9.900.000 triangular faces. The high density of the point cloud and the definition of the mesh made it possible to obtain an extremely detailed model.



Figure 10: The textured model deriving from the photogrammetric survey.

5.2 The modeling phase

The difficulties of modeling cultural heritage objects in BIM environment are several, first of all the very irregular shapes. However, in this case, the choice to operate using BIM software is aimed at testing the potential for managing information related to cultural heritage.

It's useful to refer to the LOD achieved in the realization of model. The LOD provides the degree of reliability of the geometry detail level and information level. According to the BIM Forum Level of Development Specification [48] the model of the pediment can be framed in a

LOD 300. If this level is accurate, geometric data can be measured directly on the model and any type of information (materials, decay, historical data, etc.) can be added via external references. Therefore, the three-dimensional model were made with attention to the modelling of the structure and archiving the results of the diagnostic campaign.

The pediment was modeled trying to be true to its shape and features using Autodesk Revit software. The greatest difficulty is due to the not perfectly planar conformation of the wooden frame and the pediment. Starting from a reference level, the Revit wall system families were used to model the layers that make up the artwork, in particular the Macco.



Figure 11: A general view of the BIM model.

Wall-objects were created with customized stratigraphy and materials that had suitable textures to guarantee the recognizability of the different structures (Figures 11 and 12). Instead, the wooden frame was modeled using parametric beam elements.

We have tried to use *in place* modeling as little as possible, which is often not recommended as it is a traditional methodology that goes beyond the rules of BIM, creating non-reusable objects that weigh down the file. Therefore, every object that could not be modeled with a system family, such as the beams of the frame, was inserted starting from a parameterized and customized family that can be further enriched with information.

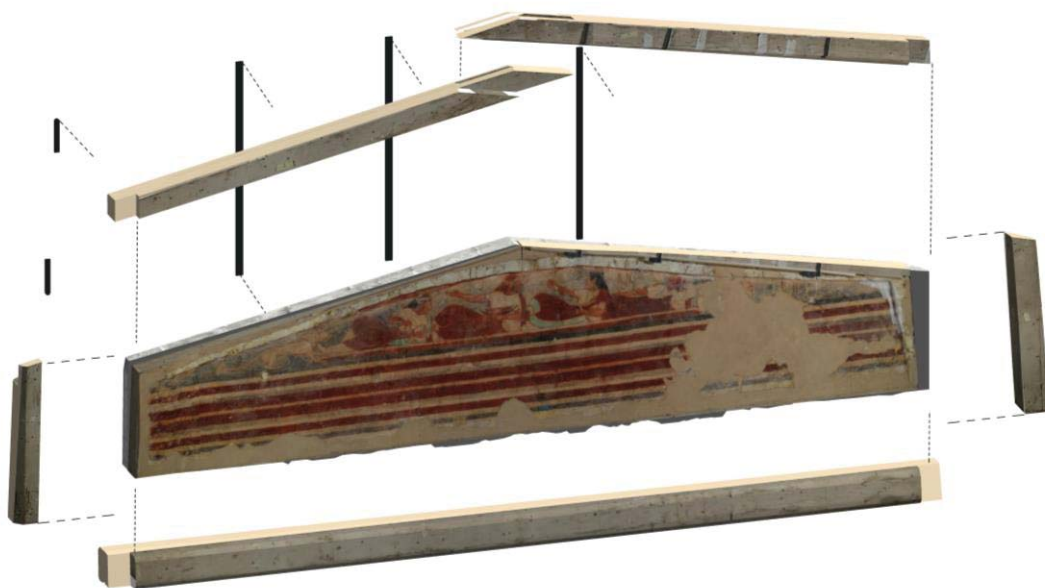


Figure 12: Exploded view of the BIM model.

The inclusion of the surveys in the model was addressed through the creation of specific families to which the parameters described in section 5.3 are linked. The geometry of the objects that represent the surveys has been studied according to its characteristics (Figures 5-8).

For example, the georadar survey was modelled on a panel of variable dimensions. This mode allows a faster and more efficient visualization and understanding of the model.

All this led to create a family library that allowed a rapid modelling of the case study and can be reused in future works.

The BIM model was designed to facilitate the understanding of the wall structure of the painting, to store information found during the diagnostic campaign and during restoration, and to allow easy viewing and consultation.

5.3 The implementation of the informative model

This work phase illustrates how the data were entered into the model and how it was assigned to each object.

For each element modeled in 3D, it is possible to connect data relating to the general characteristics of the element, to the dimensions, the results of the investigations, the materials and the monitoring data, etc. It is also possible to associate links to external files such as images, videos, documents.

Each object was created within an appropriate category, and preferably associated with instance parameters. All parameters are shared and subsequently converted into project parameters, linking them to the relevant category.

The families of the surveys have been associated with parameters that allow inserting information such as the date of execution, the description, the instrument used and the results. It was possible to create parameters to insert links to photos, documents and videos.

Parameters such as dimensions, wood essence, dating were associated to the beams of the frame, while the characteristics of the materials were associated with the layers constituting the support. Each object has been provided with an ID that identifies it and which can be viewed using the appropriate label. The creation of abacus allowed the classification of the objects by category and the interrogation of the model (Figure 13).

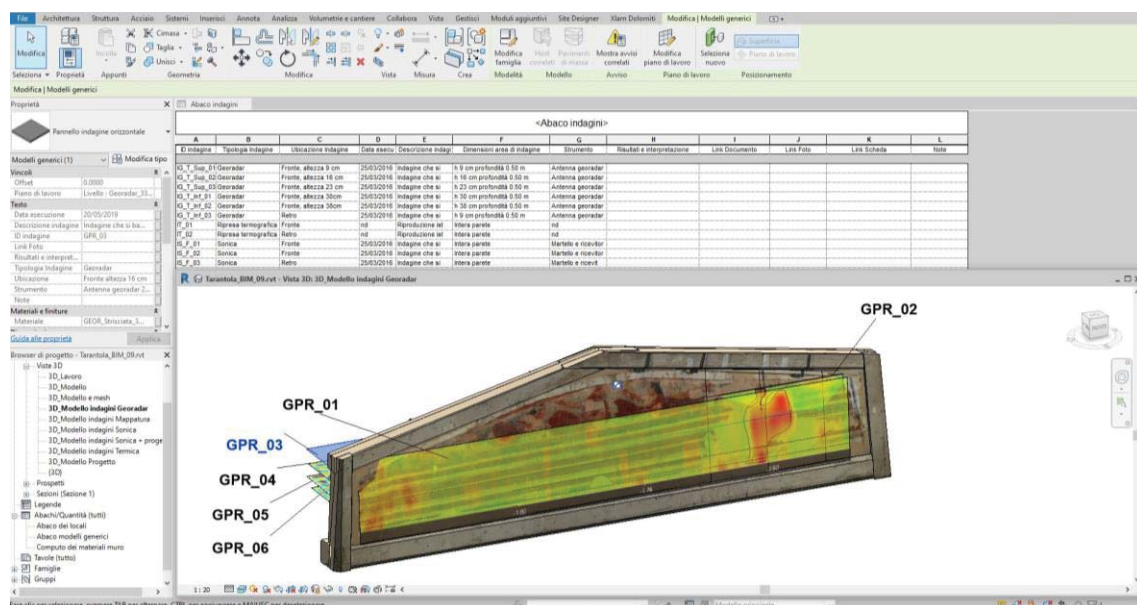


Figure 13: The identification of the surveys by label, the visualization of the parameters connected to the object, and an example of abacus that allow managing all the surveys.

By selecting an element inside the abacus, Revit allows to view it within the model. Furthermore, the objects inside the schedules can be filtered and sorted according to the parameters created, making it easy to interrogate even very complex models.

Revit software also allows managing the visualization of the model through customized views and in the 3D environment through dynamic sections and exploded view that facilitate in the modeling phase and in the public presentation phase of the research results.

The creation of specific abacus allowed the interrogation the model. The model was subsequently organized through specific views aimed at displaying the different types of information to be highlighted.

The result obtained is a digital twin of the artwork, which makes it possible to analyze the results of the investigations in close relation with the areas investigated and to locate and measure any anomalies.

6. CONCLUSIONS AND FUTURE DEVELOPMENT

The workflow presented made it possible to test the possibilities of digitization and archiving using the BIM methodology applied to a very particular case study of cultural heritage.

The result is a model that describes with a good level of detail the current state of the pediment and its wall support, while the information was stored in a simple and easily accessible way.

Even in this particular case study, BIM is a valid tool for management and storage for the speed of modeling thanks to parameterization.

Among the problems encountered are the difficulty of modeling complex elements with non-standard forms, the lack of categories related to the restoration and diagnostic process, the absence of information classification procedures and the lack of a single system that allows consultation and implementation of the model without using BIM software.

This last aspect can be partially solved using an online viewer or an IFC viewer, which however remain limited and allow consulting the information but do not always allow the visualization of the textures and many others problem.

The next steps of the DST research aim to study a way to consult the model also on mobile devices and without having to choose a BIM Authoring software.

Future developments foresee a double aspect: on the one hand, the creation of centralized models with multidisciplinary information that can be used in the field of conservation and enhancement of the single building or artwork, on the other hand complex databases will be created for management of museums as containers of artworks or, more generally, for the cultural heritage of entire cities.

REFERENCES

- [1] DPCM 9 febbraio 2011. Linee guida per la valutazione e riduzione del rischio sismico del patrimonio culturale, allineate con alle Nuove Norme Tecniche per le costruzioni 2008 (NTC 2008), Gazzetta Ufficiale n. 47 del 26-2-2011 – Suppl. Ordinario n. 54.
- [2] L. Baratin, S. Bertozzi, E. Moretti, Tecnologia GIS per la manutenzione programmata dei beni culturali. *La conservazione preventiva e programmata - PCC Conference 2014*, Monza-Mantova, 2014.
- [3] Y. Arayici, Towards building information modelling for existing structures. *Structural Survey*, **26**, 210–222, 2008. DOI: 10.1108/02630800810887108.

- [4] M. Murphy, E. McGovern, S. Pavia, Historic Building Information Modelling – Adding intelligence to laser and image-based surveys of European classical architecture. *ISPRS Journal of Photogrammetry and Remote Sensing* **76**, 89–102, 2013. DOI:10.1016/j.isprsjprs.2012.11.006.
- [5] M. Murphy, E. McGovern, S. Pavia, Historic building information modelling (HBIM). *Structural Survey*, **27**, 311–327. 2009. DOI:10.1108/02630800910985108.
- [6] S. Garagnani, A.M. Manferdini, Parametric accuracy: building information modeling process applied to the cultural heritage preservation. *ISPRS - In International Archives of the Photogrammetry, Remote Sensing and Spatial Information Sciences*, **XL-5/W1**, 87-92, 2013. DOI:10.5194/isprsarchives-XL-5-W1-87-2013.
- [7] L. Barazzetti, F. Banfi, R. Brumana, M. Previtali, Creation of parametric BIM object from point clouds using NURBS. *The photogrammetric Record*, 30 (152), 339-362, 2015. DOI: 10.1111/phor.12122.
- [8] F. I. Apollonio, M. Gaiani, Z. Sun, 3D modeling and data enrichment in digital reconstruction of architectural heritage. *ISPRS-International Archives of the Photogrammetry, Remote Sensing and Spatial Information Sciences*, **XL-5/W2**, 43–48, 2013. DOI:10.5194/isprsarchives-XL-5-W2-43-2013.
- [9] R. Brumana, D. Oreni, A. Raimondi, A. Georgopoulos, A. Bregianni, From survey to HBIM for documentation, dissemination and management of built heritage. The case study of St. Maria in Scaria d’Intelvi. *Proceedings of the DigitalHeritage 2013-Federating the 19th Int’l VSMM, 10th Eurographics GCH, and 2nd UNESCO Memory of the World Conferences, Plus Special Sessions from CAA, Arqueologica 2.0 et Al. IEEE*, 497–504, 2013. DOI:10.1109/DigitalHeritage.2013.6743789.
- [10] C. Dore, M. Murphy, Integration of Historic Building Information Modeling (HBIM) and 3D GIS for recording and managing cultural heritage sites. *18th International Conference on Virtual Systems and Multimedia. IEEE*, 69–376, 2012. DOI:10.1109/VSMM.2012.6365947.
- [11] L. Barazzetti, F. Banfi, R. Brumana, D. Oreni, M. Previtali, F. Roncoroni, HBIM and augmented information: Towards a wider user community of image and range-based reconstructions. *ISPRS-International Archives of the Photogrammetry, Remote Sensing and Spatial Information Sciences*, **XL-5/W7**, 35–42, 2015. DOI:10.5194/isprsarchives-XL-5-W7-35-2015.
- [12] F. Fassi, C. Achille, A. Mandelli, F. Rechichi, S. Parri, A new idea of BIM system for visualization, web sharing and using huge complex 3D models for facility management. *ISPRS -International Archives of the Photogrammetry, Remote Sensing and Spatial Information Sciences*, **XL-5/W4**, 359-366, 2015. DOI:10.5194/isprsarchives-XL-5-W4-359-2015.
- [13] M. Coli, A. L. Ciuffreda, M. Micheloni, An informative content 3d model for the hall holding the Resurrection of Christ by Piero della Francesca mural painting at Sansepolcro, Italy. *ISPRS - International Archives of the Photogrammetry, Remote Sensing and Spatial Information Sciences*, **XLII-2/W11**, 435-442, 2019. 10.5194/isprs-archives-XLII-2-W11-435-2019.

- [14] M. Coli, A. L. Ciuffreda, T. Donigaglia, Informative models for the cultural heritage buildings: applications and case histories. A. Conte, A. Guida, *ReUso 2019. Matera. Patrimonio in divenire. Conoscere, valorizzare, abitare*, Gangemi Editore, 2020.
- [15] Directive 2014/24/EU 26 February 2014. Directive on public procurement and repealing Directive 2004/18/EC.
- [16] UNI 11337. Edilizia e opere di ingegneria civile - Gestione digitale dei processi informativi delle costruzioni.
- [17] Historical Archive of the National Archaeological Museum of Florence, III vers. II. Part, 1904-1907, envelope 64, fasc. 9bis, N. prot. 4960. of March 18, 1904. Direction of the archaeological museum and of the excavations of antiquity in Etruria, Florence, Posiz. F / 18, Prot. 546, n. of part. 28, Object: painted tomb in Corneto Tarquinia.
- [18] M. Marzullo, The glass of farewell. Banquet and funerary space in Tarquinia, in *The symbolic banquet. Parties, symposia and bacchanals between ancient rituals and modern anachronisms*, Jouvence, Milan, 2016, p. 81 ff.
- [19] G. Simoni, The painted pediment of the Etruscan tomb of the Tarantola. Executive technique, conservation, project and restoration intervention. Thesis by SAFS / PFP1, 2020.
- [20] A. Cecchini, The painted tombs of Tarquinia conservation story, technical execution restorations. *Kermesquaderni*, Nardini Editore, Florence, 2012.
- [21] M. Marzullo, Grotte Cornetanee, Material and critical apparatus for the study of painted tombs of Tarquinia, University of Milan, TARCHNA, Excavations and research in Tarquinia, supplement 6, Ledizioni, Milan 2016, Voll. I pp. 7, 353-354 (Pediment), 106-108 (Tomb 5898 032), Voll. II pp. 658-661 (Tomb 5039-312), 745-746 (Tomb 5517-333).
- [22] L. A. Milani, The Royal Archaeological Museum of Florence, its history and illustrated guide, Deposit at Succ. B. Seeber, Florence, 1923, II vol., Pag. 245.
- [23] A. Minto, Il Regio Museo Archeologico di Firenze, La Libreria dello Stato, Roma, A. x E. F., pp. 58.
- [24] P.K. Fuliagar, D. Livleybrooks, Trial of Tunnel Radar for cavity and One Detection in the Sudbury Mining Camp, Ontario. *Proceedings of the Fifth International Conference on Ground Radar*, Waterloo centre for Groundwater research, Waterloo, Canada, 883-94, 1994.
- [25] U. Basson, Y. Enzel, R. Amit, Z. Ben-Avraham, Detecting and Mapping Recent Faults with a ground-Penetrating Radar in the Alluvial Fans of the Arava Valley. *Proceedings of the Fifth International Conference on Ground Radar*, Waterloo centre for Groundwater research, Waterloo, Canada, 777-88, 1994.
- [26] S. Van Heteren, D.M. Fitzgerald, P.S. McKinlay, Application of Ground-Penetrating Radar in the Coastal Stratigraphic Studies. *Proceedings of the Fifth International Conference on Ground Radar*, Waterloo centre for Groundwater research, Waterloo, Canada, 869-81, 1994.
- [27] S. Deng, Z. Zhengrong, H. Wang, The Application of Ground Penetrating Radar to Detection of Shallow Faults and Caves. *Proceedings of the Fifth International Conference on Ground Radar*, Waterloo centre for Groundwater research, Waterloo, Canada, 1115-33, 1994.

- [28] L. Bjelm, *Geologic Interpretation of SIR Data from Peat Deposit in Northern Sweden*. Unpublished manuscript, Department of Engineering Geology, Lund Institute Technology, Lund, Sweden, 1980.
- [29] D. Moffat, R. Puskar, A Subsurface Electromagnetic Pulse Radar. *Geophysics*, **41**, 506-18, 1976.
- [30] M.E. Collins, Soil Taxonomy: A Useful Guide for the Application of Ground Penetrating Radar. *Proceedings of the Fourth International Conference on Ground Radar*, edited by P. Hanniend and S. Autio, Rovaniemi, Finland, 125-32, 1992.
- [31] S.F. Shih, J.A. Doolittle, Using Radar to Investigate Organic Soil Thickness in the Florida Everglades. *Soil Science Society of America Journal*, **48**, 651-6, 1984.
- [32] J.A. Doolittle, L.E. Asmussen, Ten Years of Applications of Ground Penetrating Radar by the United States Department of Agriculture. *Proceedings of the Fourth International Conference on Ground Radar*, edited by P. Hanniend and S. Autio, Rovaniemi, Finland, 139-47, 1992.
- [33] L. Beres, H. Haeni, Application of Ground-Penetrating Radar Methods in Hydrogeologic Studies. *Groundwater*, **29**, 375-86, 1991.
- [34] R.A. Overmeeren, High Speed Georadar Data Acquisition for Groundwater Exploration in the Netherlands. *Proceedings of the Fifth International Conference on Ground Radar*, Waterloo centre for Groundwater research, Waterloo, Canada, 1057-73, 1994.
- [35] M. Pieraccini, M. Fratini, F. Parrini, G. Macaluso, C. Atzeni, High-Speed CW Step-Frequency Coherent Radar for Dynamic Monitoring of Civil Engineering Structures. *Electron Lett*, **40** (14), 907-8, 2004.
- [36] M. Coli, T. Donigaglia, P. Papeschi, F. Boscagli, GPR Investigation for Historical Masonry: Case Histories from Florence (Italy) Cultural Heritage Monumental Buildings. *3rd Int. Conf. on Techniques, Measurements & Materials in Art & Archaeology*, Jerusalem, Israel, 2018.
- [37] M. Coli, P. Papeschi, F. Boscagli, L. Innocenti, B. Agostini, GPR Investigation on the Masnory of the Brunelleschi's Cupola, Florence (Italy). *Giornale delle prove non distruttive, Monitoraggio, Diagnostica AIPnD*, **1**, 52-7, 2018.
- [38] A.P. Annan, W.M. Waller, D.W. Strangway, J.R. Rossiter, J.D. Redman, R.D. Watts, The Electromagnetic Response of a Low_Loss, 2-Layer, Dielectric Earth for Horizontal Electric Dipole Extraction. *Geophysics*, **40**, 285-98, 1975.
- [39] GSSI – Geophysical Survey Systems, Inc, *Operations Manual for Subsurface Interface Radar System -3*. Manual #MN83-728. Geophysical System, North Salem, New Hampshire, 1987.
- [40] N.J. Carino, *The Impact-echo method: An Overview*. Building and Fire Research Laboratory. National Institute of Standards and Technology: Gaithersburg, 2001.
- [41] ACI 228.2R 98, *Nondestructive Test Methods for Evaluation of Concrete in Structures*.
- [42] L.F. Miranda, J. Rio, J.M. Guedes, A. Costa, *Sonic impact method—a new technique for characterization of stone masonry walls*. Constr Build Mater, **36**, 27-35, 2012.

- [43] L. Miranda, L. Cantini, J. Guedes, A. Costa, *Assessment of mechanical properties of full-scale masonry panels through sonic methods. Comparison with mechanical destructive tests*. Struct Control Heal Monit., 23, 503-516, 2016.
- [44] T. Salvatici, S. Calandra, I. Centauro, E. Pecchioni, E. Intrieri, C.A. Garzonio. *Monitoring and evaluation of sandstone decay adopting non-destructive techniques: On-site application on building stones*. Heritage, 3, 1287–1301, 2021.
- [45] R. Sibson, *A Brief Description of Natural Neighbor Interpolation*, chapter 2 Interpolating Multivariate Data. New York: John Wiley & Sons, 21–36, 1981.
- [46] M. Rippa, V. Pagliarulo, A. Lanzillo, M. Grilli, G. Fatigati, P. Rossi, P. Cennamo, G. Trojsi, P. Ferraro, P. Mormile, Active Thermography for Non-invasive Inspection of an Artwork on Poplar Panel: Novel Approach Using Principal Component Thermography and Absolute Thermal Contrast, *Journal of Nondestructive Evaluation*, 2021. 40. 10.1007/s10921-021-00755-z.
- [47] G. Steenackers, J. Peeters, K. Janssens, Sublayer composition evaluation of Artwork using active thermography. *Quantitative InfraRed Thermography*, 2018, 10.21611/qirt.2018.049.
- [48] Bim Forum, Level of Development (LOD), Specification Part I & Commentary for Building Information Models and Data, April 2019.

CORRELATION OF VULNERABILITY AND CONSERVATION BETWEEN ARTISTIC ASSETS AND STRUCTURAL ELEMENTS: CAMPAIGN OF THERMOGRAPHIC SURVEYS ON THE FRESCOES OF THE TEMPLAR CHURCH OF SAN BEVIGNATE

R. Liberotti, F. Cluni, F. Faralli and V. Gusella

Department of Civil and Environmental Engineering
University of Perugia 06125 Perugia, Italy
e-mail: {riccardo.liberotti, francesco.faralli}@studenti.unipg.it

e-mail: {federico.cluni, vittorio.gusella}@unipg.it

Keywords: Heritage, NDT surveys, Museum collections, Thermography, Masonry.

Abstract. *A museum, an art collection and a heritage architecture all in one the former Church of San Bevignate is a 39.5m long masonry building that overlooks the countryside of the Umbria Region in Italy. Part of a Templar complex of the 13th century located in Perugia, it holds within a precious series of frescoes, depicting the heroic deeds of the temple's knights across crossings and borders. The safeguard of historical buildings in seismic hazard-prone Regions, as in this case, needs specific measures due, amongst other reasons, to the presence of artistic assets unmovable precisely as frescoes, valuable plasters/stuccoes or in general wall decorations. Therefore, to define a correlation of the seismic risks between masonry structural systems and artworks is a mandatory condition in order to perform safety evaluation and to identify the proper conditions for possible interventions. The efforts made to increase the level of knowledge concerning such buildings mainly through Non-Destructive Testing (NDT) are also important for such purposes. In this context, a non-invasive and contactless method was devised, which integrates the use of the thermal imaging camera with post-processing techniques and calculation algorithms, aimed at revealing the peculiarities inherent in the walls decorated with frescoes: a little-known possibility to bring out important factors for the conservation of the frescoes and also information on the seismic vulnerability of such historical masonry architectures in order to preserve the artefact from being damaged.*

1 INTRODUCTION

The protection of several types of museum collections against seismic phenomena is increasingly gaining interest among a range of stakeholders: the arts and culture sector, scientists, people working in local authorities and governments. Such approach takes into account the observation that in many cases damages to heritage buildings and art goods are irreparable and parietal art pieces e.g. frescoes, decorations and stuccos, are the example by antonomasia of such scenario. Indeed, the aftermath of the recent Italian earthquakes (L'Aquila, Amatrice etc.) in terms of destruction and harms to the historical collections and works was not secondary. Special programs of earthquake preparedness must be conducted in order to mitigate the expected hazard, especially for earthquake-prone countries, such as the Mediterranean countries and besides to avoid cultural losses that may have consequences on entire communities [1, 2, 3]. This contribution presents a contemporary approach to the theme of experimental investigations relating to the protection of heritage masonry buildings and the parietal art goods associated with it. The article constitutes the last phase of a research path started with laboratory tests [4, 5, 6] and, with the collaboration of the Municipality of Perugia, applied subsequently to a case study of value [7] and within the present contribution is examined more closely: the Italian Templar church of San Bevignate, part of an architectural complex from the 13th century located in the city of Perugia. Especially, this heritage building was selected because pose special challenges for damage detection and conservation, due to the presence of large parts of frescoed masonry surfaces. So, this heritage building represents a museum of itself, of its values and its precious original contents. The diagnostic methodology applied in this work is the passive thermography by means of an Infra-Red (IR) thermal camera that acquires the frescoes' painted surface without the emission of artificial thermal loads to the frescoes themselves backed up by the implementation of digital imaging processes. The surveys allowed identifying the main masonry damages like fissures, damages in stone elements, putlog holes, with a peculiar focus on the masonries' quality and texture. By means the data acquired it has been possible to obtain, starting from the processing of thermographic data on the wall texture and by means of a homogenization technique, an estimate of the fundamental mechanical properties of the load-bearing structures. Indeed, an adequate knowledge of the masonries' peculiarities assumes great importance for the estimation, through homogenization techniques, of the mechanical characteristics [8] and collapse conditions [9] of the heritage buildings both in the static and dynamic field [10, 11]. Besides, the in-situ measurement permitted to carry out an evaluation of the actual state of frescoes concerning other risks connected to their survivals like detachments, delamination or moist areas. So, without harming the wall frescoes, e.g. by taking the traditional essays or samples, valuable information were obtained concerning the frescoes conservation and at the same time the seismic safety of this historical former church, now a full-fledged museum site.

2 THERMOGRAPHIC ANALYSIS

An infrared camera is able to record the amount of radiated heat from a body.

The equation of Stefan–Boltzmann provides the relation between emitted radiation and surface temperature:

$$E = \varepsilon \sigma T^4 \quad (1)$$

where ε is the radiation (W/m^2), T is the absolute temperature (K), σ is the Stefan–Boltzmann constant ($5.67 \times 10^{-8} \text{ Wm}^{-2}\text{K}^{-4}$) and ϵ is the emissivity.

It is also necessary to introduce the relation between the wavelength of the maximum radia-

tion intensity λ (μm) and the temperature

$$\lambda = \frac{b}{T} \quad (2)$$

where b is the Wien displacement constant ($2897 \mu\text{mK}$).

The heat transfer in any material is affected by the presence of subsurface flaws or any other inconsistency in the material thermal properties. Localized energy gradients on the surface of a test object are due to the changes in the heat flow and can be measured using an infrared sensor.

For temperatures close to room temperature, the energy is in the infrared domain of the electromagnetic spectrum. In particular, the infrared radiation is the region of the electromagnetic spectrum located between visible light and microwaves, containing radiation characterized by wavelengths ranging from 0.75 to $10 \mu\text{m}$.

Temperature distributions are obtained by data processing from the measured infrared radiation and then recorded in the form of isotherm plots or thermograms. The electronic sensor of the instrument acquires the value of energy stored by every single pixel and generate an image, in greyscale represented by black and white shades or in a combination of levels of false colours, of the observed object. To experiment the efficiency to evaluate, by means of thermographic images, the texture of masonry walls covered with plaster or frescoes, a research program was started [4, 5, 6].

In particular, three masonry samples, which differed for the textures (periodic, quasi-periodic and random) were built. Using UNI solid bricks of dimensions $250 \times 120 \times 55 \text{ mm}$, either used as a whole or split in two or four, the periodic texture was constructed with the running bond scheme and using bricks with the same widths and heights. For the quasi-periodic texture, bricks with different widths but equal heights were used, avoiding the correspondence of the vertical mortar joints. In the last case, a random texture, made using bricks with different widths and heights, was created. The masonry walls, before applying 10 mm -thick plaster, are shown in Figure 1.

In that research, as well as for the present contribution, the thermographic camera model 885-2 manufactured by the Testo company has been used. This has a sensor of dimension 320×240 pixels. All the samples have been exposed to direct sunlight in order to improve the heat flux through the body.

To derive the masonry texture from thermographic images, the following procedure was proposed.

Assuming a T_t threshold temperature, that field is converted to a binary function, which is a “black and white image” or material binary image, by

$$b_i = b_i(x, y) = \begin{cases} 0 & \text{if } T_i \leq T_t \\ 1 & \text{if } T_i > T_t \end{cases} \quad (3)$$

where the value 1 (black) is associated with mortar pixels, the value 0 (white) with brick/stone pixels, and

$$T_i = T_i(x, y) \quad x = 1, 2, \dots, N \quad y = 1, 2, \dots, N \quad (4)$$

are the temperature data, relating to each thermographic image pixel, that can be reported as a scalar field where N is the image width in pixels (it is assumed that the image has equal width and height).

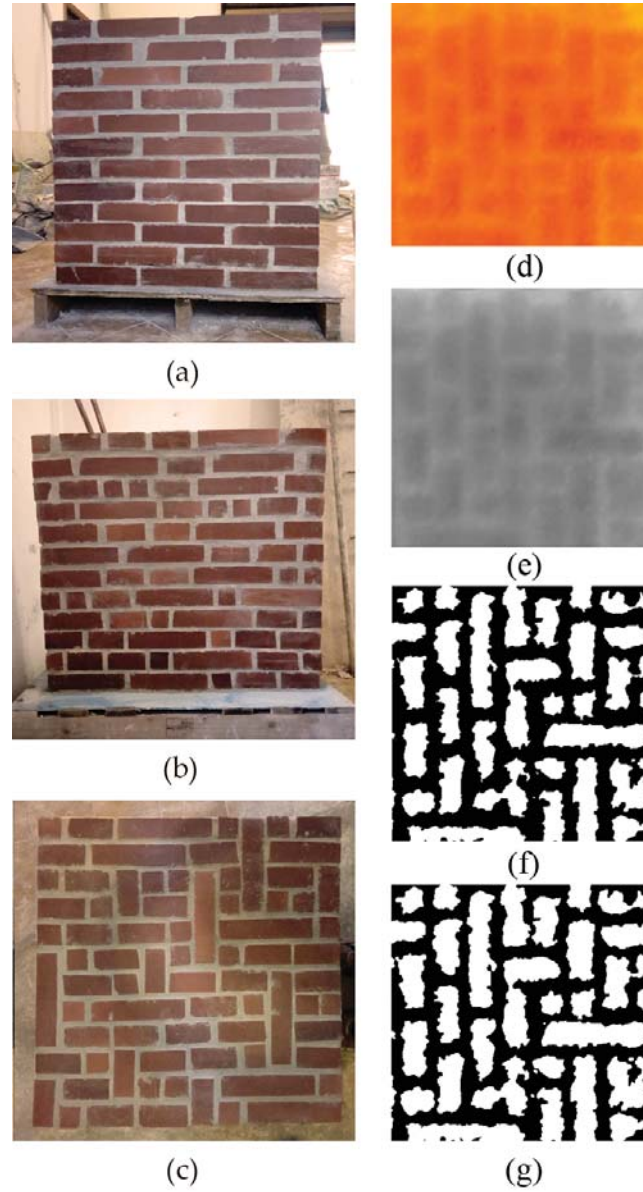


Figure 1: Samples with different masonry texture: (a) periodic, (b) quasi-periodic and (c) random. In the right column identified texture on random masonry sample: (d) thermographic image, (e) surface temperature as greyscale values $T_i(x, y)$, (f) black and white image after thresholding $b_i(x, y)$, (g) identified texture after the application of erosion and dilation factors, $b_d(x, y)$.

However, the final obtained binary image requires specific treatments in order to improve its quality. At first, mortar (black) region of pixels which are surrounded by bricks' pixels (white) are removed. Then the usage of morphological operators is required. In particular, erosion and dilation operator, in this sequence, must be used, in order to smooth the contour of the inclusions which otherwise would be very fragmented, due to the noise which belongs to the image acquisition phase.

Moreover, it was highlighted that the use of sampling Kantorovich algorithm allows to enhance remarkably the quality of the thermographic images. Furthermore, a sensitivity analysis was performed considering two sources of uncertainties: the first tied to the parameters of the morphological operator, the second related to the effects of the environmental conditions highlighting the robustness of the proposed procedure.

Applying the described process, the outcomes shown in Figure 1 were obtained; the comparison with a digital image highlights the robustness of the procedure. In fact, the resultant black and white image has a consistent separation of phases, i.e. each stone is surrounded by mortar joints and unrealistic conjunction of inclusions is obliterated as much as possible.

Nevertheless, these results were obtained in laboratory. In order to check the reliability of the proposed procedure on real cases and underline the effective importance of this tool in the historical buildings' analysis, a peculiar study on the Templar architecture of San Bevignate has been started, a former church from the 13th century, whose internal masonry walls are almost entirely covered with precious frescoes.

3 THE TEMPLAR ARCHITECTURAL COMPLEX OF SAN BEVIGNATE

3.1 History of the Church

In the countryside of the city of Perugia, and more precisely near the monumental cemetery of Monteluca, stands out for archaeological and architectural relevance the Heritage Templar asset of San Bevignate. The church, sober and austere in its external appearance with stone facades (Figure 2), is marked inside by decorations and in particular the pictorial cycles made to remind the inhabitants of the mission carried out in the Holy Ground by the Militia Templi, a.k.a. the Templars, the religious-chivalric order created in Jerusalem around 1119 on the initiative of the French knight Hugues de Payns. This exceptional artefact testifies the presence of the order in Perugia, indeed in 1256 the city's Municipality granted the authorization at the Templar diplomat friar Bonvicino to erect the religious building in place of a small church dedicated to San Girolamo. Even though the Templars, at the time, were already present in the Umbria region at the abbey of San Giustino d'Arna, since such seat was decentralized with respect to the prosperous Perugia they requested a new one. For the inhabitants of Perugia - and for the Templars - devoting the church to the figure of San Bevignate, whose history is still shrouded in mystery to this day, was important considering the popularity of its local cult back then [12]. Actually, he was not proclaimed a saint by the church of Rome but it was "laically" canonized only in 1453 by means of a decree of the Municipality of Perugia. The Templars could not see the cult of San Bevignate approved as the Congregation of Rites approved the Sanctification only in 1605, despite this they considered him already the first Templars' Saint.

In 1262 the building of the Church was finished and also that of the Romanesque bell tower with square plan. The construction of the former monastery - now used as a private residence - is coeval to the one of the octagonal well, still visible in the garden to present day. In 1312, with the suppression of the Templar Order, the monastery passed to the knights of San Giovanni of Jerusalem and in 1324 Ricco di Corbolo, a merchant of Perugia, bought the architectural complex and established a female monastic community there, likewise placed under the rule of the Order of San Giovanni. In 1517, due to economic problems, the nuns who had dwelt there were forced to leave the monastery which returned to the full possession of the Order of San Giovanni [13]. Since then, the church gradually lost its importance and in 1860, with the suppression of various religious bodies, became the property of the Municipality of Perugia and was deconsecrated. In the last century had various uses, a wood storage, a kennel and even a fire station and such peculiar events permitted to preserve - strikingly - the frescoes because they have been covered by plaster for decades. After a long and rather complex plan of consolidation and restoration in response to the 1997 earthquake, in 2009 the monumental site reopened to the public and the original decorative apparatus have also secured; result of an agreement between the municipality and the superintendence of fine arts of Perugia. In addition, in 2020 another

restoration plan concerning the frescoes of the counter-façade and part of the side walls was also performed, with particular attention to the original tones to the valuable paintings.

3.2 Architectural feature of the Church

The church of San Bevignate is located near the ancient route Spargente that was one of the five royal access road axis to Perugia. Such a distinguished monument of Gothic architecture appears as a architecture of considerable size made of sandstone and with a double sloping façade decorated with a oculus and a single round-arched portal, adorned with a marble frame with symbols typical of the Templars, while another small entrance door crowned with an ogive arch is observable on a side. At the extremity of the façade two mighty buttresses are clearly visible and recall the others located on the perimeter walls. The building ends with a quadrangular apse interrupted by a mullioned window made in travertine. The interior of the single-nave church is divided by two large spans with an ogival cross-vaulted roof and a ribbed cruise that covers the apsidal area, raised above the level of the nave. It is one of the most important documented Templar church in the world, since there is no such cycle of frescoes not even in the Chapelle des templiers de Cressac, a Templar chapel located in southwestern France that shows a valuable cycle of frescoes of reference on this theme. In addition, it is important to stress that the presence in the church of the thirteenth-century frescoes constitute the first iconographic documentation of the motion of the flagellants, also known as the disciplined, founded in Perugia in 1260 by the friar Raniero Fasani. In this same year Bonvicino became interested in the Roman Curia, under the Pope Alessandro IV, for the canonization of San Bevignate, and thus indirectly his name was linked to homonymous mysterious hermit protagonist of the “Lezenda” of Raniero Fasani itself. During the experimental campaign, the thermographic acquisitions, in conjunction with digital photography, were executed on the south wall of the nave since the opposite wall and the apse are in aggregate with other parts of the complex of San Bevignate (not the ideal environmental conditions under which passive thermal imaging must be performed), Figure 3. Furthermore, at the time of the surveys, the entrance wall and other areas were covered by scaffoldings, because there was a restoration. Among the aforementioned valuable mural paintings, the only certainly contemporaneous with the Templar period are actually those of the counter-façade and those above the apse, all the others belong therefore to other Orders. More specifically speaking, the series of the Apostles stands out on the side walls superimposed on the previous decorations, Figure 4. With reference to the counter-façade above the main entrance, is observable an unusual iconographic choice arranged in two registers inherent the efforts of the Templars in defence of the holy sepulchre. Referring to the apse, articulated decorative themes are observable portraying Biblical scenes and representations of Templar symbology and of local religious life (e.g., some flagellants can be seen and two effigies of San Bevignate), Figure 5. Concerning the apse and the decorations of the adjacent spans, geometric bands with the cornflower sign refer to the French origin of the Templar order and the presence of the nine stars surrounding the Templar cross in the fresco above the apse itself describes the nine Templars who founded the Order. At the top of the main wall of the apse the Virgin and Child are represented enthroned surrounded by angels; under the windows, there are the symbols of the four Evangelists and in the centre, immediately behind the altar, the Crucifixion is painted. On the left wall of the Last Supper is represented and on the right wall, which has no openings interruptions, the Universal Judgment is portrayed. In these portions, some flagellants can be seen and this testifies the fact that the monks of San Bevignate did not limit themselves to administering the Templar assets, but they also carried out functions of assistance and apostolate among the local inhabitants. At the end of the nave that leads to the apse, above a pointed arch

and within a complex decorative theme, fragments of the story of a miracle attributed to San Bevignate can be glimpsed, in particular the event in which he revives a child torn to pieces by a wolf. Behind the altar, a portrait of San Bevignate with a halo merits special mention and in this scene, as previously described, he receives the blessing of a bishop who seems to grant him the place in which to erect his church. In conclusion of this section, it behoves to bring up that at the same time as the restoration works following the '97 earthquake, valuable Roman ruins were discovered under the church's floorings. The finds extend for almost the entire width of the nave above and consist in an ancient fullonica characterized by the presence of five basins. The fragment of a mosaic with black and white tesserae, on the other hand, is attributable to a previous Roman domus dating back to around the second half of 1st century BC. To date, this archaeological site which also includes the crypt where was probably buried the Saint, apart from the church, is completely open to the public in a single museum itinerary.



Figure 2: External view of San Bevignate. Image taken from <https://www.iluoghidelsilenzio.it/chiesa-di-san-bevignate-perugia/>.

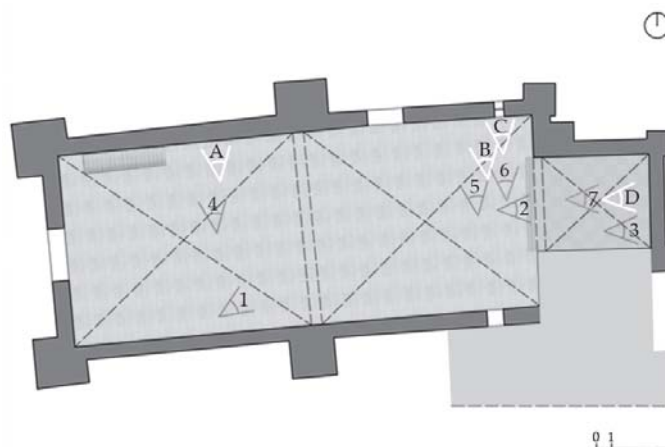


Figure 3: Schematization of the plan of the Church, inside the photographic cones of vision chosen for the survey: in white the settings of thermographic shootings, in grey the digital photography ones.



Figure 4: Inner view of the church of San Bevignate (see cone of vision 1 in Figure 3).



Figure 5: Picture of the altar, in background the lower register of the apse's frescoes (see cone of vision 2 in Figure 3).

4 INFLUENCE OF PLASTER THICKNESS

One of the key factors in assessing the correct texture of the masonry is the plaster thickness. In particular, since the plaster is made of a material which is very similar to the one the joints are made of, and it has usually a greater thermal conductivity than the stone, the plaster diffuses the thermal flux as it crosses the plaster, therefore the thermographic image, which measures the temperature differences on the surface of the wall, may not represent in detail the actual texture but could overestimate the presence of the mortar. In order to clarify this aspect, which is crucial in estimating the mechanical properties of the masonry since usually the mortar is the weaker phase, a preliminary study based on a numerical procedure using thermal finite element analysis has been developed. A masonry wall was realized with bricks having width 250 mm and height 55 mm, the thickness of the wall was 120 mm. A running bond texture was used, with mortar joints having thickness 10 mm. Several thickness of plaster were considered, from 5 mm to 15 mm. In Figure 6 the surface temperature read in the outdoor surface of the wall in steady state when the indoor temperature was 20°C and the outdoor temperature was 0°C is shown. The plaster covers only the outdoor surface of the wall.

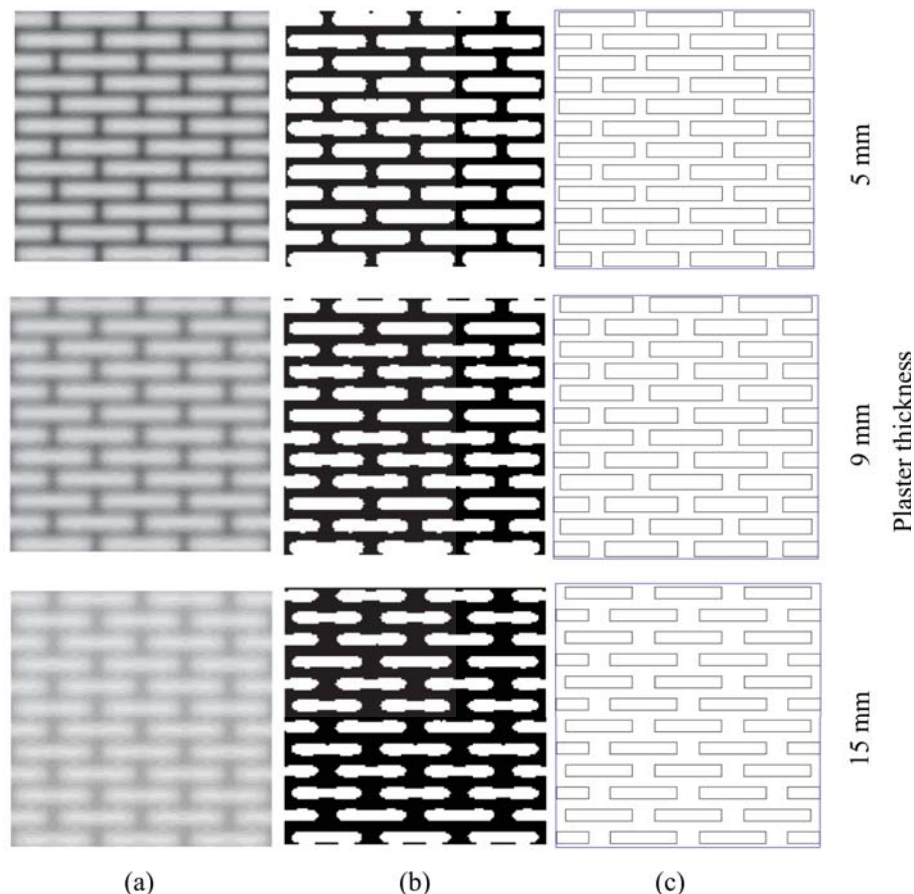


Figure 6: (a) Simulation of thermal image, (b) binary image, (c) equivalent rectangular blocks.

In the same figure, the black and white binary images obtained are shown. In order to simplify the interpretation of the results, the stones were transformed to equivalent rectangular blocks, as shown in the previous figure.

In Figure 7 the concentration ratio of the stone, which is the strong phase, is shown and compared with the reference value.

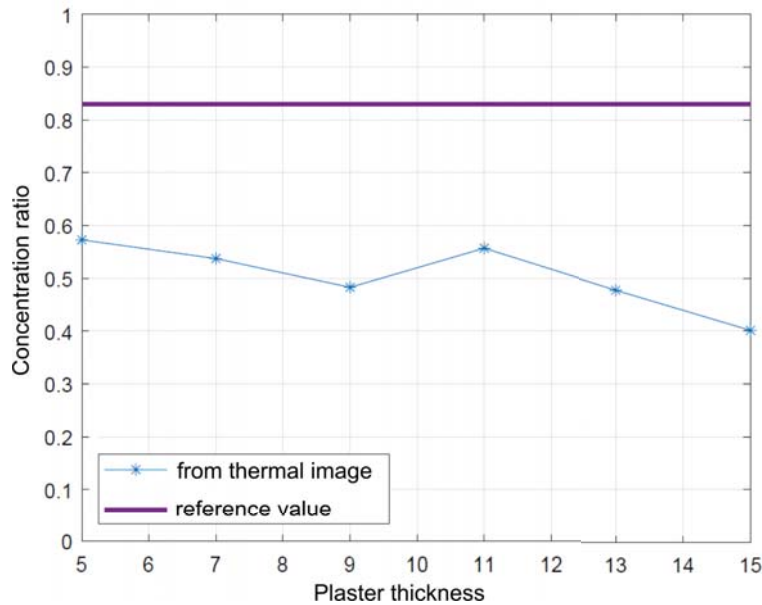


Figure 7: Concentration ratio of strong phase for various plaster thicknesses.

As can be appreciated, it seems that even small values of plaster thickness lead to a quite large decrement of the percentage estimated for the stones, and therefore further studies are necessary in order to fully assess the influence of plaster thickness when estimating the mechanical characteristics of the wall.

5 EXECUTION OF THE EXPERIMENTAL CAMPAIGN AND DIGITAL IMAGING

New technologies allow to conduct experimental investigations without harming the architectural quality of constructions, such innovations are exactly fitting with the disciplines inherent the heritage architectures [14, 15]. Among the important factors influencing the seismic response of Heritage buildings, the masonry quality and the knowledge of its processes of stratification are certainly enclosed. The acquisition of information about the non-visible masonry texture is the subject of such contribution, under the assumption that the masonry quality is the basic element to analyse and eventually improve, e.g. regarding the preferable monolithic behaviour, before to add any reinforcement intervention (metal tie-rods, mortar injections etc.).

During the actual experimental campaign, the experimental measurements were focused on the north frescoed wall of the nave and the thermographic “pictures” were taken under passive conditions: the inner wall’s surfaces were analysed without heating them, by exploiting direct sunlight and observing the thermal transient on them. This results in different responses from the elements with different thermal capacity, in particular by identifying - as mentioned earlier - with black pixels the mortar and with the white ones the stone elements.

Referring to the frescoes that decorate the examined wall, rows of overlapping ashlar are reproduced to imitate an austere wall face made of stone, this is a typical decoration of the Templar churches aimed to recall the poverty of the holy land. Moreover, the series of the twelve apostles stand out, distributed also on the other side wall, on the façade and the back walls of the apse; such pictorial cycles were superimposed on the original decoration during a second phase between 1283 and 1285. In particular, a first tranche of thermographic surveys covered the mural paintings concerning the apostle’s cycle, Figure 6.

Furthermore, dealing with a real architecture, it was necessary to add to the procedure a new

phase in order to enhance the quality of the final binary image, which is strictly connected to the sharpness of the starting thermographic image. Indeed, compared to what has been above described, an adjust contrast tool has been used aiming to improve the black-to-white mapping of the thermographic greyscale image. In visual perception, the contrast is the difference in luminance of colours that makes the elements of an image clearly distinguishable within the same field of view. In the light of the above, the thermal images recorded during the surveys were preliminarily modified by adjusting contrast so that the differences between black and white were sharp and the highlights looks brighter and the shadows looks darker, with intensity values that fill the entire range of intensities $[0, 255]$. Then, the procedure above described in Section 2, was applied.

6 MASONRY WALL TEXTURE AND PECULIAR CHARACTERISTICS OF THE FRESCOES

The approach was to have first an overview of the masonry texture and its quality and then to proceed gradually more and more closely to the wall's faces. Along with the thermographic images ordinary digital photos have been taken; in addition, reference thermal reflective elements have been placed in front of the frescoes, made by two parallel rigid meter-sticks, in order to be able to overlay subsequently the photos with the corresponding thermographic images in the next phase. Considering that in this first case the meter-sticks were separated by 2.70 m, by means of the procedure and its final binary images, elaborated by straightening photographic and measurements digital techniques, it was possible not only to seize the quality of the masonry texture but also its dimensional features, Figures 9 and 10.

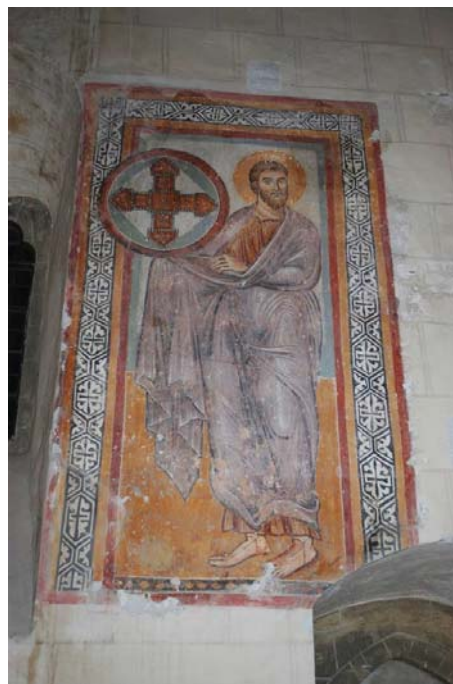


Figure 8: One of the frescoes under investigation, in particular one belonging to the apostle's cycle. 3.

A quasi-periodic texture made of stone blocks with different widths, ranging from 25 to 60 cm, but similar heights, of about 20 cm, has been observed; such results matches with what was surveyed in the apse, concerning the areas where the fresco peeled off (see Figure 5) and on the external façades.

The benefits offered by the thermal imaging methods, regarding the safeguard of frescoes, mural paintings and valuable architectonic elements, have been addressed by numerous authors [17, 18, 19, 20, 16]. In addition, it was possible to contextually ascertain that there are no detachments or infiltration phenomena in place that can afflict the health of the frescoes. Moreover, recalling the historical researches from which emerged that the frescoes of the Apostles was superimposed to the pre-existing ones, the mortar distribution (in those areas) suggests a trace of the ancient techniques of fresco-makers: the surface of the previous fresco had been probably “excavated” by the masons, allowing the new fresh plaster to cling to the ancient mortar below, a less smooth and slippery surface than the one of the wall. Then, the presence of few fragments of mortar out of the joints may show that in order to seat the new murals some holes were made by hands in the previous frescoes and so their orientation does not follow an exact pattern [17]. This, therefore, testifies that the proposed thermographic method, thanks to the possibility to improve the parameters described Section 2, allows to gain information, which must be critically analysed, even about masonries subjected to various superimposed layers of frescoes.

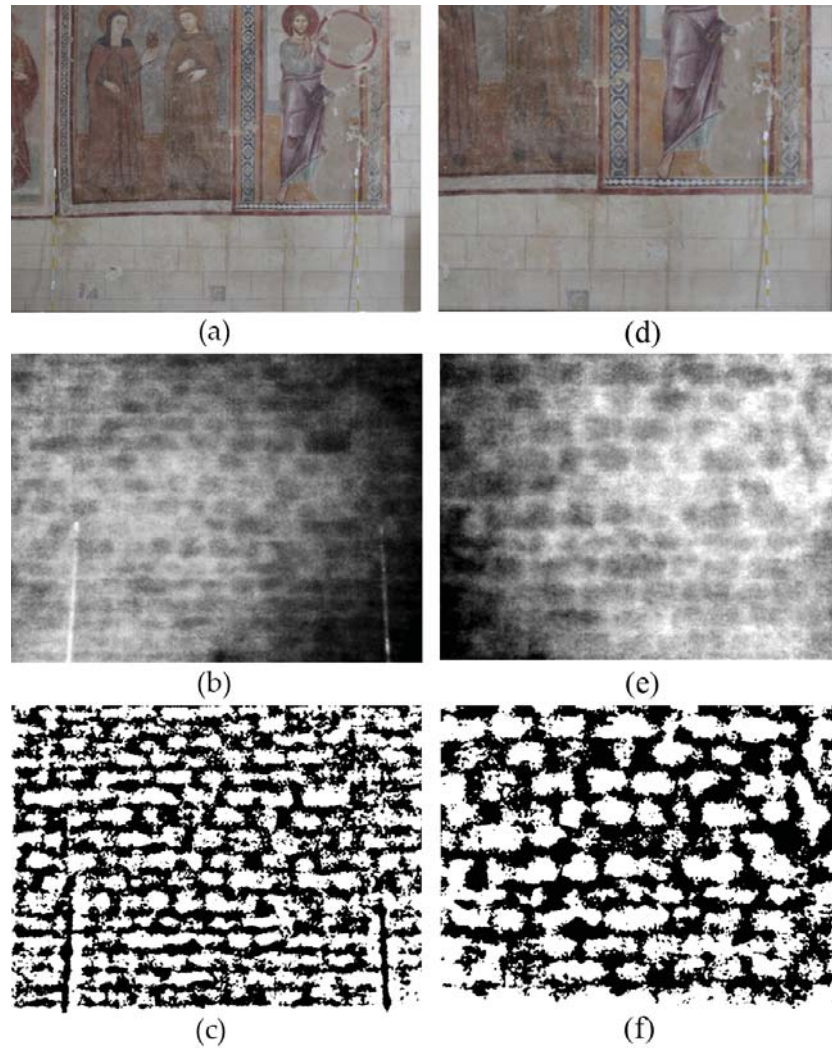


Figure 9: (a) Fresco under investigation. (b) Thermal image with improved contrast. (c) Final binary image (see the cone of vision A in Figure 3). In the right column, a thermal analysis closer to the masonry surface than the previous one: (d) Portion of the fresco under investigation. (e) Thermal image with improved contrast. (f) Final binary image (see the cone of vision B in Figure 3).

7 IDENTIFICATION OF DEFICIENCIES AND DISCONTINUITIES

The role of the latter approach in detection and qualification of deficiencies/discontinuities in the stonework is an important aspect [21, 22, 23, 24]. Through the analysis of another part of the same wall, located near the apse and in the proximity of a window, it was possible to discover the presence of a blind opening in the original masonry, which now is totally bricked up (Figure 10). In this second case the meter-sticks were placed at a distance of about 1.40 m leading to deduce a size of 65×75 cm for the part walled up with a masonry typology different from sandstone. Additionally, there was pointed out the different emissivity and the presence of an architrave made of another material (possibly wood) of about 15 cm thick. Moreover, about the constructive phases and criteria, the peculiar workmanship, and the different material were also observable on the abutments of the window.

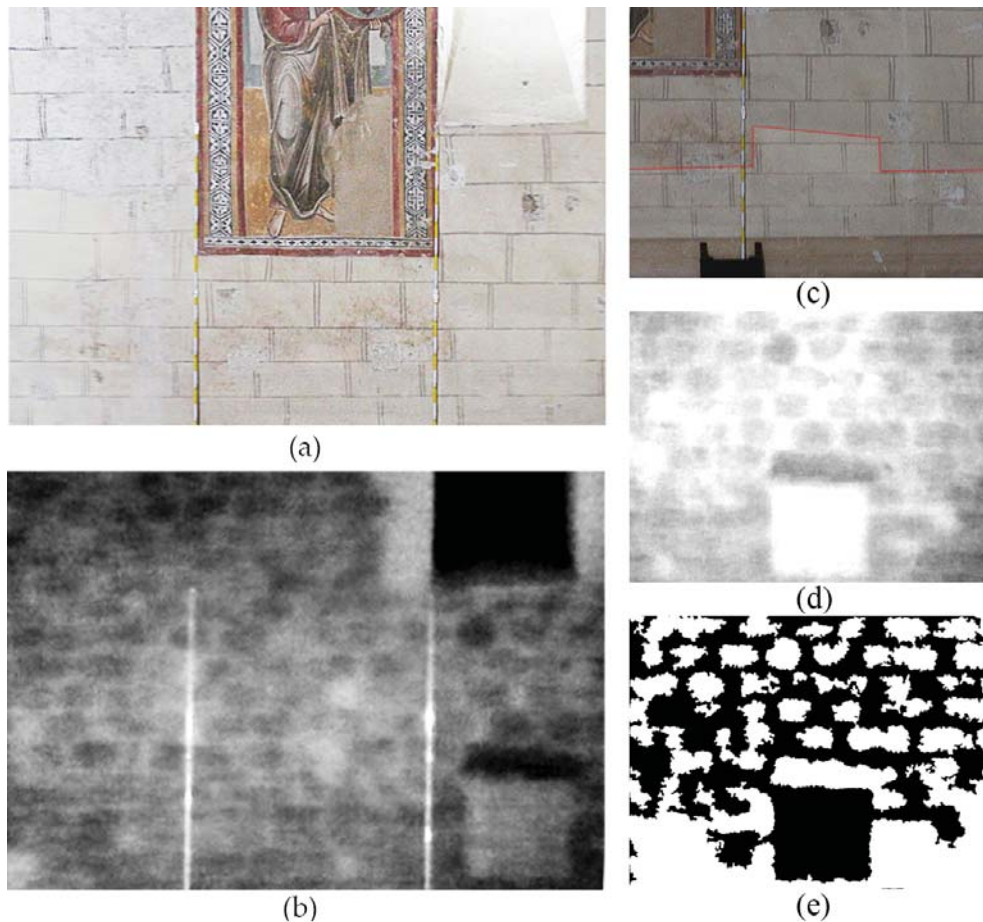


Figure 10: (a) Picture of a fresco near the apse. In the pictures, the reflective meter-sticks located as reference points for the subsequent post-processing are visible. (b) Thermal image with improved contrast in which are visible the structural peculiarities of the masonry wall, in the right corner is observable the former recess (see the cones of vision 5 and B in Figure 3). (c) Particular of the fresco under investigation, are observable colours of different gradation. (d) Thermal image with improved contrast. (e) Final binary image (see the cones of visions 6 and C in Figure 3).

Indeed, a toothing masonry has been realized, characterized by the process of leaving alternate stone "teeths" for a better adjoining block or brick wall to be started from. Even nowadays, such technique is used when windows or door openings must be made from an existing wall, by demolition and cutting of masonry, allowing the adjoining wall to develop without having to adjust or cut bricks. It is also noteworthy to notice how, already with the naked eye - can be seen in Figure 10 - portions of the fresco with colours of different gradation are observable, probably due to varied breathability of the materials making up the masonry. This scenario is also confirmed by what emerged from a closer thermographic picture: assuming a stratigraphic interpretation of the wall, arise the construction phases of the ancient site executed by different bricklayers, made by lower rows of a type of stone (which appears darker) probably of superior quality compared to that of the band between the recess and the window where instead the masonry is composed of smaller elements thus making the presence of mortar predominant. Moreover, it is interesting to remark that the filling of the recess does not present any masonry texture as if it had been filled entirely with a concretion material. Finally, a thermographic investigation involved a part of the apse wall. This portion of the church was chosen because here can be found the coexistence of portions of plaster with parts of the masonry emerging, because of the detachments of the fresco that in past centuries were witnessed by the restorers. From the

thermographic images, one of them can be seen in Figure 11, it appears that to date there are no infiltrative nor detachment or disruptive phenomena of interest undermining the safeguard of the decorations under examination.

However, such item will be taken up in the future developments of the research campaign considering also other portions of the church and to a large extent, with reference to the ongoing works of consolidation, profiting from the opportunity to deepen the knowledge about the architecture and frescoes' manufacturing techniques. Moreover, non-destructive testing (NDT) techniques can be used in regard to both evaluation of mechanical properties and for characterization of microstructural features such as grain size, texture, nucleation, defects, deformations, or damages in various contexts, also concerning historical masonries [25, 26, 27]. In particular, the pictures obtained from thermographic surveys can be used to estimate the elastic characteristics of masonry texture, by means of the method of the test-windows [28]; preliminary results are reported in [7].

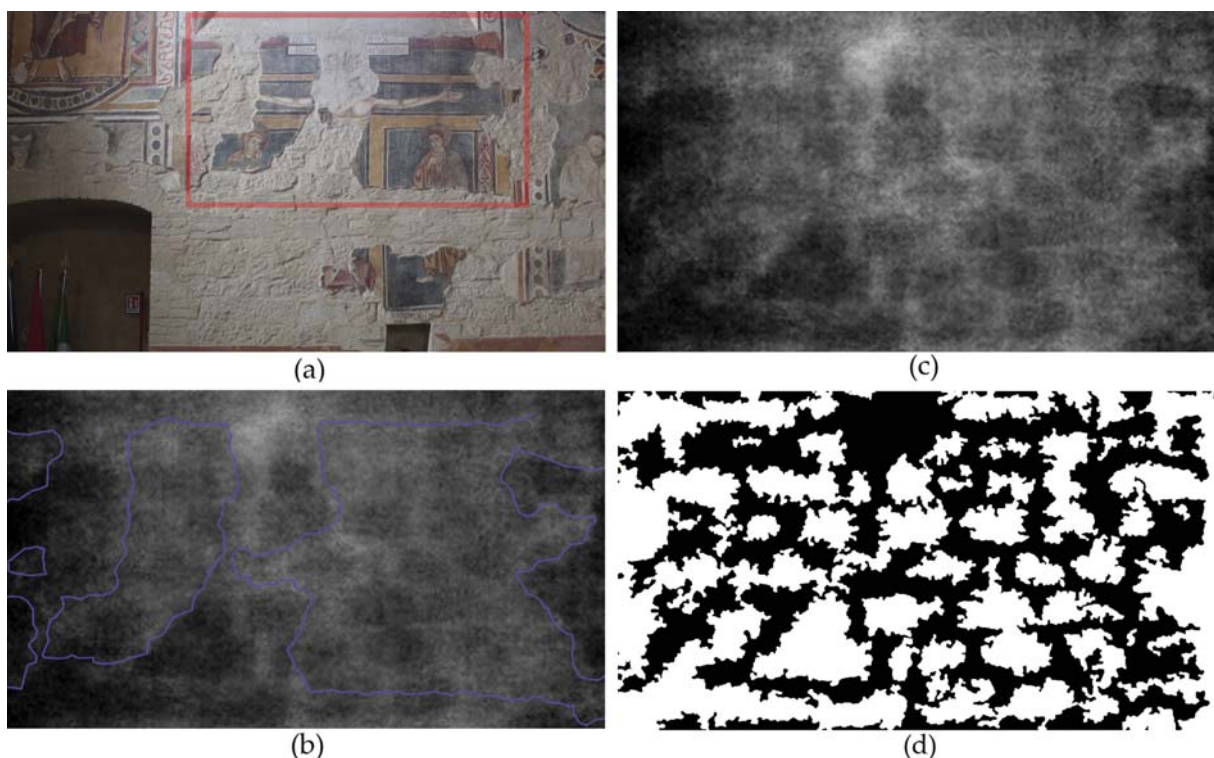


Figure 11: (a) Portion of the fresco under investigation, (b) thermal image where are highlighted in blue the edges of what remains of the frescoes, (c) thermal image with improved contrast, (d) final binary image (see the cones of vision 7 and D in Figure 3).

8 CONCLUSIONS

- A method to identify and interpret the differences of temperature in wall surfaces was proposed and applied to a heritage architecture of great value; enabling the evaluation of the historical masonry texture covered by rare frescoes;
- The outcomes highlighted the reliability of the devised procedures to identify masonry texture, a necessary information to estimate the masonry mechanical characteristics;
- A preliminary study on the influence of plaster thickness has been made;

- Moreover, the thermographic images have been very useful to detect deficiencies and discontinuities in the wall, besides to find characteristics of the frescoes in terms of realization criteria and actual conservation conditions;
- Without damaging the decorations by taking essays or samples, it was possible to obtain information not only on the risk factors concerning the frescoes conservation but also inherent to the seismic prevention, closely tied to the peculiarities and stratifications of masonry;
- From a future perspective, considering that the results are promising, the thermographic analysis will be extended to other portions of the Church.

Acknowledgements

This work was supported in part by the Italian Ministry for University and Research (P.R.I.N. National Grant 2017, Project title “Modelling of constitutive laws for traditional and innovative building materials”, Project code 2017HFPKZY; University of Perugia Research Unit). This support is gratefully acknowledged. In addition, the authors are grateful to the professional and human endeavour of the Full Professor Paolo Belardi, of the University of Perugia, and to the Dr. Catia Chiaraluce, of the municipality of the city of Perugia, aimed at the creation of a partnership with the local stakeholders.

REFERENCES

- [1] ICCROM, *International Centre for the Study of the Preservation and Restoration of Cultural Property*. 15 March 2021; accessible on <https://www.iccrom.org/news/italy-earthquakes-other-casualty-cultural-heritage>.
- [2] V. Gusella, R. Liberotti, Seismic Vulnerability of Sub-Structures: Vantitelli's Modulus in Murena Palace. *Buildings*, **10(9)**, 164, 2020.
- [3] R. Liberotti, F. Cluni, V. Gusella, Vulnerability and seismic improvement of architectural heritage: The case of Palazzo Murena. *Earthquakes and Structures*, **18(3)**, 321–335, 2020.
- [4] F. Cluni, D. Costarelli, A.M. Minotti, G. Vinti, Enhancement of thermographic images as tool for structural analysis in earthquake engineering. *NDT E Int.*, **60**, 60–72, 2015.
- [5] F. Cluni, V. Gusella, G. Vinti, Masonry elastic characteristics assessment by thermographic images. *Meccanica*, **54**, 1339–1349, 2019.
- [6] F. Cluni, D. Costarelli, V. Gusella, G. Vinti, Reliability increase of masonry characteristics estimation by a sampling algorithm applied to thermographic digital images. *Probabilistic Eng. Mech.*, **60**, 2020, 103022, ISSN 0266-8920, <https://doi.org/10.1016/j.probengmech.2020.103022>.
- [7] V. Gusella, F. Cluni, R. Liberotti, Feasibility of a Thermography Nondestructive Technique for Determining the Quality of Historical Frescoed Masonries: Applications on the Templar Church of San Bevignate. *Appl. Sci.*, **11**, 281, 2021. <https://doi.org/10.3390/app11010281>
- [8] V. Gusella, F. Cluni, Random field and homogenization for masonry with nonperiodic microstructure. *J. Mech. Mater. Struct.*, **1**, 357–386, 2006.
- [9] N. Cavalagli, F. Cluni, V. Gusella, Strength domain of non-periodic masonry by homogenization in generalized plane state. *Eur. J. Mech.-A/Solids*, **30**, 113–126, 2011.
- [10] F. Gusella, F. Cluni, V. Gusella, Homogenization of dynamic behaviour of heterogeneous beams with random Young's modulus. *Eur. J. Mech.-A/Solids*, **63**, 260–267, 2019.
- [11] F. Gusella, F. Cluni, V. Gusella, Homogenization of the heterogeneous beam dynamics: The influence of the random Young's modulus mixing law. *Compos. Part B Eng.*, **167**, 608–614, 2019.
- [12] U. Nicolini, Le canonizzazioni “facili” del comune di Perugia: Il caso di San Bevignate, già in Templari e Ospitalieri. M. Roncetti, P. Scarpellini, F. Tommasi, F. eds. *Italia. La Chiesa di San Bevignate a Perugia*, Milano, Italy, 1987, 39–45 (now In *IDEM, Scritti di storia*; pp. 337–348).
- [13] S. Merli, L'insediamento dei Templari a Perugia: da San Giustino d'Arna a San Bevignate. S. Sammarco, S., ed. *Commilitones Christi. Miscellanea di studi*; Roma, Lisanti, 9–84, 2017.

- [14] E.B. Groth, T.G.R. Clarke, G. Schumacher da Silva, I. Iturrioz, G. Lacidogna, The Elastic Wave Propagation in Rectangular Waveguide Structure: Determination of Dispersion Curves and Their Application in Nondestructive Techniques. *Appl. Sci.*, **10**, 4401, 2020.
- [15] A. Moropoulou, N.P. Avdelidis, M. Karoglou, E.T. Delegou, E. Alexakis, V. Keramidas, Multispectral Applications of Infrared Thermography in the Diagnosis and Protection of Built Cultural Heritage. *Appl. Sci.*, **8**, 284, 2018.
- [16] , E. Verstrynge, G. Lacidogna, F. Accornero, A. Tomor, A review on acoustic emission monitoring for damage detection in masonry structures. *Constr. Build. Mater.*, 121089, 2020, ISSN 0950-0618, <https://doi.org/10.1016/j.conbuildmat.2020.121089>.
- [17] G. Botticelli, *Metodologia di Restauro delle Pitture Murali. Ediz. Ampliata*. StreetLib, Florence, Italy, 2020.
- [18] E.Z. Kordatos, D.A. Exarchos, C. Stavrakos, A. Moropoulou, T.E. Matikas, Infrared thermographic inspection of murals and characterization of degradation in historic monuments. *Constr. Build. Mater.*, **48**, 1261–1265, 2013.
- [19] N. Lermé, S. Le Hégarat-Masclé, B. Zhang, E. Aldea, Fast and efficient reconstruction of digitized frescoes. *Pattern Recognit. Lett.*, **138**, 417–423, 2020.
- [20] G.M. Carlomagno, C. Meola, Comparison between thermographic techniques for frescoes NDT. *NDT E Int.*, **35**, 559–565, 2002.
- [21] S. Sfarra, S. Laureti, G. Gargiulo, H. Malekmohammadi, M.A. Sangiovanni, M. La Russa, P. Burrascano, M. Ricci, Low Thermal Conductivity Materials and Very Low Heat Power: A Demanding Challenge in the Detection of Flaws in Multi-Layer Wooden Cultural Heritage Objects Solved by Pulse-Compression Thermography Technique. *Appl. Sci.*, **10**, 4223, 2020.
- [22] F. Mercuri, N. Orazi, S. Paoloni, C. Cicero, U. Zammit, Pulsed Thermography Applied to the Study of Cultural Heritage. *Appl. Sci.*, **7**, 1010, 2017.
- [23] C. Lerma, Á. Mas, E. Gil, J. Vercher, Hygrothermal Behaviour of Continuous Air Chambers on Stone Panels Façades through CFD and IRT. *Appl. Sci.*, **9**, 3001, 2019.
- [24] I. Campione, F. Lucchi, N. Santopuoli, L. Seccia, 3D Thermal Imaging System with Decoupled Acquisition for Industrial and Cultural Heritage Applications. *Appl. Sci.*, **10**, 828, 2020.
- [25] G. Vasconcelos, P. Lourenço, C. Alves, J. Pamplona, Ultrasonic evaluation of the physical and mechanical properties of granites. *Ultrasonics*, **48**, 453–466, 2008.
- [26] S. Noor-E-Khuda, F. Albermani, Mechanical properties of clay masonry units: Destructive and ultrasonic testing. *Constr. Build. Mater.*, **219**, 111–120, 2020.
- [27] E. Vasanelli, A. Calia, D. Colangiuli, F. Micelli, M.A. Aiello, Assessing the reliability of non-destructive and moderately invasive techniques for the evaluation of uniaxial compressive strength of stone masonry units. *Constr. Build. Mater.*, **124**, 575–581, 2016.
- [28] F. Cluni, V. Gusella, Homogenization of non-periodic masonry structures. *Int. J. Solids Struct.*, **41**, 1911–1923, 2004.

EVALUATION OF A NUMERICAL MODELLING APPROACH FOR THE SIMULATION OF RETROFITTED RC ELEMENTS

I. Sousa¹, R. Couto², R. Peres¹, J.M. Castro¹ and R. Bento²

¹CONSTRUCT

Faculdade de Engenharia da Universidade do Porto
Rua Dr Roberto Frias, s/n
e-mail: {inessousa, ritaperes, miguel.castro}@fe.up.pt

²CERIS

Instituto Superior Técnico, Universidade de Lisboa
Av. Rovisco Pais, 1
e-mail: {rita.g.couto, rita.bento}@tecnico.ulisboa.pt

Abstract

The majority of the RC building stock in large cities consist of old buildings where most of them were designed with codes without any seismic provisions, thus leading, most likely, to important seismic vulnerabilities. Good knowledge about the building properties and vulnerabilities and, more importantly, on how to model the behaviour of the most relevant components, is fundamental to help analysts and practitioners in the assessment and strengthening of existing RC buildings.

This paper focuses on the numerical modelling of strengthening solutions for RC buildings, with the objective of defining a modelling approach that accurately captures the behaviour of retrofitted elements. To achieve this goal, retrofitted elements are simulated through distributed plasticity models and their seismic performance compared with the most recent experimental data available on this topic.

As a case study, an existing reinforced concrete building with typical properties of non-ductile buildings in Portugal is modelled and analysed through nonlinear static analysis to determine the building structural weaknesses. The retrofitting interventions were designed based on code recommendations.

Keywords: RC structures retrofitting, carbon fibre-reinforced polymer (CFRP), numerical modelling of strengthening solutions, seismic performance improvement.

1 INTRODUCTION

A significant number of existing reinforced concrete (RC) buildings in earthquake-prone locations require seismic retrofitting since the majority of these buildings do not meet the current seismic assessment code requirements. Several deficiencies are commonly found in this type of buildings, such as poor reinforcement details, lack of adequate transverse reinforcement and insufficient confinement reinforcement at potential plastic hinges areas. These characteristics decrease the RC members' strength to shear forces, thus leading to premature brittle failures, as have been observed on field surveys performed in areas affected by earthquakes [1]–[4].

Among the different strengthening techniques, the use of fibre-reinforced polymer (FRP) composites has become progressively suitable due to the fast installation, minimal modification to the existing architecture and satisfactory mechanical properties. Moreover, as a lightweight material, FRP does not modify the cross sectional properties of elements or the structure mass [5]. Accordingly, the seismic performance of RC elements retrofitted with FRP has been the subject of extensive investigation [6]–[13]. The majority of the studies focused on experimental campaigns carried out on RC elements retrofitted with FRP. Nonetheless, the present study will give emphasis to the modelling aspects of such type of intervention.

Since it is acknowledged that vulnerable RC buildings require retrofit, it is crucial for practitioners to have the means for modelling, with accuracy, the behaviour of the existing structures, and, more importantly, to have the tools to correctly model the response of the existing retrofitted structural elements. Therefore, the first part of this paper focuses on the numerical simulation of a RC column using the *OpenSees* [14] software, with the aim of validating the modelling approach with experimental data.

The second part of the study consists of the numerical modelling of a structure representative of the Portuguese building stock in the 1950s, also using *OpenSees*, before and after the retrofitting intervention. The structure's capacity is estimated with nonlinear static analysis and its seismic performance is evaluated through the calculation of the demand/capacity ratios recommended by Part 3 of Eurocode 8 (EC8-3) [15]. The initial assessment indicates brittle and ductile failure modes in some structural elements (columns and walls). A strengthened solution employing CFRP is designed and numerically implemented in the structural model. Afterwards, a new seismic evaluation is carried out and the structure's safety assessed once more. The results demonstrate the feasibility and effectiveness of the CFRP as a strengthening solution to eliminate brittle and ductile mechanisms.

2 MODELLING APPROACH

This section introduces a numerical modelling approach to simulate the behaviour of FRP in RC elements using *OpenSees*, which will be validated through comparison of numerical with experimental data.

2.1 Experimental data

In order to fulfil the goal of accurately representing the real behaviour of retrofitted RC elements with FRP, first it was necessary to select a RC element tested experimentally from the literature. The specimen used in this paper is available in a study performed by Del Zoppo et al. [16] and consists of a RC column tested under axial load and cyclic lateral loading. The column was designed to old construction practice in order to be representative of real existing structures. As such, the specimen is characterized by poor quality concrete, no longitudinal

reinforcement in the cross-section secondary direction and the transverse reinforcement details are not compliant with current standards.

The test specimen has a square cross-section $300 \times 300 \text{ mm}^2$ with six $\phi 18 \text{ mm}$ longitudinal steel rebars and $\phi 8 \text{ mm}$ ties spaced 150 mm apart. In the zone of the load application, the spacing between ties was reduced to avoid localized damages. The column height is 1800 mm , and the lateral load was applied at a distance of 1500 mm from the foundation block. The average concrete compressive strength for the retrofitted specimen is $f_c = 14.9 \text{ MPa}$, whilst the average yielding strength of the steel bars in both longitudinal and transverse reinforcement is $f_y = 531 \text{ MPa}$.

To what concerns the retrofit solution adopted, the column was wrapped with uniaxial carbon fibre reinforced polymers (CFRP) along 500 mm from the column base, which corresponds to the location of the plastic hinge development. The geometric properties and the reinforcement details are illustrated in Figure 1. In addition, **Erro! A origem da referência não foi encontrada.** shows the mechanical properties of the CFRP.

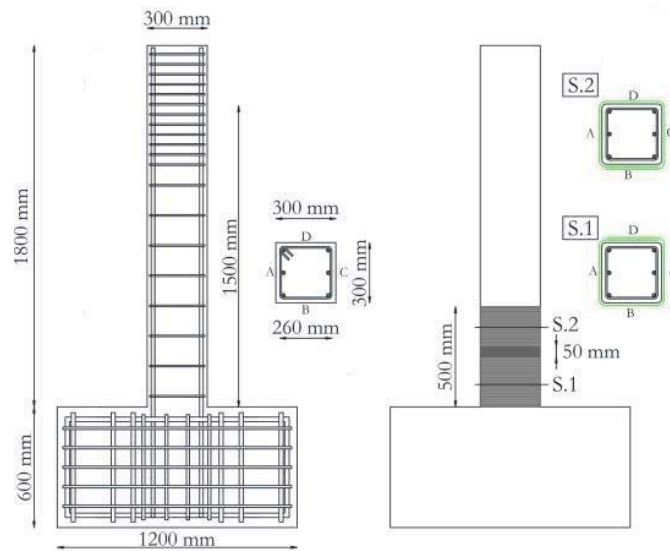


Figure 1: Specimen geometry and strengthening configuration (adapted from [16]).

Material	Number of plies	Thickness (mm)	Elastic modulus (GPa)	Ultimate strain (%)
CFRP	1	0.33	230	1.3

Table 1: Carbon fibres material properties[in Del Zoppo et al. [16]].

Regarding the axial load applied, the specimen was subjected to a constant axial load ratio of 0.1, such that $\nu = N / A_c f_c$, where N is the axial load, A_c is the concrete gross area and f_c is the mean cylindrical concrete strength.

2.2 OpenSees modelling

As mentioned before, the modelling of the specimen was conducted using *OpenSees*, an open-source software framework developed to simulate the behaviour of structures subjected seismic actions. There are two models that can be employed in *OpenSees* to simulate the inelastic response of RC elements: distributed or concentrated plasticity approaches. In this study, the column was modelled through a distributed plasticity approach, using the *nonlinear-BeamColumn* command and considering a force-based formulation with four elements, each with five integrations points.

The element's cross-section was represented by a fibre section, which in turn was subdivided into smaller fibre sections. These fibre objects are associated with uniaxial materials that express the stress-strain relationship of concrete, steel and CFRP. The behaviour of both the cover and core concrete fibres was simulated adopting the model suggested by Popovics [17], (*Concrete04* material in *OpenSees*) whilst the steel was modelled through a uniaxial bilinear hysteretic material object, translated by the command *uniaxialMaterial Hysteretic*. The stress and strain values of the steel rebars were input into this command, which also allows for the consideration of the pinching effect. Finally, the contribution of the CFRP was achieved by adding the effect of the confinement provided by the retrofit intervention.

The effect of the confinement provided by the transverse reinforcement and the CFRP acting simultaneously was determined through the confinement model proposed in Part 3 of Eurocode 8 (EC8-3) [15]. The strength of confined concrete, f_{cc} , the strain at which the strength takes place, ε_{cc} , and the ultimate strain of the extreme fibre of the compression zone, ε_{cu} , are given by the expressions (1), (2) and (3), respectively.

$$f_{cc} = f_c \left[1 + 3.7 \left(\frac{\alpha \rho_{sx} f_{yw}}{f_c} \right)^{0.86} \right] \quad (1)$$

$$\varepsilon_{cc} = \varepsilon_{c2} \left[1 + 5 \left(\frac{f_{cc}}{f_c} - 1 \right) \right] \quad (2)$$

$$\varepsilon_{cu} = 0.004 + 0.5 \frac{\alpha \rho_{sx} f_{yw}}{f_{cc}} \quad (3)$$

In the expressions above, f_c is the concrete compressive strength, f_{yw} is the transverse reinforcement yield strength, α is the confinement effectiveness factor, ρ_{sx} is the ratio of transverse reinforcement and ε_{c2} is the strain at which f_c takes place of unconfined concrete, taken as 0.002. The mechanical properties adopted for all materials are shown in **Erro! A origem da referência não foi encontrada.** The concrete tensile strength was taken as 10% of the compressive strength.

Material		f_c (MPa)	ε_c (%)	ε_{cu} (%)
Concrete (core)	ϕ 8//150	16.7	0.32	1.21
Concrete (core)	ϕ 8//50	21.8	0.67	3.5
		f_y (MPa)	f_u (MPa)	E_s (GPa)
Steel		531	627	210
		f_c (MPa)	ε_c (%)	ε_{cu} (%)
CFRP		24.6	8.4	4.41

Table 2: Mechanical properties of the materials used in the modelling.

The adequacy of this modelling approach was evaluated through comparison of the results from cyclic pushover analysis with the experimental test data. The results obtained are illustrated in Figure 2, where the black dashed line corresponds to the experimental data and the grey cyclic curves refers to the *OpenSees* results. As it can be seen, a good agreement between the experimental data and numerical modelling was achieved, not just in terms global strength but also in what concerns the ability of the model in simulating the pinching effects. These results indicate that this type of approach is adequate to model FRP interventions in existing RC buildings.

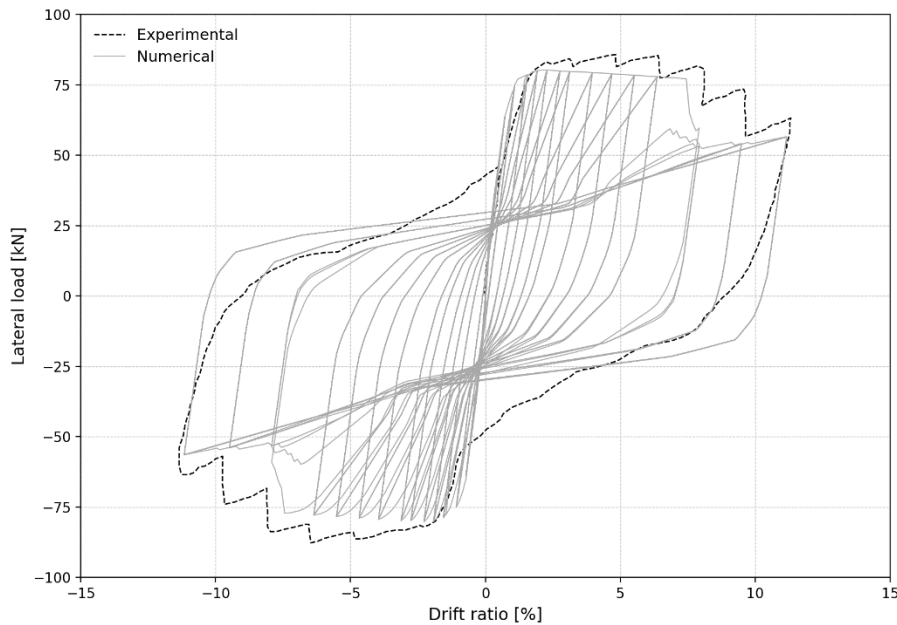


Figure 2: Comparison between experimental results and OpenSees.

An example of this FRP modelling approach application into a real existing building is described in the following sections of this paper.

3 CASE STUDY APPLICATION

3.1 Description of the building and structural modelling

The RC building selected is a five-storey wall-frame RC building, built in the 1950s. The building has a total height of 15.4m with a typical floor height of 3.0 m, except for the ground floor, for which the height is equal to 3.4 m. It has three and five frames in X and Y directions, respectively. A shear wall is positioned at the middle of the building, oriented in the X direction, on the first three storeys. The plan and elevation views of the building are shown in Figure 3.

The information about the section geometric properties and reinforcement ratios variation of the building structural elements is presented in **Erro! A origem da referência não foi encontrada.**

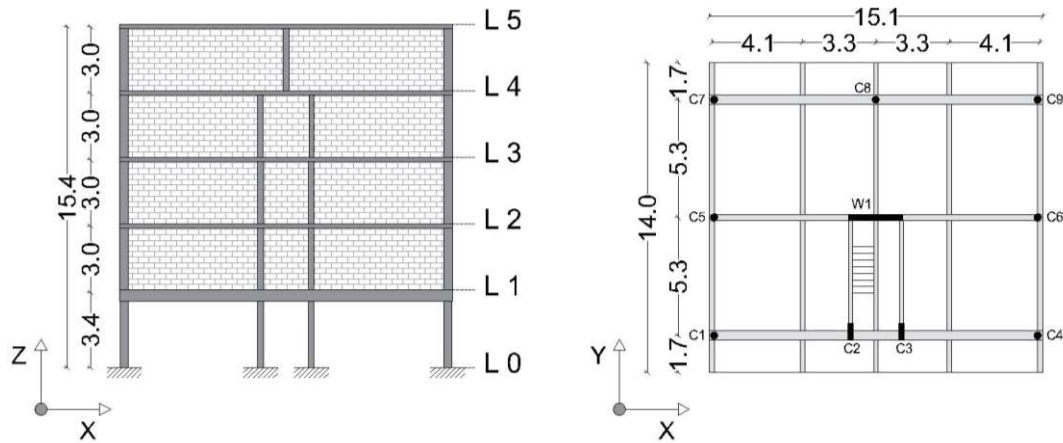


Figure 3: Elevation and plan of the selected building.

Element	Columns	Beams	Walls
Dimensions(cm)	23×25–25×87	13×31–25×68	250×25
Cross Section(cm ²)	575–2175	403–1700	6250
Longitudinal rebar (cm ²)	0.63–7.29	T: 2.26–29.76 B: 3.93–33.58	15.78
Transversal rebar (cm ²)	0.18–0.71	1.48	3.15
Spacing of stirrups(cm)	5-19	20–50	15

Table 3: Sectional geometrical properties and minimum/maximum reinforcement ratios of the structural elements (*T* and *B* refer to top and bottom beam reinforcements, respectively).

The building was modelled and analysed with *OpenSees*. All the structural elements were modelled using the *nonlinearBeamColumn* command and considering a force-based formulation considering one element per beam, column and wall. The concrete and steel stress-strain relationships adopted at the fibre level were the ones mentioned in the previous section. The mean values of the material properties used in the model are listed in Table 4. The behaviour of the smooth rebars was modelled by modifying the steel constitutive law, reducing the Young's Modulus and maximum strength of the reinforcing steel to simulate the increase in member flexibility due to strain penetration effects [18].

The torsional stiffness was incorporated in the model by computing the elements torsional stiffness and assigning it through the section aggregator program command, while the rigid in-plane stiffness of the floor slab was modelled considering a rigid diaphragm multi-point constraint, through the program command *rigid diaphragm*. Second-order effects were accounted for in the model by adopting a P-Delta geometric transformation for the columns and wall. The infill panels were also modelled by assuming the two-diagonal truss approach established in [19]. The mass, which was obtained through the conversion of dead and live loads, was lumped at the centre of mass at each floor level. The dead loads include the self-weight of the RC elements, masonry infills and coatings, i.e., 8 kN/m², while the live loads have been defined according to Part-1 of Eurocode 8 [20]. The fundamental periods of vibration of the building are 0.31s and 0.41s in X and Y directions, respectively.

Concrete	f_c (MPa)	ϵ_c (‰)	ϵ_{cu} (‰)	E_c (GPa)
Cover	28	2	4	30
Core	28	2	200	30
Steel	f_y (MPa)	f_u (MPa)	ϵ_{su} (‰)	E_s (GPa)
Ribbed rebar	370	360	240	210
Smooth rebar	222	216	168	126
Masonry	G_w (GPa)	α	τ_{cr}	E_w (GPa)
Infills	1240	0.05	280	4092

f_c -compressive maximum strength; ϵ_c -strain at maximum strength, ϵ_{cu} - concrete ultimate strain, E_c - modulus of elasticity of the concrete; f_y -yielding strength; f_u - ultimate strength; ϵ_{su} - steel ultimate strain; E_s - modulus of elasticity of steel; G_w - elastic shear modulus; α - post- capping degrading branch coefficient; τ_{cr} – shear cracking stress; E_w -modulus of elasticity of the masonry.

Table 4: Material properties

A nonlinear static analysis was performed to evaluate the lateral capacity of the structure. The analysis was performed in both the X and Y directions, with positive and negative signs and, despite the slight asymmetry in the Y direction of the building, no significant differences were observed between the positive and the negative orientations. Two load patterns were considered: i) a modal load pattern, proportional to the fundamental mode of vibration, and ii) a uniform load pattern, proportional to the masses of the floors. Only the results corresponding to the modal pattern were considered since they correspond to a capacity curve with lower resistance and, consequently, more restrictive in terms of performance.

3.2 Seismic assessment

The seismic safety of the buildings was evaluated in terms of the demand/capacity ratio (DCR) for each vertical structural element (columns and walls) following the procedure recommended in EC8-3, which consists of comparing the chord rotation and shear demand with the capacity values of ultimate chord rotation and shear strength. The target displacement was determined with the N2 method, also as prescribed in EC8-3.

As established in EC8-3, the return periods to consider in the assessment of the existing buildings are: 73, 308 and 975 years for the damage limitation (DL), the significant damage (SD) and the near-collapse (NC) limit states, respectively. According to each of the limit states, the reference ground acceleration (a_{gR}) is then multiplied by a coefficient. Only the response spectrum for the Type 1 seismic action (far-field earthquake) was considered, therefore, the a_{gR} is 0.15g (Lisbon, Zone 1.3). The Portuguese Annex of EC8-3 [21] recommends that, for existing residential buildings, the assessment should be performed considering only the significant damage (SD) limit state.

Figure 4 shows the pushover curves obtained for the X and Y directions with the indication of the target displacement attainment at the SD limit state. It can be observed that, in the X direction, brittle and ductile failures occur almost simultaneously before target displacement is reached. In the Y direction, the structure exhibits lower capacity, due to the absence of RC walls oriented in this direction, and also experiences a brittle failure before the target displacement is reached. In conclusion, the brittle failure was the conditioning mechanism for both directions,

corresponding to a displacement of 0.0036 m and 0.0079 m for the X and Y direction, respectively. The occurrence of this type of mechanism at early stages of lateral deformation is common in old RC buildings designed to resist gravity loads, as verified by [22].

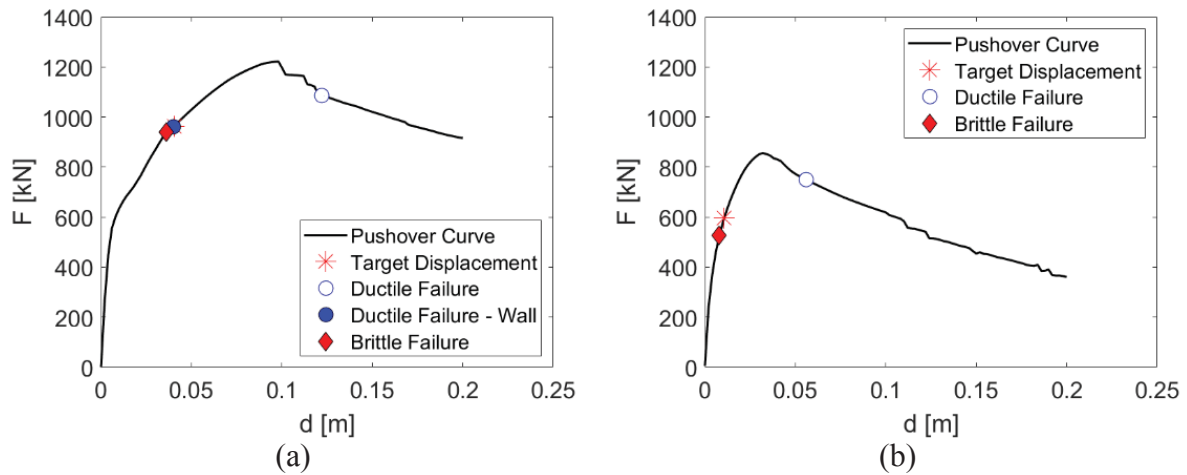


Figure 4: Pushover curves for the (a) X and (b) Y direction with the indication of the target displacement and failure mechanisms.

Figure 5 illustrates the location and type of damage experienced by the vertical RC elements when the displacement that corresponds to SD limit state is reached. As it can be seen, in direction X, some elements (columns and wall) are simultaneously affected by brittle and ductile failures on the first two storeys, while Y direction, the elements are only affected by a brittle mechanism on the ground storey.

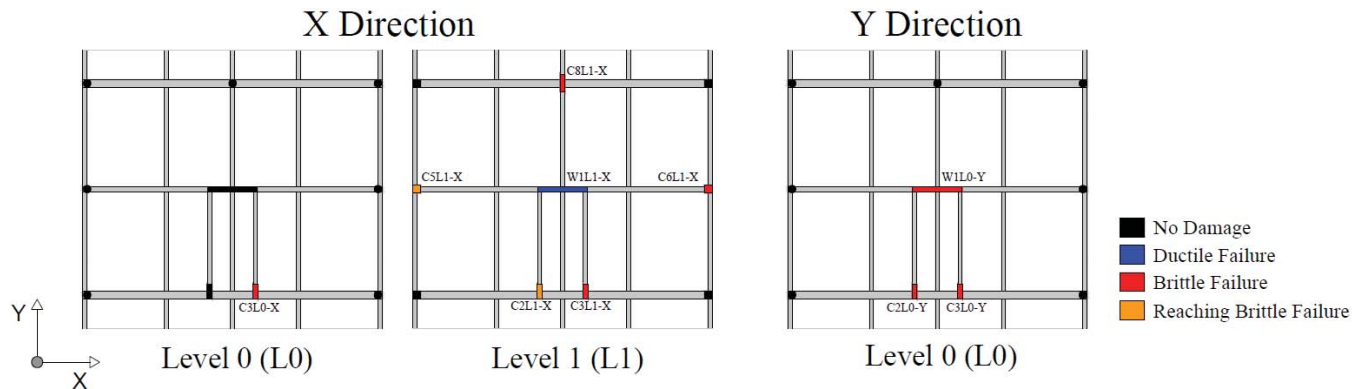


Figure 5: Location and indication of the type of damage on the vertical RC elements.

The columns C5 and C2, located in level 1, were also included in Figure 5 as “Reaching Brittle Failure” because the value of the demand/capacity ratio (DCR) associated shear failure assessment was remarkably close to the unit, which means these elements were near to develop a brittle mechanism.

4 RETROFITTED BUILDING

4.1 Design and modelling of the retrofitting solution

The initial seismic assessment performed on the case study building indicated the need for improvement of some elements flexural and shear capacities. As stated before, FRP-wrapping is widely recognised as an effective strategy for increasing the deformation and shear capacity of RC elements, without modifying the structure's stiffness [5], [23].

Following the advantages of this strengthening technique, a CFRP retrofitting strategy was developed and applied to the case study building to overcome its poor seismic performance.

The design of the CFRP solution was based on the attainment of the target displacement, for SD limit state, without failure of any vertical member. This means that chord rotation and shear capacities of the elements identified in Figure 5 need to be enhanced. **Erro! A origem da referência não foi encontrada.** shows the actual and required capacity values of chord rotation and shear of those elements.

The determination of the right amount of FRP to comply with the required values of capacity followed an iterative procedure: i) knowing the required capacity that each element needs to reach, an initial strengthening solution is adopted and the new chord rotation and shear capacity of each element is computed; ii) if the capacity values obtained are higher than the values indicated in **Erro! A origem da referência não foi encontrada.**, a solution was achieved and applied to the structural model; iii) a new assessment is carried out. Otherwise, a new tentative strengthening solution needs to be considered and the procedure repeated. The new strengthening solution can be achieved by increasing the thickness of the CFRP sheet, the number of layers or upgrading the chosen FRP material.

Direc- tion	Vertical element	Failure mecha- nism	Actual θ_{SD} [%]	Required θ_{SD} [%]	Actual V_{RD} [kN]	Required V_{RD} [Kn]
X	C ₃ L0_X	Brittle	-	-	33.41	38.1
	C ₃ L1_X	Brittle	-	-	33.0	35.8
	C ₆ L1_X	Brittle	-	-	28.31	30.05
	C ₈ L1_X	Brittle	-	-	88.5	90.2
	W ₁ L1_X	Ductile	1.26	1.33	-	-
Y	C ₂ L0_Y	Brittle	-	-	111.7	128.3
	C ₃ L0_Y	Brittle	-	-	111.7	128.6
	W ₁ L0_Y	Brittle	-	-	78.4	90.7

Table 5: Actual and required capacity values of chord rotation and shear for the damaged elements

From the iterative procedure depicted above, one layer of CFRP (with the properties described in **Erro! A origem da referência não foi encontrada.**) was found to be enough to provide the desired capacity to retrofit the identified structural elements. Since these elements are subjected to a constant shear demand, the CFRP sheets were modelled as uniformly applied through the height of the element [24]. However, due to architectural constraints, the U-shaped or side bonded striped FRPs are, in some cases, the only possible solution. To avoid the fibres premature rupture, the corners of the elements were assumed to be rounded, with a radius of 4 cm and, to improve the shear capacity of the elements, the CFRP sheets were considered to be applied with the fibres aligned along the direction in which enhancement of shear strength is pursued (i.e. horizontal) [25], [26].

Fiber thickness t_f [mm]	Tensile Strength $f_{u,f}$ [MPa]	Tensile Modulus E_f [MPa]	Elongation [%]	Ultimate strain $\varepsilon_{u,f}$
0.128	3450	230000	1.5	0.0015

Table 6: Properties of the CFRP [27]

Regarding the modelling of the retrofitted solution, the contribution of the CFRP was considered through the increase of the confinement of the retrofitted elements. The core and cover materials of these elements were replaced with an equivalent material with the properties calculated by means of Equations (1) and (3). The model of the building remains the same, except for the retrofitted elements.

4.2 Assessment of the retrofitted building

Finished the design and modelling of the retrofitting solution, a new assessment was performed to the structure to evaluate the effectiveness of the adopted solution. A pushover analysis was again carried out to evaluate the lateral capacity of the structure. Figure 6 shows a comparison between the pushover curves obtained before (pre-retrofit) and after (post-retrofit) applying the CFRP. As it can be seen, the application of the CFRP contributed to an increase of the lateral strength of the structure, in both the X and Y directions, without modifying its initial stiffness. However, the structure's capacity improvement is significantly higher in the X direction in comparison with the Y direction. This is due to fact the RC walls, which were strengthened at the first and second storey levels, are oriented in the X direction.

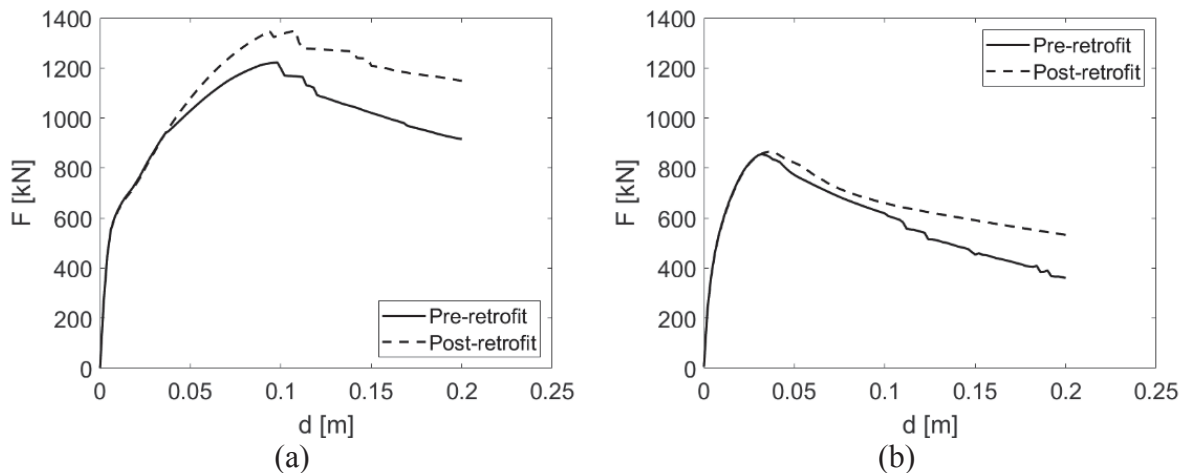


Figure 6: Pushover curves obtained pre and post retrofitting for the (a) X and (b) Y direction.

A safety assessment was also carried out in terms of demand/capacity ratio evaluation (DCR) for each vertical structural element, as established in EC8-3. Figure 7 shows the pushover curves obtained for the X and Y directions with the indication of the target displacement that corresponds to the attainment of the SD limit state. In the X direction, the development of a mechanism, either brittle or ductile, still occurs but only after the target displacement is reached. On the other hand, in the Y direction, the columns' brittle failure is not expected to develop,

and the ductile mechanism occurs for a top displacement much higher than the target displacement. These results confirm the efficiency of the CFRP and its effect in the improvement of the structure's seismic performance.

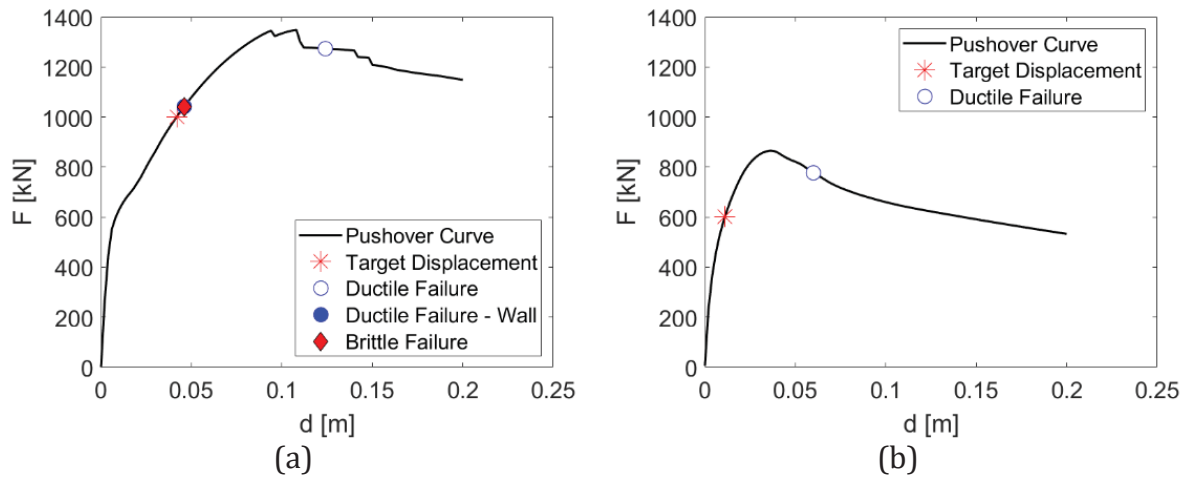


Figure 7: Pushover curves of the retrofitted structure for the (a) X and (b) Y direction with the indication of the target displacement and failure mechanisms.

5 CONCLUSIONS

This paper focused on the modelling of retrofitting solutions with carbon fibre-reinforced polymers (CFRP) to improve the seismic performance of RC structures. The first part of this research consisted of a proposal of a modelling approach to retrofit RC elements with CFRP. The CFRP was included in the model through the increase of the element's cross-section confinement.

The core and cover materials of retrofitted element were replaced with an equivalent material, whose properties were determined using the confinement model proposed in EC8-3. Afterwards, the modelling approach was validated against experimental data. The results showed a good agreement between the numerical and experimental data, indicating that the modelling approach is adequate to model FRP interventions in existing RC buildings.

The second part of this investigation focused on the application of the proposed modelling approach to an existing RC building. The selected structure corresponds to a residential building built before the introduction of modern codes without appropriate seismic resistance and characterized by (i) low confinement and tie reinforcement in vertical structural elements; (ii) insufficient longitudinal reinforcement in all structural elements; (iii) smooth longitudinal reinforcement rebars; (iv) variation in height of the vertical structural elements section and v) absence of masonry infills at the ground level. Non-linear static analyses were carried out and a seismic evaluation was performed in terms of the demand/capacity ratio (DCR), following the procedure recommended in EC8-3. This assessment exposed brittle and ductile failures in some structural elements. A retrofitting solution employing CFRP was designed and implemented numerically in the structure's model. The comparison between the pre- and post-retrofit pushover curves showed a clear improvement on the buildings' lateral strength, mainly on the X direction due to the retrofitting of the RC walls which control the behaviour of the structure in this direction. Additionally, the seismic safety of the structure, represented by the attainment of the target displacement at SD limit state without the occurrence of any failure mechanism,

highlights the effectiveness not only of the modelling approach but also of the adopted retrofitting solution.

ACKNOWLEDGMENTS

The authors would like to acknowledge the financial support of Fundação para a Ciência e a Tecnologia (FCT, Ministério da Educação e Ciência, Portugal) through the FCT Research Program: MitRisk - Framework for seismic risk reduction resorting to cost-effective retrofitting solutions, POCI-01-01456-Feder-031865.

REFERENCES

- [1] M. Del Zoppo, M. Di Ludovico, A. Balsamo, A. Prota, and G. Manfredi, "FRP for seismic strengthening of shear controlled RC columns: Experience from earthquakes and experimental analysis," *Compos. Part B Eng.*, vol. 129, pp. 47–57, 2017.
- [2] G. M. Verderame, F. De Luca, P. Ricci, and G. Manfredi, "Preliminary analysis of a soft-storey mechanism after the 2009 L'Aquila earthquake," *Earthq. Eng. Struct. Dyn.*, vol. 40, pp. 925–944, 2011.
- [3] F. De Luca, G. M. Verderame, F. Gómez-Martínez, and A. Pérez-García, "The structural role played by masonry infills on RC building performances after the 2011 Lorca, Spain, earthquake," *Bull. Earthq. Eng.*, vol. 12, no. 5, pp. 1999–2026, 2014.
- [4] J. G. Ruiz-Pinilla, J. M. Adam, R. Pérez-Cárcel, J. Yuste, and J. J. Moragues, "Learning from RC building structures damaged by the earthquake in Lorca, Spain, in 2011," *Eng. Fail. Anal.*, vol. 68, pp. 76–86, Oct. 2016.
- [5] A. S. Elnashai and R. Pinho, "Repair and retrofitting of rc walls using selective techniques," *J. Earthq. Eng.*, vol. 2, no. 4, pp. 525–568, 1998.
- [6] R. Ma, Y. Xiao, and K. N. Li, "Full-scale testing of a parking structure column retrofitted with carbon fiber reinforced composites," *Constr. Build. Mater.*, 2000.
- [7] L. P. Ye, K. Zhang, S. H. Zhao, and P. Feng, "Experimental study on seismic strengthening of RC columns with wrapped CFRP sheets," 2003.
- [8] K. Galal, A. Arafa, and A. Ghobarah, "Retrofit of RC square short columns," *Eng. Struct.*, 2005.
- [9] C. Yalcin, O. Kaya, and M. Sinangil, "Seismic retrofitting of R/C columns having plain rebars using CFRP sheets for improved strength and ductility," *Constr. Build. Mater.*, 2008.
- [10] M. ElGawady, M. Endeshaw, D. McLean, and R. Sack, "Retrofitting of Rectangular Columns with Deficient Lap Splices," *J. Compos. Constr.*, 2010.
- [11] D. A. Bournas and T. C. Triantafillou, "Bond Strength of Lap-Spliced Bars in Concrete Confined with Composite Jackets," *J. Compos. Constr.*, 2011.
- [12] R. Realfonzo and A. Napoli, "Results from cyclic tests on high aspect ratio RC columns strengthened with FRP systems," *Constr. Build. Mater.*, 2012.

- [13] H. F. Ghatte, M. Comert, C. Demir, and A. Ilki, "Evaluation of FRP confinement models for substandard rectangular RC columns based on full-scale reversed cyclic lateral loading tests in strong and weak directions," *Polymers (Basel)*., 2016.
- [14] F. McKenna, G. Fenves, and M. Scott, "OpenSees: open system for earthquake engineering simulation," *Pacific Earthquake Engineering Research Center, University of California, Berkeley*, 2007. .
- [15] CEN, "European Standard EN 1998-3:2005: Design of structures for earthquake resistance - Part 3: Assessment and retrofitting of buildings," *Com. Eur. Norm. Brussels*, 2005.
- [16] M. Del Zoppo, M. Di Ludovico, A. Balsamo, and A. Prota, "Comparative analysis of existing RC columns jacketed with CFRP or FRCC," *Polymers (Basel)*., 2018.
- [17] S. Popovics, "A numerical approach to the complete stress-strain curve of concrete," *Cem. Concr. Res.*, vol. 3, no. 5, pp. 583–599, 1973.
- [18] C. Caruso, R. Bento, R. Sousa, and A. A. Correia, "Modelling strain penetration effects in RC walls with smooth steel bars," *Mag. Concr. Res.*, vol. 71, no. 17, pp. 894–906, 2019.
- [19] D. Celarec, P. Ricci, and M. Dolšek, "The sensitivity of seismic response parameters to the uncertain modelling variables of masonry-infilled reinforced concrete frames," *Eng. Struct.*, vol. 35, pp. 165–177, 2012.
- [20] CEN, "EN 1998-1. Eurocode 8 - Design of structures for earthquake resistance - Part 1: General rules, seismic actions and rules for buildings," *Eur. Comm. Stand.*, 2004.
- [21] CEN, "European Standard NP EN 1998-3: Eurocódigo 8 – Projecto de estruturas para resistência ao sismo. Parte 3: Avaliação e Reabilitação de edifícios.," *Inst. Port. da Qualidade. Eur. Comm. Stand.*, 2017.
- [22] C. M. Ramirez and E. Miranda, "Building-specific loss estimation methods & tools for simplified performance-based. Report No. 171," , Blume Center Report. Edited by T. J. A. B. E. E. Center. Stanford, CA., 2009.
- [23] C. Caruso, "Definition of mitigation strategies for the seismic risk reduction of old RC residential buildings," Universidade de Lisboa, Instituto Superior Técnico, 2019.
- [24] C. Caruso, "Feasibility of Retrofitting Solutions for an Old Rc Wall-Frame Building in Lisbon," pp. 1–12, 2019.
- [25] M. N. Fardis, "Seismic Design, Assessment and Retrofitting of Concrete Buildings," *Geotech. Geol. Earthq. Eng.*, 2009.
- [26] B. Li and C. L. Lim, "Tests on Seismically Damaged Reinforced Concrete Structural Walls Repaired Using Fiber-Reinforced Polymers," *J. Compos. Constr.*, vol. 14, no. 5, pp. 597–608, 2010.
- [27] Sika, "SikaWrap ® Hex-230 C."

EXPERIMENTAL INVESTIGATION ON ANCHORAGE PERFORMANCE OF EMBEDDED SMOOTH REBARS SUBJECTED TO CYCLICNG LOADING

Anthony Paderno¹, Simone Pelucco¹, and Marco Preti¹

¹ University of Brescia, D.I.C.A.T.A.M.
via Branze 43, 25123, Brescia (BS), Italy
e-mail: a.paderno007@unibs.it
s.pelucco@unibs.it
marco.preti@unibs.it

Abstract

The most of the reinforced concrete frame structures of the European building stock have been built without attention to the seismic action or according to obsolete code. Before the 1970's, in all the Mediterranean area, plain rebars were employed for the longitudinal reinforcement of structural members. Due to their smooth surface, they are characterized by poor bond capacity; this results in a significant slip of the loaded bar from the surrounding concrete, which strongly increases the structural deformation capacity compared to modern ribbed rebars. Whereas the cyclic response of non-conforming reinforced concrete members and structural sub-assemblies is deeply investigated in literature, a scarce knowledge about anchored plain bar cyclic behaviour is noticed. In the recent years, detailed non-linear modelling of gravity load designed structures is widely used for the seismic vulnerability assessment; a deep investigation on full scale anchorage detailing is then fundamental for the correct modelling of such structures..

In the present paper an experimental investigation on different anchorage solution of plain rebar embedded in concrete is presented; straight, hook-ended and 45° bent rebar were analysed, monitoring their axial stress versus slip behaviour. A non-linear stress-slip behaviour was observed for all the anchorage solutions since the lower loading level. Stiffness degradation due to cyclic loading was observed; on the other hand, strength decay was visible only for straight anchorage length. Hook-end device and bar bent resulted effective in providing a good anchorage performance, on the other hand their response showed a progressive plasticization.

Keywords: Existing RC Buildings, Plain reinforcement, Bar Slip, Experimental Test, Cyclic behaviour, rebar anchorage.

1 INTRODUCTION

The Reinforced Concrete (RC) structures built from the World War II to the 1970's are significantly vulnerable against the seismic action [1]–[3]. Lack in the structural organization and in the seismic detailing, design according to obsolete codes, and interaction with structural or non-structural stiff elements are the main reasons of not adequate structural response. Moreover, smooth bars were used until the seventies as reinforcement in RC frame members.

The poor bond capacities of plain reinforcement influence the structural response since they are related to significant bar slip from the concrete embedment [4]–[8]. The main mechanisms governing the bond strength are: i) the chemical adhesion between the smooth rebar and the surrounding concrete and ii) the micro-interlocking due to concrete small particles wedging action [9]. These contributions bring to a peak bond strength value, after which the slip triggering causes a progressive degradation of the bond capacity [10]. Micro-interlocking and frictional resource reduce also under cyclic loading, like clearly shown by experimental tests on a short anchorage length [11]. Moreover, beyond the reinforcement yielding, a gradual reduction of the rebar transversal section (due to Poisson effect) causes a further loss of strength [9], [12]. Rebar straight length cannot be enough to guarantee an effective anchorage; end hooked and/or bent bar are so employed to improve the anchorage performance. In this case the bar slip depends also on the plastic deformation related its straightening, which is required for the slip development. Pull-out tests on straight smooth rebars of short anchorage length are available in the literature [11], [13], [14]; however, only one of them [11] investigates the effect of a cyclic loading. A 80cm hollow square cross section bar was also tested under pull-out force [14], showing that bond stress profile significantly varies along the bar length; more in detail, the peak bond strength is shifted inward under the increase of the axial stress.

In the present work an experimental campaign is described, aimed at clarifying some of the cited aspects. Straight long length anchorage, hook-end and bent rebars are considered. Their axial stress-slip behaviour was analysed, both before and beyond the bar yielding. In the following, the experimental campaign is described, with reference to the different specimen geometry and to the adopted loading protocol. The experimental results are then presented and discussed, paying attention to the different performances related to the investigated anchorage arrangement. The analysis of the stress-slip behaviour of smooth rebar is fundamental for the assessment of the deformation capacities of existing RC member in presence of seismic loading. Indeed, previous experimental tests on columns [11], [15]–[17], beams [18], and beam-column joints [4], [5], [8], [19] showed the great influence of plain reinforcement slip in the definition of the crack pattern and in ensuring a significant flexural deformation capacity. The same results can be also useful for the definition and the validation of analytical or numerical modelling which explicitly account for the bar slip phenomenon.

2 DESCRIPTION OF THE SPECIMENS

The reference specimens are schematized in Figure 1. For testing convenience, they are organized so as one or two anchored rebars are embedded in a concrete block; when two bars are placed in the same block, they were tested separately and they were casted at sufficient distance to avoid interference between the two tests. The same choice also allows to investigate different bond conditions effects; indeed, it is possible to qualitatively consider the lower and the upper bar as being in good and bad bond condition, respectively. No transversal reinforcement is provided since possible brittle failures were not expected, due to the adopted geometry.

A straight rebar, with no end specific detailing, characterizes the so-called SL specimens. They are designed to allow the investigation of the bond performance over a significant rebar length, on which it is expected a non-constant bond stress distribution. A total number of four

specimens were casted; two of them are instrumented with three couples of strain-gauge, with the aim of measuring the axial stress on the embedded length. A reduced adherent length is thus guaranteed in this case, due to the introduction of a local cage to protect the strain gauges around the bar at the gauge location. The specific anchorage type is representative of the bar embedment into column or beam lengths. The hook-end specimens (H type) are representative of the T-column-beam joint reinforcement anchorage and of columns rebar anchorage at any cold joint. Four out of six hook-ended bar specimens are characterized by adherent straight length (prior to the hook device); in the other two, bond in the same length is prevented a plastic pipe surrounding the bar. Finally, 45° bent rebars (B type) were tested; they were frequently used in construction practice for the beam reinforcement over the supports. To monitor the axial stress along the rebar length, two bent bars (casted in the same concrete block) are instrumented with two couple of strain gauges, respectively placed at mid-way of the inclined length and in the last straight length; a steel plate is welded on the bar end, to allow the stress reading by the end gauges couple.

2.1 Geometry

12mm diameter reinforcing bars are considered; a minimum concrete cover of 100mm and a bar distance of 250mm or 450mm are guaranteed (respectively for the H and B types). SL samples are made by a concrete block with 200mm square cross section and a length of 1000mm, in which a single bar is embedded; two out of four specimens (called SL3 and SL4 in the following) are characterized by a lower 760mm embedded length, due to strain gauges application along the rebar length (Figure 3). The H sample bar geometry is referred to the Italian Code indications [20]. A 40 diameter (480mm) straight length precedes the hook device, which is characterized by an inner bending of 5 diameters (60mm) amplitude and a 3 diameters (36mm) final straight length. The four bars with embedded straight length are called H1 and H2, the other two H3. The B specimens are characterized by a 120mm long embedded straight lengths at the bar ends; their axes distance 450mm in the vertical direction, the 45° inclined length is thus 537mm long. The inner radius of the bending is equal to 10 diameters (120mm). The two instrumented rebars are called B2.

2.2 Load frame

The self-balanced steel frame schematized in Figure 2 is used to impose the bar slip. A 3.5mm thread loading screw of 32mm diameter allows a continuous refined control of the displacement imposition. Both tensile and compressive load can be applied to the rebar, thanks to the reaction guaranteed by two steel pates; one is in contact with the concrete block head, the other one on the opposite concrete block end. These reaction plates are connected by four threaded bars, lightly prestressed to avoid relative movements.

The smooth rebar sample is anchored to the frame by means of a mechanical joint made of an hollow cylinder in which three high hardness steel screws punch the rebar surface. The rebar head-joint is fixed to a load cell; the latter is then connected by a torsion-free joint to the loading screw. The frame weight and loading torque are transmitted by the steel plates on external supports.

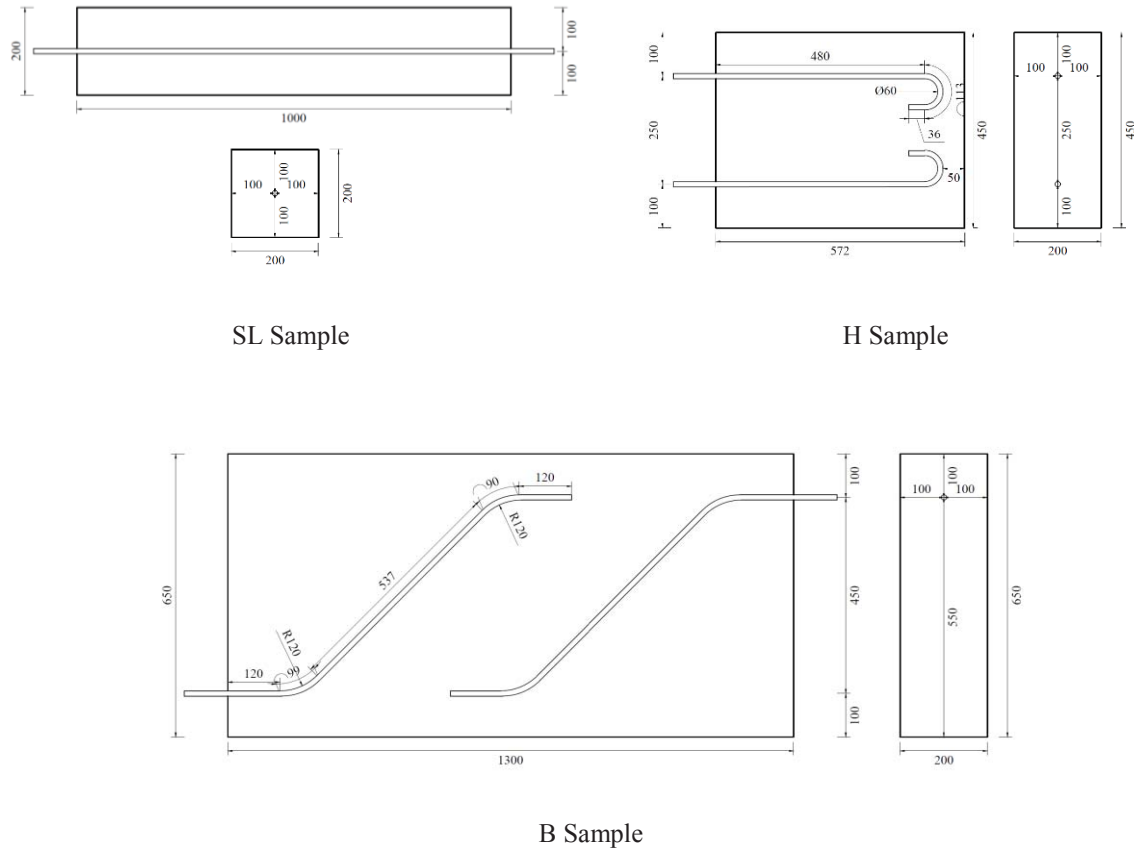
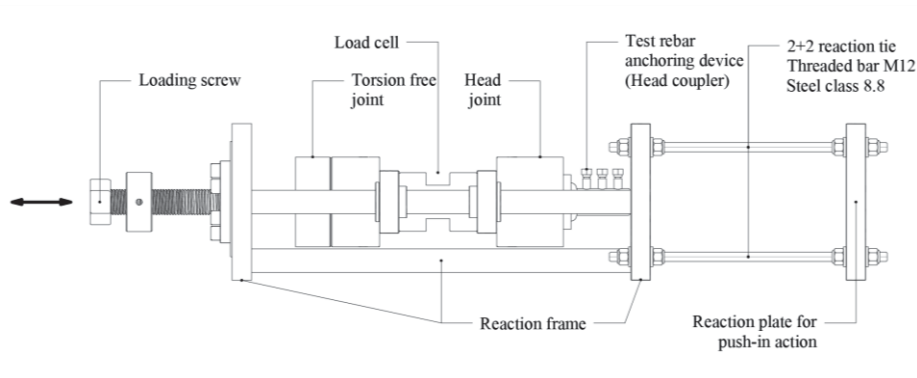


Figure 1 Geometry of the tested specimens.



2.3 Materials

Hot rolled reinforcing steel of grade S275 JR is considered [21]. Yielding, f_y , and failure, f_u , stress were investigated by a tensile test according to [22]; they were significantly different for the straight length (SL samples) bars and for the shaped (H and B samples) ones. Also the total elongation on a 10-diameter reference length across the failure section ΔL is defined.

The reference concrete mix design was the same for all the samples. Since they were casted in different times, the average compressive strength, f_c , and the elastic modulus, E_c , are defined

for each specimen type. The results are reported in Table 1 in terms of mean values; they are representative of the properties of the material employed in the reference RC frame construction.

Sample type	Steel			Concrete	
	f_y [MPa]	f_u [MPa]	ΔL	f_c [MPa]	E_c [MPa]
SL	442	535	13.70	24.71	25490
H	361	519	20.16	19.53	22810
B	363	520	18.98	22.52	25175

Table 1 Mean values of the mechanical properties of the employed materials.

3 INSTRUMENTATION AND LOADING PROTOCOL

3.1 Instrumentation

Load and displacement transducers are used to measure the bar axial stress-slip behaviour. Three different LVDTs are concentrically placed around the rebar head; they measure the displacement between the load frame head joint and the concrete block. A supplemental LVDT monitored the slip of the bar tail in SL specimens. The load cell is placed in the load frame, as it is schematized in Figure 2.

Strain-gauges are used to measure the axial strain along the rebar embedded length. An 80mm length is deactivated around the extensometer, to protect the gauges and avoid bond interference; the simplified representation of the arrangement is shown in Figure 3. On straight bars (SL3 and SL4) they are placed with a spacing of 250mm, therefore three different cross section are monitored. On bent rebars they are placed at midway of the inclined length and in the straight tail end. In this case, a mechanical anchorage is guaranteed after the last gauges, to allow a stress reading; indeed, no embedded length is present beyond the gauge deactivated length.

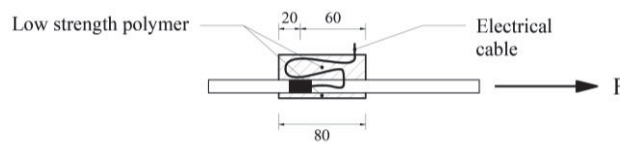


Figure 3 Detailing of the strain gauge isolation from the surrounding concrete.

3.2 Loading protocol

The straight rebars are tested in slip control during all the test. On the other hand, the shaped bars are load-controlled below the yielding point and slip-controlled beyond it. A summary of the reference loading protocol is visible in Figure 4.

The unloading phase was always characterized by the recovering of all the imposed slip; thus, also compressive loads were imposed to the rebar. For the H specimens in which the straight length was not adherent to the concrete, the unloading is stopped at the null force point since the application of compression to the rebar triggered its buckling.

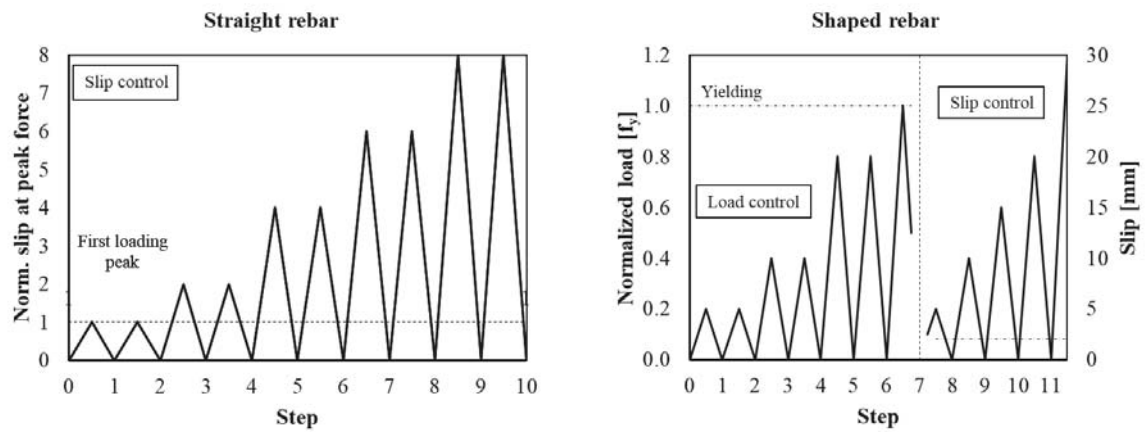


Figure 4 Loading protocol schematization for straight and shaped rebars.

4 EXPERIMENTAL RESULTS

4.1 Straight bar

The experimental results of the four tested rebars are divided according to the total embedded length (Figure 5). SL1 and SL2 samples are adherent to concrete along all the specimen length (1000mm); on the other hand, SL3 and SL4 samples are embedded for 760mm, due to strain gauge application along their length. The former showed the capacity in anchoring the bar yielding, whereas the latter showed a strength decay at a force lower than yielding. Nevertheless, the strength degradation is observed after the triggering of the bar tail slip in both the case. After the reach of the peak force, the cyclic behaviour is controlled by a lower strength. A reloading force can be observed exploring new slip of larger amplitude; cycling at a target deformation level, a residual lower strength is instead noticed. Subsequent cycles and slip amplitude within the range previously explored seemed not to influence the reference strength capacities.

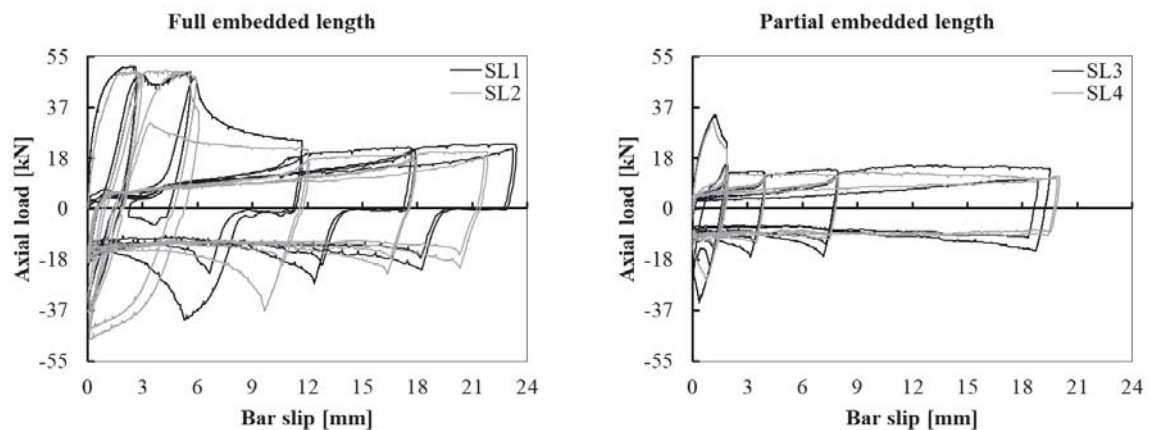


Figure 5 Stress-slip behaviour of the SL-type specimens: full and partial embedded length samples response.

4.2 Hook-end bar

In the following the bottom bars of the H specimens are qualitatively identified as being in good bond condition, whereas the top ones are considered in bad bond conditions. In Figure 6 the response of two different concrete specimens (H1 and H2) is represented up to the reach of

the bar yielding. A non-linear elastic loading branch was followed by a plastic plateau. The cyclic behaviour was characterized by a linear force-slip relationship, stiffer for the unloading and secant during the reloading (oriented to the maximum explored slip point at the previous cycle). Significant difference in the elastic stiffness is noticed with respect to the identified bond conditions. The unloading stiffness is not influenced in subsequent cycles and by the explored drift level; it is higher than the secant value at the yielding point. Good anchoring performance was observed also in presence of compressive loads; moreover, a less stiff behaviour is noticed at the load reversal.

In presence of unbonded straight length (H3 specimens), the behaviour was similar (Figure 7); however, a less stiff loading can be observed. In this case the bond conditions seemed not to affect the force-slip relationship. It is possible to conclude that the hook device alone can provide the bar anchorage; it is effective also in ensuring the bar overstrength (hardening behaviour). This is clearly visible in Figure 7, where the complete response of the upper bar of the concrete block H3 is represented up to a slip magnitude of 45mm.

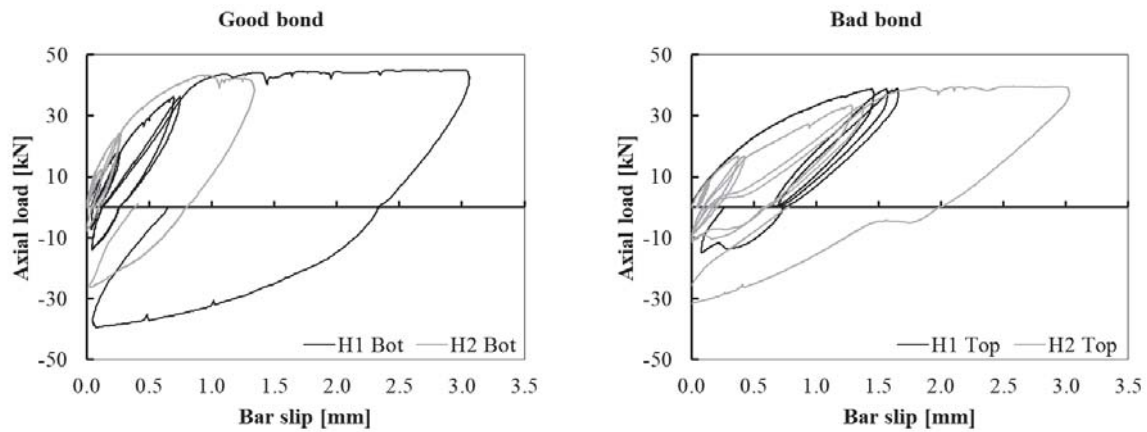


Figure 6 Experimental response of H1 and H2 samples: lower (good bond) and upper (bad bond) tested rebar responses.

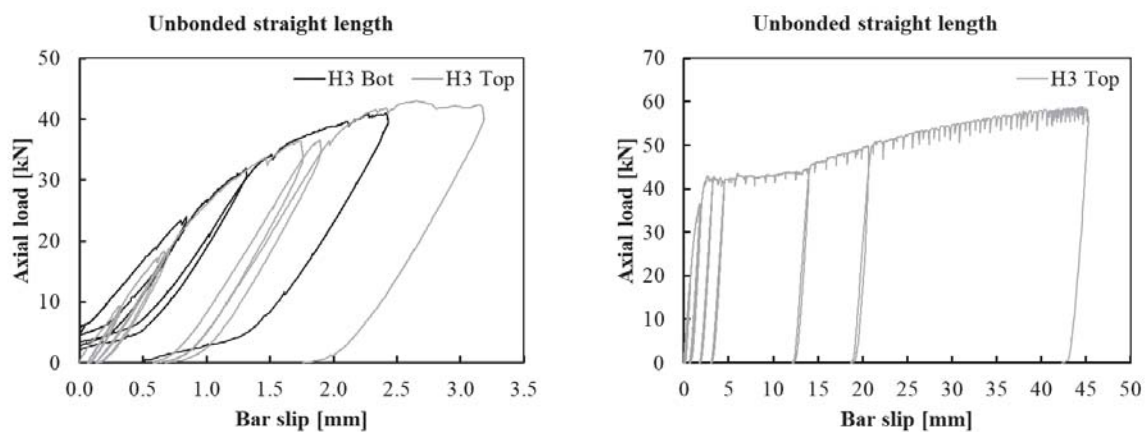


Figure 7 Cyclic response of H3 sample rebars: focus on the elastic cycles and complete response of the upper bar.

4.3 Bent rebar

Since the B type rebars cross the concrete block from top to bottom, and vice versa, in the following good or bad bond conditions refer to the bar head position (end on which the load was applied). The response of the bent rebars (Figure 8) was very close to the one of the hook-ended bars, especially in good bond conditions. The cycles in the range of the elastic stress were enveloped by a non-linear stress-slip relationship, after which a plastic plateau took place. The bending of the rebar ensures the anchorage of the bar up to yielding stress, and more, including overstrength (the graphs of Figure 8 are cut at the cycles of yielding). Only the instrumented bar (B2 sample) showed difference stress-slip response before yielding (bad bond condition); indeed it was more deformable.

The bars in bad bond conditions showed an increasing stiffness gradient (concave stress-slip curve) before yielding. This behaviour was associated with an initial sliding of the rebar, which was confirmed by a strain reading in both the strain gauge placed on the instrumented rebar in bad bond condition.

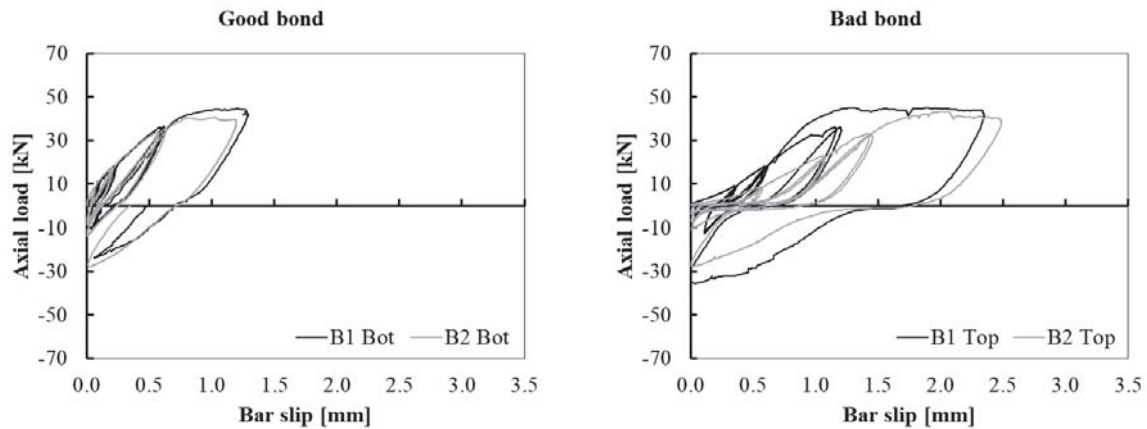


Figure 8 Stress-slip behaviour of bent rebars under cyclic loading up to the yielding point.

5 RESULTS COMPARISON

5.1 Straight length anchorage

To evaluate the anchorage performance of a straight bar, an average constant bond stress distribution along the rebar embedded length is considered, as suggested in literature. With reference to experimental measure of i) peak, ii) reloading, and iii) residual forces, the calculated bond capacities are reported in Table 2.

To help the comparison of the experimental evidences with literature available models, a normalization of the bond strength τ_b over the concrete compressive strength is taken:

$$\tau_b = C\sqrt{f_c} \quad (1)$$

with C non dimensional coefficient and f_c mean cylindrical concrete compressive strength. The values reported in Table 2 are lower with respect to the literature available model in term of peak force [11]–[13], [15]. On the other hand, the reloading and residual capacities well match with the available indications [11], [15].

Sample	Peak strength		Reloading strength		Residual strength	
	Force [kN]	Bond [MPa]	Force [kN]	Bond [MPa]	Force [kN]	Bond [MPa]
SL1	51	1.36	22	0.58	12	0.32
SL2	50	1.33	19	0.50	12	0.32
SL3	34	1.18	15	0.52	6	0.28
SL4	31	1.09	12	0.42	8	0.21
Mean	Bond [kN]	1.24	Bond [kN]	0.51	Bond [kN]	0.28
	C	0.25	C	0.10	C	0.06

Table 2 Estimation of the anchorage capacity along a straight rebar in hypothesis of constant bond stress.

5.2 Shaped anchorage

The difference in stiffness between the response of bars anchored in good or bad bond conditions is clearly visible by the observation of the graphs in Figure 9. The cyclic response below the yielding point is plot for all the shaped anchored rebars tested; it makes exception the H3 block bars, whose response was not affected by bond conditions. The stiffer behaviour showed the reach of the bar yielding at a slip level lower than 0.75mm; on the other hand, the less stiff response showed the yielding reach at a slip magnitude of about 1.50mm. Therefore, two different values of the secant stiffness at yielding can be attributed to the bars in good bond conditions. Moreover, the response in good bond conditions is very similar both for hooked or bent shape. On the other hand, in bad bond conditions the stress-slip relationships of the different anchorage solutions is strong; nevertheless, the secant stiffness at yielding is similar.

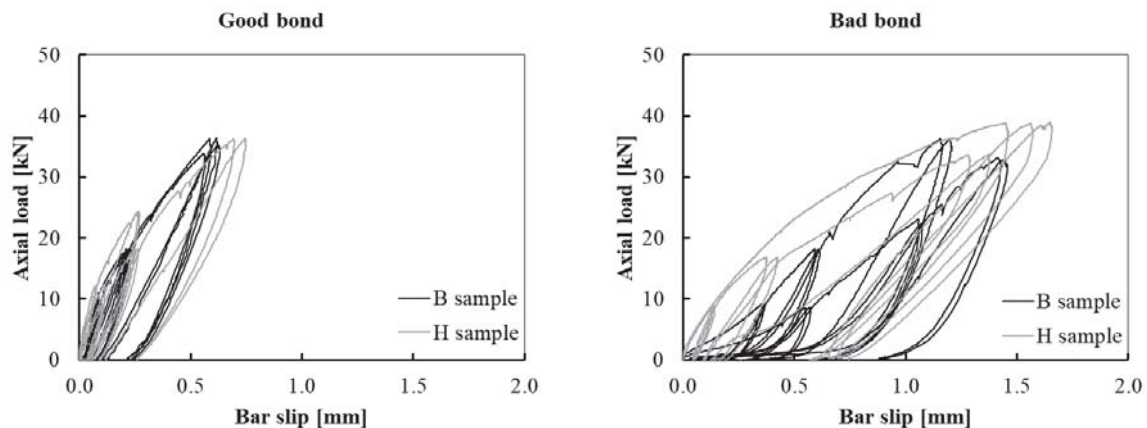


Figure 9 Focus on the elastic response of hooked (grey lines) and bent (black lines) rebars.

6 CONCLUSIONS

The experimental cyclic response of different anchorage solutions for smooth rebar is herein investigated. Long straight anchorage length, hook-end device, and bar bent were tested in presence of both tensile and compressive loads. The response, in term of force versus slip relationship, was monitored and it is herein discussed.

The straight length anchorage gave equilibrium to different applied force values, depending on its overall embedded length; in presence of the lower anchorage length (760mm) a peak strength about the 60% of the bar yielding stress was reached. In all the cases, at the triggering of the last embedded section slip, a force degradation was observed. Exploring higher slip level, a reloading bond strength can be defined, while cycling in the same slip range (of previously explored cycles) a lower residual strength was observed. Hook-end device and bar bent were

effective in ensuring the bar yielding and overstrength force. No force degradation was observed, and the response was stable, also at the highest slip imposition. The position of the shaped rebar with respect to the concrete block sample significantly influenced the stiffness of the response; the lower (good bond condition) bars reached the yielding point at slip level lower than 0.75mm, the top ones (bad bond condition) at a value of deformation twice. The unloading of the shaped anchorages showed a residual plastic deformation, also cycling at stress values lower than the yielding one. Since a straightening is required for the bar pullout under tensile force, plastic deformations are expected in the hook (or bending) length; moreover, the same straightening causes high local stress in the surrounding concrete. The different concrete porosity can affect the anchorage slip development, justifying the difference herein presented between the anchorage response in good or bad bond conditions. This aspect will be considered in future studies.

ACKNOWLEDGEMENT

The experimental campaign presented in this work has been supported within the framework of DPC/ReLUI project 2019-2021, WP5.

REFERENCES

- [1] L. D. Decanini, A. De Sortis, A. Goretti, L. Liberatore, F. Mollaioli, and P. Bazzurro, 'Performance of Reinforced Concrete Buildings during the 2002 Molise, Italy, Earthquake', *Earthquake Spectra*, vol. 20, no. 1_suppl, pp. 221–255, 2004a, doi: 10.1193/1.1765107.
- [2] C. Del Gaudio *et al.*, 'Empirical Fragility Curves From Damage Data on RC Buildings After the 2009 L'Aquila Earthquake', *Bull Earthquake Eng*, vol. 15, no. 4, pp. 1425–1450, Apr. 2017, doi: 10.1007/s10518-016-0026-1.
- [3] G. M. Verderame, I. Iervolino, and P. Ricci, 'Report on the Damages on Buildings Following the Seismic Event of 6th of April 2009 Time 1.32 (UTC) – L'Aquila M=5.8', p. 17, 2009c.
- [4] C. Beschi, P. Riva, G. Metelli, and A. Meda, 'HPFRC Jacketing of Non Seismically Detailed RC Corner Joints', *Journal of Earthquake Engineering*, vol. 19, no. 1, pp. 25–47, Jan. 2015, doi: 10.1080/13632469.2014.948646.
- [5] F. Braga, R. Gigliotti, and M. Laterza, 'R/C Existing Structures with Smooth Reinforcing Bars: Experimental Behaviour of Beam-Column Joints Subject to Cyclic Lateral Loads', *TOBCTJ*, vol. 3, no. 1, pp. 52–67, May 2009, doi: 10.2174/1874836800903010052.
- [6] G. M. Calvi, G. Magenes, and S. Pampanin, 'Experimental Test on a Three Storey RC Frame Designed for Gravity Only', *Proceedings of 12th European Conference on Earthquake Engineering*, p. 8, 2002.
- [7] S. Pampanin, G. M. Calvi, and M. Moratti, 'Seismic Behaviour of RC Beam-Column Joints Designed for Gravity Loads', p. 11, 2002.
- [8] G. Russo and M. Pauletta, 'Seismic Behavior of Exterior Beam-Column Connections with Plain Bars and Effects of Upgrade', *SJ*, vol. 109, no. 2, 2012, doi: 10.14359/51683633.

- [9] L. Feldman and M. Bartlett, 'Bond Strength Variability in Pullout Specimens with Plain Reinforcement', *ACI Structural Journal*, no. 102, 2005.
- [10] M. F. Stocker and M. A. Sozen, 'Investigation of Prestressed Reinforced Concrete for Highway Bridges - Part VI: Bond of Prestressing Strand'. 1969.
- [11] G. M. Verderame, P. Ricci, G. D. Carlo, and G. Manfredi, 'Cyclic Bond Behaviour of Plain Bars. Part I: Experimental Investigation', *Construction and Building Materials*, vol. 23, no. 12, pp. 3499–3511, Dec. 2009, doi: 10.1016/j.conbuildmat.2009.07.002.
- [12] Model Code, 'Model Code for Concrete Structures 2010 fib – International Federation for Structural Concrete'. Ernst & Sohn, Berlin, Germany, 2010.
- [13] G. Fabbrocino, G. M. Verderame, and G. Manfredi, 'Experimental behaviour of anchored smooth rebars in old type reinforced concrete buildings', *Engineering Structures*, vol. 27, no. 10, pp. 1575–1585, Aug. 2005, doi: 10.1016/j.engstruct.2005.05.002.
- [14] L. Feldman and M. Bartlett, 'Bond Stresses Along Plain Steel Reinforcing Bars in Pullout Specimens', *ACI Structural Journal*, vol. 104, no. 6, pp. 685–692, 2007.
- [15] G. M. Verderame, G. De Carlo, P. Ricci, and G. Fabbrocino, 'Cyclic Bond Behaviour of Plain Bars. Part II: Analytical Investigation', *Construction and Building Materials*, vol. 23, no. 12, pp. 3512–3522, Dec. 2009, doi: 10.1016/j.conbuildmat.2009.07.001.
- [16] M. Di Ludovico, G. M. Verderame, A. Prota, G. Manfredi, and E. Cosenza, 'Experimental Behavior of Nonconforming RC Columns with Plain Bars under Constant Axial Load and Biaxial Bending', *J. Struct. Eng.*, vol. 139, no. 6, pp. 897–914, Jun. 2013, doi: 10.1061/(ASCE)ST.1943-541X.0000703.
- [17] J. Melo, H. Varum, and T. Rossetto, 'Experimental Cyclic Behaviour of RC Columns with Plain Bars and Proposal for Eurocode 8 Formula Improvement', *Engineering Structures*, vol. 88, pp. 22–36, Apr. 2015, doi: 10.1016/j.engstruct.2015.01.033.
- [18] M. S. Marefat, S. M. Hassanzadeh Shirazi, R. Rostamshirazi, and M. Khanmohammadi, 'Cyclic Response of Concrete Beams Reinforced by Plain Bars', *Journal of Earthquake Engineering*, vol. 13, no. 4, pp. 463–481, May 2009, doi: 10.1080/13632460902837769.
- [19] S. Pampanin, G. M. Calvi, and M. Moratti, 'Seismic Behaviour of RC Beam-Column Joints Designed for Gravity Loads', p. 10, 2002.
- [20] RD 2229, 'Regio Decreto n.2229 del 19 Novembre 1939 (in italian)'. 1939.
- [21] EN 10025, 'Hot Rolled products of structural steels'. 2019.
- [22] UNI EN 10080, 'UNI EN 10080 Steel for the Reinforcement of Concrete - Weldable Reinforcing Steel'. 2005.

OUT-OF-PLANE TESTING OF MASONRY INFILL WALLS MADE WITH LIGHTWEIGHT CONCRETE BLOCKS

M. Agante^(1A), A. Furtado^(1B), H. Rodrigues⁽²⁾, A. Arêde^(1C), P. Fernandes⁽³⁾, H. Varum^(1D)

¹ CONSTRUCT-LESE, Faculdade de Engenharia da Universidade do Porto
Porto, Portugal
e-mail: A – up201700035@edu.fe.up.pt, B - afurtado@fe.up.pt, C - aarede@fe.up.pt and D -
hvarum@fe.up.pt

² RISCO, Universidade de Aveiro
Aveiro, Portugal
hrodrigues@ua.pt

³ Instituto Politécnico de Leiria
Leiria, Portugal
paulo.fernandes@ipleiria.pt

Abstract

The masonry infill walls are widely spread over the reinforced concrete buildings due to different demands. The buildings' thermal energy efficiency is a top priority nowadays since many of the existing building stock comprises buildings with low energy performance. The buildings' external envelope is suffering a transformation with the appearance of the vertical hollow concrete blocks with high thermal and acoustic demands. However, recent evidence from a strong earthquake shows that the masonry infill walls are vulnerable to out-of-plane loadings and were responsible for many casualties, injuries, and economic losses. Based on that, this work's main objective is to study the out-of-plane (OOP) behaviour of masonry infills made with vertical hollow concrete blocks. The experimental campaign comprises the OOP testing of three full-scale infill walls made up of these masonry units. One of them was as-built without previous damage, one with previous damage due to an earlier in-plane test and the third one retrofitted. All the tests consisted of applying the loading-unloading-reloading history of imposed displacements in the OOP direction through a uniformly distributed load. The results will be presented in terms of OOP force-displacement responses, deformed shapes, damage evolution, energy dissipation capacity and damping. Finally, the test results are compared to each other to assess the previous damage and the retrofit technique's effectiveness.

Keywords: Masonry infill walls, Out-of-plane behaviour, lightweight concrete blocks, Experimental testing.

1 INTRODUCTION

Masonry infill walls are widely spread over the reinforced concrete (RC) building structures. Different masonry units were developed over the years to be used to construct the RC buildings envelopes. Their geometric, thermal and acoustic characteristics followed the building code demands, neglecting the vulnerability's assessment under out-of-plane (OOP) seismic loadings. At the beginning of 1950, hollow clay horizontal bricks with different thicknesses (70mm, 110mm, 150mm and 220mm) and at the 2000 decade, clay and concrete vertical thermal blocks were developed. Their acoustic and thermal characteristics were improved to be used in the buildings façade. However, experimental studies on the seismic behaviour of lightweight concrete blocks are very scarce.

Different investigations were carried out concerning the OOP behaviour of masonry infill walls [1, 2], from which it was concluded that the OOP strength reduces with the increasing of the panel slenderness [3, 4]. Ricci, et al. [4] performed a series of OOP tests assessing the effect of the walls slenderness in their OOP behaviour. Before the OOP tests, the walls were subjected to different IP damage levels (Low – 0.30%; Medium – 0.60% and High – 1%). Hollow clay horizontal units were used to construct the scaled walls with slenderness equal to 22.9 and 15.2. It was observed during the tests a more significant decrease of the OOP maximum strength and initial stiffness for the thinner panels.

De Risi, et al. [5] carried out a testing campaign to study the effect of the panel aspect ratio (1.28 and 1) in their OOP response. The authors found that square and rectangular infills have very different damage states. For examples, the rectangular walls showed more damage than square ones. For panels previously subjected to low IP drift (0.30%), the square panel exhibited a strength reduction of 24%, while the rectangular panel reduced by about 52%.

Based on this motivation, this research work's primary goal was to study the OOP behaviour of full-scale masonry infill walls made with lightweight concrete blocks. An experimental campaign was carried out comprising three full-scale specimens. The first specimen was tested without previous damage and without strengthening. The second specimen was tested with prior damage caused by a previous IP test with a maximum drift of 0.3% without strengthening. The third wall was tested without previous damage, but it was strengthened with a TRM based solution. All the tests have been performed by imposing a half-cyclic (loading-unloading-reloading) history of displacements in the OOP direction employing a uniform distributed load provided by small pneumatic jacks. The results will be presented in terms of damage evolution and OOP force-displacement responses.

2 DESCRIPTION OF THE TESTING CAMPAIGN

2.1 Specimens characteristics

A full-scale RC frame was built in a laboratory 4.80m long and 3.30m high and was designed according to Eurocode 8 – Part 1 [6] for medium ductility class. The columns dimensions are 0.30x0.30m² with longitudinal reinforcement 4ø16+2ø12 and transversal reinforcement equal ø8//0.05m along the plastic hinge regions and ø8//0.15m in the remaining extension of the column. Regarding the beam cross-section detailing, it was defined to be 0.30x0.50m² with symmetrical longitudinal reinforcement of 5ø16+5ø16 and transversal reinforcement of ø8//0.10m along the plastic hinge length and ø8//0.20m in the remaining beam extension. The dimensions and detailing of the frame are presented in Figure 1.

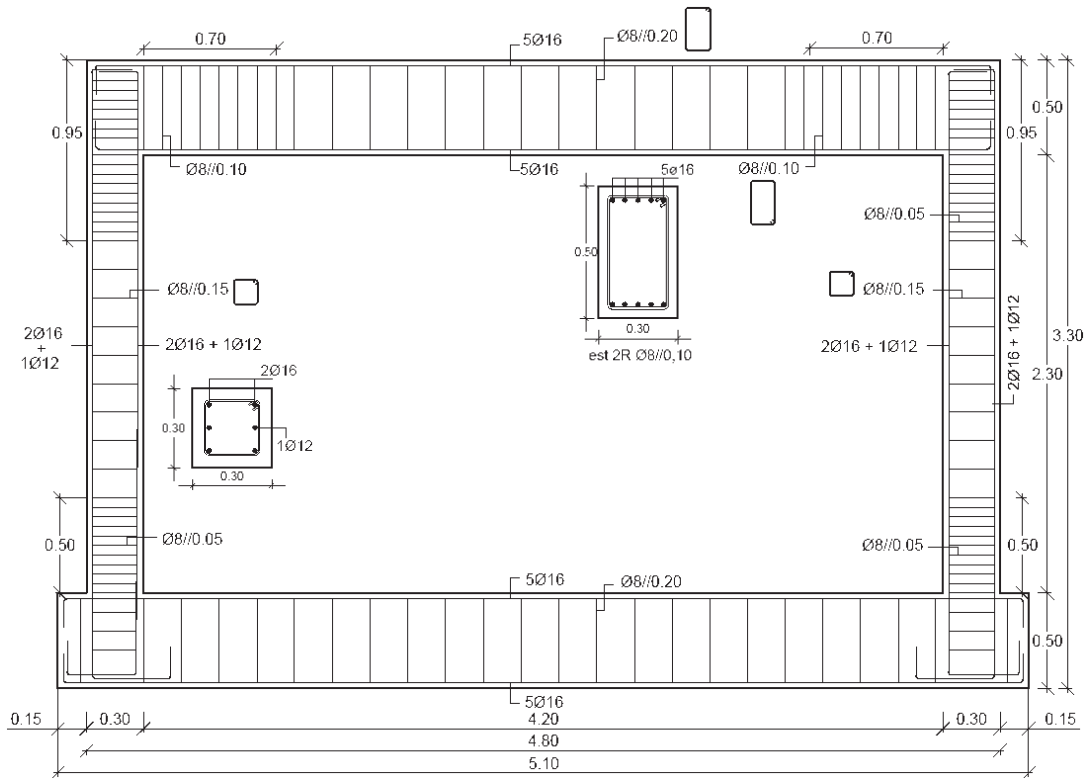


Figure 1 – RC frame dimensions and detailing.

The masonry infill walls were constructed with vertical hollow concrete blocks. These light lightweight concrete blocks (Figure 2) of expanded clay aggregates have the nominal dimensions of $400 \times 190 \times 315 \text{ mm}^3$. The thermal transmission coefficient (U) is $0.51 \text{ W/m}^2\text{°C}$ and were specially designed for simple exterior walls or in contact with unheated areas. It can also be used in partitions between fires, stairwells and elevators. Vertical compressive strength tests were carried out in masonry units according to the standard EN 772-1 [7].

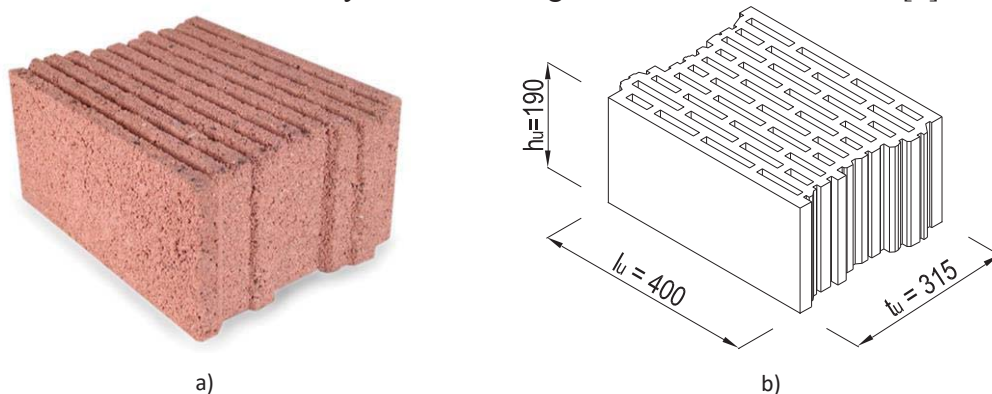


Figure 2 – Detail of the masonry unit: a) general overview; and b) geometric details (units in millimetres).

All the panels have the same geometrical dimensions, boundary conditions and materials. The construction of each wall started with the placement of a continuous layer of mortar over the entire width of the previously humidified frame. The blocks were then placed and positioned. The masonry infill walls were aligned with the external surface of the RC frame. Due to that, a short portion of the masonry infill walls remained 15 mm from the frame's back face (the thickness of the block is 315mm, and the beam width is 300mm). Discontinuous bed joints

approximately 15 mm thick were placed using a mortar box provided by the supplier. This procedure was repeated until it was impossible to fit another row of blocks, leaving about 130 mm between the panel and the lower face of the RC frame's upper beam to be filled. It was decided to close the masonry panel two or three days after its construction to guarantee stabilization in the deformation of the wall during the mortar curing, ensuring the sealing between the upper face of the masonry and the upper beam of the frame. An M5 class mortar was used to build the masonry infill walls. Vertical bed joints with 10mm thickness were assumed between the concrete masonry units.

As mentioned before, the specimens LWC_Ref and LWC_IPOOP were built with the same characteristics. The third wall LWC_S was strengthened with TRM. The reinforcing mesh was applied only on one side of the wall. The strengthening consisted of using a glass fibre textile mesh with a matrix of 4x4cm and a tensile strength equal to 70kN/m². The construction process started with the first layer of plaster (0.5cm thick) over the whole panel and 12cm in length and the RC elements. For this plaster, it was used an M10 mortar. After that, the textile mesh was placed and fixed to the panel using plastic connectors. These connectors were set all over the wall with a geometry defined in Figure 6. Also, the mesh was anchored to the RC elements using thin steel plates and steel connectors M8. According to the supplier recommendations, a textile mesh overlapping with a total length of 100mm was used. The interface wall-RC frame was used to layers of stripes with a full extension in the columns and beams of 170mm and the panel of 400mm, in agreement with the standard ACI 549 4R recommendations. After applying the textile mesh, a second layer of mortar (1cm) was applied. The schematic layout of the LWC_S strengthening is presented in Figure 3

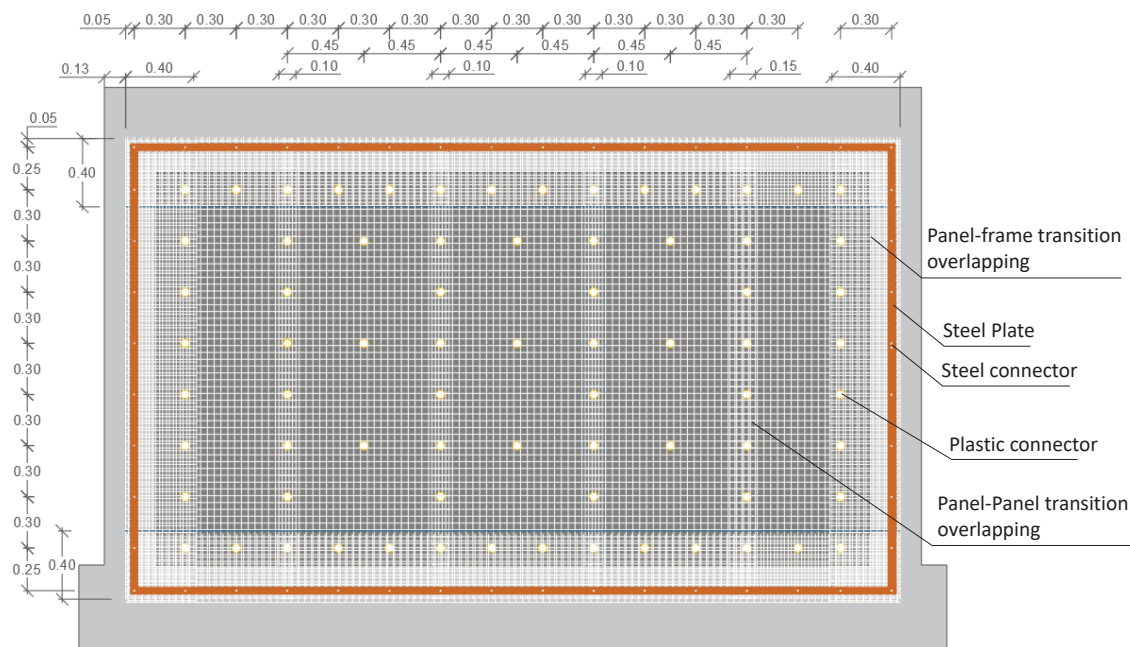


Figure 3 – Schematic layout of the strengthening solution of the wall LWC_S.

2.2 Description of the in-plane and out-of-plane test setup

The quasi-static IP cyclic test consisted of applying a horizontal force at half the height of the RC frame's upper beam through a hydraulic actuator with a capacity of approximately 500 kN and +/-150 mm travel. The hydraulic actuator is connected to a steel reaction structure. The

horizontal force transmission to ensure full-cycle tests were performed using two steel profiles positioned on the top beam's extremities linked together through four dywidag pre-stressed bars ($\phi 27$ mm), resulting in a beam compression of about 170 kN. The quasi-static cyclic test schematic layout is shown in Figure 4. A steel structure was used at the back of the RC frame, linked in two points of the frame top beam. The primary goal was to avoid OOP displacement or rotation of the structure during the test. The frame's base IP and OOP displacement were restricted using a steel profile attached to the strong slab.

The IP drift ratio was computed using the displacement of the top beam-column joint divided by the distance between the bottom and top beam-column joints. The IP displacement of the bottom beam-column joint is subtracted from the displacement of the top beam-column joint to avoid possible frame sliding effect.

The quasi-static IP cyclic loading consisted of applying a horizontal load at half-height of the RC frame upper beam, in the form of target displacements until a drift of 0.3%. Each cycle started with an increase in loading until reaching the target displacement and after unloading the inverse target, displacement was applied, ending after unloading. Three target displacements 2.8, 5.6 and 8.4 mm were imposed, corresponding to 0.1%, 0.2% and 0.3% drift, respectively, with three repetition cycles for each target displacement, totalling nine complete cycles.

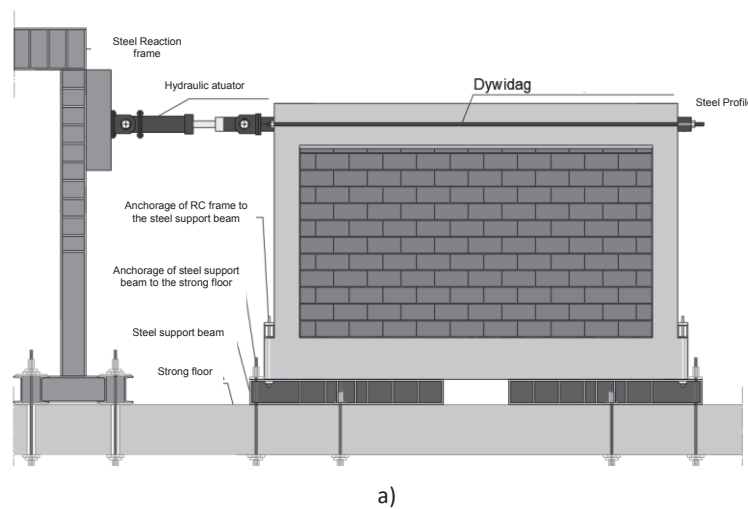


Figure 4 – Schematic layout of the IP test setup.

The OOP test consisted of applying a distributed OOP loading through twenty-eight pneumatic actuators that mobilize the entire infill panel surface resorting to wood plates (one per actuator) placed between the actuators and the panel. The maximum strength capacity of each pneumatic actuator is 20kN and a total displacement amplitude of 185mm. The system has a full-strength ability to apply a distributed load of 560kN. This testing platform can test infill panels with openings (with different configurations and dimensions). This test setup also allowed placing the instrumentation in the back of the reaction structure, which helps to perform OOP tests until the panel collapse without damaging any equipment. Identifying the panels' cracking throughout the OOP tests becomes easier as the quality of the pictures and films recording of each test improved significantly. A self-equilibrated system was used, which balances the transmission of the OOP loadings to the reaction frame attached to the RC frame. Thus, this test setup uses pneumatic jacks linked to four horizontal alignments performed by HEB140 steel profiles, which react against five vertical alignments made of

HEB200 steel profiles. The horizontal alignments are coupled with hinged devices that allow lateral sliding. The steel structure is attached to the RC frame in twelve points (5 in the bottom beam, 5 in the top beam, and 2 in middle-height columns) with steel bars coupled with load cells to monitor the OOP loadings. Figure 5a and Figure 5b present the schematic layout and the general view of the test setup. The pneumatic actuators applied the OOP loading, and the test control is ensured by monitoring their internal pressure and the imposed OOP displacements in a selected control point.

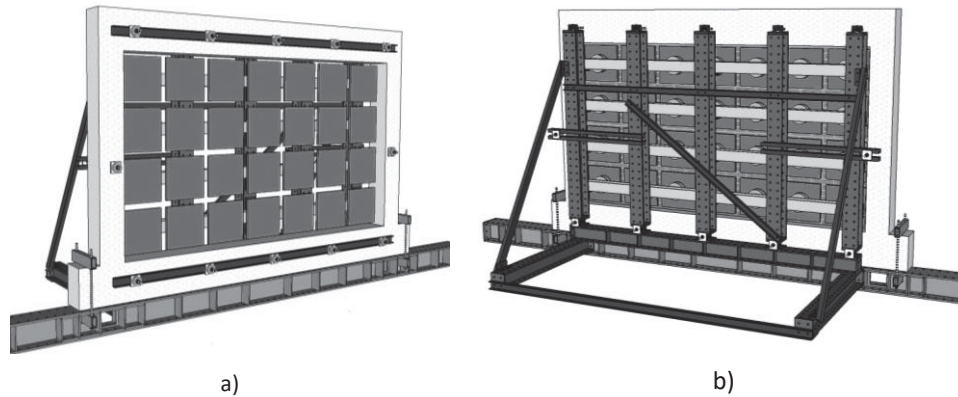


Figure 5 – Layout of the OOP test setup using pneumatic actuators: a) front and b) near view.

The loading protocol is based on the protocol used in the previous tests [8] and consisted of the application of several half-cyclic OOP displacements (loading-unloading-reloading) that were imposed with steadily increasing displacement levels, targeting the following nominal peak displacements at the control node located in the centre of the panel: 0.5, 1, 1.5, 2, 2.5, 3.5; 5; 7.5; 10 mm; and then 5 by 5 mm up to a maximum OOP displacement of 120 mm (largest capacity of the pneumatic actuators). Two half-cycles were repeated for each lateral deformation demand level. No axial load was applied on the top of the adjacent RC columns.

3 DISCUSSION OF THE EXPERIMENTAL RESULTS

3.1 Individual results

3.1.1. Specimen LWC_Ref

The undamaged and no-strengthened specimen LWC_Ref was tested under OOP loadings and reached the first cracking for a $DR_{OOP,crack}$ of 0.29% and a corresponding force equal to 76.75kN. The cracking was located at the panel centre and is horizontal with a full-length extension of 2m. The initial stiffness was estimated at 24024kN/m. After that, diagonal cracking emerged from the horizontal first one to both bottom corners of the panel. A vertical crack was also visible at the panel middle length, from the horizontal first crack to the panel's top. This cracking configuration is similar to trilinear cracking, which typically corresponds to a wall with three borders constrained, and the top boundary is unrestricted or less restricted. This phenomenon is justified by the quality and type of construction of the wall last row (top beam-panel interface), which was mortared. Similar observations were reported in the literature by other authors [8, 9].

At this stage, the specimen reached the maximum peak load of about 229.6kN for a $DR_{OOP,max}$ equal to 4.19%. When compared with the first cracking stage, it is possible to observe that the peak load and the OOP drift are 3 and 14.4 times higher, respectively. Afterwards, the panel reduced its OOP strength slightly until reaching the OOP drift of 6% in which occurred a large detachment of the panel from the top beam and a slight separation from the bottom

beam. New oblique cracks appeared. Horizontal and vertical cracks became thicker and crack developed at the bottom panel-frame interface, presenting a crack pattern maintained until the end of the test. Upon reaching the $DR_{OOP,ult}$ of 7.63% with a residual strength of 149.2kN. The panel exhibited an increase of detachment concerning the upper and lower beams of the frame and presented new vertical cracks in the panel's centre. Based on the measurements made by the vertical displacement located at the top of the frame structure and based on this cracking pattern, it can be concluded that the arching mechanism controlled the response of the wall. Two-way bending occurred similarly to a panel three borders constrained. The top panel-frame interface was not fully mortared due to difficulties in the wall constructions, which is quite common in constructing infill walls, as observed in previous research works [5, 8, 10]. Finally, it can be stated that the conventional rupture occurred for an OOP drift of 6.94%. The force-displacement curve is presented in Figure 6a. The damages observed at the end of the test are shown in Figure 6b.

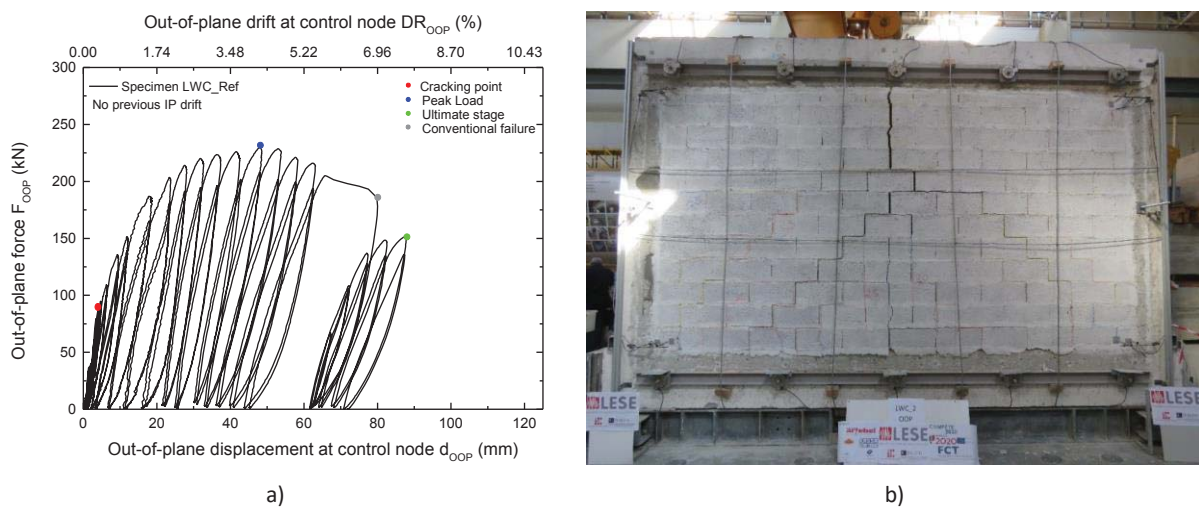


Figure 6 – Specimen LWC_Ref: a) Force-displacement curve; Damages observed at the end of test and b) Front view.

3.1.2. Specimen LWC_IPOOP

The out-of-plane load was applied after the in-plane test, in agreement with the protocol described before. From the test, it was observed that the first crack occurred for a $DR_{OOP,crack}$ equal to 0.71% and a corresponding force of 204.4kN. The first crack appeared horizontally, followed by two oblique cracks up to the panel's lower corners. The initial panel stiffness was 60427kN/m. After that, the peak load was reached for a value equal to 246.06kN and a corresponding drift of 1.39%. A vertical crack appeared at the top of the panel, and horizontal cracks develop in this stage. The OOP strength remains almost constant until 2.3%, when it started to reduce progressively. The conventional rupture was reached for an OOP drift equal to 3.87%.

After that, the panel rupture occurred through the vertical sliding and cracking of the concrete blocks from the panel upper part. The separation of the panel into two pieces resulting from the arching mechanism development becomes more evident. The trilinear cracking pattern was observed at the test end for a $DR_{OOP,ult}$ equal to 4.77% and a residual force of 155.9kN. Based on the measurements made by the vertical displacement located at the top of the frame structure and based on this cracking pattern, it can be concluded that the arching mechanism controlled the response of the wall. Again, two-way bending occurred similarly to a panel three borders constrained, as observed in previous research works [5, 8, 10]. Figure 7a shows

the force-displacement curve. The damages observed after the end of the test are shown in Figure 7b.

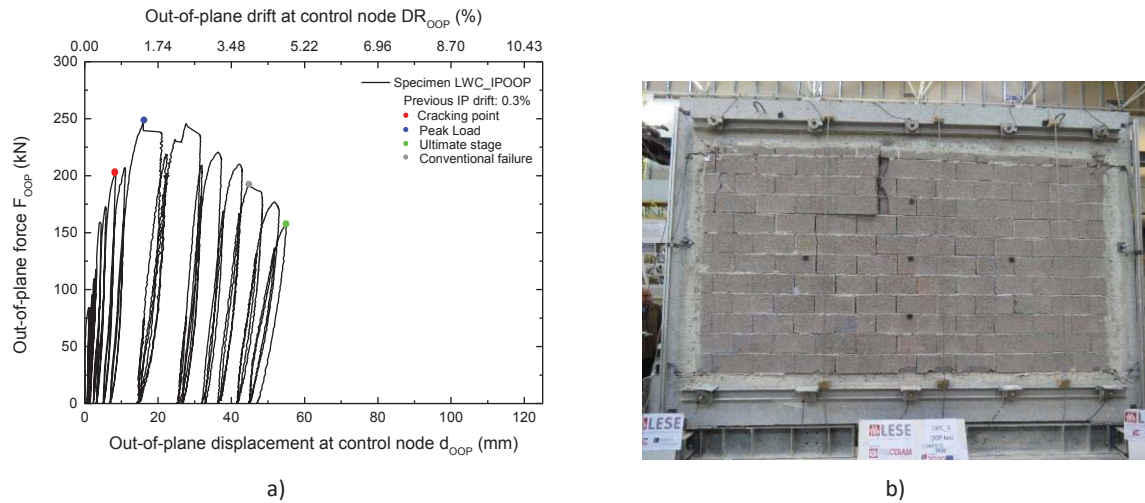


Figure 7 – Specimen LWC_IPOOP: OOP test a) Force-displacement curve; Damages observed at the end of test b) front view.

3.1.3. Specimen LWC_S

The strengthened panel LWC_S was subjected to a pure OOP test and presented an initial stiffness equal to 69250kN/m. The development of the first visible horizontal cracks occurred for a $DR_{OOP,crack}$ equal to 0.30% for a corresponding force of 171.3kN. The OOP force increased to values around 280kN and remained almost constant until reaching the maximum value of 281.28kN for a drift of 2.76%. The panel detached from the upper beam during this period and developed a vertical crack in the panel's upper part. The first diagonal cracks appear. The vertical crack is more evident at the peak stage, and new vertical cracks occur at the panel's top and bottom. Horizontal cracks become thicker, and cracks develop at the interface between the panel and the frame. After that, there is a sudden reduction of the OOP force of about 25% for a drift of 3.1%. The degradation of the OOP strength was then slow until reaching the conventional collapse for the drift of 6.17%. At this moment, it occurred again, a reduction of the panel strength of about 20% for a 6.82% of drift. After that, the panel strength was continuously reducing until the last stage, where it was observed the sliding of the glass fibers of the reinforcement mesh from the steel plate. The residual panel strength was 103.57kN for a drift of 8.21%. Based on the measurements made by the vertical displacement located at the top of the frame structure and based on this cracking pattern, it can be concluded that the arching mechanism controlled the response of the wall. Again, two-way bending occurred similarly to a panel three borders constrained. The force-displacement curve is plotted in Figure 8a. The damages observed after the end of the test are shown in Figure 8b.

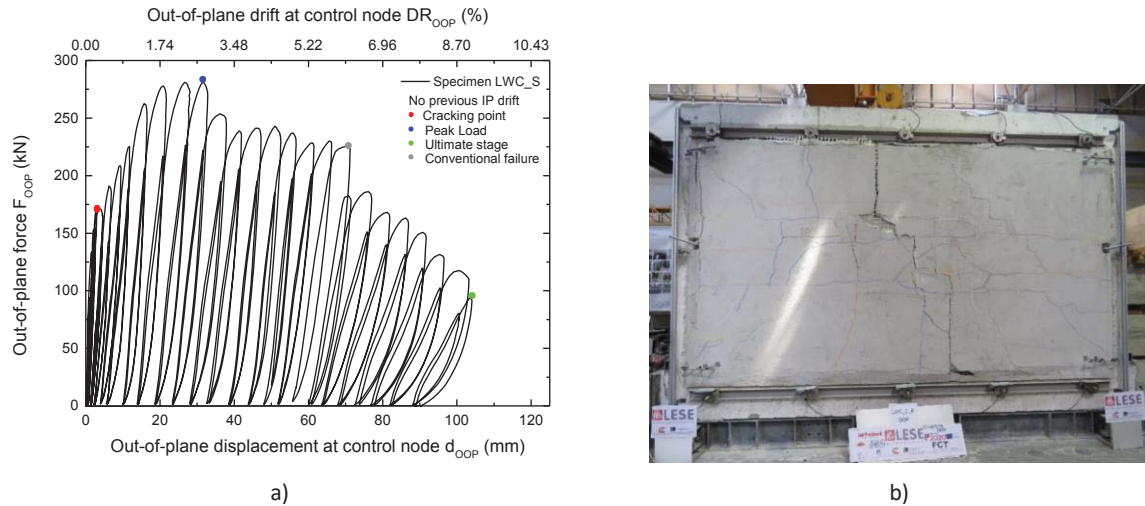


Figure 8 – Specimen LWC_S: a) Force-displacement curve; Damages observed at the end of the test; b) Front view.

3.2 Global results comparison

The initial secant stiffness, $k_{OOP,sec,ini}$, was calculated for each specimen by dividing the peak load of the first half-cycle by the respective OOP displacement. It can be observed that the LWC_S reached, as expected, the highest one. The initial stiffness of the panel LWC_S is 2.88 times higher than LWC_Ref and 14% than LWC_IPOOP. Surprisingly, LWC_IPOOP got an initial stiffness 2.52 times higher than LWC_Ref. Since this panel was damaged before the OOP test due to the IP test, it was expected that the initial stiffness would be lower than LWC_Ref. Based on this, and since no other experimental evidence can justify this result, this higher initial stiffness of LWC_IPOOP can only be attributed to experimental variability.

Regarding the first cracking development, the lowest $DR_{oop,crack}$ was 0.29%, and LWC_Ref reached it. The highest $DR_{oop,crack}$ was 0.71% achieved by the LWC_IPOOP, 2.44 times higher than LWC_Ref. The previous damage was the reason that justifies this significant variation. The cracks developed in the IP test widened and the other ones only emerged for a larger OOP drift demand. The TRM strengthening increased the $DR_{oop,crack}$ by about 3.4%. Concerning the $F_{oop,crack}$, LWC_IPOOP and LWC_Ref again reached the highest and lowest result with 204.4kN and 76.8kN, respectively. Experimental variability can justify that LWC_IPOOP $DR_{oop,crack}$ was 2.66 times higher than LWC_Ref. The strengthening increased the $F_{oop,crack}$ about 2.23 times.

The maximum peak load was reached by the strengthened specimen LWC_S with 281.3kN, proving the technique's efficiency to increase the wall strength capacity. LWC_Ref achieved the lowest peak load with 229.6kN. The TRM strengthening increased the strength capacity about 23%, but it occurred for a $DR_{oop,max}$ 35% lower. The previously damaged LWC_IPOOP reached a $F_{oop,max}$ 7% higher than the reference one due to variability often observed in experimental tests [4]. The $DR_{oop,max}$ of the specimen LWC_IPOOP was 77% lower than the reference specimen.

The conventional rupture occurred first for the specimen LWC_IPOOP ($d_{oop,conv}$ equal to 3.87%), highlighting the importance of previous damage in reducing the OOP capacity. The $DR_{oop,conv}$ of the specimen LWC_REF was two times higher than LWC_IPOOP. The strengthening solution did not contribute to the increase of the $DR_{oop,conv}$, since the panel LWC_S reached the conventional rupture at 6.17%, 11% lower than the reference specimen. However, the residual strength capacity was 22% higher.

No reliable conclusions can be extracted from the ultimate stage since the tests were interrupted for different OOP displacement demands depending on the level of damage.

Table 1 - Global results comparison.

Parameters	LWC_Ref	LWC_IPOOP	LWC_S
$k_{OOP,sec,ini}$ (kN/mm)	24024	60427	69250
$F_{OOP,crack}$ (kN)	76.75	204.41	171.3
$F_{OOP,max}$ (kN)	229.6	246.06	281.3
$F_{OOP,conv}$ (kN)	183.7	196.3	225
$F_{OOP,ult}$ (kN)	149.2	155.92	103.6
$DR_{OOP,crack}$ (%)	0.29	0.71	0.30
$DR_{OOP,max}$ (%)	4.19	1.39	2.76
$DR_{OOP,conv}$ (%)	6.94	3.87	6.17
$DR_{OOP,ult}$ (%)	7.63	4.77	8.21

CONCLUSIONS

This manuscript's primary goal was to study the OOP behaviour of full-scale masonry infill walls made with lightweight concrete blocks. An experimental campaign was carried out comprising three nominally identical full-scale specimens were built. One of them without previous damage and without strengthening. The second specimen was tested with prior damage caused by a prior IP test with a maximum drift of 0.3% without strengthening. The third wall was tested without previous damage, but it was strengthened with a TRM based solution. All the tests have been performed by imposing a half-cyclic (loading-unloading-reloading) history of displacements in the out of plane (OOP) direction employing a uniform distributed load provided by small pneumatic jacks. From the testing campaign, the following conclusions can be drawn:

- The previous damage increased the displacement corresponding to the first crack development. On the other hand, the strengthening reduced this cracking displacement. The same phenomenon was observed at the peak load, and conventional rupture stages. It should be taken into account the variability often observed in experimental tests;
- The OOP strength capacity was not affected by the previous damage, which can be associated with experimental variability. A minor increase of the panel peak load was also observed when strengthened with TRM compared with the reference specimen. Globally, it can be stated that the IP damage and strengthening affect the ductility in negative and positive manners. Only three tests were carried out to assess both effects, which are not enough to draw solid conclusions. Additional tests need be carried out to validate the findings herein extracted;
- The TRM strengthening provided no significant improvement in all the response parameters. Besides the use of a textile mesh with high tensile strength, the strength capacity was not improved. Even the strength degradation was similar to the reference specimen.

ACKNOWLEDGMENTS

This work was financially supported by: Base Funding - UIDB/04708/2020 and Programmatic Funding - UIDP/04708/2020 of the CONSTRUCT - Instituto de I&D em Estruturas e Construções - funded by national funds through the FCT/MCTES (PIDDAC). In addition, this work was also supported by the Foundation for Science and Technology (FCT) - Aveiro Research Centre for Risks and Sustainability in Construction (RISCO), Universidade de Aveiro, Portugal [FCT/UIDB/ECI/04450/2020].



REFERENCES

- [1] A. Furtado, H. Rodrigues, A. Arede, and H. Varum, "Experimental Investigation on the Possible Effect of Previous Damage, Workmanship and Test Setup on the Out-of-plane Behaviour of Masonry Infill Walls," *Journal of Earthquake Engineering*, pp. 1-32, 2021.
- [2] A. Furtado and M. Teresa de Risi, "Recent Findings and Open Issues concerning the Seismic Behaviour of Masonry Infill Walls in RC Buildings," *Advances in Civil Engineering*, vol. 2020, p. 9261716, 2020/03/13 2020.
- [3] J. Dawe and C. Seah, "Behaviour of masonry infilled steel frames," *Canadian Journal of Civil Engineering*, vol. 16, pp. 865-876, 1989.
- [4] P. Ricci, M. Di Domenico, and G. M. Verderame, "Experimental investigation of the influence of slenderness ratio and of the in-plane/out-of-plane interaction on the out-of-plane strength of URM infill walls," *Construction and Building Materials*, vol. 191, pp. 507-522, 2018/12/10/ 2018.
- [5] M. T. De Risi, M. Di Domenico, P. Ricci, G. M. Verderame, and G. Manfredi, "Experimental investigation on the influence of the aspect ratio on the in-plane/out-of-plane interaction for masonry infills in RC frames," *Engineering Structures*, vol. 189, pp. 523-540, 2019/06/15/ 2019.
- [6] *Eurocode 8: Design of structures for earthquake resistance - Part 1-1: General rules, seismic actions and rules for buildings*, B. European Committee for Standardization, Belgium, 2005.
- [7] CEN, "NP-EN 772-1 Métodos de ensaio de blocos para alvenaria Parte 1: Determinação da resistência à compressão," 2002.
- [8] A. Furtado, H. Rodrigues, A. Arêde, and H. Varum, "Effect of the Panel Width Support and Columns Axial Load on the Infill Masonry Walls Out-Of-Plane Behavior," *Journal of Earthquake Engineering*, Article vol. 24, no. 4, pp. 653-681, 2020.
- [9] F. Akhoundi, G. Vasconcelos, and P. Lourenço, "Experimental Out-Of-Plane Behavior of Brick Masonry Infilled Frames," *International Journal of Architectural Heritage*, Article vol. 14, no. 2, pp. 221-237, 2020.
- [10] M. T. De Risi *et al.*, "Experimental analysis of strengthening solutions for the out-of-plane collapse of masonry infills in RC structures through textile reinforced mortars," *Engineering Structures*, vol. 207, p. 110203, 2020/03/15/ 2020.

SELECTION OF OPTIMAL SEISMIC RETROFITTING FOR EXISTING SCHOOL BUILDINGS THROUGH MULTI-CRITERIA DECISION MAKING

**Wilson W. Carofilis¹, Nicholas Clemett¹, Giammaria Gabbianelli¹, Gerard O'Reilly¹,
and Ricardo Monteiro¹**

¹ Centre for Training and Research on Reduction of Seismic Risk (ROSE), Scuola Universitaria
Superiore IUSS Pavia

Palazzo del Broletto, Piazza della Vittoria 15, Pavia 27100, Italy

e-mail: {wilson.carofilis,nicholas.clemett,giammaria.gabbianelli,gerard.oreilly,
ricardo.monteiro}@iusspavia.it

Abstract

The poor performance of school buildings in Italy during past seismic events has underlined their high vulnerability to earthquakes. To improve their seismic performance, retrofitting interventions are commonly designed and then evaluated against a range of key decision criteria. However, more than one intervention may be found to reduce the seismic risk of the structure but it may not be clear which scheme is the most effective given the diverse evaluation criteria. In such cases, multi-criteria decision-making procedures are practical tools that can help to solve this issue, especially when multiple evaluation parameters are considered. This study conducts a full seismic assessment of two existing RC school buildings located in different regions of Italy. For both buildings, similar retrofitting interventions are proposed and designed according to the requirements specified by the Italian building code, NTC 2018. The retrofitting interventions are assessed through non-linear dynamic analyses to thoroughly estimate their overall performance and expected losses. The retrofitting interventions are then comparatively evaluated considering parameters that integrate economic, social, environmental and technical aspects that have a significant role in the decision-making process. The preferential rankings of the retrofit alternatives obtained for both buildings are used to identify the optimal retrofitting solutions for each case and are compared to determine what parameters influence such optimal solutions according to the different buildings' characteristics. The outcomes of this study can assist engineers, or general decision-makers, throughout the evaluation and subsequent selection of retrofit options for existing school buildings.

Keywords: RC school buildings, MCDM, retrofitting interventions, NTC 2018, evaluation parameters.

1 INTRODUCTION

The seismic risk of existing school buildings is an important topic that has been addressed in recent years. For instance, Perrone et al. [1] conducted an extensive performance assessment for three school building typologies adapted from the Progetto Scuole developed by the European Centre for Training and Research in Earthquake Engineering (EUCENTRE). Building upon such work, Carofilis et al. [2] proposed and assessed different retrofitting techniques to reduce the seismic risk of the same school buildings. Besides evaluating the seismic performance, Carofilis et al. [2] determined the economic feasibility of these alternatives through a cost-benefit analysis [3]. However, as further explored by Carofilis et al. [4], the consideration of a diverse set of decision variables (DV) for a set of retrofitting strategies may result in a distinct retrofitting preference, when compared to traditional economic assessments. Therefore, Carofilis et al. [4] suggested that multi-criteria decision making (MCDM) analysis is more suitable than other methodologies, which tends to focus only a few decision variables, for selecting the most advantageous option from a set of retrofitting strategies. Similarly, MCDM has been adopted in other studies focusing on the retrofitting alternatives for residential buildings (Caterino et al. [5]) and school buildings (Gentile and Galasso [6]), where technical, social, and economic aspects were evaluated.

With the current focus on reducing impact that humans have on the environment, a body of recent research has also focused on assessing the environmental impacts associated with the seismic damage of existing buildings. Recently, Caruso et al. [7] proposed a methodology for considering the life cycle costs and environmental impacts (EIs) associated with the seismic and energy efficiency retrofitting of existing buildings. Additionally, Caruso et al. [7] investigated how this methodology could be used for the selection of retrofitting alternatives.

Subsequently, Clemett et al. [8] carried out a detailed and comprehensive review of five different metrics that can be used to account for the EI of retrofitting strategies within an MCDM framework. They found that incorporating the EI into the MCDM analysis influenced the identification of the ideal retrofitting solution, as the selection of an appropriate EI DV affected the preference ranking of the retrofitting solutions. Therefore, in the selection of the most convenient retrofitting strategy for an existing school building not only traditional aspects (i.e. technical, economic and social views), but also environmental impacts should be considered. With the above aspects in mind, this paper looks at the retrofitting of two case study existing buildings in Italy, where several retrofitting alternatives are examined and the choice via an MCDM framework, considering economic, social, environmental and technical aspects, is carried out.

2 MULTI-CRITERIA DECISION MAKING (MCDM)

The MCDM framework is advantageous when considering a number of different DVs, complemented by an analytical hierarchy process (AHP) [9]. Additionally, the “technique for order preference by similarity to ideal solution” (TOPSIS) [10] can be applied to rank the assessed options according to their relative closeness to an ideal alternative, which comprises all of the most convenient characteristics (e.g. best performance, lowest cost, lowest losses, etc.). Nevertheless, the closeness to an ideal solution depends on the importance given to each DV by the analyst, as well as to their specific values.

2.1 Description of the method

At the start of an MCDM analysis, it is necessary to define the evaluation parameters or DVs. Then, the importance given to each DV is assigned. This importance is represented

through a weight vector (w), which can be defined according to a preference matrix as implemented by Caterino et al. [5] or through a survey, as performed by Carofilis et al. [11] and Gentile and Galasso [6]. The values of each retrofitting alternative associated with each DV create the decision matrix (D), which along with the weight vector (w) represent the input variables. Figure 1 summarizes the process to develop the MCDM analysis. The decision matrix is normalized since each DV may be expressed in different units. The normalized decision matrix R is determined by applying Equation 1 to the elements of the decision matrix (D). Then, the weight normalized decision matrix V is calculated through Equation 2, where r_{ij} represents the components of matrix R and w_j the elements of the weight vector (w). From the matrix V the most ideal solution A^* and negative-ideal solution A^- are determined, representing the most and least convenient values for each column of matrix V . These parameters are used to calculate the distances S_i^* and S_i^- as indicated by Equation 3. As illustrated in Figure 1, these distances represent the proximity of each alternative to a fictitious ideal and negative-ideal alternative. Finally, the relative closeness (Equation 4) is used to rank the alternatives and determine the most convenient one, i.e. the alternative with the largest relative closeness. For example, in Figure 1, it is observed that A_2 is closer to the ideal fictitious alternative in comparison with A_1 and A_3 . Consequently, A_2 will be assumed the most favourable alternative since its relative closeness would be much larger than that of the other alternatives. Further details of this method can be found in [5] and [4, 11].

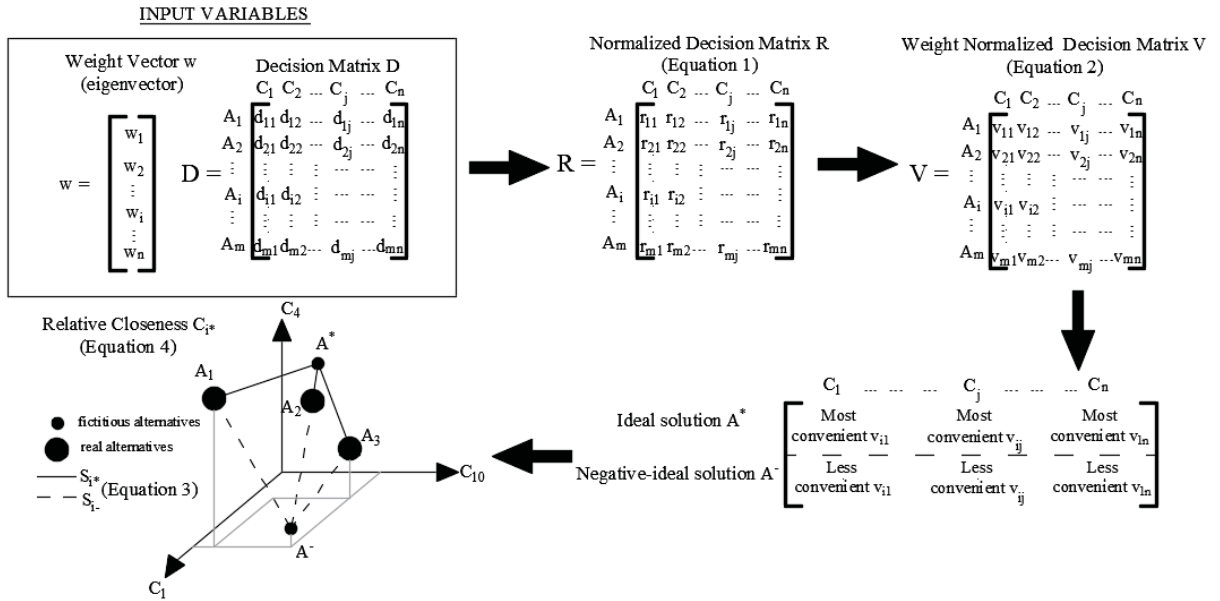


Figure 1: MCDM procedure.

$$r_{ij} = \frac{d_{ij}}{\sqrt{\sum_{k=1}^m d_{kj}^2}} \quad (1)$$

$$v_{ij} = r_{ij} * w_j \quad (2)$$

$$S_{i*} = \sqrt{\sum_{j=1}^n (v_{ij} - v_{j*})^2}; \quad S_{i-} = \sqrt{\sum_{j=1}^n (v_{ij} - v_{j-})^2} \quad (\text{Distances } S_{i*} \text{ and } S_{i-}) \quad (3)$$

$$C_{i*} = \frac{s_{i-}}{s_{i*}+s_{i-}} C_{i*} = \frac{s_{i-}}{s_{i*}+s_{i-}} (\text{Relative closeness}) \quad (4)$$

2.2 Evaluation parameters

The DVs selected for this study were in part characterised through an ad-hoc survey devised by Carofilis et al. [11], which collected information on which evaluation parameters are considered important in the assessment of retrofitting options for school buildings. These variables are reported in Table 1, where it is indicated to which aspect they are related and how they are estimated for each retrofitting configuration. Some of these variables have also been investigated in past studies [5, 6].

Label	Decision Variable	Aspect	How this DV is determined
C1	Installation Costs	Economic	Total cost of installation comprising removal, demolition, application of retrofitting technique and all other cost associated with applying the intervention
C2	Maintenance Costs	Economic	Cost of maintenance over the lifetime of the structure.
C3	Duration of Works	Economic/ Technical	Number of days needed to fully complete the intervention and start the normal operation of the building
C4	Architectural Impact	Social	Qualitative evaluated through AHP [9]
C5	Need for Specialized Labor	Technical	Qualitative evaluated through AHP [9]
C6	Foundation Intervention	Technical	Estimates of the maximum axial load ratio between the retrofitting intervention to the as-built configuration
C7	Expected Annual Losses	Technical	Evaluated as the expected annual loss obtained from the loss assessment using PACT [12].
C8	Expected Annual EI	Technical/ Social	Refer to Section 2.3

Table 1: Evaluation parameters.

2.3 Environmental impact

Clemett et al. [8] highlighted how an EI metric that captures the entire life cycle impacts can be incorporated into the MCDM. The EI of a building can be estimated in several ways. For instance, through a Process Life Cycle Assessment (PLCA) inventory, containing a list of all the processes that contribute to the life cycle of a building. PLCA is generally considered a meticulous approach for estimating the life cycle EI of a structure, however, it is particularly time-consuming to develop a full inventory accounting for all sources of EI. Therefore, PLCA is susceptible to truncation bias (i.e. 30-50% of the total life cycle impacts [13]). An alternative to PLCA is the Environmentally Extended Input-Output Life Cycle Assessment (EEIOLCA), which, unlike PLCA, is a top-down method based on economic input-output (IO) models [14]. These IO models capture the monetary transactions that occur between the different sectors of the economy and are generally represented as matrices [15] (Figure 2, point 3). If rows and columns are included for the various EI metrics of interest, these tables can be used to assess

the EI of each industrial sector. The values for each impact category are generally presented in EIs/\$ [16]. The EI of a building can be calculated by disaggregating the total cost estimate of the structure into each of the available industrial sectors and then multiplying the dollars spent in each sector by sector- unique EI/\$ value.

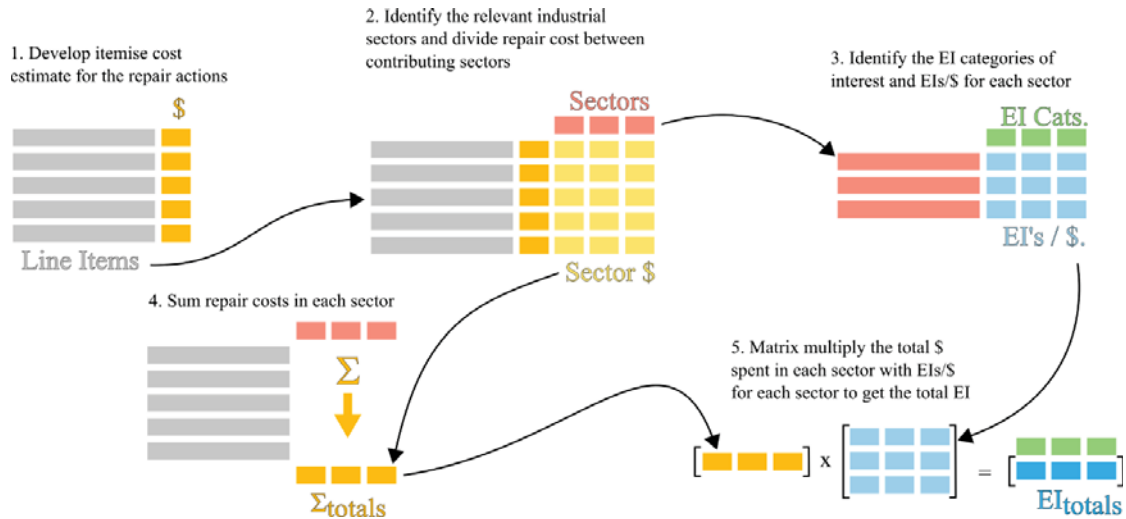


Figure 2: EEIOLCA impact assessment procedure adapted from Huang and Simonen [16].

Nevertheless, it is important to note that EEIOLCA has three primary sources of error: aggregation error (i.e. values represent a weighted average of several smaller economic sectors); the homogeneity assumption (i.e. all products produced within a specific sector have the same average EI), and; the linearity assumption (i.e. EIs are linearly correlated with the market price, meaning that a higher price leads to higher emissions) [8]. Additionally, EEIOLCA might present other limitations and potential sources of uncertainty. For example, the USEEIO [17] inventory has been developed using US economic data so that EIs derived from its use are applicable only within the United States. The application of this inventory to case studies outside of the US will likely increase the error of the impact estimate unless it can be demonstrated that the economy of interest has the same structure as the US economy. In this study, the use of the USEEIO inventory for a case-study building in Italy can be justified by the fact that the assessments performed are for comparative purposes and any error resulting from the use of a US inventory will likely have an equal effect on all of the retrofitted structures. Additionally, the USEEIO database [17] does not consider any sort of uncertainty in the EI estimates for each sector, however, uncertainty in these values is accounted for in the PACT software (version 3.1.2) [12] by assuming that the uncertainty of the EIs is related to the uncertainty of the cost estimate (refer to Equation 1 of Clemett et al. [8]).

For this study, the EI, denoted C8, was estimated using EEIOLCA which represents the ongoing cost associated with the retrofit alternatives, and is impacted by the seismic performance (i.e. the effectiveness) of the retrofit alternatives [8]. The reconstruction EI was coarsely approximated by first converting the reconstruction cost, in 2020 € to 2013 \$, then multiplying the reconstruction cost by the EIs/€ factor for “schools and vocational buildings” from the USEEIO database [17]. An additional 15% of the reconstruction EI was added to

account for the impacts associated with the demolition and disposal of the damaged structure [8].

3 CASE-STUDY BUILDINGS

Two existing reinforced concrete (RC) school buildings located in different regions of Italy with medium-high seismicity are used as case-study. These structures share the same modelling techniques (Figure 3a), as well as structural deficiencies. The first building is referred to as Building 1 (Figure 3b) and is located in central Italy, at Isola del Gran Sasso, Parozzani. This school building consists of two storeys and one underground portion (staircase section), the construction period is estimated at around 1960–1970. The area of the underground level is 133m^2 and for the subsequent levels is 631m^2 . Likewise, the inter-storey heights are 3.75, 3.75 and 4.75m, respectively for each level. The second building is denoted as Building 2 (Figure 3b) and is located on Italy's Adriatic coast, in Ancona. It is estimated that the construction period of this building dated back to the 60s. The structure is composed of three storeys including an underground level. The floor area is about 690m^2 , and inter-storey height of 3.83m for the underground level and first storey, and 3.77m for the second storey.

3.1 Structural modelling

These buildings share similarities in their configuration, size, material and year of construction. Therefore, the same assumptions were adopted for the numerical modelling of both buildings with the software OpenSees [18] as illustrated in Figure 3. The modelling techniques suggested by O'Reilly and Sullivan [19] for old RC Italian frames were implemented. For example, beams and columns were created through force-based beam-column elements with a modified Radau plastic hinge integration scheme with lumped plasticity (Scott and Fenves [20]). Even though the shear behaviour was assumed elastic, a post-processing analysis was carried out to compare the shear forces of these flexural elements to their maximum shear capacity determined through NTC -2018 [21]. On the other hand, the beam-column joints were modelled using a zero-length rotational spring to capture any potential shear failure for joints. Furthermore, the buildings also incorporate a rigid floor slab and consider second-order geometry effects ($P-\Delta$). Regarding damping, a 5% tangent-stiffness-proportional Rayleigh damping model for the periods of the fundamental modes was adopted. Additionally, the effects of the exterior masonry infills were incorporated into the model through a system of equivalent diagonal struts that represent the behaviour of the infills, following the recommendations of Sassun et al. [22]. To account for the influence of openings, the stiffness and strength of the struts were affected by a reduction factor proposed by Decanini et al. [23]. The strut models used in these analyses are only capable of modelling the in-plane behaviour of the infills and do not consider out-of-plane failure. Further details about the building configuration and modelling can be found in [8] and [1, 2] for Building 1 and 2, respectively.

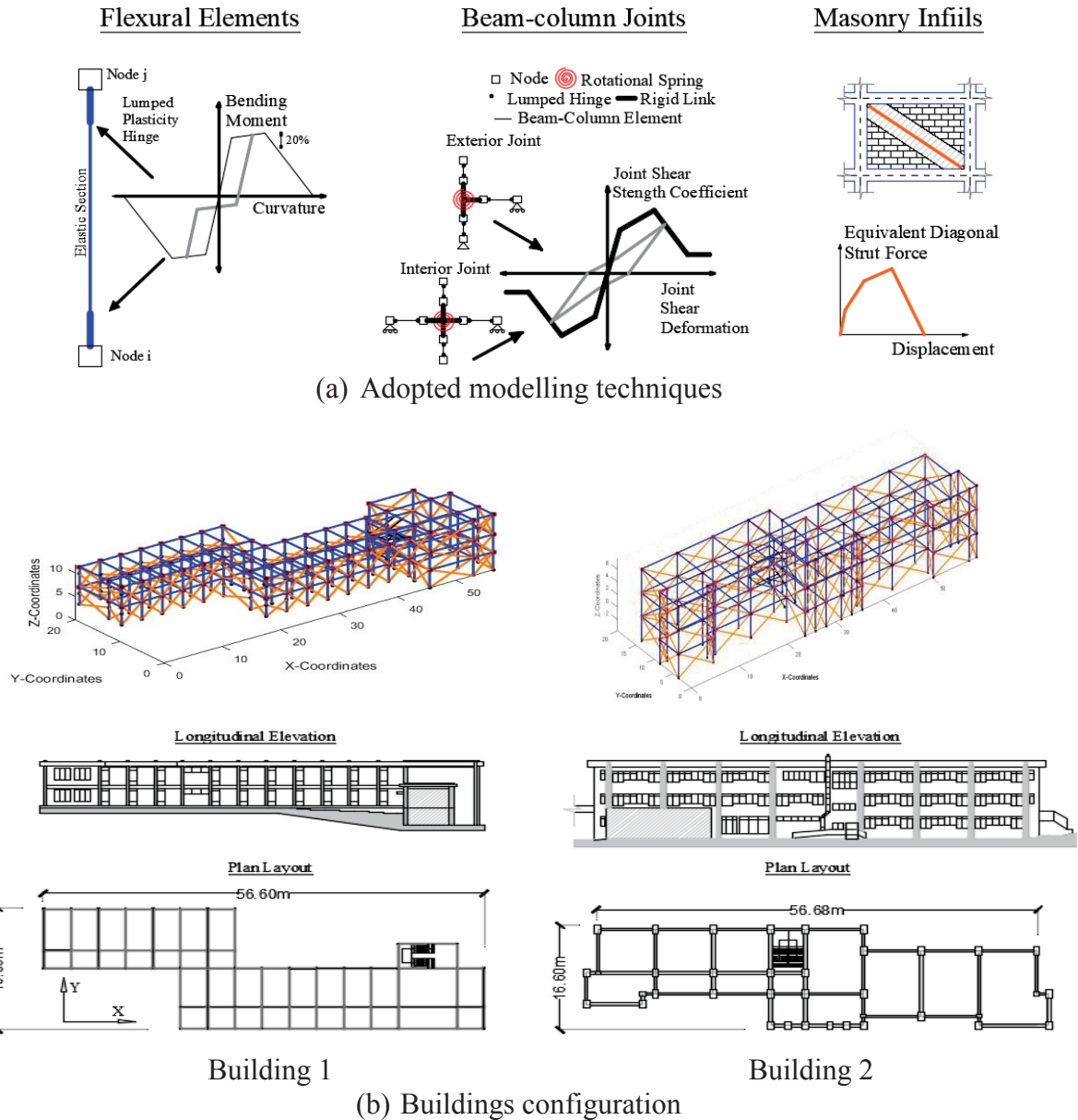


Figure 3: Schemes of case-study school buildings.

3.2 Performance assessment

A performance assessment was developed for both buildings, carrying out verifications of deformation and strength capacity for the seismic demands imposed by NTC 2018 [21] according to the site location of each building. For a school building, the NTC 2018 [21] specifies a design life of 75 years (occupancy class III) and return periods associated with four limit states: Operational limit state (SLO) 45 years; Damage limitation limit state (SLD) 75 years; Life safety limit state (SLV) 712 years, and; Collapse prevention limit state (SLC) 1463 years. For the serviceability limit states, the code imposes two drift limits 0.17% and 0.5% for SLO and SLD, respectively. For a building of occupancy class III, it is only necessary to verify the limit at SLO, however, in this study, both limits were checked.

The results of the preliminary performance assessment are illustrated in Figure 4. They are expressed in terms of the base shear coefficient (i.e. lateral capacity divided by the seismic weight of the building), building roof drift (i.e. roof displacement divided by the total height of the building) and drift profiles related to the different limit states. On the one hand, it is observed

that the capacity of both buildings is controlled by the premature failure of joints, and thereby controlling the other limit states as well. In the case of the drift profile, Building 1 meets the drift limit for both serviceability limit states in both directions. On the other hand, Building 2 exceeds these limits, especially for the Y direction. For the limit states associated with the ultimate capacity (i.e. SLV and SLC), both buildings present a soft-storey mechanism which is denoted by the drift concentration in one of their storeys, namely second storey for Building 1 and third storey for Building 2.

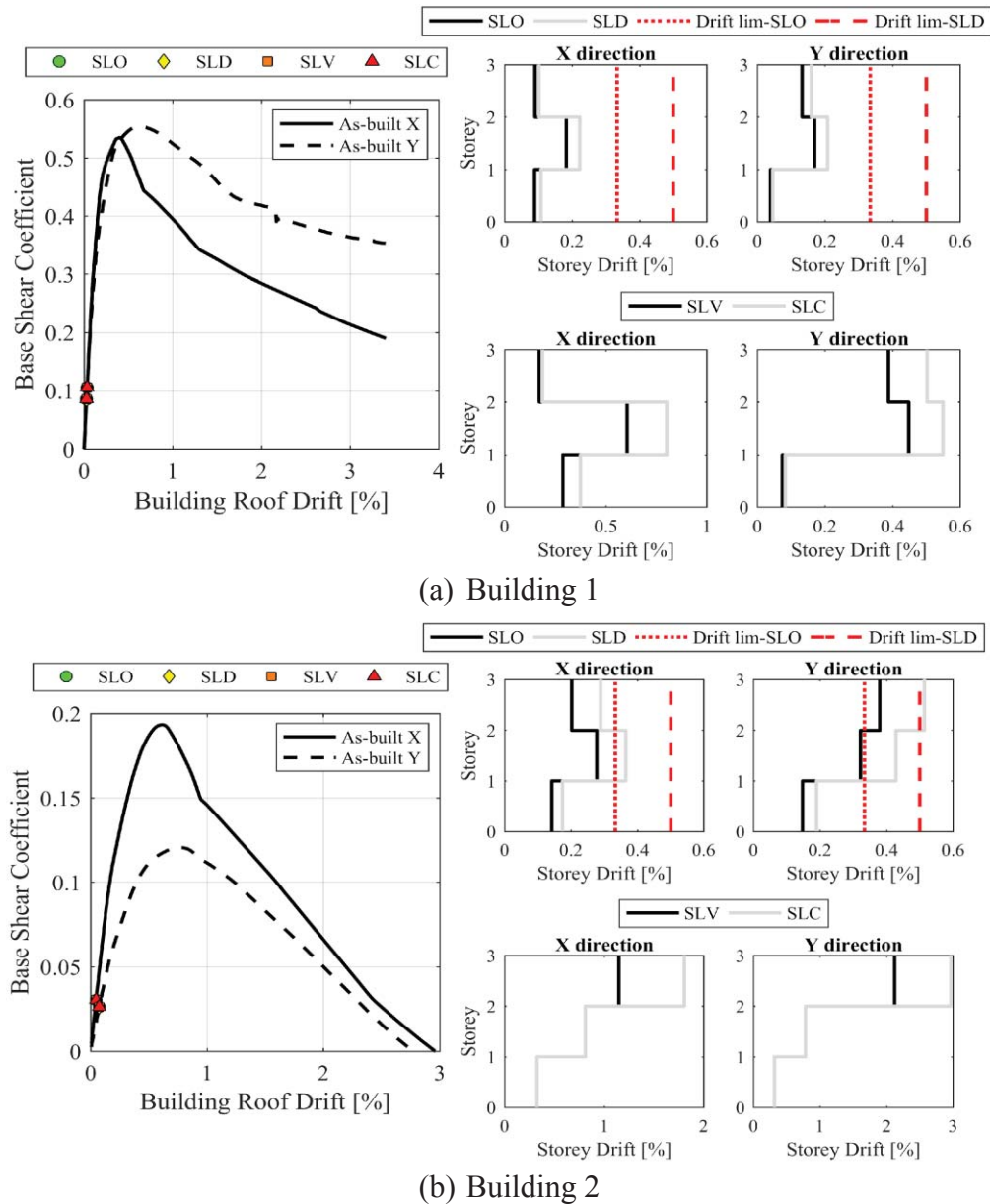


Figure 4: School buildings structural performance.

4 RETROFITTING INTERVENTIONS

Four retrofitting strategies were proposed for both school buildings. As illustrated in Figure 5, these strategies are the same for both buildings and consist of: A1 involves carbon fiber reinforced polymer (CFRP) wrapping of columns along with CFRP bars, as well as CFRP strips placed on beam-column joints; A2 implements exterior cross-steel braces in some strategic locations of the building; A3 combines the two previous interventions (i.e. CFRP and steel

braces) and, lastly; A4 combines CFRP and viscous dampers placed strategically in the building. Moreover, the infill-strut elements were removed from the models in response to the seismic separation of the infills and the frames. To accommodate this assumption, additional checks were carried out during the non-linear analyses to ensure that the estimated drifts did not exceed the 50mm seismic gap provided. Further details of the original and retrofitted configurations, as well as their design, can be found in [4, 8].

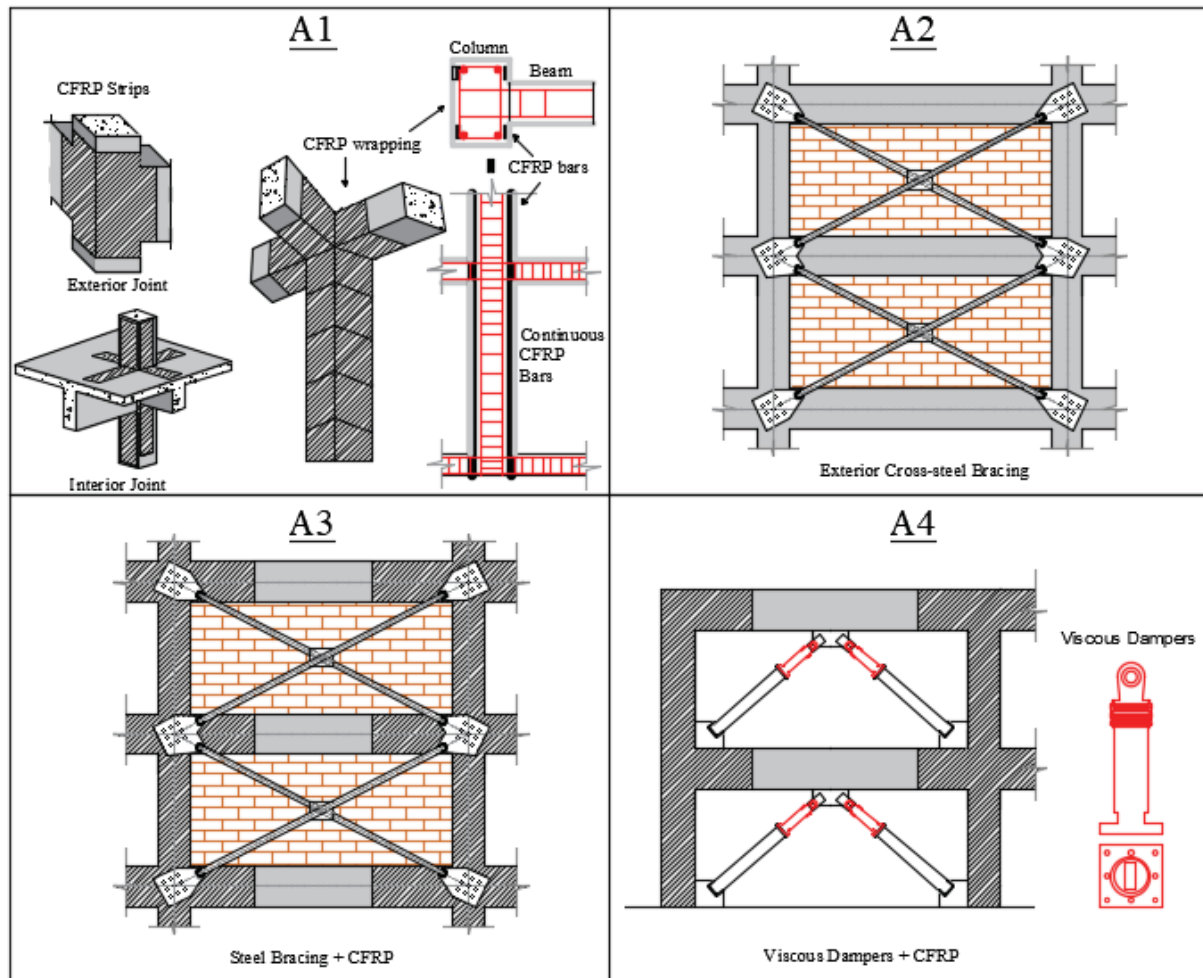


Figure 5: Proposed retrofitting configurations.

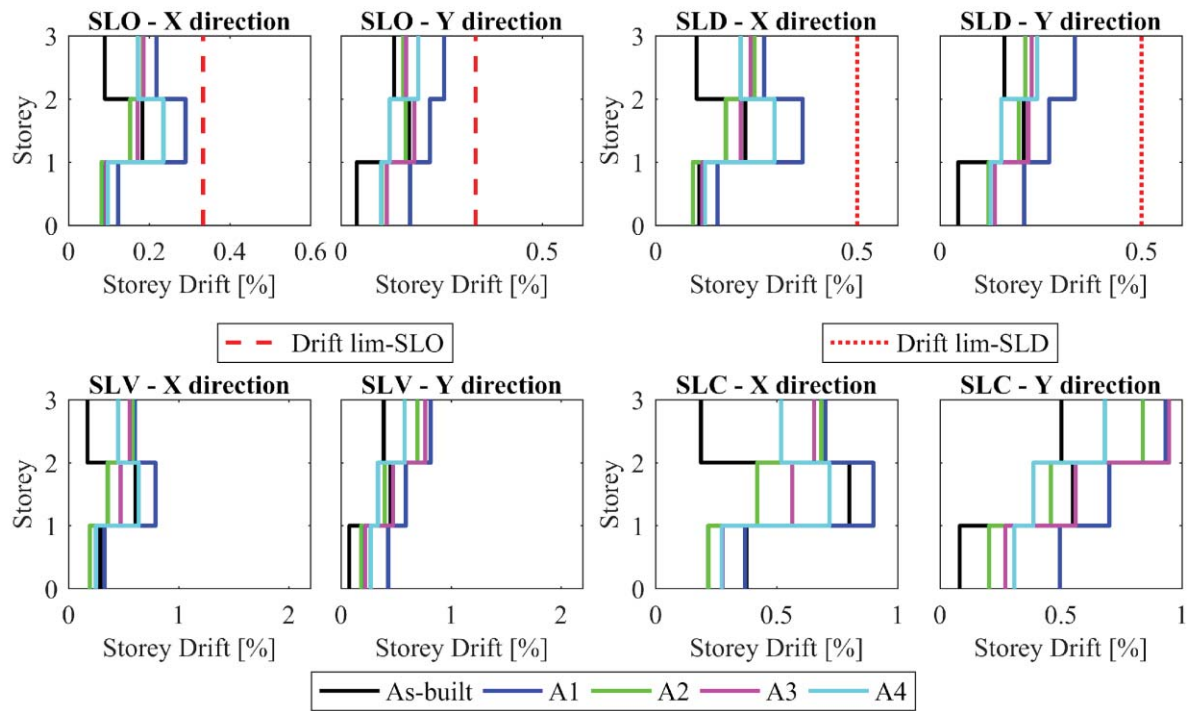
4.1 Performance assessment of retrofitting strategies

The performance assessment was applied to the retrofitting configuration, again this assessment is reported as drift profiles (Figure 6) and lateral capacity (Figure 7). For Building 1 all retrofitting interventions meet the drift limit for SLO and SLD whereas they reduce the drift concentration for SLV and SLC. In the case of Building 2, all strategies improve the drift distribution, especially for the Y direction. However, strategy A1 is slightly exceeding the drift limit at SLO and at SLD the maximum storey drift coincides with the drift limit.

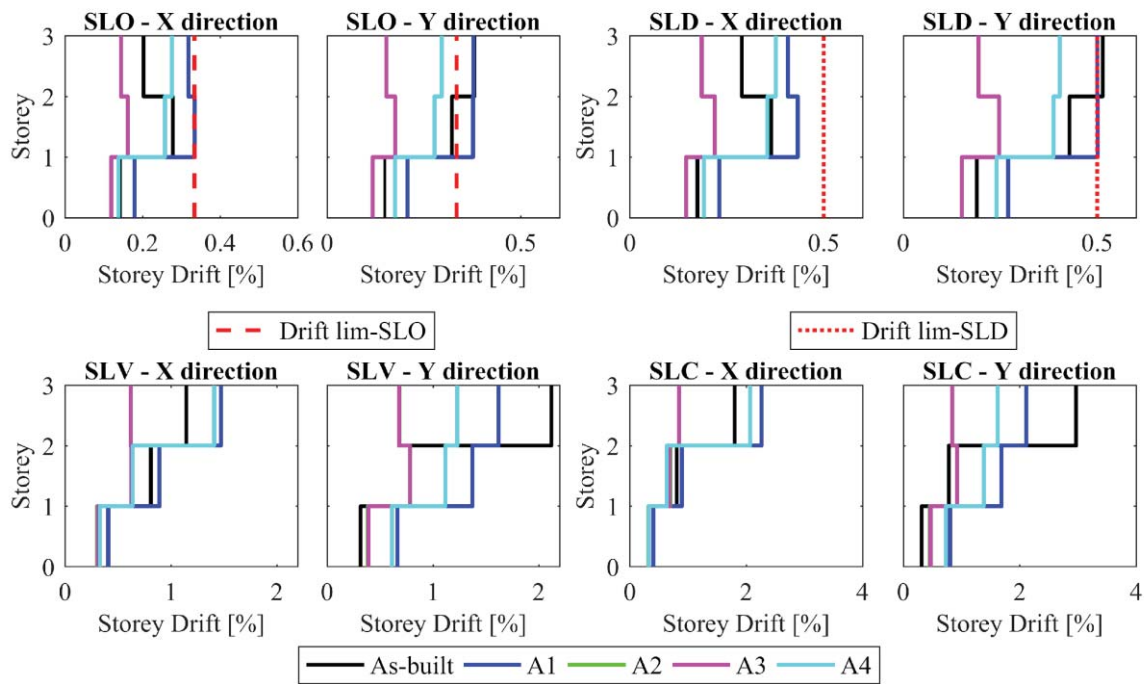
The strategies involving steel braces (A2 and A3) prove to be more effective in reducing the storey drift in both building configurations. The strategy with viscous dampers (A4) reduces the drift concentration, and the option with CFRP (A1) also reduces the drift profiles but its effect is not as substantial as the other strategies.

Moreover, the lateral capacity, as well as performance capacity points, are improved for all strategies except for A2 (steel braces). Even though this strategy boosts considerably the lateral

capacity of the buildings, in terms of local strength does not account for an improvement since the strength capacity remains unchanged and thereby the premature failure of joints still persists. Strategy A3 also boosts the lateral capacity of the buildings, the action of the CFRP increases the local capacity of the structural elements so that the capacity points are shifted to the right (i.e. a zone of better performance). The same effect is observed for A1 and A4, which also incorporate CFRP. Furthermore, a particular difference of the steel bracing options (A2 and A3) is noted in the lateral capacity of the case-study buildings (Figure 7a). The contribution of the bare frame (due to seismic separation of infills) and steel braces present a lower initial stiffness than that of the as-built configuration for Building 1. On the other hand, in Building 2, this same combination results in a stiffer building, meaning that the steel bracing system surpasses the stiffness of the infilled configuration (as-built).

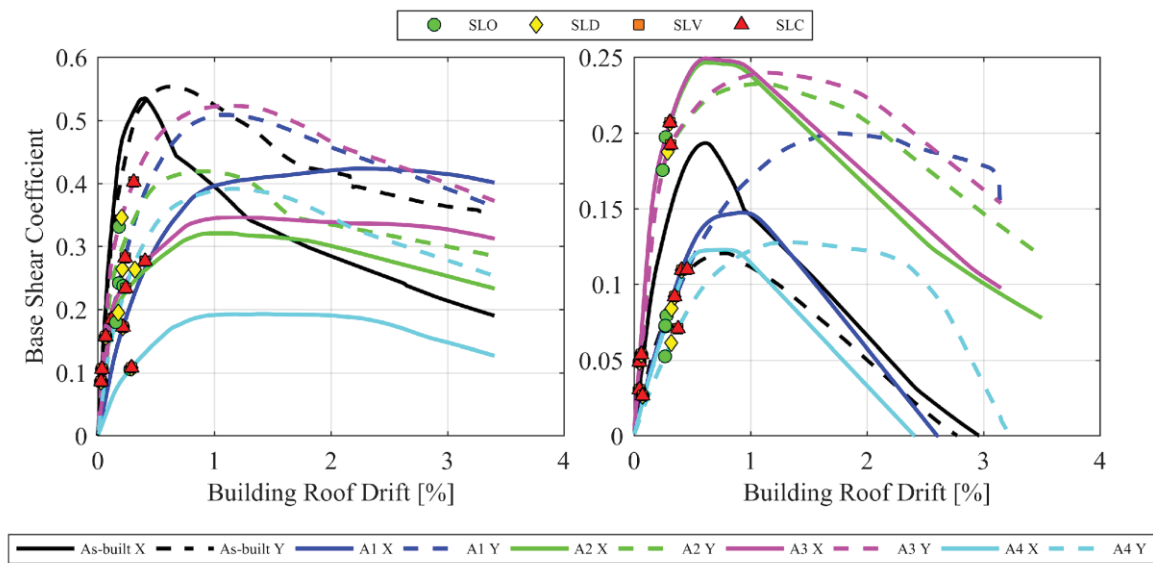


(a) Building 1



(b) Building 2

Figure 6: Drift profiles of retrofitting interventions.



(a) Building 1

(b) Building 2

Figure 7: Lateral capacity of retrofitting interventions.

4.2 Collapse vulnerability and loss estimation

The next stage in the performance assessment was to conduct refined nonlinear time history analysis (NLHA). Therefore, the fundamentals periods of all models were determined (they are reported in Table 2 and Table 1 for Building 1 and 2, respectively). Due to the period variability of the different models, the average spectral acceleration (AvgSa) was considered as intensity measure to carry out a ground motion record selection, since it is a more efficient and unbiased quantifier of response in these structural typologies, as shown by O'Reilly [24]. The software

OpenQuake [25] was used to carry out the probabilistic seismic hazard analysis (PSHA) and disaggregation analyses for the site locations defined in Section 3. The Italian seismic source model MPSO4 (Meletti et al. [26]) and the ground motion model by Akkar, Sandikkaya, and Bommer [27] and Sandikkaya, Akkar, and Bard [28] were adopted. The geometrical period (T_{gm}) was determined as the square root of the product between the two fundamental periods. The period range of $0.2T_g - 1.5T_g$ was used to perform the AvgSa-based selection, as suggested by Kohrangi et al. [29]. The period range of 0.05s to 1.0s was adopted for Building 1 whereas a range of 0.10s to 1.60s was used for Building 2. A set of 20 pairs of ground motion records in two horizontal components were selected for ten return periods: 30, 45, 75, 100, 200, 475, 712, 975, 1463 and 2475 years. Figure 8 illustrates the hazard curves for the two sites locations, expressed in terms of the mean annual frequency of exceedance (MAFE) and AvgSa, as well as a scheme of the ground motion selection at a specified intensity.

Model	$T_x[2]$	$T_y[s]$	$T_g[s]$	$0.2T_g[s]$	$1.5T_g[s]$
As-built	0.27	0.24	0.25	0.04	0.38
A1	0.60	0.37	0.47	0.09	0.71
A2	0.41	0.37	0.39	0.07	0.58
A3	0.40	0.35	0.37	0.08	0.56
A4	0.75	0.35	0.51	0.10	0.77

Table 2: Fundamental periods, geometric period, and period range for the models of Building 1.

Model	$T_x[2]$	$T_y[s]$	$T_g[s]$	$0.2T_g[s]$	$1.5T_g[s]$
As-built	0.57	0.80	0.68	0.14	1.01
A1	0.98	1.00	0.99	0.20	1.49
A2	0.53	0.59	0.56	0.11	0.84
A3	0.53	0.59	0.56	0.11	0.84
A4	0.98	1.17	1.07	0.21	1.61

Table 3: Fundamental periods, geometric period, and period range for the models of Building 2.

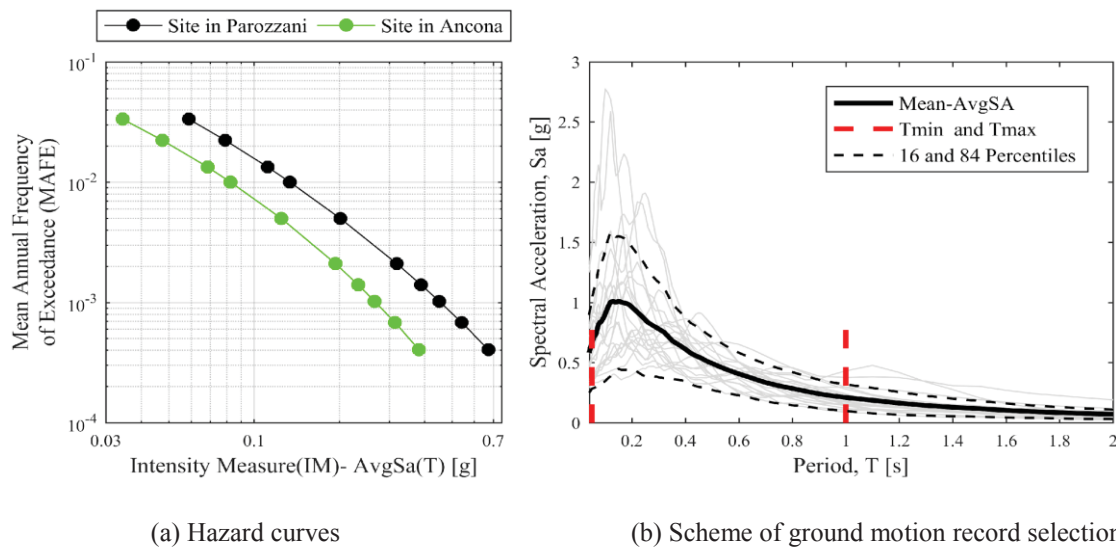
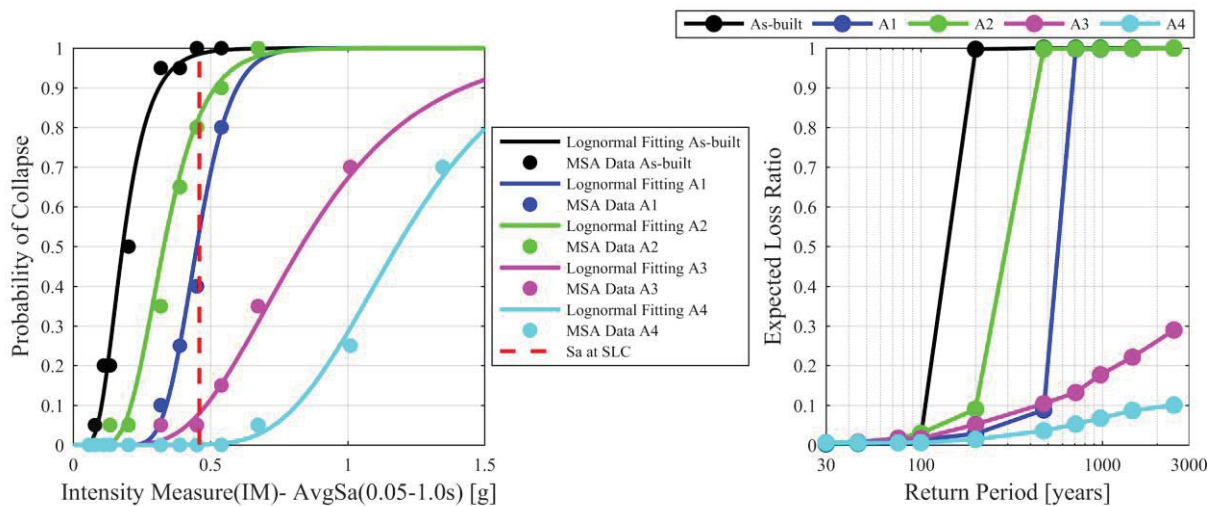


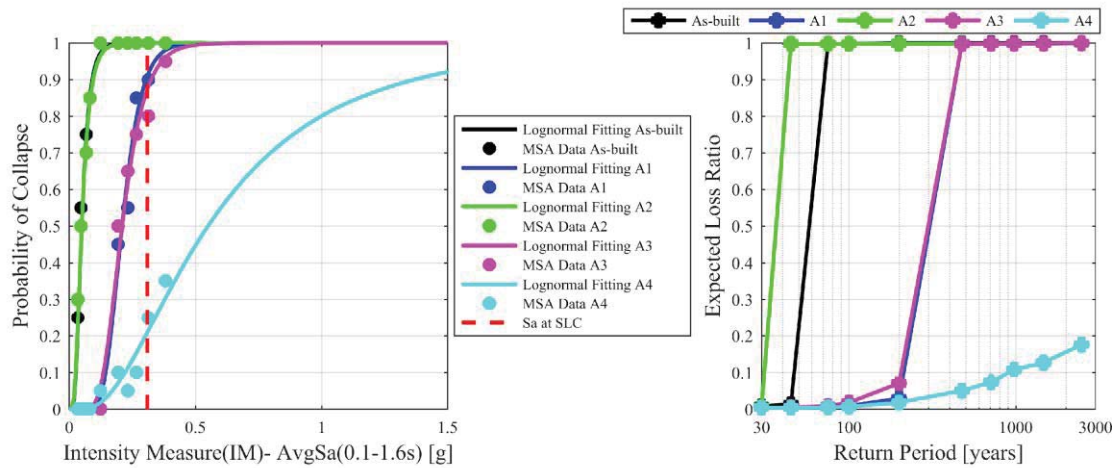
Figure 8: Hazard curves and ground motions selected using AvgSa for the site locations.

Multiple-stripe analysis (MSA) [30] was conducted to characterize the response of the structures using the records selected. The results from the MSA were used to develop collapse fragility curves, for all models for both buildings, by recording at each intensity level, the number of collapses observed. The collapse criteria adopted here was based as the first of: the shear force demand exceeds the shear resistance of one or more of the flexural elements; the rotation of one or more flexural elements exceeds the SLC deformation limits; the shear deformation in one or more of the beam-column joints exceeds 0.02 rad [19]. The curves were fitted from the MSA collapse data using a lognormal distribution and maximum-likelihood estimation [31]. The fragility curves obtained from the fitting procedure account for the record-to-record variability of the selected ground motions (Figure 9). To account for the modelling uncertainty, the median and dispersion values from the fitting procedure were modified following the recommendations of O'Reilly and Sullivan [19]. Moreover, Figure 9 also illustrates the expected economic losses, which were determined through the software PACT (version 3.1.2) [12].

The retrofitting alternatives A3 and A4 substantially reduce the collapse vulnerability and expected economic losses, especially for Building 1. A1 improves the collapse capacity of Building 1 and expected losses but this improvement is not as prominent as the one given by A3 and A4. On the other hand, A2 achieves a slight enhancement of both aspects. In case of Building 2, A4 has a considerably better performance in terms of collapse vulnerability and expected economic losses. On the other hand, A1 and A3 reach a similar reduction for both aspects, and lastly, A2 does not seem to improve these two parameters. Indeed, A2 has a worse performance compared to the as-built configuration of Building 2. Furthermore, from Figure 7b, it can be predicted that A2 would generate higher floor accelerations, as well as higher losses associated with this demand parameter. Likewise, the period shortening observed in Table 2 indicates that this strategy will be conditioned to larger inertial forces. As a result, the structural elements will be subjected to higher internal forces, which leads to more local failures. These same effects are expected for A3, however, the contribution of CFRP increases the local strength and thereby decreases the number of element failures (i.e. collapse cases).



(a) Building 1



(a) Building 2

Figure 9: Collapse vulnerability and expected economic losses.

Tables 5 and 6 report the expected annual losses (EAL) and expected annual environmental impacts (EAEI) for all configurations of both buildings. These calculations were based on the total replacement cost of the buildings. The average costs of building demolition and reconstruction were assumed as 95.50€/m² and 1805.75€/m², respectively [32]. Given an approximate floor area of 1395m², the demolition and reconstruction costs were estimated to be 133,223€ and 2,519,021€ respectively (total replacement cost of 2,652,244€) for Building 1. On the other hand, for Building 2 with an approximate floor area of 2067m² the demolition and reconstruction cost resulted in 197,427€ and 3,733,027€, respectively (total replacement cost of 3,930,454€). Furthermore, replacement EI for Building 1 is 1,830,000kg-CO₂e and 2,713,000kg-CO₂e for Building 2. For simplicity, the total replacement cost and EIs were considered to be the same for all of the alternatives in each building case.

Model	EAL [%]	Rep. Cost[€]	EAEI [%]	Rep. EI [kgCO ₂ e]
As-built	0.50	2,652,244	0.51	1,830,000
A1	0.20		0.18	
A2	0.43		0.39	
A3	0.16		0.11	
A4	0.06		0.04	

Table 5: EAL and EIs expressed as a percentage (%) of the estimated replacement cost and EI, Building 1.

Model	EAL [%]	Rep. Cost[€]	EAEI [%]	Rep. EI [kgCO ₂ e]
As-built	1.46	3,930,454	1.47	2,713,000
A1	0.33		0.33	
A2	1.77		1.77	
A3	0.38		0.34	
A4	0.13		0.12	

Table 6: EAL and EIs expressed as a percentage (%) of the estimated replacement cost and EI, Building 2.

5 APPLICATION OF MCDM

5.1 Input variables

The input variables (i.e. weight vector w and decision matrix D) are reported in Table 7 and 8 for Building 1 and 2, respectively. The values assigned to the decision matrix (D) were determined as described in Section 2.2 whereas the weight vector (w) was adopted from Carofilis et al. [11].

DV [units]	C1 [€]	C2 [€]	C3 [days]	C4	C5	C6	C7 [%]	C8 [%]
A1	850,458	1,520,883	36	0.07	0.25	1.40	0.20	0.18
A2	43,120	229,829	8	0.17	0.04	14.70	0.43	0.39
A3	389,477	794,218	28	0.28	0.25	14.80	0.16	0.11
A4	679,445	810,781	29	0.49	0.45	1.20	0.06	0.04
w	6.83	7.04	6.17	5.38	5.54	6.50	6.87	6.08

Table 7: Input variables for MCDM, Building 1.

DV [units]	C1 [€]	C2 [€]	C3 [days]	C4	C5	C6	C7 [%]	C8 [%]
A1	1,792,080	2,915,946	92	0.07	0.25	1.33	0.33	0.33
A2	41,528	43,487	16	0.17	0.04	2.90	1.77	1.77
A3	151,435	254,743	25	0.28	0.25	2.90	0.38	0.34
A4	224,661	186,082	28	0.49	0.45	1.24	0.13	0.12
w	6.83	7.04	6.17	5.38	5.54	6.50	6.87	6.08

Table 8: Input variables for MCDM, Building 2.

5.2 Ranking of retrofitting interventions

The rank of each retrofitting alternative is listed in Table 9 (Building 1) and Table 10 (Building 2). To evaluate the influence of EI, two analyses were carried out, i.e. one including EIs (all DVs of Table 1) and other without considering EIs (excluding C8). For Building 1, it is observed that when EI is integrated into the MCDM, A4 results as the most convenient retrofit alternative. The relative closeness among A4, A3 and A2 is very similar, especially between A3 and A2. On the other hand, when EI is excluded from the analysis, A2 is ranked as the first option. In this scenario, the relative closeness of A2 is larger than A3 and A4, but for A3 and A4 this parameter is close to one another.

Moreover, for Building 2, the influence of EIs does not affect the rank preferences of the retrofitting options. For both analysis scenarios, A3 is selected as the most ideal solution with a considerably larger relative closeness compared to the other strategies. Indeed, the rank remains unchanged (i.e. A3-A4-A2-A1). However, it is observed that the relative closeness decreases when EIs are not considered in the MCDM analysis. A possible reason for this same pattern is that the values associated with EI (C8) for Building 2 are very similar to EAL (C7). Therefore, this similarity does not affect considerably the rank preference, especially since C8

is considered sixth in the order of preference of the weight vector w (i.e. sixth larger weight 6.08).

One could argue that A2 should not be considered within the set of retrofitting alternatives for both buildings, given that, even though the resulting lateral capacity is considerably larger than that of the as-built configuration and the storey drifts are reduced, the performance capacity (controlled by joint failure) remains unchanged. Additionally, the nonlinear dynamic analysis showed that the collapse vulnerability and expected losses were only slightly improved or even worsened with respect to the original building. However, this depends on the analysis and/or conditions of the project. Additionally, integration of refined methods or conservative assessment approaches that are more consistent with reality may not be possible, especially for regions where prompt solutions are needed. Therefore, the MCDM may be applied to select the most appropriate solution in conjunction with simplified methods, as long as they include relevant evaluation parameters for a particular case study.

Consideration	Alternatives	A1	A2	A3	A4
With EI	Relative closeness	0.472	0.522	0.523	0.539
	Rank	IV	III	II	I
No EI	Relative closeness	0.459	0.573	0.484	0.494
	Rank	IV	I	III	II

Table 9: Rank of alternatives for Building 1.

Consideration	Alternatives	A1	A2	A3	A4
With EI	Relative closeness	0.444	0.577	0.756	0.697
	Rank	IV	III	I	II
No EI	Relative closeness	0.400	0.638	0.745	0.676
	Rank	IV	III	I	II

Table 10: Rank of alternatives for Building 2.

6 CONCLUSIONS

This paper looked at the seismic retrofitting of two case-study existing buildings in Italy. Several retrofitting alternatives were examined and the choice via a multi-criteria decision making (MCDM) framework considering economic, social, environmental and technical aspects was evaluated. Based on the results obtained, the following observations can be made:

- The influence of environmental impacts greatly affects the preference of a retrofitting strategy and can alter the rank of the options in a multi-criteria decision making analysis, highlighting the importance of also considering the environmental impacts for evaluating retrofitting options;
- The retrofitting strategy based solely on CFRP was ranked as the least convenient solution in both buildings. Even though this strategy has the lowest architectural impact, the high

values associated with installation cost, maintenance and duration of works, diminish its attractiveness;

- The strategy with steel braces and CFRP is considered as the most convenient strategy for Building 2 and second-best for Building 1; this strategy achieves a balance among all the evaluation parameters that make it stand out among the other strategies;
- The strategy involving CFRP and viscous dampers achieved the best structural performance and was selected as the most beneficial strategy for Building 1. However, this option was ranked as the second most favourable solution for Building 2;
- The retrofitting scheme composed only of exterior steel braces had an insignificant performance improvement, but its lowest implementation costs made it stand out as the most convenient strategy for Building 1 when environmental impacts were not considered. This strategy is however not practical for Building 2 since its performance resulted to be worse than that of the as-built configuration.

Lastly, MCDM can be adopted in large scale scenarios or in cases where there are limited resources (e.g. developing countries) where retrofitting options are evaluated for many buildings. In such cases, simplified methods [33] can be practical for selecting the most appropriate retrofitting strategy, as an alternative to refined nonlinear dynamics analysis.

REFERENCES

- [1] D. Perrone, G.J. O'Reilly, R. Monteiro, A. Filiatrault. Assessing seismic risk in typical Italian school buildings: From in-situ survey to loss estimation. *International Journal of Disaster Risk Reduction*, **44**, 101448, 2020, <https://doi.org/10.1016/j.ijdr.2019.101448>.
- [2] W. Carofilis, D. Perrone, G. O'Reilly, R. Monteiro, A. Filiatrault. Seismic retrofit of existing school buildings in Italy: performance evaluation and loss estimation. *Engineering Structures*, **225**, 2020, DOI: <https://doi.org/10.1016/j.engstruct.2020.111243>.
- [3] L. Sousa, M. Monteiro. 2018. Seismic retrofit options for non-structural building partition walls: Impact on loss estimation and cost-benefit analysis. *Engineering Structures*, **161**, 8–27, 2018, doi: 10.1016/j.engstruct.2018.01.028.
- [4] W. Carofilis, G. Gabbianelli, R. Monteiro. Assessment of multi-criteria evaluation procedures for identification of optimal retrofitting strategies for existing RC buildings, *Journal of Earthquake Engineering*, 2021, DOI:10.1080/13632469.2021.1878074.
- [5] Caterino N, Iervolino I, Manfredi G, Cosenza E. Multi-criteria decision making for seismic retrofitting of RC structures. *Journal of Earthquake Engineering*, **12**, 555-583, 2008, DOI: 10.1080/13632460701572872.
- [6] R. Gentile, C. Galasso, Simplified seismic loss assessment for optimal structural retrofit of RC buildings. *Earthquake Spectra*, **00**, 1-20, 2020, DOI: 10.1177/8755293020952441.
- [7] M. Caruso, R. Pinho, F. Bianchi, F. Cavalieri, M. Teresa. A Life Cycle Framework for the Identification of Optimal Building Renovation Strategies Considering Economic and Environmental Impacts. *Sustainability*, **26**, 2020.

- [8] N. Clemett, W. Carofilis, G.J. O'Reilly, G. Gabbianelli, R. Monteiro. Optimal retrofitting of existing buildings considering environmental impact. *Engineering Structures*, Submitted - Unpubl n.d.
- [9] T.L. Saaty. The Analytic Hierarchy Process McGraw-Hill. New York, 1980.
- [10] C.L. Hwang, K. Yoon. Multiple Attribute Decision Making. *Lecture Notes in Economics and Mathematical Systems*, **186**, 1981. Springer-Verlag. Berlin.
- [11] W. Carofilis, N. Clemett, G. Gabbianelli, G. O'Reilly, R. Monteiro. Influence of parameter uncertainty in multi-criteria decision-making when identifying optimal retrofitting strategies for RC buildings. *Journal of Earthquake Engineering*, Submitted - Unpubl n.d.
- [12] FEMA. Seismic Performance Assessment of Buildings, Volume 3 – Supporting Electronic Materials and Background Documentation, Third Edition, 2018. Washington D.C.: Federal Emergency Management Agency.
- [13] G. Majeau-Bettez, A.H. Strømman, E.G. Hertwich. Evaluation of Process- and Input–Output-based Life Cycle Inventory Data with Regard to Truncation and Aggregation Issues. *Environ Sci Technol*, **45**, 10170–7, 2011, <https://doi.org/10.1021/es201308x>.
- [14] W. Leontief. Input-Output Economics. Second, reprint. Oxford University Press; 1986.
- [15] C.T. Hendrickson, A. Horvath, S. Joshi, M. Klausner, L.B. Lave, F.C. McMichael. Comparing two life cycle assessment approaches: a process model vs. economic input-output-based assessment. Proc. 1997 IEEE Int. Symp. Electron. Environ. ISEE-1997, San Francisco, CA, USA: IEEE; 176–81, 1997. <https://doi.org/10.1109/ISEE.1997.605313>.
- [16] M. Huang, K. Simonen. Comparative Environmental Analysis of Seismic Damage in Buildings. *J Struct Eng*, **146**, 05019002, 2020. [https://doi.org/10.1061/\(ASCE\)ST.1943-541X.0002481](https://doi.org/10.1061/(ASCE)ST.1943-541X.0002481).
- [17] Y. Yang, W.W. Ingwersen, T.R. Hawkins, M. Srocka, D.E. Meyer. USEEIO: A new and transparent United States environmentally-extended input-output model. *J Clean Prod*, **158**, 308–18, 2017, <https://doi.org/10.1016/j.jclepro.2017.04.150>.
- [18] F. McKenna, M.H. Scott, G.L. Fenves. Nonlinear finite-element analysis software architecture using object composition. *J Comput Civ Eng*, **24**, 95–107, 2010, doi: 10.1061/ (ASCE) CP.1943-5487.0000002.
- [19] G.J. O'Reilly, T.J. Sullivan. Modeling Techniques for the Seismic Assessment of the Existing Italian RC Frame Structures. *Journal of Earthquake Engineering*, **23**(8), 1262–1296, 2019, DOI: 10.1080/13632469.2017.1360224.
- [20] M.H. Scott, G.L. Fenves. Plastic hinge integration methods for force-based beam column elements. *J Struct Eng*, **132**, 244–52, 2006, doi: 10.1061/ (ASCE)0733-9445(2006) 132:2(244).
- [21] Norme Tecniche Per Le Costruzioni (NTC). Rome, Italy, 2018.
- [22] K. Sassun, T.J. Sullivan, P. Morandi, D. Cardone. Characterising the in-plane seismic performance of infill masonry. *Bull N Z Soc Earthq Eng*, **49**, 98–115, 2016, <https://doi.org/10.5459/bnzsee.49.1.98-115>.

- [23] L.D. Decanini, L. Liberatore, F. Mollaioli. Strength and stiffness reduction factors for infilled frames with openings. *Earthq Eng Eng Vib*, **13**, 437–54, 2014, <https://doi.org/10.1007/s11803-014-0254-9>.
- [24] G.J. O'Reilly (2021). Limitations of Sa(T1) as an intensity measure when assessing non-ductile infilled RC frame structures. *Bulletin of Earthquake Engineering*. <https://doi.org/10.1007/s10518-021-01071-7>
- [25] Global Earthquake Model (GEM). The openquake-engine user manual. *Open- Quake Manual for Engine version 3.7.0*, 2019, 183. 10.13117/GEM.OPENQUAKE.MAN.ENGINE.3.7.0
- [26] C. Meletti, F. Galadini, G. Valensise, M. Stucchi, R. Basili, S. Barba, G. Vannucci, E. Boschi. A seismic source zone model for the seismic hazard assessment of the Italian territory. *Tectonophysics*, **450** (1–4), 85–108, 2008, doi: 10.1016/j. tecto.2008.01.003.
- [27] S. Akkar, M.A. Sandikkaya, J.J. Bommer. Empirical ground-motion models for point-and extended-source crustal earthquake scenarios in Europe and the Middle East. *Earthquake Engineering*, **12**, 359–387, 2014, doi:10.1007/ s10518-013-9461-4.
- [28] M. Sandikkaya, S. Akkar, P. Bard. A nonlinear site-amplification model for the next Pan-European ground-motion predictions equations. *Bulletin of the Seismology Society of America*, **130** (1): 1–32, 2013, doi: 10.1785/ 0120120008.
- [29] M. Kohrangi, P. Bazzurro, D. Vamvatsikos, A. Spillatura. Conditional spectrum-based ground motion record selection using average spectral acceleration. *Earthquake Engineering & Structural Dynamics*, **46** (10), 1667–85, 2017, doi: 10.1002/eqe.2876
- [30] K.R. Mackie, B. Stojadinović. Comparison of Incremental Dynamic, Cloud, and Stripe Methods for Computing Probabilistic Seismic Demand Models. *Struct. Congr. 2005, New York, New York, United States: American Society of Civil Engineers*, 1–11, 2005, [https://doi.org/10.1061/40753\(171\)184](https://doi.org/10.1061/40753(171)184).
- [31] J.W. Baker. Efficient Analytical Fragility Function Fitting Using Dynamic Structural Analysis. *Earthq Spectra*, **31**, 579–99, 2015, <https://doi.org/10.1193/021113EQS025M>.
- [32] G. O'Reilly, D. Perrone, M. Fox, R. Monteiro, A. Filiatrault. Seismic assessment and loss estimation of existing school buildings in Italy. *Eng Strt*, **168**,142–62, 2018, <https://doi.org/10.1016/j.engstruct.2018.04.056>.
- [33] S. Ruggieri, D. Perrone, M. Leone, G. Uva, M.A. Aiello. A prioritization RVS methodology for the seismic risk assessment of RC school buildings. *International Journal of Disaster Risk Reduction*, **51**, 101807, 2020, <https://doi.org/10.1016/j.ijdrr.2020.101807>.

NUMERICAL INVESTIGATIONS ON THE RESIDUAL CAPACITY AND ECONOMIC LOSSES OF EARTHQUAKE-DAMAGED REINFORCED CONCRETE WALL STRUCTURES

Cristiana Ceccarelli¹, Simona Bianchi¹, Livio Pedone¹, Stefano Pampanin¹

¹ Sapienza University of Rome,
Department of Structural and Geotechnical Engineering, Via Eudossiana 18, 00184, Rome, Italy,
ceccarelli.1530827@studenti.uniroma1.it, simona.bianchi@uniroma1.it,
livio.pedone@uniroma1.it, stefano.pampanin@uniroma1.it

Abstract

The substantial damage to Reinforced Concrete (RC) structural walls observed from post-earthquake reconnaissance has prompted the attention on the need for improved code-based design provisions for these structural elements as well as for detailed investigations on their residual capacity, typically neglected in the retrofit/repair evaluation. Although several research works and international guidelines focusing on the seismic performance of damaged structural walls are available from a state-of-the-art review, a specific methodology to evaluate the earthquake-related damage to structural walls is still missing in literature. Therefore, this research work investigates the seismic residual capacity of RC walls through parametric numerical analyses, aiming to provide indications on the assessment methodology to be used in practical applications. The numerical investigation is initially carried out by implementing Finite Element Modelling of RC walls with different mechanical properties and expected failure mechanisms. This allows to evaluate and collect stiffness/strength reduction coefficients to be adopted for different post-earthquake damage conditions. Then, the influence of residual capacity on the economic seismic losses of wall structures is investigated and discussed. Specifically, a multi-story case-study RC building is selected, and pre- and post-earthquake loss assessments are carried out considering alternative wall typologies and damage levels. Analytical-based nonlinear analyses highlight that the loss of stiffness and strength can lead to increasingly higher economic losses depending on the damage level of the structural wall. Moreover, substantial economic losses can be estimated if residual capacity is taken into account even at low-intensity seismic levels. Therefore, such methodology could provide valuable information to support decisions on the post-earthquake repair/retrofit/demolition.

Keywords: Residual Capacity, Seismic Assessment, Reinforced Concrete, Wall Structures, Repair Costs.

1 INTRODUCTION

The recent seismic events in seismic-prone countries have further highlighted the controversial issues related to the rehabilitation of earthquake-damaged buildings. On one hand, rapid post-earthquake surveys are needed for the evaluation of the safety level of damaged buildings and their possible re-occupancy [1]. On the other hand, a detailed assessment of the seismic residual capacity of damaged buildings, including loss investigations, is critical to support the decision-making process of repair vs. demolition and guide in the selection/design and implementation of appropriate techniques able to ‘restore’ the building to its undamaged conditions. Moreover, the crucial need to gain a better understanding of the residual capacity of earthquake-damaged buildings refers to both existing and new structures. In fact, according to the “Capacity Design” philosophy, even modern buildings are often affected by extensive structural damage after a major earthquake, as observed in *Kam et al.* [2] during the Canterbury Earthquake Sequence 2010-2011.

Focusing on Reinforced Concrete (RC) structural walls, widely used as primary lateral-force resisting systems in earthquake-resistant structures, the substantial damage to these components observed from post-earthquake reconnaissance (2010 Darfield and 2011 Lyttleton in New Zealand [2]; 2010 Chile [3]; Figure 1) has prompted the attention on the need for improved code-based design provisions for these structural elements as well as for detailed investigations on their residual capacity, typically neglected in the retrofit/repair evaluation.



Figure 1: Observed damage to RC structural walls in a) the 2010 Chile earthquake [3] and b) the 2011 Lyttleton earthquake, New Zealand [2].

Despite research works and international guidelines focusing on the seismic performance of damaged structural walls are available in literature (e.g. FEMA 306 [4]; JBDPA Guideline [5]), a specific methodology to evaluate the earthquake-related damage to structural walls as well as the consequent loss of stiffness/strength affecting the component capacity is still missing. Following this goal, this paper aims to investigate the seismic residual capacity of RC walls through numerical modelling, providing indications on both the methodology and the stiffness/strength reduction coefficients to be adopted for different post-earthquake damage levels. A parametric analysis is thus developed to study the residual capacity of RC walls with different mechanical properties and expected failure mechanisms (flexural, flexure-shear, shear). The structural walls are analyzed adopting a refined FEM modelling approach, based on the modified compression field theory, using the structural software VecTor2 (*Vecchio* [6]). Firstly, the seismic behavior of the RC walls under reversed-cyclic loads is investigated to simulate the achievement of specific damage states, assessing residual cracks and residual

displacements at each damage level. Then, a unidirectional monotonic lateral load is applied to the damaged wall to evaluate the force-displacement capacity curve for each configuration. Hence, according to the FEMA 306 approach, stiffness and strength reduction coefficients, namely λ_k and λ_Q respectively (as shown in Figure 2), are derived by comparing the pre- and post- earthquake force-displacement curves for each damage state and wall configuration. Lastly, the influence of residual capacity on the estimation of the economic seismic losses of wall structures is also investigated and discussed. Specifically, a RC case-study building is selected, and loss assessments are implemented considering different wall typologies and damage levels. For each configuration, the economic losses are computed in terms of both Expected Annual Losses (EAL) and Probable Maximum Losses (PML) to highlight the importance of including residual capacity considerations when implementing economic analyses.

2 EVALUATION OF RESIDUAL CAPACITY

In the past decades, a substantial research effort has been dedicated at international level to gain a better understanding of the post-earthquake residual capacity of buildings. In 1994 *Holmes* [7] discussed the critical need for improved seismic assessment accounting for the actual lateral load of buildings and considering different damaged levels. Following this research line, two main guidelines were developed: 1) FEMA 306 [4] in the United States, and 2) JBDPA Guideline [5] in Japan (described in English in *Nakano et al.* [8]; overview available in *Maeda et al.* [1]). Both documents propose a conceptually similar approach, based on the definition of capacity reduction factors for structural members to simulate the achievement of a specific damage state. In FEMA 306 a modification of plastic hinges' response is proposed for damaged elements, based on stiffness, strength and ductility reduction coefficients, namely λ_k , λ_Q and λ_D (Figure 2a). In the JBDPA Guideline a single capacity reduction factor for structural members, i.e. η , defined as the ratio between residual energy dissipation capacity and original energy dissipation capacity is adopted (Figure 2b).

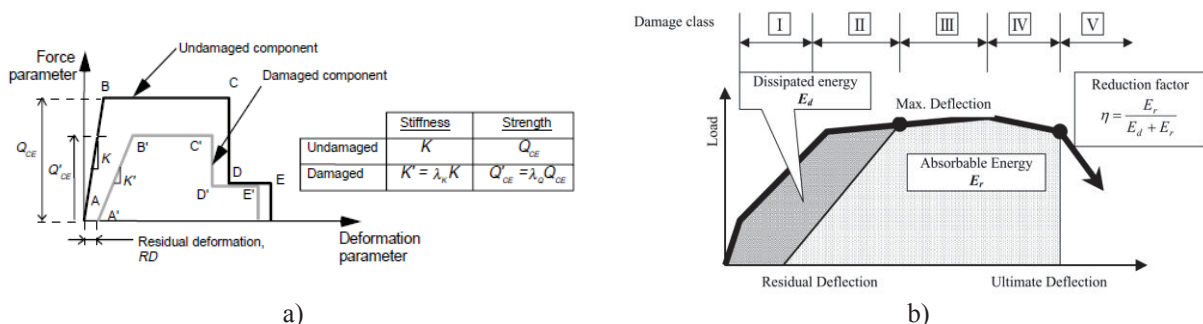


Figure 2: a) Stiffness, strength and residual displacement reduction coefficients in FEMA 306 [4]; b) capacity reduction factor for structural members in JBDPA Guideline [5].

Furthermore, FEMA 307 [9] reports background and theoretical information as well as an example of application of the FEMA 306 procedure. According to FEMA 306 (whose procedure is adopted within this research work), the most reliable approach to determine λ reduction factors would consist of performing experimental investigations on two identical specimens for each structural component. One specimen would represent the component in its pre-earthquake condition, while the other specimen would represent the component in its post-earthquake condition (i.e., earthquake-damaged). Therefore, the reduction factor values would be derived by comparing the force-displacement capacity curves of the two specimens. However, FEMA 307 highlights that at the date of the document, no such test campaigns on RC walls were available in literature to calculate the λ factors. In the absence of this type of

tests, an alternative approach was adopted, based on individual cyclic-static tests. According to this approach, the change in force-displacement response from cycle to cycle is examined as the displacement increases. As reported in FEMA 307, firstly the component type and behavior mode (e.g., flexural, shear, etc.) are defined according to the selected test. The critical damage states (e.g., spalling, cracking, etc.) are observed during the load-displacement history of the test and are correlated with the displacement ductility achieved by the component. Then, by comparing the initial and subsequent cycles, λ factors are derived. Finally, both the critical damage indicators and the associated reduction factors are discretized into six damage severity levels (from “None” to “Extreme”). An example of FEMA 306 component damage classification is reported in Figure 3a for an isolated wall with ductile flexural behavior and “Insignificant” damage level. It is worth noting that, even for “Insignificant” damage level, stiffness reduction occurs, since the component stiffness is most sensitive to damage, as shown in Figure 3b.

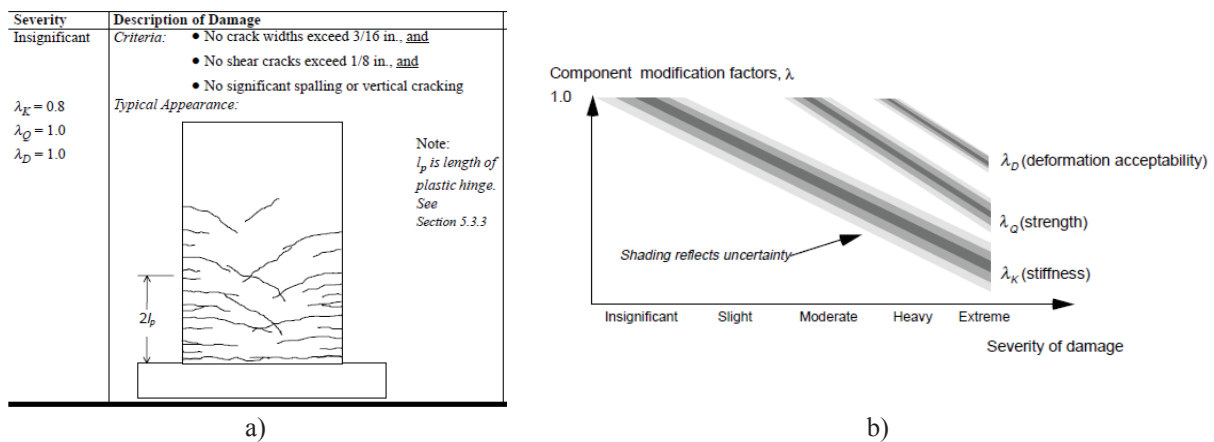


Figure 3: a) Example of component damage classification for an isolated wall with ductile flexural behavior; b) general relationship between damage severity and modification factors [4].

Following the FEMA 306/307 approach, significant research effort has been dedicated in order to derive coefficient reduction factors for damaged structural elements as well as to define a detailed general framework for the evaluation of the residual capacity of RC buildings (e.g., [10, 11]). Nevertheless, these investigations mainly focused on frame systems (e.g., [12–14]). Looking at structural walls, several experimental and numerical studies can be found in literature, however these research works focused at improving the understanding on the seismic response and performance of RC walls. *Dashti et al.* [15] developed a finite element model based on curved shell element formulation to predict the nonlinear behavior of planar RC structural walls with specific focus on out-of-plane instability mechanisms. Moreover, the same authors carried out a detailed experimental investigation on the out-of-plane instability in rectangular RC walls [16]. *Shegay et al.* [17] performed experimental testing on four flexural walls with rectangular cross sections in order to investigate the impact of the imposed axial load ratio as well as the transverse reinforcement detailing on their seismic performance. *Niroomandi et al.* [18] experimentally investigated the effects of the bi-directional loading on the seismic behavior of slender rectangular RC walls. An overview of comprehensive research programs, developed in New Zealand, following the 2010/2011 Canterbury earthquakes, and including practical recommendations for the design and assessment of RC walls, is available in *Shegay et al.* [19]. *Li and Xiang* [20] suggested a formulation for assessing the effective stiffness of RC squat structural walls by performing a comprehensive parametric study. A similar study was discussed in *Sharifi and Shafieian* [21], who proposed a formulation to de-

termine the effective stiffness of slender and squat walls, based on statistical analyses of 154 existing experiments available in literature. *Kolozvari et al.* [22] developed an analytical model able to capture the interaction between axial/flexural and shear responses for RC walls subjected to reversed-cyclic, based on a two-dimensional fiber-based macroscopic model, and the experimental calibration and validation of this analytical wall model was also carried out [23]. Finally, a special collection of 10 papers presenting recent advances in seismic design of Reinforced Concrete walls can be found in *Sritharan and Beyer* [24]. However, as mentioned above, further investigations and research efforts are required to study and better understand the post-earthquake residual capacity of structural wall systems.

3 PARAMETRIC INVESTIGATIONS ON RC WALLS

A parametric analysis is carried out to investigate the seismic residual capacity of RC walls. After the collection of experimental literature data on structural walls, refined FEM models are implemented and calibrated by comparing numerical and experimental results. Then, additional case-study walls are defined by modifying the geometrical and structural details of the selected RC walls. Non-linear static analyses are thus performed to assess the seismic performance of the walls in their undamaged and damaged configurations. Different damage conditions as well as assessment methods are indeed considered. Finally, for each case-study wall system, strength and stiffness reduction factors are derived. Detailed information about the implemented methodology and the analysis results are reported within this section.

3.1 RC wall configurations and modelling approach

The case-study structural walls are selected from experimental tests available in literature and taking into account alternative collapse modes (i.e., flexural, flexural/shear and shear). Specifically, six experimental tests on structural walls are selected. Geometrical details and material properties of these RC walls are reported in Table 1. More details about the specimens can be found in the cited papers.

Author(s)	ID Specimen	A.R. [-]	H _w /t _w [-]	S.S.R. [-]	ν [-]	f'_c [MPa]	f_y [MPa]	$\rho_{l, BE}$ [%]	$\rho_{h, web}$ [%]	Collapse mode
Thomsen and Wollace [25]	RW2	3.00	35.88	3.25	0.10	34.00	425.0	2.90	0.33	Flexural
Dazio et al. [26]	WSH6	2.25	30.00	2.25	0.11	45.60	584.0	1.54	0.25	Flexural
Tran and Wollace [27]	SP4	1.69	13.50	1.69	0.10	55.80	414.0	6.06	0.73	Flexural/shear
Vallenas et al. [28]	S6	1.26	26.73	1.59	0.05	35.00	482.0	5.60	0.55	Flexural/shear
Lefas et al. [29]	SW11	1.00	10.71	1.00	0.00	52.30	470.0	3.00	1.10	Shear
Lefas et al. [29]	SW12	1.00	10.71	1.00	0.08	52.30	470.0	3.00	1.10	Shear

Note: A.R. = Aspect Ratio; H_w = wall height; t_w = wall thickness; S.S.R. = Shear Span Ratio, ν = axial load ratio; f'_c = concrete compression strength; f_y = steel yield stress; $\rho_{l, BE}$ = boundary element longitudinal reinforcement ratio, $\rho_{h, web}$ = web horizontal reinforcement ratio.

Table 1: Geometrical details and material properties of the selected structural walls.

The structural walls are analyzed adopting a refined Finite Element Modelling approach based on the Modified Compression Field Theory (MCFT, *Vecchio and Collins* [30]). The MCFT is an analytical model for predicting the load-deformation response of reinforced concrete membrane elements subjected to shear and normal stresses. It is based on three sets of relationships: 1) compatibility relationships for concrete and reinforcement average strains; 2) equilibrium relationships involving average stresses in concrete and reinforcement; 3) constitutive relationships for cracked concrete and reinforcement [31].

The numerical analyses are performed using the structural software VecTor2 [6]. The reinforced concrete wall is modelled by plane stress rectangular elements. Steel transversal bars are modelled as smeared reinforcement in concrete elements, while steel longitudinal bars are represented by mono-dimensional “truss” elements. The *Popovics* [32] stress-strain relationship is adopted to model the (unconfined) concrete cover, while the *Mander et al.* [33] behavior is used for the (confined) concrete core. The steel stress-strain relationship is modeled according to *Seckin* [34], allowing to include the so-called Bauschinger effect. Figure 4 shows an example of structural wall numerical model in VecTor2 and the results obtained in terms of crack patterns (numerical vs. experimental).

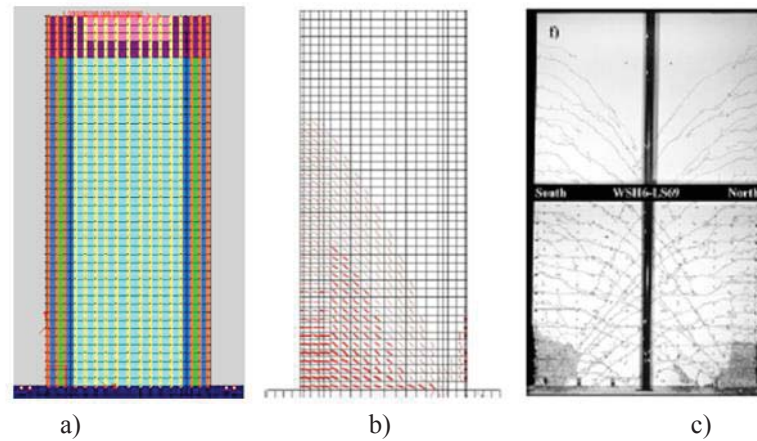


Figure 4: Example of: a) numerical model in VecTor2; b) crack patterns obtained by VecTor2 vs c) crack patterns observed during the experimental tests performed by *Dazio et al.* [26].

For all the selected walls, numerical vs. experimental comparisons in terms of cyclic response and crack patterns are carried out. Results highlight a good agreement between numerical and experimental behavior, confirming the reliability of the adopted modelling approach. In Figure 5 an example of comparison in terms of cyclic response is presented for two flexural-dominated walls (for the walls affected by shear collapse mechanisms, only monotonic experimental curves are available).

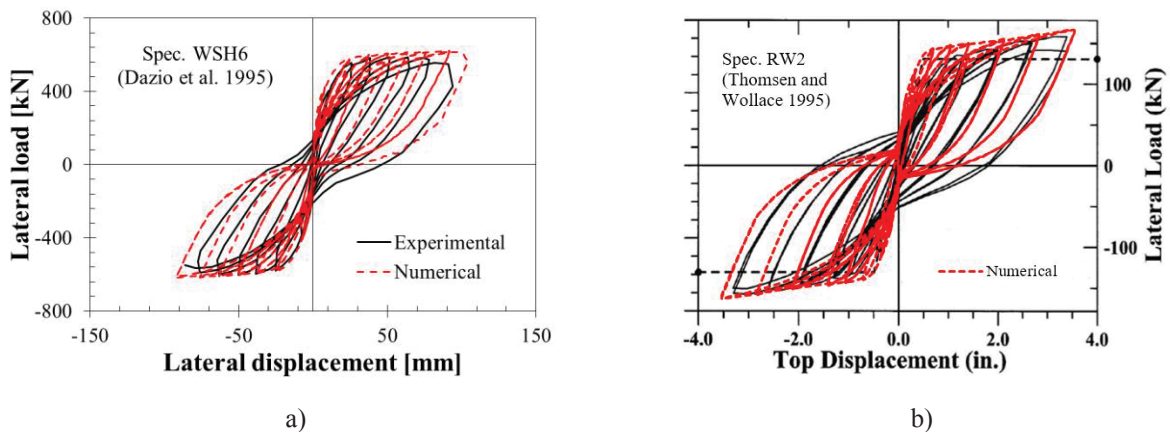


Figure 5: Example of comparison in terms of cyclic response: a) Experimental data from *Dazio et al.* [26]; b) original graph from the experimental tests by *Thomsen and Wallace* [25].

In order to increase the dataset, parametric configurations of the RC walls listed in the previous Table 1 are identified and numerical analyses are simulated for each additional case-

study adopting the same modelling approach previously described. Specifically, the walls are parameterized in terms of geometrical details (i.e., aspect ratio), applied axial load (v) and material properties. It is worth noting that the expected behavior/collapse mode of the wall (flexural or shear or flexural/shear) can thus change, especially when the aspect ratio is modified. Table 2 summarizes the main properties of each structural wall considered to develop the parametric analysis. In total 39 RC walls are involved (13 for each collapse mode).

Collapse mode	ID Case-study	A.R. [-]	H_w/t_w [-]	S.S.R. [-]	v [-]	f'_c [MPa]	f_y [MPa]	$\rho_{l, BE}$ [%]	$\rho_{h, web}$ [%]
Flexural	1	3.00	35.88	3.25	0.10	34.00	425.0	2.90	0.33
	2	3.00	35.88	3.25	0.10	45.60	425.0	2.90	0.33
	3	3.00	35.88	3.25	0.10	34.00	584.0	2.90	0.33
	4	3.00	35.88	3.25	0.10	34.00	425.0	6.00	0.33
	5	2.25	30.00	2.25	0.11	45.60	584.0	1.54	0.25
	6	2.25	30.00	2.25	0.055	45.60	584.0	1.54	0.25
	7	2.25	30.00	2.25	0.22	45.60	584.0	1.54	0.25
	8	2.25	30.00	2.25	0.11	34.00	584.0	1.54	0.25
	9	2.25	30.00	2.25	0.11	45.60	584.0	2.90	0.25
	10	3.00	32.13	3.00	0.08	52.30	470.0	3.00	1.10
	11	3.00	32.13	3.00	0.08	34.00	470.0	3.00	1.10
	12	3.00	32.13	3.00	0.08	52.30	584.0	3.00	1.10
	13	3.00	32.13	3.00	0.08	52.30	470.0	6.00	1.10
Flexural/Shear	14	1.69	13.50	1.69	0.10	55.80	414.0	6.06	0.73
	15	1.69	13.50	1.69	0.05	55.80	414.0	6.06	0.73
	16	1.69	13.50	1.69	0.20	55.80	414.0	6.06	0.73
	17	1.69	13.50	1.69	0.10	34.00	414.0	6.06	0.73
	18	1.69	13.50	1.69	0.10	55.80	500.0	6.06	0.73
	19	1.26	26.73	1.59	0.05	35.00	482.0	5.60	0.55
	20	1.26	26.73	1.59	0.05	55.80	482.0	5.60	0.55
	21	1.26	26.73	1.59	0.05	35.00	584.0	5.60	0.55
	22	1.26	26.73	1.59	0.05	35.00	482.0	6.06	0.55
	23	1.90	22.54	1.80	0.10	34.00	425.0	2.90	0.33
	24	1.90	22.54	1.80	0.10	55.80	425.0	2.90	0.33
	25	1.90	22.54	1.80	0.10	34.00	584.0	2.90	0.33
	26	1.90	22.54	1.80	0.10	34.00	425.0	2.90	0.33
Shear	27	1.00	10.71	1.00	0.00	52.30	470.0	3.00	1.10
	28	1.00	10.71	1.00	0.00	34.00	470.0	3.00	1.10
	29	1.00	10.71	1.00	0.00	52.30	584.0	3.00	1.10
	30	1.00	10.71	1.00	0.00	52.30	470.0	6.00	1.10
	31	1.00	10.71	1.00	0.08	52.30	470.0	3.00	1.10
	32	1.00	10.71	1.00	0.16	52.30	470.0	3.00	1.10
	33	1.00	10.71	1.00	0.08	45.60	470.0	3.00	1.10
	34	1.00	10.71	1.00	0.08	52.30	584.00	3.00	1.10
	35	1.00	10.71	1.00	0.08	52.30	470.0	3.00	1.10
	36	1.25	15.00	1.25	0.11	45.60	584.0	1.54	0.25
	37	1.25	15.00	1.25	0.11	52.30	584.0	1.54	0.25
	38	1.25	15.00	1.25	0.11	45.60	470.0	1.54	0.25
	39	1.25	15.00	1.25	0.11	45.60	584.0	3.00	0.25

Note: A.R. = Aspect Ratio; H_w = wall height; t_w = wall thickness; S.S.R. = Shear Span Ratio, v = axial load ratio; f'_c = concrete compression strength; f_y = steel yield stress; $\rho_{l, BE}$ = boundary element longitudinal reinforcement ratio, $\rho_{h, web}$ = web reinforcement ratio

Table 2: Selected case-study walls.

3.2 Non-linear static analyses

Non-linear static analyses are performed to assess the seismic performance of all the case-study structural walls in their pre- (undamaged) and post- earthquake (damaged) conditions. In particular, three post-earthquake damage levels are considered, namely: DS1 (limited damage), DS2 (moderate damage) and DS3 (severe damage). Nevertheless, in the international codes/guidelines practical and specific methods to identify these damage states are still under development, while only a qualitative damage description is often reported. Therefore, in this paper three alternative methods are considered and compared to identify the three damage levels for each wall configuration:

- The first method (M1) refers to the FEMA 307 [9] approach. Damage severity levels are correlated with the achievement of displacement ductility levels. More details about the FEMA 307 evaluation procedure are reported in the previous section.
- The second method (M2) refers to the fragility database of FEMA P-58 [35]. The existing repository of fragility data allows to identify the damage states by the achievement of specific drift levels and damage conditions (e.g. dimensions of cracking in concrete).
- The third method (M3) refers to the damage classification of FEMA 306 [4]. Specifically, as mentioned above, FEMA 306 provides crack pattern information associated with different damage severity levels and this description can be used to identify different damage levels.

A unidirectional monotonic lateral load is initially applied to each wall in order to evaluate the force-displacement capacity curve in its undamaged configuration. Then, a two-step procedure is adopted: 1) first, reversed-cyclic loads are applied to simulate the achievement of specific damage states (i.e., DS1, DS2, DS3) considering the identification methods described above (i.e., M1 vs. M2 vs. M3); 2) then, a unidirectional monotonic lateral load is applied to the damaged walls to evaluate the force-displacement capacity curve for each damaged configuration. This allows to derive stiffness and strength reduction coefficients (i.e., λ_K and λ_Q) by comparing the pre- and post- earthquake force-displacement curves. It is worth noting that a bilinearization of the capacity curves is needed to compute these reduction factors. In this work, two different bilinearization methods are considered, according to the procedure proposed by *Paulay and Priestley* [36] and FEMA 273 [37] (referred to as B1 and B2 respectively), and compared. The first approach provides the secant stiffness intersecting the pushover curve at $0.75 V_u$, where V_u is the average of the maximum shear values at the base of the wall, while for the second method the intersection point is identified at $0.6 V_y$, where V_y is now the wall yielding shear.

Figure 6 shows an example of load history adopted in the two-step non-linear static analysis of damaged wall configurations as well as an example of assessment of reduction factors through the capacity curves of both the undamaged and damaged wall (B2 bilinearization, DS3 level). In summary, three different damaged states are considered for each case-study wall by adopting three different damage identification methods (M1, M2, M3). Moreover, reduction factors are derived according to two alternative bilinearization methods (B1, B2). This leads to a total number of 702 values for both strength and stiffness reduction factors.

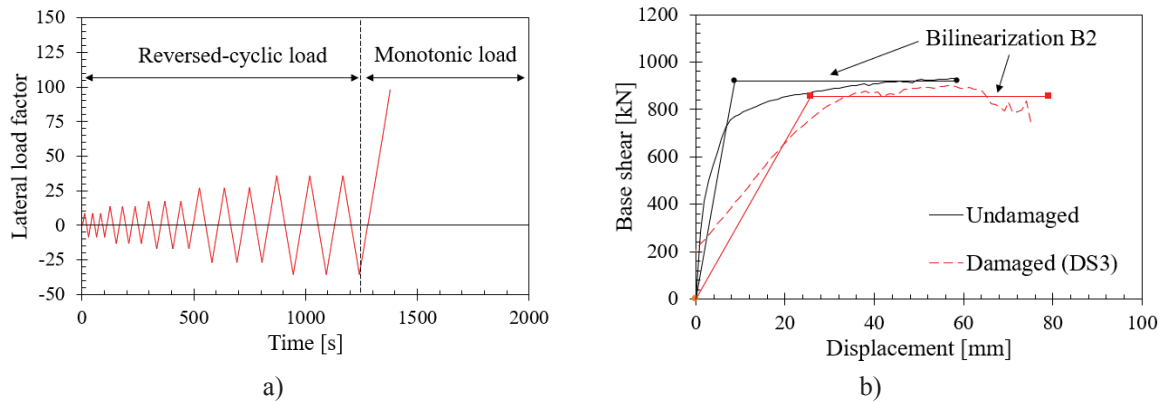


Figure 6: a) Load history for the non-linear static analysis of damaged walls; b) assessment of reduction factors by comparing the capacity curves of the undamaged and damaged wall (e.g., B2 bilinearization, DS3 level).

3.3 Reduction coefficients

Results in terms of strength and stiffness reduction factors (as percentage values [%]) are summarized in Table 3. The structural walls are classified according to their collapse mechanism mode and for each damaged state (DS1, DS2, DS3) and identification method (M1, M2, M3), as well as bilinearization procedure (B1, B2), average and dispersion (standard deviation) values of reduction factors are reported.

Method M1				Method M2				Method M3				
Type B1		Type B2		Type B1		Type B2		Type B1		Type B2		
Avg.	S.Dev.	Avg.	S.Dev.	Avg.	S.Dev.	Avg.	S.Dev.	Avg.	S.Dev.	Avg.	S.Dev.	
[%]	[-]	[%]	[-]	[%]	[-]	[%]	[-]	[%]	[-]	[%]	[-]	
Stiffness Reduction Coefficient (λ_K)												
Flexural mechanism												
DS1	74.61	0.043	77.92	0.051	71.54	0.044	58.00	0.082	66.85	0.087	53.46	0.090
DS2	42.85	0.054	47.85	0.107	50.92	0.054	41.15	0.074	51.69	0.082	40.92	0.095
DS3	35.69	0.046	34.85	0.069	41.54	0.047	34.15	0.064	41.38	0.066	33.54	0.085
Flexural/Shear mechanism												
DS1	80.08	0.036	73.42	0.051	60.69	0.086	55.23	0.064	67.85	0.119	59.85	0.079
DS2	52.92	0.097	54.42	0.057	42.08	0.058	39.08	0.070	44.69	0.094	36.46	0.090
DS3	36.69	0.085	41.75	0.098	33.00	0.074	29.69	0.089	27.46	0.078	22.15	0.096
Shear mechanism												
DS1	74.15	0.080	75.43	0.076	73.92	0.151	67.08	0.205	62.08	0.128	52.69	0.106
DS2	49.23	0.092	49.00	0.081	44.46	0.061	36.08	0.073	40.00	0.115	32.08	0.065
DS3	32.38	0.056	33.86	0.081	29.15	0.040	25.15	0.054	26.08	0.049	22.46	0.052
Strength Reduction Coefficient (λ_Q)												
Flexural mechanism												
DS1	99.77	0.004	99.92	0.003	99.62	0.005	99.38	0.007	99.46	0.005	99.38	0.007
DS2	98.69	0.006	98.69	0.011	99.15	0.008	98.38	0.012	99.15	0.007	98.46	0.012
DS3	97.54	0.014	97.69	0.015	98.46	0.007	97.85	0.013	98.46	0.010	97.46	0.011
Flexural/Shear mechanism												
DS1	99.92	0.003	99.58	0.005	91.62	0.275	98.62	0.005	99.15	0.008	98.77	0.004
DS2	97.08	0.030	98.42	0.005	87.92	0.268	95.08	0.025	95.38	0.024	96.15	0.018
DS3	93.77	0.047	96.83	0.019	85.46	0.261	91.31	0.042	89.08	0.044	88.69	0.031
Shear mechanism												
DS1	99.08	0.010	99.14	0.009	98.85	0.022	98.38	0.014	96.77	0.041	95.77	0.047
DS2	93.08	0.059	96.14	0.042	91.54	0.055	90.77	0.051	88.85	0.052	88.77	0.052
DS3	80.46	0.119	85.50	0.109	79.23	0.104	80.15	0.091	75.23	0.077	77.62	0.071

Table 3: Reduction coefficients obtained for the case-study walls.

Results highlight that stiffness is more sensitive to damage when compared to strength, and this is in agreement with FEMA 306. Moreover, the obtained mean reduction values are lower (especially in case of λ_K) when compared to DS1/DS2/DS3 reduction coefficients of 80/60/50 and 100/100/80 for λ_K and λ_Q , respectively, provided by FEMA 306 for flexural walls. Referring to the severe damage state (DS3), the strength loss obtained for flexural-dominated walls is less than 5%, while is around 10-15% for flexural/shear walls and almost 20-25% for walls affected by shear collapse. On the other hand, referring to the same damage level, higher stiffness losses can be observed for all the wall typologies, even more than 70% at DS3. The previous table also shows that walls with shear collapse mechanism have higher dispersion in the results, as highlighted in Figure 7a for the case of Method M1-Bilinearization B2. Furthermore, differences (less than 10% for M1, while less than 20% for M2, M3) can be highlighted when the two bilinearization methods (B1 vs. B2) are compared (Figure 7). Finally, it is worth noting that the damage assessment methods strongly affect the results. In fact, adopting the M1 method the lowest dispersion is found, while the M3 method leads to the highest dispersion values. This result is in agreement with the expectation, since referring to crack patterns (M3 method) can lead to higher uncertainty in the identification of damage states than using a direct indicator as the displacement ductility (M1 method).

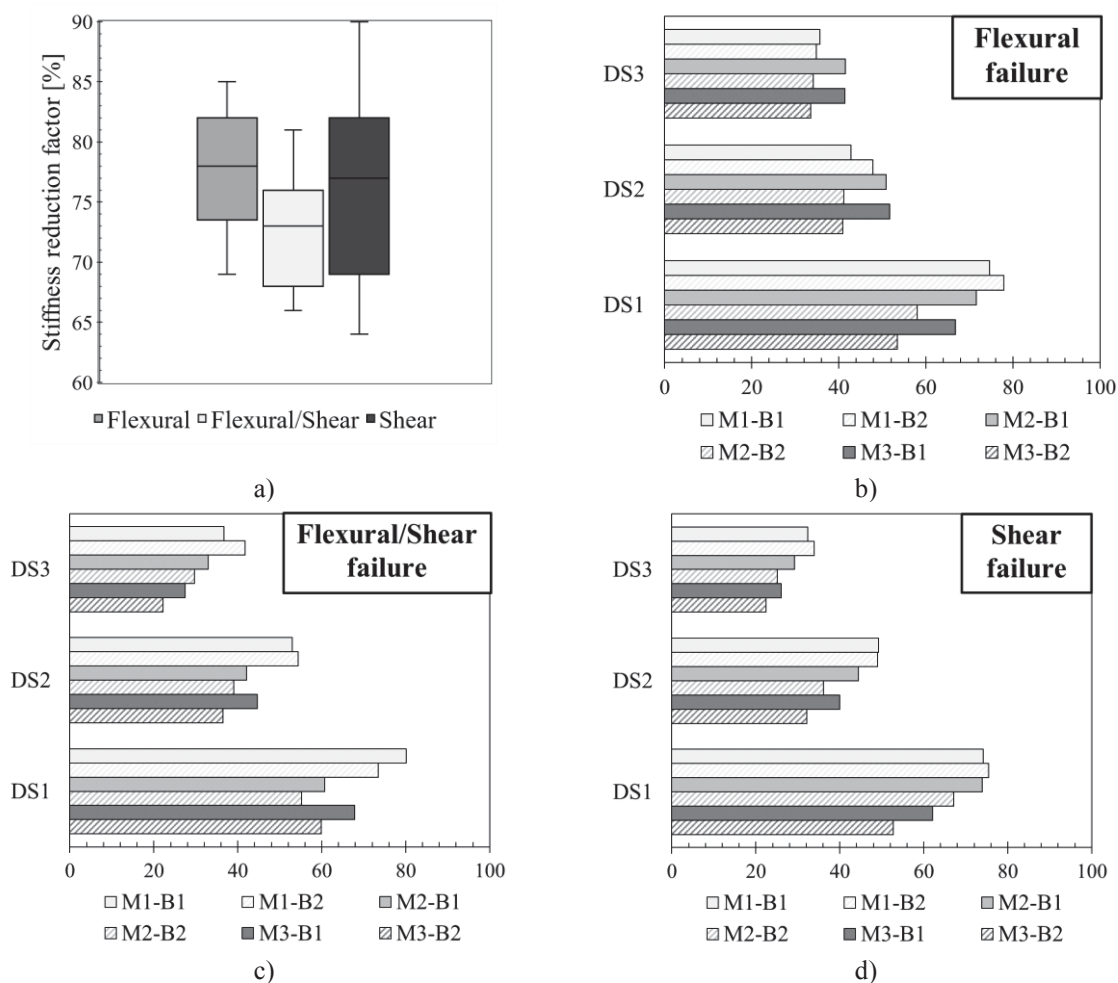


Figure 7: a) Mean and dispersion values of stiffness reduction factors λ_K (for Method M1 and Bilinearization B2); comparison between the λ_K values obtained from all the implemented approaches, in case of: b) flexural failure; c) flexural/shear failure; d) shear failure.

4 NUMERICAL ANALYSIS ON A MULTI-STORY RC BUILDING

4.1 Description of the case-study

The case-study building is a 5-story reinforced concrete structure with global dimensions and plan geometry as presented in Figure 8. This structure is selected from a previous research work developed by *Bianchi et al.* [38]. The structural skeleton consists of seismic-resistant four-bay frames in one direction and seismic-resistant walls in the orthogonal direction. The building has commercial and residential use and is located in a high-seismicity Italian zone (PGA of 0.353 g). Focusing on the wall direction, alternative typologies of structural systems are designed to provide the same Overturning Moment (OTM of 35000 kNm) of the initial reference multi-story building, namely: 1) a first case-study comprising four earthquake-resistant ductile walls, characterized by a flexural collapse mechanism (Case 1); 2) a second case-study consisting of the same geometrical configuration, but the RC walls are now affected by a brittle shear failure, i.e. no hierarchy of strengths principles is applied (Case 2). Although the reference building is a new structure, the shear-dominant walls are designed for the purpose of this study only.

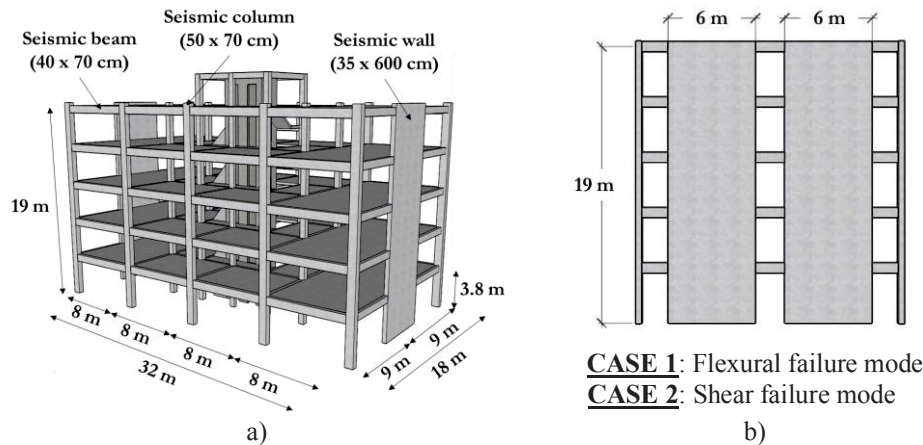


Figure 8: a) Global view of the reference building (Bianchi et al. [38]; b) new geometrical configuration designed in the wall direction (Case 1: flexural collapse; Case 2: shear collapse)

4.2 Numerical analysis

Non-linear static (pushover) analyses are performed following an analytical-based approach, the so-called Simple Lateral Mechanism Analysis (SLaMA) described in the NZSEE guidelines [39-41]. This practical methodology allows to determine the base shear-displacement (capacity) curves of the two case-study wall systems by simple analytical calculations accounting for the collapse mechanism (flexure, shear, flexure/shear) developing within the structural system. Then, following the pushover-based Capacity Spectrum Method [42, 43], the building performance points are computed at different seismic intensity levels (namely SLO, SLD, SLV, SLC, or, Immediate Operational, Damage Control, Life Safety and Collapse Prevention, respectively, as indicated in the NTC 2018 [44]).

Figure 9 (a, c) shows the demand vs. capacity results obtained in the Acceleration-Displacement Response Spectrum (ADRS) domain. This figure highlights the better behavior of the ductile flexural walls, even allowing for a greater dissipation and consequently a reduced seismic demand (response spectra at Ultimate Limit States are in fact reduced considering the building equivalent viscous damping). Instead, the shear-dominated walls are

characterized by a brittle behavior leading to a ultimate capacity point not even achieving the Life-Safety design spectrum. Finally, the damaged configurations for the two case-studies (Case 1, Case 2) are determined applying the reduction strength/stiffness coefficients already computed in the previous section (Figure 9 b, d).

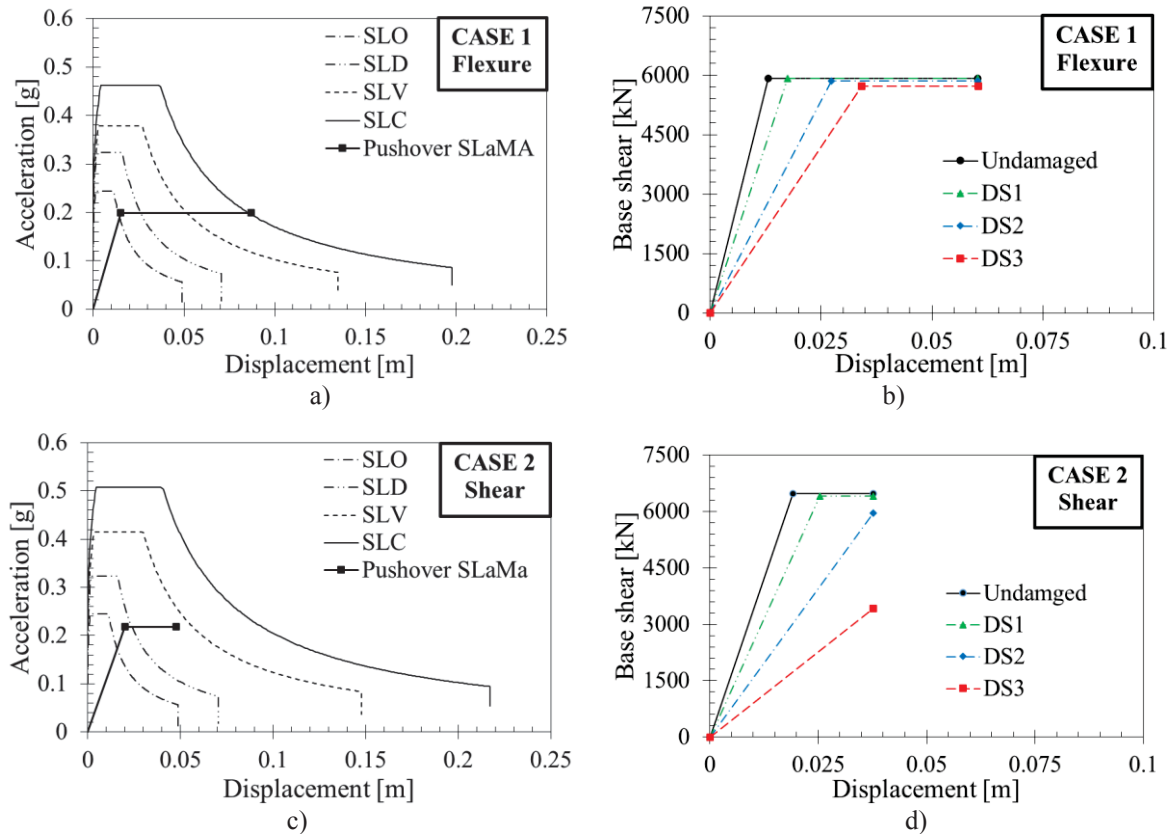


Figure 9: Capacity curves of the undamaged structure in the Acceleration-Displacement Response Spectrum (ADRS) domain and for all the damaged wall configurations (DS1, DS2, DS3): a) b) Case 1 - flexural failure mode; c) d) Case 2 - shear failure mode.

4.3 Loss assessment investigations

Loss assessment analyses are finally implemented considering as input data the floor accelerations and inter-story drift ratios (from the performance points) obtained at the various seismic intensities. Two alternative loss assessment procedures are involved: 1) the simplified approach described in the D.M. 65 [45], the “Seismic-Bonus” guidelines; 2) the rigorous probabilistic-based procedure defined in FEMA P-58 [35].

Focusing on the simplified methodology, results in terms of Expected Annual Losses (EAL) curves and values (expressed as percentage of the Replacement Cost - RC) are summarized in Figure 10 (referring to M1 damage assessment method and B1 bilinearization method) for both undamaged and damaged wall systems. The comparison highlights that the structural system comprising brittle RC walls (Case 2) leads to higher losses when compared to the structural configuration consisting of ductile walls (Case 1). Furthermore, for Case 1 and looking at DS1 damage level (and DS2 in some cases), lower economic losses are found when compared to the undamaged structure. This is due to the structural system yielding before the expulsion of the external infill walls (expected to be achieved at 0.5% drift level as per Italian NTC 2018 code [44]). Thus, the cost/frequency point at SLD is now represented by the yield-

ing of the steel rebars, causing reduced repair costs instead of the pre-fixed value imposed by D.M. 65 [45] at SLD, i.e. 15% RC (this value has been derived from the reconstruction/repair costs after L'Aquila earthquake - *White Book, Dolce and Manfredi* [46] - already including the contribution of non-structural damage, especially masonry infill walls).

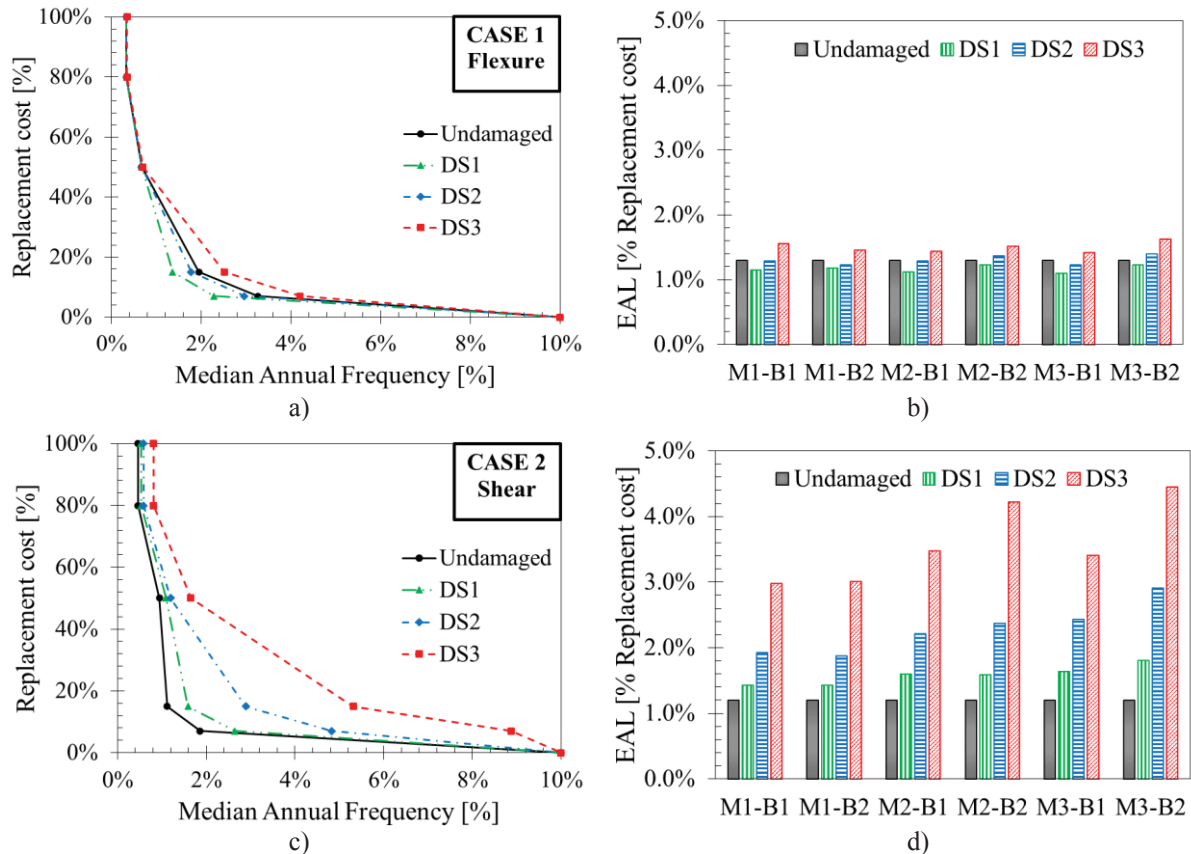


Figure 10: EAL curves and values for the undamaged and damaged wall systems: a) b) Case 1 (flexural collapse mode); c) d) Case 2 (shear collapse mode).

Consequently, looking at the yielding point as damage limit for SLD and following the analytical-based codified loss assessment approach, the lower elastic stiffness of the structure in case of DS1 (or DS2) inherently brings to lower losses (Figure 11). Therefore, losses are not properly evaluated for the flexural-dominated wall configurations at SLD (and consequently at SLO). In general, this outcome highlights the limits of the current code-compliant procedure, not accounting for the possibility of adjusting the repair cost/frequency values when a specific damage condition is achieved. In this case, the very stiff structural walls begin to damage at drift levels lower than the 0.5% (or greater) value, representing the displacement check/verification at low seismic intensity levels within the Italian Code [44]. Nevertheless, referring to international codes (as SEAOC Vision 2000 [47], NZS 1170.5 [48]), useful indications can be found to evaluate proper drift limiting values at Damage Control level for the case of wall structural typology.

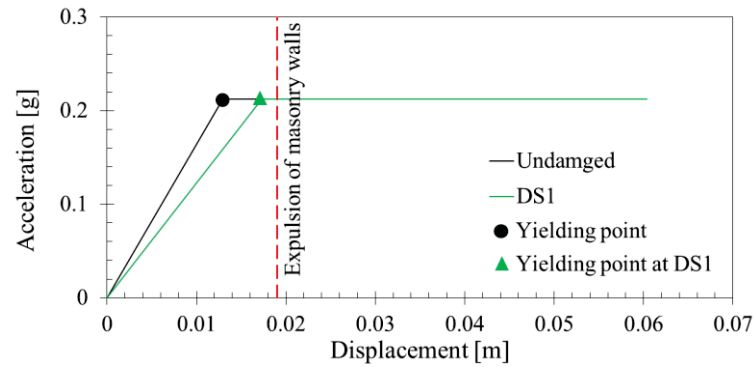


Figure 11: Comparison between undamaged and damaged (DS1) response for Case 1 (flexural collapse).

In order to obtain a more accurate evaluation of the EAL values, loss assessment analyses are also implemented using the PACT (Performance Assessment Calculation Tool) provided by the FEMA P-58[35]. This tool allows to include all the component fragilities of the building under consideration, thus the issue previously highlighted for the simplified procedure is automatically solved. In fact, the methodology is flexible and opened to the possibility of including new fragility functions, as well as consequence functions, describing the behavior of specific building structural and non-structural elements. In this case, due to the absence of fragility curves representing the Italian clay-brick masonry infill walls within the available fragility database, these functions are added by referring to the data reported in *Cardone et al.* [49]. Table 4 summarizes the EAL values obtained from both loss assessment methodology for both (undamaged) case-studies. It can be highlighted that the probabilistic procedure leads to reduced repair cost values and, consequently, an improved risk class for the building, as observed for the case of flexural collapse mechanism.

Case-study	Collapse mode	EAL [%RC]		Risk class	
		D.M. 65	FEMA P-58	D.M. 65	FEMA P-58
Case 1	Flexural	1.30	0.84	B	A
Case 2	Shear	1.20	1.04	B	B

Table 4: EAL values for D.M. 65 and FEMA P-58 loss assessment methodology for undamaged case-studies

Ultimately, another decision variable useful to provide indications on the seismic performance of a building system (as well as addressing the design of new and/or retrofitted buildings, as described in the research work by *Nuzzo et al.* [50]) is represented by the expected Probable Maximum Loss (PML). This parameter provides the maximum probable building repair cost associated with a specific intensity level. Figure 12 presents the PML curves obtained from PACT tool for both case-study structures. This graph highlights how losses can be high even at low-intensity seismic levels and that higher values are obtained for the structural walls affected by shear collapse mechanism (40% more than the flexural case when looking at the maximum expected loss of Figure 12a).

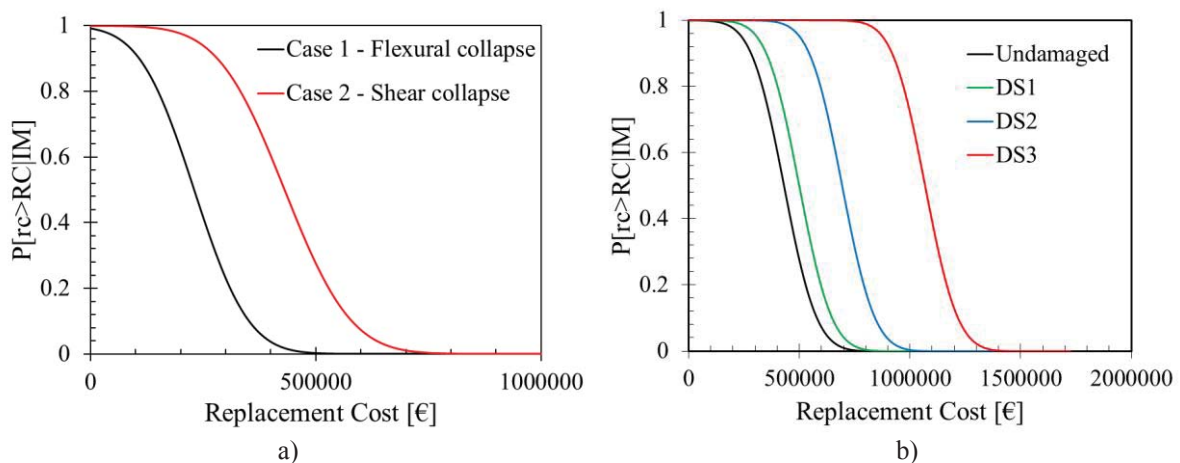


Figure 12: PML curves obtained through the FEMA P-58 methodology: a) comparison between Case 1 (flexural collapse mode) and Case 2 (shear collapse mode); b) at various damage levels for Case 2 (shear collapse mode).

The FEMA-based loss assessment results in terms of EAL/PML values are presented for the undamaged structural configurations (Case 1 vs. Case 2), with the aim of defining more reliable loss values through a more accurate prediction of the repair costs. When considering the damaged cases (DS1, DS2, DS3), the probabilistic-based procedure as developed within the PACT tool does not allow (yet) to properly consider the cumulative damage associated with the wall systems, i.e. to evaluate PML/EAL results for the damage wall configurations. In fact, modifications of the probabilistic formulations (conditional probability) as well as cumulative-based fragility/consequence functions should be considered. Therefore, in order to highlight the possible effect of the damage state into the loss assessment results (from a conceptual point of view), Figure 12b presents the PML curves obtained for the damaged structural cases when the same relative difference in losses obtained from the simplified assessment is adopted.

5 CONCLUSIONS

This paper investigated the seismic residual capacity of RC structural walls through numerical (non-linear cyclic/static, FEM/macro-modelling) analyses and loss assessment studies. The research work aimed at providing indications on the methodology to be followed in order to include residual capacity considerations in practical applications. Therefore, alternative damage assessment methods were used (or proposed) and compared to define specific damage limit states (DS1: light, DS2: moderate, DS3: severe) and the related stiffness/strength reduction coefficients for RC walls affected by either a flexural and/or shear collapse mechanism. Moreover, loss investigations on a multi-story case-study building were developed to study the effect of the damage level and type of collapse mechanism into the repair costs of structural wall systems.

The main results from the developed study are herein discussed:

- FEMA 306/307 (1998) guidelines do not provide a standardized procedure to identify the different damage states levels (DS1, DS2, DS3) in RC structural walls (e.g. in case of experimental testing, indications on the specific load history to be adopted are missing). Comparing alternative damage assessment methods, less dispersion in the results in terms of stiffness/strength reduction coefficients is related to the adoption of the

FEMA 307 procedure (describing the damage states by the achievement of specific ductility levels);

- Loss assessment results in terms of EAL highlight the importance of including residual capacity considerations in the analysis. This could provide valuable information to support decisions on the post-earthquake repair/retrofit/demolition. In fact, results highlight that greater losses are obtained even at low-intensity levels when the response of the damaged wall is considered, when compared to the undamaged wall. Moreover, when repair/rehabilitation actions need to be implemented for existing wall systems, higher attention should be paid in case of walls with brittle (shear-dominated) behavior, leading to substantial economic losses at increased damage levels.
- The simplified procedure reported in the “Sesmic-Bonus” is not able to consider realistic repair costs at low seismic intensity levels in case of stiff RC wall systems. This is due to the codified analytical procedure based on economic losses from L’Aquila 2009 earthquake accounting for alternative structural typologies and non-structural damage (especially unreinforced masonry walls). This issue could be solved by referring to post-earthquake reports and extrapolating the data related to the RC buildings only, as well as modifying the definition of the low-intensity (SLD) cost/frequency points following international codes/guidelines indications (drift limits in case of wall systems).

Nevertheless, this research work represents a preliminary parametric analysis and investigation on the residual capacity for RC walls. Further studies are needed to provide general indications on the reduction strength/stiffness coefficients to be used in practical applications, for specific wall typologies/structural response. Moreover, additional and more refined investigations (numerical modelling, time-history analysis) are needed to study the residual capacity of multi-story wall structures as well as to determine the consequent socio-economic losses - even by the implementation of a more refined procedure taking into account the cumulative damage within the building elements.

REFERENCES

- [1] M. Maeda, H. Al-Washali, K. Matsukawa, An overview of post earthquake damage and residual capacity evaluation for reinforced concrete buildings in Japan. *7th International Conference on Computational Methods in Structural Dynamics and Earthquake Engineering (COMPDYN 2019)*. Crete, Greece, June 24-26, 2019.
- [2] W.Y. Kam, S. Pampanin, K. Elwood, Seismic performance of reinforced concrete buildings in the 22 February Christchurch (Lyttelton) earthquake. *Bulletin of the New Zealand Society for Earthquake Engineering* **44(4)**, 239-278, 2011.
- [3] J.W. Wallace, L. M. Massone, P. Bonelli, J. Dragovich, R. Lagos, C. Lüders, J. Moehle, Damage and implications for seismic design of RC structural wall buildings. *Earthquake Spectra*, **28(1)**, 281-299, 2012.
- [4] Federal Emergency Management Agency, *Evaluation of Earthquake Damaged Concrete and Masonry Wall Buildings – Basic procedures manual*. FEMA 306, Washington DC, 1998.

- [5] The Japan Building Disaster Prevention Association (JBDPA), *Guideline for Post-earthquake Damage Evaluation and Rehabilitation*. (in Japanese), 1991, revised in 2001 and 2015.
- [6] F.J. Vecchio, Nonlinear finite element analysis of reinforced concrete membranes. *ACI Structural Journal*, **86(1)**, 26–35, 1989.
- [7] W.T. Holmes, Policies and standards for reoccupancy repair of earthquake-damaged buildings. *Earthquake spectra*, **10(1)**, 197-208, 1994.
- [8] Y. Nakano, M. Maeda, H. Kuramoto, M. Murakami, Guideline for post-earthquake damage evaluation and rehabilitation of RC buildings in Japan. *13th World Conference on Earthquake Engineering*. Vancouver, B.C., Canada, August 1-6, 2004.
- [9] Federal Emergency Management Agency, *Evaluation of Earthquake Damaged Concrete and Masonry Wall Buildings – Technical Resources*. FEMA 307, Washington DC, 1998.
- [10] M. Polese, M. Di Ludovico, A. Prota, G. Manfredi, Damage-dependent vulnerability curves for existing buildings. *Earthquake engineering & structural dynamics*, **42(6)**, 853-870, 2013.
- [11] K.J. Elwood, K. Marder, S. Pampanin, A. Cuevas Ramirez, M. Kral, P. Smith, A. Cattanch, M. Stannard, Draft framework for assessing residual capacity of earthquake-damaged concrete buildings. *Proceedings of The New Zealand Society for Earthquake Engineering Annual Technical Conference*, 2016.
- [12] M. Di Ludovico, M. Polese, M. Gaetani d’Aragona, A. Prota, G. Manfredi, A proposal for plastic hinges modification factors for damaged RC columns. *Engineering Structures*, **51**, 99-112, 2013.
- [13] K. Marder, C. Motter, K.J. Elwood, G. Charles Clifton, Testing of 17 identical ductile reinforced concrete beams with various loading protocols and boundary conditions. *Earthquake Spectra*, **34(3)**, 1025-1049, 2018.
- [14] K. Marder, K.J. Elwood, C.J. Motter, G. Charles Clifton. Post-earthquake assessment of moderately damaged reinforced concrete plastic hinges. *Earthquake Spectra*, **36(1)**, 299-321, 2020.
- [15] F. Dashti, R.P. Dhakal, S. Pampanin, A parametric investigation on applicability of the curved shell finite element model to nonlinear response prediction of planar RC walls. *Bulletin of Earthquake Engineering*, **17(12)**, 6515-6546, 2019.
- [16] F. Dashti, R.P. Dhakal, S. Pampanin., Evolution of out - of - plane deformation and subsequent instability in rectangular RC walls under in - plane cyclic loading: Experimental observation. *Earthquake Engineering & Structural Dynamics*, **47(15)**, 2944-2964, 2018.
- [17] A.V Shegay, C.J. Motter, K.J. Elwood, R.S. Henry. Impact of axial load on the seismic response of rectangular walls. *Journal of Structural Engineering*, **144(8)**, 04018124, 2018.
- [18] A. Niroomandi, S. Pampanin, R.P. Dhakal, M.S. Ashtiani, R. Nokes. Experimental study on the effects of bi - directional loading pattern on rectangular reinforced concrete walls. *Earthquake Engineering & Structural Dynamics*, 1-21, 2021.

- [19] A.V. Shegay, F. Dashti, L. Hogan, Y. Lu, A. Niroomandi, P. Seifi, T. Zhang, R.P. Dhal, K.J. Elwood, R.S. Henry, S. Pampanin, Research programme on seismic performance of reinforced concrete walls. *Bulletin of the New Zealand Society for Earthquake Engineering*, **53(2)**, 54-69, 2020.
- [20] B. Li, W. Xiang, Effective stiffness of squat structural walls. *Journal of Structural Engineering*, **137(12)**, 1470-1479, 2011.
- [21] M. Sharifi, M. Shafieian, Effective stiffness of concrete shear walls based on statistical analysis. *Structural Concrete*, **19(6)**, 1560-1576, 2018.
- [22] K. Kolozvari, K. Orakcal, J.W. Wallace, Modeling of cyclic shear-flexure interaction in reinforced concrete structural walls. I: Theory. *Journal of Structural Engineering*, **141(5)**, 04014135, 2015.
- [23] K. Kolozvari, T.A. Tran, K. Orakcal, J.W. Wallace, Modeling of cyclic shear-flexure interaction in reinforced concrete structural walls. II: Experimental validation. *Journal of Structural Engineering*, **141(5)**, 04014136, 2015.
- [24] S. Sritharan, K. Beyer, Special Collection on Recent Advances in Reinforced Concrete Walls Designed to Resist Seismic Loads. *Journal of Structural Engineering*, **144(9)**, 02018002, 2018.
- [25] J.H. Thomsen, J.W. Wallace, Displacement-based design of reinforced concrete structural walls: Experimental studies of walls with rectangular and T-shaped cross sections. Rep. No. CU/ CEE-95/06, Department of Civil and Environmental Engineering, Clarkson University, Potsdam, N.Y., 1995.
- [26] A. Dazio, K. Beyer, H. Bachmann, Quasi-static cyclic tests and plastic hinge analysis of RC structural walls. *Engineering Structures*, **31(7)**, 1556-1571, 2009.
- [27] T.A. Tran, J.W. Wallace, Experimental study of nonlinear flexural and shear deformations of reinforced concrete structural walls. *Proceedings, 15th World Conference on Earthquake Engineering*, Lisbon, Portugal. 2012.
- [28] J.M. Vallenias, V.V. Bertero, E.P. Popov, Hysteretic behaviour of reinforced concrete structural walls. Rep. No. UCB/EERC79/20, Earthquake Engineering Research Center, Univ. of California, Berkeley, CA, 1979.
- [29] I.D. Lefas, M.D. Kotsovos, N. N. Ambraseys, Behavior of reinforced concrete structural walls: strength, deformation characteristics, and failure mechanism. *ACI Structural Journal*, **87(1)**, 23-31, 1990.
- [30] F.J. Vecchio, M.P. Collins, M. P, The modified compression-field theory for reinforced concrete elements subjected to shear. *ACI J.*, **83(2)**, 219-231, 1986.
- [31] P.S. Wong, F.J. Vecchio, H. Trommels, Vector2 & Formworks user's manual second edition. University of Toronto, Canada, 2013.
- [32] S. Popovics. A numerical approach to the complete stress-strain curve of concrete. *Cement and concrete research*, **3(5)**, 583-599, 1973.
- [33] J.B. Mander, M.J.N. Priestley, R. Park, Theoretical stress-strain model for confined concrete. *Journal of structural engineering*, **114(8)**, 1804-1826, 1988.
- [34] M. Seckin, *Hysteretic Behavior of Cast-in-Place Exterior Beam Column Sub-Assemblies*. PhD thesis, University of Toronto, Toronto, Canada, 1981.

- [35] Federal Emergency Management Agency, *Seismic Performance Assessment of Buildings, Volume 1 – Methodology*. Technical Report FEMA-P-58-1, Washington, D.C., USA, 2012.
- [36] T. Paulay, M.J.N. Priestley. *Seismic design of reinforced concrete and masonry buildings*. Wiley, New York, 1992.
- [37] Federal Emergency Management Agency, *NEHRP Guidelines for Seismic Rehabilitation of Buildings*. FEMA-273, Building Seismic Safety Council, Washington, D.C, 1997.
- [38] S. Bianchi, J. Ciurlanti, S. Pampanin, Comparison of traditional vs low-damage structural and non-structural building systems through a cost/performance-based evaluation. *Earthquake Spectra* **37**(1), 366-385, 2021.
- [39] New Zealand Society for Earthquake Engineering, *The Seismic Assessment of Existing Building – Technical Guidelines for Engineering Assessments*. NZSEE 2017, New Zealand, 2017.
- [40] S. Pampanin, Towards the practical implementation of performance-based assessment and retrofit strategies for RC buildings: challenges and solutions. *Proceedings of the SMAR 2017*, Zurich, Switzerland, September 13-15, 2017.
- [41] C. Del Vecchio, R. Gentile, S. Pampanin, *The simple lateral mechanism analysis (SLA-MA) for the seismic performance assessment of a case study building damaged in the 2011 Christchurch earthquake*. Research report N. 2016-02, University of Canterbury, Christchurch, New Zealand, 2017
- [42] S.A. Freeman, Review of the development of the capacity spectrum method. *ISET J. Earthquake Technol.*, **41** (1), 1–13, 2004
- [43] Applied technology council, *Seismic evaluation and retrofit of concrete buildings*. ATC 40, Redwood City, CA, USA, 1996.
- [44] Ministero delle Infrastrutture, *Aggiornamento delle Norme Tecniche per le Costruzioni*, Suppl. ordinario n°8 alle G.U. n° 42 del 20/02/2018, (in Italian) serie generale, Rome, Italy, 2018.
- [45] Ministero delle Infrastrutture, *Allegato A: linee guida per la classificazione del rischio sismico delle costruzioni*. (in Italian). Decreto Ministeriale 65 del 07/03/2017, Rome, Italy, 2017
- [46] M. Dolce, G. Manfredi G, *Libro Bianco sulla ricostruzione privata fuori dai centri storici nei comuni colpiti dal sisma dell'Abruzzo del 6 Aprile 2009*. (in Italian), Doppiavoce: 210. ISBN 978-88-89972-50-2, 2015.
- [47] Structural Engineers Associate of California, *Performance-based seismic engineering*. SEAOC Vision 2000, Sacramento, California, USA, 1995.
- [48] NZS1170.:5 Structural design actions part 5: earthquake actions. New Zealand, 2004
- [49] D. Cardone, G. Perrone, Developing fragility curves and loss functions for masonry infill walls. *Earthquakes and Structures*, **9**(1), 257-279, 2015.
- [50] I. Nuzzo, N. Caterino, S. Pampanin, Seismic Design Framework Based on Loss-performance Matrix. *Journal of Earthquake Engineering*, 1-21, 2020

SIMPLIFIED LOSS ESTIMATION IN INFILLED RC BUILDINGS: MECHANICAL METHOD AND VALIDATION

Carlo Del Gaudio¹, Maria Teresa De Risi¹, Gerardo Mario Verderame¹

¹ Department of Structures for Engineering and Architecture, University of Naples Federico II
via Claudio 21, 80125 Naples, Italy
{carlo.delgaudio, mariateresa.derisi, verderam}@unina.it

Abstract

In this study a dedicated framework for seismic losses estimation in Reinforced Concrete buildings is presented, taking advantage of a simplified analytical structural analysis, a dedicated drift-based fragility curves and a specific repair cost analysis. To this aim, the mechanically based “Pushover on Shear Type model” (POST)-method, already known in the literature [1] for simplified structural analysis, has been integrated herein to obtain expected losses due to earthquakes for infilled RC buildings. On the other hand, the thoroughly cost analysis dedicated to only masonry infill panels and services (electric and plumbing system, sanitary equipment, floors, etc.) restoration presented in [2] has been used to develop an integrated formulation for loss estimation in Reinforced Concrete buildings.

The application to a wide dataset of buildings struck by L'Aquila (Italy) 2009-earthquake is used as testbed for large-scale applications. In fact, the comparison with actual damage distribution and repair cost provides a useful validation of the whole framework, from structural analysis to loss prediction.

Keywords: Seismic risk, infilled RC buildings, mechanical methodology, loss prediction, validation.

1 INTRODUCTION

The unfavorable combination of high exposure of artistic, monumental and residential assets, together with the high seismic hazard and the high vulnerability of the major part of building stock makes seismic risk in Italy and, generally in the Mediterranean area, a pivotal issue. Thus, several methodologies for losses assessment of built inventory have been developed in Italy since the end of '80 ([3]; [4]; [5]; [6]; [7]), belonging to the first generation of approaches making use of empirical Damage Probability Matrix (DPMs) and damage factor (DF) to

determine repair cost as a function of the complete replacement cost. The second generation of methods ([8]; [9]; [10]) makes use of fragility curves for different building classes ([11]; [12]; [13]; [14]; [15]; [16]) to evaluate seismic risk maps of Italy. The last generation of methods ([17]; [18]; [19]; [20]; [21]; [22]) estimates seismic losses through a component level approaches, thus requiring the use of specific component fragility functions and consequence data.

In this study, a mechanical method for regional loss estimation is presented, taking advantage of structural analyses performed through the simplified mechanical method POST ([1]) (Push-Over on Shear Type models). POST method originally developed for fragility analysis of building portfolio ([23]; [24]; [25]; [26]), has been slightly adapted to properly determine damage distribution and resultant losses within a component-based approach for economic (direct) loss estimation.

To this aim, specific drift-based fragility curves and repair cost analysis have been defined and used for three damage states (light cracking - DS1, extensive damage - DS2, severe damage - DS3), describing the evolution of damage to the masonry infills and partitions in a RC building.

The application to a wide dataset of buildings (5095 RC buildings) struck by L'Aquila (Italy) 2009-earthquake is used as testbed for large-scale applications. In fact, the comparison with actual damage distribution and repair cost provides a useful validation of the whole framework, from structural analysis to loss prediction.

2 A REGIONAL LOSS ESTIMATION FRAMEWORK VIA POST METHOD

A novel methodology for regional loss estimation at the component-level is presented herein based on structural analyses performed through the simplified mechanical method "POST" ([1]; [23]; [24]; [25]; [26]) (Push-Over on Shear Type models).

POST method is a simplified mechanical methodology for vulnerability and fragility assessment at regional scale of RC buildings, which can be applied both at single building level ([1]; [23]; [24]; [26]) or at building class level ([25]).

The mechanical framework stated above is used to evaluate repair cost for a given building considering the contribution of all its N-components:

$$E[L|IM = im] = \sum_{j=1}^N a_j \cdot E[L_j|IM = im] \quad (1)$$

The conceptual derivation of the adopted procedure is briefly recalled in Figure 1, which shows: (i) the evaluation of IM value from ground motion characterization; (ii) the assessment of spectral displacement and resultant roof displacement through IDA curves; (iii) the consequent interstorey drift ratio (IDR) profile assessment throughout the height of building by means of pushover analysis results; and (iv) lastly the definition of damage and resultant cost through their comparison with capacity values related to specific damage levels.

The seismic hazard phase can be done both with results of Probabilistic Seismic Hazard Analysis (PSHA) or from the results of ShakeMap scenario earthquakes, depending on the objective to be pursued, namely if an unconditional risk analysis (considering the seismic events could occur in a given area and in a given time interval and their mean annual frequency of exceedance) or a conditional risk analysis (referred to a specific scenario) should be performed.

The structural response phase is accomplished with the aid of POST method, which allows to relate an engineering demand parameters (edp), i.e. roof displacement, and a resultant displacement profile, given an intensity measure (IM) value, through the use of simplified Incremental Dynamic Analysis (IDA) curves within the SPO2IDA framework ([27]). The Static Pushover (SPO) analysis is carried out in closed form based on a software package on Matlab code thanks to the simplified assumption of shear-type behaviour for RC frames. In fact, the

POST method starts generating geometrical and mechanical models of buildings based on a simulated design procedure, accounting for the technical codes in force at the age of construction and the relevant seismic classification of the site. Then, the nonlinear behaviour of RC structural components is reproduced by means of a tri-linear response, with two linear ascending branches up to yielding (defined in agreement with [28]) and perfectly plastic thereafter. Note that eventual shear critical elements are not explicitly modelled (with modified plastic hinges or explicit shear springs), but their damage due to seismic loading can be detected as reported in [24].

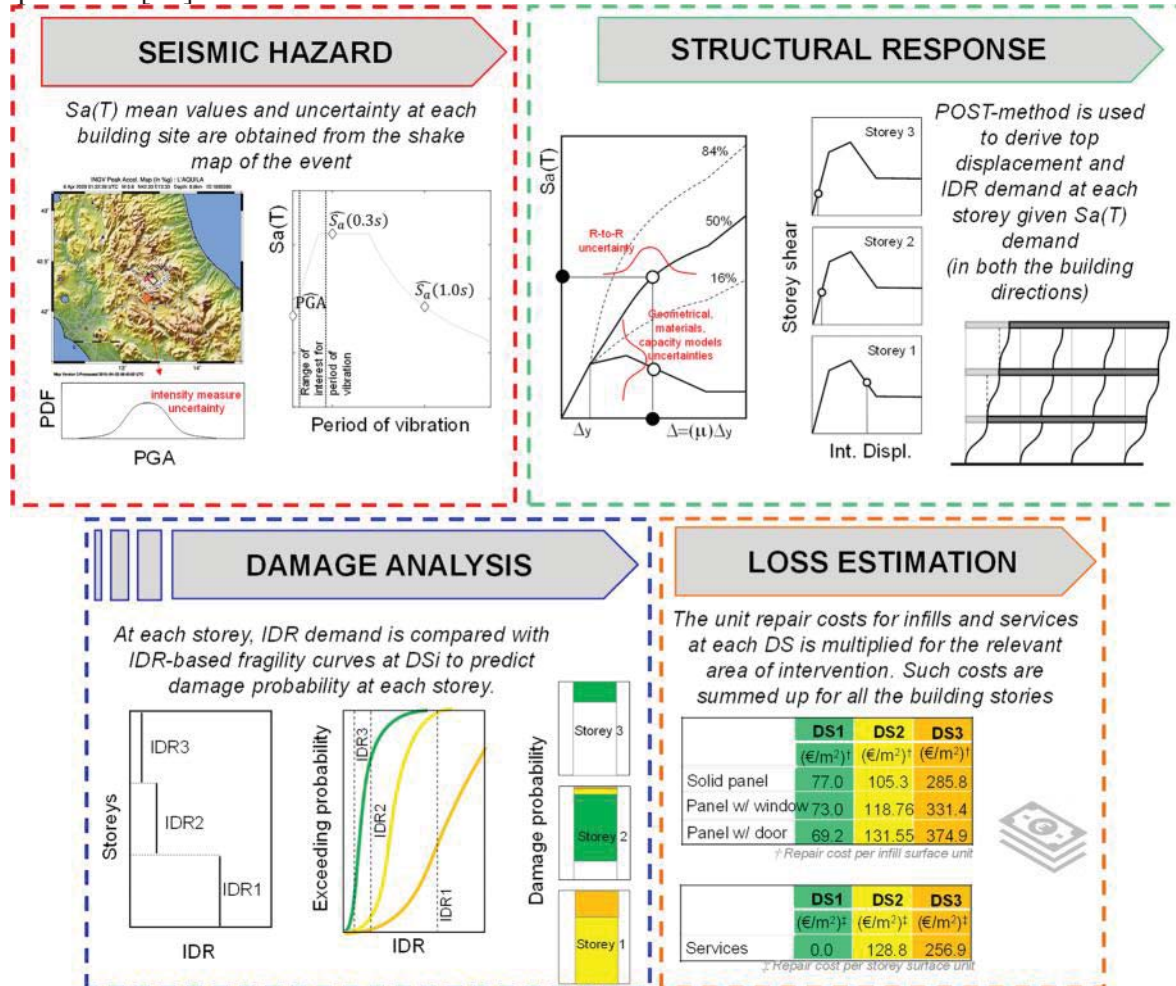


Figure 1: Flow-chart of the procedure applied in this study for loss assessment

Infills have been explicitly included in the structural models, by means of a four-branch force-displacement curve ([29]). The influence of the openings on infills' lateral force-displacement relationship is also considered, by means of the modifying behaviour parameters based on [30].

The simplified assumption of shear-type behaviour for RC frames allows obtaining a multi-linear storey shear -vs- interstorey displacement relationship at each storey by simply adding up the lateral shear-displacement relationships of all the RC columns and infill panels along longitudinal and transverse direction, separately. In such a way, seismic response via a static push-over curve is obtained in a closed-form procedure, which is force-controlled up to peak response and displacement-controlled thereafter, once the distribution of lateral forces has been set.

Therefore, the structural response estimation is entirely evaluated via POST method, which returns the evolution of the lateral displacement profile increasing the IM value through the

results of static SPO analysis for each main direction of the building. The relation between IM values and EDPs is given by the IDA curves related to the quadri-linear simplification of SPO curve.

The damage estimation phase is performed by means of specific component fragility curve, returning the probability of exceeding a discrete Damage State, DS, given the EDP.

It has to be noted, that due to the peculiarity of the building dataset considere in this work (see later), resulting to be “lightly damaged” to infills only after the 2009 Abruzzi earthquake, vertical structures will be neglected from damage and loss computation. Moreover, IDR thresholds and resultant uncertainties for infills/partitions and services have been assumed in this study from [31]’s proposal, which finds its background in [32]. In fact, the construction practices in Mediterranean region for residential RC buildings entail that services are generally allocated within building enclosure, the latter typically made up of hollow clay bricks. In this case, cascading effects could occur, such that damage to one, i.e. infills, could cause the fracture of the other one, i.e. a water or electric distribution pipes or a sanitary equipment. Thus, damage for both infill panels and services is strictly related to each other due to their firm interaction, as it will be better shown in the following application.

The comparison between IDR demand and fragility curves allows determining DS for the considered component. In such a way, the number of components suffering a given DS_i can be determined, thus evaluating its relative extension also considering the possibility of experiencing different co-existing DSs along the building height (namely at different stories).

Finally, the loss estimation phase is fulfilled taking advantage of proper repair cost analysis reproducing detailed quantity surveying considering a list of elementary actions to be performed for an area of intervention given $DM = dm$, through the use of specific unit costs from a price list (e.g., that for Public Works in Abruzzi Region - [33], as applied in the following section). Thus, the values of repair costs for infills and services per square meters of storey surface for 3 DSs reported in [2] and [22] (briefly reported in table 1 and table 2) are used.

	\bar{C}^{IP}_{DS1} (€/m ²)	\bar{C}^{IP}_{DS2} (€/m ²)	\bar{C}^{IP}_{DS3} (€/m ²)
solid panel (w/o openings)	77.0	105.3	285.8
panel with window	73.0	118.76	331.4
panel with door	69.2	131.55	374.9
interior partition	51.3	73.5	199.9

Table 1. Repair costs for double leaf hollow clay bricks for infills/partitions (IP) at each DS per infill panel unit (from [2] and [22])

	$C^{Services}_{DS1}$ (€/m ²)	$C^{Services}_{DS2}$ (€/m ²)	$C^{Services}_{DS3}$ (€/m ²)
All Services	0.0	128.8 ± 28.2*	258.9 ± 32.8*

(*) mean ± standard deviation

Table 2. Repair costs for services at each DS per plan surface unit (from [2] and [22])

Obviously, the damage and loss estimation steps have to be repeatedly calculated for all building components and for all DSs. Nonetheless, a realistic definition of losses should consider the fact that some activities should be carried out simultaneously for all the components of a given portion of the building (“minimum area of intervention”) higher than that strictly necessary for practical or aesthetic reasons which is assumed in this study as the whole storey. In other words, it is assumed that all the (structural and non-structural) components located in

a given storey are characterized by the maximum damage therein experienced, thus resultant losses are consequently evaluated, favoring an intervention that meets practical and aesthetic criteria.

3 APPLICATION OF REGIONAL LOSS ESTIMATION METHOD TO SLIGHTLY DAMAGED RC BUILDINGS AFTER L'AQUILA EARTHQUAKE

A large-scale application of the mechanical method for regional loss estimation via POST method is performed in this section, considering a building stock struck by the L'Aquila (Italy) earthquake (April 6th, 2009) and damaged to only infills, which incidence represented, for RC buildings, almost the entirety of actual losses after the most recent earthquakes occurred in Italy [34].

The main features of the event and of the analysed building stock are completely treated in previous works and briefly recalled in what follows. For further analysis the reader is referred to [2].

The seismic event investigated for this application struck the Abruzzi region, with a magnitude M_w equal to 6.3, resulting in IX-X grade of the Mercalli-Cancani-Sieberg scale.

For this application, the IM characterization is fulfilled by means of the shake map of the seismic event which struck the Abruzzi region on 6th April 2009, with a magnitude M_w equal to 6.3, resulting in IX-X grade of the Mercalli-Cancani-Sieberg scale. The latter is derived following the procedure reported in [35].

3.1 Building stock description

Building stock characterization is made available from post-earthquake reconnaissance filed trips carried out in the aftermath of L'Aquila earthquake with the supervision and coordination of Department of Civil Protection (DPC), and recently made available on the Da.D.O platform ([36]). These inspections collected data for each building about location, typology, geometry, age of construction, and suffered damage for structural components (including vertical structures, horizontal structures, stairs, roofs and infills) and non-structural components, by means of the so-called AeDES forms ([37]). Additionally, for each component damage, its severity and its extent have been recorded.

Overall, out of a total of about 7500 residential RC buildings listed in the Da.D.O. platform, only a subset of 5095 buildings have been selected, hereinafter defined as "lightly damaged buildings", since they are characterized to be damaged only to infills.

Their main geometrical properties (number of stories, N_s , and average plan surface, A), are thoroughly analyzed in ([2]), where it has been shown that a major part of considered building stock is characterized by three or four stories (about 75% of the whole database), that 92% of the building stock has been built after 1972 and that the most common average plan surfaces range between 70 and 230m² (about 80% of the building stock).

3.2 Building class definition for loss analysis via POST-method

The case study (large-scale) application is performed through a class-oriented approach to reduce the computational burden required by the derivation of structural analysis for an extensive (5095 units) building stock. In particular, 15 building classes have been considered herein as a function of number of storeys, N_s , and average plan area, A , such that their statistical characterization well reproduces data collected from post-earthquake AeDES survey forms. Thus, for each class of storey (from 1 to 5), three further sub-classes (low, medium and high) of plan area are defined.

Moreover, in order to explicitly consider the uncertainties related to seismic risk estimation, different kind of uncertainties are considered within a Monte Carlo simulation procedure approach, dealing with:

- (i) **geometrical-typological parameters**, i.e. building plan ratio, infills thickness, the type of opening (no opening; window opening; door opening).
- (ii) **material properties**, i.e. compressive strength of concrete (f_c), steel yield strength (f_y), mechanical characteristics of infill panels (shear strength - τ_{cr} , shear modulus - G_w).
- (iii) **capacity models**, both for the non-linear behaviour of both RC columns and infill panels.
- (iv) **intensity measure**, from INGV ShakeMap in terms of PGA (mean and logarithmic standard deviation values at each site);
- (v) **record to record variability**.

A summary of all the considered random variables (RV) and the parameters for their characterization are briefly reported in Table 3.

Type of R.V.	R.V.	Reference	Distribution	Median value	CoV [-]
Geometry	Building area	survey data	uniform	from survey	-
	Building plan ratio	[1]; [24]	uniform	median([1.0-2.5])	-
	Infill: Type of opening	-	discrete	[solid; window opening; door opening]	-
Material properties	f_c	[38]	lognormal	25 MPa	31%
	f_y	[39]	lognormal	Calculated	Calculated
	τ_{cr}	[40]; [41]	lognormal	[0.23-0.53] MPa**	30%
Modelling parameters	θ_v	[28]	lognormal	0.95·Calculated	28%
	$k_{elastic, infill}^*$	[29]	lognormal	1.09·Calculated	32%
	$k_{peak, infill}^*$		lognormal	1.63·Calculated	70%
	F_{cr}^*		lognormal	0.93·Calculated	19%
	F_{max}^*		lognormal	0.93·Calculated	25%
PGA	PGA value from ShakeMap	http://shakemap.rm.ingv.it [35]	lognormal	from ShakeMap	from ShakeMap
Record-to-record variability	Record-to-record variability	[27]	lognormal	Calculated	Eq. (2)

*: sampled through the simulated annealing procedure according to (Vorechovsky and Novák, 2009)

** : modified depending on the age of construction

Table 3: Summary of the considered random variables.

4 EVALUATION OF PREDICTED DAMAGE AND LOSSES FROM STRUCTURAL ANALYSIS

Maximum damage (DS_{max}) can be easily determined from results of structural analysis as the most severe DS_i suffered in all stories and in both directions. Contrarily, mean damage gathers information on both severity and damage extension – DE_i related to DS_i . To this aim, DE_i is evaluated from results of POST method as:

$$DE_i = \frac{\sum_{j=1}^{n_s} 1_i \cdot (\sum_{s=1}^{n_b} {}^x A_{j,s}^{II} + \sum_{k=1}^{n_b} {}^y A_{j,k}^{II})}{\sum_{j=1}^{n_s} (\sum_{s=1}^{n_b} {}^x A_{j,s}^{II} + \sum_{k=1}^{n_b} {}^y A_{j,k}^{II})} \quad (2)$$

where 1_i is the indicator function which is 1 if infill panels at that storey are characterized by DS_i at least in one (longitudinal or transversal) direction and 0 vice-versa. Previous equation is derived referring to the minimum area of intervention (the whole storey surface), thus

assuming that all the (structural and non-structural) components located in a given storey are characterized by the maximum damage therein (i.e. at that storey) experienced in both (longitudinal and transversal) directions. In Eq.2 A_j^{ii} is the area of j^{th} infill panel in s^{th} - or k^{th} -direction.

Obviously, since the damage distribution of infills can be characterized by the attainment of different DSs along the height of building, a synthetic information about the co-existing DS_i and its extent is represented by the “mean damage” level (hereinafter referred to as \overline{DS}), calculated as follows:

$$\overline{DS} = \sum_{i=0}^3 i \cdot DE_i \quad (3)$$

Therefore \overline{DS} is always lower than or equal to DS_{max} , and it can range between 0 and 3, since the maximum possible average damage is achieved when the maximum possible damage state (DS3) is reached in the whole building ($DE_3=1$).

Finally, the total repair cost for unit surface area (trc) is evaluated for each building as a function of specific repair costs for infills and services reported in Tables 1 and 2:

$$trc = \sum_{i=1}^3 \left\{ \sum_{j=1}^{N_s} 1_i \cdot \left[\overline{C}_{DS_i}^{IP} \left(\sum_{s=1}^{n_b} A_{j,s}^{ii} + \sum_{k=1}^{n_b} A_{j,k}^{ii} \right) / A + C_D^S \right] \right\} \quad (4)$$

The trc is evaluated by summing up the relative repair costs for each storey. The latter is determined given the maximum DS (DS_{max}) suffered by at least one infill panel in one of the two directions and extended to all the remaining one, in addition to services (plumbing systems, radiators, electrical system, floor/wall tiles), too. This circumstance is given in Eq. (6) through the indicator function (1_i) which is equal to 1 when at least one infill panel suffers DS_i at that storey and 0 vice-versa. Obviously, the repair costs of infills are first multiplied by the panel area (A^{ii}) and then divided by the floor area (A) to obtain the total repair cost for unit surface area.

5 PREDICTED-TO-OBSERVED COMPARISON OF DAMAGE AND LOSSES

Predicted damage and loss estimation presented in the section 4 are here compared with damage actually observed for the investigated buildings population (section 5.1) and with repair costs directly obtained from this damage (section 5.2) (hereinafter referred to as “observed damage” and “observed losses”, respectively). Note that all details about “observed damage” and “observed losses” can be found in [2] and [22].

5.1 Comparison between Observed and Predicted damage

The actual data about damage suffered by the collected building stock (“observed damage”) represents the anchorage to reality against which predicted data should be compared. Such a comparison will be shown in this section to “validate” the mechanical based procedure presented in this work.

The observed-versus-predicted agreement in terms of maximum achieved DS, reported in Figure 2, results very satisfying, considering the simplification of the method and its large-scale application. A slight underestimation of no-damaged ($DS_{max}=DS_0$) buildings can be noted, along with an overestimation of DS3-buildings.

“Predicted” damage well reproduces the “observed” damage, independently on the number of stories, as shown in Figure 3, where “predicted” and “observed” DS_{max} scenarios are reported depending on the number of stories, N_s , for the most frequent classes of N_s , namely from 1 to 5 stories.

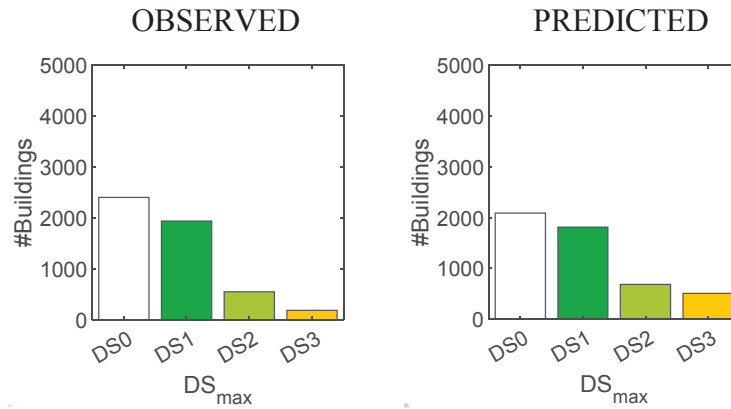


Figure 2. Comparison between observed and predicted damage scenario in terms of DS_{max}

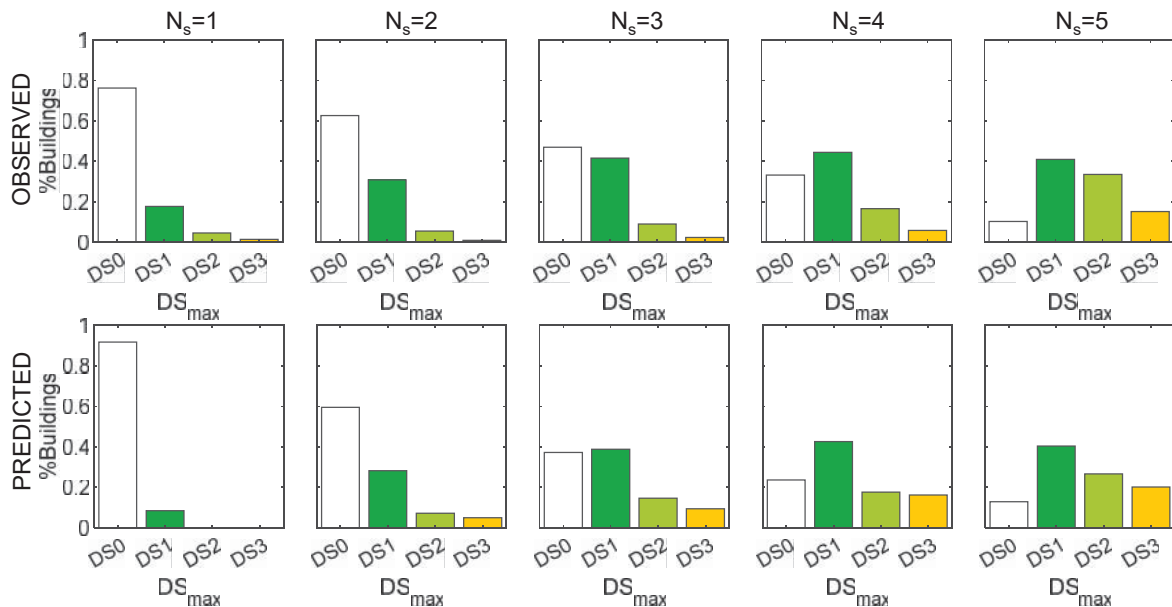


Figure 3. Comparison between observed and predicted damage scenario in terms of DS_{max} depending on the number of stories (N_s)

Figure 4 reports the comparison between observed and predicted mean damage given the maximum achieved DS, where the 16th, the 50th and the 84th percentiles are also reported. A quite good agreement between mean “predicted” and “observed” mean damage can be generally observed.

Additionally, when median values of “observed” mean damage are considered, a clear trend exists depending on the number of stories, as in Figure 5, where buildings are grouped depending on the maximum achieved DS. When DS_{max} is equal to DS1 or DS2, the average damage tends to decrease when N_s increases from 1 to 3 stories, then keeping a pseudo-constant value for taller buildings. At DS3, such a decreasing trend is observed from 1 to 5 stories. The predicted damage successes in reproducing such a trend.

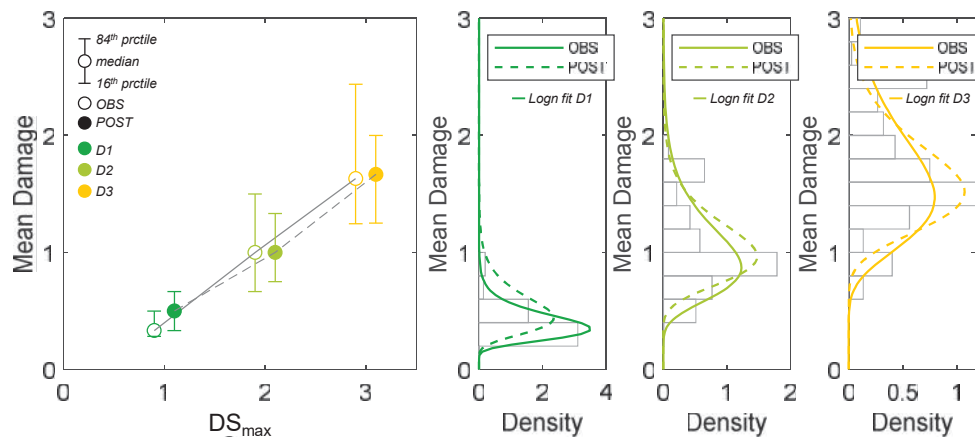


Figure 4. Predicted (POST)-versus-observed (OBS) comparison: mean damage-versus-maximum achieved DS (DS_{max}); 16th, 50th and 84th percentiles.

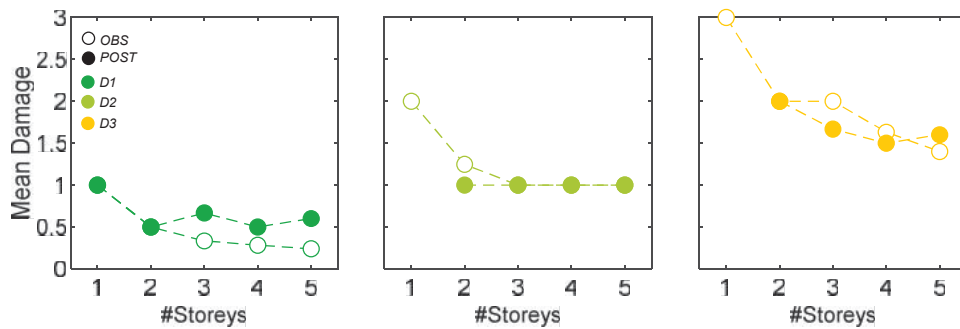


Figure 5. Predicted (POST)-versus-observed (OBS) comparison, given DS_{max} : trend of mean damage depending on the number of stories.

5.2 Comparison between Observed and Predicted losses

In this section, the comparison between observed and predicted losses (in terms of trc) is shown. In Figure 6, the 16th, 50th and 84th percentiles of observed and predicted trc are reported, showing a very good agreement, on average, especially when DS_{max} is equal to DS2 (-11%) or DS3 (-3%). A slight overestimation of the “observed” losses is obtained at DS1.

In Figure 7, the trends between the trc and N_s , given DS_{max} , are reported. It can be noted that both “observed” and “predicted” trc decrease, on average, when N_s varies from 1 to 3 when the maximum achieved damage is DS1 or DS2, then keeping an almost constant value for higher N_s . At DS3, a decreasing trend of trc is observed, on average, for N_s varying from 1 to 5, for both “observed” and “predicted” trc .

As for the “predicted” trc , “observed” trc can be also shown as a function of mean damage (Figure 8). A clear linear trend exists between the average mean damage and trc , with an increasing slope for increasing maximum damage severity. Obviously, when the average damage is exactly equal to a given maximum DS_i (with $i=1,2,3$), trc can be very easily computed as the sum of the repair costs per floor unit related to infills and services at that DS_i , equal to respectively: 142.1 €/m² for DS1; 352.9 €/m² for DS2 and 744.4 €/m² for DS3. It can be easily verified that the ratio between trc and average mean damage (= DS_i) is very close to the slope of the linear fitting plotted in Figure 8, for the “observed” trc .

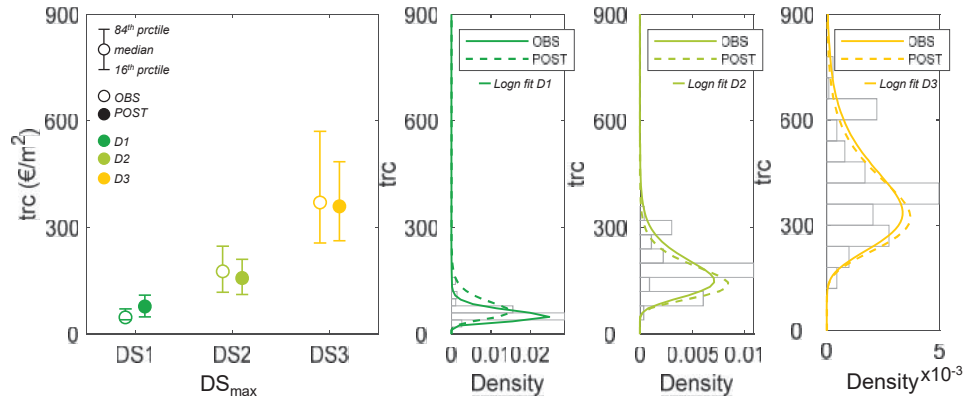


Figure 6. *trc* percentiles depending on DS_{max} : predicted (POST)-versus-observed (OBS) comparison.

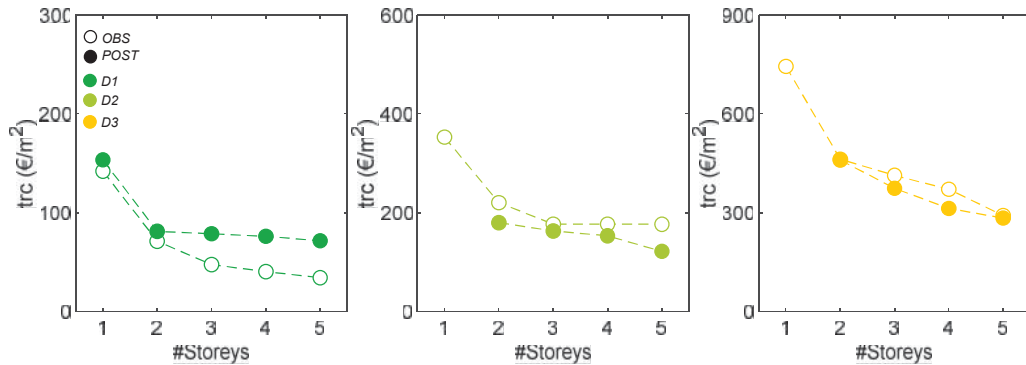


Figure 7. Predicted (POST)-versus-observed (OBS) comparison, given DS_{max} : trend of *trc* depending on the number of storeys.

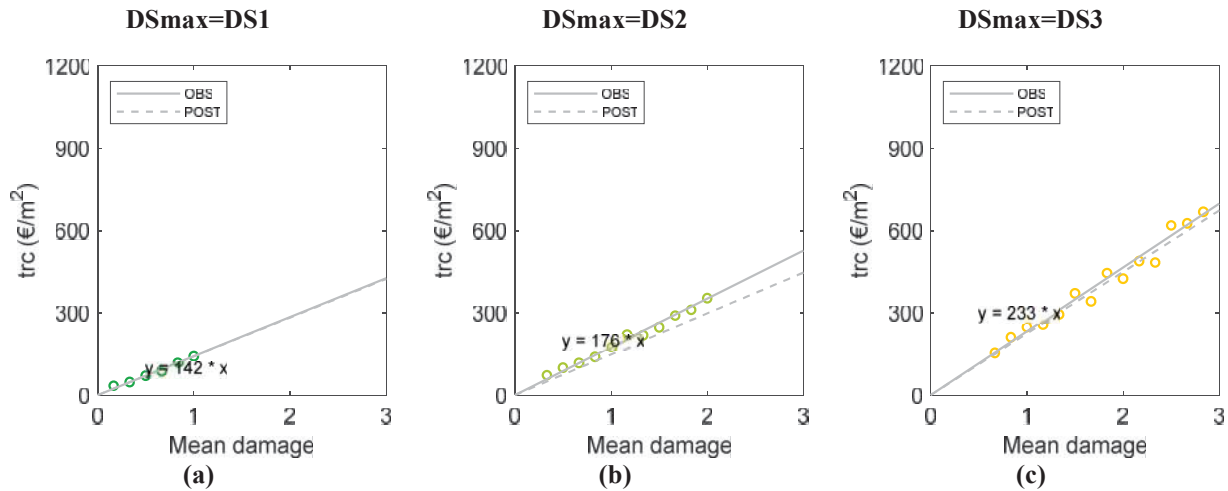


Figure 8. Predicted-versus-experimental comparison: *trc* depending on average damage level. Along x- and y-axis the distributions of mean damage and *trc* are reported.

6 CONCLUSIONS

In this work provides a regional loss estimation framework via the “Pushover on Shear Type model” (POST)-method ([1]) for residential Reinforced Concrete (RC) buildings has been shown. The proposed component-based procedure accounts for the contribution of infills/partitions and services to the buildings seismic repair costs, using dedicated drift-based fragility curves and specific repair cost analysis for masonry infills and partitions and for three damage states (DSs) proposed in [31].

The methodology has been applied to a wide dataset of real buildings, struck by L'Aquila (Italy) 2009-earthquake and resulted damaged to infills or partitions only, as testbed for its reliability and robustness.

A generally satisfying agreement between observed and predicted results was shown. In fact, predicted damage successes in well reproducing the general observed trend in terms of maximum achieved DS, also catching their trend with the number of stories, namely, the higher the number of stories, the higher the percentage of buildings with more severe damage. The mechanical method allowed to well reproduce the damage distribution observed over the buildings, beyond their maximum value; in fact, the predicted mean damage index – combining damage severity and its extent – well replicates the “observed” outcomes, along with their trends depending on the number of storeys and on maximum achieved DS. Finally, a good agreement can be found also between predicted and observed total repair costs, capable of also capturing the observed trend of loss as a function of number of storeys and mean damage values.

In conclusion, the comparison between numerically predicted and actually observed damage scenario and seismic losses allowed the validation of the implemented procedure, showing its potential for large-scale applications.

REFERENCES

- [1] Del Gaudio C., Ricci P., Verderame G.M., Manfredi G., 2015. Development and urban-scale application of a simplified method for seismic fragility assessment of RC buildings. *Eng Struct*, 91:40–57, 2015. <https://doi.org/10.1016/j.engstruct.2015.01.031>
- [2] De Risi, M. T., Del Gaudio, C., & Verderame, G. M. (2020). A component-level methodology to evaluate the seismic repair costs of infills and services for Italian RC buildings. *Bulletin of Earthquake Engineering*, 18(14), 6533–6570.
- [3] Guagenti, E., Molina, C. and Mulas, G. (1988) Seismic risk analysis with predictable models. *Earthquake Engineering and Structural Dynamics* 16, 343–359
- [4] Colonna, E., Molina, C. and Petrini, V. (1994) Criteri di valutazione della vulnerabilità sismica del patrimonio edilizio esistente sul territorio nazionale. *Ingegneria Sismica*, n. 1, Gen-Apr. 1994.
- [5] Bramerini, F., Di Pasquale, G., Orsini, G., Pugliese, A., Romeo, R.W. and Sabetta, F. (1995) Rischio sismico del territorio italiano. *Proceedings 7th National Conference on Earthquake Engineering in Italy*, Siena, September 1995, Vol. 3, pp. 1099–1108.
- [6] Di Pasquale, G. and Orsini, G. (1998) A probabilistic model for the assessment of the earthquake economic losses in Italy. *Proceedings International Conference ‘Risk Analysis 98’*, Valencia, Spain, 1998.
- [7] Di Pasquale, G., Orsini, G., & Romeo, R. W. (2005). New developments in seismic risk assessment in Italy. *Bulletin of Earthquake Engineering*, 3(1), 101–128.
- [8] Silva V., Amo-Oduro D., Calderon A., Dabbeek J., Despotaki V., Martins L., Rao A., Simionato M., Viganò D., Yepes C., Acevedo A., Horspool N., Crowley H., Jaiswal K., Journeay M., Pittore M. (2018). Global Earthquake Model (GEM) Seismic Risk Map (version 2018.1). DOI: 10.13117/GEM-GLOBAL-SEISMIC-RISK-MAP-2018.1
- [9] Dolce M., Borzi B., da Porto F., Faravelli M., Lagomarsino S., Magenes G., Moroni C., Penna A., Prota A., Speranza E., Zuccaro G., Verderame G.M., 2019. Mappe di rischio

- sismico per il territorio italiano. XVIII Convegno ANIDIS 2019 “L’ingegneria sismica in Italia” (Ascoli Piceno, 15 settembre – 19 settembre 2019).
- [10] da Porto F., Donà M., Rosti A., Rota M., Lagomarsino S., Cattari S., Borzi B., Onida M., De Gregorio D., Perelli F.L., Del Gaudio C., Ricci P., Speranza E., 2021. Comparative analysis of the fragility curves for Italian residential masonry and RC buildings. *Bulletin of earthquake engineering*
 - [11] Borzi B., Pinho R., Crowley H., 2008. Simplified pushover-based vulnerability analysis for large scale assessment of RC buildings. *Engineering Structures*, 30(3), 804-820.
 - [12] Ahmad N., Crowley H., and Pinho R., (2010). Analytical fragility functions for reinforced concrete and masonry buildings and building aggregates - UPAV-Internal Report
 - [13] Borzi, B., Faravelli, M. & Di Meo, A. Application of the SP-BELA methodology to RC residential buildings in Italy to produce seismic risk maps for the national risk assessment. *Bull Earthquake Eng* (2020). <https://doi.org/10.1007/s10518-020-00953-6>
 - [14] Del Gaudio, C., Di Ludovico, M., Polese, M. et al. Seismic fragility for Italian RC buildings based on damage data of the last 50 years. *Bull Earthquake Eng* 18, 2023–2059 (2020). <https://doi.org/10.1007/s10518-019-00762-6>
 - [15] Del Gaudio, C., Di Ludovico, M., Polese, M. et al. Correction to: Seismic fragility for Italian RC buildings based on damage data of the last 50 years. *Bull Earthquake Eng* 18, 4547–4548 (2020). <https://doi.org/10.1007/s10518-020-00890-4>
 - [16] Rosti, A., Del Gaudio, C., Rota, M. et al. Empirical fragility curves for Italian residential RC buildings. *Bull Earthquake Eng* (2020). <https://doi.org/10.1007/s10518-020-00971-4>
 - [17] ATC - Applied Technology Council. FEMA P-58 Next-generation Seismic Performance Assessment for Buildings, Volume 1 - Methodology, Federal Emergency Management Agency, Washington, DC, 2012a.
 - [18] ATC - Applied Technology Council. FEMA P-58 Next-generation Seismic Performance Assessment for Buildings, Volume 1 - Implementation, Federal Emergency Management Agency, Washington, DC, 2012b.
 - [19] Cardone D., Perrone G., (2017), Damage and loss assessment of pre-70 RC frame buildings with FEMA P-58, *Journal of Earthquake Engineering*, Vol. 21, pp. 23-61.
 - [20] Ramirez, C. M. (2009). Building-specific loss estimation methods & tools for simplified performance-based earthquake engineering. Stanford University.
 - [21] Cardone, D., Perrone, G., & Flora, A. (2020). Displacement-Based Simplified Seismic Loss Assessment of Pre-70S RC Buildings. *Journal of Earthquake Engineering*, 24(sup1), 82-113.
 - [22] Del Gaudio, C., De Risi, M. T., Verderame, G. M. (2021). Seismic Loss Prediction for Infilled RC Buildings via Simplified Analytical Method. *Journal of Earthquake Engineering*, 1-34. doi.org/10.1080/13632469.2021.1875940
 - [23] Del Gaudio C., Ricci P., Verderame G.M., Manfredi G., 2016. Observed and predicted earth-quake damage scenarios: the case study of Pettino (L’Aquila) after the 6th April 2009 event. *Bull Earthq Eng*, 2016. <https://doi.org/10.1007/s10518-016-9919-2>

- [24] Del Gaudio C., Ricci P., Verderame G.M., Manfredi G., 2017. Urban-scale seismic fragility assessment of RC buildings subjected to L'Aquila earthquake. *Soil Dyn Earthq Eng* 96:49–63, 2017. <https://doi.org/10.1016/j.soildyn.2017.02.003>
- [25] Del Gaudio C., Ricci P., Verderame G.M., 2018. A class-oriented mechanical approach for seismic damage assessment of RC buildings subjected to the 2009 L'Aquila earthquake. *Bulletin of Earthquake Engineering*, 1-25, 2018. <https://doi.org/10.1007/s10518-018-0365-1>
- [26] Masi A., L. Chiauzzi, G. Santarsiero, V. Manfredi, S. Biondi, E. Spacone, C. Del Gaudio, P. Ricci, G. Manfredi, G. M. Verderame. Seismic response of RC buildings during the Mw 6.0 August 24, 2016 Central Italy earthquake: the Amatrice case study. *Bulletin of Earthquake Engineering*, 1-24, 2017. <https://doi.org/10.1007/s10518-017-0277-5>
- [27] Vamvatsikos, D., Cornell., C.A. (2006) Direct estimation of the seismic demand and capacity of oscillators with multi-linear static pushovers through IDA. *Earthquake Engineering and Structural Dynamics*, 35(9), 1097-1117, 2006.
- [28] Biskinis D., Fardis M.N., (2010). Deformations at flexural yielding of members with continuous or lap-spliced bars. *Structural Concrete*, 11(3), 128-138.
- [29] Panagiotakos T.B., Fardis M.N., (1996). Seismic response of infilled RC frames structures. *Proceedings of the 11th World Conference on Earthquake Engineering*, Acapulco, México. Paper No. 225.
- [30] Kakaletsis D.J., Karayannis C.G., (2009). Experimental investigation of infilled reinforced concrete frames with openings. *ACI Structural Journal*, 106(2), 132-141.
- [31] Del Gaudio, M.T. De Risi, C., Ricci, P., Verderame, G. M. 2019b. Empirical drift-fragility functions and loss estimation for infills in reinforced concrete frames under seismic loading. *Bulletin of Earthquake Engineering* <https://doi.org/10.1007/s10518-018-0501-y>.
- [32] Grunthal G (1998) *Cahiers du Centre Europeen de Geodynamique et de Seismologie: volume 15—European Macroseismic Scale 1998*. European Center for Geodynamics and Seismology, Luxembourg
- [33] B.U.R.A. (Official Journal of Regione Abruzzo) (n. 10—08/03/2017—ordinary), Price List of Public Works in Abruzzi Region, Italy. 2017. (in Italian)
- [34] Del Vecchio, C., Di Ludovico, M., & Prota, A. (2019). Repair costs of RC building components: from actual data analysis to calibrated consequence functions. *Earthquake Spectra*.
- [35] Michelini, A., L. Faenza, V. Lauciani, and L. Malagnini (2008). ShakeMap implementation in Italy. *Seismological Research Letters* 79.5: 688-697.
- [36] Dolce M., Speranza E., Giordano F., Borzi B., Bocchi F., Conte C., Di Meo A., Faravelli M., and Pascale V. 2019a. Observed damage database of past Italian earthquakes: the DaDO WebGIS. *Bollettino di Geofisica Teorica ed Applicata*, 60(2).
- [37] Baggio C, Bernardini A, Colozza R, Coppari S, Corazza L, Della Bella M, Di Pasquale G, Dolce M, Goretti A, Martinelli A, Orsini G, Papa F, Zuccaro G (2007) Field manual for post-earthquake damage and safety assessment and short-term countermeasures. Translation from Italian: Goretti A., Rota M., JRC Scientific and Technical Reports, EUR 22868 EN-2007

- [38] Masi, A., Vona M., (2009). Estimation of the in-situ concrete strength: provisions of the European and Italian seismic codes and possible improvements. In: E. Cosenza (editor). Eurocode 8 perspectives from the Italian standpoint workshop. Doppiavoce, Naples, Italy, 2009. ISBN 978-88-89972-16-8. Pp. 67-77.
- [39] Verderame G.M., Ricci P., Esposito M., Manfredi G., (2012). STIL v1.0 - Software per la caratterizzazione delle proprietà meccaniche degli acciai da c.a. tra il 1950 e il 2000. ReLUIS, <http://www.reluis.it/>
- [40] Circolare del Ministero dei Lavori Pubblici. n. 617 del 2/2/2009. Istruzioni per l'applicazione delle "Nuove norme tecniche per le costruzioni" di cui al DM 14 gennaio 2008. (in Italian)
- [41] De Risi M.T., Del Gaudio C., Ricci P., Verderame G.M., 2018. In-plane behaviour and damage assessment of masonry infills with hollow clay bricks in RC frames. *Engineering Structures*, 168, 257-275.

SEISMIC PERFORMANCE ASSESSMENT OF AS-BUILT AND RETROFITTED RC BUILDINGS CONSIDERING THE INFLUENCE OF INFILLS: PRE-‘70 LOW-MIDE RISE CASE-STUDIES

Maria T. De Risi¹, Santa A. Scala¹, Carlo Del Gaudio¹, and Gerardo M. Verderame¹

¹ University of Naples Federico II,
Department of Structures for Engineering and Architecture,
{mariateresa.derisi, santaanna.scala, carlo.delgaudio, verderam}@unina.it

Abstract

The seismic assessment and retrofit of non-conforming Reinforced Concrete (RC) buildings still represent a challenge for researchers and practitioners worldwide due to several aspects. On one hand, low standards RC buildings typically present some failure typologies very different from newly designed buildings, and such failure modes should be properly modelled for a reliable seismic performance assessment. On the other hand, retrofitting strategies should be chosen carefully looking both at safety at collapse and at seismic capacity at less severe performance levels, considering non-structural components as well. Masonry infills, typically defined as non-structural components despite their structural role, significantly affect the seismic behavior of existing RC buildings, especially at low-medium intensity measures. Therefore, when the seismic performance of as-built or retrofitted RC buildings is assessed, their contribution should be considered. In this work, a preliminary analysis of two 4-storey low-standard RC buildings, different for design typology, is presented, based on static nonlinear analyses. First, case-study buildings, representative of Italian pre-70 residential buildings, have been assessed in their “bare” configuration (without infills), as common in design practice, in a code-based approach (according to Italian code). Based on the as-built assessment outcomes, their retrofit has been designed by means of two main strategies: (1) the complete resolution of all the shear failures (in columns or joints), if any; (2) the reduction of the displacement demand by means of RC column jacketing, when necessary, along with the resolution of shear failures (as for the previous strategy). Then, both the as-built and retrofitted building configurations have been modelled and analysed explicitly considering the presence of infills and shear-critical elements. Fragility curves have been obtained at different Damage States according to European Macroseismic Scale EMS-98, considering record-to-record variability, and compared to each other. Remarks about the choice among strengthening strategies are carried out, based on these outcomes and on a preliminary estimation of the expected mean annual losses for the investigated buildings.

Keywords: RC buildings; damage states; masonry infills; strengthening; fragility curves; losses.

1. INTRODUCTION

The seismic assessment and retrofit of non-conforming Reinforced Concrete (RC) buildings still represent a challenge for researchers and practitioners worldwide, due to several aspects.

On one hand, low standards RC buildings typically present some failure typologies very different from newly designed buildings [1]-[2], and such failure modes should be properly modelled for a reliable seismic performance assessment. In existing buildings, columns can likely suffer shear damage under seismic actions, due to the very poor concrete quality or the insufficient stirrups mechanical percentage, leading to reduced lateral displacement capacity, especially if shear failures are expected to occur before the member yielding ([1], [3]-[6]). Additionally, beam-column joints typically in low-standard buildings have been not designed at all and totally lack of stirrups. This means that shear failures in those connections could occur before the yielding of the adjacent members, thus limiting the overall ductility capacity of the whole building [7].

On the other hand, retrofit strategies should be chosen carefully to comply with current codes, preventing the structural collapses (e.g. [1]). Nevertheless, in addition, a proper retrofit should also guarantee an reduction in expected annual seismic losses (e.g. [8]-[11]). To this end, the retrofit design should look at collapse safety and at seismic capacity at less severe performance levels as well. Especially at less severe performance levels, i.e. at more frequent seismic events, non-structural components must be considered. Among them, masonry infills, typically defined as non-structural components despite their structural role, significantly affect seismic performance and relevant losses in existing RC buildings, both as-built and retrofitted, as recently demonstrated by ([12]-[14]). Therefore, when seismic performance of retrofitted RC buildings is assessed, their contribution should be properly considered in numerical modelling and in damage and loss assessment.

In this work, a preliminary analysis of two case-study low-standard RC buildings, different for design typology, is presented, based on static nonlinear analyses. The investigated case-study structures are 4-storey buildings representative of Italian pre-70 residential buildings, designed for gravity loads only (GLD) or according to obsolete seismic design (OSD).

First, they have been assessed in their “bare” configuration (without infills), as typical in design practice. In such a first-step-assessment only nonlinear flexural response of beams and columns has been modelled, whereas columns/joints shear failures have been detected in post-processing, based on the current Italian code [15].

Then, based on the as-built assessment outcomes, the retrofit phase has been designed by means of two alternative strategies:

1. *Strategy “A”*: the complete resolution of all the shear failures (in columns or joints), if any (by means, for example, of localised steel cages, pre-stressed steel strips or wrapping with Fiber Reinforced Polymers (FRP) fabrics);
2. *Strategy “B”*: the reduction of the displacement demand by means of RC column jacketings, when necessary, along with the resolution of shear failures (as for the previous strategy).

These two strategies represent two boundary conditions for the retrofitted buildings since in strategy “A” no modification in the lateral stiffness is produced, whereas strategy “B”, the most invasive one, necessarily leads to a higher lateral stiffness of the building.

Lastly, both the as-built and retrofitted building configurations have been modelled and re-analysed explicitly considering the presence of infills, and, in the case of as-built configurations, potential shear failures in columns/beams and joints. SPO analyses has been carried out and Incremental Dynamic Analyses (IDAs) curves have been derived by means of SPO2IDA tool [16]. Fragility curves have been finally obtained at different Damage States (DSs) according to European Macroseismic Scale EMS-98 [17], considering record-to-record variability, and compared to each other. Remarks about the choice of the strengthening strategies are carried out, based on these outcomes and on a preliminar estimation of the expected mean annual losses for the investigated buildings.

2. CASE-STUDY BUILDINGS

In this work, two residential RC buildings are investigated as case-study structures. They have the same floorplan (see Figure 1a), symmetric in both directions. 4 meters length bays are present in both directions, except than the central bay, which has a length equal to 3 meters. The interstory height is 3 m. In both cases, in the transverse direction, only two (external) frames are present, as typical for pre-70 existing buildings in Italy.

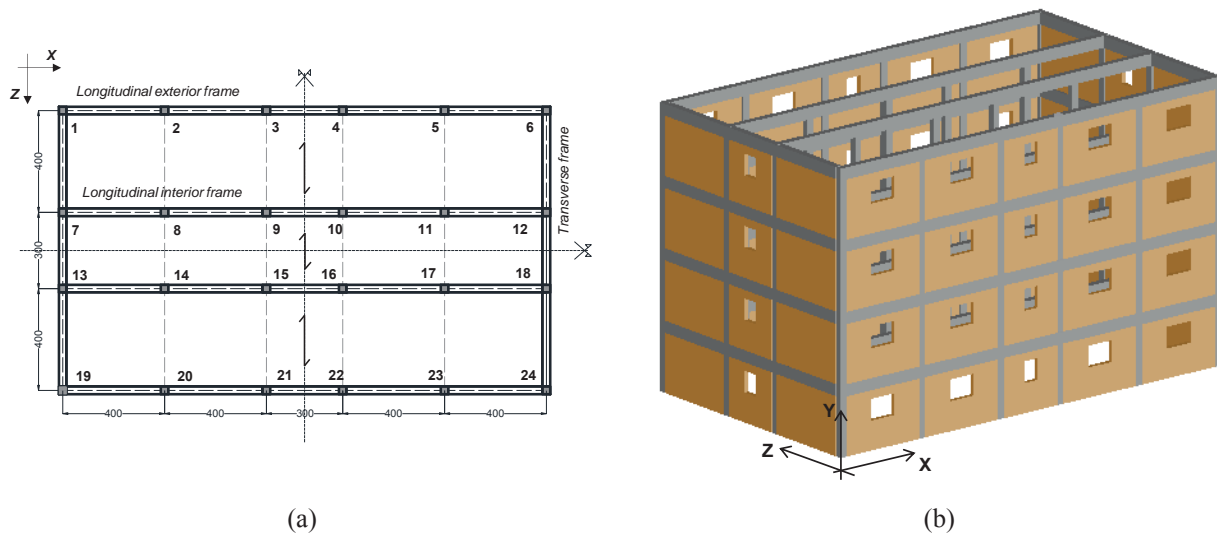


Figure 1: Plan view of the case-study buildings and column labels (a) (measures in centimetres); 3D view (b)

The two buildings differ to each other for the design typology. One building has been designed to sustain gravity loads only, as typical in Italy before '70 in most of the country. It will be referred to as Gravity Loads Designed (GLD) buildings. The other building has been designed according to an Obsolete Seismic Design (OSD) in force in Italy until the beginning of '70 and adopted for the (few) sites classified as seismic zone in that time period, as described later. Therefore, the investigated buildings are representative of the Italian building stock related to the same time period (between '50 and the very beginning of '70) but located in different sites (with different seismic hazard at the year of construction), as explained in section 2.1.

2.1 Location and seismic hazard

Both the considered buildings are in medium-high seismic hazard sites in Italy. The GLD building is located at Morra de Sanctis, in the Southern of Italy. Such location has been classified as a seismic-prone site only after the well-known Irpinia earthquake (1980) and, therefore, all the buildings realized before '80 have been designed to sustain gravity loads only.

The OSD building is assumed to be located in L'Aquila city (Abruzzi region, Italy), which has been classified as seismic-prone starting from the very beginning of the last century, and, thus, the major part of its existing RC buildings has been designed to take into account seismic actions, according to seismic prescriptions as obsolete as their age of construction.

Figure 2a shows the location of these two sites on the current seismic Italian hazard map by the National Institute of Geophysics and Vulcanology (INGV) in terms of expected ground acceleration with a 10% probability of exceedance in 50 years. Additionally, Figure 2b reports a comparison between the pseudo-accelerations ($S_a(T)$) of the two selected sites at different return period (T_R) corresponding to four limit states according to Eurocode 8-part 1 [18] and Italian code [15]

(Immediate Occupancy, $T_R=30y$; Damage Limitation, $T_R=50y$; Life-Safety, $T_R=475y$; Near Collapse, $T_R=975y$).

In both cases, it is assumed soil type “C” and soil topography “T2” [18] for the definition of the local seismic amplification effects.

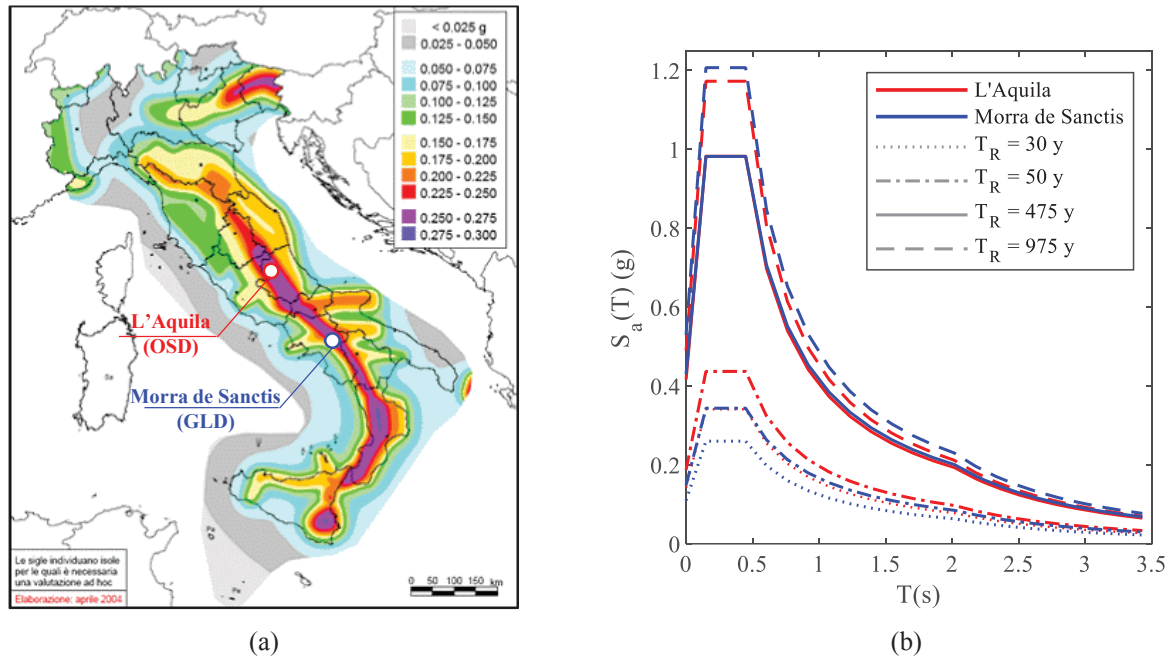


Figure 2: Buildings locations on the current hazard map by the National Institute of Geophysics and Vulcanology (INGV) (a); comparisons among pseudo-acceleration ($S_a(T)$) spectra at different return periods (T_R) (b)

2.2 Simulated design

The moment resisting frames (MRFs) system for both the buildings is characterized by 2D resisting frames in the longitudinal (X) direction, whereas, in the transverse (Z) direction, MRFs are present only along the exterior perimeter. Floors are 20 cm thick, with 4 cm RC slab. As shown in Figure 1a, the floor weight is sustained by the longitudinal frames only. Infills differ between the two directions for the openings presence: the opening percentage ranges from 0 to 15% of the infill total area, as qualitative shown in Figure 1b. An infill weight (per panel unit surface) equal to 2.00 kN/m² and 2.36 kN/m² for longitudinal and transverse direction, respectively, is assumed for exterior frames. “Maximum allowable stress method” is adopted for the “simulated design” of these buildings [19]. Since all the buildings were “located” in the same time period, the design mechanical properties of reinforcing steel and concrete are identical for all the buildings. Maximum allowable concrete strength was assumed equal to 5 MPa or 6 MPa, for purely compressive loads or bending actions, respectively (according to [21]). A maximum allowable strength equal to 140 MPa has been adopted for reinforcing bars [21] in the hypothesis that steel typology “AQ42” was used, as typical in the reference time period in Italy [20]. It is worth noting that plain bars were used as reinforcement typology, as typical in pre-‘70 RC buildings in Italy ([20], [22]). Additionally, infill panels are supposed to be identical for both the analysed buildings, and in particular made up of hollow clay bricks assembled with mortar: the presence of two coupled leaves is assumed, with 120 mm and 80 mm thickness, respectively, as typical in Italian and Mediterranean area in the reference time period [23].

GLD buildings have been designed to sustain gravity loads only and to comply code prescriptions about minimum amount of longitudinal and transverse reinforcement as defined by the Italian R.D.

[21]. On the contrary, OSD buildings are designed to sustain horizontal loads, too, the latter defined according to obsolete seismic codes in force in the reference time period ([24]-[25]), which allowed modelling the seismic actions as horizontal equivalent forces constant along the building height. The design horizontal acceleration was equal to 0.07 times the gravity acceleration ([24]-[25]). Additionally, the total design base shear is divided among resisting frames proportionally to the vertical loads supported by each of them, as typical for the reference time period. This means that transverse frames should support very low lateral actions, whereas longitudinal interior frames should sustain the highest horizontal loads. As a result, transverse frames are almost identical between GLD and OSD buildings; whereas, longitudinal frames generally result in a higher reinforcement amount, especially at the lowest stories (where columns have the highest longitudinal reinforcement percentage). The reinforcement percentage values of the first-floor columns significantly decrease at the upper stories (varying around about 0.7%). Stirrups with 250 mm maximum spacing and 8 mm diameter have been used in the beams; stirrups with 140 mm spacing and 6 mm diameter have been used in the columns (in agreement with prescriptions by [21]). All the beams resulted in a $30 \times 50 \text{ cm}^2$ cross-section, whereas column sections vary from a minimum of $30 \times 30 \text{ cm}^2$ (for most of the columns) to a maximum of $30 \times 40 \text{ cm}^2$ (for central columns). Rectangular columns are always oriented in the longitudinal direction. Further details can be found in [26].

2.3 Material properties

Lastly, a key issue for the complete assessment and modelling of the case-study structures is the definition of the strength values used for concrete, steel and infills.

As far as the as-built buildings is concerned, mean values of concrete compressive strength (f_c) and reinforcing yielding strength (f_y) have been assumed equal to 20.0 MPa and 322.4 MPa, respectively, according to suggestions by [27] and [20] for the adopted steel typology and the reference time period. Infill panels are characterized by a diagonal compressive strength (τ_{cr}) equal to 0.27 MPa and a Young modulus (parallel to the holes) of 3000 MPa. Such values are based on a subset of data collected in [28] on weak Italian infills characterised by horizontally placed hollow clay bricks with a void percentage of about 60%, as typical of the investigated case-study buildings. It is worth noting that the definition of infill mechanical properties is a complex issue, since they are characterised by a very high variability and they significantly depend on brick typology and strength, mortar mechanical properties, bricks void percentage, bricks compressive strength. Therefore, a further extension of the present work should explicitly consider the possible variability of the key infill mechanical properties and their effect on structural response (e.g. [29]).

3. CODE-BASED ASSESSMENT AND DESIGN OF RETROFIT

This section shows the first-step seismic assessment of the two case-study buildings, performed according to the current Italian code [15]. A “Normal Knowledge Level” (KL2) ([15], [30]) has been assumed; therefore, according to [15], the mean values of the mechanical properties of existing materials used in the capacity calculation have been divided by a confidence factor equal to 1.20. Two performance levels have been analysed for this code-based assessment: “Damage Limitation” (DL) and “Life Safety” (LS) limit states, corresponding to seismic actions with a return period of 50 and 475 years, respectively ([15], [30]). The building’s capacity at DL limit state is assumed to be achieved when for the first time an inter-story drift ratio (IDR) equal to 0.5% is achieved. The LS limit state is reached when for the first time a member achieves a chord-rotation equal to 3/4 of the ultimate rotation (θ_u) (flexural failure) or when a shear failure arises (in beams, columns, or joints), as explained in this section. Demand-to-capacity peak ground acceleration (PGA) ratio for each considered limit state represents the building’s safety index (SI) at that limit state. Thus, the design of retrofit has been carried out based on this index, as explained in detail in the next sub-sections.

3.1 Modelling assumptions

The seismic response of the investigated case-study buildings has been numerically reproduced in OpenSees platform [31] and analysed by means of nonlinear static pushover (SPO) analyses in N2 framework [32], according to the modelling assumptions explained herein. In particular, a lumped plasticity approach has been used for RC members by means of *zero-length elements* in OpenSees located at the ends of each beam/column element in series with *elastic BeamColumn elements* (see Figure 3).

First of all, for this code-based assessment and the relevant design of retrofit intervention, the buildings have been modelled as “bare frames”, namely, infills are not included in the numerical models, unless in the definition of masses and loads, as usual in common practice approaches. Additionally, the “code-based” numerical models only reproduce the nonlinear flexural response of the RC members; therefore, static pushover curves are derived in the hypothesis that all the elements are “ductile” members.

For elements with plain bars, the flexural (bending moment, M – versus – chord rotation, θ) response of beams and columns has been modelled by means of the (quadri-linear) proposal by [22], calibrated for RC elements reinforced with plain bars, and implemented in the adopted software with a *Zero-Length Elements* (Figure 3) characterised by the *Pinching4 uniaxial material* (F-elements). The four-point envelope represents: the yielding point (“y”), the capping point (“cap”), the softening branches’ intersection (“int”), the zero-strength condition (“0”). Such material has been slightly modified by adding an additional point corresponding to the first cracking (“cr”) point (Figure 3).

Lastly, floors are assumed to be stiff in their own plane.

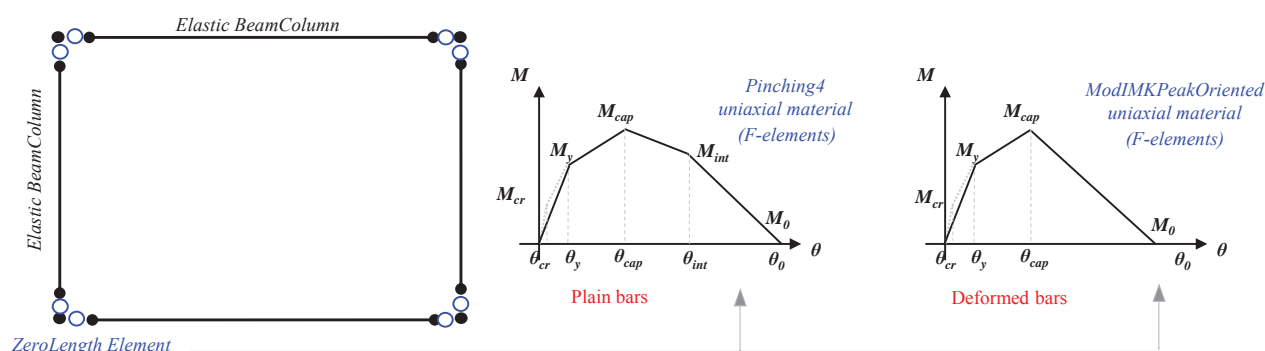


Figure 3: Schematic view of the modelling adopted for each bay in a code-based approach

In this code-based assessment phase, ductile members reach their capacity at the LS Limit State [18] when their chord rotation demand reaches $\frac{3}{4}$ of the ultimate chord rotation capacity (θ_u), the latter assessed according to the proposal by [33], as suggested by the Eurocode 8 [18] and the Italian prescriptions [34].

Nevertheless only the flexural response is modelled, as explained before, eventual shear failures in columns/beams or joints have been detected by means of a post-processing of the static pushover results, as common in practice. To this end, the Italian code-prescriptions have been adopted, so that:

- joint shear failure occurs when its principal compressive stress, p_c , overcomes 0.5 times the concrete compressive strength, f_c , or if the principal tensile stress, p_t , overcomes 0.3 times the square root of f_c [34], based on suggestions by [35] and limiting the joint failure to its shear cracking (each further strength mechanism beyond the shear cracking is neglected by this code);

- columns/beams shear failure occurs when the demand shear load overcomes the shear strength, the latter evaluated according to the model by [36] as suggested by the Eurocode 8 [18] and [34], and thus depending on the inelastic displacement demand.

3.2 As-built assessment according to Italian (D.M. 2018) code

SPO analyses have been performed separately in longitudinal (X) and transverse (Z) directions. Two lateral load patterns have been used: (i) (pseudo-)“Uniform” pattern, proportional to the storey mass distribution, and (ii) “Modal” pattern, proportional to the first-mode deformed shape in the considered direction, according to Italian prescriptions [15].

Figure 4 shows the resulting SPO curves in terms of top displacement (Δ_{top}) - versus - base shear, along with the achievement of the first joint cracking, the first shear failure in RC members, the first “ductile” failure (chord rotation demand reaches $3/4 \theta_u$), and the capacity point at the DL limit state, for GLD and OSD case-study buildings. SPO curves of OSD building generally present in the longitudinal direction higher base shear values and displacement capacity with respect to GLD building; conversely, SPO curves in the transverse direction are quite similar to each other, mainly due to the very low difference in geometry and reinforcement amount in that direction (as a consequence of the simulated design, as explained in section 2). A global collapse mechanism is observed in the transverse direction for both the case-study buildings and for both the lateral load patterns; whereas local mechanisms are observed in the longitudinal direction. In particular, for the GLD building local first- and second-floor mechanisms are observed applying respectively the “Uniform” and the “Modal” distributions; for OSD building a second- and third-floor mechanism are observed.

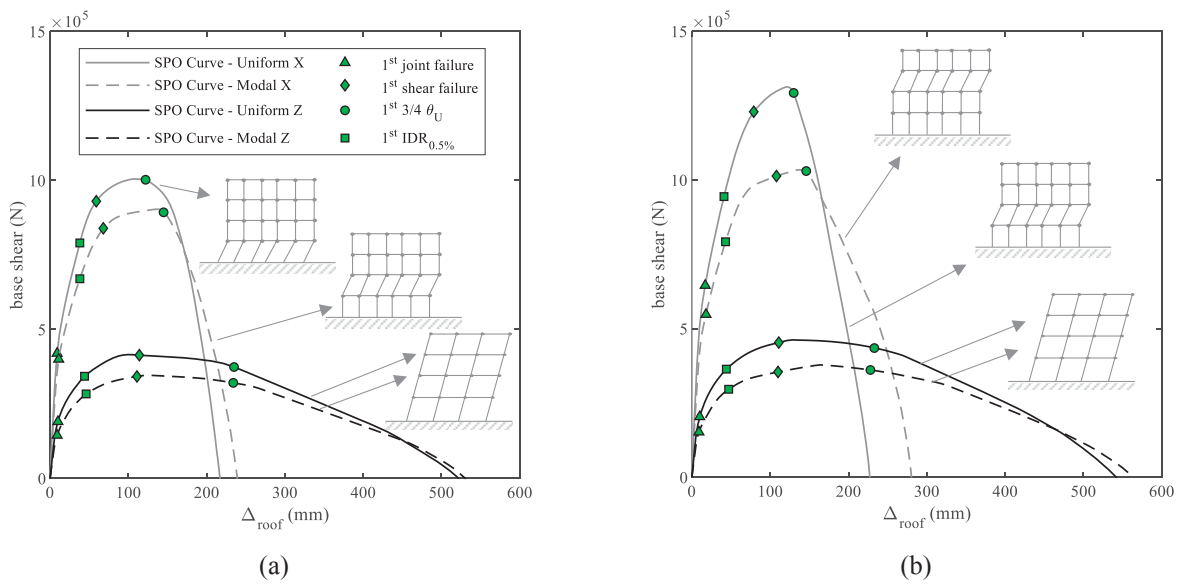


Figure 4: Static Pushover curves for (a) GLD and (b) OSD case-study buildings

Starting from each SPO curve (SPC), the capacity curve (CC) of the equivalent single-degree-of-freedom (SDOF) system [32] can be obtained dividing the abscissa and ordinates of SPO curve by the first modal participation factor in the considered direction (see Figure 5a). The CC has been bi-linearized using an equal-energy approach (according to [15]) thus obtaining an Elastic-Perfectly-Plastic (EPP) curve (whose first elastic branch is characterised by an “effective” period, T_{eff}). The EPP curve is, then, represented in the Acceleration-Displacement Response Spectrum (ADRS)

domain, where also the demand spectrum at the considered limit state can be reported (see Figure 5b).

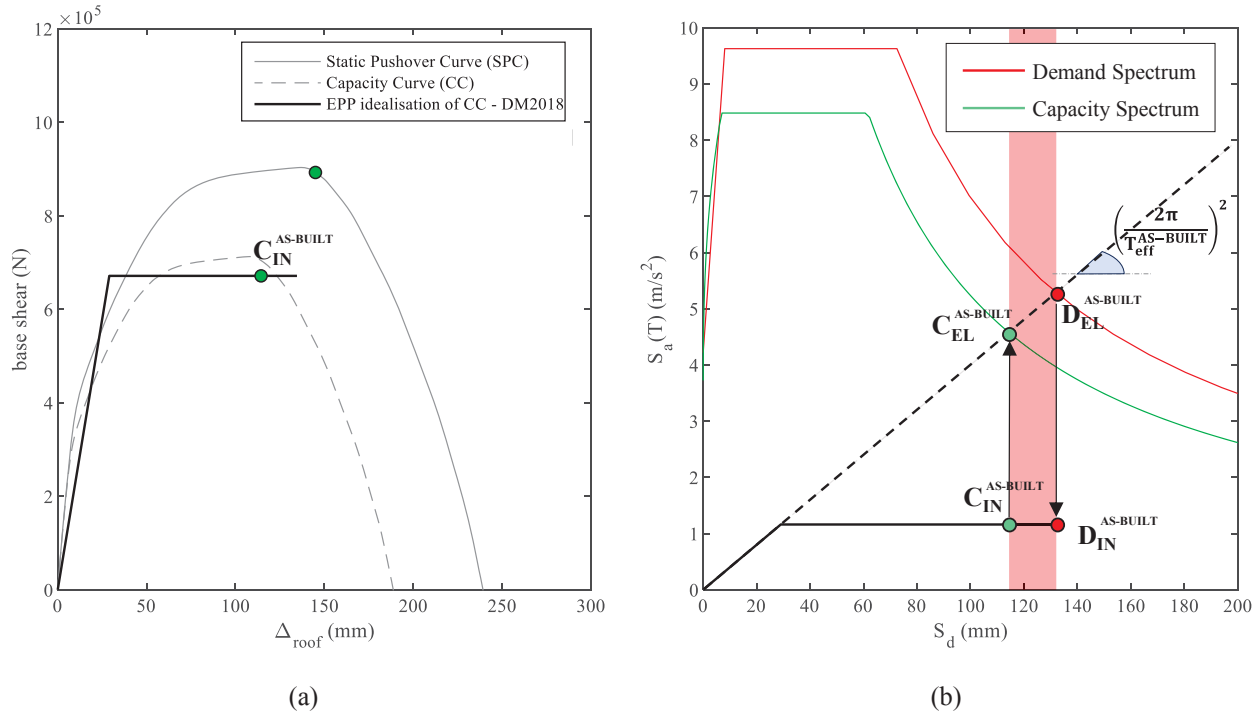


Figure 5: Example of the seismic assessment procedure: from the SPO curve to EPP capacity curve (a); from the EPP capacity curve to the capacity spectrum (b)

In order to obtain the “capacity spectrum” for a given capacity point, the elastic capacity point (i.e., $C_{\text{EL}}^{\text{AS-built}}$ for the as-built configuration) should be detected starting from the corresponding inelastic capacity point ($C_{\text{IN}}^{\text{AS-built}}$), using the equal displacement rule, modified for short period systems by [37]. In particular, in case of long or intermediate effective period of the equivalent SDOF ($T_{\text{eff}} \geq T_c$), the elastic and the inelastic displacements (i.e., the abscissas of $C_{\text{EL}}^{\text{AS-built}}$ and $C_{\text{IN}}^{\text{AS-built}}$ points) match each other, whereas the ordinate of $C_{\text{EL}}^{\text{AS-built}}$ point can be graphically obtained by intersecting the vertical line through $C_{\text{IN}}^{\text{AS-built}}$ with the elastic branch of the bi-linearization. The resulting spectrum passing by $C_{\text{EL}}^{\text{AS-built}}$ is the capacity spectrum at the considered limit state, to be compared with the demand spectrum at the analysed limit state. In particular, the demand-to-capacity ratio in terms of PGA is defined herein as the building’s safety index (SI), based on which the design of retrofit has been carried out.

In Figure 6 the above-explained seismic assessment procedure is shown for the (i) DL limit state, and the (ii) LS limit states (at the achievement of the first ductile failure (DF)), for GLD and OSD case-study buildings, separately in longitudinal (X) and transverse (Z) directions.

Quite low SI values have been obtained at DL limit state, especially in the Z direction, being SI_{DLLS} equal to 0.63 and 0.50, for GLD and OSLD buildings, respectively.

For both the buildings and in both directions, the safety index at LS limit state ($SI_{\text{LSLS,DF}}$) is quite high, if only ductile failures are considered (especially for the OSLD case-study building). Nevertheless, when shear failures are considered, too, at LS limit state, the SIs values significantly decrease, as reported in Table 1, which shows also the resulting SIs in terms of PGA at the first joint cracking and at the first shear failure in RC beams/columns for each direction and for both case-study buildings. Note that, for the first joint failure, in both directions the same SI is observed, being the corresponding capacity return periods less than 30 years for both the main directions. Thus, for both directions, the same “minimum” code-based [15] spectrum has been considered as capacity spectrum

($T_R=30y$). Based on these outcomes, the retrofit of the two case-study buildings has been designed by means of two main strategies, as explained in the next sub-section.

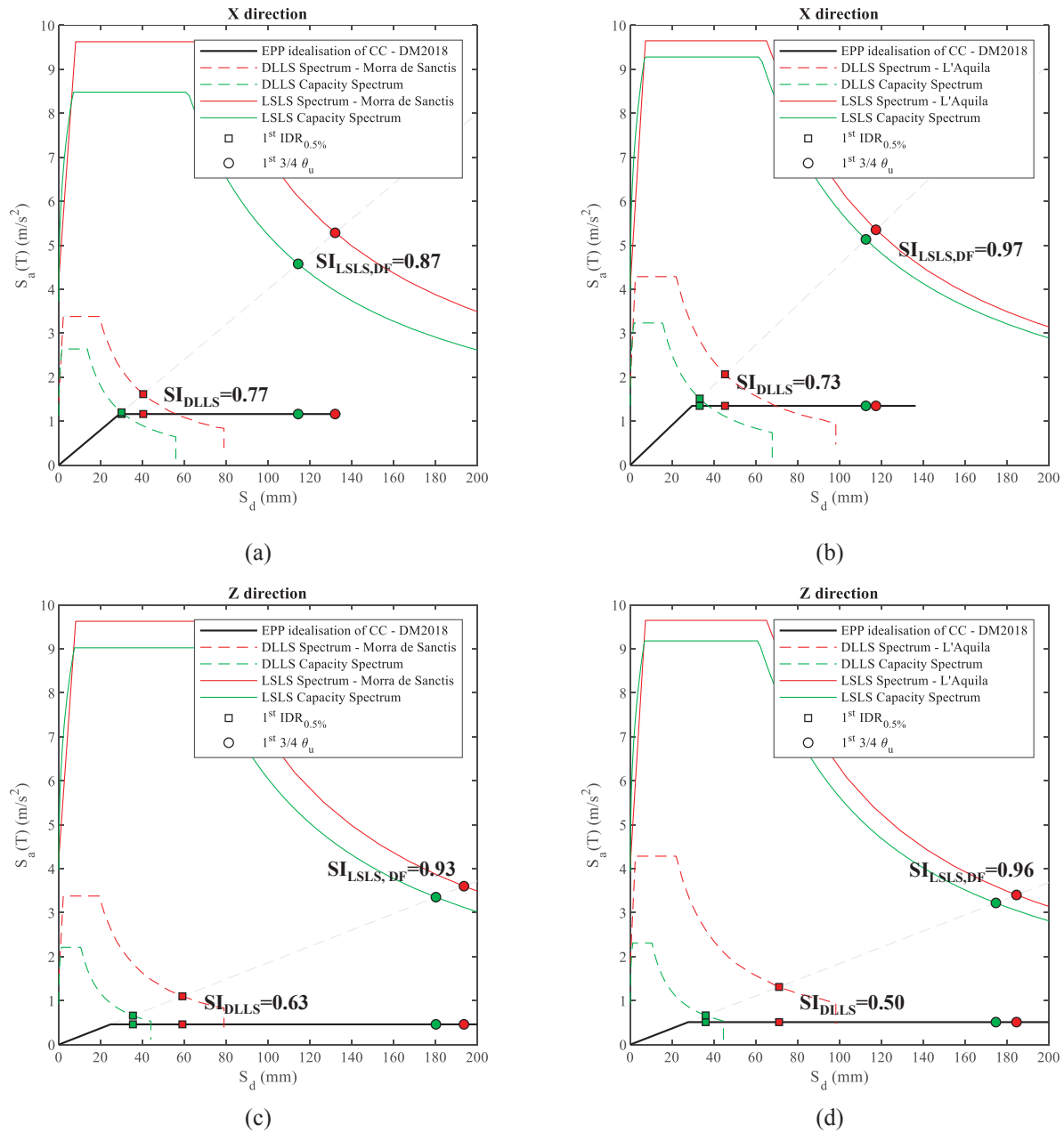


Figure 6: Seismic assessment with reference to Damage Limitation (DL) and Life Safety (LS) limit states for (a; c) GLD and (b; d) OSD case-study buildings

	GLD		OSD	
	X direction	Z direction	X direction	Z direction
1 st IDR=0.5%	0.77	0.63	0.73	0.50
1 st joint failure	0.34	0.34	0.19	0.19
1 st shear failure	0.62	0.52	0.43	0.47
1 st ductile failure	0.87	0.93	0.93	0.96

Table 1: SIs summary

3.3 Design of retrofit

The main aim of the design of the retrofit strategies is to increase the SI towards/beyond the unity, by adopting one of the available retrofitting techniques or also combining them. Mainly, these techniques are based on strategies which involve the reduction of the seismic demand or/and the increase of the building's capacity. In this work, two main strategies for the retrofit's design have been considered:

- (A) the complete resolution of all the shear failures (in columns or joints) only, by means, for example, of localised wrapping with Fiber Reinforced Polymers strips, steel cages, or pre-stressed steel strips;
- (B) the reduction of the displacement demand at DL limit state by means of RC column jacketings, when necessary, along with the resolution of shear failures (as for the strategy A).

Strategy "A" aims at the resolution of all the shear failures, both in joints and shear-critical columns, by means localised interventions. According to this strategy (see Figure 7a), any shear failure in the post-retrofit phase is solved, so that the seismic capacity moves from the first shear failure of joint - the minimum one in the as-built configuration - (at $J^{As-built}$ in Figure 7a) to the first ductile failure (at $C_{IN}^{As-built}$). This strategy does not reduce the seismic displacement demand (being $T_{eff}^{As-built} = T_{eff}^{Retrofit}$), but only increases the shear capacity and, in tune, the deformation capacity of the retrofitted members. As a result, the final SI of the building is not higher or equal to the unity, but it corresponds to the first ductile failure capacity (which in these cases is always beyond the 80%, namely already "acceptable" according to current codes [15]). Such strategy could be pursued by means of FRP fabrics, steel cages or pre-stressed steel strips. However, note that the exact definition of the technique and the material properties to be used to apply this strategy is beyond the scope of this work.

Conversely, strategy "B" is based on the decrease of the seismic demand of the entire structure by means of the increase of building's stiffness. In Figure 7b, the retrofit strategy "B" is graphically shown, starting from the elastic demand point in the as-built condition ($D_{EL}^{As-built}$). This point belongs to the demand spectrum at the considered limit state and can be detected considering the effective period of the equivalent SDOF ($T_{eff}^{As-built}$). The corresponding inelastic demand ($D_{IN}^{As-built}$) can be found through the equal displacement rule. Therefore, to achieve SI equal to one, the retrofit intervention should be able to move the inelastic demand from $D_{IN}^{As-built}$ to $C_{IN}^{As-built}$, reducing the effective period of the equivalent SDOF. This strategy may be implemented by using the RC jacketing, making an additional concrete layer outside the perimeter of the existing members, and introducing additional longitudinal and transversal reinforcements. For both the buildings, RC column jacketing are designed by assuming as $C_{IN}^{As-built}$ the capacity at DL limit state, instead than the first ductile failure at LS limit state. It is worth noting that in a code-based approach, the safety check at DL limit state is not mandatory [15], but in this study it has been analysed to create an upper bound for the lateral stiffness that can be reached for these buildings. For both the buildings, the retrofit's designed involved the columns belong to the MRFs along the exterior perimeter in Z direction (see Figure 8). The concrete overlay of the four-sided jacket is at least 100 mm, to guarantee a sufficient cover for the new reinforcement. In particular, all the jacketed columns resulted in a 50x60 cm² cross-section (starting from the original 30x30 cm²) for GLD building and in a 50x70 cm² cross-section (starting from 30x30 cm for the corner's columns and 40x30 cm for the remaining ones) for OSD building. The jacket's concrete class and the reinforcement steel type is C25/30 ($f_{ck}=25$ MPa; $f_{cm}=33$ MPa), and B450C ($f_{yk}=450$, $f_{ym}=500$ MPa) respectively [18]. The longitudinal reinforcement is 12Φ18 and 12Φ20 (i.e., about 1% of the new cross-section area) for GLD and OSD buildings, respectively. Additionally, stirrups with 140 mm spacing and 8 mm diameter have been used in both buildings; they were designed to guarantee a ductile behaviour for these new columns.

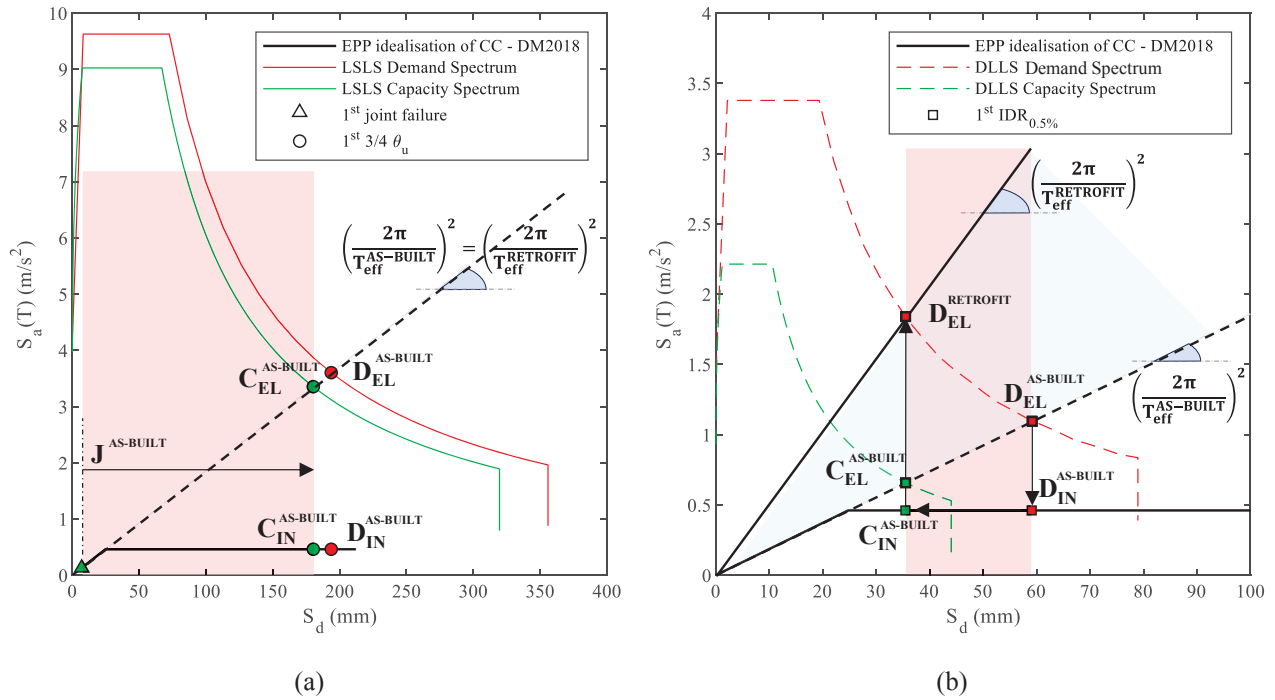


Figure 7: Strategies “A” (a) and “B” (b) for buildings’ retrofit in the ADRS domain.

These retrofit solutions allow to increase the safety indexes.

If Strategy “A” is applied, SI at LS limit state increases from 0.34 to 0.87 for the GLD building, and from 0.19 to 0.93 for the OSD building (see Table 1); the re-analysis of the retrofit buildings is not necessary since no modification in mass and stiffness are expected to occur if this strategy is applied [38]. Additionally, DL limit state safety check does not change at all, obviously.

On the contrary, if Strategy “B” is applied, the retrofitted buildings should be re-modelled and re-analysed to prove its effectiveness. In this case, for member with deformed bars, namely only for columns interested by RC jacketing in the retrofitted buildings, the nonlinear flexural response has been modelled by means of the proposal by [39]. Note that, for sake of simplicity, and according to Italian code [15], it is assumed that the “new” jacketed” sections are made up of the new steel and concrete only, and that the whole new section will sustain the total axial load (including gravity loads already present in the as-built phase). The “shape” of the moment-rotation relationship of the nonlinear response used for these elements is similar to that already described for members with plain bars, except than for the softening phase, as shown in Figure 3. It is worth noting, however, that an important difference exists between the models used herein for members with plain bars and with deformed bars: the model by [22] proposes a monotonic backbone that already reproduces the envelope of the cyclic response of columns subjected to cyclic lateral loading; on the contrary, the monotonic curve provided by [39]’s model does not account for any cyclic degradation, and some degrading rules have been suggested explicitly depending on the case-specific loading history. Such a discrepancy should be necessarily solved in future works, if a comparison based on static pushover curves has to be performed. With these modelling hypotheses, Figure 9 (a,b) shows the SIs in Z direction (the direction that conditioned the design of retrofit) for the buildings retrofitted by means of the Strategy “B”, highlighting a great reduction in the effective period of the equivalent SDOF, and resulting in SI_{DLLS} very close to the unity for both the buildings.

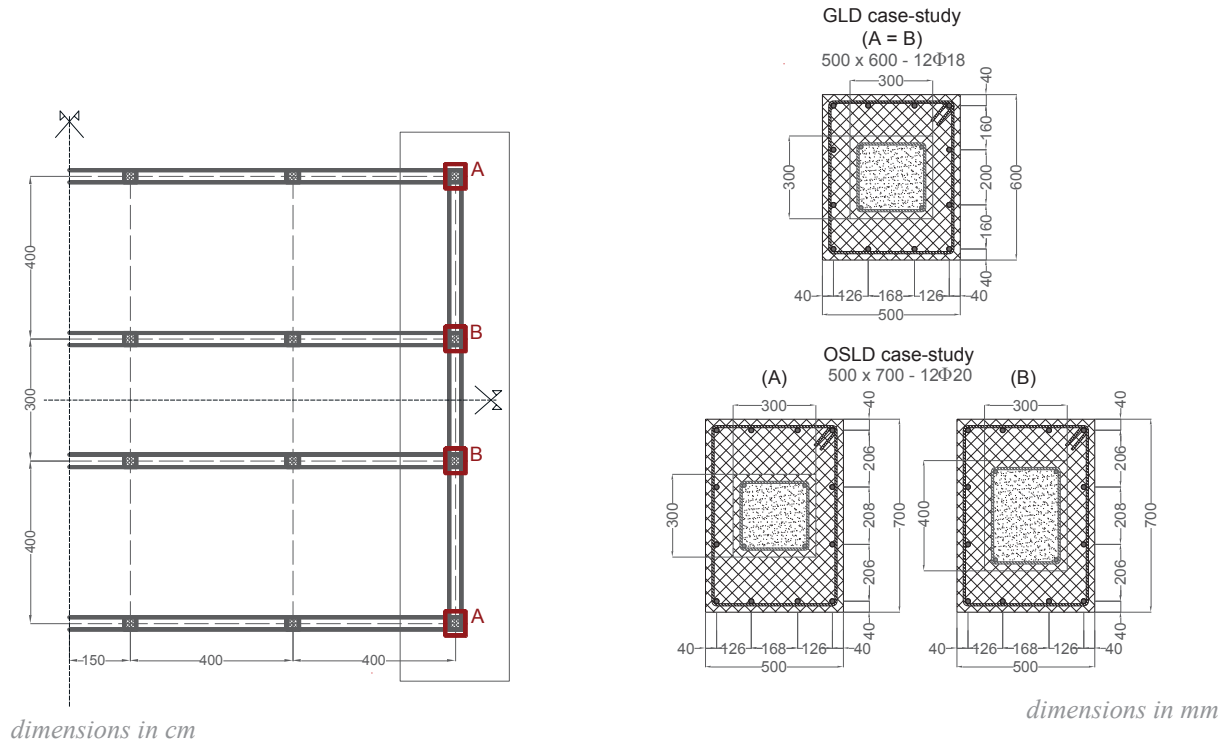


Figure 8: RC jacketing defined according to Strategy “B”

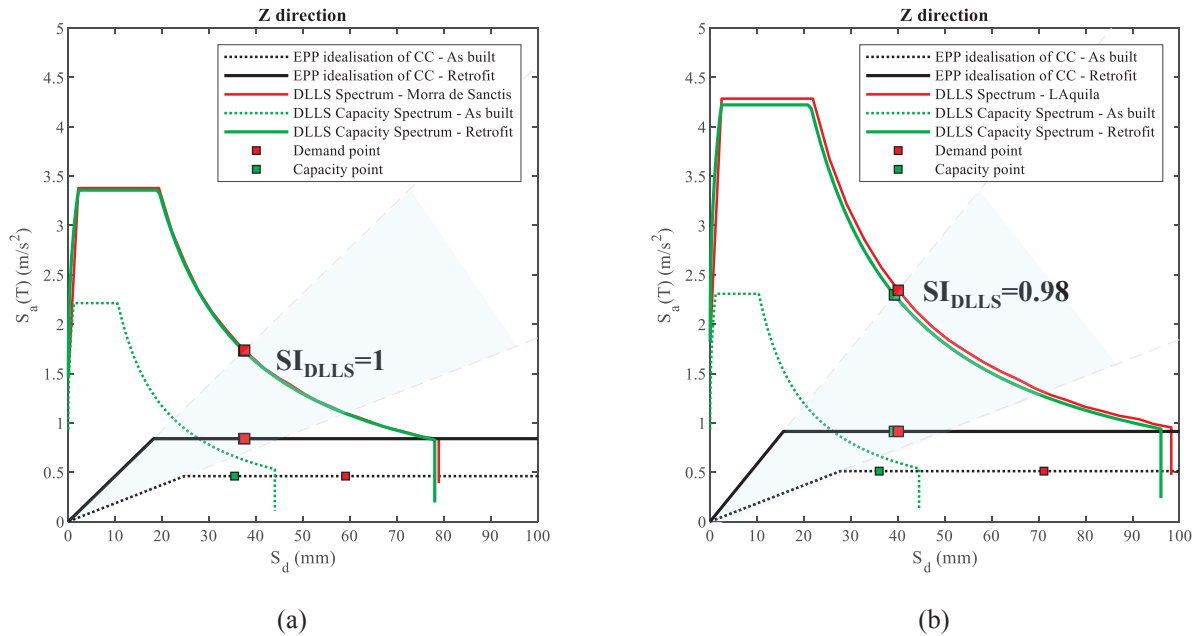


Figure 9: Seismic assessment with reference to Damage Limitation (DL) limit state for as-built and retrofitted (a) GLD and (b) OSD buildings

4. RE-ASSESSMENT OF AS-BUILT AND RETROFITTED BUILDINGS: ASSUMPTIONS

After the code-based assessment of the as-built buildings and the design of their retrofit, a re-assessment of these buildings has been performed, as explained in this section. This further phase of

assessment is aimed at the evaluation of the “real” seismic capacity of the as-built and retrofitted buildings, explicitly considering the infills contribution, the beam-column joints nonlinear behaviour, and the limited displacement capacity of columns potentially subjected to shear failures (see section 4.1). To this end, damage states definition according to EMS-98 macro-seismic scale [17] has been adopted instead than code-conforming limit states (see section 4.2).

4.1 Modelling assumption

A lumped plasticity approach has been used for RC members by means of *zero-length elements* in OpenSees located at the ends of each beam/column element in series with *elastic BeamColumn elements* (see Figure 10), as for the “code-based assessment” phase.

For member with plain bars, the flexural (bending moment, M – versus – chord rotation, θ) response of beams and columns has been modelled by means of the (quadri-linear) proposal by [22], as already explained in section 3.1. In addition, for the as-built buildings, a pre-classification of each RC member has been performed to a-priori identify its failure mode (i.e., flexural element, F; flexure-shear element, FS; purely-shear element, S), by comparing plastic shear load and shear strength, the latter calculated according to [5]’s shear strength model. When FS or S elements were detected, the relevant flexural moment-chord rotation relationship shown in Figure 10 has been modified, according to [2], by limiting the element deformation capacity according to [6]’s proposal for shear critical RC columns. For the GLD-building, only some interior columns at lower stories resulted to be FS-elements. In the case of OSD-building, almost all columns at the first floor (except than column belonging to the exterior transverse frames) resulted FS-elements. In the retrofitted buildings for both the adopted possible strategies (“A” and “B”), it is assumed that the shear failures of these elements have been solved, with a proper technique (e.g., by mean of localized steel cages or FRP fabrics), so that the shear strength of each element becomes higher than its plastic shear load. In such a hypothesis, all the elements in the retrofitted buildings have been assumed as “ductile” (“F” failure mode) with their relevant displacement capacity.

For members with deformed bars, namely for columns interested by RC jacketing (in the case of Strategy “B”), the nonlinear flexural response is modelled by means of the proposal by [39], as commented in section 3.1. Since model by [39] is used only for RC jacketed members, no further modifications are needed to account for any eventual shear failures. In fact, for each jacketed element, a proper number of stirrups can be used to prevent shear failures and ensure its ductile behavior.

Nonlinear response of beam-column joints has been modelled, too (see Figure 10). A zero-length rotational spring has been introduced in the numerical modelling at each beam-column centreline and rigid offset spreading within the joint panel have been modelled at the ends of the beams/columns. The joint moment (M_j)- shear strain (γ_j) response depends on the joint typology. The model proposed by [7] is adopted for exterior joints. For interior joints, the joint shear strain values proposed by [40] and the joint shear strength proposed by [41] have been used. For further details, see [7]. As for shear failures in columns, also for joints, it is assumed that, in the retrofitted buildings, the potential shear failure of these elements will be completely solved by means of proper strategies (e.g., by means of pre-stressed steel strips or FRP fabric in the joint core) in both the possible strategies (“A” and “B”), so that the beam-column joints become simple elastic elements.

About infill panels, two diagonal (concentric) compressive-only resisting struts (one per loading direction, as shown in Figure 10) have been implemented in each bay (with *truss element* of OpenSees library). [28]’s (tri-linear) model has been adopted herein: the corresponding axial load-axial strain (N_w - ε_w) response have been implemented with a *Hysteretic uniaxial material* (see Figure 10) for each truss element. Additionally, [42]’s reduction coefficients of infill lateral strength and stiffness have been used when openings are present.

Lastly, P-Delta effect are considered.

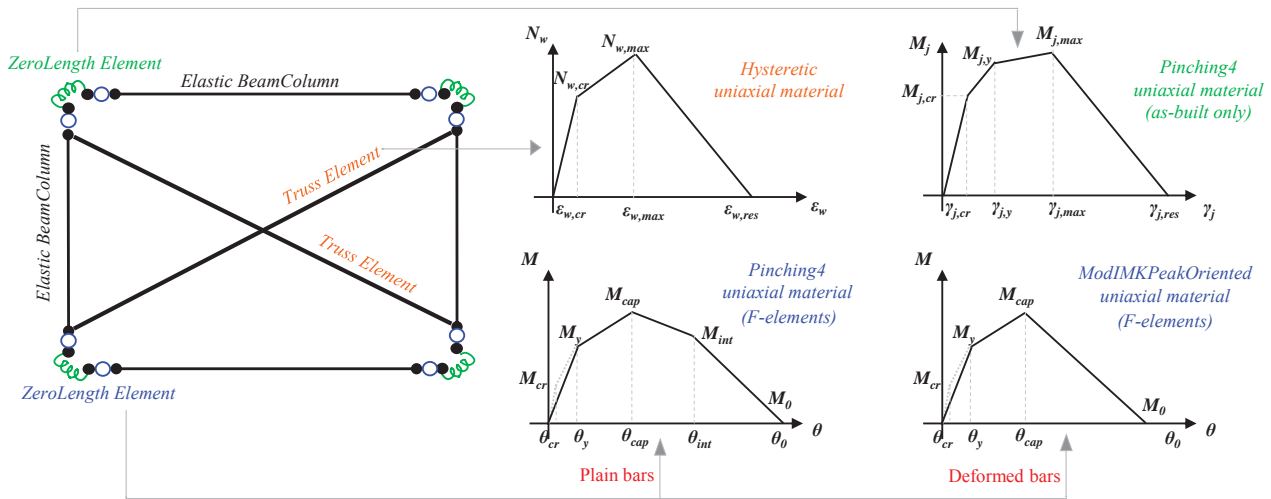


Figure 10: Schematic view of the modelling strategy adopted for each bay for the “real” assessment approach

4.2 Damage States definitions

A key issue for the assessment of the “real” seismic capacity is the definition of Damage States (DSs) for the investigated buildings. Two aspects should be considered for these buildings, in agreement with [17]’s definition Table 2), namely:

- the damage to infill panels, generally significantly affecting the relevant repair costs in the aftermath of seismic events ([12]-[14]);
- the damage to RC components (beams/columns and joints).

Therefore, each DS can be achieved due to the achievement of a certain damage level in RC members or in infill panels. The achievement of DS1, DS2, and DS3 due to infills is defined herein according to [43], namely when the interstory drift ratio (IDR) reaches the median IDR capacity at each DS (see Figure 11). In this study, the achievement of DS1, DS2, and DS3 is also associated to the achievement of the first cracking, the first yielding and the first peak load, respectively, in one element among beams, columns and beam-column joints. However, damage to infills, from light cracking to severe damage, generally condition the achievement of DS1 to DS3 in infilled RC buildings [44], as in the present applications.

DS	EMS-98 [17]	Adopted in this study
DS1	Negligible to slight damage	$\min \left\{ \begin{array}{l} \text{IDR}_{\text{infills,DS1}} \\ \text{RC beam/column/joint cracking} \end{array} \right.$
DS2	Moderate damage	$\min \left\{ \begin{array}{l} \text{IDR}_{\text{infills,DS2}} \\ \text{RC beam/column/joint yielding/pre – peak} \end{array} \right.$
DS3	Substantially to heavy damage	$\min \left\{ \begin{array}{l} \text{IDR}_{\text{infills,DS3}} \\ \text{RC beam/column/joint peak} \end{array} \right.$
DS4	Very heavy damage	RC beam/column zero-load or beam-column joint residual strenght
DS5	Collapse	RC beam/column zero-load (if “FS”) or $V_{\text{base}}=0$

Table 2. Adopted DSs definition for infills and RC members and comparison with EMS-98 macro-seismic scale

DS4 and DS5 are achieved due to damage to RC members only, since, at those DSs, infill panels should be already totally damaged. In this study, in agreement with [44], it is assumed that DS4 is achieved when a beam or a column completely losses its lateral load capacity or a beam-column joint

reaches its residual capacity. When this condition occurs in FS-elements, it is assumed that DS5 also occurs (contemporary to DS4), since, when a shear-critical element loses its lateral load capacity, it is also characterized by the onset of its axial-load failure, which reasonably leads to the collapse of, at least, a part of the building. DS5 is anyway reached when the building base shear becomes null. It is worth noting that the definition of DS4 and DS5 still deserves further investigations in future research efforts.



Figure 11: Example of damage state evolution for a masonry infilled frame for the experimental test “DIST Unina” performed at the University of Naples Federico II, adapted by [43].

5. RE-ASSESSMENT OF AS-BUILT AND RETROFITTED BUILDINGS: RESULTS

Based on the assumptions explained in section 4, in this section, the SPO curves of the as-built and retrofitted buildings are shown (section 5.1), along with the simplified Incremental Dynamic Analysis (IDA) curves obtained by means of SPO2IDA tool [16] in terms of spectral pseudo-acceleration $S_a(T)$ (section 5.2). Starting from $S_a(T)$, and assuming the spectral shape suggested by [15] for the Italian country, the corresponding PGA capacity values are obtained and fragility curves in PGA at each DS are finally shown in section 5.3. A preliminary comparison among the as-built and the retrofitted buildings is also performed in terms of Expected Annual Losses (EAL) (section 5.4).

5.1 SPO curves

SPO analyses have been performed for each case-study building separately in longitudinal (X) and transverse (Z) direction. Two lateral load distributions have been applied, as already explained in section 3. Resulting SPO curves – in terms of base shear versus Δ_{top} - and their comparison are shown in Figure 12, grouped depending on the design typology and loading direction, for the as-built and the retrofitted buildings.

It can be noted that SPO curves related to the two as-built buildings are quite similar to each other, even if, as expected, OSD presents higher base shear values and displacement capacity of GLD in the longitudinal direction, as already highlighted in section 3. It can be noted that the “Uniform” distribution leads to higher base shear values. Additionally, the most important comparison can be performed by analysing the SPO curves related to the as-built conditions and Strategy “A” case. It can be observed that the SPO curves do not significantly change when Strategy “A” is adopted, except than (slightly) in the softening branch, since FS-elements in the as-built buildings (when involved in the collapse mechanism) present a stiffer softening branch and a lower displacement capacity than the “corresponding” F-elements in Strategy “A”. On the contrary, when RC jacketing are used, obviously, the SPO curves significantly change, incrementing their base shear values and displacement capacity. A very important increment in ductility capacity is also due to the global collapse mechanisms that generally characterise these buildings when the Strategy “B” is adopted.

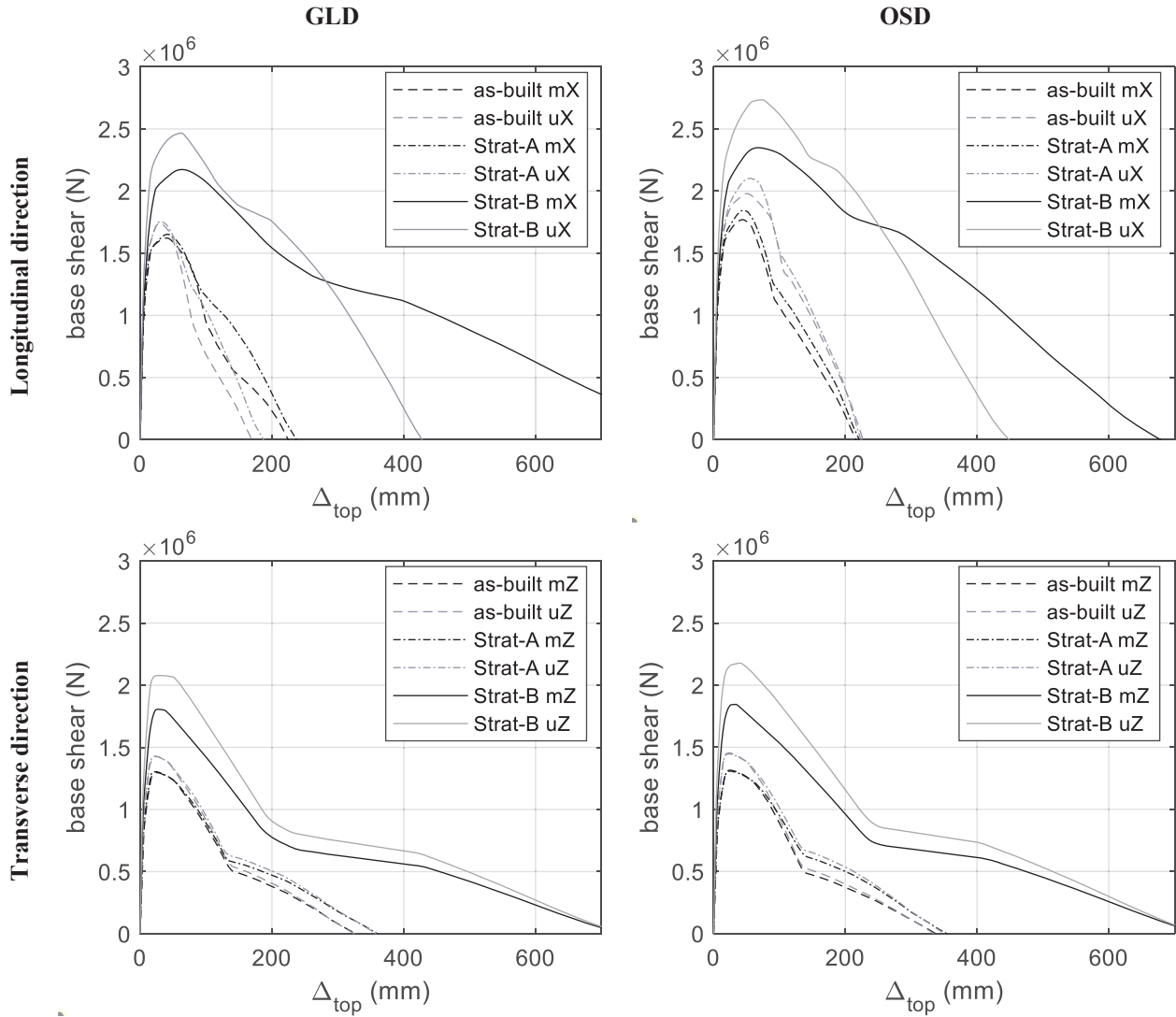


Figure 12: Comparison of SPO curves

5.2 Simplified IDA curves

SPO curves are obviously related to a multi-degree-of-freedom (MDOF) system. SPO curve' abscissa and ordinates can be divided by the first mode participation factor (Γ) of the building, in each considered direction, to obtain the capacity curve (CC) of the equivalent SDOF system [32]. Then, each CC is multi-linearized to take in due account the strength and stiffness contribution of infill panels. Nevertheless, a zero-strength residual branch is introduced, whereas the softening branch is defined based on an energy-equivalent approach between the peak load and the zero-lateral load point on the pushover curve. As a result, four-branch capacity curves are obtained for each analysed building.

Starting from each quadri-linear CC, the related Incremental Dynamic Analysis (IDA) curve have been derived thanks to the well-known SPO2IDA tool by [16], which provides the relationship between the selected engineering demand parameter (*edp*) and the seismic hazard intensity measure (*IM*). To apply the SPO2IDA tool, the CC should be first expressed in terms of ductility (μ) – strength reduction factor (*R*). The ductility μ is derived as the ratio between CC abscissas and yielding displacement. The factor *R* is the ratio between CC ordinates and yielding acceleration. SPO2IDA tool finally provides the IDA in terms of *edp* (spectral displacement) versus *IM* (spectral acceleration). Therefore, given a certain capacity *edp*, the corresponding 16th-, 50th-, and 84th- percentiles of

capacity IM can be obtained; alternatively, given a certain IM demand, the corresponding 16th-, 50th-, and 84th- percentiles of demand edp can be derived. 50th-, 16th- and 84th- percentile IDA curves also allow quantifying the record-to-record variability, which will be used later for the definition of the fragility curves “slope”.

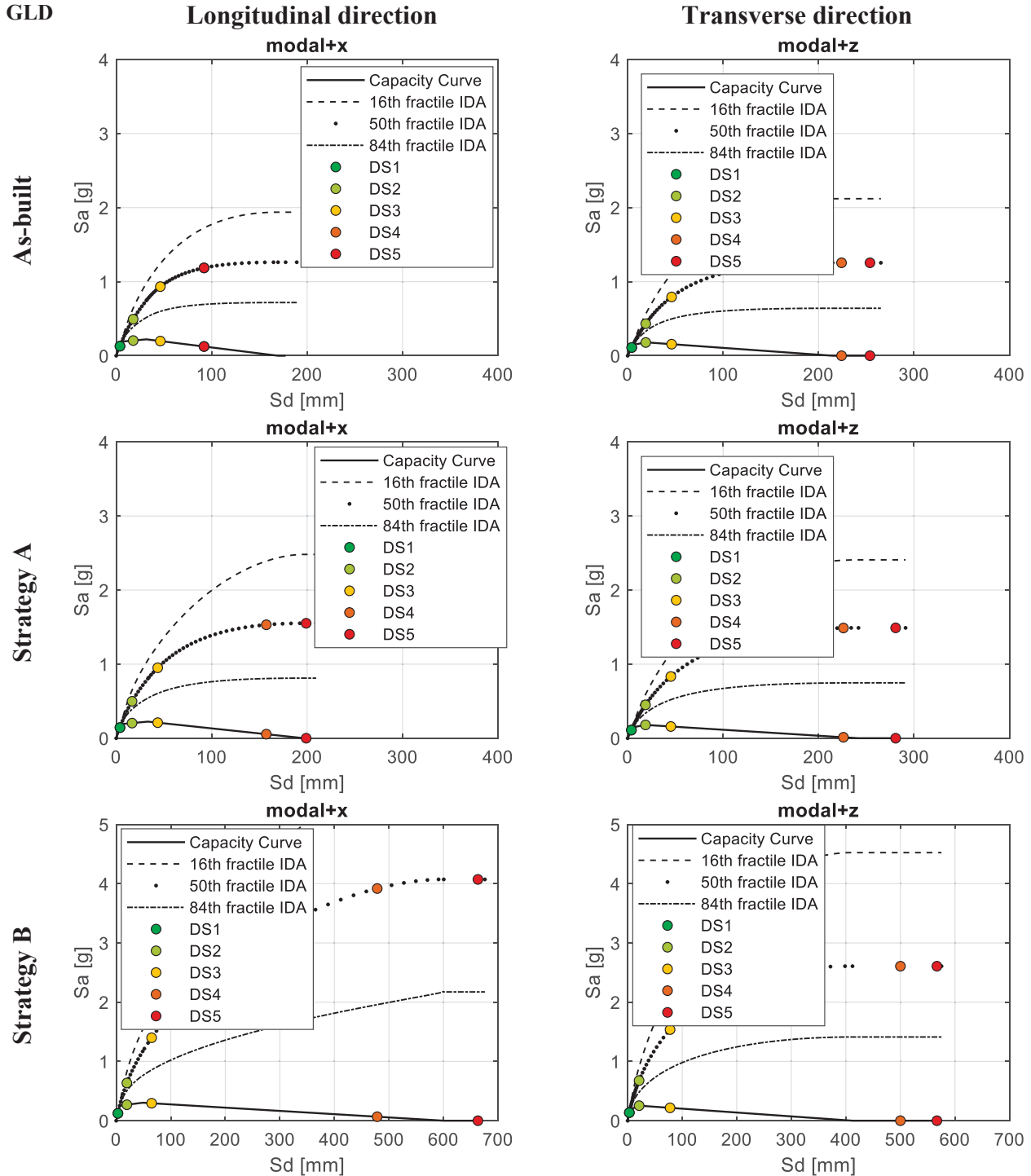


Figure 13: GLD-buildings: Multi-linearized CC, simplified IDA curves and capacity at each DS (only results for “Modal” distribution are reported, for sake of brevity)

Figure 13 and Figure 14 shows the multi-linearized CCs (reported as spectral displacement, S_d , versus spectral pseudo-acceleration, S_a , relationships) and the related (median, 16th and 84th percentiles) IDA

curves for the case-study buildings, along with the performance points related to the achievement, for the first time, of DS1 to DS5 (as defined in section 4).

OSD

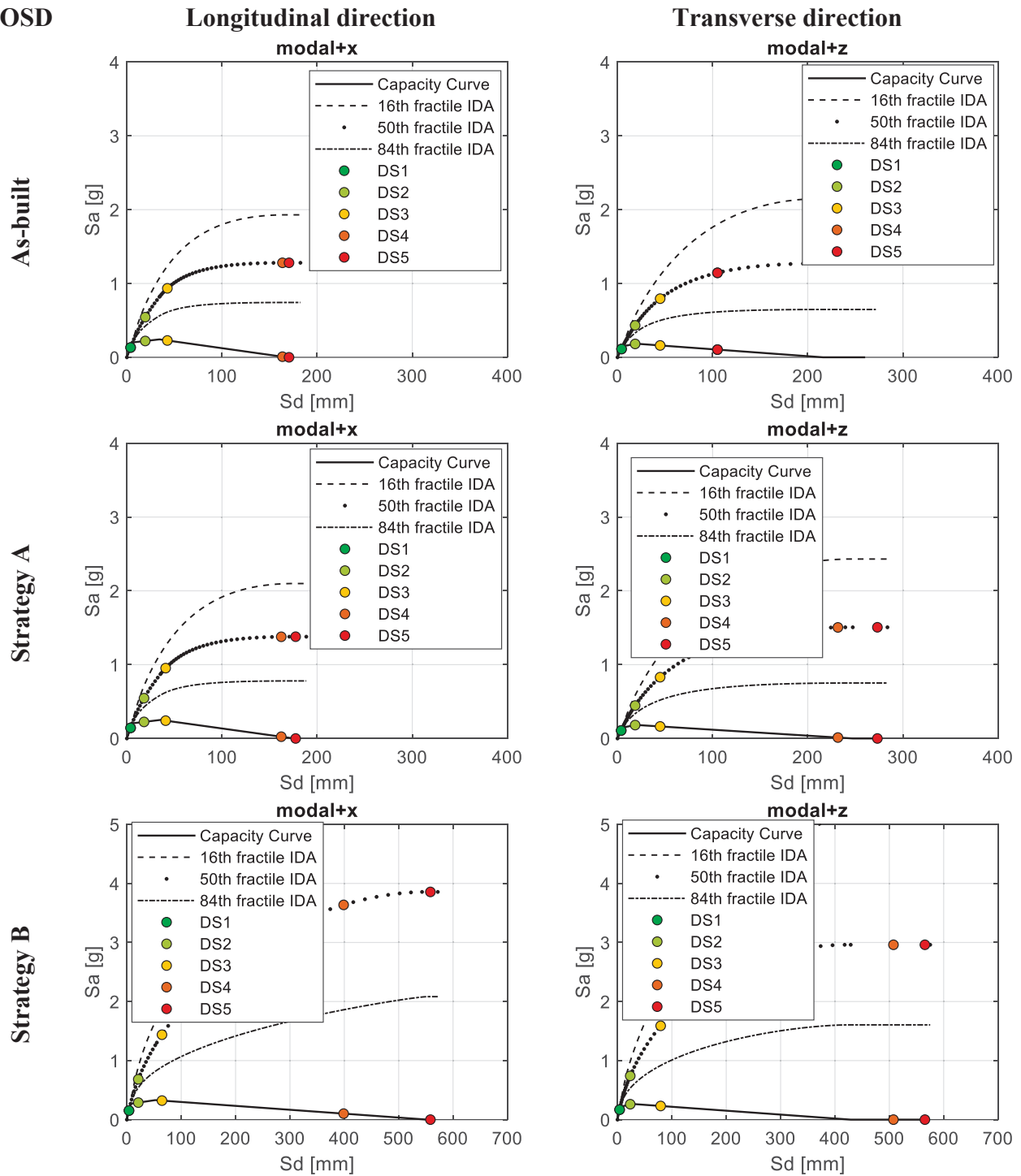


Figure 14: OSD-buildings: Multi-linearized CC, simplified IDA curves and capacity at each DS (only results from “Modal” distribution are reported, for sake of brevity)

It is worth noting that the achievement of DSi (with $i=1, 2, 3$) for infill panels is assumed to occur when the IDR demand in a panel reaches its median capacity value at that DSi. Additionally, due to the structural regularity of the case-study buildings and the same adopted capacity thresholds for all

the panels (for sake of simplicity), the achievement of DS_i “contemporary” (namely, at the same top displacement level) occurs in all the panels in a storey, in a given direction.

It can be noted that, when Strategy “A” is applied, DS1-to-DS3 remain almost unchanged, whereas displacement capacity at DS4 and DS5 can more significantly increase, especially when their achievement in the as-built buildings was strongly conditioned by the achievement of a null lateral load in shear-critical columns involved in the collapse mechanism.

On the contrary, when Strategy “B” is adopted, seismic capacity at all the DSs improves, above all at DS4 and DS5, but also at less severe DSs. This is mainly due to the increment of lateral stiffness induced by the RC jacketing and to the design approach chosen for this strategy (since it was designed to satisfy the DL limit state).

It is so clear that Strategy “A” and Strategy “B” create a range of minimum and maximum variation of the seismic capacity for these buildings, especially for what concerns the first three DSs, strongly influenced by the infill panels capacity.

5.3 Fragility curves

In this section, preliminary fragility curves have been obtained in terms of peak ground acceleration (PGA). To this end, the seismic capacity in terms of S_a has been used for each case-study, along with the spectral shape defined according to Italian code [[15]] for the sites of interest. A single fragility curve (for each DS) has been reported here for each case-study since it represents the minimum capacity between the two main directions and the two selected lateral load distributions (Uniform or Modal). Minimum values of PGA capacities for each case-study are first shown in Table 3. Fragility curves are finally shown and compared to each other in Figure 15. Only record-to-record (RtoR) variability is considered in this study. This is the reason why DS1 fragility curve is a “Z-shaped” function, since DS1 generally belongs to the first (elastic) branch of the multi-linearized CC, and no RtoR variability exists in this range of behavior. Further sources of variability should be introduced in future works.

GLD	As-built		Strategy “A”			Strategy “B”		
	β_{RtoR}	PGA (g)	β_{R2R}	PGA (g)	Retrofitted/As-built	β_{RtoR}	PGA (g)	Retrofitted/As-built
DS1	0	0.05	0	0.04	0.90	0	0.05	1.07
DS2	0.24	0.18	0.24	0.18	1.01	0.23	0.28	1.51
DS3	0.47	0.35	0.47	0.36	1.05	0.45	0.59	1.72
DS4	0.48	0.43	0.58	0.55	1.26	0.62	1.05	2.41
DS5	0.48	0.43	0.58	0.55	1.26	0.62	1.05	2.41

OSD	As-built		Strategy “A”			Strategy “B”		
	β_{RtoR}	PGA (g)	β_{RtoR}	PGA (g)	Retrofitted/As-built	β_{RtoR}	PGA (g)	Retrofitted/As-built
DS1	0	0.04	0	0.04	0.95	0	0.06	1.41
DS2	0.27	0.19	0.28	0.19	1.03	0.23	0.30	1.60
DS3	0.46	0.34	0.47	0.36	1.04	0.48	0.58	1.70
DS4	0.62	0.48	0.57	0.56	1.17	0.63	1.13	2.37
DS5	0.62	0.48	0.57	0.56	1.17	0.63	1.13	2.37

Table 3: Summary of median PGA capacity and logarithmic standard deviation due to record-to-record variability (β_{RtoR}) of fragility curves

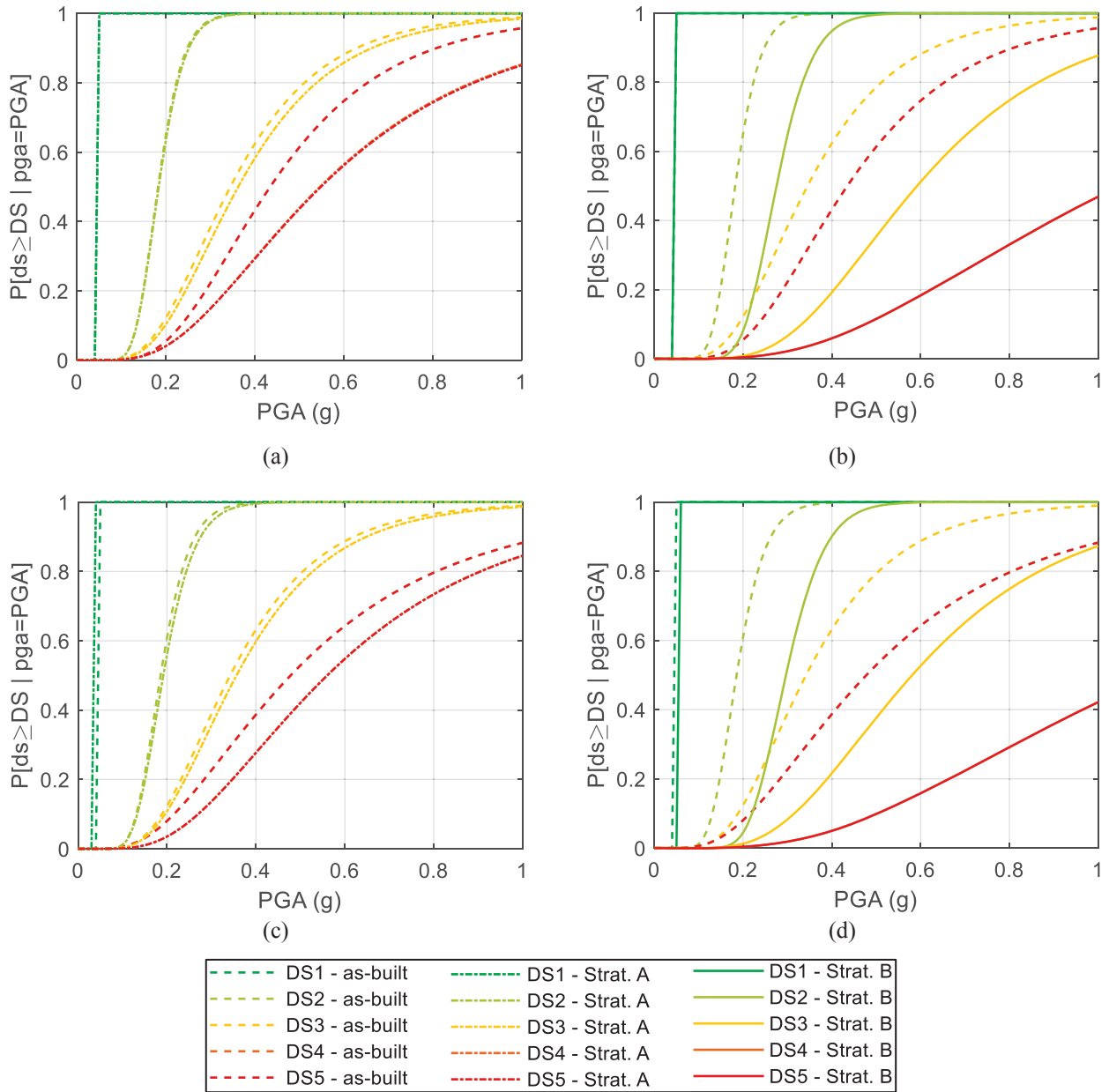


Figure 15: Comparisons among fragility curves: GLD (a,b) and OSD (c,d) buildings

The main outcomes from Table 3 and Figure 15 can be summarized as follows:

- When Strategy “A” is applied, the seismic capacity at DS1, DS2, and DS3 changes in terms PGA capacity only slightly (generally very below the 10%);
- When Strategy “A” is applied, slight changes at DS1 can be ascribable to the small differences in the very first branch of the multi-linearized CC; on the contrary, variation in PGA capacity at DS3 are generally due to some difference in the softening branches of the multi-linearized CC;
- When Strategy “A” is applied, only PGA capacity at DS4 and DS5 is more significantly affected; it can increase from +17% (OSD) to +26% (GLD), mostly due to the capability to switch off column shear failures (when they resulted shear-critical elements in the as-built buildings);

- When Strategy “B” is applied, the maximum increment in PGA capacity at DS1 to DS3 can be observed, due to the higher lateral stiffness produced by the columns RC jacketing and the way these jacketings have been designed (namely, to satisfy the DL limit state, see section 3);
- When Strategy “B” is applied, the PGA capacity at DS4 and DS5 increases significantly (more than 100%) also thanks to the global collapse mechanism they produce.

A final comment is about the difference in terms of capacity increment assessment obtained in this section and that obtained in a code-based approach (section 3). When safety check and retrofit design are performed in code-based approach, the first joint failure significantly influences the seismic capacity of the as-built building, limiting it to the first shear cracking in the joint panel in a force-based approach. When shear-critical elements, like joints as well as columns, are analyzed in a displacement-based approach, contrary to what the code prescribes, the assessment results are very different, even in the as-built configurations. Additionally, infill panels are not accounted for in typically code-conforming practice-oriented analyses. As a result, even if Strategy “A” leads to a PGA capacity increment higher than 150% for GLD and 350% for OSD (from the first joint shear failure to the first ductile failure) in a code-based approach (section 3), such a high increment cannot be found when a displacement-based safety assessment is performed; in this latter case, the capacity increment ascribable to Strategy “A” is more limited (around +20%), at least for the buildings analysed in this work.

5.4 Preliminary estimation of EAL

A final comparison among the as-built and the retrofitted buildings is performed here in terms of mean Expected Annual Losses (EAL), to emphasize the importance of the less severe damage states – and thus of masonry infills which condition the achievement of those DSs - to the seismic loss estimation. It is worth remembering that EAL represents the average amount of money (generally expressed as a percentage of the total reconstruction cost) to be spent per year to repair damage due to seismic events during the building lifetime.

First, for each DS, the expected seismic losses, expressed as a percentage of the total reconstruction cost (%CR), should be defined. A clear association between %CR and limit states defined according to Italian [15] and Eurocode 8 [18] can be found in [44] and in [46]. In this work, such an association is preliminary based on a previous study by the Authors ([13]-[14]), which considered damage to infills/partitions and services only for the same DSs adopted herein (in particular from DS1 to DS3). Therefore, 4%, 15%, and 31% of the building reconstruction cost has been assumed here at DS1, DS2, and DS3, respectively, only accounting for seismic losses due to infills/partitions and services allocated in within. DS5 is instead a physical collapse for the building and, therefore, it is associated herein to 100% of the reconstruction cost.

Additionally, the mean annual frequency of exceeding a certain DS (λ) can be obtained (as the inverse of the capacity return period at that DS), thus obtaining all the information required to calculate the EAL, as the area underneath the λ -%CR curves (Figure 16). A maximum threshold for λ (10%) has been preserved in agreement with [46].

Resulting EAL values are finally reported in Table 4. It can be noted that the EAL related to the as-built buildings and that related to the adoption of “Strategy A” are technically identical (about 3% of reduction). This means that, when seismic capacity increment affects the most severe DSs only, no benefits can be gained in terms of seismic losses. On the contrary, the increment in lateral stiffness (produced by Strategy “B”) can reduce the EAL of about 20% for both the case-study buildings.

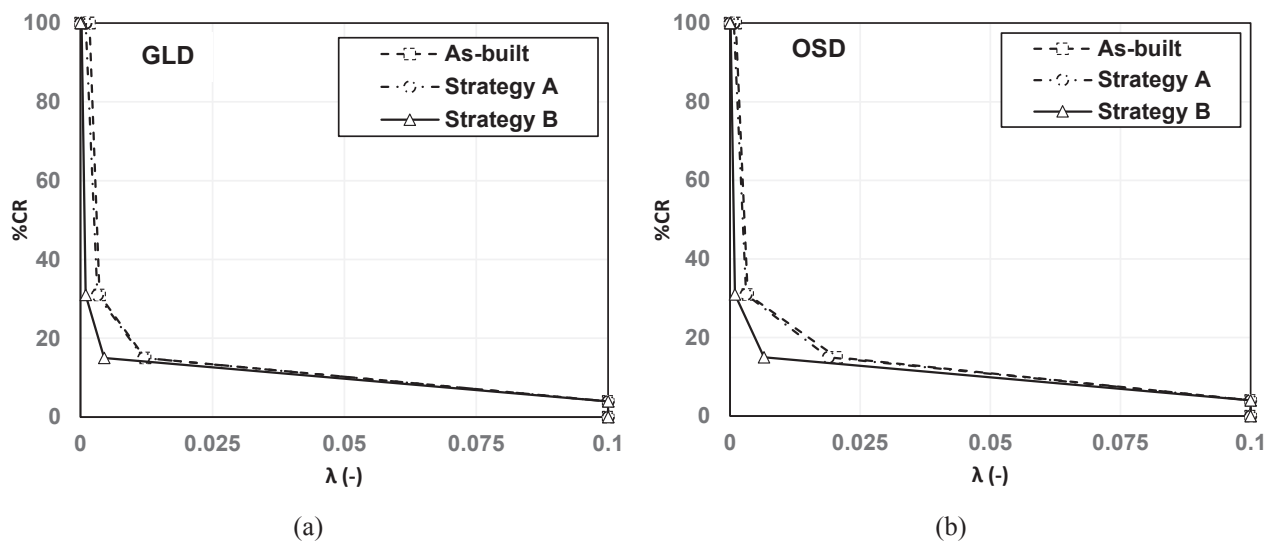


Figure 16: Percentage of the Reconstruction Cost (%CR) depending on the mean annual frequency of exceedance each DS (λ)

EAL (%)	GLD	OSD
As-built	1.33	1.41
Strategy “A”	1.28 (-3%)	1.36 (-3%)
Strategy “B”	1.06 (-20%)	1.08 (-21%)

Table 4: Expected annual losses, EAL (in grey, its percentage variation with respect to the relevant as-built building).

6. CONCLUSIONS

A preliminary seismic analysis of two case-study low-standard RC buildings has been presented, based on static nonlinear analyses. The investigated case-study structures are 4-storey buildings representative of Italian pre-70 residential buildings, designed for gravity loads only (GLD) or according to obsolete seismic design (OSD). First, they have been assessed in a code-based approach according to the current Italian code [15], namely without infills (as typical in practice) and modelling nonlinear flexural response of beams and columns only, whereas columns/joints shear failures have been detected in post-processing (in a force-based safety check). Then, based on the as-built assessment outcomes, the retrofit phase has been designed by means of two alternative strategies, representing two boundary conditions for the lateral stiffness modification of the buildings:

1. Strategy “A”: the complete resolution of all the shear failures (in columns or joints), if any, at Life Safety limit state;
2. Strategy “B”: the reduction of the displacement demand by means of RC column jacketings, designed at the Damage Limitation limit state, along with the resolution of shear failures at LS limit state.

Then, both the as-built and retrofitted building configurations have been modelled and analysed explicitly considering the presence of infills and shear-critical elements, including beam-column joints. Fragility curves have been obtained at different Damage States (DSs) according to European Macroseismic Scale EMS-98, from DS1 to DS5, considering record-to-record variability, and compared to each other. DSs from 1 to 3 were significantly affected by the infill presence; they were always achieved due to the achievement of the relevant drift capacity in infill panels.

The following conclusions can be drawn:

- when Strategy “A” is applied, the seismic capacity at DS1, DS2, and DS3 changes only slightly (generally very below the 10% in terms PGA capacity);
- when Strategy “A” is applied, only seismic capacity at DS4-5 is more significantly affected; PGA capacity at DS4 and DS5 it can increase from +17% (OSD) to +26% (GLD), mostly due to the capability to switch off column shear failures (when they resulted shear-critical elements in the as-built buildings);
- when Strategy “B” is applied, the maximum increment in PGA capacity at DS1 to DS3 can be observed, due to the higher lateral stiffness produced by the columns RC jacketing and the way these jacketings have been designed (namely, to satisfy the DL limit state);
- when Strategy “B” is applied, the PGA capacity at DS4 and DS5 increases significantly (more than 100%) also thanks to the global collapse mechanism they produce;
- if mean Expected Annual Losses (EAL) are evaluated, it can be noted that, when seismic capacity increment affects the most severe DSs only (as for Strategy “A”), no benefits can be gained in terms of economic losses (only 3% reduction); on the contrary, the increment in lateral stiffness produced by Strategy “B” can reduce the EAL of about 20% for both the case-study buildings.

It is worth noting that the present study analyses only two case-studies in a static nonlinear analyses approach and only considering record-to-record variability to obtain fragility curves. Other case-studies and sources of variability should be considered in future works, also in the context of nonlinear dynamic analyses. Additionally, the modelling strategies and DSs definition adopted herein will be deeper investigated, both about a more detailed definition of DS4 and DS5 (a topic still controversial in the literature), and about the modelling of further key shear-critical phenomena (above all involving beam-column joints), such as the joint axial load failure in as-built buildings (herein neglected). Lastly, in this study, infill panels have been considered to be identical in the as-built and in retrofitted buildings. Nevertheless, such an aspect could be modified in future works to consider the possibility of a change in infill typology to address energy-efficiency requirements, at least when invasive strategies (like Strategy “B”) are implemented.

ACKNOWLEDGEMENTS

This work was developed under the support of ReLUIIS-DPC 2019-2021 funded by the Italian Department of Civil Protection (DPC), and PON-AIM Ricerca e Innovazione 2014-2020 – Fondo Sociale Europeo, Azione I.2, “Smart, Secure and Inclusive Communities. These supports are gratefully acknowledged.

REFERENCES

- [1] Shoraka Baradaran, M. (2013). Collapse assessment of concrete buildings: an application to non-ductile reinforced concrete moment frames (Doctoral dissertation, University of British Columbia).
- [2] Ricci, P., Manfredi, V., Noto, F., Terrenzi, M., De Risi, M. T., Di Domenico, M., Camata, G., Franchin, P., Masi, A., Mollaioli, F., Spacone, E., Verderame, G.M. (2019). RINTC-e: Towards seismic risk assessment of existing residential reinforced concrete buildings in Italy. In Proceedings of the 7th ECCOMAS Thematic Conference on Computational Methods in Structural Dynamics and Earthquake Engineering, Crete, Greece (pp. 24-26).

- [3] Elwood, K. J., & Moehle, J. P. (2005). Drift capacity of reinforced concrete columns with light transverse reinforcement. *Earthquake Spectra*, 21(1), 71-89.
- [4] Elwood, K. J., & Moehle, J. P. (2005). Axial capacity model for shear-damaged columns. *ACI Structural Journal-American Concrete Institute*, 102(4), 578-587.
- [5] Sezen, H., & Moehle, J. P. (2004). Shear strength model for lightly reinforced concrete columns. *Journal of structural engineering*, 130(11), 1692-1703.
- [6] Aslani, H., Miranda, E., 2005. Probabilistic earthquake loss estimation and loss disaggregation in buildings. J. A. Blume Earthquake Engineering Center. Research report n. 157. Stanford, California, United States.
- [7] De Risi, M. T., Ricci, P., & Verderame, G. M. (2017). Modelling exterior unreinforced beam-column joints in seismic analysis of non-ductile RC frames. *Earthquake Engineering & Structural Dynamics*, 46(6), 899-923.
- [8] Liel, A. B., & Deierlein, G. G. (2008). Assessing the collapse risk of California's existing reinforced concrete frame structures: metrics for seismic safety decisions (Vol. 69, No. 05).
- [9] Pampanin, 2017. Valutazione della vulnerabilit , classificazione sismica, strategie di rinforzo e riduzione del rischio sismico di edifici esistenti in calcestruzzo armato parte iii: strategie e tecniche di rinforzo, *Structural 210 – settembre/ottobre 2017 – paper 28– ISSN 2282-3794 DOI 10.12917/Stru213.28*
- [10] Giovinazzi, S., & Pampanin, S. (2017). Simplified Approaches for the Seismic Risk Rating of Reinforced Concrete Buildings and the Selection of Retrofit Strategies.
- [11] Cardone, D., Gesualdi, G., & Perrone, G. (2019). Cost-benefit analysis of alternative retrofit strategies for RC frame buildings. *Journal of Earthquake Engineering*, 23(2), 208-241.
- [12] Del Vecchio, C., Di Ludovico, M., & Prota, A. (2019). Repair costs of RC building components: from actual data analysis to calibrated consequence functions. *Earthquake Spectra*.
- [13] De Risi, M. T., Del Gaudio, C., & Verderame, G. M. (2020). A component-level methodology to evaluate the seismic repair costs of infills and services for Italian RC buildings. *Bulletin of Earthquake Engineering*, 18(14), 6533-6570.
- [14] Del Gaudio, C., De Risi, M. T., & Verderame, G. M. (2021). Seismic Loss Prediction for Infilled RC Buildings via Simplified Analytical Method. *Journal of Earthquake Engineering*, 1-34.
- [15] D.M. 2018, Aggiornamento delle «Norme Tecniche per le Costruzioni» - D.M. 17/1/18. (in Italian)
- [16] Vamvatsikos, D., & Allin Cornell, C. (2006). Direct estimation of the seismic demand and capacity of oscillators with multi-linear static pushovers through IDA. *Earthquake engineering & structural dynamics*, 35(9), 1097-1117.
- [17] Grunthal G (1998) Cahiers du Centre Europeen de Geodynamique et de Seismologie: volume 15—European Macroseismic Scale 1998. European Center for Geodynamics and Seismology, Luxembourg
- [18] CEN 2004, Eurocode 8: Design of structures for earthquake resistance - Part 1 : General rules, seismic actions and rules for buildings, European Committee for Standardization, Ref. N. EN 1998-1 :2004

- [19] Verderame G.M., Polese M., Mariniello C., Manfredi G., (2010). A simulated design procedure for the assessment of seismic capacity of existing reinforced concrete buildings. *Advances in Engineering Software*, 41(2), 323-335.
- [20] Verderame G.M., Ricci P., Esposito M., Manfredi G., (2012). STIL v1.0 - Software per la caratterizzazione delle proprietà meccaniche degli acciai da c.a. tra il 1950 e il 2000. ReLUIS, <http://www.reluis.it/>
- [21] R.D. Regio Decreto Legge n. 2229 del 16/11/1939. Norme per la esecuzione delle opere in conglomerate cementizio semplice od armato. G.U. n. 92 del 18/04/1940 (in Italian)
- [22] Verderame, G. M., & Ricci, P. (2018). An empirical approach for nonlinear modelling and deformation capacity assessment of RC columns with plain bars. *Engineering Structures*, 176, 539-554.
- [23] Bal I.E., Crowley H., Pinho R., Gulay F.G., 2007. Structural characteristics of Turkish RC building stock in Northern Marmara region for loss assessment applications. ROSE Research Report No. 2007/03, IUSS Press, Pavia, Italy.
- [24] R.D. Regio Decreto Legge n. 2105 del 22/11/1937 - "Norme tecniche di edilizia con speciali prescrizioni per le località colpite dai terremoti", G.U. n. 298 del 27/12/1937. (in Italian)
- [25] D.M. L.1684/1962 Legge 25 novembre 1962, n. 1684, *Gazzetta Ufficiale* 22 dicembre 1962, n. 326, Provvedimenti per l'edilizia, con particolari prescrizioni per le zone sismiche. (in Italian)
- [26] Del Gaudio, C., De Risi, M. T., Scala, S. A., & Verderame, G. M. (2020). Seismic loss estimation in pre-1970 residential RC buildings: the role of infills and services in low-mid rise case-studies. *Frontiers in Built Environment*, 6, 188.
- [27] Masi, A., Digrisolo, A., and Santarsiero, G. (2014). Concrete strength variability in Italian RC buildings: analysis of a large database of core tests. In *Applied Mechanics and Materials* (Vol. 597, pp. 283-290). Trans Tech Publications Ltd.
- [28] De Risi M.T., Del Gaudio C., Ricci P., Verderame G.M., 2018. In-plane behaviour and damage assessment of masonry infills with hollow clay bricks in RC frames. *Engineering Structures*, 168, 257-275.
- [29] Mucedero, G., Perrone, D., & Monteiro, R. (2021). Nonlinear static characterisation of masonry-infilled RC building portfolios accounting for variability of infill properties. *Bulletin of Earthquake Engineering*, 1-45.
- [30] CEN (2005) EN 1998-3-1-4 Eurocode 8, Design of Structures for Earthquake Resistance, Part 3, Assessment and Retrofitting of Buildings. European Committee for Standardization.
- [31] McKenna, F. 2011. OpenSees: A framework for earthquake engineering simulation. *Computing in Science & Engineering* 13 (4): 58–66. doi: 10.1109/MCSE.2011.66.
- [32] Fajfar, P., 1999, Capacity spectrum method based on inelastic demand spectra, *Earthquake Engineering and Structural Dynamics* 28: 979-993.
- [33] Biskinis, Dionysis, and Michael N. Fardis. "Deformations at flexural yielding of members with continuous or lap-spliced bars." *Structural concrete* 11.3 (2010): 127-138.
- [34] Circolare 21 gennaio 2019, n. 7 C.S.LL.PP. Istruzioni per l'applicazione dell'«Aggiornamento delle "Norme tecniche per le costruzioni"» di cui al decreto ministeriale 17 gennaio 2018. GU n.35 del 11-2-2019 - Suppl. Ordinario n. 5. (in Italian)

- [35] Priestley MJN. Myths and fallacies in earthquake engineering, revisited. The Mallet Milne Lecture. IUSS Press: Pavia, Italy, 2003.
- [36] Biskinis DE, Roupakias GK, Fardis MN (2004) Degradation of shear strength of reinforced concrete members with inelastic cyclic displacements. *Struct J* 101(6):773–783
- [37] Vidic, T., Fajfar, P., & Fischinger, M. (1994). Consistent inelastic design spectra: strength and displacement. *Earthquake Engineering & Structural Dynamics*, 23(5), 507-521.
- [38] Frascadore, R., Di Ludovico, M., Prota, A., Verderame, G. M., Manfredi, G., Dolce, M., & Cosenza, E. (2015). Local strengthening of reinforced concrete structures as a strategy for seismic risk mitigation at regional scale. *Earthquake Spectra*, 31(2), 1083-1102.
- [39] Haselton C, Liel A, Taylor SL and Deierlein GG. Beam-Column Element Model Calibrated for Predicting Flexural Response Leading to Global Collapse of RC Frame Buildings. Pacific Earthquake Engineering Research Center 2007/03, University of California at Berkeley, 2007.
- [40] Celik OC and Ellingwood BR. Modeling Beam-Column Joints in Fragility Assessment of Gravity Load Designed Reinforced Concrete Frames. *Journal of Earthquake Engineering*, 2008, 12: 357-381.
- [41] Jeon JS, Shafieezadeh A and DesRoches R. Statistical models for shear strength of RC beam-column joints using machine-learning techniques. *Earthquake Engineering & Structural Dynamics*, 2014, 43(14): 2075-2095.
- [42] Decanini, L. D., Liberatore, L., and Mollaioli, F. (2014). Strength and stiffness reduction factors for infilled frames with openings. *Earthquake Engineering and Engineering Vibration*, 13(3), 437-454.
- [43] Del Gaudio, M.T. De Risi, C., Ricci, P., Verderame, G. M. (2019). Empirical drift-fragility functions and loss estimation for infills in reinforced concrete frames under seismic loading. *Bulletin of Earthquake Engineering* <https://doi.org/10.1007/s10518-018-0501-y>.
- [44] Del Gaudio, C., Ricci, P., Verderame, G. M., & Manfredi, G. (2015). Development and urban-scale application of a simplified method for seismic fragility assessment of RC buildings. *Engineering Structures*, 91, 40-57.
- [45] Cosenza, E., Del Vecchio, C., Di Ludovico, M., Dolce, M., Moroni, C., Prota, A., & Renzi, E. (2018). The Italian guidelines for seismic risk classification of constructions: technical principles and validation. *Bulletin of Earthquake Engineering*, 16(12), 5905-5935.
- [46] D. M. 58 28/02/2017 Allegato A: linee guida per la classificazione del rischio sismico delle costruzioni. Italian Ministry of Infrastructures and Transport, Italy. <http://www.mit.gov.it/normativa/decreto-ministeriale-numero-58-del-28022017> (in Italian).

MAPPING PERFORMANCE-TARGETED RETROFITTING TO SEISMIC FRAGILITY REDUCTION

Karim Aljawhari¹, Roberto Gentile², and Carmine Galasso^{1,2}

¹ Scuola Universitaria Superiore IUSS Pavia
Piazza della Vittoria, 15, 27100 Pavia, Italy
e-mail: karim.aljawhari@iusspavia.it

² University College London
Gower St, London WC1E 6BT, United Kingdom
e-mail: {r.gentile,c.galasso}@ucl.ac.uk

Abstract

This study investigates the improvement in the seismic performance of an archetype reinforced concrete (RC) frame due to varying structural retrofit levels. Specifically, the study attempts to map the increase of the displacement-based global ratio between capacity and life-safety demand (CDR_{LS}) to the reduction of seismic fragility. Such a reduction is characterized by the shift of the median fragility for different structure-specific damage states (DSs). The considered structure does not conform to modern seismic design requirements, and it is retrofitted using various techniques. Advanced nonlinear models are developed for the archetype frame, accounting for potential failure mechanisms, including flexural, joint, and shear failure. Three common retrofitting techniques are investigated, namely RC jacketing, steel jacketing, and fiber-reinforced polymers (FRP) wrapping of columns and joints. Each technique is specifically designed and proportioned to achieve predefined performance objectives (i.e., performance-targeted retrofitting), thus generating many retrofit alternatives. The improvement in seismic performance for the retrofitted frames is first characterized by computing the global CDR_{LS} , which can be obtained using nonlinear pushover analysis combined with the Capacity Spectrum Method. Subsequently, cloud-based nonlinear time-history analyses are performed to derive fragility relationships for the as-built and retrofitted configurations, monitoring the variation in the median fragility for all DSs. Finally, the global CDR_{LS} increase due to retrofitting is correlated with the corresponding shift in the median fragility. A linear trend is found, and it is used accordingly to develop simple models that engineers can implement to provide reasonable estimates for such shift once the global CDR_{LS} is known.

Keywords: Retrofitting strategies, fragility relationships, nonlinear analysis, reinforced-concrete frames, performance-based assessment.

1 INTRODUCTION

Many existing reinforced concrete (RC) buildings in earthquake-prone regions do not conform to modern seismic codes as they were mainly designed to resist gravity loads only. These buildings are vulnerable to severe damage or even collapse under moderate-to-high ground-shaking intensity levels [1]. This has led to significant economic and life losses, as demonstrated by numerous past earthquakes (*e.g.* [2], [3]).

To mitigate the consequences of earthquake events on such buildings and improve their seismic performance, structural retrofitting is often necessary. Such an approach has become very popular lately due to the ease of construction and cost-effectiveness compared to other drastic solutions like demolition and complete replacement.

Generally, retrofitting strategies aim to modify key structural parameters such as strength, ductility, and stiffness or reduce seismic demand. Several techniques (systems) are widely used to implement one or more strategies. For instance, adding RC shear walls (*e.g.* [4], [5]) or bracing (*e.g.* [6], [7]) to existing buildings improves both stiffness and lateral strength significantly. On the other hand, base isolation can be implemented to reduce seismic demands by simply decoupling the horizontal motion of the structure and that of the ground [8].

Many challenges may arise in adopting the above techniques, which are related to the architectural compatibility of the intervention, its invasiveness, the need to modify existing foundations or adding new ones, in addition to the high implementation costs and long duration of the work. Therefore, less-invasive retrofitting techniques, which represent the main focus of the current study, are more common and popular. Examples include wrapping structural elements with fiber-reinforced polymers (FRP), and jacketing columns using either RC or steel jackets. These local techniques are fundamentally less expensive, and they pose a minimal degree of invasiveness/business interruption compared to RC shear walls or bracing.

Most of the past research focused on the experimental investigation of different retrofitting techniques and developing analytical and numerical models to simulate their effect on existing structural elements and/or systems. For instance, some studies investigated the effects of steel jackets on RC columns experimentally and developed design procedures (*e.g.* [9]–[12]), while others explored FRP retrofitting (*e.g.* [12]–[15]) and RC jacketing for columns (*e.g.* [16], [17]).

Retrofitted buildings are expected to perform better against earthquake-induced ground shaking. However, field observations for those buildings under actual seismic events are still scarce, indicating the lack of sufficient empirical fragility and vulnerability models in the literature. This demonstrates the need for numerically developing such models considering different retrofitting techniques and geometric layouts, which are essential for applications related to seismic risk reduction and increasing resilience of earthquake-prone communities around the world. This has indeed attracted many research efforts in the past few decades, but a limited number of studies is available. A detailed review of such studies is outside of the current paper's scope, but a few are briefly discussed to provide the reader with some background.

Some studies developed fragility relationships considering FRP, RC jacketing, base isolation, and adding shear walls (*e.g.* [18], [19]). However, the fragility models accounted for collapse only, without considering other damage states (DSs). Moreover, retrofitting was either applied based on engineering judgment, *i.e.* without properly accounting for structure-specific seismic deficiencies or predefined performance objectives [18], or considering only one, rather than multiple, performance objectives (*e.g.* [19], [20]). Other studies considered applying different retrofitting techniques with varying intervention levels to achieve different performance objectives (*e.g.* [21], [22]), but only collapse fragility relationships were evaluated.

The current study investigates the improvement in seismic performance of an archetype RC frame located in a high-seismicity zone considering varying levels of retrofitting intervention

This frame does not satisfy the main seismic design provisions such as those for capacity design and strong-column-weak-beam. Beams and columns are poorly confined, and the latter elements have a very low amount of longitudinal reinforcement (*i.e.* less than 1%). Moreover, the joints lack transverse reinforcement, use smooth bars, and improper anchorage [24]–[26]. This makes the frame susceptible to developing brittle failure mechanisms such as joint failure, soft-storey, and shear failure. Typical average values for the material properties are used, which are representative of that era. Specifically, the average compressive strength of the concrete (f_{cm}) is 16.5 MPa, in compliance with other studies (*e.g.* [27], [28]). The average yield strength (f_{ym}) of reinforcing steel is 330 MPa [29]–[31].

2.2 Selected retrofitting techniques

Three different retrofitting techniques are investigated in this study: FRP wrapping, steel jacketing, and RC jacketing. Typical cross-sections for columns retrofitted using these techniques are illustrated in Figure 2.

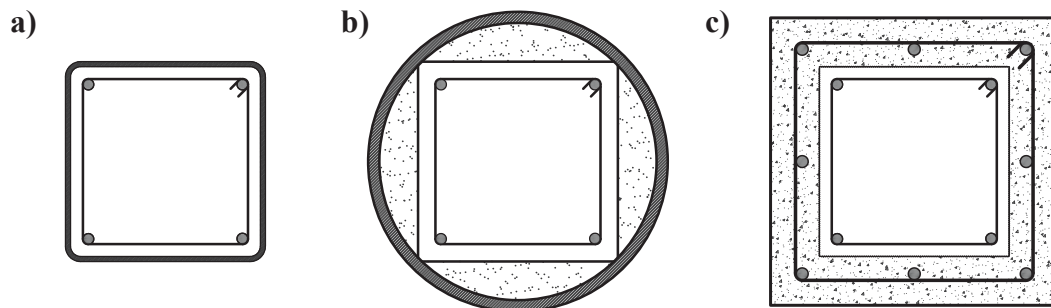


Figure 2: Typical cross-sections of a column retrofitted using (a) FRP; (b) steel jacketing; and (c) RC jacketing

FRP wrapping is mainly used for joints and columns to prevent brittle shear failure mechanisms. It also provides a high level of confinement for columns, thus improving their ductility under extreme loading conditions (*e.g.* [13], [14]). The contribution of FRP wrapping to the stiffness and flexural strength is minimal as the unidirectional fibers are placed perpendicular to the longitudinal axis of columns.

Rectangular and elliptical steel jackets are another popular option to prevent shear failure of columns. They are also able to increase lateral stiffness due to the isotropic properties of steel [12]. However, only elliptical (or circular) steel jackets are used in the current study because they are very effective in improving confinement and ductility due to the continuous confining pressure they provide [9]. This technique also offers some enhancement of flexural strength. Conversely, experiments demonstrated that rectangular steel jackets lose much of their confinement efficiency (*e.g.* [9], [16]). A gap of 50 mm is deliberately left between the edges of the steel jacket and foundations/beams to prevent excessive flexural strength enhancement, which transfers forces to adjacent members [9].

RC jacketing is the most traditional and common technique in practice as it is characterized by a low cost and does not require specialized labor. It comprises encasing existing columns with a cast-in-place RC jacket to improve confinement, ductility, and both shear and flexural strengths. Continuous column jacketing in two consecutive floors also enhances joint behavior. The thickness of an RC jacket is controlled by the size of longitudinal and transverse reinforcement to be used, in addition to the minimum cover requirement (*e.g.* [16], [32]). Compared to the other two techniques, RC jacketing poses the highest level of invasiveness. It can notably increase the size of existing columns and might require extending reinforcement through slabs, foundations, and joints.

2.3 Design of retrofitting techniques

A trial-and-error design procedure is adopted for the three retrofitting techniques, aiming to achieve a predefined set of performance objectives, as explained later. For each technique, design iterations might vary with respect to detailing, geometric characteristics, and the number of retrofitted elements to ensure incremental improvements in seismic performance.

For the FRP technique, laminated pre-cured sheets with high-strength carbon fibers (CFRP) are wrapped around the full height of existing columns. The elasticity modulus (E_f) is equal to 140 GPa, ultimate tensile strength (F_{fu}) is 2000 MPa, and rupture strain (ϵ_{fu}) is 1.2% [33], assuming that each layer has a thickness of 0.5 mm. It is considered that the maximum number of FRP layers is five to ensure confinement efficiency [34]. It should be noted that the FRP is also used for joint retrofit in cases where joint failure is observed (mainly external ones).

On the other hand, full-height elliptical/circular steel jackets are used. The space between the steel jacket and retrofitted column can be filled with either grout material or plain concrete [9], [12]. The jackets are made of structural steel grade S235 with an average yield strength (f_{yj}) of 235 MPa and a minimum thickness of 1.5 mm, which is increased during the iterative design process. As mentioned earlier, a gap of 50 mm is left between the edges of steel jackets and column ends to prevent transferring forces to adjacent members [9].

In the case of RC jacketing, a full-height encasement of existing columns is made using cast-in-situ concrete, with the possibility of extending longitudinal reinforcement through foundations and slabs. RC jackets with a minimum thickness of 50 mm are adopted, with at least 4 Φ 14 mm for external columns and 4 Φ 16 mm for internal ones (Φ refers to the diameter). Hoops with Φ 8 mm are used with a spacing not exceeding 150 mm. The reinforcement and/or jacket thickness are increased gradually during the iterative design, as stated earlier. The concrete material is characterized by f_{cm} of 33 MPa, while f_{ym} for the reinforcement is equal to 490 MPa.

2.4 Nonlinear modeling strategies

The nonlinear response of the case-study building is simulated by developing 2D numerical models using OpenSees [35]. Structural components are modeled as beam-column elements with finite-length plastic hinges to simulate the nonlinear flexural response, which is defined by performing moment-curvature analysis following the rules defined by [36] and [37]. The post-capping degrading response for the moment-curvature and the hysteretic parameters are assigned according to [38]. Additional shear springs are added in series to the beam-column element to account for potential shear failure modes, as illustrated in Figure 3. The backbone curve parameters for the shear response are calculated in accordance with [39]–[41].

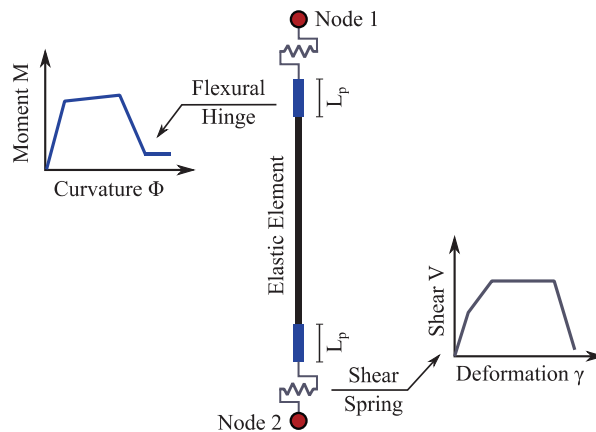


Figure 3: Modelling strategy for structural components

As mentioned earlier, joints in older Italian RC frames are characterized by the lack of transverse reinforcement and the use of smooth bars with end-hooks, particularly in external joints [24]–[26]. Therefore, the early failure of such joints leads the building to develop a brittle failure mechanism. Therefore, an additional spring is added in each beam-column joint zone. The parameters of the nonlinear material of joints are defined according to [38], which is a mechanics-based approach introduced in many other studies (*e.g.* [42], [43]).

To account for the effects of FRP on columns, the moment-curvature relationship is modified considering the confinement provided by this technique. This is achieved by first assuming that the entire column cross-section is confined rather than the core only since the FRP layers are wrapped around the external perimeter of the column. Next, the confinement pressure (f_l) due to FRP wrapping is calculated based on [13] and then the compressive strength and ultimate strain of the confined concrete (f_{cc} and ϵ_{ccu}) can be estimated based on [44] and [13], respectively. It should be noted that FRP wrapping around rectangular columns is less effective than circular ones because only inward corner forces provide the confinement in the former case instead of continuous pressure around the perimeter. Thus, a confinement effectiveness factor is used to reduce the value of f_l as per [33]. Moreover, the additional shear strength due to FRP is calculated and added to the shear strength of the as-built column in accordance with [13].

It should be noted that the unique failure modes pertaining to FRP, such as debonding and fracture mechanisms, are not explicitly modeled, assuming the FRP retrofitting is designed and installed appropriately so that the concrete and reinforcement will govern the softening behavior of the retrofitted elements at high levels of deformation (*e.g.* [22], [45]).

Steel jacketing is treated in a similar manner to FRP. The value of f_l is estimated as per [9], whilst f_{cc} and ϵ_{ccu} are found based on [44] and [16], respectively. These new values are adopted to modify the moment-curvature relationship. The additional shear strength due to the steel jacket is estimated according to [9].

Finally, columns retrofitted with RC jackets are treated as equivalent monolithic members. This assumption is deemed valid as long as the jackets are well constructed and the surface of existing columns is adequately treated (*e.g.* [45], [46]). However, to address the possibility of a poor bond between the new RC jackets and existing columns, it is recommended to use the as-built value of f_c for the entire cross-section and to assume that lateral confinement is provided solely by the hoops of the new RC jacket [16].

2.5 Damage state definition and thresholds mapping

Three structure-specific DSs are adopted in order to characterize different damage conditions, which reflect the performance level (PL) of the building. Each DS occurs when the structure attains a specific threshold defined with respect to an engineering demand parameter (EDP). This study adopts the maximum interstorey drift ratio (MIDR) as an EDP, which is a reliable and widely-used proxy to quantify global structural and nonstructural damage (at least in the case of drift-sensitive nonstructural components).

The MIDR thresholds are calibrated by assessing multiple measurable criteria during non-linear static (*i.e.* pushover) analysis using a modal-pattern incremental load. These criteria are adopted from [47] and are also summarized in Table 1. The parameters θ_y and θ_u in Table 1 represent the yield and ultimate chord rotations, respectively. The latter parameter is evaluated according to [48]. It should be noted that the MIDR threshold for each DS is based on the first occurrence of any criterion among those shown in Table 1 (*e.g.* [47]).

The three DSs are described as follows: DS1, which accounts for moderate damage levels, is characterized by moderate structural and nonstructural damages with no significant yielding. The building here maintains the limited occupancy PL, but minor repairs may be required. DS2,

which corresponds to significant damage (SD), incorporates severe damages in both structural and nonstructural components, but buildings still retain some residual strength and stiffness. The building in DS2 meets the PL of life safety (LS), in which significant repairs are needed, which might not always be feasible. Finally, DS3 represents here the collapse-prevention PL, characterized by the full exploitation of strength and ductility. Minimal residual strength and stiffness remain in DS3, and the building is in a near-collapse condition [49].

Level/DS	DS1	DS2	DS3
Section Level	Reaching yield bending in a supporting column	Max. bending strength of a column is reached	Reaching shear failure in any element
Component Level	Reaching θ_y in any supporting column	Reaching 75% of the θ_u in any component	Reaching the θ_u in any component
Global Level	Reaching the global yield point of the structure	Reaching the maximum strength	About 20% drop in the maximum strength
General description	Moderate structural and nonstructural damage. No significant yielding of members	Severe structural and nonstructural damage. Some residual strength and stiffness retained	Full exploitation of strength and ductility. Low residual strength and stiffness

Table 1: Criteria used for mapping of DSs; adopted from [47]

The analytical formulation for θ_u requires inputting the amount of transverse reinforcement. This is directly applicable for the existing structural components and those retrofitted using RC jackets. In the case of FRP or steel jacketing, the concept of equivalent transverse reinforcement is implemented (*e.g.* [12], [22], [45]). In this approach, the FRP or steel jacketing can be simply converted to standard transverse reinforcement that mimics their effect by generating a lateral confining pressure equal to that produced by either of them.

2.6 Performance-targeted retrofitting

As indicated earlier, varying retrofitting levels are designed and applied to the case-study structure to meet some predefined performance objectives (*i.e.* performance-targeted retrofitting). These objectives represent achieving specific PLs (or DSs), either fully or partially, under a selected level of seismic hazard (*e.g.* [50]). The selected hazard level in all performance objectives is the one associated with life safety, *i.e.* corresponding to a mean return period of 475 years (*e.g.* [48], [50], [51]), as it is the most relevant and widely-used hazard level for the design and assessment of buildings – and for which hazard maps/curves are readily available.

To investigate whether a retrofitting intervention achieves a particular performance objective, the displacement-based global ratio between capacity and LS seismic demand, *i.e.* CDR_{LS} is considered. The LS displacement demand is calculated by transforming the force-deformation relationship (*i.e.* capacity curve) derived from pushover analysis to a capacity spectrum of an equivalent single-degree-of-freedom (SDoF) system plotted in the acceleration-displacement response spectra (ADRS) space. Subsequently, the capacity spectrum method (CSM) is applied in order to obtain a graphical representation of the performance [52]. A summary of the selected performance objectives is provided in Table 2.

It should be highlighted that the seismic demand used to design and assess different retrofitting cases is characterized by a Type 1 response spectrum according to [53], with a peak ground acceleration (PGA) of 0.30g and ground type C to account for high-seismicity conditions.

Performance objective	Description
No-collapse performance	Achieve the collapse-prevention PL (DS3) against the LS seismic demand
Limited performance	Partially achieve significant damage PL (DS2) against LS demand ($CDR_{LS} \approx 75\%$)
Basic performance	Achieve the significant-damage PL (DS2) against LS demand (100% of CDR_{LS})
Advanced performance	Achieve moderate damage (DS1; limited occupancy) against LS seismic demand

Table 2: Selected performance objectives for seismic retrofitting

2.7 Fragility relationships and selection of ground-motion records

Retrofitting of structures can result in a significant improvement in their seismic fragility. Fragility relationships characterize the conditional probability of exceeding different building-level, structure-specific DSs given a ground-shaking intensity level (IM), *i.e.* $P(DS \geq dsi|IM)$. It is possible to derive fragility relationships by performing nonlinear time-history analysis (NLTHA) using a set of unscaled (as-recorded) ground-motion records, *i.e.* by performing cloud analysis [54], among other alternative approaches. Hence, clouds of IM vs. EDP are developed and appropriate probabilistic seismic demand models (PSDMs) are fitted via power-law regression, which allows deriving fragility relationships using a closed-form solution [55] as shown in Eq. (1)-(2).

$$EDP = aIM^b \quad (1)$$

$$P(DS \geq dsi|IM) = \Phi\left(\frac{\ln(IM/\mu)}{\beta}\right) \quad (2)$$

where a and b are the regression parameters, μ is the median IM, and β is the dispersion. The records used for the NLTHA are adopted from the SIMBAD (Selected Input Motions for displacement-Based Assessment and Design) database developed by [56], which incorporates 467 three-component records related to shallow crustal earthquakes with magnitudes between 5.0 and 7.3 and epicentral distances less than 30 km [56]. To reduce the computational effort yet maintaining the engineering significance of the analysis, only 150 records are selected following the same criteria defined in [20], [57]. Specifically, the ground motions are ranked with respect to their PGA, obtained as the geometric mean of the two horizontal components. For each ground motion, the horizontal component with the highest PGA is kept, and then the 150 records with the highest ranking are selected. Such procedure is compatible with cloud analysis, and therefore it does not require a site-specific record selection. Moreover, this approach is deemed appropriate for regional-scale seismic risk assessment of building portfolios, especially when coupled with optimal IMs.

The IM implemented in this study is the geometric mean of the 5%-damped spectral acceleration over a specific range of vibration periods (avgSa). Such an IM accounts indirectly for the effects of higher modes, in addition to the period elongation due to the strength and stiffness degradation as well as the damage of different components (*e.g.* [58]–[60]). This IM, compared to other conventional ones like the spectral acceleration at the fundamental period $Sa(T_1)$, minimizes response variability, and it has a higher relative sufficiency [61].

The avgSa in this study is calculated considering 10 equally-spaced periods ranging within $0.2T_1$ and $1.5T_1$ (e.g. [62]). However, to allow for fragility comparison between the as-built and the retrofitted case-studies, the same period range is adopted for all of them, which is based on T_1 of the as-built case. This assumption is deemed appropriate as the change in T_1 for the majority of retrofitted cases is not very significant.

3 RESULTS AND DISCUSSION

3.1 Initial assessment for the as-built structure

To understand the response and failure mechanism of the as-built case-study structure, an initial assessment is carried out using pushover analysis to identify DS thresholds and then apply the CSM to evaluate the CDR_{LS} before any intervention through retrofitting.

Figure 4(a) shows the pushover curve with the horizontal axis representing the MIDR among all stories and the vertical axis showing the base shear. The first occurrence of some damage observations are also illustrated in Figure 4(a), such as first yield for beams and columns, SD for columns and joints (θ_{SD} and γ_{SD}), and joint failure (γ_u); mainly external ones. The MIDR thresholds for all DSs are also summarized in Table 3.

It can be observed in Figure 4(a) that both DS2 and DS3 are controlled by the limit states of the joints, which take place before those pertaining to the columns. It is also noticed that the beams do not reach their θ_{SD} and θ_u despite their yielding. This demonstrates that the nonlinear deformation is concentrated in the columns and joints, which depicts a non-ductile joint and column-sway mechanism. Accordingly, retrofitting efforts must be directed towards improving the key properties (*i.e.* strength, ductility, stiffness) of these structural components in particular, which will eventually improve the overall plastic mechanism of the building towards a beam-sway one (mainly characterized by beam hinging).

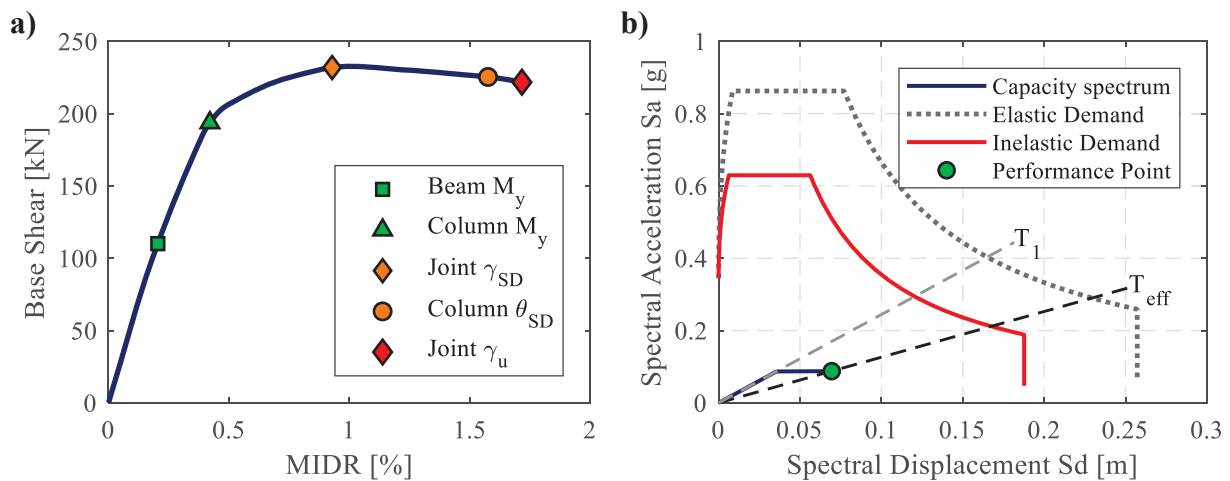


Figure 4: (a) Assessment for the as-built structure using pushover analysis and damage observations; (b) Graphical illustration for the capacity and demand spectra using the CSM

Damage state (DS)	DS1	DS2	DS3
MIDR threshold [%]	0.41	0.93	1.71

Table 3: MIDR thresholds for different DSs derived from pushover analysis

Figure 4(b) illustrates the idealized capacity spectrum of the equivalent SDoF system and the demand spectrum, both elastic and inelastic, plotted in the ADRS space. Applying the CSM, it is found that the inelastic demand spectrum significantly exceeds the capacity of the as-built structure. In other words, the performance point (PP) cannot intersect the inelastic demand spectrum, thus indicating a CDR_{LS} less than 1.0. According to Figure 4(b), the maximum capacity corresponds to a spectral displacement (S_d) of 0.07 m only. However, the expected demand displacement identified through the intersection between the secant stiffness line and the inelastic demand spectrum is nearly 0.167 m. Therefore, the CDR_{LS} of the as-built structure is very low, *i.e.* 42%, demonstrating the need for structural retrofitting.

3.2 Designed retrofitting solutions

As mentioned in section 2.3, the as-built structure is retrofitted with varying intervention levels to achieve the selected performance objectives (see Table 2). This process resulted in 13 retrofitted case studies using FRP wrapping of columns and joints, 15 cases for steel jacketing, and 18 for RC jacketing. The details, layout, and amount of retrofitted elements using FRP for all performance objective are listed in Table 4. For the sake of brevity, only one retrofitted case-study is described for each performance objective; particularly the one that satisfies the objective with the minimum possible amount of intervention.

Performance objective	Achieved CDR_{LS}	Description of FRP retrofitting	Graphical illustration
No-collapse performance	65.4%	1 layer for external columns and joints in the 1 st to 3 rd floor and 1 layer for internal columns in the 1 st and 3 rd floors	
Limited performance	75.5%	Same joint retrofitting as above. 2 layers for the 3 rd floor columns and internal columns of the 1 st floor. 1 layer for external columns in 1 st to 2 nd floor.	
Basic performance	105.0%	Same joint retrofitting as above. 1 layer for the 2 nd floor columns. 4 layers for the 1 st floor and internal columns in 3 rd floor and 5 layers for the 3 rd floor external columns.	
Advanced performance	N.A.	N.A.	N.A.

Table 4: Description of FRP retrofitting alternatives for different performance objectives

Table 4 demonstrates that the advanced performance objective could not be achieved using FRP retrofitting. This is because FRP wrapping improves ductility through confinement and increases shear strength while its contribution to the lateral strength and stiffness is minimal (less than 10% in the current study). In fact, enhancing these parameters (*i.e.* stiffness and lateral strength) is essential with respect to moderate damage PL (or DS1) as the columns will not yield quickly, especially at low IM levels. It should be noted that the maximum value of CDR_{LS}

that could be achieved is around 110% since the number of FRP layers that could be applied for the columns cannot exceed five layers (see section 2.3).

Table 5 provides similar information about the retrofitted case studies using steel jacketing. It was possible to generate many cases of retrofitted buildings with large values of CDR_{LS} , particularly up to 147%. This is related to the high effectiveness of circular/elliptical jackets with respect to the high and continuous (radial) confinement they provide. This, in turn, significantly improves the ductility of the columns, thus making them capable of sustaining large levels of inelastic deformation. This also improved the (near) collapse situation, allowing beams to undergo failure prior to columns. Like the FRP case, all these advantages are insufficient to make the structure experience moderate damage (DS1) only against the LS demand (*i.e.* the advanced performance level) for the same reasons explained previously regarding the FRP.

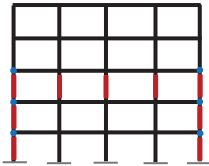
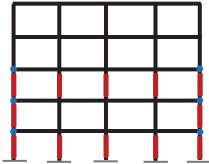
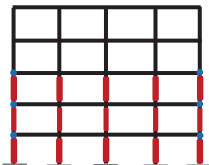
Performance objective	Achieved CDR_{LS}	Description of steel jacketing retrofitting	Graphical illustration
No-collapse performance	61%	1.5 mm thick jacket mm for the external columns in 1 st to 3 rd floor and internal ones in the 3 rd floor. Also retrofit external joints in 1 st to 3 rd floors using FRP.	
Limited performance	80%	Same joint retrofitting as above. Use 1.5 mm thick jacket for the external columns in the 1 st to 3 rd floor and internal ones in the 1 st and 3 rd floor	
Basic performance	106%	Same joint retrofitting as above. 1.5 mm thick jacket for the columns of 2 nd floor. 2.5 mm thick jackets for the 3 rd floor and external columns of 1 st floor. 3 mm jacket for the internal columns in 1 st floor	
Advanced performance	N.A.	N.A.	N.A.

Table 5: Description of steel jacketing retrofitting alternatives for different performance objectives

Finally, a summary for the case studies with RC jacketing is provided in Table 6, which shows that unlike FRP and steel jacketing, the advanced performance objective is achieved. This is because the RC jacketing provides a significant overall enhancement for the stiffness and strength, both shear and flexural, and improves the ductility through confinement. These features can also shift the building mechanism from local (*e.g.* soft-storey) to global, *i.e.* beam-sway. Therefore, the (frame-level) MIDR threshold of DS1 becomes much higher, and the retrofitted structure will not be easily subjected to yielding and moderate damages, especially at low IM levels. Nevertheless, as illustrated in Table 6, achieving the advanced performance level requires retrofitting the entire columns in the frame, thus making a global intervention to the frame rather than local, which might be expensive and technically challenging.

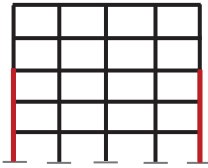
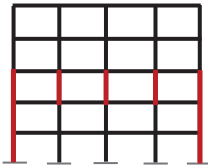
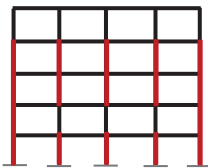
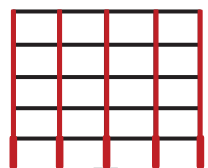
Performance objective	Achieved CDR_{LS}	Description of RC jacketing retrofitting	Graphical illustration
No-collapse performance	65%	Retrofit external columns in the 1 st to 3 rd floor with 50 mm jacket with 4 Φ 14 mm bars and 1 Φ 8/150 mm hoops.	
Limited performance	78%	50 mm jackets for the external columns in the 1 st to 3 rd floor with 4 Φ 14 mm bars and 1 Φ 8/150 mm hoops. 50 mm jackets for the internal columns of the 3 rd floor with 4 Φ 16 mm bars and 1 Φ 8/150 mm hoops	
Basic performance	105%	50 mm jackets for the external columns in the 1 st to 4 th floor with 4 Φ 14 mm bars and 1 Φ 8/150 mm hoops. 50 mm jackets for the internal columns in 1 st , 3 rd , 4 th floors with 4 Φ 16 mm bars and 1 Φ 8/150 mm hoops	
Advanced performance	181%	100 mm jackets with 8 Φ 16 mm bars and 1 Φ 8/100 mm hoops for external, and with 12 Φ 22 mm bars and 1 Φ 10/80 mm hoops for the internal columns of 1 st floor. 50 mm jackets with 8 Φ 20 mm bars and 1 Φ 8/150 mm hoops for external and with 8 Φ 22 mm bars and 1 Φ 8/150 for the internal columns of 2 nd floor. 50 mm jackets with 8 Φ 14 mm bars and 1 Φ 8/150 mm hoops for the 3 rd , 5 th and external columns of 4 th floor. Similar jackets but with 8 Φ 16 mm bars for internal columns of the 4 th floor	

Table 6: Description of RC jacketing retrofitting alternatives for different performance objectives

3.3 Fragility assessment

Upon developing all the case studies, including both the as-built and retrofitted structures, NLTHA is performed using the selected set of ground-motion records to assess the performance and derive the corresponding fragility relationships. Figure 5 shows both the IM vs. EDP cloud along with the fitted PSDM and the derived fragility relationships for the as-built structure. As demonstrated by Figure 5(a), the following points must be highlighted:

- The as-built structure remained undamaged only in 19.3% of the analysis cases.
- Moderate damage (DS1) was experienced by the frame in 23.3% of the cases.
- The frame was subjected to DS2 in a considerable portion of cases, particularly 21.3%.

- The near-collapse condition characterized by DS3 was experienced by the as-built frame in a significant number of analysis cases, which represents 36%.

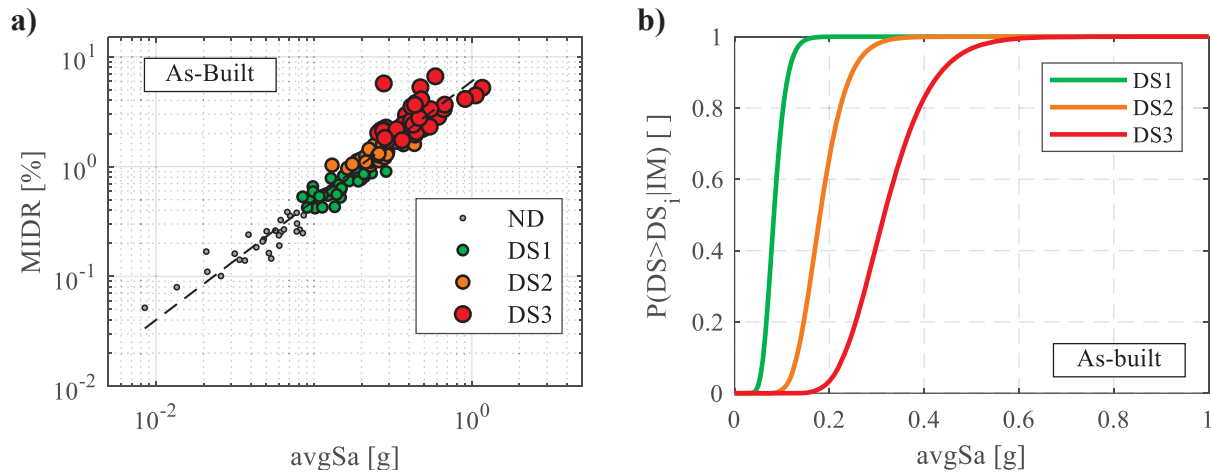


Figure 5: (a) IM vs EDP cloud; and (b) fragility relationships for the as-built structure

The poor performance of the as-built structure is reflected in the fragility relationships in Figure 5(b), which shows that the building is expected to experience high DSs, even at low IM levels. The fragility parameters including median (μ_{DS}) and dispersion (β) are given in Table 7.

DS	μ_{DS} [g]	β
DS1	0.083	
DS2	0.180	0.2504
DS3	0.316	

Table 7: Fragility parameters for the as-built structure

Fragility assessment is then carried out considering the retrofitted case studies defined previously. To illustrate the substantial impact of retrofitting, the fragility relationships for the as-built structure and the retrofitted cases are depicted in Figure 6. For each retrofitting technique, the fragility relationships for one retrofitted case only are plotted per performance objective, particularly the one that satisfied that objective with minimal intervention.

As per Figure 6, a significant improvement can be observed in the fragility relationships of DS2 and DS3 when the frames are retrofitted until satisfying the basic performance objective ($CDR_{LS} \approx 100\%$), which is represented by the rightward shift. This improvement is very similar for the three different retrofitting techniques but slightly higher for both steel and RC jacketing.

Figure 6(a),(b) demonstrate that the improvement in the fragility relationships of DS1, unlike DS2 and DS3, is relatively low when the frames are retrofitted using either FRP wrapping or steel jacketing. This can be explained by the fact that both techniques are mainly enhancing the ductility through confinement, in addition to prevention of shear failure, which is beneficial for DS2 and DS3 as they are associated with the performance of the building under high levels of inelastic deformation. On the other hand, improving DS1 fragility requires the enhancement of both lateral strength and stiffness to control the sway mechanism of the building and make it more difficult to develop moderate damages due to early yielding. However, the contribution of steel jacketing to the lateral strength and stiffness is minor compared to RC jacketing, whereas the contribution of FRP is approximately negligible.

In contrast, RC jacketing can change the mechanism of the building to a full beam-sway one. It also provides a significant overall improvement for all the aforementioned parameters, which resulted in a considerable shift in DS1 fragility relationship shown in Figure 6(c). Furthermore, the advanced performance objective could also be achieved using RC jacketing, which caused a considerable shift in the fragility relationships of the three DSs.

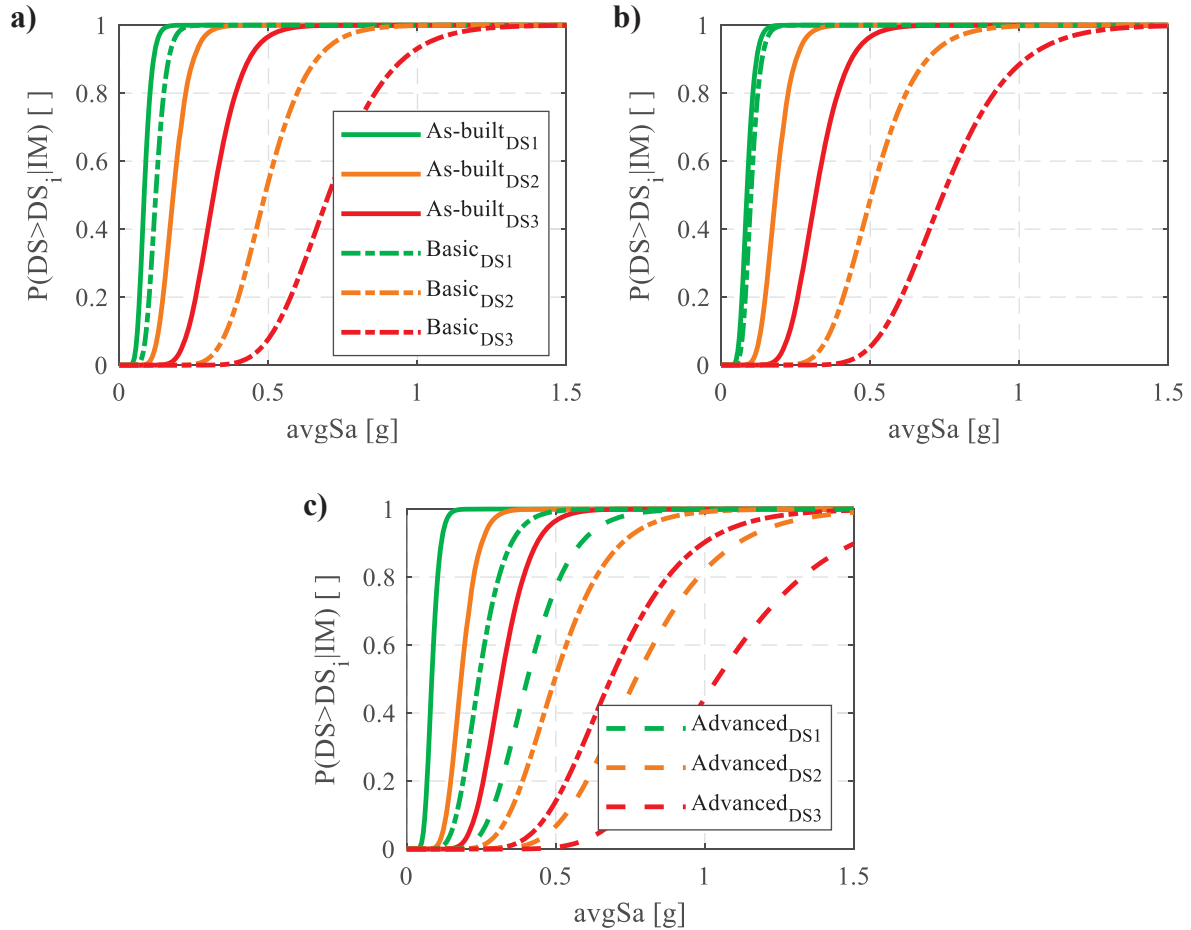


Figure 6: Fragility relationships for different performance objectives considering (a) FRP wrapping; (b) steel jacketing; and (c) RC jacketing

Overall, the previous analysis shows that the three techniques are similar with respect to improving the fragility relationships for the significant damage (DS2) and near collapse (DS3) conditions. In contrast, the improvement in DS1 fragility relationships is trivial if the FRP or steel jacketing are used. This indicates that structures retrofitted using these two techniques will remain highly susceptible to moderate damages, even at low ground-shaking levels.

4 CORRELATION BETWEEN CDR AND FRAGILITY PARAMETERS

The current study also attempts to map the improvement in the seismic performance of the case-study frame due to the varying retrofitting levels to the corresponding reduction in fragility. A reasonable approach to address this task is by correlating a simplified performance metric, which is the CDR_{LS} in this study, to the median of all fragility relationships, *i.e.* μ_{DS} . This is shown in Figure 7. A gradual increase in the values of μ_{DS} for DS2 and DS3 is observed for all the retrofitting techniques, which results from the performance improvement characterized by the CDR_{LS} . A sudden jump in the values of μ_{DS} can be also noticed in Figure 7(c) for the RC

jacketing, particularly at a CDR_{LS} close to 90%. This jump represents the case in which the RC jacketing becomes very effective due to the shift of the failure mechanism to beam sway.

In contrast, the overall increase in μ_{DS} of DS1 is trivial for both FRP wrapping and steel jacketing, as demonstrated by Figure 7(a),(b), even at very high levels of CDR_{LS} (see Section 3.3 for the discussion on this result). In fact, only the RC jacketing, with reference to Figure 7(c), is capable of significantly improving the μ_{DS} values for DS1, indicating that the structure becomes less susceptible to moderate damage, especially at low IM levels.

It should also be noticed that large values of CDR_{LS} could be reached using either steel or RC jacketing. After these levels, the retrofitting might become ineffective because the failure becomes associated with the beams rather than the columns and/or joints. However, the extent of CDR_{LS} increase in the case of the FRP technique is notably lower since a limited number of layers can be wrapped around to ensure confinement efficiency, as stated earlier.

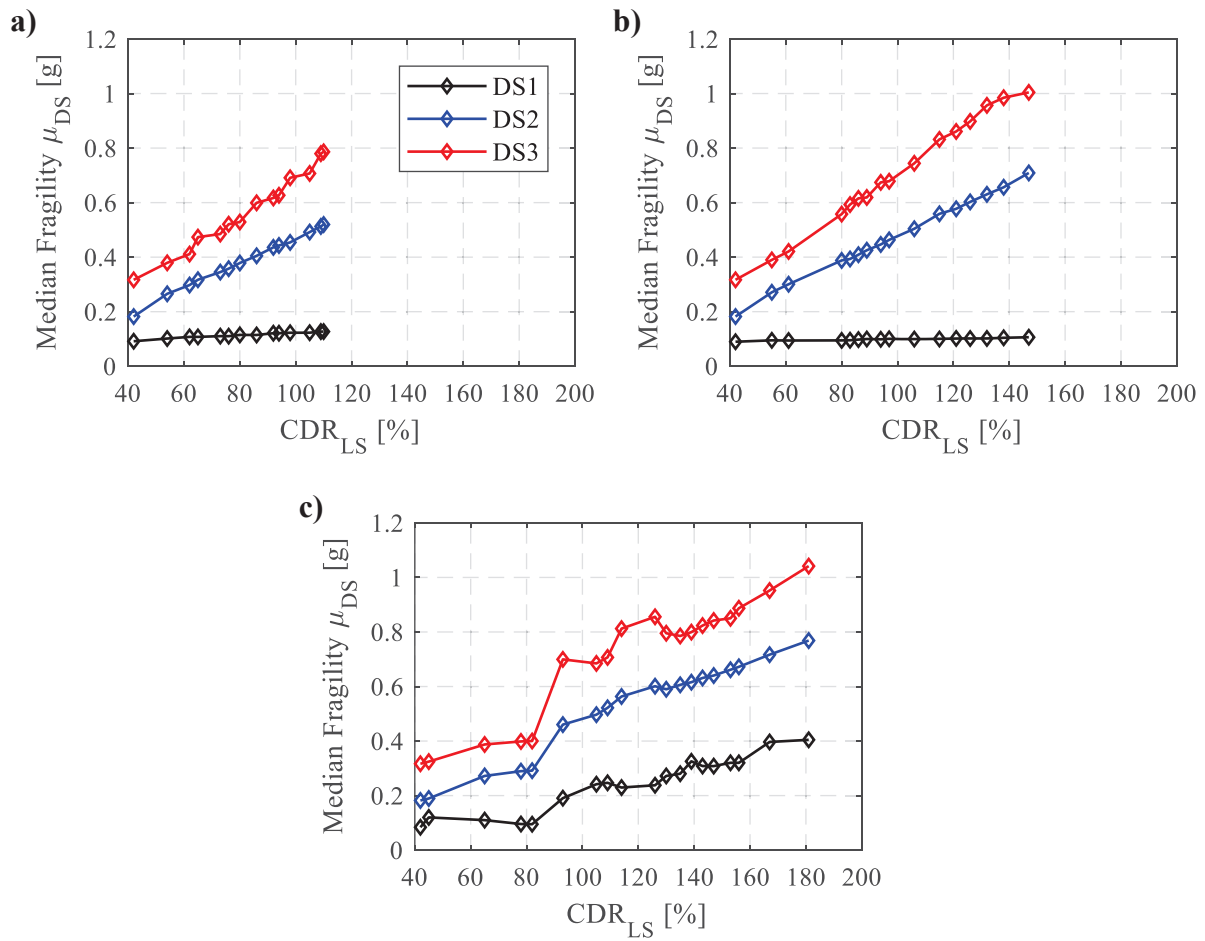


Figure 7: Variation of μ_{DS} against CDR_{LS} for (a) FRP wrapping; (b) steel jacketing; and (c) RC jacketing

A simplified model expressing the variation in μ_{DS} as a function of CDR_{LS} is defined by the best-fit line that minimizes the sum of squares of residuals (*i.e.* least-square approach). It should be noted that the variation of μ_{DS} is treated in a normalized fashion, which means that the developed expressions consider the variation in μ_{DS} resulting from retrofitting as a percentage of μ_{DS} of the as-built structure ($\Delta\mu_{DS}$). Figure 8 illustrates the fitted simplified models on the CDR_{LS} vs. $\Delta\mu_{DS}$ space, taking into account all the investigated DSs and retrofitting techniques. The coefficient of determination values (R^2) are also shown, which depict a clear linear trend between the two parameters. It must be noted that the initial CDR_{LS} is assumed equal to 42%.

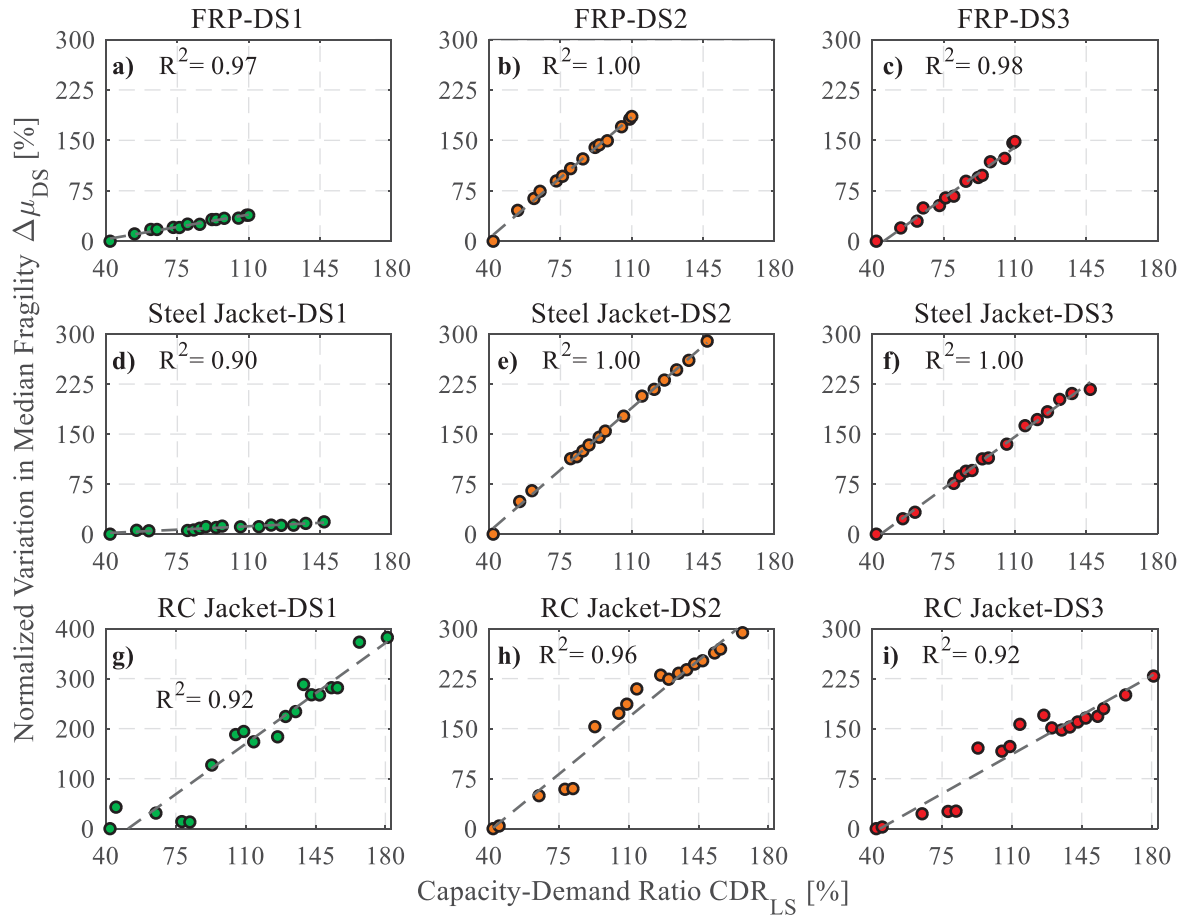


Figure 8: Correlation between the normalized variation of μ_{DS} against the CDR_{LS} for all DSs and techniques

The proposed simplified models can be easily used to provide reasonable estimates for the shift in fragility relationships of an as-built structure due to retrofitting once the CDR_{LS} is determined by just performing a pushover analysis. The outcome of these simplified models is directly used to modify the median values of the original fragility relationships to achieve the desired shift. Such an approach is deemed a quick and reasonable approximation in lieu of performing computationally expensive NLTHAs to derive new fragility relationships.

Nevertheless, it is important to highlight that the results obtained by the proposed models are limited by the uncertainties associated with the adopted modeling assumptions, material properties, geometry, layout, etc. Accordingly, additional research effort is needed to improve the accuracy of these expressions through incorporating additional case-study structures with different failure mechanisms, geometric/material properties, and layouts.

5 CONCLUSIONS

This study investigated the mapping between the improvement in seismic performance of a case-study RC frame and the seismic fragility reduction, which was achieved by designing and implementing varying structural retrofit levels. This is specifically characterized by correlating the increase in the CDR_{LS} values resulting from retrofitting to the shift of median parameters of fragility curves expressed by $\Delta\mu_{DS}$. The considered case study is an older non-ductile RC bare frame, which is designed to resist gravity loads only.

Three common and widely-used retrofitting techniques were adopted: FRP; steel jacketing, and RC jacketing. These techniques were designed via trial and error to achieve multiple

predefined performance objectives and thus generate numerous retrofitted case studies. The improvement in the seismic performance is initially quantified by applying pushover analysis in conjunction with the CSM in order to estimate CDR_{LS} for each case study.

The analysis of the as-built structure demonstrated a very poor seismic performance due to its susceptibility to high DSs, even at low IM levels. In contrast, a substantial improvement could be achieved through retrofitting. For example, fragility analysis showed that the μ_{DS} of DS2 and DS3 increased by at least 125% using any of the three techniques by just achieving the basic performance objective through retrofitting. However, only the RC jacketing was very effective in improving the DS1 fragility curves compared to FRP and steel jacketing. This is attributed to the fact that the latter two techniques improve ductility only, which is necessary for the DSs associated with high levels of nonlinear deformation, *i.e.* DS2 and DS3. Conversely, improving DS1 fragility curve requires enhancing both stiffness and lateral strength in addition to controlling lateral-sway mechanisms in order to make it difficult to develop early yielding and experience moderate damages, especially at low IM levels. This was possible to accomplish only by using the RC jacketing technique.

Finally, simple mathematical models were developed to relate the CDR_{LS} achieved by retrofitting to the $\Delta\mu_{DS}$ estimated using fragility analysis accounting for all DSs and retrofitting techniques. It is worth mentioning that these models are limited to the implemented case-study structure, modeling choices, and material properties. Therefore, additional research efforts are required in order to produce more generic models and reduce the uncertainty. After appropriate generalization, those expressions can be adopted to provide reasonable and quick quantification of the shift in median fragility parameters by just plugging in the value of CDR_{LS} , which can be calculated using simple pushover analyses. Such a simplified method can be used to analyze and/or design scenario-based retrofit implementation plans at a portfolio level, drastically reducing implementation efforts in a regional seismic risk model.

ACKNOWLEDGEMENTS

This study has received funding from project “Dipartimenti di Eccellenza”, funded by the Italian Ministry of Education, University and Research at IUSS Pavia. RG received additional funding from the European Union’s Horizon 2020 research and innovation programme under grant agreement No. 843794. (Marie Skłodowska-Curie Research Grants Scheme MSCA-IF-2018: MULTIRES, MULTI-level framework to enhance seismic RESilience of RC buildings).

REFERENCES

- [1] F. De Luca, G. E. D. Woods, C. Galasso, and D. D’Ayala, RC infilled building performance against the evidence of the 2016 EEFIT Central Italy post-earthquake reconnaissance mission: empirical fragilities and comparison with the FAST method, *Bulletin of Earthquake Engineering*, **16** (7), 2943–2969, 2018, doi: 10.1007/s10518-017-0289-1.
- [2] P. Ricci, F. de Luca, and G. M. Verderame, 6th April 2009 L’Aquila earthquake, Italy: Reinforced concrete building performance, *Bulletin of Earthquake Engineering*, **9**, 285–305, 2011, doi: 10.1007/s10518-010-9204-8.
- [3] J. P. Stewart *et al.*, Reconnaissance of 2016 central Italy earthquake sequence, *Earthquake Spectra*, **34** (4), 1547–1555, 2018, doi: 10.1193/080317EQS151M.
- [4] H. Kaplan, S. Yilmaz, N. Cetinkaya, and E. Atimtay, Seismic strengthening of RC structures with exterior shear walls, *Sadhana - Academy Proceedings in Engineering*

- Sciences*, **36** (1), 17–34, 2011, doi: 10.1007/s12046-011-0002-z.
- [5] A. Miano, H. Sezen, F. Jalayer, and A. Prota, Performance-based comparison of different retrofit methods for reinforced concrete structures, *COMPDYN 2017 - Proceedings of the 6th International Conference on Computational Methods in Structural Dynamics and Earthquake Engineering*, **1**, 1515–1535, 2017, doi: 10.7712/120117.5510.17150.
- [6] M. Badoux and J. O. Jirsa, Steel Bracing of RC Frames for Seismic Retrofitting, *Journal of Structural Engineering*, **116** (1), 55–74, 1990, doi: 10.1061/(asce)0733-9445(1990)116:1(55).
- [7] F. Freddi, E. Tubaldi, L. Ragni, and A. Dall’Asta, Probabilistic performance assessment of low-ductility reinforced concrete frames retrofitted with dissipative braces, *Earthquake Engineering and Structural Dynamics*, **42**, 993–1011, 2013, doi: 10.1002/eqe.2255.
- [8] A. Natale, C. Del Vecchio, and M. Di Ludovico, Seismic retrofit solutions using base isolation for existing RC buildings: economic feasibility and pay-back time, *Bulletin of Earthquake Engineering*, **19** (1), 483–512, 2021, doi: 10.1007/s10518-020-00988-9.
- [9] M. J. N. Priestley, F. Seible, Y. Xiao, and R. Verma, Steel jacket retrofitting of reinforced concrete bridge columns for enhanced shear strength. Part 2: Test results and comparison with theory, *ACI Materials Journal*, **91** (5), 537–551, 1994, doi: 10.14359/4168.
- [10] R. S. Aboutaha, M. U. Engelhardt, J. O. Jirsa, and M. F. Kreger, Retrofit of concrete columns with inadequate lap splices by the use of rectangular steel jackets, *Earthquake Spectra*, **12** (4), 693–714, 1996, doi: 10.1193/1.1585906.
- [11] R. S. Aboutaha, M. D. Engelhardt, J. O. Jirsa, and M. E. Kreger, Rehabilitation of shear critical concrete columns by use of rectangular steel jackets, *ACI Structural Journal*, **96** (1), 68–78, 1999, doi: 10.14359/597.
- [12] J. C. Alvarez, S. F. Breña, and S. R. Arwade, Nonlinear backbone modeling of concrete columns retrofitted with fiber-reinforced polymer or steel jackets, *ACI Structural Journal*, **115** (1), 53–64, 2018, doi: 10.14359/51700779.
- [13] M. J. N. Priestley and F. Seible, Design of seismic retrofit measures for concrete and masonry structures, *Construction and Building Materials*, **9** (6), 365–377, 1995, doi: 10.1016/0950-0618(95)00049-6.
- [14] F. Seible, M. J. N. Priestley, G. A. Hegemier, and D. Innamorato, Seismic Retrofit of RC Columns with Continuous Carbon Fiber Jackets, *Journal of Composites for Construction*, **1** (2), 52–62, 1997, doi: 10.1061/(asce)1090-0268(1997)1:2(52).
- [15] L. Lam and J. G. Teng, Design-oriented Stress – Strain Model for FRP-confined Concrete in Rectangular Columns, *Construction and Building Materials*, **17** (6–7), 471–489, 2003, doi: 10.1016/S0950-0618(03)00045-X.
- [16] M. J. N. Priestley, F. Seible, and G. M. Calvi, *Seismic Design and Retrofit of Bridges*. 1996.
- [17] M. Rodriguez and R. Park, Seismic load tests on reinforced concrete columns strengthened by jacketing, *ACI Structural Journal*, **91** (2), 150–159, 1994, doi: 10.14359/4593.
- [18] A. B. Liel and G. G. Deierlein, Cost-benefit evaluation of seismic risk mitigation alternatives for older concrete frame buildings, *Earthquake Spectra*, **29** (4), 1391–1411, 2013, doi: 10.1193/030911EQS040M.

- [19] D. Cardone, G. Gesualdi, and G. Perrone, Cost-Benefit Analysis of Alternative Retrofit Strategies for RC Frame Buildings, *Journal of Earthquake Engineering*, **23** (2), 208–241, 2019, doi: 10.1080/13632469.2017.1323041.
- [20] R. Gentile and C. Galasso, Simplified seismic loss assessment for optimal structural retrofit of RC buildings, *Earthquake Spectra*, **37** (1), 346–365, 2021, doi: 10.1177/8755293020952441.
- [21] V. Ligabue, S. Pampanin, and M. Savoia, Seismic performance of alternative risk-reduction retrofit strategies to support decision making, *Bulletin of Earthquake Engineering*, **16** (7), 3001–3030, 2018, doi: 10.1007/s10518-017-0291-7.
- [22] C. C. Harrington and A. B. Liel, Indicators of improvements in seismic performance possible through retrofit of reinforced concrete frame buildings, *Earthquake Spectra*, **37** (1), 262–283, 2021, doi: 10.1177/8755293020936707.
- [23] NZSEE, Assessment and improvement of the structural performance of buildings in earthquakes, 2006.
- [24] G. Calvi, G. Magenes, and S. Pampanin, Relevance of beam-column joint damage and collapse in rc frame assessment, *Journal of Earthquake Engineering*, **6** (1), 75–100, 2002, doi: 10.1080/13632460209350433.
- [25] G. M. Calvi, G. Magenes, and S. Pampanin, Experimental Test on a Three Storey RC Frame Designed for Gravity Only, in *Proceedings of the Twelfth European Conference on Earthquake Engineering*, 2002.
- [26] S. Pampanin, G. M. Calvi, and M. Moratti, Seismic behaviour of RC beam-column joints designed for gravity loads, in *12th European Conference on Earthquake Engineering*, 2002.
- [27] F. Braga, G. De Carlo, G. F. Corrado, R. Gigliotti, M. Laterza, and D. Nigro, Meccanismi di risposta di nodi trave-pilastro in ca di strutture non antisismiche, *X Congr. Naz. “L’ingegneria Sismica in Italia*, 9–13, 2001.
- [28] A. Masi, A. Digrisolo, and G. Santarsiero, Concrete strength variability in Italian RC buildings: Analysis of a large database of core tests, *Applied Mechanics and Materials*, **597**, 283–290, 2014, doi: 10.4028/www.scientific.net/AMM.597.283.
- [29] S. Caprili, L. Nardini, and W. Salvatore, Evaluation of seismic vulnerability of a complex RC existing building by linear and nonlinear modeling approaches, *Bulletin of Earthquake Engineering*, **10** (3), 913–954, 2012, doi: 10.1007/s10518-011-9329-4.
- [30] Verderame, A. Stella, and E. Cosenza, Le proprietà meccaniche degli acciai impiegati nelle strutture in c.a. realizzate negli anni ’60, *X Congresso Nazionale “L’Ingegneria Sismica in Italia” - ANIDIS*, 2001.
- [31] M. L. Puppio, M. Pellegrino, L. Giresini, and M. Sassu, Effect of material variability and mechanical eccentricity on the seismic vulnerability assessment of reinforced concrete buildings, *Buildings*, **7** (3), 15–17, 2017, doi: 10.3390/buildings7030066.
- [32] B. Lizundia, W. T. Holmes, K. Cobeen, J. Malley, and H. S. Lew, Techniques for the seismic rehabilitation of existing buildings, *8th US National Conference on Earthquake Engineering 2006*, **6**, 3646–3656, 2006.
- [33] ACI 440.2R, *Guide for the Design and Construction of Externally Bonded FRP Systems*. 2008.
- [34] P. E. Pinto, Istruzioni per la Valutazione Affidabilistica della Sicurezza Sismica di

- Edifici Esistenti CNR-DT 212/2013, *CNR – Commissione di studio per la predisposizione e l'analisi di norme tecniche relative alle costruzioni*, 190, 2014.
- [35] F. McKenna, OpenSees: A framework for earthquake engineering simulation, *Computing in Science and Engineering*, **13** (4), 58–66, 2011, doi: 10.1109/MCSE.2011.66.
- [36] M. J. N. Priestley, G. M. Calvi, and M. J. Kowalsky, *Displacement-Based Seismic Design of Structures*. Pavia: Fondazione EUCENTRE, IUSS Press, 2007.
- [37] M. M. Karthik and J. B. Mander, Stress-block parameters for unconfined and confined concrete based on a unified stress-strain model, *Journal of Structural Engineering*, **137** (2), 270–273, 2011, doi: 10.1061/(ASCE)ST.1943-541X.0000294.
- [38] G. J. O'Reilly and T. J. Sullivan, Modeling Techniques for the Seismic Assessment of the Existing Italian RC Frame Structures, *Journal of Earthquake Engineering*, **23** (8), 1262–1296, 2019, doi: 10.1080/13632469.2017.1360224.
- [39] H. Sezen and J. P. Moehle, Shear strength model for lightly reinforced concrete columns, *Journal of Structural Engineering*, **130** (11), 1692–1703, 2004, doi: 10.1061/(ASCE)0733-9445(2004)130:11(1692).
- [40] P. E. Mergos and A. J. Kappos, A gradual spread inelasticity model for R/C beam-columns, accounting for flexure, shear and anchorage slip, *Engineering Structures*, **44**, 94–106, 2012, doi: 10.1016/j.engstruct.2012.05.035.
- [41] D. K. Zimos, P. E. Mergos, and A. J. Kappos, Shear hysteresis model for reinforced concrete elements including the post-peak range, *COMPdyn 2015 - 5th ECCOMAS Thematic Conference on Computational Methods in Structural Dynamics and Earthquake Engineering*, (May), 2640–2658, 2015, doi: 10.7712/120115.3565.1184.
- [42] M. J. N. Priestley, *Displacement-based seismic assessment of reinforced concrete buildings*, **1** (1). 1997.
- [43] S. Pampanin, G. Magenes, and A. Carr, Modelling of shear hinge mechanism in poorly detailed RC beam-column joints, *Proceedings of the fib Symposium 2003: Concrete Structures in Seismic Regions*, (May 2014), 126–127, 2003.
- [44] J. B. Mander, M. J. Priestley, and R. Park, Theoretical stress-strain model for confined concrete, *Journal of Structural Engineering*, **114** (8), 1804–1826, 1988, doi: 10.1061/(ASCE)0733-9445(1988)114:8(1804).
- [45] C. C. Harrington and A. B. Liel, Evaluation of Seismic Performance of Reinforced Concrete Frame Buildings with Retrofitted Columns, *Journal of Structural Engineering*, **146** (11), 04020237, 2020, doi: 10.1061/(asce)st.1943-541x.0002801.
- [46] S. N. Bousias, D. Biskinis, M. N. Fardis, and A. L. Spathis, Strength, stiffness, and cyclic deformation capacity of concrete jacketed members, *ACI Structural Journal*, **104** (2), 521–531, 2007, doi: 10.14359/18854.
- [47] K. Aljawhari, R. Gentile, F. Freddi, and C. Galasso, Effects of ground-motion sequences on fragility and vulnerability of case-study reinforced concrete frames, *Bulletin of Earthquake Engineering*, 2020, doi: 10.1007/s10518-020-01006-8.
- [48] EN 1998-3, Eurocode 8: Design of structures for earthquake resistance – Part 3: Assessment and retrofitting of buildings [Authority: The European Union Per Regulation 305/2011, Directive 98/34/EC, Directive 2004/18/EC], Brussels, 2005.
- [49] K. Aljawhari, F. Freddi, and C. Galasso, State-dependent vulnerability of case-study

- reinforced concrete frames, in *7th International Conference on Computational Methods in Structural Dynamics and Earthquake Engineering, COMPDYN 2019; Crete, Greece; June 24-26, 2019*.
- [50] ASCE/SEI 41-13, American Society of Civil Engineers ASCE standard ASCE/SEI 41-13: seismic evaluation and retrofit of existing buildings, American Society of Civil Engineers, Reston, Virginia, 2013.
 - [51] FEMA, Prestandard and Commentary for the Seismic Rehabilitation of Buildings, *Rehabilitation Requirements*, (1), 1–518, 2000.
 - [52] A. Atc, 40, Seismic evaluation and retrofit of concrete buildings, *Applied Technology Council*, **1**, 334, 1996.
 - [53] EN 1998-1, Eurocode 8: Design of structures for earthquake resistance - Part 1 : General rules, seismic actions and rules for buildings [Authority: The European Union Per Regulation 305/2011, Directive 98/34/EC, Directive 2004/18/EC], Brussels, 2004.
 - [54] F. Jalayer, R. De Risi, and G. Manfredi, Bayesian Cloud Analysis: Efficient structural fragility assessment using linear regression, *Bulletin of Earthquake Engineering*, **13**, 1183–1203, 2015, doi: 10.1007/s10518-014-9692-z.
 - [55] C. A. Cornell, F. Jalayer, R. O. Hamburger, and D. A. Foutch, Probabilistic Basis for 2000 SAC Federal Emergency Management Agency Steel Moment Frame Guidelines, *Journal of Structural Engineering*, **128** (4), 526–533, 2002, doi: 10.1061/(asce)0733-9445(2002)128:4(526).
 - [56] C. Smerzini, C. Galasso, I. Iervolino, and R. Paolucci, Ground motion record selection based on broadband spectral compatibility, *Earthquake Spectra*, **30** (4), 1427–1448, 2014, doi: 10.1193/052312EQS197M.
 - [57] R. Gentile, C. Galasso, Y. Idris, I. Rusydy, and E. Meilianda, From rapid visual survey to multi-hazard risk prioritisation and numerical fragility of school buildings, *Natural Hazards and Earth System Sciences*, **19** (7), 1365–1386, 2019, doi: 10.5194/nhess-19-1365-2019.
 - [58] J. W. Baker and C. A. Cornell, Spectral shape, epsilon and record selection, *Earthquake Engineering and Structural Dynamics*, **35** (9), 1077–1095, 2006, doi: 10.1002/eqe.571.
 - [59] A. K. Kazantzi and D. Vamvatsikos, Intensity measure selection for vulnerability studies of building classes, *Earthquake Engineering and Structural Dynamics*, **44** (15), 2677–2694, 2015, doi: 10.1002/eqe.2603.
 - [60] M. Kohrangi, P. Bazzurro, D. Vamvatsikos, and A. Spillatura, Conditional spectrum-based ground motion record selection using average spectral acceleration, *Earthquake Engineering and Structural Dynamics*, **46** (10), 1667–1685, 2017, doi: 10.1002/eqe.2876.
 - [61] S. Minas and C. Galasso, Accounting for spectral shape in simplified fragility analysis of case-study reinforced concrete frames, *Soil Dynamics and Earthquake Engineering*, **119** (August 2018), 91–103, 2019, doi: 10.1016/j.soildyn.2018.12.025.
 - [62] M. Kohrangi, P. Bazzurro, and D. Vamvatsikos, Vector and scalar IMs in structural response estimation, Part II: Building demand assessment, *Earthquake Spectra*, **32** (3), 1525–1543, 2016, doi: 10.1193/053115EQS081M.

EXPERIMENTAL STUDY ON THE IN-PLANE RESPONSE OF ADOBE MASONRY WALLETS STRENGTHENED WITH TEXTILE REINFORCED MATRIX SYSTEMS

Paolino Cassese¹, Luigi Fenu², Domenico Asprone³, Antonio Occhiuzzi^{4,5} and Fulvio Parisi³

¹ National Research Council (CNR), Construction Technologies Institute (ITC)
c/o Polo Tecnologico di San Giovanni a Teduccio, Naples, Italy - paolino.cassese@itc.cnr.it

² University of Cagliari, Department of Civil Engineering, Environment Engineering and Architecture
Via Marengo 2, Cagliari, Italy - lfenu@unica.it

³ University of Naples Federico II, Department of Structures for Engineering and Architecture
Via Claudio 21, Naples, Italy - d.asprone@unina.it, fulvio.parisi@unina.it

⁴ National Research Council (CNR), Construction Technologies Institute (ITC)
Viale Lombardia, 49, San Giuliano Milanese, Italy - occhiuzzi@itc.cnr.it

⁵ University Parthenope, Department of Engineering
Centro Direzionale Isola C4, 80143 Naples, Italy - antonio.occhiuzzi@uniparthenope.it

Abstract

Seismic strengthening of existing adobe masonry (AM) buildings has been recognized as a critical issue due to the dramatic consequences of recent seismic events occurred especially in developing countries, where a great part of the population lives in those constructions. Previous studies investigated the effectiveness of different retrofitting techniques by means of experimental programs consisting of either dynamic or static tests on reduced- or full-scale specimens, representing partial or complete AM dwellings. In this study, the output of diagonal compression tests on adobe masonry panels before and after external strengthening are presented. Three series of specimens were tested, namely, unreinforced and strengthened wallets with textile reinforced matrix (TRM) systems made of either hemp or glass meshes. Those tests benefitted from the characterization of the mud mortar that was used for both masonry joints and matrix, representing typical characteristics of existing Italian AM buildings. Main testing outcomes obtained for the AM wallets, particularly in terms of observed damage and response curves, are presented and discussed. In the end, the effectiveness of the applied TRM systems in the improvement of shear strength and ductility capacity is assessed.

Keywords: Adobe masonry; Experimental tests; Textile reinforced matrix; Shear strength; Ductility; Hemp fibres; Glass fibres; Mud mortar.

1 INTRODUCTION

Since ancient times, a large part of civil and historical buildings were realized in adobe masonry (AM), representing nowadays one of the most widespread structural typology in the world, especially in developing countries [1-4]. Furthermore, such constructions are not engineered and the recent seismic events showed their vulnerability with dramatic consequences for residents [5, 6].

In the recent past, seismic strengthening of existing AM buildings has been recognized as a paramount issue. Indeed, a number of researchers investigated the effectiveness of different retrofitting techniques via experimental testing. Several studies dealt with dynamic testing on reduced-scale specimens representative of AM dwellings, strengthened by means of mesh-reinforcement embedded in mud-mortar [5, 7-10], horizontal low-cost post-tensioning straps [11-13], systems of internal/external interconnected grids [14], combined mud-grout injection of cracks and external mesh-reinforcement [15-16]. Such techniques proved to be very promising in reducing seismic vulnerability of AM constructions, even though more detailed and comprehensive assessments should be carried out.

Few experimental studies focused on the external strengthening of real-scale AM wallets, most of which based on mesh-reinforced plasters. Specifically, cyclic tests on real-scale AM walls were described in [17]. The specimens were firstly tested in the as-built configuration, then, hydraulic lime grout was injected in the cracks and synthetic mesh incorporated in the plaster was applied. The strengthening system restored the initial stiffness and improved both lateral strength and ductility. Similar findings were presented in [18]. Finally, Turanli and Saritas [19] performed diagonal compression tests on AM specimens externally strengthened with plaster reinforcement mesh placed along mortar bed joints. Despite the increased strength and energy absorption capacity, such solution appeared to be unfeasible for strengthening existing AM buildings.

Earthen dwellings can also be found in Italy, especially in Sardinia island, where such structural typology was largely adopted until mid-last century and, currently, represents a considerable part of existing buildings [20]. Sardinian AM constructions were generally realized with adobe blocks reinforced with straw fibres, according to practice rules without any seismic design [21]. Within the framework of a comprehensive research program on seismic assessment and retrofitting of existing Sardinian AM dwellings [6, 21-24], the present study deals with the results of diagonal compression tests on AM wallets. Specifically, three series of specimens were tested, namely: unreinforced and strengthened with two different textile reinforced matrix (TRM) systems, made of hemp and glass meshes, respectively. The hemp-based TRM system (HTRM hereinafter) was composed of natural and sustainable hemp fibres, which however were characterized by considerable variability in mechanical properties due to production process. Conversely, the glass-based TRM system (GTRM) was produced using a commercial glass-fibre mesh, which is usually adopted for strengthening of other traditional masonry structures. Both hemp and glass textiles were embedded in the same mud mortar detected in masonry joints of existing Italian AM buildings.

The following sections describe the experimental campaign, presenting its main outcomes in terms of observed damage, response curves, and effectiveness of the applied TRM systems in the improvement of shear strength and ductility capacity for the AM wallets.

2 EXPERIMENTAL CAMPAIGN

Diagonal compression tests were performed on 21 specimens equally divided into three series: unreinforced AM wallets (URM series); HTRM-strengthened AM wallets (HTRM series); and G-TRM-strengthened AM wallets (GTRM series). The adopted on-site

experimental set-up typology, suggested by relevant technical codes for existing masonry [25-27], allowed avoiding the handling of specimens with reduced disturbance before testing.

2.1 Materials and specimens

AM blocks used for specimens' construction were obtained by pressing a mixture of soil, water and straw fibres into moulds with grooved internal surfaces, whereas mud mortar with same composition of AM blocks (except straw fibres) was used for both masonry joints and TRM matrix, according to traditional Sardinian practice [20]. The experimental characterization of masonry was carried out in [21, 23].

The adopted hemp textile was a bidirectional grid with mesh of $20 \times 20 \text{ mm}^2$ and thickness equal to 4 mm, which was made of three twisted yarns impregnated through epoxy resin according to 70% fraction by volume, in order to preserve its durability. Tensile strength per unit length of reinforcement was obtained by testing and Young's modulus was deducted given the value of volumetric resin fraction. More details can be found in [28]. A commercial glass fibre reinforced biaxial grid was used for strengthening of GTRM specimens. The mesh was equal to $25 \times 25 \text{ mm}^2$, with yarns of thickness equal to 3 mm and 2 mm along weft and warp directions, respectively. The grid was coated with an acrylic polymer mixture. Material properties were provided by the supplier.

Main mechanical properties of the materials used for test specimens are summarized in Table 1. In detail, the mean value and coefficient of variation (*CoV*) are provided for compressive strength (f_c), tensile strength (f_t) and Young's modulus (E). It is noticed that *CoV* is not reported for material properties of glass fibre grid, given the lack of data by the supplier, and tensile strength of the hemp grid is given as force per unit length, due to diameter variability of the cord.

Property	AM block	Mortar	Hemp grid	Glass grid
$f_c \text{ (N/mm}^2\text{)}$	1.08	0.50	-	-
<i>CoV</i>	36%	14%	-	-
$f_t \text{ (N/mm}^2\text{)}$	0.56	0.45	20*	1276
<i>CoV</i>	36%	20%	15%	n.a.
$E \text{ (N/mm}^2\text{)}$	143	49	6500 - 7000	72000
<i>CoV</i>	40%	47%	n.a.	n.a.

* Tensile strength in terms of kN/mm

n.a.: not available data

Table 1: Mechanical properties of the adopted materials.

Adobe blocks used for construction of AM wallets were approximately $200 \times 400 \times 100 \text{ mm}^3$ in size. Mud mortar joints were 10 mm thick. Two-leave AM specimens were fabricated with running bond configuration, reaching a size of $410 \times 1230 \times 1230 \text{ mm}^3$. For both HTRM and GTRM series, the TRM was applied on both sides of the wallets. First, the wallet was externally hydrated. Then, a 10-mm-thick layer of mud mortar was applied. When mortar was still fresh, the textile was installed. Finally, a covering layer of mortar was applied until a total 25 mm thickness was reached. Special attention was paid to hemp-fibre grids for which an ad-hoc, on-site fabrication process was implemented. Hemp meshes were realized by means of a proper wooden frame on which nails were placed with 20 mm spacing. Yarns were arranged along both warp and weft directions by using the nails as guide, then were impregnated of res-

in. Finally, square textiles with same specimens' dimensions were obtained by cutting. Figures 1 and 2 show a schematic view of specimens and details on fabrication of hemp mesh.

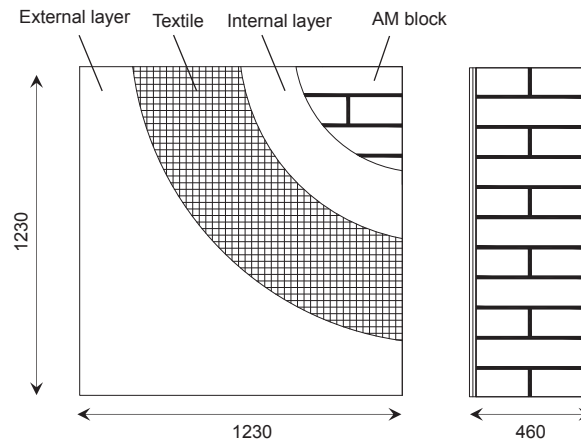


Figure 1: Layout of reinforced specimen.



Figure 2: Detail of the on-site fabrication of hemp mesh.

2.2 Testing setup and procedure

In order to reduce disturbance on specimens, the diagonal compression tests were performed directly in the manufacturing site by means of the movable system depicted in Figure 3. Specifically, the diagonal load was applied by reaction of a closed system with respect to the elongation of a hydraulic jack. Steel shoes were installed at both specimen's corners in order to distribute compressive stresses. Between such shoes and the specimen, a proper filling with shrinkage-free mortar was realized. All specimens were erected on rigid blocks. Foam sheets with low density were interposed between AM wallets and support-block, with the aim to avoid potential friction. After the installation, the loading system was self-supporting.

Diagonal compression load was applied with displacement control at 0.01 mm/s rate until failure was observed. The installed monitoring system was able to record diagonal displacements and load. In addition, four linear variable differential transformers (LVDTs) were arranged on both external surfaces of the wallet according to the typical X configuration, as shown in Figure 3. The gauge length was equal to 400 mm.

The average shear stress (τ) was derived from recorded load (F) by applying the formulation suggested by the ASTM E519-15 [29] standard (ASTM hereinafter), which is based on pure shear assumption as given in Eq. (1) in which A represents the cross-section area of the specimen (i.e., length \times thickness). The average shear strain (γ) on each side of the specimen

was obtained as the sum of the axial strains derived from LVDT displacement recordings along and perpendicular to the loading direction, respectively, as reported in Eq. (2).

$$\tau = 0.707 \frac{F}{A} \quad (1)$$

$$\gamma = \varepsilon_x + \varepsilon_y \quad (2)$$



Figure 3: Picture of the experimental set-up.

3 MECHANICAL RESPONSE AND FAILURE MODE

Shear stress versus shear strain (τ - γ) curves for series URM, HTRM and GTRM, along with crack patterns at failure, are depicted in Figure 4. In order to discuss the obtained results, for each test main mechanical parameters of the wallet were defined: the peak shear stress (τ_p), the elastic limit shear strain (γ_{cr}) corresponding to a shear stress equal to $0.7 \tau_p$, the shear strain at failure (γ_u), the latter assumed as associated to a strength drop of $0.2 \tau_p$ beyond the peak. Accordingly, the ductility capacity (μ) of the wallet was the ratio of ultimate to elastic shear strain values, as reported in Eq. (3). Such parameters are summarized in Table 2 in terms of mean and CoV for each specimen series.

$$\mu = \frac{\gamma_u}{\gamma_{cr}} \quad (3)$$

By observing Figure 4, all the specimens presented a mechanical response characterized by a first linear elastic branch up to first cracking, then a nonlinear curve up to peak stress and finally a softening until failure was observed. The recorded response was globally affected by high dispersion in displacement and force, especially in the post-peak range.

URM specimens were characterized by shear strength (τ_p) equal to 0.107 MPa on average with small dispersion (CoV = 7%). Conversely, ductility capacity (μ) resulted highly dispersed, with CoV = 41% and a mean value of 17.1. Unreinforced wallets showed similar damage patterns at failure. Large stair-stepping diagonal cracks were observed on the specimens, partially developed in joints and bricks. Shear failure occurred, resulting in quasi-brittle post-peak response.

Property	URM	GTRM	HTRM
τ_p (N/mm ²)	0.107	0.120	0.134
CoV	7%	14%	13%
γ_{cr} (-)	0.08	0.06	0.13
CoV	15%	20%	23%
γ_u (-)	1.37	2.38	7.57
CoV	52%	23%	13%
μ (-)	17.1	38.2	61.4
CoV	41%	19%	22%

Table 2: Experimental results of diagonal compression tests.

As expected, a higher shear strength was found for GTRM specimens, namely $\tau_p = 0.120$ MPa on average, in spite of a larger scatter (CoV = 14%). Generally, a more gradual post-peak softening was observed with respect to the unreinforced specimens, resulting in considerably increased ductility capacity, the mean value of which was 38.2. Failure modes were characterized by debonding of reinforcing grids after diagonal cracking onset, due to reduced mechanical compatibility of glass grid with respect to mud matrix.

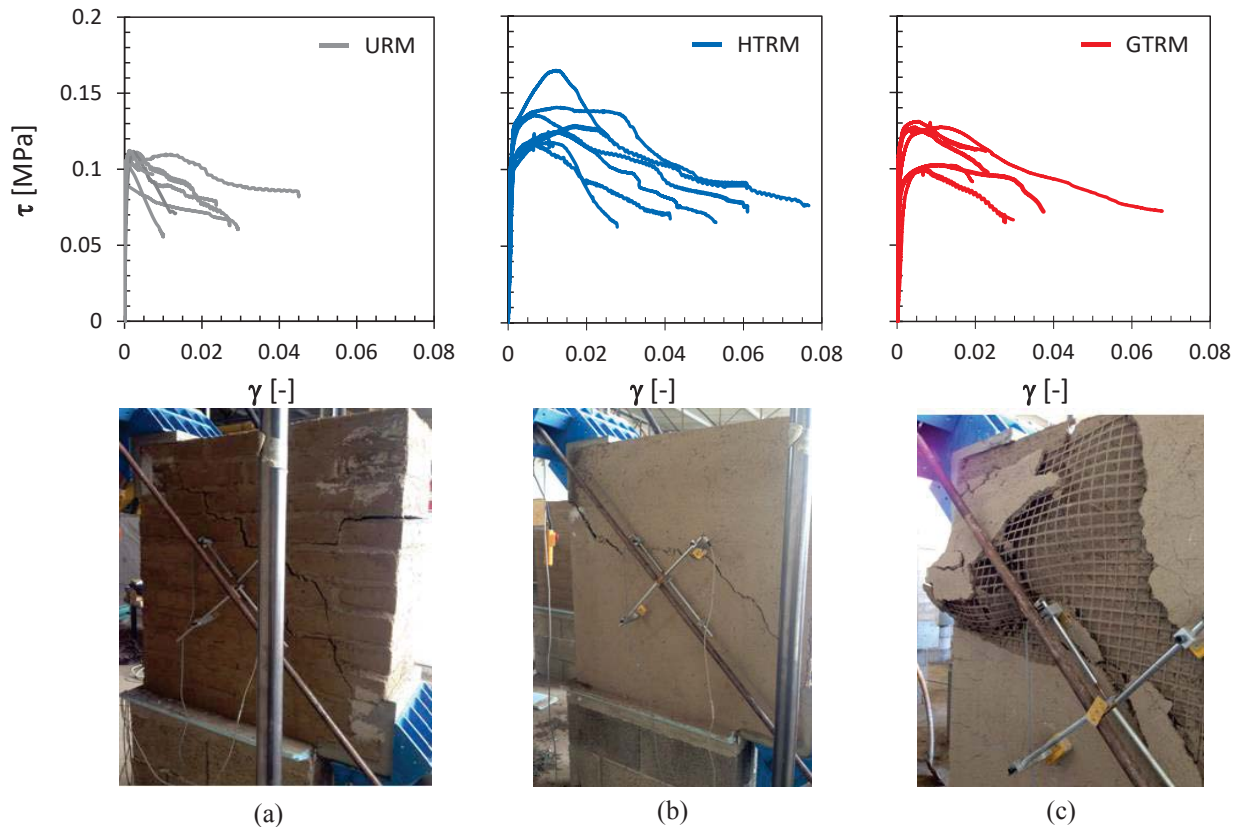


Figure 4: Experimental τ - γ curves and observed damage at the end of tests: (a) URM specimens; (b) HTRM specimens; (c) GTRM specimens.

No premature debonding occurred in the case of HTRM-strengthened wallets. The observed diagonal cracks followed the same profile of the inner unreinforced specimen; therefore, the imposed deformation was transferred to the TRM system up to global failure was

reached. HTRM-strengthened specimens showed a distinct hardening behaviour due to TRM up to peak strength, followed by a gradual strength degradation up to failure. The peak stress (τ_p) was equal to 0.134 MPa. Also in this case, significant scatter was recorded. Very high ductility capacity was obtained on average ($\mu = 61.4$) with $\text{CoV} = 22\%$.

4 STATISTICAL CONSTITUTIVE CURVES

Experimental testing confirmed a significant dispersion in the mechanical response of AM specimens. Specifically, high scattered values were recorded in terms of shear strain over all specimen series (i.e., URM, GTRM, HTRM). Regarding shear strength, considerably lower dispersion was observed with respect to strain, particularly in the case of URM specimens. With the aim of assessing the influence of such variability on TRM strengthening efficiency, a statistical analysis of the experimental results was carried out. Based on the assumption of normal distribution of the shear stress (considered as random variable) conditioned upon shear strain, τ - γ curves of the 16th, 50th (median) and 84th percentiles of conditional shear stresses were derived for each specimen series. Such curves are compared to each other in Figure 5. It is noted that diagrams are plotted up to 20% post-peak strength drop, which was assumed as ultimate limit state.

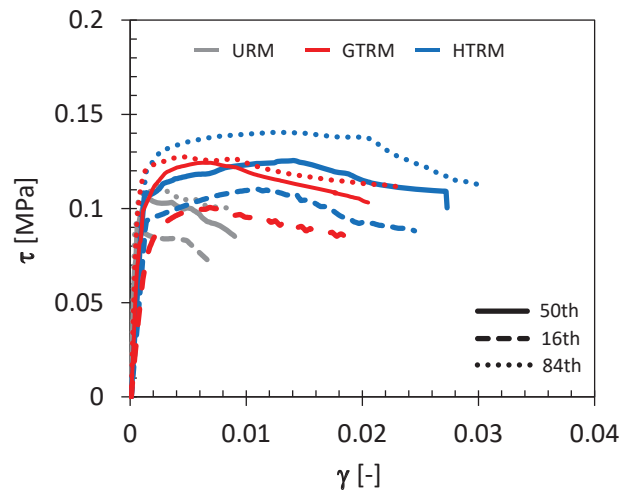


Figure 5: Statistical response curves corresponding to 16th, 50th and 84th percentiles of shear stresses.

Given the shear strain, the stress scatter (S) was computed as ratio of the difference between 84th and 16th values to the median value. Accordingly, similar scatter values were derived for URM and GTRM specimens, equal to 26% and 25%, on average, respectively. Conversely, a larger S -value was obtained for wallets strengthened by means of HTRM system ($S = 39\%$). Such result was partially expected because of the higher variability in hemp grid production process, as opposed to commercial glass-grid for which stringent quality-control protocols are implemented during manufacturing [30]. By observing the statistical τ - γ curves, some general trend can be extrapolated regarding the efficiency of the two considered TRM strengthening systems. Response curves of URM specimens were characterized by negligible hardening, with peak strength reached in the elastic phase and a subsequent sudden drop in strength, resulting in a fragile failure mode. On the contrary, τ - γ diagrams of HTRM and TTRM series show a large hardening phase with gradual softening, representative of a more ductile failure. Therefore, in general, both TRM ensured considerable improvement of shear capacity, although the HTRM solution appeared more effective. In fact, on average, the increase of shear strength (e_τ , computed as ratio of the strengthened to unstrengthened peak

stress) in this latter case was equal to 1.31, whereas the mean increasing ductility factor (e_μ , defined as ratio of the strengthened to unstrengthened ductility capacities) was 3.60. By contrast, in the case of GTRM system, mean values of e_τ and e_μ were equal to 1.12 and 2.20, respectively. Average values of stress scatter (S) and efficiency factors (e_τ and e_μ) are summarized in Table 3.

Property	URM	GTRM	HTRM
S (%)	26	25	39
e_τ (-)	-	1.12	2.20
e_μ (-)	-	1.30	3.60

Table 3: Stress scatter and efficiency factors.

5 CONCLUSIONS

In this study, the critical issue of the retrofitting of AM buildings has been experimentally investigated. Specifically, the efficiency of two TRM systems made of glass- and hemp-fibre meshes, respectively (both embedded in mud-mortar matrix) was assessed by means of diagonal compression tests on AM wallets. Overall, twenty-one specimens were tested and were equally divided into three groups: unreinforced specimens (URM), specimens strengthened with glass-based TRM (GTRM), and specimens strengthened with hemp-based TRM (HTRM).

Experimental shear stress-strain curves derived according to the ASTM E519-15 standard [29] and observed failure modes allow the following conclusions to be drawn:

- URM specimens failed in diagonal tension with wide cracks along joints and blocks, evidencing negligible pre-peak hardening and a quasi-brittle post-peak behaviour.
- The GTRM strengthening system considerably improved the mechanical behaviour of AM wallets, producing significant hardening until peak stress was reached and post-peak softening. Nevertheless, the failure mode was generally detected by the debonding of the reinforcing glass-fibre grid from the mud-mortar matrix, which limited the ductility capacity. Resulting strength increase with respect to as-built configuration was equal to 10%, on average, whereas the improved ductility was twice.
- Neither debonding nor local failure of the hemp-matrix system was observed on HTRM-strengthened specimens. Their shear behaviour was generally characterized by large hardening after cracking onset and very gradual softening in the post-peak response. Indeed, the observed diagonal cracks gradually developed until failure, the latter being caused by tensile fracture of hemp grid. Accordingly, the HTRM system ensured high efficiency, increasing the unreinforced shear strength by about 30% and resulting into a ductility capacity 3.6 times that of URM wallets.

Definitely, the feasibility of using TRM with the aim to obtain a crucial reduction of the seismic vulnerability of existing AM structures has been illustrated in this study. Both the considered TRM strengthening systems ensured considerable retrofitting efficiency with highly improved energy dissipation of AM wallets. The HTRM solution proved to be preferable due to its major mechanical compatibility with poor mud mortar and adobe blocks. Nevertheless, due to large dispersion of mechanical properties and response, great emphasis should be given on the improvement of the manufacturing process.

REFERENCES

- [1] H. Houben, H. Guillaud, *Earth construction — A comprehensive guide*. London: Intermediate Technology Publication, 1994.
- [2] B. Briseghella, V. Colasanti, L. Fenu, C. Nuti, E. Spacone, H. Varum, Seismic analysis by macroelements of Fujian Hakka Tulous, Chinese circular earth constructions listed in the UNESCO World Heritage List. *International Journal of Architectural Heritage*, **14**(10), 1551-1566, 2020.
- [3] E.L. Tolles, E.E. Kimbro, W.S. Ginell, *Planning and engineering guidelines for the seismic retrofitting of historic adobe structures*. Los Angeles: Getty Publications, 2003.
- [4] M. Blondet, G.V. Garcia, S. Brzev, A. Rubiños, *Earthquake-resistant construction of adobe buildings: A tutorial*. EERI/IAEE World Housing Encyclopedia, 2003.
- [5] R. Meli, O. Hernandez, M. Padilla, Strengthening of adobe houses for seismic actions. In: *Proceedings of the Seventh World Conference on Earthquake Engineering*, Istanbul, 1980; Vol. 4, p. 465-472.
- [6] F. Parisi, N. Augenti, Earthquake damages to cultural heritage constructions and simplified assessment of artworks. *Engineering Failure Analysis*, **34**, 735-760, 2013.
- [7] M. Blondet, J. Vargas, J. Velasquez, N. Tarque, Experimental study of synthetic mesh reinforcement of historical adobe buildings. In: *Proceedings of International Conference on Structural Analysis of Historical Constructions*, 2006; p. 715-722.
- [8] D. Torrealva, Seismic Design Criteria for Adobe Buildings Reinforced with Geogrids. In: *Proceedings of 15th World Conference on Earthquake Engineering*, Lisboa, 2012.
- [9] S. Bossio, M. Blondet, S. Rihal, Seismic behavior and shaking direction influence on adobe wall structures reinforced with geogrid. *Earthquake Spectra*, **29**(1), 59-84, 2013.
- [10] N. Sathiparan, K. Sakurai, M. Numada, K. Meguro, Seismic evaluation of earthquake resistance and retrofitting measures for two story masonry houses. *Bulletin of Earthquake Engineering*, **12**(4), 1805-1826, 2014.
- [11] E.L. Tolles, E.E. Kimbro, F.A. Webster, W.S. Ginell, *Seismic stabilization of historic adobe structures: Final report of the Getty seismic adobe project*. Los Angeles: Getty Publications, 2000.
- [12] A. Turer, S.Z. Korkmaz, H.H. Korkmaz, Performance improvement studies of masonry houses using elastic post-tensioning straps. *Earthquake Engineering & Structural Dynamics*, **36**(5), 683-705, 2007.
- [13] A. Charleson. *Seismic strengthening of earthen houses using straps cut from used car tires: a construction guide*. Oakland: Earthquake Engineering Research Institute (EERI), 2010.
- [14] D.M. Dowling, B. Samali, Low-cost and low-tech reinforcement systems for improved earthquake resistance of mud brick buildings. In: *Proceedings of the Getty seismic adobe project 2006 colloquium*, Los Angeles, 2006.
- [15] M. Blondet, J. Vargas-Neumann, R. Groenenberg, Evaluation of the efficacy of mud injection to repair seismic cracks on adobe structures via full-scale shaking table tests. In: *Proceedings of 15th World Conference on Earthquake Engineering*, Lisboa, 2012.

- [16] M. Blondet, J. Vargas, C. Sosa, J. Soto, Using mud injection and an external rope mesh to reinforce historical earthen buildings located in seismic areas. In: *Proceedings of 9th International Conference on Structural Analysis of Historical Constructions*, Mexico City, 2014. p 14-17.
- [17] C. Oliveira, H. Varum, A. Figueiredo, D. Silveira, A. Costa, Experimental tests for seismic assessment and strengthening of adobe structures. In: *Proceedings of the 14th European conference on earthquake engineering*, Ohrid, 2010.
- [18] A. Figueiredo, H. Varum, A. Costa, D. Silveira, C. Oliveira, Seismic retrofitting solution of an adobe masonry wall. *Materials and Structures*, **46**(1-2), 203-219, 2013.
- [19] L. Turanli, A. Saritas, Strengthening the structural behavior of adobe walls through the use of plaster reinforcement mesh. *Construction and Building Materials*, **25**(4), 1747-1752, 2011.
- [20] C. Atzeni, Stone masonry in rural Sardinian building. Evolution of the traditional building techniques between XIX and XX century. In: *Proceedings of the First International Congress on Construction History*, Madrid, 2003. p. 279-289.
- [21] F. Parisi, D. Asprone, L. Fenu, A. Prota, Experimental characterization of Italian composite adobe bricks reinforced with straw fibers. *Composite Structures*, **122**, 300-307, 2015.
- [22] D. Asprone, V. Colasanti, L. Fenu, F. Parisi, A. Prota, Adobe in Sardinia. Static and dynamic behaviour of the earthen material and of adobe constructions. In: *Proceedings of the 16th International Brick and Block Masonry Conference*, Padova, 2016.
- [23] A. Caporale, F. Parisi, D. Asprone, R. Luciano, A. Prota, Critical surfaces for adobe masonry: micromechanical approach. *Composites Part B: Engineering*, **56**, 790-796, 2014.
- [24] A. Caporale, F. Parisi, D. Asprone, R. Luciano, A. Prota, Comparative micromechanical assessment of adobe and clay brick masonry assemblages based on experimental data sets. *Composite Structures*, **120**, 208-220, 2014.
- [25] EN 1998-3, *Eurocode 8: design of structures for earthquake resistance – part 3: assessment and retrofitting of buildings*. Brussels: Comité Européen de Normalisation; 2005.
- [26] FEMA 356, *Prestandard and commentary for the seismic rehabilitation of buildings*. Washington (DC): Federal Emergency Management Agency; 2000.
- [27] Italian Building Code Commentary, Circolare n. 617 del 02.02.2009: *Istruzioni per l'applicazione delle «Nuove Norme Tecniche per le Costruzioni» di cui al decreto ministeriale 14 gennaio 2008*. Rome: Italian Ministry of Infrastructures and, Transportation; 2009 [in Italian].
- [28] C. Menna, D. Asprone, M. Durante, A. Zinno, A. Balsamo, A. Prota, Structural behaviour of masonry panels strengthened with an innovative hemp fibre composite grid. *Construction and Building Materials*, **100**, 111-121, 2015.
- [29] ASTM E 519-15 – *Standard test method for diagonal tension (shear) in masonry assemblages*. ASTM International, West Conshohocken, PA, USA, 2015.

- [30] A. Bonati, A. Franco, O. Coppola, G. De Luca, Strengthening of masonry structures: Current national and international approaches for qualification and design. *Key Engineering Materials* **817**, 501-506, 2019.

GENETIC OPTIMIZATION FOR THE DESIGN OF SEISMIC RETROFITTING OF PLANE RC FRAMES WITH BUCKLING RESTRAINED BRACES (BRBS)

Giovanni Minafò, Gaetano Camarda

Università degli Studi di Palermo, Dipartimento di Ingegneria
Viale delle Scienze, 90128 Palermo (Italy)

giovanni.minafo@unipa.it
gaetano.camarda@unipa.it

Abstract

The increasing development of computational power in modern digital devices has spread the use of structural optimization in design applications of different fields of engineering problems. This approach exposes engineers to challenging design procedures aimed to optimize all variables to satisfy the imposed requirements, finding the “optimal” solution. Despite this wide use, the application of optimization algorithms for the design of seismic retrofitting strategies becomes tougher, due to the difficulties in finding a mathematical expression which includes and combines all the key variables (i.e., cost, safety, sustainability, design) and the nonlinearity of the analysis. In this paper, the Genetic Algorithm search method (GA) has been used to optimize the retrofitting, using Buckling-Restrained Braces (BRBs), of a three-storeys RC structure designed to resist only gravity loads. The optimization aims to ensure the safety level required, minimizing intervention costs and use of materials, particularly finding the best topology solution for BRB positioning. To this purpose, an objective function has been applied to the model to minimize retrofit costs intervention using GA. The procedure has been implemented in Python Programming Language. In particular non-linear static analysis has been run using OpenSeesPy framework to evaluate the seismic required safety level at each simulation, while GA has been carried out with a custom design code to provide the best topology position of BRBs to minimize costs and consequently the use of materials. The method brought out the real possibility to ensure the required seismic safety level while reducing intervention cost and use of materials with an optimized and structured BRB positioning.

Keywords: Structural optimization, Genetic Algorithm, Retrofitting, BRB.

1 INTRODUCTION

Soft-computing techniques are becoming increasingly common in the field of civil engineering for structural optimization. These methods are widely used for sizing, topology optimization, and form-finding of new structures and infrastructures [1], but structural optimization is less commonly used for structural retrofitting of existing structures. Despite the growing interest in retrofit of existing framed RC structures, it is difficult to find procedures to define the optimal parameters for intervention design. It is also important to note that the displacement demand on existing structures depends on the stiffness, the mass of the structure and the dynamic characteristics of the system. The introduction of new lateral-resisting components, such as braces, shear walls, or stiffening frames, alters the force-displacement demands, and the design of the retrofit cannot be achieved in a closed-form. As a result, retrofitting applications are often designed without an "engineered process", and often lead to an overestimated retrofit solution. The scientific community has only recently begun to address this issue, and some innovative applications using soft-computing techniques and artificial intelligence have recently been proposed [2]. In this field, Genetic Algorithms (GAs) have shown to be especially useful for optimizing design processes. GA is a meta-heuristic algorithm built on Darwin's "evolution of species" [3], that has been commonly used for optimization problems [4, 5], but only a few recent applications are available for structural retrofitting. Di Trapani et al. [6] presented a GA model for designing steel jacket confinement of columns in 3D structures with a typical gravity load configuration. In the present paper a GA implementation, for structural optimization of seismic retrofitting interventions in 2D RC frames with BRBs, is presented. The aim is to use the GA approach to design BRB configurations that provide the necessary level of safety while minimizing costs. The RC frames are modeled using fiber section beam elements with force formulation and plastic hinge regions at the extremities, implemented using OpenSeesPy framework [7]. The GA was implemented using a custom code written in Python programming language [8], where a boolean integer design vector is used to assign the position of the BRB and its orientation. For each configuration, the algorithm performs a modal and a non-linear static analysis to check the safety level of the frame according to N2 verification [9]. The fitness of the solution is evaluated at each iteration combining the retrofit cost and a penalty factor, implemented to penalize infeasible solutions in terms of seismic safety. The opensource environment here proposed (Python-OpenSeesPy) allows finding the optimum BRB configuration for the frame to retrofit, ensuring seismic safety and minimizing the retrofit cost.

2 CASE OF STUDY AND NUMERICAL MODELLING

A case of study of 2D RC frame retrofitted with BRB elements is here presented, Figure 1. The chosen case of study replicates a typical situation of framed structures designed in the early 1980s in Europe. The frame has 5 storeys and 4 bays with a rectangular section for all elements, in particular, some columns are disposed to be stressed on their weak inertia axis and others are oriented on their principal strong inertia axis.

The design of reinforcing steel of the section was evaluated using elastic calculations, as usually assumed in old designs approaches, particularly a set of static lateral load was assumed as a fraction of the axial forces in the columns for each storey. The latter was a usual assumption in design process according to old codes in Italy during the 1970s.

A process of calculation of uniformly distributed load was done before the implementation of the model in the algorithm, as result the assumed load on the beams was 33.64 kN/m at first storey, 32.89 kN/m at intermediate storeys and 15.79 kN/m at last storey. The load value here assumed are calculated as a combination of seismic loads-i.e. as the sum of dead gravity loads and a fraction of the live load.

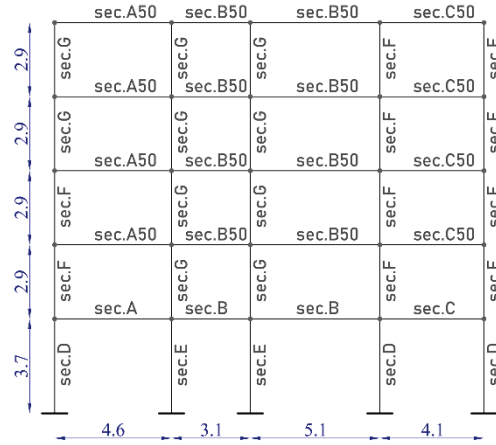


Figure 1: Studied frame geometry and sections.

The materials properties, Figure 2, of the concrete and the reinforcing steel used for the model design are reported in Table 1. The steel model used, take into account isotropic hardening of the material and needs the tangent at initial strain hardening (E_{sh}) as parameters. As regards the concrete material, it was modeled without taking into account the tensile strength. The depth of the concrete cover was set for all the sections to 25mm.

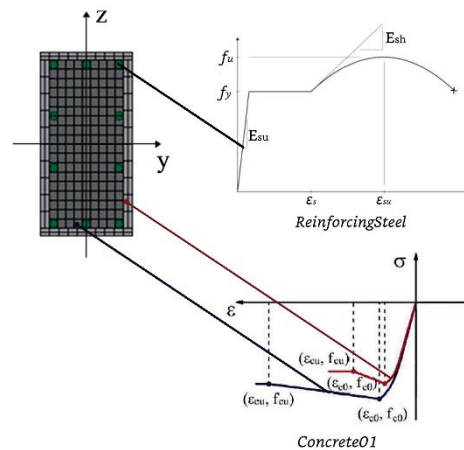


Figure 2: Fiber section discretization and materials behavior.

Steel	Unconf. Concrete	Conf. Concrete
$f_y = 319 \text{ MPa}$	$f_c = 18.4 \text{ MPa}$	$f_c = 18.4 \text{ MPa}$
$f_{su} = 365 \text{ MPa}$	$f_{cu} = 18.4 \text{ MPa}$	$f_{cu} = 20.26 \text{ MPa}$
$E_{su} = 210000 \text{ MPa}$	$E_c = 29444 \text{ MPa}$	$E_c = 32544 \text{ MPa}$
$E_{sh} = 31500 \text{ MPa}$	$\epsilon_o = 0.002$	$\epsilon_o = 0.0035$
$\epsilon_{su} = 0.06$	$\epsilon_u = 0.0035$	$\epsilon_u = 0.005$

Table 1: Materials properties.

With regards to the elements section indicated in Figure 1, the geometry details are reported in the following Table 2.

Section	Dimensions	Top reinf.	Bottom reinf.
A	600x300 mm	3 ϕ 16	2 ϕ 16
B	600x300 mm	4 ϕ 16	2 ϕ 16
C	600x300 mm	6 ϕ 16	2 ϕ 16
D	300x600 mm	3 ϕ 16	3 ϕ 16
E	600x300 mm	4 ϕ 16	4 ϕ 16
F	300x500 mm	3 ϕ 16	3 ϕ 16
G	500x300 mm	4 ϕ 16	4 ϕ 16
A50	500x300 mm	3 ϕ 16	2 ϕ 16
B50	500x300 mm	4 ϕ 16	2 ϕ 16
C50	500x300 mm	6 ϕ 16	6 ϕ 16

Table 2: Sections and reinforcement adopted.

2.1 Modelling

As mentioned before, the numerical implementation of the considered frame was done using OpenSeesPy framework, in particular using for RC beams and columns the force-based elements with flexibility formulation. A “BeamWithHinge” element, based on plastic hinge integration [10], was used for the implementation of the beams and columns with a plastic hinge length equal to half the depth of the section for the columns and the depth of the section for the beams. The element state is determined using a total of six integration points (two for each hinge and two for the interior). Two different fiber sections are assigned for each element, one for the two plastic hinge regions and one for the remaining region of the element. The confined and unconfined concrete were modeled using Concrete01 uniaxial material, while the constitutive law for the bars was implemented using the ReinforcingSteel uniaxial material (Fig. 2).

As regards the BRB, it is well known that it usually exhibits good capacity in tension and compression. During compression phase the core plate starts to buckle, but the phenomena is prevented by the reinforcing case (usually filled with concrete). The constitutive law of the element was implemented following the model suggested by Upadhyay et al. [11]. The model adopted used Steel02 material for the steel core and in order to take into account tension and compression a Pinching4 material is added in parallel to Steel02. At this point, the material model adopted was calibrated by comparing the results achieved with the experimental data available in Xu and Pantelides [12], the calibration results are presented in Figure 3. A corotational element truss formulation is used to implement the BRB in the structural model.

The design of BRB features was executed before the implementation in the nonlinear models of the frame. The dissipative length (L_c) and the elastic end length were calculated following Gelfi et al. [13] relationship:

$$L_c = \frac{\Delta_{bm}}{\varepsilon_{cu}} = L_b \left(\frac{d_r}{h} \sin\beta \cos\beta \right) \quad (1)$$

Where Δ_{bm} is the elongation of BRB, ε_{cu} is the plastic strain, d_r is the storey displacement, L_b is the overall diagonal length of the BRB, β is the inclination of the brace and h is the height of the considered storey. Two area parameters are set for the BRB and they are fixed in all the elements: $A_c = 5000 \text{ mm}^2$ for the core area, while in the elastic zone the section area is equal to $A_e = 64500 \text{ mm}^2$.

The design length core, length end, diagonal length, inclination of the brace and the elastic modulus of the BRB vary on the basis of the considered bay.

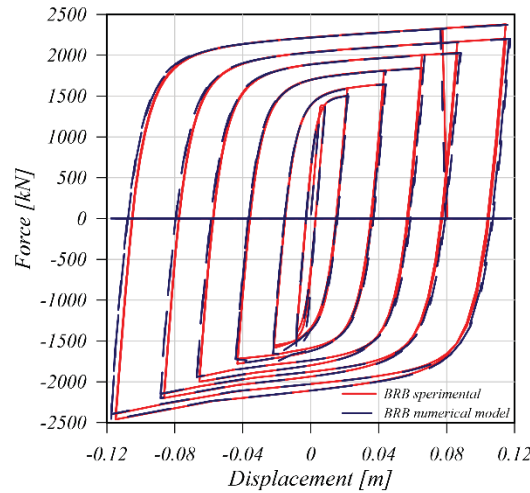


Figure 3: Calibration of BRB constitutive model.

2.2 Analyses and structural safety

The implemented environment provides a modal dynamic and a static non-linear analysis for each analyzed configuration. Modal analysis was performed to identify the lateral load profile to be applied to the structural nodes, while the NL analysis was performed to evaluate the capacity curve (force-displacement) of the analyzed configuration. The latter analysis was performed under displacement control with incremental steps of 0.05mm and load profile proportional to the first modal shape. The maximum displacement of 200mm was imposed on all analyses and the Newton-Raphson algorithm was used with a norm displacement increment check with tolerance equal to 10^{-6} .

The required seismic action was estimated based on the elastic response spectrum reported in Figure 4, assuming a high seismicity zone (type 1) and design spectral parameters ground acceleration on rock soil $a_g = 0.286g$, soil factor $S=1.332$ and damping correction factor $\eta=1$ (corresponding to 5% damping).

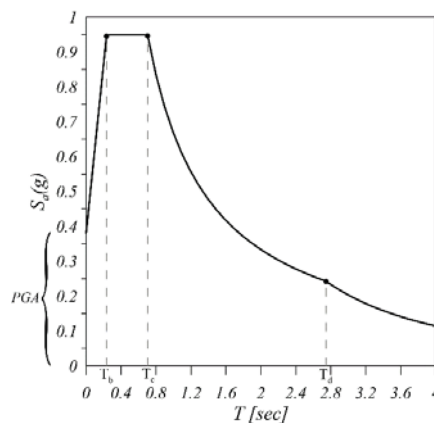


Figure 4: Pseudo acceleration response spectrum.

The safety of the structure was checked in compliance with Eurocode 8 [14] by comparing the required displacement demand with the capacity of the equivalent Single Degree of Freedom (SDOF) system, as expected in N2 method [15]. The SDOF capacity curve was linearized

with elastoplastic behavior, by the equivalent energy rule, and the seismic safety was evaluated by comparing the linearized SDOF response with the Acceleration-Displacement format (ADRS). Finally, structural safety index was evaluated as the ratio between the displacement capacity and the required displacement $\zeta = d_u^*/d_{r,max}^*$.

3 IMPLEMENTATION OF THE GA FRAMEWORK

The Genetic Algorithm is a meta-heuristic search method for optimization, based on evolutionary processes in which the algorithm simulates biological mechanisms. The aim of the GA is to find the optimal solution of a predefined objective function using the solution's fitness value. In the present work, the fitness of a solution depends on retrofit cost and structural safety, in particular, retrofit cost has to be minimized.

As mentioned before the environment was implemented on custom code written in Python programming language, while for the analysis the OpenSeesPy library has been used, so that all the processes were implemented in one code using *opensource* tools only.

The first step of the procedure begins generating an initial random population of individuals ($p_{size} = 5$ in the present work), where an individual defines the location and orientation of the BRB across the frame. Each individual of the population is identified by a design vector V_d , Figure 5, with 1 row and a number of columns depending on the number of the bays of the frame. An integer encoding type is used to enable BRB retrofit using boolean parameters from 0 to 2, where 0 means bare frame, 1 means bay retrofitted with a BRB in the tensile direction and 2 means bays retrofitted with BRB in compression.

$$V_d = \begin{bmatrix} 1 & 0 & 0 & 0 & 0 & 2 & 0 & 0 & 0 \end{bmatrix}_{1 \times 9}$$

0 1 2 3 4 5 6 7 8

Figure 5: Example of design vector.

Each design vector is decoded in a retrofit BRB topology configuration for the structural analysis to be executed. At the end of population analysis, the safety index (ζ), retrofit cost and fitness of individuals are calculated. The retrofit cost is obtained through the objective function, while the fitness value of the configuration is calculated as follows:

$$f = \frac{C + \delta}{100} \quad (2)$$

Where C represents the retrofit cost, while δ is a contribute that penalizes the solution if the safety index is less than 1. In particular, the latter coefficient is implemented as follows:

$$\delta(\zeta) = \begin{cases} 0, & \zeta \geq 1 \\ C_{max} + C \cdot e^{\zeta}, & \zeta < 1 \end{cases} \quad (3)$$

Where C_{max} is the maximum retrofit cost if all the bays of the frame were reinforced using BRB. The cost function, hence the objective function to minimize, is calculated as the sum of two main contributions:

$$C = C_m + C_s \quad (4)$$

C_m is the manpower and safety cost for each BRB (increased with the BRB number), while C_s is the cost that takes into account the scaffolding cost, demolition and rebuilding cost of infill walls and the cost of BRB. Is important to notice that C_s not only depends on the BRB geometrical properties but it is strictly related also to the geometrical parameters of the bay's walls.

For each population, that identify a generation, a *Tournament selection* (Fig. 6) is applied to selects 2 parents individuals used to generate a new possible solution (offspring). This selection method runs a series of tournaments inside the population pool, where individuals are randomly selected and the winner is chosen by its fitness value; in the present work lower the fitness and better is the solution.

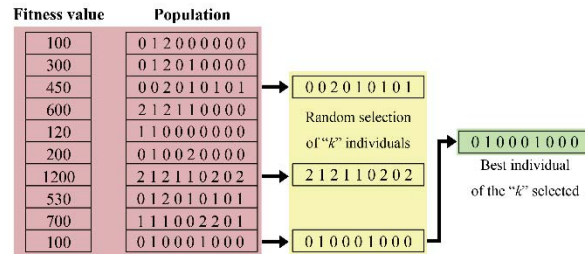


Figure 6: Example of tournament selection implemented.

The selected parents are then coupled using the *Crossover operator*, which is used to generate new offspring that will improve the exploration of the search space. In particular, *Single-point crossover* is implemented, where a random point is evaluated to cut in half the two parents and the offspring are generated cross-merging the pieces of the two individuals. At this point, the new offspring could be modified using the *Mutation operator*, which will randomly change an integer inside the design vector. In particular, if the chosen position has a value equal to 1, it can be changed in a random value inside the list (0, 2), and so on for the other cases. The mutation will happen depending on a mutation rate parameter ($m_r = 0.2$ in this work) defined by the user.

Is important to notice that the number of offspring is generally higher than population size (p_{size}), hence before the process could proceed a *Survival selection* is applied to resize the offspring individuals to the population size. The survival selection will select the first p_{size} individuals with the best fitness to move forward to the next generation and repeat the process, but before that, a convergence check is executed to evaluate if the optimal solution has been reached. In this work the convergence is reached when there is no difference between old and new populations for a certain number of generations, depending on the number of bays and storeys of the frame.

4 RESULTS AND DISCUSSION

Figure 7 shows the optimal retrofit configuration achieved by the Genetic Algorithm. Four BRB are needed to secure the frame, one per storey disposed along the tensile direction at the three bottom storeys and along the compressive direction for the fourth storey.

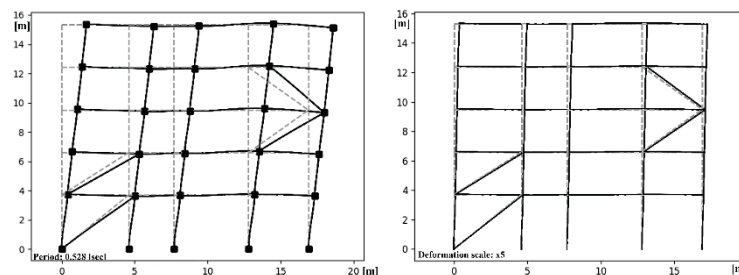


Figure 7: First modal shape and last step of static non-linear analysis of the retrofitted frame.

The optimal solution is achieved by the algorithm with a safety index $\zeta = 1.17$ and a retrofit cost of 28753€, while the total retrofit cost for all the bays of the frame with BRB is estimated to be 136597€, this means a saving cost of about 79%.

Finally, Figure 8 and 9 shows the verification of the displacement demand on the considered frame for both the bare (Fig. 8) and retrofitted (Fig. 9) configuration.

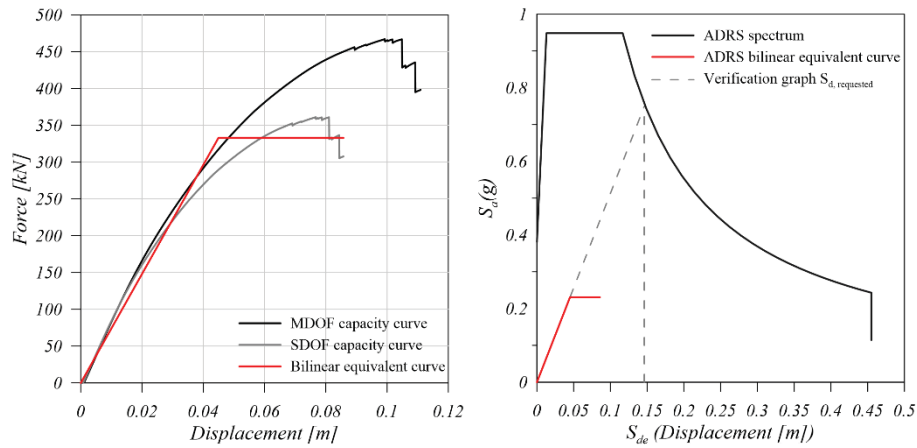


Figure 8: N2 verification of bare frame.

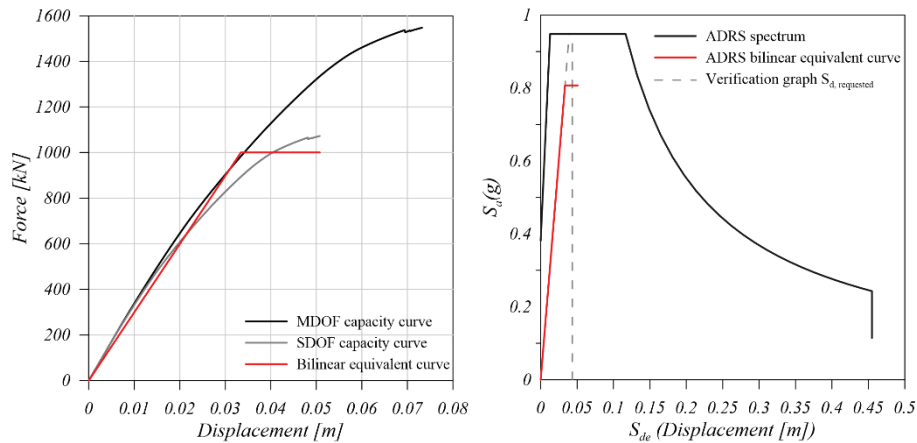


Figure 9: N2 verification of retrofitted frame.

As regards the implemented GA, the best fitness values of each generation are plotted in Figure 10(b), or for each analyzed individual in Figure 10(c), while the color of the points depends on the value of the safety index. It is observed that the solution comes after 50 generations of 5 individuals and a stable convergence is achieved with a constant value of fitness.

It is also worth noting that the solution cannot be improved, meaning that the number and disposal of braces is the minimum for ensuring the safety level. Figure 10(d) shows the best individual fitness of each generation.

Furthermore, the number of unfeasible solutions is a limited part of all the generated configurations (Fig. 10(c)), which confirms that the GA tends to select only possible solutions within the search space. The convergence of the procedure is reached after 20 generations with 5 individuals, meaning that 100 modal and pushover analyses are needing, as shown in Figure 10(d).

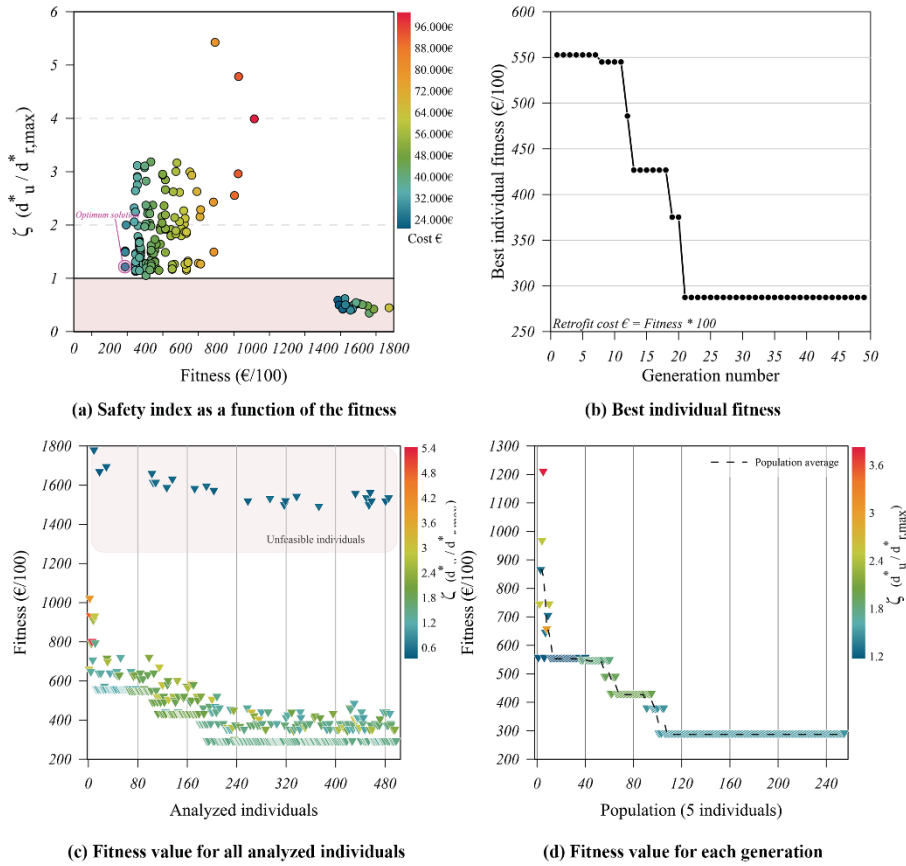


Figure 10: Results of the proposed procedure for the studied frame.

The efficacy and the stability of the proposed algorithm were assessed by comparing the results with those of multiple simulations carried out with a Monte Carlo (MC) approach. A comparison between GA retrofitted configuration, MC configuration and the bare frame is reported in Table 3.

Configuration	Period T[s]	ζ	Cost [€]	d_u^* [m]	$d_{r,max}^*$ [m]
Bare frame	1.002	0.585	-	0.09	0.146
Retrofitted (GA)	0.53	1.168	28753	0.05	0.043
Retrofitted (MC)	0.44	1.294	40439	0.04	0.0287

Table 3: Results comparison between the bare frame, retrofitted (GA) and retrofitted (MC) analysis.

The same number of analyses as GA individuals number was performed on frames with randomly disposed BRBs. In particular, the design vector was composed by generating a pseudorandom integer number in the range 0 to 2 for each bay with equal probability. The number of generated configurations was selected to keep the same computational effort in comparison with the GA and having the same number of overall structural analyses (500 simulations).

Figure 11 shows the comparison between the results obtained through the MC simulation with those achieved with the proposed GA approach. The graphs show the cost (Figures 11(a) and 11(b)) and the safety index (Figures 11(c) and 11(d)) associated with each generated configuration, while the red line indicates the moving average for each 5 individuals. It is evident that the GA quickly converges down to a minimum value of the cost of about 29000€, while

the distribution of the cost for the MC approach follows the "white noise" distribution, keeping the average cost on the starting value.

A similar consideration can be made in terms of safety index, which is almost kept constant by the GA, searching smartly the best configuration on a limited range around 1. It is also observed as the Coefficient of Variation associated with the distributions of the GA is significantly lower concerning that of the MC analysis, due to the capability of the algorithm in improving the solution progressively.

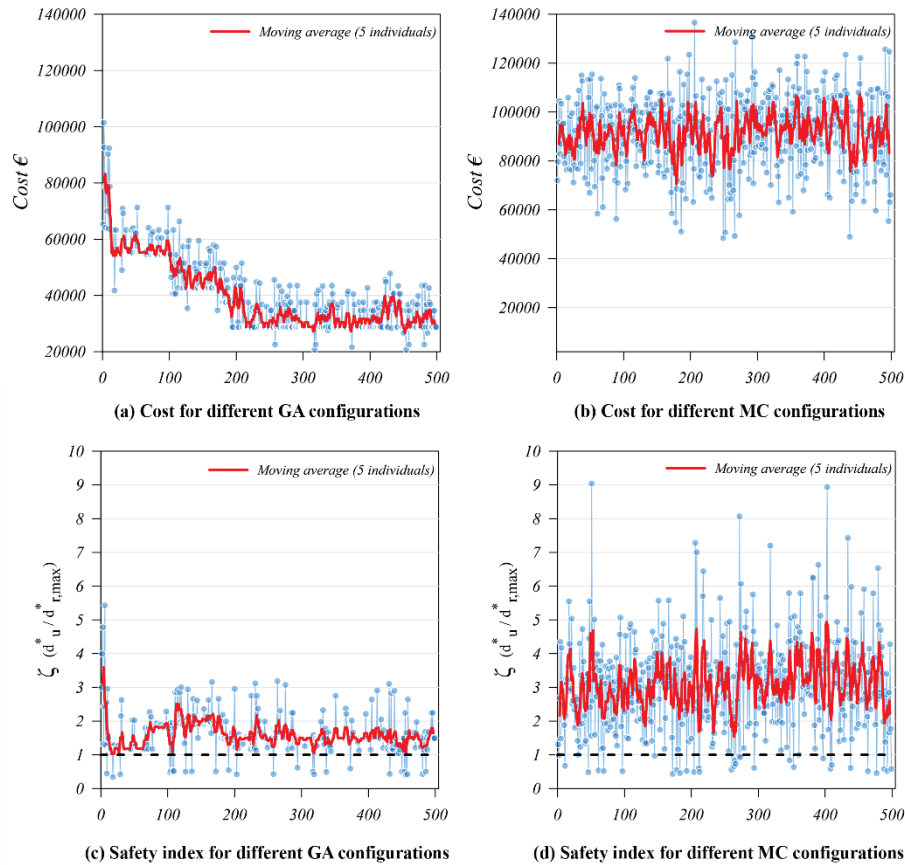


Figure 11: Comparisons between GA and Monte Carlo simulations.

It is evident that the GA allows achieving safe results with the cheapest solution. It is also to note that with the same number of analyses, hence the same computational time, the best solution of the MC simulation is more expensive than the solution found by GA of approximately 40.64% with an almost equal safety index.

5 CONCLUSIONS

This paper presented the proposal of a GA framework for designing the optimal configuration of BRBs for the seismic upgrading of plane RC frames. The algorithm allows varying the position and the direction of the braces, while the mutation and generation operations search for the most suitable configuration of the retrofitted frame. The GA was implemented in a Python environment while the OpenSeesPy library was adopted for modelling and analyzing the frames, making up a unique open-source framework for analysis and optimization.

Based on the obtained results and for the range of analyzed variables, the following conclusions can be drawn:

- the algorithm proved to be stable, finding the optimal configuration after a number of generations depending on the deformability of the structure;
- the solutions achieved for all the cases ensured the required safety level and proved to minimize the cost, on the basis of the selected features of the BRB;
- the penalty function implemented ensured the safety of the structure while the algorithm minimizes the cost;
- comparison with Monte Carlo simulations has shown the intelligence of the Genetic Algorithm in using previous information data to improve the search inside the solution space;

Further analysis has to be done to assess the algorithm behavior of the algorithm implementing 3D structural analysis and taking into account the possible shear increment at beam-column nodes.

REFERENCES

- [1] G. Bekdaş, S. M. Nigdeli, A. E. Kayabekir, X.-S. Yang, Optimization in civil engineering and metaheuristic algorithms: a review of state-of-the-art developments, *Computational intelligence, optimization and inverse problems with applications in engineering*, 2019, 111–137.
- [2] R. Falcone, C. Lima, E. Martinelli, Soft computing techniques in structural and earthquake engineering: A literature review, *Engineering Structures* 207, 2020, 110269.
- [3] J. H. Holland, et al., Adaptation in natural and artificial systems: an introductory analysis with applications to biology, control, and artificial intelligence, *MIT press*, 1992.
- [4] M. Pathan, S. Patsias, V. Tagarielli, A real-coded genetic algorithm for optimizing the damping response of composite laminates, *Computers & Structures*, 2018, 51–60.
- [5] C. Xu, S. Lin, Y. Yang, Optimal design of viscoelastic damping structures using layer-wise finite element analysis and multi-objective genetic algorithm, *Computers & Structures*, 2015, 1–8.
- [6] F. Di Trapani, M. Malavisi, G. C. Marano, A. P. Sberna, R. Greco, Optimal seismic retrofitting of reinforced concrete buildings by steel-jacketing using a genetic algorithm-based framework, *Engineering Structures* 219, 2020, 110864.
- [7] M. Zhu, F. McKenna, M. H. Scott, Openseespy: Python library for the OpenSees finite element framework, *SoftwareX*, 7, 2018, 6–11.
- [8] G. Van Rossum, F. L. Drake, Python 3 Reference Manual, *CreateSpace*, 2009.
- [9] P. Fajfar, Capacity spectrum method based on inelastic demand spectra, *Earthquake Engineering & Structural Dynamics* 28, 1999, 979–993.
- [10] M. H. Scott, G. L. Fenves, Plastic hinge integration methods for force-based beam-column elements, *Journal of Structural Engineering* 132, 2006, 244–252.
- [11] A. Upadhyay, C. Pantelides, L. Ibarra, Residual drift mitigation for bridges retrofitted with buckling restrained braces or self centering energy dissipation devices, *Engineering Structures* 199, 2019, 109663.

- [12] W. Xu, C. P. Pantelides, Strong-axis and weak-axis buckling and local bulging of buckling-restrained braces with prismatic core plates, *Engineering Structures* 153, 2017, 279–289.
- [13] P. Gelfi, G. Metelli, Prova sperimentale di un elemento diagonale di controvento ad instabilità controllata, in: Proc., *XXI Congresso CTA: Costruire con l'acciaio*, Catania, Italy, [only in Italian], 2007, pp. 169–176.
- [14] Eurocode 8: Design of structures for earthquake resistance-part 1: general rules, seismic actions and rules for buildings, *European Committee for Standardization*, Brussels, 2005.
- [15] P. Fajfar, Capacity spectrum method based on inelastic demand spectra, *Earthquake Engineering & Structural Dynamics* 28, 1999, 979–993.

INFLUENCE OF THE EFFECTIVENESS FACTORS IN ASSESSING THE SHEAR CAPACITY OF RC BEAMS STRENGTHENED WITH FRP

Piero Colajanni, and Salvatore Pagnotta

Department of Engineering, University of Palermo
Viale delle Scienze, Ed. 8, 90128, Palermo, Italy
email: {piero.colajanni, salvatore.pagnotta}@unipa.it

Abstract

Shear failure of RC beams strengthened with composite textiles is often affected by the different failure modes characterizing the FRP reinforcement. The most relevant analytical models for evaluating the shear capacity of RC beams strengthened with FRP take into account these failure modes by introducing an effectiveness factor “R”, which reduces the ultimate FRP tensile stress. Moreover, the interaction between stirrups and FRP reinforcement leads to a reduced efficiency of the transverse steel reinforcement due to the brittle failure of composite textile which hinders the yielding of all the stirrups involved by critical crack. In this regard, some analytical models introduce an effectiveness factor “r”, aiming at reducing the yielding stress of stirrups. The procedures to calculate the above two parameters represent the main differences characterizing most of analytical models, significantly influencing their results. For this reason, the present paper focuses on the comparison of the different procedures to assess the effectiveness factors, proposing a new procedure for each effectiveness factor by modification of already existing formulations. Influence of the arrangement of composite reinforcement on the efficacy of stirrups, affected by brittle failure of FRP, is considered by means of the ratio between effective strain of composite to yielding strain of steel. The proposed procedures are employed in a design-oriented analytical model able to calculate the shear strength of RC beams retrofitted with FRP reinforcement arranged in any direction. The model is formulated aiming at representing an extension of EN1992 shear model to beams strengthened with FRP. The efficacy of the proposed procedures is assessed by comparing the experimental results against the predictions obtained via the design-oriented model and the above-mentioned analytical models.

Keywords: Instructions, ECCOMAS Thematic Conference, Structural Dynamics, Earthquake Engineering, Proceedings.

1 INTRODUCTION

Over the last years, several research groups have made significant efforts to develop innovative structures, able to significantly reduce structural damage caused by destructive earthquakes [1-6]. Nevertheless, due to different factors (e.g. costs, business disruption, design limitations), a considerable share of construction market is still devoted to retrofit existing RC structures, especially those built between 1950s and 1970s, whose seismic performances are unsatisfactory if compared to recently built structures. To this aim, among the different techniques used, externally bonded Fiber-Reinforced Polymer (EB-FRP) is one of the most employed, thanks to its excellent mechanical performance to density ratio.

During the last two decades, several mechanical models have been developed to assess flexural capacity and confinement effect of RC members retrofitted with externally wrapped composite reinforcement (e.g. [7, 8]). On the contrary, it is challenging to develop analytical models able to accurately account for all the resisting mechanisms influencing shear behavior of RC members (e.g. aggregate interlock, shear span to depth ratio, size effect, dowel effect, ductility demand), and the topic is still widely debated in the literature [9-11]. Some shear capacity models (such as [12, 13]) were developed on the basis of the strut-and-tie resisting scheme, by using an additive approach. However, these models assume that there is no interaction between shear contributions provided by concrete, steel stirrups and FRP reinforcement, and each contribution is achieved at shear failure. Nevertheless, experimental results showed that this interaction occurs, and may lead to both a reduced shear contribution provided by steel stirrups due to brittle failure of FRP which can be achieved before that all stirrups passing through shear critical crack yield, and a reduced shear contribution provided by FRP due to possible limitation of the ultimate strain [14-16].

Differently from the American codes, those developed in Europe (e.g. [17-20]) evaluate shear capacity of retrofitted RC members by means of truss mechanism with variable inclination of concrete strut, consistently with that used by [21] for ordinary RC members. However, uncertainty arises when assessing shear capacity provided by concrete strut, being no common solution in the selection of the angle of reinforcement to be used in the case of simultaneous presence of steel stirrups and FRP reinforcement arranged with different inclinations.

In this framework, the present paper focuses on the comparison of the different procedures to assess the effectiveness factors, proposing new procedures for the effectiveness factors dedicated to FRP and steel stirrups, by modification of already existing formulations. Influence of the arrangement of composite reinforcement on the efficacy of stirrups, affected by brittle failure of FRP, is considered by means of the ratio between effective strain of composite to yielding strain of steel. The proposed procedures are employed in a design-oriented analytical model able to calculate the shear strength of RC beams retrofitted with FRP reinforcement arranged in any direction. The model is formulated aiming at representing an extension of EN1992-1-1 shear model to beams strengthened with FRP. The main advantage of this model is the capability of simultaneously taking into account the presence, and their mutual influence, of steel stirrups, FRP reinforcement and concrete strut, in assessing shear capacity of retrofitted members. Closed-form equations are provided, for any amount and arrangement of shear reinforcement, able to calculate stress acting at failure on steel stirrups, FRP reinforcement and concrete strut, as well as angle of inclination of concrete stress field with respect to member axis. The accuracy of the proposed procedures is assessed by comparing the experimental results against the predictions obtained via the design-oriented model and the above-mentioned analytical models.

Moreover, a modified version of the model suggested by CNR is proposed and validated, aimed at overcoming the inaccuracy of the original model when assessing shear capacity of

concrete strut. In fact, in this case CNR model considers the angle of inclination of FRP reinforcement only, neglecting the presence of stirrups. The modified version of CNR, named CNRm, proposes to calculate an equivalent angle of shear reinforcement included in the evaluation of shear strength of concrete strut, obtained as a weighted average between shear capacity provided by steel stirrups and FRP reinforcement.

2 DESIGN-ORIENTED MODEL

Colajanni et al. [22] proposed a model based on the stress field approach, able to assess the shear capacity of RC members having transverse reinforcement arranged with two different inclinations. Here, that model is modified to be applied in the case of RC beams retrofitted with FRP reinforcement inclined in any direction. The proposed model also represents the extension of a model based on the stress field approach, able to assess shear strength of retrofitted RC beams with vertically-oriented FRP reinforcement only [23]. On the basis of the same assumption of the models proposed in [22, 24], shear capacity of a strengthened RC beam can be assessed by means of three different equations, obtained by calculating the vertical equilibrium of beam segments, identified via three different sections parallel to stress field directions of concrete strut, steel stirrups, and FRP reinforcement, respectively (Figure 1).

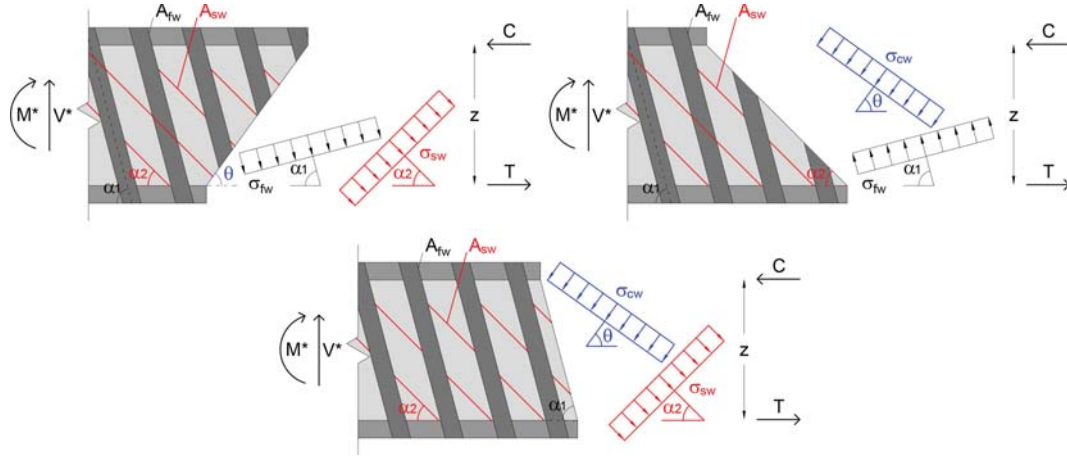


Figure 1: Different beam segments identified through three sections parallel to stress field direction of: concrete strut (a); steel stirrups (b); FRP reinforcement (c).

By doing so, each of the three equilibrium equations, which are given below, depends only on two stress fields, and can be easily solved:

$$v = R \tilde{\sigma}_{fw} \omega_{fw} (\cot \theta + \cot \alpha_1) \sin^2 \alpha_1 + r \tilde{\sigma}_{sw} \omega_{sw} (\cot \theta + \cot \alpha_2) \sin^2 \alpha_2 \quad (1)$$

$$v = \tilde{\sigma}_{cw} (\cot \theta + \cot \alpha_2) \sin^2 \theta + R \tilde{\sigma}_{fw} \omega_{fw} (\cot \alpha_1 - \cot \alpha_2) \sin^2 \alpha_1 \quad (2)$$

$$v = \tilde{\sigma}_{cw} (\cot \theta + \cot \alpha_1) \sin^2 \theta + r \tilde{\sigma}_{sw} \omega_{sw} (\cot \alpha_2 - \cot \alpha_1) \sin^2 \alpha_2 \quad (3)$$

In the above equations v is the shear strength made non-dimensional with respect to $b_w z f'_{cm}$ (b_w section width), $\tilde{\sigma}_{fw} = \sigma_{fw} / f_{fu}$, $\tilde{\sigma}_{sw} = \sigma_{sw} / f_{syw}$, $\omega_{fw} = (2 b_f t_f f_{fu}) / (b_w s_f \sin \alpha_1 f'_{cm})$, and $\omega_{sw} = (A_{sw} f_{syw}) / (b_w s_w \sin \alpha_2 f'_{cm})$ are the non-dimensional stresses and the mechanical ratios of FRP reinforcement and steel stirrups, respectively, f_{fu} is the nominal rupture stress of the fiber, R the strain and stress “effective” coefficient (effective strain $\varepsilon_{fe} = \varepsilon_{fu} R$, effective stress $f_{fe} = f_{fu} R = E_f \varepsilon_{fe}$), and r is the reduction factor

of the efficiency of the steel stirrups. The values of these efficiency coefficients will be investigated and assessed in the following sections.

The shear capacity of an RC beam is computed via the static theorem of theory of plasticity, which gives an assessment of the shear capacity as the maximum value among the possible solutions satisfying both the equilibrium condition (1)-(3) and the following inequalities of plastic admissibility:

$$0 \leq \tilde{\sigma}_{cw}, \tilde{\sigma}_{fw} \leq 1 \quad -1 \leq \tilde{\sigma}_{sw} \leq 1 \quad (4)$$

A plastic admissible condition is obtained by combining (1), (2) and (4), as follows:

$$0 \leq \tilde{\sigma}_{cw} = \left(R \tilde{\sigma}_{fw} \omega_{fw} \sin^2 \alpha_1 + r \tilde{\sigma}_{sw} \omega_{sw} \sin^2 \alpha_2 \right) (1 + \cot^2 \theta) \leq 1 \quad (5)$$

The above inequalities clarify the relation between the stress fields of the web concrete, steel stirrups and FRP reinforcement.

In this paper, only the case of major practical interest is considered, namely α_1 and $\alpha_2 \leq 90^\circ$. According to Colajanni et al. (2020), to evaluate the shear strength and $\cot\theta$ initially it is supposed that, at failure, the stress limit is reached simultaneously in the three stress fields (i.e. $\tilde{\sigma}_{cw} = \tilde{\sigma}_{fw} = \tilde{\sigma}_{sw} = 1$). Thus, on the basis of the upper limit imposed by Eq. (5), the first tentative value of the inclination of the web concrete stress field is obtained as follows:

$$\cot \theta = \sqrt{\left(R \omega_{fw} \sin^2 \alpha_1 + r \omega_{sw} \sin^2 \alpha_2 \right)^{-1} - 1} \quad (6)$$

Based on the results of the above equation, assuming $\cot\theta_{lim} = 2.5$, three cases are defined:

- $1 \leq \cot\theta \leq 2.5$: the stress limit is reached simultaneously in the three stress fields, and shear resistance can be calculated by using Eq.(1) assuming $\tilde{\sigma}_{cw} = \tilde{\sigma}_{fw} = \tilde{\sigma}_{sw} = 1$;
- $\cot\theta > 2.5$: the amount of FRP reinforcement and steel stirrups is not sufficient to induce attainment of the maximum resistance in the web concrete stress field. Thus, $\cot\theta = 2.5$ is assumed, and the shear capacity is computed through Eq. (1), assuming $\tilde{\sigma}_{fw} = \tilde{\sigma}_{sw} = 1$. The stress value in the web concrete field can be calculated by using Eq. (5), in which $\cot\theta = 2.5$;
- $\cot\theta < 1$: shear failure is due to attainment of the stress limit in the web concrete stress field and in one of the two shear reinforcements. Therefore, the other shear reinforcement is in the elastic range at beam failure. Now it is assumed that $\alpha_1 < \alpha_2$. With the aim of determining if the maximum shear is given by Eq. (2) with the FRP reinforcement reaching the effective strain in tension ($\tilde{\sigma}_{fw} = 1$) or (unlikely event) by Eq. (3) with the steel stirrups yielding in compression ($\tilde{\sigma}_{sw} = -1$), the following inequality is employed:

$$R \omega_{fw} \sin^2 \alpha_1 \leq 0.5 + r \omega_{sw} \sin^2 \alpha_2 \quad (7)$$

If the inequality is true, then the FRP reinforcement attains its stress limit, and the stress acting on the steel stirrups is computed as follows:

$$\tilde{\sigma}_{sw} = \left(0.5 - R \omega_{fw} \sin^2 \alpha_1 \right) / \left(r \omega_{sw} \sin^2 \alpha_2 \right) \quad (8)$$

Conversely, if the inequality is false, then the steel stirrups yield in compression, and the stress acting on the FRP reinforcement is calculated as follows:

$$\tilde{\sigma}_{fw} = \left(0.5 + r \omega_{sw} \sin^2 \alpha_2 \right) / \left(R \omega_{fw} \sin^2 \alpha_1 \right) \quad (9)$$

3 FRP EFFECTIVENESS FACTOR

Several experimental observations have shown that the failure of shear-strengthened RC beams with bonded FRP is often associated with achievement of a specific failure mode involving the textile material. The most common FRP failure modes reported in the literature [25, 26] are the following: failure of the FRP; debonding at the FRP-concrete interface; excessive width of the shear cracks and consequent loss of aggregate interlock; separation of the concrete cover along a vertical plane (peeling off) (e.g. [27]). To take these effects into account a reduced effective FRP design strength $f_{fe} = E_f \times \varepsilon_{fe}$, smaller than its nominal design strength $f_{fu} = E_f \times \varepsilon_{fu}$, was assumed. It was assessed by applying the effectiveness coefficient R to the nominal ultimate fiber strain. Over the last two decades, several formulations have been developed in order to estimate the above coefficient. In the proposed model, six different approaches to assessing the reduced effective FRP design strength are considered, with the aim of comparing their efficiency when introduced in the proposed model. Two of these six approaches are reported below, being assembled by using different equations reported in several papers, while the other four approaches are those suggested by ACI [12], CNR [17], fib [20], and Mofidi and Chaallal [30].

3.1 First approach: Khalifa and Nanni [28, 29] and Pellegrino and Modena [27]

According to the first approach, already used in [23], the value of R is the minimum among the three effectiveness coefficients R_i ($i=1,2,3$) proposed in [28, 29] and the fourth R_4 reported in [27], i.e. $R = \min\{R_1, R_2, R_3, R_4\}$.

The equations selected to describe the four modes of failure are reported below. The efficiency coefficient R_1 , which takes into account the tensile failure of the FRP, is computed by means of the following equation:

$$R_1 = 0.56(\rho_{fw} E_f)^2 - 1.22(\rho_{fw} E_f) + 0.78 \quad (10)$$

where E_f is the elastic modulus of the fibers. The coefficient R_2 , representing the debonding phenomenon, is calculated using the following equation:

$$R_2 = \frac{(f_{ck})^{\frac{2}{3}} (d_{ft} - \eta L_e) [738.93 - 4.06(E_f t_f)]}{\varepsilon_{fu} d_{ft} 10^6} \quad (11)$$

where L_e is the effective length, which is evaluated using the expression provided by ACI and CSA:

$$L_e = 23300 / (E_f t_f)^{0.58} \quad (12)$$

η is a parameter that takes into account the anchorage conditions, equal to 1 or 2 if the shear strengthening is U-shaped or side-only, respectively. The range of validity of Eq. (12) is $20 \leq E_f t_f \leq 90$. In case of complete wrapping or U-shaped strengthening with anchorages able to prevent a debonding effect, the coefficient R_2 is not taken into account. The coefficient R_3 , limiting the shear crack width, is set equal to:

$$R_3 = 6 \cdot 10^{-3} / \varepsilon_{fu} \quad (13)$$

In the case of side-bonding and U-jacketing reinforcement, FRP failure often involves the separation of the concrete cover along a vertical plane (peeling off). Hence, the coefficient

proposed in [27] is assumed equal to:

$$R_4 = \frac{2f_{ct}A_c \cos^2 \beta b_{c,v}}{n_f t_f L_f E_f \left[(h_f - L_e) / (h_f) \right] b_f \varepsilon_{fu}} \quad (14)$$

Further details about the parameters involved by Eq. (14) can be found in the above-mentioned paper.

3.2 Second approach: Chen and Teng [25, 26]

According to [25, 26] the coefficient of effectiveness is the minimum between two effectiveness coefficients, namely $R = \min\{R_5, R_6\}$. The effectiveness factor R_5 takes into account the tensile rupture of FRP, which usually occurs across the critical crack, correlating it with non-uniform strain distribution in the FRP along a shear crack. The authors, assuming proportionality of the fiber strain to the width of the shear crack, supposed an approximate strain linear distribution, where the FRP strain increases linearly from a minimum at the crack tip to a maximum at the lower end. Thus, R_5 can be expressed as:

$$R_5 = \frac{1 + (h_w - d_f) / z}{2} \quad (15)$$

where d_f = height of the FRP. Since experimental observations show that this kind of failure mode usually occurs in fully wrapped or U-wrapped RC beams, this coefficient must be considered only for these arrangements. Instead, the coefficient R_6 takes into account failure through debonding of FRP, which may occur when the bond length is not sufficient. According to [25] the stress in the FRP is variable along the bond length, and its maximum stress ($\sigma_{f,max}$) can be evaluated as:

$$\sigma_{f,max} = 0.427 \beta_w \beta_L \sqrt{\frac{E_f \sqrt{f'_c}}{t_f}} \leq E_f \varepsilon_{fu} \quad (16)$$

where β_w = coefficient of the FRP-to-concrete width ratio; β_L = bond length coefficient. These values can be calculated by using the following equations:

$$\beta_w = \sqrt{\frac{2 - w_f / s_f \sin \beta}{1 + w_f / s_f \sin \beta}} \quad (17)$$

$$\beta_L = \begin{cases} 1 & \text{if } \lambda \geq 1 \\ \sin \frac{\pi \lambda}{2} & \text{if } \lambda < 1 \end{cases} \quad (18)$$

where $\lambda = L_{max}/L_e$ = normalized maximum bond length; in which the maximum (L_{max}) and the effective bond length (L_e) are respectively:

$$L_{max} = \begin{cases} \frac{h_{frp,e}}{\sin \beta} & \text{for U - wrap} \\ \frac{h_{frp,e}}{2 \sin \beta} & \text{for side bonded} \end{cases} \quad (19)$$

$$L_e = \sqrt{E_f t_f / \sqrt{f'_c}} \quad (20)$$

where $h_{frp,e}$ is the effective height of the FRP (further details can be found in [25]). Thus, the effectiveness reduction factor R_6 can be expressed as:

$$R_6 = \frac{\sigma_{f,max}}{E_f \varepsilon_{fu}} \begin{cases} \frac{2}{\pi \lambda} \frac{1 - \cos \frac{\pi \lambda}{2}}{\sin \frac{\pi \lambda}{2}} & \text{for } \lambda < 1 \\ 1 - \frac{\pi - 2}{\pi \lambda} & \text{for } \lambda \geq 1 \end{cases} \quad (21)$$

4 STEEL STIRRUPS EFFECTIVENESS FACTOR

As recognized in several studies [14-16] the simultaneous presence of steel stirrups and FRP reinforcement leads to a reduction in the peak resistance provided by each shear reinforcement. The interaction between the two materials is expressed both in the decrease of the FRP shear contribution with the increase of the axial rigidity ratio between the internal steel and the external FRP [27] and in the inability of some or all of the steel stirrups, affected by critical fracture, to reach the yield strength due to FRP brittle rupture [14-16]. To overcome these drawbacks many models have been developed, connecting the interaction between the two reinforcement systems to their rigidities [30], or the shear crack width [31] or simply assuming a fixed reductive coefficient $\alpha = 0.75$ [15].

On the basis of the parameter proposed by [15], in this paper the r reduction parameter is defined by means of a bi-linear expression that relates the reduction of the contribution to the shear strength given by the steel reinforcement to the ratio between the component of FRP effective strain in the direction of the internal steel reinforcement $\varepsilon_{fe,sd}$ and the internal steel reinforcement yield strain ε_{syw} :

$$r = \begin{cases} 0.75 \frac{\varepsilon_{fe,sd}}{\varepsilon_{syw}} & \text{if } \varepsilon_{fe,sd} / \varepsilon_{syw} \leq 1.33 \\ 1 & \text{if } \varepsilon_{fe,sd} / \varepsilon_{syw} > 1.33 \end{cases} \quad (22)$$

where $\varepsilon_{fe,sd} = \varepsilon_{fe} \cos \varphi$ with φ equal to the angle between FRP reinforcement direction and steel stirrups. The reduction coefficient thus defined is able to take into account both that the strain of the most elongated steel stirrup, at beam failure, can be limited by the effective strain of the fiber, and that not all the stirrups along the critical crack are able to reach the yield strain. In particular, when $\varepsilon_{fe,sd}/\varepsilon_{sy} = 1$, only the most elongated stirrup, which intercepts the shear crack at the point of maximum width, can reach the yield strain (assuming perfect adhesion with concrete). It is also noted that r can take on a value less than 1 even if the ratio $\varepsilon_{fe,sd}/\varepsilon_{sy}$ is greater than 1. This makes it possible to take into account the second effect mentioned above, i.e. the non-uniform distribution of tension in the steel stirrups intercepted by the shear crack.

As will be seen in the following sections, the modulation of the reduction coefficient $\alpha = 0.75$ proposed in [15], through the ratio between the deformations of the interacting materials, makes it possible to minimize the inaccuracy of the proposed models due to overestimation of the steel resistance contribution.

The above effectiveness factor for steel stirrups is used in conjunction with effectiveness factors reported in sections 3.1 and 3.2 only. This is due to the fact that the effectiveness fac-

tor proposed by Mofidi and Chaallal [30] already considers reduction of contribution provided by steel stirrups, while models proposed by investigated codes do not suggest any effectiveness factor and are used in their original formulation.

5 MODIFIED VERSION OF CNR-DT 200 R1/2013 [17]

Shear capacity model suggested by CNR is developed with the purpose of representing a direct extension of the model proposed by EN1992-1-1 to evaluate shear capacity of ordinary RC members. Shear capacity of each element constituting the truss mechanism can be written in non-dimensional form, as well as shear capacity of retrofitted members, as given below:

$$\begin{aligned} v_s &= \omega_{sw} (\cot \theta + \cot \alpha) \sin^2 \alpha \\ v_f &= \omega_{fw} (\cot \theta + \cot \beta) \sin^2 \beta \\ v_c &= (\cot \theta + \cot \psi) / (1 + \cot^2 \theta) \\ v &= \min(v_s + v_f, v_c) \end{aligned} \quad (23)$$

In the third of (23), the angle α provided by CNR model is substituted with the to-be-determined angle ψ . In fact, considering the angle α would consequently neglect the presence, and its influence, of the other shear reinforcement when assessing shear strength of concrete strut. For this reason, a simple iterative procedure is proposed below to calculate angle ψ .

According to the suggestion of CNR code, in the original version of CNR model the angle ψ is set equal to angle β , while the inclination of concrete strut is assessed aiming at maximizing shear capacity of retrofitted RC member. Therefore, the sum of the first and second equation of (23) is equated to the third of (23), yielding:

$$\begin{aligned} &\cot^3 \theta (\omega_{sw} \sin^2 \alpha + \omega_{fw} \sin^2 \beta) + \cot^2 \theta (\omega_{sw} \sin^2 \alpha \cot \alpha + \omega_{fw} \sin^2 \beta \cot \beta) + \\ &+ \cot \theta (\omega_{sw} \sin^2 \alpha + \omega_{fw} \sin^2 \beta - 1) = \cot \psi - \omega_{sw} \sin^2 \alpha \cot \alpha - \omega_{fw} \sin^2 \beta \cot \beta \end{aligned} \quad (24)$$

In the proposed version of CNR model, angle ψ contained in (24) is calculated by means of the following iterative procedure:

- A tentative $\cot \theta$ value is assumed, based on the sum of the mechanical ratios of each shear reinforcement $\omega_{sw} + \omega_{fw}$ (alternatively a value of 1.75 can be used, being the average value of the range of variation of $\cot \theta$ suggested by CNR);
- By means of the first and second equation of (23) are computed shear capacities v'_s and v'_f provided by steel stirrups and FRP reinforcement, respectively. These values are employed to calculate a weighted angle ψ' as $\psi' = (\alpha v'_s + \beta v'_f) / (v'_s + v'_f)$;
- The angle ψ' obtained is inserted in (24), yielding a new $\cot \theta$ value.

This procedure can be used iteratively until the difference between two consecutive values of $\cot \theta$ is negligible. However, numerical analysis performed by means of the above procedure showed that one iteration is sufficient to obtain accurate values of $\cot \theta$.

6 DATABASE DESCRIPTION

With the aim of comparing the accuracy of the model described above, a database containing 158 specimens of RC beams having rectangular or T-shaped cross-sections, strengthened in shear by means of FRP strips or sheets was collected [14-16, 27, 32-51]. The specimen

characteristics and the test results are reported in in Table 1. The database contains beams strengthened with U-jacketing or complete wrapping schemes using carbon or glass fibers. The effective depth of the cross-section of the beams ranges between 155 and 831 mm, while the shear span is between 2.3 and 3.8. The transverse internal reinforcement is constituted by vertical steel stirrups whose maximum geometrical ratio is 0.48%. As regards FRP reinforcement, the ultimate tensile strength ranges between 106 and 4361 MPa, while the elastic modulus is comprised between 8 and 640 GPa. Lastly, the FRP geometrical ratio ranges between 0.04% and 3.00%.

The database was divided into two partial databases: DTB1, consisting of 138 specimens, in which the FRP reinforcement is arranged at right angles to the longitudinal axis of the member; DTB2, consisting of 20 specimens, in which the FRP reinforcement is arranged at an angle β different from 90° .

7 INFLUENCE OF EFFECTIVENESS FACTORS

The effectiveness factors described in previous sections are used to assess accuracy of the proposed design-oriented model, which is evaluated by means of the ratio between experimental shear capacity v_{exp} and theoretical prediction v_{the} of tests reported in Table 1. The parameters used to quantify the accuracy and reliability of the model are the average ratio between experimental and analytical values of shear capacity (Avg) and the Coefficient of Variation (CoV).

Generally speaking, all the approaches used to calculate effectiveness factor provide satisfactory results, as showed in Figure 2. Nevertheless, significant differences in the average and scatter values given by the analyzed approaches can be observed, highlighting the paramount influence of effectiveness factors in assessing shear capacity of RC beams. In fact, effectiveness factor suggested by ACI provides the best average value (0.99), while that of fib gives the worst one (0.83), overestimating significantly, in average, the shear capacity of beams. On the contrary, effectiveness factor provided by Mofidi & Chaallal leads to an overall underestimation of the shear capacity, with an average value of 1.12. With regard to effectiveness factors described in sections 3.1 and 3.2, and that suggested by CNR, they provide similar average values, showing an overall slight overestimation of shear capacity. Concerning CoV values, it can be observed that FRP effectiveness factor proposed by Chen & Teng combined with that for steel stirrups proposed in this paper provides the lowest scatter (0.20). Even if ACI effectiveness factor gives the best average value, it leads to the highest scatter (0.31), similar to that obtained by using Mofidi & Chaallal equations (0.29). As for effectiveness factor named as “first approach”, as well as those proposed by CNR and fib, scatter values range between 0.24 and 0.27. All that said, it can be stated that the procedure to calculate effectiveness factors which combines the best average accuracy (Avg value close to 1) and the highest reliability (low CoV value) is the one named “second approach”, which uses the equations proposed by Chen & Teng to evaluate effectiveness factor for FRP, and the equations proposed in section 4 to assess effectiveness factor for steel stirrups.

To provide an insight into the above-described differences, in Figure 3 are plotted the effectiveness factor values provided by the above-mentioned procedures for each specimens of the database. Moreover, power regression in the form $y = Ax^B$, as well as coefficient of determination R^2 , are given for each group of effectiveness factors in the case of U-shaped strengthening configuration. The results showed in Figure 3 help to explain the average and scatter values plotted in Figure 2. As a matter of fact, fib and Mofidi & Chaallal procedures, which averagely overestimates and underestimates the shear capacity of beams, respectively, are characterized by parameters A of power regression equal to 0.20 and 0.08, respectively.

Moreover, the high scatter in shear capacity assessment provided by ACI procedure is

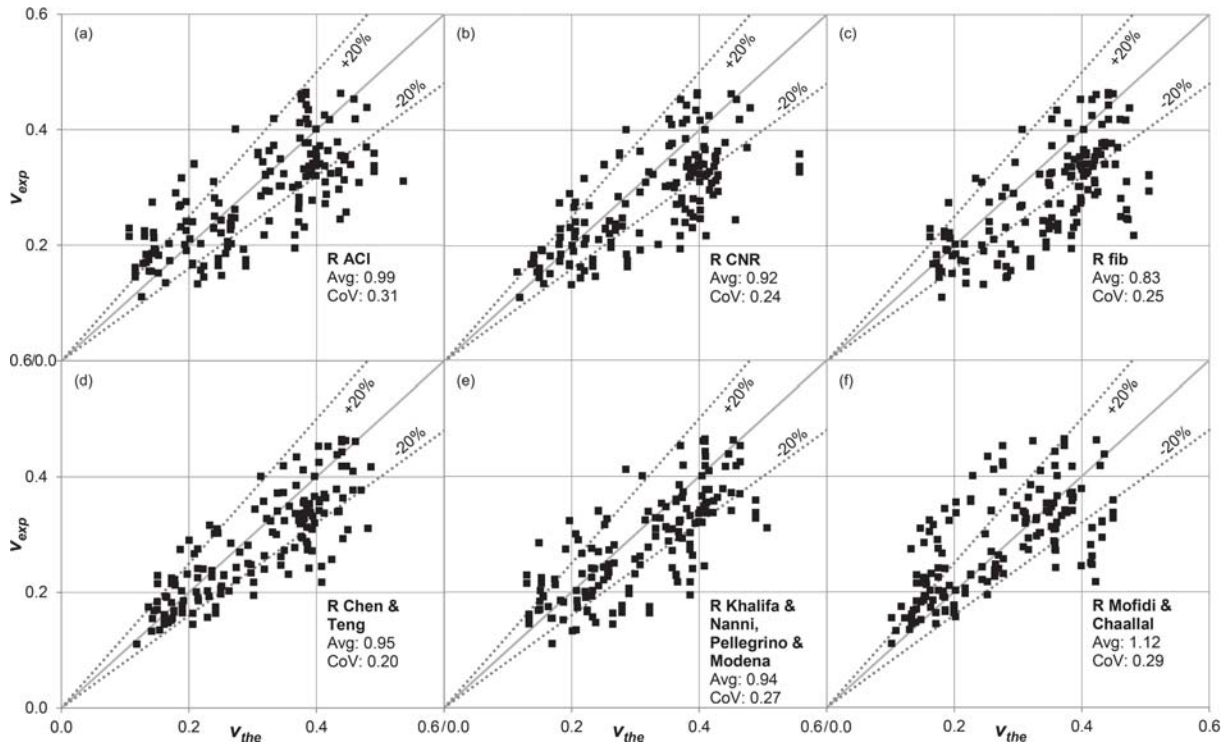


Figure 2: Experimental vs. theoretical shear capacity by using the proposed design-oriented model calculating effectiveness factors as suggested by: ACI (a); CNR (b); fib (c); Chen & Teng (second approach, sections 3.2 and 4) (d); Khalifa & Nanni, Pellegrino & Modena (first approach, sections 3.1 and 4) (e); Mofidi & Chaallal (f).

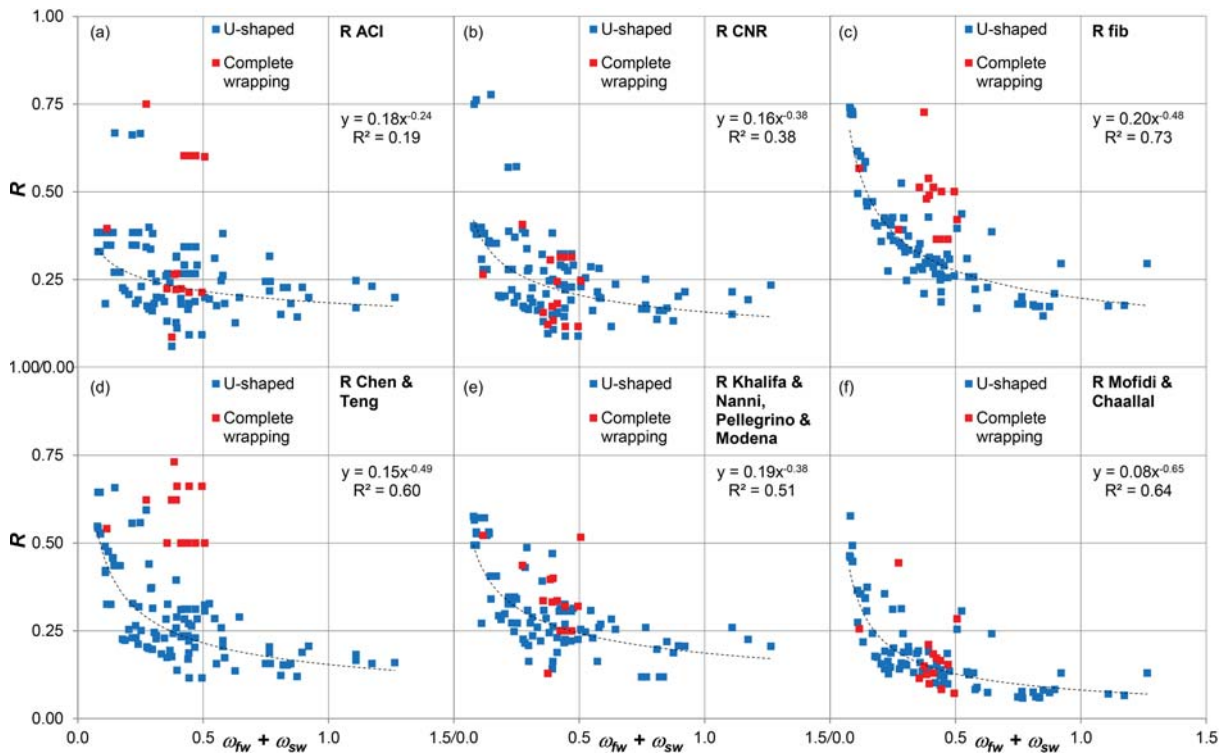


Figure 3: Effectiveness factors for FRP calculated as suggested by: ACI (a); CNR (b); fib (c); Chen & Teng (section 3.2) (d); Khalifa & Nanni, Pellegrino & Modena (section 3.1) (e); Mofidi & Chaallal (f).

confirmed by R^2 value, which is the lowest among those given by the analyzed procedures. With reference to complete wrapping configuration, it can be observed substantial differences

among the procedures. In fact, equations proposed by fib and Chen & Teng tend to provide R values higher than those given in the case of U-shaped configuration. On the contrary, equations proposed by CNR, Mofidi & Challal, and those listed in section 3.1, give R values similar to those for U-shaped strengthening scheme. With regard to ACI procedure, no trend can be noted, the R values being highly scattered.

Once the procedure to calculate effectiveness factors was selected, the proposed design-oriented model is validated against analytical results provided by code models suggested by ACI and CNR, as well as the proposed modified version of CNR, named CNRm.

In Figure 4 and Figure 5 are showed the results of the ratio between the experimental shear capacity and the theoretical prediction for each specimen belonging to the database and for each of the above-mentioned models, considering the two partial databases. Regarding results reported in Figure 4, all the models provide reliable results, even if some substantial difference can be observed. In fact, CNR model provides the best average value (1.00), to which correspond, however, the worst CoV value (0.24). With reference to the proposed model and ACI one, they provide similar values, characterized by low scatter and with a slight average overestimation of shear strength of beams. It is worth recalling that, in the case of FRP reinforcement and steel stirrups arranged with the same inclination, CNRm model gives the same results of the original CNR one.

Concerning beams having FRP reinforcement arranged with different inclination with respect to that of steel stirrups, the proposed model gives the best results. Although all the models overestimate in average shear capacity of beams, the proposed model gives the closest average to 1 and the lowest scatter. These results prove the accuracy and reliability of the proposed design-oriented model, and its superior performance in the case for which it was formulated, namely when FRP reinforcement and steel stirrups are oriented with different inclinations. It should be stressed that, in this latter case, the proposed model is the only one derived from a consistent physical model.

The results obtained in the two partial databases confirm that the use of an effectiveness factor that takes into account the strain experienced by FRP reinforcement oriented in any direction, leads to superior performance of the proposed model, which is thus able to account for the main interactions characterizing the shear resistance of a strengthened RC beam. On the contrary, model codes consider the brittle failure of FRP reinforcement, but neglect the interaction of the retrofitting system with both steel stirrups and concrete strut.

With regard to the results provided by CNR model and its modified version, CNRm, in Figure 5 it can be observed that the proposed calibration of ψ angle, which is the angle used in the evaluation of shear strength of concrete strut, slightly improves the performance of CNR model, reducing the scatter from 0.19 to 0.17. However, the proposed version of CNR model still significantly overestimates shear capacity beams, with an average value of 0.73.

To shed light on how the calibration of ψ angle influences the assessment of concrete strut inclination, in Figure 6 are illustrated $\cot\theta$ values for specimens having FRP reinforcement and steel stirrups oriented with different inclinations. It can be noted that, for high amount of mechanical ratios of shear reinforcements, $\cot\theta$ values are lower when ψ angle is computed by means of the simple procedure proposed. This contributes to reduce the overestimation of shear capacity affecting CNR model, increasing its reliability. It is worth noting that the proposed design-oriented model provides $\cot\theta$ values which are equal to 2.5 in most of the analyzed cases. This is due to the different formulation used to calculate effectiveness factor for FRP, and to the presence of the effectiveness factor for steel stirrups, which reduces the denominator value of Eq. (6).

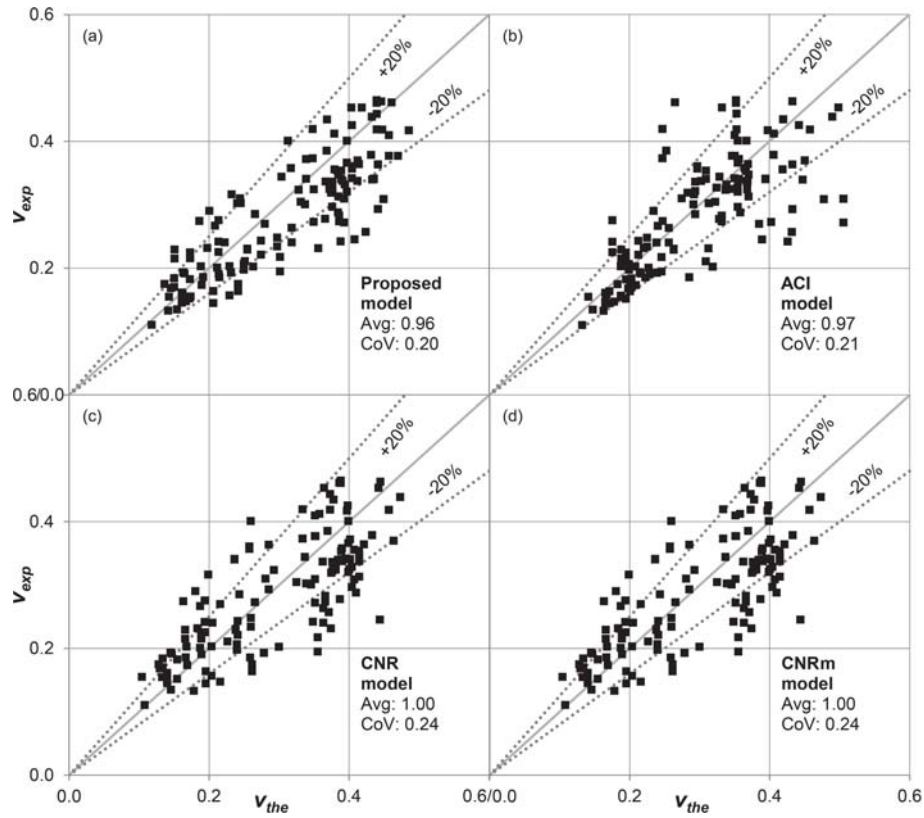


Figure 4: Experimental vs. theoretical shear capacity for DTB1: proposed design-oriented model with second approach (a); ACI (b); CNR (c); CNRm (d).

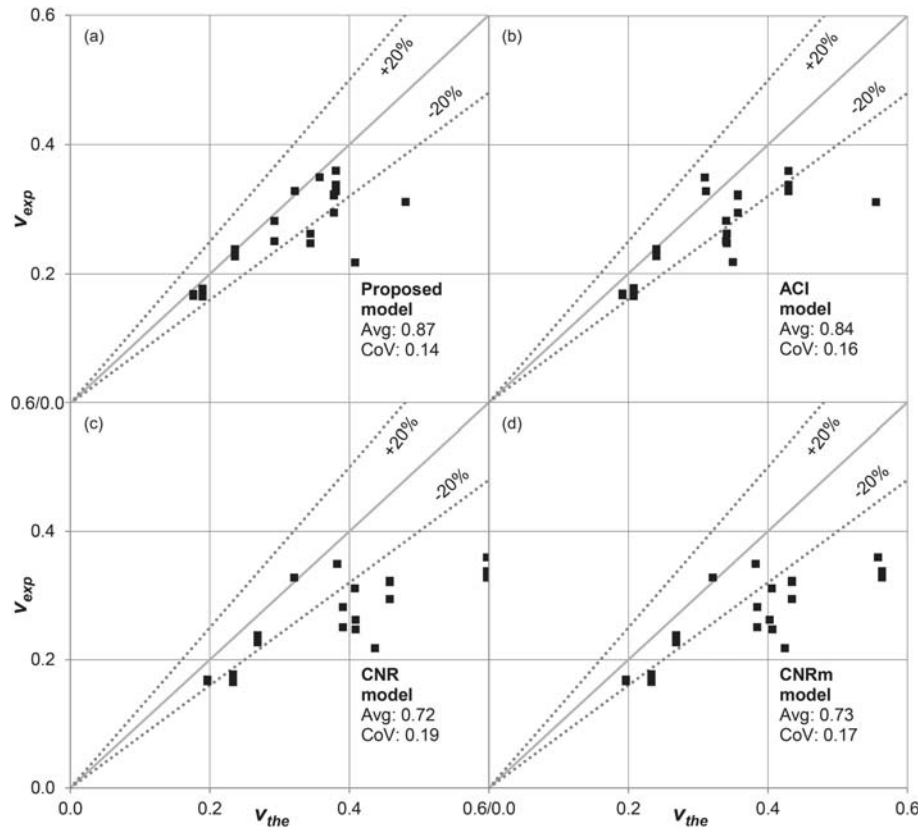


Figure 5: Experimental vs. theoretical shear capacity for DTB2: proposed design-oriented model with second approach (a); ACI (b); CNR (c); CNRm (d).

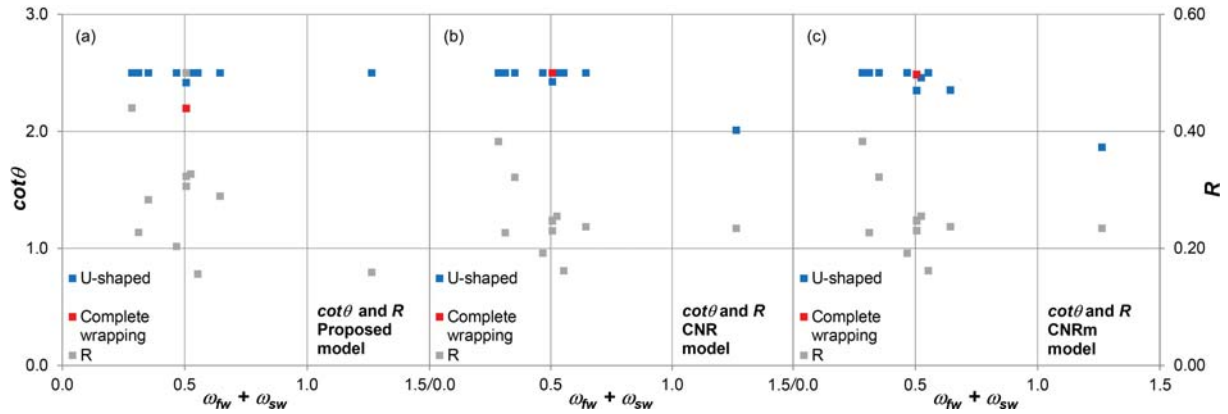


Figure 6: Inclination of concrete strut $\cot\theta$ vs. sum of mechanical ratios of shear reinforcements $\omega_{fw} + \omega_{sw}$ for DTB2: proposed design-oriented model with second approach (a); CNR (b); CNRm (c).

8 PARAMETRIC ANALYSIS

Once the accuracy and reliability of the proposed design-oriented model were proved, in this section a parametric analysis is carried out, by varying inclination of FRP reinforcement, with the aim of evaluating its influence on shear capacity of retrofitted RC beams, calculated by means of the above-mentioned models based on variable inclination of concrete strut.

Among the several parameters influencing evaluation of shear capacity, mechanical ratios of shear reinforcements (ω_{fw} and ω_{sw}), as well as inclination of steel stirrups ($\alpha = 90^\circ$), are assumed, while inclination of FRP reinforcement can vary in the range $45^\circ \leq \beta \leq 90^\circ$. To highlight some peculiar aspects of the proposed model, CNR one and its modified version CNRm, four different arrangements of shear reinforcement are assumed, considered representative of real applications: the first two, $\omega_{fw} = 0.15$; $\omega_{sw} = 0.05$ and $\omega_{fw} = 0.15$; $\omega_{sw} = 0.15$, are selected to compare the influence of the increment of steel shear reinforcement having low amount of FRP shear reinforcement; the other two, $\omega_{fw} = 0.20$; $\omega_{sw} = 0.40$ and $\omega_{fw} = 0.40$; $\omega_{sw} = 0.20$, are selected to compare shear strength in the case of high amount of steel/FRP shear reinforcement. In Figure 7 are showed curves of theoretical prediction of shear capacity obtained by means of the above models, calculated by varying angle of inclination of FRP reinforcement.

Generally speaking, the proposed model provides shear capacity values which are in most cases lower than those given by the two versions of CNR model, confirming the findings of Figure 5 against experimental results. Moreover, the proposed version of CNR model provides shear capacity values which are close to that of original CNR models for low amount of steel stirrups, while approach to those of the proposed design-oriented model when increasing amount of steel stirrups. With the exception of the case with very low amount of steel shear reinforcement (i.e. $\omega_{fw} = 0.15$; $\omega_{sw} = 0.05$), the difference between shear capacity values given by CNR and CNRm increases when angle of inclination of FRP approaches to 45° . As already stated above, this difference is due to the inability of CNR model to properly take into account the inclination of both steel stirrups and FRP reinforcement when assessing shear strength of concrete strut. This difference is magnified when contribution to shear capacity provided by steel stirrups is significant. More precisely, considering only the angle of inclination of FRP in evaluating shear capacity of concrete strut, CNR model provides shear capacity values of retrofitted beams closer to those of the other models when contribution given by FRP reinforcement prevails ($\omega_{fw} = 0.40$; $\omega_{sw} = 0.20$), while substantial differences can be noted when mechanical ratio of steel stirrups is considerably greater than that of FRP ($\omega_{fw} = 0.20$; $\omega_{sw} = 0.40$).

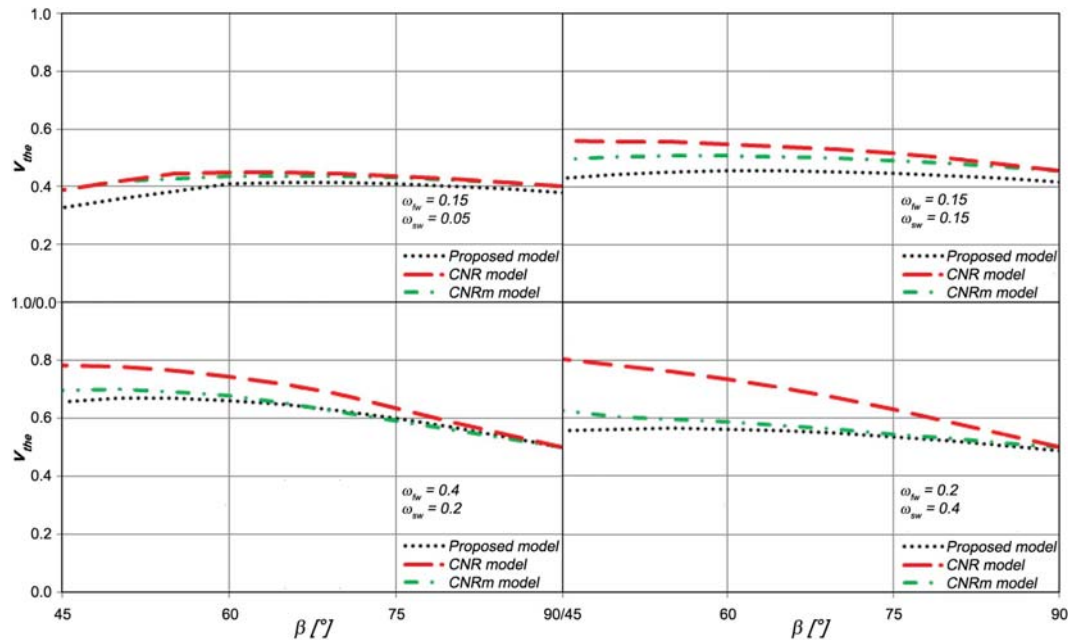


Figure 7: Shear capacity curves obtained with the proposed design-oriented model (black dotted line), CNR model (red dashed line), and CNRm model (green dash-dotted line), by varying angle of inclination of FRP reinforcement.

Focusing the attention on the variation of shear capacity by changing angle of inclination of FRP reinforcement, it can be observed that the optimal angle to obtain maximum shear strength varies on the basis of mechanical ratios of steel stirrups and FRP reinforcement assumed. For low amount of shear reinforcement, maximum shear strength is obtained for angle between 65° and 90° , while in the case of high amount of shear reinforcement, shear strength is maximized when FRP reinforcement is arranged with an angle less than 55° .

9 CONCLUSIONS

In the present paper was carried out a comparison between different procedures able to assess the effectiveness factors used to reduce shear contribution provided by FRP reinforcement when calculating shear capacity of retrofitted RC beams. In this regard, new procedures, by modification of already existing formulations, were proposed both for FRP reinforcement and steel stirrups. Concerning the latter, the proposed effectiveness factor aims to limit the strain of stirrups on the basis of the effective strain of FRP arranged in any direction. The above procedures were compared, together with those suggested by ACI, CNR, fib, and Mofidi and Chaallal [30], by calculating theoretical shear capacity of a group of 158 experimental tests, by using a proposed design-oriented model based on stress fields with variable inclination of concrete strut. This model has the advantage to simultaneously take into account the presence, and their mutual influence, of FRP reinforcement, steel stirrups, and concrete strut, when assessing the shear capacity, as well as the concrete stress field inclination. The model was formulated in order to accurately take into account FRP reinforcement and steel stirrups arranged with different inclinations in evaluating shear strength of concrete strut. In this latter case, other models based on truss mechanism, such as that proposed by CNR, fail to consider the presence of both FRP reinforcement and steel stirrups when evaluating shear capacity of concrete strut. For this reason, a new simple formulation developed for CNR model was proposed, aimed at obtaining an equivalent angle of inclination to be used in evaluation of shear capacity of concrete strut, weighted on the basis of shear contributions provided by FRP reinforcement and steel stirrups. To highlight the improvement given by the

proposed modification to CNR model, a parametric analysis was carried out, by varying inclination of FRP reinforcement, with the aim of evaluating its influence on shear capacity of retrofitted RC beams, calculated by means of the above-mentioned models based on variable inclination of concrete strut.

Once the effectiveness factors providing the best results were selected, the proposed model was compared against models proposed by ACI and CNR, as well as the proposed modified version of CNR, named CNRm. The main findings are summarized below:

- The procedure to calculate effectiveness factors which combines the best average accuracy (Avg value close to 1) and the highest reliability (low CoV value) is the one named “second approach”, which uses the equations proposed by Chen & Teng to evaluate effectiveness factor for FRP, and the equations proposed in section 4 to assess effectiveness factor for steel stirrups.
- Concerning beams having FRP reinforcement arranged with different inclination with respect to that of steel stirrups, the proposed model gives the best results. Although all the models overestimate in average shear capacity of beams, the proposed model gives the closest average to 1 and the lowest scatter. These results prove the accuracy and reliability of the proposed design-oriented model, and its superior performance in the case for which it was formulated, namely when FRP reinforcement and steel stirrups are oriented with different inclinations.
- With regard to the results provided by CNR model and its modified version, CNRm, results showed that the proposed calibration of ψ angle, which is the angle used in the evaluation of shear strength of concrete strut, slightly improves the performance of CNR model. However, the proposed version of CNR model still significantly overestimates shear capacity of RC beams.
- Regarding the parametric analysis, the proposed version of CNR model provides shear capacity values which are close to those of original CNR models for low amount of steel stirrups, while approach to that of the proposed design-oriented model when increasing the amount of steel stirrups.
- Focusing the attention on the variation of shear capacity by changing angle of inclination of FRP reinforcement, it can be observed that the optimal angle to obtain maximum shear strength varies on the basis of mechanical ratios of steel stirrups and FRP reinforcement assumed. For low amount of shear reinforcement, maximum shear strength is obtained for angle between 65° and 90° , while in the case of high amount of shear reinforcement, shear strength is maximized when FRP reinforcement is arranged with an angle less than 55° .

10 APPENDIX

	Spec. no.	f_{cm} (MPa)	$b_w \times d$ (mm)	ρ_{sw} (%)	b_f (mm)	t_f (mm)	β (°)	ρ_{fw} (%)	f_{fu} (MPa)	E_f (GPa)	v_{exp} (-)
Sato et al. (1997) [51] $a/d = 2.5$	No.2	35.7	150×240	0.42	C	0.11	90	0.15	3480	230	0.39
$E_{sw} = 183$ GPa $f_{syw} = 387$ MPa	No.3	35.3	150×240	0.42	C	0.11	90	0.15	3480	230	0.46
Deniaud & Cheng (2001) [38] $a/d = 2.8$	T6S4-C90	44.1	140×528	0.10	50	0.11	90	0.08	3400	230	0.19
	T6S4-G90	44.1	140×528	0.10	C	1.80	90	2.57	106	18	0.20

	Spec. no.	f_{cm} (MPa)	$b_w \times d$ (mm)	ρ_{sw} (%)	b_f (mm)	t_f (mm)	β (°)	ρ_{fw} (%)	f_{fu} (MPa)	E_f (GPa)	ν_{exp} (-)
$E_{sw} = 260$ GPa $f_{syw} = 520$ MPa	T6S2-C90	44.1	140×528	0.20	50	0.11	90	0.08	3400	230	0.21
Deniaud & Cheng (2003) [39]	T4S4-G90	30.0	140×362	0.10	50	1.80	90	2.57	106	18	0.30
	T4S2-G90	30.3	140×362	0.20	C	1.80	90	2.57	106	18	0.33
$a/d = 3.0$	T4S2-C45	29.4	140×362	0.20	C	0.70	45	0.50	442	45	0.33
$E_{sw} = 200$ GPa $f_{syw} = 520$ MPa	T4S2-Tri	30.4	140×362	0.20	C	2.10	60	3.00	124	8	0.35
Bousselham & Chaallal (2006) [35]	SB-S1-0.5L	25.0	152×356	0.38	C	0.06	90	0.08	3100	243	0.46
$a/d = 3.0$	SB-S1-1L	25.0	152×356	0.38	C	0.11	90	0.14	3100	243	0.42
$E_{sw} = 215$ GPa $f_{syw} = 650$ MPa	SB-S1-2L	25.0	152×356	0.38	C	0.21	90	0.28	3100	243	0.44
	A-U1-C-17	41.4	150×250	0.39	C	0.17	90	0.22	3450	230	0.34
Pellegrino & Modena (2006) [27]	A-U1-C-20	41.4	150×250	0.34	C	0.17	90	0.22	3450	230	0.32
	A-U1-S-17	41.4	150×250	0.39	C	0.17	90	0.22	3450	230	0.35
	A-U1-S-20	41.4	150×250	0.34	C	0.17	90	0.22	3450	230	0.34
$a/d = 3.0$	A-U2-C-17	41.4	150×250	0.39	C	0.33	90	0.44	3450	230	0.35
$E_{sw} = 210$ GPa	A-U2-C-20	41.4	150×250	0.34	C	0.33	90	0.44	3450	230	0.33
$f_{syw} = 534$ MPa	A-U2-S-17	41.4	150×250	0.39	C	0.33	90	0.44	3450	230	0.31
	A-U2-S-20	41.4	150×250	0.34	C	0.33	90	0.44	3450	230	0.30
	SB-U1	27.4	75×155	0.28	20	0.11	90	0.10	4200	235	0.45
	SB-F1	27.4	75×155	0.28	20	0.11	90	0.10	4200	235	0.46
Leung et al. (2007) [43]	SB-F2	27.4	75×155	0.28	20	0.11	90	0.10	4200	235	0.46
	MB-U1	27.4	150×305	0.28	40	0.22	90	0.10	4200	235	0.27
$a/d = 2.9$ (SB)	MB-U2	27.4	150×305	0.28	40	0.22	90	0.10	4200	235	0.28
$a/d = 3.0$ (MB)	MB-F1	27.4	150×305	0.28	40	0.22	90	0.10	4200	235	0.42
$a/d = 2.7$ (LB)	MB-F2	27.4	150×305	0.28	40	0.22	90	0.10	4200	235	0.44
$E_{sw} = 210$ GPa	LB-U1	27.4	300×660	0.14	80	0.44	90	0.10	4200	235	0.23
$f_{syw} = 550$ MPa	LB-U2	27.4	300×660	0.14	80	0.44	90	0.10	4200	235	0.23
	LB-F1	27.4	300×660	0.14	80	0.44	90	0.10	4200	235	0.36
	LB-F2	27.4	300×660	0.14	80	0.44	90	0.10	4200	235	0.36
	UF90	11.0	250×410	0.10	C	0.22	90	0.18	2600	390	0.25
	US60	11.0	250×410	0.10	150	0.22	60	0.08	2600	390	0.22
	US45+	11.0	250×410	0.10	150	0.22	45	0.06	2600	390	0.25
	US45++	11.0	250×410	0.10	50	0.22	45	0.06	2600	390	0.26
Monti & Liotta (2007) [14]	UF45+ A	11.0	250×410	0.10	C	0.22	45	0.18	2600	390	0.33
	UF45++ B	11.0	250×410	0.10	C	0.22	45	0.18	2600	390	0.34
$a/d = 3.5$	UF45++ C	11.0	250×410	0.10	C	0.22	45	0.18	2600	390	0.36
$E_{sw} = 210$ GPa	US45+ D	11.0	250×410	0.10	150	0.22	45	0.08	2600	390	0.32
$f_{syw} = 500$ MPa	US45++ E	11.0	250×410	0.10	150	0.22	45	0.08	2600	390	0.32
	US45++ F	11.0	250×410	0.10	150	0.22	45	0.08	2600	390	0.29
	WS45+	11.0	250×410	0.10	50	0.22	45	0.06	2600	390	0.31
	USVA	10.6	250×410	0.10	150	0.22	38	0.05	2600	390	0.25
	USVA+	10.6	250×410	0.10	150	0.22	38	0.05	2600	390	0.28
Pellegrino & Modena (2008) [15]	B-U1-C-14	46.2	150×240	0.48	C	0.17	90	0.22	3450	230	0.34
	B-U2-C-14	46.2	150×240	0.48	C	0.33	90	0.44	3450	230	0.35
$a/d = 3.0$	B-U1-C-17	46.2	150×240	0.39	C	0.17	90	0.22	3450	230	0.32
$E_{sw} = 210$ GPa $f_{syw} = 534$ MPa	B-U2-C-17	46.2	150×240	0.39	C	0.33	90	0.44	3450	230	0.33
Grande et al. (2009) [16]	RS4Wa	21.0	250×411	0.10	C	0.19	90	0.15	2600	392	0.26
	RS3Wa	21.0	250×411	0.13	C	0.19	90	0.15	2600	392	0.34
$a/d = 3.4$	RS2Wa	21.0	250×411	0.20	C	0.19	90	0.15	2600	392	0.31

	Spec. no.	f_{cm} (MPa)	$b_w \times d$ (mm)	ρ_{sw} (%)	b_f (mm)	t_f (mm)	β (°)	ρ_{fw} (%)	f_{fu} (MPa)	E_f (GPa)	v_{exp} (-)
$E_{sw} = 210$ GPa $f_{syw} = 476$ MPa	RS4Ub	21.0	250×411	0.10	C	0.19	90	0.15	2600	392	0.23
	RS3Ua	21.0	250×411	0.13	C	0.19	90	0.15	2600	392	0.28
	RS2Ua	21.0	250×411	0.20	C	0.19	90	0.15	2600	392	0.29
Belarbi et al. (2012) [34] $a/d = 3.3$ $E_{sw} = 200$ GPa $f_{syw} = 276$ MPa	8-NA	20.7	457×831	0.15	254	0.22	90	0.06	3792	228	0.24
	8-DMA	23.8	457×831	0.15	254	0.22	90	0.06	3792	228	0.23
	12-NA	28.9	457×831	0.10	254	0.22	90	0.06	3792	228	0.15
	12-DMA	30.5	457×831	0.10	254	0.22	90	0.06	3792	228	0.18
	12-PC	19.2	457×831	0.10	254	0.22	90	0.06	3792	228	0.29
	12-HS-PC	18.3	457×831	0.10	254	0.22	90	0.06	3792	228	0.27
Alzate et al. (2013) [32] $a/d = 3.5$ $E_{sw} = 200$ GPa $f_{syw} = 500$ MPa	U90S5-a(L)	37.0	250×420	0.11	300	0.29	90	0.14	4000	240	0.16
	U90S5-a(S)	37.0	250×420	0.11	300	0.29	90	0.14	4000	240	0.14
	U90S5-b(L)	28.0	250×420	0.11	300	0.29	90	0.14	4000	240	0.21
	U90S5-b(S)	28.0	250×420	0.11	300	0.29	90	0.14	4000	240	0.20
	U90C5-a(L)	24.5	250×420	0.11	C	0.29	90	0.23	4000	240	0.22
	U90C5-a(S)	24.5	250×420	0.11	C	0.29	90	0.23	4000	240	0.20
	U90C5-b(L)	22.6	250×420	0.11	C	0.29	90	0.23	4000	240	0.26
	U90C5-b(S)	22.6	250×420	0.11	C	0.29	90	0.23	4000	240	0.24
	U90S3-a(L)	20.5	250×420	0.11	300	0.17	90	0.08	3800	240	0.25
	U90S3-a(S)	20.5	250×420	0.11	300	0.17	90	0.08	3800	240	0.23
	U90S3-b(L)	22.6	250×420	0.11	300	0.17	90	0.08	3800	240	0.22
	U90S3-b(S)	22.6	250×420	0.11	300	0.17	90	0.08	3800	240	0.24
	U90S3-c(L)	28.0	250×420	0.11	300	0.17	90	0.08	3800	240	0.20
	U90S3-c(S)	28.0	250×420	0.11	300	0.17	90	0.08	3800	240	0.16
	U90C3-a(L)	30.2	250×420	0.11	C	0.17	90	0.13	3800	240	0.17
	U90C3-a(S)	30.2	250×420	0.11	C	0.17	90	0.13	3800	240	0.18
	U90C3-b(L)	30.2	250×420	0.11	C	0.17	90	0.13	3800	240	0.16
	U90C3-b(S)	30.2	250×420	0.11	C	0.17	90	0.13	3800	240	0.17
	U45S5(L)	30.7	250×420	0.11	300	0.29	45	0.14	4000	240	0.17
	U45S5(S)	30.7	250×420	0.11	300	0.29	45	0.14	4000	240	0.18
Panda et al. (2013) [49] $a/d = 3.2$ $E_{sw} = 200$ GPa $f_{syw} = 252$ MPa	U45S3-a(L)	20.5	250×420	0.11	300	0.17	45	0.08	3800	240	0.23
	U45S3-a(S)	20.5	250×420	0.11	300	0.17	45	0.08	3800	240	0.24
	U45S3-b(L)	30.7	250×420	0.11	300	0.17	45	0.08	3800	240	0.17
	U45S3-b(S)	30.7	250×420	0.11	300	0.17	45	0.08	3800	240	0.17
Baggio et al. (2014) [33] $a/d = 2.9$ $E_{sw} = 200$ GPa $f_{syw} = 384$ MPa	S300-U-90	40.4	100×230	0.19	C	0.36	90	0.72	160	13	0.22
	S300-UA-90	40.4	100×230	0.19	C	0.36	90	0.72	160	13	0.23
	S200-U-90	42.1	100×230	0.28	C	0.36	90	0.72	160	13	0.22
	S200-UA-90	42.1	100×230	0.28	C	0.36	90	0.72	160	13	0.23
Colalillo & Sheikh (2014) [37] $a/d = 3.1$ $E_{sw} = 195$ GPa $f_{syw} = 501$ MPa	6-G-N	50.1	150×310	0.21	100	0.51	90	0.34	575	26	0.16
	7-PD-G-N	50.1	150×310	0.21	100	0.51	90	0.34	575	26	0.15
	8-PD-G-CA	50.1	150×310	0.21	100	0.51	90	0.34	575	26	0.15
	9-PD-G-GA	50.1	150×310	0.21	100	0.51	90	0.34	575	26	0.16
	S5-US	47.6	400×545	0.07	100	1.00	90	0.25	961	95	0.11
Ozden et al. (2014) [48] $a/d = 3.8$ $E_{sw} = 200$ GPa $f_{syw} = 249$ MPa	S5-UA	47.6	400×545	0.07	C	1.00	90	0.50	961	95	0.13
	S5-CS	47.6	400×545	0.07	100	1.00	90	0.25	961	95	0.16
	S2-US	47.5	400×545	0.14	100	1.00	90	0.25	961	95	0.13
	S2-UA	47.5	400×545	0.14	C	1.00	90	0.50	961	95	0.15
	FBwo-C	12.4	120×339	0.14	20	0.13	90	0.05	4300	238	0.27
	FBw-C	12.4	120×339	0.14	20	0.13	90	0.05	4300	238	0.36
	PBw-C	12.4	120×339	0.14	20	0.13	90	0.05	4300	238	0.29
	FBwo-G	12.4	120×339	0.14	20	0.16	90	0.06	3400	73	0.27
	FBw-G	12.4	120×339	0.14	20	0.16	90	0.06	3400	73	0.34
	PBw-G	12.4	120×339	0.14	20	0.16	90	0.06	3400	73	0.34

	Spec. no.	f_{cm} (MPa)	$b_w \times d$ (mm)	ρ_{sw} (%)	b_f (mm)	t_f (mm)	β (°)	ρ_{fw} (%)	f_{fu} (MPa)	E_f (GPa)	ν_{exp} (-)
	FBwo-Hi-C	12.4	120×339	0.14	20	0.14	90	0.05	2600	640	0.24
	FBw-Hi-C	12.4	120×339	0.14	20	0.14	90	0.05	2600	640	0.27
	PBw-Hi-C	12.4	120×339	0.14	20	0.14	90	0.05	2600	640	0.31
Mofidi & Chaallal (2014) [44]	WT-ST-50	31.0	152×350	0.38	88	0.11	90	0.07	3450	230	0.33
$a/d = 3.0$	WT-ST-70	31.0	152×350	0.38	88	0.11	90	0.10	3450	230	0.34
$E_{sw} = 206$ GPa $f_{syw} = 540$ MPa	WT-SH-100	31.0	152×350	0.38	C	0.11	90	0.14	3450	230	0.34
Mofidi et al. (2014) [45]	S1-LS-NE	33.7	152×350	0.38	40	2.00	90	0.60	1350	90	0.34
$a/d = 3.0$	S1-LS-PE	33.7	152×350	0.38	40	2.00	90	0.60	1350	90	0.37
$E_{sw} = 205$ GPa $f_{syw} = 650$ MPa	S1-EB-NA	33.7	152×350	0.38	C	0.11	90	0.14	3450	230	0.36
El-Saikaly et al. (2014) [40]	S1-EB	28.0	152×350	0.25	C	0.38	90	0.50	894	65	0.32
$a/d = 3.0$	S1-LS	28.0	152×350	0.25	20	1.40	90	0.21	2250	120	0.30
$E_{sw} = 200$ GPa	S1-LS-Rope	28.0	152×350	0.25	20	1.40	90	0.21	2250	120	0.38
$f_{syw} = 580$ MPa	S3-EB	28.0	152×350	0.38	C	0.38	90	0.50	894	65	0.38
	S3-LS	28.0	152×350	0.38	20	1.40	90	0.21	2250	120	0.36
	S3-LS-Rope	28.0	152×350	0.38	20	1.40	90	0.21	2250	120	0.42
Qin et al. (2015) [50]	S00	29.6	125×295	0.29	C	1.00	90	1.60	986	96	0.37
$a/d = 3.1$ $E_{sw} = 210$ GPa $f_{syw} = 542$ MPa											
Chen et al. (2016) [36]	S8-U	46.1	200×320	0.25	50	0.17	90	0.08	4361	226	0.23
$a/d = 3.0$	S8-UFA1	46.1	200×320	0.25	50	0.17	90	0.08	4361	226	0.24
$E_{sw} = 200$ GPa $f_{syw} = 416$ MPa	S8-UFA2	46.1	200×320	0.25	50	0.17	90	0.08	4361	226	0.28
Frederick et al. (2017) [42]	TB2	27.2	130×235	0.17	C	0.15	90	0.23	1400	119	0.37
$a/d = 3.2$ $E_{sw} = 200$ GPa $f_{syw} = 415$ MPa	TB4	27.2	130×235	0.17	C	0.15	90	0.23	1400	119	0.42
El-Saikaly et al. (2017) [41]	EBS-NA	28.0	152×350	0.25	C	0.38	90	0.50	894	65	0.32
$a/d = 3.0$	EBL-NA	28.0	152×350	0.25	20	2.00	90	0.30	1350	90	0.30
$E_{sw} = 200$ GPa	EBS-BL	28.0	152×350	0.25	C	0.38	90	0.50	894	65	0.37
$f_{syw} = 580$ MPa	EBS-ER	28.0	152×350	0.25	C	0.38	90	0.50	894	65	0.40
	EBL-RF	28.0	152×350	0.25	20	2.00	90	0.30	1350	90	0.41
	EBL-RW	28.0	152×350	0.25	20	2.00	90	0.30	1350	90	0.38
Nguyen-Minh et al. (2018) [46]	A1-2.3-C	30.6	120×406	0.16	75	1.00	90	0.83	986	96	0.41
$a/d = 2.3$	A1-2.3-G	30.6	120×406	0.16	75	1.30	90	1.08	575	26	0.40
$E_{sw} = 205$ GPa	A1-2.3-G-C.	30.6	120×406	0.16	C	1.30	90	2.17	575	26	0.43
$f_{syw} = 342$ MPa	A1-2.3-C-C.	30.6	120×406	0.16	C	1.00	90	1.67	986	96	0.45
	A2-2.3-C	30.6	120×406	0.16	75	2.00	90	1.67	986	96	0.43
	B1-2.3-C	44.4	120×406	0.16	75	1.00	90	0.83	986	96	0.32
	B1-2.3-G	44.4	120×406	0.16	75	1.30	90	1.08	575	26	0.32
	B1-2.3-G-C.	44.4	120×406	0.16	C	1.30	90	2.17	575	26	0.34
	B1-2.3-C-C.	44.4	120×406	0.16	C	1.00	90	1.67	986	96	0.36
	B2-2.3-C	44.4	120×406	0.16	75	2.00	90	1.67	986	96	0.34
	C1-2.3-C	58.7	120×406	0.16	75	1.00	90	0.83	986	96	0.29
	C1-2.3-G	58.7	120×406	0.16	75	1.30	90	1.08	575	26	0.27
	C1-2.3-G-C.	58.7	120×406	0.16	C	1.30	90	2.17	575	26	0.31
	C1-2.3-C-C.	58.7	120×406	0.16	C	1.00	90	1.67	986	96	0.32
	C2-2.3-C	58.7	120×406	0.16	75	2.00	90	1.67	986	96	0.30

	Spec. no.	f_{cm} (MPa)	$b_w \times d$ (mm)	ρ_{sw} (%)	b_f (mm)	t_f (mm)	β (°)	ρ_{fw} (%)	f_{fu} (MPa)	E_f (GPa)	ν_{exp} (-)
	M1-a	42.8	200 × 493	0.12	50	0.17	90	0.04	2739	263	0.18
	M1-b	42.8	200 × 493	0.12	50	0.17	90	0.04	2739	263	0.17
	M1A	39.0	200 × 493	0.12	50	0.17	90	0.04	2739	263	0.19
	M1B	38.5	200 × 493	0.12	50	0.17	90	0.04	2739	263	0.19
Oller et al.	M2A	39.0	200 × 493	0.12	100	0.17	90	0.07	2739	263	0.20
(2019) [47]	M2B	38.5	200 × 493	0.12	100	0.17	90	0.07	2739	263	0.19
$a/d = 3.0$	H1-a	44.4	200 × 493	0.12	50	0.17	90	0.04	2739	263	0.17
$E_{sw} = 200$ GPa	H2-a	44.4	200 × 493	0.12	100	0.17	90	0.07	2739	263	0.17
$f_{syw} = 646$ MPa	H2-b	49.7	200 × 493	0.12	100	0.17	90	0.07	2739	263	0.15
	H2A	44.7	200 × 493	0.12	100	0.17	90	0.07	2739	263	0.20
	H2B	49.6	200 × 493	0.12	100	0.17	90	0.07	2739	263	0.18
	H3A	44.7	200 × 493	0.12	C	0.17	90	0.17	2739	263	0.19
	H3B	49.6	200 × 493	0.12	C	0.17	90	0.17	2739	263	0.19

Table 1: Characteristics of specimens and experimental results

REFERENCES

- [1] E. Elettore, F. Freddi, M. Latour, G. Rizzano, Design and analysis of a seismic resilient steel moment resisting frame equipped with damage-free self-centering column bases. *Journal of Constructional Steel Research*, **179**, 106543, 2021. <https://doi.org/10.1016/j.jcsr.2021.106543>.
- [2] S. Ramhormozian, G.C. Clifton, M. Latour, G.A. Macrae, Proposed simplified approach for the seismic analysis of multi-storey moment resisting framed buildings incorporating friction sliders. *Buildings*, **9** (5), 130, 2019. <https://doi.org/10.3390/buildings9050130>.
- [3] P. Colajanni, L. La Mendola, A. Monaco, S. Pagnotta, Design of RC joints equipped with hybrid trussed beams and friction dampers. *Engineering Structures*, **227**, 111442, 2021. <https://doi.org/10.1016/j.engstruct.2020.111442>.
- [4] P. Colajanni, L. La Mendola, A. Monaco, S. Pagnotta, Dissipative connections of rc frames with prefabricated steel-trussed-concrete beams. *Ingegneria Sismica* **37** (1), 51-63, 2020. <http://ingegneriasismica.org/product/5-2020-1-dissipative-connections-of-rc-frames-with-prefabricated-steel-trussed-concrete-beams/>
- [5] S. Pagnotta, P. Colajanni, L. La Mendola, A. Monaco, Seismic response of RC frames with HSTC beams endowed with friction damper devices. *18th Conference of the Italian National Association of Earthquake Engineering (ANIDIS 2019)*, Ascoli Piceno, Italy, September 15-19, 2019. <https://doi.org/10.1400/271271>.
- [6] P. Colajanni, L. La Mendola, A. Monaco, S. Pagnotta, Design of friction connections in R.C. structures with hybrid steel-trussed-concrete beams. *18th Conference of the Italian National Association of Earthquake Engineering (ANIDIS 2019)*, Ascoli Piceno, Italy, September 15-19, 2019. <https://doi.org/10.1400/271300>.
- [7] P. Colajanni, F. De Domenico, A. Recupero, N. Spinella, Concrete columns confined with fibre reinforced cementitious mortars: experimentation and modeling. *Construction and Building Materials*, **52**, 375-384, 2014. <https://doi.org/10.1016/j.conbuildmat.2013.11.048>.

- [8] G. Campione, F. Cannella, M.F. Ferrotto, M. Gianquinto, Compressive behavior of FRP externally wrapped R.C. column with buckling effects of longitudinal bars. *Engineering Structures*, **168**, 809-818, 2018. <https://doi.org/10.1016/j.engstruct.2018.05.027>.
- [9] N. Spinella, P. Colajanni, A. Recupero, F. Tondolo, Ultimate shear of RC beams with corroded stirrups and strengthened with FRP. *Buildings*, **9** (2), 34, 2019. <https://doi.org/10.3390/buildings9020034>.
- [10] P. Colajanni, A. Recupero, N. Spinella, Shear Strength Degradation Due to Flexural Ductility Demand in Circular R.C. Columns. *Bulletin of Earthquake Engineering*, **13** (6), 1795–1807, 2015. <https://doi.org/10.1007/s10518-014-9691-0>.
- [11] G. Campione, M.F. Ferrotto, M. Papia, Flexural response of RC beams failing in shear. *Practice Periodical on Structural Design and Construction*, **25** (4), 4020028. [https://doi.org/10.1061/\(ASCE\)SC.1943-5576.0000507](https://doi.org/10.1061/(ASCE)SC.1943-5576.0000507).
- [12] ACI (American Concrete Institute). 2017. Guide for the Design and Construction of Externally Bonded FRP Systems for Strengthening Concrete Structures. ACI 440.2R-17. Farmington Hills, MI: ACI.
- [13] CAN/CSA (Canadian Standards Association). 2006. *Canadian highway bridge design code*. S6-06. Mississauga, Canada: CAN/CSA.
- [14] G. Monti, M. Liotta, Tests and design equations for FRP strengthening in shear. *Construction and Building Materials*, **21** (4), 799–809, 2007. <https://doi.org/10.1016/j.conbuildmat.2006.06.023>.
- [15] C. Pellegrino, C. Modena, An experimentally based analytical model for the shear capacity of FRP-strengthened reinforced concrete beams. *Mechanics of Composite Materials*, **44** (3), 231-244, 2008. <https://doi.org/10.1007/s11029-008-9016-y>.
- [16] E. Grande, M. Imbimbo, A. Rasulo, Effect of transverse steel on the response of RC beams strengthened in shear by FRP: experimental study. *Journal of Composites for Construction*, **13** (5), 405-414, 2009. [https://doi.org/10.1061/\(ASCE\)1090-0268\(2009\)13:5\(405\)](https://doi.org/10.1061/(ASCE)1090-0268(2009)13:5(405)).
- [17] CNR (Consiglio Nazionale delle Ricerche – National Research Council). 2013. Istruzioni per la Progettazione, l'Esecuzione ed il Controllo di Interventi di Consolidamento Statico mediante l'utilizzo di Compositi Fibrorinforzati. CNR-DT-200/R1. Rome, Italy: CNR. [In Italian].
- [18] DAfStB (Deutscher Ausschuss für Stahlbeton - German Committee for Structural Concrete). 2012. Strengthening of Concrete Members with Adhesively Bonded Reinforcement. Beuth-Verlag, Berlin, Germany. [Original in German, English version].
- [19] A. Darby, J. Clarke, J.D. Shave, T. Ibell, 2012. “Design guidance for strengthening concrete structures using fibre composite materials: report of a Concrete Society Working Party.” Technical Report Vol. 55, 3rd ed. The Concrete Society.
- [20] Fib (Fédération internationale du béton - International Federation for Structural Concrete). 2019. *Externally applied FRP reinforcement for concrete structures*. Fib bulletin 90. Lausanne, Switzerland: Fib.
- [21] CEN (European Committee for Standardization). 2004. *Design of concrete structures, part 1.1: general rules and rules for buildings*. EN1992-1-1. Brussels, Belgium: CEN.

- [22] P. Colajanni, S. Pagnotta, A. Recupero, N. Spinella, Shear resistance analytical evaluation for RC beams with transverse reinforcement with two different inclinations. *Materials and Structures*, **53** (1), 18, 2020. <https://doi.org/10.1617/s11527-020-1452-8>.
- [23] P. Colajanni, L. La Mendola, A. Recupero, N. Spinella, Stress field model for strengthening of shear-flexure critical RC beams. *Journal of Composites for Construction*, **21** (5), 04017039, 2017. [https://doi.org/10.1061/\(ASCE\)CC.1943-5614.0000821](https://doi.org/10.1061/(ASCE)CC.1943-5614.0000821).
- [24] P. Colajanni, L. La Mendola, G. Mancini, A. Recupero, N. Spinella, Shear capacity in concrete beams reinforced by stirrups with two different inclinations. *Engineering Structures*, **81**, 444-453, 2014. <https://doi.org/10.1016/j.engstruct.2014.10.011>.
- [25] J.F. Chen, J.G. Teng, Shear capacity of FRP-strengthened RC beams: FRP debonding. *Construction and Building Materials*, **17** (1), 27-41, 2003. [https://doi.org/10.1016/S0950-0618\(02\)00091-0](https://doi.org/10.1016/S0950-0618(02)00091-0).
- [26] J.F. Chen, J.G. Teng, Shear capacity of fiber-reinforced polymer-strengthened reinforced concrete beams: fiber reinforced polymer rupture. *Journal of Structural Engineering*, **129** (5), 615-625, 2003. [https://doi.org/10.1061/\(ASCE\)0733-9445\(2003\)129:5\(615\)](https://doi.org/10.1061/(ASCE)0733-9445(2003)129:5(615)).
- [27] C. Pellegrino, C. Modena, Fiber-reinforced polymer shear strengthening of reinforced concrete beams: experimental study and analytical modeling. *ACI Structural Journal*, **103** (5), 720-728, 2006. <https://doi.org/10.14359/16924>.
- [28] A. Khalifa, A. Nanni, Improving shear capacity of existing RC T-section beams using CFRP composites. *Cement and Concrete Composites*, **22** (3), 165-174, 2000. [https://doi.org/10.1016/S0958-9465\(99\)00051-7](https://doi.org/10.1016/S0958-9465(99)00051-7).
- [29] A. Khalifa, A. Nanni, Rehabilitation of rectangular simply supported RC beams with shear deficiencies using CFRP composites. *Construction and Building Materials*, **16** (3), 135-146, 2002. [https://doi.org/10.1016/S0950-0618\(02\)00002-8](https://doi.org/10.1016/S0950-0618(02)00002-8).
- [30] A. Mofidi, O. Chaallal, Shear strengthening of RC beams with EB FRP: Influencing factors and conceptual debonding model. *Journal of Composites for Construction*, **15** (1), 62-74, 2011. [https://doi.org/10.1061/\(ASCE\)CC.1943-5614.0000153](https://doi.org/10.1061/(ASCE)CC.1943-5614.0000153).
- [31] N. Spinella, Modeling of shear behavior of reinforced concrete beams strengthened with FRP. *Composite Structures*, **215**, 351-364, 2019. <https://doi.org/10.1016/j.compstruct.2019.02.073>.
- [32] A. Alzate, A. Arteaga, A. De Diego, D. Cisneros, R. Perera, Shear strengthening of reinforced concrete members with CFRP sheets. *Materiales de Construcción*, **63** (310), 251-265, 2013. <https://doi.org/10.3989/mc.2012.06611>.
- [33] D. Baggio, K. Soudki, M. Noël, Strengthening of shear critical RC beams with various FRP systems. *Construction and Building Materials*, **66**, 634-644, 2014. <https://doi.org/10.1016/j.conbuildmat.2014.05.097>.
- [34] A. Belarbi, S.W. Bae, A. Brancaccio, Behavior of full-scale RC T-beams strengthened in shear with externally bonded FRP sheets. *Construction and Building Materials*, **32**, (10), 27-40, 2012. <https://doi.org/10.1016/j.conbuildmat.2010.11.102>.
- [35] A. Bousselham, O. Chaallal, Behavior of reinforced concrete T-beams strengthened in shear with carbon fiber-reinforced polymer - an experimental study. *ACI Structural Journal*, **103** (3), 339-347, 2006. <https://doi.org/10.14359/15311>.

- [36] G.M. Chen, Z. Zhang, Y.L. Li, X.Q. Li, C.Y. Zhou, T-section RC beams shear-strengthened with anchored CFRP U-strips. *Composite Structures*, **144**, 57-79, 2016. <https://doi.org/10.1016/j.compstruct.2016.02.033>.
- [37] M.A. Colalillo, S.A. Sheikh, Behavior of shear-critical RC beams strengthened with FRP - experimentation. *ACI Structural Journal*, **111** (6), 1373-1384, 2014. <https://doi.org/10.14359/51687035>.
- [38] C. Deniaud, J.J.R. Cheng, Shear behavior of reinforced concrete T-Beams with externally bonded fiber-reinforced polymer sheets. *ACI Structural Journal*, **98** (3): 386-394, 2001. <https://doi.org/10.14359/10227>.
- [39] C. Deniaud, J.J.R. Cheng, Reinforced concrete T-beams strengthened in shear with fiber reinforced polymer sheets. *Journal of Composites for Construction* **7** (4), 302-310, 2003. [https://doi.org/10.1061/\(ASCE\)1090-0268\(2003\)7:4\(302\)](https://doi.org/10.1061/(ASCE)1090-0268(2003)7:4(302)).
- [40] G. El-Saikaly, A. Godat, O. Chaallal, New anchorage technique for FRP shear-strengthened RC T-beams using CFRP rope. *Journal of Composites for Construction*, **19** (4), 04014064, 2014. [https://doi.org/10.1061/\(ASCE\)CC.1943-5614.0000530](https://doi.org/10.1061/(ASCE)CC.1943-5614.0000530).
- [41] G. El-Saikaly, O. Chaallal, B. Benmokrane.. "Comparison of anchorage systems for RC T-beams strengthened in shear with EB-CFRP." *6th Asia-Pacific Conference on FRP in Structures (APFIS2017)*, Singapore, 1-5, 2017.
- [42] F.F.R. Frederick, U.K. Sharma, V.K. Gupta, Influence of end anchorage on shear strengthening of reinforced concrete beams using CFRP composites, *Current Science*, **112** (5), 973-981, 2017. <https://doi.org/10.18520/cs/v112/i05/973-981>.
- [43] C.K.Y. Leung, Z. Chen, S. Lee, M. Ng, M. Xu, J. Tang, Effect of size on the failure of geometrically similar concrete beams strengthened in shear with FRP strips, *Journal of Composites for Construction*, **11** (5), 487-496, 2007. [https://doi.org/10.1061/\(ASCE\)1090-0268\(2007\)11:5\(487\)](https://doi.org/10.1061/(ASCE)1090-0268(2007)11:5(487)).
- [44] A. Mofidi, O. Chaallal, Tests and design provisions for reinforced-concrete beams strengthened in shear using FRP sheets and strips. *International Journal of Concrete Structures and Materials*, **8**, 117–128, 2014. <https://doi.org/10.1007/s40069-013-0060-1>.
- [45] A. Mofidi, S. Thivierge, O. Chaallal, Y. Shao, Behavior of reinforced concrete beams strengthened in shear using L-shaped CFRP plates: experimental investigation. *Journal of Composites for Construction*, **18** (2): 04013033, 2014. [https://doi.org/10.1061/\(ASCE\)CC.1943-5614.0000398](https://doi.org/10.1061/(ASCE)CC.1943-5614.0000398).
- [46] L. Nguyen-Minh, D. Vo-Le, D. Tran-Thanh, T.M. Pham, C. Ho-Huu, M. Rovňák, Shear capacity of unbonded post-tensioned concrete T-beams strengthened with CFRP and GFRP U-wraps. *Composite Structures*, **184**, 1011-1029, 2018. <https://doi.org/10.1016/j.compstruct.2017.10.072>.
- [47] E. Oller, M. Pujol, A. Marí, Contribution of externally bonded FRP shear reinforcement to the shear strength of RC beams. *Composites Part B: Engineering*, **164**, 235-248, 2019. <https://doi.org/10.1016/j.compositesb.2018.11.065>.
- [48] S. Ozden, H.M. Atalay, E. Akpınar, H. Erdogan, Y.Z. Vulaş, Shear strengthening of reinforced concrete T-beams with fully or partially bonded fibre-reinforced polymer composites. *Structural Concrete*, **15** (2), 229–239, 2014. <https://doi.org/10.1002/suco.201300031>.

- [49] K.C. Panda, S.K. Bhattacharyya, S.V. Barai, Effect of transverse steel on the performance of RC T-beams strengthened in shear zone with GFRP sheet. *Construction and Building Materials*, **41**, 79-90, 2013. <https://doi.org/10.1016/j.conbuildmat.2012.11.098>.
- [50] S. Qin, S. Dirar, J. Yang, A.H.C. Chan, M. Elshafie, CFRP shear strengthening of reinforced-concrete T-beams with corroded shear links. *Journal of Composites for Construction*, **19** (5), 04014081, 2015. [https://doi.org/10.1061/\(ASCE\)CC.1943-5614.0000548](https://doi.org/10.1061/(ASCE)CC.1943-5614.0000548).
- [51] Y. Sato, T. Ueda, Y. Kakuta, S. Ono, "Ultimate shear capacity of reinforced concrete beams with carbon fiber sheet." *3rd International Symposium on Non-Metallic (FRP) Reinforcement for Concrete Structures*, Tokyo, Japan, 499-506, 1997.

OPTIMIZATION OF STEEL-JACKETING RETROFITTING OF SHEAR-CRITICAL AND DUCTILITY CRITICAL RC FRAME STRUCTURES BY A NOVEL GENETIC ALGORITHM FRAMEWORK

Antonio P. Sberna¹, Fabio Di Trapani¹, and Giuseppe C. Marano¹

¹ Politecnico di Torino. Dipartimento di Ingegneria Strutturale, Edile e Geotecnica
Corso Duca degli Abruzzi 24, 10129, Turin, Italy
e-mail: {antonio.sberna, fabio.ditrapani, giuseppe.marano}@polito.it

Abstract

The paper presents a new specific optimization framework that is directed at minimizing seismic retrofitting intervention costs of reinforced concrete (RC) frame structures. A genetic algorithm routine is developed to provide as outputs the individuation of the retrofitted columns (topological optimization) and amount of steel-jacketing reinforcement. The major novelty regards the framework's capacity to perform retrofitting optimization both for RC structures with ductility-critical and shear-critical RC columns, also considering the additional shear demand due to infill-frame interaction. Modified genetic operators (population generator, elitism, and mutation) are defined and calibrated to be effective and computationally sustainable. The feasibility of each tentative solution is controlled by a static pushover analysis in the framework of the N2 method, accomplished by a 3D fiber-section model implemented in OpenSees. It is shown that the proposed procedure is sufficiently general and robust to handle structural configurations having different structural deficiencies, significantly reducing invasiveness, downtime, and costs.

Keywords: genetic algorithm, structural optimization, seismic retrofitting, existing structures

1 INTRODUCTION

Steel-jacketing (SJ) is one of the extensively used technique for retrofitting existing reinforced concrete (RC) structure designed prior to the entry into force of seismic guidelines. The arrangement of a cage made of steel angles and battens provides additional confinement and transverse reinforcement to the RC elements, also increasing the shear strength.

Even though steel-jacketing is quite effective as a seismic retrofitting technique, its application is invasive because it also involves several related operations, including the demolition and reconstruction of column-side masonries and plasters. This significantly affects the costs and the downtime associated with the intervention.

In this context, one of the major issues that structural engineers face in the design of this kind of interventions regard the determination of the optimal position and arrangement of the retrofitting system. Nowadays the design of this kind of interventions is mainly based on engineer's intuition and experience that needs several trial-and-error attempts, requiring noticeable time consumption.

In the last years, the scientific interest on the structural optimization was mainly focused on sizing and shape optimization of new structures. On the contrary, the issue of the optimization of seismic retrofitting of existing structures has not been investigated many times in the past, while noticeable interest is emerging in the last years. Available studies have been addressed to the optimization of carbon fibre reinforcement of concrete slabs (**Chaves and Cunha 2014 [1]**) or FRP jackets (**Chisari and Bedon 2016 [2]**, **Seo et al. 2018 [3]**). Other applications of seismic engineering optimization are related to fluid viscous dampers (**Pollini et al. 2017 [4]**), dissipative bracings (**Braga et al. 2019 [5]**) or both (**Lavan and Dargush 2009 [6]**) as seismic retrofitting devices for frame buildings.

More recent studies addressed the issue of pushover-based optimization of seismic retrofitting. Among these, **Falcone et al. 2019 [7]** proposed a framework implementing the optimization of FRP jacketing and steel X-bracings as possible reinforcements for existing RC structures. **Papavasileiou et al. 2020 [8]** faced seismic retrofit optimization of encased steel-concrete composite columns comparing three different retrofitting methods: concrete jacketing, steel jacketing and steel bracing.

Regarding steel-jacketing of standard RC columns, a recent study by **Di Trapani et al. 2020 [9]** proposed an innovative framework aimed at minimizing seismic retrofitting costs through genetic algorithm optimization. The framework provided both the optimization of the position of the reinforced columns and the amount of reinforcement for RC structures presenting ductility deficiencies as major vulnerability, while having adequate capacity against local shear failures. The current paper provides a significant step forward to the methodology proposed by **Di Trapani et al. 2020 [9]**.

An updated optimization framework with general validity is proposed and tested. Besides the ductility issues, the new optimization framework can deal with steel-jacketing optimization of potentially shear-critical RC columns, including also shear-induced mechanisms due to frame-infill interaction. The optimization is carried with a genetic algorithm-based algorithm. Novel genetic operators (population generator, elitism, and mutation) are defined by modifying the standard MATLAB® GA tool. The optimization framework provides as output the cheapest seismic retrofitting intervention among the feasible ones, defining the optimal configuration of the steel jacketing reinforcement of columns in terms of reinforcement location (topological optimization) and spacing between steel battens (sizing optimization). The feasibility of each solution is verified by the results of static pushover analyses in the framework of the N2 method from the results carried out a 3D fibre-section model, developed in the *OpenSees* software (**McKenna et al. 2000 [10]**).

2 DESIGN OPTIMIZATION FRAMEWORK

2.1 Problem statement and general operating principles

The proposed optimization framework works by connecting the MATLAB® genetic algorithm (GA) tool with a FE structural model developed with the *OpenSees* software platform. The framework aims at minimizing an objective function that computes the steel-jacketing retrofitting costs as a function of the design variables which define the retrofitting arrangement. These are the position of the retrofitted columns (topological optimization) and the battens spacing (sizing optimization). The feasibility of each tentative solution is assessed by evaluating the ductility capacity and demand ratio ($\xi_\mu = \mu_c / \mu_d$) after performing pushover analysis of the structure in the framework of N2 method (Fajfar 2000 [11]). An adaptive penalty function applied in the cases of unfeasible solutions.

The overall structure of the framework reflects the one proposed by Di Trapani et al. 2020 [9], for the optimization of the steel-jacketing retrofitting in case of structures with flexural ductility-related lacks. However, a strong review of the algorithm has been provided to redefine the genetic operators to generalize the framework for both flexural ductility-critical and shear-critical RC structures. The reason behind the need to update the framework is that, differently from RC structures with flexural ductility lacks, for shear-critical structures, a significant number of columns may need to be retrofitted. This is typical when the base shear demand exceeds the shear capacity of a storey. If the number of columns needing retrofitting is a high percentage of those included in the design space, a standard random selection of the individuals defining the population may have reduced probability to find feasible solutions. This condition may lead a GA to stall or to find a local minimum solution even in the unfeasible space (Fig. 1). The first remedy that could be thought to avoid this drawback is the expansion of the population of individuals (P) belonging to the design space to have a major chance to include feasible individuals. However, increasing the individuals means increasing the number on nonlinear static analyses and this very easily brings to a huge computational effort. Therefore, keeping a reduced population and a possibly restricted design space is fundamental to get an effective and affordable optimization through a genetic algorithm associated with nonlinear structural analyses.

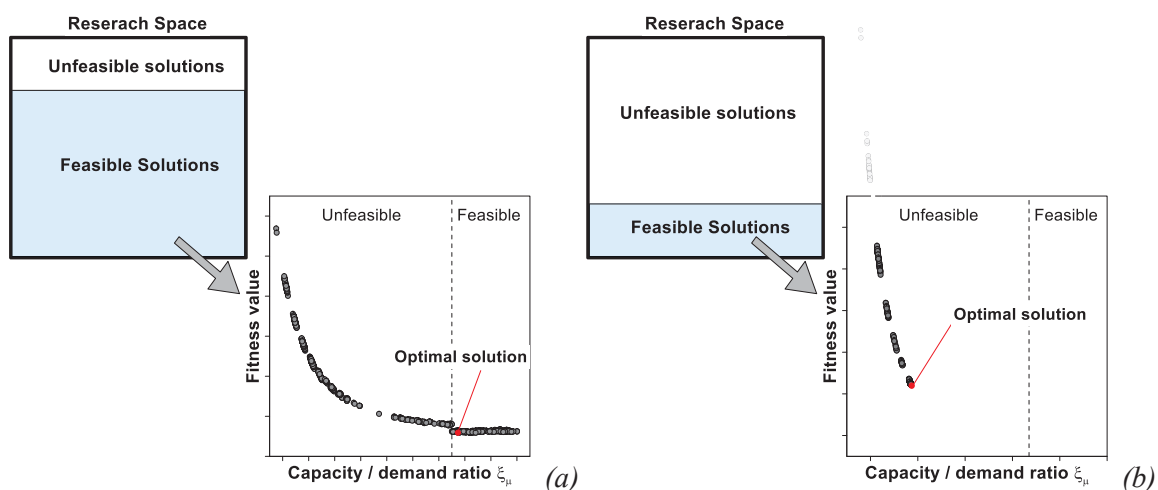


Figure 1: Possible optimization outcomes in case of: (a) design space with prevalence of feasible solutions; (b) design space with prevalence of unfeasible solutions.

2.2 Encoding of the design vector

As mentioned in the previous sections, the design optimization variables are the position of the retrofitted columns and the battens spacing (s_b), assuming that:

- i) The angles are constituted by L-shaped steel profiles having fixed lateral length (l_a) and thickness (t_a) for all the retrofitted columns.
- ii) The battens are constituted by rectangular plates having fixed thickness (t_b) and width (w_b) for all the retrofitted columns.
- iii) Battens spacing is the same for all the retrofitted columns.
- iv) The design space can be restricted to a reduced number of columns (e.g. those belonging to the lower storeys).

A schematic representation of the design variables is illustrated in **Fig. 2**.

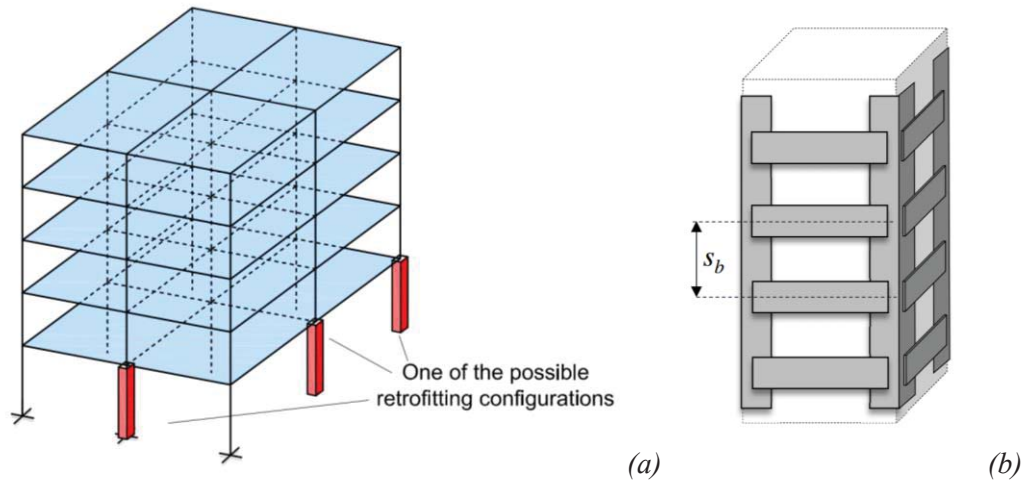


Figure 2: Representation of the optimization variables: (a) Generic column retrofitting configuration for an RC structure; (b) Typical retrofitting arrangement for a column with generic batten spacing (s_b).

The design vector collecting the design variable is formalized as follows:

$$\mathbf{b} = \begin{pmatrix} s_b \\ \mathbf{p} \end{pmatrix} \quad (1)$$

where s_b is a natural discrete number that represent the battens spacing (Fig. 4b), belonging to the interval:

$$s_b \in S = [s_{b,\min} \quad s_{b,\max}] \quad (2)$$

where $s_{b,\min}$ and $s_{b,\max}$ are the respectively the minimum and maximum battens spacing allowed. The element \mathbf{p} is the vector so defined:

$$\mathbf{p} = [\dots \quad \dots \quad c_{ij} \quad \dots]^T \quad (3)$$

in which the generic element c_{ij} , is a binary number assuming the value 1 if a column is retrofitted and 0 if not. The subscript i denotes the position of a column in plan and j the storey. In this way, each individual (namely a model) generated by the GA is univocally defined by the \mathbf{b} vector, which characterizes position and battens spacing of the retrofitted columns.

2.3 Definition of objective function and penalty function

The objective function evaluates retrofitting cost intended as the material cost and the manpower cost to realize columns steel jacketing (C_{SJ}) and necessary works for demolition and reconstruction of plasters and masonry (C_M). The general expression of the objective function is therefore:

$$C = C_M + C_{SJ} \quad (4)$$

The cost C_M is estimated considering a fixed amount (c_m) of 2000€ per column. Assuming n_c as the number of retrofitted columns and all the potentially retrofitted columns have the same cross-section dimension, one obtains:

$$\begin{cases} C_M = n_c \cdot c_m \\ C_{SJ} = n_c W_s c_s \end{cases} \quad (5)$$

where $W_{s,i}$ is the total weight of steel used to arrange a steel jacketing cage, c_s is the manpower and material cost per unit weight, which is estimated as 4.5€/kg and W_s is the weight of each steel jacketing cage. The latter can be computed as:

$$W_s = \gamma_s \cdot (V_A + V_B) \quad (6)$$

in which γ_s is the specific weight of steel ($78.5 \text{ kN} / \text{m}^3$), V_A is the total weight of the steel angles applied at the corners of a columns and V_B is the total volume of the battens belonging to a cage (on the assumption of column of square cross section), that are:

$$\begin{cases} V_A = 8 \cdot l_a \cdot t_a \cdot l_c \\ V_B = 2 \cdot t_b \cdot l_b \cdot ((b+h) - 2 \cdot l_a) \cdot \left(\frac{l_c}{s_b} \right) \end{cases} \quad (7)$$

where l_a , t_a are the width and the thickness of an angle, l_b , t_b are the width and the thickness of the batten, b , h are the dimension of the cross section of the column and l_c is the length of a column.

The feasibility of a solution is known by the evaluation of the capacity/demand ratio (ξ_μ). To effectively manage unfeasible cases a dynamic penalty approach is developed by summing to the objective function (C) above defined the penalty function (Π) into the new objective function (F) so defined:

$$F = C + \Pi \quad (8)$$

where Π is defined as:

$$\Pi = \begin{cases} 0 & \text{if } \xi_\mu \geq 1 \\ C_{\max} \cdot \left(\frac{1}{\xi_\mu} \right)^3 & \text{if } \xi_\mu < 1 \end{cases} \quad (9)$$

in which C_{\max} is the maximum possible retrofitting cost evaluated by considering retrofitting all the columns included in the design space with the minimum battens spacing. In this way, if

a solution is not feasible, the current cost is fictitiously increased by C_{\max} multiplied by the factor $(1/\xi_{\mu}^3)$ which takes into account the distance of the current solution from the feasibility condition ($\xi_{\mu} = 1$).

3 DEFINITION OF THE GENETIC OPERATORS

3.1 Population generator and elitism

The control of the population in terms of the selection of individuals is essential to the optimization effectiveness. As defined in **Eq. 1**, the genotype of each individual is a vector composed of one natural number representing the battens spacing s_b , and a sub-vector (**p**) collecting a number of binary variables which represent the retrofitted columns. In the selection phase, the parameter s_b is randomly selected by the S interval, which includes all possible spacing values as a multiple of a fixed minimum spacing variation Δs_b .

As mentioned in previous sections, and depicted in **Fig. 1**, in case of structures having shear-related deficiencies, the number of unfeasible solutions belonging to the design space can be relevant. In order to avoid algorithm stall into unfeasible design subspace, the population generator operator has been modified by introducing two subspaces in the definition of initial population (**Fig. 3**). The first subspace (p_{rand} space) collects randomly created individual. The second subspace (p_{Pr} space) is defined by a specified percentage (p_{Pr}) of individuals having an assigned probability of retrofitting (P_r). The percentage of randomly selected individuals (p_{rand}) is the complement to 100%. The probability P_r is typically high (e.g. 90%), this means that an individual included the p_{Pr} space is an individual with a high number of retrofitted column. The introduction of the p_{Pr} space within the initial population increases from the beginning the number of feasible solutions. This allows reducing population dimension and increasing the exploration efficiency of the algorithm.

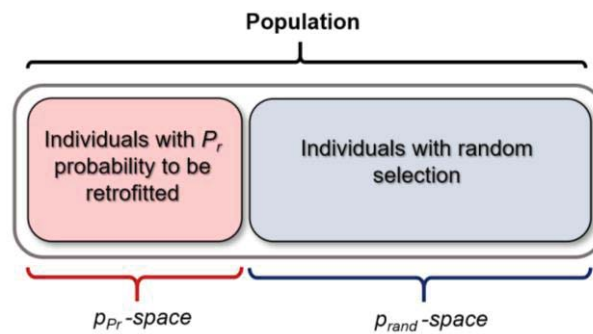


Figure 3: Definition of the population (population generator).

To further improve the algorithm performance, the *elitism* function is used. This genetic operator involves copying a small number of the fittest candidates, unchanged, into the next generation. In fact, the fittest individuals of a population can be lost during the crossover operations of consecutive generation analysis. Then, the use of the elitism function allows not losing good genetic heritage and consequently speeds up convergence.

3.2 Mutation and crossover

The crossover operator is employed to improve the genes of the individuals at the end of each generation. This is done by mixing chromosomes from parent better individuals. A uniform scatter crossover function is used in the proposed framework. The operating principle provides randomly selection of pairs of parent individuals from the previous generation. Their genomes are mixed with the generation of a random binary string of the same dimension of the parents. Base on the binary value (0 or 1) associated with each position, the gene is transferred to the child from the parent 1 or 2 (**Fig. 4a**).

The crossover function here used has a standard form, while modifications are made in the *mutation* operator. Mutation is used to bring about random changes in the population.

The standard MATLAB® mutation operator cannot handle heterogeneous vectors (e.g. vectors made of natural numbers and binaries as the vector **b**), and this made necessary the definition of a new mutation function. The latter works by fixing first a suitable mutation ratio (P_m). Then a real number u ($u \in [0,1] \subseteq \mathcal{R}$) is randomly selected for each gene. If $u \geq P_m$ the gene is maintained unchanged, otherwise if $u < P_m$ the gene is mutated. For the Boolean variables included in the design vector, the mutation of a gene is simply a switch from 0 to 1 or vice-versa. For the natural variables (the battens spacing s_b) the same procedure is applied, but in the cases in which a gene has to change ($u < P_m$) a further random number v ($v \in [0,1] \subseteq \mathcal{R}$) is chosen in order to decide if mutation will increase or decrease the battens spacing.

The new random temporary parameter v leads the mutation toward an increase or decrease of s_b if $v < 0.5$ or $v \geq 0.5$ respectively. Increases and decreases of s_b have the magnitude of the minimum spacing variation (Δs_b). A flow-chart example of the proposed mutation function is illustrated in **Fig. 4b**.

The application to the current case, in which a limited dimension of the population is used, require to increase the mutation to values which are larger than 1%. The relatively high value of mutation ratio helps in avoiding the stall of the analysis into local optimal solution.

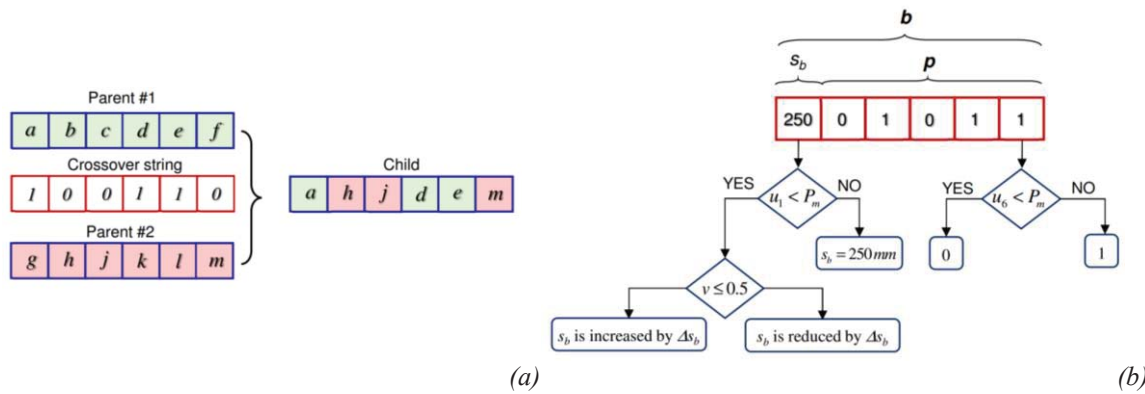


Figure 4: Example flow-charts of the: (a) uniform scatter crossover function; (b) proposed mutation function.

4 REFERENCE STRUCTURAL MODEL

The proposed optimization framework can work with any finite element program handling nonlinear static analysis. Tests and application presented in the current study are carried out using the *OpenSees* software platform and the structural modelling assumptions below described.

4.1 Modelling of RC elements with and without steel-jacketing

Frame elements are modelled adopting distributed plasticity force-based elements with five Gauss-Lobatto integration points available in OpenSees (**Fig. 5**). Fiber-section elements are modelled using a *Concrete02* uniaxial material model for the cross-section fibers. It is assumed that the effect of confinement is extended to the whole cross-section (**Fig. 5**) both for the cases of columns with and without steel jacketing reinforcement. This simplified assumption allows a formal consistency with the confinement model in the case of concrete confined by stirrups and steel jacketing (**Campione et al. 2017 [12]**) which provides uniform confinement over the cross-section. In order to simulate the crushing of the cross-section fibers, *Concrete02* material is combined with *MinMax* material. For the current case, it is assumed that crushing of fibers occurs in correspondence of the compressive strain (ϵ_{cr}) attained at a 30% reduction of the peak strength (**Fig. 8**).

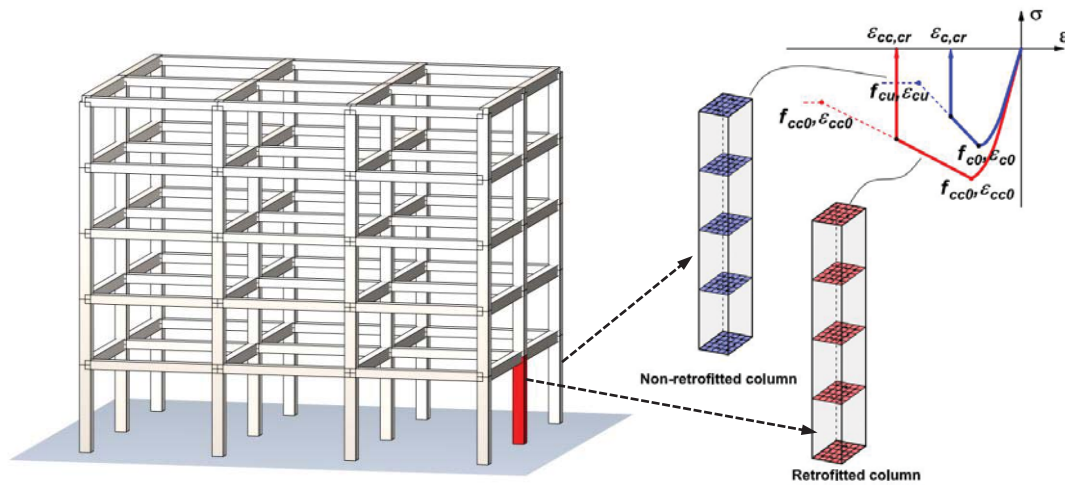


Figure 5: Definition of the frame fiber-section elements with and without steel-jacketing reinforcement.

Confined concrete for RC elements confined only by stirrups will be characterized by parameters f_{c0} , f_{cu} , ϵ_{c0} , ϵ_{cu} (**Fig. 5**), while these parameters are changed into f_{cc0} , f_{ccu} , ϵ_{cc0} , ϵ_{ccu} for RC elements confined by stirrups and steel jacketing (**Fig. 5**). Confined concrete parameters for the RC elements confined only by stirrups are evaluated using the stress-strain model by **Razvi and Saatcioglu 1992 [13]**. As for the columns with steel jacketing retrofitting, confined concrete parameters are obtained using the procedure already presented by **Di Trapani et al. 2020 [9]**, which is based on the model by **Campione et al. 2017 [12]**.

Steel rebars are modelled using the *Steel02* (Giuffrè-Menegotto-Pinto) material model (elasto-plastic with linear strain hardening). Finally, rigid diaphragm behaviour is imposed at the floor nodes.

4.2 Modelling of masonry infills

Masonry infills (if any) are modelled as equivalent diagonal struts resisting only in compression. The equivalent strut model by **Di Trapani et al. 2018 [14]** is used for the fiber-section struts. The model provides a concrete-type compression-only stress-strain relationship defined by the four parameters, peak stress (f_{md0}), ultimate stress (f_{mdu}), peak strain (ϵ_{md0}) and ultimate strain (ϵ_{mdu}) obtained by empirical equations. The infill is supposed to collapse in correspondence of the axial strain $\epsilon_{mdc} = 2 \cdot \epsilon_{mdu}$.

5 STRUCTURAL ANALYSIS AND POSTPROCESSING

5.1 Pushover curve post-processing for feasibility assessment

The feasibility of each solution is assessment by a pushover analysis of the individual. Pushover analysis is carried out in the framework of the N2 method (**Fajfar 2000 [11]**), also provided by **Eurocode 8 [15]**. The feasibility of each solution is assessed by evaluating the ductility capacity / demand ratios defined by:

$$\xi_\mu = \frac{\mu_c}{\mu_d} \quad (10)$$

Where the ductility capacity (μ_c) is obtained as the ratio between the ultimate displacement capacity (d_u^*) and the yielding displacement (d_y^*) of the single degree of freedom bilinear equivalent curve (**Fig. 6**), while the ductility demand (μ_d) of an inelastic SDOF system is evaluated as:

$$\begin{cases} \mu_d = (q^* - 1) \frac{T_c}{T^*} + 1 & \text{if } T^* \leq T_c \\ \mu_d = q^* & \text{if } T^* > T_c \end{cases} \quad (11)$$

where T^* is the period of the equivalent SDOF system having mass m^* , and stiffness k^* and reduction factor q^* evaluated as:

$$T^* = 2\pi \sqrt{\frac{m^*}{k^*}}; \quad k^* = \frac{F_y^*}{d_y^*}; \quad q^* = \frac{S_{ae}(T^*)m^*}{F_y^*} \quad (12)$$

The coefficient ξ_μ is the final output of the processing of pushover curves and is used as a discriminating factor in the optimization process in order to establish the feasibility of each a single individual ($\xi_\mu \geq 1$).

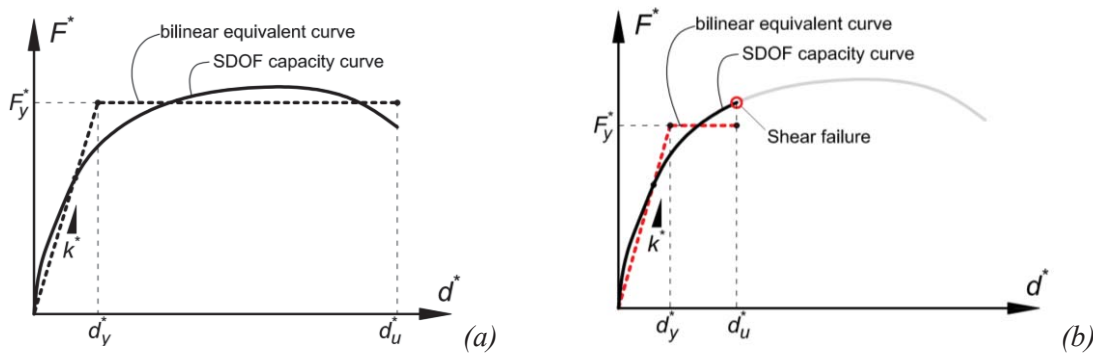


Figure 6: Typical equivalent SDOF capacity curve and bilinear equivalent curve for: (a) shear-resistant structure; (b) shear-critical structure.

5.2 Shear verification of RC elements with and without steel-jacketing

Shear verification of columns is carried out in the post-processing phase in terms of strength. The ultimate displacement capacity of assumed for the SDOF system is the one associated with the first shear failure of a column. Therefore, if shear failure of a column occurs, the capacity curve is cut in correspondence of that event (**Fig. 6b**). Shear verifications are carried out according to the model by **Biskinis et al. 2004 [16]**, also included in **Eurocode 8 [15]** and in the **Italian Technical Code [17]** for the evaluation of shear strength of element

subjected to seismic loads. Still according to **Italian Technical Code [17]**, the contribution of the steel-jacketing to the shear strength is evaluated.

5.3 Additional shear demand caused by infill-frame interaction

Masonry infills induce significant increase of shear in adjacent columns. In case of single concentric strut, the additional shear demand due to infills ($V_{C,inf}$) can be estimated as (**Di Trapani and Malavisi 2019 [18]**):

$$V_{C,inf} = P_{str} \cdot \cos \alpha - \mu \cdot P_{str} \cdot \sin \alpha \quad (13)$$

where, referring to the **Fig. 9**, P_{str} is the current value of the axial force acting on the equivalent strut, α is the angle of inclination of the strut with respect to horizontal direction, and μ the friction coefficient associated with the infill-mortar-frame interface and assumed as 0.7 in absence of more detailed evaluations. The total shear demand on a column of the frame adjacent to and infill (V_D) will be the evaluated as the sum of shear force currently acting on the column ($V_{C,fr}$) and the additional shear demand ($V_{C,inf}$) so that:

$$V_D = V_{C,fr} + V_{C,inf} \quad (14)$$

6 TEST OF THE PROPOSED FRAMEWORK

As illustrated in previous sections, modified genetic operators have been introduced in the optimization framework. Their effectiveness is here tested in comparison with the standard ones, also providing some remarks on the most suitable calibration of parameters. The tests are carried out on a reference reinforced concrete frame case study structure having column with shear deficiencies in a high seismic hazard zone.

6.1 Details of the reference structure

The case study building consists of a five-storey reinforced concrete structure designed to resist only gravity loads. The building is supposed being located in Cosenza (Italy), soil type C. The reference nominal life (V_N) is of 100 years. The resulting return period is $T_R=975$ years. The structure (**Fig. 7**) has double symmetry in plan and is regular in elevation. Modeling assumptions are those illustrated in Section 4. Reinforced concrete elements are supposed to be made of concrete having average unconfined strength $f_{c0} = 20$ MPa and steel rebars with nominal average yielding strength $f_y = 455$ MPa. Reinforcement details of beams and columns are shown in **Fig. 12b** and **Table 1**.

RC members	$b \times h$ (mm)	Longitudinal reinforcement	Transverse reinforcement
Beams	400 x 500	4+4 $\phi 18$	$\phi 6$ / 200 mm
Columns	500 x 500	12 $\phi 18$	$\phi 6$ / 200 mm

Table 1: Reinforcement details of beams and columns.

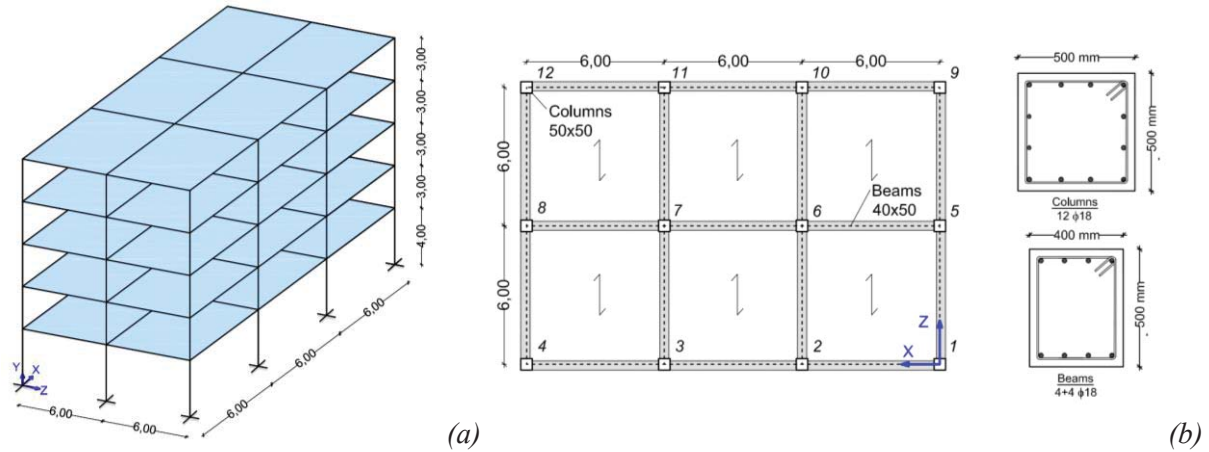


Figure 7: Geometrical dimensions of the case study structure: (a) 3D frame view; (b) dimensions in plan.

Vertical loads are modelled as point loads applied to the top node of each column as function of the respective tributary areas in plan. Pushover analyses are carried out by considering only a uniform profile for lateral loads acting along the softer direction of the structure.

A regards steel-jacketing retrofitting, it is supposed that angles and battens are made of steel having nominal yielding strength $f_{yb} = 275$ MPa and the same dimension for angles and battens (**Table 2**), while the battens spacing (s_b) range of optimization is 150-400 mm.

Angles		Battens		
Lateral length l_a (mm)	Thickness w_a (mm)	Width w_b (mm)	Thickness t_b (mm)	Spacing s_b (mm)
Columns	5	50	5	150–400

Table 2: Steel-jacketing arrangement details.

Moreover, to reduce the computational effort the following restriction have been applied to the design space:

- Retrofitted columns can be only located within the first the second floor.
- Battens spacing optimization can vary with a minimum step size Δs_b of 50 mm

6.2 Case study structural configurations description

An application of the proposed framework is carried out for a case study structure supposing two different configurations of the infills. The reference reinforced concrete frame structure is the same as the one described in the previous section. Infills are supposed made clay hollow masonry having thickness $t = 250$ mm, elastic modulus $E_m = 6400$ MPa compressive strength $f_m = 8.6$ MPa and shear strength $f_{vm} = 1.07$ MPa. Equivalent strut properties defined according to the model by **Di Trapani et al. 2018 [14]** are reported in **Table 3**.

t (mm)	w (mm)	f_{md0} (MPa)	f_{md0} (MPa)	ϵ_{md0} (-)	ϵ_{mdu} (-)
250	1053	1.88	0.86	0.010	0.073

Table 3: Geometric and mechanical details of the equivalent struts.

In the first infilled frame configuration (IFC-1), infills are located on the side frames with symmetric arrangement (**Fig. 8a**). In this configuration, infills are not provided on the ground floor. In the second configuration (IFC-2), infills are provided only in one of the external side frames and extended to the ground floor (**Fig. 8b**). The reason for the choice of these two infills configurations is related to the fact that they tend to induce a significantly different seismic demand to structures in terms of shear and ductility. Furthermore, the optimization of the two structures is carried out supposing the RC frame columns being shear-critical (SC) or shear-resistant (SR). In the first case, shear reinforcement of columns is supposed to be as described in **Table 1**. In the second case, columns are supposed to have adequate shear resistance to carry seismic loads. This further test allows examining the general efficacy of the proposed algorithm to work with both the typologies of structures.

Moreover, to reduce the computational burden, the design space of retrofitted columns is limited to the first two floors (24 columns), where the maximum seismic demand is expected in terms of shear and ductility. Optimization tests are carried out considering a pushover analysis with a uniform distribution of lateral forces along z direction.

The adopted settings for the GA optimization framework are summarized in **Table 4**.

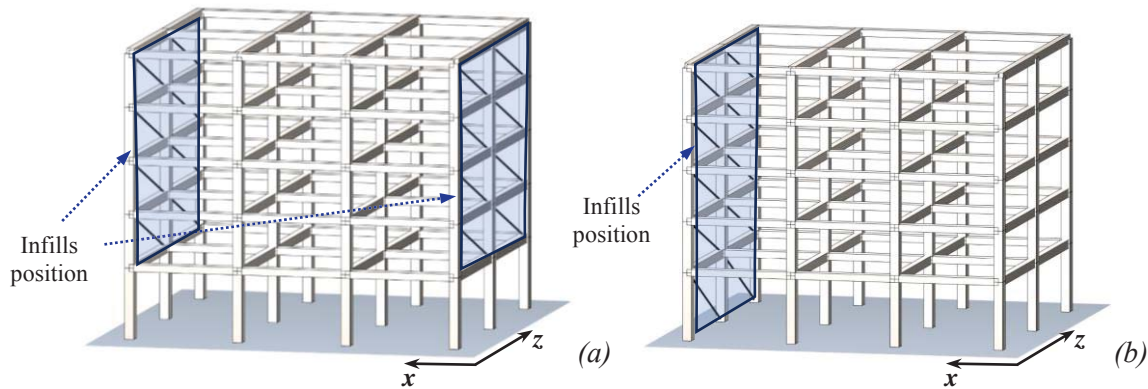


Figure 8: Case study structures: (a) IFC 1: symmetric positioning of infills with pilotis storey; (b) IFC2: asymmetric positioning of infills.

Dimension of the design vector $\text{dim}(b)$	Population size P	Dimension of the p_{Pr} space p_{Pr}	Prob. of retrofitting of an element in the p_{Pr} space P_r	Probability of mutation P_m	No. of indiv. subject to Elitism per gen. E
25	80	50%	90%	10	5%

Table 4: GA framework settings used for the case studies.

6.3 Optimization results and discussion

As previously mentioned, four optimization tests have been carried out with the aim of assessing first the responsiveness of the proposed framework in finding optimal retrofitting solution under different potential damage scenarios (IFC-1 and IFC-2 configurations). Secondly, the general validity of the framework, and in particular of the modified genetic operators, has been tested by considering both shear-critical (SC) and shear resistant (SR) configurations for the columns. This allows understanding the algorithm performance as a function of the variety of the population.

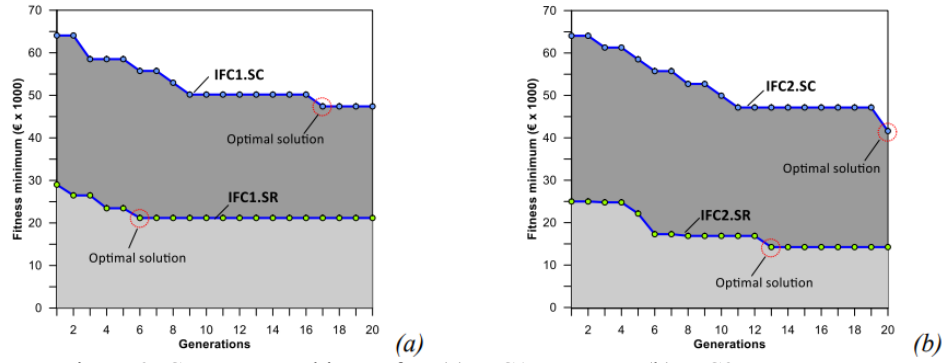


Figure 9: Convergence history for: (a) IFC1 structure; (b) IFC2 structure.

The convergence histories of the tests are depicted in **Figs. 9**. As it can be observed, the proposed framework is able to pinpoint an optimal solution for each examined cases efficiently. The performances of the optimal retrofitting configurations in terms of capacity curves are displayed in **Figs. 10**.

The consistency of the optimal retrofitting arrangements with the expected structural deficiencies is very clear from **Figs. 11**, showing the structural deformed shapes under $z+$ pushover loads and depicting in red the retrofitted columns. In fact, for both IFC-1 and IFC-2 shear resistant structures, retrofitting was provided for central columns that have reduced ductility because of the significant axial force, and leeward columns subjected to axial force increases because of the base moment. The significant amount of retrofitted columns for the IFC-1.SR configuration is related to the more severe damage mechanism (soft storey) induced by lateral loads. For what concerns shear-critical configurations IFC-1.SC and IFC-2.SC, more retrofitted columns were found. The shear deficiency of columns and the associated retrofitting demand is more evident observing **Figs. 11b, 11d**. This highlights that the additional shear demand due to the pushing action of infills plays a relevant role. In fact, retrofitting was requested to every leeward column adjoined to the equivalent struts.

For all the retrofitting configurations low battens spacing was found ($s_b=150\div 200$ mm). This can be justified considering that fixed costs influenced more than steel cage related costs. Therefore, the framework tends to prefer solutions providing the minimum possible number of columns even with reducing the spacing of battens.

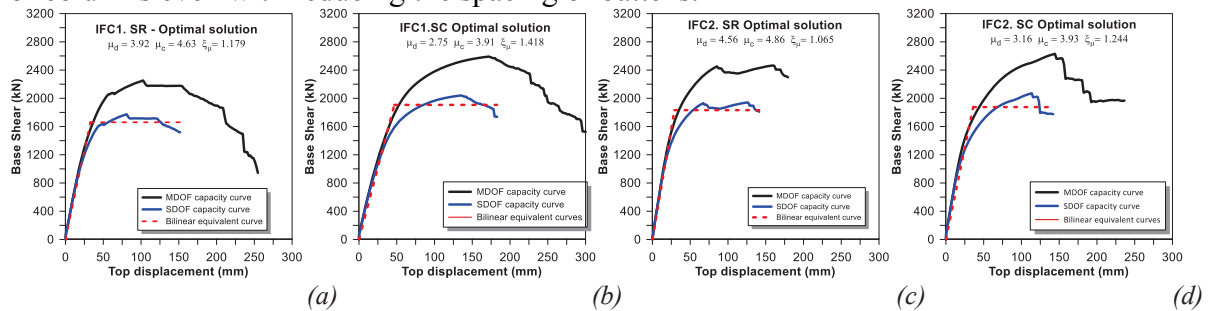


Figure 10: Optimal solutions capacity curves for: (a) IFC1.SR; (b) IFC1.SC; (c) IFC2.SR; (d) IFC2.SC

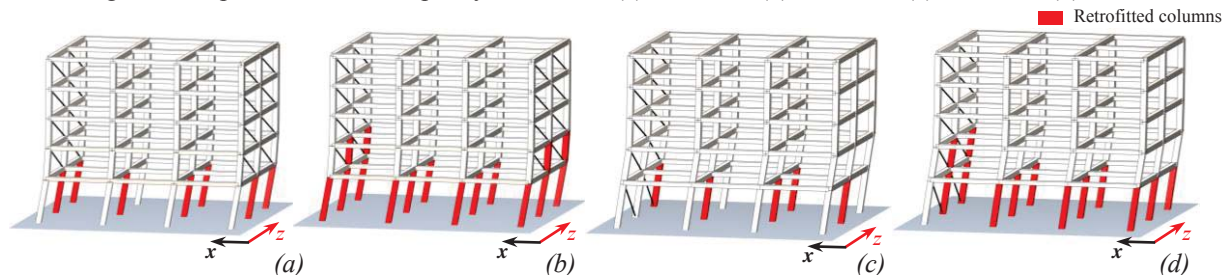


Figure 11: Optimal retrofitting arrangements for: (a) IFC1.SR; (b) IFC1.SC; (c) IFC2.SR; (d) IFC2.SC

Results of the optimization test in terms of cost, performance and arrangement are summarized in **Table 5**. Based on the previously discussed results the proposed framework has demonstrated to be sufficiently robust against the heterogeneity of the populations.

The advantages in terms of economical cost savings can certainly justify the application of a retrofitting optimization framework in the current practice. Of course, this is even more true for larger reinforced concrete frames structures, where retrofitting and downtime costs become a crucial issue.

Structural configuration	s_b (mm)	n_c (-)	C (€)	μ_d (-)	μ_c (-)	ξ_μ (-)
IFC1.SR	150	7	21 171	3.92	4.63	1.179
IFC1.SC	150	16	47 402	2.75	3.90	1.419
IFC2.SR	200	5	14 239	4.56	4.86	1.065
IFC2.SC	150	13	38 823	3.15	3.93	1.244

Table 5: Results of the optimization.

7 CONCLUSIONS

The paper presented a new genetic algorithm-based framework aimed at the optimization of steel-jacketing retrofitting interventions costs in reinforced concrete frame structures subjected to seismic loads. The proposed optimization framework can effectively handle both in the cases of shear resistance and flexural ductility lacks, providing as output the retrofitted columns' position and the amount of reinforcement associated with the minimum cost.

The development of the optimization framework was based on the MATLAB® GA tool, addressing special effort in revising the standard genetic operators (population generator, elitism, and mutation) to effectively handle retrofitting optimization of RC frame structures in the cases of lacks in ductility, shear or combined shear and ductility.

The proposed framework has been tested with a reference structure with different infills configurations and assuming the columns to be shear-critical or shear-resistant. Results have shown that the optimization algorithm is sufficiently general and robust both for the cases of shear-deficient or ductility-deficient structures. Economic and downtime gains are not clearly evident for structures with reduced size (as the ones examined in the paper); however substantial savings can be expected for larger RC structures with a noticeable number of columns.

REFERENCES

- [1] L.P. Chaves, J. Cunha, Design of carbon fiber reinforcement of concrete slabs using topology optimization. *Construction and Building Materials*, **73**, 688-98, 2014.
- [2] C. Chisari, C. Bedon, Multi-Objective Optimization of FRP Jackets for Improving the Seismic Response of Reinforced Concrete Frames. *American Journal of Engineering and Applied Sciences*, **9(3)**, 669-679, 2016.
- [3] H. Seo, J. Kim, M. Kwon, Optimal seismic retrofitted RC column distribution for an existing school building. *Engineering Structures*, **168**, 399-404, 2018.
- [4] N. Pollini, O. Lavan, O. Amir, Minimum-cost optimization of nonlinear fluid viscous dampers and their supporting members for seismic retrofitting. *Earthquake Engineering & Structural Dynamics*, **46**, 1941-1961, 2017.
- [5] F. Braga, R. Gigliotti, R. Laguardia, Intervention cost optimization of bracing systems with multiperformance criteria. *Engineering Structures*, **182**, 185-197, 2019.

- [6] O. Lavan, G.F. Dargush, Multi-objective evolutionary seismic design with passive energy dissipation systems. *Journal of Earthquake Engineering*, **13(6)**, 758-790, 2009.
- [7] R. Falcone, F. Carrabs, R. Cerulli, C. Lima, E. Martinelli, Seismic retrofitting of existing rc buildings: a rational selection procedure based on genetic algorithms. *Structures*, **22**, 310–326, 2019.
- [8] G.S. Papavasileiou, D.C. Charmpis, N.D. Lagaros, Optimized seismic retrofit of steel-concrete composite buildings. *Engineering Structures*, **213**, 110573, 2020.
- [9] F. Di Trapani, M. Malavisi, G.C. Marano, A.P. Sberna, R. Greco, Optimal seismic retrofitting of reinforced concrete buildings by steel-jacketing using a genetic algorithm-based framework. *Engineering Structures*, **219**, 110864, 2020.
- [10] F. McKenna, G.L. Fenves, M.H. Scott, *Open system for earthquake engineering simulation*. University of California Berkeley, 2000.
- [11] P. Fajfar, A Nonlinear Analysis Method for Performance-Based Seismic Design. *Earthquake Spectra* **16(3)**, 573-592, 2000.
- [12] G. Campione, L. Cavaleri, F. Di Trapani, M.F. Ferrotto, Frictional effects in structural behavior of no end-connected steel-jacketed RC columns: experimental results and new approaches to model numerical and analytical response. *Journal of Structural Engineering*, **143(8)**, 04017070, 2017.
- [13] S.R. Razvi, M. Saatcioglu, Strength and Ductility of Confined Concrete. *Journal of Structural Engineering*, **125(3)**, 281-298, 1992.
- [14] F. Di Trapani, G. Bertagnoli, M.F. Ferrotto, D. Gino, Empirical equations for the direct definition of stress–strain laws for fiber-section-based macro-modeling of infilled frames. *Journal of Engineering Mechanics*, **144(11)**, 04018101, 2018.
- [15] *Eurocode 8. Design of structures for earthquake resistance - Part 1: general rules, seismic actions and rules for buildings*. European Committee for Standardization, 2004.
- [16] D.E. Biskinis, G.K. Roupakias, M.N. Fardis, Degradation of shear strength of reinforced concrete members with inelastic cyclic displacements. *Structural Journal*, **101(6)**, 773–783, 2004.
- [17] *Norme tecniche per le costruzioni. Decreto ministeriale 17 gennaio 2018*. Ministero delle infrastrutture e dei trasporti, 2018.
- [18] F. Di Trapani, M. Malavisi, Seismic fragility assessment of infilled frames subject to mainshock/aftershock sequences using a double incremental dynamic analysis approach. *Bulletin of Earthquake Engineering*, **17(1)**, 211–235, 2019.
- [19] F. Di Trapani, V. Bolis, F. Basone, M. Preti, Seismic reliability and loss assessment of RC frame structures with traditional and innovative masonry infills. *Engineering Structures*, **208**, 110306, 2020.
- [20] L. Cavaleri, F. Di Trapani, M.F. Ferrotto, A new hybrid procedure for the definition of seismic vulnerability in Mediterranean cross-border urban areas. *Natural Hazards*, **86(2)**, 517–541, 2017.
- [21] L. Cavaleri, F. Di Trapani, M.F. Ferrotto, L. Davì, Stress-strain models for normal and high strength confined concrete: Test and comparison of literature models reliability in reproducing experimental results. *Ingegneria Sismica*, **34(3-4)**, 114-137, 2017.

EXPECTED ANNUAL LOSS ORIENTED SEISMIC RETROFITTING OPTIMIZATION OF RC FRAME STRUCTURES USING A NEW AI-BASED FRAMEWORK

Fabio Di Trapani¹, Antonio Pio Sberna¹ and Giuseppe Carlo Marano¹

¹ Politecnico di Torino. Dipartimento di Ingegneria Strutturale, Edile e Geotecnica
Corso Duca degli Abruzzi 24, 10129, Turin, Italy
e-mail: {fabio.ditrapani, antonio.sberna, giuseppe.marano}@polito.it

Abstract

The paper proposes a new genetic algorithm-based framework aimed at efficiently design multiple seismic retrofitting interventions for reinforced concrete (RC) frame structures minimizing the costs of intervention. The feasibility of each tentative solution is assessed by considering in indirect way the expected annual loss (EAL). EAL evaluation is performed referring to different limit states whose repairing costs are expressed as a percentage of reconstruction costs and evaluating the respective mean annual frequency of exceedance. To effectively engage both serviceability and ultimate limit states, the compresence of two different retrofitting systems is considered. Steel bracings are used to increase the global stiffness of the structure and improve operational and damage limit states performance. FRP wrapping of columns is used to manage the life safety and collapse limit state demands. The optimization carried out by the novel AI-based framework implementing a genetic algorithm (GA). For both the retrofitting systems, their position within the structure (topological optimization) and their sizing are provided as output. Results will show that seismic retrofitting can be effectively optimized to minimize costs controlling the expected annual loss.

Keywords: structural optimization, genetic algorithm, seismic retrofitting, expected annual loss, FRP, bracing

1 INTRODUCTION

The pressing necessity of reducing the seismic vulnerability of existing structures located in earthquake-prone regions has motivated the last decade of research activities to address the seismic retrofitting techniques. Despite the large availability of retrofitting solutions with different materials and arrangement techniques, nowadays, there are no formal methods for designing this kind of interventions simultaneously controlling the resulting overall seismic performance. Therefore, in most cases, the choice of retrofitting position and amount are

exclusively entrusted to the experience and intuition of the designer. A first consequence of this empirical approach is that several trial-and-error attempts are required to find a feasible retrofitting solution. This also requires considerable time consumption to get a sufficient compromise between safety and costs. Secondly, results so obtained are not controlled in cost or in performance, therefore, obtained retrofitting solutions are feasible do not ensure maximum exploitation or the retrofitting with a consequent increase of intervention costs, invasiveness, and downtime.

In the last years, the scientific interest in structural optimization was mainly focused on sizing and shape optimization of new structures. On the contrary, the optimization of seismic retrofitting of existing structures has not been investigated many times, while noticeable interest is emerging in the last years. Few researchers have addressed the problem of the optimization of FRP jackets (Chisari and Bedon 2016 [1], Seo et al. 2018 [2]) or other applications of seismic retrofitting devices for RC buildings by using fluid viscous dampers (Pollini et al. 2017 [3]), dissipative bracings (Braga et al. 2019 [4]) or both (Lavan and Dargush 2009 [5]). More recent studies addressed the issue of optimization of seismic retrofitting costs. Among these, Falcone et al. 2019 [6] proposed a framework for optimizing the realization costs of FRP jacketing and steel bracings for existing RC frame structures through genetic algorithm optimization. Papavasileiou et al. 2020 [7] faced retrofitting optimization of encased steel-concrete composite columns comparing three different retrofitting methods: concrete jacketing, steel jacketing and steel bracing. A similar approach was followed by Di Trapani et al. 2020 [8] who proposed an innovative framework based on genetic algorithm aimed at minimizing steel jacketing seismic retrofitting costs for ductility deficient RC structures. These very recent research activities addressed their efforts in defining new effective algorithms focused on the optimization of the retrofitting interventions to minimize their cost. This provided an answer to the issue raised above, that is getting the control of the design to achieve an output goal. A more generalized view of this problem is faced in this paper, whose purpose is the development of a new optimization framework aimed at optimizing service-life costs of structures subject to retrofitting interventions, with special regard to RC frame structures. The expected annual loss (EAL) has been proved as valid tool to compare structure seismic performance during their service life Calvi (2013) [9]. It estimates the overall behaviour of the construction in terms of expected economic annual losses associated with seismic events that could take place during the reference service life.

The goal of the proposed framework is to determine, for a non-seismically conforming RC building, the best retrofitting configuration in terms of position (topological optimization) and amount of reinforcement (sizing optimization). Optimization focuses on the minimization of retrofitting costs considering in an indirect way the resulting EAL value.

Since EAL assessment involves different limit states satisfaction, the proposed framework considers multiple retrofitting interventions. In particular, the case study of a 3D multistorey RC building is considered supposing FRP jacketing of RC columns (to increase ductility) and steel bracings (to reduce lateral deformability) as retrofitting interventions to optimize.

The optimization process is carried out by a genetic algorithm (GA) developed in MatLab®. The structural performance of each solution is assessed from the results of static pushover analyses in the framework of the N2 method. The validity and efficiency of the proposed method is proved by implementing it on a case study structure. Eventually, the results are compared with the outcomes of a cost optimization that does not consider EAL control. The presented methodology is still under development, but it constitutes a novel contribution towards the use of artificial intelligence techniques to improve design effectiveness and sustainability.

2 OPTIMIZATION FRAMEWORK

The optimization framework herein proposed is based on a genetic algorithm (GA) optimization routine developed in MatLab®. The optimization algorithm relates a structural model developed with the *OpenSees* software platform (McKenna et al. 2000 [10]) with the GA process. The genetic algorithm is an evolutionary algorithm inspired by the evolution theory, therefore, it generates a *population* of *individuals* representing different tentative retrofitting arrangements. Each individual handled by algorithm is characterized by a *design vector* collecting all the decision variable to be optimized. Each design vector is associated with a potential retrofitting configuration. The optimization involves the definition of a proper *objective function*, taking into account both the feasibility of a solution (namely the passing safety checks) and cost associated to the retrofitting intervention. A schematic flowchart of the proposed framework is depicted in Fig. 1, which structure is discussed in detail in the following sections.

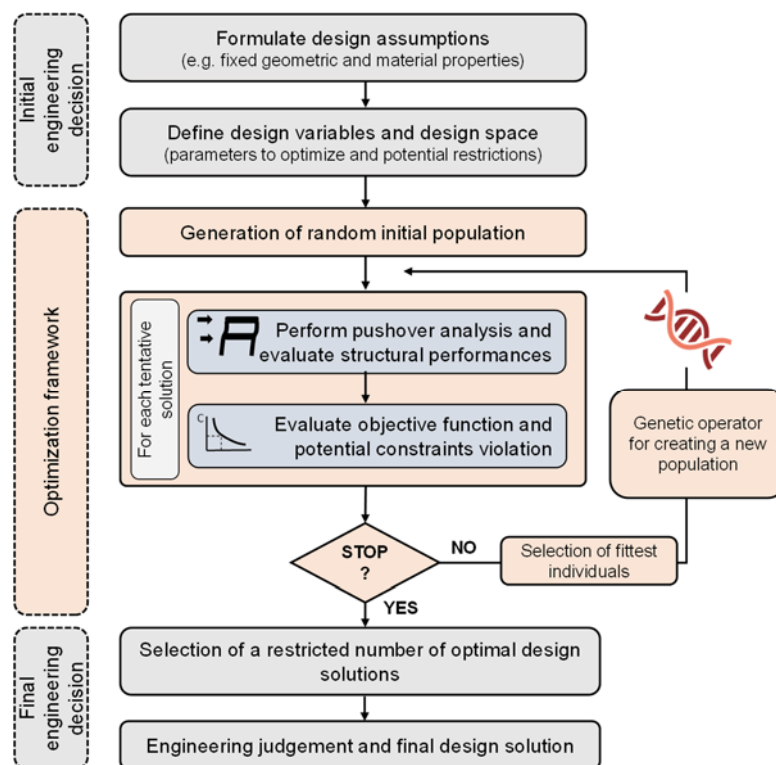


Figure 1: Flowchart of the optimization framework.

2.1 Definition of the EAL

The expected annual loss represents percentage annual loss of economic value of a structure in its reference life taking into account the associated seismic risk, which basically depends on the site hazard and on the structure seismic vulnerability. The determination of the EAL requires therefore the assessment of the performance of the structure to different limit states, associated with the respective return periods $T_{r,LS}$ and annual rates of failure, expressed as the inverse of the return periods ($\lambda_{LS} = 1/T_{r,LS}$). The achievement of a limit state is associated with a specific repair cost. The EAL curve connects the annual rate of failure of each limit state with the respective repairing cost. A simplified method to compute EAL has been proposed by Cosenza et al. (2018) [11]. According to this approach repair costs are expressed as percentages of the

repair costs (%RC) with respect to the reconstruction cost (reconstruction limit state (RLS)) and are fixed for each limit state (Fig. 2a).

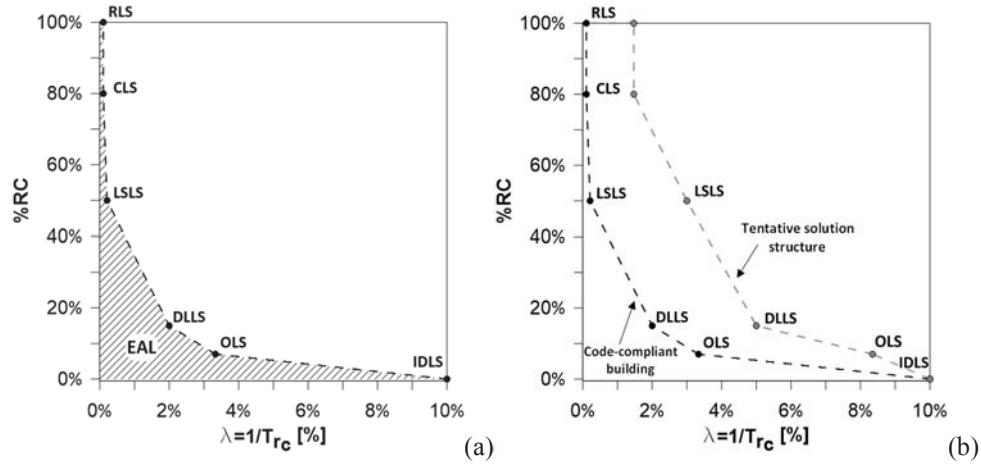


Figure 2: Expected Annual Loss curve: (a) formal EAL determination; (b) code compliant building EAL curve and generic EAL curve for a building.

According to Cosenza et al. (2018) [11], eight limit states are identified by reconstruction limit state (RLS) and collapse limit state (CLS) which are associated with repair cost (%RC) equal to 100% and 80%, respectively. Moreover, the %RC for the life safety limit state (LSLS) is set to 50%. Service limit states are the damage limitation limit state (DLLS) and the operational limit state (OLS). These two former limit states have a %RC of 15% and 7% respectively. The initial damage limit state (IDLS) is characterized by repair costs equal to zero and a mean annual frequency of exceedance that is conventionally assumed as $\lambda_{IDLS} = 10\%$. For a code-compliant structure, namely a structure having for each limit state a capacity that is exactly equivalent to the demand, the annual rates of exceedance of each limit states for the associated (fixed) reconstruction costs and are those reported in Table 1. Considering values in Table 1, the EAL of the code compliant building is 1.13%.

Limit state	%RC	$T_{r,LS}$ [years]	$\lambda_{LS}=1/T_{r,LS}$ [%]	EAL _{cc}
RLS	100	∞	0.00	1.13%
CLS	80	975	0.10	
LSLS	50	475	0.21	
DLLS	15	50	2.00	
OLS	7	30	3.33	
IDLS	0	10	10.0	

Table 1: Mean annual frequency of exceedance (λ) and repair costs (%RC) associated with each LS for a code-compliant building.

Formally the EAL is evaluated as the area under the curve that connect the points (λ , %RC) for each limit state (Fig. 1a), so that:

$$EAL = \sum_{i=2}^5 \left[\lambda_{LS(i-1)} = \lambda_{LS(i)} \right] \cdot \left[\%RC_{LS(i)} = \%RC_{LS(i-1)} \right] / 2 + \lambda_{CLS} \cdot \%RC_{RLS} \quad (1)$$

For the code-compliant building Eq. 1 results in EAL=1.13%. The evaluation of the EAL for a generic structure can be carried out performing a pushover results to determine return period associated with occurrence of each limit state ($T_{rc,LS}$). A simplified expression [11], based on the determination of the safety factor ($\zeta_{E,LS}$) can be used to evaluate capacity return period for each limit state as follows:

$$T_{rC,LS} = T_{rD,LS} \cdot (\zeta_{E,LS})^\eta \quad (2)$$

where the parameter η can be approximated to $\eta = 1 / 0.41$ and the safety factors can be calculated for the damage limitation limit state (DLLS) and life safety limit state (LSLS) as:

$$\begin{cases} \zeta_{E,LSLS} = \frac{PGA_{c,LSLS}}{PGA_{d,LSLS}} \\ \zeta_{E,DLLS} = \frac{d_{max,DLLS}^*}{S_{de,DLLS}(T^*)} \end{cases} \quad (3)$$

where $PGA_{d,LSLS}$ is the peak ground acceleration demand and $PGA_{c,LSLS}$ is the peak ground acceleration capacity, that is the one associated with the earthquake inducing LS limit state. The latter can be evaluated from the results of a pushover analysis in the framework of the N2 method (Fajfar 2000 [12]). In Eq. 3, $S_{de,DLLS}(T^*)$ is the displacement demand associated with elastic DLLS spectrum, and $d_{max,DLLS}^*$ is the top displacement associated with the achievement of the DLLS condition. This can be assessed by evaluating the maximum interstory drift. For instance, the value of $d_{max,DLLS}^*$ can be evaluated as the top displacement of the structure at which the larger interstory drift exceeds a limit drift $\delta_{i,max}$.

The corresponding annual rates of failure are then obtained as $\lambda_{LS} = 1/T_{rC,LS}$. According to [11], the annual rates of failure for the operational and collapse limit states are obtained as a function of those evaluated for DL and LS limit state, so that:

$$\begin{cases} \lambda_{OLS} = 1.67 \cdot \lambda_{DLLS} \\ \lambda_{CLS} = 0.49 \cdot \lambda_{LSLS} \end{cases} \quad (4)$$

Therefore, EAL is known once obtained λ_{DLLS} and λ_{LSLS} .

2.2 Definition of the design vector

The framework aims at optimizing the intervention cost of two different retrofitting systems: FRP wrappings of columns and concentric steel bracings. The decision variables that encode the position and sizing of both retrofit are collected together into a so-called design vector. With reference to Fig. 3, the selected design variables are the number of braced frame fields (n_{br}), the diameter of braces (ϕ_{br}), the number of layers of FRP (n_{FRP}), and the position of the columns retrofitted by the FRP. Design variables are gathered in the design vector \mathbf{b} so defined:

$$\mathbf{b} = (n_{br} \quad \phi_{br} \quad n_{FRP} \quad \mathbf{p})^T \quad (5)$$

in which the term \mathbf{p} is an array of binary numbers representing the position of the FRP retrofitted columns defined as:

$$\mathbf{p} = [\dots \quad \dots \quad c_{ij} \quad \dots]^T \quad (6)$$

in which the generic element c_{ij} , is a Boolean number assuming the value 1 if a column is retrofitted and 0 if not. The subscript i indicates the position of a column in plan and j the storey. The term n_{FRP} , instead, is a natural value that represents the number of overlapping layers of FRP on each column belonging to the interval:

$$n_{FRP} \in [1, n_{FRP,max}] \quad (7)$$

where $n_{FRP,max}$ is the maximum number of FRP layers allowed.

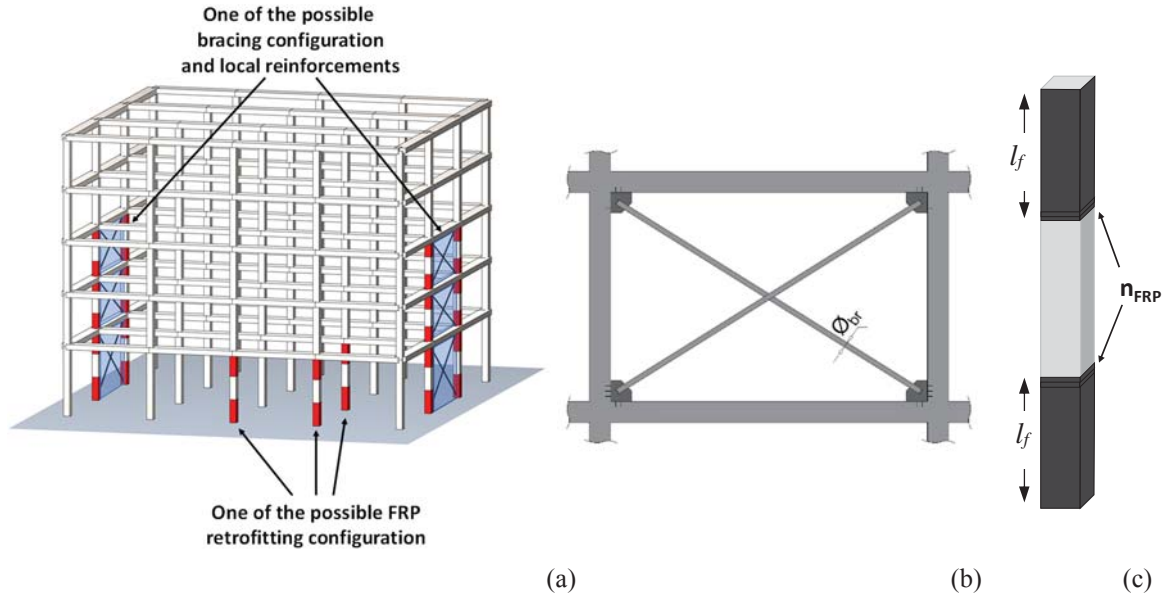


Figure 3: Representation of the design variables: (a) Generic FRP and bracing retrofitting configuration for a RC frame structure; (b) Usual circular steel bracings installation with generic diameter (ϕ_{br}); (c) Typical FRP arrangement for ductility reasons with a generic number of fabric layers (n_{FRP}).

To prevent premature collapse of columns that are adjoining to the bracing systems due to the additional shear demand, it is provided that they are reinforced with at least one layer of FRP. To introduce this local reinforcement into the design vector (if not already present in the retrofitting configuration) a heuristic repair technique is employed. By controlling the position of the bracings, the algorithm adjusts the vector \mathbf{p} so that the columns adjacent to the bracings are reinforced with FRP.

To reduce the computational effort, the following simplifying hypotheses are introduced for the retrofitting system:

- i) FRP fabrics have fixed height (h_f) and thickness ($t_{f,i}$).
- ii) Confinement of columns is realised by applying the FRP for a length (l_f) at both terminal part of the column where the maximum ductility demand is expected.
- iii) The number of FRP layers is constant for all the retrofitted columns.
- iv) Bracings are realised with circular cross-section steel elements. Their characteristics are constant for every frame.

2.3 Definition of the objective function

The objective function is aimed at the minimization the retrofitting intervention considering the realization of the two retrofitting systems as:

$$F = C_{br} + C_{FRP} \quad (8)$$

where C_{br} is the cost related to the arrangement of bracings and C_{FRP} is the one for the realization of the FRP wrapping of the columns. Both terms consider the material and manpower costs and the necessary works for the demolition and restoration of adjoining plaster and masonry. The first one can be evaluated as:

$$C_{br} = \sum_{i=1}^{n_{br}} (W_{br,i} \cdot c_{br}) + n_{br} \cdot c_{br,m} \quad (9)$$

where c_{br} is the manpower and material cost per unit weight (estimated in $c_{br} = 6 \text{ €/kg}$), $c_{br,m}$ is the fixed cost related to the demolition and reconstruction of masonry (2000€ every braced frame fields), and $W_{br,i}$ is the weight of the bracings in the i -th frame field that can be evaluated as:

$$W_{br} = 2 \cdot L_{br} \cdot \left(\frac{\phi_{br}}{2} \right)^2 \cdot \pi \cdot \gamma_s \quad (10)$$

in which L_{br} is the length of one bracing and γ_s is the specific weight of the steel (78.5 kN/m^3).

As regards FRP retrofitting the cost is computed as follows: C_{FRP} is computed as:

$$C_{FRP} = \sum_{i=1}^{n_c} (A_{FRP,i} \cdot c_{FRP}) + n_c \cdot c_{FRP,m} \quad (11)$$

where n_c is the number of retrofitted columns taking into account also the local reinforcement of the columns adjoining the steel bracings systems as presented in the previous section, c_{FRP} is the unit cost of the FRP (estimated in $c_{FRP} = 300 \text{ €/m}^2$), $c_{FRP,m}$ is the cost per column for the demolition and reconstruction of adjacent masonries and plasters and A_{FRP} is the area of the FRP fabric used to retrofit the generic column. The latter can be computed starting from the geometric dimensions of each column cross-section (b and h); supposing that the edges of the columns are rounded with a r_c radius, and the fabrics are applied for a length l_f at both end of the columns:

$$A_{FRP} = [2 \cdot (b + h) - (4 - \pi) \cdot r_c^2] \cdot 2l_f \quad (12)$$

As presented in the previous section, the EAL assessment is ruled only by the evaluation of λ_{DLLS} and λ_{LSLS} , thus the feasibility of each solution is restrained by the simultaneous verification that:

$$\lambda_{t_{DLLS}} \leq \lambda_{ccb_{DLLS}} \quad \& \quad \lambda_{t_{LSLS}} \leq \lambda_{ccb_{LSLS}} \quad (13)$$

which implies:

$$EAL \leq EAL_{cc} \quad (14)$$

A non-penalty approach is developed to take into account the feasibility (or not) of each tentative solution as explained in the following section.

2.4 Optimization algorithm subroutines

The search for the optimal solution through the use of GA algorithms proceeds generating a first population by randomly creating a series of individuals encoded by design vectors as

presented in the previous section. Analysing each of the population's tentative solutions, the value of fitness and the number of violated constraints is estimated.

Two different genetic operators are employed to improve the genes of the individuals at the end of each generation, the crossover, which mixes the genomes of the best individuals and the mutation, preventing local optima stuck by introducing random slight changes. The framework proceeds until one of the stopping criteria is achieved. For the current cases, only two stopping criteria on maximum number of generations and stall are imposed. In the ensuing Figure 4 a schematic flowchart of the subroutines is depicted.

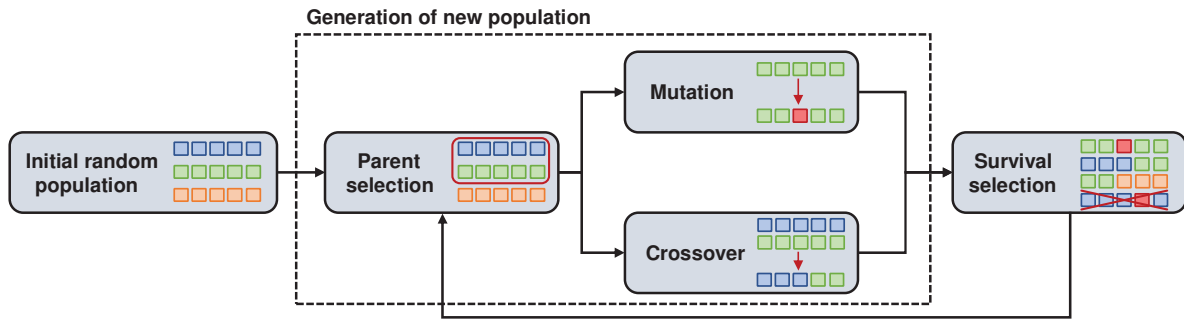


Figure 4: Schematic flowchart of the genetic algorithm process.

2.4.1. Parent selection

Parent selection is the subroutine entrusted with selecting individuals that have to be handled by other genetic operators (mutation and crossover). For the current application, random tournament selection is employed. It is based on a direct comparison of individual's performance. Within the individuals of the generation, k individuals are randomly selected (where k is called *tournament size*), among them the best individual is chosen as parent for the ensuing mating process. The comparison is carried out firstly by checking the number of violated constraints and then with respect to the fitness value. In this way, individuals with the lowest number of constraints violated are preferred. If the individuals have the same number of constraint violations the individual with the best fitness is chosen.

2.4.2. Crossover and mutation

Crossover and mutation operators are employed to improve the chromosomes at each generation. While the former works by mixing chromosomes selected by the parent selection, the latter is the genetic operator who is mainly entrusted with introducing the random component in creating offspring.

A single point mutation function is employed in the proposed GA framework. It works by selecting one random position along the design vector and changing the value of that design variable. For Boolean variables included in the \mathbf{p} sub-vector (Eq. 10) the mutation of a gene is simply a switch from 0 to 1 or vice-versa. In case the mutation has

to be achieved on the discrete values of the design vector, a new random number among the possible ones is chosen.

For the crossover subroutine, a new specific procedure has been defined to correctly handle heterogeneous genomes such as those of the proposed framework. For the binary string \mathbf{p} , a single point crossover is employed (Fig. 5). The operating principle provides the random selection of a locus along the string called crossover point. The child individual is constructed by

picking from the beginning of the chromosome to the crossover point from one parent; the rest is copied from the second one.

The crossover of the natural decision variables is conducted by randomly choosing a new value among the corresponding values of the parents. This new crossover function, which can be called *random intermediate value crossover*, is implemented to smoothly mix the parents chromosomes. An example of the proposed crossover procedure is depicted in Fig. 5.

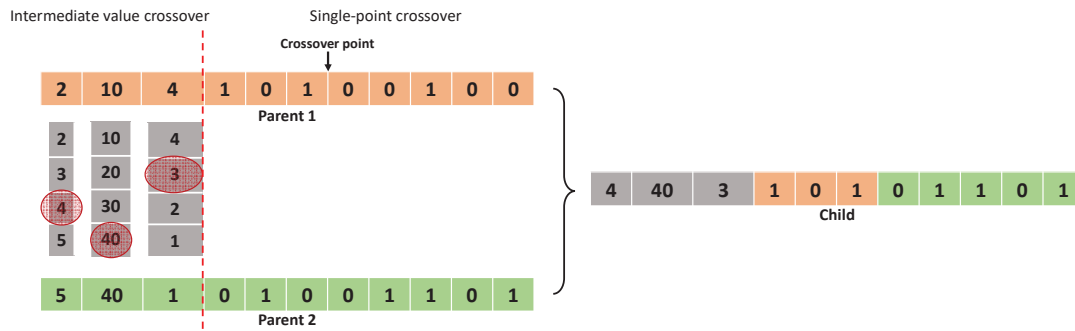


Figure 5: Example of the proposed crossover procedure.

2.4.3. Survival selection

The selection of the best individuals at the end of each generation is a fundamental step for optimization process success. The function entrusted with this task has to reject the individuals with low fitness to allow the best individuals to spread their genome. Moreover, as defined in Eq.5, the fitness evaluation does not consider the feasibility of tentative solutions; hence the selection function is responsible for managing the two constraints (Eq. 7).

A new survival selection function is developed to handle both individual's fitness and feasibility constraints efficaciously. The operating principle provides a double sorting process, first ordering the individuals with respect to the number of violated constraints and then among the individuals with the same number of constraint violation for the fitness value.

Eventually, only the best individuals are taken for the next generation. This new function that can be called *sorting and truncation selection*, has proved a valid operator to manage constrained optimization problems without requiring penalty approaches.

3 REFERENCE STRUCTURAL MODEL

The proposed framework is interfaced with a FE software to execute structural analysis. For the current application the *OpenSees* software platform. Modelling assumptions are described in detail in this section.

3.1 Modelling of reinforced concrete elements with and without FRP and of steel braces

Frame elements are modelled adopting distributed plasticity force-based elements with five Gauss-Lobatto integration points present in OpenSees (Fig. 6).

Concrete elements are modelled using a *Concrete01* uniaxial material model for the cross-section fibers. In order to simulate the crushing of the cross-section fibers, *Concrete01* material is combined with *MinMax* material, which removes the contribution of a fiber when a specified strain threshold is achieved. Steel rebars are modelled using the *Steel02* Giuffrè-Menegotto-Pinto material model (elasto-plastic with linear strain hardening).

The confined concrete model adopted for RC elements with and without retrofitting is the standard confined parabola-rectangle. According to the Italian Technical Code [13] and

Eurocode 8 [14] this model can be adopted for concrete elements confined by stirrups only or stirrups and FRP wrapping.

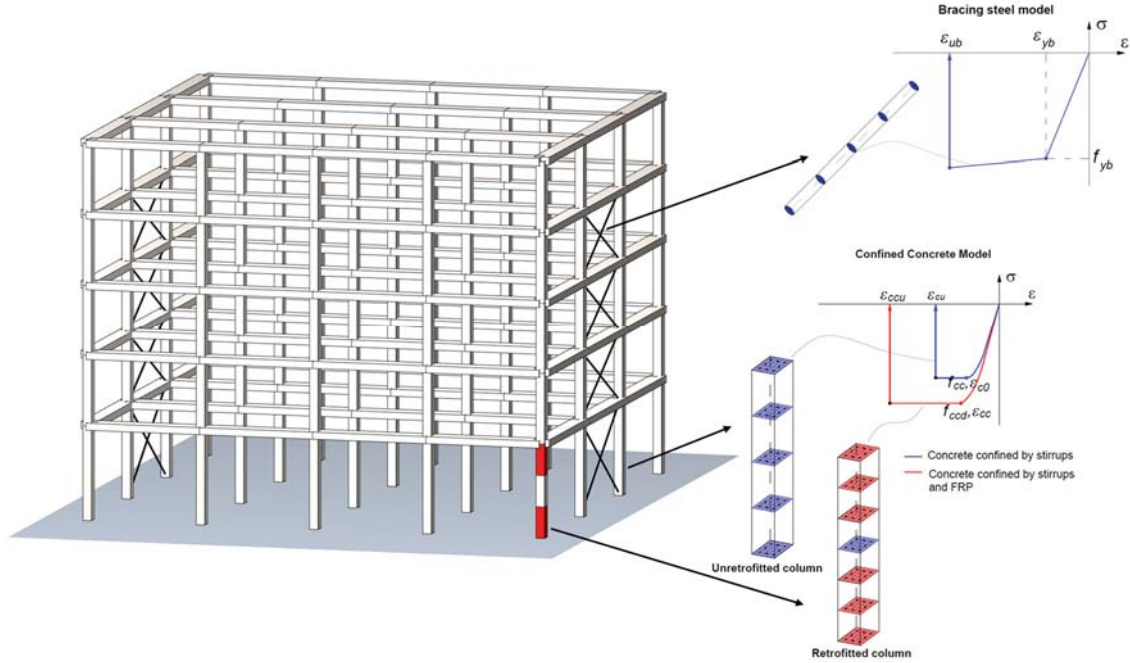


Figure 6: Definition of the fiber-section elements in OpenSees, concrete elements with and without FRP wrapping and steel bracings.

For the sake of brevity, the formulation of the model is here briefly recalled only for the RC elements wrapped by FRP. In detail, the confined peak stress is obtained as:

$$f_{ccd} = f_{cd} \cdot \left(1 + 2.6 \cdot \left(\frac{f_{l,eff}}{f_{cd}} \right) \right) \quad (15)$$

where f_{cd} is the peak stress of the concrete confined by stirrups and $f_{l,eff}$ is the effective lateral confinement pressure that can be evaluated as:

$$f_{l,eff} = k_{eff} \cdot f_l \quad (16)$$

where f_l is the confinement pressure exerted by the FRP that can be calculated as:

$$f_l = \frac{1}{2} \cdot \rho_f \cdot E_f \cdot \varepsilon_{fd,red} \quad (17)$$

in which E_f is the elastic modulus of the FRP (along the fiber direction), $\varepsilon_{fd,red}$ is the reduced FRP peak strain that, in case of ductility evaluations, can be obtained as:

$$\varepsilon_{fd,red} = \eta_a \cdot \frac{\varepsilon_{fk}}{\gamma_f} \leq 0.6 \cdot \varepsilon_{fk} \quad (18)$$

where ε_{fk} is the design rupture strain of FRP reinforcement, η_a is the environmental reduction factor, and γ_f is the partial factor of FRP materials. In Eq. 15, ρ_f is the geometric reinforcement percentage that, in case of rectangular cross-section and continuous confinement (FRP is not applied in strips), can be calculated as:

$$\rho_f = \frac{2 \cdot t_f \cdot (b + h)}{(b + h)} \quad (19)$$

where b and h are the cross-section dimensions, and t_f is the thickness of FRP wrapping. The latter is calculated as the number of layers (n_{FRP}) encoded into the design vector (Eq. 5) that multiple the thickness of the FRP fabric ($t_f = n_{\text{FRP}} \cdot t_{f,1}$).

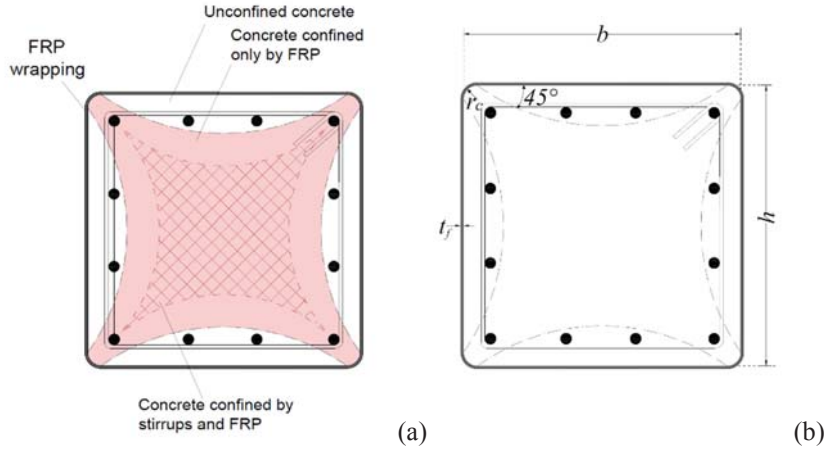


Figure 7: Configuration of the cross-section of columns retrofitted by FRP wrapping: (a) effectively confined area by stirrups and FRP; (b) geometric dimensions.

In Eq. 14 the coefficient k_{eff} represents the confining efficiency that can be calculated as the product of three different factors:

$$k_{\text{eff}} = k_v \cdot k_\alpha \cdot k_h \quad (20)$$

where k_v is the vertical confining efficiency, k_α is related to the fabric tilt, and k_h is the coefficient that represent the confining effect on the cross-section. They can be calculated in accordance with Eurocode [14], for a rectangular cross-section as:

$$k_v = \left(1 - \frac{p'_f}{2 \cdot \min\{b, h\}} \right)^2; \quad k_\alpha = \frac{1}{1 + (\tan \alpha_f)^2}; \quad k_h = 1 - \frac{(b - 2r_c)^2 + (h - 2r_c)^2}{3 \cdot b \cdot h} \quad (21)$$

In the previous equations p'_f is the distance between FRP strips, α_f is the tilt angle with respect the horizontal axis, r_c is the radius of the rounded corner.

The confined peak strain ε_{cc} and the confined ultimate strain ε_{ccu} can be evaluated as:

$$\varepsilon_{\text{cc}} = \varepsilon_{c0} \cdot \left(\frac{f_{\text{ccd}}}{f_{\text{cd}}} \right)^2; \quad \varepsilon_{\text{ccu}} = 0.0035 + 0.015 \cdot \sqrt{\frac{f_{\text{l,eff}}}{f_{\text{cd}}}} \quad (22)$$

where ε_{c0} is the peak strain of the concrete confined by the stirrups. The FRP reinforcement is supposed to be applied at both end of the columns for a length l_f (Fig. 8a). This arrangement is aimed at concentrating the confinement effect of retrofitting system in the portion of element where the major ductility is required.

The effect of FRP retrofitting is introduced into reinforced concrete elements by simply modifying the constitutive model of concrete fibers. For sake of simplicity, given that the confining effect exerted by the FRP wrapping is prevailing, the model considers only one single concrete constitutive law for the whole section.

Moreover, it is assumed that the effect of confinement is extended to the entire cross-section both for the cases of columns with and without steel jacketing reinforcement. Samples of the resulting stress–strain response in compression for a reference column cross-section fiber are reported in Fig. 8b considering different FRP layers.

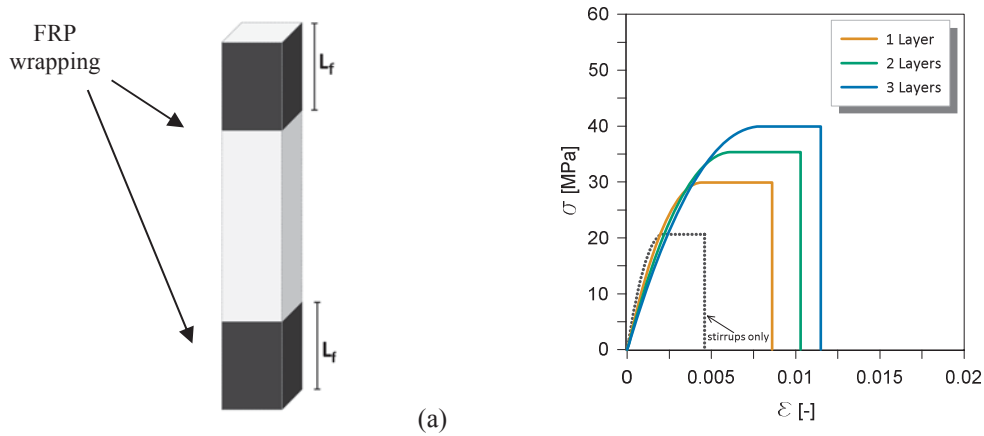


Figure 8: Details of FRP reinforcement of concrete elements: (a) Typical FRP arrangement for a column with generic confined height (l_a); (b) Samples of confined concrete stress–strain responses by varying the number of FRP layers.

3.2 Modelling of steel braces

Steel bracings are modelled using truss elements available in OpenSees. The steel is modelled adopting *Steel02* elastic-plastic with isotropic strain hardening (Giuffrè-Menegotto-Pinto material model). The model provides elastic linear behaviour and strain hardening defined by the yielding stress and strain (respectively f_{yb} and ϵ_{yb}), strain hardening factor (k), and ultimate strain (ϵ_{ub}). Steel elements are assumed to have a circular cross-section whose diameter is defined by the decision variable ϕ_{br} .

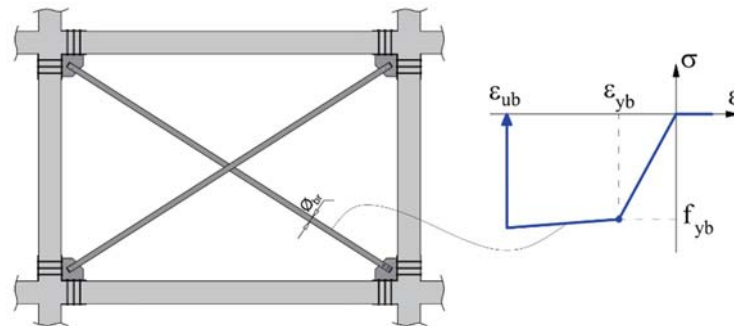


Figure 9: Typical arrangement of the concentric steel bracings.

Given that the constitutive law used provides strain hardening, so in order to limit the strain value of elements, *Steel02* is combined with *MinMax* material. The bracings elements are modelled using the OpenSees *trussSection* command. In Figure 9 the typical arrangement of bracing is reported together with the representation of the constitutive law of the material.

4 CASE-STUDY TEST OF THE OPTIMIZATION FRAMEWORK

4.1 Details of the reference structural and performance of the as-built structure

The effectiveness of the proposed framework is tested by performing the retrofitting optimization for a RC structure having structural configuration typical of buildings designed prior to the entry into force of seismic guidelines. In detail, the building consists of a five-storey reinforced concrete frames structure presenting uni-directional frames (Fig. 10). Reinforcement details of beams and columns are reported in Table 2.

RC mem- bers	<i>b</i> (mm)	<i>h</i> (mm)	Longitudinal reinforcement	Transverse reinforcement
Beams	800	300	4+4 Ø18	Ø6 / 200 mm
Columns	450	450	12 Ø18	Ø6 / 200 mm

Table 2: Geometrical dimensions and reinforcement details of RC elements.

Reinforced concrete elements are assumed to be made of poor resistance concrete having average unconfined strength $f_{c0} = 20$ MPa and steel rebars with nominal average yielding strength $f_y = 455$ MPa and strain hardening ratio is assumed equal to $\eta = 0.01$.

As regards seismic hazards, the building is supposed to be located in Cosenza (Italy), soil type C, the nominal life (V_N) is 100 years. The resulting return period is $T_R = 975$ years. The structure has double symmetry in plan and it is regular in elevation. Vertical loads are modelled as point loads applied to the top node of each column as function of the respective tributary areas in plan. Rigid diaphragm behaviour is imposed at every floor.

The maximum interstory drift ratio, at which the DLLS condition is achieved, is set to $\delta_{i,max} = 0.005$. Interstory drifts are monitored at each step of pushover analysis so that the damage limitation limit state is associated with top displacement of the structure which corresponds to the first exceeding of $\delta_{i,max}$.

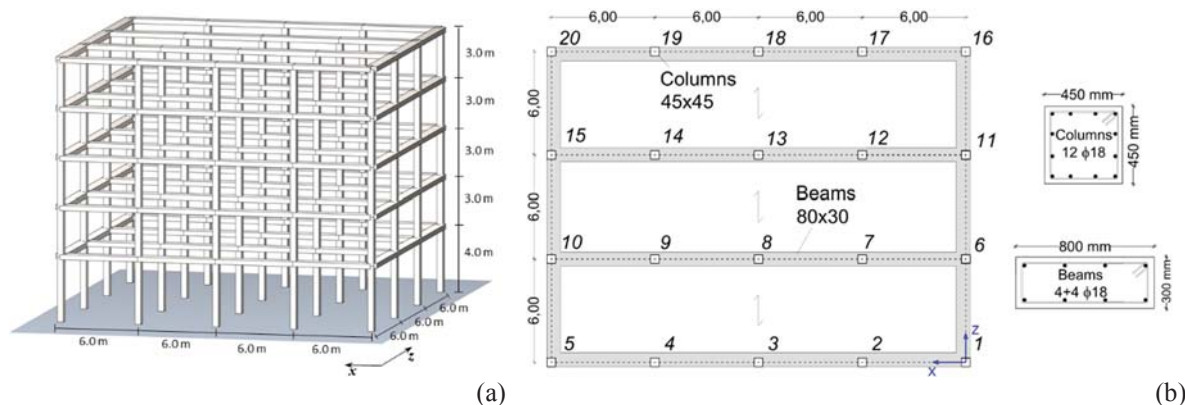


Figure 10: Geometrical dimension of the reference structural model: (a) 3D frame view; (b) in plane dimensions.

A preliminary assessment of the as-built structure has been carried out to test its performance against the reference earthquake loads. For the sake of simplicity, pushover analysis is carried out by considering only a uniform profile for lateral loads acting along the z direction of the structure, which is supposed being the most vulnerable to seismic actions. As can be seen from Fig. 11, depicting the pushover curve in the ADRS plane together with and EAL curve compared to the one associated to code compliant building, the structure shows both reduced ductility and propension to be vulnerable against damage limit states.

$\zeta_{E,DLLS}$	$\zeta_{E,LSLS}$	λ_{DLLS}	λ_{LSLS}	EAL
0.906	0.812	0.0263	0.0027	1.381

Table 3: GA analysis parameters set up for the case study.

Results are also shown in the Table 3, showing the as-built configuration safety factors related to DLLS and LSLS smaller than unity ($\zeta_{E,DLLS} = 0.9$ and $\zeta_{E,DLLS} = 0.8$). This leads to a EAL value that is equal to 1.381. Seismic retrofitting interventions are therefore needed.

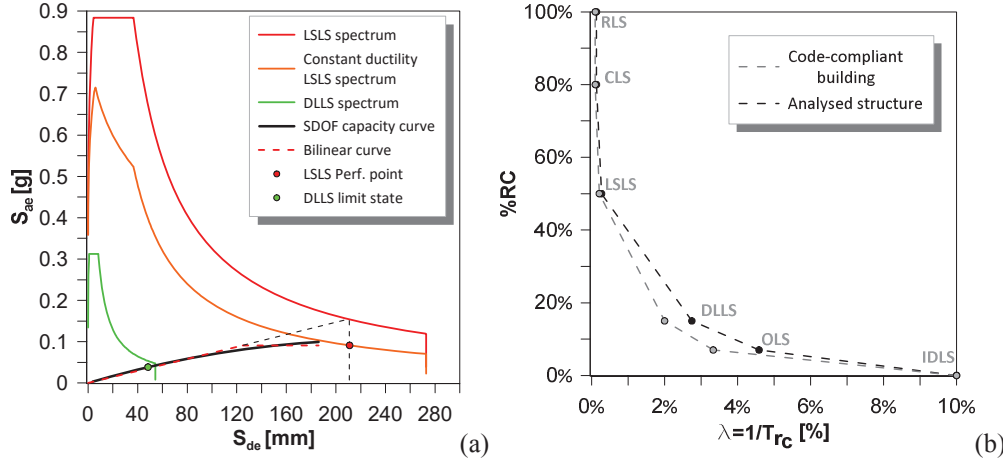


Figure 11: As-built preliminary test: (a) pushover curve in ADRS plane; (b) EAL curve compared with the curve related to code-compliant building.

4.2 Retrofitting system and hypotheses on the design space

The retrofitting system is composed of FRP wrapping of columns and concentric steel bracings. In order to reduce the computational effort of the analysis, the following restrictions are applied. Since the structure has a double symmetry in plane, the bracings are defined symmetrically on the two external transversal frames. In this way the n_{br} is the number of floors where the bracing systems are defined, starting from the ground floor, and ϕ_{br} is the diameter of the bracing, so that:

$$\begin{cases} n_{br} \in [0, n_{floor,max}] \\ \phi_{br} \in [\phi_{min}, \phi_{max}] \end{cases} \quad (23)$$

where $n_{floor,max}$ is the maximum number of floors of the structure to be potentially retrofitted (for the current case $n_{floor,max} = 5$), ϕ_{min} and ϕ_{max} are the minimum and maximum bracing diameters allowed respectively.

The FRP sheets have a thickness of $t_{f,1} = 0.337 \text{ mm}$ per layer, elastic modulus $E_f = 230 \text{ GPa}$, ultimate stress referred to net area of the fibers $f_{fib,k} = 3250 \text{ MPa}$ and ultimate strain $\epsilon_{fib} = 1.3\%$. For the implementation of FRP wrapping, it is assumed that a rounding of the column edges with a radius equal to $r_c = 25 \text{ mm}$ is carried out. The bracings are supposed to be made of S275 structural steel with $f_{yb} = 275 \text{ MPa}$, and elastic modulus $E_{sb} = 210 \text{ GPa}$.

To decrease the design space dimension, the analysis has been constrained to a limited number of columns for the confinement systems and to a restricted number of frames for the bracings. The following hypotheses are being placed:

- i) The optimization space for retrofitted columns by FRP jacketing is limited to the first two floors (red area Fig. 12).
- ii) The maximum number of FRP layers is 4.
- iii) The design space for the bracings is restricted to the central transversal frames (blue area Fig. 12).
- iv) Bracing diameter range of optimization is 20-100 mm and it vary with a minimum step size $\Delta\phi_{br}$ of 10 mm.

The resulting size of the design space is then of 6 integers that encode the number of floors where the bracings are defined (n_{br}), 9 discrete natural variables for the bracings diameter (ϕ_{br}), 4 naturals encoding the number of FRP layers (n_{FRP}), and 40 Boolean variables for the FRP position (\mathbf{p}). Therefore, the research space consists of 2×10^{14} different solutions.

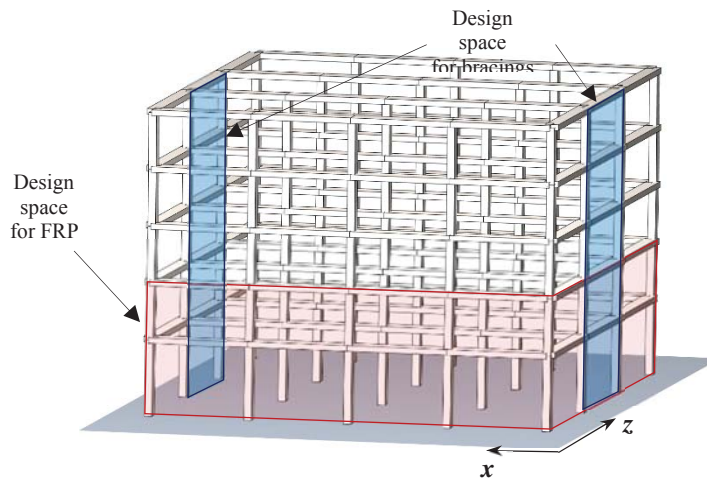


Figure 12: Design space representation on the case study structure.

4.3 Optimization results

The analysis was carried out starting from a first generation of 100 randomly generated. Individuals. The algorithm proceeds by creating 100 new child every generation selecting the parents from a tournament selection on three randomly selected parents. In the following Table 4 a summary of the GA framework parameter settings is reported.

Generation dimension	Number of off-spring	Tournament size \mathbf{k}	Max generations	Max stall
100	100	3	20	5

Table 4: GA analysis parameters set up for the case study.

The convergence history of the optimization is also shown in Fig. 13, where the optimal solution is found in correspondence of the eighteenth generation with a stagnation equal to two. As shown in the convergence Fig. 13a, the proper definition of the genetic operators allows a gradual transition between the exploration and exploitation phases.

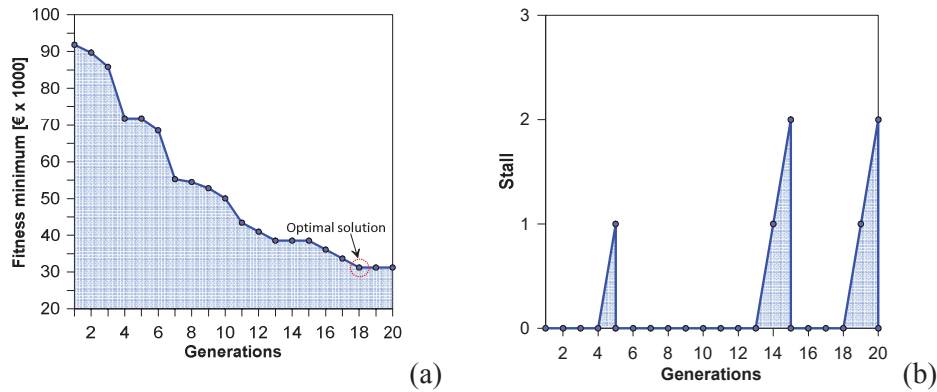


Figure 13: GA analysis performance results: (a) Convergence history; (b) Progressive optimal results stall.

The optimal solution obtained is represented in Fig. 14. It can be observed that the latter is characterized by only steel bracing retrofitting on the external frames for the first two floors, while no specific FRP interventions were required except from local reinforcement of braced frame columns. The optimal configuration bracings had a diameter $\varnothing_{br} = 50$ mm, which is equivalent to a cross-section area of $A_{br} = 19.6 \text{ cm}^2$. The overall cost of this intervention was 31299€.

Bracings were basically introduced to reduce lateral deformability of the frames, especially in along z direction, and prevent DLLS. However, bracings also provide additional strength and deformation capacity, so their contribution is also reflected on the LSLS. This double effect, combined with the overall lower cost of bracings with respect to FRP wrapping, has led the algorithm to individuate only steel bracings (as in Fig. 14) as the minimum cost solution.

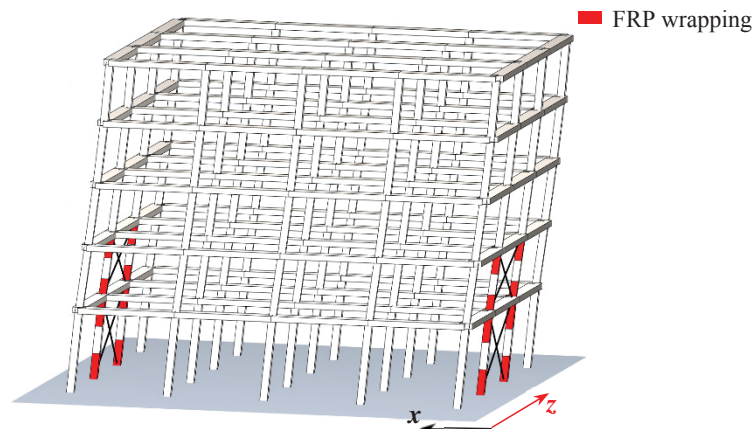


Figure 14: Retrofitting configuration of the optimal solution (deformed shape).

The performance of the optimal solution is shown in Figure 15 in terms of pushover and EAL curves. The increase in stiffness due to the retrofitting system led to a reduced displacement demand, which combined with the additional resistance and ductility provided by the steel bracing allowed satisfying both LS and DL limit states. As reported in Table 5, safety factor related to damage limit state is barely close to the unity ($\zeta_{E,DLLS} = 1.025$) whereas the safety factor related to LSLS is $\zeta_{E,LSLS} = 1.585$.

The EAL curve displayed in Fig. 15b shows a noteworthy reduction with respect to as-built configuration EAL, resulting in $EAL = 1.01\%$. Given that the objective function does not directly consider the value of the EAL associated with each tentative solution (only the cost is minimized), the optimal configuration does not lead to EAL value that is optimized with respect

to the code compliant building. However, the proposed framework improves the quality of the retrofitting design by providing a cost-optimized intervention with a control on the EAL.

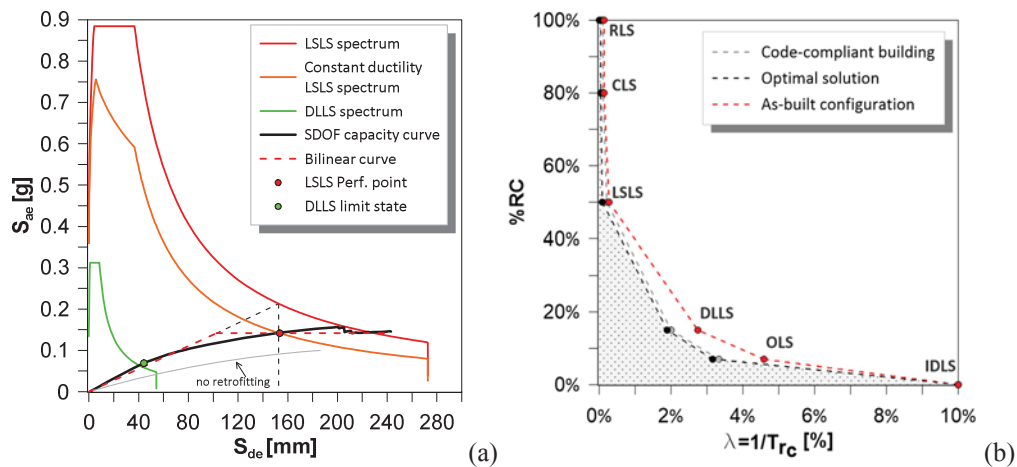


Figure 14: Optimal solution: (a) pushover curve in ADRS plane; (b) EAL curve.

n_{FRP}	n_{br}	ϕ_{br} (mm)	$\zeta_{E,DLLS}$	$\zeta_{E,LSLS}$	EAL (%RC)	Cost (€)
1	2	50	1.025	1.585	1.009	31229

Table 5: Optimization analysis results

5 CONCLUSIONS

The paper has presented a novel optimization framework aims to minimize costs related to retrofitting intervention on RC frame structures. The framework is based on genetic algorithm developed in MatLab® which interfaces with a 3D fiber-section model realized in OpenSEES. Two different typology of retrofitting system are considered: FRP jacketing of columns and steel bracings.

The main target of the algorithm is to seek the retrofitting configuration that optimize the intervention costs taking into account in indirect way of the expected annual loss value referring to that requested by the reference technical code. The performance of each tentative solution is evaluated starting from the results of non-linear static analysis in the framework of N2 method. Through a case study implementation, it has been shown that the proposed framework can pinpoint optimal retrofitting arrangement in efficient way. Eventually, the results obtained have been compared with the outcomes of an optimization procedure that neglect the EAL assessment.

An extensively usage of the framework will allow improving the management of the funds allocated to seismic retrofitting of existing structures enhancing the overall structural safety of building heritage.

REFERENCES

- [1] C. Chisari, C. Bedon, Multi-Objective Optimization of FRP Jackets for Improving the Seismic Response of Reinforced Concrete Frames. *American Journal of Engineering and Applied Sciences*, **9**(3), 669-79, 2016.

- [2] H. Seo, J. Kim, M. Kwon, Optimal seismic retrofitted RC column distribution for an existing school building. *Engineering Structures*, **168**, 399-404, 2018.
- [3] N. Pollini, O. Lavan, O. Amir, Minimum-cost optimization of nonlinear fluid viscous dampers and their supporting members for seismic retrofitting. *Earthquake Engineering & Structural Dynamics*, **46**, 1941–61, 2017.
- [4] F. Braga, R. Gigliotti, R. Laguardia, Intervention cost optimization of bracing systems with multiperformance criteria. *Engineering Structures*, **182**, 185-197, 2019.
- [5] O. Lavan, G.F. Dargush, Multi-objective evolutionary seismic design with passive energy dissipation systems. *Journal of Earthquake Engineering*, **13(6)**, 758-90, 2009.
- [6] R. Falcone, F. Carrabs, R. Cerulli, C. Lima, E. Martinelli, Seismic retrofitting of existing rc buildings: a rational selection procedure based on genetic algorithms. *Structures*, **22**, 310–326, 2019.
- [7] G.S. Papavasileiou, D.C. Charmpis, N.D. Lagaros, Optimized seismic retrofit of steel-concrete composite buildings. *Engineering Structures*, **213**, 110573, 2020.
- [8] F. Di Trapani, M. Malavisi, G.C. Marano, A.P. Sberna, R. Greco, Optimal seismic retrofitting of reinforced concrete buildings by steel-jacketing using a genetic algorithm-based framework. *Engineering Structures*, **219**, 110864, 2020.
- [9] G.M. Calvi, Choices and criteria for seismic strengthening. *Journal of Earthquake Engineering*, **17(6)**, 769-802, 2013.
- [10] F. McKenna, G.L. Fenves, M.H. Scott, *Open system for earthquake engineering simulation*. University of California Berkley, 2000.
- [11] E. Cosenza, C. Del Vecchio, M. Di Ludovico, M. Dolce, C. Moroni, A. Prota, E. Renzi, The Italian guidelines for seismic risk classification of constructions: technical principles and validation. *Bulletin of Earthquake Engineering*, **16**, 5905–5935, 2018.
- [12] P. Fajfar, A Nonlinear Analysis Method for Performance-Based Seismic Design. *Earthquake Spectra*, **16(3)**, 573-92, 2000.
- [13] *Norme tecniche per le costruzioni. Decreto ministeriale 17 gennaio 2018*, Ministero delle infrastrutture e dei trasporti, 2018.
- [14] *Eurocode 8. Design of structures for earthquake resistance - Part 3: Assessment and retrofitting of buildings*, European Committee for Standardization, 2005.

THE ROLE OF THE SUSTAINED LOADS ON THE BEARING CAPACITY OF REINFORCED CONCRETE COLUMNS RETROFITTED BY STEEL JACKETS

Marco Filippo Ferrotto, Bharat Pradhan and Liborio Cavaleri

University of Palermo
Viale delle Scienze, Palermo, Italy
{marcofilippo.ferrotto, bharat.pradhan, liborio.cavaleri}@unipa.it

Abstract

Strengthening of reinforced concrete structures by steel jackets is a common retrofitting technique widely used in engineering practice. In most cases, reinforced concrete columns are strengthened under service loads while the columns are subjected to a certain amount of compressive stress caused by gravitational loads. In such cases, the bearing capacity for strengthened columns can be different from that obtained without existing stresses. In this paper, the effect of sustained loads in the prediction of the bearing capacity for strengthened columns is assessed by experimental, numerical, and analytical approaches. The results of the investigation revealed that the level of sustained loads at the moment of strengthening reduces the bearing capacity of columns, influencing the overall performances of retrofitted structures.

Keywords: Steel Jacketing, Confined Concrete, Sustained Loads, Preloading, Retrofitting.

1 INTRODUCTION

Retrofitting of existing RC frame structures by strengthening members such as beams and columns is among the commonly adopted strategies to improve the seismic capacity of existing buildings subjected to seismic actions [1-3]. Different approaches are available nowadays and each method provides different capacity improvement depending on the mechanical behavior of the confining device [3]. For example, Fiber Reinforced Polymers (FRP) sheets provide to the columns passive confining mechanism [4-9], and steel jackets provide semi-active or active confinement [8-15]. Other techniques can be used to increase the cross-section of the existing columns i.e. reinforced concrete jackets [18,19].

Most of the available analytical and mechanical models are provided without considering the effect of existing sustained loads on the members during the strengthening, that is a common situation for reinforced concrete structures. The consequence is that, when these formulations are used for the assessment of buildings, it is not possible to consider whether the elements are already in a stressed/strained state able to change the effectiveness of the adding reinforcement [8,17].

In the last years, few studies dealt with the modification of the capacity of strengthened members while loaded. In the case of FRP jacketing, the findings do not always lead to the same conclusions. Some authors state that there is no significant capacity modification [7], other authors state that there is a capacity reduction depending on the level of stress/strain acting on the columns at the moment of strengthening [20]. In the case of steel jackets, it was demonstrated that there is a reduction of the capacity depending on the level of sustained loads in the columns when the reinforcement is applied [17]. An important role belongs also to the time-dependent effects to consider the modification of the compressive strength of the concrete.

This paper focuses on the evaluation of the compressive behavior of columns strengthened by means of external steel cages considering the effect of the presence of service loads, and how this effect can change the compressive capacity with respect to the commonly known compressive behavior of confined members without preload.

A numerical model is assessed by the finite element software Abaqus CAE to realistically reproduce the physical process. Results by a recent experimental investigation are used for the calibration and the validation of the FE model, demonstrating the reliability of the proposed procedure.

2 THEORETICAL FRAMEWORK

Retrofitting by strengthening on existing structures is usually performed under serviceability loads (gravitational loads from beams and slabs with no live loads): the consequence is that the concrete columns are subjected to a certain stress-strain level when become strengthened. The ratio between the acting stress $\sigma(\varepsilon)$ and the compressive concrete strength f_{c0} can identify the preloading level as follows [6,17]:

$$n_p = \frac{P}{P_{\max}} = \frac{\sigma(\varepsilon)}{f_{c0}} \quad \text{for } 0 \leq n_p \leq 1 \quad (1)$$

After the strengthening, the column became confined only if further increasing of loads are applied, changing the behavior from plain concrete to confined concrete. This differs from the case of columns strengthened without preload and different results in terms of load-carrying capacity were found to be depending on the preloading level acting while the columns are strengthened.

In the following sections, the physical problem is faced by means of the finite element modeling software package *Simulia* Abaqus CAE, reproducing the pre-loading, the confinement, and the failure compressive tests. The plasticity parameters for the concrete as well as the constitutive material modeling of steel and concrete are discussed also considering the influence of the time-dependent effects due to the concrete subjected to sustained stresses. The finite element model was calibrated on the basis of a previous experimental investigation carried out by the authors. A further validation has been made with further new experimental tests presented in the second part of the paper, demonstrating the reliability of the findings and the suitability of the realistic prediction of the process carried out by numerical approach.

It is worth stating that the authors assessed this numerical procedure in the case of FRP-confined concrete cylinders subjected to preload [6].

3 NUMERICAL MODEL

The finite element software ABAQUS CAE version 6.13 [21] was used to build a FE model of reinforced concrete columns externally confined with steel angles and plates according to the study of Ferrotto et al. [16].

The column and the steel cage were modeled with C3D8-R elements (8-node linear brick, reduced integration, hourglass control). Mesh convergence studies were carried out to observe the influence of the aspect ratio of the C3D8-R elements on the global response and to determine optimal FE mesh that provides a relatively accurate solution with low computational efforts. Elements with aspect ratio not higher than 1.5 resulted to be optimal for the numerical simulations.

Concrete prismatic specimen having dimensions of 200x200x750 mm and compressive strength of 25 MPa was used. The steel cage was composed by steel angles and strips with yielding stress of 275 MPa, having dimensions of 50/50/5 (mm) and 40/4 (mm) respectively. Details of the specimen are shown in Fig. 1.

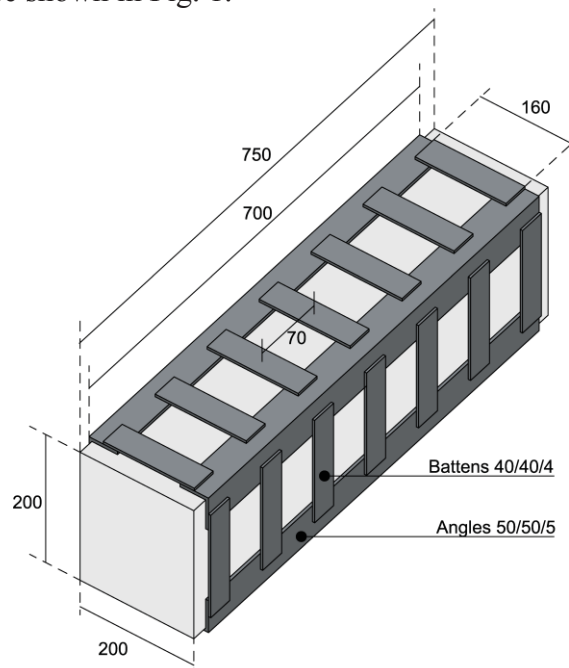


Figure 1: Geometrical configuration of the strengthened specimen.

3.1 Boundary conditions and interactions

Two rigid bodies at the top and the bottom of the specimen with the translational degrees of freedom restrained for the ends except for the vertical displacement (direction of loading) were defined. “Tie-constrain” interactions were used to define the contact properties between the steel battens and the steel angles to simulate the welding of the steel so that there was no relative motion between them. The same interactions were defined also between the concrete column and the steel angles. The latter assumption allows to define a perfect contact between steel angles and concrete (avoiding potential convergence problems due to other types of contact modeling) provided that an adequate material constitutive law is defined for the steel angles.

3.2 Material modeling of steel

According to Ferrotto et al. [16], during compression tests, RC Steel Jacketed columns can be loaded in two different ways, that are applying the load both to the steel angles and the concrete (angles fully-loaded) or to the concrete column only (angles indirectly-loaded). Buckling or frictional effects need to be considered in the constitutive modeling of the steel if tie-constrain interaction is used.

To take into account tangential stresses along the contact surfaces between steel angles and concrete (in the case of angles indirectly-loaded), Mohr-Coulomb criterion was adopted according to Campione et al. [15] and Ferrotto et. al. [16, 17]. If 0.5 is used as a friction coefficient μ , the equivalent normal stress in the angles (fictitious yielding stress corresponding to the concrete-angles sliding) can be expressed as follows:

$$f_y^* = \frac{2 \cdot n_a \cdot l_1 \cdot l_0 \cdot (\mu \cdot f_{l_{\max}})}{n_a \cdot t_1 \cdot (L_1 + t_1)} = \frac{l_1 \cdot l_0 \cdot f_{l_{\max}}}{t_1 \cdot (L_1 + t_1)} \quad (2)$$

in which n_a is the number of the angles, L_1 and l_1 are the external and the internal sides of the angles in contact with the concrete column respectively, l_0 is the overall vertical length along the columns and t_1 is the thickness of the angles. For more details, please refer to the original treatment of the authors.

In the case of angles fully loaded, the model allows the evaluation of the critical stress taking into account possible buckling by the following equations:

$$\sigma_c = \frac{1}{s_b \cdot l_t \cdot t} \cdot \frac{1}{\sqrt{2\varepsilon_s - \varepsilon_s^2}} \cdot \left\{ 2 \left[\frac{l_t^2 \cdot t \cdot f_{yb}}{4} - \frac{(N_u^*)^2}{16 f_{yb} \cdot t} \right] - \sqrt{2} f_{le} \cdot l_t \frac{s_b^2}{4} \right\} \quad (3)$$

$$N_u^* = \varepsilon_s \cdot 2 \cdot l_t \cdot t \cdot E_s \leq 2 \cdot l_t \cdot t \cdot f_{yb} \quad (4)$$

with s_b being the spacing of the horizontal steel battens, l_t the transversal width of the angles, t the thickness of the angles, and ε_s the axial strain in the angle.

3.3 Material modeling of concrete

Material modeling of concrete has been performed according to Ferrotto et. al. [16] by using Concrete Damaged Plasticity (CDP) model available in the software package, by considering modifications for the plasticity parameters to overcome problems related to the triaxial stress state of concrete under high confining stresses. In detail, modification to the yield criterion, the hardening/softening rule and the flow rule are provided by adequate laws for:

- the dilation angle ψ that defines the plastic flow potential;

- the ratio between the compressive strength under biaxial loading and uni-axial compressive strength f_{b0}/f_{c0} ;
- the ratio Kc between the second stress invariant on the tensile meridian and that on the compressive meridian for the yield function.

In the present work, CDP model was used to perform simulation in the case of confinement under monotonic loads only, therefore the damage variables were not defined.

The parameter Kc is evaluated according to Ozbakkaloglu et al. [22] depending on the ratio f_{b0}/f_{c0} as follows:

$$\frac{f_{b0}}{f_{c0}} = 1.57 \cdot f_{c0}^{-0.09} \quad (5)$$

$$Kc = 0.71 \cdot f_{c0}^{-0.025} \quad (6)$$

The dilation angle is evaluated depending on the external transverse mechanical confinement ratio ω_{st} .

$$\omega_{st} = \omega_{st,x} + \omega_{st,y} = \left(\frac{A_{st,x}}{h \cdot s_b} + \frac{A_{st,y}}{b \cdot s_b} \right) \frac{f_{yb}}{f_{c0}} \quad (7)$$

$$\psi = 56.3e^{-0.594 \cdot \omega_{st}} \quad (8)$$

In Eqs. (7) $A_{st,x}$ and $A_{st,y}$ are the area of the transverse steel bars along x and y direction respectively, b and h are the dimensions of the concrete cross-section, s_b and f_{yb} are the spacing of the horizontal steel battens and the yielding stress, f_{c0} is the unconfined concrete strength.

A three-stage stress-strain relationship for the plain concrete is therefore used to take into account the modification proposal by Ferrotto et al. [16] depending on the external transverse mechanical confinement ratio ω_{st} as well as the dilation angle.

$$\frac{f_c(\varepsilon)}{f_{c0}} = \begin{cases} \frac{x_1 \cdot \gamma_1}{\gamma_1 - 1 + x_1^{\gamma_1}} & 0 \leq \varepsilon \leq \varepsilon_{c0} \\ 1 & \varepsilon_{c0} \leq \varepsilon \leq \varepsilon_{c1} \\ \frac{x_2 \cdot \gamma_2}{\gamma_2 - 1 + x_2^{\gamma_2}} & \varepsilon \geq \varepsilon_{c1} \end{cases} \quad (9)$$

$$\gamma_1 = \frac{E_c}{E_c - \frac{f_{c0}}{\varepsilon_{c0}}}, \gamma_2 = \frac{E_c}{E_c - \frac{f_{c0}}{\varepsilon_{c1}}}, x_1 = \frac{\varepsilon}{\varepsilon_{c0}}, x_2 = \frac{\varepsilon}{\varepsilon_{c1}} \quad (10)$$

$$\frac{\varepsilon_{c1}}{\varepsilon_{c0}} = 0.2107 \cdot \ln(\omega_{st}) + 1.6455 \quad (11)$$

In the above equations, ε_{c0} is the unconfined concrete peak strain, ε_{c1} is the increasing peak strain affected by the confinement, and E_c is the modulus of elasticity of the plain concrete.

3.4 Simulation of the preloading

Differently to the case of strengthening of columns without preload, in the presence of loads (a situation that reflects several cases of reinforcement of existing buildings), the con-

fining element gives its contribution starting from a certain stress/strain level. The external reinforcement should be modeled/activated as soon as the concrete reaches the state of stress at the moment of the application of the reinforcement.

The problem is solved by using the deactivation/reactivation elements technique identified in the software by the “model change interactions”. It is thus possible to define the assembled system in such a way to activate the wrapping contribution only when desired.

The simulation of the preload conditions is obtained by articulating the analysis into two steps: i) force applied to the top section of the specimen according to the fixed preload level, ii) the external steel cage is activated and the load test continues until the failure of element.

Specifically, simulations under preload conditions require that in the first step a force/displacement is applied to the non-confined element (with the reinforcement device deactivated) and the stress/strain state at the end of the analysis corresponds to the tensional state relative to the preload level. In the second step, the confinement device becomes active in deformed conditions, characterized by the congruence of the nodal displacements of the concrete meshes, but with zero stress/strain state.

Axial stresses, lateral stresses and axial total strains corresponding to the middle section were recorded during the analysis.

The time analysis-stress and the stress-strain response are plotted in Fig. 2 for the case of compression test with no preload and with two different levels of preloading i.e. np 0.7 and 0.9. It is possible to see that, coupled with the strain lag activation of the steel cage (and therefore the providing of the lateral confinement pressure), the strength decreases as the imposed preload level increases (Fig. 2).

In Fig. 3 the stress and strain distributions in the specimen confined with steel jackets are shown for three significant steps of the numerical process:

- The end of the first step (Fig. 3 a-b) in which the unconfined concrete reached the preload without any contribution of the jacket;
- The beginning of the second step at increment 0 (Fig. 3 c-d) in which the concrete keeps the same stress/strain configuration of the previous step and the jacket becomes “active” in a virgin stress/strain state but having the same shape of the column;
- A certain increment of the second step (Fig. 3 e-f) in which the steel jackets contribute to the global response. In this phase, the strain compatibility is still given by “tie constrains interaction” and the strains in the jackets are lower than the cylinders because they are computed in the analysis before the preloading step.

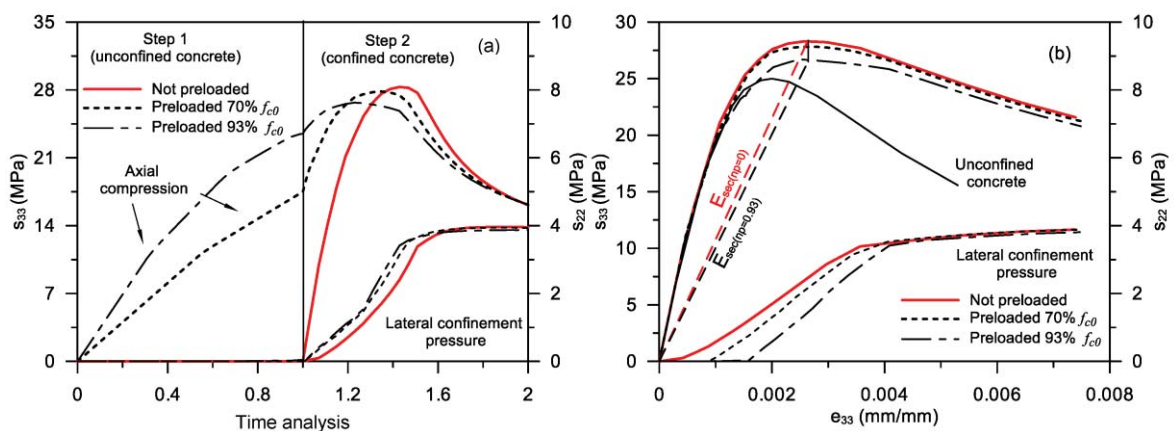


Figure 2: FE computational process (a) and Axial stress-strain behavior and lateral pressure evolution (b).

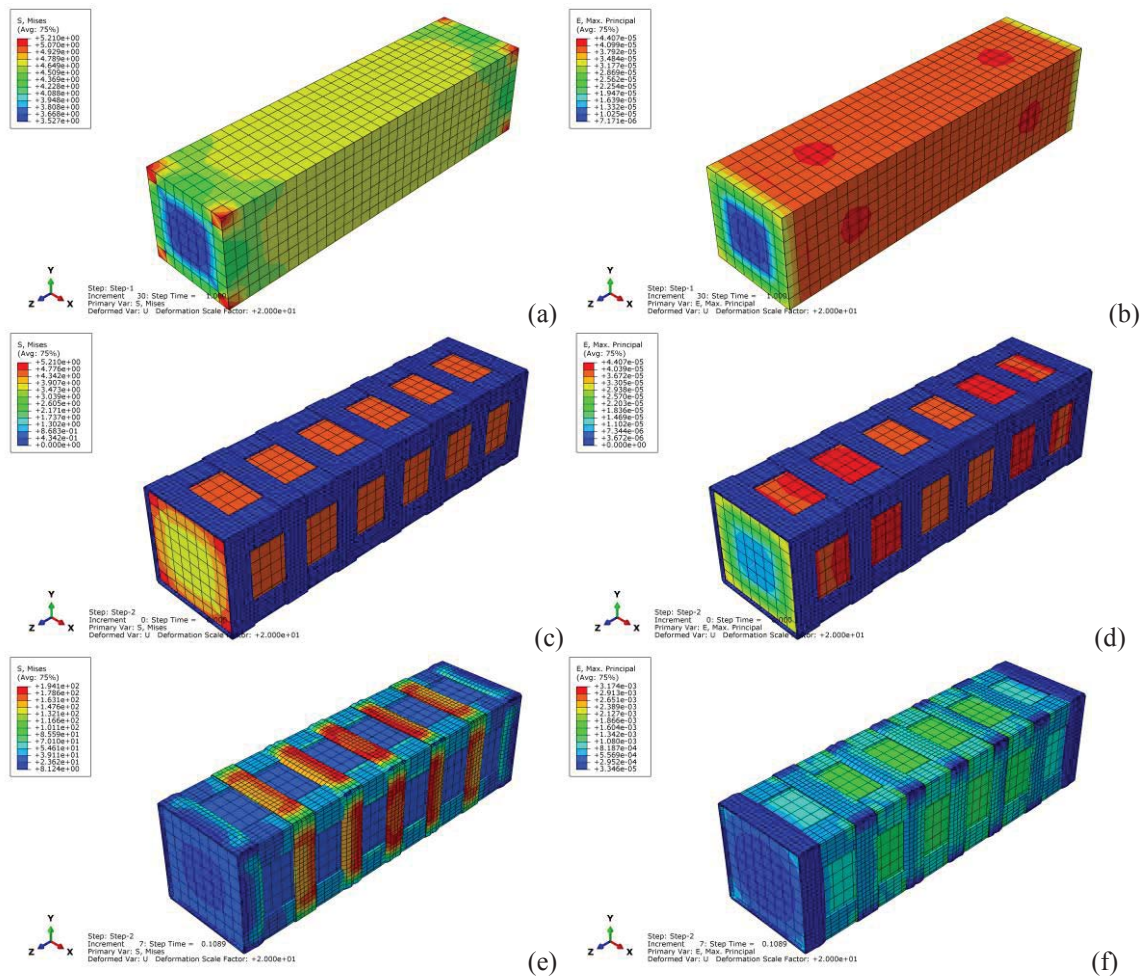


Figure 3: Stresses and strains distribution in the model (case 2) during: end of first step (a and b); second step at increment 0 (c and d) and increment 7 (e and f)

4 EXPERIMENTAL TESTING

In the following, a brief description of an experimental investigation previously carried out by the authors is provided. For more details, please refer to the original paper by Ferrotto et al. [17]. It has to be pointed out that, in the frame of the present paper, additional tests carried out for different concrete age specimens are presented to improve the number of data and the reliability of the findings.

The experimental program consisted of compression tests on columns strengthened by means of steel cages under different load conditions. Tests on unreinforced, reinforced before any loading and reinforced after axial loading at a fixed rate of the capacity were performed for low, medium and high level of the preload.

Fifteen compressive tests were performed. Among the total number of tests, ten columns were tested with an average concrete age of 146 days, while five additional columns were tested with an average concrete age of 530 days. The reason was to observe the effect of the aging of the concrete on the compressive capacity including sustained loads.

The external steel cages used for the strengthening were defined according to Fig. 1, connecting angles and battens by welding. For both angles and battens, no mortar was used at the contact surfaces with the concrete columns.

The steps of the tests of the preloaded specimens are listed hereinafter:

- Preloading: during this stage, the measuring of the shortening in the middle height of the specimens allowed to identify the stress-strain behavior of the unconfined concrete. Once the target preload was reached, stabilization of the load and acquisition of creep strains were performed;
- Strengthening: After preloading, digital transducers were removed from the concrete specimens and steel jackets were applied by welding;
- Unloading: specimens were unloaded and transferred to the load testing machine, strain gauges were applied to the steel cages and the digital transducers to the concrete specimens as in the case of the preload tests. Moreover, long digital transducers were assembled at the four corners of the specimens;
- Collapse test: the specimens were loaded up to collapse, recording axial strains of the columns and axial and lateral strains on the steel jackets.

Preloading was applied in a three-dimensional steel testing frame system composed by three rigid steel beams and four steel bars (diameter of 80 mm) fixed to the lower floor structure. Hydraulic jack and a load cell were placed between the central steel beam and the concrete specimen to apply the compressive force monitored by a digital data acquisition system.

The welding of the steel cages was done while specimens were under a certain assigned stress/strain state. The apparatus for the preloading is shown in Fig. 4 coupled with a picture of a specimen reinforced under sustained loads.

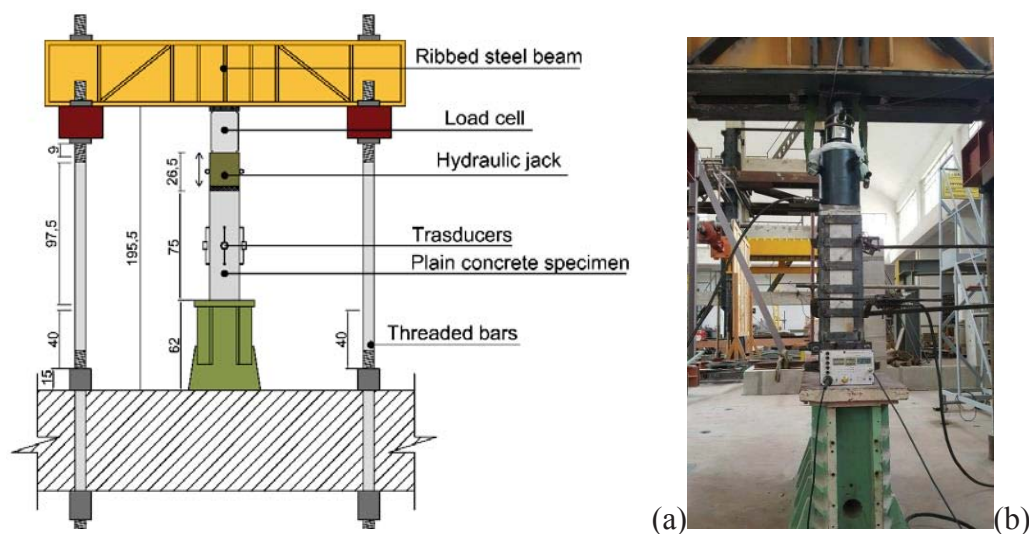


Figure 4: Preloading frame device (a); Strengthening of a specimen under sustained load.

Axial strains on the column specimens were measured by using two systems of digital transducers. Four of these had a gauge length equal to the internal length of the specimen (750 mm) and were placed at the corners. Four other transducers were placed on the lateral faces of the column at the middle height, with a gauge length of 220 mm. The double system of transducers allowed the recognition of strain concentration in the middle of the specimens. Strains on the steel cages were also recorded by means of “linear type” strain gauges with a gauge length of 13 mm. Horizontal and vertical strain gauges were bonded to the steel battens in correspondence of the middle height of the column and on the external surface of the steel angles at the top, middle and bottom respectively. This measurement layout allowed to obtain average strains and stresses of the battens (controlling, therefore, the evolution of the lateral pres-

sure) and average strains and stresses of the angles (obtaining the axial load carried out by the angles). Details of the measurement setup are reported in Fig. 5.

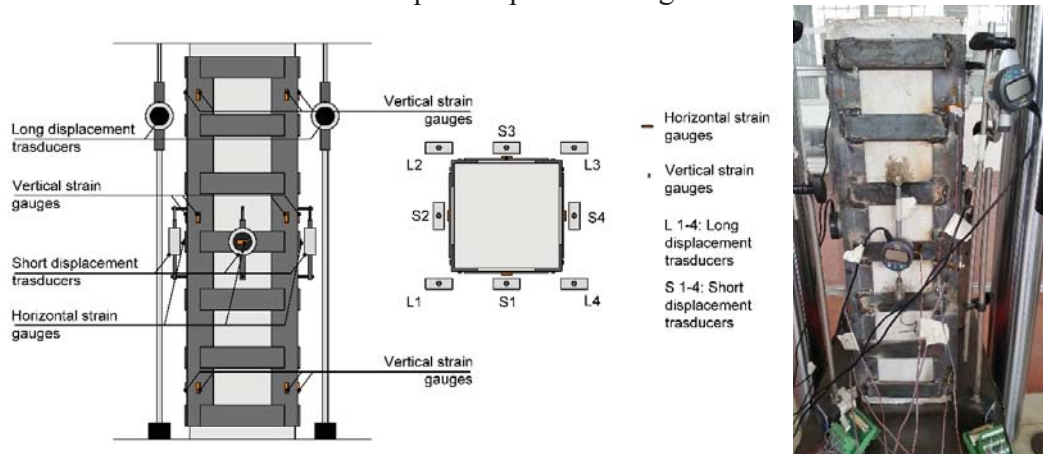


Figure 5: Arrangement of the measurement system.

4.1 Testing under sustained loads

The target strength for the concrete was 20 MPa. Concrete mixture was composed by CEM I 32.5 R, water, sand and aggregate with size varying from 0 to 20 mm, having proportion in weight 1:1.51:0.384:0.353. Concrete cubes having size of 150 mm were made during the concrete casting, for testing the compression strength after 28 days. The tests were performed according to UNI EN 12390 Standards. Test results provided for the plain concrete a cubic compressive strength of 19.99 MPa (and therefore, a cylinder compressive strength of 16.59 MPa), while the target strength f_{c0} was considered equal to 16.75 MPa based on the average from cubes and two full-scale plain concrete specimens (633.94 kN and 715.27 kN with average max load and stress of 674.58 kN and 16.86 MPa respectively).

Specimens were labeled depending on the type of preload (P#), the type of reinforcement (S) and the number of the specimen #. For example, specimen P0S1 referred to 0 preload force, specimen strengthened with steel jackets (S), specimen n1, while P60S2 refers to a preload force nominally equal to the 60% of the strength, specimen strengthened with steel jackets, specimen n 2. Table 1 lists the details of each test.

Specimen	Type of test	Preload level (%) and force (kN)	Average concrete age (days)
NC1-2	Plain concrete	/	146
P0S1-2	Confined	/	146
P0S3		/	146
P40S1	Preloaded and confined	40 / 270	146
P60S1-2	Preloaded and confined	60 / 402	146
P60S3			530
P70S1	Preloaded and confined	70 / 483	146
P70S2			530
P80S1-2	Preloaded and confined	80 / 530	146
P80S3			530
P90S1	Preloaded and confined	90 / 603	530

Table 1: Type of tests.

Preload tests had variable duration depending on the evolution of creep strains after the maximum load was reached. The time of preloading for each specimen was: specimen P40S1, 10 hours, P60S1-3, 11, 10 and 12 hours respectively, P70S1-2 6.5 and 8 hours respectively, P80S1-3 7.5, 5 and 8 hours respectively, and P90S1 7 hours.

In the case of low preload levels, i.e. for preloaded specimens at 40% and 60% of the strength, creep strains evolution was restricted and stable. Otherwise, for high preload forces (i.e. 70-90%), higher creep strains evolution was observed followed by smeared cracking of the specimens.

During the last stage of the preloading, specimens were strengthened by the steel jackets; then, after the unloading and the transferring to the load testing machine, specimens were equipped with digital transducers and strain gauges before the final collapse tests. For more details, please refer to the original treatment of the authors [17].

4.2 Failure compressive tests

Compressive load-strain response of the strengthened specimens was characterized by load increasing behavior up to the maximum load capacity, followed by a strain-softening behavior. Compression tests were terminated in correspondence to a reduction of 85% of the maximum load. In some cases, a premature failure of the confinement device occurred by the failure of the welding between steel angle and strip causing a high loss of load (as for specimen P0S2). Some pictures of strengthened specimens at failure are shown in Fig. 6.

The results showed a significant increase in load and deformational capacity compared to the compression response of unconfined specimens. It is important to note that this increase in the load capacity was due to the global contribution provided by the response of the confined concrete and the angles.

Compression tests of preloaded specimens showed differences with respect to the non-preloaded ones. Load-strain curves were affected by a reduction of the maximum load-bearing capacity and a significant reduction in the secant stiffness. This effect was caused by the strain-lag (lower confinement lateral pressure for a given value of axial strain with respect to the non-preloaded specimens) directly proportional to the applied preload level as for the load carried out by the angles. These reductions can be observed in Table 2 that summarizes the experimental results (and subsequently the comparisons with the FE predictions).



Figure 6: Strengthened specimens at failure.

5 COMPARISONS BETWEEN EXPERIMENTAL RESULTS AND FE PREDICTIONS

The comparisons between experimental results and FE predictions are presented hereinafter. The plasticity parameters of the concrete for the numerical model were calculated by using Eqs. (5-9), while the steel angles equivalent yielding stress was calculated by using Eq. (2). An equivalent elasticity modulus has been assigned to the steel angles to consider indirectly the sliding between the steel and concrete contact surfaces according to Ferrotto et al. [17].

The effect of the sustained loads on the compressive strength of concrete need to be considered for the modification of the compressive response of the plain concrete depending on:

- i) the level of sustained load applied before strengthening (preloading): this aspect modifies, according to the statements presented in section 3.4, the load-strain response of the confined concrete because of the strain-lag effects;
- ii) the modification of the plain concrete strength due to high sustained stresses: this aspect was considered according to the findings of Rüsç [23] and Tasevski et al. [24].

The first aspect was assessed by a modification of the hardening/softening function to consider the reduction of the confinement effects due to the strain-lag. This causes a lower equivalent compressive peak strain compared to confined concrete without preload. Besides, this effect resulted in much higher strain as the preload level increases. Differently from Eq. (11), in the frame of this study, a new equation (Eq. 12) is proposed based on non-linear regression of the numerical results depending on the mechanical confinement ratio and the preloading level. The proposed equation considers the increasing of the concrete peak strain due to the confinement and, at the same time, the reduction of the latter due to the preloading effects by the parameter $k_{(np)}$. It is remarked that, by using Eq. (12), in the case of columns without any external reinforcement and no preload, the behavior of the plain concrete is obtained.

$$\frac{\varepsilon_{c1}}{\varepsilon_{c0}} = k_{(np)} \cdot (1 + 1.6877 \cdot \omega_{st}) \quad (12)$$

$$k_{(np)} = 1 + 0.0785 \cdot n_p - 0.4695 \cdot n_p^2$$

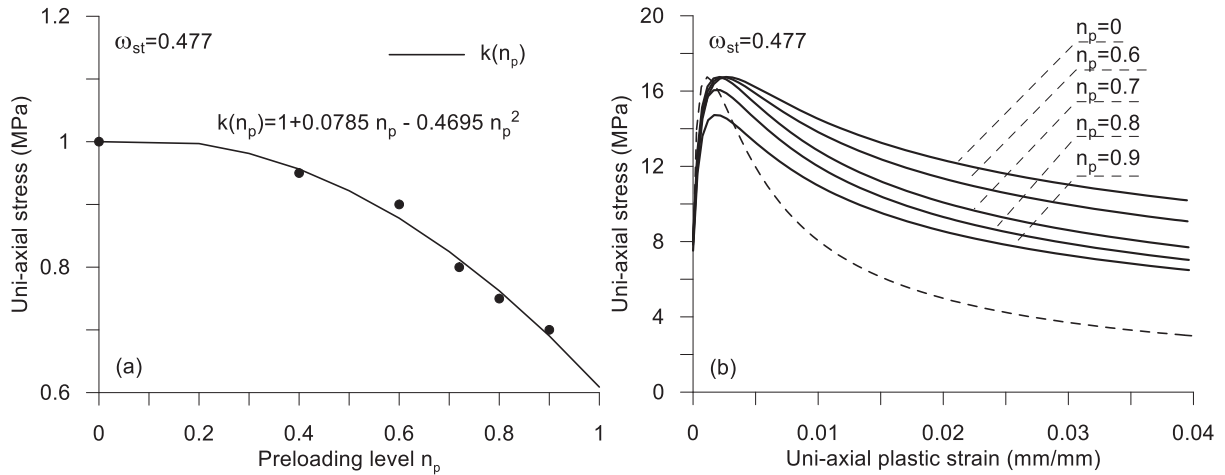
The second aspect is assessed by a simplified analytical equation to predict the compressive strength of concrete influenced by high sustained loads according to Tasevski et al. [24]. The proposed equation is selected in the present study to be used for the assessment of the numerical model.

$$\begin{aligned} f_c(np) &= 1 \cdot f_{c0} & \text{if } n_p &\leq 0.75 \\ f_c(np) &= (1.6 - 0.8 \cdot n_p) \cdot f_{c0} & \text{if } n_p &\geq 0.75 \end{aligned} \quad (13)$$

As a result, in Fig. 7 a-b, the reduction parameter $k_{(np)}$ and the uni-axial stress-plastic strain laws used for the analyses are shown for the different preloading levels according to the experimental tests. The others plasticity parameters as well as the plain concrete strengths used for the numerical analyses are shown in Table 3. Finally, the experimental-numerical comparisons in terms of load-strain response are shown in Fig. 8, highlighting the suitability of the FE model to reproduce the compressive behavior of the strengthened columns under the different levels of preload.

Specimen	P_{\max} -Exp (kN)	FE (kN)	FE/ P_{\max} -Exp
P0S1	1364.80		0.97
P0S2	1402.97	1317.88	0.94
P0S3	1341.60		0.98
P40S1	1297.30	1295.00	1.00
P60S1	1274.14		1.00
P60S2	1237.31	1271.40	1.03
P60S3	1214.10		1.05
P70S1	1179.80		1.04
P70S2	1224.59	1222.48	1.00
P80S1	1203.01		0.98
P80S2	1323.13	1182.37	0.89
P80S3	1141.30		1.04
P90S1	1153.24	1120.00	0.97

Table 2: Experimental and numerical results.


 Figure 7: Reduction parameter $k(n_p)$ (a); uni-axial stress-plastic strain laws used for the analyses (b).

Specimen	Concrete strength (MPa)	Dilation angle	Kc	f_{b0}/f_{c0}	ε_{c1}
P0S	16.75	42.45	0.736	1.21	0.00362
P40S	16.75	42.45	0.736	1.21	0.00350
P60S	16.75	42.45	0.736	1.21	0.00320
P70S	16.75	42.45	0.736	1.21	0.00289
P80S	16.08	41.89	0.736	1.22	0.00275
P90S	14.74	40.85	0.738	1.23	0.00257

Table 3: Plasticity parameters for the different case analyses.

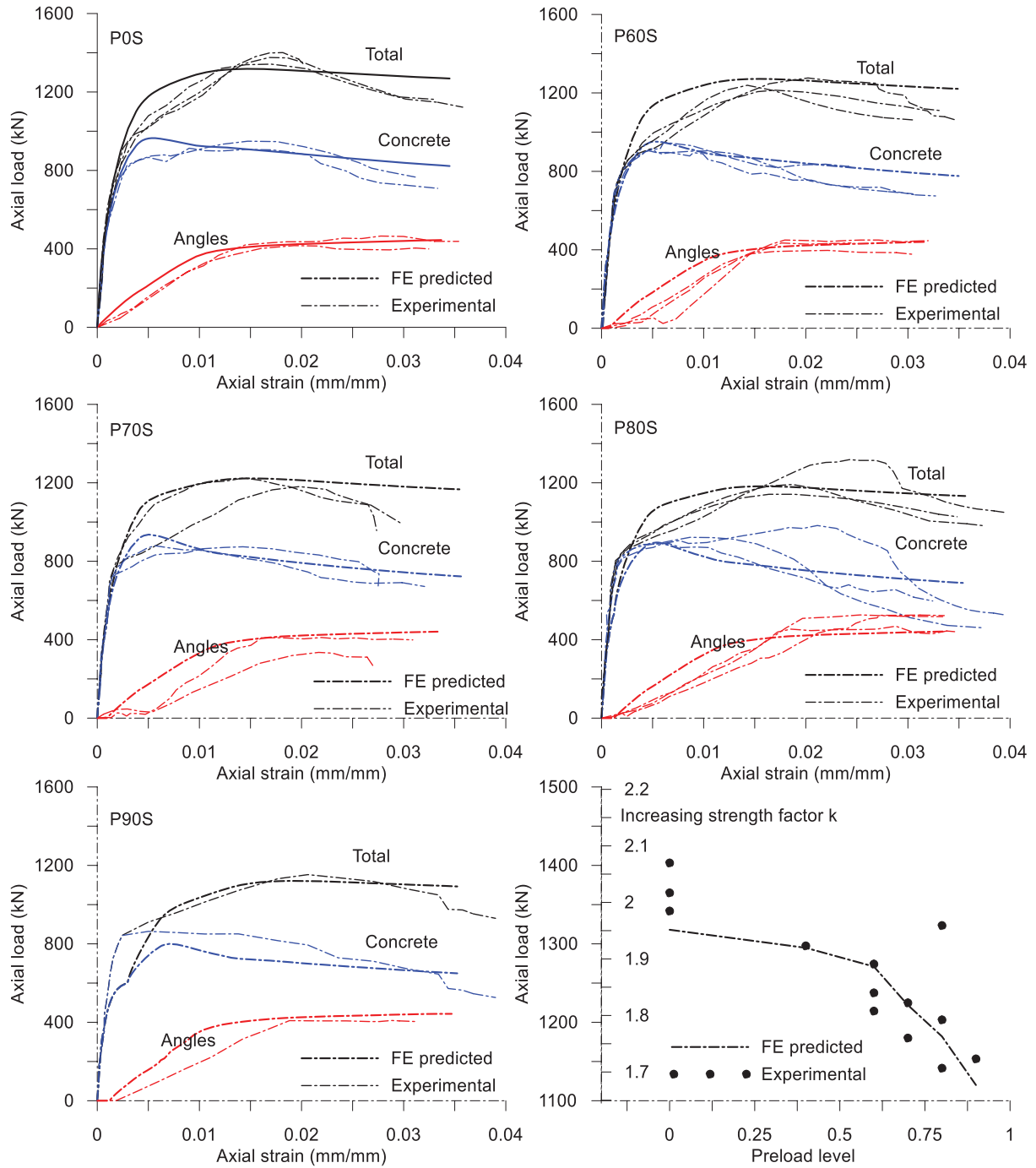


Figure 8: Experimental-numerical comparisons.

6 CONCLUSIONS

In this paper, the evaluation of the compressive behavior of columns strengthened by means of external steel cages considering the effect of the preload at the moment of strengthening was investigated by experimental and numerical approaches. Compared to the load-bearing capacity of columns strengthened without preload, it was observed that there is a reduction of the capacity because of the preload depending on:

- A reduction of the compressive strength of the concrete induced by high sustained loading;
- The strain-lag effects of the confining device due to the preload.

Moreover, the above-mentioned effects are more significant with the increasing of the levels of preload.

A numerical FE model was assessed and used for the experimental-numerical comparisons, showing its reliability on the realistic prediction of the physical process and the results. The FE model can be used for subsequent accurate predictive scenarios including different mechanical properties for the concrete and the steel cages.

REFERENCES

- [1] C. Ma, N.M. Apandi, C.S.Y. Sofrie, J.H. Ng, W.H. Lo, A.Z. Awang, W. Omar, Repair and rehabilitation of concrete structures using confinement: a review. *Construction and Building Material*, **133**, 502–515, 2017.
- [2] P. Colajanni, S. Pagnotta, G. Testa, Comparison of fully non-stationary artificial accelerogram generation methods in reproducing seismicity at a given site. *Soil Dynamics and Earthquake Engineering*, **133**, 106135, 2020. <https://doi.org/10.1016/j.soildyn.2020.106135>.
- [3] P. Colajanni, S. Pagnotta, A. Recupero, N. Spinella, Shear resistance analytical evaluation for RC beams with transverse reinforcement with two different inclinations. *Materials and Structures*, **53** (1), 18, 2020. <https://doi.org/10.1617/s11527-020-1452-8>.
- [4] R. Benzaid, H. Mesbah, N. Chikh. FRP-confined concrete cylinders: axial compression-experiments and strength model. *Journal of Reinforced Plastic Composites*, **29**(16), 2469–88, 2010.
- [5] F. Micelli, R. Modarelli. Experimental and analytical study on properties affecting the behavior of FRP-confined concrete. *Composites Part B*, **45**(1):1420–31, 2013.
- [6] M.F. Ferrotto, O. Fischer, L. Cavaleri. A strategy for the finite element modeling of FRP-confined concrete columns subjected to preload. *Engineering Structures*, **173**, 1054-1067, 2018.
- [7] M.F. Ferrotto, O. Fischer, R. Niedermeier, Experimental investigation on the compressive behavior of short term preloaded CFRP-confined concrete columns, *Structural Concrete*, 1–14, 2017. <https://doi.org/10.1002/suco.201700072>.
- [8] M.F. Ferrotto, O. Fischer, L. Cavaleri, Analysis-oriented stress-strain model of CRFP-confined circular concrete columns with applied preload. *Materials and Structures*, **51**(44), 2018. <https://doi.org/10.1617/s11527-018-1169-0>.
- [9] G. Campione, F. Cannella, M.F. Ferrotto, M. Gianquinto, Compressive behavior of FRP externally wrapped R.C. column with buckling effects of longitudinal bars. *Engineering Structures*, **168**, 809–818, 2018.
- [10] J.M. Adam, S. Ivorra, E. Giménez, J.J. Moragues, C. Mirigall, P.A. Calderón, Behaviour of axially loaded RC columns strengthened by steel angles and strips. *Steel Composite Structures*, **7**, 405–419, 2007.

- [11] J.M. Adam, S. Ivorra, F.J. Pallarés, E. Giménez, P.A. Calderón, Axially loaded RC columns strengthened by steel caging. Finite element modelling. *Construction and Building Material*, **23**, 2265–2276, 2009.
- [12] R. Montuori, V. Piluso, Reinforced concrete columns strengthened with angles and battens subjected to eccentric load, *Engineering Structures*. **31**, 539–550, 2009.
- [13] V. Badalamenti, G. Campione, M.L. Mangiavillano, Simplified Model for Compressive Behavior of Concrete Columns Strengthened by Steel Angles and Strips. *Journal of Engineering Mechanics ASCE*, **136**, 230–238, 2010.
- [14] G. Campione, L. Cavaleri, M.F. Ferrotto, G. Macaluso, M. Papia, Efficiency of stress-strain models of confined concrete with and without steel jacketing to reproduce experimental results. *The Open Construction and Building Technology Journal*, **10** (Suppl 1: M4) (2016) 65–86.
- [15] G. Campione, L. Cavaleri, F. Di Trapani, M.F. Ferrotto, Frictional effects on structural behavior of no-end-connected steel-jacketed RC columns: Experimental results and new approaches to model numerical and analytical response. *Journal of Structural Engineering ASCE* **143**, 04017070, 2017, [https://doi.org/10.1061/\(ASCE\)ST.1943-541X.0001796](https://doi.org/10.1061/(ASCE)ST.1943-541X.0001796).
- [16] M.F. Ferrotto, L. Cavaleri, F. Di Trapani, FE modeling of Partially Steel-Jacketed (PSJ) RC columns using CDP model. *Computers and Concrete*, **22**(2), 143-152, 2018.
- [17] M.F. Ferrotto, L. Cavaleri, M. Papia, Compressive response of substandard steel jacketed RC columns strengthened under sustained loads: from the local to the global behavior, *Construction and Building Materials*. **179**, 500-511, 2018.
- [18] A.R. Takeuti, J.B. de Hanai, A. Mirmiran, Preloaded RC columns strengthened with high-strength concrete jackets under uniaxial compression. *Materials and Structures*, **41**, 1251–1262, 2008.
- [19] G.K. Vondoros, S.E. Dritsos, Axial preloading effects when reinforced concrete columns are strengthened by concrete jackets. *Progress in Structural Engineering Materials* **8**, 79–92, 2006.
- [20] Y. Pan, L. Wan, X. Wu. Analysis-oriented stress-strain model of CFRP confined concrete with preload. *Journal of Southwest Jiaotong University*; **50**(3):461–5, 2015. (In Chinese).
- [21] ABAQUS (2013), ABAQUS Theory and User Manuals, Version 6.13-1.
- [22] T. Ozbakkaloglu, A. Gholampour, J.C. Lim, Damage-plasticity model for FRP-confined normal-strength and high-strength concrete, *Journal of Composites for Construction ASCE*, **20**(6), 04016053, 2016.
- [23] H. Rüsç. Experimental determination of the effect of the duration of loading on the resistance and deflection. (in German: "Versuche zur Bestimmung des Einflusses der Zeit auf Festigkeit und Verformung."). Report. IABSE congress report, **5**, 237–244, 1956.
- [24] D. Tasevski, M. Fernández Ruiz, A. Muttoni, Assessing the compressive strength of concrete under sustained actions: From refined models to simple design expressions. *Structural Concrete*. 1–15, 2019. <https://doi.org/10.1002/suco.201800303>

CASE STUDY OF CONNECTIVITY OF DIGITAL TWINS AND EXPERIMENTAL SYSTEMS

Matthew Bonney¹, Paul Gardner¹, David Wagg¹ and Robin Mills¹

¹Dynamics Research Group, Department of Mechanical Engineering
University of Sheffield, Sheffield S1 3JD, UK
e-mail: m.bonney@sheffield.ac.uk

Keywords: Digital Twins, Operational Platform, 6-DOF Excitations, Environmental Testing

Abstract. *One of the main usages for a digital twin is the centralization and utilization of numerical, physics, and experimental based data. While there has been a large amount of research in the definition and utilization of computer simulations, there exists a gap in research in the interaction between experimental setups and digital twins. This work focuses on an example of how an experimental setup can interact with a digital twin via an operational platform. The experimental setup for this work is a scaled 3 storey building excited with a 6-DOF ground shaker under various controlled environmental conditions. For the digital twin, a server-based operational platform is used to allow for interactions with the digital twin from any remote operation site. The work in this paper gives an example of how the digital twin and experimental setup interacts and explores the added benefits of using a digital twin in experimental research.*

1 Introduction

In the current state-of-the-art, digital twins are typically comprised of purely experimental (pre-digital twins), or physics (numerical twins) based models [1]. It is currently rare for digital twins to incorporate both types of models in a meaningful capacity. This has led to a greater desire in research to incorporate both experimental results and physics based simulations into a single digital twin to be useful for an analyst. The research presented in this paper is a case study for the centralization of experimental and numerical models into a digital twin.

The concept of “twinning”, the art of using a one-to-one surrogate for generating diagnostic/predictive information, dates back to the NASA Apollo missions used for training astronauts and diagnostic testing [2]. However, recently there has been a greater focus on the development of digital twins that allows easy access to both accurate physics based simulations and experimental data performed. This will lead to the utilization for decision making, such as determining a maintenance schedule [3].

Some initial work has been done in the combination of experimental data and numerical simulations, such as the work done in [3, 4, 5]. The majority of this work is focused on what is termed “grey-box modelling” that uses a combination of physics based models and experimental data to create a surrogate model. While this work is important for the use in digital twins, the work presented in this paper focuses on how the information is passed between the experimental data, physics based models, and the analyst via an operational platform.

The Digital Twin Operational Platform (DTOP) is the interface that an analyst uses to create models, investigates numerical and experimental results, and create predictions based on the available information. There are multiple methods researchers and companies have used to develop operational platforms. Currently, a majority of available digital twins are operated via an executable that can interact with a database or live sensor data. This, although designed as such, limits both the number of people and whom can interact with the digital twin. Using an executable is useful if only a small number of analysts are expected to use it, for example in a power generating facility, however researchers tend to have a larger number of analysts at various locations. In order to aide researchers in using a digital twin, this work focuses on a web based platform that is accessible to any approved analyst with internet access.

With a web based platform, there is greater access to the DTOP, even at remote locations such as test sites. However, there are connectivity issues between local hardware and the DTOP. This work will demonstrate a case study for one method to combine the local hardware used in experimental testing with the web based DTOP. Section 2 will describe the hardware setup and testing conditions tested on the demonstration system discussed in Section 2.1. To discuss the web based DTOP, Section 3 shows the generated digital twin for the demonstration system and discusses some of the selected options used for the demonstration system and alternatives for each option. Section 4 discusses the interactions between the DTOP and experimental setup and demonstrates some of the added benefits to using a digital twin with experimental systems in Section 4.1. Some concluding remarks are presented in Section 5.

2 Experimental Setup

The main purpose of these experiments are to characterize the combined effects of environmental temperature and added masses on a civil structure. More information about this system is given in Section 2.1. To test this combined effects, the advanced facilities at the Laboratory for Verification and Validation (LVV) at the University of Sheffield. The LVV is equipped with multiple environmental chambers with one specifically designed for shaker based vibration test-

ing. This specific chamber is able to operate from -50 to 50°C with a shaker able to exert a maximum acceleration of $3g$.

To study the combined effects on this structure, a suite of tests are performed at multiple temperatures with various added masses. For each temperature, the four values of added mass are $0.0, 5.72, 11.44$, and 18.2 Kg. Relative to the structure mass, this is $0\%, 4.0\%, 8.0\%$, and 12.7% respectively. These proportions are thought of as a high percentage, but still realistic for civil structures. The temperature range of interest is based on yearly range in a seismically active region. Specifically, northern Japan is used that has a typical range between -10 and 30°C , so the testing is performed on a slightly expanded range of -15 to 35°C .

For each combinations of temperature and added mass, a swept sine excitation is applied via the 6 degree of freedom shaker. This excitation was applied in a single direction with frequencies ranging from 3 to 30 Hz with a linear rate of 0.1 Hz/s and an amplitude of 0.8 m/s^2 . This range is based on the first three bending modes obtained by preliminary tap tests where the third natural frequency is near 25 Hz. Although this paper focuses on the connectivity between the experiment and DTOP, these tests are also used for other work that focuses more on the grey-box modelling.

2.1 Demonstration System

The experimental system tested in this work is a scaled 3 storey building. This is constructed using extruded T-slot aluminium that is mounted to the shaker table. The general dimensions of this building are 2.42 m tall with a cross-section of 930×820 mm. A photo of the test system mounted to the shaker table within the environmental chamber is seen in Figure 1.



Figure 1: 3 storey building

One aspect of the experimental system is the sensor layout. For these tests, there are two single-axis accelerometers for each pillar on each floor with a total of 24 accelerometers. In

addition to these 24, there is also a baseline accelerometer on the shaker table to measure the input and additional sensors on a single pillar at the half floors to identify if there are any local modes in the support pillars experienced for this system in the range of interest. As a validation for this system, a calibrated beam model is generated. This model has an adjusted Young's modulus because the exact heat treatment of the aluminium is unknown, to match the first three bending frequencies that was obtained through some preliminary impact hammer testing. The accuracy of the calibrated model for the first three natural frequencies are within 1.5%.

3 Digital Twin Operational Platform

The most import aspect of communication between a user of the digital twin, the stored information, and the experimental system is the Digital Twin Operational Platform (DTOP). Using a DTOP is a useful method to inspecting information for the digital twin, with an emphasis on the ease-of-use. The main goals of a DTOP is to perform six main operations.

1. Access the collection of simulation, experimental, and historical results to aid in decision making
2. Provide access to approved users
3. Maintain data security and redundancy
4. Schedule/perform novel simulations for the digital twin
5. Access real-time data from live sensors
6. Interact directly with the physical twin

These six goals of a DTOP represent all the needs expressed for the operational platform aspect of the digital twin. While there is currently a large amount of work being done in order to ensure that the digital and physical twins perfectly correlate, this work focuses on the access to information and the user experience (the so-called human-computer interaction). For this particular work, a large focus is placed on the first two operations listed above.

While discussing the access to digital twins via a DTOP, it is import to denote some of the different frameworks available. One of the most important frameworks is the accessibility of the DTOP to users. To discuss how a user can access a digital twin, Figure 2 shows the 3 main methods to access a digital twin via a DTOP. There are both advantages and disadvantages for each method.

The first method to access a DTOP is based on being stand-alone. This method is where a local version of the digital twin is accessed, typically through an executable. All the information from experiments, simulations, and sensors are all stored on a single machine. This provides maximum information security, however, it greatly limits the amount of work that can be performed. A common use for a stand-alone DTOP is in an energy producing plant. This example is more focused on the daily operation and predicting the needed controls under various circumstances. These types of use-cases require extremely high security and doesn't have a large number of simultaneous users.

The second method to access a DTOP is through a Local Area Network (LAN). This method is an expansion of the stand-alone by allowing access to the DTOP for multiple users on the same network. In addition to having multiple users, the LAN method also allows the utilization of distributed computing. If the site has a local high performance computer, this method can

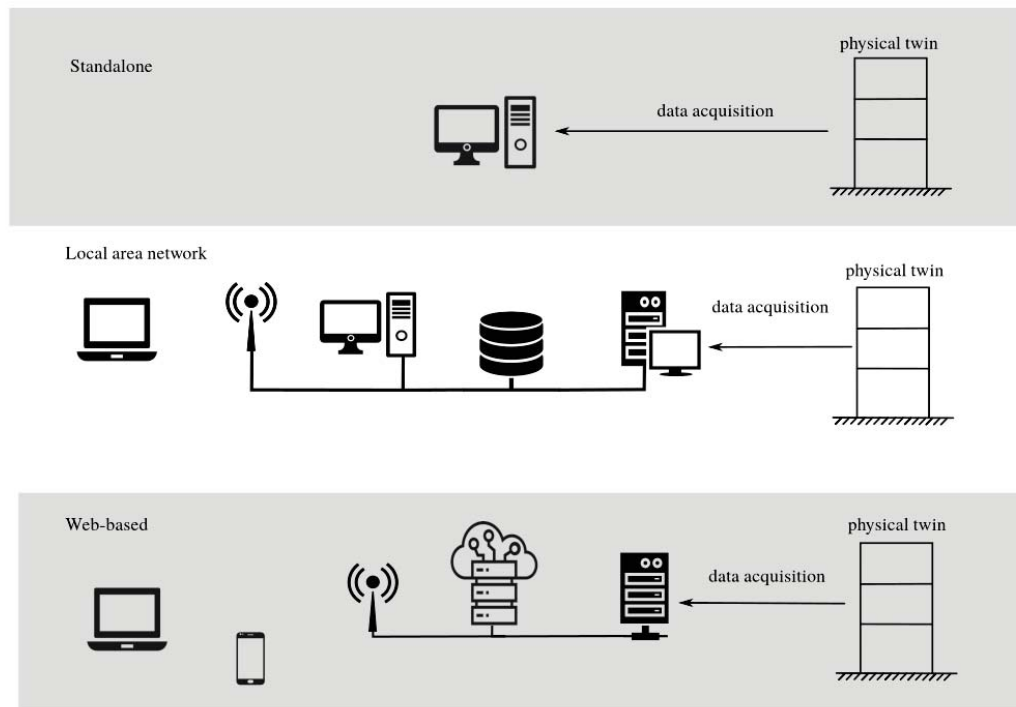


Figure 2: Different methods to access digital twins via a DTOP

utilise it in making predictions and other calculations. This method is an expected use case for the design and operation of complex systems. One example would be an aircraft, where there are multiple aspects being evaluated simultaneously, such as structural and electrical design/repair. While there is the ability for multiple users, this method also has high data security by only allowing people physically on the network to access this information.

The final method is the web-based DTOP. This greatly expands the number of possible users to anyone allowed access and internet access. Having this large accessibility encourages collaborative work and greatly expands the possibilities available. One such possibility is the ability to easily have remote sensors and monitoring a system after deployment. This method is particularly of interest for research systems, civil structures such as bridges, and large scale designs to incorporate multiple facilities at various locations.

4 Connectivity Example of Digital Twin and Experimental System

In order to demonstrate the connectivity aspects of a DTOP, an example DTOP is created using the demonstration system. This DTOP utilizes the web-based method since the testing and analysis are performed at separate locations due to social distancing requirements. To structure the web-based framework, two actions are performed. The first action is the utilization of the python code FLASK to create a webpage template to act as the user interface. FLASK uses python as a programming framework and HTML/CSS for visualization and navigation. This framework using FLASK can be used for any of the previously mentioned access methods (stand-alone, LAN, or web-based).

It is simple to utilise FLASK for a stand-alone or LAN version, but to use it as a web-based DTOP, a hosting service is required. This hosting can be done through a supporting organization, such as an University, or via a private host. For the second action of this example DTOP, a

service called Heroku is used to host the DTOP. Heroku was chosen for a few reasons including a free tier of hosting for demonstration purposes, virtual computations, and database hosting, but there are many other possible hosting services available that may fit other applications better.

There are two main simulations currently implemented in this DTOP, the first being a parametric beam finite element model. This simulation produces an ABAQUS run script then calls ABAQUS to run the simulation. The other simulation, and the main focus of this paper, is for post-processing the raw experimental data. A PostgreSQL database is utilized to store the raw experimental data and is implemented using the Heroku service.

To demonstrate this example DTOP, the main navigation page is displayed in Figure 3. This contains two main sections; The first section on the left side is a selection of the implemented simulations. This section allows the user to select which simulation they wish to perform. The other section on the right is an interactive visualization for the system of interest. This gives an “as-designed” geometric understanding of the system. One interesting aspect is that the extruded aluminium portions of the system are given directly from the manufacturer.

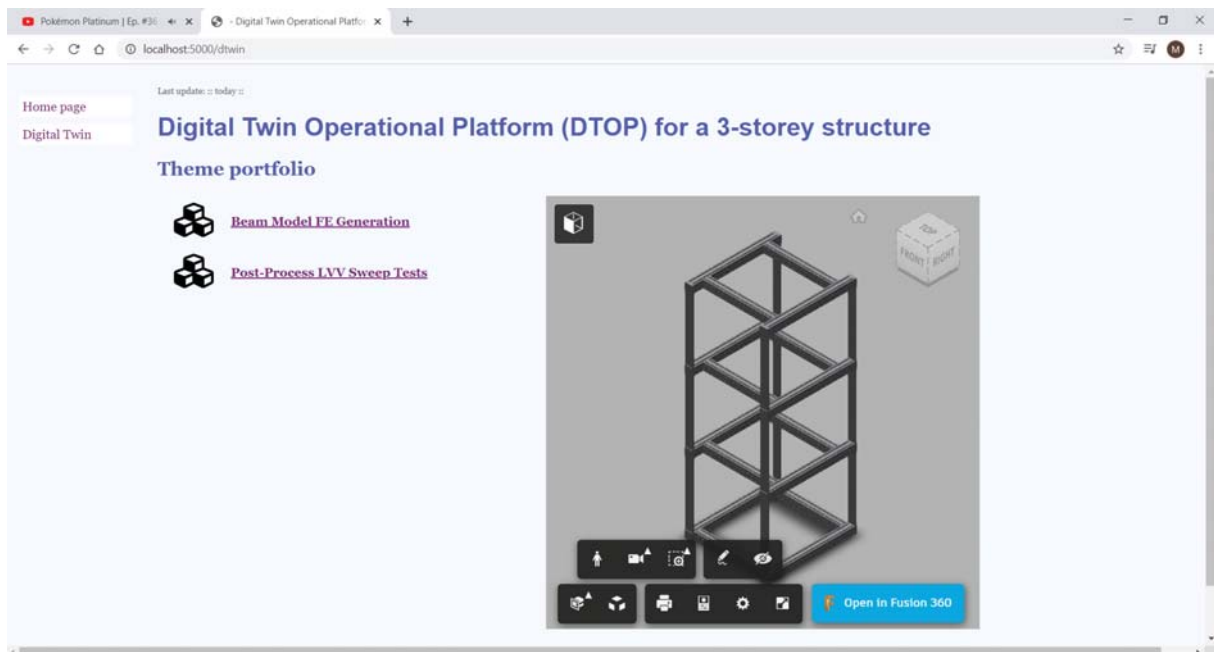


Figure 3: Main Navigation Page of DTOP

In the current implementation, there is no live streaming of the sensor information. This is primarily due to some of the proprietary software associated with controlling the environmental chamber and shaker. A prototype of streaming the sensor information is currently in development but is not the focus of this work. Instead, the data from the sensors is recorded then uploaded to the digital twin database. This upload is possible to implement within the DTOP, but currently is not to ensure a consistent data-structure. Currently, a separate python script is run that gathers the correct meta-data and stores that information and sensor data to the database.

For the post-processing aspect of the DTOP, there are two steps to perform this analysis. The first step is the selection of what experimental data to process. To aid the user with this selection, the DTOP queries the database to produce a list of available experimental tests that the user can select via a drop-down menu option. Once a test is selected, the next step is performing the

post-processing and visualization. This visualization is displayed to the user with an example shown in Figure 4. The results shown are for a test at 25°C with no added mass.



Figure 4: Post-processing page of DTOP

There are five main parts to the screen in Figure 4. The first part is an expression of the meta-data. This part gives users the testing parameters such as temperature and added mass, along with the testing date and name. Part 2 gives the scalar post-processing values. These values are the natural frequency and damping ratio for each of the three bending modes. The natural frequency is calculated via a peak picking routine and the damping is determined by a half-power method. Part 2 shows the values for these quantities by averaging all the excitation direction sensor results for the 3 repeated tests per configuration. Both of these are shown in greater details in Figure 5.

Part 4 allows for downloading the database entry onto the local drive, and can be seen in more detail in Figure 5c. This saves 6 pieces of information in a dictionary that is saved via a .npy file. These are lists containing the sensor names, time history, and PSDs. Additionally, it also saves the meta-data and vectors containing the time and frequency for the time history and PSD information. Part 3 of Figure 4, with a closer view in Figure 6, shows the auto Power Spectral Density (PSD) for a number of the sensors to denote some of the differences between sensors and tests. Since there are a large amount of sensors, this part is categorized based on the sensor location. In the current implementation, these sensors are categorized based on which floor they measure. The user can select which floor to visualize via the drop-down menu.

The final part is a measure of the variability for the calculated scalar post-processing values, specifically the natural frequencies. This shows a histogram of the calculated frequencies used in part 2 and a fitted Gaussian distribution to the same data. The first natural frequency is shown in Figure 7 with the histogram in blue and the fitted Gaussian distribution in red. This plot takes a total of 54 sensor readings to create this histogram.

Testing Parameters:

Test Name	: 25C with 0.0 Kg
Test Date	: 28 Jan 2021
Environmental Temperature [° C]	: 25.0
Added Mass [kg]	: 0.0

(a) Part 1 - Testing parameters

Average Modal Properties:

Ω_1 : 5.54 [Hz]	ζ_1 : 1.53 [%]
Ω_2 : 16.39 [Hz]	ζ_2 : 0.54 [%]
Ω_3 : 25.06 [Hz]	ζ_3 : 0.31 [%]

(b) Part 2 - Average scalar post-processing values

Local Save

File Name (.npz will be added automatically)

Load via "np.load('Filename.npz',allow_pickle=True).item()"

(c) Part 4 - Local save option

Figure 5: Text-based reported post-processing

4.1 Added Benefits

Using a DTOP with an experimental system provides several benefits to both the testing engineer and the analyst. One of the greatest benefits is the data storage and access. In a traditional approach, the data is stored locally in a variety of formats depending on the software used and engineering preference. After the data is collected, it is then transferred to the analyst either via email or physical transfer such as with an USB removable drive. This requires the analyst to understand the format used by the test engineer and be able to transform it into a usable format for the analysis.

For a large amount of cases, the data is too large to send via email and the analyst is typically not at the testing location. In some cases, the analyst might be in a different country where the delivering of a physical transfer would introduce large amount of wasted time. Using a DTOP centralizes the data and allows access to an analyst at any location in an easy to understand format. This only requires the testing engineer to submit the test results to the database, and the analyst can investigate the results via the DTOP. After investigating the results, the analyst can ensure the accuracy of the tests, suggest additional testing configurations, and perform advanced calculations/predictions in a timely manner.

In addition to the efficiency increase, using a DTOP also greatly increases the collaborative nature of projects and increases visibility of the project for marketing purposes. Because the data is stored virtually, access can be granted to any collaborators regardless of physical location. In the same sense, the DTOP can be used for demonstrating the project potential, show preliminary results without the need to transfer information, and to give a live demonstration of the digital twin.

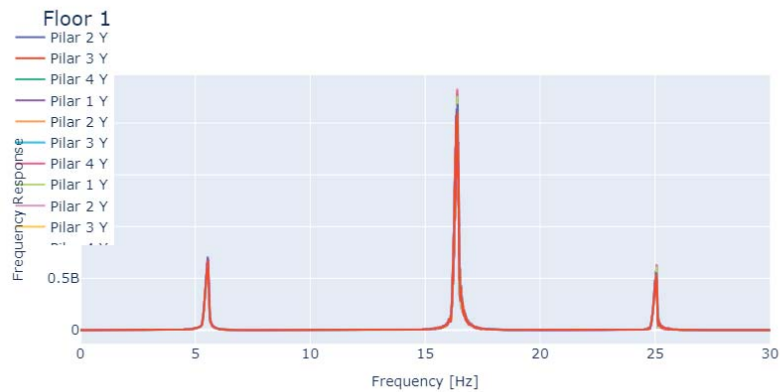


Figure 6: Part 3 - Power spectrum densities

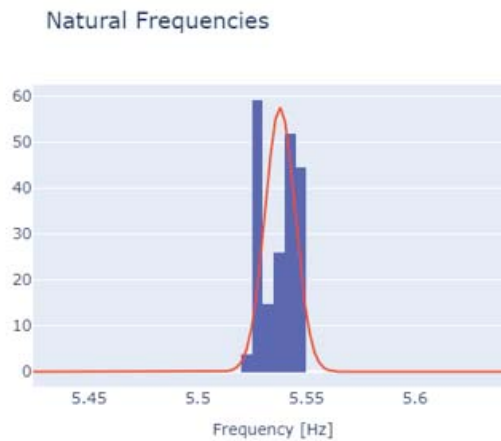


Figure 7: Part 5 - Histogram of fundamental frequency

5 Conclusions/Remarks

This work demonstrates a case study of how an operational platform can benefit experimental operations through increased connectivity to analysts and simulations. The connectivity is based on the use of a web-based digital twin operational platform. This allows the experimentalist to upload experimental results and for an analyst to access this information via an easy to use interface with high time efficiency due to the reduced data transfer time.

This paper presents an example operational platform that gathers the experimental data from the database and performs post-processing on it from any device that has an internet connection. These calculations are performed virtually so there are no hardware requirements to view the data. This is particularly useful for demonstration purposes to present results without the need to ensure correct data transfer.

The operational platform also highly encourages collaborative works where researchers from different universities or companies are able to access and supplement all the collected simulation and experimental data. With all of these benefits, an operational platform, particularly for digital twin purposes, provides a useful user-interface for the collected data, perform additional simulations, directly interact with the physical system, and promote collaboration and efficiency

with both local and global partners.

Acknowledgements

The authors would like to acknowledge the support of EPSRC via grant number(s) EP/R006768/1. This research made use of The Laboratory for Verification and Validation (LVV) which was funded by the EPSRC (grant numbers EP/R006768/1 and EP/N010884/1), the European Regional Development Fund (ERDF) and the University of Sheffield.

REFERENCES

- [1] D. J. Wagg, K. Worden, R. J. Barthorpe, and P. Gardner. Digital Twins: State-of-the-Art and Future Directions for Modeling and Simulation in Engineering Dynamics Applications. *ASCE-ASME Journal of Risk and Uncertainty in Engineering Systems Part B Mechanical Engineering*, 6(3), 05 2020. 030901.
- [2] M. S. Bonney and D. J. Wagg. Historical perspective of the development of digital twins. In *Proceedings of the 39th International Modal Analysis Conference*, 2021.
- [3] E. J. Tuegel, A. R. Ingrassia, T. G. Eason, and S. M. Spottswood. Reengineering aircraft structural life prediction using a digital twin. *International Journal of Aerospace Engineering*, 2011, 2011.
- [4] K. Worden, E. J. Cross, R. J. Barthorpe, D. J. Wagg, and P. Gardner. On Digital Twins, Mirrors, and Virtualizations: Frameworks for Model Verification and Validation. *ASCE-ASME Journal of Risk and Uncertainty in Engineering Systems Part B Mechanical Engineering*, 6(3), 05 2020. 030902.
- [5] F. Tao, F. Sui, A. Liu, Q. Qi, M. Zhang, B. Song, Z. Guo, S. C.-Y. Lu, and A. Y. C. Nee. Digital twin-driven product design framework. *International Journal of Production Research*, 57(12):3935–3953, 2019.

AN ADAPTIVE FAST NONLINEAR ANALYSIS (AFNA) ALGORITHM FOR RAPID TIME HISTORY ANALYSIS

Bowei Li¹, Wei-Chu Chuang¹, and Seymour M.J. Spence¹

¹Department of Civil and Environmental Engineering, University of Michigan
2350 Hayward St, Ann Arbor, MI, USA
e-mail: {jacklbw, wechuang, smjs}@umich.edu

Keywords: Performance-based Earthquake Engineering, Inelastic Systems, Structural Dynamics.

Abstract. *Performance-based earthquake engineering is becoming ever-more popular due to its capability to deliver structures that rationally meet society's need for a safe built environment. An important barrier to the application of this approach is the high computational demand required for providing detailed and accurate response characterization through nonlinear time history analysis. In this paper, an efficient adaptive fast nonlinear analysis (AFNA) algorithm is proposed to address this issue. This novel step-by-step integration scheme adaptively updates all solver configurations in real-time, including number of pseudo modes considered in the analysis, time step size, and potential nonlinear elements, in order to efficiently evaluate the nonlinear dynamic responses. In particular, in modeling potential inelasticity, a distributed plasticity model is considered to allow inelasticity to distribute along the length and height of the elements. The practicality and potential of the proposed algorithm are illustrated on a full scale archetype building subject to stochastic seismic excitations. The proposed algorithm is shown to be around an order of magnitude faster than traditional direct integration schemes while achieving a remarkable accuracy in both global response time histories and local hysteretic responses, therefore enabling efficient application of probabilistic performance-based design frameworks that often require repeated evaluation of nonlinear dynamic systems.*

1 INTRODUCTION

Performance-based earthquake engineering (PBEE) has gained immense interest in the past decades [1, 2, 3, 4, 5], and has recently been extended to wind engineering[6, 7, 8, 9, 10, 11, 12, 13, 14]. The popularity of PBEE can be traced back to its ability to meet society's desire for a safe built environment at reasonable economic cost. One of the key difficulties in the applications of PBEE in practice is the potentially significant computational demand associated with evaluating nonlinear responses of structural systems subject to extreme seismic events through nonlinear analysis. This computational demand can become intractable in the case of probabilistic PBEE based on stochastic simulation as such approaches generally require the repeated evaluation of the system. The most straightforward solution for this issue is to improve analysis efficiency by replacing traditional time consuming nonlinear time history analysis with computationally tractable alternatives. While approaches such as pushover analysis can meet the efficiency requirement, these approaches are generally incapable of capturing cumulative damage mechanisms or effects of higher modes [15, 16, 11], nor are they able to provide full time history responses.

Fast nonlinear analysis (FNA) [17] is a promising nonlinear time history analysis approach to overcome the aforementioned limitations. This approach keeps the concept of modal coordinate transformation and truncation, as in linear elastic analysis, which not only allows the equations of motion to be partially decoupled, such that more accurate and efficient piece-wise exact solutions can be used, but also enables the possibility to exclude unnecessary modes to lower the dimensionality of the problem for better efficiency. Based on a pre-designated set of elements that are expected to be nonlinear, this approach only considers these elements during the solution process, and thus enjoys significant gains in computational efficiency. However, the need to pre-designate elements that will experience inelasticity greatly reduces the general applicability of the FNA approach. In this work, an adaptive FNA (AFNA) is developed to address this limitation, while preserving almost all the advantages of the FNA approach. The resulting approach provides remarkably accurate full time history results at a fraction of the computational demand required by state-of-the-art direct integration schemes. The proposed approach adjusts the solver configurations, e.g. number of pseudo modes, time step size, and potential nonlinear elements, in real-time based on the state of the system, such that unnecessary computations and the need of a pre-designated set of potential nonlinear elements are eliminated. In modeling inelasticity, a distributed plasticity model is considered in this work, allowing inelasticity to distribute along the length and depth of the elements. A full scale archetype building subject to stochastic seismic excitations is presented to illustrate the efficiency and potential of the proposed approach.

2 PROBLEM SETUP

A structural system subject to dynamic load effects can in general be modeled as a multi-degree-of-freedom (MDOF) system subject to stochastic excitations:

$$M\ddot{\mathbf{u}}(t) + C\dot{\mathbf{u}}(t) + \mathbf{f}_{nl}(t) = \mathbf{F}(t) \quad (1)$$

where M , C are respectively the structural mass and damping matrices; $\mathbf{u}(t)$ is the displacement vector while $\dot{\mathbf{u}}(t)$ and $\ddot{\mathbf{u}}(t)$ are its first and second derivatives with respect to time, i.e. the velocity and acceleration vectors; $\mathbf{F}(t)$ is the external force vector while, considering a fiber-based discretization, $\mathbf{f}_{nl}(t)$ is the following nonlinear force vector:

$$\mathbf{f}_{nl}(t) = \mathbf{B}^T \mathbf{W} \boldsymbol{\sigma}(t) \quad (2)$$

where \mathbf{B} is the compatibility matrix transforming responses at global degree of freedoms (DOF) to fiber responses; \mathbf{W} is a diagonal matrix collecting multiplication factors to perform numerical integration for each of the fiber stress, typically obtained from the integration weights, fiber areas, as well as element lengths; and $\boldsymbol{\sigma}(t)$ is the vector that collects the fiber stress at all integration points of finite element discretization.

3 The adaptive fast nonlinear analysis method

In this section, the AFNA method is developed by making the solver configurations, including time step size, number of pseudo modes, and set of potential nonlinear elements, of the FNA approach adaptive in time. This eliminates the requirement of a pre-designated set of potential nonlinear elements. Methods are outlined to this end that do not compromise the original merits of the FNA approach.

3.1 The fast nonlinear analysis method

By moving the nonlinear force vector $\mathbf{f}_{\text{nl}}(t)$ to the right hand side, and introducing an pseudo positive definite stiffness matrix \mathbf{K}_e to prevent singularity, Equation (1) can be rewritten as:

$$\mathbf{M}\ddot{\mathbf{u}}(t) + \mathbf{C}\dot{\mathbf{u}}(t) + \mathbf{K}_e\mathbf{u}(t) = \mathbf{F}(t) + \mathbf{K}_e\mathbf{u}(t) - \mathbf{f}_{\text{nl}}(t) \quad (3)$$

It should be noted that, despite how the pseudo stiffness matrix \mathbf{K}_e can be any arbitrary positive definite matrix, it is recommended to be taken as the initial elastic stiffness matrix of the structural system. The P-Delta effect can be further taken into account by considering a reduced stiffness matrix [17, 18].

By denoting $\mathbf{f}_{\text{nlc}}(t) = \mathbf{K}_e\mathbf{u}(t) - \mathbf{f}_{\text{nl}}(t)$ as the nonlinear correction force, Equation (3) can be decoupled on the left hand side using the modal approach, as follows:

$$\boldsymbol{\Theta}\ddot{\mathbf{q}}(t) + \boldsymbol{\Lambda}\dot{\mathbf{q}}(t) + \boldsymbol{\Omega}\mathbf{q}(t) = \hat{\mathbf{F}}(t) + \hat{\mathbf{f}}_{\text{nlc}}(t) \quad (4)$$

where $\mathbf{q}(t)$ is the modal displacements while $\dot{\mathbf{q}}(t)$ and $\ddot{\mathbf{q}}(t)$ are its first and second derivatives with respect to time; $\boldsymbol{\Theta} = \boldsymbol{\Phi}^T \mathbf{M} \boldsymbol{\Phi}$, $\boldsymbol{\Lambda} = \boldsymbol{\Phi}^T \mathbf{C} \boldsymbol{\Phi}$, and $\boldsymbol{\Omega} = \boldsymbol{\Phi}^T \mathbf{K}_e \boldsymbol{\Phi}$ are respectively the diagonal generalized mass, damping and stiffness matrices; $\boldsymbol{\Phi}$ is the pseudo mode matrix consisting of the generalized eigenvectors of \mathbf{M} and \mathbf{K}_e . It is worth noting that the generalized masses representing inertial effects can be non-zero or zero, which correspond to dynamic or static modes respectively. In practice, higher order dynamic modes can be considered as static modes by ignoring their inertial effects in order to enhance both the efficiency and stability of dynamic solvers. In Equation (3), $\hat{\mathbf{F}}(t) = \boldsymbol{\Phi}^T \mathbf{F}(t)$ is the generalized force vector; $\hat{\mathbf{f}}_{\text{nlc}}(t) = \boldsymbol{\Phi}^T \mathbf{f}_{\text{nlc}}(t)$ is the generalized nonlinear correction force vector, which can be evaluated as:

$$\hat{\mathbf{f}}_{\text{nlc}}(t) = \boldsymbol{\Psi}^T \mathbf{W} [\boldsymbol{\sigma}_e(t) - \boldsymbol{\sigma}(t)] \quad (5)$$

where $\boldsymbol{\Psi} = \mathbf{B} \boldsymbol{\Phi}$ is the modal strain matrix; $\boldsymbol{\sigma}_e(t)$ is the fiber stress elastic predictor for all fibers evaluated with the elastic modulus and fiber strains $\boldsymbol{\epsilon}(t)$ as:

$$\boldsymbol{\epsilon}(t) = \boldsymbol{\Psi} \mathbf{q}(t) \quad (6)$$

It can be noted that when a fiber stress is in the linear elastic range, it does not contribute to $\hat{\mathbf{f}}_{\text{nlc}}(t)$, and thus can be ignored. In practice, the FNA only considers a pre-designated set of potential nonlinear elements, such that Equation (5) can be evaluated with much higher efficiency if only a portion of the elements are potentially nonlinear.

The FNA solves Equation (3) in a step by step manner, with a step size of Δt , and starts with an initial guess solution at each of the time step through the Taylor expansion:

$$\begin{aligned} \mathbf{q}^{(0)}(t + \Delta t) &= \mathbf{q}(t) + \Delta t \dot{\mathbf{q}}(t) + \frac{\Delta t^2}{2} \ddot{\mathbf{q}}(t) \\ \dot{\mathbf{q}}^{(0)}(t + \Delta t) &= \dot{\mathbf{q}}(t) + \Delta t \ddot{\mathbf{q}}(t) \end{aligned} \quad (7)$$

where the superscripts on the left hand side indicates the number of iterations. At the k th iteration, $\mathbf{q}^{(k)}(t + \Delta t)$ and $\dot{\mathbf{q}}^{(k)}(t + \Delta t)$ will be used to determine fiber strains and subsequently fiber stresses $\sigma_e(t)$ and $\sigma(t)$ through the fiber material constitutive law. Finally, $\hat{\mathbf{f}}_{\text{nle}}^{(k)}(t)$ can be estimated through integration. The solution at the next iteration, i.e. $\mathbf{q}^{(k+1)}(t + \Delta t)$ and $\dot{\mathbf{q}}^{(k+1)}(t + \Delta t)$, is obtained by the piece-wise exact solution [19] with the external loads considered as $\hat{\mathbf{F}}(t) + \hat{\mathbf{f}}_{\text{nle}}^{(k)}(t)$. This iterative process continues until convergence is reached. The algorithm performs the process described above for each time step over the time range of interest to provide response time histories.

3.2 The adaptive solution procedure

The main limitation of the FNA approach is the requirement of a pre-designated set of potential nonlinear elements. The AFNA presented in this section addresses this issue by determining the potential nonlinear elements during analyses in real-time. This feature allows AFNA to detect the existence of nonlinear elements, and further enables AFNA to shift between linear elastic and nonlinear solvers with different time steps and number of pseudo modes.

In the implementation, modes with natural frequencies greater than a threshold of interest, f_{st} , will be considered as static by ignoring their generalized mass or inertial effect, while the remaining modes are considered as dynamic. In solving the response time histories, the algorithm first assumes that the structural system is linear elastic and moves ahead with a relatively large time step $\Delta^L t$ while considering only the dynamic modes. At the end of each time step $\Delta^L t$, fiber strains and stresses are determined based on the estimated solutions $\mathbf{q}(t + \Delta^L t)$ and $\dot{\mathbf{q}}(t + \Delta^L t)$ for the assumed linear elastic step. The algorithm will proceed to the next time step if all fibers remain in their linear elastic loading/unloading/reloading range. Otherwise, the algorithm moves back to the previous time step t and solves until reaching the time $t + \Delta^L t$ using a smaller time step $\Delta^S t = \Delta^L t / \eta$, in which η is an integer such that the $\Delta^S t$ is not greater than half the natural period of the highest dynamic mode T_{\min} , i.e. $\Delta^S t \leq T_{\min} / 2$, to ensure stability of the approach. In general, the choice of $\eta = 4$ will provide a good balance between accuracy and efficiency. Within each small time step $\Delta^S t$ the algorithm first forms a list of potential nonlinear elements by checking the fiber strains or stresses based on the predicted solutions of Equation (7). The solution process then enters the iterative scheme as in the FNA with all modes considered, if the list of potential nonlinear elements is not empty. Otherwise, it proceeds to the next small time step using the piece-wise exact solution considering the dynamic modes of the larger time step phase without iteration. Within this context, when the algorithm reaches $t + \Delta^L t$, the solution process then proceeds to the next time step considering the initial step size $\Delta^L t$ and starts another adaptive process if necessary. The entire process is then terminated when reaching the end of the time sequence, providing a full range of inelastic response histories for structures subject to dynamic external loads. The overall solution process is illustrated in the flow chart of Figure 1.

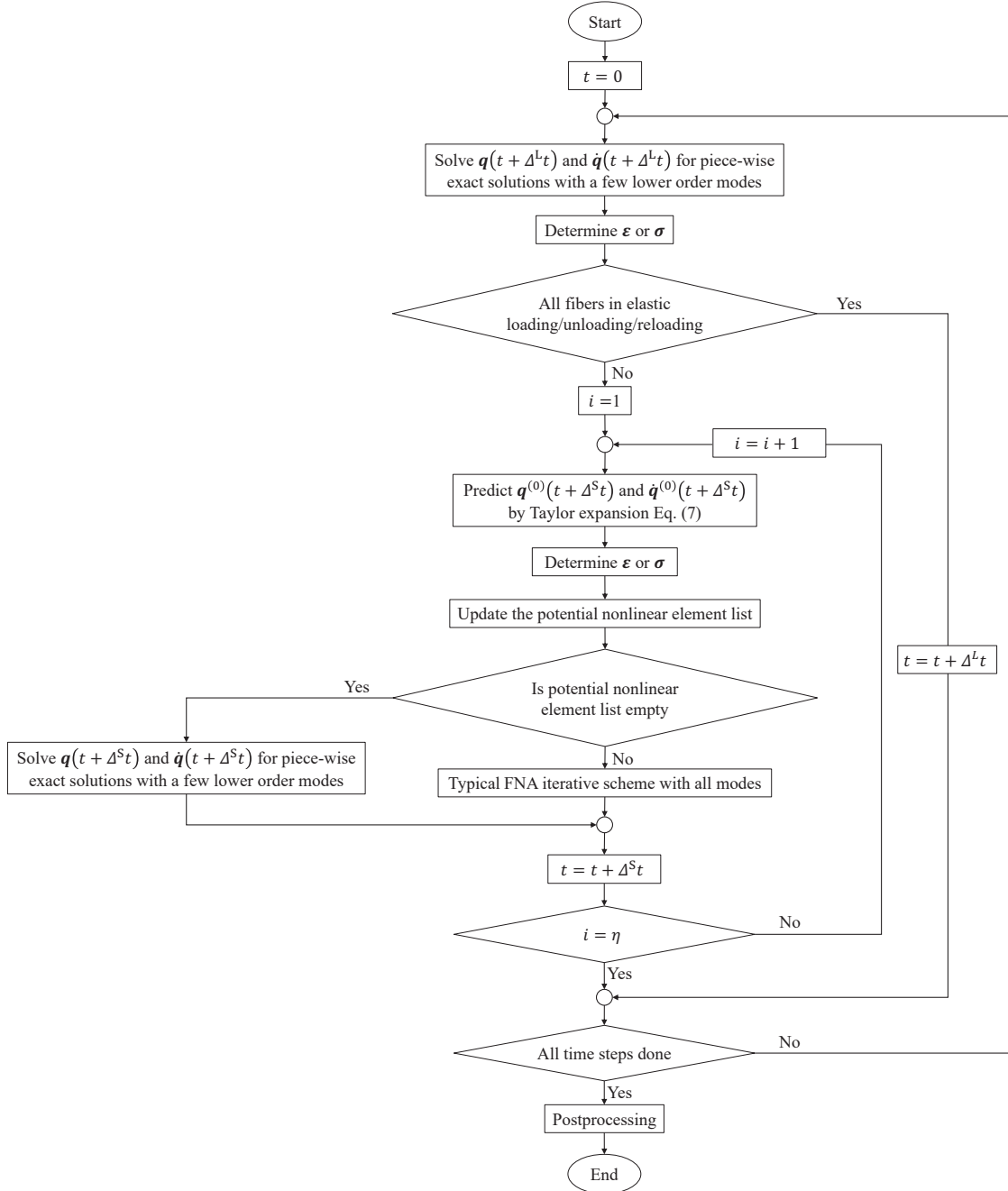


Figure 1: Flowchart illustrating the steps of the AFNA algorithm.

4 CASE STUDY

A 37-story 6 span steel moment resisting frame assumed to be located in downtown San Francisco is considered in this case study. The width of each span is 5 m while the story height is 6 m for the first floor and 4 m for the remaining floors, leading to a total height of 150 m. Box sections and W24 sections are considered respectively for columns and beams, with section sizes summarized in Table 1. The elastic modulus and the yield stress are respectively taken as $E_s = 200$ GPa and $\sigma_y = 355$ MPa. The structural mass is modeled to be lumped at each floor considering combined self and carried mass of 100 kg/m^3 , and super dead load of 23.5 kN/m .

Floor	Beams	Columns*
1-20	W 24 \times 192	50 ² \times 2.5
21-30	W 24 \times 103	40 ² \times 2.0
31-40	W 24 \times 103	35 ² \times 1.8

*(outer side size)² \times (wall thickness)

Table 1: Sections with dimensions in (cm).

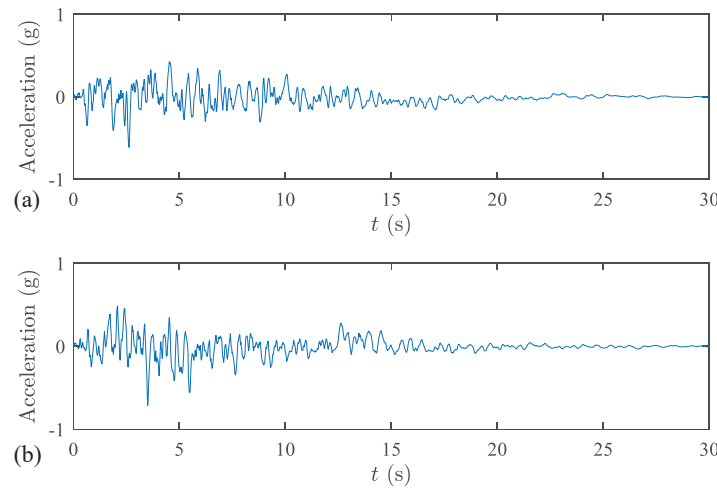


Figure 2: The two synthetic ground motion samples used in the case study: (a) GM1 (b) GM2.

The structure is assumed to be subjected to a 10% exceedance probability in 50-year seismic hazard. Synthetic ground motions are generated via the model proposed by Rezaeian and Der kiureghian [20], with the filter frequency and damping optimized to fit the target spectrum constructed from the USGS unified hazard tool [21] for the building site, with the rest of the parameters chosen to be consistent with Loma Prieta records (Moment magnitude = 6.93, Rupture distance = 18.3 km). The two representative synthetic ground motion (GM) samples used in this work are shown in Figure 2. For comparison, nonlinear time history analyses based on the GM samples was carried out by direct integration in OpenSees. Elements experiencing inelasticity subject to the two GM samples are marked in red in Figure 3. It can be seen that for the two cases (GM1 and GM2) the structure experiences, respectively, moderate and significant nonlinearity.

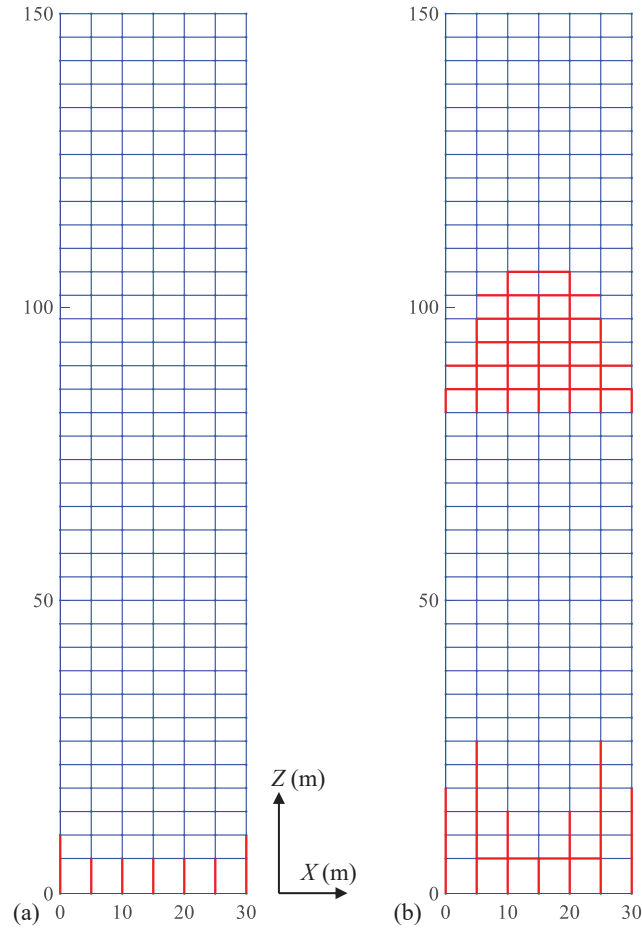


Figure 3: Elements experiencing nonlinearity (in red): (a) GM1 (b) GM2.

All results were estimated using a machine with Intel(R) Core(TM) i7-8750H CPU @ 2.20GHz processor and 16 GB RAM. The comparison in terms of computational times is reported in Table 2. It is seen that the AFNA is around an order of magnitude faster than the state-of-the-art nonlinear analysis approach used in OpenSees for GM1, i.e. for moderate nonlinearity. Despite how a lower gain in efficiency is achieved for GM2 (significant nonlinearity), the AFNA is still notably faster. It should also be noted that the AFNA approach was programmed in Matlab and, unlike the OpenSees solvers, was not fully optimized for computational efficiency. Thus, based on the results, the AFNA algorithm is expected to be around an order of magnitude faster than the direct integration even in the case of significant nonlinearity.

The comparison between the displacements under GM1 and GM2 at the 10th, 20th, and 37th floor obtained from direct integration and the AFNA approaches are reported in Figure 4. A perfect correspondence can be observed over the entire time history. In addition, Figure 5 reports the comparison between the fiber strain and stress time histories and hysteretic curves for an extreme fiber of the exterior first floor column for the two ground motions. It is seen that the AFNA approach still achieves remarkable accuracy, even for highly localized responses, e.g. nonlinear fiber strains or stresses, which are generally challenging to compute accurately and efficiently due to the potentially large number of modes involved. Lastly, it is worth noting that, despite how an elastic perfectly plastic (EPP) material was considered in the case study,

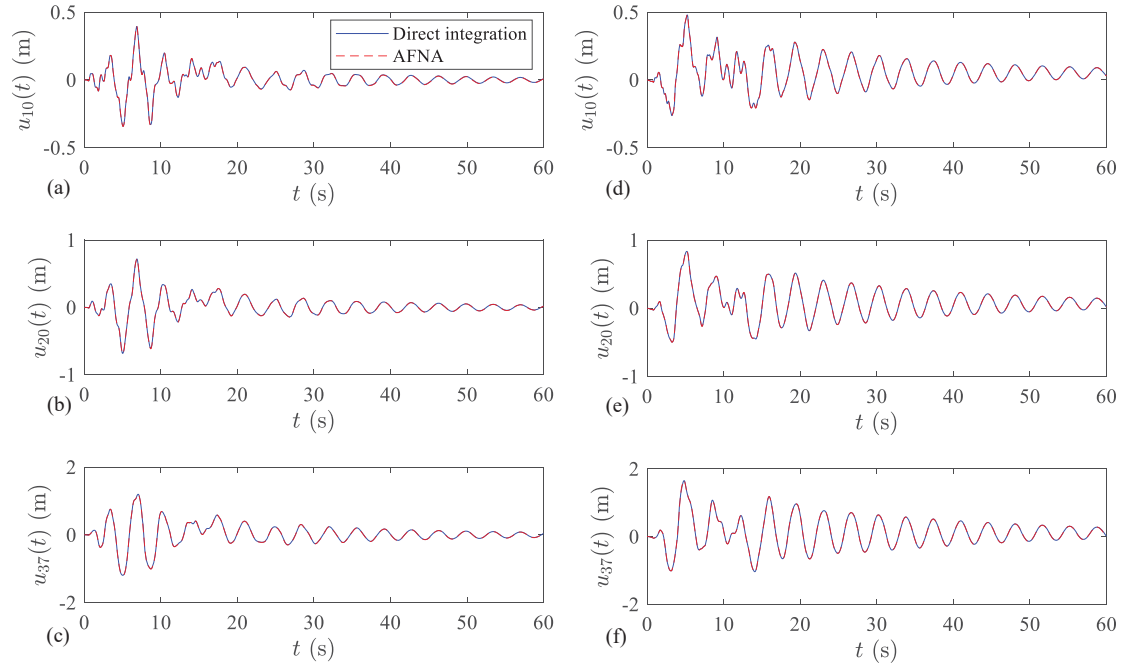


Figure 4: Comparison of displacements obtained by direct integration and AFNA for: GM1 at (a) the 10th floor, (b) the 20th floor (c), the 37th floor; and for GM2 at (d) the 10th floor, (e) the 20th floor, (f) and the 37th floor.

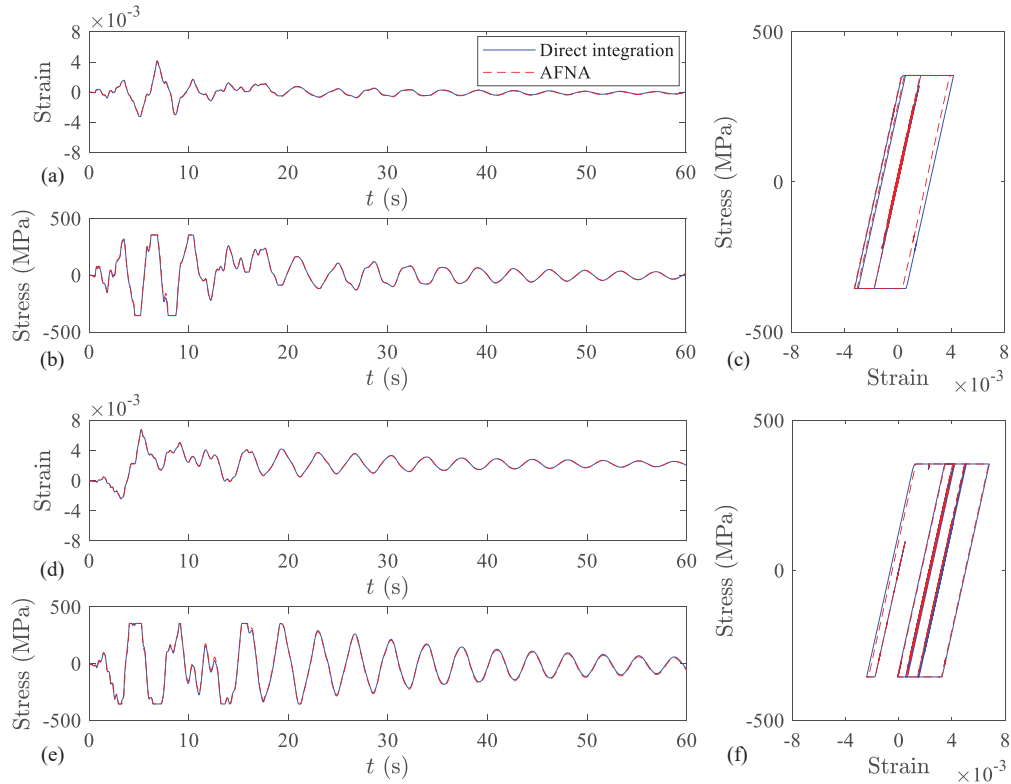


Figure 5: Extreme fiber responses for the exterior first floor column. Comparison between direct integration and AFNA: (a) strain time history for GM1; (b) stress time history for GM1; (c) hysteric curve for GM1; (d) strain time history for GM2; (e) stress time history for GM2; (f) hysteric curve for GM2.

Ground motions	GM1	GM2
Computational time: Direct integration (s)	64.58	63.90
Computational time: AFNA (s)	7.03	15.10

Table 2: Computational time for the nonlinear time history analyses.

the proposed algorithm can be used for materials with general constitutive relations.

5 CONCLUSION

In this work, a highly efficient adaptive fast nonlinear analysis (AFNA) algorithm was developed, as a computational efficient alternative to the direct integration approach to provide full time history responses for computationally intensive engineering applications, e.g. performance-based earthquake engineering. The algorithm implements the modal analysis concept that partially decouples the equation of motions, such that piece-wise linear solutions are applicable. Meanwhile, the algorithm updates the potential nonlinear elements, time step size, as well as the number of pseudo modes to be considered in real-time during the solution process. In particular, in defining the structural model, fiber-based distributed plasticity models were considered. The results show that the AFNA algorithm is capable of accurately estimating both the global response time histories and local hysteretic behaviors with around an order of magnitude less computational time as compared to state-of-the-art direct integration approaches. Finally, it is worth noting that even though only seismic input was considered in the case study, the proposed algorithm can also be directly applied to cases subject to stochastic wind loads. In this case, the algorithm is expected to provide even greater time savings, as typically less nonlinearity is experienced by structures subject to winds. Overall, the notable efficiency and accuracy of the proposed AFNA approach illustrates its potential in computationally intensive applications, such as probabilistic performance-based design frameworks, that require repeated evaluation of nonlinear dynamic systems.

6 ACKNOWLEDGEMENT

This research effort was supported in part by the Magnusson Klemencic Associates (MKA) Foundation through Research Grant Agreement No. 101 and the National Science Foundation through grant number CMMI-1750339. This support is gratefully acknowledged.

REFERENCES

- [1] H. Krawinkler. Challenges and progress in performance-based earthquake engineering. In *International Seminar on Seismic Engineering for Tomorrow—In Honor of Professor Hiroshi Akiyama*, volume 26, 1999.
- [2] K.A. Porter. An overview of peer’s performance-based earthquake engineering methodology. In *Proceedings of ninth international conference on applications of statistics and probability in civil engineering*, pages 1–8, 2003.
- [3] J. Moehle and G.G. Deierlein. A framework methodology for performance-based earthquake engineering. In *13th world conference on earthquake engineering*, volume 679, 2004.

- [4] S. Günay and K.M. Mosalam. Peer performance-based earthquake engineering methodology, revisited. *Journal of Earthquake Engineering*, 17(6):829–858, 2013.
- [5] Federal Emergency Management Agency (FEMA). Seismic performance assessment of buildings volume 1-methodology. *Rep. No. FEMA P-58-1*, 2012.
- [6] M. Ciampoli, F. Petrini, and G. Augusti. Performance-based wind engineering: towards a general procedure. *Structural Safety*, 33(6):367–378, 2011.
- [7] S.M.J. Spence and A. Kareem. Performance-based design and optimization of uncertain wind-excited dynamic building systems. *Engineering Structures*, 78:133–144, 2014.
- [8] S.M.J. Spence, E. Bernardini, and A. Kareem. A first step towards a general methodology for the performance-based design of wind-excited structures. In *Structures Congress 2015*, pages 1482–1493, 2015.
- [9] S.M.J. Spence, W.C. Chuang, P. Tabbuso, E. Bernardini, A. Kareem, L. Palizzolo, and A. Pirrotta. Performance-based engineering of wind-excited structures: A general methodology. In *Geotechnical and Structural Engineering Congress 2016*, pages 1269–1282, 2016.
- [10] W.C. Chuang and S.M.J. Spence. A performance-based design framework for the integrated collapse and non-collapse assessment of wind excited buildings. *Engineering Structures*, 150:746–758, 2017.
- [11] W.C. Chuang and S.M.J. Spence. An efficient framework for the inelastic performance assessment of structural systems subject to stochastic wind loads. *Engineering Structures*, 179:92–105, 2019.
- [12] Z. Ouyang and S.M.J. Spence. A performance-based damage estimation framework for the building envelope of wind-excited engineered structures. *Journal of Wind Engineering and Industrial Aerodynamics*, 186:139–154, 2019.
- [13] A. Suksuwan and S.M.J. Spence. Performance-based design optimization of uncertain wind excited systems under system-level loss constraints. *Structural Safety*, 80:13–31, 2019.
- [14] W.C. Chuang and S.M.J. Spence. Probabilistic performance assessment of inelastic wind excited structures within the setting of distributed plasticity. *Structural Safety*, 84:101923, 2020.
- [15] H. Krawinkler and G.D.P.K. Seneviratna. Pros and cons of a pushover analysis of seismic performance evaluation. *Engineering structures*, 20(4-6):452–464, 1998.
- [16] S. Antoniou and R. Pinho. Advantages and limitations of adaptive and non-adaptive force-based pushover procedures. *Journal of Earthquake Engineering*, 8(04):497–522, 2004.
- [17] E.L. Wilson. Three-dimensional static and dynamic analysis of structures. 2002.
- [18] E.L. Wilson and A. Habibullah. Static and dynamic analysis of multi-story buildings, including p-delta effects. *Earthquake spectra*, 3(2):289–298, 1987.

- [19] A.K. Chopra. *Dynamics of Structures: Theory and Applications to Earthquake Engineering*. Prentice-Hall, 2001.
- [20] S. Rezaeian and A. Der Kiureghian. Simulation of synthetic ground motions for specified earthquake and site characteristics. *Earthquake Engineering & Structural Dynamics*, 39(10):1155–1180, 2010.
- [21] United States Geological Survey (USGS). Unified hazard tool, 2017.

A NOVEL METHOD FOR THE GENERATION OF FULLY NON-STATIONARY SPECTRUM COMPATIBLE ARTIFICIAL ACCELEROGRAMS

F. Genovese*, G. Muscolino, G. Biondi and E. Cascone

Department of Engineering, University of Messina, Villaggio S. Agata, 98166 Messina, Italy
e-mail: fedgenovese@unime.it, gmuscolino@unime.it, gbiondi@unime.it, ecascone@unime.it

Abstract

The increasing availability of strong motion records makes the use of real accelerograms an attractive option for a proper definition of the input motions in the dynamic analysis of structural and geotechnical systems. Despite different real accelerograms selection procedures have been proposed in the literature, there are situations in which it may be impossible to select a suitable code-required number of accelerograms without applying large scale factors which distort the actual characteristics of selected motions leading to unrealistic input. In these situations, the use of artificial accelerograms could represent a possible alternative.

A novel procedure for generating fully non-stationary spectrum compatible artificial accelerograms, is presented in this paper.

Depending on the aim to be achieved, it is possible to obtain the spectrum-compatibility between the generated samples and the target action in terms of response spectrum or Fourier spectrum, using two different corrective Power Spectral density function terms.

A numerical application shows the validity of the generation procedure and the accuracy of the model in reproducing realizations with statistical characteristics similar to those of the target motion.

Keywords: Artificial accelerograms, Fully non-stationary stochastic process, Real ground motion records, Spectrum-Compatibility.

1 INTRODUCTION

The worldwide increasing availability of strong motion records makes the use of actual acceleration time-histories an attractive option to properly define the input motions for dynamic analysis of both structural and geotechnical (*S&G*) systems [1,2].

The characteristics of the expected ground motion at a given site are strongly affected by the possible coupling between the frequency content of the input ground motion and the frequencies of vibration of the soil deposit which, in turn, depend on the non-linear behaviour exhibited by soils when subjected to cyclic and dynamic loadings. Consequently, soil mechanical properties considerably influence the site response to the motion imposed by an earthquake at the bedrock level and, thus, should be properly accounted for in the definition of the interval of periods of interest for the accelerogram selection [3].

In this vein and with reference to one dimensional site response analysis problems, a method for the selection of proper sets of input ground motions accounting for most of these relevant issues has been proposed in Ref. [4]; Refs[5] and [6] showed that the soil heterogeneity in terms of shear wave velocity profile and the soil non-linear behaviour under cyclic loading significantly affect: *i*) the interval of vibration periods relevant for the accelerogram selection; *ii*) the characteristics of the selected input motions. However, despite the availability of earthquake records, frequently it is not possible to find sets of time histories that satisfy the compatibility criteria between the selected records and a target code-prescribed response spectrum, without applying large scale factors to each record of the set [7]. For this reason, different numerical procedures capable to generate artificial accelerograms with energy and frequency content consistent with those of actual acceleration records have been proposed in literature.

In [8], the authors proposed a deterministic modification method based on the harmonic wavelet transform, aimed at matching the elastic response spectrum of a given accelerogram to a target code-prescribed elastic response spectrum, while in [9], a novel formulation based on the wavelet transform has been used for the stochastic generation of fully non-stationary spectrum-compatible accelerograms. In [10] the evolutionary power spectra of seismic accelerograms, estimated using the method of separation, have been used to produce artificial accelerograms compatible with given recordings while, an iterative procedure based on the spectral representation of stochastic processes in which the ground motion is constituted by two waveforms, a real record and an artificial accelerogram, has been proposed in [11].

A new method for generating fully non-stationary spectrum compatible artificial accelerograms, that requires only the knowledge of the numbers of peaks, zero level up-crossings and the value of the total energy of the target signal, is presented in this paper.

Depending on the aim to be achieved, it is possible to obtain the spectrum-compatibility between the generated samples and the target action in terms of response spectrum or Fourier spectrum, using two different corrective Power Spectral density function (*PSD*) terms.

The proposed procedure requires the following steps: *i*) subdivide a selected target accelerogram in many contiguous time intervals in which appropriate unimodal Power Spectral density functions and polynomial form of modulating function have been chosen to obtain the same energy and frequency content of real accelerograms expected at the site of interest, applying the stochastic generation method recently proposed in [12]; *ii*) evaluate the mean elastic response spectrum and the Fourier spectrum of a set of generated fully non-stationary accelerograms samples; *iii*) satisfy the compatibility of so determined spectra to target ones by means of an iterative procedure.

A numerical application shows the validity of the spectrum-compatible generation procedure and the accuracy of the proposed model in reproducing realizations with statistical characteristics similar to those of the target motion both in time and frequency domain.

2 EVOLUTIONARY POWER SPECTRAL DENSITY FUNCTION METHOD FOR MODELLING SEISMIC ACTION

The procedure for generating a set of *fully non-stationary* artificial accelerograms compatible with a target spectrum and having the same characteristics of an earthquake induced ground motion \ddot{U}_g , consist of the following four steps:

1) divide the time duration $0 \div T_D$ of the analysed accelerogram \ddot{U}_g , in n contiguous time intervals of amplitude $\Delta T_k = t_k - t_{k-1}$ ($k=1, 2, \dots, n$), in each of which a uniformly modulated process is introduced as the product of a deterministic modulating function, $a(t)$, times a stationary zero-mean Gaussian sub-process $X_k(t)$, whose power spectral density (PSD) function $G_{X_k}(\omega)$ is filtered by two Butterworth filters:

$$G_{X_k}(\omega) = \beta_k \left(\frac{\omega^2}{\omega^2 + \omega_{H,k}^2} \right) \left(\frac{\omega_{L,k}^4}{\omega^4 + \omega_{L,k}^4} \right) \frac{\rho_k}{\pi} \left(\frac{1}{\rho_k^2 + (\omega + \Omega_k)^2} + \frac{1}{\rho_k^2 + (\omega - \Omega_k)^2} \right); \quad k=1, \dots, n \quad (1)$$

where β_k is a coefficient, given in closed form solution in [12], that makes unitary the variance of each sub-process $X_k(t)$ while the predominant circular frequency Ω_k and the frequency bandwidth ρ_k can be evaluated by the following expressions:

$$\Omega_k \cong \frac{2\pi N_{0,k}^+}{\Delta T_k}; \quad \rho_k \cong \frac{\pi N_{0,k}^+}{2\Delta T_k} \left[\pi - 2 \frac{N_{0,k}^+}{P_k} \right] \quad (2)$$

being P_k and $N_{0,k}^+$ respectively the number of *maxima* and of *zero-level up-crossings* of each k -th part in which the target accelerogram is subdivided;

2) evaluate the modulating function $a(t)$ by least-square fitting the *cumulative expected energy function* of the stochastic process to the cumulative energy function $E_{\ddot{U}_g}(t)$ of the target accelerogram subdivided in three-time intervals, according to [12]:

$$a(t) = \sum_{j=1}^2 \bar{a}_j(t) \mathbb{W}(t_{j-1}, t_j) + a(t_2) \exp \left[\frac{t - t_2}{T_D - t_2} \ln \left(\frac{|\ddot{U}_g(T_D)|}{a(t_2)} \right) \right] \mathbb{W}(t_2, t_3). \quad (3)$$

being $\mathbb{W}(t_{j-1}, t_j) = \mathbb{U}(t - t_j) - \mathbb{U}(t - t_{j-1})$ the window function and $\mathbb{U}(t)$ the unit step function;

3) generate the i^{th} *fully non-stationary* sample of the stochastic process $F_0^{(i)}(t)$ via the formula:

$$F_0^{(i)}(t) = a(t) \sqrt{2\Delta\omega} \left[\sum_{k=1}^n \sum_{r=1}^{m_N} \mathbb{W}(t_{k-1}, t_k) \sin \left(r \Delta\omega t + \theta_r^{(i)} \right) \sqrt{G_{X_k}(r \Delta\omega)} \right] \quad (4)$$

$\theta_r^{(i)}$ being the random phase angles, uniformly distributed over the interval $[0, 2\pi]$ and m_N being the number of parts in which the k -th PSD function $G_{X_k}(\omega)$ is discretized with a $\Delta\omega$ frequency sampling interval;

4) obtain the spectrum-compatibility reducing the gap between the mean spectrum of the generated samples $\bar{S}^{(j-1)}(\omega, \zeta_0)$ and the target one $S^{(T)}(\omega, \zeta_0)$, through the introduction of a corrective iterative *PSD* function $\bar{G}_{X_k}^{(j)}(\omega)$:

$$\bar{G}_{X_k}^{(j)}(\omega) = \bar{G}_{X_k}^{(j-1)}(\omega) \frac{S^{(T)}(\omega, \zeta_0)^2}{\bar{S}^{(j-1)}(\omega, \zeta_0)^2} \quad (5)$$

being $\bar{G}_{X_k}^{(0)}(\omega) = 1$ [14] and ζ_0 the viscous damping.

According to the formulation described in [13], the generic spectrum-compatible sample can be generated as:

$$\bar{F}_0^{(i)}(t) = a(t) \sqrt{2\Delta\omega} \left[\sum_{k=1}^n \sum_{r=1}^{m_N} \mathbb{W}(t_{k-1}, t_k) \sin(r \Delta\omega t + \theta_r^{(i)}) \sqrt{\bar{G}_{X_k}^{(j)}(r \Delta\omega) G_{X_k}(r \Delta\omega)} \right]. \quad (6)$$

2.1 Spectrum-compatibility

Depending on the purposes of the accelerogram generation procedure, the spectrum compatibility can be checked against the following targets:

- i) the pseudo acceleration response spectrum $S_R^{(T)}(\omega, \zeta_0)$ of the target accelerogram;
- ii) the Fourier spectrum $S_F^{(T)}(\omega)$ of the target accelerogram;
- iii) the code-prescribed elastic response spectrum $S_C^{(T)}(\omega, \zeta_0)$.

To achieve the Fourier-spectrum compatibility $S^{(T)}(\omega, \zeta_0) = S_F^{(T)}(\omega)$, the corrective iterative *PSD* function $\bar{G}_{X_k}^{(j)}(\omega)$ term can be particularized as follows:

$$\bar{G}_{X_k}^{(j)}(\omega) = \bar{G}_{X_k}^{(j-1)}(\omega) \frac{S_V^{(T)}(\omega, 0)^2}{\bar{S}_V^{(j-1)}(\omega, 0)^2} \quad (7)$$

being $S_V^{(T)}(\omega, 0)$ and $\bar{S}_V^{(j-1)}(\omega, 0)$ the velocity response spectra for $\zeta_0 = 0$.

3 NUMERICAL APPLICATION

In this section, in order to verify the accuracy of the proposed method, two different sets of one hundred artificial accelerograms spectrum-compatible with the pseudo acceleration response spectrum and the Fourier spectrum of the target accelerogram, have been generated.

3.1 Target accelerogram

The North-South component of the time history recorded at Vasquez Rocks Park ($R_{JB} = 23.1$ km [15]) during the $M_w = 6.7$ 1994 Northridge earthquake has been used as target accelerogram.

The selected accelerogram, having an overall duration $T_D = 36.6$ s and a sampling interval $\Delta t = 0.02$ s, has been recorded by a station with an average shear wave velocity in the upper 30 m equal to $V_{s,30} = 996$ m/s.

The target ground motion is characterized by a peak ground acceleration $PGA = 0.132$ g, a total intensity equal to $I_0 = 1.9$ m²/s³, a significant strong motion duration (i.e. interval of time elapsed between the 5% and 95% of I_0) $SMD = 7.3$ s and a total number of zero-level up-crossings and of peaks equal to $N_0^+ = 196$ and $P_0 = 212$, respectively.

As highlighted in [12], to obtain accurate results, the analysed accelerogram must be subdivided into n time intervals, each of which containing a number of *zero level up crossings* at least equal to one; consequently, in this application, the target accelerogram is subdivided in 73-time intervals with a constant time step of 0.5 s.

Further details about the parameters used to characterize the modulating function $a(t)$ and the *PSD* function $G_{X_k}(\omega)$ associated with each time interval, have been detailed in [13].

3.2 Spectrum compatibility

According to the procedure described in Section 2, a set of one hundred artificial accelerograms has been generated by using Eq. (4).

Then, to satisfy the spectrum compatibility in terms of pseudo acceleration response spectrum (*RSC*) or Fourier Spectrum (*FSC*), the iterative procedure has been applied four times and two different sets of one hundred accelerograms, have been obtained by Eq. (6).

Figure 1 shows a comparison between the time history of the target accelerogram and the i -th generated sample $\bar{F}_0^{(i)}(t)$, after 4 iterations, using the pseudo acceleration response spectrum compatibility (*RSC*) model (a) and the Fourier spectrum-compatibility (*FSC*) model (b). In both cases the variation in amplitude of the generated samples appears to be preserved in the time domain.

In Figure 2, the mean value of the cumulative energy function $I_0(t)$ and the cumulative *zero level up crossing* function $N_0^+(t)$ of the generated samples applying the pseudo acceleration response spectrum compatibility (*RSC*) model or the Fourier spectrum compatibility (*FSC*) model, after 4-th iterations, have been compared with the trend of the target functions.

In Figure 3 and 4 the average acceleration response spectrum $Sa(T)$ and the average Fourier spectrum module $|\mathcal{F}[\ddot{U}_g(t)]|$ of the two sets of artificial accelerograms, generated after 4 iterations by the *RSC* and *FSC* model, are compared with the corresponding target spectrum, respectively.

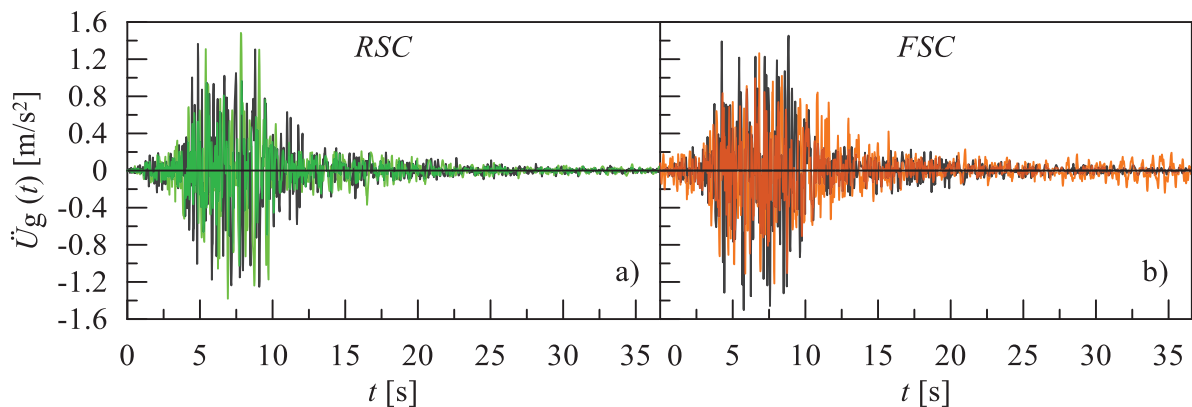


Figure 1: Comparison among the selected accelerogram (black line) and the corresponding i -th generated sample by the proposed fully non-stationary spectrum-compatible model, after 4 iterations: a) pseudo acceleration response spectrum-compatibility (*RSC*) model, b) Fourier spectrum-compatibility (*FSC*) model.

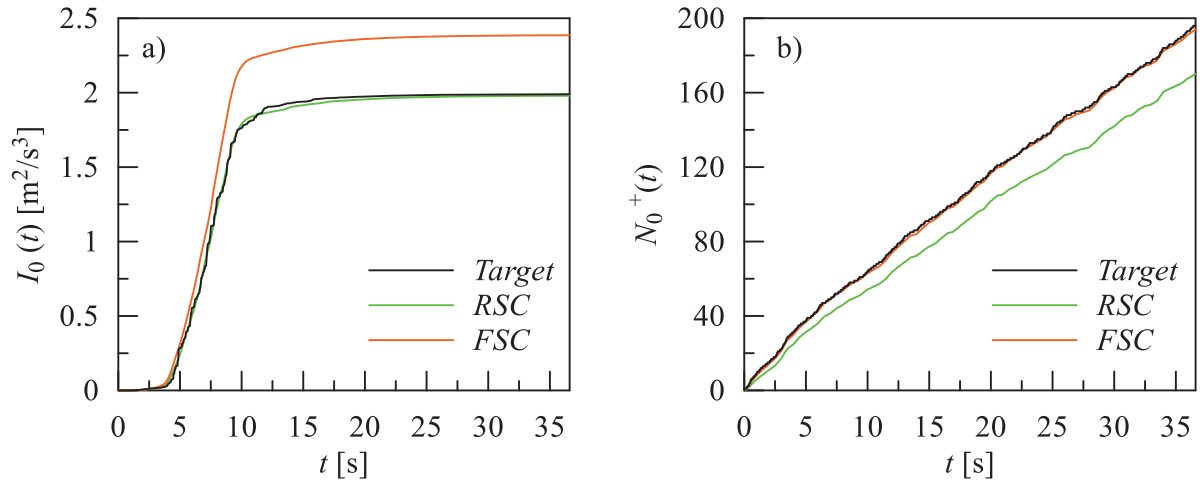


Figure 2: Comparison among the cumulative energy function (a) or cumulative zero level up crossing function (b) between the *target* accelerogram and the corresponding mean cumulative functions of the 100 samples, evaluated using *RSC* model and the *FSC* model, after 4-th iterations.

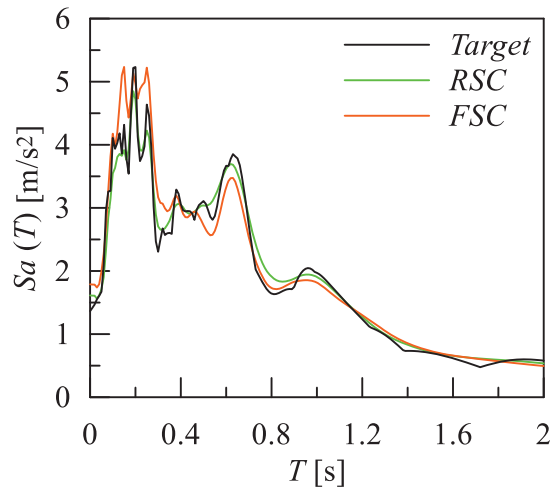


Figure 3: Comparison between the pseudo acceleration response spectrum and the mean response spectra of the 100 samples, evaluated using the *RSC* model and *FSC* model after 4-th iterations.

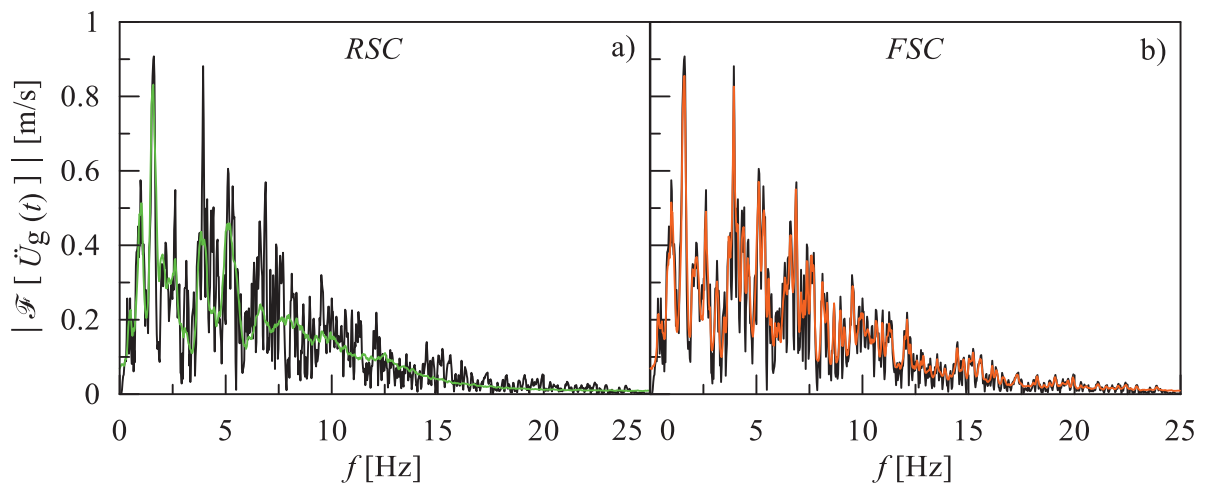


Figure 4: Comparison among the Fourier spectrum module of the selected accelerogram and the mean Fourier spectrum module of the generated sample, evaluated after 4 iterations by the: a) *RSC* model, b) *FSC* model.

From the observation of the numerical results obtained in the time and frequency domain, it emerges that:

- the use of the pseudo acceleration response spectrum-compatibility (*RSC*) model leads to outcomes statistically closer to those of the target one in terms of cumulative energy function $I_0(t)$ and pseudo-acceleration response spectrum $Sa(T)$ respect to the trends obtained by the application of the *FSC* model;
- the application of the Fourier-compatibility (*FSC*) model allows to obtain samples having an average *zero level up crossing function* $N_0^+(t)$ and Fourier spectrum closer to target one trend respect to those evaluated though the *RSC* model.

4 CONCLUSIONS

In this paper, a new procedure for generating fully non-stationary artificial spectrum-compatible artificial accelerograms, has been presented.

Firstly, the target accelerogram is subdivided in many contiguous time intervals in which the modulating and the unimodal Power Spectral density functions have been evaluated to obtain an average trend of the cumulative energy function $I_0(t)$ and *zero-level up crossing function* $N_0^+(t)$ very close to the ones of the target accelerogram.

Then, depending on the type of spectrum compatibility to be achieved (response spectrum compatibility or Fourier spectrum compatibility), an iterative procedure based on the use of different corrective iterative *PSD* function terms, has been implemented.

The numerical results show that using the acceleration response spectrum compatible (*RSC*) model, the generated samples have been characterized by an average cumulative energy function and pseudo-acceleration response spectrum very close to those of the target one, while the use of the Fourier spectrum model (*FRC*) leads to samples having an average *zero level up crossing function* and Fourier spectrum in good agreement with the target one.

ACKNOWLEDGEMENTS

This work is part of the research activities carried out in the framework of the research project of major national interest, PRIN n. 2017YPMBWJ, on “Risk assessment of Earth Dams and River Embankments to Earthquakes and Floods (REDREEF)” funded by the Italian Ministry of Education University and Research (MIUR).

REFERENCES

- [1] J.J. Bommer, B. Acevedo, The use of real earthquake accelerograms as input to dynamic analysis. *Journal of Earthquake Engineering*, **8**, Special issue, 1, pp. 43-91, 2004.
- [2] E.I. Katsanos, A.G. Sextos, G.D. Manolis. Selection of earthquake ground motion records: a state-of-the-art review from a structural engineering perspective. *Soil Dynamics and Earthquake Engineering*, **30**: pp. 157–169, 2010.
- [3] F. Genovese, D. Aliberti, G. Biondi, E. Cascone. Geotechnical aspects affecting the selection of input motion for seismic site response analysis. *7th COMPDYN 2019, 24-26 June 2019, Crete, Greece*, **1**, pp. 151-161, 2019.

- [4] F. Genovese, D. Aliberti, G. Biondi, E. Cascone, A procedure for the selection of input ground motion for 1D seismic response analysis. *Earthquake Geotechnical Engineering for Protection and Development of Environment and construction*. F. Silvestri and N. Moraci eds. *7th International Conference on Earthquake Geotechnical Engineering (ICEGE 2019)*, Rome, Italy, June 17-20, 2019, pp. 2591-2598, 2019.
- [5] F. Genovese, D. Aliberti, G. Biondi, E. Cascone, Influence of Soil Heterogeneity on the Selection of Input Motion for 1D Seismic Response Analysis, *Lecture Notes in Civil Engineering*, **40**, pp. 694–704, 2020.
- [6] F. Genovese, Influence of Soil Non-linear Behaviour on the Selection of Input Motion for Dynamic Geotechnical Analysis. M. Barla, A. Di Donna, D. Sterpi eds, *Challenges and Innovations in Geomechanics, 16th International Conference of the International Association for Computer Methods and Advances in Geomechanics (IACMAG 2021)*, *Lecture Notes in Civil Engineering*, Springer, Cham, **126**, pp. 588-596, 2021.
- [7] I. Iervolino, C. Galasso, E. Cosenza, REXEL: computer aided record selection for code-based seismic structural analysis, *Bulletin of Earthquake Engineering*, **8**, pp. 339–362, 2010.
- [8] D. Cecini, A. Palmeri, Spectrum-compatible accelerograms with harmonic wavelets, *Computers and Structures*, **147**, pp.26-35, 2015.
- [9] F. Genovese, G. Muscolino, A. Palmeri, Influence of different fully non-stationary artificial time histories generation methods on the seismic response of frequency-dependent structures, *4th International Conference on Uncertainty Quantification in Computational Sciences and Engineering, UNCECOMP 2021*, Streamed from Athens, Greece, 28-30 June 2021.
- [10] G. Stefanou, S. Tsiliopoulos, Estimation of evolutionary power spectra of seismic accelerograms. M. Papadrakakis, M. Fragiadakis eds, *7th International Conference on Computational Methods in Structural Dynamics and Earthquake Engineering*, **3**, pp. 5880–5888, 2019.
- [11] P. Cacciola, A stochastic approach for generating spectrum-compatible fully non-stationary earthquakes, *Computers and Structures*, **88**, pp. 889-901, 2010.
- [12] G. Muscolino, F. Genovese, G. Biondi, E. Cascone, Generation of Fully Non-Stationary Random Processes Consistent with Target Seismic Accelerograms, *Soil Dynamics and Earthquake Engineering*, **141**(106467), pp. 1-14, 2021.
- [13] F. Genovese, G. Muscolino, G. Biondi and E. Cascone. Generation of artificial accelerograms consistent with earthquake-induced ground motions. M. Papadrakakis, M. Fragiadakis, C. Papadimitriou eds, *11th International Conference on Structural Dynamic, (EURODYN 2020)*, Virtual, Athens, Greece, November 23-26 2020; Code 165382, **2**, pp. 3027-3042, 2020.
- [14] E.H. Vanmarcke, D.A. Gasparini, Simulated earthquake ground motions. *K - Seismic Response Analysis of Nuclear Power Plant Systems K1 - Ground Motion and Design Criteria SMiRT 4*, San Francisco, USA, 1977.
- [15] W.B. Joyner, D.M. Boore, Peak horizontal acceleration and velocity from strong motion records including records from the 1979 Imperial Valley, California, earthquake. *Bulletin of the Seismological Society of America*; **71**, pp. 2011–2038, 1981.

AN APPLICATION OF THE PROPER ORTHOGONAL DECOMPOSITION METHOD FOR NONLINEAR DYNAMIC ANALYSIS OF REINFORCED CONCRETE STRUCTURES SUBJECTED TO EARTHQUAKES

Naim AYOUB^{1,2}, Walid LARBI¹, Joseph PAIS², Lucie ROULEAU¹,
and Jean-François DEÜ¹

¹ Laboratoire de Mécanique des Structures et des Systèmes Couplés (LMSSC)
Conservatoire national des arts et métiers (Cnam)
292 rue Saint-Martin – 75141 Paris cedex3
naim.ayoub@lecnam.net, walid.larbi@lecnam.net, lucie.rouleau@lecnam.net,
jean-francois.deu@cnam.fr

² GRAITEC INNOVATION
17 Burospace – 91572 Bièvres cedex
naim.ayoub@graitec.com, joseph.pais@graitec.com

Abstract

This paper presents an extension of the Proper Orthogonal Decomposition method (POD) to nonlinear dynamic analysis of reinforced concrete multistory frame structure where the material nonlinearity is modeled by the multi-fiber section. To test the effectiveness of this approach, we first perform a nonlinear dynamic analysis under a seismic excitation using a direct implicit time integration scheme. Then, based on structural response observations, POD modes were extracted and used to reduce the structural system subjected to different earthquakes. A comparison was made between full model and reduced model analysis in order to assess the effectiveness of this technique.

Keywords: Reinforced concrete beam, Material nonlinearity, Multi-fiber section, Dynamic analysis, Reduced model, Proper Orthogonal Decomposition.

1 INTRODUCTION

This paper presents an extension of the Proper Orthogonal Decomposition method (POD) to nonlinear dynamic analysis of reinforced concrete multistory frame structure where the material nonlinearity is modeled by the multi-fiber section.

The multi-fiber section model consists in dividing the structural element cross section into a set of longitudinal fibers. Each fiber is made up of a single material and has the potential to undergo nonlinear inelastic longitudinal deformation according to the uniaxial stress-strain behavior of its corresponding material [1-4]. The layered shell element consists in dividing the 2D structural element into layers along its thickness. Each layer is made up of a single material and can behave nonlinearly in 2D [5-7]. When dealing with nonlinearities, nonlinear solving techniques should be adopted. The classical and most used nonlinear solvers are the Newton-Raphson method and its derivatives, displacement control approach and the arc length technique.

Dynamic excitations in structures are usually studied using direct integration time history analysis. In this approach, temporal discretization is considered and the direct time integration is conducted using implicit methods like Newmark- β [8], Wilson θ [9], HHT- α [10] or explicit methods like central difference and Runge-Kutta. The main concern in using the direct time integration analysis for linear and nonlinear models is its high computational cost especially when applied in structural seismic analysis. In fact for seismic analysis, the structure is subjected to dynamic excitations at its base. These excitations are generally based on the accelerograms of previously recorded quakes in the region. In order to cover all probable scenarios, the structure should be subjected to multiple accelerograms vibrating in all different directions which greatly increases the time cost of this analysis technique.

Due to this setback, several model reduction techniques have been proposed to decrease the time cost of the dynamic time history analysis. For linear systems, modal truncation can be used to define the most influential mode shapes of the structure and then this truncated modal base is used to reduce the dynamic equation of the structural system [11-12]. For nonlinear structures, research based on the work of [13] has been conducted to determine an analogy between nonlinear normal modes and linear ones. However, this nonlinear modal analysis is not widely used due to the limitation when non-smooth nonlinearities are present in the structure [14].

The Proper Orthogonal Decomposition (POD) is a data driven method based on the statistical Principal Component Analysis (PCA) of observations dataset. In other words, data obtained from observations at different time intervals (snapshots) are analyzed to determine the optimal subspace that can be used to recreate the entire dataset with minimum errors. This subspace is later used to reduce the model under consideration in calculation. The POD method dates back to the 1930's and today is applied in fluid mechanics for model reduction of turbulent flow, model reduction of structural dynamics, damage detection, reduction of dynamic models for microelectromechanical systems and in lots of other domains.

Seismic analysis considering nonlinear material behavior of reinforced concrete structures is classically conducted by two approaches. The first one is the pushover analysis which is a static nonlinear approach that tries mimicking the dynamic behavior of the structure by considering it to respond dynamically according to its fundamental mode shape only. Horizontal loads are distributed on the structure proportionally to this fundamental mode shape vector and are increased progressively while nonlinear material behavior is taken into account. This approach is limited to structures where the fundamental mode shape is the dominant mode of vibration and thus limiting it to regular low-rise buildings where no response in function of

time is required (only maximum values are provided). For other cases, the previously mentioned direct integration nonlinear time history analysis is used.

According to the authors' knowledge, the POD method was never used for reducing the direct integration nonlinear time history analysis of a Reinforced Concrete (RC) structure where material nonlinearity is modelled by the multi-fiber section approach. This paper presents a nonlinear multi-fiber RC multistory frame structure subjected to seismic excitations at its base and the POD is used to reduce the direct integration time history analysis cost. Section 2 presents the modeling of material nonlinear behavior for a RC beam element using the multi-fiber section approach. Section 3 is dedicated to the dynamic analysis of a RC element with material nonlinearities using classical and reduced POD procedures. Section 4 presents an application of the POD reduction method to the multistory frame structure under consideration while comparing the results with full model analysis. Section 5 summarizes the conclusions and future perspectives.

2 MULTI-FIBER BEAM MODEL

The concentrated (lumped) plasticity is the simplest and most popular approach to model material nonlinearity in structural elements. However, this technique is based on the assumption that nonlinear material behavior occurs only at specified concentrated points of the structural member (which is a major simplification). In addition, interaction between bending moments and varying axial forces at the plastic hinge is not taken into account. Moreover, the plastic hinges behavior is defined by characteristic curves (Moment versus Rotation or Force versus Displacement) provided by the seismic codes. These curves are based on rough estimations and assumptions which reduce their accuracy. On the other hand and as we will detail in this section, the multi-fiber beam model assures the distribution of nonlinear material behavior all along the structural element length and all over its cross section (distributed plasticity approach). In addition, this technique takes into account the interaction between bending moments and axial loads and can be applied to elements having non-typical cross sections. The fiber model approach is more computationally demanding than the concentrated plastic hinge technique however it remains efficient and very beneficial especially for wall elements modeled by the equivalent beam approach.

Since 2D finite elements are not addressed in this paper, the multi-fiber beam approach is adopted in this work to model the nonlinear material in 1D finite elements (beams, columns, equivalent beam model for walls) while considering the Euler-Bernoulli hypothesis (planar sections before deformation remain planar and perpendicular to the element's center line after deformation).

As already mentioned, the multi-fiber beam approach consists in dividing the structural element cross section into a set of longitudinal fibers. As a consequence, using this modeling technique requires a 3-level analysis.

Fibers are the fundamental level of analysis. Each fiber is made up of only one single material: for reinforced concrete members, the fibers can be made of steel reinforcements, confined or unconfined concrete. The fiber axial stress σ_{fiber} and the longitudinal tangent Young modulus $E_{T fiber}$ are determined as a function of the longitudinal fiber axial strain ϵ_{fiber} .

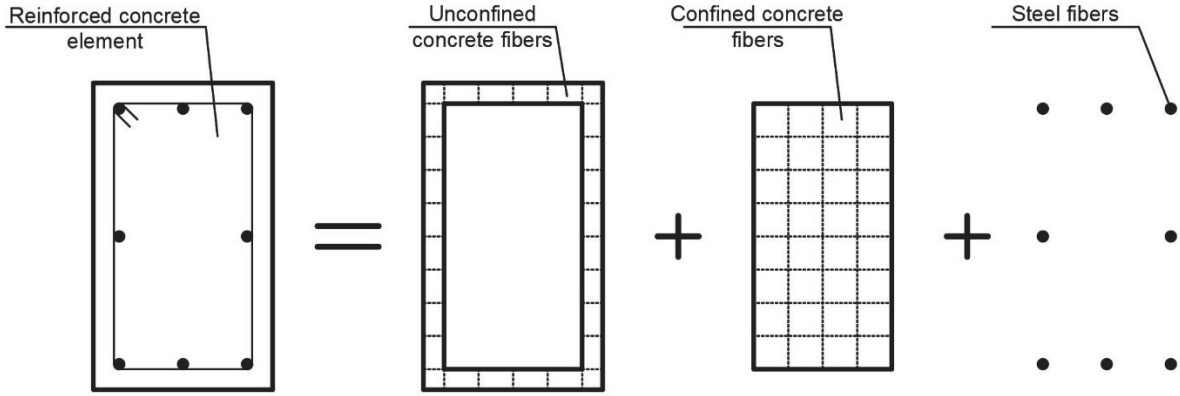


Figure 1. Multi-fiber reinforced concrete section

The element's cross section is the second level of analysis. Applying the Euler-Bernoulli hypothesis will result in perfect bond conditions between fibers (no sliding of a fiber with respect to another is allowed). In 2D structural analysis, for a fiber having its centroid located at the ordinate y in the section reference, the axial longitudinal strain in the fiber $\varepsilon(y)$ can be determined as a function of the section's uniform axial strain along x axis ε_x and the section's curvature along z axis ϕ_z

$$\varepsilon(y) = \varepsilon_x - y\phi_z = \begin{Bmatrix} 1 & -y \end{Bmatrix} \begin{Bmatrix} \varepsilon_x \\ \phi_z \end{Bmatrix} \quad (1)$$

since in nonlinear analysis the calculation is done by increments, we get:

$$\Delta\varepsilon(y) = \Delta\varepsilon_x - y\Delta\phi_z = \begin{Bmatrix} 1 & -y \end{Bmatrix} \begin{Bmatrix} \Delta\varepsilon_x \\ \Delta\phi_z \end{Bmatrix} \quad (2)$$

this axial strain increment of the fiber $\Delta\varepsilon(y)$ causes an increment in the section's internal axial force ΔN and bending moment along z axis ΔM_z .

$$\Delta N = E_{T \text{ fiber}} A_{\text{fiber}} \Delta\varepsilon(y) \quad (3.a)$$

$$\Delta M_z = -y\Delta N = -yE_{T \text{ fiber}} A_{\text{fiber}} \Delta\varepsilon(y) \quad (3.b)$$

for a single fiber, the resulting increment of internal forces in the section is

$$\{\Delta F_{\text{Section}}\} = \begin{Bmatrix} \Delta N \\ \Delta M_z \end{Bmatrix} = E_{T \text{ fiber}} A_{\text{fiber}} \begin{bmatrix} 1 & -y \\ -y & y^2 \end{bmatrix} \begin{Bmatrix} \Delta\varepsilon_x \\ \Delta\phi_z \end{Bmatrix} \quad (4)$$

for all the fibers, the entire resulting increment of internal forces in the section is

$$\{\Delta F_{\text{Section}}\} = \begin{Bmatrix} \Delta N \\ \Delta M_z \end{Bmatrix} = \underbrace{\sum_{i=1}^{n_{\text{fiber}}} E_{T \text{ fiber } i} A_{\text{fiber } i}}_{[K_T]} \begin{bmatrix} 1 & -y_i \\ -y_i & y_i^2 \end{bmatrix} \begin{Bmatrix} \Delta\varepsilon_x \\ \Delta\phi_z \end{Bmatrix} \quad (5)$$

where n_{fiber} is the total number of fibers in the section and $[K_T]$ is the section's tangent stiffness matrix.

The entire element is the third level of analysis. Linear shape functions are considered for longitudinal translation and Hermite cubic shape functions are used for bending. Applying the principle of virtual work we get

$$\{F_{\text{int}}\} = \int [B(x)]^T \begin{Bmatrix} 1 \\ -y \end{Bmatrix} \sigma_{\text{fiber}}(x, y) dV \quad (5)$$

$$[K_T] = \int [B(x)]^T \begin{Bmatrix} 1 \\ -y \end{Bmatrix} E_{T \text{ fiber}}(x, y) \{1 \quad -y\} [B(x)] dV \quad (6)$$

where $\{F_{int}\}$ is the internal nodal force vector of the element, $[K_T]$ is the element's tangent stiffness matrix and $[B(x)]$ is the gradient operator containing the derivatives of shape functions.

The volume integral required for the calculation of $\{F_{int}\}$ and $[K_T]$ is split into a surface integral on the cross section and a 1D integral along the longitudinal axis of the element. Since the element's cross section is already divided into fibers, we substitute the surface integration by the summation of fiber areas. Next, the longitudinal 1D integration is done by Gauss points.

3 FULL AND REDUCED DYNAMIC MODELS

As already mentioned, the classical time costly approach for capturing the nonlinear seismic response of a structure in function of time is the full model implicit direct integration nonlinear time history analysis. The Newmark- β method [8] is one of the famous implicit direct integration techniques used for linear and nonlinear time history analysis. For this method, knowing the structural system state at instant t_i (displacement, velocity and acceleration vectors) and assuming a variation pattern for acceleration between instants t_i and t_{i+1} (i.e. constant average acceleration) makes it possible to express the dynamic equation of the structural system at instant t_{i+1} with only one unknown (the displacement vector at instant t_{i+1}) and thus solving easily the system.

The proper orthogonal decomposition POD also known as the Principal Component Analysis PCA and the Karhunen-Loève Decomposition KLD is a statistical analysis of observation data. Let's consider a data matrix $[X]$ containing n observation vectors $[X] = [\{X_1\} \quad \dots \quad \{X_n\}]$ and each observation vector is made of m dimension

$$[X] = [\{X_1\} \quad \dots \quad \{X_n\}] = \begin{bmatrix} x_{11} & \dots & x_{1n} \\ \vdots & \ddots & \vdots \\ x_{m1} & \dots & x_{mn} \end{bmatrix} \quad (7)$$

$\{S_i\} = \{x_{i1} \quad \dots \quad x_{in}\}$ is row i in matrix $[X]$ and represents all the data collected on dimension i . If data set $\{S_i\} \forall i$ has a zero mean, the variance of $\{S_i\}$ becomes

$$\sigma^2(\{S_i\}) = \frac{1}{n-1} \times \sum_{k=1}^n (x_{ik} - \text{mean}(\{S_i\}))^2 = \frac{1}{n-1} \times \sum_{k=1}^n (x_{ik})^2 = \frac{1}{n-1} \{S_i\} \{S_i\}^T \quad (8)$$

and the covariance of $\{S_i\}$ and $\{S_j\}$ becomes

$$\text{COV}(\{S_i\}, \{S_j\}) = \frac{1}{n-1} \times \sum_{k=1}^n (x_{ik} - \text{mean}(\{S_i\})) (x_{jk} - \text{mean}(\{S_j\})) \quad (9.a)$$

$$\text{COV}(\{S_i\}, \{S_j\}) = \frac{1}{n-1} \times \sum_{k=1}^n (x_{ik})(x_{jk}) = \frac{1}{n-1} \{S_i\} \{S_j\}^T \quad (9.b)$$

High value of $\sigma^2(\{S_i\})$ indicates high action on dimension i and vice versa. High value of $\text{COV}(\{S_i\}, \{S_j\})$ indicates high similarity between the actions on dimension i and dimension j . On the other hand, $\text{COV}(\{S_i\}, \{S_j\}) = 0$ indicates zero resemblance (total independence) between the actions on dimension i and dimension j .

If data set $\{S_i\} \forall i$ has a zero mean, the covariance of matrix $[X]$ becomes

$$\text{COV}([X]) = \frac{1}{n-1} [X][X]^T \quad (10.a)$$

$$COV([X]) = \begin{bmatrix} \sigma^2(\{S_1\}) & COV(\{S_1\}, \{S_2\}) & \cdots & COV(\{S_1\}, \{S_n\}) \\ COV(\{S_2\}, \{S_1\}) & \sigma^2(\{S_2\}) & \cdots & COV(\{S_2\}, \{S_n\}) \\ \vdots & \vdots & \ddots & \vdots \\ COV(\{S_n\}, \{S_1\}) & COV(\{S_n\}, \{S_2\}) & \cdots & \sigma^2(\{S_n\}) \end{bmatrix} \quad (10.b)$$

Determining the principal components of data matrix $[X]$ starts by finding a new orthonormal reference $[N]$. The initial data matrix $[X]$ is expressed in this new reference as $[X'] = [N]^T [X]$. For $[N]$ to be containing the principal components of the data observation, $COV([X'])$ should be a diagonal matrix. In other words, we have zero similarity between actions on different new dimensions in reference $[N]$ ($COV(\{S'_i\}, \{S'_j\}) = 0$ for $i \neq j$).

Since $COV([X])$ is made up of $[X][X]^T$ it is a symmetrical matrix and thus has real eigenvalues.

$$[X][X]^T [\emptyset] = [\emptyset][\lambda] \quad (11)$$

where $[\emptyset]$ is the eigenvectors matrix and $[\lambda]$ is the diagonal matrix containing the eigenvalues. Eigenvectors are orthonormal vectors and we can demonstrate that the new reference $[N]$ we were talking about in the previous paragraph is in fact the eigenvectors matrix ($[N] = [\emptyset]$) of $[X][X]^T$. In fact for $[X'] = [\emptyset]^T [X]$ we get

$$COV([X']) = \frac{1}{n-1} [X'] [X']^T = \frac{1}{n-1} [\emptyset]^T \underbrace{[X][X]^T [\emptyset]}_{[\emptyset][\lambda]} = [\lambda] \quad (12)$$

$COV([X'])$ is a diagonal matrix and $\sigma^2(\{S'_i\}) = \lambda_i$. We notice that the higher λ_i is the more we have actions on dimension i in the eigenvectors reference. As a conclusion, principal components of the data set $[X]$ are the eigenvectors of $[X][X]^T$ and modes with high eigenvalues are the most influential in representing $[X]$.

The orthogonal eigenvectors obtained are called POD modes and the corresponding eigenvalues are called proper orthogonal values. The POD modes can be used to reconstruct the initial data matrix $[X]$. The higher the eigenvalue of a POD mode is, the more essential this mode is in recreating $[X]$.

By considering the most important s POD modes ($s < m$) and placing them in $[T] \in \mathbb{R}^{m \times s}$, the $\{X_t\}$ snapshot vector previously expressed in m dimensions can now be approximated in the lower s dimensions

$$\underbrace{\{X_t\}}_{\in \mathbb{R}^{m \times 1}} \cong \underbrace{[T]}_{\in \mathbb{R}^{m \times s}} \underbrace{\{Q_t\}}_{\in \mathbb{R}^{s \times 1}} \quad (13)$$

where $\{Q_t\}$ contains the coordinates of the snapshot vector in the new reference $[T]$. The choice of the number s of POD modes to consider in the reduced new reference should satisfy 2 conditions:

- 1- The representation in the new reference should be accurate so the error should be minimal. The higher s is, the more accurate the approximation is.

$$error = \sum_{t=1}^n \|\{X_{t_i}\} - [T]\{Q_{t_i}\}\| \quad (14)$$

- 2- For the dimensions reduction to be efficient, the number of chosen POD modes s should be relatively small.

In order to balance between accuracy and efficiency, an energy criterion is considered to determine the optimal value of s . The Proper Orthogonal Value of a mode gives an indication on the energy carried by this mode. Generally, the first s POD modes carrying at least 99% of the total system energy are considered for the new reduced reference.

$$\frac{\sum_{i=1}^s \lambda_i}{\sum_{j=1}^m \lambda_j} \geq 99\% \quad (15)$$

In structural dynamics, the POD reduction can be applied to the direct integration time history analysis for linear or nonlinear structures. In order to get the observation data required for the POD, we initially do a classical implicit direct integration time history analysis of the full structural finite element model subjected to a specific base excitation. Let's consider a nonlinear structural system with m degrees of freedom and n snapshots were taken. We calculate the POD modes and proper orthogonal values of the data matrix $[X]$ and then choose the subspace $[T] \in \mathbb{R}^{m \times s}$ containing the first s POD modes satisfying the 99% energy criterion. The dynamic equation of the system is

$$[M]\{\ddot{X}(t)\} + [C]\{\dot{X}(t)\} + R(\{X(t)\}) = \{F(t)\} \quad (16)$$

By replacing $\{X(t)\}$ and its derivatives by $[T]\{Q(t)\}$ and multiplying both sides of the dynamic equation by $[T]^T$ we get

$$\underbrace{[T]^T [M] [T]}_{[M_r] \in \mathbb{R}^{s \times s}} \{\ddot{Q}(t)\} + \underbrace{[T]^T [C] [T]}_{[C_r] \in \mathbb{R}^{s \times s}} \{\dot{Q}(t)\} + \underbrace{[T]^T R([T]\{Q(t)\})}_{R_r([T]\{Q(t)\}) \in \mathbb{R}^{s \times 1}} = \underbrace{[T]^T \{F(t)\}}_{\{F_r(t)\} \in \mathbb{R}^{s \times 1}} \quad (17)$$

The previously m degrees of freedom dynamic system is reduced to s degrees of freedom. However, the nonlinear restoring force $R([T]\{Q(t)\})$ cannot be reduced and always needs to be calculated in the full coordinate model which makes this step the most time consuming part of the entire process. In this case, the most effective direct time integration technique to adopt will be the one with the least recurrence for the expensive nonlinear restoring force calculation.

Implicit direct time integration techniques are usually used in conjunction with the Newton-Raphson approach for solving nonlinear systems. In order to reach convergence with this approach, multiple iterations are required at each time step and for every iteration we need to calculate the tangent stiffness matrix, its inverse and the nonlinear restoring force which are all time costly. Using the constant stiffness Newton-Raphson approach will save us the need for the tangent stiffness calculation and its inverse but will increase the number of iterations required for convergence.

On the other hand and for explicit direct time integration techniques, the popular central difference method requires only one iteration per time step and no expensive calculation of the tangent stiffness matrix and its inverse are needed (only the nonlinear restoring force is required). However, the central difference approach is conditionally stable and needs to satisfy the following stability condition

$$\Delta t < \frac{2}{\omega_{max}} \quad (18)$$

where Δt is the time step and ω_{max} is the largest natural pulsation of the system. Generally, the full model of the structure has a relatively large number of degrees of freedom and will result in high natural pulsations (for high modes) hence requiring small time steps to maintain calculation stability and consequently increasing the computational cost. Nevertheless, when working with a reduced structural model, significantly fewer number of degrees of freedom are considered and thus the reduced system will have smaller natural pulsations which makes it possible to use larger time steps while maintaining numerical stability. For this reason, in this work the central difference method is considered to be the most effective direct time integration technique for reduced models.

Various applications of this POD nonlinear dynamic model reduction are possible. As already mentioned for the dynamic seismic analysis, the structure is studied for a range of possible earthquakes and is analyzed and checked for each excitation (earthquake record)

separately. Since we need to conduct an analysis for each excitation, we start with the classic full model implicit direct integration nonlinear time history analysis for the first excitation. By collecting snapshots from this initial analysis, we can determine the essential POD modes and use them to reduce the dynamic model in the analysis of the remaining excitations. [15] proposed this approach and applied it on a small scale steel frame in addition to using it for studying seismic base isolators. In the current article, we will use this approach and extend it on a reinforced concrete multistory frame structure while the material nonlinearity is modeled by the multi-fiber section technique.

4 APPLICATION

At first we need to consider the base vibrations to use. The following 4 earthquake recordings obtained from the Center of Engineering for Strong Motion Data CESMD (www.strongmotioncenter.org) were considered (refer to Table 1).

Earthquake	Location	Date	Magnitude	Measurement station	Vibration direction	Total duration	Time step
Northridge	Los Angeles, USA	01/17/1994	6.4 ML	Newhall LA county fire station	0°	60s	20ms
Elcentro	California, USA	05/18/1940	6.9 Mw	Elcentro	0°	53.74s	20ms
L'Aquila	L'Aquila, Italy	04/06/2009	6.3 Mw	L'Aquila V.Aterno Centro Valle	90°	60s	20ms
Chile	Off the coast of central Chile	02/27/2010	8.8 Mw	Constitution city	90°	120s	20ms

Table 1: Considered earthquakes.

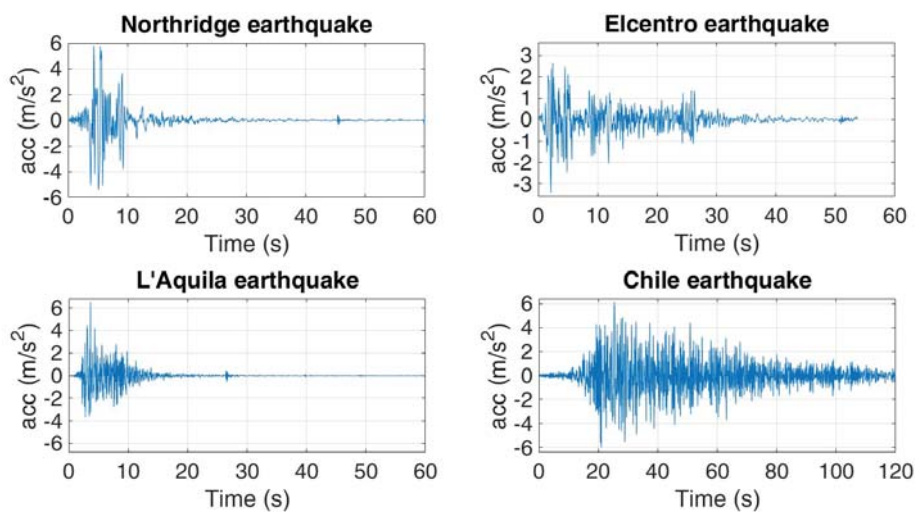


Figure 2. Earthquakes accelerograms

The structure is a 2D Reinforced Concrete (RC) multistory frame made up of 10 stories and 5 spans with a 3 m story height, a 5 m span length, a 4 t/m linear load is considered on beams and the structural self-weight is neglected (refer to Figure 3). All concrete columns and beams are divided into 1 m length finite elements and considered to have the same square cross section 40x40 cm with four 20 mm High Bond HB reinforcing bars at both top and bottom sides (refer to Figure 5). The cross section is divided into 4 concrete fibers and 2 steel fibers. Rayleigh damping was used to get a 5% damping ratio for the first two eigenmodes (more than 90% of the total mass is participating in the first two eigenmodes). The energy criteria for POD modes selection is set to 99.9% (higher than 99% due to the complexity of reinforced concrete elements).

Material nonlinearity is considered to occur in the elements near the beam column connections at the first 5 stories (refer to Figure 4). The steel rebar is considered to have a bilinear backbone curve (initially linear elastic then plastic with strain hardening) with a yielding stress of 400 MPa, a yielding strain of 2‰, an elastic Young modulus of 200 GPa, an ultimate stress of 420 MPa and an ultimate strain of 2.5‰. Under cyclic loading, if nonlinearity is reached, the steel material will undergo a kinematic hysteresis behavior (refer to Figure 6). Concrete is considered to be unconfined and modeled according to a simplified version of Mander model [16] that takes into account the damaging phenomena. The maximum concrete compressive strength is 25 MPa at a corresponding strain of 2‰, the ultimate compressive strain is 4‰, the maximum tensile strength is considered 2.5 MPa (10% of the compressive strength) at a corresponding strain of 0.1‰ and the elastic Young modulus is 25 GPa (refer to Figure 7).

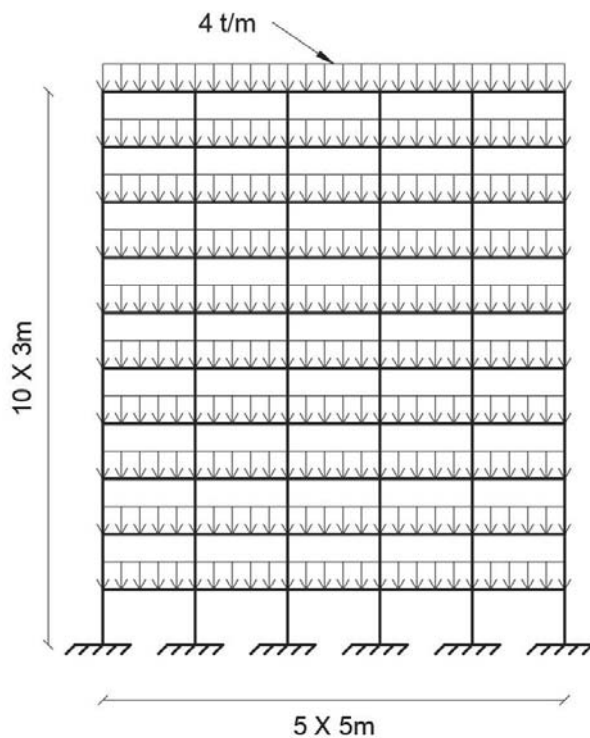


Figure 3. RC frame geometry and loading

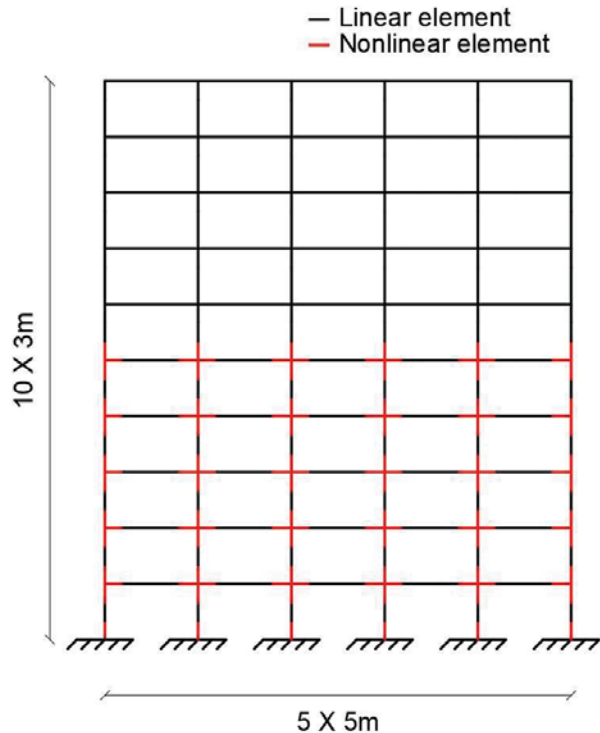


Figure 4. Position of nonlinear elements in RC frame

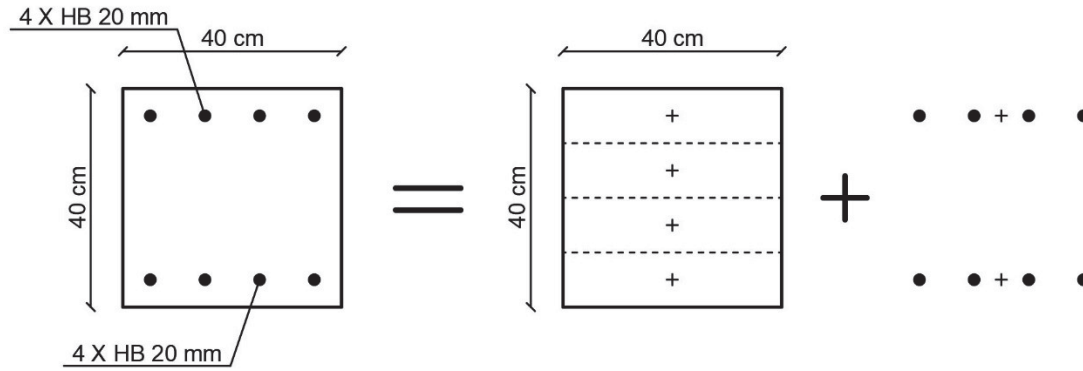


Figure 5. RC element multi-fiber section

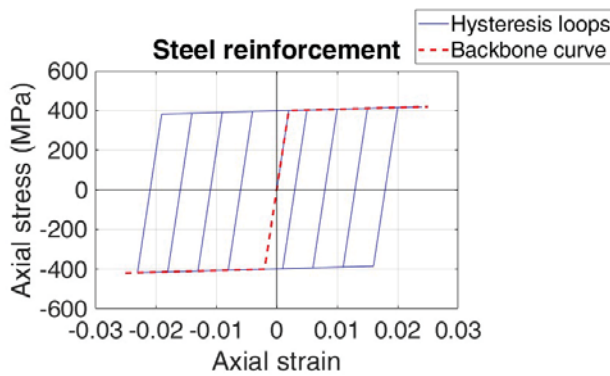


Figure 6. Steel reinforcement axial stress-strain curve

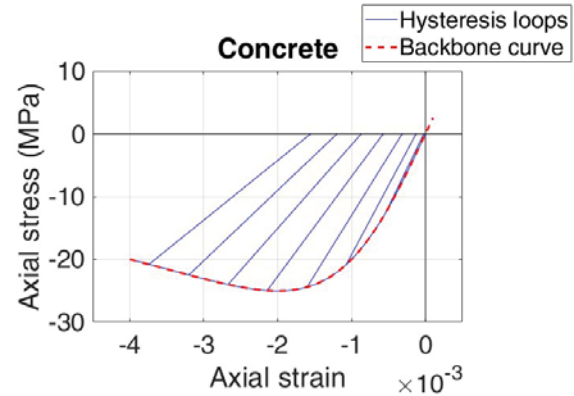


Figure 7. concrete axial stress-strain curve

Northridge earthquake is considered as the initial vibration. Full Model (FM) implicit nonlinear time history analysis with a 20 ms time step was carried out for this earthquake. 50 snapshots were taken for the resulting displacement vector during the first 15 seconds of the vibration (where most of the powerful excitation occurs) and at equally spaced time intervals. POD modes were extracted from the snapshot matrix and the dynamic system was reduced based on Northridge earthquake results. Then, Reduced Model (RM) explicit nonlinear time history analysis with a 20 ms time step was carried out for the remaining earthquakes (Elcentro, L'Aquila and Chile).

It should be noted that for comparison purpose, FM implicit nonlinear time history analysis was conducted separately for Elcentro, L'Aquila and Chile earthquakes in order to have a base reference. Also RM analysis was performed for the Northridge earthquake for comparison with the initially calculated full dynamic model.

For this structure, the reduced base is made of the first 4 POD modes since they represent more than 99.9% of the system's energy. As a result, this structure with initially 1140 degrees of freedom is reduced to only 4.

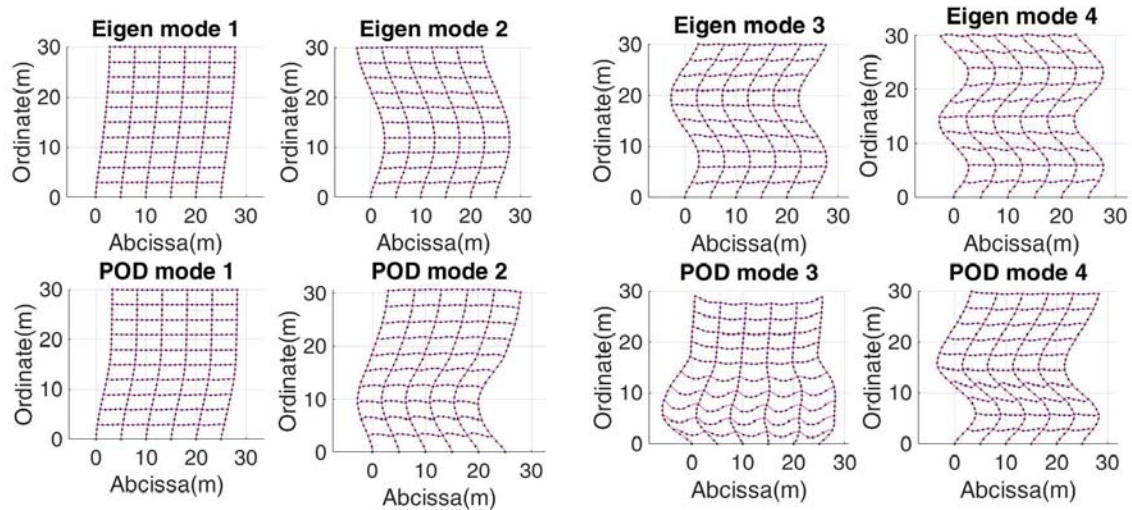


Figure 8. Classic structural eigenmodes Vs POD modes

By comparing the POD modes with the classical eigenmodes of the structure, we can clearly see the nonlinearity effect in the POD modes at the first 5 stories of the structure especially for modes 2 and 3.

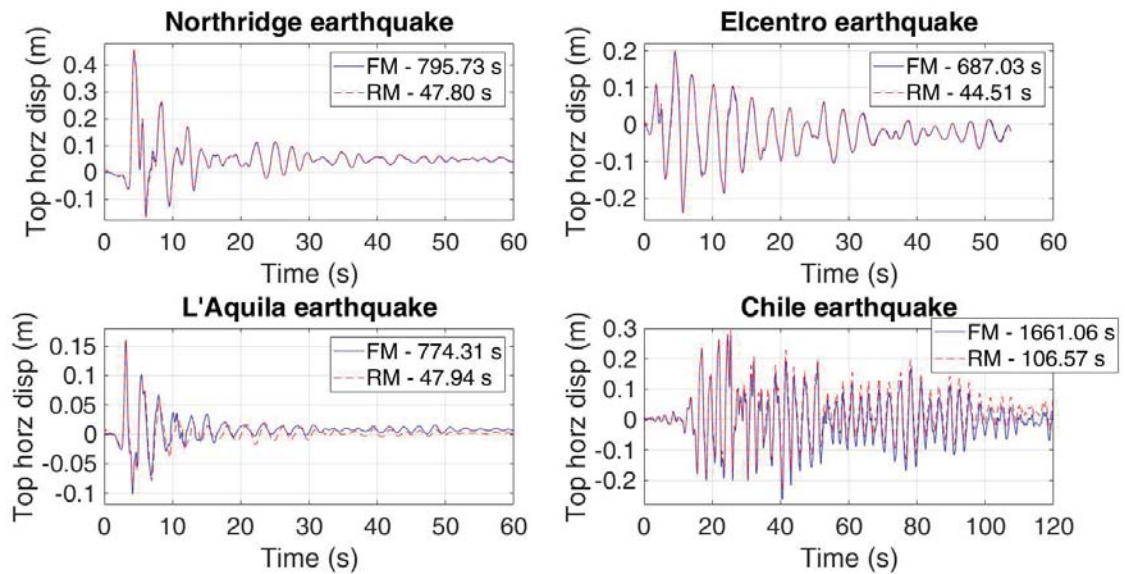


Figure 9. Structural top left corner horizontal displacement in function of time for Full Models (FM) and Reduced Models (RM)

As we can see in Figure 9 the reduced models results are very close to the full models and at a fraction of the time cost, for further details refer to the following table 2.

Earthquake	FM time	RM time	Time saving	Speedup	Average error	Max horiz displacement
Northridge	795.73 s	47.80 s	93.99%	16.6	0.28 cm	45.06 cm
Elcentro	687.03 s	44.51 s	93.52%	15.4	0.36 cm	23.96 cm
L'Aquila	774.31 s	47.94 s	93.81%	16.2	0.79 cm	15.85 cm
Chile	1661.06 s	106.57 s	93.58%	15.6	2.71 cm	27.24 cm

Table 2: Accuracy and time saving of the Reduced Model (RM) with respect to the Full Model (FM).

We can clearly see the time saving benefits of the POD modes in reducing the nonlinear structural system. In addition, the POD modes extracted from the Full Model (FM) analysis of Northridge earthquake are working well in the reduction of the structural model subjected to other excitations (Elcentro, L'Aquila and Chile Earthquake).

5 CONCLUSIONS AND PERSPECTIVES

In this paper we extended the application of the Proper Orthogonal Decomposition to reduce nonlinear dynamic analysis of reinforced concrete multistory frame structure where the material nonlinearity was modeled by the multifiber section approach. We succeeded in reducing a 1140 degrees of freedom system to only 4 degrees while achieving a speedup of around 16 (the reduced model calculation is 16 times faster than the full model) and maintaining an acceptable accuracy level. It was also shown that POD modes obtained from the analysis of a full structural model subjected to a certain base vibration were also convenient for reducing the same model when subjected to different base excitations. The key point here is having a well representative snapshot matrix of the dynamic system.

As perspectives for future work, we are looking forward for increasing the time saving, results accuracy and applying this approach on 2D reinforced concrete structural elements (plates, shells and membranes) by using the layered 2D element model.

REFERENCES

- [1] K.M.S. Mark, J.M. Roesset, *Nonlinear Dynamic Response of Reinforced Concrete Frames*, Publication R76-38, Department of Civil Engineering, M.I.T, 1976.
- [2] E. Spacone, F.C. Filippou, F.F. Taucer, Fibre beam-column model for non-linear analysis of R/C frames: Part I. Formulation, *Earthquake Engineering and Structural Dynamics*, **25**, 711-725, 1996.
- [3] P. Kotronis, J. Mazars, Simplified modelling strategies to simulate the dynamic behaviour of RC walls. *Journal of Earthquake Engineering*, **9(2)**, 285–306, 2005.
- [4] C. Zerbis, S.A. Mahin, Analysis of reinforced concrete beam-columns under uniaxial excitation, *Journal of Structural Engineering*, **114(4)**, 804–820, 1988.
- [5] M.A. Polak, Modeling Punching Shear of Reinforced Concrete Slabs Using Layered Finite Elements, *ACI structural journal*, **95-S08(1)**, 71-80, 1998.
- [6] R. Cerioni, I. Iori, E. Michelini, P. Bernardi, Multi-directional modeling of crack pattern in 2D R/C members, *Engineering Fracture Mechanics*, **75**, 615–628, 2008.
- [7] F. Rojas, J.C. Anderson, L.M Massone, A nonlinear quadrilateral thin flat layered shell element for the modeling of reinforced concrete wall structures, *Bulletin of Earthquake Engineering*, **17**, 6491–6513, 2019.
- [8] N.M. Newmark, A method of computation for structural dynamics, *Journal of Engineering Mechanics*, **85(3)**, 67-94, 1959.
- [9] E.L. Wilson, *A Computer Program for the Dynamic Stress Analysis of Underground Structures*, SESM Report No.68-1, Division of Structural Engineering Structural Mechanics, University of California, 1968.

- [10] H.M. Hilber, T.J.R. Hughes, R.L. Taylor, Improved numerical dissipation for time integration algorithms in structural dynamics. *Earthquake Engineering and Structural Dynamics*, **25**, 283-292, 1977.
- [11] W. Larbi, J.-F. Deü, Reduced order finite element formulations for vibration reduction using piezoelectric shunt damping, *Applied Acoustics*, **147**, 111-120, 2019.
- [12] W. Larbi, J.-F. Deü, R. Ohayon, Finite element reduced order model for noise and vibration reduction of double sandwich panels using shunted piezoelectric patches, *Applied Acoustics*, **108**, 40-49, 2016.
- [13] R. Rosenberg, On Nonlinear Vibrations of Systems with Many Degrees of Freedom, *Advances in Applied Mechanics*, **9**, 155-242, 1966.
- [14] S. Shaw, P. Holmes, A periodically forced piecewise linear oscillator, *Journal of Sound and Vibration*, **90**, 129-155, 1983.
- [15] F. Bamer, A.K. Amiri, C. Bucher, A new model order reduction strategy adapted to nonlinear problems in earthquake engineering, *Earthquake Engineering and Structural Dynamics*, **46**, 537–559, 2017.
- [16] J.B. Mander, M.J.N. Priestley, R. Park, Theoretical stress-strain model for confined concrete, *Journal of Structural Engineering*, **114(8)**, 1804-1826, 1988.

MULTI-RESOLUTION FINITE WAVELET DOMAIN METHOD FOR FAST TRANSIENT DYNAMIC ANALYSIS IN HOMOGENEOUS AND HETEROGENEOUS RODS AND BEAMS

Dimitris K. Dimitriou¹, Christos V. Nastos² and Dimitris A. Saravanos³

Dept. of Mechanical Engineering & Aeronautics, University of Patras
GR-26500, Rion-Patras, Greece

¹e-mail: d.dimitriou@upnet.gr

² e-mail: xnastos@upatras.gr

³ e-mail: saravanos@mech.upatras.gr

Keywords: Daubechies wavelets, Multi-resolution analysis, Wavelet-based elements, Composite structures, Guided waves.

Abstract

A Multi-resolution wavelet-based numerical method is developed for the fast prediction of transient response in elastic homogeneous and heterogeneous rods and beams. The method takes advantage of the remarkable mathematical properties of Daubechies wavelet and scaling functions as basis functions for the spatial approximation of state variables. The Multi-resolution capability of the Daubechies wavelet family, provides the hierarchical computational framework that incorporates both scaling and wavelet functions. An uncoupled solution system between each resolution is formulated, using an explicit time integration scheme. The first level of analysis provides the coarse solution, while finer approximations are sequentially calculated and superimposed on the coarse solution, until the desired level of accuracy is achieved, without discarding the previous results obtained at coarser resolutions. Additionally, due to the orthogonality and compact support of Daubechies wavelet family, the decoupled mass matrices of each resolution are diagonal, or block diagonal and the stiffness matrices are banded. The proposed method uses a uniform grid which remains practically unchanged when increasing the order of interpolation (p-method), owing to its meshless character. Numerical results for the simulation of high-frequency wave propagation in isotropic and orthotropic rods and beams are presented and compared against confirmed models, demonstrating substantial reduction in computational effort. Furthermore, additional benefits of the proposed method are shown, such as the localization capabilities of the fine solutions, which exhibit high sensitivity in detecting discontinuities resulted from material inhomogeneity.

1 INTRODUCTION

The transient dynamic response of isotropic and composite materials and structures is attracting intensive research over the last decade, as it is central to classical problems and applications. For instance, the design of passive and active Structural Health Monitoring (SHM) systems based on linear guided waves is an emerging technology, which requires rapid and robust simulation tools for ultrasonic wave propagation in healthy and damaged structures. However, the modeling of wave propagation in light-weight structures is computationally demanding, because of the high frequencies and wavenumbers involved in SHM applications. In addition, the anisotropy and inhomogeneity of composite light-weight structures, adds further complexity and makes the analysis of such problems even more challenging. Traditional methods, such as the Finite Element (FE) and Finite Difference Method, require very fine spatial and temporal discretization, mandated by the small wavelengths and the high frequencies. Remeshing techniques are implemented for the increase of the results accuracy, but using the h- or p-refinement method requires the introduction of intermediate nodes which render the simulation of Lamb or guided waves practically intractable in terms of required computation time. Computational efficiency is further deteriorated in damage detection applications, where most of the widely used detection methods have been developed independently, without sharing common features and synergies with numerical methods.

A powerful and multifunctional mathematical tool, which is mainly used in signal processing, pattern recognition and data compression, is wavelet analysis. During the past three decades, various researchers have studied the use of wavelets to solve partial differential equations (PDEs) [1]. Also, numerous works have investigated the application of several wavelets in computational mechanics and structural analysis. Patton and Marks [2] created a wavelet-based rod element for static and free vibration problems. Ma et al. [3] constructed a beam element based on Daubechies scaling functions, that exhibited great results in static analyses. Diaz et al. [4] have also developed a Daubechies wavelet-based Euler-Bernoulli beam element and a Mindlin-Reisner plate element for static problems. Except from Daubechies wavelets, Deslauries-Dubuc interpolating wavelets, known as interpolets, have been employed for the construction of beam elements for static [5] and wave propagation analysis [6]. Ko, Kurdila and Pilant [7] have developed a class of finite elements based on orthonormal compactly supported wavelets, and used Daubechies wavelets to solve a second order Neumann problem. In a different direction, wavelets have been used in dynamic problems for the reduction of PDEs to ODEs [8],[9] and for the development of wavelet-based time integration schemes [10]. Furthermore, B-spline wavelets have been studied for the construction of rod, beam, and plate elements for static and dynamic problems [11],[12],[13],[14],[15]. Moreover, Hermitian interpolation wavelets have been exploited for the simulation of wave propagation in isotropic structures [16]. Nastos et al. have implemented the Daubechies scaling functions and introduced the Finite Wavelet Domain (FWD) method for the simulation of wave propagation problems in rods, beams, membranes and plates [17],[18],[19]. Due to the orthogonality of Daubechies scaling functions, diagonal or block diagonal consistent mass matrices are created, and the equivalent wavelet domain algebraic system is rapidly solved using explicit time integration, evincing high accuracy and convergence rates. The FWD method incorporated first order shear and higher order layerwise theories either for beam or for plate structures, to achieve rapid and efficient simulation of symmetric and antisymmetric guided waves in thin and thick laminated composites.

All the forenamed wavelet-based methods are confined to the utilization of the scaling functions of each wavelet family; hence they can be termed as single-resolution (SR) approaches. However, the most distinct property of many wavelet families is the Multi-

resolution (MR) property. This property has mainly been investigated by numerous scientists in the fields of image and signal processing, feature extraction, data compression and denoising, et cetera [20],[21]. During the last decade, many researchers implemented the MR approximation in the field of computational mechanics. Quraishi and Sandeep [22] have created customized second generation wavelets that lead to a scale-decoupled system for the hierarchical static analysis of beams and plates, because of the stiffness decoupling. Jang et al. [23] used hat interpolation wavelets to solve Neumann and Dirichlet boundary value problems. Liu et al. [24] have developed a wavelet MR interpolation Galerkin method for the targeted enrichment of the solution of plane elastic problems. Also, several research works in the field of fracture mechanics using wavelet MR approaches have also been reported [25],[26],[27]. Additionally, Shen, Li and Ou [28] have studied the wave dispersion characteristics of 2D elastic waves using multiscale B-spline wavelets on interval (BSWI) method.

The present work takes advantage of the MR property of Daubechies wavelet family, to develop a hierarchical computational method as an expansion of the FWD method. The proposed method is termed as Multi-resolution Finite Wavelet Domain method (MR-FWD) and employs both Daubechies wavelet and scaling functions as basis functions for the generalized displacement field approximation. Due to the orthogonality and the MR property of Daubechies wavelet family, the solution system is uncoupled for each resolution in the wavelet space. In the present paper, the concept of the MR-FWD method is introduced for 1D cases, and its performance and functionalities are evaluated towards the simulation of longitudinal and guided waves in rods and beams.

In the following sections, the concept of the MR analysis and the mathematical properties of Daubechies scaling functions (SF) and wavelet functions (WF) are introduced. Then, the development of the MR-FWD approximation for rods and beams is described and the hierarchical solution scheme is formulated using explicit time integration. The final physical solution consists of the coarse resolution component and the superposition of sequential finer resolution components that incrementally improve the accuracy of the analysis. Finally, numerical results for transient dynamic analysis in homogeneous and inhomogeneous rod and beam structures are presented and evaluated.

2 MATHEMATICAL PROPERTIES OF DAUBECHIES WAVELET FAMILY

Daubechies scaling functions have been employed as basis functions for the FWD and other methods, owing to their remarkable mathematical properties [21],[29]. The Daubechies wavelet family consists of compactly supported orthogonal scaling functions $\varphi(x)$ and wavelet functions $\psi(x)$. Both SF (also called father wavelet) and WF (also called mother wavelet) are needed to form the Multi-resolution approximation. Also, both SF, WF and their derivatives are algorithmically constructed and do not have analytical expressions [30]. Many researchers have studied the computation of wavelet integrals, also termed as connection coefficients, which is a challenging task because of the highly oscillatory and noisy nature of many SF and WF [7],[31],[32]. The basic mathematical properties of Daubechies SF and WF are summarized below.

Compact Support. Both SF and WF are bounded within an interval, which spans over a compact support domain of grid points $[0, 2L - 1]$, where L is the order of the SF/WF. For the sake of conciseness, Daubechies WF/SF of order L are termed as DBL. This can be visualized in Figure 1. The values of SF and WF beyond their support are zero by definition. So, the influence of each SF/WF is limited within their support domain, that depends on the order L . Also, SF/WF of order L can be defined in the wavelet domain, either by translating the parent

SF/WF at other integer points j , thus creating new SF/WF $\phi(x-j)$, $\psi(x-j)$, or by shrinking/dilating the parent functions to form new ones $\phi(2^j x)$, $\psi(2^j x)$.

Orthogonality. The integer translates of the SF/WF are orthogonal to each other, hence, they form an orthogonal basis in the functional space,

$$\int_{-\infty}^{\infty} \phi(x-i)\phi(x-j)dx = \delta_{ij} \quad (1)$$

$$\int_{-\infty}^{\infty} \psi(x-i)\psi(x-j)dx = \delta_{ij} \quad (2)$$

$$\int_{-\infty}^{\infty} \phi(x-i)\psi(x-j)dx = 0 \quad (3)$$

Vanishing moments. The number of vanishing moments signifies the maximum degree of polynomial that can be exactly approximated by SF/WF. Daubechies SF/WF of order L have L vanishing moments, which are the highest amongst first generation wavelets. It should be noted, that a SF/WF with L vanishing moments can exactly represent polynomials up to $L-1$ order.

Two scale relation/ Dilation property. Provided by the dilation equations,

$$\phi(2^j x) = \sqrt{2} \cdot \sum_{k=0}^{2L-1} h_k \cdot \phi(2^{j+1} x - k) \quad (4)$$

$$\psi(2^j x) = \sqrt{2} \sum_{k=0}^{2L-1} (-1)^k h_{2L-k-1} \cdot \phi(2^{j+1} x - k) \quad (5)$$

where h_k is the set of $2L$ filter coefficients, and j is the resolution or scale. The dilation property constitutes the basis for the MR analysis since it mathematically connects the scaling and the wavelet function. Also, SF and WF can be calculated at dyadic points from the dilation equations.

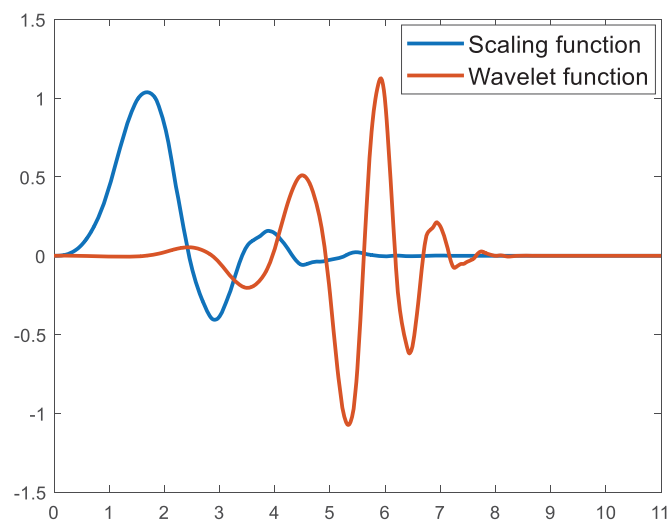


Figure 1: Example of Daubechies scaling $\phi(x)$ and wavelet $\psi(x)$ functions of order $L=6$ (DB6).

3 THE 1D MULTI-RESOLUTION FINITE WAVELET DOMAIN METHOD

In the present section, the basic concepts of the MR-FWD method for 1D problems and the construction of MR wavelet-based elements for rods and beams are presented. Besides that, the MR hierarchical procedure using explicit time integration scheme and the achievement of effective resolution decoupling are described.

3.1 Generalized approximation of field variables

For a generalized 1D problem, Figure 2 depicts a rod or beam structure that is subdivided into 2 segments, using a uniform grid of 3 grid points. Additional $2L-2$ nodes (where L is the order of the SF/WF) are introduced at the left side of the physical domain, and so the wavelet domain is formed. The case of DB3 discretization is shown in Figure 2, so the additional nodes are 4. The approximation of the generalized displacements $u(x, t)$ in the segment between 2 grid points, also called a wavelet-based element, for R resolutions can be expressed as:

$$u(x, t) = \sum_{n=-(2L-2)}^0 \hat{u}_{Cn}^0(t) \varphi(\xi - n) + \sum_{n=-(2L-2)}^0 \left\{ \sum_{S=0}^R \hat{u}_{Fn}^S(t) \psi(2^S \xi - n) \right\} \quad (6)$$

where L is the order of Daubechies SF/WF, \hat{u}_{Cn}^0 are the coarse wavelet coefficients of generalized displacements at resolution 0, and \hat{u}_{Fn}^S are the fine wavelet coefficients of generalized displacements at resolution S . Also, apart from the global coordinate system, a normalized local coordinate system is associated with each element, as shown in Figure 2. The local dimensionless coordinate variable ξ is given in terms of the global coordinate variable x as:

$$\xi = \frac{x - x_i}{x_{i+1} - x_i} = \frac{x - x_i}{l_e} \quad (7)$$

so, in Equation (6) the spatial variables x and ξ are limited to the ranges $0 \leq x \leq l_e$ and $0 \leq \xi \leq 1$, respectively. Also, l_e is the elemental length.

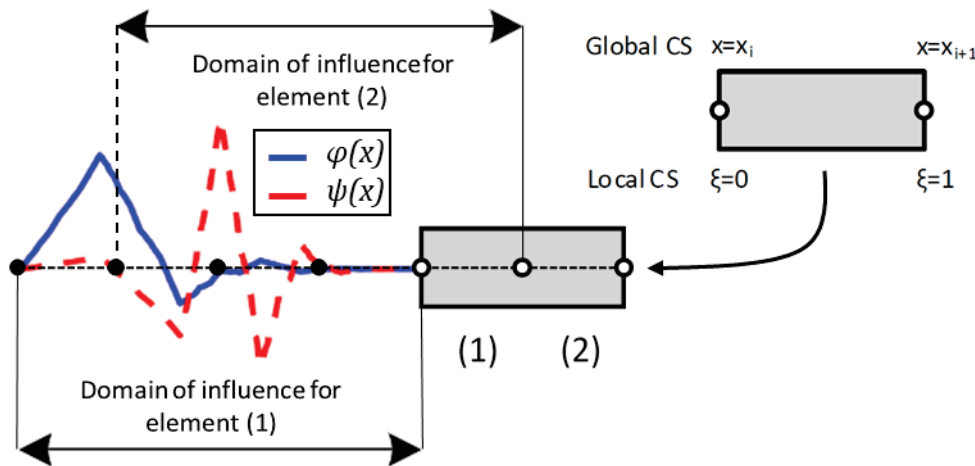


Figure 2: Discretization of the wavelet domain for 2 DB3 MR wavelet-based elements.

3.2 MR-FWD Rod-Beam element

The aforementioned MR approximation is implemented for the construction of Timoshenko beam elements. It should be noted, that the rod element is basically included in the beam element, since the rod kinematics are comprehended in the first shear deformation theory

(FSDT). Specifically, the proposed wavelet-based shear beam element encompasses transverse displacement and rotational degrees of freedom, except from axial displacement. According to the FSDT, the axial and transverse displacement, u and w respectively are expressed by the following equations:

$$u(x, z, t) = u^0(x, t) + \beta_x(x, t) \cdot z \quad (8)$$

$$w(x, z, t) = w^0(x, t) \quad (9)$$

where u^0 and w^0 are the axial and transverse displacement at the beam midplane, respectively, and β_x is the rotation of the neutral line. The axial and shear strain, ε_x and ε_{xz} , respectively, are calculated as:

$$\varepsilon_x(x, z, t) = \varepsilon_x^0(x, t) + k_x(x, t) \cdot z \quad (10)$$

$$\varepsilon_{xz}(x, z, t) = \varepsilon_{xz}^0(x, t) \quad (11)$$

in which $\varepsilon_x^0 = u_{,x}^0$, $k_x = \beta_{x,x}$ and $\varepsilon_{xz}^0 = \beta_x + w_{,x}^0$. The generalized Hooke's law takes the form:

$$\begin{Bmatrix} N_x \\ N_{xz} \\ M_x \end{Bmatrix} = \begin{bmatrix} A_{11} & B_{11} & 0 \\ B_{11} & A_{55} & 0 \\ 0 & 0 & D_{11} \end{bmatrix} \begin{Bmatrix} \varepsilon_x^0 \\ \varepsilon_{xz}^0 \\ k_x \end{Bmatrix} \Leftrightarrow \sigma_{gen} = [ABD] \varepsilon_{gen} \quad (12)$$

where N_x , N_{xz} and M_x are the axial force, shear force and bending moment, and A_{11} , A_{55} , B_{11} and D_{11} are the extensional, shear, coupling and flexural stiffness terms, respectively. As shown in Eq. (12) the generalized Hooke's law can take compact form, introducing the generalized stress $\sigma_{gen} = [N_x, N_{xz}, M_x]^T$, the generalized strain $\varepsilon_{gen} = [\varepsilon_x^0, \varepsilon_{xz}^0, k_x]^T$ and the well-known $[ABD]$ matrix of the beam. The Principle of Virtual Work provides the variational form of the equation of motion for the FSDT beam:

$$-\int_0^l \delta \varepsilon_{gen}^T \cdot \sigma_{gen} dx + \int_0^l \delta u_{gen}^T \cdot \rho_{total} \cdot \ddot{u}_{gen} dx + \int_S \delta \bar{u}_{gen}^T \cdot \bar{\tau} dS = 0 \quad (13)$$

where $u_{gen} = [u^0, w^0, \beta_x]^T$ are the generalized displacements, $\rho_{total} = \text{diag}[\rho^A, \rho^A, \rho^D]$ is the diagonal total density matrix of the beam, in which ρ^A is the linear density and ρ^D is the rotational inertia, and overbar variables are tractions and displacement on the boundary S . The approximation of generalized displacements of a MR-FWD shear beam element for R resolutions is:

$$\begin{Bmatrix} u^0 \\ w^0 \\ \beta_x \end{Bmatrix} = \sum_{n=-(2L-2)}^0 \begin{Bmatrix} \hat{u}_{Cn}^0 \\ \hat{w}_{Cn}^0 \\ \hat{\beta}_{xCn} \end{Bmatrix} \cdot \varphi(\xi - n) + \sum_{S=0}^R \sum_{n=-(2L-2)}^0 \begin{Bmatrix} \hat{u}_{Fn}^{0,S} \\ \hat{w}_{Fn}^{0,S} \\ \hat{\beta}_{xFn}^{0,S} \end{Bmatrix} \cdot \psi(2^S \xi - n) \quad (14)$$

and the generalized strains for resolution R , are expressed as:

$$\begin{Bmatrix} \varepsilon_x^0 \\ \varepsilon_{xz}^0 \\ k_x \end{Bmatrix} = \sum_{n=-(2L-2)}^0 [\Phi_{,x}] \cdot \begin{Bmatrix} \hat{u}_{Cn}^0 \\ \hat{w}_{Cn}^0 \\ \hat{\beta}_{xCn} \end{Bmatrix} + \sum_{S=0}^R \sum_{n=-(2L-2)}^0 [\Psi_{,x}] \cdot \begin{Bmatrix} \hat{u}_{Fn}^0 \\ \hat{w}_{Fn}^0 \\ \hat{\beta}_{xFn} \end{Bmatrix} \quad (15)$$

where matrix $\Phi_{,x}$ is the coarse strain shape function matrix:

$$[\Phi_{,x}] = \frac{1}{l_e} \begin{bmatrix} \varphi_{,\xi}(\xi - n) & 0 & 0 \\ 0 & \varphi_{,\xi}(\xi - n) & l_e \cdot \varphi(\xi - n) \\ 0 & 0 & \varphi_{,\xi}(\xi - n) \end{bmatrix} \quad (16)$$

and matrix $\Psi_{,x}$ is the fine strain shape function matrix for resolution R:

$$[\Psi_{,x}] = \frac{1}{l_e} \begin{bmatrix} \psi_{,\xi}(2^S \xi - n) & 0 & 0 \\ 0 & \psi_{,\xi}(2^S \xi - n) & l_e \cdot \psi(2^S \xi - n) \\ 0 & 0 & \psi_{,\xi}(2^S \xi - n) \end{bmatrix} \quad (17)$$

The implementation of Eqs. (14), (15), (16) and (17) to Eq. (13) yields the MR stiffness and mass matrices of the shear beam element. For simplicity, the hierarchical MR process for resolution 1 will be presented, considering that the generalized displacement field is termed as u in the physical space.

Resolution 1 ($C^0 + F^0$). Following the hierarchical MR scheme, the fine approximation at resolution 0 (F^0) needs to be calculated and added to the coarse solution at resolution 0 (C^0) in order to obtain C^1 solution. The MR discretized solution system is:

$$\begin{bmatrix} M_{CC} & 0 \\ 0 & M_{FF} \end{bmatrix} \begin{Bmatrix} \ddot{\hat{u}}_C(t) \\ \ddot{\hat{u}}_F(t) \end{Bmatrix} + \begin{bmatrix} K_{CC} & K_{CF} \\ K_{FC} & K_{FF} \end{bmatrix} \begin{Bmatrix} \hat{u}_C(t) \\ \hat{u}_F(t) \end{Bmatrix} = \begin{Bmatrix} F_C(t) \\ F_F(t) \end{Bmatrix} \quad (18)$$

where \hat{u}_F are the generalized fine wavelet coefficients and \hat{u}_C are the generalized coarse wavelet coefficients of the coupled equations of motion for resolution 1. The coarse solution at resolution 0 (C^0) is obtained assuming that $\hat{u}_F = 0$. In that way, this single-resolution coarse solution, termed as \hat{u}_{CC} , is basically the same solution that the FWD method provides, employing only the Daubechies SF $\varphi(x)$. It is important to point out that \hat{u}_C is not equal to \hat{u}_{CC} , because of the coupling between the coarse and fine equations of motion. That coupling emanates from the coupling stiffness matrices $[K_{CF}]$ and $[K_{FC}]$ that are nonzero in opposition to $[M_{CF}]$ and $[M_{FC}]$ that are equal to zero because of the orthogonality between $\varphi(x)$ and $\psi(x)$. Also, $[K_{FF}]$ and $[M_{FF}]$ are the fine resolution stiffness and mass matrices, respectively, and F_F is the fine resolution load vector. More specifically, all the aforementioned MR stiffness and mass matrices are calculated as:

$$[K_{CC}^e] = \begin{bmatrix} \frac{A_{11}}{l_e} \Gamma_{kl}^{11} & \frac{B_{11}}{l_e} \Gamma_{kl}^{11} & 0 \\ & \frac{A_{55}}{l_e} \Gamma_{kl}^{11} & A_{55} \Gamma_{kl}^{01} \\ (S) & & A_{55} l_e \Gamma_{kl}^{00} + \frac{D_{11}}{l_e} \Gamma_{kl}^{11} \end{bmatrix} \quad (19)$$

$$[K_{CF}^e] = \begin{bmatrix} \frac{A_{11}}{l_e} \Gamma 1_{kl}^{11} & \frac{B_{11}}{l_e} \Gamma 1_{kl}^{11} & 0 \\ & \frac{A_{55}}{l_e} \Gamma 1_{kl}^{11} & A_{55} \Gamma 1_{kl}^{01} \\ (S) & & A_{55} l_e \Gamma 1_{kl}^{00} + \frac{D_{11}}{l_e} \Gamma 1_{kl}^{11} \end{bmatrix} \quad (20)$$

$$[K_{FC}^e] = [K_{CF}^e]^T \quad (21)$$

$$[K_{FF}^e] = \begin{bmatrix} \frac{A_{11}}{l_e} \Gamma 2_{kl}^{11} & \frac{B_{11}}{l_e} \Gamma 2_{kl}^{11} & 0 \\ & \frac{A_{55}}{l_e} \Gamma 2_{kl}^{11} & A_{55} \Gamma 2_{kl}^{01} \\ (S) & & A_{55} l_e \Gamma 2_{kl}^{00} + \frac{D_{11}}{l_e} \Gamma 2_{kl}^{11} \end{bmatrix} \quad (22)$$

$$[M_{CC}^e] = \rho_{total} \cdot l_e \cdot \Gamma_{kl}^{00} \quad (23)$$

$$[M_{FF}^e] = \rho_{total} \cdot l_e \cdot \Gamma 2_{kl}^{00} \quad (24)$$

where $\Gamma_{kl}^{ij}, \Gamma 1_{kl}^{ij}, \Gamma 2_{kl}^{ij}$ in which $i, j = 1, 2$, determine the order of the derivation of the SF and WF, are the so called connection coefficients [17]. The computation of the connection coefficients is a challenging numerical procedure that is rigorously explained on [31],[32],[7]. Considering the previous equations, the wavelet integrals are given as:

$$\begin{aligned} \int_0^1 \varphi^{(i)}(\xi - k) \varphi^{(j)}(\xi - l) d\xi &= \Gamma_{kl}^{ij} \\ \int_0^1 \varphi^{(i)}(\xi - k) \psi^{(j)}(\xi - l) d\xi &= \Gamma 1_{kl}^{ij} \\ \int_0^1 \psi^{(i)}(\xi - k) \psi^{(j)}(\xi - l) d\xi &= \Gamma 2_{kl}^{ij} \end{aligned} \quad (25)$$

Due to the orthogonality of SF and WF, there are no coupling mass matrices because:

$$[M_{CF}^e] = [M_{FC}^e]^T = \rho_{total} l_e \int_0^1 \varphi(\xi - k) \cdot \psi(\xi - l) d\xi = 0 \quad (26)$$

The mass decoupling and the fact that the mass matrices are consistent and diagonal, leads to crucial computational benefits in the transient dynamic structural analysis. The mass decoupling feature is further discussed in section 3.3 for the hierarchical MR procedure using explicit time integration.

Another important feature of the novel MR-FWD method, is that when the traditional p-refinement method is utilized, the mesh remains practically unchanged [17]. Due to the meshless character of the proposed method, increasing the order of Daubechies SF/WF only leads to an increase in the additional grid points to the left side of the physical domain (Figure 2) and the rest of the mesh remains intact.

Moreover, the hierarchical MR solution system that is shown in Eq. (18) can be generalized for $S+I$ resolutions. The $S+I$ resolution stiffness matrices, mass matrices, generalized displacement vectors and load vectors are formed as:

$$\begin{bmatrix} K_{CC}^{s+1} \end{bmatrix} = \begin{bmatrix} K_{CC}^s & K_{CF}^s \\ K_{FC}^s & K_{FF}^s \end{bmatrix}, \begin{bmatrix} M_{CC}^{s+1} \end{bmatrix} = \begin{bmatrix} M_{CC}^s & 0 \\ 0 & M_{FF}^s \end{bmatrix}, \begin{bmatrix} F_C^{s+1} \end{bmatrix} = \begin{bmatrix} F_C^s \\ F_F^s \end{bmatrix}, \begin{bmatrix} \hat{u}_{CC}^{s+1} \end{bmatrix} = \begin{bmatrix} \hat{u}_C^s \\ \hat{u}_F^s \end{bmatrix} \quad (27)$$

It should be noted, that the MR procedure that is presented for the FSDT beam case in Eq. (18) is the same for the rod case, and so is the generalized form of the MR matrices and vectors in Eq. (27).

3.3 Hierarchical MR process using Explicit time integration scheme

The hierarchical MR process is shown in Eq. (18) for resolution 1. Essentially, the solution at resolution $S+1$ is the superposition of two different solutions (coarse and fine) at resolution S , that are obtained in two independent steps. The first step is always the SR solution that provides the coarse component approximation. For generality, the MR procedure will be described for resolution $S+1$. Considering Eq. (27), the following mass uncoupled MR solution system, that involves both coarse and fine approximation is obtained at resolution $S+1$:

$$\begin{bmatrix} M_{CC}^s & 0 \\ 0 & M_{FF}^s \end{bmatrix} \begin{Bmatrix} \ddot{\hat{u}}_C^{s,t} \\ \ddot{\hat{u}}_F^{s,t} \end{Bmatrix} + \begin{bmatrix} K_{CC}^s & K_{CF}^s \\ K_{FC}^s & K_{FF}^s \end{bmatrix} \begin{Bmatrix} \hat{u}_C^{s,t} \\ \hat{u}_F^{s,t} \end{Bmatrix} = \begin{bmatrix} F_C^{s,t} \\ F_F^{s,t} \end{bmatrix} \quad (28)$$

The component \hat{u}_C^s is set as:

$$\hat{u}_C^s = \Delta \hat{u}^s + \hat{u}_{CC}^s \quad (29)$$

where \hat{u}_{CC}^s is the already calculated single-resolution coarse approximation, and $\Delta \hat{u}^s$ is the residual between \hat{u}_C^s and \hat{u}_{CC}^s , called correction component. It is already mentioned that the multi-resolution coarse component \hat{u}_C^s is not equal to the single-resolution coarse component \hat{u}_{CC}^s because of the stiffness coupling terms. Combining Eqs. (28) and (29), leads to:

$$\begin{bmatrix} M_{CC}^s & 0 \\ 0 & M_{FF}^s \end{bmatrix} \begin{Bmatrix} \Delta \ddot{\hat{u}}^{s,t} \\ \ddot{\hat{u}}_F^{s,t} \end{Bmatrix} + \begin{bmatrix} K_{CC}^s & K_{CF}^s \\ K_{FC}^s & K_{FF}^s \end{bmatrix} \begin{Bmatrix} \Delta \hat{u}^{s,t} \\ \hat{u}_F^{s,t} \end{Bmatrix} = \begin{bmatrix} 0 \\ F_F^{s,t} - K_{FC}^s \hat{u}_{CC}^{s,t} \end{bmatrix} \quad (30)$$

The diagonality of the total MR mass matrix of Eq. (30) results in two uncoupled equations for the prediction of $\Delta \hat{u}^s$ and \hat{u}_F^s , using the central differences explicit time integration scheme. Those are calculated as:

$$\Delta \hat{u}^{s,t+1} = \frac{\begin{bmatrix} M_{CC}^s \end{bmatrix} (a_2 \Delta \hat{u}^{s,t} - a_0 \Delta \hat{u}^{s,t-1}) - \begin{bmatrix} K_{CC}^s \end{bmatrix} \Delta \hat{u}^{s,t} - \begin{bmatrix} K_{CF}^s \end{bmatrix} \hat{u}_F^{s,t}}{a_0 \begin{bmatrix} M_{CC}^s \end{bmatrix}} \quad (31)$$

$$\hat{u}_F^{s,t+1} = \frac{F_F^{s,t} + \begin{bmatrix} M_{FF}^s \end{bmatrix} (a_2 \hat{u}_F^{s,t} - a_0 \hat{u}_F^{s,t-1}) - \begin{bmatrix} K_{FC}^s \end{bmatrix} (\hat{u}_{CC}^{s,t} + \Delta \hat{u}^{s,t}) - \begin{bmatrix} K_{FF}^s \end{bmatrix} \hat{u}_F^{s,t}}{a_0 \begin{bmatrix} M_{FF}^s \end{bmatrix}} \quad (32)$$

where $a_0 = 1/\Delta t^2$ and $a_2 = 2/\Delta t^2$, in which Δt is the time step for the explicit dynamic solver. The superposition of the three components \hat{u}_{CC}^s , $\Delta \hat{u}^s$ and \hat{u}_F^s at resolution S , forms the coarse approximation of the next resolution $S+1$, as:

$$\hat{u}_{CC}^{s+1,t+1} = \hat{u}_{CC}^{s,t+1} + \Delta \hat{u}^{s,t+1} + \hat{u}_F^{s,t+1} \quad (33)$$

4 NUMERICAL RESULTS

The efficiency and the functionalities of the MR-FWD method are evaluated towards the simulation of longitudinal and guided waves in homogeneous and heterogeneous aluminum rods and laminated carbon/epoxy beams. The mechanical properties of the involved materials are shown in Table 1.

	E_{11} (GPa)	$E_{22}=E_{33}$ (GPa)	$G_{12}=G_{23}=G_{13}$ (GPa)	$\nu_{12}=\nu_{13}=\nu_{23}$	ρ (kg/m ³)
Aluminum	70	70	26.923	0.3	2700
Damaged Aluminum	7	7	2.6923	0.3	2700
Carbon/Epoxy	120	7.9	5.5	0.3	1580
Damaged Carbon/Epoxy	114	7.505	5.225	0.3	1580

Table 1: Material properties.

4.1 Homogeneous Aluminum Rod

An aluminum rod with length $l=4m$, cross section $A=10^{-4}m^2$ and mechanical properties that are shown in Table 1, is modeled. The rod is clamped at its left edge and it is excited at its center ($x=2m$), by a 5-cycle tone burst with 25 kHz central frequency. The analysis duration is 0.3 milliseconds (ms). The effectiveness of the MR hierarchical procedure is investigated for resolution up to 2, for DB3 wavelet-based elements. A converged 3-node FE analysis with 401 nodes is considered the reference solution. It is worth mentioning that both the 3-node FE and the DB3 wavelet-based elements, are quadratic approximation elements. The hierarchical process is shown in Figure 3, following top-down sequence.

The first step of the analysis is the SR approximation (C^0) that involves 54 grid points. It is obvious that this coarse solution \hat{u}_{CC}^0 diverges a lot from the reference solution. Moving to resolution 1, the components $\Delta\hat{u}^0$ and \hat{u}_F^0 are calculated and superimposed to \hat{u}_{CC}^0 , using the same grid points. In that way, the coarse solution at resolution 1 (C^1) is obtained, and it is shown that crucial correction is provided by $\Delta\hat{u}^0$ and \hat{u}_F^0 . The same procedure is repeated for resolution 2, but the shrinking of the DB3 WF requires the use of 104 grid points, for the calculation of $\Delta\hat{u}^1$ and \hat{u}_F^1 . The total summation of the above 5 components ($\hat{u}_{CC}^0, \Delta\hat{u}^0, \hat{u}_F^0, \Delta\hat{u}^1, \hat{u}_F^1$) provides the overall solution at resolution 2 (C^2), which has converged to the reference solution. It can be concluded, that the components $\Delta\hat{u}^s$ mainly improve the frequency and the time of flight of the wave packets, whereas the components \hat{u}_F^s provide a small correction on the amplitude of the wave packets. The functionalities of the fine components will be extensively assessed at the inhomogeneous cases.

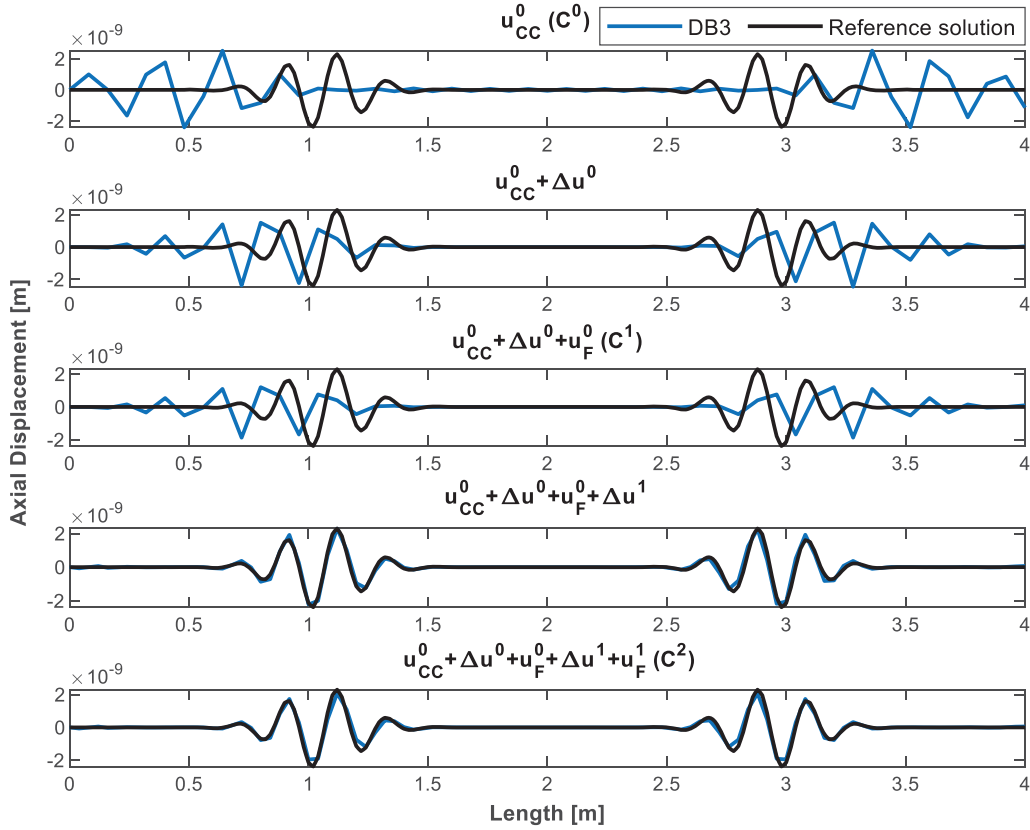


Figure 3: Predicted axial displacement field of the aluminum rod. The MR hierarchical procedure is shown from resolution 0 to resolution 2 (top-down sequence).

The MR hierarchical process demonstrates substantial reduction in the computational effort, because not only the required grid points for a converged solution are much fewer compared to the 3-node FE, but also the mass diagonality permits the initial $2N \times 2N$ algebraic system (Eq. (28)) to be solved as two $N \times N$ algebraic systems (Eq. (31) and (32)), using explicit time integration. Considering the computational cost in terms of floating-point operations (flops), a matrix inversion using LU decomposition requires approximately $2n^3/3$ flops. So, inverting two $N \times N$ matrices requires approximately 75% less flops in comparison with inverting a $2N \times 2N$ matrix. In that way, additional computational benefits arise from the hierarchical MR procedure, apart from the exploitation of the already calculated coarse solution.

4.2 Laminated Composite Beam

A 1m long unidirectional $[0]_8$ carbon/epoxy beam with cross section $A=10^{-4}m^2$ and mechanical properties shown in Table 1, is modeled. The beam is clamped at its left edge and it is transversely excited at its center ($x=0.5m$), by a 5-cycle tone burst with 50 kHz central frequency. The analysis duration is 0.15 ms. The simulation of antisymmetric guided waves is more challenging than the simulation of pressure waves, owing to the smaller wavelengths and the dispersive nature of the antisymmetric mode. In this case, the effectiveness of the p-method for resolution 1 solutions (C^1) is demonstrated. As shown in Figure 4, MR-FWD models with DB3, DB6, DB8 and DB11 wavelet-based elements are used to predict the transverse displacement field of the composite beam. The reference solution is a converged and validated FWD analysis (C^0) that employs DB3 elements with 434 grid points.

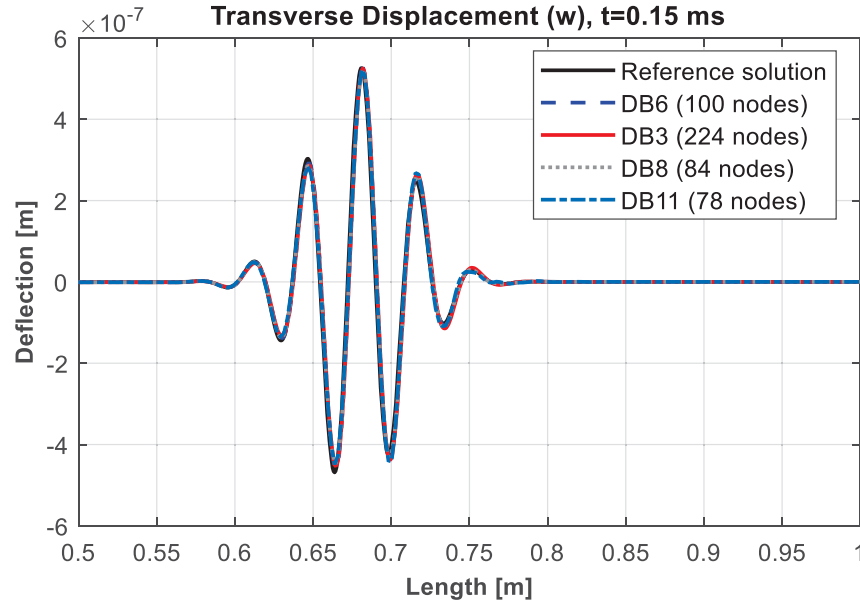


Figure 4: Predicted transverse displacement of the right half of the laminated beam. Minimum number of nodes required for a converged solution are illustrated for each discretization case inside the parentheses.

The superiority of the high order MR DB elements is depicted in Figure 4, where it is obvious that higher order MR models require substantially fewer nodes to obtain an accurate solution. Moreover, observing the case of DB3 discretization, the MR hierarchical method demonstrates remarkable precision and critically decreases the already decreased computational effort required by the single-resolution FWD method. Considering the grid points needed for a converged solution, there is a reduction of almost 50% for the C^I DB3 case and up to 82% for the C^I DB11 case, compared to the C^0 DB3 analysis. Finally, it should be noted that the wavelet-based FSDT beam elements do not exhibit shear locking effects, which is another significant advantage compared to traditional shear beam FE [17].

4.3 Inhomogeneous Aluminum Rod

An inhomogeneous aluminum rod with length $l=4m$ and cross section $A=10^{-4}m^2$ is modeled. The rod consists of two different materials, aluminum, and damaged aluminum, and their mechanical properties are shown in Table 1. The damaged area spans from $2m \leq x \leq 2.2m$, as depicted with dark grey in Figure 5a. The rod is clamped at the left edge and it is excited at its right free end ($x=4m$), by a 5-cycle tone burst with 25 kHz central frequency. The duration of the simulation is 0.8 ms. The reference solution is a converged SR analysis of 800 DB3 elements. Figure 5b depicts the axial displacement of the MR process, for 200 DB3 elements and resolutions from 0 to 2.

It is obvious that the initial scale of analysis (C^0) exhibits substantial error compared to the reference solution. Moving up to the C^I there is crucial correction of the predicted displacement field, but there is still divergence from the reference solution. Finally, the C^2 solution shows excellent agreement with the reference solution. The examination of the fine components introduces certain critical results and reveals some of their extraordinary benefits.

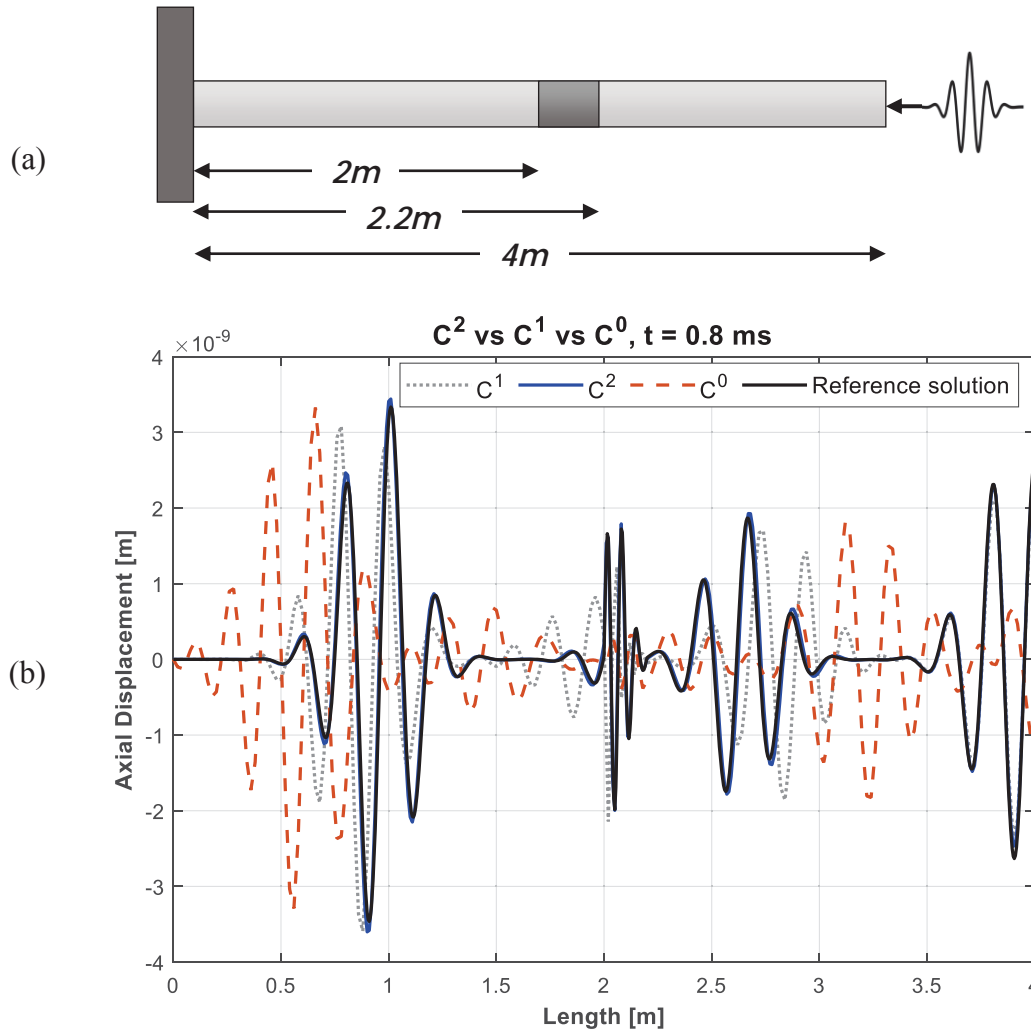


Figure 5: (a) Wave propagation in damaged rod structure. (b) Axial displacement field of the inhomogeneous rod for resolutions 0, 1 and 2.

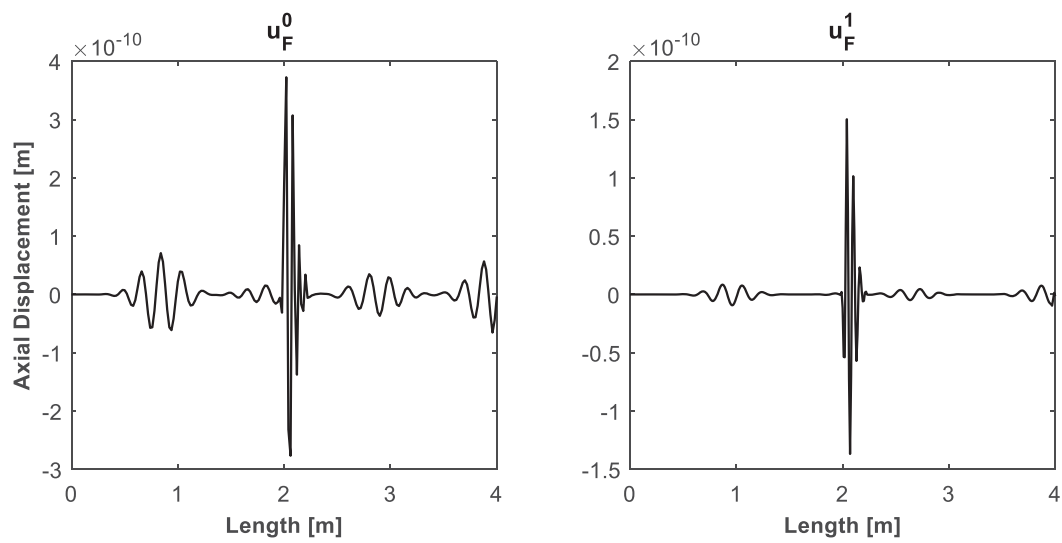


Figure 6: Contribution of the fine components of resolutions 0 (left) and 1 (right), in which the inhomogeneity is precisely detected and also the higher wavenumber inside the damaged area is accurately predicted.

As shown in Figure 6, the fine components \hat{u}_F^0, \hat{u}_F^1 exactly localize the span of the damage and capture the higher wavenumbers inside the inhomogeneity due to the high frequency nature of Daubechies WF. In particular, the \hat{u}_F^0 component uses the same nodes as the \hat{u}_{CC}^0 , but efficiently approaches the smaller wavelengths that arise from the lower Young modulus of the damaged region. Apparently, the \hat{u}_F^1 component that uses double nodes in comparison with the \hat{u}_{CC}^0 solution, precisely predicts the higher wavenumbers inside the inhomogeneity. Thus, besides the critical benefits of the MR-FWD method in terms of accuracy and computational effectiveness, there are additional gains concerning the fine components, which are extremely sensitive in detecting discontinuities and can numerically simulate steep gradients, even at coarse discretization cases.

4.4 Damaged Composite Beam

A 1m long cross-ply [0/90/0/90]_s carbon/epoxy beam with cross section $A=10^{-4}m^2$ is modeled. The beam consists of two different regions, the pristine carbon/epoxy, and the damaged carbon/epoxy region. The mechanical properties of those materials are shown in Table 1. The damage is assumed to induce 5% degradation to all the elastic moduli. The damaged area ranges from $0.75m \leq x \leq 0.8m$, as illustrated with dark grey in Figure 7a. The beam is clamped at its left edge and it is excited at its center ($x=0.5m$), by a 5-cycle tone burst with 50 kHz central frequency. The analysis duration is 0.2 ms. The efficiency of the MR hierarchical scheme is highlighted in the previous sections. In this section, the sensitivity of the fine components is exhibited. A converged discretization of 314 grid points of DB8 elements is used for resolution up to 1.

Figure 7b depicts the predicted deflection of the beam for the converged solutions C^0, C^I and the fine component w_F^0 . The objective of this analysis is not to emphasize the computational gains of the MR-FWD method in terms of the required grid points, since C^0 and C^I approximations are in excellent agreement. Hence, moving up to resolution 1 does not offer any correction at the C^0 solution. Nevertheless, the existence of the damaged area is not perceptible at C^0 or C^I solution, even though the right wave packet passes through the heterogeneity at $t=2ms$. The fine component w_F^0 provides precise detection of the interfaces between the damaged and the pristine composite beam despite the small degradation of its mechanical properties by 5%. In this case, the fine component does not capture a dissimilar wavenumber inside the heterogeneity, because of the insignificant difference among the material properties of the damaged and the pristine carbon/epoxy. Also, w_F^0 does not practically participate in the total solution in quantitative terms, since the C^0 solution is meticulous due to the dense discretization. However, the fine solution can exactly localize the boundaries between the two materials, introducing a pioneering additional property of the proposed numerical method.

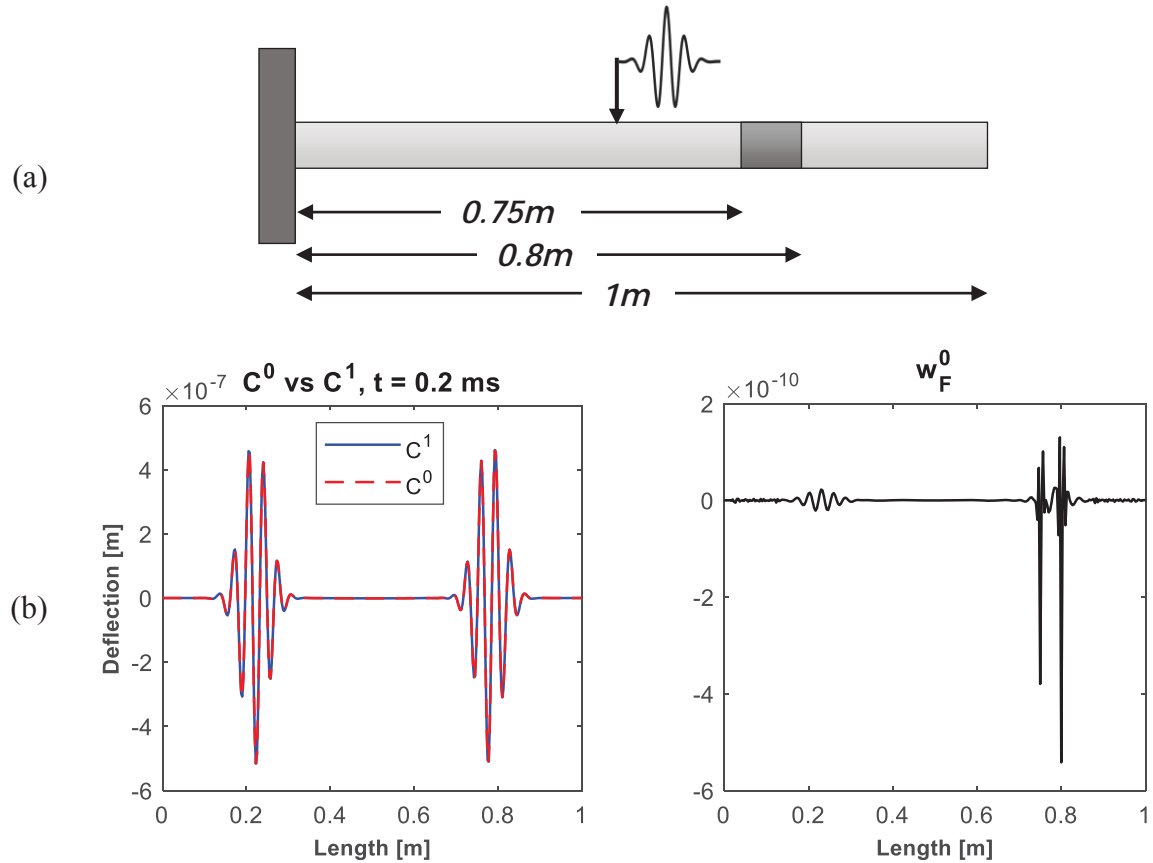


Figure 7: (a) Wave propagation in damaged composite beam. (b) C^0 and C^1 solutions are converged (left) but the inhomogeneity is not visible. The fine component accurately delimits the damage span (right).

5 CONCLUSIONS

A novel Multi-resolution hierarchical wavelet-based method for the efficient simulation of transient dynamic response of rods and beams, is presented. Taking advantage of the remarkable mathematical properties and the unique MR capability of Daubechies wavelet and scaling functions, the proposed 1D MR-FWD method has been developed, as an expansion of the single-resolution FWD method. The MR approximation includes two types of variables, the coarse and fine wavelet coefficients of each resolution. The implementation of the MR approximation at the equations of motion, yields a MR solution system that involves both coarse and fine resolution degrees of freedom. The hierarchical process starts with the coarse solution (C^0), which basically is the FWD method, and then a fine approximation (F^0) is calculated and superimposed on the coarse solution, forming the 1st improved solution (C^1). This procedure can be continued until the desired level of accuracy is achieved. Therefore, the proposed MR-FWD method exploits the non-converged solutions that are obtained at coarser resolutions, compared to traditional numerical methods that discard them. Due to the orthogonality of the Daubechies wavelet and scaling functions, the consistent mass matrices of each resolution are diagonal or at least block diagonal. Also, the mass diagonality results in decoupling of the discretized dynamic equations with the use of explicit time integration scheme. It should be emphasized, that the approximation C^1 provides a much more accurate prediction than C^0 , using the same grid points as the approximation C^0 . Additionally, it should be noted, that performing p-refinement to the proposed method, leaves the mesh practically unaffected. The precision and computational efficiency of the developed method were evaluated by com-

paring the predicted longitudinal and guided wave responses of homogeneous and heterogeneous rods and beams, with validated FE and single-resolution FWD models.

The numerical results demonstrated 4 key advantages of the MR-FWD method: (1) the MR property of Daubechies wavelets leads to a hierarchical MR set of dynamic equations, that introduce a new type of refinement which utilizes the solution of an already obtained coarser analysis; (2) the hierarchical MR procedure in synergy with the advantageous use of the classical p-method, enables the exact solution of demanding transient dynamic problems, using smaller size algebraic systems compared to the single-resolution FWD method; (3) the consistent diagonal mass matrices of each resolution in conjunction with the mass decoupling, lead to faster analyses with the use of explicit time integration; and (4) the fine components of the MR analysis introduce additional benefits to the MR-FWD method, such as the efficient capture of the higher wavenumbers and the exact localization of inhomogeneities and interfaces. Future work may focus on the inclusion of a higher order layerwise theory to the proposed MR-FWD method, for the accurate simulation of both symmetric and antisymmetric modes in thick composites and sandwich structures.

REFERENCES

- [1] S. Jaffard, “Wavelet methods for fast resolution of elliptic problems,” *SIAM J. Numer. Anal.*, vol. 29, no. 4, pp. 965–986, 1992, doi: 10.1137/0729059.
- [2] R. D. Patton and P. C. Marks, “One-dimensional finite elements based on the Daubechies family of wavelets,” *AIAA J.*, vol. 34, no. 8, pp. 1696–1698, 1996, doi: 10.2514/3.13291.
- [3] J. Ma, J. Xue, S. Yang, and Z. He, “A study of the construction and application of a Daubechies wavelet-based beam element,” *Finite Elem. Anal. Des.*, vol. 39, no. 10, pp. 965–975, 2003, doi: 10.1016/S0168-874X(02)00141-5.
- [4] L. A. Díaz, M. T. Martín, and V. Vampa, “Daubechies wavelet beam and plate finite elements,” *Finite Elem. Anal. Des.*, vol. 45, no. 3, pp. 200–209, 2009, doi: 10.1016/j.finel.2008.09.006.
- [5] R. B. Burgos, M. A. Cetale Santos, and R. R. E. Silva, “Deslauriers-Dubuc interpolating wavelet beam finite element,” *Finite Elem. Anal. Des.*, vol. 75, pp. 71–77, 2013, doi: 10.1016/j.finel.2013.07.004.
- [6] R. B. Burgos and M. A. C. Santos, “Finite Elements Based on Deslauriers-Dubuc Wavelets for Wave Propagation Problems,” *Appl. Math.*, vol. 07, no. 14, pp. 1490–1497, 2016, doi: 10.4236/am.2016.714128.
- [7] J. Ko, A. J. Kurdila, and M. S. Pilant, “A class of finite element methods based on orthonormal, compactly supported wavelets,” *Comput. Mech.*, vol. 16, no. 4, pp. 235–244, 1995, doi: 10.1007/BF00369868.
- [8] M. Mitra and S. Gopalakrishnan, “Spectrally formulated wavelet finite element for wave propagation and impact force identification in connected 1-D waveguides,” *Int. J. Solids Struct.*, vol. 42, no. 16–17, pp. 4695–4721, 2005, doi: 10.1016/j.ijsolstr.2005.02.007.
- [9] D. Samaratunga, R. Jha, and S. Gopalakrishnan, “Wavelet spectral finite element for wave propagation in shear deformable laminated composite plates,” *Compos. Struct.*,

- vol. 108, no. 1, pp. 341–353, 2014, doi: 10.1016/j.compstruct.2013.09.027.
- [10] L. Pahlavan, C. Kassapoglou, and Z. Gürdal, “Spectral formulation of finite element methods using Daubechies compactly-supported wavelets for elastic wave propagation simulation,” *Wave Motion*, vol. 50, no. 3, pp. 558–578, 2013, doi: 10.1016/j.wavemoti.2012.12.006.
 - [11] J. W. Xiang, X. F. Chen, Z. J. He, and H. B. Dong, “The construction of 1D wavelet finite elements for structural analysis,” *Comput. Mech.*, vol. 40, no. 2, pp. 325–339, 2007, doi: 10.1007/s00466-006-0102-5.
 - [12] Z. B. Yang, X. F. Chen, Y. Xie, H. Zuo, H. H. Miao, and X. W. Zhang, “Wave motion analysis and modeling of membrane structures using the wavelet finite element method,” *Appl. Math. Model.*, vol. 40, no. 3, pp. 2407–2420, 2016, doi: 10.1016/j.apm.2015.09.071.
 - [13] X. Zhang, X. Chen, X. Wang, and Z. He, “Multivariable finite elements based on B-spline wavelet on the interval for thin plate static and vibration analysis,” *Finite Elem. Anal. Des.*, vol. 46, no. 5, pp. 416–427, 2010, doi: 10.1016/j.finel.2010.01.002.
 - [14] X. Wei, W. Chen, and B. Chen, “B-spline wavelet on interval finite element method for static and vibration analysis of stiffened flexible thin plate,” *Comput. Mater. Contin.*, vol. 52, no. 1, pp. 53–71, 2016, doi: 10.3970/cmc.2016.052.053.pdf.
 - [15] W. Shen, D. Li, and J. Ou, “Modeling dispersive waves in cracked rods using the wavelet-based higher-order rod elements,” *Int. J. Mech. Sci.*, vol. 166, no. October 2019, 2020, doi: 10.1016/j.ijmecsci.2019.105236.
 - [16] X. Xue, X. Chen, X. Zhang, and B. Qiao, “Hermitian plane wavelet finite element method: Wave propagation and load identification,” *Comput. Math. with Appl.*, vol. 72, no. 12, pp. 2920–2942, 2016, doi: 10.1016/j.camwa.2016.10.019.
 - [17] C. V. Nastos, T. C. Theodosiou, C. S. Rekatsinas, and D. A. Saravanos, “A finite wavelet domain method for the rapid analysis of transient dynamic response in rods and beams,” *C. - Comput. Model. Eng. Sci.*, vol. 107, no. 5, pp. 379–409, 2015, doi: 10.3970/cmes.2015.107.379.
 - [18] C. V. Nastos, T. C. Theodosiou, C. S. Rekatsinas, and D. A. Saravanos, “A 2D Daubechies finite wavelet domain method for transient wave response analysis in shear deformable laminated composite plates,” *Comput. Mech.*, vol. 62, no. 5, pp. 1187–1198, 2018, doi: 10.1007/s00466-018-1558-9.
 - [19] C. V. Nastos and D. A. Saravanos, “A finite wavelet domain method for wave propagation analysis in thick laminated composite and sandwich plates,” *Wave Motion*, vol. 95, p. 102543, 2020, doi: 10.1016/j.wavemoti.2020.102543.
 - [20] S. G. Mallat, “A theory for multiresolution signal decomposition: The wavelet representation,” *Fundam. Pap. Wavelet Theory*, vol. II, no. 7, pp. 494–513, 2009, doi: 10.1515/9781400827268.494.
 - [21] I. Daubechies, “Ten Lectures on Wavelets - Ingrid Daubechies (1992).pdf.” 1998.
 - [22] S. M. Quraishi and K. Sandeep, “Multiscale modeling of beam and plates using customized second-generation wavelets,” *J. Eng. Math.*, vol. 83, no. 1, pp. 185–202, 2013, doi: 10.1007/s10665-012-9579-4.
 - [23] G. W. Jang, J. E. Kim, and Y. Y. Kim, “Multiscale Galerkin method using

- interpolation wavelets for two-dimensional elliptic problems in general domains,” *Int. J. Numer. Methods Eng.*, vol. 59, no. 2, pp. 225–253, 2004, doi: 10.1002/nme.872.
- [24] X. Liu, G. R. Liu, J. Wang, and Y. Zhou, “A wavelet multiresolution interpolation Galerkin method for targeted local solution enrichment,” *Comput. Mech.*, vol. 64, no. 4, pp. 989–1016, 2019, doi: 10.1007/s00466-019-01691-6.
- [25] S. Tanaka, H. Suzuki, S. Ueda, and S. Sannomaru, “An extended wavelet Galerkin method with a high-order B-spline for 2D crack problems,” *Acta Mech.*, vol. 226, no. 7, pp. 2159–2175, 2015, doi: 10.1007/s00707-015-1306-6.
- [26] X. Liu, G. R. Liu, J. Wang, and Y. Zhou, “A wavelet multiresolution interpolation Galerkin method with effective treatments for discontinuity for crack growth analyses,” *Eng. Fract. Mech.*, vol. 225, no. November 2019, p. 106836, 2020, doi: 10.1016/j.engfracmech.2019.106836.
- [27] S. Tanaka, S. Sannomaru, M. Imachi, S. Hagihara, S. Okazawa, and H. Okada, “Analysis of dynamic stress concentration problems employing spline-based wavelet Galerkin method,” *Eng. Anal. Bound. Elem.*, vol. 58, pp. 129–139, 2015, doi: 10.1016/j.enganabound.2015.04.003.
- [28] W. Shen, D. Li, and J. Ou, “Dispersion Analysis of Multiscale Wavelet Finite Element for 2D Elastic Wave Propagation,” *J. Eng. Mech.*, vol. 146, no. 4, pp. 1–17, 2020, doi: 10.1061/(ASCE)EM.1943-7889.0001756.
- [29] B. Li and X. Chen, “Wavelet-based numerical analysis: A review and classification,” *Finite Elem. Anal. Des.*, vol. 81, pp. 14–31, 2014, doi: 10.1016/j.finel.2013.11.001.
- [30] W. Lin, N. Kovvali, and L. Carin, “Direct algorithm for computation of derivatives of the Daubechies basis functions,” *Appl. Math. Comput.*, vol. 170, no. 2, pp. 1006–1013, 2005, doi: 10.1016/j.amc.2004.12.038.
- [31] M.-Q. CHEN, C. HWANG, and Y.-P. SHIH, “the Computation of Wavelet-Galerkin Approximation on a Bounded Interval,” *Int. J. Numer. Methods Eng.*, vol. 39, no. 17, pp. 2921–2944, 1996, doi: 10.1002/(sici)1097-0207(19960915)39:17<2921::aid-nme983>3.3.co;2-4.
- [32] T. Zhang, Y. C. Tian, M. O. Tadé, and J. Utomo, “Comments on ‘The computation of wavelet-Galerkin approximation on a bounded interval,’” *Int. J. Numer. Methods Eng.*, vol. 72, no. 2, pp. 244–251, 2007, doi: 10.1002/nme.2022.

A TECHNIQUE FOR TIME INTEGRATION WITH STEPS LARGER THAN THE EXCITATION STEPS: REVIEW OF THE PAST ADDRESSING THE EXISTING CHALLENGES AND A PERSPECTIVE OF THE FUTURE

Aram Soroushian

¹ International Institute of Earthquake Engineering and Seismology (IIEES)
No. 21, West Arghavan St., North Dibajee St., S. Lavasani St., Tehran 19537, Iran
e-mail: a.soroushian@iiees.ac.ir

Abstract

Time history analysis using a time integration method is a powerful broadly accepted tool for structural dynamic analysis. In practical areas, such as earthquake engineering, computations based on time history analysis might be computationally very expensive. In 2008, a technique was proposed to considerably reduce the computational effort by reducing the data in the earthquake record. This technique, which is recently named as a SEB THAAT, is reviewed in this paper. After a brief review on the formulation and implementation, the positive points, the limitations, and the challenges facing versatile implementation of the SEB THAAT are addressed, and a future perspective is presented.

Keywords: Time History Analysis, Earthquake Engineering, Computational Effort, SEB THAAT, Existing Challenges, Future Perspective.

1 INTRODUCTION

The true behavior of structural systems is nonlinear and dynamic. Time history analysis using a time integration method is a versatile tool to study structures' nonlinear dynamic behavior. The analysis process is briefly reviewed in Fig. 1. Evidently, the analysis leads to approximate responses and is computationally expensive. Specifically, the run-time may be considerable in many real analyses. The significance of these features highlights in earthquake engineering, where seismic codes require structures' time history analysis considering several ground acceleration records. Also there exist advanced seismic computations such as IDA

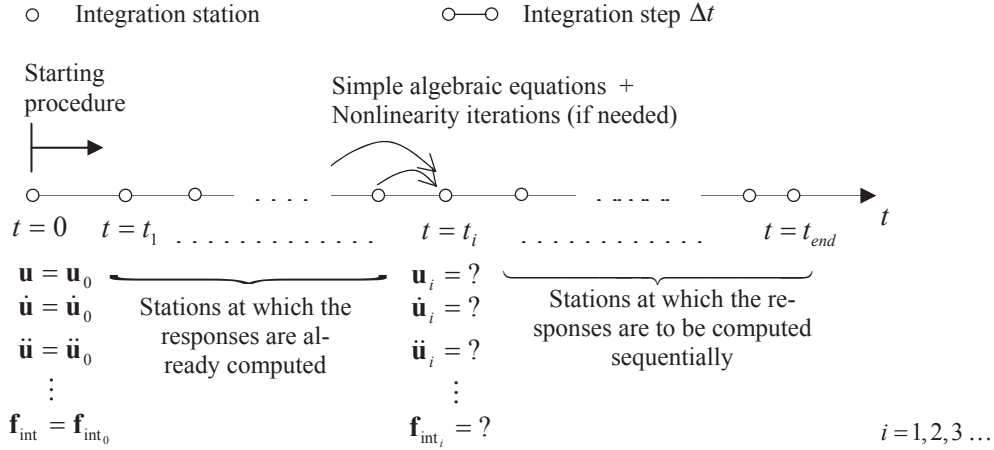


Figure 1: Brief description of the process of time history analysis using a time integration method [1].

(Incremental Dynamic Analysis) [2], for which many time history analyses are essential and the computational effort can be very high. Some main approaches to lessen the computational effort are: (1) reducing the structural systems by replacing the structures finite element models with models with less degrees of freedom [3, 4], (2) reducing the number of essential earthquake records, e.g. see [5-7], (3) reducing the number of oscillatory modes [8, 9], and (4) using higher order time integration methods [10-12]. Meanwhile, in the last two decades, approaches are developed to reduce the computational effort by reducing the earthquake records' data [13-15].

The semi-discretized equation of motion can be expressed as [1, 11, 16-19]:

$$\mathbf{M}\ddot{\mathbf{u}}(t) + \mathbf{f}_{\text{int}}(t) = \mathbf{f}(t) \quad 0 \leq t \leq t_{\text{end}}$$

$$\text{Initial Conditions : } \begin{cases} \mathbf{u}(t=0) = \mathbf{u}_0 \\ \dot{\mathbf{u}}(t=0) = \dot{\mathbf{u}}_0 \\ \mathbf{f}_{\text{int}}(t=0) = \mathbf{f}_{\text{int}_0} \end{cases} \quad (1)$$

Additional Constraints : \mathbf{Q}

where, t and t_{end} imply the time and the duration of the dynamic behavior; \mathbf{M} is the mass matrix; \mathbf{f}_{int} and $\mathbf{f}(t)$ stand for the vectors of internal force and excitation; $\mathbf{u}(t)$, $\dot{\mathbf{u}}(t)$, and $\ddot{\mathbf{u}}(t)$, denote the vectors of displacement, velocity, and acceleration; \mathbf{u}_0 , $\dot{\mathbf{u}}_0$, and $\mathbf{f}_{\text{int}_0}$, define the initial status of the model ($\mathbf{f}_{\text{int}_0}$ is essential in presence of material nonlinearity; see [20]); and finally, \mathbf{Q} represents restricting conditions, e.g., additional constraints in problems involved in impact or elastic-plastic behavior [21, 22].

For time history analysis of Eq. (1), using a time integration method, the broadly recommended integration-step [1, 23-26] is as follows:

$$\Delta t = \text{Min} \left(\frac{T}{\chi}, \Delta t_{cr}, f \Delta t \right) \quad (2)$$

where, T is the smallest oscillatory period with worthwhile contribution in the response [26], Δt_{cr} stands for the largest integration step leading to numerically stable responses [10, 11, 23], $f \Delta t$ is the step by which the excitation is digitized [13, 25], and as addressed in [1, 23-26],

$$\chi = \begin{cases} 10 & \text{when the behavior is linear} \\ 100 & \text{when the behavior is nonlinear and there is no impact} \\ 1000 & \text{when the behavior is nonlinear and there is impact} \end{cases} \quad (3)$$

In view of Eqs. (1)-(3), there are techniques [14] that replace the earthquake digitized record and specifically replace t_{end} with $(t_{end})_{new}$, such that: (1) after an ordinary time integration analysis, the main features of the response remain almost unchanged, and (2)

$$(t_{end})_{new} < t_{end} \quad (4)$$

There are also techniques [13, 15] that replace the excitation record, such that: (1) the main features of the response, e.g. peak response and frequency content, are almost preserved, and (2) the integration-step Δt , can be replaced with $(\Delta t)_{new}$, satisfying

$$(\Delta t)_{new} > \Delta t \quad (5)$$

The purpose of both of these groups of techniques is to reduce the number of integration steps, and accordingly, lessen the computational run-time and effort; also see [1].

With attention to the following features of a technique in the second group, i.e. the SEB THAAT (Step-Enlargement-Based Time History Analysis Acceleration Technique) [13, 27]:

1. Significant reduction in computational effort; see Table 1,
2. Simple implementation; see [1, 13, 28]
3. Good accuracy for the time history of the response [28]
4. Versatility (see Table 1) [1, 28, 31-34],
5. Having a mathematical basis [13].

the objective of this paper is to review the SEB THAAT, address the existing challenges, and present a perspective of the future.

2 THE SEB THAAT AND ITS PAST

The SEB THAAT is developed, based on two mathematical statements, a broadly accepted convention, and a realistic assumption, such that to preserve convergence and its order, for responses obtained from time integration. The two statements are:

1. Consider analysis of Eq. (1) by a time integration method of order q . Consider an approximation of the $\mathbf{f}(t)$ in Eq. (1), i.e. $\mathbf{f}_{new}(t)$, which converges to $\mathbf{f}(t)$ with respect to the integration step, with an order q' satisfying $q' \geq q$. Analysis of Eq. (1) by that integration method, after replacing $\mathbf{f}(t)$ with $\mathbf{f}_{new}(t)$, would lead to responses converging with order q (see [13, 35]).

System	Effort reduced in the price of negligible change in accuracy (%)	Details
Shear frames	60-80	A few linear shear frames subjected to different excitations
Residential buildings	50-90	More than 200 buildings structures with linear and nonlinear behavior and regularity and irregularity in plan or height subjected to different excitations
A thirty-storey building	50	A thirty-storey steel three-dimensional frame subjected to two different excitations
Bridges	30-80	About 20 real bridges with linear and nonlinear behaviors, some with pre-stressed elements, subjected to different excitations
Power station, Cooling tower, Space structure, Silo	>50	One or two of each special structure, considering linear and nonlinear behavior and different near-field and far-field excitations and different integration schemes
Earth dams	<80	Several earth dams each subjected to many earthquake records
Milad telecommunication tower	50-70	Considering linear and nonlinear behavior, near-field and far-field excitations, and different integration schemes
Structural systems damped non-classically	30-90	Considering linear and nonlinear behavior, and different integration schemes

Table 1: A summary of the tests carried out on the SEB THAAT [1, 27-30].

2. In view of the Taylor series expansion [36], for an arbitrary continuous function of x , i.e. $H(x)$,

$$H(x + \Delta x) + H(x - \Delta x) = 2H(x) + O(\Delta x^2) \quad (6)$$

The convention is the second order of accuracy of majority of time integration methods [1, 10, 11]. An extension of the SEB THAAT disregarding this convention is addressed in [13], the numerical tests are however few; see [37]. And finally, the realistic assumption is:

The $\mathbf{f}(t)$ in the right hand side of Eq. (1), though is available in digitized format, can be considered originally continuous with respect to time.

Provided these considerations, implementation of the SEB THAAT means ordinary time integration analysis after replacing the $\mathbf{f}(t)$ in Eq. (1), digitized in step ${}_f\Delta t$, with a new excitation $\mathbf{f}_{new}(t)$, digitized in step $({}_f\Delta t)_{new}$,

$$({}_f\Delta t)_{new} = n {}_f\Delta t \quad (7.1)$$

$$n = 2, 3, 4, \dots \quad (7.2)$$

where, n stands for the enlargement scale of the digitization-step (see also Fig. 2), and

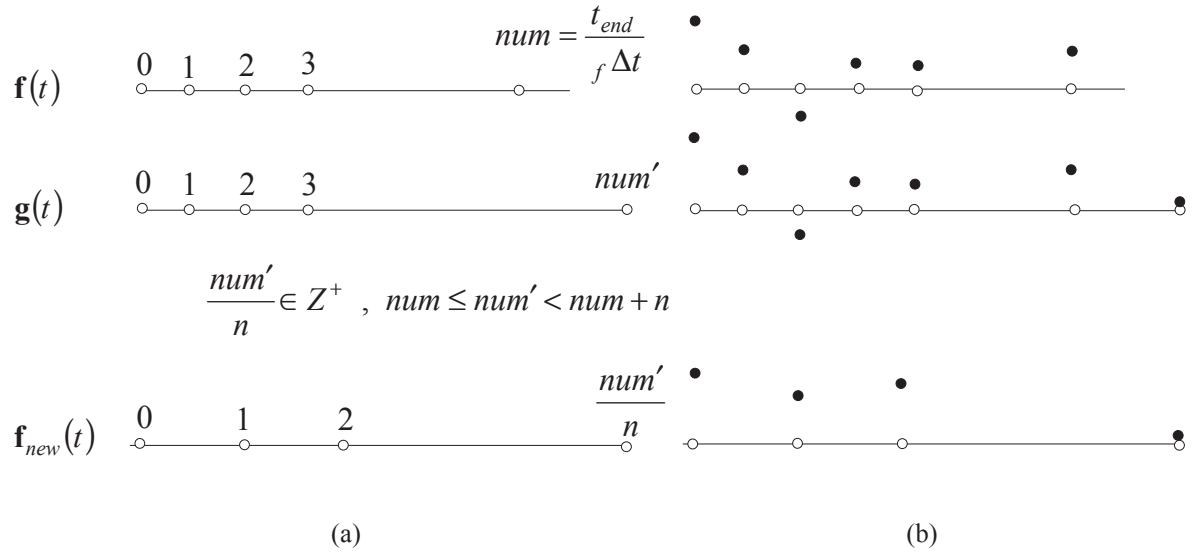


Figure 2: Typical changes in the $\mathbf{f}(t)$ in Eq. (1) because of implementation of the SEB THAAT:
 (a) Digitization stations, (b) Digitized data.

$$\mathbf{f}_{new}(t) = 0, \quad \text{unless when } t = t_0, t_1, t_2, \dots (\text{the digitization stations}) \quad (8.1)$$

$$\mathbf{f}_{new}(t = t_i) = \begin{cases} \mathbf{g}(t_i) & \text{when } t_i = t_0 = 0 \\ a\mathbf{g}(t_i) + (1-a) \sum_{k=1}^{n'} b_k [\mathbf{g}(t_i + k_f \Delta t) + \mathbf{g}(t_i - k_f \Delta t)] & \text{when } 0 < t_i < t'_{end} \\ \mathbf{g}(t_i) & \text{when } t_i = t'_{end} \end{cases} \quad (8.2)$$

$i = 0, 1, 2, \dots$

$$t_i = i(n_f \Delta t) = 0, n_f \Delta t, 2n_f \Delta t, 3n_f \Delta t, \dots t'_{end} \quad (9)$$

$$\mathbf{g}(t_i) = \begin{cases} \mathbf{f}(t_i) & \text{when } 0 \leq t_i \leq t_{end} \\ \mathbf{0} & \text{when } t_{end} < t_i \leq t'_{end} \end{cases} \quad (10)$$

$$a = \frac{1}{2} \quad (11.1)$$

$$b_k = \frac{1}{2n'} \quad (11.2)$$

$$n' = \begin{cases} n-1 & \text{when } t_i = t_1 = n_f \Delta t \text{ or } t_i = t'_{end} - n_f \Delta t \\ \left\{ \begin{array}{l} \frac{n}{2} \text{ (even values of } n) \\ \frac{n-1}{2} \text{ (odd values of } n) \end{array} \right. & \text{when } n_f \Delta t < t_i < t'_{end} - n_f \Delta t \end{cases} \quad (12)$$

$$t'_{end} = \begin{cases} t_{end} & \text{when } \frac{t_{end}}{n_f \Delta t} \in Z^+ \text{ (} Z^+ \text{ implies the set of positive integers)} \\ l(n_f \Delta t) & \text{when } \frac{t_{end}}{n_f \Delta t} \notin Z^+, \exists l \in Z^+, t_{end} < l(n_f \Delta t) < t_{end} + n_f \Delta t \end{cases} \quad (13)$$

and extension of Eqs. (8-13) to fractional/real values of n (see Eq. (7.2)), is discussed in [1, 38, 39]. Evidently, in view of Eq. (2), the SEB THAAT is effective and may reduce the run-time, only when

$$_f \Delta t < \text{Min} \left(\frac{T}{\chi}, \Delta t_{cr} \right) \quad (14)$$

and more, in view of Eqs. (8-13), the effort needed for computing $\mathbf{f}_{new}(t)$ is negligible compared to that of the time history analysis. Accordingly, the enlargement scale n implies reduction in run-time for linear analyses, where no additional computation is needed to model the nonlinearities. Furthermore, in view of Fig. 1 and notion of computational effort [40, 41], the reductions in run-time and computational effort because of the SEB THAAT are identical, for linear analyses.

There is no guarantee about sufficiency of the accuracy of the results of the SEB THAAT when using arbitrary value of n . The reason is that convergence (and its rate) is the only accuracy-related basis of the SEB THAAT. Furthermore, when the SEB THAAT is successful for some value of n , upper-bounds will exist on n . Considering this and some different theoretical questions, research on the SEB THAAT has been followed in two directions. In one direction, to study the performance of the SEB THAAT, many cases are studied, considering changes of structural system, time integration method, digitized excitation (e.g. far- and near-field earthquakes), etc.. For each case, responses are investigated for the following three questions:

- (1) Does $_f \Delta t$ governs Eq. (2), for the case under study (see Eq. (14))?
- (2) For cases with $_f \Delta t$ as the governing term of Eq. (2), can, for some value of n , implementation of the SEB THAAT cause no notable loss of accuracy, i.e. is the following statement correct?

$$\exists n > 1: \mathbf{R}_{new} \cong \mathbf{R} \quad (15)$$

where, \mathbf{R}_{new} and \mathbf{R} are the responses obtained from time integration with and without implementation of the SEB THAAT, respectively.

- (3) For cases, where $_f \Delta t$ governs Eq. (2), is the largest value of n satisfying Eq. (15) (n_{max}) consistent with Eq. (2), i.e. is the following statement correct?

$$\forall n \quad \mathbf{R}_{new} \cong \mathbf{R}: \exists n_{max} \cong \frac{1}{_f \Delta t} \text{Min} \left(\frac{T}{\chi}, \Delta t_{cr} \right): 1 < n \leq n_{max} \quad (16)$$

The consequence was positive responses in almost all cases [1, 27-30, 37-39, 42-56]. Specifically, a very interesting numerical observation, for two cases reported in [42, 43], was the more accuracy after implementation of the SEB THAAT (compared to that of the ordinary analysis). This leads to the fact that the inaccuracy because of the SEB THAAT can be added or subtracted from the inaccuracy originated in the approximate time integration, and accordingly,

$$\exists \text{ Cases : } \|\mathbf{R}_{new} - \mathbf{R}_{exact}\| < \|\mathbf{R} - \mathbf{R}_{exact}\| \quad (17)$$

where, \mathbf{R}_{exact} stands for the exact response and $\|\cdot\|$ represents arbitrary norm [57]. Finally, it is worth noting that the reduction in run-time because of the SEB THAAT is generally considerable, as addressed in Table 1 and Fig. 3. And, as already stated, for linear analyses, the reduction in run-time is equal to the reduction in computational effort.

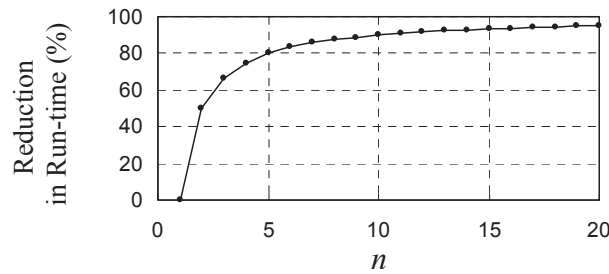


Figure 3: Reduction in the run-time with respect to the enlargement scale n , for linear analyses accelerated by the SEB THAAT.

In the other direction, some theoretical studies were carried out. First, enlarging the digitization step, without changing the record at the non-eliminated time stations (see Fig. 4), which is implemented as a simple approach for faster analysis since decades e.g. [58], was studied. It was demonstrated that though in some cases the simple approach leads to good accuracy and reduced computational effort compared to the ordinary analysis, the efficiency is in all cases better, when using the SEB THAAT [59]. Specially, cases were observed, where the result of the simple approach was totally erroneous, while the corresponding result of the SEB THAAT was satisfactory [59].

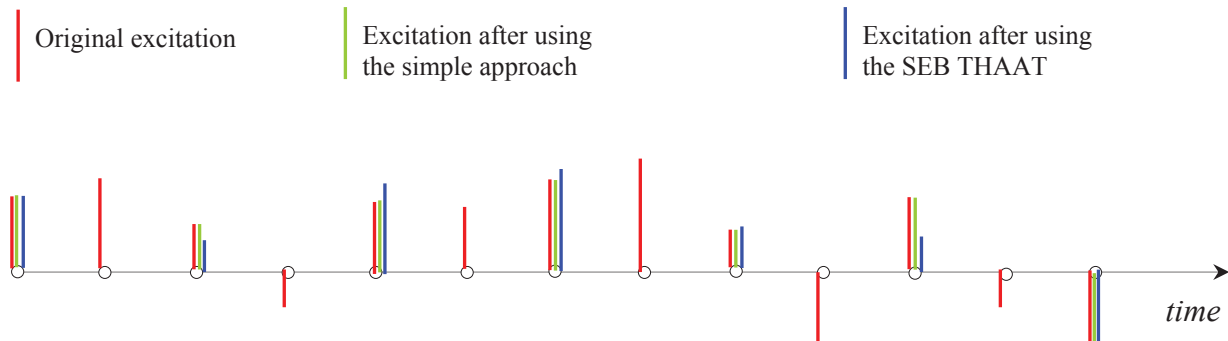


Figure 4: Typical comparison between excitation records in implementation of the SEB THAAT and the traditional simple step enlargement approach considering $n = 2$.

It is then studied whether the inaccuracy because of the SEB THAAT can lead to instability, or in other words, whether the SEB THAAT may negatively affect the responses stability. The response was negative [1, 60], i.e. when Eq. (2) is satisfied the responses are numerically stable regardless of implementation of the SEB THAAT. The main reasons are the convergence basis of the SEB THAAT and the relation between convergence and numerical stability in time integration analyses [61-63]. In the next step, selecting values for a and b in Eq. (8.2), different from those stated in Eqs. (11), and subjected to (see [13]):

$$\sum_{k=1}^{n'} b_k = \frac{1}{2} \quad (18)$$

was studied [64]. As the result, though in some examples Eqs. (11) did not present the best alternative, the overall best selection can be considered as stated in Eqs. (11). Another question was on how to consider non-integer values as the enlargement scale n . This is essential especially with attention to Fig. 3 and when the n_{\max} available from Eq. (16) satisfies:

$$1 < n_{\max} < 2 \quad (19)$$

Two simple approaches to extend the SEB THAAT to:

$$n, n_{\max} = \frac{p}{q} \quad , \quad p, q \in \mathbb{Z}^+ \quad (20)$$

and

$$n, n_{\max} \in \mathbb{R}^+ \quad (\mathbb{R}^+ \text{ stands for the set of positive real numbers}) \quad (21)$$

can be found in [38, 39].

The effect of nonlinear behavior on the performance of the SEB THAAT was another area for theoretical study. The carried out brief study led to the good performance of the SEB THAAT, when adequate values are assigned to the nonlinearity parameters [49, 65]. Further study seems essential.

Meanwhile, in response to a question, after a conference presentation, it was demonstrated that the T in Eq. (2) should be related to the response, the accuracy of which, is under study [66]. Some initial study was also carried out on the frequency content of the inaccuracies because of the SEB THAAT [67].

And finally, the most recent study was on the performance of the SEB THAAT when the structural viscous damping is non-classical. The study had a numerical/theoretical nature. As the consequence, for majority of integration methods, the performances of the SEB THAAT in application to classically and non-classically damped analyses are conceptually similar [27]. For other integration methods, the case may be the same as well, though can not be guaranteed before the analysis [27].

3 THE EXISTING CHALLENGES

As implied in the previous sections and specifically in Table 1 and Fig. 3, the reduction in computational effort because of implementation of the SEB THAAT can be considerable. Considering this, the simplicity and versatility of the SEB THAAT, the comparisons made between the SEB THAAT and other analysis acceleration methods [1, 68], the importance of computational effort in practical structural analyses, and the fact that structural systems become larger and more complicated every new day, the SEB THAAT can be considered a successful analysis acceleration technique in need of further research for broad practical

implementation. Accordingly, special attention should be paid to the challenges facing the SEB THAAT. Some of the most important challenges are as follows:

The first challenge relates to the T in Eqs. (2), (14) and (16). The T is not only vague, because of the expression “worthwhile contribution” in its definition (see the definition just after Eq. (2)), but also is not computable prior to the analysis. The consequence is a serious problem in determination of n_{\max} and n ; see Eq. (16). Practical implementation of the SEB THAAT will hence be significantly affected and indeed becomes complicated, the least; i.e. what is the value to be assigned to step enlargement scale n resulting in the determination of the $(\int \Delta t)_{\text{new}}$ and $\mathbf{f}_{\text{new}}(t)$? Recently, efforts for overcoming this problem are reported (see [31]). These efforts make use of a convergence-based conventional error-control method [23, 69, 70] and the practical suggestions stated in seismic standards [25, 71]. According to these efforts, the analysis is carried out via sequential time history analyses, each throughout $[0 \ t'_{\text{end}}]$ using a special enlargement scale. The repetitive analyses are continued, till two sequential responses are sufficiently close. The resulting analysis seems powerful and versatile, in the limits of structural dynamics problems, but not restricted to satisfaction of Eq. (14). More study on this effort and analyzing problems in real need of run-time reduction are essential.

The second challenge relates to the true nature of many oscillatory behaviors, which is a combination of inertial (structural dynamics) behavior and wave propagation. As implied in Eqs. (1) and (2) and Table 1, the SEB THAAT is mostly applied to analysis of structural dynamic problems. Study on application of the SEB THAAT in analysis of wave propagation problems is complicated, especially because of the CFL condition [72] (this condition upper-bounds the time integration step by a coefficient of the element sizes in spatial discretization by finite elements). Despite, successful numerical efforts presented in this regard [29, 30, 48], further detailed study is essential, both in theory, as well as in application. The relaxation method recently proposed for the CFL condition [73, 74] seems a good starting point.

The third challenge returns to the purpose of the SEB THAAT, i.e. reduction of the computational effort in time integration analysis of structural systems against digitized excitations. As implied in Eqs. (2) and (14), the SEB THAAT cannot reduce the analysis computational effort, when the excitation digitization step $\int \Delta t$ does not dominate Eq. (2), i.e.

$$\text{Min}\left(\frac{T}{\chi}, \Delta t_{cr}\right) \leq \int \Delta t \quad (22)$$

Overcoming this restriction is a main challenge facing the SEB THAAT for highly oscillatory and highly nonlinear problems, for which T can be sufficiently small to satisfy Eq. (22). Though the ongoing efforts on the first challenge seem effective in easing this challenge, direct efforts to cancel this restriction would be instructive and reasonable. No such effort is reported yet. Enhancement in the accuracy or order of accuracy of the integration scheme and/or the SEB THAAT seems an appropriate solution.

A fourth challenge is implementation of the SEB THAAT in analysis of structural systems subjected simultaneously to several excitations digitized in completely different step-sizes. Considering that many important structural systems, e.g. offshore or super-tall structures, are in this group, overcoming this challenge is of high practical importance. No special effort is reported yet.

And finally, for practical implementation of the SEB THAAT, besides clear determination of the enlargement scale (n) discussed as the first challenge, it is important to have an idea about the resulting reduction in computational effort. Figure 3 clarifies this ambiguity for lin-

ear analyses. The case is however different for nonlinear analyses, and even there is yet no theoretical guarantee for the reduction of the run-time and computational effort. Especially the method of nonlinearity iteration and the related parameters can significantly affect the reductions. Though in many nonlinear analyses, the reduction in run-time is less than that reported in Fig. 3, the opposite can be correct, as well; see [42, 43, 75]. Considering that nowadays structural dynamic analyses are generally nonlinear, without overcoming this challenge, implementation of the SEB THAAT would hardly be accepted in practice. Yet, no effort is reported.

4 A LOOK AT THE FUTURE

In view of the discussions presented in Sections 1-3, the SEB THAAT can be considered as a successful analysis acceleration technique in need of further research. Nevertheless, especially to manage and access the research resources, it is important to have a perspective of the future of the SEB THAAT and the probable needs to this technique.

With attention to Section 3, the SEB THAAT seems in progress in both numerical experiments' direction, as well as the theoretical aspects' direction. The growing sizes of structural models, and complicatedness of analysis requirements from different points of view, e.g. material and excitation, highlight the significance of analysis acceleration. In addition, the seismic recording instrumentation is in progress towards smaller digitization step $f_s \Delta t$ [76]. Besides, because of the everyday advancement in structural design optimization and the growing popularity of the optimization, the T in Eq. (2) will likely become larger in future. These lead to more chance for $f_s \Delta t$ to be the governing term in Eq. (2). The consequence is more need to the SEB THAAT, in near- and mid-future. Accordingly, it is reasonable to anticipate efforts to overcome the first challenge addressed in Section 3, i.e. clear determination of the enlargement scale n , in near future. The study reported in [31] implies an initial step that should be established, after which extending the SEB THAAT to wave propagation problems can be anticipated for future studies. The next step can be plugging the SEB THAAT in a commercial soft ware, e.g. seismo-struct [77]. With an analysis soft ware equipped with the SEB THAAT, many different numerical tests, considering different structural materials, such as wood, aluminum, epoxy glass composites, different nonlinear behaviors, interaction with completely different behaviors, subjected to different earthquake records, temperature changes, soil-structure-interaction, etc. can be simply carried out. Specifically, efforts on the fourth challenge addressed in Section 3 can be carried out much simpler. In mid- and far-future, it will be reasonable to try for improving the SEB THAAT, especially to overcome the third challenge addressed in Section 3. This seems possible, either directly with attention to the very details of the technique [1], the integration methods, or even by combining the SEB THAAT with other techniques, such as those proposed in [5-7, 14].

Furthermore, and in view of the mathematical basis of the SEB THAAT [1, 13], this technique can be tested in non-seismic problems, where the excitation is not originated in earthquakes. First steps in this area are already taken; see [32, 78]. Even more, the digitization might be limited to some part or some components of the $\mathbf{f}(t)$ in Eq. (1), or more, to terms of Eq. (1) other than the excitation. Some related studies are already reported [33, 34]. In far future, the SEB THAAT seems having the potential to be accepted as a general tool for data simplification for arbitrary numerical computation. The most important pre-requisite is however to overcome the first challenge addressed in Section 3.

Meanwhile, no anticipation is possible for the future of the fifth challenge, addressed in Section 3. The reason is the same ambiguity for ordinary time history analysis, persisting since decades. A unique solution can however be anticipated for both ambiguities.

5 CONCLUDING REMARKS

As a technique for accelerating time history analysis, by enlarging the excitation records' digitization steps ($\int \Delta t$),

1. The SEB THAAT can be considered a successful analysis acceleration technique, in need of further research.
2. For practical implementation in real problems, there are still challenges to be overcome; the most important challenges can be summarized as:
 - (a) clear determination of the enlargement scale (n),
 - (b) providing the capability to successfully implement the SEB THAAT in analysis of wave propagation problems,
 - (c) providing the capability to successfully implement the SEB THAAT in analysis of highly oscillatory/nonlinear problems,
 - (d) providing the capability to successfully implement the SEB THAAT in analysis of problems with several excitations completely different in digitization step and time length,
 - (e) clarifying the amount of run-time and computational effort reduction in nonlinear analyses prior to the analyses.
3. The future of the SEB THAAT is promising, especially considering the improvements in the recording instrumentation.
4. Besides, the challenges addressed in the Point 2 above, some areas for further research are:
 - (a) Combination of the SEB THAAT, with other analysis acceleration techniques.
 - (b) Plugging the SEB THAAT in commercial structural analysis soft ware, and application of the SEB THAAT to different time history analyses.
 - (c) Applying the SEB THAAT to computations other than those in structural and earthquake engineering.
 - (d) Study on the details of the SEB THAAT, to improve the results accuracies.

Finally, the author anticipates that the SEB THAAT will eventually be extended to a data simplification technique.

REFERENCES

- [1] A. Soroushian, Integration step size and its adequate selection in analysis of structural systems against earthquakes. M. Papadrakakis, V. Plevris, N.D. Lagaros, eds. *Computational Methods in Earthquake Engineering Vol 3*, Springer, USA, pp. 285-329, 2017.
- [2] D. Vamvatsikos, C.A. Cornell, Incremental dynamic analysis. *Earthquake Engineering & Structural Dynamics*, **31**, 491-514, 2002.
- [3] N. Teunisse, L. Demasi, P. Tiso, R. Cavallaro, Reduced basis methods for structurally nonlinear Joined Wings. *Aerospace Science and Technology*, **68**, 486-495, 2017.
- [4] Y. Lee, B. Seo, E.T. Lee, Application of model reduction techniques to jacket structures. *International Journal of Steel Structures*, **15**, 1-6, 2015.
- [5] J. Kiani, C. Camp, S. Pezeshk, N. Khoshnevis, Application of pool-based active learning in reducing the number of required response history analyses. *Computers & Structures*, **241**, Article 106355, 2020.

-
- [6] M. Mousavi, M. Ghafory-Ashtiany, A. Azarbakht, A new indicator of elastic spectral shape for the reliable selection of ground motion records. *Earthquake Engineering & Structural Dynamics*, **40**, 1403-1416, 2011.
 - [7] S.A. Moghaddam, M. Ghafory-Ashtiany, Evaluation of a recently proposed ground motion selection method in case of vertically irregular frames. *Journal of Seismology and Earthquake Engineering*, **17**, 165-180, 2015.
 - [8] D.N. Herting, A general purpose, multi-stage, component modal synthesis method. *Finite Elements in Analysis and Design*, **1**, 153-164, 1985.
 - [9] D. Rixen, A Lanczos procedure for efficient mode superposition in dynamic analysis. *43rd AIAA/ASME/ASCE/AHS/ASC Structures, Structural Dynamics, and Materials Conference*, Denver, Colorado, USA, April 22-25, 2002.
 - [10] W.L. Wood, *Practical time stepping schemes*. Oxford, 1990.
 - [11] T. Belytschko, T.J.R. Hughes, *Computational methods for transient analysis*. Elsevier, 1983.
 - [12] W. Kim, J.N. Reddy, A new family of higher-order time integration algorithms for the analysis of structural dynamics. *Journal of Applied Mechanics*, **84**, 071008, 2017.
 - [13] A. Soroushian, A technique for time integration with steps larger than the excitation steps. *Communication in Numerical Methods in Engineering*, **24**, 2087-2111, 2008.
 - [14] J.C. Reyes, E. Kalkan, A. Sierra, Fast nonlinear response history analysis. *16th World Conference on Earthquake Engineering (16WCEE)*, Santiago, Chile, January 9-13, 2017.
 - [15] M. Hosseini, I. Mirzaei, Simplification of earthquake accelerograms for rapid time history analysis based on the impulsive load concept. M. Papadrakakis, V. Papadopoulos, V. Plevris eds. *4th ECCOMAS Thematic Conference on Computational Methods in Structural Dynamics and Earthquake Engineering (COMPDYN 2013)*, Kos Island, Greece, June 12-14, 2013.
 - [16] J. Henrych, *Finite models and methods of dynamics in structures*. Elsevier, 1990.
 - [17] K.J. Bathe, *Finite element procedures*. Prentice-Hall, 2006.
 - [18] H. Kardestuncer, *Finite element handbook*. McGraw Hill, 1987.
 - [19] T. Belytschko, W.K. Liu, B. Moran, *Non-linear finite elements for continua and structures*. John Wiley & Sons, 2000.
 - [20] A. Soroushian, *New methods to maintain responses' convergence and control responses' errors in analysis of nonlinear dynamic models of structural systems*. Ph.D. Thesis, University of Tehran, Iran, 2003. (in Persian)
 - [21] P. Wriggers, *Computational contact mechanics*. John Wiley & Sons, 2002.
 - [22] T.J.R. Hughes, K.S. Pister, R.L. Taylor, Implicit-explicit finite elements in nonlinear transient analysis. *Computer Methods in Applied Mechanics and Engineering*, **17**, 159-182, 1979.
 - [23] R.W. Clough, J. Penzien, *Dynamics of structures*. McGraw-Hill, 1993.
 - [24] J.F. McNamara, Solution schemes for problems of nonlinear structural dynamics. *ASME Journal of Pressure Vessel Technology*, **96**, 147-155, 1974.

-
- [25] NZS 1170. Structural Design Actions, Part 5: Earthquake Actions-New Zealand. New Zealand, 2004.
 - [26] C.C. Chen, A.R. Robinson, Improved time history analysis for structural dynamics: I. Treatment of rapid variation of excitation and material nonlinearity. *ASCE Journal of Structural Engineering*, **12**, 2496-2513, 1993.
 - [27] A. Soroushian, On performance of a time integration acceleration technique applied to seismic analysis of non-classically damped structural dynamics. *Iranian Journal of Science and Technology, Transactions of Civil Engineering* (just accepted).
 - [28] A. Soroushian, *Direct time integration with steps larger than the steps by which the excitations are digitized*, Technical Report No. 7510. International Institute of Earthquake Engineering and Seismology (IIEES), Iran, 2011. (In Persian)
 - [29] M. Erfaninia, A. Soroushian. On reduction of computational cost in analysis of soil-structural-interaction. M. Papadrakakis, M. Fragiadakis eds. *6th ECCOMAS Thematic Conference on Computational Methods in Structural Dynamics and Earthquake Engineering (COMPdyn 2017)*, Rhodes Island, Greece, June 15-17, 2017.
 - [30] M-A. Daziano, *Evaluation of seismic vulnerability of dams constructed of loose material*. Ph.D. Thesis, National University of Tucuman, Argentina, 2017. (in Spanish)
 - [31] A. Soroushian, *Direct time integration from earthquake induced equations of motion with steps larger than conventional and least dependence to the frequency content of the response*, Technical Report No. 7537. International Institute of Earthquake Engineering and Seismology (IIEES), Iran, 2018. (In Persian)
 - [32] A. Soroushian, E.M. Farahani, Efficient static analysis of assemblies of beam-columns subjected to continuous loadings available as digitized records. *Frontiers in Built Environment*, **4**, 215-229, 2019.
 - [33] A. Soroushian, S. Amiri, Reduction in space for dynamic finite element analysis of assemblies of beam-columns when the mass is available in digitized format. *Journal of Applied and Computational Mechanics*, DOI: 10.22055/JACM.2019.31603.1898. (in press)
 - [34] A. Soroushian, S. Amiri, Simultaneous reduction in time and space for dynamic finite element models of beam-column assemblies. *Iranian Journal of Science and Technology, Transactions of Civil Engineering*, **45**, 1265-1279, 2021.
 - [35] S.N. Penry, W.L. Wood, Comparison of some single-step methods for the numerical solution of the structural dynamic equation. *International Journal for Numerical Methods in Engineering*, **21**, 1941-1955, 1985
 - [36] T.M. Apostol, *Calculus, Vol. I*. John Wiley & Sons, 1967.
 - [37] S. Azad, A.A. Hadad, S., Amiri, A. Soroushian, Case studies on the performance of a transient analysis computational cost reduction technique when applied to analyses with integration methods of order one two and four. D.T. Tsahalis ed. *6th International Conference from "Scientific Computing to Computational Engineering" (6th IC-SCCE)*, Athens, Greece, July 9-12, 2014.
 - [38] A. Sabzei., A. Y. Reziakolaei, A. Soroushian, On more versatility for an integration step size enlargement technique in time integration analysis. M. Papadrakakis, V. Papadopoulos, V. Plevris eds. *4th ECCOMAS Thematic Conference on Computational Methods*

- in Structural Dynamics and Earthquake Engineering (COMPDYN 2013)*, Kos Island, Greece, June 12-14, 2013.
- [39] A. Soroushian, Y. Zarabimanesh, K. Soleymani, S.M. Khalkhali, A new technique for fractional enlargement of integration steps in transient analysis against digitized excitations. S. Braun, N. Maia, M. de Matos Neves eds. *International Conference on Structural Engineering Dynamics (ICEDyn 2017)*, Ericeira, Portugal, July 3-5, 2017.
 - [40] X. Zhou, K.K. Tamma, A new unified theory underlying time dependent linear first-order systems: a prelude to algorithms by design. *International Journal for Numerical Methods in Engineering*, **60**, 1699–740, 2004
 - [41] D.M. Monro, *Fortran 77*. Edward Arnold, 1987.
 - [42] Y. Zarabimanesh, *On the possibility to reduce the computational cost of time history analysis of the Milad telecommunication tower*. Ms.c. Thesis, International Institute of Earthquake Engineering and Seismology (IIEES), Iran, 2017. (in Persian)
 - [43] A.A. Hadad, *Reducing computational costs in time integration analyses of buildings with irregularities in height because of mass*. Ms.c. Thesis, International Institute of Earthquake Engineering and Seismology (IIEES), Iran, 2015. (in Persian)
 - [44] S. Azad, *A study on accelerating time history analysis of bridges*. Ms.c. Thesis, International Institute of Earthquake Engineering and Seismology (IIEES), Iran, 2015. (in Persian)
 - [45] A. Baiani, *On the possibility to accelerate time history analysis of buildings with irregularities in plan because of mass distribution*. M.Sc. Thesis, University of Pooyandegan Danesh, Iran, 2018. (in press, in Persian)
 - [46] H. Ghondaghsaz, *A Study on a recent technique for more efficient seismic analysis applied to concrete and steel buildings*. M.Sc. Thesis, Islamic Azad University West Tehran Branch, Tehran, 2018. (in Persian)
 - [47] A. Soroushian, A. Jahani Mehrnoosh, Y. Zarabimanesh., M.H. Ghondaghsaz., A. Baiani, A. Zakizadeh, *On the performance of a computational cost reduction technique when applied to cooling towers transient analysis*. M. Papadrakakis, V. Papadopoulos, G. Stefanou, V. Plevris eds. *7th European Congress on Computational Methods in Applied Sciences and Engineering (ECCOMAS VII)*, Crete Island, Greece, June 5-10, 2016.
 - [48] M-A. Daziano, A. Soroushian, *On faster transient analysis of structural systems against earthquakes: case study of an earth dam*. *8th International Conference on Seismology and Earthquake Engineering (SEE8)*, Tehran, Iran, November 11-13, 2019.
 - [49] A. Garakaninezhad, A. Yahyapour, A.A. Hadad, A. Soroushian, A comparison between linear and nonlinear time history analyses after implementing a recent computational cost reduction technique. E. Onate, X. Oliver, A. Huerta eds. *11th World Congress on Computational Mechanics (WCCM2014)*, Barcelona, Spain, July 25-29, 2014.
 - [50] A. Garakaninezhad, R.K. Moghadas, *On the Performance of a Technique to Accelerate Time Integration when Applied to Space Structures Analyses*. M. Papadrakakis, V. Papadopoulos, V. Plevris eds. *4th ECCOMAS Thematic Conference on Computational Methods in Structural Dynamics and Earthquake Engineering (COMPDYN 2013)*, Kos Island, Greece, June 12-14, 2013.

- [51] O. Bahar, S. Ramezani, Faster time integration analysis for building structures subjected to 3-component earthquakes. M. Papadrakakis, M. Fragiadakis, V. Plevris eds. *3rd ECCOMAS Thematic Conference on Computational Methods in Structural Dynamics and Earthquake Engineering (COMPDYN 2011)*, Corfu, Greece, May 25-28, 2011.
- [52] F. Nateghi, M. Yakhchalian, On less computational costs for analysis of silos seismic behaviors by time integration. M. Papadrakakis, M. Fragiadakis, V. Plevris eds. *3rd ECCOMAS Thematic Conference on Computational Methods in Structural Dynamics and Earthquake Engineering (COMPDYN 2011)*, Corfu, Greece, May 25-28, 2011.
- [53] F. Nateghi, M. Yakhchalian, An investigation into the effectiveness of a technique proposed for reducing computational cost of time integration in the analysis of silos seismic behaviors. *11th US national congress on computational mechanics (USNCCM 2011)*, Minneapolis, USA, July 25-28, 2011.
- [54] A. Soroushian, A. Saaed, M. Arghavani, M. Rajabi, M.M. Sharifpour, Less computational costs in the analysis of reservoirs seismic behaviours by time integration. J. Náprstek, J. Horáček, M. Okrouhlík, B. Marvalová, F. Verhulst, J.T. Sawicki eds. *10th biennial conference on vibration problems (ICoVP-2011)*, Prague, Czech Republic, September 5-8, 2011.
- [55] M. Bastami, A technique for more efficient time integration applied to seismic analysis of power substation equipment. E. Onate, X. Oliver, A. Huerta eds. *11th World Congress on Computational Mechanics (WCCM2014)*, Barcelona, Spain, July 25-29, 2014.
- [56] A.Y. Reziakolaei, A. Sabzei, A. Soroushian, On the performance of a structural analysis cost reduction technique when applied to residential buildings. M. Papadrakakis, V. Papadopoulos, V. Plevris eds. *4th ECCOMAS Thematic Conference on Computational Methods in Structural Dynamics and Earthquake Engineering (COMPDYN 2013)*, Kos Island, Greece, June 12-14, 2013.
- [57] B. Noble, J.W. Daniel, *Applied linear algebra*. Prentice Hall, 1977.
- [58] O. Azizpour, *Evaluating the seismic vulnerability of and proposing multi-variable fragility curves for on pipe-way piping in petrochemical plants*. Ph.D. Thesis, International Institute of Earthquake Engineering and Seismology (IIEES), Iran, 2011. (in Persian)
- [59] A. Soroushian, P. Farshadmanesh, S. Azad. On the essentiality of techniques to enlarge integration steps in transient analysis against digitized excitations. *Journal of Seismology and Earthquake Engineering*, **17**, 43-60, 2015.
- [60] A. Soroushian, A. Garakaninezhad, A. Yahyapour, A.A. Hadad, Performance of a computational cost reduction technique in lengthy time interval analyses. E. Onate, X. Oliver, A. Huerta eds. *11th World Congress on Computational Mechanics (WCCM2014)*, Barcelona, Spain, July 25-29, 2014.
- [61] P. Henrici, *Discrete variable methods in ordinary differential equations*. Prentice-Hall, 1962.
- [62] J.C. Strikwerda, *Finite difference schemes and partial differential equations*. Wadsworth & Books/Cole, Pacific Grove, 1989.
- [63] R.D. Richtmyer, K.W. Morton, *Difference methods for initial value problems*. John Wiley & Sons, 1967.

- [64] A. Zakizadeh, *Investigation on the role of the parameter representing the influence of the eliminated excitation stations in the performance of a transient analysis computational cost reduction technique*. M.Sc. Thesis, International Institute of Earthquake Engineering and Seismology (IIEES), Iran, 2017. (in Persian)
- [65] A. Soroushian, On the performance of a recent technique for more efficient time integration in severe seismic conditions. C-K. Choi ed. *1st International Conference on Advances in Structural Engineering and Mechanics (ASEM'11)*, Seoul, South Korea, September 18-23, 2011.
- [66] A. Soroushian, On the accuracy of accelerations in general implementation of a recently proposed seismic analysis computational cost reduction technique. D.T. Tsahalis ed. *5th International Conference from "Scientific Computing to Computational Engineering" (5th IC-SCCE)*, Athens, Greece, July 4-7, 2012.
- [67] A. Soroushian, M. Hosseini, S.M.K. Khalkhali, On the frequency content of errors originated in a time integration computational cost reduction technique. M. Papadrakakis, V. Papadopoulos, G. Stefanou, V. Plevris eds. *7th European Congress on Computational Methods in Applied Sciences and Engineering (ECCOMAS VII)*, Crete Island, Greece, June 5-10, 2016.
- [68] A. Saaed, *A technique for faster seismic analysis of MDOF structural systems*. M.Sc. Thesis, International Institute of Earthquake Engineering and Seismology (IIEES), Iran, 2012. (in Persian)
- [69] E. Hairer, G. Wanner, *Solving ordinary differential equations II: stiff and differential-algebraic problems*. Springer, 1996.
- [70] A. Soroushian, J. Farjoodi, More reliable responses for time integration analyses. *Structural Engineering and Mechanics, An International Journal*, **16**, 219–240, 2003.
- [71] NZS 1170.5 Supp 1. Structural Design Actions - Part 5: Earthquake Actions. Standards New-Zealand, New Zealand, 2004.
- [72] R. Courant, K. Friedrichs, H. Lewy, Über die partiellen differenzengleichungen der mathematischen physik. *Mathematische Annalen*, **100**, 32–74, 1928.
- [73] D. Peterseim, M. Schedensack, Relaxing the CFL condition for the wave equation on adaptive meshes. *Journal of Scientific Computing*, **72**, 1196-1213, 2017.
- [74] R. Maier, D. Peterseim, Explicit computational wave propagation in micro-heterogeneous media. *BIT Numerical Mathematics*, **59**, 443-462, 2019.
- [75] A. Soroushian, S.R. Mirghaderi, Y. Zarabimanesh, A. Jahani Mehrnoosh, A. Zakizadeh, M.H. Ghondaghsaz, On the possibility to accelerate time history analysis of the Milad telecommunication tower, *10th National Conference on Civil Engineering (10NCCE)*, Tehran, Iran, April 19-21, 2017. (in Persian)
- [76] J. Havskov, G. Alguacil, *Instrumentation in earthquake seismology (modern approaches in geophysics)*. Springer, 2004.
- [77] S. Antoniu, R. Pinho, *Seismostruct – seismic analysis program by seismosoft, technical manual and user manual*. University of Pavia, 2003.
- [78] E.M. Farahani, A. Ganji, S. Maalek, A. Soroushian, Reduction of computational cost in FEM analysis of beams subjected to digitized static loadings. *10th National Congress on Civil Engineering (10NCCE)*, Tehran, Iran, April 19-21, 2017.

A SIMPLIFIED APPROACH FOR THE ESTIMATION OF SEISMIC VULNERABILITY OF STEEL MOMENT RESISTING FRAMES

Rosario Montuori¹, Elide Nastri², Vincenzo Piluso², Paolo Todisco^{2,*}

¹ University of Salerno, Department of Pharmacy
Via Giovanni Paolo II, 132, 84084 Fisciano (SA)
e-mail: r.montuori@unisa.it

² University of Salerno, Department of Civil Engineering
Via Giovanni Paolo II, 132, 84084 Fisciano (SA)
{enastri,v.piluso, ptodisco}@unisa.it

Abstract

In recent years, the numerous seismic events occurred have pointed out the need for a prompt classification of the built heritage in terms of seismic vulnerability. the concept of vulnerability is closely linked to the definition of the capacity curve, requiring sophisticated numerical procedures to be performed, such as the inelastic incremental analysis.

Therefore, the simplified method herein proposed requires use of only analytically simple analyses such as the elastic analysis and the rigid-plastic analysis. For this reason, this method can be used in the immediate aftermath of an earthquake and also for a large-scale classification of the buildings. The proposed methodology has been set up by a wide parametric analysis, carried out on 420 frames designed according to 3 different approaches: the first one is linked to the Theory of Plastic Mechanism Control (TPMC), assuring the design of structures showing global collapse mechanism (GMRFs), the second is based on the Eurocode 8 requirements (SMRFs) while the third is a non-seismic design, based on vertical loads (OMRFs).

Keywords: Pushovers, Capacity, Performances, Vulnerability, Simplified methods.

1 INTRODUCTION

The evaluation of seismic performances of existing buildings has gained, in recent years, an increasingly interest in seismic and structural engineering [1]-[11]. In particular, the setting up of design rules based on the so-called hierarchy criteria has changed the designer approach to let building able to withstand seismic events with an adequate level of reliability [12]-[22]. In the safeguard of the built heritage the knowledge of the seismic response of the structures plays a fundamental role [24]-[25]. Therefore, any seismic retrofitting or improvement of an existing building should be preceded by a strength evaluation phase before the intervention. The evolution of codes, numerical methods and calculation tools has provided designers the access to advanced methodologies of seismic assessment [26]. The seismic performances of buildings are evaluated by comparing the capacity of dissipating incoming seismic energy with the seismic demand. The main difficulties that arise from developing a performance checking procedure, are linked to the definition of damage levels corresponding to predetermined performance levels, in a methodology that can be applied in everyday practice [27]-[30]. Resorting to non-linear static analysis, through a structural analysis programme, is conditioned by the precision of the structural model, having to be adequately accurate to catch the non-linear behaviour. The whole process is not easy to standardise and for this reason a simplified methodology, able to define the capacity curve analytically, has been defined. This model shows a full inclination to code liability not requiring complicated analyses and being uniquely defined. To this scope, several parametric analyses, in terms of pushover, on 420 frames, designed according to three different approaches, were made and their results in terms of capacity curves were analysed. In particular, each capacity curve has been simplified by defining 3 branches: the elastic response curve, the maximum horizontal forces multiplier curve and the mechanism equilibrium curve. In this evaluation, the role of the beam-to-column joints has not been considered considering that the beam ends are equipped with full strength-full stiff joints [31]-[38].

2 TRILINEAR MODEL OF THE CAPACITY CURVE

2.1 Definition of the three branches

One of the most common tools adopted to assess the capacity of a structure is the pushover analysis. The simplified method herein proposed only requires use of common analyses such as the elastic structural analysis and the rigid-plastic analysis. For this reason, it lends itself well to be used in the immediate aftermath of an earthquake, not requiring any static or dynamic non-linear analyses. Therefore, the user can quickly obtain the capacity curve through the intersection of three linear branches (Fig. 1), computed by means of simple equations reported in the following. The shape of the capacity curve, for a given structure, is affected by the occurring collapse mechanism. The first branch is affected by the elastic behavior of the structure. The knee depends on the plastic capacity distribution, appearing sharper as more as the plastic hinges develop simultaneously while the slope of softening branch is linked to the second-order effects.

Referring to the trilinear model proposed, the first branch of the curve can be approximated by the elastic response curve; the horizontal one is provided by the maximum load bearing capacity, while, the softening branch is given by the collapse mechanism equilibrium curve of the structure, influenced by the second order effects. The definition of the third branch, is linked to the concept of mechanism equilibrium curve [40], [41]. Therefore, the mechanism equilibrium curve is a straight line, expressed in the following form:

$$\alpha = \alpha_0 - \gamma_s \delta \quad (1)$$

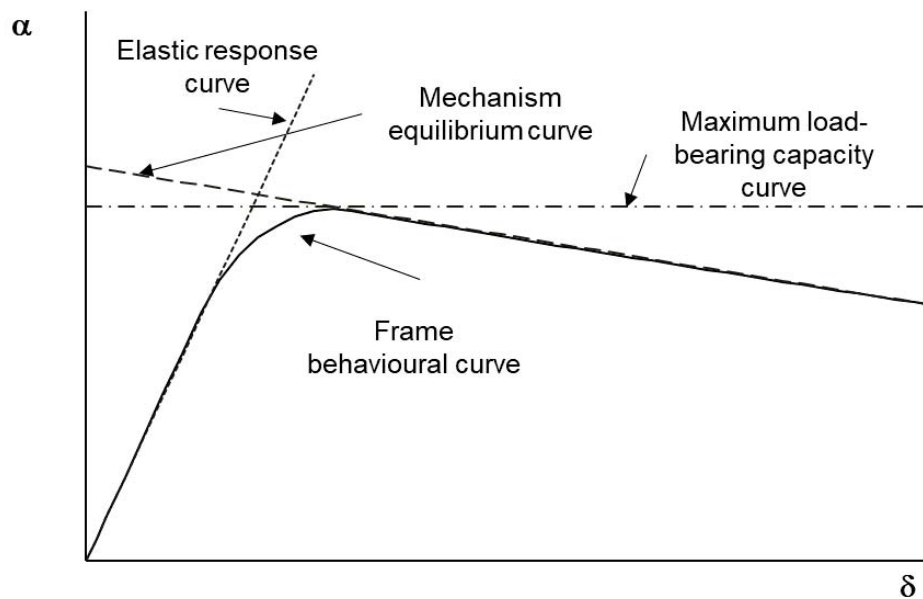


Figure 1: Trilinear model of the capacity curve.

where α_0 is the kinematically admissible multiplier of horizontal forces due to first-order rigid-plastic analysis and γ_s is the slope of the mechanism equilibrium curve [42]-[51]. Providing input data about mechanical and geometric properties of structural members, acting forces [52]-[54] and the potential collapse configurations, both α_0 and γ_s can be computed for each type of possible collapse mechanism. According to the extension of the kinematic theorem of plastic collapse to the concept of mechanism equilibrium curve, the triggering mechanism will be the one characterized by the curve located below the others into a given displacement range compatible with the local ductility supply.

2.2 Parametric analysis

The definition of the horizontal branch of the trilinear curve and the plastic rotation demand corresponding to the collapse condition was achieved through a wide parametric analysis on moment resisting steel frames (MRFs) and calibrated by regression analysis according to the results obtained by the pushovers performed on MRFs.

The parametric analysis has been carried out with reference to three categories of frames:

- GMRFs (Global moment resisting frames) designed according to TPMC procedure (showing global collapse mechanisms);
- SMRFs (Special moment resisting frames) designed according to hierarchy criterion as suggested by Eurocode 8 [53], able to avoid “soft storey” collapse mechanisms;
- OMRFs (Ordinary moment resisting frames) designed without any requirement aimed at the control of the collapse mechanism and usually showing “soft storey” collapse mechanism.

The parametric analysis regarded 140 geometrical schemes of low-rise frames by varying the *number of bays*, n_b from 2 to 6, the *number of storeys*, n_s from 2 to 8, the *bay span*, equal to 3,00 m, 4.50 m, 6.00 m, 7.50m and the three different design approaches for a total number of

420 designed structures. All the combinations were analysed considering dead loads (G_k) equal to $3.5kN/m^2$, live loads (Q_k) equal to $3kN/m^2$ and interstorey height of 3.5m [54].

2.3 Calibration of maximum multiplier formula

To define the horizontal branch of the trilinear curve and the point corresponding to the collapse condition, wide parametric and regression analyses on moment resisting steel frames (MRFs) have been carried out. In particular, MRFs are analysed through pushover analyses - [56] in order to check the correspondence between their results and the aforementioned trilinear model. The maximum multiplier corresponding to the maximum bearing capacity is derived by the Merchant-Rankine formula [57] as a combination of the collapse multiplier obtained by the rigid-plastic analysis α_0 and the critical collapse multiplier for vertical loads. Introducing a calibration factor, useful to ensure a large application of the method, the relation has been rearranged as:

$$\alpha = \alpha_0 - \gamma_s \delta \quad (2)$$

where:

$$\alpha = \alpha_0 - \gamma_s \delta \quad (3)$$

$$\alpha = \alpha_0 - \gamma_s \delta \quad (4)$$

I_b and L_b are the inertia and the length of the beam, respectively; I_c e L_c are the inertia and the height of the column; E is the elastic modulus; a and b are the regression coefficients. The parameter ξ is calculated with reference to the first storey members.

The coefficient Ψ can be computed according to the following relation, which guarantees an accurate evaluation of the α_{max} as Figure 2 testifies:

$$\alpha = \alpha_0 - \gamma_s \delta \quad (5)$$

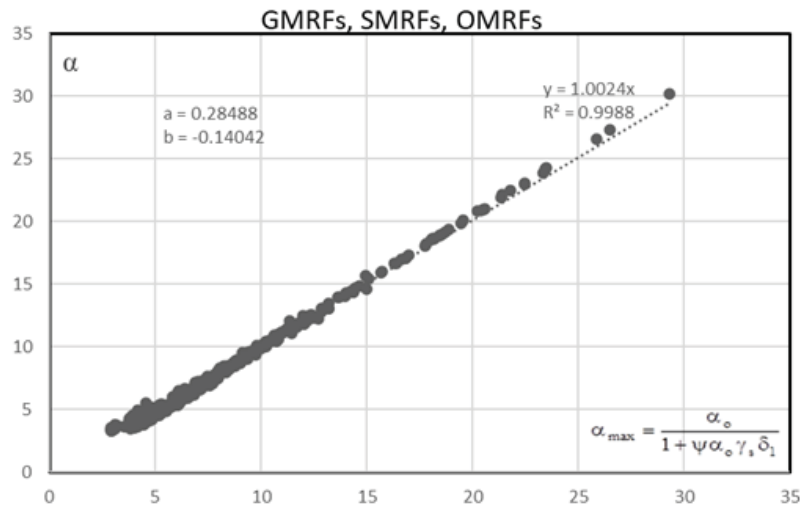


Figure 2: Regression analysis for the maximum multiplier formula.

2.4 Characteristic points of the trilinear model

Starting from the trilinear approximation model, four characteristic points of the simplified capacity curve (points A, B, C, D of Fig. (3)) have been identified. These points are associated to limit states with the meaning of identifying a target performance [58]-[61].

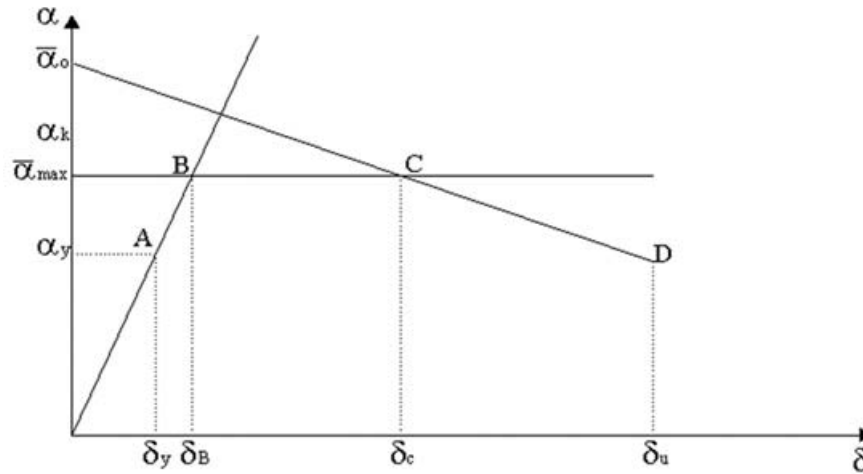


Figure 3: Characteristic points of the trilinear capacity curve

▪ Point A

This point corresponds to the minimum value between the maximum storey displacement under serviceability conditions and the multiplier of the horizontal forces corresponding to the formation of the first plastic hinge. It is associated with the "Fully Operational" limit state.

The multiplier corresponding to point A, will be calculated as follows:

$$\alpha = \alpha_0 - \gamma_s \delta \quad (6)$$

▪ Point B

Point B corresponds to the development of the maximum bearing capacity of the structure and to the elastic limit of the structure and is associated with the "Operational" limit state. To locate point B, the maximum multiplier ($\alpha_{max} = \alpha_B$) has to be computed, by means of the Merchant-Rankine formula (Eq. (2)).

Therefore, it can be stated that:

$$\alpha_{max} = \alpha_B = \frac{1}{\delta_1} \delta_B \quad (7)$$

where the unknown is the top sway displacement δ_B

▪ Point C

Point C corresponds to the development of the collapse mechanism and is associated with the "Life Safety" limit state.

The corresponding top sway displacement δ_C can be derived as follows:

$$\delta_C = \delta_{mecc} = \frac{\alpha_0 - \alpha_{max}}{\gamma_s} + \delta_y \quad (8)$$

▪ Point D

Point D corresponds to the overcoming, at least in one member, of the local ductility supplies and is associated with the "Near Collapse" limit state. This is the case of very rare seismic events in which considerable local ductility is required.

The corresponding top sway displacement $\delta_D = \delta_u$, is calculated as follows:

$$\delta_D = \delta_C + (\vartheta_{p.u} - \vartheta_{p.mecc})H_0 \quad (9)$$

where $\vartheta_{p.u}$ is the plastic hinge rotation assumed equal to $8.0 \vartheta_y$ according to Eurocode 8 [60], $\vartheta_{p.mecc}$ is the plastic hinge rotation corresponding to the formation of the collapse mechanism, H_0 is the total height of storeys involved into the collapse mechanism.

For the evaluation of plastic rotations occurring in the critical members, an analytical formulation is proposed, based on a simplified Grinter's (shear type) single storey portal in which it is assumed that the plastic moments are different at the top and at the base of the columns, to represent the plastic redistribution capacity characterizing frames with more storeys and bays. The relationships for the evaluation of the plastic rotation corresponding to the development of the collapse mechanism are proposed as follows:

$$\frac{\theta_{p.mec} H_0}{n_s \delta_y} = \frac{\Psi_1}{\Psi_2} \Psi_3 \left(\frac{\alpha_{max}}{\alpha_y} - 1 \right)^{\Psi_4} \frac{1 - \Psi_5 \gamma_s}{1 - \Psi_6 \gamma_s} \quad (10)$$

$$\frac{\theta_{p.mec} H_0}{n_s \delta_y} = \frac{\Psi'_1}{\Psi'_2} \Psi'_3 \left(\frac{\alpha_{max}}{\alpha_y} - 1 \right)^{\Psi'_4} \frac{1 - \Psi'_5 \gamma_s}{1 - \Psi'_6 \gamma_s} \quad (11)$$

where H_0 is the total height of storeys involved into the collapse mechanism, n_s is the number of storeys, α_y is the multiplier of the horizontal forces corresponding to the formation of the first plastic hinge, δ_y is the displacement corresponding to the formation of the first plastic hinge. The Ψ_i coefficients, determined by regression analyses, are given by:

$$\Psi_1 = a_1 + b_1 n_b \quad \Psi'_1 = a'_1 + b'_1 n_b \quad (12)$$

$$\Psi_2 = a_2 + b_2 n_s \quad \Psi'_2 = a'_2 + b'_2 n_s \quad (13)$$

$$\Psi_i = a_i + b_i \xi \quad i = 3, \dots, 6 \quad \Psi'_i = a'_i + b'_i \xi \quad i = 3, \dots, 6 \quad (14)$$

The results of linear regression on GMRFs and SMRFs, are reported in Figs. (4-7).

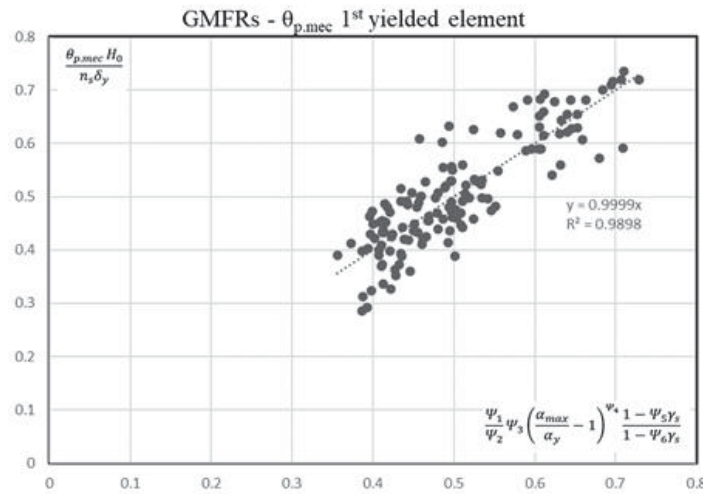


Figure 4: Regression analysis GMRFs - $\theta_{p.mec}$, 1st yielded element.

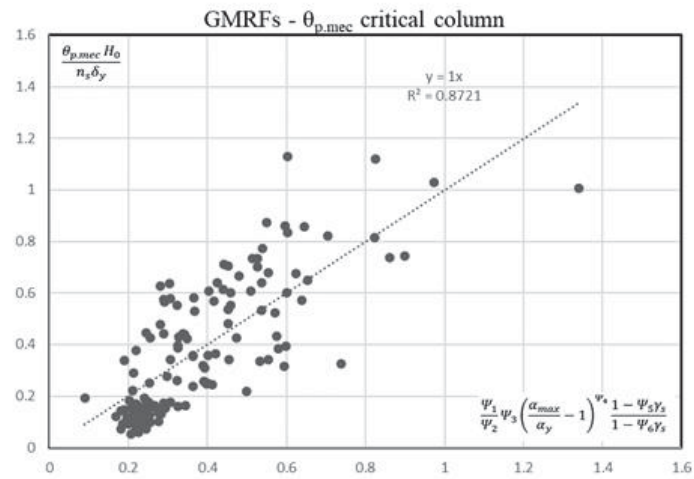


Figure 5: Regression analysis GMRFs - $\theta_{p.mec}$, critical column.

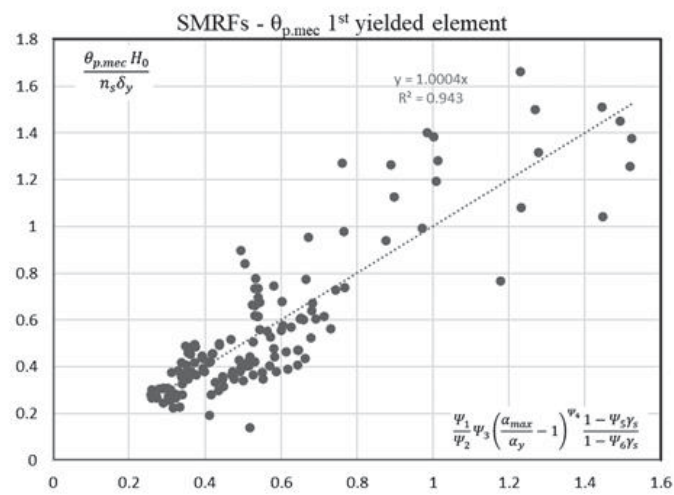


Figure 6: Regression analysis SMRFs - $\theta_{p.mec}$, 1st yielded element.

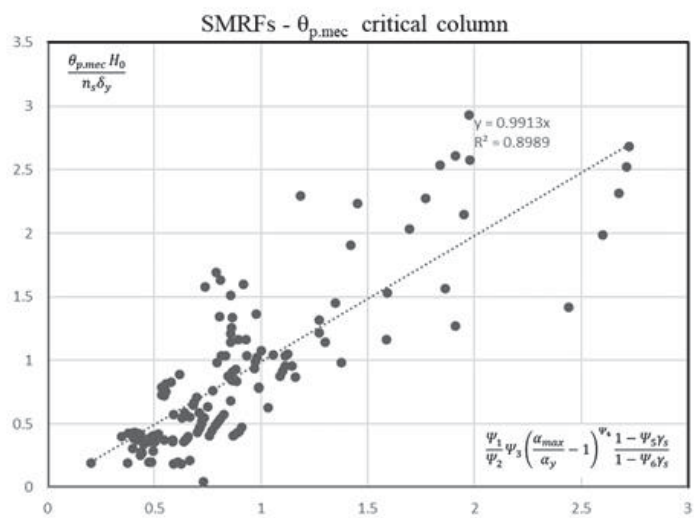


Figure 7: Regression analysis SMRFs - $\theta_{p.mec}$, critical column.

3 ASSESSMENT PROCEDURES IN TERMS OF SPECTRAL ACCELERATIONS

3.1 ADRS spectrum approach

According to the ADRS spectrum approach, for each limit state, the spectrum $S_a - S_{De}$ will be defined by means of the relationship $S_{De}(T) = S_a(T)(T/2\pi)^2$. For the definition of the capacity it is necessary to represent the characteristic points of the trilinear curve of the structure, in the ADRS plane through the abscissa, that is the displacement $d_{LS}^* = d_{LS}/\Gamma$.

It is necessary to distinguish between the cases $T^* > T_C$ e $T^* < T_C$. If $T^* > T_C$. The capacity in terms of spectral acceleration, for a specific limit state, can be obtained through the following relationship:

$$S_{aSL} = d_{LS}^* \omega_0^{*2} \quad (15)$$

The demand is represented by the spectral acceleration provided by the code, for the specific limit state, considering the equivalent period of vibration T^* .

For the assessment procedure, the inequality $S_{als} \geq S_a(T^*)$ has to be satisfied.

If $T^* < T_C$ and $q > 1$, according to equality of energy criteria, there is a different procedure to evaluate the capacity that leads to the anelastic spectrum:

$$F_{ls}^* = \frac{m^* S_a(T^*)}{q_{ls}} \quad (16)$$

$$q_{ls} = 1 + (\mu_{ls} - 1) \frac{T^*}{T_C} \quad (17)$$

$$S_{aSL} = q_{ls} \frac{F_{ls}^*}{m^*} \quad (18)$$

3.2 Nassar & Krawinkler approach

The proposed approach overcomes the limits of the verification methodology proposed by the current seismic codes. In addition, it accounts for second-order effects, occurring when the collapse mechanism is fully developed.

In the framework of capacity-demand checking procedure, the MDOF actual system is replaced by an equivalent SDOF system an equivalent SDOF system introducing the modal participation factor Γ . Multiplying the multiplier of horizontal forces α with the design base shear the capacity curve is reported in a $F_b - d_c$ plane (base shear force-top-sway displacement).

The capacity curve must be reduced through the modal participation factor and represented in a $F^* - d^*$ plane through the relations $F^* = F_b/\Gamma$, $d^* = d_c/\Gamma$.

The demand can be estimated through the period T^* and the equivalent mass m^* . In the following, the verification procedure for each characteristic point of the capacity curve approximated with trilinear model is reported.

- Point A (Fully operational)

The capacity in terms of spectral acceleration for the point A is given as follows:

$$F_{FO}^* = m^* S_{aFO}(T^*) \quad (19)$$

- Point B (Operational)

The capacity in terms of spectral acceleration for the point B is given as follows:

$$S_{aO}(T^*) = \frac{F_O^*}{m^*} \quad (20)$$

▪ Point C (Life Safe)

The capacity in terms of spectral acceleration for the point C is given as follows:

$$S_{aLS}(T^*) = \frac{F_{LS}^*}{m^*} q_{LS} \quad (21)$$

$$q_{LS} = q_0(\mu, T, \gamma=0) = [c(\mu_{LS} - 1) + 1]^{1/c} \quad (22)$$

where $c = \frac{T^*}{1+T^*} + \frac{0.42}{T^*}$ and $\mu_{LS} = \frac{d_{LS}^*}{d_O^*}$.

In the case of point C (and point D), the structure draws on its own plastic resources to dissipate incoming seismic energy. Consequently, the q structure factor comes into play, expressed according to the formulation of Nassar and Krawinkler [30], as a function of the ductility μ_{LS} .

▪ Point D (Near Collapse)

The capacity in terms of spectral acceleration for the point D is given as follows:

$$S_{aNC}(T^*) = \frac{F_{NC}^*}{m^*} q_{NC} \quad (23)$$

$$q_{NC} = \frac{q_0}{\varphi} \quad (24)$$

To take these into account, the coefficient φ which is a function of the ductility μ and the slope of the equilibrium curve γ (expressing the sensitivity of the structure to second-order effects), has been introduced:

$$q_0(\mu, T, \gamma=0) = [c(\mu_{NC} - 1) + 1]^{1/c} \quad (25)$$

where $c = \frac{T^*}{1+T^*} + \frac{0.42}{T^*}$ and $\mu_{NC} = \frac{d_{NC}^*}{d_O^*}$

$$\varphi = \frac{1+0.62(\mu_{NC}-1)^{1.45}\gamma}{(1-\gamma)} \quad (26)$$

4 CONCLUSIONS

In conclusion, the proposed methodology opens-up new scenarios regarding the seismic classification of the built heritage. An analytical methodology allows to evaluate uniquely the seismic vulnerability of buildings without passing through complex analyses not manageable by means of codes and prescriptions. The trilinear model seems to be the right compromise between accuracy in analysis and computational speed and fits well in all the major seismic codes. The assessment of structure performances, in terms of comparison capacity-demand, has been performed by means of the Nassar & Krawinkler approach, characterized by a wide generality because it does not discriminate between high and low periods of vibration and accounts for second-order effects by means of the stability coefficient φ . Finally, it is important to note that discretization in characteristic points of the capacity curve makes easy the comparison capacity-demand and already shows inclination towards the generality of the application of the method, being associated with behavioural characteristics of structures that are independent of the structural type.

ACKNOWLEDGEMENTS

The research leading to the results presented in this paper has received funding from the Italian Department of Civil Protection (DPC-Reluis). The support of DPC-RELUIS 2019-2021 is gratefully acknowledged.

REFERENCES

- [1] H.-C. Jung, J.-S. Jung, K.S. Lee “Seismic performance evaluation of internal steel frame connection method for seismic strengthening by cycling load test and nonlinear analysis” (2019) *Journal of the Korea Concrete Institute*, **31** (1), pp. 79-88.
- [2] R. Montuori, E. Nastri, V. Piluso, P. Todisco, “A simplified performance based approach for the evaluation of seismic performances of steel frames”, *Engineering Structures*, **224**, art. no. 111222, (2020).
- [3] R. Montuori, E. Nastri, V. Piluso, P. Todisco, “Evaluation of the seismic capacity of existing moment resisting frames by a simplified approach: Examples and numerical application” (2021) *Applied Sciences (Switzerland)*, **11**(6), art. no. 2594.
- [4] R. Montuori, E. Nastri, V. Piluso, "Problems of modeling for the analysis of the seismic vulnerability of existing buildings" (2019) *Ingegneria Sismica*, **36** (2), pp. 53-85.
- [5] F. Barbagallo, M. Bosco, A. Floridia, E.M. Marino, P.P. Rossi, “Design for seismic upgrading of existing RC frames by friction dampers”, (2020) *Ingegneria Sismica*, **37** (1), pp. 5-18.
- [6] M. Ferraioli, A. Lavino, A. Mandara, “Seismic retrofit design method of RC buildings using metallic yielding dampers” (2020) *Ingegneria Sismica*, **37** (1), pp. 19-32.
- [7] M. Ferraioli, A. Lavino, A. Mandara, “Effectiveness of multi-mode pushover analysis procedure for the estimation of seismic demands of steel moment frames” (2018) *Ingegneria Sismica*, **35** (2), pp. 78-90.
- [8] C. Bernuzzi, D. Rodigari, M. Simoncelli, “Post-earthquake damage assessment of moment resisting steel frames” (2019) *Ingegneria Sismica*, **36** (4), pp. 35-55.
- [9] D. De Domenico, N. Impollonia, G. Ricciardi, “Seismic retrofitting of confined masonry-RC buildings: The case study of the university hall of residence in Messina, Italy” (2019) *Ingegneria Sismica*, **36** (1), pp. 54-85.
- [10] E. Nastri, M. Vergato, M. Latour, "Performance evaluation of a seismic retrofitted R.C. precast industrial building" (2017) *Earthquake and Structures*, **12** (1), pp. 13-21.
- [11] S. Wang, J.-W. Lai, M.J. Schoettler, S.A. Mahin, “Seismic assessment of existing tall buildings: A case study of a 35-story steel building with pre-Northridge connection” (2017) *Engineering Structures*, **141**, pp. 624-633.
- [12] S. Costanzo, M. D’Aniello, R. Landolfo, Proposal of design rules for ductile X-CBFS in the framework of EUROCODE 8. *Earthquake Engng Struct Dyn*. Volume 48, Issue 1, Pages 124-151, January 2019. <https://doi.org/10.1002/eqe.3128>
- [13] R. Tartaglia, M. D’Aniello, G.A. Rassati, (2019) Proposal of AISC-compliant seismic design criteria for ductile partially-restrained end-plate bolted joints. *Journal of Constructional Steel Research* Volume 159, August 2019, Pages 364-383

- [14] D. Vamvatsikos, K. Bakalis, M. Kohrangi, S. Pyrza, C. Castiglioni, A. Kanyilmaz, F. Morelli, A. Stratan, M. D' Aniello, L. Calado, J.M. Proença, H. Degee, B. Hoffmeister, M. Pinkawa, P. Thanopoulos, I. Vayas, (2020). A risk-consistent approach to determine EN1998 behaviour factors for lateral load resisting systems. *Soil Dynamics and Earthquake Engineering* 131, 106008
- [15] S. Shakeel, L. Fiorino, R. Landolfo, Behavior factor evaluation of CFS wood sheathed shear walls according to FEMA P695 for Eurocodes. *Engineering Structures*, 2020, 221, 111042
- [16] L. Fiorino, S. Shakeel, R. Landolfo, Seismic behaviour of a bracing system for LWS suspended ceilings: Preliminary experimental evaluation through cyclic tests. *Thin-Walled Structures*, 2020, 155, 106956
- [17] A. Campiche, L. Fiorino, R. Landolfo, Numerical modelling of CFS two-storey sheathing-braced building under shaking-table excitations. *Journal of Constructional Steel Research*, 2020, 170, 106110
- [18] A. Campiche, Numerical modelling of cfs three-story strap-braced building under shaking-table excitations. *Materials*, 2021, 14(1), pp. 1–13, 118
- [19] A. Poursadrollah, M. D'Aniello, R. Landolfo, A. De Martino (2020), “Preliminary Study on The Seismic Performance of Hybrid Steel Structures with Truss Lightweight Girders and Plug-and-Play Connections” (2020) *Ingegneria Sismica: International Journal of Earthquake Engineering*, **37**(1), pp. 103-113.
- [20] Costanzo S, D'Aniello M, Landolfo R. Seismic design rules for ductile Eurocode compliant two storey X concentrically braced frames. *Steel and Composite Structures*, Vol. 36, No. 3 (2020) 273-291. DOI: <https://doi.org/10.12989/scs.2020.36.3.273>
- [21] S. Costanzo, M. D'Aniello, R. Landolfo, (2017). Seismic Design Criteria for Chevron CBFs: European vs North American Codes (PART-1). *Journal of Constructional Steel Research*, Volume 135, August 2017, Pages 83–96. 10.1016/j.jcsr.2017.04.018
- [22] M. Bruneau, C.M. Uang, R.S.E. Sabelli, (2011). *Ductile Design of Steel Structures*. McGraw-Hill.
- [23] S. Costanzo, M. D'Aniello, R. Landolfo, A. De Martino, (2018). Critical discussion on seismic design criteria for X concentrically braced frames. *Ingegneria Sismica: International Journal of Earthquake Engineering*, Volume 35, Issue 2, 2018, Pages 23-36.
- [24] S.-H. Hwang, J.-S. Jeon, K. Lee, “Evaluation of economic losses and collapse safety of steel moment frame buildings designed for risk categories II and IV” (2019) *Engineering Structures*, **201**, art. no. 10983.
- [25] E. Romano, L. Cascini, M. D'Aniello, F. Portioli, R. Landolfo, (2020) simplified multi-performance approach to life-cycle assessment of steel structures. *Structures* 27 (2020) 371–382
- [26] A. Gupta, H. Krawinkler, “Feasibility of push-over analyses for estimation of strength demand”, Stessa 2003, - *Behaviour of Steel Structures in Seismic Areas: Proceedings of the 4th International Specialty Conference*, Naples, Italy, 9-12 June 2003.
- [27] NTC 2018 Italian Code: Chapter 7 “Design for seismic actions”.
- [28] P. Fajfar, “A Nonlinear Analysis Method for Performance-Based Seismic Design,” *Earthq. Spectra*, 2000.

- [29] FEMA, “Seismic performance assessment of buildings. Volume 1- Methodology,” Fema P-58-1, 2012
- [30] A. Gupta and H. Krawinkler, “Seismic Demands for Performance Evaluation of Steel Moment Resisting Frame Structures,” (1999).
- [31] D. Cassiano, M. D’Aniello, C. Rebelo, (2017) Parametric finite element analyses on flush end-plate joints under column removal. *Journal of Constructional Steel Research*, Volume 137, October 2017, Pages 77–92
- [32] R. Tartaglia, M. D’Aniello, M. Zimbru, R. Landolfo, (2018). Finite element simulations on the ultimate response of extended stiffened end-plate joints. *Steel and Composite Structures, An International Journal* Vol. 27 No. 6, June25 2018. pages 727-745. DOI: 10.12989/scs.2018.27.6.727
- [33] S. Costanzo, M. D’Aniello, R. Landolfo (2018). The influence of moment resisting beam-to-column connections on seismic behavior of chevron concentrically braced frames. *Soil Dynamics and Earthquake Engineering* 113 (2018) 136–147
- [34] R. Tartaglia, M. D’Aniello, R. Landolfo, (2018). The influence of rib stiffeners on the response of extended end-plate joints. *Journal of Constructional Steel Research* 148 (2018) 669–690.
- [35] M. D’Aniello, R. Tartaglia, D. Cassiano, (2020) Experimental Investigation of The Inelastic Tensile Behaviour of Non-Preloadable Grade 8.8 Bolts. *Ingegneria Sismica: International Journal of Earthquake Engineering*, Volume 37, Issue 2, 2020, Pages 92-110
- [36] R. Tartaglia, M. D’Aniello, M. Zimbru, (2020). Experimental and numerical study on the T-Stub behaviour with preloaded bolts under large Deformations. *Structures* Volume 27, October 2020, Pages 2137-2155 <https://doi.org/10.1016/j.istruc.2020.08.039>
- [37] M. Pongiglione, C. Calderini, M. D’Aniello, R. Landolfo, Novel Reversible Seismic-Resistant Joint for Sustainable and Deconstructable Steel Structures, *Journal of Building Engineering*, 2021, 35, 101989 <https://doi.org/10.1016/j.jobbe.2020.101989>
- [38] R. Tartaglia, M. D’Aniello, R. Landolfo, (2020). Numerical Simulations to Predict the Seismic Performance of a 2-Story Steel Moment-Resisting Frame. *Materials* 2020, 13(21), 4831; doi:10.3390/ma13214831
- [39] R. Montuori, E. Nastri, P.Todisco, “Influence of the seismic shear proportioning factor on steel MRFs seismic performances”, *Soil Dynamics and Earthquake Engineering*, 2020, 106498, ISSN 0267-7261, <https://doi.org/10.1016/j.soildyn.2020.106498>.
- [40] R. Montuori, G. Gabbianelli, E. Nastri, M. Simoncelli, “Rigid plastic analysis for the seismic performance evaluation of steel storage racks” (2019) *Steel and Composite Structures*, **32** (1), pp. 1-19.
- [41] R. Montuori, E. Nastri, V. Piluso, “Advances in theory of plastic mechanism control: Closed form solution for MR-Frames”, (2015) *Earthquake Engineering and Structural Dynamics*, **44** (7), pp. 1035-1054.
- [42] E. Nastri, M. D’Aniello, M. Zimbru, S. Streppone, R. Landolfo, R. Montuori, V. Piluso, “Seismic response of steel Moment Resisting Frames equipped with friction beam-to-column joints”, *Soil Dynamics and Earthquake Engineering*, **119**, 144-157, (2019).

- [43] G. Dell’Aglio, R. Montuori, E. Nastri, V. Piluso, “Consideration of second-order effects on plastic design of steel moment resisting frames” *Bulletin of Earthquake Engineering*, **17** (6), pp. 3041-3070, (2019).
- [44] V. Piluso, R. Montuori, E. Nastri, A. Paciello, “Seismic response of MRF-CBF dual systems equipped with low damage friction connections”, *Journal of Constructional Steel Research*, **154**, pp. 263-277, (2019).
- [45] S. Krishnan, M. Muto, “Mechanism of collapse of Tall Steel Moment-Frame Buildings under Earthquake Excitation”, *Journal of Structural Engineering*, ASCE, November 2012, **138**: 1361-1387.
- [46] A. Pisapia, E. Nastri, Probabilistic theory of plastic mechanism control: Design and seismic assessment (2019) COMPDYN Proceedings, 3, pp. 4201-4212.
- [47] E. Nastri, P. Tsarpalis, Seismic analyses of dual concentrically braced frames accounting for the presence of haunched connections (2019) COMPDYN Proceedings, 1, pp. 73-95.
- [48] A. Catapano, E. Nastri, S. Streppone, Design and analysis of dual EBFs equipped with prequalified connections (2019) COMPDYN Proceedings, 1, pp. 96-130.
- [49] E. Nastri, “The influence of geometry, loads and steel grade for the development of a specific collapse type of MR-Frames” (2017) *COMPDYN 2017 - Proceedings of the 6th International Conference on Computational Methods in Structural Dynamics and Earthquake Engineering*, **2**, pp. 5014-5025.
- [50] E. Nastri, “Eccentrically braced frames designed for the energy dissipation optimization”, (2016) *ECCOMAS Congress 2016 - Proceedings of the 7th European Congress on Computational Methods in Applied Sciences and Engineering*, **4**, pp. 8476-8491.
- [51] V. Piluso, A. Pisapia, P. Castaldo, E. Nastri, “Probabilistic Theory of Plastic Mechanism Control for Steel Moment Resisting Frames”, (2019) *Structural Safety*, **76**, pp. 95-107.
- [52] M. J. N. Priestley, “Performance based seismic design” *Bull. New Zeal. Soc. Earthq. Eng.*, 2000.
- [53] Eurocode 8 (2004). EN 1998-1: Design of Structures for Earthquake Resistance – Part 1: general Rules, Seismic Actions and Rules for Buildings, CEN.
- [54] Eurocode 3 (2005). UNI EN 1993-1-1: Design of steel structures Part 1-1: General rules and rules for buildings, CEN.
- [55] R. Montuori, E. Nastri, B. Tagliafierro, “An optimal seismic force pattern for uniform drift distribution” (2019) *Buildings*, **9** (11), art. no. 231.
- [56] F.M. Mazzolani, V. Piluso, (1997). Plastic Design of Seismic Resistant Steel Frames. *Earthquake Engineering and Structural Dynamics*, **26**, 167-191.
- [57] F.M. Mazzolani, V. Piluso, (1996). Theory and Design of Seismic Resistant Steel Frames. E&FN Spon, London.
- [58] D. Grecea, F. Dinu, D. Dubina, “Performance Criteria for MR Steel Frames in Seismic Zones”, *Journal of Constructional Steel Research*, **60**, 739-749, 2004.
- [59] N. Newmark, & W. Hall (1982). *Earthquake Spectra and Design*. In EERI Monographs.
- [60] Eurocode 8 (2004). EN 1998-3: Design of Structures for Earthquake Resistance – Part 3: Assessment and retrofitting of buildings, CEN.

- [61] F. Naeim, “Earthquake Engineering-From Engineering Seismology to Performance-Based Engineering”, *Earthq. Spectra*, 2005.

PRELIMINARY NUMERICAL ANALYSIS OF THE SEISMIC RESPONSE OF STEEL FRAMES WITH MASONRY INFILLS RETROFITTED BY BUCKLING RESTRAINED BRACES

Fernando Gutiérrez-Urzúa¹, Fabio Freddi¹, Luigi Di Sarno², Jing-Ren Wu², Mario D’Aniello³, Raffaele Landolfo³, and Stathis Bousias⁴

¹ Dept. of Civil, Environmental & Geomatic Engineering, University College London
Gower St., London, WC1E 6BT, U.K.
{f.urzua,f.freddi}@ucl.ac.uk

² Dept. of Civil Eng. & Industrial Design, University of Liverpool
Brownlow Hill, Liverpool, L69 3GH, U.K.
{Luigi.Di-Sarno,Jingren.Wu}@liverpool.ac.uk

³ Dept. of Structures for Eng. & Architecture, University of Naples Federico II
Corso Umberto I, Naples, 80134, Italy
{mdaniel,raffaele.landolfo}@unina.it

⁴ Structures Laboratory (STRULAB), Civil Eng. Dept., University of Patras
Rio Patras, Patras, 265 04, Greece
sbousias@upatras.gr

Abstract

Existing steel moment-resisting frames in several seismic regions worldwide are often characterised by high vulnerability to earthquakes due to insufficient local and/or global ductility. Nowadays, it is of paramount importance to assess their response under strong motions and provide cost-effective retrofitting strategies. Amongst others, the seismic behaviour of these frames is often strongly affected by the presence of masonry infills which, from one side, if adequately distributed, beneficially contribute to the seismic resistance of the structure providing stiffness and strength to the frame, from the other side often experience a brittle behaviour and are very vulnerable to seismic actions. To this end, the H2020-INFRAIA-SERA project HITFRAMES (i.e., Hybrid Testing of an Existing Steel Frame with Infills under Multiple EarthquakeS) experimentally evaluated a case study building representative of non-seismically designed European steel frames with masonry infills and investigated a possible retrofit strategy. This paper takes advantage of the experimental results of the HITFRAMES project to calibrate numerical models in OpenSees of a case study building which is analysed as bare, infilled and retrofitted frame with buckling-restrained braces (BRBs). The impact of masonry infills and BRB-retrofit is investigated by comparing the response of models with different configurations.

The numerical results provide some insights on the ability of BRB-retrofit option in protecting not only the steel frames from experiencing critical damage during earthquakes but also the masonry infills and on the importance of using appropriate models for the masonry infills in the assessment procedures.

Keywords: Existing steel frames, Retrofitting, Buckling-restrained braces, Masonry infills, Seismic response, Numerical Simulations.

1 INTRODUCTION

Many existing steel structures worldwide were built before the introduction of modern seismic design provisions and may exhibit high seismic vulnerability due to lack of proper lateral resisting systems and detailing, as well as inadequate energy dissipation capacity [1,2]. Among others, Di Sarno *et al.* [3] investigated the failure patterns of an existing steel moment resisting frames (MRFs) located in Amatrice and damaged by the 2016 Central Italy earthquakes. The case study structure was characterised by large residual lateral drifts with significant yielding at beam-column connections and soft storey mechanisms. Severe damage was also noted in non-structural components, including in-plane and out-of-plane failure of masonry infill walls. This damage is consistent with damage reported in previous earthquakes (*e.g.*, [4–6]). Although masonry infills can significantly contribute to the overall strength and stiffness of a steel MRF [7–9], their structural properties easily degrade with strong or long ground motions (GMs), as well as with cumulative demands, such as foreshock-mainshock-aftershock sequences, as in the case of the 2016 Central Italy Earthquake [10–13].

In this context, the H2020-SERA project HITFRAMES (Hybrid Testing of an Existing Steel Frame with Infills under Multiple Earthquakes) is aimed on assessing the seismic performance of existing steel frames with masonry infills under multiple earthquakes and the feasibility of retrofitting with buckling restrained braces (BRBs) [14–18]. Among others, the objectives of the HITFRAMES project include: (1) to experimentally assess the seismic performance of non-seismically designed steel frames with masonry infills under earthquake sequences, including the effects of cumulative damage; (2) to evaluate the existing masonry infill models and to develop new calibrated models aimed at describing the behaviour of masonry panels within infilled steel MRFs; and (3) to experimentally evaluate the contribution and effectiveness of BRB-based retrofitting strategies in steel MRFs.

Figure 1 shows the set-up of the experimental test carried out as part of the HITFRAMES project. It consists of a 75% scaled, two-storey steel MRF, designed primarily for gravity loads with insufficient seismic detailing [19,20]. The test was conducted at the Structures Laboratory (STRULAB) of the University of Patras, Greece, and it included a pseudo-dynamic (PsD) testing procedure. The prototype building was designed to be a representative of non-seismically designed steel frames based on the characteristics observed in the Amatrice building [3]. The specimen was subjected to GM sequences, based on GMs recorded at Norcia (NRC) station, in Central Italy, and summarised in Table 1.

The present paper proposes a preliminary numerical study of the seismic response of the steel building tested during the HITFRAMES experimental campaign. First, a preliminary calibrated masonry strut model is developed, based on the observations of the HITFRAMES experiment. This model is compared with three widely used single strut masonry models available in literature, through time history analysis and by considering GM1. Then, the numerical model is retrofitted by means of BRBs, in order to evaluate the effectiveness of the devices when interacting with the masonry panels. Finally, conclusions are drawn highlighting the relevance of accurately modelling the masonry infills while assessing the performance of the retrofitted structure.

Event	Date & time	Mw	R _{epi} [km]	PGA [g]
GM1	24/08/2016 1:36	6.0	15.3	0.35
GM2	30/10/2016 6:40	6.5	4.6	0.48
GM3	26/10/2016 17:10	5.4	9.4	0.3

Table 1: Main characteristics of the GMs used during the HITFRAMES experimental campaign.

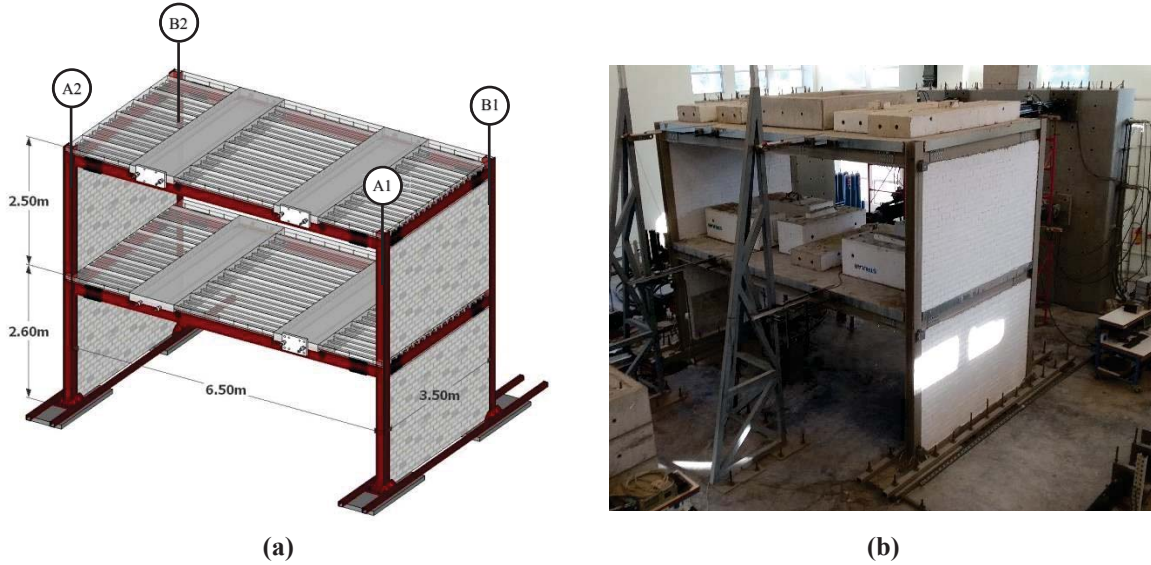


Figure 1: Experiment set-up: (a) 3D model of lab specimen; (b) constructed lab specimen.

2 EVALUATION OF EXISTING MASONRY INFILL MODELS

For the present paper, a non-linear OpenSees numerical model [21] is developed. Columns are modelled with a distributed plasticity approach (*Steel01*), while the beams are modelled by considering a lumped plasticity approach. In the latter approach, plastic hinges are modelled by considering the formulation by Lignos and Krawinkler [22] and modified according to Zareian and Medina [23]. Material properties are consistent with the characterisation tests performed on the steel members after the experiments.

Masonry panels are included by considering a macro-modelling approach, which consists of one simple compression-only diagonal strut on each direction (*i.e.* in X shape). The behaviour of the masonry infills is represented by using a *pinching4* OpenSees material.

2.1 Calibration of masonry infill struts based on experimental results

The calibration of masonry struts is carried out by reproducing the deformation history imposed during the PsD testing in an OpenSees numerical model. The full GM sequence comprises six records in the following order: GM1, GM1, GM2, GM3, GM1 and GM2, with the last two upscaled to 300% in the acceleration axis. As the 75% scaling rules followed for the lab specimen consider constant stress, the time axis in the accelerogram is also multiplied by $0.75^{1/2} = 0.87$ in all GMs.

The masonry strut displacement values (δ_n) are directly obtained from the horizontal floor deformation (Δ_n), assuming negligible vertical deformation and by considering a simple geometric transformation, as follows

$$\delta_n = d_n - d_0 = \sqrt{d_0^2 + 2L\Delta_n + \Delta_n^2} - d_0 \quad (1)$$

where d_0 is the undeformed diagonal length, d_n is the deformed diagonal length at step n , and L is the span length of the frame. Forces are estimated under the assumption that the MRF system works in parallel with the masonry strut, which effectively creates a truss-like mechanism with the steel frame (*i.e.*, the infill-frame interaction does not modify the frame deformation pattern), therefore, the forces assigned to the masonry strut in the numerical model are simply a subtraction of the total storey shear minus the storey shear exhibited by the bare frame at the same level of storey drift.

For this purpose, the elastic and modal properties of the bare frame OpenSees model are validated by comparing the results of the lab characterisation tests (*i.e.*, material testing, snap-back test) [13] with the numerical model. The validated numerical model of the bare frame is then subjected to the storey displacement history observed during the PsD testing in a displacement-controlled manner, with the resulting storey shear values (V_n) recorded. The resulting horizontal shear values at each storey (V_n) are approximated to diagonal equivalent forces (F_n), as follows

$$F_n = \frac{V_n \sqrt{h^2 + (\Delta_n + L)^2}}{\Delta_n + L} \quad (2)$$

where h is the inter storey height.

Figure 2 shows the forces and deformations attributed to one masonry panel (*i.e.*, one compression-only strut on each direction) in comparison with the calibrated model. Four masonry panels per storey are considered in the numerical model (*i.e.*, two double layer walls), therefore, the struts shown in Figure 2 only withstand one quarter of the total load. The masonry struts are calibrated on the *pinching4* material in OpenSees, and their properties are summarised in Table 2.

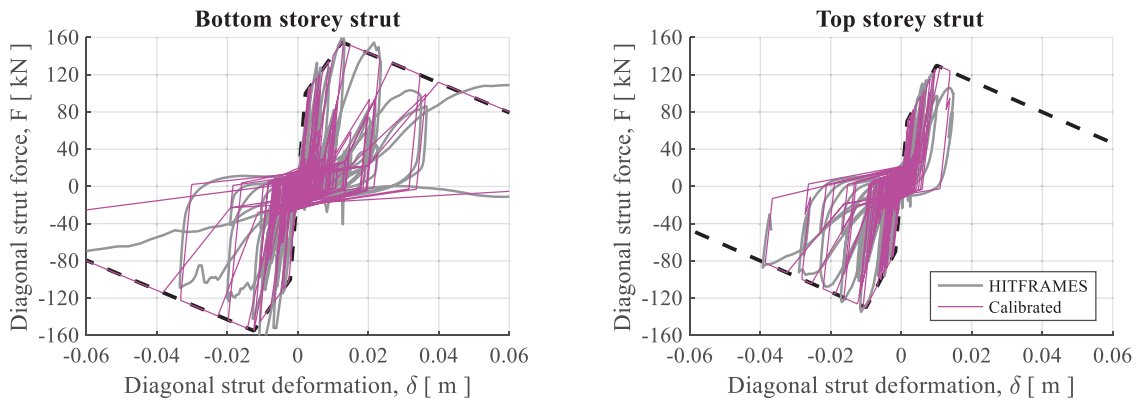


Figure 2: Hysteretic behaviour of the masonry struts during the HITFRAMES experiments, in comparison with the calibrated model. The calibrated pinching parameters are $rDisp = 0.5$, $rForce = 0.2$, $uForce = 0.05$. The calibrated degradation parameters are $gK1 = 0.15$, $gD1 = 0.15$, while all the others keep their default values.

2.2 Comparison of existing masonry infill models with experimental results

Several masonry strut models have been proposed in literature, nonetheless, most of them have been calibrated for reinforced concrete (RC) frames and their application to steel frames is not yet validated. Some of these models comprise complex strut configurations (*e.g.*, multiple struts, additional shear springs, etc.), nonetheless, the most common ones are based on a single strut approach.

Panagiotakos and Fardis (PF) [7,24] proposed a single-strut constitutive model to represent the behaviour of solid (*i.e.*, with no openings) masonry infills in RC frames. This model is characterised by four stress states: (1) initial elastic behaviour of the uncracked masonry infill; (2) post-elastic linear response, characterised by a reduced stiffness; (3) softening of the masonry panel after the maximum force; and, (4) residual axial strength region. The strut resistance is calculated based on the area of the masonry strut, which is the product of the wall thickness and the theoretical width of the strut. This measure depends not only on the properties of the masonry wall, but also on the surrounding frame. Dolšek and Fajfar (DF) [8] proposed a similar model whose main difference is to have a strut resistance implicitly calculated in the capacity formulations. In addition, this model considers that the masonry strut possesses no residual capacity. Decanini and Fantin [25] proposed a model, successively updated by Liberatore and

Decanini (LD) [26], for the evaluation of the seismic response of high-rise RC buildings designed as bare frames but with significant infill contribution. This model considers empirical relationships to define the horizontal capacity and stiffness of the struts.

A comparison of the calibrated masonry strut model is made with the aforementioned models proposed in literature and is shown in Figure 3. The basic material properties of the masonry were obtained from material characterisation tests: compressive strength, $\sigma_{w0} = 2.85$ MPa; shear strength, $\tau_{w0} = 0.653$ MPa. The elastic modulus was estimated by using the relationship proposed by FEMA 356 [27], $E_{w0} = 550\sigma_{w0}$, while the shear modulus is considered to be $G_{w0} = 0.4E_{w0}$. The following observations can be made from the comparison with the calibrated masonry struts: (1) the calibrated model for the bottom storey seems to have more similarities in terms of forces with the PF model and the DF model; (2) the LD model tends to underestimate the force capacity and to overestimate the deformation capacity; regardless of the similar inter-storey heights, the top masonry strut exhibits lower capacity; and (4) the calibrated model exhibits lower initial and post-yielding stiffness than any of the models available in literature. A comparison of the backbone properties for each model is detailed in Table 2.

Figure 4 shows a comparison of the storey shear response obtained during the GM1 of the displacement-based test, by considering the LD and the calibrated models. As observed, the LD shows larger force at low values of displacement, in comparison with the calibrated model. On the other hand, forces are larger in the calibrated model at large displacement values. These observations are consistent with the larger initial stiffness and lower maximum force capacity of the LD model.

Storey	Properties [kN, m]	Calibrated	PF	DF	LD
1	F_y (eNf1)	-100	-132.6	-88.9	-75.5
	F_m (eNf2)	-155	-172.3	-148.2	-94.4
	F_u (eNf3)	-15.5	-13.3	0	-32.6
	k_1	45455	60273	59267	94375
	k_2	5340	14704	21179	4974
	k_3	-1594	-2972	-2976	-415
	δ_y (eNd1)	-0.0022	-0.0022	-0.0015	-0.0008
	δ_m (eNd2)	-0.0125	-0.0049	-0.0043	-0.0046
	δ_u (eNd3)	-0.1	-0.0584	-0.0541	-0.1535
2	F_y (eNf1)	-70	-132.6	-88.9	-78.2
	F_m (eNf2)	-130	-172.3	-148.2	-97.7
	F_u (eNf3)	-13	-13.3	0	-33.6
	k_1	41176	60273	59267	86889
	k_2	7229	14704	21179	4875
	k_3	-1671	-2972	-2976	-400
	δ_y (eNd1)	-0.0017	-0.0022	-0.0015	-0.0009
	δ_m (eNd2)	-0.01	-0.0049	-0.0043	-0.0049
	δ_u (eNd3)	-0.08	-0.0584	-0.0541	-0.1653

Table 2: Comparison among the parameters of the masonry strut calibrated model and the models of Panagiotakos and Fardis (PF) [7,24], Dolšek and Fajfar (DF) [8] and Liberatore and Decanini (LD) [26].

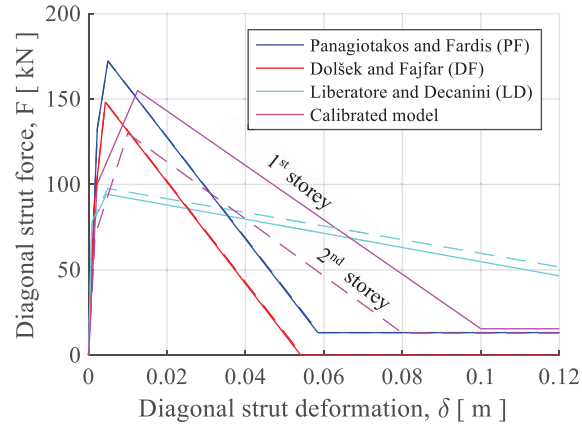


Figure 3. Comparison among the force-displacement curves of the masonry strut calibrated model and the models of Panagiotakos and Fardis (PF) [7,24], Dolšek and Fajfar (DF) [8] and Liberatore and Decanini (LD) [26].

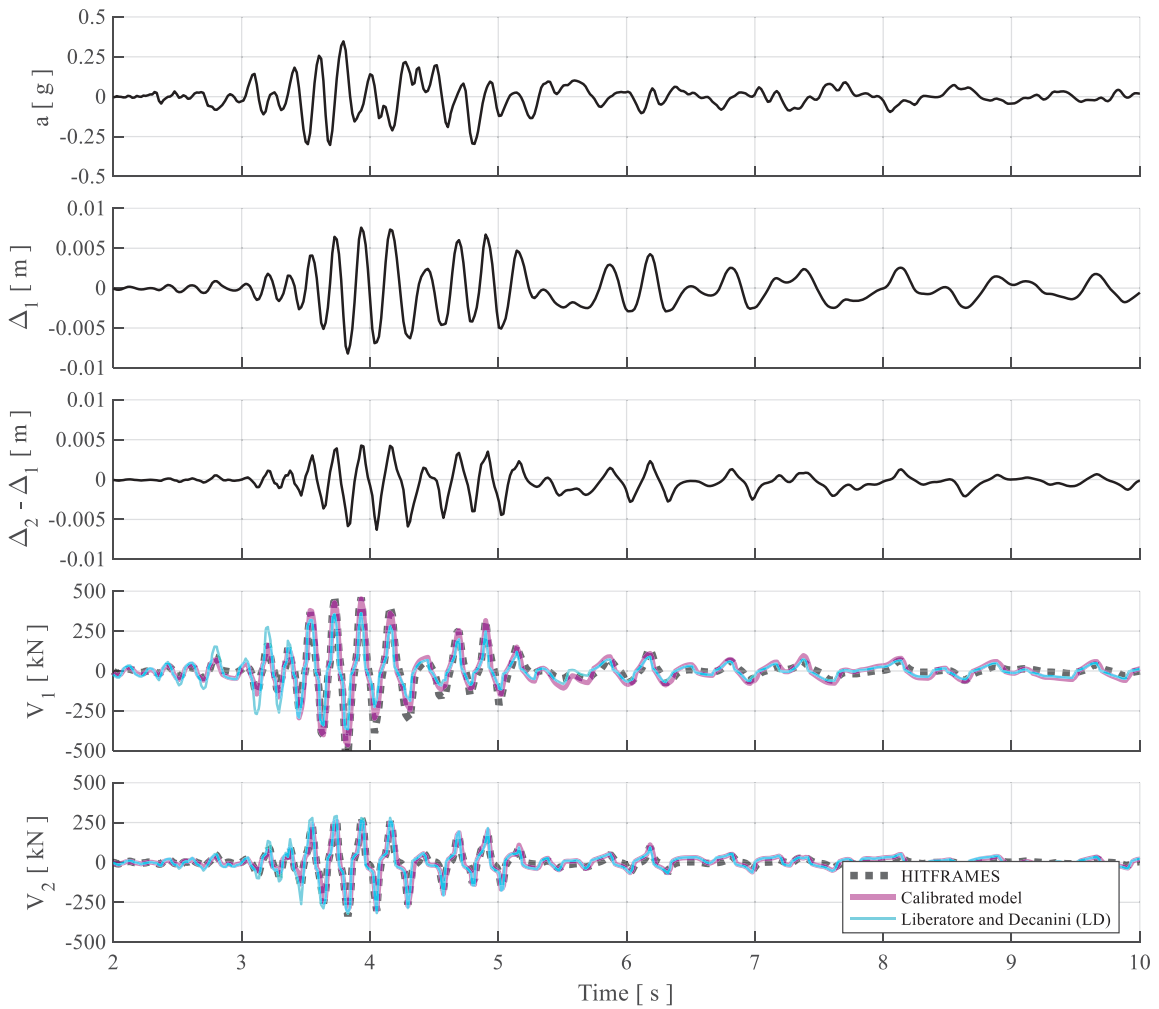


Figure 4. Storey shear output during GM1, considering the frame with the masonry strut calibrated model and the Liberatore and Decanini (LD) [26] model subjected to a displacement-controlled test.

3 ASSESSMENT OF THE RETROFITTED STRUCTURE

The frame with calibrated masonry struts is retrofitted by including diagonal steel braces equipped with BRBs. The sizing of the device is carried out by a simplified code-based design approach. For this matter, the structure is considered to be located in Central Italy and the design of the retrofitting was done in accordance with the recommendations of the Eurocode 8 Part 1 (EC8-1) [28] and Eurocode 3 Part 1-1 (EC3-1-1) [29]. The design is performed for the Ultimate Limit State (*i.e.*, probability of exceedance of 10% in 50 years), considering a Type 1 spectrum, with soil Type B, and Peak Ground Acceleration (PGA) equal to 0.25g. The structure is designed by considering a basic behaviour factor $q_0 = 3$. The design requirements are paired with a commercial catalogue of BRB devices, and result on a device with an initial yielding force $F_{y0-BRB} = 143$ kN. The device is included in the numerical model by using the *SteelBRB* model [30] in OpenSees. The monotonic and hysteretic properties of the device are validated with a characterisation test made by the manufacturer. The hysteretic behaviour of the BRB model is shown in Figure 5. The length of the BRB is 1.535m, therefore, the device is connected in series to a steel tubular section ($\varnothing = 0.16$ m, $t = 0.01$ m) which completes the diagonal length. The full BRB and elastic brace system is pinned at the ends.

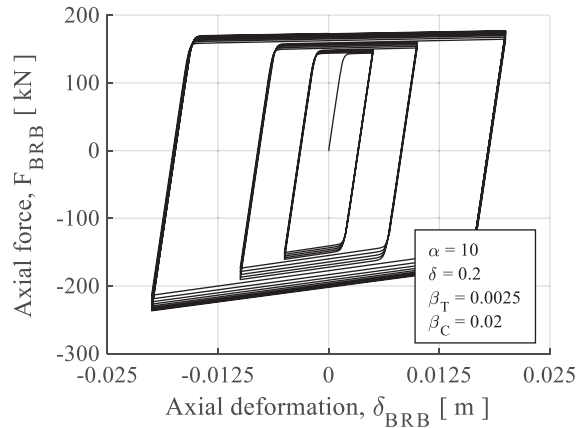


Figure 5. BRB model in OpenSees by using the *SteelBRB* material. $F_{y0-BRB} = 143$ kN; $F_{1-BRB-C} = 178$ kN; $F_{1-BRB-T} = 151$ kN.

Time history analyses based on GM1 were performed on the unretrofitted and retrofitted structures, by considering the calibrated masonry strut model and the LD model. Figure 6 shows the spectrum of GM1 and the comparison of the spectral accelerations (S_a) corresponding to the fundamental period of each structure. The period of the unretrofitted calibrated structure matches the observed fundamental period during the characterisation test of the lab specimen. The addition of the BRBs further reduces its fundamental period to 0.11 s. While considering the LD model, the fundamental period is shorter in the unretrofitted structure due to the higher initial stiffness of the struts and reaches a value of 0.09 s with the addition of BRBs. As observed in Figure 6, for the considered GM, the retrofitted structures benefit from a slight reduction on the demand due to the increased stiffness.

Figure 7, Figure 8, Figure 9 show the inter-storey deformation and storey shear demands during the time history analysis of GM1, for the calibrated and LD masonry strut models, considering the unretrofitted and retrofitted conditions. The deformation in the struts is compared with their own cracking deformation (δ_y), as suggested by the ASCE 41-17 [31] as a limit for the Immediate Occupancy Performance Level. When comparing the unretrofitted cases, the LD model exhibits lower deformation and force values than the calibrated model, as it avoids the strut deformation to reach significant levels of cracking. Nonetheless, the calibrated model (as

well as the lab specimen during the testing) exhibited extensive cracking in the struts. When comparing the retrofitted models, the addition of BRBs significantly reduce the demands on the masonry infills of the calibrated model. Nonetheless, the improvement is not as noticeable in the case of the LD model.

These observations highlight the sensitivity of considering higher values of initial stiffness in the masonry strut model. On one side, the larger stiffness underestimates the damage that the masonry panel could experience in the unretrofitted case. On the other side, it underestimates the capacity of the BRBs in protecting the masonry infills from damage in moderate intensity earthquakes.

Therefore, when the masonry strut properties are properly accounted for, the BRBs can protect the case-study structure from damage at lower and moderate intensity earthquakes, while they simultaneously increase the energy dissipation capacity of the structure at higher levels of demands.

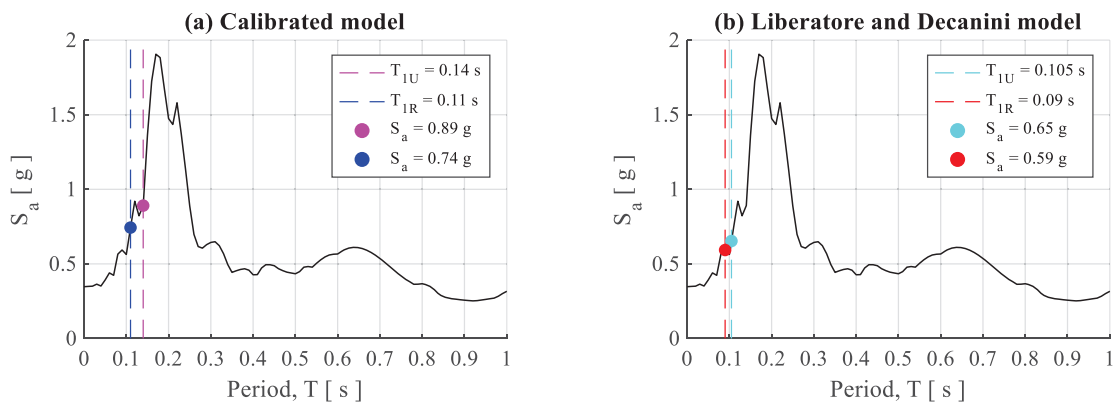


Figure 6. Response spectrum for GM1, considering 3.3% damping, along with the fundamental period of the infilled frame model considering (a) the calibrated strut model and (b) the Liberatore and Decanini strut model [26].

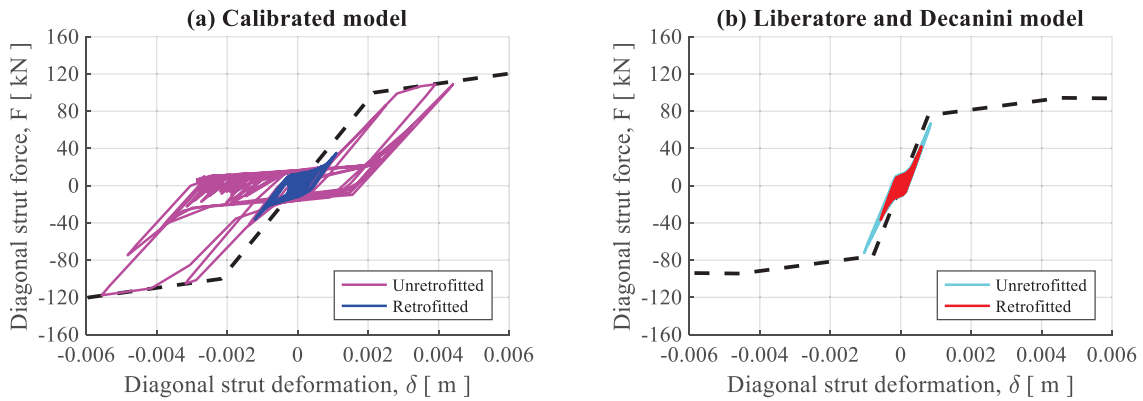


Figure 7. Hysteretic behaviour of masonry struts in the first storey during GM1 considering the (a) calibrated strut model and (b) Liberatore and Decanini strut model [26].

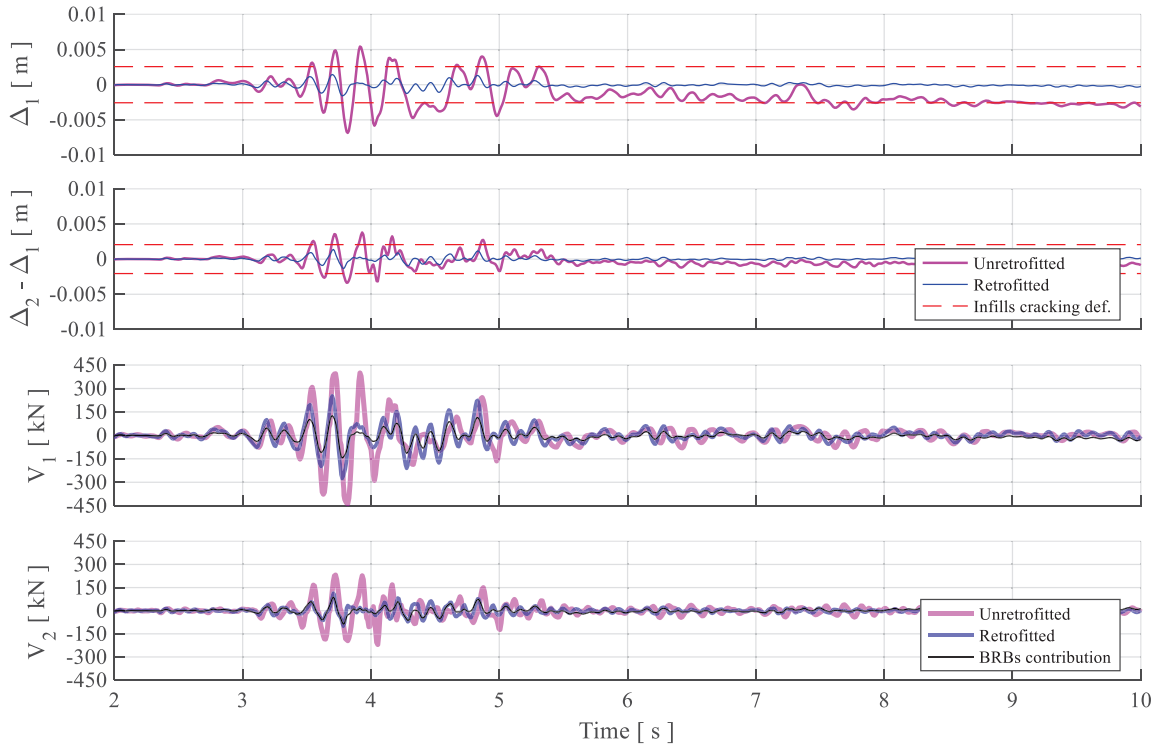


Figure 8. Inter-storey drift and storey shear comparison between the unretrofitted and retrofitted structures when considering the calibrated model for masonry struts.

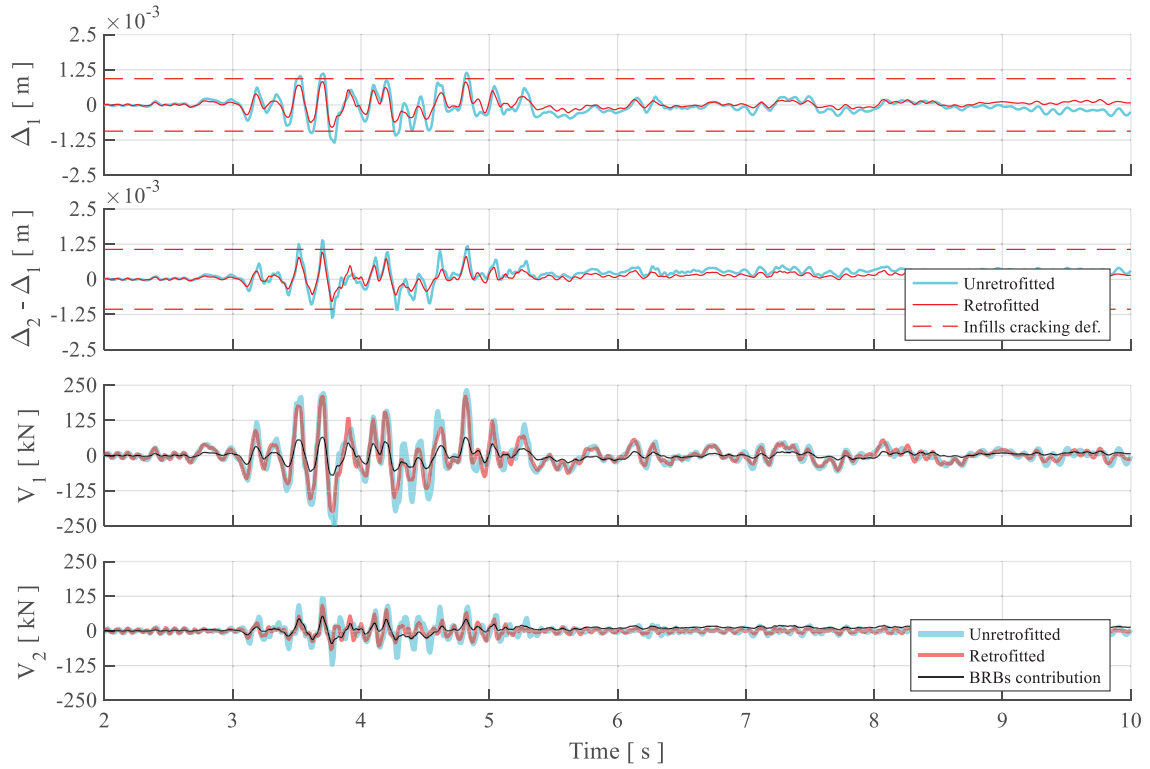


Figure 9. Inter-storey drift and storey shear comparison between the unretrofitted and retrofitted structures when considering the Liberatore and Decanini [26] model for masonry struts.

4 CONCLUSIONS

The present paper investigates the interaction of masonry infills and buckling restrained braces (BRBs) when these are used as a retrofit measure in existing steel moment resisting frames (MRFs). The study takes advantage of the experimental results of the HITFRAMES project to calibrate numerical models in OpenSees for a case study steel MRF which has been analysed as bare, infilled and retrofitted frame with BRBs. The impact of masonry infills and BRB-retrofit is investigated by comparing the response of different infills models. The numerical results provide some insights on the ability of BRB-retrofit option in protecting not only the steel frames from experiencing critical damage during earthquakes but also the masonry infills and on the importance of using appropriate modelling strategies for the masonry infills during the assessment procedures. The following conclusions can be drawn:

- All of the considered masonry strut models exhibited larger values of initial stiffness, in comparison with the calibrated model. The Panagiotakos and Fardis (PF) model, and the Dolšek and Fajfar (DF) model, exhibited larger force capacity but lower deformation capacity than the calibrated model. The Liberatore and Decanini (LD) model exhibited lower force capacity but higher deformation capacity than the calibrated model.
- Large values of initial stiffness were translated in an underestimation of the seismic demands (for GM1) and an overestimation of the capacity. This could lead to larger than expected levels of damage in masonry panels. The calibrated model is able to capture the cracking observed during GM1 in the pseudo-dynamic testing carried out on the lab specimen.
- The addition of BRBs as a retrofit measure for masonry infilled steel MRFs can reduce the damage in the masonry infills at low and moderate seismic demands. Nonetheless, it is necessary to consider a more accurate masonry strut model in the numerical analysis, as the relative stiffness between the masonry and BRB system will dictate the capacity of the BRB to protect the infills.

ACKNOWLEDGEMENTS

The financial support of the Seismic Engineering Research Infrastructure (SERA) project (European Commission, H2020-INFRAIA-2016-2017, Agreement No.730900) to HITFRAMES project is greatly acknowledged. FGU acknowledges the partial funding provided by partially funded by CONACYT-FiiDEM (Grant No. 2018-000013-01EXTF-00148). Any opinions, findings and conclusions, or recommendations expressed in this paper are those of the Authors and do not necessarily reflect those of the sponsors.

REFERENCES

- [1] Federal Emergency Management Agency, State of the Art Report on Past Performance of Steel Moment-Frame Buildings in Earthquakes, FEMA 355E. (2000).
- [2] F. Freddi, V. Novelli, R. Gentile, E. Velu, S. Andreev, A. Andonov, F. Greco, E. Zhuleku, Observations from the 26th November 2019 Albania earthquake: the earthquake engineering field investigation team (EEFIT) mission, Bull. Earthq. Eng. 19 (2021) 2013–2044. <https://doi.org/10.1007/s10518-021-01062-8>.
- [3] L. Di Sarno, F. Paolacci, A.G. Sextos, Seismic performance assessment of existing steel buildings: A case study, Key Eng. Mater. 763 (2018) 1067–1076. <https://doi.org/10.4028/www.scientific.net/KEM.763.1067>.
- [4] S.A. Mahin, Lessons from damage to steel buildings during the Northridge earthquake,

- Eng. Struct. 20 (1998) 261–270. [https://doi.org/10.1016/S0141-0296\(97\)00032-1](https://doi.org/10.1016/S0141-0296(97)00032-1).
- [5] R. Tremblay, P. Timler, M. Bruneau, A. Filiatrault, Performance of lifelines during the 1994 Northridge earthquake, *Can. J. Civ. Eng.* 22 (1995) 338–360. <https://doi.org/10.1139/l95-052>.
- [6] T. Okazaki, D.G. Lignos, M. Midorikawa, J.M. Ricles, J. Love, Damage to steel buildings observed after the 2011 Tohoku-oki earthquake, *Earthq. Spectra*. 29 (2013) 219–243. <https://doi.org/10.1193/1.4000124>.
- [7] T.B. Panagiotakos, M.N. Fardis, Seismic response of infilled RC frame structures, in: 11th World Conf. Earthq. Eng., Acapulco, Mexico, 1996.
- [8] M. Dolšek, P. Fajfar, The effect of masonry infills on the seismic response of a four storey reinforced concrete frame-a probabilistic assessment, *Eng. Struct.* 30 (2008) 3186–3192. <https://doi.org/10.1016/j.engstruct.2008.04.031>.
- [9] M. Mohammadi, S.M. Motovali Emami, Multi-bay and pinned connection steel infilled frames; an experimental and numerical study, *Eng. Struct.* 188 (2019) 43–59. <https://doi.org/10.1016/j.engstruct.2019.03.028>.
- [10] L. Di Sarno, J.R. Wu, Seismic assessment of existing steel frames with masonry infills, *J. Constr. Steel Res.* 169 (2020) 106040. <https://doi.org/10.1016/j.jcsr.2020.106040>.
- [11] K. Aljawhari, R. Gentile, F. Freddi, C. Galasso, Effects of ground-motion sequences on fragility and vulnerability of case-study reinforced concrete frames, *Bull. Earthq. Eng.* (2020). <https://doi.org/10.1007/s10518-020-01006-8>.
- [12] L. Di Sarno, J.R. Wu, Fragility assessment of existing low-rise steel moment-resisting frames with masonry infills under mainshock-aftershock earthquake sequences, *Bull. Earthq. Eng.* 19 (2021) 2483–2504. <https://doi.org/10.1007/s10518-021-01080-6>.
- [13] L. Di Sarno, J.R. Wu, F. Gutiérrez-Urzúa, F. Freddi, M. D’Aniello, O.S. Kwon, S. Bousias, M. Dolšek, Dynamic response of existing steel frames with masonry infills under multiple earthquakes, *Proc. Int. Conf. Struct. Dyn. , EURODYN*. 2 (2020) 3671–3685. <https://doi.org/10.47964/1120.9301.19738>.
- [14] L. Di Sarno, G. Manfredi, Seismic retrofitting with buckling restrained braces: Application to an existing non-ductile RC framed building, *Soil Dyn. Earthq. Eng.* 30 (2010) 1279–1297. <https://doi.org/10.1016/j.soildyn.2010.06.001>.
- [15] G. Della Corte, M. D’Aniello, R. Landolfo, Field Testing of All-Steel Buckling-Restrained Braces Applied to a Damaged Reinforced Concrete Building, *J. Struct. Eng.* 141 (2015) 1–11. [https://doi.org/10.1061/\(asce\)st.1943-541x.0001080](https://doi.org/10.1061/(asce)st.1943-541x.0001080).
- [16] F. Freddi, E. Tubaldi, A. Zona, A. Dall’Asta, Seismic performance of dual systems coupling moment-resisting and buckling-restrained braced frames, *Earthq. Eng. Struct. Dyn.* 50 (2021) 329–353. <https://doi.org/10.1002/eqe.3332>.
- [17] F. Freddi, J. Ghosh, N. Kotoky, M. Raghunandan, Device uncertainty propagation in low-ductility RC frames retrofitted with BRBs for seismic risk mitigation, *Earthq. Eng. Struct. Dyn.* (2021) eqe.3456. <https://doi.org/10.1002/eqe.3456>.
- [18] P. Castaldo, E. Tubaldi, F. Selvi, L. Gioiella, Seismic performance of an existing RC structure retrofitted with buckling restrained braces, *J. Build. Eng.* 33 (2021) 101688. <https://doi.org/10.1016/j.jobe.2020.101688>.

- [19] L. Di Sarno, J.R. Wu, M. D’Aniello, S. Costanzo, R. Landolfo, O.S. Kwon, F. Freddi, Assessment of existing steel frames with infills under multiple earthquakes, *COMPDYN Proc.* 3 (2019) 5813–5824. <https://doi.org/10.7712/120119.7347.19837>.
- [20] F. Gutiérrez-Urzúa, F. Freddi, L. Di Sarno, Comparative analysis of code-based approaches for seismic assessment of existing steel moment resisting frames, *J. Constr. Steel Res.* 181 (2021) 106589. <https://doi.org/10.1016/j.jcsr.2021.106589>.
- [21] F. McKenna, G.L. Fenves, M.H. Scott, Open system for earthquake engineering simulation (OpenSees), (2000).
- [22] D.G. Lignos, H. Krawinkler, Deterioration modeling of steel components in support of collapse prediction of steel moment frames under earthquake loading, *J. Struct. Eng.* 137 (2011) 1291–1302. [https://doi.org/10.1061/\(ASCE\)ST.1943-541X.0000376](https://doi.org/10.1061/(ASCE)ST.1943-541X.0000376).
- [23] F. Zareian, R.A. Medina, A practical method for proper modeling of structural damping in inelastic plane structural systems, *Comput. Struct.* 88 (2010) 45–53. <https://doi.org/10.1016/j.compstruc.2009.08.001>.
- [24] T.B. Panagiotakos, M.N. Fardis, Proposed nonlinear strut model for infill panels, 1st Year Prog. Rep. HCM-PREC8 Proj. Univ. Patras. (1994).
- [25] L.D. Decanini, G. Fantin, Modelos simplificados de la mampostería incluida en porticos. Características de resistencia en el estado límite., in: VI Jornadas Argentinas Ing. Estructural, Buenos Aires, Argentina., 1986.
- [26] L. Liberatore, L.D. Decanini, Effect of infills on the seismic response of high-rise RC buildings designed as bare according to Eurocode 8, *Ing. Sismica.* 28 (2011) 7–23. <http://www.scopus.com/inward/record.url?eid=2-s2.0-84859059861&partnerID=40&md5=5eab990ef5b233a5d5a7477c382f1ea9>.
- [27] Federal Emergency Management Agency, Prestandard and Commentary for the Seismic Rehabilitation of Buildings, FEMA 356. (2000).
- [28] European Committee for Standardization (CEN), Eurocode 8: Design of structures for earthquake resistance - Part 1: General rules, seismic actions and rules for buildings, EN 1998-1. (2004).
- [29] European Committee for Standardization (CEN), Eurocode 3: Design of Steel Structures - Part 1-1: General Rules and Rules for Buildings, EN 1993-1-1. (2005).
- [30] A. Zona, A. Dall’Asta, Elastoplastic model for steel buckling-restrained braces, *J. Constr. Steel Res.* 68 (2012) 118–125. <https://doi.org/10.1016/j.jcsr.2011.07.017>.
- [31] American Society of Civil Engineers, Seismic Evaluation and Retrofit of Existing Buildings, ASCE/SEI 41-17. (2017). <https://doi.org/10.1061/9780784414859>.

NUMERICAL MODELLING OF MASONRY INFILL WALLS IN EXISTING STEEL FRAMES

Luigi Di Sarno^{1*}, Jing-Ren Wu¹, Fabio Freddi², Mario D’Aniello³, Stathis Bousias⁴, Fernando Gutiérrez-Urzúa², Raffaele Landolfo³ and Nikolaos Stathas⁴

¹ Department of Civil Engineering and Industrial Design, University of Liverpool
The Quadrangle, Brownlow Hill, Liverpool, L69 3GH, UK
e-mail: {luigi.di-sarno,jingren.wu}@liverpool.ac.uk

² Department of Civil, Environmental and Geomatic Engineering, University College London
Gower Street, London, WC1E 6BT, UK
{f.freddi,f.urzua}@ucl.ac.uk

³ 3Department of Structures for Engineering and Architecture, University of Naples Federico II
Corso Umberto I, 40, 80138 Napoli NA, Italy
{mdaniel,raffaele.landolfo}@unina.it

⁴ Structures Laboratory, Department of Civil Engineering, University of Patras
265 04 Patras, Greece
{sbousias,stathas}@upatras.gr

Abstract

It is now widely recognised that masonry infill plays an essential role in the seismic behaviour of existing steel buildings; however, there is still a lack of clear guidance on the modelling of masonry infill in the current Eurocode 8-Part 3. Several methods for the numerical modelling of masonry infills have been proposed in literature over the past few decades, which either adopt a detailed approach (micro-model) or a simplified approach (macro-model). In the former case, bricks are individually modelled, taking into account the brick-mortar cohesive interface, which is able to provide detailed insights of the behaviour of masonry infills and the frame-wall interaction but usually at a high computational cost. On the other hand, a simplified model can be easily built within finite element software, most of which replace the infill wall panel with one or more equivalent struts in the diagonal direction. It has been demonstrated that the strut models can simulate RC infilled structures’ global response with acceptable accuracy; however, there are still no adequate recommendations for their modelling within steel frames. Besides, these models are generally incapable of capturing the interactions between the infills and the frame members. To this end, the present paper numerically investigates an Abaqus macro-model of the infilled steel frame, which was experimentally tested as part of the recent SERA HITFRAMES project. The preliminary re-

sults shows that the different detailing of steel frames could lead to different damage patterns in the infill walls when compared to RC frames. In particular, instead of a single diagonal strut, at most three struts were observed in this study. The results also suggested that the number and geometry of struts could change with increasing displacement demands, hence it might not be appropriate to use the same strut model for infill walls on different floors.

Keywords: Seismic Behaviour, Masonry Infill, Existing Steel Frame, Experimental Test

1 INTRODUCTION

Masonry infill walls were widely used in existing steel frame structures as exterior walls mainly for insulation and aesthetic purposes; hence in the code-based assessment procedures of existing buildings, *e.g.*, Eurocode 8-Part 3 [1], they are typically considered as non-structural components. As a consequence, only the self-weight of infill walls is usually considered during the assessment, while their effects on the structural behaviour under lateral load are often neglected. However, it has been widely recognised that masonry infill can significantly affect the seismic response of structures, as they considerably influence the lateral stiffness and strength of structures (and their distribution), as well as the energy dissipation capacity under seismic loading [2-8]. In addition, the strut action of infill wall panels may also exert concentrated force to beams, columns and beam-column joints, increasing local seismic demands. Besides, in the case of infill walls not uniformly distributed, *e.g.*, non-infilled ground floor, severe soft-storey mechanisms can also be triggered [9-11], leading to complete failure of the non-infilled storey.

Currently, a considerable number of studies focused on the behaviour of masonry infills within reinforced concrete (RC) frames, while the current knowledge level on the behaviour of infilled steel frames is still inadequate. Although the masonry infill confined by RC and steel frames share some commons in their seismic response, the different characteristics of steel frames may significantly alter masonry infill response. Steel frames are usually more flexible and more ductile and have different features and detailing compared to RC members, such as the aspect ratio of the frames and the geometries of steel beams and columns. Moreover, when involved in the infill-frame interactions, some local details typical of steel structures, *e.g.*, stiffener plates and connections, may cause local stress concentration in the wall and, consequently, lead to a different response and failure mode of the masonry infills. Despite some experimental tests investigated the behaviour of infilled steel frame over the past few decades [*e.g.*, 6, 12, 13], and a few simplified models have been proposed [*e.g.*, 14, 15], further research is still of great necessity for the development of simplified models that can be used in practice for the assessment of infilled steel buildings. In addition, within the European context, there is an urgent need for additional and detailed rules and recommendations for the assessment of existing steel structures [*e.g.*, 16] to be implemented within an updated version of the Eurocode 8-Part 3. These should include and consider the interaction with the masonry infills, thus promoting reliable assessment procedures.

Finite element modelling of masonry infill can be classified into two groups, namely *micro-* and *macro-modelling*. Detailed micro-modelling approaches usually include a detailed description of brick units and mortar as continuum elements and the brick-mortar interfaces to simulate the cohesive behaviour between brick units and mortar. Such models are able to reproduce the basic mechanisms of the masonry unit, hence are more likely to capture the complex damage patterns of masonry infill accurately. However, the high computational cost of detailed micro-models usually constrains their application to small structures. To this end, simplified micro-models were proposed as an alternative to detailed micro-models, which usually neglect the geometry of mortar and utilise expanded brick units to account for the thickness of mortar [17-19]. Subsequently, the material properties are often defined based on masonry samples, and the interactions between expanded brick units are simulated through cohesive elements or surface-based cohesive behaviour. The simplified micro-modelling can effectively reduce the computational cost but may lead to less accurate results. On the other hand, macro-modelling approaches consider the masonry infill as homogeneous isotropic material, whose mechanical properties can be defined based on various material tests of masonry triplets [11, 20, 21]. As a cost-effective computational strategy, macro-models are usually

adopted while investigating the global response of infilled frames and/or to perform preliminary analyses of the stress distribution in the infill wall panel.

The present paper investigates the behaviour of infilled steel moment frames through the macro-modelling approach. The finite element models are validated based on the results of large-scale experimental tests conducted on a one-bay two-storey infilled steel frame as part of the HITFRAMES SERA project. The steel frame was designed to be representative of typical existing steel frames with inadequate seismic detailing at joints. A pushover analysis is carried out, providing insights into the response of masonry infills. In particular, the change of number and geometry of struts formed in the infill walls were investigated considering increasing displacement demands.

2 EXPERIMENTAL TEST

2.1 Description of the steel frame

A two-storey single-bay 3:4 scaled steel frame was experimentally tested to investigate the behaviour of masonry infill confined by steel members. The test frame had a storey height of 2.5 m, and span of 3.5 and 6.5 m in the transverse (X) and longitudinal (Y) direction, respectively. A sketch of the steel frame is shown in Figure 1. The columns, primary and secondary beams profiles were HE 180A, IPE 200 and IPE 140, respectively. The test was performed in the X-direction with the columns placed along with their weak axis; beam-to-column joints were made through full penetration welds with stiffeners installed to increase joints’ rigidity, while beam-to-beam connections, for the primary beams, were placed at a distance of 400 mm with respect to the column axis. Besides, the columns’ bases were welded to 30 mm-thick steel plates with stiffeners to ensure their rigidity. The stiffened beam-column joints, the beam-to-beam connection and column bases are shown in Figure 2.

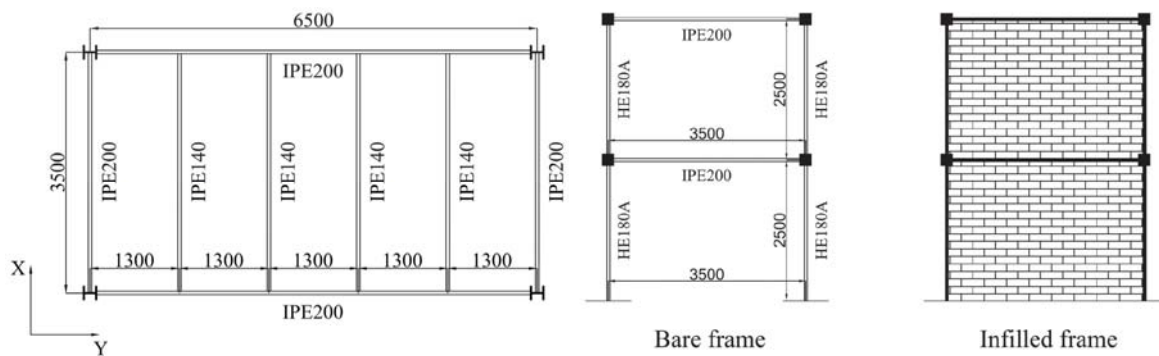


Figure 1: Plan and side view of the steel frame experimentally tested in the laboratory.



Figure 2: Detailing at the beam-column joints (left) and column base (right) of the test frame.

The test frame included a composite slab at both storeys, consisting of 150 mm-thick concrete slabs poured on a 1.25 mm-thick corrugated steel sheet. Shear studs were implemented on both external and internal beams to ensure the transfer of applied horizontal loads to the steel frame through the slab. However, shear studs were omitted in the 0.5-m-wide regions around the columns to avoid the development of composite actions in the joints. Finally, only the masonry infill in the transverse direction of the steel frame were included in the experimental test, each consisting of two layers of 58 mm-thick perforated bricks of size $58 \times 83 \times 190$ mm.

2.2 Experimental setup

The test frame is shown in Figure 3 and was built in the laboratory, according to standard European constructional practice. The steel members were prepared in the workshop and fully assembled in the lab. Two parallel tubular beams were placed on top of each steel base plates and anchored to the strong floor in order to increase the rigidity of the base restraints of the test frame. Besides, the composite slab was built following the assembly of the bare steel frame, where the corrugated steel sheets were installed on the beams and fixed with the shear connectors, with the concrete slab subsequently cast and poured on-site.



Figure 3: Experimental setup and positions of the actuators.

As shown in Figure 3, two actuators were placed at each storey of the test frame and connected to the reaction wall. Additionally, pre-cast concrete blocks were placed on the slab of each storey to simulate the gravity loads imposed on the structure, which would influence beams and columns' behaviour. It is noteworthy that additional concrete blocks were used to represent the mass of infill walls in the preliminary dynamic characterisation tests and were successively removed upon the installation of infill walls.

2.3 Experimental test scheme

A snap-back test was performed to capture the frame's modal properties for both the bare and infilled configurations. The initial displacement imposed on the frame also allowed the definition of the test frame's lateral stiffness. Both stiffness and modal properties were used for the numerical models' calibration.

After the modal characterisation test, pseudo-dynamic (PsD) displacements' control tests were performed to investigate the infilled frame's behaviour subjected to an earthquake sequence. Three ground motions, recorded during the 2016 Central Italy earthquakes, were selected to define the earthquake sequence used in the PsD tests. The time-history of accelerations of the earthquake sequence is shown in Figure 4. Two scaling factors (SF) of the earthquake sequence, $SF = 1.0$ and 3.0 , were used during the PsD tests. The scaling factors were decided based on comparisons of the response spectra of selected ground motions with

the code-based elastic response spectrum, where the use of unit scaling factor was to investigate the behaviour of the test frame subjected to real earthquakes, while the scaling factor of 3.0 was adopted to ensure the failure of the test frame, *i.e.*, the collapse of infill walls and severe yielding of steel members.

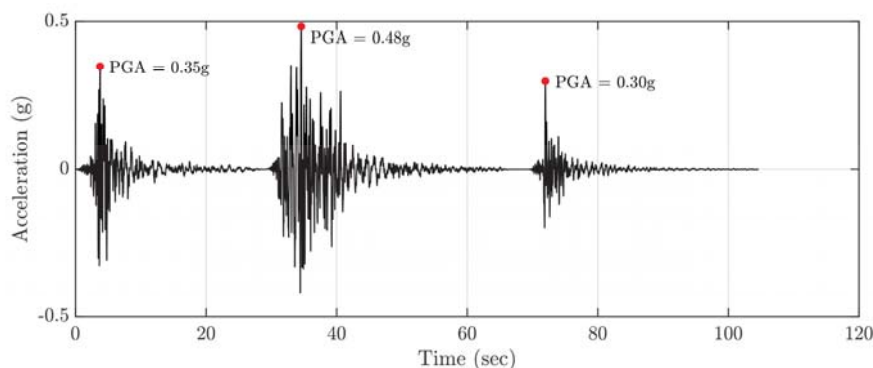


Figure 4: Accelerogram of the selected earthquake sequence.

2.4 Experimental results

The response of the infilled steel frame recorded during the entire PsD test, *i.e.*, top storey displacement against base shear, is shown in Figure 5(a). Aside from the response curve, envelopes are also presented individually for the positive and negative direction. Subsequently, the corresponding backbone curve could also be derived based on the envelopes, which was assumed to be symmetric in the positive and negative direction.

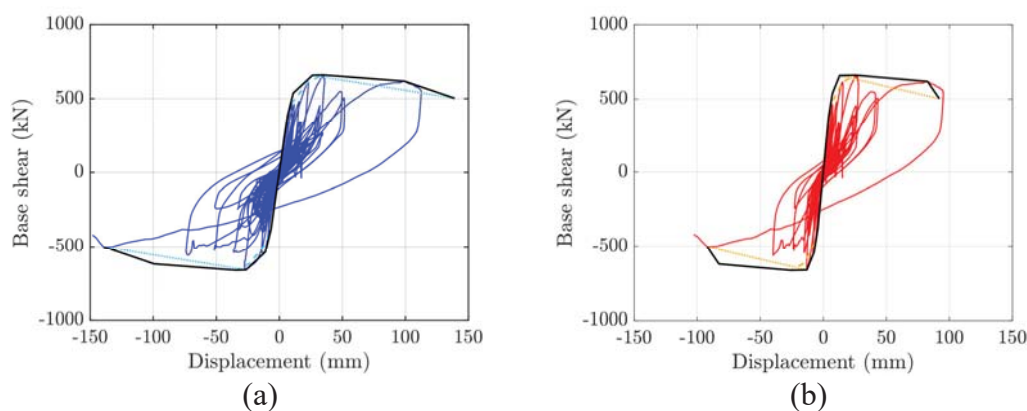


Figure 5: Response of the infilled steel frame with backbone curves: a) global response; b) first storey displacement against base shear.

As shown in Figure 5(a), the first significant change of the frame's lateral stiffness corresponds to a 10 mm top storey displacement. Then the steel frame reached the maximum base shear of around 650 kN when the lateral displacement at the top storey was approximately 25 mm. This also marked the onset of negative stiffness in the backbone curve of the steel frame. In addition, degradation of strength was also noticed at 100 mm of top floor displacement, where the capacity of base shear dropped by about 8% to 600 kN. Lastly, the largest top storey displacement experienced during the PsD test corresponds to 140 mm, when the collapse of infill occurred, and the test was terminated.

The pushover numerical analysis requires the knowledge of the forces and displacements' distribution at both storeys. To this end, the response history at the first storey was determined and is shown in Figure 5(b). This also included the envelopes for the definition of the corre-

sponding backbone curve. The comparison of the backbone curves for both storeys is shown in Figure 6, and six points were selected for the determination of displacement ratios of the top storey to the first storey, as also summarised in Table 1. It can be concluded that initially the displacement ratio was around 1.5, however, when the displacements were increased, the ratio was slightly reduced to 1.34 at point D and 1.20 at point E, which was attributed to the concentrated damage at the first storey. Consequently, it can be anticipated that soft storey mechanism might be triggered at some point beyond 140 mm top floor displacement.

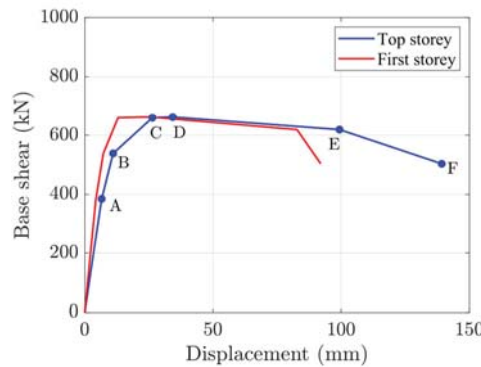


Figure 6: Comparison of backbone curves for the first and top storey of the steel frame (symmetric in the positive and negative directions). See Table 1 for more details.

	A	B	C	D	E	F
Top storey, d_2	6.61	11.09	26.39	35.31	99.37	139.25
First storey, d_1	4.36	7.27	13.01	25.60	82.78	92.06
d_2/d_1	1.52	1.53	2.03	1.34	1.20	1.51

Table 1: Distribution of displacement demands along with the height of the steel frame.

3 NUMERICAL STUDY

3.1 Finite element modelling of masonry infill and steel frame

Finite element models of the bare and infilled steel frame were built in Abaqus [22]. Only half of the 3D steel frame was modelled due to symmetry conditions and to reduce the computational cost. Meanwhile, all the internal secondary beams were excluded from the model as their contribution to the lateral resistance of the steel frame were considered negligible. All steel and masonry components were modelled using the solid element C3D8R. Figure 7 shows an overview of the Abaqus model.

The material properties were defined based on the results of material tests when possible. For parameters that could not be obtained from the tests conducted, typical values recommended in literature were adopted. The yield and ultimate strength of steel were defined to be 433 and 575 MPa, respectively, while the Young's modulus was assumed to be 210,000 MPa. On the other hand, as the masonry infill walls were modelled using macro-modelling approaches, the Young's modulus of masonry was manually adjusted to be about 3,000 MPa based on model calibration.

The concrete damaged plasticity model was used to simulate the inelastic behaviour of masonry. This model is characterised by five parameters: 1) dilation angle (ψ); 2) the flow potential eccentricity (ϵ); 3) the ratio between initial equibiaxial compressive yield stress to initial

uniaxial compressive yield stress (f_{b0}/f_{c0}); 4) the ratio between second stress invariant on the tensile meridian to that on the compressive meridian at initial yield (K), and 5) the viscosity parameter (μ). Values recommended by D’Altri *et al.* [19], reported in Table 2 were adopted in this study as typical assumptions for masonry infill. Besides, the compressive and tensile strength of masonry were defined to be 5.70 and 1.30 MPa, respectively. Furthermore, the composite slabs were modelled as rigid bodies to simulate the rigid diaphragm behaviour and ensure a smooth transfer of load to the steel frame. Lastly, a 75 mm-thick concrete block was included in the model as the base of ground floor masonry infill. Since no damage was observed on this concrete base during the experimental test, it was assumed to behave in the elastic range with a Young’s modulus of 35,000 MPa.

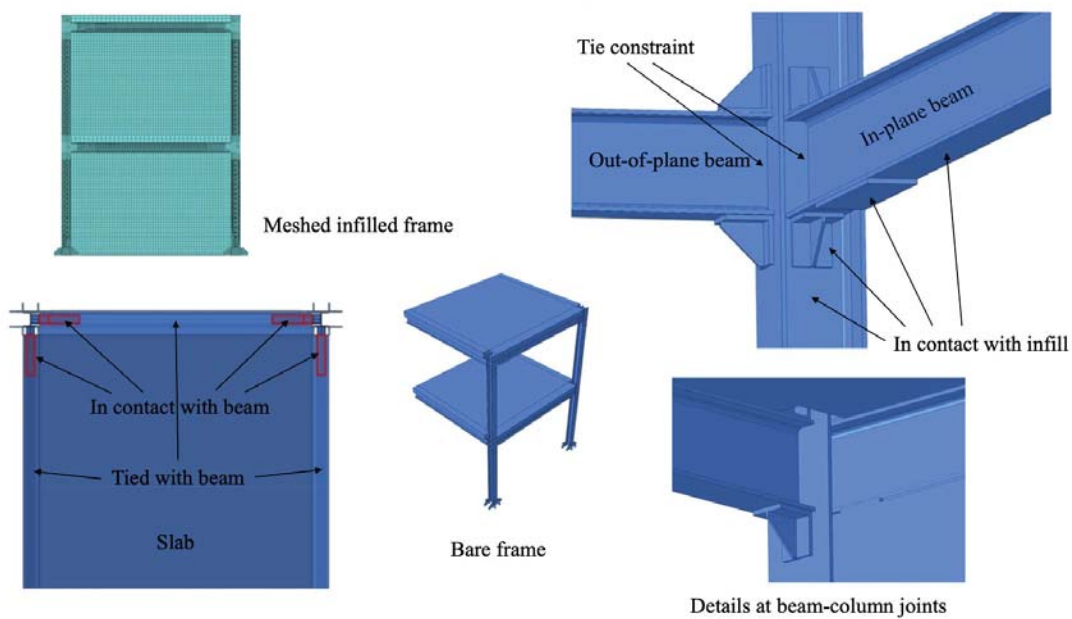


Figure 7: Numerical models of the steel frame in Abaqus using macro-model of masonry infill.

ψ	ε	f_{b0}/f_{c0}	K	μ
10°	0.1	1.16	0.667	0.0005

Table 2: Parameter to define the inelastic behaviour of masonry infill using concrete damaged plasticity model in Abaqus [21].

Beam-to-column joints, stiffeners, and cover plates of the beam-to-beam connections were modelled through tie constraint. Appropriate boundary conditions were applied at the end of the transverse beams to simulate the structure’s symmetric condition. Besides, in the region with shear connectors, a tie constraint was used to simulate the slab-beam interaction. Conversely, for the region without shear studs, a surface-to-surface contact interaction was defined between the slab and the beam with ‘Hard’ normal behaviour and a friction coefficient of 0.7 for the tangential behaviour. Lastly, a surface-to-surface contact (with the same properties as above) was also introduced to simulate the masonry infill and steel frame interaction.

3.2 Model validation

The numerical models’ validation was performed with respect to the stiffness and dynamic properties observed during the snap-back tests. During this test, lateral loads of 13 and 31 kN were imposed on the top storey of the bare and infilled frame, respectively. The comparisons of the numerical and experimental lateral displacement profiles are shown in Figure 8 and reported in Table 3.

As shown in Figure 8, both the bare and infilled frame models achieved a ‘good’ match of lateral displacements with the test mockup, and the discrepancies were all within 10%. In both cases, the comparison of the numerical and experimental results show a nearly identical initial lateral stiffness at the first storey. Conversely, the top storey’s lateral stiffness was slightly underestimated in the bare frame and slightly overestimated when the masonry infills were present.

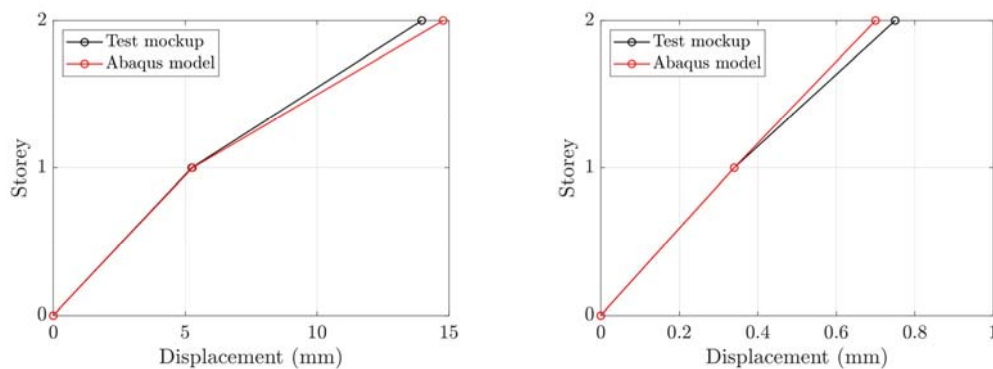


Figure 8: Comparisons of lateral displacement profile of the bare frame (left) and the infilled frame (right) during the modal characterisation test.

	Test		Abaqus			
	First floor	Top floor	First floor		Top floor	
Bare	5.25	13.97	5.28	+0.57%	14.78	+5.80%
Infilled	0.34	0.75	0.34	0.00%	0.70	-6.67%

Table 3: Comparisons of the lateral displacements of the steel frame obtained numerically and experimentally.

3.3 Pushover analysis

The results of the pushover analysis is presented hereafter. The numerical model was pushed up to 140 mm at the top storey, which was the maximum lateral displacement measured during the test. The pushover analysis was done assuming three displacement ratios of top storey to first storey (d_2/d_1). When the top storey displacement was less than 30 mm, the ratio d_2/d_1 was assumed to be 1.5. Then when the top storey displacement was between 30 and 100 mm, the ratio d_2/d_1 reduced linearly from 1.5 to 1.2. Eventually, when the top storey displacement was larger than 100, the ratio d_2/d_1 was equal to 1.2. Figure 9 presents the comparison between the pushover curve, *i.e.*, the top storey displacement-base shear relation, and the structural response of the steel frame measured during the experimental test, while Figure 10 shows the evolution of stress distribution in the infill walls during the pushover analysis.

It can be seen that in general the numerical model were in good agreement with the test results when the displacement was smaller than 30 mm. However, the numerical model failed to capture the deterioration of strength which took place beyond 30 mm top storey displacement.

This is because that firstly a bi-linear relation was assumed for the mechanical property of masonry, which did not account for the strength degradation. Besides, the simplified modelling approach adopted was unable to simulate the falling of crushed bricks at the top corners. Consequently, the base shear of the numerical model continued to increase beyond the actual point of the onset of strength and stiffness degradation.

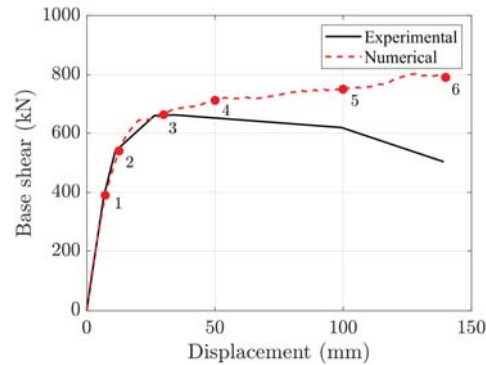


Figure 9: Pushover curve of infilled steel frame.

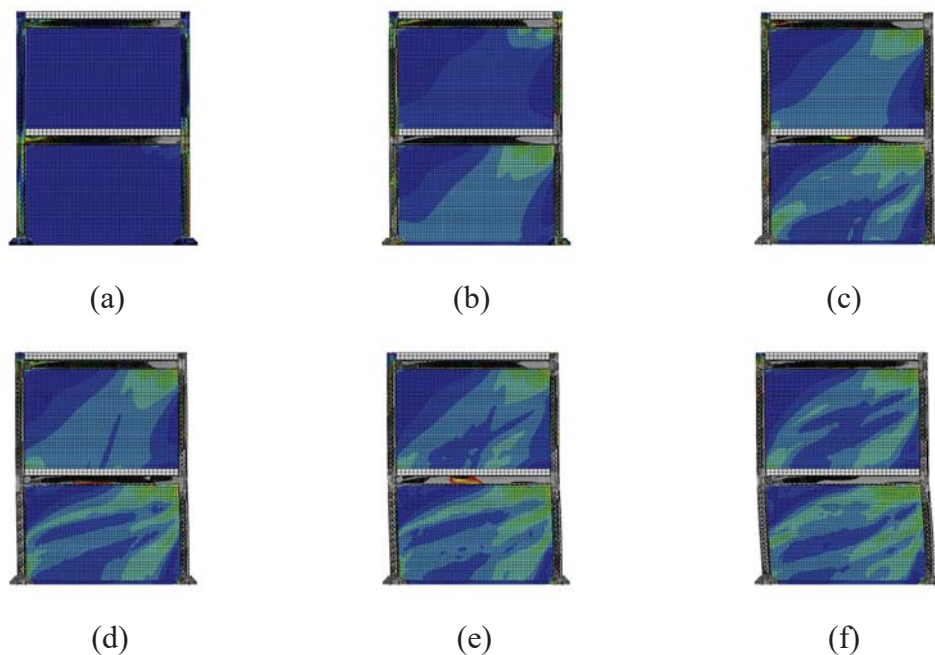


Figure 10: Stress contour of the masonry infill walls during the pushover analysis (See Figure 9): a) Point 1; b) Point 2; c) Point 3; d) Point 4; e) Point 5; f) Point 6.

As can be seen in Figure 10(a), initially when the model was within the elastic range, stress concentration was noticed at both storeys surrounding the beam splice connections before any struts were formed in the infill walls. This illustrated the occurrence of cracks at the top corners of each infill wall, which were due to the interlock between the bolts of beam splice connections and the top layer of bricks. When the displacement demand was increased, an inclined strut was formed within the lower storey infill wall, as can be seen in Figure 10(b). Successively, when the top floor displacement was approaching 30 mm (Point 3 in Figure 9), the previous strut was split into a diagonal strut and an off-diagonal strut, as shown in Figure 10(c), and the diagonal strut appeared to be wider than the off-diagonal strut. In the meantime, an inclined strut started to form in the top floor infill wall as well, which had a similar shape

to the one previously formed in the lower storey infill wall. When the displacements at both storeys of the infilled steel frame were further increased, as shown in Figure 10(d) to (f), the contact length between the infill and the surrounding steel members remained almost unchanged, and the diagonal strut in the lower storey infill wall was further split into two smaller struts. It is clear that the upper strut connected the top corner and the end of contact length over the other column, while the middle strut connected the bottom corner and the mid-point of the contact length over the other column. Figure 10(f) also shows the tendency that with increasing lateral displacement, the upper strut would become wider, and the middle and lower struts might eventually become one single strut that has approximately the same width as the upper strut. It was also noticed that despite the infill wall on the top floor exhibited the same behaviour as that on the lower floor, the two infill walls contained different numbers and geometries of struts at the same step of pushover, which indicated that it might not be appropriate to use the same simplified strut model to represent the infill walls on different floors.

4 CONCLUSIONS

This paper presented numerical modelling of infilled steel frame using a macro-model of masonry infill. It was concluded that the steel joints that were in contact with masonry infill caused local stress concentration in the part of infill wall adjacent to the joints. Besides, a single inclined strut was noticed at small displacement, when the overall structural was within the elastic range. Subsequently, when the displacements at both storeys became larger, the single strut was firstly split into two struts and eventually became three struts. The width of struts was also found to be changing during the pushover analysis. Moreover, the contact length over beams and columns were also observed, which initially increased with increasing displacement and then remained approximately constant. Lastly, it was also concluded that the masonry infill on different floors could form different numbers of struts with varying geometries, which should be taken into consideration when developing simplified strut models.

Future studies should be conducted using a more detailed micro-model of masonry infill to investigate the development of cracks in the infill walls and achieve more accurate observation of infill-frame interactions.

REFERENCES

- [1] British Standards Institution, BS EN 1998-3:2005, Eurocode 8. *Design of structures for earthquake resistance - Part 3: Assessment and retrofitting of buildings*. London, 2005.
- [2] J.L. Dawe, C.K. Seah, Behaviour of masonry infilled steel frames. *Canadian Journal of Civil Engineering*, **16**(6), 865-876, 1989.
- [3] M.N. Fardis, T.B. Panagiotakos, Seismic design and response of bare and masonry-infilled reinforced concrete buildings part II: infilled structures. *Journal of Earthquake Engineering*, **1**(03), 475-503, 1997.
- [4] M. Dolšek, P. Fajfar, The effect of masonry infills on the seismic response of a four-storey reinforced concrete frame - a deterministic assessment. *Engineering Structures*, **30**(7), 1991-2001, 2008.
- [5] L. Liberatore, L.D. Decanini, Effect of infills on the seismic response of high-rise RC buildings designed as bare according to Eurocode 8. *Ingegneria Sismica*, **3**, 7-23, 2011.

- [6] D. Markulak, I. Radić, V. Sigmund, Cyclic testing of single bay steel frames with various types of masonry infill. *Engineering Structures*, **51**, 267-277, 2013.
- [7] L. Di Sarno, J.-R. Wu, M. D’Aniello, S. Costanzo, R. Landolfo, O.-S. Kwon, F. Freddi, Assessment of existing steel frames with infills under multiple earthquakes. M. Papadrakakis, M. Fragiadakis eds. *7th ECCOMAS Thematic Conference on Computational Methods in Structural Dynamics and Earthquake Engineering (COMPDYN 2019)*, Crete, Greece, June 24-26, 2019.
- [8] L. Di Sarno, J.-R. Wu, Seismic assessment of existing steel frames with masonry infills. *Journal of Constructional Steel Research*, **169**, 106040, 2020.
- [9] M. Dolšek, P. Fajfar, Soft storey effects in uniformly infilled reinforced concrete frames. *Journal of Earthquake Engineering*, **5**(01), 1-2, 2001.
- [10] G.M. Verderame, F. De Luca, P. Ricci, G. Manfredi, Preliminary analysis of a soft-storey mechanism after the 2009 L’ Aquila earthquake. *Earthquake Engineering and Structural Dynamics*, **40**(8), 925-944, 2011.
- [11] H. Zuo, W. Zhang, B. Wang, X. Gu, Seismic behaviour of masonry infilled hinged steel frames with openings: experimental and numerical studies. *Bulletin of Earthquake Engineering*, **19**(3), 1311-1335, 2021.
- [12] M.M. Ghazimahalleh, Stiffness and damping of infilled steel frames. *Proceedings of the Institution of Civil Engineers-Structures and Buildings*, **160**(2), 105-118, 2007.
- [13] K.F. Najarkolaie, M. Mohammadi, N. Fanaie, Realistic behavior of infilled steel frames in seismic events: experimental and analytical study. *Bulletin of Earthquake Engineering*, **15**(12), 5365-5392, 2017.
- [14] W.W. El-Dakhkhni, M. Elgaaly, A.A. Hamid, Three-strut model for concrete masonry-infilled steel frames. *Journal of Structural Engineering*, **129**(2), 177-185, 2003.
- [15] M. Yekrangnia, M. Mohammadi, A new strut model for solid masonry infills in steel frames. *Engineering Structures*, **135**, 222-235, 2017.
- [16] L.F. Gutiérrez-Urzúa, F. Freddi, L. Di Sarno, Comparative Analysis of Code Based Approaches for the Seismic Assessment of Existing Steel Moment Resisting Frames. *Journal of Constructional Steel Research*, **181**, 106589, 2021.
- [17] P.B. Lourenço, J.G. Rots, Multisurface interface model for analysis of masonry structures. *Journal of engineering mechanics*, **123**(7), 660-668, 1997.
- [18] K.F. Abdulla, L.S. Cunningham, M. Gillie, Simulating masonry wall behaviour using a simplified micro-model approach. *Engineering Structures*, **151**, 349-365, 2017.
- [19] A.M. D’Altri, S. de Miranda, G. Castellazzi, V. Sarhosis, A 3D detailed micro-model for the in-plane and out-of-plane numerical analysis of masonry panels. *Computers and Structures*, **206**, 18-30, 2018.
- [20] P.B. Lourenço, J.G. Rots, J. Blaauwendraad, Continuum model for masonry: parameter estimation and validation. *Journal of Structural Engineering*, **124**(6), 642-652, 1998.
- [21] J. Yacila, G. Camata, J. Salsavilca, N. Tarque, Pushover analysis of confined masonry walls using a 3D macro-modelling approach. *Engineering Structures*, **201**, 109731, 2019.

- [22] Dassault Systèmes, ABAQUS/Standard User's Guide, Version 6.14. Dassault Systèmes Simulia Corp., Providence, RI, USA.

HYBRID COLD-FORMED/TUBULAR MODULAR STRUCTURAL SYSTEM WITH INNOVATIVE JOINTS

**Luís Carlos Silva^a, Hélder David Craveiro^a, Trayana Tankova^{a*}, Rui Simões^a, Ricardo
Costa^a, Mario D’Aniello^b, Raffaele Landolfo^b, Luís Simões da Silva^a**

¹ University of Coimbra, ISISE, Department of Civil Engineering
Polo II, Rua Luís Reis Santos, 3030-788 Coimbra, Portugal
e-mail: {luis.c.silva, heldercraveiro.eng, ttankova }@uc.pt {rads, rjcosta, luisss }@dec.uc.pt

² Department of Civil Engineering, University Federico II
Naples, Italy
{ mdaniel, landolfo }@unina.it

Abstract

In recent years, modular construction has been used in low-to medium rise multi-story and even high-rise buildings. Pre-fabrication by off-site manufacture leads to faster and safer construction, improved quality, reduced resources and waste.

The research activity summarized in this paper is carried out within the European project INNO3DJOINTS and it aims at developing innovative plug-and-play joints which enable modularity, faster construction and deconstruction. The developed modular construction system is hybrid, whereby tubular columns are combined with cold-formed lightweight steel profiles using plug-and-play connections to provide an efficient structural system.

The influence of the type of floor system, the horizontal and vertical load-bearing systems and the type of truss on the structural performance are investigated. The results obtained from numerical analyses allowed optimizing the geometry of the examined hybrid modular system. To highlight its effectiveness and versatility, a case study building was used to compare the proposed hybrid system with other conventional structural solutions.

Keywords: Plug-and-play joints, Steel Construction, Cold-formed steel, Hybrid system, Modular construction, Eurocode 3.

1 INTRODUCTION

Sustainability is a key driver in the construction sector requiring innovative solutions to face the existing challenges in terms of consumption of natural resources (responsible for the consumption of 40% of the global materials) and construction waste management and treatment. Prefabricated modular construction system can greatly contribute to minimizing waste, improving the overall quality, with shorter construction times, lower resources, and on-site labour costs [1], promoting the development of structural solutions that are suitable for deconstruction and possible reuse of the entire structure or part of the structure in multiple life cycles.

The level of prefabrication may refer to components, subframes or even the whole building [2], [3]. Recently prefabricated modular solutions have been presented for high-rise and multi-storey buildings [4], but its applicability is still limited [5]. It is recognized that one of the biggest challenges is related to inter and intra module connections, ensuring that adequate performance requirements are attained [6]. The competitiveness of these innovative modular systems relies on several parameters, such as span, span, floor height and type, number of floors, resistance to lateral loads and connections, which are a critical part of the overall structural stability and robustness of the building.

Light gauge cold-formed steel (CFS) structural solutions, due to its versatility, are very efficient systems that lead to relevant weight savings of up to 35% when compared to an equivalent hot-rolled solution [7]. Light Steel Framing (LSF) systems comprising CFS members are panelised construction systems using close spaced studs and different types of sheathing (OSB, gypsum, lightweight concrete panels) providing adequate in-plate stiffness. Typically, standard CFS construction is very efficient for low-rise buildings and spans in the 4 m range. Several panelised modular systems using CFS are available, which are delivered on-site and easily erected. At the European level, several research projects were devoted to this topic. In the scope of the research project, DRYCONDIS the capabilities of light-weight steel dry construction system [8] was assessed. Others were devoted to the study of light-weight steel systems for prefabricated steel buildings and their integration with the steel skeletal system (e.g. ETHICS; InFaSo; FrameUp; PRECASTEEL, [9]-[12]). However, few have considered the erection stage and ease of assembly and disassembly as critical parameters in the development and optimization of the system.

The extension of the light-weight steel solutions to medium rise construction brings new challenges due to the higher demands in terms of lateral load strength and stiffness. For CFS multistorey buildings, reinforced concrete cores may also be considered as a lateral force resisting system, ensuring that the CFS modular part only carries gravity loading [3]. Other solutions have been developed and investigated. Hong et al. [13] developed a modular building solution using double skin steel panels as the lateral force-resisting system and concluded that the steel panel system greatly increases the initial lateral stiffness of the system. More recently, the performance of light steel framing wall panels with Oriented Strand-Boards (OSB) [14] was assessed through experimental tests. It was observed that OSB can be considered as an effective sheathing solution to enhance the lateral stability of CFS structures. Lightweight steel frames with OSB panels are also effective systems to resist seismic actions by means of energy dissipation in the OSB sheathing-to-frame connections as shown by experimental tests formerly carried out at the University of Naples Federico II [15], [16].

New buildings using CFS construction often require larger free spans and the possibility of large openings (of the order of the span length) within the alignments of the load bearing panelised walls. In these cases, tightly spaced CFS trusses [16]. The use of CFS trusses is attractive but their generalized application in the same structure may lead to a reduction of the lateral

stiffness of the structure. This can be a critical issue if no auxiliary lateral load resisting systems are not used.

In the scope of the European research project INNO3DJOINTS [18], a new hybrid, prefabricated structural system was developed, aiming to address existing challenges related to modular construction. The modular hybrid system consists of cold-formed steel trusses combined with tubular columns using innovative plug-and-play joints. The investigation reported in this paper aims to characterize the innovative hybrid system, assessing the use of such system in multi-storey buildings. The innovative hybrid structural system was developed to address the following objectives:

- To allow the specification of architectural plans with 4 m to 6 m free spans and similar sized openings in the load-bearing wall alignments.
- To provide adequate lateral stiffness through a combination of cold-formed trusses and tubular sections for the column positions at the intersection of the main grid axes and load-bearing light steel framing walls with diagonal steel straps as cross-bracings. Tubular sections have some advantages over “I” or “H” sections, such as higher torsional rigidity, possible replication of the configuration of the joints in both plan directions, availability in high-strength steel and better aesthetic quality [18];
- Developing innovative hybrid plug-and-play joints between the truss and the tubular column, easy to assemble and disassemble using simple tools and erection equipment.

2 THE INNO3DJOINTS HYBRID MODULAR CONSTRUCTION SYSTEM

The main components of the developed structural system (Figure 1) are:

- Tubular columns: cold-formed circular, rectangular, or square hollow profiles, as the main vertical structural elements.
- Truss-girders: span up to 6 m, light-gauge CFS profiles, as the main horizontal structural elements. For spans without openings, the LSF walls are stiffened by OSB panels.
- Plug-and-play joints: devices connecting the columns and the truss-girders that guarantee a fast and safe on-site execution.
- CLT slab: the floor is constructed using CLT panels, providing the necessary gravity load-bearing capacity and in plane diaphragm effect.

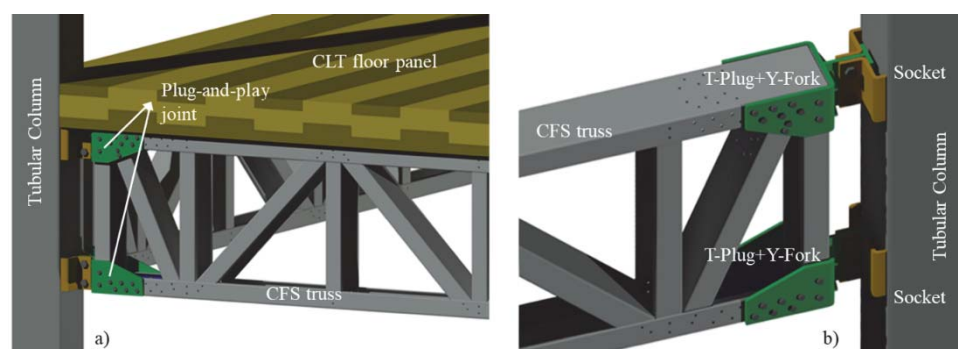


Figure 1: INNO3DJOINTS system a) Global view with the prescribed floor system. b) Detailed view of the plug-and-play joint.

The plug-and-play joint is composed by parts that connect the columns and the truss-girders: a socket, which is welded to the column, and a T-plug with a Y-fork (plug), where the T-plug

is bolted to the socket and Y-fork is connected to the truss by a bolted simple lap joint. The socket comprises a set of two cold bent plates welded to the tubular column with a spacing equal to the thickness of the T-plug plus the necessary tolerances. The spacing between the two pieces allows the positioning of the T-plug. Stiffeners can be added to the socket and/or to the Y-fork depending on the performance requirements. During fabrication of the structure in a steel workshop, the T-plug with Y-fork are assembled to the truss girder and the socket is welded to column.

3 INFLUENCE OF THE GEOMETRICAL AND MECHANICAL FEATURES ON THE DESIGN OF THE BASIC MODULE OF THE INNO3DJOINTS SYSTEM

The development of the structural system comprised the analysis of several aspects, such as: the configuration of the trusses; the floor system; and the layout of the lateral force resisting system.

3.1 Description of the numerical model and design verifications

The assessment of the structural behaviour was based on numerical linear elastic analyses developed using SAP2000 [19]. Beam elements were used for the modelling of the 2D and 3D structures. The 2D frame models were implemented according to the scheme illustrated in Figure 2. The chords were modelled with releases at their extremities, to impose pinned members (in plane rotations are free).

The joints between the trusses and the columns are modelled using a rigid link that prevents relative translations between the column and the truss-girder. Pinned boundary conditions were considered at the column bases.

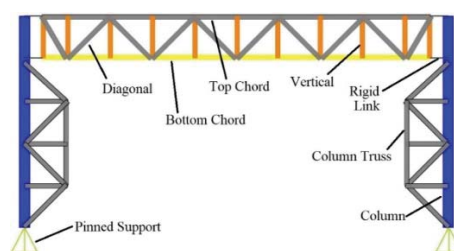


Figure 2: Schematic representation of the 2D FEM models

The 3D FEM models were implemented using the same modelling assumptions. The floor system and the sheathing panels were modelled using orthotropic shell elements. The connection between the sheathing panels and the framing was modelled using linear links.

3.2 The influence of the type of truss girder

Different types of truss-girder arrangements were tested: the cross-diagonal truss with flat plates as diagonals and the Howe, Pratt Warren trusses, with C profiles as diagonals, all shown in Figure 3.

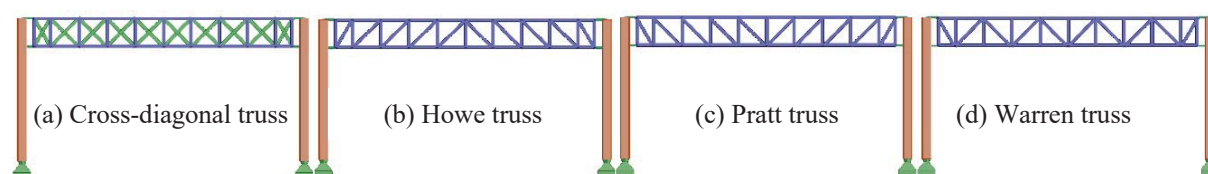


Figure 3: Selected types of truss girder.

The truss elements were designed according to EN 1993-1 parts 1 and 3, satisfying strength and serviceability limits and corresponding to similar utilization ratios and the solutions were compared based on their performance and weight.

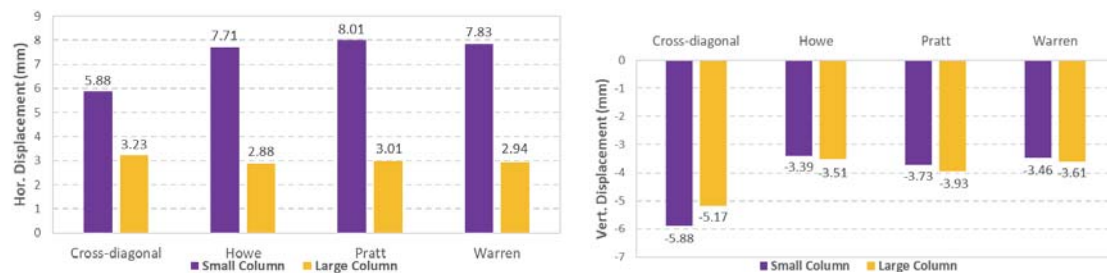


Figure 4: Horizontal and vertical displacements for the selected truss configurations

The displacements at the middle of the top chord were used to compare the deformability of the frames (Figure 4), confirming that smaller vertical displacements occurred for the Howe truss and Warren truss types, followed by the Pratt truss, while the cross-diagonal truss deforms the most.

The weight comparison of the tested typologies showed that the cross-diagonal truss is slightly lighter, yet it is characterized by the greater deformability.

3.3 The influence of the floor system

A regular building with three spans and 3 floors was used to analyse the type of floor system to be employed with the proposed structural system. This was exploited on the basis of three examples – MRF (moment resisting frame) or conventional hot-rolled solution, HF (hybrid frame) or the proposed solution using tubular column and CFS truss and HF+CT (Hybrid frame + column truss). The structural systems were considered together with three types of floor structure:

cold-formed steel joist with OSB sheathing; composite reinforced concrete-steel deck slab; cross laminated timber slab (CLT).

The structures were subjected to the same actions (varying only their self-weight) and the utilization ratios were used as comparison parameters. The steel and total weights of the structures are shown in Figure 5. Based on the results obtained, the CLT solution was considered the best since it is light solution, which can be easily erected on site and it can provide sufficient diaphragm effect [27, 28].

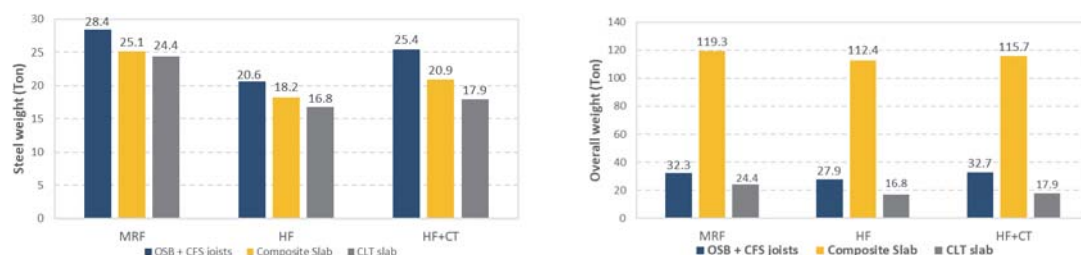


Figure 5: Weight comparison (tonnes)

3.4 The influence of lateral force resisting system

Within the development of the structural system, it was important to define the lateral force resisting system. In this case it was sought to understand if the solution using column truss (CT) can be viable and on a second step the use of structural walls with OSB panels was addressed.

For these analyses: the steel classes for hot-rolled and for CFS are S355 and S350GD, respectively; the height of the storey is 3 m; the new plug-and-play joints are simulated by Rigid Links; and the supports of the columns are assumed as pinned. Only the horizontal displacement, lateral stiffness and weight were considered for the assessment of the performance of the systems.

Regarding the solution using CT four options were considered: (i) no column truss (no CT); (ii) no interaction between the column truss and the truss-girder (CT 1); (iii) full-interaction (CT 2); and (iv) full-interaction with battened profiles (CT 3), (Figure 6). The analysis was based on these four main reference frames with column cross-section SHS150x6.3. These solutions were compared to the configuration no CT but changing the column dimension in order to find the same stiffness as if one of the column truss configurations were used..

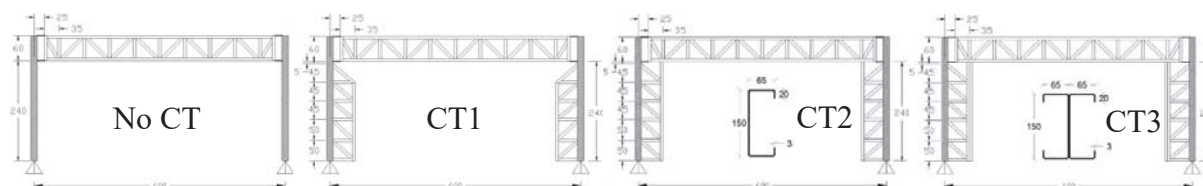


Figure 6: Summary of the reference frame layouts (dimensions in centimetres).

The analyses were conducted for frames with 4, 5 and 6-meter spans, where the span length was not found as influencing parameters. A summary of the results for the 6 m frames is shown in Figure 7.

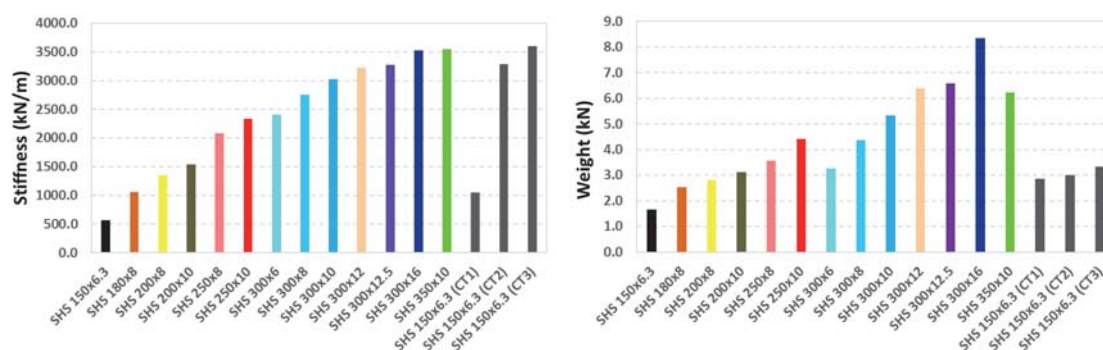


Figure 7: Lateral stiffness and weight for the frames 6m

The results showed that the SHS180x8 section matches the lateral stiffness given by the utilization of SHS150x6.3 with the CT1, the sections SHS300x12 and SHS300x12.5 reach similar lateral stiffness values as the SHS150x6.3 with the CT2 and the SHS300x16 and SHS350x10 sections are comparable to the SHS150x6.3 with the CT3 solution. Even though the CT2 and CT3 configuration result in much higher stiffness, they were not considered practical from construction point of view, hence these configurations were disregarded.

A possibility of using LSF wall with OSB panel was also exploited. In this assessment, the solution CT1 was compared with the configuration without CT and also with the solution using OSB panel.

The span length varied between 4, 5 and 6 m and single, double, and triple-span frames were considered (Figure 8)

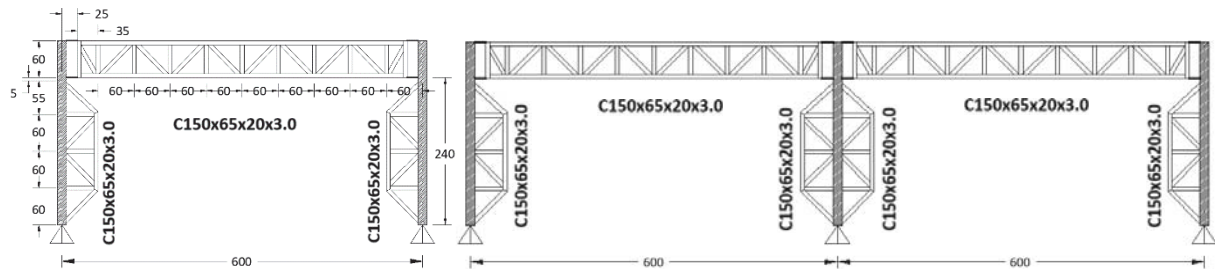


Figure 8: Reference cases – 6-meter span

Figure 9 summarizes the obtained weight and stiffness for each of the studied cases. As expected, the adoption of the wall with OSB panel led to significant increase in the lateral stiffness. In addition, the consideration of CT1 type was not considered economical since it does not bring significant increase in lateral stiffness and it is harder to produce.

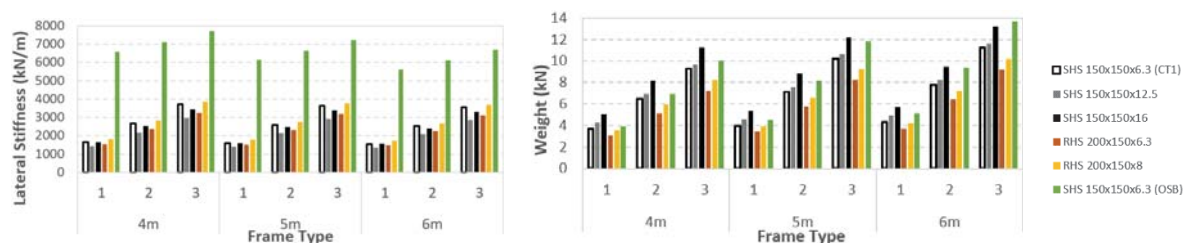


Figure 9: Lateral Stiffness and weight (2nd Set)

4 CASE STUDY

After defining the main structural components, a real building was used to analyse the performance of the system. For the assessment, three structural configurations were used: SC 1 – tubular columns with cold-formed truss beams; SC 2 – tubular columns with envelope walls with OSB panels; and MRF (moment resisting frame) – hot rolled structure using IPE and HE profiles.

The building was adapted from a real residential case built in Angola, but it was designed as if it was located in Coimbra (Portugal). The structure is 3-meter four-storey building with an area of 456 m². The structure is shown in Figure 10.

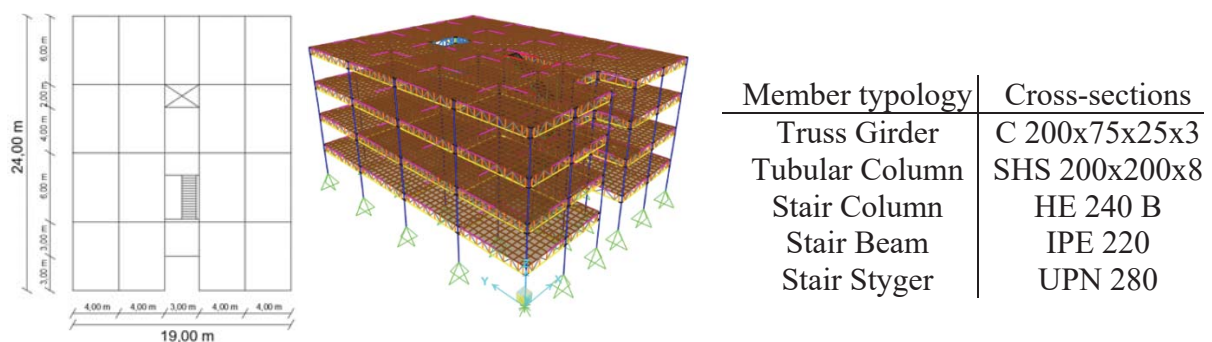


Figure 10: Plan, 3D view and cross-sections for SC1 and SC2

The building was designed in accordance with the Structural Eurocodes [22-25]; its fire performance was verified using a prescriptive approach EC3-1-2 [26]; and its seismic performance was considered for low seismicity conditions according EC8-1 [21]. For fire safety, gypsum boards 12.5 mm thick were chosen, providing fire resistance periods longer than 60 minutes. In

this case, the critical temperature is 662.5°C, reached after 69.08 minutes. For the floor system, CLT, the fire resistance is provided by the manufacturer, and an appropriate fire-resistant solution was chosen for the loads [23] and spans considered (max. 6 m), resulting a 160mm-thick panel. A fire resistance of at least EI 60 minutes is achieved.

A seismic action is considered [21], assuming a low seismicity zone and a $q > 1.5$, for low ductility structures. The reference PGA for this site is $a_g = 0.12g$, and a type C ground and Type I spectrum were adopted.

The performance of the three structural solutions was evaluated on the basis of their stiffness and weight. Table 3 summarizes the result obtained.

The MRF was used as a reference solution, where it is concluded that SC1 is lighter (78% of the MRF) while SC2 resulted in a similar weight of steel (96%). When the lateral stiffness of the three configurations for the x and y directions is compared, SC1 is 1.5 / 1.62 times stiffer and SC2 is 2.78 / 2.18 stiffer.

Structural System	Weight		Stiffness y-y					Stiffness x-x				
	Steel	Total	$k_{y,1}$	$k_{y,2}$	$k_{y,3}$	$k_{y,4}$	K_y	$k_{x,1}$	$k_{x,2}$	$k_{x,3}$	$k_{x,4}$	K_x
MRF	92.93	356.3	58	37	33	26	13	73	50	44	35	17
SC 1	62.42	167.9	46	120	126	122	26	45	117	128	121	27
SC 2	75.26	193.9	143	221	218	202	62	98	212	219	196	51

Table 1: Weight and lateral stiffness (kN/mm).

5 CONCLUSIONS

A new hybrid modular structural system comprising lightweight cold-formed steel trusses and tubular columns connected using innovative plug-and-play joints was presented. To assess the global structural performance of the innovative structural building, a parametric study was undertaken, examining the following parameters: the type of truss, different spans, the lateral force-resisting system and the type of floor system.

The truss-girders with better performance in terms of deformability, when subjected to horizontal and vertical loading, are the Howe truss and Warren truss.

From the conducted analysis the solutions incorporating the column truss connected to the tubular column and truss-girder (CT2 and CT3), were discarded due to assembly difficulties and possible localized problems. Meanwhile, the adoption of OSB panels significantly increases the stiffness of the frames

Considering the selected case study, it was found that the highest lateral stiffness was attained for the solution with the envelope walls and OSB sheathing (SC2 solution). Also, the innovative structural systems (SC1 and SC2) provide the lightest solutions in terms of steel consumption.

6 ACKNOWLEDGEMENT

The research leading to these results has received funding from:

- This work was partly financed by FCT / MCTES through national funds (PIDDAC) under the R&D Unit Institute for Sustainability and Innovation in Structural Engineering (ISISE), under reference UIDB / 04029/2020;
- the Research Fund for Coal and Steel under grant agreement No. 749959 (INNO3DJOINTS)

- and the Portuguese Ministry of Science, Technology and Higher Education (Ministério da Ciência, Tecnologia e Ensino Superior) under the project contract Grant INNO3DJOINTS (031834).

REFERENCES

- [1] Lawson R.M. and Ogden R.G. (2006). Hybrid Systems in Light Steel and Modular Construction,”7, 252–256.
- [2] Boafó F. E., Kim, J.H. and Kim J.T. (2016), Performance of modular prefabricated architecture: Case study-based review and future pathways,” *Sustain.*, 8, 1–16.
- [3] Lawson R.M., “Light Steel Modular Construction.” [Online]. Available: <https://www.steel-sci.com/assets/downloads/LSF/ED014 Download.pdf>.
- [4] Zhai Y., Chen K., Zhou J.X., Cao, Lyu Zhongyuan L., Jin X., Shen G.Q.P., Lu W., Huang G.Q. (2019). An internet of Things-enabled BIM platform for modular integrated construction: A case study in Hong Kong. In: *Advanced Engineering Informatics*, 42, 100997
- [5] Zhai Y.; Chen K.; Zhou J.X.; Cao L.; Zhongyuan L.; Jin X.; Shen G.Q.P.; Lu W.; Huang G.Q. (2019) An internet of Things-enabled BIM platform for modular integrated construction: A case study in Hong Kong. *Advanced Engineering Informatics*, 42, 100997
- [6] Perampalam Gatheeshgar, Keerthan Poologanathan, Shanmuganathan Gunalan, Islam Shyha, Paul Sherlock, Heshachanaa Rajanayagam, Brabha Nagaratnam (2021). Development of affordable steel-framed modular buildings for emergency situations (Covid-19), *Structures*, Volume 31, pages 862-875.
- [7] Santos, P., Simões da Silva, L., Ungureanu, (2012). Energy efficiency of light weight steel framed buildings, P129, ECCS, Brussels.
- [8] J. Kesti, et al. Dissemination of knowledge in the use of steel-intensive dry construction systems in housing, Final Report, Research Fund for Coal and Steel, European Commission, 2008
- [9] Optimization of frames for effective assembling, FRAMEUP, RFSR-CT-2011-00035, final report
- [10] New market chances for steel structures by innovative fastening solutions, INFASO, RFSR-CT-2007-00051, final report
- [11] Energy and thermal improvements for construction in steel, ETHICS, RFSR-CT-2008-00038, final report
- [12] Prefabricated steel structures for low-rise buildings in seismic areas, PRECASTEEL, RFSR-CT-2007-00038, final report
- [13] Hong, S., Cho, B., Chung, K., Moon, J., Behavior of framed modular building system with double skin steel panels, *Journal of Constructional Steel Research*, 67, 936-946, 2011.
- [14] Henriques, J., Rosa, N., Gervásio, H., Santos, P, Simões da Silva, L., (2017) Structural performance of light steel framing panels using screw connections subjected to lateral loading, *Thin-Walled Structures*, 121, 67-88
- [15] Landolfo R. (2019) Lightweight steel framed systems in seismic areas: Current achievements and future challenges. *Thin-Walled Structures* 140: 114-131
- [16] Landolfo R., Fiorino L., Della Corte G. (2006) Seismic behavior of sheathed cold-formed structures: Physical tests *Journal of Structural Engineering* 132(4): 570-581
- [17] J. B. Scalzi, “Light-gage cold-formed structures,” *IABSE Congr. Rep.*, 8, 1968.

- [18] Innovative 3D joints for economic and robust hybrid tubular construction, INNO3DJOINTS, Research Fund for Coal and Steel, 749959
- [19] Simões R., Jordão S., Diogo J., and Fernandes J., Development and design of a concealed splice joint configuration between tubular sections, *Eng. Struct.*, 137, 181–193.
- [20] Computers and Structures, SAP2000, v.20.1.0, Integrated Software for structural analysis and design, <https://www.csiportugal.com/software/2/sap2000>
- [21] Autodesk, Robot Structural Analysis Professional, <https://www.autodesk.com/products/robot-structural-analysis/>
- [22] CEN (2004), EN 1998-1, Eurocode 8: Design of structures for earthquake resistance – Part 1: General rules, seismic action and design of buildings. CEN, Brussels.
- [23] CEN (2005), EN 1990, Eurocode 0: Basis of structural design. CEN, Brussels.
- [24] CEN (2002), EN 1991-1-1, Eurocode 1: Actions on structures – Part 1-1: General actions – Densities, self-weight, imposed loads for buildings. CEN, Brussels.
- [25] CEN (2005), EN 1993-1-1, Eurocode 3: Design of steel structures – Part 1-1: General rules and rules for buildings. CEN, Brussels.
- [26] CEN (2006), EN 1993-1-3, Eurocode 3: Design of steel structures – Part 1-3: General rules – Supplementary rules for cold-formed members and sheeting. CEN, Brussels.
- [27] CEN (2005), EN 1993-1-2, Eurocode 3: Design of steel structures – Part 1-2: General rules – Structural fire design. CEN, Brussels.
- [28] WoodWorks, An Approach to CLT Diaphragm Modelling for Seismic Design Application to a US High-Rise Project, <https://www.woodworks.org/wp-content/uploads/Approach-to-CLT-Diaphragm-Modeling-for-Seismic-WoodWorks-Jan-2017.pdf>, Accessed: 06/07/2020.
- [29] Sullivan K., Miller T.H., Gupta R., (2018). Behaviour of cross-laminated timber diaphragm connections with self-tapping screws. In: *Engineering Structures*, 168, 505-524
- [30] The Regional Price List for Public Works year 2018 of the region of Campania <http://regione.campania.it>

SEISMIC ASSESSMENT OF BEAM-TO-COLUMN JOINTS FOR A NON-CONFORMING MRF EXISTING STRUCTURE

R. Tartaglia¹, M. D’Aniello², A. Milone³, R. Landolfo⁴

¹Department of Structures for Engineering and Architecture, University of Naples “Federico II”, Via Forno Vecchio 36, 80134 Naples, Italy; roberto.tartaglia@unina.it

²Department of Structures for Engineering and Architecture, University of Naples “Federico II”, Via Forno Vecchio 36, 80134 Naples, Italy; mdaniel@unina.it

³Department of Structures for Engineering and Architecture, University of Naples “Federico II”, Via Forno Vecchio 36, 80134 Naples, Italy; aldo.milone@unina.it

⁴Department of Structures for Engineering and Architecture, University of Naples “Federico II”, Via Forno Vecchio 36, 80134 Naples, Italy; landolfo@unina.it

Abstract

As widely investigated in literature, the local behavior of the joints strongly influences the whole performance of the steel structures; thus, both in the design and assessment of the moment resisting frame (MRF) the joint performance should be properly accounted for. The present work is focused on local assessment and retrofit the beam-to-column joints of an existing non-conforming steel building. Therefore, the monotonic and cyclic behaviors of internal beam-to-column joints are investigated by means of finite element analyses (FEAs). The main peculiarities of these joints are the continuity of beams and hollow square columns interrupted at each level and connected both by bolts and fillet welds to the tapered flanges of the beams. On-site surveys allowed fully characterizing the geometry of the joints. The joint assemblies were sub-structured from the moment resisting frames and analyzed against both the vertical loads and seismic actions. The results showed that these types of joints exhibit very poor seismic behavior, concentrating most of the damage within the welds. Therefore, different local strengthening interventions were designed and numerically checked. The comparison between the response of the unreinforced and the various strengthening joints is described, and the best solutions in terms of both cyclic behavior and technological feasibility are subsequently identified.

Keywords: Existing structures, Beam-to-column joints, Seismic retrofit, ductile behavior, finite element model.

1 INTRODUCTION

Nowadays many studies investigated the behavior of the steel structures in seismic areas [1-12], with the aim to obtain ductile structures that could resist to the earthquake action without showing any brittle behavior; however, in many cases, these studies and innovative solutions could be applied not only to the new structures but could represent a viable solution also for the existing structures.

The existing steel buildings are characterized by a great variability in terms of structural conception, typology and distribution of resisting systems, and details adopted for the connections. Moreover, old steel buildings were often designed without considering any seismic action or, even when some lateral loads were considered, no hierarchy criteria between structural members were adopted. Thus, in the assessment of the existing steel building particular attention should be given to the joint's details; indeed, as deeply investigated in literature for the new structures [13-22], also in the analyses of the existing buildings the joint could influence the global structural behavior.

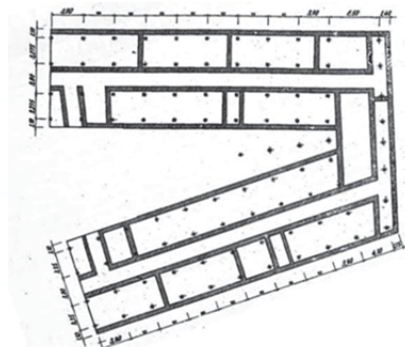
In this framework, an existing steel multi-storey building located in Naples has been selected as a case study due to its structural peculiarities. The design was carried out in accordance to the Italian provisions that were in force during the 1960 as reported in [23]; therefore, only gravity and wind loads were considered at that time. The P-Delta effects were also completely neglected despite of the height of the building (22.5 m). The structure was conceived and manufactured not in conformity with the majority of similar contemporary buildings.

The main aim of this research is to investigate the local behavior of the moment resisting joints and to investigate the efficiency of some local intervention to strengthen and improve the joint behavior. The paper is divided in four main parts; initially the structural feature of the building is described; then the main aspects of the finite element model (FEM) are presented. The third part is mainly focused on the results of beam-to-column joints under both vertical and horizontal action. Finally, the efficiency of four possible retrofitting solutions is presented.

2 DESCRIPTION OF THE STRUCTURE

2.1 History and general features

The multi-storey building serves for offices and depository of documents. The structure was built between 1960 and 1961 to replace a former two-storeys masonry construction used as public office. The V-shape of the original plan of the building was preserved (see Figure 1), with a footprint of about 1400 m². The design was carried out in accordance to the Italian provisions that were in force during the 1960; therefore, only gravity and wind loads were considered. MRFs were adopted on the longitudinal axes of the construction, while various types of concentric braces (X and Y shaped) were located in the transverse direction.



2.2 History and general features

The columns of the MRF systems have a hollow squared tubes cross section, with a constant external size along the height of the building (140x140 mm), but the thickness of the tubes varies from 18 to 6 mm from the bottom to the top. The main beams are made with IPN 320 profiles at all storeys. Floors were made using corrugated steel sheets filled with concrete for a total height of 55 mm. Geometrical features of MRF joints are summarised in Fig. 2.

According to the design report [23], all members are made with Aq 42 Steel, with an allowable stress of 1600 kg/cm², with the only exception of the tubes, which are manufactured with Aq 55 Steel, with an allowable stress of 2000 kg/cm². High-strength bolts (8.8) has been considered.

A total of six beam-to-column joints (one for each floor) have been investigated under both vertical and horizontal actions. Therefore, a specified nomenclature was introduced to identify each investigated joint in function of the floor ("Fx") and the load scenario (vertical or seismic).

3 MODELING ASSUMPTIONS

The finite element models (FEMs) were developed using ABAQUS 6.14 [24]. The modelling assumptions are the same as described by the Authors in previous publications [25-26]. Therefore, only the main features of the models are summarized in the following for the sake of brevity.

The beam-to-column joints were modelled considering a sub-assembly of the whole structure, which is obtained by extracting both the columns and the beams at the inflection points of the bending moment diagram induced by gravity and horizontal loads on the MRF. All elements were discretized using C3D8R solid element type. The characteristic dimension of mesh was set equal to 5 mm for bolts, welds and plates, and 20 mm for the beams and the columns.

According to the design report, a yield stress of 240 MPa was assigned to all the existing members, with the only exception of the columns, for which the yield stress was set to 300 MPa.

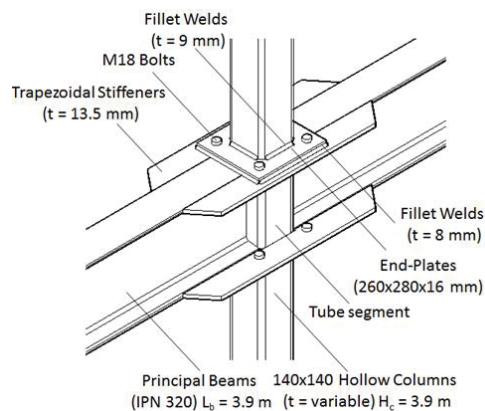


Figure 2: Detail of investigated MRF beam-to-column joints.

Steel yielding was modelled using the Von Mises criterion. The kinematic and isotropic hardening were implemented. The constitutive law for high-strength bolts (class 8.8) was modelled according to D'Aniello et al. [27]. The weld steel was modelled with the Ramberg-Osgood constitutive law; in absence of more detailed information from the design report, the yielding strength of existing welds was assumed to be equal to the highest between the existing members (300 MPa). Finally, an European S355 steel grade was used for all strengthening elements.

Displacement histories were applied at the tip of the beams in the sub-assemblages, reaching a maximum chord rotation of 0.06 rad. AISC 341 [28] protocol was adopted for cyclic analyses.

4 RESULTS FROM FINITE ELEMENT ANALYSES

4.1 Behavior of MRF beam-to column joints under vertical loads

The behaviour of MRF beam-to-column joints under vertical loads was investigated imposing maximum vertical displacements at the beam tips equal to 120 mm.

As expected, the internal beam-to column joints showed a good overall response, with the activation of plastic hinges at the extremity of the beams with basically no involvement of the column that remains in elastic range (see Fig. 3). Plastic hinges start to develop nearby the continuity restraint, while increasing the vertical displacements also the activation other two plastic hinges at the beam extremity can be observed. Moreover, since the beam profiles do not change among the different floors, the response in terms of bending resistance is almost the same for all the investigated joints, as shown in Fig. 3a.

However, a very small difference in terms of elastic stiffness can be observed owing to the variation of the column bending stiffness at each floor.

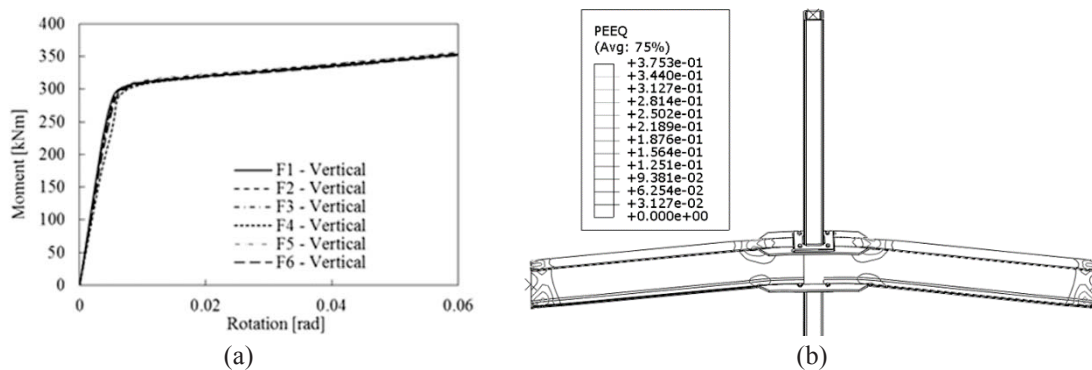


Figure 3: Results of MRF joints at 3rd floor under vertical loads in terms of moment-rotation curve (a) and PEEQ distribution of joint (b).

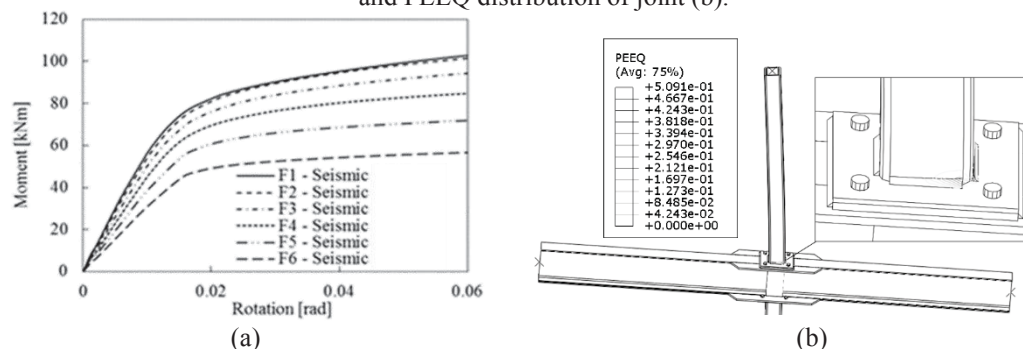


Figure 4: Results of MRF joints at 3rd floor under seismic loads in terms of moment-rotation curve (a) and PEEQ distribution of joint (b).

4.2 Seismic behavior of MRF beam-to column joints

The seismic behaviour of MRF beam-to-column joints is depicted in Fig. 4 in terms of moment-rotation curves and distribution of equivalent plastic strains (PEEQ); in Fig. 4b it can be notice that all plastic deformations are concentrated in the columns and in the fillet welds. The beams always remain in an elastic range; the same type of failure mode can be observed at each floor of the building. The maximum bending resistance is showed by the joint at the first floor, as shown in Fig. 4a; indeed, due to the variation of the column thickness a reduction of the resistance along the structural height can be observed.

In Table 2 results from each scenario are reported in terms of maximum bending moments.

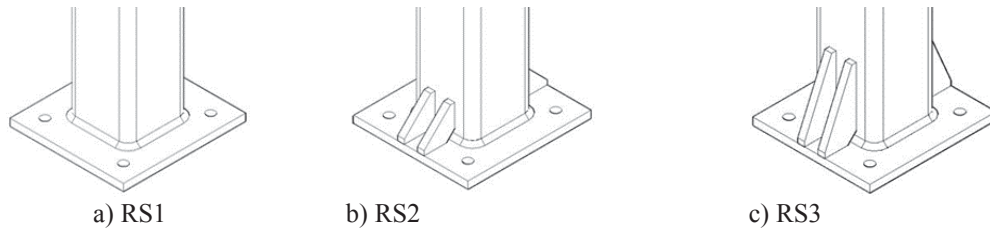


Figure 5: Different retrofitting solutions for the beam-to-column joint: weld collar (a), 65 mm high ribs (b), 150 mm high ribs (c)

Floor	Vertical [kNm]	Seismic [kNm]
Floor 1	356.1	102.8
Floor 2	355.4	101.4
Floor 3	355.0	94.8
Floor 4	354.3	85.2
Floor 5	353.9	72.2
Floor 6	351.9	56.5

Table 2: Results from numerical analyses in terms of maximum bending moments.

4.3 Strengthening solutions

The results of the numerical analyses showed that MRF joints have a good behaviour under gravity loads while exhibit a poor ductile response, with a large plastic concentration in the column's tip and in the adjacent fillet welds (see Fig. 4b). Therefore, three different strengthening interventions have been designed and numerically tested to improve the seismic performance of the joints by preventing welds brittle failure. For sake of brevity only results of the joint at the third floor (with the medium value of column thickness) are reported hereinafter.

The main geometrical features of the interventions (see Fig. 5) are summarised as follows:

1. Complete replacement of the fillet welds with a continuous weld collar made with stronger material (e.g. yielding stress equal to 450 MPa), see Fig. 5a (RS1).
2. Replacement of the welds and introduction of four 65x10 mm rib stiffeners made with steel S355, two on each side of the column, shaped with an angle of 40°, see Fig. 5b (RS2).
3. Replacement of the welds and introduction of four 150x10 mm rib stiffeners made with steel S355, two on each side of the column, see Fig. 5c (RS3).

The results of monotonic analysis for each RS scenario are depicted in Fig. 6. Maximum bending moments and the relative increment with respect to unreinforced joint response are also reported in Table 3. As it can be observed, the retrofitting solutions provide a large variation of both resistance and elastic stiffness; indeed, with the only exception of RS1, that only implies the change of the welds, the introduction of the rib stiffeners increases the assembly stiffness and the resistance. The maximum increase of the bending capacity is not very high (RS3, 17% with respect to the unreinforced joint) but the real benefit of the presence of the ribs is to obtain a more ductile mechanism moving the failure from the weld to the column allowing a larger rotational capacity. This aspect can be better observed in case of cyclic analyses (see Fig. 7).

Thus, comparing the unreinforced solution with the RS3 (the one with two ribs) it can be observed that the first case a large concentration of plastic deformation appears in the welds and at the column tip. Contrariwise, the reinforced solution provides a slightly larger resistance and a more stable energy dissipation without pinching. In this case plastic strains are concentrated in the columns, leaving the welds in elastic range.

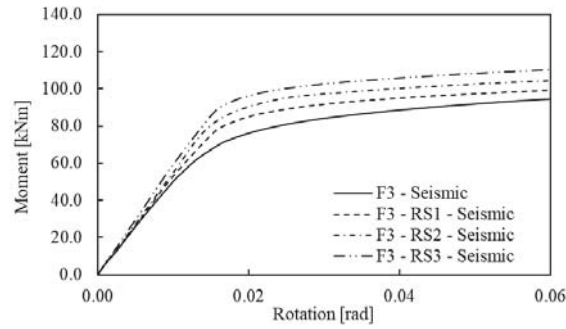


Figure 6: Moment – rotation curves for all different strengthening solutions.

Intervention	$M_{i,Max}$ [kNm]	Resistance increment [%]
RS0 (Unreinforced)	94.8	-
RS1 (Replaced Welds)	99.2	+5%
RS2 (Ribs 65 mm)	104.5	+10%
RS3 (Ribs 150 mm)	110.2	+16%

Table 3: Comparison between different scenarios in terms of bending moments.

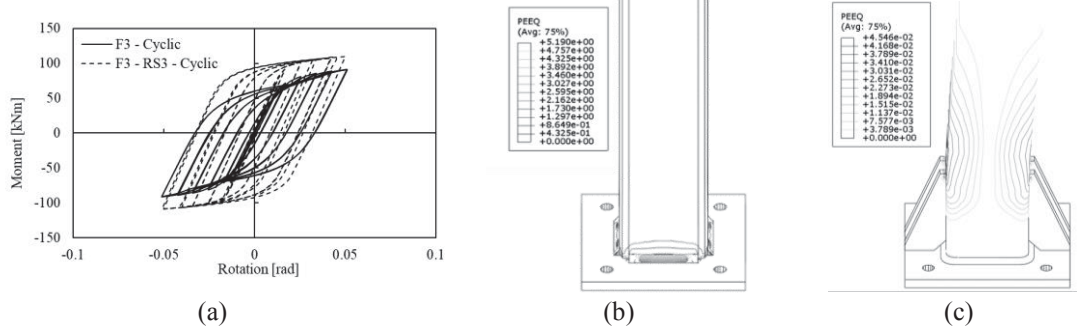


Figure 7: Moment-rotation curves for the unreinforced column and the RS3 proposal (a) and distribution of equivalent plastic strains under cyclical horizontal actions for the same cases (b-c).

5 CONCLUSIONS

An existing non-code conforming six-storey steel building has been investigated. Particular attention was paid on both vertical and lateral behaviour of the MRF beam-to-column joints. From the results of FEAs the following observations can be pointed out:

- Moment resisting joints are able to support the vertical loads showing only the activation of the plastic hinges at very large value of chord rotation.
- Lateral loads induce stress concentration in the welds around the columns, which represent a brittle component. Therefore, local interventions have been designed to retrofit joints.
- The first retrofitting intervention (RS1) involves the replacement of the original welds; results show that the increment of weld resistance is not enough to change the failure mode.
- The second (RS2) and third (RS3) interventions consist in the use of rib stiffeners to increase the resistance of the connection. The numerical results show that both under monotonic and cyclic action the introduction of rib stiffeners allows to reduce the plastic demand within the welds. Therefore, the local ductility of the joints is preserved despite additional consideration should be done from a global point of view.

REFERENCES

- [1] F. Di Lauro, R. Montuori, E. Nastri, V. Piluso, Partial safety factors and overstrength coefficient evaluation for the design of connections equipped with friction dampers. *Engineering Structures*, **178**, 645-655, 2019.
- [2] R. Montuori, E. Nastri, V. Piluso, Problems of modeling for the analysis of the seismic vulnerability of existing buildings. *Ingegneria Sismica*, **36**(2), 53-85, 2019.
- [3] A. Poursadrollah, M. D’Aniello, A. De Martino, R. Landolfo, Preliminary study on the seismic performance of hybrid steel structures with truss lightweight girders and plug-and-play connections. *Ingegneria sismica* **37**, 102-114, 2020.
- [4] L. Fiorino, T. Pali, R. Landolfo, Out-of-plane seismic design by testing of non-structural lightweight steel drywall partition walls. *Thin-Walled Structures*, **130**, 213-230, 2018.
- [5] V. Macillo, S. Shakeel, L. Fiorino, R. Landolfo, Development and Calibration of Hysteretic Model for CFS Strap braced stud walls. *International Journal of Advanced Steel Construction*, **14**(3), 337-360, 2018.
- [6] A. Campiche, Numerical modelling of CFS three-story strap-braced building under shaking-table excitations. *Materials*, **14**(1), 1–13, 2021
- [7] A. Campiche, L. Fiorino, R. Landolfo, Numerical modelling of CFS two-storey sheathing-braced building under shaking-table excitations, *J. Constr. Steel Res.* **170**, 2020.
- [8] S. Shakeel, L. Fiorino, R. Landolfo, Behavior factor evaluation of CFS wood sheathed shear walls according to FEMA P695 for Eurocodes. *Engineering Structures*, **221**, 111042, 2020.
- [9] L. Fiorino, O. Iuorio, V. Macillo, R. Landolfo, Performance-based design of sheathed CFS buildings in seismic area. *Thin-Walled Structures*, **61**, 248-257, 2012
- [10] R. Montuori, G. Gabbianelli, E. Nastri, M. Simoncelli, Rigid plastic analysis for the seismic performance evaluation of steel storage racks. *Steel and Composite Structures*, **32** (1), 1-19, 2019.
- [11] R. Montuori, E. Nastri, V. Piluso, Modelling of floor joists contribution to the lateral stiffness of RC buildings designed for gravity loads. *Engineering Structures*, **121**, 85-96, 2016.
- [12] A. Campiche, S. Shakeel, V. Macillo, M.T. Terracciano, B. Bucciero, T. Pali, L. Fiorino, R. Landolfo, Seismic behaviour of sheathed CFS buildings: Shake table tests and numerical modelling. *Ingegneria sismica*, **35**, 106-123, 2018.
- [13] E. Elettore, F. Freddi, M. Latour, G. Rizzano, Design and analysis of a seismic resilient steel moment resisting frame equipped with damage-free self-centering column bases. *Journal of Constructional Steel Research*, **179**, 2021.
- [14] S. Di Benedetto, A.B. Francavilla, M. Latour, G. Ferrante Cavallaro, V. Piluso, G. Rizzano, Pseudo-dynamic testing of a full-scale two-storey steel building with RBS connections. *Engineering Structures*, **212**, 2020.
- [15] G. Ferrante Cavallaro, A.B. Francavilla, M. Latour, V. Piluso, G. Rizzano, Cyclic response of low yielding connections using different friction materials. *Soil Dynamics and Earthquake Engineering*, **114**, 404-42, 2018.

- [16] A. Lemos, L.S. da Silva, M. Latour, G. Rizzano, Numerical modelling of innovative DST steel joint under cyclic loading. *Archives of Civil and Mechanical Engineering*, **18** (3), 687-701, 2018
- [17] M. D'Antimo, J.F. Demonceau, J.P. Jaspart, M. Latour, G. Rizzano, Experimental and theoretical analysis of shear bolted connections for tubular structures. *Journal of Constructional Steel Research*, **138**, 264-282, 2017.
- [18] M. Latour, G. Rizzano, Mechanical modelling of exposed column base plate joints under cyclic loads. *Journal of Constructional Steel Research*, 2019.
- [19] A.F. Santos, A. Santiago, M. Latour, G. Rizzano, Analytical assessment of the friction dampers behaviour under different loading rates. *Journal of Constructional Steel Research*, **158**, 443-459, 2019.
- [20] S. Di Benedetto, M. Latour, G. Rizzano, Assessment of the stiffness of 3D cut welded connections with CHS columns and through I-BEAMS. *Structures*, **27**, 247-258, 2020
- [21] S. Di Benedetto, M. Latour, G. Rizzano, Chord failure resistance of 3D cut welded connections with CHS columns and through I-BEAMS. *Thin-Walled Structures*, **154**, 2020.
- [22] R. Tartaglia, M. D'Aniello, G.A. Rassati, J.A. Swanson, R. Landolfo, Full strength extended stiffened end-plate joints: AISC vs recent European design criteria. *Engineering Structures*, **159**, 155-171, 2018.
- [23] G. Travaglini, F. De Miranda, L'ampliamento della sede uffici del Genio Civile di Napoli, *Costruzioni Metalliche*, **2**, 198-209, 1962 [in Italian].
- [24] Dassault (2014), Abaqus 6.14 User's Manual, Dassault Systèmes Simulia Corp.
- [25] R. Tartaglia, M. D'Aniello, M. Zimbru, Experimental and numerical study on the T-Stub behaviour with preloaded bolts under large deformations. *Structures*, **27**, 2137-2155, 2020.
- [26] R. Tartaglia, M. D'Aniello, Influence of Transverse Beams On the Ultimate Behaviour of Seismic Resistant Partial Strength Beam-To-Column Joints. *Ingegneria Sismica*, **37**(3), 50-65, 2020.
- [27] M. D'Aniello, D. Cassiano, R. Landolfo, Simplified criteria for finite element modelling of European preloadable bolts. *Steel and Composite Structure*, **24**, 643-658, 2017.
- [28] AISC (American Institute of Steel Construction) (2016), Seismic Provisions for Structural Steel Buildings, ANSI/AISC 341-16.

APPLICATION AND ASSESSMENT OF A DYNAMIC SOIL-BRIDGE-TRAIN INTERACTION MODEL

Benjamin Hirzinger^{1,2} and Christoph Adam²

¹VCE Vienna Consulting Engineers, Department of Railway Engineering
Untere Viaduktgasse 2, 1030 Vienna, Austria
e-mail: hirzinger@vce.at

² University of Innsbruck, Unit of Applied Mechanics
Technikerstr. 13, 6020 Innsbruck, Austria
e-mail: christoph.adam@uibk.ac.at

Keywords: Bridge Dynamics, Soil-Structure-Vehicle Interaction, Approach and Departure Phase, Dynamic Substructuring.

Abstract. *In this contribution, the dynamic response of two railway bridges, represented by a viscoelastically supported Euler-Bernoulli model, subjected to high-speed trains is analyzed and discussed. Different types of high-speed trains are considered, which are modeled as moving mass-spring-damper (MSD) system. The structural response is determined by a dynamic substructuring approach, in which the equation of motion of the beam bridge model and the equations of motion of the MSD system, both written in state space, are coupled using a generalized corresponding assumption. The coupled set of equations of motion representing the dynamic soil-structure-vehicle interaction model are solved by time history analysis. The utilized approach captures all essential features of dynamic soil-structure-vehicle interaction and allows for a numerically efficient evaluation of the dynamic responses of the structure. Particular attention is paid to the influence of the MSD system on the beam bridge during approach and after departure. The structural response of the considered beam bridges is compared and discussed for the different types of high-speed trains and different subsoil conditions.*

1 INTRODUCTION

The increasing operational speed along train lines involves new challenges on the design of railway bridges and on the assessment of existing bridges. At certain train speeds, especially short-to-medium span railway bridges are excited to resonance, which leads to a significant structural acceleration response at the deck level [1]. Resonance effects can lead to destabilization of the ballast, to increased wearing of the rails which is associated with increased maintenance costs of the line, and in extreme cases even to the hazard of train derailment. These aspects demand a detailed dynamic analysis of the response behavior within the framework of a reliability assessment of bridge structures for trains with high-speed. In common computational models the subsoil of the bridge is assumed to be rigid and only a few studies deal with the influence of SSI on the dynamic response behavior of the bridge (e.g. [2, 3, 4, 5]). However, dynamic soil-structure interaction (SSI) effects may have a significant influence on the structural response of high-speed railway bridges and therefore should to be taken into account when performing a reliability analysis.

The most general modeling approach for the prediction of the structural response including SSI is provided by three-dimensional (3D) finite element (FE) models [4, 6, 7]. A 3D FE bridge model offers the possibility of taking the full coupling between the track and the soil into account, the geometry of the bridge can be modeled in detail, and in a time domain formulation nonlinear constitutive behavior can be implemented [3]. In a numerically more efficient but more elaborate approach, an FE model of the bridge is coupled with a boundary element (BE) model of the subsoil [3, 5, 8]. For instance, [5] investigated the influence of SSI on the structural responses of a single-span railway bridge subjected to moving trains at different speeds. In this study, a mass-spring-damper (MSD) train model is coupled with a 3D FE track and bridge model in combination with the BE soil model. The prediction of the structural bridge response using FE or BE-FE formulations involves a significant computational effort, and in the context of reliability assessment, where many limit state function evaluations are required, it is not feasible to use such complex and computationally expensive models. For this reason, the authors of this paper have recently developed a numerically efficient dynamic soil-structure and bridge-train interaction model [9] that allows for a large number of computations in the context of a reliability analysis.

In this contribution, this model is utilized to determine the structural response of beam bridges subjected to moving high-speed trains. The trains are modeled as a planar MSD system, and the bridges as an Euler-Bernoulli beam resting at both ends on spring-damper elements that capture the effect of the subsoil. A dynamic substructuring approach is used to determine the system response, in which the equation of motion of the beam bridge model and the equations of motion of the MSD system are written separately in state space and then coupled via a generalized corresponding assumption. Particular emphasis is paid to the influence of the MSD system on the bridge response during approach and after departure of the bridge. In two application examples, the structural response of two existing bridge structures subjected to three different German high-speed InterCity Express (ICE) trains is assessed.

2 DYNAMIC SOIL-BRIDGE-TRAIN INTERACTION MODEL

2.1 Dynamic substructuring approach

The response of the coupled bridge-MSD system is found by a dynamic substructuring technique [9]. In this approach, the equations of motion of the two subsystems (i.e., the bridge and the MSD system) are derived separately and then coupled utilizing a coupling condition at the interfaces of the subsystems. The beam bridge is subjected to a planar viscoelastic

MSD system representing the moving train at constant speed v (see Figure 1). To account for soil-structure interaction effects, the bridge is modeled as an Euler-Bernoulli beam with spring-dashpot elements at both ends, which is thus non-classically damped. In addition, the rotational springs consider the bending stiffness of the rails and the lumped masses account for the mass of the foundation (see Figure 1).

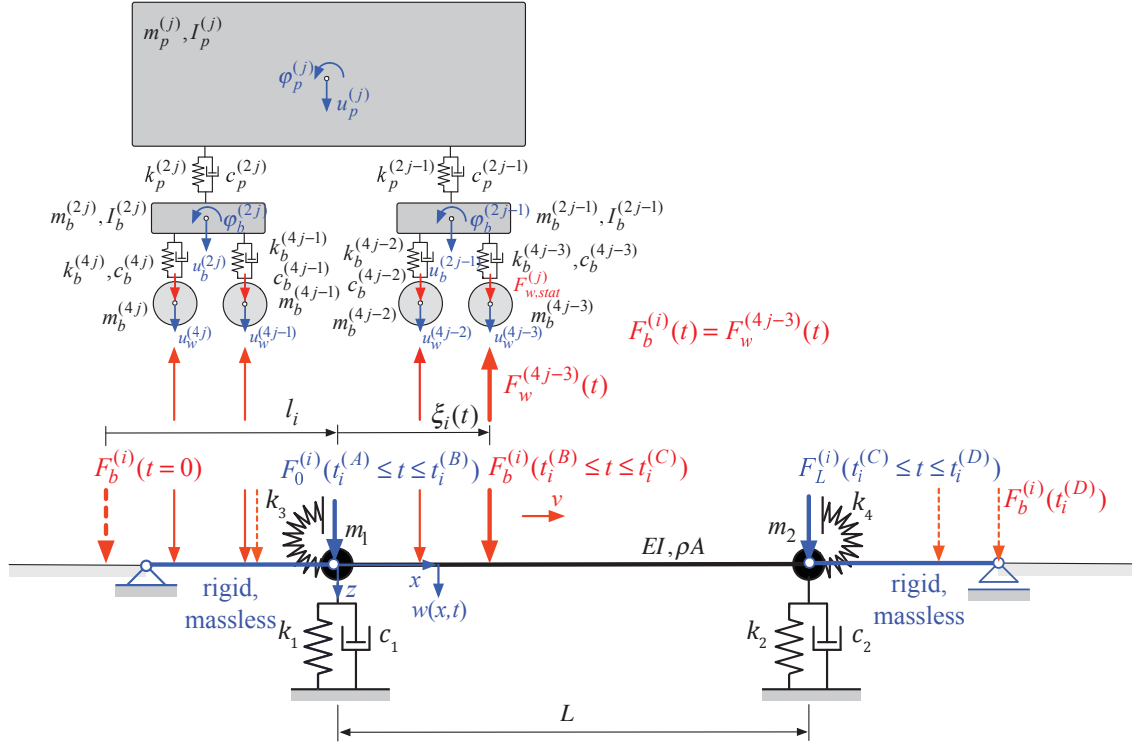


Figure 1: Viscoelastically supported Euler-Bernoulli beam model and planar MSD model, modified from [9]

The procedure described in [9] is based on a complex modal series representation of the beam bridge displacement $w(x, t)$ and the acceleration $\ddot{w}(x, t)$,

$$w(x, t) \approx 2\mathcal{R} \left\{ \sum_{r=1}^{N_\Phi} \Phi_r(x) y_r(t) \right\}, \quad \ddot{w}(x, t) \approx 2\mathcal{R} \left\{ \sum_{r=1}^{N_\Phi} \Phi_r(x) s_r \dot{y}_r(t) \right\} \quad (1)$$

with $\Phi_r(x)$ denoting the r -th complex eigenfunction of the non-classically damped beam and s_r is the corresponding complex natural frequency. The modal equations of motion in state space for the first N_Φ modes of the Euler-Bernoulli beam read [9]

$$\mathbf{A}_b \dot{\mathbf{y}} + \mathbf{B}_b \mathbf{y} = \mathbf{f}_b \quad (2)$$

where \mathbf{y} is the vector of the complex modal coordinates y_r , $r = 1, \dots, N_\Phi$, and their conjugate complex counterparts \bar{y}_r , matrix \mathbf{A}_b contains the coefficients of the decoupled first order differential equations related with $\dot{\mathbf{y}}$, matrix \mathbf{B}_b the coefficients related with \mathbf{y} , and \mathbf{f}_b denotes the vector of the modal interaction forces f_r and \bar{f}_r , $r = 1, \dots, N_\Phi$, between the bridge and the train model,

$$\begin{aligned} \mathbf{y} &= [y_1, \dots, y_r, \dots, y_{N_\Phi}, \bar{y}_1, \dots, \bar{y}_r, \dots, \bar{y}_{N_\Phi}]^T, \\ \mathbf{A}_b &= \text{diag}[a_1, \dots, a_r, \dots, a_{N_\Phi}, \bar{a}_1, \dots, \bar{a}_r, \dots, \bar{a}_{N_\Phi}], \\ \mathbf{B}_b &= \text{diag}[b_1, \dots, b_r, \dots, b_{N_\Phi}, \bar{b}_1, \dots, \bar{b}_r, \dots, \bar{b}_{N_\Phi}], \\ \mathbf{f}_b &= [f_1, \dots, f_r, \dots, f_{N_\Phi}, \bar{f}_1, \dots, \bar{f}_r, \dots, \bar{f}_{N_\Phi}]^T \end{aligned} \quad (3)$$

The MSD train system is composed of rigid bodies with mass representing the passenger stage, two bogies, and four wheel pairs connected with spring-dashpot elements, as shown in Figure 1 [10, 11]. The equations of motion of this MSD system with 10 degrees of freedom (DOFs) in state space representation are given as [11, 12],

$$\mathbf{A}_c \dot{\mathbf{d}}_c(t) + \mathbf{B}_c \mathbf{d}_c(t) = \mathbf{f}_c(t) \quad (4)$$

with the matrices \mathbf{A}_c , \mathbf{B}_c , and vector \mathbf{f}_c

$$\mathbf{A}_c = \begin{bmatrix} \mathbf{C}_c & \mathbf{M}_c \\ \mathbf{I}_c & \mathbf{0} \end{bmatrix}, \quad \mathbf{B}_c = \begin{bmatrix} \mathbf{K}_c & \mathbf{0} \\ \mathbf{0} & -\mathbf{I}_c \end{bmatrix}, \quad \mathbf{f}_c = \begin{bmatrix} \mathbf{F}_c \\ \mathbf{0} \end{bmatrix} \quad (5)$$

composed of the mass matrix \mathbf{M}_c , the damping matrix \mathbf{C}_c , the stiffness matrix \mathbf{K}_c , the vector \mathbf{F}_c comprising the axle forces, and the identity matrix \mathbf{I}_c . The vector $\mathbf{d}_c = \{\mathbf{u}_c^{(1)}, \dots, \mathbf{u}_c^{(j)}, \dots, \mathbf{u}_c^{(N_c)}, \dot{\mathbf{u}}_c^{(1)}, \dots, \dot{\mathbf{u}}_c^{(j)}, \dots, \dot{\mathbf{u}}_c^{(N_c)}\}^T$ contains all DOFs of the MSD system and their first derivative in time of the DOFs.

The equation of motions of beam and MSD system are coupled with the so-called generalized corresponding assumption [9, 13], where it is assumed that the displacement in the vertical direction of the beam and the MSD system at the contact point are equal. Consequently, lift-off of the wheels is not possible, see Figure 2. The generalized corresponding assumption yields the following expression for the vertical displacement $u_w^{(i)}$ of the i -th wheel, which is at time t at position $\xi_i(t)$, together with Eq. (1) [9],

$$u_w^{(i)}(\xi_i) = w(\xi_i, t) \approx \sum_{r=1}^{N_\Phi} \Phi_r(\xi_i) y_r(t) + \sum_{r=1}^{N_\Phi} \bar{\Phi}_r(\xi_i) \bar{y}_r(t) \quad (6)$$

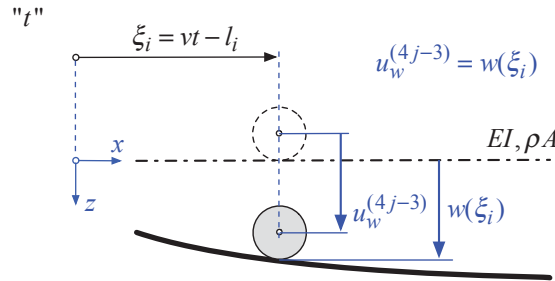


Figure 2: Generalized corresponding assumption for beam and wheel contact at position $\xi_i(t)$ [9]

Finally, the resulting coupled set of equations of motion in state space reads as [9, 13]

$$\mathbf{A}^*(t) \dot{\mathbf{x}}^*(t) + \mathbf{B}^*(t) \mathbf{x}^*(t) = \mathbf{f}^*(t) \quad (7)$$

with the time-dependent system matrices

$$\begin{aligned} \mathbf{A}^*(t) &= \mathbf{\Gamma}_1^T(t) \left[\mathbf{A} \mathbf{\Gamma}_1(t) + \mathbf{A} \dot{\mathbf{\Gamma}}_2(t) + \mathbf{A} \mathbf{\Gamma}_2(t) \mathbf{S} + \mathbf{B} \mathbf{\Gamma}_2(t) \right], \\ \mathbf{B}^*(t) &= \mathbf{\Gamma}_1^T(t) \left[\mathbf{A} \dot{\mathbf{\Gamma}}_1(t) + \mathbf{B} \mathbf{\Gamma}_1(t) \right] \end{aligned} \quad (8)$$

and

$$\mathbf{f}^*(t) = \mathbf{\Gamma}_1^T(t) \left[\mathbf{f}(t) - \mathbf{A} \dot{\mathbf{\Upsilon}}(t) - \mathbf{B} \mathbf{\Upsilon}(t) \right] \quad (9)$$

The time-dependent transformation matrices $\Gamma_1(t)$, $\Gamma_2(t)$ include terms that consider the interaction between the subsystems. This system of equations is solved for the vector \mathbf{x}^* utilizing the 4-th order numerical Runge-Kutta time-step integration scheme of the explicit form of Eq. (7), i.e. $\dot{\mathbf{x}}^*(t) = \mathbf{A}^*(t)^{-1} (\mathbf{f}^*(t) - \mathbf{B}^*(t)\mathbf{x}^*(t))$. A detailed derivation of the equations of motions of the beam bridge model and the MSD system can be found in [9, 13].

2.2 Modeling of the approach and departure phase of the train

When the train approaches the bridge, the bridge is lowered slightly due to the flexibility of the subsoil. This lowering must be taken into account in the mechanical model to avoid a physically unreasonable acceleration jump in the calculation. The same applies accordingly after the train has left the bridge. As described in [14], in the mechanical model the lowering of the bridge in the approach and departure phases is achieved by two fictitious massless rigid beams placed before and after the bridge, respectively, as shown in Figure 1. The effect of N_w axle loads of the MSD system in the approach phase on the first massless beam and in further consequence on the bridge model can be simply described by a force on the left support $F_0(t)$ (at $x = 0$) that increases linearly in this phase [14],

$$F_0(t) = \sum_{i=1}^{N_w} F_b^{(i)}(t) \left(1 + \frac{vt - l_i}{L_a} \right) \delta(x) \Pi(t, t_i^{(A)}, t_i^{(B)}) \quad (10)$$

where the Dirac delta function $\delta(x)$ indicates the position of $F_0(t)$ at $x = 0$, i.e. at the left beam support. The i -th force $F_b^{(i)}$ is activated at time $t_i^{(A)} = (l_i - L_a)/v$ by the Heaviside function $H(t - t_i^{(A)})$ when it enters the fictitious rigid beam, and at time $t_i^{(B)} = l_i/v$ deactivated by the Heaviside function $H(t - t_i^{(B)})$ when $F_b^{(i)}$ runs onto the flexible support, i.e., $\Pi(t, t_i^{(A)}, t_i^{(B)}) = H(t - t_i^{(A)}) - H(t - t_i^{(B)})$. Accordingly, a single force $F_L(t)$ on the right support (at $x = L$) captures the movement of the train away from the bridge [9],

$$F_L(t) = \sum_{i=1}^{N_w} F_b^{(i)}(t) \left(1 - \frac{vt - l_i - L}{L_d} \right) \delta(x - L) \Pi(t, t_i^{(C)}, t_i^{(D)}) \quad (11)$$

At time $t_i^{(C)} = (l_i + L)/v$ the i -th force of the MSD system leaves the beam bridge, and at time $t_i^{(D)} = (l_i + L + L_d)/v$ it leaves the fictitious rigid beam of length L_d , consequently, $\Pi(t, t_i^{(C)}, t_i^{(D)}) = H(t - t_i^{(C)}) - H(t - t_i^{(D)})$.

The r -th modal form of these forces read as [9]

$$\begin{aligned} f_0^{(r)}(t) &= \int_L \sum_{i=1}^{N_w} F_b^{(i)} \left(1 + \frac{vt - l_i}{L_a} \right) \delta(x) \Pi(t, t_i^{(A)}, t_i^{(B)}) \Phi_r(x) dx = \\ &= \sum_{i=1}^{N_w} F_b^{(i)} \left(1 + \frac{vt - l_i}{L_a} \right) \Pi(t, t_i^{(A)}, t_i^{(B)}) \Phi_r(0) \\ f_L^{(r)}(t) &= \int_L \sum_{i=1}^{N_w} F_b^{(i)} \left(1 - \frac{vt - l_i - L}{L_d} \right) \delta(x - L) \Pi(t, t_i^{(C)}, t_i^{(D)}) \Phi_r(x) dx = \\ &= \sum_{i=1}^{N_w} F_b^{(i)} \left(1 - \frac{vt - l_i - L}{L_d} \right) \Pi(t, t_i^{(C)}, t_i^{(D)}) \Phi_r(L) \end{aligned} \quad (12)$$

Consequently, the r -th modal load in Eq. (3) is given as $f_r = f_0^{(r)} + f_b^{(r)} + f_L^{(r)}$, where $f_b^{(r)}(t) = \int_L \sum_{i=1}^{N_w} F_b^{(i)}(t) \delta(x - \xi_i) \Pi(t, t_i^{(B)}, t_i^{(C)}) \Phi_r(x) dx = \sum_{i=1}^{N_w} F_b^{(i)}(t) \Pi(t, t_i^{(B)}, t_i^{(C)}) \Phi_r(\xi_i)$ accounts for the modal form of the series of N_w moving single forces crossing the beam bridge. During the approach and departure phase of the MSD system the dynamic interaction between the beam and the MSD system is explicitly considered in the transformation matrices $\Gamma_1(t)$, $\Gamma_2(t)$, see [9, 13].

3 Application

This dynamic substructuring approach is used to efficiently evaluate the acceleration response of two example bridges subjected to the German InterCity Express trains ICE 2, ICE 3, and ICE 4. In the considered configuration, the ICE 2 train with a maximum train speed of $v_{\max} = 77.8$ m/s (280 km/h) and a total length of $L_{\text{train}} = 205.4$ m is composed of one power car followed by seven passenger cars. The UIC axle classification [15] of this train with in total 32 axles thus reads $\text{Bo}'\text{Bo}' + 2'2' + 2'2' + 2'2' + 2'2' + 2'2' + 2'2' + 2'2'$, with Bo' representing one pair of axles of the power car and $2'$ representing one pair of axles of the passenger car. The considered ICE 3 train contains four power cars and four passenger cars with an UIC axle classification of $\text{Bo}'\text{Bo}' + 2'2' + \text{Bo}'\text{Bo}' + 2'2' + 2'2' + \text{Bo}'\text{Bo}' + 2'2' + \text{Bo}'\text{Bo}'$. The length of this train with 32 axles and a maximum speed of $v_{\max} = 91.4$ m/s (330 km/h) is $L_{\text{train}} = 200.8$ m. The considered ICE 4 train with a maximum speed of $v_{\max} = 69.4$ m/s (250 km/h) has 3 power cars and 4 passenger cars, which add up to 28 axles and a total length of $L_{\text{train}} = 202$ m. The corresponding UIC axle classification is $2'2' + \text{Bo}'\text{Bo}' + 2'2' + \text{Bo}'\text{Bo}' + \text{Bo}'\text{Bo}' + 2'2' + 2'2'$. The parameters of the MSD model of the ICE 2 and ICE 3 can be found in [16, 17], and of the ICE 4 train in [18].

In general, the maximum acceleration of the bridge deck is decisive for the assessment of the reliability of the railway bridge exposed to high-speed trains [19]. Therefore, the acceleration response of the two beam bridges subjected to the MSD system representing the considered trains is computed for five different subsoil conditions. In this study, the time history of the beam bridge response at closely spaced beam locations x is analyzed for a given speed v of the train models in the observation period $T = (l_1 + L_{\text{train}} + L_a + L + L_d)/v$, and subsequently the absolute value of the peak response is recorded, i.e. the peak acceleration $a(v) = \max \{ |\ddot{w}(x, t, v)| : 0 \leq x \leq L, 0 \leq t \leq T \}$. The modal expansions are approximated by seven modes, i.e. $N_\Phi = 7$. Structural modal damping of $\tilde{\zeta}_r = 0.25\%$ ($r = 1, \dots, N_\Phi$) is taken into account and the surface of the beam is assumed to be perfectly smooth.

The properties of the soil under the bridge foundation are varied, representing a range from moderately soft to stiff soils. Five homogeneous soils with different stiffness are considered, whose soil parameters (constrained modulus E_s , Poisson's ratio ν , mass density ρ) are summarized in Table 1 [13, 20]. Soil 1 with the lowest stiffness corresponds to a medium stiff soil and soil 5 to a stiff soil (rock). Since the required contact area A_0 of the foundations depends on the soil stiffness (i.e. the stiffer the soil the smaller the required area), the product of the base area of the foundation A_0 and the root of the constrained modulus of the soil E_s is kept constant when determining k and c , i.e., $A_0 \sqrt{E_s} = 2.289 \cdot 10^4 \sqrt{\text{Nm}}$ [14]. It is assumed that the foundation has the same mass for all soils considered: $m = 1.5 \cdot 10^5$ kg.

	E_s [MN/m ²]	ν [-]	ρ [kg/m ³]	k [N/m]	c [kg/s]
1	200	0,30	2263	$5,895 \cdot 10^8$	$1,089 \cdot 10^6$
2	250	0,28	2300	$7,662 \cdot 10^8$	$1,098 \cdot 10^6$
3	300	0,26	2333	$9,495 \cdot 10^8$	$1,106 \cdot 10^6$
4	400	0,25	2367	$1,284 \cdot 10^9$	$1,114 \cdot 10^6$
5	500	0,25	2400	$1,605 \cdot 10^9$	$1,121 \cdot 10^6$

Table 1: Soil parameters and corresponding parameters of the spring-dashpot elements [13]

3.1 Example bridge 1

Example bridge 1 models an existing single-span ballasted steel railway bridge located in Austria with a span length of $L = 16.8$ m. Its bending stiffness is $EI = 3.262 \cdot 10^{10}$ Nm² and its mass per unit length $\rho A = 1.220 \cdot 10^4$ kg/m. Table 2 presents the first four natural frequencies $f_r (= \mathcal{I}(s_r)/2\pi = \Omega_r/2\pi)$, $r = 1, \dots, 4$, and equivalent damping coefficients $\zeta_r + \tilde{\zeta}_r$ for the beam model on viscoelastic supports representing various subsoil conditions, and for the simply supported beam bridge model (i.e., in this case the subsoil is rigid). In this context, it should be noted that higher modes, associated with higher frequencies, are less critical for bridge failure [13].

Table 2: First four natural frequencies and damping coefficients of bridge model 1 resting on soils 1 to 5 and on rigid soil

	soil no. 1	soil no. 2	soil no. 3	soil no. 4	soil no. 5	simply supported beam
f_1 [Hz]	6.59	7.12	7.49	7.94	8.19	9.10
f_2 [Hz]	8.96	10.19	11.34	13.16	14.68	36.39
f_3 [Hz]	12.96	13.68	14.45	15.87	17.19	81.90
f_4 [Hz]	38.80	38.85	38.89	38.99	39.08	145.60
$\zeta_1 + \tilde{\zeta}_1$ [%]	2.71	1.96	1.46	0.94	0.69	0.25
$\zeta_2 + \tilde{\zeta}_2$ [%]	5.41	4.79	4.35	3.77	3.39	0.25
$\zeta_3 + \tilde{\zeta}_3$ [%]	2.94	3.17	3.20	3.18	3.08	0.25
$\zeta_4 + \tilde{\zeta}_4$ [%]	0.42	0.43	0.44	0.45	0.46	0.25

Figure 3 shows the maximum acceleration response $a(v)$ of example bridge 1 subjected (a) to the ICE 2 train and (b) to the ICE 3 train as a function of the train speed v . The local response peaks of these so-called response spectra are referred to as resonance peaks, and the associated train speeds are known as critical speeds or resonance speeds. At such a critical train speed, defined as $v_j^{(r)} = df_r/dj$, $j = 1, 2, 3, \dots$, the r -th natural bridge frequency is excited to a state of resonance due to the repetitive axle loads with constant distance d [21].

When the beam is rigidly supported, the ICE 2 train induces a maximum bridge deck acceleration $a = 6.6$ m/s² at speed $v = 79.5$ m/s (which is close to the resonance speed $v_3^{(1)} = 80.1$ m/s, based on the wagon length of the ICE 2 train $d = 26.4$ m). For the beam resting on soil 5, the maximum acceleration $a = 3.6$ m/s² occurs at the train speed $v = 71$ m/s, which is close to the resonance speed $v_3^{(1)} = 72.1$ m/s. Soil 4 and soil 3 lead to the acceleration maxima $a = 2.9$ m/s² and $a = 1.9$ m/s² at the train speeds $v = 68.8$ m/s, $v = 66.7$ m/s, respectively. Due to the considerable geometric damping at soil 1 and soil 2, no pronounced resonance peak is visible in these cases. These results show that SSI reduces the peak accelerations at resonance compared to the rigidly supported beam bridge model. Simultaneously, the corresponding critical train speeds

also decrease, which could be of concern because these speeds are below the maximum train speed (cf. Figure 3(a)).

The overall response behavior of this example bridge is very similar when subjected to the ICE 3 train, see Figure 3. In the rigidly supported beam bridge model, the global acceleration maximum at $v = 74.6$ m/s is $a = 10.3$ m/s², which is close to the resonance speed $v_3^{(1)} = 75.2$ m/s, based on the ICE 3 wagon length $d = 24.8$ m. The global resonance peak of the bridge resting on soil 5 is $a = 5.7$ m/s² at $v = 66.7$ m/s (close to resonance speed $v_3^{(1)} = 67.6$ m/s). The structure in combination with soil 4 yields the maximum acceleration $a = 4.1$ m/s² at $v = 64.7$ m/s, and in combination with soil 3 $a = 2.6$ m/s² at $v = 60.4$ m/s. As in the case of the ICE 2 train, no distinct acceleration peaks can be observed for the structure resting on soil 1 and soil 2.

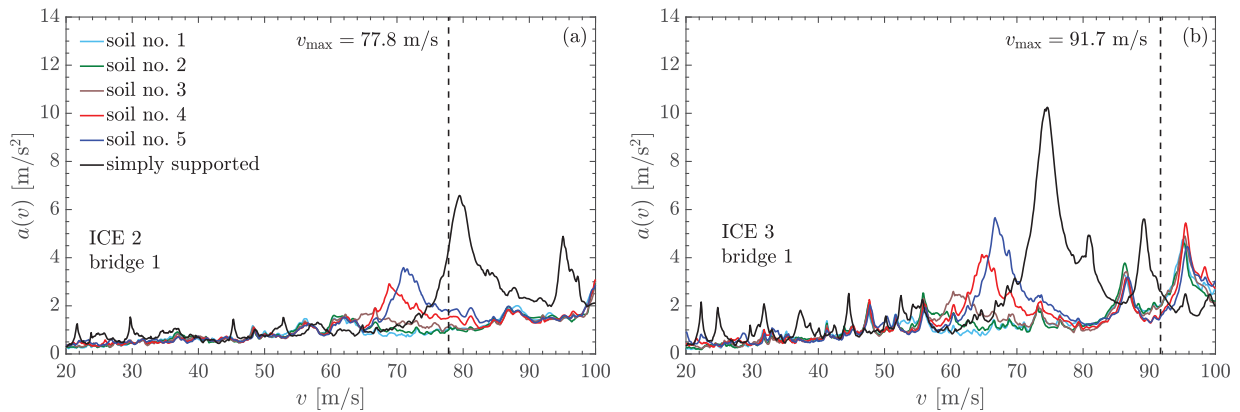


Figure 3: Maximum bridge acceleration of example bridge 1 subjected (a) to the ICE 2 train and (b) to the ICE 3 train as a function of the train speed for different soil conditions.

Figure 4 presents the maximum acceleration response of example bridge 1 subjected to the MSD system of the ICE 4 train. As before, the rigidly supported beam bridge model exhibits the largest bridge deck acceleration $a = 12.6$ m/s² at $v = 86.4$ m/s (close to the resonance speed $v_3^{(1)} = 87.7$ m/s; wagon length $d = 28.9$ m). Likewise, the maximum bridge acceleration and the associated resonant speed decrease with decreasing base stiffness (soil 5: $a = 7.9$ m/s² at $v = 77.7$ m/s; soil 4: $a = 6.7$ m/s² at $v = 74.5$ m/s; soil 3: $a = 4.9$ m/s² at $v = 70.7$ m/s; soils 1 and 2: no pronounced response peaks).

Comparison of Figures 3 and 4 reveals that at bridge 1 on rigid soil the ICE 3 train leads to the dominant resonance peak at the lowest speed, while the ICE 2 train induces the lowest bridge accelerations. On the other hand, the ICE 4 train excites the bridge to the largest accelerations, however, at the largest resonance speed compared to the other train models.

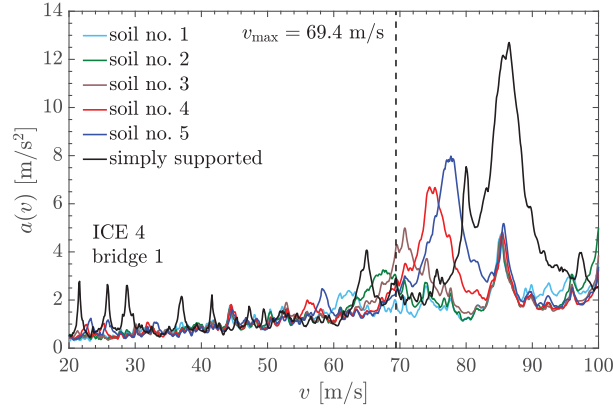


Figure 4: Maximum bridge acceleration of example bridge 1 subjected to the ICE 4 as a function of the train speed for different soil conditions.

3.2 Example bridge 2

With $L = 21$ m, the span length of example bridge 2, which is also the model of an existing single-span ballasted steel railway bridge, is larger than that of bridge 1. The flexural stiffness is $EI = 2.6 \cdot 10^{10}$ Nm² and the mass per unit length $\rho A = 7083 \cdot 10^4$ kg/m. The first four natural frequencies of example bridge 2 f_r , $r = 1, \dots, 4$, and corresponding equivalent damping coefficients $\zeta_r + \tilde{\zeta}_r$ depending on the subsoil conditions are compiled in Table 3.

Table 3: First four natural frequencies and damping coefficients of bridge model 2 resting on soils 1 to 5 and on rigid soil

	soil no. 1	soil no. 2	soil no. 3	soil no. 4	soil no. 5	simply supported beam
f_1 [Hz]	5.96	6.19	6.33	6.47	6.55	6.80
f_2 [Hz]	9.18	10.45	11.61	13.44	14.96	27.20
f_3 [Hz]	10.88	11.95	13.01	14.79	16.35	61.20
f_4 [Hz]	28.62	28.67	28.73	28.85	28.99	108.80
$\zeta_1 + \tilde{\zeta}_1$ [%]	1.40	0.91	0.67	0.46	0.38	0.25
$\zeta_2 + \tilde{\zeta}_2$ [%]	5.52	4.88	4.4	3.79	3.37	0.25
$\zeta_3 + \tilde{\zeta}_3$ [%]	4.46	4.34	4.15	3.79	3.50	0.25
$\zeta_4 + \tilde{\zeta}_4$ [%]	0.45	0.47	0.49	0.52	0.56	0.25

Figures 5(a),(b) and 6 show the peak acceleration response of this structure subjected to the ICE 2, ICE 3 and ICE 4 train models. In all cases, the maximum peak acceleration occurs at the rigidly supported beam. The ICE 2 train induces large responses of the bridge resting on soil 1 (smallest stiffness) compared to structure on the stiffer soils 5, 4, 3, and 2, as can be seen from Figure 5(a). However, in general the ICE 2 train does not cause significant acceleration responses of this structure. Another observation is that the peak acceleration of bridge 2 on soil 3 induced by the ICE 3 train is larger than for the bridge on soils 5 and 4, cf. Figure 5(b). Clearly, the ICE 4 train yields the largest bridge accelerations, as can be seen from Figure 6. For instance, the rigidly supported beam bridge model exhibits the largest acceleration $a = 17.4$ m/s² at $v = 64.7$ m/s, which is close to the resonance speed $v_3^{(1)} = 65.5$ m/s. The peak acceleration and the corresponding resonance speed for the bridge on flexible soil decrease with decreasing soil stiffness. Soil 5: $a = 13.2$ m/s² at $v = 62$ m/s (close to $v_3^{(1)} = 63.1$ m/s); soil 4: $a = 12.2$ m/s²

at $v = 61.3$ m/s; soil 3: $a = 10.1$ m/s² at $v = 59.8$ m/s; soil 2: $a = 8.2$ m/s² at $v = 58.5$ m/s; soil 1: $a = 5.9$ m/s² at $v = 56.4$ m/s.

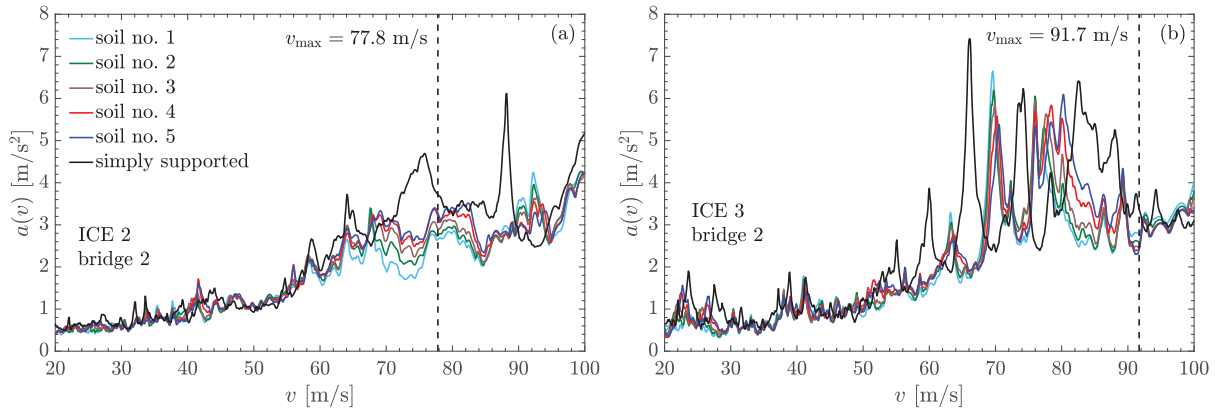


Figure 5: Maximum bridge acceleration of example bridge 2 subjected (a) to the ICE 2 train and (b) to the ICE 3 train as a function of the train speed for different soil conditions.

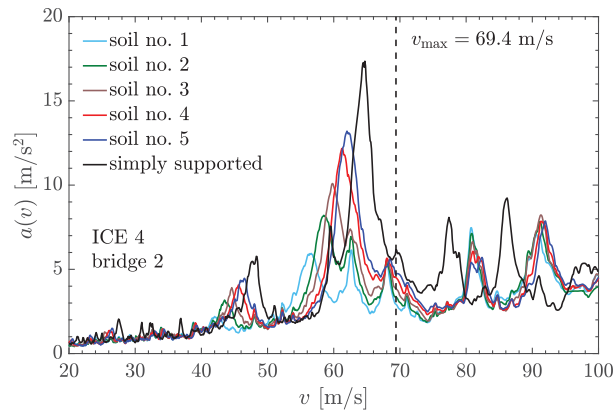


Figure 6: Maximum bridge acceleration of example bridge 2 subjected to the ICE 4 as a function of the train speed for different soil conditions.

4 CONCLUSIONS

In this study, a soil-bridge-train interaction model recently developed by the authors was used to efficiently evaluate the structural response of two example bridges subjected to the German high-speed trains ICE 2, ICE 3 and ICE 4. This model is based on a dynamic substructuring approach in which the bridge is modeled as a beam and the train as a mass-spring-damper system. To obtain physically meaningful results, the arrival and departure phases of the train were considered. Train-bridge interaction was explicitly considered in the approach and departure phases.

The influence of the soil-structure interaction and the bridge-train interaction on the response of the example bridges subjected to the three different train types was shown. When the soil-structure interaction is considered, the maximum acceleration at resonance is reduced due to the additional damping of the system, but simultaneously also the resonance peaks are shifted to lower train speeds. This trend is visible for the two example bridges and all three train types considered.

ACKNOWLEDGEMENTS

The computational results presented have been achieved (in part) using the HPC infrastructure LEO of the University of Innsbruck.

REFERENCES

- [1] J. Li, M. Su, The resonant vibration for a simply supported girder bridge under high-speed trains. *Journal of Sound and Vibration*, **224**(5), 897–915, 1999.
- [2] A. Doménech, M.D. Martínez-Rodrigo, A. Romero, P. Galvín, Soil-structure interaction effects on the resonant response of railway bridges under high-speed traffic. *International Journal of Rail Transportation*, **3**(4), 201–214, 2015.
- [3] P. Galvín, A. Romero, J. Domínguez, Fully three-dimensional analysis of high-speed train-track-soil-structure dynamic interaction. *Journal of Sound and Vibration*, **329**, 5147–5163, 2010.
- [4] A.M. Gharad, R.S. Sonparote, Study of direct finite element method of analysing soil-structure interaction in a simply supported railway bridge subjected to resonance. *Iranian Journal of Science and Technology, Transactions of Civil Engineering*, **43**, 273–286, 2019.
- [5] A. Romero, M. Solís, J. Domínguez, P. Galvín, Soil-structure interaction in resonant railway bridges. *Soil Dynamics and Earthquake Engineering*, **47**, 108–116, 2013.
- [6] J.Y. Shih, D.J. Thompson, A. Zervos, The effect of boundary conditions, model size and damping models in the finite element modelling of a moving load on a track/ground system. *Soil Dynamics and Earthquake Engineering*, **89**, 12–27, 2016.
- [7] A. Martínez-De la Concha, H. Cifuentes, F. Medina, A finite element methodology to study soil-structure interaction in high-speed. *Journal of Computational and Nonlinear Dynamics*, **13**(3), 031010, 2018.
- [8] P. Galvín, S. François, M. Schevenels, E. Bongini, G. Degrande, G. Lombaert, A 2.5D coupled FE-BE model for the prediction of railway induced vibrations. *Soil Dynamics and Earthquake Engineering*, **30**, 1500–1512, 2010.
- [9] B. Hirzinger, C. Adam, P. Salcher, Dynamic response of a non-classically damped beam with general boundary conditions subjected to a moving mass-spring-damper system. *International Journal of Mechanical Sciences*, **185**, 105877, 2020.
- [10] K. Knothe, S. Stichel, *Railway Vehicle Dynamics*. Springer International, 2017.
- [11] K. Popp, W. Schiehlen, *Ground Vehicle Dynamics*. Springer International, 2010.
- [12] A. Brandt, *Noise and Vibration Analysis*. John Wiley and Sons, Ltd., 2010.
- [13] B. Hirzinger, *Contributions to modeling and assessment strategies in railway bridge dynamics*. Dissertation, University of Innsbruck, 2020.

- [14] C. Adam, B. Hirzinger, Simplified dynamic response analysis of a railway bridge considering soil-structure interaction. In: *Proc. XI European Conference on Structural Dynamics (EURODYN 2020)*, virtual conference (Papadrakakis, M., Fragiadakis, M., Papadimitriou, C., eds.), November 23-26 2020, 9 pp, 2020.
- [15] UIC Leaflet 650, *Standard designation of axle arrangement on locomotives and multiple-unit sets*. 5th edition of 1.1.83.
- [16] A. Doménech, *Influencia del modelo de vehículo en la predicción del comportamiento a flexión de puentes isostáticos de ferrocarril para tráfico de alta velocidad (in Spanish)*. Dissertation, Universitat Politècnica de Valencia, 2014.
- [17] M. Hädrich, *Untersuchungen zur dynamischen Bauwerk-Fahrzeug-Wechselwirkung bei Eisenbahnbrücken kurzer Spannweite (in German)*. Masterthesis, Bauhaus-Universität Weimar, 2008.
- [18] A. Firus, H. Berthold, J. Schneider, G. Grunert, Untersuchungen zum dynamischen Verhalten einer Eisenbahnbrücke bei Anregung durch den neuen ICE 4 6. *VDI-Fachtagung Baudynamik*, 233–248, 2018.
- [19] L. Frýba, *Dynamic of Railway Bridges*. Thomas Telford, 1996.
- [20] C. Adam, B. Hirzinger, Ein Modell mit Boden-Bauwerk-Interaktion zur dynamischen Berechnung von Eisenbahnbrücken (in German) [A model with soil-structure interaction for the dynamic analysis of railway bridges]. *Bauingenieur*, **95**, 289–298, 2020.
- [21] Y.B. Yang, J.D. Yau, Y.S. Wu, *Vehicle-Bridge Interaction Dynamics*. World Scientific Publishing Company Incorporated, 2004.

SEISMIC FRAGILITY ANALYSIS OF RAILWAY RC BRIDGES ACCOUNTING FOR BRIDGE-TRAIN INTERACTION BASED ON A NOVEL FORMULATION FOR CONSTRAINED DYNAMICAL SYSTEMS AND A CO-SIMULATION TECHNIQUE

Sotiria P. Stefanidou, and Elias A. Paraskevopoulos²

¹ Postdoctoral Researcher, School of Civil Engineering, Aristotle University of Thessaloniki
Thessaloniki, 54124, Greece
e-mail: ssotiria@civil.auth.gr

² Postdoctoral Researcher, School of Mechanical Engineering, Aristotle University of Thessaloniki
Thessaloniki, 54124, Greece
e-mail: eapcivil@gmail.com

Abstract

Based on past earthquake events, bridges are the most critical and usually the most vulnerable component of road and rail transport systems, while bridge damage is related to substantial direct and indirect losses. For the case of railway bridges, the estimation of seismic fragility is a rather complex and computationally demanding procedure due to the real-time interaction of the train movement and the bridge and the different failure modes of subsystems. Several methodologies are available in the literature to estimate train-bridge systems' seismic fragility, ignoring the nonlinear behavior of the bridge during earthquake loading and the different failure modes of critical components. The scope of this research paper is to propose a component-based methodology for the estimation of bridge fragility curves, considering all critical components and failure modes of subsystems. The coupled VBI (vehicle bridge interaction) is solved in a software platform using the co-simulation approach, based on a force-displacement coupling technique and a Gauss-Seidel communication pattern. The co-simulation implementation, i.e., the orchestrator and the functional mockup units (FMUs), were developed in the environment of PyFMI. The vehicle-rail system is solved using a C++ tailor-made code based on a novel mathematical formulation of constrained dynamical systems with a set of pure ordinary differential equations and is wrapped in an independent FMU. The inelastic bridge model is developed and solved using OpenSees.py, which is wrapped in an independent FMU. Also, an ad-hoc software for implementing the probabilistic framework and the derivation of fragility curves is developed in Python. The methodology and the software developed are described and applied to a case study bridge of the Greek railway network, and the fragility curves are provided and discussed.

Keywords: Railway bridges, vehicle-bridge interaction (VBI), Co-simulation, fragility curves

1 INTRODUCTION

Roadway and railway bridges are considered the most critical infrastructure of relevant networks exposed to multiple hazards, while damage at their critical components is related to substantial direct and indirect losses. Furthermore, decision-making for upgrade and expansion of existing roadway and railway networks should be based on detailed technical studies accounting for various social and economic parameters, infrastructure robustness and reliability data. In this context, a robust and reliable assessment of railway bridges is a valuable tool for both retrofit prioritization and investment planning. Several methodologies for seismic fragility assessment of railway bridges are available, however a detailed framework considering both the vehicle bridge-interaction and the coupled system's limit states incorporated within a fully parameterized, tailor-made software for the derivation of fragility curves has not yet been proposed.

The dynamic behavior of a train-bridge system is a coupled and complex model consisting of two main subsystems, the train, and the bridge. The train subsystem can be described as a multibody assembly and the bridge subsystem can be modeled using classical structural finite element formulations. The subsystems interact through forces between the vehicle wheels and the rail on the bridge deck. Several researchers worldwide have worked on train-bridge interaction problems integrating the train, track and bridge as a single system [1,2]. Vehicle-rail-bridge (VRBI) models have been introduced to analyze dynamic interaction between moving trains and railway bridges, based on the dynamic integration methods [3,4,5,6,7]. Due to the nonlinear interaction of subsystems, it is widely accepted that the dynamic analysis of train-bridge system during earthquakes cannot be a simple combination of bridge seismic design and train-bridge interaction calculation. Therefore, several studies have investigated the response of coupled systems under dynamic (earthquake) loading [8] as well as the seismic performance for different levels of earthquake intensity (fragility analysis) [9].

Based on the above, the scope of this paper is to propose and develop a novel methodology for the modeling and analysis of the coupled train-railway bridge system, considering an appropriate numerical discretization scheme and a solution strategy based on a co-simulation approach. Efficient modeling of the vehicle multibody assembly is proposed using a tailor-made C++ code, while the nonlinear bridge model is developed and analyzed using open-source software. Interaction between the vehicle and the bridge is proposed via an integrated approach that employs co-simulation techniques and FMI (functional mockup interface) for the communication and joint solution of subsystems in the time domain considering different time steps for analysis and selecting Gauss Seidel communication pattern. All the above are incorporated into a holistic methodology proposed herein for seismic fragility analysis of the coupled train-bridge system considering VBI, multiple critical components, and appropriate limit states that account for the running safety of high-speed trains along with the possibility for derailment. The novel methodology for fragility analysis and the relevant software developed are applied to a representative bridge of the Greek railway network, providing the subsystems' and coupled systems' fragility curves. The results are discussed and assessed, providing insight regarding seismic fragility analysis of coupled train-bridge systems and the computational framework required for their estimation.

2 VEHICLE-BRIDGE SYSTEM INTERACTION (VBI)

2.1 Description of vehicle modeling

A typical railway vehicle consists of car bodies, bogies, wheelsets and spring-damper primary and secondary suspensions. A car body is connected to the bogie frame through the sec-

ondary suspension system, whereas the bogie is connected to the wheelsets through the primary suspension system [10]. The vehicle system can be seen as an assembly of rigid and flexible parts subjected to a set of kinematic constraints and connected through springs and dampers. This assembly constitutes a multibody system with bodies that can undergo large rotations, move at high speed, and interact with each other inducing large forces and moments. The target is to study the dynamical synergy between a moving train and a rail when the latter is attached to the bridge and may be subjected to seismic loads (and/or high lateral winds). Realistic modeling of derailment constitutes a crucial step for evaluating train running safety and should be accordingly considered.

Each vehicle of the high-speed train consists of two bogie sub-systems, connected to the car-body via an inline joint and spring-damper elements (SPDP). The latter constitutes the vertical and lateral secondary suspension system. At the lower part of each bogie, two wheelsets are placed, connected to the bogie via the axle boxes. The axle boxes are connected to the bogie with vertical and lateral spring-damper elements, forming the primary suspension system. There is a revolute joint linking the two axle boxes to the wheelset at both ends of the wheelset. The revolute joints allow the wheelsets to rotate freely to the axle boxes and vice versa. The direction of rotation is the wheelset's centerline and the wheelset-axle boxes system has eight degrees of freedom. Six of those DOFs include its rigid body motion, while the last two leave the relative rotation free between the axle boxes and the bogie, bringing the functionality of the primary suspension system. Therefore, each vehicle consists of 15 rigid bodies. The geometric cubic splines of the wheel and rail profiles and that of the track centerline generate the wheel and rail surfaces. To form the entire high-speed train a specific number of vehicles are considered, placed at a predefined distance from each other, connected through a selected type of constraint joint. A practical selection is that of the spherical joint leaving all three rotational degrees of freedom free, while the remaining three translational are unconstrained. Finally, the front vehicle has the constraint of constant linear velocity along the direction of the train movement, simulating the driving motion of the entire train assembly. The resultant contact force between the wheel and the rail can be decomposed in two component forces. The first is the normal contact force which is always perpendicular to the common tangent plane of the two surfaces at the contact point. The second component is the friction force acting in the tangent plane. This friction force is described by Kalker's linear theory.

The analysis described above is based on the assumption that the normal direction \underline{n} is known. Knowing the position and orientation of the wheelset along with the analytical forms of the surfaces for the wheel and rail, a minimization problem can be formulated to determine \underline{n} . The minimization function is defined in the form of the square of the Euclidian distance between a point on the wheel and a point on the rail. The local minimum determines the points on the two surfaces with the shortest distance. The unit vector along the line connecting these two points provides the contact normal direction. This is the direction used to calculate the value of the contact constraint needed for the numerical integration of the equations of motion.

A dully tailored software in C++ is developed to apply the methodology described above for the vehicle analysis. The numerical algorithm for the solution of the constrained multibody system is based on the methodology developed in [11] and [12]. The software is wrapped in an FMU and is used within the proposed co-simulation framework for the analysis of the coupled vehicle and bridge system for earthquake loading.

2.2 Description of bridge modeling

The bridge structure is modeled using an open-source FEM program, OpenSees.py [13]. The detailed inelastic model of the bridge system is developed, considering all critical parameters and boundary conditions. The deck is commonly prestressed and intended to remain elastic during earthquake loading; therefore, it is modeled using elastic beam elements with the relevant properties. Bridge piers are modeled using inelastic beam-column elements considering concentrated plastic hinges at pier bottom for the case of cantilever piers and at pier top and bottom for multicolumn piers or piers with monolithic pier-to-deck connection. Based on the results of moment-curvature analysis the secant stiffness of the fully cracked section at yield ($EI_{\text{eff}} = M_y / \phi_y$) is estimated and used for the consideration of cracked elastic pier section. Regarding bearings of railway bridges, it is noted that elastomeric bearings are commonly used for the support of bridge deck on piers and seat-type abutments, while the use of pot bearings and stoppers, lead rubber bearings (with increased damping) and isolation devices are also common. For the modeling of bearings, either the linear effective stiffness or the non-linear hysteretic behavior may be considered with the parameters calculated based on literature recommendations [14], [15], etc. Regarding pier shallow or pile foundation, linear or nonlinear springs are used for the modeling of soil-structure-interaction (SSI), playing an important role in both component and system seismic performance and fragility, as mentioned in [16]. Piles are modeled using elastic beam-column elements, while vertical (friction) and horizontal (p-y) springs are calculated considering SSI. Modeling of boundary conditions at abutment location is crucial; therefore both the gap in the longitudinal direction and the inelastic abutment-embankment system behavior (described in detail in [17]) are modeled. It should be highlighted that for the case of railway bridges there is no gap in the transverse direction, in order to prevent derailment phenomena. Response history analysis of the inelastic bridge model is performed using OpenSees.py, in order to calculate inelastic bridge responses and bridge fragility.

3 EARTHQUAKE ANALYSIS CONSIDERING VBI PROPOSING A CO-SIMULATION APPROACH

Coupled simulation or co-simulation has been proposed as a solution to overcome the challenges emerging in complex, coupled engineering systems. The holistic problem is being broken down into two or more individual subsystems and the coupling variables between the subsystems could be either in force terms (applied-force coupling), or in force-kinematic terms (displacement-displacement (X-X) and displacement-force (X-T) respectively) [18]. The co-simulation process is being carried out by a third simulator, named orchestrator, that is responsible for the integration, coupling, and communication between subsystems. The orchestrator leads each co-simulation step (communication interval), exchanges variables with the subsystems simulators, and checks the coupling conditions (convergence).

Regarding the communication scheme, the Gauss-Seidel (serial) communication scheme is proposed for the solution of the vehicle(train)-bridge system in the time domain. Applying an iterative Gauss-Seidel approach, the vehicle subdomain is first solved for the communication interval H (starting point $T_N = t_{0, \text{tr}}$), assuming a known solution for the bridge subdomain. The vehicle subdomain is integrated until the next communication step, i.e. $T_{N+1} = t_{1, \text{tr}}$. At this time point, the output variables of the vehicle subdomain are being used by the orchestrator in order to calculate new inputs for the bridge subdomain. The bridge subdomain is solved until $T_{N+1} = t_{1, \text{br}}$ (starting point $T_N = t_{0, \text{tr}}$). The process described above is repeated until the coupling conditions are satisfied (convergence) and the co-simulation can proceed to the next communication point. The vehicle subdomain is solved using a multibody dynamics method devel-

oped at the Laboratory of Machine Dynamics (AUTH), whereas the bridge subdomain is solved via OpenSees, a general FEM open-source code. The coupled vehicle-bridge systems' analysis procedure is described in Figure 1, explaining the analysis of every subsystem at every distinct step and the communication pattern.

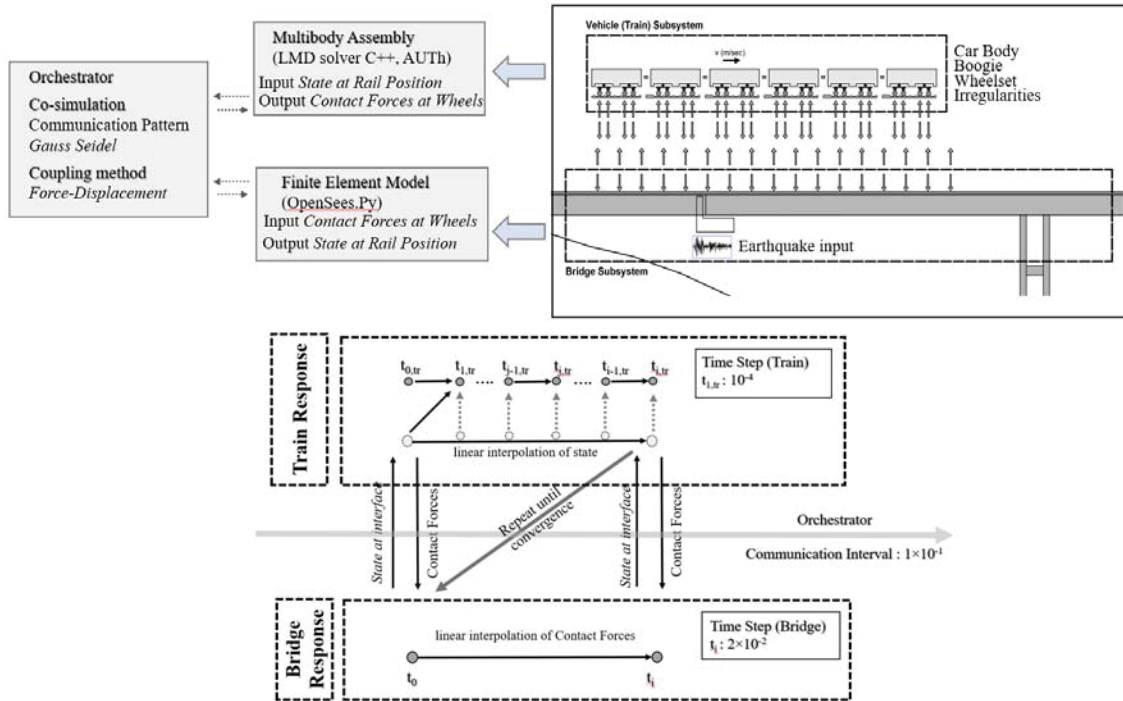


Figure 1: Outline of the methodology for dynamic high-speed train -bridge interaction

4 SEISMIC FRAGILITY ANALYSIS OF COUPLED RAILWAY BRIDGE SYSTEMS CONSIDERING VBI

The framework proposed for seismic fragility analysis of bridges is based on analysis results of the coupled vehicle-bridge system for different levels of earthquake intensity, estimating the probability of damage of critical bridge components and the vehicle for various limit states (minor damage to collapse) [10]. The methodology proposed is outlined in Figure 2.

For the estimation of *vehicle subsystem* fragility, serviceability and ultimate limit state thresholds are defined, based on the recommendations of EN1990-prANNEX A2, (2001) and BS EN 14363: (2016), as described in Table 1. The vehicle limit states proposed consider vehicle stability (LS1), the dynamic performance of the bridge (LS2) and vehicle safety (derailment LS3 &4) (Table 1). The *vehicle subsystem* properties (i.e., number of boogies), speed, and time step that the vehicle enters the bridge are initially defined, and analysis of the subsystem is performed considering real-time vehicle-bridge interaction via co-simulation techniques. The threshold values are compared to the ones monitored at the vehicle during the coupled system analysis for the selected earthquake ground motions to estimate the probability of exceedance and plot the relevant fragility curves (Figure 2).

Regarding the *railway bridge subsystem* fragility estimation, the engineering demand parameters and their threshold values are initially defined at component level for different limit states, as described in detail in [17]. The structural type of the railway bridge is selected, along with varying properties (random variables selection), for probabilistic treatment and

derivation of bridge samples using Latin Hypercube Sampling (LHS). The bridge samples are analysed considering real-time train-bridge interaction for accelerograms of varying intensity (0.1~1.0g), selected applying Multiple Stripe Analysis (details for Multiple Stripe Analysis and accelerogram selection are available in [16]). The engineering demand parameters values at component control points are monitored to estimate the probability of limit state threshold exceedance and plot fragility curves at component and system level. Based on the above, fragility curves for the subsystems and the coupled system are proposed accounting for series connection and complete correlation of critical components.

	Criteria for train running stability			Criteria for bridge dynamic performance		Criteria for train running safety		
	Lateral accel. (boogie)	Lateral accel. (veh.body)	Vertical accel. (veh.body)	Accel-eration	Transverse deformation & vibration of deck	Overturn Coefficient	Overturn Criterion	
Parameter	Accel. (m/s ²)	Accel. (m/s ²)	Accel. (m/s ²)	Accel-eration (m/s ²)	Curvature (1/m) [<i>r</i> = <i>l</i> ² /8· <i>δ_h</i>]	<i>D</i> = <i>P_d</i> / <i>P_{st}</i>	$\kappa = \frac{\sum_{boogie} Q_{JA} - \sum_{boogie} Q_{JB}}{\sum_{boogie} Q_{JA} + \sum_{boogie} Q_{JB}}$	
Limit Values	12.0 m/s ² – (m ⁺ /5t) = 11.392 m/s ²	3.0	5.0	0.35g (3.5m/s ²) for ballasted track	<i>Speed range (km h⁻¹)</i>	<i>Limits</i>	0.80 (for all wheels at the same time)	1.0
					V≤120	1700		
					120≤V≤200	6000		
					V>200	14000		

Table 1: Limit values for vehicle and fragility analysis of the coupled train-bridge system

For the estimation of the coupled systems' fragility curves, seismic analysis of the coupled system is performed considering earthquake loading of varying intensity (0.1~1g). The analysis results are recorded at the vehicle and the bridge control points for the all the coupled (train-bridge) system samples. The values are compared to the limit state thresholds of each subsystem (and component) and statistical analysis of the results is performed estimating the mean and standard deviation of capacity over demand exceedance and, eventually, the seismic fragility curves of the vehicle and bridge subsystem. For the estimation of uncertainty in capacity and demand the methodology described in [17] is followed. The fragility curves of the coupled system are calculated assuming series connection between subsystems (vehicle and bridge) according to Eq. 1 (upper and lower bound, Zhang &Huo, (2009)):

$$\max_{i=1}^n [P(F_i)] \leq P(F_{system}) \leq 1 - \prod_{i=1}^n [1 - P(F_i)] \quad (1)$$

The lower bound corresponds to completely correlated components, while the upper bound assumes no correlation between components. Therefore, the coupled system's fragility lies within these two bounds and the exact value is dependent on the correlation of the component response.

5 APPLICATION TO A CASE STUDY RAILWAY BRIDGE FOR THE ESTIMATION OF SEISMIC FRAGILITY OF THE COUPLED SYSTEM

The methodology presented above is applied to a representative bridge of the Greek railway network with simply supported deck, using the software developed for real-time bridge-vehicle analysis. A five boogies Vehicle is considered to cross the bridge during the earthquake. The vehicle is entering the bridge about 3[sec] before the earthquake peak. Based on the coupled system analysis results, fragility analysis is performed, and fragility curves are provided for all the critical bridge components, the bridge subsystem, the vehicle subsystem and the coupled system. The effect of VBI consideration on seismic fragility of critical bridge

components (piers and abutments since pot bearings are used in combination with stoppers, rendering the bearings a non-critical component) is evaluated providing relevant fragility curves for the cases of earthquake only analysis and earthquake analysis accounting for VBI. Moreover, the seismic fragility curves of the bridge subsystem with and without VBI consideration are provided for both longitudinal and transverse direction, highlighting the effect of VBI on the subsystem's fragility. The seismic fragility of the vehicle subsystem is also provided for both directions along with the fragility curves of the coupled (vehicle and bridge) system based on series connection assumption. The effect of the consideration or ignorance of vehicle subsystem limit states and fragility, i.e. the consideration of the coupled system instead of the bridge system solely, is evaluated and discussed.

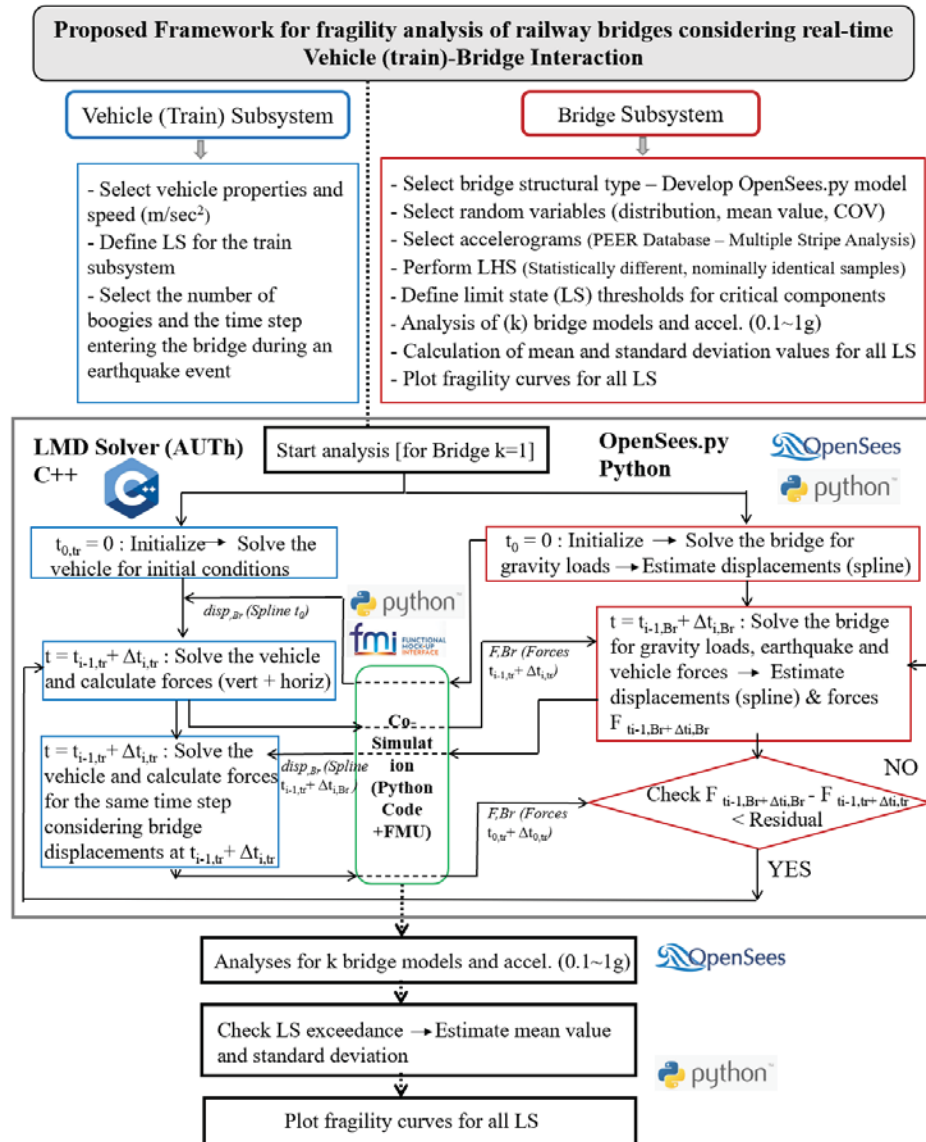


Figure 2: Outline of the methodology for dynamic high-speed train-track-bridge interaction.

The Tirothea - Domokos bridge is a two-way railway bridge of the Athens-Thessaloniki railway network, located at Central Greece, near Lamia (Figure 3). Responsible for the management of the project is ERGOSE SA, Greece. The bridge is designed for train speed equal to $v \leq 200$ km/h and PGA equal to 0.24g, while it should be outlined that it is located at a 175m distance from the seismically active Atalanti fault; therefore, the probability of the occurrence

of an earthquake event when the train crossing the bridge is relatively higher. The Tirothea - Domokos bridge has a total length of 505.26 (m) and fifteen (15) spans (approx. 34.0m length each) consisting of precast-prestressed beams simply supported on single and multicolumn piers with heights ranging from 2.67(m) to 6.57(m). All multicolumn piers consist of two cylindrical piers supporting the two decks through pot bearings and stoppers. The first five pairs of piers are single column cylindrical (or rectangular) piers (Fig. 3), supporting the deck through pot bearings and stoppers. The abutments are seat type; the seismic gap is considered along the longitudinal direction but not the transverse one to prevent derailment. The bridge is modelled using linear and nonlinear elements and material laws, as described at the relevant section above and depicted in Fig.3.

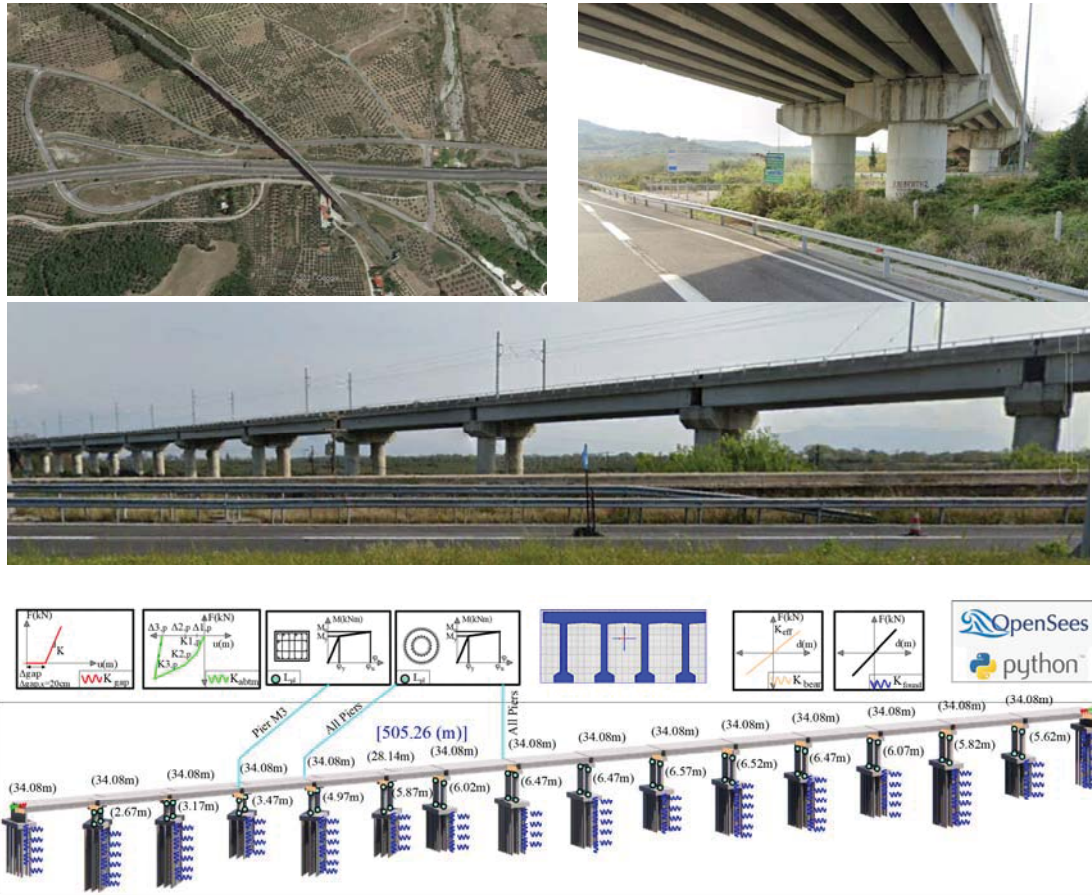


Figure 3: Description of Tirothea-Domokos railway bridge and details of the structural model

Regarding the effect of VBI consideration on the seismic fragility of critical bridge components, it is obvious from Fig.4 that the component seismic fragility (i.e. the probability of damage for different levels of earthquake intensity) is decreased, mainly for higher limit states, in case that the train is considered to move on the bridge during the earthquake and vehicle-bridge interaction is accounted for. The latter is attributed to the fact that the consideration of the vehicle during analysis differentiates the dynamic characteristics of the bridge, resulting in a different earthquake response that is additionally related to the structural system and the properties (ductility, inelastic performance, etc.) of the components.

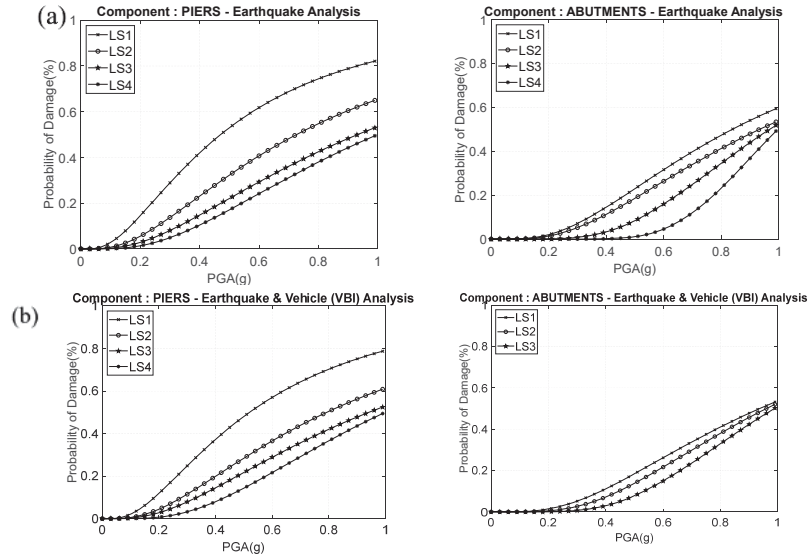


Figure 4: Seismic fragility curves of the critical components of the bridge subsystem with (a) and without (b) VBI consideration for the Tirothea-Domokos Railway Bridge and x-direction

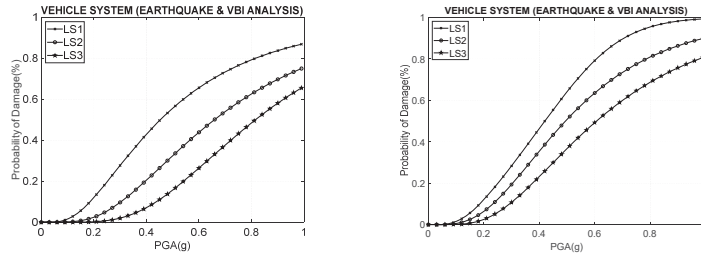
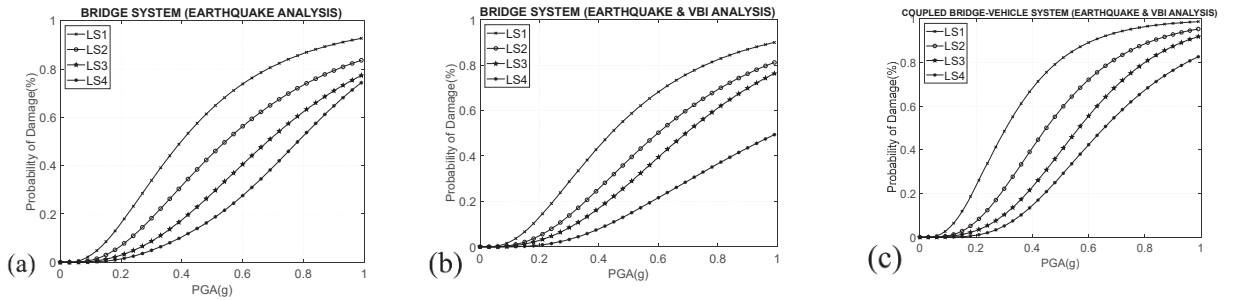


Figure 5: Seismic fragility curves of the vehicle subsystem for the Tirothea-Domokos Railway Bridge (x- and y-direction)

Fragility Curves (X-direction) – Bridge System & Coupled Bridge-Vehicle System



Fragility Curves (Y-direction) – Bridge System & Coupled Bridge-Vehicle System

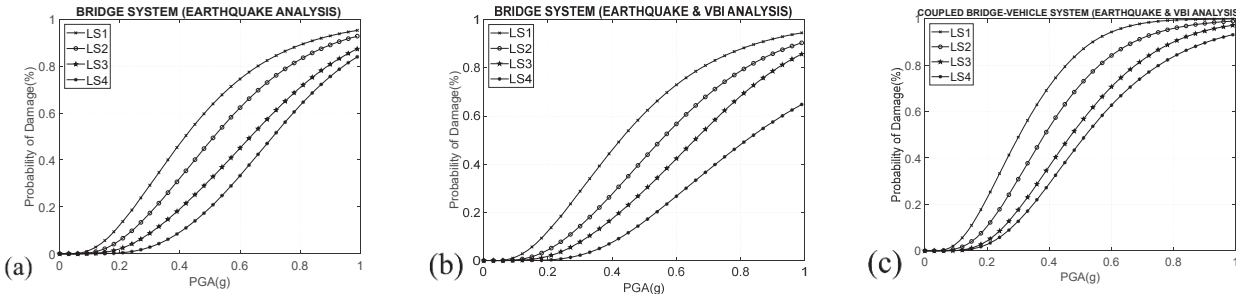


Figure 6: Seismic fragility curves of the bridge subsystem with and without VBI consideration (a,b) and of the coupled train-bridge system with VBI consideration for the Tirothea-Domokos Railway Bridge (x- and y-direction)

Respectively, VBI consideration was found to reduce the seismic fragility of the bridge system and both the longitudinal and transverse direction, compared to the relevant without

the train movement and VBI consideration. The reduction is greater for the higher limit states and the transverse direction of the bridge and is consistent with the previous comment regarding the effect of VBI on the seismic fragility of components, since series connection is assumed for the estimation of the bridge system's fragility.

The seismic fragility of the vehicle subsystem, i.e. the probability of damage related to the exceedance of the limit state defined for running stability, dynamic bridge performance and running safety, are presented for LS1 to LS3 (same with LS4) in Figure 5. The consideration of the aforementioned limit states in the frame of the coupled system analysis and the derivation of relevant fragility curves is obviously critical, based on Fig.6 (c). The seismic fragility of the coupled vehicle-bridge system for both the longitudinal and transverse direction is obviously higher for all the damage states when the limit states related to the vehicle performance are considered in the frame of fragility analysis (accounting for series connection between subsystems). Therefore, it was found crucial to account for VBI and for limit states related to the vehicle performance for the estimation of the coupled systems' fragility since the system is practically coupled and the train safety, stability, etc affects the total performance. However, for resilience, restoration and loss assessment, all the subsystem and component fragility curves should be considered.

6 CONCLUSIONS

A novel methodology for fragility analysis of the coupled vehicle-bridge system is presented herein, accounting for the fragility of subsystems (vehicle and bridge). Limit state thresholds are defined at component and subsystem level and the probabilistic framework is applied, analyzing the coupled system on the basis of a co-simulation technique. A fully parameterized, software is developed including a tailor-made module for vehicle analysis (multibody system), the use of an open-source software for bridge analysis and a module developed for fragility analysis based on the proposed framework. The methodology and framework proposed are applied to a representative, simply supported bridge of the Greek railway network, providing the coupled systems' fragility curves. The most important conclusions from the application of the methodology to the case study bridge are summarized below:

- The seismic fragility of critical bridge *components* is decreased for the case that VBI is considered, mainly for higher limit states. The latter is attributed to the differentiation of the dynamic characteristics of the bridge due to VBI resulting in a different earthquake response, also related to the structural system and the properties (ductility, inelastic performance, etc.) of the components.
- VBI consideration was found to reduce the seismic fragility of the *bridge system* and both the longitudinal and transverse direction, compared to the relevant without the train movement and VBI consideration. The reduction is greater for the higher limit states and the transverse direction of the bridge.
- The seismic fragility of the coupled vehicle-bridge system for both the longitudinal and transverse direction is higher for all the damage states when the limit states related to the vehicle performance are considered. Therefore, it was found crucial to account for VBI and for limit states related to the vehicle performance for the estimation of the coupled systems' fragility.

ACKNOWLEDGEMENTS

The authors would like to thank ERGOSE SA & METESEISM SA for providing access to the data (drawings, technical reports) of the case study bridges.

This project has received funding from the Hellenic Foundation for Research and Innovation (HFRI) and the General Secretariat for Research and Innovation (GSRT), under grant agreement No 617”



REFERENCES

- [1] H. Xia, N. Zhang, N., W.W. Guo, *Dynamic Interaction of Train-Bridge Systems in High-Speed Railways*. Springer-Verlag, 2018.
- [2] A.A. Shabana, K.E. Zaazaa, H. Sugiyama, *Railroad Vehicle Dynamics: A Computational Approach. Flexible Multibody Dynamics*. CRC Press, 2010.
- [3] Q. Zeng, and E.G. Dimitrakopoulos, Vehicle-bridge interaction analysis modeling derailment during earthquakes. *Nonlinear Dynamics*, **93-4**, 2315-2237, 2018.
- [4] Q. Zeng, C.D. Stoura, E.G. Dimitrakopoulos, A localized lagrange multipliers approach for the problem of vehicle-bridge-interaction. *Engineering Structures*, **168**, 82-92, 2018.
- [5] Y.E. Wu, Y.B. Yang, J.D. Yau, Three-Dimensional Analysis of Train-Rail-Bridge Interaction Problems. *Vehicle System Dynamics*, **36-1**, 1-35, 2001.
- [6] X.Y. Lei, *High Speed Railway Track Dynamics. Models, Algorithms and Applications*. Springer Verlag, 2017.
- [7] C. D. Stoura, E. Paraskevopoulos, E.G. Dimitrakopoulos & S. Natsiavas. A Dynamic Partitioning Method to solve the vehicle-bridge interaction problem. *Computers and Structures*, **251**, 2021.
- [8] T.S. Paraskeva, E.G. Dimitrakopoulos, Q. Zeng, Dynamic vehicle-bridge interaction under simultaneous vertical earthquake excitation. *Bull. Earthquake Eng*, **15**, 71-95, 2017.
- [9] Y.F. Mehmet, C.O. Barlas, Seismic assessment of a multi-span steel railway bridge in Turkey based in nonlinear time history. *Nat. Hazards Earth Syst. Sci*, **18**, 231-240, 2018.
- [10] E. Paraskevopoulos, S. Stefanidou, S. Natsiavas, (2019). A novel approach for the analysis of a coupled train-railway bridge system: Basic Principles and Methodology. 7th ECCOMAS Thematic Conf on Computational Methods, COMPDYN 2019, 24-26 June, Crete, Greece.
- [11] E. Paraskevopoulos, S. Natsiavas. On applications of Newton's law to mechanical systems with motion constraints. *Nonlinear Dynamics*, **72 (1-2)**, 455-475, 2013
- [12] S. Natsiavas, E. Paraskevopoulos. A set of ordinary differential equations of motion for constrained mechanical systems. *Nonlinear Dynamics*, **79(3)**, 2015.

- [13] M. Zhu, F. McKenna, & M. H. Scott, OpenSeesPy: Python library for the OpenSees finite element framework. *SoftwareX*, 7, 6–11., 2018
- [14] F. Naeim, & J. M. Kelly, *Design of Seismic Isolated Structures*. John Wiley & Sons, INC., U.S.A., 1999.
- [15] Zhang, J., & Huo, Y. Evaluating effectiveness and optimum design of isolation devices for highway bridges using the fragility function method. *Engineering Structures*, 31(8), 1648–1660, 2009.
- [16] Stefanidou, S.P., Sextos, A. G., Kotsoglou, A. N., Lesgidis, N., & Kappos, A. J., Soil-structure interaction effects in analysis of seismic fragility of bridges using an intensity-based ground motion selection procedure. *Engineering Structures*, **151**, 366-380, 2017.
- [17] Stefanidou, S.P., & Kappos, A. J. Methodology for the development of bridge-specific fragility curves. *Earthquake Engineering & Structural Dynamics*, **46**, 73–93, 2017.
- [18] Olivier, B., Verlinden, O., & Kouroussis, G. Effect of applied force cosimulation schemes on recoupled vehicle/track problems. *Multibody System Dynamics*, 50(4), 337–353, 2020

REDUCTION OF LOCAL DAMAGES IN PRECAST POST-TENSIONED SEGMENTAL BRIDGE PIERS

Parya Ahmadi¹, Ehsan Ahmadi², and Mohammad M. Kashani³

¹ MSc, University of Mohaghegh Ardabili, Ardabil, Iran
Ahmadii.Parya@gmail.com

² Lecturer, Birmingham City University, Birmingham, UK
Ehsan.Ahmadi@bcu.ac.uk

³ Associate Professor, University of Southampton, Southampton, UK
Mehdi.Kashani@soton.ac.uk

Abstract

The application of precast post-tensioned segmental (PPS) bridge piers is growing in order to reduce global damages through rocking motion of the segments when subject to lateral excitations. However, local damages still exist in form of concrete spalling and crushing at the compression zones when one segment rocks on top of the underlying segment. Hence, this work will address reduction of these local damages in PPS piers through confinement of concrete segments by glass-fibre reinforced polymer (GFRP) tubes and use of elastic layers between segments at the joints. To achieve this goal, a robust Finite Element (FE) model is first developed in ABAQUS software, and is experimentally validated using the existing literature. The cyclic behaviour of the experimentally-validated FE model is then determined. It was found that the GFRP tubes and elastic layers significantly reduce local damages of PPS piers at the joints.

Keywords: Precast Post-Tensioned Segmental Piers, Glass-Fibre Reinforced Polymer, Finite Element Model, Elastic Layer, Cyclic Loading.

1 INTRODUCTION

Bridges are one of the crucial components of any transport network and any small disruption in their functionality can result in enormous economic damages and life losses. In particular, lateral excitations such as earthquake, can cause severe damages in bridge structures. Conventional cast-in-place (CIP) reinforced concrete (RC) piers are constructed monolithically with the bridge deck, and experience permanent damages in form of plastic hinges during

severe earthquake loadings. One of the most effective solutions to avoid any plastic hinge, widely considered by researchers in accelerated bridge construction (ABC) [1], is precast post-tensioned segmental (PPS) piers [2]. In ABC, the concrete segments are manufactured offsite with higher quality, and then transferred to the construction site to be assembled. Additionally, the construction process is expedited, and environmental pollution is reduced. The rocking mechanism of the segments and self-centering effect of the post-tensioned tendon decrease the residual deformation of the PPS piers [3].

On the other hand, application of fibre reinforced polymer (FRP) material is growing in concrete piers due to its high stiffness and resistance against corrosion, weathering, and chemical attacks [4,5]. Using FRP around concrete piers enhances their performance by adding extra confinement to the concrete. In existing piers, FRP tubes are used to strengthen the pier, and in design of new piers, FRP tubes increase axial loading capacity of the pier [4]. FRP tubes also prevent the cover concrete from spalling, and significantly increase the ductility and lateral strength of the pier subject to seismic loading events [6]. The FRP tubes have larger flexural strength and higher strength-to-weight ratio compared to steel tubes, and reduce the creep strain of the confined concrete [7,8].

In moderate- and high-seismicity regions, each segment of the PPS piers may still experience local damages at the contact interfaces (e.g. compression zones at the joints) in form of concrete spalling and crushing [4]. This is because of high stress concentration at the joints due to high compressive stresses [9]. To reduce or even eliminate concrete spalling and crushing at the joints, the segments were confined with steel jackets [10,11,12]. However, the steel jackets yield, and thus induce permanent residual deformations in the pier. Therefore, this study adopts a new approach in order to reduce the local damages and a damage-free PPS pier. The current study numerically investigates PPS piers confined with glass fibre reinforced polymer (GFRP) tubes, where elastic layers are used between the segments. To achieve this aim, a robust FE model is first developed and validated. Then, cyclic behavior of the pier is studied to investigate the effects of GFRP tubes around the segments and elastic layers between the segments.

2 NUMERICAL MODELLING

Four PPS specimens are modelled: (1) PPS pier without GFRP tube and elastic layer, P, (2) PPS pier with GFRP tubes, PT, (3) PPS pier with elastic layers, PL, and (4) PPS pier with GFRP tubes and elastic layers, PTL. To study the effects of the flexibility of the elastic layers between the segments, three values of Young's modulus are considered for the elastic layers: 05, 10 and 15 GPa. All the PPS specimens are summarized in Table 1, and the FE models of the PPS piers are shown in Figure 1.

Pier Name	Pier Description	GFRP Tube	Elastic Layer (E_{layer})
P	Without GFRP tube and elastic layer	-	-
PT	With GFRP tubes	✓	-
PL05	With elastic layers	-	✓ (05 GPa)
PL10		-	✓ (10 GPa)
PL15		-	✓ (15 GPa)
PTL05	With GFRP tubes and elastic layers	✓	✓ (05 GPa)
PTL10		✓	✓ (10 GPa)
PTL15		✓	✓ (15 GPa)

Table 1: PPS specimens with different configurations of GFRP tubes and elastic layers.

Figure 1 compares all the PPS pier specimens considered in this study. A 3D FE modelling of the PPS pier is developed in ABAQUS [13]. Figure 2 shows geometric details of the PPS piers. The 3D FE model of the piers is defined with n segments ($n = 6$), of width B ($B = 0.5$ m) and height h ($h = 0.5$ m). To provide the self-centering mechanism under a lateral cyclic loading, an unbounded post-tensioned tendon passes through a duct in the segments, and is fixed to the top of the pier and the bottom of the foundation. The duct has a diameter of 80 mm, and the post-tensioned tendon area is considered 20 % of the segment area [14]. The elastic layers of height of h_L ($h_L = 5$ cm) are used between the segments.

The segments, foundation, and tendon are modelled using eight-node 3D brick elements (C3D8R). The segments, layers, and tendons are deformable solids while the foundation is a discrete rigid element. The GFRP tubes are modelled as shell elements around the concrete segments. To model the joints, the surface-to-surface contact elements are adopted. The tangential friction between the surfaces is taken 0.5 [15]. To model the normal contact between the surfaces, the hard contact is used. To model the unboundedness of the tendon, the frictionless surface-to-surface contact element is adopted between the tendon and the inside face of the ducts, through the segments and layers. The unbounded tendon is embedded in a load stub at the top of the pier and in the foundation.

Figure 1: The FE models of: (a) P, without GFRP tubes and elastic layer, (b) PT, with GFRP tubes, (c) PL, with elastic layers, and (d) PTL, with GFRP tubes and elastic layers.

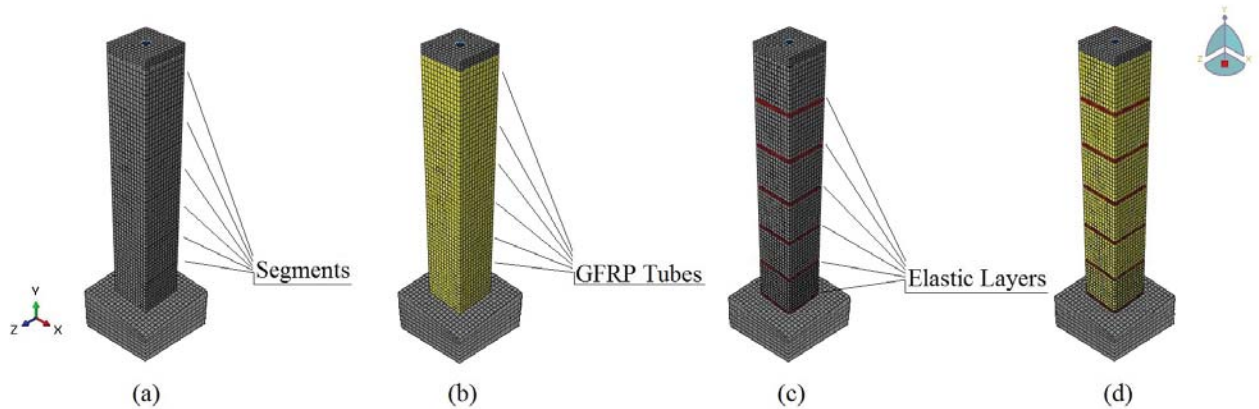


Figure 2: Geometric details of the piers: (a) P and PT, and (b) PL, and PTL.

To define concrete material of the segments, there are two models in ABAQUS: (i) smeared cracking model, and (ii) damaged plasticity model. The concrete damage plasticity is recommended for concrete piers subject to monotonic, cyclic and dynamic loading as used in this study [13,16]. Figure 3a shows the stress-strain of concrete for both confined (with GFRP tubes) and unconfined (without GFRP tubes) concrete [17]. The concrete's modulus of elasticity, Poisson's ratio, and density are 34.6 GPa, 0.2, and 22 kN/m³, respectively. To simulate the opening between the joints, tension strength of concrete is taken zero. The post-tensioning tendon is modelled by a bilinear elastic-plastic model, shown in Figure 3b. The initial post-tensioning of the tendon is $T_0 = \alpha f_y$, where α is the yield force ratio of the tendon, 0.2, and f_y is yield stress of the tendon. The tendon's modulus of elasticity, yielding stress, Poisson's ratio, and density, 200 GPa, 2000 MPa, 0.3, and 78.4 kN/m³, respectively. To model the GFRP tubes, the elastic behavior of Lamina type is used [13]. To develop the material properties, five constants are required: three shear moduli (G_{12} ; G_{13} ; G_{23}) and two Young's moduli

(E_{11} ; E_{22}). Each shear modulus is taken 3 MN/m^2 , and each Young's modulus is considered 65 GN/m^2 .

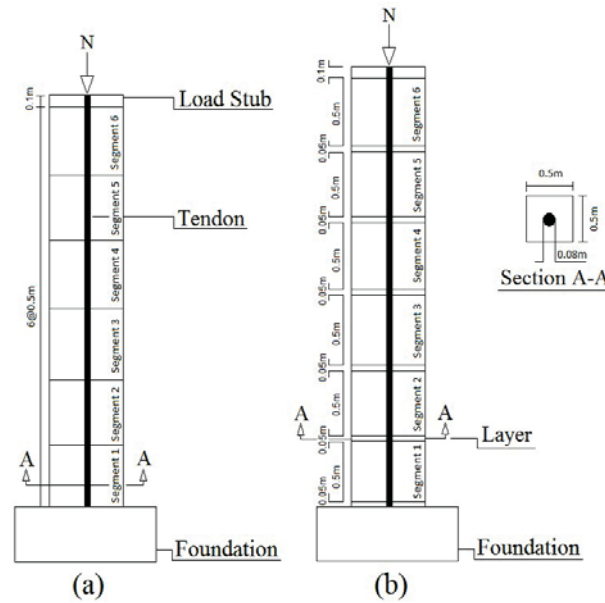


Figure 3: Stress-Strain models of: (a) concrete, and (b) steel.

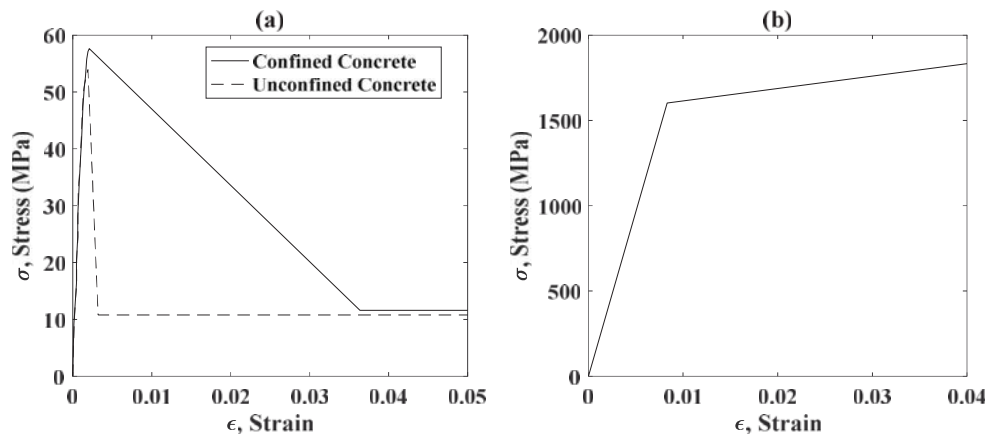
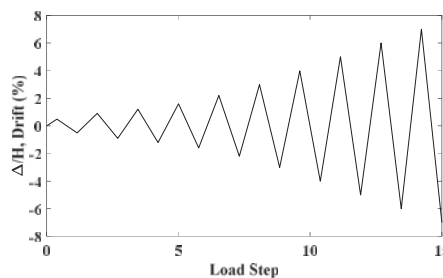


Figure 4: Cyclic loading pattern.



3 VALIDATION

The modelling approach, explained in Section 2, is validated through comparing with the experimental results by Palermo et al. [16,18]. The tested pier is composed of one concrete segment of height 1.6 m, and width 0.35 m without any elastic layer or GFRP tubes. The model has two $\phi 12.7$ mm tendons, which pass through a pair of ducts in the segment and are fixed to a load stub at the top of the pier and a foundation at the bottom of the pier, as shown in Figure 5. The post-tensioning force ratio, α , is 0.3, and the compressive strength of concrete, f'_c , is 54.1 MPa. The yield stress, f_y , and ultimate stress, f_u , of the post-tensioned tendons are assumed 1600 MPa and 1870 MPa, respectively. All the details of the modelling and loading are the same with those in the Palermo's test [16]. As Figure 6 shows, the lateral force-drift of the FE model and the test are very compatible, which demonstrates the robustness of the FE model in capturing lateral behavior of post-tensioned rocking piers. This comparison validates the reliable simulating of the models to study the behavior of the PPS piers.

Figure 5: Geometric details of the tested pier.

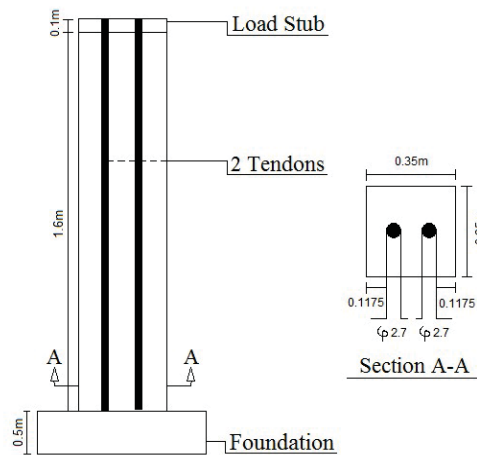
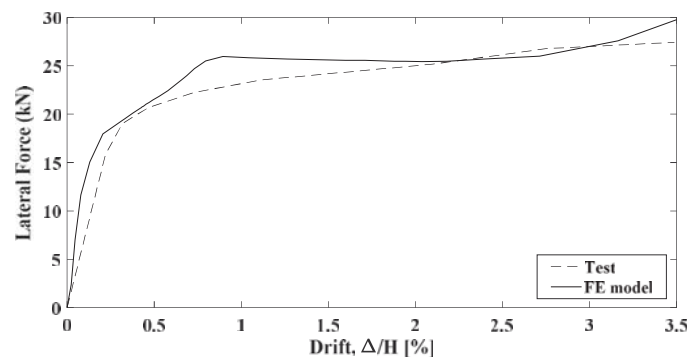


Figure 6: Comparison of FE modelling and test pushover curves.



4 ANALYSIS AND RESULT

In this section, the cyclic behaviors of the eight piers, summarized in Table 1, are compared. Figure 7 demonstrates hysteretic response curves of the piers: the base shear, V , versus drift, Δ/H ; Δ is the tip displacement of the pier, and H is the total height of the pier. The results demonstrate different cyclic behavior for each pier. The pier, P, without any tube and layer, demonstrates a sudden reduction in its stiffness as the slope of the hysteretic loops suddenly drops after a few cycles at small drift ratios, less than 1% (Figure 7a). This stiffness re-

duction is due to the concrete spalling and crushing at small drift ratios at the toe of the segments (see Figure 3a). Adding GFRP tubes around the pier's segment, enhances the strength and slightly the ductility of the pier (Figure 7b). However, significant residual drifts are seen, particularly for the last cycles of the loading. Adding elastic layers between the segments slightly affects the strength of the pier, and gives zero-residual drift for the pier (Figure 7c). The simultaneous use of elastic layers and GFRP tubes increases ultimate strength of the pier, and results in zero-residual drift. This is very desirable in a PPS pier as it is intended to be a damage-free pier (zero-residual drifts).

Figure 7: Hysteretic response curves of the piers: (a) P, (b) PT, (c) PL15, and (d) PTL15.

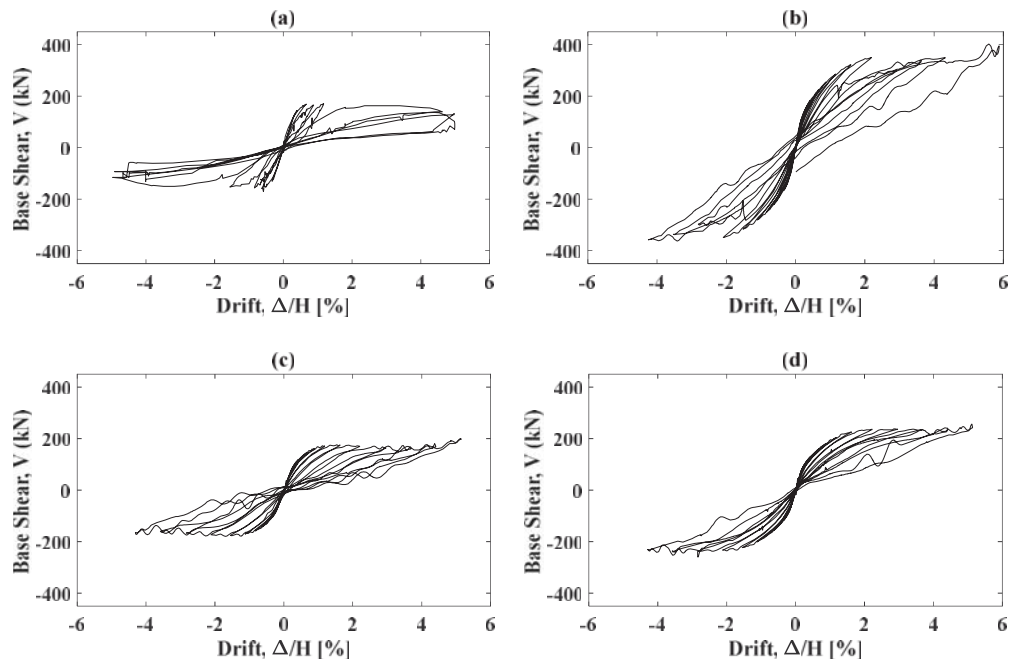


Figure 8 shows hysteretic response curves of the piers with different values of Young's modulus for the elastic layer. It is seen that the models with both GFRP tubes and elastic layers reach higher lateral strength. For the piers, PL and PTL, (Figures 8a and 8b), larger Young's modulus of the elastic layers gives higher lateral strength; The maximum value of base shear for Young's modulus of 15 GPa are 200 and 273.8 kN, for the piers PL and PTL, respectively.

Figure 8: The effect of Young's modulus of the layer on the hysteretic response curves of the piers: (a) PL, and (b) PTL.

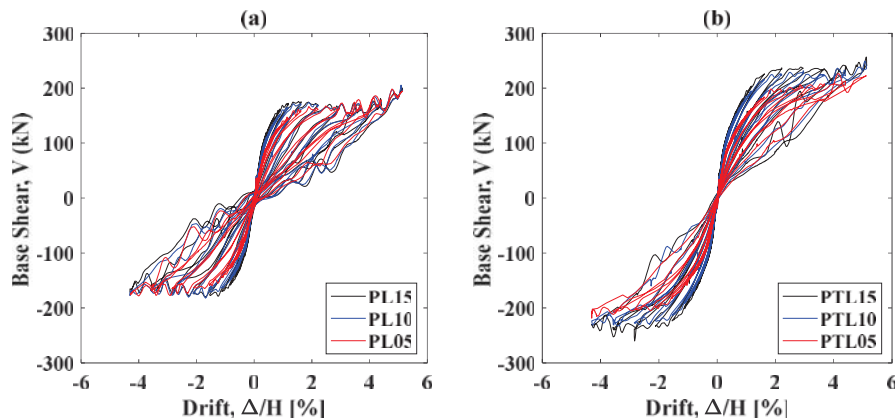


Figure 9 shows the stress at the toe of the bottommost joint (base joint), located between the bottom segment and the foundation, for the piers P, PT, PL15, and PTL15. For the pier P, after a few cycles of loading, the concrete crushes at the toe subject to high value of strain (see Figure 3a), and consequently, an abrupt drop is seen in the compressive stress at very small drifts, less than 1% (Figure 9a). Using GFRP tubes around the segments delays the stress drop by adding confinement to the concrete (Figure 9b). Adding elastic layers to the pier eliminates the sudden drop in the compressive strength of concrete (Figure 9c). The pier with both GFRP tubes and elastic layers (Figure 9d) reaches to higher compressive strength for higher values of drift compared to when using elastic layers only (Figure 9c). Figures 10 and 11 show the stress at the topmost, second bottom, and bottommost joints of the piers, PL and PLT. For both piers, the bottommost joint experiences the highest stress and local damage at their toes. The maximum values of stress is obtained for the models with Young's modulus of 15 GPa (PL15 and PTL15).

Figure 9: Compressive stress at the toe of the bottommost joint for the piers: (a) P, (b) PT, (c) PL15, and (d) PTL15.

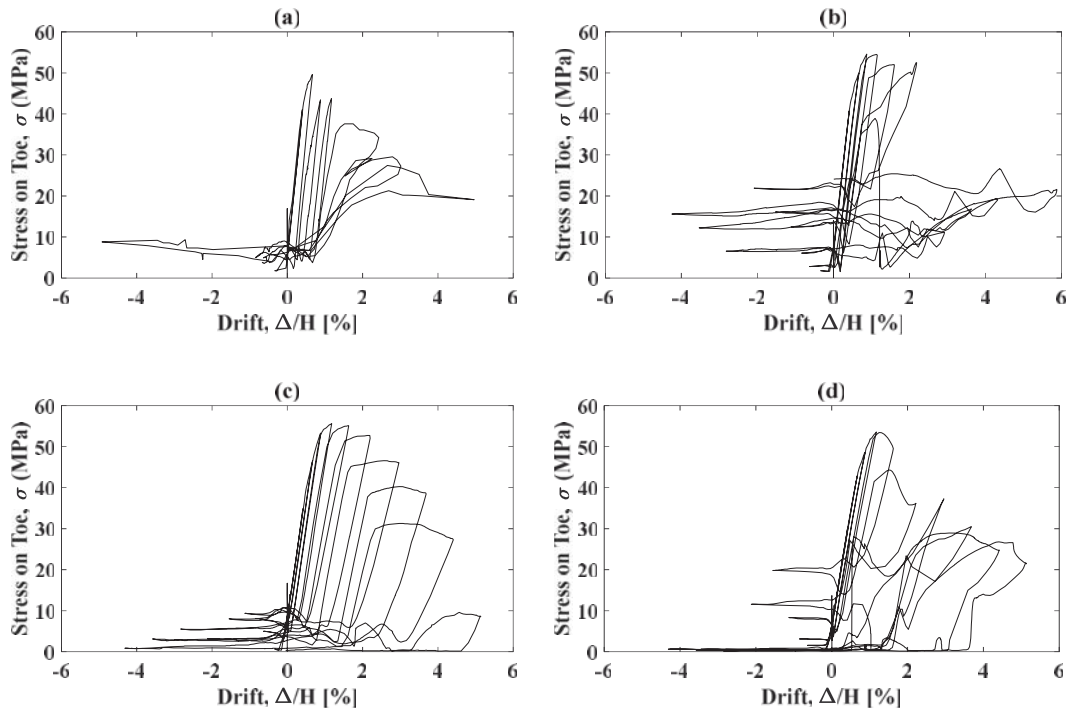


Figure 10: The effect of Young's modulus of the layer on the stress at: (a) the topmost joint, (b) the second bottom joint, and (c) the bottommost joint of the pier PL.

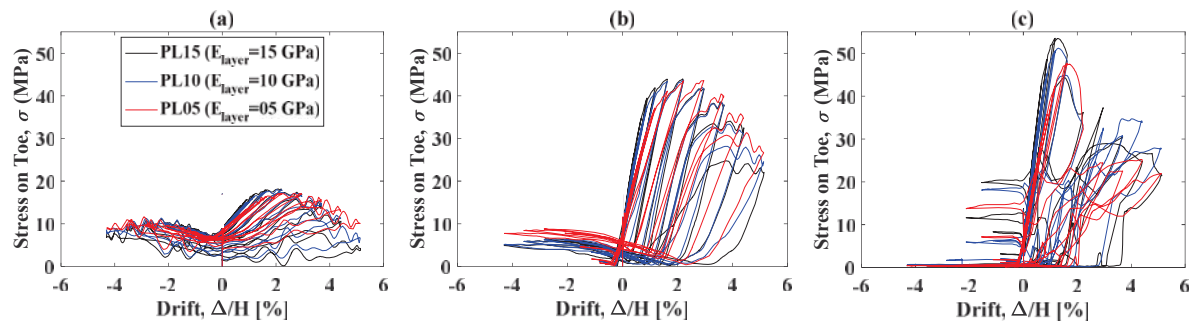
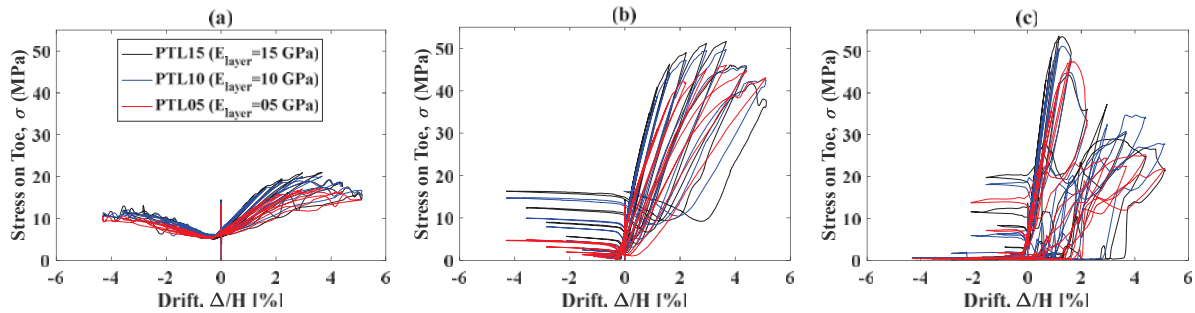


Figure 11: The effect of Young's modulus of the layer on the stress at: (a) the topmost joint, (b) the second bottom joint, and (c) the bottommost joint of the pier PLT.



5 CONCLUSIONS

In this study, the effects of GFRP tubes and elastic layers on local damage of PPS piers were investigated. Hence, an FE model including GFRP tubes around segments and elastic layers in joints between segments were modelled using ABAQUS software.

It is found that elastic layers significantly reduce local damages at the joints, and GFRP tubes improve the results for large drifts. The results also show that GFRP tubes increase strength of the PPS piers, and both elastic layers and GFRP tubes give a zero-residual drift for the pier. These conclusions are very promising in designing a damage-free PPS pier. Hence, elastic layers need to be designed, and experimental tests need to be conducted for further investigation and validation of the proposed strategy.

REFERENCES

- [1] M. Tazarv, M. Saiid Saiidi. Low-damage precast columns for accelerated bridge construction in high seismic zones. *Journal of Bridge Engineering*, **21(3)**, 04015056, 2016 Mar 1.
- [2] H. Dawood, M. ElGawady, J. Hewes, Behavior of segmental precast posttensioned bridge piers under lateral loads. *Journal of Bridge Engineering*, **17(5)**, 735-46, 2012 Sep 1.
- [3] SL. Billington, RW. Barnes, JE. Breen, A precast segmental substructure system for standard bridges. *PCI journal*, **44(4)**, 56-73, 1999 Jul 1.
- [4] MA. ElGawady, A. Sha'lan, Seismic behavior of self-centering precast segmental bridge bents. *Journal of Bridge Engineering*, **16(3)**, 328-39, 2011 May 1.
- [5] AA. Maghsoudi, R. Rahgozar, SH. Hashemi, Flexural testing of high strength reinforced concrete beams strengthened with CFRP sheets. *International Journal of Engineering*, **1, 22(2)**, 131-46, 2009 Aug.
- [6] SA. Sheikh, SA. Jaffry, C. Cui, Investigation of glass-fibre-reinforced-polymer shells as formwork and reinforcement for concrete columns. *Canadian Journal of Civil Engineering*, **34(3)**, 389-402, 2007 Mar 1.
- [7] KA. Soudki, MF. Green, Performance of CFRP retrofitted concrete columns at low temperatures. *In2nd International Conference on Advanced Composite Materials in Bridges and Structures*, Montreal, Quebec, 11-14, 1996 Aug 11.

- [8] O. Youssf, MA. ElGawady, JE. Mills, X. Ma, Finite element modelling and dilation of FRP-confined concrete columns. *Engineering Structures*, **79**, 70-85, 2014 Nov 15.
- [9] Hewes JT, Priestley MJN., Seismic design and performance of precast concrete segmental bridge columns. *Report no. SSRP-2001/25*, University of California, San Diego, 2002.
- [10] M. ElGawady, AJ. Booker, HM. Dawood, Seismic behavior of posttensioned concrete-filled fiber tubes. *Journal of Composites for Construction*, **14(5)**, 616-28, 2010 Oct.
- [11] MA. ElGawady, A. Sha'lan, Seismic behavior of self-centering precast segmental bridge bents. *Journal of Bridge Engineering*, **16(3)**, 328-39, 2011 May 1.
- [12] CC. Chou, YC. Chen, Cyclic tests of post-tensioned precast CFT segmental bridge columns with unbonded strands. *Earthquake engineering & structural dynamics*, **35(2)**, 159-75, 2006 Feb.
- [13] SL. Billington, JK. Yoon, Cyclic response of unbonded posttensioned precast columns with ductile fiber-reinforced concrete. *Journal of Bridge Engineering*, **9(4)**, 353-63, 2004 Jul.
- [14] Simulia DS. Abaqus 2017, Documentation. Providence, Rhode Island, US, 2017.
- [15] E. Ahmadi, MM. Kashani, Numerical investigation of nonlinear static and dynamic behaviour of self-centring rocking segmental bridge piers. *Soil Dynamics and Earthquake Engineering*, **128**, 105876, 2020 Jan 1.
- [16] H. Zhu, MT. Stephens, CW. Roeder, DE. Lehman, Inelastic response prediction of CFST columns and connections subjected to lateral loading. *J. Constr. Steel Res.*, **40**, 132:130, 2017,
- [17] BD. Scott, R. Park, MJ. Priestley, Stress-strain behavior of concrete confined by overlapping hoops at low and high strain rates. *InJournal Proceedings*, **79.1**, 13-27, 1982 Jan 1.
- [18] A. Palermo, S. Pampanin, D. Marriott, Design, modeling, and experimental response of seismic resistant bridge piers with posttensioned dissipating connections. *Journal of Structural Engineering*, **133.11**, 1648-61, 2007 Nov.

BASE VERSUS TOP ACTIVE CONTROL TO IMPROVE DYNAMIC AND SEISMIC PERFORMANCES OF RIGID BLOCKS

A. Di Egidio¹, A. Contento², and S. Pagliaro³

¹University of L'Aquila - DICEAA
via G. Gronchi 19, 64100 L'Aquila - Italy
e-mail: angelo.diegidio@univaq.it

²University of L'Aquila - DICEAA
via G. Gronchi 19, 64100 L'Aquila - Italy
e-mail: alessandro.contento@univaq.it

³University of L'Aquila - DICEAA
via G. Gronchi 19, 64100 L'Aquila - Italy
e-mail: stefano.pagliaro@graduate.univaq.it

Keywords: Rigid block-like structures, base active control, active mass damper, pole placement method, rocking motion, overturning.

Abstract. *This paper compares the efficiency of two active control systems based on the same control algorithm in protecting rigid block-like structures from overturning. The control algorithm is the Pole Placement Method that is aimed at transforming the rest position of a rigid block into a stable equilibrium point. The two control systems differ in the position of the actuator driven by the active control algorithm. In the first case, the block is placed on a horizontally translating support that is connected to the ground by an actuator able to provide a controlled displacement. In the second case, a small mass able to run at the top of the block is driven by an actuator capable of applying a controlled displacement. This kind of protection system is commonly called Active Mass Damper. The effectiveness of the two control systems is analysed by comparing the overturning spectra that represent the amplitude of the harmonic excitation able to overturn the block versus its circular frequency. Several simulations have been conducted using different recorded earthquakes to evaluate the performances of the two control methods in the reduction of the rocking angle and the protection from the overturning of the block. The results show the excellent performance of both the considered control systems.*

1 INTRODUCTION

The protection of rigid block-like elements such as obelisks, statues, storage boxes, transformers, cabinets, and racks for both civil and industrial use is a challenging topic for civil engineers. The most common failure of such elements is the overturning caused by base excitation. Different techniques have been proposed to prevent such overturning. The majority of the researchers proposed protection techniques that are based on passive control systems.

For example, in [1, 2], the authors studied the effectiveness of base anchorages. Some papers investigated the efficiency of base isolated systems [3, 4, 5, 6, 7]. Several authors used mass-dampers that have been modeled either in the shape of a pendulum [8, 9, 10, 11] or as a single degree of freedom mass running on the top of the rigid block [12, 13, 14]. Some papers presented the coupling of rigid bodies with inerter devices [15, 16]. Lately, some researchers studied the use of semi-active anchorages [17, 18], and active control techniques [19, 20, 21] to increase the amplitude of base excitation required to topple a rigid block.

This paper compares the efficiency of two active control systems based on the same control algorithm in protecting rigid block-like structures from overturning. The control algorithm is the Pole Placement Method that is aimed at transforming the rest position of a rigid block into a stable equilibrium point. In fact, in the classical rocking equations of rigid blocks based on Housners model [22], the rest position is not an equilibrium point. The two control systems differ in the position of the actuator driven by the active control algorithm. In the first control system, the block is placed on a horizontally translating support. Such support has a mass that is negligible compared to the mass of the block and it is connected to the ground by an actuator able to provide a controlled displacement. This protection system was already studied in [20]. In the second control system, a small mass able to run at the top of the block is driven by an actuator capable of applying a controlled displacement. This protection system is commonly called Active Mass Damper (AMD).

For both methods, the linearized rocking equations are used to derive the control laws. The optimal coefficients of the control laws are selected assuming the overshoot as the key parameter. Both the control systems exhibit a low sensitivity to the geometrical characteristics of the rigid block so that the same optimized control coefficients can be used for a wide class of rigid blocks. The robustness of the two control systems is also investigated by considering the limitations of the control forces and different sampling and delay times.

The effectiveness of the two control systems is analyzed by comparing the overturning spectra that are obtained with and without control. Such overturning spectra provide the amplitude of the harmonic excitation able to overturn the block versus its circular frequency. Several simulations have also been conducted using different recorded earthquakes to evaluate the performances of the two control methods in the reduction of the rocking angle and the protection from the overturning of the block under seismic excitation.

The results show the excellent performance of both the considered control systems. Consequently, since the performances of the control systems are comparable for all the working conditions considered, the choice between the two methods is dictated by the technical and technological aspects of each specific application.

2 ACTIVE CONTROL METHODS

In both the control methods the mechanical system is a rigid block in the shape of a parallelepiped with a height $2h$ and a base $2b$ (Fig. 1). The base dimension orthogonal to the rocking plane has unitary length. The mass of the block is $M = \rho \times 2b \times 2h \times 1.0$, where the mass den-

sity $\rho = 1800\text{kg/m}^3$. The block cannot slide, so its motion is described by only the Lagrangian parameter $\theta(t)$ that is the rocking angle. In the first control method, the block is placed on a horizontally translating support. Such support has a mass that is negligible compared to the mass of the block and it is connected to the ground by an actuator able to provide the controlled displacement $u^B(t)$ (Fig. 1a). In the second control scheme, a small mass m , able to run at the top of the block, is driven by an actuator capable of applying the controlled displacement $u^T(t)$ (Fig. 1b).

The control algorithm used in this paper is the Pole Placement Method (PPM) that is aimed at transforming the rest position of a rigid block into a stable equilibrium point. It is worth observing that, the two rocking equations describing the motion around the two base pivots of a stand-alone rigid block, do not admit the rest position ($\theta(t) = 0$) as an equilibrium point. The PPM algorithm makes the rest position a stable equilibrium point in both the rocking equations.

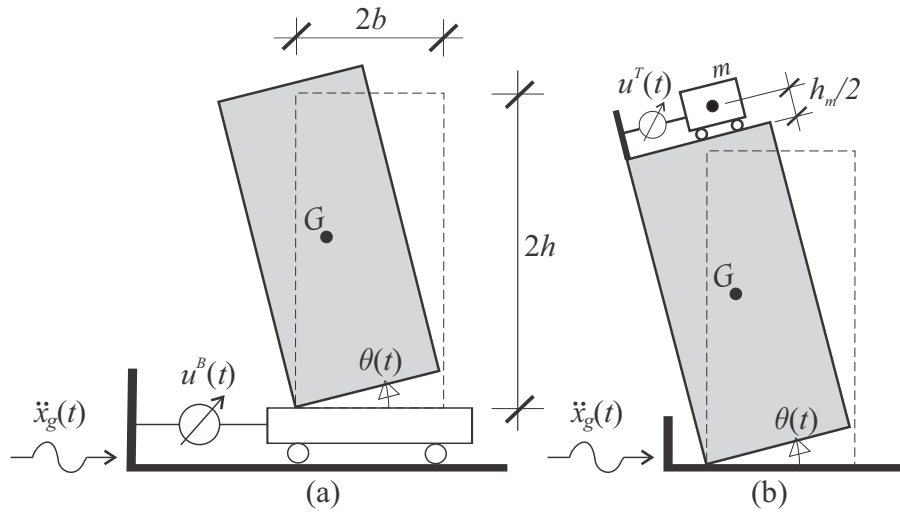


Figure 1: Active control systems: (a) Base Active Control (BAC); (b) Top Active Control (TAC) or active mass damper.

2.1 Base active control system

Since the active control system applied to the base of the rigid block and based on the Pole Placement Method was already studied in [20], in this subsection only the main governing equations are reported. The system shown in Fig. 1a can be described by the same equations of a stand-alone block with an additional term due to the control device. The control displacement $u^B(t)$ applies an acceleration $\ddot{u}^B(t)$ at the base of the block that works as the external excitation. Hence, it appears in the equations of motion as a contribution added to external acceleration \ddot{x}_g . The equations of motion read

$$\begin{aligned} (J_G + MR^2) \ddot{\theta}(t) + gMR \sin(\alpha_{cr} - \theta(t)) - MR \cos(\alpha_{cr} - \theta(t)) (\ddot{x}_g(t) + \ddot{u}^B(t)) &= 0 \\ (J_G + MR^2) \ddot{\theta}(t) - gMR \sin(\alpha_{cr} + \theta(t)) - MR \cos(\alpha_{cr} + \theta(t)) (\ddot{x}_g(t) + \ddot{u}^B(t)) &= 0 \end{aligned} \quad (1)$$

where g is the gravity acceleration; J_G is the polar momentum evaluated with respect to the mass centre G ; α_{cr} is the value of $\theta(t)$ in which the vertical projection of the mass centre G passes through the base rocking corner; R is the distance between the mass centre G and the base rocking corner.

The control algorithm is obtained by linearising the equations of rocking motion with respect to $\theta(t)$. This assumption leads to an excellent approximation in the case where $\theta(t)$ is very small. This fact occurs in sufficiently tall blocks where θ has to be smaller than the critical angle α_{cr} .

The Pole Placement Method has two main objectives: (i) to vanish the external excitation at each instant and (ii) to make the rest position of the block a stable point. The first objective is achieved by providing a control force opposite to the external one to the system. For the second objective, the rest position of the block can be considered a stable point if the Jacobian matrix is modified in such a way that the eigenvalues have negative real part. The control law $\ddot{u}^B(t)$, representing the control acceleration that the actuator has to apply to the system at each time t reads

$$\ddot{u}^B(t) = \pm g\alpha_{cr} - \ddot{x}_g(t) - \frac{1}{4} \left(4 + q_{22}^2 \right) \vartheta(t) - \frac{g}{\omega_o} q_{22} \dot{\vartheta}(t) \quad (2)$$

where q_{22} is a control coefficient that has to be determined. The sign $(-)$ refers to the rocking motion around the left corner, whereas the sign $(+)$ refers to rocking motion around the right corner.

2.2 Active mass damper system

The equations of motion of the controlled system in Fig. 1b are obtained via a Lagrangian approach

$$\begin{aligned} 0.25 [\theta''(t)(4b^2(m+M) + m(4u(t)(2b+u(t)) + h_m^2 + 8hh_m) + 4h^2(4m+M)) + \\ 4m(2b\dot{\theta}(t)\dot{u}(t) + u(t)(g\cos(\theta(t)) + 2\dot{\theta}(t)\dot{u}(t)) - 2h\ddot{u}(t)) + \\ 4\ddot{x}_g(t)(-\sin(\theta(t))(b(m+M) + mu(t)) - h(2m+M)\cos(\theta(t))) - \\ 2mh_m(g\sin(\theta(t)) + \ddot{u}(t) + \cos(\theta(t))\ddot{x}_g(t))] + \\ bg(m+M)\cos(\theta(t)) - gh(2m+M)\sin(\theta(t)) + J_G\ddot{\theta}(t) = 0 \end{aligned} \quad (3)$$

$$\begin{aligned} 0.25 [\ddot{\theta}(t)(4b^2(m+M) + m(4u(t)(u(t)-2b) + h_m^2 + 8hh_m) + 4h^2(4m+M)) - \\ 2m(4b\dot{\theta}(t)\dot{u}(t) + gh_m\sin(\theta(t)) - 2gu(t)\cos(\theta(t)) + (h_m + 4h)\ddot{u}(t) - \\ 4u(t)\dot{\theta}(t)\dot{u}(t) + 2\ddot{x}_g(t)(2\sin(\theta(t))(b(m+M) - mu(t)) - \\ (2h(2m+M) + mh_m)\cos(\theta(t)))) - \\ bg(m+M)\cos(\theta(t)) - gh(2m+M)\sin(\theta(t)) + J_G\ddot{\theta}(t) = 0 \end{aligned}$$

where $h_m/2$ is the vertical distance between the centre of the small mass m and the top of the block (see Fig. 1b.) Also in this case the control algorithm is obtained by linearising the equations of rocking motion with respect to the variables $\theta(t)$ as

$$\dot{\mathbf{Z}}(t) = \mathbf{A}_1(t)\mathbf{Z}(t) + \mathbf{A}_2 + \mathbf{A}_3\ddot{x}_g(t) + \mathbf{A}_4\ddot{u}^T(t) \quad (4)$$

where $\mathbf{Z}(t) = \left\{ \begin{matrix} \theta(t) & \dot{\vartheta}(t) \end{matrix} \right\}^T$ is the state variables vector and the matrices \mathbf{A}_1 , \mathbf{A}_2 , \mathbf{A}_3 , and \mathbf{A}_4 read

$$\begin{aligned} \mathbf{A}_1(t) = \begin{bmatrix} 0 & 1 \\ \omega_0^2 & \mp \frac{2bm}{J_{A,B}}\dot{u}^T(t) \end{bmatrix}; \quad \mathbf{A}_2 = \begin{bmatrix} 0 \\ \mp \frac{bg(m+M)}{J_{A,B}} \end{bmatrix} \\ \mathbf{A}_3 = \begin{bmatrix} 0 \\ \frac{\omega_0^2}{g} \end{bmatrix}; \quad \mathbf{A}_4 = \begin{bmatrix} 0 \\ \frac{\omega_0^2}{g} - \frac{hM}{J_{A,B}} \end{bmatrix} \end{aligned} \quad (5)$$

where $\omega_0^2 = (hM + (2h + h_m/2)m)g/J_{A,B}$ is the linear frequency associated to the motion of the block and $J_A = J_B$ is the total polar momentum evaluated with respect to one of the base rocking corners. The following control law is assumed:

$$\mathbf{A}_4 \ddot{u}^T(t) = -\mathbf{A}_2 - \mathbf{A}_3 \ddot{x}_g(t) - \mathbf{Q}(t) \mathbf{Z}(t) \quad (6)$$

where $\mathbf{Q}(t)$ is a weighting matrix

$$\mathbf{Q}(t) = \begin{bmatrix} 0 & 1 \\ \omega_0^2 q_{12} & \omega_0 q_{22} \mp \frac{2bm}{J_{A,B}} \dot{u}^T(t) \end{bmatrix} \quad (7)$$

By introducing Eq. 6 into the linearised equations Eq. 4, the linearised controlled system becomes

$$\dot{\mathbf{Z}}(t) = (\mathbf{A}_1(t) - \mathbf{Q}(t)) \mathbf{Z}(t) \quad (8)$$

where the Jacobian matrix of the controlled system $\mathbf{A}_1(t) - \mathbf{Q}(t)$ does not depend on time. The linearised system Eq. 8 admits the rest position $\theta(t) = 0$ as stable equilibrium point if the eigenvalues of the linearised Jacobian matrix are real, negative, and coincident. This fact occurs for the control coefficient $q_{12} = 1/4(4 + q_{22}^2)$.

By expanding Eq. 6, it is possible to observe that the control displacement $u^T(t)$ has to satisfy the following differential equation:

$$\ddot{u}^T(t) \mp c_u(\dot{\theta}) \dot{u}^T(t) \mp c_0 + c_g(\ddot{x}_g) + c_\theta(\theta) + c_{\dot{\theta}}(\dot{\theta}) = 0 \quad (9)$$

where the coefficients in the equation are

$$\begin{aligned} c_u(\dot{\theta}) &= \frac{2bmg}{J_{A,B} - hMg} \dot{\theta}; & c_0 &= \frac{bg^2(M+m)}{J_{A,B} - hMg}; & c_g(\ddot{x}_g) &= \frac{J_{A,B}\omega_0^2}{J_{A,B} - hMg} \ddot{x}_g \\ c_\theta(\theta) &= \frac{1}{4} \frac{J_{A,B}g\omega_0^2}{J_{A,B} - hMg} (4 - q_{22}^2) \theta; & c_{\dot{\theta}}(\dot{\theta}) &= \frac{1}{4} \frac{J_{A,B}g\omega_0}{J_{A,B} - hMg} q_{22} \dot{\theta} \end{aligned} \quad (10)$$

2.3 Ideal and real controlled system

The real working conditions of the controlled system differ from the ideal case because (i) the control accelerations $\ddot{u}^{B,T}$ have to be limited to a threshold value that depend on the characteristics of the actuator, (ii) the control device applies the accelerations $\ddot{u}^{B,T}$ with a delay that depends on the characteristics of the control system, and (iii) the control algorithm is obtained from the linearised equations of motion, hence it works sufficiently well with the nonlinear mechanical system if the smallness of the rocking angle θ can be considered a valid approximation.

It is considered that the actuators can reach the maximum acceleration $\ddot{u}_{max}^B = 0.2g$ and $\ddot{u}_{max}^T = 2.0g$, respectively for the base and the top active control system. Therefore, by taking the moving mass of Fig. 1b $m = \gamma M$, with $\gamma = 0.1$, it follows that the maximum control forces $F_{max}^B = M0.2g$ and $F_{max}^T = m2.0g = \gamma M2.0g$ are equal. In the simulations performed in the paper, it is always considered this threshold value of the controlled accelerations.

As it is known, real control systems suffer of time-delays between the real time and the application of the control displacement. One of the delays is the so-called sampling time δt_c , which measures the time-step between two successive data acquisitions of the state variables necessary to evaluate the control displacement. The other type of delay is the time-delay δt_d , which is related to the speed of the control system and of the actuator to evaluate and to apply

the control displacement to the system. An analysis to evaluate the robustness of the control systems to a variation of the time-delays is performed below.

Both active control systems depend only on the coefficient q_{22} (Eq. 2 and Eqs. 9-10). The search of the optimal value of such coefficient can be usually performed in terms of step response of the system ([23]). In a rigid block system the step input cannot assume any value because the block overturns over a threshold of the base acceleration. Hence, a small constant base acceleration, capable of uplifting the block but not sufficient to overturn it, is considered. The efficiency of the control system can be measured by evaluating the so called *overshoot*. Under a step excitation, the block uplifts, reaches the overshoot, that is the maximum rocking amplitude, and comes back to the rest position, thanks to the control apparatus. A parametric analysis is performed in order to evaluate the overshoot as a function of the sole control coefficient q_{22} , in both the considered control systems. Such parametric analysis provide the same value of the control coefficient $q_{22} = 7$ for both control systems.

3 UPLIFT AND IMPACT CONDITIONS

In order to correctly describe the behaviour of the system, the knowledge of the transition conditions among the different possible phases of motion is needed. The system at hand presents two transition conditions: uplift and impact.

The uplift condition provides the minimum base acceleration a_{up} capable of uplifting the block. It is assumed that the control system works after the beginning of the rocking motion. The minimum value of the horizontal acceleration able to uplift the block can be obtained from the balance between the resisting moment (due to the weight of the block) and the overturning moment (due to the inertial forces).

During the rocking motion, when the rotation $\theta(t)$ approaches to zero, an impact between the block and the support occurs. Consequently, the pivot of the rocking motion changes and it is necessary to evaluate the angular velocity of the block after the impact. Post-impact conditions of the rocking motion can be found assuming that the impact happens instantly, the block position remains unchanged, and the conservation of the angular momentum is imposed.

3.1 Base Active Control system

Since the control system works only after the beginning of rocking motion, the uplift and impact conditions are the same as those of a stand-alone rigid block. The uplift condition reads

$$|a_{up}| \geq \frac{g}{\lambda} \quad (11)$$

where $\lambda = h/b$ is the slenderness of the block. An uplift occurs around the left (right) base corner when $a_{up} > 0$ ($a_{up} < 0$).

The impact condition provides the following restitution coefficient

$$\mu = \frac{\dot{\vartheta}^+}{\dot{\vartheta}^-} = \frac{(J_O - 2bS_y)}{J_O} \quad (12)$$

where J_O is the polar inertia of the block with respect one of the two base corners; $S_y = \pm Mb$ (sign minus in case of re-uplift around the left base corner, sign plus in case of re-uplift around the right corner) is the static moment of the block with respect to a vertical axis passing through one of the two base corners and superscript $(\cdot)^-$ and superscript $(\cdot)^+$ denote pre- and post-impact quantities respectively.

3.2 Top Active Control system

The acceleration able to uplift the system can be found from the balance between the resisting and the overturning momenta as

$$|a_{up}| \geq \frac{(M + m)bg}{Mh + m\left(2h + \frac{h_m}{2}\right)} \quad (13)$$

An uplift occurs around the left (right) base corner when $a_{up} > 0$ ($a_{up} < 0$). By imposing the conservation of the angular momentum before and after an impact, both evaluated respect to the re-uplifting corner, the following restitution coefficient is obtained:

$$\mu = \frac{\dot{y}^+}{\dot{y}^-} = \frac{4\left(J_O - 2bS_y + m\left(-b^2 + 4h^2 + u(t)^2\right)\right) + mh_m^2 + 8h_mh_m}{4\left(J_O + m\left(b^2 + 2bu(t) + 4h^2 + u(t)^2\right)\right) + mh_m^2 + 8h_mh_m} \quad (14)$$

It is worth observing that, if $m = 0$ the uplift and the impact conditions given by Eq. 13 and Eq. 14 becomes the same as those of a stand-alone rigid block.

4 PARAMETRIC ANALYSIS

4.1 Harmonic excitation

An harmonic base excitation is first considered. It reads

$$\ddot{x}_g(t) = A_s \sin(\Omega t) \quad 0 \leq t \leq t_{\max} \quad (15)$$

where $\Omega = 2\pi/T_s$ is the circular frequency of the excitation, T_s is the period of the harmonic cycle, A_s is its amplitude, and $t_{\max} = 10s$ is the maximum time used in the numerical integrations. The assessment of the efficiency of the two control algorithms in protecting the block from the overturning is performed by comparing the results obtained with those of the uncontrolled system. A parametric analysis is performed to obtain overturning spectra, where the overturning amplitude A_s of the excitation is plotted versus the frequency Ω . The single overturning spectrum is obtained for blocks with fixed base $2b$, fixed slenderness λ , and fixed upper limit of the control forces $F_{max}^B = F_{max}^T$ (as explained in Subsection 2.3).

The overturning spectra referring to two blocks with different geometrical characteristics are shown in Fig. 2. Specifically, the spectra in the first row of the figure refer to a block with $2b = 0.4$ m and $\lambda = 5$, whereas the spectra in the second row refer to a block with $2b = 0.6$ m and $\lambda = 7$. Figure 2a shows the spectra of both the blocks obtained for three different couples of time delays and where the Base Active Control (BAC) is used. As can be observed, the spectra obtained for different time-delays are very close to each other. This means that the BAC system manifest a good robustness to time-delays. In Figure 2b the spectra of both blocks with the Top Active Control (TAC) and different time-delays are reported. The results show that the TAC system is more sensible to time-delays than the BAC system. This means that the TAC does not manifest a good robustness to time-delays. However, when the time-delays increase (from the dashed curve to the dotted curve), the distance among the spectra reduces.

Finally, the comparison among overturning spectra with the BAC system, the TAC system, and with No Active Control (NAC) are shown in Fig. 2c. These spectra refer to a fixed couple of time-delays ($\delta t_c = 0.1s$ and $\delta t_d = 0.05s$), that refer to a control apparatus of mean characteristics as in [17] and [18]. As can be observed, both the control systems exhibit a better performance than the case without active control. Nevertheless, the TAC system assures the

best performances in reducing the overturning of the block, since for each frequency Ω of the harmonic excitation the overturning of the block occurs for higher amplitude A_s of the excitation.

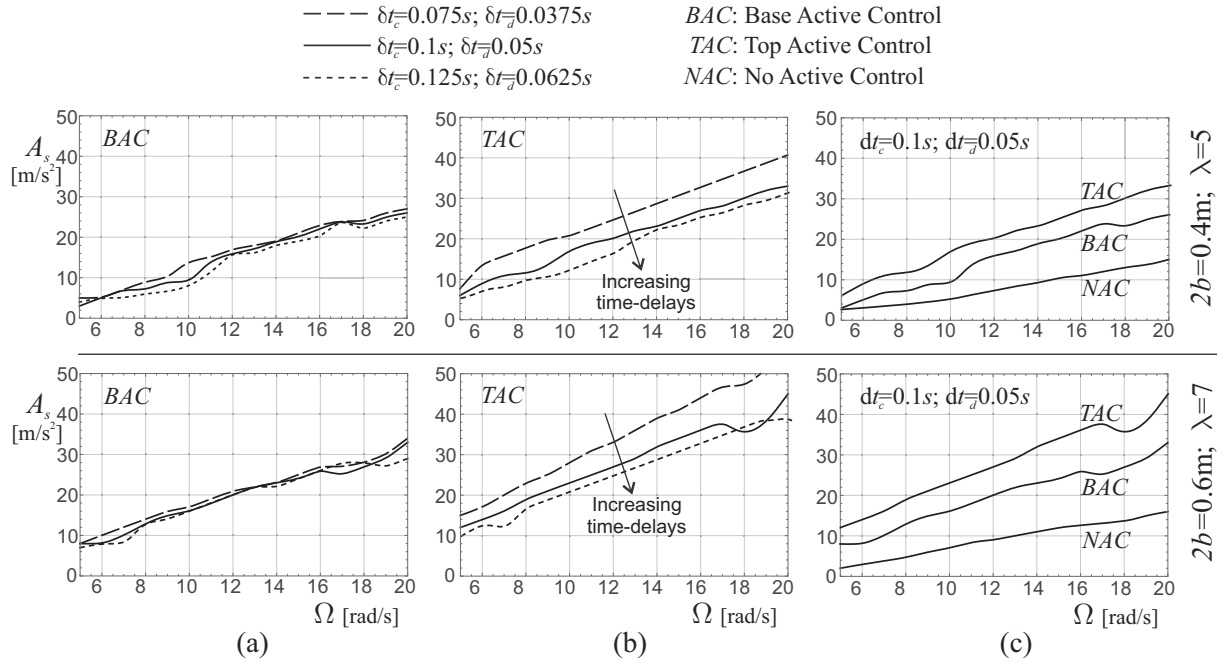


Figure 2: Overturning spectra: (a) spectra of the Base Active Control (BAC) system obtained for different time-delays; (b) spectra of the Top Active Control (TAC) system obtained for different time-delays; (c) comparison among spectra for fixed time-delays ($F_{max}^B = F_{max}^T$, $F_{max}^B = 0.2Mg$, $F_{max}^T = 2.0mg$, $m = \gamma M$, $\gamma = 0.1$).

4.2 Seismic excitation

Two earthquake records are used as seismic input. The earthquake records are

- Kobe, Takarazuka-000 station, ground motion recorded during the 1995 Japan earthquake;
- Parkfield, CO2-065 ground motion recorded during the California earthquake 1966.

Figure 3 shows the time-histories (left graphs) and the pseudo-acceleration elastic spectra (right graphs) of the two earthquake records. The results of the parametric analyses are shown by means of rocking maps that represent the contour plots (for a single seismic record) of the maximum rocking angle in the parameter plane ($2b - \lambda$). The regions where the block overturns (*i.e.*, where the maximum rocking angle is $\theta_{max} = \pi/2$) are colored in dark grey; the regions where the block does not overturn are colored in light grey, and the contour levels represent the maximum values of $\theta(t)$. For each earthquake, the rocking maps of the two control systems and the map obtained without active control are compared. In the analysis, the sampling time and time-delay are assumed as $\delta t_c = 0.1s$ $\delta t_d = 0.05s$, respectively, as in ([17] and [18]).

In Fig. 4 the rocking maps are organized in matrix form. Along the two columns there are the maps of the earthquake records (Kobe and Pacoima), whereas the rows refer to NAC, BAC, and TAC. As can be observed, the active control systems drastically reduce the overturning regions (dark grey regions) with respect to the case without active control. However, the TAC appears to

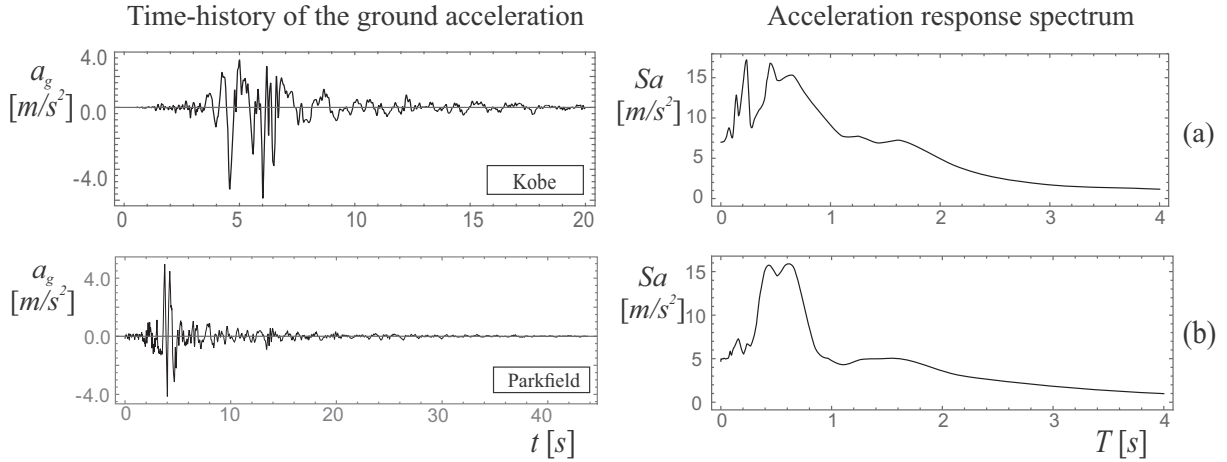


Figure 3: Time-histories (left graphs) and pseudo-acceleration elastic spectra (right graphs) of the earthquakes analysed: (a) Kobe; (b) Parkfield.

be able to extend the safety region (i.e., the regions where no overturning occurs) to the whole parameter $(2b - \lambda)$ plane. In fact, the BAC is not able to protect the block from overturning in the whole parameter plane under Kobe earthquake, as done by the TAC (see maps of the second row in Fig. 4).

Fig. 5 shows sections of the rocking maps that help to understand the efficiency of the control systems in reducing θ_{max} . The sections are identified by paths *I* and *II* in Fig. 4. Specifically, Fig. 5a shows the two section along path *I*, referring to Kobe earthquake, obtained for the Base and the Top Active Control systems. Instead, Fig. 5b shows the two section along path *II*, referring to Parkfield earthquake, obtained for the BAC and the TAC systems. As can be observed, the use of the TAC system generally leads to values of θ_{max} smaller than those obtained by using the BAC system.

5 CONCLUSIONS

The performances in protecting rigid blocks from the overturning of two different active control systems, both based on the same active control algorithm (i.e., the Pole Placement Method), were investigated and compared. In the first control system, the block is placed on a horizontally translating support that is connected to the ground by an actuator able to provide a controlled displacement. In the second control system, a small mass able to run on the top of the block is driven by an actuator capable of applying a controlled displacement. The control algorithm based on the Pole Placement Method acts both vanishing the external excitation at each instant by imposing a control force opposite to the external one and making the rest position of the block a stable point by suitably modifying the Jacobian matrix of the system and its eigenvalues. A preliminary analysis that considers the overshoot as key parameter was performed to evaluate the optimal coefficients of the control law for the two systems. The optimal value of such coefficients weakly depends on the parameters characterizing the mechanical system and is the same for the two different control systems.

The effectiveness of the two control systems was analysed by comparing the overturning spectra that represent the amplitude of the harmonic excitation able to overturn the block versus its circular frequency. Results showed that both control systems significantly improve the behaviour of the rigid block with respect to the case without control. Nevertheless, if on the

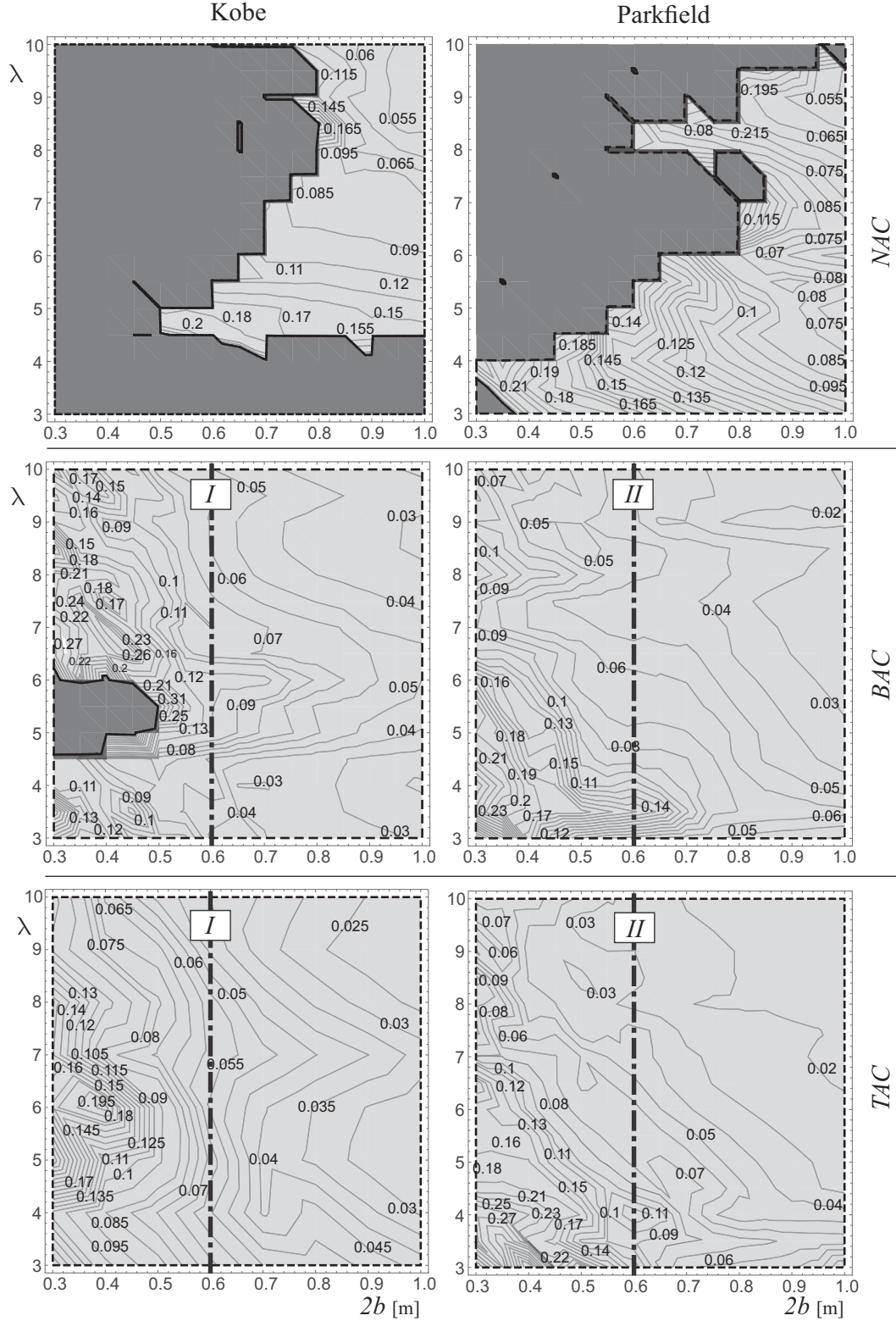


Figure 4: Rocking maps for two different earthquakes (Kobe e Parkfield) and three different configurations: No Active Control (NAC), Base Active Control (BAC), and Top Active Control (TAC).

one hand, the Top Active Control system manifests better performances than the Base Active Control system, on the other hand, this last exhibits an higher robustness to time-delays. Other

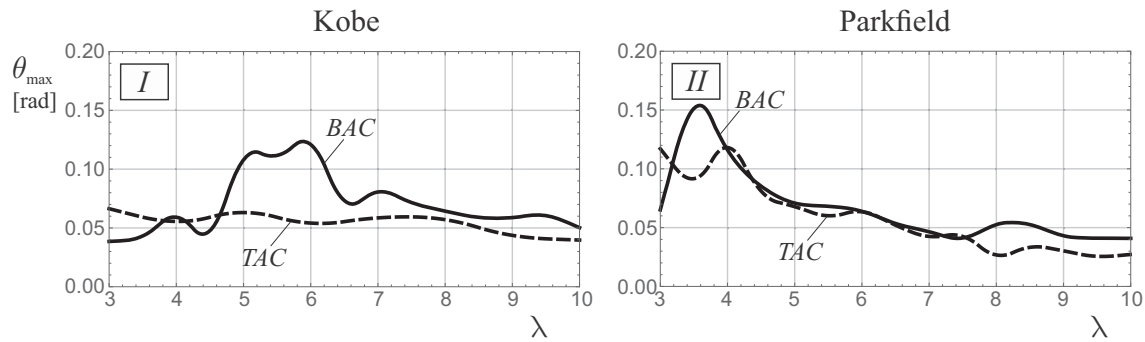


Figure 5: Sections of rocking maps for two different earthquakes (Kobe e Parkfield) and two different configurations: Base Active Control (BAC), and Top Active Control (TAC); ($2b = 0.6$ m).

simulations were also conducted using two recorded earthquakes to evaluate the performances of the control methods in the reduction of the rocking angle and the protection from the overturning of the block. The results showed the excellent performance of both the considered control systems. To conclude, since the performances of the control systems are comparable for all the working conditions considered, the choice between the two methods is dictated by the technical and technological aspects of each specific application.

References

- [1] N. Makris and J. Zhang. Rocking response of anchored blocks under pulse-type motions. *Journal of Engineering Mechanics*, 127(5):484–493, 2001.
- [2] E.G. Dimitrakopoulos and M.J. DeJong. Overturning of retrofitted rocking structures under pulse-type excitations. *Journal of Engineering Mechanics*, 138:963–972, 2012.
- [3] A. Di Egidio and A. Contento. Base isolation of sliding-rocking non-symmetry rigid blocks subjected to impulsive and seismic excitations. *Engineering Structures*, 31:2723–2734, 2009.
- [4] A. Di Egidio and A. Contento. Seismic response of a non-symmetric rigid block on a constrained oscillating base. *Engineering Structures*, 32:3028–3039, 2010.
- [5] A. Contento and A. Di Egidio. On the use of base isolation for the protection of rigid bodies placed on a multi-storey frame under seismic excitation. *Engineering Structures*, 62-63:1–10, 2014.
- [6] I. Calìo and M. Marletta. Passive control of the seismic response of art objects. *Engineering Structures*, 25:1009–1018, 2003.
- [7] M.F. Vassiliou and N. Makris. Analysis of the rocking response of rigid blocks standing free on a seismically isolated base. *Earthquake engineering and structural dynamics*, 41(2):177–196, 2012.
- [8] L. Collini, R. Garziera, K. Riabova, M. Munitsyna, and A. Tasora. Oscillations control of rocking-block-type buildings by the addition of a tuned pendulum. *Shock and Vibration*, 2016:Article ID 8570538, 2016.

- [9] P. Brzeski, T. Kapitaniak, and P. Perlikowski. The use of tuned mass absorber to prevent overturning of the rigid block during earthquake. *International Journal of Structural Stability and Dynamics*, 6(10):Article ID 1550075, 2016.
- [10] A. de Leo, G. Simoneschi, C. Fabrizio, and A. Di Egidio. On the use of a pendulum as mass damper to control the rocking motion of a non-symmetric rigid block. *Meccanica*, 51:2727–2740, 2016.
- [11] A. Di Egidio, R. Alaggio, A. Aloisio, A.M. de Leo, A. Contento, and M. Tursini. Analytical and experimental investigation into the effectiveness of a pendulum dynamic absorber to protect rigid blocks from overturning. *Int. Journal of Non-Linear Mechanics*, 115:1–10, 2019.
- [12] G. Simoneschi, A. de Leo, and A. Di Egidio. Effectiveness of oscillating mass damper system in the protection of rigid blocks under impulsive excitation. *Engineering Structures*, 137:285–295, 2017.
- [13] G. Simoneschi, A. Geniola, A. de Leo, and A. Di Egidio. On the seismic performances of rigid blocks coupled with an oscillating mass working as tmd. *Earthquake Engineering and Structural Dynamics*, 46:1453–1469, 2017.
- [14] A. Di Egidio, A. de Leo, and G. Simoneschi. Effectiveness of mass-damper dynamic absorber on rocking block under one-sine pulse ground motion. *International Limits of Non-Linear Mechanics*, 98:154–162, 2018.
- [15] R. Thiers-Moggia and M. Mlaga-Chuquitaype. Seismic protection of rocking structures with inerters. *Earthquake Engineering and Structural Dynamics*, 48(5):528–457, 2019.
- [16] A. Di Egidio, S. Pagliaro, and C. Fabrizio. Combined use of rocking wall and inerters to improve the seismic response of frame structures. *Journal of Engineering Mechanics*, 2021 (accepted, in press).
- [17] R. Ceravolo, M.L. Pecorelli, and L. Zanotti Fragonara. Semi-active control of the rocking motion of monolithic art objects. *Journal of Sound and Vibration*, 374:1–16, 2016.
- [18] R. Ceravolo, M.L. Pecorelli, and L. Zanotti Fragonara. Comparison of semi-active control strategies for rocking objects under pulse and harmonic excitations. *Mechanical Systems and Signal Processing*, 90:175–188, 2017.
- [19] A. Di Egidio, G. Simoneschi, C. Olivieri, and A.M. de Leo. Protection of slender rigid blocks from the overturning by using an active control system. In *Proceedings of the XXIII Conference The Italian Association of Theoretical and Applied Mechanics*, 2014.
- [20] G. Simoneschi, C. Olivieri, A.M. de Leo, and A. Di Egidio. Pole placement method to control the rocking motion of rigid blocks. *Engineering Structures*, 167:39–47, 2018.
- [21] A. Di Egidio, C. Olivieri, and A.M. de Leo. Protection from overturning of rigid block-like objects with linear quadratic regulator active control. *Structural Control and Health Monitoring*, 27, 2020.
- [22] G.W. Housner. The behavior of inverted pendulum structures during earthquakes. *Bulletin of the Seismological Society of America*, 53(2):404–417, 1963.

- [23] R.C. Dorf and R.H. Bishop. *Modern control system*, 2008.

UNIFORM RISK SPECTRA FOR NEGATIVE STIFFNESS SYSTEMS

Natalia Reggiani Manzo¹, Christos G. Lachanas², Michalis F. Vassiliou¹, and
Dimitrios Vamvatsikos²

¹ ETH Zürich
Institute of Structural Engineering
Stefano-Franscini-Platz 5, 8093 Zürich, Switzerland
{reggianimanzo,vassiliou}@ibk.baug.ethz.ch

² National Technical University of Athens
School of Civil Engineering
9, Iroon Polytechniou str., Zografou Campus, GR-15780, Athens, Greece
{lahanasch,divamva}@central.ntua.gr

Abstract

This paper presents uniform risk spectra for negative stiffness systems that do not exhibit hysteretic damping, named Negative Stiffness Bilinear Elastic (NSBE) systems. The NSBE oscillator can be used to describe the dynamics of deformable rocking systems with or without restraining systems flexible enough to lead to an overall negative stiffness. It can also be used to describe rocking systems equipped with curved extensions at their base. It has been shown that the response of an NSBE system can be well predicted using the response of a Zero Stiffness Bilinear Elastic (ZSBE) system, which is a bilinear system of constant restoring force. The ZSBE system is a single parameter system; therefore it is simple to construct design spectra for it.

For a wide range of ZSBE system strength values, this paper employs Incremental Dynamic Analysis using 105 ordinary (non-pulse-like, non-long-duration) ground motions to obtain the fragility functions for predefined limit-states of the ZSBE seismic response. Fragility functions per limit-state are convolved with the seismic hazard to compute the Mean Annual Frequency of exceedance (MAF). For this study, the seismic hazard curve for a site at Athens Greece is used as it is obtained via probabilistic seismic hazard analysis. Finally, uniform risk spectra per limit-state are obtained by computing the MAF for all the ZSBE oscillators. These spectra can be used for the design of NSBE systems, including rocking oscillators.

Keywords: Uniform Risk Spectra, nonlinear dynamics, negative stiffness, rocking, rocking spectra

1 INTRODUCTION

Rocking has been proposed as an alternative design method in seismic prone regions because it reduces foundation moments and results in resilient structures [1-19]. Differently from structures designed to yield, rocking systems present negative lateral stiffness after uplift.

The negative stiffness value of the free-standing block is defined by its geometry (Fig. 1). Its negative stiffness, however, can be modified by the introduction of restrainers flexible enough to keep the post-uplift stiffness negative (Fig. 2a) [3, 5, 13, 20-22], or by equipping the blocks with extended curved ends (Fig. 2b) [14, 15]. These solutions increase the maximum displacement the rocking system can achieve before overturning, without affecting its uplifting force. The flexible restrainers also act as a redundant mechanism for the rocking structures, a desired mechanism by practicing engineers.

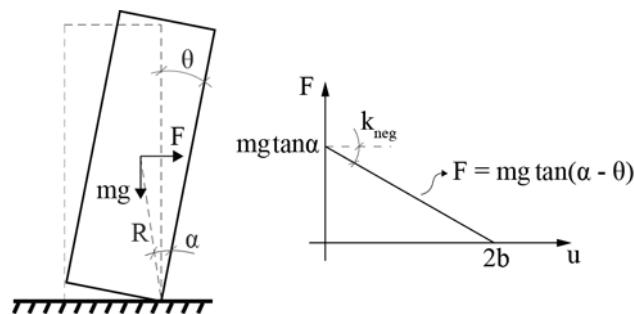


Figure 1. Free-standing rigid rocking block.

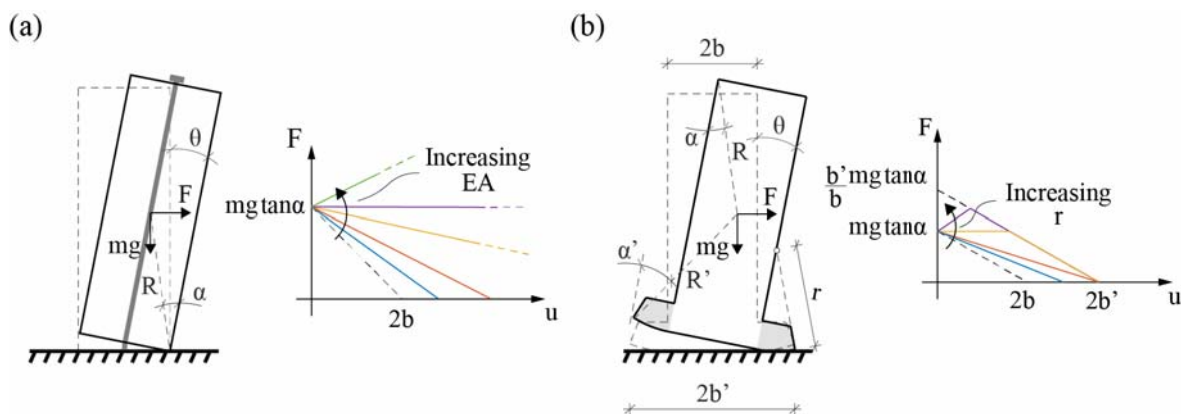


Figure 2. (a) Restrained rigid rocking block, and (b) Curved-base rigid rocking block.

Seismic codes adopt the uniform hazard spectrum concept. The spectrum is constructed using a probabilistic framework and provides seismic actions with a given probability of exceedance. Recently, Luco et al. [23] proposed the Uniform Risk Spectra (URS), which provides seismic actions that results in structures with uniform risk of damage and/or collapse, an indicator much more meaningful for decision makers and users of the designed structure.

Both the uniform hazard spectrum and uniform risk spectrum are useful tools that allow engineers to design structures by only estimating its fundamental period and damping ratio. The elastic spectra, however, cannot be used for designing rocking structures [24]. The inherent negative stiffness of rocking systems would oblige engineers to carry out time-consuming time history analyses when designing such structures.

Reggiani Manzo and Vassiliou [25, 26] have observed that rocking systems having the same uplifting force and being far from their failure point will exhibit roughly equal displace-

ment demand, independently of their post uplift stiffness. Therefore, the displacement of rocking structures of uplift force f_{up} can be computed using as a proxy the displacement of a bilinear oscillator of uplift force f_{up} and infinite displacement capacity (Zero Stiffness Bilinear Elastic (ZSBE) oscillators). This simplification allows the construction of spectra for a range of negative stiffness systems: free-standing rocking frames, restrained rocking frames, or rocking frames with curved ends. Therefore, the design of negative stiffness systems can be accomplished using a spectrum and avoiding time history analysis.

In an attempt to propose a simplified design methodology for negative stiffness systems that also introduces the uncertainty of seismic action, this paper presents uniform risk spectra for rocking structures, using the ZSBE oscillator proxy.

Previous studies have presented fragility curves for rocking structures [27-37], which also consider the random characteristic of seismic actions. These curves, however, were constructed using complex models, or in other cases, considering the classical description of the motion of rocking blocks by its tilt angle. Neither approach allows the construction of a single rocking spectrum that covers all range of systems with negative post-uplift stiffness. On the other hand, the uniform risk spectra proposed herein can be used for any system that presents negative post-uplift stiffness and does not present hysteretic damping.

2 THE ZERO STIFFNESS BILINEAR ELASTIC SYSTEM (ZSBE) AS PROXY FOR NEGATIVE STIFFNESS BILINEAR ELASTIC SYSTEMS (NSBE)

2.1 The Negative Stiffness Bilinear Elastic System

The Negative Stiffness Bilinear Elastic (NSBE) system can describe the dynamics of free-standing (Fig.1), restrained (Fig.2a), and curved-based (Fig.2b) rocking structures, or any other deformable system that presents negative post-uplift stiffness and does not exhibit hysteretic damping.

Fig.3 presents the NSBE oscillator, and its displacement-restoring force relationship. Up until uplift, the system behaves linearly with a positive stiffness (k_{pos}), representing any deformability the system might present before uplifting. After uplifting, the tangent stiffness becomes negative (k_{neg}). The displacement capacity (u_{cap}) is defined not by material failure, but by the displacement where the restoring force becomes negative. Therefore, for an unrestrained rocking column, the displacement capacity is equal to its width.

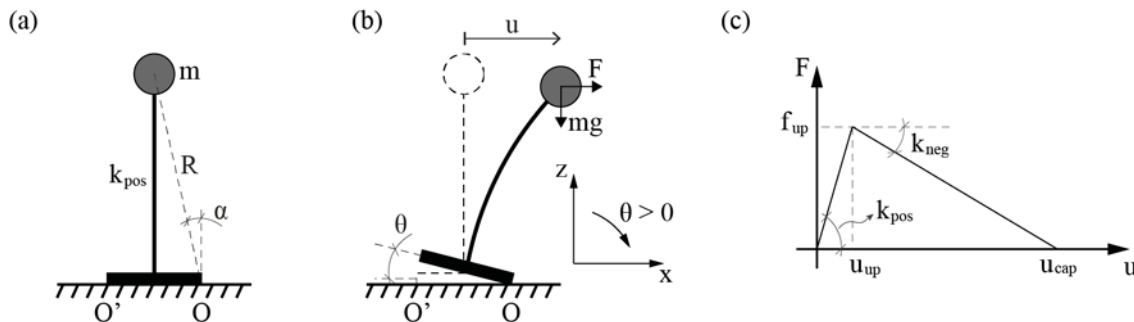


Figure 3. (a,b) NSBE system; and (c) its displacement-restoring force relationship.

Based on its displacement-force relationship (Fig.3c), the oscillator's equation of motion is:

$$m \cdot \ddot{u}(t) + f_{up} \cdot \frac{u(t)}{u_{up}} = -m \cdot \ddot{u}_g(t), \quad |u(t)| \leq u_{up} \quad (1)$$

$$m \cdot \ddot{u}(t) \pm f_{up} \cdot \left(\frac{u_{cap} - u(t)}{u_{cap} - u_{up}} \right) = -m \cdot \ddot{u}_g(t), \quad |u(t)| > u_{up} \quad (2)$$

The upper sign in Eq.2 corresponds to positive displacements, and the lower sign to negative displacements.

Impact damping is the only source of energy dissipation, implying that the ends of the rocking element are protected from damage [38]. When the system's displacement equals to the uplift displacement (u_{up}), the integration is halted, and its post-impact velocity is calculated by a coefficient of restitution (r_c):

$$r_c = \frac{\dot{u}_{postimpact}}{\dot{u}_{preimpact}} \quad (3)$$

Herein, a coefficient of restitution equal to 0.95 is assumed, corresponding to relatively slender structures.

2.2 The Zero Stiffness Bilinear Elastic System

Fig. 4 presents the displacement-force relationship of the Zero Stiffness Bilinear Elastic (ZSBE) system. The system presents the same equation of motion and assumptions of the NSBE system when its displacement capacity tends to infinity, resulting in a system with zero post-uplift stiffness ($k_{neg} = 0$).

The ZSBE can be used as a proxy for the prediction of the response of the NSBE [25,26]. Hence, studying the response of a ZSBE of a given f_{up} and u_{up} suffices for the description of the response of all NSBE of the same f_{up} and u_{up} , independently of their u_{cap} . Therefore, spectra providing u_{max} of the ZSBE as a function of f_{up} for a given u_{up} can be used for the design of NSBE systems. Fig. 5 presents such a spectrum, extracted from Reggiani Manzo and Vassiliou [26]. It refers to $u_{up}=0.0005\text{m}$ and it gives the median response for a set of ground motions selected and scaled as discussed in [26].

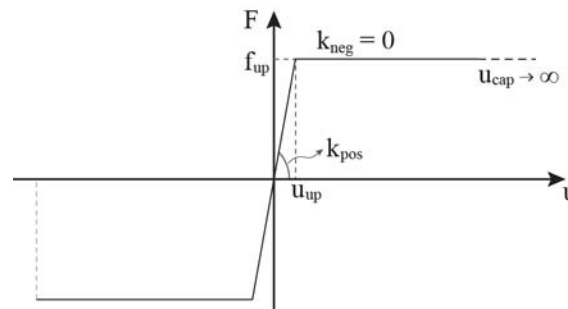


Figure 4. Displacement-restoring force relationship of the ZSBE systems.

2.3 Equal Displacement and Equal Energy Rules for Negative Stiffness Systems

Reggiani Manzo and Vassiliou [25, 26] proposed that the displacement demand of NSBE and ZSBE systems can be related by two different rules: the Equal Displacement rule and the Equal Energy rule.

The Equal Displacement rule assumes that the NSBE and ZSBE system will experience the same displacement demand (Fig. 6a):

$$u_{dem,NS} = u_{dem,ZS} \rightarrow \gamma_{ED} = \frac{u_{dem,NS}}{u_{dem,ZS}} = 1 \quad (4)$$

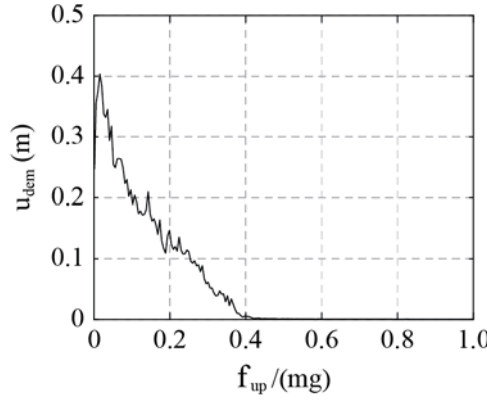


Figure 5. Design spectrum for negative stiffness systems.

In which, γ_{ED} is the ratio of the displacement demand of the NSBE system ($u_{dem,NS}$) to the displacement demand of the ZSBE system ($u_{dem,ZS}$).

The Equal Energy rule assumes that the displacement-force curves of both systems produce the same work. In other words, it assumes that the shaded areas of Fig. 6b are equal. Therefore, the ratio (γ_{EE}) of $u_{dem,NS}$ to $u_{dem,ZS}$ is:

$$\gamma_{EE} = \frac{u_{dem,NS}}{u_{dem,ZS}} = \frac{u_{cap}}{u_{dem,ZS}} - \sqrt{\frac{(u_{cap} - u_{up})}{u_{dem,ZS}} \cdot \frac{(u_{cap} - 2 \cdot u_{dem,ZS} + u_{up})}{u_{dem,ZS}}} \quad (5)$$

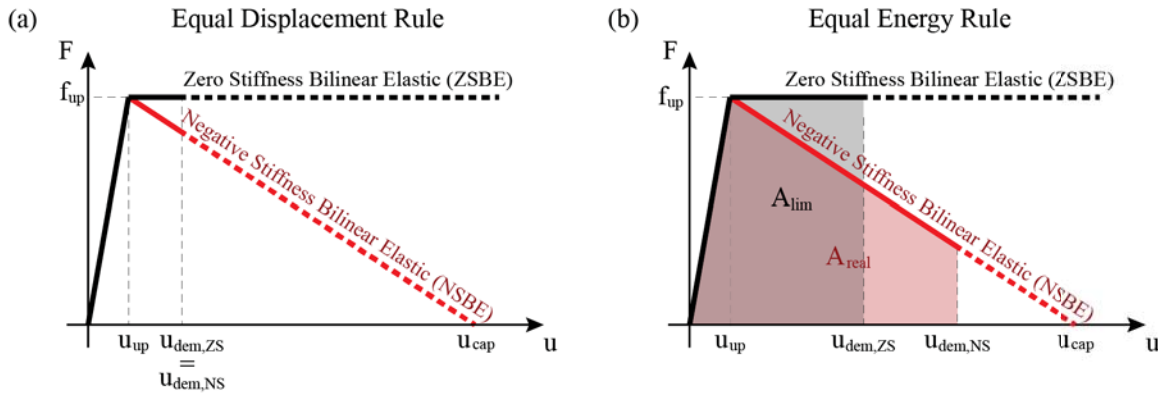


Figure 6. (a) Equal Displacement rule; and (b) Equal Energy rule.

3 PROBABILISTIC FRAMEWORK

Using the ZSBE proxy, the uniform risk spectrum for negative stiffness systems is a plot of the displacement demand of the system as a function of its normalized strength, in which all ordinates of the plot present the same mean annual frequency (MAF) of exceedance (Fig. 7b). It can also be interpreted as an iso-MAF contour plot of the seismic risk surface, which is a 3D plot of the probability of exceeding a displacement demand for a range of systems with different normalized strengths (Fig. 7a).

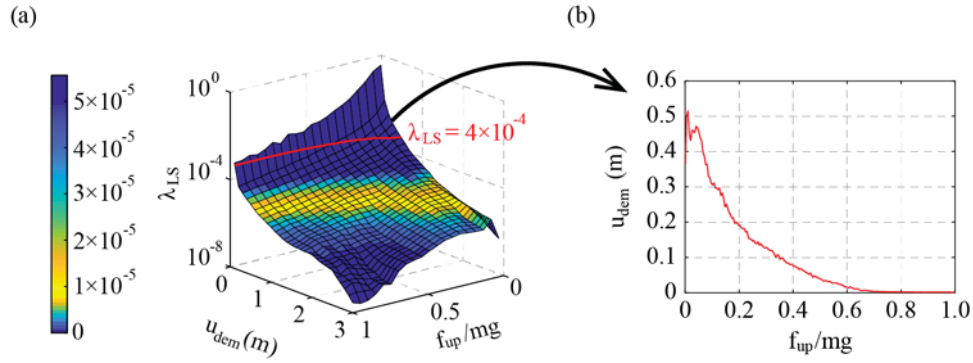


Figure 7. (a) Seismic risk surface with an iso-MAF contour plot highlighted; (b) Uniform risk spectrum.

The calculation of the probability of exceedance, also known as risk assessment, can be performed using the risk integral, the same framing equation of PBEE (Performance Based Earthquake Engineering) framework [39]:

$$\lambda_{LS} = \lambda(EDP > EDP_C) = \int P(EDP > EDP_C | IM) \cdot |d\lambda(IM)| \quad (6)$$

In Eq. 6, λ_{LS} is the mean annual frequency (MAF) of exceeding (i.e., violating) a limit state (LS). $P(EDP > EDP_C | IM)$ is the fragility function, which represents the probability that the engineering demand parameter (EDP) exceeds the capacity threshold of EDP_C associated with LS for any given level of the ground motion intensity measure (IM), and $\lambda(IM)$ is the MAF of exceeding a given value of IM, which can be retrieved from the site-specific seismic hazard curve.

In this paper, the maximum horizontal displacement of the system, or as mentioned before, the displacement demand, was adopted as EDP. Note that Eq.6 gives a single-point of the seismic risk surface. To construct the complete surface, the equation had to be evaluated for several limit states and a range of systems with different normalized uplifting strength. Herein, the probability of exceedance was calculated for 3001 limit states, ranging from 0 to 3m, in steps of 0.001m; and 301 different systems with a normalized strength varying from 0.1 to 1.0, in steps of 0.05.

Based on Eq.6, λ_{LS} combines the structural response and the seismic hazard at the site. The fragility function, or vulnerability analysis, gives us information about the structural response of the system, connecting the EDP to the IM. Given that all results are conditioned on the IM, the IM has to be carefully chosen [40]. The adequate IM for rocking structures, however, is still an open discussion in the engineering community [27–30, 36]. Herein, the peak ground velocity (PGV) was adopted as IM, with further studies pending.

Incremental dynamic analyses (IDA) [41] were carried out to obtain the fragility functions for each predefined limit state and different system. A set of 105 ordinary (non-pulse-like, non-long-duration) ground motions was used in each incremental dynamic analysis. The ground motions were gradually scaled so that their PGV is equal to $\overline{PGV} = [(1:0.5:20), (25:5:200)]$ cm/s, in which \overline{PGV} is the geometric mean of the PGV of the two horizontal components x and y of the individual ground motion:

$$\overline{PGV} = \sqrt{PGV_x \cdot PGV_y} \quad (7)$$

The model considers only planar response. Therefore, the nonlinear dynamic analysis was carried out only for one of the components of each ground motion (arbitrary component); the component was once chosen randomly, and then used for all analyses. After carrying out the analyses for all different scales and ground motions, the fragility function for each limit state

and system can be easily obtained on an EDP-basis or an IM-basis approach [40]. Here, the first was employed where for each IM-step value (stripe) the probability of exceeding the deterministic EDP capacity threshold is calculated as:

$$P(EDP > EDP_c | IM) = \frac{\text{number of records with } EDP > EDP_c}{\text{total number of records}} \quad (8)$$

The second curve necessary for the convolution represented by Eq.6 is the site-specific seismic hazard curve. In this study, a seismic hazard curve for a site at Athens, Greece was assessed via the open source platform OpenQuake [42]. The 2013 European seismic source model [43] was used for the calculations. The site-specific seismic hazard curve for the \overline{PGV} is presented in Fig. 8.

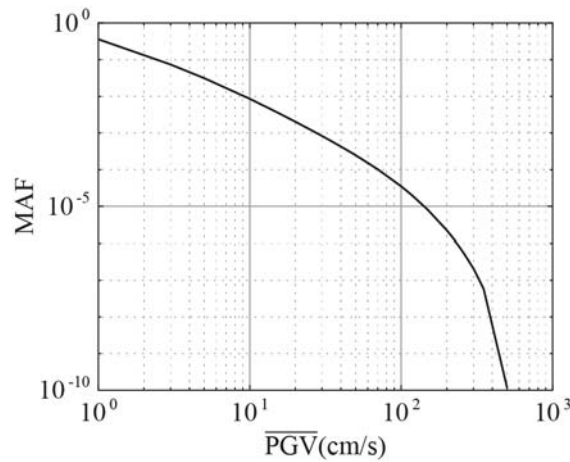


Figure 8. Site-specific seismic hazard curve for \overline{PGV} in Athens, Greece.

At last, after carrying out the vulnerability analysis for all desired systems and limit states, the uniform risk spectrum for a given MAF can be obtained as a cross-section of the seismic risk surface.

4 RISK ASSESSMENT

Herein, uniform risk spectra for quasi-rigid ZSBE systems ($u_{up} = 0.0005$ m), computed using the probabilistic framework of the previous section, is presented.

4.1 Fragility Curves

As the first step of the vulnerability analysis, fragility curves were computed for the different limit states and systems. As mentioned before, the ground motions were gradually scaled in stripes of $\overline{PGV} = [(1 : 0.5 : 20), (25 : 5 : 200)]$ cm/s. A finer discretization for smaller values of \overline{PGV} was necessary because low PGV ground motions might have small overturning potential, but they have large probability of occurrence resulting in significant contribution to the convolution of Equation 6.

Fig. 9 presents the fragility curve obtained using a coarse mesh (ranging from 1 to 100 cm/s, in steps of 5 cm/s) and using the finer mesh for a system with normalized strength $f_{up}/(mg) = 0.15$ and limit state of 9.0 cm. Because the fragility curve is created by a linear interpolation between the values for which the probability was calculated, the coarse mesh cannot capture the peaks and troughs as accurately as the finer mesh. If the risk quantity is

calculated using both fragility curves presented in Fig.9, the one with the coarse mesh overestimates the risk by 12%.

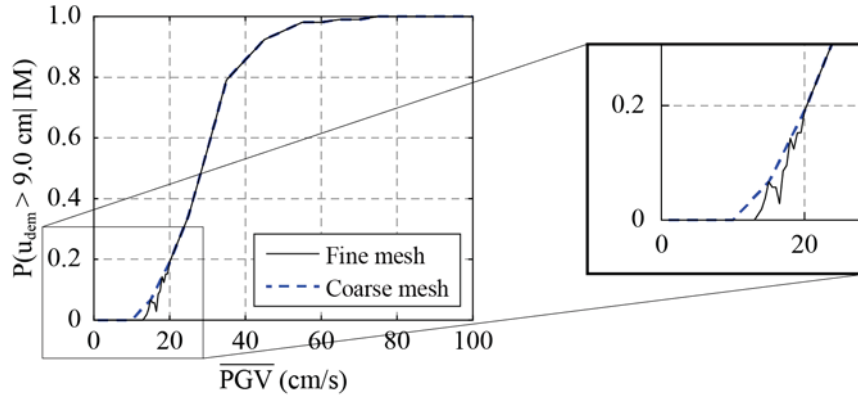


Figure 9. Fragility curves obtained for coarse and fine mesh.

4.2 Uniform Risk Spectra

Fig. 10 presents the uniform risk spectra for negative stiffness systems with 2%, 10%, and 50% probability of exceedance in 50 years, for a site in Athens, Greece. These probabilities correspond to a MAF of 0.0004, 0.0021, and 0.0139 per year, as given by Eq. 9, in which p is the probability of exceedance and T , the number of years considered.

$$\text{MAF} = \frac{-\ln(1-p)}{T} \quad (9)$$

It can be observed that the spectrum with smaller probability of exceedance (2% in 50 years) predicts larger displacement demands, while the spectrum with larger probability of exceedance (50% in 50 years) predicts smaller displacement demands.

The figure also depicts an interesting characteristic: if the curves were scaled by two distinct factors at x- and y-axes, they would collapse into a unique curve. This a very remarkable characteristic that might allow negative stiffness systems to be designed for different performance scenarios using a unique curve.

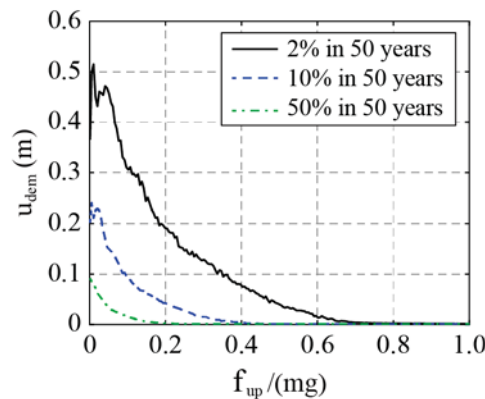


Figure 10. Uniform risk spectra for negative stiffness systems with 2%, 10%, and 50% probability of exceedance in 50 years, for a site in Athens, Greece.

5 CONCLUSIONS

This paper presented uniform risk spectra for negative stiffness systems, using the ZSBE proxy. It explains in detail the probabilistic framework necessary to construct such spectra, highlighting possible source of errors. It presents uniform risk spectra for three probabilities of exceedance: 2%, 10%, and 50% in 50 years. The uniform risk spectrum, however, can be computed for any given MAF and site, following the framework presented herein.

Interestingly, it seems that the uniform risk spectra for different MAF can be scaled in the x- and y-axes, collapsing to a unique curve. This characteristic would make the design of negative stiffness systems even simpler: one “master” curve could be used to design negative stiffness systems with different displacement capacities for different performance scenarios.

Further studies are still necessary on which is the adequate intensity measure to be adopted for these spectra.

REFERENCES

- [1] N. Makris, M. Vassiliou. Planar rocking response and stability analysis of an array of free-standing columns capped with a freely supported rigid beam. *Earthq. Eng. Struct. Dyn.*, **42**, 431–449, 2013.
- [2] N. Makris, M. F. Vassiliou. Are Some Top-Heavy Structures More Stable?. *J. Struct. Eng.*, **140** (5), 06014001, 2014.
- [3] N. Makris, M. F. Vassiliou. Dynamics of the Rocking Frame with Vertical Restrainers. *J. Struct. Eng.*, **141** (10), 04014245, 2015.
- [4] E. G. Dimitrakopoulos, A. I. Giouvanidis. Seismic Response Analysis of the Planar Rocking Frame. *J. Eng. Mech.*, **141** (7), 04015003, 2015.
- [5] M. F. Vassiliou, N. Makris. Dynamics of the Vertically Restrained Rocking Column. *J. Eng. Mech.*, **141** (12), 04015049, 2015.
- [6] A. I. Giouvanidis, E. G. Dimitrakopoulos. Seismic Performance of Rocking Frames with Flag-Shaped Hysteretic Behavior. *J. Eng. Mech.*, **143** (5), 04017008, 2017.
- [7] A. Agalianos, A. Psychari, M. F. Vassiliou, B. Stojadinovic, I. Anastasopoulos. Comparative assessment of two rocking isolation techniques for a motorway overpass bridge. *Front. Built Environ.*, **3**, 1–19, 2017.
- [8] M. F. Vassiliou, K. R. Mackie, B. Stojadinovic. A finite element model for seismic response analysis of deformable rocking frames. *Earthq. Eng. Struct. Dyn.*, **46** (3), 447–466, 2016.
- [9] M. F. Vassiliou, S. Burger, M. Egger, J. A. Bachmann, M. Broccardo, B. Stojadinovic. The three-dimensional behavior of inverted pendulum cylindrical structures during earthquakes. *Earthq. Eng. Struct. Dyn.*, **46** (14), 2261–2280, 2017.
- [10] M. F. Vassiliou. Seismic response of a wobbling 3D frame. *Earthq. Eng. Struct. Dyn.*, **47** (5), 1212–1228, 2018.
- [11] A. Dar, D. Konstantinidis, W. El-Dakhakhni. Seismic response of rocking frames with top support eccentricity. *Earthq. Eng. Struct. Dyn.*, **47** (12), 2496–2518, 2018.
- [12] I. M. Thomaidis, A. J. Kappos, A. Camara. Dynamics and seismic performance of rocking bridges accounting for the abutment-backfill contribution. *Earthq. Eng. Struct. Dyn.*, **49** (12), 1161–1179, 2020.
- [13] R. Thiers-Moggia, C. Málaga-Chuquitaype. Seismic protection of rocking structures with inerters. *Earthq. Eng. Struct. Dyn.*, **48** (5), 528–547, 2019.
- [14] J. A. Bachmann, M. F. Vassiliou, B. Stojadinovic. Rolling and rocking of rigid

- uplifting structures. *Earthq. Eng. Struct. Dyn.*, **48** (14), 1556–1574, 2019.
- [15] J. A. Bachmann, M. F. Vassiliou, B. Stojadinovic. Dynamics of rocking podium structures. *Earthq. Eng. Struct. Dyn.*, **46** (14), 2499–2517, 2017.
- [16] G. Ríos-García, A. Benavent-Climent. New rocking column with control of negative stiffness displacement range and its application to RC frames. *Eng. Struct.*, **206**, 110133, 2020.
- [17] M. Aghagholizadeh, N. Makris. Earthquake response analysis of yielding structures coupled with vertically restrained rocking walls. *Earthq. Eng. Struct. Dyn.*, **47** (15), 2965–2984, 2018.
- [18] M. Sieber, S. Klar, M. F. Vassiliou, I. Anastasopoulos. Robustness of simplified analysis methods for rocking structures on compliant soil. *Earthq. Eng. Struct. Dyn.*, **49** (14), 1388–1405, 2020.
- [19] Giouvanidis, A. I., & Dong, Y. (2020). Seismic loss and resilience assessment of single-column rocking bridges. *Bulletin of earthquake engineering*, 18, 4481-4513.
- [20] Y. L. Zhou, Q. Han, X. L. Du, J. Q. Zhang, S. S. Cheng, J. Y. Chen. Additional viscous dampers for double-column rocking bridge system: Seismic response and overturning analysis. *Soil Dyn. Earthq. Eng.*, **141**, 106504, 2021.
- [21] Y.-L. Zhou, Q. Han, X.-L. Du, Z. Jia. Shaking Table Tests of Post-Tensioned Rocking Bridge with Double-Column Bents. *J. Bridg. Eng.*, **24** (8), 04019080, 2019.
- [22] Giouvanidis, A. I., & Dimitrakopoulos, E. G. (2017). Seismic performance of rocking frames with flag-shaped hysteretic behavior. *Journal of Engineering Mechanics*, 143(5), 04017008.
- [23] N. Luco, B. R. Ellingwood, R. O. Hamburger, J. D. Hooper, J. K. Kimball, and C. A. Kircher. Risk-targeted versus current seismic design maps for the conterminous united states. *Struct. Eng. Assoc. Calif. 2007 Conv. Proc.*, Squaw Creek, California, United States, September, 26-29, 2007.
- [24] N. Makris, D. Konstantinidis. The rocking spectrum and the limitations of practical design methodologies. *Earthq. Eng. Struct. Dyn.*, **32** (2), 265–289, 2003.
- [25] N. Reggiani Manzo, M. F. Vassiliou. Displacement-based analysis and design of rocking structures. *Earthq. Eng. Struct. Dyn.*, **48** (14), 1613-1629, 2019.
- [26] N. Reggiani Manzo, M. F. Vassiliou. Simplified analysis of bilinear elastic systems exhibiting negative stiffness behavior. *Earthq. Eng. Struct. Dyn.*, **50** (2), 580–600, 2021.
- [27] S. Acikgoz, M. J. DeJong. The rocking response of large flexible structures to earthquakes. *Bull. Earthq. Eng.*, **12** (2), 875–908, 2014.
- [28] E. G. Dimitrakopoulos, T. S. Paraskeva. Dimensionless fragility curves for rocking response to near-fault excitations. *Earthq. Eng. Struct. Dyn.*, **44** (12), 2015–2033, 2015.
- [29] A. I. Giouvanidis, E. G. Dimitrakopoulos. Rocking amplification and strong-motion duration. *Earthq. Eng. Struct. Dyn.*, **47** (10), 2094–2116, 2018.
- [30] Y. Xie, J. Zhang, R. DesRoches, J. E. Padgett. Seismic fragilities of single-column highway bridges with rocking column-footing. *Earthq. Eng. Struct. Dyn.*, **48** (7), 843–864, 2019.
- [31] M. Ebad Sichani, J. E. Padgett, V. Bisadi. Probabilistic seismic analysis of concrete dry cask structures. *Struct. Saf.*, **73**, 87–98, 2018.
- [32] E. Bakhtariy, P. Gardoni. Probabilistic seismic demand model and fragility estimates for rocking symmetric blocks. *Eng. Struct.*, **114**, 25–34, 2016.
- [33] B. Kafle, N. T. K. Lam, E. F. Gad, J. Wilson. Displacement controlled rocking behaviour of rigid objects. *Earthq. Eng. Struct. Dyn.*, **40** (15), 1653–1669, 2011.
- [34] H. Roh, G. P. Cimellaro. Seismic fragility evaluation of RC frame structures retrofitted

- with controlled concrete rocking column and damping technique. *J. Earthq. Eng.*, **15** (7), 1069–1082, 2011.
- [35] L. Deng, B. L. Kutter, S. K. Kunnath. Probabilistic Seismic Performance of Rocking-Foundation and Hinging-Column Bridges. *Earthq. Spectra*, **28** (4), 1423–1446, 2012.
- [36] I. N. Psycharis, M. Fragiadakis, I. Stefanou. Seismic reliability assessment of classical columns subjected to near-fault ground motions. *Earthq. Eng. Struct. Dyn.*, **42** (14), 2061–2079, 2013.
- [37] K. Bakalis, A. K. Kazantzi, D. Vamvatsikos, M. Fragiadakis. Seismic Performance Evaluation of Liquid Storage Tanks Using Nonlinear Static Procedures. *J. Press. Vessel Technol. Trans. ASME*, **141** (1), 1–13, 2019.
- [38] D. Kalliontzis, S. Sritharan, A. Schultz. Improved Coefficient of Restitution Estimation for Free Rocking Members. *J. Struct. Eng.*, **142** (12), 06016002, 2016.
- [39] C. A. Cornell, H. Krawinkler. Progress and challenges in seismic performance assessment. *PEER Cent. News*, **3** (2), 1–2, 2000.
- [40] A. K. Kazantzi, D. Vamvatsikos. Intensity measure selection for vulnerability studies of building classes. *Earthq. Eng. Struct. Dyn.*, **44** (15), 2677–2694, 2015.
- [41] D. Vamvatsikos, C. A. Cornell. Incremental dynamic analysis. *Earthq. Eng. Struct. Dyn.*, **31** (3), 491–514, 2002.
- [42] Global Earthquake Model (GEM). OpenQuake Engine User Instruction Manual, 2016.
- [43] J. Woessner, D. Laurentiu, D. Giardini *et al.*, The 2013 European Seismic Hazard Model: key components and results. *Bull. Earthquake Eng.*, **13**, 3553–3596, 2015.

SEISMIC BEHAVIOR OF ARCHAEOLOGICAL MULTIDRUM COLUMNS AT THE POMPEII SITE

F. Autiero^{1*}, G. De Martino¹, M. Di Ludovico¹, A. Prota¹

¹ Department of Structures for Engineering and Architecture, University of Naples Federico II, Italy
e-mail: francesca.autiero@unina.it
giuseppina.demartino2@unina.it
diludovi@unina.it
aprota@unina.it

Abstract

Free-standing multidrum stone columns are widespread elements in archaeological areas. The present study aims at investigating the behavior of these elements under seismic excitations. The dynamic behavior of free-standing multidrum columns is greatly affected by geometrical properties, constitutive materials, state of preservation, and amplitude and frequency of the seismic action. The first step of the research involved a wide and detailed survey for the definition of the mean geometrical properties affecting the seismic behavior of these columns in the archeological Pompeii site. To this end, a wide range of grey-tuff columns (103 elements) from four different areas of the site involving private and public areas, were investigated. Then, numerical analyses were carried out based on the Finite Element Method (FEM) to investigate the seismic behavior of such elements. A column from the tetrastyle atrium of Casa del Fauno was selected for the analysis. The house is one of the largest and most visited private buildings at the Pompeii archeological site. The selected column presented deep degradation and needed specific and urgent attention for its assessment. In the following, the detailed survey and the modeling phases of the investigated element are described and the outcomes of the numerical analysis are reported and discussed.

Keywords

Pompeii archaeological site; cultural heritage; multidrum stone columns; geometrical properties; seismic assessment

1 INTRODUCTION

Understanding the seismic behavior of typical ancient structures is crucial for the conservation of historical and archaeological assets. In particular, many important Greek and Roman archaeological sites are located in the Mediterranean area which is characterized by a notable seismic activity.

Columns are typical elements of ancient Greek and Roman architecture. In many cases, they were built with dry-overlapped stone pieces, namely the drums, placed above a stylobate, and typically carrying the load transmitted by a stone architrave or a wooden beam. Nowadays, multidrum stone columns are often free-standing elements, i.e. with no axial load except for their self-weight.

When subjected to a seismic motion, the single drums can rock and slide independently or in groups, resulting in a complex and highly non-linear behavior of the whole column. The first systematic and landmark study on the analysis of the rocking response of a single rigid block was proposed by Housner in 1963 [1]. From then, numerous investigations focused on the analysis of the dynamic response of free-standing multidrum columns, by following analytical [2–5], experimental [6,7], or more recent numerical approaches [8–11]. The main findings of these studies can be summarized in the following points: i) when subjected to seismic excitation, multidrum columns show many patterns of the rocking motion, whose number increase with the number of constituent blocks, and continuously move from one of them to another, thus natural modes of vibration in the classical meaning cannot be defined [12]; ii) the dynamic behavior of these elements is extremely sensitive to even trivial changes of the parameters of the structure or seismic input; iii) the slenderness and size of the columns affect their stability, with the higher slenderness, the higher the probability of collapse, and the higher size, for the same slenderness, the higher the stability; iv) low-frequency earthquakes are generally more dangerous than high-frequency ones [2,4,11,13]. Moreover, it was found that this type of structure, if well-preserved, is generally able to sustain notable seismic inputs [8,12]. However, typical forms of degradation can significantly affect the state of preservation and the stability of these elements. These are: material degradation; the presence of cracks; missing portions; deterioration of the contact surfaces among the drums; uneven profile of the column; misplaced drums after their re-erection; permanent relative displacements among the drums caused by past seismic events.

This paper presents a part of a wide study aimed at the investigation of the seismic vulnerability of free-standing multidrum tuff columns at the Pompeii archaeological site. This was a part of a scientific collaboration between the Archaeological Pompeii Park (PAP) and the Department of Structures for Engineering and Architecture (DiSt) of the University of Naples Federico II aimed to support the monitoring of the state of preservation of the columns at the site and the development of programs of interventions. The investigation included 103 columns from four different areas of the site. The first phase of the research involved detailed surveys, archival researches and visual inspections to define the main geometrical properties of the columns and the most common forms of degradation and damage, that may affect their seismic behavior. After that, an analysis of the seismic behavior of such structures was implemented with a column from one of the largest and most visited private buildings at the site, *Casa del Fauno*. Indeed, when the investigation has been started, the selected column presented deep degradation and needed specific and urgent attention for its assessment. The study was carried out based on the Finite Element Method (FEM). Eight seismic records were selected for the analyses, to investigate the influence of different frequencies and amplitudes of the seismic input. The following sections firstly focus on the main geometric characteristics and common forms of degradation of the Pompeian multidrum tuff columns; then discuss the modeling phases of the investigated element and the outcomes of the numerical analyses.

2 FREE-STANDING MULTIDRUM TUFF COLUMNS

According to the results of previous studies, the main geometrical properties and the state of preservation of multidrum columns significantly affect their seismic response [1,12]. Therefore, the following sections present the results of a systematic and detailed survey of a wide number of

multidrum stone columns representative of a typical typology at the Pompeii archaeological site. In particular, free-standing Corinthian and Doric tuff columns were studied.

2.1. Localization of the columns

This part of the investigation involved structures from four different private and public areas of the site: a private house at *Regio VI*, *Casa del Fauno* (CF) and public areas at *Regio VIII*, *Quadriportico dei Teatri* (Q), *Palestra Sannitica* (PS), and *Foro Triangolare* (FT) (Figure 1). Note that the picture related to the *Tetrastyle atrium* of *Casa del Fauno* predates the recent restoration intervention (January 2021), that allowed removing the lateral supporting props shown in the picture.



Tetrastyle atrium, Casa del Fauno (CF), Regio VI, Insula 12.



Quadriportico dei teatri (Q), Regio VIII, Insula 7.



Palestra Sannitica (PS), Regio VIII, Insula 7.



Foro triangolare (FT), Regio VIII, Insula 7.

Figure 1: Research areas.

As shown in Figure 1 several columns are incomplete and in a state of ruins. This was probably related to the fact that throughout the excavation and/or the execution of later interventions certain parts were significantly damaged. In detail, 55 out of 103 columns were complete, i.e. all the parts from the base to the capital stand today, while the other 48 columns were incomplete, i.e. had missing parts. One incomplete column was found at the tetrastyle atrium of the *Casa del Fauno*, for which only the capital was missing. Table 1 reports the total number of investigated columns for each area and the relative numbers of complete and incomplete elements.

Table 1: Number of investigated columns for each area and complete and incomplete elements.

	CF	Q	PS	FT	Total
number of free-standing columns	4	54	19	26	103
number of complete columns	3	28	13	11	55
number of incomplete columns	1	26	6	15	48

2.2. Geometry and state of preservation

The slenderness and the size of a column greatly affect its dynamic response [1,12,13]. The number of constituting drums is also relevant because it affects the energy dissipation due to friction. Literature studies showed that, on hard soil, it is possible to observe the effect of higher stability for a higher number of drums [8,10].

Table 2 summarizes the mean geometric parameters and mass of the investigated complete columns. In particular, Table 2 reports: the total height, H ; the diameter at the base, d ; the aspect ratio, H/d , which is a measure of the column slenderness; the quote of the center of mass, y_{CM} ; the distance from the center of mass of the column to the circumference at the base, R , which is a measure of the column size; the number of drums; the volume; the mass.

Table 2: Main overall characteristics of the complete columns.

	CF	Q	PS	FT
Total height, H [m]	5.74	3.56	3.30	3.99
Diameter at the base, d [m]	0.71	0.49	0.39	0.53
Aspect ratio, H/d [-]	8.09	7.27	8.53	7.50
Quote of the center of mass, y_{CM} [m]	2.79	1.70	1.58	1.88
Distance center of mass - base perimeter, R [m]	2.82	1.72	1.59	1.90
Number of drums	6	5	5	5
Volume, V [m ³]	1.70	0.63	0.37	0.85
Mass, M [kg]	4407	1634	972	2214

The presence of material degradation and damage must be also taken into account for structural modeling since they can significantly alter the dynamic response of a multidrum column. Common forms of degradation and damage were found among the investigated columns at the Pompeii site: the presence of cracks; missing portions; contact surface between the drums reduced by weathering, the presence of invasive and incompatible interventions (see Figure 2).

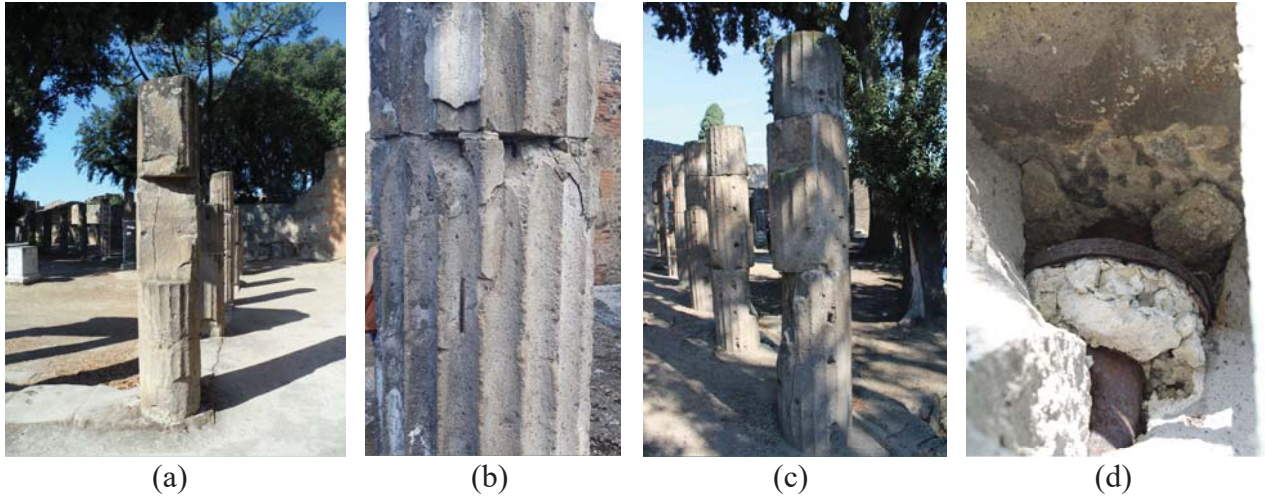


Figure 2: Most common imperfections, damage and deterioration forms in the columns: the presence of cracks, missing portions, reduced contact surface between the drums (a), (b), (c), invasive and incompatible interventions (b), and (d).

3 INVESTIGATION OF THE SEISMIC RESPONSE OF MULTIDRUM COLUMNS

3.1. Description of the model

The analyses herein presented refer to one column at the *Casa del Fauno*. The analyses were carried out with finite element modeling (FEM), by using the software Abaqus/CAE. Therefore, the column was modeled as an assembly of overlapping deformable blocks, i.e. the drums. The geometric characteristics used in the model are listed in Table 3.

Table 3: Geometrical parameters used in the model.

Free-standing multidrum column at the <i>Casa del Fauno</i>			
	h [m]	d_{inf} [m]	d_{sup} [m]
drum 1	0.55	0.73	-
drum 2	0.99	-	-
drum 3	0.11	-	-
drum 4	0.76	-	-
drum 5	0.17	-	0.66
capital	0.67	0.66	0.66
column	5.72	0.73	0.66

Each drum was modeled as an isotropic and elastic semi-conical solid (Figure 3 (a)) with material properties defined based on information from the technical archive of the Pompeii archeological site (Table 4).

Table 4: Material parameters used in the model.

Grey tuff	
Bulk density, ρ [kg/m ³]	1230
Elastic modulus, E [GPa]	4.5
Poisson ratio, ν	0.25
Coefficient of friction, μ	0.5

The discretization of each drum was performed with 8-node hexahedra elements (Figure 3 (c)). Each drum was partitioned into eight portions, to obtain a regular and correct formation of the meshes (Figure 3 (b)).

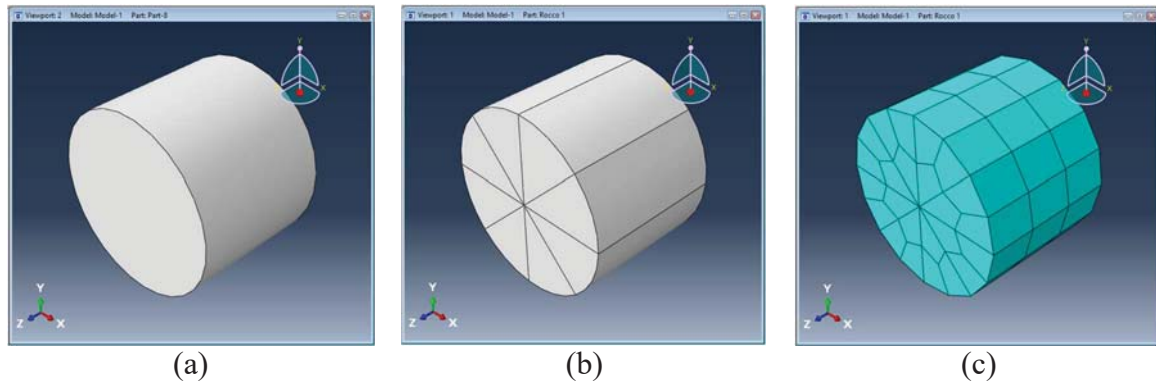


Figure 3: The geometric model of a drum: semi-conical solid (a), partition in eight parts (b), and mesh configuration (c).

The contact interaction between two consecutive drums was considered as governed by friction. Thus, it was modeled by adopting the Mohr-Coulomb criterion for the tangential stress along the surfaces, with dynamic coefficient friction equal to the static one (i.e. 0.5). This was consistent with the assumption made in other literature studies showing that the value of the dynamic coefficient friction has a negligible role in the analyses to capture columns seismic behavior [8,13]. Moreover, the hard contact behavior was set for the interaction between the drums in the normal direction, with compressive stress developed on the contact surface between two drums and zero stress when the drums are not in contact. Finally, the interactions between consecutive drums and between the first drum and the base of the column were defined by a “master” surface and a “slave” surface. A boundary condition of fully fixed connection was applied at the base of the column as well as the input seismic signals. Figure 4 shows the geometric assembly of the entire column; the defined interactions between adjacent surfaces; the boundary condition of fully fixed connection at the base; the application of a seismic input at the base; the final numerical model of the column with meshes.

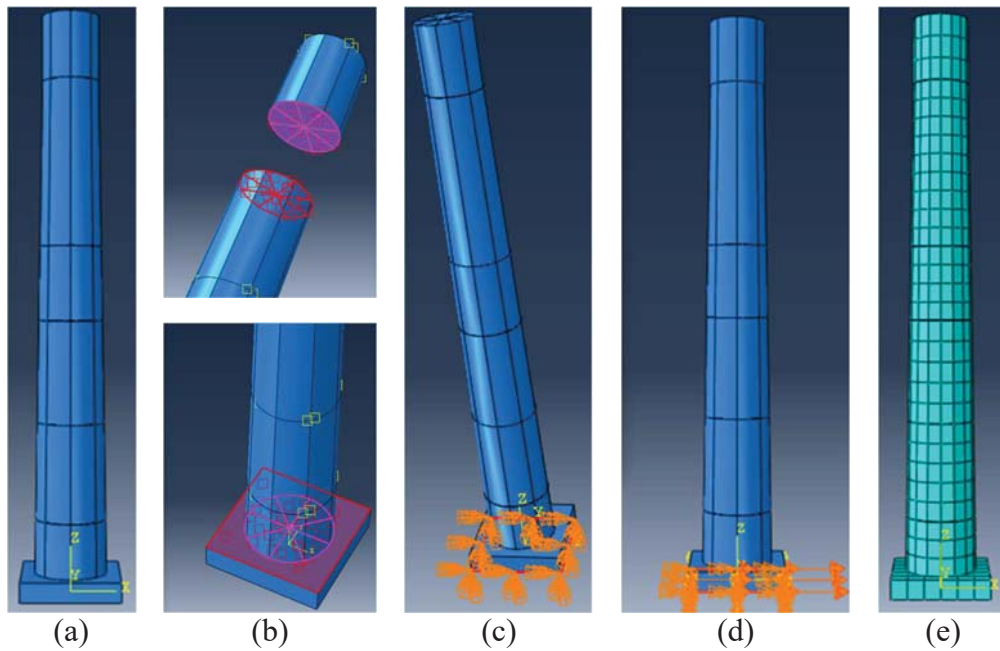


Figure 4: Phases of the modeling process: assembling of the single parts of the column (a); definition of the interactions between adjacent surfaces (b); definition of the boundary condition at the base (c); application of the seismic input at the base (d); final numerical model of the column with meshes (e).

Each analysis involved two steps: the assignment of the geometrical and material properties, interactions and the acceleration of gravity; and the seismic input signal applied at the base of the column. The analyses were performed according to the dynamic implicit method, with the time of each step set equal to 0.005s. This latter was equal to the time step of the selected seismic records.

3.2. Seismic input motions

Eight seismic records with different frequencies and amplitudes were selected for the analyses: i) Irpinia, Italy (1980), recorded at Sturno, close to the epicenter and ii) Irpinia, Italy (1980), recorded at Torre del Greco, about 15km from Pompeii; iii) Molise, Italy (2002), recorded at San Severo, about 50 km from the epicenter; L'Aquila, Italy (2009), recorded at v. Aterno – Centro Valle, close to the epicenter; Kalamata, Greece (1986), recorded at Kalamata; Edessa, Greece (1990), recorded at Edessa; Aigio (1995), recorded at Aigio; Athens, Greece (1999), recorded at Athens. Table 5 reports the intensity measures and frequency content indicator of the seismic input motions selected for the analysis. In particular, the intensity measures PHA, PHV and PHD represent the maximum vector sums of the accelerations, velocities and displacements, respectively, in the two horizontal directions of the seismic records. The predominant period, T_g , was evaluated as the period corresponding to the maximum ordinate of the 5% damped pseudo-velocity spectrum.

Table 5: Intensity measures and frequency content indicator of the seismic input motions selected for the analysis.

Seismic record	PGA	PGV	PGD	PHA*	PHV*	PHD*	T_g [s]**		
	[g]	[cm/s]	[cm]	[g]	[cm/s]	[cm]	E-W	N-S	mean
Irpinia_Str	0.32	70.0	27.8	0.33	72.2	27.8	3.00	3.20	3.10
Irpinia_TdG	0.06	8.1	6.1	0.06	8.8	7.1	6.49	0.67	3.58
L'Aquila	0.66	42.7	6.8	0.77	46.7	6.8	0.67	0.50	0.58
Molise	0.06	2.1	0.3	0.06	2.4	0.3	0.50	0.38	0.44
Kalamata	0.27	31.7	6.5	0.35	38.5	6.7	0.67	0.55	0.61
Edessa	0.10	11.2	1.1	0.11	12.0	1.2	0.67	0.70	0.68
Aigio	0.52	51.3	8.3	0.53	51.3	8.6	0.55	0.55	0.55
Athens	0.31	16.9	2.1	0.38	16.3	2.9	0.65	0.22	0.44

*The maximum vector sum of the two relative components

**Predominant period corresponding to the maximum ordinate of the 5% damped relative velocity spectrum

4 RESULTS AND DISCUSSION

The model of the column of *Casa del Fauno* was excited with the eight selected seismic records. To define the maxim ground acceleration sustained by the column for each seismic input without collapsing, a specific parametric analysis was performed by progressively increasing a scale factor applied to the intensities of the seismic records. Indeed, for each seismic input, the minimum value of the scaling factor leading to the collapse of the column was determined. Table 6 summarizes the outcomes of the analyses in terms of parameters of the seismic input motions leading to the collapse of the column and the number of collapsed drums beside the capital.

Table 6: Parameters of the seismic input motions leading to the collapse of the column.

Seismic record	Scaling factor	PHA [g]	PHV [cm/s]	PHD [cm]	Collapsed parts
Irpinia_Str	0.5	0.17	36	13.9	Capital and 2 drums
Irpinia_TdG	4	0.24	35	28.2	Capital and 4 drums
L'Aquila	1.5	1.16	70	10.2	Capital and 2 drums
Molise	16.8	1.01	41	5.6	Capital and 2 drums
Kalamata	1.1	0.38	42	7.4	Capital and 3 drums
Edessa	3.45	0.38	41	4.2	Capital and 2 drums
Aigio	1.05	0.55	54	9.0	Capital and 2 drums
Athens	3.3	1.24	54	9.5	Capital and 1 drum

The studied column showed different dynamic responses for the different input motions. Seismic motions with the higher predominant periods were found to be more dangerous, leading to the collapse with lower values of PHA, and confirming fundamental conclusions found in previous numerical and experimental studies [11,12]. Indeed, two records of the Irpinia earthquake, characterized by a high value of T_g , led to the collapse with the lowest intensities. Moreover, according to Italian territorial classification [14], the Pompeii site falls in a seismic zone whose acceleration with a probability of exceeding equal to 10% in 50 years ranges between 0.15g and 0.25g. Therefore, considering the maximum vectorial sum, PHA, ranging between 0.21g and 0.35g, only the two records of the Irpinia earthquakes produced PHA at the collapse falling in this range or below it. Figure 5 plots the value of the PHA that produced the collapse of the column for each seismic record, represented by the value of its predominant period, and the range of expected PHA derived by Italian seismic classification.

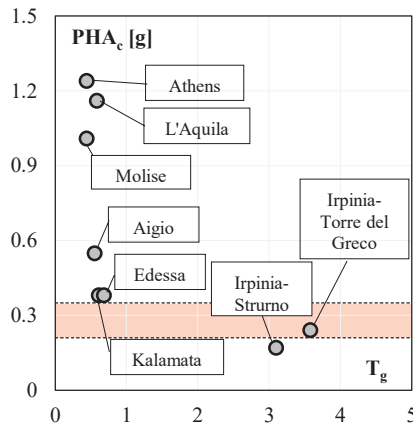
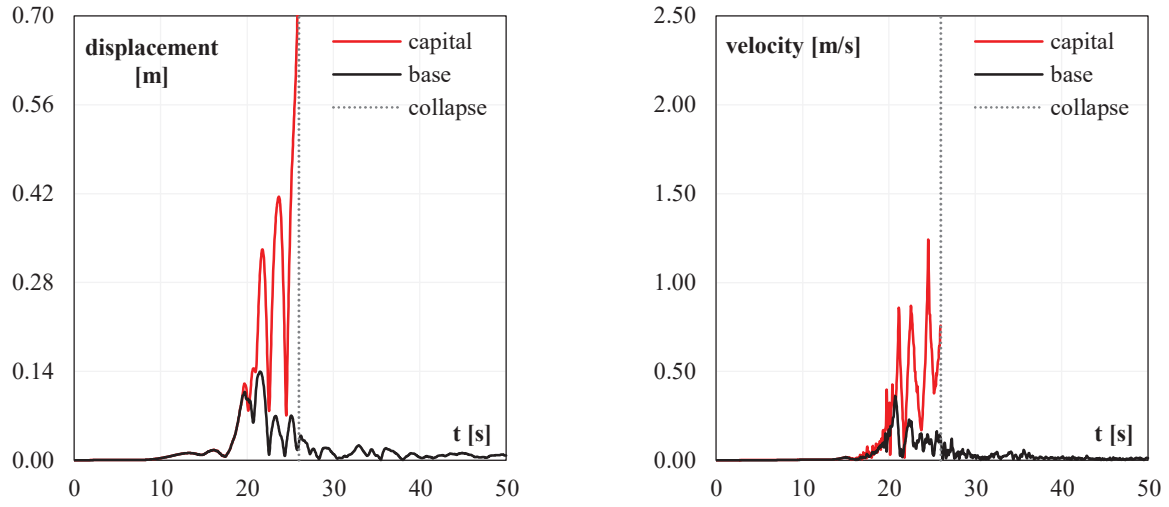


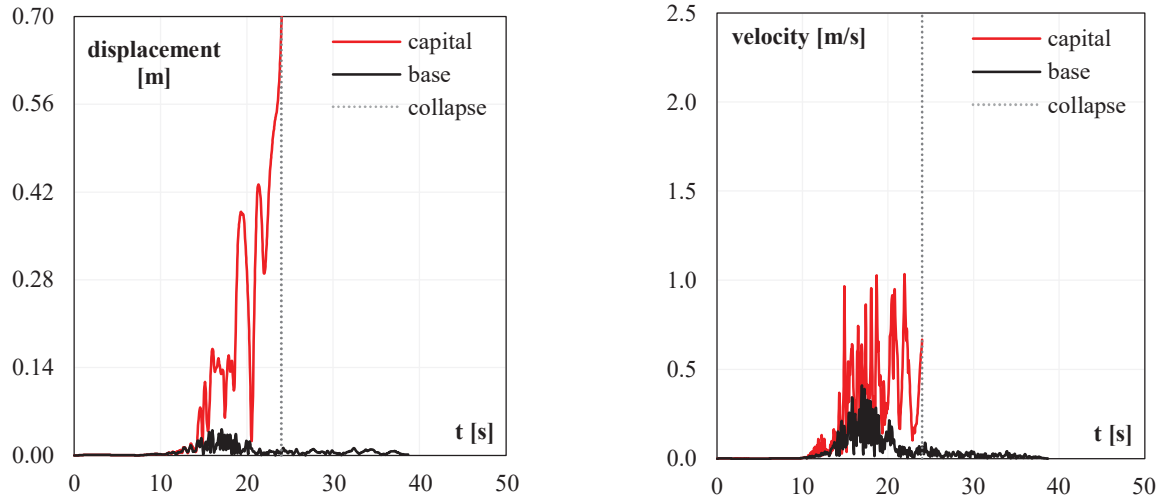
Figure 5: PHA that produced the collapse of the column for each value of the predominant period corresponding to the different seismic inputs and range of expected PHA derived by Italian seismic classification.

The responses were characterized by different combinations of relative sliding and rocking among the drums. As assessed by previous studies [11], low-frequency earthquakes led to prevalent rocking, while high-frequency earthquakes led to significant sliding. Indeed, as an example, Figure 6 shows the displacements and velocities at the capital and base of the column under the Irpinia-Sturno and Edessa records. Figure 7 shows the failure process of the column within the last four seconds until the collapse. Both the records led to the collapse of the capital and two drums. However, the Irpinia-Sturno record initially induced the rocking of the entire column as a single block, then the failure process involved the rocking of the last two drums and the capital without permanent displacements

in the standing part of the column. The second input (i.e. Edessa) induced relative sliding between the drums, other than rocking. Unlike the first case, permanent relative displacements were produced.

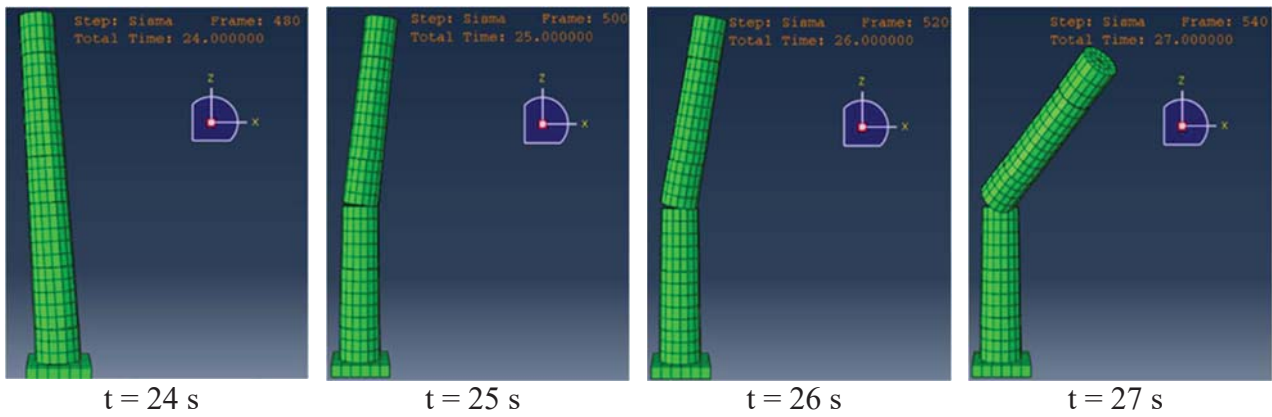


(a)



(b)

Figure 6: Displacements and velocities at the capital and base of the column under the Irpinia-Struno (a) and Edessa (b) input motions.



(a)

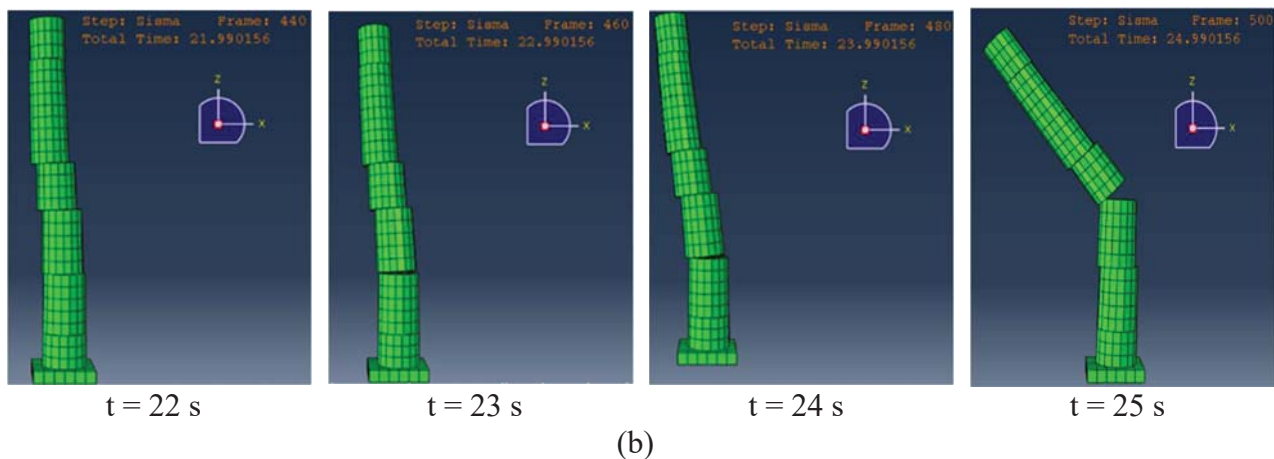


Figure 7: Failure process of the column under the Irpinia-Struno (a) and Edessa (b) input motions.

5 CONCLUSIONS

This paper presents a part of a wide study focused on the investigation of the seismic stability of multidrum free-standing tuff columns at the Pompeii archeological site. The study involved, at first, extensive surveys and visual inspection aimed at the knowledge of the main geometrical properties and most common forms of degradation of such structures at the site. The study involved 103 grey-tuff columns from four different areas of the site in private and public areas, selected as representative of typical column-type at the site. A study of the seismic behavior of one column from the tetrastyle atrium of *Casa del Fauno* was performed. This structure was selected for the analyses since it showed a high level of degradation and needed specific and urgent actions. The study was carried out based on the Finite Element Method (FEM). The performed investigations led to the following main conclusions:

- A considerable number of the surveyed columns were incomplete with missing parts, while 55 out of 103 columns were completely preserved;
- The main geometrical parameters of complete columns, affecting their seismic behavior ranged between: mean aspect ratio, H/d , 7.27m - 8.53m; mean distance from the center of mass of the column to the base perimeter, R , 1.59m - 2.82m; mean number of drums was equal to 5 or 6;
- Eight seismic records with different frequencies and amplitudes were selected for the numerical analyses aimed at investigating one multidrum column seismic behavior; the minimum scale factors applied to the intensities of the seismic records producing the collapse of the column was determined;
- Two seismic records with the higher predominant periods were found to be most dangerous, leading to the collapse with the minimum critical intensity measures, PHA. These intensity values at the collapse fall into and below the range of expected values derived from the Italian seismic zoning;
- The studied column showed different dynamic responses for the different input motions, with low-frequency records leading to prevalent rocking and high-frequency ones leading to significant sliding and permanent relative displacements among the drums.

Information on the geometrical properties and the state of preservation of typical archaeological multidrum columns are useful for the assessment of the seismic vulnerability of these structural elements. Further research could be performed to assess the effect of different geometrical properties of the structures on their seismic behavior (i.e. slenderness and size of the column and number and size of the drums) and different forms of degradation, particularly considering the presence of cracks, missing portions, eroded surfaces, permanent relative displacements between the drums and/or uneven profile of the column.

ACKNOWLEDGMENTS

The authors acknowledge the former director of *Parco Archeologico di Pompei* (PAP), Prof. Massimo Osanna and Arch. Annamaria Mauro for the support provided to this research. We would also like to thank Mr. Andrea Torre for his undergraduate thesis on the research topic presented in the paper and for his collaboration on the development of the analyses.

REFERENCES

- [1] G.W. Housner, The behavior of inverted pendulum structures during earthquakes, *Bull. Seismol. Soc. Am.* 53 (1963) 403–417. <https://doi.org/10.1017/CBO9781107415324.004>.
- [2] I.N. Psycharis, Dynamic behaviour of rocking two-block assemblies, *Earthq. Eng. Struct. Dyn.* 19 (1990) 555–575.
- [3] P.D. Spanos, P.C. Roussis, N.P.A. Politis, Dynamic analysis of stacked rigid blocks, *Soil Dyn. Earthq. Eng.* 21 (2001) 559–578. [https://doi.org/10.1016/S0267-7261\(01\)00038-0](https://doi.org/10.1016/S0267-7261(01)00038-0).
- [4] G. Minafò, G. Amato, L. Stella, Rocking Behaviour of Multi-Block Columns Subjected to Pulse-Type Ground Motion Accelerations, *Open Constr. Build. Technol. J.* 10 (2016) 150–157. <https://doi.org/10.2174/1874836801610010150>.
- [5] M.J. DeJong, E.G. Dimitrakopoulos, Dynamically equivalent rocking structures, *Earthq. Eng. Struct. Dyn.* 43 (2014) 1543–1563. <https://doi.org/10.1002/eqe.2410>.
- [6] H.P. Mouzakis, I.N. Psycharis, D.Y. Papastamatiou, P.G. Carydis, C. Papantonopoulos, C. Zambas, Experimental investigation of the earthquake response of a model of a marble classical column, *Earthq. Eng. Struct. Dyn.* 31 (2002) 1681–1698. <https://doi.org/10.1002/eqe.184>.
- [7] V. Drosos, I. Anastasopoulos, Shaking table testing of multidrum columns and portals, *Earthq. Eng. Struct. Dyn.* 43 (2014) 1703–1723. <https://doi.org/10.1002/eqe.2418>.
- [8] K. Papadopoulos, E. Vintzileou, I.N. Psycharis, Finite element analysis of the seismic response of ancient columns, *Earthq. Eng. Struct. Dyn.* 48 (2019) 1432–1450. <https://doi.org/10.1002/eqe.3207>.
- [9] V. Sarhosis, G.P. Lignola, P.G. Asteris, Seismic Vulnerability of Ancient Colonnade, in: *Civ. Environ. Eng.*, IGI Global, 2016: pp. 950–974. <https://doi.org/10.4018/978-1-4666-9619-8.ch041>.
- [10] A. Pappas, F. da Porto, C. Modena, Seismic vulnerability assessment form for free-standing columns based on a simplified numerical analysis, *Int. J. Archit. Herit.* 10 (2016) 15583058.2015.1113336. <https://doi.org/10.1080/15583058.2015.1113336>.
- [11] I.N. Psycharis, J. V. Lemos, D.Y. Papastamatiou, C. Zambas, C. Papantonopoulos, Numerical study of the seismic behaviour of a part of the Parthenon Pronaos, *Earthq. Eng. Struct. Dyn.* 32 (2003) 2063–2084. <https://doi.org/10.1002/eqe.315>.
- [12] I.N. Psycharis, Seismic Vulnerability of Classical Monuments, in: *Recent Adv. Earthq. Eng. Eur. 16th Eur. Conf. Earthq. Eng.*, Thessaloniki, Greece, 2018: pp. 563–582. https://doi.org/10.1007/978-3-319-75741-4_24.
- [13] K. Pitilakis, E. Tavouktsi, Seismic Response of the Columns of Two Ancient Greek Temples in Rhodes and Lindos, 8th Int. Symp. Conserv. Monum. Mediterr. Basin, Patra. (2010) Vol. 31. http://library.tee.gr/digital/m2616/m2616_pitilakis.pdf.
- [14] Italian Presidency of the Council of Ministers, Ordinance n. 3519. Criteri generali per l'individuazione delle zone sismiche e per la formazione e l'aggiornamento degli elenchi delle medesime zone, G.U. n.108 del 11/05/2006, (2006).

THE INFLUENCE OF IMPACT MODELLING ASSUMPTIONS ON THE DYNAMIC BEHAVIOUR OF FLEXIBLE ROCKING OSCILLATORS

Huanian Zhu¹, Manolis Chatzis², and Sinan Acikgoz²

¹Phd Candidate, Department of Engineering Science, The University of Oxford
Parks Road, Oxford OX1 3PJ
e-mail: huanian.zhu@eng.ox.ac.uk

² Associate Professor, Department of Engineering Science, The University of Oxford
Parks Road, Oxford OX1 3PJ
e-mail: {manolis.chatzis, sinan.acikgoz}@eng.ox.ac.uk

Keywords: rocking, lateral flexibility, impact, analytical model.

Abstract. *For rigid rocking models, energy dissipation relies solely on impact. Consequently, the position of the impulse acting on the rocking body determines the magnitude of energy loss and strongly influences the subsequent dynamic response. This paper evaluates the corresponding influence of the location of the vertical impulse on the dynamic behaviour of flexible rocking oscillators. The dynamic behaviour of a rocking flexible oscillator is explored in this study with an impact model that parametrically considers the position of impulse. The influence of the position of impulse on the expected energy loss during impact, and on the overturning stability of the flexible rocking oscillator are then examined. It is shown that the energy loss at impact reduces and the potential for overturning instability increases, for impulses located at increasing distances from the future rocking corner.*

1 INTRODUCTION

The rocking problem of a rigid body was first systematically studied by Housner [1] with the inverted pendulum model (IPM). Several idealisations were made: the rocking body and the support medium are rigid; sliding and complete separation of the body from the support are prevented; the motion is restricted to be planar; dissipation of energy depends exclusively on impact. The impulse forces at impact were assumed to act on the future rocking corner. Consequently, the resulting energy loss can be described as a function of the geometry of the rigid body, and is often quantified with a coefficient of restitution parameter.

The coefficient of restitution arising from the assumption of impulses being applied at the future rocking corner was found to overestimate the energy dissipation during impact by various experimental investigations [2, 3, 4]. Modified values for the coefficient of restitution were used in numerical simulations to achieve a better fit with experimental data. A similar approach was followed for flexible oscillators by Acikgoz et al. [5, 6]. Kalliontzis et al. [7] modified coefficient of restitution in a different way. A new width of the body was adopted by noting the varying location of the instantaneous rocking corner of the rigid rocking body. The coefficient of restitution was obtained by conserving angular momentum with the new future rocking corner. Furthermore, coefficient of restitution was noticed to be velocity-dependent [3, 4, 8].

However, Shenton and Jones [9] noted that conserving angular momentum with a point other than the future rocking corner is not a necessity dictated by mechanics: they hinted the ratio of the impulse at the future rocking corner and the one at the previous rocking corner can be a non-zero value (though a ratio of zero was adopted). Chatzis et al. [8] further extended this observation and quantified the influence of the location of the vertical impulse on the overturning stability of rigid bodies: the future rocking corner was determined to be the least conservative location. These results have later been extended to stacked rocking bodies [10].

The aforementioned publications show that the modelling of coefficient of restitution is of significant importance to model the dynamics of rigid rocking bodies. This paper is devoted to exploring the influence of modelling the coefficient of restitution for the flexible rocking oscillator. In particular, it investigates how the coefficient of restitution is influenced by the position of impulses, and how coefficient of restitution further influences the rocking response.

2 ANALYTICAL MODEL

The model is illustrated in Figure 1(a). There are two masses: the top one is a concentrated mass m with negligible rotational mass moment of inertia at point P; the bottom one is a concentrated mass m_A with mass moment of inertia I_A at point A. The bottom mass takes the form of a rigid ‘U’ structure with a centroid at A; while the top mass is connected to the ‘U’ structure by a spring (with stiffness, k) and a viscous damper (with damping coefficient, c).

The body is symmetrical about a central vertical axis. The half width of the base is denoted by b . The slenderness of the bottom mass, centroid, and top mass are given by α_A , α_{cg} , and α . The height of the corresponding positions are h_A , h_{cg} , and h while their distances to either base corner are given by R_A , R_{cg} , and R , where cg refers to the centre of gravity.

There are three motion phases in this model: full contact phase, rocking around the left corner o’, and rocking around the right corner o. The mechanical constraint for each phase is illustrated in Figure 1(b)-1(d). Two degrees of freedom exist: the rotation of the body θ and the lateral displacement u of the top mass. The system is subjected to horizontal ground accelerations \ddot{x}_g . Based on the mechanical constraints and excitations, the equations of motion for each phase is derived using Newton’s law. They are similar to the ones proposed by Acikgoz

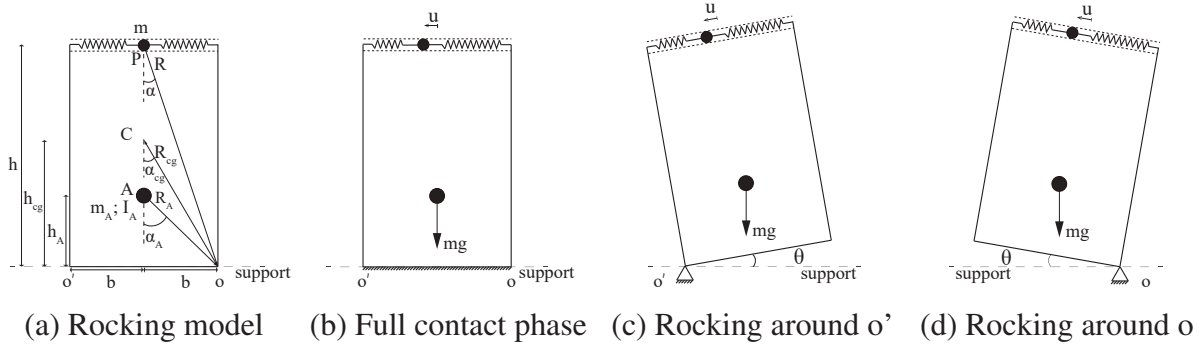


Figure 1: Rocking model and phases.

and DeJong [11], with the difference of the bottom mass at non-zero height.

After obtaining the equations of motion, phase transition rules are defined. There are two types of transition: uplift and impact, with the former indicating a transition from full contact phase to a rocking phase, and the latter a transition from a rocking phase to another rocking phase or to a full contact phase.

During full contact, the reaction forces from the support medium move along the base of the body. Uplift happens when the position of the vertical reaction force coincides with one of the corners of the base. Uplift involves a smooth transition between two phases of motion. In contrast, impact involves impulsive forces and features a non-smooth transition. The horizontal impulse experienced by the top mass is zero, as the spring and damper cannot transmit impulsive forces over an infinitesimally small duration impact. Using this information and noting that angular momentum is conserved around the locus of the impulsive force (located at a distance λb from the future rocking corner) allows the calculation of the post-impact angular velocity $\dot{\theta}^+$. The following equation expresses the coefficient of restitution e which relates pre-impact and post-impact angular velocities (i.e. $\dot{\theta}^+ = e\dot{\theta}^-$) for the body transitioning from a pure-rocking phase to another pure-rocking phase:

$$e = \frac{I_A + m_A h_A^2 + mu(\mp b + u) + b(1 - \lambda)(-m_A b - mb \pm mu)}{I_A + m_A h_A^2 + mu(\pm b + u) + b(1 - \lambda)(+m_A b + mb \pm mu)} \quad (1)$$

Here, the upper sign refers to transitions from rocking around the left corner to rocking around the right corner, and the lower sign refers to vice versa. If e is positive, a new rocking phases follows. A negative value is mechanically inadmissible; in this case, a transition to full contact phase is assumed. For this to occur, $e = 0$ and this implies that λ attains a specific value λ_0 . In the absence of any horizontal impulsive forces applied to the top mass, its post-impact velocity is determined by the conservation of horizontal momentum.

3 INFLUENCE OF IMPULSE POSITION ON ROCKING BEHAVIOUR

3.1 Dimensional analysis

To obtain the effects of the position of impulses on rocking behaviour systematically, dimensional analysis is employed. Single cycle sine and cosine pulses are used as excitations:

$$\ddot{x}_g = \begin{cases} AP(\omega t) & t \leq 2\pi/\omega \\ 0 & t > 2\pi/\omega \end{cases} \quad (2)$$

where \mathbf{P} denotes either sin or cos; A and ω denote the amplitude and frequency of the pulse.

Under the excitations shown in Equation (2), the response of the rocking oscillator can be characterised by Equation (3).

$$(u, \theta) = f(\omega_n, \zeta_n, \alpha, \alpha_A, \omega, A, t, m, m_A, I_A, g, b, \lambda) \quad (3)$$

With 13 parameters and 3 fundamental dimensions involved, the two non-dimensional response parameters can be expressed by $13 - 3 = 10$ non-dimensional parameters according to Buckingham's Π theorem [12]. The chosen three repeating parameters are: p , g and m , while the Π groups are shown in Table 1. Note p is the frequency for rocking ($p = \sqrt{(m + m_A)gR_{cg}/(I_A + m_A R_A^2 + mR^2)}$). Thus, the dimensionless response parameters u/u_{cr} and θ/α_{cg} can be obtained by Equation (4). u_{cr} is a displacement used to nondimensionalise lateral displacement, which corresponds to the critical lateral displacement when an undamped body with a zero bottom mass height uplifts ($u_{cr} = \pm \frac{(m_A/m+1)gb}{\omega_n^2 h}$).

Table 1: Π groups

Π groups	Π_1	Π_2	Π_3	Π_4	Π_5	Π_6	Π_7	Π_8	Π_9	Π_{10}
Quantity	ω_n/p	ζ_n	α_{cg}	α_A	ω/p	$A/(g \tan \alpha_{cg})$	pt	m_A/m	$I_A/(m_A R_A^2)$	λ

$$(u/u_{cr}, \theta/\alpha_{cg}) = f(\omega_n/p, \zeta_n, \alpha_{cg}, \alpha_A, \omega/p, A/(g \tan \alpha_{cg}), pt, m_A/m, I_A/(m_A R_A^2), \lambda) \quad (4)$$

3.2 Coefficient of restitution

The influence of the position of the vertical impulse, as expressed through the value of λ , on the coefficient of restitution can be estimated by evaluating Equation (1) numerically for a chosen rocking body. After defining the Π groups, a stocky but laterally flexible body is chosen to investigate the relationship between the coefficient of restitution, the position of the impulse and lateral displacement of the top mass at the moment of impact. The parameters chosen for the rocking body are given in Table 2. The relationship between e , λ and u/u_{cr} is illustrated in Figure 2 for a range of plausible values.

Table 2: Simulation parameters for investigation of coefficient of restitution

	Π_1	Π_2	Π_3	Π_4	Π_8	Π_9	Π_{10}
Figure 2	2.43	0.05	0.35	0.6	0.47	0.56	[0, 1]

Figure 2(a) shows that e is monotonically increasing with respect to λ . This can be confirmed to be true for all flexible rocking bodies. The partial derivative of e with respect to λ is shown in Equation (5) and is always positive. Thus, the increasing trend is confirmed. Chatzis et al. [8] established that the increase of λ within the expected physical bounds $[0, 2]$ leads to an increased coefficient of restitution for rigid rocking bodies. It is shown the trend is the same for flexible bodies.

$$\frac{\partial e}{\partial \lambda} = \frac{2(m + m_A)b^2(I_A + m_A h_A^2) + 2mm_A b^2 u^2}{[I_A + m_A h_A^2 + mu(\pm b + u) + b(1 - \lambda)(+m_A b + mb \pm mu)]^2} \quad (5)$$

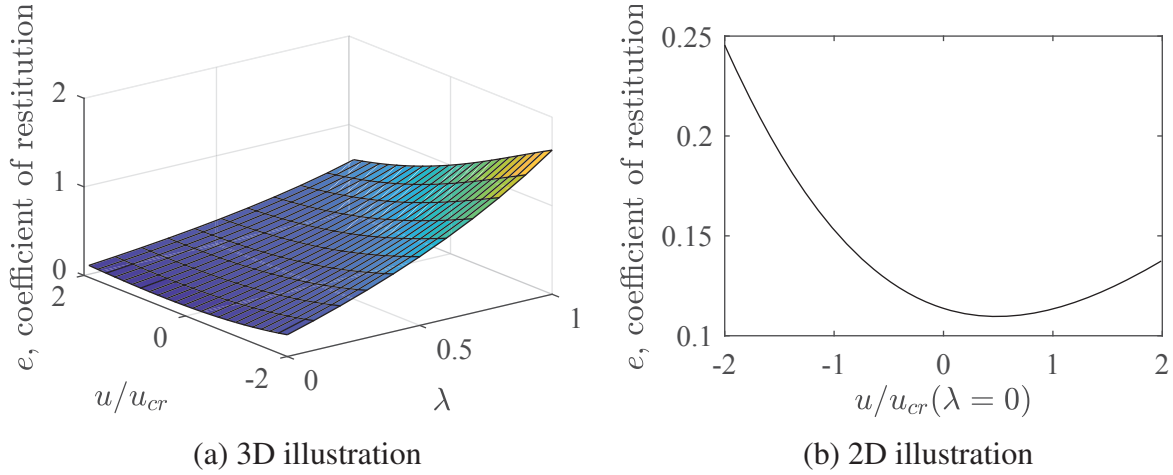


Figure 2: Illustration of the relation between e , λ and u/u_{cr} .

Figure 2(a) indicates the noteworthy influence of lateral deformations u/u_{cr} on the coefficient of restitution e ; while Figure 2(b) further investigates this relationship for an impulsive force locus at the future rocking corner, i.e. when $\lambda = 0$. Coefficient of restitution is clearly not a monotonic function of lateral deformation according to Figure 2(b). The lateral displacement u at impact, can reduce or increase the coefficient of restitution depending on its sign and magnitude.

For the example given in Figure 2, e is greater than 1 in some cases (e.g. $\lambda = 1$, $u/u_{cr} = -2$). However, different from the rigid body scenario, an e greater than 1 does not necessarily mean gaining energy during impact. Similarly, an e smaller than 1 can still lead to increase of energy. Furthermore, e with $\lambda = 0$, $u/u_{cr} = 0$ is much smaller than Housner's coefficient of restitution. This mainly reflects the effect of the absence of horizontal impulse applied at the top mass.

3.3 Stability analysis

A slender body is chosen to examine the influence of the impulse locus on overturning instability. The parameters are presented in Table 3. In the experiment by Espinosa [13], it is noticed $\lambda = 0.3$ is a reasonable value for the specific flat-base steel body placed on a sufficiently-stiff rubber mat. According to this, only three values of λ around 0.3 are included (0, 0.2, 0.4) in the following simulations. Figure 3 shows the stability diagram of a stiffer body; while Figure 4 illustrates that of a more flexible body. For both bodies, a sine and a cosine pulse excitation is applied separately. Each point on the diagram corresponds to the result under a pulse with a specific nondimensional frequency (horizontal axis) and nondimensional amplitude (vertical axis). Three types of results are involved as indicated in Figure 3(a) (annotations are omitted in other figures as the location of different types of results are similar): mode 1 failure (overturning with one or more impacts), mode 2 failure (overturning without impact), safe case (no overturning). It can be seen from all the figures that an increase in λ leads to an expansion of mode 1 failure area.

Table 3: Simulation parameters for stability analysis

	Π_1	Π_2	Π_3	Π_4	Π_5	Π_6	Π_8	Π_9	Π_{10}
Figure 3(a)	2.43	0.05	0.15	0.28	$[0, 6]$	$[0, 8]$	0.47	0.56	0, 0.2, 0.4
Figure 3(b)	2.43	0.05	0.15	0.28	$[0, 6]$	$[0, 8]$	0.47	0.56	0, 0.2, 0.4
Figure 4(a)	9.82	0.05	0.15	0.28	$[0, 12]$	$[0, 24]$	0.47	0.56	0, 0.2, 0.4
Figure 4(b)	9.82	0.05	0.15	0.28	$[0, 6]$	$[0, 10]$	0.47	0.56	0, 0.2, 0.4

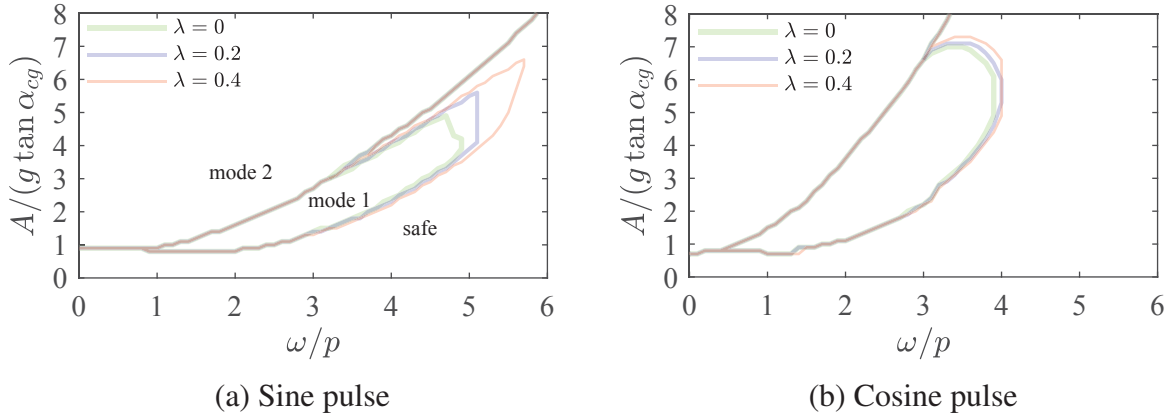


Figure 3: Effects of position of impulse on stability (flexible case).

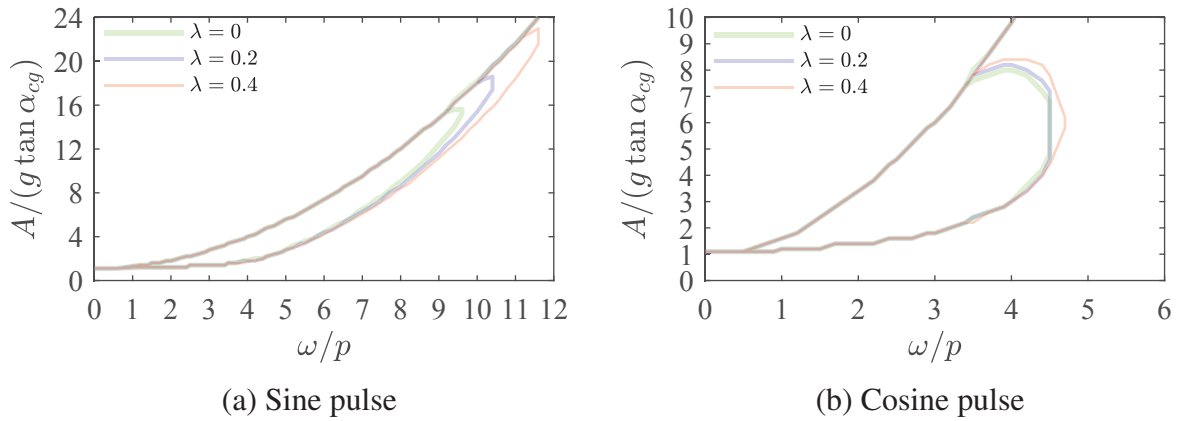


Figure 4: Effects of position of impulse on stability (stiff case).

The stability of the flexible rocking bodies is less sensitive to the change of λ under cosine pulse excitations. The trends are similar in Figures 3 and 4, indicating that the influence of λ on the stiff and flexible oscillators are qualitatively similar.

The increasing λ leads to more instances of overturning for the investigated flexible bodies, similar to the results obtained for rigid bodies [8]. In the rigid case, a reduced dissipation of energy can be predicted by the increase of λ since it directly determines energy loss. However, both rotational motion and lateral motion need to be considered to estimate energy loss at impact for the flexible body. Thus, a numerical example is chosen to demonstrate the total energy

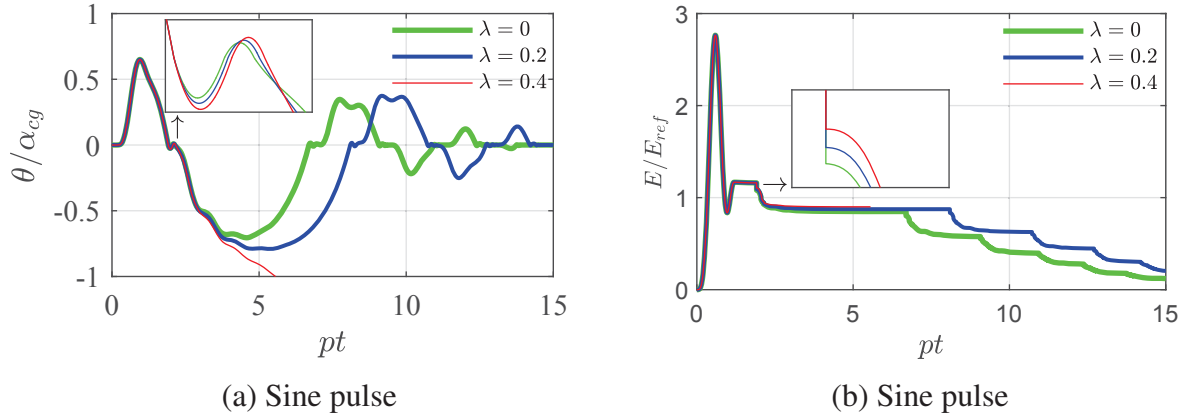


Figure 5: Time history example.

dissipation. The investigated rocking body is identical to the one shown in Figure 3(a), and its properties are provided in Table 3. The excitation that was considered is a sinusoidal pulse with $\omega/p = 5.3$ and $A/(g \tan(\alpha_{cg})) = 5$.

Figure 5(a)-5(b) show the time histories for rocking angle and total energy, which are all in normalised forms. Note that E_{ref} is the potential energy difference between the unstable and stable equilibrium points of a rigid body with a similar geometry [11]. It can be seen from the inset figure in Figure 5(b) that less energy was dissipated for larger λ , which leads to failure of the rocking body for $\lambda = 0.4$.

To generalise this result further, the total energy dissipation is investigated analytically. The following equation (6) shows the dissipated energy during impact (E_d); while the following equation (7) shows the partial derivative of E_d with respect to e , which is always negative for $e > 0$. Therefore, the dissipated energy is a monotonically decreasing function of e . Since a greater λ invariably leads to a greater e , the dissipated energy also decreases with the rise of λ . Therefore, it is reasonable to postulate that an increase in λ is likely to increase the risk of overturning for most types of excitations.

Nonetheless, due to the coupling between u and θ , it is possible for the rocking body to go directly from rocking into full contact [11]. The energy based considerations above do not account for this behaviour.

$$E_d = -\frac{1}{2}(I_A + m_A R_A^2 + mb^2 + mu^2)(e^2 - 1)(\dot{\theta}^-)^2 \mp mbu(e^2 + 1)(\dot{\theta}^-)^2 \quad (6)$$

$$\frac{\partial E_d}{\partial e} = -[I_A + m_A R_A^2 + m(b \pm u)^2]e(\dot{\theta}^-)^2 \quad (7)$$

It is also possible that a chosen value of λ may lead to an overall increase of the energy of the system during impact. Such values need to be avoided as the system would be gaining energy during impact. Similarly to [10], it is possible for this to happen for values of λ smaller than unity.

4 CONCLUSIONS

- A flexible rocking model and an impact model parametrising the location of the vertical impulse during impact is introduced.

- The effect of the position of the impulse on the coefficient of restitution is analytically and numerically examined, through studying the effect of changing the parameter λ .
- As the vertical impulse moves away from the future rocking corner, less energy is dissipated during impact. This is likely to lead to a higher risk of overturning instability.

REFERENCES

- [1] G.W. Housner, The behavior of inverted pendulum structures during earthquakes. *Bulletin of the seismological society of America*, **53**, 403–417 1963.
- [2] M. Aslam, W.G. Godden, D.T. Scalise, Earthquake rocking response of rigid bodies. *Journal of the Structural Division*, **106**, 377-392, 1980.
- [3] Q. Ma, The mechanics of rocking structures subjected to ground motion. PhD diss., ResearchSpace@ Auckland, 2010.
- [4] M.A. ElGawady, Q. Ma, J.W. Butterworth, J. Ingham, Effects of interface material on the performance of free rocking blocks. *Earthquake Engineering & Structural Dynamics*, **40**, 375-392, 2011.
- [5] S. Acikgoz, Q. Ma, A. Palermo, M.J. DeJong, Experimental identification of the dynamic characteristics of a flexible rocking structure. *Journal of Earthquake Engineering*, **20**, 1199-1221, 2016.
- [6] S. Acikgoz, M.J. DeJong, Analytical modelling of multi-mass flexible rocking structures. *Earthquake engineering & structural dynamics*, **45**, 2103-2122, 2016.
- [7] D. Kalliontzis, S. Sritharan, A. Schultz, Improved coefficient of restitution estimation for free rocking members. *Journal of Structural Engineering* **142**, 06016002, 2016.
- [8] M.N. Chatzis, M.G. Espinosa, A. Smyth, Examining the energy loss in the inverted pendulum model for rocking bodies. *Journal of Engineering Mechanics*, **143**, 04017013, 2017.
- [9] H.W. Shenton III, N.P. Jones, Base excitation of rigid bodies. I: Formulation. *Journal of Engineering Mechanics* **117**, 2286-2306, 1991.
- [10] M.N. Chatzis, M.G. Espinosa, C. Needham, M. S. Williams, Energy loss in systems of stacked rocking bodies. *Journal of Engineering Mechanics* **144**, 04018044, 2018.
- [11] S. Acikgoz, M.J. DeJong, The interaction of elasticity and rocking in flexible structures allowed to uplift. *Earthquake Engineering & Structural Dynamics*, **41**, 2177–2194, 2012.
- [12] E. Buckingham, On physically similar systems; illustrations of the use of dimensional equations. *Physical review*, **4**, 345, 1914.
- [13] M.G. Espinosa, Risk estimation of rocking components subjected to ground motions. PhD diss., University of Oxford, 2018.

QUANTIFYING SEISMIC RESILIENCE OF SINGLE-COLUMN ROCKING BRIDGES – A COMPARATIVE STUDY

Anastasios I. Giouvanidis¹, and You Dong²

¹University of Minho, ISE, Department of Civil Engineering
Guimarães, Portugal
e-mail: agiouvanidis@civil.uminho.pt

² Department of Civil and Environmental Engineering, The Hong Kong Polytechnic University
Hung Hom, Hong Kong
e-mail: you.dong@polyu.edu.hk

Keywords: Rocking, Analytical dynamics, Fragility, Seismic loss, Resilience.

Abstract. *This study focuses on structural systems which are particularly attractive for bridge design. Specifically, it investigates the seismic performance of single-column bridges, which are either conventionally designed, with the column monolithically connected with the ground (i.e. fixed-base), or designed with the column-footing system able to uplift and exhibit planar rocking motion during an earthquake. Conventionally designed bridges sustain considerable damage at the column ends after severe earthquakes. Seismic damage often determines whether the bridge remains functional after a seismic event. On the contrary, rocking design implies that a structure under seismic loading performs rigid body rotation around pre-defined pivot points. Thus, in principle, it relieves the structure from excessive deformations and damage. However, rocking isolation is not often applied in bridge engineering practice, mainly due to the lack of thorough understanding of its dynamic (seismic) performance and its potential post-earthquake financial benefits. This paper redirects our attention to the main benefits of rocking design over the conventional (fixed-base) design and conducts a comparative study between the two design methodologies in terms of their seismic losses and resilience in the aftermath of severe seismic hazard scenarios. The analysis reveals the mitigated seismic losses and the remarkable resilience that rocking design offers compared to the conventional (fixed-base) design after all the examined seismic hazard scenarios. The above findings reinforce the potential of the rocking design as an alternative seismic design paradigm for future bridge engineering applications and serve as the basis for a more rational and holistic seismic assessment of single-column rocking bridges.*

1 INTRODUCTION

Conventional bridge seismic design implies the column remains fixed with its foundation, and subsequently with the ground, offering the necessary strength and ductility to the structure to withstand seismic forces and avoid collapse. After severe earthquakes though, such a design concept leads to sustainable seismic damage and, thus, residual displacements. Seismic damage is an important measure of post-earthquake functionality that often dictates whether a bridge remains operational following a seismic event. On the other hand, rocking design allows the structure to uplift and pivot during an earthquake relieving the structure from stresses and subsequently seismic damage. The seminal work of Housner [1] first revealed the benefits of rocking design over the conventional (fixed-base) design after the Chilean earthquake in 1960, and many studies have followed [2, 3, 4, 5, 6, 7, 8, 9, 10, 11, 12, 13, 14, 15, 16, 17], among others.

The structural configuration of Fig. 1(a), in which the column is monolithically connected with the ground (i.e. fixed-base), is widely used for bridge design. On the contrary, the configuration of Fig. 1(b) is designed in such a way that the column is monolithically connected with the footing (or base) but the column-base system can detach from the (assumed rigid) ground when subjected to a ground motion. Hence, the rocking structural system of Fig. 1(b) is gaining momentum as an alternative bridge design paradigm, since it combines the benefits of rocking isolation with the merits of the *accelerated bridge construction* method. To illustrate its superior behavior, various studies have compared its seismic performance with the pertinent performance of its fixed-base counterpart [18, 19, 20, 21, 22, 23, 24, 25], and references therein.

This work is motivated by the lack of analytical studies that thoroughly evaluate the post-earthquake performance of the rocking system of Fig. 1. Hence, it extends the well-established performance-based earthquake engineering framework to compare the post-earthquake performance of the conventional design method with the rocking design in terms of: (i) the accumulated seismic (repair) losses, and (ii) the resilience in the aftermath of severe seismic hazard scenarios.

2 ANALYTICAL MODELLING

Fig. 1 illustrates the examined single-column structural systems. Fig. 1(a) shows the conventional (fixed-base) design, while Fig. 1(b) illustrates the rocking column-base system that is designed for bridges. Assuming rigid ground conditions and no sliding at the rocking interface allow the structure of Fig. 1(b) to uplift and pivot during an earthquake exhibiting planar rocking motion. When the rocking structure of Fig. 1(b) remains in full contact with the ground, from a dynamics perspective, it behaves as a single degree-of-freedom system (i.e. similar to the fixed-base structure of Fig. 1(a)). Thus, its motion is captured by the deformation of the column u . After rocking commences, the motion of the rocking structure is captured by both the deformation of the column u and the rocking rotation ϕ of the base [26, 27].

Consider the rocking oscillator of Fig. 1(b) with a concentrated mass m at height h . The column has a total mass of m_c and elastic stiffness of EI uniformly distributed along its length. The rigid base has mass m_b and width $2b$, while its height is considered negligible compared to its width. For simplicity, assume the lumped mass m creates no moment of inertia, while the rigid base creates moment of inertia with respect to its center of mass equal to $I_{m_b} = (1/3) m_b b^2$.

The equations of motion of the rocking oscillator of Fig. 1 can be derived using the general

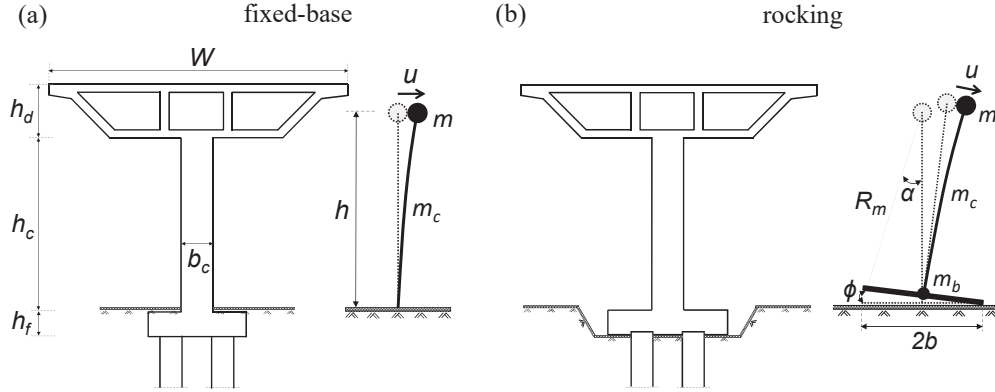


Figure 1: Single-column bridge: (a) designed conventionally with the column monolithically connected with the ground (i.e. fixed-base); and (b) designed with the column-base system able to uplift and pivot during an earthquake

form of the Lagrange's equation:

$$\frac{d}{dt} \left(\frac{\partial L}{\partial \dot{u}} \right) - \frac{\partial L}{\partial u} = Q, \quad \frac{d}{dt} \left(\frac{\partial L}{\partial \dot{\phi}} \right) - \frac{\partial L}{\partial \phi} = 0 \quad (1)$$

where $L = T - V$, with T the kinetic energy, V the potential energy and Q the generalized force, whose mathematical derivations are omitted herein for brevity (see [25] for more details). While the structure of Fig. 1(b) exhibits planar rocking, the equations that describe its motion are [25]:

$$\begin{aligned} & \left(m + \frac{33}{140} m_c \right) \ddot{u} + \left(m + \frac{11}{40} m_c \right) h \ddot{\phi} = \\ & -C\dot{u} - \frac{3EI}{h^3} u + \left[\left(m + \frac{33}{140} m_c \right) u - \text{sgn}(\phi) \left(m + \frac{3}{8} m_c \right) b \right] \dot{\phi}^2 \\ & -\ddot{u}_g \left(m + \frac{3}{8} m_c \right) \cos \phi + g \left(m + \frac{3}{8} m_c \right) \sin \phi \\ & \left(m + \frac{11}{40} m_c \right) h \ddot{u} + \left[\begin{aligned} & (I_{m_b} + m_b b^2) + m(h^2 + b^2) + mu^2 - \text{sgn}(\phi) 2mbu \\ & + m_c \left(\frac{1}{3} h^2 + b^2 \right) + \frac{33}{140} m_c u^2 - \text{sgn}(\phi) \frac{3}{4} m_c bu \end{aligned} \right] \ddot{\phi} = \\ & - \left(2m + \frac{33}{70} m_c \right) u \dot{\phi} + \text{sgn}(\phi) \left(2m + \frac{3}{4} m_c \right) b \dot{\phi} \\ & + \ddot{u}_g \left[\begin{aligned} & -\text{sgn}(\phi) (m + m_b + m_c) b \sin \phi \\ & - \left(m + \frac{1}{2} m_c \right) h \cos \phi + \left(m + \frac{3}{8} m_c \right) u \sin \phi \end{aligned} \right] \\ & + g \left[\begin{aligned} & -\text{sgn}(\phi) (m + m_b + m_c) b \cos \phi \\ & + \left(m + \frac{1}{2} m_c \right) h \sin \phi + \left(m + \frac{3}{8} m_c \right) u \cos \phi \end{aligned} \right] \end{aligned} \quad (2)$$

whereas when it remains in full contact with the ground, the pertinent equation of motion becomes:

$$\left(m + \frac{33}{140} m_c \right) \ddot{u} = -C\dot{u} - \frac{3EI}{h^3} u - \ddot{u}_g \left(m + \frac{3}{8} m_c \right) \quad (4)$$

where C is the damping coefficient responsible for the energy dissipation while the structure vibrates. \ddot{u} and $\ddot{\phi}$ denote the flexural and angular acceleration, while \ddot{u}_g and g are the ground and gravitational acceleration, respectively.

Rocking initiates when the overturning moment due to the external forces exceeds the restoring moment of the structural system. Therefore, uplift occurs when [25]:

$$\pm h \frac{m + \frac{11}{40} m_c}{m + \frac{33}{140} m_c} \left[\begin{aligned} & C\dot{u} + \frac{3EI}{h^3} u \\ & + \ddot{u}_g \left(m + \frac{3}{8} m_c \right) \end{aligned} \right] \mp \ddot{u}_g \left(m + \frac{1}{2} m_c \right) h - g \left[\begin{aligned} & (m + m_b + m_c) b \\ & \mp \left(m + \frac{3}{8} m_c \right) u \end{aligned} \right] > 0 \quad (5)$$

where the upper sign denotes clockwise (positive) rotations and the lower sign counter-clockwise (negative) rotations.

When during rocking, impact occurs, $\phi = 0$ and energy is lost. Following [28, 29, 25], this work assumes that after impact the rocking structure remains in full contact with the ground and uplifts when Eq. (5) is satisfied. Under this assumption and through conservation of angular momentum, the post-impact flexural velocity \dot{u}^+ can be expressed as [25]:

$$\dot{u}^+ = \dot{u}^- + \frac{I_{mb} - m_b b^2 + m_c \left(-b^2 + \frac{1}{3} h^2 + \frac{33}{140} u^2 \right) + m \left(-b^2 + h^2 + u^2 \right)}{\left(m + \frac{11}{40} m_c \right) h} \dot{\phi}^- \quad (6)$$

where \dot{u}^- and $\dot{\phi}^-$ denote the pre-impact flexural and angular velocity, respectively.

3 RESILIENCE-BASED EARTHQUAKE ENGINEERING ASSESSMENT

To evaluate the seismic performance of a structural system, the Pacific Earthquake Engineering Research (PEER) Center formulated the *performance-based earthquake engineering* (PBEE) framework [30, 31]. The PBEE framework encompasses four steps: (i) hazard analysis, (ii) structural analysis, (iii) damage analysis, and (iv) loss analysis. On the other hand, the resilience-based earthquake engineering (RBEE) framework illustrated in Fig. 2 appears to be a more holistic approach and it is considered as an extension of the PBEE in the design process. Specifically, the RBEE additionally incorporates the post-earthquake functionality and resilience of the structure, which are also important indicators to evaluate its seismic performance.

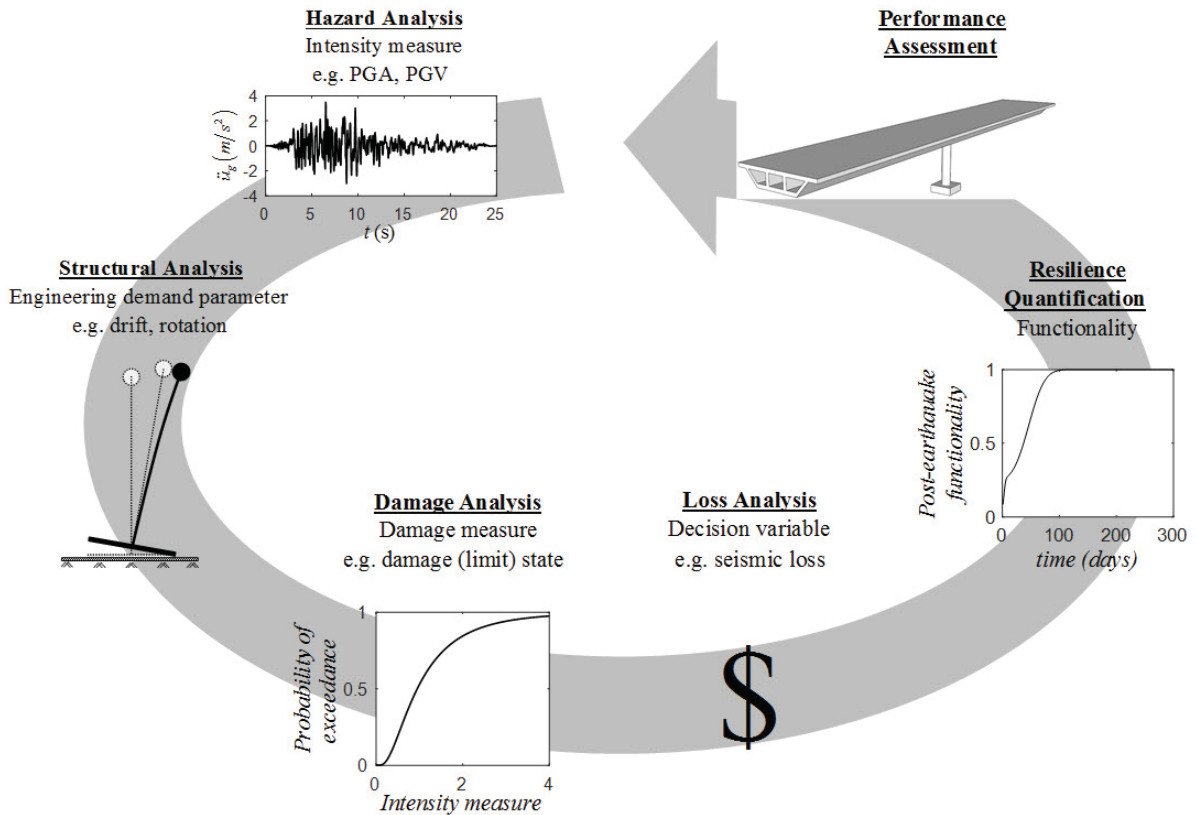


Figure 2: Resilience-based earthquake engineering framework

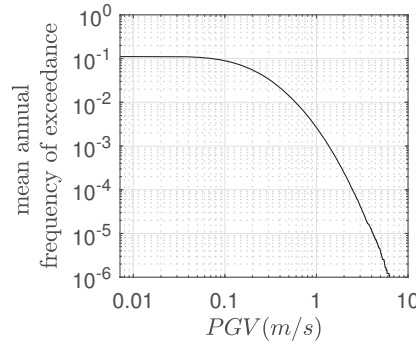


Figure 3: Hazard curve (in logarithmic scale) for the area of focus after conducting probabilistic seismic hazard analysis

3.1 Hazard Analysis

Assume that the examined structures of Fig. 1 are located in California laying on a strike-slip fault. The minimum and maximum moment magnitudes M_w are taken as 5.5 and 8, respectively, while the shear wave velocity averaged over the top 30 m $V_{s,30}$ is 480 m/s. The Joyner-Boore distance R_{JB} is 5 km. The IM considered herein is the peak ground velocity (PGV) [32, 33]. The PSHA provides a sample of 1,000,000 PGV values of ground excitations that are probable to appear in the area of focus [34]. To connect the earthquake events that are likely to appear in the examined area (i.e. California) with their annual frequency of exceedance, the Gutenberg-Richter recurrence law is adopted: $\log_{10}\lambda_M = 3.94 - 0.89M$, where λ_M is the frequency of the earthquakes with magnitudes greater than M . Fig. 3 plots the hazard curve (in logarithmic scale) that provides the mean annual frequency of exceedance λ_M of every earthquake that is likely to occur in the area of focus characterized by the adopted PGV.

3.2 Structural Analysis

This section investigates the seismic response of the single-column structural systems of Fig. 1. Each structure is considered to be part of a two-span box-girder bridge of total length $L = 60$ m and width $W = 10$ m. Assume that the total mass of the column is $m_c = 0.25m$, while the total mass of the base is $m_b = 0.17m$. The lumped mass m is located at height $h = 8$ m. The rocking structure of Fig. 1(b) has base-width $2b = 4.6$ m and slenderness $\alpha = 0.28$ rad. In addition, the examined structural systems have identical natural frequency $\omega_n = 8p$, where $p = \sqrt{g/R_m}$ is the frequency parameter of the rocking oscillator with R_m being the diagonal distance of the lumped mass from the pivot point (Fig. 1(b)). The damping ratio ζ is taken equal to 5% for the fixed-base oscillator of Fig. 1(a). For the rocking oscillator of Fig. 1(b), this study follows [27, 28] and assumes a constant damping ratio of 5% during rocking and a reduced damping ratio value during full contact (see [27] for further details).

To conduct the structural analysis, appropriate engineering demand parameters (EDPs) need first to be defined. The two EDPs are: (i) the absolute peak flexural deformation $|u_{max}|$ normalized with respect to the height h , and (ii) the absolute peak rocking rotation $|\phi_{max}|$ normalized with respect to the slenderness α .

$$EDP_1 = \frac{|u_{max}|}{h} \quad EDP_2 = \frac{|\phi_{max}|}{\alpha} \quad (7)$$

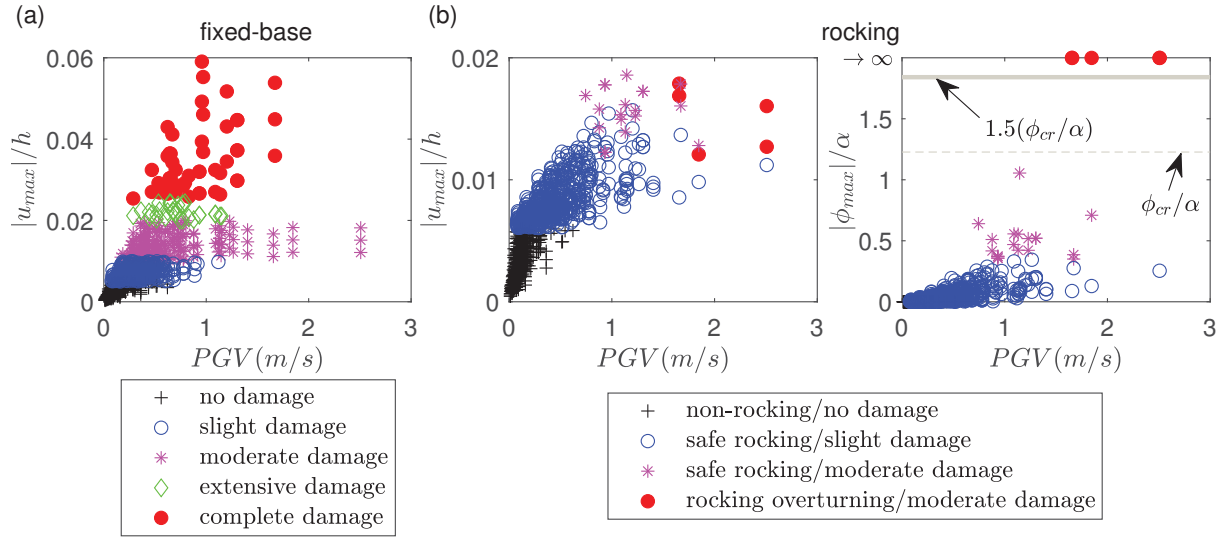


Figure 4: Seismic response analysis of (a) the fixed-base bridge bent of Fig. 1(a), and (b) the rocking bridge bent of Fig. 1(b)

Each of the structural systems of Fig. 1 is subjected to a series of strong ground motions adopted from the Pacific Earthquake Engineering Research (PEER) Center database [35]. The database covers a wide range of both pulse-type and nonpulse-type ground motions with magnitudes $6 \leq M_w \leq 8$ and distance from the fault $R_{rup} \leq 50$ km. To induce higher levels of demand, a scale factor of 1, 1.25 and 1.5 is, respectively, assigned to the accelerograms of the adopted database. Therefore, 960 response-history analyses are conducted for each of the examined structural systems of Fig. 1.

Fig. 4 illustrates the seismic response of both structural systems of Fig. 1. As a first approach, Fig. 4 reveals that uplift considerably reduces the structural deformation $|u_{max}|/h$ and therefore damage at the column. However, it makes the structure prone to excessive rocking rotations $|\phi_{max}|/\alpha$, and thus, overturning. Therefore, Fig. 4 reveals the importance of a proper design for a rocking bridge bent to avoid overturning (or collapse) and at the same time minimize structural damage at the column.

3.3 Damage Analysis

The seismic response of a structure is related to the damage occurred at the structure through appropriate damage measures. When excessive damage occurs, the structure collapses (or overturns for the case of a rocking structure) and subsequently it needs to be reconstructed. This work assumes that damage is occurred only at the column of the structure due to seismic forces. To quantify the seismic damage on the fixed-base structure of Fig. 1(a), this section adopts the damage limit states (or limit values of column damage) proposed by [37, 36], according to which damage is categorized into four levels/states, i.e. *slight*, *moderate*, *extensive* and *complete*. Table 1 presents the damage limits states of the fixed-base structure of Fig. 1(a).

On the other hand, the seismic response of the rocking structural system can be adequately described by three damage limit states. This work adopts the damage limits states proposed in [25], which proposed damage limit states for rocking bridge bents based on equivalence of their flexural deformation ($|u_{max}|/h$) with the pertinent deformation of their fixed-base counterparts. Table 2 presents these damage limits states. In Table 2, u_{cr} is the critical deformation of the column when rocking initiates (i.e. when the condition of Eq. (5) is met), and ϕ_{cr} is the critical

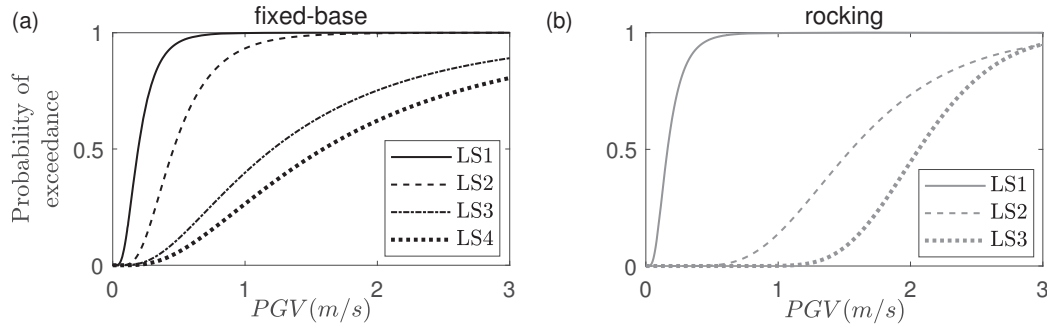


Figure 5: Fragility curves of (a) the fixed-base bridge bent of Fig. 1(a), and (b) the rocking bridge bent of Fig. 1(b) with respect to the adopted intensity measure

rotation for which the structure becomes dynamically unstable [27].

Based on Tables 1, 2, this section employs the *maximum likelihood estimation* approach [38] to estimate the probability of the examined structural systems to exceed the certain damage limit states. Fig. 5 plots the fragility curves of the structures of Fig. 1. Note from Fig. 5 and Fig. 4 that, uplift mitigates both structural deformations and the structure's probability to excessive rocking rotations and thus overturning.

3.4 Loss Analysis

The structural damage of the examined structures of Fig. 1 accumulated in the aftermath of a seismic event is connected with the seismic losses through decision variables such as: (i) the seismic (repair) losses, (ii) downtime, i.e. the time that is required for the bridge to restore its functionality, and (iii) resilience, i.e. the ability of the bridge to sustain a level of functionality

Damage limit state	Capacity limit [36]	Damage description [37]
LS1	$\frac{ u_{\max} }{h} = 0.005$	<i>Slight</i> concrete cracking and spalling at the column. Onset of yielding of the reinforcing bars. Column in operational condition (damage requires no more than cosmetic repair)
LS2	$\frac{ u_{\max} }{h} = 0.010$	<i>Moderate</i> concrete cracking and spalling at the column. Damage to the exposed reinforcing bars. Minimal residual displacements. Column is still operational (column is structurally sound, damage is repairable)
LS3	$\frac{ u_{\max} }{h} = 0.020$	<i>Extensive</i> flexural damage at the column in the form of buckling and/or fracture of the longitudinal reinforcing bars, transverse steel loss, etc. Considerable residual displacements. Column is not operational (column is structurally unsafe, damage is considerable and repairs are immediate)
LS4	$\frac{ u_{\max} }{h} = 0.025$	<i>Complete</i> damage and collapse of the column (column and the whole bridge need to be reconstructed)

Table 1: Damage limit states of the fixed-base bridge bent of Fig. 1(a).

Damage limit state	Capacity limit [25]	Response mode	Damage description [37]
LS1	$\frac{ u_{\max} }{h} = \frac{u_{cr}}{h}$	Rocking initiation	<i>Slight</i> concrete cracking and spalling at the column. Onset of yielding of the reinforcing bars. Column in operational condition (damage requires no more than cosmetic repair)
LS2	$\frac{ \phi_{\max} }{\alpha} = 0.35$	Safe rocking	<i>Moderate</i> concrete cracking and spalling at the column. Damage to the exposed reinforcing bars. Minimal residual displacements. Column is still operational. Damage at the pivot points and the abutments due to rocking motion (column is structurally sound, damage is repairable)
LS3	$\frac{ \phi_{\max} }{\alpha} = 1.5 \left(\frac{\phi_{cr}}{\alpha} \right)$	Rocking overturning	<i>Moderate</i> concrete cracking and spalling at the column. Damage to the exposed reinforcing bars. Minimal residual displacements. Column is still operational. Damage at the pivot points and the abutments due to rocking motion (column is structurally sound, damage is repairable, the column-base system can be reused after the applied repair methods, the whole bridge needs to be reconstructed)

Table 2: Damage limit states of the rocking bridge bent of Fig. 1(b) [25].

for over a period of time.

Seismic losses are defined as the sum of the seismic consequences weighted with their probability of occurrence. Therefore, the expected seismic losses under a given IM can be expressed as [39, 40]:

$$E(l) = \sum_{i=1}^n C_i \cdot P_{LSi|IM} \quad (8)$$

where C_i represents the seismic consequences, e.g. the repair cost associated with the given damage limit state i , and $P_{LSi|IM}$ is the conditional probability of the structure to be at the given damage limit state (see Fig. 5). The seismic consequences associated with the given damage limit states are assumed proportional to the reconstruction cost of the bridge [41, 39]:

$$C_i = RCR_i \cdot c_{rec} \cdot W \cdot L \quad (9)$$

where W and L are the bridge width and length, respectively. c_{rec} is the reconstruction cost, which for the fixed-base structure of Fig. 1(a) is translated into 2,306 \$/m² in present monetary values [42]. RCR_i is the repair cost ratio that corresponds to each damage limit state. The repair cost ratios are expressed as a percentage of the reconstruction cost of the bridge, and differ from damage limit state to damage limit state — the more severe the damage, the larger the repair cost ratio. Tables 3, 4 present the pertinent repair cost ratio values for each damage limit state of the examined structures of Fig. 1.

Damage limit state	Repair cost ratio [37]	Repair methods description [43, 44]	Downtime (days) [37]	
			Mean	Standard deviation
LS1	0.03	Repair slight concrete cracking/spalling at the column (epoxy injection, patch with concrete, etc.)	0.6	0.6
LS2	0.08	Repair moderate concrete cracking/spalling at the column, repair damaged reinforcing bars (patch with concrete, reinforce and recast, etc.)	2.5	2.7
LS3	0.25	Repair extensive concrete cracking/spalling at the column, replace/repair longitudinal/transverse reinforcing bars (reinforce and recast, potential replacement of the column)	75	42
LS4	1	Demolition and reconstruction of the column and the whole bridge	230	110

Table 3: Repair cost ratio and downtime values for each damage limit state of the fixed-base bridge bent of Fig. 1(a).

This study considers nine different seismic hazard scenarios with $T_R = 40, 72, 125, 225, 475, 975, 1,485, 2,475$ and $4,975$ -year return period, which translate into a probability of 71%, 50%, 33%, 20%, 10%, 5%, 3%, 2% and 1%, respectively, that at least one such event will occur in the next 50 years in the area of focus. The hazard curve of Fig. 3 provides the intensities in terms of PGV values that correspond to the adopted seismic hazard scenarios, i.e. 0.37, 0.51, 0.65, 0.83, 1.08, 1.36, 1.53, 1.76 and 2.11 m/s, respectively. Fig. 6 presents a comparison of the examined structural systems in terms of their expected seismic losses accumulated after the considered seismic hazard scenarios. As a first approach, Fig. 6 shows that for all of the examined seismic hazard scenarios, the rocking bridge bent of Fig. 1(b) provides a significant post-earthquake financial benefit compared to its fixed-base counterpart. In particular, even after a severe seismic event (i.e. with $T_R = 4,975$ -year return period), the rocking bridge bent yields seismic losses which correspond to around 50% of the construction cost of the structure — a considerable post-earthquake financial benefit.

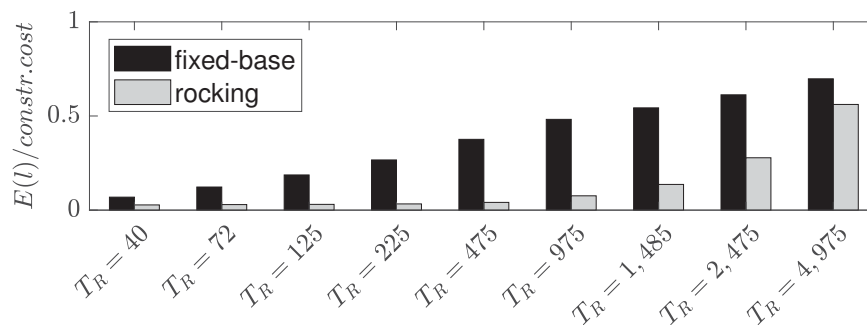


Figure 6: Expected (seismic) losses of the examined bridge bents of Fig. 1 in the aftermath of various seismic hazard scenarios

Damage limit state	Repair cost ratio [37]	Repair methods description	Downtime (days) [37, 45]	
			Mean	Standard deviation
LS1	0.03	Repair slight concrete cracking/spalling at the column (epoxy injection, patch with concrete, etc.)	0.6	0.6
LS2	0.08	Repair moderate concrete cracking/spalling at the column, repair damaged reinforcing bars (patch with concrete, reinforce and recast, etc.). Repair damage at the pivot points and the abutments	2.5	2.7
LS3	1	Repair moderate concrete cracking/spalling at the column, repair damaged reinforcing bars (patch with concrete, reinforce and recast, etc.). Repair damage at the pivot points and the abutments. Reuse the column-base system after the applied repair methods. Reconstruction of the whole bridge	46	22

Table 4: Repair cost ratio and downtime values for each damage limit state of the rocking bridge bent of Fig. 1 [25].

3.5 Resilience Quantification

Resilience, as a performance indicator, quantifies the recovery (or restoration) functions of a structural system following a seismic event. These recovery functions depend on the associated damage limit states. For instance, a bridge completely damaged needs more time to restore its functionality compared to a slightly damaged bridge. The resilience of the structural systems of Fig. 1 can be quantified under the investigated time-interval (e.g. $\Delta t = 365$ days) as [46]:

$$R = \frac{1}{\Delta t} \int_{t_0}^{t_0 + \Delta t} Q(t) dt \quad (10)$$

where t_0 indicates the time-instant the seismic event occurs, and $Q(t)$ is time-variant functionality which herein is expressed as [47]:

$$Q(t) = \sum_{i=1}^n FR_i(t) \cdot P_{LSi|IM} \quad (11)$$

where $P_{LSi|IM}$ is the conditional probability of the structure to be at the given damage limit state, and $FR_i(t)$ denotes the functionality restoration process of the structure for each damage limit state. This study models the functionality restoration process of the examined rocking structure as a normal cumulative distribution function corresponding to each damage limit state i [37]:

$$FR_i(t) = \frac{1}{2} \left[1 + \operatorname{erf} \left(\frac{t - \mu_{d_i}}{\sqrt{2}\sigma_{d_i}} \right) \right] \quad (12)$$

where μ_{d_i} and σ_{d_i} represent the mean and standard deviation of the time during which the bridge is under restoration (i.e. downtime). Table 3 presents values mean and standard deviation

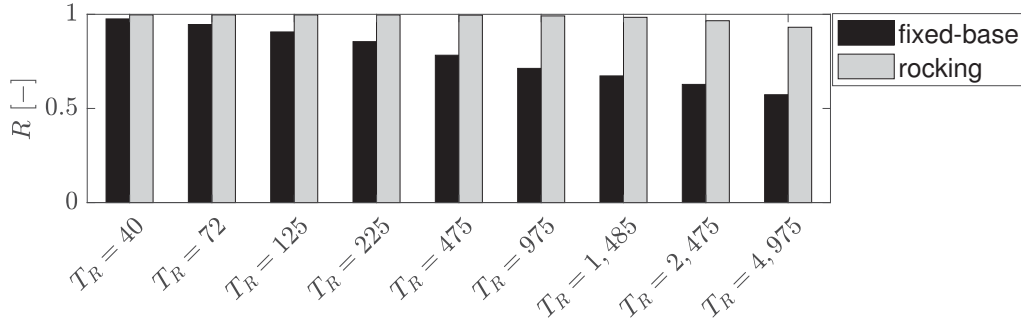


Figure 7: Resilience of the examined bridge bents of Fig. 1 in the aftermath of various seismic hazard scenarios under the investigated time-interval of $\Delta t = 365$ days

values of downtime (in days) for the fixed-base bridge bent of Fig. 1(a) proposed by HAZUS [37]. To estimate the corresponding downtime values for a rocking bridge, Mantawy et al. [45] experimentally compared the seismic performance of a rocking versus a conventionally designed (fixed-base) bridge. That study revealed that the construction time of the rocking bridge is, on average, 5 times lower than the construction time of the fixed-base bridge. In other words, when the fixed-base and the rocking bridge bent of Fig. 1 need to be reconstructed (i.e. when LS4 in Table 3 and LS3 in Table 4 are exceeded), the downtime of the rocking structure is considered as 1/5 of the downtime of the fixed-base structure. Table 4 presents the pertinent mean and standard deviation values of downtime for the rocking bridge bent of Fig. 1(b) [25].

Fig. 7 plots the resilience of each structural system and illustrates the dominance of the rocking structure over the conventionally designed (fixed-base) structure after all the examined seismic hazard scenarios. Note that the resilience of the rocking structure starts deteriorating only when a maximum considered earthquake occurs (i.e. with $T_R = 2,475$ -year return period). On the contrary, the resilience of the fixed-base structure is impaired even when a low intensity earthquake occurs (i.e. with $T_R = 72$ -year return period).

In sum, Figs 6, 7 reveal the remarkable financial benefits (i.e. decreased seismic losses and increased seismic resilience) that rocking design offers compared to the conventional fixed-base design, illustrating its potential as a seismic-avoidance design paradigm for bridges.

4 CONCLUSIONS

This work evaluates the seismic performance of structural systems, which are particularly attractive for bridge design. It focuses on single-column bridge bents either monolithically connected with the ground (i.e. fixed-base) or able to uplift and exhibit planar rocking motion during an earthquake. It extends the well-established performance-based earthquake engineering framework to compare the examined structural systems in terms of their accumulated seismic losses and resilience in the aftermath of severe seismic hazard scenarios.

The analysis reveals the considerably mitigated (seismic) losses of the examined rocking structure compared to the pertinent losses of the fixed-base structure, illustrating its potential as an economically feasible design solution. Further, results show that even under an extreme seismic hazard event, i.e. with 1% probability of occurrence in the next 50 years (i.e. $T_R = 4,975$ -year return period), the rocking bridge bent yields financial losses equivalent to 50% of the construction cost of the bridge — a considerable post-earthquake financial benefit. Further, this paper also unveils the remarkable post-earthquake resilience of the examined rocking structure after various seismic hazard scenarios. Importantly, the rocking bridge bent sustains

its resilience at the highest level till a maximum considered earthquake occurs (i.e. with $T_R = 2,475$ -year return period and 2% probability of occurrence in the next 50 years). On the contrary, the resilience of the fixed-base bridge bent is deteriorated even when a low intensity earthquake occurs (i.e. with $T_R = 72$ -year return period and 50% probability of occurrence in the next 50 years). The above findings redirect our attention to the main post-earthquake benefits of rocking design when used as a seismic isolation technique for bridges and pave the way for a more rational and holistic seismic assessment framework of single-column rocking bridges.

REFERENCES

- [1] G.W. Housner, The behavior of inverted pendulum structures during earthquakes. *Bulletin of the Seismological Society of America* **53**(2), 403–417 (1963).
- [2] E.G. Dimitrakopoulos, M.J. DeJong, Revisiting the rocking block: closed-form solutions and similarity laws. *Proceedings of the Royal Society A: Mathematical, Physical and Engineering Science* **468**(2144), 2294–2318 (2012).
- [3] M.J. DeJong, E.G. Dimitrakopoulos, Dynamically equivalent rocking structures, *Earthquake Engineering & Structural Dynamics*, **43**(10), 1543–1563 (2014).
- [4] E.G. Dimitrakopoulos, A.I. Giouvanidis, Seismic response analysis of the planar rocking frame. *Journal of Engineering Mechanics* **141**(7), 04015003 (2015).
- [5] E.G. Dimitrakopoulos, E.D.W. Fung, Closed-form rocking overturning conditions for a family of pulse ground motions. *Proceedings of the Royal Society A: Mathematical, Physical and Engineering Science* **472**(2196), 20160662 (2016).
- [6] M.F. Vassiliou, K.R. Mackie, B. Stojadinovic, A finite element model for seismic response analysis of deformable rocking frames. *Earthquake Engineering & Structural Dynamics* **46**(3), 447–466 (2017).
- [7] M.F. Vassiliou, Seismic response of a wobbling 3D frame. *Earthquake Engineering & Structural Dynamics* **47**(5), 1212–1228 (2017).
- [8] A.I. Giouvanidis, E.G. Dimitrakopoulos, Seismic performance of rocking frames with flag-shaped hysteretic behavior. *Journal of Engineering Mechanics* **143**(5), 04017008 (2017).
- [9] J.A. Bachmann, M.F. Vassiliou, B. Stojadinovic, Dynamics of rocking podium structures. *Earthquake Engineering & Structural Dynamics* **46**(14), 2499–2517 (2017).
- [10] J.A. Bachmann, M. Strand, M.F. Vassiliou, M. Broccardo, B. Stojadinovic, Is rocking motion predictable? *Earthquake Engineering & Structural Dynamics* **47**(2), 535–552 (2018).
- [11] A. Dar, D. Konstantinidis, W. El-Dakhakhni, Seismic response of rocking frames with top support eccentricity. *Earthquake Engineering & Structural Dynamics* **47**(12), 2496–2518 (2018).

- [12] J.A. Bachmann, M.F. Vassiliou, B. Stojadinovic, Rolling and rocking of rigid uplifting structures. *Earthquake Engineering & Structural Dynamics* **48**(14), 1556–1574 (2019).
- [13] N. Reggiani Manzo, M.F. Vassiliou, Displacement-based analysis and design of rocking structures. *Earthquake Engineering & Structural Dynamics* **48**(14), 1613–1629 (2019).
- [14] S. Diamantopoulos, M. Fragiadakis, Seismic response assessment of rocking systems using single degree-of-freedom oscillators. *Earthquake Engineering & Structural Dynamics* **48**(7), 689–708 (2019).
- [15] E. Avgenakis, I.N. Psycharis, An integrated macroelement formulation for the dynamic response of inelastic deformable rocking bodies. *Earthquake Engineering & Structural Dynamics* **49**(11), 1072–1094 (2020).
- [16] K.E. Bantilas, I.E. Kavvadias, L.K. Vasiliadis, Seismic response of elastic multidegree of freedom oscillators placed on the top of rocking storey. *Earthquake Engineering & Structural Dynamics* **50**(5), 1315–1333 (2021).
- [17] G. Vlachakis, A.I. Giouvanidis, A. Mehrotra, P.B. Lourenço, Numerical block-based simulation of rocking structures using a novel universal viscous damping model. *Journal of Engineering Mechanics* (under review).
- [18] A. Palermo, S. Pampanin, Enhanced seismic performance of hybrid bridge systems: Comparison with traditional monolithic solutions. *Journal of Earthquake Engineering* **12**(8), 1267–1295 (2008).
- [19] G. Antonellis, M. Panagiotou, Seismic response of bridges with rocking foundations compared to fixed-base bridges at a near-fault site. *Journal of Bridge Engineering* **19**(5), 04014007 (2014).
- [20] A. Agalianos, A. Psychari, M.F. Vassiliou, B. Stojadinovic, I. Anastasopoulos, Comparative assessment of two rocking isolation techniques for a motorway overpass bridge. *Frontiers in Built Environment* **3**, 47 (2017).
- [21] D. Marriott, S. Pampanin, A. Palermo, Quasi-static and pseudo-dynamic testing of unbonded post-tensioned rocking bridge piers with external replaceable dissipaters. *Earthquake Engineering & Structural Dynamics* **38**(3), 331–354 (2009).
- [22] M. Panagiotou, W. Trono, G. Jen, P. Kumar, C.P. Ostertag, Experimental seismic response of hybrid fiber-reinforced concrete bridge columns with novel longitudinal reinforcement detailing. *Journal of Bridge Engineering* **20**(7), 04014090 (2014).
- [23] A.S. Saad, D.H. Sanders, I.G. Buckle, Experimental evaluation of bridge column foundation rocking behavior. *Journal of Bridge Engineering* **23**(11), 04018088 (2018).
- [24] Y. Xie, J. Zhang, R. DesRoches, J.E. Padgett, Seismic fragilities of single-column highway bridges with rocking column-footing. *Earthquake Engineering & Structural Dynamics* **48**(7), 843–864 (2019).
- [25] A.I. Giouvanidis, Y. Dong, Seismic loss and resilience assessment of single-column rocking bridges. *Bulletin of Earthquake Engineering* **18**(9), 4481–4513 (2020).

- [26] S. Acikgoz, M.J. DeJong, : The interaction of elasticity and rocking in flexible structures allowed to uplift. *Earthquake Engineering & Structural Dynamics* **41**(15), 2177–2194 (2012).
- [27] M.F. Vassiliou, R. Truniger, B. Stojadinovic, An analytical model of a deformable cantilever structure rocking on a rigid surface: development and verification. *Earthquake Engineering & Structural Dynamics* **44**(15), 2775–2794 (2015).
- [28] A.I. Giouvanidis, E.G. Dimitrakopoulos, Nonsmooth dynamic analysis of sticking impacts in rocking structures. *Bulletin of Earthquake Engineering* **15**(5), 2273–2304 (2017).
- [29] J. Zhang, Y. Xie, G. Wu, Seismic responses of bridges with rocking column-foundation: A dimensionless regression analysis. *Earthquake Engineering & Structural Dynamics* **48**(1), 152–170 (2019).
- [30] P. Fajfar, H. Krawinkler, *Seismic design methodologies for the next generation of codes*. Taylor & Francis (1997).
- [31] J. Moehle, G.G. Deierlein, A framework methodology for performance-based earthquake engineering. In: *Proceedings of the 13th World Conference on Earthquake Engineering*, Paper No 679. Vancouver, B.C., Canada (2004).
- [32] E.G. Dimitrakopoulos, T.S. Paraskeva, Dimensionless fragility curves for rocking response to near-fault excitations. *Earthquake Engineering & Structural Dynamics* **44**(12), 2015–2033 (2015).
- [33] A.I. Giouvanidis, E.G. Dimitrakopoulos, Rocking amplification and strong-motion duration. *Earthquake Engineering & Structural Dynamics* **47**(10), 2094–2116 (2018).
- [34] J.W. Baker, *An introduction to probabilistic seismic hazard analysis*. White Paper Version 2.1 **2**(1), 79 (2015).
- [35] J.W. Baker, T. Lin, S.K. Shahi, N. Jayaram, *New ground motion selection procedures and selected motions for the peer transportation research program*. Tech. Rep. PEER Report 2011/3, Pacific Earthquake Engineering Research Center, University of California, Berkeley, CA (2011).
- [36] J.S. Jeon, A. Shafieezadeh, D.H. Lee, E. Choi, R. DesRoches, Damage assessment of older highway bridges subjected to three-dimensional ground motions: characterization of shear–axial force interaction on seismic fragilities. *Engineering Structures* **87**, 47–57 (2015).
- [37] HAZUS-MH: *Multi-hazard loss estimation methodology - earthquake model (technical manual)*. Tech. Rep. MH MR5, Federal Emergency Management Agency, Washington (2010).
- [38] J.W. Baker, Efficient analytical fragility function fitting using dynamic structural analysis. *Earthquake Spectra* **31**(1), 579–599 (2015).
- [39] Y. Dong, D.M. Frangopol, D. Saydam, Time-variant sustainability assessment of seismically vulnerable bridges subjected to multiple hazards. *Earthquake Engineering & Structural Dynamics* **42**(10), 1451–1467 (2013).

- [40] G.A. Anwar, Y. Dong, Y. Li, Performance-based decision-making of buildings under seismic hazard considering long-term loss, sustainability, and resilience. *Structure and Infrastructure Engineering* **17**(4), 454–470 (2020).
- [41] J.B. Mander, *Fragility curve development for assessing the seismic vulnerability of highway bridges*. Tech. rep., University at Buffalo (1999).
- [42] Y. Zheng, Y. Dong, Y. Li, Resilience and life-cycle performance of smart bridges with shape memory alloy (SMA)-cable-based bearings. *Construction and Building Materials* **158**, 389–400 (2018).
- [43] J. Ghosh, J.E. Padgett, Probabilistic seismic loss assessment of aging bridges using a component-level cost estimation approach. *Earthquake Engineering & Structural Dynamics* **40**(15), 1743–1761 (2011).
- [44] W.K. Lee, S.L. Billington, Performance-based earthquake engineering assessment of a self-centering, post-tensioned concrete bridge system. *Earthquake Engineering & Structural Dynamics* **40**(8), 887–902 (2011).
- [45] I.M. Mantawy, T. Thonstad, D.H. Sanders, J.F. Stanton, M.O. Eberhard, Seismic performance of precast, pretensioned, and cast-in-place bridges: Shake table test comparison. *Journal of Bridge Engineering* **21**(10), 04016071 (2016).
- [46] G.P. Cimellaro, A.M. Reinhorn, M. Bruneau, Framework for analytical quantification of disaster resilience. *Engineering Structures* **32**(11), 3639–3649 (2010).
- [47] Y. Dong, D.M. Frangopol, Risk and resilience assessment of bridges under mainshock and aftershocks incorporating uncertainties. *Engineering Structures* **83**, 198–208 (2015).

DYNAMIC RESPONSE OF MULTI-STOREY STRUCTURES SEISMICALLY ISOLATED USING KINEMATIC BEARINGS

Kosmas E. Bantilas¹, Ioannis E. Kavvadias¹, Lazaros Vasiliadis¹, Anaxagoras Elenas¹

¹ Department of Civil Engineering, Democritus University of Thrace
Campus of Kimmeria, Xanthi 67100, Greece
e-mail: {kbantila, ikavvadi, lvasilia, elenas}@civil.duth.gr

Abstract

A storey comprised of free-standing columns that may uplift under ground motion excitations can be regarded as a seismic isolation technique. These columns are referred to the literature as “kinematic bearings” and have been used in Russia and the wider region of the former Soviet Union over the past 40 years. Despite the extensive use of kinematic bearings, there are only limited studies based on the results obtained by the analytical solution of the dynamic response of such structural systems. From this point of view, in the present study the dynamic response of multi-storey structures placed on the top of a kinematic storey is examined. For this purpose an analytical model that describes the dynamic response of such structures is introduced. As long as the curved configuration of the ends of the kinematic bearings can affect the post-uplift stiffness of the kinematic storey, modal analysis is performed and the dynamic properties after the uplift are demonstrated. Subsequently, dynamic time history analyses are performed and the effect of post uplift stiffness of the kinematic storey on the displacement response of the base is investigated. Finally, the seismic demands of the superstructure, as well as their distribution throughout the storeys are examined.

Keywords: Rocking structures; Kinematic bearings; Seismic isolation;

1 INTRODUCTION

The dynamic response of rigid blocks rocking on a rigid ground was first studied by Housner [1], who highlighted the parameters that affect the stability of rigid bodies which can be uplifted under horizontal excitations. Since then, with the recognition of the remarkable properties of the rocking response, various forms of rocking systems have been studied, such as flexible rocking oscillators on solid [2-6] and flexible ground [7, 8], rocking structures on the foundations [9], rocking bridge piers [10-12], rocking frames [13-17], coupled conventional structures with rocking walls [18-20] and seismic isolation by forming a rocking floor at the base [21-24]. Despite the remarkable stability of free-to-rock large-scale systems, the basic requirement for the practical application of rocking systems is the prevention of overturning [25]. Along with the study of free rocking structural systems, the dynamic response of controlled and energy dissipative rocking systems have also been studied. Pre-tensioned tendons [26-29] and energy dissipation mechanisms [30-32] have been implemented onto rocking systems in order to limit the seismic demands and increase the deformation capacity. At the same time, due to the strongly non-linear behavior of the rocking motion, small changes in both the rocking system and the ground motion parameters can lead to large variations in the response, so that the study of the phenomenon under a probabilistic framework yields more reliable conclusions [33]. To this end, various intensity measures have been proposed to describe the influence of ground excitations on the response of rocking systems [34-39].

Although the rocking isolation design strategy has been implemented in a limited number of bridges [40, 41] and tall chimneys [42], hundreds of rocking podium structures (RPSs) have been constructed over the past 40 years in Russia and the wider region of the former Soviet Union [43]. RPSs are comprised of a superstructure placed on the top of a rocking story. The freestanding columns of the rocking story, referred to as "kinematic bearings" in Russian literature, can uplift under earthquake excitations, limiting the earthquake-induced loads on the superstructure. A complete presentation of the application of kinematic bearings in conjunction with energy dissipation mechanisms in Russia is provided by Smirnov et al. [44], while practical recommendations for the design of structures with kinematic foundations can be found in Cherepinskiy's book on kinematic foundations [45].

The first detailed study of the dynamic response of structures seismically isolated using a purely rocking floor at the base, considering that the superstructure behaves like a single degree of freedom elastic oscillator, was carried out by Bachmann et al. [21]. The developed analytical model has also been verified by experiments [22]. Through the analytical model, the forenamed study concentrates mainly on the investigation of parameters related to the stability of such systems, under pulse-type and natural seismic excitations. Based on the sdof model of the superstructure, Bantilas et al. [23] investigated the parameters that affect the elastic demands of RPSs. Later studies of Bantilas et al. [24] highlighted the critical effect of the higher vibration modes on the dynamic response of RPSs consisted of multiple degree of freedom (mdof) elastic superstructure. Due to the coupling between rocking and elastic vibrations, RPSs present a more complex response compared to solely rocking oscillators.

At this point, it should be emphasized that despite the wide use of kinematic bearings, their dynamic response differs from that of purely rocking systems, since the bearing base of the former is configured concave in opposition to the flat base of the latter. The aforementioned configuration of the rocking base results in a rolling response of the kinematic bearing onto the foundation, with positive or negative stiffness, before it starts to purely rock. An analytical model of the dynamic response of rigid bodies rolling and rocking on rigid ground is presented by Bachmann et al. [46] and Bachmann et al. [47].

In the present study an analytical model that describes the dynamic response of multi-storey structures placed on the top of a rocking base comprised of kinematic bearings is presented. As long as the curved configuration of the ends of the kinematic bearings can affect the post-uplift stiffness of the rocking storey, modal analysis is performed and the vibration mode properties after the uplift are demonstrated. In addition, dynamic time history analyses are performed on three typical multi-storey structures using the proposed analytical model. Considering three different rocking columns configurations, the effect of post uplift stiffness of the rocking storey on the response of the base is investigated. Finally, of particular interest are also the determination of the magnitude and the distribution of the seismic demands throughout the storeys of the superstructure. For this purpose the seismic demands of the nine structural systems are also presented.

2 DYNAMIC RESPONSE OF ROCKING PODIUM STRUCTURES

In the present section, the analytical model of the dynamic response of frame structures, seismically isolated using kinematic bearings, is presented. The model is based on the assumption that the superstructure can be described by a mdof elastic oscillator, fixed on the top of a rocking frame comprised of kinematic bearings. The rigid frame consists of a cap beam with mass m_b and N freestanding columns with mass m_c , semi-diagonal length $R = \sqrt{H^2 + B^2}$, rotational moment of inertia around its center of mass I_{cm} , and slenderness $\alpha = \tan(B/H)$. During the dynamic response, the rocking columns are considered to be in contact with the cap beam and the ground, while the friction coefficient at the contact surfaces is large enough to prevent any sliding. The idealization of the model is illustrated in Figure 1(a).

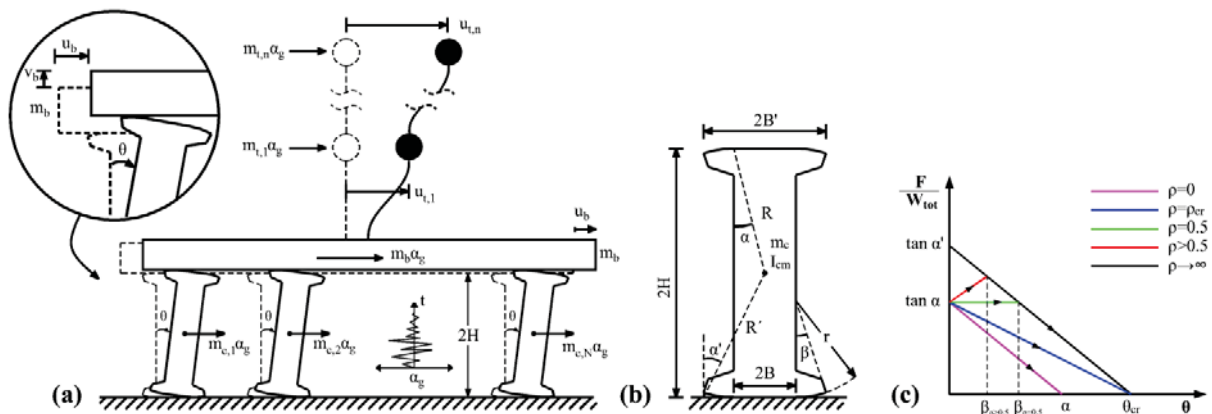


Figure 1: (a) Schematic representation of the analytical model, (b) geometric configuration of a typical kinematic bearing, and (c) static pushover curves of the kinematic storey.

A typical configuration of the kinematic bearings that comprise the rocking storey is presented in Figure 1(b). After the uplift occurrence, the curved extensions at the ends of the rocking columns result in the rolling response of the base storey before it starts to rock purely. With reference to Figures 1(b) and 1(c), the post uplift stiffness during rolling response depends on the radius of curvature r of the extensions, while the wedge's angle β sets the limit between rolling and rocking response. According to Bachman et al. [47], the critical rotation of the rocking storey is given by the following equation:

$$\theta_{cr} = \begin{cases} \arctan \frac{\tan \alpha}{1-2\rho}, & \rho \leq \rho_{cr} \text{ (overturning during rolling)} \\ \arctan \frac{\tan \alpha'}{1-2\rho(1-\cos \beta)}, & \rho > \rho_{cr} \text{ (overturning during rocking)} \end{cases} \quad (1)$$

where $\rho=r/(2H)$ is the non-dimensional radius of curvature of the extensions; $\rho_{cr} = 0.5(1 - \tan \alpha / \tan \alpha')$; $\beta = \arcsin((\tan \alpha' - \tan \alpha)/(2\rho))$; and $\tan \alpha' = B'/H$ (see Figure 1(b)).

The equations of motion of the RPS, as it is depicted in Figure 1 are expressed as follows:

$$A\ddot{\theta} = -B\frac{g}{R}(1+2\gamma+2\eta\gamma) - C\left(\frac{\alpha_g}{R}(1+2\gamma) - \frac{2\eta\gamma V}{M_{tot}R}\right) - D\dot{\theta}^2 \quad (2)$$

$$\mathbf{M}\ddot{\mathbf{u}}_t + \mathbf{C}\dot{\mathbf{u}}_t + \mathbf{K}\mathbf{u}_t = -\mathbf{M}\delta\alpha_g + \mathbf{K}\delta\mathbf{u}_b + \mathbf{C}\delta\dot{\mathbf{u}}_b \quad (3)$$

where A, B, C, and D are the coefficients listed in Table 1 for rolling and rocking response; γ is the mass ratio of the cap beam (m_b) divided by the total mass of rocking columns (Nm_c); η is the mass ratio of the superstructure (M_{tot}) divided by the mass of cap beam (m_b); α is the slenderness of rocking columns; \mathbf{u}_t , $\dot{\mathbf{u}}_t$ and $\ddot{\mathbf{u}}_t$ are the displacements, velocities, and accelerations of the mdof oscillator with respect to the undeformed configuration of the system (see Figure 1(a)); \mathbf{K} and \mathbf{C} are the stiffness and damping matrices of the mdof oscillator, respectively; δ is the influence vector of the ground motion ($\delta=1$); α_g is the ground acceleration; and \mathbf{u}_b and $\dot{\mathbf{u}}_b$ are the cap beam displacement and velocity, respectively. The base shear of the superstructure (V) is given by:

$$V = \delta^T \mathbf{K}(\mathbf{u}_t - \delta\mathbf{u}_b) + \delta^T \mathbf{C}(\dot{\mathbf{u}}_t - \delta\dot{\mathbf{u}}_b) \quad (4)$$

	Rolling Phase	Rocking Phase
$A^{*,\dagger}$	$\bar{I}_o + (1+4\gamma)\left(4\rho\cos\alpha(\cos(\pm\alpha-\theta)-\cos\alpha)\right) + 8\rho^2\cos^2\alpha(1-\cos\theta) + 4\gamma\left(1+\eta(\sin(\pm\alpha-\theta)+2\rho\cos\alpha\sin\theta)^2\right)$	$\bar{I}_o + (1+4\gamma)\left(4\rho\cos\alpha(\cos(\alpha-\beta)-\cos\alpha)\right) + 8\rho^2\cos^2\alpha(1-\cos\beta) + 4\gamma\left(1+\eta\left(\frac{\sin(\pm\alpha-\theta)+2\rho\cos\alpha(\sin(\pm\beta-\theta)+\sin\theta)}{2}\right)^2\right)$
B^\dagger	$\sin(\pm\alpha-\theta)+2\rho\cos\alpha\sin\theta$	$\sin(\pm\alpha-\theta)+2\rho\cos\alpha(\sin(\pm\beta-\theta)+\sin\theta)$
C^\dagger	$\cos(\pm\alpha-\theta)+2\rho\cos\alpha(1-\cos\theta)$	$\cos(\pm\alpha-\theta)+2\rho\cos\alpha(\cos(\pm\beta-\theta)-\cos\theta)$
D^\dagger	$(\sin(\pm\alpha-\theta)+2\rho\cos\alpha\sin\theta) \cdot \left(2\rho\cos\alpha(1+4\gamma)-4\eta\gamma\begin{pmatrix}\cos(\pm\alpha-\theta) \\ -2\rho\cos\alpha\cos\theta\end{pmatrix}\right)$	$-(\cos(\pm\alpha-\theta)+2\rho\cos\alpha(\cos(\pm\beta-\theta)-\cos\theta)) \cdot (\sin(\pm\alpha-\theta)+2\rho\cos\alpha(\sin(\pm\beta-\theta)+\sin\theta))$
\mathbf{u}_b^\dagger	$2(R(\sin(\pm\alpha)-\sin(\pm\alpha-\theta))+r(\theta-\sin\theta))$	$2(R(\sin(\pm\alpha)-\sin(\pm\alpha-\theta))+r(\pm\beta-\sin\theta-\sin(\pm\beta-\theta)))$
$\dot{\mathbf{u}}_b^\dagger$	$2(R\cos(\pm\alpha-\theta)+r(1-\cos\theta))\dot{\theta}$	$2(R\cos(\pm\alpha-\theta)+r(\cos(\pm\beta-\theta)-\cos\theta))\dot{\theta}$

* $\bar{I}_o = I_o/(m_c R^2)$ and I_o is the rotational inertia of the column with respect to the pivot point.

† The upper and lower signs define rolling/rocking around the right ($\theta>0$) and left ($\theta<0$) pivot points.

Table 1: Coefficients of the rocking storey equation of motion.

Until uplift occurs, the rocking base is assumed to remain inactive ($\theta = \dot{\theta} = 0$). Thus the superstructure behaves as a fixed base mdof oscillator, and the equations of motion are given by

Eq. (3), considering $u_b = \dot{u}_b = 0$. When the horizontal overturning actions overcome the restoring forces of the RPS, uplift occurs, and the rocking story starts to roll. The uplift criteria can be summarized as follows:

$$\mp \frac{\alpha_g}{g} \geq \left(1 + \frac{2\eta\gamma}{1+2\gamma}\right) \tan \alpha \mp \frac{2\eta\gamma}{(1+2\gamma)M_{tot}g} V \quad (5)$$

where V is the superstructure's base shear given by Eq. (4) considering $u_b = \dot{u}_b = 0$. The upper and lower signs define rolling initiation around the right ($\theta > 0$) and left ($\theta < 0$) pivot points.

In the particular case where the superstructure is rigid, Eq. (2) and the coefficients of Table 1 results in the equation of motion of rigid rolling and rocking frames[47], whose cap beam mass is equal to the sum of the mass of the superstructure and the mass of the cap beam of the RPS. On the other hand, if $\rho=0$, Eqs. (2) and (3) are equivalent to the equations of motion of pure rocking RPSs [24].

In the rolling/rocking response of rigid blocks, energy dissipation occurs during impact when the tilt angle of the rocking columns reverses the sign. The solution of the impact problem results in the coefficient of restitution of the rocking base, as well as in the post-impact velocities of the floors of the superstructure as follows [24]:

$$c = \left(\frac{\dot{\theta}^+}{\dot{\theta}^-}\right)^2 = \left[1 - 2\sin^2 \alpha \frac{1+4\gamma(1+\eta)}{I_0 + 4\gamma(1+\eta)}\right]^2 \quad \text{and} \quad \dot{\mathbf{u}}_t^+ = \dot{\mathbf{u}}_t^- - \delta 2R \cos \alpha (1 - \sqrt{c}) \dot{\theta}^- \quad (6)$$

where $\dot{\mathbf{u}}_t^-$ and $\dot{\mathbf{u}}_t^+$ are the superstructure's absolute velocity vectors before (-) and after (+) impact, respectively.

	Rolling Phase (I)	Rocking Phase (II)
\mathbf{M}_L	$\begin{bmatrix} Nm_c \bar{I}_0/4 + m_b + M_{tot} \alpha^2 & \mathbf{0} \\ \mathbf{0} & \mathbf{M} \end{bmatrix}$	$\begin{bmatrix} Nm_c \bar{I}_0/4 + m_b + M_{tot} \alpha'^2 & \mathbf{0} \\ \mathbf{0} & \mathbf{M} \end{bmatrix}$
\mathbf{C}_L	$\begin{bmatrix} \delta^T \mathbf{C} \delta & -\delta^T \mathbf{C} \\ -\mathbf{C} \delta & \mathbf{C} \end{bmatrix}$	$\begin{bmatrix} \delta^T \mathbf{C} \delta & -\delta^T \mathbf{C} \\ -\mathbf{C} \delta & \mathbf{C} \end{bmatrix}$
\mathbf{K}_L	$\begin{bmatrix} \delta^T \mathbf{K} \delta & -\frac{Nm_c/2 + m_b + M_{tot}}{2R} g (2\rho - 1) & -\delta^T \mathbf{K} \\ -\mathbf{K} \delta & \mathbf{K} \end{bmatrix}$	$\begin{bmatrix} \delta^T \mathbf{K} \delta & -\frac{Nm_c/2 + m_b + M_{tot}}{2R} g & -\delta^T \mathbf{K} \\ -\mathbf{K} \delta & \mathbf{K} \end{bmatrix}$
\mathbf{B}_{ag}	$\begin{bmatrix} Nm_c/2 + m_b \\ \mathbf{M} \delta \end{bmatrix}$	$\begin{bmatrix} Nm_c/2 + m_b \\ \mathbf{M} \delta \end{bmatrix}$
\mathbf{F}_L	$\begin{bmatrix} (Nm_c/2 + m_b + M_{tot}) g \alpha \\ \mathbf{0} \end{bmatrix}$	$\begin{bmatrix} (Nm_c/2 + m_b + M_{tot}) g \alpha' \\ \mathbf{0} \end{bmatrix}$

Table 2: Linearized matrices of Eq. (7) during rolling and rocking phase.

3 THE EIGENVALUE PROBLEM

In order to obtain the linearized equations of motion of a RPS once uplift occurs, the non-linear terms of Eqs. (2) and (3) expand into Taylor series about the static rest position of the

system ($\theta=0, \dot{\theta}=0, \mathbf{u}_t = \mathbf{0}, \dot{\mathbf{u}}_t = \mathbf{0}$) and the higher order terms are omitted. The linearized equations of motion can be represented as follows:

$$\mathbf{M}_L^{III} \ddot{\mathbf{u}}_L + \mathbf{C}_L^{III} \dot{\mathbf{u}}_L + \mathbf{K}_L^{III} \mathbf{u}_L = -\mathbf{B}_{ag}^{III} \alpha_g(t) \mp \mathbf{F}_L^{III} \quad (7)$$

where $\mathbf{u}_L = [u_{b,R} \ \mathbf{u}_t]^T$ and $u_{b,R}=2R\theta$ is the displacement of the cap beam in direction perpendicular to the diagonal of the rocking columns. The linearized matrices of mass (\mathbf{M}_L), damping (\mathbf{C}_L), stiffness (\mathbf{K}_L) as well as the load vectors (\mathbf{B}_{ag}) and (\mathbf{F}_L) during rolling (I) and rocking (II) are given in Table 2.

The eigenvalues and eigenvectors that correspond to the vibration modes of the superstructure after uplift occurrence, as well as the eigenvalues correspond to the rocking and rolling vibration modes are calculated following the process applied for RPSs consisted of purely rocking columns by Bantilas et al. [24].

4 VIBRATION PRPERTIES

In order to study the modification of dynamic properties of typical structures of one to 10 floors isolated using kinematic bearings, the eigenvalue problem is solved numerically. Superstructures with shear displacement profile are considered. The construction of mass (\mathbf{M}), stiffness (\mathbf{K}) and the damping (\mathbf{C}) matrices is based on the procedure presented by Thermou et al. [48] and has been also applied in RPSs [24]. Assuming that the superstructures are fixed on the top of a typical rocking frame, which consists of rectangular columns ($\bar{I}_0 = 4/3$) of size $R = 1.5$ m, slenderness $\tan(\alpha) = 0.15$ and $\tan(\alpha') = 0.30$, $\gamma = 10$ and cap beam mass m_b equal to the mass of the standard floor m ($\eta = \eta$), the linearized matrices (\mathbf{M}_L), (\mathbf{K}_L), and (\mathbf{C}_L) are constructed. Then, the eigenvalue problem is solved and the dynamic properties ($\omega_{u,i}$ and $\xi_{u,i}$) of the uplifted structures are determined. The amplification factors of the natural frequency ($\omega_{u,i}/\omega_{o,i}$) and damping ($\xi_{u,i}/\xi_{o,i}$) that correspond to the first ($i = 1$) vibration mode of typical superstructures from one to 10 floors ($n = 1 \div 10$) are presented in Figures 2. The amplification of the natural frequency is more intense during rolling phase compared to rocking phase. Regarding the nondimensional radius of the curved extensions, superstructures placed on the top of a rocking base with negative ($\rho=\rho_{cr}$) or zero stiffness ($\rho=0.5$) during rolling present identical modification of their dynamic properties. However, kinematic bearings with positive stiffness ($\rho=1.5$) results in higher values of amplification. Regardless the radius of the curved extensions, the damping amplification factors take lower values compared to corresponding frequency ones.

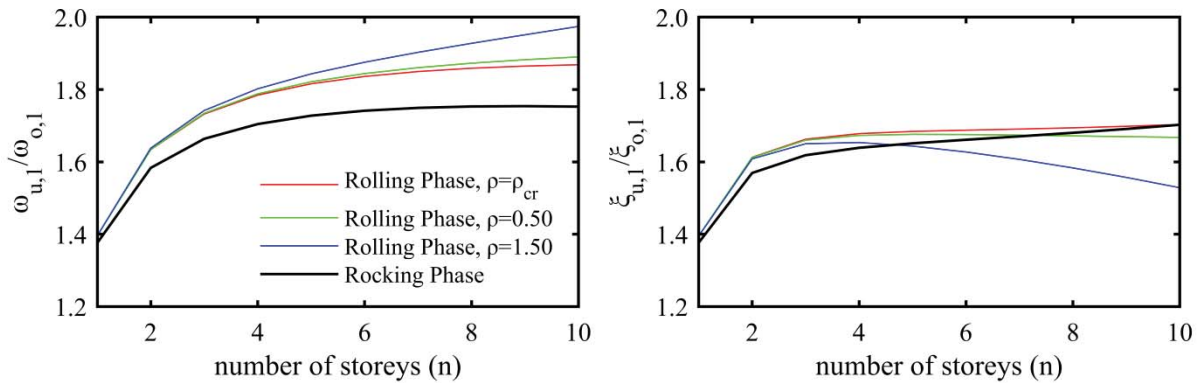


Figure 3: Amplification factors of the natural frequency (left) and damping ratio (right) of the first vibration mode, as a function of superstructure storeys (n) for rocking podium structures.

In Figure 4 (α) the eigenvalues (\bar{p}_{ext}) that correspond to the rolling and the rocking mode for RPSs with columns with nondimensional radius of curvature $\rho = \{\rho_{\text{cr}}, 0.5 \text{ and } 1.5\}$, as a function of size R , are presented. It has to be mentioned that these values correspond to the frequency parameter of the rocking base during rolling and rocking. Moreover, in Figure 4 (β) the frequency parameter during rolling phase is presented as a function of the radius of the curved wedges. The eigenvalues correspond to a six storey superstructure ($n = 6$) with shear deformation profile. In Figure 4 is also depicted, with dashed lines, the frequency parameter (\hat{p}_{ext}) of a rigid rocking frame with cap beam mass is equal to the sum of the mass of the superstructure and the mass of the cap beam of the RPS ($\gamma_{\text{tot}} = \gamma(1 + \eta)$). The frequency parameter \hat{p}_{ext} is given by the following expression:

$$\hat{p}_{\text{ext}} = \hat{p} \sqrt{k_1^*} \quad (5)$$

where \hat{p} the frequency parameter of a rigid rocking frame without curved extensions at the rocking columns; and $k_1^* = 2\rho - 1$ the dimensionless stiffness of the rocking base during rolling.

It is observed that the frequency parameter \bar{p}_{ext} , which is calculated by the modal analysis, is estimated with high accuracy by the frequency parameter \hat{p}_{ext} of the rigid rocking frame, in cases of negative and zero stiffness ($\rho \leq 0.5$) during rolling phase. In case of systems with positive stiffness, the frequency parameter values differ from the analytically calculated parameter, especially for small rocking columns ($R < 1.5 \text{ m}$) with large radius of the curved extensions ($\rho > 1.5$). Moreover, in structural systems with radius of curvature $\rho \leq 0.5$ the frequency parameter take lowers values in rolling than in rocking phase. In the special case where $\rho = 0.5$ (zero stiffness), the frequency parameter take value $\bar{p}_{\text{ext}} = 0$.

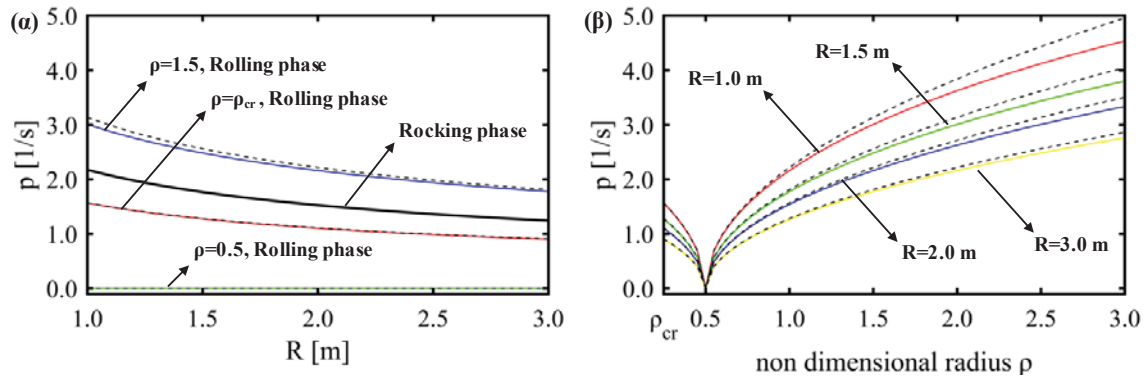


Figure 4: Frequency parameter: (α) as a function of size R and (β) as a function of the wedge's radius (ρ), of a seismic isolated six storey shear structure ($\gamma = 10$, $\eta = 6$, $\tan(\alpha) = 0.15$, $\tan(\alpha') = 0.30$ and $\bar{I}_0 = 4/3$).

The effect of the superstructures flexibility on the frequency parameters is presented in Figure 5 (α) and (β) for negative ($\rho = \rho_{\text{cr}}$) and positive stiffness ($\rho = 1.5$), respectively. The frequency parameter values of isolated shear superstructures with structural features $R = \{1.00, 1.50, 2.00 \text{ and } 3.00\} \text{ m}$, $\gamma = 10$, $\eta = n$, $\tan(\alpha) = 0.15$, $\tan(\alpha') = 0.30$ and $\bar{I}_0 = 4/3$, are illustrated as a function of the number of the floors (n). In dashed lines the frequency parameter (\hat{p}_{ext}) of a rigid rocking frame with curved extensions and beams mass $\gamma_{\text{tot}} = \gamma(1 + \eta)$ is also provided in the Figures. The flexibility of the superstructure do not affect the frequency parameter values in case of negative stiffness systems. However, in systems with positive stiffness during rolling, as the flexibility of the superstructure increases the frequency parameter of the rigid rocking

frame differs substantially from the values of the analytical solution, especially for rocking columns of small size.

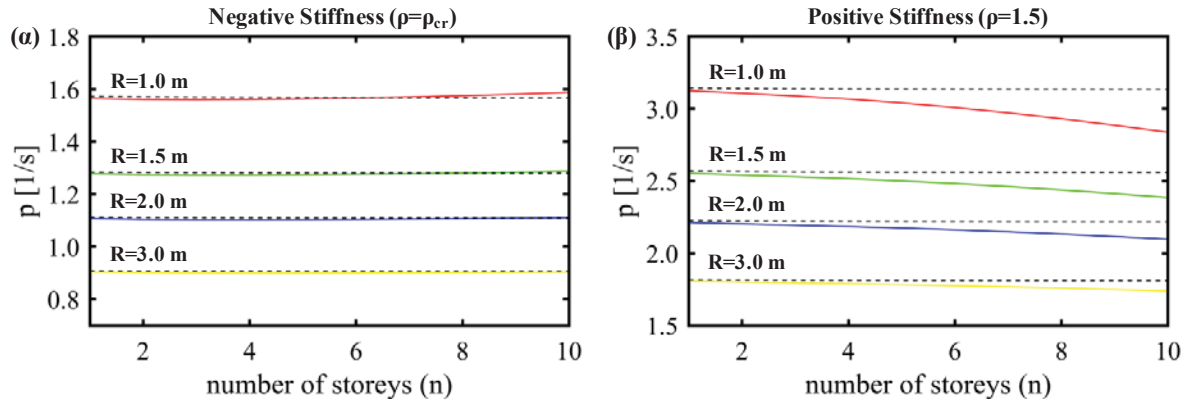


Figure 5: Frequency parameter as a function of the number of the floors (n), of rocking base with (a) negative and (b) positive stiffness during rolling phase.

The vibration mode eigenvectors of a typical three-story RPS ($n = \eta = 3$) isolated using kinematic bearings are presented in Figure 6. Specifically, the vibration modes during rolling phase, considering wedges with nondimensional radius of curvature $\rho = \{\rho_{cr}, 0.5 \text{ and } 1.5\}$, and rocking phase are displayed. The dashed black lines correspond to the full-contact eigenvectors of the superstructure, while the continuous black lines correspond to the horizontal components of the uplifted state eigenvectors of the RPS. The elastic components of the uplifted state eigenvectors are also presented in Figure 6 with continuous red lines. The calculation of the horizontal components of the eigenvectors herein is presented by Bantilas et al. [24].

The vibration mode eigenvectors of the uplifted structures present a compound shape that comprises an elastic component and a rigid body displacement due to the oscillation of the superstructure and the rocking action, respectively. Moreover, during the pure rolling/rocking vibration mode the elastic component eigenvector is negligible. Regardless the radius of the curved extensions the eigenvectors are identical during rolling and rocking phase. In any case, the magnitude of both the rigid body displacements of the uplifted state eigenvectors and the natural frequency amplification factors indicate the coupling between the response of the rocking base and the elastic vibration modes of the superstructure.

5 SEISMIC RESPONSE UNDER NATURAL GROUND MOTIONS

In this section, the seismic response of multi-storey structures seismically isolated using kinematic bearings subjected to natural ground motions is examined. Specifically, the effect of the stiffness of the rocking storey on the overall response of the PRS is investigated. For this purpose, the three sets of ground motions proposed by FEMA P695 [49] are used to perform dynamic time history analyses.

Dynamic time history analysis are performed on three typical shear structures with number of storeys $n = \{3, 6 \text{ and } 9\}$. The fundamental vibration period of the mdof oscillators is assumed to be given by the empirical relation $T_{t,1} = n/10$. Rayleigh damping with critical damping ratio $\xi = 5\%$ for the first two vibration modes is considered for the mdof oscillators. The mass (\mathbf{M}), stiffness (\mathbf{K}) and damping (\mathbf{C}) matrices are constructed based on the procedure applied by Bantilas et al. [24]. Every superstructure is considered to be fixed on the top of a rocking storey comprised of rectangular columns ($\bar{I}_0 = 4/3$) with semi-diagonal length $R = 1.50 \text{ m}$, slenderness $\tan(\alpha) = \{0.10, 0.15 \text{ and } 0.20\}$ and $\tan(\alpha') = 2 \cdot \tan(\alpha)$, and curved extensions

with nondimensional radius of curvature $\rho = \{\rho_{cr}, 0.5 \text{ and } 1.5\}$. Moreover, mass ratios $\eta/T_t = 10$ and $\gamma = 10$ are considered.

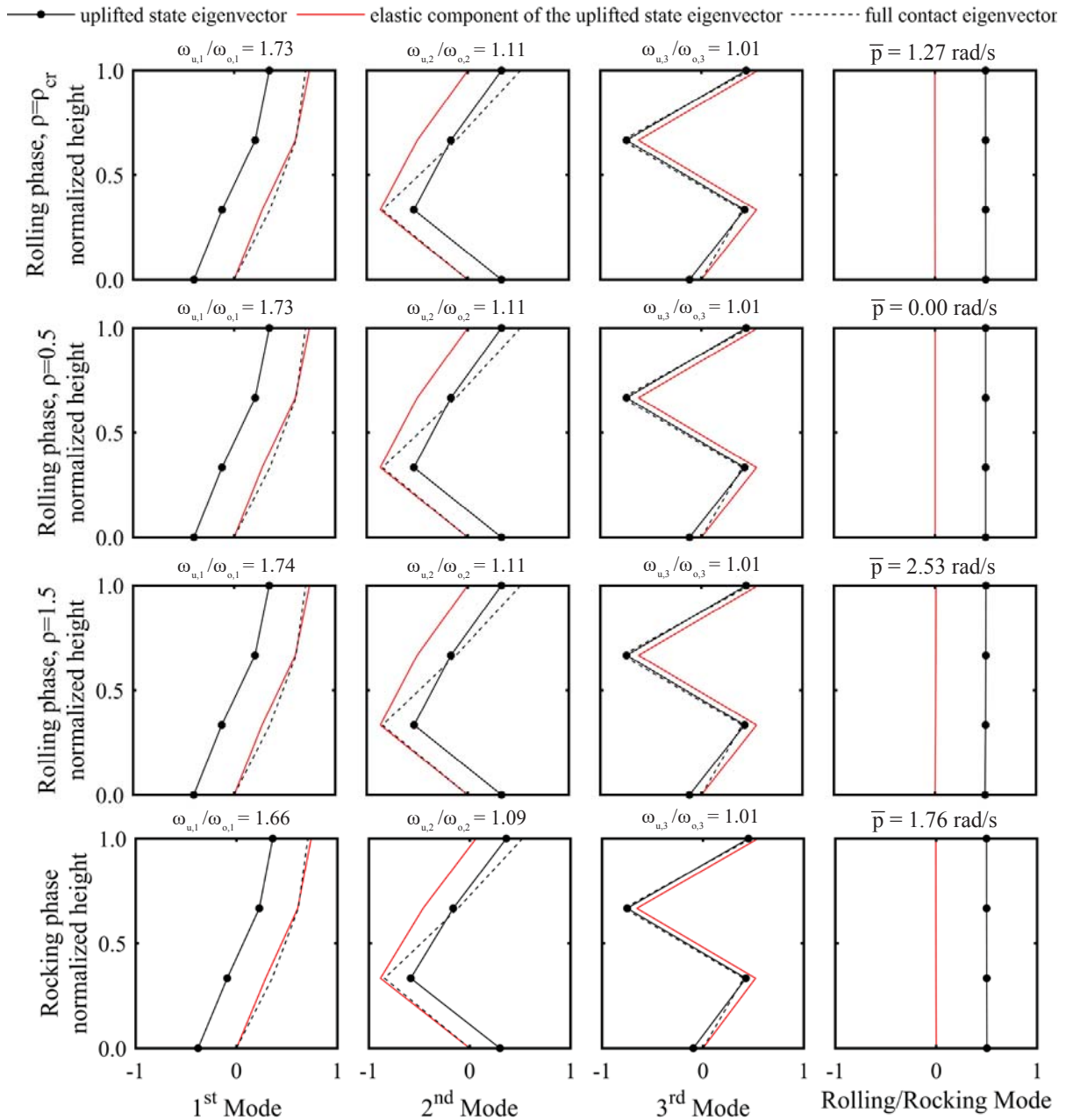


Figure 6: Vibration modes of a typical three-storey rocking podium structure ($\bar{I}_0 = 4/3$, $R = 1.5$ m, $\gamma = 10$, $\eta = 3$, $\tan(\alpha) = 0.15$ and $\tan(\alpha') = 0.30$).

The effect of curvature of the free standing column's curved wedges on the seismic response of the rocking base is presented in Figure 7. Specifically, the maximum rocking response of rocking base with curved extensions $(|\theta_{\max}|/\alpha)_{\text{ext}}$, compared with the response of rocking base without curved extensions $(|\theta_{\max}|/\alpha)_{\text{flat}}$ is displayed. For small rocking rotations $(|\theta_{\max}|/\alpha)_{\text{flat}} < 0.5$ the maximum response is almost identical. In general, the structures with curved extensions present increased stability. Due to the high nonlinearity there are only few cases where the structure without curved extensions develop finite rocking rotations $(|\theta_{\max}|/\alpha)_{\text{flat}} < 1$, while the structure with curved extensions overturns. However, enhanced dis-

placement capacity is achieved using columns with curved extensions. In Table 3 the rocking overturn probabilities of the examined structural systems are listed. It is obvious that rocking columns with curved extensions lead to significantly decreased probabilities of overturn. Moreover, the increase of the stiffness of the rocking base (larger radius of curvature), as well as the increase of the flexibility of the superstructure results in greater stability.

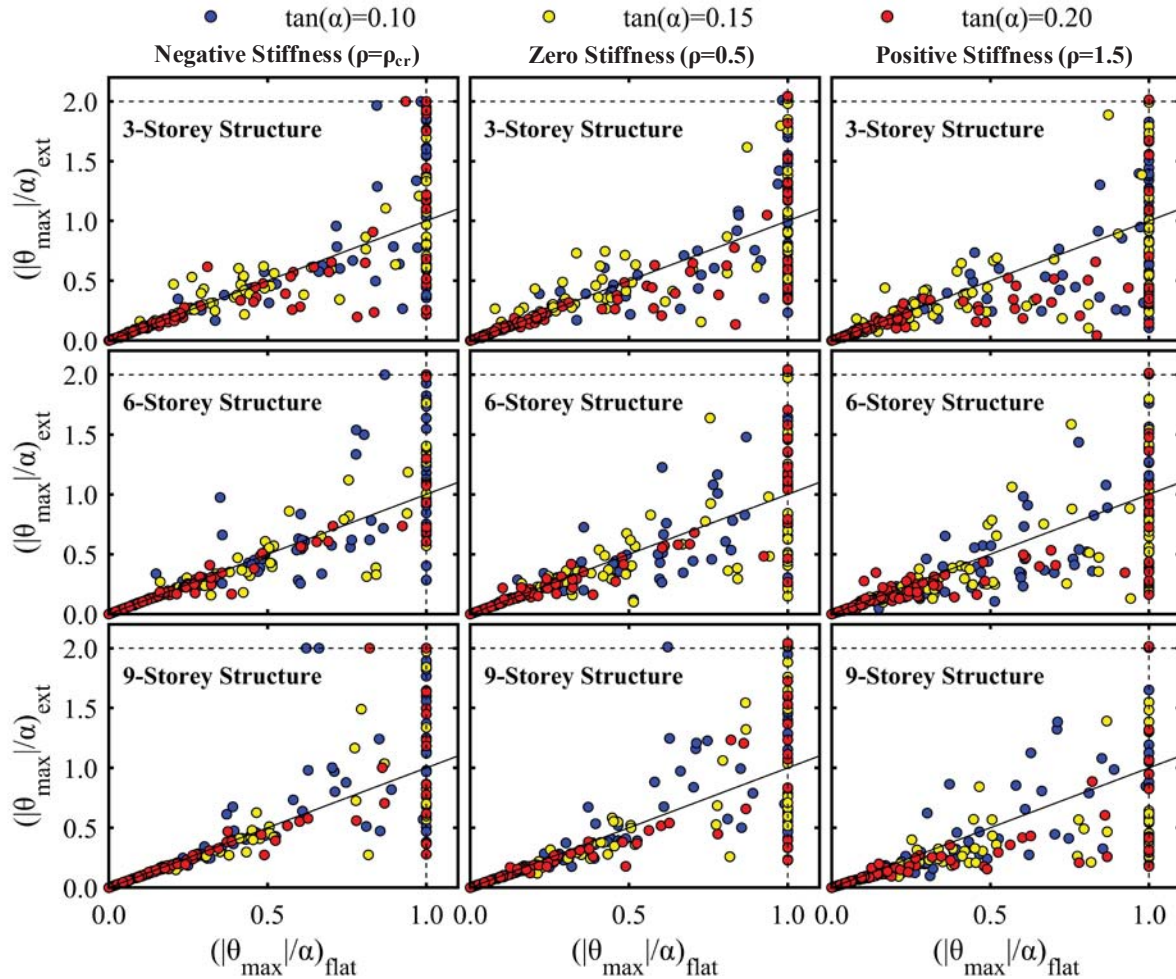


Figure 7: Comparison of the maximum rocking rotations between the isolated systems with $(|\theta_{\max}|/\alpha)_{\text{ext}}$ and without $(|\theta_{\max}|/\alpha)_{\text{flat}}$ curves extensions, under the 100 natural ground motions of FEMA P695.

$\tan(\alpha)$	η	Negative Stiffness ($\rho=\rho_{\text{cr}}$)	Zero Stiffness ($\rho=0.5$)	Positive Stiffness ($\rho=1.5$)	Without Wedges
0.10	3	0.37	0.34	0.29	0.67
	6	0.32	0.33	0.30	0.52
	9	0.31	0.30	0.23	0.49
0.15	3	0.20	0.13	0.09	0.39
	6	0.17	0.13	0.09	0.29
	9	0.16	0.12	0.07	0.25
0.20	3	0.06	0.02	0.02	0.17
	6	0.08	0.02	0.01	0.15
	9	0.03	0.01	0.01	0.13

Table 3: Rocking overturn probabilities of the examined structural systems under the 100 natural ground motions of FEMA P695.

Since rocking initiation, the seismic demands of RPSs present a lower bound of V_{st} [23]. Thus, Figure 8 presents the normalized seismic demands of the podium systems $(V_b/V_{st})_{Pod}$ as a function of the maximum tilt angle of the rocking base $(|\theta_{max}|/\theta_{cr})$. In cases where fairly small rocking rotations are developed $(|\theta_{max}|/\theta_{cr} \approx 0)$, the normalized seismic demands of the superstructure take values $V_b/V_{st} \approx 1$. As the rocking rotation of the base increases, the demands of the superstructure also increase until saturation occurs $(\theta/\theta_{cr})_{sat}$. In order to illustrate the effect of the dynamic characteristics of the superstructure on the elastic response, without a mean to quantify the problem, the seismic demand-tilt angle relationship is summarized in Figure 8 through a bilinear curve. The values of the normalized seismic demands $(V_b/V_{st})_{sat}$ and the critical tilt angle $(\theta/\theta_{cr})_{sat}$ beyond which the slope (k_s) changes, are also presented. It is observed that in cases of kinematic bearings with negative and zero stiffness the seismic demands are stable ($k_s = 0$) for rocking rotations $(|\theta_{max}|/\theta_{cr}) > (\theta/\theta_{cr})_{sat}$. On the other hand, in case of kinematic bearings with positive stiffness the seismic demands increases ($k_s > 0$) beyond $(\theta/\theta_{cr})_{sat}$. Additionally, in case of rocking storey with positive stiffness, increasing the flexibility of the superstructure leads to higher values of the slope coefficient k_s . In all cases, as the stiffness of the superstructure increases, the critical tilt angle $(\theta/\theta_{cr})_{sat}$ increases too, regardless the stiffness of the rocking base.

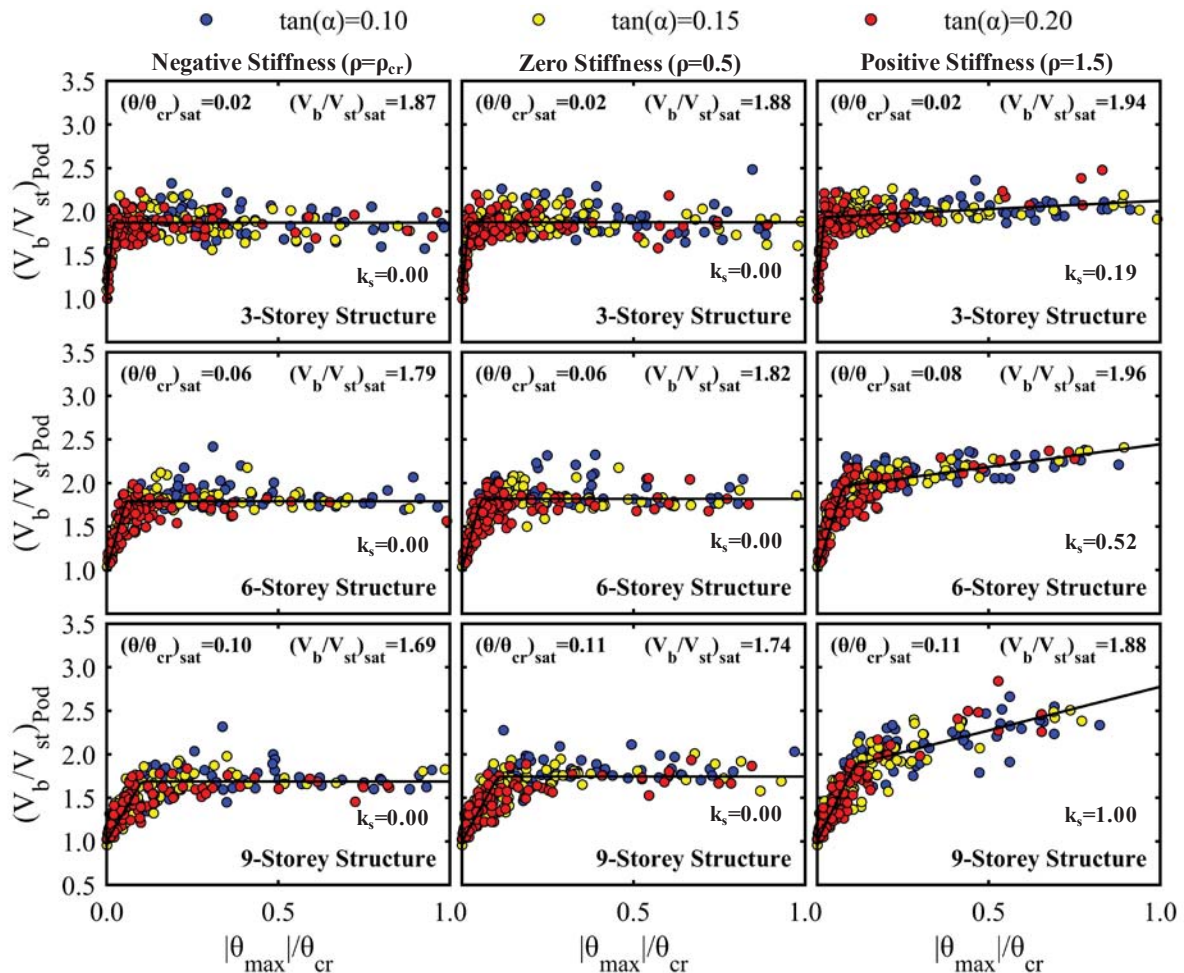


Figure 8: Normalized seismic demands $(V_b/V_{st})_{Pod}$ of the nine multi-storey podium structures as a function of the maximum tilt angle of the rocking floor (θ_{max}/α) .

The effect of the rocking base stiffness on the distribution of the elastic seismic demands throughout the superstructure is also examined. Figure 9 presents the storey shear (V_i) of

structures isolated with kinematic bearings of slenderness $\tan(\alpha) = 0.15$ and $\tan(\alpha') = 0.30$. The black and red lines correspond to the average and maximum values of the storey seismic demands, respectively. In the same figure, the seismic demands of the fixed-base superstructures are presented with dashed lines. The results obtained by ground motions that cause overturning of the rocking base are omitted. In the case of isolated systems, the differences between the mean and maximum values of the storey shear are much smaller than those of the fixed-base systems. Regarding the distribution of seismic demands throughout the superstructure, the maximum shear of the RPSs is developed on the intermediate floors, in contrast to the fixed-base structures in which the maximum seismic demand appears at the base. The completely different distribution pattern of the seismic demands presented by podium structures, regardless the rocking base stiffness, indicates the excitation of higher modes of the superstructure during impact [24]. Moreover, the differences between the mean and the maximum values of the storey shears are lower in cases of zero and negative stiffness than in case of positive stiffness of the base. That fact emerges due to the dependence of the elastic demands on the maximum rocking rotations, in case of rocking base with positive stiffness. Although positive stiffness of the rocking base results in slightly higher values of seismic demands in the superstructure, it should be preferable due to the fact that it significantly decreases the overturning probability.

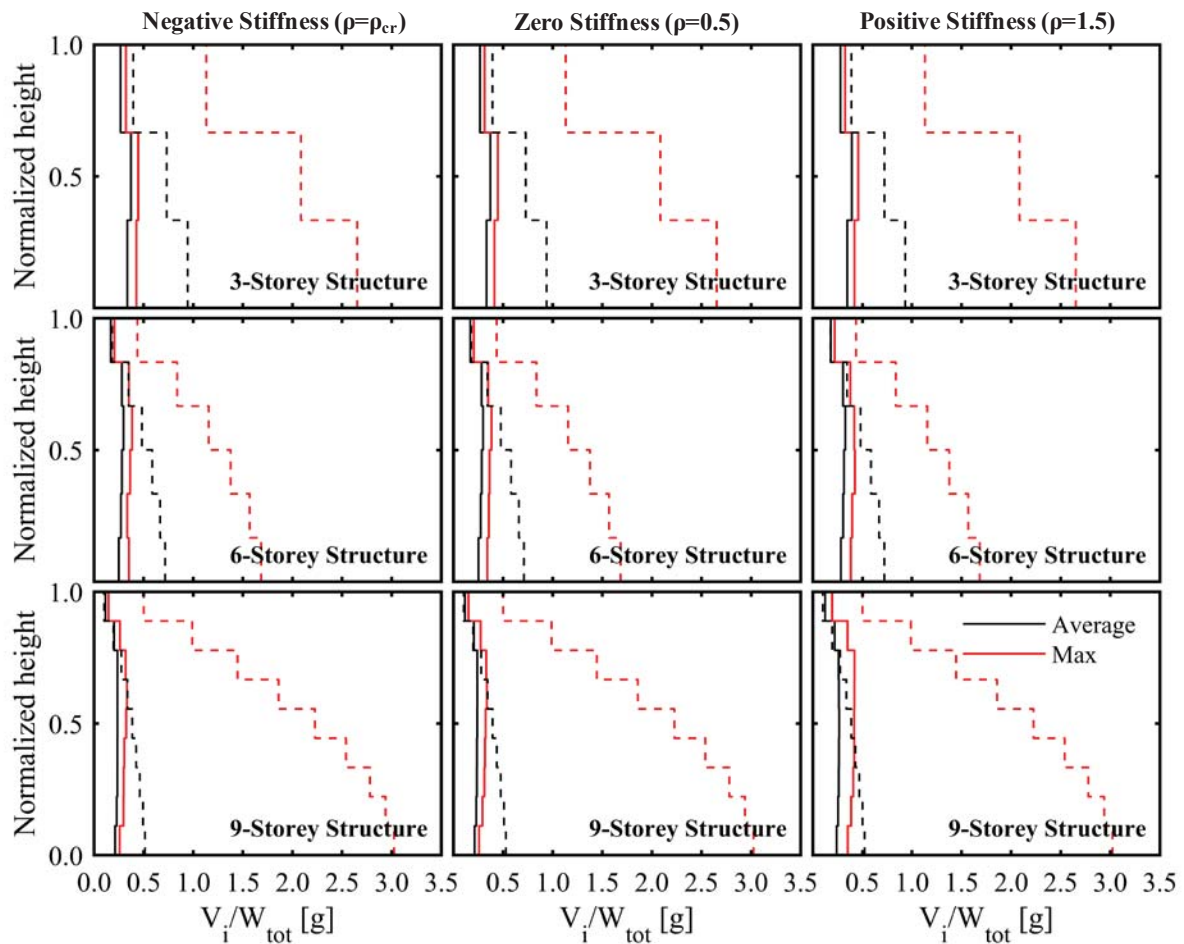


Figure 9: Average and maximum storey shear profiles (V_i).

CONCLUSIONS

In the present study, the dynamic response of seismic isolated multi-storey structures using kinematic bearings was studied. For this purpose, an analytical model that describes the dynamic response of multi-storey podium structures under rolling and rocking phase of the base was proposed. In addition, the effect of the radius of the curved extensions on the response of the rocking base and the seismic demands of the superstructure was investigated. The conclusions of the present work can be summarized as follows:

1. The uplift of the rocking base results in an increase in both the natural frequency and the damping ratio of the first vibration mode of the superstructure. During rolling phase the dynamic properties amplification depends on the curvature of the columns' curved extensions.
2. The curved extensions of the kinematic bearings results in enhanced stability. Moreover, as the stiffness of the rocking base increases the seismic stability increases too.
3. The magnitude of seismic demands depends mainly on the slenderness of the rocking columns. In case of a rocking base with negative or zero stiffness the seismic demands are independent of the features of the curved extensions. On the other hand, considering rocking base with positive stiffness, the elastic seismic demands depends on the radius of the curved extensions and on the developed displacements of the base.
4. Since rocking initiation, the distribution of the seismic demands throughout the superstructure differs substantially from that of a fixed-base structure, regardless the stiffness of the kinematic bearings.

ACKNOWLEDGEMENTS

The research work was supported by the Hellenic Foundation for Research and Innovation (HFRI) under the HFRI PhD Fellowship grant (Fellowship Number: 1048).

REFERENCES

- [1] G.W. Housner, The behavior of inverted pendulum structures during earthquakes. *Bulletin of the Seismological Society of America*, **53**(2), 403-417, 1963.
- [2] S. Acikgoz, M.J. DeJong, The rocking response of large flexible structures to earthquakes. *Bulletin of Earthquake Engineering*, **12**(2), 875-908, 2014.
- [3] S. Acikgoz, M.J. DeJong, Analytical modelling of multi-mass flexible rocking structures. *Earthquake Engineering and Structural Dynamics*, **45**(13), 2103-2122, 2016.
- [4] E. Avgenakis, I.N. Psycharis, Modeling of inelastic rocking bodies under cyclic loading. *Journal of Engineering Mechanics*, **146**(4), 04020020, 2020.
- [5] S. Diamantopoulos, M. Fragiadakis, Seismic response assessment of rocking systems using single degree-of-freedom oscillators. *Earthquake Engineering and Structural Dynamics*, **48**(7), 689-708, 2019.

- [6] M.F. Vassiliou, R. Truniger, B. Stojadinović, An analytical model of a deformable cantilever structure rocking on a rigid surface: development and verification. *Earthquake Engineering and Structural Dynamics*, **44**(15), 2775-2794, 2015.
- [7] I.N. Psycharis, Dynamics of flexible systems with partial lift-off. *Earthquake Engineering and Structural Dynamics*, **11**(4), 501-521, 1983.
- [8] C.S. Yim, A.K. Chopra, Simplified earthquake analysis of multistorey structures with foundation uplift. *Journal of Structural Engineering*, **111**(12), 2708-2731, 1985.
- [9] F. Gelagoti, R. Kourkoulis, I. Anastasopoulos, G. Gazetas, Rocking-isolated frame structures: margins of safety against toppling collapse and simplified design approach. *Soil Dynamics and Earthquake Engineering*, **32**(1), 87-102, 2012.
- [10] A. Palermo, S. Pampanin, D. Marriott, Design, modeling, and experimental response of seismic resistant bridge piers with post tensioned dissipating connections. *Journal of Structural Engineering*, **133**(11), 1648-1661, 2007.
- [11] J.A. Schaefer, B. Kennedy, M.O. Eberhard, J.F. Stanton, *Unbonded pretensioned bridge columns with rocking detail*. Technical Report PEER 2014/08, University of Washington, USA, 2014.
- [12] A. Agalianos, A. Psychari, M.F. Vassiliou, B. Stojadinovic, I. Anastasopoulos, Comparative assessment of two rocking isolation techniques for a motorway overpass bridge. *Frontiers in Built Environment*, **3**, 47, 2017.
- [13] N. Makris, M.F. Vassiliou, Planar rocking response and stability analysis of an array of free-standing columns capped with a freely supported rigid beam. *Earthquake Engineering and Structural Dynamics*, **42**(3), 431-449, 2013.
- [14] N. Makris, M.F. Vassiliou, Are some top-heavy structures more stable?. *Journal of Structural Engineering*, **140**(5), 06014001, 2014.
- [15] E.G. Dimitrakopoulos, A.I. Giouvanidis, Seismic response analysis of the planar rocking frame. *Journal of Engineering Mechanics*, **141**(7), 04015003, 2015.
- [16] A. Dar, D. Konstantinidis, W. El-Dakhakhni, Seismic response of rocking frames with top support eccentricity. *Earthquake Engineering and Structural Dynamics*, **47**(12), 2496-2518, 2018.
- [17] I.M. Thomaidis, A.J. Kappos, A. Camara, Dynamics and seismic performance of rocking bridges accounting for the abutment-backfill contribution. *Earthquake Engineering and Structural Dynamics*, **49**(12), 1161-1179, 2020.
- [18] A. Wada, Z. Qu, S. Motoyui, H. Sakata, Seismic retrofit of existing SRC frames using rocking walls and steel dampers. *Frontiers of Architecture and Civil Engineering in China*, **5**(3), 259, 2011.
- [19] N. Makris, M. Aghagholizadeh, The dynamics of an elastic structure coupled with a rocking wall. *Earthquake Engineering and Structural Dynamics*, **46**(6), 945-962, 2017.
- [20] M. Aghagholizadeh, N. Makris, Seismic response of a yielding structure coupled with a Rocking Wall. *Journal of Structural Engineering*, **144**(2), 04017196, 2017.
- [21] Bachmann J.A., Jost C., Studemann Q., Vassiliou M.F., Stojadinović B., An analytical model for the dynamic response of an elastic SDOF system fixed on top of a rocking

- single-storey frame structure: experimental validation. *7th European Congress on Computational Methods in Applied Sciences and Engineering*, Crete Island, Greece, 2016.
- [22] J.A. Bachmann, M.F. Vassiliou, B. Stojadinović, Dynamics of rocking podium structures. *Earthquake Engineering and Structural Dynamics*, **46(14)**, 2499-2517, 2017.
 - [23] K.E. Bantilas, I.E. Kavvadias, L.K. Vasiliadis, Analytical investigation of the seismic response of elastic oscillators placed on the top of rocking storey. *Bulletin of Earthquake Engineering*, **19**, 1249-1270, 2021.
 - [24] K.E. Bantilas, I.E. Kavvadias, L.K. Vasiliadis, Seismic response of elastic multidegree of freedom oscillators placed on the top of rocking storey. *Earthquake Engineering and Structural Dynamics*, **50(5)**, 1315-1333, 2021.
 - [25] N. Makris, M.F. Vassiliou, Sizing the slenderness of free-standing rocking columns to withstand earthquake shaking. *Archive of Applied Mechanics*, **82(10-11)**, 1497-1511, 2012.
 - [26] E.G. Dimitrakopoulos, M.J. DeJong, Overturning of retrofitted rocking structures under pulse-type excitations. *Journal of Engineering Mechanics*, **138(8)**, 963-972, 2012.
 - [27] N. Makris, M.F. Vassiliou, Dynamics of the rocking frame with vertical restrainers. *Journal of Structural Engineering*, **141(10)**, 04014245, 2014.
 - [28] M.F. Vassiliou, N. Makris, Dynamics of the vertically restrained rocking column. *Journal of Engineering Mechanics*, **141(12)**, 04015049, 2015.
 - [29] M. Aghagholizadeh, N. Makris, Earthquake response analysis of yielding structures coupled with vertically restrained rocking walls. *Earthquake Engineering and Structural Dynamics*, **47(15)**, 2965-2984, 2018.
 - [30] D. Marriott, S. Pampanin, A. Palermo, Quasi-static and pseudo-dynamic testing of unbonded post-tensioned rocking bridge piers with external replaceable dissipaters. *Earthquake Engineering and Structural Dynamics*, **38(3)**, 331-354, 2009.
 - [31] W.Y. Kam, S. Pampanin, A. Palermo, A.J. Carr, Self-centering structural systems with combination of hysteretic and viscous energy dissipations. *Earthquake Engineering and Structural Dynamics*, **39(10)**, 1083-1108, 2010.
 - [32] A.I. Giouvanidis, E.G. Dimitrakopoulos, Seismic performance of rocking frames with flag-shaped hysteretic behavior. *Journal of Engineering Mechanics*, **143(5)**, 04017008, 2017.
 - [33] C.S. Yim, A.K. Chopra, J. Penzien, Rocking response of rigid blocks to earthquakes. *Earthquake Engineering and Structural Dynamics*, **8(6)**, 565-587, 1980.
 - [34] I.E. Kavvadias, L.K. Vasiliadis, A. Elenas, Seismic response parametric study of ancient rocking columns. *International Journal of Architectural Heritage*, **11(6)**, 791-804, 2017.
 - [35] I.E. Kavvadias, G.A. Papachatzakis, K.E. Bantilas, L.K. Vasiliadis, A. Elenas, Rocking spectrum intensity measures for seismic assessment of rocking rigid blocks. *Soil Dynamics and Earthquake Engineering*, **101**, 116-124, 2017.
 - [36] E.G. Dimitrakopoulos, T.S. Paraskeva, Dimensionless fragility curves for rocking response to near-fault excitations. *Earthquake Engineering and Structural Dynamics*, **44(12)**, 2015-2033, 2015.

- [37] I. Psycharis, M. Fragiadakis, I. Stefanou, Seismic reliability assessment of classical columns subjected to near-fault ground motions. *Earthquake Engineering and Structural Dynamics*, **42(14)**, 2061-2079, 2013.
- [38] M. Fragiadakis, S. Diamantopoulos, Fragility and risk assessment of freestanding building contents. *Earthquake Engineering and Structural Dynamics*, **49(10)**, 1028-1048, 2020.
- [39] A. Pappas, A. Sextos, F. Da Porto, C. Modena, Efficiency of alternative intensity measures for the seismic assessment of monolithic free-standing columns. *Bulletin of Earthquake Engineering*, **15(4)**, 1635-1659, 2017.
- [40] J.L. Beck, R.I. Skinner, The seismic response of a reinforced concrete bridge pier designed to step. *Earthquake Engineering and Structural Dynamics*, **2(4)**, 343-358, 1973.
- [41] P.J. Routledge, M.J. Cowan, A. Palermo, Low-damage detailing for bridges—a case study of Wigram–Magdala bridge. *New Zealand Society for Earthquake Engineering Conference*, Christchurch, New Zealand, 2016.
- [42] R.D. Sharpe, R.I. Skinner, The seismic design of an industrial chimney with rocking base. *Bulletin of the New Zealand Society for Earthquake Engineering*, **16(2)**, 98–106, 1983.
- [43] Y. Cherepinskiy, Seismic isolation of buildings with application of the kinematics bases. *13th World Conference on Earthquake Engineering*, Vancouver, Canada, 2004.
- [44] V. Smirnov, J. Eisenberg, A. Vasileva, Seismic isolation of buildings and historical monuments. Recent developments in Russia. *13th World Conference on Earthquake Engineering*, Vancouver, Canada, 2009.
- [45] Y. Cherepinskiy, *Seismic isolation of buildings. Construction on kinematic foundations*. Blue Apple, 2009.
- [46] J.A. Bachmann, P. Blöchliger, M. Wellauer, M.F. Vassiliou, B. Stojadinovic, Experimental investigation of the seismic response of a column rocking and rolling on a concave base. *7th European Congress on Computational Methods in Applied Sciences and Engineering*, Crete Island, Greece, 2016.
- [47] J.A. Bachmann, M.F. Vassiliou, B. Stojadinović, Rolling and rocking of rigid uplifting structures. *Earthquake Engineering and Structural Dynamics*, **48(14)**, 1556-1574, 2019.
- [48] G.E. Thermou, S.J. Pantazopoulou, A.S. Elnashai, Global interventions for seismic upgrading of substandard RC buildings. *Journal of Structural Engineering*, **138(3)**, 387-401, 2012.
- [49] FEMA P695, *Quantification of Building Seismic Performance Factors*. Federal Emergency Management Agency, Washington DC, 2009.

THE EFFECT OF IMPACT MODELING ON THE SEISMIC RESPONSE OF MULTI-STOREY PODIUM STRUCTURES

Ioannis E. Kavvadias¹, Kosmas E. Bantilas¹, Lazaros Vasiliadis¹, Anaxagoras Elenas¹

¹ Department of Civil Engineering, Democritus University of Thrace
Campus of Kimmeria, Xanthi 67100, Greece
e-mail: {ikavvadi, kbantila, lvasilia, elenas}@civil.duth.gr

Abstract

In the present study the effect of impact modeling on the seismic response of multi-storey structures placed on the top of a rocking storey is examined. For this purpose, two impact models are introduced, where the energy dissipation is treated using the angular momentum-impulse theorem combined with different assumptions regarding the post-impact state of the superstructure. The effect of the examined impact models on the dynamic response of nine typical multi-storey podium structures is assessed using synthetic pulse-like ground motion records. The superstructures are divided in three classes based on the lateral displacement profile of their fundamental vibration mode. Thus, the effect of the impact model on the maximum rocking rotations and elastic seismic demands as a function of the superstructure's dynamic properties is investigated. The study concludes that the impact model presents a minor effect on the rocking response of the podium structure. On the contrary, it might substantially affect both the magnitude and the distribution of the seismic demands, especially in cases of stiff superstructures with flexural displacement profile.

Keywords: Rocking structures; Podium structures; Impact model; Synthetic ground motions

1 INTRODUCTION

The dynamic response of rigid blocks rocking on a rigid ground was first studied by Housner [1], who highlighted the parameters that affect the stability of rigid bodies which can be uplifted under horizontal excitations. Since then, with the recognition of the remarkable properties of the rocking response, various forms of rocking systems have been studied, such as flexible rocking oscillators on solid [2-6] and flexible ground [7, 8], rocking structures on the foundations [9], rocking bridge piers [10-12], rocking frames [13-17], coupled conventional structures with rocking walls [18-20]. Regarding the seismic isolation by forming a rocking floor at the base [21-24], the first analytical study was carried out by Bachmann et al. [21]. Subsequently, Bantilas et al. [22] investigated the structural and the ground motion parameters that affect the elastic demands of rocking podium structures (RPSs), while Bantilas et al. [23] examined the effect of the higher vibration modes of multi-storey superstructures on the dynamic response of RPSs.

Due to the strongly non-linear behavior of the rocking motion, small changes in both the rocking system and the ground motion parameters can lead to large variations in the response, so that the study of the phenomenon under a probabilistic framework yields more reliable conclusions [24]. To this end, except of the investigation of the influence of ground excitation characteristics on the dynamic response of rocking systems [25-30], the effect of modeling assumptions on the rocking response is of great interest.

In the rocking response of rigid blocks, energy dissipation occurs during impact when the tilt angle of the rocking columns reverses the sign. Although different models for energy dissipation have been proposed [31-33], Housner's coefficient of restitution [1] has been widely used. Regarding the energy dissipation during impact, various conservation rules have been proposed in order to evaluate the post impact state of a rocking system. In the case of deformable rocking cantilevers, such approaches involve the conservation of the horizontal momentum [34], conservation of the moment of momentum [35] and conservation of kinetic energy at the horizontal direction [6] combined with the assumption that the vertical velocity of the model is completely dissipated. The above conservation rules led to an increase in the elastic demands especially when applied to stiff systems [6, 36]. Due to this fact the conservation of horizontal momentum combined with the assumption that the relative velocity between the deformable oscillator and the base is constant during impact were introduced by Oliveto et al. [36]. Since then, the assumption of constant relative velocity has been adopted by other researchers to study the response of both deformable rocking cantilevers [2-3]. Later studies of Giouvanidis and Dimitrakopoulos [37] prove that the relative velocity of a deformable rocking cantilever before and after the impact does not remain constant.

Regarding the podium structures, assuming instantaneous impact and all the impact forces concentrated at the pivot points, the system can be considered isolated and conservation of angular momentum can be applied. Bachmann et al. [21] and Bantilas et al. [23] examined the response of sdof and mdof RPSs respectively, assuming that the relative horizontal velocity of the superstructure with respect to the cap beam of the rocking frame before and after the impact remains constant. Moreover, Bantilas et al. [22] assumed constant absolute horizontal velocity of the superstructure during impact, in order to investigate the effect of the impact modeling assumption on the response of sdof RPSs. In the present study the effect of the two aforementioned impact assumptions on the response of multi-storey RPSs is investigated. Thus, nine multi-storey RPSs are examined under a set of synthetic pulse-like ground motion records, in order to assess the effect of the energy dissipation model on the response of the rocking base, as well as the elastic seismic demands.

2 DYNAMIC RESPONSE OF ROCKING PODIUM STRUCTURES

In the present section, the analytical model of the dynamic response of frame structures, seismically isolated using a rocking story, is presented. The model is based on the assumption that the superstructure is described by a mdof elastic oscillator, fixed on the top of a rigid rocking frame. The rigid frame consists of a cap beam with mass m_b and N freestanding columns with mass m_c , semi-diagonal length $R = \sqrt{H^2 + B^2}$, rotational moment of inertia around its center of mass I_{cm} , and slenderness $\alpha = \tan(B/H)$. During the dynamic response, the rocking columns are considered to be in contact with the cap beam and the ground, while the friction coefficient at the contact surfaces is large enough to prevent any sliding. The schematic representation of the model is illustrated in Figure 1.

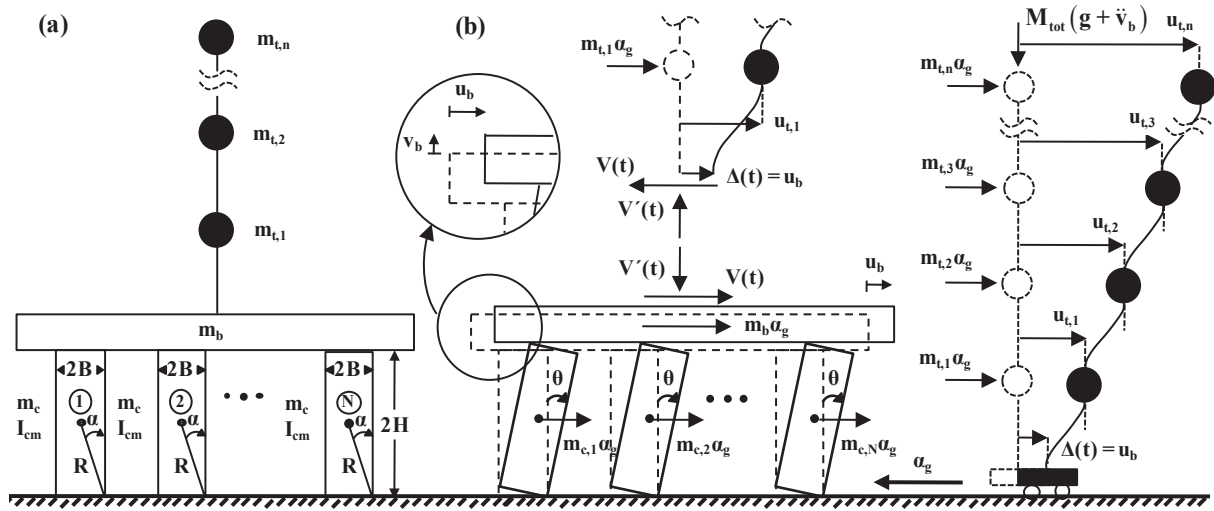


Figure 1: Schematic representation of the analytical model of multi-storey rocking isolated structures (a) and interaction of the rocking base with the superstructure (b).

The analytical presentation of the assumptions related to the model used herein is provided by Bantilas et al. [23]. The equations of motion of the sub-system of the rocking base, as well as the superstructure are given by Equation (1) and (2), respectively.

$$\begin{aligned} & \left[\bar{I}_0 + 4\gamma + 4\eta\gamma \sin^2(\alpha \mp \theta) \right] R\ddot{\theta} = \pm 2\eta\gamma R \sin[2(\alpha \mp \theta)] \dot{\theta}^2 \mp \\ & \mp (1 + 2\eta\gamma + 2\gamma)g \sin(\alpha \mp \theta) - (1 + 2\gamma)\alpha_g \cos(\alpha \mp \theta) + \frac{V}{M_{tot}} 2\eta\gamma \cos(\alpha \mp \theta) \end{aligned} \quad (1)$$

$$\mathbf{M}\ddot{\mathbf{u}}_t + \mathbf{C}\dot{\mathbf{u}}_t + \mathbf{K}\mathbf{u}_t = -\mathbf{M}\delta\alpha_g + \mathbf{K}\delta \underbrace{\left[\pm 2R(\sin(\alpha) - \sin(\alpha \mp \theta)) \right]}_{u_b} + \mathbf{C}\delta \underbrace{2R\cos(\alpha \mp \theta)\dot{\theta}}_{\dot{u}_b} \quad (2)$$

where γ is the mass ratio of the cap beam (m_b) divided by the total mass of rocking columns (Nm_c); η is the mass ratio of the superstructure (M_{tot}) divided by the mass of cap beam (m_b); $\bar{I}_0 = I_0/(m_c R^2)$ and I_0 is the rotational inertia of the column with respect to the pivot point; θ , $\dot{\theta}$ and $\ddot{\theta}$ are the title angle, the rotational velocity and the rotational acceleration of the rocking columns; u_t , \dot{u}_t and \ddot{u}_t are the floor displacements, velocities and accelerations with respect to the undeformed configuration of the system; \mathbf{M} , \mathbf{K} and \mathbf{C} are the mass the stiffness and the damping matrix of the superstructure; δ is the influence vector of the ground motion ($\delta=\mathbf{1}$); α_g is the ground acceleration; u_b and v_b the horizontal and vertical displacements of the center of mass of the cap beam; and the base shear of the superstructure (V) is given by:

$$V = \delta^T \mathbf{K}(\mathbf{u}_t \mp \delta \mathbf{u}_b) + \delta^T \mathbf{C}(\dot{\mathbf{u}}_t - \delta \dot{\mathbf{u}}_b) \quad (3)$$

The terms $\mathbf{K}\delta \mathbf{u}_b$ and $\mathbf{C}\delta \dot{\mathbf{u}}_b$ correspond to the dynamic loads applied to the superstructure due to the continuous displacement of the cap beam of the rocking base. The upper and lower signs in Eqs. (1)-(3) define rocking around the right ($\theta > 0$) and left ($\theta < 0$) pivot points of the rocking columns respectively.

Until uplift occurs, the rocking base is assumed to remain inactive ($\theta = \dot{\theta} = 0$). Thus the superstructure behaves as a fixed base mdof oscillator, and the equations of motion are given by Eq. (2), considering $\mathbf{u}_b = \dot{\mathbf{u}}_b = 0$. When the horizontal overturning actions overcome the restoring forces of the podium structure, uplift occurs, and the rocking story starts to roll. The uplift criteria can be summarized as follows:

$$\mp \frac{\alpha_g}{g} \geq \left(1 + \frac{2\eta\gamma}{1+2\gamma}\right) \tan \alpha \mp \frac{2\eta\gamma}{(1+2\gamma)M_{tot}g} V \quad (4)$$

where V is the superstructure's base shear given by Eq. (3) considering $\mathbf{u}_b = \dot{\mathbf{u}}_b = 0$. The upper and lower signs define rolling initiation around the right ($\theta > 0$) and left ($\theta < 0$) pivot points.

3 IMPACT MODELING

In the present study, in order to evaluate the influence of the adopted energy dissipation model on the elastic response of multi-storey RPSs, two different assumptions regarding the velocity of the superstructure during impact are examined.

Due to the constant relative horizontal velocity (CRV) of the superstructure with respect to the cap beam of the rocking frame before and after the impact assumption, the coefficient of restitution (COR_{CRV}) and post-impact horizontal velocities of the floors of the superstructure are given by Eqs. (5.a) and (5.b), respectively.

$$COR_{CRV} = \frac{\dot{\theta}^+}{\dot{\theta}^-} = 1 - 2\sin^2 \alpha \frac{1 + 4\gamma(1 + \eta)}{I_0 + 4\gamma(1 + \eta)} \quad (5.a)$$

$$\dot{\mathbf{u}}_t^+ = \dot{\mathbf{u}}_t^- - 2R \cos(\alpha) \dot{\theta}^- (1 - COR_{CRV}) \quad (5.b)$$

Additionally, the solution of the impact problem adopting the constant absolute velocity (CAV) assumption results in the coefficient of restitution of the rocking base (COR_{CAV}) as well as in the post impact velocities of the superstructure as follows:

$$COR_{CAV} = \frac{\dot{\theta}^+}{\dot{\theta}^-} = 1 - 2\sin^2(\alpha) \frac{1 + 4\gamma + 4\gamma\eta}{I_0 + 4\gamma + 4\gamma\eta \sin^2(\alpha)} \quad (6.a)$$

$$\dot{\mathbf{u}}_t^+ = \dot{\mathbf{u}}_t^- \quad (6.b)$$

where $\dot{\mathbf{u}}_t^-$ and $\dot{\mathbf{u}}_t^+$ are the superstructure's absolute velocity vectors before (-) and after (+) impact, respectively.

In contrast to the CRV assumption (Eq. 5.b), the CAV assumption (Eq. 6.b) implies that no horizontal impulsive loads are developed on the superstructure which might be crucial for the elastic deformation of the superstructure [36]. In the limit case of an extremely flexible superstructure ($T_t \rightarrow \infty$) the CAV assumption seems well-founded. On the contrary, in the case of a quasi-rigid superstructure ($T_t \rightarrow 0$) the relative velocity between the superstructure and the cap beam cannot change and as a consequence the CRV assumption is more appropriate.

4 SYNTETIC GROUND MOTION RECORDS

Near-fault ground motions often contain distinct velocity and acceleration pulses, caused primarily by the rapture forward directivity effect [38]. The impulsive characteristics of such ground motions are quite destructive for most civil engineering structures [39] as well as rocking systems [1]. Due to the limited number of recorded pulse-like ground motions, the Mavroeidis and Papageorgiou [40] procedure was adopted to generate synthetic ground motions for a wide range of moment magnitude–distance scenarios (M_w – R_e). According to the model, a pulse-like ground motion can be synthesized by properly superimposing low and high-frequency signals that simulate the coherent directivity pulse and the incoherent seismic radiation, respectively.

The low-frequency component of the synthetic ground motion is modeled using the Mavroeidis and Papageorgiou [40] wavelet. In terms of velocity, the closed-form expression of the analytical pulse is given by:

$$v(t) = \begin{cases} \frac{A_p}{2} \left[1 + \cos \left(\frac{2\pi}{\gamma_p T_p} (t - t_0) \right) \right] \cos \left(\frac{2\pi}{T_p} (t - t_0) + v_p \right), & t_0 - \gamma_p \frac{T_p}{2} \leq t \leq t_0 + \gamma_p \frac{T_p}{2} \\ 0, & \text{otherwise} \end{cases} \quad (7)$$

where A_p controls the amplitude of the signal envelope; T_p is the prevailing period of the signal; v_p is the phase; γ_p is a parameter that defines the oscillatory character of the signal ($\gamma > 1$), and t_0 defines the epoch of the peak of the envelope. For every magnitude–distance (M_w – R_e) scenario, a certain low-frequency signal is assumed using the mean values of the Mavroeidis and Papageorgiou pulse parameters (A_p , T_p , v_p , γ_p). The mean values of the parameters v_p and γ_p are 1.93 and 1.83, respectively [41]. Moreover, the mean values of the velocity amplitude (V_p) and the prevailing period (T_p) of the pulse are given by Eqs. (8) and (9) [27]. The envelope parameter A_p of Eq. (7) is calculated using the velocity amplitude and the phase of the signal.

$$\log(V_p) = -5.17 + 1.98 \min(M_w, 7) - 0.14 \min(M_w, 7)^2 - 0.10 \log(R_e^2 + 0.562), \quad V_p \text{ in cm/s} \quad (8)$$

$$\log(T_p) = -2.87 + 0.47 M_w, \quad T_p \text{ in s} \quad (9)$$

The high-frequency component of the synthetic ground motion is modeled using the stochastic method. In this approach, the Fourier amplitude spectrum of a windowed white noise is fitted on a "target" amplitude spectrum $Y(M_w, R_e, f)$. The "target" spectrum is expressed as a product of quantities which represent the earthquake source radiation $E(M_w, f)$, the propagation path effects $P(R, f)$, the site response $G(f)$, and the type of motion $I(f)$. The fitted amplitude spectrum is transformed back to the time domain, yielding the synthetic high-frequency signal. A detailed review of the method can be found in Boore [42]. In the present study, the model parameters of Atkinson and Silva [43] is adopted to generate high-frequency synthetic time histories for different M_w – R_e scenarios.

According to Mavroeidis and Papageorgiou [40], the simulation of a pulse-like synthetic ground motion requires the evaluation of the low and high-frequency components for a given M_w – R_e scenario. Subsequently, the Fourier amplitude spectrum of the high-frequency component is subtracted from that of the coherent pulse. Then, the resulting "residual" amplitude spectrum is transformed back to the time domain by considering that its phase coincides with the phase of the Fourier transform of the high-frequency component. Finally, the "residual" high-frequency signal and the low-frequency component are superimposed, yielding the synthetic pulse-like time history.

In the present study, magnitudes M_w in the range 5.5–7.5 with a step of 0.5 and distances from the fault R_e in the range 5–20km with a step of 2.5 km were considered [27, 28]. For every M_w - R_e scenario, 100 simulations of pulse-like synthetic ground motions were generated using the aforementioned procedure. For the scope of this study a specific low-frequency signal is assumed for every M_w - R_e scenario, using the mean values of the pulse parameters, in order to restrict the ground motion variability and as such to minimize the dependency of the time history analysis results on the characteristics of the signal.

5 EVALUATION OF IMPACT ASSUMPTIONS

The effect of the assumptions regarding the velocity of the superstructure during impact on the response of multi-storey RPSs is examined in the present study. The considered multi-storey podium structures are divided into three classes, based on the lateral displacement profile of the fundamental vibration mode of the superstructure. For this purpose superstructures with flexural, shear and triangular lateral displacement profile are considered (Figure 2). Considering that in typical multi-storey structures the distribution of floor masses is constant and that the fundamental vibration period of the superstructure is $T_{t,1} = n/10$, where n is the number of the floors, the definition of the mass (\mathbf{M}) and stiffness (\mathbf{K}) matrices are defined, given the lateral displacement profile [23, 44]. The damping matrix (\mathbf{C}) of each structure is assumed to be proportional to the mass and stiffness matrices (Rayleigh damping) considering critical damping ratio $\xi = 5\%$ for the first two vibration modes. In total nine different superstructures are examined. Specifically, for every displacement profile superstructures with $n=\{3, 6, 9\}$ floors are considered. All the structures are assumed to be fixed on the top of a typical rocking frame which consists of rectangular columns ($\bar{I}_0=4/3$) of size $R = 1.5$ m, slenderness $\tan(\alpha) = 0.15$, $\gamma = 10$ and cap beam mass m_b equal to the mass of the standard floor m ($\eta = n$).

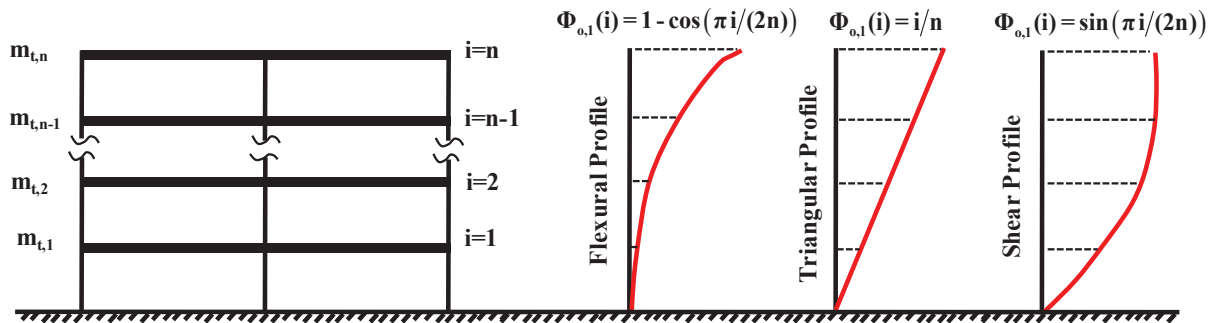


Figure 2: Lateral displacement profiles of the examined multi-storey structures [44].

The values of the coefficient of restitution as obtained by CAV and CRV assumptions are presented in Figure 3. The only feature of the superstructure that affects the coefficient of restitution is the mass ratio η . The values of the coefficient of restitution obtained by the CAV assumption are much smaller than the corresponding values under the assumption of CRV. Additionally, the superstructure's mass ratio (η) seems to significantly affect the coefficient of restitution under the assumption of CAV. On the other hand the coefficient of restitution under CRV assumption is saturated if the term " $\gamma(1+\eta)$ " of Eq.(5.a) takes values greater than 10. Thus, for typical RPSs with $\gamma=10$, the coefficient of restitution using CRV assumption is identical for $\eta \geq 1$.

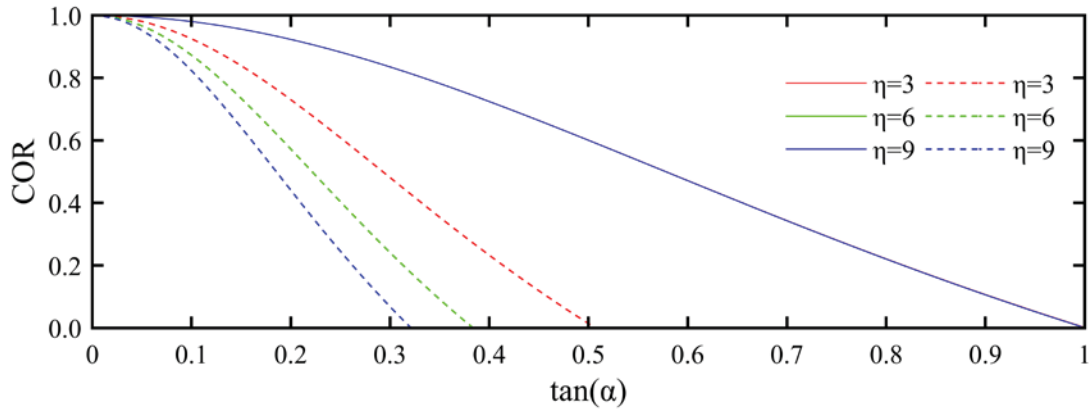


Figure 3: Values of the coefficient of restitution, calculated by the two examined assumptions, as a function of the slenderness (α) of the rocking columns for different values of the superstructure's mass ratio (η).

Figure 4 illustrates the responses of three RPSs under free oscillation of the rocking base with initial conditions $\theta_0/\alpha = 0.9$ and superstructure's relative deformation $\mathbf{u}_{t,0} - \delta \mathbf{u}_{b,0} = 0$. The mDOF elastic oscillators correspond to superstructures with $n = \{3, 6 \text{ and } 9\}$ floors and shear displacement profile. The results are presented comparatively between the CAV and CRV impact assumption. The dynamic response of the rocking base is similar in both models. Despite the different values of the coefficient of restitution between the CAV and CAR assumptions, the energy loss during impact is comparable in both models. In the former case energy is dissipated exclusively by the rocking base while in the latter case energy is dissipated by the rocking base and the superstructure. Regarding the response of the superstructure the CAV assumption results in slightly larger elastic deformations.

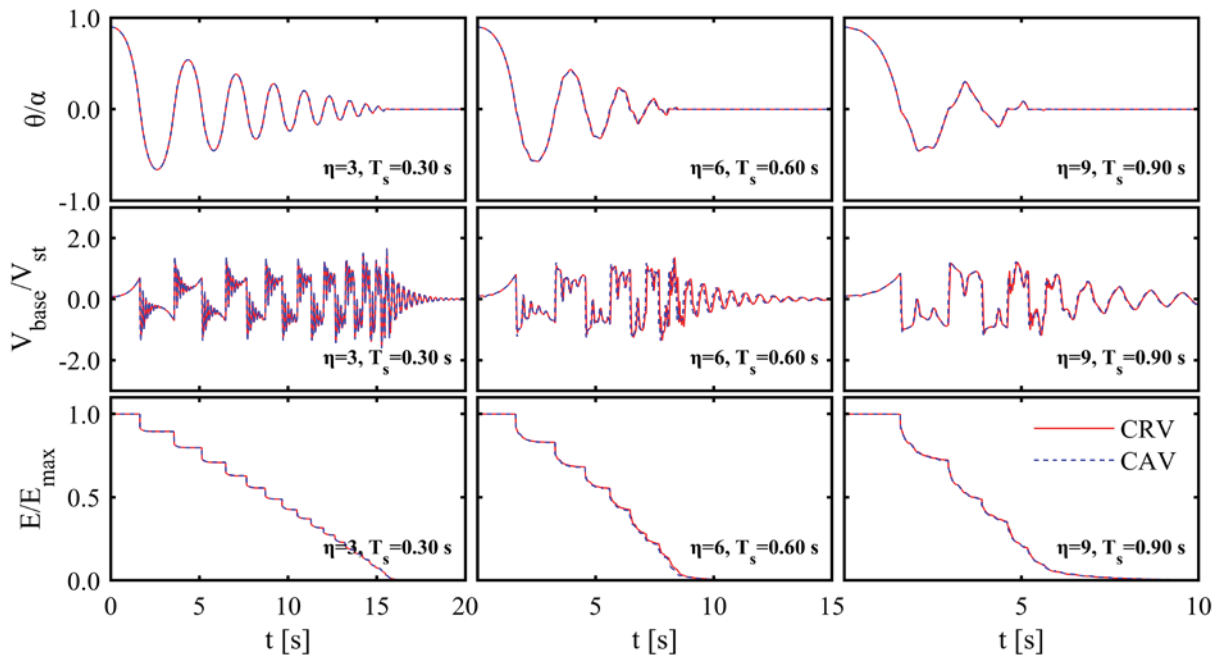


Figure 4: Response time histories under free rocking oscillations of the rocking base.

The maximum rocking response (θ_{\max}/α) for each of the examined structures considering CRV and CAV assumption, under the set of the synthetic pulse-like ground motions, are presented in Figure 5. It can be observed that the majority of the data follows a trend. However, there are many cases where RPSs considering CRV assumption overturns, while assuming

CAV assumption survives and vice versa. That fact is more intense in case of the 3-storey superstructure. As the flexibility of the superstructure increases, the dispersion between the responses seems to be significantly decreased. However, the displacement profile of the superstructure seems not to affect the developed rocking rotations.

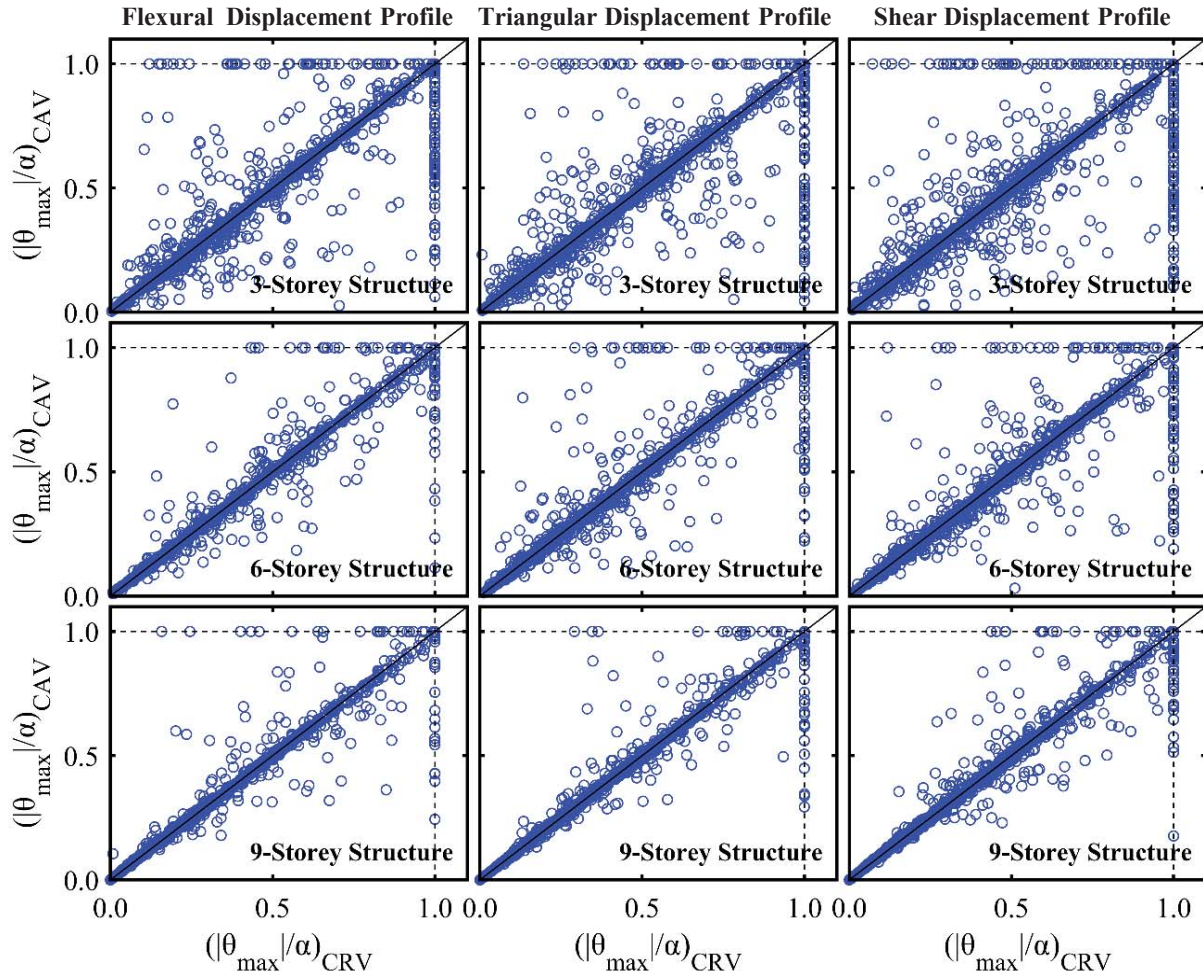


Figure 5: Comparison of the maximum rocking rotation calculated by the CRV and CAV assumption under the pulse like synthetic ground motions.

In order to examine the effect of the adopted assumption regarding the velocity of the superstructure during impact on the elastic seismic demands of mdof oscillators, the maximum shears developed on the multi-storey superstructures are presented in Figure 6. The seismic demands normalized to the horizontal base shear (V_{st}), required to activate the rocking base under static conditions [22], as calculated using both impact assumptions are presented comparatively. The results obtained by ground motions that cause overturning of the rocking base are omitted. As emerged by the results of the tilt angles, the responses of the stiffer superstructure present higher dispersion. Moreover, the displacement profile of the superstructures seems to affect the estimated maximum shear. Specifically, the increase of the effective mass of the superstructure's first mode (from flexural to shear displacement profile) results in higher correlation between the maximum responses obtained by the two energy dissipation models.

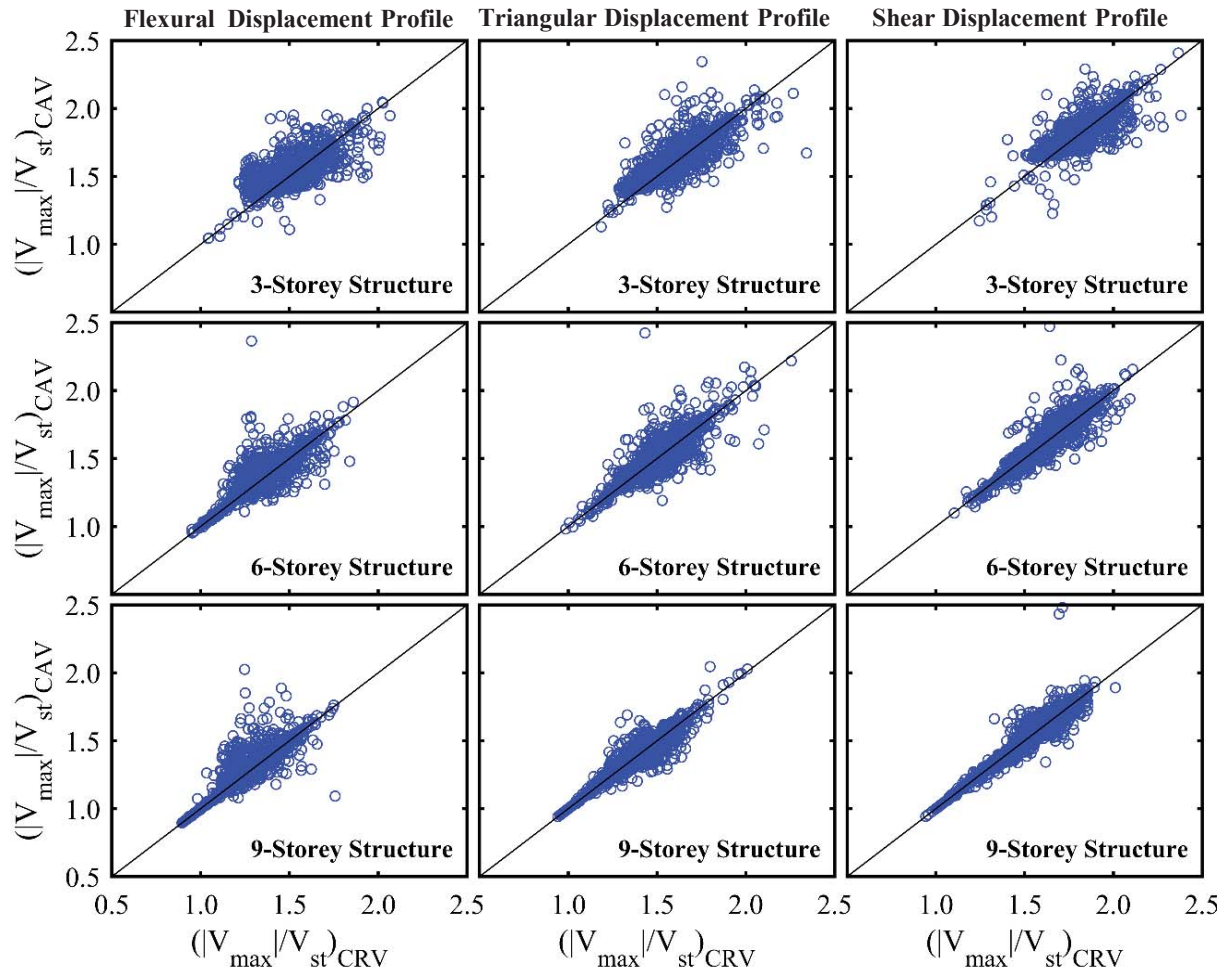
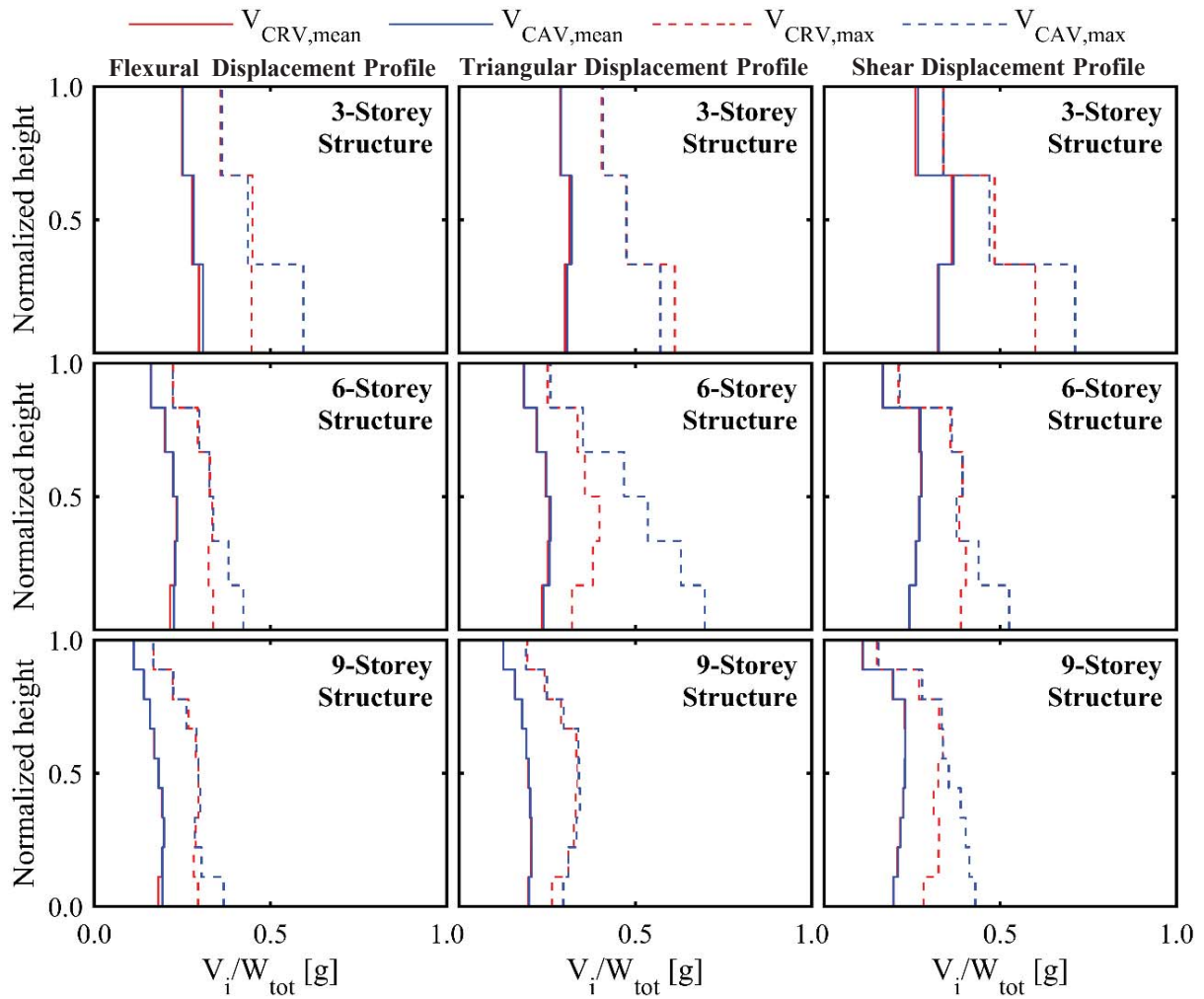


Figure 6: Comparison of the maximum normalized shear calculated by the CRV and CAV assumption under the pulse like synthetic ground motions.

In addition to the seismic demands in terms of maximum shear forces, their distribution throughout the superstructure is also of particular interest. Figure 7 presents the storey shears (V_i) of the nine podium structures. The solid and dashed lines correspond to the average and maximum values of the storey seismic demands, respectively. In the same figure, the seismic demands of the superstructures considering CRV and CAV assumptions are presented comparatively. The results obtained by ground motions that cause overturning of the rocking base are omitted. The differences of the maximum values of the storey shears between the two impact assumptions seems to be important. However, regarding the mean values slight differences are depicted. In general, the CAV assumption results in increase of the shear in the lower floors. In upper floors the shears seems to be identical. The distribution pattern of the mean seismic demands presented by podium structures, regardless the impact assumption, indicates the excitation of higher modes of the superstructure during impact [23].

Figure 7: Average and maximum storey shear profiles (V_i).

In order to statistically assess the effect of the impact assumption on the dynamic response of the RPSs, following Bachmann et al. [45], empirical cumulative distribution functions (ECDFs) are constructed. In Figures 8 and 9 the ECDFs of the maximum rocking rotations of the base, as well as the maximum elastic seismic demands are presented, respectively. In each figure the ECDFs considering both CRV and CAV impact assumption is depicted. Moreover, the 95% confidence interval is reported for the ECDF calculated by the response results assuming CRV assumption. These plots illustrate the probability that the maximum response is smaller than a specific value of the response, in terms of tilt angle of the base ($|\theta_{\max}|/\alpha$) or maximum shear of the superstructure ($|V_{\max}|/V_{st}$).

The ECDFs of the response of the rocking base considering CRV and CAV assumption are almost identical (Figure 8). Thus, statistically the two different assumptions regarding the velocity of the superstructure during impact do not affect the rocking response of RPSs. The effect of the superstructure's flexibility and lateral displacement profile on the response of the base can be observed throughout Figure 8. It has to be mentioned that the ECDFs of the 9-storey superstructure indicate the lack of rocking initiation under a large amount of ground motion excitations ($>15\%$).

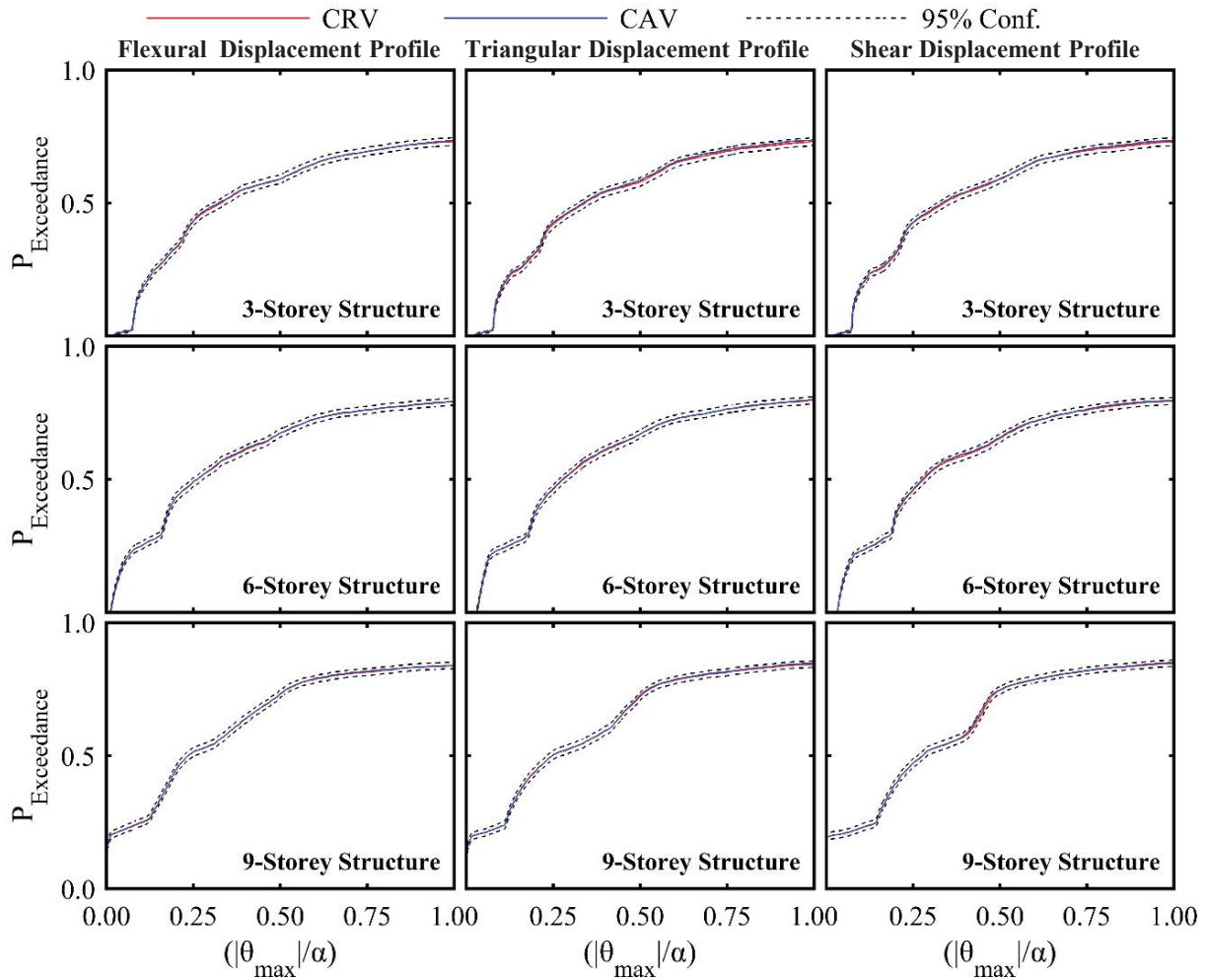


Figure 8: Cumulative distribution functions of the normalized maximum tilt angle θ_{\max}/α for the synthetic pulse like ground motions.

In Figure 9 the ECDFs of the maximum superstructure's shear forces are presented. Unlike the response of the rocking base, the ECDFs of the seismic elastic demands considering the two impact assumptions present considerable differences. The variance of the responses is more intense in the 3-storey superstructure. As the flexibility of the superstructure increases the differences are diminished. The differences between the two impact models also tend to decrease as the effective mass of the superstructure's first vibration mode increases. The ECDF by the CAV assumption is inside the confidence interval of the CRV assumption ECDF only in case of the 9-storey superstructure. In general, it is evident that CAV assumption results in increased elastic seismic demands. That fact is more intense in case of stiff superstructures.

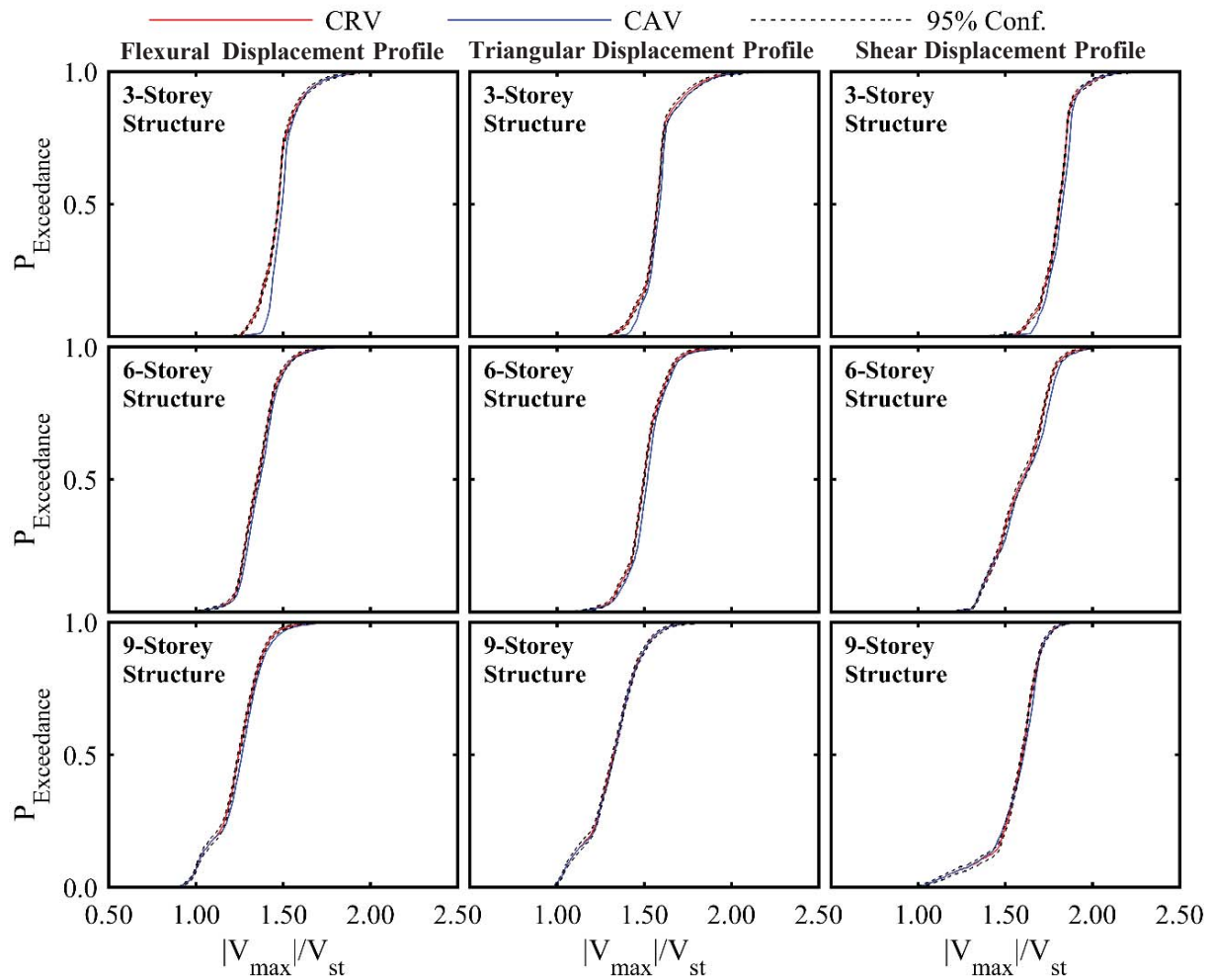


Figure 9: Cumulative distribution functions of the normalized base shear V_{\max}/V_{st} for the pulse like synthetic ground motions.

6 CONCLUSION

In the present study, the effect of the adopted energy dissipation modeling during impact on the response of multi-storey rocking podium systems are examined. Thus, two different assumptions regarding the velocity of the superstructure during impact is examined. Specifically, the assumptions of constant relative horizontal velocity and constant absolute horizontal velocity of the superstructure with respect to the cap beam of the rocking frame before and after the impact were considered.

The response time histories indicate that the assumptions regarding the impact model may result in diverging estimates of the tilt angle, especially in case of stiff superstructures. However, the response of the rocking base in terms of empirical cumulative density functions is not affected by the assumptions regarding the velocity of the superstructure during impact.

The effect of the impact assumption on the elastic seismic demands depends on the stiffness and the lateral displacements profile of the fundamental vibration mode of the superstructure. As the flexibility and the effective mass of the first mode of the superstructure increases, the effect of the two impact assumptions on the superstructure's response tend to be less notable. Examining especially stiff superstructures the CAV assumption results in higher elastic demands.

ACKNOWLEDGEMENTS

This research is co-financed by Greece and the European Union (European Social Fund-ESF) through the Operational Programme «Human Resources Development, Education and Lifelong Learning» in the context of the project "Reinforcement of Postdoctoral Researchers - 2nd Cycle" (MIS-5033021), implemented by the State Scholarships Foundation (IKY).

REFERENCES

- [1] G.W. Housner, The behavior of inverted pendulum structures during earthquakes. *Bulletin of the Seismological Society of America*, **53(2)**, 403-417, 1963.
- [2] S. Acikgoz, M.J. DeJong, The rocking response of large flexible structures to earthquakes. *Bulletin of Earthquake Engineering*, **12(2)**, 875-908, 2014.
- [3] S. Acikgoz, M.J. DeJong, Analytical modelling of multi - mass flexible rocking structures. *Earthquake Engineering and Structural Dynamics*, **45(13)**, 2103-2122, 2016.
- [4] E. Avgenakis, I.N. Psycharis, Modeling of inelastic rocking bodies under cyclic loading. *Journal of Engineering Mechanics*, **146(4)**, 04020020, 2020.
- [5] S. Diamantopoulos, M. Fragiadakis, Seismic response assessment of rocking systems using single degree-of-freedom oscillators. *Earthquake Engineering and Structural Dynamics*, **48(7)**, 689-708, 2019.
- [6] M.F. Vassiliou, R. Truniger, B. Stojadinović, An analytical model of a deformable cantilever structure rocking on a rigid surface: development and verification. *Earthquake Engineering and Structural Dynamics*, **44(15)**, 2775-2794, 2015.
- [7] I.N. Psycharis, Dynamics of flexible systems with partial lift-off. *Earthquake Engineering and Structural Dynamics*, **11(4)**, 501-521, 1983.
- [8] C.S. Yim, A.K. Chopra, Simplified earthquake analysis of multistorey structures with foundation uplift. *Journal of Structural Engineering*, **111(12)**, 2708-2731, 1985.
- [9] F. Gelagoti, R. Kourkoulis, I. Anastasopoulos, G. Gazetas, Rocking-isolated frame structures: margins of safety against toppling collapse and simplified design approach. *Soil Dynamics and Earthquake Engineering*, **32(1)**, 87-102, 2012.
- [10] A. Palermo, S. Pampanin, D. Marriott, Design, modeling, and experimental response of seismic resistant bridge piers with post tensioned dissipating connections. *Journal of Structural Engineering*, **133(11)**, 1648-1661, 2007.
- [11] J.A. Schaefer, B. Kennedy, M.O. Eberhard, J.F. Stanton, *Unbonded pretensioned bridge columns with rocking detail*. Technical Report PEER 2014/08, University of Washington, USA, 2014.
- [12] A. Agalianos, A. Psychari, M.F. Vassiliou, B. Stojadinovic, I. Anastasopoulos, Comparative assessment of two rocking isolation techniques for a motorway overpass bridge. *Frontiers in Built Environment*, **3**, 47, 2017.
- [13] N. Makris, M.F. Vassiliou, Planar rocking response and stability analysis of an array of free-standing columns capped with a freely supported rigid beam. *Earthquake Engineering and Structural Dynamics*, **42(3)**, 431-449, 2013.

- [14] N. Makris, M.F. Vassiliou, Are some top-heavy structures more stable?. *Journal of Structural Engineering*, **140(5)**, 06014001, 2014.
- [15] E.G. Dimitrakopoulos, A.I. Giouvanidis, Seismic response analysis of the planar rocking frame. *Journal of Engineering Mechanics*, **141(7)**, 04015003, 2015.
- [16] A. Dar, D. Konstantinidis, W. El-Dakhakhni, Seismic response of rocking frames with top support eccentricity. *Earthquake Engineering and Structural Dynamics*, **47(12)**, 2496-2518, 2018.
- [17] I.M. Thomaidis, A.J. Kappos, A. Camara, Dynamics and seismic performance of rocking bridges accounting for the abutment-backfill contribution. *Earthquake Engineering and Structural Dynamics*, **49(12)**, 1161-1179, 2020.
- [18] A. Wada, Z. Qu, S. Motoyui, H. Sakata, Seismic retrofit of existing SRC frames using rocking walls and steel dampers. *Frontiers of Architecture and Civil Engineering in China*, **5(3)**, 259, 2011.
- [19] N. Makris, M. Aghagholizadeh, The dynamics of an elastic structure coupled with a rocking wall. *Earthquake Engineering and Structural Dynamics*, **46(6)**, 945-962, 2017.
- [20] M. Aghagholizadeh, N. Makris, Seismic response of a yielding structure coupled with a Rocking Wall. *Journal of Structural Engineering*, **144(2)**, 04017196, 2017.
- [21] J.A. Bachmann, M.F. Vassiliou, B. Stojadinović, Dynamics of rocking podium structures. *Earthquake Engineering and Structural Dynamics*, **46(14)**, 2499-2517, 2017.
- [22] K.E. Bantilas, I.E. Kavvadias, L.K. Vasiliadis, Analytical investigation of the seismic response of elastic oscillators placed on the top of rocking storey. *Bulletin of Earthquake Engineering*, **19**, 1249-1270, 2021.
- [23] K.E. Bantilas, I.E. Kavvadias, L.K. Vasiliadis, Seismic response of elastic multidegree of freedom oscillators placed on the top of rocking storey. *Earthquake Engineering and Structural Dynamics*, **50(5)**, 1315-1333, 2021.
- [24] C.S. Yim, A.K. Chopra, J. Penzien, Rocking response of rigid blocks to earthquakes. *Earthquake Engineering and Structural Dynamics*, **8(6)**, 565-587, 1980.
- [25] I.E. Kavvadias, L.K. Vasiliadis, A. Elenas, Seismic response parametric study of ancient rocking columns. *International Journal of Architectural Heritage*, **11(6)**, 791-804, 2017.
- [26] I.E. Kavvadias, G.A. Papachatzakis, K.E. Bantilas, L.K. Vasiliadis, A. Elenas, Rocking spectrum intensity measures for seismic assessment of rocking rigid blocks. *Soil Dynamics and Earthquake Engineering*, **101**, 116-124, 2017.
- [27] E.G. Dimitrakopoulos, T.S. Paraskeva, Dimensionless fragility curves for rocking response to near-fault excitations. *Earthquake Engineering and Structural Dynamics*, **44(12)**, 2015-2033, 2015.
- [28] I. Psycharis, M. Fragiadakis, I. Stefanou, Seismic reliability assessment of classical columns subjected to near-fault ground motions. *Earthquake Engineering and Structural Dynamics*, **42(14)**, 2061-2079, 2013.
- [29] M. Fragiadakis, S. Diamantopoulos, Fragility and risk assessment of freestanding building contents. *Earthquake Engineering and Structural Dynamics*, **49(10)**, 1028-1048, 2020.

- [30] A. Pappas, A. Sextos, F. Da Porto, C. Modena, Efficiency of alternative intensity measures for the seismic assessment of monolithic free-standing columns. *Bulletin of Earthquake Engineering*, **15(4)**, 1635-1659, 2017.
- [31] F. Prieto, P.B. Lourenço, C.S. Oliveira, Impulsive Dirac-delta forces in the rocking motion. *Earthquake Engineering and Structural Dynamics*, **33(7)**, 839-857, 2004
- [32] D. Kalliontzis, S. Sriharan, A. Schultz, Improved coefficient of restitution estimation for free rocking members. *Journal of Structural Engineering*, **142(12)**, 06016002, 2016.
- [33] M.N. Chatzis, M.G. Espinosa, A.W. Smyth, Examining the energy loss in the inverted pendulum model for rocking bodies. *Journal of Engineering Mechanics*, **143(5)**, 04017013, 2017.
- [34] A.K. Chopra, C.S. Yim, Simplified earthquake analysis of structures with foundation uplift. *Journal of Structural Engineering*, **111(4)**, 906-930, 1985.
- [35] I.N. Psycharis, Effect of base uplift on dynamic response of SDOF structures. *Journal of Structural Engineering*, **117(3)**, 733-754, 1991.
- [36] G. Oliveto, I. Calio, A. Greco, Large displacement behaviour of a structural model with foundation uplift under impulsive and earthquake excitations. *Earthquake Engineering and Structural Dynamics*, **32(3)**, 369-393, 2003.
- [37] A.I. Giouvanidis, E.G. Dimitrakopoulos, Nonsmooth dynamic analysis of sticking impacts in rocking structures. *Bulletin of Earthquake Engineering*, **15(5)**, 2273-2304, 2017.
- [38] P.G. Somerville, N.F. Smith, R.W. Graves, N.A. Abrahamson, Modification of empirical strong ground motion attenuation relations to include the amplitude and duration effects of rupture directivity. *Seismological Research Letters*, **68(1)**, 199-222, 1997.
- [39] N. Makris, C.J. Black, Evaluation of peak ground velocity as a "good" intensity measure for near-source ground motions. *Journal of Engineering Mechanics*, **130(9)**, 1032-1044, 2004.
- [40] G.P. Mavroeidis, A.S. Papageorgiou, A mathematical representation of near-fault ground motions. *Bulletin of the seismological society of America*, **93(3)**, 1099-1131, 2003.
- [41] R. Rupakhety, S.U. Sigurdsson, A.S. Papageorgiou, R. Sigbjörnsson, Quantification of ground-motion parameters and response spectra in the near-fault region. *Bulletin of Earthquake Engineering*, **9(4)**, 893-930, 2011.
- [42] D.M. Boore, Simulation of ground motion using the stochastic method. *Pure and Applied Geophysics*, **160(3)**, 635-676, 2003.
- [43] G.M. Atkinson, W. Silva, Stochastic modeling of California ground motions. *Bulletin of the Seismological Society of America*, **90(2)**, 255-274, 2000.
- [44] G.E. Thermou, S.J. Pantazopoulou, A.S. Elnashai, Global interventions for seismic upgrading of substandard RC buildings. *Journal of Structural Engineering*, **138(3)**, 387-401, 2012.
- [45] J.A. Bachmann, M. Strand, M.F. Vassiliou, M. Broccardo, B. Stojadinović, Is rocking motion predictable?. *Earthquake Engineering and Structural Dynamics*, **47(2)**, 535-552, 2018.

3D ROCKING MOTION: BLIND PREDICTION CONTEST RESULTS AND INFLUENCE OF EVALUATION METRIC ON THE RANKINGS

M. F. Vassiliou¹, M. Broccardo², C. Cengiz³, M. Dietz⁴, L. Dihoru⁵, S. Gunay⁶,
K. M. Mosalam⁷, G. Mylonakis⁸, A. Sextos⁹, B. Stojadinovic¹⁰

¹ ETH Zurich
{vassiliou, stojadinovic}@ibk.baug.ethz.ch

² University of Trento
marco.broccardo@unitn.it

³ University of Bristol
c.cihancengiz@gmail.com

⁴ University of Bristol
{m.dietz,Luiza.Dihuru,g.mylonakis,a.sextos}@bristol.ac.uk

⁵ UC Berkeley
{selimgunay, mosalam}@berkeley.edu

Abstract

It has been claimed that numerical rocking motion models are not only inaccurate, but that all rocking structures behave unpredictably. This paper revisits the issue of rocking motion unpredictability and explores whether not the response to a single ground motion, but the statistics of the responses to an ensemble of ground motions is predictable.

To this end, a 3D rocking podium structure was constructed and tested on a shake table. A blind prediction contest was organized, where the contestants were invited to predict the CDF of the time-maxima of the responses. There were 13 participant teams that used FEM, DEM and rigid body models.

It was found that several teams were able to predict the CDF with a decent accuracy. Both FEM and DEM can perform well, depending on the input parameters. Hence, it can be concluded that 3D rocking motion is predictable in the statistical sense.

Keywords: Rocking, Blind Prediction Contest, Shake table testing, Model Validation

1 INTRODUCTION

Rocking structures are the ones that can uplift from their base when subject to an earthquake. Such structures attracted the attention of the research community after the powerful 1960 Valdivia (Chile) earthquakes, when Housner presented his seminal work [1] on the dynamics of the archetype rocking block (Figure 1). The rocking block dynamic model is useful because it can also describe the seismic behavior of non-anchored equipment [2-12], masonry structures [13-20], and ancient Greco-Roman and Chinese temples [20-22].

Motivated by the increasing stability of larger rocking blocks with identical aspect ratios, researchers have suggested using rocking as a seismic design strategy because the uplift of the block acts as a mechanical fuse and limits the design forces of both the superstructure and the foundation. The idea is applicable to both buildings [23-25] and bridges [26-40].

However, seismic analysis of rocking structures is not straightforward because, during the uplift, such structures have negative stiffness (in terms of the relation between the lateral force F and displacement u , shown in Figure 1). This is why their seismic response cannot be described by any “equivalent linear” system such as those employed for ordinary yielding structures [41]. Even though attempts to create non-linear spectrum-based methods to present the maxima of the seismic displacement of rocking structures (not related to elastic response spectrum) have been made [43-43], these spectra were created by performing multiple time-history seismic response analyses using Housner’s model. Therefore, Housner’s model is as useful for rocking structures as the elastic SDOF oscillator is for the fixed-base ones.

2 THREE-DIMENSIONAL ROCKING – “WOBBLING” UNDER 2D/3D GROUND EXCITATION

Housner’s model describes planar rocking of a rigid body excited by horizontal excitation. However, many real uplifting structures (e.g., bridges, statues, or ancient temples) would undergo a 3-dimensional motion characterized by simultaneous uplift from the ground (rocking) and change of the contact point with the ground (nutation) without twisting or sliding out of its original position, called “wobbling” in this study. Real uplifting structures may also twist and slide out of their positions, a phenomenon not investigated in this study.

There have been attempts to study wobbling using rigid body analytical dynamics. In [44], the motion of a rigid cylinder under seismic excitation was studied. Other researchers studied the 3D response of ancient conical or cylindrical columns [20, 45-48]. Makris et al. [49] experimentally tested scaled models of uplifting bridges that exhibited wobbling. All the above studies conclude that wobbling motion is present, even under planar initial conditions and/or

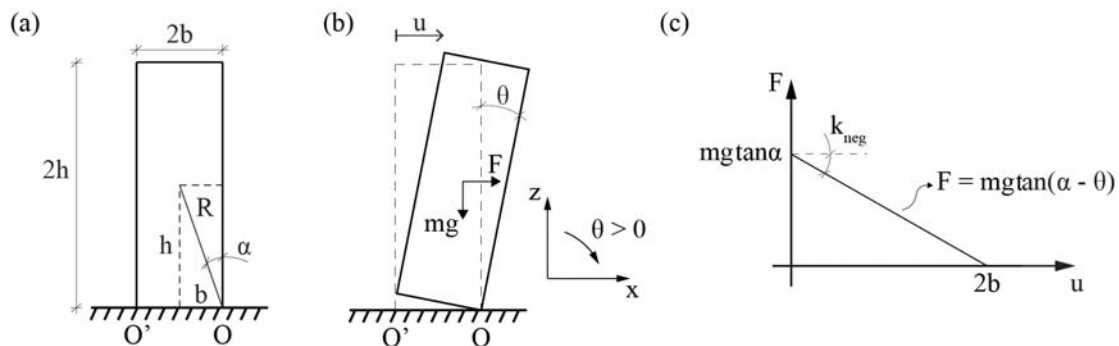


Figure 1: Geometric characteristics of a rigid rocking body (a,b); Lateral force-deformation relation of an uplifted rigid rocking body (c).

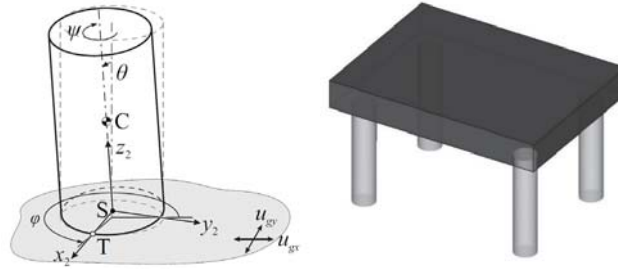


Figure 2: Cylinder allowed to wobble without twist [56] (Left); Wobbling frame [68] (Right).

under planar ground excitation. Stefanou et al. [50] provided theoretical justification for the above observation.

The 3D behavior of non-cylindrical rocking bodies received attention recently. Konstantinidis and Makris [51] and Zulli et al. [52] studied the rocking motion of a 3D prism. Chatzis and Smyth [53] studied the motion of a 3D prism on a deformable base, taking sliding into account as well as the 3D dynamics of a rigid body with wheels on a moving base [54]. Mathey et al. [55] studied the influence of geometric defects on the 3D response of small-size blocks. They concluded that the blocks with imperfections are less stable than the theoretically perfect ones.

Vassiliou et al. [56] studied a 2DOF rigid cylinder constrained to wobble above its initial position without twisting or sliding, i.e. without stepping out of its original position (Figure 2, left). Subsequently, Vassiliou [57] extended this model to include a slab on top of a set of cylindrical columns (Figure 2, right). This is a model of a wobbling bridge, where the columns are physically constrained to wobble above their initial position without stepping out, under the assumption that wobbling is smooth and sliding on the ground does not occur.

3 STATISTICAL SEISMIC RESPONSE MODEL VALIDATION

A major drawback for rocking seismic response models is that they are not validated - at least not by means of the conventional approach of deterministically comparing the displacement response of the model and the prototype to a given ground excitation. This is further hindered by the fact that the seismic response of a rocking block is particularly sensitive to all of the parameters that define it and as such it has been characterized as “chaotic” (i.e. non-reproducible and non-predictable). In fact, small model parameter perturbations lead to substantially different time-history responses. For this reason, experiments involving seismically or dynamically excited rocking specimens are seldom repeatable.

This lack of validation effectively means that Housner’s model should not be used as its ability to represent the physical reality has not been proven. Consequently, rocking cannot be used as a seismic design strategy, given that the seismic response of such structures would be effectively unpredictable, by analytical or numerical methods.

Bachmann et al. [58, 59] and Del Giudice et al. [60] suggested that the conventional seismic response model validation procedure focused on deterministic reproduction of the experimentally obtained response to a particular ground motion with acceptable accuracy is too strict of a test. Instead, they proposed a weaker, but sufficient, concept of statistical validation of structural seismic response models. This novel model validation procedure comprises two steps. *First*, an experimental benchmark dataset, measuring the recorded dynamic response of the same specimen (or essentially identical specimens) subjected to ensembles of consistently generated and scaled ground motions that represent a given seismic hazard, is developed. *Second*, a model is used to produce a dataset comprising its dynamic responses to the same ground motion ensembles. Validation is conducted by comparing statistical distributions of

the pertinent response quantities of the model and the benchmark using the two datasets. Statistical seismic response model validation is a weak method in that it involves the statistics of model predictions of the response to ensembles of ground motions, rather than predicting the responses to every single ground motion deterministically. Bachmann et al. [58], [59] applied the statistical seismic response model validation procedure to validate the Housner [1] rocking response model. They performed 600 shaking table tests using a well-defined and repeatable uplifting structure as well as 600 numerical simulations for the same tests, and compared both the individual test responses and the statistical aggregates of these responses focused on predicting limit states such as overturning or maximum tilt angle. They showed that the 1963 Housner model passes the weak validation test, even though it fails the strong validation test. Therefore, the Housner model was found to be good enough for the use in the scope of seismic design.

4 WOBBLING SEISMIC RESPONSE BENCHMARK DATASET

Wobbling (three-dimensional rocking without sliding) is even harder to predict than planar rocking. Thus, developing seismic wobbling models is challenging, but is necessary in order to further develop seismic design of rocking structures as well as of non-structural elements, such as equipment, as outlined in the introduction of this paper. Validation of wobbling models is a key step in this development process. To facilitate statistical seismic response model validation of wobbling response models, a series of shake table tests was performed at the University of Bristol to create the benchmark response dataset.

4.1 Specimen Description

The wobbling specimen was designed at ETH Zurich and built in Bristol in the framework of the EU-funded research project SERA [61,62]. It comprises an aluminum slab supported on four wobbling circular structural steel columns resting on the shake table platform (Figure 3). The four columns had a height, diameter and wall thickness of 1000 mm, 244.5 mm and 8 mm, respectively, with a corresponding slenderness (i.e., diameter to height) ratio of $\tan\alpha = 0.2445$ (Figure 4). Note that the size of the wobbling specimen is not representative of the size of a prototype bridge or a prototype podium building. The ground motion excitations used in the



Figure 3: Wobbling specimen on the University of Bristol shake table.

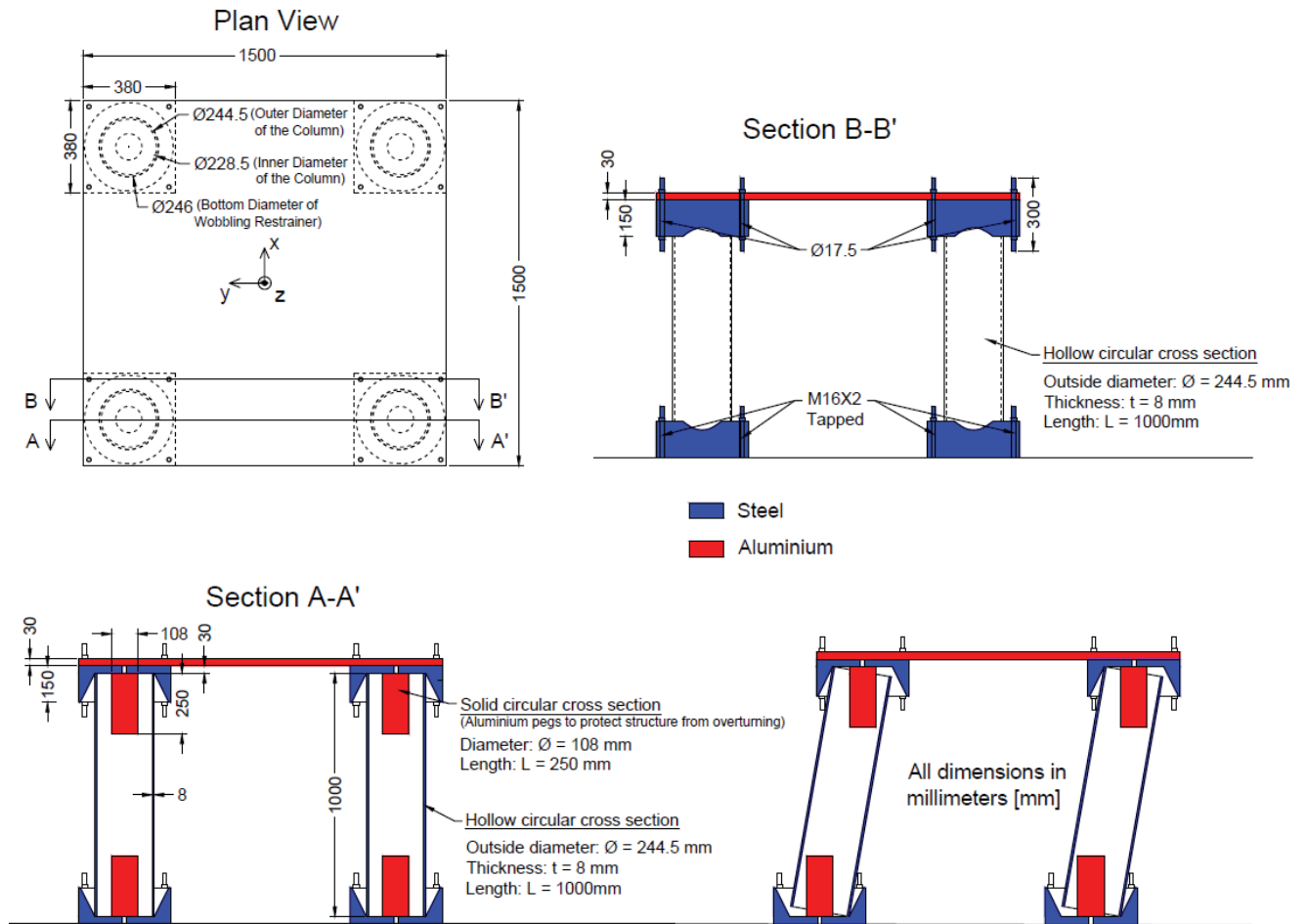


Figure 4: Details of the wobbling specimen.

shake table experiments were scaled to preserve acceleration scaling (as discussed later in this paper) so that the model represents a structure with a height similar to an actual bridge. The intent of the specimen detailing was to mimic the assumptions in Vassiliou's [57] "wobbling bridge" model, namely that the structure is rigid and that the columns wobble without sliding or twisting about their longitudinal axis. Conical end restraints were placed at each end of each column to stop the columns from wobbling out of their original position (Figure 5). After the tests, scratches on the conical restrainers were observed, showing that the columns tried to "climb out" (Figure 5). Aluminum pegs were installed inside the columns (Figure 5) with enough clearance to enable unrestrained wobbling up to overturning, but engage early enough to enable easy recovery of the specimen to its original position after a test that resulted in overturning. Moreover, padded frames were placed under and around the specimen to protect the shake table platform (Figure 3).

4.2 Specimen Excitation Using A Shake Table

The wobbling response of the specimen was induced by a dynamic bi-directional (two orthogonal horizontal components) excitation of its support. This was achieved by placing the specimen on the top of the 6DOF 3 m×3 m shake table of the University of Bristol [63].

4.3 Ground Motions and Scaling

To constrain the uncertainty in the ground motion excitation, ensembles of bi-directional

ground motions were synthesized using a spectral version of the Rezaeian and Der Kiureghian stochastic ground motion model [64-66]). More info on the ground motions used can be found in [61].

Two recorded ground motions, the 1940 El Centro Array #9 record and the 1999 Chi-Chi CHY080 record, were used as the "seed" ground motions for the experimental campaign. Next, two bi-directional (two orthogonal horizontal components) ground motion ensembles, each comprising 100 synthetic ground motions, were generated from the two seed ground motions. These two ground motion ensembles were used to drive the shake table during the conducted tests. Vertical ground motion translational and the three rotational excitations were not considered.

A detailed discussion on the scaling parameters of the tests can be found in [61]: The frequency of the excitations was scaled by a factor of $\sqrt{9.67} = 3.11$, so that the size of the structure in the prototype scale is 9.67 times larger and its height is 9.67m and representative of a typical overpass bridge.

It should be noted that the wobbling specimen is only a distorted model of a prototype structure because the stress similitude is not preserved. Thus, the elastic modulus of the material and the natural frequencies of the prototype are not correctly scaled. In addition, the wobbling specimen columns are not perfectly rigid, as Vassiliou [57] assumes, nor are any realistic foundation condition modelled. However, it has been shown that the deformability of large structures does not qualitatively change their rocking behavior [67-74]. Ultimately, the conducted experiments serve to generate a benchmark dataset for wobbling seismic response model validation and do not aim at representing the nuances of a prototype structure without distortion.

4.4 Motion Measurement

The response of the wobbling specimen was measured using displacement and acceleration sensors.



Figure 5: Conical restraint and an aluminum peg at the bottom of the wobbling specimen column before installation (left). Metal shavings found after the shake table tests showing that the steel column scratched against the conical restrainer during the tests (right).



Figure 6: Marker positions on top of the aluminum slab used for wobbling specimen displacement measurements.

The displacements were measured using an infrared tracking system, with six infrared passive markers installed on the top of the aluminum slab, as shown in Figure 6. The accelerations were measured using three-dimensional accelerometers. These sensors were placed on the shake table platform to record the actually applied excitation.

4.5 Relevant Wobbling Response Quantity

The horizontal displacement of the slab is the relevant response quantity in the created benchmark dataset, which was measured using the markers shown in Figure 6. The following maximum absolute average displacement (MAAD) of the wobbling specimen slab is defined as the relevant measure of the wobbling specimen response:

$$u = \max_t \left(\frac{u_1(t) + u_3(t) + u_4(t) + u_6(t)}{4} \right) \quad (1)$$

where u_i is the Euclidean norm of the horizontal displacement at points M_i of Figure 6, relative to the shake table. Figure 7 plots the Cumulative Distribution Functions (CDFs) of the specimen MAAD (i.e. of u) for the El Centro and the Chi-Chi ground motion ensembles using thick black lines.

5 WOBBLING SEISMIC RESPONSE BLIND PREDICTION CONTEST

Statistical seismic response model validation was conducted for a number of wobbling response models in the scope of a blind prediction contest organized by the Pacific Earthquake Engineering Research center (PEER), the University of Bristol, and ETH Zurich, launched in October 2019 with a prediction submission deadline on November 20th, 2019. The contestants were asked to use their models to predict not the wobbling specimen seismic displacement (Equation 1) to each of the 200 ground motions in the two ground motion ensembles, but the experimental CDFs of the wobbling specimen MAAD u response, as shown in Figure 7 using thick black lines. The as-built geometry of the wobbling specimen and the recorded shake table accelerations were provided to the contestants, but no tests were performed to mechanically characterize the materials of the wobbling specimen (i.e., the steel of the columns and conical restrainers), as these were not essential in terms of affecting the response and use of common modulus of elasticity for steel and aluminum was sufficient.

In the blind prediction contest, for each set of ground motion ensembles, the competing models were ranked according to the maximum vertical distance, i.e. the Kolmogorov-Smirnov (K-S) distance [75], between their predicted and the experimentally obtained CDFs [61]. This paper revisits the ranking by using a different metric to rank the contesting models: Instead of the K-S distance, the models are ranked according to their performance in predicting the median response along each ground motion ensemble. Given that two ensembles of ground motions were used, the average normalized error is taken as a best-fit performance indicator.

Thirteen contestants participated in the blind prediction contest. The models they used can be grouped into three categories, as follows:

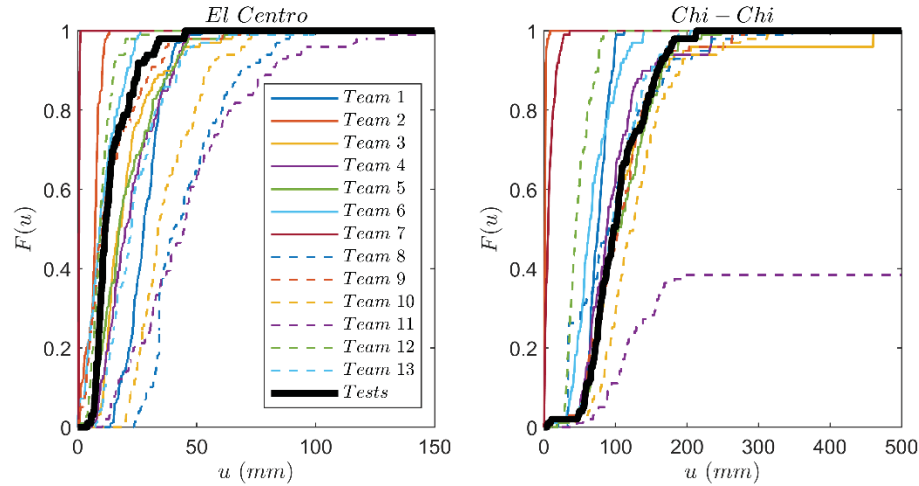


Figure 7: MAAD CDFs obtained from shake table tests (thick black lines) and CDFs of the same response quantity obtained using the 13 contesting models for the El Centro and Chi-Chi ground motion examples.

	El Centro		Chi-Chi		Average	
	Team number (method used)	$e_{50,EC} = \frac{ u_{50,m,EC} - u_{50,exp,EC} }{u_{50,exp,EC}}$	Team number method used)	$e_{50,CC} = \frac{ u_{50,m,CC} - u_{50,exp,CC} }{u_{50,exp,CC}}$	Team number (method used)	$e_{50} = \frac{(e_{50,EC} + e_{50,CC})}{2}$
1	9 (FEM)	0.12	3 (DEM)	0.01	9 (FEM)	0.09
2	12 (FEM)	0.18	13 (DEM)	0.01	3 (DEM)	0.24
3	6 (FEM)	0.21	9 (FEM)	0.06	6 (FEM)	0.28
4	2 (FEM)	0.37	5 (DEM)	0.07	5 (DEM)	0.29
5	3 (DEM)	0.48	8 (DEM)	0.07	12 (FEM)	0.36
6	5 (DEM)	0.52	4 (FEM)	0.10	4 (FEM)	0.41
7	4 (FEM)	0.73	1 (FEM)	0.22	13 (DEM)	0.48
8	13 (DEM)	0.94	10 (FEM)	0.27	2 (FEM)	0.67
9	7 (FEM)	0.95	6 (FEM)	0.35	1 (FEM)	0.82
10	1 (FEM)	1.41	12 (FEM)	0.54	7 (FEM)	0.94
11	10 (FEM)	1.92	7 (FEM)	0.94	10 (FEM)	1.10
12	8 (DEM)	2.50	2 (FEM)	0.98	8 (DEM)	1.29
13	11 (RB)	2.87	11 (RB)	overturn	11 (RB)	n/a

Table 1. Contestant model ranking based on the error of predicting the median MAAD CDFs

- 8 contestants developed models based on the Finite Element Method (FEM), out of which 4 used ABAQUS [76] (Teams #7, #9, #10, and #12), 2 used SAP2000 [77] (Teams #2 and #4), 1 used Midas GEN [78] (Team #1) and 1 used OpenSees [79] (Team #6);
- 4 contestants used the Discrete Element Method (DEM) to build their models, out of which 3 used 3DEC [80] (Teams #3, #5 and #8), and 1 used Code Aster [81] (Team #13);
- 1 contestant (#Team 11) used Vassiliou's [57] Rigid Body (RB) model (independently, as Vassiliou was one of the contest organizers and did not take part in the contest).

The outcomes of the statistical seismic response validation of the contesting models are shown in Figure 7 and Table 1. Figure 7 graphically compares the predicted wobbling specimen MAAD response CDFs ($F(u)$) to the experimentally obtained wobbling specimen dis-

placement response CDFs. Table 1 ranks the contestant predictions based on the u_{50} distance: Column 1 gives the ranking for the El Centro ensemble, column 2 for Chi-Chi ensemble, and column 3 gives the overall model ranking based on the average normalized u_{50} distance for the two ensembles of ground motions.

Using a different metric than the one used in the blind prediction contest does change the overall ranking. However, the two models that scored the best in term of their K-S distance, continue to score the best in the u_{50} distance: a) The model with the best score is the one submitted by Team #9 (Myron Chiyun Zhong and Constantin Christopoulos from the University of Toronto). They used FE software ABAQUS 6.13 with C3D20R quadratic brick element, with reduced integration. They assumed a coefficient of friction of 0.3 and no Rayleigh damping [82]. The second best model was the one submitted by Team #3 (Daniele Malomo, Anjali Mehrotra, and Matthew DeJong from UC Berkeley). They used Distinct (or Discrete) element software 3DEC. The frictional mechanisms were modeled using a simplified Mohr-Coulomb criterion with tension cut-off [83]. Zero Rayleigh damping was used.

Both FEM and DEM models used in this blind prediction contest performed well or poorly, depending on the modeling parameters. For example, of the two best models, Team #9 developed an FEM and Team #3 used a DEM model. Thus, there is no basis to recommend FEM or DEM to model wobbling structures seismic response. However, it should be mentioned that MAAD CDFs produced by DEM models were close to the experimental benchmark CDFs, except in the case of the model developed by Team #8 which clearly underpredicted the response for the El Centro ground motion ensemble. Similarly, the FEM models of Teams #2 and #7 grossly underestimated the response, as can be seen in Figure 7. This does not mean that FEM models cannot perform well, or that such models would underestimate the response; the FEM model of Team #9 performed the best in all metrics. This is merely an indication that, when it comes to uplifting and rocking structures, modeling decisions should be made with care. This is more important for FEM models, as such models originate from continua, as opposed to DEM models that inherently assume the structure comprises of discrete parts.

The specific Rigid Block model proposed by Vassiliou [57] and used by Team #11 consistently overestimates the response. Hence it is conservative, but not accurate. It should be noted that the Rigid Block model formulation does not include any form of energy dissipation. Apparently, disregarding the energy dissipated in the tests through scratching of the conical restrainers leads to overestimation of the response. Therefore, this model can only be used to obtain conservative estimates of the response.

6 ROLE OF ENERGY DISSIPATION IN MODELING OF WOBBLING RESPONSE

Modelling of energy dissipation in structures is an open problem, not only for rocking structures, but for fixed base structures as well. The widely used Rayleigh model, although numerically convenient (akin to viscous damping in SDOF oscillators), is not validated experimentally and can create implausible forces and moments, especially when the initial stiffness proportional component is included [84-86]. In the wobbling system discussed herein, energy is dissipated mainly through sliding (that created the metal shavings shown in Figure 5) and through radiation damping, through the interaction with the supporting wave transmitting structure [87]. Inherent material damping also exists, but since the stresses are relatively small, this form of energy dissipation is not expected to be significant when compared to the other mechanisms. Therefore, creating a mass and/or stiffness proportional damping matrix clearly has no physical meaning, especially if assigned to all degrees of freedom, including the rocking interface.

Based on the above, it is not a surprise that the best models by Teams #9 and #3 do not use Rayleigh damping and rely only on modelling friction to dissipate energy. On the contrary, Team #1 model that assumed a damping ratio of 1% at 0.05s and 1.5s clearly underestimated the response. Team #4 model used Rayleigh damping, but with damping ratio set to very low values (0.1%), which was low enough not to suppress the response.

Even though the Rayleigh damping model is not suitable for modeling the seismic response of rocking or wobbling structures, this does not imply that the model should not incorporate any energy dissipation. The tests showed that the input seismic energy is dissipated by friction and radiation, and that it should be modelled explicitly. Neglecting energy dissipation completely, like in the Team #11 Rigid Body dynamics model, grossly overestimates the response. The above observations on energy dissipation, corroborate that numerical models should respect the physics of the system, to the extent possible. This is does not hold for Rayleigh damping applied in rocking.

7 CONCLUSIONS

The seismic response of rocking structures is notoriously sensitive to all of the parameters that define it. As expected, numerical models often fail to adequately predict the seismic response of a rocking structure to a single ground motion. Based on this, researchers have claimed that not only are current models inaccurate, but that a numerical model accurate enough to predict the seismic response of rocking structures is not feasible. Hence, rocking is not used as a seismic design approach, and virtually all engineered structures are designed as fixed to the ground.

Along these lines, this paper revisits the issue of seismic response predictability in seismic design. It claims that predicting the response to a single ground motion is too strong of an acceptance test for a model. Instead, the minimum precondition for a valid model to be used in seismic design is the ability to predict the statistical characteristics of the seismic responses to an ensemble of ground motions that are compatible to the seismic hazard of interest. This is a weaker, but sufficient model validation test.

The objective of this study is to answer the question: Are seismic tests of three-dimensional rocking structures predictable using numerical models? To answer the above question in a statistical sense, an experimental campaign has been designed to obtain observations of the seismic response of a rocking podium structure that was able to sustain three-dimensional rocking motion without sliding. A stochastic model was used to generate two synthetic ground motion ensembles that match the physical characteristics of two recorded ground motions. These two ensembles were used to excite a rocking podium structure.

A blind prediction contest was organized to evaluate the ability of several models submitted by the contestants to predict the response of the rocking podium structure statistically. The models were evaluated based on their ability to predict not the time history response to each single ground motion, but the CDF of the maxima of the specimen displacement response time histories. Contestants used FEM, DEM and Rigid Body Dynamics models.

The winning model, developed by means of the FEM, scored the best of all models in terms of its K-S distance from the experimental CDF. This paper shows that it performs the best when a different metric (the median displacement u_{50}) is used to evaluate its performance. However, this is not sufficient to conclude that FEM models were uniformly better than the submitted DEM models, because some DEM submissions were also very accurate, plus some of the least accurate models were FEM. Therefore, both FEM and DEM can perform well or poorly in simulating the wobbling (three-dimensional rocking) seismic response, depending on the parameters used and the assumptions made.

Therefore, it can be concluded that the response of a 3-dimensional rocking structure is predictable in terms of a CDF of the maxima of the time-history responses to a set of ground motions.

In terms of rocking and wobbling seismic response modelling guidelines, this blind prediction contest confirmed that energy dissipation is a key factor that needs to be modelled, though not by means of Rayleigh damping. The models that best predicted the response used zero Rayleigh damping, but modeled energy dissipation directly through friction elements. A model with 0.1% Rayleigh damping that explicitly modelled friction as well also performed relatively well, but a model with 1% Rayleigh damping clearly underestimated the response. The rigid body model which modelled no energy dissipation at all, overestimated the response and should only be used only to obtain conservative wobbling response estimates.

8 ACKNOWLEDGEMENT

This research was conducted under the auspices of the project “Statistical verification and validation of 3D seismic rocking motion models (3DROCK)”, funded by the EU H2020 programme under grant agreement number 730900 [SERA]. Additional funding from ETH Zurich, University of Bristol and the Pacific Earthquake Engineering Research Center, as well as the contribution of the personnel at EQUALS laboratory, University of Bristol, and Erika Donald and Amarnath Kasalanti of PEER Center and UC Berkeley are gratefully acknowledged.

We also acknowledge the participation of the following teams in the blind prediction contest, herein listed alphabetically (not following the team numbering in this paper for reasons of anonymity):

1) Turki Alalawi, Abduaziz S. Al-Hazmi, Majd R. Zain, Jahad I. Al-harbi, Maha M. Hassan, and Mohamed S. Laissy; 2) Yu Bao and Dimitrios Konstantinidis; 3) Shanshan Chen, JingCong Lin, Yanfei Cai, Hanbin Lin, Xiaomin Liang, Jiatun Deng, Haoyun Lin, Lei Zhang, Difang Huang, Zinan Wu, and Xiancai Chen; 4) Ioannis P. Christovasilis, Lorenzo Riparbelli, Dimitris Papaevangelou, Gabriele Pini; 5) Tamás Forgács, Daniel Joó, Sándor Ádány, Vasilis Sarhosis, and José V. Lemos; 6) Jincheng Liu and Xinxin Wei; 7) Royce Liu; 8) Daniele Malomo, Anjali Mehrotra, and Matthew J. DeJong; 9) Yi Peng, Jianian Wen, Zhenlei Jia, Yazhou Xie, Jian Zhang; 10) P. Ravi Prakash, Bora Pulatsu, Nuno Mendes and Paulo B. Lourenço; 11) Chiyun Zhong and Constantin Christopoulos, as well as the 2 participating teams that wished to remain anonymous.

9 REFERENCES

- [1] Housner, GW (1963): The behaviour of inverted pendulum structures during earthquakes, *Bull. Seismol. Soc. Am.* **53**, 404–417.
- [2] Konstantinidis, D., & Makris, N. (2010). Experimental and analytical studies on the response of 1/4-scale models of freestanding laboratory equipment subjected to strong earthquake shaking. *Bull. Earth. Eng.*, 8(6), 1457-1477.
- [3] Di Egidio, A., Alaggio, R., Contento, A., Tursini, M., & Della Loggia, E. (2015). Experimental characterization of the overturning of three-dimensional square based rigid block. *Int. J. Non Linear Mech.*, 69, 137-145
- [4] Wittich, C. E., & Hutchinson, T. C. (2015). Shake table tests of stiff, unattached, asymmetric structures. *Earthq Eng Struct Dynam*, 44(14), 2425-2443.

- [5] Dar, A., Konstantinidis, D., & El-Dakhakhni, W. W. (2016). Evaluation of ASCE 43-05 seismic design criteria for rocking objects in nuclear facilities. *J Struct Eng*, 142(11), 04016110.
- [6] Sextos, A. G., Manolis, G. D., Ioannidis, N., & Athanasiou, A. (2017). Seismically induced uplift effects on nuclear power plants. Part 2: Demand on internal equipment. *Nuclear Engineering and Design*, 318, 288-296.
- [7] Dar, A., Konstantinidis, D., & El-Dakhakhni, W. (2018). Seismic response of rocking frames with top support eccentricity. *Earthq Eng Struct Dynam*, 47(12), 2496-2518.
- [8] Voyagaki E, Psycharis IN, & Mylonakis G. (2013). Rocking Response and Overturning Criteria for Free Standing Rigid Blocks to Single – Lobe Pulses. *Soil Dynamics & Earthquake Engineering*, 46, 85–95.
- [9] Voyagaki E, Psycharis IN, & Mylonakis G. (2014). Complex Response of a Rocking Block to a Full-Cycle Pulse. *Journal of Engineering Mechanics ASCE*, 140(16)
- [10] Voyagaki, E., Kloukinas, P., Dietz, M., Dihoru, L., Horseman, T., Oddbjornsson, O., ... & Steer, A. (2018). Earthquake response of a multiblock nuclear reactor graphite core: Experimental model vs simulations. *Earthq Eng Struct Dynam*, 47(13), 2601-2626.
- [11] Di Sarno, L., Magliulo, G., D'Angela, D., & Cosenza, E. (2019). Experimental assessment of the seismic performance of hospital cabinets using shake table testing. *Earthq Eng Struct Dynam*, 48(1), 103-123.
- [12] Bao, Y., & Konstantinidis, D. (2020). Dynamics of a sliding-rocking block considering impact with an adjacent wall. *Earthquake Engineering & Structural Dynamics*, 49(5), 498-523.
- [13] Stefanou, I., Psycharis, I., & Georgopoulos, I. O. (2011). Dynamic response of reinforced masonry columns in classical monuments. *Constr. Build. Mater.* 25(12), 4325-4337.
- [14] Tondelli, M., Beyer, K., & DeJong, M. (2016). Influence of boundary conditions on the out-of-plane response of brick masonry walls in buildings with RC slabs. *Earthq Eng Struct Dynam*, 45(8), 1337-1356.
- [15] Casapulla, C., Giresini, L., & Lourenço, P. B. (2017). Rocking and Kinematic Approaches for Rigid Block Analysis of Masonry Walls: State of the Art and Recent Developments. *Buildings*, 7(3), 69.
- [16] Kalliontzis, D., & Schultz, A. E. (2017). Characterizing the In-Plane Rocking Response of Masonry Walls with Unbonded Posttensioning. *J Struct Eng* 143(9), 04017110.
- [17] Mehrotra, A., & DeJong, M. J. (2018). The influence of interface geometry, stiffness, and crushing on the dynamic response of masonry collapse mechanisms. *Earthq Eng Struct Dynam*, 47(13), 2661-2681.
- [18] Shawa, O. A., de Felice, G., Mauro, A., & Sorrentino, L. (2012). Out-of-plane seismic behaviour of rocking masonry walls. *Earthquake Engineering & Structural Dynamics*, 41(5), 949-968.
- [19] Giresini, L., Sassu, M., & Sorrentino, L. (2018). In situ free-vibration tests on unrestrained and restrained rocking masonry walls. *Earthquake Engineering & Structural Dynamics*, 47(15), 3006-3025.
- [20] Mouzakis, H. P., Psycharis, I. N., Papastamatiou, D. Y., Carydis, P. G., Papantonopoulos, C., & Zambas, C. (2002). Experimental investigation of the earthquake response of a model of a marble classical column. *Earthq Eng Struct Dynam*, 31(9), 1681-1698.
- [21] Papantonopoulos, C., Psycharis, I. N., Papastamatiou, D. Y., Lemos, J. V., & Mouzakis, H. P. (2002). Numerical prediction of the earthquake response of classical columns using the distinct element method. *Earthq Eng Struct Dynam*, 31(9), 1699-1717.

- [22] Vassiliou, M. F., & Makris, N. (2012). Analysis of the rocking response of rigid blocks standing free on a seismically isolated base. *Earthq Eng Struct Dynam*, 41(2), 177-196.
- [23] Bachmann, J. A., Vassiliou, M. F., & Stojadinović, B. (2018). Dynamics of rocking podium structures. *Earthq Eng Struct Dynam*, 46(14), 2499-2517.
- [24] Bachmann, J. A., Vassiliou, M. F., & Stojadinovic, B. (2019). Rolling and rocking of rigid uplifting structures. *Earthq Eng Struct Dynam*, 48(14), 1556-1574.
- [25] Ríos-García, G., & Benavent-Climent, A. (2020). New rocking column with control of negative stiffness displacement range and its application to RC frames. *Eng. Struct.*, 206, 110133.
- [26] Makris N. and Vassiliou M.F. (2013), Planar rocking response and stability analysis of an array of free standing columns capped with a freely supported rigid beam, *Earthquake Engng. Struct. Dyn*, 42(3), 431-449.
- [27] Makris, N., & Vassiliou, M. F. (2014). Are Some Top-Heavy Structures More Stable?. *J Struct Eng*, 140(5).
- [28] Dimitrakopoulos, E. G., & Giouvanidis, A. I. (2015). Seismic Response Analysis of the Planar Rocking Frame. *J. Eng. Mech.*, 141(7), 04015003.
- [29] Agalianos, A., Psychari, A., Vassiliou, M. F., Stojadinovic, B., & Anastasopoulos, I. (2017). Comparative Assessment of Two Rocking Isolation Techniques for a Motorway Overpass Bridge. *Front. Built Environ.* 3, 47.
- [30] Vassiliou, M. F., Mackie, K. R., and Stojadinović, B. (2017) A finite element model for seismic response analysis of deformable rocking frames. *Earthquake Engng Struct. Dyn.*, 46: 447–466.
- [31] Sideris, P., Aref, A. J., & Filiatrault, A. (2014). Quasi-static cyclic testing of a large-scale hybrid sliding-rocking segmental column with slip-dominant joints. *Journal of Bridge Engineering*, 19(10), 04014036.
- [32] Sideris, P., Aref, A. J., & Filiatrault, A. (2014). Large-scale seismic testing of a hybrid sliding-rocking posttensioned segmental bridge system. *Journal of Structural Engineering*, 140(6), 04014025.
- [33] Sideris, P., Aref, A. J., & Filiatrault, A. (2015). Experimental seismic performance of a hybrid sliding–rocking bridge for various specimen configurations and seismic loading conditions. *Journal of Bridge Engineering*, 20(11), 04015009.
- [34] Sideris, P. (2015). Nonlinear quasi-static analysis of hybrid sliding–rocking bridge columns subjected to lateral loading. *Engineering Structures*, 101, 125-137.
- [35] Salehi, M., Sideris, P., & Liel, A. B. (2017). Numerical simulation of hybrid sliding-rocking columns subjected to earthquake excitation. *Journal of Structural Engineering*, 143(11), 04017149.
- [36] Marriott, D., Pampanin, S., & Palermo, A. (2009). Quasi-static and pseudo-dynamic testing of unbonded post-tensioned rocking bridge piers with external replaceable dissipaters. *Earthquake engineering & structural dynamics*, 38(3), 331-354.
- [37] Palermo, A., Pampanin, S., & Calvi, G. M. (2004). The use of controlled rocking in the seismic design of bridges. *Doctate Thesis, Technical Institute of Milan, Milan, I*, 1-5.
- [38] Routledge, P., McHaffie, B., Cowan, M., & Palermo, A. (2020). Wigram–Magdala Link Bridge: Low-Damage Details for a More Efficient Seismic Design Philosophy. *Structural Engineering International*, 30(2), 177-184.
- [39] Mashal, M., & Palermo, A. (2019). Low-damage seismic design for accelerated bridge construction. *Journal of Bridge Engineering*, 24(7), 04019066.
- [40] Thonstad, T., Mantawy, I. M., Stanton, J. F., Eberhard, M. O., & Sanders, D. H. (2016). Shaking table performance of a new bridge system with pretensioned rocking columns. *Journal of Bridge Engineering*, 21(4), 04015079.

- [41] Makris, N., & Konstantinidis, D. (2003). The rocking spectrum and the limitations of practical design methodologies. *Earthq Eng Struct Dynam*, 32(2), 265-289.
- [42] Reggiani Manzo, N., & Vassiliou, M. F. (2019). Displacement-based analysis and design of rocking structures. *Earthq Eng Struct Dynam*, 48(14), 1613-1629.
- [43] Reggiani Manzo, N., & Vassiliou, M. F. (2020). Dimensional analysis of negative stiffness bilinear systems under pulse like excitations. *Earthq Eng Struct Dynam*, DOI: [10.1002/eqe.3347](https://doi.org/10.1002/eqe.3347)
- [44] Koh AS and Hsiung CM (1991): Base isolation benefits of 3-D rocking and uplift. I: Theory. *J. Eng. Mech.*, 117(1), 1-18.
- [45] Ambraseys, N., & Psycharis, I. N. (2011). Earthquake stability of columns and statues. *Journal of Earthquake Engineering*, 15(5), 685-710.
- [46] Psycharis, I. N., Fragiadakis, M., & Stefanou, I. (2013). Seismic reliability assessment of classical columns subjected to near-fault ground motions. *Earthquake engineering & structural dynamics*, 42(14), 2061-2079.
- [47] Drosos, V., & Anastasopoulos, I. (2014). Shaking table testing of multidrum columns and portals. *Earthq Eng Struct Dynam*, 43(11), 1703-1723.
- [48] Pappas, A., Sextos, A., Da Porto, F., & Modena, C. (2017). Efficiency of alternative intensity measures for the seismic assessment of monolithic free-standing columns. *Bull. Earthquake Eng.*, 15(4), 1635-1659.
- [49] Makris N, Alexakis H, Kampas G, Strepelias I, Kolonas C and Bousias S (2015): *Seismic protection of bridges with rocking piers which recenter with gravity*, Report EEAM, 2015-01, University of Patras Dept of Civil Engng
- [50] Stefanou, I., Vardoulakis, I., & Mavraganis, A. (2011). Dynamic motion of a conical frustum over a rough horizontal plane. *Int. J. Nonlinear Mech.*, 46(1), 114-124.
- [51] Konstantinidis D and Makris N (2007): The dynamics of a rocking block in three dimensions, 8th Hell. Soc. Theor. Appl. Mech. Int. Congr. Mech. Patras, Greece 9/2015.
- [52] Zulli D, Contento A, and Di Egidio A (2102): 3D model of rigid block with a rectangular base subject to pulse-type excitation, *Int. J. Non. Linear. Mech.*, 47 (6), 679–687.
- [53] Chatzis, MN, and Smyth AW (2012). Modeling of the 3D rocking problem. *International Journal of Non-Linear Mechanics*, 47(4) 85-98.
- [54] Chatzis, M. N., & Smyth, A. W. (2012). Three-dimensional dynamics of a rigid body with wheels on a moving base. *Journal of Engineering Mechanics*, 139(4), 496-511.
- [55] Mathey, C., Feau, C., Politopoulos, I., Clair, D., Baillet, L., & Fogli, M. (2016). Behavior of rigid blocks with geometrical defects under seismic motion: an experimental and numerical study. *Earthquake Engineering & Structural Dynamics*, 45(15), 2455-2474.
- [56] Vassiliou, M. F., Burger, S., Egger, M., Bachmann, J. A., Broccardo, M., & Stojadinovic, B. (2017). The three-dimensional behavior of inverted pendulum cylindrical structures during earthquakes. *Earthq Eng Struct Dynam*, 46(14), 2261-2280.
- [57] Vassiliou, M. F. (2018). Seismic response of a wobbling 3D frame. *Earthquake Engineering & Structural Dynamics*, 47(5), 1212-1228.
- [58] Bachmann, J. A., Strand, M., Vassiliou, M. F., Broccardo, M., & Stojadinović, B. (2018). Is rocking motion predictable?. *Earthq Eng Struct Dynam*, 47(2), 535-552.
- [59] Bachmann, J., Strand, M., Vassiliou, M. F., Broccardo, M., & Stojadinovic, B. (2019) "Modelling of rocking structures: Are our models good enough?," *Proceedings of 2nd International Conference on Natural Hazards & Infrastructure*, Crete, Greece.
- [60] Del Giudice, L., Wrobel, R., Leinenbach, C., & Vassiliou, M. F. (2020). Static Testing of Additively Manufactured Microreinforced Concrete Specimens for Statistical Structural Model Validation at a Small Scale. In *8th International Conference on Advances in Experimental Structural Engineering (8AESE)*.

- [61] Vassiliou, M. F., Broccardo, M., Cengiz, C., Dietz, M., Dihoru, L., Gunay, S., ... & Stojadinovic, B. (2021). Shake table testing of a rocking podium: Results of a blind prediction contest. *Earthq Eng Struct Dyn.* **50**(4):1043-1062
- [62] Vassiliou, M. F., Cengiz, C., Dietz, M., Dihoru, L., Broccardo, M., Mylonakis, G., ... & Stojadinovic, B. (2020). Dataset from the shake table tests of a rocking podium structure. *Earthquake Spectra*, 8755293020988017.
- [63] <http://www.bris.ac.uk/engineering/research/earthquakegeo/equip/tablespect/> (accessed on April 29th 2020)
- [64] Rezaeian S, Der Kiureghian A. (2008) A stochastic ground motion model with separable temporal and spectral nonstationarities. *Earthq Eng Struct Dyn* **37**(13):1565-1584.
- [65] Broccardo M, Dabaghi M. (2017) A spectral-based stochastic ground motion model with a non-parametric time-modulating function. In: 12th International Conference on Structural Safety and Reliability; Vienna; 2017:1-10.
- [66] Broccardo M, Der Kiureghian A. (2014) Simulation of near-fault ground motions using frequency-domain discretization. In: Proceedings of the 10th NCEE; Anchorage, Alaska; 2014:1-11.
- [67] Chopra AK, Yim SCS. Simplified earthquake analysis of structures with foundation uplift. *J Struct Eng.* 1985;111(4):906-930.
- [68] Psycharis IN. Effect of base uplift on dynamic response of SDOF structures. *J Struct Eng.* 1991;117(3):733-754.
- [69] Oliveto G, Calì I, Greco A. Large displacement behaviour of a structural model with foundation uplift under impulsive and earthquake excitations. *Earthq Eng Struct Dynam.* 2003;32(3):369-393.
- [70] Ma QTM. The mechanics of rocking structures subjected to ground motion (Doctoral dissertation, ResearchSpace@ Auckland) 2010.
- [71] Acikgoz S, DeJong MJ. The interaction of elasticity and rocking in flexible structures allowed to uplift. *Earthq Eng Struct Dynam.* 2012;41(15):2177-2194.
- [72] Vassiliou, M. F., Mackie, K. R., & Stojadinović, B. (2014). Dynamic response analysis of solitary flexible rocking bodies: modeling and behavior under pulse-like ground excitation. *Earthq Eng Struct Dyn.*, 43(10), 1463-1481.
- [73] Vassiliou, M. F., Truniger, R., & Stojadinović, B. (2015). An analytical model of a deformable cantilever structure rocking on a rigid surface: development and verification. *Earthq Eng Struct Dynam.*, 44(15), 2775-2794.
- [74] Truniger, R., Vassiliou, M. F., & Stojadinović, B. (2015). An analytical model of a deformable cantilever structure rocking on a rigid surface: experimental validation. *Earthq Eng Struct Dynam.*, 44(15), 2795-2815.
- [75] Kolmogorov A.N. (1933) Sulla determinazione empirica di una legge di distribuzione. *Giornale dell'Istituto Italiano degli Attuari.*, 4, 83-91.
- [76] ABAQUS (2012). *Standard User's Manual*. Providence, RI: Dassault Systèmes Simulia Corp.,
- [77] CSI (2019), *SAP2000 Integrated Software for Structural Analysis and Design* Computers and Structures Inc., Berkeley, California.
- [78] MIDAS (2019), *Design of General Structures, Integrated Design System for Building and General Structures*, MIDASoft, Inc.
- [79] Mazzoni, S., McKenna, F., Scott, M. H., & Fenves, G. L. (2006). OpenSees command language manual. *Pacific Earthquake Engineering Research (PEER) Center*, 264.
- [80] Itasca, C. G. (2007). 3DEC Version 4.1 User's Guide. *Minneapolis, Minnesota USA*.
- [81] Aster, C. (2001). General public licensed structural mechanics finite element software.

- [82] Zhong, C., & Christopoulos, C. (2021). Finite element analysis of the seismic shake-table response of a rocking podium structure. *Earthquake Engineering & Structural Dynamics*, 50(4), 1223-1230.
- [83] Malomo, D., Mehrotra, A., & DeJong, M. J. (2020). Distinct element modeling of the dynamic response of a rocking podium tested on a shake table. *Earthquake Engineering & Structural Dynamics*. 50(5),1469-1475
- [84] Chopra, A. K., & McKenna, F. (2016). Modeling viscous damping in nonlinear response history analysis of buildings for earthquake excitation. *Earthq Eng Struct Dynam*, 45(2), 193-211.
- [85] Cruz, C., & Miranda, E. (2017). *Evaluation of the Rayleigh damping model for buildings*. *Eng.Struct.*, 138, 324-336.
- [86] Hall, John F. (2018) *Performance of Viscous Damping in Inelastic Seismic Analysis of Moment-Frame Buildings*. *EERL Report, 2018-01*. California Institute of Technology, Pasadena, CA.
- [87] Stewart, J., Crouse, C. B., Hutchinson, T. C., Lizundia, B., Naeim, F., & Ostadan, F. (2012). *Soil-structure interaction for building structures (No. Grant/Contract Reports (NISTGCR)-12-917-21)*.

FINITE ELEMENT MODELLING OF A RC ROCKING WALL WITH ADDITIONAL STEEL REBARS

M.E. Bressanelli¹, A. Belleri², J.I. Restrepo²

¹ University of Bergamo, Department of Engineering and Applied Sciences.
Dalmine, Italy
{michele.bressanelli, andrea.belleri}@unibg.it

² University of California, Department of Structural Engineering
San Diego, La Jolla, USA
jrestrepo@ucsd.edu

Abstract

Hybrid walls, i.e. rocking walls with additional energy dissipation, represent a valid lateral force resisting system in seismic regions, due to the limited seismic damage experienced by this system and to the self-centering ability provided by unbounded post-tensioned tendons. These systems accommodate the displacement seismic demand by the development of a single gap opening at the wall base.

A sensitivity analysis of the various parameters has been carried out with the purpose to evaluate their influence on the finite element dynamic response of a selected case study. Three types of models are considered in order to describe the behaviour of the wall-foundation interaction: fiber beam elements, compression-only springs and lumped rotational spring. The main parameters investigated are the damping model and damping magnitude, the elastic modulus of the concrete at the wall-foundation interface, the stiffness and number of the compression only springs, the unbonded length of the rebars used as dissipating device and their hysteresis model. The sensitivity analysis was carried out with the OpenSees finite element software and allowed to preliminary address the influence of the selected parameters by comparison with a reference case study.

Keywords: Rocking walls, Nonlinear Static Analyses, Nonlinear Time History analyses, Acceleration Spikes, Steel Dissipators.

1 INTRODUCTION

To reduce the seismic vulnerability of existing buildings it is possible to use different intervention techniques including rocking systems obtained with the insertion of unbonded post-tension cables inside precast structural elements, typically walls or columns [1][2][3][4][5]. These systems are characterized by a bilinear elastic hysterical behavior, that is characterized by a limited ability to dissipate energy in the case of seismic events [6]. For this reason, additional energy dissipation systems are placed [7], including mild steel rebars [8][9], hysteretic devices [10][11], linear and non-linear fluid-viscous damping [12][13] and friction devices [14][15][16] among others. They are defined as hybrid systems and are characterized by a flag-shaped hysterical curve [9].

In these systems the demand for horizontal displacement is guaranteed by the development of a gap at the wall-to-foundation interface [17]. The unbonded post-tension tendons are sized to ensure no residual displacements at the end of the seismic event [18], allowing the structure to be fully operational after the seismic event [19][20][21]. Numerous studies on these systems have proved their performance under both quasi static and dynamic loading [22][7][23][24][25][26][27] and parametric analyses have carried out to highlight the influence of post-tension tendons [28] and dissipative devices [29][30][31].

The present paper focuses on numerical modeling of hybrid walls by investigating the effects of different modeling techniques in dynamic non-linear analyses. The considered rocking wall panel is taken from the DSDM project [32][23][33] in which shake table tests were conducted on a three story half-scale precast concrete structure whose lateral force resisting system consisted entirely on rocking and hybrid walls. Herein, focus is placed on numerical modeling of a single hybrid wall panel and the effects of different modeling techniques in both nonlinear static and dynamic analyses [34][23][17] are investigated. The comparison between the investigated modeling techniques and the experimental tests is carried out in terms of bending moment, rotation at the base and accelerations.

2 SELECTED CASE STUDY

The selected case study considers the hybrid walls adopted as lateral force resisting system for a three-story half-scale precast concrete structure resembling a parking garage tested on the Network for Earthquake Engineering Simulation (NEES) Large High-Performance Outdoor Shake Table at the University of California at San Diego. Detailed information on the test specimen geometry, material tests and loading sequence can be found elsewhere [35][32][23]. The total mass of each floor, considering the tributary mass of the columns, is 36.795ton, 38.999ton and 34.230ton for the 1st, 2nd and 3rd floor, respectively [17]; it is worth noting that a vertical slotted connection between the wall and the floors allowed to transfer only horizontal loads from the floors to the walls.

This work focuses on the study of the single wall panel with additional steel rebars at the wall to foundation interface. The wall panel is 7.010m height, 2.438m long and 0.203m thick. 2 sets of tendons (each of them made by five 12.7mm diameter low-relaxation tendons) are placed on each wall with a total prestressing force in each wall was equal to 642kN. Two longitudinal reinforcing bars are used as hysteretic energy dissipators.

The relevant data for the finite element analyses are reported in Table 1.

Unconfined concrete	
Strength (f_c')	54MPa
Elastic modulus (E_c)	37000MPa
Strain at maximum strength (ϵ_{c0})	0.2%
Ultimate compressive strain	0.55%
Confined concrete	
Strength (f_{cc}')	80.8MPa
Strain at maximum strength (ϵ_{cc})	0.67%
Ultimate compressive strain (ϵ_{cu})	3.77%
Unbonded prestress tendons	
Tendon set	5x0.5" strands
Prestressing force for each tendon set	235.75kN
Unbonded length (ϵ_{cu})	8529mm

Table 1: Summary of the wall properties.

The input motion adopted for the selected case study represent a design basis earthquake for Seattle, i.e. a moderate seismic hazard [32]. It is worth noting that similitude law was not achieved by mass substitution but only by scaling the input ground motions, horizontal acceleration field amplified by 1.855 and ground motions time step compressed by 1.855.

3 FINITE ELEMENT MODELS

The finite element models presented herein represent a single hybrid wall panel. The tributary mass of each floor is modelled as lumped horizontal mass at the wall center line corresponding to the floor height. The foundation is herein assumed as rigid.

Three different types of 2D-models have been developed with the software OpenSees [36]: fiber beam elements model (FM), lumped rotational spring model (RS), and compression-only springs model (MS) (Figure 1). For all the models, a Rayleigh damping with mass proportionality is considered (damping coefficient equal to 0.01).

In the FM model (Figure 1a), different fiber sections are used to capture the hysteretic behavior of the elements. Regular fiber sections are adopted in the wall panel considering non-linear stress-strain relationship for the confined and unconfined concrete and the reinforcing rebars. No fiber elements are placed above the first floor being the response in that region essentially elastic. To simulate the wall-to-foundation rocking interaction, a fiber section with no reinforcing bars and no tensile strength concrete is positioned between the wall base and the ground. Each tendon set is constituted by a truss element fixed at the base and rigidly connected at the top of the wall by rigid elements [37][27].

In the MS model (Figure 1b) the support of the wall is schematized with a series of axial springs acting only in compression to allow separation between the wall and the foundation during rocking. A total of 25 springs has been considered [17]. The elastic stiffness of each spring is calculated as $E_c A/L$, where E_c is the elastic modulus of the foundation, A is the influence area of each spring and L is half the length of the wall. Yielding of concrete in compression is also introduced in each axial spring with a normal bilinear model.

In the RS model (Figure 1c), the wall panel is modeled with an elastic beam with a nonlinear rotational spring connecting the wall base to the ground with a multilinear hysteretic model. The analytical formulations proposed by Restrepo and Rahman [9] is used for the definition of nonlinear properties of the rotational spring. An additional spring was placed in parallel to capture the behaviour of the dissipative devices [9][38][34].

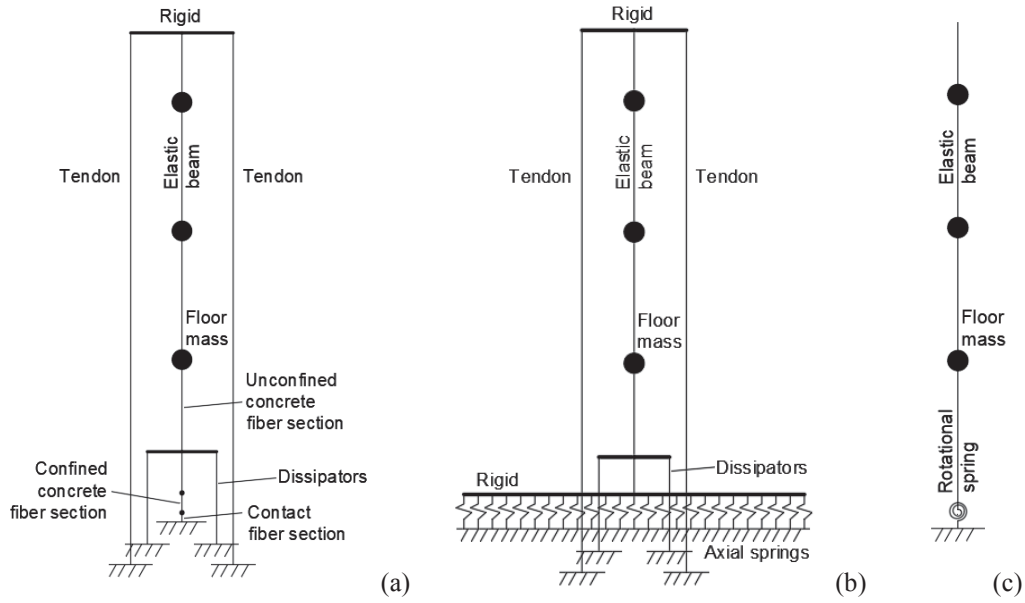


Figure 1: Representation of the 1D elements models: fiber elements, FM, (a), multi-springs, MS, (b), rotational spring, RS, (c).

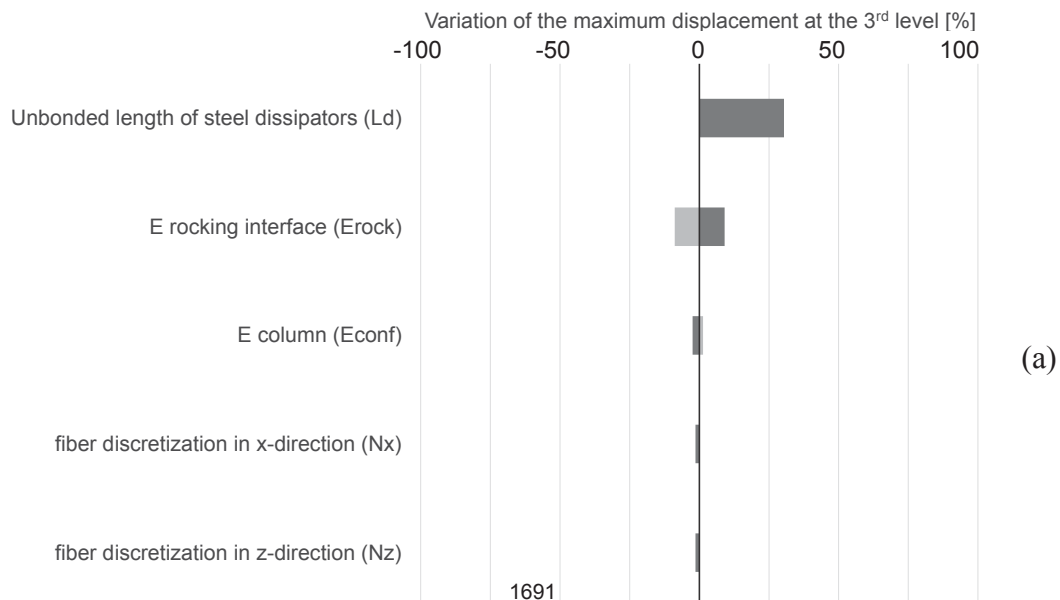
In all models, the uniaxial material properties of the dissipative device are inserted with the Dodd-Restrepo model [39], with the factor Ω for the Bauschinger effect equal to 1.15. In MS and FB models, each dissipator set is constituted by a truss element fixed at the base and rigidly connected to the wall.

3.1 Sensitivity analysis of the parameters

A sensitivity analysis was conducted to investigate the main parameters affecting the dynamic response of the selected case study: elastic modulus of the concrete at the wall-to-foundation interface, stiffness of the compression only springs, unbonded length of the rebars used as dissipating device and their hysteresis model. For both FM and MS models the effective debonded length is equal to 302mm.

The results of the sensitivity analysis are represented by means of a tornado diagram; Figure 2a shows the variation of the maximum displacement of the 3rd level for FM model, while Figure 2b for MS model.

FM model



MS model

(b)

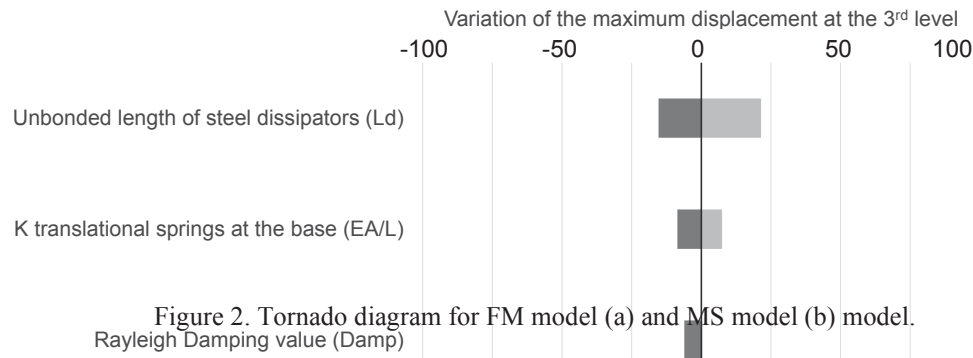


Figure 2. Tornado diagram for FM model (a) and MS model (b) model.

The parameters that mainly affect the horizontal displacements of the rocking wall are the total unbonded length of the mild-steel rebars and the stiffness of the compression-only springs for MS model (Figure 2b) and the elastic modulus at the rocking interface for FM model (Figure 2a).

4 FINITE ELEMENT ANALYSES RESULTS

In this section, the results of the nonlinear static and dynamic analyses are presented in terms of moment-rotation at the base and relative acceleration on the 3rd floor, both horizontal and vertical. The bending moment is calculated as the product between inertial forces and the distance to the rocking interface.

The nonlinear static results of the considered models are shown in Figure 3, where θ is the rotation at the base, i.e. at the gap developing at the wall-to-foundation interface, V is the shear at the base and W is the half-weight of the model structure equal to 621.3kN [17].

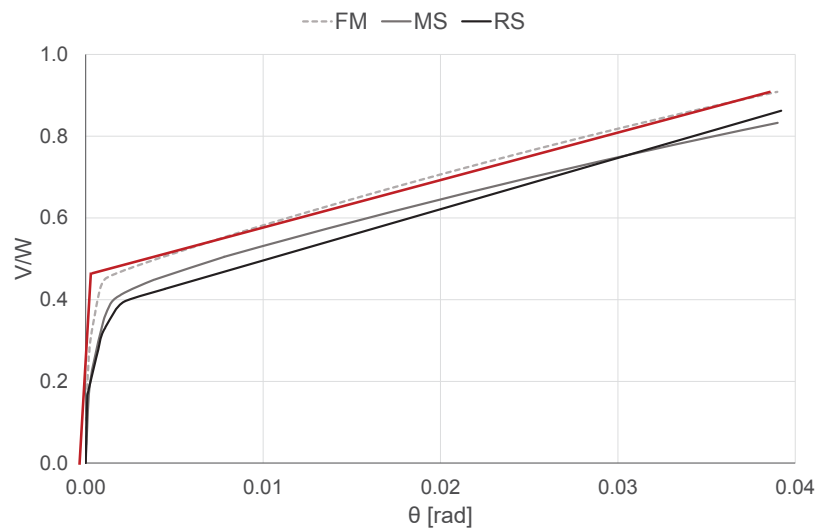
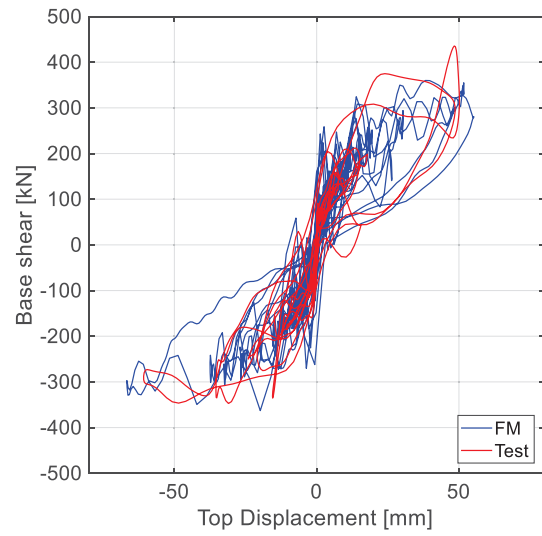
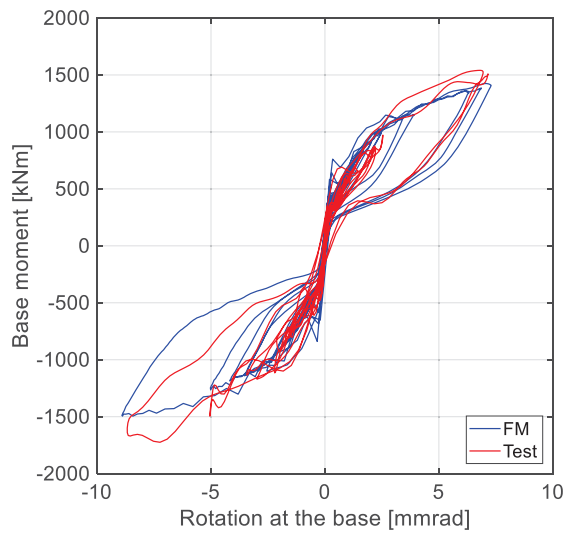


Figure 3: Base shear–base rotation elements models with energy dissipators at the wall-to-foundation interface.

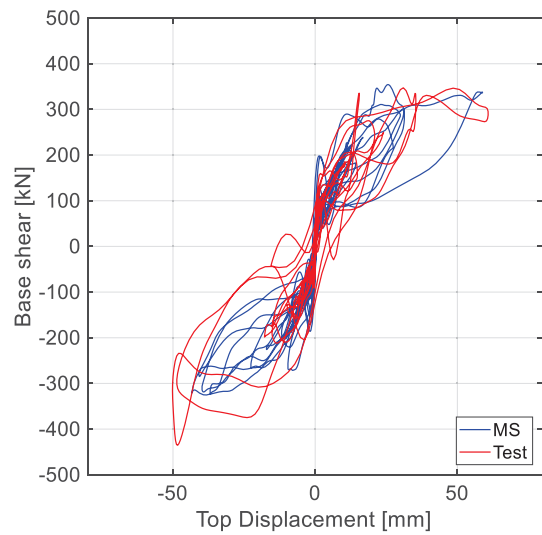
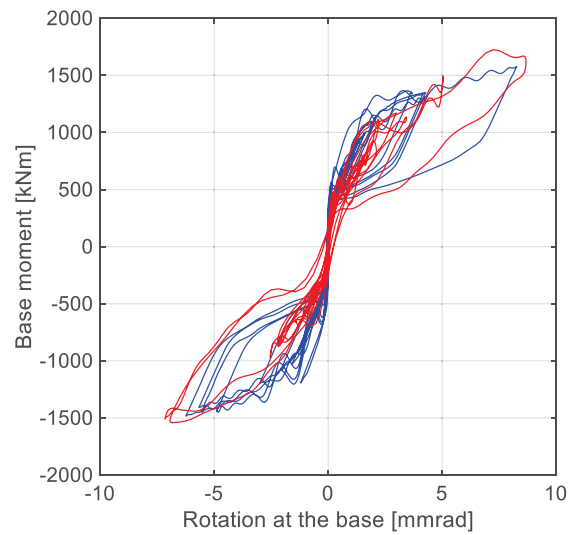
The red line in Figure 3 indicates the bilinear response of hybrid walls [9]. It shows a good approximation to the idealized bilinear response.

Nonlinear dynamic analyses were conducted. The sequence of the actual input ground motions used during the experimental tests is considered. Figure 4, Figure 5 and Figure 6 show the results of the three models, indicating how the models are able to reasonably describe the

global wall behavior. In these figures, the red line indicates the results of the experimental tests, while the blue line indicates the results obtained from the finite element model.



(a)



(b)

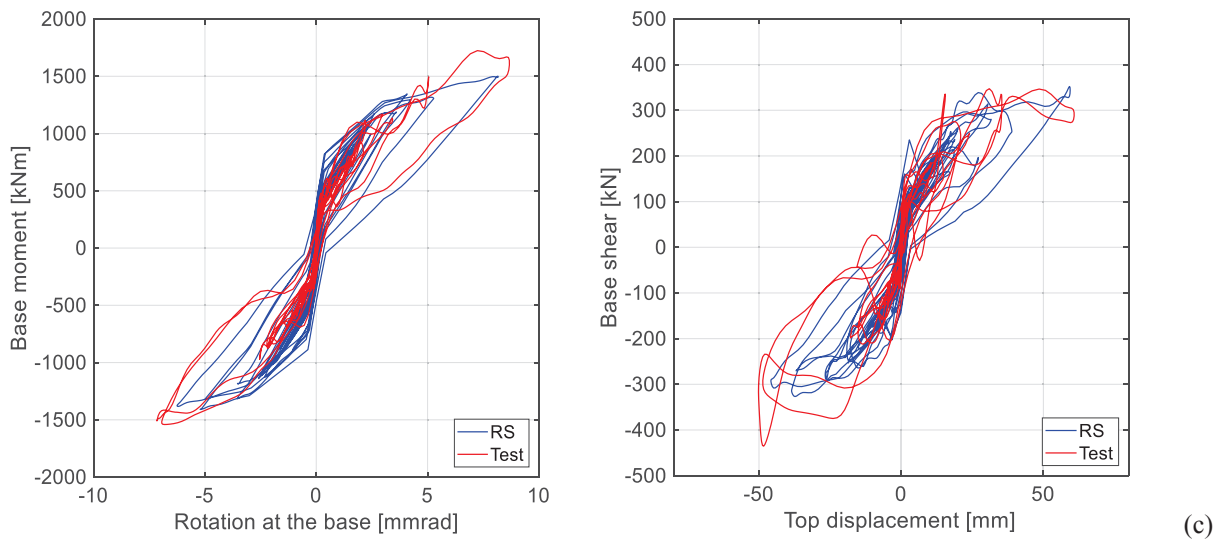
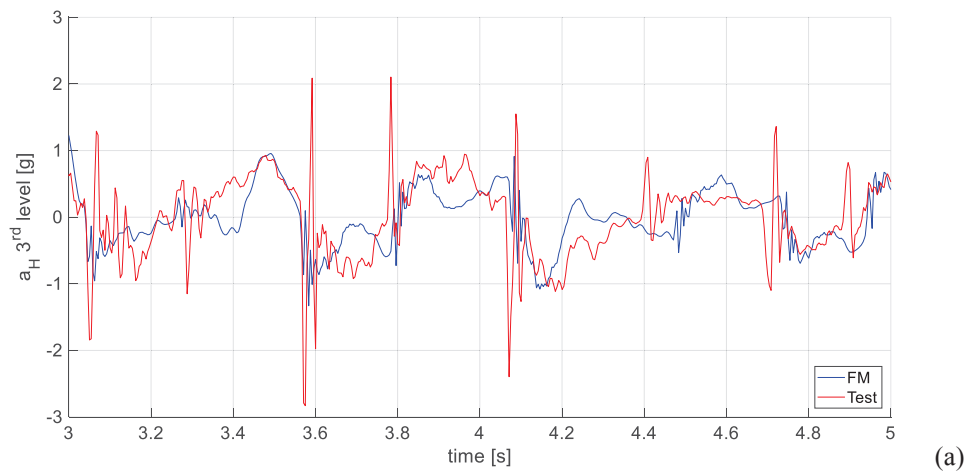
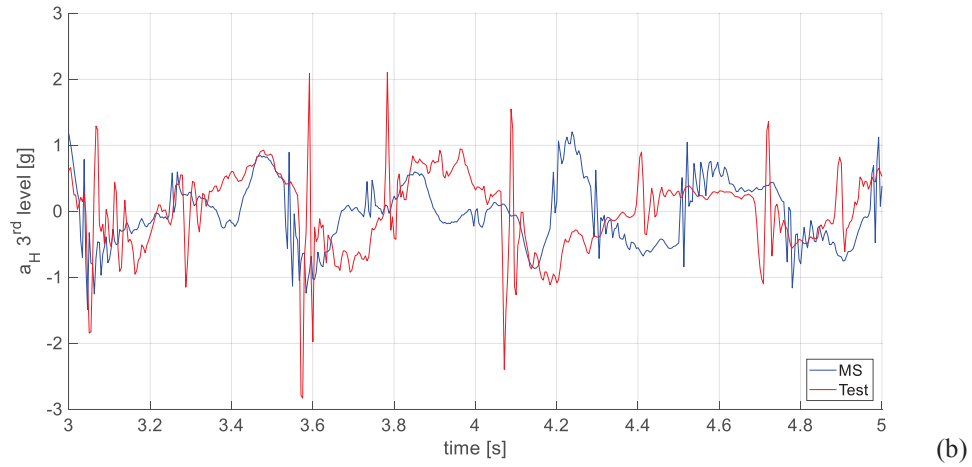


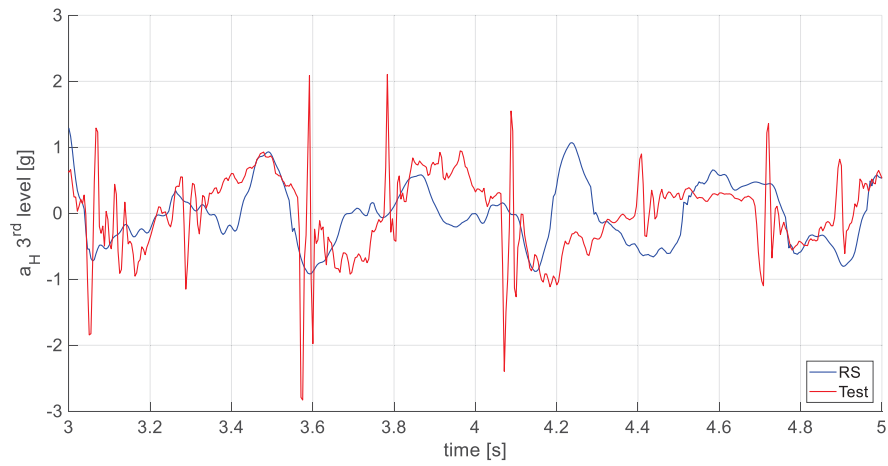
Figure 4: Moment-rotation for fiber elements 'FM' (a), multi-springs only-compression 'MS' (b) and rotational lumped spring 'RS' (c) model. Note: in red the experimental test and in blue the numerical results.

Figure 5 shows the horizontal accelerations. The models capture the acceleration trend, but not the exact peak values. These peaks are associated with horizontal acceleration spikes arising when the wall gains horizontal lateral stiffness in the unloading phase [23][40], which happens in proximity of zero-base rotation.





(b)



(c)

Figure 5: Horizontal acceleration [g] for fiber elements (a), multi-springs only-compression (b) and rotational lumped spring (c) model for the hybrid wall. Note: in red the experimental test and in blue the numerical results.

Figure 6 shows the vertical accelerations. The peaks observed arise when the wall base gap closes [23]. A good approximation is obtained compared to the experimental test. Vertical accelerations are not investigated in the RS model.

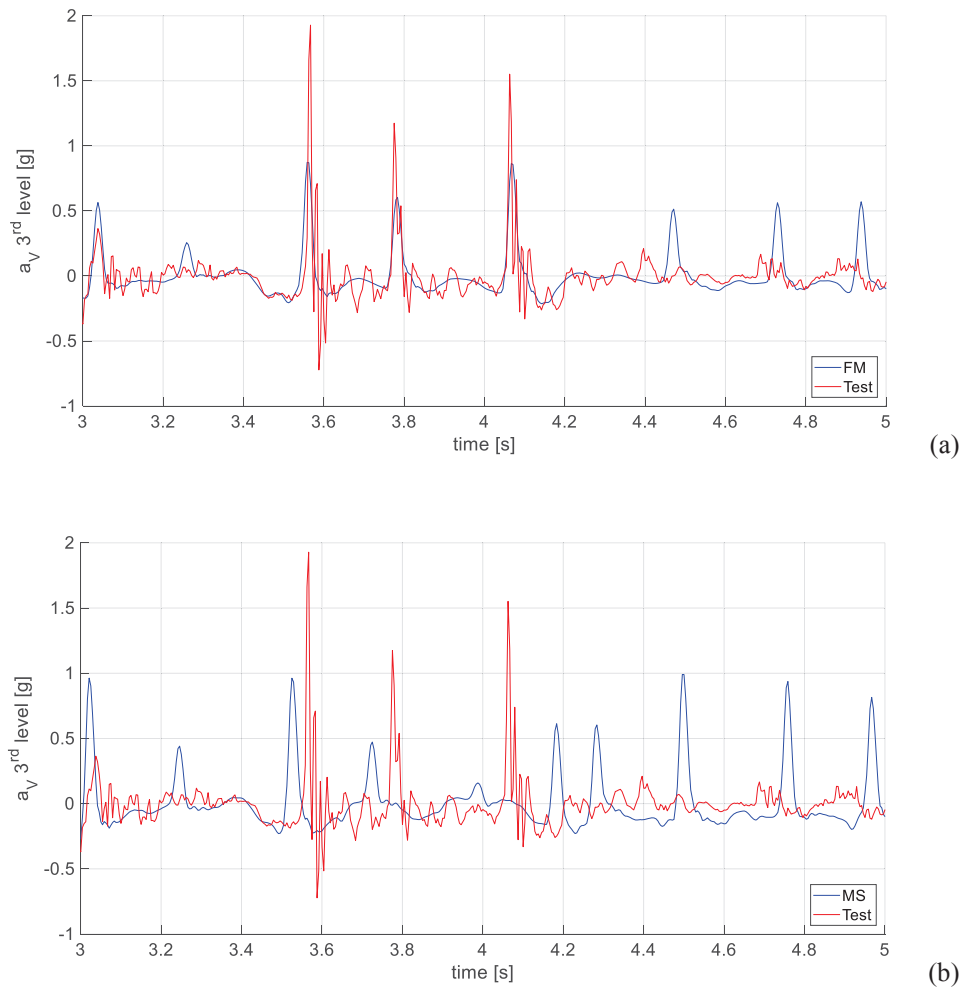


Figure 6: Vertical acceleration [g] for fiber elements (a) and multi-springs only-compression (b) model for the hybrid wall. Note: in red the experimental test and in blue the numerical results.

Overall, the results show how the considered planar models predict quite well the rocking wall behavior in terms of moment-rotation, although significant differences are present close to zero base rotation where horizontal acceleration spikes arise.

5 CONCLUSIONS

In the present paper, the finite element modeling of hybrid walls, i.e. rocking walls with additional energy dissipation, is considered to highlight differences between different modeling techniques: fiber beam elements (FM), lumped rotational spring (RS) and compression-only springs at the base (MS). The dynamic interaction between the wall and the building and the influence of the foundation was not considered. Mass proportional damping formulation is used with a damping coefficient equal to 0.01.

The RS model is the least suitable for capturing the rocking behavior, despite being the easiest to implement model. The sensitivity analysis shows that the main parameters affecting the results in terms of lateral displacements are the stiffness of the compression only springs, the elastic modulus of the concrete at the wall-to-foundation interface in the fiber model, the unbonded length of the mild steel rebars and the amount of damping.

After the sensitivity analysis, a reduced elastic modulus of concrete (0.6 of the elastic modulus of plain concrete) has been considered. The total unbonded length of the energy dissipators are equal to the unbonded length at the wall-to-foundation interface plus six times the value of the diameter of the rebars to account for strain penetration. For the definition of the stiffness of the springs, a value of half length of the wall has been considered.

Regarding nonlinear dynamic analyses, the models provide results qualitatively similar to the experimental test.

REFERENCES

- [1] M.J.N., Priestley, Overview of PRESSS research program. *PCI Journal*, **36**(4):50-57, 1991.
- [2] Y.C. Kurama, S. Pessiki, R. Sause, L.-W. Lu, Seismic behavior and design of unbonded posttensioned precast concrete walls. *PCI Journal*, **44**(3):72–89, 1999.
- [3] Y.C. Kurama, R. Sause, S. Pessiki, L.-W. Lu, Lateral load behavior and seismic design of unbonded posttensioned precast concrete walls.” *ACI Struct. J.*, **96**(4):622–632, 1999.
- [4] Y.C. Kurama, Seismic design of unbonded post-tensioned precast walls with supplemental viscous damping. *ACI Structural Journal*, **97**(4):648-658, 2000.
- [5] Y.C. Kurama, Seismic design of partially post-tensioned precast concrete walls. *PCI Journal*, **50**(4):100-125, 2005.
- [6] T. Holden, J.I. Restrepo, J.B. Mander, Seismic performance of precast reinforced and prestressed concrete walls. *J Struct Eng*, **129**(3):286-296, 2003.
- [7] D. Marriott, S. Pampanin, D. Bull, A. Palermo, Dynamic testing of precast, post-tensioned rocking wall systems with alternative dissipating solutions. *Bull N Z Soc Earthq Eng* 41(2):90-103, 2008.
- [8] W.C. Stone, G.S. Cheok, J.F. Stanton, Performance of hybrid moment-resisting precast beam–column concrete connection subjected to cyclic loading, *ACI Structural Journal*, **92**(2):229–249, 1995.
- [9] J.I. Restrepo, A. Rahman, Seismic performance of self-centering structural walls incorporating energy dissipators. *J Struct Eng*, **133**(11):1560-1570, 2007.
- [10] J.J. Ajrab, G. Pekcan, J.B. Mander, Rocking wall-frame structures with supplemental tendon systems, *Journal of Structural Engineering*, 2004.
- [11] L. Li, J.B. Mander, R.P. Dhakal, Bidirectional cyclic loading experiment on a 3D beam–column joint designed for damage avoidance, *Journal of Structural Engineering*, **134**(11):1733–1742, 2008.
- [12] G.W. Rodgers, K.M. Solberg, J.G. Chase, J.B. Mander, B.A. Bradley, R.P. Dhakal, L. Li, Performance of a damage-protected beam–column subassembly utilizing external HF2V energy dissipation devices, *Earthquake Engineering and Structural Dynamics*, **37**(13):1549–1564, 2008.
- [13] G.W. Rodgers, K.M. Solberg, J.B. Mander, J.G. Chase, B.A. Bradley, R.P. Dhakal, High-force-to-volume seismic dissipators embedded in a jointed precast concrete frame, *Journal of Structural Engineering*, **138**(3):375–386, 2010.

- [14] T. Koshikawa, Moment and energy dissipation capacities of post-tensioned precast concrete connections employing a friction device, *Engineering Structures*, **138**:170–180, 2017.
- [15] L.L. Song, T. Guo, Study on seismic performance of self-centering prestressed frames with web friction devices, *Engineering Mechanics*, **31**(12):47–55, 2014.
- [16] L.L. Song, T. Guo, Z.L. Cao, Seismic response of self-centering prestressed concrete moment resisting frames with web friction devices, *Soil Dynamics and Earthquake Engineering*, **71**:151–162, 2015.
- [17] A. Belleri, M. Torquati, P. Riva, Finite Element Modeling of “Rocking Walls”, M. Papadrakakis, N.D. Lagaros, V. Plevris eds. *4th ECCOMAS Thematic Conference on Computational Methods in Structural Dynamics and Earthquake Engineering*, Kos Island, Greece, 2013.
- [18] M.J.N. Priestley, J.R.T. Tao, Seismic response of precast prestressed concrete frames with partially debonded tendons, *PCI Journal*, **38**(1):58-69, 1993.
- [19] L.G. Cormack, The design and construction of the major bridges on the Mangaweka Rail deviation, *Transactions of the Institute of Professional Engineers of New Zealand*, **15**:6-23, 1998.
- [20] Q.T. Ma, M.H. Khan, Shake table tests of a stepping bridge model, *The 14th World Conference on Earthquake Engineering*, 2008.
- [21] Q.T. Ma, M.H. Khan, Free vibration tests of a scale model of the South Rangitikei railway bridge, *NZSEE Conference*, 2008.
- [22] M.J.N. Priestley, S. Sritharan, J.R. Conley, S. Pampanin, Preliminary results and conclusions from the PRESSS five-story precast concrete test building. *PCI J*, **44**(6):42-67, 1999.
- [23] A. Belleri, M.J. Schoettler, J.I. Restrepo, R.B. Fleischman, Dynamic Behavior of Rocking and Hybrid Cantilever Walls in a Precast Concrete Building, *ACI Structural Journal*, **111**(3):661-671, 2014.
- [24] M. Nazari, Seismic performance of unbonded post-tensioned precast wall systems subjected to shake table testing. *Ph.D. Thesis, Department of Civil, Construction and Environmental Engineering*, Iowa State University, Ames, Iowa, 2016.
- [25] S. Gavridou, J.W. Wallace, T. Nagae, T. Matsumori, K. Tahara, K. Fukuyama, Shake-table test of a full-scale 4-story precast concrete building. I: overview and experimental results, *J Struct Eng*, **143**(6), 2017.
- [26] K.M. Twigden, R.S. Henry, Shake table testing of unbonded post-tensioned concrete walls with and without additional energy dissipation. *Soil Dyn Earthq Eng*, 2018.
- [27] D. Kalliontzis, M. Nazari, Unbonded post-tensioned precast concrete walls with rocking connections: Modeling approaches and impact damping. *Frontiers in Built Environment*, 2021.
- [28] B. Erkmen, A.E. Schultz, Self-centering behavior of unbonded, post-tensioned precast concrete shear walls. *J Earthq Eng*, **13**(7):1047-1064, 2009.

- [29] V. Mpampatsikos, M.E. Bressanelli, A. Belleri, R. Nascimbene, A non-dimensional parametric approach for the design of PT tendons and mild steel dissipaters in precast rocking walls, *Engineering Structures*, 2020.
- [30] V. Mpampatsikos, DDBD of Rocking Walls with Mild Steel Dissipaters, *A Thesis Submitted in Partial Fulfilment of the Requirements for the Degree of Doctor of Philosophy in Earthquake Engineering*, 2009.
- [31] H. Wu, Y. Zhou, W. Liu, Collapse fragility analysis of self-centering precast concrete walls with different post-tensioning and energy dissipation designs, *Bulletin of Earthquake Engineering*, 2019.
- [32] M. Schoettler, A. Belleri, D. Zhang, J.I. Restrepo, R.B. Fleischman, Preliminary results of the shake-table testing for the development of a diaphragm seismic design Methodology, *PCI Journal*, 2009.
- [33] R.B. Fleischman, C. Naito, J. Restrepo, R. Sause, S. K. Ghosh, G. Wan, M. Schoettler, L. Cao, Precast Diaphragm Seismic Design Methodology (DSDM) Project, Part 2: Research Program. *PCI Journal*, **50**(6):14–31, 2005.
- [34] D. Kalliontzis, M. Nazari, Unbonded post-tensioned precast concrete walls with rocking connections: Modeling approaches and impact damping. *Frontiers in Built Environment*, 2021.
- [35] A. Belleri, B. Moaveni, J.I. Restrepo, Damage assessment through structural identification of a three-story large-scale precast concrete structure, *Earthquake Engineering Structural Dynamics*, **43**:61–76, 2014.
- [36] F. McKenna, G.L. Fenves, OpenSees Manual. *Pacific earthquake engineering research center*, 2013.
- [37] G. Guerrini, J.I. Restrepo, A. Vervelidis, M. Massari, Self-centering precast concrete dual-steel-shell columns for accelerated bridge construction: seismic performance, analysis. *Pacific Earthquake Engineering Research Center*, 2015.
- [38] M. Nazari, S. Sritharan, S. Aaleti, Single Precast Concrete Rocking Walls as Earthquake Force resisting elements. *Earthquake Engineering and Structural Dynamics*, **46**(5):753-759, 2007.
- [39] J.I. Restrepo, L.L. Dodd, R. Park, N. Cooke, Variables Affecting Cyclic Behavior of Reinforcing Steel. *Journal of Structural Engineering*, **3178**, 1994.
- [40] L. Wiebe, C. Christopoulos, Characterizing acceleration spikes due to stiffness changes in nonlinear systems, *Earthquake Engineering and Structural Dynamics*, **39**:1653-1670, 2010.

CYCLIC TEST OF A PRECAST BRIDGE COLUMN FOR SUSTAINABLE BRIDGE DESIGN

Natalia Reggiani Manzo¹, and Michalis F. Vassiliou¹

¹ ETH Zürich
Institute of Structural Engineering
Stefano-Franscini-Platz 5, 8093 Zürich, Switzerland
{reggianimanzo,vassiliou}@ibk.baug.ethz.ch

Abstract

In seismic regions, more often than never the dogma that bridge columns need to be firmly connected to the ground leads to huge pile foundations that require as much concrete as the superstructure. This is clearly a non-sustainable design method. To reduce the foundation design moment and possibly avoid the piles foundation, it has been proposed to let the bridge columns uplift and rock.

This paper presents quasi-static testing of a 1:5 scale precast restrained rocking bridge column exhibiting negative stiffness. The proposed system is resilient, able to achieve limited to no damage during design earthquakes. It allows prefabrication and quick on-site assembly, which reduces the on-site construction time and traffic impact.

As part of this experimental campaign, quasi-static cyclic tests were carried out on a reinforced concrete column allowed to rock on its interface with the foundation and cap-beam. An unbonded tendon was adopted to restrain the columns. The tendon was connected in series to a Belleville spring system to keep the overall post-uplift stiffness of the system negative. Large drifts lead to stress concentrations at the ends of the columns, therefore they were protected by steel jackets.

The column was subjected to drift ratios up to 15%. The results show that it returned to its original position with negligible to no residual displacement.

Keywords: rocking bridges, Accelerated Bridge Construction, sustainable seismic design, precast bridges

1 INTRODUCTION

Accelerated Bridge Construction (ABC) has emerged as a convenient method to reduce onsite construction time and traffic impact, as well as providing elements of higher quality due to its prefabrication offsite [1–23].

Within ABC two seismic design methods exist: (a) emulating connections of conventional reinforced concrete structures by creating fixed connections of the precast elements with cast in situ concrete or, (b) letting the precast elements rock by adopting dry connections combined with prestressed or posttensioned unbonded tendons passing through the columns. The advantage of the former method is that it results in bridges that behave like the traditional cast in place ones, this it is an established and easily acceptable technology. The advantage of the latter method is that it is more resilient as it presents minimal damage and residual displacement. Some of the techniques developed to emulate connections are: bar coupling [6, 7], pocket and socket connections [5, 10, 21, 23], and grouted duct connections [9, 22, 23].

As an alternative to emulated connections, rocking systems provide the additional advantage of reducing residual displacements and damage after the earthquake event ceases. Priestley and Tao [1] and Stone et al. [2] studied the behavior of precast posttensioned beam columns designed to rock in the connections. Mander and Cheng [13] developed the *Damage Avoidance Design* methodology for bridge piers, introducing the concept of precast posttensioned elements to bridge systems. Following on, Hewes and Priestley [17] and Billington and Yoon [18] also explored the adoption of posttensioned rocking elements to segmental columns.

To control design displacements, researchers proposed introducing energy dissipation devices to the system. Davis et al. [3], Finnson [4], Thonstad et al. [11] and Thonstad et al. [12] conducted an experimental campaign exploring the behavior of prestressed rocking piers with mild reinforcing bars connecting the foundation and column, and/or column and cap beam, which provided energy dissipation. With similar goal, Marriott et al. [20], Guerrini et al. [8], White and Palermo [24] and Mashal and Palermo [14] explored rocking piers equipped with external energy dissipaters.

Sideris et al. [25–27] also proposed a posttensioned segmental column with a rock-dominant connection at the bottom, and intermediate slip-dominant connections, which provided energy dissipation with low damage.

The works mentioned above led to the development of systems with small residual displacements and low damage after a ground motion excitation. Hence, they succeed in the goal of resilience. However, they result in foundation design moments that are on the same order with their plastic design counterparts. These design moments often require huge pile foundations which can comprise up to 50% of the total Reinforced Concrete used in the whole project. Aiming at decreasing the foundation design moments and obtaining a more sustainable system, it has been suggested either to not restrain the bridge columns at all [28–42] or to restrain them with flexible restraining systems [43–46]. In an effort to bring the concept of negative stiffness closer to practice, this paper presents quasi-static cyclic tests of a restrained RC concrete column exhibiting negative post-uplift stiffness. The column is allowed to rock freely on its interface with the foundation, while the cap beam and column are connected through a non-prestressed tendon in series with disc springs.

2 BEHAVIOR OF NEGATIVE STIFFNESS BILINEAR ELASTIC SYSTEMS

Rocking systems of negative stiffness present the Negative Stiffness Bilinear Elastic (NSBE) force deformation loop shown in Fig. 1, and discussed extensively in [30]. Up until uplift the system behaves linearly with a stiffness representing any deformability the system

might present before uplifting. After uplifting, the tangent stiffness becomes negative. The displacement capacity is defined not by material failure, but by the displacement where the restoring force becomes negative. Therefore, for an unrestrained rocking column the displacement capacity is equal to its width. One can increase it by equipping the column with extended curved ends [47–49] or by adopting a flexible restraining system. Herein, a flexible restraining system was adopted for the proposed column.

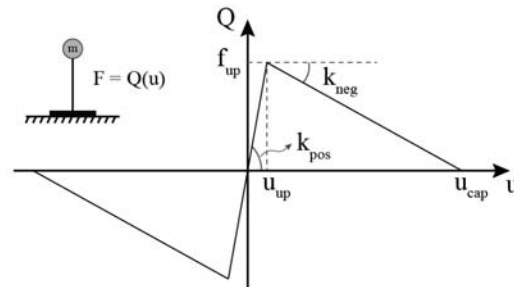


Figure 1: Characteristic Pushover Curve of a NSBE Oscillator (figure from [30])

3 SPECIMEN DESIGN

In the tests discussed in this paper, the restraining system of the column was designed to double the displacement capacity of the free rocking column, assuming that u_{up} is negligible. The system was composed of an unbonded tendon in series with disc (“Belleville”) springs (Fig. 2). The disc springs were adopted to avoid yielding of the tendon in large displacements.

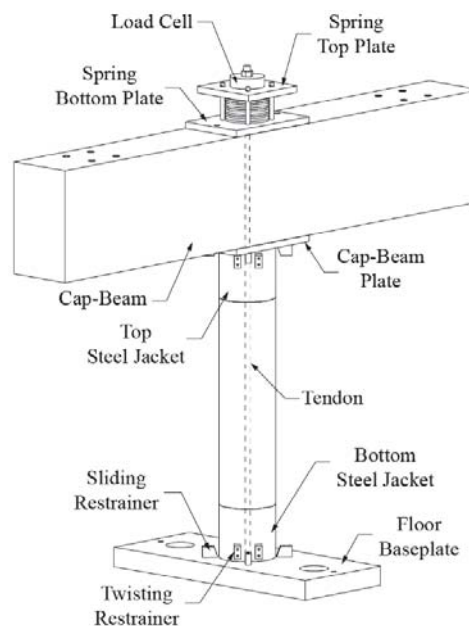


Figure 2: Specimen

The ungrouted tendon passed through the centerline of the column. One end was anchored in the bottom of the column, providing no connection between the foundation and the column. The other end was anchored above the beam, in series with the disc springs. No prestress loading was applied to the restraining system.

The columns were protected by steel jackets at their ends. The jackets comprised a steel tube welded to a circular end plate. Steel jackets were also used by [11, 14]. However, in the tests discussed in this work, the stresses are expected to be smaller because of the springs.

Steel plates were also fixed to the floor and to the cap beam to avoid damage due to stress concentrations. The plates were equipped with sliding restrainers, which limited the sliding motion of the column. A restrainer was also provided to avoid twisting of the columns. Fig. 2 presents the tested system, in which the elements discussed in this section are identified.

The geometry of the column is shown in Fig. 3-4 and follows from scaling to 1:5 a typical overpass bridge column.

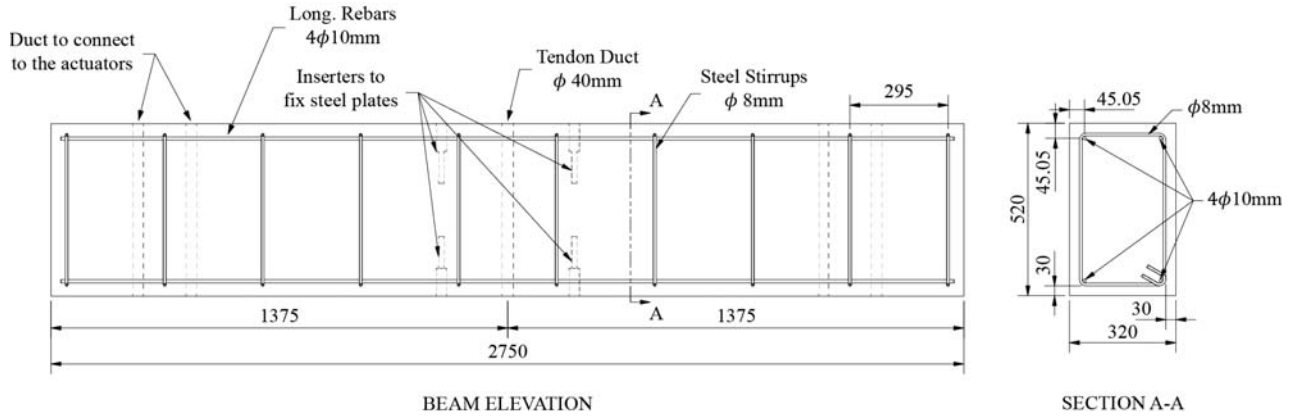


Figure 3: Cap-beam elevation and cross-section (dimensions in mm)

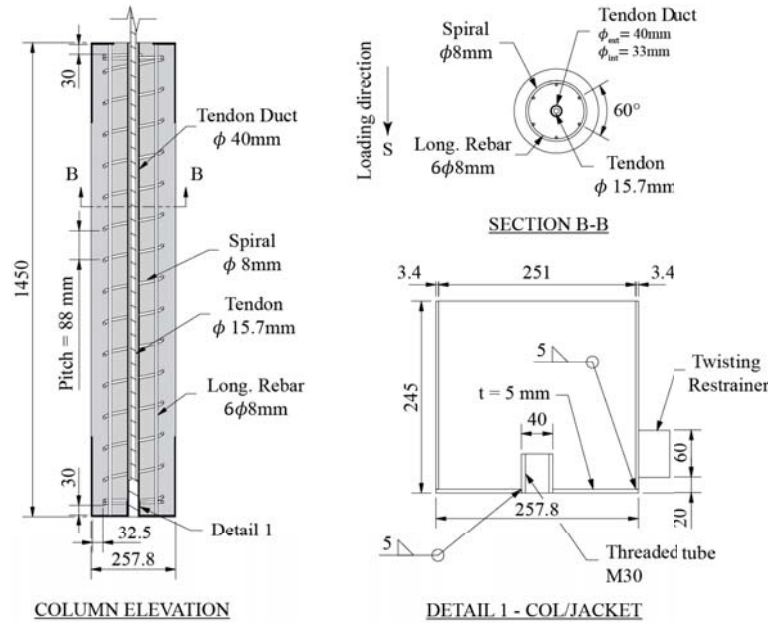


Figure 4: Column elevation and critical cross-sections (dimensions in mm)

3.1 Restraining System

The stiffness of the restraining system (k_{res}) was obtained based on the force deformation curve discussed in [30], under the assumption that the pre uplift deformation is negligible. For small rotations, one can linearize and get the desired stiffness of the restraining system as:

$$k_{res} = \frac{4V}{ab} \cdot \frac{(\lambda - 1)}{\lambda} \quad (1)$$

where V is the total vertical loading acting on the column plus half of its self-weight, α is the slenderness angle of the column (i.e. width to height ratio), $b=257.8$ mm is the diameter of the

column, and λ is the factor by which the displacement capacity of a free rocking column with equivalent slenderness should be increased (i.e. $\lambda = u_{cap}/b$).

The tests were performed under a vertical load $V=52.2$ kN that would correspond to a normalized axial load (ν) of 5% in the columns, which is typical for bridge columns. Then, Eq. (1) gives the target stiffness of the restraining system that would result in doubling the displacement capacity of the column ($\lambda = 2$): $k_{res}=2302$ kN/m. The restraining system was composed of a tendon with nominal cross-section area of 150 mm^2 in series with 11 disc springs of individual deformation capacity of 5.6 mm (Fig. 2). This design gives an overall stiffness of the restraining system of 2613 kN/m until 44 mm axial displacement.

The tendon had threaded sockets at its ends. Therefore, it was anchored in the bottom end of the column, as Detail 1 of Fig. 4 shows. The other end was anchored at the top of the springs with a nut. The tendon was unbonded through its entire length.

3.2 Steel Reinforcement

The column reinforcement was designed to resist the internal moment generated when the column rotates to a displacement equal to $2b=515.6$ mm. It resulted in a longitudinal reinforcement composed of 6 B500B rebars of 8 mm-diameter ($A_s = 3.02 \text{ cm}^2$) distributed uniformly along the circular perimeter of the column. The longitudinal reinforcement was welded on the steel plate at the column ends.

The transverse reinforcement comprised an 8 mm-diameter B500B spiral, which is the minimum according to Eurocode 2 [50] ($A_{sw}/s = 0.022 \text{ cm}^2/\text{cm}$).

3.3 Column steel parts

The steel jackets consisted of a S355 steel tube 3.4 mm-thick, 245 mm-high and 257.8 mm in external diameter. The steel tube was welded in its base to a S355 steel plate 5 mm-thick. The detailing of the steel plate is different in the bottom and top part of the column. In the steel plate placed at the bottom of the column, a threaded steel tube was welded to it for anchoring the tendon. In the top part, a circular annular plate was used to allow casting of the column.

3.4 Slide and twist restrainers

To limit sliding, the steel plates fixed to the ground and to the cap-beam were equipped with sliding restrainers that limited sliding to 5 mm in each direction (Fig. 5).

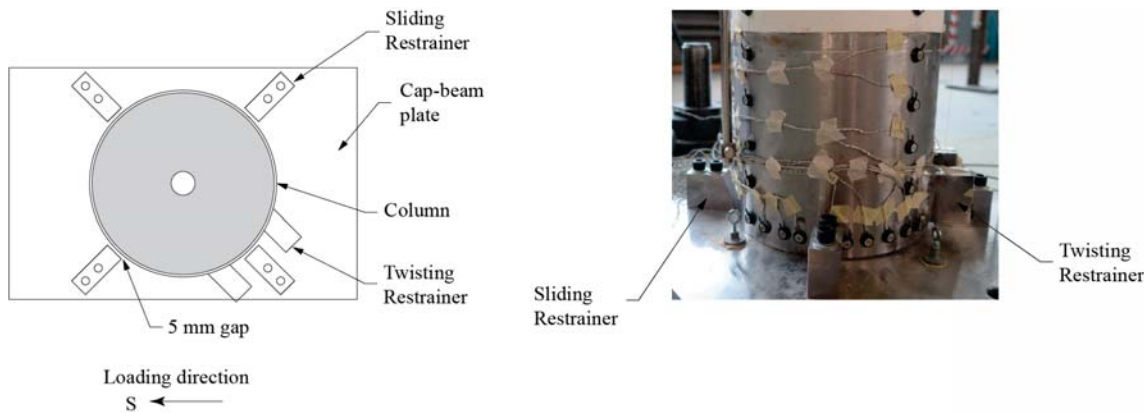


Figure 5: Schematic illustration of the motion restrainers

3.5 Concrete mix

The columns were casted in-house using a commercial dry mixture of self-compacting concrete of strength class C30/37 ($f_{ck} = 30$ MPa). Although the water/cement ratio suggested in the pack of the dry mixture was initially respected, the concrete workability was not the one expected, and more water had to be added to the mixture.

Three standard cylindrical specimens of 150mm-diameter and 300mm-high were casted to define the strength and Young's modulus of the concrete. The measured mean strength and Young's modulus of the specimen were 45.4 MPa and 30 GPa, respectively.

4 TEST SETUP AND INSTRUMENTATION

The test setup is shown in Fig. 6a. It consisted of two vertical actuators and a horizontal actuator. The three actuators applied forces or displacements to a steel beam, which was connected to the cap-beam with short wide flange steel beams. The steel beam is constrained, and out-of-plane displacement is not allowed.

The setup kept the vertical force applied to the column constant and equal to 52.20 kN, simulating the gravitational loads of the super-structure. The rotation of the cap and steel beam was kept constant and equal to zero. For the cyclic test, the horizontal actuator applied the displacements defined in the loading protocol shown in Fig. 6b. The loading protocol consisted of two consecutive cycles of same drift ratio, followed by a subsequent cycle of 1.25 times the previous drift ratio. In total, the columns were subjected to 18 sets of two cycles each. The loading protocol was based on the American Concrete Institute recommendations. Since the most recent report [51] specifies that the drift ratio must be increased based on the yield strain, the increase of the drift ratios was based on an older report [52].

The displacement of the column and cap-beam were measured by an optical measurement device that tracks the positions of markers fixed in the specimen. The forces and strokes of all actuators were recorded by load cells and lasers installed on them. A load cell was also installed in series with the springs and tendon, recording the forces in the restraining system. Rosettes measured the strain in the steel jacket.

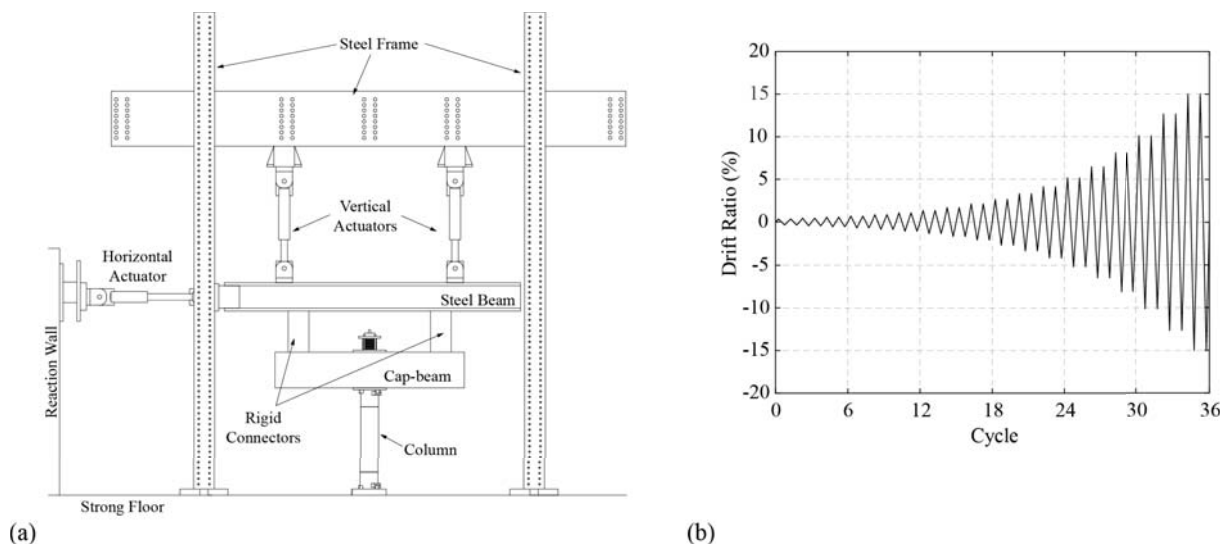


Figure 6: (a) Test setup, and (b) Cyclic time history.

5 FORCE-DRIFT LOOPS

Fig. 7 presents the force-drift response for low drift ratios (up to 1.1%), medium drift ratios (up to 4.2%), and high drift ratios (up to 15%). The drift ratio is defined herein as the ratio between the horizontal displacement of the beam and the height of the column (1450 mm).

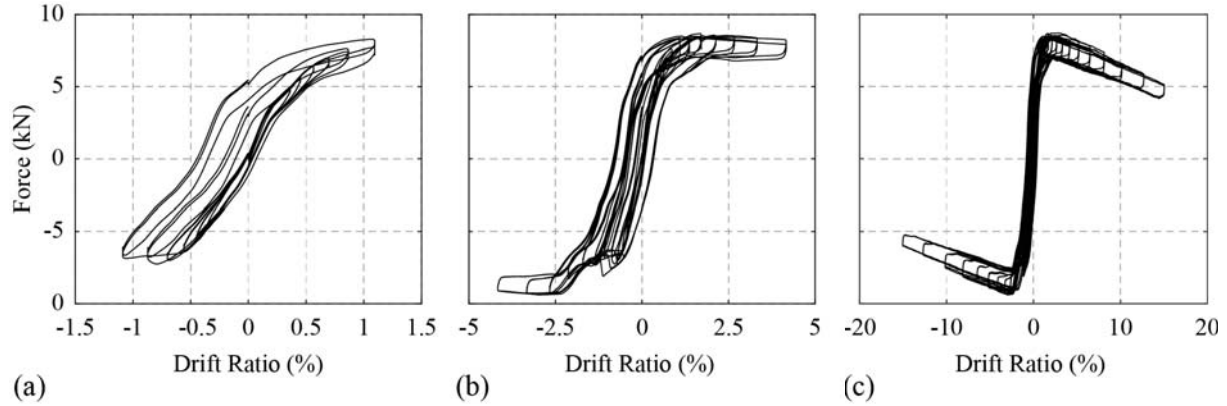


Figure 7. Force-drift relation for: (a) low drift ratio, (b) medium drift ratio, and (c) high drift ratio

One can observe that the column presents almost no strength reduction. It is not clear whether the energy dissipation deduced from the area of the loops comes from the column itself or from friction of the set up. More tests are currently performed to quantify the friction of the spring and of the setup itself. In any case, there was only minimal damage in the columns, so it is difficult to imagine a physically plausible way of energy dissipation within the column.

Sliding and twisting of the specimen were limited, but not zero. Both motions could be observed and measured with the optical position trackers fixed in several points of the column and cap-beam. Twisting was negligible. Sliding, however, was observed and it is also depicted in the force-drift relations (Fig.7a-b).

Fig. 8 shows the envelope of the force-drift response. As the protocol defined two cycles per drift amplitude, the envelope for both cycles is plotted. The same plot shows the envelope predicted by rigid body calculations, assuming a rigid column with same dimensions of the tested column (257.8 mm-diameter and 1450 mm-height), constant vertical load of 52.20 kN and restraining system stiffness of 2613 kN/m. The flexibility of the tested system only causes a slight deviation from the rigid body model that is non-negligible only for very small drift ratios, essentially before the column uplifts.

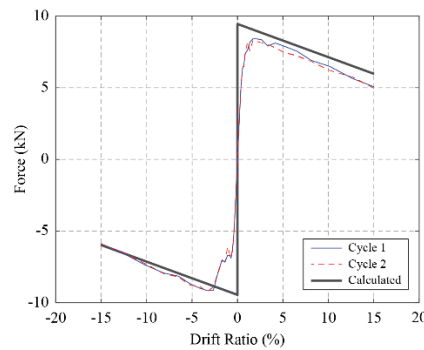


Figure 8: Force-drift envelope

6 OBSERVED DAMAGE

At the end of the test, almost no damage could be noticed at the column (Fig. 9c-d). No cracks or spalling of the column was observed. The top steel jacket, however, presented some minimal damage. The steel plate slightly bent (Fig. 9a) and the steel tube presented a dent (Fig. 9b), as a result of local buckling. Both damages occurred close to the end of the very end of the column, at drift of 12.7%. The bottom steel jacket did not present any damage visually observed, as the contact force there is smaller.

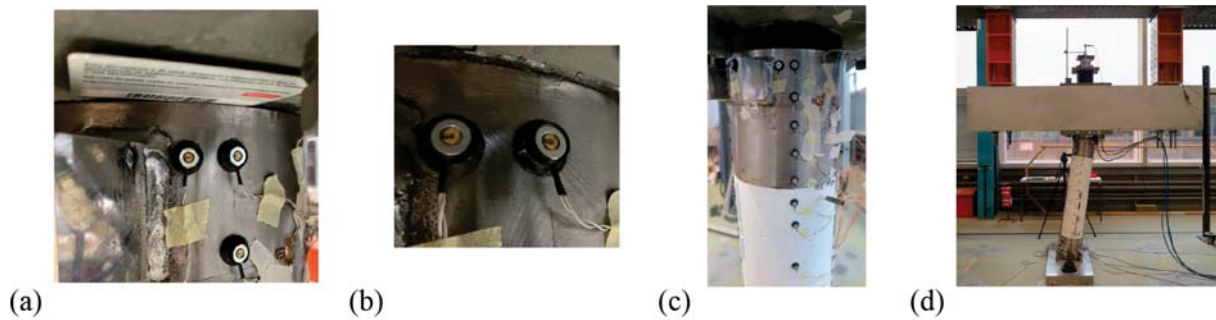


Figure 9: (a) Bending of the steel plate, and (b) dent of the steel tube of the steel jacket at the end of test; (c) column, and (d) overall view of the system at 15% drift ratio.

7 CONCLUSIONS

Negative stiffness restrained rocking columns can be used in bridge design in an effort to reduce the design moment of the foundation and possibly save the piles. Such a system using disc springs in series with a steel tendon as a restraining system was tested to drift ratios up to 15%. Negligible visual damage was observed. Since the force deformation loops did not change during the tests, no strength degradation was observed. Thus the system is resilient.

As the aim of the proposed design approach is to reduce the design moment of the foundation and avoid the huge pile foundations that are often designed in seismic areas, the system contributes to sustainable seismic design.

8 ACKNOWLEDGEMENT

This work was supported by the ETH Zurich under grant ETH-10 18-1.

REFERENCES

- [1] M. J. N. Priestley and J. R. Tao, Seismic Response of Precast Prestressed Concrete Frames With Partially Debonded Tendons. *PCI J.*, **38** (1), 58–69, 1993.
- [2] W. C. Stone, S. Geraldine, and J. F. Stanton, Beam-Column Concrete Connections Subjected to Cyclic Loading. *ACI Struct. J.*, **92** (2), 229–249, 1995.
- [3] P. M. Davis, T. M. Janes, M. O. Eberhard, and J. F. Stanton, Unbonded pre-tensioned columns for bridges in seismic regions, *Rep. No. 2012/04*, Pacific Earthquake Engineering Research Center, Berkeley, CA, 2012.
- [4] G. Finnson, Unbonded Pre-Tensioned Bridge Columns with Hybrid Fiber-Reinforced Concrete Shells. University of Washington, 2013.
- [5] O. S. Haraldsson, T. M. Janes, M. O. Eberhard, and J. F. Stanton, Seismic Resistance of Socket Connection between Footing and Precast Column. *J. Bridg. Eng.*, **18** (9), 910–919, 2013.
- [6] Z. B. Haber, M. S. Saiidi, and D. H. Sanders, Seismic performance of precast columns with mechanically spliced column-footing connections. *ACI Struct. J.*, **111** (3), 639–650, 2014.
- [7] M. J. Ameli, J. E. Parks, D. N. Brown, and C. P. Pantelides, Seismic evaluation of grouted splice sleeve connections for reinforced precast concrete column-to-cap beam joints in accelerated bridge construction. *PCI J.*, **60** (2), 80–103, 2015.
- [8] G. Guerrini, J. I. Restrepo, M. Massari, and A. Vervelidis, Seismic Behavior of Posttensioned Self-Centering Precast Concrete Dual-Shell Steel Columns. *J. Struct. Eng.*, **141** (4), 04014115, 2015.
- [9] M. Tazarv and M. S. Saiidi, UHPC-filled duct connections for accelerated bridge construction of RC columns in high seismic zones. *Eng. Struct.*, **99**, 413–422, 2015.
- [10] H. Tran, “Drilled Shaft Socket Connections for Precast Columns in Seismic Regions,” University of Washington, 2015.
- [11] T. Thonstad, I. M. Mantawy, J. F. Stanton, M. O. Eberhard, and D. H. Sanders, Shaking Table Performance of a New Bridge System with Pretensioned Rocking Columns. *J. Bridg. Eng.*, **21** (4), 04015079, 2016.
- [12] T. Thonstad, B. J. Kennedy, J. A. Schaefer, M. O. Eberhard, and J. F. Stanton, Cyclic Tests of Precast Pretensioned Rocking Bridge-Column Subassemblies. *J. Struct. Eng.*, **143** (9), 04017094, 2017.
- [13] J. B. Mander and C. T. Cheng, Seismic Resistance of Bridge Piers Based on Damage Avoidance Design. *Rep. No. NCEER-97-0014*, National Center for Earthquake Engineering and Research, Buffalo, NY, 1997.
- [14] M. Mashal and A. Palermo, Low-Damage Seismic Design for Accelerated Bridge Construction. *J. Bridg. Eng.*, **24** (7), 04019066, 2019.
- [15] J. Jia, K. Zhang, M. S. Saiidi, Y. Guo, S. Wu, K. Bi, X. Du, Seismic evaluation of precast bridge columns with built-in elastomeric pads. *Soil Dyn. Earthq. Eng.*, **128**, 105868, 2020.
- [16] R. Liu and A. Palermo, Ten Years of Experiments on Bridges Using Resilient Damage-Resistant Systems and Accelerated Construction Techniques. *Struct. Eng. Int.*, **30** (2),

224–231, 2020.

- [17] J. T. Hewes and M. J. N. Priestley, Seismic design and performance of precast concrete segmental bridge columns. *Rep. No. SSRP-2001/25*, California Department of Transportation, Sacramento, California, 2002.
- [18] S. L. Billington and J. K. Yoon, Cyclic Response of Unbonded Posttensioned Precast Columns with Ductile Fiber-Reinforced Concrete. *J. Bridg. Eng.*, **9** (4), 353–363, 2004.
- [19] A. Palermo, S. Pampanin, and D. Marriott, Design, Modeling, and Experimental Response of Seismic Resistant Bridge Piers with Posttensioned Dissipating Connections. *J. Struct. Eng.*, 133 (11), 1648–1661, 2007.
- [20] D. Marriott, S. Pampanin, and A. Palermo, Quasi-static and pseudo-dynamic testing of unbonded post-tensioned rocking bridge piers with external replaceable dissipaters. *Earthq. Eng. Struct. Dyn.*, **38**, 331–354, 2009.
- [21] E. E. Matsumoto, M. C. Waggoner, M. E. Kreger, J. Vogel, and L. Wolf, Development of a precast concrete bent-cap system. *PCI J.*, **53** (3), 74–99, 2008.
- [22] J. B. K. Pang, M. O. Eberhard, and J. F. Stanton, Large-Bar Connection for Precast Bridge Bents in Seismic Regions. *J. Bridg. Eng.*, **15** (3), 231–239, 2010.
- [23] J. I. Restrepo, E. E. Matsumoto, and M. J. Tobolski, Development of a Precast Bent Cap System for Seismic Regions, *NCHRP Rep. No. 681*, Transportation Research Board, Washington, DC, 2011.
- [24] S. White and A. Palermo, Quasi-Static Testing of Posttensioned Nonemulative Column-Footing Connections for Bridge Piers. *J. Bridg. Eng.*, **21** (6), 04016025, 2016.
- [25] P. Sideris, A. J. Aref, and A. Filiatrault, Quasi-Static Cyclic Testing of a Large-Scale Hybrid Sliding-Rocking Segmental Column with Slip-Dominant Joints. *J. Bridg. Eng.*, **19** (10), 04014036, 2014.
- [26] P. Sideris, A. J. Aref, and A. Filiatrault, Large-Scale Seismic Testing of a Hybrid Sliding-Rocking Posttensioned Segmental Bridge System. *J. Struct. Eng.*, **140** (6), 04014025, 2014.
- [27] P. Sideris, A. J. Aref, and A. Filiatrault, Experimental Seismic Performance of a Hybrid Sliding–Rocking Bridge for Various Specimen Configurations and Seismic Loading Conditions. *J. Bridg. Eng.*, **20** (11), 04015009, 2015.
- [28] N. Makris and M. Vassiliou, Planar rocking response and stability analysis of an array of free-standing columns capped with a freely supported rigid beam. *Earthq. Eng. Struct. Dyn.*, **42**, 431–449, 2012.
- [29] N. Makris and M. F. Vassiliou, Are Some Top-Heavy Structures More Stable?. *J. Struct. Eng.*, **140** (5), 06014001, 2014.
- [30] N. Reggiani Manzo and M. F. Vassiliou, Simplified analysis of bilinear elastic systems exhibiting negative stiffness behavior. *Earthq. Eng. Struct. Dyn.*, **50** (2), 580–600, 2021.
- [31] Y. Xie, J. Zhang, R. DesRoches, and J. E. Padgett, Seismic fragilities of single-column highway bridges with rocking column-footing. *Earthq. Eng. Struct. Dyn.*, **48** (7), 843–864, 2019.
- [32] A. I. Giouvanidis and Y. Dong, Seismic loss and resilience assessment of single-

- column rocking bridges- *Bull. Earthq. Eng.*, **18** (9), 4481–4513, 2020.
- [33] M. Sieber, S. Klar, M. F. Vassiliou, and I. Anastasopoulos, Robustness of simplified analysis methods for rocking structures on compliant soil. *Earthq. Eng. Struct. Dyn.*, **49** (14), 1388–1405, 2020.
- [34] I. M. Thomaidis, A. J. Kappos, and A. Camara, Dynamics and seismic performance of rocking bridges accounting for the abutment-backfill contribution. *Earthq. Eng. Struct. Dyn.*, **49** (12), 1161–1179, 2020.
- [35] E. G. Dimitrakopoulos and A. I. Giouvanidis, Seismic Response Analysis of the Planar Rocking Frame. *J. Eng. Mech.*, 141 (7), 04015003, 2015.
- [36] A. I. Giouvanidis, Non-smooth seismic response analysis of the rocking frame. The Hong Kong University, 2015.
- [37] A. Agalianos, A. Psychari, M. F. Vassiliou, B. Stojadinovic, and I. Anastasopoulos, Comparative assessment of two rocking isolation techniques for a motorway overpass bridge. *Front. Built Environ.*, **3**, 1–19, 2017.
- [38] M. F. Vassiliou, K. R. Mackie, and B. Stojadinovic, A finite element model for seismic response analysis of deformable rocking frames. *Earthq. Eng. Struct. Dyn.*, **46** (3), 447–466, 2016.
- [39] M. F. Vassiliou, S. Burger, M. Egger, J. A. Bachmann, M. Broccardo, and B. Stojadinovic, The three-dimensional behavior of inverted pendulum cylindrical structures during earthquakes. *Earthq. Eng. Struct. Dyn.*, **46** (14), 2261–2280, 2017.
- [40] M. F. Vassiliou, M. Broccardo, C. Cengiz, M. Dietz, L. Dihoru, S. Gunay, K. M. Mosalam, G. Mylonakis, A. Sextos, B. Stojadinovic, Shake table testing of a rocking podium: Results of a blind prediction contest. *Earthq. Eng. Struct. Dyn.*, **50** (4), 1043–1062, 2021.
- [41] M. F. Vassiliou, Seismic response of a wobbling 3D frame. *Earthq. Eng. Struct. Dyn.*, **47** (5), 1212–1228, 2018.
- [42] N. Reggiani Manzo and M. F. Vassiliou, Displacement-based analysis and design of rocking structures. *Earthq. Eng. Struct. Dyn.*, **48** (14), 1613–1629, 2019.
- [43] N. Makris and M. F. Vassiliou, Dynamics of the Rocking Frame with Vertical Restrainers. *J. Struct. Eng.*, **141** (10), 04014245, 2015.
- [44] M. F. Vassiliou and N. Makris, Dynamics of the Vertically Restrained Rocking Column. *J. Eng. Mech.*, **141** (12), 04015049, 2015.
- [45] R. Thiers-Moggia and C. Málaga-Chuquitaype, Seismic protection of rocking structures with inerters. *Earthq. Eng. Struct. Dyn.*, **48** (5), 528–547, 2019.
- [46] Y. L. Zhou, Q. Han, X. L. Du, J. Q. Zhang, S. S. Cheng, and J. Y. Chen, Additional viscous dampers for double-column rocking bridge system: Seismic response and overturning analysis. *Soil Dyn. Earthq. Eng.*, **141**, 106504, 2021.
- [47] S. Polyakov, *Design of Earthquake Resistant Structures*. Mir. Publishers., 1974.
- [48] J. A. Bachmann, M. F. Vassiliou, and B. Stojadinovic, Dynamics of rocking podium structures. *Earthq. Eng. Struct. Dyn.*, **46** (14), 2499–2517, 2017.
- [49] J. A. Bachmann, M. F. Vassiliou, and B. Stojadinovic, “Rolling and rocking of rigid uplifting structures,” *Earthq. Eng. Struct. Dyn.*, **48** (14), 1556–1574, 2019.

- [50] CEN, Eurocode 2: Design of concrete structures - Part 1-1: General rules and rules for buildings. *Comité Européen de Normalisation*, Brussels, Belgium, 2004.
- [51] ACI, Guide for Testing Reinforced Concrete Structural Elements under Slowly Applied Simulated Seismic Loads. Farmington Hills, MI, 2013.
- [52] ACI, Acceptance criteria for moment frames based on structural testing. Farmington Hills, MI, 2001.

STUDY OF THE INFLUENCE OF SEISMIC ACTION ON THE CONSTRUCTION COST OF THE LOAD-BEARING STRUCTURE OF A TEN-STOREY R/C BUILDING

Panagiotis A. Sioulas¹, Theodoros A. Chrysanidis¹, Nikolaos O. Alamanis², Grigorios P. Papageorgiou³

¹ Hellenic Open University
Parodos Aristotelous 18, P.C. 26335, Patra, Greece
pan.sioulas@yahoo.gr, theodoros_gr@yahoo.com

² University of Thessaly
P.C. 41110, Larissa, Greece
alam@teilar.gr

³ University of Thessaly
V. Griva 11, P.C. 41300, Karditsa, Greece
gpapageor@uth.gr

Abstract

Greece is divided into three seismic hazard zones ZI, ZII, ZIII. In the present research work, the same building in the three seismic zones of Greece is modeled, analysed and dimensioned and then the construction cost of its structural body is estimated. The building modeling was performed in SAP2000 using linear finite elements. The analysis of the building was performed by dynamic spectral analysis methods using the design spectrum of EC8. A ten-storey building with a standard floor plan per floor was used. The purpose of this research paper is through comparative analytical estimation of construction costs to demonstrate whether the cost of construction of the bearing structure of a reinforced concrete building is affected by the area seismic hazard, if this influence is significant and to what extent. Useful conclusions are drawn regarding the influence of seismicity on the construction cost of the load-bearing structure of reinforced concrete buildings.

Keywords: Seismicity, Cost, Reinforced Concrete, Seismic Hazard.

1 INTRODUCTION

One matter that has troubled consultant engineers worldwide is the correct design and detailing of a reinforced concrete (R/C) building [1]–[16]. However, another matter that has troubled engineers is the economical design of a R/C building, as far as the construction cost of the load-bearing structure is concerned. Several studies worldwide have taken place on this matter in order to find the most economical way of designing and detailing the load-bearing structure of structures, whether these structures are buildings [17]–[19], bridges [20]–[24] or other types of structures [25], [26].

2 DESCRIPTION OF BUILDING

The reinforced concrete structure that is simulated and dimensioned in the three seismic zones is a symmetrical ten-storey building, without a basement. The floor plan of the building is 25 m x 25 m, so its area is $E = 625.00 \text{ m}^2$, and is the same for each floor (Figure 1). The height of the ground floor is 4.5 m and the rest of the floors 3 m. In the center of each floor, there is a strong core and two ductile walls around the center of the Y direction.

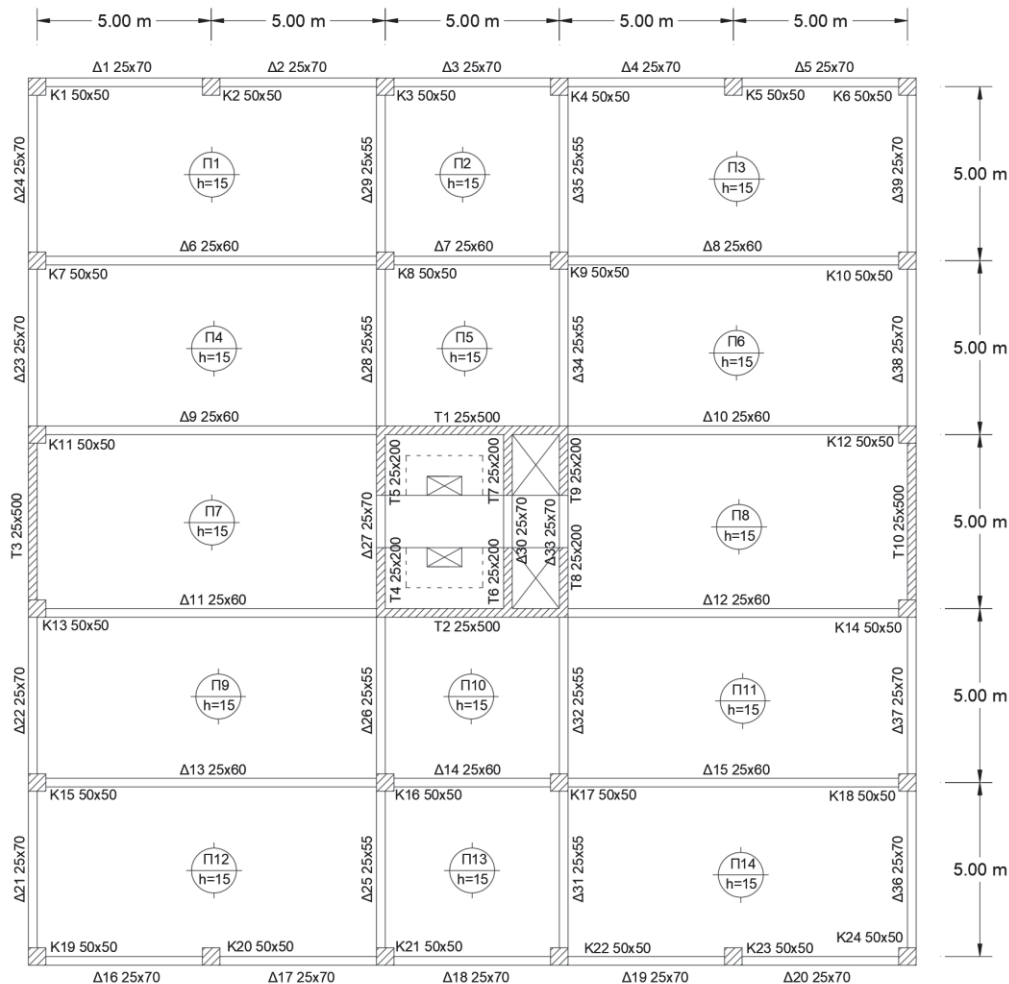


Figure 1: Floor plan.

The dimensions of the beams' cross sections of the building do not change per floor. The perimeter beams have dimensions 25 cm x 70 cm and the inner ones 25 cm x 60 cm in the X direction and 25 cm x 55 cm in the Y direction, apart from the core where they are also 25 cm x 70 cm. The cross section of the columns varies in height; for the first two floors is 75 cm x 75 cm and then decreases by 5 cm per floor. The thickness of the ductile wall sections varies with height and changes every five floors. On the first five floors, it is 37.5 cm and for the last five it is 25 cm. Enlarged boundary elements are used at both ends of the ductile walls T3 and T10 to avoid lateral buckling of structural walls under extreme seismic actions [27]–[34]. The thickness of the slabs is 15 cm.

3 MODEL DESCRIPTION

The modeling of the load-bearing structure is performed with the program SAP 2000. The ductile walls are modeled through the equivalent frame method (Figure 2). A vertical element is used, equivalent to a column, in the center of the wall, which is connected to the other structural elements with horizontal elements; rigid bodies at the level of the floors, with special properties. These bodies have increased values of their characteristics so that they appear as rigid in relation to the neighboring elements. The nodes at the base of the structure have rigid supports so that the superstructure is not affected by the foundation structure [35], [36].

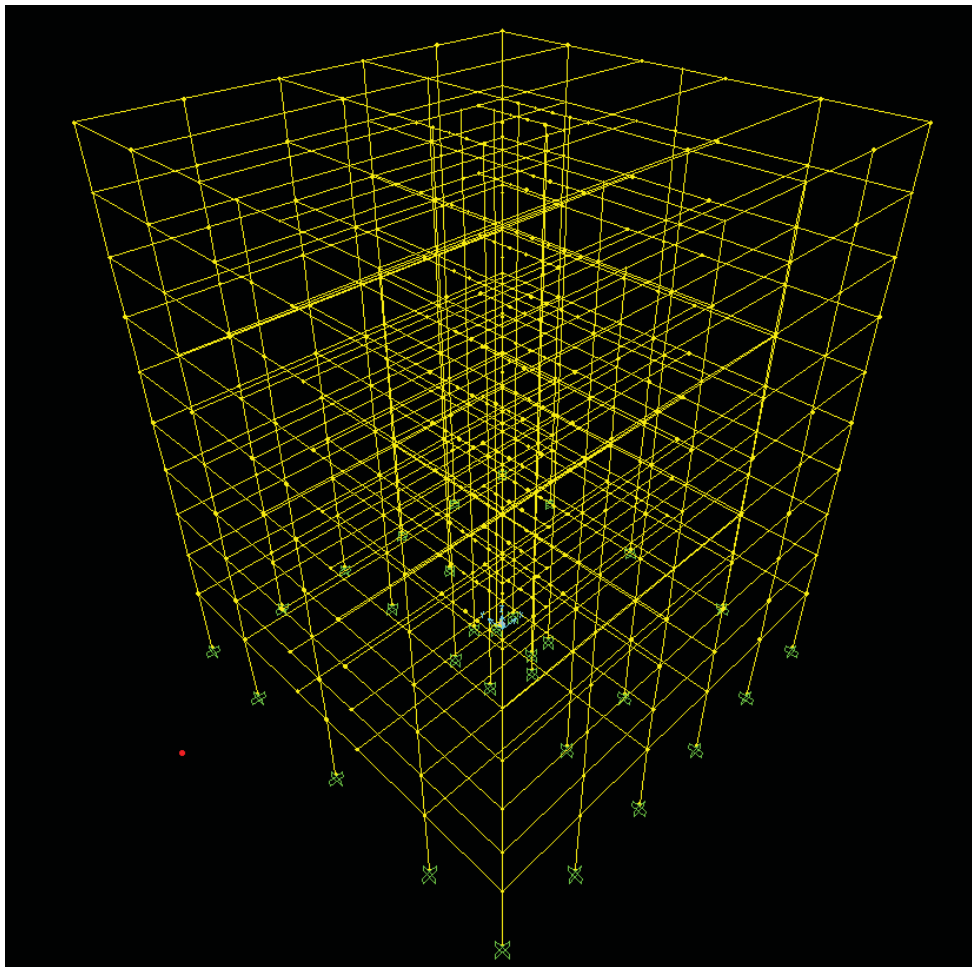


Figure 2: 3D building simulation.

The construction materials of the load-bearing structure have the following characteristics:

- Concrete quality C30/37
- Steel quality B500C

The modulus of elasticity of concrete is 33 GPa, according to Eurocode 2 [37]. The value of the Poisson ratio is set equal to 0, according to the specifications of Eurocode 2 [37], for cracked sections of reinforced concrete. The beams are modeled as linear finite elements in space, placed on the centroid axis of the structural element. As the diaphragm action of the slabs is ensured, the beams are considered as T or L beams. The columns are modeled as linear finite elements in space, placed on the centroid axis of the structural element, like the beams.

4 DIMENSIONING

4.1 Slabs

All slabs are quadrilateral and are reinforced in both directions and the calculation was done with Czerny tables. The maximum torque at middle of the slabs is $M = 15.80 \text{ kNm}$. Therefore, reinforcement $\emptyset 10/190$ ($A_s = 4,13 \text{ cm}^2$) is placed in the openings of the slabs. The supports that require additional reinforcement are $\Pi 1-\Pi 4$, $\Pi 3-\Pi 6$, $\Pi 9-\Pi 12$, $\Pi 11-\Pi 14$, as well as the core support and so additional reinforcement $\emptyset 10/250$ is placed.

4.2 Beams

The detailing of the beams has been performed in the openings and the supports for the most unfavorable combination and according to the minimum requirements of Eurocodes 2 and 8 [37], [38].

4.3 Columns

Detailing against biaxial bending with axial force is performed according to Eurocode 2 [37]. Similar to the beams, the most unfavorable combinations, the minimum requirements of Eurocodes 2 and 8 [37], [38] and the capacity design were used (Table 1).

ZONE II				
Column	vd	$\mu 1$	$\mu 2$	Reinforcement
K1, K6, K19, 24	-0.07570	0.01544	0.00564	12 \emptyset 25
K2, K5, K20, K23	-0.12780	0.01795	0.00360	12 \emptyset 25
K3, K4, K21, K22	-0.17002	0.01773	0.00281	12 \emptyset 25
K8, K9, K16, K17	-0.16832	0.01783	0.00273	12 \emptyset 25
K7, K10, K15, K18	-0.12499	0.01787	0.00341	12 \emptyset 25

Table 1: Longitudinal reinforcement of ground floor columns of Zone II

4.3 Structural walls

The detailing of the ductile walls has been performed according to the provisions of Eurocodes 2 and 8 (Table 2) [37], [38].

ZONE III				
Structural Walls	vd	μ_x	μ_y	Reinforcement
T1, T2	0.0690	0.1200	0.0043	12 Φ 32
T3, T10	-0.1380	0.1750	0.0160	12 Φ 32
T4, T5	0.2420	0.0805	0.0052	8 Φ 25
T6, T7	0.1200	0.0755	0.0051	8 Φ 25
T8, T9	0.2631	0.0772	0.0052	8 Φ 25

Table 2: Tension reinforcement of ground floor ductile walls of Zone III

5 CONCRETE AND STEEL MEASUREMENTS

The amount of concrete does not change in the three seismic zones, as the dimensions of the elements remain constant. The measurement of the steel reinforcement of the slabs, beams, columns and walls took place after the completion of the detailing for all three seismic zones.

6 ANALYSIS OF RESULTS

6.1 Analysis of concrete results

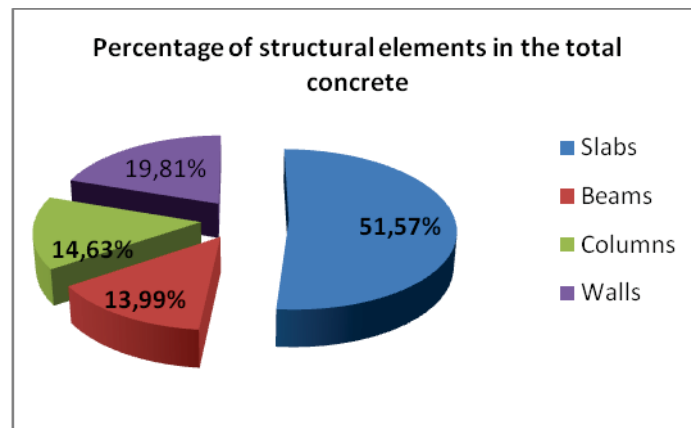


Figure 3: Percentage of structural elements concrete column compared to the total volume of concrete.

From Figure 3, it appears that the slabs have the largest percentage of the structural elements with a percentage of 51.57%. Then there are the walls with a percentage of 19.81%, the columns with a percentage of 14.63% and finally the beams with a percentage of 13.99%.

6.2 Analysis of reinforcement results for the ground floor

The following Table 3 and Figures 4-11 display the weight of steel of the structural elements of the ground floor for each zone.

Zone	Slab steel (kgr)	Beam steel (kgr)	Column steel (Kgr)	Structural wall steel (kgr)	Sum
Z1	10381.83	6739.43	6391.74	5538.13	29051.13
Z2	10381.83	8028.39	6405.58	7573.54	32389.35
Z3	10381.83	8561.27	7370.15	8784.73	35097.98

Table 3: Weight of steel of structural elements

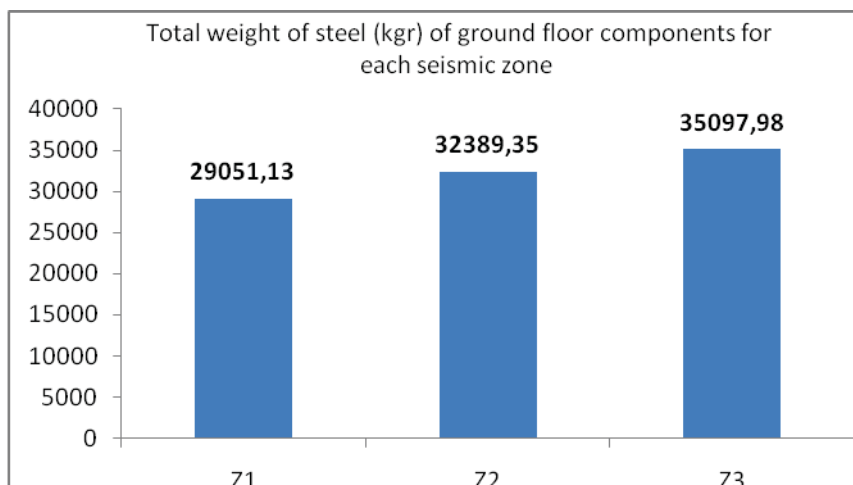


Figure 4: Total weight of steel of ground floor components for each seismic zone.

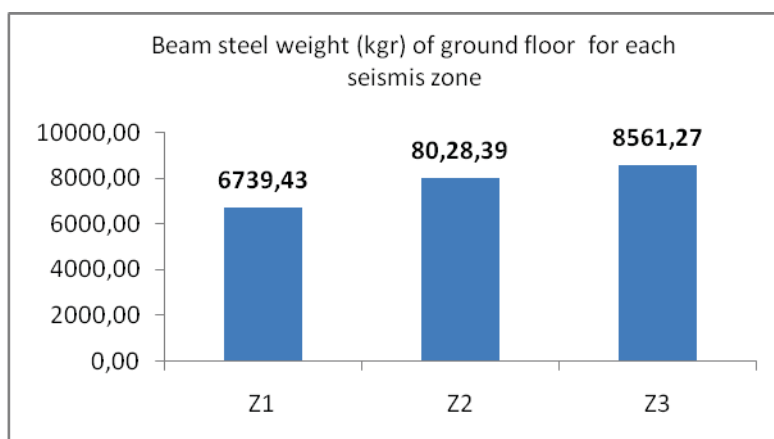


Figure 5: Beam steel weight of ground floor for each seismic zone.

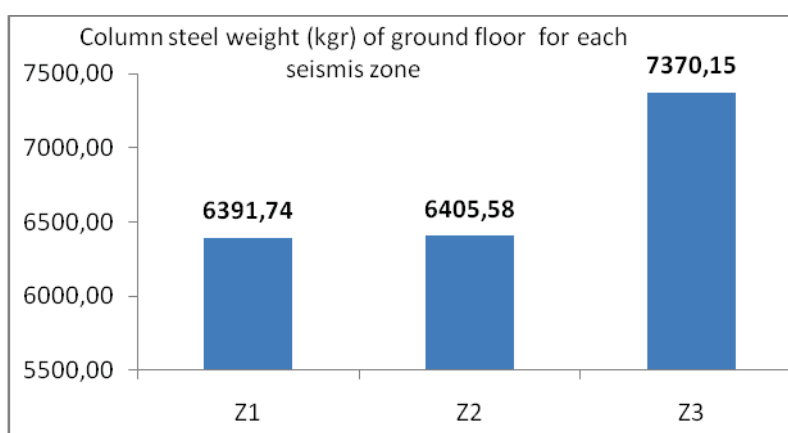


Figure 6: Column steel weight of ground floor for each seismic zone.

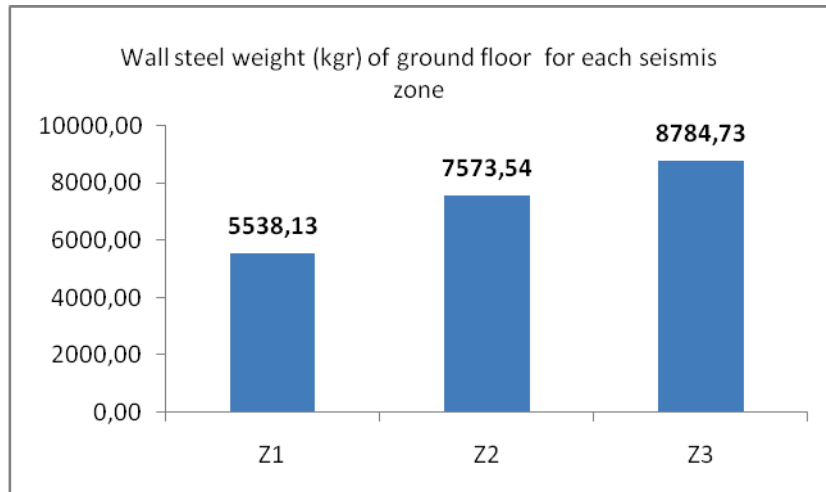


Figure 7: Wall steel weight of ground floor for each seismic zone.

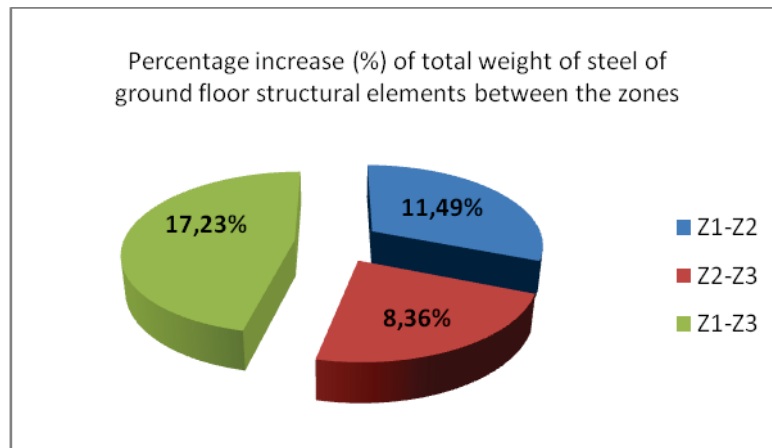


Figure 8: Percentage increase of total weight of steel of ground floor structural elements per zone.

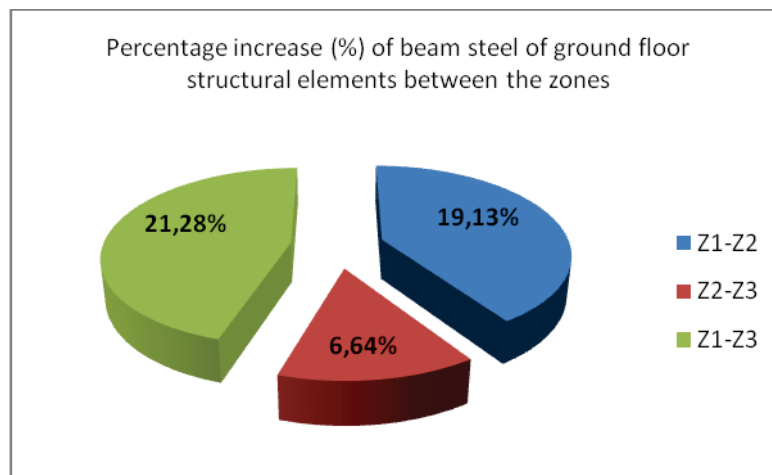


Figure 9: Percentage increase of beam steel of ground floor structural elements per zone.

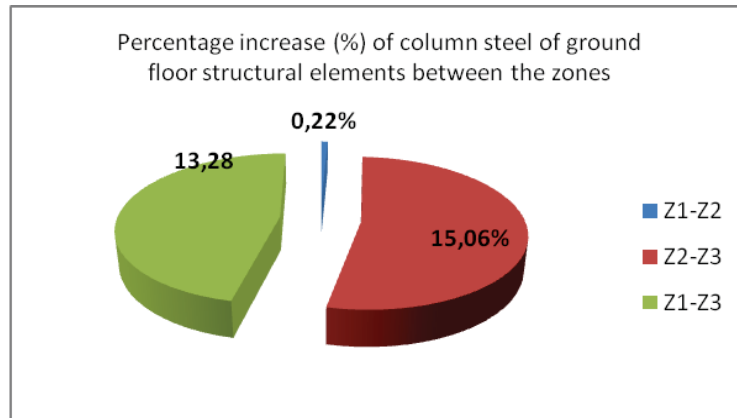


Figure 10: Percentage increase of column steel of ground floor structural elements per zone.

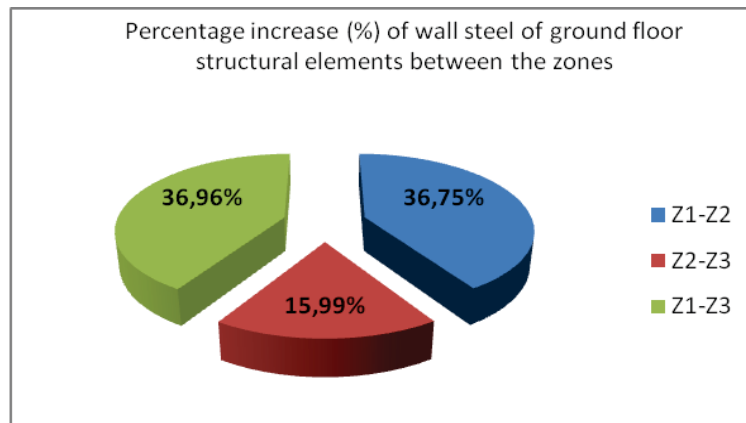


Figure 11: Percentage increase of wall steel of ground floor structural elements per zone.

The analysis of the above diagrams shows the following:

- **Transition from ZI seismic acceleration 0.16g, to ZII seismic acceleration 0.24g**
 - Increase of 11.49% of the total weight of steel of all structural elements
 - Increase of 19.13% in the steel weight of the beams
 - Increase of 0.22% in the steel weight of the columns
 - Increase of 36.75% of the steel weight of the walls
- **Transition from ZII seismic acceleration 0.24g, to ZIII seismic acceleration 0.36g**
 - Increase of 8.36% of the total weight of steel of all structural elements
 - Increase of 6.64% in the steel weight of the beams
 - Increase of 15.06% in the steel weight of the columns
 - Increase of 15.99% of the steel weight of the walls
- **Transition from ZI seismic acceleration 0.16g, to ZIII seismic acceleration 0.36g**
 - Increase of 17.23% of the total weight of steel of all structural elements
 - Increase of 21.28% in the steel weight of the beams
 - Increase of 13.28% in the steel weight of the columns
 - Increase of 21.28% of the steel weight of the walls

- **Increase in seismic acceleration**

- Zone I to Zone II $(0.24-0.16)/0.16 = 50\%$
- Zone II to Zone III $(0.36-0.24)/0.24 = 50\%$
- Zone I to Zone III $(0.24-0.16)/0.16 = 125\%$

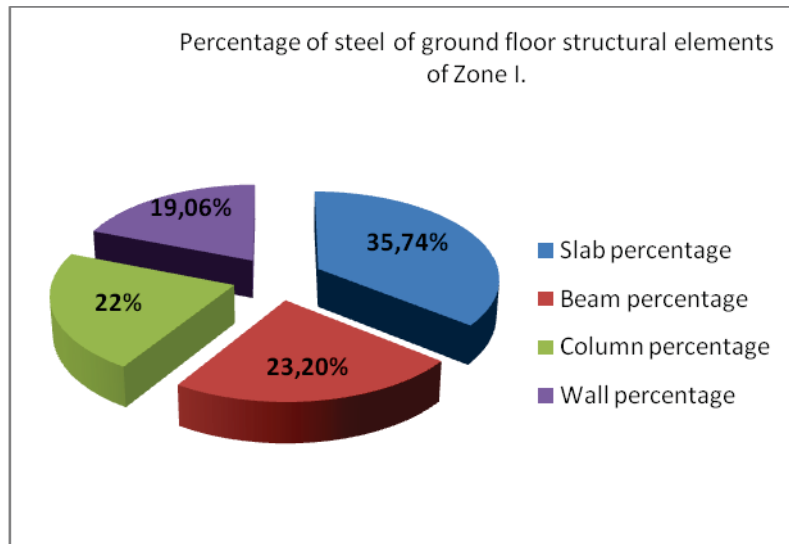


Figure 12: Percentage of steel of ground floor structural elements of Zone I.

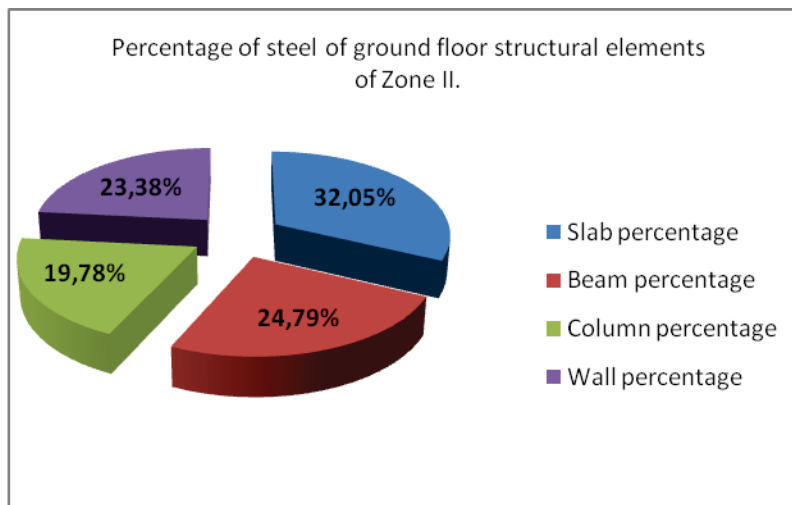


Figure 13: Percentage of steel of ground floor structural elements of Zone II.

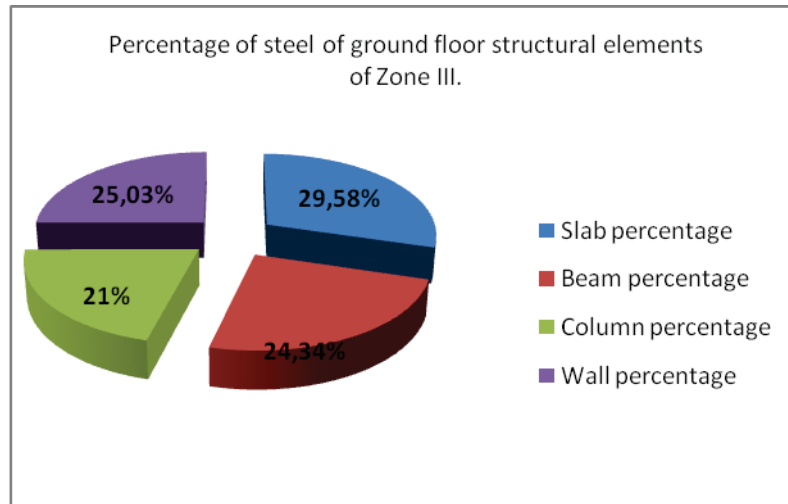


Figure 14: Percentage of steel of ground floor structural elements of Zone III.

From the Figures 12-14, it is concluded that:

- Slabs occupy their largest percentage in steel in ZI 35.74%, then in ZII 32.05% and finally in ZIII 29.58%.
- Beams occupy their largest percentage in steel in ZII 24.79%, then in ZIII 24.34% and finally in ZI 23.20%.
- Columns occupy their largest percentage in steel in ZI 22%, then ZIII 21% and finally in ZII 19.78%.
- Structural walls occupy their largest percentage in steel in ZII 25.03%, then in ZIII 23.38% and finally in ZI 19.06%.

7 CONCLUSIONS

In the present work, a ten-storey reinforced concrete building, without a basement, of rectangular conventional floor plan, was analyzed and detailed in the three seismic zones ZI, ZII, ZIII. The following conclusions emerged:

1. As the seismic hazard in the building increases, the largest percentage increase in steel occurs in the seismic walls. Specifically:
 - ZI ($\alpha_g = 0.16g$) \rightarrow ZII ($\alpha_g = 0.24g$) percentage increase 36.75%
 - ZII ($\alpha_g = 0.16g$) \rightarrow ZIII ($\alpha_g = 0.36g$) percentage increase 15.99%
 - ZI ($\alpha_g = 0.16g$) \rightarrow ZIII ($\alpha_g = 0.36g$) percentage increase 36.96%
2. The increase in seismic acceleration:
 - From ZI to ZII is a percentage of 50%, while respectively the increase in the total amount of steel is 11.49%, significantly smaller.
 - From ZII to ZIII is a percentage of 50%, while respectively the increase in the total amount of steel is 8.36%, an even greater difference compared to the previous transition.
 - From ZI to ZIII is a percentage by 125%, while respectively the increase in the total amount of steel is only 17.23%.
3. In a reinforced concrete building designed in accordance with the Eurocodes, seismicity affects the construction cost of the building but certainly the increase in construction costs

is significantly smaller compared to the increase in seismic risk. The increase in the total cost of materials is much smaller than the increase in seismic accelerations.

4. A building may be detailed for a seismic hazard zone greater than that provided for in the respective code, taking into account that there is a difference in construction costs.

REFERENCES

- [1] K. J. Elwood and M. O. Eberhard, "Effective stiffness of reinforced concrete columns," *ACI Structural Journal*, vol. 106, no. 4, pp. 476–484, 2009.
- [2] S. Watson, F. A. Zahn, and R. Park, "Confining Reinforcement for Concrete Columns," *Journal of Structural Engineering*, vol. 120, no. 6, pp. 1798–1824, 2006, doi: 10.1061/(asce)0733-9445(1994)120:6(1798).
- [3] J. M. Barron and M. B. D. Hueste, "Diaphragm effects in rectangular reinforced concrete buildings," *ACI Structural Journal*, vol. 101, no. 5, pp. 615–624, 2004.
- [4] Tavio and S. Teng, "Effective Torsional Rigidity of Reinforced Concrete Members," *ACI Structural Journal*, vol. 101, no. 2, pp. 252–260, 2004.
- [5] M. Mansour and T. T. C. Hsu, "Behavior of Reinforced Concrete Elements under Cyclic Shear. II: Theoretical Model," *Journal of Structural Engineering*, vol. 131, no. 1, pp. 54–65, 2004, doi: 10.1061/(asce)0733-9445(2005)131:1(54).
- [6] J. A. Pincheira, F. S. Dotiwala, and J. T. D'Souza, "Seismic analysis of older reinforced concrete columns," *Earthquake Spectra*, vol. 15, no. 2, pp. 245–272, 1999, doi: 10.1193/1.1586040.
- [7] J. A. Munshi and S. K. Ghosh, "Analyses of seismic performance of a code designed reinforced concrete building," *Engineering Structures*, vol. 20, no. 7, pp. 608–616, 1998, doi: 10.1016/S0141-0296(97)00055-2.
- [8] A. P. Harasimowicz and R. K. Goel, "Seismic code analysis of multi-storey asymmetric buildings," *Earthquake Engineering and Structural Dynamics*, vol. 27, no. 2, pp. 173–185, 1998, doi: 10.1002/(SICI)1096-9845(199802)27:2<173::AID-EQE724>3.0.CO;2-W.
- [9] C. C. Shu and N. M. Hawkins, "Behavior of columns continuous through concrete floors," *ACI Structural Journal*, vol. 89, no. 4, pp. 405–416, 1992.
- [10] G. Ozcebe and M. Saatcioglu, "Confinement of concrete columns for seismic loading," *ACI Structural Journal*, vol. 84, no. 4, pp. 308–315, 1987.
- [11] T. H. Tan and W. K. Yip, "Behavior of axially loaded concrete columns confined by elliptical hoops," *ACI Structural Journal*, vol. 96, no. 6, pp. 967–971, 1999.
- [12] G. G. Penelis and A. J. Kappos, *Earthquake-resistant Concrete Structures*. London, UK: E & F N SPON (Chapman & Hall), 1996.
- [13] G. Penelis, K. Stylianidis, A. Kappos, and C. Ignatakis, *Reinforced Concrete Structures*. Thessaloniki, Greece: A.U.Th. Press, 1995.
- [14] G. N. Devi, K. Subramanian, and A. R. Santhakumar, "Experimental investigations on reinforced concrete lateral load resisting systems under lateral loads," *Experimental*

- Techniques*, vol. 35, no. 4, pp. 59–73, 2011, doi: 10.1111/j.1747-1567.2010.00634.x.
- [15] H. Bechtoula, M. Sakashita, S. Kono, F. Watanabe, and M. O. Eberhard, “Cyclic performance of lower stories of mid-rise reinforced concrete frame buildings,” *ACI Structural Journal*, vol. 103, no. 4, pp. 513–521, 2006.
- [16] S. Francisco, “Response analysis of reinforced concrete c-bent columns,” *Spring*, vol. 23, no. 420, 2006.
- [17] T. Chrysanidis, V. Panoskaltsis, and I. Tegos, “Preliminary design and analysis of cost parameters of a high-rise building: Braced shear wall core system,” *International Journal of Civil Engineering and Technology*, vol. 7, no. 5, pp. 137–152, 2016.
- [18] T. Chrysanidis, V. Panoskaltsis, and I. Tegos, “Parametrical cost analysis of an ultra high-rise building: Detailed design,” *International Journal of Applied Engineering Research*, vol. 11, no. 18, pp. 9644–9650, 2016.
- [19] T. Chrysanidis and I. Tegos, “Cost Comparison and Parametrical Investigation of the R/C Shear Wall Core of a Tall Building,” *International Journal of Engineering Research and Technology*, vol. 5, no. 09, pp. 592–595, 2016.
- [20] I. Tegos, N. Giannakas, and T. Chrysanidis, “Serviceability cracking check of circular section piers,” *Bridge Structures*, vol. 7, no. 1, pp. 43–52, 2011, doi: 10.3233/BRS-2011-018.
- [21] I. Tegos, N. Giannakas, and T. Chrysanidis, “Cross-correlation of stresses in the transverse reinforcement under shear load and confinement,” in *Proceedings of the 2013 International Van Earthquake Symposium*, 2013.
- [22] A. Parapanisiou, D. Argyropoulou, E. Andreadou, X. Demertzi, T. Chrysanidis, and I. Tegos, “A suggestion of a quick and economic method of strengthening bridge piers,” in *Proceedings of the International Conference: Innovations on Bridges and Soil-Bridge Interaction (IBSBI 2011)*, 2011, pp. 419–426.
- [23] I. Tegos, N. Giannakas, and T. Chrysanidis, “Seismic design of circular section piers under axial load and biaxial bending belonging to low ductility bridges: Analytical and experimental investigation of bending resistance,” in *Proceedings of the International Conference: Innovations on Bridges and Soil-Bridge Interaction (IBSBI 2011)*, 2011, pp. 141–148.
- [24] I. Tegos, D. Kifokeris, and T. Chrysanidis, “Seismic design of R/C piers of hollow circular cross sections,” in *Proceedings of the 2013 International Van Earthquake Symposium*, 2013.
- [25] G. Papageorgiou, “Economic assessment of pavement maintenance and strengthening techniques in view of implementation cost,” *European Transport*, no. 78, Article 5, 2020.
- [26] A. Tsiknas, A. Athanasopoulou, and G. Papageorgiou, “Evaluation of flexible pavement construction cost according to the design method,” *Proceedings of the Institution of Civil Engineers (ICE) - Transport*, vol. 173, no. 1, pp. 3–12, 2020.
- [27] T. Chrysanidis, “Evaluation of Out-of-Plane Response of R/C Structural Wall Boundary Edges Detailed with Maximum Code-Prescribed Longitudinal Reinforcement Ratio,” *International Journal of Concrete Structures and Materials*, vol. 14, no. 1. 2020, doi: 10.1186/s40069-019-0378-4.

- [28] T. Chrysanidis, "Influence of elongation degree on transverse buckling of confined boundary regions of R/C seismic walls," *Construction and Building Materials*, vol. 211, pp. 703–720, Jun. 2019, doi: 10.1016/J.CONBUILDMAT.2019.03.271.
- [29] T. Chrysanidis and I. Tegos, "Does reinforcement ratio affect displacements due to lateral buckling behavior of concrete walls?," *International Journal of Applied Engineering Research*, vol. 12, no. 3, pp. 382–388, 2017.
- [30] T. Chrysanidis and I. Tegos, "Influence of elongation degree on out-of-plane buckling of R/C structural walls with a medium high reinforcement ratio," *International Journal of Civil Engineering and Technology*, vol. 7, no. 4, pp. 358–364, 2016.
- [31] T. Chrysanidis and I. Tegos, "Displacements and mode of failure of medium high reinforced walls due to transverse buckling," *International Journal of Engineering Development and Research*, vol. 4, no. 3, pp. 628–634, 2016.
- [32] T. Chrysanidis and I. Tegos, "Size of seismic tensile strain and its influence on the displacements due to transverse buckling of ultra-highly reinforced structural walls," *ARPJ Journal of Engineering and Applied Sciences*, vol. 11, no. 23, pp. 13884–13890, 2016.
- [33] T. Chrysanidis, "Low Reinforced Shear Walls: Displacements and Failure Modes Due to Lateral Buckling," *International Journal of Science and Engineering Investigations*, vol. 5, no. 55, pp. 143–148, 2016.
- [34] T. Chrysanidis, "Degree of Elongation of Maximum Code-Prescribed Reinforced Walls: Modes of Failure and Displacements of Lateral Buckling Phenomenon," *International Journal of Trend in Research and Development*, vol. 3, no. 4, pp. 435–440, 2016.
- [35] N. Alamanis and P. Dakoulas, "Simulation of random soil properties by the Local Average Subdivision method and engineering applications," *Energy Systems*, pp. 1–21, 2019, doi: 10.1007/s12667-019-00362-y.
- [36] N. Alamanis, "Uncertainties and optimization in geotechnical engineering," *American Scientific Research Journal for Engineering, Technology, and Sciences*, vol. 38, no. 1, pp. 92–111, 2017.
- [37] European Committee for Standardization, "EN 1992-1-1:2004, Eurocode 2: Design of concrete structures - Part 1-1: General rules and rules for buildings," Brussels, Belgium, 2004.
- [38] European Committee for Standardization, "EN 1998-1:2004, Eurocode 8: Design of structures for earthquake resistance - Part 1: General rules, seismic actions and rules for buildings," Brussels, Belgium, 2004.

ASSESSMENT AND RETROFITTING OF A RC BUILDING THROUGH A MULTI-HAZARD APPROACH: SEISMIC RESISTANCE AND ROBUSTNESS

M. Scalvenzi¹, F. Freddi² and F. Parisi¹

¹ Dept. of Structures for Engineering and Architecture, University of Naples Federico II, Naples, Italy
e-mail: martina.scalvenzi@unina.it, fulvio.parisi@unina.it

² Dept. of Civil, Environmental & Geomatic Engineering, University College London, London, UK
e-mail: f.freddi@ucl.ac.uk

Abstract

Most of the existing buildings in seismic prone regions have been built before the publication of modern design provisions against seismic events and progressive collapse. Nonetheless, some studies have highlighted the possible interaction between earthquake resistance and structural robustness, the latter being of interest to either individual extreme hazards (e.g., blast, impact, fire) or interacting hazards (e.g., landslides produced by seismic events). While retrofit strategies to improve the seismic performance of reinforced concrete (RC) structures have been widely investigated since many years, the topic of mitigation strategies against progressive collapse received very little attention. Progressive collapse can be described as a special type of structural collapse that involves several components of the structure as consequence of an initial localised damage. The present study aims at investigating whether and how much seismic retrofitting may improve not only the earthquake resistance but also robustness. A four-storey, five-bay, RC frame building designed according to Eurocode 2 is considered as a case study. The frame was assessed by evaluating: 1) the capacity of the structure to redistribute loads after a local damaging event; 2) the seismic capacity of the structure. Non-linear static analyses, i.e., PushDown and PushOver analyses, were carried out in OpenSees to evaluate the robustness and seismic resistance of the structure, respectively. The progressive collapse capacity was evaluated under two relevant column-removal scenarios, i.e., the sudden loss of an internal and an external column, while the seismic resistance was assessed under two load distributions, i.e., proportional to the first vibration mode and to the inertia masses. Subsequently, the impact of retrofitting with carbon fibre-reinforced polymers on both structural robustness and seismic resistance was evaluated. The use of the retrofit measure allowed, on the one hand, the removal of all the shear failures due to horizontal seismic actions and, on the other hand, to increase the robustness of the structure.

Keywords: Reinforced concrete buildings, structural robustness, retrofit operation, progressive collapse, non-linear static analysis.

1 INTRODUCTION

Some iconic cases, such as the collapse of the Ronan Point Building (London, 1968) [1], the Murrah Federal Building (Oklahoma City, 1995) [2], and the World Trade Centre (New York, 2001) [3] highlighted the high consequences of progressive collapse, in terms of loss of lives and properties, significantly increasing the interest of the research community in this topic [4]. Since the 1940s, many studies focused on this research area, widely investigating various aspects of the problem by performing components [e.g., [5], [6], [7]] and large-scale experimental tests [e.g., [8], [9], [10], [11]], numerical modelling and simulations [e.g., [12], [13], [14], [15], [16], [17]] and investigating several aspects of the design against progressive collapse [e.g., [18], [19]]. These studies allowed to build up an increasing understanding of the structural response in progressive collapse scenarios, along with the definition of possible design strategies. However, design guidelines and codes [[20], [21], [22]] have been introduced only in recent years, and most of the existing buildings worldwide do not incorporate design provisions to achieve structural robustness.

Besides, existing reinforced concrete (RC) structures are often vulnerable to seismic actions, as demonstrated by many events worldwide [e.g., [23]]. However, in the last few decades, there has been a significant effort from the research community in order to address these issues, and many seismic retrofit strategies are currently available and implemented in practice [e.g., [24], [25], [26], [27], [28], [29]].

In contrast, a very limited number of research studies focused on the development and investigation of retrofit strategies to avoid progressive collapse for both RC and steel structures. Among the few studies addressing this problem, Vieira *et al.* [7] experimentally investigated the effectiveness of the Textile-Reinforced Mortar and Near-Surface-Mounted reinforcement techniques when applied for the strengthening of existing RC frames against disproportionate collapse, showing an increase of the ductility by a factor of 1.95. Shayanfar *et al.* [30] numerically investigated the use of several combinations of additional rebars and Carbon Fiber Reinforced Polymer (CFRP) layers for the retrofitting of 2-storey RC frame showing the improved catenary effects and the reduction of vertical displacements. Jinkoo *et al.* [31] investigated the effect of prestressing tendons on the progressive collapse performance of a RC structure by performing non-linear static and dynamic analyses investigating a 6- and a 20-storey RC structure subjected to a sudden column loss scenario.

Although the above-mentioned studies (and a few more) investigate retrofit strategies for progressive collapse resistance, the knowledge level in this field is still very limited and there is a significant need for additional studies in this direction. Moreover, the vulnerability of these structures against multiple hazards offers the opportunity for integrated retrofit strategies that otherwise would often not be economically sustainable if directed toward the improvement of the structural response against a single hazard.

Within this context and given the high vulnerability of RC buildings towards the two considered hazards (*i.e.*, seismic actions and progressive collapse scenarios), the present study investigates the influence of the seismic retrofitting based on the use of CFRP on the structural robustness of a case study RC structure.

2 CASE-STUDY STRUCTURE AND FINITE ELEMENT MODELLING

A five-storey, six-bay by four-bay RC building, designed according to Eurocode 2 [32] and only to gravity loads, and previously investigated by the authors [[33], [34], [35]] was considered for case study purposes (see Figure 1). The building has a constant inter-storey height of 3 m and span lengths along the x - and y -directions equal to 5 m. Columns have a 400×400 mm² square section, whereas beams are 300×500 mm² at each floor. Concrete class C20/25

and steel reinforcement bars B450C were employed in the design. Uniform longitudinal reinforcement consisting of $6\phi 18$ and $8\phi 18$ were used for columns and beams, respectively. The same transverse steel reinforcement of $\phi 18$ stirrups with 200 mm spacing and a concrete cover of 40 mm were used for both beams and columns.

A two-dimensional Finite Element (FE) model of the external frame in x -direction was developed in OpenSees [36]. A spread plasticity approach with displacement-based fibre formulation was used, and each cross-section was discretised in 120 fibres: one hundred fibres relating to the confined concrete (*i.e.*, the concrete core) and twenty for the concrete cover. The stress-strain concrete behaviour was simulated through the uniaxial Kent-Scott-Park concrete model [37] (*i.e.*, ‘Concrete01’ in OpenSees), while a uniaxial bilinear model with kinematic hardening set to 0.01 was adopted to simulate the steel behaviour (*i.e.*, ‘Steel01’ in OpenSees). The characteristic cylinder compressive strength of concrete, f_{ck} , was set to 20 MPa. The characteristic yield strength, f_{yk} , and Young’s modulus of the reinforcing steel, E_0 , were set equal to 450 MPa and 200 GPa, respectively. The loads were applied as concentrated loads on the beams following a discretisation of the structure in which each beam element was subdivided into 5 parts. Masses were concentrated at beam-column intersections while beam-column joints were modelled as rigid. Geometric non-linearities in the form of both large displacements/rotations and P-Delta effects were considered by means of a total corotational transformation.

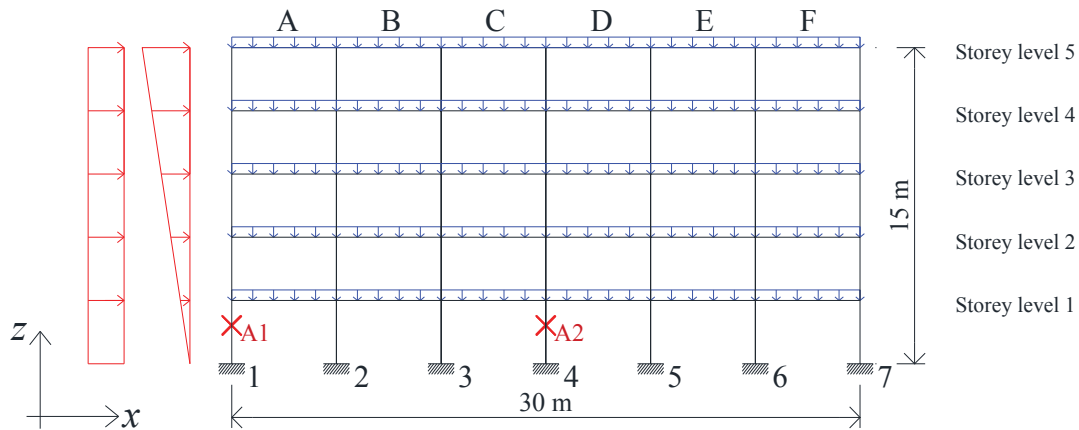


Figure 1: Reference frame model

3 PROGRESSIVE COLLAPSE ANALYSIS METHODS

The present Section investigates three different strategies for progressive collapse simulations. As shown in Figure 1, two different column removal scenarios were considered, *i.e.*, scenario A1 and A2. Loads were applied according to the accidental load combination, as per UFC [21] guidelines:

$$Q_{bd} = 1.2 DL + 0.5LL \quad (1)$$

where DL and LL indicate the dead and live loads, respectively equal to 3 kN/m^2 and 2 kN/m^2 .

A FE model in Seismostruct [38] was previously developed by the authors [35] for the case study frame, allowing the comparison of the numerical results and increasing confidence in the modelling strategy. The comparison was initially carried out in terms of modal properties showing a good match, *i.e.*, the first vibration periods were 0.35 sec and 0.37 sec for the Seismostruct and OpenSees model, respectively, while the second and third vibration periods

were coincident. A further comparison was carried out investigating the behaviour under the progressive collapse scenarios. In particular, the results of Incremental Dynamic Analysis (IDA) carried out in the previous study [35] were compared with the PushDown Analysis (PDA) carried out in this study. The Dynamic Amplification Factor (DAF) is used in the PDAs in order to simulate the dynamic effects. Figure 2 shows three different approaches used to carry out the PDAs, allowing the identification of the most appropriate one in terms of convergence and analysis' accuracy. The following approaches are evaluated:

- The '*Approach A*' is characterised by two Analyses (see Figure 2(a)). '*Analysis 1*' consists of a standard load control static analysis of the 'undamaged' structure, allowing the definition of the reaction force (R) of the column where the column loss is successively simulated. During '*Analysis 2*' the column removal is simulated by two steps. '*Step 1*', represented in Figure 2(a), allows simulating the presence of the column before the removal. The equivalent upward force F is applied to the frame, which entity corresponds to the vertical load previously detected on that column. In this Step, the gravity loads and the force F, are monotonically increased until the target value. In the following '*Step 2*', represented in Figure 2(a), a downward force F (equal to R in terms of values and opposite in terms of direction) is applied to simulate the column removal. Moreover, the loads on the beams adjacent to the removal are amplified with the DAF. This second set of loads are thus gradually applied.
- The '*Approach B*' is characterised by a single step (see Figure 2(b)), consisting in a displacement control analysis with the application of design loads amplified by the DAF. This approach, differently from '*Approach A*' neglects the initial condition before the collapse but allows an easier implementation of the analysis. In addition, the displacement control strategy allows the convergence of the analysis for larger displacements hence better simulating the catenary effects.
- The '*Approach C*' is characterised by two Steps (see Figure 2(c)). '*Step 1*' represented in Figure 2(c) consists of a standard load control static analysis of the 'damaged' structure with the application of the design loads. In the following '*Step 2*' a displacement control analysis is performed with the design loads amplified by the DAF.

The present Section of the work investigates the intensity of the DAF parameter by the comparison of the results of the PDAs and IDA. For this reason, the DAF was considered unitary during these preliminary analyses.

The results of the PDAs were obtained in terms of α - θ curves, in which α represents the design load multiplier and θ the vertical drift of the control point. Specifically, α was obtained, according to Eq. 2, as the ratio between the sum of the reaction values, relative to the base constraints, and the sum of the loads applied to the structure. The vertical drift was obtained as the ratio between the vertical displacement of the control point, v , and the beam length, L , according to Eq. 3; the control point was coincident with the upper joint of the removed column.

$$\alpha = \frac{\sum_i R_i}{\sum_i R_i(Qbd)} \quad (2)$$

$$\theta = \arctg \frac{v}{L} \quad (3)$$

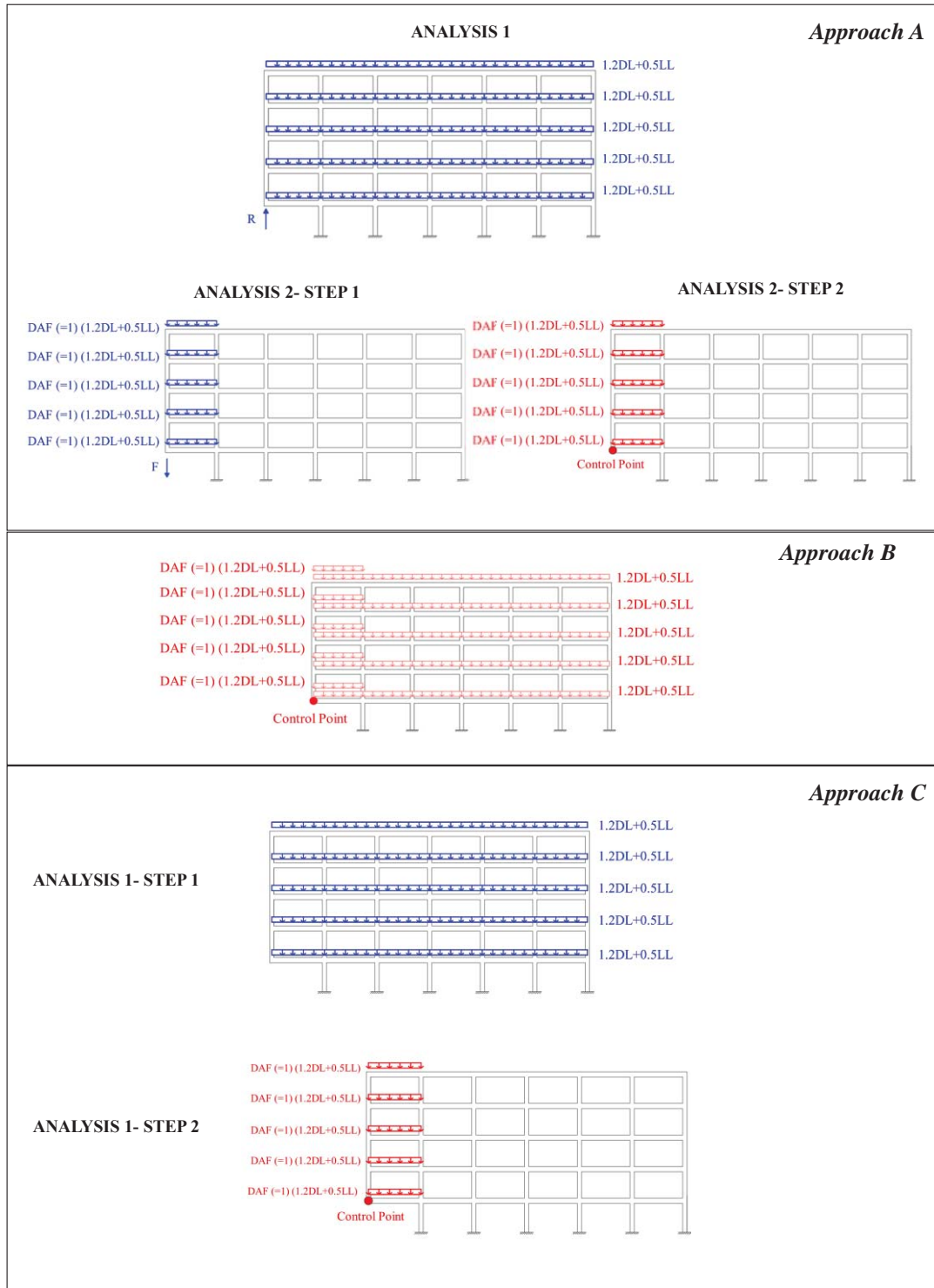


Figure 2: Approaches used for PushDown Analysis (PDA) (scenario A1).

The comparison between PDAs and IDA is shown in Figure 3. Through these results, the specific DAF (DAF_{sp}) was assessed as the ratio between the values of the load multipliers, α , obtained from both analyses, as follows:

$$DAF_{sp} = \frac{\alpha_{PDA}}{\alpha_{IDA}} \quad (4)$$

The results of the PDAs overestimated the design load multiplier, α , overestimating the capacity of the structure. This is related to the lack of consideration of the dynamic amplification during these analyses since the DAF was set equal to 1. However, this preliminary assumption allowed the evaluation of the DAF (DAF_{sp}) based on the results of the PDAs and IDA according to Eq. 4. The DAF_{sp} for the three Approaches and for the two removal Scenarios is shown in Figure 4. Figure 4 shows that Approaches A and C provide DAF values lower than the unit for high values of θ . The Approach B, on the other hand, led to a more realistic estimate of the DAF. Indeed, its value is always higher than the unit for both scenarios up to large vertical drift values and is aligned with DAF values obtained from other studies in the literature [40]. Approach B, with the corresponding value of the DAF, was chosen as the analysis method for the following part of the study. The DAF was set equal to 1.16, corresponding to a value of plastic rotation of 0.03 rads, as suggested by UFC (table 4-1); the yield rotation was calculated based on the recommendations of the Eurocode 8 [39].

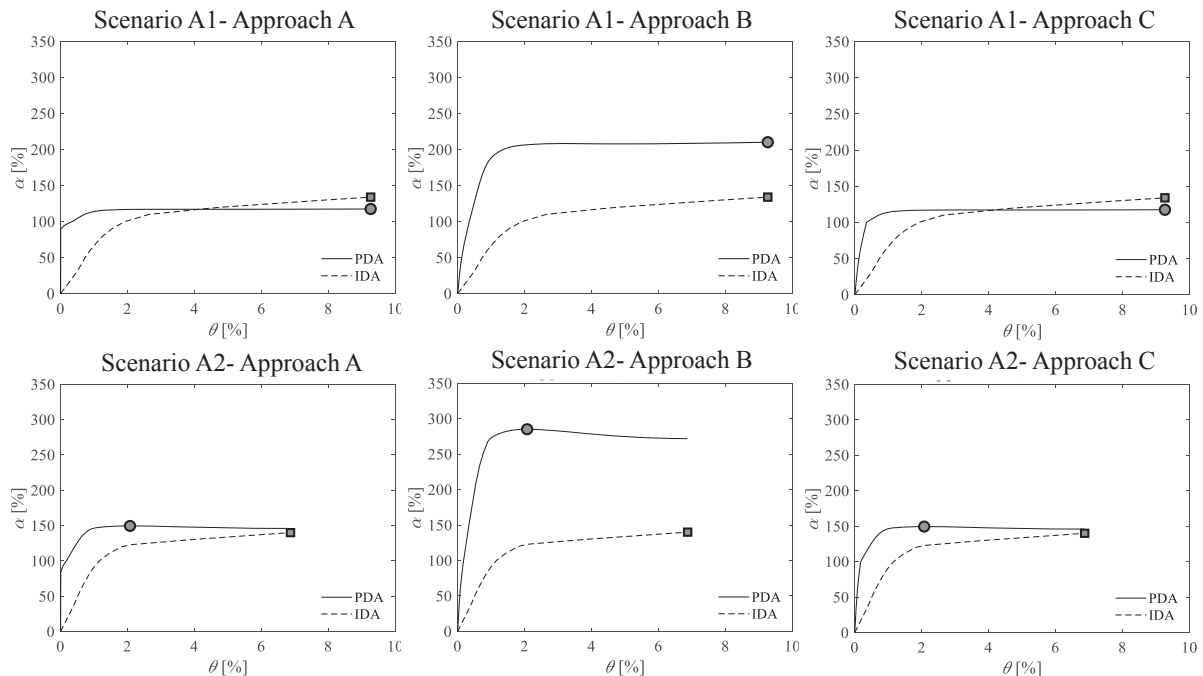


Figure 3: Comparison between PushDown analysis (PDA) and Incremental Dynamic Analysis (IDA).

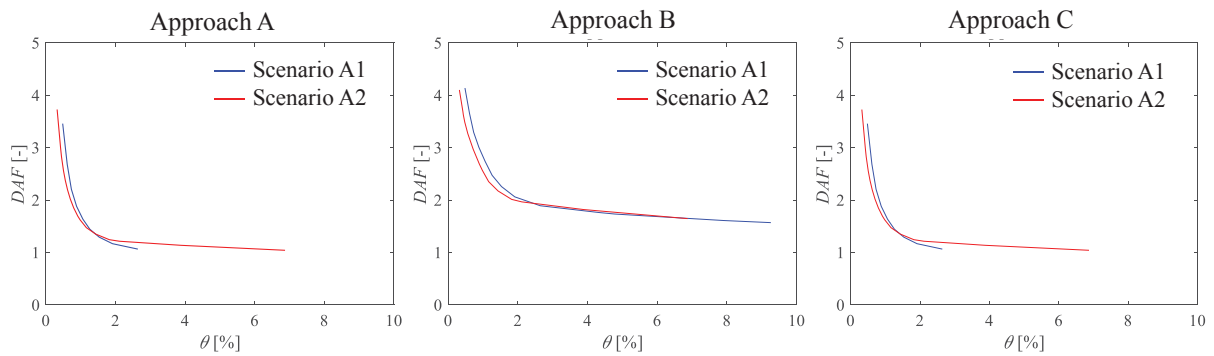


Figure 4: Dynamic Amplification Factor (DAF) assessment.

4 PROGRESSIVE COLLAPSE AND SEISMIC ANALYSIS

4.1 Progressive collapse resistance assessment

Progressive collapse analyses were carried out to assess structural robustness under the two column-removal scenarios previously discussed and shown in Figure 1. Unlike previous studies [[33], [34], [35]], in which a building perimeter frame was considered, the structural system is herein supposed to be an internal primary frame. This led to an increase of design loads applied on beams equal to 23 kN/m according to Eq. 1.

The α - θ curves for the two scenarios and obtained with the PDAs are shown in Figure 5. For both scenarios, Figure 5 shows that the structure lack of robustness with shear failures of the beams corresponding to α values of 33.05 and 47.61, respectively, for scenarios A1 and A2. The degrading model of Biskinis and Fardis [41] was used for shear checks.

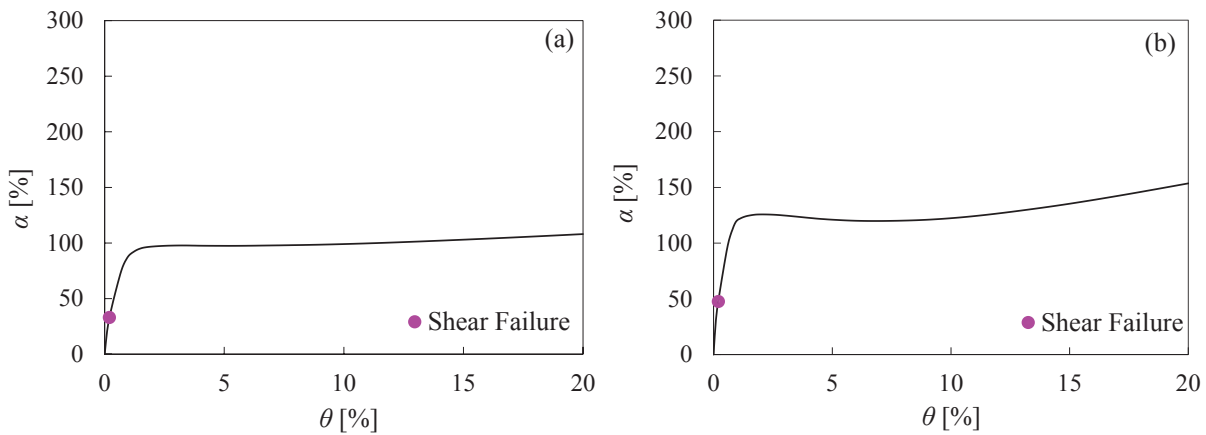


Figure 5: Pushdown analysis results: (a) scenario A1, (b) scenario A2.

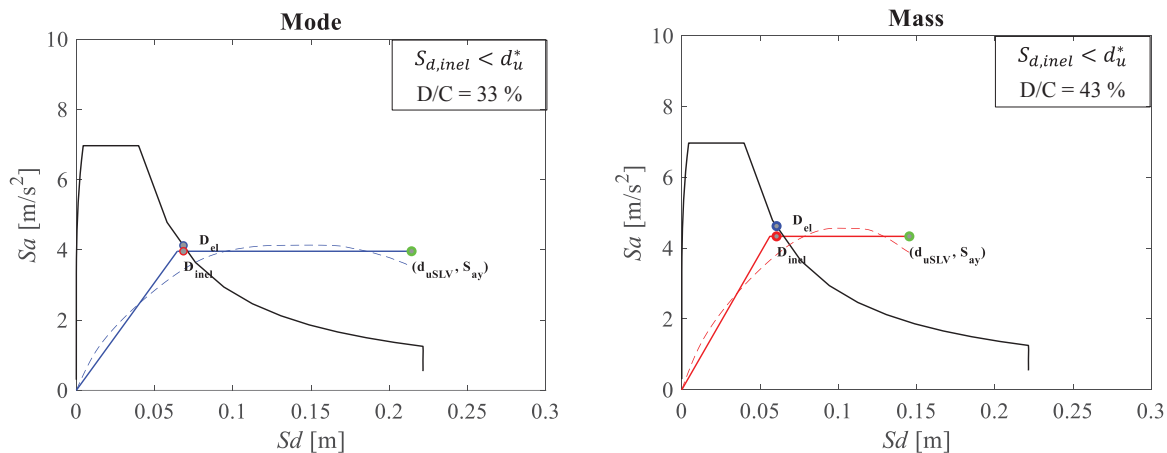
4.1 Seismic safety assessment

In order to evaluate the seismic capacity of the structure, global and local checks were carried out through non-linear static analysis performed according to NTC 2018 [42]. The construction site was coincident with L'Aquila (Abruzzo, Italy), the reference life of the structure, V_R , was 50 years and soil and topographic category were B and T_I , respectively; the PGA was equal to 0,301g. Two different load distribution, such as the MODE and a MASS distribution, were considered. Local checks showed that almost all elements, vertical and horizontal, were subjected to brittle failures, as underlined by the demand/capacity ratios collected in Tables 2 and 3 (Bold values in the tables indicate demand/capacity ratios greater than 1). These checks were carried out step-by-step, and they were performed in correspondence of a single step, *i.e.*, that related to the identified performance point. The global checks compared the required inelastic displacement, $S_{d,inel}$ with the ultimate displacement of the structure, d_u . This comparison was performed in the ADRS plane, allowing the comparison between the demand spectrum and the capacity curve. The intersection between the demand spectrum with the extension of the elastic branch provided the performance point. The results are shown in Figure 6, with the relative demand/capacity ratios.

Floor level	Column Line													
	Mass distribution							Mode distribution						
	1	2	3	4	5	6	7	1	2	3	4	5	6	7
1	2.03	2.07	2.14	2.19	2.25	2.32	2.04	1.59	1.81	1.93	2.03	2.12	2.21	1.89
2	1.60	2.20	2.14	2.09	2.04	1.98	0.90	1.80	2.25	2.24	2.20	2.16	2.12	0.98
3	1.15	1.86	1.77	1.68	1.58	1.48	1.02	1.46	2.16	2.07	1.98	1.88	1.78	1.17
4	0.70	1.39	1.32	1.25	1.19	1.13	0.74	1.04	1.76	1.67	1.58	1.50	1.42	0.91
5	0.02	0.81	0.79	0.75	0.71	0.63	0.60	0.18	1.12	1.05	0.99	0.93	0.81	0.65

Table 1: Columns' demand/capacity ratios.

Floor level	Beam Span											
	Mass distribution						Mode distribution					
	A	B	C	D	E	F	A	B	C	D	E	F
1	2.36	2.24	2.25	2.25	2.24	2.28	2.24	2.18	2.21	2.23	2.25	2.28
2	2.20	2.06	2.02	1.97	1.92	1.89	2.32	2.18	2.14	2.10	2.06	2.03
3	1.82	1.70	1.66	1.61	1.56	1.53	2.05	1.90	1.85	1.80	1.74	1.72
4	1.36	1.33	1.29	1.26	1.23	1.19	1.58	1.51	1.46	1.42	1.37	1.32
5	1.36	1.33	1.29	1.26	1.23	1.19	1.13	1.01	1.00	0.98	0.98	0.89

Table 2: Beams' demand/capacity ratios.**Figure 6:** Global checks

5 INFLUENCE OF SEISMIC RETROFITTING ON STRUCTURAL ROBUSTNESS

The analysis results outlined the need to adopt a retrofit measure in order to prevent brittle failures occurring as a consequence of both considered hazards. In this study, the application of CFRP was investigated as it represents a widely used strategy to improve the seismic performances of RC frames. The impact of this retrofit strategy on the structural robustness was successively evaluated. The CFRP were applied differently on vertical and horizontal elements so as to eliminate brittle failures. A single bandage ply was used for the beams, while a different composition was considered for the columns. Five layers of CFRP plies, coinciding with the limit set by CNR-DT 200 R1/2013 [43], were used for the first floor level; three and two layers of plies were used for second and third floor level, respectively, while a single layer of ply was applied for fourth and fifth floor level. The analysis results showed that the application of CFRP allowed the removal of all the shear failures due to the seismic action, obtaining values of demand/capacity ratios lower than the unit.

Additionally, this retrofit measure had a beneficial effect, also improving the structural robustness of the frame under both column removal scenarios, as shown in figure 7. The first brittle failure, for both cases, occurred for a higher multiplier value than in the case of the existing structure. In scenario

A2, the retrofitted structure is able to avoid progressive collapse and at the same time was characterised by little damage, as low drift values were reached. A lower increase of structural performance was observed for scenario A1 where shear failures are observed for α values just above 100% *i.e.*, $\alpha = 101.64$, yet achieving structural robustness under the considered design loads. In this case, however, the activation of the alternative load path required large displacements, *i.e.*, exceeded 10% of vertical drift, corresponding to a damage level significantly greater than in the previous scenario.

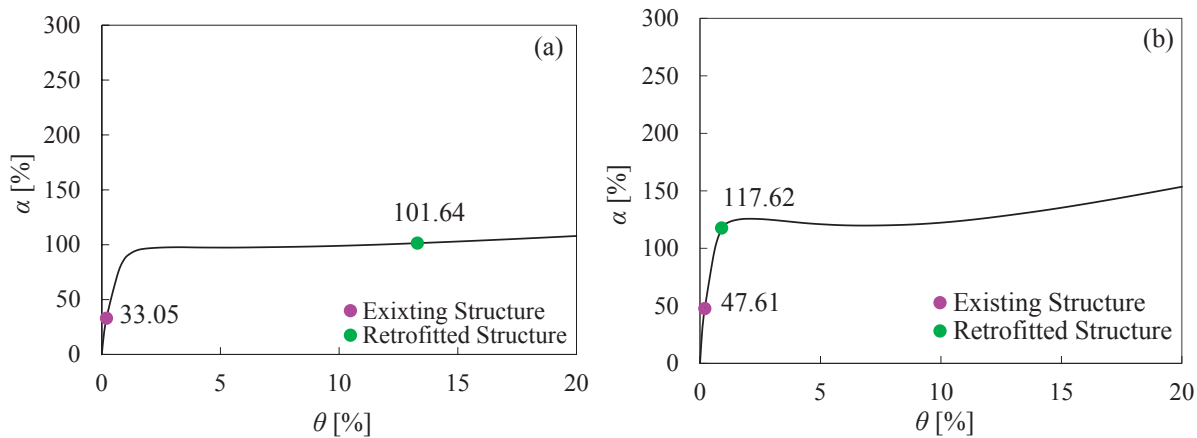


Figure 7: Impact of retrofit measure on structural robustness: (a) scenario A1, (b) scenario A2.

6 CONCLUSIONS

In this study, the structural capacity of RC framed structure through a multi-hazard approach was investigated. The impact of a retrofit measure, by the application of Carbon Fibre Reinforced Polymer (CFRP), on structural robustness was assessed. Non-linear static analyses were carried out to evaluate the structure's seismic capacity and its resistance to progressive collapse. The results of the analyses showed the need for retrofitting in order to eliminate brittle failures and to increase the structural capacity. The study also provided some insights into the methodologies for progressive collapse analysis using non-linear static procedures. Three Approaches (*i.e.*, A, B and C) were investigated and compared with the results of non-linear dynamic analysis previously performed on the same case study structure. The following conclusions can be drawn: (i) among the alternative options for progressive collapse resistance assessment, a more realistic estimate of the dynamic amplification factor was obtained with Approach B; (ii) the seismic safety and structural robustness are limited by premature brittle failures and (iii) the use of CFRP as a retrofit measure was efficient for the case study structure, leading to the removal of all the shear failures due to the seismic action. On the other hand, the introduction of this retrofit measure allows obtaining a positive result also in terms of structural robustness.

REFERENCES

- [1] C. Pearson, N. Delatte, Ronan point apartment tower collapse and its effect on building codes. *Journal of Performance of Constructed Facilities*, **19**, 172–177, 2005.
- [2] A. Kazemi-Moghaddam, M. Sasani, Progressive collapse evaluation of Murrah Federal Building following sudden loss of column G20. *Engineering Structures*, **89**, 162–171, 2015.

- [3] Z. Bažant, M. Verdure, Mechanics of progressive collapse: Learning from World Trade Center and building demolitions. *Journal of Engineering Mechanics*, **133**, 308–319, 2007.
- [4] J.M. Adam, F. Parisi, J. Sagaseta, X. Lu, Research and practice on progressive collapse and robustness of building structures in the 21st century. *Engineering Structures*, **173**, 122–149, 2018.
- [5] J. Yu, K.H. Tan, Experimental and numerical investigation on progressive collapse resistance of reinforced concrete beam column sub-assemblages. *Engineering Structures*, **55**, 90–106, 2013.
- [6] M. D’Antimo, M. Latour, G. Rizzano, J.F. Demonceau, Experimental and numerical assessment of steel beams under impact loadings. *Journal of Constructional Steel Research*, **158**, 230–247, 2019.
- [7] A.D.A. Vieira, S.P. Triantafyllou, D.A. Bournas, Strengthening of RC frame subassemblies against progressive collapse using TRM and NSM reinforcement. *Engineering Structures*, **207**, 110002, 2020.
- [8] R. Zandonini, N. Baldassino, F. Freddi, Robustness of steel-concrete flooring systems. An experimental assessment. *Stahlbau*, **83**(9), 608–613, 2014.
- [9] E.S. Johnson, J.E. Meissner, L.A. Fahnestock, Experimental Behavior of a Half-Scale Steel Concrete Composite Floor System Subjected to Column Removal Scenarios. *Journal of Structural Engineering (ASCE)*, **142**(2), 04015133, 1–12, 2016.
- [10] R. Zandonini, N. Baldassino, F. Freddi, G. Roverso, Steel-Concrete Composite Frames under the Column Loss Scenario: an Experimental study. *Journal of Constructional Steel Research*, **162**, 105527, 2019.
- [11] N. Stathas, I. Karakasis, E. Strepelias, X. Palios, S. Bousias, M.N. Fardis. Tests and analysis of RC building, with or without masonry infills, for instant column loss. *Engineering Structures*, **193**, 57–67, 2019.
- [12] H.Z. Jahromi, A.G. Vlassis, B.A. Izzuddin, Modelling approaches for robustness assessment of multi-storey steel-composite buildings. *Engineering Structures*, **51**, 278–294, 2013.
- [13] V. De Biagi, F. Parisi, D. Asprone, B. Chiaia, G. Manfredi, Collapse resistance assessment through the implementation of progressive damage in finite element codes. *Engineering Structures*, **136**, 523–534, 2017.
- [14] D. Stephen, D. Lam, J. Forth, J. Ye, K.D. Tsavdaridis, An evaluation of modelling approaches and column removal time on progressive collapse of building. *Journal of Constructional Steel Research*, **153**, 243–253, 2019.
- [15] C. Dimopoulos, F. Freddi, T.L. Karavasilis, G. Vasdravellis, Progressive collapse of Self-Centering moment resisting frames. *Engineering Structures*, **208**: 109923, 2020.
- [16] G. Mucedero, E. Brunesi, F. Parisi, Non-linear material modelling for fibre-based progressive collapse analysis of RC framed buildings. *Engineering Failure Analysis*, **118**, 104901, 2020.
- [17] A.F. Santos, A. Santiago, M. Latour, G. Rizzano, Robustness analysis of steel frames subjected to vehicle collisions, *Structures*, **25**, 930–942, 2020.

- [18] A.G. Vlassis, B.A. Izzuddin, A.Y. Elghazouli, D.A. Nethercot, Design oriented approach for progressive collapse assessment of steel framed buildings. *Structural Engineering International*, **16**(2), 129-136, 2006.
- [19] N. Hoffman, U. Kuhlmann, J.F. Demonceau, J.P. Jaspart, N. Baldassino, F. Freddi, R. Zandonini, Robust impact design of steel and composite building structures: The Alternate Load Path Approach. *IABSE Workshop 2015, Safety, Robustness and Condition Assessments of Structures*, Helsinki, Finland, 2015.
- [20] EN1991–1–7. Eurocode 1: Actions on structures – Part 1–7: General actions – Accidental actions. European Standard EN 1991–1–7. *European Committee for Standardization* (CEN), Brussels, Belgium, 2006.
- [21] DoD. Unified Facilities Criteria (UFC) – Design of structures to resist progressive collapse. 4-023-0314, July 2009 – Change 3, 1 November 2016. *United States Department of Defense* (DoD), 2016.
- [22] GSA. Progressive collapse analysis and design guidelines for new federal office buildings and major modernization projects. *General Services Administration*, Washington, DC, 2003.
- [23] F. Freddi, V. Novelli, R. Gentile, E. Velu, A. Andonov, S. Andreev, F. Greco, E. Zhuleku, Observations from the 26th November 2019 Albania Earthquake: the Earthquake Engineering Field Investigation Team (EEFIT) mission. *Bulletin of Earthquake Engineering* 2021. <https://doi.org/10.1007/s10518-021-01062-8>
- [24] S. Pampanin, D. Bolognini, A. Pavese. Performance-Based Seismic Retrofit Strategy for Existing Reinforced Concrete Frame Systems Using Fiber-Reinforced Polymer Composites. *Journal of Composites for Construction*, **11**(2), 211-226, 2007.
- [25] F. Freddi, E. Tubaldi, L. Ragni, A. Dall'Asta, Probabilistic Performance Assessment of low-ductility RC frames retrofitted with dissipative braces. *Earthquake Engineering and Structural Dynamics*, **42**(7), 993-1011, 2013.
- [26] N. Augenti, A. Nanni, F. Parisi, Construction failures and innovative retrofitting. *Buildings*, **3**(1), 100-121, 2013.
- [27] L. Gioiella, E. Tubaldi, F. Gara, L. Dezi, A. Dall'Asta. Modal properties and seismic behaviour of buildings equipped with external dissipative pinned rocking braced frames. *Engineering Structures*, **172**, 807-819, 2018.
- [28] F. Freddi, E. Tubaldi, A. Zona, A. Dall'Asta. Seismic performance of dual systems coupling moment-resisting frames and buckling-restrained braced frames. *Earthquake Engineering and Structural Dynamics*, **50**(2): 329–353, 2021.
- [29] R. Gentile, C. Galasso, Simplified seismic loss assessment for optimal structural retrofit of RC buildings. *Earthquake Spectra*, **37**(1), 346-365, 2021.
- [30] M. Shayanfar, M. Bigonah, D. Sobhani, M. Zabihi-Samani. The Effectiveness Investigation of New Retrofitting Techniques for RC Frame against Progressive Collapse. *Civil Engineering Journal*, **4**(9), 2018.
- [31] K. Jinkoo, S. Woo-Seung, Retrofit of RC frames against progressive collapse using prestressing tendons. *The Structural Design of Tall and Special Buildings*, **22**, 349–361, 2013.

- [32] CEN, European Committee for Standardization. EN 1992-1-1. Eurocode 2 (EC2): design of concrete structures – Part 1. 1: General rules and rules for buildings. Brussels; 2004.
- [33] E. Brunesi, R. Nascimbene, F. Parisi, N. Augenti, Progressive collapse fragility of reinforced concrete framed structures through incremental dynamic analysis. *Engineering Structures*, **104**, 65–79, 2015.
- [34] E. Brunesi, F. Parisi, Progressive collapse fragility models of European reinforced concrete framed buildings based on pushdown analysis. *Engineering Structures*, **152**, 579–596, 2017.
- [35] F. Parisi, M. Scalvenzi, E. Brunesi, Performance limit states for progressive collapse analysis of reinforced concrete framed buildings. *Structural Concrete*, **20**, 68–84, 2019.
- [36] F. McKenna, G.L. Fenves, M.H. Scott. Open system for earthquake engineering simulation (OpenSees) 2000.
- [37] B.D. Scott, R. Park, M.J.N. Priestley, Stress–strain behavior of concrete confined by overlapping hoops at low and high strain rates. *ACI Journal*, **79**(1), 13–27, 1982.
- [38] Seismosoft. SeismoStruct—A computer program for static and dynamic non-linear analysis of framed structures. 2016. Available from: www.seismosoft.com.
- [39] EN 1998-1 (2004) (English): Eurocode 8: Design of structures for earthquake resistance – Part 1: General rules, seismic actions and rules for buildings
- [40] E. Brunesi and F. Parisi. Progressive collapse fragility models of European reinforced concrete framed buildings based on pushdown analysis. *Engineering Structures*, **152**, 579-596, 2017.
- [41] D.E. Biskinis, G.K. Roupakias, M.N. Fardis, Degradation of shear strength of reinforced concrete members with inelastic cyclic displacement. *ACI Structural Journal*, **101**(6), 773-783, 2004.
- [42] CS.LL.PP. NTC 2018, Aggiornamento delle «Norme tecniche per le costruzioni», *Gazzetta Ufficiale della Repubblica Italiana* 42, 2018.
- [43] CNR-DT 200 R1/2013. Guide for the Design and Construction of Externally Bonded FRP Systems for Strengthening Existing Structures. *CNR – Advisory Committee on Technical Recommendations for Construction*, 2013.

OPTIMAL LATERAL RESISTING SYSTEMS FOR HIGH-RISE BUILDINGS UNDER SEISMIC EXCITATIONS

Giulia Angelucci¹, Giuseppe Quaranta², and Fabrizio Mollaioli¹

¹Department of Structural and Geotechnical Engineering, Sapienza University of Rome
via Gramsci 53, 00197 Rome, Italy
e-mail: {giulia.angelucci,fabrizio.mollaioli}@uniroma1.it

² Department of Structural and Geotechnical Engineering, Sapienza University of Rome
via Eudossiana 18, 00184 Rome
e-mail: giuseppe.quaranta@uniroma1.it

Keywords: Lateral bracing system, Seismic design, Stochastic optimization, Tall building, Topology optimization.

Abstract. *It is generally presumed that the design of tall buildings is mainly dictated by wind loads rather than seismic actions because of the high flexibility and, therefore, long natural periods. However, slender buildings exhibit a complex dynamic behavior, and the involvement of higher modes can result in higher flexural and shear demands than expected. Overlooking the importance of strength, stiffness, and stability requirements in seismic design of tall buildings can thus lead to excessive damage, large residual deformations, and even failure. In this regard, since pure rigid frames alone are not sufficient to withstand lateral loads, as those due to earthquakes, bracing systems are often introduced to stiffen the steel frameworks of tall buildings. The design of lateral bracing systems, in turn, calls for the selection of a suitable pattern for the diagonals arrangement, which is commonly performed through trial-and-error procedures that can require many iteration cycles. It is too evident that this approach does not neither ensure the convergence towards a design solution able to fulfill all requirements, nor the achievement of an optimal solution that minimizes the consumption of structural material and thus the total construction costs. In this context, topology optimization might represent an effective tool for improving the design of tall buildings under earthquake. Therefore, a topology optimization methodology is here presented to support the selection of the most effective design solution for the lateral bracing systems of tall buildings, in such a way to meet minimum weight requirement while ensuring the highest structural performance. Specifically, a density-based approach is adopted to establish an optimization design procedure able to generate optimal lateral-resisting systems for tall buildings subjected to earthquakes. The optimum design is formulated in terms of minimum compliance, also to facilitate the comparison of the material distribution results with those already available in the literature. Numerical results presented in this work are concerned with two-dimensional case studies, which are envisioned as part of realistic tall buildings.*

1 INTRODUCTION

The introduction of automated optimization approaches has demonstrated great potential in assisting designers to achieve more efficient and advanced structural systems than those obtained using traditional iterative procedures. Specifically, topology optimization has attracted significant attention in the last decades as a robust computational tool for the identification of high-performing design solutions at reduced material consumption. Efficiency and effectiveness of topology optimization for defining bracing systems in multi-story buildings has been widely demonstrated in recent research works, most of which refer to wind loading within deterministic frameworks [1–5].

Although interesting results have been successfully achieved under static loading conditions, slender buildings exhibit a complex dynamic behavior where the involvement of higher modes can result in high flexural and shear demands. To this end, a great effort has been devoted to incorporate the topology optimization problem in a dynamic setting. Previous attempts targeted at enhancing the dynamic performance of structural systems through topology optimization have addressed the maximization of the natural eigenfrequencies of structures under free vibration [6–9] and the minimization of the dynamic compliance [10–12]. Because element-wise design variables operate on both stiffness and self-mass of the continuum domain, the mitigation of the overall dynamic response can be properly performed within a topological optimization approach via density-based formulations. However, it is easy to observe that optimizing the topology of large-scale models, as the case of tall buildings, inevitably involves a huge number of degrees of freedom. Hence, the limitations associated with the use of computationally expensive finite element models have led recently to the implementation of model reduction techniques based on modal decomposition methods [13–15]. In dynamic topology optimization problems, the seismic ground motion is usually modeled as stochastic process using the random vibration theory. In most of the existing works, seismic loading conditions are commonly simulated using a stationary Gaussian-type stochastic excitation whereas the design criterion is concerned with the compliance minimization [16–18] or the strain energy minimization [19].

This paper presents a computational framework for the minimization of the dynamic compliance in linear elastic multi-story buildings subjected to seismic ground motion. The optimization procedure integrates the random vibration theory together with the Solid Isotropic Material with Penalization (SIMP) technique whereas a gradient-based optimizer is employed for updating the design variables. Particularly, the use of the random vibration theory offers several advantages as compared to traditional time-history analyses since it allows to perform iterative optimization procedures at affordable computational cost. Compared to response analysis based on integration schemes in the time domain, in fact, this allows to speed up the optimization routines while accurately identifying the stochastic features of the seismic behavior of the building without performing time consuming Monte Carlo simulations. Finally, numerical examples are presented to demonstrate the influence of the mass modeling on the final topologies. The applicability of the formulation within topology optimization procedures as well as stability and effectiveness of the proposed approach in finding the optimum solutions are discussed with reference to a paradigmatic case study. Mesh independent solutions are monitored by operating a gradual refinement of the mesh structure over the design domain.

2 OPTIMUM DESIGN UNDER DETERMINISTIC CONDITIONS

This work is meant to optimize the lateral loading resisting systems for seismically excited large structures by means of topology optimization. For a better understanding of the optimiza-

tion problem, the topology optimization problem in static and dynamic settings are sequentially discussed henceforth.

For a linear elastic structure with a continuous domain discretized into n_d degrees of freedom and n_f finite elements, the most common topology optimization problem formulation in case of static loads aims at minimizing the compliance of the structural system under volume constraints, that is:

$$\begin{aligned} \min_{\boldsymbol{\rho}} \{ & \mathbf{u}^\top \mathbf{K} \mathbf{u} \} \\ \text{s.t.} & \\ & \sum_{e=1}^{n_f} V_e = V_{max} \\ & \boldsymbol{\rho}_\ell \leq \boldsymbol{\rho} \leq \boldsymbol{\rho}_u, \end{aligned} \quad (1)$$

where V_e is the volume of the generic finite element e within the meshed domain whereas $\boldsymbol{\rho} = \{d_1 \dots \rho_e \dots \rho_{n_f}\}$ represents the set of design variables with lower and upper bounds $\boldsymbol{\rho}_\ell$ and $\boldsymbol{\rho}_u$, respectively. Moreover, \mathbf{K} and \mathbf{u} are global stiffness matrix and static displacements vector, respectively. The constrain in Eq. (1) ensures that the volume of the final optimal solution does not exceed a threshold value equal to V_{max} .

In order to formulate the topology optimization for dynamic problems, a linear viscous elastic structure is assumed according to the Rayleigh damping model:

$$\mathbf{C} = a_0 \mathbf{M} + a_1 \mathbf{K}, \quad (2)$$

where \mathbf{M} is the constant global mass matrix whereas a_0 and a_1 are two positive constants calculated by imposing that the damping ratio ξ_s is the same for the first two modes of the structure. Therefore, the following relationships hold:

$$a_0 = \xi_s \frac{2\omega_1\omega_2}{\omega_1 + \omega_2}, \quad (3a)$$

$$a_1 = \xi_s \frac{2}{\omega_1 + \omega_2}, \quad (3b)$$

where ω_1 and ω_2 are the first two circular natural frequencies of the structure. If the structural system is subjected to a seismic ground acceleration \ddot{u}_g within the time window $[0, t_f]$, then the motion equation reads:

$$\ddot{\mathbf{u}} + \mathbf{M}^{-1} \mathbf{C} \dot{\mathbf{u}} + \mathbf{M}^{-1} \mathbf{K} \mathbf{u} = -\mathbf{r} \ddot{u}_g, \quad (4)$$

where \mathbf{u} are now the dynamic displacements of the structure, \mathbf{r} is the incidence vector and the dots indicate the derivative with respect to time. Formally, the statement of the topology optimization problem for dynamical systems can thus be expressed by rearranging the static compliance problem in Equation (1) as follows:

$$\begin{aligned} \min_{\boldsymbol{\rho}} \left\{ \int_0^{t_f} \mathbf{u}^\top \mathbf{K} \mathbf{u} dt \right\} \\ \text{s.t.} & \\ & \sum_{e=1}^{n_f} V_e = V_{max} \\ & \boldsymbol{\rho}_\ell \leq \boldsymbol{\rho} \leq \boldsymbol{\rho}_u. \end{aligned} \quad (5)$$

3 OPTIMUM DESIGN FOR STOCHASTIC SEISMIC LOADING

The topology optimization problem for structures subjected to stationary stochastic seismic loading is now discussed. The seismic ground motion model is a filtered white Gaussian noise, and the structural system dynamics is described using the state-space representation. Once the covariance matrix of the stochastic response is obtained, the topology optimization problem is presented.

3.1 Stochastic seismic excitation model

Random vibration theory allows to assess the probabilistic response of dynamical systems under random dynamic loads without the need of performing extensive Monte Carlo simulations based on direct integration of the motion equations. This makes random vibration theory especially attractive for topology optimization of large structures under dynamic loads characterized by inherent randomness. Therefore, the seismic ground motion \ddot{u}_g is herein modeled as a stationary filtered white Gaussian noise through the Clough-Penzien filter as follows:

$$\ddot{u}_g = \mathbf{a}_p^\top \mathbf{z}_p, \quad (6a)$$

$$\dot{\mathbf{z}}_p = \mathbf{D}_p \mathbf{z}_p + \mathbf{v}_p W, \quad (6b)$$

where

$$\mathbf{a}_p = \{-\omega_p^2 \quad -2\xi_p\omega_p \quad \omega_k^2 \quad 2\xi_k\omega_k\}^\top, \quad (7a)$$

$$\mathbf{z}_p = \{u_p \quad \dot{u}_p \quad u_k \quad \dot{u}_k\}^\top, \quad (7b)$$

$$\mathbf{D}_p = \begin{bmatrix} 0 & 1 & 0 & 0 \\ -\omega_p^2 & -2\xi_p\omega_p & \omega_k^2 & 2\xi_k\omega_k \\ 0 & 0 & 0 & 1 \\ 0 & 0 & -\omega_k^2 & -2\xi_k\omega_k \end{bmatrix}, \quad (7c)$$

$$\mathbf{v}_p = \{0 \quad 0 \quad 0 \quad -1\}^\top. \quad (7d)$$

where ω_p and ξ_p , ω_k and ξ_k are the filter parameters whereas W is a zero-mean white Gaussian noise having constant power spectral density S_0 . It is evaluated as function of the peak ground acceleration \ddot{u}_g^{max} according to the following relationship:

$$S_0 = \frac{(\ddot{u}_g^{max})^2}{\gamma^2 \left[\pi \omega_k \left(2\xi_k + \frac{1}{2\xi_k} \right) \right]}, \quad (8)$$

where $\gamma = 2.8$ denotes the peak factor, see for instance Liu et al. [20].

3.2 Covariance analysis

By assembling the equation of motion in Eq. (4) and the filter equation in Eq. (6), the state-space representation of the overall dynamics is obtained as follows:

$$\underbrace{\begin{Bmatrix} \dot{\mathbf{z}}_s \\ \dot{\mathbf{z}}_p \end{Bmatrix}}_{\dot{\mathbf{z}}} = \underbrace{\begin{bmatrix} \mathbf{A}_s & \mathbf{H}_p \\ \mathbf{0}_{4 \times 2n_d} & \mathbf{D}_p \end{bmatrix}}_{\mathbf{A}} \underbrace{\begin{Bmatrix} \mathbf{z}_s \\ \mathbf{z}_p \end{Bmatrix}}_{\mathbf{z}} + \underbrace{\begin{Bmatrix} \mathbf{0}_{2n_d \times 1} \\ \mathbf{v}_p W \end{Bmatrix}}_{\mathbf{f}}, \quad (9)$$

where

$$\mathbf{z}_s = \{\mathbf{u} \quad \dot{\mathbf{u}}\}^\top, \quad (10)$$

$$\mathbf{A}_s = \begin{bmatrix} \mathbf{0}_{n_d} & \mathbf{I}_{n_d} \\ -\mathbf{M}^{-1}\mathbf{K} & -\mathbf{M}^{-1}\mathbf{C} \end{bmatrix}, \quad (11)$$

$$\mathbf{H}_p = [\mathbf{0}_{n_d \times 4} \quad -\mathbf{r}\mathbf{a}_p^\top]^\top, \quad (12)$$

while $\mathbf{0}$ is a (square or rectangular) null matrix or vector and \mathbf{I} is the (square) identity matrix, respectively (their size is explicated in the corresponding subscripts, where a single number is used for a square matrix). Given this state-space representation, the response covariance matrix of the resulting linear time-invariant system is defined as follows:

$$\mathbf{R} = \mathbb{E}[\mathbf{z}\mathbf{z}^\top] = \mathbb{E}\left[\begin{Bmatrix} \mathbf{z}_s \\ \mathbf{z}_p \end{Bmatrix} \begin{Bmatrix} \mathbf{z}_s & \mathbf{z}_p \end{Bmatrix}\right] = \begin{bmatrix} \mathbf{R}_{\mathbf{z}_s\mathbf{z}_s} & \mathbf{R}_{\mathbf{z}_s\mathbf{z}_p} \\ \mathbf{R}_{\mathbf{z}_p\mathbf{z}_s} & \mathbf{R}_{\mathbf{z}_p\mathbf{z}_p} \end{bmatrix}, \quad (13)$$

where

$$\mathbf{R}_{\mathbf{z}_s\mathbf{z}_s} = \begin{bmatrix} \mathbf{R}_{\mathbf{uu}} & \mathbf{R}_{\mathbf{u}\dot{\mathbf{u}}} \\ \mathbf{R}_{\dot{\mathbf{u}}\mathbf{u}} & \mathbf{R}_{\dot{\mathbf{u}}\dot{\mathbf{u}}} \end{bmatrix}. \quad (14)$$

The matrix \mathbf{R} , in turn, is the solution of the Lyapunov equation in stationary conditions, which reads:

$$\mathbf{A}\mathbf{R} + \mathbf{R}\mathbf{A}^\top + \mathbf{B} = \mathbf{0}_{2n_d+4 \times 2n_d+4}, \quad (15)$$

where \mathbf{B} is a matrix whose elements are equal to zero except that the element whose index is $(2n_d + 4, 2n_d + 4)$, which is equal to $2\pi S_0$.

3.3 Optimum design under stochastic seismic loads

By applying the mean value operator $\mathbb{E}[\cdot]$ to the objective function \mathcal{F} of the optimization problem formulated in Eq. (5), it can be found that:

$$\mathbb{E}[\mathcal{F}] = \mathbb{E}\left[\int_0^T \mathbf{u}^\top \mathbf{K} \mathbf{u} dt\right] = \int_0^T \mathbf{r}^\top (\mathbf{K} \otimes \mathbf{R}_{\mathbf{uu}}) \mathbf{r} dt, \quad (16)$$

where \otimes is the term-by-term product and $\mathbf{R}_{\mathbf{uu}}$ is the covariance matrix of the structural displacements (i.e., the square block of size $n_d \times n_d$ of the matrix \mathbf{R} in Eq. (14) whose elements index lies between 1 and n_d). Hence, by recalling that a stationary ground motion is here assumed, the topology optimization problem in Eq. (5) can be simplified as follows:

$$\begin{aligned} & \min_{\boldsymbol{\rho}} \{\mathbf{r}^\top (\mathbf{K} \otimes \mathbf{R}_{\mathbf{uu}}) \mathbf{r}\} \\ & \text{s.t.} \\ & \sum_{e=1}^{n_f} V_e = V_{max} \\ & \boldsymbol{\rho}_\ell \leq \boldsymbol{\rho} \leq \boldsymbol{\rho}_u \end{aligned} \quad (17)$$

4 COMPUTATIONAL ISSUES

4.1 Topology design via Solid Isotropic Material with Penalization

The Solid Isotropic Material with Penalization (SIMP) approach is adopted in this work in order to find efficiently the optimal solution for the topology optimization problem formulated in Eq. 17. The computational procedure starts with a spatial discretization of the continuum design domain. The SIMP approach [21] is thus performed by assuming that the design variable is constant over the finite element with a resulting uniform distribution of the structural material. The mechanical properties of each element are determined using a heuristic power-law interpolation that relates the element-wise design variable with the element elastic properties as follows:

$$E_e(\rho_e) = \rho_e^p E_0 \text{ with } \rho_{min} \leq \rho_e(d_j) \leq 1, \quad (18)$$

where E_0 is the elastic modulus of the base material and ρ_{min} is a non-zero minimum value for $\rho_e(d_j)$ that serves at preventing the singularity of the stiffness matrix. A coefficient $p > 1$ is introduced to penalize the presence of intermediate densities in the relaxed setting and steer the solution to discrete integer values (i.e., black-and-white digital image).

It is well recognized that topology optimization problems are especially sensitive to numerical instabilities, which are related to the possible non-existence/non-uniqueness of the optimal solution as well as to the lack of convergence, thereby resulting in some anomalies into the final design. The presence of checkerboarding, mesh dependence and local minima makes the interpretation of the optimal layout unfeasible and should be avoided by adopting a proper regularization scheme. To circumvent the occurrence of such problems, the density-filter proposed in [22] is adopted in the present work. It relies on the convolution product between a filter kernel and the design density vector, which leads to:

$$\rho_e(d_j) = \frac{\sum_{j \in \mathcal{N}_e} H_{ej} d_j}{\sum_{j \in \mathcal{N}_e} H_{ej}}, \quad (19)$$

where H_{ej} are weighting functions defined through a linearly decaying function of fixed-length radius r_{min} . The linear density filter function modifies the densities of the element e to be a function of the design variable d_j and of its neighborhood \mathcal{N}_e .

Because the density variable is assumed to be constant over each finite element, the relationship in Eq. (18) can be implemented for the finite element stiffness matrix by simply scaling it before the global stiffness matrix is assembled. The finite element stiffness matrix is interpolated and expressed in terms of E_0 as follows:

$$\mathbf{K}_e(\rho_e) = E_e(\rho_e) \mathbf{K}_e^0 = \rho_e^p \mathbf{K}_e^0, \quad (20)$$

where \mathbf{K}_e^0 is the finite element stiffness matrix with unit elastic modulus. The adoption of the SIMP approach is particularly beneficial if implemented in iterative algorithms since it allows calculating the finite element stiffness matrices at the beginning of the procedure. For each loop, finite element stiffness matrices are simply updated using the fictitious elasticity modulus E_e and then assembled to solve for the system covariance matrix.

4.2 SENSITIVITY ANALYSIS

The derivative of the objective function f in Eq. (17) with respect to the design variable ρ_e is:

$$\frac{\partial f}{\partial \rho_e} = \mathbf{r}^\top \left(\frac{\partial \mathbf{K}}{\partial \rho_e} \otimes \mathbf{R}_{uu} \right) \mathbf{r} + \mathbf{r}^\top \left(\mathbf{K} \otimes \frac{\partial \mathbf{R}_{uu}}{\partial \rho_e} \right) \mathbf{r}. \quad (21)$$

For this preliminary study, a direct differentiation approach is adopted. The calculation of the derivatives $\partial \mathbf{R}_{uu} / \partial \rho_e$ requires the solution of the following associate stationary Lyapunov equation:

$$\mathbf{A} \frac{\partial \mathbf{R}}{\partial \rho_e} + \frac{\partial \mathbf{R}}{\partial \rho_e} \mathbf{A}^\top + \bar{\mathbf{B}} = \mathbf{0}_{2n_d+4 \times 2n_d+4} \text{ for } e = 1, \dots, n_f, \quad (22)$$

with

$$\bar{\mathbf{B}} = \frac{\partial \mathbf{A}}{\partial \rho_e} \mathbf{R} + \mathbf{R} \frac{\partial \mathbf{A}^\top}{\partial \rho_e}. \quad (23)$$

It is also noted that:

$$\frac{\partial \mathbf{A}}{\partial \rho_e} = \begin{bmatrix} \frac{\partial \mathbf{A}_s}{\partial \rho_e} & \mathbf{0}_{2n_d \times 4} \\ \mathbf{0}_{4 \times 2n_d} & \mathbf{0}_4 \end{bmatrix}, \quad (24)$$

in which

$$\frac{\partial \mathbf{A}_s}{\partial \rho_e} = \begin{bmatrix} \mathbf{0}_{n_d} & \mathbf{0}_{n_d} \\ \mathbf{M}^{-1} \frac{\partial \mathbf{M}}{\partial \rho_e} \mathbf{M}^{-1} \mathbf{K} - \mathbf{M}^{-1} \frac{\partial \mathbf{K}}{\partial \rho_e} & \mathbf{M}^{-1} \frac{\partial \mathbf{M}}{\partial \rho_e} \mathbf{M}^{-1} - \mathbf{M}^{-1} \frac{\partial \mathbf{C}}{\partial \rho_e} \end{bmatrix}. \quad (25)$$

The derivative of \mathbf{C} with respect to ρ_e is calculated as follows:

$$\frac{\partial \mathbf{C}}{\partial \rho_e} = \frac{\partial a_0}{\partial \rho_e} \mathbf{M} + a_0 \frac{\partial \mathbf{M}}{\partial \rho_e} + \frac{\partial a_1}{\partial \rho_e} \mathbf{K} + a_1 \frac{\partial \mathbf{K}}{\partial \rho_e}, \quad (26)$$

where

$$\frac{\partial a_0}{\partial \rho_e} = \frac{\partial a_0}{\partial \omega_1} \frac{\partial \omega_1}{\partial \rho_e} + \frac{\partial a_0}{\partial \omega_2} \frac{\partial \omega_2}{\partial \rho_e}, \quad (27a)$$

$$\frac{\partial a_1}{\partial \rho_e} = \frac{\partial a_1}{\partial \omega_1} \frac{\partial \omega_1}{\partial \rho_e} + \frac{\partial a_1}{\partial \omega_2} \frac{\partial \omega_2}{\partial \rho_e}. \quad (27b)$$

The derivatives of the constants a_0 and a_1 with respect to ρ_e are calculated as follows:

$$\frac{\partial a_0}{\partial \omega_1} = \frac{2\xi_s \omega_2^2}{(\omega_1 + \omega_2)^2}, \quad \frac{\partial a_0}{\partial \omega_2} = \frac{2\xi_s \omega_1^2}{(\omega_1 + \omega_2)^2}, \quad (28)$$

$$\frac{\partial a_1}{\partial \omega_1} = \frac{-2\xi_s}{(\omega_1 + \omega_2)^2}, \quad \frac{\partial a_1}{\partial \omega_2} = \frac{-2\xi_s}{(\omega_1 + \omega_2)^2}, \quad (29)$$

whereas

$$\frac{\partial \omega_1}{\partial \rho_e} = \frac{1}{2\omega_1} \frac{\partial \lambda_1}{\partial \rho_e}, \quad \frac{\partial \omega_2}{\partial \rho_e} = \frac{1}{2\omega_2} \frac{\partial \lambda_2}{\partial \rho_e} \quad (30)$$

are the derivatives of the first two circular natural frequencies of the structure. The terms λ_1 and λ_2 are the first two eigenvalues of the following eigenproblem:

$$\phi_k^\top \mathbf{K} \phi_k = \lambda_k \phi_k^\top \mathbf{M} \phi_k, \quad (31)$$

in which ϕ_k is the k th eigenvector. The derivatives of λ_1 and λ_2 with respect to ρ_e are evaluated as follows:

$$\frac{\partial \lambda_1}{\partial \rho_e} = \phi_1^\top \left[\frac{\partial \mathbf{K}}{\partial \rho_e} - \lambda_1 \frac{\partial \mathbf{M}}{\partial \rho_e} \right] \phi_1, \quad \frac{\partial \lambda_2}{\partial \rho_e} = \phi_2^\top \left[\frac{\partial \mathbf{K}}{\partial \rho_e} - \lambda_2 \frac{\partial \mathbf{M}}{\partial \rho_e} \right] \phi_2, \quad (32)$$

under the assumption of distinct real eigenvalues and the mass orthonormalization condition.

Finally, by virtue of the SIMP method, it is obtained that:

$$\frac{\partial \mathbf{K}}{\partial \rho_e} = \bigwedge_{e=1}^{n_f} \frac{\partial \mathbf{K}_e}{\partial \rho_e} = \bigwedge_{e=1}^{n_f} p \rho_e^{p-1} \mathbf{K}_{e,0}, \quad (33a)$$

$$\frac{\partial \mathbf{M}}{\partial \rho_e} = \bigwedge_{e=1}^{n_f} \frac{\partial \mathbf{M}_e}{\partial \rho_e} = \bigwedge_{e=1}^{n_f} q \rho_e^{q-1} \mathbf{M}_{e,0}, \quad (33b)$$

where \bigwedge stands for standard finite element assembly operator.

5 EFFECTS OF SEISMIC MASS MODELING ON FINAL TOPOLOGIES

In seismic topology design of structural systems, the dynamic load is design-dependent because the inertial load is function of position and value of the structural mass within the domain. In order to obtain objective, reliable, and feasible optimal solutions, a proper modeling of the seismic mass is, therefore, of primary importance and deserves a thorough understanding. Some examples are discussed in such a way to highlight the significance of the mass modeling assumptions on the final topologies.

The reference model is based on a two-dimensional domain with single bay and high equal to 5 m and 15 m, respectively. The inter-story height is equal to 5 m, thereby resulting in three levels along the building elevation. The floors are made of concrete decks and their mass is calculated considering dead and live loads equal to 7.0 kN/m² and 2.0 kN/m², respectively. The design domain is discretized using 4-node quadrilateral Lagrangian (Q4) elements with a uniform thickness equal to 0.15 m and a mesh size 0.25 m \times 0.25 m (which implies a total of 1,200 finite elements). The continuum domain is modeled using steel as building material, with elastic modulus $E_0 = 210$ GPa. The algorithm is executed with constant penalization factor $p = 3$, projection radius $r_{min} = 0.3$ m and initial volume fraction over the Q4 domain equal to 30%. The Rayleigh damping model is assumed with damping ratio equal to 5%. Fixed supports are considered at the base and a symmetry constraint with respect to the centerline is enforced. A seismic ground motion with $\ddot{u}_g^{max} = 0.3g$ is assumed, with $\xi_p = \xi_k = 0.6$, $\omega_p = 1.5$ rad/s and $\omega_k = 15$ rad/s.

A complete system is fully defined by combining the continuum domain with the discrete elements of the gravity load-bearing frame, as already proposed in previous works [2, 23]. The introduction of a non-designable secondary system improves the feasibility of the final solution (e.g., clearer identification of the working points, disappearance of small multiple horizontal elements) and makes the topological results independent from the direct application of the external load on the domain, whether it is static or dynamic. For a deeper understanding of the role of the secondary systems and symmetry constraints on optimal topologies of lateral resisting systems for tall buildings, the reader is referred to the work by Angelucci et al. [15].

For the seismic design of tall buildings, and multi-story buildings in general, the structural mass of the system \mathbf{M} can be decomposed into two contributions $\mathbf{M} = \mathbf{M}_f + \mathbf{M}_\Omega$, where \mathbf{M}_f is the seismic mass of the building components estimated by considering the floor tributary areas and \mathbf{M}_Ω is the mass of the designable lateral resisting system. Nevertheless, it is straightforward to recognize that, in multi-story buildings and especially for concrete slabs, the mass is primarily located at the floor levels and the lateral resisting system contributes only for a small fraction of the overall building mass. Since the seismic excitation produces inertial forces mostly associated with the tributary mass of the building \mathbf{M}_f , the introduction of the

floor mass within the optimizable domain is incorrect from a conceptual standpoint. During the optimization routines, in fact, the dynamic characteristics of the domain representing the lateral resisting system are iteratively updated according to the new material distribution and the inherent structural mass is partially removed. Additionally, it can be demonstrated that when the seismic mass is included in the designable domain, updating the mass arrangement at each iteration slows down the rate of convergence and compromises the stability of the whole topology optimization procedure. Therefore, it is required to allocate the tributary mass within a non-optimizable domain, which remains constant during the optimization routines and expediently relaxes the design-dependency of the tributary mass on the element variables (i.e., $\partial \mathbf{M}_f / \partial \rho_e$ is null). Moreover, since the weight of the bracing members is negligible compared to the mass of the story levels, it is possible to assume a massless optimizable domain in the seismic analysis, without any significant loss of accuracy. The structural mass is thus kept constant during the iterative process, and this allows to state that the final topologies are almost exclusively dependent on the stiffness properties of the continuum elements. Within the scope of this work, the tributary mass is located at each floor level in the horizontal direction only, provided that the dynamic excitation does not include external forces at the nodes in the vertical and rotational degrees of freedom.

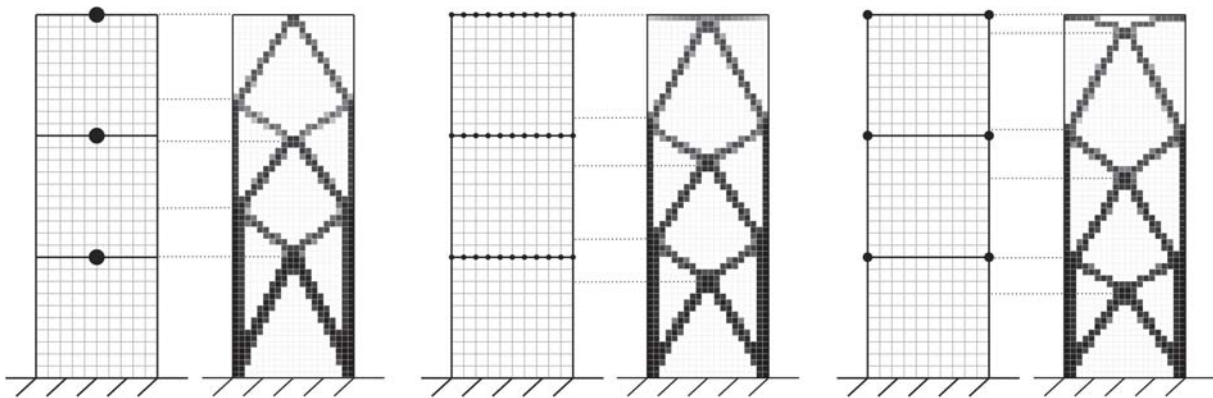


Figure 1: Reference models and optimal topologies for different mass modelling: lumped mass at the floor diaphragms (a, b); distributed mass at story levels (c, d); lumped mass at master nodes (e, f).

In the analysis and design of tall buildings subjected to lateral loads, floor slabs are usually assumed to possess high in-plane stiffness, and the assumption of diaphragm constraints reflects quite well the real behavior. This assumption justifies the concentration of the structural mass in a single point at each floor as illustrated in Figure 1a, and allows to further reduce the degrees of freedom of the structural system, thereby simplifying the seismic analysis. However, in case of topology optimization, the introduction of a displacement constraint undermines the objectivity of the final solution because the rigidity/flexibility of the floor diaphragms has a significant influence on the building model. As illustrated in Figure 1b, the optimized layout shows a design-dependent topology, where the diagonal arrangement of the lateral resisting system is affected by the specific location of the tributary mass in the middle of each story level.

Since rigid diaphragm constraints lead to flawed solutions, the effects of floor deformability cannot be disregarded and a reasonable stiffness must be assigned to each floor. Figure 1c illustrates the designable and non-designable domains of the reference model, in which the tributary mass is uniformly distributed at the floor levels. The beams are discretized into smaller ele-

ments, which allows the mass nodes to be coincident with the interior joints of the quadrilateral mesh. The optimal layout presented in Figure 1d results in a K-brace arrangement at the top of the building, due to the development of inertial forces along the line. The top member, in fact, is needed to transfer the load along the bay between the far sided columns. Although correct from a topological standpoint, this solution is theoretically inaccurate since the presence of floor beams at each story level contributes to transmit gravity loads to the vertical members of the unbraced frame. The reference model is thus modified accordingly to reduce the tributary mass to a discrete number of master nodes of the floor system located at the intersections of the secondary system (extreme corners of the quadrilateral mesh in Figure 1e). The resulting topology in Figure 1f shows the optimal solution where theoretical concepts and modeling assumptions are both fulfilled.

Because inertial loads originate at master nodes of the secondary system only and assuming that the auxiliary perimeter framework is not included in the optimizable domain, the final topologies are independent from the master nodes definition. This allows to choose arbitrarily the secondary system bounding the continuum domain. Additionally, the distribution of the seismic mass at a discrete number of nodes suggests the adoption of a reduced-order model during the dynamic analysis of the structural system. Through static condensation, stiffness and mass matrices (and implicitly the damping matrix) of the complete system can be properly reduced to the degrees of freedom of the master nodes.

The demanding computational cost of the dynamic topology optimization process certainly benefits from the sub-structuring technique, where inversion and eigenanalysis of large-size matrices are generally involved. Without any loss of objectivity, the eigenvalue analysis can be performed on the reduced-order system since natural frequencies and modal shapes are defined at the master node locations only.

6 CASE STUDY

The topology optimization problem is solved next to define the lateral resisting system of a multi-story building subjected to ground motion excitation. Particularly, given a stationary-type support excitation described as filtered white Gaussian noise, the optimal material distribution is attained by minimizing the dynamic compliance in the continuum design domain under a volume constraint. The reference model is a regular multi-story building with height and width equal to 40 m and 20 m, respectively. The external skin of the building is split into four panels, such that each façade can be analyzed as a continuous optimizable design domain discretized by using Q4 elements with uniform thickness equal to 0.15 m. A two-dimensional case study is deemed accurate enough. The structure is idealized with fixed supports and symmetry constraints are imposed.

An auxiliary load-bearing framework bounding the continuum domain is designed with bay width and inter-story height equal to 5 m and 4 m, respectively. W8x21 steel cross-sections are preliminary designed to model columns and beams of the unbraced frame, which is considered as a non-designable domain during the optimization process. The frame members are discretized into smaller elements, so that the nodes of the beam-column elements (thick black lines in Figure 2) and those of the Q4 elements (grid area in Figure 2) coincide each other. This operation results in a continuous connection between the discrete frame and the continuum domain throughout height and width of the building. Floor slabs are placed every 4 m. The associated seismic mass is calculated considering gravity loads equal to 9.0 kN/m² and tributary influence areas. The floor mass is lumped at the master nodes at 5 locations for each floor level, corresponding to the intersection of floor beam and column lines (black nodes in Figure

2). The algorithm is executed once again with constant penalization factor $p = 3$, projection radius $r_{min} = 0.3$ m and initial volume fraction over the Q4 domain equal to 30%.

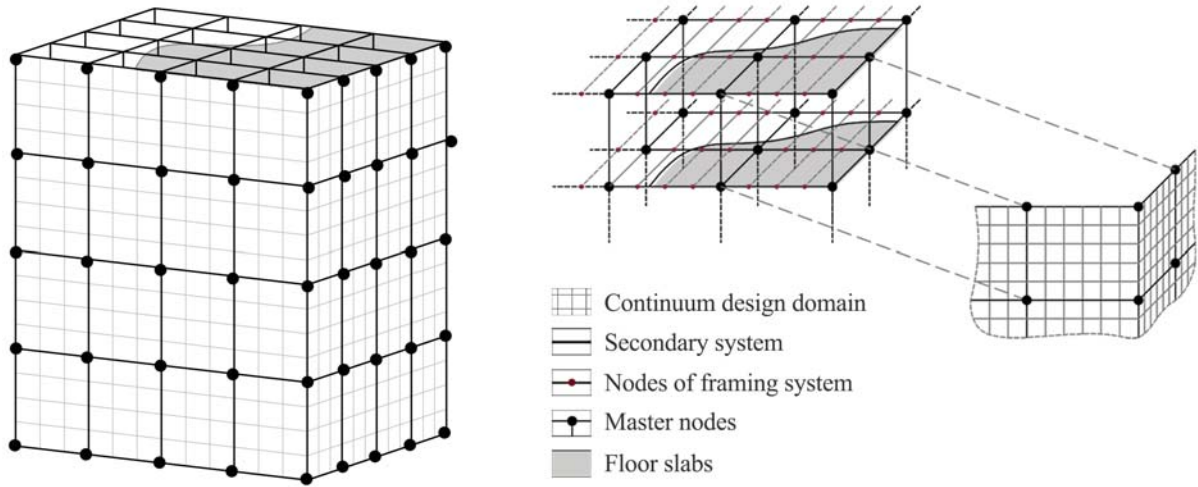


Figure 2: Schematic of the constitutive elements of the numerical model.

The topology optimization is first performed for the reference model with unit mesh size ($1 \text{ m} \times 1 \text{ m}$, resulting in 800 finite elements). The optimal topology is displayed in Figure 3b in terms of filtered design variables. Figure 3c shows the optimal layout obtained when refining the design domain using a mesh size equal to $0.5 \text{ m} \times 0.5 \text{ m}$ (total of 3,200 finite elements). The results clearly demonstrate that the optimal topologies are qualitatively the same, with the possible exception of major differences at the domain boundaries, which become gradually smoother with the mesh refinement. The material distribution within the design domain assumes a precise arrangement composed by two lateral columns and two pairs of full-width diagonal braces. The optimized domain is post-processed to physically appreciate the results of the topology optimization process and correctly identify the location of the working points of brace-to-brace and brace-to-column nodes. It is worth noticing here that the optimal topology does not include the presence of a secondary framed system (which is constituted by intermediate beams and columns), and thus it can be omitted from the final layout. The evolution of the optimal solution during the optimization routines is illustrated in Figure 4 by plotting objective function (dynamic compliance) and constraint function (material volume) values with respect to the number of iterations required until a tolerance of 1% is met (the filled circle marks the convergence). The efficiency of the topology optimization framework is confirmed by the steady convergence as well as the limited number of iterations.

7 CONCLUSIONS

The minimum compliance formulation for the topology optimization of large structures under seismic excitation has been discussed in this work. The huge computational effort required, even for the case of linear elastic systems, has made the adoption of classical time-history dynamic analyses prohibitive. To overcome this challenge and deal with the topology optimization of tall buildings under seismic loads, random vibration theory has been explored in this study. The well-posedness of the optimization problem has been ensured through the adoption of the SIMP approach. A sensitivity analysis of the objective function with respect to the ele-

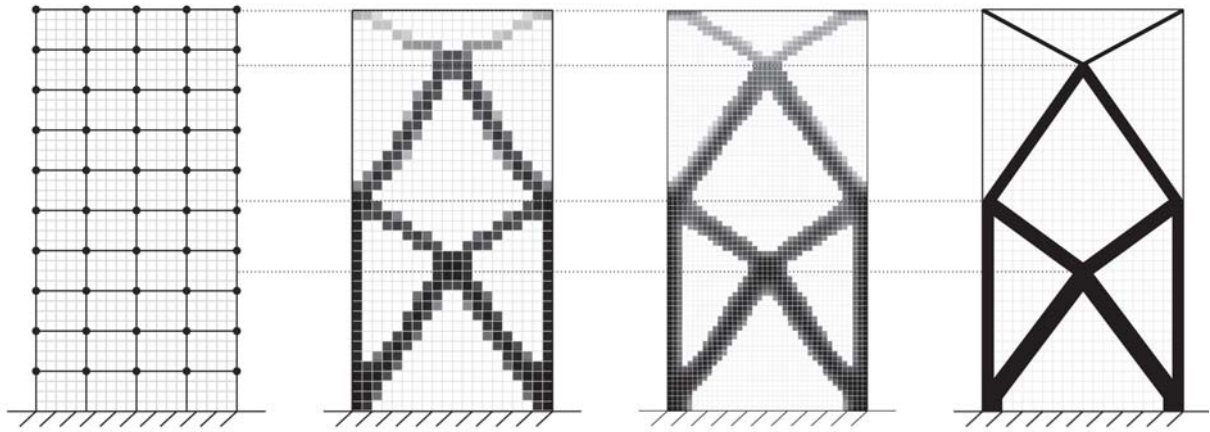


Figure 3: Reference model of the $40\text{ m} \times 20\text{ m}$ tall building (a), optimal topologies for mesh sizes $1\text{ m} \times 1\text{ m}$ (b) and $0.5\text{ m} \times 0.5\text{ m}$ (c), post-processed refined layout (d).

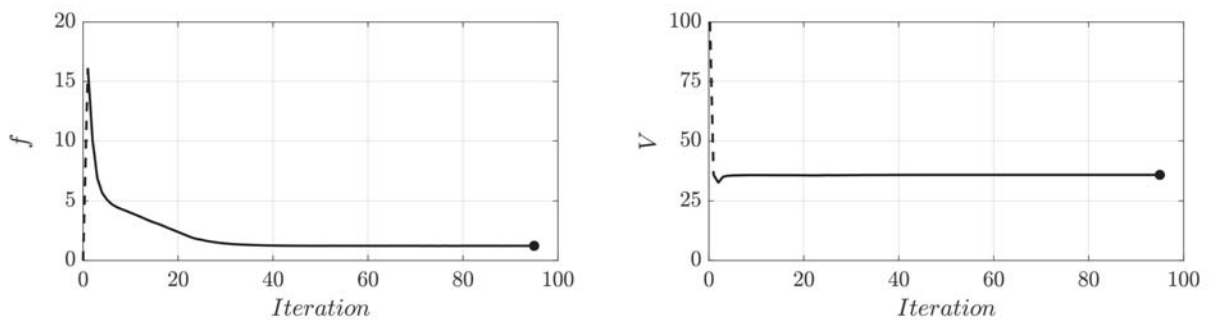


Figure 4: Objective function (left) and constraint function (right) value for mesh size $1\text{ m} \times 1\text{ m}$.

ment design variables has been assessed analytically to foster the employment of gradient-based methods.

The present study has paid special attention to mass modeling techniques for tall buildings under earthquakes within topology optimization procedures. Numerical examples have been presented to validate the effects of preliminary theoretical assumptions on the final layouts. Finally, a paradigmatic case study has been discussed to demonstrate effectiveness and stability of the proposed framework in finding the optimum solutions. A gradually refined mesh process has been also presented to explore the efficiency of the optimization procedure in avoiding numerical mesh-dependency instabilities.

The findings presented here should be considered as a first attempt toward the development of more sophisticated dynamic formulations within topology optimization frameworks. Further improvements and extensions will be included in future works to identify optimal lateral resisting systems for multi-story buildings subjected to stochastic processes, where fully non-stationary models will be considered to simulate the seismic ground motion more accurately.

REFERENCES

- [1] O. Sigmund, A 99 line topology optimization code written in Matlab. *Structural and Multidisciplinary Optimization*, **21**(2), 120–127, 2001.

- [2] L.L. Stromberg, A. Beghini, W.F. Baker, G.H. Paulino, Topology optimization for braced frames: combining continuum and beam / column elements. *Engineering Structures*, **37**, 106–124, 2012.
- [3] C. Talischi, G.H. Paulino, A. Pereira, I.F.M. Menezes, PolyTop: a Matlab implementation of a general topology optimization framework using unstructured polygonal finite element meshes. *Structural and Multidisciplinary Optimization*, **45**(3), 329–357, 2012.
- [4] K. Liu, A. Tovar, An efficient 3D topology optimization code written in Matlab. *Structural and Multidisciplinary Optimization*, **50**(6), 1175–1196, 2014.
- [5] G. Angelucci, S.M.J. Spence, F. Mollaioli, An integrated topology optimization framework for three-dimensional domains using shell elements. *Structural Design of Tall and Special Buildings*, **30**(1), 1–17, 2021.
- [6] A.R. Díaz, N. Kikuchi, Solutions to shape and topology eigenvalue optimization problems using a homogenization method. *International Journal for Numerical Methods in Engineering*, **35**(7), 1487–1502, 1992.
- [7] A.P. Seyranian, E. Lund, N. Olhoff, Multiple eigenvalues in structural optimization problems. *Structural Optimization*, **8**(4), 207–227, 1994.
- [8] N.L. Pedersen, Maximization of eigenvalues using topology optimization. *Structural and Multidisciplinary Optimization*, **20**(1), 2–11, 2000.
- [9] G.H. Yoon, Structural topology optimization for frequency response problem using model reduction schemes. *Computer Methods in Applied Mechanics and Engineering*, **199**(25–28), 1744–1763, 2010.
- [10] S. Min, N. Kikuchi, Y.C. Park, S. Kim, S. Chang, Optimal topology design of structures under dynamic loads. *Structural Optimization*, **17**(2–3), 208–218, 1999.
- [11] Y. Maeda, S. Nishiwaki, K. Izui, M. Yoshimura, K. Matsui, K. Terada, Structural topology optimization of vibrating structures with specified eigenfrequencies and eigenmode shapes. *International Journal for Numerical Methods in Engineering*, **67**(5), 597–628, 2006.
- [12] E.T. Filipov, J. Chun, G.H. Paulino, J. Song, Polygonal multiresolution topology optimization (PolyMTOP) for structural dynamics. *Structural and Multidisciplinary Optimization*, **53**(4), 673–694, 2016.
- [13] W.H. Greene, R.T. Haftka, Computational aspects of sensitivity calculations in linear transient structural analysis. *Structural Optimization*, **3**(3), 176–201, 1991.
- [14] J. Zhao, C. Wang, Dynamic response topology optimization in the time domain using model reduction method. *Structural and Multidisciplinary Optimization*, **53**(1), 101–114, 2016.
- [15] G. Angelucci, F. Mollaioli, O. AlShawa, Evaluation of optimal lateral resisting systems for tall buildings subject to horizontal loads. *Procedia Manufacturing*, **44**, 457–464, 2020.

- [16] Y. Yang, M. Zhu, M.D. Shields, J.K. Guest, Topology optimization of continuum structures subjected to filtered white noise stochastic excitations. *Computer Methods in Applied Mechanics and Engineering*, **324**, 438–456, 2017.
- [17] M. Zhu, Y. Yang, J.K. Guest, M.D. Shields, Topology optimization for linear stationary stochastic dynamics: applications to frame structures. *Structural Safety*, **67**, 116–131, 2017.
- [18] J. Chun, J. Song, G.H. Paulino, System-reliability-based design and topology optimization of structures under constraints on first-passage probability. *Structural Safety*, **76**, 81–94, 2019.
- [19] B.S. Kang, G.J. Park, J.S. Arora, A review of optimization of structures subjected to transient loads. *Structural and Multidisciplinary Optimization*, **31**(2), 81–95, 2006.
- [20] Z. Liu, W. Liu, Y. Peng, Random function based spectral representation of stationary and non-stationary stochastic processes. *Probabilistic Engineering Mechanics*, **45**, 115–126, 2016.
- [21] M.P. Bendsøe, O. Sigmund, Material interpolation schemes in topology optimization. *Archive of Applied Mechanics*, **69**(9), 635–654, 1999.
- [22] B. Bourdin, Filters in topology optimization. *International journal for numerical methods in engineering*, **50**(9), 2143–2158, 2001.
- [23] S. Bobby, S.M. Spence, A. Kareem, Data-driven performance-based topology optimization of uncertain wind-excited tall buildings. *Structural and Multidisciplinary Optimization*, **54**(6), 1379–1402, 2016.

NON-INVASIVE VIBRATING CONTROL OF THE ZOSER PYRAMID

M. Shadlou¹, P. Cacciola¹, A. Ayoub², Y.F. Rashed³ and A. Tombari¹

¹ School of Environment and Technology, University of Brighton, Brighton, UK

e-mail: {m.shadlou, p.cacciola, a.tombari}@brighton.ac.uk

² School of Mathematics, Computer Science and Engineering, City University of London, UK

email: ashraf.ayoub.1@city.ac.uk

³ Department of Structural Engineering, Cairo University, Giza, Egypt,

email: youssef@eng.cu.edu.eg

Abstract

The historical sites and monuments in Egypt are among the most important in the world and conserving this cultural heritage is crucial. The large damages observed in hundreds of monuments and in the Zoser Pyramid after the Cairo Earthquake in 1992 unveiled the fragility of the Egyptian heritage asset to seismic hazards. This paper aims to investigate the use of the innovative non-invasive vibration control device, the vibrating barrier (ViBa) as a potential strategy to mitigate the effects of the seismic action on the Zoser Pyramid. In this regard, a finite element model of the Zoser Pyramid and surrounding soil has been developed. A pertinent ground motion acceleration induced by the 1992 Cairo earthquake event has been simulated through spectral representation method with power spectral density function defined by seismological data available for Saqqara. Moreover, a reduced-order model is implemented to facilitate the design of the ViBa device. The efficiency of the ViBa is assessed by numerical simulation of the finite element model of the ViBa-Soil-Pyramid system. Results show an evident reduction of the acceleration and stresses on the Pyramid, especially in those areas where the damages have been observed.

Keywords: Vibrating Barriers, Zoser Pyramid, Soil-Structure Interaction.

1 INTRODUCTION

Egypt has an extensive cultural heritage, reaching back more than five thousand years, with a plethora of archaeological sites considered among the most important in the world. The archaeological site of Saqqara, located at a distance of about 20 km from Cairo city, is appraised as the world's most extensive burial ground with monuments of almost every period of ancient Egyptian civilization. In this area, the Step Pyramid of Djoser or Zoser's pyramid is located. It is therefore an important legacy of ancient construction to be preserved.

Although Egypt is a region of small to moderate magnitude earthquakes [1], several events that occurred in the area from the late 1980s, with two main events, the 1992 Cairo earthquake and the 1995 Gulf of Aqaba earthquake, partly damaged the Zoser pyramid that needed of an important restoration activity to avoid the risk of collapse leading to its closure to visitors for a long time [1]. Therefore, it becomes evident that the preservation and conservation of archaeological monuments and sites require unconventional and exceptional seismic analysis and design. Conventional seismic protection systems mainly based on strengthening techniques or local devices such as dampers or seismic isolators are based on structural invasive interventions whose application clearly might risk compromising the historical value of heritage structures such as the pyramid. Those techniques are generally applied to heritage structures as a repairing technique (as done to the Zoser pyramid) rather than as a preventive strategy to mitigate future seismic actions. Ancient monuments, therefore, are left generally unprotected from future catastrophic events due to the difficulty to protect them without altering their historical value.

In this paper, the novel non-invasive seismic passive control device [2] called Vibrating Barrier (ViBa) is proposed as a mean of protection for the Zoser Pyramid. The ViBa is a device buried in the soil and detached from the surrounding structure able to absorb a significant portion of the dynamic energy arising from the ground motion. It exploits the basic principle of the structure-soil-structure interaction introduced in the early 70's [3][4]. To date, several studies on the efficiency of the ViBa have been carried out to mitigate the seismic vulnerability of different structures: Cacciola et al. [5] investigated the potential of ViBa for the seismic protection of monopiled structures, Tombari et al. [6] considered ViBa to mitigate the seismic risk of a nuclear reactor, Cacciola et al. [7] and Andreozzi et al. [8] applied ViBa to control the seismic response of heritage buildings, while the ViBa device was used to protect a large urban area in Coronado et al. [9] as well as a cluster of buildings in Tombari et al. [10]. Therefore, to mitigate the seismic response of the Zoser pyramid, the ViBa device has to be properly designed. In this regard, due to the lack of ground motion records in the area, a stochastic approach following the Boore method [11], has been adopted to determine the power spectral density function of the ground motion at the bedrock underneath the Zoser pyramid. The model has been calibrated using the seismological parameters related to the Cairo 1992 earthquake [12]. The stochastic model has been then used as seismic input for the design of the ViBa device.

Furthermore, a sub-structuring method is proposed in the paper to reduce the large order of the complete system composed of Pyramid and soil and the ViBa. Following this approach, it is possible to optimize the ViBa to minimize the effect of the ground motion on selected-response parameters (e.g. displacement, stresses). Several configurations of ViBas are proposed and their impact on the seismic response of the Pyramid is computed employing a pertinent Monte Carlo Simulation. The efficiency of the ViBa is assessed in terms of mitigation of the peak acceleration of the top of the pyramid and Von Mises stresses over one of the areas that has been damaged during the 1992 Cairo Earthquake.

2 NUMERICAL MODELLING OF ZOSER PYRAMID

The Zoser pyramid is modelled in this study as a stepped solid structure (Figure 1a) with a rectangular base of about $108\text{ m} \times 120\text{ m}$ and a total height of about 63 m . Surveying with a 3D scanner has been carried on to determine the geometry of the Zoser pyramid. Soil investigations have been also conducted at the site. Specifically, samples from the stones inside the site were tested in the laboratory for determining the properties of the materials used in building the pyramid. Moreover, a borehole with a depth of 10 meters was dug to determine the soil properties in Saqqara. The total borehole was limestone or sandy limestone interspersed with layers of silt at the depth of the borehole. No groundwater has been observed during the borehole. Geometrical dimensions of the simplified geometry used in this study pertinent to North and West sections are reported in Figure 1b and 1c, respectively. The Pyramid is made of polished white limestone modelled as an isotropic linear material defined by the elastic modulus, $E_p = 45\text{ GPa}$, Poisson's ratio, $\nu_p = 0.25$ as well as unit density, ρ_p , of 2900 kg/m^3 . The position of the bed-rock has been determined from previous studies available in the literature [13], [14] and it is considered to be located at 35m depth. The soil stratum between the bedrock and the base of the pyramid is assumed homogeneous with a shear wave velocity of 3000 m/sec considering the site investigation undertaken in the first 10m . Material properties used to define the linear elastic behaviour of the soil and Pyramid are shown in Table 1.

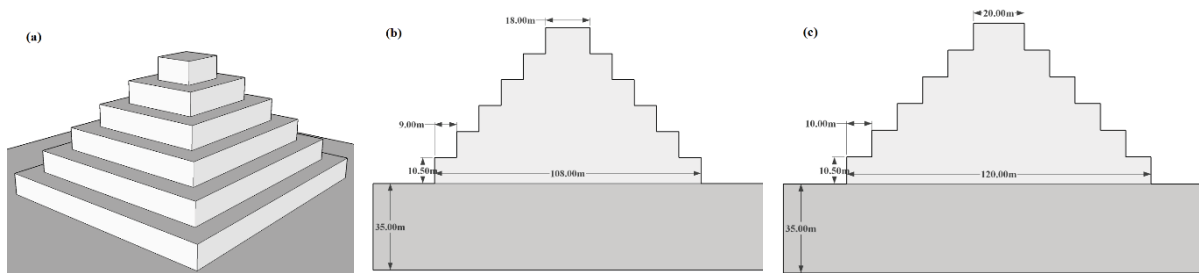


Figure 1. Zoser Pyramid, (a) 3D view, (b) North and (c) West sections of the stepped Pyramid

Soil			Pyramid		
$\rho_s\text{ (kg/m}^3\text{)}$	$E_s\text{ (kPa)}$	ν_s	$\rho_p\text{ (kg/m}^3\text{)}$	$E_p\text{ (kPa)}$	ν_p
2200	45×10^6	0.25	2900	45×10^6	0.25

Table 1. Material properties for Soil and Pyramid

Numerical Finite Element models of the fixed-base Pyramid (Figure 2a) and of the full Pyramid-Soil system (Figure 2b) are created through the software SAP2000 by using 8-node elements. A large soil model with lateral free boundaries, 500m far away from each edge of the Pyramid, is considered to mitigate the spurious waves reflected back to the system. Fully fixed restraints are used on the bottom of the soil to simulate the rigid bedrock.

A modal analysis is first carried out for the fixed-base Pyramid model: the first mode, associated with its smallest width (Figure 3a) has a natural frequency of 14.6 Hz , while the second mode, associated with the largest width (Figure 3b) is characterized by the natural frequency of 14.95 Hz .

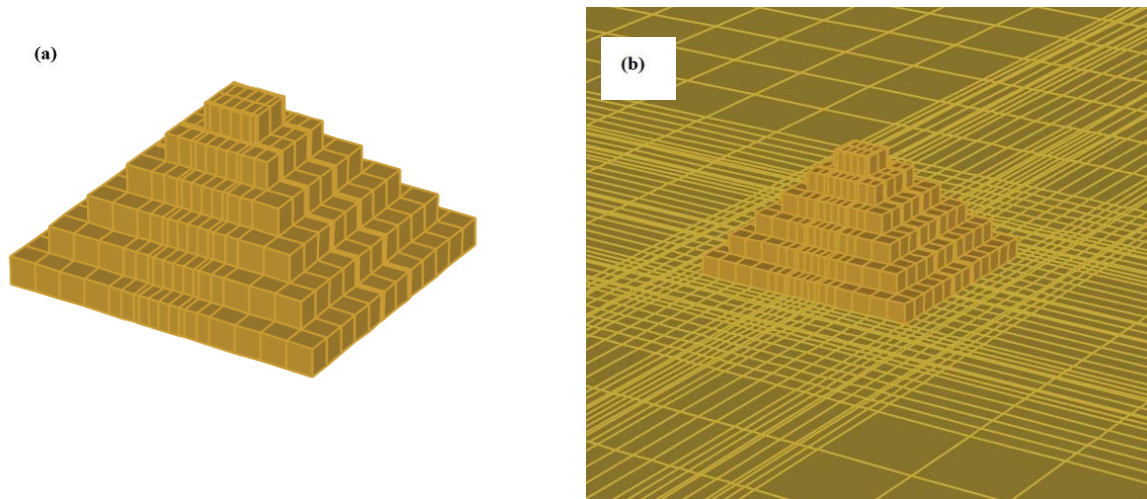


Figure 2. a) Mesh configuration of the fixed-base pyramid and b) soil-pyramid system

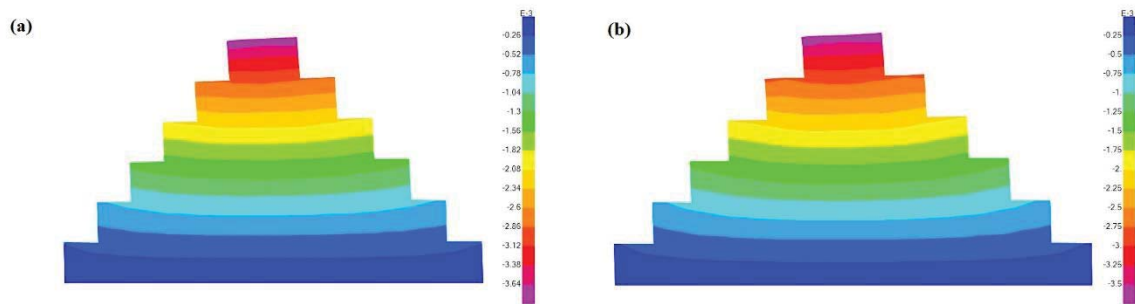


Figure 3. The amplitude of the modal vector for a) the first and b) the second mode of the Pyramid.

Successively, the modal analysis is carried out on the full Soil-Pyramid system to account for the soil-structure interaction effects: the first natural frequency of the pyramid is shifted from 14.6 Hz to 10.54 Hz, while the second natural frequency changed from 14.95 to 10.73 because of the soil flexibility (Figure 4a and b).

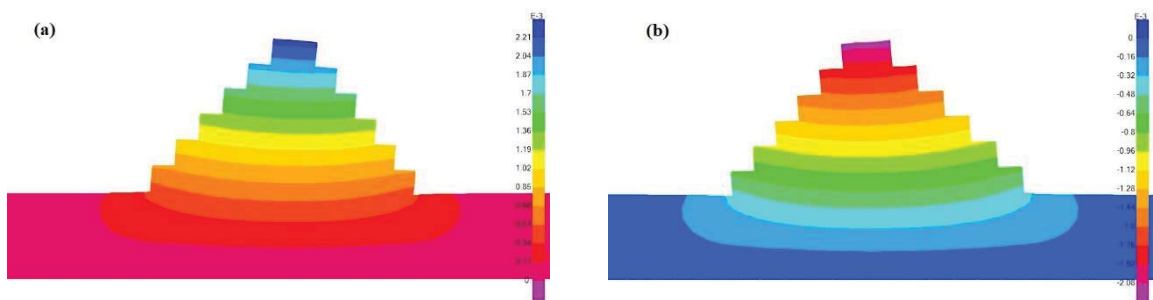


Figure 4. The amplitude of the modal vector for a) the first and b) the second mode of the soil-Pyramid system.

3 PROPOSED METHOD FOR THE DESIGN OF THE VIBRATING BARRIERS

To mitigate the seismic response of the Zoser Pyramid, the non-localised system denoted Vibrating Barrier is employed in this section. Figure 5 shows a potential implementation of the Vibrating Barrier to protect the Zoser pyramid.

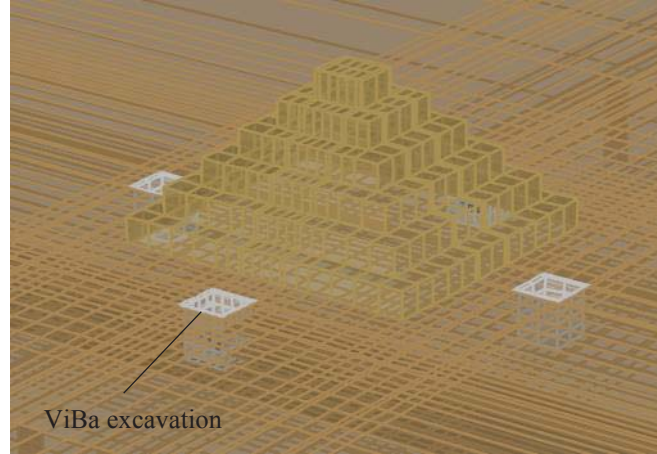


Figure 5. A potential configuration of the Vibrating Barriers to protect the Zoser pyramid

For a selected configuration, the problem to design the ViBa is therefore reduced to determine the mechanical parameters of the devices so that relevant response quantities (e.g., stresses, accelerations) are reduced.

A reduced-order model capturing the ViBa(s)-Soil-Pyramid interaction is developed to reduce the computational complexity of the optimization problem used to design the ViBa mechanical parameters. Specifically, a sub-structuring method [15], determined in the frequency domain, is used to condensate the Soil-Pyramid system into complex-valued transfer functions and, to reduce the order of the full system to just 2 translational degrees of freedom related to the translational ViBa displacement, X_v and to the displacement, X_f , of its box foundation.

Although the design method proposed in the next section is developed by considering one ViBa device, the approach can be easily extended for any number of ViBas and any possible configuration and location, by adopting the superposition principle.

3.1 A Multi-Step Approach to Evaluate the ViBa-Soil-Structure Interaction

The proposed method consists to subdivide the full domain into 2 partitions: the first subdomain represents the Soil-Pyramid system with any rigid excavations where the ViBas will be installed (Figure 6a); the second subdomain comprises the internal structure of the ViBa contained by the rigid box-foundation resting on a flexible soil medium modelled through soil-foundation impedance functions (Figure 6b). In the design approach proposed in this paper, only the translational degrees of freedom of the ViBa and its foundation, are considered. A 4-step analysis is devised as follows: i) a steady-state analysis of the first subdomain subjected to bedrock ground motion displacement, $U_b(\omega)$, modelled as unitary constant function to derive the foundation input motion of the rigid excavation, $U_{FIM}^V(\omega)$, as well as the normalized displacement in a relevant point of the Pyramid, $U_p^{(1)}(\omega)$; ii) a steady-state analysis of the first subdomain where a unitary displacement, $X_0(\omega)$, is applied to the centre of the rigidity of the excavation (Figure 7) to derive the displacement in a relevant point of the Pyramid, $U_p^{(2)}(\omega)$, as well as the complex-valued soil-foundation impedance, $\tilde{K}_h(\omega)$; iii) an inertial analysis of the ViBa-Soil subdomain where the soil is modelled through the impedance $\tilde{K}_h(\omega)$; and iv)

recovery of the complete displacement of the relevant point of the Pyramid by adopting the superposition principle. It is worth noting the control parameter of the Pyramid can be represented not just in terms of displacements but even stresses, strains, internal forces, or any relevant measure, without compromising the generality of the presented method.

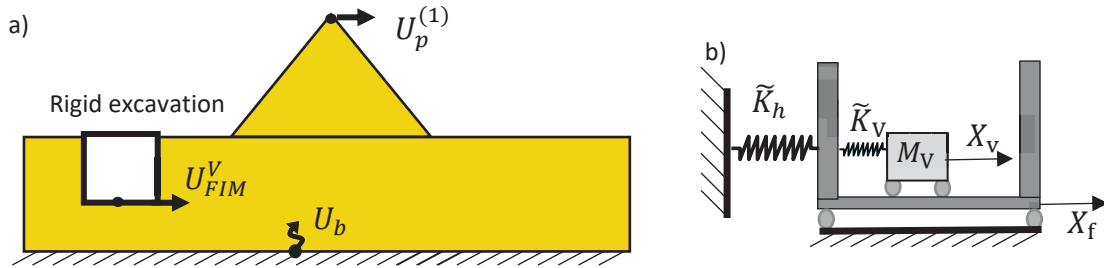


Figure 6. Sub-structuring method: a) Soil-Pyramid System; and b) ViBa-Soil System

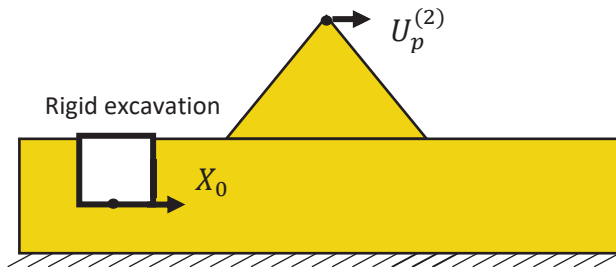


Figure 7. Steady-state analysis to condensate the Soil-Pyramid system into transfer functions

3.2 Reduced-Order ViBa-Soil-Pyramid Model Governing Equations

After computing the various complex-valued transfer functions, $U_p^{(1)}(\omega)$ in step i) and $U_p^{(2)}(\omega)$ in step ii), the design of the optimal ViBa parameters is performed on the reduced-order model of step iii) and iv) in which an extremely fast optimization analysis can be implemented. Considering the mechanical system of Figure 6b, the governing equations of the reduced-order model can be written in the frequency domain as follows:

$$\begin{cases} \tilde{K}_V X_V - \tilde{K}_V X_f - \omega^2 M_V X_V = 0 \\ (\tilde{K}_h + \tilde{K}_V) X_f - \tilde{K}_V X_V - \omega^2 M_0 X_f = \tilde{K}_h U_{FIM}^V \end{cases} \quad (1)$$

where the dependencies from the frequency ω have been omitted. Eq. (1) represents a system of algebraic equations in which X_V and X_f , are the unknown ViBa's displacement and foundation displacement, respectively, whilst \tilde{K}_V is the ViBa parameter to be optimized. To perform the optimal design of the ViBa, the complete displacement of the relevant point of the Pyramid, U_p , must be computed by superposition in step iv), as follows:

$$U_p(\omega) = \left(U_p^{(1)}(\omega) + \frac{U_p^{(2)}(\omega)}{X_0(\omega)} X_f(\omega) \right) U_g(\omega) \quad (2)$$

where $U_g(\omega)$ is the Fourier transform of the earthquake ground motion displacement applied at the bedrock. It is worth mentioning that in Eq. (2), the terms within the brackets, $H(\omega) =$

$\left(U_p^{(1)}(\omega) + U_p^{(2)}(\omega) X_f(\omega)/X_0(\omega) \right)$ represents the non-dimensional transfer function $H(\omega) = \frac{U_p}{U_g}$ between the response output of the Pyramid and the input ground motion at the bedrock.

Because of the derivation rule in the frequency domain, $H(\omega) = \frac{U_p}{U_g} = \frac{\dot{U}_p}{\dot{U}_g} = \frac{\ddot{U}_p}{\ddot{U}_g}$.

3.3 Optimal design of the ViBa

The design of the ViBa, once the mass, M_V , is assigned, involves the determination of the optimal value of the internal device, \tilde{K}_V , which can be expressed as $\tilde{K}_V = K_V(1 + i\eta_V)$ with i as an imaginary unit, K_V , real-valued stiffness of the internal device and, η_V as its loss factor.

Therefore, Eq. (2) can be re-written as

$$U_p(\omega, \alpha) = H(\omega, \alpha)U_g(\omega) \quad (3)$$

in which the parameters to be optimised, listed in the design vector $\alpha = [K_V, \eta_V]$, are made explicit in the transfer function. The optimization approach adopted in this paper involves the mitigation of the stochastic response of the Pyramid. Considering a ground motion acceleration modelled as Gaussian zero-mean stochastic process with zero mean, fully defined by the knowledge of the power spectral density function $PSD(\omega)$, it becomes straightforward to extend Eq. (3) by using the Random Vibration Theory, as follows:

$$G(\omega, \alpha) = H^*(\omega, \alpha)PSD(\omega)H(\omega, \alpha) \quad (4)$$

where $G(\omega, \alpha)$ is the PSD function in terms of acceleration at the reference point of the Pyramid and $*$ is the complex conjugate operator.

The largest value of the response in terms of acceleration, $\ddot{u}_{p,ViBa}^{max}$, of the reference point of the Pyramid protected by the ViBa technology, can be derived from Eq. (4) in approximated fashion [8] as:

$$\ddot{u}_{p,ViBa}^{max}(\alpha) \cong \eta_p \sqrt{\int_0^\infty G(\omega, \alpha) d\omega} = \eta_p \sqrt{\lambda_0(\alpha)} \quad (5)$$

where λ_0 is the zeroth-order spectral moment and η_p is the peak factor.

The objective function of the optimization approach determined on the Reduced Order Model (ROM) is defined as follows:

$$\min_{\alpha > 0} (\ddot{u}_{p,ViBa}^{max}(\alpha)) \quad (6)$$

Clearly, other response parameters can be used such as the maximum stress in a specific element or the top displacement. The efficiency of the ViBa device is then measured through the reduction factor in terms of acceleration, $R_{\ddot{u}_p}^{ROM}$, as follows:

$$R_{\ddot{u}_p}^{ROM}(\alpha) = \frac{|\ddot{u}_p^{max} - \ddot{u}_{p,ViBa}^{max}(\alpha)|}{\ddot{u}_p^{max}(\alpha)} \times 100 \quad (7)$$

Therefore, the optimization problem can be written as minimization of the objective function which can be solved with standard iterative algorithms for constrained optimization, such as the derivative-free method [16].

4 NUMERICAL RESULTS

In this study, the method proposed in Section 3 is applied to mitigate the seismic response of the Zoser Pyramid. Three ViBa configurations (hereinafter called, Case 1-2-3), oriented in the North-South (N-S) direction as depicted in Figure 8, are proposed.

Case 1 is represented by one ViBa on the Southern side of the Pyramid realized in a rigid excavation of size 20 m x 20 m x 20 m; in Case 2, one ViBa for each side of the Pyramid is considered; Case 3 considers one ViBa for each side of the Pyramid as in Case 2 but placed inside a larger rigid excavation of 60 m long, 20 wide and 20 m deep. Furthermore, in Case 3, each box-foundation contains three internal vibrating masses supposed to oscillate synchronously.

In every configuration, the excavations where the ViBas are located, are realized at a minimum distance of 15 m from each side of the Pyramid. The box foundation of the ViBa is made of four concrete retaining walls and a matt foundation. The reference point used for the optimization procedure of Section 3, indicated by point 'p' in Figure 8, is selected at the top of the Pyramid. Moreover, an area of interest is to calculate the stresses induced by the seismic event, denoted as representative element (RE) in Figure 8. Because of the damages that the Zoser Pyramid experienced over that area during the 1992 Cairo Earthquake [12], RE is employed on the edge of the pyramid.

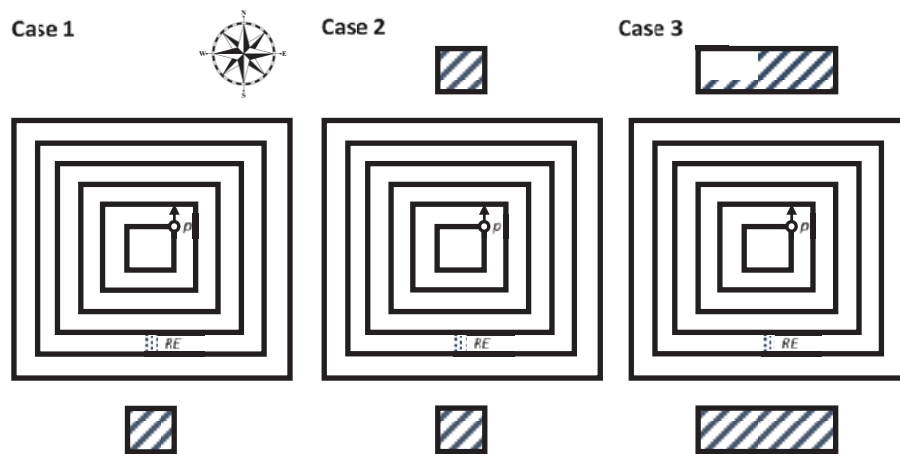


Figure 8. Top view of ViBa configurations for Case 1-2-3

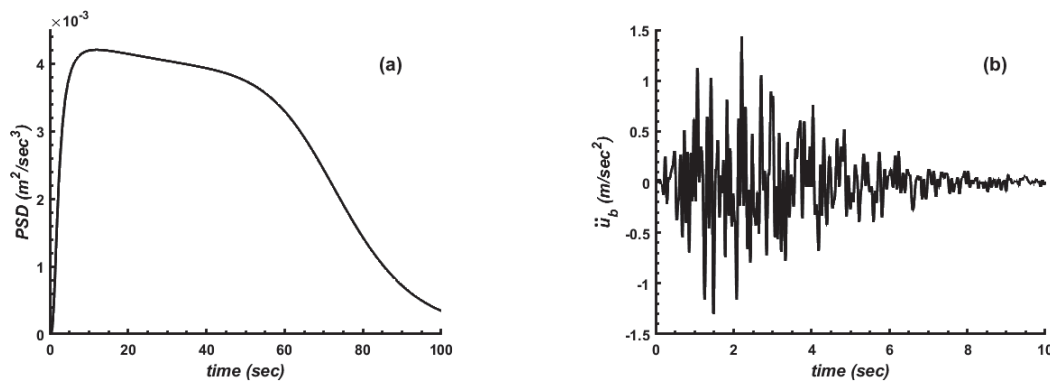


Figure 9. (a) the unilateral PSD function at the bedrock underneath the Zoser Pyramid, (b) a sample of the acceleration time series obtained by the spectral representation method

The unilateral PSD function (Figure 9a) at the bedrock, $PSD(\omega)$, determined using the Boore method [11] and the relevant seismological parameters determined in [12], is used in Eq. (4) of the proposed approach to perform the optimal design of the ViBa. Furthermore, the same PSD function is also used to generate 30 realizations of the time-history acceleration functions using the spectral representation method; these realizations are used to calculate the statistics of the seismic response of the Pyramid before and after being protected by the ViBa technology. A random sample is shown in Figure 9b for illustration purposes.

For each case, the proposed 4-step approach is performed. Results of the steady-state analyses of step i), $U_p^{(1)}(\omega)$, are shown in Figure 10a, while results from step ii), $U_p^{(2)}(\omega)$, are shown in Figure 10b. Also, in step ii) the soil-foundation impedance, $K_h(\omega)$, of Eq. (1) can be computed. In this paper, the static values, $K_h(0)=4320$ GN/m (Case 1-2) and $K_h(0)=8077$ GN/m (Case 3) are used.

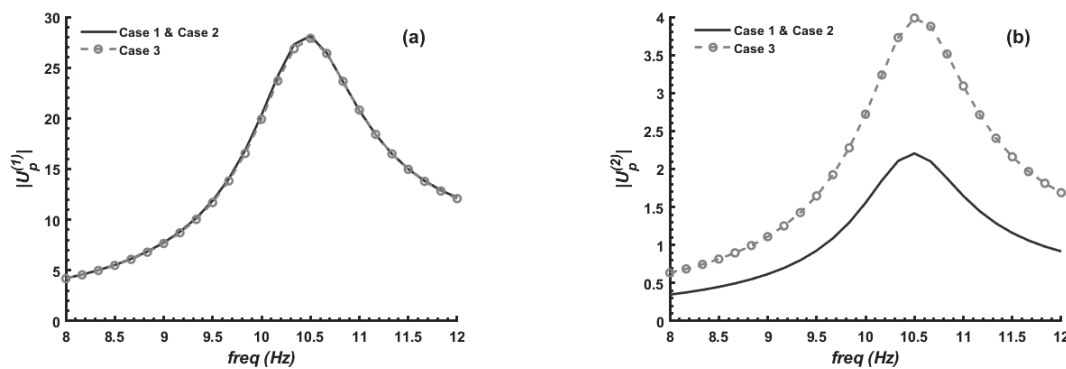


Figure 10. Results of the steady-state analysis in terms of a) $|U_p^{(1)}|$ and b) $|U_p^{(2)}|$ for Case 1-2-3

The optimization problem of Eq. (7) is performed for the 3 cases by considering the total mass of the ViBa devices, M_V , equal to 80% of the Pyramid mass, and by fixing the loss factor, η_V , to 0.1. To minimize the computational effort, a limited range of frequencies from 8 to 12 Hz, hence, around the first natural frequency of the Pyramid, is considered. Optimal parameters computed by using the proposed approach are reported in Table 2.

Case	ViBa 1			ViBa 2		
	M_V/M_p	K_V GN/m	$\eta_{n,V}$	M_V/M_p	K_V GN/m	$\eta_{n,V}$
1	0.8	7190.6	0.1	-	-	-
2	0.4	2394	0.1	0.4	1696	0.1
3	0.4	1883.4	0.1	0.3	1464.2	0.1

Table 2. Optimal design of the ViBa for Case 1-2-3.

Figure 11 shows the results of steady-state analyses in terms of power spectral density functions, $G(\omega) = G(\omega, \hat{a})$ for Case 1-2-3, where \hat{a} is the optimal design vector listing the parameters of Table 2. Results, obtained from the full FEM and ROM, are also depicted for a visual comparison. The reduced-order model with just 2 degrees of freedom captures satisfactorily the response of the full ViBa-Soil-Pyramid system. Furthermore, a comparison with the existing scenario without ViBa is reported with a grey dashed line. It can be seen that the ViBa technology greatly modifies the Pyramid's response by decreasing the total energy experienced by the Pyramid.

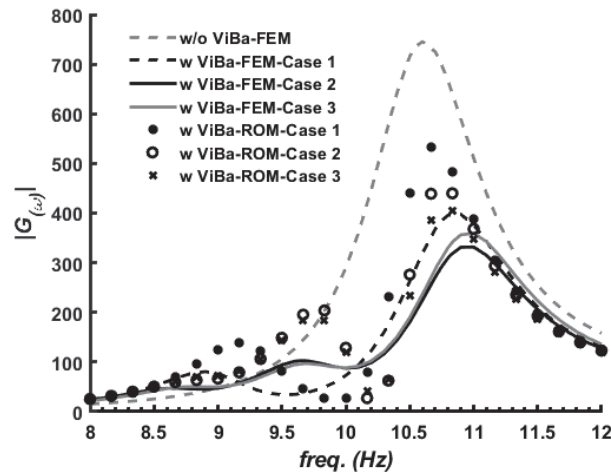


Figure 11. Steady-state response of the pyramid for different cases.

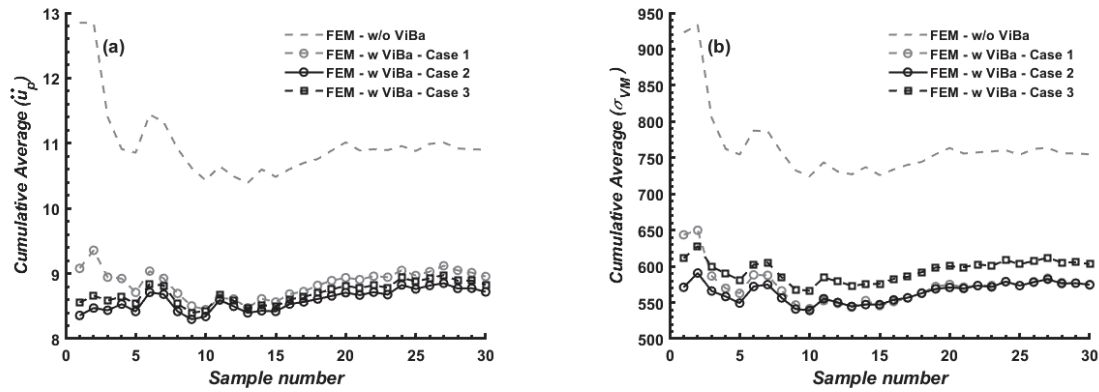


Figure 12. Cumulative average of acceleration recorded at the top of the pyramid (a) and Von Mises Stress (b) recorded at the specific element in respect of the number of realizations.

To assess the effects of the mitigation induced by the ViBa technology on the seismic response of the Pyramid, a modal time-history Monte Carlo Simulation (MCS) is performed by using the $n=30$ generated realizations. The three Cases are compared to the existing scenario of the Zoser Pyramid with no seismic protection. Figure 12 shows the convergence of the results in terms of average acceleration and Von Mises stress at the control point and reference element indicated in Figure 8.

In Figure 13, the mitigating effect of the ViBa technology against the existing scenario without the protection of the ViBa, is shown as acceleration and Von Mises time history functions for Case 1-2-3 for a randomly generated sample.

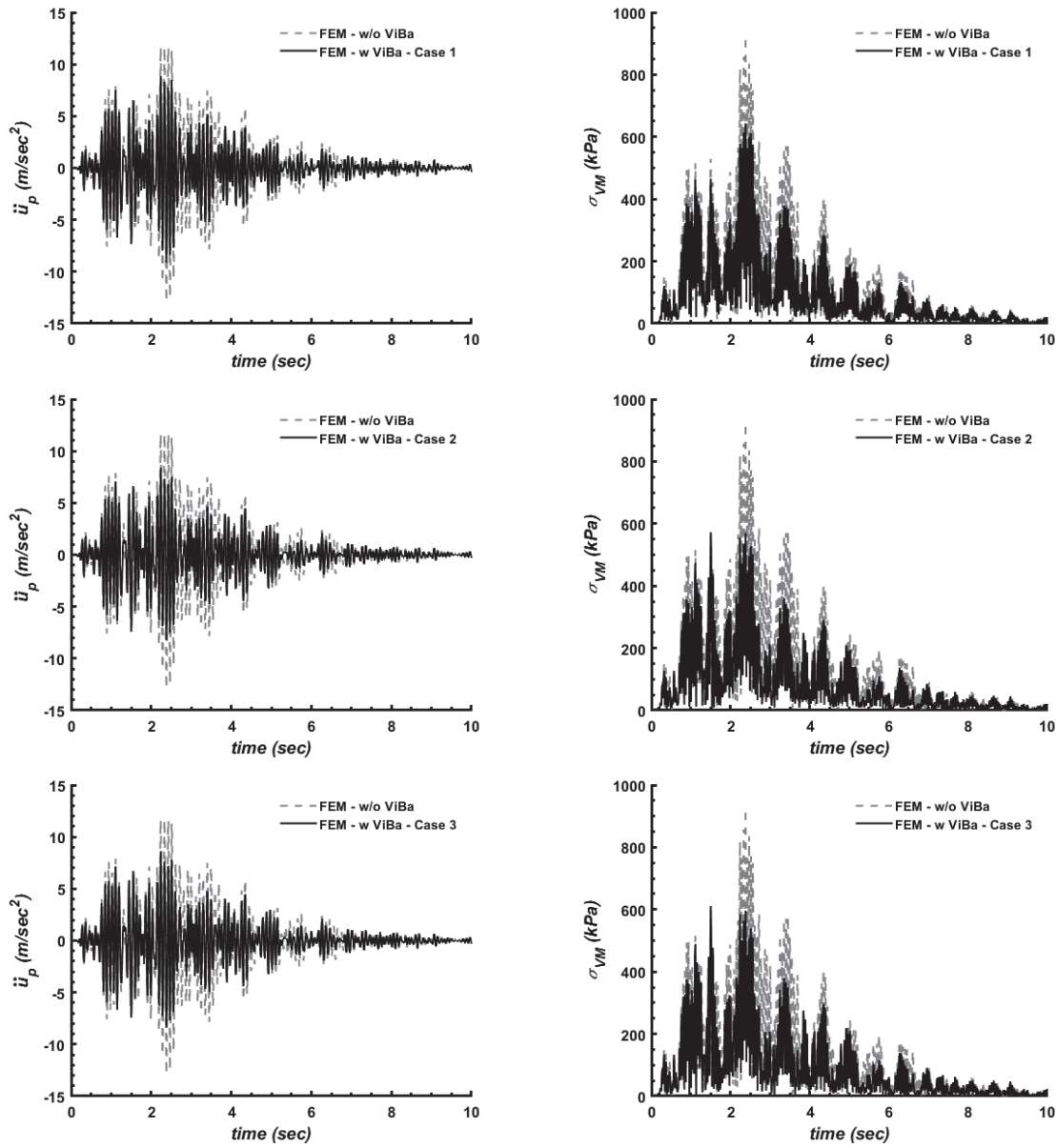


Figure 13. Acceleration time series and Von Mises Stress (σ_{VM}) time series for the top of the pyramid and specified element of the pyramid (RE), respectively, for different cases.

The mitigation of the seismic response is evaluated through a reduction factor in terms of acceleration defined as:

$$R_{\ddot{u}_p}^j = \frac{|\max(|\ddot{u}_p^j(t)|) - \max(|\ddot{u}_{p,ViBa}^j(t)|)|}{\max(|\ddot{u}_p^j(t)|)} \times 100 \quad (8)$$

where $\ddot{u}_p^j(t)$ and $\ddot{u}_{p,ViBa}^j(t)$ are the accelerations computed at the reference point of the Pyramid induced by the j -th realization for the full FEM model, before and after being protected by the ViBa technology, respectively. Therefore, the mean value is expressed as:

$$\bar{R}_{\ddot{u}_p}^{FEM} = \frac{1}{n} \sum_{j=1}^n R_{\ddot{u}_p}^j \quad (9)$$

A further expression of the reduction factor in terms of Von Mises stresses is defined as follows:

$$R_{\sigma}^j = \frac{\left| \max(|\sigma_{VM}^j(t)|) - \max(|\sigma_{VM,ViBa}^j(t)|) \right|}{\max(|\sigma_{VM}^j(t)|)} \times 100 \quad (10)$$

where $\sigma_{VM}^j(t)$ and $\sigma_{VM,ViBa}^j(t)$ are the Von Mises stresses computed at the horizontally central-second row-edge element of the pyramid induced by the j-th realization for the full FEM model, before and after being protected by the ViBa technology, respectively. Accordingly, the mean value is determined as:

$$\bar{R}_{\sigma}^{FEM} = \frac{1}{n} \sum_{j=1}^n R_{\sigma}^j \quad (11)$$

The mitigation induced by the ViBa on the seismic response of the Pyramid is shown in Figure 14a-b for both coefficients determined by Eq. (8) and (10). It is worth noting that the effect of the ViBa is beneficial for most of the events (only a few cases have been observed in which the ViBa was ineffective or slightly detrimental <2%) with a maximum reduction equal to 35 % on the peak acceleration and 39 % on the Von Mises stresses.

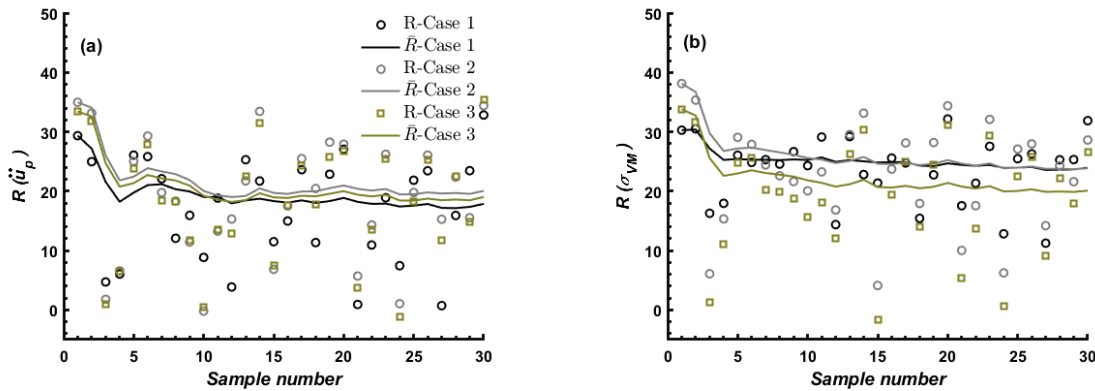


Figure 14. The mitigation provided by ViBa on the seismic response of the Pyramid; (a) mitigation on maximum acceleration, (b) mitigation on maximum Von Mises Stress.

A summary of the results is reported in Table 3 in which the computed averages of Eq. (9) and (11) from the MCS are compared with the target reduction obtained by the ROM through Eq. (7). Therefore, good reductions around 19% on the peak acceleration and about 23% on the Von Mises stress are observed for all three Cases. A slight improvement of the reduction of the peak acceleration is obtained for Case 3 (about 25%) whilst a higher reduction of the stresses on the reference element is obtained for Case 1-2 (about 24%). Remarkably, the three configurations used in this paper do not significantly affect the outcome once the same mass ratio is used, hence, more ViBas with smaller individual masses might be used to efficiently mitigate the seismic response of the Pyramid.

Case	$R_{\ddot{u}_p}^{ROM} (\%)$	$\bar{R}_{\ddot{u}_p}^{FEM} (\%)$	Rel. err (%)	$\bar{R}_{\sigma}^{FEM} (\%)$	Rel. err (%)
1	20.95	17.86	14.75	23.94	-14.27%
2	23.219	20.04	13.69	23.86	-2.76%
3	24.46	19.02	22.24	20.08	17.91%

Table 3. Reduction of the Pyramid response in terms of max acceleration and stresses

It is worth mentioning that the ViBa technology affects the whole behaviour of the Pyramid and not just the investigated control point and reference element. Therefore, the complete contour map of the Von Mises stresses is also shown for a specific instant, $t = 2.38 \text{ s}$, in which the Pyramid experienced the maximum stress at the reference element. Figure 15 shows the distribution of the stresses for the existing situation subjected to the first realization; the maximum stresses occur in the same region where the Pyramid has been largely damaged during the 1992 Cairo earthquake event.

Figure 16 shows the impact of the excavation on the stresses of the Pyramid for Case 1 and 3 for the same realization used for Figure 15. In both cases, the changes in the distribution of the stresses on the Pyramid is minimal, indicating that the excavation on its own cannot reduce the seismic body waves as opposed to the effect of trenches on surface waves (see e.g. [17]).

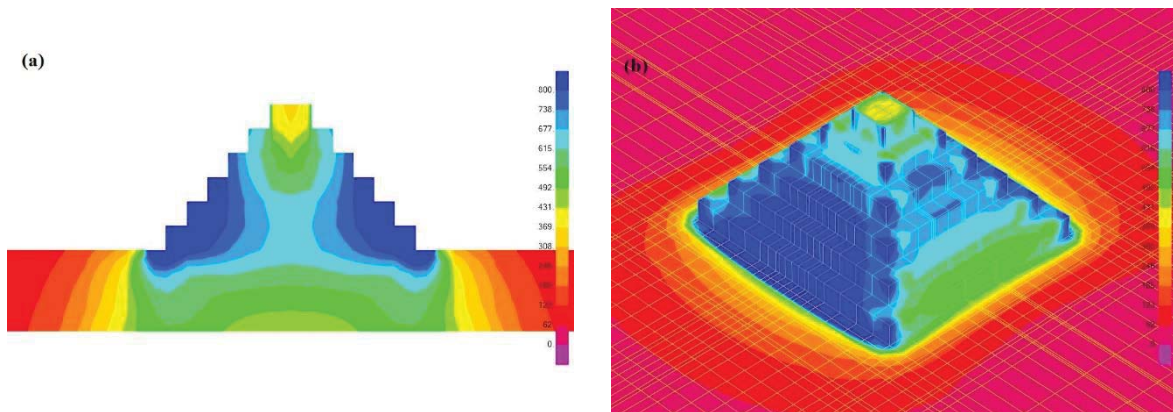


Figure 15. Instantaneous Von Mises stress contour map of a) the central cross-section and, b) the 3D soil-pyramid system for the first generated earthquake.

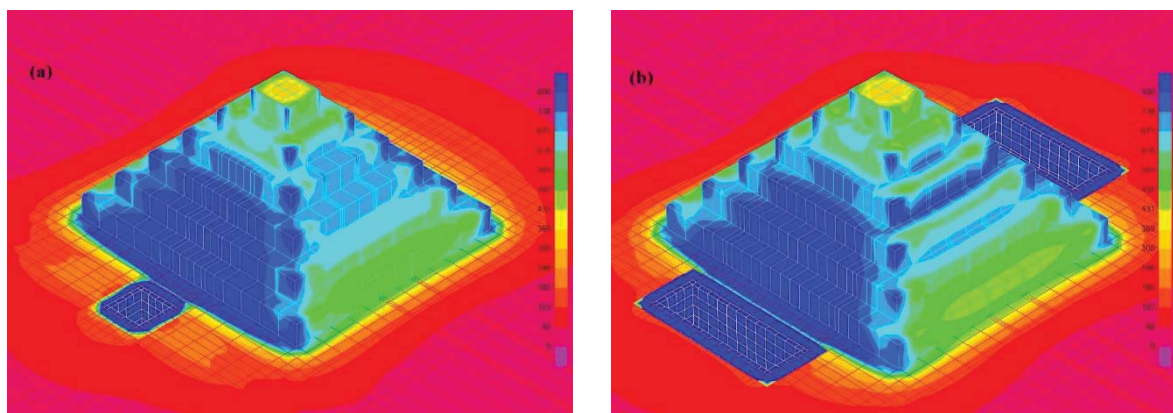


Figure 16. Effect of excavation on the response of the pyramid, (a) small excavation on one side of the pyramid, (b) large excavation on both sides of the pyramid.

Figures 17-18-19 show the response of the Pyramid protected by the ViBa device. As it can be seen, the Von Mises stresses are reduced over a large volume of the Pyramid. Particularly in Case 2, the ViBas have a narrower but greater influence over the central area whilst the large ViBas on Case 3 act in a more uniform fashion.

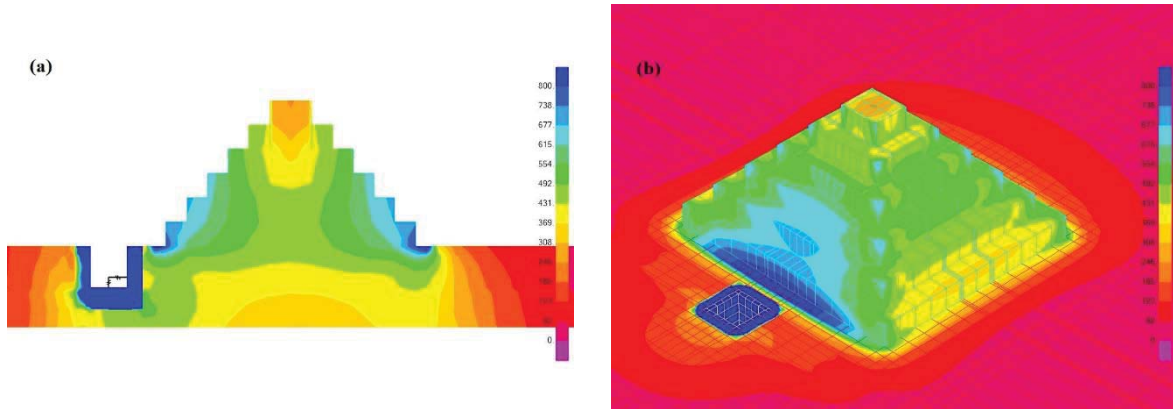


Figure 17. Maximum Von Mises stress contour map in the central cross-section and 3D for case 1 for the first generated earthquake.

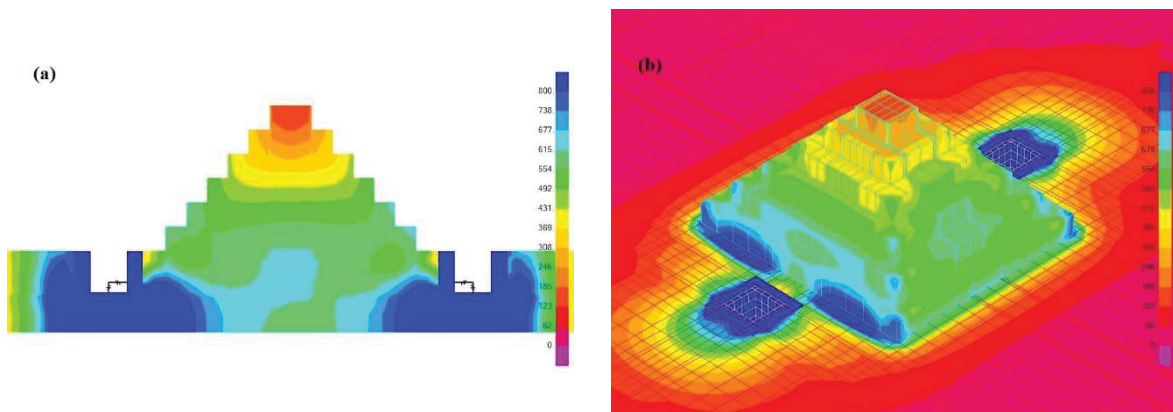


Figure 18. Maximum Von Mises stress contour map in the central cross-section and 3D for case 2 for the first generated earthquake.

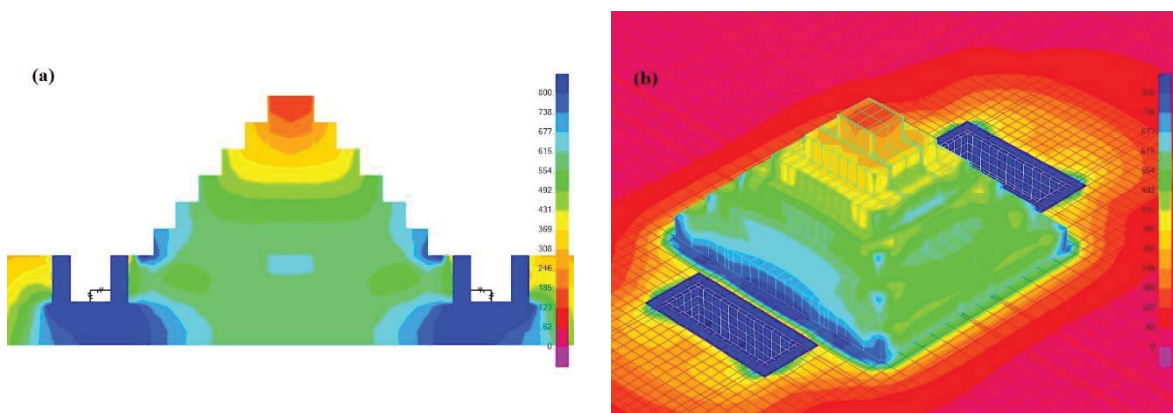


Figure 19. Maximum Von Mises stress contour map in the central cross-section and 3D for case 3 for the first generated earthquake.

5 CONCLUSIONS

In this paper, the innovative non-invasive vibration control technology called Vibrating Barrier has been applied to reduce the seismic response of the Step Pyramid of Zoser. The Pyramid has been severely damaged during the 1992 Cairo Earthquake and to guarantee its preservation, the seismic risk should be mitigated. To reduce the computational complexity of the model during the design stage of the ViBa parameters, a 4-step approach has been proposed to derive a Reduce-Order Model by adopting a sub-structuring technique. Only 2-DOFs capturing the ViBa translations of the internal device and its foundation is required. The result of the inertial analysis is then related to the seismic behaviour of the Pyramid through non-dimensional transfer functions obtained from steady-state analyses on the full FEM Soil-Pyramid system. Because the transfer functions are computed only once, this proposed approach allows performing an optimization analysis on the several parameters of the ViBa through a very fast and robust procedure. By considering a spectral representation of the 1992 Cairo earthquake, the results in terms of peak acceleration and stresses on particular control points have shown a significant reduction of the seismic response of the Pyramid when the ViBa device is used. An average reduction ranging from 20% to 24% has been observed on the Von Mises stresses with maximum mitigation of up to 39%. Remarkably, reductions have been observed in those areas where the damages have been observed. Parametric studies changing the configuration of the ViBa with one or two box-foundations and small and large individual masses were also conducted to assess their impact on efficiency. Whilst results have been obtained with a large overall mass of 80% of the Pyramid mass, the parametric analysis shows that several ViBa devices can be used with smaller masses or by improving its technology through inerters as done in [16]. Therefore, because of the impossibility to use conventional seismic control solutions without affecting its cultural heritage, the ViBa technology can be seen as a viable solution to guarantee the preservation of the ancient monuments as the Zoser pyramid.

6 ACKNOWLEDGEMENTS

This research was supported by the AHRC Grant AH/R007934/1 Preserving Egypt's Cultural Heritage from Earthquake Damage through Vibrating Barriers (ViBa).

REFERENCES

- [1] E.D. Johnson, The Need for Seismic Analysis and Planning as Part of Ongoing Archaeological Site Management and Conservation: A Case Study of the Necropolis of Saqqara, *J. Am. Res. Cent. Egypt.* 36 (1999) 135–147. <https://doi.org/https://doi.org/10.2307/40000207>.
- [2] P. Cacciola, A. Tombari, Vibrating barrier: a novel device for the passive control of structures under ground motion, *Proc. R. Soc. London A Math. Phys. Eng. Sci.* 471 (2015). <https://doi.org/https://doi.org/10.1098/rspa.2015.0075>.
- [3] G. Warburton, J. Richardson, J. Webster, Forced Vibrations of Two Masses on an Elastic Half Space, *J. Appl. Mech. ASME.* 38 (1971) 148–156. <https://doi.org/10.1115/1.3408735>.
- [4] J. Luco, L. Contesse, Dynamic structure–soil–structure interaction., *Bull. Seismol. Soc. Am.* 63 (1973) 1289–1303.
- [5] P. Cacciola, M.G. Espinosa, A. Tombari, Vibration control of piled-structures through structure-soil-structure-interaction, *Soil Dyn. Earthq. Eng.* 77 (2015) 47–57.
- [6] A. Tombari, I. Zentner, P. Cacciola, Sensitivity of the stochastic response of structures

- coupled with vibrating barriers, *Probabilistic Eng. Mech.* 44 (2016) 183–193.
- [7] P. Cacciola, N. Banjanac, A. Tombari, Vibration Control of an existing building through the Vibrating Barrier, in: *Procedia Eng.*, 2017. <https://doi.org/10.1016/j.proeng.2017.09.065>.
 - [8] M. Andreozzi, A. Tombari, A. Lampropoulos, P. Cacciola, Seismic protection of the Messina Cathedral Bell Tower through Vibrating Barriers, in: *SECED 2019 Earthq. Risk Eng. Towar. a Resilient World*, Greenwich, UK, 2019.
 - [9] J.D. Coronado, R. Lomurno, A. Tombari, P. Cacciola, Improving Urban Seismic Resilience through Vibrating Barriers, in: *ICOSSAR*, Vienna, Austria, 2017.
 - [10] A. Tombari, M. Garcia Espinosa, N.A. Alexander, P. Cacciola, Vibration control of a cluster of buildings through the Vibrating Barrier, *Mech. Syst. Signal Process.* (2018). <https://doi.org/10.1016/j.ymssp.2017.08.034>.
 - [11] D. Boore, Simulation of Ground Motion Using the Stochastic Method, *Pure Appl. Geophys.* 160 (2003) 635–676.
 - [12] A.E. Khalil, H.E. Abdel Hafiez, M. Girgis, M.A. Taha, Earthquake ground motion simulation at Zoser pyramid using the stochastic method: A step toward the preservation of an ancient Egyptian heritage, *NRIAG J. Astron. Geophys.* 6 (2017) 52–59. <https://doi.org/https://doi.org/10.1016/j.nrjag.2016.11.003>.
 - [13] M. Metwaly, A.G. Green, H. Horstmeyer, H. Maurer, A.M. Abbas, A.R.G. Hassaneen, Combined seismic tomographic and ultra-shallow seismic reflection study of an early dynastic mastaba, Saqqara, Egypt, *Archaeol. Prospect.* 12 (2005) 245–256. <https://doi.org/10.1002/arp.261>.
 - [14] G.M. El-Qady, F.A. Monteiro Santos, A.G. Hassaneen, L. Trindade, 3D inversion of VES data from the Saqqara archaeological area, Egypt: a case study, *Near Surf. Geophys.* 3 (2005) 227–233. <https://doi.org/10.3997/1873-0604.2005018>.
 - [15] J. Lysmer, F. Ostandan, C.C. Chin, SASSI 2000—A System for Analysis of Soil-Structure Interaction-User's Manual, Berkeley, California: University of California., 1999.
 - [16] P. Cacciola, A. Tombari, A. Giaralis, An inerter-equipped vibrating barrier for noninvasive motion control of seismically excited structures, *Struct. Control Heal. Monit.* 27 (2019) 1–21.
 - [17] E. Çelebi, S. Firat, I. Çankaya, The effectiveness of wave barriers on the dynamic stiffness coefficients of foundations using boundary element method, *Appl. Math. Comput.* 180 (2006) 683–699.

OPTIMUM DESIGN OF A HYBRID ISOLATION DEVICE FOR SERVER RACKS USING CONSTRAINED DIFFERENTIAL EVOLUTION ALGORITHM

Luca Aceto¹, Giuseppe Quaranta², Guido Camata¹, Bruno Briseghella³, Enrico Spacone¹

¹ Department of Engineering and Geology
University G. D'Annunzio of Chieti-Pescara
Viale Pindaro 42, 65127 Pescara, Italy
e-mail: luca.aceto@unich.it, guido.camata@unich.it, enrico.spacone@unich.it

² Department of Structural and Geotechnical Engineering
Sapienza University of Rome
Via Eudossiana 18, 00184 Rome, Italy
e-mail: giuseppe.quaranta@uniroma1.it

³ College of Civil Engineering
Fuzhou University
Fuzhou 350108, China
e-mail: bruno@fzu.edu.cn

Abstract

Nonstructural elements and contents often constitute a large fraction of the economic investment in ordinary buildings. In case of seismic events, damage to nonstructural elements not only contributes to the overall direct material costs but can also significantly impact the indirect costs. The latter are especially affected by earthquake-induced damage if production and business flows depend on proper functioning of such nonstructural components, since consequent downtime costs turn out to be very high. Within this framework, server racks' performance under seismic loading is of interest in the present work. The economic relevance of these nonstructural components requires the implementation of proper design solutions so that their performance under earthquakes can fulfill specific requirements. In this perspective, including isolation devices between server racks and building floors is deemed effective for enhancing the stability of the protected equipment, preserving the computer components' integrity and, minimizing downtime losses. Hence, the present work is meant to optimize a hybrid isolation system for server racks. Specifically, the hybrid isolation device designed for such application combines at least two elastomeric isolators and three sliders, and it is intended for the seismic protection of server racks characterized by different configurations. The objective function is formulated to minimize the accelerations transmitted to server racks and manufacturing cost.

Keywords: Constrained optimization – Cost minimization – Nonstructural elements – Optimum structural design – Server rack – Seismic isolation

1 INTRODUCTION

Nonstructural elements and contents contribute to large part of the initial economic investments in typical buildings, but they often undergo disproportional damage due to seismic actions even if the structure in which they are placed exhibits satisfactory performances [1]. Apart from contributing directly to final material costs after an earthquake, damage to contents housed in most buildings can cause inestimable losses (in case of objects of historical value) or the interruption of production/business flows (when damage occur in industrial equipments, computer servers, etc.) along with extremely high downtime costs. For example, the economic cost due to the five-days of downtime for a single data center following the 1989 Loma Prieta earthquake or the 1994 Northridge and 1995 Kobe seismic events amounted to 5%-10% of the entire rebuilding cost [2]. In this regards, it is opportune to point out that many building contents – such as computer servers or museum artifacts – are acceleration-sensitive, i.e., they are especially vulnerable to damage when subject to high accelerations [3]. In this perspective, there has been growing interest about the use of seismic isolators at the floor level because, in most cases, this can cope efficiently with the need of protecting acceleration-sensitive building equipments under earthquake, provided that the building structure is properly designed against seismic loads. In fact, it is recognized that seismic isolation of server racks would improve business resiliency at a low cost as compared to downtime losses [4].

Within this framework, the present paper proposes a novel design procedure in order to optimize a hybrid isolation system for server racks combining at least two elastomeric isolators and three sliders. The objective function is selected to minimize the accelerations transmitted to the servers placed in the racks as well as the material cost of the isolation system. Design variables include number, compound, and geometric dimensions of the elastomeric elements and slider position. The final optimization problem is then solved using a suitable variant of the differential evolution algorithm [5] to handle the design constraints. The search for the optimal hybrid isolation system is carried out in two phases. The first phase is concerned with the identification of the optimal device to be deployed on all floors of a given building. The standardized optimal design is addressed next in the second phase, in which the design procedure is extended to determine which isolation device is best suited for all floors of the building stock under investigation. The sliders optimal topology is also investigated parallel to that in such a way to minimize the overturning moment. This final design phase is motivated by the fact that standardization and generalization of an industrial device during the development stage are crucial to reduce engineering and production costs. As a matter of fact, they allow to circumvent the redesign phase should any design condition changes and to reduce the costs related to the acceptance tests required in the development stage. Hence, it means no waste of any other devices except the installed ones, thereby saving materials and overall unitary industrial costs.

2 OVERVIEW ABOUT COMMON PRACTICES IN DATA CENTER DESIGN

Most of the world's largest data centers are housed within dedicated one-story buildings, which usually host some offices serving as technical or control rooms. Medium to large data centers are often located within the upper floor of a commercial building. The position of small data centers can vary considerably in terms of, both, building type and location within the host structure. Standard models exist for large data centers placement only, whereas they lack for small to medium-large ones [6].

The distribution of racks in the data center varies significantly, regardless of the size. The most common racks configuration in large data centers is based on rows of racks installed side-by-side with alternating cold aisles and hot aisles [7]. Generally, the rows of racks are placed back-to-back, and all the holes through the rack are blocked off to create barriers that reduce

recirculation and divide hot aisles from cold aisles efficiently [8]. In some cases, hot aisles or cold aisles between two rows of racks are covered with a modular system of cooling containment. This choice reduces the energy cost and concentrates the refrigerated airflow on the rack when the server room is vast or the inter-floor space is large enough compared to the vertical dimension of the racks [9].

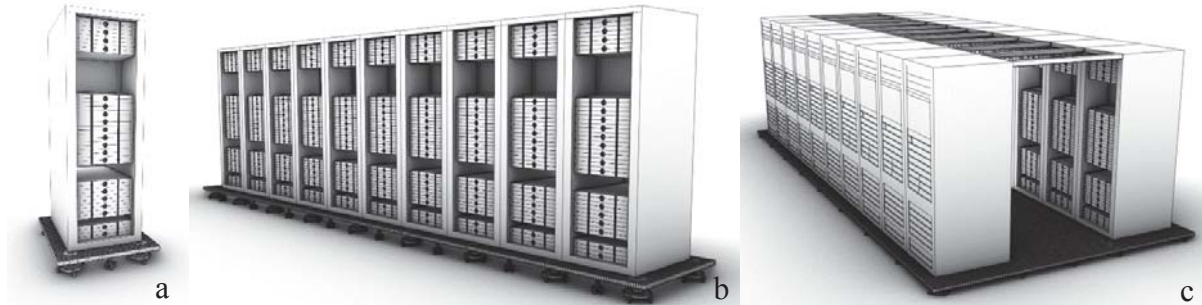


Figure 1 – Most common server racks configurations: a) single rack; b) row of racks; c) rows of racks with covered aisle.

The aisle containment system is composed of a series of light aluminum frames that do not have a structural function. Generally, these systems are scalable, and thus there is no a fixed number of racks that compose the covered aisle. Server rooms can host multiple rows of racks and multiple covered aisles.

Data center density is usually measured in terms of W/m^2 or $W/rack$, which represent the electric power consumed per square meter and the electric power consumed per rack, respectively. It means that a low-density data center is characterized by a configuration that consumes few Watts per square meter of the server room. If a data center employs this configuration, then the rows are commonly composed of sparsely populated racks or spaced full single racks [10].

As reported in many guidelines, scalability brings added value to the data center. The scalability requirement implies that the data center can be conceived and built according to a low-density architecture able to meet current needs and to expand for fulfilling higher future demands that require the postponed installation of further infrastructures such as UPS systems, air conditioners, and other racks [10]. This means that the data center layout can eventually evolve during its lifetime, with the possible exception of large and predefined configurations.

It is anticipated that this study addresses the seismic protection of a single rack, whereas the remaining configurations will be considered in future works. The configuration consisting of a single rack device is the most flexible one and facilitates later installations when data center scaling is needed. Some available commercial proposals for server rack seismic isolation are intended for a single item. They are generally modular systems, which means that it is possible to isolate more racks in a row by combining more devices [11–19]. Many other commercial devices propose total raised floor isolation [13,19,20]. Another solution adopted to achieve server rack seismic protection is obtained through the direct introduction of damping to the rack's steel structure or in the raised floor [21,22]. The main guidelines and codes that refer to electronic equipments installed in earthquake-prone areas suggest the use of a cabinet rack that has passed a codified seismic test, usually named "seismic rack" [23–30]. On the other hand, to make a non-conforming cabinet resistant against seismic actions, the installation of a "seismic kit" composed of steel braces is common. Both solutions are meant to enhance the rack resistance and stiffness. Furthermore, technical codes in force indicate that racks in seismic areas have to be anchored to the floor by fasteners together with shear keys. Although these specifications already existed during the 2010 Chile earthquake, the lack of fasteners and shear keys

was common in both new and old buildings [31]. It is worthy highlight that code requirements that target at increasing the system stiffness to reduce the drift generally lead to an increment of the acceleration demands in the electronic components of the racks, thereby amplifying the potential risk of interrupting the business continuity.

3 ANALYSIS OF ELASTOMERIC ISOLATORS

Design rules provided by EN 15129 [32] and EN 1337-3 [33] for seismic actions and static conditions, respectively, are the constraints of the optimization procedure.

The use of slender elastomeric elements is required to ensure a suitable level of isolation for light nonstructural elements. This condition turns out to be very binding for axial loads, since it makes elastomeric elements vulnerable to buckling phenomena. In order to overcome this issue, a hybrid isolation system is adopted, which combines elastomers with at least three sliders that aims at absorbing the axial load. Thanks to these features, elastomeric elements integrity under seismic loads is governed primarily by shear deformability limits. In operating conditions, the racks positioned inside the building are protected against horizontal environmental actions, such as wind. Therefore, only an accidental rotation equal to 0.03 rad and a horizontal force equal to 1 kN are considered during the optimization procedure to account for anthropic interferences. According to EN 15129, the design shear strain $\varepsilon_{q,E}$ due to earthquake-imposed design displacement d_{bd} is given by:

$$\varepsilon_{q,E} = \frac{d_{bd}}{T_q}, \quad (1)$$

where T_q is the total thickness of the active elastomer during shear. The design shear strain calculated using Eq. (1) has to be compared with the maximum shear strain equal to 2.5.

4 SEISMIC ACTION

The floor response spectrum method is a convenient way to find the nonstructural element acceleration on the floor during an optimization procedure because it is less computationally expensive than a time history analysis [34]. The Italian building code (NTC18) floor spectrum formulation [35] is here employed, which demonstrated a good agreement with the Newmark response spectrum derived from a compatible time history analysis.

According to NTC18, the seismic demand on nonstructural elements can be determined by applying a horizontal force F_a defined as follows:

$$F_a = \frac{(S_a \cdot W_a)}{q_a}, \quad (2)$$

where F_a is the horizontal seismic force applied in the center of mass of the nonstructural element, S_a is the maximum dimensionless acceleration, W_a is the weight of the element, and q_a is the quality factor. The following relationship is adopted to determine the acceleration at the j th floor of the structure corresponding to the i th mode:

$$S_{ij} = \varphi_{ij} \Gamma_i S_i(T_i), \quad (3)$$

where $S_i(T_i)$ is the ordinate of the spectrum relative to the i th mode. Herein, Γ_i is the modal participation factor, which is defined by the relationship:

$$\Gamma_i = \frac{\varphi_i^T M \tau}{\varphi_i^T M \varphi_i}, \quad (4)$$

where τ is the drag vector, φ_i is the i th normalized modal shape, and M is the mass matrix.

A ground spectrum for a high seismic risk zone with $a_g=0.26g$ is considered in the present work (Figure 2a). Additionally, it is assumed that the building containing the racks has to undergo slight damage levels or to behave elastically; otherwise, business continuity would be jeopardized in any case. Therefore, the design of the isolation system will not rely on the ductility reserve that the structure would provide by adopting a unit quality factor.

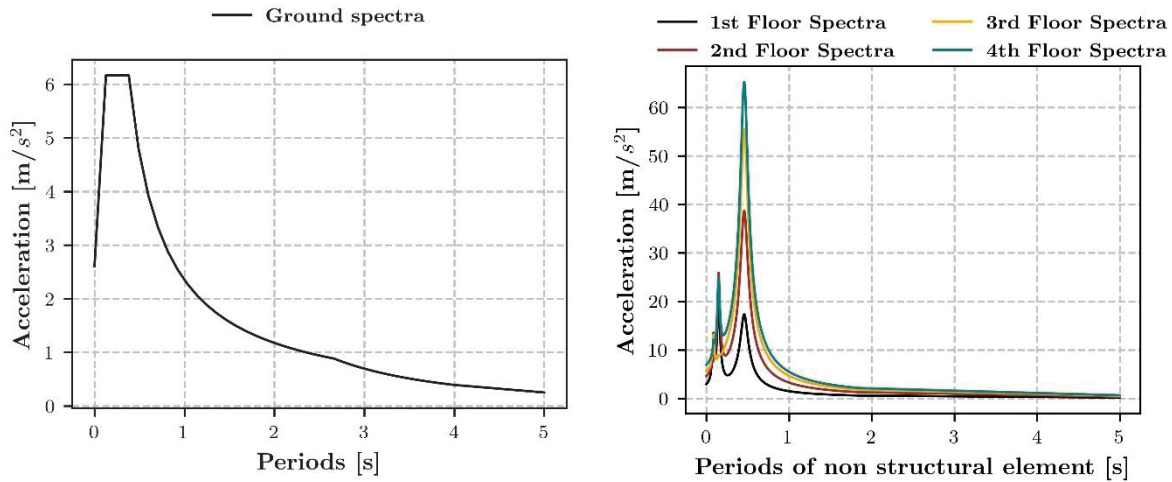


Figure 2 – Reference ground spectrum (left) and floor spectra for a 4-story building (right).

The floor spectra for ten buildings with an increasing number of floors were generated accordingly. As an example, the floor spectra for a 4-story building are shown in Figure 2b. All buildings have a concrete frame structure and $5\text{ m} \times 5\text{ m}$ square floor plan with an inter-floor height equal to 3.5 m. The first frame is replicated to obtain all buildings (Figure 3).

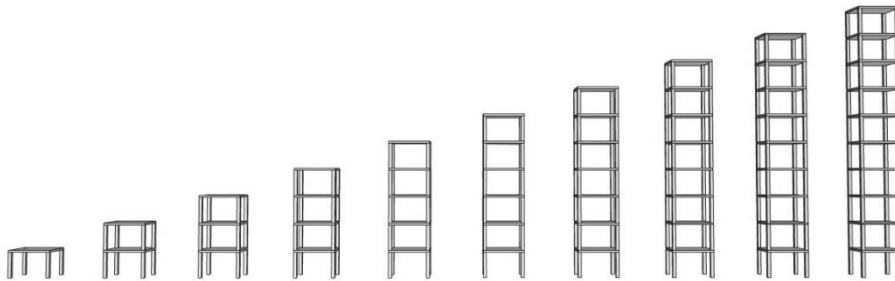


Figure 3 – Stock of buildings under consideration.

5 OPTIMIZATION PROCEDURE

The optimization problem is formulated, taking into account both, integrity of the isolated servers and system cost-effectiveness. Within the present work, the elastomeric isolator's behavior and the seismic actions are evaluated through an iterative search considering the mechanical characteristics of the elastomeric compound and the floor response spectra for each floor. The elastomer's lateral stiffness was calibrated by considering the damping related to the shear deformation calculated through the floor spectral displacement until convergence. The optimization procedure is divided into two phases. In the first phase, the optimum isolation system is identified separately for the ten buildings under consideration (Figure 4). Thus, for each candidate solution generated by the differential evolution algorithm, the iterative procedure required to identify the isolation system's properties was conducted for each floor of the

considered building. In the second phase, all ten buildings are examined simultaneously in the attempt to determine the optimal isolator that complies with all constraints on all floors of all buildings. In this case, the isolator properties were identified for all floors of the ten buildings for each generation. The design variables in the optimization problem are diameter of the elastomeric isolators, rubber height, type of compound, and number of isolators. From these quantities, it is thus possible to derive number of rubber layers and number of steel layers for the isolator. The algorithm employs primary and derived design variables in order to calculate the material cost of the isolation system. The problem constraints are defined in compliance with the design rules in EN 1337-3 and EN 15129. Furthermore, the maximum acceleration at the top of the rack is required to be less than 0.20g, whereas the isolation system period is forced to be larger than 1 s. The limitation about the maximum acceleration transmitted to the servers by the rack is necessary to ensure that the hard disks would remain operational during seismic events.

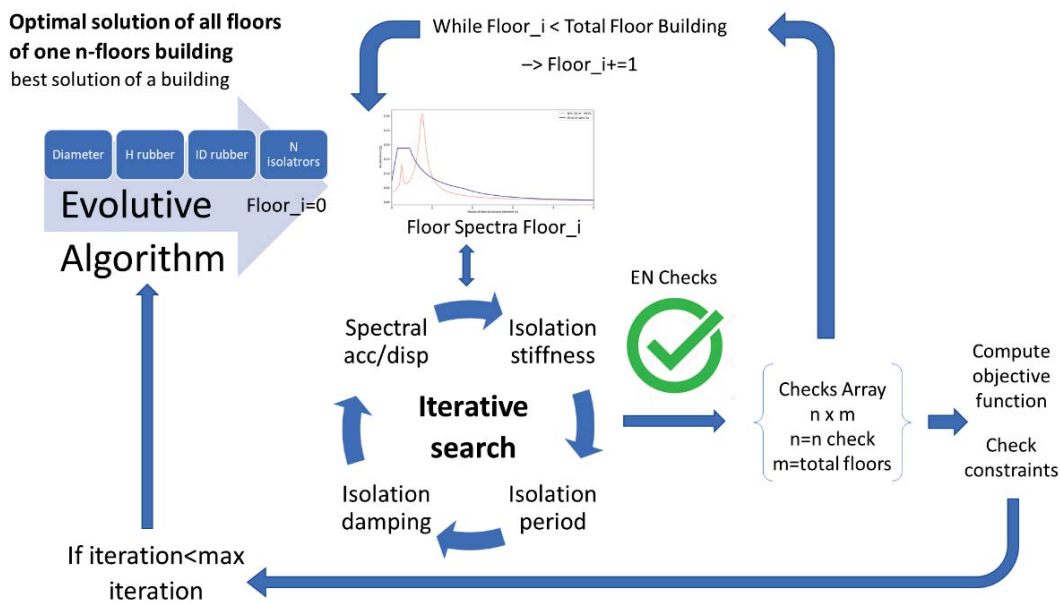


Figure 4 –Workflow of the optimization procedure for a single building

A special $(\mu+\lambda)$ -constrained differential evolution algorithm is adopted to solve the optimization problem. This algorithm uses a robust nature-inspired strategy that focuses on finding the best solution iteratively by checking a set of candidate solutions [36,37]. The objective function of the optimization problem $ObjF$ is formulated as follows:

$$ObjF = \left(\frac{C_{Mat} + C_{Fixed}}{C_{Fixed}} \right) \cdot \gamma_c + Acc_{max} \cdot \gamma_{Acc} \quad (5)$$

where C_{Mat} is the material cost of the isolation system, C_{Fix} are the fixed costs, Acc_{Max} is the maximum acceleration recorded on the floors of each building. The two terms included in the objective function are weighted using two user-defined coefficients (i.e., γ_C and γ_{Acc}). The constrained differential evolution algorithm's iterative strategy runs until the maximum number of fitness evaluations is reached. Meanwhile, the sliders position is optimized to reduce the overturning moment due to the seismic action. The only design variable is the position of the sliders as related to the dimensions of each individual rack. In this case, the optimum design is formulated as a single-objective constrained optimization problem, and the $ObjF$ $f(x_i)$ is calculated as follows:

$$ObjF = \frac{M_{Stab}}{M_{Ov}} \quad (6)$$

where M_{stab} is the stabilizing moment, and M_{ov} is the overturning moment under seismic action.

6 RESULTS

Figure 5a shows the results for all the analyses performed in the first design phase by overlaying the trends in the devices' geometric dimensions with the maximum acceleration values recorded for each building. Figure 5b illustrates the maximum acceleration among all floors of each building, and compare them to the acceleration of a floor-fixed rack. All results are listed in Table 1. A fundamental period equal to 0.33 s is considered for the non-isolated seismic rack [38]. The numerical value of the weights are $\gamma_C=3$ and $\gamma_{Acc}=0.30$ [1/g]. The optimal number of elastomeric devices was found equal to 2 for all cases (it corresponds to the lower bound).

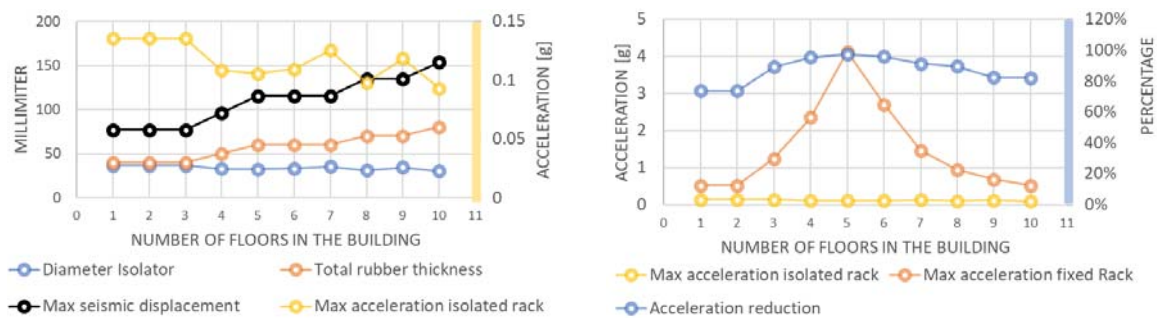


Figure 5 – Results of the optimization performed in the first phase (left) and comparison between maximum acceleration on the isolated rack and that of a fixed-floor rack (right).

Number of floors	Isolator diameter [mm]	Total rubber thickness [mm]	Cost of isolation system [€]	Objective function	Max seismic displacement [mm]	Max acceleration isolated rack [g]
1	37	40	288	1.29	77	0.1354
2	37	40	288	1.29	77	0.1354
3	37	40	288	1.29	77	0.1354
4	33	50	301	1.31	96	0.1083
5	32	60	313	1.36	115	0.1054
6	33	60	313	1.36	115	0.1094
7	35	60	313	1.38	115	0.1253
8	31	70	326	1.40	135	0.0981
9	34	70	326	1.42	135	0.1184
10	30	80	338	1.45	154	0.0930

Table 1 – Results of the optimization procedure in the first design phase.

The second phase of the optimization procedure is performed by assuming the same variables and constraints already employed in the first phase. The results are listed in Table 2.

Finally, the search for the sliders optimal position has been performed alongside the elastomeric elements sizing optimization. The search space area is limited to a single rack size equal to 800 mm × 1000 mm. The minimum number of sliders required for an equilibrium configuration is three. In this study, the 4-slider scheme is also investigated.

Isolator diameter [mm]	Total rubber thickness [mm]	Cost of isolation system [€]	Objective function	Max seismic displacement [mm]	Max acceleration isolated rack [g]
30	80	338	1.45	154	0.0930

Table 2 – Results of the optimization procedure in the second design phase.

Figure 6 shows all feasible positions generated by the differential evolution algorithm during the optimization process in case of 4 sliders (color intensity indicates the age of the sliders' candidate positions during the optimization procedure, which means that lighter dots indicate earlier generations than darker ones). The final results for both the 4-sliders and 3-sliders problems are shown in Figure 7.

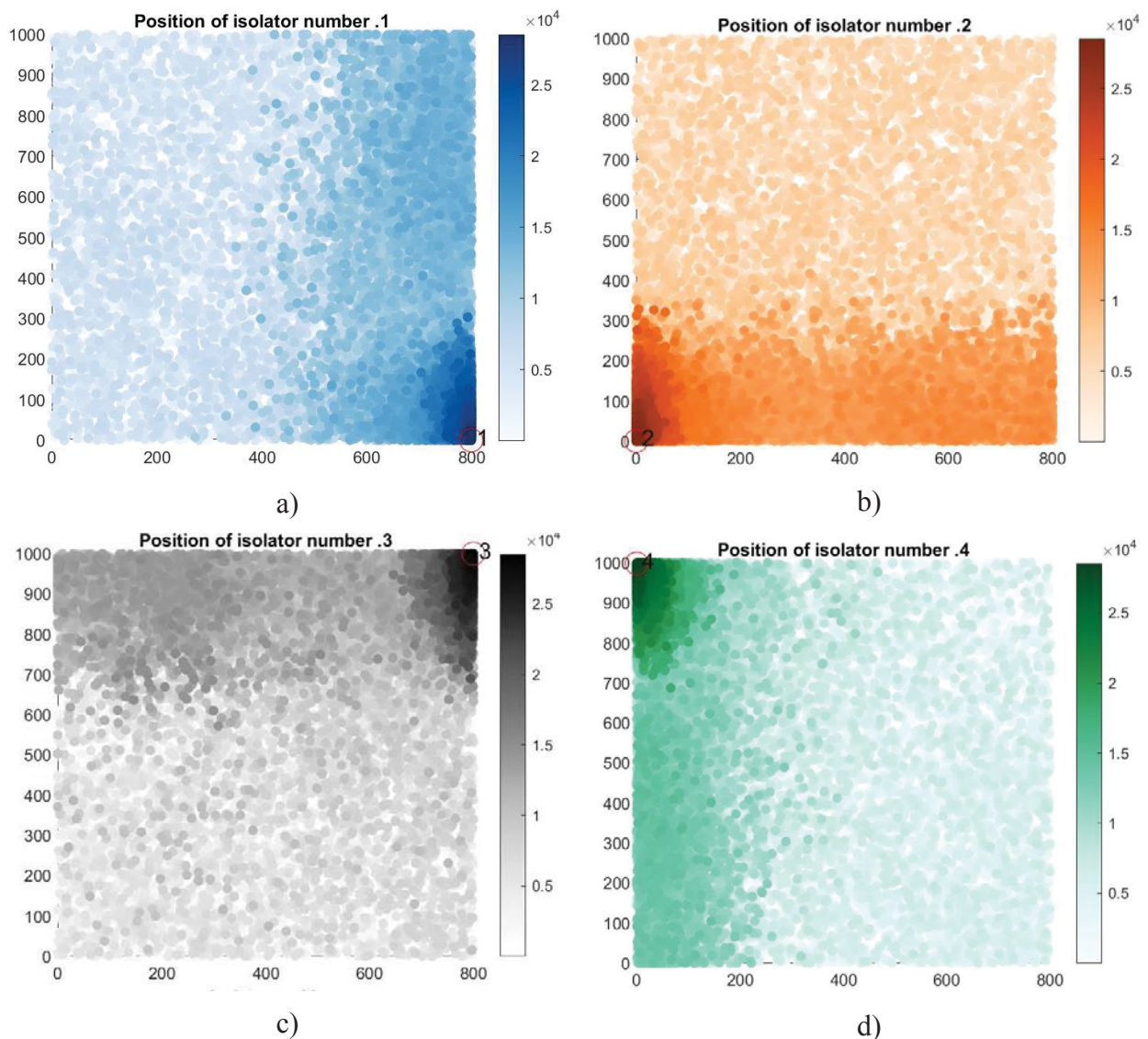


Figure 6 – Position of the sliders during the optimization procedure (the color gradient indicates the position during the evolutionary search): a) position of slider number 1; b) position of slider number 2; c) position of slider number 3; d) position of slider number 4.

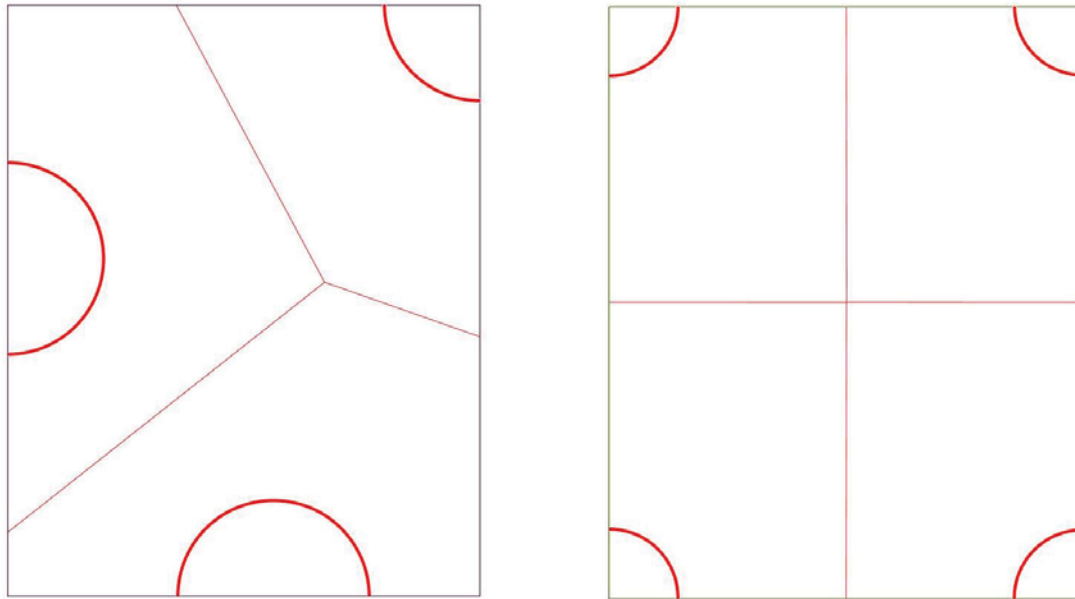


Figure 7 – Optimal positions of the sliders in case of 3 (left) or 4 (right) devices.

7 CONCLUSIONS

This paper has explored the application of the constrained differential evolution algorithm for the optimum and standardized design of a hybrid seismic isolation device for a server rack. The device is designed in compliance with EN 15129 and EN 1337-3. Size of the elastomeric devices and positions of the sliders have been optimized.

The sizing optimization of elastomeric devices allow to draw the following general conclusions:

- the most important seismic demand parameter for the integrity of the elastomeric isolators is the lateral seismic displacement, which increases as the number of floors grows up and ultimately governs the total height of the device;
- the isolator diameter is almost constant for all buildings under consideration and is close to the lower bound of the search space;
- the optimum design of the isolation system performed taking into account all buildings simultaneously leads to the same results carried out considering the tallest building only, which therefore rules the whole design because of the largest value of the seismic demand.

As regards the sliders position, an intuitive layout is obtained for the configuration consisting of 4 devices, whereas the optimal arrangement for 3 devices is less predictable.

The optimization of the isolation system has been here performed through a constrained differential evolution algorithm. This numerical technique was able to reduce the total computational time and to provide a better solution as compared to a parametric analysis-aided approach. Therefore, the constrained differential evolution algorithm proved to be suitable for this optimization problem.

The design procedure herein proposed will be further extended in future works so as to enable the optimization of the other racks configurations typically encountered in data centers.

REFERENCES

- [1] R. Villaverde, Seismic Design of Secondary Structures: State of the Art, J. Struct. Eng.

- 123 (1997) 1011–1019. [https://doi.org/10.1061/\(asce\)0733-9445\(1997\)123:8\(1011\)](https://doi.org/10.1061/(asce)0733-9445(1997)123:8(1011)).
- [2] C. Alhan, H.P. Gavin, Reliability of base isolation for the protection of critical equipment from earthquake hazards, *Eng. Struct.* 27 (2005) 1435–1449. <https://doi.org/10.1016/j.engstruct.2005.04.007>.
- [3] S. Taghavi, E. Miranda, Response Assessment of Nonstructural Building Elements, *Pacific Earthq. Eng. Res.* (2003) 96.
- [4] E. Makwae, An assessment of disaster recovery planning: A strategy for data security, *Researchgate*. (2018).
- [5] G. Quaranta, W. Lacarbonara, S.F. Masri, A review on computational intelligence for identification of nonlinear dynamical systems, Springer Netherlands, 2020. <https://doi.org/10.1007/s11071-019-05430-7>.
- [6] F.F. Tajirian, SEISMIC VULNERABILITY OF DATA CENTERS, in: 2009: pp. 616–626.
- [7] M.K. Patterson, D.G. Costello, P.F. Grimm, M. Loeffler, Data center TCO ; a comparison of high-density and low-density spaces, *Chart.* (2007) 1–12. <http://www.pentium.ch/technology/eep/datacenter.pdf>.
- [8] W. Lintner, B. Tschudi, O. VanGeet, Best Practices Guide for Energy-Efficient Data Center Design, U.S Dep. Energy. (2011) i–24. <http://www1.eere.energy.gov/femp/pdfs/eedatacenterbestpractices.pdf>.
- [9] H. Geng, Data Center Handbook, 2014. <https://doi.org/10.1002/9781118937563>.
- [10] N. Rasmussen, Guidelines for Specification of Data Center Power Density, APC White Pap. #120. (2005) 1–21.
- [11] THK, Seismic Isolation Module Model TGS, Japan, Japan, n.d.
- [12] THK, Seismic Isolation Table Model TSD, Japan, n.d.
- [13] DIS, Non-Structural Isolation - DIS Catalogue, McCarran, Nevada, n.d. www.dis-inc.com.
- [14] P.S. Harvey, H.P. Gavin, Double rolling isolation systems: A mathematical model and experimental validation, *Int. J. Non. Linear. Mech.* 61 (2014) 80–92. <https://doi.org/10.1016/j.ijnonlinmec.2014.01.011>.
- [15] M. Nacamuli, Seismic protection of data centers using Ball-N-cone base isolation, *Struct. Congr. 2012 - Proc. 2012 Struct. Congr.* (2012) 1373–1384. <https://doi.org/10.1061/9780784412367.123>.
- [16] MAURER, Maurer Vibration Isolation Catalogue, n.d.
- [17] Mu-Solator, Mu-Solator DataCenter - Catalogue, 2019.
- [18] Mu-Solator, Mu-Solator Server Rack - Catalogue, 2019.
- [19] LG Earthquake Defense, Seismic Isolation for Machines - LG Catalogue, n.d.
- [20] LG Earthquake Defense, Seismic Mount for Data Centers, n.d.
- [21] I.-K. Chang, S.-C. Liu, H.C. Shah, Seismic support of electronic and computer equipment on raised floors, *Soil Dyn. Earthq. Eng.* 5 (1986) 159–169. [https://doi.org/10.1016/0267-7261\(86\)90019-9](https://doi.org/10.1016/0267-7261(86)90019-9).

- [22] LG Eartquake Defense, Interstory Isolation For Buildings, n.d.
- [23] A. Filiatrault, P.S. Higgins, A. Wanitkorkul, J.A. Courtwright, R. Michael, Experimental seismic response of base isolated pallet-type steel storage racks, *Earthq. Spectra*. 24 (2008) 617–639. <https://doi.org/10.1193/1.2942375>.
- [24] F. 461, FEMA 461 / June 2007, (2007).
- [25] S. Committee of the IEEE Power Engineering Society, IEEE Std 693TM-2005 (Revision of IEEE Std 693-1997) IEEE Recommended Practice for Seismic Design of Substations, 2006.
- [26] JIS C6011-2-2011 JIS C6010, (n.d.).
- [27] N. Equipment, P. Grounding, ATT-TP-76200, 14 (2016) 1–73.
- [28] D. Version, N.O.T.F.O.R. Resale, ANSI/BICSI 002-2014 - Data Center Design and Implementation Best Practices, (2014).
- [29] Telcordia Technologies Generic Requirements, NEBS TM Requirements: Physical ProtectTelcordia Technologies Generic Requirements GR-63-CORE Issue 4, 2012. <http://telecom-info.telcordia.com>. (accessed April 21, 2020).
- [30] C. DiMinico, Telecommunications Infrastructure Standard for Data Centers, MC Commun. (2010) 36.
- [31] E. Miranda, G. Mosqueda, R. Retamales, G. Pekcan, Performance of nonstructural components during the 27 February 2010 Chile earthquake, *Earthq. Spectra*. 28 (2012) 453–471. <https://doi.org/10.1193/1.4000032>.
- [32] CEN, EN 15129:2018 - Anti-seismic devices, (2018).
- [33] CEN, EN 1337-3 - Structural bearings - Part 3: Elastomeric bearings, (2005).
- [34] P.M. Calvi, Relative displacement floor spectra for seismic design of non structural elements, *J. Earthq. Eng.* 18 (2014) 1037–1059. <https://doi.org/10.1080/13632469.2014.923795>.
- [35] Ministero delle Infrastrutture e dei Trasporti, Aggiornamento delle “Norme tecniche per le costruzioni” (in Italian), (2018) 1–198.
- [36] A. Scodeggio, G. Quaranta, G.C. Marano, G. Monti, R.B. Fleischman, Optimization of force-limiting seismic devices connecting structural subsystems, *Comput. Struct.* 162 (2016) 16–27. <https://doi.org/10.1016/j.compstruc.2015.09.008>.
- [37] G. Quaranta, A. Fiore, G.C. Marano, Optimum design of prestressed concrete beams using constrained differential evolution algorithm, *Struct. Multidiscip. Optim.* 49 (2014) 441–453. <https://doi.org/10.1007/s00158-013-0979-5>.
- [38] S. Canfield, Seismic Evaluation of Large Server Computer Structure, (2016) 1–6.

INNOVATIVE MASS-DAMPING-BASED APPROACHES FOR SEISMIC DESIGN OF TALL BUILDINGS

Elena Mele^{1,*}, Diana Faiella², and Mario Argenziano³

^{1,*} University of Naples Federico II
Dept. Structures for Engineering and Architecture
P.le Tecchio 80
elenmele@unina.it (corresponding author)

² University of Naples Federico II
Dept. Structures for Engineering and Architecture
P.le Tecchio 80
diana.faiella@unina.it

³ University of Naples Federico II
Dept. Structures for Engineering and Architecture
P.le Tecchio 80
mario.argenziano@unina.it

Abstract

Mass damping is a well known principle for the reduction of structural vibrations and applied in tall building design in a variety of configurations. With mass usually small (around 1% of building mass), the properly “tuned” mass damper (TMD) shows great effectiveness in reducing wind vibrations, but minor advantages under earthquake excitations.

The above limitation can be surpassed by utilizing relatively large mass TMD. For this purpose, two different solutions are here proposed. In both cases, the idea is to separate the building into two or more parts, thus allowing for a relative motion between them, and activating the mass damping mechanism.

In the first solution, the building is subdivided along elevation into an upper and a lower structure, separated by means of an intermediate isolation system (IIS). In the second solution, by revisiting the classical mega-frame typology, the exterior full-height structure provides the global strength and stiffness, and secondary structures, extending between two transfer levels, are physically detached from the main structure at each floor and isolated at transfer level.

Simplified lumped-mass models are developed for illustrating the dynamic behaviour of the two solutions and carrying out parametric analyses. Procedures for deriving optimum values of design parameters are also proposed and compared to the parametric study.

Keywords: mass damping, motion based design, vibrations control, tall buildings, Mega Sub-structure Control System, Intermediate Isolation Systems.

1. INTRODUCTION

Mass Damping (MD) is nowadays a consolidated passive strategy, widely applied in tall building design since 1976 (John Hancock Tower in Boston) for mitigating structural vibrations and improve serviceability and occupant comfort [1]. A Tuned Mass Damper (TMD) is an auxiliary device attached to the main structure, consisting in a mass, spring, and damper. While TMDs with relatively small mass are very effective for reducing wind-induced response, they are not equally interesting under earthquake excitations [1 - 4].

In order to improve their seismic effectiveness, large mass TMDs can be utilized. With this choice, in fact, the system becomes most robust against deviations from design parameters and less dependent on the earthquake frequency content and the impulsive character of the seismic input [5]. This large mass can be obtained by converting a part of the structure into a huge mass damper, also appointed as non-conventional mass damper [5 - 9], thus combining control and structural functions. For this purpose, two different solutions are here proposed, by separating the building into two or more parts that vibrate out of phase and, thus, activate the mass damping mechanism.

In the first solution, the building is divided into two substructures, a lower and an upper structure, separated by means of a flexible horizontal disconnection, the isolation system, thus realizing an Intermediate Isolation System (IIS, Figure 1a). This configuration is widely utilized in Japan, where more than 60 buildings have been already realized [10], both for the seismic design of new buildings [11 - 17], and retrofit of existing buildings by means of vertical addition [13, 14]. While the IIS represents an extension of the Base Isolation System (BIS), its dynamics is more complicated due to the flexibility of the lower structure. In fact, the isolated upper structure behaves like a base isolated structure and as a large mass TMD for the lower structure [5 - 9, 18 - 26].

In the second solution, starting from the classical mega-frame typology for tall building structures [27 - 29], the building is subdivided in an exterior primary megastructure that provides the global strength and stiffness, and several interior secondary substructures, extending between two transfer levels, physically disconnected from the main structure at each floor and isolated at transfer level. Therefore, a Mega Substructure Control System (MSCS, Figure 1b) is realized, in which each isolated substructure behaves like a base isolated structure and the mass damping mechanism is activated by allowing the relative motion between the substructures and the main structure. This approach has been firstly proposed by Feng and Mita in 1995 [30], and then developed by the same authors [30 - 32] and by other researchers in a variety of solutions [34 - 45].

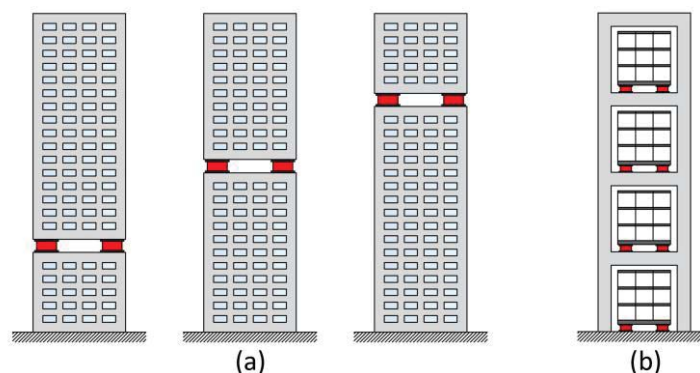


Figure 1: (a) Intermediate Isolation System (IIS) and (b) Mega-Substructure Control System (MSCS).

Both the mass damping solutions can be preliminary analysed by means of a simplified two-degree of freedom lumped mass model (2DOF MD, Figure 2b). For the Mega Substructure Control System, the main system accounts for the exterior megastructure, while the absorber globally represents the internal secondary substructures; instead, for the Intermediate Isolation System, the main and secondary system respectively refers to the lower structure and isolated upper structure. It is worth recalling that the IIS is generally analysed by means of a 3DOF model, accounting the DOFs

of the lower structure, the isolation system, and the upper structure. However, for evaluating its global dynamic behaviour, a 2DOF model can be adopted by satisfying the following two requirements: the upper structure is rigid with respect to the isolation system [46, 47], and the higher modes coupling is avoided [25, 48, 49].

In the present paper the dynamic behaviour of the two solutions is explored by carrying out parametric analyses on the simplified lumped mass model. The authors also propose procedures for deriving optimum values of the mass damper's design parameters, by minimizing the displacement amplitude of the main system under white noise. Finally, the optimal procedures are compared to the parametric study.

2. OPTIMIZATION PROCEDURE FOR NON-CONVENTIONAL MASS-DAMPING (MD) CONFIGURATIONS

Non-conventional mass-damping (MD) configurations utilising isolation system, such as Mega Substructure Control Systems and Intermediate Isolation Systems, can be preliminary analyzed by means of a simplified two degree-of-freedom (2DOF) lumped mass model, as depicted in Figure 2b. The first oscillator represents the main system with mass, stiffness, and damping coefficients named as m_1 , k_1 , and c_1 , while the second oscillator represents the absorber (or secondary system) with mass, stiffness, and damping coefficients named as m_2 , k_2 , and c_2 .

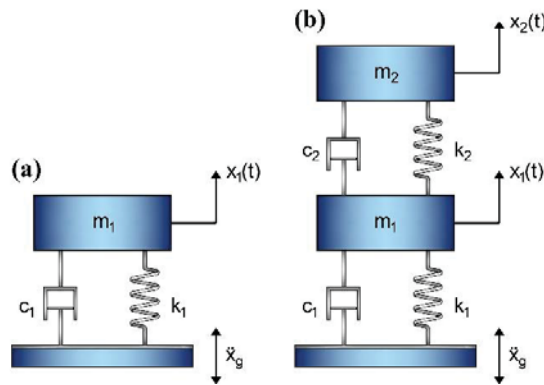


Figure 2: (a) simplified SDOF FB model, (b) simplified 2DOF MD model.

The equations of motion of the 2DOF MD model are:

$$\begin{cases} m_1 \ddot{x}_1 + c_1 \dot{x}_1 + k_1 x_1 - c_2 (\dot{x}_2 - \dot{x}_1) - k_2 (x_2 - x_1) = -m_1 \ddot{x}_g \\ m_2 \ddot{x}_2 + c_2 (\dot{x}_2 - \dot{x}_1) + k_2 (x_2 - x_1) = -m_2 \ddot{x}_g \end{cases} \quad (1)$$

being x_1 and x_2 the relative displacements of the two oscillators with respect to the ground and \ddot{x}_g the ground acceleration.

By considering the stochastic nature of earthquake, the ground acceleration \ddot{x}_g is modelled as a stationary Gaussian random process characterized by zero mean and white noise power spectral density $S_{\ddot{x}_g}(\omega) = S_0$, in which there is no statistical correlation on what happens in two subsequent instants t_0 and $t_0 + \tau$. Although it is neglected the dependency on the excitation frequency content, this process seems to be acceptable in an initial design phase, [e.g. 5].

For the 2DOF MD model shown in Figure 2, the optimization procedure provided by the authors is based on the minimization of the variance of the response x_1 , $E[x_1^2]$ given by:

$$E[x_1^2] = S_0 \int_{-\infty}^{+\infty} |H_1(\omega)|^2 d\omega \quad (2)$$

where $H_1(\omega)$ is the transfer function of the displacement of the main system expressed in the frequency domain ω and obtained by means of the Fourier Transform of the linear differential equations (1) as a function of some dimensionless parameters:

$$H_1(\omega) = \frac{-i\omega^3 B_3 - \omega^2 B_2 + i\omega B_1 + B_0}{\omega^4 A_4 - i\omega^3 A_3 - \omega^2 A_2 + i\omega A_1 + A_0}, \quad (3)$$

where the coefficients $B_1 - B_3$ and $A_1 - A_4$ are:

$$\begin{aligned} B_0 &= -\nu^2 \omega_1^2 (1 + \mu); & A_0 &= \nu^2 \omega_1^4 \\ B_1 &= -2\xi_2 \nu (1 + \mu) \omega_1 + 2\xi_1 \omega_1; & A_1 &= 2\xi_2 \nu \omega_1^3 + 2\xi_1 \nu^2 \omega_1^3 \\ B_2 &= -1; & A_2 &= \omega_1^2 + (1 + \mu) \nu^2 \omega_1^2 + 4\xi_1 \xi_2 \nu \omega_1^2 \\ B_3 &= 0; & A_3 &= 2\xi_2 \nu \omega_1 (1 + \mu) + 2\xi_1 \\ & & A_4 &= 1 \end{aligned}$$

and $\mu = m_2/m_1$ is the mass ratio, $\nu = \omega_2/\omega_1$ is the tuning ratio, ω_1 and ω_2 are the natural circular frequencies while $\xi_1 = c_1/(2m_1\omega_1)$ and $\xi_2 = c_2/(2m_2\omega_2)$ are the damping ratios of the main and secondary system, respectively.

The ranges of values selected for the non-dimensional parameters, covering a wide range of civil engineering applications, are: $\mu =]0, 2]$, $\nu =]0, 2]$, $\xi_1 = [0, 0.1]$, $\xi_2 = [0, 1]$.

By applying the Cauchy's residue theorem, the integral (2) can be analytically obtained [50, 51], leading to the following expression of $E[x_1^2]$:

$$E[x_1^2] = \frac{\pi S_0 \left(\frac{(A_2 A_3 - A_1 A_4) B_0^2}{A_0} + A_3 (B_1^2 - 2B_0 B_2) + \frac{(A_1 A_2 - A_0 A_3) B_3^2}{A_4} + A_1 (B_2^2 - 2B_1 B_3) \right)}{-A_0 A_3^2 + A_1 (A_2 A_3 - A_1 A_4)} \quad (4)$$

The square root of $E[x_1^2]$ is provided in Figure 3a and b, respectively for a damping ratio ξ_1 equal to 0 and 0.05. Each triplet of charts refers to mass ratios equal to 0.01, 0.1, and 1, by assuming unit values of the spectral density S_0 and the circular frequency ω_1 . From Figure 3 it can be noticed that, by increasing the damping of the first oscillator for the same value of mass ratio, the variance of x_1 is reduced, highlighting the beneficial effect of ξ_1 in reducing the response of the main system. Instead, by increasing the mass ratio for the same value of ξ_1 , the number of couples ξ_2 - ν characterized by the same variance increases, leading to lower dependance of the response on the design parameters, and thus, to a major robustness of the system.

The minimization of the variance $E[x_1^2]$ (4) is implemented by imposing that its gradient is null with respect to the tuning ratio ν and the damping ratio ξ_2 , i.e.:

$$\begin{cases} \frac{\partial E[x_1^2]}{\partial \nu} = 0 \\ \frac{\partial E[x_1^2]}{\partial \xi_2} = 0 \end{cases} \quad (5)$$

The optimal values of the tuning ratio ν_{opt} and the damping ratio $\xi_{2,\text{opt}}$, obtained from Eq. (5), are presented in graphical form in Figure 4 by varying the damping ratio ξ_1 and considering the range of validity of the mass ratio μ equal to 0 – 1. In particular, the optimal tuning ratio decreases, and the optimal damping ratio increases, by increasing the mass ratio. From Figure 4 the effect of the first damping ratio on the trend of the optimal parameters can be also evaluated. While the distance between the optimal tuning curves becomes significant for ξ_1 equal to 0.05 and 0.1, with scatters up to 44% for medium-high mass ratios (Figure 4a), in terms of optimal damping curves, only for $\xi_1 = 0.1$ and for mass ratios approaching to 1, considerable scatters, up to 56%, are obtained (Figure 4b).

Depending on project specific considerations, related to both architectural/functional and constructive aspects, as well as to structural and dynamic requirements, the values of the optimal pa-

parameters cannot always be simultaneously adopted. In order to account these cases, starting from the optimizing conditions of Eq. (5), a single design variable is assumed, either the tuning ratio ν_{opt} or the damping ratio $\xi_{2,\text{opt}}$, while the other variable and the mass ratio are assumed as design data.

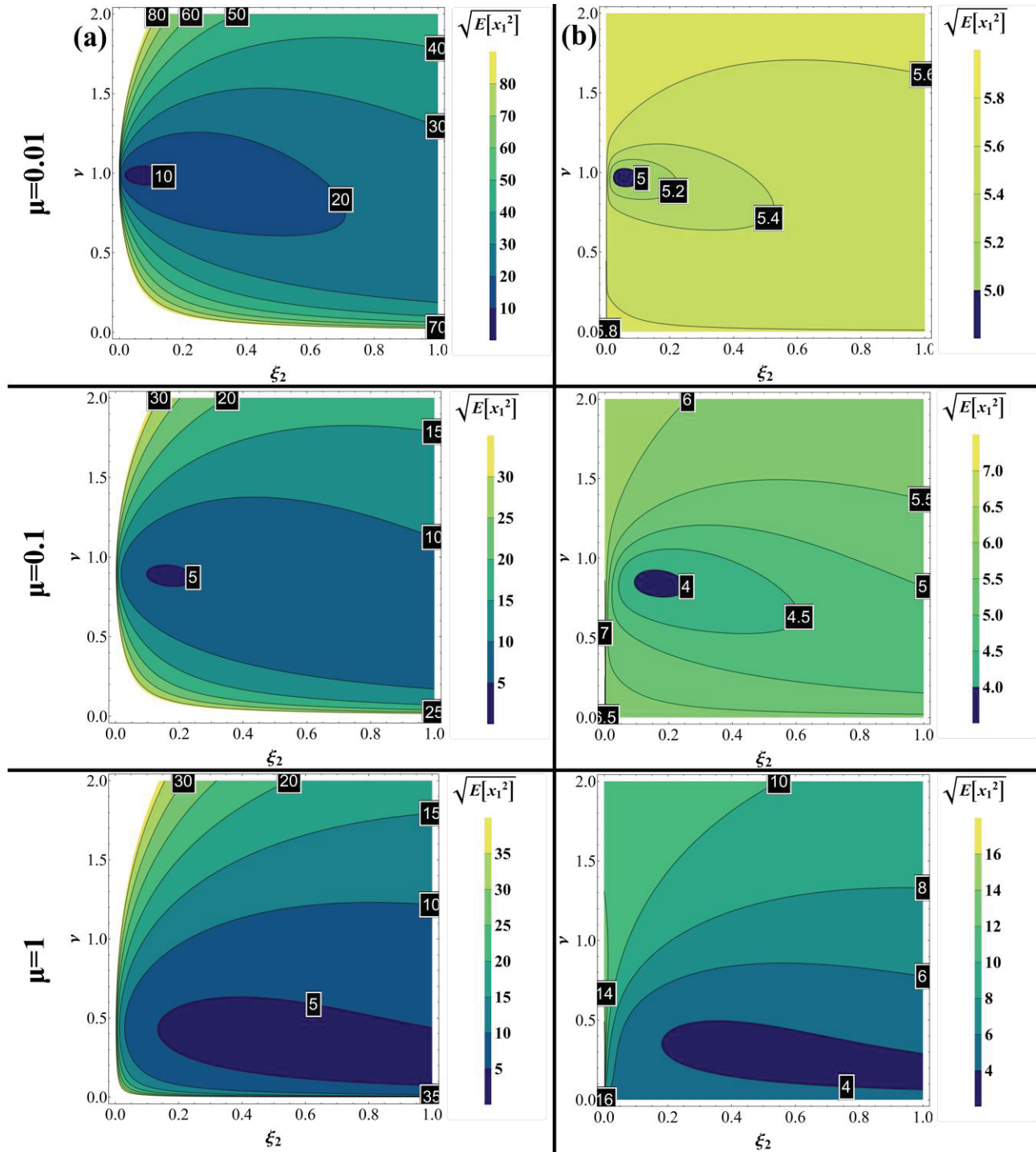


Figure 3: Response displacement of the main system: (a) first column $\xi_1 = 0$, (b) second column $\xi_1 = 0.05$.

Also for these optimization procedures, the values of the optimal parameters are provided in graphic form (Figure 5), by assuming the damping ratio ξ_1 equal to 0.05.

It is worth emphasizing that the first procedure proposed in this paper represents the generalization of the optimization algorithm implemented by [52]. In fact, by neglecting the damping of the main system, Warburton [52] imposes the minimization of the variance of the main system subjected to a white-noise input, with respect to ξ_2 and ν , thus analytically deriving optimal parameters.

Additionally, by considering a single design variable, ξ_2 or ν (Figure 5), the optimization method degenerates into the procedure proposed by [30], when the damping ratio of the main structure is assumed equal to 0 and ξ_2 is set equal to $(2m_2\omega_1)^{-1}$.

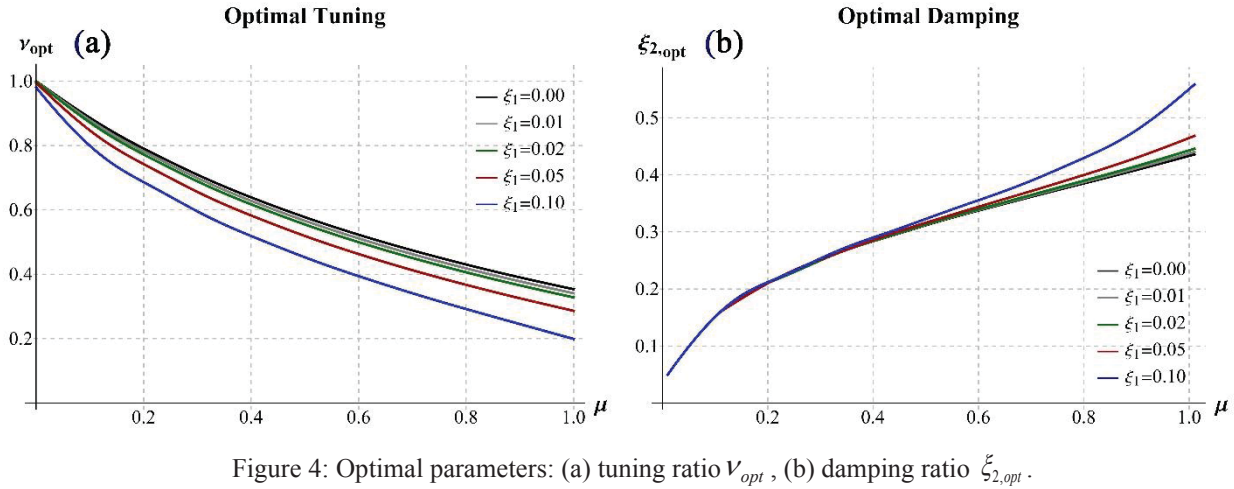


Figure 4: Optimal parameters: (a) tuning ratio ν_{opt} , (b) damping ratio $\xi_{2,opt}$.

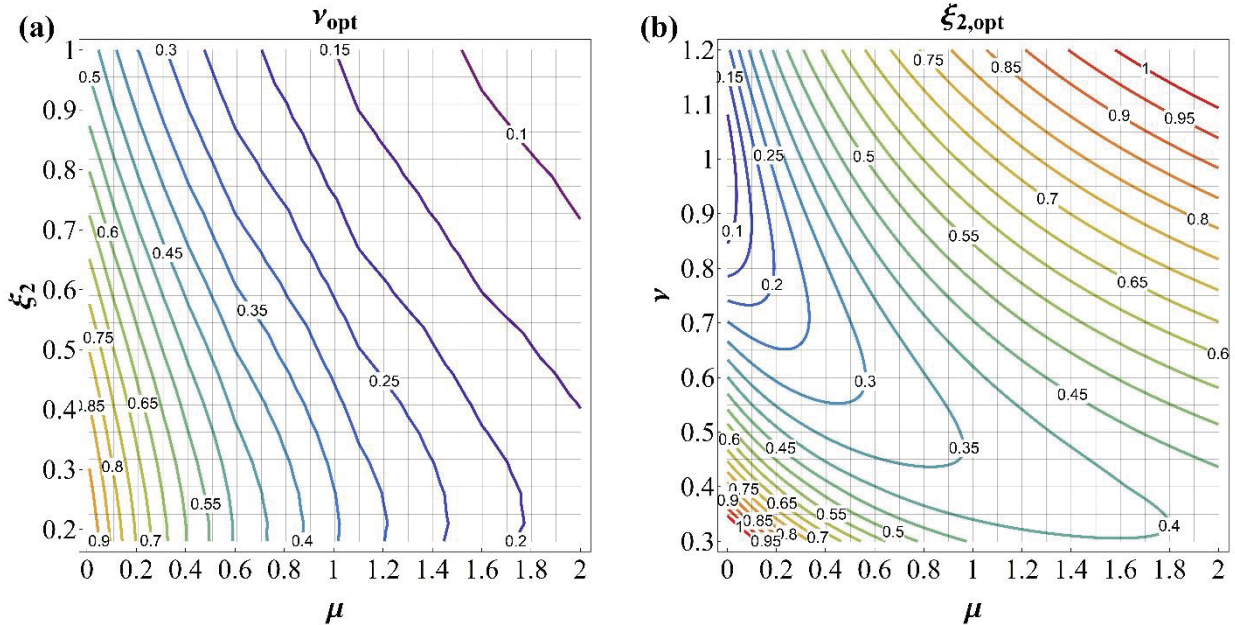


Figure 5: (a) optimal tuning ν_{opt} by varying ξ_2 and μ , (b) optimal damping $\xi_{2,opt}$ by varying ν and μ .

3. PARAMETRIC ANALYSIS

A wide parametric analysis is carried out for analysing the dynamic behaviour of non-conventional MD configurations and their potential benefits in reducing the seismic response of tall buildings, by adopting the simplified 2DOF model defined in the previous section 2 (Figure 2b). In particular, the dynamic characteristics of the MD models (periods and participating masses) are derived from classical modal analyses of the undamped system, while the complex eigenvalue problem has been solved in the state space for accounting the effect of the non-proportional damping. Then, response spectrum analyses are carried out by considering the complex modal superposition methods, in order to derive the base shear and displacement demands. Finally, time history analyses are performed for highlighting the effect of the seismic input (frequency content, duration, etc.), for discussing the effectiveness and robustness of the system, and for comparing different procedures of optimization.

3.1. Simplified models and design parameters

A 40-story tall building is adopted as a reference for the fixed-base (FB) single-degree of freedom model, by assuming the mass m_1 equal to 80000 kNs²/m and the damping ratio ξ_1 equal to 0.05. Three baseline SDOF FB (Figure 2a) models are defined by varying the fundamental vibration period T_1 , thus accounting for different structural solutions, from very rigid (*e.g. stiff diagrid structures or diagonalized mega-frame*) to more flexible structural systems (*e.g. moment resisting frames or frame tubes*). In particular, the fundamental vibration periods T_1 are assumed equal to 1.62 s, 2.5 s, 3.5 s.

The design parameters adopted for exploring the dynamic behaviour of the controlled 2DOF MD configurations (Figure 2b) are the mass ratio μ , the isolation period T_2 , and the damping ratio of the isolation system ξ_2 , which vary in the following ranges:

- $T_2 = 0.05 - 10$ s (50 values);
- $\mu = 0.1, 0.5, 1.0, 1.5$;
- $\xi_2 = 0.05 - 0.5$ (26 values).

Hence, by varying all the design parameters, a total of 15600 models have been generated.

It is worth observing that, while some values of the mass ratios and of the isolation periods are not realistic, they are considered herein to fully characterize the behaviour of the system and provide a comprehensive view of its potential applications and limitations. The range for the damping ratio ξ_2 has been chosen considering different isolation systems, composed either by high damping rubber bearings or by natural rubber bearings plus viscous or hysteretic dampers.

3.2. Non-proportional damping and complex mode superposition method

In the controlled MD configurations, the structural damping ξ_1 is assumed equal to 0.05 while the damping of the isolation system ξ_2 varies between 0.05 and 0.50. Structures with very different values of damping ratios represent non-proportional (or non-classical) damped system, characterized by complex-valued natural modes. In this case, the off-diagonal terms in the damping matrix \mathbf{C} cannot be neglected, since the system does not satisfy the Caughey and O' Kelly identity: $\mathbf{C}\mathbf{M}^{-1}\mathbf{K} = \mathbf{K}\mathbf{M}^{-1}\mathbf{C}$ (with \mathbf{M} , \mathbf{K} , and \mathbf{C} the mass, stiffness and damping matrices) [53]. Furthermore, when \mathbf{C} is an arbitrary symmetric positive-definite matrix, the expansion in terms of the eigenvectors for the undamped system and real modal coordinates does not lead to uncoupled modal equations. Therefore, rather than working with a second-order equation, it is more convenient to transform the equations of motion into a set of first-order equations involving complex modal coordinates and complex state eigenvectors, and working in the state space [54].

In the response spectrum analyses carried out in the following section, the complete-quadratic-combination (CQC) rule is utilized in order to obtain the maximum responses associated to each degree of freedom. Being the system non-classically damped, the method described by Sinha and Igusa [55] is utilized in order to consider the complex-valued nature of the vibration mode shapes. Therefore, the maximum system response, R , is given by:

$$R = \sqrt{\sum_{i=1}^n \sum_{j=1}^n B_i B_j \rho_{ij} R_i R_j} \quad (6)$$

with n the number of the considered vibration mode; B_i and B_j real-valued participation factors; R_i and R_j spectral displacements; ρ_{ij} real-valued modal correlation factors. The participation factors and modal correlation factors depend on the vector that defines which DOF is being considered; therefore, they assume different values when evaluating the response of each floor, differently to what is done in the case of CQC rule for classically damped systems, where these parameters are fixed quantities [56].

3.3. Response spectrum analysis (RSA)

Response spectrum analyses (RSA) are carried out on all the simplified MD and FB models by utilizing the acceleration response spectrum defined by the Eurocode 8 [57] for the design earthquake, characterised by 10 % probability of exceedance in 50 years (475 years Return Period).

The spectrum is depicted in Figure 6a, for $a_g = 0.35$ g, soil type B ($S = 1.2$; $T_B = 0.15$ s; $T_C = 0.5$ s; $T_D = 2$ s), damping ratio equal to 0.05. The complex mode superposition method proposed by Sinha and Igusa [55], briefly recalled in section 3.2, has been used to consider the complex-valued nature of the vibration mode shapes. In Figures 6b and 7 the results of the analyses are firstly presented for the case of $\xi_2 = 0.30$; then the effect of the damping ratio of the isolation system is evaluated in Figure 8.

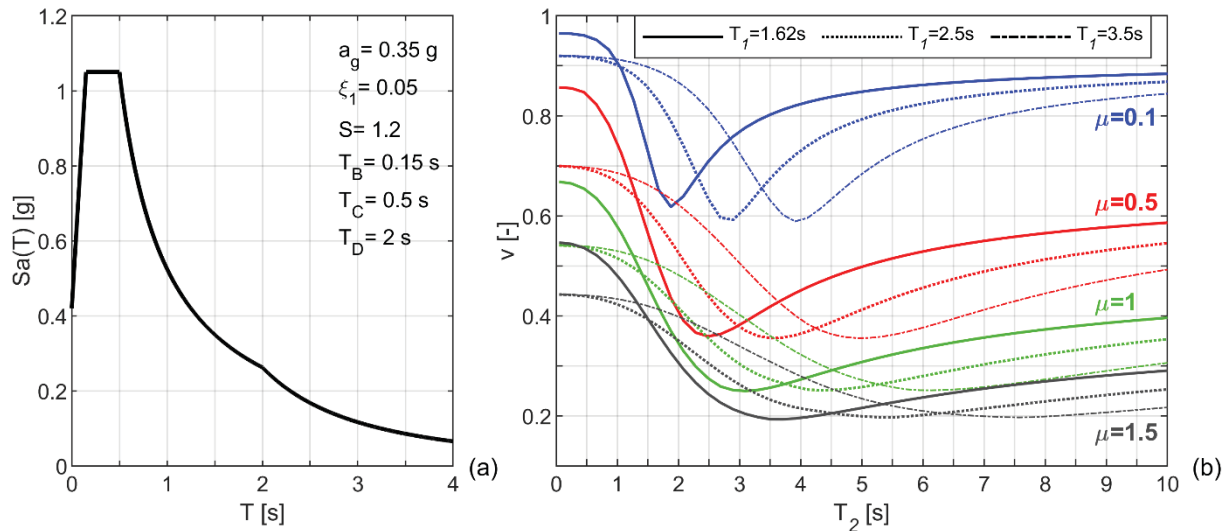


Figure 6: (a) EC8 elastic acceleration response spectrum, (b) base shear ratio v vs. T_{ISO} . for $\xi_2 = 0.30$.

The Figure 6b depicts the base shear ratio between the base shear controlled MD configuration and the uncontrolled FB counterpart, i.e. $v = V_{MD}/V_{FB}$, as a function of the isolation period T_2 . From the chart, it can be immediately observed that the base shear ratio v is always less than one, approximately between 0.95 e 0.85 for $\mu=0.1$, between 0.85 e 0.50 for $\mu=0.5$, between 0.68 e 0.30 for $\mu=1$, between 0.55 e 0.20 for $\mu=1.5$, showing significant reduction by increasing the mass ratio.

Considering the trend of v for each mass ratio, three behavioural zone can be clearly identified. The *first zone* (e.g. very small values of T_2) corresponds to the largest values of v , since the two parts are rigidly connected, thus no relative motion is allowed and no mass-damping mechanism arises. In particular, the first mode is the mode of the main structure, which activates all the mass of the system and, due to the presence of the secondary system, shows a period slightly elongated with respect to the uncontrolled baseline counterpart. Therefore, the base shear assumes values slightly lower than the FB counterpart and the ratio becomes less than one. The *second zone* (e.g. very large values of T_2) shows base shear ratios that reach the relevant mass fractions of the primary system $m_1/(m_1+m_2)$. In particular, the dynamic behaviour of the system tends to a condition of “perfect isolation”, with the masses of the two systems almost completely decoupled, and the first and second mode respectively corresponding to the mode of the secondary and main system. The *third zone* (e.g. intermediate values of T_2) presents the minimum values of v , thanks to maximum exploitation of the mass damping mechanism. In this zone, the first and second modes are still the modes of the secondary and primary system. However, the interaction between the two parts leads to a transfer of a fraction of the main system’s mass from the second to the first mode, with a consequent significant reduction of the ratio v .

In Figure 7 the shear ratio charts (v - T_2) for three values of T_1 (1.62, 2.5, 3.5 s) are coupled to the analogous charts depicting the displacement of the primary system in the MD configuration normalized to the FB counterpart, i.e. $d = d_{I,MD}/d_{I,FB}$, and the deformation in the isolation system δ_2 , as a

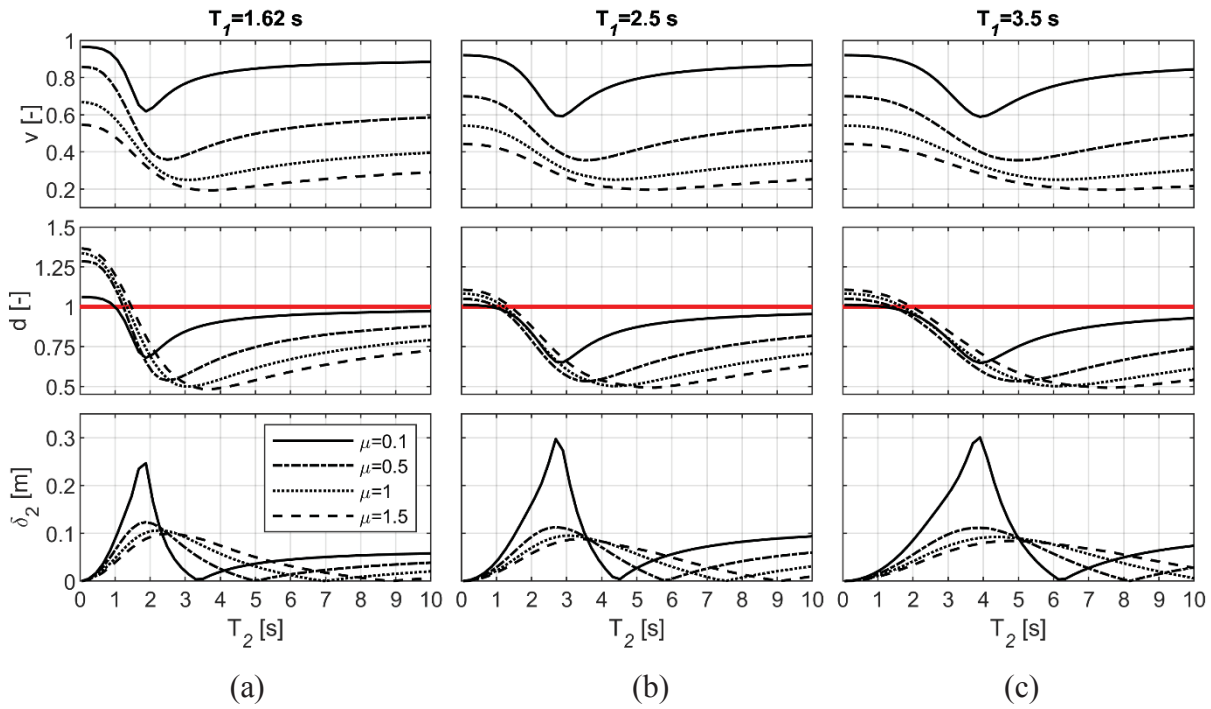


Figure 7: Ratios v , d , and relative displacement δ_2 for $\xi_2 = 0.30$: (a) $T_I = 1.62$ s, (b) $T_I = 2.5$ s, (c) $T_I = 3.5$ s.

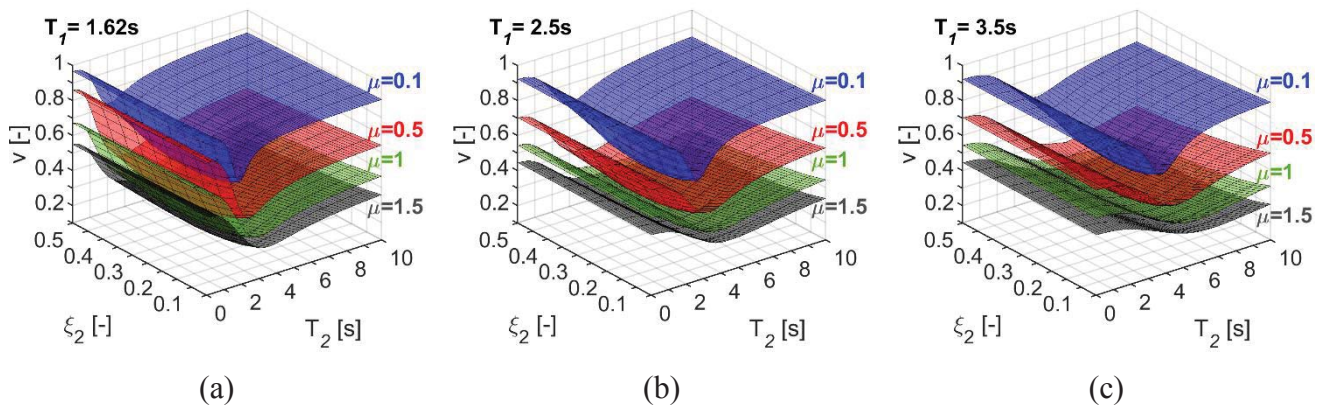


Figure 8: Base shear ratio v as a function of ξ_2 and T_2 for (a) $T_I = 1.62$ s, (b) $T_I = 2.5$ s, (c) $T_I = 3.5$ s.

function of T_2 . Quite trivially, it can be observed that the minimum values of v and d are obtained for the same value of T_2 , which also corresponds to the maximum deformation in the isolation system.

For the three baseline models, Figure 8 provides the trend of the shear ratio v as a function of the isolation period T_2 and the damping ratio ξ_2 , for each value of the mass ratio μ . It can be observed that, in the third zone of “perfect isolation”, the shear ratio v is reduced by increasing T_I , therefore the effect of ξ_2 becomes more significant for more flexible baseline models and isolation systems. In the second zone in which the mass damping mechanism is maximized and the primary and secondary systems are strongly coupled, the minimum values of v are obtained for values of ξ_2 between 0.2 – 0.4, as discussed in detail in the following section.

3.4. Comparison between the results of optimal procedures and of the parametric analysis

In this section the optimal values of the parameters v e ξ_2 derived from the results of the RSA are compared to the ones calculated by means of the optimal procedures provided in section 2. For the sake of brevity, only the results obtained for the MD controlled configuration characterized by $T_I = 1.62$ s and $\mu = 1$ are presented in the following.

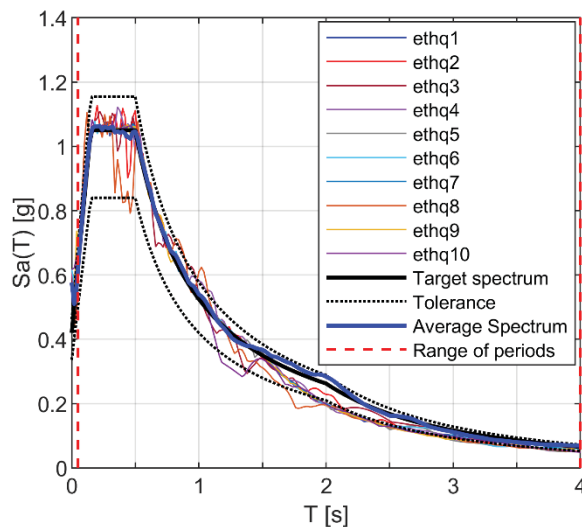
In particular, six optimal configurations are defined and named as A, B, C, D, FM, W. The solution A represents the optimal configuration that gives rise to the minimum values of the base shear, and of the displacement of the primary system, obtained through the RSA. The solutions B and C are derived by assuming respectively ξ_{2opt} or v_{opt} from the optimal procedures of section 2, while the other one is retrieved from the parametric analysis (Figure 5); the solution D is entirely derived through the optimization procedure, i.e. the optimal values of both parameters are simultaneously considered (Figure 4). The solutions FM and W are derived by adopting the optimal parameters of the procedures suggested by Feng and Mita [30] and Warburton [52], respectively. The values of the optimal parameters, of the corresponding two complex modal damping ratios η_1 and η_2 , as well as of the shear ratio v , of the six solutions are reported in Table 1. It can be observed that, the solutions A and B provide the minimum shear ratio v , equal to 0.25, while the other solutions show values of the shear ratio varying between 0.28 and 0.34.

Ref.	Optimal Solutions	v_{opt} -	ξ_{2opt} -	T_{2opt} s	η_1 -	η_2 -	v -	
This paper	RSA	A	0.523	0.33	3.10	0.207	0.267	0.25
	RSA+OPT	B	0.523	0.36	3.10	0.225	0.289	0.25
	OPT+RSA	C	0.330	0.33	4.91	0.281	0.172	0.30
	OPT	D	0.325	0.47	4.98	0.409	0.220	0.29
Feng and Mita	FM	0.353	0.15	4.59	0.124	0.108	0.34	
Warburton	W	0.353	0.43	4.59	0.365	0.225	0.28	

Table 1: Dynamic properties of the six optimal solutions.

3.5. Time history analyses

In order to assess and compare the response of the six controlled configurations under real seismic inputs, time history analyses are carried out on the relevant MD and FB models. A set of ten records registered during real earthquakes is used and scaled by means of the software SeismoMatch [58], by checking the closeness of their average response spectrum to the target elastic spectrum (provided in Figure 6a) in the period range 0.05 - 4 s. Data of the ten scaled ground motions and corresponding acceleration response spectra, with the average spectrum, are given in Figure 9.



Earthquake name	Date	Comp.	PGA [g]
ethq1	Imperial Valley	18/05/1940	S00E 0.425
ethq2	Taft	21/07/1952	S69E 0.482
ethq3	Hachinohe	16/05/1968	NS 0.490
ethq4	Loma Prieta	17/10/1989	NS 0.511
ethq5	Northridge	17/01/1994	S90W 0.547
ethq6	Kobe	17/01/1995	000 0.571
ethq7	L'Aquila	04/04/2009	EW 0.472
ethq8	Chile	27/02/2010	NS 0.437
ethq9	Christchurch	22/02/2011	N55W 0.551
ethq10	Amatrice	24/08/2016	EW 0.617

Figure 9: Major data and acceleration response spectra of the scaled acceleration records.

The results of the analyses are here provided in Figures 10 and 11 in terms of base shear, relative displacements, floor absolute accelerations, by comparing the six controlled configurations and each MD configuration to the FB counterpart.

The Figure 10 depicts for each optimal solution the average peak response registered during the ten acceleration histories in terms of some response parameters. These parameters express the response of the controlled configuration normalized to the uncontrolled counterpart, considering the base shear, v , the relative displacement, d , and absolute acceleration, a , of the primary structure. The remarkable effectiveness of the controlled configurations emerges in terms of all the response parameters. In fact, the shear ratio v varies between 0.194 and 0.345, the displacement ratio d between 0.388 and 0.689, and the acceleration ratio a between 0.553 and 0.726. In particular, the solution B provides the maximum reductions, with values very close to the ones of the solution A, while the solution FM shows the minimum reductions and thus it represents the less efficient solution. The average envelopes of the peak displacements and absolute accelerations, obtained from the time history analyses of the controlled configurations and baseline structure, are shown in Figure 11. From the graphs it can be observed that, for all the optimal solutions the average values of story drift and absolute acceleration in the MD models are reduced with respect to the FB uncontrolled structure. The solutions A and B are confirmed the most effective in reducing the seismic response of the primary system.

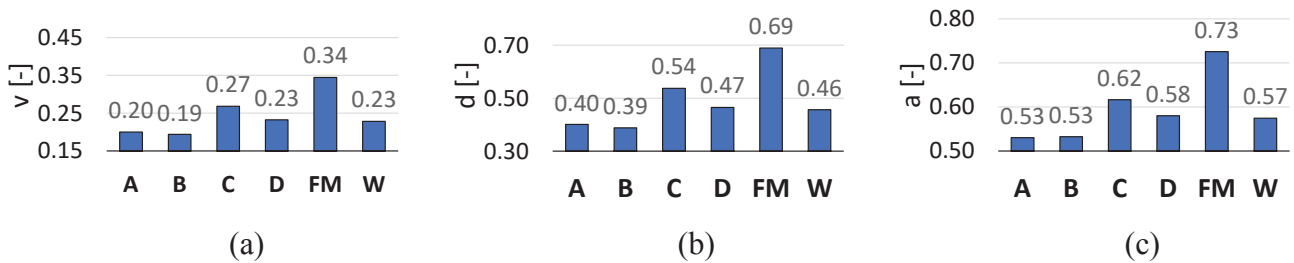


Figure 10. Comparison between the six optimal solutions: (a) base shear ratio v , (b) displacement ratio d , (c) acceleration ratio a .

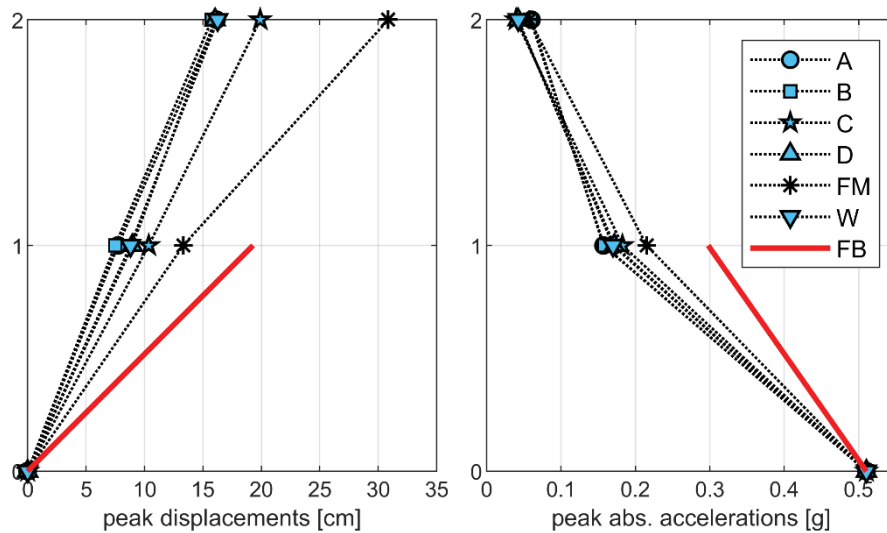


Figure 11: Peak story displacements and absolute accelerations for the six optimal solutions.

4. SUMMARY AND CONCLUSIONS

In the present paper, the authors investigate the dynamic behaviour of mass damping (MD) configurations utilising isolation system, such as Mega Substructure Control Systems and Intermediate Isolation Systems, by preliminary adopting simplified lumped mass 2-DOF models. By considering a stochastic approach, the seismic acceleration is modelled as a white noise and the variance of the displacement of the first degree of freedom is minimized in the first instance with respect to both design variables, i.e. the tuning ratio and the damping ratio of the secondary system and secondly with respect to only one of these two variables. Furthermore, in order to validate this general proce-

ture, a wide parametric analysis is carried out on simplified lumped mass models and the potential benefits of such systems in reducing the seismic response of tall buildings is examined.

In particular, by selecting a 40-story tall building and by varying the mass ratio, classical and complex modal analyses show three different dynamic behavioural zones as a function of the isolation period: the first zone is characterized by a “fixed-base” behaviour, in the second zone the interaction between the two masses gives rise to the mass damping effect, while in the third zone for very long isolation periods, the two structural parts are almost dynamically decoupled.

Then, response spectrum analyses with complex modal superposition methods are performed, with the aim to compare the base shear and the displacement demands with the fixed-base counterpart simplified SDOF model. More in detail, a significant reduction of the seismic demand on the main system is observed when large mass ratios are adopted for the whole range of the isolation period, thus confirming the structural robustness of such systems. Finally, time history analyses are implemented for underlining the effects of the seismic input (amplitude, frequency content, duration, etc.) and for comparing the results of different procedures of optimization, both those proposed in the present work and those of existing literature.

References

- [1] Holmes D., Listing of installations, *Engineering Structures* 1995, 17(9):676–678.
- [2] Kaynia A.M., Veneziano D., Seismic effectiveness of tuned mass dampers, *Journal of the Structural Division* 1981, ASCE, 107(8):1465–1484.
- [3] Sladek J.R., Klingner R.E., Effect of tuned mass dampers on seismic response. *Journal of Structural Engineering* 1983, ASCE; 109(8):2004–2009.
- [4] Soto-Brito R., Ruiz S.E., Influence of ground motion intensity on the effectiveness of tuned mass dampers, *Earthquake Engineering and Structural Dynamics* 1999, 28(11):1255–1271.
- [5] De Angelis M., Perno S., Reggio A. ‘Dynamic response and optimal design of structures with large mass ratio TMD’. *Earthquake Engng Struct. Dyn.* 2012, vol. 41(1), pp. 41–60. <https://doi.org/10.1002/eqe.2548>
- [6] Reggio A. and De Angelis M. ‘Optimization of a Non-Conventional TMD implemented via Inter-story Isolation’. *Proceedings of the EUROLYN 2014 – IX International Conference of Structural Dynamics*; Porto, Portugal, 30 June – 2 July 2014. pp. 1713–1720
- [7] Reggio A. and De Angelis M. ‘Optimal energy-based seismic design of non-conventional tuned mass damper (TMD) implemented via inter-story isolation’. *Earthquake Eng Struct. Dyn.* 2015, vol. 44(10), pp. 1623–1642. <https://doi.org/10.1002/eqe.2548>
- [8] Wang S.J., Lee B.H., Chuang W.C., Chang K.C. ‘Optimum dynamic characteristic control approach for building mass damper design’. *Earthquake Engng Struct Dyn.* 2018, vol. 47(4), pp. 872–888. <https://doi.org/10.1002/eqe.2995>
- [9] Wang S.J., Lee B.H., Chuang W.C., Chiu I.C., Chang K.C. ‘Building mass damper design based on optimum dynamic response control approach’. *Eng Struct.* 2019; vol. 187, pp. 85–100. <https://doi.org/10.1016/j.engstruct.2019.02.053>
- [10] Kobayashi M. and Sasaki D. ‘Making a seismic design database of mid-story isolated buildings and structural property evaluation based on response prediction method’. *AIIJ Technol Des*, Feb 2009, vol. 15(29), pp. 65–70. <https://doi.org/10.3130/aijt.15.65> (in Japanese)
- [11] Murakami K., Kitamura H., Ozaki H., Teramoto T. ‘Design and analysis of a building with the middle-story isolation structural system’. *Proceeding of the 12th World Conference on Earthquake Engineering*; Auckland, New Zealand, 30 Jan – 4 Feb 2000, paper 0857
- [12] Sueoka T., Torii S., Tsuneki Y. ‘The application of response control design using middle-story isolation system to high-rise building’. *Proceeding of the 13th World Conference on Earthquake Engineering*; Vancouver, B.C., Canada, Aug 2004, paper 3457
- [13] Tsuneki Y., Torii S., Murakami K., Sueoka T. ‘Middle-story Isolated Structural System of High-Rise Building’. *Proceedings of the 14th World Conference on Earthquake Engineering*; Beijing, China, Oct 2008, paper S05-01-023.f

- [14] Tsuneki Y., Torii S., Murakami K., Sueoka T. 'Middle-story isolated structural system of high-rise building'. *J Disaster Res.* 2009, vol. 4(3), pp. 229–238. <https://doi.org/10.20965/jdr.2009.p0229>
- [15] Okada K., Yoshida S. 'Structural design of Nakanoshima festival tower'. *Int J High-Rise Build.* 2014, vol. 3(3), pp. 173–183
- [16] Nakagawa K., Shimazaki D., Yoshida S., Okada K. 'Application of Seismic Isolation Systems in Japanese high-rise buildings'. *International Journal of High-Rise Buildings.* 2015. Seismic Design Issue II. pp. 36–38.
- [17] Tamari M., Yoshihara T., Miyashita M., Ariyama N., Nonoyama M. 'Structural Design and Performance Evaluation of a Mid-story Seismic Isolated High-Rise Building'. *International Journal of High-Rise Buildings.* 2017. Vol. 6(3), pp. 227–235. <https://doi.org/10.21022/IJHRB.2017.6.3.227>
- [18] Villaverde R. 'Reduction seismic response with heavily-damped vibration absorbers'. *Earthquake Eng Struct Dyn.* 1985, vol. 13(3), pp. 33–42. <https://doi.org/10.1002/eqe.4290130105>
- [19] Sadek F., Mohraz B., Taylor A.W., Chung R.M. 'A method of estimating the parameters of tuned mass dampers for seismic applications'. *Earthquake Engng Struct Dyn.* 1997, vol. 26(6), pp. 617–635. [https://doi.org/10.1002/\(SICI\)1096-9845\(199706\)26:6%3C617:AID-EQE664%3E3.0.CO;2-Z](https://doi.org/10.1002/(SICI)1096-9845(199706)26:6%3C617:AID-EQE664%3E3.0.CO;2-Z)
- [20] Tan P., Zhang Y, Zhou F. 'Optimal Design and Control Mechanism Study on Story Isolation System'. *Proceedings of the 14th World Conference on Earthquake Engineering*; Beijing, China, Oct 2008, paper 0060.
- [21] Chey M., Chase J.G., Mander J.B., Carr A.J. 'Innovative seismic retrofitting strategy of added stories isolation system'. *Front Struct Civ Eng.* 2013, vol. 7(1), pp. 13–23. <https://doi.org/10.1007/s11709-013-0195-9>
- [22] Miranda J.C. 'A method for tuning tuned mass dampers for seismic applications'. *Earthquake Engng Struct Dyn.* 2013, vol. 42(7), pp. 1103–1110. <https://doi.org/10.1002/eqe.2271>
- [23] Zhou Q, Singh MP, Huang XY (2016) Model reduction of mid-story isolation systems. *Eng Struct* 124:36–48. <https://doi.org/10.1016/j.engstruct.2016.06.011>
- [24] Argenziano M., Faiella D., Fraldi M., Mele E. 'Optimum tuning frequency and damping ratios in Inter-story Isolation Systems (IIS): a closed form solution'. *XVIII Convegno Anidis*; Ascoli Piceno, Italy, Sept 2019.
- [25] Faiella D., Mele E. 'Vibration Characteristics and Higher Mode Coupling in Intermediate Isolation Systems (IIS). A Parametric Analysis'. *Bull Earthq Eng.* 2019, vol. 17(7), pp. 4347–87. <https://doi.org/10.1007/s10518-019-00637-w>.
- [26] Faiella D., Mele E. 'Insights into inter-story isolation design through the analysis of two case studies'. *Eng Struct.* 2020, vol. 215, pp. 1–21. <https://doi.org/10.1016/j.engstruct.2020.110660>
- [27] Goldsmith M. 'The tall buildings: the effect of scale'. Master's thesis, Illinois Institute of Technology, Chicago, Illinois, 1953.
- [28] Ali M.M. (2001). *Art of the skyscraper. The genius of Fazlur Khan*. Rizzoli International Publications Inc, New York.
- [29] Khan Y.S. (2004). *Engineering Architecture. The vision of Fazlur R. Khan*. W W Norton & Co Inc, New York.
- [30] Feng M.Q, Mita A. (1995). Vibration control of tall buildings using mega subconfiguration, *Journal of Engineering Mechanics*, 121(10):1082–1088.
- [31] Chai W., Feng M.Q.. (1996). Seismic performance of mega-sub controlled buildings. The 11th World Conference on Earthquake Engineering, June 23–28, 1996, Acapulco, Mexico. Paper no. 789.
- [32] Chai W., Feng M.Q.. (1997). Vibration control of super tall buildings subjected to wind loads. *International Journal of Non-Linear Mechanics*, 32(4): 657–668. [https://doi.org/10.1016/S0020-7462\(96\)00094-7](https://doi.org/10.1016/S0020-7462(96)00094-7)

- [33] Feng M.Q., Chai W.. (1997). Design of mega-sub controlled building system under stochastic wind loads. *Probabilistic Engineering Mechanics*, 12(3): 149-162. [https://doi.org/10.1016/S0266-8920\(96\)00035-5](https://doi.org/10.1016/S0266-8920(96)00035-5)
- [34] Zhang X.A, Wang D., Jiang J. (2005) The controlling mechanism and the controlling effectiveness of passive mega-sub-controlled frame subjected to random wind loads. *Journal of Sound and Vibration* 283(3-5), 543–560. <https://doi.org/10.1016/j.jsv.2004.04.038>
- [35] Zhang X.A., Zhang J., Wang D., Jiang J. (2005) Controlling Characteristics of Passive Mega-Subcontrolled Frame Subjected to Random Wind Loads. *Journal of Engineering Mechanics*, 131(10):1046-1055.
- [36] Zhang X.A, Qin X., Cherry S., Lian Y., Zhang J., Jiang J. (2009) A New Proposed Passive Mega-Sub Controlled Structure and Response Control, *Journal of Earthquake Engineering*, 13:2, 252-274. <https://doi.org/10.1080/13632460802347422>
- [37] Kalehsar H.E, Khodaie N. (2018) Wind-induced vibration control of super-tall buildings using a new combined structural system. *Journal of Wind Engineering & Industrial Aerodynamics*, 172, 256–266.
- [38] Li T., Zhang X.A, Wang Q. (2011) Control Characteristics of Mega-sub Controlled Structure System with Friction Damper under Rare Earthquake. *Proceedings of the International MultiConference of Engineers and Computer Scientists 2011 Vol II*; Hong Kong, China, Mar 2011. pp. 791 – 796.
- [39] Li X., Tan P., Li X., Liu A. (2016) Mechanism Analysis and Parameter Optimization of Mega-Sub-Isolation System. *Shock and Vibration*. Vol. 2016, pp. 1-12. Article ID 2605839. <https://doi.org/10.1155/2016/2605839>
- [40] Tan P., Zhang Y., Li X., Li X., Liu A., Zhou F. (2016) Experimental investigation of mega-sub isolation structure'. *Struct Design Tall Spec Build*, vol. 26(16), e1360. <https://doi.org/10.1002/tal.1360>
- [41] Ye Z. and Wu G. (2017) Optimal lateral aseismic performance analysis of mega-substructure system with modularized secondary structures. *Struct Design Tall Spec Build.*, vol. 26, e1387. pp. 1-14. <https://doi.org/10.1002/tal.1387>
- [42] Huang J.Q, Chong X. Jiang Q., Ye X.G, Wang H.Q. (2018) Seismic Response Reduction of Megaframe with Vibration Control Substructure. *Shock and Vibration Volume 2018*, Article ID 9427908.
- [43] Martinez-Paneda M, Elghazouli A.Y (2020) An integrated damping system for tall buildings. *The Structural Design of Tall and Special Buildings*, vol. 29(7), e1724. <https://doi.org/10.1002/tal.1724>
- [44] Kawai A., T. Maeda, Takewaki I. (2020) Smart Seismic Control System for High-Rise Buildings Using Large-Stroke Viscous Dampers Through Connection to Strong-Back Core Frame. *Front. Built Environ.*, vol. 6(29), pp. 6-29. <https://doi.org/10.3389/fbuil.2020.00029>
- [45] Liang Q., Li L., Yang Q. (2020) Seismic analysis of the tuned-inerter-damper enhanced mega-sub structure system'. *Struct Control Health Monit.*, e2658. pp. 1-15. <https://doi.org/10.1002/stc.2658>
- [46] Kelly J (1997) *Earthquake resistant design with rubber*. Springer, Berlin
- [47] Naeim F, Kelly J (1999) *Design of seismic isolated structures: from theory to practice*. Wiley, Hoboken
- Wang et al., 2012
- [48] Wang SJ, Chang KC, Hwang JS, Hsiao JY, Lee BH, Hung YC (2012) Dynamic behaviour of a building structure tested with base and mid-story isolation systems. *Eng Struct* 42:420–433. <https://doi.org/10.1016/j.engstruct.2012.04.035>
- [49] Kobayashi M, Koh T (2008) Modal coupling effects of mid-story isolated buildings. In: 14th World conference on earthquake engineering, Beijing, China, paper 05-01-0230
- [50] James, H. M., Nichols, N. B., & Phillips, R. S. (Eds.). (1947). *Theory of servomechanisms* (Vol. 25). New York:

- [51] Crandall, S. H., & Mark, W. D. (2014). *Random vibration in mechanical systems*. Academic Press.
- [52] Warburton G.B., Optimum absorber parameters for various combinations of response and excitation parameters, *Earthquake Engineering and Structural Dynamics* 1982, 10(3):381-401.
- [53] Veletsos A.S., Ventura C.E. 'Modal Analysis of non-classically damped linear systems', *Earthquake Engng Struct Dyn.* 1986, vol. 14(2), pp. 217–243.
<https://doi.org/10.1002/eqe.4290140205>
- [54] Connor J., Laflamme S. *Structural Motion Engineering*. Berlin: Springer; 2014.
- [55] Sinha R. and Igusa T. 'CQC and SRSS methods for non-classically damped structures'. *Earthquake Engng Struct Dyn.* 2012, vol. 24(4), pp. 615-619. <https://doi.org/10.1002/eqe.4290240410>
- [56] Moutinho C. 'An alternative methodology for designing tuned mass dampers to reduce seismic vibrations in building structures'. *Earthquake Engng Struct Dyn.* 2012, vol. 41(14), pp. 2059-2073.
<https://doi.org/10.1002/eqe.2174>
- [57] Code, P. (2005). Eurocode 8: Design of structures for earthquake resistance-part 1: general rules, seismic actions and rules for buildings. *Brussels: European Committee for Standardization*.
- [58] SeismoMatch, SEISMOSOFT, Earthquake Engineering Software Solutions.

DIAGRID SYSTEM COUPLED WITH SHEAR WALLS: ANALYTICAL INVESTIGATION ON THE DYNAMICAL RESPONSE IN TALL BUILDINGS

G. Lacidogna^{1*}, G. Nitti¹, D. Scaramozzino¹, and A. Carpinteri¹

¹ Department of Structural, Geotechnical and Building Engineering, Politecnico di Torino, Corso Duca degli Abruzzi 24, 10129, Torino, Italy
e-mail: giuseppe.lacidogna@polito.it, giuseppe.nitti@polito.it, domenico.scaramozzino@polito.it, alberto.carpinteri@polito.it

*Corresponding author: giuseppe.lacidogna@polito.it

Abstract

Diagrids are tubular structural systems made up of mega-diagonals arranged in a triangular or tetrahedral pattern, which are placed all over the external surface of the building and usually span across several floors. In the last two decades, diagrids have experienced a remarkable development as efficient structural systems in tall building design and construction. This was mainly due to their high lateral stiffness, capability to realize complex-shaped structures and obtain impressive aesthetic results, flexibility of the external diagonals' layout, etc. The structural analysis of these systems is usually carried out by the Finite Element Method (FEM) or by numerical calculations based on simplified assumptions. Recently, we developed a matrix-based method (MBM) to perform the structural analysis of diagrid systems under static forces. The MBM was then coupled with an analytical formulation developed in the past years by some of the authors, the so-called General Algorithm (GA), in order to study the structural response of an external diagrid tube coupled with an internal shear wall under lateral and torque static actions. The study allowed to investigate the influence of the diagonal inclination on the lateral and torsional flexibility of the diagrid-core system. In the past years, the analytical formulation of the GA was also made suitable to analyze the response of three-dimensional tall building in the dynamic regime. In this contribution, we show new results regarding the dynamical behavior of an external diagrid structural system coupled with an internal shear wall, as obtained from the GA calculations. Modal analysis was carried out in order to obtain the natural frequencies and mode shapes of the tall building, and the influence of the diagonal inclination on the results was also investigated. Moreover, by applying different harmonic oscillations at different frequencies at the base of the building, the damped dynamical response of the different diagrid-core systems was investigated.

Keywords: diagrid, matrix-based method, general algorithm, dynamic analysis, analytical method.

1 INTRODUCTION

In the last decades, the field of tall buildings has undergone a major development due to the introduction of new structural systems able to resist lateral loads very efficiently [1]. Among these, diagrid systems have been exploited worldwide due to their high lateral stiffness and aesthetic potential. The diagrid is a tubular structure placed over the external surface of the building, made up of inclined mega-diagonals [2,3] or tetrahedral configuration [4] which are designed to withstand both lateral and vertical loads. Therefore, in diagrid structures the conventional vertical columns are completely removed from the external tube, as the gravitational loads can be directly transferred to the ground via the mega-diagonals.

Besides the conventional application of Finite Element (FE) calculations, a variety of analytical and simplified methodologies have been proposed in the last years for the structural analysis of diagrid systems under lateral loads. All these methods usually rely on the following basic assumptions: (1) the deformation mechanism of the building is governed by the axial elongation and shortening of the mega-diagonals, (2) the stress-strain relationship of the diagonals lies within the linear elastic regime, and (3) the floor slabs of the building remain plane after deformation. Based on these assumptions, Moon et al. [5] developed a stiffness-based methodology for the structural analysis and preliminary design of rectangular diagrid tubes under horizontal forces. Mele et al. [6] proposed a hand-based method for the calculation of axial stresses in the diagonals under both lateral and vertical loads. Liu and Ma [7] suggested a modular method for the structural analysis of arbitrary polygonal diagrid tubes, where the shear and bending stiffness of the diagrid modules were analytically calculated.

More recently, we developed a stiffness-based approach based on matrix calculus, which was called the matrix-based method (MBM), for the analysis of generic diagrid systems [8]. The MBM is based on the direct calculation of the global stiffness matrix of the diagrid, by considering the kinematic and equilibrium equations at the level of the rigid floors. The MBM allows to perform very quickly the structural analysis of diagrids under both lateral, vertical and torsional actions. Furthermore, the MBM has been recently integrated within a more general semi-analytical framework, the so-called General Algorithm (GA). The GA has been developed by some of the authors in the last decades and allows to investigate the structural behavior of three-dimensional buildings made up of several vertical resisting elements, such as frames, tubes and shear walls [9-12]. Very recently, we have inserted the MBM within the GA environment in order to perform the structural analysis of an external diagrid tube coupled with internal shear walls [13].

One of the main interesting features of diagrid structures is that their structural response is significantly affected by the layout of external diagonals. This means that the diagonal layout can undergo optimization processes, finding the optimal diagonal arrangement to optimize certain responses of the building. Moon [14] has early shown that there exists an optimal inclination of the external diagonals able to minimize the lateral building deflection under horizontal loads. Various diagonal layouts have been proposed in the following years and the corresponding building efficiency under lateral loads has been investigated [15-18]. Attention has also been paid to torsional actions and the role that these might have in the parametric investigation of the diagrid structural response [13].

In this contribution, we make use of the MBM coupled with the GA in order to investigate how the dynamic response of an external diagrid tube coupled with an internal closed-section shear wall changes according to a change in the inclination of the external diagrid diagonals. The natural frequencies and fundamental mode shapes of the building are extracted by solving the multi-degree-of-freedom (MDOF) unforced undamped equations of motion. The analysis of the natural frequencies and mode shapes of the buildings with different inclinations of the

diagonals reveals the influence of the diagrid geometry on the overall dynamic response of the system. Furthermore, the damped dynamic response of the diagrid-core structure is also studied under the application of harmonic oscillations of the base of the building. Comparisons between the obtained maximum displacements, velocities, accelerations, inter-story drifts and base shear values are finally made.

2 METHODOLOGY

As shown in [13], the MBM can be coupled to the GA in order to carry out the structural analysis of a diagrid-core system under lateral and torsional static actions. More details about the basic assumptions and the applications of the MBM and the GA can be found in [8-13]. In the GA environment the building is assumed to be subjected to two horizontal forces (along the horizontal X and Y axes) and one torque moment (around the vertical Z axis) acting at the level of the floor centroids. It follows that the total number of DOFs in the GA is equal to $3N$, N being the total number of floors.

In this paper, the MBM-GA framework has been adapted in order to investigate the dynamic response of a diagrid-core system. First of all, the natural frequencies and fundamental mode shapes of the building are evaluated according to the MDOF undamped unforced equations of motion. Then, we apply harmonic oscillations at various frequencies at the base of the building and solve the dynamical problem based on the MDOF forced oscillations in presence of damping.

The first problem can be formulated in simple mathematical terms via the following matrix relationship related to the modal eigenvalue-eigenvector solution:

$$(\mathbf{K} - \omega_n^2 \mathbf{M}) \mathbf{u}_n = \mathbf{0} \quad (1)$$

where \mathbf{K} and \mathbf{M} represent the stiffness and mass matrix of the structure, \mathbf{u}_n is the mass-weighted eigenvector associated to the n -th mode shape ($n = 1, 2, \dots, 3N$) and ω_n is the angular frequency associated to the n -th mode of vibration. The angular frequency ω_n is related to the vibrational frequency f_n and period of vibration T_n by $\omega_n = 2\pi f_n = 2\pi/T_n$. More details about the calculation of the stiffness matrix \mathbf{K} and mass matrix \mathbf{M} can be found in [9,11]. After the construction of these matrices, equation (1) immediately yields the natural frequencies and mode shapes of the structure.

After evaluating the fundamental vibrational features of the diagrid-core building (frequencies and mode shapes), we also want to investigate the dynamic response of the structure under the application of harmonic oscillations at the base of the structure. This can be done by considering the complete dynamic equation, which includes the contribution of inertia, damping, elastic and external forces:

$$\mathbf{M}\delta''(t) + \mathbf{C}\delta'(t) + \mathbf{K}\delta(t) = \mathbf{F}_{\text{ext}}(t) \quad (2)$$

where \mathbf{C} is the damping matrix of the structure, $\mathbf{F}_{\text{ext}}(t)$ is the vector of external dynamic forces and $\delta''(t)$, $\delta'(t)$ and $\delta(t)$ represent the vectors of floor accelerations, velocities and displacements (the apex ' stands for the time-derivative). One can then separate the spatial and temporal contribution within the dynamic displacements $\delta(t)$, as $\delta(t) = \mathbf{U}\mathbf{p}(t)$, where \mathbf{U} is the matrix whose columns contain the time-independent mode shapes \mathbf{u}_n obtained from equation (1) and $\mathbf{p}(t)$ is the vector containing the time-dependent principal coordinates associated to each mode shape. Hence, we obtain:

$$\mathbf{M}\mathbf{U}\mathbf{p}''(t) + \mathbf{C}\mathbf{U}\mathbf{p}'(t) + \mathbf{K}\mathbf{U}\mathbf{p}(t) = \mathbf{F}_{\text{ext}}(t) \quad (3)$$

Multiplying each term of equation (3) by \mathbf{U}^T and remembering that, due to the mass-normalization of \mathbf{U} , $\mathbf{U}^T \mathbf{M} \mathbf{U} = \mathbf{I}$ and $\mathbf{U}^T \mathbf{K} \mathbf{U} = \mathbf{\Omega}$, \mathbf{I} being the identity matrix and $\mathbf{\Omega}$ the matrix containing the eigenvalues ω_n^2 on the diagonal and zero outside, it follows that:

$$\mathbf{p}''(t) + \mathbf{U}^T \mathbf{C} \mathbf{U} \mathbf{p}'(t) + \mathbf{\Omega} \mathbf{p}(t) = \mathbf{U}^T \mathbf{F}_{\text{ext}}(t) \quad (4)$$

The problem can now be decoupled with respect to each individual mode n if one assumes that the matrix $\mathbf{U}^T \mathbf{C} \mathbf{U}$ is diagonal, with diagonal elements equal to $2\xi_n \omega_n$, where ξ_n represents the damping ratio associated to the n -th mode of vibration. Then, one finally obtains the set of $3N$ scalar equations whose unknowns are the temporal principal coordinates $p_n(t)$:

$$p_n''(t) + 2\xi_n \omega_n p_n'(t) + \omega_n^2 p_n(t) = \mathbf{u}_n^T \mathbf{F}_{\text{ext}}(t) \quad (5)$$

Since we apply harmonic oscillations at the base of the building, the vector of external forces $\mathbf{F}_{\text{ext}}(t)$ can be simply written as $\mathbf{F}_{\text{ext}}(t) = \mathbf{M} \mathbf{u}_g''(t) = \mathbf{M} \mathbf{u}_g'' \sin(\omega_g t)$, where \mathbf{u}_g'' is the vector associated to the ground acceleration and ω_g the angular frequency of the ground oscillation. The solution of the single-degree-of-freedom (SDOF) equation of motion (5), with the application of the initial resting conditions, leads to:

$$p_n(t) = e^{-\xi_n \omega_n t} \left[A_n \cos(\omega_{d,n} t) + B_n \sin(\omega_{d,n} t) \right] + C_n \cos(\omega_g t + \phi_n) \quad (6)$$

where $\omega_{d,n} = \omega_n \sqrt{1 - \xi_n^2}$ is the reduced frequency of the n -th mode of vibration due to its damping, and the coefficients A_n , B_n , C_n and ϕ_n take the following form:

$$\begin{cases} A_n = -C_n \sin(\phi_n) \\ B_n = \frac{\xi_n \omega_n A_n - C_n \omega_n \cos(\phi_n)}{\omega_{d,n}} \\ C_n = \frac{\mathbf{u}_n^T \mathbf{M} \mathbf{u}_g''}{\omega_n^2 \sqrt{(1 - \beta_n^2)^2 + (2\xi_n \beta_n)^2}} \\ \phi_n = -\arctan\left(\frac{2\xi_n \beta_n}{1 - \beta_n^2}\right) \end{cases} \quad (7)$$

where $\beta_n = \omega_g / \omega_n$ is the ratio between the angular frequency of the external excitation and the one associated to the n -th mode shape. Once all the $3N$ principal coordinates are evaluated from equations (6-7), the displacements of the structure $\delta(t)$ are immediately obtained as $\delta(t) = \mathbf{U} \mathbf{p}(t)$. Known the time-dependent displacements of the building floors one can easily find the velocities $\delta'(t)$ and accelerations $\delta''(t)$ by single and double time-differentiation. The inter-story drifts can also be evaluated directly from the vector $\delta(t)$. Finally, the total time-dependent base shear $V(t)$ is calculated by summing all the horizontal elastic forces at the level of the floors, which can be computed as $\mathbf{F}_{el}(t) = \mathbf{K} \delta(t)$.

The analytical procedure described in the above paragraphs is applied to a tall building made up of an external steel diagrid tube coupled with an internal closed-section concrete core. Figure 1a shows the dimensions (in meters) of the building plane, while figure 1b reports the six different lateral views by considering six different inclinations of the external diagonals [13]. The building has 40 stories and the inter-story height is equal to 4 meters, leading to a total height of the building of 160 meters. The internal core is a 9 m \times 9 m closed-section shear wall made of concrete (Young's modulus of 30 GPa) and 0.80 m thick. The ex-

ternal diagonals are made of steel (Young's modulus of 210 GPa) and their cross-sectional area is equal to 0.1 m^2 [13]. The different diagonal inclinations of the models (figure 1b) range from 32.6° (model 1) up to 81.1° (model 6). The mass of the structure is calculated assuming a dead load for the floors equal to 7 kN/m^2 . Finally, the damping ratio ξ_n is considered equal to 0.05 for all the modes of vibration.

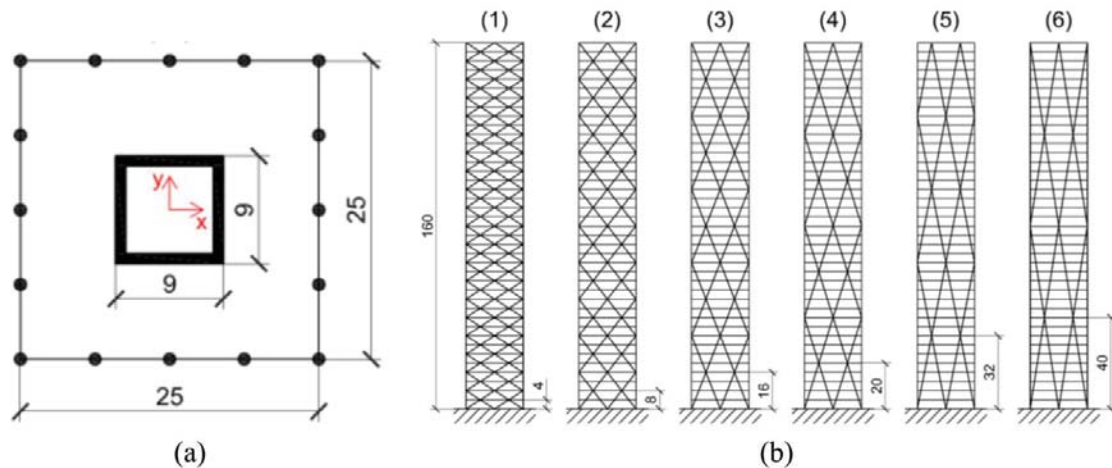


Figure 1: Building geometry: (a) floor plan; (b) lateral views. From Lacidogna et al. [13].

3 RESULTS AND DISCUSSION

Table 1 shows the first ten values of the natural frequencies (in Hz) arising from the MDOF unforced oscillation problem reported in equation (1) for the six models. The letters X, Y and Z in the parentheses describe the predominance direction of the mode shape: X and Y refer to lateral oscillations of the building along the X and Y direction, respectively, while T means that there is a not negligible contribution due to the torsional rotation of the building.

As can be seen, due to the symmetry of the building (figure 1a), the first two modes involve lateral oscillations along the X and Y axis at the same frequency for all models. The absolute value of this fundamental frequency is found to be maximum (0.364 Hz) for model 3 and minimum (0.243 Hz) for model 1. The first frequency of model 4 (0.362 Hz) is close to that of model 3, whereas the first frequencies of models 2 (0.321 Hz), 5 (0.339 Hz) and 6 (0.320 Hz) lie in between. Since higher frequencies are associated to stiffer responses, these results reflect a feature already found from the static analysis performed in [13], i.e. model 1 (the one with the shallowest diagonals) has the lowest lateral rigidity, whereas models 3 and 4 (with diagonal inclinations around 70°) are the stiffest under lateral loads.

For higher mode numbers an important torsional contribution is found to appear associated with displacements of the structure along the Y direction. It is interesting to notice how the first mode shapes involving significant torsional rotations are found at the fifth mode for models 1 and 2 and at the third mode for the other models. Moreover, the fundamental frequency values associated to these first torsional oscillations are found to decrease as the number of the model increases, i.e. it is maximum for model 1 (2.313 Hz) and it decreases up to the minimum value for model 6 (1.186 Hz). Again, since higher frequencies correspond to stiffer responses, these results show that increasing the diagonal inclination of the diagrid leads to higher torsional flexibility, as already shown by the static analysis reported in [13].

Mode number	Model 1	Model 2	Model 3	Model 4	Model 5	Model6
1	0.243 (X)	0.321 (X)	0.364 (X)	0.362 (X)	0.339 (X)	0.320 (Y)
2	0.243 (Y)	0.321 (Y)	0.364 (Y)	0.362 (Y)	0.399 (Y)	0.320 (X)
3	1.499 (X)	1.857 (Y)	1.581 (Y+T)	1.442 (Y+T)	1.243 (Y+T)	1.186 (Y+T)
4	1.499 (Y)	1.857 (X)	1.834 (X)	1.746 (Y)	1.539 (Y)	1.458 (Y)
5	2.313 (Y+T)	2.105 (Y+T)	1.834 (Y)	1.746 (X)	1.539 (X)	1.458 (X)
6	4.115 (X)	4.777 (Y)	4.432 (Y+T)	4.200 (Y+T)	3.688 (Y+T)	3.520 (Y+T)
7	4.115 (Y)	4.777 (X)	4.432 (X)	4.200 (Y+T)	3.769 (Y)	3.607 (Y)
8	6.935 (Y+T)	6.281 (Y+T)	4.701 (Y+T)	4.284 (X)	3.769 (X)	3.607 (X)
9	7.879 (Y)	8.641 (Y)	7.698 (Y+T)	7.005 (Y+T)	6.027 (Y+T)	5.757 (Y+T)
10	7.879 (X)	8.641 (X)	7.834 (Y+T)	7.508 (Y+T)	6.961 (Y+T)	6.820 (Y+T)

Table 1: Natural frequencies (in Hz) of the diagrid-core system depending on the diagrid diagonal inclination.

After evaluating the natural dynamic response of the diagrid-core system, various harmonic oscillations at different frequencies are applied to the base of the building and the dynamic structural response examined as obtained from equations (2-7). The time-dependent acceleration applied at the base of the building is of the form $u_g'' \sin(\omega_g t)$, being $u_g'' = 0.03 \text{ m/s}^2$ the maximum ground acceleration in the X direction and $\omega_g = 2\pi/T_g$ the ground angular frequency, with T_g varying in the range $0.01 \text{ s} - 8 \text{ s}$. Figures 2-6 show the results in terms of maximum story displacement, maximum story velocity, maximum story acceleration, maximum inter-story drift and maximum base shear, respectively, as a function of the applied ground oscillation period T_g and diagrid model.

Figure 2 shows that each diagrid-core system exhibits the largest value of the lateral displacement when the period of the ground oscillation matches the fundamental period of vibration of the building. With reference to the frequency values reported in table 1, this is found to occur when T_g is approximately equal to 4.1 s, 3.1 s, 2.8 s, 2.8 s, 2.9 s, and 3.1 s for models 1, 2, 3, 4, 5 and 6, respectively. Therefore the high peaks in the graphs of figure 1 refer to resonance phenomena related to the first modes of vibrations of the diagrid-core system. Clearly, adopting different diagonal inclinations makes the position of this resonance peak to translate horizontally with respect to the variable T_g , as the fundamental frequency of vibration of the system changes (table 1). It is also interesting to notice that the amplitude of this resonance peak is maximum for model 1 (blue curve), while it reaches a minimum value for models 3 (orange curve) and 4 (purple curve). This result is again in agreement with the above-mentioned fact that models 3 and 4 are indeed the most rigid ones against lateral forces, whereas model 1 is the most flexible. Therefore, the maximum dynamic displacements of the building floors are the highest for model 1, lowest for models 3 and 4, and exhibit intermediate values for models 2 (red curve), 5 (green curve) and 6 (light blue curve).

Figures 3 and 4 report the corresponding spectra of maximum story velocities and accelerations, respectively. Again, we find the largest resonance peaks in correspondence of the fundamental periods of the structure. However, in these cases we also start to see additional resonance peaks at lower periods (higher frequencies). The velocity response spectrum shows secondary resonance peaks around $0.5 - 0.7 \text{ s}$ (figure 3), which correspond to the activation of the second lateral vibrational modes (table 1). These secondary peaks are also found in the acceleration response spectrum (figure 4).

This spectrum is also found to exhibit tertiary resonance peaks around $0.2 - 0.3 \text{ s}$, which correspond to the resonance conditions along the third modes of vibration along the X direction (table 1). The amplitudes of the resonance peaks in the velocity spectrum (figure 3) exhibit similar trends of those reported in the displacement spectrum (figure 2), but here the

difference between the peaks corresponding to the different diagrid models is reduced. In the acceleration spectrum (figure 4), the amplitudes of the fundamental resonance peaks get somewhat inverted, since model 1 is the one experiencing the lowest acceleration, whereas models 3 and 4 are the ones undergoing the highest value. This is mainly due to the fact that, being models 3 and 4 the stiffest ones, they are not highly deformable but can undergo high accelerations due to their stiffer response.

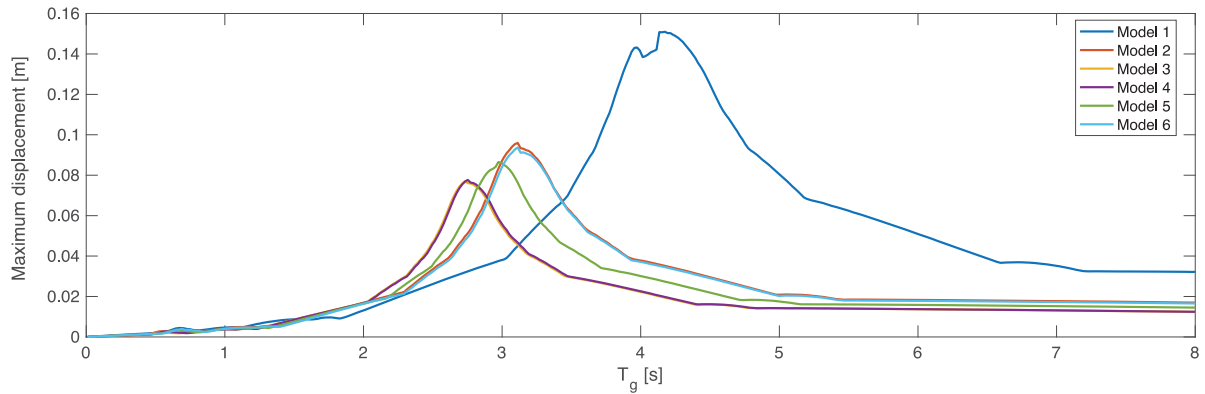


Figure 2: Maximum story displacement of the diagrid-core system.

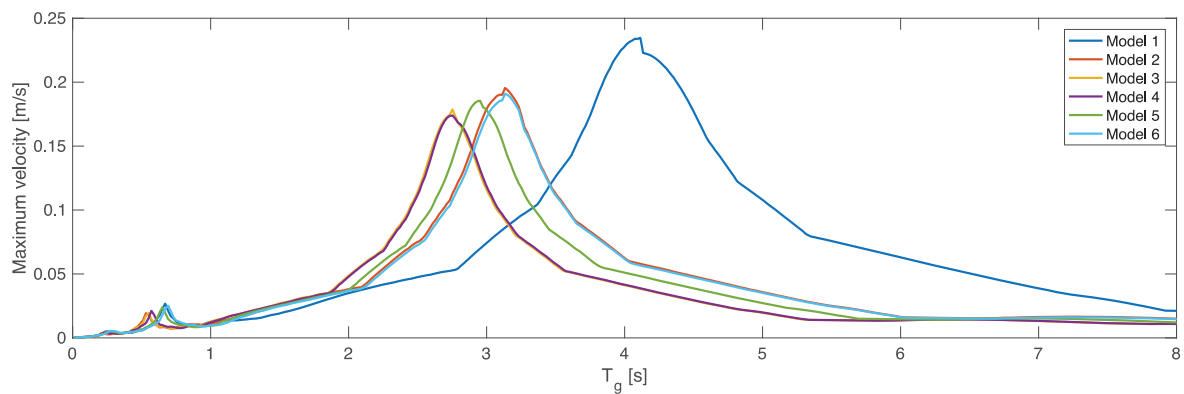


Figure 3: Maximum story velocity of the diagrid-core system.

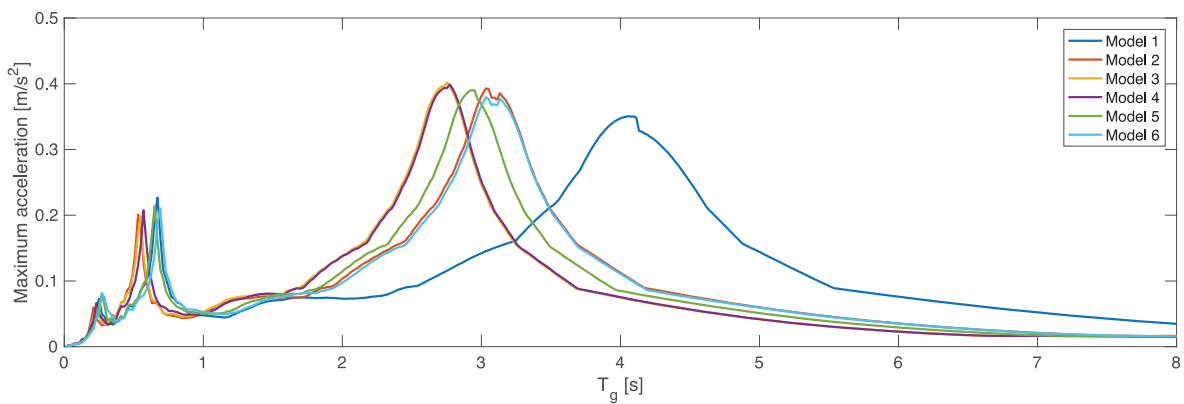


Figure 4: Maximum story acceleration of the diagrid-core system.

Figure 5 shows the maximum inter-story drifts depending on the diagrid-core model and the value of the ground oscillation period T_g . As can be seen, this spectrum strictly resembles the one of absolute displacements. However, in this case a somewhat clearer occurrence of the second resonance peaks at 0.5 – 0.7 s can be observed.

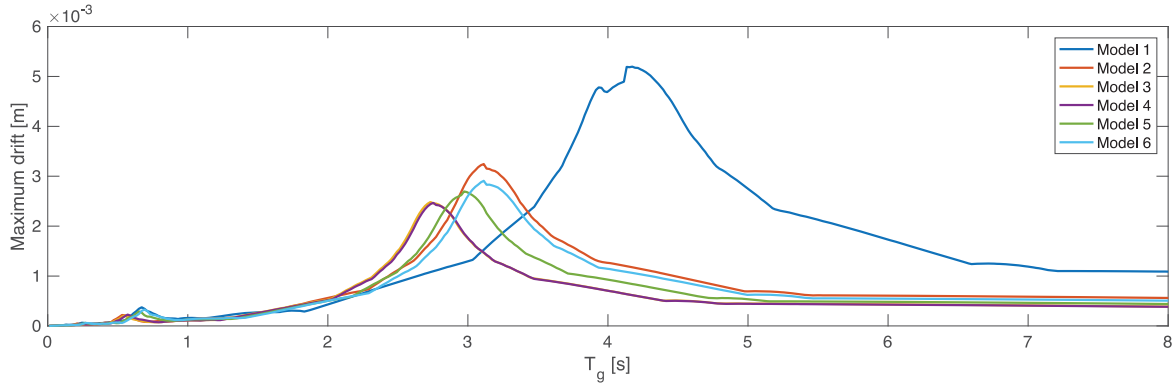


Figure 5: Maximum inter-story drift of the diagrid-core system.

Finally, figure 6 reports the maximum value of the total shear at the base of the building obtained for each oscillation period T_g and each diagrid-core model. In this case, three clear resonance peaks can again be observed, in analogy with the acceleration spectrum reported in figure 3. From the graph of the base shears, it can be seen that model 1 is the one absorbing the least amount of elastic force, as it is already known to be the most flexible under lateral loads. On the other hand, since the other models are stiffer, they exhibit a higher value of the base shear. These results reflect the fact that, under dynamic excitations, there is a general trade-off between the displacement-based and force-based demand. Stiffer structures obviously lead to lower displacements but they usually are required to withstand higher amounts of force. On the other hand, more flexible solutions undergo larger displacements but they are less loaded. However, this is also strongly affected by the frequency of the external excitation. Large dynamic responses, with high dynamic amplifications, are obviously generated if the excitation frequency is close to the fundamental ones of the structure. Conversely, if we are far from the resonance condition, the dynamic response of the building might lead to low values of the displacements as well as elastic forces.

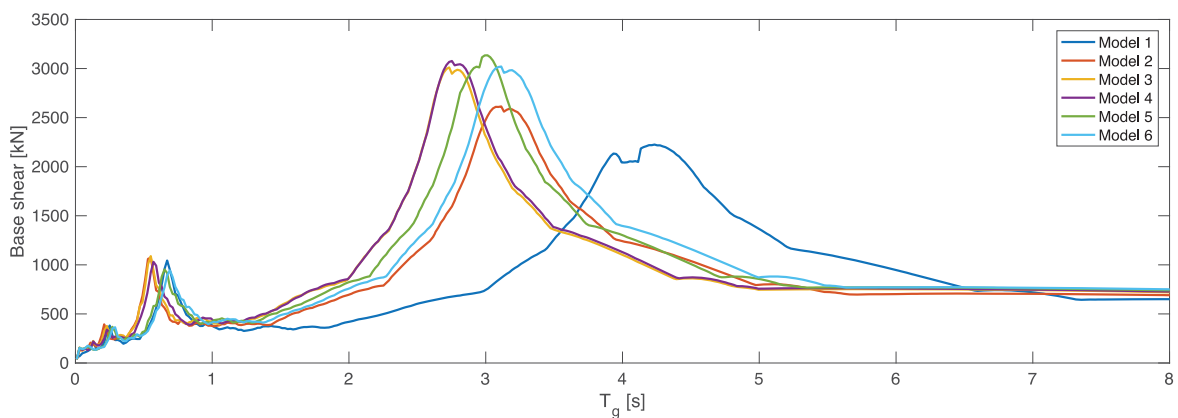


Figure 6: Maximum base shear of the diagrid-core system.

4 CONCLUSIONS

In this contribution we presented the analytical investigation of the dynamic response of a diagrid-core system for tall buildings. For this purpose, a matrix-based method (MBM) was employed within the framework of a General Algorithm (GA). For a set of diagrid-core systems with different inclinations of the external diagonals, the analytical formulation allowed to quickly evaluate the natural frequencies and mode shapes of the structure, as well as the damped response under harmonic oscillations at different frequencies. The semi-analytical formulation led to the investigation of the maximum values of the story displacements, velocities and accelerations under the external excitations, as well as the inter-story drifts and generated base shears.

It was found that diagrid solutions with very shallow diagonals lead to the highest lateral flexibility and lowest torsional deformability. Conversely, the lowest lateral flexibility was found for diagonal inclinations close to 70° . These diagrid solutions led to the lowest values of lateral displacements, but they were the ones experiencing the highest amount of elastic shear force in resonance conditions. Conversely, the most flexible solutions (with very shallow diagonals) were found to undergo the highest dynamic displacements, but experienced the least amount of elastic force. From these considerations, it follows that the dynamic response of a diagrid-core tall building strongly depends on the geometry of the external diagrid tube. However, great attention must also be paid to the fundamental frequency of the external excitation. When far from resonance conditions, each structural solution might have its advantages in terms of minimizing the lateral displacements and generated elastic forces.

REFERENCES

- [1] M.M. Ali, K.S. Moon, Advances in structural systems for tall buildings: Emerging developments for contemporary urban giants. *Buildings*, **8**, 104, 2018.
- [2] E. Asadi, H. Adeli, Diagrid: An innovative, sustainable, and efficient structural system. *Structural Design of Tall and Special Buildings*, **26**, e1358, 2017.
- [3] D. Scaramozzino, G. Lacidogna, A. Carpinteri, New trends towards enhanced structural efficiency and aesthetic potential in tall buildings: The case of diagrids. *Applied Sciences*, **10**, 3917, 2020.
- [4] G. Angelucci, F. Mollaioli, R. Tardocchi, A new modular structural system for tall buildings based on tetrahedral configuration. *Buildings*, **10**, 240, 2020.
- [5] K.S. Moon, J.J. Connor, J.E. Fernandez, Diagrid structural systems for tall buildings: Characteristics and methodology for preliminary design. *Structural Design of Tall and Special Buildings*, **16**, 205-230, 2007.
- [6] E. Mele, M. Torenò, G. Brandonisio, A. De Luca, Diagrid structures for tall buildings: Case studies and design considerations. *Structural Design of Tall and Special Buildings*, **23**, 124-145, 2014.
- [7] C. Liu, K. Ma, Calculation model of the lateral stiffness of high-rise diagrid tube structures based on the modular method. *Structural Design of Tall and Special Buildings*, **26**, e1333, 2017.
- [8] G. Lacidogna, D. Scaramozzino, A. Carpinteri, A matrix-based method for the structural analysis of diagrid systems. *Engineering Structures*, **193**, 340-352, 2019.

- [9] A. Carpinteri, G. Lacidogna, S. Puzzi, A global approach for the three-dimensional analysis of tall buildings. *Structural Design of Tall and Special Buildings*, **19**, 518-536, 2010.
- [10] A. Carpinteri, G. Lacidogna, G. Nitti, Open and closed shear-walls in high-rise structural systems: Static and dynamic analysis. *Curved and Layered Structures*, **3**, 154-171, 2016.
- [11] G. Nitti, G. Lacidogna, A. Carpinteri, Tall buildings subjected to horizontal loading: Analysis of two case studies by an in-house numerical code. *Proceedings of the 23rd Conference of the Italian Association of Theoretical and Applied Mechanics (AIMETA)*, Salerno, Italy, September 4-7, 292-300, 2017.
- [12] G. Nitti, G. Lacidogna, A. Carpinteri, Structural Analysis of High-rise Buildings under Horizontal Loads: A Study on the Piedmont Region Headquarters Tower in Turin. *The Open Construction and Building Technology Journal*, **13**, 81-96, 2019.
- [13] G. Lacidogna, G. Nitti, D. Scaramozzino, A. Carpinteri, Diagrid systems coupled with closed- and open-section shear walls: Optimization of geometrical characteristics in tall buildings. *Procedia Manufacturing*, **44**, 402-409, 2020.
- [14] K. S. Moon, Optimal grid geometry of diagrid structures for tall buildings. *Architectural Science Review*, **51**, 239-251, 2008.
- [15] G. Angelucci, F. Mollaioli, Diagrid structural systems for tall buildings: Changing pattern configuration through topological assessments. *Structural Design of Tall and Special Buildings*, **26**, e1396, 2017.
- [16] V. Tomei, M. Imbimbo, E. Mele, Optimization of structural patterns for tall buildings: The case of diagrid. *Engineering Structures*, **171**, 280-297, 2018.
- [17] G. Angelucci, F. Mollaioli, Voronoi-like grid systems for tall buildings. *Frontiers in the Built Environment*, **4**, 1-20, 2018.
- [18] G. Angelucci, F. Mollaioli, O. A. Shawa, Evaluation of optimal lateral resisting systems for tall buildings subject to horizontal loads. *Procedia Manufacturing*, **44**, 457-464, 2020.

OPTIMUM DAMPING OF SLENDER MONOPOLE TOWERS BY GYROSCOPIC STABILIZER

Gian Felice Giaccu¹ Luigi Fenu² Bruno Briseghella³ Camillo Nuti^{3,4}

¹ Department of Architecture, Design and Urban Planning, University of Sassari, Alghero, Italy

e-mail: [gf.giaccu@uniss.it](mailto:g.f.giaccu@uniss.it)

² Department of Civil and Environmental Engineering, and Architecture, University of Cagliari, Cagliari, Italy

e-mail: lfenu@unica.it

³ College of Civil Engineering, Fuzhou University, Fuzhou, Fujian Province, China

e-mail: bruno@fzu.edu.cn

⁴ Department of Architecture, Roma Tre University, Rome, Italy

e-mail: camillo.nuti@uniroma3.it

Abstract

Slender structures as lighting poles and telecommunication towers are usually very sensitive to wind effects due their dynamic characteristics and due to their notable exposure to wind forces. Wind-induced forces produce fluctuating stress, which, despite the assessment of dynamic properties and the study of the environmental conditions, can lead to damage accumulation and consequent collapse of these structures. Careful attention to wind forces has, therefore, to be paid for these typologies of structures, since several damages have been attributed to fatigue issues. It is well known that damping and structural frequencies play a fundamental role in the structural response under wind loads; in fact, an increase of damping would lead to remarkable beneficial effects on the dynamic response of these structures. This paper focuses the attention on a mathematical model of a damped gyroscopic device conceived as a dynamic stabilizer for such slender structures; the proposed mechanical device allows for an increase of structural damping with a consequent improvement of dynamic performances of the tower subjected to wind loads. A parametric study for different mechanical properties of the gyroscopic device has been conducted in the present paper aiming to assess the effectiveness of the proposed apparatus for different configurations of the proposed device.

Keywords: Monopole towers, Slender structures, Gyroscopic stabilizer, Frequency increment, Damping increment.

1 INTRODUCTION

The Monopole towers are slender structures usually employed for supporting communication devices or lighting poles. It is generally recognized that these structures are very sensitive to wind effects and to uncertainties related to wind forces and to structural dynamic features [1, 2]. In past years, the authors have studied the dynamics of the monopole towers [3], among wind sensitive structures, ensuring the presence of specific design problems related to the definition of wind load and the dynamic characteristics of the structure as shown in [4, 5]. Dynamic performances of these structures are therefore strongly affected by environmental conditions and by dynamic and geometrical properties of these structures [6, 7].

Proper assessment of environmental conditions (ground roughness, exposition, orographic placement) combined to dynamic structural characteristics of the mast, is an important topic since these factors deeply affect the structural dynamic behavior of these systems [3, 7, 8]. However, despite the assessment of dynamic characteristics and the examination of the environmental conditions, cautious attention to fatigue problems has to be paid for this typology of slender structures e.g. [7-9].

Gyroscopic systems have been always studied in automotive and in mechanical systems [10-14]; moreover, the interaction between the beam and gyroscopic devices has been studied by several authors for examining their dynamic behavior [15-18] moreover recently gyroscopic devices were applied as structural isolation device in seismic engineering [19].

This paper proposes a direct integration approach for simulating the structural interaction between the gyroscopic device and the vertical mast of the tower, utilizing a mathematical model of the gyroscopic device applied to lumped mass mast model already developed by the author in a previous paper [20], in the present work, a parametric study performed on mechanical properties of the gyroscopic device has been performed, aiming to assesses and to optimizes the performances of the proposed device.

The principal component of the gyroscopic system is a rotating mass, having a horizontal angular momentum Ω perpendicular to the mast axis; the rotating mass is connected to the vertical shaft by a mechanical system provided with rotational damped spring system, which allows relative rotations (in the horizontal plane) between the vertical shaft and the rotating mass. The gyroscopic system reacts to the mast horizontal oscillations by coupling its vibrations with the relative rotation of the gyroscopic device, consequently transferring the energy from the mast to the damped gyroscopic device [11].

Results show that the gyroscopic stabilizer allows, for an increasing of the natural frequency of the system, as confirmed by Yamanaka [21] and Carta et al. [17, 19] and for a remarkable increasing of damping of the tower; which, plays an important role in the reduction of wind-induced vibrations amplitude of slender structures [22-24]. The study demonstrates that the effectiveness of the device depends on the mechanical properties of the gyroscopic device which have to be properly set in order to optimize the efficiency of the proposed apparatus.

2 BACKGROUND MATHEMATICAL MODELS AND BENCHMARK SYSTEM

The present approach is based on the dynamic equilibrium equations of the gyroscopic lumped system with gyricity Ω described by D'Eleuterio [11] and on the hypothesis of the continuous Euler-Bernoulli beam dynamic equation; in the present work, the structural damping of the mast is not taken into account. The proposed formulation is valid for a gyroscopic device positioned at the elevation H_Q of the mast, the equation considers the bending mo-

ments M_{uu} , M_{vv} and of the torsional moment M_{ww} of the mast acting on the gyroscopic device. In case of small oscillations dynamic equation of the lumped gyroscopic device can be written as:

$$\begin{aligned} J_{\Omega,11}\ddot{\alpha} + C_{\alpha}\dot{\alpha} + K_{\alpha}\alpha + M_{ww}^{do} - M_{ww}^{up} &= -\Omega\dot{v}' \\ J_{\Omega,22}\ddot{v}' + M_{uu}^{do} - M_{uu}^{up} &= \Omega\dot{\alpha} \\ J_{\Omega,33}\ddot{u}' + M_{ww}^{do} - M_{ww}^{up} &= 0 \end{aligned} \quad (1)$$

Where u and v respectively indicate displacements in the horizontal and transversal direction, the dot \cdot indicates time derivative, the superscripts ' indicate derivative with respect to the vertical axis w and the superscripts up and do indicate the position “up” and “down” of the cross-section respect to the position of the gyroscopic device. According to above-mentioned hypotheses and after a proper static matrix condensation dynamic equilibrium of the undamped free vibrations of the system can be written in matrix form as:

$$\mathbf{M}\ddot{\mathbf{x}} + \mathbf{K}\mathbf{x} = \mathbf{0} \quad (2)$$

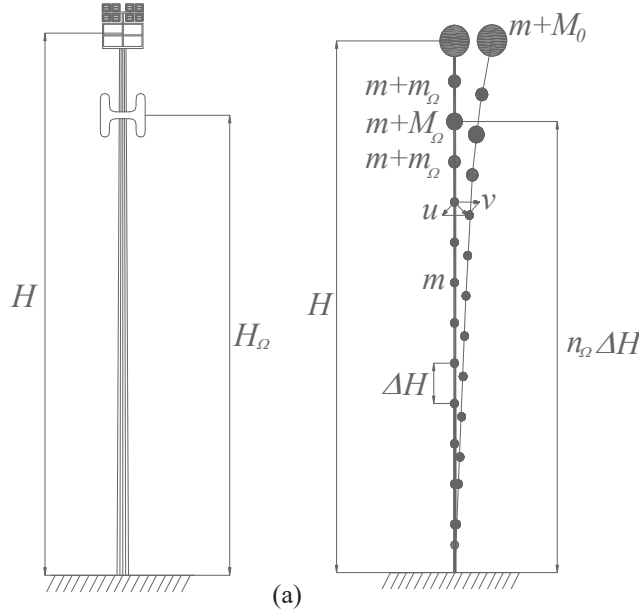


Figure 1: Monopole tower with gyroscopic device: (a) Schematic of the structure, (b) Generalized lumped mass model, orientation and displacements.

Where \mathbf{M} , and \mathbf{K} represent respectively the $2N \times 2N$ mass and stiffness matrix of the system depicted in Fig.1 $\ddot{\mathbf{x}}$ and \mathbf{x} symbolize respectively generalized accelerations and displacements vectors of the $2N$ degrees of freedom (DOF) of the structure in the two directions u and v , being N the number of lumped masses of the system.

Accounting on the further DOF α of the gyroscopic device and according to above mentioned hypotheses Eq.1 and Eq.2 [20], can be conveniently combined as a function of a non-dimensional time $\tau = \bar{\omega}_0 t$ and converted to non-dimensional displacements $\chi_j = x_j / D$ in a matrix forma as:

$$\mathbf{M}_n \chi'' + \frac{C_{\alpha}}{M_0} \mathbf{C}_n \chi' + \bar{\omega}_0^2 \mathbf{K}_n \chi = \mathbf{K}_{n,\Omega}(\chi, \chi') \quad (3)$$

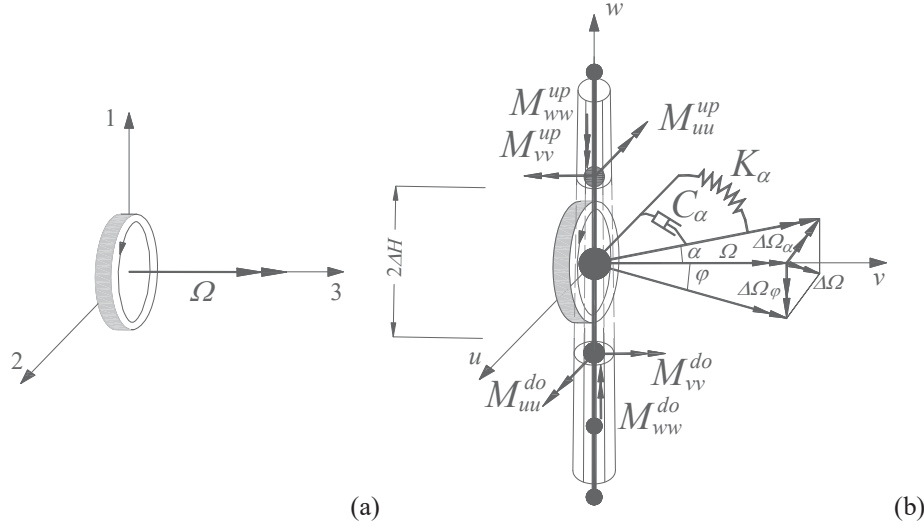


Figure 2: (a) Rotating mass with the local reference axes, (b) schematic of the gyroscopic device placed on the mast.

Where \mathbf{M}_n , \mathbf{C}_n and \mathbf{K}_n represent respectively the normalized mass damping and stiffness $(N+1) \times (N+1)$ matrix of the system depicted in Fig.1, were the additional DOF present in the matrices is due to the further DOF α of the gyroscopic device and $\bar{\omega}_0 = \sqrt{k_0/M_0}$ is the reference pulsation of a single DOF with reference mass M_0 and stiffness $k_0 = 3EI/H^3$, $\mathbf{M}_n = \mathbf{M}/M_0$, \mathbf{C}_n and $\mathbf{K}_n = \mathbf{K}/M_0$ represents respectively the normalized mass matrix, damping matrix and stiffness matrix of the system. The quantities χ'' , χ' and χ are respectively the unknown non-dimensional vectors of the generalized accelerations, velocities and displacements with respect to the dimensionless time τ , $C_\alpha = 2\bar{\omega}_0 J_\alpha \zeta_\alpha$ is the damping coefficient of the of the gyroscopic device with stiffness K_α , inertia $J_\alpha = J_{\Omega,11}$, undamped pulsation $\bar{\omega}_\alpha = \sqrt{k_\alpha/J_\alpha}$ and damping ratio ζ_α . Normalized undamped pulsation of the gyroscopic device can therefore written as function of the reference system pulsation $\bar{\omega}_0$ as $\alpha_\alpha = \bar{\omega}_\alpha/\bar{\omega}_0$ [20].

As it can be noticed from an examination of Eq. (1), displacements in the u - w plane do not involve the gyricity of the system, moreover, given the hypothesis of a lumped mass model having their barycenter coincident with the mast shear center cross-section; displacement u (in the u - w plane) can, therefore, considered decoupled from the remaining degrees of freedom of the structure [25]. The model described in section 2.1 with $2 \times (N+1)$ DOF, can be consequently reduced to a $N+1$ DOF system for proper boundary conditions which does not involve displacements in the u - w plane. Accounting of the above-mentioned hypotheses the lumped mass model with the gyroscopic device will be treated in the following as a $N+1$ DOF system.

To assess the effectiveness of the proposed apparatus, numerical integration of the discrete dynamic equations has been conducted, similar verification approaches were already utilized by the authors in [20, 26-28].

3 NUMERICAL RESULTS

The prototype of the proposed gyroscopic device applied to the lumped mass system depicted in Fig. 1 is examined in this section. Without any loss of generality, the lumped masses are constant and equally distributed in the shaft with $m_i=m$; in order to perform a parametric study, generalized properties of the system are defined as a function of the reference system having mass M_0 (mass of upper platform), stiffness k_0 (stiffness of a cantilever beam with height H and flexural stiffness EI), reference pulsation $\bar{\omega}_0$.

The gyroscopic system has been placed in the N -1- th mass of the lumped mass model with $N=16$. The considered structure is a slender lighting pole typically utilized for illumination of large areas, sizes and structural properties are shown in Table 1:

H (m)	ρ_{mast} (kg/m)	M_0 (kg)	D (mm)	z_Ω (m)	EI (N×m ²)	N (-)	Δz (m)	m (kg)	$\bar{\omega}_0$ (rad/s)
22	71.47	687.9	211.2	20.6	3.07e+7	16	1.37	98.27	1.88

Table 1: Structural properties of the monopole tower and of the corresponding lumped mass model.

Generalized properties of the gyroscopic system (refer to Table 2) are defined as a function of the structural characteristics of the mast, therefore non-dimensional magnitudes defining the gyroscopic device are: the mass ratio $\mu_{M,\Omega}=M_{\Omega,TOT}/M_0$ (respect to the reference mass M_0), the radius of gyration ratio $\mu_{\rho,\Omega}=\rho_\Omega/D$ (respect to mast diameter D), so that $J_{\Omega,p} = M_0\mu_{M,\Omega}(D\mu_{\rho,\Omega})$ and $J_{\Omega,11} = J_{\Omega,22} = 0.5J_{\Omega,p}$. Mechanical properties of the gyroscopic apparatus as stiffness k_a , damping coefficient C_a , damping ratio ζ_a , pulsation $\bar{\omega}_a$ and normalized pulsation α_a are illustrated in Table 2.

$\mu_{M,\Omega}$ (-)	$M_{\Omega,TOT}$ (kg)	M_Ω (kg)	m_Ω (kg)	$\mu_{\rho,\Omega}$ (-)	ρ_Ω (m)	$J_{\Omega,p}$ (kg×m ²)	$J_{\Omega,11}=J_{\Omega,22}$ (kg×m ²)	K_a (N×m)	C_a (N×m×s)	ζ_a (-)	$\bar{\omega}_a$ (rad/s)	α_a (-)
0.10	68.79	67.15	0.82	1.42	0.30	6.14	3.07	-	11.66	10	0.19	0.10

Table 2: Mechanical properties of the gyroscopic device.

It must be noted that the presence of the mass of the gyroscopic device affects the global behavior of the original structure, is therefore important to reduce as much as possible the additional mass of the gyroscopic device $M_{\Omega,TOT}$ and its radius of gyration ρ_Ω which respectively influence the structure natural frequency and its aerodynamic behavior. Therefore, careful attention must be paid for the design of the gyroscopic apparatus especially regarding the additional mass increment for possible buckling effects and frequency reduction and its size for a suitable aerodynamic design. Equation 3 has been solved by fourth-order Runge-Kutta algorithm [34] which requires appropriate initial boundary conditions at $\tau=0$ selected to examine the dynamic response of the first mode by imposing zero velocities and initial displacements in the y - z plane, proportional to linear eigenvector Φ of the structure without gyricity ($\Omega=0$) according to a preselected amplitude parameter $\delta = y/D$.

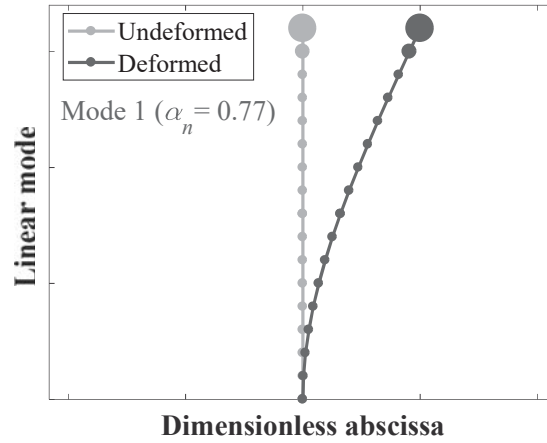


Fig. 3. First vibration mode of the examined lumped mass model for $\mu_{M,\Omega}=0.10$, without gyricity ($\Omega=0$).

Free vibrations corresponding to the first mode of the dynamic system with the gyroscopic device are illustrated in Fig. 4. Fig. 4a shows normalized displacements x/D of the top of the tower and angular rotations α of the gyroscopic device acting with gyricity $\Omega=\omega J_{\Omega,p}$ ($\omega=180$ rad/sec) for different stiffness K_α of the spring device. Results illustrate the effectiveness of the proposed device in increasing the total damping of the mast, low values of stiffness K_α involve higher values of angular rotations α (refer to Fig. 4b), which in turn allow higher equivalent damping ratios ζ_Ω of the tower. As can be observed by the inspection of Fig. 4a, the effectiveness of the device increases with the decreasing of the device spring K_α , which allows (for a constant gyricity Ω) the maximum effectiveness for $K_\alpha=0.01$, by an inspection of Fig.4b, it must be noted that a further decreasing of the K_α would led, as expected, to unacceptable angular rotations which it would not satisfy the hypotheses of small oscillations on which Equation 1 is based.

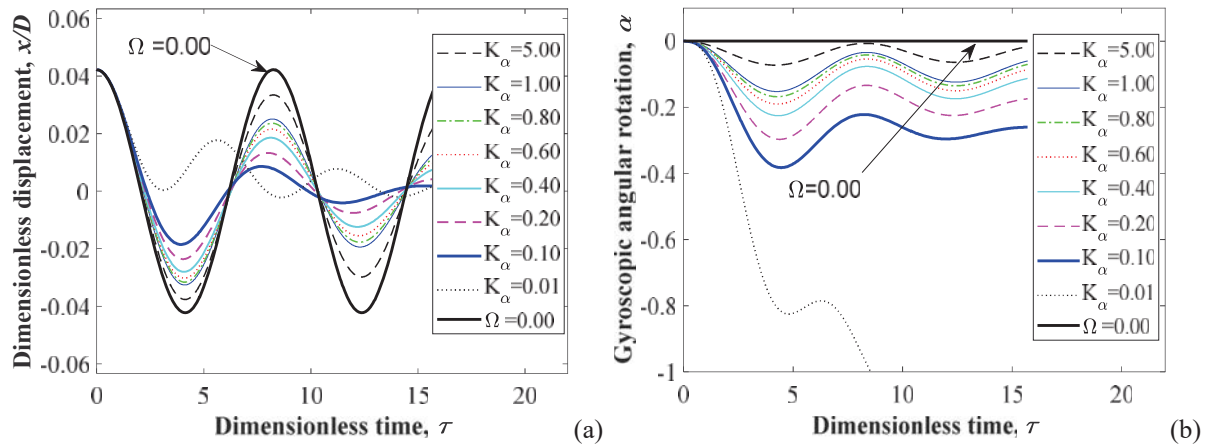


Figure 4. Time history analysis of the free vibrations of the first mode of the tower with $\mu_{M,\Omega}=0.10$, $\mu_{p,\Omega}=1.42$, corresponding to an amplitude parameter $\delta=y/D=0.20$ with constant gyricity $\Omega=\omega J_{\Omega,p}$ ($\omega=180$ rad/sec) for different stiffness of the gyroscopic device spring K_α : (a) normalized horizontal displacements y/D of the N -th point and (b) rotations α of the gyroscopic device.

The results of Fig.4 are corroborated by the data illustrated in Fig.5. which show an increasing of α_Ω and of ζ_Ω with the decreasing of the spring stiffness K_α . The effectiveness of the proposed gyroscopic device acting with the same gyricity, is therefore directly connected to the spring stiffness K_α .

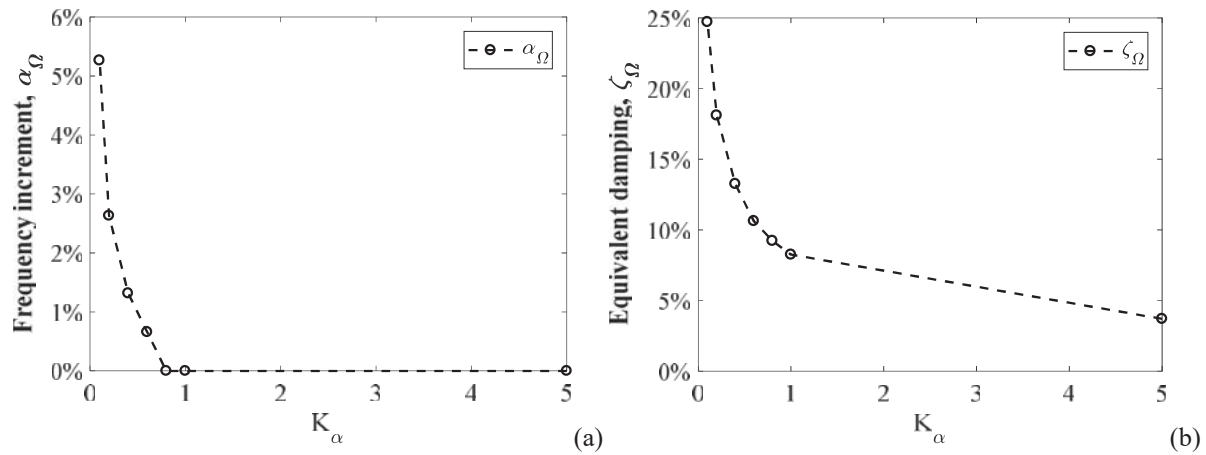


Figure 5. Parametric analysis as function of the stiffness of the gyroscopic device spring K_α for the first mode of the tower with $\mu_{M,\Omega}=0.10$, $\mu_{p,\Omega}=1.42$, $\delta=y/D=0.20$ and constant gyricity $\Omega=\omega J_{\Omega,p}$ ($\omega=180$ rad/sec), (a) Normalized damped frequency α_Ω and (b) equivalent damping ζ_Ω of the tower.

4 CONCLUSIONS

This paper investigated the effects of a prototype of a gyroscopic device installed in slender monopole tower. Results show that the presence of the device allows for an increase of the frequency and for a remarkable increase of damping of the tower; the effectiveness of the device depends on its mechanical properties. A further parametric study assesses and optimizes the performances of the gyroscopic device as a function of the angular spring stiffness K_α which connects the gyroscope to the mast. Results illustrate that stiffness spring K_α can be considered a key parameter for adjusting and setting the mechanical properties of the gyroscopic device.

REFERENCES

- [1] I. Venanzi, A.L. Materazzi, L. Ierimonti, Robust and reliable optimization of wind-excited cable stayed masts, *Journal of Wind Engineering and Industrial Aerodynamics* 147 (2015) 368-379.
- [2] G. Solari, L.C. Pagnini, Gust buffeting and aeroelastic behaviour of poles and monotubular towers, *Journal of Fluids and Structures* 13(7-8) (1999) 877-905.
- [3] G.F. Giaccu, L. Caracoglia, Wind-load fragility analysis of monopole towers by Layered Stochastic-Approximation-Monte-Carlo method, *Engineering Structures* 174 (2018) 462-477.
- [4] M. Pavan Kumar, Effect of wind speed on structural behaviour of Monopole and self-support telecommunication towers, *Asian Journal of Civil Engineering* 18(6) (2017) 911-927.
- [5] U. Støttrup, Masts and towers, *Journal of the International Association for Shell and Spatial Structures* 55 (2014) 79-88.
- [6] L. Pagnini, G. Solari, Gust buffeting and turbulence uncertainties, *Journal of Wind Engineering and Industrial Aerodynamics* 90(4) (2002) 441-459.

- [7] M.P. Repetto, G. Solari, Dynamic alongwind fatigue of slender vertical structures, *Engineering Structures* 23(12) (2001) 1622-1633.
- [8] M.P. Repetto, G. Solari, Dynamic crosswind fatigue of slender vertical structures, *Wind and Structures* 5(6) (2002) 527-542.
- [9] M.P. Repetto, G. Solari, Wind-induced fatigue of slender vertical structures, 11th International Conference on Wind Engineering, Wind Science and Engineering Research Center, Texas Tech University, Lubbock, Texas, USA, 2003, pp. 1803-1810.
- [10] Y. Kan, Y. Psinh, A.-C. Lee, Investigation on the steady-state response of a symmetric rotors, *Journal of Vibration and acoustics* 114 (1992).
- [11] G.M.T. D'Eleuterio, Dynamics of gyroelastic vehicles, Institute for aerospace studies, Toronto, 1986.
- [12] M. Ghommema, A.H. Nayfeh , S. Choura, F. Najar, E.M. Abdel-Rahman, Modeling and performance study of a beam micro gyroscope, *Journal of Sound and Vibration* 329 (2010) 4970-4979.
- [13] J. Li, D. Chen, G. Liu, Y. Li, B. Xu, Analysis of the gyroscopic effect on the hydro-turbine generator unit, *Mechanical Systems and Signal Processing* 132 (2019) 138-152.
- [14] R. Lot, J. Fleming, Gyroscopic stabilisers for powered two-wheeled vehicles, *Vehicle System Dynamics* 57(9) (2019) 1381-1406.
- [15] A. Sinha, S. Bose, A. Nandi, S. Neogy, A precessing and nutating beam with a tip mass, *Mechanics Research Communications* 53 (2013) 75- 84.
- [16] M. Esmaeilia, N. Jalilib, M. Duralia, Dynamic modeling and performance evaluation of a vibrating beam microgyroscope under general support motion, *Journal of Sound and Vibration* 301 (2007) 146-164.
- [17] M. Garau, G. Carta, M.J. Nieves, I.S. Jones, N.V. Movchan, A.B. Movchan, Interfacial waveforms in chiral lattices with gyroscopic spinners, *Proc. R. Soc.A* 474 (2018) 20180132.
- [18] M.J. Nieves, G. Carta, I.S. Jones, A.B. Movchan, N.V. Movchan, D.M. Sykes, Vibrations and elastic waves in chiral multi-structures, *Journal of the Mechanics and Physics of Solids* 121 (2018) 387–408.
- [19] G. Carta, I.S. Jones, N.V. Movchan, A.B. Movchan, M.J. Nieves, Gyro-elastic beams for the vibration reduction of long flexural systems, *Proceedings of the Royal Society A: Mathematical, Physical and Engineering Sciences* 473 (2017) 1-17.
- [20] G.F. Giaccu, Modeling a gyroscopic stabilizer for the improvement of the dynamic performances of slender monopole towers, *Engineering Structures* 215 (2020) 110607.
- [21] K. Yamanaka, G. Heppler, K. Huseyin, Stability of gyroelastic beams, *AIAA J.* 34 (1996) 1270-1278.
- [22] L.C. Pagnini, S. Lagomarsino, G. Solari, Experimental assessment of the damping of steel poles and monotubular towers (in Italian), "Costruzioni Metalliche", *Journal of the Italian Technical Association for Steel Construction (CTA)* LI(1) (1999) 39-51.
- [23] G. Solari, Evaluation and role of damping and periods for the calculation of structural response under wind loads, *Journal of Wind Engineering and Industrial Aerodynamics* 59(2-3) (1996) 191-210.
- [24] G. Solari, C. Pagnini, The action and effects of wind on poles and monotubular towers (in Italian), "Costruzioni Metalliche", *Journal of the Italian Technical Association for Steel Construction (CTA)* L(4) (1998) 29-51.
- [25] C. Senthamaraiannan, R. Ramesh, Experimental investigation on vibration characteristics of woven carbon fabric-reinforced composite beams of various cross-sectional shapes, *Proceedings of the Institution of Mechanical Engineers Part L Journal of Materials Design and Applications* 230(1) (2014) 64-74.

- [26] G.F. Giaccu, L. Caracoglia, B. Barbiellini, Modeling unilateral response in the cross-ties of a cable network: deterministic vibration, *Journal of Sound and Vibration* 333(19) (2014) 4427–4443.
- [27] G.F. Giaccu, L. Caracoglia, Generalized power-law stiffness model for nonlinear dynamics of in-plane cable networks, *Journal of Sound and Vibration* 332(8) (2013) 1961-1981.
- [28] G.F. Giaccu, L. Caracoglia, A displacement-based approach for determining non-linear effects on pre-tensioned-cable cross-braced structures *Journal of Sound and Vibration* 394 (2017) 465-481.

VIBRATION CONTROL OF WIND TURBINE TOWERS WITH KDAMPER-BASED DESIGNS

Konstantinos A. Kapasakalis¹, Ioannis A. Antoniadis², and Evangelos J. Sapountzakis¹

¹ Institute of Structural Analysis and Antiseismic Research, School of Civil Engineering,
National Technical University of Athens, Zografou Campus, GR-157 80 Athens, Greece
e-mail: kapasakalis@mail.ntua.gr, cvsapoun@central.ntua.gr

² Dynamics and Structures Laboratory, School of Mechanical Engineering,
National Technical University of Athens, Zografou Campus, GR-157 80 Athens, Greece
e-mail: antogian@central.ntua.gr

Abstract

The application of dynamic vibration absorbers (DVA) to Wind Turbine (WT) towers has the potential to significantly improve the damping of the tower and the nacelle dynamic responses, thus increasing the reliability of WTs. The Tuned Mass Damper (TMD) is considered a benchmark for vibration absorption of WT. However, its effectiveness is limited by the requirement of large masses, in association to its installation location. Thus, an alternative concept is introduced, which is based on a novel passive vibration absorption configuration, the extended KDamper concept. The KDamper is essentially an extension of the conventional TMD, introducing appropriate negative stiffness (NS) elements. Instead of increasing the additional mass, the vibration absorption capability of the KDamper can be increased by increasing the value of the NS element. Therefore, the KDamper always indicates better isolation properties than a TMD with the same additional mass. In this paper, the performance of these concepts is examined for increasing the damping of WT towers. A constrained optimization procedure is presented, from which the optimal design parameters are obtained. Although both concepts present a good behavior, the KDamper-based design significantly increases the effective damping of the WT tower, retaining the additional masses in reasonable ranges.

Keywords: Wind Turbines, KDamper, Negative Stiffness, Vibration Control, Damping, Tuned Mass Damped.

1 INTRODUCTION

Wind power continues its rapid growth worldwide and as a result, wind farms are likely to comprise a significant portion of the total production of wind energy. The high-quality wind resource and the proximity to load centres make wind energy a compelling proposition. The WWEA predicts that offshore wind farms of 150GW will operate in the EU by 2030, contributing 14% of the EU's total electricity consumption. However, the above prediction is very ambitious. In recent years, several failures have been recorded in existing wind turbines (WT). It is estimated that the structural failure (tower, foundation) of the installed WT amounts up to 10% [1]. In addition, the structural and foundation costs are excessively high, reaching up to 17% for land based (onshore) and fixed bottom offshore WT.

From the above comments, and according to the International Energy Agency [2], it emerges as top priority to enhance research to avoid WT structural failures. A way to extend the feasibility of Wind Turbine towers is by means of structural control.

The concept of a resonant damper, like a Tuned Mass Damper (TMD) is among the approaches that have received the most attention in the literature. The principal of the TMD system [3] is the degradation of the dynamic response of the system through energy transfer to a system of an additional mass, designed with optimum characteristics and adapted in a suitable position in the structure [4,5]. Active [6,7] and semi-active [8–12] TMD have been examined thoroughly in the latest year, enhancing the damping performance of the passive TMD. The downside of such designs is that their performance is directly (or obliquely) depended by the accuracy of the actuators output, which over time can have an alternation in its performance. In addition, the essential limitations of all the aforementioned TMD-related concepts, are related with the location and the selected mass of these devices. TMD should be installed at the top of the tower or inside the nacelle in order to be effective, and is associated with large additional masses, which constitutes a major limitation, since additional mass is highly undesirable at the top of the WT. In addition, a slight alteration in the system parameters can alter the TMD tuning and reduce the system performance [13].

In this paper, the (extended) KDamper is intervened between the nacelle and the WT tower. The KDamper, introduced in [14], is essentially an extension of the TMD, by incorporating appropriate negative stiffness (NS) elements. Instead of increasing the additional mass, the vibration isolation capability of the KDamper can be increased by the NS, overcoming the sensitivity problems of TMDs as the tuning is mainly controlled by the NS. Thus, the KDamper always indicates better isolation properties than a TMD with the same mass, finding numerous applications for vibration absorption in structural systems [15–24]. Although the KDamper incorporates a NS element, it is designed to be statically and dynamically stable.

Section 2 of the paper presents the dynamic model of the WT tower. The developed model is an assemblage of prismatic beam elements with sway DoFs considered to be the dynamic ones. In order to verify the validity and the efficiency of the developed model, a set of simplified analyses were conducted and compared with a commercial software package based on FEM. The aerodynamic load is taken into account by generating artificial basic wind velocities following the corresponding regulations of EC1 and applying it at the WT following the procedure described in [25]. Section 3, presents the optimization procedure for the EKD. The independent design variables are presented, and proper limitations and constraints are imposed on the design variables and the system main dynamic responses, based on the proposed constrained engineering-criteria driven optimization procedure. In section 4, the numerical results are presented, where the effectiveness of the EKD is verified. A comparison with a conventional TMD (2% mass) confirms that the EKD manages to significantly increase the effective damping of the WT tower, and thus mitigate the WT dynamic responses, with small

additional masses and a realistically designed configuration. In section 5, the conclusive remarks are presented, based on the nonlinear dynamic responses of the controlled WT tower with the proposed VCS and the comparison with the conventional TMD.

2 MATHEMATICAL MODELLING OF WIND TURBINE FOUNDED ON MONOPILE FOUNDATION

2.1 Dynamic Model of WT with Monopile Foundation

An onshore wind turbine (WT) tower of length l_t and variable tubular cross-section $A_t(x)$ is examined, as presented in Figure 1. The tower supports the NREL baseline 5MW nacelle and rotor [26,27]. In order to account the inertial forces applied by the mechanical parts (nacelle, rotor, and blades) an additional concentrated mass m_{top} is added at the top of the tower [27]. The WT is founded on a monopile of length l_p of cylindrical cross-section A_p . The monopile is embedded in a layered Winkler type soil profile represented by a Kelvin-Voigt element (i.e. elastic spring - dashpot parallel configuration $k_s - c$).

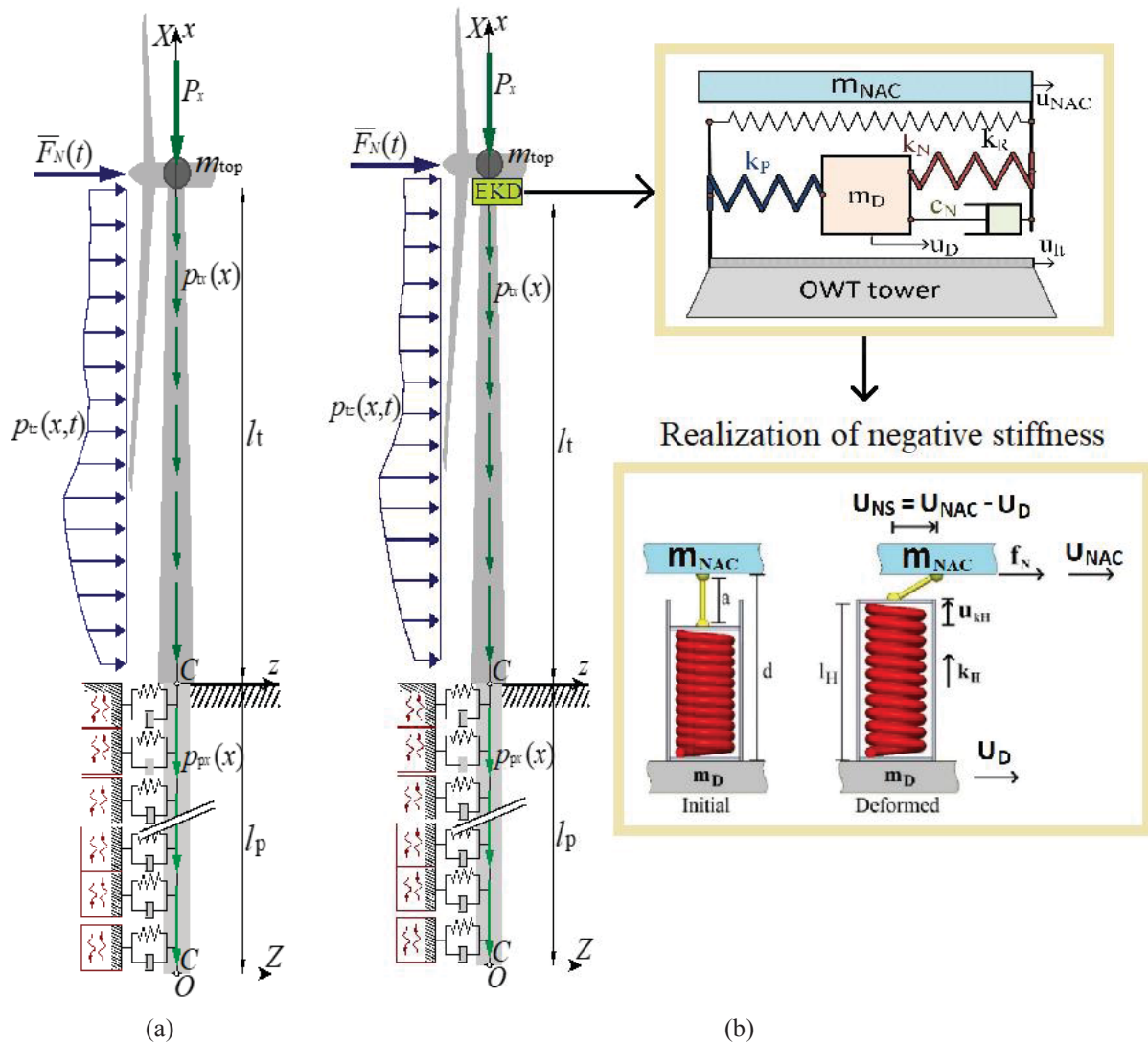


Figure 1: Wind turbine tower of variable cross section founded on monopile foundation. (a) Uncontrolled structure, and (b) controlled structure with EKD at the top of the WT tower.

The transient nonlinear dynamic response analysis of the tower-pile system is investigated through a *Beam of Variable Cross Section* over a *Beam on Winkler Foundation* formulation accounting for both kinematic and inertia interaction. Considering large displacements and employing the second Piola-Kirchhoff stress tensor, the geometrically nonlinear equations of motion of the WT are obtained as follows:

$$\begin{bmatrix} \mathbf{M}_t & \mathbf{0} \\ \mathbf{0} & \mathbf{M}_p \end{bmatrix} \begin{Bmatrix} \ddot{u}_t \\ \ddot{u}_p \end{Bmatrix} + \begin{bmatrix} \mathbf{C}_t & \mathbf{0} \\ \mathbf{0} & \mathbf{C}_p \end{bmatrix} \begin{Bmatrix} \dot{u}_t \\ \dot{u}_p \end{Bmatrix} + \begin{bmatrix} \mathbf{K}_t(x) & \mathbf{K}_{tp}(x) \\ \mathbf{K}_{pt}(x) & \mathbf{K}_p(x) \end{bmatrix} \begin{Bmatrix} u_t \\ u_p \end{Bmatrix} = \begin{Bmatrix} F_t(x) \\ F_p(x) \end{Bmatrix} \quad (1)$$

where (\cdot) denotes differentiation with respect to the time t . Moreover, $[M_t]$, $[M_p]$, $[C_t]$ and $[C_p]$ are the matrices of mass and damping of the WT tower and monopile, respectively. $[K_t]$, $[K_p]$ and $[F_t]$, $[F_p]$ are the nonlinear stiffness matrices and force vectors containing the geometrically nonlinear terms, while $\{u_t, u_p\}^T$ denotes the vector of unknown nodal displacements. By introducing a vibration control system (VCS) at the top of the tower, the tower related matrices of Equation 1 are modified as:

$$[\mathbf{M}_t] = \begin{bmatrix} [\mathbf{M}_s]_{N \times N} & [\mathbf{0}]_{N \times n} \\ [\mathbf{0}]_{n \times N} & [\mathbf{0}]_{n \times n} \end{bmatrix} + \begin{bmatrix} [\mathbf{M}_{n,a}]_{N \times N} & [\mathbf{0}]_{N \times n} \\ [\mathbf{0}]_{n \times N} & [\mathbf{M}_{n,d}]_{n \times n} \end{bmatrix}_{(N+n) \times (N+n)} \quad (2.a)$$

$$[\mathbf{K}_t] = \begin{bmatrix} [\mathbf{K}_s]_{N \times N} & [\mathbf{0}]_{N \times n} \\ [\mathbf{0}]_{n \times N} & [\mathbf{0}]_{n \times n} \end{bmatrix} + \begin{bmatrix} [\mathbf{K}_{n,a}]_{N \times N} & -[\mathbf{K}_{n,b}]_{N \times n} \\ -[\mathbf{K}_{n,c}]_{n \times N} & [\mathbf{K}_{n,d}]_{n \times n} \end{bmatrix}_{(N+n) \times (N+n)} \quad (2.b)$$

$$[\mathbf{C}_t] = \begin{bmatrix} [\mathbf{C}_s]_{N \times N} & [\mathbf{0}]_{N \times n} \\ [\mathbf{0}]_{n \times N} & [\mathbf{0}]_{n \times n} \end{bmatrix} + \begin{bmatrix} [\mathbf{C}_{n,a}]_{N \times N} & -[\mathbf{C}_{n,b}]_{N \times n} \\ -[\mathbf{C}_{n,c}]_{n \times N} & [\mathbf{C}_{n,d}]_{n \times n} \end{bmatrix}_{(N+n) \times (N+n)} \quad (2.c)$$

where $[M_N]$ is the $N \times N$ mass matrix of the uncontrolled WT tower with N DoF while $[M_n]$ indicates the $n \times n$ mass matrix of the VCS. Similarly, $[C_N]$ and $[K_N]$ are the Rayleigh damping matrix and the condensed stiffness matrix corresponding to the sway DoF. The expressions of the matrices in Equation 2 depend on the VCS of choice (TMD, EKD).

2.2 Wind Loads

In this paper, the aerodynamic load is taken into account by employing a basic wind velocity at the altitude of 10 m, V_b and applying the corresponding regulations of (*EN 1991 - Wind actions*, 2010). Moreover, in order to account the wind velocity fluctuation at the altitude of l_t , an artificial velocity time history is generated by applying the procedures presented in [29–32] assuming a standard deviation σ . The total concentrated force exerted on the top of the tower is computed as in [27]. Apart from the concentrated force applied on the top of the steel tower due to operation of the turbine, an additional distributed loading along the tower height is taken into account due to the fact that a portion of wind forced is exerted directly on the tower. The spatial and time distribution of this loading is obtained by employing the procedures of (*EN 1991 - Wind actions*, 2010) and of the studies [29–31]. The basic wind velocity that is employed has corresponding standard deviation $V_b = 27.0$ m/s with $\sigma = 3.30$ m/s ($V_m(120m) = 39.93$ m/s). The rotor is assumed to develop a constant angular velocity $\Omega_{bl} = 12.1$ rpm, while all the necessary blade profile characteristics are retrieved from [26,32]. Figure 2.a presents the mean wind velocity, and Figure 2.b the time history of the evaluated total forces $\bar{F}_N(t)$ for the aforementioned basic wind velocity ($V_b = 27.0$ m/s, $\sigma = 3.30$ m/s).

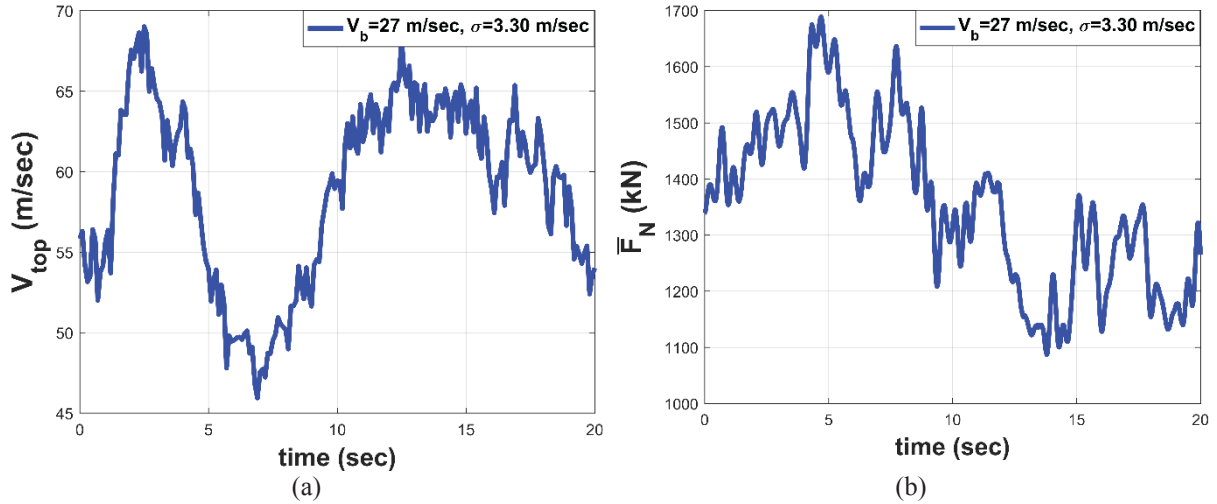


Figure 2: (a) Wind velocity at the top of the WT tower, and (b) total concentrated force exerted on the top of the WT tower $\bar{F}_N(t)$.

3 IMPLEMENTATION OF VIBRATION CONTROL SYSTEMS

3.1 VCS Considered

The first vibration mitigation approach is based on the classical TMD. The additional mass (m_D) of the TMD is attached at the top of the WT tower or inside the nacelle, using a positive stiffness element and a linear damper (k_D , c_D). This concept is employed as a benchmark because it has received the most attention in the literature due to the simplicity of its implementation. The main drawback of this option is the need for large additional masses, in order for the TMD to achieve significant effective damping, as will be observed in the numerical results. The parameters of the TMD configuration are presented below:

$$\mu_D = m_D / m_{top} \quad (3.a)$$

$$\omega_D = 2\pi f_D = \sqrt{k_D / m_D} \quad (3.b)$$

$$\zeta_D = c_D / (2\omega_D m_D) = c_D / (2\sqrt{k_D m_D}) \quad (3.c)$$

The TMD tuning frequency is selected to equal to the fundamental frequency of the primary structure $f_D = f_l$. The damping ratio affects the transferred vibrating energy to the oscillating mass of the TMD, and the TMD stroke. As the damping ratio decreases, more energy is transferred to m_D , as the oscillating mass has an increased stroke. As a result, the TMD is more effective. However, the TMD stroke is upper bounded due to the geometrical limitation that the oscillating mass is placed at the top of the tower. For this reason, the damping ratio is selected to be equal to 10% in order to be as effective as possible, and at the same time realistic. The mass of the TMD is be equal to 2%, an extreme value selected only for comparison reasons.

In this paper, an extended version of KDamper [21], will be employed at the top of the WT in order to protect the WT tower from environmental vibrations (wind), as presented in Figure 1. The additional mass, m_{top} , of the nacelle, rotor and blades is no longer rigidly attached to the WT tower but is mounted on an extended KDamper device. In this concept, the additional oscillating mass of the EKD (m_D) is connected with the nacelle with a negative stiffness element and a linear damper (k_{NS} , c_{NS}), and with the steel tower with a positive stiffness element (k_{PS}), and the steel tower is connected with the nacelle with a positive stiffness connection (k_R). This way, the EKD aims to isolate the vibrations of the nacelle from the steel tower. In

addition, the EKD aims to increase the effective damping of the WT tower compared to the TMD with the same additional mass, as it has been proven that the KDamper always presents an improved dynamic behavior as compared to the TMD.

The configuration of the extended KDamper (EKD) implemented at the top of the WT tower is illustrated in Figure 1. The positions regarding the EKD are presented below:

$$\mu_D = m_D / m_{top} \quad (4.a)$$

$$k_D = k_{NS} + k_{PS} \quad (4.b)$$

$$\omega_D = 2\pi f_D = \sqrt{k_D / m_D} = \sqrt{\frac{k_{NS} + k_{PS}}{m_D}} \quad (4.c)$$

$$k_0 = k_R + \frac{k_{NS}k_{PS}}{k_{NS} + k_{PS}} \quad (4.d)$$

$$\omega_0 = 2\pi f_0 = \sqrt{k_0 / (m_D + m_{top})} = \sqrt{\left(k_R + \frac{k_{NS}k_{PS}}{k_{NS} + k_{PS}}\right) / (m_D + m_{top})} \quad (4.e)$$

$$\zeta_{NS} = c_{NS} / (2m_D\omega_D) = c_{NS} / (2\sqrt{k_D m_D}) \quad (4.f)$$

where μ_D is the EKD additional mass ratio. In order for the proposed configuration to be realistic, the design of the EKD concept foresees variation in all the stiffness elements to ensure that the system remain statically and dynamically stable:

$$(1 - \varepsilon_R)k_R + \frac{(1 - \varepsilon_{PS})k_{PS}(1 + \varepsilon_{NS})k_{NS}}{(1 - \varepsilon_{PS})k_{PS} + (1 + \varepsilon_{NS})k_{NS}} = 0 \quad (5)$$

Assuming that the m_D , and the values of the stability factors ε_{NS} , ε_{PS} , and ε_R are supposed known, the stiffness elements k_{PS} and k_R , result from Equations (4.e, 5) as a function of f_0 , and k_{NS} . Therefore, the independent design variables sought in the optimization are:

1. the nominal frequency f_0 ;
2. the value of the negative stiffness (NS) element k_{NS} ;
3. the value of the damping coefficient c_{NS} ;

For the optimization process, the Harmony Search (HS) algorithm, a novel metaheuristic algorithm is used [33].

3.2 Optimal Design of EKD

Having established the nonlinear equations of motion Equation 1 for the controlled WT, the next objective is to determine the optimal EKD parameters in order to attain the best possible vibration control strategy. The objective function and the constraints are selected from the geometrically non-linear time domain responses, are described below:

- i. Assign values to the known parameters (initial guess).
 - a) EKD is implemented at the top of the WT tower, and as a result the additional oscillating mass is desired to be the minimum possible. Thus, m_D varies in the range [0.1 0.5] %, one order of magnitude lower as compared to that of the TMD.
 - b) The stability factors of the k_{PS} , k_R are conservatively selected as 5%. The variation of the NS element k_{NS} , is selected equal to 10%, as indicated in [21].

- ii. Set the objective function (OF) as the minimization of the relative displacement of the WT tower. (obtained from geometrically nonlinear dynamic analysis)

$$\min: u_{top}^{Rel} = u_{l_t} - u_{l=0} \quad (\text{OF}) \quad (6)$$

- iii. Set the geometrical constraint regarding the relative displacement of the oscillating mass of the EKD and the top of the WT tower. The upper limit is equal to half of the top tower diameter.

$$u_D^{Rel} = u_D - u_{l_t} \leq D_{top} / 2 \quad (\text{Constraint 1}) \quad (7)$$

- iv. To ensure the effective operation of the WT. another geometrical limitation regarding the relative displacement of the nacelle and the top of the WT tower is set:

$$u_{Nac}^{Rel} = u_{nac} - u_{l_t} \leq 0.5 \text{ m} \quad (\text{Constraint 2}) \quad (8)$$

- v. Set an upper limit for the damping coefficients c_{NS} with respect to the superstructure mass. This constraint is based on previous works [47] as well as on manufacturing restrictions:

$$c_{NS} \leq 1000 \text{ kNs} / \text{m} \quad (\text{Constraint 3}) \quad (9)$$

- vi. Set an upper limit for the NS per 1 *tn* of structure mass [14]:

$$k_{NS} \geq -50 \text{ kN} / \text{m} \quad (\text{Constraint 4}) \quad (10)$$

- vii. The nominal frequency f_0 of the SBA varies in the range $[0.1 \text{ } 5] \text{ Hz}$, (Constraint 5).

Finally, the limits of the free design variables are: a) nominal frequency $f_0 \text{ (Hz)}$ $[0.1 \text{ } 5.0]$, b) value of the NS element $k_{NS} \text{ (kN/m)}$ $[-20000 \text{ } -1]$, and c) damping coefficient $c_{NS} \text{ (kNs/m)}$ $[1 \text{ } 1000]$. As for the parameters inherently involved in the HS algorithm, the commonly used values in relative literature are employed: HMS=75, HMC=0.5, and PAR=0.1.

4 NUMERICAL APPLICATION

4.1 Considered WT tower and monopile systems

In this section, the NREL baseline 5-MW nacelle and rotor, supported by a steel tower of 120 m height is examined. This choice is made due to the fact that is widely used in the literature as a benchmark option for vibration control of WT towers. The key properties of the wind turbine and the steel tower are listed in Table 1 and Table 2 respectively.

As far as monopile system is concerned, a steel tubular pile of constant cross section ($E_p=2.1 \times 10^8 \text{ kN/m}^2$, $\rho_p=7.8 \text{ tn/m}^3$, $\nu_p=0.3$, $G_p=8.0769 \times 10^7 \text{ kN/m}^2$, $l_p=30.0 \text{ m}$, $D_p=5.0 \text{ m}$, $t_p=0.08 \text{ m}$) is considered. The undrained shear strength of the soil profile is assumed to follow a parabolic distribution with depth with mean $S_u=60 \text{ kPa}$, , mass density $\gamma=1 \text{ tn/m}^3$ and modulus of elasticity $E=1800S_u$. The whole structure is subjected to the action of its total weight (including mechanical parts). More specifically, a distributed axial load along the length of the structure and a concentrated axial force at its top are applied, which are evaluated according to the corresponding masses.

Property	Value
<i>Rating</i>	<i>5 MW</i>
<i>Rotor diameter</i>	<i>126 m</i>
<i>Hub diameter</i>	<i>3 m</i>
<i>Cut-in wind speed</i>	<i>3 m/sec</i>
<i>Rated wind speed</i>	<i>11.4 m/sec</i>
<i>Cut-out wind speed</i>	<i>25 m/sec</i>
<i>Cut-in rotor speed</i>	<i>6.9 rpm</i>
<i>Rated rotor speed</i>	<i>12.1 rpm</i>
<i>Nacelle mass</i>	<i>240,000 kg</i>
<i>Rotor mass</i>	<i>110,000 kg</i>
<i>Blade material</i>	<i>Glass-fibre</i>
<i>Blade length</i>	<i>61.5 m</i>
<i>Blade mass</i>	<i>17,740 kg</i>
<i>Blade CM (from blade root)</i>	<i>20.475 m</i>
<i>Blade damping ratio (all modes)</i>	<i>0.48%</i>

Table 1: Key properties of NREL baseline 5 MW wind turbine.

Property	Value
<i>Height</i>	<i>120 m</i>
<i>Base diameter</i>	<i>8.43 m</i>
<i>Base steel thickness</i>	<i>0.048 m</i>
<i>Top diameter</i>	<i>3.87 m</i>
<i>Top steel thickness</i>	<i>0.025 m</i>
<i>Young's modulus</i>	<i>210 GPa</i>
<i>Steel density</i>	<i>8,500 kg/m³</i>
<i>Total mass</i>	<i>798,640 kg</i>
<i>Location of CM (above base)</i>	<i>43.042 m</i>
<i>Tower damping ratio (all modes)</i>	<i>1%</i>

Table 2: Key properties of the considered steel tower.

4.2 Nonlinear dynamic model verification

In order to verify the validity and the efficiency of the developed formulation, a set of simplified analyses were conducted and the obtained results were compared with those obtained from the commercial software package SOFiSTiK [34] based on FEM. More specifically, in Table 3, the first 5 eigenperiods of vibration, are presented using SOFiSTiK, and are com-

pared with those obtained from a FEM solution employing 24 prismatic beam elements for the tower and 60 for the monopile. Furthermore, the response of each tower configuration is examined performing a simplified linear static analysis, applying a concentrated force at the top of the tower. Table 3 presents the static deflections X_{top} at the top of the WT tower obtained from the developed model of the WT tower as compared with the aforementioned FEM solution, using SOFiSTiK software. It can be observed that the validity of the developed model of the WT tower is verified, as both the values of the WT eigenperiods and the static deflection of the top of the WT tower are in a very good agreement.

	Eigenperiods (sec)					Static deflection at the top of the tower X_{top} (m)
	T1	T2	T3	T4	T5	
Present Study	4.315	0.727	0.243	0.122	0.076	1.225
SOFiSTiK	4.310	0.726	0.246	0.128	0.081	1.233

Table 3: Eigenperiods of the WT tower, and static deflection at the top of the tower under static analysis.

4.3 Dynamic responses

The design parameters selected for the TMD system are $\mu_D=2\%$, $\zeta_D=10\%$, and $f_D=f_I$, where f_I is the fundamental frequency of the primary structure. Regarding the EKD system, the selected additional mass is equal to $\mu_D=0.1\%$, 20 times lower as compared to that of the TMD, and the stability factors ε_{NS} , ε_{PS} , and ε_R are selected as 10%, 5%, and 5%, respectively. The optimal EKD parameters obtained following the procedure presented in Section 3.2, are presented in Table 4.

Fixed values		Independent design variables			Resulting stiffnesses	
m_D (tn)	$\varepsilon_{NS}, \varepsilon_{PS}, \varepsilon_R$ (%)	f_0 (Hz)	k_{NS} (kN/m)	c_{NS} (kN/m)	k_R (kN/m)	k_{PS} (kN/m)
0.403	10, 5, 5	0.3664	-9089.7	511.69	13057	54275

Table 4: Optimal EKD parameters.

The dynamic response of the WT tower relative displacement is presented in Figure 3.a, for the uncontrolled WT, as well as the controlled WT with a conventional TMD (2%), and the proposed EKD (0.1%) implemented at the top of the WT. It is observed that due to the nature of the external load, the first peak of the dynamic response is not affected by either system, however, the 2nd peak is greatly reduced with the EKD system. As a result, the effective damping of the controlled system is significantly increased. In order to calculate the exact value of the effective damping, the initial and the controlled structures are subjected to a free vibration with initial conditions, as illustrated in Figure 4, and more specifically to that of the first modal eigenform of the uncontrolled structure. The effective damping is then calculated with the following logarithmic rule:

$$\ln \left[\frac{u_{top}^{Rel}(t)}{u_{top}^{Rel}(t+T)} \right] = \frac{2\pi\zeta_{eff}}{\sqrt{1-\zeta_{eff}^2}} \quad (1)$$

where T is the time between two consecutive peaks of the dynamic response, and u_{top}^{Rel} is the top tower relative displacement. The effective damping of the initial structure, the TMD and the EKD systems are 2.67 %, 2.98 %, and 8.36 %. The TMD system slightly increases the effective damping, while the EKD system has more than 3 times the initial effective damping.

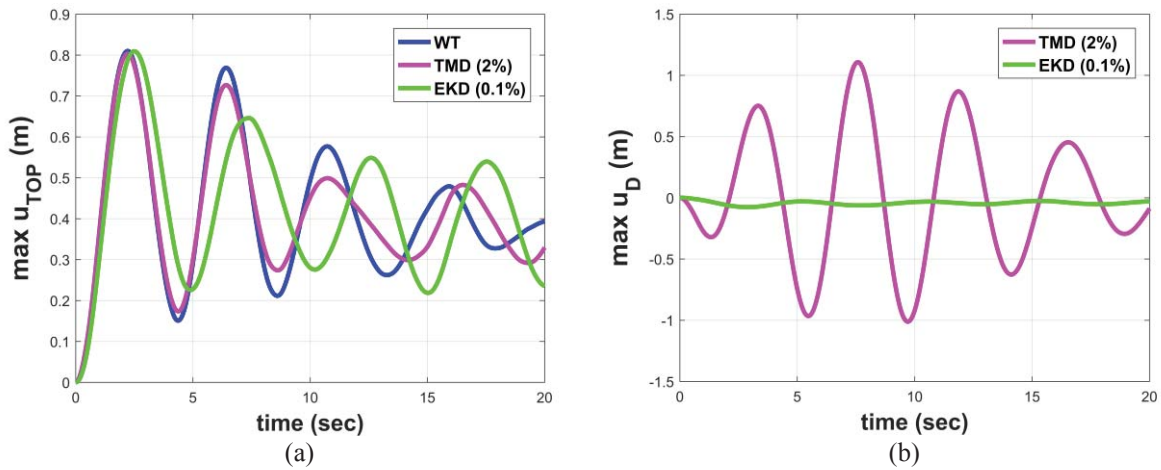


Figure 3: (a) Dynamic response of the WT tower top relative displacement of the initial, the TMD and the EKD systems. (b) Additional oscillating mass relative to the tower displacement of the TMD and EKD systems.

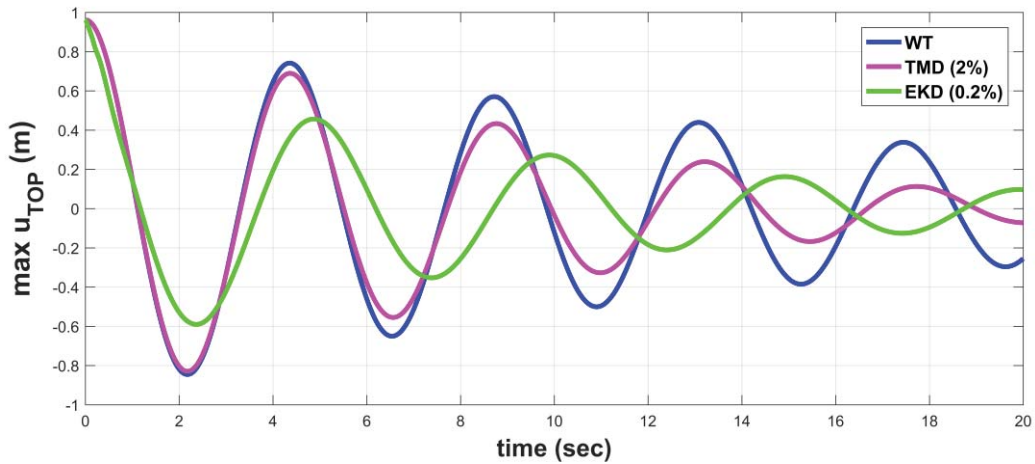


Figure 4: Free vibration of the top WT tower of the initial uncontrolled structure, the TMD system, and the EKD. The initial displacement conditions imposed are according to the first modal eigenform of the initial WT.

Finally, the relative displacement of the additional oscillating mass of the TMD and EKD systems, is presented in Figure 3.b. The additional mass of the EKD has a stroke more than one order of magnitude smaller, as compared to that of the TMD. More specifically, the peak of the additional mass stroke is 1.11 m with the TMD system, and 0.076 m with the EKD system.

5 CONCLUSIONS

In this paper, a novel passive vibration absorption and damping concept, the extended KDamper, is examined for improving the WT tower dynamic behavior and increasing the effective damping. A wind turbine of 5MW supported by a steel tower of 120 m founded on a monopile was analyzed under a horizontal aerodynamic load due to the wind. The developed nonlinear dynamic model is an assemblage of prismatic beam elements, the validity of which is verified based on a comparison with a commercial software package on FEM. The aerodynamic load is taken into account by generating artificial basic wind velocities applying the corresponding regulations of EC1, Part1,4. The proposed vibration control system (VCS) is designed based on a constrained optimization procedure, that accounts for geometrical, con-

structional and manufacturing limitations. Based on the performed nonlinear dynamic analysis, the following conclusive remarks can be made:

- i. The proposed nonlinear dynamic model is effective and efficient in implementing VCS for vibration control of WT.
- ii. The employed additional mass is significantly lower (0.1%, 0.403 *tn*) as compared to a conventional TMD (2%, 8.6 *tn*).
- iii. The EKD increases the effective damping (8.36 %) of the WT tower more than 3 times compared to the initial WT (2.67 %), while the TMD system achieves only a slight increase (2.98 %).
- iv. The additional mass stroke in the EKD is in the order of a few centimeters (7.6 *cm*), overcoming the fundamental disadvantage of the TMD that requires large strokes, more than 1 *m*.

6 ACKNOWLEDGMENTS

This research has been co-financed by the European Union and Greek national funds through the Operational Program Competitiveness, Entrepreneurship and Innovation, under the call RESEARCH – CREATE – INNOVATE (project code: T1EDK-02827).



Co-financed by Greece and the European Union

7 REFERENCES

- [1] Li, Y., 2018, “Research and Development of the Wind Turbine Reliability,” *Int. J. Mech. Eng. Appl.*, **6**(2), p. 35.
- [2] “Sustainable Development Scenario – World Energy Model – Analysis - IEA” [Online]. Available: <https://www.iea.org/reports/world-energy-model/sustainable-development-scenario>. [Accessed: 24-Apr-2020].
- [3] Frahm, H., 1911, “Device for Damping of Bodies,” U.S. Pat., (989).
- [4] Soong, T. T., and Dargush, G. F., 1997, *Passive Energy Dissipation Systems in Structural Engineering*, Wiley.
- [5] Casciati, F., and Giuliano, F., 2009, “Performance of Multi-TMD in the Towers of Suspension Bridges,” *J. Vib. Control*, **15**(6), pp. 821–847.
- [6] Ricciardelli, F., Pizzimenti, A. D., and Mattei, M., 2003, “Passive and Active Mass Damper Control of the Response of Tall Buildings to Wind Gustiness,” *Eng. Struct.*, **25**(9), pp. 1199–1209.
- [7] Ankireddi, S., and Yang, H. T. Y., 1996, “Simple ATMD Control Methodology for Tall Buildings Subject to Wind Loads,” *J. Struct. Eng.*, **122**(1), pp. 83–91.
- [8] Liao, G. J., Gong, X. L., Kang, C. J., and Xuan, S. H., 2011, “The Design of an Active-Adaptive Tuned Vibration Absorber Based on Magnetorheological Elastomer and Its Vibration Attenuation Performance,” *Smart Mater. Struct.*, **20**(7), p. 075015.
- [9] Weber, F., Boston, C., and Maślanka, M., 2011, “An Adaptive Tuned Mass Damper Based on the Emulation of Positive and Negative Stiffness with an MR Damper,” *Smart Mater. Struct.*, **20**(1), p. 015012.
- [10] Casciati, F., Rodellar, J., and Yildirim, U., 2012, “Active and Semi-Active Control of

- Structures – Theory and Applications: A Review of Recent Advances,” *J. Intell. Mater. Syst. Struct.*, **23**(11), pp. 1181–1195.
- [11] Acar, M. A., and Yilmaz, C., 2013, “Design of an Adaptive-Passive Dynamic Vibration Absorber Composed of a String-Mass System Equipped with Negative Stiffness Tension Adjusting Mechanism,” *J. Sound Vib.*, **332**(2), pp. 231–245.
 - [12] Weber, F., 2014, “Optimal Semi-Active Vibration Absorber for Harmonic Excitation Based on Controlled Semi-Active Damper,” *Smart Mater. Struct.*, **23**(9), p. 095033.
 - [13] Weber, B., and Feltrin, G., 2010, “Assessment of Long-Term Behavior of Tuned Mass Dampers by System Identification,” *Eng. Struct.*, **32**(11), pp. 3670–3682.
 - [14] Antoniadis, I. A., Kanarachos, S. A., Gryllias, K., and Sapountzakis, I. E., 2018, “KDamping: A Stiffness Based Vibration Absorption Concept,” *JVC/Journal Vib. Control*, **24**(3), pp. 588–606.
 - [15] Kapasakalis, K., Sapountzakis, E., and Antoniadis, I., 2017, “Implementation of the KDamper Concept to Wind Turbine Towers,” *Proceedings of the 6th International Conference on Computational Methods in Structural Dynamics and Earthquake Engineering (COMPDYN 2017)*.
 - [16] Kapasakalis, K., Antoniadis, I., and Sapountzakis, E., 2019, “Control of Multi Storey Building Structures with a New Passive Vibration Control System Com-Bining Base Isolation with KDamper,” *Proceedings of the 7th International Conference on Computational Methods in Structural Dynamics and Earthquake Engineering (COMPDYN 2019)*.
 - [17] Antoniadis, I., Kapasakalis, K., and Sapountzakis, E., 2019, “Advanced Negative Stiffness Absorbers for the Seismic Protection of Structures,” *Proceedings of the International Conference on Key Enabling Technologies 2019 (KEYTECH2019)*.
 - [18] Kapasakalis, K., Antoniadis, I., and Sapountzakis, E., 2019, “Performance Assessment of the KDamper as a Seismic Absorption Base,” *Struct. Control Heal. Monit.*
 - [19] Kapasakalis, K., Antoniadis, I., and Sapountzakis, E., 2019, “KDamper Concept for Base Isolation and Damping of High-Rise Building Structures,” *Proceedings of the 14th International Conference on Vibration Problems (ICOVP 2019)*.
 - [20] Kapasakalis, K., Sapountzakis, E., and Antoniadis, I., 2018, “Optimal Design of the KDamper Concept for Structures on Compliant Supports,” *Proceedings of the 16th European Conference on Earthquake Engineering (16ECEE 2018)*.
 - [21] Kapasakalis, K. A., Antoniadis, I. A., and Sapountzakis, E. J., 2021, “Constrained Optimal Design of Seismic Base Absorbers Based on an Extended KDamper Concept,” *Eng. Struct.*, **226**.
 - [22] Kapasakalis, K. A., Alvertos, A. E., Mantakas, A. G., Antoniadis, I. A., and Sapountzakis, E. J., 2020, “Advanced Negative Stiffness Vibration Absorber Coupled with Soil-Structure Interaction for Seismic Protection of Buildings,” *Proceedings of the International Conference on Structural Dynamic , EURODYN*, European Association for Structural Dynamics, pp. 4160–4176.
 - [23] Kapasakalis, K. A., Bollano, P. O. N., Sapountzakis, E. J., and Antoniadis, I. A., 2020, “Comparison of Alternative Dynamic Vibration Mitigation Approaches for Wind Turbine Towers,” *Proceedings of the International Conference on Structural Dynamic , EURODYN*, European Association for Structural Dynamics, pp. 1358–1372.
 - [24] Kapasakalis, K. A., Antoniadis, I. A., and Sapountzakis, E. J., 2020, “Optimal Design of Advanced Negative Stiffness Absorbers,” *Proceedings of the International Conference on Structural Dynamic , EURODYN*, European Association for Structural Dynamics, pp. 4177–4188.
 - [25] Hansen, M. O. L., 2008, *Aerodynamics of Wind Turbines*, Earthscan.

- [26] Quilligan, A., O'Connor, A., and Pakrashi, V., 2012, "Fragility Analysis of Steel and Concrete Wind Turbine Towers," *Eng. Struct.*, **36**, pp. 270–282.
- [27] Sapountzakis, E. J., Dikaros, I. C., Kampitsis, A. E., and Koroneou, A. D., 2015, "Nonlinear Response of Wind Turbines under Wind and Seismic Excitations with Soil-Structure Interaction," *J. Comput. Nonlinear Dyn.*, **10**(4).
- [28] 2010, *EN 1991-1-4: Eurocode 1: Actions on Structures - Part 1-4: General Actions - Wind Actions*.
- [29] Koulatsou, K., Petrini, F., Vernardos, S., and Gantes, C. J., 2013, *Artificial Time Histories of Wind Actions For Structural Analysis of Wind Turbines*.
- [30] M, D. P., 1998, "Digital Simulation of Wind Field Velocity," *J. Wind Eng. Ind. Aerodyn.*, (74–76), pp. 91–109.
- [31] Norske Veritas (Organization), and Forskningscenter Risø., 2002, *Guidelines for Design of Wind Turbines.*, Det Norske Veritas, Copenhagen ;[Roskilde Denmark].
- [32] Jonkman, J. M., 2007, *Dynamics Modeling and Loads Analysis of an Offshore Floating Wind Turbine. Technical Report No. NREL/TP-500-41958*.
- [33] Zong Woo Geem, Joong Hoon Kim, and Loganathan, G. V., 2001, "A New Heuristic Optimization Algorithm: Harmony Search," *Simulation*, **76**(2), pp. 60–68.
- [34] "FEM, BIM and CAD Software for Structural Engineers | SOFiSTiK AG" [Online]. Available:
https://www.sofistik.com/?__hstc=136929903.778d8a8e3515c0a0f7da049d7f27258a.1587748377743.1587748377743.1587748377743.1&__hssc=136929903.2.1587748377744&__hsfp=4014916924. [Accessed: 24-Apr-2020].

ADAPTIVE BENDING-ACTIVE MODULES FOR A TENSILE SOLAR SHADING SYSTEM

Alessandro D'Ambrosio¹, Maria Matheou², Rosario Montuori¹, Elide Nastri¹

¹ Department of Civil Engineering, University of Salerno
Via Giovanni Paolo II, 132, 84084 Fisciano SA, Italy
e-mail: alexdam.nli@gmail.com; r.montuori@unisa.it; enastri@unisa.it

² Institute of Lightweight Structures and Conceptual Design, Faculty of Civil and Environmental Engineering
Pfaffenwaldring 14, 70569 Stuttgart, F.R. Germany
e-mail: maria.matheou@ilek.uni-stuttgart.de

Keywords: Adaptive Façade, Bending-Active Elements, Daylight Performance, Parametric Design.

Abstract. *Adaptive façades can be a solution to many urban aspects such as sustainability and energy efficiency. Along these lines, a parametric analysis has been conducted to investigate the geometrical reconfigurations of the proposed adaptive solar shading system, the daylight performance with Rhinoceros and the plugins Grasshopper and ClimateStudio as well as the structural behaviour with Karamba3D. A skeleton structure synthesized by GFRP bending-active elements and stabilized by a secondary system of cables with variable length and a PTFE tensile skin leads to a lightweight modular structure with embedded actuation. The control system is capable of flexible patterns and multi-stages of open, semi and close configurations for different sun shading effects, depending on the changeable weather conditions and the relative response required in every part of the façade. The mechanism recalls a Class-2 Tensegrity system with springed hinges, where the rigid members and the hinges are substituted by lamellas, which can be bend by controlling the length of the cables. Furthermore, the ever-changing modular structure, especially to the plethora of different configurations, results in an aesthetically pleasing and organic dynamic filter for a tall building. Further research can be carried out about the wind load, how the structure can be naturally wind-resistant, and convective factors triggered by air movements between the façade and the building itself.*

1 INTRODUCTION

Adaptive building envelope design may provide a real-time process of reconfiguration on a daily and seasonal basis enlivening the environmental performance of the building and enhancing the end-users' internal comfort. A viable design for adaptive shading systems is necessary, especially when the building sector absorbs 40 % of the total energy use, even greater than the transport and industry sectors [1]. Current numerical studies evaluate the performance of external shades by scoping the impact of them with regard to the building envelope and the indoor environment [2-6]. Different typologies of shadings such as overhangs, vertical fins, horizontal shading, egg-crate shading, perforated screens and exterior blinds are giving potential opportunities for energy savings and improvement of indoor environment.

The sustainability role of the external shading elements can be further extended by means of adaptability either following environmental spaces and user needs or increasing the efficiency and optimizing the materials in order to reduce energy consumptions [7]. The effectiveness of kinetic façades in terms of energy savings is demonstrated in [8] with three existing buildings, Al Bahar Towers, Council House 2 and Q1 Headquarters Building. Adaptive folding shading systems placed externally on the Al-Bahar Tower in Abu Dhabi obtain different configurations, in order to regulate solar radiation and maximize the energy savings on cooling. In tracking the sun position, the kinetic system applied on the western façade of the Council House 2 in Australia provides full shading while minimizing the electricity consumption by 85 %. Following the sun path with three different configurations by the motorized swivel vertical louvers of the Q1 Headquarters Building in Germany, the adaptive external shading system succeeds in minimizing the electricity consumption, glare, as well as maximizing the heat gain and natural air ventilation.

A systematic analysis for daylight performance of an adaptive façade shading system integrated on a multi-storey office proves that rotation of the external shades and inclination of the slats may considerably influence the indoor daylight performance. Furthermore, shades can control the amount of incoming solar radiation and block the solar heat gain admitted into the open-space offices, while their impact on the air indoor temperature is significant by reducing the overheating and cooling loads [9-10]. Indoor environment is related to the comfort of the occupants and inevitably affects the well-being, productivity and consequently provokes the economic benefit. For example, the rising demand for lighting energy is also associated with the visual discomfort. Adaptive façade systems can lower the thermal load of the building by blocking the sunlight effectively, while daylight can be used properly during the day enhancing occupant comfort [11].

Adaptive sun shading systems can meet the changing solar radiation and provide an optimal shading as well as maximization of the daylight use [12]. Relevant adaptive and kinetic systems that reflect principles of embedded actuation and meditated to sustainable issues, functionality and aesthetics considerations are presented in this paper. An experimental prototype in full-scale of a tensegrity structure is actuated in obtaining a responsive behavior through adjustment of tension members and actuators [13]. In this context, a conceptual development of an adaptable structure aiming at structural simplicity and reduced energy consumption during the reconfiguration is presented in [14]. The proposed actuation method conveys the ability to the structure to obtain different geometrical reconfigurations. The methodology approach of the responsive skylight modules leading to the integration of architectural kinetic elements and computational devices is presented in [15]. Design requirements of the project are the optimization of the thermal and daylighting conditions. The prototype system is based on tensegrity principles incorporated with photovoltaic panels in its structure.

A similar approach on adaptive tensegrity architecture mimics the dynamics of a blinking sail as a dynamic sun-screen harvesting device presented in [16].

The current research project refers to the design and analysis of adaptive bending-active modules for a tensile solar shading system using as a case study the SFB1244 demonstrator tower located in the campus Vaihingen of the University of Stuttgart in Germany. A synergistic architectural and engineering approach of the adaptive bending-active modules leads to the design of a high efficiency envelope system with improved load-bearing performance. Essentially, the goal was to increase energy efficiency by controlling the light transmission and thus provide energy savings on cooling, heating and lighting demands. The characters of lightness, aesthetic quality and utilization flexibility were the most important to consider at the beginning of the designing process. The software used for the parametric analysis include Rhinoceros and Grasshopper for the 3D modeling, ClimateStudio for the daylight analysis and Karamba3D for the structural analysis; both ClimateStudio and Karamba3D work in the Rhino/Grasshopper environment. The daylight simulations were carried out on different days and times throughout the year, to test the response and effectiveness of the various configurations that the adaptive system is capable of, using the parameterization of the Grasshopper model.

2 DESIGN

2.1 Adaptive bending-active modules

The first idea was to use tensegrity for the mechanism of each module - specifically, a Class-2 tensegrity system for the vertical ribs of the shells, consisting of two cable-controlled rigid bars connected by a springed hinge. This approach, though, would have required a change of shape through approximation; this is why, at the end, the bending-active approach was chosen. This approach could keep the structure in the lightweight range, providing almost the same mechanism and the possibility of keeping the shape just as it was designed. The bending-active solution for the module mechanism recalls the bow-and-string principle; the original frame of bending-active elements consisted of a single vertically oriented bow in the middle. This disposition was eventually modified (as shown in Figure 1) to have two vertical elements instead, spaced enough to have a more even area distribution of the membrane.

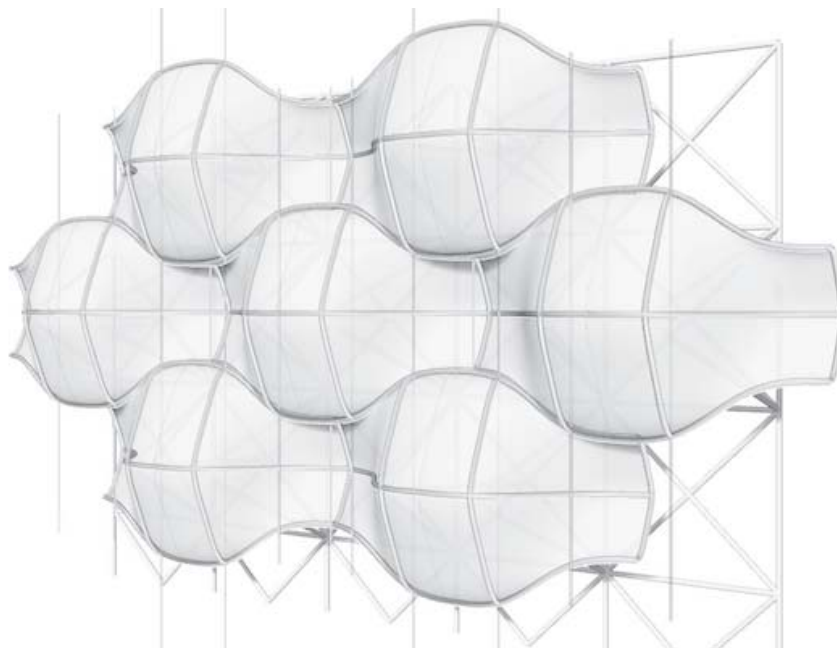


Figure 1: Adaptive bending-active system.

Each sun-shielding module is 2,00m wide and 0,90m tall, and its shape allows for each row to aesthetically interlock with the previous ones, with a 1,00m horizontal offset. The modules open and close by being constrained to the horizontal plane (identified with the midpoints of each row) by controlling the length of cables.

Glass Fiber Reinforced Polymer (GFRP) was chosen as the material for the bending-active frame; this material allows good behavior on long-term deformation cycles and a very high strength-to-weight ratio. Architectural Polytetrafluoroethylene (PTFE) was chosen as the material for the membrane; the resin-painted fiberglass has excellent properties for a second skin facade, thanks to its weather resistance and self-cleaning behavior.

2.2 Reconfigurations and integration to the Demonstrator

The system is designed to flexibly work in various sunlight conditions, thanks to the ability of each module to change in configuration to a certain degree, from completely closed to completely open. This is possible thanks to the GFRP skeleton of each module, stabilized by cables and a PTFE membrane. The embedded actuation system, controlled by sensors, makes it possible to have different sun shading (and aesthetic) effects, visible as gradients on the façade throughout the day (as shown in Figure 2).

The connection with the Demonstrator tower is realized through a steel space grid-like structure that gives the needed support to the panels and keeps the whole system lightweight, without obstructing the view from and to the building.

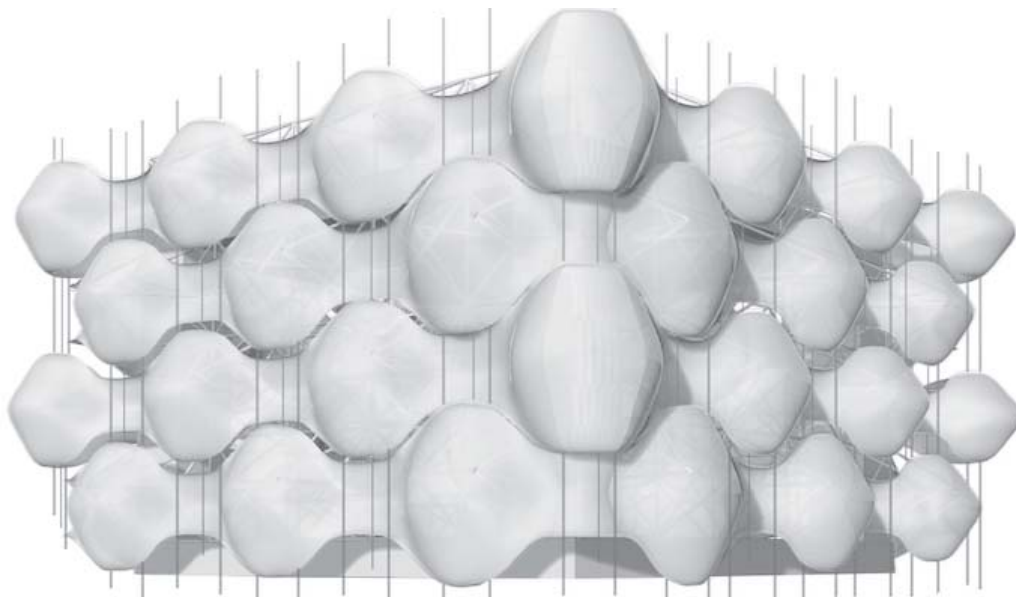


Figure 2: Gradients in the adaptive configuration model.

3 STRUCTURAL ANALYSIS

The structural analysis was originally intended to be carried out in SAP2000; in order to do that, the 3D model had to be assembled in GeometryGym, a software that works in the Rhino/Grasshopper environment and helps exporting the model to SAP2000, thanks to the controlled IFC conversion of the files. The issues had with such a work outline were in the double curvature of the shell elements. Said software works best when synthesizing big models, deconstructing them in smaller parts; when the mathematical conversion needed, from the Grasshopper boundary representation to a mesh, interests smaller elements with tighter toler-

ances it becomes a problem. The approximation was excessive and it resulted in troubles related to the bijective individuation of points; this was especially an obstacle for the external forces and support placement. The ideal solution was to control the degree of approximation of the curvature of each element through a software that was closer to the Grasshopper native environment. For this reason, in the present work, it was decided to carry out the analysis in the Rhino environment with Karamba3D; this software made it possible to better control the approximation of the original shape, for both the frame and the membrane. The membrane was meshed, and its area was used for the wind load; its support was the frame, deformed, while the supports of the frame itself were placed in the intersection between the central vertical and horizontal elements. The support structure was designed as a space grid structure, in order to be well distributed and light in both aesthetic and structural terms, while allowing for the full movement of each module.

3.1 Wind load

The main loads considered were self-weight and wind load; the latter was calculated from the local legislation and the Eurocodes. The obtained wind load was related to a wind speed of 81km/h; this was the worst-case scenario, and in Stuttgart this condition is very rare (less than 30 hours per year). Another scenario was taken into account, imagining the request of the client to have the structure designed for 50km/h and 60km/h (wind conditions still rare for the city), to consider the advantages in terms of lightness and economy at the expense of having the façade closed when said wind velocities are reached. Tangential wind was also considered.

3.2 Results

After having the model assembled in Karamba3D, a strict hierarchy was followed in the relationship between each element of the façade, so to have their structural behavior connected just as expected in working conditions. A nonlinear analysis was needed, because of the bending-active approach used; after solving using the specific analysis tool, the ModelView tool allowed the visualization of displacements (Figure 3) and stress on each of the models. A specific set of tools was placed on the Grasshopper canvas to get the axial stress results on each element. The highest displacements measured on the module frame were 2,83mm at the extremes, without considering the stabilizing effect of the steel cables. The highest value of tension measured on the support system is 0,61 kN, while the highest value of compression is 0,43kN.

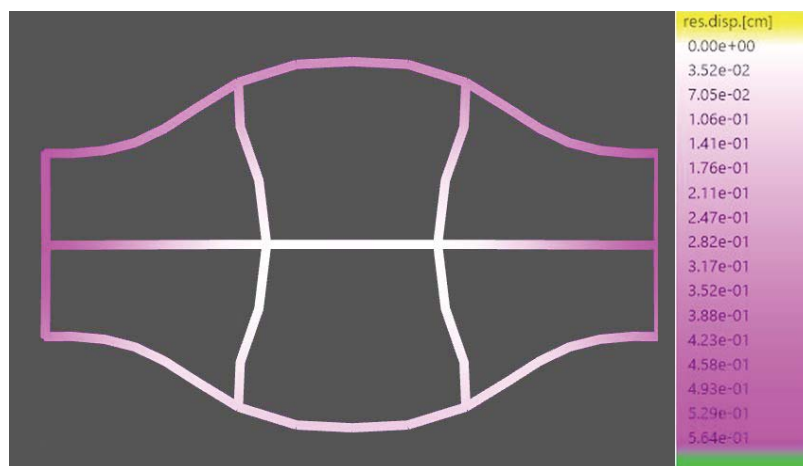


Figure 3: Karamba3D result window.

3.3 Support system sections

Following positive outcomes related to buckling, displacement and axial stress tests, the profiles chosen for the original wind condition (81km/h) were the EN10210 33,7x3,2mm with circular section. The provided results for a lower wind condition (60km/h) have led to a thinning of the profile section, now the circular EN10210 26,9x3,2mm, which leads to increased lightness and economic convenience.

4 DAYLIGHT ANALYSIS

The daylight analysis was carried out in ClimateStudio; the chosen days for the simulations were the two solstices and the two equinoxes, and for each day the hour chosen was 9:30 am, 12:30 am and 15:30 pm.

All materials have been assigned to each element of the 3D model. Three case studies have been considered in this project: the bare structure, fully open configuration and adaptive configuration.

4.1 Parameterization

The parameterization of the façade allowed each corner to independently open and close, causing a dynamic gradient on each side of the building. By changing the corner values in order to follow the sun position at a certain time, the ideal overall configuration was researched each time (as shown in Figure 4 for March 20th, 15:30). Issues with the model were related to the cable slits, excessively large, and the BRep approximation from Grasshopper to ClimateStudio, that caused some light to creep in. The solution was to reduce the slits and to mesh the entire façade, so the software could read it properly.

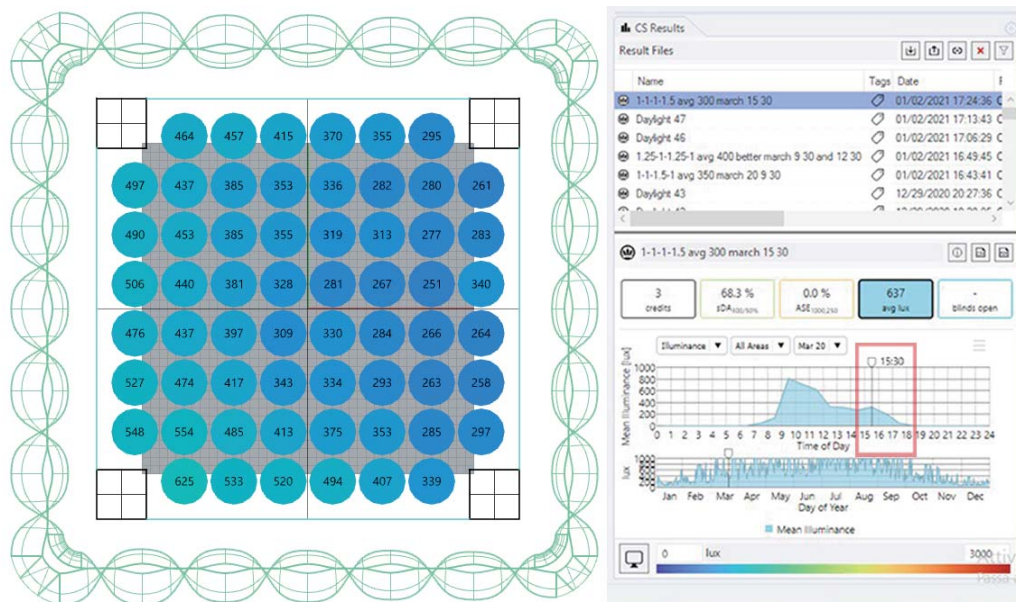


Figure 4: ClimateStudio test environment.

4.2 Results

The results (Figure 5) show that the adaptive configuration always respects the ideal lux range (350–450), with peak values hardly over 500; the completely open configuration has worse results, especially during the cold months. The worst condition is, by far, the bare

structure, with average peak values of over 600lux. Furthermore, the façade shows its dynamic aesthetic value the most when following the sun position in the adaptive configuration.

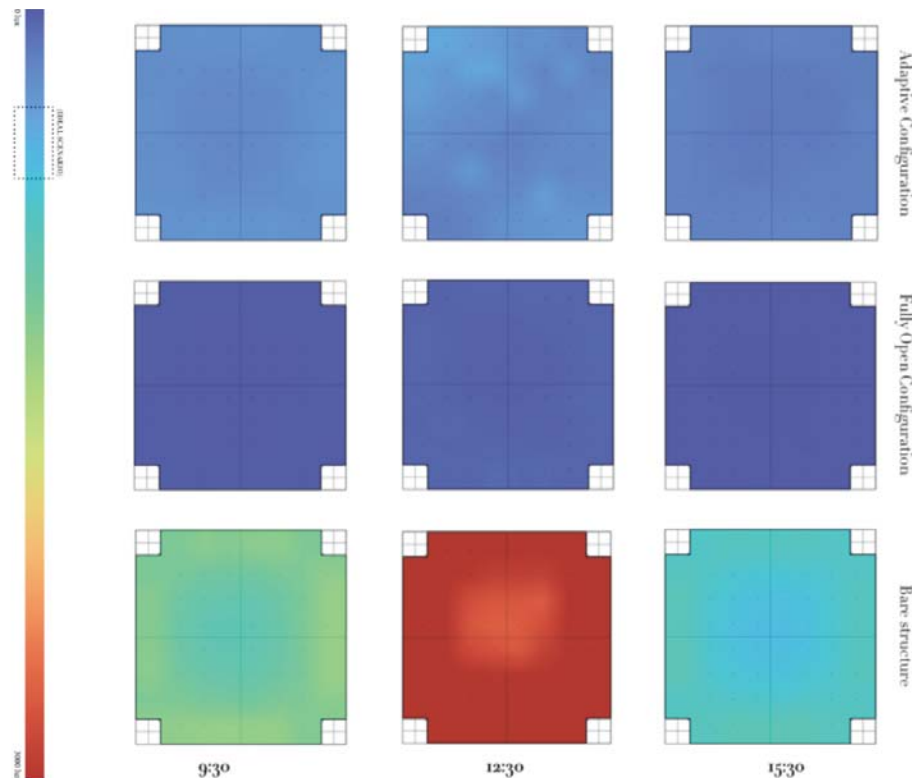


Figure 5: Daylight simulation results (21st of December).

5 CONCLUSIONS

5.1 Overall results

The designed adaptive façade proved to be very effective in its dynamic sun-shielding behavior, providing the right amount of daylight even when most exposed to the sun radiation. The structure, including the support system, is lightweight and thin, which is convenient for both its cost and aesthetic value. Furthermore, the sculpted feel given to the building helps create a sense of dynamism and the character of the façade becomes the character of the building.

5.2 Further considerations

The structure, especially the support system frame, can benefit from form-finding approaches aimed at optimizing the mass and geometry distribution of its elements. Furthermore, a tensegrity solution for the same space grid can be researched.

Form-finding can also be used for the modules, to consider a change of shape related to the dynamic action of the wind in any configuration. This requires a new parameterization and the use of accessory tools in the Grasshopper environment.

ACKNOWLEDGEMENTS

Partly funded by the Deutsche Forschungsgemeinschaft (DFG, German Research Foundation) – Project-ID 279064222 – SFB 1244.

REFERENCES

- [1] *Energy Saving and CO2 Reduction Potential From Solar Shading Systems and Shutters in the EU-25 (ESCORP-EU25), a research project commissioned by ES-SO*, the European Solar Shading Organization, ES-SO 2006
- [2] A.A.M. Ali, and T.M.F. Ahmed. *Evaluating the impact of shading devices on the indoor thermal comfort of residential buildings in Egypt. Fifth National Conference of IBPSA-USA*, Madison, Wisconsin, 2012, pp. 603–612.
- [3] A.A.M. Ali. *Using simulation for studying the influence of vertical shading devices on the thermal performance of residential buildings (Case study: New Assiut City)*. *Ain Shams Engineering Journal*, **3**(2), 2012, pp. 163–174.
- [4] N.A. Al-Tamimi, and S.F.S. Fadzil. *The potential of shading devices for temperature reduction in high-rise residential buildings in the tropics*. *Procedia Engineering*. **21**, 2011, pp. 273–282.
- [5] M.A. Hegazy, S. Attia, and J.L. Moro. *Parametric analysis for daylight autonomy and energy consumption in hot climates*. *Proceedings of BS2013: 13th Conference of International Building Performance Simulation Association*, Chambéry, France, 2013, pp. 2232–2240.
- [6] F. Mazzichi, and M. Manzan. *Energy and daylighting interaction in offices with shading devices*, *Proceedings of Building Simulation Applications BSA 2013*. Bozen-Bolzano University Press, Bolzano, 2013, pp. 385–393.
- [7] M. Barozzi, J. Lienhard, A. Zanelli, and C. Monticelli. *The sustainability of adaptive envelopes: developments of kinetic architecture*. *Procedia Engineering*, **155**, 2016, pp. 275–284.
- [8] F. Alotaibi. *The role of kinetic envelopes to improve energy performance in buildings*. *Journal of Architectural Engineering Technology*. **4**(3), 2015, pp. 1–5.
- [9] A. Couvelas, M.C. Phocas, F. Maden, M. Matheou, and D. Olmez. *Daylight performance of an adaptive shading system integrated on a multi-storey office building*. *13th Conference on Advanced Building Skins*, Bern, Switzerland, October 2018.
- [10] A. Couvelas, M. Matheou, and M.C. Phocas. *Analysis and development of an adaptive façade system integrated on a multi-storey office building*. *The Tenth International Conference on Engineering Computational Technology*, Sitges, Barcelona, Spain, September 2018.
- [11] G. Yun, D.Y. Park und K.S. Kim. *Appropriate activation threshold of the external blind for visual comfort and lighting energy saving in different climate conditions*. *Building and Environment*. **13**, 2017, pp. 247–266
- [12] Schnittich, R. Krippner, W. Lang, *Building Skins, Detail*, Birkhäuser, Basel, 2006F.
- [13] T.E. Sterk., *CAAD for Responsive Architecture, The Office of Robotic Architectural Media*. Canada, 2006.
- [14] M.C. Phocas, O. Kontovourkis, M. Matheou. *Kinetic Hybrid Structure Development and Simulation*, *International Journal of Architectural Computing*. **10**(1), 2012, pp. 68–86.

- [15] M. Fox. *Sustainable Applications of Intelligent Kinetic Systems. Second International Conference on Transportable Environments*. Singapore National University, Singapore, 2001.
- [16] M.C. Cimmino, R. Miranda, E. Sicignano, A.J.M. Ferreira, R.E. Skelton, and F. Fraternali. *Composite solar façades and wind generators with tensegrity architecture. Composites Part B*. 115, 2017, pp. 275-281.

A MESOSCALE TENSEGRITY MODEL OF SPIDER DRAGLINE SILK FIBER

A. Amendola^{1*}, N. Sigh¹, C. Rodenburg², C. Holland², F. Fraternali¹

¹Department of Civil Engineering, University of Salerno, via Giovanni Paolo II, 132, 84084, Fisciano (SA), Italy

[{adaamendola1, snarinder, f.fraternali}@unisa.it}](mailto:{adaamendola1, snarinder, f.fraternali}@unisa.it)

²Department of Materials Science & Engineering, University of Sheffield
Sir Robert Hadfield Building, Mappin Street, Sheffield, S1 3JD, UK

[{c.rodenburg, christopher.holland}@sheffield.ac.uk}](mailto:{c.rodenburg, christopher.holland}@sheffield.ac.uk)

Abstract

Tensegrity concepts are common in nature and are recognizable, e.g., in every cell, in the microstructure of the spider silk, and in the pattern of bones and tendons for control of locomotion. This work deals with the formulation of a tensegrity model of spider dragline silk fiber at the mesoscale through a multi-domain network approach with tensegrity architecture. The fiber is described as a multi-walled tube formed by coaxial cylindrical networks of beta-sheet crystals (crystalline domains) and polypeptide (amorphous) chains (noncrystalline domains). The given model generalizes a previous one recently appeared in the literature and paves the way to the optimal design of innovative biomimetic fibers with tensegrity architecture.

Keywords: Tensegrity, Spider Silk, Multiscale Modeling, Tensile Response.

1 INTRODUCTION

Tensegrity principles are common in nature and exist, e.g., in every cell, in the micro-structure of the spider silk, and in the arrangement of bones and tendons for control of locomotion. The present study deals with the formulation of a tensegrity model of spider dragline silk fiber at the mesoscale through a multi-domain network approach [1],[2] with tensegrity architecture [3].

The fiber is described as a multi-walled tube made of coaxial cylindrical networks of β -sheet crystals (crystalline domains) [4] and polypeptide (amorphous) chains (noncrystalline domains) [5]. Each tube is composed of a network of helical-shaped elements, loaded in tension (or strings) [6] and circumferential elements, loaded in compression (or bars).

The strings correspond to domains of amorphous chains attached to crystalline domains at their extremities, while the bars reproduce the compressive stiffening effect that is played by beta-sheet plated crystals in the circumferential direction, when the fiber is longitudinally stretched [3],[6]. Radial links transfer the compressive stresses from one tube to another.

2 MESOSCALE MECHANICAL MODELING OF A SPIDER SILK FIBER

We now illustrate the mechanical behavior of the dragline silk fiber at the mesoscopic scale through a multi-domain network approach [1],[2] with tensegrity architecture [3]. The fibre is described as a multi-walled tube made of coaxial cylindrical networks of β -sheet crystals (crystalline domains) [4] and polypeptide (amorphous) chains (noncrystalline domains, see Fig. 1) [5]. Each tube consists of a network of helical-shaped elements loaded in tension (or strings) [6] and circumferential elements loaded in compression (or bars). The strings are used to model amorphous chains attached to crystalline domains at their extremities, while the bars are introduced to simulate the compressive stiffening effect of the β -sheet plated crystals in the circumferential direction, when the fibre is stretched along its direction [3],[6]. Radial links reproduce the stresses of compression from one tube to another. The different tubes forming the fibre model describe the homogenised properties of different sections of the core of the fibre. It is indeed largely accepted in the up-to-date literature that the outer lipid, glycol and skin layers minimally contribute to the overall mechanical response of the fibre [6]-[8].

We now focus the attention on the response of the fibre under an isochoric longitudinal stretching deformation, which stretches the fibre up to an engineering strain $\hat{\epsilon} = (\ell - L)/L$, where L denotes the unstretched length of the fibre, and ℓ denotes the stretched length. If we consider that the volume of the fibre remains constant under stretching, as it is written in many experimental studies (refer, e.g., to [9],[10]), the length variation along the longitudinal axis occurs in association with a radial contraction of the fibre. The radial engineering strain $\hat{\epsilon}_r = (r - R)/R$, where R is the radius of the fibre in the unstretched configuration, and r is the stretched radius, is related to the longitudinal strain $\hat{\epsilon}$ through

$$\hat{\epsilon}_r = \frac{1}{\sqrt{1+\hat{\epsilon}}} - 1 \quad (1)$$

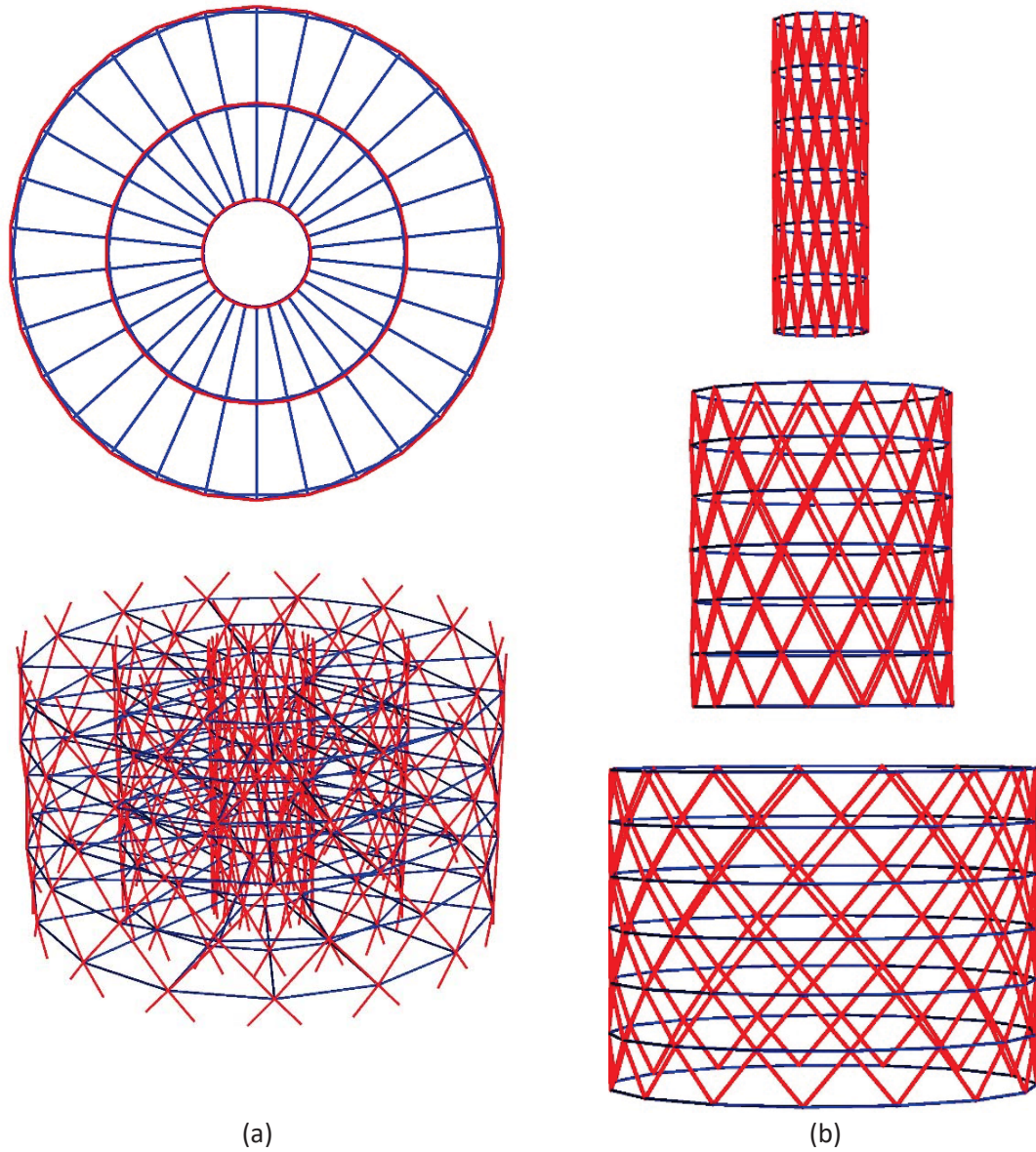


Fig. 1: Triple-walled tensegrity model of a portion of the dragline silk fiber at the mesoscopic scale: (a) overall views; (b) exploded view of the different walls. The red members are strings or tendons while the blue members are bars or struts.

We characterise the initial elastic response of the strings forming the multiwalled model in Fig. 1 through the following Young modulus:

$$E_s^{(1)} = x E_a + (1 - x) E_b, \quad (2)$$

where E_a is the elastic modulus of β -sheet crystal domains, E_b is the initial (pre-yielding) elastic modulus of the noncrystalline domanins and x is the volume fraction of β -sheet crystals within the strings.

The generic string yielding occurs when the engineering strain $\hat{\epsilon}_s$ of the element reaches a threshold value $\hat{\epsilon}_{s_y}$. The mechanical response of the string in the post-yielding regime is described through the following incremental Young modulus:

$$E_s^{(2)} = x E_a + (1 - x) E_c, \quad (3)$$

where E_c denotes the post-yield tangent modulus of the noncrystalline domains.

We consider that the bars are characterized by a constant compressive modulus equal to E_a , being not affected by yielding phenomena.

Both the strings and the bars of the model (Fig. 1) are considered as rods with rectangular cross section with width b and thickness t . By considering the strings of the i -th wall, we consider $b = b_{s_i} = L_{b_i}$, where L_{b_i} refers to the initial (undeformed) length of the circumferential bars, and t denotes the radial dimension t_i of the layer. Considering the circumferential bars of the i -th wall, we assume $b = b_{b_i} = s_c/10$ and $t = t_{b_i} = t_{s_i}$, where s_c indicates the longitudinal spacing of such elements. Finally, for what concerns the radial bars we assume $b = b_r = L_{b_r}$ and $t = t_r = s_c/10$. The geometrical and mechanical parameters that describe the proposed model (Fig. 1) are provided in Table 1. Such properties are imported from Refs. [6]-[7] for what concerns the radial dimensions of the layers forming a dragline silk fibre with overall diameter of $5 \mu\text{m}$. The mechanical properties of the fibre elements are instead the following (elastic modulus of the β -sheet crystals and mechanical properties of the links connecting the crystalline domains, in pre- and post-yielding conditions).

wall	d (nm)	t (nm)	L_b (nm)	x	E_a (GPa)	E_b (GPa)	$\hat{\varepsilon}_{s_y}$ (%)	E_c (MPa)
1	4100	800	859	0.40	20	4	0.4	7
2	2500	800	524	0.40	20	4	0.4	7
3	900	800	189	0.40	20	4	0.4	7

Table 1. Geometrical and mechanical properties of the model in Fig. 1.

3 TENSILE RESPONSE

The use of the properties in Table 1 leads us to predict the engineering and true stress-strain curves illustrated in Fig. 2. The engineering stress $\hat{\sigma}$ is obtained by dividing the total pulling force acting on the fibre by the initial cross section area \hat{A} . The true stress σ is related to the engineering stress through the equation $\sigma = (1 + \hat{\varepsilon})\hat{\sigma}$, while the true strain ε is related to the engineering strain through $\varepsilon = \log(1 + \hat{\varepsilon})$ [12].

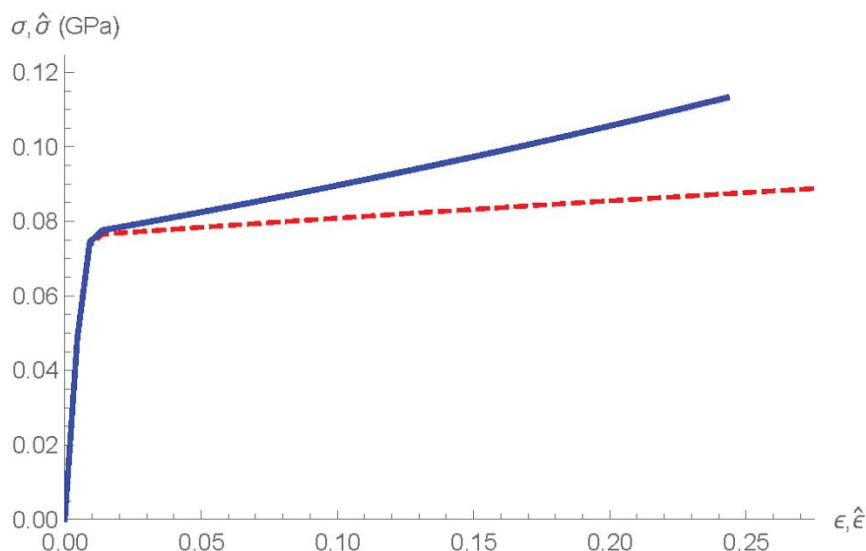


Fig. 2: Engineering (dashed line) and true (solid line) stress-strain responses of the multiwalled silk fibre model.

4 CONCLUDING REMARKS

We have illustrated a multi-walled generalization of the tensegrity model recently proposed for the spider dragline silk fiber. The different tubes forming the fiber model describe the homogenized properties of different sections of the core of the fiber. It is indeed largely accepted in the recent literature that the outer lipid, glycol and skin layers contribute very little to the global mechanical behavior of the fiber [6]–[8].

The presented model generalizes the one proposed in [9] and paves the way to the optimal design of innovative biomimetic fibers with tensegrity architecture.

REFERENCES

- [1] Lin N, Liu XY. Correlation between hierarchical structure of crystal networks and macroscopic performance of mesoscopic soft materials and engineering principles. *Chem Soc Rev* 2015;44(21):7881-915.
- [2] Xu G, Gong L, Yang Z, Liu XY. What makes spider silk fibers so strong? from molecular-crystallite network to hierarchical network structures. *Soft Matter* 2014;10(13):2116-23.
- [3] Skelton RE, Nagase K. Tensile tensegrity structures. *Int J Space Struct* 2012;27(2-3):131-7.
- [4] Keten S, Xu Z, Ihle B, Buehler MJ. Nanoconfinement controls stiffness, strength and mechanical toughness of B-sheet crystals in silk. *Nat Mater* 2010;9(4):359-67.
- [5] Du N, Xiang YL, Narayanan J, Li L, Lim MLM, Li D. Design of superior spider silk: From nanostructure to mechanical properties. *Biophys J* 2006;91(12):4528-35.
- [6] Sponner A, Vater W, Monajembashi S, Unger E, Grosse F, Weisshart K. Composition and hierarchical organisation of a spider silk. *PLoS ONE* 2007;2(10).

- [7] Stehling N, Abrams KJ, Holland C, Rodenburg C. Revealing spider silk's 3D nanostructure through low temperature plasma etching and advanced low-voltage SEM. *Front Mater* 2019;5.
- [8] Yazawa K, Malay AD, Masunaga H, Numata K. Role of skin layers on mechanical properties and supercontraction of spider dragline silk fiber. *Macromol Biosci* 2019;19(3).
- [9] Fraternali, F., Stehling, N., Amendola, A., Tiban Anrango, B.A., Holland, C., Rodenburg, C. Tensegrity modelling and the high toughness of spider dragline silk. *Nanomaterials*, 10, 1510, 2020

GEOMETRIC PATTERNS AND DYNAMICS OF FOLDABLE MODULI FOR ADAPTIVE FAÇADES

Veronica Abbate¹, Enrico Babilio², Filipe Amarante dos Santos³, Narinder Singh¹ and
Fernando Fraternali¹

¹Department of Civil Engineering, University of Salerno,
via Giovanni Paolo II, 132, 84084, Fisciano (SA), Italy
{vabbate,snarinder,f.fraternali}@unisa.it

²Department of Structures for Engineering and Architecture (DiSt), University of Naples “Federico II”,
via Forno Vecchio 36, 80134, Naples, Italy
enrico.babilio@unina.it

³CERIS and Departamento de Engenharia Civil da Faculdade de Ciências e Tecnologia,
Universidade NOVA de Lisboa,
Quinta da Torre, 2829-516 Caparica, Portugal
fpas@fct.unl.pt

Keywords: Tensegrity, Solar Façades, Mashrabiya, Deployability, Dynamic Response.

Abstract. *The design of buildings with a limited environmental impact and improved energy efficiency is nowadays of fundamental importance to face the challenge of reducing pollution and saving natural resources, without giving up comfort, indoor air quality and well-being. In fact, it is well known that the building industry is one of the largest consumers of material and energy resources and, among the many parts that make up a building, façades are responsible for a huge energy exchange with the surrounding environment. Therefore, both the research world and industry are very interested in effective solutions for smart and climate adaptable façades. A variety of concepts and solutions, which are competing with each other, have indeed already been developed. However, the field is not yet mature and an increase in emerging and innovative solutions is expected and requires future research and further challenges to be addressed. Recent studies have paid attention to the mechanics of folding sunscreens made with origami panels activated by stretching or releasing strings, following the tensegrity design philosophy. The present contribution is aimed at promoting innovative technological solutions based on the study of new models for foldable façade modules, paying attention to geometric patterns, deployability and mechanical properties.*

1 INTRODUCTION

One of the main challenges that contemporary architecture and civil engineering have to face is the construction of sustainable buildings with high energy efficiency, capable of limiting their environmental impact by minimizing the pollution they produce and the consumption of natural resources. It is well known, in fact, that the building industry is among the largest consumers of material resources and energy, accounting for about 40% of final energy consumption in the European Union (EU) [1]. Sustainability is thus among the main objectives of Horizon 2020 [2], the EU program for research and innovation. The challenge of the EU is maintaining the current standards of living while decreasing the energy dependence on fossil fuels and reducing CO₂ emissions by between 80% and 85% compared to 1990 [3].

Since the energy consumption of buildings is mostly related to air conditioning and domestic hot water, electricity and gas [4], increasing importance has been given to the concept of energy efficient buildings (EEBs), able to guarantee a condition of well-being inside, minimizing the use of non-renewable energy sources, through the integration of “active” and “passive” typological solutions. Among the many parts that make up a building, façades are responsible for a huge energy exchange with the surrounding environment. Hence, to save energy, the building envelope must perform more than the simple function of separating the external space from the inside, with insulation. The envelope is thus assigned the task of regulating the energy flow related to the passage of heat, the transmission of light and solar radiation and minimizing energy consumption due to air conditioning. Therefore, both the research world and industry are very interested in effective solutions for smart and climate adaptable facades. A variety of concepts and solutions, as for instance double envelope systems, which are considered with increasing interest in the EEB design [5, 6], have indeed already been developed. However, the field is not yet mature and an increase in emerging and innovative solutions is expected and requires future research and further challenges to be addressed [7]. Recent studies have paid attention to the mechanics of folding sunscreens made with origami panels activated by stretching or releasing strings, following the tensegrity design philosophy [8]. Glazing systems with morphing capabilities controlled by pairs of superelastic cables reversibly actuated against each other have also been considered, where superelasticity is also exploited to improve the structural behavior of the façade system subjected to wind loads [9]. The possibility of harvesting energy under the action of wind loads or partially recovering energy from the folding/unfolding mechanism has also been considered in the literature [10].

The present paper, which is focused on dynamic solar screens and shading systems for façades improving energy performance of buildings, is organized as follows. In Sect. 2, we briefly report about two of the existing state-of-the-art dynamic solar shading systems. Then, Sect. 3 is devoted to the operating principles of tensegrity structures and the possible advantages in using them as building envelopes. Basics on dynamics and foldability of tensegrity are reported in Sect. 4. Finally, some remarks given in Sect. 5 conclude the paper.

2 STATE OF THE ART OF DYNAMIC SOLAR FAÇADES

The present section is devoted to a brief description of two significant examples of adaptive dynamic façades, that indeed constitute the state of the art of contemporary architectural research about the building envelope, that, over time, has been transformed from a static and energetically passive element into a dynamic, permeable, and selective interface, designed to adapt to changes in external environmental conditions and positively affect the thermo-hygrometric and environmental parameters that guarantee comfort of users. Both examples are interesting,

modern reinterpretations of the traditional, wooden shading façades, the so-called “mashrabiyas” [11], common in Arab culture. Mashrabiyas are able to filter the light and control the air flow to reduce the temperature and increase the humidity of the internal environments of a building.

The first example we consider is the building of the Institut du Monde Arabe (IMA). Located in Paris, France, the building of the IMA, designed by Jean Nouvel, Pierre Soria, Gilbert Lezénés and Architecture Studio, has become a fundamental reference for dynamic façades. In particular, the rectangular, south-west façade of IMA is a lattice made up of square modules equipped with motorized steel diaphragms, connected to photosensitive sensors. The diaphragms open and close every hour to regulate the amount of natural light that enters the building, resulting in a dynamic shading system. It is emphasized in [12], to which we refer for further details, that the adaptive façade of the IMA exemplifies the strengths and limitations of mechanically operated designs.

The second example is the adaptive dynamic façade of the Al Bahar Towers, located in Abu Dhabi, where the climate is very hot and humid, especially in the summer, with up to 100% humidity and temperatures that reach 50°C, thus making a cooling system an equipment of paramount importance for buildings. The cooling of the glass façades of the buildings is guaranteed by a system of panels activated by low consumption electric linear actuators and which dynamically responds to the position of the sun during the day. The result is a scalable hexagonal shading device that acts as a solar barrier. This shading system allows the building to reach and maintain optimal thermo-hygrometric well-being, protecting the inhabitants from the glare of the sun rays and, at the same time, guaranteeing the right privacy. The shading system is based on modules made of six panels, coated in polytetrafluoroethylene (PTFE), mounted on a supporting structure made up of duplex stainless-steel frames [13, 14].

3 TENSEGRITY SOLAR FAÇADES

The design of active solar façades may exploit the advantages of tensegrity paradigm, that leads to light, deployable and foldable structures. If well designed, the core module quickly becomes scalable and is capable of being replicated to generate large-scale patterns.

Among the many different possible definition of “tensegrity”, the most widely accepted [15] is that can be given by quoting words by Motro [16], i.e. “tensegrity system is a system in a stable self-equilibrated state comprising a discontinuous set of compressed components inside a continuum of tensioned components.”

Theoretical and experimental studies [17] have highlighted that lightness, modularity, synergy, self-stability, fractal properties, enantimorphism, distributability and foldability are typical characteristics of tensegrity structures.

In particular, foldability makes tensegrity structures useful in many applications in which transport and storage must be considered. For instance, in the field of extra-terrestrial applications, transport costs, lightness of materials and optimization of the available space are of paramount importance [16].

The tensegrity structural paradigm can be exploited at different levels in the design of EEBs, since tensegrity assemblies are minimum mass structures able to carry many different load conditions, including compressive, tensile (under given stiffness constraints) and torsional loads without yielding and instability phenomena [18–20].

Thanks to their special ability to act as extremely light systems with “morphing” abilities [8, 21–24], tensegrity structures allow designing dynamic solar screens leading to a limited use of materials accompanied by a low level of energy consumption. A tensegrity reinterpretation of

the system adopted in Al Bahar Towers is considered in [8, 25].

Furthermore, tensegrity-based dynamic façades can also be exploited to harvest energy from the environment, by converting mechanical energy stored in strings into electrical energy [10, 21, 26] or from solar panels, that can be endowed in the structure and modeled as special rigid members [21, 27].

Finally, tensegrity lattices may be designed to operate as multi-scale actuators, capable of transferring energy through compact solitary waves thanks to their highly non-linear dynamic behavior [28–31].

4 DYNAMICS AND DEPLOYABILITY

This section illustrates a model for the numerical simulation of the dynamics of tensegrity systems. The procedure, already applied to solar façades in [32], with appropriate changes generalizes that presented in [33, 34] to account for the presence of wind forces [10, 35, 36].

Let us assume that the tensegrity structure is composed of n_n frictionless nodes, n_b straight, uniform, rigid bars, and n_s elastic strings, which carry only tensile forces.

The positions of nodes $\mathbf{n}_i \in \mathbb{R}^3$, $i \in [1, \dots, n_n]$, and external forces acting on them are respectively stored in node and load matrices

$$\mathbf{N} = [\mathbf{n}_1 \quad \mathbf{n}_2 \quad \cdots \quad \mathbf{n}_i \quad \cdots \quad \mathbf{n}_{n_n}] \in \mathbb{R}^{3 \times n_n}, \quad (1)$$

$$\mathbf{W} = [\mathbf{w}_1 \quad \mathbf{w}_2 \quad \cdots \quad \mathbf{w}_i \quad \cdots \quad \mathbf{w}_{n_n}] \in \mathbb{R}^{3 \times n_n}. \quad (2)$$

By calling \mathbf{b}_i and \mathbf{s}_i the vectors connecting the end nodes of the i^{th} bar and i^{th} string, respectively, and \mathbf{r}_i the position vector of the center of mass of the i^{th} bar, all of them are grouped in matrices

$$\mathbf{B} = [\mathbf{b}_1 \quad \mathbf{b}_2 \quad \cdots \quad \mathbf{b}_i \quad \cdots \quad \mathbf{b}_{n_b}] \in \mathbb{R}^{3 \times n_b}, \quad (3)$$

$$\mathbf{S} = [\mathbf{s}_1 \quad \mathbf{s}_2 \quad \cdots \quad \mathbf{s}_i \quad \cdots \quad \mathbf{s}_{n_s}] \in \mathbb{R}^{3 \times n_s}, \quad (4)$$

$$\mathbf{R} = [\mathbf{r}_1 \quad \mathbf{r}_2 \quad \cdots \quad \mathbf{r}_i \quad \cdots \quad \mathbf{r}_{n_b}] \in \mathbb{R}^{3 \times n_b}. \quad (5)$$

Let us introduce the connectivity matrices of bars $\mathbf{C}_B \in \mathbb{R}^{n_b \times n_n}$, cables $\mathbf{C}_S \in \mathbb{R}^{n_s \times n_n}$, and centers of mass $\mathbf{C}_R \in \mathbb{R}^{n_b \times n_n}$. The generic $(i, j)^{\text{th}}$ entry of \mathbf{C}_B (or of \mathbf{C}_S) takes values -1 or 1 , if \mathbf{b}_i (or \mathbf{s}_i) is directed away from, or toward node j^{th} , respectively, or 0 if \mathbf{b}_i (or \mathbf{s}_i) does not touch node j . Similarly to \mathbf{C}_B and \mathbf{C}_S , matrix $\mathbf{C}_R \in \mathbb{R}^{n_b \times n_n}$ is a connectivity matrix. Its i^{th} row stores the bar \mathbf{b}_i and its $(i, j)^{\text{th}}$ entry takes values $1/2$, if \mathbf{b}_i touches node j , or 0 , otherwise [37]. The connectivity matrices allows rewriting Eqns. (3)–(5) as

$$\mathbf{B} = \mathbf{N} \mathbf{C}_B^T, \quad (6)$$

$$\mathbf{S} = \mathbf{N} \mathbf{C}_S^T, \quad (7)$$

$$\mathbf{R} = \mathbf{N} \mathbf{C}_R^T. \quad (8)$$

The matrix equation of motion of a tensegrity system is written as [38]

$$\ddot{\mathbf{N}} \mathbf{M} + \mathbf{N} \mathbf{K} = \mathbf{W}, \quad (9)$$

where \mathbf{N} and \mathbf{W} have been already defined by Eqn. (1) and Eqn. (2), respectively, $\ddot{\mathbf{N}}$ stands for the second derivative of \mathbf{N} with respect to time, \mathbf{M} is the mass matrix and \mathbf{K} is the stiffness

matrix. The last two are computed as

$$\mathbf{M} = \frac{1}{12} \mathbf{C}_B^T \hat{\mathbf{m}} \mathbf{C}_B + \mathbf{C}_R^T \hat{\mathbf{m}} \mathbf{C}_R \in \mathbb{R}^{n_n \times n_n}, \quad (10)$$

$$\mathbf{K} = \mathbf{C}_S^T \hat{\gamma} \mathbf{C}_S - \mathbf{C}_B^T \hat{\lambda} \mathbf{C}_B \in \mathbb{R}^{n_n \times n_n}, \quad (11)$$

where $\hat{\mathbf{m}} \in \mathbb{R}^{n_b \times n_b}$ and $\hat{\gamma} \in \mathbb{R}^{n_s \times n_s}$ are diagonal matrices. The generic entry $(i, i)^{\text{th}}$ of $\hat{\mathbf{m}}$ is the mass m_i , $i \in [1, \dots, n_b]$ of the i^{th} bar, while entry $(i, i)^{\text{th}}$ of $\hat{\gamma}$ stands for the force density γ_i , $i \in [1, \dots, n_s]$ along the i^{th} string, given by

$$\gamma_i = \max \left[0, K_i \left(1 - \frac{L_i}{s_i} \right) \right] + \gamma_{ci}, \quad (12)$$

where K_i , L_i , and $s_i = \|\mathbf{s}_i\|$ are the axial stiffness, the rest length, and the current length of the string, respectively, and γ_{ci} is the damping force density, computed as

$$\gamma_{ci} = \begin{cases} c_i \frac{\dot{s}_i}{s_i}, & \text{if } s_i \geq L_i, \\ 0, & \text{otherwise.} \end{cases} \quad (13)$$

The diagonal matrix $\hat{\lambda} \in \mathbb{R}^{n_b \times n_b}$ in Eqn. (11) collects force densities in bars and is given by

$$\hat{\lambda} = -\frac{1}{12} \left[\dot{\mathbf{B}}^T \dot{\mathbf{B}} \right] \hat{\mathbf{m}} \hat{\ell}^{-2} - \frac{1}{2} \left[\mathbf{B}^T (\mathbf{W} - \mathbf{S} \hat{\gamma} \mathbf{C}_S) \mathbf{C}_B^T \right] \hat{\ell}^{-2}, \quad (14)$$

where $\hat{\ell}^{-2} \in \mathbb{R}^{n_b \times n_b}$ is a diagonal matrix, whose entries are $\ell_k^{-2} = \|\mathbf{b}_k\|^{-2}$, and $[\mathbf{A}]$ is a matrix keeping the diagonal terms of the generic square matrix \mathbf{A} , while all the off-diagonal entries are set to zero.

The stiffness matrix \mathbf{K} is not constant, being a function of time and the mechanical variables \mathbf{N} , $\dot{\mathbf{N}}$, and $\hat{\gamma}$, i.e. $\mathbf{K} = \mathbf{K}(t, \mathbf{N}, \dot{\mathbf{N}}, \hat{\gamma})$.

The numerical integration of Eqn. (9) is made by employing the algorithm described in [33, 34], which is based on fourth-order Runge-Kutta schemes.

As a basic module of a façade one can consider the deployable structure reported in Fig.1, which is a tensegrity system of class 6, meaning that the maximum number of bars concurring in each node is at most 6 (see the classification introduced in [18]).

5 CONCLUDING REMARKS

The present contribution aims to promote innovative technological solutions to design shading façades of energy efficient buildings through tensegrity systems, which can also be exploited as actuators to orient solar panels and as devices to harvest the wind-generated energy.

Recent studies have paid attention to the mechanics of tensegrity sunscreens activated by stretching or releasing strings, also exploring the possibility of wind energy harvesting. Glazing systems, with morphing capabilities, actuated with superelastic strings have also been considered in literature.

Future research in the field of tensegrity structures will focus on the possibility of using composite materials to design of dynamic shading façades, also using rapid prototyping of different architectural shapes through 3D and 4D printing technologies, at laboratory and full scales.

In conclusion, lightness, controllability and even the high artistic value of tensegrity structure are distinguished characteristics that can be exploited in the near future applications to building façades. Research in the field of tensegrity applied to buildings must necessarily take into account functionality and eco-sustainability.

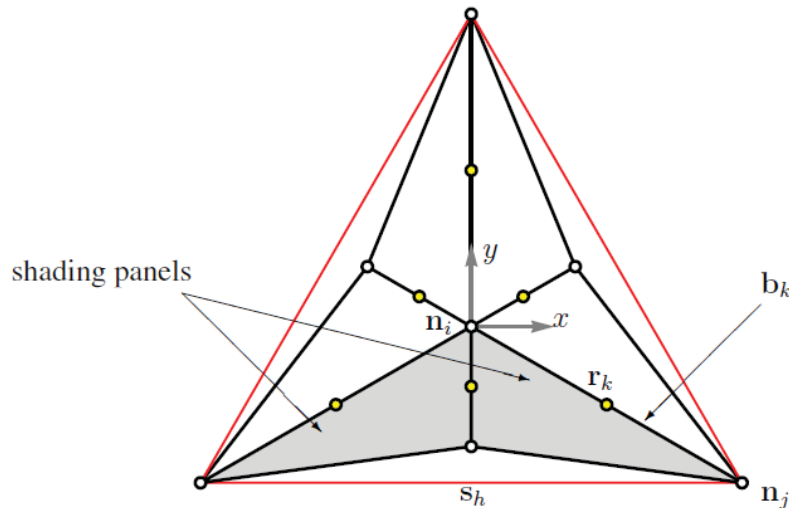


Figure 1: Schematic view of a foldable class 6 sunscreen tensegrity system: nodes are depicted as white disks (as n_i and n_j); red colored members are strings (as the generic s_h); black colored members are bars (as b_k); yellow disks (as r_k) stand for centers of mass of bars.

REFERENCES

- [1] L. Pérez-Lombard, J. Ortiz, C. Pout, A review on buildings energy consumption information. *Energy and Buildings*, **40** (3), 394–398, 2008.
- [2] *European Commission, HORIZON 2020 Work Programme 2014-2015, EU Decision C (2014) 4995 of 22 July 2014.*
- [3] *Directive (UE) 2018/844 of the European Parliament and of the Council of 30 May 2018 on energy efficiency, amending Directives 2012/27/UE and 2010/31/EU.*
- [4] D. Urge Vorsatz, L. F. Cabeza, S. Serrano, C. Barreneche, K. Petrichenko, Heating and cooling energy trends and drivers in buildings. *Renewable and Sustainable Energy Reviews*, **41**, 85–98, 2015.
- [5] T. Meyer Boake, K. Harrison, A. Chatham, The tectonics of the double skin: green building or just more hi-tech hi-jinx? *ARCC Conference Repository*, **1** (1), 2019.
- [6] H. S. M. Shahin, Adaptive building envelopes of multistory buildings as an example of high performance building skins. *Alexandria Engineering Journal*, **58** (1), 345–352, 2019.
- [7] R. Loonen, M. Trčka, D. Cóstola, J. Hensen, Climate adaptive building shells: State-of-the-art and future challenges. *Renewable and Sustainable Energy Reviews*, **25**, 483–493, 2013.
- [8] E. Babilio, R. Miranda, F. Fraternali, On the kinematics and actuation of dynamic sunscreens with tensegrity architecture. *Frontiers in Materials*, **6**, 7, 2019.
- [9] F. Amarante dos Santos, C. Bedon, A. Micheletti, Explorative study on adaptive facades with superelastic antagonistic actuation. *Structural Control and Health Monitoring*, **27** (4). e2463 stc.2463, e2463, 2020.

- [10] R. Miranda, E. Babilio, N. Singh, F. Santos, F. Fraternali, Mechanics of smart origami sunscreens with energy harvesting ability. *Mechanics Research Communications*, **105**, 103503, 2020.
- [11] A. F. Ashour, Islamic architectural heritage: mashrabiya. *WIT Transactions on the Built Environment*, **177**, 245–253, 2018.
- [12] M. Decker, A. Zarzycki, Designing Resilient Buildings with Emergent Materials, *Fusion - 32nd ECAADe Conference Proceedings*. Vol. 2. Northumbria University, Newcastle upon Tyne, England, 179–184, 2014.
- [13] A. Armstrong, G. Buffoni, D. Eames, R. James, L. Lang, J. Lyle, K. Xuereb, The Al Bahar towers: multidisciplinary design for Middle East high-rise, Abu Dhabi, United Arab Emirates. *The Arup Journal*, **2**, 60–73, 2013.
- [14] A. Karanouh, E. Kerber, Innovations in dynamic architecture. *Journal of Façade Design and Engineering*, **3**(2), 185–221, 2015.
- [15] A. Fraddosio, S. Marzano, G. Pavone, M. D. Piccioni, Morphology and self-stress design of V-Expander tensegrity cells. *Composites Part B: Engineering*, **115**. Composite lattices and multiscale innovative materials and structures, 102–116, 2017.
- [16] R. Motro, *Tensegrity: Structural Systems for the Future*. Elsevier Science, 2003.
- [17] V. Gómez Jáuregui, Tensegrity structures and their application to architecture. PhD thesis, Sept. 2004.
- [18] R. Skelton, M. de Oliveira, *Tensegrity Systems*. Springer US, 2010.
- [19] R. Skelton, F. Fraternali, G. Carpentieri, A. Micheletti, Minimum mass design of tensegrity bridges with parametric architecture and multiscale complexity. *Mechanics Research Communications*, **58**, 124–132, 2014.
- [20] G. Carpentieri, R. E. Skelton, F. Fraternali, Minimum Mass and Optimal Complexity of Planar Tensegrity Bridges. *International Journal of Space Structures*, **30** (3-4), 221–243, 2015.
- [21] M. Cimmino, R. Miranda, E. Sicignano, A. Ferreira, R. Skelton, F. Fraternali, Composite solar façades and wind generators with tensegrity architecture. *Composites Part B: Engineering*, **115**, 275–281, 2017.
- [22] J. Cai, X. Wang, R. Yang, J. Feng, Mechanical behavior of tensegrity structures with High-mode imperfections. *Mechanics Research Communications*, **94**, 58–63, 2018.
- [23] Y. Chen, J. Yan, J. Feng, Stiffness contributions of tension structures evaluated from the levels of components and symmetry subspaces. *Mechanics Research Communications*, **100**, 103401, 2019.
- [24] S. Ma, X.-F. Yuan, A. Samy, Shape optimization of a new tensegrity torus. *Mechanics Research Communications*, **100**, 103396, 2019.
- [25] R. Miranda, A. Amendola, I. Mascolo, F. Fraternali, E. Babilio, Design and control of adaptive tensegrity sunscreens. A. Zingoni, ed., *Advances in Engineering Materials, Structures and Systems: Innovations, Mechanics and Applications - Proceedings of the*

- 7th International Conference on Structural Engineering, Mechanics and Computation*. Cape Town, South Africa: CRC Press/Balkema, 1027–1032, 2019.
- [26] E Arroyo, S Foong, K. L. Wood, Modeling and experimental characterization of a fluttering windbelt for energy harvesting. *Journal of Physics: Conference Series*, **557**, 012089, Nov. 2014.
 - [27] F. Fraternali, E. De Chiara, R. Skelton, On the use of tensegrity structures for kinetic solar facades of smart buildings. *Smart Materials and Structures*, **24** (10), 2015.
 - [28] F. Fraternali, L. Senatore, C. Daraio, Solitary waves on tensegrity lattices. *Journal of the Mechanics and Physics of Solids*, **60** (6), 1137–1144, 2012.
 - [29] F. Fraternali, G. Carpentieri, A. Amendola, R. E. Skelton, V. F. Nesterenko, Multiscale tunability of solitary wave dynamics in tensegrity metamaterials. *Applied Physics Letters*, **105** (20), 201903, 2014.
 - [30] A. Amendola, G. Carpentieri, M. de Oliveira, R. Skelton, F. Fraternali, Experimental investigation of the softening-stiffening response of tensegrity prisms under compressive loading. *Composite Structures*, **117**, 234–243, 2014.
 - [31] F. Fraternali, G. Carpentieri, A. Amendola, On the mechanical modeling of the extreme softening/stiffening response of axially loaded tensegrity prisms. *Journal of the Mechanics and Physics of Solids*, **74**, 136–157, 2015.
 - [32] E. Babilio, R. Miranda, G. Carpentieri, F. Fraternali, Computational modeling of the dynamics of active sunscreens with tensegrity architecture. M. Papadrakakis, M. Fragiadakis, eds., *Proceedings of COMPDYN 2019 - 7th International Conference on Computational Methods in Structural Dynamics and Earthquake Engineering*. Vol. 2. National Technical University of Athens, 2159–2166, 2019.
 - [33] K. Nagase, R. Skelton, Network and vector forms of tensegrity system dynamics. *Mechanics Research Communications*, **59**, 14–25, 2014.
 - [34] F. Fabbrocino, G. Carpentieri, Three-dimensional modeling of the wave dynamics of tensegrity lattices. *Composite Structures*, **173**, 9–16, 2017.
 - [35] R. Miranda, E. Babilio, N. Singh, D. Villamil, F. Santos, F. Fraternali, Mechanics of energy harvesters based on tensegrity solar facades. *IOP Conference Series: Materials Science and Engineering*, **999**, 012003, Dec. 2020.
 - [36] R. Miranda, E. Babilio, N. Singh, D. Villamil, F. Santos, F. Fraternali, Dynamics of tensegrity solar Façades operating as mechanical energy harvesters. M. Papadrakakis, M. Fragiadakis, C. Papadimitriou, eds., *Proceedings of EUROLYN 2020 - 11th International Conference on Structural Dynamics*. Vol. 1. European Association for Structural Dynamics, 2113–2122, 2020.
 - [37] G. Carpentieri, R. Skelton, On the Dynamics of Tensegrity Bridges. *Journal of Aerospace Engineering and Mechanics*, **1** (1), 48–62, 2017.
 - [38] R. Skelton, Dynamics and control of tensegrity systems., *IUTAM Symposium on Vibration Control of Nonlinear Mechanisms and Structures*. Springer Netherlands, 309–318, 2005.

MODELING AND DESIGN OF PERIODIC LATTICES WITH TENSEGRITY ARCHITECTURE AND HIGHLY NONLINEAR RESPONSE

Andrea Micheletti¹, Claudio Intrigila¹, Nicola Nodargi¹, Edoardo Artioli¹, Fernando Fraternali², and Paolo Bisegna¹

¹Dipartimento di Ingegneria Civile e Ingegneria Informatica, University of Rome Tor Vergata
Via Politecnico 1, 00133, Rome, Italy
e-mail: micheletti, intrigila, nodargi, artioli@ing.uniroma2.it, bisegna@uniroma2.it

² Department of Civil Engineering, University of Salerno, Italy
84084 Fisciano (SA), Italy
e-mail: f.fraternali@unisa.it

Keywords: Bistable Systems, Nonlinear Systems, Additive Manufacturing, Experimental Testing, Solitary Waves.

Abstract. *In recent years, the nonlinear response of tensegrity systems has attracted increasing attention in the study of mechanical metamaterials. It has been shown in the literature that geometry and prestress of an elastic tensegrity structure can be designed to obtain different behaviors: stiffening, softening, and snap-through behavior in statics; propagation of solitary waves in dynamics. However, the realization of tensegrity systems is challenging, because of their prestressed state and the presence of tension-only cable members. A design method for periodic lattices with null prestress and no cables is here proposed, in which the repeating unit is at, or close to, a tensegrity configuration, maintaining the nonlinear types of response aforementioned. These structures can be realized by conventional additive manufacturing techniques, while the static and dynamic response can be predicted by means of stick-and-spring models.*

1 INTRODUCTION

Nonlinear mechanical metamaterials have been the subject of numerous studies aimed at discovering and exploiting new structural architectures with unprecedented properties [1–3]. Among lattice metamaterials, tensegrity periodic lattices have been found to possess a peculiar types of behavior, owing to the highly nonlinear mechanical response of the constituting tensegrity units, and to the fact that such response can be tuned by changing their geometry or prestress level [4–12]. In particular, in [4, 5], the nonlinear static and dynamic response of the triangular tensegrity prims (T3) was examined. In [6, 7], it was shown that a T3 can feature a stiffening or a softening response to applied loads in dependence of its aspect ratio. In [8], two distinct regimes of bistability have been highlighted in a case study. In [9, 11], the impact dynamics of tensegrity columns was investigated, finding that such periodic structures support the propagation of solitary waves. In addition, it was shown in [10] that such solitary waves can be either compression or rarefaction waves according to the geometry of the repeating unit. In [12], compression compact waves were obtained in numerical simulations of tensegrity beams in two- and three-dimensions.

While tensegrity units have a rich collection of mechanical responses which are attractive for applications, prototyping and realization of tensegrity metamaterials are challenging, since they are largely composed of tension-only prestressed cables [13]. Taking the cue from the study reported in [14], where bistable lattices with tensegrity architecture were designed, fabricated at the microscale using multiphoton lithography, and subsequently subjected to loading-unloading compression testing, in this work we aimed at showing that similar structures can be realized at higher scales with relatively inexpensive additive manufacturing techniques, such as fused deposition modeling (FDM), in order to obtain lattice metamaterials with customizable nonlinear response, possessing no cables and no prestress. We considered one of the systems analyzed in [14], a double-T3 structure, and we fabricated it by FDM after redesigning its geometry. More specifically, the system was conceived as a compliant mechanism by realizing nodal member connections as flexible hinges [15, 16]. The fabricated structure was then subjected to compression testing for determining its static response. The results of this test were used to validate a Stick-and-Spring reduced-order model of the structure [17, 18] and its predictions. The validated model was then used to perform impact dynamics simulations on lattice columns composed of T3 units.

This paper is organized as follows. After outlining the basic properties of tensegrity systems which can be inherited by tensegrity-like lattices in Section 2, the additive manufacturing process and compression testing results are described in Section 3. Afterward, the reduced-order Stick-and-Spring model, and the results of corresponding static and dynamic simulations are presented in Section 4, while our concluding remarks follow in Section 5.

2 NONLINEAR LATTICES WITH TENSEGRITY ARCHITECTURE

Tensegrity structures are prestressed pin-connected frameworks composed of cables and bars, which in many instances possess internal mechanisms stabilized by their prestress state. In these cases, the mechanical response is mainly geometrical, that is, it is associated to large configuration changes. The two-bar system depicted in Fig. 1(a) exemplifies this situation. In the reference configuration (in black in Fig. 1(a)), the two bars are aligned and subjected to a tensile prestressing axial force. The relation between the vertical load F and the corresponding displacement δ is well approximated by a cubic whose slope in the origin, $\tan \alpha$, is directly proportional to the prestressing axial force, while a stiffening effect can be observed when F

increases.

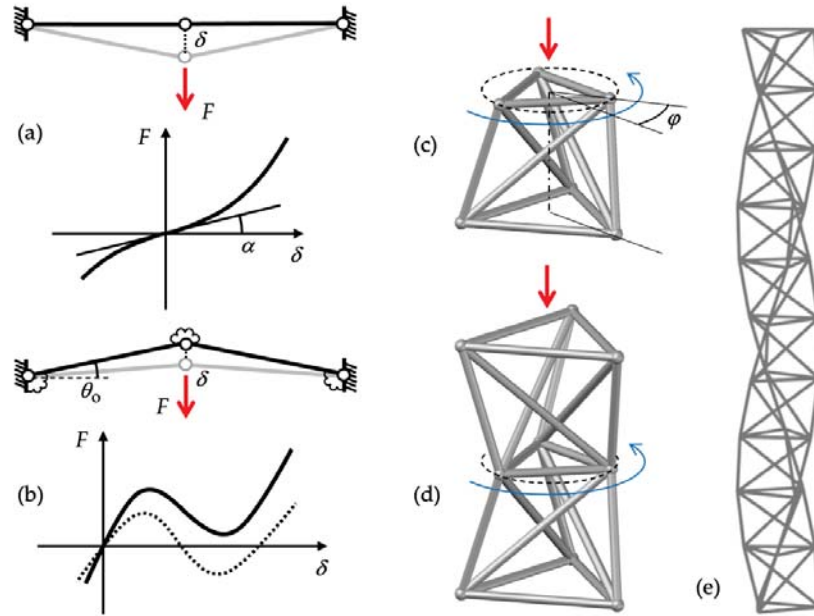


Figure 1: Nonlinear lattices with tensegrity architecture. Two-bar systems with stiffening response (a). Two-bar system with snapping response (b). Single unit (c) and double unit (d) subjected to a vertical load. Column composed of several units (e).

For the two-bar system in Fig. 1(b), the reference configuration is slightly misaligned and unstressed, with each bar inclined by an angle θ_0 . Bars are inflexible and unshearable, while remaining elastically extensible, and additional angular linearly elastic springs respond to changes in angle at nodes. Such angular springs account for the fact that the fabricated structures are monolithic, and bars nodal connections are realized as compliant hinges. If the elastic constant of rotational springs is null, this system constitutes a classic example of bistable snapping system (dotted curve in the F -vs- δ plot in Fig. 1,b). When the elastic constants take positive values in a certain range, the system has just one stable configuration in absence of loads, while retaining a snapping response (solid curve in the F -vs- δ plot in Fig. 1,b).

Figure 1(c) shows a truss unit shaped as a T3 tensegrity system subjected to a vertical load, and the associated deformation mode, in which a relative rotation between the top and bottom bases occurs. The properties of such system depend on the initial twist angle φ between the top and bottom bases. When $\varphi = \pi/6$, the system behaves similarly to the two-bar system in Fig. 1(a) with null prestress [4]. When $\varphi = \pi/6 + \theta_0$, with $\theta_0 < 0$ a small overtwist angle, the system behaves similarly to the two-bar system in Fig. 1(b). Figure 1(d) shows a truss shaped as a double T3 system, obtained by assembling together two mirror images of the unit shown in Fig. 1(c) [14]. In this way, under a vertical force, the relative rotations between the bases of the units compensate each other, and in the resulting deformation mode, the top and bottom bases undergo just a vertical relative displacement, and only the middle base rotates. Several units can be assembled together in columns (Figure 1,e) so as to realize periodic lattices supporting the propagation of solitary or compact waves [12, 14].

3 ADDITIVE MANUFACTURING AND EXPERIMENTAL TESTING

The geometry of the double unit is shown in Fig. 2 (left, center). The top and bottom triangular bases are inscribed in circles of radius $a = 40$ mm, while $b = 30$ mm is the corresponding radius for the middle triangle. Each unit has height $h = 60$ mm, and overtwist angle $\theta_0 = -7$ degrees. Nodes were realized as spheres of diameter $d_s = 6$ mm; the bars forming the bottom, middle, and horizontal triangles are realized with a solid circular cross section of diameter $d_b = 4$ mm. The bars placed between the top and middle triangles, and between the middle and bottom triangle, are subdivided into three segments: the bar main body, with same cross section as mentioned above, and two terminal links to form the connections with nodal spheres. The terminal links have a solid circular cross section of diameter $d_l = 2.2$ mm, and net length $l_l = 4.7$ mm.

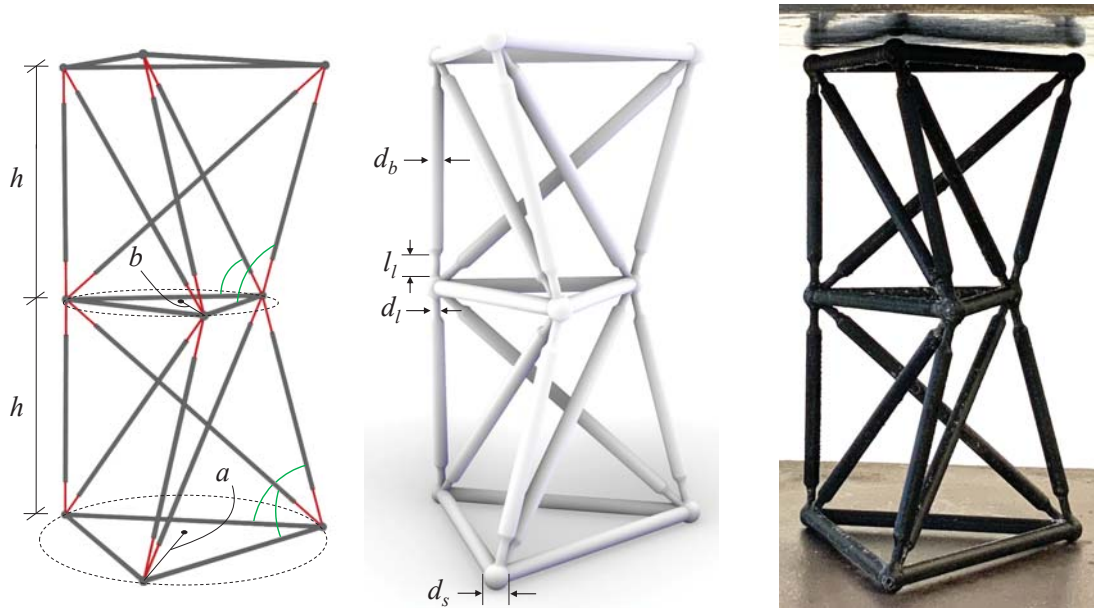


Figure 2: Geometry of a double unit and fabricated sample.

Test samples were fabricated by FDM using the UltimakerTM S5 dual extruder 3D printer, employing the Ultimaker Cura slicing software. The material chosen for the samples is polylactic acid (PLA Tough Ultimaker), while polyvinyl alcohol (PVA Ultimaker) has been used as water-soluble support material for fabrication. Figure 3(a) displays the fabrication process preview and main setup parameters in Cura, while Figure 3(b) shows one sample immediately after the fabrication process.

After removal of the supporting material, samples were subjected to a quasi-static displacement-control compression test. An Instron 4482 testing machine, equipped with a 10 kN load cell, was employed to carry out the experiments, setting a testing speed of 1 mm/min. Data were collected with an acquisition frequency of 20 Hz, while the test was recorded with a camera sampling rate of 60 fps at 1080 p resolution. The recorded motion of the structure and the force-vs-displacement curve depicted in Fig. 4 confirm the expected snapping behavior of the double unit.

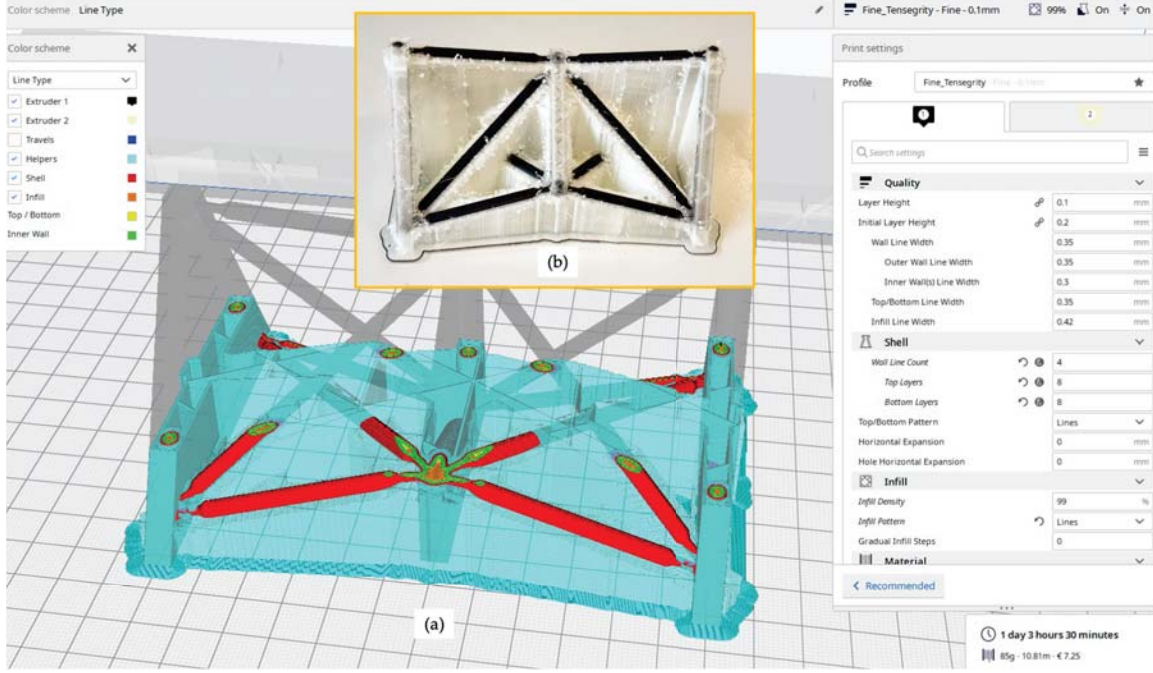


Figure 3: Fabrication preview display in Ultimaker Cura (a), and sample before removal of the supporting PVA (b).

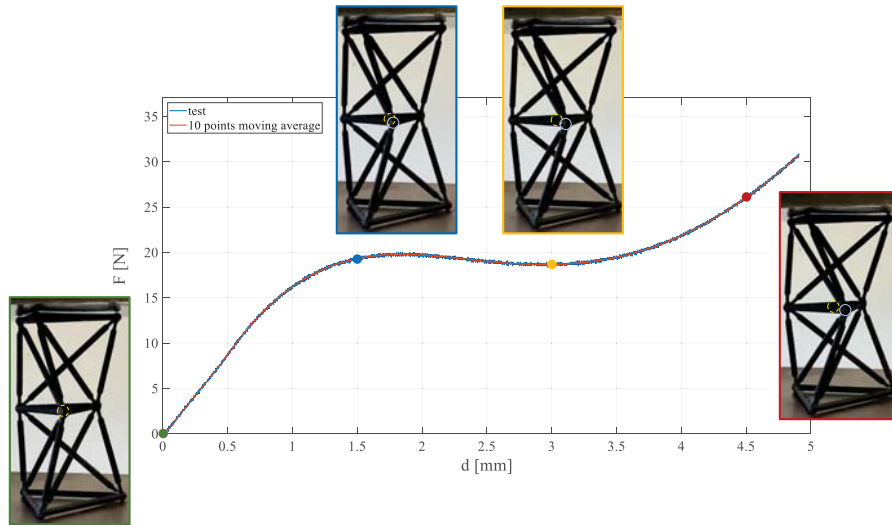


Figure 4: Compression testing results: force-vs-displacement curve.

4 NUMERICAL SIMULATIONS

We consider a Stick-and-Spring model [17, 18] in which bars are extensible but otherwise undeformable, behaving as axial springs, and equipped with angular springs responding to changes in angle between pairs of adjacent bars. Figure 2 (left) shows the location of such angular springs (green arcs, symmetric copies not shown). The axial spring constants for the bars of the horizontal triangles are computed as EA/l_f , with E the Young's modulus, A the cross-sectional area, and l_f their fabrication length (inter-nodal distance). For the remaining bars, equivalent

axial spring constants are computed considering each of them composed of three springs in series, corresponding to the three segments (two terminal links and the central bar body) they are divided in, taking into account cross-sectional area and length of each segment. Angular springs account for the bending stiffness of the terminal links, and their spring constants are computed as EJ/l_l , with J the inertia moment of the cross section and l_l the link fabrication length.

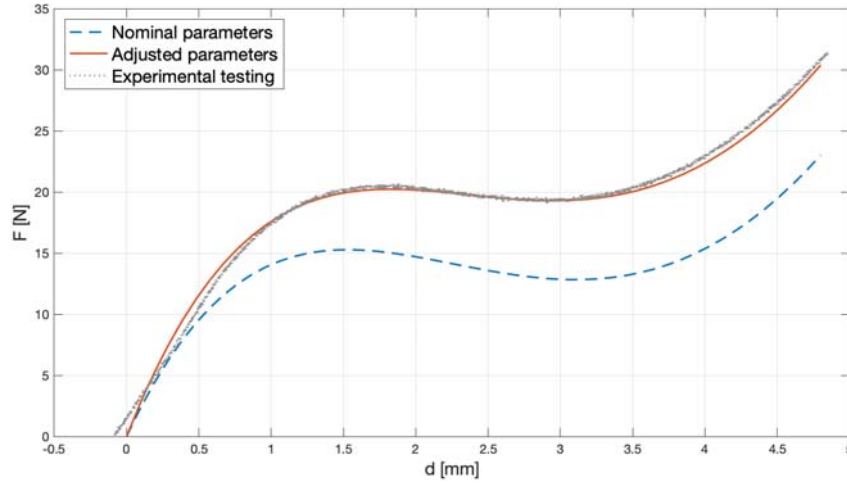


Figure 5: Test-vs-simulation results comparison.

Displacement-control numerical simulations were carried out in a regime of large displacements and rotations by imposing the vertical relative displacement between the top and bottom bases, and by computing the balancing nodal forces applied to them. In calculations, we considered the value $E = 1820$ MPa for the Young's modulus, as given in the Ultimaker PLA Tough specifications. Figure 5 compares simulation results to experimental ones, and it can be observed that the simulated curve follows the experimental one qualitatively when nominal values of the geometric parameters are considered. By adjusting slightly simulation parameters, setting $\theta_0 = -7.25$ degrees, $d_l = 2.5$ mm, $l_l = 5.0$ mm (nominal values, $\theta_0 = -7.00$ degrees, $d_l = 2.2$ mm, $l_l = 4.7$ mm), the simulated curve can be brought to be almost superposed to the numerical curve.

Impact dynamics simulations were carried out on arrays composed of several units with constant base radius a (Fig. 1,e), by integrating the equations of motion written for Stick-and-Spring model [18], considering nodal lumped masses $m = 0.01$ kg. Figure 6 shows simulation results for an array of 20 units, in which the rightmost base is fixed, while the leftmost base is imposed a longitudinal velocity $v_0 = 2$ m/s, and an angular velocity about the longitudinal axis $\omega = 150$ rad/s, so as to trig the snapping of the leftmost unit. The nodal speed v_n at each triangular base is represented in Fig. 6 at three time instants, showing a localized wave propagating along the array.

5 CONCLUSIONS

In this work, we showed that lattice metamaterials with tensegrity architecture and a highly nonlinear behavior can be effectively fabricated by simple additive manufacturing techniques, such as FDM, and that these types of nonlinear lattice units can constitute the building blocks of three-dimensional arrays with a customized mechanical response. In particular, we redesigned the double unit with snapping behavior studied in [14] by reducing bars cross section near

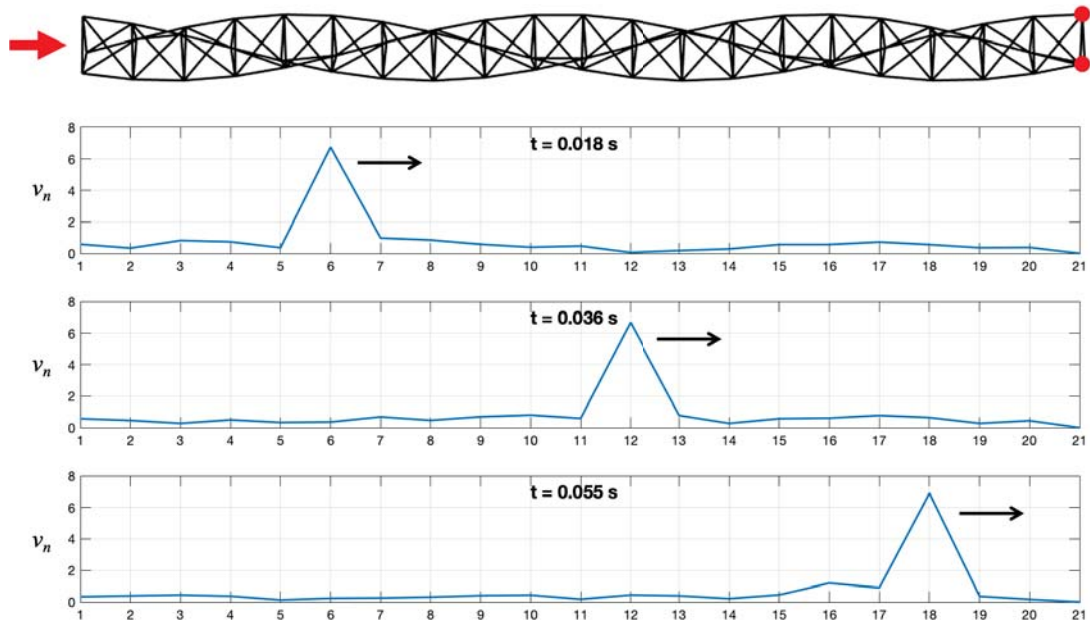


Figure 6: Impact dynamics simulation on an array of 20 units: profile of the nodal speed (m/s).

the nodes, so as to obtain an easy-to-model compliant mechanism. Fabricated samples were subjected to compression tests which confirmed the snapping behavior. The static response of the double unit was accurately simulated by calibrating a Stick-and-Spring numerical model. Such calibrated model was then employed for predicting the dynamical response of an array of several units subjected to impact loading, confirming that these type of systems support the propagation of solitary or compact waves, and that they can be realized by additive manufacturing techniques. These results can be extended to other types of tensegrity architectures and fabrication techniques to widen the range of mechanical behaviors achievable by lattice meta-materials.

ACKNOWLEDGEMENTS

A.M., C.I., N.N., E.A., and P.B. acknowledge financial support from the Italian Ministry of Education, University, and Research (MIUR) under the PRIN 2017 National Grant "3D printing: a bridge to the future" (grant number 2017L7X3CS_004).

REFERENCES

- [1] Z. Liu, X. Zhang, Y. Mao, Y. Y. Zhu, Z. Yang, C. T. Chan, P. Sheng, Locally resonant sonic materials. *Science*, **289**, 1734–1736, 2000.
- [2] L.R. Meza, S. Das, J.R. Greer, Strong, lightweight, and recoverable three-dimensional ceramic nanolattices, *Science*, **345**, 1322–1326, 2014.
- [3] S. Walia, C.M. Shah, P. Gutruf, H. Nili, D.R. Chowdhury, W. Withayachumnankul, M. Bhaskaran, and S. Sriram, Flexible metasurfaces and metamaterials: A review of materials and fabrication processes at micro- and nano-scales. *Applied Physics Reviews*, **2**(1), 011303, 2015.

- [4] I.J. Oppenheim, W.O. Williams, Geometric Effects in an Elastic Tensegrity Structure, *J. Elasticity* **59**, 51–65, 2000.
- [5] Oppenheim, I.J., Williams, W.O. Vibration of an Elastic Tensegrity Structure, *Eur. J. Mech. A* **20**, 1023–1031, 2001.
- [6] F. Fraternali, G. Carpentieri, A. Amendola, On the mechanical modeling of the extreme softening/stiffening response of axially loaded tensegrity prisms. *J. Mech. Phys. Solids*, **74**, 136–157, 2014, 2015.
- [7] A. Amendola, G. Carpentieri, M. De Oliveira, R.E. Skelton, F. Fraternali, Experimental investigation of the softening-stiffening response of tensegrity prisms under compressive loading. *Compos. Struct.* **117**, 234–243, 2014.
- [8] A. Micheletti, Bistable regimes in an elastic tensegrity system. *Proc. R. Soc. A*, **469**, 2013.
- [9] F. Fraternali, L. Senatore, C. Daraio, Solitary waves on tensegrity lattices. *Journal of the Mechanics and Physics of Solids*, **60**, 1137–1144, 2012.
- [10] F. Fraternali, G. Carpentieri, A. Amendola, R.E. Skelton, V.F. Nesterenko, Multiscale tunability of solitary wave dynamics in tensegrity metamaterials. *Applied Physics Letters*, **105**, 201903, 2014.
- [11] C. Davini, A. Micheletti, P. Podio-Guidugli, On the impulsive dynamics of T3 tensegrity chains, *Meccanica*, **51**, 2763–2776, 2016.
- [12] A. Micheletti, G. Ruscica, F. Fraternali, On the compact wave dynamics of tensegrity beams in multiple dimensions. *Nonlinear Dynamics*, **98**, 2737–2753, 2019.
- [13] A. Amendola, E.H. Nava, R. Goodall, I. Todd, R.E. Skelton, F. Fraternali, On the additive manufacturing and testing of tensegrity structures. *Compos. Struct.*, **131**, 66–71, 2015.
- [14] Z. Vangelatos, A. Micheletti, C.P. Grigoropoulos, F. Fraternali, Design and testing of bistable lattices with tensegrity architecture and nanoscale features fabricated by multi-photon lithography. *Nanomaterials*, **10**(4), 652, 2020.
- [15] L.L. Howell, Compliant Mechanisms. In: McCarthy J. eds. *21st Century Kinematics*. Springer, 2013.
- [16] M.S. Baker, L.L. Howell, On-chip actuation of an in-plane compliant bistable micromechanism. *Journal of microelectromechanical systems*, **11**(5), 566–573, 2002.
- [17] A. Favata, A. Micheletti, P. Podio-Guidugli, A Nonlinear Theory of Prestressed Elastic Stick-and-Spring Structures, *International Journal of Engineering Sciences*, **80**, 4–20, 2014.
- [18] A. Amendola, A. Favata, A. Micheletti, On the mechanical modeling of tensegrity columns subject to impact loading. *Frontiers in Materials*, **5**, 1–22, 2018.

A DYNAMIC-STIFFNESS APPROACH FOR DAMPED LOCALLY-RESONANT TIMOSHENKO BEAMS

A.F. Russillo¹, G. Failla¹, A. Pirrotta² and F. Fraternali³

¹University of Reggio Calabria
Via Graziella, Località Feo di Vito, 89124 Reggio Calabria, Italy
e-mail: {andrea.f.russillo, giuseppe.failla}@unirc.it

² University of Palermo
Viale delle Scienze, 90100 Palermo
e-mail: antonina.pirrotta@unipa.it

³ University of Salerno
Via Giovanni Paolo II, 132, Fisciano, 94084 Salerno
e-mail: f.fraternali@unisa.it

Keywords: Local Resonance, Timoshenko Beam, Dynamic-Stiffness Matrix, Contour-Integral Algorithm

Abstract. *A dynamic-stiffness matrix approach is presented for locally-resonant Timoshenko beams with a periodic array of viscously-damped multi-degree-of-freedom resonators. First, an exact dynamic condensation of the resonator degrees of freedom is pursued, expressing the resonator reaction forces in terms of the deflections of the attachment points via pertinent frequency-dependent stiffness terms. On this basis, a direct integration deriving from the theory of generalized functions provides the exact dynamic-stiffness matrix of the beam, whose size is 4×4 for any the number of resonators and degrees of freedom within the resonators. The dynamic-stiffness matrix is used to calculate the complex eigenvalues of the beam by a recently introduced contour-integral algorithm, without missing anyone. Further, it provides the transmittance for an insight into the elastic wave attenuation properties of the beam.*

1 INTRODUCTION

A great deal of attention was devoted in the last decade to the concept of locally-resonant (LR) beams, i.e. beams coupled with a periodic array of resonators with one or multiple degrees of freedom (DOFs). Indeed, as a result of the periodic resonance induced by the resonators, these beams exhibit considerable mitigation properties of elastic waves over so called frequency band gaps, whose position and amplitude determined by mass, stiffness and mutual distance of the resonators. The typical model of LR beam adopted in the literature involves Euler-Bernoulli or Timoshenko continuous beams coupled with mass-spring subsystems modelling the resonators. Several numerical studies confirmed by experimental results were published in this respect [1, 2, 3, 4, 5, 6, 7, 8, 9].

Here, the focus is on LR Timoshenko beams, when viscous damping is present within the resonators. The exact dynamic-stiffness matrix (DSM) of the beam is obtained with size 4×4 for any the number of resonators and DOFs within the resonators using, for this purpose, (1) a dynamic condensation of the DOFs within the resonators to express their reaction forces in terms of pertinent frequency-dependent stiffness terms and (2) a direct integration of the beam motion equations based on the theory of generalized functions. The DSM is used to compute the complex eigenvalues of the beam by a recently introduced contour-integral algorithm. The interest in the proposed approach is twofold. The dynamic-stiffness formulation involves a reduced number of variables compared with a standard finite-element (FE) approach while the contour-integral algorithm proves successful in evaluating all complex eigenvalues, without missing anyone, with remarkable computational efficiency. Additionally, the dynamic-stiffness matrix allows a straightforward evaluation of the transmittance of the beam, for an insight into its elastic wave attenuation properties due to local resonance.

2 DYNAMIC-STIFFNESS MATRIX FORMULATION

Consider the beam in Figure 1 under harmonic loads $p_v(x, t) = f_v(x)e^{i\omega t}$ and $p_\phi(x, t) = f_\phi(x)e^{i\omega t}$. Using generalized functions, the motion equations in the frequency domain are:

$$GA \left(\frac{\bar{d}^2 V}{dx^2} + \frac{\bar{d}\Phi}{dx} \right) + \rho A \omega^2 V + \sum_{j=1}^N R_j \delta(x - x_j) + f_v = 0 \quad (1)$$

$$EI \frac{\bar{d}^2 \Phi}{dx^2} - GA \left(\frac{\bar{d}V}{dx} + \Phi \right) + \rho I \omega^2 \Phi + f_\phi = 0 \quad (2)$$

where bar means generalized derivative and R_j is the reaction force of the j^{th} resonator, given as

$$R_j = -k_{eq}(\omega)V(x_j) \quad (3)$$

In Eq. (3), $k_{eq}(\omega)$ is the frequency-dependent stiffness of the resonator, which can be obtained from its motion equations by an exact dynamic condensation in the frequency domain. For instance, for a mass-spring-dashpot resonator

$$k_{eq}(\omega) = \frac{(k + i c \omega) m \omega^2}{k + i c \omega - m \omega^2} \quad (4)$$

where k , c and m are the spring stiffness, damping coefficient and mass of the resonator. Analytical expressions for the frequency-dependent stiffness are available also for various types of multi-DOF resonators, see ref. [1].

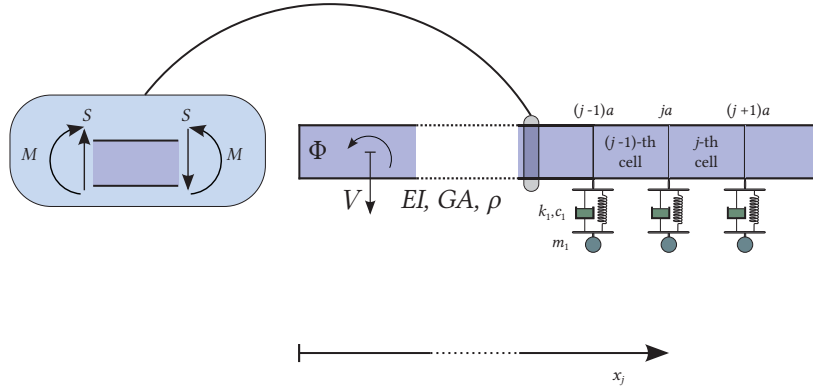


Figure 1: LR Timoshenko beam with 1-DOF viscous resonators.

The solution is built observing that Eqs. (1)-(2) can be reverted to two decoupled 4th order differential equations only, whose general form is:

$$\frac{\bar{d}^4 Z}{dx^4} + p_1 \frac{\bar{d}^2 Z}{dx^2} + p_2 Z + p_3 = 0 \quad (5)$$

In Eq. (5), symbol Z stands for either V (deflection) or Φ (rotation); symbols p_1 and p_2 are defined as

$$p_1 = \left(\frac{\rho EI \omega^2}{G} + \rho I \omega^2 \right) / EI \quad (6)$$

$$p_2 = \left(\frac{\rho^2 I \omega^4}{G} - \rho A \omega^2 \right) / EI \quad (7)$$

and p_3 denotes the following functions:

$$p_3 = \begin{cases} \frac{1}{GA} \left(\frac{\bar{d}^2 q}{dx^2} + \frac{\bar{d}^2 f_v}{dx^2} \right) + \left(\frac{\rho \omega^2}{EGA} - \frac{1}{EI} \right) (q + f_v) - \frac{1}{EI} \frac{\bar{d} f_\phi}{dx} & \text{if } Z = V \\ -\frac{1}{EI} \left(\frac{\bar{d}^2 f_\phi}{dx^2} + \frac{\rho \omega^2}{G} f_\phi + \frac{\bar{d} f_v}{dx} + \frac{\bar{d} q}{dx} \right) & \text{if } Z = \Phi \end{cases} \quad (8)$$

Recognize that f_v and f_ϕ in Eq. (8) the spatial load functions in Eqs. (1)-(2) while q depends on the reaction forces R_j in Eq. (1), i.e.

$$q = \sum_{j=1}^N R_j \delta(x - x_j) \quad (9)$$

The solution of Eq. (5) is

$$Z = Z_{om} + \sum_{j=1}^N R_j J_{Z,j} + \tilde{Y}_Z^{(f)} \quad (10)$$

whose details are given in Appendix A for brevity.

Now, using $Z = V$ given by Eq. (10) for $V(x_j)$ in Eq. (3), it is noticed that every reaction force R_j depends only on the 4 integration constants $c_{i,0}$ involved in Z_{om} and the reaction forces R_k at $x_k < x_j$. This means that all the reaction forces R_j can be expressed as functions of $c_{i,0}$, providing the frequency response function (FRF) vector $\mathbf{Y}(x, \omega)$

$$\mathbf{Y}(x, \omega) = \mathbf{W}(x, \omega) \mathbf{c}_0 + \mathbf{Y}^{(f)}(x, \omega) \quad (11)$$

In Eq. (11), \mathbf{W} is a 4×4 matrix involving the solution of the homogeneous equation associated with Eq. (5), $\mathbf{c}_0 = [c_{1,0} \ c_{2,0} \ c_{3,0} \ c_{4,0}]^T$, $\mathbf{Y}^{(f)}$ is a 4×1 load-dependent vector. Elements in \mathbf{W} and $\mathbf{Y}^{(f)}$ are available in analytical form, see Appendix A for conciseness; in particular, here they are given for arbitrary polynomial loading functions f_v and f_ϕ . Vector \mathbf{c}_0 in Eq. (11) is derived by enforcing the beam boundary conditions (B.C.), i.e.

$$\mathbf{B}\mathbf{c}_0 = \mathbf{e} \rightarrow \mathbf{c}_0 = \mathbf{B}^{-1}\mathbf{e} \quad (12)$$

where \mathbf{B} and \mathbf{e} are a 4×4 matrix and 4×1 vector, built from \mathbf{W} and $\mathbf{Y}^{(f)}$ computed at $x = 0$ and $x = L$. The inverse matrix \mathbf{B}^{-1} takes a closed analytical form, as shown in ref. [10]. Hence, replacing Eq. (12) for \mathbf{c}_0 in Eq. (11) provides an analytical expression for the FRF vector $\mathbf{Y}(x, \omega)$ of the beam in Figure 1, which can be implemented in any symbolic software package.

Eq. (11) is an exact analytical expression for the FRF vector $\mathbf{Y}(x, \omega)$. It holds for any number of resonators and DOFs within the resonators, any loads and positions of the loads relative to the resonators, with significant advantages w.r.t. to the FE method where the mesh has to be chosen depending also on the applied loads.

Here, Eq. (11) is used for two purposes. First, Eq. (11) is used to build the exact DSM $\mathbf{D}(\omega)$ of the beam, adopting the method in ref. [10]. Specifically, the procedure provides $\mathbf{D}(\omega)$ in exact analytical form and its size depends only on the number of DOFs at the beam ends, regardless of the number of resonators and number of DOFs within the resonators. Second, Eq. (11) can be used to calculate the transmittance of a cantilever beam [11, 12]. In this case, being $V_g e^{i\omega t}$ the harmonic deflection at the clamped end $x = 0$, $V(x)$ in Eqs.(1)-(2) is the beam deflection relative to the ground and transverse load $f_v = \rho A \omega^2 V_g$ is included in Eq. (1); accordingly

$$R_j = -k_{eq}(\omega)(V(x_j) + V_g) \quad (13)$$

while the B.C. are

$$V(0) = 0 \quad \Phi(0) = 0 \quad M(L) = 0 \quad T(L) = 0 \quad (14)$$

Using Eq. (13), changes to matrix \mathbf{W} and vector $\mathbf{Y}^{(f)}$ reported in Appendix A for Eq. (11) are simple. The transmittance is $|V(L) + V_g|/V_g$.

3 CONTOUR-INTEGRAL ALGORITHM FOR EIGENVALUE CALCULATION

Computing the complex eigenvalues for the LR Timoshenko beam under study, without missing anyone and with the required accuracy, is a particularly challenging task since several modes are expected to be close to each other, as a result of local resonance [17, 18, 19].

Specifically, the eigenvalues are calculated by the following key steps [17, 18, 19]:

1. Select a circle $\Gamma = \gamma_0 + \rho_0 e^{i\theta}$ on the complex plane with center γ_0 , radius ρ_0 and $0 \leq \theta \leq 2\pi$.
2. Compute two complex random source matrices \mathbf{U} and \mathbf{V} with dimensions $n_0 \times L_0$, being n_0 the size of the DSM $\mathbf{D}(\omega)$ and L_0 the number of source vectors in \mathbf{U} and \mathbf{V} .
3. Calculate the shifted and scaled moments \mathbf{M}_k using a N_0 -point trapezoidal rule:

$$\mathbf{S}_k = \frac{1}{N_0} \sum_{j=0}^{N_0-1} \left(\frac{\eta_j - \gamma_0}{\rho_0} \right)^{k+1} \mathbf{D}(\eta_j)^{-1} \mathbf{V}, \quad k = 0, 1, \dots, 2K-1$$

$$\mathbf{M}_k = \mathbf{U}^H \mathbf{S}_k$$

where $\eta_j = \gamma_0 + \rho_0 \exp 2\pi i(j + 1/2)/N_0$ for $j = 0, 1, \dots, N_0 - 1$, K is the maximum moment degree assumed for the moment and \mathbf{U}^H denotes the Hermitian transpose of \mathbf{U} .

4. Construct of the Hankel matrices $\hat{\mathbf{H}}_{KL_0}$ and $\hat{\mathbf{H}}_{KL_0}^< \in \mathbb{C}^{KL_0 \times KL_0}$ so that:

$$\hat{\mathbf{H}}_{KL_0} = [\mathbf{M}_{i+j-2}]_{i,j=1}^K \quad \hat{\mathbf{H}}_{KL_0}^< = [\mathbf{M}_{i+j-1}]_{i,j=1}^K$$

5. Carry out a singular value decomposition of $\hat{\mathbf{H}}_{KL_0}$.
6. Eliminate small singular value components $\sigma_i < \epsilon \cdot \max_i \sigma_i$, set \tilde{m} as the number of remaining singular value components ($\tilde{m} < KL_0$) and build $\hat{\mathbf{H}}_{\tilde{m}}$ and $\hat{\mathbf{H}}_{\tilde{m}}^<$ extracting the principal submatrix with maximum index \tilde{m} from $\hat{\mathbf{H}}_{KL_0}$ and $\hat{\mathbf{H}}_{KL_0}^<$, that is

$$\hat{\mathbf{H}}_{\tilde{m}} = \hat{\mathbf{H}}_{KL_0}(1 : \tilde{m}, 1 : \tilde{m}); \quad \hat{\mathbf{H}}_{\tilde{m}}^< = \hat{\mathbf{H}}_{KL_0}^<(1 : \tilde{m}, 1 : \tilde{m})$$

7. Calculate the eigenvalues ζ_j of the linear pencil:

$$\hat{\mathbf{H}}_{\tilde{m}}^< = \zeta \hat{\mathbf{H}}_{\tilde{m}}$$

8. Compute the eigenvalues

$$\omega_j = \gamma_0 + \rho_0 \zeta_j, \quad j = 1, \dots, \tilde{m}$$

The algorithm captures all the eigenvalues ω_j falling within the selected circle Γ , including multiple ones [17, 18, 19]. Circles of increasing radius and centred at the origin can be considered to explore the whole complex plane and calculate all the requested eigenvalues.

The accuracy of the algorithm is determined by the selection of the parameters K , L_0 , N_0 . The maximum moment degree K can be set at least equal to $N_0/4$ [20], while the minimum number of source vectors L_0 is such that $\sigma_{\min}/\sigma_1 < \epsilon$ with small $\epsilon > 0$; the number of quadrature points N_0 determines the quadrature error and can be set in advance.

The eigenfunction associated with every eigenvalue can be derived as non-trivial solution of the eigenvalue problem involving the DSM $\mathbf{D}(\omega)$, as evaluated for that eigenvalue [10].

4 NUMERICAL APPLICATION

Focus on the cantilever LR Timoshenko beam with 1-DOF resonators in Figure 2. Parameters of the beam are: $E = 30 \times 10^9 \text{ N m}^{-2}$; $G = 11.53 \times 10^9 \text{ N m}^{-2}$; $\rho = 2500 \text{ kg m}^{-3}$; $a = 0.125 \text{ m}$, $N = 8$ is the number of the resonators, $L = 1.0 \text{ m}$ is the beam length. Further, the parameters of the resonators are $k = 1 \times 10^5 \text{ N m}^{-1}$, $c_1 = 0.01 \text{ N s m}^{-1}$, $m_1 = 0.1 \text{ kg}$.

Table 1 shows the first 13 complex eigenvalues, as computed from the proposed DSM approach via the contour-integral algorithm, along with the corresponding ones obtained by a standard FE model, implemented in ABAQUS employing a two-node shear-deformable linear FE for every beam segment between two resonators. Specifically, $K = 20$, $L_0 = 30$ (with $\epsilon = 10^{-10}$) and $N_0 = 700$ are selected for the implementation of the contour-integral algorithm (to calculate every eigenvalue, regardless of its position on the complex plane), while an automatic multi-level substructuring eigensolver is used in ABAQUS. The results in Table 1 are in excellent agreement, confirming the accuracy of the DSM approach. Further, the eigenvalue calculation via contour-integral algorithm is very expeditious, with savings up to 30 % – 40 % with respect to the eigenvalue calculation in ABAQUS.

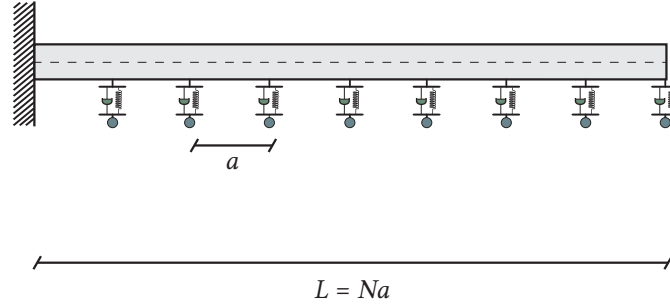


Figure 2: Cantilever LR Timoshenko beam hosting viscously-damped 1-DOF resonators.

Mode	Eigenvalue ($\cdot 10^4$) [DSM]			Eigenvalue ($\cdot 10^4$) [FE]		
1	± 68.39	+	0.000i	± 68.38	+	0.000i
2	± 410.86	+	0.001i	± 410.86	+	0.001i
3	± 846.54	+	0.023i	± 846.55	+	0.023i
4	± 962.77	+	0.043i	± 962.77	+	0.043i
5	± 986.62	+	0.047i	± 986.62	+	0.047i
6	± 993.74	+	0.049i	± 993.74	+	0.049i
7	± 996.37	+	0.049i	± 996.37	+	0.049i
8	± 997.39	+	0.049i	± 997.39	+	0.049i
9	± 1245.36	+	0.076i	± 1245.39	+	0.076i
10	± 1348.97	+	0.082i	± 1348.99	+	0.082i
11	± 1826.05	+	0.064i	± 1826.12	+	0.064i
12	± 3106.14	+	0.043i	± 3106.85	+	0.043i
13	± 4956.25	+	0.039i	± 4956.87	+	0.039i

Table 1: Complex eigenvalues of the cantilever LR Timoshenko beam in Figure 2 computed by the proposed DSM approach and the FE method in ABAQUS.

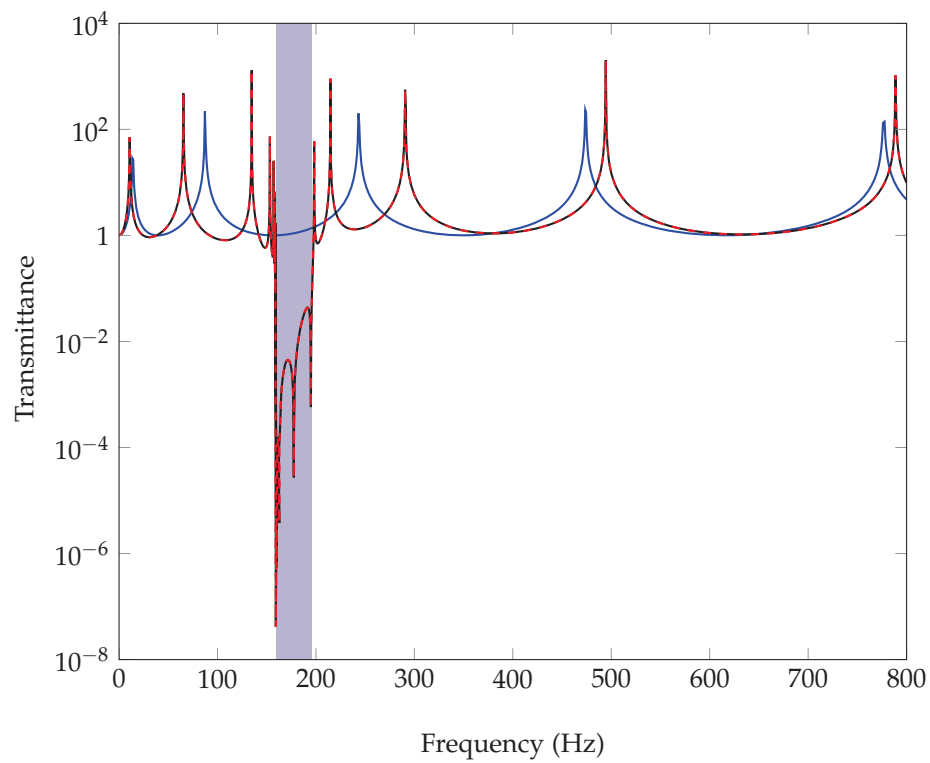


Figure 3: Transmittance of the cantilever LR Timoshenko beam in Figure 2: exact response without resonators (blue continuous line); exact response with resonators by the proposed DSM approach (black continuous line) and corresponding FE response in ABAQUS (red dashed line).

5 CONCLUSIONS

Here, a DSM approach has been presented to calculate complex eigenvalues and frequency response of LR Timoshenko beams, featuring a periodic array of viscously-damped multi-DOF resonators. The approach relies on an exact dynamic condensation of the resonator DOFs and a direct integration approach based on the theory of generalized functions, which provide the exact DSM of the beam with size 4×4 for any number of resonators and DOFs within the resonators. The DSM has been used to evaluate the complex eigenvalues, without missing anyone, by a contour-integral algorithm of remarkable accuracy and, additionally, to evaluate the transmittance of the beam.

6 Appendix A

This Appendix contains various formulas and expressions referred to in the main text.

In Eq. (10), Z_{om} is the solution of the homogeneous differential equation associated with Eq. (5), i.e.

$$Z_{om}(x) = \sum_{i=1}^4 c_{i,0} \alpha_i e^{\lambda_i x} \quad (15)$$

where $c_{i,0}$ are integration constants, λ_i are

$$\lambda_{1,2} = \mp \left(\left(-p_1 - \sqrt{p_1^2 - 4p_2} \right) / 2 \right)^{1/2} \quad (16)$$

$$\lambda_{3,4} = \mp \left(\left(-p_1 + \sqrt{p_1^2 - 4p_2} \right) / 2 \right)^{1/2} \quad (17)$$

and the coefficients α_i are

$$\alpha_i = \begin{cases} 1 & \text{if } Z = \Phi \\ -\frac{GA\lambda_i}{\rho A \omega^2 + GA\lambda_i^2} & \text{if } Z = V \end{cases} \quad (18)$$

Further, $J_{Z,j} = J_Z(x, x_j)$ in Eq. (10) is the particular integral of Eq. (5) that is associated with the Dirac's delta $\delta(x - x_j)$ and its derivatives (see Eq. (8) and Eq. (9)). Based on the approach in ref. [16], $J_Z(x, x_j)$ can be obtained via direct and inverse Laplace Transforms of Eq. (5), on setting $f_v = f_\phi = 0$ in p_3 given by Eq. (8). Specifically, $J_V(x, x_j)$ is

$$J_V(x, x_j) = -(\sqrt{2}GA\Sigma_1)^{-1} [B \sinh(C(x - x_j)) + D \sinh(E(x - x_j))] \mathcal{H}(x - x_j) \quad (19)$$

for

$$\begin{aligned} B &= \left(\sqrt{2}C \right)^{-1} [\Sigma_1 + \Sigma_2 - 2(GA)^2] \\ C &= ((\Sigma_1 - \Sigma_3) / (2EI GA))^{1/2} \\ D &= -\left(\sqrt{2}C \right)^{-1} [\Sigma_1 - \Sigma_2 + 2(GA)^2] \\ F &= -(\Sigma_1 + \Sigma_3) / (2EI GA)^{1/2} \\ \Sigma_1 &= [(EI)^2(\rho A)^2\omega^4 + 2EIGA\rho A\omega^2 (2GA - I\rho\omega^2) \\ &\quad + (GA)^2 I^2 \rho^2 \omega^4]^{1/2} \\ \Sigma_2 &= GAI\rho\omega^2 - EI\rho A\omega^2 \quad \Sigma_3 = GAI\rho\omega^2 + EI\rho A\omega^2 \end{aligned} \quad (20)$$

being $\mathcal{H}(x) = 1$ if $x > 0$ and $\mathcal{H}(x) = 0$ if $x < 0$. Also, $J_\Phi(x, x_j)$ is:

$$J_\Phi(x, x_j) = -GA\Upsilon_1^{-1} \{ \cosh[S_1(x - x_j)] - \cosh[S_2(x - x_j)] \} \mathcal{H}(x - x_j) \quad (21)$$

$$\begin{aligned} S_1 &= ((\Upsilon_1 - \Upsilon_2)/(2EI GA))^{1/2} \\ S_2 &= (- (\Upsilon_1 + \Upsilon_2)/(2EI GA))^{1/2} \\ \Upsilon_1 &= \{ \rho\omega^2 [(A EI)^2 \rho\omega^2 + 2AEIGA (2GA - I\rho\omega^2)] \\ &\quad + (GA I)^2 \rho\omega^2 \}^{1/2} \\ \Upsilon_2 &= AEI\rho\omega^2 + GAI\rho\omega^2 \end{aligned} \quad (22)$$

Finally, $\tilde{Y}_Z^{(f)}(x)$ in Eq. (10) is the particular integral of Eq. (5) that is associated with the loading functions f_v and f_ϕ and their derivatives (see Eq. (8)), given as

$$\tilde{Y}_Z^{(f)}(x) = \int_0^L \tilde{J}(x, \xi) f_Z(\xi) d\xi \quad (23)$$

Based on Eq. (8), f_Z in Eq. (23) is

$$f_Z = \begin{cases} \frac{1}{GA} \left(\frac{d^2 f_v}{dx^2} \right) + \left(\frac{\rho\omega^2}{EGA} - \frac{1}{EI} \right) f_v - \frac{1}{EI} \frac{d f_\phi}{dx} & \text{if } Z = V \\ -\frac{1}{EI} \left(\frac{d^2 f_\phi}{dx^2} + \frac{\rho\omega^2}{G} f_\phi + \frac{d f_v}{dx} \right) & \text{if } Z = \Phi \end{cases} \quad (24)$$

and $\tilde{J}(x, \xi)$ is

$$\begin{aligned} \tilde{J}(x, \xi) &= \sqrt{2} \mathcal{A}_1^{-1} (\mathcal{A}_2^{-1} \sinh(2^{-1/2} \mathcal{A}_2(x - \xi)) \\ &\quad - \mathcal{A}_3^{-1} \sinh(2^{-1/2} \mathcal{A}_3(x - \xi))) \mathcal{H}(x - \xi) \end{aligned} \quad (25)$$

$$\begin{aligned} \mathcal{A}_1 &= (p_1^2 - 4p_2)^{1/2} \\ \mathcal{A}_2 &= (-p_1 - \mathcal{A}_1)^{1/2} \\ \mathcal{A}_3 &= (-p_1 + \mathcal{A}_1)^{1/2} \end{aligned} \quad (26)$$

Notice that $\tilde{J}(x, \xi)$ is the particular integral of Eq. (5) acted upon by $p_3 = \delta(x - \xi)$; its form (25) is obtained, again, by applying direct and inverse Laplace Transforms to Eq. (5).

REFERENCES

- [1] G. Failla, R. Santoro, A. Burlon, A.F. Russillo, An exact approach to the dynamics of locally-resonant beams, *Mechanics Research Communications*, **103**, 103460, 2020.
- [2] A.F. Russillo, G. Failla, On the free vibrations of locally-resonant structures. *Computers & Structures*, **241**, 106356, 2020.
- [3] Y. Xiao, J. Wen, X. Wen, Broadband locally resonant beams containing multiple periodic arrays of attached resonators, *Physics Letters A*, **376**, 1384–1390, 2012.

- [4] Y. Xiao, J. Wen, D. Yu, X. Wen, Flexural wave propagation in beams with periodically attached vibration absorbers: band-gap behavior and band formation mechanisms, *Journal of Sound and Vibration*, **332**, 867–893, 2013.
- [5] M. Modano, F. Fabbrocino, A. Gesualdo, G. Matrone, I. Farina, F. Fraternali, On the forced vibration test by vibrodyne, *Paper presented at the COMPDYN 2015 - 5th EC-COMAS Thematic Conference on Computational Methods in Structural Dynamics and Earthquake Engineering*, 209-217, 2015.
- [6] A.F. Russillo, G. Failla, F. Fraternali, Free and forced vibrations of damped locally-resonant sandwich beams. *European Journal of Mechanics, A/Solids*, **86**, 2021.
- [7] Y. Xiao, J. Wen, G. Wang, X. Wen, Theoretical and experimental study of locally resonant and Bragg band gaps in flexural beams carrying periodic arrays of beam-like resonators, *Journal of Vibration and Acoustics*, **135**, 2013.
- [8] P.F. Pai, Metamaterial-based broadband elastic wave absorber, *Journal of Intelligent Material Systems and Structures*, **21**, 517–528, 2010.
- [9] A. Casalotti, S. El-Borgi, W. Lacarbonara, Metamaterial beam with embedded nonlinear vibration absorbers, *International Journal of Non-Linear Mechanics*, **98**, 2018.
- [10] G. Failla, Stationary response of beams and frames with fractional dampers through exact frequency response functions. *Journal of Engineering Mechanics*, **143(5)**, D4016004, 2017.
- [11] G. Hu, L. Tang, R. Das, Internally coupled metamaterial beam for simultaneous vibration suppression and low frequency energy harvesting, *Journal of Applied Physics*, **123**, 055107, 2018.
- [12] Y. Liu, D. Yu, L. Li, H. Zhao, J. Wen, X. Wen, Design guidelines for flexural wave attenuation of slender beams with local resonators, *Physics Letters A*, **362**, 344–347, 2007.
- [13] D. Bestle, L. Abbas, X. Rui, Recursive eigenvalue search algorithm for transfer matrix method of linear flexible multibody systems, *Multibody System Dynamics*, **32**, 429–444, 2014.
- [14] S. Kawashima, T. Fujimoto, Vibration analysis of frames with semi-rigid connections, *Computers & Structures*, **19**, 85–92, 1984.
- [15] A. Mukherjee, S. Sarkar, A. Banerjee, Nonlinear eigenvalue analysis for spectral element method, *Computers & Structures*, **242**, 106367, 2021.
- [16] J. Wang, P. Qiao, Vibration of beams with arbitrary discontinuities and boundary conditions, *Journal of Sound and Vibration*, **308**, 12–27, 2007.
- [17] T. Sakurai, H. Sugiura, A projection method for generalized eigenvalue problems using numerical integration, *Journal of computational and applied mathematics*, **159**, 119–128, 2003.
- [18] J. Asakura, T. Sakurai, H. Tadano, T. Ikegami, K. Kimura, A numerical method for non-linear eigenvalue problems using contour integrals, *JSIAM Letters*, 52–55, 2009.

- [19] T. Ikegami, T. Sakurai, U. Nagashima, A filter diagonalization for generalized eigenvalue problems based on the Sakurai–Sugiura projection method, *Journal of Computational and Applied Mathematics*, **233**, 1927–1936, 2010.
- [20] T. Sakurai, Y. Futamura, H. Tadano, Efficient parameter estimation and implementation of a contour integral-based eigensolver, *Journal of Algorithms & Computational Technology*, **7**, 249–269, 2013.

SEISMIC METAMATERIALS WITH TENSEGRITY ARCHITECTURE

Filipe Santos^{1*}, Narinder Singh², Ada Amendola², Fernando Fraternali² and Andrea Micheletti³

¹Department of Civil Engineering
CERIS, NOVA School of Science and Technology-FCT NOVA, Universidade NOVA de Lisboa
2829-516 Caparica, Portugal
e-mail: fpas@fct.unl.pt

² Department of Civil Engineering
University of Salerno, Via Giovanni Paolo II, 132 - 84084 Fisciano (Salerno), Italy
e-mail: {snarinder, adaamendola1, f.fraternali}@unisa.it

³ Deptt. of Civil and computer Science Engineering
University of Rome, Tor Vergata, Italy
e-mail: micheletti@ing.uniroma2.it

Keywords: metamaterials, Seismic isolators, Tensegrity, Shape memory alloys.

Abstract. *The class of nonlinear metamaterials with tensegrity architecture is particularly interesting, since the mechanical behavior of such systems can be effectively adjusted by acting on internal and external prestress, as well as the usual controls of geometry, topology, and mechanical properties of the members. This work is focused on the development of 3D versions of the tensegrity braces (T-braces) recently proposed in the literature. The examined structures are aimed at forming novel seismic isolators, reinforcing seismic-resistant frames of steel and reinforced concrete buildings, as well as introducing the energy dissipation mechanisms of masonry walls, floor slabs, and junctions between seismic-resistant structures. This technology consists of lightweight and high-strength systems with re-centering capabilities formed by a variety of tensegrity systems. The tensegrity bracing systems incorporate superelastic shape memory bars/wires acting as pre-tensioned dissipative elements. The struts are prevented from buckling through the internal pretension of the braces via self-stress, and/or by contrasting them against the elements of the structure (external pre-tension). Using fractal geometry concepts, such systems can be designed through bio-inspired self-similar divisions of tensegrity brace modules to enhance both the energy dissipation capacity and the buckling resistance of the bracing system. Their development will significantly impact currently available techniques for the seismic protection of masonry and framed structures.*

1 INTRODUCTION

A novel area of research has emerged over the last few years regarding the highly non-linear dynamics of mechanical metamaterials formed by assembling tensegrity units and lumped masses [4]. Experimental and theoretical studies have shown that the geometrically non-linear response of several tensegrity units may gradually change from stiffening to softening, depending on mechanical, geometrical, and prestress variables. Such behavior, which can be dynamically tuned, supports highly-controllable bandgap and solitary wave dynamics. For this particular reason, various tensegrity devices are being designed also for seismic protection [5]. A Tensegrity System is defined as a set of rigid bodies (subject to compression) that can be stabilized (therefore balanced) by a set of cables (or tense elements), in the absence of external forces [6]. The strings are in pretension and that pretension helps the system to be in equilibrium. There are several known examples of tensegrity structures, for example in nature (the bone-tendon system), in the art (for aesthetic beauty), in architecture (for their properties). These structures are nowadays usually referred to as “mechanical metamaterials”. It has been found that linear elastic meta-materials can exhibit peculiar behaviors in the dynamical regime, like, e.g., negative effective elastic moduli, negative effective mass density, phononic band gaps, to name just a few examples [7]. The seismic response of strongly non-linear meta-materials has been particularly investigated in this article. The tensegrity structures can be 3D printed it is the system comprises of the bars and the strings. The strings are in tension and bars in compression. When we try to change the position, the strings experience some forces which put more compression on the bars and the strings face more tension. These systems which are useful in dissipating the seismic energy are called passive energy dissipation devices. Various designs were studied before adopting the scissor-Jack design (SJD) by replacing the viscous damper with the SMA wires [6]. The reason behind SJD is it has magnification factors substantially greater than unity. Toggle-brace-damper (C & d) systems can also achieve the magnification factor greater than the unity. Viscous dampers used in these systems are pretty heavy [8] -[9]. To reduce the weight and to enhance the amplification, shape memory alloy (SMA) wires have been used in the current version of seismic devices. These SMA wires act as energy dissipators inside the braces because of their shape memory effect and super-elastic effect without having major deformation [11]. When stretched, the energy is dissipated in a considerable amount [12]- [14]. Further SMA effect of the wire amplifies the even infinitesimal movement in bars thus acting as sensors for energy dissipation device. In this article, two different types of seismic systems have been described one is named a 2D bracing system and another is 3D bracing system. In addition to the design, the experimental analysis of the 2D and 3D braces has been discussed in the next sections. It has been seen that 3D braces are far more efficient in terms of stability and dissipation because of the out-of-plane energy dissipation and the SMA effect of the strings [10].

2 Materials and methods

The key focus of this study was on the design and development of an anti-seismic system based on SMA wires. Furthermore, as discussed above, SMA wires have been used as restitution components instead of liquid viscous dampers to serve as passive energy dissipation (PED) equipment. The dissipation in this system is solely elastic due to the peculiar nature of the SMA wires. In this study, two types of bracing systems have been studied, namely the 2D bracing system (Figure. 1) and the 3D bracing system. In the 2D bracing method, the SJD model was used as shown in Figure 1 and was studied for its effectiveness. It was able to dissipate energy,

but some limitations were observed. To overcome these drawbacks, particularly instability, less energy dissipation compared to the 3D brace model, and amplification, a 3D tensegrity bar model has been developed and theoretical results discussed in the following sections.

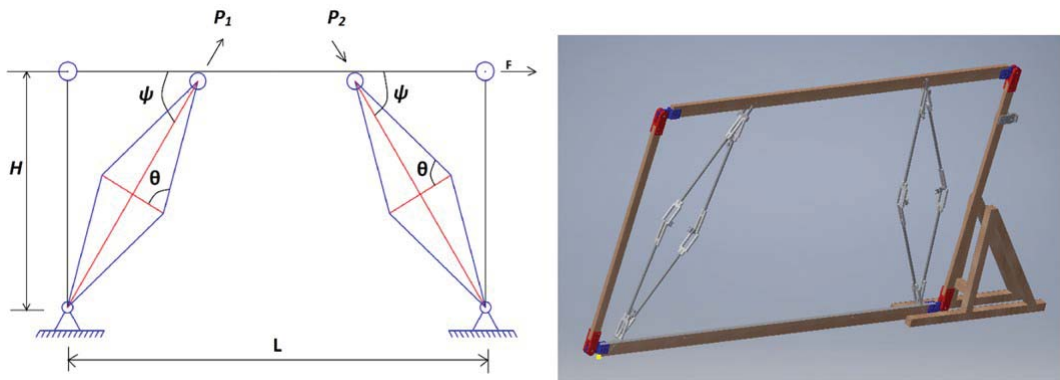


Figure 1: SMAD braces inserted into a frame structure

3 Anti-seismic response of developed 2D bracing system

After the design and development of the 2D tensegrity bar, theoretical tests were performed to access the necessary information. In Figure. 2 of Ref. [3] the amplification properties of the 2D tensegrity bar have shown and quite high amplification has been seen. In this system of braces, the system can achieve extreme position, unlike the liquid viscous dampers. Further, displacement in both the directions i.e, lateral and longitudinal directions has been seen, which makes it a better energy dissipation device by dissipation a fair amount of energy. In this, u and v represent the longitudinal and the lateral displacements of the framework. In a special case of $u/v = \tan\theta$, β approaches to 0 i.e, $\beta \rightarrow 0$, which signifies the negligible displacement from reference or original configuration. The variation of u/v with θ for different values of β is depicted in ref [3]. where u and v , denote the longitudinal and the transverse displacements of the structure respectively.

Also, in Figure 3 of Ref. [3], the experimental and theoretical results were obtained and compared. It can be observed that the experimental and theoretical results are nearly identical. It is worth noting that minute residual strains are observed at unloading (not greater than 0.03 max) in experimental conditions.

4 Anti-seismic response of developed 3D bracing system

As discussed in previous sections, the extension to this work by designing a novel 3D tensegrity brace has been provided (see Figure. 2). Both physical and constitutive models have been developed and tested to characterize the force-displacement behavior of the bracing system. Due to the 3D shape of this configuration, it is possible to obtain a tensegrity element with increased stability towards out-of-plane buckling, and more effective in terms of energy dissipation. Researchers have found that triangular cross-section is by far the most effective configuration for a tensegrity element, where $N=3$ [10].

Next, we show some numerical simulations of a 3D tensegrity bracing system, which enabled us to characterize its force-displacement response to cyclic loading (Fig. 3). In Figure. 4) it is displayed the geometric layout of the tested bracing. For further information about the



Figure 2: 3D model of the tensegrity bracing

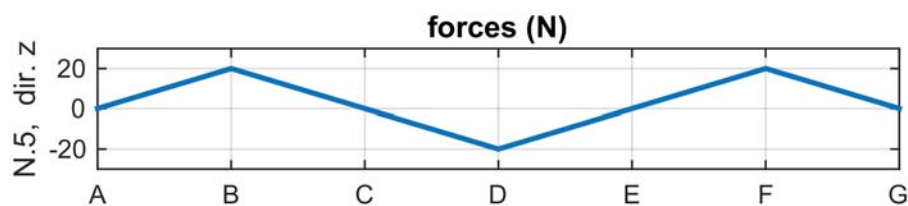


Figure 3: Mechanical loading cycle.

numerical implementation which was used for these simulations please refer to [15].

An initial pre-strain is introduced in the SMA wires (State A), prior to the implementation of the mechanical loading cycle, shown in Figure. 3. In Figure. 5 we show a compilation of the stress-strain-temperature responses of the SMA wires acting as ties in the 3D tensegrity bracing, during the imposed loading cycle. We assume isothermal conditions during the mechanical cycle, for an ambient temperature of 20 °C. Finally, in Figure. 6 we show the force-displacement plot for the proposed 3D tensegrity bracing, during the mechanical loading. Due to the fact that the horizontal (cables 1) and vertical (cable 2) ties are working in phase opposition, it is possible to obtain a wide superelastic hysteresis, highlighting the great energy dissipating capabilities of the proposed system.

5 CONCLUSIONS

In present work a novel method of developing seismic bracing systems with tensegrity architecture has been shown. Computational calculations of 2D and 3D tensegrity braces have been carried out to prove the effectiveness of the proposed systems. This research work is an extension of previous research focused on the development of a 2D PED device with tensegrity architecture incorporating SMA wires, which is a competitive alternative to viscous damper systems. SMA effects of the restitution elements has been proved to be very effective in terms

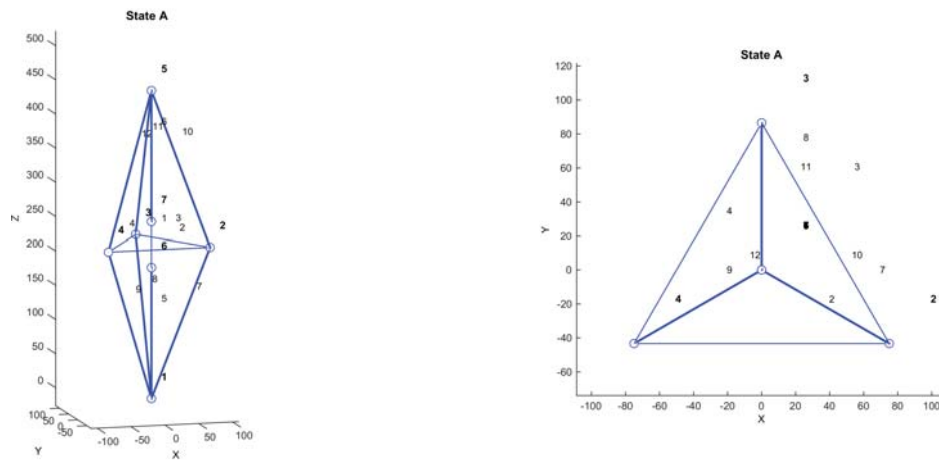


Figure 4: 3D numerical model of the tensegrity bracing (3D view and top view).

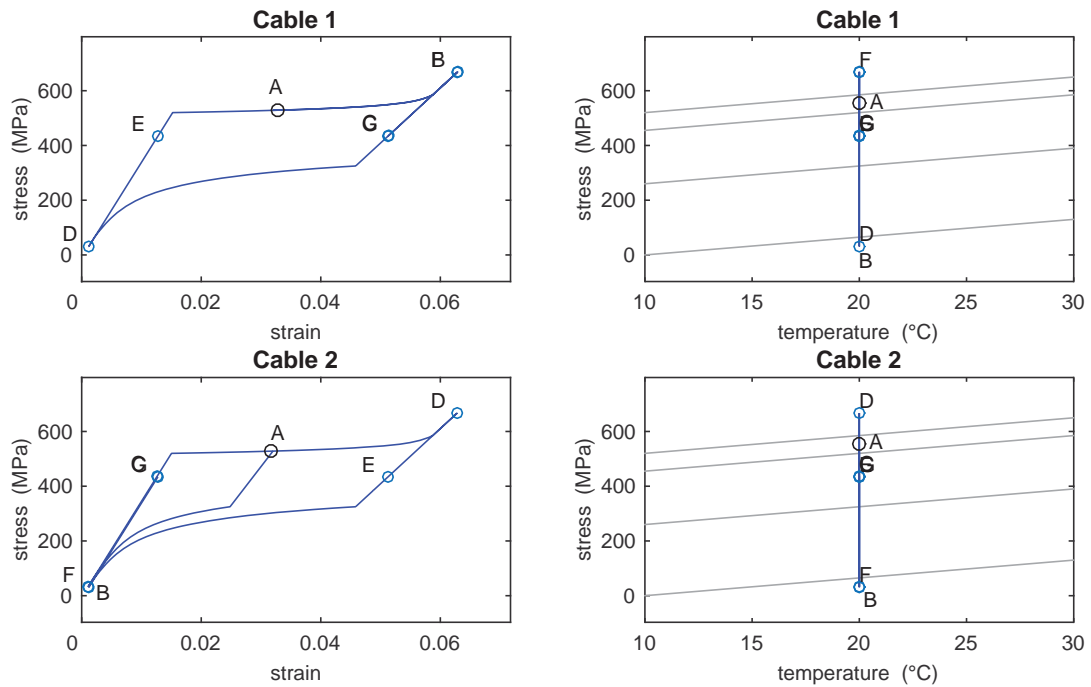


Figure 5: Stress-strain-temperature response of the SMA ties.

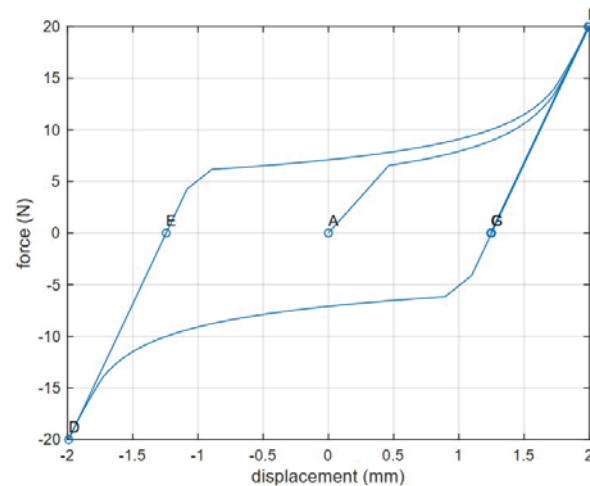


Figure 6: Force-displacement responses of a model frame reinforced with symmetrical SMAD braces.

of the displacement amplification factor and the energy dissipation capacity, because of the super-elastic properties of the SMA wires without experiencing permanent deformations. A 3D tensegrity bracing has been developed to multiply the existing effectiveness, such as energy dissipation and the stability of the bars. It has been seen from the theoretical results published in Ref. [3] that the amplification factor of the 2D brace is enhanced when the SMA wires are incorporated. In addition, in the case of the 3D brace, it is possible to obtain even more important energy dissipation features with additional lateral buckling restraints, as shown in the Figure. 6. The non viscous nature of the SMA wires makes the system lightweight and provide the opportunity to achieve extreme positions of the bar i.e., when the aspect angle is nearly 90 degrees. These features of the tensegrity bracing system would be very effective in technical applications, and indeed future steps are being taken to develop real scale models to be validated against experimental results by using various other meta materials and polymer materials and techniques [16]-[19].

REFERENCES

- [1] A. Micheletti, G. Ruscica, F. Fraternali On the compact wave dynamics of tensegrity beams in multiple COMPDYN 2021 dimensions. *Non linear dynamics*, **98**, 2737–2753, 2019.
- [2] F. Santos, G. Benzoni, F. Fraternali, Seismic performance of superelastic tensegrity braces. *Ingegneria sismica/international journal of earthquake engineering*, **36(3)**, 20-37, 2019.
- [3] F. Fraternali, F. Santos, Mechanical modeling of superelastic tensegrity braces for earthquake-proof structures. *Extreme mechanics letters*, **33**, 100578, 2019.
- [4] F. Fraternali, G. Carpentieri, A. Amendola, R.E. Skelton, & V. F. Nesterenko, V. F. Multiscale tunability of solitary wave dynamics in tensegrity metamaterials. *Applied Physics Letters*, **105(20)**, 201903, 2014.
- [5] B. Basu, O. S. Bursi, F. Casciati, S. Casciati, A. E. Del Grosso, M. Domaneschi , ... & J. Rodellar, A European Association for the Control of Structures joint perspective.

- Recent studies in civil structural control across Europe. Structural Control and Health Monitoring*, **21(12)**, 1414-1436, 2014.
- [6] AN. Sigaher, MC. Constantinou, Scissor-jack-damper energy dissipation system, *Earthquake Spectra*, **19(1)**, 133–158, 2003.
 - [7] F. Fraternali, F. Santos, Mechanical modeling of superelastic tensegrity braces for earthquake-proof structures, *Extreme Mechanics Letters*, 33, 100578, 2019.
 - [8] M. Dolce, R. Marnetto, Passive seismic devices based on shape memory alloys, *12th World Conference on Earthquake Engineering*, 1–8, 2000.
 - [9] Z. Xu, AK. Agrawal, WL. He, P. Tan, Performance of passive energy dissipation systems during near-field ground motion type pulses. *Engineering Structure*, **29(2)**, 224-236, 2007.
 - [10] RE. Skelton, MC. de Oliveira, Tensegrity Systems, *Springer*, 2010.
 - [11] V. Mercuri, Shape memory alloy strands: Conventional 3D FEM modeling and simplified models, *MSc Thesis, University of Pavia*, 2014.
 - [12] A. Alipour, M. Kadkhodaei, & M. Safaei, Design, analysis, and manufacture of a tension–compression self-centering damper based on energy dissipation of pre-stretched superelastic shape memory alloy wires. *Journal of Intelligent Material Systems and Structures*, **28(15)**, 2129-2139, 2017
 - [13] R. DesRoches, & M. Delemont, Seismic retrofit of simply supported bridges using shape memory alloys. *Engineering Structures* **24(3)**, 325-332, 2002.
 - [14] D. Liang, Y. Zheng, C. Fang, M. C. Yam, & C. Zhang, Shape memory alloy (SMA)-cable-controlled sliding bearings: development, testing, and system behavior. *Smart Materials and Structures* **29(8)**, 08500, 2002.
 - [15] A. Micheletti, F. Amarante dos Santos & P. Sittner, Superelastic tensegrities: matrix formulation and antagonistic actuation. *Smart Materials and Structures* **27(10)**, 105028, 2018.
 - [16] N. Singh, R. Singh, I.P.S. Ahuja, On Development of Functionally Graded Material Through Fused Deposition Modelling Assisted Investment Casting from Al₂O₃/SiC Reinforced Waste Low Density Polyethylene. *Trans Indian Inst Met* **71**, 2479–2485, 2018.
 - [17] R. Miranda, E. Babilio, N. Singh, F. Santos, F. Fraternali, . Mechanics of smart origami sunscreens with energy harvesting ability. *Mechanics Research Communications* **105**, 103503, 2020.
 - [18] R. Kumar, J. S. Chohan, R. Kumar, A. Yadav, N. Singh, Hybrid fused filament fabrication for manufacturing of Al microfilm reinforced PLA structures. *Journal of the Brazilian Society of Mechanical Sciences and Engineering* **42(9)**, 1-13, 2020.
 - [19] I. Farina, N. Singh , F. Colangelo, R. Luciano , G. Bonazzi F. Fraternali High-Performance Nylon-6 Sustainable Filaments for Additive Manufacturing. *Materials* **12(23)**, 3955, 2019.

RECONSTRUCTION OF MATERIAL STIFFNESS PROPERTIES FROM DISPERSION RELATIONS USING GENETIC ALGORITHMS

V.Thierry¹, W.Wu¹, D.Chronopoulos¹, S.Cantero Chinchilla²

¹*Institute for Aerospace Technology & The Composites Research Group, The University of Nottingham, NG7 2RD, UK*

²*Department of Mechanical Engineering, University of Bristol, Bristol, BS8 1TR, UK*

Abstract

The widespread use of composite materials has led to the development of characteristics identification methods for composite materials. This paper presents an inverse technique based on genetic algorithms to reconstruct material stiffness properties of composites from dispersion relations of three fundamental modes of guided Lamb waves (A_0 , SH_0 and S_0). The discrepancy between the mesoscopic dispersion relations computed for a textile composites and the macroscopic dispersion characteristics computed for a tentative set of elastic moduli defines the objective function. The proposed scheme is presented to obtain the elastic moduli of unidirectional carbon fibre reinforced polymer composite. The results show that the proposed method can effectively inverse the dispersion curves to get mechanical properties of composites.

Keywords: Textile composites, Guided Lamb wave, Dispersion relations, Genetic Algorithm

1. Introduction

Carbon fiber composite materials have been widely used in modern industries due to the characteristics of high specific strength and high specific stiffness [1, 2]. Different types of damage can occur in composites structures, which potentially leads to catastrophic failure of the whole system. Therefore effective and reliable Non-Destructive Evaluation (NDE) and Structural Health Monitoring (SHM) techniques are of utter importance to develop. Various algorithms were developed for damage identification, including time-of-flight, time reversal, migration technique, tomography and phased-array beamforming [3, 4, 5, 6]. All of the above algorithms require prior knowledge of elastic moduli particularly in anisotropic materials.

The traditional tests for determining the elastic properties of materials are generally expensive and time-consuming. Over years, non-destructive techniques have been done to identify the elastic constants of composite plates as these techniques are robust and quick to perform, especially guided wave technique [7, 8]. The use of guided wave for material characterization yields a frequency-dependent behaviour of the waves that can be used in inverse identification procedures. Different parameters, such as wave velocity [9], group delay curves [10], wavenumber [11], and dynamic displacement response [12] are used to identify the elastic constants in the inverse process.

The solution of dispersion relations is the premise of the inversion process. Methods such as SAFE [13, 14, 15], or WFE [16, 17, 18] using macroscale modelling are extremely efficient to compute the dispersion relations of laminates as long as the elastic moduli are known for each individual layer. The methodology presented in [18] provides a reduced formulation for WFE approach which in itself is a hybridization between periodic structure theory and finite elements. This methodology, while revealing itself to provide accurate dispersion predictions, needs much more computational resources than a macroscale model. Given that macro is superior to meso in terms of the computational time, but from the perspective of accuracy, it is opposite. Therefore, there is considerable motivation to bridge them. The approach proposed in this manuscript takes advantage of the accuracy of the methodology for computing dispersion relations in complex textile composites from [18] and the efficiency of the SAFE method to compute the dispersion characteristics of macroscale laminate models.

Different inversion procedures have been used to identify the elastic constants of composite plates [12, 19, 20, 21]. Balasubramaniam [19] was the first to employ genetic algorithms (GAs) for inverting unidirectional composite

material elastic moduli with significant success. The advantage of GAs over other search algorithms is that GAs do not need an initial guess but rather a valid search space; GAs are also robust and avoid entrapment at local minima. Neural network techniques have also been applied in solving inverse problems [12, 20]. More recently, a Bayesian identification technique based on finite element modelling and the properties of propagating waves in multilayered structures is proposed, which overcomes the limitations of ill-conditioning and non-uniqueness associated with the conventional approaches [21]. Considering the advantages of GAs, GAs are adopted in this paper.

The paper is structured as follows. In Sec. 2, the proposed methodology is thoroughly described. In Sec. 3, the scheme is validated using a simple orthotropic plate structure. Finally, Sec. 4 provides concluding remarks.

2. Inverse methodology based on a genetic algorithm

In this section, the GA is used to determine the elastic moduli of a material from its dispersion relations. A schematic representation of the elastic moduli identification framework based on the GA method is shown in Fig. 1. The mesoscale model based on modified WFE approach [18] is used to calculate the mesoscale dispersion characteristics, which is regarded as the input of an inverse algorithm. The macroscale model based on SAFE method is used to calculate the iterative dispersion relations. The GWs-based identification of elastic properties is realized through the minimization of an objective function, which is built on the relative discrepancies between the dispersion characteristics computed using the mesoscale model and the SAFE method for a tentative set of elastic moduli at the macroscale. The GA procedure iteratively updates the sets of elastic moduli in the SAFE formulation in order to minimise the objective function as presented in [22]. The iteration terminates when the stopping-conditions are fulfilled; these can be when the value of the objective function for a tentative set of elastic moduli overcomes a threshold or after completing a predefined number of iterations.

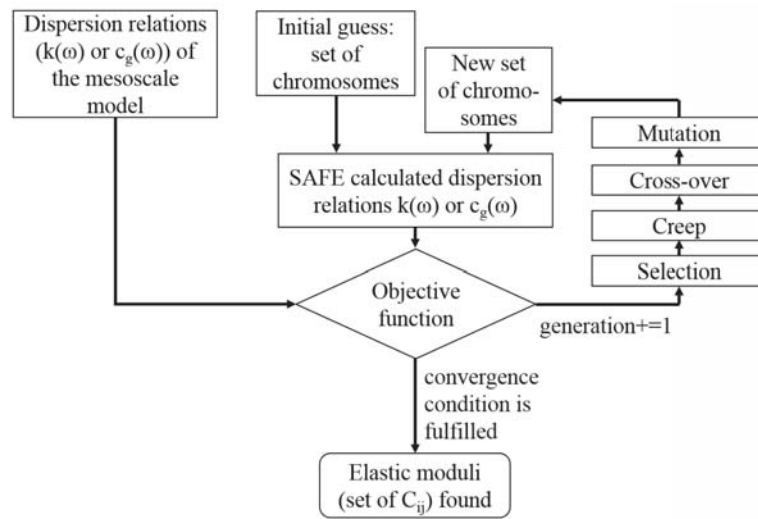


Figure 1: Schematic representation of the elastic moduli (C_{ij}) identification framework based on a genetic algorithm. The starting point for the optimization process are the nine statically determined mechanical moduli for the textile composite. The mesoscale wave propagation properties computed through a modified WFE scheme are compared to the macroscale SAFE estimations incorporating the mechanical moduli. The moduli are updated iteratively until the mesoscale and macroscale wave propagation properties converge.

In this study, a chromosome is a set of nine elastic moduli (also called C_{ij}) describing the stiffness matrix of the homogenised orthotropic material. Each individual modulus is a gene. A set of multiple chromosomes is called a population, as depicted in Fig. 2.

2.1. Initialisation of the homogenisation process

Although it is not necessary for attaining convergence, using an initial guess allows for speeding up the process (that is given that the initial guess is not far from the solution). Since the material is modelled to obtain its mesoscale

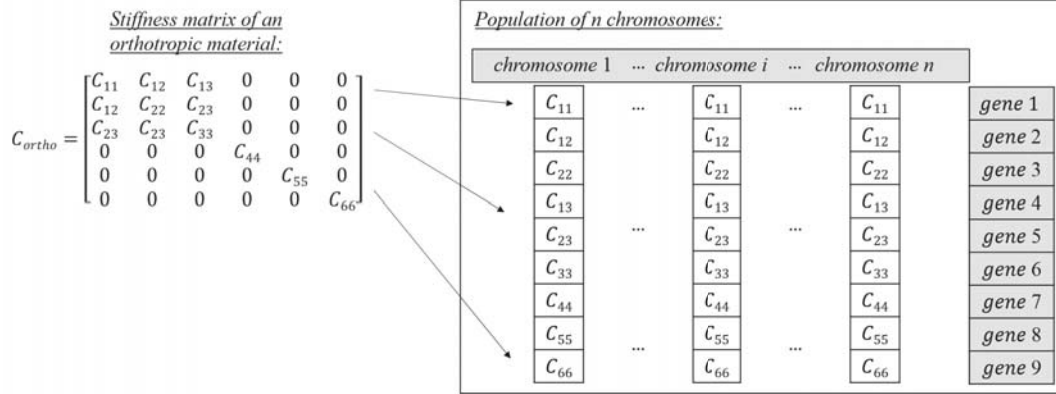


Figure 2: Chromosomes incorporating the elastic moduli of an orthotropic textile layer. Multilayer structures can be considered with the size of chromosomes varying accordingly. Nine independent elastic moduli are included for each layer. These moduli are injected within a macroscale SAFE calculation and results are compared against the mesoscale derived wave dispersion properties.

dispersion characteristics, it is convenient to use its effective elastic moduli obtained by static virtual testing (method detailed in [23, 24, 18]) as initial guess but not necessary. A small set of chromosomes of the initial population is set equal to the initial guess while the rest of the population is randomly generated from a small neighborly interval whose median value is the initial guess.

2.2. Objective function

The objective function defines the discrepancy between the mesoscopic dispersion relations computed for a textile composite and the macroscopic dispersion characteristics computed for a tentative set of elastic moduli. It is noted that any property directly related to the dispersion characteristics of the structure (i.e. the computed wavelength, wavenumber of wave speed) can be employed within the objective function in Eq. (1) with such correlated quantities being expected to provide the same effective properties. The identification of the optimal set of elastic moduli is realised through the minimisation of this objective function. The mesoscale dispersion relations are input to the GA procedure and are not updated while the macroscale dispersion curves are computed iteratively using the SAFE method for each updated set of elastic moduli. Different types of dispersion characteristics can be used for comparison: the wavenumber or the group velocity displayed in Fig. 3 are two possibilities. While the group velocity values are traditionally used [25, 26, 27] for GA-based homogenisation methods (for the simple reason that this parameter is straightforward to obtain experimentally), the wavenumber parameter is also a good candidate. In this study, the wavenumber is used to explore more possibilities.

The error function to be minimised is the Mean of the Relative Error (MRE) for each point of an individual dispersion curve and is written as follows:

$$\text{MRE}(\theta) = \sum_{i=1}^n \left| \frac{\lambda_i^{\text{meso}}(\theta) - \lambda_i^{\text{macro}}(\theta)}{\lambda_i^{\text{meso}}(\theta)} \right| / n. \quad (1)$$

with λ the dispersion parameter which is hereby taken as the computed wavelength (equivalently the phase velocity) of the considered wave mode. Moreover θ the angle of propagation of consideration and n the number of compared data points.

The relative error function is computed separately for the three fundamental modes (S_0 , SH_0 and A_0) and in a few directions of propagation. The objective function is set to the maximum of any of these values, thus minimising all modes simultaneously. All modes have to be considered as it would be useless to obtain a set of moduli that reconstructs one mode only considering that results will be employed within wave interaction with damage modelling or multiple ray reflection modelling where wave conversion phenomena are predominant. Using the sum of all relative errors has been considered but revealed itself to slow down the optimisation process. It is noted that while the formulation is globally applicable to frequency ranges including higher order modes, this study focuses on matching

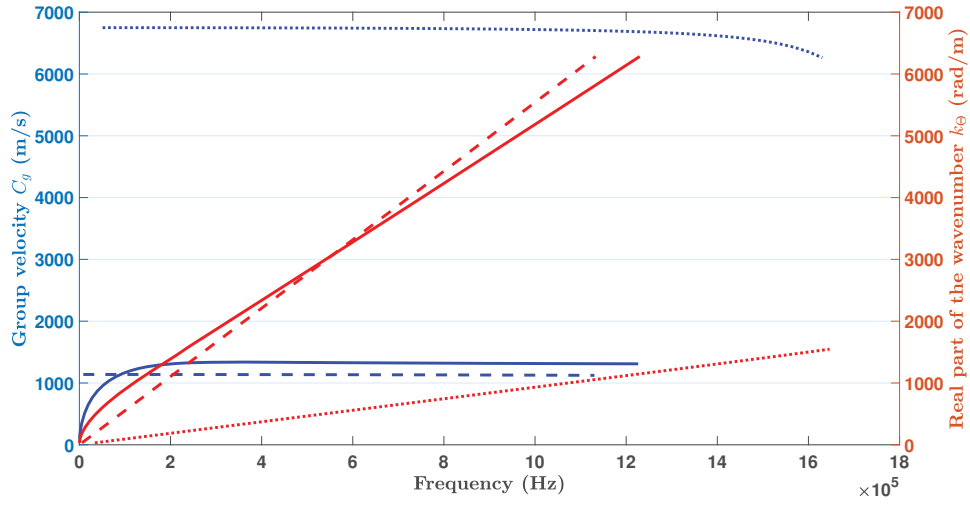


Figure 3: Dispersion relations (group velocity plotted in blue and wavenumber in red) of the three first modes in the x -direction of propagation for a plate constituted of an orthotropic material. Comparisons on the sensitivity of both parameters are provided in Sec. 3 to determine which is best for this application. (—) A_0 , (---) SH_0 , (...) S_0 .

the dispersion characteristics within the range where only fundamental Lamb wave modes propagate, since this is the range typically employed for damage identification.

2.3. Selection and genetic operators

Selection of the portion of existing population to breed. The fitness function is directly derived from the objective function and determines the likeliness of a chromosome to be selected for the next generation. The selection process can be visualised as a roulette wheel in which each chromosome covers an area of the wheel proportional to its probability to be selected. The chromosomes for the next generation are selected one by one by turning the wheel. All generations population contain an equal number of chromosomes thus a chromosome with a high probability of selection might be selected more than once to be passed on to the next generation.

Creeping operation. A creeping operation is performed on each new candidate solution. A threshold is established and a random number is generated. If the random number exceeds the threshold then the considered set of elastic moduli is randomly scaled in the range of $[1-\delta_{creep}, 1+\delta_{creep}]$, δ_{creep} being the creep amount. Using this approach also allows for a search outside the search space.

Single-point crossover of parent chromosomes. Some of the selected chromosomes mate through the crossover process to create new offspring whose genes are a combination of its parent's genes. The crossover rate defines the number of parent chromosomes to be selected for cross-over. Two parent chromosomes are 'cut' at a single random crossover point and their genes are interchanged.

Mutation of parent chromosomes. Finally some of the chromosomes are mutated to avoid stagnation of the solution to a local minima. The mutation rate defines the number of genes to be mutated and their positions across the chromosomes are selected randomly. The genes selected for mutations are each replaced by a newly generated one.

3. Case studies

To show the applicability of the method, it is firstly performed on a simulated orthotropic plate whose theoretical elastic moduli are known. Its dispersion characteristics are computed using the WFE method similarly to the way it would for a textile composite. In the following subsections, the elastic moduli are approximated using two different approaches to validate and compare them. The approach called 'brute-force' with the ambitious task of reconstructing all nine parameters at once is adopted here.

3.1. Brute-force approach

The thickness of the plate and the density of the material are fixed (0.5 mm and 3212 kg/m^3) as known and the nine elastic moduli presented in Table1 in the ‘theoretical’ column are sought. These moduli represent a unidirectional carbon fibre reinforced polymer composite whose fibre arrangement makes it slightly non-transverse isotropic. Table1 shows the results obtained for five different runs of the GA and the percentage of error to the theoretical value. In order to validate the method, a random set of elastic moduli was used as initial guess for each run. The crossover and mutation rates are both set to 0.1, the creep amount is set to 0.3 and the generated population size is 50 chromosomes. The algorithm is launched considering the wavenumber dispersion relations for five runs. Parallel computing is performed on a 4 cores and 8 Gb RAM system and the algorithm is coded in Python language.

	Theoretical	#1	#2	#3	#4	#5
C_{11} (GPa)	147.36	146.18	147.61	146.93	147.39	148.12
error (%)		0.80	0.18	0.29	0.02	0.52
C_{12} (GPa)	3.43	2.46	2.93	3.85	3.63	8.64
error (%)		28.23	14.49	12.18	5.68	151.65
C_{22} (GPa)	9.51	8.68	8.21	8.34	9.31	10.11
error (%)		8.71	13.70	12.29	2.15	6.30
C_{13} (GPa)	3.47	1.11	0.73	1.18	1.77	5.88
error (%)		67.84	78.84	65.85	48.83	69.59
C_{23} (GPa)	4.02	1.49	1.31	1.01	1.89	4.87
error (%)		63.04	67.49	74.94	52.98	21.17
C_{33} (GPa)	11.66	5.77	5.19	5.53	4.80	12.89
error (%)		50.52	55.49	52.54	58.85	10.54
C_{44} (GPa)	3.19	3.18	3.36	3.30	3.20	3.21
error (%)		0.20	5.44	3.44	0.31	0.56
C_{55} (GPa)	5.58	5.60	5.69	5.72	5.48	5.59
error (%)		0.35	1.99	2.52	1.88	0.22
C_{66} (GPa)	4.16	4.13	4.14	4.10	4.13	4.09
error (%)		0.72	0.41	1.51	0.57	1.54
Generations	-	103	118	286	222	222
Time (h)	-	25	30	59	49	46

Table 1: Results of the GA for five independent runs for the reconstruction of the elastic moduli of an orthotropic material whose real moduli are displayed on the left-hand side, when $k(\omega)$ is considered.

The results are displayed for the wavenumber approach in Table1. It can be observed that this methodology, while providing a realistic order of magnitude for the elastic moduli, yields strong relative error for many of them ($> 10\%$). Some elastic moduli such as C_{11} and C_{66} however, are in all five runs approximated with a very low relative error ($< 2\%$), while C_{44} and C_{55} are approximated with a tolerable error ($< 6\%$). One can conclude that these parameters are extremely sensible in comparison to the others.

Trying to optimise nine coefficients at once is a very ambitious task and the convergence is obtained after many generations (at least 100) as seen in Fig. 4.a, and thus is computationally taxing. Moreover, only two elastic moduli are reconstructed with good accuracy and two more with a relatively low error. One can conclude that this approach is neither time efficient, nor yields accurate results. However, the objective function value is smaller than 1% at convergence for each of the runs. This indicates that even though the correct solution was not found, at least a solution does exist. Therefore, there is a considerable motivation to employ the sensitivity of each individual mode to the different moduli to optimise a reduced number of parameters at once in the future work.

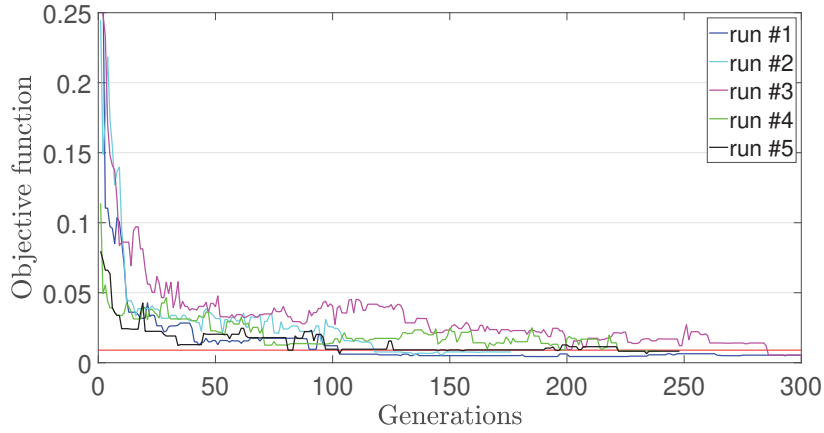


Figure 4: Value of the objective function as a function of the generation for the five GA independent runs for the reconstruction of the elastic moduli of the orthotropic material. $k(\omega)$ is considered. Convergence is observed for all runs after 290 generations. 100 generations were needed for at least one run to converge. The horizontal red line is plotted at 1% of error.

4. Conclusions

The GA is presented to reconstruct material stiffness properties of composites based on dispersion characteristics of Lamb wave in this paper, which combines the advantages of WFE and SAFE. Case study has been selected to illustrate the strengths of proposed approach. While the brute-force approach showed that the dispersion relations have a very low sensitivity to some of the moduli if considered altogether. A sensitivity study is therefore hereby performed in order to uncover the effect of each parameters to be optimised on the dispersion relations in the future.

5. Acknowledgments

- This work is funded by the INNOVATIVE doctoral programme. The INNOVATIVE programme is partially funded by the Marie Curie Initial Training Networks (ITN) action (project number 665468) and partially by the Institute for Aerospace Technology (IAT) at the University of Nottingham. This project has also received funding from the European Union's Horizon 2020 research and innovation programme under the Marie Skłodowska-Curie grant agreement No. 859957.
- We are grateful for access to the University of Nottingham's Augusta HPC service.

References

- [1] R. Bai, J. Guo, Z. Lei, D. Liu, Y. Ma, and C. Yan, "Compression after impact behavior of composite foam-core sandwich panels," *Composite Structures*, vol. 225, p. 111181, 2019.
- [2] R. Bai, Z. Lei, X. Wei, W. Tao, and C. Yan, "Numerical and experimental study of dynamic buckling behavior of a j-stiffened composite panel under in-plane shear," *Composite Structures*, vol. 166, pp. 96–103, 2017.
- [3] S. Cantero-Chinchilla, J. Chiachío, M. Chiachío, D. Chronopoulos, and A. Jones, "A robust bayesian methodology for damage localization in plate-like structures using ultrasonic guided-waves," *Mechanical Systems and Signal Processing*, vol. 122, pp. 192–205, 2019.
- [4] P. Malinowski, T. Wandowski, I. Trendafilova, and W. Ostachowicz, "A phased array-based method for damage detection and localization in thin plates," *Structural Health Monitoring*, vol. 8, no. 1, pp. 5–15, 2009.
- [5] Z. Su and L. Ye, "Selective generation of lamb wave modes and their propagation characteristics in defective composite laminates," *Proceedings of the Institution of Mechanical Engineers, Part L: Journal of Materials: Design and Applications*, vol. 218, no. 2, pp. 95–110, 2004.
- [6] H. W. Park, S. B. Kim, and H. Sohn, "Understanding a time reversal process in lamb wave propagation," *Wave Motion*, vol. 46, no. 7, pp. 451–467, 2009.
- [7] L. Pagnotta, "Recent progress in identification methods for the elastic characterization of materials," *International Journal of mechanics*, vol. 2, no. 4, pp. 129–140, 2008.
- [8] J. H. Tam, Z. C. Ong, Z. Ismail, B. C. Ang, and S. Y. Khoo, "Identification of material properties of composite materials using nondestructive vibrational evaluation approaches: A review," *Mechanics of Advanced Materials and Structures*, vol. 24, no. 12, pp. 971–986, 2017.
- [9] J. Vishnuvardhan, C. Krishnamurthy, and K. Balasubramaniam, "Blind inversion method using lamb waves for the complete elastic property characterization of anisotropic plates," *The Journal of the Acoustical Society of America*, vol. 125, no. 2, pp. 761–771, 2009.
- [10] A. Marzani and L. De Marchi, "Characterization of the elastic moduli in composite plates via dispersive guided waves data and genetic algorithms," *Journal of intelligent material systems and structures*, vol. 24, no. 17, pp. 2135–2147, 2013.
- [11] A. A. Eremin, E. Glushkov, N. Glushkova, and R. Lammering, "Evaluation of effective elastic properties of layered composite fiber-reinforced plastic plates by piezoelectrically induced guided waves and laser doppler vibrometry," *Composite Structures*, vol. 125, pp. 449–458, 2015.
- [12] G. Liu, K. Lam, and X. Han, "Determination of elastic constants of anisotropic laminated plates using elastic waves and a progressive neural network," *Journal of Sound and Vibration*, vol. 252, no. 2, pp. 239–259, 2002.
- [13] I. Bartoli, A. Marzani, F. Lanza di Scalea, and E. Viola, "Modeling wave propagation in damped waveguides of arbitrary cross-section," *Journal of Sound and Vibration*, vol. 295, no. 3–5, pp. 685–707, 2006.
- [14] A. Marzani, E. Viola, I. Bartoli, F. L. Di Scalea, and P. Rizzo, "A semi-analytical finite element formulation for modeling stress wave propagation in axisymmetric damped waveguides," *Journal of Sound and Vibration*, vol. 318, no. 3, pp. 488–505, 2008.
- [15] K.-L. Nguyen, F. Treyssède, and C. Hazard, "Numerical modeling of three-dimensional open elastic waveguides combining semi-analytical finite element and perfectly matched layer methods," *Journal of Sound and Vibration*, vol. 344, pp. 158–178, 2015.
- [16] D. Mead, "Wave propagation in continuous periodic structures: research contributions from southampton, 1964–1995," *Journal of sound and vibration*, vol. 190, no. 3, pp. 495–524, 1996.
- [17] B. R. Mace, D. Duhamel, M. J. Brennan, and L. Hinke, "Finite element prediction of wave motion in structural waveguides," *The Journal of the Acoustical Society of America*, vol. 117, no. 5, pp. 2835–2843, 2005.
- [18] V. Thierry, L. Brown, and D. Chronopoulos, "Multi-scale wave propagation modelling for two-dimensional periodic textile composites," *Composites Part B: Engineering*, vol. 150, pp. 144–156, 2018.
- [19] K. Balasubramaniam and N. S. Rao, "Inversion of composite material elastic constants from ultrasonic bulk wave phase velocity data using genetic algorithms," *Composites Part B: Engineering*, vol. 29, no. 2, pp. 171–180, 1998.
- [20] G. Liu, W. Ma, and X. Han, "An inverse procedure for determination of material constants of composite laminates using elastic waves," *Computer Methods in Applied Mechanics and Engineering*, vol. 191, no. 33, pp. 3543–3554, 2002.
- [21] W.-J. Yan, D. Chronopoulos, S. Cantero-Chinchilla, K.-V. Yuen, and C. Papadimitriou, "A fast bayesian inference scheme for identification of local structural properties of layered composites based on wave and finite element-assisted metamodeling strategy and ultrasound measurements," *Mechanical Systems and Signal Processing*, vol. 143, p. 106802, 2020.
- [22] A. Marzani and L. De Marchi, "Characterization of the elastic moduli in composite plates via dispersive guided waves data and genetic algorithms," *Journal of Intelligent Material Systems and Structures*, vol. 24, no. 17, pp. 2135–2147, 2012.
- [23] S. Li and A. Wongsto, "Unit cells for micromechanical analyses of particle-reinforced composites," *Mechanics of Materials*, vol. 36, no. 7, pp. 543–572, 2004.
- [24] S. Li and E. Sitnikova, *1.18 An Excursion into Representative Volume Elements and Unit Cells*, pp. 451–489. Oxford: Elsevier, 2018.
- [25] J. Vishnuvardhan, C. V. Krishnamurthy, and K. Balasubramaniam, "Genetic algorithm based reconstruction of the elastic moduli of orthotropic plates using an ultrasonic guided wave single-transmitter-multiple-receiver shm array," *Smart Materials and Structures*, vol. 16, no. 5, p. 1639, 2007.
- [26] M. Sale, P. Rizzo, and A. Marzani, "Semi-analytical formulation for the guided waves-based reconstruction of elastic moduli," *Mechanical Systems and Signal Processing*, vol. 25, no. 6, pp. 2241–2256, 2011.
- [27] A. A. Eremin, E. V. Glushkov, N. V. Glushkova, and R. Lammering, "Evaluation of effective elastic properties of layered composite fiber-reinforced plastic plates by piezoelectrically induced guided waves and laser doppler vibrometry," *Composite Structures*, vol. 125, pp. 449–458, 2015.

PARTICLE FILTER-BASED HYBRID DAMAGE PROGNOSIS CONSIDERING BIAS

Tianzhi Li¹, Francesco Cadini¹, and Claudio Sbarufatti¹

¹ Dipartimento di Meccanica, Politecnico di Milano
Milan, via La Masa 1, 20156, Italy

tianzhi.li@polimi.it, francesco.cadini@polimi.it, claudio.sbarufatti@polimi.it

Abstract

Hybrid prognosis combining both the physical knowledge and data-driven techniques has shown great potential for damage prognosis in structural health monitoring (SHM). Current practices consider the physics-based process and data-driven measurement equations to describe the damage evolution and the mapping between the damage state and the SHM signal (or the feature extracted from SHM signal), respectively. However, the bias between the measurements predicted by data-driven equation and the actual SHM measurements, arising from uncertainties like damage geometries and sensor placement or noise, can lead to inaccurate prognosis results. To account for this problem, this paper adopts a methodology typically applied for sensor fault diagnosis, and develops a new hybrid state space model with a bias parameter included into the state vector and the measurement equation. Particle filter (PF) serves as the estimation technique to identify the state and parameters relating to the damage as well as the bias parameter, and RUL can be predicted by the PF estimates and physics-based process equation. The numerical study about the fatigue crack growth shows the new model together with PF can provide satisfactory estimation and prediction results in case of bias in the measurement model.

Keywords: Structural Health monitoring, Fault Prognosis, Hybrid Model, Measurement Equation, Particle Filter.

1 INTRODUCTION

Prognostic is the process of predicting the future state and the remaining useful life (RUL) of a component or system. In the last decades, a great variety of damage prognosis techniques have been developed in SHM depending on the availability of physics knowledge and data. From the perspective of how the prognosis models are formulated, they can be distinguished into physics-based [1-3], data-driven [4-8] and hybrid methods [9-13]. Physics-based methods utilize specific mechanistic knowledge and theories to formulate a pure physics-based model, which describes the structural degradation phenomena as well as the links between the damage states and the SHM measurements. On the other hand, data-driven methods, resorting to data-driven modelling techniques such as neural networks [6] and Markov chains [8], attempt to use amounts of data to build the relationship between the internal degradation behaviour and the external observations. Hybrid methods, taken as a combination of the two above methods, usually consider the physics-based process and data-driven measurement equations to describe the damage evolution and the mapping between the damage state and measurement, respectively.

The right method (or model) should probably be case specific, as each type of method has its pros and cons [14, 15]. However, given the uncertainties arising from the complex structural degradation behaviour, the environment effects and the sensor health conditions [16, 17], both the deterministic physic-based and data-driven models are unable to provide an accurate prognostic result. A well-acknowledged strategy for both the physics-based [1-3] and data-driven methods [6, 8] to improve their prognostic performance is to set the parameters within the corresponding models as unknown components to be updated by a state estimation technique, such as particle filter (PF) given its good performance in nonlinear and non-Gaussian problem. On the other hand, this strategy is not fully exploited in hybrid methods, where the parameters in physics-based process equation are usually taken as unknown variables to be estimated by PF, while the parameters relating to the data-driven measurement equation are not [11, 18, 19].

The relationship between the damage state and the SHM measurement should probably vary in different specimens of same structure [9] due to the uncertainties mentioned above. As a consequence, the bias between the measurements predicted by data-driven measurement equation, often derived from training data, and the measurements from testing specimen is unavoidable. In this context, the measurement equation, that fails to be online updated or take the bias into account, will lead to inaccurate damage estimation [20] and prognosis [9] in case of large-level bias. Only a few studies relating to hybrid prognosis [9, 13] field attempt to solve this bias problem, where an additional measurement system is adopted to collect or calculate the true damage state and to update the measurement equation.

The bias between the predicted measurements and the actual measurements can be regarded as a typical sensor fault, which can be detected, localized and identified by adding a parameter representing a bias in both the process and measurement equations for estimation [21-23]. It has been verified that this bias can have little effect on the estimation of other state components

when it can be accurately estimated by a state estimation technique [22, 23]. However, such idea, that has been validated for the sensor fault diagnosis problem [21-23] and the state estimation considering bias [22, 23], has not been used for hybrid damage prognosis.

This paper develops a new particle filter-based hybrid prognosis framework that combines the methods from sensor fault diagnosis and current hybrid prognosis investigations. The process equation is formulated resorting to the physical law describing damage propagation and a bias parameter, while the measurement equation representing the relationship between the damage state and the measurements is built by a polynomial fitting function and the bias parameter. Then, PF is used to estimate the damage state, damage parameters and the bias parameter. Finally, the future states and, consequently, the RUL can be estimated on the basis of the process equation and the estimated damage state and parameters.

The rest of this paper is organized as follows: Section 2 introduces the traditional and new models as well as the prognosis framework. The numerical validation is discussed in Section 3. Finally, Section 4 concludes this paper with some topics for future work.

2 DAMAGE PROGNOSIS FRAMEWORK

Particle filter-based damage prognosis framework generally has three main steps, namely, (i) formulating a state space model, (ii) estimating the unknown state components using PF and (iii) calculating the future state and RUL by the PF estimates and the physic-based process equation.

2.1 Traditional and new models

Current PF-based prognosis investigations in SHM usually have the hybrid state space model formulated as

$$\begin{cases} \mathbf{z}_k = \begin{bmatrix} \boldsymbol{\theta}_k \\ x_k \end{bmatrix} = \begin{bmatrix} \boldsymbol{\theta}_{k-1} + \boldsymbol{\omega}_{\theta(k)} \\ f(x_{k-1}, \boldsymbol{\theta}_k, \omega_k) \end{bmatrix} \\ y_k = h(x_k) + v_k \end{cases} \quad (1)$$

where $f(\cdot)$ is the physics-based function describing the evolution of the damage state, and $h(\cdot)$ is a function mapping the relationship between the damage state and the measurement, the subscript k is the time step, \mathbf{z} represents the state vector, y is the output that is given by the measurement system, such as strain [11] and guided wave [9, 10], $\boldsymbol{\theta}$ includes evolution parameters and x is the state relating to the damage (hereafter focusing on crack damage), ω and $\boldsymbol{\omega}_{\theta}$ are the process noises, v is the measurement noise.

The relationship between the damage extent and measurement will inevitably vary in different specimens of same structure [9], due to the uncertainties like damage geometries and sensor error, which means the bias between the measurement predicted by a data-driven measurement equation derived from some specimens and the actual measurements from another one is typically unavoidable. Inaccurate estimation [20] and prognosis [9] may occur in case of large-level bias. Inspired from the sensor fault diagnosis investigations [21-23] and hybrid prognosis studies [9, 10, 13], a novel hybrid state space model is thus developed with the bias parameter b included as

$$\begin{cases} \mathbf{z}_k = \begin{bmatrix} \boldsymbol{\theta}_k \\ x_k \\ b_k \end{bmatrix} = \begin{bmatrix} \boldsymbol{\theta}_{k-1} + \boldsymbol{\omega}_{\boldsymbol{\theta}(k)} \\ f(x_{k-1}, \boldsymbol{\theta}_k, \omega_k) \\ b_{k-1} + \omega_{b(k)} \end{bmatrix} \\ y_k = h(x_k) + b_k + v_k \end{cases} \quad (2)$$

where ω_b is the process noise for the parameter b . This model can provide satisfactory estimated damage state and parameters, because the bias between the output calculated from the function $h(\cdot)$ and the actual measurement y can be on-line estimated by the parameter b , as will be validated in Section 3.4.

2.2 Particle filter and RUL prediction

Particle filter serves as the state estimation technique in this study, due to its good performance in nonlinear and non-Gaussian problem.

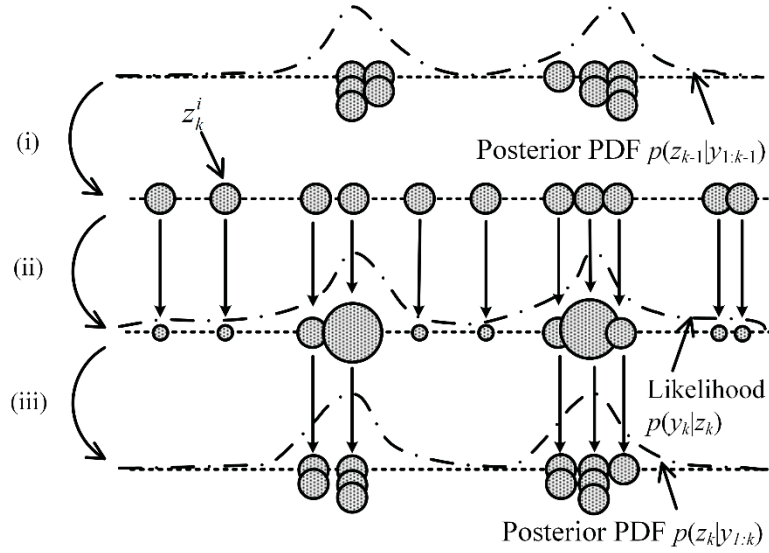


Figure 1 Sampling importance resampling (SIR) particle filter [24]

The sampling importance resampling (SIR) PF [25] with systematic resampling, as presented in Figure 1, is used in this study, and it consists of the three steps, i.e.,

- (i) draw N_p particles $\{\mathbf{z}_k^i: i = 1, 2, \dots, N_p\}$ from the prior probability density function (PDF) $p(\mathbf{z}_k|\mathbf{z}_{k-1})$,
- (ii) calculate the weight w_k^i by the likelihood function $p(\mathbf{y}_k|\mathbf{z}_k^i)$ as

$$w_k^i \propto p(\mathbf{y}_k|\mathbf{z}_k^i) \quad (3)$$

and assign its normalized form \tilde{w}_k^i to each particle \mathbf{z}_k^i ,

- (iii) Resample for $\{\mathbf{z}_k^i: i = 1, 2, \dots, N\}$ using particle weights.

In addition, the kernel smoothing method [26] is adopted for the parameters $\boldsymbol{\theta}$ due to its good performance in current investigations [3],

$$\boldsymbol{\theta}_k^i = \sqrt{1 - h^2} \boldsymbol{\theta}_{k-1}^i + (1 - \sqrt{1 - h^2}) \hat{\boldsymbol{\theta}}_{k-1} + \boldsymbol{\omega}_{\boldsymbol{\theta}(k)}^i \quad (4)$$

where $\hat{\theta}_{k-1}$ are the means of the samples.

The prediction for future state and RUL is summarized in Table 1. At each time step k , the posterior PDFs of the state and parameters are adopted to calculate the future evolution of the particles. The RUL of each particle can be defined when its future state reaches a predefined threshold.

Initialization: set $\{x_k^{i,0} : i = 1, 2, \dots, N_p\}$ as $\{x_k^i : i = 1, 2, \dots, N_p\}$
For $i = 1 : N_p$
$j = 0$
While $x_k^{i,j} < l_{th}$
Calculate the future state $x_k^{i,j+1}$ by $x_k^{i,j+1} = f(x_k^{i,j}, \theta_k^i)$
$j = j + 1$
End
$RUL_k^i = \Delta N j$
End

Table 1 Calculation of future state and RUL at time step k

3 APPLICATION

3.1 Crack growth and measurement

The crack growth data, as presented in Figure 2(a), are created by Paris' law with parameters as in Table 2.

$$x_k = x_{k-1} + e^{\omega_k} C (F \Delta S \sqrt{\pi x_{k-1}})^m \Delta N \quad (5)$$

where x is the crack length, the subscript k means the k -th time step, ΔN , ΔS and F represent the load cycle increment, the applied fatigue stress range and the crack shape function, respectively, C and m are two empirical values governing damage progression and $\omega \sim \mathcal{N}\left(-\frac{\sigma^2}{2}, \sigma^2\right)$ is the unbiased log-normal process noise with standard deviation σ . The crack length 35 mm is set as the threshold for damage prognosis.

Initial crack length x_0	Parameter C	Parameter m	Noise ω
15 mm	$1.1994 \times 10^{-14} \text{ mm/cycle(MPa}\sqrt{\text{mm}})^{-m}$	3.79	$\mathcal{N}\left(-\frac{0.6^2}{2}, 0.6^2\right)$
Crack shape function F	Applied fatigue stress ΔS	Load cycles ΔN	
1	60 MPa	500	

Table 2 Details for crack growth

Given the difficulty in directly measuring the crack length, current SHM applications usually have advanced measurement system, e.g., guided wave [9, 10], strain gauge [11], adopted for online monitoring to estimate the crack length. In this study, the measurements at different crack

lengths (Figure 2(b)) are created via two steps:

- (i) calculate the measurements without the bias and noise by a polynomial fitting function $h(\cdot)$, representing the relationship between the crack lengths and the SHM measurements

$$h(x_k) = (-0.00001x_k^4 + 0.0025x_k^3 + 0.05x_k^2 + 0.3x_k - 0.4)/40 \quad (6)$$

- (ii) add the varying bias, as given in Eq. (7), and 33dB signal-to-noise ratio white Gaussian noise to the above measurements.

$$b_k = -0.12 \sin\left(\frac{k}{100}\right) + 0.0001k \quad (7)$$

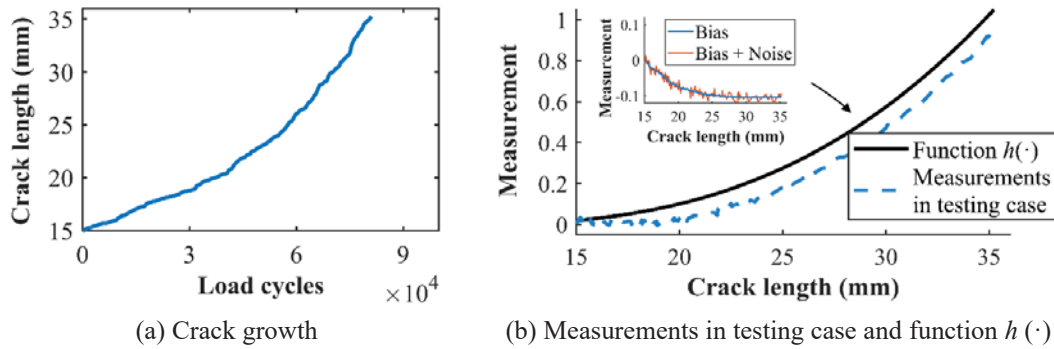


Figure 2 Testing data.

Note: the x -axis for the bias in Figure 2(b) is changed as crack length.

3.2 Formulation of traditional and new models

Given the two parameters C and m will also vary in different specimens, they are taken as unknown variables and added to the state vector to form the traditional augmented state space model as

$$\begin{cases} \mathbf{z}_k = \begin{bmatrix} C_k \\ m_k \\ x_k \end{bmatrix} = \begin{bmatrix} \sqrt{1-h^2}C_{k-1} + (1-\sqrt{1-h^2})\hat{C}_{k-1} + \omega_{1(k)} \\ \sqrt{1-h^2}m_{k-1} + (1-\sqrt{1-h^2})\hat{m}_{k-1} + \omega_{2(k)} \\ x_{k-1} + e^{\omega_k}C_k(F\Delta S\sqrt{\pi x_{k-1}})^{m_k}\Delta N \end{bmatrix} \\ y_k = h(x_k) + v_k \end{cases} \quad (8)$$

where $\omega \sim \mathcal{N}\left(-\frac{\sigma^2}{2}, \sigma^2\right)$ is log-normal process noise with the standard deviation σ [3], while ω_1 and ω_2 are zero-mean Gaussian process noises.

The new hybrid model with a bias parameter included is given as

$$\begin{cases} \mathbf{z}_k = \begin{bmatrix} C_k \\ m_k \\ x_k \\ b_k \end{bmatrix} = \begin{bmatrix} \sqrt{1-h^2}C_{k-1} + (1-\sqrt{1-h^2})\hat{C}_{k-1} + \omega_{1(k)} \\ \sqrt{1-h^2}m_{k-1} + (1-\sqrt{1-h^2})\hat{m}_{k-1} + \omega_{2(k)} \\ x_{k-1} + e^{\omega_k}C_k(F\Delta S\sqrt{\pi x_{k-1}})^{m_k}\Delta N \\ b_{k-1} + \omega_{b(k)} \end{bmatrix} \\ y_k = h(x_k) + b_k + v_k \end{cases} \quad (9)$$

where b is the parameter representing the bias, and ω_b is its process noise.

3.3 Particle filter parameters

All the PF parameters used in this study are reported in Table 3. The strategies about the distributions of initial intervals for C and m and the process noise ω are determined from [3, 11, 12].

Number of particles N_p	STD in likelihood function	h in Kernel smoothing	
2000	0.04	0.1	
Initial distributions for C, m		Initial range for x , mm	Initial value for b
$\begin{bmatrix} C_0 \\ m_0 \end{bmatrix} \sim \mathcal{N} \left(\begin{bmatrix} 1.14e - 14 \\ 3.86 \end{bmatrix}, \begin{bmatrix} 1 \times 10^{-30} & -8 \times 10^{-17} \\ -8 \times 10^{-17} & 0.01 \end{bmatrix} \right)$		$x_0 \in (14.5, 15.5)$	$b_0 = 0$
Distributions of process noises $\{\omega, \omega_1, \omega_2, \omega_3, \omega_4\}$ for x, C, m, b			
x, ω	C, ω_1	m, ω_2	b, ω_3
$\mathcal{N} \left(-\frac{0.04^2}{2}, 0.04^2 \right)$	$\mathcal{N}(0, (1 \times 10^{-17})^2)$	$\mathcal{N}(0, 0.003^2)$	$\mathcal{N}(0, 0.008^2)$

Table 3 PF parameters.

3.4 Results from estimation and RUL prediction

Figures 3 (a) and (b) present the estimation results using traditional model. The estimated crack length remains close to the true values until reaching about 17 mm, when the bias grows large enough to hamper damage estimation, as visible in Figure 2. The narrow confidence boundaries after about 6×10^4 load cycles show the existence of a poor particle diversity. In addition, the samples of the parameters C and m also fail to accumulate around the true values. The observation that the bias between the output of the measurement equation and the actual measurement will lead to inaccurate estimation is confirmed in [9, 20]. Figures 3 (c), (d) and (e) present the estimation results using the new model with included bias parameter. The estimated crack length, C and m are noticeably more accurate than those in Figures 3 (a) and (b), as the bias is correctly identified by the PF and is taken into consideration for the estimation for the other state components. Moreover, given the presence of measurement noise and the difficulty in estimating the time-varying parameter, the bias parameters from the 3×10^4 to 7×10^4 load cycles are not accurately estimated, which leads to less accurate estimation for crack length at these load cycles.

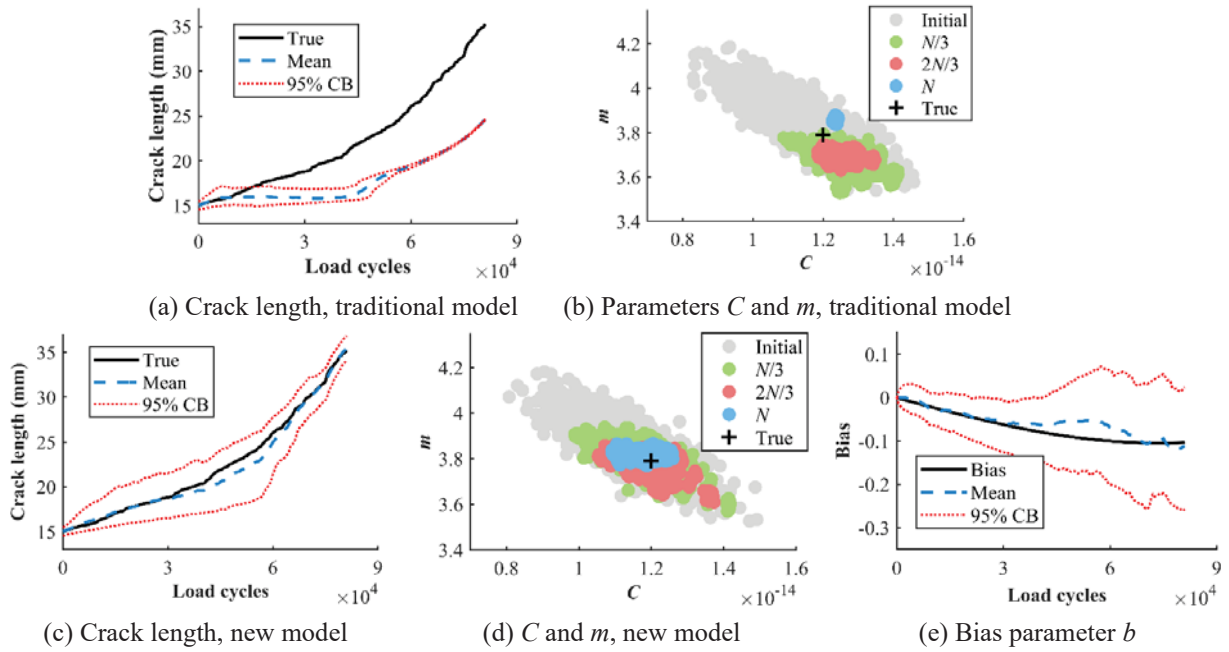
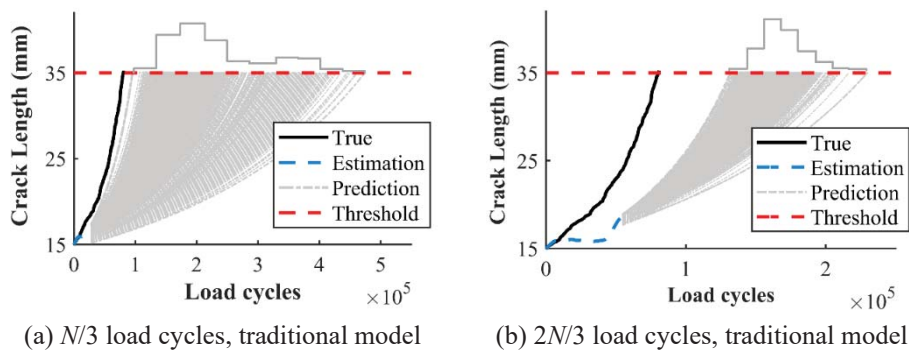


Figure 3 Estimation using traditional and new models

Figures 4 (a)(b) and (c)(d) present the prediction for future states at some selected load cycles using the traditional and new models, respectively. The grey dotted lines are the crack length trajectories predicted by the particles at the selected load cycles, and the grey histogram at the end of life (identified as a critical crack length) is the RUL posterior PDF. Figures 5 (a) and (b) present the RUL predictions using the traditional and new models, respectively, along with their 95% confidence boundary. The predicted states and RULs from the new model always keep close to the true values, while those from the traditional model don't. It can be concluded that the new model can provide more accurate estimation and prognosis results within a PF framework than the traditional model, for which the bias existing between the measurement equation and the actual observation prevents a correct estimation.



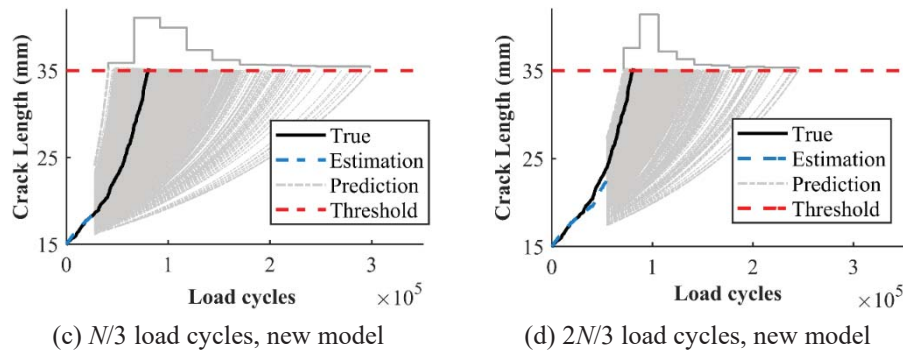


Figure 4 Prediction at two selected load cycles from traditional and new models.

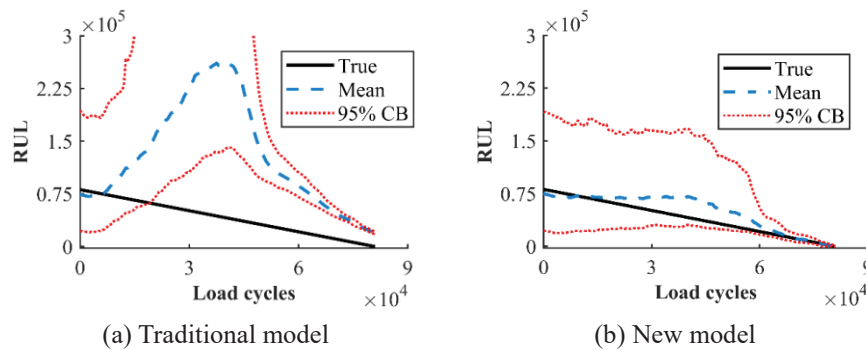


Figure 5 RUL Prediction from traditional and new models.

4 CONCLUSIONS

The bias between the measurements predicted by any data-driven measurement equation and the actual SHM measurements is unavoidable in hybrid prognostic investigations, which might lead to inaccurate prognostic results. Combining the ideas from sensor fault diagnosis and hybrid prognosis, this paper proposes a new hybrid state space model that always includes an adaptive bias parameter in both the state vector and measurement equation. The numerical study proves the new model can provide accurate estimation and prognosis for crack length when the bias can be accurately estimated. Our future work intends to validate this framework by experimental study.

ACKNOWLEDGEMENTS

This project has received funding from the European Union's Horizon 2020 research and innovation programme under the Marie Skłodowska-Curie grant agreement No. 859957.

REFERENCES

- [1] J. Chiachío, M. Chiachío, S. Sankararaman, A. Saxena, K. Goebel, Condition-based prediction of time-dependent reliability in composites, *Reliability Engineering & System Safety*, 142 (2015) 134-147.
- [2] M. Chiachío, J. Chiachío, S. Sankararaman, K. Goebel, J. Andrews, A new algorithm for prognostics using Subset Simulation, *Reliability Engineering & System Safety*, 168 (2017) 189-199.

- [3] M. Corbetta, C. Sbarufatti, M. Giglio, M.D. Todd, Optimization of nonlinear, non-Gaussian Bayesian filtering for diagnosis and prognosis of monotonic degradation processes, *Mechanical Systems and Signal Processing*, 104 (2018) 305-322.
- [4] N. Eleftheroglou, D. Zarouchas, T. Loutas, R. Alderliesten, R. Benedictus, Structural health monitoring data fusion for in-situ life prognosis of composite structures, *Reliability Engineering & System Safety*, 178 (2018) 40-54.
- [5] N. Eleftheroglou, D. Zarouchas, R. Benedictus, An adaptive probabilistic data-driven methodology for prognosis of the fatigue life of composite structures, *Composite Structures*, 245 (2020) 112386.
- [6] F. Cadini, C. Sbarufatti, M. Corbetta, F. Cancelliere, M. Giglio, Particle filtering-based adaptive training of neural networks for real-time structural damage diagnosis and prognosis, *Structural Control and Health Monitoring*, 26 (2019).
- [7] C. Chen, G. Vachtsevanos, M.E. Orchard, Machine remaining useful life prediction: An integrated adaptive neuro-fuzzy and high-order particle filtering approach, *Mechanical Systems and Signal Processing*, 28 (2012) 597-607.
- [8] J. Chiachío, M.L. Jalón, M. Chiachío, A. Kolios, A Markov chains prognostics framework for complex degradation processes, *Reliability Engineering & System Safety*, 195 (2020) 106621.
- [9] J. Chen, S. Yuan, H. Wang, On-line updating Gaussian process measurement model for crack prognosis using the particle filter, *Mechanical Systems and Signal Processing*, 140 (2020) 106646.
- [10] J. Chen, S. Yuan, X. Jin, On-line prognosis of fatigue cracking via a regularized particle filter and guided wave monitoring, *Mechanical Systems and Signal Processing*, 131 (2019) 1-17.
- [11] D. Cristiani, C. Sbarufatti, M. Giglio, Damage diagnosis and prognosis in composite double cantilever beam coupons by particle filtering and surrogate modelling, *Structural Health Monitoring*, (2020) 1475921720960067.
- [12] D. Cristiani, C. Sbarufatti, F. Cadini, M. Giglio, Fatigue damage diagnosis and prognosis of an aeronautical structure based on surrogate modelling and particle filter, *Structural Health Monitoring*, 0 1475921720971551.
- [13] M.E. Orchard, G.J. Vachtsevanos, A particle-filtering approach for on-line fault diagnosis and failure prognosis, *Transactions of the Institute of Measurement and Control*, 31 (2009) 221-246.
- [14] Y. Peng, M. Dong, M.J. Zuo, Current status of machine prognostics in condition-based maintenance: a review, *The International Journal of Advanced Manufacturing Technology*, 50 (2010) 297-313.
- [15] L. Liao, F. Köttig, Review of Hybrid Prognostics Approaches for Remaining Useful Life Prediction of Engineered Systems, and an Application to Battery Life Prediction, *IEEE Transactions on Reliability*, 63 (2014) 191-207.
- [16] I. Lopez, N. Sarigul-Klijn, A review of uncertainty in flight vehicle structural damage monitoring, diagnosis and control: Challenges and opportunities, *Progress in Aerospace*

- Sciences, 46 (2010) 247-273.
- [17] P. Baraldi, F. Mangili, E. Zio, Investigation of uncertainty treatment capability of model-based and data-driven prognostic methods using simulated data, *Reliability Engineering & System Safety*, 112 (2013) 94-108.
 - [18] S. Yuan, J. Chen, W. Yang, L. Qiu, On-line crack prognosis in attachment lug using Lamb wave-deterministic resampling particle filter-based method, *Smart Materials and Structures*, 26 (2017) 085016.
 - [19] S.-L. Ma, S.-F. Jiang, J. Li, Structural damage detection considering sensor performance degradation and measurement noise effect, *Measurement*, 131 (2019) 431-442.
 - [20] F. Cadini, C. Sbarufatti, M. Corbetta, M. Giglio, A particle filter-based model selection algorithm for fatigue damage identification on aeronautical structures, *Structural Control & Health Monitoring*, (2017) e2002.
 - [21] M. Gálvez-Carrillo, M. Kinnaert, Sensor fault detection and isolation in doubly-fed induction generators accounting for parameter variations, *Renewable Energy*, 36 (2011) 1447-1457.
 - [22] A. Giremus, J.-Y. Tournet, V. Calmettes, A particle filtering approach for joint detection/estimation of multipath effects on GPS measurements, *IEEE Transactions on Signal Processing*, 55 (2007) 1275-1285.
 - [23] J.A. Grauer, Real-Time Data-Compatibility Analysis Using Output-Error Parameter Estimation, *Journal of Aircraft*, 52 (2015) 940-947.
 - [24] E.N. Chatzi, A.W. Smyth, The unscented Kalman filter and particle filter methods for nonlinear structural system identification with non-collocated heterogeneous sensing, *Structural Control & Health Monitoring*, 16 (2010) 99-123.
 - [25] M.S. Arulampalam, S. Maskell, N. Gordon, T. Clapp, A tutorial on particle filters for online nonlinear/non-Gaussian Bayesian tracking, *IEEE Transactions on Signal Processing*, 50 (2002) 174-188.
 - [26] J. Liu, M. West, Combined parameter and state estimation in simulation-based filtering, *Sequential Monte Carlo methods in practice*, Springer, 2001, pp. 197-223.

DISPERSION ANALYSIS OF BULK ACOUSTIC WAVES IN PIEZOELECTRIC MEDIA DISCRETIZED BY ENERGY- ORTHOGONAL FINITE ELEMENTS

Francisco J. Brito Castro

Departamento de Ingeniería Industrial, Universidad de La Laguna
Calle Méndez Núñez 67-2C, Santa Cruz de Tenerife 38001, Spain
e-mail: fjbrito@ull.edu.es

Abstract

This contribution studies the propagation of bulk acoustic waves in piezoelectric media discretized by the finite element method. The element elastic and dielectric stiffness matrices are split into basic and higher order components which are related to the mean and deviatoric components of the element strain and electric fields, respectively. This decomposition is applied to the total energy of the finite element assemblage. By a dispersion analysis the higher order total energy is related to the total energy error for the propagating waves. An averaged correlation is proposed as an error indicator for the finite element vibration eigenmodes in piezoelectric solids.

Keywords: energy-orthogonal stiffness, numerical dispersion, piezoelectric media, vibration eigenmodes.

1 INTRODUCTION

It is well known that the wave scattering at boundaries creates an interference field that, if composed solely of waves of frequency equal to a natural frequency of the bounded medium, takes the form of a standing-wave field which is an eigenmode of the continuum [1]. For homogeneous piezoelectric solids, whose three dimensions are comparable, this standing-wave field could be considered essentially composed of propagating quasi-longitudinal and quasi-shear bulk acoustic waves. In this case the goal of determining the finite element mesh required to accurately represent a given number of eigenmodes could be approached by analysing the effect of the spatial discretization over the propagation of such bulk acoustic waves in unbounded media. This effect becomes apparent by observing the dispersive behavior of the waves, a phenomenon that is not present in the physical system [2]. This contribution extends the author's previous research about homogeneous isotropic elastic solids [3].

The piezoelectric media covered in this research include PZT (Lead zirconate titanate ($\text{Pb}(\text{Zr,Ti})\text{O}_3$)) piezoceramics [4]. These are transversely isotropic and they behave the same as crystals in class Hexagonal (6mm). The poling direction is supposed along the Z-axis. The material constants for the piezoceramics selected (PZT-5H, PZT-8 and PZT-5A) can be found in reference [5]. Also PMN-PT (Lead magnesium niobate-lead titanate ($\text{Pb}(\text{Mg}_{1/3}\text{Nb}_{2/3})\text{O}_3\text{-PbTiO}_3$)) <001> poled single crystals are covered [6]: the single crystal PMN-30PT from reference [7], and the commercial grade single crystals PMN-31PT and PIN-PMN-PT (TRS X2B and TRS X4B) from TRS Technologies Inc. [8] have been selected. These single crystals exhibit Tetragonal (4mm) symmetry in macroscopic material properties. See Appendix 1 for the material constants of the PZT piezoceramics and PMN-PT single crystals selected.

An enlightening discussion about PZT piezoceramics and PMN-PT single crystals in the context of sonar applications can be found in reference [9].

1.1 Finite element formulation

In a lossless piezoelectric medium discretized by the finite element method the equations of equilibrium governing its linear dynamic response for time-harmonic waves will be [10],

$$\begin{pmatrix} \mathbf{K}_{uu} - \omega^2 \mathbf{M} & \mathbf{K}_{u\phi} \\ -\mathbf{K}_{\phi u} & \mathbf{K}_{\phi\phi} \end{pmatrix} \begin{pmatrix} \mathbf{x} \\ \boldsymbol{\phi} \end{pmatrix} = \begin{pmatrix} \mathbf{F} \\ \mathbf{Q} \end{pmatrix}, \quad \mathbf{K}_{\phi u} = \mathbf{K}_{u\phi}^T; \quad \begin{matrix} \mathbf{x} = \tilde{\mathbf{x}} \exp(-i\omega t), & \mathbf{F} = \tilde{\mathbf{F}} \exp(-i\omega t) \\ \boldsymbol{\phi} = \tilde{\boldsymbol{\phi}} \exp(-i\omega t), & \mathbf{Q} = \tilde{\mathbf{Q}} \exp(-i\omega t) \end{matrix} \quad (1)$$

where: \mathbf{M} , consistent mass matrix; \mathbf{K}_{uu} ($\mathbf{K}_{\phi\phi}$, $\mathbf{K}_{u\phi}$), elastic (dielectric, piezoelectric) stiffness matrix of the finite element assemblage; $\tilde{\mathbf{x}}$ ($\tilde{\mathbf{F}}$, $\tilde{\boldsymbol{\phi}}$, $\tilde{\mathbf{Q}}$), column matrix containing the complex amplitude of the nodal displacements (external loads, electric potentials, free electric charges); $\omega = 2\pi/T$, circular frequency; T , period of wave; t , time.

The total energy will be equal to the sum of pure elastic energy and pure electric energy [11],

$$E^M = \frac{1}{2} \text{Re}[\mathbf{x}^T] \mathbf{K}_{uu} \text{Re}[\mathbf{x}] \quad (a) \quad E^E = \frac{1}{2} \text{Re}[\boldsymbol{\phi}^T] \mathbf{K}_{\phi\phi} \text{Re}[\boldsymbol{\phi}] \quad (b) \quad (2)$$

At element level

$$\begin{aligned} \mathbf{K}_{uu}^e &= \int_{V_e} \mathbf{B}_u^T [\mathbf{C}^E] \mathbf{B}_u dV \quad (a) & \mathbf{K}_{\phi\phi}^e &= \int_{V_e} \mathbf{B}_\phi^T [\boldsymbol{\epsilon}^S] \mathbf{B}_\phi dV \quad (b) \\ \mathbf{K}_{u\phi}^e &= \int_{V_e} \mathbf{B}_u^T [\mathbf{e}]^T \mathbf{B}_\phi dV \quad (c) & \mathbf{K}_{\phi u}^e &= \int_{V_e} \mathbf{B}_\phi^T [\mathbf{e}] \mathbf{B}_u dV \quad (d) \end{aligned} \quad (3)$$

where: \mathbf{B}_u (\mathbf{B}_ϕ), matrix relating the strain components (gradient of electric potential) to the nodal values of displacement (electric potential); \mathbf{C}^E , elasticity matrix evaluated at constant electric field; $\boldsymbol{\epsilon}^S$, dielectric matrix evaluated at constant mechanical strain; \mathbf{e} , piezoelectric matrix.

If the matrices \mathbf{B}_u and \mathbf{B}_ϕ are partitioned into mean and deviatoric components,

$$\begin{aligned} \mathbf{B}_u &= \bar{\mathbf{B}}_u + \mathbf{B}_{u,d}; \quad \bar{\mathbf{B}}_u V^e = \int_{V_e} \mathbf{B}_u dV, \quad \mathbf{B}_{u,d} = \mathbf{B} - \bar{\mathbf{B}}_u \quad (a) \\ \mathbf{B}_\phi &= \bar{\mathbf{B}}_\phi + \mathbf{B}_{\phi,d}; \quad \bar{\mathbf{B}}_\phi V^e = \int_{V_e} \mathbf{B}_\phi dV, \quad \mathbf{B}_{\phi,d} = \mathbf{B} - \bar{\mathbf{B}}_\phi \quad (b) \end{aligned} \quad (4)$$

the matrices Eq. (3a) and Eq. (3b) would be respectively decomposed as addition of basic and higher order components,

$$\begin{aligned} \mathbf{K}_{uu}^e &= \mathbf{K}_{uu,b}^e + \mathbf{K}_{uu,h}^e; \quad \mathbf{K}_{uu,b}^e = \bar{\mathbf{B}}_u^T [\mathbf{C}^E] \bar{\mathbf{B}}_u V^e, \quad \mathbf{K}_{uu,h}^e = \int_{V_e} \mathbf{B}_{u,d}^T [\mathbf{C}^E] \mathbf{B}_{u,d} dV \quad (a) \\ \mathbf{K}_{\phi\phi}^e &= \mathbf{K}_{\phi\phi,b}^e + \mathbf{K}_{\phi\phi,h}^e; \quad \mathbf{K}_{\phi\phi,b}^e = \bar{\mathbf{B}}_\phi^T [\boldsymbol{\varepsilon}^S] \bar{\mathbf{B}}_\phi V^e, \quad \mathbf{K}_{\phi\phi,h}^e = \int_{V_e} \mathbf{B}_{\phi,d}^T [\boldsymbol{\varepsilon}^S] \mathbf{B}_{\phi,d} dV \quad (b) \end{aligned} \quad (5)$$

In this case it is said that the element stiffness matrices are formulated in energy-orthogonal form [12]. The decomposition in Eq. (5) holds for the complete model,

$$\mathbf{K}_{uu} = \mathbf{K}_{uu,b} + \mathbf{K}_{uu,h} \quad (a) \quad \mathbf{K}_{\phi\phi} = \mathbf{K}_{\phi\phi,b} + \mathbf{K}_{\phi\phi,h} \quad (b) \quad (6)$$

For a stationary wave the amplitudes of nodal displacements and electric potentials are real-valued vectors in Eq. (1). Then, from Eq. (2a) and Eq. (2b), the period-averaged elastic and electric energies for the discretized domain will be, respectively,

$$\bar{E}^M = \frac{1}{4} \tilde{\mathbf{x}}^T \mathbf{K}_{uu} \tilde{\mathbf{x}} \quad (a) \quad \bar{E}^E = \frac{1}{4} \tilde{\boldsymbol{\phi}}^T \mathbf{K}_{\phi\phi} \tilde{\boldsymbol{\phi}} \quad (b) \quad (7)$$

By introducing Eq. (6) into Eq. (7), the basic and higher order period-averaged energies will be obtained. The latter components will be

$$\bar{E}_h^M = \frac{1}{4} \tilde{\mathbf{x}}^T \mathbf{K}_{uu,h} \tilde{\mathbf{x}} \quad (a) \quad \bar{E}_h^E = \frac{1}{4} \tilde{\boldsymbol{\phi}}^T \mathbf{K}_{\phi\phi,h} \tilde{\boldsymbol{\phi}} \quad (b) \quad (8)$$

2 DISPERSION ANALYSIS

The unbounded piezoelectric domain is discretized by a regular mesh of finite elements. Two different isoparametric finite elements with consistent mass matrix are considered: the hexahedron with twenty nodes and brick geometry HE20, Fig. 1, and the pentahedron with fifteen nodes and right prismatic isosceles geometry PE15, Fig. 2 [13]. The nodal lattice formed by the finite element assemblage has four and five nodes per unit cell, respectively. Different meshes with the same element volume can be selected by the aspect ratio parameter, $0 < \gamma \leq 1$; the skew angle, $0 \leq \beta < 90^\circ$ (only HE 20 element); and the distortion-Z parameter, $\varepsilon > 0$.

For uniform plane harmonic bulk waves at the continuum piezoelectric medium, the displacement vector field and the electric potential field will be, respectively,

$$\mathbf{u} = A^u \hat{\mathbf{a}} \exp(i\kappa \mathbf{n} \cdot \mathbf{r}) \exp(-i\omega t) \quad (a) \quad \phi = A^\phi \exp(i\kappa \mathbf{n} \cdot \mathbf{r}) \exp(-i\omega t) \quad (b) \quad (9)$$

where: A^u and A^ϕ , amplitudes of the wave; $\hat{\mathbf{a}}$, polarization vector; \mathbf{n} , wave normal, unit vector indicating the direction of the wave propagation; \mathbf{r} , position vector; $\kappa = 2\pi/\lambda = \omega/c$, wave number; λ , wavelength; c , phase velocity at the continuum medium.

The wave normal has the components $n_1 = \cos\phi \sin\theta$, $n_2 = \sin\phi \sin\theta$ and $n_3 = \cos\theta$, where: ϕ , azimuthal angle, $0 \leq \phi \leq 180^\circ$; θ , polar angle, $0 \leq \theta \leq 180^\circ$, Fig. 1.

The polarization vectors and phase velocities are solution of the stiffened Christoffel equation, which is expressed in abbreviated subscript notation [14],

$$(l_{iK}(C_{KL}^E + [e_{Kj} n_j][n_i e_{iL}]) / (n_i \varepsilon_{ij}^S n_j)) l_{Lj} \hat{a}_j = \rho c^2 \hat{a}_i, \quad i, j = 1, \dots, 3; \quad K, L = 1, \dots, 6 \quad (10)$$

where the non-null values of l_{iK} are: $l_{11} = n_1$, $l_{15} = n_3$, $l_{16} = n_2$, $l_{22} = n_2$, $l_{24} = n_3$, $l_{26} = n_1$, $l_{33} = n_3$, $l_{34} = n_2$, and $l_{35} = n_1$.

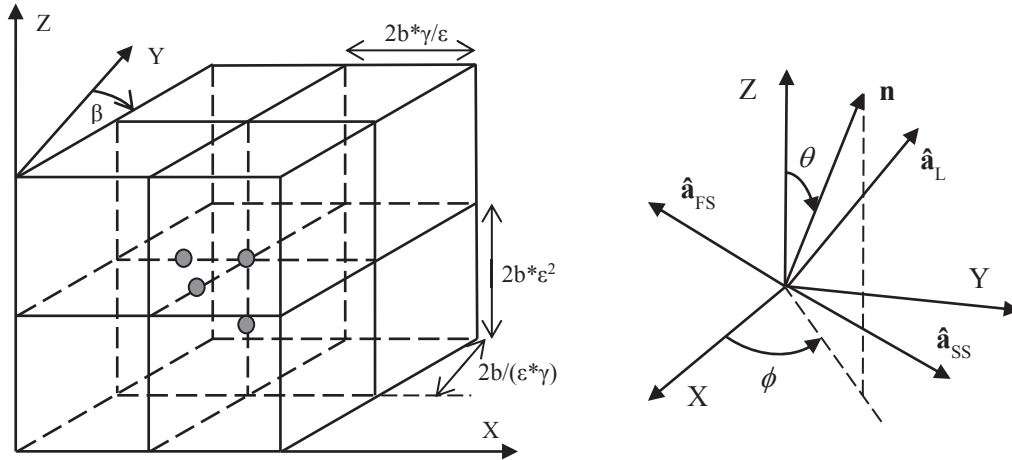


Figure 1: Piezoelectric domain discretized by a regular mesh of HE20 elements and unit cell with four nodes. Polarization vectors.

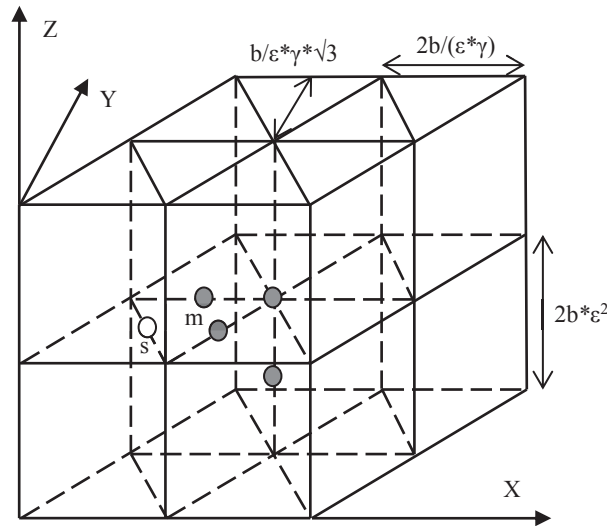


Figure 2: Piezoelectric domain discretized by a regular mesh of PE15 elements and unit cell with four master nodes (m) and one slave node (s).

By solving the eigenproblem Eq. (10), three mutually orthogonal waves at the continuum medium are computed, Fig. 1: ($\hat{\mathbf{a}}_{SS}$, c_{SS}), slow quasi-shear wave, SS; ($\hat{\mathbf{a}}_{FS}$, c_{FS}), fast quasi-shear wave, FS; and ($\hat{\mathbf{a}}_L$, c_L), quasi-longitudinal wave, L.

Then, the electric potential at the continuum medium can be computed for each wave,

$$A^\phi = A^u (n_i e_{iK} l_{Kj} / (n_i \epsilon_{ij}^S n_j) \hat{\mathbf{a}}_j), \quad i, j = 1, \dots, 3; \quad K = 1, \dots, 6 \quad (11)$$

For the displacement vector field Eq. (9a) and for the electric potential field Eq. (9b), the densities of period-averaged pure elastic energy and period-averaged pure electric energy at the continuum medium can be respectively computed by the equations [14]

$$\bar{E}_0^M = \frac{1}{4} \omega^2 (A^u)^2 l_{Ki} C_{KL}^E l_{Lj} \hat{\mathbf{a}}_j / c^2 \quad (a) \quad \bar{E}_0^E = \frac{1}{4} \omega^2 (A^\phi)^2 n_i \epsilon_{ij}^S n_j / c^2 \quad (b) \quad (12)$$

2.1 Characteristic equations

The characteristic equations can be found assuming harmonic waves Eq. (9) with different amplitudes in each node of the unit cell,

$$\tilde{\mathbf{u}} = A_j^u \hat{\mathbf{a}} \exp(i\kappa \mathbf{n} \cdot \mathbf{r}) \quad (a) \quad \tilde{\phi} = A_j^\phi \exp(i\kappa \mathbf{n} \cdot \mathbf{r}) \quad (b); \quad j = 1, \dots, N \quad (13)$$

where: N , number of nodes per unit cell.

Inserting the solutions Eq. (13) into the homogeneous part of Eq. (1), the characteristic equation for each node of the unit cell is yielded by equilibrium of nodal forces into the direction of the particle displacement [15],

$$\mathbf{F}_K^{uu} \cdot \hat{\mathbf{a}} - \omega^2 \mathbf{F}_M \cdot \hat{\mathbf{a}} + \mathbf{F}_K^{u\phi} \cdot \hat{\mathbf{a}} = 0, \quad -F_K^{\phi u} + F_K^{\phi\phi} = 0 \quad (14)$$

By considering Eq. (14) for each node of the unit cell, a homogeneous system of $2N$ algebraic equations is formed,

$$\begin{pmatrix} \mathbf{a}^{uu}(m, \phi, \theta, \boldsymbol{\alpha}) + \varpi^2 \mathbf{b}^{uu}(m, \phi, \theta, \boldsymbol{\alpha}) & \mathbf{a}^{u\phi}(m, \phi, \theta, \boldsymbol{\alpha}) \\ \mathbf{a}^{\phi u}(m, \phi, \theta, \boldsymbol{\alpha}) & \mathbf{a}^{\phi\phi}(m, \phi, \theta, \boldsymbol{\alpha}) \end{pmatrix} \begin{pmatrix} \mathbf{A}^u \\ \mathbf{A}^\phi \end{pmatrix} = \begin{pmatrix} \mathbf{0} \\ \mathbf{0} \end{pmatrix} \quad (15)$$

$$m = b\kappa/\pi = 2b/\lambda, \quad \varpi = (2b/c)\omega \quad (16)$$

where: m , dimensionless wave number, $0 < m < 1$; b , half of the element size; ϖ , dimensionless frequency of the discretized piezoelectric medium; $\boldsymbol{\alpha} = (\gamma, \beta, \varepsilon)$ form parameter for HE20 mesh, or $\boldsymbol{\alpha} = (\gamma, \varepsilon)$ form parameter for PE15 mesh.

In this procedure both the global stiffness matrices and the global mass matrix have been expressed in a suitable form,

$$\mathbf{K}_{xx} = \rho c^2 (2b) \mathbf{K}_{xx}^0 \quad xx = (uu, u\phi, \phi u, \phi\phi), \quad \mathbf{M} = \rho (2b)^3 \mathbf{M}^0 \quad (17)$$

The homogeneous system of $2N$ algebraic equations Eq. (15) can be reduced to a homogeneous system of N equations by static condensation [16]. So, from Eq. (15),

$$(\mathbf{a}^{uu} + \varpi^2 \mathbf{b}^{uu}) \mathbf{A}^u + \mathbf{a}^{u\phi} \mathbf{A}^\phi = \mathbf{0} \quad (a) \quad \mathbf{A}^\phi = -(\mathbf{a}^{\phi\phi})^{-1} \mathbf{a}^{\phi u} \mathbf{A}^u \quad (b) \quad (18)$$

Inserting Eq. (18b) into (18a), the condensate system of characteristic equations is formed,

$$(\mathbf{a}^{uu} - \mathbf{a}^{u\phi} (\mathbf{a}^{\phi\phi})^{-1} \mathbf{a}^{\phi u} + \varpi^2 \mathbf{b}^{uu}) \mathbf{A}^u = \mathbf{0} \quad \Leftrightarrow \quad \mathbf{Z} \mathbf{A}^u = \mathbf{0} \quad (19)$$

2.2 Dispersion equations

The system of homogeneous algebraic equations given in Eq. (19) has a non-trivial solution only if the matrix \mathbf{Z} is singular; that is, $\det[\mathbf{Z}] = 0$. Then it is yielded the following polynomial equation which is called the characteristic frequency equation for the plane wave propagation,

$$\sum_{r=0}^N c_r(m, \phi, \theta, \boldsymbol{\alpha}) \varpi^{2r} = 0, \quad c_N = 1 \quad (20)$$

It is an important fact that the N zeroes of a polynomial of degree $N \geq 1$ with complex coefficients depend continuously upon the coefficients [17]. Thus, sufficiently small changes in the coefficients of a polynomial can lead only to small changes in any zero. However, if the zeros are numerically computed, there is no simple way to define a function which takes the N coefficients (all but the leading 1) of a monic polynomial of degree N to the N zeroes of the polynomial, since there is no natural way to define an ordering among the N zeroes. In the case of the HE20 mesh, for which the polynomial Eq. (20) is quartic, the above difficulty has been

overcome by computing the zeroes in closed form as functions of its coefficients. Then, the components

$$\varpi_k = \varpi_k(m, \phi, \theta, \alpha), \quad k = 1, \dots, 4 \quad (21)$$

will be continuous functions precisely defined. They are called the dispersion equations.

Substituting Eq. (21) into Eq. (19), the displacement wave amplitudes corresponding to the nodes of the unit cell are yielded for each dispersion equation. Then, by Eq. (18b), the corresponding electric potential amplitudes are recovered.

To find the zeros of a polynomial equation as functions of its coefficients beyond the quartic equation is a very difficult mathematical problem [18]. Then, for the mesh PE15 which has five nodes per unit cell, if the zeros of Eq. (20) are numerically computed, the above mentioned ordering difficulty could be a problem. In this case, by considering the initial condition,

$$\lim_{m \rightarrow 0} \varpi_1(m, \phi, \theta, \alpha) = 0 \quad (22)$$

it is proposed to compute the first dispersion equation by a reduced unit cell obtained by a procedure of exact dynamic condensation [16].

Assume that the total nodes at the unit cell are categorized as master nodes (m) and slave nodes (s), where the number of master nodes is four and the number of slave nodes is one, Fig 2. With this arrangement, the system of characteristic equations Eq. (19) may be partitioned as

$$\begin{pmatrix} \mathbf{Z}_{mm}(q) & \mathbf{Z}_{ms}(q) \\ \mathbf{Z}_{sm}(q) & \mathbf{Z}_{ss}(q) \end{pmatrix} \begin{pmatrix} \mathbf{A}_m^u \\ \mathbf{A}_s^u \end{pmatrix} = \begin{pmatrix} \mathbf{0} \\ \mathbf{0} \end{pmatrix}, \quad q = \varpi^2 \quad (23)$$

From Eq. (23) the relation of wave amplitudes between the master and slave nodes may be obtained as

$$\mathbf{A}_s^u = -\mathbf{Z}_{ss}^{-1}(q) \mathbf{Z}_{sm}(q) \mathbf{A}_m^u \quad (24)$$

Then, by back-substituting, the system of characteristic equations of the reduced unit cell is obtained as

$$\mathbf{Z}_R(q) \mathbf{A}_m^u = \mathbf{0}, \quad [\mathbf{K}_R(q) + q \mathbf{M}_R(q)] \mathbf{A}_m^u = \mathbf{0} \quad (25)$$

Then, from Eq. (25), the reduced form of the characteristic frequency equation is obtained

$$q^4 + c_{3R}q^3 + c_{2R}q^2 + c_{1R}q + c_{0R} = 0, \quad c_{rR}(m, \phi, \theta, \alpha, q), \quad r = 0, \dots, 3 \quad (26)$$

The first dispersion equation is computed by the following iterative procedure:

Set by Eq. (22) the initial value $q_{i1} = 0$.

Do for $0 < m < 1$, step Δm

1. Compute the coefficients $c_{rR}(m, \phi, \theta, \alpha, q_{i1})$ of Eq. (26).

2. Compute the zero q_1 of the quartic polynomial Eq. (26).

Do while $(|q_1 - q_{i1}|/q_1) \geq \delta$

1. Refresh initial value $q_{i1} = q_1$.

2. Compute the coefficients $c_{rR}(m, \phi, \theta, \alpha, q_{i1})$ of Eq. (26).

3. Compute the zero q_1 of the quartic polynomial Eq. (26).

End do

3. Substituting q_1 into Eq. (25) to compute the wave amplitudes at the master nodes.

4. Substituting q_1 into Eq. (24) to compute the wave amplitudes at the slave nodes.
5. Refresh initial value $q_{i1} = q_1$ for the next step.

End do

It must be recall the equality of the energy and group velocities for bulk acoustic waves in a lossless piezoelectric medium [19], and the equality of the normal component of the group velocity and the phase velocity at the anisotropic continuum [20]. Then, the indicators of numerical dispersion for the phase velocity and the normal component of the group velocity are yielded for each dispersion equation. From Eq. (16),

$$e_p = c_p/c = (2\pi)^{-1} \varpi/m \quad (a) \quad e_{gn} = c_{gn}/c = (2\pi)^{-1} \partial \varpi / \partial m \quad (b) \quad (27)$$

The range of dimensionless wave number values where each dispersion equation represents the propagation of acoustic waves in the discretized medium will be called the acoustical branch of the dispersion equation. In order to determine the acoustical branches the following constraint conditions are imposed,

$$A_1^u = 1, \quad A_j^u(m, \phi, \theta, \alpha) > 0 \quad j = 2, \dots, N \quad (a) \quad (\partial \varpi / \partial m)_{\phi, \theta, \alpha} > 0 \quad (b) \quad (28)$$

In molecular physics the condition Eq. (28a) is called the restriction of the lattice spectrum to the acoustical branch [21]. By considering Eq. (27b), the constraint condition Eq. (28b) imposes that the normal component of the group velocity or energy velocity must have the wave direction. The preliminary constraint condition $\dim[\mathbf{N}(\mathbf{Z})] = 1$, over the dimension of the null space of matrix \mathbf{Z} for the HE20 mesh, or $\dim[\mathbf{N}(\mathbf{Z}_R)] = 1$ for the PE15 mesh, must be imposed in order to Eq. (28a) would be a meaningful constraint condition. For each dispersion equation only the acoustical branch will be considered.

2.3 Energy at the unit cell

From Eq. (2), Eq. (16) and Eq. (17), the densities of period-averaged elastic and electric energies at the unit cell are computed,

$$\begin{aligned} \bar{E}^M &= \frac{1}{2} \rho(\omega/\varpi)^2 C \int_0^1 \text{Re}[\tilde{\mathbf{x}}^T \exp(-i2\pi\tau)] \text{Re}[\tilde{\mathbf{F}}_{uu}^0 \exp(-i2\pi\tau)] d\tau \quad (a) \\ \bar{E}^E &= \frac{1}{2} \rho(\omega/\varpi)^2 C \int_0^1 \text{Re}[\tilde{\boldsymbol{\phi}}^T \exp(-i2\pi\tau)] \text{Re}[\tilde{\mathbf{F}}_{\phi\phi}^0 \exp(-i2\pi\tau)] d\tau \quad (b) \end{aligned} \quad (29)$$

where: $\tau = t/T$, $0 \leq \tau \leq 1$, dimensionless time; $\tilde{\mathbf{F}}_{uu}^0$ and $\tilde{\mathbf{F}}_{\phi\phi}^0$ are column matrices of forces at the nodes of the unit cell; $C = 1$ for the HE20 mesh, $C = 2/(3)^{1/2}$ for the PE15 mesh.

From the decomposition in Eq. (6), the above computed densities of period-averaged energies Eq. (29) can be partitioned as addition of basic and higher order components. Then, the percentage of period-averaged higher order total energy can be defined as

$$e_h = (\bar{E}_h^M + \bar{E}_h^E) / (\bar{E}^M + \bar{E}^E) = \bar{E}_h / \bar{E}, \quad e_h = e_h(m, \phi, \theta, \alpha) \quad (30)$$

From Eq. (29) and Eq. (12), the percentage indicator of total energy error associated with the spatial discretization that is introduced by the finite element model is defined as

$$e_T = ((\bar{E}^M + \bar{E}^E) / (\bar{E}_0^M + \bar{E}_0^E)) - 1 = (\bar{E} / \bar{E}_0) - 1, \quad e_T = e_T(m, \phi, \theta, \alpha) \quad (31)$$

From Eq. (30) and Eq. (31), a mapping between the total energy error and the percentage of higher order total energy can be also computed,

$$e_T = e_T(e_h, \phi, \theta, \alpha) \quad (32)$$

2.4 Substitute wave field

It is clear that the harmonic acoustic waves cannot be exactly captured by a regular mesh of finite elements HE20 or PE15. This fact is a consequence of the element interpolation which is quadratic. A substitute wave field [22] or alias field [13] has been obtained in the discretized unbounded medium by performing a dispersion analysis in terms of allowable polarizations of the continuum. The substitute wave field is obtained by collocating Eq. (13a) and Eq. (13b) in each node of the unit cell. The assumption of different amplitudes is introduced because the equation of equilibrium is different for each node. The analysis yields the relative wave amplitudes and the dispersion relation under which the alias field may propagate in the discretized medium. The alias wave field will be

$$\tilde{\mathbf{u}}^a = \sum N_{s,i} \tilde{\mathbf{u}}_i, \quad \tilde{\phi}^a = \sum N_{s,i} \tilde{\phi}_i \quad (33)$$

where: $\tilde{\mathbf{u}}_i$, the values of Eq. (13a) at the nodes; $\tilde{\phi}_i$, the values of Eq. (13b) at the nodes; $N_{s,i}$, the nodal shape functions.

By computing the wave amplitude distortion, the discretization error of the wave field Eq. (33) can be decomposed as addition of interpolation and pollution errors [23].

2.5 Numerical research

For the waves and media considered the indicators Eq. (27), Eq. (30) and Eq. (31) are computed versus dimensionless wave number for different meshes and directions of wave propagation. Five meshes having the same element volume will be considered for each of the elements analyzed. Specifically, for HE20 element, Fig. 1:

Q1: square section; $\gamma = 1$, $\beta = 0$, $\varepsilon = 1$.

Q2: rectangular section with aspect ratio 1:2; $\gamma = 1/\sqrt{2}$, $\beta = 0$, $\varepsilon = 1$.

Q3: skewed section; $\gamma = 1$, $\beta = 45^\circ$, $\varepsilon = 1$.

Q4: distorted in the poling Z-direction with aspect ratio 2:1; $\gamma = 1$, $\beta = 0$, $\varepsilon = 2^{1/3}$.

Q5: distorted in the poling Z-direction with aspect ratio 1:2; $\gamma = 1$, $\beta = 0$, $\varepsilon = 1/2^{1/3}$.

and, for PE15 element, Fig. 2:

T1: triangular section of equilateral geometry; $\gamma = 1$, $\varepsilon = 1$.

T2: triangular section of right geometry; $\gamma^2 = 1/(3)^{1/2}$, $\varepsilon = 1$.

T3: triangular section with angle of 30° opposite to the base; $\gamma^2 = 1/(3)^{1/2} \tan 75^\circ$, $\varepsilon = 1$.

T4: distorted in the poling Z-direction with aspect ratio 2:1; $\gamma = 1$, $\varepsilon = 2^{1/3}$.

T5: distorted in the poling Z-direction with aspect ratio 1:2; $\gamma = 1$, $\varepsilon = 1/2^{1/3}$.

Given the mesh and the piezoelectric medium, the dispersion analysis is numerically carried out by a step of $\pi/36$ for the azimuthal and polar angles, and a step of $1/10000$ for the dimensionless wave number. As result the indicators Eq. (27), Eq. (30) and Eq. (31), are computed as finite sets of values. An example of the indicators Eq. (30) and Eq. (32) is shown in Fig. 3. It is observed that Eq. (30) and it is deduced that Eq. (31) both vanish as dimensionless wave number goes to zero; that is, as the mesh is refined and in the limit of long waves. It must be remarked that the behavior of the higher order total energy as dimensionless wave number goes to zero is a consequence that both the strain field and the electric field inside each element becomes uniform. That is, given the mesh, in the limit of long waves, the density of total energy

approaches to zero more slowly than its higher order component; and, given the wavelength, as the solution converges on account of mesh refinement, the density of total energy is increasingly dominated by its basic component.

Investigating the relationship between the total energy error and the percentage of higher order total energy Eq. (32), it can be observed from Fig. 3 that both variables could be related by a cubic function for moderate values of the higher order total energy,

$$e_T = [A(\phi, \theta, \alpha) * e_h + B(\phi, \theta, \alpha)] * e_h^2 \quad (34)$$

For each of the waves (SS, FS, and L) and piezoelectric media considered in this research, an averaged correlation between the total energy error and the percentage of higher order total energy is sought by computing averaged values for the coefficients A and B .

First, two reference values of the percentage of higher order total energy are selected,

$$HE20: e_{h1} = 0.10 \quad e_{h2} = 0.20; \quad PE15: e_{h1} = 0.075 \quad e_{h2} = 0.15 \quad (35)$$

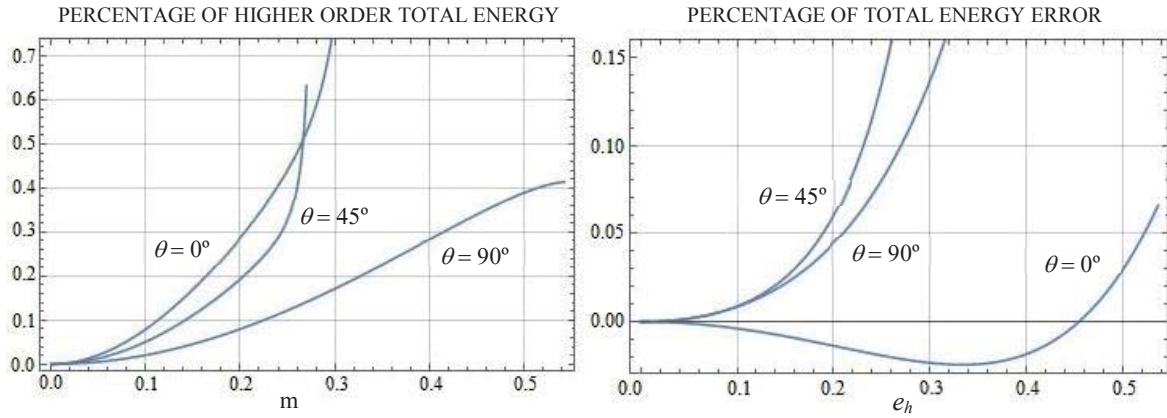


Figure 3: Percentage of higher order total energy versus dimensionless wave number and versus percentage of total energy error. PMN-30PT, MESH Q4, L-WAVES, $\phi = 45^\circ$.

Then, by Eq. (30) and Eq. (32), the reference values related of dimensionless wave number and percentage of total energy error are respectively computed,

$$m_{1,2} = m_{1,2}(\phi, \theta, \alpha), \quad e_{T1,2} = e_{T1,2}(\phi, \theta, \alpha) \quad (36)$$

The mean value of each reference dimensionless wave number, and the root mean square value (based on the L_2 -norm) and the sup-norm value [24] of each reference total energy error are next computed on the range of propagation angles,

$$\begin{aligned} m_{1,2}^M(\alpha) &= \frac{1}{\pi^2} \int_0^\pi \int_0^\pi m_{1,2} d\phi d\theta \quad (a) \quad e_{T1,2}^{RMS}(\alpha) = \sqrt{\frac{1}{\pi^2} \int_0^\pi \int_0^\pi |e_{1,2}|^2 d\phi d\theta} \quad (b) \\ e_{T1,2}^{SUP}(\alpha) &= \sup \{|e_{1,2}(\phi, \theta, \alpha)| : 0 \leq \phi, \theta \leq \pi\} \quad (c) \end{aligned} \quad (37)$$

Consistent with the discrete analysis carried out, the integrals in Eq. (37a) and Eq. (37b) are numerically computed. Mean values of the indicators of numerical dispersion for the phase velocity and the normal component of the group velocity Eq. (27) have been also computed. Detailed values are presented in the Appendix 2 attached to this manuscript.

As a next step, the values computed in Eq. (37a) and Eq. (37b) are mesh-averaged,

$$\begin{aligned}
HE20: \quad \overline{m_{1,2}^M} &= \frac{1}{5} \sum_{j=1}^5 m_{1,2}^M(Q_j) & HE20: \quad \overline{e_{T1,2}^{RMS}} &= \frac{1}{5} \sum_{j=1}^5 e_{T1,2}^{RMS}(Q_j) \\
PE15: \quad \overline{m_{1,2}^M} &= \frac{1}{5} \sum_{j=1}^5 m_{1,2}^M(T_j) & PE15: \quad \overline{e_{T1,2}^{RMS}} &= \frac{1}{5} \sum_{j=1}^5 e_{T1,2}^{RMS}(T_j)
\end{aligned} \tag{38}$$

The results of Eq. (38a) and Eq. (38b) are displayed in Table 1 and Table 2, respectively, for each of the piezoelectric media and waves investigated. Similar mesh-averaged values of the indicators of numerical dispersion for the phase velocity and the normal component of the group velocity Eq. (27) have been also computed, Table 3.

From Table 1 and Table 2, it is deduced that the mesh-averaged root mean square values of the first and the second reference percentage of total energy error roughly correspond, in an averaged sense, to six and four elements per wavelength, respectively. In such averaged sense, the total energy error of the quasi-longitudinal waves is greater than the one of the quasi-shear waves. An opposite behavior is shown by the indicators of numerical dispersion. It is deduced from Table 3 that the numerical dispersion of the quasi-shear waves is greater than the one of the quasi-longitudinal waves.

		HE20				HE20	
		PZT-5H	PZT-8	PZT-5A	PMN-30PT	PMN-31PT	PIN-PMN-PT
$\overline{m_1^M}$	SS	0.1758	0.1756	0.1755	0.1751	0.1753	0.1753
	FS	0.1756	0.1758	0.1759	0.1754	0.1754	0.1754
	L	0.1748	0.1749	0.1748	0.1745	0.1745	0.1745
$\overline{m_2^M}$	SS	0.2576	0.2571	0.2567	0.2553	0.2558	0.2557
	FS	0.2568	0.2574	0.2577	0.2564	0.2563	0.2563
	L	0.2542	0.2545	0.2543	0.2530	0.2531	0.2532
		PE15				PE15	
		PZT-5H	PZT-8	PZT-5A	PMN-30PT	PMN-31PT	PIN-PMN-PT
$\overline{m_1^M}$	SS	0.1804	0.1804	0.1802	0.1794	0.1797	0.1797
	FS	0.1804	0.1806	0.1807	0.1803	0.1804	0.1803
	L	0.1797	0.1798	0.1798	0.1796	0.1796	0.1795
$\overline{m_2^M}$	SS	0.2628	0.2627	0.2623	0.2599	0.2607	0.2606
	FS	0.2627	0.2632	0.2634	0.2624	0.2625	0.2624
	L	0.2606	0.2608	0.2607	0.2599	0.2599	0.2598

Table 1: Mesh-average of the mean values of the first and second reference dimensionless wave number.

Finally, by the mesh-averaged reference values of total energy error Eq. (38b), the averaged values of the coefficients A and B for the cubic correlation Eq. (34) can be computed,

$$\overline{e_{T1,2}^{RMS}} = [\overline{A} * e_{h1,2} + \overline{B}] * e_{h1,2}^2 \tag{39}$$

Then the averaged correlation between the total energy error and the percentage of higher order total energy will be yielded

$$e_T^{RMS} = (\overline{A} * e_h + \overline{B}) * e_h^2, \quad 0 < e_h \leq e_{h2} \tag{40}$$

3 MODAL ANALYSIS

As application it is explored the use of the averaged correlation Eq. (40) as a reference to apply the higher order total energy as an indicator of discretization error for the finite element vibration eigenmodes. These ones are the solution of the eigenproblem obtained by considering the homogeneous part of Eq. (1) and assuming stationary waves. In condensed form [10],

$$\mathbf{K}^* \tilde{\mathbf{x}}_j = \omega_j^2 \mathbf{M} \tilde{\mathbf{x}}_j, \quad \mathbf{K}^* = \mathbf{K}_{uu} + \mathbf{K}_{u\phi} \mathbf{K}_{\phi\phi}^{-1} \mathbf{K}_{\phi u}^T \quad (a) \quad \tilde{\boldsymbol{\phi}}_j = \mathbf{K}_{\phi\phi}^{-1} \mathbf{K}_{\phi u}^T \tilde{\mathbf{x}}_j \quad (b) \quad j = 1, \dots, n \quad (41)$$

$$\tilde{\mathbf{x}}_i^T \mathbf{K}^* \tilde{\mathbf{x}}_j = \delta_{ij} \omega_j^2 \quad i, j = 1, \dots, n \quad (42)$$

where: ω_j and $(\tilde{\mathbf{x}}_j, \tilde{\boldsymbol{\phi}}_j)^T$ are the finite element natural frequencies and eigenvectors.

		HE20				HE20	
		PZT-5H	PZT-8	PZT-5A	PMN-30PT	PMN-31PT	PIN-PMN-PT
$\overline{e_{T1}^{RMS}}$	SS	0.003122	0.002918	0.002759	0.003173	0.003013	0.002986
	FS	0.002698	0.002818	0.003055	0.002731	0.002780	0.002761
	L	0.005648	0.005287	0.005546	0.006690	0.006288	0.006223
$\overline{e_{T2}^{RMS}}$	SS	0.013157	0.012431	0.011570	0.012833	0.012206	0.012081
	FS	0.011348	0.011925	0.012891	0.011663	0.011962	0.011782
	L	0.029571	0.026939	0.028789	0.038235	0.034769	0.034268
		PE15				PE15	
		PZT-5H	PZT-8	PZT-5A	PMN-30PT	PMN-31PT	PIN-PMN-PT
$\overline{e_{T1}^{RMS}}$	SS	0.005515	0.005209	0.005389	0.006292	0.006286	0.006180
	FS	0.005529	0.005393	0.005588	0.005483	0.005412	0.005505
	L	0.007119	0.006555	0.007139	0.008989	0.007935	0.007664
$\overline{e_{T2}^{RMS}}$	SS	0.022301	0.021252	0.021783	0.023798	0.024103	0.023750
	FS	0.022770	0.022237	0.023049	0.022635	0.022367	0.022743
	L	0.033449	0.029710	0.033447	0.052871	0.043976	0.043680

Table 2: Mesh-average of the rms values of the first and second reference percentage of total energy error.

		HE20				HE20	
		PZT-5H	PZT-8	PZT-5A	PMN-30PT	PMN-31PT	PIN-PMN-PT
$\overline{e_{p2}^M}$	SS	1.00392	1.00326	1.00342	1.00752	1.00665	1.00654
	FS	1.00356	1.00352	1.00385	1.00321	1.00304	1.00310
	L	1.00194	1.00199	1.00196	1.00168	1.00170	1.00171
$\overline{e_{gn2}^M}$	SS	1.01941	1.01614	1.01692	1.03698	1.03269	1.03219
	FS	1.01759	1.01740	1.01902	1.01583	1.01497	1.01525
	L	1.00936	1.00964	1.00947	1.00795	1.00809	1.00815
		PE15				PE15	
		PZT-5H	PZT-8	PZT-5A	PMN-30PT	PMN-31PT	PIN-PMN-PT
$\overline{e_{p2}^M}$	SS	1.00386	1.00330	1.00354	1.00640	1.00568	1.00575
	FS	1.00352	1.00339	1.00365	1.00340	1.00322	1.00328
	L	1.00185	1.00191	1.00187	1.00164	1.00167	1.00165
$\overline{e_{gn2}^M}$	SS	1.01864	1.01596	1.01708	1.03090	1.02748	1.02783
	FS	1.01718	1.01653	1.01781	1.01652	1.01561	1.01588
	L	1.00897	1.00914	1.00891	1.00673	1.00739	1.00717

Table 3: Second mesh-averaged reference values of the indicators of numerical dispersion.

Eq. (41a) and Eq. (41b) are solved by LAPACK routines [25]. By considering the relation of \mathbf{K} -orthogonality Eq. (42) for the condensed eigenproblem Eq. (40a), and taking into account Eq. (41b) and Eq. (7), it can be yielded the following expression for the modal total energy

$$\frac{1}{4} \tilde{\mathbf{x}}_j^T \mathbf{K}_{uu} \tilde{\mathbf{x}}_j + \frac{1}{4} \tilde{\boldsymbol{\phi}}_j^T \mathbf{K}_{\phi\phi} \tilde{\boldsymbol{\phi}}_j = \frac{1}{4} \omega_j^2 \rightarrow \bar{E}_j = \frac{1}{4} \omega_j^2, \quad j = 1, \dots, n \quad (43)$$

The error for the modal total energy computed with the discretized piezoelectric domain is estimated by a reference model that will be obtained by dividing each element of the actual mesh into eight elements. The modal total energy computed with the actual model and the one computed with the reference model will be compared for each eigenmode by

$$TEE = (\bar{E}/\bar{E}^{REF}) - 1, \quad TEE = (\omega/\omega^{REF})^2 - 1 \quad (44)$$

The modal total energy error Eq. (44) will be compared with a proposed total energy error indicator which is computed either by averaging the correlation Eq. (40) for the slow and fast quasi-shear waves, or by the correlation Eq. (40) for the quasi-longitudinal waves,

$$TEES(PHE) = \frac{1}{2}(e_{T,SS}^{RMS} + e_{T,FS}^{RMS}) \quad (a) \quad TEEL(PHE) = e_{T,L}^{RMS} \quad (b), \quad 0 < PHE \leq e_{h2} \quad (45)$$

where PHE is the percentage of higher order total energy computed with the actual model.

From Table 2, the following inequality is clearly fulfilled,

$$TEES(PHE) < TEEL(PHE) \quad (46)$$

Finally, by taking into account Eq. (7), the percentage of modal electric energy will be also computed with the actual model,

$$PEE = \bar{E}^E / (\bar{E}^M + \bar{E}^E) \quad (47)$$

It must be remarked that, for plane bulk acoustic waves, Eq. (47) would be an accepted definition of electromechanical coupling coefficient from energy consideration [26].

3.1 Numerical research

Two test problems discretized by the HE20 element have been analyzed, Fig. 4: a piezoelectric cantilever bimorph connected in parallel configuration made of PZT-5A ($L = 16$ mm, $b = 3$ mm, $t = 2$ mm) [27, 28], and a piezoelectric cube laterally clamped made of PZT-5H or, alternatively, PMN-30PT single crystal ($L = 1$ mm) [29]. A piezoelectric disk laterally clamped, discretized by the PE15 element, is also analyzed, Fig. 5 ($R = 12$ mm, $t = 6$ mm). The piezoelectric disk is made of PZT-8 or, alternatively, PIN-PMN-PT single crystal. In each test problem the electrodes are shorted and their mechanical effects are neglected.

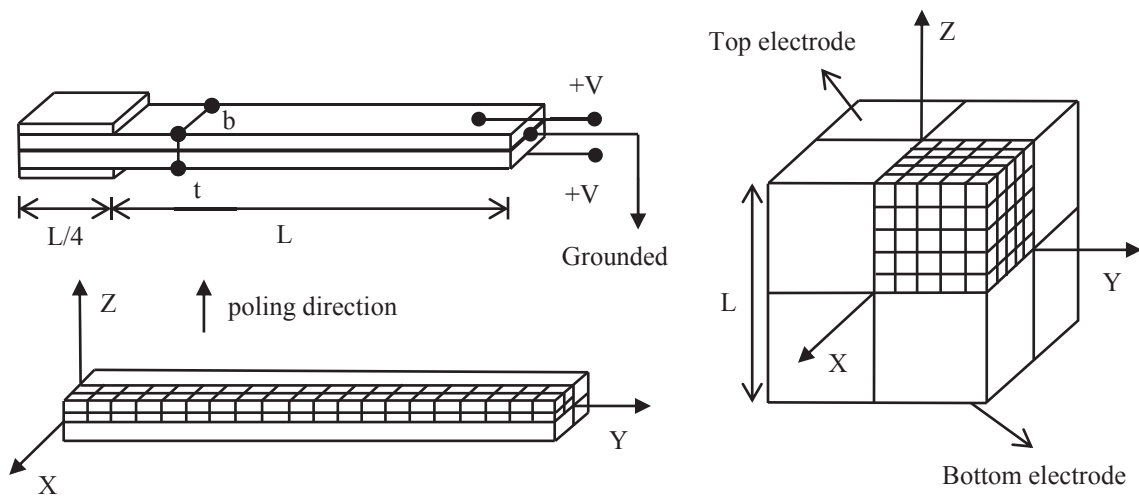


Figure 4: Piezoelectric cantilever bimorph and cube laterally clamped discretized by the HE20 element.

Since the piezoelectric bimorph has two planes of symmetry, which are XY and YZ , the modes can be computed by idealizing one quarter of it and applying four combinations of boundary conditions on the two planes for symmetric motion (S) and for antisymmetric motion (A), see details in reference [30]. In this test problem, the swaying modes in the Z -direction (AS) and the torsion modes about the Y -axis (AA) have been computed, Table 4.

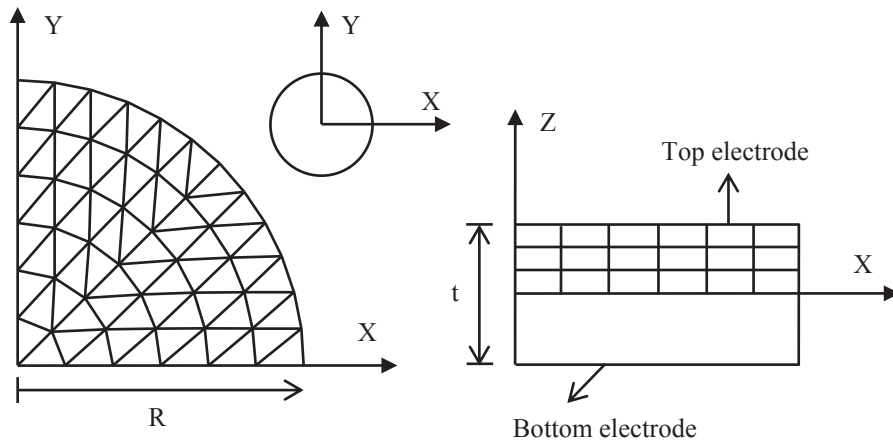


Figure 5: Piezoelectric disk laterally clamped discretized by the PE15 element.

Similarly, since both the piezoelectric cube and the piezoelectric disk have three planes of symmetry, which are YZ , XZ and XY , the modes can be computed by idealizing one eighth of them, and applying six combinations of boundary conditions on the three planes for symmetric motion (S) and for antisymmetric motion (A). Also see details in reference [30]. In both test problems, the antisymmetric and symmetric longitudinal modes in the Z -direction (SSA and SSS), the antisymmetric and symmetric swaying modes in the Y -direction (SAA and SAS), and the antisymmetric and symmetric torsion modes about the Z -axis (AAA and AAS) have been computed. The results are displayed in Tables 5-16.

For each test problem it is selected the set of consecutive eigenmodes for which the following condition is fulfilled: $0 < PHE \leq e_{h2}$ (see Eq. (35)).

#MODE		FR (Hz)	PHE	TEE	TEES	PHE REF	PEE
1	AS	3631.35	0.088188	0.005768	0.002247	0.026710	0.027781
2	AS	21217.95	0.092730	0.005303	0.002490	0.027706	0.031491
3	AA	22773.80	0.139349	0.002560	0.005760	0.039546	0.006289
4	AS	54358.47	0.103447	0.004919	0.003116	0.030374	0.038010
5	AA	68479.08	0.146347	0.002731	0.006376	0.041704	0.008586
6	AS	96273.68	0.120632	0.004907	0.004276	0.034929	0.046683
7	AA	114645.43	0.160009	0.003132	0.007674	0.045951	0.012958
8	AS	143956.67	0.143424	0.005613	0.006114	0.041300	0.056198
8	AA	161540.12	0.179748	0.003882	0.009780	0.052171	0.019010
10	AS	195356.94	0.170984	0.007262	0.008811	0.049380	0.065731
11	AA	209366.65	0.204825	0.005154	0.012858	0.026253	0.060229
12	AS	249168.34	0.201768	0.009994	0.012459	0.074345	0.058857

Table 4: PZT-5A cantilever bimorph. Proposed total energy error indicator TEES versus total energy error computed by mesh halving TEE.

#MODE		FR (Hz)	PHE	TEE	TEES	PHE REF	PEE
1	A	1494798.75	0.044947	0.001012	0.000571	0.012649	0.378348
2	S	2253607.19	0.054692	0.000674	0.000850	0.014552	0.257970
3	A	2911828.99	0.103631	0.002572	0.003131	0.030457	0.160737
4	S	2925280.47	0.104319	0.003437	0.003174	0.031274	0.075176
5	A	2949444.83	0.103972	0.003440	0.003152	0.031517	0.070138
6	S	3219709.13	0.111434	0.002536	0.003635	0.030942	0.194094
7	A	3269260.33	0.132101	0.003350	0.005164	0.037684	0.242467
8	S	3293030.56	0.122009	0.004621	0.004382	0.037425	0.138397
9	S	3343606.11	0.123991	0.003496	0.004530	0.035570	0.043260
10	A	3407876.53	0.106406	0.002466	0.003306	0.029866	0.345914
11	S	3470792.89	0.108399	0.002632	0.003434	0.030465	0.269794
12	A	3546463.33	0.102105	0.001708	0.003037	0.027275	0.170078
13	A	3727337.34	0.127277	0.003860	0.004782	0.035938	0.082845
14	A	3730441.23	0.120325	0.004203	0.004258	0.034218	0.098911
15	S	3785874.14	0.130364	0.002186	0.005024	0.035527	0.050604
16	S	4064314.52	0.163973	0.005918	0.008088	0.050438	0.115876
17	A	4115269.62	0.191198	0.005907	0.011148	0.059473	0.164358
18	S	4218250.54	0.142201	0.004665	0.006015	0.039927	0.084108
19	A	4223091.77	0.165183	0.002378	0.008212	0.045304	0.032168
20	S	4354513.22	0.178546	0.006200	0.009660	0.051740	0.173579
21	S	4440349.35	0.154910	0.005003	0.007185	0.044617	0.090900
22	S	4475618.52	0.170321	0.006235	0.008754	0.047812	0.066334
23	A	4481882.47	0.171154	0.006331	0.008844	0.050257	0.167460
24	A	4530610.59	0.166572	0.005410	0.008357	0.050164	0.293279
25	S	4569360.37	0.204520	0.008802	0.012841	0.059976	0.112327
26	A	4691002.54	0.200371	0.009031	0.012300	0.058179	0.099302
27	A	4755510.15	0.192601	0.005597	0.011321	0.055896	0.129024
28	S	4796773.25	0.170910	0.007932	0.008817	0.052541	0.097511

Table 5: PZT-5H cube laterally clamped. Proposed total energy error indicator TEES versus total energy error computed by mesh halving TEE. Modes SS (S) and SS (A).

#MODE		FR (Hz)	PHE	TEE	TEEL	PHE REF	PEE
1	A	1955083.91	0.047784	0.004777	0.001186	0.014847	0.285874
2	S	2070385.14	0.105834	0.009124	0.007681	0.028318	0.006049
3	S	2347003.92	0.062630	0.002363	0.002204	0.016782	0.332819
4	A	2368802.89	0.113605	0.008700	0.009138	0.032137	0.029402
5	A	2594239.22	0.119986	0.009462	0.010457	0.037010	0.229177
6	S	2904544.18	0.144480	0.013562	0.016629	0.043907	0.180060
7	S	2947810.19	0.169046	0.026569	0.024778	0.055882	0.098489

Table 6: PMN-30PT cube laterally clamped. Proposed total energy error indicator TEEL versus total energy error computed by mesh halving TEE. Modes SS (S) and SS (A).

From Tables 4-16 it is deduced that the percentage of higher order total energy decreases as the mesh is refined. Then, it is verified that this energy component behaves as a modal error indicator, which is in accordance with the numerical dispersion analysis.

From Tables 4, 5, 7, 9, 11, 13 and 15 it can be deduced that, for the solids made of PZT piezoceramics, the proposed total energy error indicator based on S-waves Eq. (45a) and the

total energy error computed by mesh halving Eq. (44) generally exhibit a similar evolution pattern as the modal order increases. Also, the proposed total energy error indicator Eq. (45a) generally overestimates the total energy error computed by mesh halving Eq. (44). Clearly, by the proposed total energy error indicator based on S-waves Eq. (45a), the accuracy of the finite element eigenmodes could be confidently verified in order to select a cutoff modal order given an upper bound for the total energy error close to one per cent.

The above behavior for the solids made of PZT piezoceramics could be expected based on the heuristic that, given the natural frequency, both the percentage of higher order total energy and the spatial discretization error should be mainly influenced by the error induced by the slowest quasi-shear waves which have the shortest wavelengths.

#MODE		FR (Hz)	PHE	TEE	TEES	PHE REF	PEE
1	S	1940056.24	0.037057	0.001392	0.000386	0.011346	0.131090
2	A	2089555.22	0.037879	0.000869	0.000404	0.010915	0.195819
3	A	2434954.09	0.079598	0.002009	0.001824	0.023051	0.374945
4	S	2487876.85	0.069741	0.001248	0.001393	0.019433	0.238560
5	S	2828993.11	0.080055	0.001657	0.001845	0.021692	0.044895
6	A	2982767.69	0.088200	0.001334	0.002250	0.023570	0.057256
7	S	3140640.11	0.090835	0.001926	0.002389	0.025225	0.186659
8	A	3297569.35	0.102153	0.002622	0.003040	0.029069	0.188117
9	S	3421891.52	0.123931	0.002632	0.004526	0.035635	0.075841
10	A	3467280.17	0.139115	0.003948	0.005748	0.041684	0.124472
11	S	3612688.32	0.126168	0.003720	0.004696	0.036407	0.106855
12	A	3775918.50	0.141560	0.003737	0.005959	0.040244	0.174574
13	S	3780264.69	0.128603	0.002931	0.004885	0.036160	0.190129
14	S	3901737.88	0.164548	0.005014	0.008147	0.047153	0.089534
15	A	3904222.86	0.151162	0.003813	0.006828	0.044073	0.255638
16	A	4005566.29	0.159113	0.003850	0.007596	0.045297	0.124791
17	S	4136640.68	0.181068	0.006140	0.009948	0.053140	0.203126
18	A	4178781.08	0.155419	0.003933	0.007234	0.044197	0.193035
19	A	4228182.19	0.167523	0.004781	0.008457	0.047798	0.067265
20	S	4249965.73	0.187775	0.007818	0.010734	0.057300	0.198316
21	S	4364136.58	0.167402	0.005350	0.008444	0.046784	0.079209
22	S	4501655.31	0.182042	0.006794	0.010060	0.050711	0.066730
23	A	4540145.24	0.163551	0.005669	0.008044	0.047357	0.312658
24	A	4620112.25	0.190505	0.007098	0.011064	0.052324	0.055107
25	S	4633649.48	0.179765	0.005468	0.009798	0.050850	0.123484
26	S	4688950.56	0.174831	0.005880	0.009245	0.049616	0.161655
27	A	4758178.95	0.185452	0.006966	0.010458	0.054770	0.122037
28	S	4795991.67	0.195165	0.005529	0.011639	0.056789	0.092402
29	A	4858675.43	0.203334	0.007203	0.012686	0.060966	0.174814

Table 7: PZT-5H cube laterally clamped. Proposed total energy error indicator TEES versus total energy error computed by mesh halving TEE. Modes SA (S) and SA (A).

From Tables 5-16, it can be deduced that the modal total energy errors computed by mesh halving for the solids made of PMN-PT <001> poled single crystals are significantly greater than the ones computed for the solids made of PZT. This behavior is similar to the dilatational locking phenomenon that is most commonly associated with nearly incompressible isotropic materials, i.e., with those for which the Poisson's ratio approaches one-half very closely [13].

From Tables 6, 8, 10, 12, 14 and 16 it can be deduced that, for the solids made of PMN-PT single crystals, only the proposed total energy error indicator based on L-waves Eq. (45b) overestimates for some eigenmodes the total energy error computed by mesh halving Eq. (44); however, by the proposed total energy error indicator based on L-waves Eq. (45b), an upper bound for the total energy error generally can be satisfactorily estimated for the set of eigenmodes selected. Clearly, for the PMN-PT solids, the modal total energy error should be mainly influenced by the error induced by the quasi-longitudinal waves. Both for PMN-30PT cube and for the PIN-PMN-PT disk laterally clamped, the total energy errors computed by mesh halving, for the eigenmodes selected, generally can be accepted for all practical purposes from the engineering point of view.

#MODE		FR (Hz)	PHE	TEE	TEEL	PHE REF	PEE
1	S	1831206.39	0.056366	0.007051	0.001728	0.016903	0.079782
2	A	2215758.70	0.046708	0.004171	0.001126	0.014119	0.221063
3	S	2405588.22	0.110802	0.012973	0.008594	0.032335	0.076049
4	A	2664535.32	0.117330	0.010324	0.009894	0.034096	0.103798
5	S	2794592.00	0.126270	0.014561	0.011868	0.035678	0.121444
6	S	2949954.65	0.090059	0.009531	0.005195	0.025816	0.179932
7	A	3046735.64	0.097286	0.005731	0.006258	0.028028	0.330363
8	A	3090706.07	0.150862	0.016097	0.018547	0.042078	0.033922

Table 8: PMN-30PT cube laterally clamped. Proposed total energy error indicator TEEL versus total energy error computed by mesh halving TEE. Modes SA (S) and SA (A).

#MODE		FR (Hz)	PHE	TEE	TEES	PHE REF	PEE
1	S	2024859.86	0.044406	0.000407	0.000557	0.011471	0.000216
2	A	2303313.34	0.052876	0.000465	0.000793	0.014074	0.082242
3	S	2724869.55	0.070839	0.002311	0.001438	0.020973	0.147724
4	A	2809855.32	0.062111	0.001722	0.001100	0.018002	0.144506
5	S	2937759.52	0.082856	0.001065	0.001980	0.022996	0.152725
6	S	3039991.26	0.090128	0.001847	0.002352	0.025490	0.190031
7	A	3050295.13	0.112990	0.002373	0.003741	0.032682	0.375057
8	S	3549794.00	0.122028	0.003297	0.004383	0.034450	0.164487
9	A	3617277.27	0.125511	0.001897	0.004646	0.034861	0.136241
10	S	3635257.08	0.129175	0.003529	0.004930	0.034367	0.000358
11	A	3668364.29	0.115199	0.002482	0.003893	0.032078	0.189753
12	A	3765104.77	0.136739	0.003342	0.005546	0.036684	0.015491
13	A	3887782.42	0.136244	0.003633	0.005505	0.037601	0.063732
14	S	3893669.38	0.122578	0.003667	0.004424	0.033558	0.054943
15	S	4121863.35	0.159137	0.003041	0.007599	0.043516	0.038288
16	S	4262559.26	0.157842	0.003452	0.007471	0.044082	0.125908
17	A	4269201.31	0.175189	0.004846	0.009284	0.052109	0.234513
18	S	4270499.91	0.184011	0.007730	0.010289	0.053881	0.049026
19	A	4305152.76	0.191207	0.007863	0.011150	0.057651	0.078252
20	S	4430778.46	0.185779	0.004550	0.010497	0.052688	0.141208
21	S	4452728.08	0.186311	0.005351	0.010560	0.053636	0.169705

Table 9: PZT-5H cube laterally clamped. Proposed total energy error indicator TEES versus total energy error computed by mesh halving TEE. Modes AA (S) and AA (A).

#MODE		FR (Hz)	PHE	TEE	TEEL	PHE REF	PEE
1	S	1696277.98	0.043646	0.001614	0.000966	0.011304	0.000239
2	A	2288255.39	0.051260	0.001024	0.001390	0.013540	0.118416
3	S	2600469.55	0.187436	0.027305	0.032316	0.049783	0.002476
4	S	2835507.34	0.091854	0.011700	0.005447	0.027974	0.036460
5	A	2943475.43	0.191199	0.021385	0.034021	0.052110	0.048119
6	A	3031360.11	0.092986	0.011084	0.005610	0.029612	0.107099
7	S	3437664.02	0.173580	0.041123	0.026517	0.067656	0.032985
8	S	3474206.51	0.106232	0.005290	0.007752	0.023311	0.134139
9	S	3491292.14	0.113828	0.005874	0.009182	0.032752	0.246306

Table 10: PMN-30PT cube laterally clamped. Proposed total energy error indicator TEEL versus total energy error computed by mesh halving TEE. Modes AA (S) and AA (A).

#MODE		FR (Hz)	PHE	TEE	TEES	PHE REF	PEE
1	A	51541.31	0.048021	0.002249	0.002153	0.013658	0.177725
2	A	124164.61	0.068596	0.003176	0.004425	0.019245	0.209649
3	A	136836.01	0.079258	0.003836	0.005929	0.022247	0.215999
4	S	150662.77	0.030442	0.001521	0.000860	0.008708	0.053842
5	S	189790.61	0.030784	0.001357	0.000880	0.008937	0.116753
6	S	194972.83	0.045667	0.002401	0.001946	0.012235	0.029768
7	A	198719.09	0.094287	0.005113	0.008433	0.026825	0.221408
8	A	217589.92	0.072451	0.004112	0.004942	0.020729	0.105793
9	S	229412.09	0.064027	0.004506	0.003849	0.017764	0.023877
10	A	230820.02	0.116057	0.008231	0.012870	0.033558	0.201034
11	A	231941.28	0.099038	0.005996	0.009319	0.027954	0.123675
12	A	251548.75	0.069560	0.003639	0.004551	0.019548	0.035352
13	A	257018.78	0.070986	0.001782	0.004742	0.018867	0.003714
14	A	272961.42	0.134343	0.009464	0.017351	0.039191	0.228955
15	S	273635.96	0.101763	0.006729	0.009848	0.027661	0.070426
16	S	277908.60	0.089192	0.006175	0.007533	0.024691	0.090064
17	A	281742.73	0.080465	0.004068	0.006113	0.022439	0.015318
18	S	287413.21	0.110412	0.003803	0.011627	0.030509	0.175302
19	S	287709.83	0.105576	0.006213	0.010613	0.029050	0.105030
20	S	298220.48	0.104759	0.010929	0.010447	0.029507	0.021874

Table 11: PZT-8 disk laterally clamped. Proposed total energy error indicator TEES versus total energy error computed by mesh halving TEE. Modes SS (S) and SS (A).

#MODE		FR (Hz)	PHE	TEE	TEEL	PHE REF	PEE
1	A	50070.97	0.061813	0.012118	0.004817	0.020158	0.282503
2	S	92783.92	0.043018	0.003907	0.002065	0.011601	0.116988
3	S	122410.01	0.064886	0.011353	0.005408	0.019192	0.183122
4	A	123322.12	0.076182	0.013804	0.007960	0.024150	0.262586
5	A	138967.48	0.086335	0.014515	0.010808	0.026849	0.245642
6	S	146426.59	0.050728	0.005403	0.003024	0.014895	0.390335
7	S	147337.01	0.112765	0.022865	0.021031	0.030776	0.057746
8	S	154795.39	0.081233	0.009450	0.009308	0.022474	0.086916

Table 12: PIN-PMN-PT disk laterally clamped. Proposed total energy error indicator TEEL versus total energy error computed by mesh halving TEE. Modes SS (S) and SS (A).

#MODE		FR (Hz)	PHE	TEE	TEES	PHE REF	PEE
1	A	87719.21	0.058070	0.002506	0.003160	0.016293	0.201956
2	S	99192.21	0.011349	0.000872	0.000119	0.003663	0.084222
3	S	150752.21	0.026183	0.001172	0.000635	0.006924	0.009380
4	A	161484.50	0.081146	0.004074	0.006218	0.022875	0.217459
5	A	181107.96	0.096651	0.005297	0.008868	0.027251	0.225069
6	S	192771.32	0.046451	0.002909	0.002014	0.013028	0.035684
7	A	205686.40	0.044962	0.001804	0.001886	0.012630	0.076821
8	A	232909.21	0.060667	0.001457	0.003452	0.016920	0.054281
9	A	236444.46	0.110036	0.006662	0.011546	0.030906	0.217513
10	S	237038.78	0.075228	0.004841	0.005334	0.020399	0.021474
11	S	239632.74	0.063123	0.004437	0.003740	0.017414	0.059033
12	S	251119.89	0.062182	0.002908	0.003628	0.017460	0.138893
13	A	253819.79	0.071411	0.003699	0.004800	0.020122	0.061200
14	S	264704.16	0.084074	0.007583	0.006682	0.023419	0.021252
15	A	270231.84	0.138254	0.010584	0.018400	0.040243	0.187533

Table 13: PZT-8 disk laterally clamped. Proposed total energy error indicator TEES versus total energy error computed by mesh halving TEE. Modes SA (S) and SA (A).

#MODE		FR (Hz)	PHE	TEE	TEEL	PHE REF	PEE
1	S	76742.94	0.021142	0.003894	0.000423	0.006963	0.223332
2	A	88923.44	0.071038	0.013679	0.006721	0.023099	0.245894
3	S	97133.76	0.035209	0.004302	0.001308	0.009999	0.093410
4	S	125002.91	0.066811	0.008671	0.005800	0.018029	0.027904
5	S	145553.70	0.087838	0.014946	0.011277	0.024319	0.073728
6	A	163712.89	0.079371	0.012223	0.008796	0.024630	0.236595
7	S	167542.09	0.138053	0.030572	0.035242	0.039285	0.027827
8	S	172478.18	0.092090	0.016765	0.012673	0.026622	0.172292
9	A	185128.17	0.091919	0.014160	0.012615	0.028045	0.226468
10	S	188251.10	0.091829	0.012304	0.012584	0.025898	0.216315
11	S	193595.02	0.090701	0.012885	0.012206	0.026752	0.294166

Table 14: PIN-PMN-PT disk laterally clamped. Proposed total energy error indicator TEEL versus total energy error computed by mesh halving TEE. Modes SA (S) and SA (A).

4 CONCLUSIONS

For piezoelectric media discretized either by the energy-orthogonal twenty-node hexahedral finite element or by the energy-orthogonal fifteen-node pentahedral finite element, by a dispersion analysis of plane harmonic bulk waves, an averaged correlation between the percentage of higher order total energy and the total energy error is yielded in each case both for the quasi-longitudinal waves and the quasi-shear waves. The use of such correlations as reference to apply the higher order total energy as an error indicator for the finite element vibration eigenmodes in piezoelectric solids is explored. As noteworthy conclusions:

- For PZT piezoceramics discretized by regular meshes the numerical research reveals that, by the correlation based on quasi-shear waves, the accuracy of the finite element eigenmodes can be confidently verified in order to select a cutoff modal order given an upper bound for the total energy error close to one per cent.

- For PMN-PT <001> poled single crystals a phenomenon similar to the dilatational locking could affect the accuracy of the eigenmodes computed. In this case, the correlation based on the quasi-longitudinal waves will be more accurate than the one based on the quasi-shear waves. An upper bound for the total energy error generally can be satisfactorily estimated for the set of eigenmodes selected.

#MODE		FR (Hz)	PHE	TEE	TEES	PHE REF	PEE
1	S	107006.40	0.009654	0.000537	0.000086	0.002590	0.000000
2	A	124403.79	0.068477	0.003158	0.004409	0.019188	0.213427
3	S	151530.13	0.029858	0.001511	0.000827	0.008527	0.060573
4	S	195671.83	0.045609	0.002416	0.001941	0.012245	0.035823
5	S	196124.61	0.052478	0.002468	0.002575	0.013839	0.000000
6	A	198897.48	0.097682	0.005574	0.009061	0.027787	0.218012
7	A	210858.61	0.043840	0.000851	0.001792	0.011718	0.084750
8	A	222906.51	0.099339	0.006712	0.009377	0.028718	0.208479
9	S	230153.98	0.065812	0.005252	0.004069	0.018289	0.026005
10	A	235937.00	0.076905	0.003900	0.005577	0.021555	0.080925
11	A	267146.81	0.081979	0.001640	0.006348	0.021983	0.051653
12	A	268071.13	0.082903	0.003441	0.006494	0.023966	0.089605
13	A	274323.99	0.125060	0.008319	0.014990	0.035278	0.222572
14	S	275419.64	0.103464	0.007639	0.010186	0.028167	0.058666
15	S	280164.97	0.084483	0.006603	0.006748	0.023722	0.102002
16	S	285448.64	0.117184	0.009301	0.013127	0.032024	0.000010
17	A	285499.46	0.084125	0.004895	0.006690	0.023488	0.039281
18	S	290762.64	0.100089	0.005552	0.009521	0.027868	0.147950
19	S	298812.82	0.103531	0.010995	0.010199	0.029058	0.021948

Table 15: PZT-8 disk laterally clamped. Proposed total energy error indicator TEES versus total energy error computed by mesh halving TEE. Modes AA (S) and AA (A).

#MODE		FR (Hz)	PHE	TEE	TEEL	PHE REF	PEE
1	S	71517.07	0.011112	0.001080	0.000107	0.003099	0.002713
2	S	113223.26	0.065395	0.008555	0.005510	0.017477	0.036065
3	S	124328.82	0.046330	0.005056	0.002450	0.013523	0.078704
4	A	130000.47	0.076123	0.012807	0.007946	0.024218	0.209863
5	S	147607.11	0.102151	0.017659	0.016404	0.028347	0.008013
6	S	150955.83	0.045439	0.004820	0.002342	0.013091	0.207442
7	S	176987.11	0.138696	0.036624	0.035666	0.038798	0.011464
8	S	178151.03	0.122330	0.020303	0.025855	0.033400	0.034825
9	S	195577.92	0.149584	0.036575	0.043366	0.042748	0.047200
10	A	201509.80	0.084117	0.011303	0.010138	0.025406	0.232569
11	S	216241.21	0.102550	0.011888	0.016565	0.029350	0.296416
12	S	216933.95	0.153221	0.033238	0.046159	0.046630	0.033856
16	A	227918.97	0.089985	0.011581	0.011969	0.026235	0.202592
14	S	228379.91	0.132431	0.023074	0.031669	0.038939	0.354035

Table 16: PIN-PMN-PT disk laterally clamped. Proposed total energy error indicator TEEL versus total energy error computed by mesh halving TEE. Modes AA (S) and AA (A).

REFERENCES

- [1] F. Fahy, *Sound and structural vibration*. Academic Press, 1985.
- [2] H.L. Schreyer, Dispersion of semidiscretized and fully discretized systems. T. Belytschko, T.J.R. Hughes eds. *Computational methods for transient analysis*. Elsevier Science, 1983.
- [3] F.J. Brito Castro, An error indicator based on a wave dispersion analysis for the vibration modes of isotropic elastic solids discretized by energy-orthogonal finite elements. *European Journal of Computational Mechanics*, **28**, 171-206, 2019.
- [4] M. Kimura, A. Ando (revised by D. Maurya, S. Priya), Lead zirconate titanate-based piezoceramics. K. Uchino ed. *Advances piezoelectric materials*. Woodhead Publishing, 2017.
- [5] J. Yang, *Analysis of piezoelectric devices*. World Scientific, 2006.
- [6] L. Luo, X. Zhao, H. Luo, Single crystal PZN-PT, PMN-PT, PSN-PT, and PIN-PT-based piezoelectric materials. K. Uchino ed. *Advances piezoelectric materials*. Woodhead Publishing, 2017.
- [7] J. Peng, H. Luo, T. He, H. Xu, D. Lin, Elastic, dielectric, and piezoelectric characterization of 0.70Pb(Mg_{1/3}Nb_{2/3})O₃-0.30PbTiO₃ single crystals. *Materials Letters*, **59**, 640-643, 2005.
- [8] <http://www.trstechnologies.com/Resources>.
- [9] D. Stanfield, A. Elliot, *Underwater electroacoustic transducers*. Peninsula Publishing, 2017.
- [10] H. Allik, T.J.R. Hughes, Finite element method for piezoelectric vibration. *International Journal for Numerical Methods in Engineering*, **2**, 151-157, 1970.
- [11] B.D. Zaitsev, I.E. Kuznetsova, The energy density and power flow of acoustic waves propagating in piezoelectric materials. *IEEE Transactions on Ultrasonics, Ferroelectrics, and Frequency Control*, **50**, 1762-1765, 2003.
- [12] C.A. Felippa, B. Haugen, C. Militello, From the individual element test to finite element templates: evolution of the Patch Test. *International Journal for Numerical Methods in Engineering*, **38**, 199-229, 1995.
- [13] R.H. MacNeal, *Finite elements: their design and performance*. Marcel Dekker, 1994.
- [14] B.A. Auld, *Acoustic fields and waves in solids. Volume I*. Krieger Publishing Company, 1990.
- [15] M. Okrouhlík, C. Höschl, A contribution to the study of dispersive properties of one-dimensional lagrangian and hermitian elements. *Computers and Structures*, **49**, 779-795, 1993.
- [16] Z.-Q. Qu, *Model order reduction techniques: with applications in finite element analysis*. Springer, 2004.
- [17] R.A. Horn, C.R. Johnson, *Matrix analysis*. Cambridge University Press, 1992.
- [18] R.B. King, *Beyond the quartic equation*. Birkhäuser, 1996.

- [19] V. Laude, A. Reinhardt, A. Khelif, Equality of the energy and group velocities of bulk acoustic waves in piezoelectric media. *IEEE Transactions on Ultrasonics, Ferroelectrics, and Frequency Control*, **52**, 1869-1871, 2005.
- [20] D. Royer, E. Dieulesaint, *Elastic waves in solids I*. Springer, 2000.
- [21] L. Brillouin, *Wave propagation in periodic structures*. Dover Publications, 2003.
- [22] J. Barlow, More on optimal stress points-reduced integration, element distortions, and error estimation. *International Journal for Numerical Methods in Engineering*, **28**, 1487-1504, 1989.
- [23] M. Kaltenbacher, *Numerical simulation of mechatronic sensors and actuators*. Springer, 2015.
- [24] J. N. Reddy, *Applied functional analysis and variational methods in engineering*. Krieger Publishing Company, 1991.
- [25] E. Anderson, Z. Bai, C. Bischof, S. Blackford, J. Demmel, J. Dongarra, J. Du Croz, A. Greenbaum, S. Hammarling, A. McKenney, D. Sorensen, *LAPACK user's guide*. Society for Industrial and Applied Mathematics, 1999.
- [26] B.D. Zaitsev, I.E. Kuznetsova, A.A. Teplykh, Definition of electromechanical coupling coefficient of bulk acoustic waves from energy consideration. *IEEE Symposium on Ultrasonics*, 1467-1470, 2003.
- [27] F. Lowrie, M. Cain, M. Stewart, Finite element modelling of electroceramics. NPL Report CMMT(A)150, 1999.
- [28] M.S. Vijaya, *Piezoelectric materials and devices*. CRC Press, 2013.
- [29] A. Loussert, J-C. Debus, G. Vanderborck, Studying the behavior of piezoelectric single crystals for sonar using ATILA. K. Uchino ed. *Applications of ATILA FEM software to smart materials*. Woodhead Publishing, 2013.
- [30] M. Petyt, *Introduction to finite element vibration analysis*. Cambridge University Press, 2010.

Appendix 1. Materials constants for selected piezoelectric media.

C_{IJ}^E (GPa)	PZT-5H	PZT-8	PZT-5A	PMN-30PT	PMN.31PT	PIN-PMN-PT
11	126.0	137.0	121.0	160.4	124.0	119.0
12	79.1	69.9	75.9	149.6	111.0	105.0
13	83.9	71.1	75.4	124.0	104.0	104.0
22	126.0	137.0	121.0	160.4	124.0	119.0
23	83.9	71.1	75.4	124.0	104.0	104.0
33	117.0	123.0	111.0	120.0	108.0	114.0
44	23.0	31.3	21.1	53.8	63.0	66.0
55	23.0	31.3	21.1	53.8	63.0	66.0
66	23.5	33.6	22.6	28.7	35.0	25.0
$\varepsilon_{ij}^S \times 10^8$ (C/Vm)	PZT-5H	PZT-8	PZT-5A	PMN-30PT	PMN.31PT	PIN-PMN-PT
11	1.505	0.797	0.811	4.394	1.186	1.062
22	1.505	0.797	0.811	4.394	1.186	1.062
33	1.302	0.514	0.735	1.227	0.806	0.645
e_{ij} (C/m ²)	PZT-5H	PZT-8	PZT-5A	PMN-30PT	PMN.31PT	PIN-PMN-PT
15	17.00	10.40	12.30	31.84	10.30	6.90
24	17.00	10.40	12.30	31.84	10.30	6.90
31	-6.50	-4.00	-5.40	-5.22	-3.90	-4.80
32	-6.50	-4.00	-5.40	-5.22	-3.90	-4.80
33	23.30	13.20	15.80	30.40	22.30	18.60
ρ (kg/m ³)	7500	7600	7750	7740	7740	8000

Table A1.1: Material constants for PZT piezoceramics and PMN-PT <001> poled single crystals.

Appendix 2. Detailed results of the numerical dispersion analysis carried out for media and meshes selected.

		HE20				HE20	
m_l^M		PZT-5H	PZT-8	PZT-5A	PMN-30PT	PMN-31PT	PIN-PMN-PT
M-Q1	SS	0.1802	0.1800	0.1799	0.1796	0.1798	0.1798
	FS	0.1799	0.1801	0.1802	0.1797	0.1797	0.1797
	L	0.1791	0.1791	0.1791	0.1788	0.1788	0.1788
M-Q2	SS	0.1756	0.1754	0.1753	0.1749	0.1751	0.1751
	FS	0.1753	0.1755	0.1756	0.1752	0.1751	0.1752
	L	0.1745	0.1745	0.1745	0.1742	0.1742	0.1742
M-Q3	SS	0.1710	0.1709	0.1707	0.1703	0.1706	0.1705
	FS	0.1711	0.1713	0.1714	0.1709	0.1709	0.1709
	L	0.1706	0.1707	0.1706	0.1704	0.1704	0.1704
M-Q4	SS	0.1559	0.1557	0.1557	0.1552	0.1554	0.1554
	FS	0.1556	0.1558	0.1558	0.1554	0.1554	0.1554
	L	0.1548	0.1549	0.1548	0.1545	0.1545	0.1545
M-Q5	SS	0.1963	0.1962	0.1961	0.1956	0.1957	0.1957
	FS	0.1961	0.1962	0.1963	0.1960	0.1959	0.1960
	L	0.1951	0.1952	0.1952	0.1948	0.1948	0.1948
		PE15				PE15	
m_l^M		PZT-5H	PZT-8	PZT-5A	PMN-30PT	PMN-31PT	PIN-PMN-PT
M-T1	SS	0.1835	0.1834	0.1833	0.1826	0.1829	0.1829
	FS	0.1834	0.1836	0.1837	0.1834	0.1834	0.1833
	L	0.1827	0.1828	0.1828	0.1826	0.1826	0.1825
M-T2	SS	0.1804	0.1804	0.1802	0.1799	0.1803	0.1801
	FS	0.1806	0.1808	0.1808	0.1804	0.1805	0.1804
	L	0.1799	0.1800	0.1800	0.1798	0.1798	0.1798
M-T3	SS	0.1779	0.1778	0.1777	0.1761	0.1766	0.1767
	FS	0.1780	0.1782	0.1782	0.1779	0.1779	0.1779
	L	0.1774	0.1775	0.1774	0.1772	0.1772	0.1772
M-T4	SS	0.1542	0.1541	0.1540	0.1533	0.1535	0.1536
	FS	0.1540	0.1542	0.1542	0.1538	0.1539	0.1538
	L	0.1534	0.1535	0.1535	0.1533	0.1533	0.1532
M-T5	SS	0.2062	0.2061	0.2060	0.2051	0.2053	0.2053
	FS	0.2062	0.2063	0.2064	0.2061	0.2061	0.2061
	L	0.2052	0.2053	0.2052	0.2050	0.2050	0.2049

Table A2.1: Piezoelectric ceramics PZT and PMN-PT <001> poled single crystals. Mean values of the first reference dimensionless wave number computed over the range of azimuthal and polar angles.

		HE20				HE20	
m_2^M		PZT-5H	PZT-8	PZT-5A	PMN-30PT	PMN-31PT	PIN-PMN-PT
M-Q1	SS	0.2642	0.2635	0.2633	0.2620	0.2624	0.2624
	FS	0.2631	0.2638	0.2641	0.2627	0.2626	0.2626
	L	0.2604	0.2607	0.2605	0.2594	0.2594	0.2595
M-Q2	SS	0.2574	0.2569	0.2565	0.2551	0.2555	0.2555
	FS	0.2565	0.2571	0.2574	0.2561	0.2560	0.2560
	L	0.2536	0.2539	0.2537	0.2523	0.2524	0.2525
M-Q3	SS	0.2499	0.2497	0.2490	0.2478	0.2485	0.2484
	FS	0.2502	0.2507	0.2511	0.2495	0.2495	0.2495
	L	0.2484	0.2486	0.2485	0.2477	0.2478	0.2478
M-Q4	SS	0.2287	0.2281	0.2279	0.2265	0.2269	0.2268
	FS	0.2274	0.2282	0.2283	0.2268	0.2269	0.2268
	L	0.2247	0.2252	0.2249	0.2234	0.2237	0.2238
M-Q5	SS	0.2877	0.2873	0.2870	0.2853	0.2856	0.2855
	FS	0.2870	0.2873	0.2878	0.2867	0.2866	0.2867
	L	0.2838	0.2841	0.2839	0.2822	0.2823	0.2823
		PE15				PE15	
m_2^M		PZT-5H	PZT-8	PZT-5A	PMN-30PT	PMN-31PT	PIN-PMN-PT
M-T1	SS	0.2675	0.2672	0.2669	0.2647	0.2655	0.2655
	FS	0.2671	0.2676	0.2678	0.2668	0.2669	0.2668
	L	0.2650	0.2652	0.2651	0.2645	0.2644	0.2643
M-T2	SS	0.2625	0.2624	0.2619	0.2608	0.2619	0.2614
	FS	0.2629	0.2634	0.2636	0.2624	0.2625	0.2624
	L	0.2610	0.2612	0.2611	0.2603	0.2603	0.2603
M-T3	SS	0.2589	0.2588	0.2583	0.2544	0.2554	0.2557
	FS	0.2591	0.2597	0.2598	0.2589	0.2589	0.2588
	L	0.2572	0.2575	0.2573	0.2569	0.2569	0.2568
M-T4	SS	0.2246	0.2244	0.2242	0.2222	0.2228	0.2228
	FS	0.2240	0.2245	0.2246	0.2234	0.2236	0.2234
	L	0.2222	0.2225	0.2223	0.2214	0.2216	0.2215
M-T5	SS	0.3007	0.3005	0.3001	0.2972	0.2980	0.2978
	FS	0.3005	0.3009	0.3012	0.3004	0.3004	0.3004
	L	0.2974	0.2978	0.2976	0.2965	0.2964	0.2961

Table A2.2: Piezoelectric ceramics PZT and PMN-PT <001> poled single crystals. Mean values of the second reference dimensionless wave number computed over the range of azimuthal and polar angles.

		HE20				HE20	
e_{T1}^{RMS}		PZT-5H	PZT-8	PZT-5A	PMN-30PT	PMN-31PT	PIN-PMN-PT
M-Q1	SS	0.003111	0.002951	0.002747	0.002781	0.002615	0.002589
	FS	0.002440	0.002590	0.002839	0.002930	0.002996	0.002967
	L	0.005436	0.005160	0.005353	0.006342	0.006091	0.006031
M-Q2	SS	0.003213	0.003019	0.002903	0.003171	0.003015	0.003008
	FS	0.002519	0.002608	0.002856	0.002773	0.002799	0.002787
	L	0.005893	0.005474	0.005792	0.007055	0.006668	0.006613
M-Q3	SS	0.003109	0.002987	0.002823	0.002940	0.002816	0.002774
	FS	0.002493	0.002586	0.002803	0.002673	0.002728	0.002738
	L	0.004525	0.004330	0.004461	0.005224	0.004918	0.004890
M-Q4	SS	0.003788	0.002963	0.002673	0.004246	0.003890	0.003829
	FS	0.003075	0.003603	0.004038	0.002462	0.002583	0.002598
	L	0.006038	0.005626	0.005959	0.007375	0.006487	0.006303
M-Q5	SS	0.002391	0.002670	0.002647	0.002729	0.002731	0.002728
	FS	0.002962	0.002702	0.002738	0.002819	0.002793	0.002717
	L	0.006349	0.005853	0.006163	0.007449	0.007278	0.007277
		PE15				PE15	
e_{T1}^{RMS}		PZT-5H	PZT-8	PZT-5A	PMN-30PT	PMN-31PT	PIN-PMN-PT
M-T1	SS	0.005204	0.004864	0.005081	0.005872	0.005807	0.005738
	FS	0.004828	0.004707	0.004887	0.004947	0.004918	0.005011
	L	0.006325	0.005857	0.006344	0.007948	0.007223	0.006921
M-T2	SS	0.005582	0.005380	0.005476	0.006839	0.006869	0.006442
	FS	0.005509	0.005401	0.005555	0.005756	0.005776	0.005813
	L	0.006614	0.006188	0.006638	0.010839	0.009606	0.008615
M-T3	SS	0.005859	0.005642	0.005765	0.005729	0.005891	0.005936
	FS	0.006131	0.005981	0.006151	0.006018	0.005922	0.006063
	L	0.009322	0.008403	0.009355	0.009636	0.008012	0.008553
M-T4	SS	0.004190	0.003745	0.003880	0.004819	0.004663	0.004619
	FS	0.003617	0.003699	0.003907	0.003422	0.003417	0.003452
	L	0.005639	0.005138	0.005625	0.007236	0.006429	0.006180
M-T5	SS	0.006740	0.006416	0.006742	0.008203	0.008201	0.008165
	FS	0.007562	0.007175	0.007438	0.007272	0.007028	0.007186
	L	0.007694	0.007187	0.007731	0.009288	0.008404	0.008053

Table A2.3: Piezoelectric ceramics PZT and PMN-PT <001> poled single crystals. Root-mean-square values of the first reference percentage of total energy error computed over the range of azimuthal and polar angles.

		HE20				HE20	
e_{T2}^{RMS}		PZT-5H	PZT-8	PZT-5A	PMN-30PT	PMN-31PT	PIN-PMN-PT
M-Q1	SS	0.013381	0.012952	0.011943	0.011387	0.010701	0.010581
	FS	0.010521	0.011113	0.012135	0.012881	0.013263	0.013028
	L	0.026983	0.025343	0.026457	0.032994	0.031433	0.031055
M-Q2	SS	0.013659	0.013025	0.012411	0.012765	0.012112	0.012084
	FS	0.010365	0.010741	0.011795	0.011805	0.012004	0.011841
	L	0.031094	0.027931	0.030371	0.040943	0.037724	0.037389
M-Q3	SS	0.013164	0.012886	0.011972	0.011998	0.011539	0.011337
	FS	0.010731	0.011173	0.012022	0.011668	0.012057	0.012025
	L	0.022453	0.021275	0.022036	0.027481	0.025402	0.025162
M-Q4	SS	0.015347	0.011635	0.009988	0.017049	0.015701	0.015482
	FS	0.012378	0.014993	0.016828	0.009974	0.010623	0.010723
	L	0.033683	0.030260	0.032918	0.047561	0.037925	0.036204
M-Q5	SS	0.010234	0.011658	0.011535	0.010967	0.010975	0.010923
	FS	0.012743	0.011603	0.011675	0.011987	0.011861	0.011295
	L	0.033641	0.029885	0.032162	0.042194	0.041363	0.041531
		PE15				PE15	
e_{T2}^{RMS}		PZT-5H	PZT-8	PZT-5A	PMN-30PT	PMN-31PT	PIN-PMN-PT
M-T1	SS	0.021343	0.020127	0.020836	0.022352	0.022299	0.022229
	FS	0.019872	0.019338	0.020127	0.020431	0.020349	0.020722
	L	0.028526	0.025765	0.028627	0.039510	0.034663	0.032725
M-T2	SS	0.021951	0.021364	0.021493	0.025771	0.026720	0.024810
	FS	0.022818	0.022377	0.023026	0.023755	0.023791	0.023963
	L	0.030466	0.028074	0.030559	0.043109	0.037112	0.035260
M-T3	SS	0.023094	0.022519	0.022695	0.020830	0.021604	0.021877
	FS	0.025246	0.024654	0.025354	0.024875	0.024519	0.025062
	L	0.044886	0.038575	0.045003	0.094928	0.073876	0.079793
M-T4	SS	0.017826	0.015975	0.016563	0.018830	0.018301	0.018200
	FS	0.014637	0.015075	0.015944	0.013936	0.013951	0.014109
	L	0.028755	0.025083	0.028547	0.040516	0.033460	0.031638
M-T5	SS	0.027293	0.026275	0.027327	0.031205	0.031590	0.031633
	FS	0.031278	0.029741	0.030795	0.030180	0.029226	0.029860
	L	0.034614	0.031055	0.034500	0.046293	0.040770	0.038983

Table A2.4: Piezoelectric ceramics PZT and PMN-PT <001> poled single crystals. Root-mean-square values of the second reference percentage of total energy error computed over the range of azimuthal and polar angles.

		HE20				HE20	
e_{T1}^{SUP}		PZT-5H	PZT-8	PZT-5A	PMN-30PT	PMN-31PT	PIN-PMN-PT
M-Q1	SS	0.004946	0.005104	0.004941	0.004871	0.004458	0.004589
	FS	0.004842	0.005008	0.004932	0.004646	0.004730	0.004652
	L	0.010287	0.009793	0.010192	0.011434	0.010889	0.010801
M-Q2	SS	0.006064	0.005429	0.006061	0.007097	0.006597	0.006802
	FS	0.004773	0.004942	0.005058	0.004894	0.005017	0.005071
	L	0.011419	0.010569	0.011289	0.012986	0.012092	0.011983
M-Q3	SS	0.006280	0.006588	0.006278	0.006705	0.006410	0.006537
	FS	0.007473	0.007473	0.007473	0.007473	0.007473	0.007473
	L	0.012429	0.011731	0.012293	0.013516	0.012878	0.012787
M-Q4	SS	0.006267	0.005117	0.004463	0.006485	0.005851	0.005693
	FS	0.005446	0.005645	0.006180	0.004974	0.004977	0.004905
	L	0.012539	0.011542	0.012451	0.014192	0.012454	0.012105
M-Q5	SS	0.004866	0.005098	0.004990	0.005691	0.005962	0.006050
	FS	0.005615	0.005225	0.005453	0.005857	0.005873	0.005952
	L	0.011288	0.010573	0.011035	0.012766	0.012186	0.012215
		PE15				PE15	
e_{T1}^{SUP}		PZT-5H	PZT-8	PZT-5A	PMN-30PT	PMN-31PT	PIN-PMN-PT
M-T1	SS	0.017162	0.016391	0.017158	0.017801	0.018963	0.018396
	FS	0.010875	0.010875	0.010875	0.010875	0.010960	0.011192
	L	0.022223	0.019957	0.022213	0.033930	0.033048	0.030928
M-T2	SS	0.017410	0.017854	0.017448	0.020036	0.021348	0.019359
	FS	0.017457	0.017457	0.017457	0.017457	0.017457	0.017468
	L	0.030500	0.028698	0.030492	0.060299	0.050362	0.046393
M-T3	SS	0.018419	0.018323	0.018417	0.016684	0.017354	0.017172
	FS	0.020527	0.020527	0.020527	0.020527	0.020527	0.020527
	L	0.051384	0.044223	0.051347	0.058955	0.047983	0.053773
M-T4	SS	0.017173	0.016383	0.017168	0.017784	0.018966	0.018397
	FS	0.010875	0.010875	0.010875	0.010875	0.010875	0.010875
	L	0.022248	0.019952	0.022238	0.033900	0.033078	0.030923
M-T5	SS	0.017177	0.016386	0.017172	0.017794	0.018978	0.018397
	FS	0.013150	0.012228	0.012845	0.014029	0.014507	0.014523
	L	0.022229	0.019925	0.022219	0.033913	0.033080	0.030943

Table A2.5: Piezoelectric ceramics PZT and PMN-PT <001> poled single crystals. Sup-norm of the first reference percentage of total energy error computed over the range of azimuthal and polar angles.

		HE20				HE20	
e_{T2}^{SUP}		PZT-5H	PZT-8	PZT-5A	PMN-30PT	PMN-31PT	PIN-PMN-PT
M-Q1	SS	0.023199	0.024125	0.023117	0.020298	0.020892	0.020491
	FS	0.023037	0.023882	0.023467	0.022050	0.022476	0.022309
	L	0.053215	0.050128	0.052505	0.060786	0.057137	0.056547
M-Q2	SS	0.025362	0.024742	0.025350	0.029209	0.027160	0.027970
	FS	0.021637	0.022538	0.022121	0.022383	0.023682	0.024075
	L	0.066331	0.057934	0.065265	0.095463	0.078166	0.083769
M-Q3	SS	0.030076	0.031723	0.030035	0.027694	0.028404	0.028348
	FS	0.038762	0.038762	0.038762	0.038762	0.038762	0.038762
	L	0.068921	0.063519	0.067837	0.079279	0.072882	0.072098
M-Q4	SS	0.026212	0.020792	0.016989	0.026779	0.024285	0.023593
	FS	0.025050	0.025642	0.025882	0.023777	0.023850	0.023456
	L	0.077414	0.067116	0.076350	0.100073	0.075566	0.071586
M-Q5	SS	0.023427	0.024327	0.023882	0.023406	0.024710	0.024995
	FS	0.023853	0.021739	0.022733	0.024290	0.024316	0.024581
	L	0.062078	0.056119	0.060119	0.073130	0.068866	0.069332
		PE15				PE15	
e_{T2}^{SUP}		PZT-5H	PZT-8	PZT-5A	PMN-30PT	PMN-31PT	PIN-PMN-PT
M-T1	SS	0.068776	0.067332	0.068762	0.068879	0.068204	0.068301
	FS	0.045641	0.045641	0.045641	0.045641	0.046194	0.046726
	L	0.109239	0.092908	0.109166	0.217268	0.193448	0.182894
M-T2	SS	0.063741	0.064894	0.063723	0.076098	0.082671	0.075965
	FS	0.076963	0.076963	0.076963	0.076963	0.078231	0.079146
	L	0.193846	0.170351	0.193762	0.211705	0.171666	0.183435
M-T3	SS	0.069605	0.071006	0.069599	0.058999	0.062114	0.062565
	FS	0.084933	0.084933	0.084933	0.084933	0.084933	0.084965
	L	0.249039	0.202924	0.248812	0.735536	0.732378	0.723363
M-T4	SS	0.068788	0.067344	0.068775	0.068894	0.068208	0.068322
	FS	0.045638	0.045638	0.045638	0.045638	0.045638	0.045638
	L	0.109306	0.092869	0.109233	0.217447	0.193475	0.182868
M-T5	SS	0.068803	0.067317	0.068790	0.068830	0.068148	0.068261
	FS	0.055850	0.051635	0.054473	0.060503	0.063464	0.062776
	L	0.109354	0.092874	0.109111	0.217424	0.193497	0.183005

Table A2.6: Piezoelectric ceramics PZT and PMN-PT <001> poled single crystals. Sup-norm of the second reference percentage of total energy error computed over the range of azimuthal and polar angles.

		HE20			HE20		
e_{p2}^M		PZT-5H	PZT-8	PZT-5A	PMN-30PT	PMN-31PT	PIN-PMN-PT
M-Q1	SS	1.00355	1.00294	1.00301	1.00716	1.00639	1.00624
	FS	1.00337	1.00338	1.00370	1.00299	1.00284	1.00291
	L	1.00195	1.00200	1.00197	1.00169	1.00170	1.00171
M-Q2	SS	1.00359	1.00297	1.00307	1.00724	1.00642	1.00626
	FS	1.00336	1.00335	1.00367	1.00297	1.00282	1.00288
	L	1.00189	1.00194	1.00191	1.00163	1.00164	1.00165
M-Q3	SS	1.00555	1.00464	1.00510	1.00876	1.00757	1.00759
	FS	1.00415	1.00405	1.00438	1.00419	1.00392	1.00398
	L	1.00216	1.00223	1.00218	1.00191	1.00196	1.00195
M-Q4	SS	1.00361	1.00291	1.00292	1.00768	1.00692	1.00690
	FS	1.00360	1.00369	1.00402	1.00310	1.00302	1.00309
	L	1.00202	1.00205	1.00204	1.00170	1.00175	1.00177
M-Q5	SS	1.00332	1.00285	1.00298	1.00674	1.00595	1.00573
	FS	1.00331	1.00315	1.00348	1.00278	1.00258	1.00262
	L	1.00168	1.00175	1.00171	1.00147	1.00146	1.00147
		PE15			PE15		
e_{p2}^M		PZT-5H	PZT-8	PZT-5A	PMN-30PT	PMN-31PT	PIN-PMN-PT
M-T1	SS	1.00360	1.00308	1.00327	1.00599	1.00534	1.00540
	FS	1.00335	1.00325	1.00350	1.00326	1.00310	1.00317
	L	1.00185	1.00191	1.00187	1.00167	1.00168	1.00166
M-T2	SS	1.00436	1.00373	1.00405	1.00605	1.00530	1.00557
	FS	1.00367	1.00354	1.00380	1.00377	1.00358	1.00363
	L	1.00194	1.00201	1.00197	1.00176	1.00180	1.00178
M-T3	SS	1.00418	1.00357	1.00387	1.00766	1.00680	1.00667
	FS	1.00361	1.00348	1.00373	1.00346	1.00327	1.00335
	L	1.00189	1.00197	1.00192	1.00159	1.00164	1.00163
M-T4	SS	1.00292	1.00245	1.00255	1.00539	1.00480	1.00490
	FS	1.00278	1.00278	1.00298	1.00253	1.00248	1.00254
	L	1.00160	1.00163	1.00161	1.00141	1.00145	1.00144
M-T5	SS	1.00423	1.00368	1.00397	1.00690	1.00614	1.00620
	FS	1.00421	1.00390	1.00425	1.00400	1.00367	1.00370
	L	1.00195	1.00205	1.00199	1.00177	1.00177	1.00174

Table A2.7: Piezoelectric ceramics PZT and PMN-PT <001> poled single crystals. Mean values of the second reference value for the indicator of dispersion associated with the phase velocity.

		HE20			HE20		
e_{gn2}^M		PZT-5H	PZT-8	PZT-5A	PMN-30PT	PMN-31PT	PIN-PMN-PT
M-Q1	SS	1.01756	1.01453	1.01490	1.03521	1.03136	1.03066
	FS	1.01666	1.01668	1.01828	1.01476	1.01402	1.01433
	L	1.00943	1.00966	1.00953	1.00808	1.00813	1.00821
M-Q2	SS	1.01770	1.01467	1.01515	1.03557	1.03153	1.03078
	FS	1.01661	1.01654	1.01814	1.01465	1.01389	1.01419
	L	1.00909	1.00936	1.00920	1.00768	1.00776	1.00784
M-Q3	SS	1.02754	1.02304	1.02534	1.04321	1.03735	1.03747
	FS	1.02062	1.02006	1.02174	1.02075	1.01938	1.01965
	L	1.01052	1.01090	1.01064	1.00924	1.00950	1.00946
M-Q4	SS	1.01778	1.01434	1.01444	1.03767	1.03389	1.03378
	FS	1.01765	1.01810	1.01971	1.01519	1.01477	1.01510
	L	1.00965	1.00983	1.00973	1.00782	1.00818	1.00831
M-Q5	SS	1.01647	1.01410	1.01479	1.03322	1.02933	1.02828
	FS	1.01642	1.01562	1.01724	1.01381	1.01281	1.01299
	L	1.00812	1.00847	1.00827	1.00695	1.00690	1.00695
		PE15			PE15		
e_{gn2}^M		PZT-5H	PZT-8	PZT-5A	PMN-30PT	PMN-31PT	PIN-PMN-PT
M-T1	SS	1.01745	1.01492	1.01584	1.02901	1.02590	1.02623
	FS	1.01639	1.01588	1.01710	1.01585	1.01507	1.01539
	L	1.00885	1.00915	1.00896	1.00785	1.00796	1.00790
M-T2	SS	1.02099	1.01798	1.01945	1.02925	1.02574	1.02701
	FS	1.01789	1.01725	1.01850	1.01825	1.01727	1.01754
	L	1.00928	1.00965	1.00940	1.00832	1.00859	1.00845
M-T3	SS	1.02015	1.01723	1.01862	1.03682	1.03275	1.03211
	FS	1.01760	1.01695	1.01821	1.01680	1.01588	1.01625
	L	1.00894	1.00936	1.00906	1.00271	1.00534	1.00456
M-T4	SS	1.01426	1.01194	1.01243	1.02615	1.02334	1.02384
	FS	1.01358	1.01359	1.01457	1.01237	1.01210	1.01236
	L	1.00764	1.00782	1.00770	1.00658	1.00683	1.00683
M-T5	SS	1.02035	1.01772	1.01908	1.03325	1.02968	1.02997
	FS	1.02045	1.01899	1.02066	1.01931	1.01772	1.01786
	L	1.00922	1.00974	1.00942	1.00818	1.00824	1.00811

Table A2.8: Piezoelectric ceramics PZT and PMN-PT <001> poled single crystals. Mean values of the second reference value for the indicator of dispersion associated with the normal component of the group velocity.

DISPERSION DESIGN OF 1D PERIODIC DISCRETE SYSTEMS USING LOG-DET HEURISTICS

Anton Tkachuk¹, and Mykola Tkachuk²

¹Mechanical and Materials Engineering, Karlstad University
651 88 Karlstad, Sweden
e-mail: anton.tkachuk@kau.se

² Department of Theory and Computer-Aided Design of Mechanisms and Machines
National Technical University “Kharkiv Polytechnic Institute”
Kyrpychova str., 2, Kharkiv, Ukraine, 61002
e-mail: m.tkachuk@tmm-sapr.org

Keywords: Periodic systems, rank minimization heuristics, optimization-based material design, log-det heuristics, reduced-order modeling.

Abstract. *A new class of performance functions for dispersion design of 1D periodic discrete systems using matrix rank is considered, and its regularization using existent log-det heuristics is proposed. As an input, the desired dispersion dependency of a branch is used. The design space is defined by a finite set of continuous parameters such as mass or stiffness constants. The mass and stiffness matrices are assumed to depend linearly on these parameters. Ideally, the representative dynamic stiffness matrix is singular at every point of the desired branch. Instead, the sum of ranks for the representative dynamic stiffness matrix evaluated at several discrete points is minimized using a surrogate log-det objective. This approach avoids ordering or tracking of eigenfrequencies and reduces the design problem to a sequence of quadratic programming problems. The considered periodic discrete systems are simplified objects for method development with a future goal of dispersion design of acoustic metamaterials. Also, a combination with reduced-order techniques is conceptually tested.*

1 INTRODUCTION

Dispersion design in acoustics seeks a material or a system that interacts with acoustic waves in desired manner. Typical examples of desired behavior are prohibiting wave propagation in a specific frequency range via stopping bands in metamaterials and elimination of reflected waves with anechoic tiles. Usually, these designs are realized as an array of repeating heterogeneous cells. Different options are available for manufacturing heterogeneous cells and they can use solid-solid, solid-liquid or solid-air interfaces. Each cell can be described by a large number of design parameters, which makes finding the design a challenging problem.

A common approach is to introduce a performance function that relates the design variables to desired performances and to use it in a gradient-based optimization or integer programming, see examples for maximizing relative band gap in [2] or design of self-collimating materials in [10]. Unfortunately, the common performance functions are implicit functions of dynamic equilibrium equations and their sensitivities are sometimes difficult to obtain, see [13] and references herein. Alternative integer programming approaches need very large number of iterations, e.g. of genetic algorithms. In this contribution a new class of performance functions based on matrix rank is proposed and discussed. An advantage of using matrix rank is that several explicit surrogate functions for rank approximation are available simplifying computation of the performance functions and their sensitivities.

The problem of minimizing the rank of a matrix is known to be computationally hard, see [12, 7.3] and it is attributed to be NP-hard in general case [11]. Fortunately, several available heuristics can efficiently solve it. These heuristics rely on different tractable relaxations of the problem, e.g. a nuclear norm minimization, weighted norm minimization or minimization of the logarithm of the determinant [4, 5, 9]. Tractable means here that one quadratic function minimization or SVD per an iteration step is required and the number of such iterations is affordable. Unfortunately, these heuristic methods guarantee the minimum rank solution only in case of well-conditioned equality constraints on the matrix, see the proof in [11]. Various numerical experiments show a satisfactory quality of the solutions obtained by the heuristics for applications as low-rank matrix completion [5, 9], low-order system realization [5] and lowest-dimension embedding of points in Euclidean space [5]. However, these methods are not wide spread for design in vibration or acoustic systems so far. An example in [1] uses rank minimization for reducing dispersion error in spatial discretizations of reciprocal mass matrices. Therefore, exploring rank minimization formulations in dispersion design is promising.

For simplicity, examples here are limited to 1D periodic undamped systems consisting of point masses and springs. Only continuous parameters for mass and stiffness constants are used. Constraints are applied only on upper and lower limits of parameter values.

The contribution is organized as follows. First, equations of motion for a repetitive patch are introduced and a rank minimization objective is formulated in Section 2. A log-det heuristic is applied to the rank minimization problem and two illustrative algebraic examples are discussed in Section 3. A combination of log-det heuristic with the reduced-order techniques is described and illustrated with one algebraic example in Section 4. A numerical example for a uniform back-bone mass-spring chain with a side branch at every second mass element are considered in Section (5). Conclusions are presented in Section 6.

2 EQUATION OF MOTION AND RANK MINIMIZATION OBJECTIVE

The equations of motion for an infinite periodic mechanical system can be formulated in different ways, see a comprehensive textbook [3]. Here, a form following [8] is considered for

1D case. The representative patch of the periodic structure is assumed to have n_{rep} unknown amplitudes denoted as $\tilde{\mathbf{U}}$. These amplitudes satisfy equations

$$\mathbf{Q} (\mathbf{K}(\mathbf{s}) - \omega^2 \mathbf{M}(\mathbf{s})) \mathbf{S}(k) \tilde{\mathbf{U}} = \mathbf{0}, \quad (1)$$

where ω and k are the angular frequency and wavenumber, \mathbf{K} and \mathbf{M} are the stiffness and mass matrix. Herein, affine dependence of the stiffness and mass matrix on n_s parameters \mathbf{s} is assumed with

$$\mathbf{K}(\mathbf{s}) = \mathbf{K}_0 + \sum_{j=1}^{n_s} \mathbf{K}_j s_j, \quad \mathbf{M}(\mathbf{s}) = \mathbf{M}_0 + \sum_{j=1}^{n_s} \mathbf{M}_j s_j. \quad (2)$$

These matrices are assembled for the periodic cell and a layer of neighboring elements. The periodic boundary conditions are enforced via a shift matrix \mathbf{S} whose entries on the slave side are proportional to the phase shift $\exp(ik \cdot \Delta x)$ along the lattice vector for the periodic cell Δx . The matrix \mathbf{Q} filters degrees of freedom of the representative patch $\tilde{\mathbf{U}}$ from the total model. Thus, the equation of motion as in equation (1) allows us to define the representative dynamic stiffness matrix (RDSM) with

$$\mathbf{A}(\mathbf{s}, k, \omega) = \mathbf{Q} (\mathbf{K}(\mathbf{s}) - \omega^2 \mathbf{M}(\mathbf{s})) \mathbf{S}(k). \quad (3)$$

We denote with $\mathbf{A}_j := \mathbf{A}(\mathbf{s}, k_j, \omega_j)$ the RDSM evaluated at a specific frequency-wavenumber pair (k_j, ω_j) . Solvability of the equation of motion (1) at a frequency-wavenumber pair requires that the corresponding RDSM is singular or it has a deficit of rank with

$$\text{rank } \mathbf{A}_j < \dim(\mathbf{A}_j) = n_{\text{rep}}, \quad j = \overline{1, n_w}, \quad (4)$$

where n_w is the number of sampled frequency-wavenumber pairs. Inspection of all n_w inequalities is still a hard problem. Instead, a *good* solution is sought that minimizes the *sum of the ranks* of RDSM for all pairs j with respect to parameters \mathbf{s} . Such a sum now defines the objective of the dispersion design. This sum is equal to the product $(n_{\text{rep}} n_w)$ at an initial value of parameters \mathbf{s}_0 . During the optimization process, for certain values of the parameters \mathbf{s}_k the rank of some of the matrices $\mathbf{K}_{\text{dyn,rep}}(\mathbf{s}_k, \omega_j, \mathbf{k}_j)$ reduces to $(n_{\text{rep}} - 1)$ meaning that exactly one branch of the dispersion relation crosses the prescribed frequency-wavevector pair (ω_j, \mathbf{k}_j) . Reduction of the rank to $(n_{\text{rep}} - 2)$ or less would require that more than one branch of the dispersion relation crosses the prescribed frequency-wavevector pair, i.e. two or more waves can propagate with the same wavenumber and frequency, but a different mode. Such a multiple crossing is possible but it does not significantly influence the design for a sufficiently large number of target pairs per branch. Therefore, reduction of the objective increases the number of the frequency-wavevector pairs at which the designed material follows the wanted dispersion behavior. Thus, this objective can estimate the *quality of the design*.

To bring the objective to a concise form, let us define the rank identity for a block diagonal matrix with

$$\sum_{j=1}^{n_w} \text{rank } \mathbf{A}_j = \text{rank } \text{diag}_{j=\overline{1, n_w}}(\mathbf{A}_j) \quad (5)$$

is valid for any set of square matrices \mathbf{A}_j . Here, an operator diag denotes a constructor of a block diagonal matrix from a list of rectangular matrices. Finally, the objective reads

$$J(\mathbf{s}) = \text{rank } \text{diag}_{j=\overline{1, n_w}}(\mathbf{A}_j). \quad (6)$$

The latter problem is still an affine rank minimization problem. Affinity easily follows from the definition of individual subblocks of the objective matrix. Recasting leads to

$$\begin{aligned} \text{diag}_{j=\overline{1, n_w}}(\mathbf{A}_j) &= \text{diag}_{j=\overline{1, n_w}}(\mathbf{Q}(\mathbf{K}(\mathbf{s}) - \omega_j^2 \mathbf{M}(\mathbf{s})) \mathbf{S}(k_j)) \\ &= \text{diag}_{j=\overline{1, n_w}}\left(\mathbf{Q}\left(\mathbf{K}_0 + \sum_{l=1}^{n_s} \mathbf{K}_l s_l - \omega_j^2 \left[\mathbf{M}_0 + \sum_{l=1}^{n_s} \mathbf{M}_l s_l\right]\right) \mathbf{S}(k_j)\right) = \mathbf{B}_0 + \sum_{l=1}^{n_s} \mathbf{B}_l s_l, \end{aligned} \quad (7)$$

where matrices $\{\mathbf{B}_l\}_{l=0}^{n_s}$ are defined

$$\mathbf{B}_l = \text{diag}_{j=\overline{1, n_w}}(\mathbf{Q}(\mathbf{K}_l - \omega_j^2 \mathbf{M}_l) \mathbf{S}(k_j)). \quad (8)$$

3 HEURISTIC RANK MINIMIZATION

Herein, a focus on log-det heuristics is made because of its simplicity and robustness. The rank minimization problem stated above is solved approximately by log-det heuristics from [5]. A substantial difference to the original method is due to complex entries of the RDSM matrices. These complex entries originate from the shift matrix \mathbf{S} even for the case without damping. The original rank minimization algorithm is valid for real semi-definite matrices. To bring our problem to an appropriated shape, a matrix \mathbf{X} is introduced with

$$\mathbf{X} = \text{diag}_{j=\overline{1, n_w}}(\mathbf{A}^H(\mathbf{s}, \omega_j, k_j) \mathbf{A}(\mathbf{s}, \omega_j, k_j)) \quad (9)$$

where superscript \square^H denotes Hermitian transpose (the conjugate transpose). The resultant matrix is a Hermitian positive semi-definite matrix, which is sufficient for the original log-det heuristics. The rank of matrix \mathbf{X} coincides with the objective function (6), but dependency on the free parameters is quadratic. A similar trick is used in [1] for dispersion error minimization on a regular spatial grid of finite elements. Now, a rank minimization problem (RMP) is formulated for matrix \mathbf{X} with

$$\mathbf{s}^* = \arg \min_{\mathbf{s} \in \mathcal{K}} (\text{rank}(\mathbf{X})), \quad (10)$$

where \mathcal{K} denotes an admissible convex set for parameters \mathbf{s} . Rather than solving a RMP, a *log-det smooth surrogate* for $\text{rank}(\mathbf{X})$ is used

$$\mathbf{s}^* = \arg \min_{\mathbf{s} \in \mathcal{K}} (\log \det (\mathbf{X} + \delta \mathbf{I})), \quad (11)$$

where $\delta > 0$ is a small regularization constant and \mathbf{I} is as the identity matrix. Despite complex entries of the matrix \mathbf{X} , the determinant of a Hermitian positive definite matrix $(\mathbf{X} + \delta \mathbf{I})$ is real and positive. Therefore, the objective function above is real and the optimization problem well defined. Here, we follow the paper [5] and reduce the optimization to a series of quadratic programming problems. First, a Taylor expansion of the objective function in the vicinity of the current value \mathbf{X}_k is carried out

$$\log \det(\mathbf{X} + \delta \mathbf{I}) \approx \log \det(\mathbf{X}_k + \delta \mathbf{I}) + \text{trace}(\mathbf{W}_k(\mathbf{X} - \mathbf{X}_k)), \quad (12)$$

where $\mathbf{W}_k = (\mathbf{X}_k + \delta \mathbf{I})^{-1}$ denotes the weighting matrix. The weighting matrix is evaluated numerically. Thus, the linearization of the surrogate function (12) has only a dependence on design parameters in the second factor $(\mathbf{X} - \mathbf{X}_k)$. The algorithm is illustrated in Box 1. The linearization of objective leads to real-valued Hessian H_{jl} and real-valued linear part f_j with

$$H_{jl} = \text{Re} [\text{trace}(\mathbf{W}_k(\mathbf{B}_j^H \mathbf{B}_l))] \quad f_j = \text{Re} [\text{trace}(\mathbf{W}_k(\mathbf{B}_j^H \mathbf{B}_0))] \quad (13)$$

Algorithm 1 Algorithm for dispersion design based on log-det heuristic proposed in [5].

Require: $\mathbf{X} \succcurlyeq 0$, $\delta > 0$, $\epsilon \geq 0$, $\mathcal{K} \neq \emptyset$

$\triangleright \succcurlyeq$ denotes semi-definite matrix

```

1: procedure MINRANKLOGDET( $\mathbf{X}(\mathbf{s})$ ,  $\mathcal{K}$ ,  $\mathbf{s}_0$ ,  $\delta$ ,  $\epsilon$ , maxiter)
2:    $\mathbf{X}_0 \leftarrow \mathbf{X}(\mathbf{s}_0)$ 
3:    $k \leftarrow 0$ 
4:   repeat
5:      $\mathbf{W}_k \leftarrow (\mathbf{X}_k + \delta \mathbf{I})^{-1}$ 
6:      $\mathbf{s}_{k+1} = \arg \min_{\mathbf{s} \in \mathcal{K}} \text{trace}(\mathbf{W}_k(\mathbf{X} - \mathbf{X}_k))$   $\triangleright$  Call quadratic programming solver
7:      $\mathbf{X}_{k+1} \leftarrow \mathbf{X}(\mathbf{s}_{k+1})$ 
8:      $k \leftarrow k + 1$ 
9:   until ( $k > \text{maxiter}$ )  $\vee$  ( $\|\mathbf{s}_{k+1} - \mathbf{s}_k\|_2 < \epsilon$ )
10:  return  $\mathbf{s}_k$ 
11: end procedure

```

Computation with double precision leads to tiny imaginary parts in the coefficients. Therefore, taking the real part is necessary.

The presented above algorithm is illustrated now with two algebraic examples. Both example use double precision arithmetic and a value of the regularization parameter $\delta = 10^{-3}$.

Algebraic example 1. First, a real-valued example is considered, where Hermitian transpose and usual transpose coincide. Find values of two parameters $\mathbf{s} = [s_1, s_2]$ within an admissible set $\mathcal{K} = [0, 1] \times [0, 1]$ that minimize the rank of a square matrix $\mathbf{X} \in \mathbb{R}^{4 \times 4}$ given as

$$\mathbf{X} = \mathbf{A}^T \mathbf{A}, \quad \mathbf{A} = \mathbf{B}_0 + s_1 \mathbf{B}_1 + s_2 \mathbf{B}_2 \quad (14)$$

with affine representation of matrix \mathbf{A} with matrices \mathbf{B}_i defined as

$$\mathbf{B}_0 = \begin{bmatrix} 5000 & 20 & 1/3 & 1/3 \\ 20 & 5/4 & 1/3 & 1/4 \\ 1/3 & 1/3 & 1/3 & 1/3 \\ 1/3 & 1/4 & 1/3 & 1/4 \end{bmatrix} \quad \mathbf{B}_2 = \begin{bmatrix} -1 & -1 & -1 & -1 \\ -1 & 0 & -1 & 0 \\ -1 & -1 & -1 & -1 \\ -1 & 0 & -1 & 0 \end{bmatrix} \quad \mathbf{B}_3 = \begin{bmatrix} 0 & 0 & 0 & 0 \\ 0 & -2 & 0 & -2 \\ 0 & 0 & 0 & 0 \\ 0 & -2 & 0 & -2 \end{bmatrix}. \quad (15)$$

This RMP has the global minimum

$$\mathbf{A} \left(s_1 = \frac{1}{3}, s_2 = \frac{1}{8} \right) = \begin{bmatrix} \frac{224973482}{9} & \frac{885118}{9} & 0 & 0 \\ \frac{885118}{9} & \frac{3490}{9} & 0 & 0 \\ 0 & 0 & 0 & 0 \\ 0 & 0 & 0 & 0 \end{bmatrix} \Rightarrow \text{rank}(\mathbf{X}) = \text{rank}(\mathbf{A}^T \mathbf{A}) = 2. \quad (16)$$

The log-det surrogate function shown in Figure 1 has its global minimum very close to the global minimum of the original problem. The global minimum is observed at the cross-section of two valleys where deficit of rank is one. Decreasing the regularization parameter would make the valley flanks steeper but it does not change qualitatively the shape of the objective function. The evolution of the surrogate objective over iterations is also shown in Figure 1. Convergence

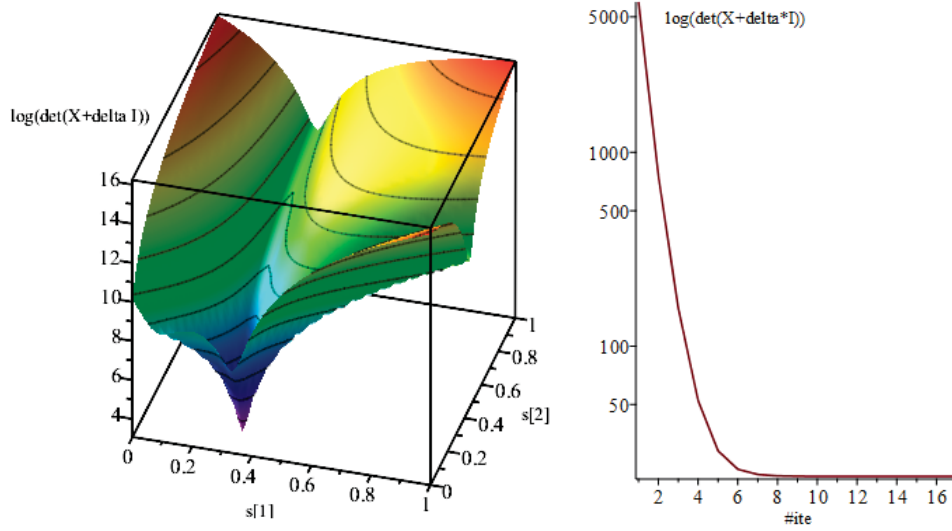


Figure 1: Surrogate objective function $\log \det (\mathbf{X} + \delta \mathbf{I})$ for the algebraic example with a regularization $\delta = 10^{-3}$ (left). Convergence of the surrogate objective (right) from starting value $[1/6, 1/12]$.

is achieved from starting value $[1/6, 1/12]$ to the rank-2 solution

$$\mathbf{X}^*(s_1=0.333328, s_2=0.125539) \approx \begin{bmatrix} 2.5e7 & 9.83e4 & 0.0264 & 0.00515 \\ 9.83e4 & 388.0 & 1.09e-4 & -9.72e-4 \\ 0.0264 & 1.09e-4 & 1.11e-9 & -1.13e-8 \\ 0.00515 & -9.72e-4 & -1.13e-8 & 2.32e-6 \end{bmatrix} \quad (17)$$

with two lowest eigenvalues below 10^{-5} within ten iterations.

Algebraic example 2. The second algebraic example treats a complex-valued square matrix $\mathbf{X} \in \mathbb{C}^{3 \times 3}$ depending on two parameters $\mathbf{s} = [s_1, s_2]$ within an admissible set $\mathcal{K} = [0, 1] \times [0, 1]$. Hermitian semi-positive matrix \mathbf{X} is defined as

$$\mathbf{X} = \mathbf{A}^H \mathbf{A}, \quad \mathbf{A} = \mathbf{B}_0 + s_1 \mathbf{B}_1 + s_2 \mathbf{B}_2 \quad (18)$$

with matrices \mathbf{B}_i defined

$$\mathbf{B}_0 = \begin{bmatrix} 5/4 & 1/3 & -1/12 + i/3 \\ 1/3 & 1/3 & i/3 \\ -1/12 + i/3 & i/3 & -5/12 \end{bmatrix} \quad (19)$$

$$\mathbf{B}_2 = \begin{bmatrix} 0 & -1 & 1-i \\ -1 & -1 & -i \\ 1-i & -i & 2 \end{bmatrix} \quad \mathbf{B}_3 = \begin{bmatrix} 0 & -1 & 1-i \\ -1 & -1 & -i \\ 1-i & -i & 2 \end{bmatrix}. \quad (20)$$

This RMP has the global minimum

$$\mathbf{A} \left(s_1 = \frac{1}{3}, s_2 = \frac{1}{8} \right) = \begin{bmatrix} 1 & 0 & 0 \\ 0 & 0 & 0 \\ 0 & 0 & 0 \end{bmatrix} \Rightarrow \text{rank}(\mathbf{X}) = \text{rank}(\mathbf{A}^H \mathbf{A}) = 1. \quad (21)$$

Log-det heuristic approximates this solution within ten iterations $s_1 = 0.334057$, $s_2 = 0.126277$ from starting value $[1/6, 1/12]$

$$\mathbf{X}^* = \begin{bmatrix} 0.995 & -0.000721 + 0.00000133i & -0.00182 - 0.000722i \\ -0.000721 - 0.00000133i & 0.00000157 & (1.33 + 0.247i)e - 6 \\ -0.00182 + 0.000722i & (1.33 - 0.247i)e - 6 & 5.62e - 6 \end{bmatrix}. \quad (22)$$

and it demonstrates work of the log-det heuristic for a Hermitian semi-positive matrix.

4 COMBINATION WITH REDUCED-ORDER TECHNIQUES

Increasing size of the representative patch increases rapidly cost of evaluation of the coefficient of quadratic programming problem in (13). Therefore, reducing dimension of the final RMP is very important. Here, a naive projection of the problem onto a reduced basis $\Phi \in \mathbb{C}^{n_{\text{rep}} n_w \times n_r}$, $n_r \ll n_{\text{rep}} n_w$ is proposed in form

$$\bar{J}(\mathbf{s}) = \text{rank}(\Phi^H \mathbf{X}(\mathbf{s}) \Phi). \quad (23)$$

Accuracy and efficiency of the reduced problem depends strongly on the reduced basis. Ideally, it should contain the kernel of the matrix \mathbf{X} at the solution point \mathbf{s}^* and have comparable dimension. Practically, using few consequent eigenmodes of \mathbf{A} at the initial approximation \mathbf{s}_0 is possible and used herein. Formally, this reduce basis can be written in block-diagonal format with

$$\Phi = \text{diag}_{j=\overline{1, n_w}} \left([\text{eig}(\mathbf{A}_j(\mathbf{s}_0))]_{:, n_l \dots n_u} \right), \quad (24)$$

where eig is an operator returning in columns eigenmodes in ascending order w.r.t. real part and an operation $\square_{:, n_l \dots n_u}$ returns columns $\overline{n_l}, \overline{n_u}$ of a matrix. This construction of the reduced basis yields the reduced dimension

$$n_r = n_w(n_u - n_l + 1) \quad (25)$$

The surrogate log-det function for the rank is computed in the same manner as for the full problem. Finally, a following minimization problem is solved

$$\mathbf{s}^* = \arg \min_{\mathbf{s} \in \mathcal{K}} (\log \det (\Phi^H \mathbf{X}(\mathbf{s}) \Phi + \delta \mathbf{I})), \quad (26)$$

where the dimension of identity matrix is adjusted to n_r .

We expect that the influence of reduced-order technique is two-fold. First, the dimension of the problem significantly reduces. Second, the conditioning of the matrix $\Phi^H \mathbf{X}(\mathbf{s}) \Phi$ is better than for full matrix $\mathbf{X}(\mathbf{s})$, which helps log-det heuristic to converge faster and allows lower values of the regularization parameter δ . However, checking these two hypothesis goes beyond the contribution.

Algebraic example 3. This example uses setup of algebraic example 1. The influence of the reduced basis on the quality of the solution is studied in for two reduced bases

$$\Phi_1 = \begin{bmatrix} 0 & 0 \\ 0 & 1/5 \\ 1 & -1 \\ 1 & 1 \end{bmatrix}, \quad \Phi_2 = \begin{bmatrix} 1 & 0 \\ 0 & 1 \\ -1 & 0 \\ 0 & -1 \end{bmatrix}. \quad (27)$$

The former basis is very close to the kernel of the matrix \mathbf{X} at the solution point

$$\ker(\mathbf{X}) = \begin{bmatrix} 0 & 0 \\ 0 & 0 \\ 1 & -1 \\ 1 & 1 \end{bmatrix}. \quad (28)$$

The surrogate objective function for the reduced basis Φ_1 is shown in Figure 2 (left). It has a global minimum close the exact one. The surrogate objective function for the reduced basis Φ_2 does not depend on the parameters and it cannot be used. It is an example of extremely unfavorable choice of the reduced basis. Convergence to a solution $s_1 = 0.333337$, $s_2 = 0.125002$ is obtained within 10 iterations. Evolution of the objective during iteration process is shown in Figure 2 (right). The absolute values of objective for the reduced problem are different the full one, which is also clear from comparison of Figure 2 and 1.

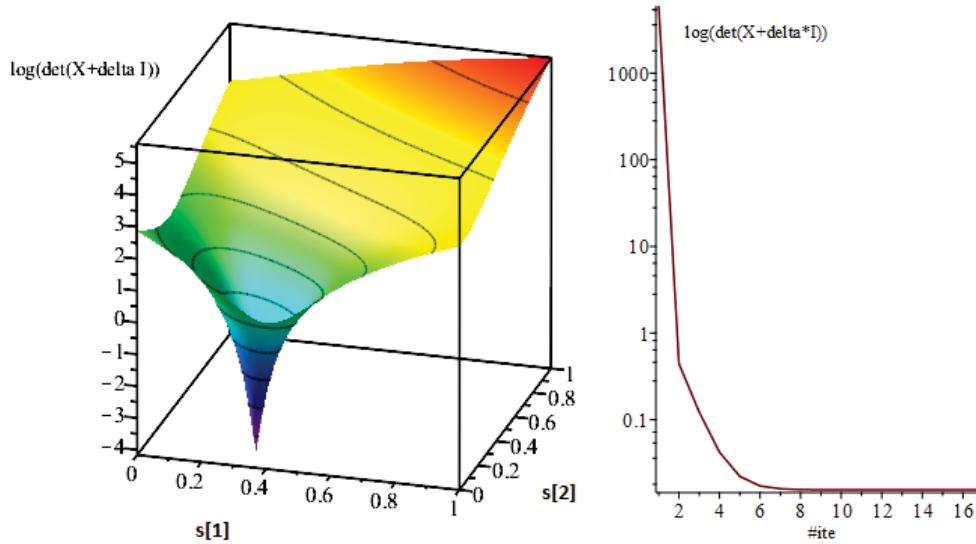


Figure 2: Surrogate objective function $\log \det (\Phi^H \mathbf{X}(\mathbf{s}) \Phi + \delta \mathbf{I})$ for the algebraic example with a regularization $\delta = 10^{-3}$ using the reduced basis Φ_1 (left). Convergence of the reduced surrogate objective (right) from starting value $[1/6, 1/12]$.

5 NUMERICAL EXAMPLE

A mechanical example illustrates performance of the proposed approach. A periodic system with a uniform back-bone mass-spring chain and a side branch at every second mass element is shown in Figure 3. Dimension of the representative patch is five, while seven continuous parameters define system properties. The mass and stiffness constants in the back-bone are fixed. Three mass and four stiffness parameters of the side branch can be varied within ranges given in Figure 3. Stiffness parameters are denoted with letter β to avoid any confusion with the wavenumber denoted with letter k .

The aim is to obtain a dispersion design with an almost *constant frequency branch*, which also provides a near to zero group velocity. Five target wavenumber-frequency pairs are used

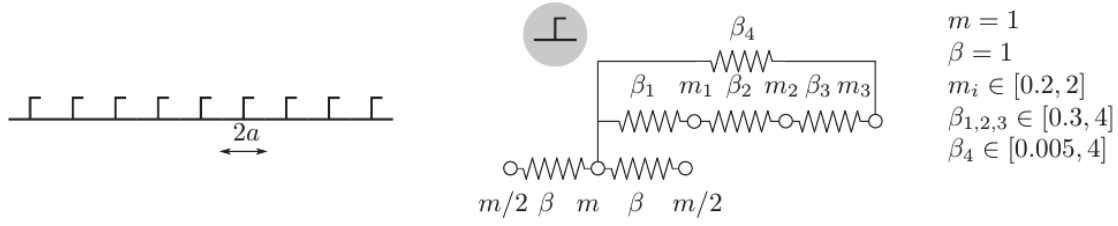


Figure 3: Setup for a periodic discrete system. Overall view on 1D linear mass-spring system with side branch (left) and a zoom in a repetitive structure with topology, parameters and their ranges (right).

with

$$n_w = 5, \quad ak_j = \frac{\pi j}{n_w + 1}, \quad \omega_j = 1.58, \quad j = \overline{1, n_w}, \quad (29)$$

where $2a$ is the physical length of repetitive structure, as shown in Figure 3. At these pairs, the RDSM should be singular and it is achieved by minimizing the rank of the corresponding matrix via log-det heuristic. Three starting value sets for design parameters are listed in Table 1. The regularization parameter $\delta = 3 \cdot 10^{-8}$, convergence tolerance $\epsilon = 10^{-10}$ and maximum 15 iterations is used in the log-det heuristic.

A solution is obtained after 15 iterations and the final values are given in Table 1. Reduction of the surrogate objective over iterations is given in Figure 4. These curves have very steep initial phase. Eventually, they flatten and come to saturation. If the convergence tolerance ϵ for the increment of parameter vector is not reached then the algorithm iterates until the maximum iteration number is reached.

Case	β_1	β_2	β_3	β_4	m_1	m_2	m_3
Starting values, set I	1.000	1.300	.6000	.1000	1.000	2.000	1.200
Starting values, set II	1.000	.5000	.6000	.1000	.5000	1.000	1.200
Starting values, set III	.3000	.5000	.6000	.1000	.5000	2.000	2.000
Result, set I	1.098	.3000	.3009	.3245	.4443	.5395	.2848
Result, set II	1.089	.3000	.3001	.2883	.4359	.5731	.2676
Result, set III	.3000	.3000	.3000	.0009	.2681	.8135	.2009
Result for ROM, set I	.3558	.3000	.3000	.2932	.2000	.3950	.2759
Result for ROM, set II	.3752	.3000	.3000	.2735	.2000	.2700	.2912
Result for ROM, set III	.3442	.3153	.3000	.2483	.2000	.3209	.2646

Table 1: Starting and final values for dispersion design parameters of the periodic discrete systems.

Figure 5 illustrates the dispersion behavior for the obtained system for starting set I and III. Result obtained with set II is very similar to one obtained for set I. The obtained system satisfies the desired property of having a constant frequency branch for initial set I and II. Notably, this branch is crossed by another branch and it is formed by third frequency for wavenumbers $ak < 2.02$ and fourth frequency otherwise. Information about the order of frequencies was not specified in the algorithm. Such a behavior illustrates the advantage of the proposed approach over standard methods, where the objective is formulated with respect to a specific frequency. Solution obtained from the starting set III is different and it satisfies the rank deficit condition only at four out of five points.

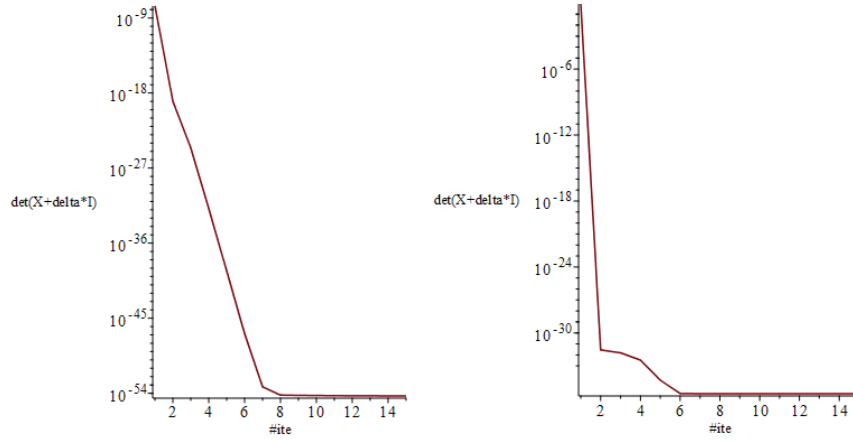


Figure 4: Convergence of the surrogate objective for initial parameter set I (left) and set III (right).

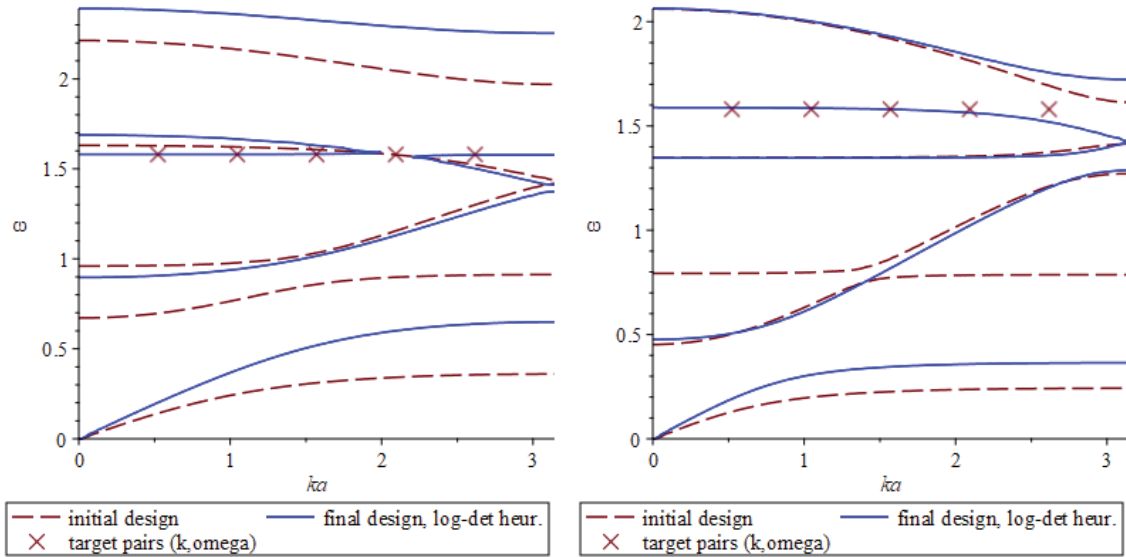


Figure 5: Dispersion behavior of the designed periodic discrete system with prescribed constant frequency $\omega = 1.58$. Initial and final dispersion behavior for initial parameter set I (left) and set III (right).

Reduced-order technique presented in Section 4 is now applied to dispersion design problem. Dimension of the original system is $n_w n_{\text{rep}} = 25$. Here, three eigenmodes in span $n_l = 2$ and $n_u = 4$ per sampling pair is used. Thus, the problem is reduced to the size $n_w(n_u - n_l + 1) = 15$ as explained in equation (25). This reduction is not drastic and it only served to check algebraic correctness of the approach.

Similar results are obtained for three starting parameter sets, see Table 1 and Figure 6. For all initial sets, third branch crosses all target pairs and these solutions are considered as satisfactory.

The considered example is undetermined, i.e. it has seven parameters and five conditions to be fulfilled. It is not a surprise that more than one solution is inside the admissible set \mathcal{K} and they are obtained with the proposed approach. It is also clear that the influence of starting approximation and algorithm setting is significant.

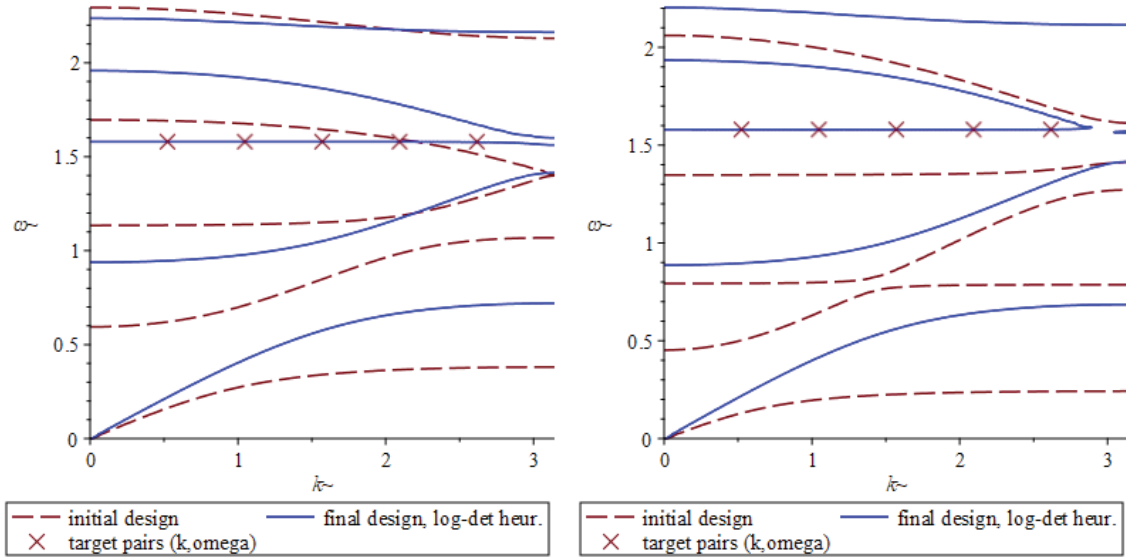


Figure 6: Dispersion behavior of the designed periodic discrete system with prescribed constant frequency $\omega = 1.58$. Initial and final dispersion behavior for initial parameter set II (left) and set III (right) obtained with reduced-order technique.

6 CONCLUSIONS

This contribution considers a special problem of design of 1D periodic discrete systems whose dispersion branch matches a prescribed dependency. For this problem, a new class of performance functions is proposed that explicitly depends on the design variables and does not require tracking of eigenmodes. This performance function is derived in several steps. First, a match to a dispersion branch is collocated in few discrete wavenumber-frequency pairs. Second, this match at discrete pairs is understood as the deficit of the representative dynamic stiffness matrix's rank. Thus, sum of these ranks is identified as a possible performance function and its reduction means quality improvement of the design. Third, the latter rank minimization problem is solved using log-det heuristics. Here, a modification for a case of square complex-valued matrices is proposed. Fourth, the log-det heuristics reduces the problem to a series of quadratic programming problems. The coefficients of the objective quadratic function are obtained here for the case of affine dependency of the mass and stiffness matrices on the free parameters.

Combining the proposed approach with reduced-order techniques is shortly discussed and a version of the reduced basis is proposed.

This approach is illustrated with several algebraic examples and one mechanical example. First algebraic example demonstrates the basic features of the rank minimization using log-det heuristic. Second algebraic example confirms the extension of the log-det heuristic for Hermitian semi-positive matrices. Third algebraic example demonstrates validity of projection-based reduction for rank minimization problems. Finally, a mechanical periodic system is considered and the concept of the dispersion design using log-det heuristic is demonstrated.

Further efforts may be focused on extending the approach to damped systems (achieving so-called metadamping [7]) and exploring the method for larger or multidimensional systems. Also, finding further explicit performance functions for different types of target dispersion behavior is of high scientific interest.

ACKNOWLEDGMENT

The work of Anton Tkachuk was supported by the Deutsche Forschungsgemeinschaft (DFG - German Research Foundation) Projektnummer 442679063 (TK 63/3-1).

REFERENCES

- [1] A. Tkachuk. Customization of reciprocal mass matrices via log-det heuristic. *IJNME*, 2020, volume 121, pages 690–711.
- [2] A. Bacigalupo, G. Gnecco, M. Lepidi, and L. Gambarotta. Machine-learning techniques for the optimal design of acoustic metamaterials. *Journal of Optimization Theory and Applications*, 2019, 1–24.
- [3] P. A. Deymier. *Acoustic metamaterials and phononic crystals*. Springer Science & Business Media, 2013.
- [4] M. Fazel, H. Hindi, and S. Boyd. A rank minimization heuristic with application to minimum order system approximation. 6:4734–4739, 2001.
- [5] M. Fazel, H. Hindi, and S. P. Boyd. Log-det heuristic for matrix rank minimization with applications to hankel and euclidean distance matrices. In *Proceedings of the 2003 American Control Conference, 2003*, volume 3, pages 2156–2162. IEEE, 2003.
- [6] M. J. Frazier and M. I. Hussein. Viscous-to-viscoelastic transition in phononic crystal and metamaterial band structures. *JASA*, 138(5):3169–3180, 2015.
- [7] M. I. Hussein and M. J. Frazier. Metadamping: An emergent phenomenon in dissipative metamaterials. *JSV*, 332(20):4767–4774, 2013.
- [8] D. Mead. A general theory of harmonic wave propagation in linear periodic systems with multiple coupling. *JSV*, 27(2):235–260, 1973.
- [9] K. Mohan and M. Fazel. Iterative reweighted algorithms for matrix rank minimization. *Journal of Machine Learning Research*, 13(Nov):3441–3473, 2012.
- [10] J. H. Park, P. S. Ma, and Y. Y. Kim. Design of phononic crystals for self-collimation of elastic waves using topology optimization method. *Structural and Multidisciplinary Optimization*, 51(6):1199–1209, 2015.
- [11] B. Recht, M. Fazel, and P. A. Parrilo. Guaranteed minimum-rank solutions of linear matrix equations via nuclear norm minimization. *SIAM review*, 52(3):471–501, 2010.
- [12] L. Vandenberghe and S. Boyd. Semidefinite programming. *SIAM review*, 38:49–95, 1996.
- [13] G. Yi and B. D. Youn. A comprehensive survey on topology optimization of phononic crystals. *Structural and Multidisciplinary Optimization*, 54(5):1315–1344, 2016.

AN EFFICIENT PRECONDITIONER FOR MODAL FREQUENCY RESPONSE

T. Willerding

INTES GmbH
Breitwiesenstraße 28
70565 Stuttgart, Germany
e-mail: tobias.willerding@intes.de

Keywords: Preconditioner, modal frequency response, iterative solver, complex eigenvalue problem

Abstract. *In frequency response analysis, it is of interest to simulate the dynamic response of a system for many excitation frequencies. In order to accelerate the calculation, the system is first transformed to modal space by calculating a limited set of eigenvectors and eigenvalues. In this way, the number of degrees of freedom can be reduced from e.g. 50 million to 50,000. However, due to the existence of structural and viscous damping, the system matrix in modal space is dense in a general case.*

In this work, a method to generate a preconditioner for the solution of modal frequency response is proposed. First, a decomposition of the system matrix at one excitation frequency is performed using a direct method (e. g. LU decomposition). In a second step, this decomposition is modified for different excitation frequencies in an efficient way, by using a complex eigenvalue problem. Although the modified decomposition is no longer exact, it has excellent characteristics to be used as a preconditioner in an iterative method. Using a complex eigenvalue problem and a decomposition update has already been proposed in [1] for a direct solution method. However, in this work, the focus is on an iterative method.

By making use of the structure of the system matrix, it is possible to split the product \mathbf{Ax} in the iterative solver in multiple parts to iterate many right hand sides (for equal or different excitation frequencies) at once. In this way, the iterative solver can make use of dense matrix-matrix multiplications, using BLAS Level-3 [6], which results in better performance.

1 INTRODUCTION

In modern finite element software (e.g. PERMAS [9]), an important problem is the calculation of the response of a system subject to harmonic loading. The system can represent a large finite element model such as a car (see figure 1), an aircraft or a ship. It is also important in the design of machine tools [3], spaceflight [4] or in acoustic analysis [5]. The dynamic response is calculated with frequency response analysis. This analysis is performed for many (e.g. 1000 or more) excitation frequencies. The solution at each excitation frequency requires the solution of a linear equation system with millions of unknowns in modern applications. In order to speed up the calculation, the dynamic system is typically transformed to modal space. This is achieved by calculating a limited number of eigenvalues and eigenvectors of the original system. The quality of the transformation depends on the dimension of the modal space, e.g. the number of calculated eigenvalues. !

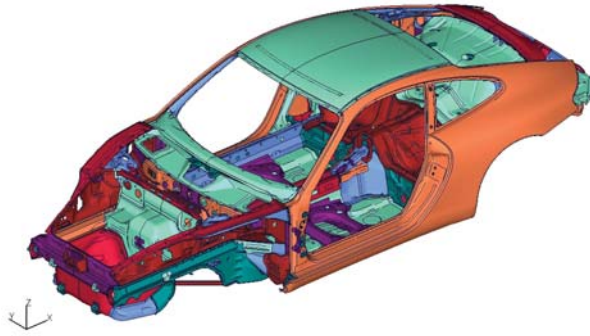


Figure 1: Porsche 996, by courtesy of Dr. Ing. h.c. F. Porsche AG

In modal space, the mass and stiffness matrix are diagonal matrices, which is very convenient for the frequency response analysis. However, a finite element model also often contains damper elements or structural damping, which results in dense damping matrices in modal space. Kim and Benninghof [1] noted, one of the two dense matrices can be diagonalized in modal space by solving another complex eigenvalue problem. However, one dense matrix remains. If this matrix is of low rank, the inverse can be updated easily with the Woodbury matrix identity as noted by Kim and Bennighof. However, if the viscous damping matrix has full rank, there is no advantage in doing this.

In this work, an idea is presented to solve this problem with an iterative solver, where the inverse of the system matrix at a reference frequency is calculated and this solution is modified by solving a complex eigenvalue problem, similar to the work by Kim and Bennighof. The iterative solver could be a purely iterative method (e.g. Jacobi iteration) or a more sophisticated method like GMRES [2].

2 THEORY

In frequency response, the solutions $\tilde{\mathbf{x}} \in \mathbb{C}^n$ to the equation

$$\left(-\omega^2 \tilde{\mathbf{M}} + i\omega \tilde{\mathbf{D}} + i\tilde{\mathbf{H}} + \tilde{\mathbf{K}}\right) \tilde{\mathbf{x}} = \tilde{\mathbf{A}}(\omega) \tilde{\mathbf{x}} = \tilde{\mathbf{b}} \quad (1)$$

for different $\omega \in \mathbb{R}$ have to be calculated. $\tilde{\mathbf{M}} \in \mathbb{R}^{n \times n}$ is the mass matrix, $\tilde{\mathbf{D}} \in \mathbb{R}^{n \times n}$ is the viscous damping matrix, $\tilde{\mathbf{H}} \in \mathbb{R}^{n \times n}$ is the structural damping matrix and $\tilde{\mathbf{K}} \in \mathbb{R}^{n \times n}$ is

the stiffness matrix. In addition, on the right hand side, there is a loading vector $\tilde{\mathbf{b}} \in \mathbb{C}^n$. i represents the imaginary unit. The matrices $\tilde{\mathbf{M}}$, $\tilde{\mathbf{K}}$, $\tilde{\mathbf{D}}$ and $\tilde{\mathbf{H}}$ are symmetric in most cases, but they may also include rotational effects or special elements, that result in a non-symmetric problem. In this work, only the symmetric case is considered. Furthermore, it is assumed that the matrices $\tilde{\mathbf{D}}$ and $\tilde{\mathbf{H}}$ are positive semi-definite.

In modal frequency response, a generalized eigenvalue problem for $\tilde{\mathbf{K}}$ and $\tilde{\mathbf{M}}$ is solved for a limited number of eigenvalues m and the system is transformed to modal space. Using a transformation matrix Φ , we can transform the matrices to modal space: $\mathbf{M} = \Phi^T \tilde{\mathbf{M}} \Phi$, $\mathbf{D} = \Phi^T \tilde{\mathbf{D}} \Phi$, $\mathbf{H} = \Phi^T \tilde{\mathbf{H}} \Phi$, $\mathbf{K} = \Phi^T \tilde{\mathbf{K}} \Phi$. The load is transformed as $\mathbf{b} = \Phi^T \tilde{\mathbf{b}}$ and the displacement vector is $\mathbf{x} = \Phi^T \tilde{\mathbf{x}}$. Finally we arrive at the following equation system in modal space:

$$(-\omega^2 \mathbf{M} + i\omega \mathbf{D} + i\mathbf{H} + \mathbf{K}) \mathbf{x} = \mathbf{A}(\omega) \mathbf{x} = \mathbf{b}. \quad (2)$$

The transformed system has a diagonal mass matrix \mathbf{M} , a diagonal stiffness matrix \mathbf{K} and a dense viscous damping matrix \mathbf{D} and a dense structural damping matrix \mathbf{H} . The system size is reduced from $n \times n$ to $m \times m$. In this work, this system is investigated to be solved with an iterative method. In general, iterative methods need a preconditioner to converge within an acceptable number of iterations.

3 PRECONDITIONING

In order to judge the quality of the preconditioner, the convergence criterion of a purely iterative solver is used, because it is very simple and easy to understand. The equation $\mathbf{A}\mathbf{x} = \mathbf{b}$ is iteratively solved using a preconditioner \mathbf{P} . This means that every eigenvalue λ of $\mathbf{I} - \mathbf{P}^{-1}\mathbf{A}$ must fulfill

$$|\lambda(\mathbf{I} - \mathbf{P}^{-1}\mathbf{A})| < 1. \quad (3)$$

It is desirable to construct a preconditioner that works for k values $\omega_1 < \omega_i < \omega_k$. First, a reference circular frequency ω_{ref} with $\omega_1 < \omega_{\text{ref}} < \omega_k$ is selected and a direct solution method (e.g. LU decomposition) is used to calculate the inverse of $\mathbf{A}_{\text{ref}} = \mathbf{A}(\omega_{\text{ref}})$. However, this reference inverse is insufficient as a general preconditioner and it must be modified to adapt it to each individual circular frequency ω_i as will be seen later.

The idea consists of approximating the difference between $\mathbf{A}(\omega)$ and $\mathbf{A}(\omega_{\text{ref}})$ with a matrix \mathbf{S} and an ω -dependent scalar factor $f(\omega)$. This approximation of $\mathbf{A}(\omega) \approx \mathbf{P} = \mathbf{A}(\omega_{\text{ref}}) + f(\omega) \mathbf{S}$ is taken as preconditioner.

In general, the difference between $\mathbf{A}(\omega)$ and $\mathbf{A}(\omega_{\text{ref}})$ can be expressed as

$$\begin{aligned} \mathbf{A}(\omega) &= \mathbf{A}(\omega_{\text{ref}}) + ((\mathbf{A}(\omega) - \mathbf{A}(\omega_{\text{ref}}))) \\ &= \mathbf{A}(\omega_{\text{ref}}) + (-\omega^2 + \omega_{\text{ref}}^2) \mathbf{M} + i(\omega - \omega_{\text{ref}}) \mathbf{D} \end{aligned} \quad (4)$$

In this work, only an approximation of the mass matrix is considered. The reference matrix \mathbf{A}_{ref} is modified with the mass matrix \mathbf{M} , multiplied with a scalar function $f(\omega)$.

$$\mathbf{A}(\omega) \approx \mathbf{A}(\omega_{\text{ref}}) + (-\omega^2 + \omega_{\text{ref}}^2) \mathbf{M} = \mathbf{A}(\omega_{\text{ref}}) + f(\omega) \mathbf{M} = \mathbf{P} \quad (5)$$

The expression is now transformed as follows,

$$\begin{aligned} \mathbf{P}^{-1} &= (\mathbf{A}_{\text{ref}} + f(\omega) \mathbf{M})^{-1} = (\mathbf{A}_{\text{ref}} (\mathbf{I} + \mathbf{A}_{\text{ref}}^{-1} \mathbf{M} f(\omega)))^{-1} \\ &= (\mathbf{I} + \mathbf{A}_{\text{ref}}^{-1} \mathbf{M} f(\omega))^{-1} \mathbf{A}_{\text{ref}}^{-1} \end{aligned} \quad (6)$$

Next, we solve a complex eigenvalue problem of $\mathbf{A}_{\text{ref}}^{-1} \mathbf{M} = \mathbf{Q} \mathbf{\Lambda} \mathbf{Q}^{-1}$. We can now replace $\mathbf{A}_{\text{ref}}^{-1} \mathbf{M}$ with an orthonormal eigenvector matrix \mathbf{Q} and the eigenvalue diagonal matrix $\mathbf{\Lambda}$:

$$\begin{aligned} \mathbf{P}^{-1} &= (\mathbf{A}_{\text{ref}} + f(\omega) \mathbf{M})^{-1} = (\mathbf{Q} \mathbf{Q}^{-1} + f(\omega) \mathbf{Q} \mathbf{\Lambda} \mathbf{Q}^{-1})^{-1} \mathbf{A}_{\text{ref}}^{-1} \\ &= \mathbf{Q} (\mathbf{I} + f(\omega) \mathbf{\Lambda})^{-1} \mathbf{Q}^{-1} \mathbf{A}_{\text{ref}}^{-1}. \end{aligned} \quad (7)$$

This expression for \mathbf{P}^{-1} is quite interesting, because first the right hand side is multiplied with the reference inverse $\mathbf{A}(\omega_{\text{ref}})^{-1}$ and then with the eigenvector matrices \mathbf{Q} and a diagonal matrix, that is different for each ω . With the definitions $\mathbf{U} = \mathbf{Q}$, $\mathbf{V} = \mathbf{Q}^{-1} \mathbf{A}_{\text{ref}}^{-1}$ and $\mathbf{G}(\omega) = (\mathbf{I} + f(\omega) \mathbf{\Lambda})^{-1}$, we can write this as

$$\mathbf{P}^{-1} = (\mathbf{A}_{\text{ref}} + f(\omega) \mathbf{M})^{-1} = \mathbf{U} \mathbf{G}(\omega) \mathbf{V}. \quad (8)$$

As can be seen, the only term that is ω -dependent is \mathbf{G} , which is a diagonal matrix. In the next section, it will be shown that this preconditioner can be evaluated in a very efficient manner.

However, first, the preconditioner quality is discussed. GNU Octave [7] is used for the evaluation of the eigenvalues. A matrix \mathbf{A} of the size $m = 100$ is selected, which corresponds to 100 modes calculated. The stiffness matrix \mathbf{K} is the identity matrix in modal space. The mass matrix \mathbf{M} is also diagonal and we set the value of \mathbf{M} equal to $M_{ii} = 1/i^2$, which corresponds to circular eigenfrequencies $\omega_i = i$. Furthermore symmetric, positiv semi-definite matrices are chosen for \mathbf{H} and \mathbf{D} . The eigenvalues of \mathbf{H} and \mathbf{D} are set to be randomly equally distributed between 0 and d_{max} or h_{max} , respectively. In addition, we select a reference frequency $\omega = 50$ and look at the absolute largest eigenvalue between $\omega = 0$ and $\omega = 100$. Depending on the seed of the random generator, the eigenvalues of $\mathbf{I} - \mathbf{P}^{-1}(\omega) \mathbf{A}(\omega)$ look slightly different, but the general picture is as seen in figure 2 and 3.

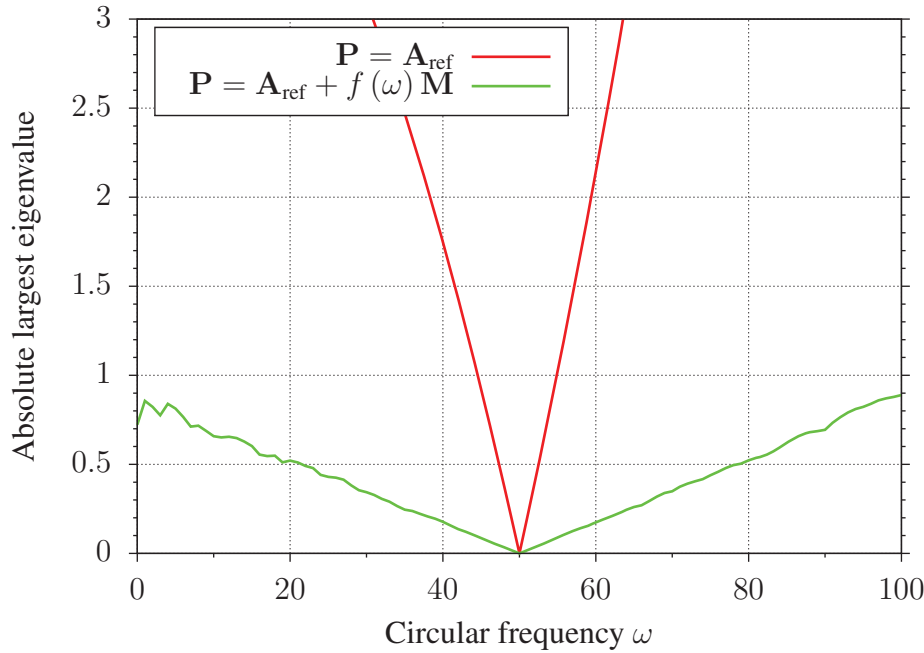


Figure 2: Plot of the absolute largest eigenvalue of $\mathbf{I} - \mathbf{P}^{-1}(\omega) \mathbf{A}(\omega)$ for two different preconditioners, inverse only and inverse with mass matrix modification. $d_{\text{max}} = 1.0 \times 10^{-4}$

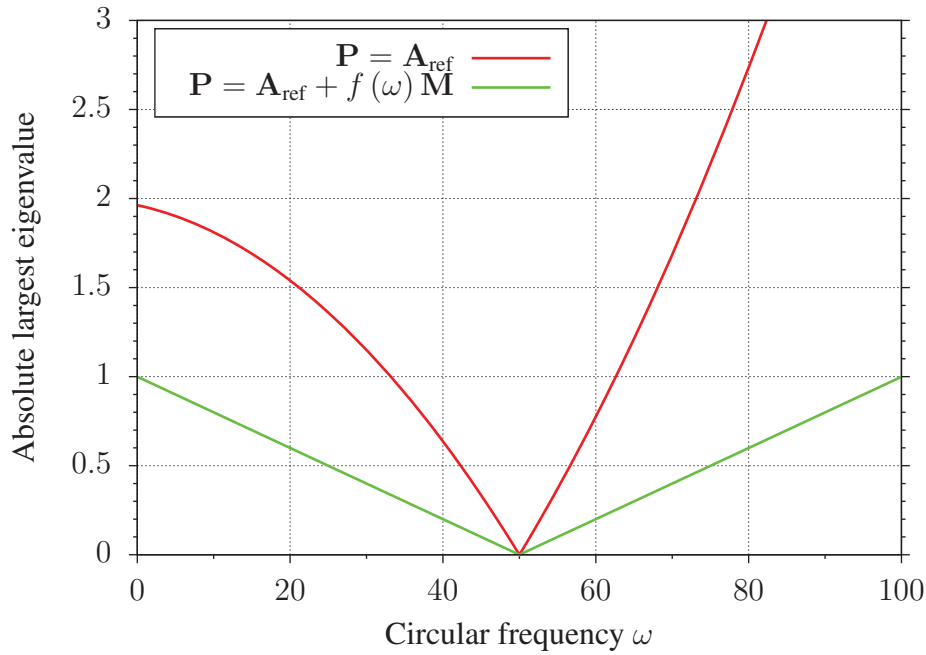


Figure 3: Plot of the absolute largest eigenvalue of $\mathbf{I} - \mathbf{P}^{-1}(\omega) \mathbf{A}(\omega)$ for two different preconditioners, inverse only and inverse with mass matrix modification. $d_{\max} = 1.0 \times 10^{-2}$

Using these definitions for \mathbf{M} , \mathbf{D} , \mathbf{H} and \mathbf{K} , figures 2 and 3 show the absolute largest eigenvalue of $\mathbf{I} - \mathbf{P}^{-1}(\omega) \mathbf{A}(\omega)$ for different values of d_{\max} . As can be seen in the figure, at $\omega = \omega_{\text{ref}}$, the absolute largest eigenvalue is zero as expected. The inverse is - of course - the perfect preconditioner. For other frequencies the absolute largest eigenvalue is monotonously rising with ω . If only the inverse at the reference circular frequency ω_{ref} is taken as preconditioner, it can be seen that the absolute largest eigenvalue is rising quickly, depending on damping d_{\max} . The higher the damping, the better the inverse for neighbouring frequencies. If the inverse is modified with the above mentioned approach, the largest absolute eigenvalue is rising much more slowly and remains below or equal to 1 in the investigated interval. Even in cases, where the inverse-only preconditioner rises quickly as seen in figure 2, the absolute largest eigenvalue of the modified inverse stays below 1. The reason for this will be investigated in future work.

4 IMPLEMENTATION

In order to use this formulaton, it is useful to have an efficient evaluation of the product $\mathbf{A}(\omega) \mathbf{x}$ and the application of the preconditioner. The matrix is defined as

$$(-\omega^2 \mathbf{M} + i\omega \mathbf{D} + i\mathbf{H} + \mathbf{K}) \mathbf{x} = \mathbf{b}. \quad (9)$$

In an iterative solver, the desired value is the residual \mathbf{r} with

$$\mathbf{r} = \mathbf{b} - (-\omega^2 \mathbf{M} + i\omega \mathbf{D} + i\mathbf{H} + \mathbf{K}) \mathbf{x}. \quad (10)$$

This can be rearranged to

$$\mathbf{r} = \mathbf{b} + \mathbf{M}\mathbf{x}\omega^2 - i\mathbf{D}\mathbf{x}\omega - i\mathbf{H}\mathbf{x} - \mathbf{K}\mathbf{x}. \quad (11)$$

By defining the matrix

$$\mathbf{\Omega} = \begin{bmatrix} \omega_1 & 0 & \cdots & 0 \\ 0 & \omega_2 & \ddots & 0 \\ \vdots & \ddots & \ddots & \vdots \\ 0 & \cdots & 0 & \omega_q \end{bmatrix} \quad (12)$$

and assembling q right hand sides

$$\mathbf{B} = [\mathbf{b}(\omega_1) \quad \mathbf{b}(\omega_2) \quad \cdots \quad \mathbf{b}(\omega_q)], \quad (13)$$

it is possible to calculate residuals for multiple right hand sides with different ω_i at once instead of calculating each vector \mathbf{x} with a different $\mathbf{A}(\omega)$. With the iteration vectors

$$\mathbf{X} = [\mathbf{x}(\omega_1) \quad \mathbf{x}(\omega_2) \quad \cdots \quad \mathbf{x}(\omega_q)] \quad (14)$$

the \mathbf{R} can be expressed as

$$\mathbf{R} = \mathbf{B} + \mathbf{MX}\mathbf{\Omega}^2 - i\mathbf{DX}\mathbf{\Omega} - i\mathbf{HX} - \mathbf{KX}. \quad (15)$$

The preconditioner is applied to the residual \mathbf{r} in order to get an increment on \mathbf{x} :

$$d\mathbf{x} = \mathbf{P}^{-1}\mathbf{r} = \mathbf{UG}(\omega)\mathbf{Vr}. \quad (16)$$

The diagonal matrix $\mathbf{G}(\omega)$ can be converted to a column vector \mathbf{g} . Next, preconditioner vectors for multiple right hand sides can be assembled to form a matrix

$$\mathbf{G}_R = [\mathbf{g}(\omega_1) \quad \mathbf{g}(\omega_2) \quad \cdots \quad \mathbf{g}(\omega_q)]. \quad (17)$$

In other words, just like the product $\mathbf{A}(\omega)\mathbf{x}$, also in this case multiple vectors can be iterated at once:

$$d\mathbf{X} = \mathbf{P}^{-1}\mathbf{R} = \mathbf{U}(\mathbf{G}_R \odot (\mathbf{VR})). \quad (18)$$

Here \odot symbolizes the Hadamard product [8]. The Hadamard product is a entry-wise multiplication of matrices. Both matrices must have the same dimension. The total operation count per iteration and vector is a bit higher than compared to the case, where each vector is iterated with the assembled matrix. However, modern CPU architecture is limited by memory bandwidth and the proposed method can make full use of the CPU as only dense matrix multiplication are performed. These can be efficiently performed with Level-3 BLAS [6], for example. A benchmark test case will be performed in future work.

5 CONCLUSIONS

In this work, the construction of a preconditioner for modal frequency response has been presented. The inverse of the system matrix is calculated at a reference frequency with a direct solution method (e.g. LU decomposition). The decomposition is modified by first solving a complex eigenvalue problem. By solving a complex eigenvalue problem, the frequency specific modification information is limited to diagonal matrices. These diagonal matrices can be transformed to a column vector and efficiently evaluated by performing a Hadamard product with the iteration vectors. The absolute value of the eigenvalues of $\mathbf{I} - \mathbf{P}^{-1}\mathbf{A}$ are below or equal 1, if the reference frequency is in the middle of the interval of interest. The absolute largest eigenvalue of $\mathbf{I} - \mathbf{P}^{-1}\mathbf{A}$ is slowly rising from zero at the reference frequency to 1 at the integration bounds.

REFERENCES

- [1] Chang-Wan Kim, J.K. Bennighof, Fast frequency response analysis of partially damped structures with non-proportional viscous damping, *Journal of Sound and Vibration*, Volume 297, Issues 35, 2006, Pages 1075-1081.
- [2] Saad, Youcef and Schultz, Martin H., GMRES: A Generalized Minimal Residual Algorithm for Solving Nonsymmetric Linear Systems, *SIAM Journal on Scientific and Statistical Computing*, Volume 7, Number 3, Pages 856-859, 1986
- [3] R. Helfrich, B. Kirchgäßner, G. Nötzel-Steidle, Optimizing the Dynamic System Behaviour of Machine Tools, *NAFEMS World Congress 2019*, Quebec 17-20 June 2019 (PDF).
- [4] R. Helfrich, J. Marchesini, Dynamic substructuring with mixed boundary conditions to cope with complex structural assemblies, *European Conference on Spacecraft Structures, Materials & Environmental Testing*, Braunschweig, Germany, 1-4 April 2014
- [5] R. Helfrich, M. Spiegel, Noise propagation from vibrating structures, *NAFEMS World Congress 2015*, San Diego 21-24 June 2015
- [6] Basic Linear Algebra Subprograms, <http://www.netlib.org/blas/>
- [7] GNU Octave, <https://www.gnu.org/software/octave/>
- [8] For more details on the Hadamard product, see [https://en.wikipedia.org/wiki/Hadamard_product_\(matrices\)](https://en.wikipedia.org/wiki/Hadamard_product_(matrices))
- [9] PERMAS Users Reference Manual, INTES Publication No. 450

FRAGILITY ASSESSMENT OF WIND-EXCITED VIDEO SCREEN ROOMS IN HIGH-RISE BUILDINGS

Fabio Rizzo ^{1*}, Laura Ierimonti ², Stefano Sacconi ², Ilaria Venanzi ²

¹Gabriele D'Annunzio University, Pescara, Italy, fabio.rizzo@unich.it

²University of Perugia, Perugia, Italy, laura.ierimonti@unipg.it, stefano.sacconi@collaboratori.unipg.it, ilaria.venanzi@unipg.it

Abstract

High-rise buildings with unusual shapes and high-technological systems are commonly used by companies to represent their economic power. In many cases, equipment consisting of LED screen walls is frequently not compatible with wind-induced displacements and accelerations experienced at high floors. The aim of the research work is to design and optimize a control device for response reduction of a prismatic room equipped with LED screen walls on all sides. The control system is a passive sliding device located at the base of the room disconnecting the LED supporting frame from the building's floor. Fragility analysis is carried out to compute the probability of exceeding predetermined displacements and acceleration thresholds with and without the control system.

Keywords: Video walls, high-rise building, wind-induced vibration, wind tunnel tests, base isolation.

1 INTRODUCTION

The wind induced vibration is an important topic for high-rise building with unusual shape because torsional effects and large oscillation along and across wind may affect the occupants' comfort largely discussed in literature [1-7]. A few information and recommendations are given by codes and literature for non-structural elements inside buildings that can be severely damaged and therefore can influence costs of construction and maintenance. This is the case of LED screen walls which are used to disseminate entertainment messages and information. They are sensitive to the floor wind induced vibration that can give significant deformation to the wall and a consequent malfunctioning or collapse.

The LED screen walls operation is frequently not compatible with wind-induced displacements and accelerations experienced at high floors in high-rise buildings. The proper functioning of these high-technological devices can therefore require the installation of local control systems to reduce wind induced vibrations.

In this paper, the wind-induced response of a LED video screen room was reduced by means of passive control system consisting in a base isolated floor which disconnects the substructure from the building. The probability of exceeding predetermined displacements and acceleration thresholds with and without the control system was investigated through fragility analysis based on the PEER integral equation [8-10]. This allows to consider all the possible sources un uncertainties involved in the problem, like those related to wind load characterization, structural modeling and analysis and damage occurrence [11-14]. Calculation was computed on the high-rise building illustrated in Fig.1 and discussed in Section 3. Metti un riferimento ad un tuo articolo precedente

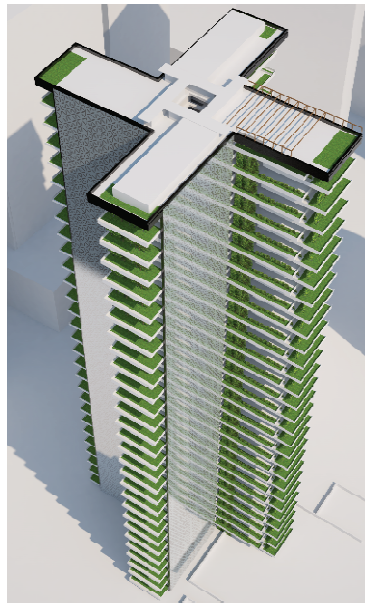


Fig. 1 Numerical model of the pultruded GRP-Tubes substructure Metti un riferimento all'articolo da dove hai preso la figura (se già pubblicata)

2 PROBABILITY-BASED DESIGN APPROACH

The proposed methodology for the design of video screen rooms inserted in high-rise buildings accounts for randomness in the load characterization, the structural response estimation and the damage occurrence and exploits the PEER (Pacific Earthquake Engineering Research) equation [8, 9]. The annual probability of exceeding a selected level of damage is computed as follows:

$$P_f\left(\frac{Z}{H}, DS\right) = \int \int P(DS|EDP) f\left(EDP|IM, \frac{Z}{H}\right) f\left(IM|\frac{Z}{H}\right) dEDP dIM \quad (1)$$

where DS is the selected damage state; EDP is the engineering demand parameter associated to the i -th DS ; $P(DS|EDP)$ is the fragility curve, i.e. the complementary cumulative distribution function (CCDF) evaluated for the specific $EDP(DS)$ under investigation; the term $f(IM|Z/H)$ represents the probability density function (PDF) of the intensity measure (IM), i.e., the reference mean wind speed evaluated at Z/H ; the term $f(EDP|IM, Z/H)$ represents

the probability density function (PDF) of the selected *EDP* conditional on the value of IM. This probability is evaluated by considering the *N* experimental realizations of the structural response components (*EDP*) evaluated from the FE model.

The *EDP* are associated to the lateral deformation of a video component (i.e. with and without isolation system); the hammer effect on the corner (i.e. with and without isolation system); acceleration-dependent damages on mechanical components (i.e. with and without isolation system); the achievement of the maximum allowable stroke of the base isolation system.

3 THE CASE STUDY

3.1 The structural setup

The case study structure is a 300 m high building with 138×138 m footprint. The building has 60 floors above ground and interstory height of 5.00 m [15]. It is assumed that inside the building a technological equipment is inserted consisting in LED screens joined to one another to reproduce screen walls on the lateral surfaces of the room, on the ceiling and on the floor. The screens are supported by a pultruded GRP-Tubes substructure (Fig.2) that is pinned to the building floors. A Finite Element Model of the substructure has been built, using frame and shell elements to perform dynamic analyses.

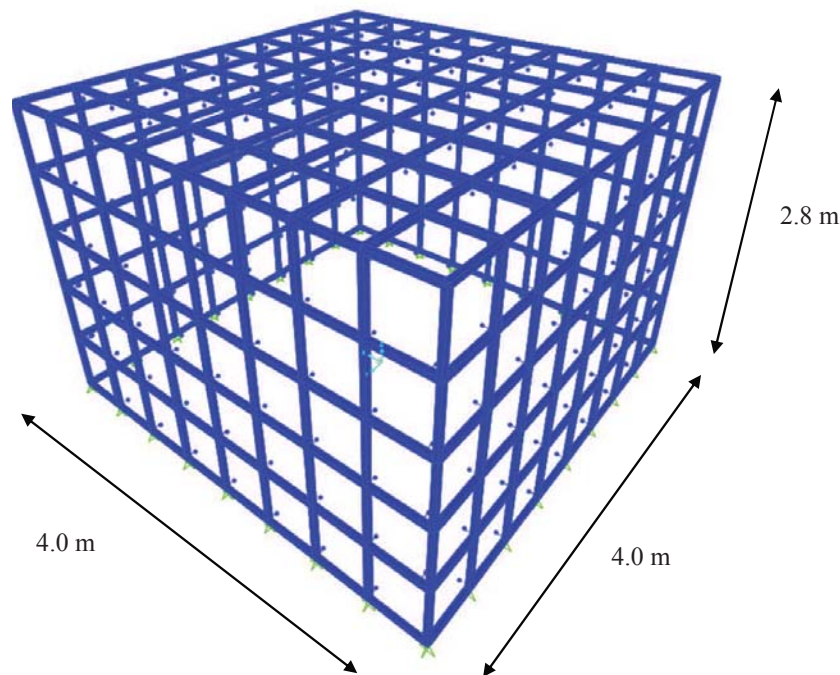


Fig. 2 Numerical model of the pultruded GRP-Tubes substructure

3.2 Wind tunnel setup

The floors' accelerations obtained from wind tunnel tests on a 1:400 reduced scale aeroelastic model of the tall building are used to evaluate the response of the substructure. Accelerations were acquired on an aeroelastic model with a sampling frequency equal to 1000 Hz for a time length equal to 180 s. At the prototype scale it corresponds to a time step equal to 0.05 s and a time length equal to 9000 s (i.e. 15 intervals 10 minutes long). Figure 3 shows a picture of the

test model during experiments. The model was equipped with 6 mono-directional accelerometers fixed on 6 floors. The main frequency of the aeroelastic model was equal to 5.86 Hz and the structural damping ratio was around 2%. The wind velocity profile was assumed equal to the Terrain IV given by [16].



Figure 3: Test model during experiments.

Figure 4 shows the relative peak displacements at the corner of the substructure illustrated in Fig.2. Results illustrated in Fig.4 suggest that after the 30th floor and for a wind speed bigger than 40 m/s at the building top, the substructure's displacements and accelerations are not compatible with the proper functioning of the video screens. Indeed, to avoid damage to video wall components, the relative displacements should be contained within a few millimeters. Therefore, it can be suitable equipping the substructure with devices able to reduce the video room response, to avoid damage and ensure proper operating conditions.

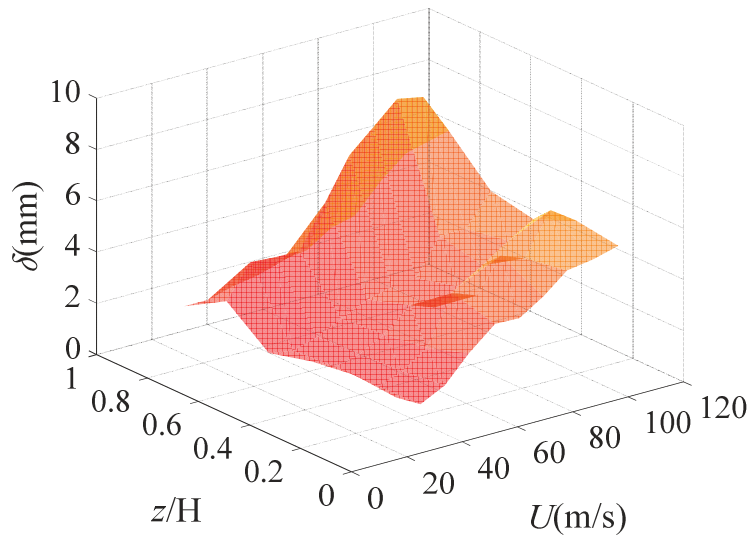


Figure 4: Relative (δ) peak displacements as a function of wind velocity (U) and height above ground (z/H) at corner of the substructure.

3.3 The base isolation system

To reduce the wind-induced vibration response, a passive control system is designed, consisting in a base isolated floor which disconnects the substructure from the building. The behavior of the base isolation devices has been modeled by a bilinear force-displacement hysteretic model, with K_s being the stiffness associated to the second branch. The model consists of a spring and a slider and it is similar to devices used for the protection of industrial equipment [17]. The period of the system is defined as $T=2\pi(M/K_s)^{0.5}$ where M is the structure's mass and K_s represents the spring's stiffness.

Figure 5 shows the results of the parametric analysis on the variation of the device's period T and the friction coefficient μ for the case $z/H=1$ and $U = 111.8$ m/s, in terms of relative displacements δ (Fig. 5). The period T varies with the change of K_s , whose interval of investigation ranges from 0.18 to 2793 kN/m. Three different values of the friction coefficients $\mu = 0.1$, $\mu = 0.3$, $\mu = 0.5$ are considered. From the figure it is possible to observe that the relative displacements (δ) are closely reduced with respect to those obtained without the isolation system.

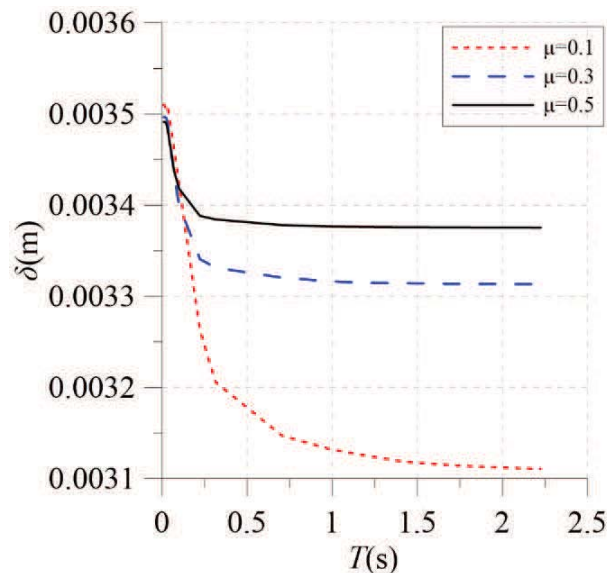


Figure 5: Corner's relative displacements δ as a function of the period T of the base isolation device.

3.4 The damage limit states

The main objective of the present paper is the evaluation of the probability-based performance of a video wall room integrated in a high-rise building by accounting for the occurrence of damages associated to the video components with and without a base isolation system. Hence, four different DS are considered (Table 1): the lateral deformation of a video component; the hammer effect on the corner; acceleration-dependent damages on mechanical components; the achievement of the maximum allowable stroke of the base isolation system.

The isolator has the capacity of providing the restoring force (given by the spring) and the capacity of limiting the maximum displacements (given by the friction force originated at the slider). Consequently, a force is transmitted to the structure equal to the combination of the friction force, due to the friction of the slider, and the reaction force of the spring as a function of the stiffness of the spring.

Table 1 Damage limit states and thresholds considered for the design of the video wall room.

Type of damage (DS)	Classification	<i>EDP</i>
DS1: Lateral deformation of a video component	Non-structural	Δ
DS2: Hammer effect on the corner	Non-structural	δ
DS3: acceleration-dependent damages on mechanical components	Non-structural	a
DS4: achievement of the maximum allowable stroke of the base isolation system	Structural	ΔL

In Table 1, Δ and a represent the absolute displacement and acceleration of the video's supporting structure, δ is relative displacement of two orthogonal faces of the supporting structures, ΔL refers to the base isolation system's stroke.

4 EVALUATION OF DAMAGE PROBABILITY

The calculation of $P_f(\frac{Z}{H}, DS)$ defined in Eq. 1 can be summarized according to the following steps:

1. Select the damage state DS and evaluate the corresponding fragility curve $P(DS|EDP)$ by means of a lognormal distribution. The selected values of μ and σ are reported in Table 2.
2. Evaluate the PDF of mean wind speed annual maxima $f(IM|Z/H)$ at the reference height Z/H according to [18] for suburban terrain, which is compatible with the mean wind profile of the wind tunnel tests.
3. Evaluate the maximum structural response component EDP for each realization of the experimentally recorded acceleration, i.e., 15 values.
4. Assess the PDF of EDP by means of a GEV distribution that gives the best fitting of the experimental values.
5. Repeat steps 4-5 for all possible IM values to find P_f by sampling.

Table 2 Fragility curves: mean values and standard deviations [14].

Parameters	Δ	δ	a	ΔL
μ	0.01 m	0.002 m	0.5 g	0.1 m
σ	0.5	0.5	0.6	0.5

5 NUMERICAL RESULTS

Figure 6 shows the annual damage probabilities P_f of DS1, DS2, DS3 and DS4, as a function of the height above ground z/H for video wall room integrated in a high-rise building by accounting for the occurrence of damages associated to the video components with and without a base isolation system. Reductions of more than 50% are noticeable at the top floor for DS1, DS2 and DS3. It is worth noticing that higher values associated to $z/H=0.83$ are due to relevant peak accelerations recorded during the wind tunnel tests. For this reason, the damage probability associated to DS4, which represent the exceeding of the maximum stroke of the base isolations system, is significant only for $z/H=0.83$.

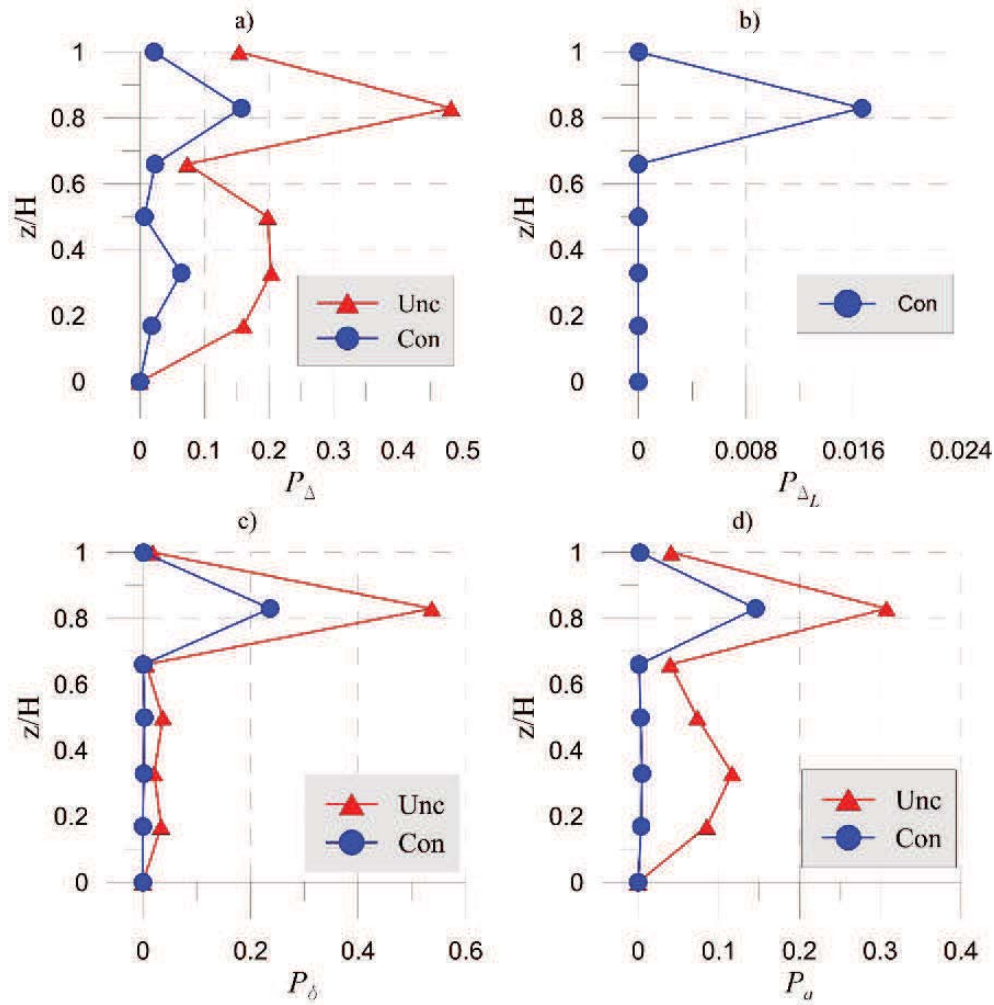


Fig. 6 Annual damage probability as a function of the floor height z/H varying between 0 and 1 with (Con) and without (Unc) the base isolation system: a) DS1; b) DS4; c) DS2; d) DS3.

6 CONCLUSIONS

The paper investigates the behavior of a base isolation system calibrated to increase the reliability of non-structural elements affected by wind induced acceleration at building's floors. A probabilistic framework for fragility assessment has been developed whose main features are:

- numerical simulations are carried out on a FE model of the video room by using the floors' accelerations measured during aeroelastic wind tunnel tests on a scaled model of the high-rise building .;
- uncertainties associated with the experimental assessment of the wind-induced accelerations and with the structural modeling and the damage estimation are considered;
- the parameters of the base isolation system with hysteretic non-linear behavior are calibrated as a function of location along the building height to avoid the excessive lateral deformation of the video components, the hammer effect at the corner, the acceleration-related damage and the exceedance of displacement limits of the isolation devices;
- the isolation system performance was discussed through a fragility analysis to compute the probability of exceeding predetermined displacements and acceleration

thresholds with and without the control system. It was observed that on the building top the reliability was increased of more than 50%.

7 ACKNOWLEDGEMENTS

A special thanks to the H-Sign srl company to sponsoring this research, to Prof. Giuseppe Piccardo and Dr. Andrea Freda for their advice and assistance during the experimental tests in the DICCA Wind Tunnel of the University of Genoa. Mr. Davide Perazzetti is grateful for his support during the model construction. Prof. Giuseppe Maddaloni, Prof. Antonio Occhiuzzi and Prof. Andrea Prota are gratefully acknowledged for their support during the experimental model dynamic identification through shaking table experiments at the University of Napoli Federico II, Italy.

REFERENCES

- [1] The International Organisation for Standardization. ISO 6897:1984. Guidelines for the evaluation of the response of occupants of fixed structures, especially buildings and off-shore structures, to low-frequency horizontal motion (0,063 to 1 Hz) (1982).
- [2] The International Organisation for Standardization. ISO 10137. Bases for design of structures - Serviceability of buildings and walkways against vibrations. Ethiopian standard agency (2012).
- [3] AIJ-GEH-2004. Guidelines for the evaluation of habitability to building vibration. Architectural institute of Japan (2004).
- [4] National Research Council of Canada. National Building Code of Canada. Canadian commission on building and re codes (2016).
- [5] Hansen R., Reed J., Vanmarcke E., Human response to wind-induced motion of buildings. *Journal of Structural Engineering* (1973) 99, 66-74.
- [6] Guidelines for the evaluation of the response of occupants of fixed structures, especially buildings and offshore structures, to low frequency horizontal motion (0.063 to 1.0 Hz) ISO 6897:1984
- [7] Bases for design of structures - Serviceability of buildings and walkways against vibrations (ISO 10137:2007). Smith, Bryan Stafford, Coull Alex, 1991. *Tall Building Structures: Analysis and Design*, Wiley, July (1991).
- [8] Iemura H., Taghikhany T., Jain S.K., 2007. Optimum design of resilient sliding isolation system for seismic protection of equipment, *Bull. Earthq. Eng.* 5 (1) 85-103.
- [9] Cornell, C. and Krawinkler, H., 2000. Progress and challenges in seismic performance assessment. PEER Center News, 3(2), 1–3.
- [10] Kunnath, S. 2006. Application of the PEER PBEE methodology to the I-880 viaduct. Rep. No. 2006/10. Davis, CA: Univ. of California.
- [11] Venanzi I., Ierimonti L., Caracoglia L., 2020. Life-cycle-cost optimization for the wind load design of tall buildings equipped with TMDs. *Wind and Structures, An International Journal*, 30(4), pp. 379-392
- [12] Ierimonti L., Venanzi I., Caracoglia L., 2018. Life-cycle damage-based cost analysis of tall buildings equipped with tuned mass dampers. *Journal of Wind Engineering and Industrial Aerodynamics*, ISSN: 01676105, 176, 54-64.
- [13] Ierimonti L., Caracoglia L., Venanzi I., Materazzi A. L., 2017. Investigation on life-cycle damage cost of wind-excited tall buildings considering directionality effects. *Journal of Wind Engineering and Industrial Aerodynamics*, ISSN: 01676105, 171, 207-218.
- [14] Venanzi I., Lavan O., Ierimonti L., Fabrizio S., 2018. Multi-hazard loss analysis of tall buildings under wind and seismic loads. *Structure and Infrastructure Engineering*, ISSN: 15732479, 4(10), pp. 1295-1311.

-
- [15] Rizzo F, Ricciardelli F, Maddaloni G, Bonati A, Occhiuzzi A, 2020. Experimental error analysis of dynamic properties for a reduced-scale high-rise building model and implications on full-scale behavior. *Journal of Building Engineering*, 28.
- [16] CEN (Comité Européen de Normalization), Eurocode 1: Actions on structures - Part 1-4: General actions - Wind actions, EN-1991-1-4, 2005.
- [17] Aslani H., Miranda E., 2005. Probabilistic earthquake loss estimation and loss disaggregation in buildings, Report no. 157, in: The John A. Blume Earthquake Engineering Center, 2005.
- [18] ASCE/SEI 7-16, 2017. Minimum Design Loads and Associated Criteria for Buildings and Other Structures. *American Society of Civil Engineers*.

FRAGILITY OF EXISTING ITALIAN BRIDGES TO TRAFFIC LOADS

G. Miluccio¹, D. Losanno¹, F. Parisi¹, and E. Cosenza¹

¹ Department of Structures for Engineering and Architecture, University of Naples Federico II
Via Claudio 21, 80125 Naples, Italy
e-mails: giacomo.miluccio@unina.it, daniele.losanno@unina.it, fulvio.pariasi@unina.it,
cosenza@unina.it

Abstract

Fragility curves are a well-established tool to define probabilistically the vulnerability of an asset to a prescribed hazard. The majority of previous studies have investigated the seismic fragility of structures and infrastructures. Nonetheless, recent disasters have highlighted the need to assess the vulnerability of aging bridges to gravity loads. Based on existing data from the literature and novel data from some real case studies, the present work presents analytical fragility curves of Italian bridges to traffic loads. The class of simply supported, beam-type, prestressed concrete bridges constructed between 1960 and 1980 was considered, given that those structures are the most recurrent type of existing Italian bridges. Then, a fragility analysis was performed through a fully automated procedure implemented in MATLAB. Geometric, material and load parameters were defined as random variables considering their probability distribution and correlation through either univariate or multivariate models. Structural fragility was evaluated with respect to the limit state of collapse. The output of this study can be of interest to engineers and decisions makers who must manage existing bridges, considering their probability of collapse under traffic loads and eventually limiting their use before structural retrofitting.

Keywords: Prestressed concrete bridges; traffic loads; fragility; collapse limit state.

1 INTRODUCTION

Structural safety of existing bridges is involving the worldwide engineering community during the last years due to recent casualties. In the aftermath of the Polcevera bridge collapse in Genoa in 2018 [1], an increasing attention has been paid towards safety evaluation and monitoring of existing bridges with a service life approaching to or even exceeding 50 years. This trend also led to new Italian guidelines for classification, safety checks and monitoring of existing bridges issued by the High Council of Public Works in April 2020 [2]-[4]. During the last years, overloads, collisions, flood and environmental degradation caused more than 80% of the total collapse cases [5]–[7][7]. Furthermore, the structural assessment and retrofiting of existing bridges is urgently needed also because of aging and material deterioration, lacking or ineffective maintenance, and climate change in multi-hazard environments involving both human-related and natural events.

The study of existing bridges should take into account the following points:

- (i) Traffic load conditions have been changing over time, i.e. different traffic loads were prescribed during original design in comparison with current code provisions.
- (ii) Materials adopted in the past are not compliant with modern building codes and may be affected by significant variability and deterioration.

In this study, the structural fragility of a class of existing Italian bridges subjected to traffic loads is studied according to code-conforming capacity models and analysis procedures [8][8]. The most important properties of the bridge decks were probabilistically modelled based on available data, randomly sampled via Monte Carlo technique, and propagated through structural analysis. Fragility analysis was fully implemented in MATLAB software [9][9], providing the conditional probability of collapse given the intensity level of code-conforming traffic loads.

2 METHODOLOGY

This study aims to define the vulnerability of existing Italian bridges subjected to code-compliant traffic loads. Previous studies investigated the seismic fragility of bridges, but recent disasters highlighted the need for a comprehensive investigation on their vulnerability to human-induced loads. A class of simply supported, beam-type, prestressed concrete (PC) bridges was considered, since they represent more than 90% of the total bridge population in Italy [10][10]. Previous studies [10][10]–[12][12] also reported that the time frame 1960–1980 is the period when the highest number of bridges were built due to Italian economic growth and infrastructure development. In those decades, a relevant part of the Italian road network was built. Based on available data collected by the authors on real case-study bridges, the period 1970–1980 was chosen in order to carry out the fragility analysis of existing bridges. Figure 1 outlines the methodology used in this study to assess the vulnerability of existing bridges to traffic loads, the distribution and design values of which was defined according to the Italian building code [8][8].

The material, geometric and load uncertainty models were defined in order to generate a set of case studies through a Monte Carlo simulation. Demand and capacity analysis were carried out and the performance level of each model was calculated. The counted fragility was evaluated applying a frequentist approach. A lognormal distribution function was then fitted to fragility points in order to obtain fragility curves.

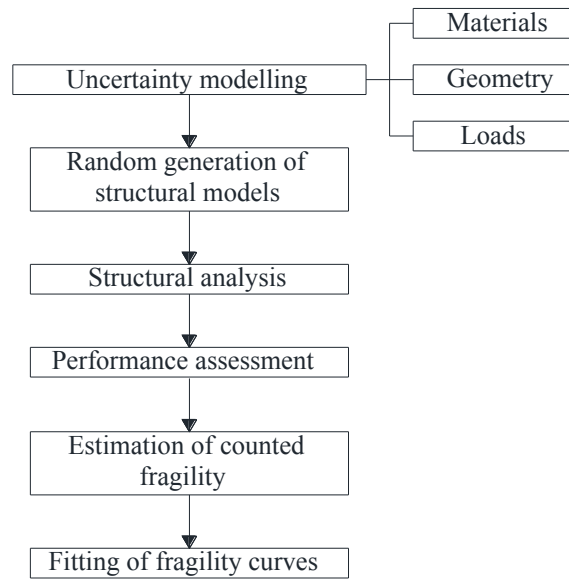


Figure 1: Flowchart of fragility analysis.

3 UNCERTAINTY MODELLING

Random variables (RVs) included both geometric and material properties. Based on [10][10] and some real case-studies, a subset of RVs were modelled through probability distributions, whereas other RVs were assumed to be statistically dependent upon the former RVs according to regression models. To that aim, the authors examined:

- geometric properties of 14 bridges built in the period 1960 to 1980;
- experimental data on mechanical properties of concrete (100 data), mild reinforcing steel (65 data), and prestressing steel (21 data) of bridges dating back to the period 1970–1980.

Case-study bridges have different locations in Italy and were built by different construction companies to be representative of the selected class of bridges. In the following sections, probability distributions and regression models are described.

3.1 Material properties

The database of material properties was based on laboratory test results of real case-studies collected by the authors. Figure 2a shows three alternative probability distributions fitted to experimental data to model the uncertainty in concrete compressive strength f_c , namely normal, lognormal and Weibull distribution. Based on best fitting, the lognormal distribution with mean value of 38.5 MPa and coefficient of variation (CoV) of 11.4% was assumed.

The same procedure was applied to derive a probability distribution for the yield strength f_y of mild steel (Figure 2b). Best fitting produced a lognormal distribution with a mean value and CoV equal to 436 MPa and 6.4%, respectively.

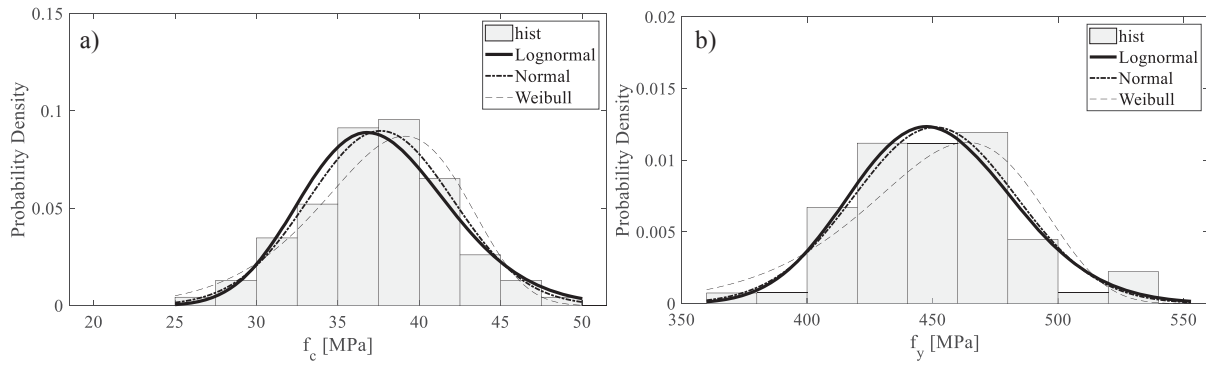


Figure 2: Probability distributions for (a) concrete compressive strength and (b) yield strength of mild steel.

A probability distribution was also fitted to experimental data on the conventional yield strength of prestressing steel $f_{p,01}$ (i.e., the tensile stress associated with a residual strain of 0.1%). A limited amount of data was collected by the authors and data were fitted by a lognormal distribution (Figure 3) with a mean value and CoV equal to 1665 MPa and 2.5%, respectively. These statistics agree well with different studies available in the literature (e.g., [13][13]–[15][15]).

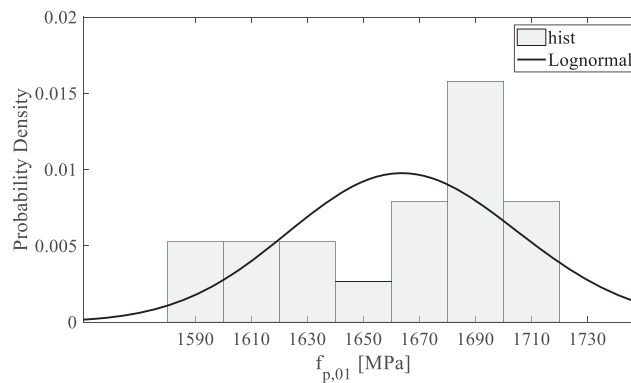


Figure 3: Probability distribution for conventional yield strength of prestressing steel.

The weight per unit volume of reinforced concrete (RC) was modelled through normal distribution with mean and CoV equal to 25 kN/m³ and 5%, respectively, in order to account for the variability of permanent loads (G_{1k}). Non-structural permanent loads (G_{2k}) were modelled via a normal distribution with mean value and CoV equal to 2 kN/m² and 10%, respectively.

3.2 Geometry

Geometric properties were defined for simply-supported PC bridge decks built between 1960 and 1980. The cross sections of the deck and longitudinal girders are shown in Figure 4, highlighting the most relevant geometric properties considered in the analysis.

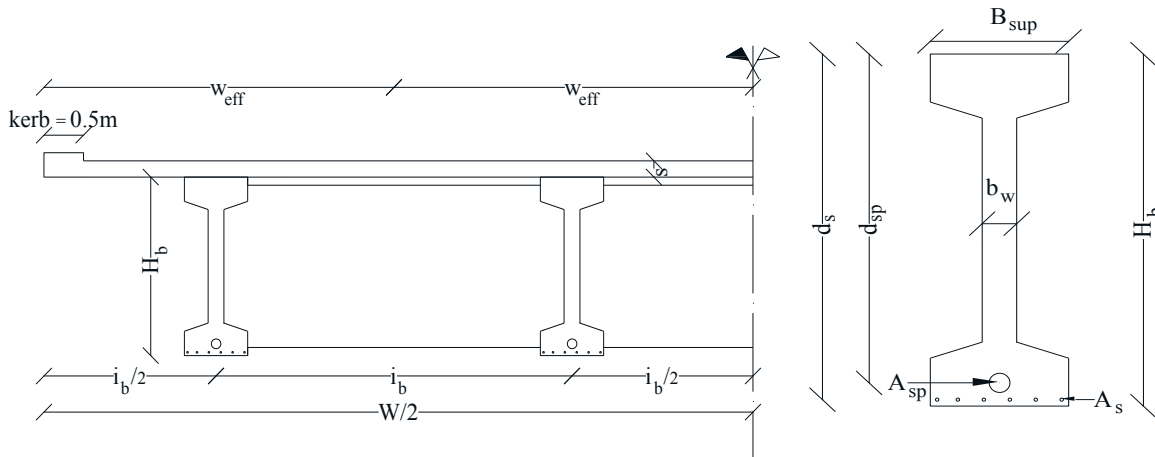


Figure 4: Cross sections of the bridge deck and longitudinal girder.

The span length (L) and width (W) of the deck were assumed as main independent RVs. Based on both literature [10][10] and case studies, the histogram of the bridge span length was derived. Approximately half of the existing bridges have a length between 30 m and 35 m, as depicted in Figure 5. A lognormal distribution was assumed, with a mean value equal to 33.2 m and $\text{CoV} = 13.6\%$. The distribution was truncated at 15 m and 45 m to obtain realistic values of the bridge length in subsequent probabilistic simulation.

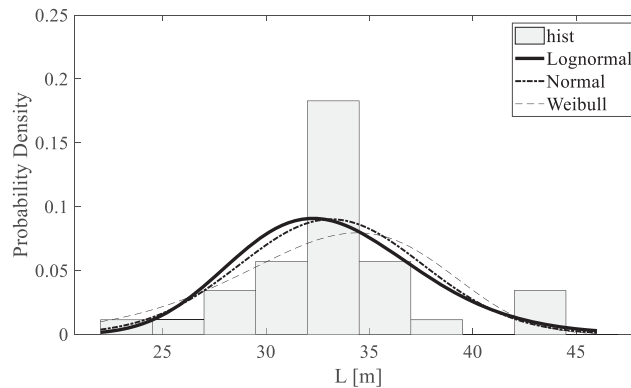


Figure 5: Probability distribution of girder span length.

Regarding the deck width W , a probability mass function (PMF) with three values equal to 8.5, 12.25 and 16 m having the same probability of occurrence was assumed. The slab thickness (denoted by s) was modelled through a uniform distribution with a mean value and CoV equal to 0.25 m and 12%, respectively, in the range [0.2 m, 0.3 m].

The transverse reinforcement ratio ρ_{sw} (A_{sw}/p , where p is the distance between stirrups) and prestressing ratio of the tendons $\sigma_{sp}/f_{p,01}$ were considered as additional independent RVs. The former was modelled through a uniform distribution between 300 mm²/m (corresponding to 8-mm-diameter stirrups with 330mm spacing as per minimum code requirement) and 1130 mm²/m (corresponding to 12-mm-diameter stirrups with 200 mm spacing as maximum recorded value). The prestressing ratio was modelled in two different ways: (i) uniform distribution between 40% and 60%, (ii) PMF with 3 equally probable values equal to 40%, 50% and 60%. In this study, degradation of prestressing steel was not taken into account. The residual stress levels σ_{sp} take into account average values of relaxation loss due to concrete creep, shrinkage and relaxation of steel under tension [17][17].

The set of independent RVs is listed in Table 1, providing their distributions, mean μ and CoV.

Random variable	μ or discrete values	CoV [%]	Distribution
f_c [MPa]	34.70	24.40	Lognormal
f_y [MPa]	436.00	6.40	Lognormal
$f_{p,01}$ [MPa]	1665.00	2.50	Lognormal
L [m]	33.20	13.60	Lognormal
W [m]	8.50 – 12.25 – 16.00	-	PMF
s [m]	0.25	12.00	Uniform
ρ_{sw} [mm ² /m]	715.00	34.00	Uniform
$\sigma_{sp}/f_{p,01}$ [%]	50.00	12.00	Uniform
$\sigma_{sp}/f_{p,01}$ [%]	40.00 – 50.00 – 60.00	-	PMF
γ_c [kN/m ³]	25.00	5	Normal
G_{2k} [kN/m ²]	2.00	10	Normal

Table 1: Distributions and statistics of independent random variables.

3.3 Correlation models

Based on case-studies, regression models were developed in order to model RVs conditioned upon independent RVs. The following dependent variables were considered:

- number of longitudinal girders, n_b ;
- height of longitudinal girder, H_b ;
- area of girder cross-section, A_b ;
- width of girder top flange, B_{sup} ;
- distance of equivalent total prestressing area from top of girder cross-section, d_{sp} ;
- geometric ratio of prestressing steel ρ_{sp} multiplied by d_{sp} , $\rho_{sp} \cdot d_{sp}$.

In Table 2, the regression models used in this study are listed together with their coefficient of determination R^2 and boundaries.

RV	Regression model	R^2	Lower bound	Upper bound
$n_b (W)$	$n_b = 0.33 \cdot W$	0.51	2	8
$H_b (i_b, L)$	$H_b = 0.28 \cdot \frac{W}{n_b} + 0.03 \cdot L$	0.81	$H_b \geq L/20$	3.2 m
$A_b (H_b)$	$A_b = 0.43 + 0.06 \cdot H_b^2$	0.84	-	-
$B_{sup} (H_b) (G_{1k})$	$B_{sup} = 0.34 \cdot H_b + 0.02 \cdot G_{1k} - 0.02 \cdot H_b \cdot G_{1k} + 0.002 \cdot G_{1k}^2$	0.71	-	1.2
$d_{sp} (H_b)$	$d_{sp} = 0.98 \cdot H_b$	0.97	-	-
$d_{sp} \cdot \rho_{sp} (L)$	$\rho_{sp} \cdot d_{sp} = 8.16 \cdot 10^{-5} \cdot L + 1.85 \cdot 10^{-5} \cdot L^2$	0.88	$0.007 d_{sp}$	-

Table 2: Regression models

The following deterministic variables were assumed:

- concrete cover equal to 0.03 m;
- girder web equal to 0.2 m;
- bottom flange thickness equal to 0.3 m;
- geometric ratio of longitudinal reinforcing mild steel equal to 0.1%;

- Young's modulus of steel equal to 200 GPa.

4 STRUCTURAL ANALYSIS

The first stage of structural analysis consisted in the modelling of loads on the bridge deck. Self-weight of deck components was evaluated according to G_{1k} , sectional area of longitudinal girders and their effective width w_{eff} (which was equal to i_{beam}). Non-structural permanent loads were obtained according to G_{2k} and w_{eff} .

Traffic loads were defined according to the Italian building code [8][8] and Eurocode 1 – Part 2 [16][16]. The number of lanes adopted in the present study is either two or three, depending on the randomly generated geometry of the deck in order to maximize the strength demands on the edge girders (i.e., bending moment at mid-span or shear force at girder ends). The deck cross section was assumed to be rigid, according to design calculations at the time of construction and Engesser formulation [18][18]. The structural analysis procedure was implemented in MATLAB [9] in order to automatically define traffic load distributions which maximize bending moment and shear force on the edge girder.

Flexural and shear capacity models were also programmed in MATLAB to evaluate the collapse capacity of the edge girder as representative of the deck structural behaviour. The ultimate limit state (ULS) of the deck was thus defined as the attainment of either flexural or shear capacity in the edge girder.

The flexural capacity of the girder was evaluated on the basis of the following assumptions:

1. Plane cross section and perfect steel-concrete bond after flexural deformation;
2. maximum compressive concrete strain equal to 0.35%;
3. uniform stress distribution and zero tensile strength of concrete;
4. mild and prestressing steel with elastic-perfectly plastic behaviour and unlimited ductility;
5. yielded steel (i.e., to be checked in all cases after neutral axis is found).

Mild steel was defined through its geometric ratio ρ_s (e.g., 0.1%). The flexural capacity M_r of girder cross section was basically predicted through sectional analysis at ULS.

The shear capacity V_r of the girder was evaluated by enveloping three different capacity models provided by current codes ([8][8], [17][17]). The first model describes the capacity of a RC member in cracked conditions without shear reinforcement. The second model adopted in this study applies to PC beams in uncracked conditions. The third model applies to cracked RC beams with internal stirrups based on a strut-and-tie resisting mechanism.

5 COLLAPSE FRAGILITY OF CASE-STUDY BRIDGES

Fragility analysis was based on Monte Carlo sampling of independent RVs, which allowed the random generation of 10,000 model realizations based on their probability distributions. Regression models were then used to generate statistically dependent variables, considering the model error of each regression equation. The magnitude of traffic loads was defined through an intensity measure (IM) denoted as α and defined as the ratio between the incremental and design first-lane tandem load, i.e. $\alpha = Q_1/Q_{1d}$ with $Q_{1d} = 600$ kN. Structural analysis of each set of 10,000 deck models was carried out under varying α from 0 to 2.5 with step of 0.1. For each deck model, both flexural and shear capacities were computed.

The output of fragility analysis was the conditional probability of exceeding ULS given IM. The maximum demand-to-capacity ratio (DCR) between flexural DCR ($DCR_f = M_e/M_r$) and shear DCR ($DCR_s = V_e/V_r$) was assumed as limit state function. Accordingly, ULS was assumed to be attained or exceeded if DCR was equal to or greater than unity. Fragility was thus defined as follows:

$$P[DCR \geq 1 | IM = im] \quad (1)$$

After that counted fragilities were computed over the whole range of IM levels, fragility curves were fitted through a lognormal distribution.

Fragility curves associated with flexural and shear failure modes were initially derived separately, considering either discrete values (Figure 6a) and uniformly distributed values (Figure 6b) of prestressing ratio. In Figure 6, the lower x -axis indicates the selected IM chosen (i.e., α), whereas the upper x -axis provides the corresponding the first-lane tandem load Q_1 . Figure 6 shows the higher fragility of the existing Italian bridges under study in terms of flexural failure. Indeed, the median value η of the flexural fragility curve is lower than that of the shear fragility curve, regardless of the prestressing ratio. This means that the attainment of ULS is governed by flexural failure. As shown in Figure 6(a), shear fragility significantly reduces under increasing prestressing ratio. Table 3 outlines the median value, dispersion β (i.e., the logarithmic standard deviation) and R^2 of each fragility curve, evidencing that the lognormal distribution fits very well the fragility points as demonstrated by R^2 very close to unity.

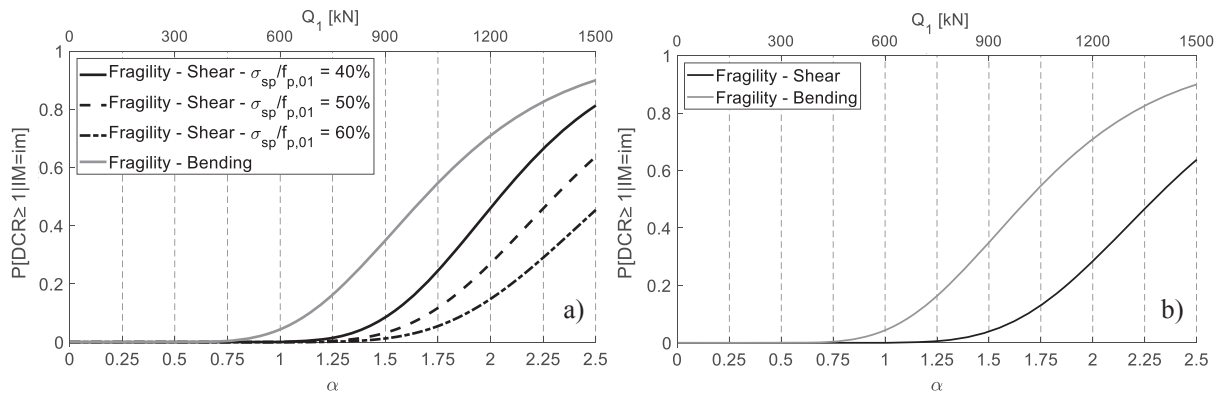


Figure 6: Fragility curves associated with flexural and shear failure modes: (a) discrete distribution of prestressing ratio; (b) uniform distribution of prestressing ratio.

Failure mode or limit state	η	β	R^2
Flexural failure	1.69	0.31	0.99
Shear failure ($\sigma_{sp}/f_{p,01} = 40\%$)	2.04	0.23	
Shear failure ($\sigma_{sp}/f_{p,01} = 50\%$)	2.30	0.23	
Shear failure ($\sigma_{sp}/f_{p,01} = 60\%$)	2.57	0.24	
Shear failure ($\sigma_{sp}/f_{p,01}$ uniformly distributed)	2.30	0.24	
ULS	1.68	0.30	0.99

Table 3: Fragility parameters corresponding to flexural failure, shear failure, and ULS.

Figure 7 shows the fragility curve of the case-study bridges for the limit state of collapse, which is almost totally overlapped to that associated with flexural failure mode. However, the median value and dispersion are slightly different from those related to the flexural fragility curve because of a very rare occurrence of shear failure in some model realizations. Table 3 shows that the selected bridges have a median collapse traffic load equal to 1.68 times the design load, with a dispersion $\beta = 0.30$. It is also found that the conditional probability of collapse under design traffic load (corresponding to $\alpha = 1$) is $4.4 \cdot 10^{-2}$. Further studies are needed to assess the unconditional failure probability of collapse, namely, the failure probability derived as a convolution of fragility and traffic load hazard.

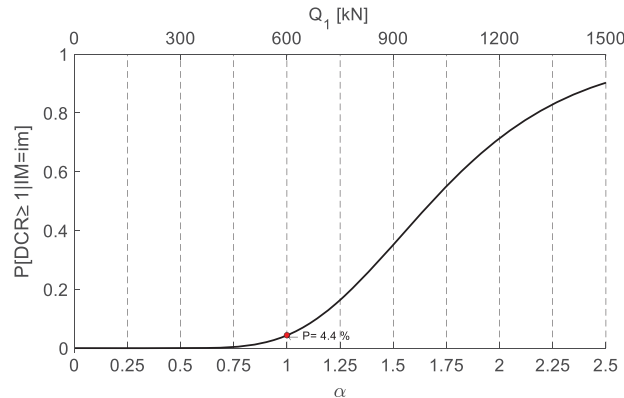


Figure 7: Collapse fragility curve of case-study bridges.

6 CONCLUSIONS

This study aimed at evaluating the fragility of existing Italian, simply supported, beam-type, prestressed concrete bridges. A fragility analysis procedure was implemented in MATLAB software to generate a set of 10,000 random samples of bridge deck models and carry out their structural performance assessment. The procedure starts considering a set of variables, including independent variables modelled through probability distributions, dependent variables evaluated through regression models, and deterministic variables. Assuming code-conforming traffic-load models, each bridge model was randomly generated according to Monte Carlo sampling technique and was analysed under incremental loading to detect the attainment of both flexural and shear failure modes. In this regard, three alternative capacity models were considered to predict shear resistance of edge longitudinal girders.

The fragility of Italian existing bridges was calculated by assuming the scale factor α of traffic loads as intensity measure IM, which was gradually incremented from 0 to 2.5. The demand-to-capacity ratio DCR was considered as limit state function, hence identifying the occurrence of flexure or shear failure modes. These latter were first probabilistically assessed separately and then considered altogether to develop the collapse fragility curve of the selected bridges. The large number of random samples allowed the estimation of collapse fragility according to a frequentist approach.

Analysis results show that the case-study bridges are significantly more vulnerable to flexural failure than to its shear counterpart. In addition, shear fragility reduces under increasing prestressing ratio.

On the basis of these outcomes, it can be inferred that flexural behaviour has a remarkable effect on the vulnerability of the considered class of existing bridges. These preliminary results suggest a prioritization scheme for structural retrofitting of existing bridges against traffic loads.

ACKNOWLEDGEMENTS

This study was supported by GRISIS research project (Gestione dei Rischi e Sicurezza delle Infrastrutture a Scala regionale, *Cup: B63D18000280007*) funded by Regione Campania.

REFERENCES

- [1] C. Nuti, B. Briseghella, T. Iori, I. Vanzi, Alcune riflessioni sul Viadotto Polcevera, dal progetto ai giorni nostri (*Accessed online on March 8th, 2021, at <https://www.enea.it/it/seguici/events/save-the-date-monitoraggio-e-valutazione-di-ponti-e-viadotti-1/NutiCEnea14febb2014.pdf>*), 2019 (in Italian).
- [2] E. Cosenza, D. Losanno, A focus on the new Italian guidelines for safety assessment of existing bridges. In: *Proceedings of Capacity Assessment of Corroded Reinforced Concrete Structures Conference (CACRCS 2021)*, Online, November-December 30-3, 2021.
- [3] Italian High Council of Public Works, Linee Guida per la classificazione e gestione del rischio, la valutazione della sicurezza ed il monitoraggio dei ponti esistenti. Italy, 2020 (in Italian).
- [4] Italian Ministry of Infrastructures and Transportation, Decreto ministeriale numero 578 del 17/12/2020. <https://www.mit.gov.it/normativa/decreto-ministeriale-numero-578-del-17/12/2020>, Italy, 2020 (in Italian).
- [5] W. Cook, P.J. Barr, M.W. Halling, Bridge failure rate. *Journal of Performance of Constructed Facilities*, **29**, 2013.
- [6] L. Deng, W. Wang, Y. Yu, State-of-the-art review on the causes and mechanisms of bridge collapse. *Journal of Performance of Constructed Facilities*, **30**, 2016.
- [7] K. Wardhana, F.C. Hadipriono, Analysis of recent bridge failures in the United States. *Journal of Performance of Constructed Facilities*, **17**, 144-150, 2003.
- [8] Italian Ministry of Infrastructures and Transportation, Aggiornamento delle «Norme tecniche per le costruzioni». *Supplemento ordinario n. 8 alla Gazzetta ufficiale del 20-2-2018*, Italy, 2018 (in Italian).
- [9] MATLAB, 2018. 9.7.0.1190202 (R2019b), Natick, Massachusetts: The MathWorks Inc.
- [10] B. Borzi, P. Ceresa, P. Franchin, F. Noto, G.M. Calvi, P.E. Pinto, Seismic Vulnerability of the Italian Roadway Bridge Stock. *Earthquake Spectra*, **31**, 2137-2161, 2015.
- [11] P.E. Pinto, P. Franchin, Issues in the Upgrade of Italian Highway Structures. *Journal of Earthquake Engineering*, **14**, 1221-1252, 2010.
- [12] P. Baratono, A. Cosentino, S. Puggelli, E. Renzi, W. Salvatore. Le nuove linee guida per la classificazione e gestione del rischio, la valutazione della sicurezza ed il monitoraggio dei ponti esistenti approvate dal Consup. *Ingenio*, 2020 (in Italian).
- [13] F.D. Wiśniewski , P.J.S. Cruz , A. Abel, R. Henriques, R.A.D. Simões, Probabilistic models for mechanical properties of concrete, reinforcing steel and pre-stressing steel. *Structure and Infrastructure Engineering*, **8**(2), 111-123, 2012.
- [14] L. Jacinto, M. Pipa, L.A.C. Neves, L. Oliveira Santos, Probabilistic models for mechanical properties of prestressing strands. *Construction and Building Materials*, **36**, 84-89, 2012.
- [15] A. Naaman, A. Siriaksorn, Reliability of partially prestressed beams at serviceability limit states. *PCI Journal*, **27**, 66-85, 1982.
- [16] CEN, EN1991-2. Eurocode 1: Actions on structures – Part 2: Traffic loads on bridges. Committee Européen de Normalisation, Brussels, 2003.

- [17] CEN, EN1992-1-1. Eurocode 2: Design of concrete structures – Part 1-1: General rules and rules for buildings. Committee Européen de Normalisation, Brussels, 2004.
- [18] C. Cestelli Guidi, *Cemento armato precompresso*. 7th edition, Hoepli, Milan (in Italian).

TOWARDS THE DEVELOPMENT OF A COMPREHENSIVE FRAMEWORK FOR LIFE CYCLE COST ANALYSIS OF BRIDGES SUBJECTED TO MULTIPLE HAZARDS

S. Sacconi¹, L. Ierimonti¹, I. Venanzi¹ and F. Ubertini¹

¹ Department of Civil and Environmental Engineering of University of Perugia
Via G. Duranti, 93, 06125 Perugia, Italy
e-mail: stefano.sacconi@collaboratori.unipg.it; laura.ierimonti@unipg.it; ilaria.venanzi@unipg.it;
filippo.ubertini@unipg.it

Abstract

Life-cycle cost analysis (LCCA) is used as a decision-making tool in the design phase to predict the expenses required over the lifetime of the bridge. The application of LCCA to bridges allows to consider different types of uncertainties such as those on loads, resistances, degradation and on the numerical modelling and structural response analysis. In this context, the present paper proposes a general framework for bridges' LCCA under multiple hazards based on the use of the PEER equation. It allows to account for the random nature of hazards and for structural and modelling uncertainties, considering in a unified manner different hazards concurring to damage occurrence. The approach is for the first time applied to cost and fragility analysis of bridges subjected to fatigue, highlighting the possibility of treating the problem of fatigue damage estimation with an approach similar to the one currently adopted for damage induced by other hazards, like earthquake and wind. Starting from the knowledge of the traffic load model, the gross vehicles weight is assumed as intensity measure (IM) and a fatigue damage index calculated through the Palmgren-Miner's rule is adopted as engineering demand parameter (EDP). The damage accumulation is evaluated by considering the time dependency of the fatigue damage index. The framework is applied to the case study of a composite steel-reinforced concrete multi-span roadway bridge located in central Italy. The evolution over time of the probability of failure and the life-cycle costs due to fatigue damage induced by heavy traffic loads are investigated.

Keywords: Life cycle cost, PEER equation, multi hazard analysis, fatigue damage.

1 INTRODUCTION

The correct definition of a life-cycle cost model for a bridge requires the preliminary selection of the limit states that could lead to bridge damage or collapse. The loads acting on the bridge are of different nature (earthquake, wind, traffic, degradation) and each one of them can lead to the achievement of more than one limit state. The main limit states which are taken into consideration in bridges are usually the achievement of the ultimate strength for bending and shear, the achievement of the serviceability limit states of deformation and stresses and the achievement of fatigue limit state [1]. In case of long-span bridges, aeroelastic limit states may also become important [2].

In this context, the fragility and cost assessment must be done exploiting a probabilistic approach to account for the random nature of hazards and for structural and modeling uncertainties, also considering in a unified manner different hazards concurring to damage occurrence. [3]. Several studies have addressed the problem of evaluating the expected life cycle cost of structures [4,5,6], including design applications of the main structure [7] and/or auxiliary damping systems [8,9,10], which is related to the probability of failure calculated through the PEER convolution integral [11] or through a reliability analysis based on the calculation of the reliability index [12].

The objective of this paper is the estimation of lifetime costs of roadway bridges with specific focus on costs related to fatigue damage. The paper presents a general and comprehensive methodology accounting for multiple-hazards and several limit states, exploiting the PEER convolution integral to compute the probabilities of failure related to life-cycle costs. The application of the PEER equation is subordinate to the definition of a hazard curve for each type of load (i.e. earthquake, traffic) and to the selection of the engineering response parameters characterizing the damage limit states (forces, deformations, tensions and accelerations). The limit state conditions are expressed through fragility functions which lead to the determination of the probability that a damage threshold is exceeded [13].

The proposed framework is particularized to the case of bridges subjected to fatigue damage. The estimation of fatigue-related probability of failure using the PEER framework is a novelty in the scientific literature and allows to insert the evaluation of fatigue-damage induced costs in a comprehensive and unified framework for life-cycle cost assessment of bridges.

2 METHODOLOGY FOR LCCA OF BRIDGES

2.1 General LCCA methodology in case of multiple-hazards

The general formulation of the expected value of the total cost in the lifetime of a bridge, considering several hazard types and limit states at the same time, can be expressed through the following expression:

$$E[C(L_t)] = C_0 + \sum_{t=1}^{L_t} \left[\frac{C_m(t) + C_i(t)}{(1+r)^t} + \sum_{h=1}^H \sum_{j=1}^J \sum_{s=1}^S \frac{E[C_{j,s,h}(t)]}{(1+r)^t} \right] \quad (1)$$

where $E[.]$ denotes the expected value operator; L_t is the lifetime of the bridge expressed in years; J is the total number of the considered limit states; S is the total number of analyzed sections; H is the total number of the considered hazards; C_0 is the initial cost of the bridge that includes the costs for design, testing, construction, terrain purchase and safety burdens; $E[C_{j,s,h}]$ is the expected value of the cost of the j -th limit state being reached in the s -th section of the bridge and due to the h -th hazard, including cost of damage and repair; C_m is the maintenance cost per year; C_i is the inspection cost per year; r is the discount rate.

The total expected normalized cost is evaluated through normalization of the Eq. (1) with respect to the initial cost C_0 as follows:

$$c(L_t) = E \left[\frac{C(L_t) - C_0}{C_0} \right] = \sum_{t=1}^{L_t} \left[\frac{c_m(t) + c_i(t)}{(1+r)^t} + \sum_{h=1}^H \sum_{j=1}^J \sum_{s=1}^S \frac{E[k_{j,s,h}(t)]}{(1+r)^t} \right] \quad (2)$$

where $c_m = C_m / C_0$, $c_i = C_i / C_0$ and $k_{j,s,h}$ can be defined as follows:

$$k_{j,s,h} = \begin{cases} \frac{c_j P_{j,s,h}}{C_0} & \text{if } P_{j,s,h} < \bar{P} \\ \frac{c_r}{C_0} & \text{if } P_{j,s,h} = \bar{P} \end{cases} \quad (3)$$

where c_j is the failure cost related to the j -th limit state, c_r is the repair cost per unit length, \bar{P} is the probability threshold beyond which the repair cost is required and $P_{j,s,h}$ can be evaluated by using the PEER convolution integral, as follows:

$$P_{j,s,h} = \int \int P(DS|EDP) f(EDP|IM) f(IM) dEDP dIM \quad (4)$$

where IM is the intensity measure related to the h -th hazard; EDP is the engineering demand parameter at section s ; DS is the damage state associated to the achievement of the j -th limit state; $P(DS|EDP)$ is the fragility curve (the complementary cumulative distribution function of DS conditioned to the occurrence of EDP); $f(EDP|IM)$ is the probability density function (PDF) of EDP conditional on IM; $f(IM)$ is the PDF of IM.

The earthquake and the traffic are the main hazards stressing a bridge. For seismic risk assessment, it is necessary to conduct a probabilistic analysis considering the site where the structure is located, the possible presence of nearby faults and the different magnitudes associated with the return period. By knowing this information, it is possible to determine the hazard curve that shows the variation of IM parameter versus the annual average of exceedance. In the earthquake case, the intensity measure (IM) can be defined as the spectral acceleration, the peak ground acceleration or the magnitude. The engineering parameters demand (EDPs) can be represented by internal forces, deformations, displacements or accelerations. The use of an EDP is specifically related to the analyzed limit state. For example, in the case of piers it is possible to use as EDP the displacement of the piers, which is closely linked to the bending and shear stresses that occur due to the seismic event.

2.2 LCCA methodology for bridges subjected to fatigue limit state

In this Section, the methodology is particularized to the LCC analysis of bridges subjected to fatigue damage due to traffic load.

The proposed methodology adopts as IM the gross vehicle weight (GVW). The traffic hazard curve, whose first derivative is the $f(IM)$ in the PEER equation, is specific for the analyzed bridge and represents the annual relative frequency of vehicles passages as a function of the GVW. It can be obtained following two different procedures:

1. exploiting information provided by the National Standards that give the annual traffic composition;
2. using monitoring data obtained from a Weight-In-Motion (WIM) system capable of detecting the total weights and the number of the vehicles that annually pass through the bridge.

The proposed methodology adopts the fatigue damage index (D) calculated through the Palmgren-Miner's rule, as EDP [14]:

$$D = \sum_i \frac{n_i}{N_i} \quad (5)$$

where n_i is the number of cycles associated with the stress range $\Delta\sigma_i$ and N_i is the corresponding cycles to failure obtained from the S-N Wöhler curve [15]. The time histories of the internal forces and the corresponding stresses at the analyzed sections are determined from the knowledge of the influence line of each type of vehicle and using the rainflow cycle counting method [16].

Exploiting Eq. (4) it is possible to determine the annual probability of exceeding the fatigue limit state due to traffic load. The following steps are carried out for the computation of the PEER equation:

- partition of the GVW range, available from WIM data or from National Standards, in a set of intervals. Knowing the annual number of passages corresponding to the vehicles comprised in each subinterval, it is possible to determine a relative frequency diagram of GVW which is used to obtain the probability distribution of GVW, i.e., $f(\text{IM})$ (Figure 1 (a));

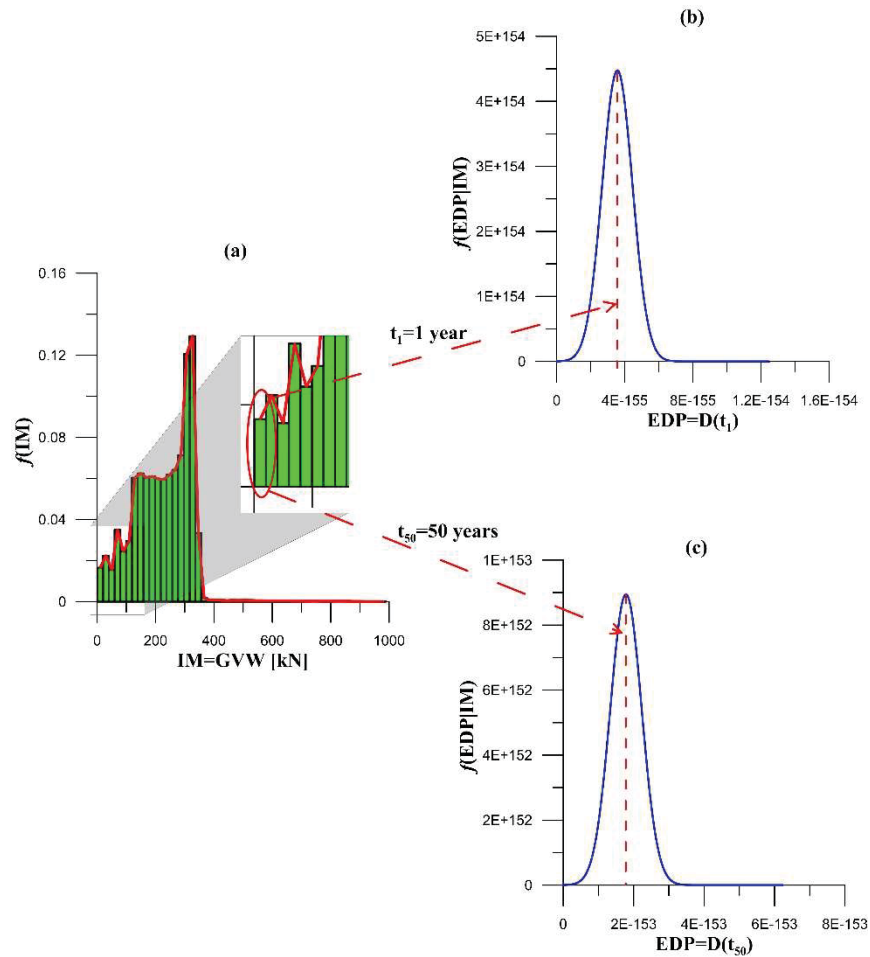


Figure 1. Probability density function of IM (a), probability density functions of EDP for different operating years: $t_1 = 1$ year (b) and $t_{50} = 50$ years (c).

- for each k -th subinterval of GVW, a damage index D_k is computed as the sum of the damage indices of the vehicles belonging to the k -th subinterval, exploiting Eq. (5). D_k is assumed as the mean value of the EDP conditional on IM, $f(\text{EDP}|\text{IM})$. A normal distribution is adopted for $f(\text{EDP}|\text{IM})$, with mean value equal to D_k and a coefficient

of variation (COV) taken from literature, accounting for uncertainties in traffic load model characterization and response parameters estimation (Figure 1 (b-c)). To account for damage accumulation over time, the probability distribution of EDP is modified over years. In particular, for each k -th subinterval of GVW, the mean value of D at time t_i , is obtained as the sum of $D_k(t_{i-1})$ and $D_k(t_i)$. Moreover, if the traffic model is constant with time $D_k(t_{Lt}) = L_t \cdot D_k(t_1)$;

- definition of the fragility curve $P(DS|EDP)$; the fatigue damage occurs when the damage value D (calculated through Eq. (5)) equals its critical value D_{crit} :

$$D_{crit} - D = 0 \quad (6)$$

Due to the random nature of fatigue damage, D_{crit} can be considered as a random variable with mean value equal to unity. Therefore, the fragility curve is determined by defining an uncertainty on the critical damage value distributed with a log-normal distribution, as shown in Figure 2.

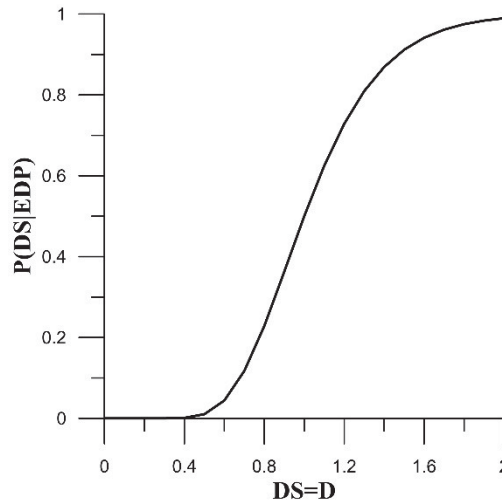


Figure 2. Fragility curve.

3 THE CASE STUDY

The proposed framework has been applied to a continuous steel-concrete composite highway bridge located in central Italy. The structure is 570 meters long and includes 10 spans of varying lengths, represented in Figure 3. The cross section consists of two double-T welded steel girders. The PEER convolution integral is calculated on 57 sections, uniformly spaced every 10 meters over the bridge length. The detail category considered for the fatigue limit state is a continuous longitudinal weld between the web and the flange of the girder.

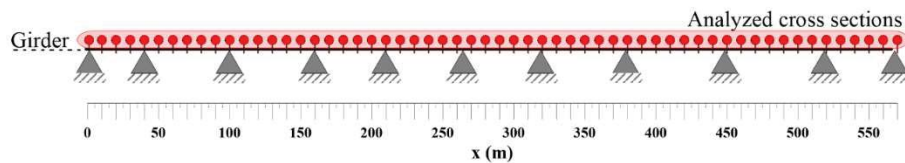


Figure 3. Schematic representation of the bridge with the indication of the analyzed cross sections.

3.1 Hazard model

For the evaluation of the fatigue limit state it is necessary to probabilistically characterize the traffic model through the hazard curve. For the sake of demonstrating the influence of the traffic model on the LCCA results, the analyses have been carried out considering two different types of traffic hazard curves:

- the first hazard curve has been constructed from traffic data obtained from a WIM monitoring system located along the Interstate 80, Iowa, USA, known to the authors from a separate research study. The traffic hazard curve has been defined experimentally by choosing as the parameter that describes the load the GVW according to its annual frequency of exceeding. The traffic hazard curve obtained from WIM data is shown in Figure 4 (a);
- the second hazard curve has been obtained considering the Fatigue Load Model 4 used by the European Technical Standard (Eurocode 1 – Part 2) [17] for the estimation of fatigue damage on bridges (Figure 4 (b)). The Eurocode provides, for each one of the five vehicles specified in Fatigue Load Model 4 and for a specific type of road, the weight of the single axles and the percentage of the number of passages with respect to the total number of annual passages. The IM is the GVW calculated as the sum of the weights of the individual vehicle axles provided by the Eurocode. The total number of vehicles is assumed equal to the one provided by the WIM system, to consider the effect of the sole traffic distribution, being equal the traffic intensity.

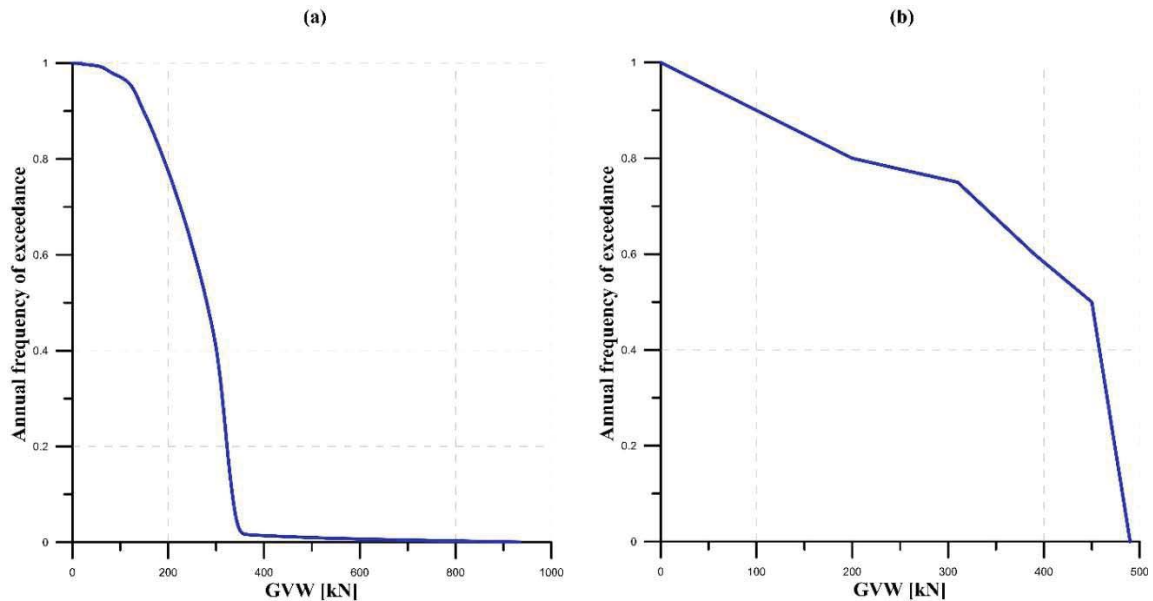


Figure 4 Traffic hazard curve obtained from WIM system (a) and from Eurocode (b).

It is assumed that the annual composition of traffic does not change over time, so the PDF(IM) is the same for all years. On the other hand, the value of the EDP changes over time due to the accumulation of damage.

3.2 Fatigue damage assessment

The calculation of the damage index D is done through Eq. (5), where n_i is determined from WIM data in case of use of the monitoring system while n_i is defined as a percentage of the total number of vehicle passage in the case of adoption of Eurocode Fatigue Load Model 4. In both

cases, in addition to providing information regarding the total weight of the vehicles, the weight distribution of the axles and their spacing are provided. This information is necessary for the determination of the influence line which allows to evaluate the time histories of the internal forces and the corresponding stresses at the analyzed sections. The stress ranges are determined by the rainflow method [16] and the corresponding cycles to failure obtained from the S-N curve.

The damage index D calculated for each range of GVW is assumed to have a normal distribution with a $COV=0.25$. The uncertainty assumed on the Palmgren-Miner damage accumulation rule (D_{crit}) is assumed to be lognormal distributed with mean 1.0 and $COV=0.3$ [18].

Figure 5 shows the probability of exceeding the fatigue limit state over time of one of the most critical bridge sections (no. 43, at the midspan of the 8th span), calculated by Eq. (4). Figure 5 (a) represents the probability calculated from the hazard traffic curve obtained from the WIM system and Figure 4 (b) shows the probability referred to the hazard traffic curve obtained from the Eurocode. The increase in probability over time is due to the accumulation of damage caused by the passage of vehicles across the bridge.

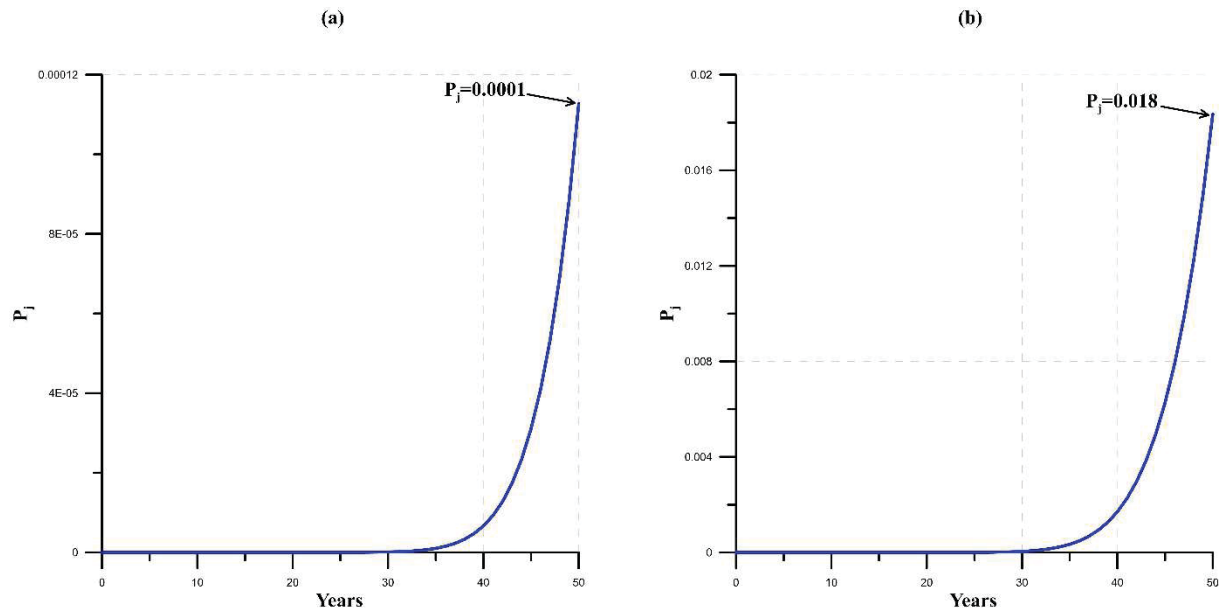


Figure 5 Probability of exceeding the fatigue limit state over the lifetime of the bridge in section no. 43 obtained using traffic model from WIM system (a) and from Eurocode (b).

3.3 Life-cycle cost analysis

LCCA is carried out by applying Eqs. (2-3). The initial cost C_0 is taken from design documentation [12]. The maintenance cost C_m is considered as a percentage of the initial cost of the bridge. The annual percentage value is assumed to be equal to 1% [19]. The unit c_j can be computed as a percentage v of the initial cost C_0 [12], as follows:

$$c_j = v C_0 \quad (7)$$

while the repair cost c_r is taken as the 10% of c_j ($c_r = 0.1 c_j$). The coefficient v is taken to be equal to 1.1 to account for demolition and disposal costs [12]. The annual inspection cost is defined through the price list of Italian National Autonomous Roads Corporation (ANAS) [20]. The cost items are summarized in Table 1 and Table 2.

Cost item	Cost
C_0 [12]	€ 4.084.801
C_m [19]	€ 40.848,01
C_i [20]	€ 11.439,65
c_j [12]	€ 4.493.281,10

Table 1: Costs of the bridge.

C_i	Cost
Inspection of bridges and viaducts [20]	15.52 €/m
Inspection of piers [20]	235.75 €/pier

Table 2: Inspection Costs.

The discount rate is assumed equal to $r = 0.05$ and the threshold of the probability beyond which a repair intervention is required is 10^{-2} [21].

Figure 6(a) illustrates the expected life cycle cost over time of the bridge normalized with respect to the initial construction costs (Eqs. (2-3)) and Figure 6(b) shows the corresponding cumulated probability of failure as a function of time by comparing the case in which the hazard traffic curve is obtained from the monitoring system and when it is obtained from the Eurocode. In the case of Eurocode, it can be noted the cost increase associated to the attainment of the probability threshold.

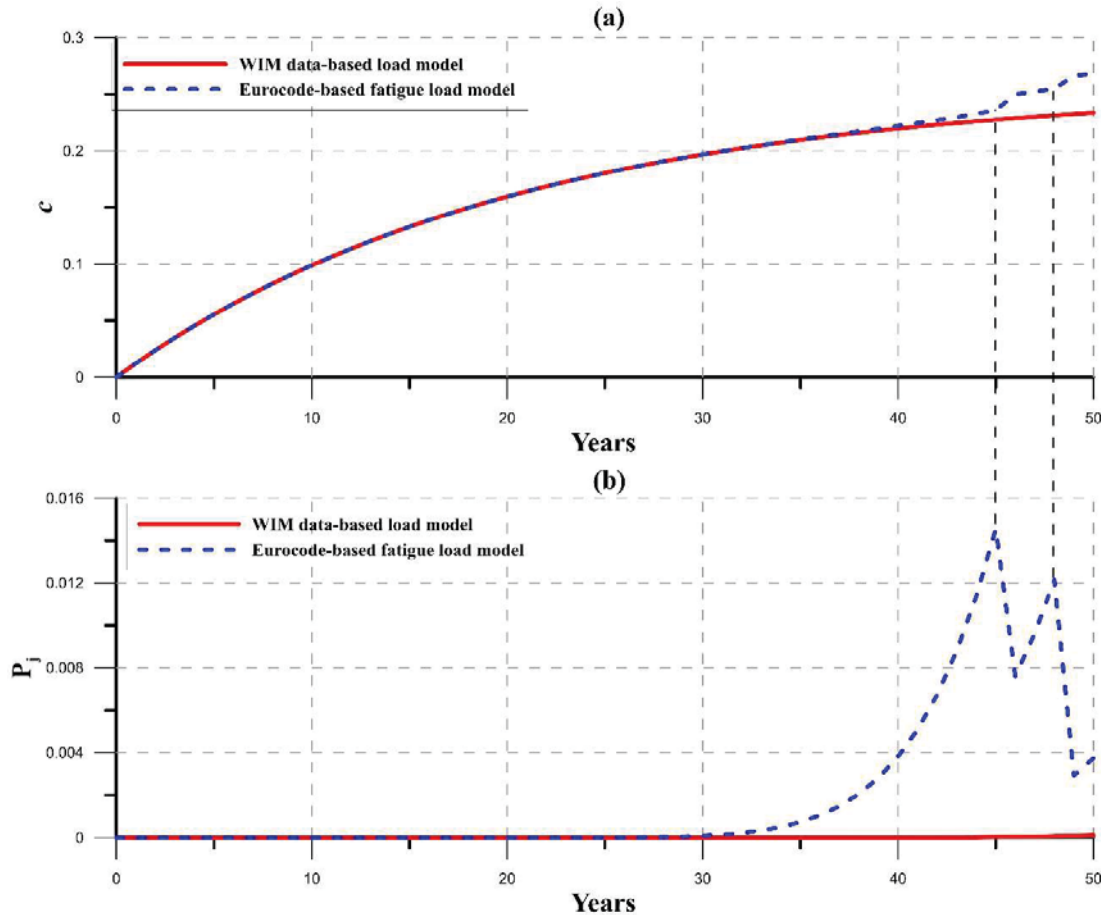


Figure 6 Expected normalized costs over the lifetime of the bridge (a) and the related probability (b).

Since the choice of the probability distributions of EDP and D_{crit} significantly influence the expected costs, parametric analyses have been carried out on the variations of the COVs of EDP and D_{crit} . Figures 7 (a) and 7 (b) show the normalized expected cost, evaluated for different values of COV of EDP (0.25, 0.5 and 0.8) for D_{crit} lognormally distributed with mean 1.0 and $COV = 0.3$, for the case of Eurocode-based fatigue load model and WIM-based monitoring data load model, respectively. Figures 7 (c) and 7 (d) represent the normalized expected cost, evaluated with mean 1.0 and for different values of COV of D_{crit} (0.1, 0.2 and 0.3) and for a fixed value of COV of EDP equal to 0.8, for the case of Eurocode-based fatigue load model and WIM-based monitoring data load model, respectively. It is visible from Figures 7 (a-b) that the expected cost increases over time and is greater when the uncertainty on the EDP is equal to 0.8. On the other hand, Figures 7 (c-d) show that the cost is higher when the uncertainty on COV of D_{crit} equals 0.3.

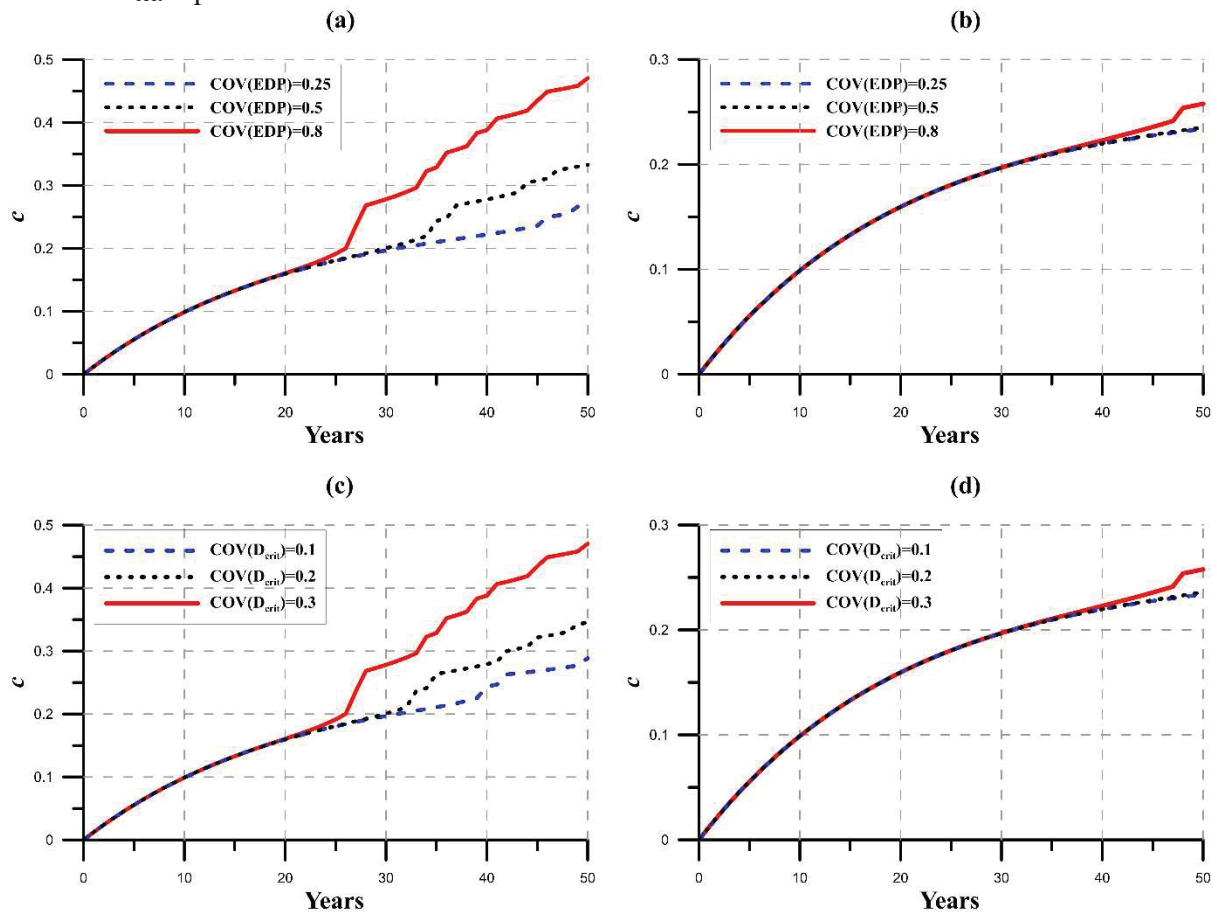


Figure 7 Expected normalized costs over the bridge's lifetime for different values of COV of EDP (a-b) and D_{crit} (c-d).

Figure 8 shows the results in terms of expected normalized costs (a-b) and the corresponding trends of the fatigue failure probabilities (c-d) considering COV of EDP equal to 0.8 (mean value equal to D) and D_{crit} equal to 0.3 (mean value equal to 1.0). Figures 8 (a-c) are obtained with the Eurocode-based fatigue load model and Figures 8 (b-d) are obtained with the WIM data-based load model. In both cases it is possible to observe that the costs increase when the probability threshold is reached, as there is the need for a repair action. From results, it can also be noted that the Eurocode-based hazard traffic curve overestimates the cost with respect to the case in which the hazard curve is obtained from WIM data.

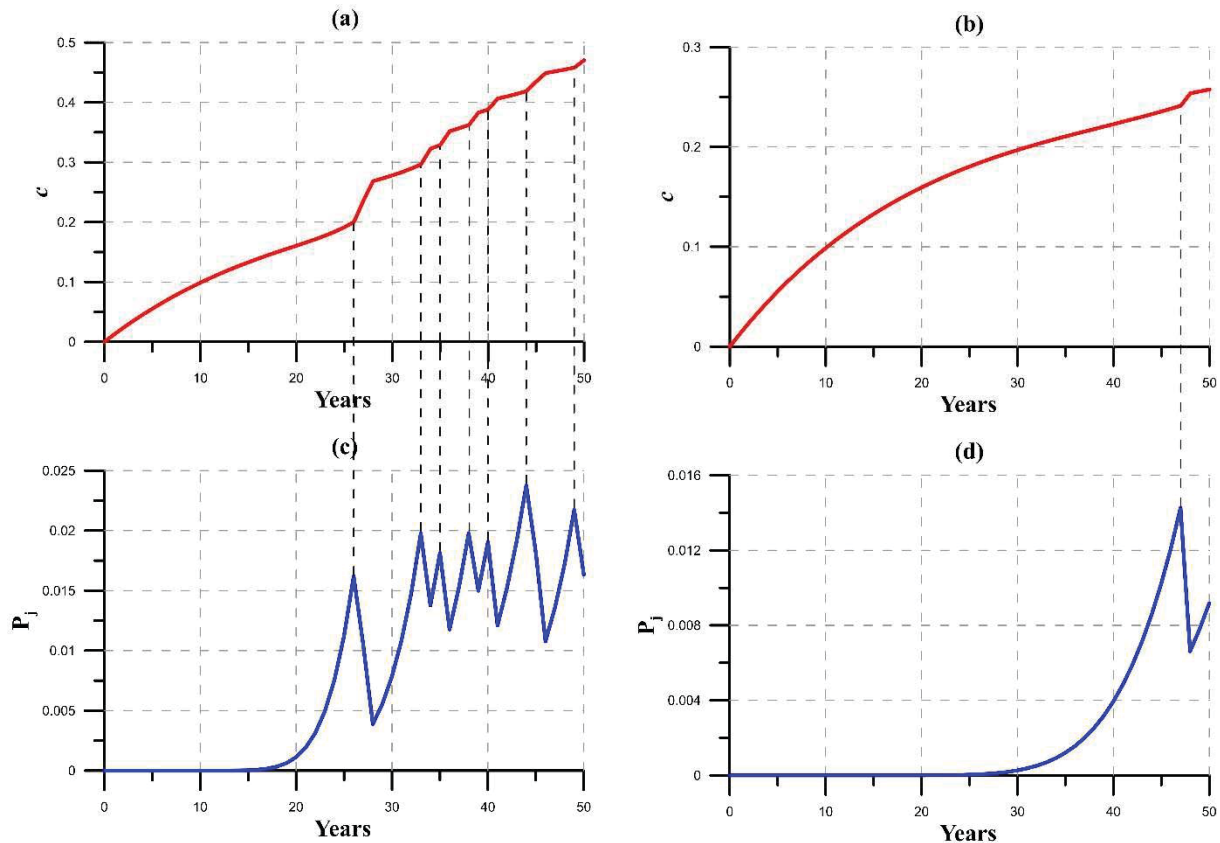


Figure 8 Expected normalized costs over the lifetime of the bridge (a-b) and the respective trends of the probabilities (c-d).

4 CONCLUSIONS

In this paper a general methodology for the computation of the expected total life-cycle cost of bridges is proposed, based on the PEER equation for failure probability estimation. The approach is for the first time applied to cost and fragility analysis of bridges subjected to fatigue, highlighting the possibility of treating the problem of fatigue damage estimation with an approach similar to the one currently adopted for damage induced by other hazards, like earthquake and wind. Starting from the knowledge of the traffic load model, the gross vehicles weight is assumed as IM and the fatigue damage index calculated through the Palmgren-Miner's rule is adopted as EDP. The damage accumulation is evaluated by considering the time dependency of the fatigue damage index.

The framework was applied to a continuous steel-concrete composite highway bridge located in central Italy by evaluating the fatigue limit state from the traffic loads defined by the Eurocode and obtained through a WIM monitoring system, for different probability distributions of the EDP and for different fragility models. The comparison between the fatigue failure probabilities and the life-cycle costs obtained with the two traffic models highlighted that the Eurocode-based hazard traffic curve overestimates the cost with respect to the case in which the hazard curve is obtained from WIM data, encouraging the adoption of traffic monitoring systems for a correct damage estimation.

ACKNOWLEDGMENTS

The authors gratefully acknowledge the support of the “Cassa di Risparmio di Perugia” Foundation, that funded this study through the Project “Development of an original life-cycle cost model for the optimal management of bridges and viaducts equipped with SHM systems” (Grant number 2019.0338.029), and the support of Brent Phares at Iowa State University and the Iowa Department of Transportation that provided the field monitoring system data.

REFERENCES

- [1] A. C. Estes, D. M. Frangopol, Bridge lifetime system reliability under multiple limit states. *Journal of Bridge Engineering*, **6**(6), 2001.
- [2] F. Ubertini, Prevention of suspension bridge flutter using multiple tuned mass dampers. *Wind & Structures*, **13**(3), 235-256, 2010.
- [3] K. M. Lee, H. N. Cho, Y. M. Choi, Life-cycle cost-effective optimum design of steel bridges. *Journal of Constructional Steel Research*, **60**(11), 1585-1613, 2004.
- [4] I. Venanzi, O. Lavan, L. Ierimonti, S. Fabrizi, Multi-hazard loss analysis of tall buildings under wind and seismic loads. *Structure and Infrastructure Engineering*, **14**(10), 1295-1311, 2018.
- [5] I. Venanzi, L. Ierimonti, L. Caracoglia, Life-cycle-cost optimization for the wind load design of tall building equipped with TMDs. *Wind and Structures*, **30**(4), 379-392, 2020.
- [6] S. H. Kim, M. S. Choi, K. I. Cho, S. J. Park, Determining the Optimal Structural Target reliability of a Structure with a Minimal Life-Cycle Cost Perspective. *Advances in Structural Engineering*, **16**(12), 2013.
- [7] L. Micheli, A. Alipour, S. Laflamme, Life-cycle-cost optimization of wind-excited tall buildings using surrogate models. *Structural Design of Tall and Special Buildings*, **30**(6), e1840, 2021.
- [8] L. Micheli, A. Alipour, S. Laflamme, P. Sarkar, Performance-based design with life-cycle cost assessment for damping systems integrated in wind excited tall buildings. *Engineering Structures*, **195**, 438-451, 2019.
- [9] L. Micheli, L. Cao, S. Laflamme, A. Alipour, Life-Cycle Cost Evaluation Strategy for High-Performance Control Systems under Uncertainties. *Journal of Engineering Mechanics*, **146**(2), 04019134, 2020.
- [10] S. Kleingesinds, O. Lavan, I. Venanzi, Life-Cycle cost-based optimization of MTMDs for tall buildings under multiple hazards. *Structure and Infrastructure Engineering*, 1-20, 2020.
- [11] L. Ierimonti, I. Venanzi, L. Caracoglia, A.L. Materazzi, Cost-Based Design of Nonstructural Element for Tall Buildings under Extreme Wind Environments. *Journal of Aerospace Engineering*, **32**(3), 2019.
- [12] I. Venanzi, R. Castellani, L. Ierimonti, F. Ubertini, An automated procedure for assessing local reliability index and life-cycle cost of alternative girder bridge solutions. *Advances in Civil Engineering*, 1-17, 2019.

- [13] S. Kunnath, *Application of the PEER PBEE methodology to the I-880 viaduct*. Rep. No. 2006/10. Davis, California: University of California.
- [14] M. Miner, Cumulative damage in fatigue. *Journal of Applied Mechanics*, **12**(3), 159-164, 1945.
- [15] Eurocode 3, *Design of steel structures-Part 1-9: Fatigue*, Eurocode 3: EN 1993-1-9, Brussels, Belgium: European Committee for Standardization, 2005.
- [16] S. D. Downing, D.F. Socie, Simple rainflow counting algorithms. *Journal of Fatigue*, **4**(1), 31-40, 1982.
- [17] Eurocode 1, *Actions on structures-Part 2: Traffic load on bridges*, Eurocode 1: EN 1991-2, Brussels, Belgium: European Committee for Standardization, 2003.
- [18] Det Norske Veritas (DNV), *Fatigue Design of Offshore Steel Structures*. No. DNV-RP-C203.
- [19] M. Wicke, Inspection, assessment and maintenance. *Proceedings of the 13th International Association of Bridge and Structural Engineering Congress on Challenges to Structural Engineering*, Helsinki, Finland, Vol.2 pp.91-105, 1988.
- [20] ANAS S.p.A., *Listino prezzi 2020*. Prove, Indagini e Monitoraggio, 2020.
- [21] R. Rackwitz, Optimization-the basis of code-making and reliability verification. *Structural Safety*, **22**(1), 27-60, 2000.

LIFE-CYCLE COST ANALYSIS OF TALL BUILDINGS IN SYNOPTIC, MIXED WIND LOAD CLIMATES BY LAYERED STOCHASTIC APPROXIMATION MONTE-CARLO METHOD

Lei Zhang¹, Luca Caracoglia²

¹PhD Candidate, Dept. of Civil and Environmental Engineering, Northeastern University
Boston, MA 02115, USA
e-mail: zhang.lei1@northeastern.edu

² Associate Professor, Dept. of Civil and Environmental Engineering, Northeastern University
Boston, MA 02115, USA
e-mail: lucac@coe.neu.edu

Keywords: Mixed Wind Load Climates; Layered Stochastic Approximation Monte-Carlo Method; Wind Directionality; Life-cycle Cost Analysis.

Abstract. *This paper extends the existing formulation for life-cycle cost analysis (LCCA) of tall buildings subjected to synoptic, mixed wind load climates. This situation arises, for example, if the site is characterized by the presence of both tropical cyclones and extra-tropical depressions. A parametric study is conducted to examine the dependence of building's intervention cost, due to wind-induced damage, on the building height. Special attention is paid to the influence of wind load directionality, enabled by the modeling of the joint probability of mean-wind speed and direction using an angular-linear model. Furthermore, the Layered Stochastic Approximation Monte-Carlo (LSAMC) method is implemented for fragility analysis, as an alternate, surrogate approach compared to the standard Monte-Carlo simulation via physical building model. The results of the LSAMC simulations are validated by Monte-Carlo sampling. The study demonstrates that the LSAMC method is eligible for wind-induced fragility analysis while simultaneously achieving a remarkable reduction in computing time.*

1 INTRODUCTION

Tall buildings tend to oscillate in the along-wind, across-wind and torsional directions under the effect of dynamic wind loads, arising from variable pressure distribution on the building surface [1]. Due to the aleatory nature of the wind flow, efficiently quantifying wind loads can be problematic for structural design. Great efforts have been devoted to the estimation of wind load effects in the presence of uncertainties [2, 3, 4]. Adapted from performance-based design that was introduced for seismic engineering, the field of performance-based wind engineering (PBWE) has been introduced as an efficient approach that accounts for various uncertainties, inherent in the interactions between structures and wind loads. PBWE has been implemented for a wide range of structures and extreme wind phenomena; examples include low-rise, light-frame wood structures subjected to hurricanes [5], tall buildings [6, 7, 8], long-span bridges [9, 10], and various structures affected by non-stationary wind loads (e.g. tornadoes, thunderstorms) [11].

At the core of the PBWE is the uncertainty evaluation and fragility determination. Uncertainty sources may incorporate wind turbulence, structural deterioration and experimental conditions, used for wind load estimation. Some of these factors are aleatory, e.g. wind turbulence, and thus cannot be eliminated, while uncertainties related to experiments can be minimized by improving testing facilities and protocols. The concept of “fragility” is used to examine likelihood of failure occurrence contingent on the prescribed uncertainties. In practice, the fragility is expressed as the exceedance probability of a predefined performance objective, conditional on a variable (e.g. mean wind speed) describing the intensity of the demand on the structure. Performance objectives are described as limit-state conditions by a resultant structural effect, for example, in tall buildings the top-floor lateral drift and acceleration for a serviceability limit state and the internal stresses in a corner column for an ultimate limit state.

Currently, Monte-Carlo simulation is widely used for the assessment of fragility because it is applicable to any structural, physical model and it is simple to implement. However, an entrenched problem that the Monte-Carlo-based approach faces is that the process requires the generation of a large number of realizations and, consequently, is time consuming and computationally expensive. To overcome this limitation, attempts have been made by using sophisticated techniques [12] and improved algorithms, e.g. the Layered Stochastic Approximation Monte-Carlo (LSAMC) method [13]. The LSAMC method is based on the Stochastic Approximation algorithm [14]; it can derive the statistics of the performance objective indicator, expediting the procedure for fragility evaluation while preserving fidelity. The objectives of this paper are to: (i) describe the results of a parametric study implementing LSAMC-based fragility analysis for a benchmark tall building with variable heights and (ii) investigate the dependency of life-cycle cost assessment on the building height within the PBWE framework [15].

2 BACKGROUND THEORY

2.1 Multi-directional aerodynamic response of tall buildings

Capitalizing on the frequency-domain random vibration analysis for estimating wind-induced loads and structural response of tall buildings, a linear, quasi-steady model for multi-directional wind analysis allows a practitioner to simultaneously examine vibrations in along-wind, across-wind and torsional directions [16]. Multi-directionality is necessary for dynamic analysis because wind load effects are multi-directional. Furthermore, several studies [15, 17] demonstrate that there is a strong correlation between the local building orientation, another factor that influences directionality effect, and the structural performance.

For a linear elastic building subjected to turbulent wind loads with a mean-wind, horizontal incidence angle Ψ , the PSD of the generalized quasi-steady buffeting forces is

$$S_{Q_b Q_b}(n) = \iint_0^h \frac{\rho^2 D^2}{4} \bar{U}(z_1) \bar{U}(z_2) \Phi^T \mathbf{C}^* \begin{bmatrix} S_{uu}(n, z_1, z_2) & 0 \\ 0 & S_{vv}(n, z_1, z_2) \end{bmatrix} \mathbf{C}^{*,T} \Phi dz_1 dz_2 \quad (1)$$

where

$$\mathbf{C}^* = \begin{bmatrix} \cos \Psi & -\sin \Psi & 0 \\ \sin \Psi & \cos \Psi & 0 \\ 0 & 0 & 1 \end{bmatrix} \begin{bmatrix} 2C_D(\Psi) & C'_D(\Psi) - C_L(\Psi) \\ 2C_L(\Psi) & C'_L(\Psi) + C_D(\Psi) \\ 2DC_M(\Psi) & DC'_M(\Psi) \end{bmatrix} \quad (2)$$

In the previous equations, $S_{Q_b Q_b}$ is the PSD matrix of the generalized buffeting forces; ρ is the air density; D is a reference floor-plan dimension (usually in the across-wind direction at $\Psi = 0$); $\bar{U}(z)$ is the mean wind speed profile evaluated at height z ; Φ is the mode shape matrix of the structure that can lead to inter-modal coupling arising from non-uniplanar, complex structural modes shapes; $C_D(\Psi)$, $C_L(\Psi)$, $C_M(\Psi)$ is the aerodynamic coefficients of drag force, transverse (lift) force and torque about z , respectively; $C'_D(\Psi)$, $C'_L(\Psi)$, $C'_M(\Psi)$ are the corresponding derivatives with respect to Ψ ; $S_{uu}(n, z_1, z_2)$ is the cross spectral density function of the along-wind turbulence component, evaluated at elevations z_1 and z_2 , and $S_{vv}(n, z_1, z_2)$ is the across-wind turbulence component. The cross-spectral density function between the two turbulence components is omitted due to a weak correlation. Furthermore, a set of dimensionless “model curves” in Eq. (3)–Eq. (4) are utilized to facilitate the parametric study of wind loads, extracted from HFFB wind tunnel tests [18].

$$\frac{n S_{Q_x Q_x}(n)}{\left(\frac{1}{2} \rho \bar{U}^2(h) D h\right)^2} = \frac{a_D f}{1 + b_D f^{c_D}} \quad (3)$$

$$\frac{n S_{Q_y Q_y}(n)}{\left(\frac{1}{2} \rho \bar{U}^2(h) D h\right)^2} = \frac{a_L f}{1 + b_L f^{c_L}} + d_L f^2 \exp \left[- \left(\frac{f - e_L}{f_L} \right)^2 \right] \quad (4)$$

2.2 Brief introduction to PBWE analysis

A general procedure for PBWE [19] analysis is summarized in Fig. 1, which describes the key steps that are usually involved in the assessment for structural design. The evaluation of each of the joint probability density functions (PDFs) represents a particular step: $f(IM)$ for site and structure-specific hazard analysis, $f(SP)$ for structural characterization, $f(IP|IM, SP)$ for interaction analysis, $f(EDP|IM, IP, SP)$ for structural analysis, $f(DM|EDP)$ for damage analysis and $f(DV|DM)$ for loss analysis. When the performance related to a decision variable DV is expressed by a limit state, which can be associated with an EDP (e.g. the top-floor lateral drift), the procedure of PBWE assumes $DV = EDP$ and can be concisely summarized in Eq. (5) below, where $G(\cdot)$ is a complementary cumulative distribution function (CCDF).

$$G(EDP) = \iiint G(EDP|IM, IP, SP) f(IP|IM, SP) f(IM) f(SP) dIM dIP dSP \quad (5)$$

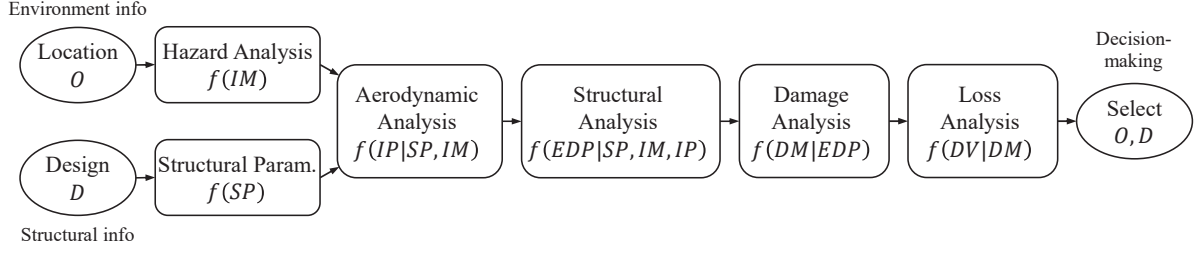


Figure 1: PBWE flowchart, reproduced from [19]. *IM*: intensity measures; *SP*: structural parameters; *IP*: interaction parameters; *EDP*: engineering demand parameters; *DM*: damage measures; *DV*: decision variables.

3 NOVEL, LSAMC-BASED SIMULATION METHOD

3.1 Wind load modeling in mixed wind climates

A parametric angular-linear distribution model [20] can be employed for the description of mean-wind speed and direction at a reference height (e.g. building's rooftop). Based on the marginal distributions of the two random variables (speed and direction), the general form of the joint PDF is given by Eq. (6), where the two marginal PDFs are combined using a third angular PDF $g(\zeta)$.

$$f_{V,\theta}(v, \theta) = 2\pi g(\zeta) f_V(v) f_\theta(\theta) \quad 0 \leq v < \infty, 0 \leq \theta, \zeta < 2\pi \quad (6)$$

In the previous equation, $g(\zeta) = 2\pi[F_\theta(\theta) - F_V(v)]$ and $F_\theta(\theta)$, $F_V(v)$ are the marginal CDFs of the wind direction and wind speed, respectively. The Gumbel distribution can be used to model the magnitude of wind speeds (annual maxima) for non-hurricane winds, and a Weibull distribution for hurricane winds, specified in Eq. (7) and Eq. (8), respectively. For the corresponding wind direction, a model based on a mixture of von Mises distributions [21], as expressed in Eq. (9) below, enables the inclusion of several prevailing wind directions.

$$f_V(v; \mu, \gamma) = \frac{1}{\gamma} \exp \left\{ - \left[\frac{v - \mu}{\gamma} + \exp \left(- \frac{v - \mu}{\gamma} \right) \right] \right\} \quad (7)$$

$$f_V(v; k, \lambda) = \frac{k}{\lambda} \left(\frac{v}{\lambda} \right)^{k-1} \exp \left[- (v/\lambda)^k \right] \quad (8)$$

$$f_\theta(\theta) = \sum_{j=1}^{N_m} \frac{\omega_j}{2\pi I_0(\kappa_j)} \exp [\kappa_j \cos (\theta - \mu_j)] \quad (9)$$

In Eq. (9), N_m is the number of components in the mixture model; ω_j are the nonnegative weights for each component that must satisfy the condition $\sum_{j=0}^{N_m} \omega_j = 1$; $I_0(\kappa_j)$ is the modified Bessel function of the first kind and order zero, evaluated at a nonnegative quantity κ_j ; μ_j is the mean directions for each prevailing wind [21].

For a site that is subjected to more than one type of extreme wind events, the wind modeling is better achieved by separately examining each meteorological phenomenon, thus yielding a comprehensive probabilistic description of the local wind environment [22]. This study examines a local wind climate typical of the Mid-Atlantic coast of the United States of America that

is subjected to both extra-tropical depressions and hurricanes. Therefore, the joint CDF of the annual maxima of the wind speed and direction, is formulated as:

$$F_m(v, \theta) = F_H(v, \theta)F_{NH}(v, \theta) \quad (10)$$

where $f_m(v, \theta)$, $f_H(v, \theta)$, $f_{NH}(v, \theta)$ are the joint PDFs of the annual maximum mean-wind speed and direction in mixed, hurricane and non-hurricane wind climates, respectively; $f_H(v)$, $f_{NH}(v)$ are the marginal PDFs of the magnitude of the maximum mean-wind speeds for hurricane winds and non-hurricane winds; $f_H(\theta)$, $f_{NH}(\theta)$ are the marginal PDFs of the corresponding directions, respectively.

$$\begin{aligned} f_m(v, \theta) &= \frac{\partial^2 F_m(v, \theta)}{\partial v \partial \theta} \\ &= f_H(v, \theta)F_{NH}(v, \theta) + f_H(v)f_{NH}(\theta) + F_H(v, \theta)f_{NH}(v, \theta) + f_H(\theta)f_{NH}(v) \end{aligned} \quad (11)$$

where $f_m(v, \theta)$, $f_H(v, \theta)$, $f_{NH}(v, \theta)$ = the joint PDFs of annual maximum wind speed and direction in mixed, hurricane and non-hurricane wind climates, respectively; $f_H(v)$, $f_{NH}(v)$ = the marginal PDFs of the magnitude of the maximum speeds for hurricane winds and non-hurricane winds; and $f_H(\theta)$, $f_{NH}(\theta)$ = the marginal PDFs of the corresponding directions, respectively.

3.2 Structural failure probability and LCCA

The objective of the fragility analysis is to estimate the probability that a specific *EDP*, conditional on the examined *IM*, exceeds a preselected threshold. Following previous studies, the *EDP* is chosen as the lateral rooftop drift; the vector *IM* consists of two random variables, the mean wind speed at the building rooftop, \bar{U}_h , and the corresponding mean wind direction, $\bar{\theta}$. Structural fragility can be explicitly expressed by Eq. (12), where d_j is the preselected threshold for the *j*-th *EDP*. In this study, the threshold for the lateral drift of a building can be set as 1/400 of the building height [23]. Note that the obtained fragility is a fragility surface, allowing for the assessment of the multi-directionality effect induced by the wind.

$$f_j(v, \theta) = P(EDP_j > d_j | \bar{U}_h = v, \bar{\theta} = \theta) \quad (12)$$

Having obtained the joint PDF of intensity measures $f(IM)$ and the fragility, the structural failure probability with respect to the *j*-th *EDP* can be estimated by Eq. (13). Finally, the annual probability of *j*-th *EDP* exceeding the preselected threshold is described by Eq. (14) [24].

$$P_{j,\text{event}} = \int_0^{2\pi} \int_0^\infty f_j(v, \theta) f_{V,\Theta}(v, \theta) dv d\theta \quad (13)$$

$$P_{j,\text{annual}} = 1 - \exp(-\nu P_{j,\text{event}}) \quad (14)$$

In Eq. (14) ν is the average annual number of occurrences in the local mixed climate. Assuming independence between hurricane and non-hurricane incidents, ν is estimated as the summation of the annual rate of hurricane landfall and the number of monthly maximum non-hurricane wind speeds occurring in any one year.

Capitalizing on the quantification of structural failure probability, the LCCA can be implemented to predict damage-induced monetary losses over the structural life-time (with *t* unit

time in years). The normalized, expectation of the relative intervention (maintenance, repair, retrofitting, etc.) cost $C_E(t)$, adapted from the cost function in [25], can be calculated as:

$$C_E(t) = \mathbf{E} \left[\frac{C(t) - C_0}{C_0} \right] = \mathbf{E} \left[\sum_{i=1}^{N(t)} \sum_{j=1}^k \epsilon_j e^{-\lambda t_i} P_j \right] \quad (15)$$

In the previous equation, $\mathbf{E}[\cdot]$ denotes the expectation operation; $C(t)$ is the expected total cost induced by damages; C_0 is the initial construction cost of a structure; $0 \leq t_i \leq t$ is the random variable describing the time when the i -th hazard occurs; $\epsilon_j = C_j/C_0$ is a normalized relative cost of the j -th limit state being violated at time t_i calculated as the ratio of the expected intervention cost related to the j -th limit state, C_j , to the initial cost; λ is the constant discount rate, which places more weight on hazards occurring closer to the completion date of the structure over those that are not; $P_j = P_{j,\text{annual}}$ is the failure probability of the j -th limit state, i.e. the probability that intervention relating to the j -th limit state is desired; k is the total number of limit states considered; $N(t)$ is the number of wind occurrences, which is a function of ν during the lifetime.

3.3 LSAMC method

Similar to the idea of the Latin Hypercube sampling, the LSAMC method uses the layered sampling of random variables within a Monte-Carlo simulation environment. As proposed by [13], the key steps of the LSAMC method include: (i) dividing the range of each random variable into a finite number of adjacent non-overlapping equally-probable intervals; (ii) constructing a subspace of the random variables for each iteration, consisting of one of the equally-probable intervals for every random variable; (iii) feeding the subspace to the standard Stochastic Approximation algorithm, which has the form of Eq. (16), to find one root of the examined problem subjected to perturbation. Iterating through all the possible subspaces of the original random variables set yields a sequence of roots to the perturbed problem; this allows to approximate the effects of the noises in a structural system through statistical moments derived from the root sequence. By contrast, the "exact" values are determined by a standard "brute-force" Monte-Carlo simulation.

$$\begin{aligned} \hat{\mathbf{x}}_{k+1} &= \hat{\mathbf{x}}_k - a_k \mathbf{Y}_k \\ \mathbf{Y}_k &= \mathbf{g}(\hat{\mathbf{x}}_k) + \mathbf{e}_k(\hat{\mathbf{x}}_k) \end{aligned} \quad (16)$$

In the previous equation, $\hat{\mathbf{x}}_k$ is the estimate of the root \mathbf{x} at the k -th iteration; \mathbf{Y}_k is the noisy measurement at the k -th iteration; $\mathbf{g}(\cdot)$ is the general vector-valued function from which the root-finding equation $\mathbf{g}(\mathbf{x}) = \mathbf{0}$ is constructed; \mathbf{e}_k is the noise introduced by the input of the k -th iteration; a_k is the gain sequence controlling the step size, which is subject to the convergence conditions $\sum_{k=0}^{\infty} a_k = \infty$ and $\sum_{k=0}^{\infty} a_k^2 = 0$. Eq. (17) utilizes recommended values of the gain sequence [14], where α is a constant belonging to the range $(0.5, 1]$ and a , A are a strictly positive constant and a nonnegative constant, respectively.

$$a_k = \frac{a}{(k + 1 + A)^\alpha} \quad (17)$$

The main advantage of the LSAMC method is the avoidance of time-consuming, computationally-expensive Monte-Carlo simulations. However, it is worth noting that the advantage could be

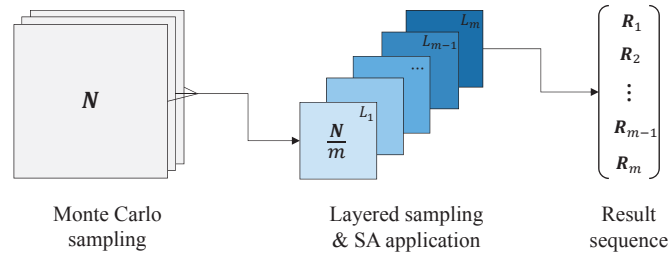


Figure 2: Key steps of the LSAMC method (workflow).

lost if the number of the random variables included were large. To illustrate the potential of the LSAMC method, the reduction of computing time achieved by the LSAMC method, in the case of two input random variables, can be as large as 88% compared to brute-force Monte-Carlo simulation for a monopole tower structure under wind loads [13].

4 NUMERICAL APPLICATION

In this section, the application of the proposed LSAMC-based simulation to a set of variants of a benchmark tall building is discussed. The LSAMC method is employed for the fragility analysis and the estimation of P_j in Eq. (15). Furthermore, dependency of the life-cycle cost variable $C_E(t)$ in Eq. (15) on the variable building height is examined.

4.1 Description of reference building structure and its variants

Based on the benchmark tall building model of the Commonwealth Advisory Aeronautical Research Council (CAARC), a set of building variants is parametrically constructed. The variants share the same structural parameters (floor plan dimensions, unit mass and mass moment of inertia, etc.) as the CAARC building, except for the building height h , which is set to vary as $h \in \{100, 150, 200, 250, 300\}$ [m]. The structural properties of the benchmark CAARC building are listed in Table 1.

Table 1: Structural properties of the original benchmark CAARC building.

Quantity	Unit	Values
Height h_0	[m]	183.0
Depth D	[m]	45.7
Width B	[m]	30.5
Unit-height mass m	[kg/m]	2.23×10^5
Unit-height mass moment of inertia I_m	[kgm ² /m]	5.62×10^7
Lateral-mode fundamental freq. $n_{0,x}, n_{0,y}$	[Hz]	0.20
Torsional-mode fundamental freq. $n_{0,z}$	[Hz]	0.40
Structural damping ratio $\xi_{0,x}, \xi_{0,y}$	—	0.01

For simplification, the fundamental lateral-mode frequencies of the building variants are modifications of the original values, $n_{0,x}$ and $n_{0,y}$ in Table 1, inversely proportional to the building height, as expressed by Eq. (18) below. The torsional-mode frequency is not modified. In addition, all mode shapes are assumed as dimensionless, monotonic functions, linearly varying

along the building height.

$$n'_{0,i} \approx \frac{h_0}{h} n_{0,i} \quad (i = x, y) \quad (18)$$

4.2 Modeling of site wind climate

The buildings are assumed to be located in Miami, Florida (USA) where hurricanes are frequent. To evaluate the probability distribution of the hurricane wind speed and direction (at landing), a total number of 20 019 synthetic hurricane records, simulated in the Miami region over a period of 20 000 years [17], are utilized. The angular-linear model for the hurricane wind is obtained by fitting a Weibull model to the magnitudes of the wind speed and a two-component mixture of von Mises model to describe the corresponding directions of the approaching storm; the $g(\zeta)$ function in (6) is modeled as a two-component von Mises mixture model. The resultant joint PDF of the hurricane mean wind speed and direction, evaluated at the rooftop of the original CAARC building with $h = 183$ m, is illustrated in Fig. 3, which is characterized by two peaks. The predominant peak corresponds to the high probability of winds coming from the east coast and the Atlantic Ocean, whereas the secondary peak is linked to the westerly winds, originating from the Gulf of Mexico and crossing the peninsula.

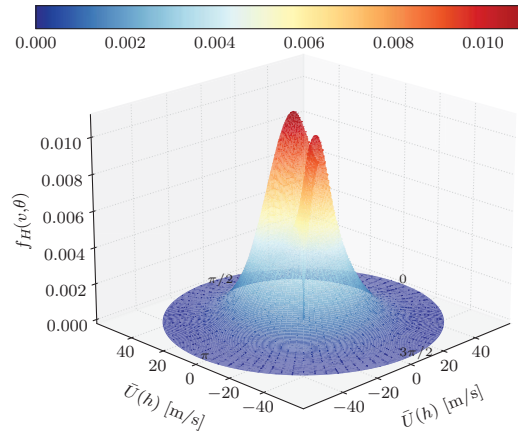


Figure 3: Joint PDF of the mean wind speed and direction for hurricane winds (Miami, Florida, USA) at the reference elevation of the original CAARC building, $h = 183$ m.

For the non-hurricane winds, the joint PDF of the mean wind speed and direction is obtained by using wind record data collected at an offshore buoy station near the Miami site. The data can be accessed by the National Oceanic and Atmospheric Administration (NOAA) [26]. In order to eliminate the influence of hurricanes, the Atlantic hurricane tracking database, HURDAT2 [27], is used to manually remove the buoy data records related to days when a hurricane approaches within a 500 km radius of the building site. In particular, the monthly maxima of the gust speed and the corresponding direction are selected from the filtered buoy data records to form a non-hurricane extreme wind dataset. The averaging time interval of the speed is transformed from 3600 seconds to 600 seconds for consistence with hurricane wind data. By fitting a Gumbel distribution to the magnitudes of the wind speeds and likewise a two-component von Mises mixture model to describe the directions, the joint PDF for the non-hurricane wind speed and direction, is illustrated in Fig. 4; quantities are also evaluated at the rooftop of the original

CAARC building with $h = 183$ m. Fig. 4 indicates that easterly winds, coming from the sea, play a prominent role in the local non-hurricane climate.

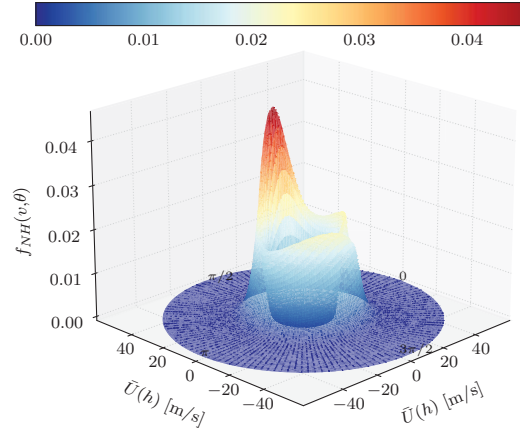


Figure 4: Joint PDF of the mean wind speed and direction for non-hurricane winds (Miami, Florida, USA) at the reference elevation of the original CAARC building, $h = 183$ m.

The joint PDF of the wind in the mixed climates can be consequently estimated from the Figs. 3 and 4 through Eq. (11). Since an analytical form of the CDF for the von Mises distribution is unavailable, the joint CDFs $F_H(v, \theta)$ and $F_{NH}(v, \theta)$ are found through numerical integrations. The joint PDF is plotted in Fig. 5. It is clear that the compound joint PDF combines features of the two separate PDFs related to both hurricane and non-hurricane climate.

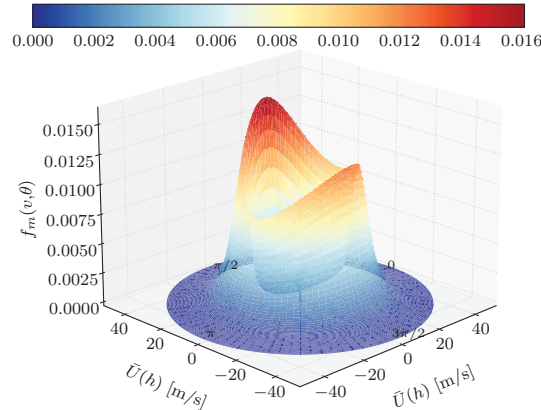


Figure 5: Joint PDF of the mean wind speed and direction for the mixed wind climate of Miami, Florida (USA) at the reference elevation of the original CAARC building, $h = 183$ m.

4.3 Characterization of uncertainty in the wind loads

As an example, this study analyzes uncertainty propagation due to experimental wind load errors by considering a parameter denoted by ΔC_D ; this quantity describes the deviation of experimentally estimated drag coefficient C_D from an average, measured value at a particular incidence angle, i.e., $\Delta C_D = C_D(\Psi) - \mathbf{E}[C_D(\Psi)]$. Data points of the drag coefficients are extracted from wind tunnel tests on a rigid, scale model of the original CAARC building [18];

eleven incidence angles are tested with $\Psi \in \{0^\circ, 5^\circ, 10^\circ, 15^\circ, 30^\circ, 45^\circ, 60^\circ, 75^\circ, 80^\circ, 85^\circ, 90^\circ\}$. Experimental data points of C_D along with a Fourier series fitting are illustrated in Fig. 6.

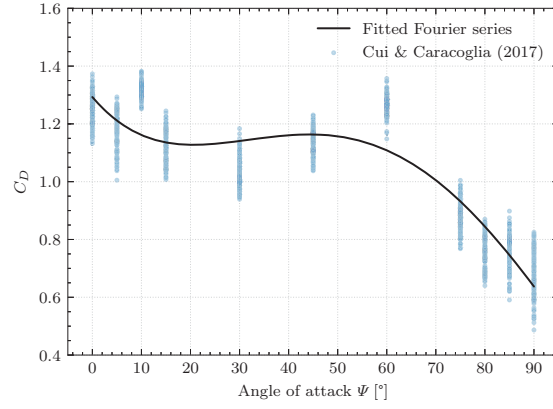


Figure 6: Drag coefficients C_D measured at various incidence angles, reproduced from [18].

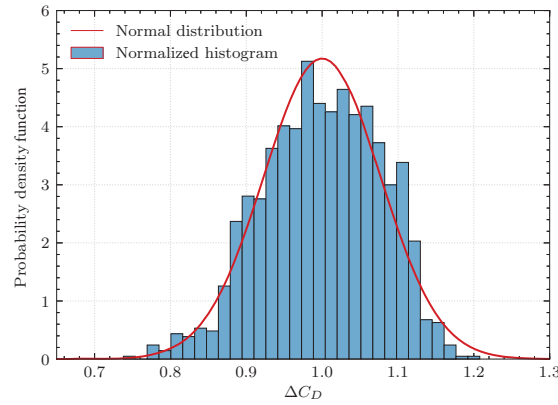


Figure 7: Histogram of the dimensionless uncertainty parameter ΔC_D .

Assuming that ΔC_D , collected from all the measured data points, is independent of Ψ and that ΔC_D is identically distributed for different angles, a suitable distribution model can be determined through Kolmogorov-Smirnov goodness-of-fit test. A normal distribution, parameterized by a mean value of 1.000 and a standard deviation STD of 0.077, can adequately describe the empirical histogram (and distribution) of the ΔC_D in Fig. 7.

4.4 Structural fragility analysis

Both the standard brute-force Monte-Carlo simulation and the LSAMC method are employed. For the LSAMC method, the number of equally-probable subsets is 10; the parameters of the gain sequence are set as $a = 10$, $A = 0$, $\alpha = 0.95$. Structural fragilities against the limit state of rooftop lateral drift are illustrated in Fig. 8; fragility curves related to mean incidence angle $\Psi = \{0^\circ, 45^\circ, 90^\circ\}$ are exclusively shown for the sake of brevity. The LSAMC results, represented by dashed, non-solid lines, are very close to those found by brute-force Monte-Carlo method plotted as solid lines. By comparing the fragility curves corresponding to different building heights, it is concluded that the wind speed required to reach the prescribed

performance limit ($h/400$) decreases as the building height increases, indicating that a higher building is more sensitive to wind-induced damage as the limit state is probabilistically violated at a lower wind speed.

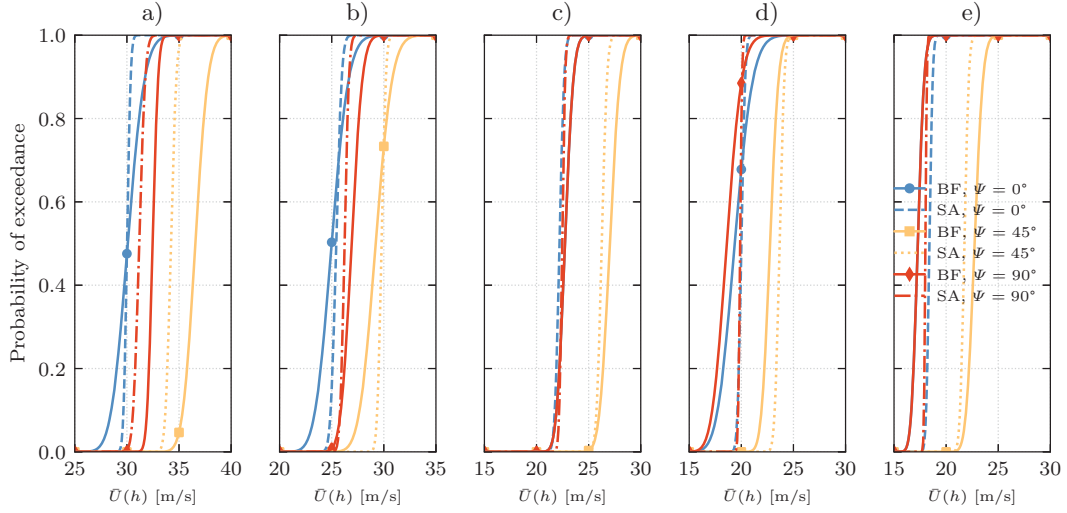


Figure 8: Fragility curves against the limit state of lateral drift with uncertainty parameter ΔC_D : a) $h = 100$ m, b) $h = 150$ m, c) $h = 200$ m, d) $h = 250$ m, e) $h = 300$ m (BF=brute force, SA=LSAMC).

Fig. 9 depicts the fragility surface of the CAARC building variant of height $h = 200$ m; other examples of fragility surface for other building variants can be similarly derived and, thus, are not included. The fragility surface is generated by linear interpolation among the fragility curves (Fig. 8) related to the eleven incidence angles. As shown, the fragility surface has an irregular, “ragged” shape, which is attributed to the directionality of the wind load. In Fig. 8c, the curves corresponding to different incident wind directions seem to shift back and forth along the horizontal axis, because the wind-induced force is directional, thus leading to a variation of fragility even for a same performance objective (EDP).

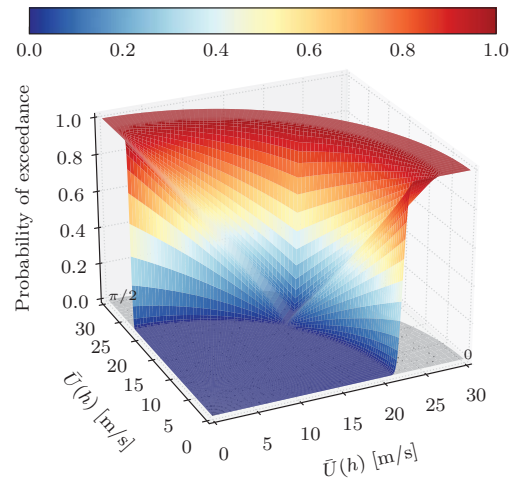


Figure 9: Fragility surface of the CAARC building variant of height $h = 200$ m.

4.5 Expected relative lifetime cost analysis

Fragility surfaces are used to calculate the failure probability and the expected lifetime cost. According to the Eq. (15), the relative intervention costs due to wind-induced damage, associated with nonstructural failures on the building façade and triggered by disproportionate lateral drift, is $\epsilon = 0.02$ and the discount rate is $\lambda = 0.05$. Numerical values have been calibrated according to previous studies [15, 17]. Using the above results of the joint PDF of the mean wind speed and direction in mixed climates and the fragility surfaces, the expected relative lifetime intervention costs due to failures associated with lateral drift are illustrated in Fig. 10. The maximum relative lifetime cost (asymptotic value as t tends to 100 years) is observed for the building variant of height $h = 300$ m and is approximately a quarter of the initial cost, while the minimum relative lifetime cost is found for the building with height $h = 100$ m, which is roughly 2% of the initial cost. This remark suggests a superlinear relationship between building height and expected relative lifetime cost (i.e. a superlinear increment of $C_E(t)$ with height). This behavior can be associated to two aspects. First, due to the wind profile the wind loading on a higher building is generally larger, thus causing larger-magnitude, wind-induced vibrations; second, as discussed in the previous section, a higher building is more slender and exhibits greater sensitivity to wind loads of same intensity because of the concurrent decrement of fundamental frequencies. Consequently, the probability of exceeding the lateral drift limit state and damage is superlinearly higher in a taller building, e.g. $h = 300$ m, vs. $h = 100$ m in Fig. 8.

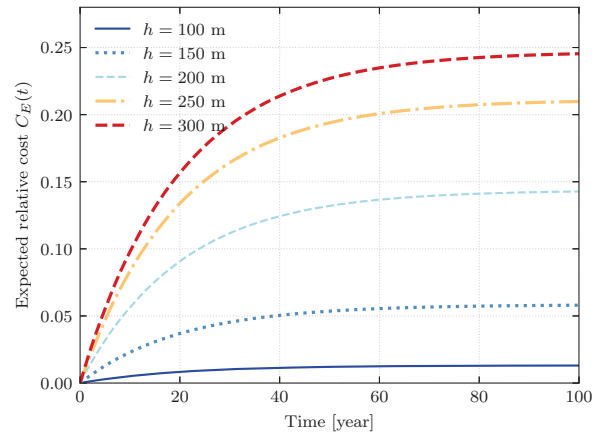


Figure 10: CAARC building variants: expected relative, lifetime intervention cost due to wind-induced damage, associated with nonstructural failures on building façade and triggered by disproportionate lateral drift.

5 CONCLUSIONS

This study examined the comprehensive application of the novel LSAMC method in the context of PBWE. Special attention was paid to lifetime intervention cost analysis. A parametric study was conducted, examining a set of variants of the benchmark CAARC building with equal floor-plan dimensions but variable heights. The LSAMC method was used to estimate structural fragilities; results were compared against standard Monte-Carlo simulation. The LSAMC method is adequate for the fragility analysis. The life-cycle cost assessment revealed a superlinear relationship between asymptotic, expected relative cost and building height; this trend can be ascribed to the reduction in structural stiffness and the increase in the sensitivity to wind-

induced resonant response. This study confirmed the particular significance of nonstructural facade damage caused by wind for operations and maintenance of a high-rise building.

ACKNOWLEDGEMENTS

This material is based upon work supported in part by the National Science Foundation (NSF) of the United States of America under grant CMMI-1852678 in 2019-2022. Any opinions, findings and conclusions or recommendations are those of the authors and do not necessarily reflect the views of the NSF.

REFERENCES

- [1] A. Kareem, Lateral-torsional motion of tall buildings to wind loads. *Journal of Structural Engineering*, **111(11)**, 2479–2496, 1985.
- [2] A. Davenport, On the assessment of the reliability of wind loading on low buildings. *Journal of Wind Engineering and Industrial Aerodynamics*, **11(1-3)**, 21–37, 1983.
- [3] J. D. Holmes, Wind loading of structures: application of probabilistic methods. *Progress in Structural Engineering and Materials*, **1(2)**, 193–199, 1998.
- [4] F. Minciarelli, M. Giofrè, M. Grigoriu, E. Simiu, Estimates of extreme wind effects and wind load factors: influence of knowledge uncertainties. *Probabilistic engineering mechanics*, **16(4)**, 331–340, 2001.
- [5] B. Ellingwood, D. Rosowsky, Y. Li, J. Kim, Fragility assessment of light-frame wood construction subjected to wind and earthquake hazards. *Journal of Structural Engineering, ASCE*, **130(12)**, 1921–1930, 2004.
- [6] K. C. Kwok, P. A. Hitchcock, M. D. Burton, Perception of vibration and occupant comfort in wind-excited tall buildings. *Journal of Wind Engineering and Industrial Aerodynamics*, **97(7-8)**, 368–380, 2009.
- [7] E. Bernardini, S. Spence, M. Giofrè, A. Kareem, A reliability approach for the wind-induced response assessment of tall buildings using the high frequency force balance. In *7th International Colloquium on Bluff Bodies Aerodynamics and Applications (BBAA7)*, pp. 2–6, 2012.
- [8] W. Cui, L. Caracoglia, Simulation and analysis of intervention costs due to wind-induced damage on tall buildings. *Engineering Structures*, **87**, 183–197, 2015.
- [9] D.-W. Seo, L. Caracoglia, Statistical buffeting response of flexible bridges influenced by errors in aeroelastic loading estimation. *Journal of Wind Engineering and Industrial Aerodynamics*, **104**, 129–140, 2012.
- [10] D.-W. Seo, L. Caracoglia, Estimating life-cycle monetary losses due to wind hazards: Fragility analysis of long-span bridges. *Engineering Structures*, **56**, 1593–1606, 2013.
- [11] V. Le, L. Caracoglia, Life-cycle cost analysis of a point-like structure subjected to tornadic wind loads. *Journal of Structural Engineering, ASCE*, **146(2)**, 04019194, 2020.

- [12] V. Le, L. Caracoglia, A neural network surrogate model for the performance assessment of a vertical structure subjected to non-stationary, tornadic wind loads. *Computers & Structures*, **231**, 106208, 2020.
- [13] G. F. Giaccu, L. Caracoglia, Wind-load fragility analysis of monopole towers by layered Stochastic-Approximation-Monte-Carlo method. *Engineering Structures*, **174**, 462–477, 2018.
- [14] J. C. Spall, *Introduction to stochastic search and optimization: estimation, simulation, and control*, vol. 65. John Wiley & Sons, 2005.
- [15] L. Ierimonti, L. Caracoglia, I. Venanzi, A. L. Materazzi, Investigation on life-cycle damage cost of wind-excited tall buildings considering directionality effects. *Journal of Wind Engineering and Industrial Aerodynamics*, **171**, 207–218, 2017.
- [16] W. Cui, L. Caracoglia, A fully-coupled generalized model for multi-directional wind loads on tall buildings: A development of the quasi-steady theory. *Journal of Fluids and Structures*, **78**, 52–68, 2018.
- [17] W. Cui, L. Caracoglia, A unified framework for performance-based wind engineering of tall buildings in hurricane-prone regions based on lifetime intervention-cost estimation. *Structural Safety*, **73**, 75–86, 2018.
- [18] W. Cui, L. Caracoglia, Examination of experimental variability in HFFB testing of a tall building under multi-directional winds. *Journal of Wind Engineering and Industrial Aerodynamics*, **171**, 34–49, 2017.
- [19] M. Ciampoli, F. Petrini, G. Augusti, Performance-based wind engineering: towards a general procedure. *Structural Safety*, **33(6)**, 367–378, 2011.
- [20] R. A. Johnson, T. E. Wehrly, Some angular-linear distributions and related regression models. *Journal of the American Statistical Association*, **73(363)**, 602–606, 1978.
- [21] J. A. Carta, P. Ramírez, C. Bueno, A joint probability density function of wind speed and direction for wind energy analysis. *Energy Conversion and Management*, **49(6)**, 1309–1320, 2008.
- [22] L. Gomes, B. Vickery, Extreme wind speeds in mixed wind climates. *Journal of Wind Engineering and Industrial Aerodynamics*, **2(4)**, 331–344, 1978.
- [23] ASCE, *Prestandard for Performance-Based Wind Design*. American Society of Civil Engineers, Reston, VA, USA, 2019.
- [24] P. J. Vickery, P. F. Skerlj, L. A. Twisdale, Simulation of hurricane risk in the U.S. using empirical track model. *Journal of Structural Engineering, ASCE*, **126(10)**, 1222–1237, 2000.
- [25] Y.-K. Wen, Y. Kang, Minimum building life-cycle cost design criteria. i: Methodology. *Journal of Structural Engineering*, **127(3)**, 330–337, 2001.
- [26] NOAA, National Data Buoy Center. <http://www.ndbc.noaa.gov/>, (accessed April 2, 2020).

- [27] NOAA, National Hurricane Center and Central Pacific Hurricane Center. <https://www.nhc.noaa.gov/>, (accessed December 15, 2020).

APPLICATION OF BAYESIAN FE MODEL SELECTION FOR SHM OF A MONUMENTAL MASONRY PALACE THROUGH SEMI-SUPERVISED LEARNING

L. Ierimonti¹, N. Cavalagli², E. García-Macías², I. Venanzi², F. Ubertini²

^{1 2} Department of Civil and Environmental Engineering, University of Perugia.
address: Via G. Duranti, 93 - 06125 Perugia, Italy
e-mail: {laura.ierimonti,nicola.cavalagli,enrique.garciamacias,ilaria.venanzi,filippo.ubertini}@unipg.it

Keywords: Transfer learning, Bayesian model updating, Model Class Selection, Surrogate model, Damage classification, Continuous monitoring.

Abstract. *The identification of high-fidelity surrogate models for real-time updating based on continuous monitoring data, is an emerging and challenging topic in the structural system identification of historical structures with a special focus on damage identification and structural health monitoring. Indeed, the protection of the historical and cultural heritage aimed at developing cost-effective and long-lasting dynamic monitoring systems in regions characterized by high seismic risk, has received a growing attention in civil engineering. A dynamic monitoring system is usually composed by a selected number of sensors installed in strategic positions within the building which enable a continuous assessment of the structural conditions over time. Then, the observation of the recorded data allows to identify any variations due to possible damages, i.e. novelty detection, which is classified as unsupervised learning. The basic idea behind the present paper is to transfer knowledge from data to updated numerical models with varying levels of complexity developed from the engineering judgment in order to detect and localize damage in a probabilistic manner, moving on to semi-supervised learning. In order to accomplish this challenging task, a transfer Bayesian-based learning (TBL) methodology is proposed by means of model class selection. For the purpose, different classes of FE (finite elements) models, with a low level of complexity, are preliminary defined in such a way to reproduce the structural dynamic behavior as a function of damage-dependent mechanical characteristics (such as average elastic moduli) of pre-selected regions within the structure. Such regions, designated as damage-sensitive, are defined on the basis of nonlinear static analyses and/or Engineering judgment. Then, the large amount of measured data is periodically used for the automatic Bayesian model selection procedure, i.e., the inverse problem to derive the posterior statistics of the uncertain parameters over the space of the FE models classes. For verifying the proposed methodology, an iconic monumental palace, located in Gubbio, Italy, named Consoli Palace which has been monitored by the Authors since 2017, is used. The dynamic monitoring system, updated in July 2020, comprises 12 uniaxial accelerometers installed at different levels within the building.*

1 INTRODUCTION

The non-destructive nature and the relatively low economic impact of the technology make SHM particularly suitable for the detection of structural damages suffered by monumental structures. Nowadays, the most common procedure in civil SHM concerns the data acquisition and feature extraction (system eigenfrequencies and modal shapes) through signal processing [20], while damage identification problems can be classified as a five-level hierarchical approaches [9]: (i) detection; (ii) localization; (iii) classification ; (iv) assessment; (v) prediction. On the one hand, variations over time (novelty detection) in the dynamic response of an healthy structure can be associated to material's damage and deterioration [26], with a special attention to proper techniques able to remove the environmental effects such as temperature and humidity [14] and the different sources of uncertainties related to SHM can be accounted for by means of Bayesian statistical frameworks [28, 1, 27]. On the other hand, long-term monitored data and labeled features able to define the meaning of novelties detection to localize, classify, assess and eventually predict damage are usually not available. Indeed, only a few recent contributions deal with long-term SHM data and damage detection so far [4, 3, 23, 2, 12].

In this context, SHM-based technologies are encompassing machine learning (ML) techniques [18, 17, 24], devoting the attention to the semi-supervised learning paradigm, which allows the use of large amount of monitoring data with and without descriptive labels [5, 6]. The process of prioritizing the acquired data can be accomplished by using numerical models, i.e. precalibrated surrogate models [11, 10], in order to transfer knowledge from the trained model to the data and build a labeled training set. Such methods can be classified as transfer learning (TL) techniques [21, 9, 19].

The present work presents a TBL methodology based on long-term monitoring data aimed at evaluating the possible damage of monumental structures in a probabilistic way. In this framework, TL concepts allow to compensate the lack of labeled structural data, especially in the case of damage occurrence, by means of a trained surrogate model, which is used as a formal prior belief for damage assessment. Then, a Bayesian-based procedure allows to associate a probability of damage occurrence.

The effectiveness of the proposed methodology is demonstrated by making use of a real complex historical masonry building as a case study, the Consoli Palace located in Gubbio, near Perugia, in Italy. The structure has been monitored by the Authors since 2015. The continuous monitoring data are used for the Bayesian-based updating of specific mechanical properties of some pre-selected damage-sensitive regions by means of non-linear static analysis (NLSA) and Engineering judgment (EJ). A trained surrogate model allows to reconstruct different classes of FE models, with a low level of complexity, i.e., depending on a single uncertain parameter. The results show the advantage of having long-term monitoring data on the correct estimation of the uncertain parameters' distribution enabling informed model-based decisions and providing a basis to mitigate the risk of a false alarm. The rest of the paper is organized as follows. Section 2 presents the proposed methodology. Section 3 presents the case study. Section 4 summarizes numerical results. Section 5 concludes the paper.

2 THE PROPOSED METHODOLOGY

The proposed methodology, designated as TBL, schematically represented in Figure 1, embraces different consequential steps which can be summarized as follows:

1. Start continuous SHM.

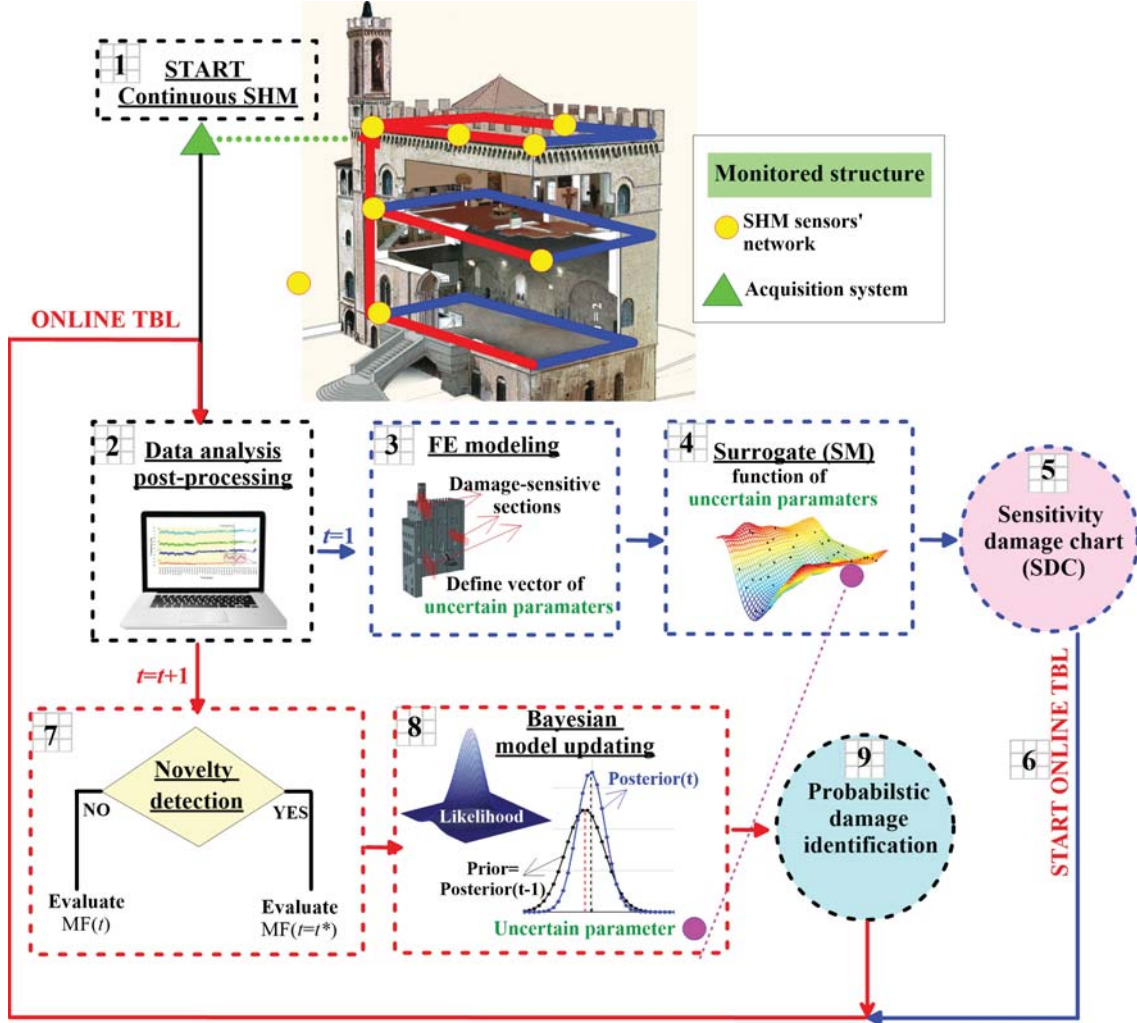


Figure 1: The proposed TBL methodology.

2. Data analysis and post-processing consisting of acquiring data from the monitoring system (acceleration data, temperature information, crack amplitudes) and post-processing data continuously over time to estimate the modal features (MF), such as natural frequencies f_i^{exp} , mode shapes Φ_i^{exp} and damping coefficients ζ_i^{exp} associated with each natural vibration mode.
3. If $t=1$, where the term t stands for discrete time (days): FE modeling and evaluation of damage-sensitive regions. The calibration process consists of solving the following optimization problem:

$$\mathbf{Y}^{\text{opt}} = \arg \min_{\mathbf{Y}} \sum_{i=1}^M p_1 \eta_{f,i}(\mathbf{Y}) + p_2 \eta_{\Phi,i}(\mathbf{Y}) \quad (1)$$

where M is the number of vibration modes; $\mathbf{Y} = \{\mathbf{Y}_1, \dots, \mathbf{Y}_u, \dots, \mathbf{Y}_U\}$ is the vector collecting the n^{th} parameter to be calibrated with N total number of uncertain parameters; p_1 and p_2 are the weights of the objective function; $\eta_{f,i}(\mathbf{Y}) = |f_i^{\text{exp}} - f_i^{\text{FEM}}|/f_i^{\text{exp}}$ and $\eta_{\Phi,i}(\mathbf{Y}) = 1 - \text{MAC}_i(\mathbf{Y})$ are the frequency-based and mode shape-based residual func-

tions, where the term MAC_i refers to the Modal Assurance Criterion (MAC) between the i^{th} experimental Φ_i^{exp} and numerical Φ_i^{FEM} mode shape.

With the main objective of selecting j^{th} damage-prone regions $\mathcal{R} = \{\mathcal{R}_1, \dots, \mathcal{R}_j, \dots, \mathcal{R}_N\}$ with $j = 1, \dots, N$, both EJ and NLSA are used. Then, each region is considered as an homogeneous portion of the structure in terms of material and, consequently, potential damage. Hence vector $\mathbf{X} = \{k_1, \dots, k_j, \dots, k_N\}$ is defined, collecting the multipliers of the Young moduli (k_j) of all the elements comprised in each region, with $0 \leq k_j \leq 1$.

4. Calibration of the surrogate model as a function of \mathbf{X} . For the present paper, the Kriging model is used, whose effectiveness in spatial interpolation was demonstrated in previous works by the Authors [11]. According to the Kriging model, the FE model-based data \mathbf{X} can be numerically interpolated by considering a regression model \mathcal{F} , i.e., the deterministic component, and an approximation error α , i.e., the stochastic component [15]:

$$y(\mathbf{X}) = \mathcal{F}(\beta, \mathbf{X}) + \alpha(\mathbf{X}) \quad (2)$$

where β are the regression parameters of \mathcal{F} . The approximation error α is assumed as a random process with zero mean and covariance $\text{cov}(X_i, X_j) = \sigma^2 \mathcal{R}(\boldsymbol{\theta}, X_i, X_j)$, with σ^2 variance of $\mathcal{F}(\beta, \mathbf{X})$ and \mathcal{R} the matrix of stochastic-process correlations with components $r(\boldsymbol{\theta}, X_i, X_j)$, where $\boldsymbol{\theta}$ are the correlation parameters.

5. Construction of the SDC, i.e., a graphical chart able to directly associate a stiffness reduction to each frequency/MAC decay for the selected damage-prone region.
6. if $t > 1$: novelty detection on a daily basis t , i.e. daily average values of MF. If a novelty is detected, i.e., a frequency or MAC anomaly, increase the frequency of the modal tests on a hourly basis $t = t^*$, i.e., $\text{MF}(t^*)$.
7. Bayesian model updating of the uncertain parameters by means of the surrogate model. Assuming that the identified model parameters k_j are statistically independent [13, 4], the surrogate model $\text{SM}(\mathbf{X})$ can be subdivided in j surrogate models with a low level of complexity, depending on k_j , i.e., $\text{SM}(k_j)$. Hence, the t - and k_j -dependent posterior probability density function (PDF) can be evaluated as follows:

$$p(k_j | \mathbf{d}, t) = c \cdot p(\mathbf{d} | k_j, t) \cdot p(k_j | \mu(t-1)) \quad (3)$$

where $c = 1 / \int p(\mathbf{d} | k_j, t) p(k_j | \mu(t-1)) dx$ is a normalizing factor called the evidence of the $\text{SM}(k_j)$; $p(\mathbf{d} | k_j, t)$ is the likelihood function that quantifies the agreement between the measured data \mathbf{d} and the surrogate-based data; $p(k_j | \mu(t-1))$ is the prior PDF of k_j function of the mean value of the posterior k_j evaluated at $t-1$.

More in depth, the likelihood function $p(\mathbf{d} | k_j, t)$ is modeled as a Gaussian distribution with zero mean [13, 4] as follows:

$$p(\mathbf{d} | k_j, t) = \frac{1}{\left[2\pi \prod_{i=1}^M (\sigma_{f_i} \sigma_{\Phi_i})^2 \right]^{(MD)/2}} \exp \left(-\frac{1}{2} \sum_{m=1}^D \sum_{i=1}^M J_i^{\text{err}}(k_j, d_k, t) \right) \quad (4)$$

where index $i = 1, \dots, M$ refers to the reference parameter associated to the i^{th} vibration mode; index $k = 1, \dots, D$ represents the number of measured data collected in the vector \mathbf{d} ; $J_i^{\text{err}} = (\sigma_{f_i})^{-2} e_{f_i}^2(\mathbf{X}, \mathbf{d}) + (\sigma_{\Phi_i})^{-2} e_{\Phi_i}^2(\mathbf{X}, \mathbf{d})$ is the measure of the fit function (error function) which quantifies the discrepancy between the experimental data and the FE model results with σ_{f_i} , σ_{Φ_i} standard deviations associated to the i^{th} natural frequency and vibration mode, $e_{f_i} = f_i^{\text{exp}} - \hat{f}_i(\mathbf{X})$ and $e_{\Phi_i} = 1 - MAC_i$.

Finally, it is noteworthy that, theoretically, the prior distribution acts as a regulator in the Bayesian-based model updating process and the more the number of data increases, the less new data influences the updating process. This aspect can be counter-productive, especially in the case of possible damage occurrence. Hence, the co-variance of the prior distribution is assumed as known, while the mean value μ is updated step by step, given the evidence of the knowledge acquired at the previous step.

8. Probabilistic damage identification which consists of calculating the probability P_j^{dam} that the updated j^{th} parameter k_j^{up} in a possibly damaged state is reduced from the undamaged state k_j^{ref} [4, 25]:

$$P_j^{\text{dam}} = P(k_j^{\text{up}} \leq (1 - \bar{k}_j)k_j^{\text{ref}} | \mathbf{d}^{\text{ref}}, \mathbf{d}^{\text{dam}}) = F\left(\frac{(1 - \bar{k}_j)k_j^{\text{ref}} - k_j^{\text{up}}}{\sqrt{(1 - \bar{k}_j)^2 \sigma_{k_j^{\text{ref}}}^2 + \sigma_{k_j^{\text{up}}}^2}}\right) \quad (5)$$

where $F(\cdot)$ is the standard Gaussian cumulative distribution function; $\bar{k}_j \in [0, 1]$ is the damage threshold selected for the j^{th} damage-prone region and quantifies the reduction of k_j^{ref} ; $k_j^{\text{ref}} = 1$ is the reference undamaged state. The possible outcomes of Eq. (5) are summarized in Table 1, where P_j^{al} is defined as probability alarm threshold.

No.	Outcome	P_j^{dam}	Meaning
1	$k_j^{\text{up}} = (1 - \bar{k}_j)k_j^{\text{ref}}$	$P_j^{\text{dam}} = 0.5 = P_j^{\text{al}}$	the damage threshold is reached
2	$k_j^{\text{up}} > (1 - \bar{k}_j)k_j^{\text{ref}}$	$P_j^{\text{dam}} < 0.5$	the damage threshold is not reached
3	$k_j^{\text{up}} < (1 - \bar{k}_j)k_j^{\text{ref}}$	$P_j^{\text{dam}} > 0.5$	the damage threshold is exceeded

Table 1: Possible outcomes of Eq. (5).

Additionally, in order to capture a possible damage occurrence, the damage factor DF is introduced and defined as follows:

$$DF = \frac{k_j^{\text{ref}} - k_j^{\text{up}}}{\bar{k}_j} \quad (6)$$

From Eq. (6) it is possible to obtain $DF=0$ if $k_j^{\text{up}} = k_j^{\text{ref}}$ and $DF=1$ if $k_j^{\text{ref}} - k_j^{\text{up}} = \bar{k}_j$. If $DF>1$, it means that k_j^{up} is strongly reduced with respect to the threshold \bar{k}_j , which is a sign of a possible high level of damage for region j or a possible false alarm due the lack of consistency with a damage in the j^{th} region. Hence, the case of $DF>1$ needs to be carefully checked in real world in order to avoid false alarms.

3 THE CASE STUDY: THE CONSOLI PALACE

The Consoli Palace is a medieval building with a rectangular plan and a height of 60 meters above the square level, located in Gubbio, Umbria, central Italy. With reference to Figure 2, three structural components can be identified: a central body; a loggia, connected to the main structure along the south wall; a bell tower. The architectural style of each façade (East and West side), is characterized by round arched windows and merlons in the rooftop. The load-bearing walls have a thickness of about 1.2 m and they are connected through horizontal masonry vaults. The Palace is built in calcareous stone masonry with a regular and homogeneous texture.

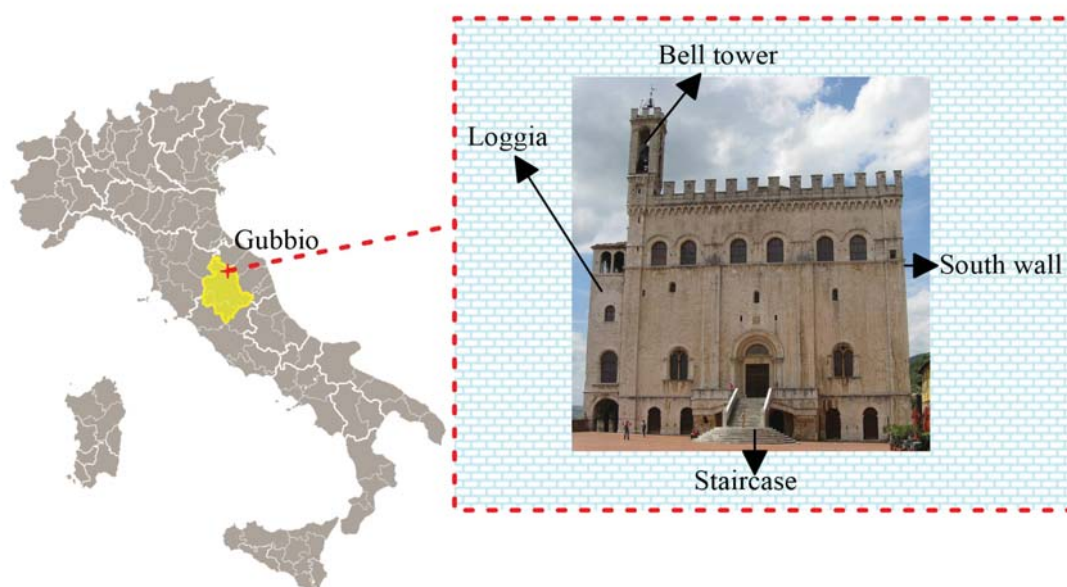


Figure 2: The Consoli Palace, located in Gubbio, Umbria, central Italy.

3.1 The SHM system

The monitoring system (Figure 3) was installed and activated by the Department of Civil and Environmental Engineering of University of Perugia in July 2020. Data are stored every 30 minutes with an acquisition sampling frequency of 40 Hz. The SHM system is characterized by:

1. No. 1 NI CompactDAQ-9132 data acquisition system to which sensors A1-A12, C1-C2 and T1-T2 are wired;
2. No. 1 wireless gateway to which sensors C3,C4,T3-T6 are connected;
3. No. 12 PCB393B12 unidirectional accelerometers A1-A12, differently oriented, installed at the 3rd (A7, A8 and A9), 5th (A4, A5 and A6), roof level (A1, A2, A3, A11 and A12) and wired to the acquisition system through NI 9234 acquisition module;
4. No. 4 S-series linear variable transducers (LVDTs), denoted as C1-C4. Sensors C1-C2 are wired to the acquisition system by means of a NI 9219 acquisition modules;
5. No. 6 temperature sensors T1-T6.

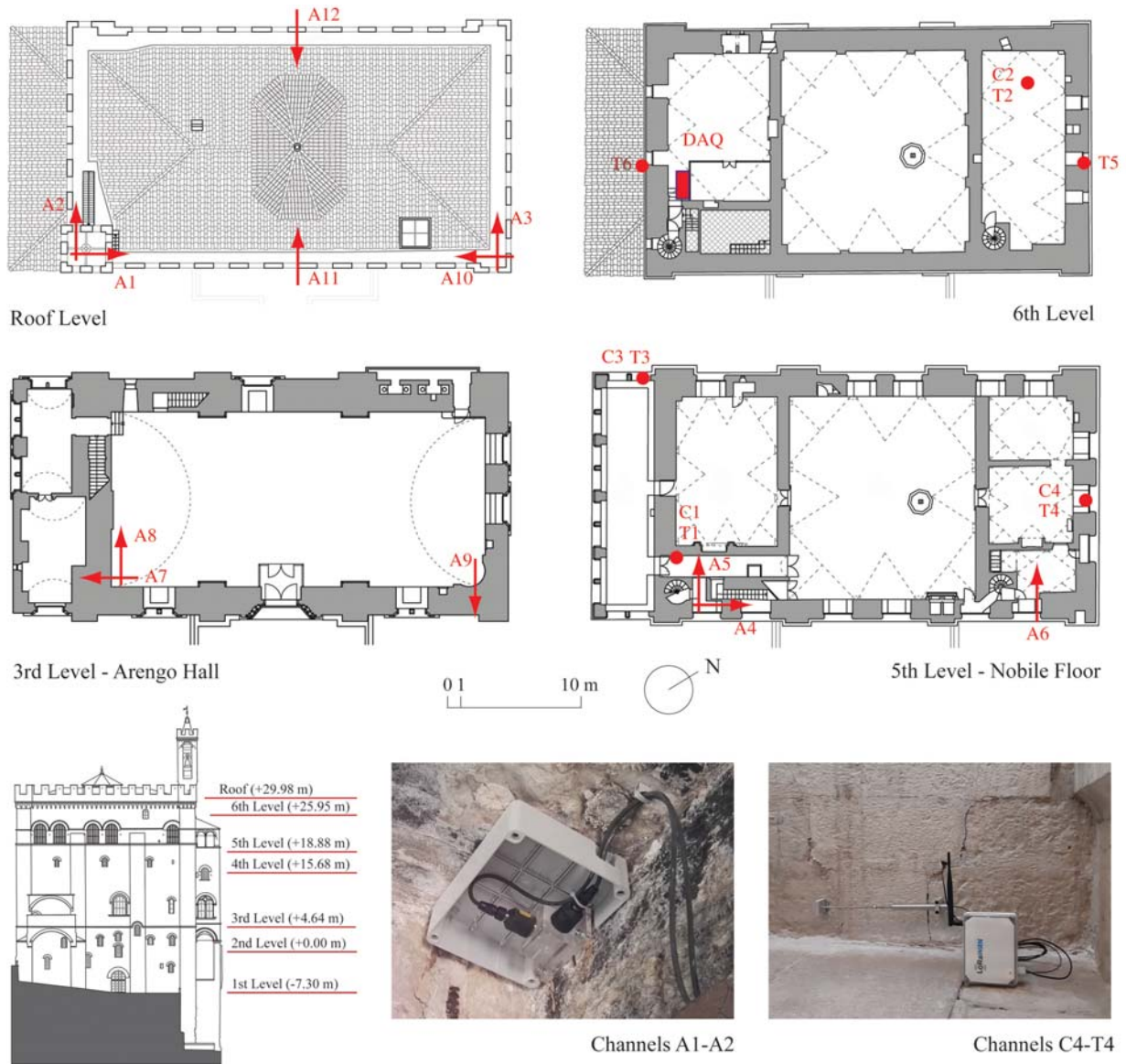


Figure 3: Continuous monitoring configuration.

For the numerical simulations, data stored between July 20th 2020 and December 21th 2020 are used. The training period is set between July 20th 2020 and November 15th 2020). Environmental effects are removed by using Multiple Linear Regression (MLR) by means of the least-angle regression (LAR) algorithm [8], which allows to efficiently select the predictors. It is worth noticing that a training period of 1 year would be more appropriate in order to effectively remove environmental effects.

3.2 FE model

According to Sect 2, step 3, a 3D FE model of the structure has been built and calibrated within the Abaqus environment [22] in order to reproduce local and global modes of vibration identified at $t = 1$. The masonry of the Palace is modeled by means of tetrahedral elements with isotropic materials. The well known concrete damage plasticity (CDP) model is assigned to reproduce the non-linear behavior and the assumed mechanical parameters are summarized as follows [16]:

- parameter which regulates the shape of the yield surface $K_c = 0.667$ (Lubliner criterion);
- eccentricity term $e = 0.1$;
- ratio between the ultimate compression strength in biaxial stress states and in uniaxial conditions $r = 1.16$;
- viscosity parameter $\nu = 0.002$.

Table 2 illustrates the principal vibration modes of the Consoli Palace: Fx1 is a global flexural mode along the x direction ; Fy1 is a global flexural mode along the y direction; L1 is a local mode which pertains to the bell tower; T1 is a global torsional mode. The x and y directions develop along the longer side and the shorter side of the Palace, respectively. The relatively low quality of model calibration, i.e., values of MAC lower than 0.8, has been already discussed in [14, 7].





Mode Fx1	Mode Fy1	Mode L1	Mode T1
			
$f_1 = 2.35 \text{ Hz}$ $MAC_1 = 0.98$	$f_2 = 3.05 \text{ Hz}$ $MAC_2 = 0.76$	$f_3 = 3.46 \text{ Hz}$ $MAC_3 = 0.64$	$f_4 = 4.17 \text{ Hz}$ $MAC_4 = 0.97$

Table 2: FE model-based frequencies and MAC of principal vibration modes.

3.3 FE model-based damage prone regions

Damage-prone regions are selected by means of NLSA and EJ. More in detail, each selected region allows to define a one-parameter dependent model. The different models (1-6) are described in Table 3.

Model No.	Region	Description	Uncertain Parameter	Source
1	R1	Loggia	k_1	EJ
2	R2	Crack pattern x	k_2	NLSA
3	R3	Crack pattern y	k_3	NLSA
4	R4	Bell tower	k_4	EJ
5	R5	Staircase	k_5	EJ
6	R6	main façade's degradation	k_6	EJ

Table 3: The different model selected by means of NLSA and EJ.

In particular: R1 represents the poor connection exerted between the loggia and the central body of the Consoli Palace (Figure 4a); R2 represents the crack pattern resulting from NLSA along x direction capable of reproducing the existing pattern, especially along the south wall

(Figure 4b); R3 refers to the crack pattern resulting from NLSA along the y direction (Figure 4c); R4 pertains to the bell tower (Figure 4d); R5 represents a possible damage to the principal staircase (Figure 4e); R6, which represents degradation of the exterior texture of the main façade of the building (Figure 4f) due to climate-induced material aging [7].

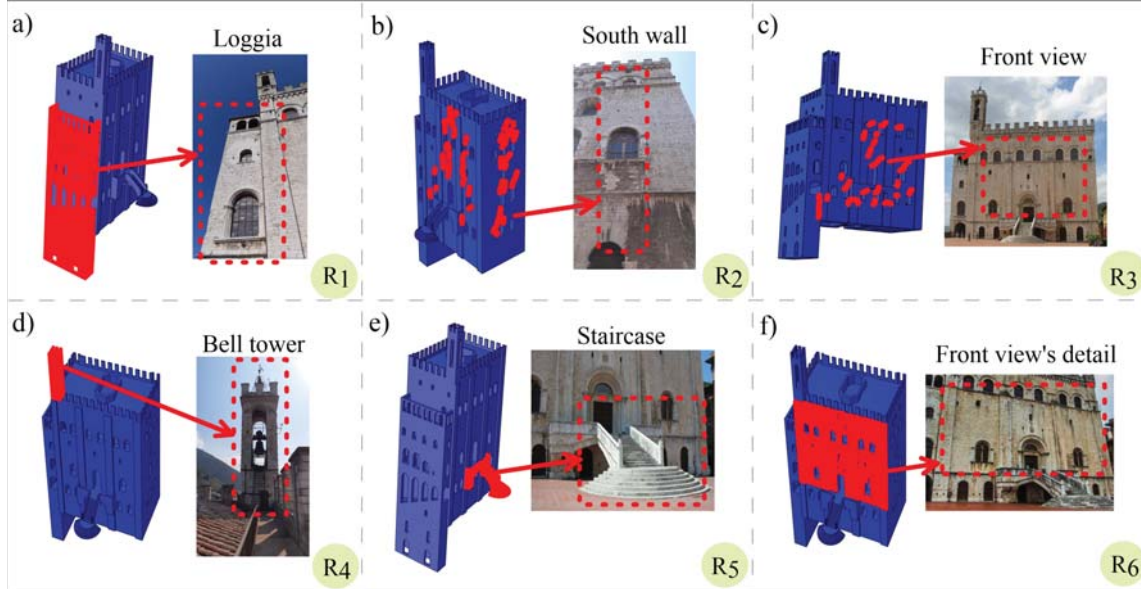


Figure 4: Selected damage sensitive areas with reference to both FE model and real structure: a) R1, the loggia; b) R2, crack pattern y ; c) R3, crack pattern x ; d) R4, the bell tower; e) R5, the staircase; f) R6, the façade degradation.

As reported in Table 3, in such areas, the multipliers of the Young's moduli (k_1, \dots, k_6) assigned to the isotropic material of each region are assumed as uncertain.

In order to calibrate the surrogate model, a total number of 500 samples (N_s) are randomly simulated for the uncertain parameters collected in vector \mathbf{X} . The correspondence between both frequencies and mode shapes is quantified by calculating the coefficient of determination R^2 and the function $J_{MAC} = 1/N_s \sum_i (1 - MAC_i)$ by comparing the FE and the Kriging models, respectively. Values of R^2 and J_{MAC} are summarized in Table 4. From the Table it can be noted

Parameter	Vibration modes			
	Fx1	Fy1	L1	T1
R^2	0.9833	0.997	0.999	0.9968
J_{MAC}	0.0142	0.0015	0.0156	5.85E-5

Table 4: Values of R^2 and (J_{MAC} associated with the calibrated surrogate model.

that the surrogate-predicted frequencies and mode shapes (Kriging estimate) well fit the corresponding FE values.

4 NUMERICAL RESULTS

The SM-based sensitivity damage chart SDC, which relates frequency and MAC values with the uncertain parameters for each Model, is depicted in Figure 5. On the one hand, due to the observed frequency decay, Fx1 (flexural mode along the x direction) appears as the most

damage-sensitive vibration mode for damage-prone regions R2 and R5, Fy1 (flexural mode along the y direction) for R1, R3, R4 and R6, L1 (local mode which pertains to the bell tower) for R4 and R6, and T1 (torsional mode) for R1 and R2. On the other hand, it can be observed that MAC variations can be considered negligible for all damage-prone regions except for R1 and R4. Indeed, a reduction of k_1 provokes a modification in the local L1 mode shapes and a reduction of k_4 induces a huge reduction of Fy1 and L1 MAC values.

Finally, a damage scenarios (Table 5), designated as DII, is selected for the numerical analyses

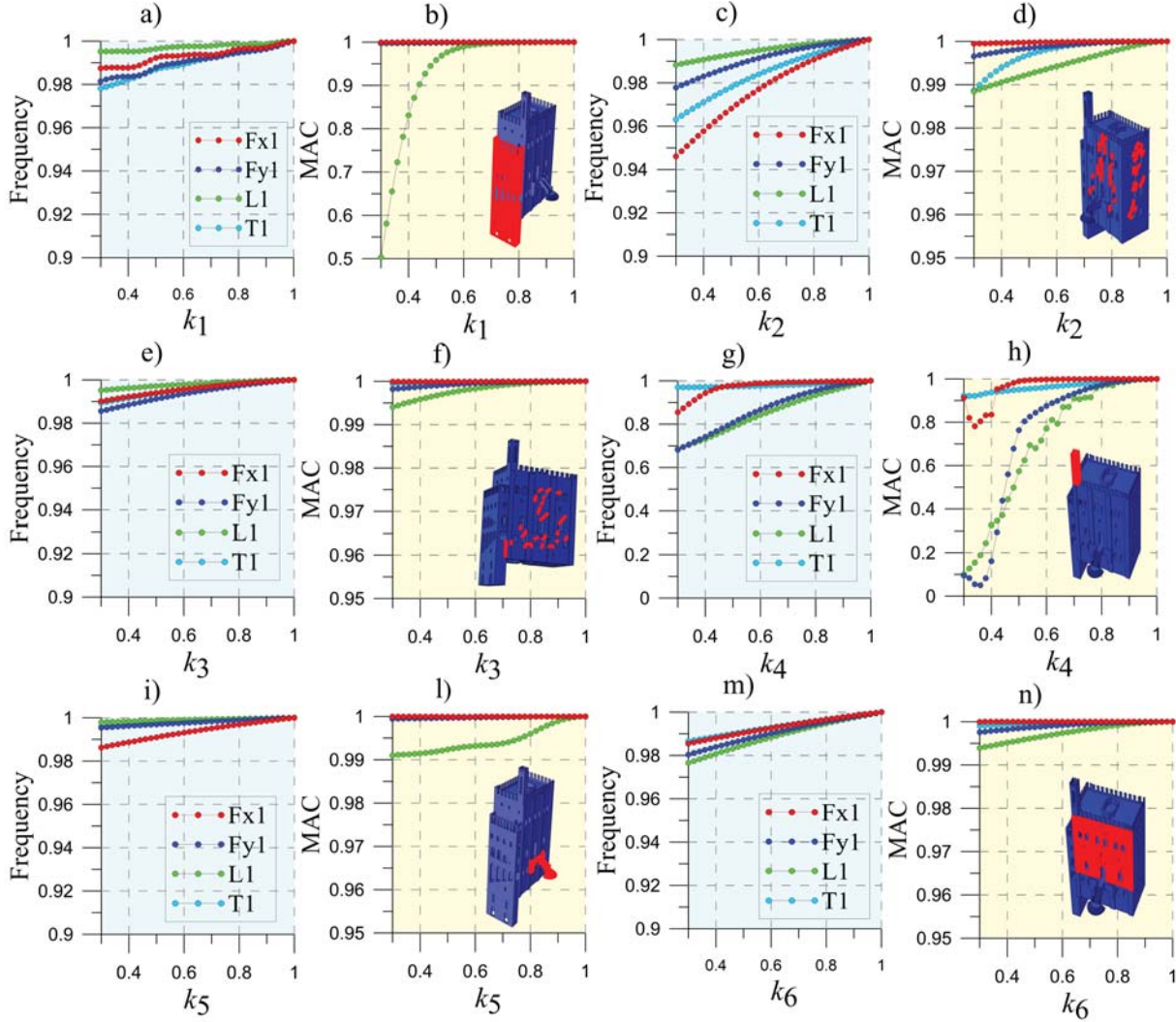


Figure 5: SDC for frequency and MAC decays: a)-b) R1; c)-d) R2; e)-f) R3; g)-h) R4; i)-l) R5; m)-n) R6.

by artificially simulating the frequencies decays (reported in Table 5) extracted from the SDC of region R2 in correspondence with the value of $k_2 = 0.3$, while MAC decays are negligible.

Following, the main results of the Bayesian model updating are summarized by simulating damage scenario DII. The uncertain parameter k_2 is updated once the model is trained, i.e., starting from November 15th 2020. From that moment on, the monitored data are gathered together in subgroups of daily data-sets (t) in order to perform the Bayesian model updating continuously over time on a daily basis. The first 20 days are considered as undamaged. Then, a damage scenario is simulated and the frequency of the model updating is incremented on an hourly basis (t^*), as described in Sect. 2.

Damage scenario	Uncertain parameter						Frequency decays			
	k_1	k_2	k_3	k_4	k_5	k_6	Fx1	Fy1	L1	T1
DII	1	0.3	1	1	1	1	0.054	0.022	0.012	0.037

Table 5: Values of k_j representing the different damage scenarios and corresponding frequency and MAC decays (%).

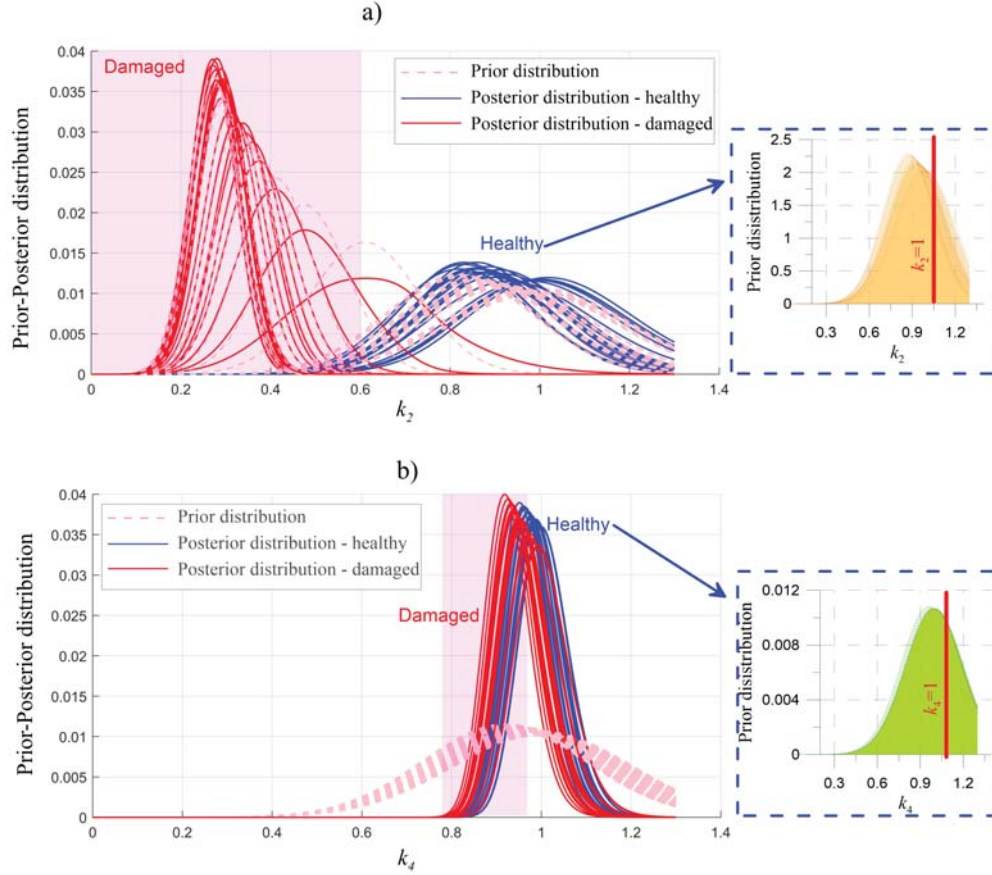


Figure 6: Bayesian-based prior and posterior distributions by simulating damage scenario DII for $k_2 = 0.3$: a) R2; b) R4.

Results in terms of prior and posterior distributions for k_2 and k_4 , when DII is simulated, are depicted in Figures 6a)-b). From the results it can be observed that the posterior distributions associated to the uncertain parameters k_2 and k_4 in the undamaged time period present a fluctuation of the mean value of k_j between about 0.9 and 1. This aspect can be related to the fact that k_j is sensitive to the slight variations which can daily occur in the frequency and, eventually, MAC tracking as confirm by the SDC. This sensitivity to changing environmental conditions can be considerably reduced by considering an appropriate training period, i.e., 1 year. Moreover, consistently with the SDC, the occurrence of a damage for region R2 is clearly highlighted by a translation of the posterior curves towards reduced values of the selected uncertain parameter k_2 (Figure 6a). In detail, it can be observed that the Bayesian-based procedure is able to tracing back to the simulated damage scenario associated to R2, i.e., $k_2^{\text{up}} \approx 0.3$. However, as expected, the simulation of DII barely affects k_4 (bell tower) in the damaged state (Figure 6b), since the mean value of the posterior distribution doesn't significantly change between healthy and damaged conditions.

As concerns the probabilistic damage identification, Figures 7a)-f) illustrate the updated values

of the uncertain parameters k_j^{up} over the number of updates, while Figures 7g)-n) show the trend of DF vs P^{dam} , when simulating the occurrence of damage scenario DII. According to the SDC, the simulated frequency decays are reported in Table 5. The values of \bar{k}_j selected for the eval-

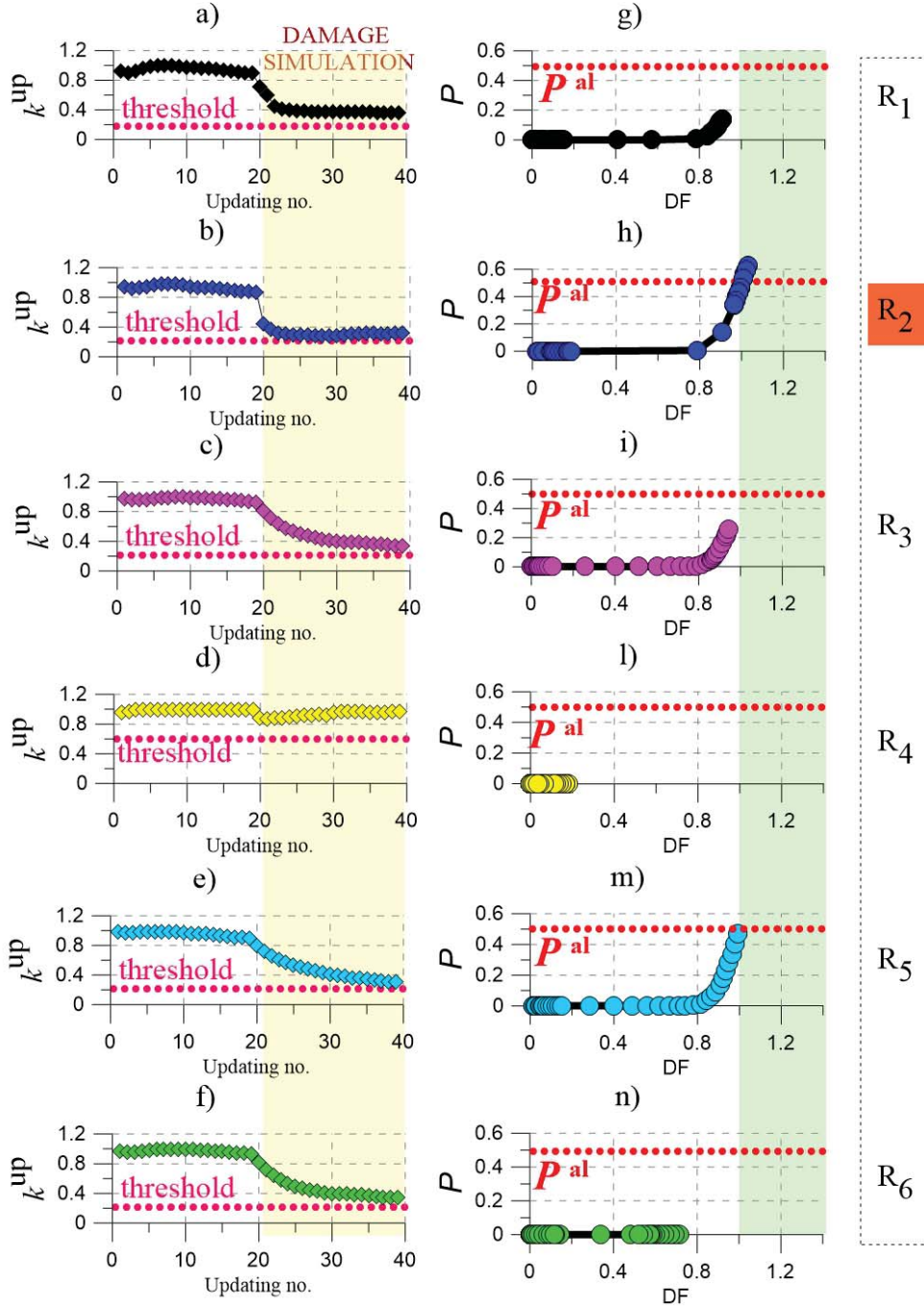


Figure 7: Time series of k_j^{up} over the number of updates by simulating the occurrence of the damage scenario DII (Table 5 for each damage-prone region, with the indication of P^{al} and \bar{k}_j : a) R1; b) R2; c) R3; d) R4; e) R5; f) R6.

uation of DF and P^{dam} are the following: a) R1: $\bar{k}_1 = 0.7$; b) R2: $\bar{k}_2 = 0.7$; c) R3: $\bar{k}_3 = 0.7$; d) R4: $\bar{k}_4 = 0.4$; e) R5: $\bar{k}_5 = 0.7$; f) R6: $\bar{k}_6 = 0.7$. Region R4 pertains to the bell tower and a reduction of the bell tower's stiffness corresponding to 40 % ($k_4 = 0.6$) is assumed sufficient to simulate a damage occurrence. From the Figures it can be noted that P^{al} is reached for region

R2, as expected, and for region R5. This result is consistent with the SDC-based results, since both regions R2-R5 can be designated to damage when a frequency decay of mode Fx1 occurs. The case of R5 deserves a particular attention and needs to be checked in the real-world structure with the main objective to avoid a false alarm. Indeed, after a certain number of updates (see the multiple points in the damaged area), P^{dam} tends to 1, DF approaches 1 and k_5^{up} faces up to $1 - \bar{k}_5$. This fact is due to the higher sensitivity of k_5 to small variations associated to Fx1. On the contrary, the remaining regions exhibit a smaller probability of being damaged, which is consistent with the simulated scenario.

5 CONCLUSIONS

The present paper has presented the numerical results of a transfer learning Bayesian methodology in the context of integrated SHM aimed at the probabilistic damage assessment of monumental structures.

The case study building is the Consoli Palace, located in Gubbio, Umbria (Italy), which has been monitored by the Authors since 2015 with an enhancement of the SHM sensors' network in 2020. The dynamic behavior of the Palace is reproduced on a calibrated FE model and NLSA in conjunction with EJ enabled to pick damage-sensitive regions within the structure. Then, each selected region allows to define a one-parameter dependent model, i.e., the multiplier of the Young's Modulus assigned to the isotropic material associated with each region. The surrogate modeling has been performed by using the Kriging model in order to define the region-dependent SDC as a prior knowledge of possible damage. Finally, a real time Bayesian model updating of the selected uncertain parameters has been developed in order to continuously identify the probability of damage occurrence over the selected regions. The main advantages and innovations of the proposed approach concern:

- the use of real-time long-term monitoring data within the context of Bayesian TL where the surrogate modeling allows real-time data;
- the use of damage factors and damage probabilities enabling informed model-based decisions and providing a basis to mitigate the risk of a false alarm.
- the use of NLSA to generate estimates of potentially vulnerable structural regions alongside with EJ.
- the possibility to continuously identify the probability of damage occurrence over time in a timely manner.

Acknowledgments

The Authors would like to acknowledge the support of the PRIN 2017 project, "DETECT-AGING" (Prot. 201747y73L), funded by the Italian ministry of university and research.

REFERENCES

- [1] S-K. Au. Uncertainty law in ambient modal identification-part ii: Implication and field verification. *Mechanical Systems and Signal Processing*, 48(1-2):34–48, 2014.

- [2] G. Bartoli, M. Betti, A.M. Marra, and S. Monchetti. A bayesian model updating framework for robust seismic fragility analysis of non-isolated historic masonry towers. *Philosophical Transactions of the Royal Society A: Mathematical, Physical and Engineering Sciences*, 377(2155), 2019.
- [3] I. Behmanesh and B. Moaveni. Accounting for environmental variability, modeling errors, and parameter estimation uncertainties in structural identification. *Journal of Sound and Vibration*, 374:92–110, 2016.
- [4] I. Behmanesh, B. Moaveni, G. Lombaert, and C. Papadimitriou. Hierarchical bayesian model updating for structural identification. *Mechanical Systems and Signal Processing*, 64–65:360–376, 2015.
- [5] L.A. Bull, T.J. Rogers, C. Wickramarachchi, E.J. Cross, K. Worden, and N. Dervilis. Probabilistic active learning: An online framework for structural health monitoring. *Mechanical Systems and Signal Processing*, 134:106294, 2019.
- [6] L.A. Bull, K. Worden, and N. Dervilis. Towards semi-supervised and probabilistic classification in structural health monitoring. *Mechanical Systems and Signal Processing*, 140:106653, 2020.
- [7] N. Cavalagli, A. Kita, V.L. Castaldo, A.L. Pisello, and F. Ubertini. Hierarchical environmental risk mapping of material degradation in historic masonry buildings: An integrated approach considering climate change and structural damage. *Construction and Building Materials*, 215:998–1014, 2019.
- [8] Bradley Efron, Trevor Hastie, Iain Johnstone, and Robert Tibshirani. Least angle regression. *Annals of statistics*, 32(2):407–499, 2004.
- [9] C.R. Farrar and K. Worden. *Structural Health Monitoring: A Machine Learning Perspective*. 2012. John Wiley & Sons, Ltd.
- [10] E. García-Macías, L. Ierimonti, I. Venanzi, and F. Ubertini. Comparison of surrogate models for handling uncertainties in shm of historic buildings. *Lecture Notes in Mechanical Engineering*, pages 1645–1657, 2020.
- [11] E. García-Macías, L. Ierimonti, I. Venanzi, and F. Ubertini. An innovative methodology for online surrogate-based model updating of historic buildings using monitoring data. *International Journal of Architectural Heritage*, 15(1):92–112, 2021.
- [12] L. Ierimonti, I. Venanzi, N. Cavalagli, F. Comodini, and F. Ubertini. An innovative continuous bayesian model updating method for base-isolated RC buildings using vibration monitoring data. *Mechanical Systems and Signal Processing*, 139:106600, 2020.
- [13] J. Jang and A. Smyth. Bayesian model updating of a full-scale finite element model with sensitivity-based clustering. *Structural Control and Health Monitoring*, 24(11):e2004, 2017.
- [14] A. Kita, N. Cavalagli, and F. Ubertini. Temperature effects on static and dynamic behavior of consoli palace in gubbio, italy. *Mechanical Systems and Signal Processing*, 120:180–202, 2019.

- [15] S.N. Lophaven, H.B. Nielsen, and J. Søndergaard. A matlab kriging toolbox, version 2.0. Technical Report IMM-TR-2002-12, Kongens Lyngby, Copenhagen, Denmark: Informatics and Mathematical Modelling, Technical University of Denmark, DTU., 2002.
- [16] G. Milani, M. Valente, and C. Alessandri. The narthex of the church of the nativity in bethlehem: A non-linear finite element approach to predict the structural damage. *Computers and Structures*, 207:3–18, 2018.
- [17] A.C. Neves, I. González, J. Leander, and R. Karoumi. A new approach to damage detection in bridges using machine learning. *Lecture Notes in Civil Engineering*, 5:73–84, 2018.
- [18] A.C. Neves, I. Gonzalez, J. Leander, and R. Karoumi. Structural health monitoring of bridges: a model-free ann-based approach to damage detection. *Journal of Civil Structural Health Monitoring*, 7(5):689–702, 2017.
- [19] T.J. Rogers, K. Worden, R. Fuentes, N. Dervilis, U.T. Tygesen, and E.J. Cross. A bayesian non-parametric clustering approach for semi-supervised structural health monitoring. *Mechanical Systems and Signal Processing*, 119:100–119, 2019.
- [20] L. Rosafalco, A. Manzoni, S. Mariani, and A. Corigliano. Fully convolutional networks for structural health monitoring through multivariate time series classification. *Advanced Modeling and Simulation in Engineering Sciences*, 7(1):38, 2020.
- [21] F. Schwenker and E. Trentin. Pattern classification and clustering: A review of partially supervised learning approaches. *Pattern Recognition Letters*, 37(1):4–14, 2014.
- [22] Simulia. *Abaqus Analysis User’s Manual. Volume III: Materials*. Dessault Systèmes, USA, 2010.
- [23] H. Sun, A. Mordret, G.A. Prieto, M.N. Toksz, and O. Bykztrk. Bayesian characterization of buildings using seismic interferometry on ambient vibrations. *Mechanical Systems and Signal Processing*, 85:468–486, 2017.
- [24] L. Sun, Z. Shang, Y. Xia, S. Bhowmick, and S. Nagarajaiah. Review of bridge structural health monitoring aided by big data and artificial intelligence: From condition assessment to damage detection. *Journal of Structural Engineering (United States)*, 146(5):04020073, 2020.
- [25] M.-W. Vanik, J.-L. Beck, and S.-K. Au. Bayesian probabilistic approach to structural health monitoring. *Journal of Engineering Mechanics*, 126(7):738–745, 2000.
- [26] I. Venanzi, A. Kita, N. Cavalagli, L. Ierimonti, and F. Ubertini. Earthquake-induced damage localization in an historic masonry tower through long-term dynamic monitoring and fe model calibration. *Bulletin of Earthquake Engineering*, 18(5):2247–2274, 2020.
- [27] W.-J. Yan and L.S. Katafygiotis. An analytical investigation into the propagation properties of uncertainty in a two-stage fast bayesian spectral density approach for ambient modal analysis. *Mechanical Systems and Signal Processing*, 118:503–533, 2019.
- [28] K.-V. Yuen and L.S. Katafygiotis. Bayesian time-domain approach for modal updating using ambient data. *Probabilistic Engineering Mechanics*, 16(3):219–231, 2001.

A NEURAL NETWORK-BASED APPROACH FOR SEISMIC-INDUCED DAMAGE ASSESSMENT OF STEEL LIQUID STORAGE TANKS

Laura Micheli¹ and Mahmoud Faytarouni²

¹ Dept. of Civil and Environmental Engineering, Catholic University of America
Washington, DC, USA
e-mail: michelil@cua.edu

² Genex Systems, Turner Fairbank Highway Research Center
McLean, VA, USA

Abstract

Surrogate models, including neural network (NN), machine learning, and Kriging, are used in various fields to reduce the computational demand of risk assessment and uncertainty analysis. In civil engineering applications, surrogate models are usually trained on synthetic data generated with numerical simulation models, which might yield approximate responses and significant computational burdens. Post-disaster reconnaissance observations represent an alternative source of data that could be used to train a surrogate model without the need for numerical models. However, the limited number of reconnaissance observations available in the literature might yield challenges, such as unbalanced data distributions. This paper presents a surrogate-based approach for seismic-induced damage prediction, where post-earthquake reconnaissance data are exploited to train a NN model. The approach is demonstrated on steel liquid storage tanks. Field data from past earthquake reconnaissance reports are first collected. Then, features representative of tank characteristics, seismic hazard parameters, and seismic-induced damage are extracted. A traditional two-layers NN model is built to map the relationship between tank characteristics, seismic hazard parameters, and seismic-induced damage. To tackle the challenge of unbalanced dataset, a cascade NN approach is proposed. In the cascade approach, two NN models are employed to predict the damage level of the steel tanks. The first NN returns a binary classification of the tank damage (i.e., damage, no damage). If the tank results damaged, a second NN identifies the level of damage (i.e., minor, severe, collapse). The performance of traditional and cascade NN approaches is compared using different metrics. Results demonstrate that the cascade NN strategy leads to more accurate damage predictions than the traditional NN approach.

Keywords: neural network, reconnaissance data, damage classification, steel tanks, surrogate model, seismic risk-assessment

1 INTRODUCTION

Performance-Based Design (PBD) is gaining prominence in the civil engineering community [1]. PBD allows to holistically evaluate a structure for potential risks and engage building owners in cost-effective risk-mitigation strategies [2-4]. It follows that risk assessment is a key component of PBD, as it enables the estimation of the probability of occurrence of a certain damage state, considering a variety of hazard scenarios [1,5]. Typically, the performance of civil structures is assessed through nonlinear numerical models (e.g., finite element models), which permit the evaluation of the structure's response beyond the elastic regime [2,6,7]. However, the computational demand of high-fidelity numerical simulation models, coupled with the necessity to simulate the structure under a large number of hazard and uncertainty scenarios, makes risk assessment a computationally demanding, if not impractical task.

Data-driven surrogate models [8-10], including neural network (NN), Kriging, and machine learning, have been proposed to reduce the computational burden of risk assessment [11,12]. Surrogate models, or metamodels, are simplified mathematical relationships trained based on input/output observations to represent the physical system under consideration. In civil engineering applications, metamodels have been used to replace computationally expensive numerical models for uncertainty and risk analyses. For example, Sudret and Mai [13] employed polynomial chaos expansion to generate fragility curves of a 3-story structure subjected to seismic hazard. Later, Gidaris *et al.* [14] developed a Kriging surrogate model for seismic risk assessment of civil structures. The authors exploited the metamodel to construct fragility functions of a 4-story building under stochastic ground motions and uncertain structural parameters. Recently, Micheli *et al.* [15] proposed a multiple-surrogate models framework for risk assessment of wind-excited tall buildings. The proposed framework exploits a set of Kriging surrogates to reduce the computational demand of risk assessment of high-rise structures subjected to wind load time histories. A drawback of using surrogate models for civil structures is the necessity to generate input/output observations to train the metamodel. Synthetic input/output observations are usually derived from numerical simulation models, which might lead to approximate responses. Furthermore, when the response of the structure is highly nonlinear, a large data pool might be required to train a reliable surrogate model [15-17], yielding a significant computational burden. A solution to this drawback could be to extract input/output observations directly from field data [18]. In this context, post-disaster field reconnaissance reports could be a valuable source of information, enabling a realistic representation of damage mechanisms and hazard characteristics. However, the use of post-disaster reconnaissance observations presents some challenges. For example, the limited number of records available could yield unbalanced datasets, eventually reducing the accuracy of the surrogate model.

This paper investigates a surrogate-based approach for damage assessment of civil structures, where the metamodel is trained based on reconnaissance observations. The approach is demonstrated on aboveground, cylindrical, steel liquid storage tanks subjected to seismic hazard. The seismic risk of storage tanks is significantly higher than ordinary structures, as damage to liquid storage tanks could cause irreparable consequences to built and natural environments, including the release of hazardous materials, uncontrolled fires, and soil contaminations [19-21]. In the proposed approach, features representative of tank characteristics (e.g., diameter, height, thickness, liquid level) and seismic excitation parameters (e.g., peak ground acceleration, magnitude) are extracted directly from reconnaissance reports, along with the corresponding damage levels. Then, a surrogate model consisting of a two-layers NN is built to map the relationship between inputs (i.e., tank and hazard features) and output (i.e., damage level). To tackle the unbalanced dataset challenge, a cascade approach is proposed,

where two NN models are employed to estimate the damage level of steel tanks. The first NN exploits a binary classification to guess if the tank is damaged or not. If the tank results damaged, a second NN identifies the damage level between minor damage, severe damage, and collapse. The accuracy of the NNs is assessed on a testing dataset using different performance metrics, such as accuracy, precision, and recall. The performance at predicting seismic-induced damage of the traditional two-layers NN and the cascade NN models is compared.

The remainder of the paper is organized as follows. First, the collected post-earthquake reconnaissance data are described. Then, traditional and cascade NN approaches are introduced. After, the metrics employed to quantify the performance of the NNs are discussed. Finally, the damage prediction capability of traditional and cascade NNs is compared.

2 METHODOLOGY

2.1 Dataset Description and Features Extraction

In this study, post-earthquake reconnaissance observations are employed as data pool for training a NN model. Such observations were derived from existing post-earthquake reconnaissance report [22] and survey [23]. Both anchored and unanchored cylindrical steel tanks were taken in consideration. Features representative of tank and seismic hazard properties were extracted and used as inputs of the NN models described in Section 2.2. Tank features include geometric characteristics, such as diameter (D), height (H), shell thickness (t), and height of the liquid at the moment of the earthquake (H_L). Peak ground acceleration (PGA) and magnitude (M) were selected as seismic hazard features. For some of the tanks, the thickness was not documented in the post-earthquake report in reference [22]. The thickness of these tanks was estimated based on the work of Cortes and Prinz [24]. Similarly, for some earthquake events, the PGA was not reported, and it was estimated based on the location of the tank and the corresponding ground motion records [25]. The material properties of the steel tanks were not enclosed in the reports. Therefore, yielding stress and modulus of elasticity of steel were assumed to be the same for all tanks and were not included between the input variables. A total of $n = 247$ aboveground, cylindrical, steel liquid storage tanks observations were collected. Table 1 reports the statistics of the dataset, while Figure 1 (a) shows a schematic representation of a storage tank, including the features selected to represent tank and seismic hazard characteristics.

	Min.	Max.	Mean	Standard dev.
Diameter, D (m)	2.0	83	22	14.3
Height, H (m)	3.0	45	11	4.0
Thickness, t (m)	0.001	0.098	0.01	0.01
Liquid height, H_L (m)	0.0	44	10	8.4
Magnitude, M	5.5	8.4	7.0	0.64
Peak ground acc., PGA (g)	0.02	2.0	0.41	0.40

Table 1: Statistics of the dataset.

A description of the damage reported by each tank was also retrieved from the reconnaissance reports [20, 21], along with the corresponding values of tank and seismic features. The

steel tanks experienced various types of seismic-induced damage, including elephant foot buckling, roof damage, shell buckling, and complete collapse [20, 21]. The damage types were assembled in four main classes: class 0, no damage; class 1, minor damage; class 2, severe damage; and class 3, collapse. Minor damage includes damage to the seal, minor roof damage, damaged valves, and, in general, damage that requires simple repairs. Severe damage comprises elephant foot buckling, shell buckling, local buckling caused by roof collapse, and floor plate rupture. Collapse is intended as the tank's total failure, or widely spread damage that necessitates the replacement of the tank. Note that, if more reconnaissance observations become available, additional damage mechanisms could be included and the damage classes may be further refined. Figure 1 (b) shows the distribution of the steel tank observations among the four damage classes, where n_0 represents the number of data in class 0, n_1 in class 1, n_2 in class 2, and n_3 in class 3, respectively. Figure 1 demonstrates that the dataset is severely skewed toward one class only, with the majority of data lying in class 0, and a smaller number of observations belonging to class 3. Such an unbalanced dataset could cause poor performance of traditional NN models, as the majority of the NN algorithms available in the literature were developed considering a balanced data distribution [26].

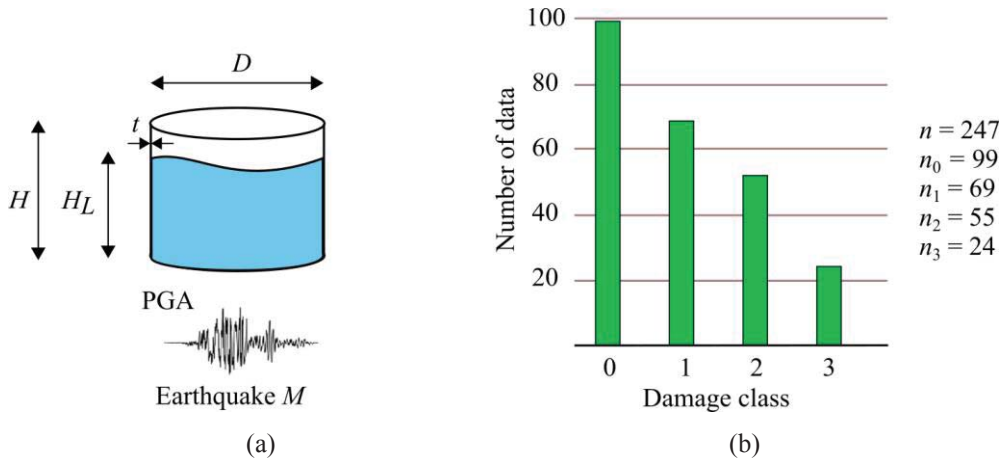


Figure 1: (a) Schematic representation of an aboveground, cylindrical, steel liquid storage tank and input variables; (b) distribution of the data among the four damage classes.

2.2 Neural Network for Damage Prediction

A traditional two-layers NN is first used to map the relationship between tank and seismic hazard characteristics (i.e., inputs) and the corresponding damage class (i.e., output). The NN is composed of a hidden and an output layer, with sigmoid and softmax activation functions, respectively. Figure 2 illustrates a representation of the NN architecture. In the figure, k_1 and k_2 indicate the number of neurons in the hidden and output layers, respectively. The NN has six inputs, corresponding to tank and seismic hazard features, and one output, representing the damage class. The output of the NN can be expressed as [27]:

$$y = g(f(\mathbf{w}_1 \mathbf{x} + \mathbf{b}_1)) \mathbf{w}_2 + \mathbf{b}_2$$

where \mathbf{x} is the input vector, \mathbf{w}_1 and \mathbf{w}_2 are the hidden and the output layers' weights, \mathbf{b}_1 and \mathbf{b}_2 are the hidden and the output layers' biases, f and g are the sigmoid and softmax activation

functions, respectively. The weights and biases are tuned based on the training dataset using a gradient backpropagation algorithm [27].

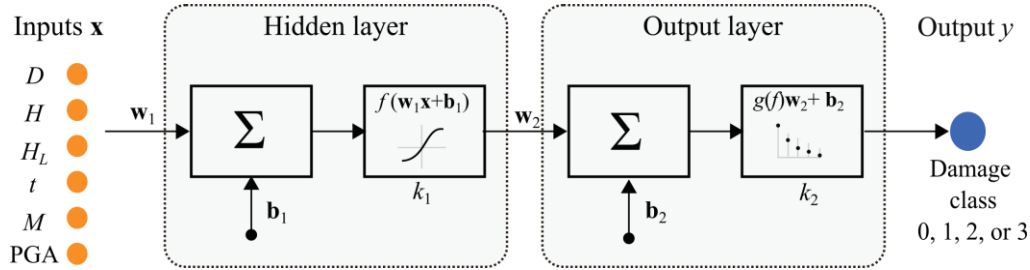


Figure 2: Neural Network configuration.

To tackle the unbalanced dataset issue (Figure 1 (b)), a cascade NN approach is proposed as an alternative for seismic-induced damage prediction. Instead of a single NN, the cascade approach employs two consecutive NN algorithms to estimate the damage class experienced by a steel tank as a function of the input variables. The first NN is trained based on a binary classification of the data among class 0 (no damage) and class 1 (damage). Note that in the binary classification, all the damaged tanks are lumped in class 1, independently of the type of damage they experienced. A second NN classifies the type of damage among classes 1, 2, and 3, eliminating the data in class 0, and thus, the source of unbalance. Both NN models have the same inputs (tank and seismic hazard features), but different outputs and number of training data. The proposed approach is schematically represented in Figure 3 (a).

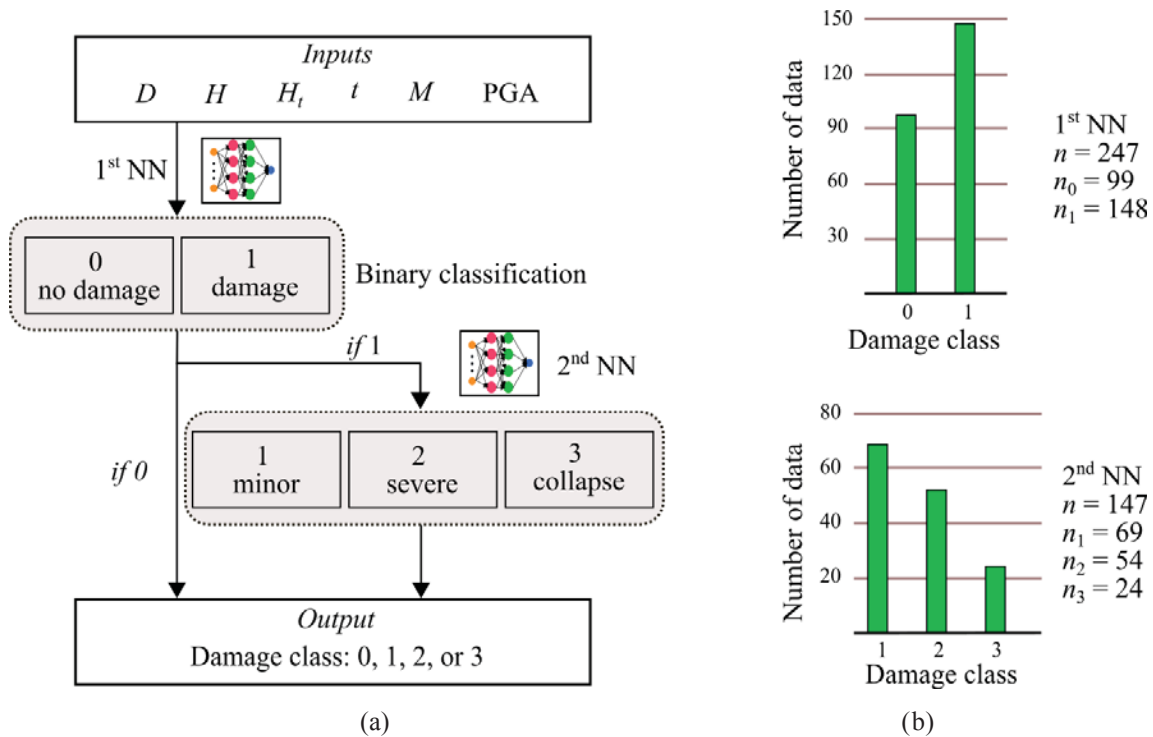


Figure 3: (a) Cascade neural network representation; (b) data distribution among damage classes for the 1st and the 2nd NN models in the cascade approach.

It is worth noting that the cascade approach uses the dataset described in Section 2.1, where data were first rearranged in the binary classification damage/no damage. Then, for training the second NN, data belonging to class 0 were eliminated, leaving only observations lying in classes 1, 2, and 3. The distribution of the data among different damage classes is reported in Figure 3 (b) for the two NN models. Furthermore, the architecture of the two NNs of the cascade approach is the same as the one shown in Figure 2.

2.3 Performance Metrics

The effectiveness of both traditional NN and cascade NNs approaches at predicting the damage experienced by steel liquid storage tanks subjected to seismic hazard is assessed on a testing subset. Specifically, the tank dataset composed of n observations is divided into three subsets: training, validation, and testing. The training data (size $n_{tr} = 70\% n$) is used to train the NN models. The validation subset (size $n_{val} = 15\% n$) is employed to validate the models, while the testing subset (size $n_{ts} = 15\% n$) is exploited to test the prediction capability of the NNs. The performance of the NNs at predicting the damage class in correspondence with the testing data is taken as an indication of the model's performance on unseen data.

		n	n_{tr}	n_{val}	n_{ts}
Traditional	NN	247	173	37	37
	1 st NN	247	173	37	37
Cascade	2 nd NN	147	103	22	22

Table 2: Dataset sizes for the traditional NN and cascade NN models.

The performance of the NNs is evaluated using different metrics, including precision, recall, and accuracy. The precision can be defined as the percentage of damage cases correctly assigned by the NN. The recall represents the percentage of the true damage classes correctly predicted by the algorithm, also referred to as true positives. The accuracy is defined as the ratio between the number of correct predictions and the total number of observations. Precision and recall can be computed for each class, while accuracy is a global performance metric.

3 RESULTS AND DISCUSSION

3.1 Neural Network

The two-layer NN model described in Figure 2 was trained to predict the damage class experienced by the tanks between 0 (no damage), 1 (minor damage), 2 (severe damage), and 3 (collapse) with the dataset described in Section 2.1 and reported in Figure 1(b). MATLAB Toolbox [28] was used to build, train, and test all the NN models developed in this study. The number of neurons k_1 and k_2 were selected iteratively to maximize the accuracy on the validation subset and set as $k_1 = 40$ and $k_2 = 3$. The values of weights and biases obtained from the training process can be found in reference [29]. Note that the trained NN model can be employed to predict the damage level of steel tanks with characteristics lying in the ranges reported in Table 1 only.

Precision, recall, and accuracy for training, validation, and testing datasets are reported in the confusion matrices in Figure 4. Each element of the confusion matrix C_{ij} indicates the

number of data known to be in class i and predicted in class j . The diagonal elements in green are the damage classes correctly guessed by the NN model, while the off-diagonal elements in red are the categories predicted incorrectly. The confusion matrices also contain precision and recall for each class, along with overall accuracy of the model.

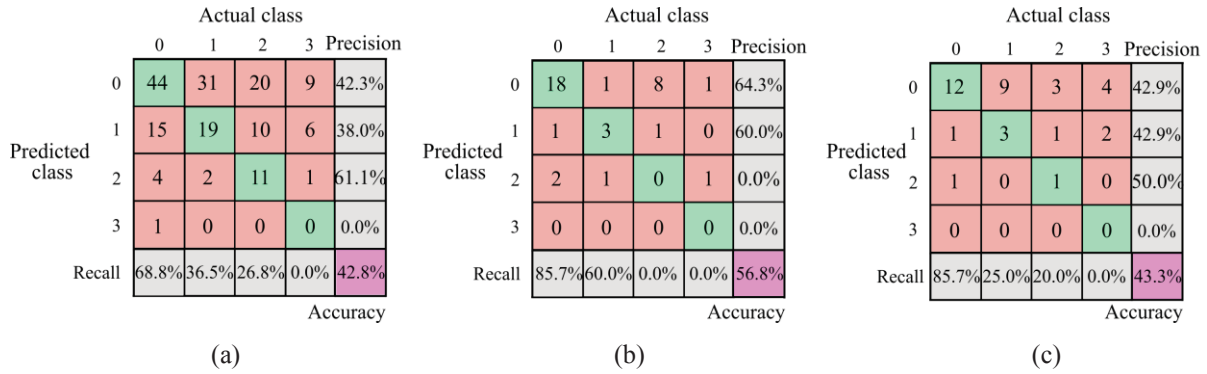


Figure 4: Confusion matrix for the traditional NN: (a) training, (b) validation, and (c) testing datasets.

Results in Figure 4 indicate a relatively poor performance of the NN at predicting the damage classes, with an average accuracy of 47.6% (accuracy averaged over training, validation, and testing datasets). Looking at recall and precision, it can be observed that the simplest class to predict is class 0, where the majority of the data is concentrated. The lowest values of precision and recall correspond to class 3, which corresponds to the class with the smallest number of observations available (Figure 1(b)). The poor performance of the NN can be attributed to the unbalance in the distribution of the data, which are severely skewed toward class 0. In particular, Figure 4 (a) shows that a very small number of data were used to train the NN in class 3, which might translate to poor accuracy of the model over both validation and testing datasets, as demonstrated by Figure 4 (b) and (c).

3.2 Cascade Neural Networks

In the cascade approach, two NN models were built and employed to classify the damage level of steel tanks, following the procedure summarized in Figure 3 (a). The first NN model was trained to predict the binary damage classification 0 (no damage) and 1 (damage) based on the data distribution reported in Figure 3 (b). The second NN was trained to identify the damage level of the tank between class 1 (minor damage), class 2 (severe damage), and class 3 (collapse). For both NN models, the number of neurons was selected iteratively as $k_1 = 10$ and $k_2 = 3$, while weights and biases values can be found in reference [29]. Figure 5 illustrates the confusion matrices for the first NN, while Figure 6 reports the second NN results.

Results in Figures 5 and 6 show that both NN models yield similar performance, with an average accuracy of 73.4% for the first NN and 71% for the second model. For the first NN, the highest values of precision are reached in class 1, while the largest recall correspond to class 0 in training and validation datasets, and class 1 in the testing subset. On the other hand, results in Figure 6 show that class 1 seems to be the simplest class to predict with the second NN model, corresponding to relatively high values of precision and recall over training, validation, and testing datasets.

A cross-comparison between the performance of the traditional and the cascade NN approaches demonstrate that the cascade NNs are 51.7% more accurate than the single NN. This

could be attributed to the more balanced distribution of the observations among different damage classes in the cascade approach. Overall, the performance of the models in terms of recall and precision varies with the damage class under consideration, with the highest values attained by the two cascade NN models. Based on the overall accuracy and the fair performance at identifying different damage classes, the cascade NN approach is recommended as the method to use to estimate the damage level of steel storage tanks as a function of tank and seismic hazard characteristics.

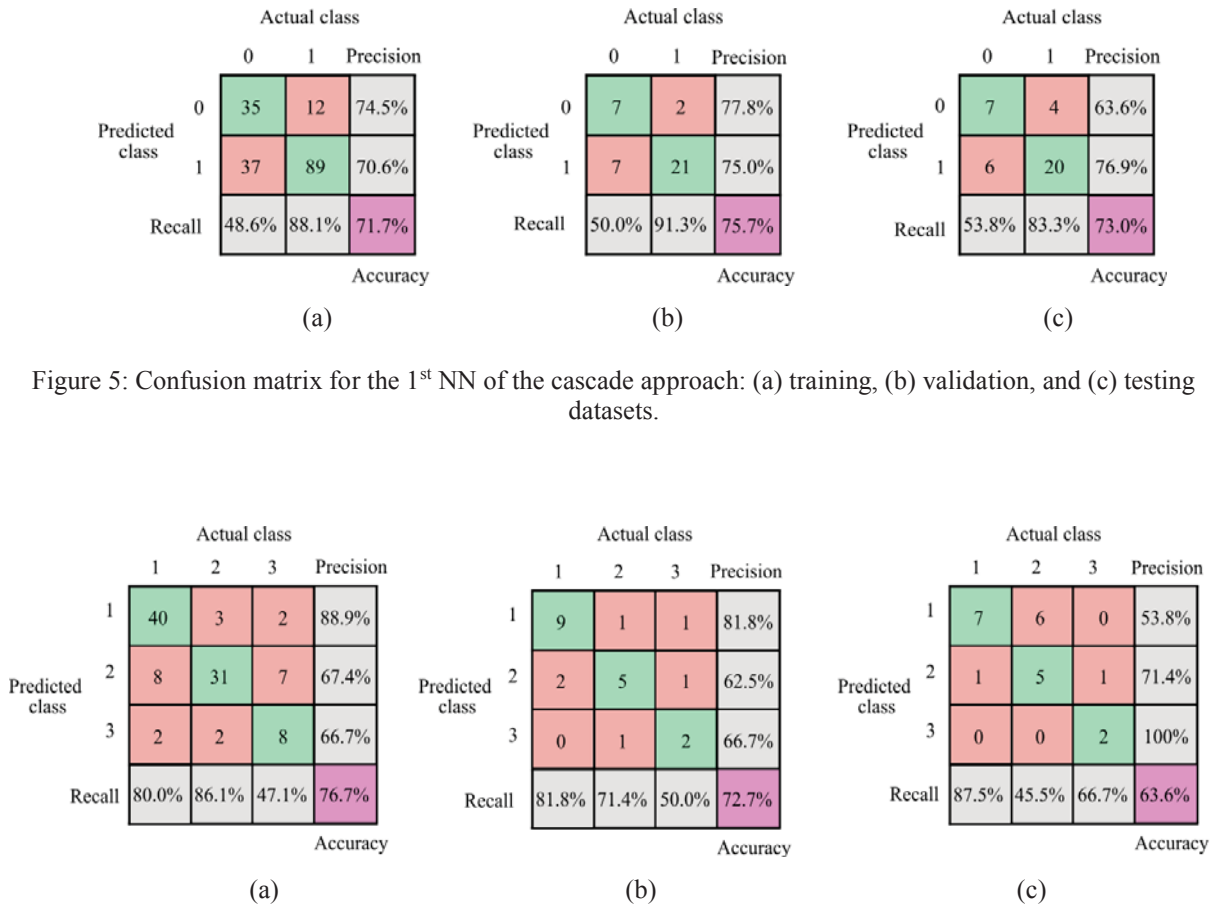


Figure 5: Confusion matrix for the 1st NN of the cascade approach: (a) training, (b) validation, and (c) testing datasets.

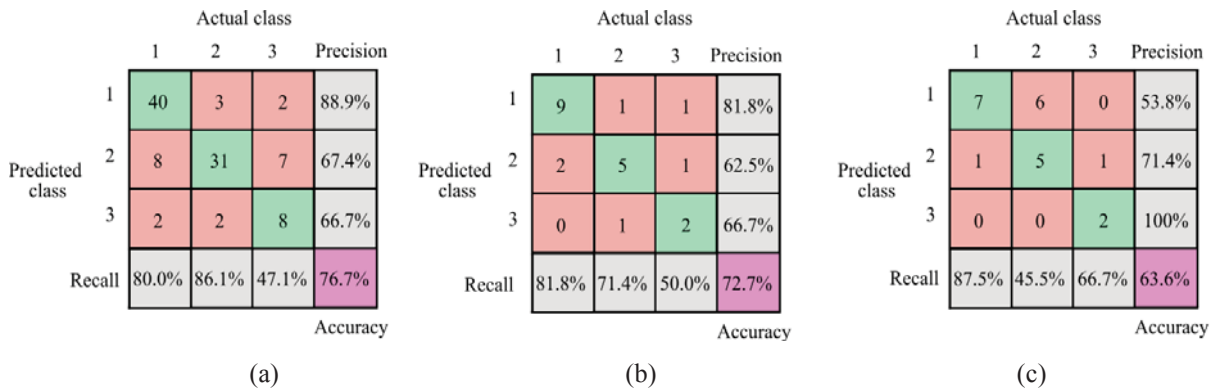


Figure 6: Confusion matrix for the 2nd NN of the cascade approach: (a) training, (b) validation, and (c) testing datasets.

4 CONCLUSIONS

In this paper, an NN-based approach for damage prediction of aboveground, cylindrical, steel liquid storage tanks was investigated. In the proposed method, data were derived from post-earthquake reconnaissance reports and surveys. Features representative of tank and seismic hazard characteristics were extracted from the reconnaissance reports, along with a description of the corresponding damage modes. The different types of damage were initially classified into four classes, ranging from no damage to collapse. The limited number of reconnaissance observations available in the literature yielded an unbalanced dataset, with the majority of the data skewed toward one class. First, a traditional two-layers NN was constructed to infer the unknown relationship between tank and seismic features (inputs of the

NN model), and corresponding damage class (output). Then, to tackle the unbalanced dataset challenge, a cascade NN approach was proposed, where two NN models were utilized to guess the damage class of the tanks. The first NN was trained based on a binary classification of the reconnaissance observations (i.e., damage, no damage). If the tank resulted in the damage class from the first model, a second NN refined the damage guess between minor damage, severe damage, and collapse. The performance of traditional and cascade NN methods was assessed with different metrics, such as accuracy, precision, and recall.

Results demonstrated that the cascade NN approach led to a better performance than the conventional NN model, with an average accuracy of 73.4% for the first and 71% for the second NN models. On the other hand, the traditional NN yielded a relatively poor performance, with an average accuracy of 47.6%. The values of recall and precision vary with the damage class under consideration. Overall, the two NNs in the cascade approach resulted in the largest values of both precision and recall compared to the traditional model. The enhanced performance of the cascade NNs can be attributed to the more balanced distribution of the data relatively to the traditional NN dataset.

Overall, the paper showed that the cascade NN approach could be a viable alternative to traditional NN models, in particular when unbalanced datasets are available, such as for post-disaster reconnaissance observations. Nevertheless, the accuracy of the cascade NN models could to be further improved by increasing the number of training data or using different data learning algorithms. Future investigations will entail exploring different machine learning algorithms, applying other techniques to solve the issue of imbalanced data, and integrating the cascade NNs into a seismic risk assessment framework for steel liquid storage tanks.

ACKNOWLEDGEMENTS

This study was supported by Catholic University of America's 2020 Burns Junior Faculty Fellowship. Any opinions, finding, and conclusion or recommendation expressed in this material are those of the authors and do not necessarily reflects the view of the sponsors.

REFERENCES

- [1] Federal Emergency Management Agency (FEMA), "Seismic performance assessment of buildings, Volume 1 - Methodology," FEMA Publication P-58-1, Washington, DC, 2012.
- [2] Yang, T. Y., Moehle, J., Stojadinovic, B., & Der Kiureghian, A., "Seismic performance evaluation of facilities: methodology and implementation," *Journal of Structural Engineering*, pp. 135(10), 1146-1154, 2009.
- [3] Ierimonti, L., Caracoglia, L., Venanzi, I., & Materazzi, A. L., "Investigation on life-cycle damage cost of wind-excited tall buildings considering directionality effects," *Journal of Wind Engineering and Industrial Aerodynamics*, pp. 171, 207-218, 2017.
- [4] Micheli, L., Alipour, A., Laflamme, S., & Sarkar, P., "Performance-Based Design with Life-Cycle Cost Assessment for Damping Systems Integrated in Wind Excited Tall Buildings," *Engineering Structures*, pp. 195, 438-451, 2019 b.
- [5] Faytarouni, M., Shen, J., Seker, O., & Akbas, B., "Seismic demand on column splices in concentrically braced frames considering brace fracture," *Journal of Constructional Steel Research*, pp. 175, 106350, 2020.
- [6] Faytarouni, M., Seker, O., Akbas, B., & Shen, J., "Impact of Brace Fracture on Column Splice Demands in Braced Frames," *Journal of Structural Engineering*, pp. 146(8),

- 04020152, 2020.
- [7] Caprili, S., Panzera, I., & Salvatore, W., "Resilience-based methodologies for design of steel structures equipped with dissipative devices," *Engineering Structures*, vol. 228, p. 111539, 2021.
 - [8] Sun, H., Burton, H., & Wallace, J. , "Reconstructing seismic response demands across multiple tall buildings using kernel-based machine learning methods," *Structural Control and Health Monitoring*, vol. 26(7), p. e2359, 2019.
 - [9] Kiani, J., Camp, C., & Pezeshk, S. , "On the application of machine learning techniques to derive seismic fragility curves," *Computers & Structures*, vol. 218, pp. 108-122, 2019.
 - [10] Sun, H., Burton, H. V., & Huang, H. , "Machine learning applications for building structural design and performance assessment: state-of-the-art review," *Journal of Building Engineering*, p. 101816, 2020.
 - [11] Moustapha, M., Bourinet, J. M., Guillaume, B., & Sudret, B., "Comparative Study of Kriging and Support Vector Regression for Structural Engineering Applications," *ASCE-ASME Journal of Risk and Uncertainty in Engineering Systems, Part A: Civil Engineering*, pp. 4(2), 04018005, 2018.
 - [12] Abdallah, I., Lataniotis, C., & Sudret, B., "Parametric hierarchical kriging for multi-fidelity aero-servo-elastic simulators—Application to extreme loads on wind turbines," *Probabilistic Engineering Mechanics*, pp. 55, 67-77, 2019.
 - [13] Sudret, B., & Mai, C. V., "Computing seismic fragility curves using polynomial chaos expansions," in *11th International Conference on Structural Safety and Reliability (ICOSSAR)*, Zürich, 2013.
 - [14] Gidaris, I., Taflanidis, A. A., & Mavroeidis, G. P., "Kriging metamodeling in seismic risk assessment based on stochastic ground motion models," *Earthquake Engineering & Structural Dynamics*, pp. 44(14), 2377-2399, 2015.
 - [15] Micheli, L., Alipour, A., & Laflamme, S. , "Multiple-Surrogate Models for Probabilistic Performance Assessment of Wind-Excited Tall Buildings under Uncertainties," *ASCE-ASME Journal of Risk and Uncertainty in Engineering Systems, Part A: Civil Engineering*, vol. 6(4), p. 04020042, 2020.
 - [16] Le, V., & Caracoglia, L. , "A neural network surrogate model for the performance assessment of a vertical structure subjected to non-stationary, tornadic wind loads," *Computers & Structures*, vol. 231, p. 106208, 2020.
 - [17] Micheli, L., & Laflamme, S, "Kriging-based design for robust high-performance control systems," *ASCE-ASME Journal of Risk and Uncertainty in Engineering Systems, Part A: Civil Engineering*, pp. 6(4), 04020037, 2020.
 - [18] Mangalathu, S., Sun, H., Nweke, C. C., Yi, Z., & Burton, H. V. , "Classifying earthquake damage to buildings using machine learning," *Earthquake Spectra*, vol. 36(1), pp. 183-208, 2020.
 - [19] Bakalis, K., Kazantzi, A. K., Vamvatsikos, D., & Fragiadakis, M, "Seismic performance evaluation of liquid storage tanks using nonlinear static procedures," *Journal of Pressure Vessel Technology*, p. 141(1), 2019.
 - [20] Bakalis, K., Fragiadakis, M., & Vamvatsikos, D. , "Surrogate modeling for the seismic performance assessment of liquid storage tanks," *Journal of Structural Engineering*, vol. 143(4), p. 04016199, 2017.
 - [21] Bohra, H., Azzuni, E., & Guzey, S. , "Seismic analysis of open-top storage tanks with

- flexible foundation," *Journal of Pressure Vessel Technology*, vol. 141(4), 2019.
- [22] Cooper, T. W, "A study of the performance of petroleum storage tanks during earthquakes, 1933-1995," US National Institute of Standards and Technology, 1997.
- [23] Hamdan, F. H, "Seismic behaviour of cylindrical steel liquid storage tanks," *Journal of Constructional steel research*, pp. 53(3), 307-333., 2000.
- [24] Cortes, G., & Prinz, G. S, "Seismic fragility analysis of large unanchored steel tanks considering local instability and fatigue damage," *Bulletin of Earthquake Engineering*, pp. 15(3), 1279-1295, 2017.
- [25] Pacific Earthquake Engineering Research Center, " PEER ground motion database," 2020. [Online]. Available: <https://ngawest2.berkeley.edu/>.
- [26] Gu, Q., Cai, Z., Zhu, L., & Huang, B. , "Data mining on imbalanced data sets," in *In 2008 International Conference on Advanced Computer Theory and Engineering* , (pp. 1020-1024). IEEE, 2008.
- [27] Beale, M. H., Hagan, M. T., & Demuth, H. B. , "Neural network toolbox. User's Guide," MathWorks, 2010.
- [28] MathWorks, "MATLAB Machine Learning and Deep Learning Toolbox Release 2020b," MathWorks, Inc., Natick, Massachusetts, United States, 2021.
- [29] Micheli, L., "GitHub," 2021. [Online]. Available: <https://github.com/lauramch/COMPDYN2021>.

APPLICATION OF WAVELET TRANSFORMS ON ACCELERATION RECORDS: PRACTICAL APPROACH

Vladimir Vukobratović¹, Trevor Yeow², and Koichi Kusunoki²

¹ Faculty of Technical Sciences, University of Novi Sad
Trg Dositeja Obradovića 6, 21000 Novi Sad, Serbia
e-mail: vladavuk@uns.ac.rs

² Earthquake Research Institute, The University of Tokyo
1-1-1 Yayoi, Bunkyo-ku, Tokyo 113-0032, Japan
e-mail: {trevoryeow, kusunoki}@eri.u-tokyo.ac.jp

Abstract

Building floor accelerations recorded during earthquakes represent valuable data which contribute to the improved understanding of structural dynamic behavior and the state of the art and practice. After recording, all accelerations are considered to be “raw” (or unprocessed, uncorrected, unfiltered), and need to be processed before they can be used. In practice, the most common approach is to apply the conventional high- and low-pass filtering methods. However, some records cannot be corrected in such a manner and remain practically useless. The problems which may occur when conventional filtering methods are applied are: (1) inability to distinguish frequencies of noise and signal, (2) change of noise characteristics in time, and (3) a need to estimate and pre-select the parameters of a chosen filter function. These issues can be avoided if wavelets are used for signal processing. In mathematical terms, wavelets are finite wave-like functions which are able to capture local changes, and are used to transform a signal into a representation which shows its properties in the time-frequency domain. Such transformation is known as a wavelet transform. The continuous wavelet transform (CWT) was applied to recordings obtained from a 3-storey reinforced concrete building shake table test performed at the E-Defense facility in Kobe, Japan. It was demonstrated that the CWT represents a useful tool for the visual interpretation of the energy localization in the time-frequency domain, and that there is a large potential for the CWT application in earthquake engineering.

Keywords: Wavelet, Transform, Acceleration, Noise, Filtering.

1 INTRODUCTION

Accelerations recorded during earthquakes provide valuable data which can be utilized in various analyses to contribute to the expansion of knowledge and the improvement of the states of the art and practice. After they are recorded, all accelerations are considered to be “raw” (or unprocessed, uncorrected, unfiltered). So, in order to make them applicable, they need to be processed (i.e. “corrected”). In practice, the most common approach is to apply conventional high- and low-pass filtering methods. However, some records cannot be corrected in such a manner, and they practically remain useless.

An overview of the conventional filtering methods’ shortcomings can be found elsewhere [1] and will not be discussed here in detail. Nevertheless, the main problems which usually occur are: (1) an inability to distinguish frequencies of noise and signal, (2) the change of noise characteristics in time, and (3) a need to estimate and pre-select the parameters of the chosen filter function. These issues are avoided if wavelets are used for signal processing, and this fact was recognized by researchers and engineers [2, 3]. In mathematical terms, wavelets are wavelike functions that satisfy certain requirements, and they are used to transform a signal into a representation which shows the information of the signal in a more useful form. Such transformation is known as a wavelet transform, which is basically a convolution of the wavelet with the signal [4].

Analysis of a signal by using a wavelet transform starts with the selection of a single wavelet, usually referred to as an “analyzing” or “mother wavelet”. Wavelets are manipulated by translation (i.e. movement along the time axis) and dilation (i.e. stretching or compressing), and they are used to decompose the signal into a series of basis functions of the finite length. Understanding the concepts of the scale-varying basis functions is key to understanding wavelets [5]. In a way, roughly speaking, the process can be seen as the “time-frequency” decomposition of the signal, where “modes” represent individual parts of the signal. The essential difference between the wavelet transform and the well-known Fourier analysis is that the former can distinguish localized events at different times at the same frequency [6]. There is a wide selection of wavelets that can be used in practice, and they can roughly be divided into real and complex ones. The choice of wavelet depends on the signal properties and the purpose of analysis. The most commonly used wavelets are Haar, Daubechies, Mexican Hat, Morlet, Meyer, Morse (some of these are shown in Fig. 1), and information about them is widely available in the literature.

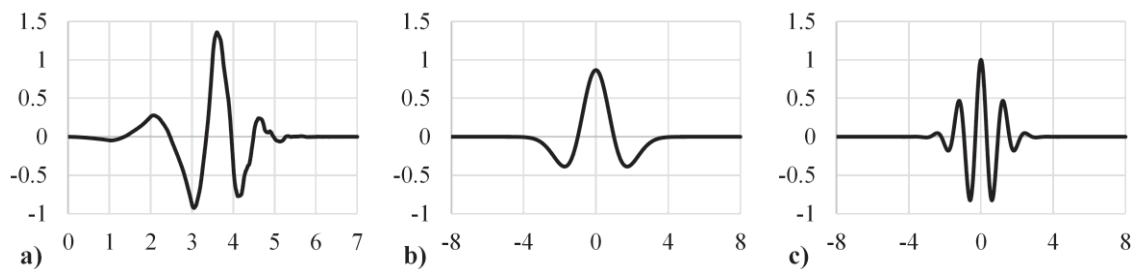


Figure 1: Often used wavelets: (a) Daubechies of order 4, (b) Mexican hat, and (c) Morlet.

This paper provides an insight into the practicality and possible benefits of using wavelets for raw acceleration processing. The paper is written from a practical point of view rather than in a mathematical manner, though the following two sections cover fundamental mathematical terms related to the continuous and discrete wavelet transforms. The benefits of the application of wavelets in the processing of acceleration records will be highlighted to encourage their usage in engineering practice.

2 CONTINUOUS WAVELET TRANSFORM

As previously noted, a function must fulfil certain criteria in order to be classified as a wavelet. These are: (1) its energy is finite, (2) it has a zero mean, and (3) the Fourier transform must be both real and vanish for negative frequencies for complex wavelets [4]. If the mother wavelet is denoted as $\psi(t)$, the continuous wavelet transform (CWT), $T(a,b)$, is defined as:

$$T(a,b) = \frac{1}{\sqrt{a}} \int_{-\infty}^{+\infty} \psi^* \left(\frac{t-b}{a} \right) f(t) dt \quad (1)$$

where $f(t)$ is a signal function, and a and b denote the dilation and translation parameters, respectively. Both parameters are real numbers, and a is always positive. It should be noted that the asterisk denotes that the complex conjugate of the wavelet is used, which needs to be taken into account only when complex wavelets are applied. The plot of $T(a,b)$ against a and b is commonly referred to as “transform plot”.

Integration of the wavelet and signal product described by Eq. (1) represents a convolution. In the sense of its energy, the normalized wavelet function can be written as

$$\psi_{a,b}(t) = \frac{1}{\sqrt{a}} \psi \left(\frac{t-b}{a} \right) \quad (2)$$

and so Eq. (1) becomes

$$T(a,b) = \int_{-\infty}^{+\infty} \psi_{a,b}^* f(t) dt \quad (3)$$

CWTs are operable at every scale, they are performed over a continuous range of a and b , and the wavelet is shifted smoothly over a full domain of the considered signal. There are several advantages in applying the CWT. For example, the movement of wavelet along the signal enables identification of the “coherent structures” within the signal, whereas the Fourier transform does not provide any information on the nature of the signal local features. Also, sudden discontinuities in the signal can be easily identified by the CWT. Furthermore, the selection of $\psi(t)$ can be such that the $T(a,b)$ contains sufficient information for the reconstruction of the signal function $f(t)$, and this is possible by using the inverse wavelet transform. However, it should be mentioned that in the inverse transform the original wavelet function is used, not the conjugate one. Thus, the integration over a range of a scales rather than all a scales makes basic filtering of the original signal possible [4].

Under the assumption that the signal contains a finite energy, the signal’s total energy can be obtained by integrating its squared magnitude

$$E = \int_{-\infty}^{+\infty} |f(t)|^2 dt \quad (4)$$

It is possible to determine the part of the energy corresponding to the particular scale a and location b as

$$E(a,b) = |T(a,b)|^2 \quad (5)$$

Graphical representation of $E(a,b)$ is called “scalogram”, and it provides a useful picture of the non-stationary process nature and energy distribution, which is shown in the application

example later in the paper. It should be noted that scalograms and transform plots have similar forms, which is a consequence of their definitions.

A known issue with the CWT analysis is the so called “edge” or “boundary” effect. It arises from the fact that the signal data set is finite and that it usually needs to be analyzed as a whole. Practically speaking, wavelets extend beyond the signal edges, and the transform is disrupted. In transform plots and scalograms, the region that is potentially affected by the edge effect is called the “cone of influence”. Its extent is proportional to the wavelet width (i.e. it increases linearly with parameter a). However, since logarithmic scale is usually used for a , the cone of influence becomes curved. The extension of the cone depends on the wavelet scale. Unfortunately, the precise way to determine the extent of cone at each scale does not exist, so it is rather a subjective decision. For instance, for Morse wavelets, which are used in the example in this paper, a useful proposal is available in the literature [7].

3 DISCRETE WAVELET TRANSFORM

In order to present the basics of the discrete wavelet transform (DWT), firstly consider Eq. (2), a continuous signal $f(t)$, and the discrete values of parameters a and b , which are linked to each other [4]. Thus, the discretization of the wavelet has the following form:

$$\psi_{m,n}(t) = \frac{1}{\sqrt{a_0^m}} \psi\left(\frac{t - nb_0 a_0^m}{a_0^m}\right) \quad (6)$$

where a_0 is the selected dilation step larger than 1, b_0 is the location parameter larger than 0, and m and n are integers that control the wavelet dilation and translation, respectively.

By considering Eq. (6), the wavelet transform of the signal $f(t)$ becomes

$$T_{m,n} = \int_{-\infty}^{+\infty} \frac{1}{a_0^{m/2}} \psi(a_0^{-m}t - nb_0) f(t) dt \quad (7)$$

In the case of the DWT, the values of $T_{m,n}$ are known as “wavelet coefficients”. In practice, the values of a_0 and b_0 are often chosen to amount to 2 and 1, respectively. These values lead to the so called “dyadic grid” arrangement, a simple and efficient discretization which leads to an orthonormal wavelet basis. By considering $a_0 = 2$ and $b_0 = 1$, Eq. (6) becomes

$$\psi_{m,n}(t) = 2^{-m/2} \psi(2^{-m}t - n) \quad (8)$$

Moreover, it is common to select the discrete dyadic grid wavelets to be orthonormal (i.e. orthogonal to each other) and normalized so that they have unit energy. In other words, the product of each wavelet with all others in the same dyadic system is zero. This way, the information contained in each coefficient $T_{m,n}$ is not repeated elsewhere, which provides the possibility to fully recover the original signal. If Eq. (8) is considered, the DWT can be expressed as

$$T_{m,n} = \int_{-\infty}^{+\infty} \psi_{m,n}(t) f(t) dt \quad (9)$$

The considered signal can be reconstructed from the inverse DWT:

$$f(t) = \sum_{m=-\infty}^{\infty} \sum_{n=-\infty}^{\infty} T_{m,n} \psi_{m,n}(t) \quad (10)$$

Note that for the DWT described by Eq. (9) the transform integral is continuous over the discretized grid. Thus, the summation in Eq. (10) provides the return of the exact signal. It is important to note though that there is a difference between the DWT and the so called discretized CWT, in which the discrete approximation of the transform integral is usually involved, in order to be able to perform its computation. Such computing of the CWT is quite robust, and in practice the fast Fourier transform is used instead.

Finally, the energy of the signal can be determined as

$$E = \int_{-\infty}^{+\infty} |f(t)|^2 dt = \sum_{m=-\infty}^{\infty} \sum_{n=-\infty}^{\infty} |T_{m,n}|^2 \quad (11)$$

4 EXAMPLE OF APPLICATION

In this section an example of application of the CWT is presented, and the application of the DWT may be found in the works of Pan and Kusunoki [2] and Kusunoki et al. [8], who used it to extract the predominant building response for structural health monitoring purposes. The signal that was analyzed is the absolute acceleration at the second floor of a 3-storey reinforced concrete frame building specimen recorded during shake table tests at the E-Defense facility in Kobe, conducted between the 3rd and 7th December 2019. The test was a part of the Tokyo Metropolitan Resilience Project, Subproject C, Theme 2 [9]. Some other recordings from the same building were previously subjected to the CWT by Yeow and Kusunoki [10].

The building properties and the description of ground motions used as input during the test are available in Yeow et al. [11]. For the analysis presented in this paper, the fourth applied motion was considered (denoted as 1.5–2 in [11]). During that input motion the structural response was highly nonlinear. Raw absolute acceleration under consideration is shown in Fig. 2. It was normalized with the respect to its absolute peak value, so it is dimensionless.

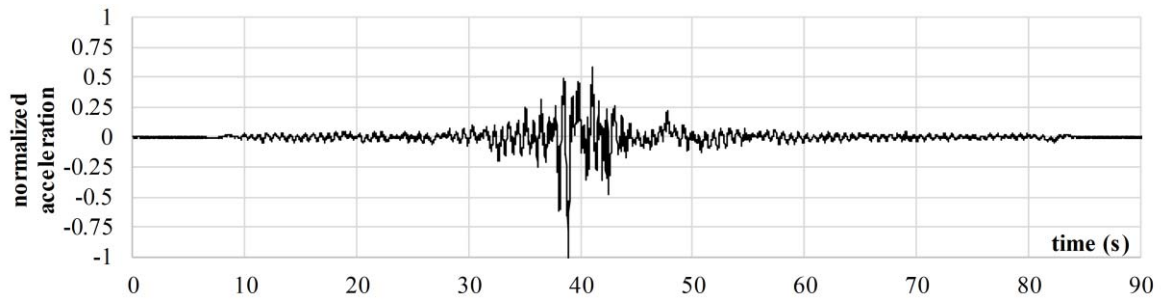


Figure 2: Normalized absolute acceleration recorded at the second floor of the considered building.

The CWT was applied to the recorded signal by using the *cwt* function which is integrated in the Wavelet Toolbox of MATLAB R2019b. The analytic Morse wavelet was adopted as the mother wavelet. The reconstruction of the signal was obtained by using the *icwt* function, which inverts the CWT coefficient matrix, by using the same predefined default parameters of the Morse wavelet as the *cwt* function. In order to perform filtering using the *icwt* function the frequency range of interest needs to be specified. This can be obtained using scalogram plots.

The scalogram obtained for the considered record is shown in Fig. 3. The dashed white line marks the cone of influence described earlier. Horizontal and vertical axes show time and frequency in the logarithmic scale, respectively, and the wavelet transform magnitude scale is shown on the right. The interpretation of the scalogram presented in Fig. 3 is quite straightforward. The parts of it in which the magnitude is sizeable are either related to the response of the structure, or to the noise and certain anomalies (e.g. a loose cable moving during shaking).

In the considered case, the influence of the response in the fundamental mode is localized at approximately 1.5 Hz, whereas the influence of the second mode is obvious at 10 Hz. It can be seen that the scalogram can be used for the visualization of modes.

As noted above, in order to perform filtering, it is necessary to select the frequency range of interest. It is usually done intuitively, which may be seen as a limitation of the CWT approach. Herein, the frequency range of 0.2 to 12 Hz was chosen. In this way, the noise at frequencies above 12 Hz was eliminated. A comparison of the raw and corrected accelerations, normalized to their absolute peak values, is shown in Fig. 4. It is obvious that the spikes are eliminated, and that the original signal is successfully recovered.

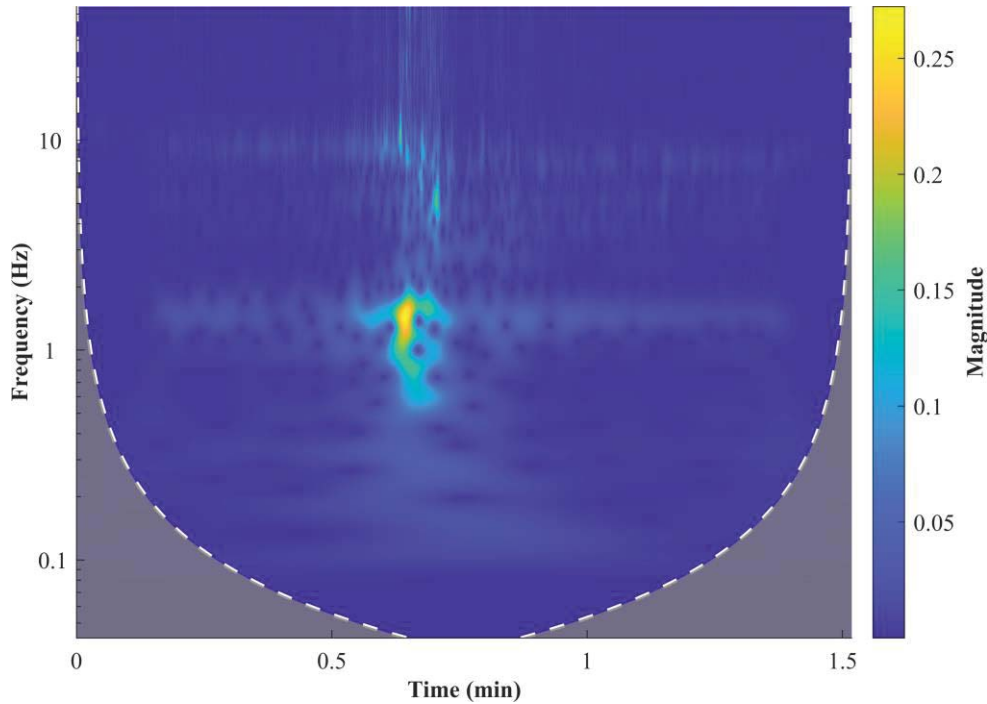


Figure 3: Scalogram of the considered absolute acceleration record.

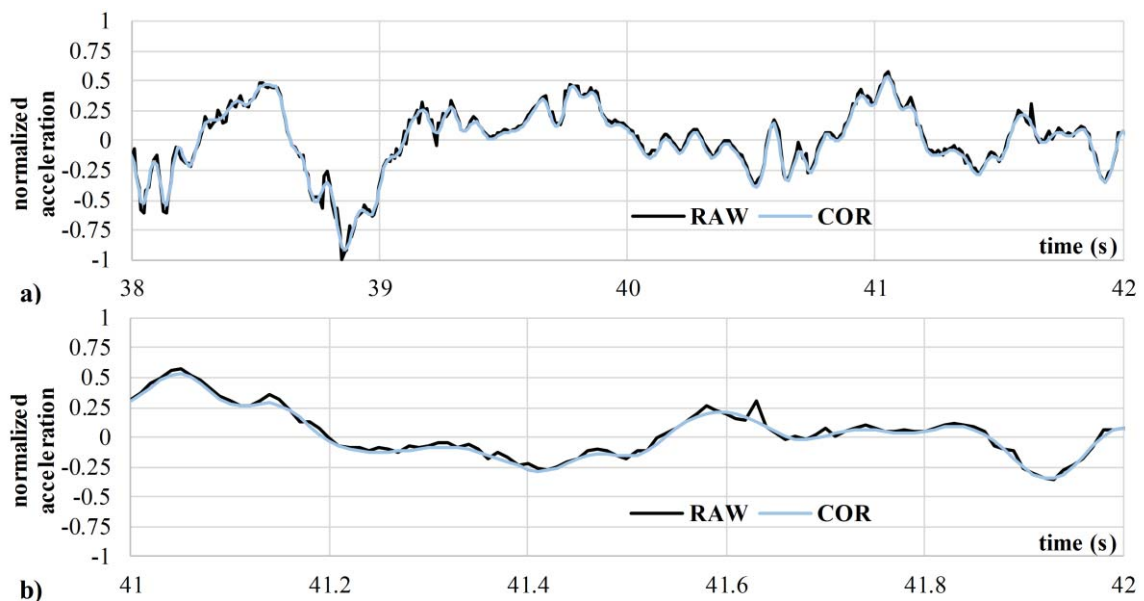


Figure 4: Comparison of the raw and corrected absolute accelerations in (a) the interval of 38 to 42 s, and (b) between 41 and 42 s.

The corrected acceleration can be integrated in order to obtain velocity and displacement, but it usually needs to be baseline-corrected first. This known issue is beyond the scope of the paper, and more details can be found elsewhere [1]. Another issue is that wavelets have zero-mean, meaning that the acceleration signal and its integrals (i.e. velocity and displacement) will always eventually return to zero. This poses an issue with obtaining residual deformations, though such issues already exist when obtaining displacements from acceleration data using conventional means [12]. Alternatives such as using Kalman filters could be an option [13, 14], but this is outside the scope of this research and will not be elaborated upon further here.

While not shown here, the DWT approach has been used in literature to extract out the predominant hysteretic response of buildings based on floor acceleration recordings. This is done by: (i) decomposing the acceleration recordings of each floor using the DWT, (ii) obtaining the relative floor acceleration and displacement response for each decomposition level, (iii) simplifying the multi-degree-of-freedom response into an equivalent single-degree-of-freedom response for each decomposition level, (iv) using the equivalent response of each decomposition level to identify which should be eliminated, and (v) re-computing the equivalent single-degree-of-freedom response using the remaining decomposition levels. Examples of the application are available in literature [2, 3, 8].

5 CONCLUSIONS

Wavelet transforms represent an alternative to the conventional high- and low-pass filtering methods, with whose application it is sometimes not possible to correct the acceleration data recorded during earthquakes. Mathematical background of the continuous and discrete wavelet transforms was briefly provided, along with the example of application of the former on the acceleration recorded during the shake table test. Application of the continuous wavelet transform by using the available commercial software was demonstrated, along with interpretation of the scalogram data and discussion on the pros and cons of the approach. Even though the use of wavelet transforms in earthquake engineering started only relatively recently, their large potential is already recognized.

ACKNOWLEDGMENTS

The present work is partially supported by the Tokyo Metropolitan Resilience Project of the National Research Institute for Earth Science and Disaster Resilience (NIED). The first author is grateful for the opportunity to participate in the Long-term visiting program organized by the Earthquake Research Institute (ERI), The University of Tokyo, where he spent four months working as a Project Researcher.

REFERENCES

- [1] A. Ansari, A. Noorzad, M. Zare, Application of wavelet multi-resolution analysis for correction of seismic acceleration records. *Journal of Geophysics and Engineering*, **4**, 362-377, 2007.
- [2] H. Pan, K. Kusunoki, A wavelet transform-based capacity curve estimation approach using seismic response data. *Structural Control and Health Monitoring*, **25**, 1-13, 2018.

- [3] H. Pan, K. Kusunoki, Y. Hattori, Capacity-curve-based damage evaluation approach for reinforced concrete buildings using seismic response data. *Engineering Structures*, **197**, 1-8, 2019.
- [4] P.S. Addison, *The Illustrated Wavelet Transform Handbook – Introductory Theory and Applications in Science, Engineering, Medicine and Finance*. Institute of Physics Publishing, Bristol and Philadelphia, 2002.
- [5] A. Graps, An Introduction to Wavelets. *IEEE Computational Science and Engineering*, **2**, 50-61, 1995.
- [6] K. Gurley, A. Kareem, Application of wavelet transforms in earthquake, wind and ocean engineering. *Engineering Structures*, **21**, 149-167, 1999.
- [7] J.M. Lilly, Element analysis: a wavelet-based method for analysing time-localized events in noisy time series. *Proceedings of the Royal Society A*, **473**, 1-28, 2017.
- [8] K. Kusunoki, D. Hinata, Y. Hattori, A. Tasai, A new method for evaluating the real-time residual seismic capacity of existing structures using accelerometers: Structures with multiple degrees of freedom. *Japan Architectural Review*, **1**, 77-86, 2018.
- [9] N. Hirata, Introduction to the Tokyo Metropolitan Resilience Project. *NHERI-NIED Plenary Session Presentations*, Tokyo, Japan, July 13-14, 2017.
- [10] T. Yeow, K. Kusunoki, A new safety evaluation system and the continuous functionality of buildings with post-disaster functions following earthquakes (Part 5 – verification of peak total floor acceleration using CWT). *Proceedings of the AIJ 2020 Conference*, Chiba, Japan, 2020.
- [11] T.Z. Yeow, K. Kusunoki, I. Nakamura, Y. Hibino, S. Fukai, W.A. Safi, E-Defense shake-table test of a building designed for post-disaster functionality. *Journal of Earthquake Engineering*, published online, 1-22, 2021.
- [12] D.A. Skolnik, J.W. Wallace, Critical Assessment of Interstory Drift Measurements. *Journal of Structural Engineering*, **136**, 1574-1584, 2010.
- [13] J.N. Yang, S. Lin, H. Huang, L. Zhou, An adaptive extended Kalman filter for structural damage identification. *Structural Control and Health Monitoring*, **13**, 849-867, 2006.
- [14] M. Wu, A.W. Smyth, Application of the unscented Kalman filter for real-time nonlinear structural system identification. *Structural Control and Health Monitoring*, **14**, 971-990, 2007.

NUMERICAL INVESTIGATION ON THE PRINCIPAL STRESS ROTATION EFFECT UNDER EARTHQUAKE LOADINGS

Zhe Wang¹, Yunming Yang²

¹ Department of Civil Engineering, Engineering College, Lishui University
Lishui 323000, China
e-mail: wangzhe@lsu.edu.cn

² Ningbo Nottingham New Materials Institute, the University of Nottingham Ningbo China
Ningbo 315100, China
Ming.yang@nottingham.edu.cn

Abstract

Earthquake loadings can cause significant principal stress rotation (PSR) in the sand bed. Even the pure PSR (rotation of principal stress axis with constant principal stress magnitudes) can lead to the build-up of excess pore water pressures and accumulation of plastic strains, thus accelerating sand liquefaction in undrained conditions. This paper conducts the fully coupled finite element simulations of a centrifuge test to investigate the PSR effect under earthquake loadings. The PSR is considered by using a PSR model developed based on an elastoplastic sand model with kinematic hardening and bounding surface concepts. The numerical predictions from the PSR model and base model are compared with the experimental results. The comparative study shows that the PSR model performs better than the base model at capturing the sand responses and liquefactions behaviors. The investigation also finds obvious PSR in the sand bed and demonstrates the importance of considering the PSR effect under earthquake loadings in undrained conditions.

Keywords: Earthquake loading, Principal stress rotation, Elastoplastic model, Liquefaction, Finite element simulation

1 INTRODUCTION

Earthquake loadings can lead to quite complicated stress conditions in the soil bed, such as conditions with principal stress rotation (PSR). Early in 1983, Ishihara and Towhata found that the PSR at fixed principal stress magnitudes can also cause the build-up of excess pore water pressure, the reduction of effective confining pressure and the increase of plastic strain in undrained conditions, which could further accelerate sand liquefaction and lead to catastrophic failure of foundations [1]. Similar conclusion and the importance of considering the PSR were also proposed by other researchers [2-5]. Ignoring the PSR effect can lead to inaccurate computations and unsafe designs. During last decades, numerous experimental and numerical attempts have been made to investigate the earthquake induced soil behaviors, such as VELACS (Verification of Liquefaction Analysis using Centrifuge Studies) [6], LEAP (Liquefaction Experiments and Analysis Projects) [7], etc. Although a number of numerical simulations have been conducted for these projects [7-10], there are few of them focusing on the PSR effect under earthquake loadings.

Therefore, this paper aims to investigate the effect of PSR induced by earthquake loadings in the sand with a series of numerical studies using an elastoplastic constitutive model considering the PSR, which is improved based on a bounding surface model with the critical state theory. The model will be verified in the numerical simulations of geotechnical laboratory tests and then implemented in the finite element simulations of the VELACS centrifuge model test. The numerical predictions from the original base model, the improved PSR model and the experimental results will be compared.

2 THE ORIGINAL BASE MODEL

The bounding surface model proposed by Dafalias & Manzari [11] is chosen as the base model. This model adopts the critical state theory, the kinematic hardening rule and state parameter to represent sand with different initial states. To better illustrate and focus on the PSR effect, the fabric change effect in their original work is not considered in this paper. The basic model formulations are briefly introduced as follows.

The yield surface of the model is given as:

$$f = [(\mathbf{s} - p\boldsymbol{\alpha}) : (\mathbf{s} - p\boldsymbol{\alpha})]^{1/2} - \sqrt{2/3} pm = 0 \quad (1)$$

where \mathbf{s} and $\boldsymbol{\alpha}$ are the deviatoric stress and back-stress ratio tensor, respectively. p is the confining pressure and m represents the radius of yield surface. The normal to the yield surface is given as:

$$\mathbf{l} = \frac{\partial f}{\partial \boldsymbol{\sigma}} = \mathbf{n} - \frac{1}{3} (\mathbf{n} : \mathbf{r}) \mathbf{I} \quad (2)$$

where \mathbf{n} is defined as the normal to the yield surface on the deviatoric plane. \mathbf{r} equals to \mathbf{s}/p and \mathbf{I} is the isotropic tensor. The elastic volumetric strain increment $d\boldsymbol{\epsilon}_v^e$ and elastic deviatoric strain increment $d\boldsymbol{\epsilon}^e$ are given as:

$$d\boldsymbol{\epsilon}_v^e = dp / K \quad (3)$$

$$d\boldsymbol{\epsilon}^e = d\mathbf{s} / 2G \quad (4)$$

The plastic strain increment $d\boldsymbol{\epsilon}^p$ is given as:

$$d\boldsymbol{\epsilon}^p = \langle L \rangle \mathbf{R}; \quad L = \frac{1}{\kappa_p} \left(\frac{\partial f}{\partial \boldsymbol{\sigma}} \right) : d\boldsymbol{\sigma}; \quad \mathbf{R} = \mathbf{n} + \frac{1}{3} D \mathbf{I} \quad (5)$$

where L is loading index and \mathbf{R} represents the direction of $d\boldsymbol{\epsilon}^p$. The plastic modulus K_p and the dilatancy ratio D are given as:

$$K_p = \frac{2}{3} p \left[G_0 h_0 (1 - c_h e) \left(\frac{p}{p_{at}} \right)^{-1/2} \right] \left[\frac{|\mathbf{b} : \mathbf{n}|}{|(\boldsymbol{\alpha} - \boldsymbol{\alpha}_{in}) : \mathbf{n}|} \right] \quad (6)$$

$$D = A_d \mathbf{d} : \mathbf{n} \quad (7)$$

where \mathbf{b} and \mathbf{d} are distances between the back-stress ratio and bounding surface and dilatancy surface back-stress ratio, respectively. $\boldsymbol{\alpha}_{in}$ represents the value of $\boldsymbol{\alpha}$ at the very beginning of each loading stage and requires update when the negative denominator occurs. h_0 , c_h and A_d are model parameters.

3 THE MODIFIED PSR MODEL

In the PSR model, the plastic strain increment is split into two parts—the monotonic strain increment $d\boldsymbol{\epsilon}_m^p$ and the PSR strain increment $d\boldsymbol{\epsilon}_r^p$. The model formulations are briefly introduced here and details can be found in Yang and Yu [12]. The subscript m and r represent monotonic and PSR loading hereinafter. The plastic strain increment is defined as:

$$d\boldsymbol{\epsilon}_m^p = \langle L_m \rangle \mathbf{R}_m = \frac{1}{K_p} \left(\frac{\partial f}{\partial \boldsymbol{\sigma}} d\boldsymbol{\sigma}_m \right) \mathbf{R} \quad (8)$$

$$d\boldsymbol{\epsilon}_r^p = \langle L_r \rangle \mathbf{R}_r = \frac{1}{K_{pr}} \left(\frac{\partial f}{\partial \boldsymbol{\sigma}} d\boldsymbol{\sigma}_r \right) \mathbf{R}_r \quad (9)$$

\mathbf{R}_r represents the direction of PSR strain increment and is given as:

$$\mathbf{R}_r = \mathbf{n} + \frac{1}{3} D_r \mathbf{I}; \quad D_r = A_r (1 - \alpha / \alpha_\theta^b) \alpha \quad (10)$$

where D_r is the PSR dilatancy ratio and A_r is model parameter for the PSR effect on dilatancy. The PSR plastic modulus K_{pr} is given as:

$$K_{pr} = \frac{2}{3} p \left[G_0 h_{0r} (1 - c_h e) \left(\frac{p}{p_{at}} \right)^{-1/2} \right] \left(\frac{|\mathbf{b} : \mathbf{n}|}{|(\boldsymbol{\alpha} - \boldsymbol{\alpha}_{in}) : \mathbf{n}|} \right)^{\xi_r} \quad (11)$$

where h_{0r} and ξ_r are new model parameters for the PSR effect. The final relationship between the stress and strain increments can be derived as:

$$d\boldsymbol{\sigma} = \mathbf{E}^{ep} d\boldsymbol{\epsilon} \quad (12)$$

$$\mathbf{E}^{ep} = \mathbf{E} - B_1 \left[\frac{(\mathbf{E}\mathbf{R})(\mathbf{I}\mathbf{N}_r^*)}{K_{pr} + \mathbf{I}\mathbf{N}_r^* \mathbf{R}_r} - \frac{(\mathbf{E}\mathbf{R})(\mathbf{I}\mathbf{E})}{K_{pr} + \mathbf{I}\mathbf{E}\mathbf{R}_r} \right] - B_2 \left[\frac{(\mathbf{E}\mathbf{R}_r)(\mathbf{I}\mathbf{N}_r^*)}{\mathbf{I}\mathbf{N}_r^* \mathbf{R}_r} - \frac{(\mathbf{E}\mathbf{R}_r)(\mathbf{I}\mathbf{E})}{K_p + \mathbf{I}\mathbf{E}\mathbf{R}_r} \right] \quad (13)$$

$$\mathbf{N}_r^* = 2G \mathbf{N}_r \quad (14)$$

$$B_1 = \left(\frac{\mathbf{I}\mathbf{N}_r^* \mathbf{R}_r}{K_{pr} + \mathbf{I}\mathbf{N}_r^* \mathbf{R}_r} - \frac{K_p + \mathbf{I}\mathbf{E}\mathbf{R}_r}{K_{pr} + \mathbf{I}\mathbf{E}\mathbf{R}_r} \right)^{-1} \quad (15)$$

$$B_2 = \left(\frac{K_{pr} + \mathbf{I}\mathbf{N}_r^* \mathbf{R}_r}{\mathbf{I}\mathbf{N}_r^* \mathbf{R}_r} - \frac{K_{pr} + \mathbf{I}\mathbf{E}\mathbf{R}_r}{K_p + \mathbf{I}\mathbf{E}\mathbf{R}_r} \right)^{-1} \quad (16)$$

where \mathbf{E} is the elastic stiffness and \mathbf{N}_r is defined to project the total stress increment to the PSR direction. It can be seen that the modified PSR model obtained a stiffness tensor independent of stress increments and the linear relationship between the stress and strain increments, thus facilitating its finite element applications in boundary value problems.

4 MODEL CALIBRATION AND SIMULATIONS OF LABORATORY TESTS

The sand used in the VELACS centrifuge model test chosen to be simulated is Nevada sand. Its specific gravity is 2.67 and has maximum and minimum void ratios of 0.887 and 0.511, respectively. Therefore, a series of undrained triaxial tests (N50U1, N60U1002, N60U2501) and rotational shear tests using Nevada sand from Chen and Kutter [13] are adopted to calibrate the model parameters and verify the model. Some typical results are presented in Figure 1 & 2 and model parameters calibrated are listed in Table 1. The first 13 parameters are calibrated using the method proposed by Dafalias and Manzari [11, 14]. The PSR parameters h_{0r} and ξ_r are calibrated by the shear stress-strain relationships in undrained rotational shear tests while A_r is determined from the volumetric responses.

	Constant	Parameters	Value
Base model	Elasticity	G_0	150
		ν	0.25
	Critical state	M	1.45
		c	0.712
		λ_c	0.005
		e_0	0.807
		ξ	0.5
	Yield surface	m	0.05
	Plastic modulus	h_0	5.5
		c_h	0.968
		n^b	0.55
	Dilatency	A_0	0.6
		n^d	3.5
Modified model	Plastic modulus	h_{0r}	0.9
		ξ^r	1.1
	Dilatancy	A_r	0.5

Table 1: Model parameters of Nevada sand used in the numerical simulation.

Figure 1 presents the numerical predicted results along with the experimental results of undrained triaxial tests. The numerical simulations have successfully reproduced the sand responses under undrained monotonic loadings, including the contractive-dilative phase transformation, the peak stress ratio q/p' around 1.45 and the increase of axial strains with deviatoric stresses. It should be noted that there is no difference between the predicted results from the base model and modified PSR model because the direction of principal stresses does not change in the monotonic triaxial tests.

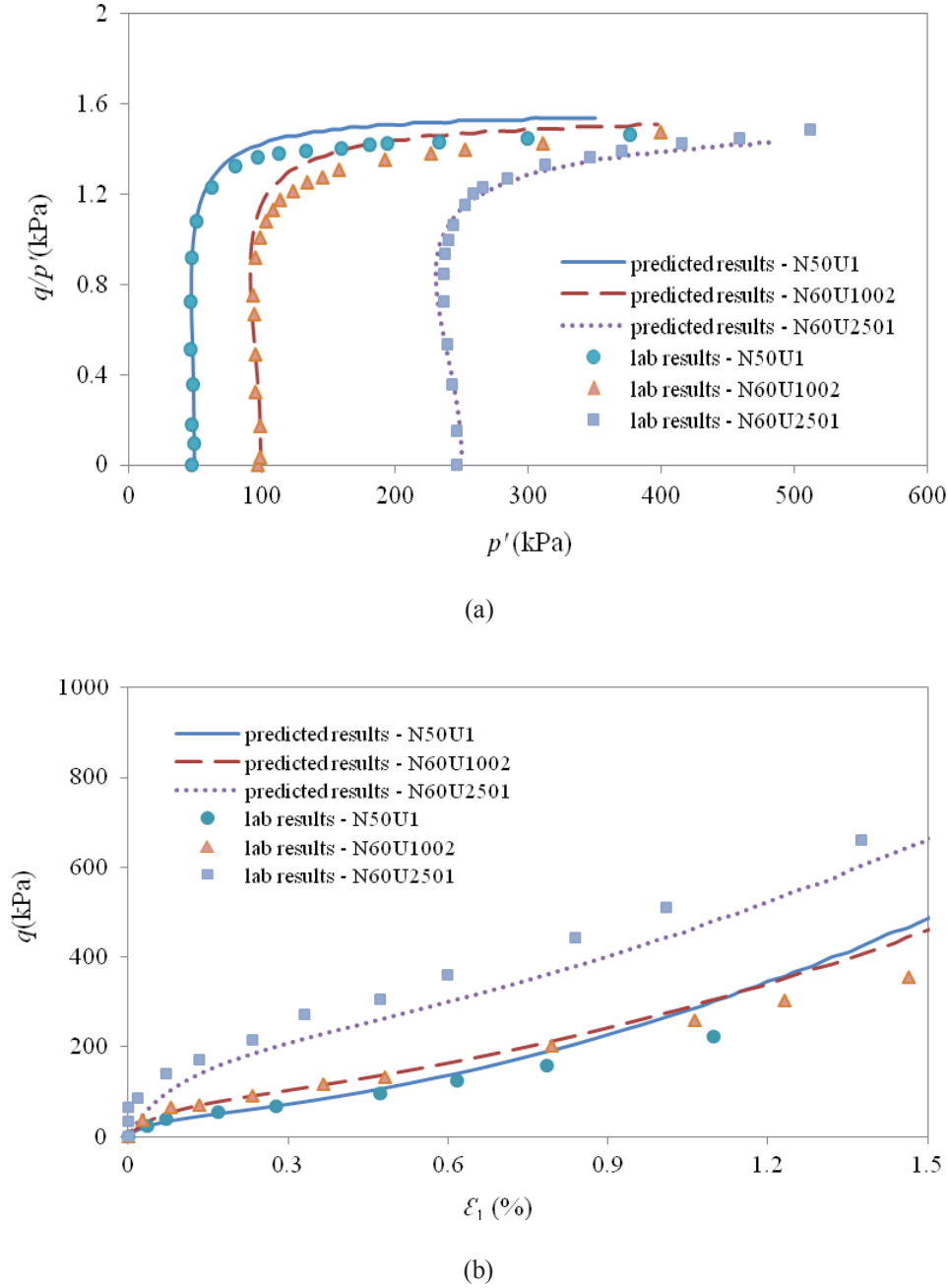
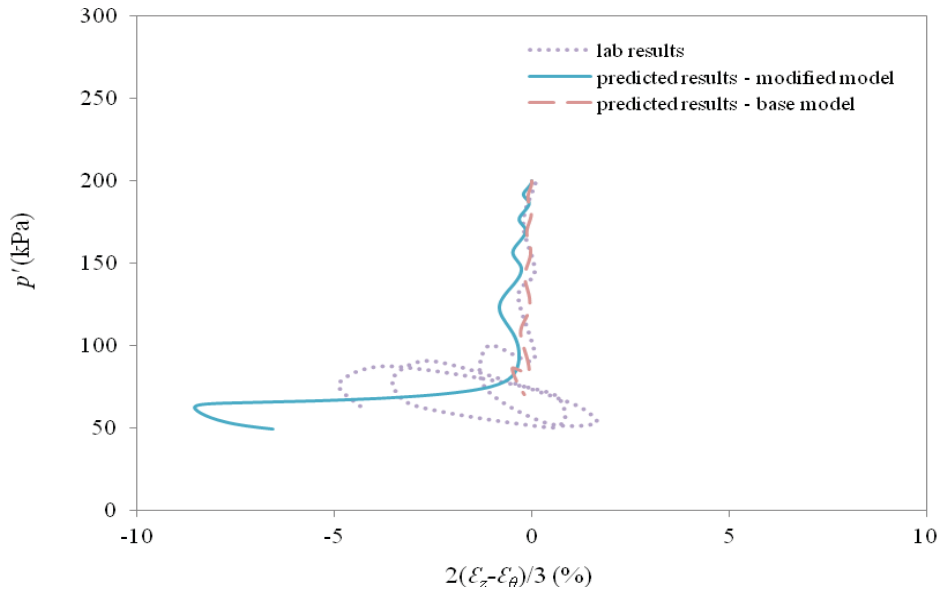
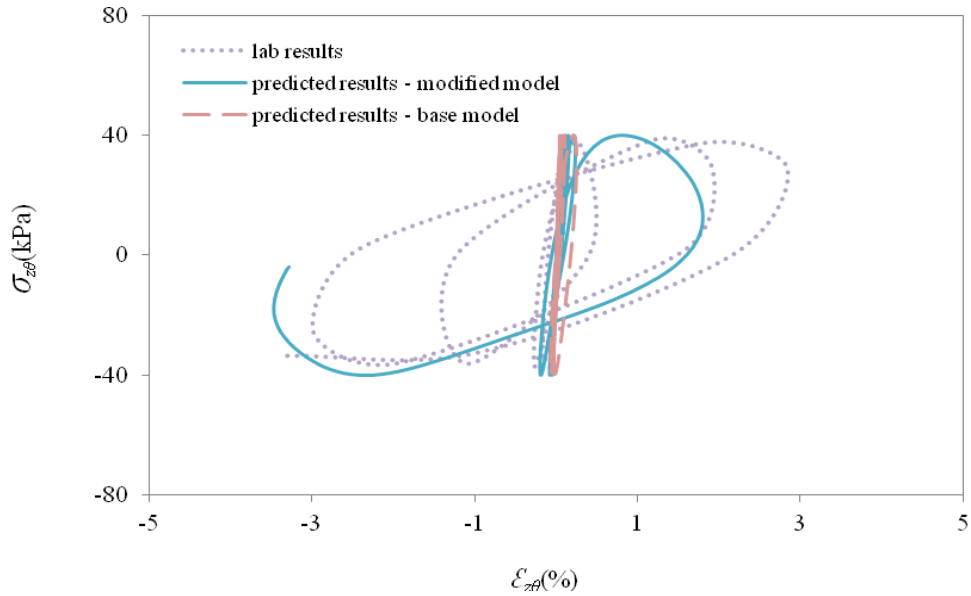


Figure 1: Predicted results and experimental results of stress-strain behaviors for undrained triaxial tests.

Figure 2 shows the numerical predicted results of the undrained rotational shear test from the base model and the modified model, as well as the experimental results. In Figure 2a, the effective confining pressure p' in the predicted results from the modified model reduced to the lowest value of 50 kPa, which agrees well with the experimental results. However, in the predicted results from the base model, both the reduction of p' and accumulation of deviatoric strain were underestimated. In the shear stress-strain behaviors in Figure 2b, the modified model has reproduced the accumulation of shear strain and dramatic shear strain increase in the last few cycles, which indicates the occurrence of liquefaction and agrees well with the experimental results. However, the base model still underestimates the shear strain accumulation because it is not able consider the PSR effect, which is important in cyclic loading conditions such as in the rotational shear test.



(a)



(b)

Figure 2: Predicted results and experimental results of stress-strain behaviors for undrained rotational shear test.

5 FINITE ELEMENT ANALYSIS

5.1 Problem definition

Model No.3 in VELACS centrifuge testing project is chosen to investigate the PSR effect and verify the modified model in boundary value conditions under earthquake loadings. The centrifuge model contains a 220 mm deep laminar box deposited with saturated sand, which is further horizontally divided into two layers with the relative density of 40% and 70%, respec-

tively (Figure 3). The soil sample is measured with 7 accelerometers, 10 pore water pressure transducers and 6 displacement LVDT transducers. Horizontal base shaking is then applied to the laminar box.

The numerical simulation is conducted using a fully coupled finite element computer code, which adopts the Hilber-Hughes-Taylor α time integration method and a predictor-multi-corrector algorithm to achieve quadratic accuracy [15]. The model scale gravitational acceleration of 50 g is used in the simulation and 30 seconds is considered in total, as the liquefaction occurs at the majority of the sand bed after 30 seconds.

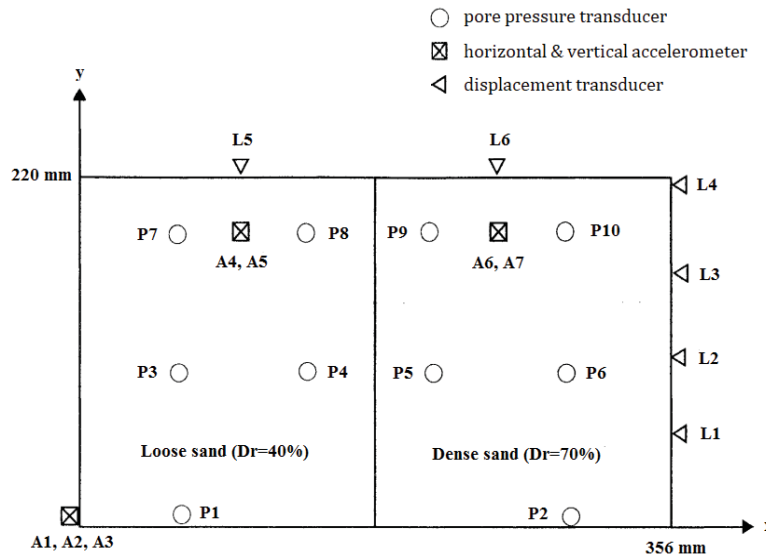


Figure 3: The front view configuration and the location of measuring instruments for the centrifuge model test.

5.2 Predicted results and comparison with the experimental data

The time histories of excess pore water pressure at typical locations are shown in Figure 4. Generally, the predicted results from the modified model have reached nearly the same peak value as the experimental data and agree well with the experimental results. In contrast, the base model has significantly underestimated the build-up of excess pore water pressures. For example, the peak value of excess pore water pressure from the base model only reached 27 kPa in location P3, which is 15 kPa lower than the experimental data. The stress path in the p' - q space at a typical location is presented in Figure 5. It is obvious that the modified model has brought the soil to liquefaction and captured the critical features such as the zero p' and the butterfly shape stress path in the liquefaction state while the base model only achieved the lowest p' value of 5 kPa and does not reach the liquefaction state. Figure 6 shows the predicted results of the displacement along with the experimental results in typical locations of L1 and L2. It can be seen that there are again significant differences between the predicted results from the two models. The modified model has reproduced the increase of displacement after the base shaking started and generally agrees with the experimental data, although slight overestimation can be observed at location L2 in the last few seconds. However, the maximum displacements in predicted results from the base model are 0.51 mm at location L1 and 1.52 mm at location L2, respectively, which is far from the experimental data. This is because the base model has failed in reproducing the PSR effect and liquefaction behaviors. The comparative study above has demonstrated that it is important to consider the PSR effect as ignoring it can cause the underestimation of the build-up of excess pore water pressure, the decrease of effective confining pressure and the increase of displacement, thus leading to inaccurate computations and unsafe designs.

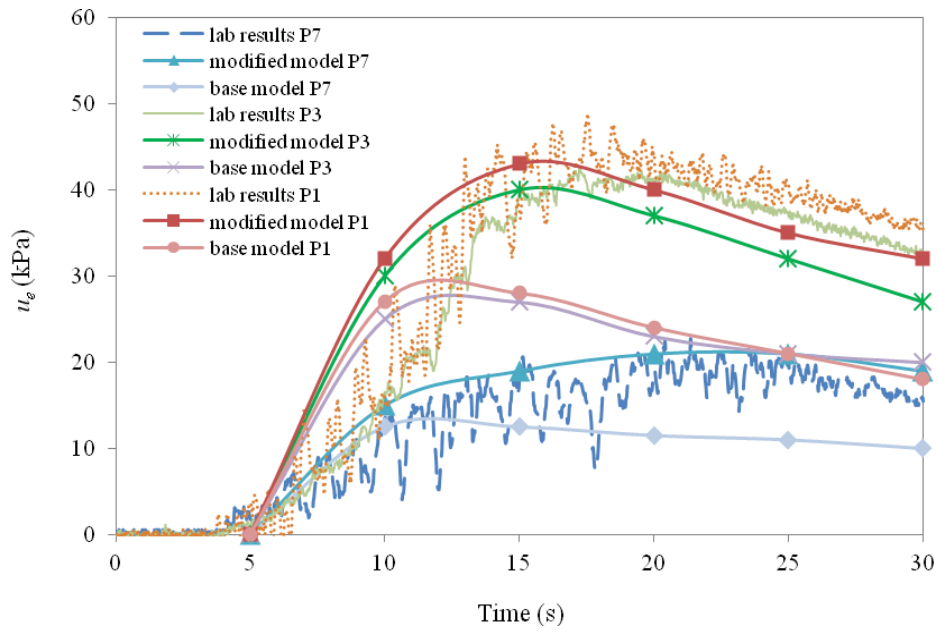
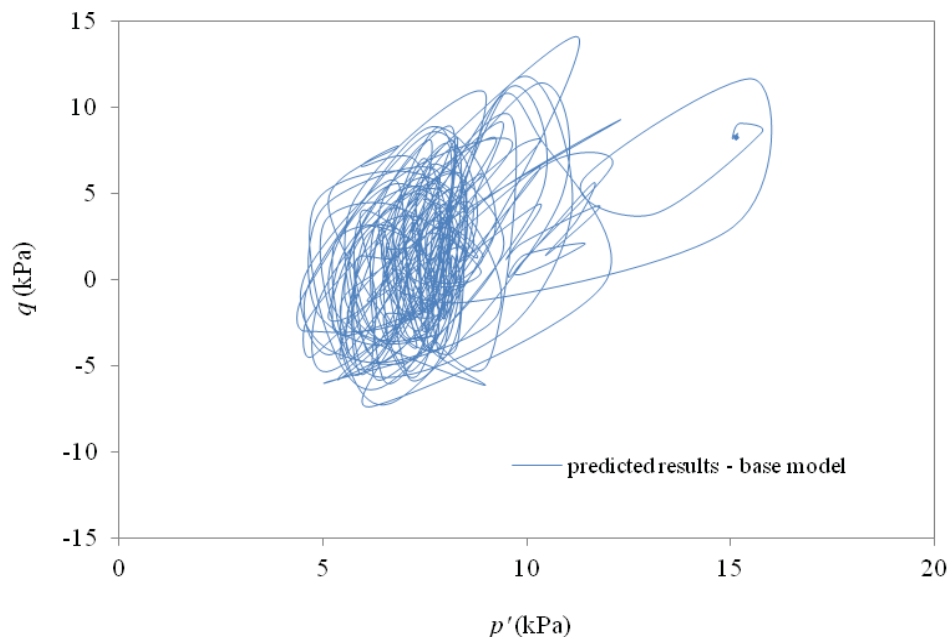
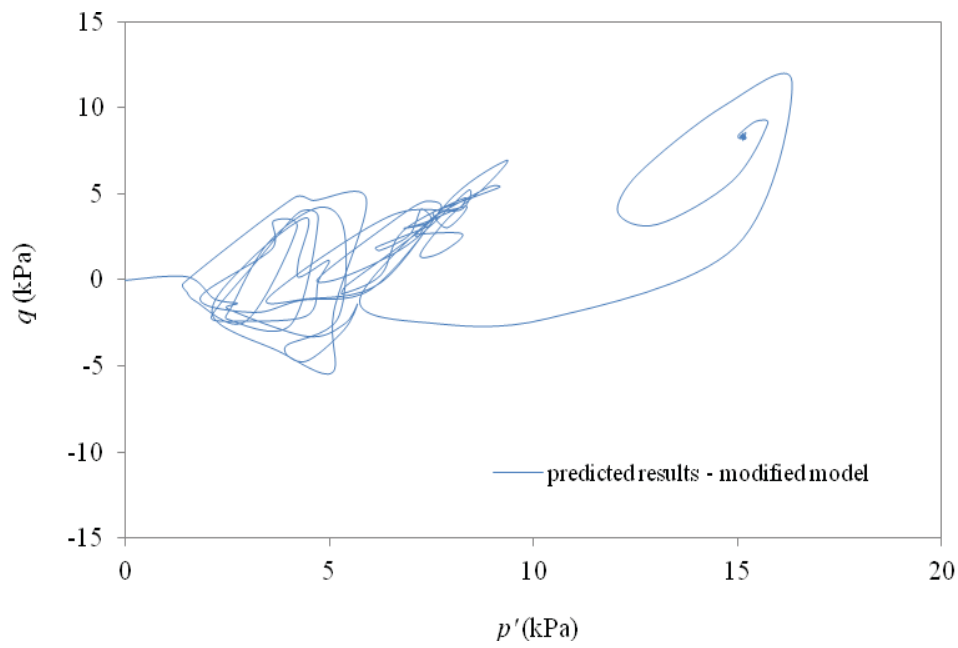


Figure 4: Predicted results and experimental results of the excess pore water pressure build-up in location P1, P3 and P7.

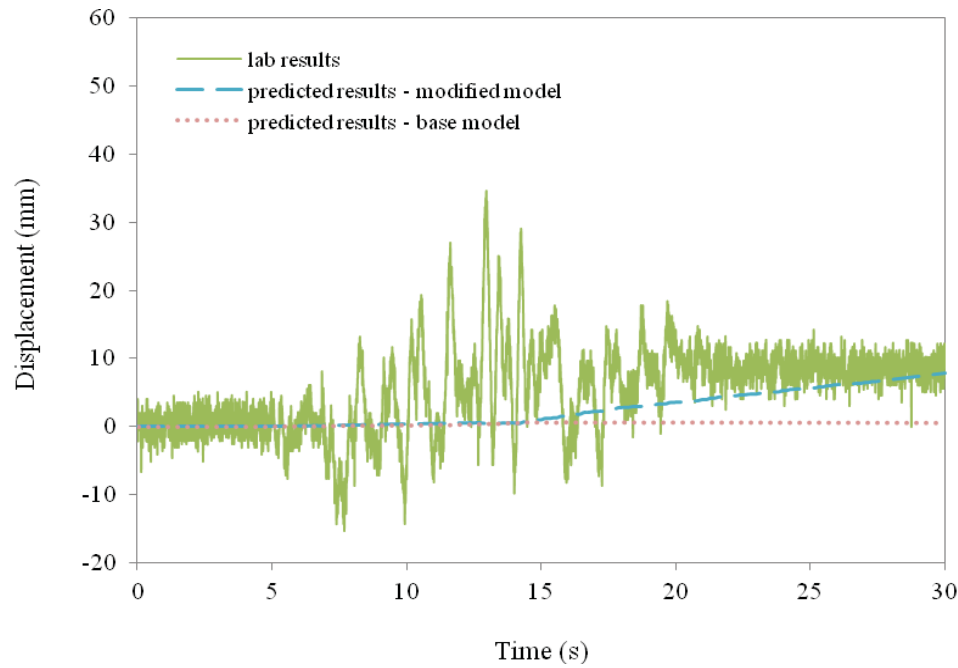


(a)

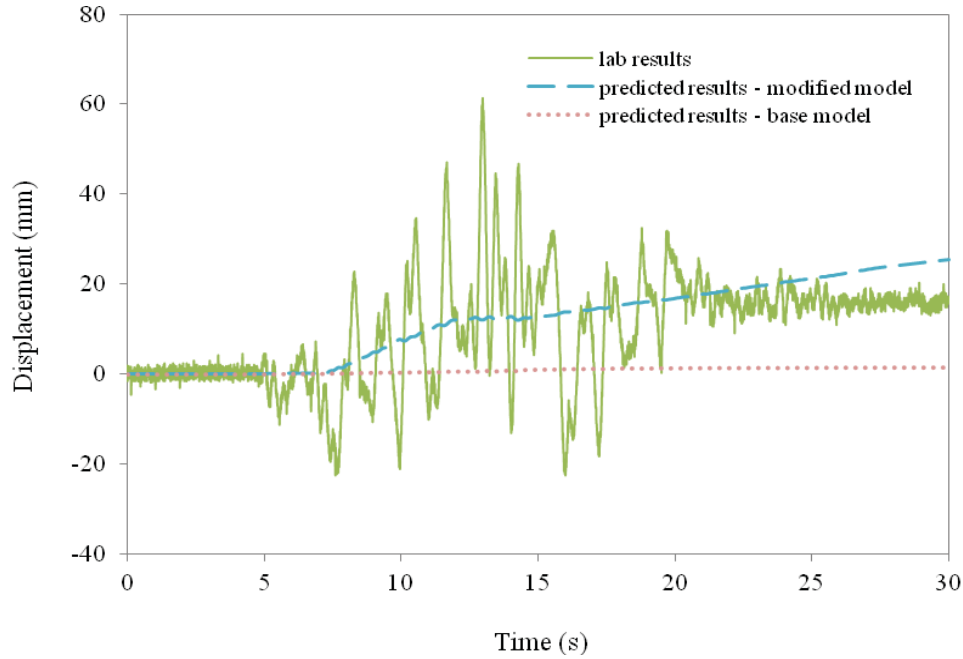


(b)

Figure 5: Predicted stress paths in location P7.



(a) Location L1



(b) Location L2

Figure 6: Predicted results and experimental results of the lateral displacement increase in location L1 and L2.

6 CONCLUSION

This paper presents the numerical investigation of the principal stress rotation under earthquake loadings using an elastoplastic sand model considering the PSR effect, which is improved from a bounding surface model with the critical state theory. The modified model is verified by a series of triaxial and rotational shear tests and then implement in the numerical simulation of a centrifuge model test under earthquake loadings involving the PSR. The predicted results from the base model and the modified model as well as the experimental results are presented and compared. The analysis shows that the base model can reproduce sand responses under monotonic loading conditions without the PSR but in most cases underestimates the build-up of excess pore water pressure, the decrease of effective confining pressure, the increase of displacement and fails to predict the liquefaction under loading conditions involving the PSR, which may lead to unsafe designs. In contrast, the modified PSR model provides much more accurate predictions than the base model as its predictions generally agree well with the experimental results and capture most of critical features of sand behaviors under the PSR. The comparative investigation demonstrates that it is important to consider the PSR effect in the simulation of geotechnical boundary value problems under earthquake loadings.

ACKNOWLEDGEMENTS

This research is supported by Zhejiang Natural Science Foundation, China (Project Code LQ19E090003), National Natural Science Foundation of China (NSFC Contract No. 51708040), and the post doctoral research program (236527) of Zhejiang University of Technology. These supports are appreciated.

REFERENCES

- [1] K. Ishihara, I. Towhata, Sand response to cyclic rotation of principal stress directions as induced by wave loads. *Soils and Foundations*, 23(4), 11-26, 1983.
- [2] K. Ishihara, A. Yamazaki, Analysis of wave-induced liquefaction in seabed deposits of sand. *Soils and Foundations*, 24(3), 85-100, 1984.
- [3] S.K. Bhatia, J. Schwab, I. Ishibashi, Cyclic simple shear, torsional shear and triaxial—A comparative study. *Advanced in the Art of Testing Soils Under Cyclic Conditions*, ASCE, New York, 232-254, 2015.
- [4] K. Miura, S. Miura, S. Toki, Deformation behavior of anisotropic dense sand under principal stress axes rotation. *Soils and Foundations*, 26(1), 36-52, 1986.
- [5] M. Gutierrez, K. Ishihara, I. Towhata, Flow theory for sand during rotation of principal stress direction, *Soils and Foundations*, 31(4), 121-132, 1991.
- [6] K. Arulanandan, F.R. Scott, Verification of numerical procedures for the analysis of soil Liquefaction problems. *Verification of Numerical Procedures for the Analysis of Soil Liquefaction Problems*. California, USA, 1993.
- [7] B. He, J.M. Zhang, W. Li, R. Wang, Numerical analysis of LEAP centrifuge tests on sloping liquefiable ground: Influence of dilatancy and post-liquefaction shear deformation. *Soil Dynamics and Earthquake Engineering*, 137, 106288, 2020.
- [8] K.I. Andrianopoulos, A.G. Papadimitriou, G.D. Bouckovalas, Bounding surface plasticity model for the seismic liquefaction analysis of geostructures. *Soil Dynamics and Earthquake Engineering*, 30, 895-911, 2010.
- [9] S. Sadeghian, L.N. Namin, Using state parameter to improve numerical prediction of a generalized plasticity constitutive model. *Computers and Geosciences*, 51, 255-268, 2013.
- [10] A. Pak, S. Seyfi, A. Ghassemi, Numerical investigation into the effects of geometrical and loading parameters on lateral spreading behavior of liquefied layer. *Acta Geotechnica*, 9, 1059-1071, 2014.
- [11] Y.F. Dafalias, M.T. Manzari, Simple plasticity sand model accounting for fabric change effects. *Journal of Engineering Mechanics*, ASCE, 130(6), 622-634, 2004.
- [12] Y. Yang, H.S. Yu, A kinematic hardening soil model considering the principal stress rotation. *International Journal for Numerical and Analytical Methods in Geomechanics*, 37, 2106-2134, 2013.
- [13] Y.R. Chen, B.L. Kutter, Contraction, dilation, and failure of sand in triaxial, torsional, and rotational shear tests. *Journal of Engineering Mechanics*, 135(10), 1155-1165, 2009.
- [14] M.T. Manzari, Y.F. Dafalias, A critical state two-surface plasticity model for sands. *Geotechnique*, 47(2), 255-272, 1997.
- [15] K.K. Muraleetharan, K.D. Mish, K. Arulanandan, A fully coupled non-linear dynamic analysis procedure and its verification using centrifuge test results. *International Journal for Numerical and Analytical Methods in Geomechanics*, 18, 305-325, 1994.

ENRICHED BEAM FINITE ELEMENT MODELS WITH TORSION AND SHEAR WARPING FOR DYNAMIC ANALYSIS OF FRAME STRUCTURES

Daniela Addessi, Paolo Di Re and Cristina Gatta

Department of Structural and Geotechnical Engineering, Sapienza University of Rome
via Eudossiana 18, 00184, Rome, Italy
e-mail: {daniela.addessi,paolo.dire,cristina.gatta}@uniroma1.it

Keywords: Seismic assessment, Dynamic analysis, Shear and torsion, Warping, Beam Finite Element.

Abstract. *This work investigates the performance of the enhanced beam Finite Element (FE) formulations proposed in [20] for the dynamic response of frame structures subjected to shear and torsional actions. These formulations introduce enriched kinematic descriptions to describe the out-of-plane deformations of beam cross-sections, in addition to the standard in-plane rigid modes. First model is based on the Vlasov's theory, enriched to include shear induced warping, and is developed according to a displacement-based approach. To this end, additional degrees of freedom (DOFs) are introduced at the two element end nodes and are used to interpolate warping along the element axis, so that the influence of warping restraints at the element boundaries are properly accounted for. Second model is based on the Benscoter's warping theory, also enriched to include shear warping, and is developed according to a mixed formulation free from shear-locking. Third model is the extension of second formulation and considers a general and accurate warping description. Indeed, a variable number of additional DOFs is introduced over the element cross-section and the warping displacement field is interpolated at two levels, along the beam axis and over the cross-section plane.*

Numerical analyses are presented to assess the performances of the three models in describing the seismic response of frame structures, when shear/torsional actions dominate the structural behavior. Results are compared with the solutions obtained from standard beam and more involving shell and brick FE models.

1 INTRODUCTION

Simulation of the mechanical behavior of large scale structures is a challenging task, although significant advances in computer technology were made during the last decades and increasingly accurate computational models were proposed. In particular, civil engineering structures subjected to seismic actions deserve special efforts, as the dynamic response to ground motions is strongly influenced by the material complex nonlinear behavior and multi-axial stress interaction. Many works have focused on the effects of in-plane and out-of plane cross-section deformation modes due to shear and torsional actions and, by employing enhanced beam models, they have proved that these phenomena can significantly reduce the element stiffness, influencing the natural frequencies of the structure [1] and producing local and global buckling under both static [2, 3, 4] and dynamic loading conditions [5]. Despite their considerable accuracy, full generalization of these models and their introduction in numerical codes for the analysis of large scale structures is hard to accomplish. Hence, more demanding two-dimensional (2D) plate/shell or three-dimensional (3D) Finite Element (FE) approaches are often used, although their lower efficiency and high computational cost. The adoption of beam FEs is to now the most convenient choice for the analysis of large scale framed structures. However, standard models are often based on classical rigid cross-section assumption and fail in correctly reproducing the structural response, even more when thin-walled members subjected to shear and torsion are considered.

Starting from the first proposals by Vlasov [6] and Bescoter [7], several enhanced beam theories and numerical models were presented [8, 9, 10, 11]. An extensive review of the first proposals is reported in [12], while more sophisticated formulations were recently developed, to include also effects due to shear forces, e.g. [13, 14, 15, 16, 17, 18]. However, only in few cases these models were focused on the analysis of large structures under dynamic loading conditions, e.g [19].

This work explores the application to dynamic field of the 3D beam FE formulations presented in [20] and originally developed for the static analysis of frame structures subjected to shear and torsional actions. Enriched kinematic descriptions are considered to include out-of-plane deformations of beam cross-sections, in addition to the classical in-plane rigid modes. Hence, warping effects related to both torsion and shear are accounted for.

First model is based on an extended Vlasov's theory that includes both torsional and shear warping and relies on an enriched displacement-based approach that prevents shear-locking [21]. The out-of-plane cross-section displacement field is assumed as the linear combination of three warping functions, a priori defined over the element cross-section, and the generalized cross-section torsional curvature and shear strains. By introducing additional degrees of freedom (DOFs) at the element end nodes, these generalized strains are interpolated along the axis as parabolic and linear functions, respectively. The model is referred to as Enhanced Vlasov Displacement-based Element (EVDE).

Second model is based on Bescoter's warping theory, also enriched to include both torsional and shear warping. As opposed to the first model, warping variables defined along the axis are assumed as independent kinematic quantities from cross-section strains. Hence, a mixed approach is followed, where the warping displacement field is interpolated along the element, together with the generalized cross-section stresses. The model is referred to as Simplified Warping Mixed Element (SWME).

Third model is the general extension of the above latter formulation. Indeed, in addition to the warping displacement interpolation along the element axis, this considers a 2D interpolation

over the cross-section plane, thus allowing for higher order descriptions of the out-of-plane deformations and full coupling of all stress components. The model is referred to as Enhanced Warping Mixed Element (EWME).

Main details of the adopted beam FE models are reviewed, discussing their extension to dynamic field. For EVDE and EWME, detailed derivation of the element governing equations under dynamic effects is reported in [22] and [23], respectively, and is briefly recalled here. More focus is dedicated to the dynamic extension of SWME, which is presented as a simplified case of that proposed for the EWME.

Numerical analyses on a steel L frame and a reinforced concrete (RC) shear wall are presented to assess the performances of the three models in describing the seismic response of the structures, when shear/torsional actions dominate the structural behavior. Elasto-plastic and plastic-damage nonlinear material behavior is considered. Results are compared with the solutions obtained from standard beam and more involving shell and brick FE models.

2 BEAM FINITE ELEMENT FORMULATIONS

The adopted model formulations are described referring to a straight beam with the local intrinsic reference system (x, y, z) , being x the axis parallel to the section centroid locus and y and z two general orthogonal axes lying on the cross-section plane. The element length and the 2D domain of the cross-section are indicated as L and $A(x)$, respectively.

Under the assumption of small displacements and strains, all models introduce the description of the out-of-plane deformations partially removing the classical hypothesis of rigid cross-sections. Hence, displacements $\mathbf{u}_m(x, y, z)$ of the generic point m are defined as the sum of cross-section rigid body motions, $\mathbf{u}_r(x, y, z)$, and warping displacements, $\mathbf{u}_w(x, y, z)$, i.e.:

$$\mathbf{u}_m(x, y, z) = \mathbf{u}_r(x, y, z) + \mathbf{u}_w(x, y, z) = \begin{Bmatrix} u_r(x, y, z) \\ v_r(x, y, z) \\ w_r(x, y, z) \end{Bmatrix} + \begin{Bmatrix} u_w(x, y, z) \\ 0 \\ 0 \end{Bmatrix} \quad (1)$$

Accordingly, three non-zero strain components are introduced, that is the axial elongation $\varepsilon_{xx}(x, y, z)$ and the two transverse shear strains, $\gamma_{xy}(x, y, z)$ and $\gamma_{xz}(x, y, z)$. These are collected in vector $\boldsymbol{\varepsilon}_m(x, y, z)$ and are work-conjugate to the axial, $\sigma_{xx}(x, y, z)$, and shear stresses in the cross-section plane, $\tau_{xy}(x, y, z)$ and $\tau_{xz}(x, y, z)$, collected in vector $\boldsymbol{\sigma}_m(x, y, z)$.

Based on the above assumptions, three enriched beam FE formulations are derived. These are presented in detail in [20] and are summarized in the following, focusing the attention on the warping description hypotheses and the derivation of the element governing equations including inertia effects.

2.1 Enhanced Vlasov Displacement-based Element (EVDE)

The EVDE formulation considers nine DOFs at each of the two end nodes, i and j , of the element, being these the six standard translations and rotations, collected in vectors $\mathbf{u}_{i/j}$ and $\boldsymbol{\theta}_{i/j}$, respectively, and three additional DOFs used to describe cross-section warping, i.e. the end cross-section torsional curvature, $\chi_{xi/j}$, and shear strains, $\gamma_{yi/j}$ and $\gamma_{zi/j}$, collected in vectors $\boldsymbol{\eta}_i = \{\chi_{xi} \ \gamma_{yi} \ \gamma_{zi}\}^T$ and $\boldsymbol{\eta}_j = \{\chi_{xj} \ \gamma_{yj} \ \gamma_{zj}\}^T$ (Figure 1). Hence, the nodal displacement vector is written as:

$$\hat{\mathbf{u}} = \{\mathbf{u}^T \ \boldsymbol{\eta}^T\}^T = \{\mathbf{u}_i^T \ \boldsymbol{\theta}_i^T \ \mathbf{u}_j^T \ \boldsymbol{\theta}_j^T \ \boldsymbol{\eta}_i^T \ \boldsymbol{\eta}_j^T\}^T \quad (2)$$

vectors \mathbf{u}^T and $\boldsymbol{\eta}^T$ collecting the standard and warping DOFs, respectively.

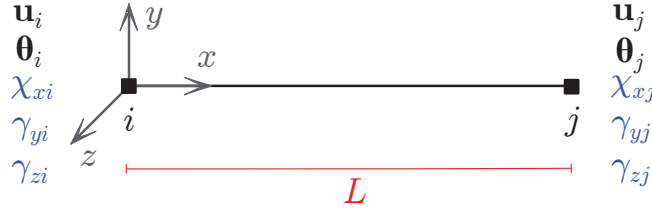


Figure 1: Standard (black) and warping (blue) nodal DOFs for the EVDE

A reference basic configuration is introduced to remove the element rigid body motions and only twelve basic displacements are used to define the element behavior. These are listed in vector $\hat{\mathbf{v}}$, that results as:

$$\hat{\mathbf{v}} = \{u_j \quad \theta_{zi} \quad \theta_{zj} \quad \theta_{xj} \quad \theta_{yi} \quad \theta_{yj} \quad \chi_{xi} \quad \gamma_{yi} \quad \gamma_{zi} \quad \chi_{xj} \quad \gamma_{yj} \quad \gamma_{zj}\}^T = \hat{\mathbf{a}}_v \hat{\mathbf{u}} \quad (3)$$

being $\hat{\mathbf{a}}_v$ the kinematic operator that removes the rigid body motions [20].

To avoid shear locking issues, generalized cross-section displacement interpolation is performed by assuming the two cross-section shear strain fields, $\gamma_y(x)$ and $\gamma_z(x)$, as independent quantities, instead of the bending rotations, $\theta_y(x)$ and $\theta_z(x)$ [21]. Thus, cross-section kinematic vector results as:

$$\hat{\mathbf{u}}_s(x) = \{u(x) \quad v(x) \quad \theta_x(x) \quad w(x) \quad \gamma_y(x) \quad \gamma_z(x)\}^T \quad (4)$$

being $u(x)$, $v(x)$ and $w(x)$ the rigid traslations and $\theta_x(x)$ the rigid torsional rotation. The nodal DOFs introduced permit to express the displacement fields $u(x)$, $\gamma_y(x)$ and $\gamma_z(x)$ as linear functions along the element axis, and $v(x)$, $w(x)$ and $\theta_x(x)$ as cubic polynomials. The relations between $\hat{\mathbf{u}}_s(x)$ and $\hat{\mathbf{v}}$ is written in compact form as:

$$\hat{\mathbf{u}}_s(x) = \hat{\mathbf{N}}(x) \hat{\mathbf{v}} \quad (5)$$

where $\hat{\mathbf{N}}(x)$ is the element shape function matrix containing the polynomial interpolations for the displacement and shear strain fields [20].

By enforcing the cross-section compatibility conditions, the generalized cross-section strain vector, $\hat{\mathbf{e}}(x) = \mathbf{D}(x) \hat{\mathbf{u}}_s(x)$, is introduced, being $\mathbf{D}(x)$ the compatibility differential operator. Vector $\hat{\mathbf{e}}(x)$ collects the axial strain, $\varepsilon_G(x)$, flexural curvatures, $\chi_z(x)$ and $\chi_y(x)$, torsional curvature, $\chi_x(x)$, shear strains, $\gamma_y(x)$ and $\gamma_z(x)$, and additional warping strains, $\zeta_x(x) = \chi'_x(x)$, $\zeta_y(x) = \gamma'_y(x)$, $\zeta_z(x) = \gamma'_z(x)$, related to warping, i.e.:

$$\hat{\mathbf{e}}(x) = \{\varepsilon_G(x) \quad \chi_z(x) \quad \gamma_y(x) \quad \chi_x(x) \quad \chi_y(x) \quad \gamma_z(x) \quad \zeta_x(x) \quad \zeta_y(x) \quad \zeta_z(x)\}^T \quad (6)$$

where the apex denotes the derivative with respect to x . Hence, the following relationship holds between the generalized cross-section strains and the nodal basic displacement vector:

$$\hat{\mathbf{e}}(x) = \hat{\mathbf{D}}(x) \hat{\mathbf{N}}(x) \hat{\mathbf{v}} = \hat{\mathbf{a}}(x) \hat{\mathbf{v}} \quad (7)$$

where $\hat{\mathbf{a}}(x) = \hat{\mathbf{D}}(x) \hat{\mathbf{N}}(x)$ is the cross-section strain compatibility matrix.

According to Vlasov's warping description [6], strain fields $\gamma_y(x)$, $\gamma_z(x)$ and $\chi_x(x)$ are used to describe cross-section out-of-plane displacements. Indeed, displacement field $u_w(x, y, z)$ is defined as the linear combination of assigned 2D warping functions, defined over the cross-section area and collected in vector $\mathbf{M}_\eta(y, z) = \{M_{\eta x}(y, z) \quad M_{\eta y}(y, z) \quad M_{\eta z}(y, z)\}$. These

are associated to torsion and shear along y - and z -directions, respectively, and, thus, are combined by means of the corresponding strain fields, assumed as warping parameters, $\eta_s(x) = \{\chi_x(x) \ \gamma_y(x) \ \gamma_z(x)\}^T$, i.e.:

$$u_w(x, y, z) = \mathbf{M}_\eta(y, z) \eta_s(x) \quad (8)$$

The warping functions $M_{\eta_x}(y, z)$, $M_{\eta_y}(y, z)$ and $M_{\eta_z}(y, z)$ are determined according to the numerical procedure described in [20], which ensures the orthogonality conditions between rigid and warping displacements, as required by Equation (1). Examples of warping functions are depicted in Figure 2 for a S-shaped cross-section.

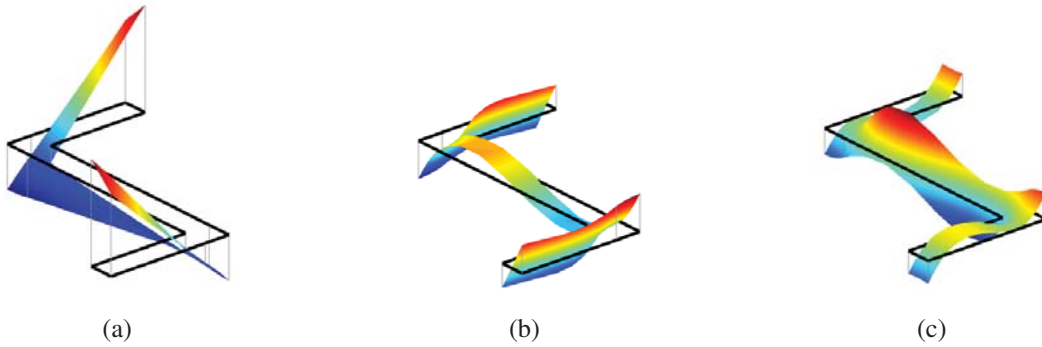


Figure 2: Warping functions for a S-shaped cross-section related to (a) torsion, $M_{\eta_x}(y, z)$, (b) shear along y -axis, $M_{\eta_y}(y, z)$, and (c) shear along z -axis, $M_{\eta_z}(y, z)$

Accounting for the warping description in Equation (8), material strains are determined as:

$$\epsilon_m(x, y, z) = \hat{\alpha}(y, z) \hat{e}(x) \quad (9)$$

where $\hat{\alpha}(y, z)$ is the cross-section compatibility operator. By enforcing the virtual work principle, the generalized section stresses, $\hat{s}(x)$, are defined as:

$$\hat{s}(x) = \int_{A(x)} \hat{\alpha}^T(y, z) \sigma_m(x, y, z) dA \quad (10)$$

with:

$$\hat{s}(x) = \{N(x) \ M_z(x) \ T_y^p(x) \ M_x^p(x) \ M_y(x) \ T_z^p(x) \ B_x(x) \ B_y(x) \ B_z(x)\}^T \quad (11)$$

being $N(x)$ the axial stress, $M_z(x)$ and $M_y(x)$ the bending moments and $B_x(x)$, $B_y(x)$ and $B_z(x)$ the bi-moments, work-conjugate to $\zeta_x(x)$, $\zeta_y(x)$, $\zeta_z(x)$ [6, 13], i.e.:

$$B_k(x) = \int_{A(x)} M_{\eta_k}(y, z) \sigma_{xx}(x, y, z) dA, \quad \text{with } k = x, y, z \quad (12)$$

Quantities $M_x^p(x)$, $T_y^p(x)$ and $T_z^p(x)$ are the *primary* torsional moment and shear stresses, each resulting as the sum of the corresponding standard stress, $M_x(x)$, $T_y(x)$ or $T_z(x)$, and bi-shear, $M_x^s(x)$, $T_y^s(x)$ or $T_z^s(x)$.

2.1.1 Derivation of the element governing equations

According to the displacement-based formulations [24], element equilibrium equations are derived from the stationarity of a Lagrangian functional, $\mathcal{L} [\mathbf{u}_m(x, y, z), \dot{\mathbf{u}}_m(x, y, z)]$, function of the displacements, $\mathbf{u}_m(x, y, z)$, and velocities, $\dot{\mathbf{u}}_m(x, y, z)$, and expressed as the difference of the element kinetic, $T [\dot{\mathbf{u}}_m(x, y, z)]$, and potential energy, $\Pi [\mathbf{u}_m(x, y, z)]$, that is:

$$\mathcal{L} [\mathbf{u}_m(x, y, z), \dot{\mathbf{u}}_m(x, y, z)] = T [\dot{\mathbf{u}}_m(x, y, z)] - \Pi [\mathbf{u}_m(x, y, z)] \quad (13)$$

Kinetic energy is expressed first in terms of cross-section velocities, $\dot{\hat{\mathbf{u}}}_s(x)$, and then in terms of nodal velocities, $\dot{\hat{\mathbf{u}}}$, as reported in details in [22]. Hence, it finally results as:

$$T (\dot{\hat{\mathbf{u}}}) = \frac{1}{2} \dot{\hat{\mathbf{u}}}^T (\mathbf{m}_r + \mathbf{m}_w) \dot{\hat{\mathbf{u}}} = \frac{1}{2} \dot{\hat{\mathbf{u}}}^T \mathbf{m} \dot{\hat{\mathbf{u}}} \quad (14)$$

where \mathbf{m}_r and \mathbf{m}_w are the element rigid and warping mass matrices related to the inertia effects due to $\mathbf{u}_r(x, y, z)$ and $u_w(x, y, z)$, respectively, while $\mathbf{m} = \mathbf{m}_r + \mathbf{m}_w$ is the total element consistent mass matrix.

Similarly, potential energy is expressed first in terms of cross-section quantities, $\hat{\mathbf{e}}(x)$ and $\hat{\mathbf{s}}(x)$, and then in terms of nodal quantities, $\hat{\mathbf{u}}$ and $\hat{\mathbf{p}}$, this latter collecting in vector \mathbf{p} the standard forces and couples, $\mathbf{p}_{i/j}$ and $\mathbf{m}_{i/j}$, work-conjugate to $\mathbf{u}_{i/j}$ and $\theta_{i/j}$, and in vector β the additional generalized forces, β_i and β_j , work-conjugate to the warping DOFs, η_i and η_j , that is:

$$\hat{\mathbf{p}} = \{\mathbf{p}^T \quad \beta^T\}^T = \{\mathbf{p}_i^T \quad \mathbf{m}_i^T \quad \mathbf{p}_j^T \quad \mathbf{m}_j^T \quad \beta_i^T \quad \beta_j^T\}^T \quad (15)$$

Hence, it results:

$$\Pi (\hat{\mathbf{u}}) = \hat{\mathbf{u}}^T \left\{ \hat{\mathbf{a}}_v^T \left[\int_L \hat{\mathbf{a}}^T(x) \hat{\mathbf{s}}(x) dx - \int_L \hat{\mathbf{N}}^T(x) \hat{\mathbf{q}}_s(x) dx \right] - \hat{\mathbf{p}} + \hat{\mathbf{p}}_{rq} \right\} \quad (16)$$

where $\hat{\mathbf{p}}_{rq}$ is the vector collecting the basic reaction forces due to distributed loads, $\hat{\mathbf{q}}_s(x)$. Under static loading conditions, the element equilibrium equations state that the term in brackets must equal the basic nodal force vector, $\hat{\mathbf{q}}$, work-conjugate to $\hat{\mathbf{v}}$ [20]. Hence, by considering Equations (14) and (16), expression of \mathcal{L} in terms of nodal quantities is obtained as:

$$\mathcal{L} (\dot{\hat{\mathbf{u}}}, \hat{\mathbf{u}}) = \frac{1}{2} \dot{\hat{\mathbf{u}}}^T \mathbf{m} \dot{\hat{\mathbf{u}}} - \hat{\mathbf{u}}^T (\hat{\mathbf{a}}_v^T \hat{\mathbf{q}} - \hat{\mathbf{p}} + \hat{\mathbf{p}}_{rq}) \quad (17)$$

and the element governing equations are derived by enforcing its stationarity as:

$$\frac{d}{dt} \frac{\partial \mathcal{L} (\dot{\hat{\mathbf{u}}}, \hat{\mathbf{u}})}{\partial \dot{\hat{\mathbf{u}}}} - \frac{\partial \mathcal{L} (\dot{\hat{\mathbf{u}}}, \hat{\mathbf{u}})}{\partial \hat{\mathbf{u}}} = \frac{d}{dt} \frac{\partial T (\dot{\hat{\mathbf{u}}})}{\partial \dot{\hat{\mathbf{u}}}} + \frac{\partial \Pi (\hat{\mathbf{u}})}{\partial \hat{\mathbf{u}}} = \mathbf{0} \quad (18)$$

which gives the element equilibrium equations in the form:

$$\mathbf{m} \ddot{\hat{\mathbf{u}}} + \hat{\mathbf{a}}_v^T \hat{\mathbf{q}} + \hat{\mathbf{p}}_{rq} = \hat{\mathbf{p}} \quad (19)$$

Linearization of Equation (19) results as:

$$\mathbf{m} \Delta \ddot{\hat{\mathbf{u}}} + \hat{\mathbf{a}}_v^T \Delta \hat{\mathbf{q}} = \mathbf{m} \Delta \ddot{\hat{\mathbf{u}}} + \hat{\mathbf{a}}_v^T \hat{\mathbf{k}}_v \Delta \hat{\mathbf{v}} = \mathbf{m} \Delta \ddot{\hat{\mathbf{u}}} + \underbrace{\hat{\mathbf{a}}_v^T \hat{\mathbf{k}}_v \hat{\mathbf{a}}_v}_{\hat{\mathbf{k}}} \Delta \hat{\mathbf{u}} = \Delta \hat{\mathbf{p}} \quad (20)$$

where Δ indicates the quantity increment and $\hat{\mathbf{k}}$ is the element tangent stiffness matrix, being:

$$\hat{\mathbf{k}}_v = \frac{\partial \hat{\mathbf{q}}}{\partial \hat{\mathbf{v}}} = \int_L \hat{\mathbf{a}}^T(x) \frac{\partial \hat{\mathbf{s}}(x)}{\partial \hat{\mathbf{e}}(x)} \frac{\partial \hat{\mathbf{e}}(x)}{\partial \hat{\mathbf{v}}} dx = \int_L \hat{\mathbf{a}}^T(x) \frac{\partial \hat{\mathbf{s}}(x)}{\partial \hat{\mathbf{e}}(x)} \hat{\mathbf{a}}(x) dx \quad (21)$$

2.2 Simplified Warping Mixed Element

The SWME formulation considers an arbitrary number of nodes, n_w , located along the element axis (Figure 3), always including end nodes, i and j . At each node, three DOFs are added

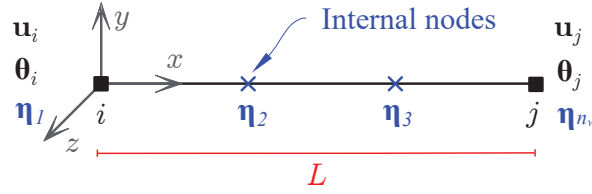


Figure 3: Standard (black) and warping (blue) nodal DOFs for the SWME model

and used to interpolate cross-section warping due to torsion and shear. These are collected in vector $\eta_n = \{\eta_{xn} \ \eta_{yn} \ \eta_{zn}\}^T$, where subscript $n = 1, \dots, n_w$ indicates the node number. Hence, the nodal displacement vector is written as:

$$\hat{\mathbf{u}} = \{\mathbf{u}^T \ \boldsymbol{\eta}^T\}^T = \{\mathbf{u}_i^T \ \boldsymbol{\theta}_i^T \ \mathbf{u}_j^T \ \boldsymbol{\theta}_j^T \ \boldsymbol{\eta}_1^T \ \boldsymbol{\eta}_2^T \ \dots \ \boldsymbol{\eta}_{n_w}^T\}^T \quad (22)$$

The element rigid body motions are removed from the standard DOFs, \mathbf{u} , and vector \mathbf{v} , collecting the standard basic nodal displacements, is obtained as follows:

$$\mathbf{v} = \{u_j \ \theta_{zi} \ \theta_{zj} \ \theta_{xj} \ \theta_{yi} \ \theta_{yj}\}^T = \mathbf{a}_v \mathbf{u} \quad (23)$$

being \mathbf{a}_v the standard element compatibility matrix [18]. The total basic deformation displacement vector $\hat{\mathbf{v}}$ reads:

$$\hat{\mathbf{v}} = \{\mathbf{v}^T \ \eta_{x1} \ \eta_{y1} \ \eta_{z1} \ \dots \ \eta_{xn_w} \ \eta_{yn_w} \ \eta_{zn_w}\}^T = \{\mathbf{v}^T \ \boldsymbol{\eta}^T\}^T \quad (24)$$

The SWME model follows a mixed beam formulation [25] where standard generalized cross-section stresses, $\mathbf{s}(x) = \{N(x) \ M_z(x) \ T_y(x) \ M_x(x) \ M_y(x) \ T_z(x)\}^T$, are interpolated along the element axis, by enforcing the equilibrium conditions in strong form, i.e.:

$$\mathbf{s}(x) = \mathbf{b}(x) \mathbf{q} + \mathbf{s}_q(x) \quad (25)$$

being $\mathbf{q} = \{p_{xj} \ m_{zi} \ m_{zj} \ m_{xj} \ m_{yi} \ m_{yj}\}^T$ the vector collecting the basic nodal forces work-conjugate to \mathbf{v} , $\mathbf{b}(x)$ the equilibrium matrix [23] and $\mathbf{s}_q(x)$ the generalized section stress vector due to distributed loads.

In addition, the warping displacement field $u_w(x, y, z)$ is interpolated. To this end, Benscoter's warping description is adopted [7], where, similarly to Equation (8), $u_w(x, y, z)$ is defined as the linear combination of warping functions, $\mathbf{M}_\eta(y, z)$. However, independent warping parameters, $\eta_s(x) = \{\eta_x(x) \ \eta_y(x) \ \eta_z(x)\}^T$, are considered to describe warping variation along x . Hence, by exploiting the additional warping DOFs, η_{xn} , η_{yn} and η_{zn} at the element nodes, polynomial interpolation of fields $\eta_x(x)$, $\eta_y(x)$ and $\eta_z(x)$, respectively, is introduced and Equation (8) is written as:

$$u_w(x, y, z) = \sum_{n=1}^{n_w} N_n(x) \mathbf{M}_\eta(y, z) \boldsymbol{\eta}_n \quad (26)$$

being $N_n(x)$ the Lagrange polynomial shape function associated to node n .

The material strains $\epsilon_m(x, y, z)$ are, thus, determined as:

$$\begin{aligned}\epsilon_m(x, y, z) &= \alpha(y, z) \mathbf{e}(x) + \alpha_\zeta(y, z) \zeta_s(x) + \alpha_\eta(y, z) \eta_s(x) = \\ &= \alpha(y, z) \mathbf{e}(x) + \sum_{n=1}^{n_w} \left[\frac{\partial N_n(x)}{\partial x} \alpha_\zeta(y, z) + N_n(x) \alpha_\eta(y, z) \right] \eta_n\end{aligned}\quad (27)$$

where three contributions are distinguished, the first related to rigid cross-section displacements and the others to warping. Vector $\mathbf{e}(x)$ collects the standard generalized cross-section strains work-conjugate to $\mathbf{s}(x)$ and matrix $\alpha(y, z)$ is the compatibility operator, while vector $\zeta_s(x) = \{\zeta_x(x) \ \zeta_y(x) \ \zeta_z(x)\}^T$ contains the strain quantities assumed as equal to the derivatives of the warping parameters with respect to x (see also Equation (6)). Matrices $\alpha_\zeta(y, z)$ and $\alpha_\eta(y, z)$ are compatibility operators related to the warping field with size 3×3 [20].

The virtual work equivalence, enforced by alternatively assigning a virtual variation to the three fields composing $\epsilon_m(x, y, z)$ [20], leads to the definition of standard, $\mathbf{s}(x)$, and warping, $\mathbf{b}_w(x)$ and $\mathbf{t}_w(x)$, generalized cross-section stresses, that is:

$$\mathbf{s}(x) = \int_{A(x)} \alpha^T(y, z) \boldsymbol{\sigma}_m(x, y, z) dA \quad (28)$$

$$\mathbf{b}_w(x) = \int_{A(x)} \alpha_\zeta(y, z)^T \boldsymbol{\sigma}_m(x, y, z) dA, \quad \mathbf{t}_w(x) = \int_{A(x)} \alpha_\eta(y, z)^T \boldsymbol{\sigma}_m(x, y, z) dA \quad (29)$$

The latter are work-conjugate to $\zeta_s(x)$ and $\eta_s(x)$, respectively, and are equivalent to the *bi-moments* and *bi-shears* introduced in the EVDE model.

2.2.1 Derivation of the element governing equations

The element governing equations are derived from the stationarity of an extended Lagrangian functional, expressed as function of four independent fields, being these the material rigid displacements, $\mathbf{u}_r(x, y, z)$, total strains, $\epsilon_m(x, y, z)$, and stresses, $\boldsymbol{\sigma}_m(x, y, z)$, and warping displacement, $u_w(x, y, z)$, i.e.:

$$\mathcal{L}(\mathbf{u}_r, \epsilon_m, \boldsymbol{\sigma}_m, u_w, \dot{\mathbf{u}}_r, \dot{u}_w) = T(\dot{\mathbf{u}}_r, \dot{u}_w) - \Pi(\mathbf{u}_r, \epsilon_m, \boldsymbol{\sigma}_m, u_w) \quad (30)$$

where dependency of the quantities from spatial coordinates x, y and z is omitted for brevity. The kinetic energy is expressed first in terms of rigid cross-section velocities, $\dot{\mathbf{u}}_s(x)$, being $\mathbf{u}_s(x) = \{u(x) \ v(x) \ \theta_x(x) \ w(x) \ \theta_y(x) \ \theta_z(x)\}^T$, and then in terms of all nodal velocities, $\dot{\mathbf{u}}$ and $\dot{\boldsymbol{\eta}}$, following [23]. This is accomplished by accounting for Equation (26) and by expressing the rigid cross-section displacements and velocities in terms of nodal DOFs as follows:

$$\mathbf{u}_s(x) = \mathbf{N}_s(x) \mathbf{u} + \mathbf{N}_w(x) \boldsymbol{\eta} \quad \text{and} \quad \dot{\mathbf{u}}_s(x) = \mathbf{N}_s(x) \dot{\mathbf{u}} + \mathbf{N}_w(x) \dot{\boldsymbol{\eta}} \quad (31)$$

where $\mathbf{N}_s(x)$ and $\mathbf{N}_w(x)$ are the shape function matrices relating $\mathbf{u}_s(x)$ to the standard and warping nodal DOFs, \mathbf{u} and $\boldsymbol{\eta}$, respectively. These are derived by using the unit load method, described in more detail in [23] for the EWME. Hence, the kinetic energy results as:

$$T(\dot{\mathbf{u}}, \dot{\boldsymbol{\eta}}) = \frac{1}{2} \dot{\mathbf{u}}^T \mathbf{m}_{rr} \dot{\mathbf{u}} + \dot{\mathbf{u}}^T \mathbf{m}_{rw} \dot{\boldsymbol{\eta}} + \dot{\boldsymbol{\eta}}^T \mathbf{m}_{wr} \dot{\mathbf{u}} + \frac{1}{2} \dot{\boldsymbol{\eta}}^T (\mathbf{m}_{ww}^r + \mathbf{m}_{ww}) \dot{\boldsymbol{\eta}} \quad (32)$$

where \mathbf{m}_{rr} , \mathbf{m}_{rw} , \mathbf{m}_{wr} and \mathbf{m}_{ww}^r are the element mass matrices associated to the generalized rigid cross-section velocity $\dot{\mathbf{u}}_s(x)$ and are defined as:

$$\begin{aligned} \mathbf{m}_{rr} &= \int_L \mathbf{N}_s^T(x) \mathbf{m}_s(x) \mathbf{N}_s(x) dx, & \mathbf{m}_{rw} &= \int_L \mathbf{N}_s^T(x) \mathbf{m}_s(x) \mathbf{N}_w(x) dx = \mathbf{m}_{wr}^T \\ \mathbf{m}_{ww}^r &= \int_L \mathbf{N}_w^T(x) \mathbf{m}_s(x) \mathbf{N}_w(x) dx \end{aligned} \quad (33)$$

being $\mathbf{m}_s(x)$ the standard rigid cross-section mass matrix [23], while \mathbf{m}_{ww} is the element mass matrix associated to the warping velocity $\dot{u}_w(x, y, z)$ and is defined as:

$$\mathbf{m}_{ww} = \int_L \begin{bmatrix} N_1(x) \mathbf{m}_{sw}(x) N_1(x) & \dots & N_1(x) \mathbf{m}_{sw}(x) N_{n_w}(x) \\ \vdots & \ddots & \vdots \\ N_{n_w}(x) \mathbf{m}_{sw}(x) N_1(x) & \dots & N_{n_w}(x) \mathbf{m}_{sw}(x) N_{n_w}(x) \end{bmatrix} dx \quad (34)$$

being $\mathbf{m}_{sw}(x)$ the cross-section mass matrix associated to $\dot{u}_w(x, y, z)$, that results as:

$$\mathbf{m}_{sw}(x) = \int_{A(x)} \rho(x, y, z) \mathbf{M}_\eta^T(y, z) \mathbf{M}_\eta(y, z) dA \quad (35)$$

where $\rho(x, y, z)$ indicates the material density.

Similarly, the potential energy is expressed first in terms of the standard cross-section quantities, $\mathbf{u}_s(x)$, $\mathbf{e}(x)$ and $\mathbf{s}(x)$, and warping displacements, $u_w(x, y, z)$, and then in terms of standard cross-section strains and stresses, $\mathbf{e}(x)$ and $\mathbf{s}(x)$, and nodal DOFs, \mathbf{u} and $\boldsymbol{\eta}$. Hence, it results:

$$\begin{aligned} \Pi(\mathbf{u}, \mathbf{e}, \mathbf{s}, \boldsymbol{\eta}) &= \int_V \boldsymbol{\varepsilon}_m^T[\mathbf{e}, u_w(\boldsymbol{\eta})] \boldsymbol{\sigma}_m(\boldsymbol{\varepsilon}_m) dV + \int_L \mathbf{s}^T \{ \mathbf{e}[\mathbf{u}_s(\mathbf{u}, \boldsymbol{\eta})] - \mathbf{e} \} dx + \\ &+ \Pi_{ext}[\mathbf{u}, \boldsymbol{\eta}, \mathbf{u}_s(\mathbf{u}, \boldsymbol{\eta})] \end{aligned} \quad (36)$$

where $\Pi_{ext}[\mathbf{u}, \boldsymbol{\eta}, \mathbf{u}_s(\mathbf{u}, \boldsymbol{\eta})]$ is the external load potential.

By considering Equations (32) and (36), expression of \mathcal{L} results as:

$$\begin{aligned} \mathcal{L}(\mathbf{u}, \mathbf{e}, \mathbf{s}, \mathbf{u}_w, \dot{\mathbf{u}}, \dot{\boldsymbol{\eta}}) &= \frac{1}{2} \dot{\mathbf{u}}^T \mathbf{m}_{rr} \dot{\mathbf{u}} + \dot{\mathbf{u}}^T \mathbf{m}_{rw} \dot{\boldsymbol{\eta}} + \dot{\boldsymbol{\eta}}^T \mathbf{m}_{wr} \dot{\mathbf{u}} + \frac{1}{2} \dot{\boldsymbol{\eta}}^T (\mathbf{m}_{ww}^r + \mathbf{m}_{ww}) \dot{\boldsymbol{\eta}} + \\ &+ \int_V \boldsymbol{\varepsilon}_m^T[\mathbf{e}, u_w(\boldsymbol{\eta})] \boldsymbol{\sigma}_m(\boldsymbol{\varepsilon}_m) dV + \int_L \mathbf{s}^T \{ \mathbf{e}[\mathbf{u}_s(\mathbf{u}, \boldsymbol{\eta})] - \mathbf{e} \} dx + \Pi_{ext}[\mathbf{u}, \boldsymbol{\eta}, \mathbf{u}_s(\mathbf{u}, \boldsymbol{\eta})] \end{aligned} \quad (37)$$

and four element governing equations are derived, by assuming \mathbf{u} , $\mathbf{e}(x)$, $\mathbf{s}(x)$ and \mathbf{u}_w as independent variables, that is by imposing the following four stationarity conditions:

$$\frac{d}{dt} \frac{\partial \mathcal{L}(\mathbf{u}, \mathbf{e}, \mathbf{s}, \mathbf{u}_w, \dot{\mathbf{u}}, \dot{\boldsymbol{\eta}})}{\partial \dot{q}_h} - \frac{\partial \mathcal{L}(\mathbf{u}, \mathbf{e}, \mathbf{s}, \mathbf{u}_w, \dot{\mathbf{u}}, \dot{\boldsymbol{\eta}})}{\partial q_h} = \frac{d}{dt} \frac{\partial T(\dot{\mathbf{u}}, \dot{\boldsymbol{\eta}})}{\partial \dot{q}_h} + \frac{\partial \Pi(\mathbf{u}, \mathbf{e}, \mathbf{s}, \boldsymbol{\eta})}{\partial q_h} = \mathbf{0} \quad (38)$$

with $q_h \equiv \mathbf{u}, \mathbf{e}, \mathbf{s}, \boldsymbol{\eta}$.

For $q_h \equiv \mathbf{e}, \mathbf{s}$, the term related to the kinetic energy vanishes and the resulting equations are those holding for static loading conditions, that is the nonlinear material constitutive law and element compatibility enforced in weak form as:

$$\boldsymbol{\sigma}_m(x, y, z) = \hat{\boldsymbol{\sigma}}_m[\boldsymbol{\varepsilon}_m(x, y, z)] \quad (39)$$

$$\mathbf{v} = \int_L \mathbf{b}^T(x) \mathbf{e}(x) dx \quad (40)$$

By contrast, for $q_h \equiv \mathbf{u}$, η the dynamic equilibrium equations result, related to rigid and warping motions, respectively, and written as:

$$\mathbf{m}_{rr} \ddot{\mathbf{u}} + \mathbf{m}_{rw} \ddot{\mathbf{u}}_w + \mathbf{a}_v^T \mathbf{q} - \mathbf{p}_{rq} = \mathbf{p} \quad (41)$$

$$\mathbf{m}_{wr} \ddot{\mathbf{u}} + (\mathbf{m}_{ww}^r + \mathbf{m}_{ww}) \ddot{\mathbf{u}}_w + \int_L \begin{bmatrix} \frac{\partial N_1(x)}{\partial x} \\ \dots \\ \frac{\partial N_{n_w}(x)}{\partial x} \end{bmatrix} \mathbf{b}_w(x) dx + \int_L \begin{bmatrix} N_1(x) \\ \dots \\ N_{n_w}(x) \end{bmatrix} \mathbf{t}_w(x) dx = \boldsymbol{\beta} \quad (42)$$

where \mathbf{p}_{rq} is the vector collecting the basic reaction forces due to distributed loads, written considering only the twelve standard nodal components, while vectors \mathbf{p} and $\boldsymbol{\beta}$ contain the element nodal forces work-conjugate to \mathbf{u} and η , respectively. These are arranged in the total nodal force vector $\hat{\mathbf{p}}$, resulting as:

$$\hat{\mathbf{p}} = \{\mathbf{p}^T \quad \boldsymbol{\beta}^T\}^T = \{\mathbf{p}_i^T \quad \mathbf{m}_i^T \quad \mathbf{p}_j^T \quad \mathbf{m}_j^T \quad \boldsymbol{\beta}_1^T \quad \boldsymbol{\beta}_2^T \quad \dots \quad \boldsymbol{\beta}_{n_w}^T\}^T \quad (43)$$

Linearization of Equations (41) and (42) is written in compact form as [23]:

$$\underbrace{\begin{bmatrix} \mathbf{m}_{rr} & \mathbf{m}_{rw} \\ \mathbf{m}_{wr} & \mathbf{m}_{ww}^r + \mathbf{m}_{ww} \end{bmatrix}}_{\mathbf{m}} \underbrace{\begin{Bmatrix} \Delta \ddot{\mathbf{u}} \\ \Delta \ddot{\eta} \end{Bmatrix}}_{\Delta \hat{\ddot{\mathbf{u}}}} + \underbrace{\begin{bmatrix} \mathbf{k}_{rr} & \mathbf{k}_{rw} \\ \mathbf{k}_{wr} & \mathbf{k}_{ww}^r + \mathbf{k}_{ww} \end{bmatrix}}_{\mathbf{k}} \underbrace{\begin{Bmatrix} \Delta \mathbf{u} \\ \Delta \eta \end{Bmatrix}}_{\Delta \hat{\mathbf{u}}} = \underbrace{\begin{Bmatrix} \Delta \mathbf{p} \\ \Delta \boldsymbol{\beta} \end{Bmatrix}}_{\Delta \hat{\mathbf{p}}} \quad (44)$$

and gives the definition of the total consistent element mass, \mathbf{m} , and stiffness matrix, \mathbf{k} . Similarly to \mathbf{m} , matrix \mathbf{k} is composed by five contributions. First four, \mathbf{k}_{rr} , \mathbf{k}_{rw} , \mathbf{k}_{wr} and \mathbf{k}_{ww}^r are the element stiffness matrices associated to the generalized rigid cross-section displacement $\mathbf{u}_s(x)$ and are defined as:

$$\mathbf{k}_{rr} = \mathbf{a}_v^T \mathbf{f}^{-1} \mathbf{a}_v, \quad \mathbf{k}_{rw} = \mathbf{a}_v^T \mathbf{f}^{-1} \mathbf{b}_{sw}, \quad \mathbf{k}_{wr} = \mathbf{b}_{ws} \mathbf{f}^{-1} \mathbf{a}_v, \quad \mathbf{k}_{ww}^r = \mathbf{b}_{ws} \mathbf{f}^{-1} \mathbf{b}_{sw} \quad (45)$$

where \mathbf{f} is the standard consistent element flexibility matrix [25] and \mathbf{b}_{sw} and \mathbf{b}_{ws} are the element warping compatibility and equilibrium matrices, respectively [18, 23]. While, \mathbf{k}_{ww} is the element stiffness matrix associated to warping.

2.3 Enhanced Warping Mixed Element

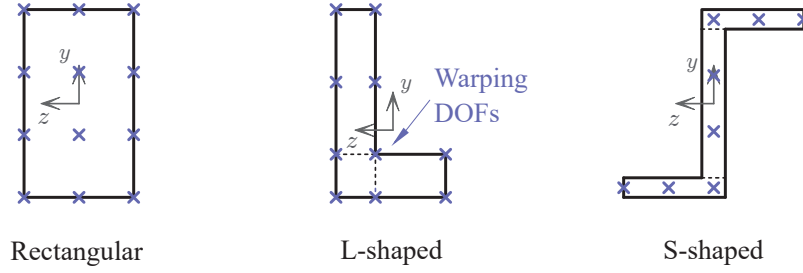
The EWME formulation is the enhanced version of the SWME model. Indeed, a richer warping interpolation is performed in this case, by introducing an arbitrary number, m_w , of DOFs at each of the n_w element nodes. These are located at uniformly distributed points over the cross-section, as depicted in the examples of Figure 4. Hence, vector η_n collecting all DOFs, u_{wnm} , with $m = 1, \dots, m_w$, for node n , now reads as:

$$\eta_n = \{u_{wn1} \quad u_{wn2} \quad \dots \quad u_{wnm_w}\}^T \quad (46)$$

while nodal displacement vector $\hat{\mathbf{u}}$ is arranged as in Equation (22).

As opposed to the SWME, where warping profiles, $\mathbf{M}_\eta(y, z)$, over the cross-section are assigned, for the EWME, warping interpolation involves all three spatial dimensions. Hence, instead of Equation (26), this assumes:

$$u_w(x, y, z) = \sum_{n=1}^{n_w} N_n(x) \left[\sum_{m=1}^{m_w} M_m(y, z) u_{wnm} \right] = \sum_{n=1}^{n_w} N_n(x) \mathbf{M}_\eta(y, z) \eta_n \quad (47)$$


 Figure 4: Examples of EWME warping DOFs for typical cross-sections at element node n

where $\mathbf{M}_\eta(y, z)$ is now a row vector containing 2D Lagrange polynomials $M_m(y, z)$ used to interpolate $u_w(x, y, z)$ over the cross-section plane.

The material strains, $\epsilon_m(x, y, z)$, are expressed in a similar fashion to Equation (27), i.e.:

$$\epsilon_m(x, y, z) = \alpha(y, z) \mathbf{e}(x) + \sum_{n=1}^{n_w} \left[\frac{\partial N_n(x)}{\partial x} \alpha_\zeta(y, z) + N_n(x) \alpha_\eta(y, z) \right] \eta_n \quad (48)$$

although matrices $\alpha_\zeta(y, z)$ and $\alpha_\eta(y, z)$ have, now, size $3 \times m_w$ and contain polynomials $M_m(y, z)$ and their derivatives with respects to y and z [20].

Generalized cross-section stresses playing the role of *bi-moments* and *bi-shears*, $\mathbf{b}_w(x)$ and $\mathbf{t}_w(x)$, are derived as in Equation (29) and all other fundamental relationships and governing equations are obtained through similar derivations performed for the SWME, that lead to formal identical expressions. Complete details of the element formulation are described in [23].

3 NUMERICAL APPLICATIONS

To validate and compare the performances of the adopted beam formulations, two numerical applications are considered. First application simulates the behavior of a steel L frame with beam and column having symmetric cross-sections and subjected to a base earthquake excitation. Second application reproduces the response of a RC U-shaped shear wall under similar loading conditions.

3.1 Steel L frame with flange continuity

The behavior of the steel frame depicted in Figure 5 is analyzed. The specimen is composed by a 4 m long column and 3 m long beam having same I-shaped cross-section geometry. Cross-section orientation is such that flange continuity is obtained at the beam-column connection joint (point C in the figure) and rigid and warping displacements are prevented at the ends of the frame (points A and E). Transverse displacement along y direction of point C is also restrained. Similar specimen was studied in [26, 27] under static loading conditions, while, here, dynamic response to ground acceleration is investigated. To this end, in addition to the mass of the frame, a lumped mass $M = 7645$ kg is considered, applied at mid-span of the beam (point D) and representing the mass of a typical slab supported by the frame. A small vertical eccentricity e is assumed between mass and centroidal axis of the beam, being equal to 0.05 m, that is half of the cross-section width.

Elasto-plastic material response is assumed. Thus, J2 plasticity model with linear kinematic hardening is adopted, with Young's modulus $E^s = 205000$ MPa, Poisson ratio $\nu^s = 0.3$, yielding stress $\sigma_y^s = 150$ MPa and hardening modulus $H_k^s = 0.01 E^s$. Material density is assumed as equal to $\rho = 7850$ kg/m³.

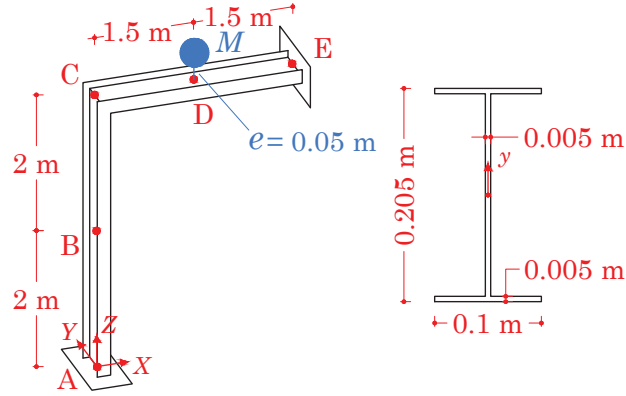


Figure 5: Geometry of the steel L frame with flange continuity.

A uniform mesh made of 10 and 14 FEs for beam and column, respectively, is used to model the frame. For the SWME and EWME, parabolic warping interpolation is assumed along the element axis, i.e. $n_w = 3$. Same order of interpolation is considered for torsional warping in the EVDE, while shear warping is assumed as linear (Equations (5) and (8)). Over the cross-section plane, EWME considers parabolic and cubic warping interpolation along web and flanges, respectively, and linear interpolation across the membrature thickness, i.e. $m_w = 28$, on the basis of the findings reported in [10, 18, 23, 20]. Same interpolation order is used to compute warping profile functions $M_\eta(y, z)$, adopted in the EVDE and SWME.

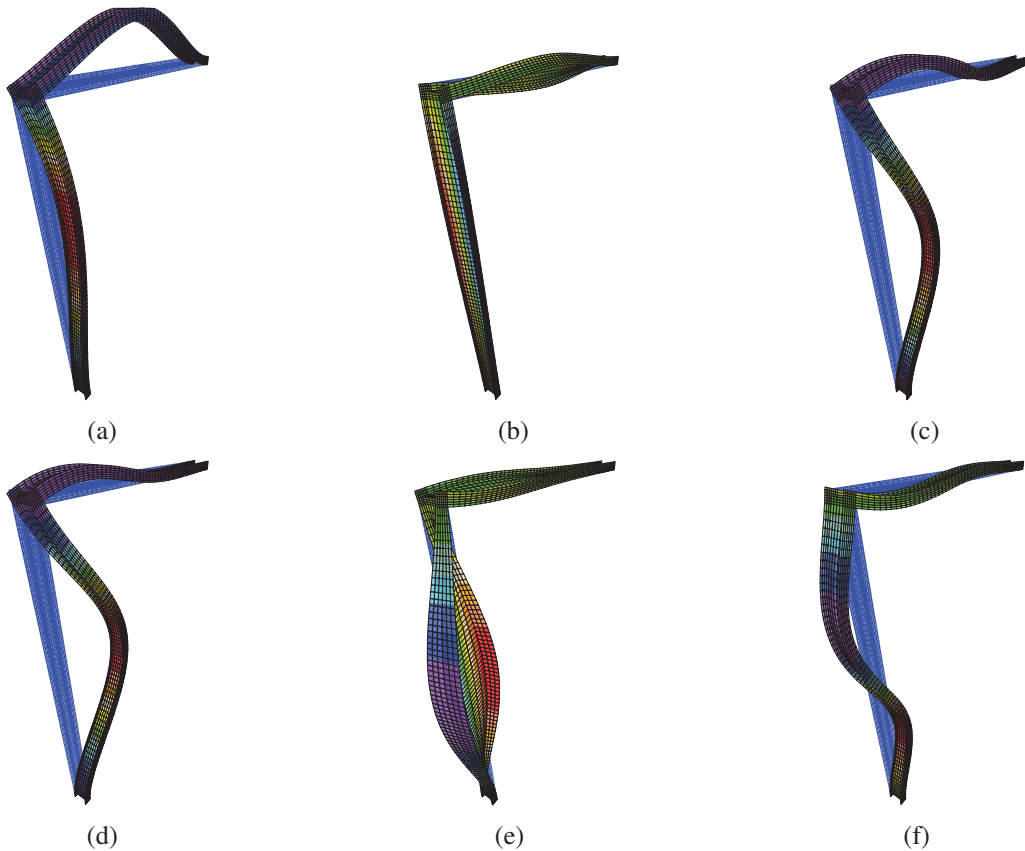


Figure 6: Steel L frame: deformed shape for mode (a) 1, (b) 2, (c) 3, (d) 4, (e) 5, (f) 6

Fiber discretization is used to compute nonlinear cross-section response, that is to evaluate cross-section resultant forces and stiffness. In this case, fibers are distributed according to the Gauss-Legendre rule, as exact integration of the element torsional stiffness is required to obtain the correct response of the frame. Fiber grid is arranged to have 6 fibers placed along web and flanges and 3 across the membrature thickness.

Table 1: Elastic circular frequency ω_i [rad/s] obtained for the L portal frame

FE type	Mode					
	1 st Flex.	1 st Tors.	2 nd Flex.	3 rd Flex.	2 nd Tors.	4 th Flex.
Shell	10.55	20.03	123.01	140.28	176.37	356.54
EWME	10.49	19.80	123.67	143.36	176.70	358.47
SWME	10.48	19.80	123.66	143.35	176.61	358.41
EVDE	10.49	19.87	123.68	143.37	176.28	358.54
Rigid section beam	10.48	9.07	123.64	143.33	84.70	358.27

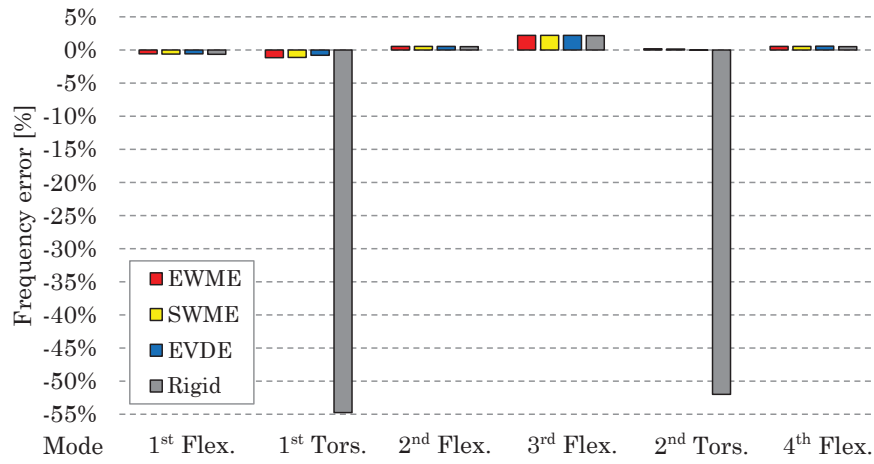


Figure 7: Steel L frame: circular frequency errors obtained with beam models with respect to the shell solution

For all models, damping ratio is set equal to 2% and introduced through Rayleigh method on the basis of the first two elastic frequencies of the frame [28]. These correspond to the first in plane flexural and torsional natural modes, respectively, as depicted in Figures 6(a) and 6(b). Indeed, Figure 6 shows the deformed shapes for the first 6 elastic modes obtained with a reference model made of 2268 4-node Discrete Kirchhoff Quadrilateral shell elements. The blue and colored configurations indicate the undeformed and deformed shapes, respectively. The circular frequencies ω_i are reported in Table 1 and are compared with the values obtained from the adopted enhanced beam models and with a standard beam model assuming rigid cross-section. For this latter, cross-section torsional inertia is computed according to the thin-walled beam theory and results equal to $J = \kappa_t I_\rho$, being I_ρ the cross-section polar inertia and $\kappa_t = 0.001153$ the correction coefficient. Figure 7 shows the solution differences in terms of percentage error for ω_i with respect to the reference results. As shown, all enhanced beam formulations give similar results that perfectly agree with the shell solution. By contrast, the standard beam model provides incorrect frequency values for the torsional modes. Indeed, this model neglects warping and, thus, warping restraints at the boundaries. Moreover, due to the particular orientation, the

end cross-sections of beam and column that meet at the joint C undergo equal warping profile. As a result, when beam twists, warping of the end cross-section at C produces warping in the column, which twists as well (see, for instance, Figure 6(e)). As opposed to the standard model, in the enhanced beam formulations, the additional nodal warping DOFs placed at the nodes permit to correctly account for boundary restraints. Moreover, mesh connectivity ensures warping continuity between column and beam and, thus, the correct warping transmission at the joint C.

The frame dynamic response is also investigated by applying to the frame the ground acceleration history depicted in Figure 8(a), and considering both linear elastic and elasto-plastic constitutive behavior. Peak ground acceleration results equal to 0.4167 g, where g indicates the gravity acceleration. Figure 8(b) shows the resulting Fourier transform and, thus, indicates the frequency content of the acceleration signal. In the same figure, the green dotted vertical line indicates the value of the first torsional natural frequency of the frame. Ground acceleration is assumed to act in the direction Y transverse to the frame plane. Newmark method [28] is adopted for time integration of the structure global equilibrium equations, with coefficients $\beta = 0.25$ and $\gamma = 0.5$ and time step set equal to 0.001 s.

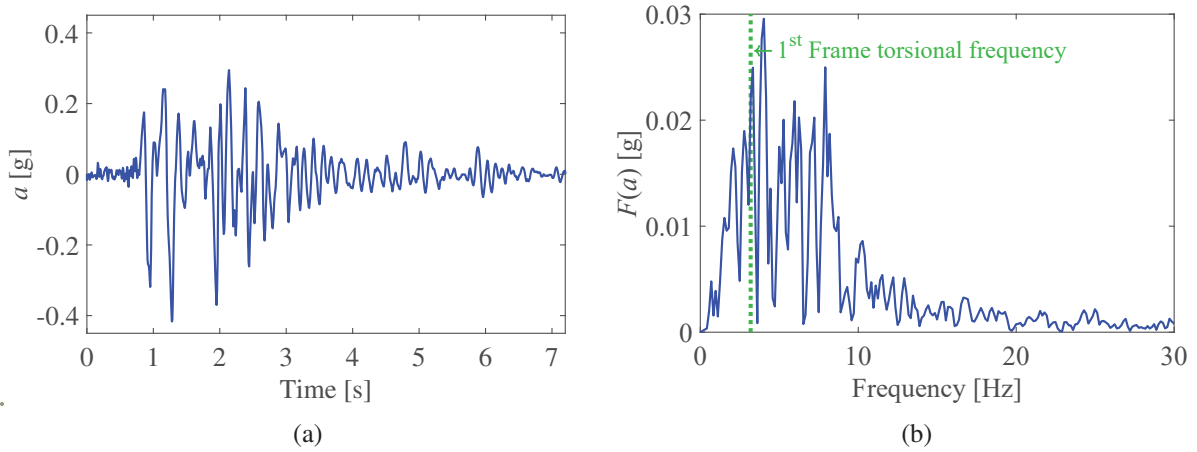


Figure 8: Base excitation signal: ground acceleration (a) history and (b) Fourier transform

Although mass eccentricity, e , is small, the applied ground acceleration mainly induces torsional deformation of the beam and, due to warping continuity, torsion is transmitted to the column. By contrast, transverse flexural deformation are mainly limited to the beam, as expected, given the assumed boundary restraints. Figure 9 plots the time-evolution of (a) the torsional rotation, θ_x^B , of the column mid-height cross-section, (b) the torsional rotation, θ_x^D , and (c) transverse displacement, v^D , of the beam mid-span cross-section, respectively, under the assumption of linear elastic material. Solid black curves represent the reference solutions obtained with the shell FEs. Red, yellow and blue curves refer to those obtained with the EWME, SWME and EVDE models, respectively. Finally, dotted dark gray curves indicate the response obtained with the standard beam formulations. As observed in the modal decomposition analysis, standard beam model, not considering the boundary warping restraints, provides a significantly more flexible response, as opposed to all enhanced models that perfectly agree with the reference response. In addition, standard model does not account for warping transmission at the joint and, thus, gives null rotations for the column (horizontal line at zero in Figures 9(a)), as opposed to the enhanced beam models that correctly capture the column torsional deformation.

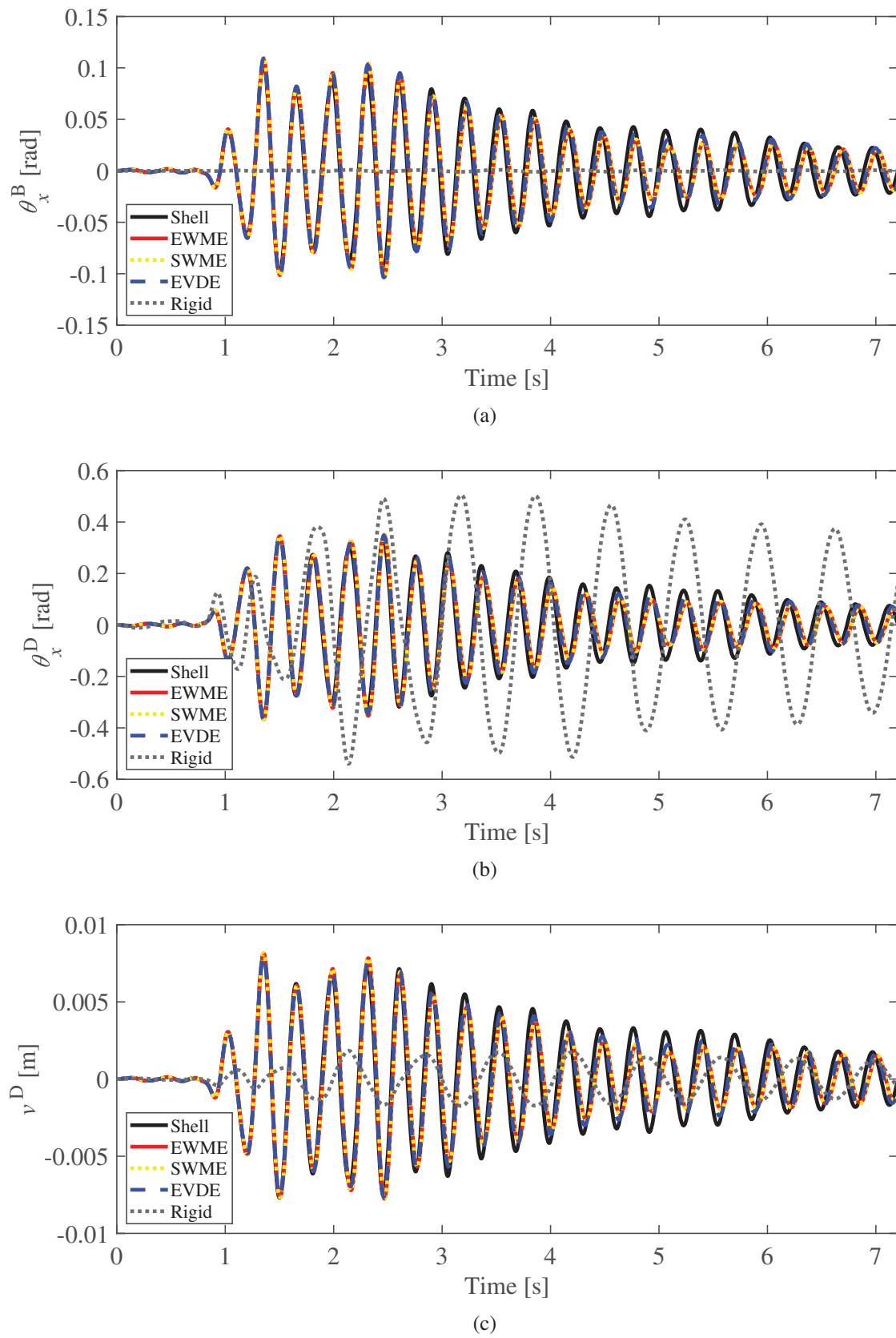


Figure 9: Linear elastic response of the steel L frame: time history of (a) the torsional rotation of the column at mid-height (point B), (b) torsional rotation and (c) transverse displacement of the beam at mid-span (point D)

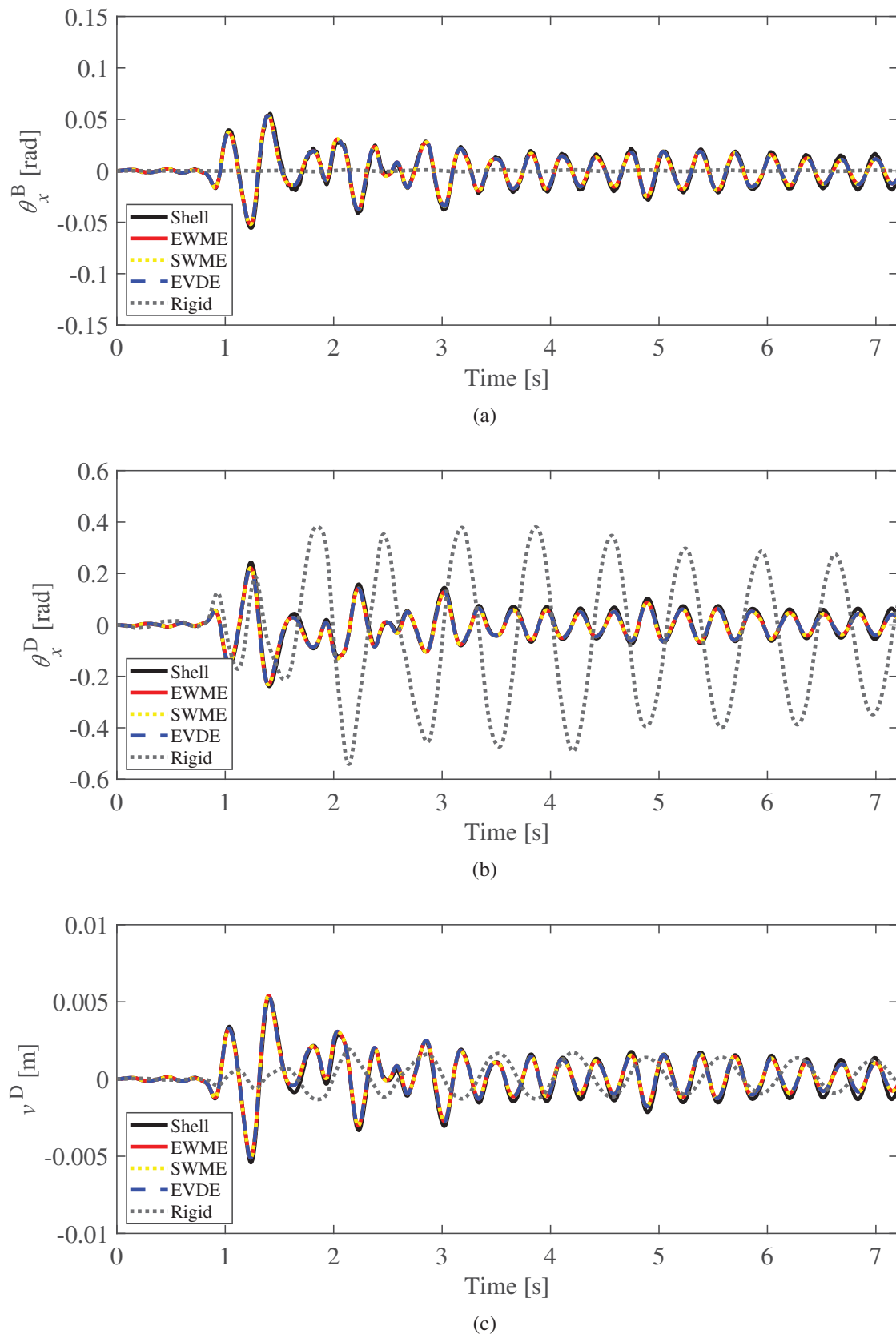


Figure 10: Nonlinear response of the steel L frame: time history of (a) the torsional rotation of the column at mid-height (point B), (b) torsional rotation and (c) transverse displacement of the beam at mid-span (point D)

Similar results are plotted in Figure 10 for elasto-plastic material response, showing that all enhanced beam formulations correctly simulate the evolution of the plastic effects in the material. Indeed, due to warping constraints, torsion of the members induces significant shear-lag effects and, thus, when ground acceleration reaches the peak value, at almost 1.3 s, axial stress exceeds material yield stress, at both ends and mid-height of the beam. Consequently, plastic strains affect the remaining part of the time-history response. As opposed to the beam model formulations accounting for warping, the standard beam model does not capture shear-lag and shows yielding of the material caused by severe torsional shear stresses acting in the cross-section plane.

Fourier transforms of the beam and column rotation histories, θ_x^B and θ_x^D , are plotted in Figure 11, for (a-b) linear elastic and (c-d) nonlinear material response, respectively. These confirm that main frequency content of the response is associated to torsional deformation mode of the frame. First torsional frequency of the frame is indicated by the green dotted vertical lines.

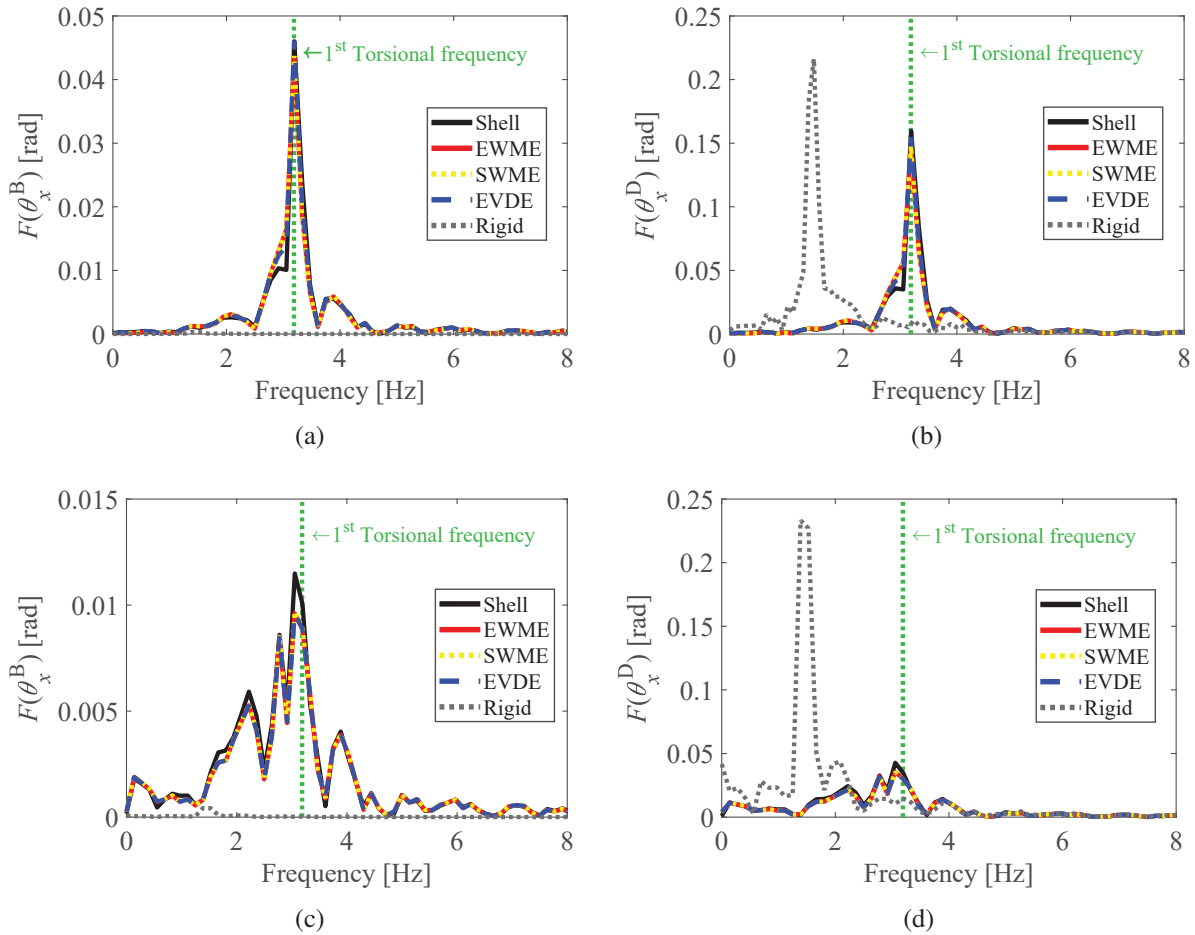


Figure 11: Steel L frame: Fourier transform of the torsional rotation of (a-c) the column mid-height (point B) and (b-d) beam mid-span cross-section (point D), for (a-b) linear elastic and (c-d) nonlinear material response

3.2 RC U-shaped shear wall

To investigate the performances of the presented enhanced beam models describing the interaction between warping and damaging mechanisms, the response of the RC U-shaped shear wall in Figure 12 is analyzed under dynamic loadings. Same specimen was experimental tested

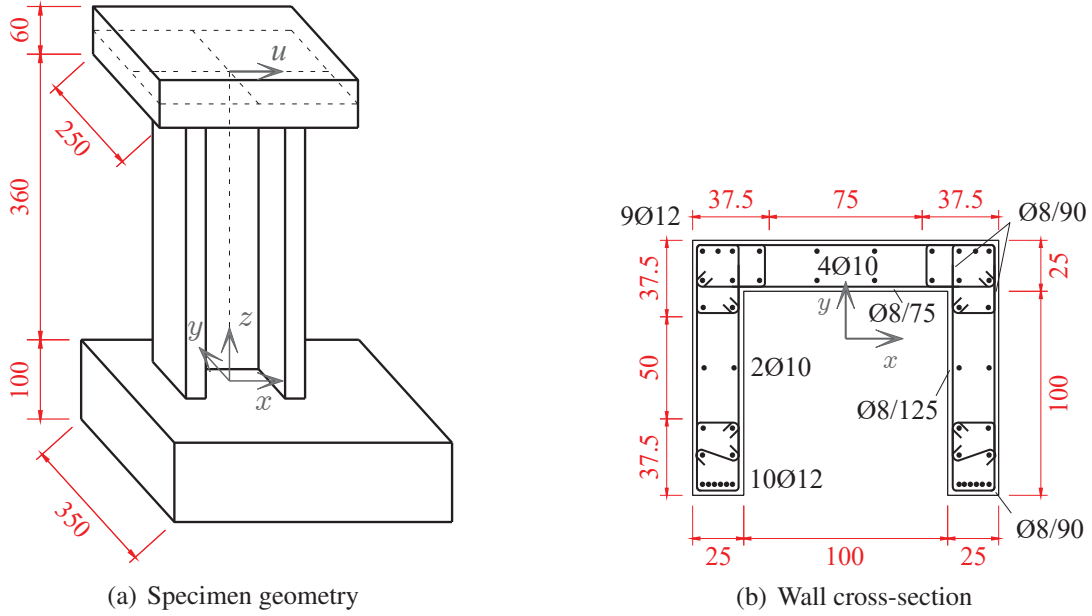


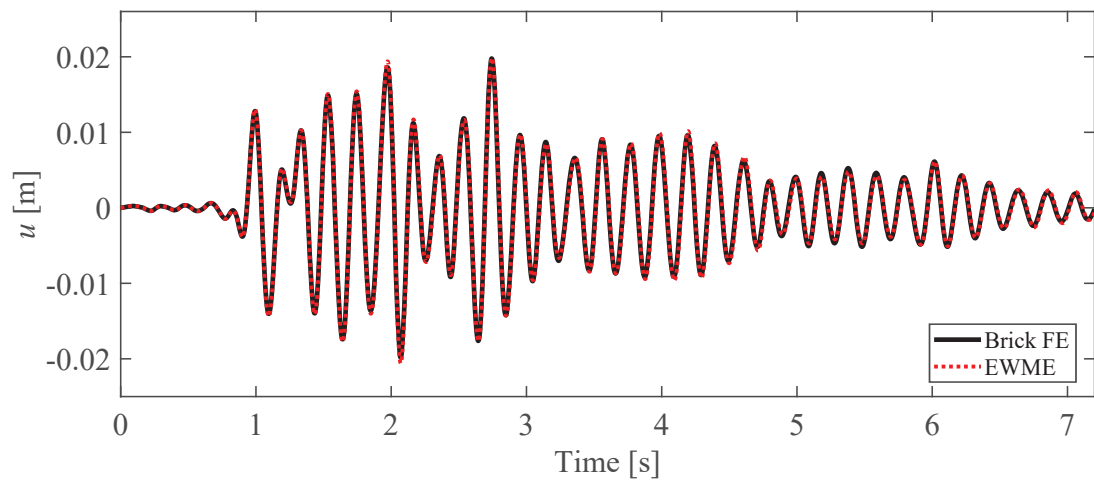
Figure 12: RC U-shaped shear wall: (a) specimen and (b) cross-section geometry (dimensions in cm)

by Pegon et al. [29] under cyclic transverse loads applied at the top slab, while ground acceleration is considered, here, as base excitation, i.e. the same signal reported in Figure 8 but scaled so that peak ground acceleration results equal to 0.8334 g. This is assumed to act in the x direction, parallel to the wall web.

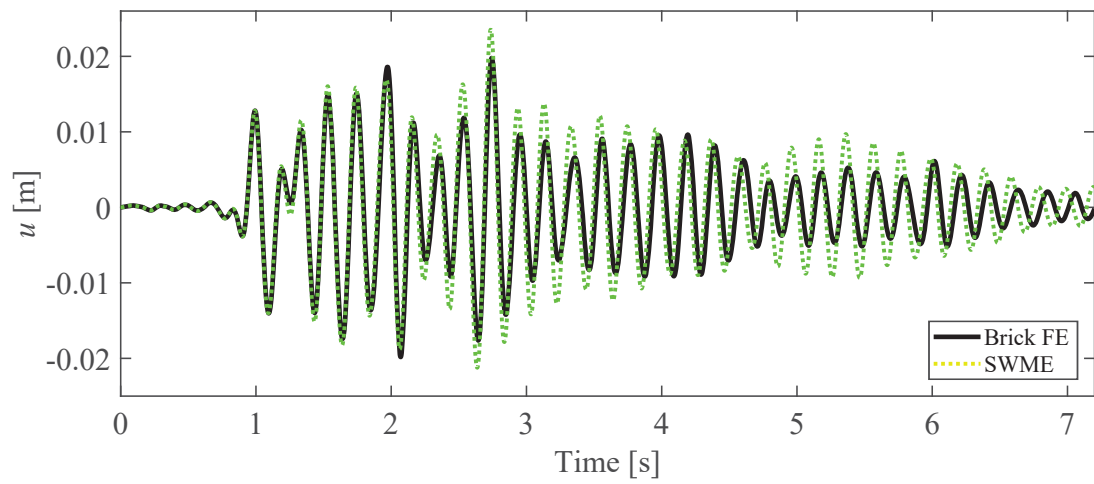
In addition to the weight of the top slab, the wall is vertically loaded by a constant compression force equal to 2000 kN. As a result, a lumped mass $M = 203969$ kg is applied at the top of the wall (at $z = 3.90$ m), representing the mass of the slab and that of the additional vertical load. Concrete density is assumed as equal to $\rho = 2548.42$ kg/m³.

The wall is modeled as a vertical cantilever, where square slabs are assumed to fully prevent warping deformations of the bottom and top cross-sections. A uniform mesh made of 4 FEs is used. For the SWME and EWME, parabolic warping interpolation is assumed along the element axis, i.e. $n_w = 3$. Over the cross-section plane, EWME considers cubic warping interpolation along web and flanges and linear interpolation across the membrature thickness, i.e. $m_w = 24$. Same interpolation order is used to compute warping profile functions $M_\eta(y, z)$, adopted in the EVDE and SWME.

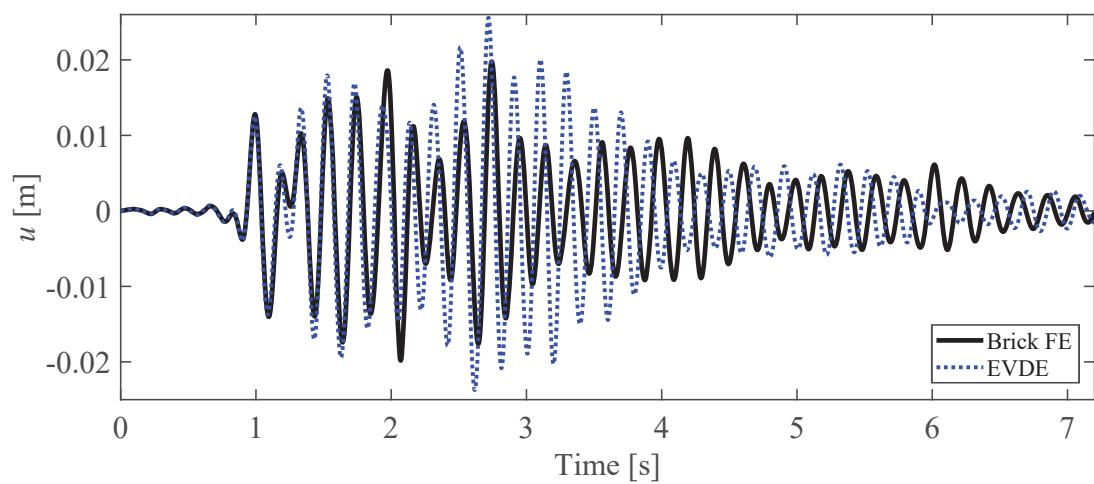
A cross-section fiber discretization is defined so that 9 fibers are placed along web and flanges and 3 across the membrature thickness, while concrete response is reproduced by adopting the damage-plastic model proposed in [18]. Table 2 lists the material parameters, being σ_t and σ_c the uniaxial plastic limit stress in tension and compression, respectively, H_k and H_i the kinematic and isotropic hardening moduli, respectively, Y_{0t} and Y_{0c} the damage thresholds in tension and compression, respectively, k_t , a_t , k_c , a_c and β parameters governing the damage evolution. Young's modulus and Poisson ratio are assumed as equal to $E = 28000$ MPa and $\nu = 0.25$, respectively. The Giuffrè-Menegotto-Pinto model [30] describes the behavior of the steel reinforcing bars, with $E^s = 200\,000$ MPa, $\sigma_y^s = 540$ MPa and $b = 1.0\%$ being the Young's modulus, plastic yield strength and ratio between hardening and elastic stiffness, respectively. The transition coefficient R from the elastic to the plastic state required in the model results from the following parameters: $R_0 = 20$, $a_1 = 18.5$ and $a_2 = 0.15$ and no isotropic hardening is assumed.



(a)



(b)



(c)

Figure 13: Linear elastic response of the RC U-shaped shear wall: time history of the transverse displacement u , along x , of the top slab obtained with (a) EWME (red dotted curve), (b) SWME (green dotted curve) and (c) EVDE (blue dotted curve), compared with the reference brick FE solution (black curves)

Table 2: Material parameters for concrete model in RC U-shaped wall.

σ_t	σ_c	H_k	H_i	Y_{0t}	k_t	a_t	Y_{0c}	k_c	a_c	β
3.3 MPa	30 MPa	$0.8 E$	$0.001 E$	$6.7 \cdot 10^{-5}$	$2.0 \cdot 10^{-5}$	0.8	$4.0 \cdot 10^{-4}$	$2.8 \cdot 10^{-3}$	0.8	0.5

Damping ratio is set equal to 2% and introduced through Rayleigh method [28] on the basis of the first two elastic frequencies of the frame and Newmark method [28] is adopted for time integration of the structure global equilibrium equations, with coefficients $\beta = 0.25$ and $\gamma = 0.5$ and time step set equal to 0.001 s.

Figure 13 shows the evolution of the transverse displacement u , along x , of the top slab, under linear elastic material behavior, for (a) EWME model (red dotted curve), (b) SWME model (green dotted curve) and (c) EVDE model (blue dotted curve). Each response is compared with a reference solution (black curve) obtained with a FE model made by 24480 8-node bricks.

As opposed to the steel portal frame analyzed in Section 3.1, in this test, the asymmetric geometry of the wall cross-section induces significant coupling between shear/bending in the x - z plane and torsional behavior. As a consequence, only the most sophisticated EWME model is able to correctly capture the shear/torsional warping interaction and provide the same solution as that obtained by the brick 3D model. The SWME provides a correct response only for the first 2 s of the history, while it slightly overestimates the wall horizontal displacement for the remaining part. Worse results are obtained with the EVDE, whose response also shows a significant overestimation of the maximum displacements occurring during oscillations. However, if compared with the solution provided by a standard beam model assuming rigid cross-sections, that obtained with the SWME results significantly more accurate, proving that this model can be considered as a good compromise between more sophisticated, but onerous, formulations and simpler, but less demanding, approaches. The standard beam solution is plotted in Figure 14 as gray dotted curve. For this model, shear areas in the x and y directions are set equal to $A_t^x = 0.4286 A$ and $A_t^y = 0.7142 A$, being A the cross-section area, while torsional inertia is assumed as $J = 0.05495 I_\rho$, being I_ρ the cross-section polar inertia.

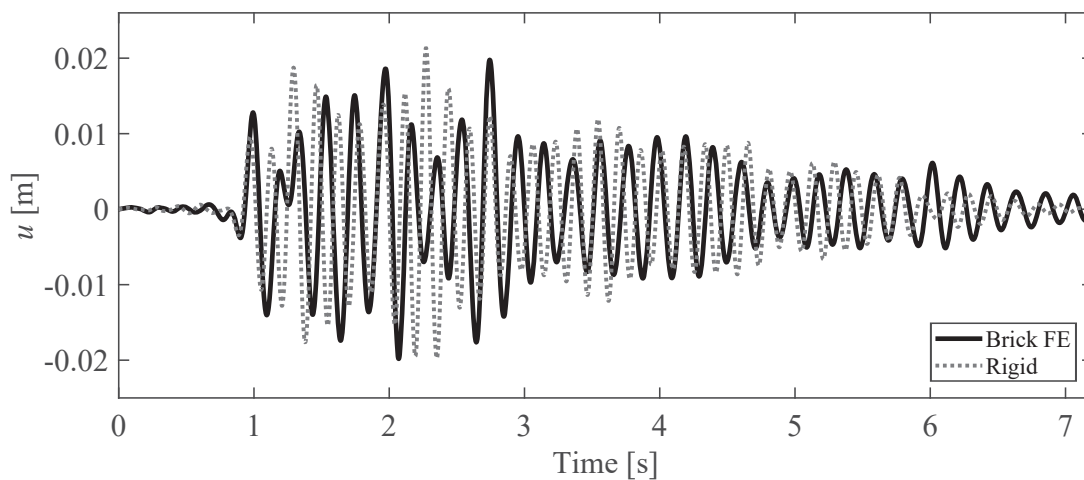


Figure 14: Linear elastic response of the RC U-shaped shear wall: time history of the transverse displacement u , along x , of the top slab obtained with reference brick FE (black curve) and standard beam (gray dotted curve) solutions

Different trend is observed for nonlinear material behavior. Figure 15 shows the displacement time histories along x of the top slab, obtained by considering the nonlinear response of concrete and steel. Figure 15(a) compares the solution obtained with the EWME (red curve) with the linear elastic response provided by the brick FE model (gray curve). When ground acceleration reaches the peak value, at almost 1.3 s, the wall significantly damages at the base, without collapsing. As a result, structural response with lower frequency content is observed compared to the linear elastic behavior. As expected, higher peak displacements occur in the first part of the history, around the peak acceleration, while lower amplitude oscillations are shown in the remaining part.

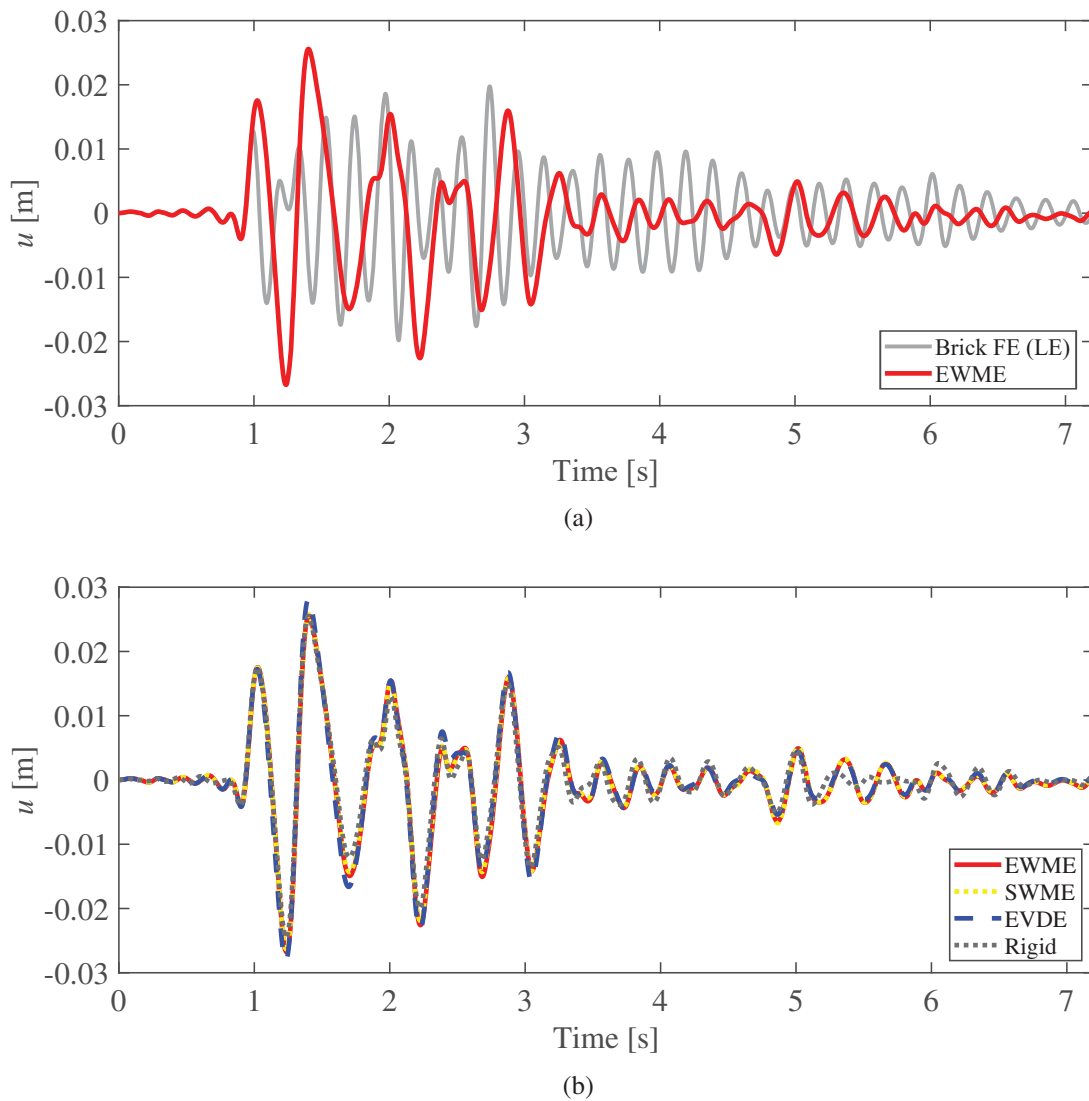


Figure 15: Nonlinear response of the RC U-shaped shear wall: time history of the transverse displacement u , along x , of the top slab obtained with (a) EWME (red curve) and (b) SWME (yellow dotted curve), EVDE (blue dashed curve) and standard beam (gray dotted curve)

In this case, all beam formulations, including the standard model, are able to correctly reproduce the wall response, as shown in Figure 15(b). This compares solutions obtained with the other beam models (SWME as yellow dotted curve, EVDE as blue dashed curve and standard beam as gray dotted curve) with the EWME results (red curve). Indeed, after damaging, wall behavior is

mainly governed by the nonlinear hinge that forms at the base and, although shear contribution is not negligible, warping effects become less important.

Fourier transforms of the displacement histories are plotted in Figures 16, using same curve styles of Figure 15. Green dotted vertical line indicates the value of the first elastic natural frequency of the wall involving shear/bending in the x direction, coupled with torsion.

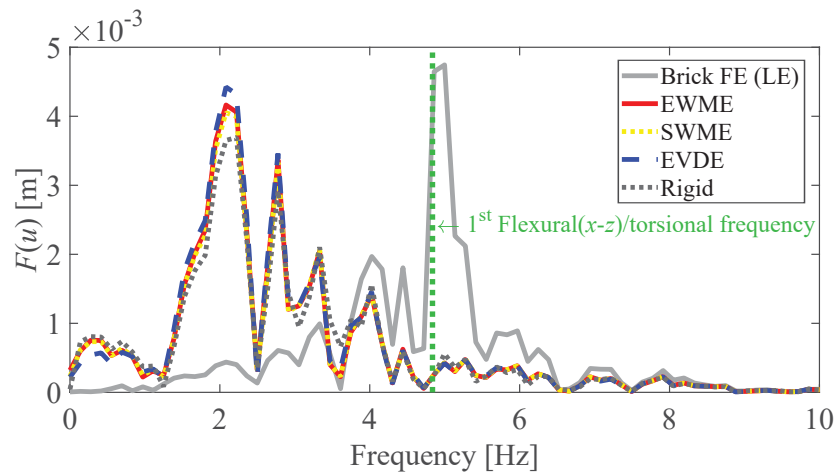


Figure 16: RC U-shaped shear wall: Fourier transform of the transverse displacement histories of the top slab

This plot confirms that, for the nonlinear behavior, natural modes of the wall that are excited by the seismic action are associated to lower frequencies, compared to the linear elastic response, as damage reduces the stiffness of the structure.

The values of the first four elastic circular frequencies ω_i obtained from all models are reported in Table 3.

Table 3: Elastic circular frequency ω_i [rad/s] obtained for the RC U-shaped shear wall

FE type	Mode			
	1 st Flex.(y-z)	1 st Flex.(x-z)/Tors.	1 st Axial.	2 nd Flex.(x-z)/Tors.
Brick	28.24	30.39	181.91	465.05
EWME	29.03	31.02	185.08	490.81
SWME	29.01	31.60	185.08	510.73
EVDE	29.18	32.61	185.08	542.53
Rigid section beam	28.86	35.32	185.08	205.75

4 CONCLUSIONS

- This paper presented three beam FE formulations for the analysis of frame structures subjected to dynamic shear and torsional actions. These are derived by extending to the dynamic analysis previously proposed enriched models, where kinematic description includes shear and torsional cross-section warping and, thus, coupling between axial/bending and shear/torsional stress components.
- More sophisticated EWME model considers a detailed two-level warping displacement field interpolation. By contrast, SWME model considers pre-defined profile functions

to describe warping variation over the cross-section and interpolates warping along the element axis only, by means of independent quantities, according to Benscoter's theory. Similar assumptions are made in the EVDE model, but warping axis variation is directly linked to torsional curvature and shear strains, according to Vlasov's theory.

- Numerical analyses performed on the steel L frame showed that, when torsional effects dominate the response, standard beam formulations based on rigid cross-section assumption fail in reproducing the correct structural behavior. By contrast, all three enhanced FEs result highly accurate and are preferable to higher order shell/brick FE models for the analysis of large scale structures, due to the lower computational cost these require. This is particularly true for the simplest model of the three, EVDE, which, however, gives satisfactory results only for open symmetric cross-section geometries, as proven in [20]. For closed and/or un-symmetric profiles, SWME model is the best alternative of the set, as this involves a lower number of additional nodal DOFs than EWME.
- Numerical analyses performed on the RC U-shaped shear wall confirm the findings observed for the steel L frame. Linear elastic response predicted with EWME model perfectly matches that evaluated with the 3D brick FE model. Good approximation is also obtained with the SWME model. Instead, major discrepancies are detected with the EDVE formulation, as a consequence of the non-symmetric cross-section geometry. However, tests also showed that nonlinear phenomena due to onset of damage can significantly modify the structural response, making the warping effects less important. As a result, correct structural response may be obtained also with simpler models and even standard formulations.

REFERENCES

- [1] P. Di Re, E. Lofrano, D. Addessi, A. Paolone, Enhanced beam formulation with cross-section warping under large displacements. *Proceedings of the XXIV AIMETA Conference 2019. Lecture Notes in Mechanical Engineering*, 1217–1229, Springer, Cham, 2020. DOI: 10.1007/978-3-030-41057-5_99.
- [2] N.L. Rizzi, V. Varano, The effects of warping on the postbuckling behaviour of thin-walled structures. *Thin-Walled Structures*, **49**(9), 1091–1097, 2011, DOI: 10.1016/j.tws.2011.04.001.
- [3] N.L. Rizzi, V. Varano, S. Gabriele, Initial postbuckling behavior of thin-walled frames under mode interaction. *Thin-Walled Structures*, **68**, 124–134, 2013, DOI: 10.1016/j.tws.2013.03.004.
- [4] Rinchen, G.J Hancock, K.J.R. Rasmussen, Geometric and material nonlinear analysis of thin-walled members with arbitrary open cross-section. *Thin-Walled Structures*, **153**, 106783, 2020.
- [5] M. Brunetti, E. Lofrano, A. Paolone, G. Ruta, Warping and Ljapounov stability of non-trivial equilibria of non-symmetric open thin-walled beams. *Thin-Walled Structures*, **86**, 73–82, 2015, DOI: 10.1016/j.tws.2014.10.004.
- [6] V.Z. Vlasov, *Thin-walled elastic beams*. National Technical Information Service, 1984.

- [7] S.U. Benscoter, A theory of torsion bending for multicell beams. *Journal of Applied Mechanics*, **21**(1), 25–34, 1954.
- [8] S.W. Lee, Y.H. Kim, A new approach to the finite element modelling of beams with warping effect. *International Journal for Numerical Methods in Engineering*, **24**(12), 2327–2341, 1987.
- [9] K. Yoon, Y. Lee, P.-S. Lee, A continuum mechanics based 3-D beam finite element with warping displacements and its modeling capabilities. *Structural Engineering and Mechanics*, **43**(4), 411–437, 2012.
- [10] P. Di Re, D. Addessi, F.C. Filippou, 3D beam-column finite element under non-uniform shear stress distribution due to shear and torsion. *VII European Congress on Computational Methods in Applied Sciences and Engineering (ECCOMAS 2016)*, Crete Island, Greece, June 5-10, 2016, **3**, 4467–4480, 2016, DOI: 10.7712/100016.2125.9035.
- [11] P. Di Re, D. Addessi, A mixed 3D corotational beam with cross-section warping for the analysis of damaging structures under large displacements. *Meccanica*, **53**(6), 1313–1332, 2018, DOI: 10.1007/s11012-017-0749-3.
- [12] R.E. Erkmen, M. Mohareb, Torsion analysis of thin-walled beams including shear deformation effects. *Thin-Walled Structures*, **44**(10), 1096–1108, 2006, DOI: 10.1016/j.tws.2006.10.012.
- [13] R. El Fatmi, Non-uniform warping including the effects of torsion and shear forces. Part I: A general beam theory. *International Journal of Solids and Structures*, **44**, 5912–5929, 2007.
- [14] P. Ceresa, L. Petrini, R. Pinho, Flexure-shear fiber beam-column elements for modeling frame structures under seismic loading - State of the art. *Journal of Earthquake Engineering*, **11**, 46–88, 2007, DOI: 10.1080/13632460701280237.
- [15] D. Camotim, C. Basaglia, N. Silvestre, GBT buckling analysis of thin-walled steel frames: a state-of-the-art report. *Thin-Walled Structures*, **48**(10-11), 726–743, 2010.
- [16] A. Genoese, A. Bilotta, G. Garcea, A generalized model for heterogeneous and anisotropic beams including section distortions. *Thin-Walled Structures*, **74**, 85–103, 2014.
- [17] A. Kagermanov, P. Ceresa, Fiber-section model with an exact shear strain profile for two-dimensional RC frame structures. *Journal of Structural Engineering*, **143**(10), 04017132, 2017.
- [18] P. Di Re, D. Addessi, F.C. Filippou, Mixed 3D Beam Element with Damage Plasticity for the Analysis of RC Members under Warping Torsion. *Journal of Structural Engineering*, **144**(6), 04018064, 2018, DOI: 10.1061/(ASCE)ST.1943-541X.0002039.
- [19] L. Librescu, O. Song, *Thin-walled composite beams: theory and application*. Springer Science & Business Media, 2006.

- [20] D. Addessi, P. Di Re, G. Cimarello, Enriched beam finite element models with torsion and shear warping for the analysis of thin-walled structures. *Thin-Walled Structures*, **159**, 107259, 2021, DOI: 10.1016/j.tws.2020.107259.
- [21] D.L. Thomas, J.M. Wilson, R.R. Wilson, Timoshenko beam finite elements. *Journal of Sound and Vibration*, **31**(3), 315–330, 1973.
- [22] P. Di Re, D. Addessi, C. Gatta, Enriched Vlasov beam model for nonlinear dynamic analysis of thin-walled structures. *Second International Nonlinear Dynamic Conference (NODYCON 2021)*, Rome, Italy, February 16-19, 2021, *In press*.
- [23] P. Di Re, D. Addessi, A. Paolone, Mixed beam formulation with cross-section warping for dynamic analysis of thin-walled structures. *Thin-Walled Structures*, **141**, 554–575, 2019, DOI: 10.1016/j.tws.2019.04.014.
- [24] K.J. Bathe, *Finite Element Procedures*. K.J. Bathe, Watertown, MA, 2016.
- [25] R.L. Taylor, F.C. Filippou, A. Saritas, F. Auricchio, A mixed finite element method for beam and frame problems. *Computational mechanics*, **31**(1-2), 192–203, 2003.
- [26] C. Basaglia, D. Camotim, N. Silvestre, Torsion warping transmission at thin-walled frame joints: Kinematics, modelling and structural response. *Journal of Constructional Steel Research*, **69**(1), 139–53, 2012.
- [27] A. Genoese, A. Genoese, A. Bilotta, G. Garcea, A mixed beam model with non-uniform warpings derived from the Saint Venant rod. *Computers & Structures*, **121**, 87–98, 2013.
- [28] A. K. Chopra, *Dynamics of Structures. Theory and Applications to Earthquake Engineering*. Prentice Hall, Pearson, 2012.
- [29] P. Pégon, C. Plumier, A. Pinto, J. Molina, P. Gonzalez, P. Tognoli, and O. Hubert, U-shaped walls: quasi-static bi-axial test in the X and Y directions - Test report. *TMR-ICONSTOPIC5*, JRC, Ispra, Italy (2000)
- [30] M. Menegotto, P. Pinto, Method of analysis for cyclically loaded reinforced concrete plane frames including changes in geometry and nonelastic behavior of elements under combined normal force and bending. *IABSE symposium*, Lisbon, Portugal, 1973.

EARTHQUAKE-INDUCED STRUCTURAL POUNDING BETWEEN TWO INELASTIC SDOF STRUCTURAL SYSTEMS

Folhento P. Pedro¹, Barros C. Rui¹, and Braz-César T. Manuel²

¹ CONSTRUCT, Faculdade de Engenharia, Universidade do Porto
FEUP, Porto, Portugal
{up201811645, rcb}@fe.up.pt

² CONSTRUCT, Instituto Politécnico de Bragança
IPB, Bragança, Portugal
brazcesar@ipb.pt

Abstract

Earthquake-induced pounding among contiguous building structures with insufficient separation distance, common in highly populated areas, may generate large impact forces that can significantly modify the overall dynamic behavior of the intervenient buildings. Serious structural damage or global collapse is among the negative consequences of building pounding. Inelastic behavior is inherent in building structures subjected to moderate to severe seismic excitations. Hence, the consideration of the inelastic behavior of building structures in the occurrence of pounding is extremely important to obtain more realistic results in the study and modeling of these phenomena. To this end, a Matlab-Simulink model was developed to emulate the elastic and inelastic behavior of two lumped mass SDOF structural systems under an earthquake excitation, where pounding is likely to occur. Using a smooth hysteresis model different hysteresis cases will be considered in the inelastic behavior of the structural systems, namely, stiffness degradation, strength deterioration, and pinching effect, arising in cyclic behavior of materials that compose civil engineering structures. A non-linear viscoelastic impact model will be used to assess the magnitude of pounding forces and their relation with the interpenetration depth. It was verified that the consideration of elastic behavior in buildings prone to pounding overestimates the magnitude and number of impacts that the structures experience, and underestimates structural displacements, especially in flexible structures.

Keywords: Building pounding, Earthquake-induced structural pounding, Impact modeling, Inelastic behavior, Hysteretic model.

1 INTRODUCTION

The world has been impacted by numerous earthquake hazard events that cause in a few amounts of time total or partial destruction of built patrimony and human activity, and potential loss of human lives. In this sense, civil and earthquake engineering came along to develop methods of analysis and design of structures, that essentially establish certain requirements to avoid the structure's collapse and minimizing damage to allow possible repair.

The seismic design of structures is primarily based on an elastic analysis to compute the seismic strength of structures. However, non-linear behavior with significant inelastic deformation is generally observed in structures under seismic events. Thus, in more advanced methods of analysis but not exclusively, this non-linear inelastic behavior can be considered in the critical zones, or plastic hinges, which within buildings are commonly located at the beams' ends, emulating in this way its behavior with an appropriate hysteresis model.

One phenomenon that has been recognized and studied for the last three decades gaining increasing importance is earthquake-induced structural pounding between adjacent buildings that are insufficiently separated.

When building pounding is likely to occur, i.e., in a situation where the buildings are very close to each other, leaving insufficient space or gaps between them or even without space, something common in metropolitan cities, great impact forces and acceleration spikes can be generated at the building floors, leading to substantial damage at the vicinity of the impact and in the worst-case scenario, it can cause the complete collapse of the structural system. Besides, and in these conditions, buildings with very different dynamic properties and consequent dynamic behavior will vibrate out-of-phase increasing the possibilities of collisions between buildings under earthquake loads.

It is known that pounding can considerably amplify the structural responses of the buildings, but in some situations, it was also found that can lead to the reduction of lateral displacements. The effects of this phenomenon are very dispersed, some in agreement, others in contradiction, while it can decrease the displacements due to the mutual blocking of the adjacent buildings it can still cause significant local damage.

And due to the high non-linearities in this contact phenomenon, pounding is very difficult to model with high accuracy since it depends on a lot of variables and their relationships. This insurgent phenomenon involves a non-linear relationship between the contact area, pressure, and deformations; local inelastic deformations; propagation of stress waves within the colliding structures; tangential and friction forces; vibrations resulting in thermal and acoustic effects; and other complex situations that makes this phenomenon extremely difficult to model.

Earthquake-induced structural pounding is usually assessed considering that the structures are within the elastic regime. This oversimplification can lead to an overestimation of the magnitude of the pounding forces and can underestimate the displacements that the structures actually experience. Some researchers already addressed this matter ([1], [2]), although additional research is required to further understand the consequences of pounding when inelastic behavior is considered.

The overall dynamic behavior of two SDOF systems with very different dynamic behavior is assessed in the following sections. These systems will represent two building structures under an earthquake excitation, in which the gap between is modified to evaluate its responses when pounding is likely to occur. The elastic and inelastic behavior of the structures will be considered. A smooth hysteresis model will be applied to emulate the non-linear hysteresis of the given structural systems.

The ultimate objective will be the understanding of the influence of the structures' non-linear inelastic behavior in the occurrence of earthquake-induced structural pounding.

2 NON-LINEAR HYSTERESIS MODEL

Hysteresis is a phenomenological concept and thus it is based on experimental data relating an input-output couple. This relationship in the present scope will represent the lateral restoring force in function of the inelastic displacement experienced by the structures.

Hysteresis is regarded as a rate-independent memory effect. However, and in reality, the response of structural systems depends always on the rate of the applied load. When this rate is significant, viscosity must be introduced. In the seismic response of structures, viscosity and hysteresis will contribute to the overall energy dissipated by the structure. Hence, the following equations of motion can be derived for the elastic and inelastic cases, respectively,

$$m\ddot{x}(t) + c\dot{x}(t) + kx(t) = -m\ddot{x}_g(t) \quad (1)$$

$$m\ddot{x}(t) + c\dot{x}(t) + ak_0x(t) + f_r^*[x(t), \dot{x}(t)] = -m\ddot{x}_g(t), \quad (2)$$

where m is the mass of the structure, c is the viscous damping, k is the elastic stiffness of the structure, $\ddot{x}_g(t)$ is the ground acceleration, $x(t)$ is the structure's displacement, \dot{x} is the structure's velocity, $\ddot{x}(t)$ is the structural acceleration. Parameters k_0 and f_r^* for the inelastic case are, respectively, the initial elastic stiffness and the restoring force comprising the hysteresis stiffness and which depends on the displacements and velocities.

More realistic hysteresis models are essential to accurately characterize an inelastic response analysis of a structural system subjected to dynamic loads, such as seismic excitations. The hysteresis models in the literature can be broadly characterized in polygonal (PHM) and smooth hysteresis models (SHM).

In this study, an SHM is used. This model was initially developed by Bouc ([3]-[6]), modified by Wen ([7], [8]), and further modified by many others ([9]-[12]). The modification used herein is the one developed by Sivaselvan and Reinhorn ([13], [14]).

Figure 1 displays the scheme used in this hysteresis model. This model is capable of simulating different behaviors of a structural system under cyclic loading, viz., strength hardening, the Bauschinger effect, stiffness degradation, strength deterioration, and the pinching effect.

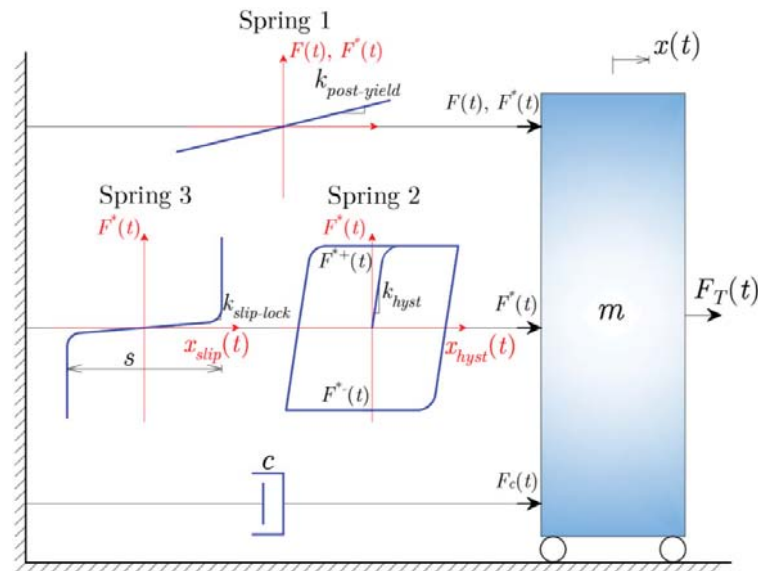


Figure 1: Sivaselvan and Reinhorn's smooth hysteresis model schematic representation.

Three different springs are used within the model: a post-yield spring (Spring 1); a hysteresis spring (Spring 2), and a slip-lock spring (Spring 3).

This modification to the original Bouc-Wen provides a more physical understanding than the previous modifications since the parameters are chosen in such a way to carry a physical meaning. A brief description of the model is presented below based on [14].

Spring 1 and Spring 2 are used in parallel to model post-yield strength hardening, and stiffness degradation, respectively. Hence, upon the application of a load, the springs undergo the same deformation, although they share this force in proportion to their instantaneous stiffness,

$$k = k_{post-yield} + k_{hyst} \quad (3)$$

in which the post-yielding stiffness, $k_{post-yield}$, is represented by a linear elastic spring (Spring 1), and the hysteresis spring, k_{hyst} , is represented by a pure elasto-plastic spring with a smooth transition from the elastic to the inelastic range (Spring 2), that may display degradation phenomena. The linear elastic stiffness and the non-degrading hysteresis stiffness are given by the following expressions, respectively,

$$k_{post-yield} = ak_0 \quad (4)$$

$$k_{hyst} = (1-a)k_0 \left\{ 1 - \left| \frac{F^*}{F_Y^*} \right|^{n_w} \left[\eta_1 \operatorname{sgn}(F^* dx) + \eta_2 \right] \right\} \quad (5)$$

where a is the post to pre-yielding stiffness ratio, n_w controls the smoothness of the transition from elastic to plastic stages, η_1 and η_2 are parameters that control the shape of the unloading curve, F^* and F_Y^* are the portion of the applied force shared by the hysteresis spring and its respective yield value, which are given, respectively, by

$$F^* = (x - x_0)(1-a)k_0 \quad (6)$$

$$F_Y^* = (1-a)F_Y \quad (7)$$

To model stiffness degradation, parameter α is introduced in factor R_K which is a positive parameter with the unity as its possible maximum value. This factor is given by the following expression

$$R_K = \frac{F^* + \alpha F_Y^*}{k_0 x + \alpha F_Y^*} \quad (8)$$

is implemented in the present SHM in the hysteresis spring, in this way only the hysteresis stiffness is modified in the following way

$$k_{hyst} = (R_K - a)k_0 \left\{ 1 - \left| \frac{F^*}{F_Y^*} \right|^{n_w} \left[\eta_1 \operatorname{sgn}(F^* dx) + \eta_2 \right] \right\} \quad (9)$$

To include strength deterioration a rule based on a continuous energy-based degradation, and on a backbone degradation which occurs when the maximum deformation value attained in the past is exceeded and is given by the following expression

$$F_Y^{+/-} = F_{Y0}^{+/-} \left[1 - \left(\frac{x_{\max}^{+/-}}{x_{\text{ult}}^{+/-}} \right)^{\frac{1}{\beta_1}} \right] \left[1 - \frac{\beta_2}{1 - \beta_2} \frac{E_h}{E_{h\text{ult}}} \right] \quad (10)$$

where $F_Y^{+/-}$ is the positive or negative yield force, $F_{Y0}^{+/-}$ is the initial positive or negative yield force, $x_{\max}^{+/-}$ is the maximum positive or negative displacement, $x_{\text{ult}}^{+/-}$ is the ultimate positive or negative displacement, E_h is the hysteresis energy dissipated, $E_{h\text{ult}}$ is the hysteresis energy dissipated when loaded monotonically until the ultimate displacement without any degradation, β_1 is a parameter based on ductility demands, and β_2 is a parameter based on energy demands. The second term on the right side of Equation 10 is related to strength deterioration based on increased deformation and the last term is related to the hysteresis energy dissipated.

The hysteresis energy dissipated can be given in incremental form as follows

$$\Delta E_h = \left[\frac{F + (F + \Delta F)}{2} \right] \left(\Delta x - \frac{\Delta F}{R_k k_0} \right) \quad (11)$$

A “slip-lock” spring (Spring 3) represented in Figure 1 was implemented in the hysteresis model to simulate pinching behavior. The combined stiffness from the three springs can be given as

$$k = k_{\text{post-yield}} + \frac{k_{\text{hyst}} k_{\text{slip-lock}}}{k_{\text{hyst}} + k_{\text{slip-lock}}} \quad (12)$$

where

$$k_{\text{slip-lock}} = \left\{ \sqrt{\frac{2}{\pi}} \frac{s}{F_\sigma^*} \exp \left[-\frac{1}{2} \left(\frac{F^* - F_m^*}{F_\sigma^*} \right)^2 \right] \right\}^{-1} \quad (13)$$

in which s is the slip length, F_σ^* is a measure of the force range over which slip occurs, and F_m^* is the mean force level on either side about which slip occurs, being these three parameters given, respectively, as follows

$$s = R_s (x_{\max}^+ - x_{\max}^-) \quad (14)$$

$$F_\sigma^* = \sigma F_Y^* \quad (15)$$

$$F_m^* = \lambda_s F_Y^* \quad (16)$$

where parameters R_s , σ_s , and λ_s are parameters that control each of the resulting values of the previous three equations.

With the right tuned hysteresis parameters presented in Equations 3 to 16 different hysteretic behaviors can be achieved and replicated, representing different structural systems, elements, or with different materials.

3 IMPACT MODELS REVIEW

As mentioned in the introduction section, structural pounding involves different and complex phenomena that make the problem of earthquake-induced structural building pounding extremely complicated to model.

When modeling structural pounding between buildings it is enough to accurately estimate the magnitude of the pounding forces to understand how these forces will influence the overall dynamic behavior of the intervenient structures. Hence, in the literature two possible ways to model these forces are available: stereomechanics or the classical theory of impact, and the use of impact or contact elements [15].

The first approach is limited to the specification of the initial and final impact velocity states of the colliding rigid bodies (Equations 17 and 18), as well as the applied linear or angular impulse-momentum.

$$\dot{x}_{1,f} = \dot{x}_{1,0} - (1 + CR) \frac{m_2 \dot{x}_{1,0} - m_2 \dot{x}_{2,0}}{m_1 + m_2} \quad (17)$$

$$\dot{x}_{2,f} = \dot{x}_{2,0} + (1 + CR) \frac{m_1 \dot{x}_{1,0} - m_1 \dot{x}_{2,0}}{m_1 + m_2} \quad (18)$$

This approach cannot describe transient stresses or forces and fails to account for local deformations at the contact point of the bodies assuming that a negligibly part of the initial kinetic energy of the system is transformed into vibrations of the colliding bodies [16].

The impact velocities are related to the very important parameter, coefficient of restitution (CR),

$$CR = \frac{\dot{x}_{2,f} - \dot{x}_{1,f}}{\dot{x}_{1,0} - \dot{x}_{2,0}} \quad (19)$$

in which its value represents the energy losses and degree of inelasticity of the collision being directly related with the kinetic energy loss ($-\Delta E_k$) during impact, as follows

$$-\Delta E_k = \frac{1}{2} \left(\frac{m_1 m_2}{m_1 + m_2} \right) (1 - CR^2) (\dot{x}_{1,0} - \dot{x}_{2,0})^2 \quad (20)$$

A coefficient of restitution equal to one represents a perfectly elastic impact and equal to zero represents a perfectly plastic impact. This coefficient is found to be intrinsically correlated with the prior-impact velocity ([16], [17]).

The classical theory of impact is generally not used in structural pounding due to referred limitations. In addition, it neglects the existence of the period of impact failing to directly assess the evolution of the pounding forces during contact [18].

In reality, the period of impact exists and is divided into the approach (compression, loading, deformation) and restitution (unloading, elastic) periods. These periods are explicitly considered in most of the impact models that constitute the second approach available in modeling structural pounding between buildings under seismic excitations.

This approach is essentially based on a penalty method, i.e., when the buildings interpenetrate, the impact element is activated generating the pounding forces that push the structures apart. Considering the unidirectional relative displacements of the colliding structures, the impact element becomes active when

$$\delta(t) > 0 \quad \text{where} \quad \delta(t) = x_1(t) - x_2(t) - \text{Gap} \quad (21)$$

in which $\delta(t)$ is the interpenetration depth of the colliding structures.

These models are compression-only zero-length elements comprising a massless spring and dashpot in parallel. The structures involving large masses can be considered as rigid bodies, having the masses lumped at the stories' levels.

The use of these elements is based on Hertz's theory and oversimplified assumptions that make the analysis of the problem simpler yet less accurate [19].

According to theories of contact mechanics [19], in impact problems, the stress wave propagation will have a significant influence on the distribution of forces within the structure. However, if one can assume that the stress waves will travel through the structures being re-

flected many times before any of them is brought to rest, then the state of stress in the structures at any instant can be considered approximately uniform throughout its length. Thus, the sudden changes in stress associated with the passage of the elastic stress waves within the structure are small compared with the general stress level. This justifies the use of the well-known spring-dashpot element with acceptable accuracy, ignoring the dynamic effects in the structures due to wave propagation and assuming that structural pounding between buildings can be approximately quasi-static if the duration of the impact is long enough to allow stress waves to transverse the length of the body many times.

In addition, the contact area is in general elliptical and is assumed to be small in comparison with the main dimensions of the bodies; deformations are restricted to the vicinity of the impact; contact surfaces are non-conforming, smooth, continuous, and frictionless; and the contact regions are assumed to remain elastic and unaltered after impact events.

During impact, the spring will control the elastic restoring force and deformation, and the dashpot will account for the energy radiated due to impact by wave motion. With these impact models is thus possible to determine with reasonable accuracy the magnitude of the impact forces at any instant during structural pounding between buildings, which is the fundamental information to understand how pounding influences the overall dynamic response of the colliding buildings.

Nonetheless, and cumulative to the oversimplified assumptions, the effectiveness of the impact models largely depends on its parameters, viz., impact stiffness and impact damping ratio. The impact stiffness (k_{imp}) namely depends on the material properties and geometric characteristics of the region of impact, and hence it presents high levels of uncertainties. The impact damping ratio (ξ_{imp}) depends mostly on the coefficient of restitution and is generally derived from energy considerations.

Based on the relations between these parameters several impact models were developed in the literature.

The most basic impact model is the linear elastic model (Figure 2a), comprising only a spring and lacking the ability to account for energy loss during impacts which is inevitable in this kind of phenomenon. The pounding force, $f_P(t)$, can then be determined by the following expression

$$f_P(t) = \begin{cases} k_{imp} \delta(t), & \text{for } \delta(t) > 0 \\ 0 & \text{for } \delta(t) \leq 0 \end{cases} \quad (22)$$

The non-linear elastic model or Hertz's contact model follows Hertz's contact law [20], which describes the static compression between two isotropic elastic bodies according to the previously defined assumptions. It essentially consists of a non-linear spring as represented in Figure 2b. The spring non-linearity is capable of modeling the force-deformation relation more realistically, i.e., the contact area between neighboring structures is expected to increase as the contact force grows, leading to a non-linear stiffness. In other words, the impact force increases with the interpenetration depth to the power of 3/2 [19],

$$f_P(t) = \begin{cases} \beta_{imp} [\delta(t)]^{\frac{3}{2}} & \text{for } \delta(t) > 0 \\ 0 & \text{for } \delta(t) \leq 0 \end{cases} \quad (23)$$

in which β_{imp} is a parameter indicating the non-linear impact stiffness depending on material properties and geometry of the colliding structures. Simplified formulae were developed by Goldsmith [16] to compute the impact stiffness parameters depending on the shape of the colliding bodies.

Alternatively, a linear viscoelastic impact model (also called Kelvin-Voigt model) as represented in Figure 2c, can be used accounting for the energy dissipation during impact ([21], [22]). The pounding force can be computed using the following system of equations

$$f_p(t) = \begin{cases} k_{imp} \delta(t) + c_{imp} \dot{\delta}(t), & \text{for } \delta(t) > 0 \\ 0 & \text{for } \delta(t) \leq 0 \end{cases} \quad (24)$$

where c_{imp} is the damping constant of the pounding contact element computed by the following expression ([22], [23])

$$c_{imp} = 2 \xi_{imp} \sqrt{k_{imp} \frac{m_1 m_2}{m_1 + m_2}} \quad \text{where} \quad \xi_{imp} = \frac{-\ln(CR)}{\sqrt{\pi^2 + [\ln(CR)]^2}} \quad (25)$$

A shortcoming to this model is the tension stress verified at the end of the restitution period, i.e., immediately before separation of the bodies, produces a negative pounding force, pulling the bodies together in the unloading phase not having a physical meaning. This happens since the parallel association in the Kelvin solid means that the total stresses are obtained as the summation of the stresses in the spring and dashpot, i.e., all elements will suffer the same deformation, meaning that the stress-strain curves produced in both periods of impact will have the same damping coefficient. This will produce a uniform dissipation of energy on both periods of impact, which in reality does not happen ([15], [16]). Also, it is observed that the elastic strain energy stored in the first period of impact is released in the second period without major plastic effects, being that most of the energy dissipated is verified to be lost in the approach period, while in the restitution period only a relatively small quantity is observed to be dissipated.

To address and solve these drawbacks some modifications to the Kelvin-Voigt impact model have been developed. Komodromos et al. [24] proposed the following modification

$$f_p(t) = \begin{cases} k_{imp} \delta(t) + c_{imp} \dot{\delta}(t), & \text{for } f_p(t) > 0 \\ 0 & \text{for } f_p(t) \leq 0 \end{cases} \quad (26)$$

Valles and Reinhorn [25], modified the Kelvin-Voigt model by considering the damping term to be activated only for positive velocities during impact which means only activated during the approach period (Figure 2e). The following compact expression was suggested

$$f_p(t) = \left\{ k_{imp} \delta(t) + c_{imp} \dot{\delta}(t) H[\dot{\delta}(t)] \right\} H[\delta(t)] \quad (27)$$

where H is the unit step or Heaviside function. The expressions used to compute the impact damping coefficient and ratio are the same as in Equation 25, and an expression to compute an equivalent coefficient of restitution was derived based on the instant of time of maximum deformation (end of approach period), impact frequency (ω_{imp}), impact damped frequency ($\omega_{d,imp}$), and impact damping ratio

$$CR = \sin(\omega_{d,imp} t_{max}) e^{-\xi_{imp} \omega_{imp} t_{max}} \quad \text{where} \quad t_{max} = \frac{1}{\omega_{d,imp}} \tan^{-1} \left(\frac{\omega_{d,imp}}{\xi_{imp} \omega_{imp}} \right) \quad (28)$$

Mahmoud [26] addressed the drawbacks of the linear viscoelastic impact model by redefining the pounding force depending on the two periods of impact. The author considered a similar approach to Valles and Reinhorn [25] (Figure 2e), and the following equivalent expression was suggested

$$f_p(t) = \begin{cases} k_{imp} \delta(t) + c_{imp} \dot{\delta}(t) & \text{for } \delta(t) > 0, \dot{\delta}(t) > 0 \\ k_{imp} \delta(t) & \text{for } \delta(t) > 0, \dot{\delta}(t) \leq 0 \\ 0 & \text{for } \delta(t) \leq 0, \end{cases} \quad (29)$$

The relationship between the damping ratio and the CR was reevaluated since the energy dissipation properties depend on the damping term, which now is only active in the first period of impact. The author used the same procedure as Jankowski in [27] using energy considerations, arriving at the following expression

$$\xi_{imp} = \frac{1}{\pi} \frac{1 - CR^2}{CR} \quad (30)$$

Ye et al. [28] proposed the following modification to the Kelvin-Voigt model (Figure 2e) at the impact damping coefficient and ratio

$$c_{imp} = \xi_{imp} \delta(t) \quad \text{where} \quad \xi_{imp} = \frac{3 k_{imp} (1 - CR)}{2CR (\dot{x}_{1,0} - \dot{x}_{2,0})}. \quad (31)$$

Pant et al. ([29], [30]) developed a modification on the Kelvin-Voigt impact model (Figure 2e) considering the same expression presented by Mahmoud in Equation 29, by modifying the expression of the impact damping ratio as follows

$$\xi_{imp} = \frac{3 k_{imp} (1 - CR^2)}{2CR^2 (\dot{x}_{1,0} - \dot{x}_{2,0})} \quad (32)$$

Following the research in Mahmoud [26], Mahmoud and Jankowski [31] suggested a further modification to the linear viscoelastic model (Figure 2e) using a different approach to arrive at an improved formula for the impact damping ratio

$$\xi_{imp} = \frac{1 - CR^2}{CR [CR (\pi - 2) + 2]} \quad (33)$$

In the modifications to the Hertz contact model, the lack of energy dissipation properties was addressed by the addition of non-linear damping becoming now a non-linear viscoelastic model. Lankarani and Nikraves ([32], [33]) proposed a contact model considering a non-linear spring using Hertz's law in parallel with non-linear damping in hysteresis form proposed by Hunt and Crossley [34] (Figure 2d) to better represent impacts between mechanical systems. The authors considered the pounding force to be computed as follows

$$f_p(t) = \beta_{imp} [\delta(t)]^n + c_H \dot{\delta}(t) \quad (34)$$

where c_H is the non-linear damping coefficient given by

$$c_H = \mu_d [\delta(t)]^n \quad \text{where} \quad \mu_d = \frac{3 \beta_{imp} (1 - CR^2)}{4 (\dot{x}_{1,0} - \dot{x}_{2,0})} \dot{\delta}(t) \quad (35)$$

in which μ_d is the hysteresis damping factor and $n=3/2$ to represent Hertz's law. Muthukumar and DesRoches ([35], [36]) proposed an impact model, the "Hertzdamp" impact model represented in Figure 2d, using the previous considerations applied to civil engineering structures

$$f_P(t) = \begin{cases} \beta_{imp} [\delta(t)]^{\frac{3}{2}} + c_H \dot{\delta}(t) & \text{for } \delta(t) \geq 0 \\ 0 & \text{for } \delta(t) < 0 \end{cases} \quad (36)$$

where the impact damping ratio is now

$$\xi_{imp} = \frac{3\beta_{imp}(1-CR^2)}{4(\dot{x}_{1,0} - \dot{x}_{2,0})} \dot{\delta}(t) \quad (37)$$

Jankowski [37] proposed a modification to Hertz's non-linear impact model by considering that the non-linear damping component is only active in the approach period (Figure 2f) since it is in this period of the impact that most energy is dissipated. Thus, the pounding force is obtained using the following piecewise function

$$f_P(t) = \begin{cases} \beta_{imp} [\delta(t)]^{\frac{3}{2}} + c_H(t) \dot{\delta}(t) & \text{for } \delta(t) > 0 \text{ and } \dot{\delta}(t) > 0 \\ \beta_{imp} [\delta(t)]^{\frac{3}{2}} & \text{for } \delta(t) > 0 \text{ and } \dot{\delta}(t) \leq 0 \\ 0 & \text{for } \delta(t) \leq 0 \end{cases} \quad (38)$$

The impact element's damping can be considered as an extension of the linear viscoelastic model (modified Kelvin-Voigt) and is obtained with the following expression

$$c_H(t) = 2\xi_{imp} \sqrt{k_{imp} \frac{m_1 m_2}{m_1 + m_2}} \quad \text{where} \quad k_{imp} = \beta_{imp} \sqrt{\delta(t)} \quad (39)$$

The second of Equation 39 can be seen as an effective impact stiffness for a given value of the interpenetration depth. Additionally, Jankowski ([27], [37]) redefined the expression for the damping ratio which is related to the coefficient of restitution since now the non-linear damping is only active in the approach period. To do this the author developed two algebraic expressions (with approximating functions) for the impact damping ratio and then compared them with numerical results to verify its validity. The two expressions are

$$\xi_{imp} = \frac{\sqrt{5}}{2\pi} \frac{1-CR^2}{CR} \quad \text{and} \quad \xi_{imp} = \frac{9\sqrt{5}}{2} \frac{1-CR^2}{CR[CR(9\pi-16)+16]} \quad (40)$$

in which the second was found to provide better approximations. The approximating functions used by Jankowski in [27] served as the base to the procedure adopted by Mahmoud and Mahmoud and Jankowski in [26] and [31], respectively. Also, the results regarding the relationship between the impact damping ratio and the coefficient of restitution in impact models drew attention to the fact that when the coefficient of restitution becomes zero the impact damping ratio should go to infinity. This was addressed by Ye et al. [28] for the modification to the original Kelvin-Voigt that provided the unit value of the impact damping ratio for zero value of the coefficient of restitution, and by the same authors [38] for the modification of the Hertz damp model that gave a finite value for the impact damping ratio for perfectly plastic collisions. Besides, all models corroborated the fact that a coefficient of restitution of one corresponds to the obvious zero value of the impact damping ratio.

Ye et al. [38] then arrived at a more accurate expression to approximate the damping constant given by

$$\xi_{imp} = \frac{8 \beta_{imp} (1 - CR)}{5CR (\dot{x}_{1,0} - \dot{x}_{2,0})} \quad (41)$$

which confirms the aforementioned premises by Jankowski [27] and was then validated through numerical simulations.

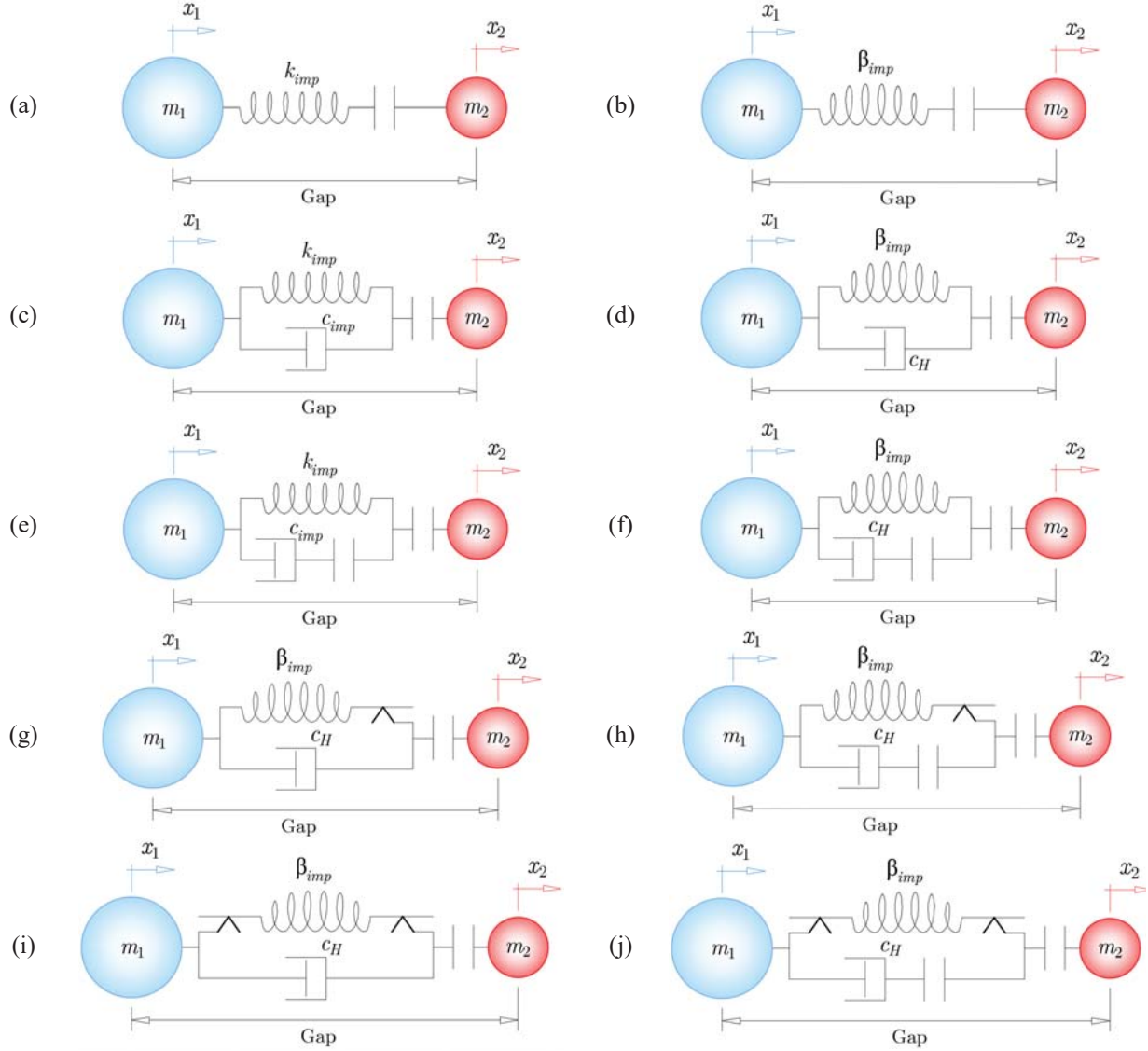


Figure 2: Schematic representation of state-of-the-art impact models.

More recently, Naderpour et al. [39] considered an equivalent expression to Equation 34 and the first of Equation 35 to compute the pounding force between buildings. Ultimately, a new expression for the impact damping ratio for the non-linear viscoelastic model (Figure 2f) related to the coefficient of restitution was obtained by an iterative procedure that attempts to equate the energy dissipated by the non-linear damping in the approach period (translated by the area of the impact hysteresis loop) to the kinetic energy loss (of the stereomechanical impact), resulting in

$$\xi_{imp} = \left[\frac{2}{CR\sqrt{\pi}} (1 - CR^2) \right]^2 \quad (42)$$

A further study by Naderpour et al. [40] suggested a new expression (see Equation 43) for the impact damping coefficient that depends on the prior-impact velocity and coefficient of restitution.

$$c_{imp}(t) = \alpha \frac{CR^\beta \dot{\delta}_{imp}(1-CR)}{\ddot{\delta}(t)} k_{imp} \delta^n(t) \quad (43)$$

Bamer [41] and Bamer and Markert [42], respectively, proposed an extension to the Hertz-damp and Jankowski's non-linear viscoelastic model by including a dry friction element in series with the non-linear spring (Figure 2g and 2h) to address one of the mentioned oversimplified assumptions, the unaltered contact surface which is tacitly known to experience damage and material dissipation caused by numerous and repeated impacts. The authors modified the condition of collision (see Equation 21), first by considering the equivalent condition of collision when $\delta < 0$ (when the Gap is added instead of subtracted) and then by including an additional increase in the gap due to damage, material loss, or plastic deformation, yielding

$$\delta_T(t) = \delta(t) + \delta_s(t) < 0 \quad \text{where} \quad \delta(t) = x_1(t) - x_2(t) + \text{Gap} \quad (44)$$

in which the non-negative parameter δ_s is the additional offset to the position of the initial pounded surface. Three states were then considered within the periods of impact: state 0 refers to the case without impact; state I corresponds to the activation of the impact model satisfying the condition in Equation 44; state II when a limit value of the elastic Hertz's contact force is exceeded (sliding). A constant friction force R obeying Coulomb's friction law is considered based on the material and geometric properties of the colliding surfaces, together with the non-linear damping term. An additional state, state III considered in the case of Jankowski's non-linear viscoelastic model, where the damping term is no longer active in the restitution period. Equations 45 represents, the improved models of Hertz-damp and Jankowski's non-linear viscoelastic model, according to the states defined ([41], [42])

$$f_P(t) = \begin{cases} f_k + f_c & \text{for } \delta_T(t) < 0 \quad \text{and} \quad \dot{\delta}_T(t) < 0 \quad \text{and} \quad f_k < f_R \quad (\text{State I}) \\ f_R + f_c & \text{for } \delta_T(t) < 0 \quad \text{and} \quad \dot{\delta}_T(t) < 0 \quad \text{and} \quad f_k \geq f_R \quad (\text{State II}) \\ f_k & \text{for } \delta_T(t) < 0 \quad \text{and} \quad \dot{\delta}_T(t) \geq 0 \quad (\text{State III}) \\ 0 & \text{for } \delta_T(t) \geq 0 \quad (\text{State 0}) \end{cases} \quad (45)$$

$$\text{where} \quad f_k = \beta_{imp} \left[|\delta(t)| - \delta_s(t) \right]^{\frac{3}{2}}, \quad f_c = c_H(t) \dot{\delta}_T(t), \quad f_R = -\text{sgn}(\dot{\delta}_T(t)) R$$

Later Bamer et al. [43] went further to include in the previous model a decrease in the stiffness depending on the sliding gap which now is divided into two and attributed to each frame. A simple damage curve was then assumed to allow structural damage description. The impact model may then be represented, respectively, for the modified Hertz-damp and Jankowski's non-linear viscoelastic model in Figures 2i and 2j.

Khatami et al. [44] developed an effective formula for the impact damping ratio included in the non-linear viscoelastic impact model (Figure 2f). The authors used a program developed called the Coefficient of Restitution-Velocity-Stiffness (CRVK), which performs several dynamic analyses and solves impact problems. The accuracy of this new formula was assessed based on four different approaches that include energy-based considerations, numerical simulations, and comparisons with experimental results. The expression proposed by the authors is

$$\xi_{imp} = \frac{(1 - CR)}{CR^{(\alpha + 0.204)} + 3.351\pi CR} CR^{0.204} \quad \text{where} \quad \alpha = 1.05 CR^{0.653} \quad (46)$$

Based on the previous studies regarding impact models it is possible to verify that the main modifications are at the parameters impact stiffness and impact damping ratio. These parameters along with the coefficient of restitution, which generally is the only independent variable of the impact damping ratio constitute the core of the impact models and its accuracy depends on how accurate is the estimation of these parameters.

Some experimental tests regarding pounding between structures have been carried out ([17], [45]-[49]) essentially concerning reduced-scale models. These experimental tests motivated several investigations comparing the effectiveness of the previous impact models and other comparisons between them.

For instance, based on different experimental results available in the literature regarding pounding-involved structural responses, Jankowski [37] made comparisons between Jankowski's non-linear viscoelastic model, Kelvin-Voigt model, and Hertz's non-linear model. The author verified that the Kelvin-Voigt and the non-linear viscoelastic model gave the smallest simulation errors in the pounding force time-histories during impact and that further research confirmed that Jankowski's model provided smaller errors in the response time-histories with the structural pounding.

Jankowski and Mahmoud ([15], [17]) performed experimental tests based on dropping different balls of different materials (steel, concrete, timber, and ceramic), and on the impact between reduced-scale models excited by shake tables. The results corroborated with the study addressed in the previous paragraph and revealed that the improved version of the linear viscoelastic model by Jankowski and Mahmoud did not lead to increased accuracy and that the Hertz damp also furnished small errors in the response time-histories of earthquake-induced structural pounding.

Bamer et al. ([41]-[43]) proposed a new strategy using state-of-the-art impact models that includes damage description and failure of the pounding-involved structures. The authors verified through sensitivity analysis the importance of the consideration of the damage state of the adjacent structures.

Khatami et al. [44] compared their impact damping ratio formula with the ones of different impact models in the literature and based on different experimental tests and numerical simulations, presenting the lowest errors and proving its accuracy in the study of earthquake-induced structural pounding.

Still, most of the impact models in the literature lack the ability to emulate structural pounding between three-dimensional structures. The central impact is defined as the collision between two non-rotating objects at a point belonging to a line that connects the two centroids. An oblique impact considering a two-dimensional impact model may be possible to develop to emulate three-dimensional pounding that considers in addition to the two directions of translation of the buildings, their rotation. One good example is the model developed by Polycarpou et al. [50] that considers tangential forces and friction during impact, and the material properties and geometry of the contact area without the need to previously determine the location of the impact. The model proved to furnish good results and close to the results obtained with commercial software.

4 NUMERICAL MODELING

Two adjacent structural systems will be considered in this earthquake-induced structural pounding study, one flexible building, and the other building stiffer as represented in Figure 3.

The structures are assumed to be in shear configuration, and thus can be reduced to lumped mass models with the masses lumped at the floor levels. The structural properties of the representative buildings are considered to be the same as in [15] and are summarized in Table 1.

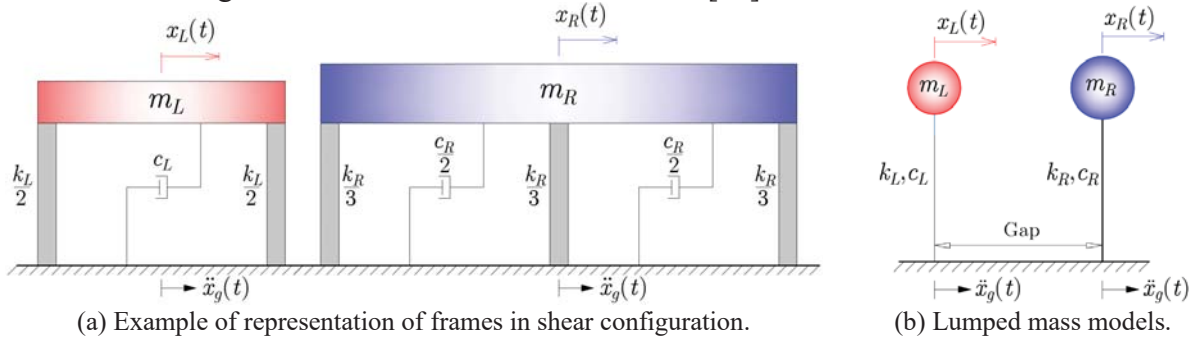


Figure 3: Representation of the two SDOF structural systems separated by a gap size.

Structural properties	Flexible building	Stiffer building
Mass (kg)	$m_L=75000$	$m_R=3000 \times 10^3$
Stiffness (kN/m)	$k_L=2056$	$k_R=1.316 \times 10^6$
Natural period (s)	$T_L=1.2$	$T_R=0.3$
Damping coefficient (kg/s)	$c_L=39270$	$c_R=6.283 \times 10^6$
Damping ratio (%)	$\xi_L=5$	$\xi_R=5$

Table 1: Structural properties of the adjacent buildings.

Among the different types of building pounding, impacts will be assumed to happen exclusively between floors. The impact model used in this study is the one developed by Jankowski ([27], [37]), the non-linear viscoelastic model which is illustrated in Figure 2f, and so the expressions to be used are Equations 38, 39 and the second of 40. These expressions are then implemented in the equations of motion in Equations 1 and 2, being modified, respectively, for the elastic and inelastic case as follows

$$m\ddot{x}(t) + c\dot{x}(t) + kx(t) + f_p(t) = -m\ddot{x}_g(t) \quad (47)$$

$$m\ddot{x}(t) + c\dot{x}(t) + ak_0x(t) + f_r^*[x(t), \dot{x}(t)] + f_p(t) = -m\ddot{x}_g(t), \quad (48)$$

Depending on the structural behavior one of the two previous equations will be solved for each building. The term regarding the pounding force becomes activated when the buildings interpenetrate satisfying Equation 21.

The stiffness of the impact element is usually taken as the same order of magnitude as the axial stiffness of the stiffer story. This parameter depends on the geometry of the impact surfaces, material properties, variable impact velocities, and uncertainties concerning its value arising from these factors [22]. Goldsmith [16] referred that for steel-to-steel impacts the impact stiffness generally takes higher values than concrete-to-concrete impacts. Van Mier et al. [45] experiments reveal that impacts between concrete bodies depend mostly on the contact surface geometry and ranges typically between $40 \text{ kN/mm}^{3/2}$ and $80 \text{ kN/mm}^{3/2}$ (respectively, $1.2 \times 10^9 \text{ N/m}^{3/2}$ and $2.6 \times 10^9 \text{ N/m}^{3/2}$). Cole et al. [51] refer that the impact stiffness is typically set as ten times the stiffness of the larger axial floor.

The values used for the impact stiffness and the coefficient of restitution are, respectively, $2.75 \times 10^9 \text{ N/m}^{3/2}$ and 0.65. These values were provided by Jankowski [37] based on comparisons between numerical simulations using the author's non-linear viscoelastic model and experimental data available in the literature.

The hysteresis parameter values considered for the present study are: $a=0.1$; $\eta_1=\eta_2=0.5$; $\alpha=4$; $\beta_1=0.30$; $\beta_2=0.15$; $\sigma_s=0.2$; $R_s=0.1$; $\lambda_s=0$; $n_W=3$. In addition, the yield force and displacement of the left building are, respectively, $F_{YL}=70 \text{ kN}$, $x_{YL}=3.4 \text{ cm}$, the yield force and displacement of the right building are, respectively, $F_{YR}=7000 \text{ kN}$, $x_{YR}=0.53 \text{ cm}$, and the ductility is $\mu=10$. The values were chosen according to the information furnished in [14] and are intended to be representative of a reinforced concrete (RC) frame, although the values are not the result of direct calibration with experimental data. Hence, for the RC frame a severe stiffness degradation, moderate strength deterioration, and mild to moderate pinching effect.

A Matlab/Simulink [52] model was developed and used to emulate structural pounding between the elastic and inelastic SDOF systems under the El Centro earthquake represented in Figure 4. The simulations were performed for the following values of the gap between the adjacent structures: 0 cm , 3 cm , 5 cm , 10 cm , and 15 cm . To solve the differential equations of motion the Runge-Kutta of 4th order was used with a fixed time step of $5 \times 10^{-4} \text{ s}$.

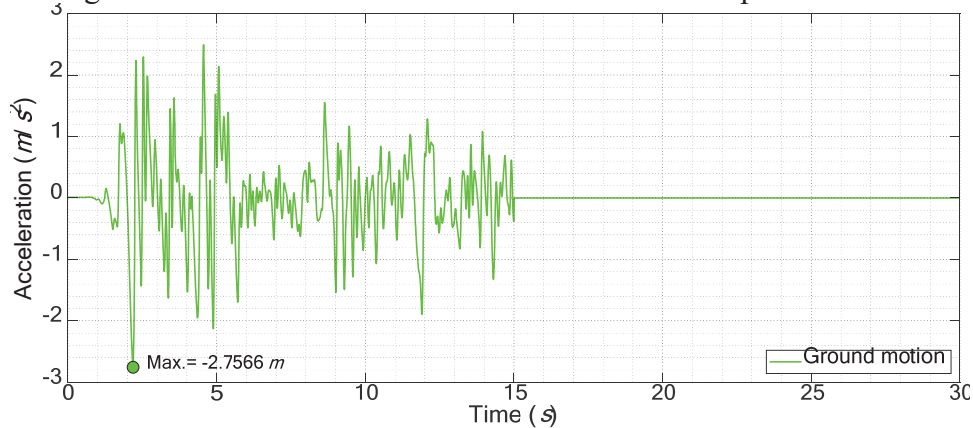


Figure 4: NS component of El Centro seismic accelerations - Station: El Centro, CA - Sta9; Imperial Valley-02 [53].

5 RESULTS AND DISCUSSION

As an example, the following results in form of graphs are presented only for the situations where the buildings have no gap in between and are separated by 3 cm and for the elastic and inelastic structural systems described in the previous section. Nevertheless, and for the purpose of comparisons Table 2 presents the peak responses (displacements, velocities, accelerations, and pounding forces and number of impacts) of both buildings for the different situations of the separation distance and structural behavior cases. It should be pointed out that in the case where the gap is 10 cm and the structural system has inelastic behavior no impacts were verified and so its response is the same as for the case with 15 cm of gap size, thus its results do not explicitly appear in the table.

Hence, Figures 5 to 8 present the displacement and pounding force time-history responses for the 0 cm and 3 cm of gap size and for the elastic and inelastic case. Correspondingly the graphs of Figure 9 present the pounding force vs interpenetration depth cycles for the 0 cm and 3 cm of gap size for the elastic and inelastic case. Figures 10 and 11 present comparisons between the displacements and impact forces time-history responses for the different gap sizes considered (except for the 10 cm for the mentioned reason).

The graphs of Figures 12 and 13 present the hysteresis cycles of the left and right structural systems obtained with the aforementioned hysteresis model for the two gap cases considered, respectively.

Additionally, the acceleration time-history responses are also presented in Figures 14 to 18 for the mentioned cases to assess the acceleration spikes.

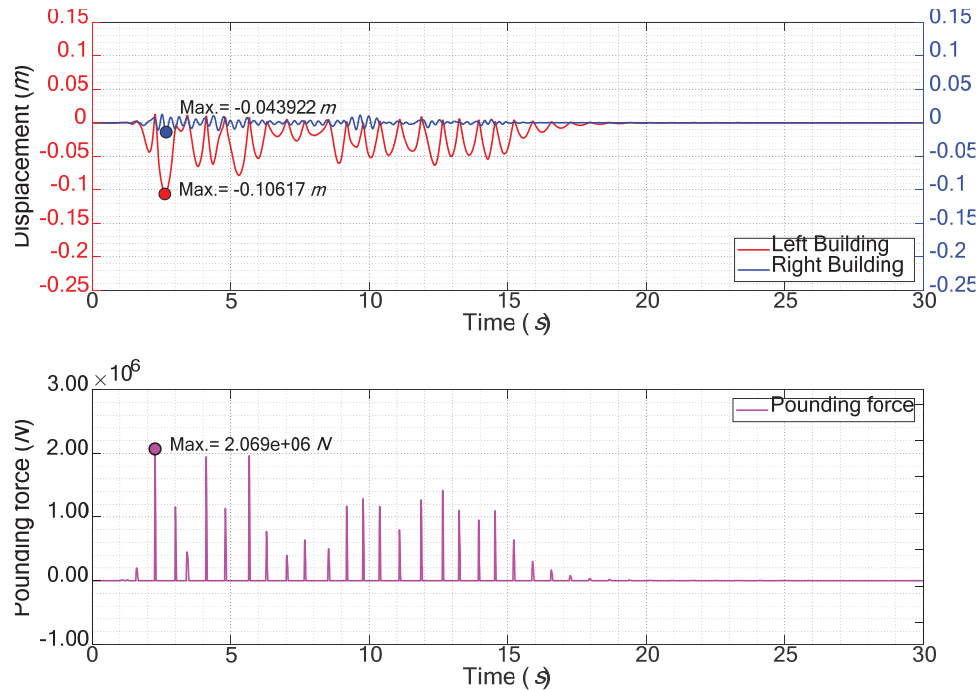


Figure 5: Displacements and pounding forces time-history responses for the elastic case of the representative structural systems with no gap in between.

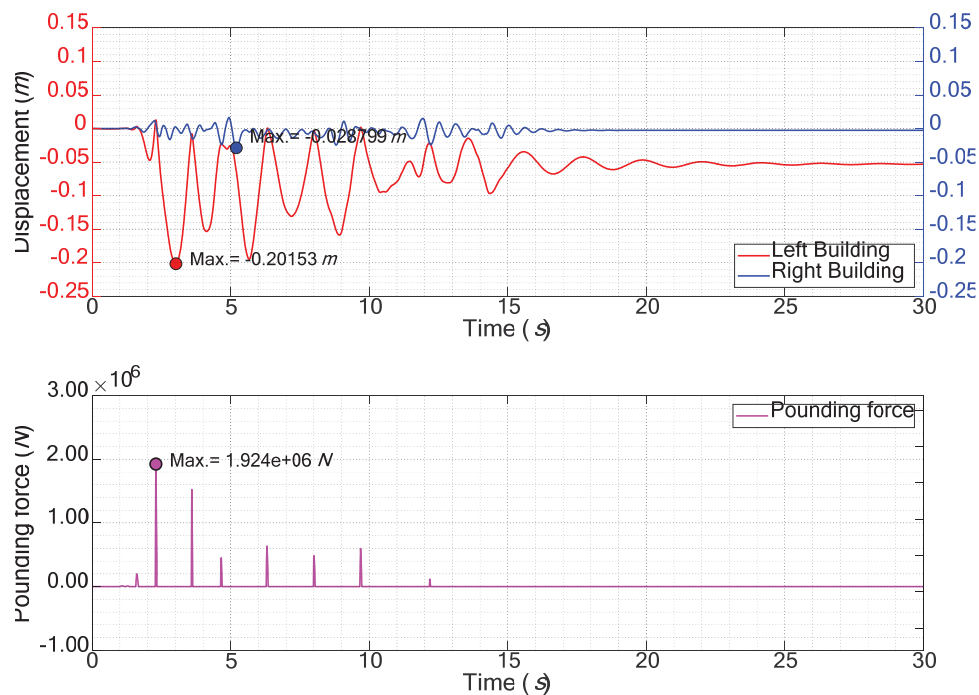


Figure 6: Displacements and pounding forces time-history responses for the inelastic case of the representative structural systems with no gap in between.

The huge differences in stiffness and mass of the structures allow for better conclusions regarding the effects of pounding between these buildings. In general, and as expected, it can be verified for every response considered that the most flexible structure is the most affected, and thus, the most sensitive to the ground motion excitation and the pounding forces.

In general, as the gap between the buildings decreases, the number of impacts increases. No distance between buildings with very different dynamic properties may constitute one of

the worst situations when pounding is likely to occur. This situation presents the biggest number of impacts between the buildings, and the intensity of the pounding forces is closer to the maximum verified in the situation with a 3 cm of gap size.

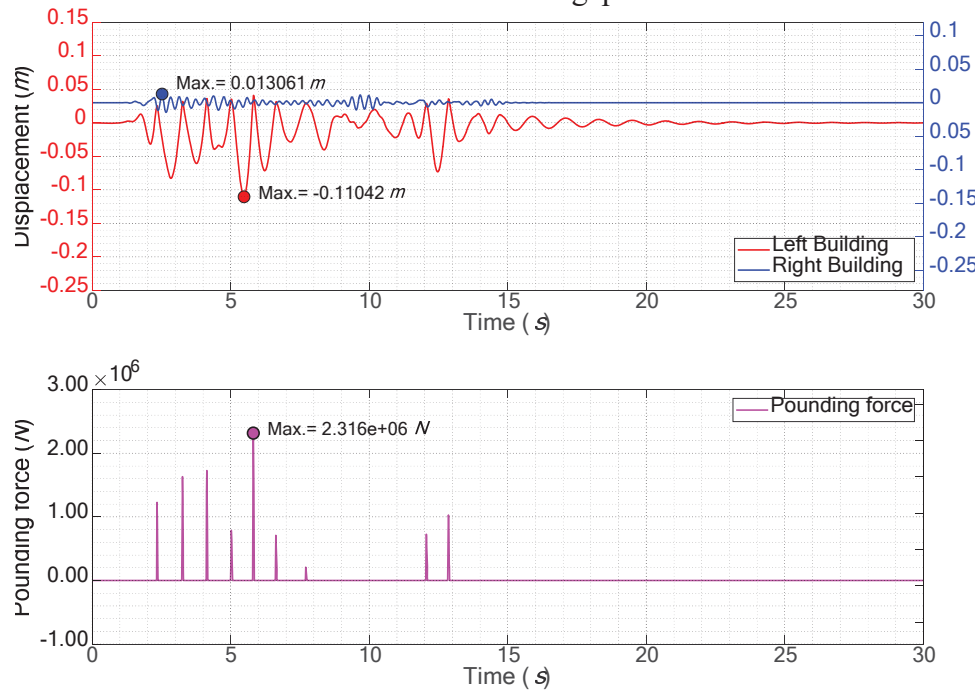


Figure 7: Displacements and pounding forces time-history responses for the elastic case of the representative structural systems separated by a distance of 3 cm.

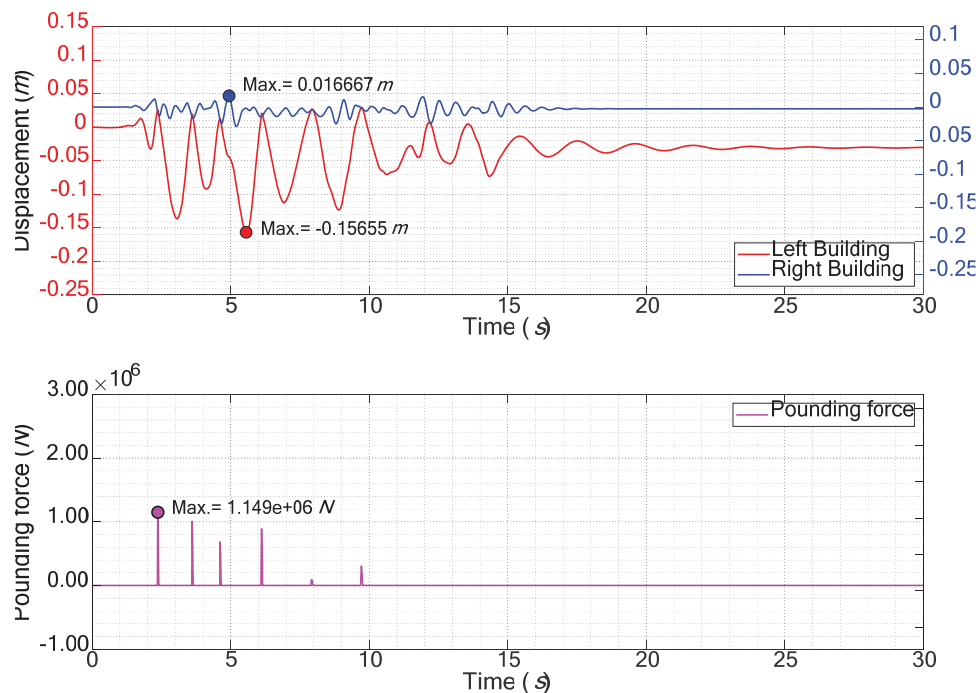


Figure 8: Displacements and pounding forces time-history responses for the inelastic case of the representative structural systems separated by a distance of 3 cm.

Attention should be drawn to the acceleration spikes, that in comparison with no pounding display huge percentages of increase. The sudden changes in the velocity response of the

buildings due to impacts cause these short-duration acceleration spikes in the opposite direction that can cause greater damage to the buildings' structures and contents. The graphs of Figures 14 to 17 show these acceleration spikes due to pounding between the building during the seismic hazard event.

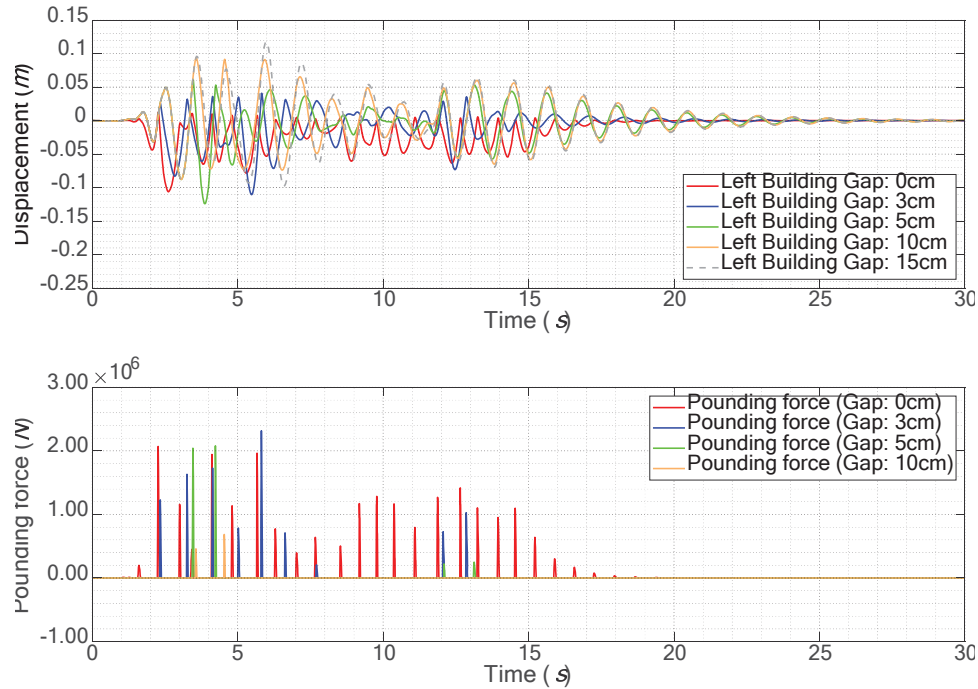


Figure 9: Comparison of the displacements and pounding forces time-history responses for the elastic case of the left building for different gap sizes.

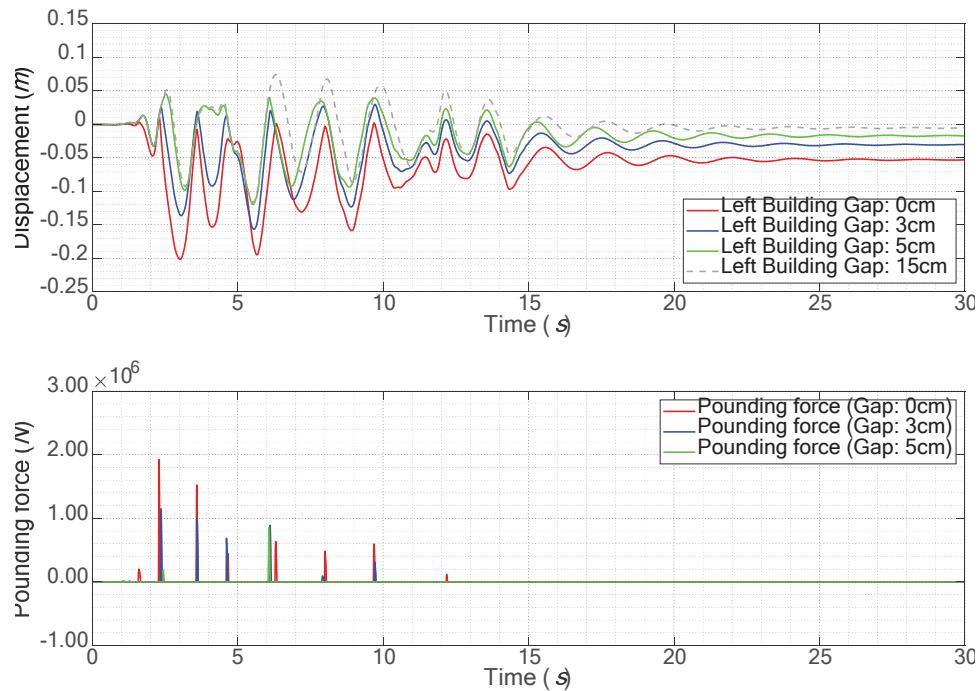


Figure 10: Comparison of the displacements and pounding forces time-history responses for the inelastic case of the left building for different gap sizes.

Observing the elastic case (Figure 5, 8, and 9) it can be seen that the mutual blocking of the buildings explains the peak displacement reductions in Table 2. It is known that pounding tends to reduce the inbound structural displacements due to building blocking. Conversely, it tends to increase the rebound displacements. This is evident in the flexible structure as can be seen in Figure 9, although the same cannot be verified in the stiffer building which experiences great reductions in the peak structural displacements (Table 2). In terms of peak velocities, the flexible structure tends to suffer increases (gap sizes of 10 cm and 5 cm), and the stiffer structure only experiences a slight decrease in the case of no separation distance. It should be stated that although there is a reduction in the peak responses when pounding is considered, this is not beneficial since great local damages at the regions of impact are implicitly known and damage in the structures due to structural inelastic behavior should be expected and aggravated due to pounding, as will be discussed in the next paragraphs.

The inelastic behavior of the structural systems has a significant influence on the structural overall dynamic behavior. As can be seen by comparing Figures 9 and 10, the inelastic case experiences fewer impacts and its intensity is also smaller. However, the presence of permanent deformations is inevitable and increases with decreasing gap size. In addition, the rebound displacements are also increased concerning the elastic case, particularly, in the flexible structure for the gap sizes of 0 cm and 3 cm since in the corresponding 5 cm of gap size a reduction is verified. In the case of the stiffer structure, permanent deformations are still expected although much smaller than in the flexible structure, increases were verified in the gap sizes of 3 cm and 5 cm and a decrease in the case with no gap.

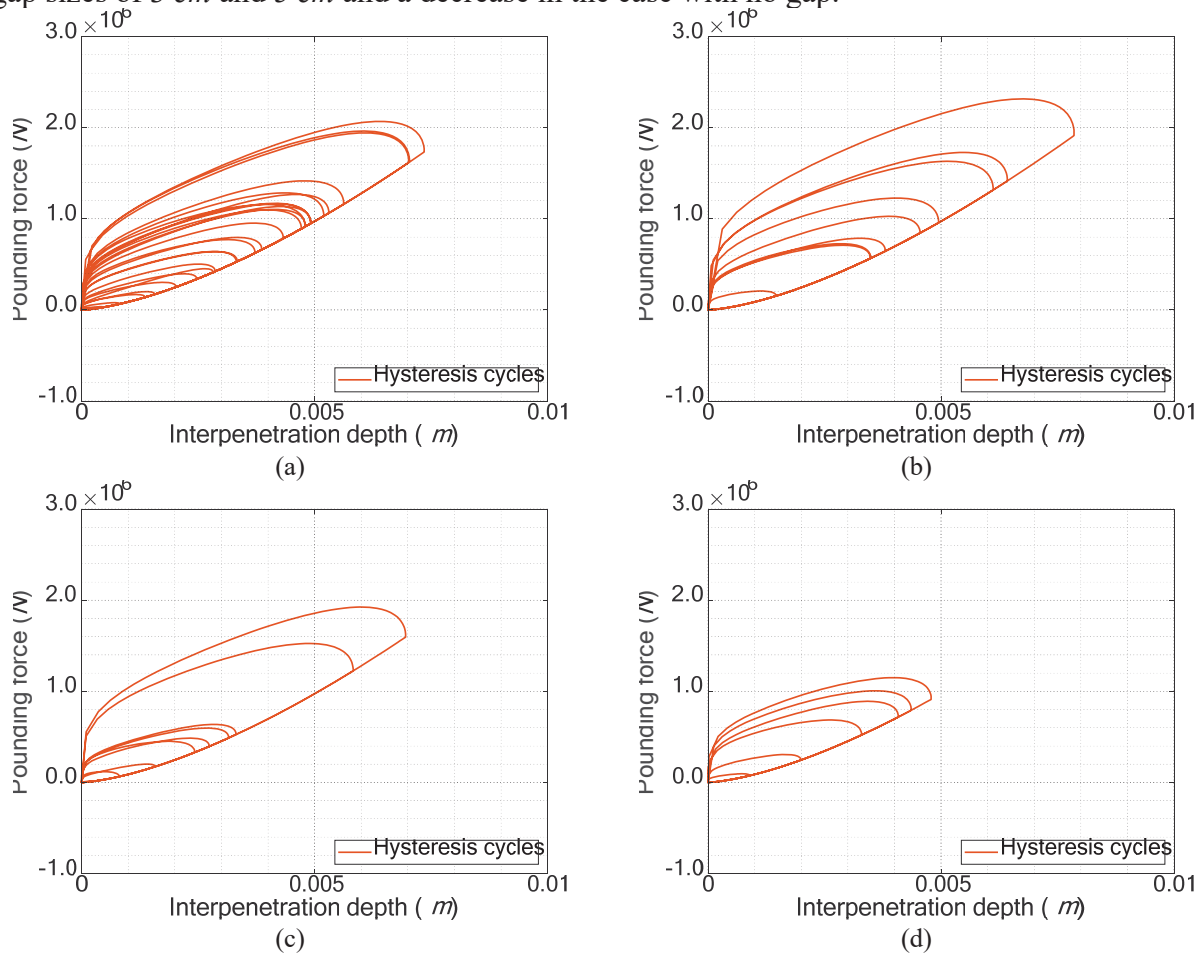


Figure 11: Pounding cycles for the elastic case of the structural systems: (a) 0 cm, (b) 3 cm; and for the inelastic case of the structural systems: (c) 0 cm, (d) 3 cm.

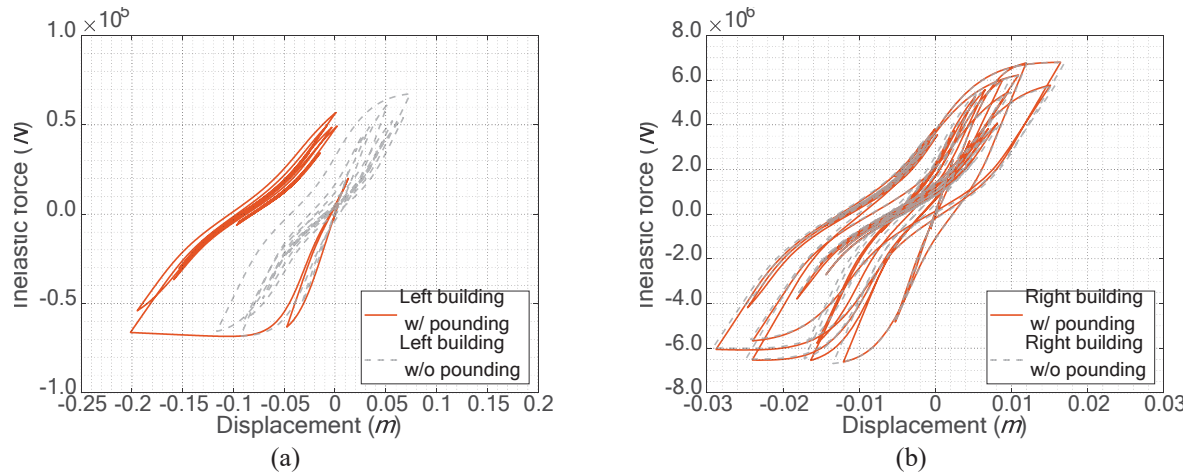


Figure 12: Hysteresis cycles when the structural systems have no gap in between: (a) Left and (b) Right building.

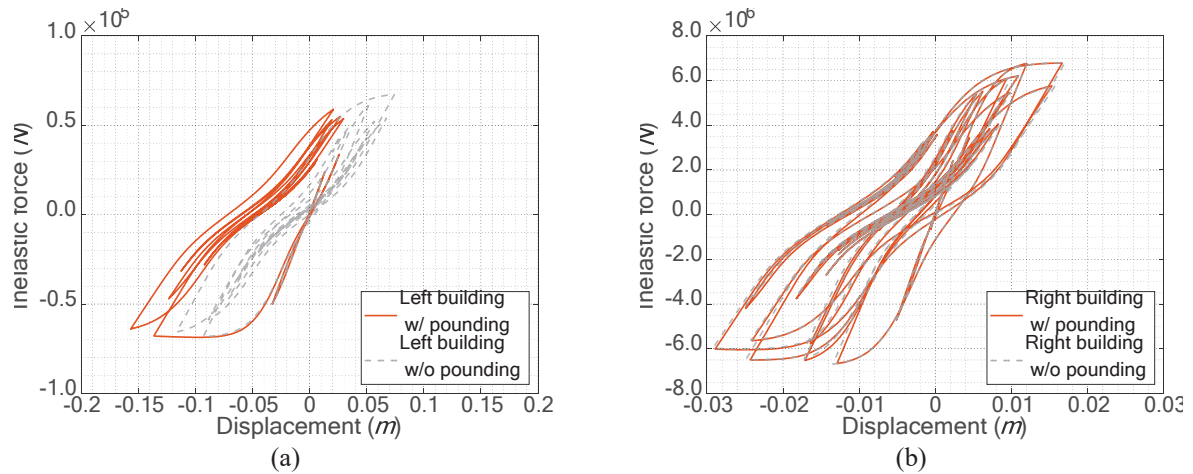


Figure 13: Hysteresis cycles when the structural systems are separated by a distance of 3 cm: (a) Left and (b) Right building.

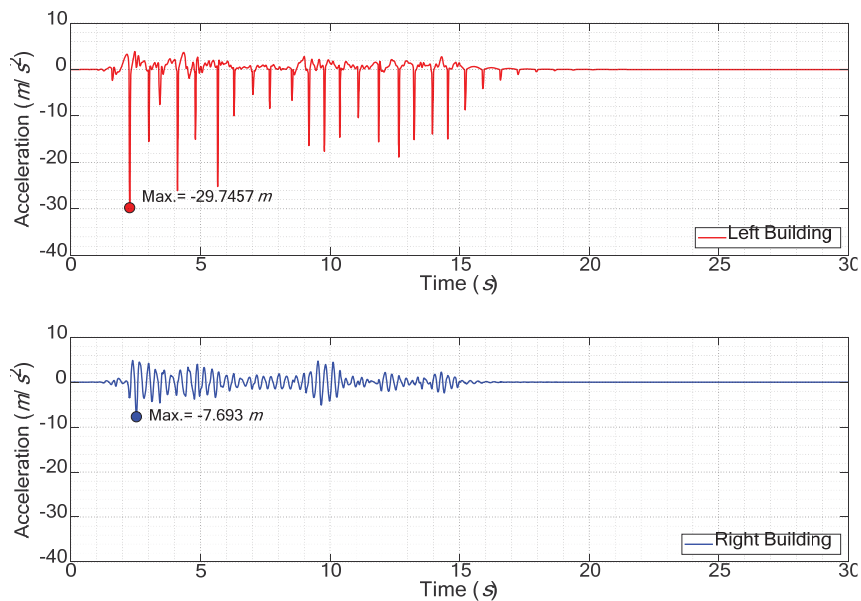


Figure 14: Acceleration time-history responses for the elastic case of the structural systems with no space in between.

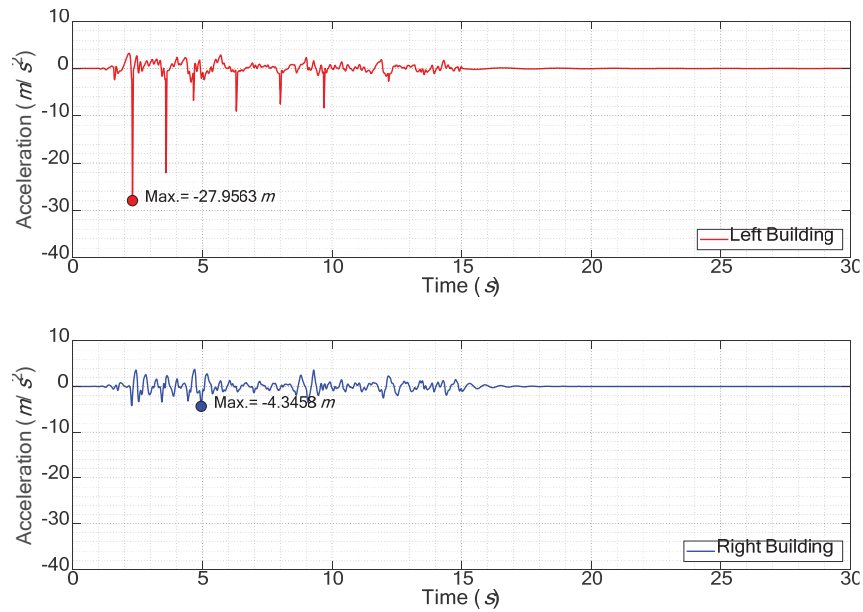


Figure 15: Acceleration time-history responses for the inelastic case of the structural systems with no space in between.

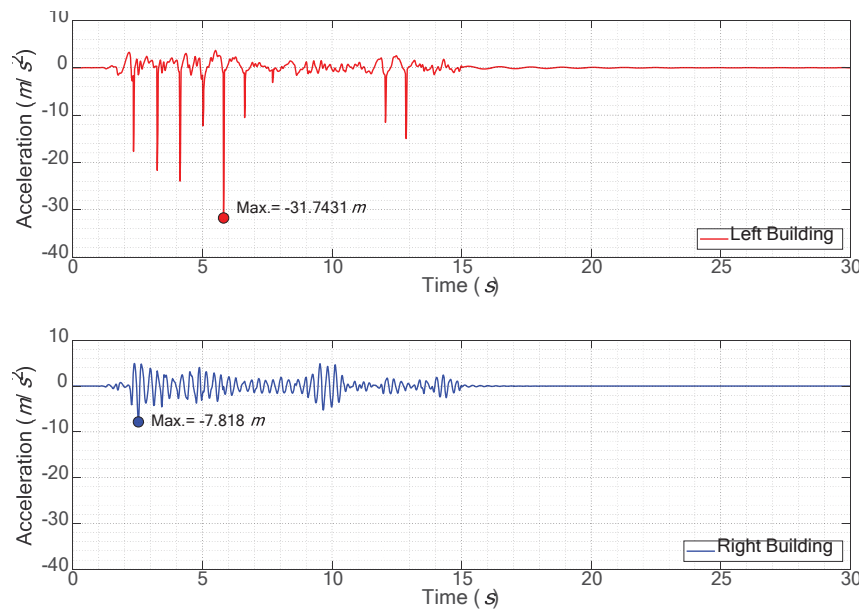


Figure 16: Acceleration time-history responses for the elastic case of the structural systems separated by a distance of 3 cm.

Figure 11 shows the pounding cycles that display the reduced number of cycles and the relatively small magnitude of impacts in the inelastic case. The influence of the gap size when inelastic behavior is considered can also be seen in the graphs of Figures 12 and 13 in which in the right building corresponding to the stiffer structure there is no clear difference between the responses with and without pounding. On the contrary, the flexible structure exhibits clear increases in the rebound displacements and hysteresis energy dissipation as well as the presence of permanent deformations which increase for smaller gap sizes.

Single-degree-of-freedom structural systems with elastic and inelastic behavior were considered in this study and the differences between these were addressed. Although it should be pointed out that further research is required to better investigate this complex behavior with

building pounding that should include more degrees of freedom, three-dimensional analysis including tangential/friction forces, different ground motion excitations, parametric and sensitivity analysis to understand the influence of intervenient input parameters on the output responses, presence of non-structural elements such as infill walls which are common in building structures, and the consideration of different pounding scenarios.

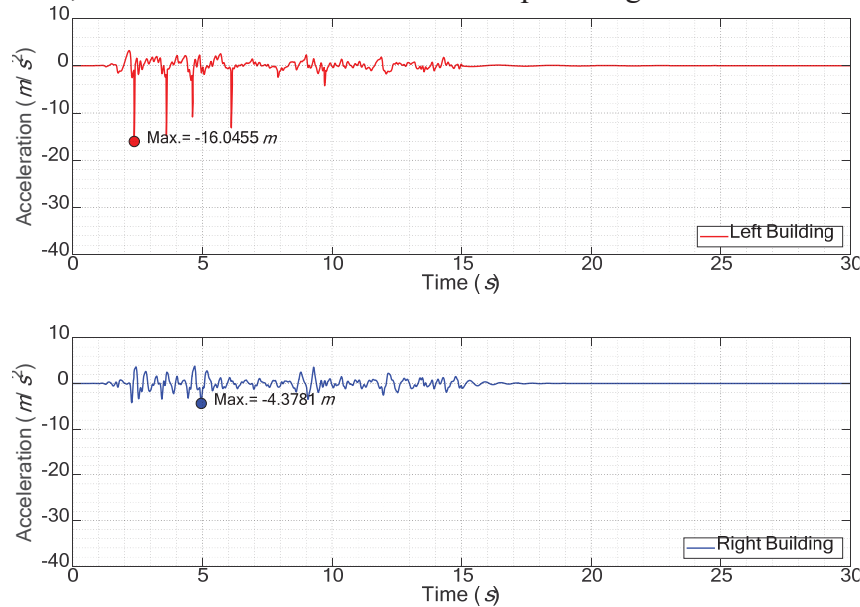


Figure 17: Acceleration time-history responses for the inelastic case of the structural systems separated by a distance of 3 cm.

Behavior of frame structure	Gap (cm)	Peak absolute values							N° of impacts
		x_L (m)	x_R (m)	\dot{x}_L (m/s)	\dot{x}_R (m/s)	\ddot{x}_L (m/s²)	\ddot{x}_R (m/s²)	F_P (kN)	
Linear Elastic	15	0.118	0.133	0.598	-0.312	-4.588	-7.961	0	0
	10	0.094 (-20%)	0.013 (-90%)	0.579 (-3%)	-0.312 (0%)	-13.837 (202%)	-7.961 (0%)	683.72	2
	5	-0.124 (5%)	0.013 (-90%)	0.694 (16%)	-0.312 (0%)	-29.877 (551%)	-7.961 (0%)	2077.7	4
	3	-0.110 (-6%)	0.013 (-90%)	0.704 (18%)	-0.309 (-1%)	-31.743 (592%)	-7.818 (-2%)	2315.8	9
	0	-0.106 (-10%)	-0.044 (-67%)	-0.589 (-1%)	-0.296 (-5%)	-29.746 (548%)	-7.693 (-3%)	2069	29
Non-linear Inelastic	15	-0.117	0.017	0.424	-0.276	-3.274	-4.447	0	0
	5	-0.120 (3%) (-4%)	0.017 (0%) (28%)	0.423 (0%) (-39%)	-0.277 (0%) (-11%)	-12.070 (269%) (-60%)	-4.449 (0%) (-44%)	849.87 (-59%)	2 (-50%)
	3	-0.157 (34%) (42%)	0.017 (-2%) (28%)	0.467 (10%) (-34%)	-0.271 (-2%) (-12%)	-16.046 (390%) (-49%)	-4.378 (-2%) (-44%)	1149.3 (-50%)	6 (-33%)
	0	-0.202 (73%) (90%)	-0.029 (69%) (-34%)	-0.573 (35%) (-3%)	-0.269 (-3%) (-9%)	-27.956 (754%) (-6%)	-4.346 (-2%) (-44%)	1924.1 (-7%)	10 (-66%)

- The percentage below the values in blue color stands for the absolute percentage of increase or decrease regarding the case with no pounding.
- The percentage below the values in green color stands for the absolute percentage of increase or decrease regarding the corresponding linear elastic behavior case.

Table 2: Relevant results of the simulations carried out.

6 CONCLUSIONS

The present study concerns earthquake-induced structural building pounding considering two SDOF systems with elastic and inelastic behavior. Building pounding can be simulated by the use of impact models which rely on the proper establishment of its parameters. Several analytical expressions were provided to calculate each of the parameters of the impact models which depend essentially on the impact stiffness, impact damping, and coefficient of restitution. The uncertainties regarding these parameters are intrinsically connected with the over-simplified assumptions considered as well as the unknown geometry and material properties of the contact region. Experimental data and parametric sensitivity studies may reduce the level of uncertainties and/or redirect the investigations for particular input parameters to obtain more reliable results.

One of the factors that may influence pounding-involved results is the consideration of the inelastic behavior of the colliding structures. Pounding forces caused permanent damage on the buildings in the rebound direction, especially in the flexible structure, increasing for smaller gap sizes. In addition, it was observed that the inelastic behavior should be considered since the most flexible structure presents higher increases of displacements when pounding is considered, and the acceleration spikes continue to have large peak values. The positive effect is the reduction of the number of impacts and their intensity compared with the elastic case. Hence, the neglect of the structural inelastic behavior may overestimate the magnitude of pounding forces and underestimate the displacement amplitude as well as neglect the permanent deformations that will certainly arise during earthquakes.

Further research is necessary since it is not possible to find a clear pattern or trend in the results concerning the input parameters and the desired output results using only SDOF systems with representative inelastic behavior under a specific ground motion. Future studies should address more degrees of freedom and possibly a three-dimensional spatial model (to account for forces in the tangential direction), calibration of the hysteresis model with experimental data, and the consideration of several different ground motions to validate the presented results as well and contribute with additional information on the matter of earthquake-induced structural building pounding.

ACKNOWLEDGEMENTS

This paper is within the scope of the first author's Ph.D. degree in progress, financially supported by the Portuguese Foundation for Science and Technology (FCT) through the PhD grant reference SFRH/BD/139570/2018 under the programme POCH (N2020 – P2020) and subsidized by the European Social Fund (FSE) and national funds from MCTES. This work was financially supported by: Base Funding - UIDB/04708/2020 of the CONSTRUCT - Instituto de I&D em Estruturas e Construções - funded by national funds through the FCT/MCTES (PIDDAC).

REFERENCES

- [1] N. Mate, S. Bakre, O. Jaiswal and K. Sayyad, "Elastic and Inelastic Response of Structural Systems in Seismic Pounding," *Open Journal of Civil Engineering*, vol. 6, pp. 50-73, 2016.
- [2] N. Mate, S. Bakre and O. Jaiswal, "Seismic Pounding Response of Singled-Degree-of-Freedom Elastic and Inelastic Structures Using Passive Tuned Mass Damper," *International Journal of Civil Engineering*, vol. 15, pp. 991-1005, 2017.

- [3] Bouc, R. "Forced vibration of mechanical systems with hysteresis". Proceedings of the Fourth Conference on Non-linear oscillation. Prague, Czechoslovakia. 1967.
- [4] Bouc, R. "Modele mathematique d'hysteresis et application aux systems un degre de liberte". These de Doctorat. Marseille, France. 1969.
- [5] Bouc, R. "Modele mathematique d'hysteresis". Application au circuit oscillant self saturable. Cinquieme Congres Oscillations Non-Lineaires. Volume 4, pp. 100-112. Kiev, Ukraine 1969.
- [6] Bouc, R. "Modele mathematique d'hysteresis. Acustica". Volume 24, pp. 16-25. 1971.
- [7] Y.-K. Wen, "Method for Random Vibration of Hysteretic Systems," *Journal of the Engineering Mechanics Division, ASCE*, vol. 102, no. 2, pp. 249-263, 1976.
- [8] Y.-K. Wen, "Equivalent Linearization for Hysteretic System under Random Excitation," *Journal of Applied Mechanics, ASME*, vol. 47, no. 1, pp. 150-154, 1980.
- [9] T. T. Baber and Y.-K. Wen, "Random Vibration of Hysteretic, Degrading Systems," *Journal of the Engineering Mechanics Division, ASCE*, vol. 107, no. 6, pp. 1069-1087, 1981.
- [10] T. T. Baber and M.-N. Noori, "Random Vibration of Degrading Pinching Systems," *Journal of the Engineering Mechanics Division, ASCE*, vol. 11, no. 8, pp. 1010-1026, 1985.
- [11] T. T. Baber and M.-N. Noori, "Modeling General Hysteresis Behavior and Random Vibration Application," *Journal of Vibration, Acoustic, Stress, and Reliability in Design, ASME*, vol. 108, no. 4, pp. 411-420, 1986.
- [12] G. C. Foliente, "Hysteresis Modeling of Wood Joints and Structural Systems," *Journal of Structural Engineering, ASCE*, vol. 121, no. 6, pp. 1013-1022, 1995.
- [13] M. V. Sivaselvan and A. M. Reinhorn, "Hysteretic Models for Cyclic Behavior of Deteriorating Inelastic Structures," Technical Report MCEER-99-0018, Multidisciplinary Center for Earthquake Engineering Research, State University of New York at Buffalo, Buffalo, New York, 1999.
- [14] M. V. Sivaselven and A. M. Reinhorn, "Hysteretic models for deteriorating inelastic structures," *Journal of Engineering Mechanics*, vol. 126, no. 6, pp. 633-640, 2000.
- [15] R. Jankowski and S. Mahmoud, *Earthquake-Induced Structural Pounding*, Switzerland: Springer, 2015.
- [16] Goldsmith, W. *Impact: The Theory and Physical Behaviour of Colliding Solids*. Edward Arnold (Publishers) LTD: London. 1960.
- [17] R. Jankowski, "Experimental study on earthquake-induced pounding between structural elements made of different building materials," *Earthquake Engineering and Structural Dynamics*, vol. 39, pp. 349-354, 2010.
- [18] M. Mahmoud, K. Choong, and R. Jankowski, "Seismic pounding between adjacent buildings: Identification of parameters, soil interaction issues and mitigation measures," *Soil Dynamics and Earthquake Engineering*, vol. 121, pp. 135-150, 2019.
- [19] K. Johnson, "Contact Mechanics," Cambridge university press, 1987.

- [20] H. Hertz, "Über die Berührung fester elastischer Körper (On the contact of elastic solids)," *J. für die Reine und Angewandte Mathematik*, vol. 29, pp. 156-171, 1881. (in German)
- [21] J. Wolf and P. Skrikerud, "Mutual pounding of adjacent structures during earthquakes," *Nuclear Engineering and Design*, vol. 57, pp. 253-275, 1980.
- [22] S. Anagnostopoulos, "Pounding of buildings in series during earthquakes," *Earthquake Engineering and Structural Dynamics*, vol. 16, pp. 443-456, 1988.
- [23] S. Anagnostopoulos, "Equivalent viscous damping for modeling inelastic impacts in earthquake pounding problems," *Earthquake Engineering and Structural Dynamics*, vol. 33, pp. 897-902, 2004.
- [24] P. Komodromos, P. Polycarpou, L. Papaloizo, and M. Phocas, "Response of seismically isolated buildings considering poundings," *Earthquake Engineering and Structural Dynamics*, vol. 36, pp. 1605-1622, 2007.
- [25] R. Valles and A. Reinhorn, "Evaluation, prevention and mitigation of pounding effects in building structures," Technical Report NCEER-97-0001, *National Center for Earthquake Engineering Research*, State University of New York, Buffalo, USA, 1997.
- [26] S. Mahmoud, "Modified linear viscoelastic model for elimination of the tension force in the linear viscoelastic," in *The Fourteenth World Conference on Earthquake Engineering, October 12-17, 2008*, Beijing, China, 2008.
- [27] R. Jankowski, "Analytical expression between the impact damping ratio and the coefficient of restitution in the non-linear viscoelastic model of structural pounding," *Earthquake Engineering and Structural Dynamics*, vol. 35, pp. 517-524, 2006.
- [28] K. Ye, L. Li and H. Zhu, "A modified Kelvin impact model for pounding simulation of base-isolated building with adjacent structures," *Earthquake Engineering and Engineering Vibration*, vol. 8, pp. 433-446, 2009.
- [29] D. Pant, A. Wijeyewickrema and T. Ohmachi, "Three dimensional nonlinear analysis of seismic pounding between multi-story reinforced concrete buildings," in *Proceedings of the Seventh International Conference on Urban Earthquake Engineering (7CUEE) and Fifth International Conference on Earthquake Engineering (5ICEE)*, Vol II: 1829-1840, 2010.
- [30] D. Pant, A. Wijeyewickrema and T. Ohmachi, "Seismic Pounding between Reinforced Concrete Buildings: A Study using two recently proposed Contact Element Models," in *Proceeding of the 14th European Conference on Earthquake Engineering, European Conference on Earthquake Engineering*, Republic of Macedonia, 2010.
- [31] S. Mahmoud and R. Jankowski, "Modified linear viscoelastic model of earthquake-induced structural pounding," *Iranian Journal of Science and Technology*, vol. 35, no. C1, pp. 51-62, 2011.
- [32] H. Lankarani and P. Nikraves, "A Contact Force Model With Hysteresis Damping for Impact Analysis of Multibody Systems," *Journal of Mechanical Design*, vol. 112, pp. 369-376, 1990.
- [33] H. Lankarani and P. Nikraves, "Continuous Contact Force Models for Impact Analysis in Multibody Systems," *Nonlinear Dynamics*, vol. 5, pp. 193-207, 1994.

- [34] K. Hunt and F. Crossley, "Coefficient of restitution interpreted as damping in vibroimpact," *Journal of Applied Mechanics, American Society of Mechanical Engineers*, vol. 42, pp. 440-445, 1975.
- [35] S. Muthukumar, "A contact element approach with hysteresis damping for the analysis and design of pounding in bridges," Ph.D. Thesis, Georgia Institute of Technology, Georgia, EUA, 2003.
- [36] S. Muthukumar and R. DesRoches, "A Hertz contact model with non-linear damping for pounding simulation," *Earthquake Engineering and Structural Dynamics*, vol. 35, pp. 811-829, 2006.
- [37] R. Jankowski, "Non-linear viscoelastic modelling of earthquake-induced structural pounding," *Earthquake Engineering and Structural Dynamics*, vol. 34, pp. 595-611, 2005.
- [38] K. Ye, L. Li and H. Zhu, "A note on the Hertz contact model with nonlinear damping for pounding simulation," *Earthquake Engineering and Structural Dynamics*, vol. 38, pp. 1135-1142, 2009.
- [39] H. Naderpour, R. Barros, and S. Khatami, "A new model for calculating impact force and energy dissipation based on the CR-factor and impact velocity," *Scientia Iranica A*, vol. 22, pp. 59-68, 2015.
- [40] H. Naderpour, R. Barros, R. Khatami, and R. Jankowski, "Numerical Study on Pounding between Two Adjacent Buildings under Earthquake Excitation," *Hindawi Publishing Corporation: Shock and Vibration*, vol. 2016, 2016.
- [41] F. Bamer, "A Hertz-pounding formulation with a nonlinear damping and a dry friction element," *Acta Mechanica*, vol. 229, pp. 4485-4494, 2018.
- [42] F. Bamer and B. Markert, "A nonlinear visco-elastoplastic model for structural pounding," *Earthquake Engineering and Structural Dynamics*, vol. 47(12), pp. 2490-2495, 2018.
- [43] F. Bamer, N. Strubel, J. Shi and B. Markert, "A visco-elastoplastic pounding damage formulation," *Engineering Structures*, vol. 197, 2019.
- [44] S. Khatami, H. Naderpour, R. C. Barros, A. Jakubczyk-Gałczynska and R. Jankowski, "Effective Formula for Impact Damping Ratio for Simulation of Earthquake-induced Structural Pounding," *Geosciences, MDPI*, vol. 9, no. 8: 347, 2019.
- [45] J. van Mier, A. F. Pruijssers, H. Reinhardt and T. Monnier, "Load-Time Response of Colliding Concrete Bodies," *Journal of Structural Engineering*, Vols. 117, No. 2, no. 25544, pp. 354-374, 1991.
- [46] K. Chau, X. Wei, X. Guo and C. Shen, "Experimental and theoretical simulations of seismic poundings between two adjacent structures," *Earthquake Engineering and Structural Dynamics*, vol. 32, pp. 537-554, 2003.
- [47] M. Goland, P. Wickersham, and M. Dengler, "Propagation of elastic impact in beams in bending," *Journal of Applied Mechanics*, vol. 22, pp. 1-7, 1955.
- [48] P. Zhu, M. Abe, and Y. Fujino, "Modelling three-dimensional non-linear seismic performance of elevated bridges with emphasis on pounding of girders," *Earthquake Engineering and Structural Dynamics*, vol. 31, pp. 1891-1913, 2002.

- [49] Y. Kajita, T. Kitahara, Y. Nishimoto, and H. Otsuka, “Estimation of Maximum Impact Force on Natural Rubber during Collision of Two Steel Bars,” In Proceedings of the First European Conference on Earthquake Engineering and Seismology (1st ECEES), Geneva, Switzerland, 3–8 September 2006; p. 488.
- [50] P. Polycarpou, L. Papaloizou, P. Komodromos, “An efficient methodology for simulating earthquake-induced 3D pounding of buildings”, *Earthquake Engineering and Structural Dynamics*, vol. 43, pp. 985–1003, 2014.
- [51] G. L. Cole, R. P. Dhakal, A. J. Carr and D. K. Bull, “Building pounding state of the art: Identifying structures vulnerable to pounding damage,” in *New Zealand Society of Earthquake Engineerings (NZSEE) Conference, 26-28 March*, Wellington, NZ, 2010.
- [52] MATLAB 2014a., Natick, Massachusetts, USA: MathWorks, Inc., 2014.
- [53] Pacific Earthquake Engineering Research Center (PEER) strong ground motion database, [Online]. Available: <https://peer.berkeley.edu/peer-strong-ground-motion-databases>.

INFLUENCE OF STRUCTURAL INELASTIC BEHAVIOR IN THE STUDY OF COLLIDING SDOF STRUCTURES

Folhento P. Pedro¹, Barros C. Rui¹, and Braz-César T. Manuel²

¹ CONSTRUCT, Faculdade de Engenharia, Universidade do Porto
FEUP, Porto, Portugal
{up201811645, rcb}@fe.up.pt

² CONSTRUCT, Politécnico Instituto de Bragança
IPB, Bragança, Portugal
brazcesar@ipb.pt

Abstract

Earthquake-induced structural pounding between buildings is an insurgent field of investigation since in metropolitan areas it is very common to construct buildings very close to each other leaving small gap distances in between or even no space at all, increasing the likelihood of structural collisions in an earthquake event. These impacts can provoke substantial structural damage or global collapse of building structures. The overall dynamic behavior is thus greatly affected by this phenomenon and so importance should be given in the study of the respective consequences. The most practical and simple approach is to model buildings as SDOF lumped mass models considering elastic behavior. However, it has been verified previously that neglecting inelastic behavior in these situations can lead to significant overestimations of the magnitude and number of impacts between the adjacent structures and underestimations of the displacement responses, especially in flexible structures. In this sense, the influence of inelastic behavior in SDOF structural systems is carried out using a smooth hysteresis model, implemented in a Matlab-Simulink model, for different levels of hysteresis degradation phenomena under cyclic loading. This parametric study will enable a further understanding of the inelastic behavior of structures under pounding forces.

Keywords: Building structural pounding, Earthquake-induced pounding, Impact modeling, Inelastic behavior, Parametric study.

1 INTRODUCTION

Non-linear inelastic behavior and significant damage are usually observed in building structures when subjected to earthquake events.

Loss of human lives, total or partial destruction of built patrimony, and human activity are consequences that seismic design seeks to avoid and in the case of significant structural damage to limit it to permit for possible repair and/or substitution of damaged elements in the structures.

Seismic design of building structures can be performed using linear or non-linear, static or dynamic analysis. When inelastic behavior is considered it is usually assumed to be lumped at beam's ends, critical regions, commonly called plastic hinges that require an adequate structural detail to possess acceptable ductility, while other zones should be kept in the elastic range with overstrength, forming the strong links in the structural system, the case of columns and the middle span of beams. Nevertheless, the behavior of columns should be assessed since, in reality, these elements will suffer some inelastic deformation (due to redistribution of forces within the structure) that should be evaluated by analyzing its lateral restoring forces.

To reproduce this inelastic behavior, the common assumption is to consider for plastic hinges known constitutive behavior translated by a suitable hysteresis model capable of emulating different physical phenomena such as stiffness degradation, strength deterioration, and the pinching effect.

Hence, it is well known and expected that permanent damage will occur under moderate to severe earthquakes. One phenomenon that has been progressively studied over recent years is structural pounding between buildings that have very limited separation distance or no distance at all. Earthquake-induced structural pounding between buildings has revealed significant negative effects that may lead to the global collapse of the structural systems. Large ductility and energy dissipation demands are verified in buildings under earthquake-induced pounding.

To emulate structural building pounding several approaches have been developed and are present in the literature. The simplest approach is the consideration of impact models based on some simplifications and assumptions that capture the essence of the impacts, i.e., its magnitude. This phenomenon is extremely or virtually impossible to emulate with perfect accuracy, being associated with non-linear relationships between the contact area, stresses, and deformations; local inelastic deformations; propagation of stress waves in the involved structures; friction forces; vibrations resulting in thermal and acoustic effects; etc.

Due to these short-duration impulses, i.e., huge forces involving large masses in an incredibly short amount of time, it is known to cause inevitable local and global structural damage and thus, influencing the overall dynamic responses of the colliding buildings.

Thus, this paper intends to analyze how different kinds of hysteresis behaviors may influence the pounding-involved response of buildings under seismic events.

To achieve this the usual approach of assuming two single-degree-of-freedom (SDOF) lumped mass models with very different dynamic behavior is considered. These structural systems are connected by a zero-length element, an impact model.

A smooth hysteresis model is implemented to emulate the non-linear inelastic behavior of the structures.

The elastic case and the inelastic behavior with different levels/cases of hysteresis degradation phenomena under cyclic loading and structural pounding are then simulated using a developed Matlab-Simulink model. The results are then presented in terms of graphs and peak responses to enable a further understanding of the inelastic behavior of building structures under earthquake-induced pounding forces.

2 HYSTERESIS BEHAVIOR CASES

The relationship between the input and the output in the inelastic range is controlled by the rate-independent memory effect concept, that is, a hysteresis operator, that takes in an input function and returns an output function. This phenomenological concept is based on experimental data relating the input-output pair.

The response of structural systems depends always on the rate of the applied load when this needs to be considered viscosity is introduced along with the rate-independent restoring force. Hence, the usual dynamic equation of motion is modified, including the lateral restoring force (in this study) term, f_r^* , that depends on the displacements and velocities of the system, to become

$$m\ddot{x}(t) + c\dot{x}(t) + kx(t) = -m\ddot{x}_g(t) \Leftrightarrow m\ddot{x}(t) + c\dot{x}(t) + ak_0x(t) + f_r^*(t) = -m\ddot{x}_g(t) \quad (1)$$

where m , k , and c are, respectively, the mass, the elastic stiffness and the viscous damping of the structure, $\ddot{x}_g(t)$ is the earthquake's acceleration, $x(t)$ is the structural displacement, \dot{x} is the structural velocity, and $\ddot{x}(t)$ is the structure's acceleration.

To account for the inelastic behavior several empirical hysteresis models were developed by many researchers and can be broadly categorized into polygonal and smooth hysteresis models. In the present study, a smooth hysteresis model is considered. This model was developed by Sivaselvan and Reinhorn [1] and is a subsequent modification of the original Bouc-Wen model ([2]-[4]).

A schematic representation of the abovementioned hysteresis model is presented in Figure 1 which is capable of simulating different behaviors of a structural system under cyclic loading, viz., strength hardening, the Bauschinger effect, stiffness degradation, strength deterioration, and the pinching effect.

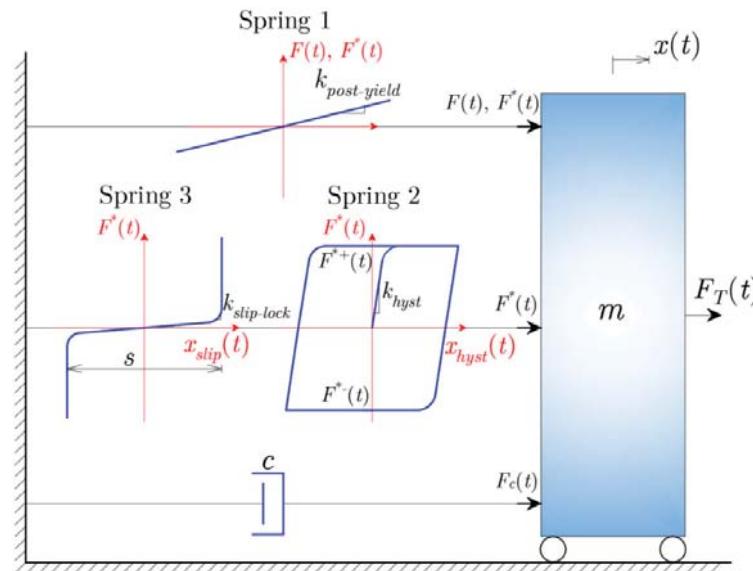


Figure 1: Sivaselvan and Reinhorn's smooth hysteresis model schematic representation.

The following subsections describe the model in [1] and present different hysteresis behavior cases that can be considered depending on the type of structural system and material used for simulation. Three springs define the model and the different hysteresis cases: a post-yield spring (Spring 1), a hysteresis spring (Spring 2), and a slip-lock spring (Spring 3) as can be observed in Figure 1.

2.1 Plain hysteresis

Plain hysteresis behavior is characterized by a case of hysteresis that can account for strength hardening and possess no degradation features. In the present investigation, this will be denominated by Case 0 of hysteresis behavior. This behavior is suitable for well-detailed steel structures, e.g., special moment resisting frames (SMRFs) [5].

Upon the application of a load, the springs 1 and 2 in parallel undergo the same deformation, although they share this force in proportion to their instantaneous stiffness,

$$k = k_{post-yield} + k_{hyst} \quad (2)$$

in which the post-yielding stiffness, $k_{post-yield}$, is represented by a linear elastic spring (Spring 1), and the hysteresis spring, k_{hyst} , is represented by a pure elasto-plastic spring with a smooth transition from the elastic to the inelastic range (Spring 2).

The previous stiffnesses terms, the elastic stiffness, and the non-degrading hysteresis stiffness are given, respectively, by the following expressions

$$k_{post-yield} = ak_0 \quad (3)$$

$$k_{hyst} = (1-a)k_0 \left\{ 1 - \left| \frac{F^*}{F_Y^*} \right|^{n_W} \left[\eta_1 \operatorname{sgn}(F^* dx) + \eta_2 \right] \right\} \quad (4)$$

in which a is the post to pre-yielding stiffness ratio, n_W controls the smoothness of the transition from elastic to plastic stages, η_1 and η_2 are parameters that control the shape of the unloading curve, F^* and F_Y^* are the portion of the applied force shared by the hysteresis spring and its respective yield value.

2.2 Stiffness degradation

Stiffness degradation is considered by the introduction of an additional parameter, R_K , a positive parameter with the unity as its possible maximum value. This factor is given by the following expression

$$R_K = \frac{F^* + \alpha F_Y^*}{k_0 x + \alpha F_Y^*} \quad (5)$$

The stiffness degradation is implemented in the Matlab-Simulink model through the so-called pivot rule [6]. This degradation phenomenon is observed in several structural elements and systems under cyclic loading and occurs due to non-linear geometric effects [7] and the elastic stiffness degrades with increasing ductility [1]. The degree of stiffness decay depends on the characteristics of the structure, e.g., material properties, geometry, ductility capacity, and connection type; and on the loading history, e.g., the intensity in each cycle, number of cycles, and sequence of loading cycles [8].

In the case of reinforced concrete (RC) components under severe cyclic loading, this degradation can be the result of cracking, loss of bond, or interaction with high shear or axial stresses [8]. Reduced stiffness in steel elements can be attributed to the Bauschinger effect [9] and is caused by accumulated damage or fatigue.

This type of hysteresis behavior in this study will be designated as Case 1. Hence, the hysteresis stiffness in Equation 4 is modified by including parameter R_K in Equation 5 which depends on parameter α (measuring the degree of stiffness degradation), as follows

$$k_{hyst} = (R_K - a) k_0 \left\{ 1 - \left| \frac{F^*}{F_Y} \right|^{n_w} \left[\eta_1 \operatorname{sgn}(F^* dx) + \eta_2 \right] \right\} \quad (6)$$

2.3 Strength deterioration

Two main types of strength deterioration can be identified: cyclic strength degradation and in-cycle strength degradation [8]. Cyclic strength degradation refers to the loss of strength and stiffness in subsequent cycles. As for the in-cyclic strength, degradation is characterized by a reduction of strength during the current cycle, leading to a negative stiffness. This type of behavior occurs when a structural component subjected to increasing deformation reaches the capacity boundary. Since a cyclic load-path cannot pass through this limit, the response continues along the boundary until unloading occurs, producing the in-cycle strength degradation.

According to FEMA's report [8], cyclic reduction of lateral strength is based on the increasing inelastic displacement and ultimately on the peak displacement, and on the total hysteresis energy demands of the system translated by the area enclosed by the hysteresis cycles. On the other hand, in-cycle strength degradation along with stiffness degradation may occur due to geometric (P-delta effects) and/or material non-linearities. Material nonlinearities that may cause in-cycle strength degradation include concrete crushing, shear failure, buckling or fracture of longitudinal reinforcement, and splice failures for RC components; and for steel components include buckling of bracing elements, local buckling in flanges of columns or beams, and fracture of bolts, or welds. The first type of deterioration usually specifies this decay in terms of the ductility ratio, and the second is the result of a single level of inelastic displacement imposed many times (along with the cycles), reducing the lateral strength level as the number of cycles increases.

The authors [1] considered in the current model a deterioration rule that reduces the capacity of the backbone curve. This rule of deterioration is based on a continuous energy-based degradation, and on a backbone degradation which occurs when the maximum deformation value attained in the past is exceeded and is given by the following expression

$$F_Y^{+/-} = F_{Y0}^{+/-} \left[1 - \left(\frac{x_{\max}^{+/-}}{x_{\text{ult}}^{+/-}} \right)^{\frac{1}{\beta_1}} \right] \left[1 - \frac{\beta_2}{1 - \beta_2} \frac{E_h}{E_{h\text{ult}}} \right] \quad (7)$$

where $F_Y^{+/-}$ is the positive or negative yield force, $F_{Y0}^{+/-}$ is the initial positive or negative yield force, $x_{\max}^{+/-}$ is the maximum positive or negative displacement, $x_{\text{ult}}^{+/-}$ is the ultimate positive or negative displacement, E_h is the hysteresis energy dissipated, $E_{h\text{ult}}$ is the hysteresis energy dissipated when loaded monotonically until the ultimate displacement without any degradation, β_1 is a parameter based on ductility demands, and β_2 is a parameter based on energy demands. The second term on the right side of Equation 7 is related to strength deterioration based on increased deformation and the last term is related to the hysteresis energy dissipated.

Stiffness and strength degradation will be considered together as Case 2 of hysteresis behavior for the present investigation.

2.4 Pinching effect

The pinching effect is another phenomenon observed in structural components and connections subjected to cyclic lateral load. The name pinching arises from the effect that has on the hysteresis loops. Pinched or compressed hysteresis cycles are obtained by great reductions in stiffness during reloading and stiffness recovery when the opposite displacement is imposed.

This phenomenon is mostly observed in brittle materials, viz., RC elements, timber components, and some types of masonry components. Some connections in steel structures also exhibit this kind of effect. In RC elements, pinching is the consequence of cracks that open when the element deforms in a certain direction. On load reversal, the deformation in the opposite direction closes the cracks and the stiffness is partially recovered. In timber structures, the main cause of pinching is the opening and closing of gaps in bordering elements due to nail pullout. Reinforced masonry also experiences pinching due to the opening and closing of flexural cracks, gaps between the masonry infill and the bordering structural frame, and between plates in steel-end connections [8]. In addition, the degree of pinching essential depends on the material properties, geometry, ductility, and connections of the structure, as well as the loading history, in terms of the intensity and sequence of the loading cycles.

An additional spring (Spring 3) is thus implemented in the hysteresis model to simulate pinching behavior [1]. A “slip-lock” spring is added in series to the hysteresis spring as illustrated in Figure 1. The combined stiffness now becomes

$$k = k_{post-yield} + \frac{k_{hyst} k_{slip-lock}}{k_{hyst} + k_{slip-lock}} \quad \text{where} \quad k_{slip-lock} = \left\{ \sqrt{\frac{2}{\pi}} \frac{s}{F_{\sigma}^*} \exp \left[-\frac{1}{2} \left(\frac{F^* - F_m^*}{F_{\sigma}^*} \right)^2 \right] \right\}^{-1} \quad (8)$$

in which s is the slip length, F_{σ}^* is a measure of the force range over which slip occurs, and F_m^* is the mean force level on either side about which slip occurs, being these three parameters given, respectively, as follows

$$s = R_s (x_{\max}^+ - x_{\max}^-) \quad (9)$$

$$F_{\sigma}^* = \sigma F_Y^* \quad (10)$$

$$F_m^* = \lambda_s F_Y^* \quad (11)$$

where parameters R_s , σ_s , and λ_s are parameters that control each of the resulting values of the previous three equations.

Proper calibration of these hysteresis parameters presented in the present section (in Equations 2-11) can model different hysteresis behaviors depending on material properties and structural systems.

This hysteretic model will be further implemented in this investigation to assess the inelastic behavior of the structures under the earthquake-induced pounding.

Stiffness and strength degradation with the pinching effect will be denoted as Case 3 of hysteresis behavior in the following sections.

3 STRUCTURAL POUNDING MODELING

Structural pounding involves complex phenomena making the problem of earthquake-induced structural building pounding extremely difficult to model with high accuracy. However, in structural pounding, the estimation of the magnitude of pounding forces with satisfactory accuracy is enough to verify its influence on the overall dynamic response of the colliding structures.

Two possible ways of earthquake-induced structural pounding modeling are available in the literature: the classical theory of impact and the use of impact or contact elements [10].

The classical theory of impact fails to describe transient stresses and to account for local deformations at the contact point of the bodies assuming that a negligibly part of the initial kinetic energy of the system is transformed into vibrations of the colliding bodies [11]. Addi-

tionally, it does not consider the existence of the period of impact failing to directly assess the evolution of the pounding forces during collision [12].

The coefficient of restitution (CR) is a parameter derived in the first approach of pounding modeling. This parameter depends on the relative final ($\dot{x}_{2,f} - \dot{x}_{1,f}$) and initial ($\dot{x}_{2,0} - \dot{x}_{1,0}$) impact velocities and represents the energy losses and degree of plasticity of the impact being directly related with the kinetic energy loss during impact. CR is given by the following expression

$$CR = \frac{\dot{x}_{2,f} - \dot{x}_{1,f}}{\dot{x}_{1,0} - \dot{x}_{2,0}} \quad (12)$$

Impact models constitute the second approach to model building pounding, largely used in many investigations to assess the detrimental effects of impacts in building structures. From the consideration of two periods of impact, approach and restitution periods, to the penalty method and establishment of parameters such as impact stiffness and impact damping ratio, the impact models have been widely used providing relative satisfactory accuracy in replicating the pounding forces arising from the contact of buildings during earthquake events. Although, the formulation of these elements is based on Hertz's theory and oversimplified assumptions making the problem simpler yet less accurate.

Among these simplifications, one can mention [13]: the stress wave propagation is neglected and the state of stress in the structures at any instant can be considered approximately uniform. This ignores the dynamic effects in the structures due to wave propagation, assuming that structural pounding between buildings can be approximately quasi-static if the duration of the impact is long enough to allow stress waves to transverse the length of the body many times, justifying in this way the use of spring-dashpot elements; the contact area is in general elliptical and is assumed to be small in comparison with the principal dimensions of the bodies; deformations are restricted to the vicinity of the impact; contact surfaces are non-conforming, smooth, continuous and frictionless; and the contact regions are assumed to remain elastic and unaltered after impact events.

In these compression-only impact models with zero-length, the spring will control the restoring force and deformation, and the dashpot will account for the energy radiated due to impact by wave motion. Hence, these two elements in the model represent the impact stiffness (k_{imp}) which depends on material properties and the contact geometry, and the impact damping ratio (ξ_{imp}) that depends mostly on the CR being derived from energy considerations.

Different impact models have been developed. The simplest model is the consideration of a spring, hence possessing only the elastic part of the impact correspondent to the impact spring and lacking the ability to account for energy dissipation during a collision. Similarly, the non-linear elastic model following Hertz's contact law [14], describes the static compression between two isotropic elastic bodies and is also limited by the lack of energy dissipation during impact. The spring non-linearity is capable of modeling the force-deformation relation more realistically. The impact force increases with the interpenetration depth to the power of 1.5

$$f_p(t) = \begin{cases} \beta_{imp} [\delta(t)]^{\frac{3}{2}} & \text{for } \delta(t) > 0 \\ 0 & \text{for } \delta(t) \leq 0 \end{cases} \quad (13)$$

in which β_{imp} is a parameter indicating the non-linear impact stiffness depending on material properties and geometry of the colliding structures.

The two impact models mentioned in the previous paragraph were the target of many modifications through the years, mostly to correct its drawbacks and increase the accuracy in modeling pounding forces.

A central modification to the linear elastic model was carried out giving rise to the linear viscoelastic or Kelvin-Voigt impact model [15], having now the ability to account for the loss of energy during impact. Pounding forces are thus computed using the following expressions

$$f_p(t) = \begin{cases} k_{imp} \delta(t) + c_{imp} \dot{\delta}(t), & \text{for } \delta(t) > 0 \\ 0 & \text{for } \delta(t) \leq 0 \end{cases} \quad (14)$$

where c_{imp} is the damping constant of the pounding contact element computed by the following expression ([16], [17])

$$c_{imp} = 2 \xi_{imp} \sqrt{k_{imp} \frac{m_1 m_2}{m_1 + m_2}} \quad \text{where} \quad \xi_{imp} = \frac{-\ln(CR)}{\sqrt{\pi^2 + [\ln(CR)]^2}} \quad (15)$$

However, this modification revealed a tensile force at the end of the impact period due to the uniform dissipation of energy on both periods of impact, which in reality does not happen ([10], [11]). This model further suffered different modifications to address this drawback. Komodromos et al. [18] modified the linear viscoelastic model by eliminating the negative force making it zero. Valles and Reinhorn [19], modified the Kelvin-Voigt model by assuming that the damping term is activated only for positive velocities during impact, which means only activated during the approach period. Mahmoud [20] addressed the drawbacks of the linear viscoelastic impact model with the same line of reasoning in [19] but redefining the expression of the impact damping ratio through energy considerations. Ye et al. [21] and Pant et al. ([22], [23]) proposed different modifications providing a different expression for the impact damping ratio. Following the research in [20], Mahmoud and Jankowski [24] suggested a further modification to the linear viscoelastic model using a different approach to arrive at an improved formula for the impact damping ratio.

Hertz's model (Equation 13) was modified by Lankarani and Nikraves ([25], [26]), to address the matter of the lack of energy dissipation properties by including in parallel with the non-linear spring a non-linear damping proposed by Hunt and Crossley [27] to better represent impacts between mechanical systems. Similar to the previous modifications, this model now becomes a non-linear viscoelastic impact model. Muthukumar and DesRoches ([28], [29]) considered the previous model applied to civil engineering structures being designated by the "Hertzdamp" impact model. An important modification to the Hertzdamp model was carried out by Jankowski [30] suggesting that the non-linear damping component becomes active only in the approach period where most energy is dissipated. Figure 2 presents a representation of Jankowski's non-linear viscoelastic model.

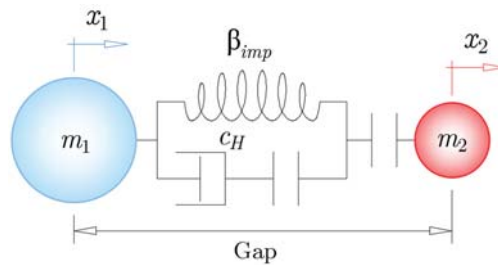


Figure 2: Schematic representation of Jankowski's non-linear viscoelastic model.

The pounding force can thus be calculated using the following system of equations [30]

$$f_P(t) = \begin{cases} \beta_{imp} [\delta(t)]^{\frac{3}{2}} + c_H(t) \dot{\delta}(t) & \text{for } \delta(t) > 0 \text{ and } \dot{\delta}(t) > 0 \\ \beta_{imp} [\delta(t)]^{\frac{3}{2}} & \text{for } \delta(t) > 0 \text{ and } \dot{\delta}(t) \leq 0 \\ 0 & \text{for } \delta(t) \leq 0 \end{cases} \quad (16)$$

where the damping coefficient is determined as follows

$$c_H(t) = 2\xi_{imp} \sqrt{k_{imp} \frac{m_1 m_2}{m_1 + m_2}} \quad \text{where } k_{imp} = \beta_{imp} \sqrt{\delta(t)} \quad (17)$$

and the impact damping ratio, which had to be redefined was approached by using two different approximating functions in the process, leading to two expressions from which one was found more accurate and is thus shown below [31]

$$\xi_{imp} = \frac{9\sqrt{5}}{2} \frac{1 - CR^2}{CR[CR(9\pi - 16) + 16]} \quad (18)$$

Further modifications were carried out to the Hertz damp impact model. Ye et al. [32] based on the resulting relationship between the CR and the impact damping ratio developed a new and more rational expression for the damping ratio.

More recent modifications to the core impact models presented in previous paragraphs were carried out, mostly modifications to the relation between the impact damping ratio and the CR, e.g., Naderpour et al. ([33], [34]) and Khatami et al. [35].

A different modification was carried out by Bamer et al. ([36]-[38]) to include damage provoked by repetitive impacts which are known to happen in inelastic impacts translated implicitly by parameter CR. This was made by the inclusion of a dry friction element in series with the non-linear spring from the Hertz damp model or the Jankowski's non-linear viscoelastic model (respectively, [36] and [37]).

Hence, most of the investigations concerning the development of impact models are based on the correct establishment or calibration of the impact stiffness and impact damping ratio. These parameters along with the coefficient of restitution, are the core of the impact models and their accuracy depends on how accurate is the estimation of these parameters. Unfortunately, these parameters are also subjected to great sources of uncertainties, viz., the geometry of the region of impact, material properties, impact velocities, stiffness and mass properties of the involved buildings, etc. These uncertainties may be addressed by performing validation experimental tests and performing parametric sensitivity analysis, which allows for additional information reducing the epistemic error in the models and understanding which parameters are important and relevant to consider and the ones that have no or little influence in the model. Some experimental tests regarding impacts and the calibration of the abovementioned parameters have been carried out ([39]-[43]).

It should be referred that the previous models mostly addressed central impact, i.e., impacts in one direction and a predefined location and geometry of impact. In reality, buildings will have correlated translational and rotational responses which makes the location and geometry of impacts unknown being a more complex model to study. In addition, the neglect of tangential forces and friction constitutes one of the assumptions of the previous models that may have a substantial effect on the overall dynamic response of building structures under earthquake-induced pounding. The work of Polycarpou et al. [44] addressed these situations by using a rational three-dimensional spatial model supported by previous considerations of impact models and by classical theory of contact mechanics considerations.

4 NUMERICAL MODELING PROCEDURE

The numerical models consist of two SDOF systems that can have elastic or inelastic behavior. The inelastic behavior will be considered by four representative cases of frame behavior. The two SDOF systems will represent two buildings with very different dynamic properties and are assumed as lumped mass models as sketched in Figure 3.

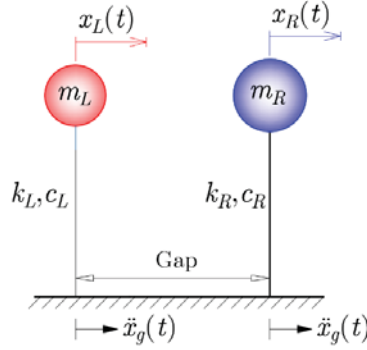


Figure 3: Representation of the two SDOF lumped mass models separated by a certain distance.

Table 1 presents the considered dynamic properties of each SDOF structural system according to [10].

Structural properties	Flexible building	Stiffer building
Mass (kg)	$m_L=75000$	$m_R=3000 \times 10^3$
Stiffness (kN/m)	$k_L=2056$	$k_R=1.316 \times 10^6$
Natural period (s)	$T_L=1.2$	$T_R=0.3$
Damping coefficient (kg/s)	$c_L=39270$	$c_R=6.283 \times 10^6$
Damping ratio (%)	$\xi_L=5$	$\xi_R=5$

Table 1: Structural properties of the adjacent buildings.

Equation 1 is modified to include the pounding force according to Equations 16 to 18, becoming now, respectively, for the elastic and inelastic case as follows

$$m\ddot{x}(t) + c\dot{x}(t) + kx(t) + f_p(t) = -m\ddot{x}_g(t) \quad (19)$$

$$m\ddot{x}(t) + c\dot{x}(t) + ak_0x(t) + f_r^*[x(t), \dot{x}(t)] + f_p(t) = -m\ddot{x}_g(t), \quad (20)$$

These structural systems will be subjected to a seismic ground motion, the El Centro's earthquake, whose acceleration signal is presented in Figure 4.

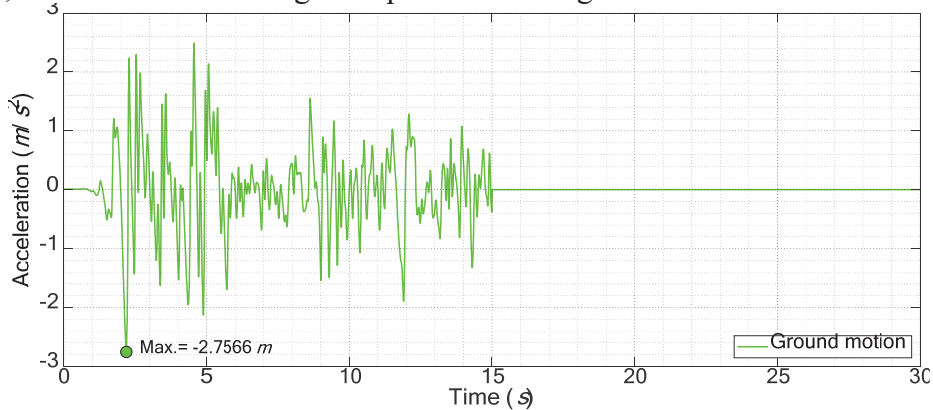


Figure 4: NS component of El Centro seismic accelerations - Station: El Centro, CA - Sta9; Imperial Valley-02 [45].

Equation 19 or 20 is used to emulate, respectively, the elastic and inelastic behavior of the considered structural systems. The hysteresis cases presented in section 2 will be considered. Table 2 presents the values considered to account for each case of hysteresis behavior. These values were based on the considerations given in [5].

Case	Hysteresis behavior	α	β_1	β_2	σ_s	R_s	λ_s
0	Plain	50	0	0	1	0	0
1	Stiffness degradation	1	0	0	1	0	0
2	Stiffness and strength degradation	1	0.3	0.3	1	0	0
3	Stiffness and strength degradation with pinching effect	1	0.3	0.3	0.2	0.1	0

Table 2: Non-linear hysteresis parameters for the structural system for different hysteresis behavior cases (in all cases: $\eta_1 = \eta_2 = 0.5$, $n_W = 5$, $a = 0.03$, $F_{YL} = 70 \text{ kN}$, $x_{YL} = 3.4 \text{ cm}$, $F_{YR} = 7000 \text{ kN}$, $x_{YR} = 0.53 \text{ cm}$, $\mu = 10$).

The pounding will be considered between the buildings' slabs and as implicitly mentioned the impact model will be the non-linear viscoelastic model developed by Jankowski ([30], [31]). The impact stiffness and the coefficient of restitution are, respectively, $2.75 \times 10^9 \text{ N/m}^{3/2}$ and 0.65 [30].

A Matlab/Simulink [46] model was developed to simulate structural pounding between the elastic and inelastic SDOF systems subjected to the El Centro Earthquake. The Simulink model is represented in Figure 5 and contemplates the case of structural pounding between SDOF systems. The gap between the adjacent structures was varied: 0 cm, 3 cm, 5 cm, 10 cm, and 15 cm. To solve the differential equations of motion the Runge-Kutta of 4th order was used with a fixed time step of $5 \times 10^{-4} \text{ s}$.

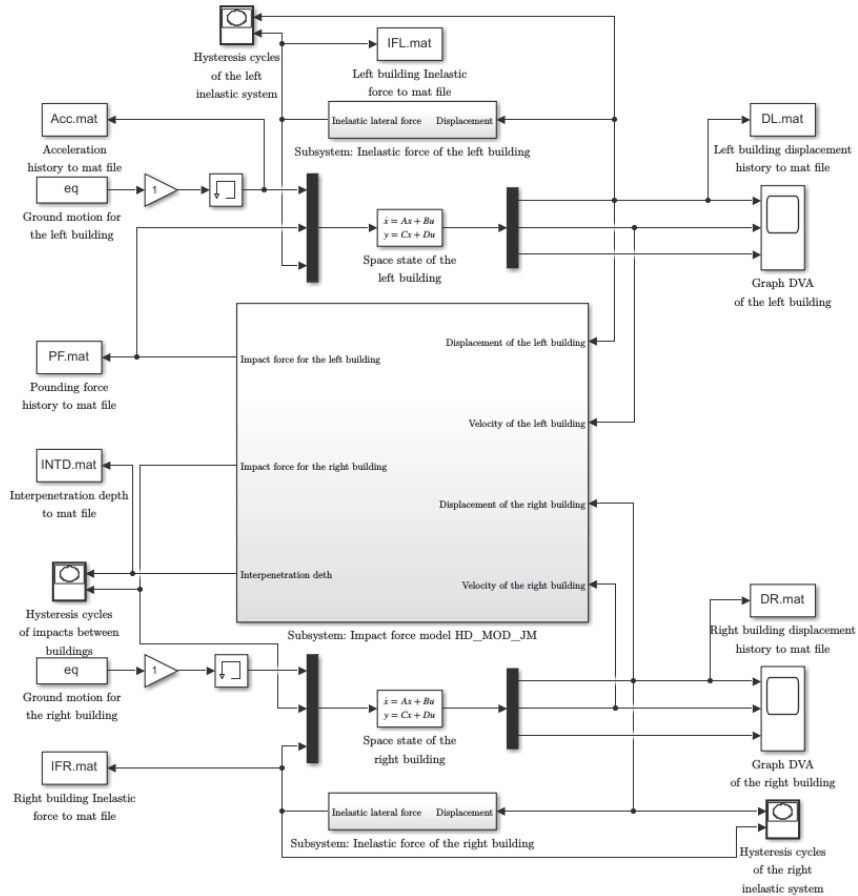


Figure 5: Layout of the macro Matlab/Simulink model using the non-linear viscoelastic impact model modified by Jankowski for pounding between non-linear systems.

5 RESULTS AND DISCUSSION

For convenience, only the results concerning the gap size between the adjacent buildings of 0 cm and 3 cm are presented in graphical form, except for the hysteresis cycles for the four hysteresis cases in which only the worst case was presented, for the case of no gap distance. The graphs of the acceleration time-histories are presented only for case 3 of hysteresis behavior compared with the elastic case for both the gaps of 0 cm and 3 cm. Nonetheless, Table 3 shows the peak values regarding displacements, velocities, accelerations, and pounding forces for each building and for the hysteresis cases considered and every value for the gap size studied. In addition, the number of impacts associated with each case is also presented. The percentages of increase or decrease depending on the cases being compared are shown below the peak values for better comparisons and understanding of the influence of the inelastic behavior in earthquake-induced pounding between buildings.

Attention is drawn to the fact that the gap size of 10 cm when the structural system has inelastic behavior does not appear in Table 3 since it didn't produce any impact and thus the responses are exactly the same as for the gap size of 15 cm.

Figures 6 to 10 present the graphic results regarding the displacement time-histories of the two colliding structures with no space in between and the corresponding resulting pounding forces for the elastic case and the different hysteresis cases considered. In the same way Figures 11 to 15 present the same graphs mentioned but for the gap size of 3 cm.

The graphs of Figures 16 to 20 present relevant comparisons between the displacements and pounding forces histories of the left structure, the most sensible to impacts and the ground motion for the different hysteresis behaviors considered and the elastic case.

The pounding cycles in Figure 21 are presented for both the elastic case and the different hysteresis cases considered.

Figure 22 shows the hysteresis cycles of each colliding building in comparison with the case of no pounding.

Finally, Figure 23 presents the acceleration response histories of both buildings for case 3 of hysteresis compared with the elastic case.

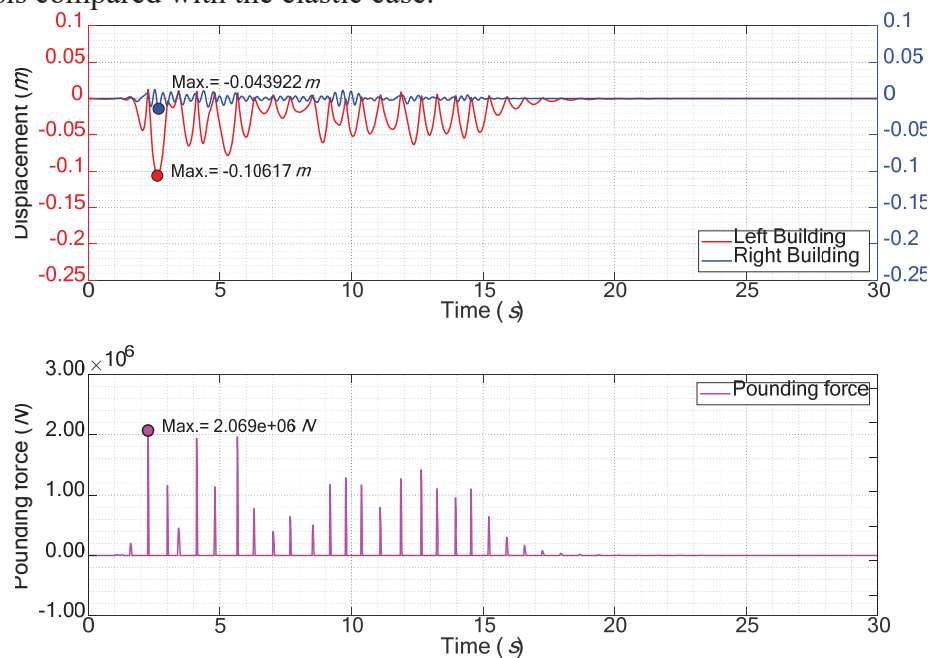


Figure 6: Displacements and pounding forces time-history responses for the elastic case of the representative structural systems with no gap in between.

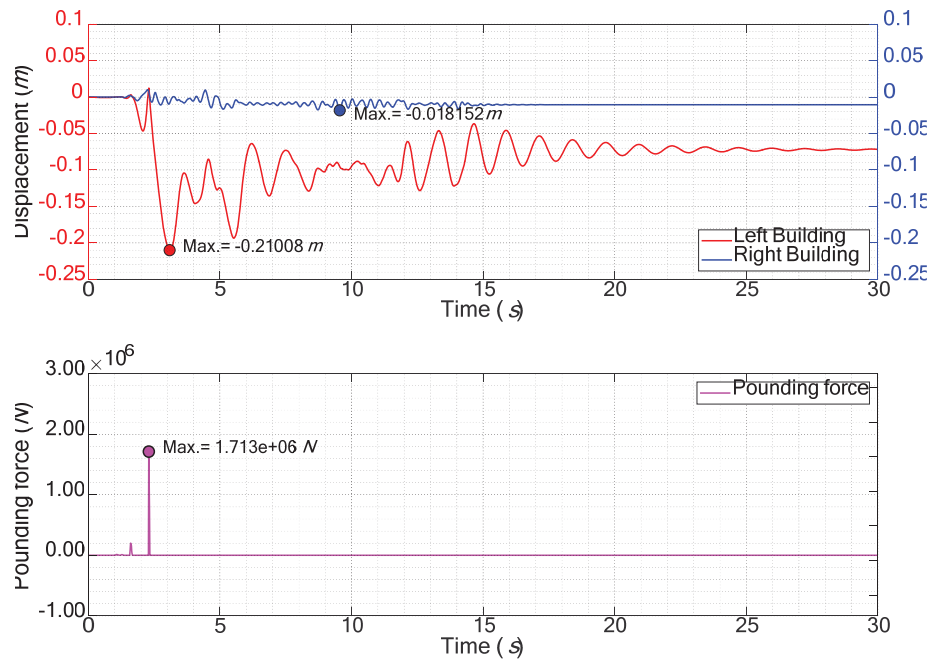


Figure 7: Displacements and pounding forces time-history responses for the hysteresis case 0 of the representative structural systems with no gap in between.

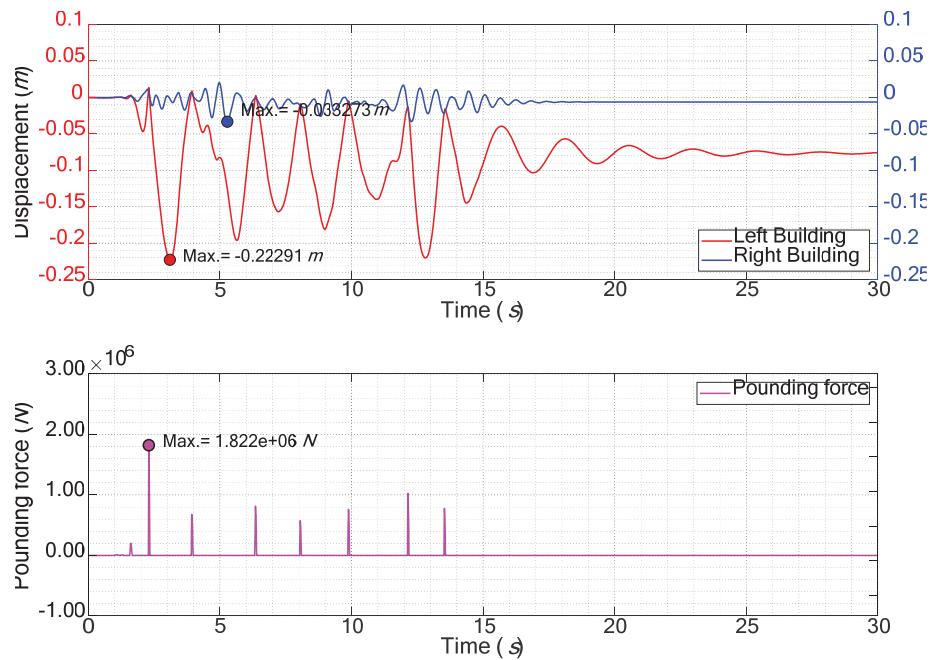


Figure 8: Displacements and pounding forces time-history responses for the hysteresis case 1 of the representative structural systems with no gap in between.

As expected, it is possible to verify the sensitiveness of the flexible building to both pounding forces and the ground motion. It is clear by the analysis of the results in Figures 6 to 15 that the inelastic cases present fewer impacts and the magnitude of the forces is smaller. However, the amplitude of the inelastic displacements, generally, exceeds the displacements in the elastic case, as can be validated by the peak values presented in Table 3. This is particularly true when the responses involve pounding and for hysteresis cases with degradation fea-

tures. When pinching is considered is possible to verify the largest inelastic displacements and magnitude of the pounding forces.

Analyzing the graphs from Figures 16 to 20 regarding the flexible building, one can verify that the case with no gap presents larger displacements and impact forces, as well as an increased number of impacts.

In the graphs of Figures 7 to 10 and 12 to 20, it is possible to verify the permanent displacements in the rebound direction caused by the action of the ground excitation and aggravated by the impact forces.

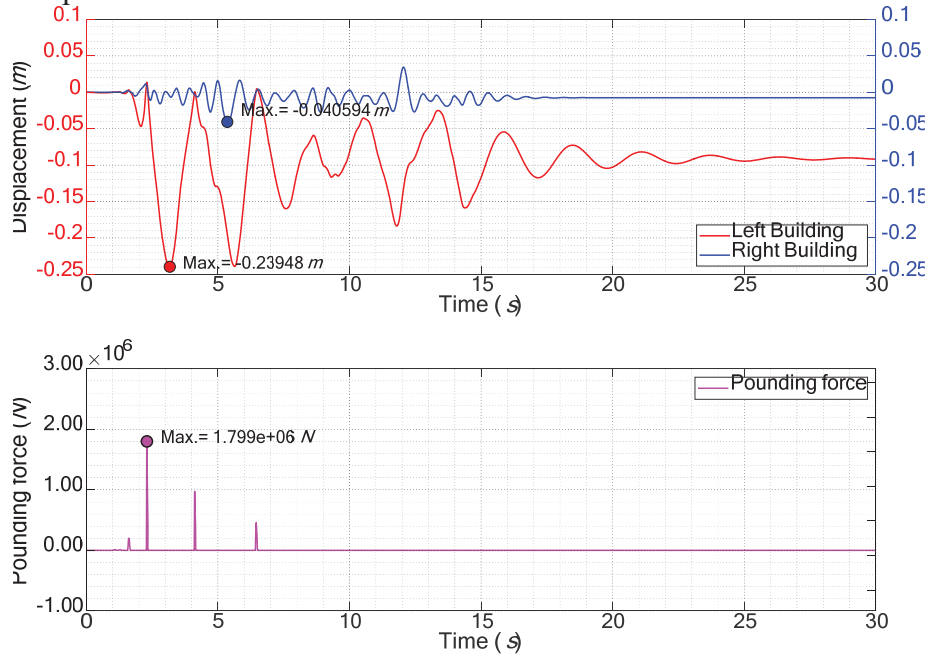


Figure 9: Displacements and pounding forces time-history responses for the hysteresis case 2 of the representative structural systems with no gap in between.

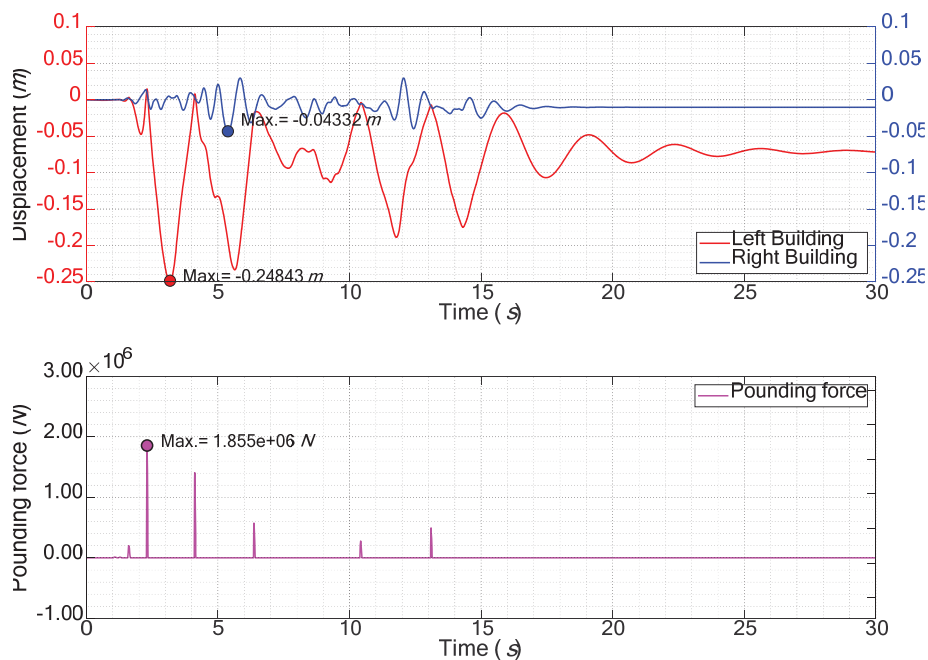


Figure 10: Displacements and pounding forces time-history responses for the hysteresis case 3 of the representative structural systems with no gap in between.

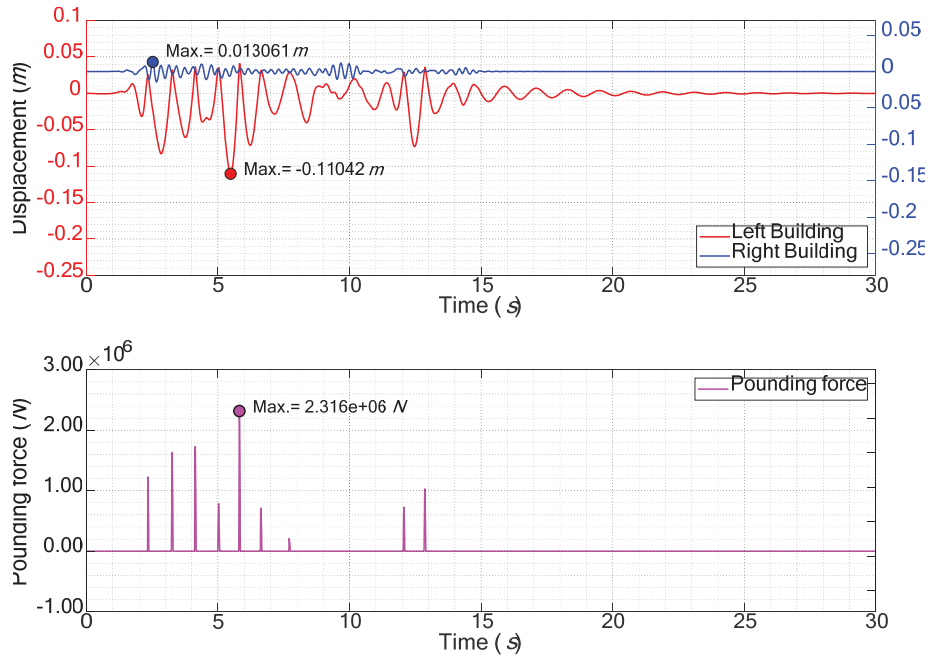


Figure 11: Displacements and pounding forces time-history responses for the elastic case of the representative structural systems separated by a distance of 3 cm.

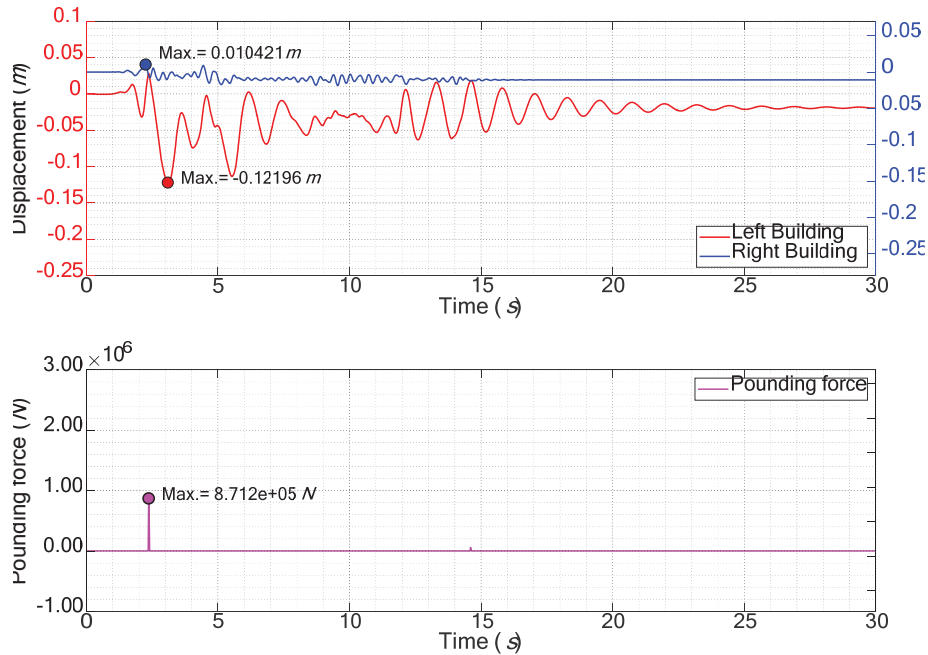


Figure 12: Displacements and pounding forces time-history responses for the hysteresis case 0 of the representative structural systems separated by a distance of 3 cm.

These permanent displacements are most visible in the flexible structure which proves once more the sensitiveness of the flexible building to pounding forces.

The residual displacements increase as the gap between the adjacent structures decreases, and since the number of impacts and its magnitude increases for these scenarios then it proves and supports the influence that the pounding forces have when inelastic behavior is considered. Such a fact would not be noticed when elastic behavior is considered.

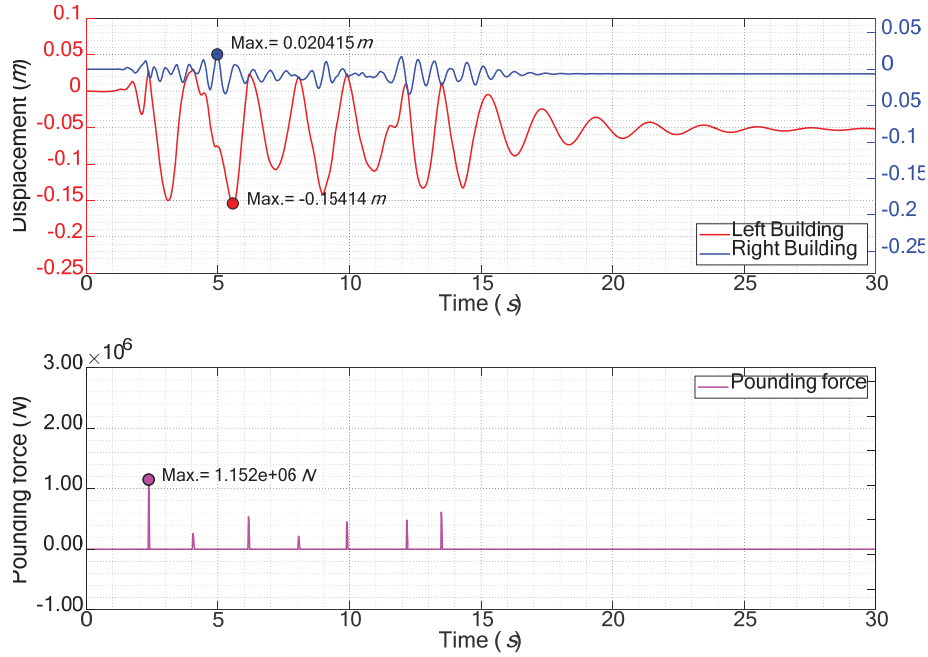


Figure 13: Displacements and pounding forces time-history responses for the hysteresis case 1 of the representative structural systems separated by a distance of 3 cm.

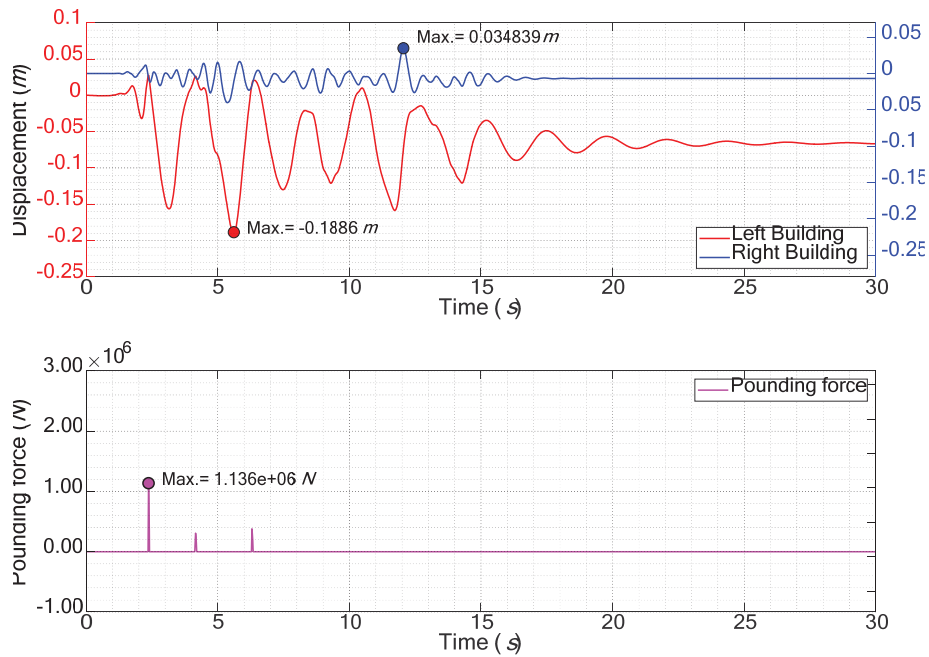


Figure 14: Displacements and pounding forces time-history responses for the hysteresis case 2 of the representative structural systems separated by a distance of 3 cm.

It is not clear for which case of hysteresis behavior the unrecoverable displacements are bigger since it also depends on the separation distance between the adjacent buildings. Nevertheless, these tend to be slightly bigger in case 2 of hysteresis behavior, when stiffness and strength degradation are considered.

Observing the graphs of Figure 21 regarding the pounding cycles, it is evident the difference between the magnitude of impacts when elastic and inelastic cases are considered. The number of cycles for the elastic case is also bigger for the inelastic cases. The number of im-

pacts is smaller for the hysteresis case 0 and bigger for the cases where stiffness degradation, strength deterioration, and the pinching effect are considered. In addition, the increase in the gap size decreased the magnitude of impacts as already mentioned by the observation of other graphs. Hence, with a few exceptions within the inelastic cases, case 3 presented slightly higher magnitudes for the impact forces.

The hysteresis loops for the different cases considered and for the scenario of no gap confirm the conclusions withdrawn previously, viz., the presence of permanent deformations in the rebound direction in the left building.

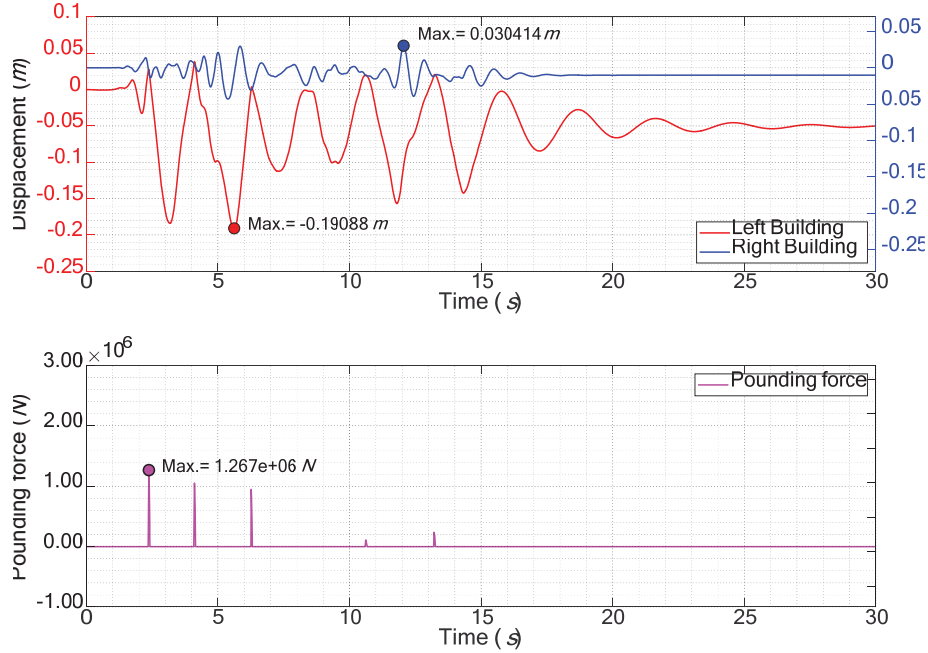


Figure 15: Displacements and pounding forces time-history responses for the hysteresis case 3 of the representative structural systems separated by a distance of 3 cm.

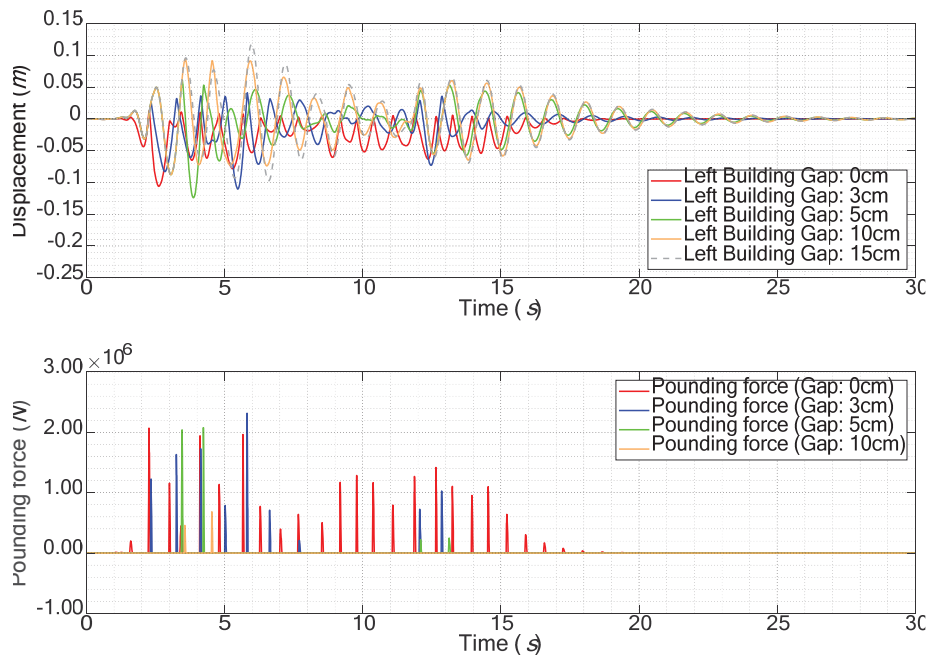


Figure 16: Comparison of the displacements and pounding forces time-history responses for the elastic case of the left building for different gap sizes.

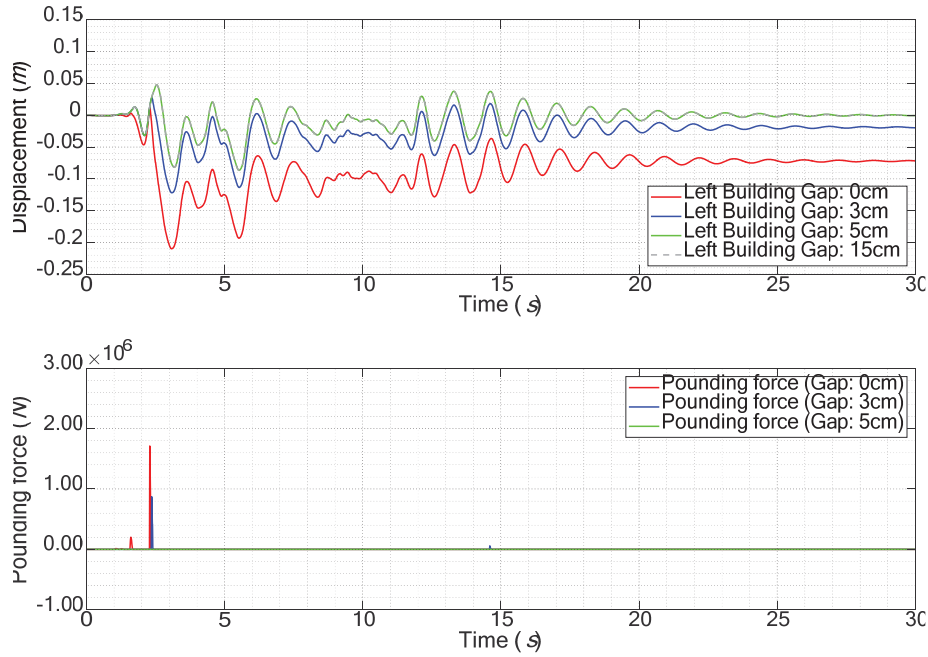


Figure 17: Comparison of the displacements and pounding forces time-history responses for the hysteresis case 0 of the left building for different gap sizes.

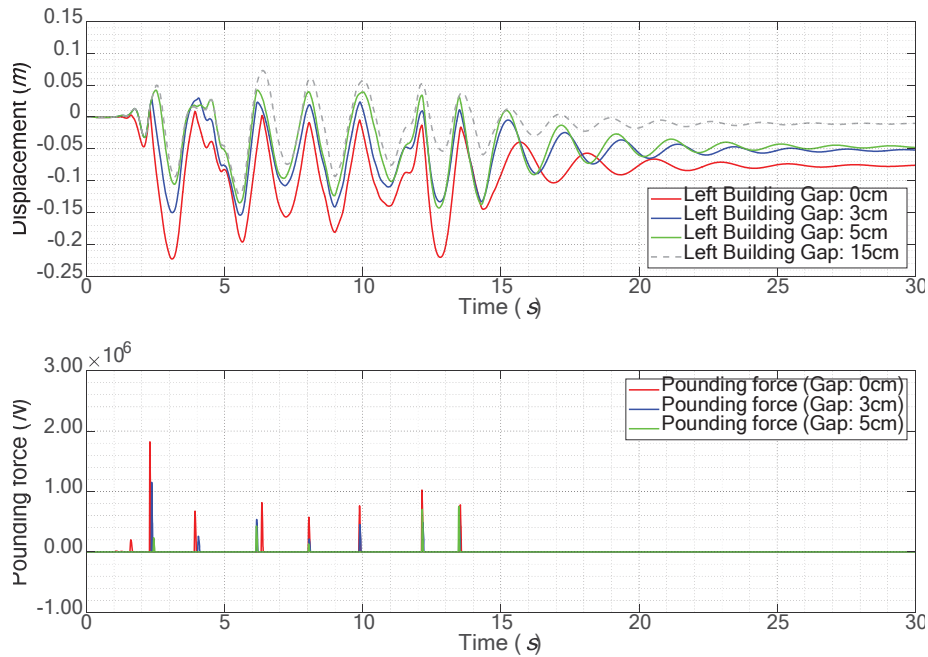


Figure 18: Comparison of the displacements and pounding forces time-history responses for the hysteresis case 1 of the left building for different gap sizes.

The hysteresis cycles also reveal that pounding has very little or no effect on the right structure. The hysteresis loops when pounding is considered are almost coincident showing very little deviation from the case with no pounding.

Table 3 also shows that the stiffer structure with inelastic behavior generally presents percentages of increase or decrease of the peak displacement with respect to the case with no pounding, which are approximately zero concerning the hysteresis cases and the gap sizes presenting impacts, viz., 3 cm and 5 cm. The exception is the scenario without space in be-

tween the structures that present an increase of the peak displacement in every hysteresis case. This increase corresponds to the case presented in Figure 22.

Table 3 also shows that in the elastic case the stiffer structure exhibits a reduction of the peak displacements for every gap size when pounding is considered.

Regarding the acceleration responses in Figures 23 and 24, it is possible to verify the reduction of the number and magnitude of the acceleration spikes of both the left and right structures when the inelastic behavior (Case 3 of hysteresis behavior) is considered with respect to the elastic case.

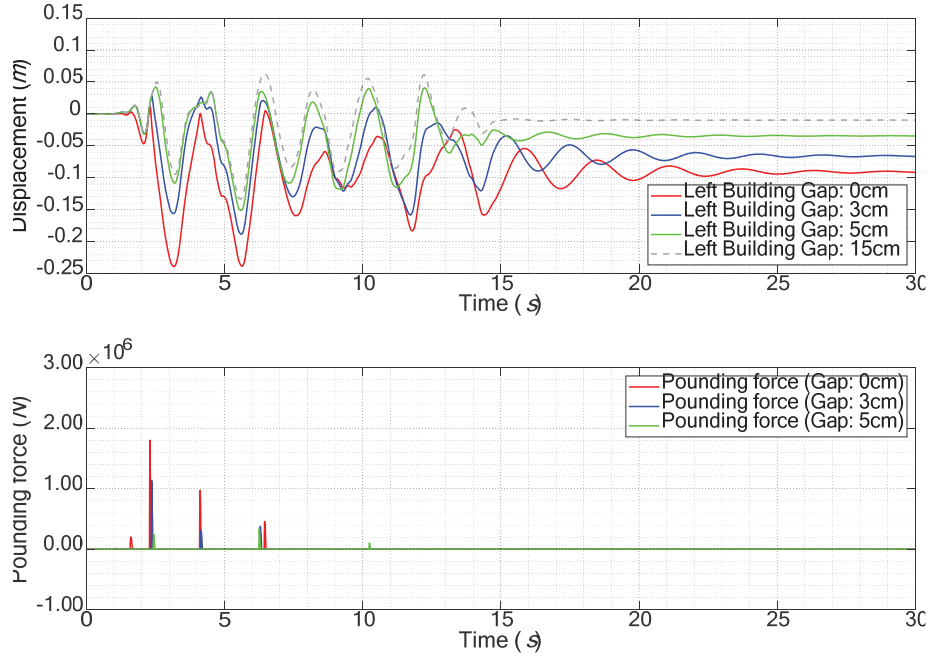


Figure 19: Comparison of the displacements and pounding forces time-history responses for the hysteresis case 2 of the left building for different gap sizes.

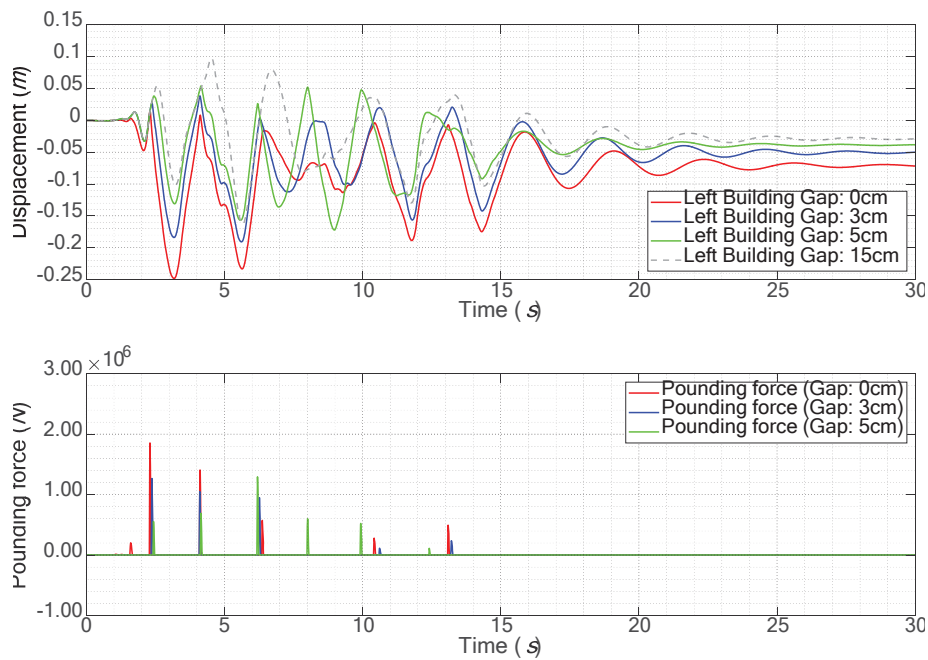


Figure 20: Comparison of the displacements and pounding forces time-history responses for the hysteresis case 3 of the left building for different gap sizes.

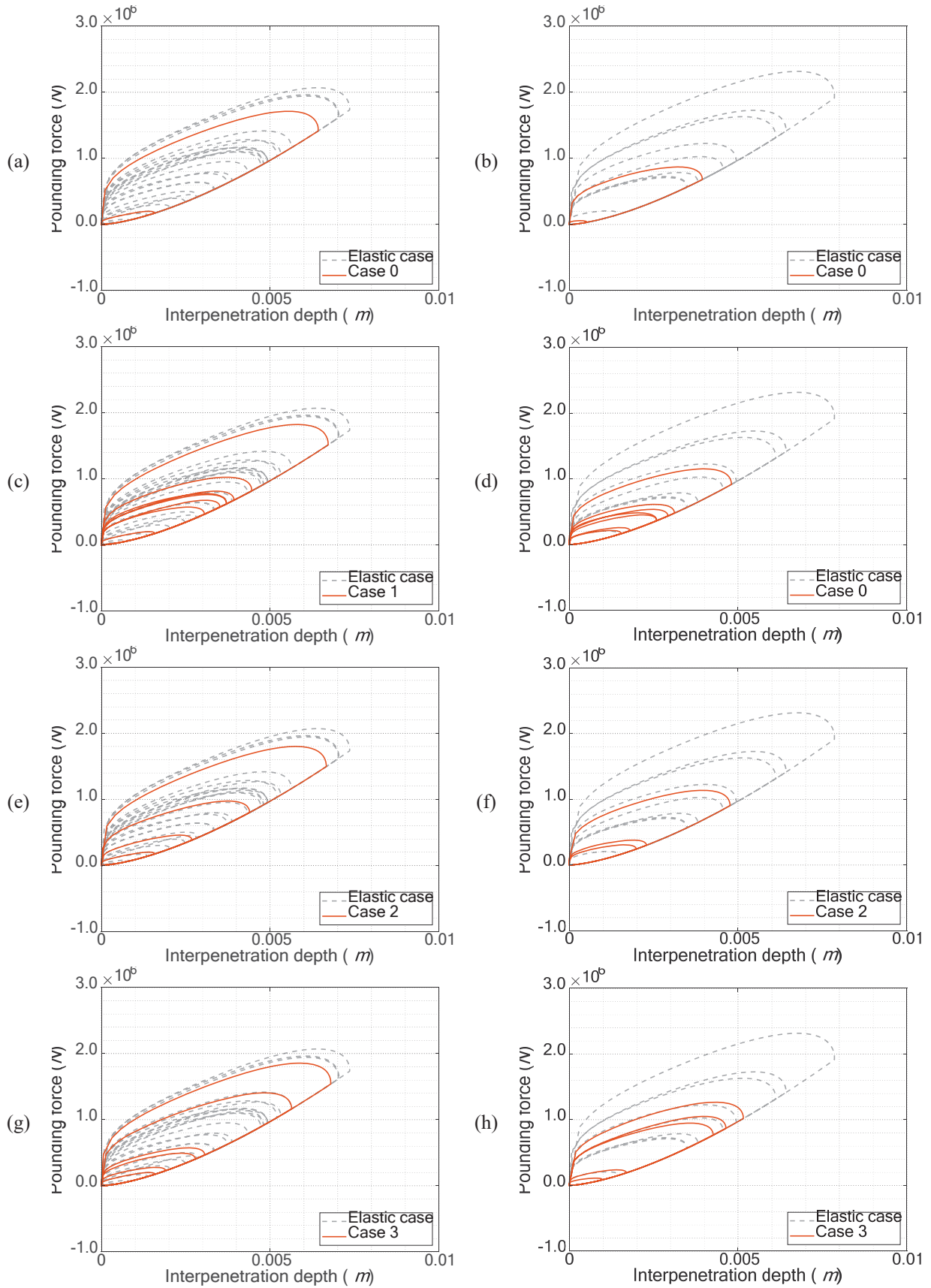


Figure 21: Pounding cycles for the hysteresis cases of the frame structures compared to the elastic case: (a), (c), (e), and (g) 0 cm; (b), (d), (f) and (h) 3 cm.

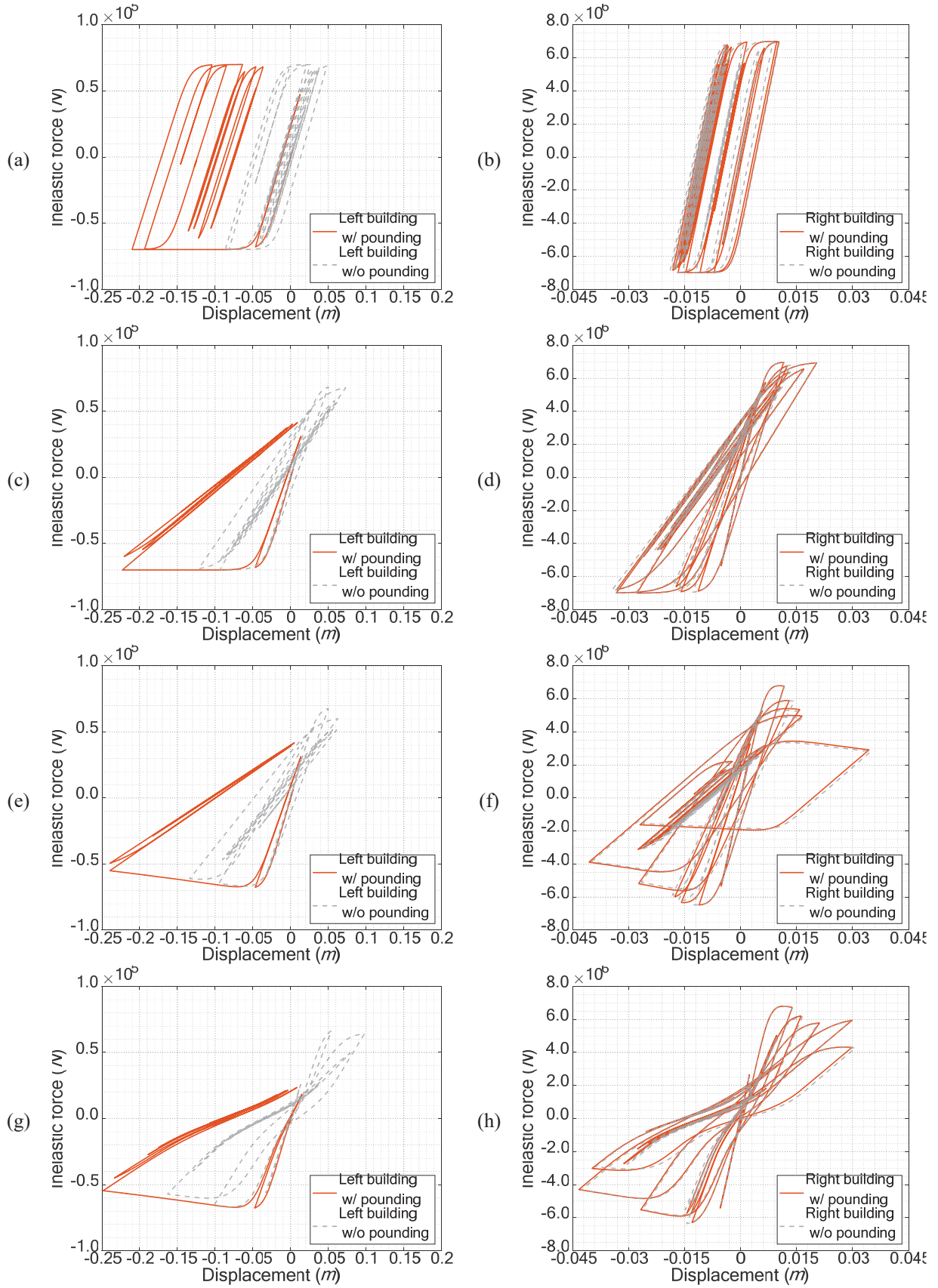


Figure 22: Hysteresis cycles when the structural systems have no gap in between: (a) and (b) Case 0; (c) and (d) Case 1; (e) and (f) Case 2; (g) and (h) Case 3.

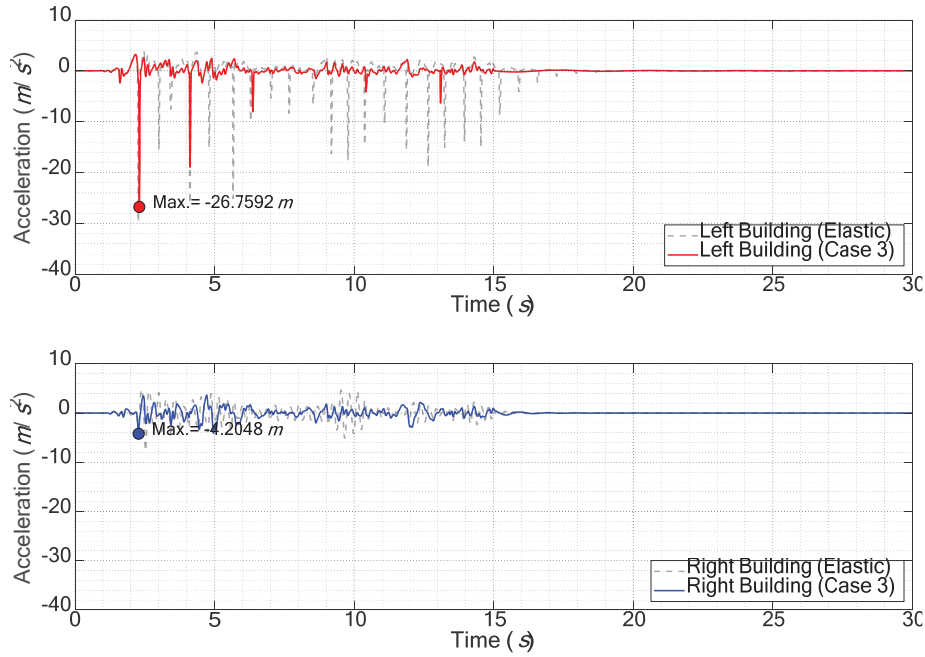


Figure 23: Acceleration time-history responses for the hysteresis case 3 of the structural systems with no space in between.

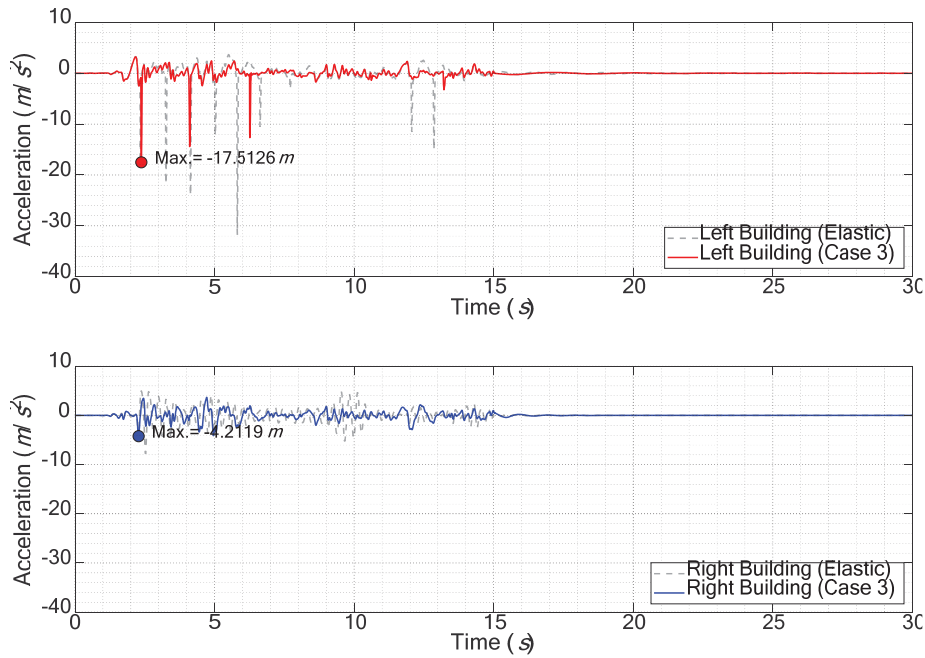


Figure 24: Acceleration time-history responses for the hysteresis case 3 of the structural systems separated by a distance of 3 cm.

From the peak acceleration values presented in Table 3 with particular emphasis on the flexible structure, it is possible to see the influence of the pounding forces in the large increases of the peak acceleration values for both the elastic and inelastic cases (except for the case 0 cm with 5 cm of gap size that presented no impact – see Figure 17). However, the acceleration spikes are smaller when the hysteresis cases are considered as can be seen in the percentages in green color that present negative values.

Behavior of frame structure	Gap (cm)	Peak absolute values							Nº of impacts
		x_L (m)	x_R (m)	\dot{x}_L (m/s)	\dot{x}_R (m/s)	\ddot{x}_L (m/s ²)	\ddot{x}_R (m/s ²)	F_P (kN)	
Linear Elastic	15	0.118	0.133	0.598	-0.312	-4.588	-7.961	0	0
	10	0.094 (-20%)	0.013 (-90%)	0.579 (-3%)	-0.312 (0%)	-13.837 (202%)	-7.961 (0%)	683.716	2
	5	-0.124 (5%)	0.013 (-90%)	0.694 (16%)	-0.312 (0%)	-29.877 (551%)	-7.961 (0%)	2077.72	4
	3	-0.110 (-6%)	0.013 (-90%)	0.704 (18%)	-0.309 (-1%)	-31.743 (592%)	-7.818 (-2%)	2315.8	9
	0	-0.106 (-10%)	-0.044 (-67%)	-0.589 (-1%)	-0.296 (-5%)	-29.746 (548%)	-7.693 (-3%)	2069.01	29
Non-linear Inelastic (Case 0)	15	-0.087	0.010	0.375	-0.197	-3.441	-4.584	0	0
	5	-0.087 (0%) (-30%)	0.010 (0%) (-22%)	0.375 (0%) (-46%)	-0.197 (0%) (-37%)	-3.441 (0%) (-88%)	-4.584 (0%) (-42%)	0 (-100%)	0 (-100%)
	3	-0.122 (41%) (10%)	0.010 (0%) (-20%)	0.375 (0%) (-47%)	-0.197 (0%) (-36%)	-12.639 (267%) (-60%)	-4.621 (1%) (-41%)	871.159 (-62%)	1 (-89%)
	0	-0.210 (143%) (98%)	-0.018 (74%) (-59%)	-0.523 (40%) (-11%)	-0.181 (-8%) (-39%)	-25.553 (643%) (-14%)	-4.624 (1%) (-40%)	1713.191 (-17%)	2 (-93%)
Non-linear Inelastic (Case 1)	15	-0.122	0.020	0.408	-0.313	-3.261	-4.387	0	0
	5	-0.143 (17%) (15%)	0.020 (0%) (53%)	-0.483 (18%) (-30%)	-0.313 (0%) (0%)	-10.777 (230%) (-64%)	-4.388 (0%) (-45%)	753.36 (-64%)	5 (25%)
	3	-0.154 (27%) (40%)	0.020 (0%) (56%)	0.434 (6%) (-38%)	-0.314 (0%) (1%)	-16.311 (400%) (-49%)	-4.386 (0%) (-44%)	1151.6 (-50%)	7 (-22%)
	0	-0.223 (83%) (110%)	-0.033 (63%) (-24%)	-0.550 (35%) (-7%)	-0.312 (0%) (5%)	-26.749 (720%) (-10%)	-4.374 (0%) (-43%)	1821.593 (-12%)	8 (-72%)
Non-linear Inelastic (Case 2)	15	-0.134	0.035	0.394	-0.276	-3.252	-4.157	0	0
	5	-0.152 (13%) (22%)	0.035 (0%) (162%)	0.425 (8%) (-39%)	-0.275 (0%) (-12%)	-5.068 (56%) (-83%)	-4.157 (0%) (-48%)	336.41 (-84%)	3 (-25%)
	3	-0.189 (41%) (71%)	0.035 (0%) (167%)	0.411 (4%) (-42%)	-0.276 (0%) (-11%)	-16.098 (395%) (-49%)	-4.157 (0%) (-47%)	1136.4 (-51%)	3 (-67%)
	0	-0.239 (79%) (126%)	-0.041 (17%) (-8%)	-0.544 (38%) (-8%)	-0.281 (2%) (-5%)	-26.419 (712%) (-11%)	-4.149 (0%) (-46%)	1799.359 (-13%)	4 (-86%)
Non-linear Inelastic (Case 3)	15	-0.163	0.031	0.368	-0.297	-3.377	-4.212	0	0
	5	-0.172 (6%) (39%)	0.031 (0%) (132%)	0.394 (7%) (-43%)	-0.298 (0%) (-4%)	-17.690 (424%) (-41%)	-4.212 (0%) (-47%)	1291.7 (-38%)	6 (50%)
	3	-0.191 (17%) (73%)	0.030 (-1%) (133%)	-0.387 (5%) (-45%)	-0.299 (1%) (-3%)	-17.513 (419%) (-45%)	-4.212 (0%) (-46%)	1266.6 (-45%)	5 (-44%)
	0	-0.248 (52%) (134%)	-0.043 (41%) (-1%)	-0.555 (51%) (-6%)	-0.300 (1%) (1%)	-26.759 (692%) (-10%)	-4.205 (0%) (-45%)	1855.221 (-10%)	6 (-79%)

a. The percentage below the values in blue color stands for the absolute percentage of increase or decrease regarding the corresponding case with no pounding. The percentage below the values in green color stands for the absolute percentage of increase or decrease regarding the corresponding linear elastic behavior case.

Table 3: Relevant results of the simulations carried out.

6 CONCLUSIONS

Earthquake-induced structural pounding between two SDOF structural systems was investigated. These systems can have elastic behavior or one of the four different types of hysteresis behavior considered with and without degradation features.

Inelastic behavior was found to be very relevant when impacts between the SDOF structures occurred. Ultimately, elastic behavior overestimates the number and magnitude of impact forces and underestimates the displacements and accelerations that the structures might experience. These conclusions are particularly relevant for the case of the flexible structure.

It was found that the amplitude of the inelastic displacements, generally, exceeds the displacements in the elastic case, particularly, when the responses involve pounding and for hysteresis cases with degradation features. Among the hysteresis cases, the case with pinching presented the largest peak displacement and magnitude of the pounding forces for the scenario without space between the structures.

Permanent displacements were verified in the rebound direction, viz., in the flexible structure, caused by the action of the ground excitation and aggravated by the impact forces. These residual displacements increase as the gap between the adjacent structures decreases. Although there is no clear understanding of which hysteresis behavior the unrecoverable displacements are bigger since it also depends on the separation distance between the adjacent buildings. However, these tend to be slightly bigger for the case where stiffness and strength degradation are considered.

The hysteresis cycles revealed that pounding has very little or no effect on the right structure. The hysteresis loops when pounding is considered are almost coincident with the case of no pounding, showing very little deviation from it.

Regarding the acceleration responses, it is possible to verify the reduction of the number and magnitude of the acceleration spikes of both the left and right structures when the inelastic behavior is considered with respect to the elastic case.

This study only comprises SDOF structural systems under a specific ground motion. Further studies should include multiple DOFs, a three-dimensional spatial model, calibration of the hysteresis model with experimental data, and the consideration of several different ground motions to further validate the results presented in this study and add more relevant information to the problem of earthquake-induced structural building pounding.

ACKNOWLEDGEMENTS

This paper is within the scope of the first author's Ph.D. degree in progress, financially supported by the Portuguese Foundation for Science and Technology (FCT) through the PhD grant reference SFRH/BD/139570/2018 under the programme POCH (N2020 – P2020) and subsidized by the European Social Fund (FSE) and national funds from MCTES. This work was financially supported by: Base Funding - UIDB/04708/2020 of the CONSTRUCT - Instituto de I&D em Estruturas e Construções - funded by national funds through the FCT/MCTES (PIDDAC).

REFERENCES

- [1] M. V. Sivaselven and A. M. Reinhorn, "Hysteretic models for deteriorating inelastic structures," *Journal of Engineering Mechanics*, vol. 126, no. 6, pp. 633-640, 2000.
- [2] Bouc, R. "Forced vibration of mechanical systems with hysteresis". Proceedings of the Fourth Conference on Non-linear oscillation. Prague, Czechoslovakia. 1967.
- [3] Y.-K. Wen, "Method for Random Vibration of Hysteretic Systems," *Journal of the Engineering Mechanics Division, ASCE*, vol. 102, no. 2, pp. 249-263, 1976.

- [4] Y.-K. Wen, "Equivalent Linearization for Hysteretic System under Random Excitation," *Journal of Applied Mechanics, ASME*, vol. 47, no. 1, pp. 150-154, 1980.
- [5] S. A. Mousavi, S. M. Zahrai, and M. Saatcioglu, "Toward buckling free tension-only braces using slack free connections," *Journal of Constructional Steel Research*, vol. 115, pp. 329-345, 2015.
- [6] Y. J. Park, A. M. Reinhorn and S. K. Kunnath, "IDARC: Inelastic Damage Analysis of Reinforced Concrete Frame - Shear-Wall Structures," *Technical Report NCEER-87-0008, National Center for Earthquake Engineering Research, University at Buffalo, State University of New York, Buffalo, New York, USA*, 1987.
- [7] S. K. Kunnath, A. M. Reinhorn and Y. J. Park, "Analytical modeling of inelastic seismic response of RC structures," *Journal of Structural Engineering, ASCE*, vol. 116, no. 4, pp. 996-1017, 1990.
- [8] Federal Emergency Management Agency (FEMA) P440A, *Effects of Strength and Stiffness Degradation on Seismic Response*, Redwood City, California: Applied Technology Council, 2009.
- [9] S. Otani, *Nonlinear Earthquake Response Analysis of Reinforced Concrete Buildings (Lecture Notes)*, Tokyo, Japan: Department of Architecture, Graduate School of Engineering, University of Tokyo, 2002.
- [10] R. Jankowski and S. Mahmoud, *Earthquake-Induced Structural Pounding*, Switzerland: Springer, 2015.
- [11] Goldsmith, W. *Impact: The Theory and Physical Behaviour of Colliding Solids*. Edward Arnold (Publishers) LTD: London. 1960.
- [12] M. Mahmoud, K. Choong, and R. Jankowski, "Seismic pounding between adjacent buildings: Identification of parameters, soil interaction issues and mitigation measures," *Soil Dynamics and Earthquake Engineering*, vol. 121, pp. 135-150, 2019.
- [13] K. Johnson, "Contact Mechanics," Cambridge university press, 1987.
- [14] H. Hertz, "Über die Berührung fester elastischer Körper (On the contact of elastic solids)," *J. für die Reine und Angewandte Mathematik*, vol. 29, pp. 156-171, 1881. (in German)
- [15] J. Wolf and P. Skrikerud, "Mutual pounding of adjacent structures during earthquakes," *Nuclear Engineering and Design*, vol. 57, pp. 253-275, 1980.
- [16] S. Anagnostopoulos, "Pounding of buildings in series during earthquakes," *Earthquake Engineering and Structural Dynamics*, vol. 16, pp. 443-456, 1988.
- [17] S. Anagnostopoulos, "Equivalent viscous damping for modeling inelastic impacts in earthquake pounding problems," *Earthquake Engineering and Structural Dynamics*, vol. 33, pp. 897-902, 2004.
- [18] P. Komodromos, P. Polycarpou, L. Papaloizo, and M. Phocas, "Response of seismically isolated buildings considering poundings," *Earthquake Engineering and Structural Dynamics*, vol. 36, pp. 1605-1622, 2007.
- [19] R. Valles and A. Reinhorn, "Evaluation, prevention and mitigation of pounding effects in building structures," Technical Report NCEER-97-0001, *National Center for Earthquake Engineering Research*, State University of New York, Buffalo, USA, 1997.

- [20] S. Mahmoud, "Modified linear viscoelastic model for elimination of the tension force in the linear viscoelastic," in *The Fourteenth World Conference on Earthquake Engineering, October 12-17, 2008, Beijing, China, 2008*.
- [21] K. Ye, L. Li and H. Zhu, "A modified Kelvin impact model for pounding simulation of base-isolated building with adjacent structures," *Earthquake Engineering and Engineering Vibration*, vol. 8, pp. 433-446, 2009.
- [22] D. Pant, A. Wijeyewickrema and T. Ohmachi, "Three dimensional nonlinear analysis of seismic pounding between multi-story reinforced concrete buildings," in *Proceedings of the Seventh International Conference on Urban Earthquake Engineering (7CUEE) and Fifth International Conference on Earthquake Engineering (5ICEE)*, Vol II: 1829-1840, 2010.
- [23] D. Pant, A. Wijeyewickrema and T. Ohmachi, "Seismic Pounding between Reinforced Concrete Buildings: A Study using two recently proposed Contact Element Models," in *Proceeding of the 14th European Conference on Earthquake Engineering, European Conference on Earthquake Engineering*, Republic of Macedonia, 2010.
- [24] S. Mahmoud and R. Jankowski, "Modified linear viscoelastic model of earthquake-induced structural pounding," *Iranian Journal of Science and Technology*, vol. 35, no. C1, pp. 51-62, 2011.
- [25] H. Lankarani and P. Nikraves, "A Contact Force Model With Hysteresis Damping for Impact Analysis of Multibody Systems," *Journal of Mechanical Design*, vol. 112, pp. 369-376, 1990.
- [26] H. Lankarani and P. Nikraves, "Continuous Contact Force Models for Impact Analysis in Multibody Systems," *Nonlinear Dynamics*, vol. 5, pp. 193-207, 1994.
- [27] K. Hunt and F. Crossley, "Coefficient of restitution interpreted as damping in vibroimpact," *Journal of Applied Mechanics, American Society of Mechanical Engineers*, vol. 42, pp. 440-445, 1975.
- [28] S. Muthukumar, "A contact element approach with hysteresis damping for the analysis and design of pounding in bridges," Ph.D. Thesis, Georgia Institute of Technology, Georgia, EUA, 2003.
- [29] S. Muthukumar and R. DesRoches, "A Hertz contact model with non-linear damping for pounding simulation," *Earthquake Engineering and Structural Dynamics*, vol. 35, pp. 811-829, 2006.
- [30] R. Jankowski, "Non-linear viscoelastic modelling of earthquake-induced structural pounding," *Earthquake Engineering and Structural Dynamics*, vol. 34, pp. 595-611, 2005.
- [31] R. Jankowski, "Analytical expression between the impact damping ratio and the coefficient of restitution in the non-linear viscoelastic model of structural pounding," *Earthquake Engineering and Structural Dynamics*, vol. 35, pp. 517-524, 2006.
- [32] K. Ye, L. Li and H. Zhu, "A note on the Hertz contact model with nonlinear damping for pounding simulation," *Earthquake Engineering and Structural Dynamics*, vol. 38, pp. 1135-1142, 2009.

- [33] H. Naderpour, R. Barros, and S. Khatami, "A new model for calculating impact force and energy dissipation based on the CR-factor and impact velocity," *Scientia Iranica A*, vol. 22, pp. 59-68, 2015.
- [34] H. Naderpour, R. Barros, R. Khatami, and R. Jankowski, "Numerical Study on Pounding between Two Adjacent Buildings under Earthquake Excitation," *Hindawi Publishing Corporation: Shock and Vibration*, vol. 2016, 2016.
- [35] S. Khatami, H. Naderpour, R. C. Barros, A. Jakubczyk-Gałczyńska and R. Jankowski, "Effective Formula for Impact Damping Ratio for Simulation of Earthquake-induced Structural Pounding," *Geosciences, MDPI*, vol. 9, no. 8: 347, 2019.
- [36] F. Bamer, "A Hertz-pounding formulation with a nonlinear damping and a dry friction element," *Acta Mechanica*, vol. 229, pp. 4485-4494, 2018.
- [37] F. Bamer and B. Markert, "A nonlinear visco-elastoplastic model for structural pounding," *Earthquake Engineering and Structural Dynamics*, vol. 47(12), pp. 2490-2495, 2018.
- [38] F. Bamer, N. Strubel, J. Shi and B. Markert, "A visco-elastoplastic pounding damage formulation," *Engineering Structures*, vol. 197, 2019.
- [39] R. Jankowski, "Experimental study on earthquake-induced pounding between structural elements made of different building materials," *Earthquake Engineering and Structural Dynamics*, vol. 39, pp. 349-354, 2010.
- [40] J. van Mier, A. F. Pruijssers, H. Reinhardt and T. Monnier, "Load-Time Response of Colliding Concrete Bodies," *Journal of Structural Engineering*, Vols. 117, No. 2, no. 25544, pp. 354-374, 1991.
- [41] K. Chau, X. Wei, X. Guo and C. Shen, "Experimental and theoretical simulations of seismic poundings between two adjacent structures," *Earthquake Engineering and Structural Dynamics*, vol. 32, pp. 537-554, 2003.
- [42] M. Goland, P. Wickersham, and M. Dengler, "Propagation of elastic impact in beams in bending," *Journal of Applied Mechanics*, vol. 22, pp. 1-7, 1955.
- [43] P. Zhu, M. Abe, and Y. Fujino, "Modelling three-dimensional non-linear seismic performance of elevated bridges with emphasis on pounding of girders," *Earthquake Engineering and Structural Dynamics*, vol. 31, pp. 1891-1913, 2002.
- [44] P. Polycarpou, L. Papaloizou, P. Komodromos, "An efficient methodology for simulating earthquake-induced 3D pounding of buildings", *Earthquake Engineering and Structural Dynamics*, vol. 43, pp. 985–1003, 2014.
- [45] Pacific Earthquake Engineering Research Center (PEER) strong ground motion database, [Online]. Available: <https://peer.berkeley.edu/peer-strong-ground-motion-databases>.
- [46] MATLAB 2014a., Natick, Massachusetts, USA: MathWorks, Inc., 2014.

VIRTUAL SENSING AND STRAIN ESTIMATION ON AN OFFSHORE WIND TURBINE USING SUPERVISED LEARNING

Marius Tarpø¹, Sandro Amador¹, Evangelos Katsanos¹, Mattias Skog¹, Johan Gjødvad²,
and Rune Brincker¹

¹Technical University of Denmark
Brovej B. 118, Kgs. Lyngby, Denmark
e-mail: mariotarpoe@gmail.com, sdio@byg.dtu.dk, vakat@byg.dtu.dk, runebr@byg.dtu.dk

²Sigicom
Glasfibergatan 8, 125 45 Älvsjö, Sweden
e-mail: mattias.skog@sigicom.com, johan.gjodvad@sigicom.com

Keywords: Data-driven model, virtual sensing, stress estimation, structural health monitoring, principal component analysis

Abstract. *Virtual sensing enables expansion and transformation of measured quantities from physical sensors into new quantities at unmeasured locations. This allows for estimating the strain and stress in unmeasured locations of a system by transforming the physical sensors (input) into the desired strain and stress response (output). This transformation model can be based on either knowledge of the systems, data from the system, or any combination of these. In this paper, supervised learning and data-driven models are applied to strain estimation of an offshore wind turbine through Principal Component Analysis (PCA). Training data are used to establish the data-driven model that enables a versatile strain estimation that functions well under different wind scenarios than the training data set.*

1 INTRODUCTION

Virtual sensing transforms measured data into other quantities and/or expands the data to unmeasured locations through virtual sensors [1]. We can categorise stress/strain estimation technique as a subcategory within virtual sensing that estimates the full-field stress/strain response of a system [2]. The reader should note that there is unfortunately not a consensus or common terminology in the field of virtual sensing and stress/strain estimation [2].

Stress/strain estimation started in the 1950s with models of analytical relationships between response and strain [3]. In the 1990s, transformation matrices started to replace the analytical relationships with Okubo and Yamaguchi [4] introducing a displacement-to-strain transformation matrix, which is based on data of both strain and displacement. Hjelm et al. [5] used mode shapes to create a transformation matrix - called the modal expansion technique - that enabled full-field strain estimation. The techniques of stress/strain estimation were expanded to include adaptive filters as Papadimitriou et al. [6] introduced the Kalman filter to full-field strain estimation in 2011. In 2016, Maes et al. [7] compared the different techniques of the transformation matrix (modal expansion) and adaptive filters (Kalman filter and the joint input-state estimation algorithm) for strain estimation on an offshore monopile wind turbine and they found the technique to be equal performance-wise. Accounting for the quasi-static response, Iliopoulos et al. [8] fused both accelerometers and strain gauges into the modal expansion technique while Skaftø et al. [9] applied Ritz vectors to the modal expansion technique. Risaliti et al. [10] introduced the augmented extended Kalman filter on a nonlinear system using the implicit equation of motion. Tarpø et al. [11] studied expansions of experimental mode shapes used for stress estimation and they concluded that expansions of mode shapes is equivalent to updating the system model. Nabuco et al. [12] estimated the dynamic full-field strain of an offshore tripod structure during operation with high accuracy. Tarpø et al. [13] proved that the modal expansion technique applies to a subsystem within a nonlinear and time-varying system when the nonlinear and time-varying effects act externally on the subsystem. At the end of the 2010s, machine learning and data-driven models enter the portfolio of stress/strain estimation techniques where Lu et al. [14] applied pattern recognition and Deng et al. [15] applied deep learning to modal expansion.

In this paper, we will study data-driven strain estimation on an operating offshore wind turbine in the Great Belt in Denmark. In general, a data-driven model consists of relationships between input and output of a system and is constructed through training data without any explicit knowledge of the system [16]. Therefore, data-driven strain estimation enables a transformation from physical sensors (input) to strain (output) at locations where temporary strain gauges were placed during the training data. Thus, this form of strain estimation is unextendable to other locations without adding information or new data to the model. This is the main drawback of data-driven strain estimation. Data-driven strain estimation, however, has the advantage over strain gauges in the form of prolonged service life. Strain gauges are known to be unreliable over long-term monitoring - especially in an offshore environment where they are damaged by the corrosive seawater. The service life of the data-driven strain estimation depends on the utilised physical sensors (eg. geophones or accelerometers) and these often have longer service life and are easier to replace than strain gauges. Furthermore, data-driven strain estimation is independent of a system model (often a finite element model) and the accuracy of this model.

In this paper, we utilize training data to construct a data-driven model that can estimate the strain response with high accuracy and reliability. The model works for different wind scenarios than the one from the training data.

2 STRAIN ESTIMATION USING PRINCIPAL COMPONENT ANALYSIS

In this paper, we apply the Principal Component Analysis (PCA) [17] in a supervised learning approach to find a transformation matrix between the displacement (the input) and the strain response of that system (the output) based on training data. Essentially, principal component analysis is a dimensionality reduction of data to set of uncorrelated principal components ordered by contribution [17].

In this technique, we will stack the displacement vector, $\mathbf{y}(t)$, and the strain response, $\boldsymbol{\varepsilon}(t)$, in a vector.

$$\mathbf{y}_c(t) = \begin{bmatrix} \mathbf{y}(t) \\ \boldsymbol{\varepsilon}(t) \end{bmatrix} \quad (1)$$

We estimate the covariance matrix of this stacked response and apply the singular value decomposition on the covariance matrix.

$$\mathbf{U}\mathbf{S}\mathbf{U}^T = \mathbb{E} [\mathbf{y}_c(t)\mathbf{y}_c(t)^T] \quad (2)$$

where \mathbf{S} is a diagonal matrix holding the singular values, \mathbf{U} holds the singular vectors as column vectors, $\mathbb{E}[\cdot]$ denotes the expectation operator, and $(\cdot)^T$ denotes the transpose of a vector or matrix.

We use the singular values, \mathbf{S} , to find the dominating principal components to represent the majority of the response. Then we can create a displacement-to-strain matrix, \mathbf{H} , using the singular vectors corresponding to these dominating singular components. We can estimate the strain response in other data set by the displacement-to-strain matrix.

$$\widehat{\boldsymbol{\varepsilon}}(t) = \mathbf{H}\mathbf{y}(t) \quad (3)$$

We must avoid an ill-posed problem, which requires a redundant sensor network with more physical sensors than included singular vectors in $\widehat{\mathbf{U}}$. Fortunately, we can separate the data into multiple frequency bands and find a set of singular vectors for each band.

3 CASE STUDY

3.1 Quality measures

In the literature or industry, there are no rules or guidelines for an evaluation of virtual sensors. The most common approach is to compare the virtual sensors with a set of reference sensors through different quality measurements. In this paper, we will use two different quality measurements.

3.1.1 Coefficient of determination (R^2)

The coefficient of determination (R^2) [18] is a popular quality measure in statistics and modal validation where a value of one indicates perfect correlation with the same amplitudes.

$$R_i^2 = 1 - \frac{\mathbb{E} [(\boldsymbol{\varepsilon}_i(t) - \widehat{\boldsymbol{\varepsilon}}_i(t))^2]}{\text{Var} [\boldsymbol{\varepsilon}_i(t)]} \quad (4)$$

where $\boldsymbol{\varepsilon}_i(t)$ is the measured strain response for the i^{th} strain gauge, $\widehat{\boldsymbol{\varepsilon}}_i(t)$ is the estimated strain response at the same location, and $\text{Var} [\cdot]$ denotes the variance operator.



Figure 1: Wind turbine near Sprogø and the Great Belt Bridge in Denmark

3.1.2 Normalised error in equivalent stress range

It is important to evaluate stress estimation in terms of the fatigue damage when the estimation is intended for a fatigue analysis. When we have varying stress amplitudes, we must apply cycle counting [19], like rainflow counting [20]. Sometimes, we might prefer to access fatigue damage for variable amplitude loading in the form of a damage equivalent stress range, which leads to the same fatigue damage as all stress cycles [19]. We calculate the damage equivalent stress range for both reference and the estimated as follows

$$\Delta\sigma_{eq} = \left(\frac{1}{n_{cycles}} \sum_{j=1}^{n_{cycles}} \Delta\sigma_j^m \right)^{1/m}, \quad \Delta\hat{\sigma}_{eq} = \left(\frac{1}{\hat{n}_{cycles}} \sum_{j=1}^{\hat{n}_{cycles}} \Delta\hat{\sigma}_j^m \right)^{1/m} \quad (5)$$

where n_{cycles} and \hat{n}_{cycles} are the total number of counted cycles for the measured and estimated signal, respectively, $\Delta\sigma_j$ and $\Delta\hat{\sigma}_j$ denote the stress range from cycle counting, and m is the "slope" of the SN curve. For this paper, we will assume $m = 3$, which corresponds to welded steel structures [19].

The normalised error of the equivalent stress range is given as

$$\eta_i = \frac{\Delta\hat{\sigma}_{eq} - \Delta\sigma_{eq}}{\Delta\sigma_{eq}} \quad (6)$$

Here $\eta_i = 0$ indicates a correct strain estimation in terms of equivalent fatigue damage while a negative value suggests an underestimation and a positive value suggests an overestimation of fatigue damage.

3.2 Wind turbine

The case study is an offshore wind turbine in the Great Belt in Denmark and the model of the wind turbine is a Vestas V90, 3 MW installed on a gravitation foundation, see Fig. 1. The wind turbine is equipped with a sensor network consisting of four Sigicom triaxial geophones

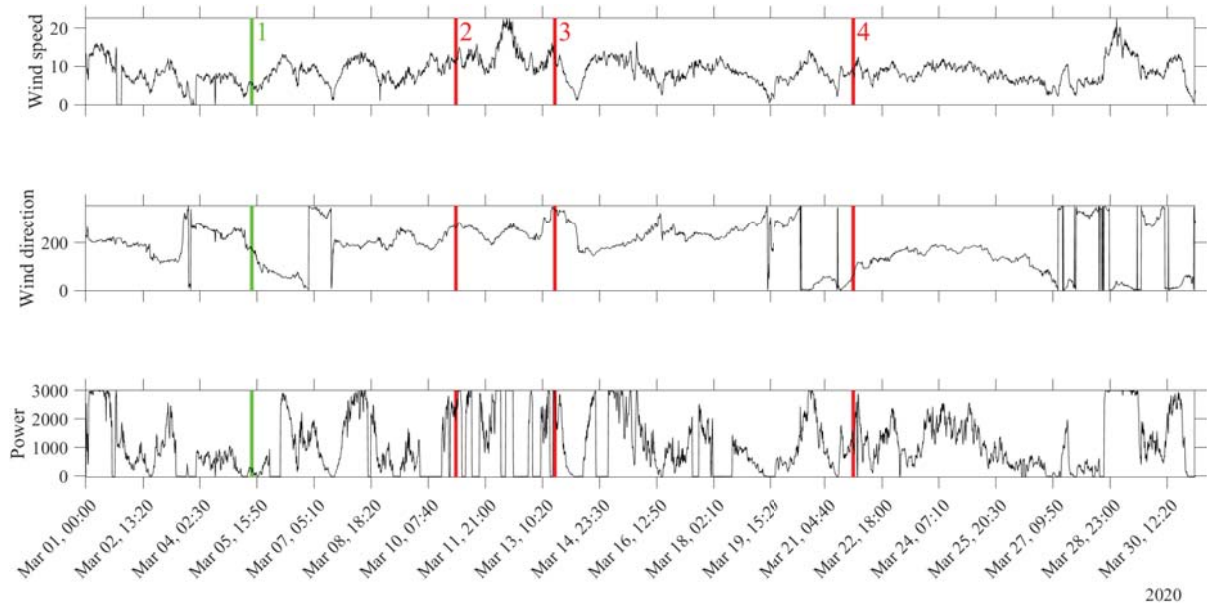


Figure 2: Monitoring campaign during a month with the measured wind speed, wind direction, and the production of power of the wind turbine. The chosen data sets are marked with a line and numbered where the training data set is marked with a green line and the others are marked with red.

attached at the lower part of the tower and two strain gauges located just above the foundation. The monitoring campaign was during a one month period, see Fig. 2, with a sampling frequency of 20 Hz.

To exclude the quasi-static response of the wind turbine, we apply a high-pass filter to all data with a cut-off frequency of 0.2 Hz. We calibrate the geophones using digital correlation [21] and we reduce the tilt effects on the geophones through the vertical geophones [22]. We integrate signals from the geophones into displacement by the integration theorem for the Fourier transformation [23]. Then, the data is divided into 3 frequency bands: 0.2-0.7, 0.7-4.5, and 4.5-10 Hz using complementary filters. These filters are applied to avoid an ill-posed problem for the strain estimation. We applied 40 minutes of training data to the principal component analysis, as explained in Section 2, to generate the transformation matrix for each frequency band. The training data set is marked with green in Fig. 2 and it has a wind direction of 180° and a low power production. The results of the strain estimation is shown in Fig. 3 for the training data sets. This displacement-to-strain matrix is saved as the data-driven model for the strain estimation for the entire monitoring period.

To illustrate the accuracy of the data-driven model, we apply the strain estimation model to three other data sets with different wind direction and power production distributed over the entire monitoring campaign, see the data sets marked with red in Fig. 2. Figs. 4, 5, and 6 show the strain estimation in both time and frequency domain for the three data sets. Finally, Fig. 7 (a) shows the coefficient of determination (R^2), Eq. (4), for all three data sets while Fig. 7 (b) displays the normalised error of equivalent strain range, Eq. (6).

All coefficient of determination values are above 0.965 and the estimated equivalent stress range is within $\pm 7\%$ of the measured one. All these values indicate that the data-driven model estimates the strain response with high accuracy and low uncertainty. Furthermore, strain estimation of the training data has similar quality measurements as the other data sets. This indicates that the displacement-to-strain matrix is versatile and applies to different wind scenarios of wind directions, wind speeds, and power production than the original training data set,

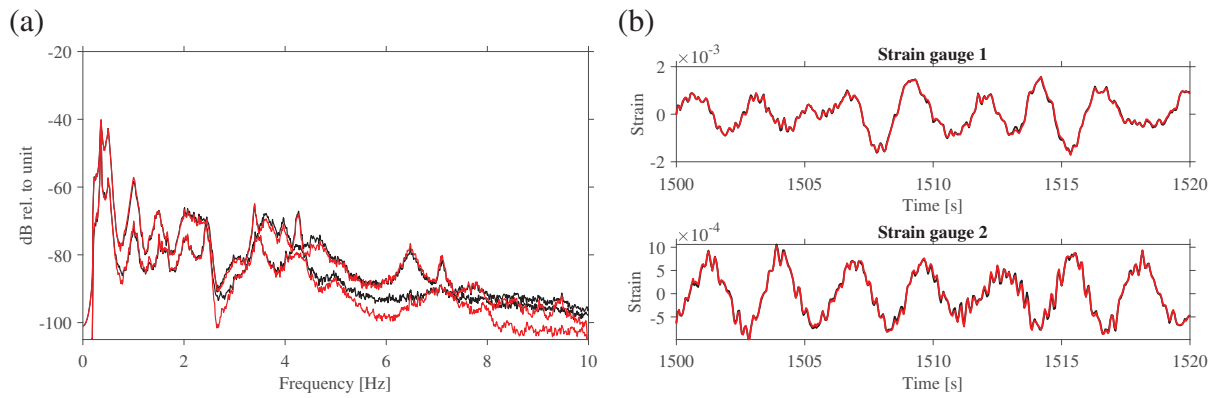


Figure 3: First data-set (training data) corresponding to the marking in Fig. 2 with measured strain (*black line*) and estimated strain (*red line*): (a) frequency domain with the first two singular values of the spectral density matrix calculated using Welch averaging method with segments of 2048 data points and 50 % overlap and (b) time domain with a zoom on the strain response.

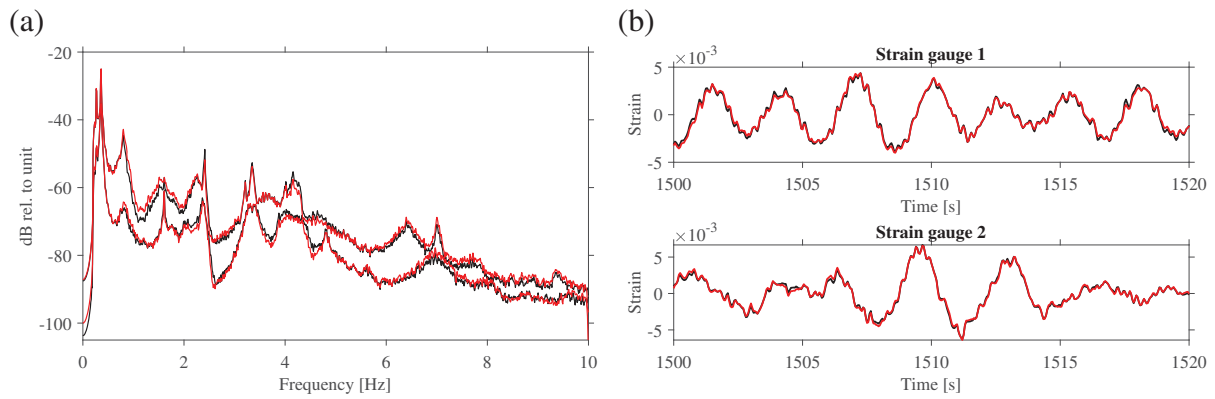


Figure 4: Second data-set corresponding to the marking in Fig. 2 with measured strain (*black line*) and estimated strain (*red line*): (a) frequency domain with the first two singular values of the spectral density matrix calculated using Welch averaging method with segments of 2048 data points and 50 % overlap and (b) time domain with a zoom on the strain response.

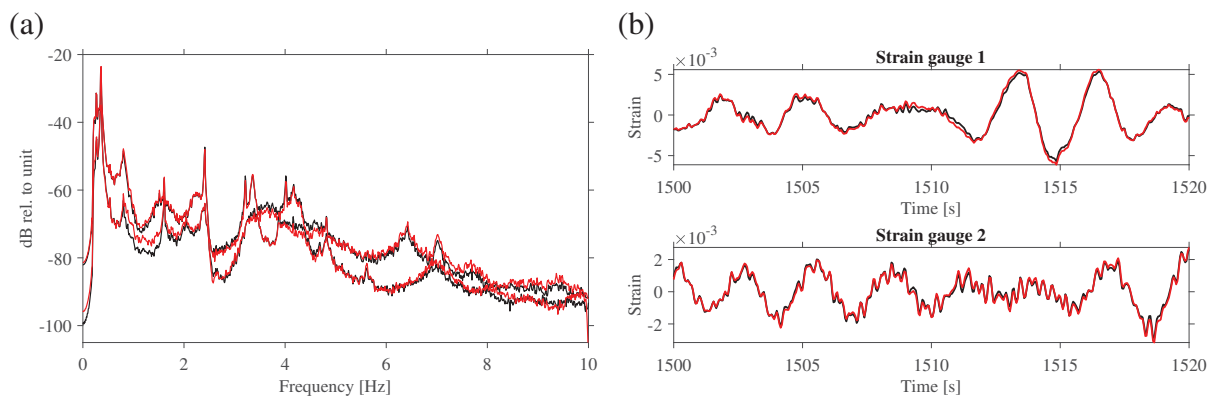


Figure 5: Third data-set corresponding to the marking in Fig. 2 with measured strain (*black line*) and estimated strain (*red line*): (a) frequency domain with the first two singular values of the spectral density matrix calculated using Welch averaging method with segments of 2048 data points and 50 % overlap and (b) time domain with a zoom on the strain response.

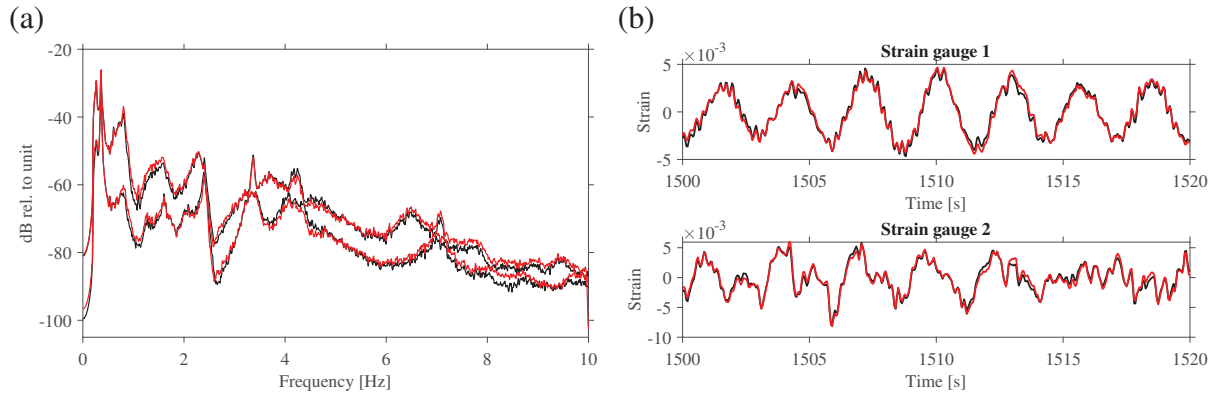


Figure 6: Fourth data-set corresponding to the marking in Fig. 2 with measured strain (*black line*) and estimated strain (*red line*): (a) frequency domain with the first two singular values of the spectral density matrix calculated using Welch averaging method with segments of 2048 data points and 50 % overlap and (b) time domain with a zoom on the strain response.

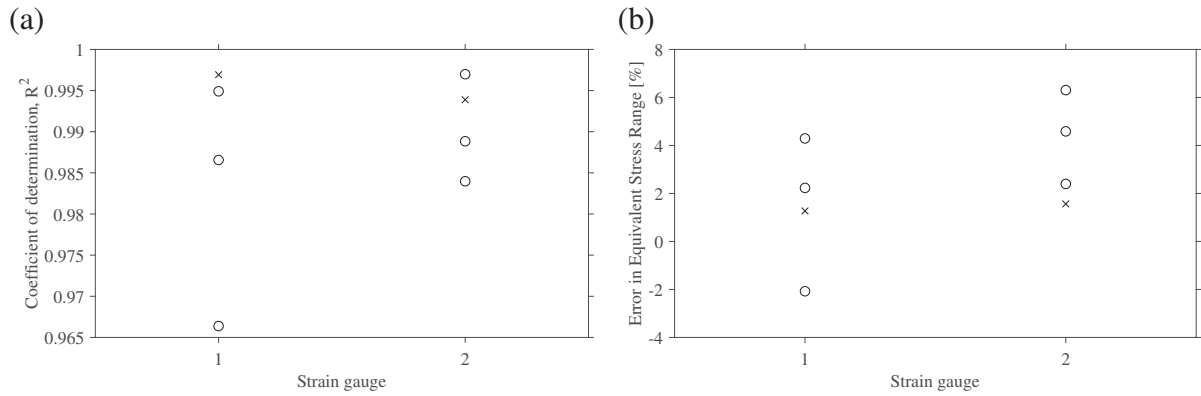


Figure 7: Quality measurements where training data set is marked with \times and the other data sets are marked with \circ : (a) the coefficient of determination (R^2), Eq. (4), for the estimated and measured strain, and (b) the normalised error in equivalent strain range, Eq. (6), for the estimated and measured strain.

which was constructed from.

4 CONCLUSION

In this paper, a data-driven strain estimation technique was introduced based on principal component analysis and temporary strain gauges. After the creation of the data-driven model, the temporary strain gauges become unessential for the future monitoring of the strain response and they can be removed. The technique was applied to an offshore wind turbine equipped with both triaxial geophone and strain gauges. A single data set was used to generate the data-driven model that could estimate the strain response - using only vibration responses from the geophones - with high precision in other data sets under different wind scenarios. Recapitulating, the virtual sensors were reliable and robust regardless of wind direction, wind speed, and power production of the wind turbine.

ACKNOWLEDGEMENTS

The authors acknowledge the funding received from the Centre for Oil and Gas - DTU/Danish Hydrocarbon Research and Technology Centre (DHRTC).

REFERENCES

- [1] L. Liu, S. M. Kuo, and M. Zhou. Virtual sensing techniques and their applications. In *2009 International Conference on Networking, Sensing and Control*, pages 31–36, March 2009.
- [2] Marius Tarpø. *Stress estimation of offshore structures*. PhD thesis, Aarhus University, 2020.
- [3] Denis Gordon Karczub. *The prediction of dynamic stress and strain in randomly vibrating structures using vibrational velocity measurements*. PhD thesis, The University of Western Australia, 1996. This thesis has been made available in the UWA Profiles and Research Repository as part of a UWA Library project to digitise and make available theses completed before 2003. If you are the author of this thesis and would like it removed from the UWA Profiles and Research Repository, please contact digitaltheses-lib@uwa.edu.au.
- [4] N. Okubo and K. Yamaguchi. Prediction of strain distribution under operating condition by the use of modal analysis. *Proceedings of the International Modal Analysis Conference XIII*, 210(5):91–96, 1995.
- [5] H.P. Hjelm, R. Brincker, J. Gaugaard-Jensen, and K. Munch. Determination of stress histories in structures by natural input modal analysis. *Proceedings of IMAC XXIII International Modal Analysis Conference*, 12:838–844, 2006.
- [6] C. Papadimitriou, C.P. Fritzen, P. Kraemer, and E. Ntotsios. Fatigue predictions in entire body of metallic structures from a limited number of vibration sensors using kalman filtering. *Structural Control and Health Monitoring*, 18(5):554–573, 2011.
- [7] K. Maes, A. Iliopoulos, W. Weijtjens, C. Devriendt, and G. Lombaert. Dynamic strain estimation for fatigue assessment of an offshore monopile wind turbine using filtering and modal expansion algorithms. *Mechanical Systems and Signal Processing*, 76-77:592–611, 2016.
- [8] Alexandros Iliopoulos, Wout Weijtjens, Danny Van Hemelrijck, and Christof Devriendt. Fatigue assessment of offshore wind turbines on monopile foundations using multi-band modal expansion. *Wind Energy*, 20(8):1463–1479, 2017.
- [9] A. Skaftø, J. Kristoffersen, J. Vestermark, U. T. Tygesen, and R. Brincker. Experimental study of strain prediction on wave induced structures using modal decomposition and quasi static ritz vectors. *Engineering Structures*, 136:261–276, 4/1 2017.
- [10] Enrico Risaliti, Tommaso Tamarozzi, Martijn Vermaut, Bram Cornelis, and Wim Desmet. Multibody model based estimation of multiple loads and strain field on a vehicle suspension system. *Mechanical Systems and Signal Processing*, 123:1 – 25, 2019.
- [11] M. Tarpø, B. Nabuco, C. Georgakis, and R. Brincker. Expansion of experimental mode shape from operational modal analysis and virtual sensing for fatigue analysis using the modal expansion method. *International Journal of Fatigue*, 130:105280, 2020.
- [12] Bruna Nabuco, Marius Tarpø, Ulf T. Tygesen, and Rune Brincker. Fatigue stress estimation of an offshore jacket structure based on operational modal analysis. *Shock and Vibration*, 2020:12, 2020.

- [13] Marius Tarpø, Tobias Friis, Christos Georgakis, and Rune Brincker. Full-field strain estimation of subsystems within time-varying and nonlinear systems using modal expansion. *Mechanical Systems and Signal Processing*, 153:107505, 2021.
- [14] Wei Lu, Jun Teng, Qiushi Zhou, and Qiexin Peng. Stress prediction for distributed structural health monitoring using existing measurements and pattern recognition. *Sensors*, 18(2), 2018.
- [15] Huaxia Deng, Haicong Zhang, Jun Wang, Jin Zhang, Mengchao Ma, and Xiang Zhong. Modal learning displacement–strain transformation. *Review of Scientific Instruments*, 90(7):075113, 2019.
- [16] Kevin P. Murphy. *Machine Learning: A Probabilistic Perspective*. MIT Press, Cambridge, Mass., USA, 2012.
- [17] Ian Jolliffe. *Principal component analysis*. Springer Verlag, New York, USA, 2nd revised edition, 2002.
- [18] P. C. Hansen, V. Pereyra, and G. Scherer. *Least squares data fitting with applications*. Johns Hopkins University Press, Baltimore, MD, 2013.
- [19] M.M. Pedersen. Introduction to metal fatigue - concepts and engineering approaches. Technical report, Department of Engineering, Aarhus University, 2018.
- [20] C. Amzallag, J.P. Gerey, J.L. Robert, and J. Bahuaud. Standardization of the rainflow counting method for fatigue analysis. *International Journal of Fatigue*, 16(4):287 – 293, 1994.
- [21] Rune Brincker, Thomas Lagö, Palle Andersen, and Carlos Ventura. Improving the classical geophone sensor element by digital correction. 01 2005.
- [22] M. Tarpø, B. Nabuco, R. Boroscek, and R. Brincker. Tilt errors of translational accelerometers attached to dynamic systems with tilt motion caused by the system response. *In revision at Journal of Sound and Vibration*.
- [23] R. Brincker and C. Ventura. *Introduction to operational modal analysis*. John Wiley and Sons, Inc., Chichester, West Sussex, UK, 2015.

SIMPLIFIED METHODS FOR FREQUENCY ESTIMATION OF SMALL WIND TURBINE TOWER

Dick Anelise¹, Carneiro-Barros Rui¹, and Braz-César T. Manuel²

¹ CONSTRUCT, Faculdade de Engenharia, Universidade do Porto
FEUP, Porto, Portugal
{anelise.dick, rcb}@fe.up.pt

² CONSTRUCT, Instituto Politécnico de Bragança
IPB, Bragança, Portugal
brazcesar@ipb.pt

Abstract

The design process of a slender structure, such as a wind turbine tower, goes through the analysis of the natural frequency, since it is important that this frequency is away from the frequencies generated by the excitation sources. The simplified analysis models and formulations are an important tool in the frequency evaluation on design phase, even though most formulations consider the structure with constant mass and inertia, which is not the case of wind turbine tower, that have a tapered shape. The main objective of this study is to evaluate the accuracy of the simplified models when applied to structures with variable inertia. The results of the simplified models applied to a small wind tower were compared with the finite element method and experimental results. The large scatter of the simplified method's results, frequencies in the range of 0.8 – 2.12 Hz, emphasizes the importance of a reliable model to evaluate the frequency. The Rayleigh and SDOF reduction methods were found to be accurate in evaluating the first frequency of the investigated tower under consideration.

Keywords: Wind turbine tower, Simplified frequency estimation, Eigenfrequency.

1 INTRODUCTION

Wind energy is one of the sources of renewable energy that has been used by mankind since the dawn of civilization. Recent wind turbine towers (WTT) studies intend to optimize the costs of installation and production, not only for large ones but also for small ones; the later can be used for domestic or specific energy production. The wind turbine tower is a part of the system that affects energy production efficiency, and because of being usually slender and flexible structures, is considered the critical part of the wind turbine since it should support the dead loads of equipment and additional loads caused by wind. There are essentially two types of towers used for this purpose: lattice towers and tapered hollow towers. Tapered hollow towers are usually preferable because they require less implantation area and are aesthetically more pleasant. For modeling these structures, it is necessary the estimate the natural frequency in the lowest sway mode of the structure.

The importance of the natural frequency determination for wind turbine towers design is because it must be away from the frequencies generate by the excitation sources as wind, the rotor (1P) or blade passing (3P-for 3 blades turbines)[1]. For complex structures finite-element computer programs will be used to access this information, however, for cost reduction and in the early design the simplified methods are quite useful.

In literature can be found several methods for frequency estimation, like empirical formulas [2] simplified formulas [1, 3] as well as Rayleigh's method [4, 5]. The tower can be considered as a generalized single-degree-of-freedom structure with a concentrated tip mass on top, that is analyzed with SDOF reduction [5] or through the solution of the transcendental equation. The main problem is that the mass of the rotor and nacelle located on top of the tower is usually neglected, and generally tapered towers have a behavior different from the tubular towers; these are sufficient sources capable of causing certain errors.

The objective of this research work is to analyze the accuracy of simplified models for the determination of the first eigenfrequency of a cantilever metallic hollow tower (used as a small WTT), by evaluating the differences between them and the results obtained by finite-element model analysis in established computational software; still comparing these results, with those of evaluated frequencies from ambient or structural health monitoring vibrations measurements on the real structure. The analysis shows that the main difficulty of simplified formulas is the determination of the mass and moment of inertia that should be used, which can significantly affect the results.

2 SIMPLIFIED MODELS REVIEW

The studies of standard vibratory movements of structures are based on the hypothesis that for small amplitudes of vibration the structures exhibit a linear behavior; that is, the forces of inertia, stiffness and damping are respectively proportional to acceleration, displacement and velocity, defining a linear systems [6]. The equation of motion (on the displacement variable $w(t)$) of an elastic linear undamped system (mass M and stiffness K) in the absence of external forces (Eq.1), leads to the natural frequency f (in Hz) expressed by Eq.2.

$$M\ddot{w}(t) + Kw(t) = 0 \quad (1)$$

$$f = \frac{1}{2\pi} \sqrt{\frac{K}{M}} \quad (2)$$

The simplest way to determine the frequency of a cantilever tower is to consider the structure as a beam with a concentrated mass at the top and with constant stiffness and mass, that is, as a structure with one degree of freedom (SDOF). In such case for towers of height H with constant inertia and constant distributed flexural stiffness EI , the lateral stiffness is calculated by

$$K_L = \frac{3EI}{H^3} \quad (3)$$

According to Ko [1] if the tower is modelled as a SDOF system with a tip mass, using a constant cross-section than the natural frequency is,

$$f = \frac{1}{2\pi} \sqrt{\frac{K_L}{M_{tip} + \alpha M}} \quad (4)$$

where α is the equivalent mass ratio of the tower concentrated at the top. The wind turbine design standard DNV-OS-J101 [7] establishes $\alpha = 0.25$, while the IEC 61400-1 standard [8] indicates that $\alpha = 0.5$; another value of $\alpha = 33/140$ is proposed by Blevins [9].

A different procedure is to model the wind turbine tower as Euler-Bernoulli beam system [10], with distributed mass m and distributed flexural stiffness EI . The governing equation of motion for undamped free vibrations of a uniform Euler-Bernoulli beam [11, 12, 13] is,

$$EI \frac{\partial^4 w(z, t)}{\partial z^4} + m \frac{\partial^2 w(z, t)}{\partial t^2} = 0 \quad (5)$$

and, the clamped-free boundary conditions with a tip mass are,

$$w(0, t) = 0, \quad \left[\frac{\partial w(z, t)}{\partial z} \right]_{z=0} = 0 \quad (6)$$

$$\left[EI \frac{\partial^2 w(z, t)}{\partial z^2} + I_{tip} \frac{\partial^3 w(z, t)}{\partial t^2 \partial z} \right]_{z=L} = 0, \quad \left[EI \frac{\partial^3 w(z, t)}{\partial z^3} - M_{tip} \frac{\partial^2 w(z, t)}{\partial t^2} \right]_{z=L} = 0 \quad (7)$$

Separating the spatial and temporal functions using the method of separation of variables [11], applying Eq. 8 leads to Eq. 9

$$w(z, t) = \Phi(z)\eta(t) \quad (8)$$

$$\frac{EI}{m} \frac{1}{\Phi(z)} \frac{\partial^4 \Phi(z)}{\partial z^4} = -\frac{1}{\eta(t)} \frac{\partial^2 \eta(t)}{\partial t^2} = \gamma = \omega^2 \quad (9)$$

From which, the solution for Eq. 8 can be expressed as follows,

$$\Phi(z) = A \cos\left(\frac{\lambda}{H} z\right) + B \cosh\left(\frac{\lambda}{H} z\right) + C \sin\left(\frac{\lambda}{H} z\right) + D \sinh\left(\frac{\lambda}{H} z\right) \quad (10)$$

$$\eta(t) = E \cos(\omega t) + F \sin(\omega t) \quad (11)$$

where A, B, C, D, E and F are unknown constants and,

$$\lambda^4 = \frac{\omega^2 m H^4}{EI} \rightarrow \omega = \frac{\lambda^2}{H^2} \sqrt{\frac{EI}{m}} \quad (12)$$

The non-trivial solution for $\Phi(z)$ is obtained by the differential eigenvalue problem, using the spatial form of the boundary conditions to find the values of λ [12]. Then the characteristic equation of the system is,

$$1 + \cos \lambda \cosh \lambda + \frac{\lambda M_{tip}}{mH} [\cos \lambda \sinh \lambda - \sin \lambda \cosh \lambda] - \frac{\lambda^3 I_{tip}}{mH^3} [\cosh \lambda \sin \lambda + \sinh \lambda \cos \lambda] + \frac{\lambda^4 M_{tip} I_{tip}}{mH^4} [1 - \cos \lambda \cos \lambda] = 0 \quad (13)$$

If the tip mass is modeled as a point mass, the rotational inertia of the tip mass is negligible, $I_{tip} = 0$. The first root of the characteristic equation is the first natural frequency, calculated by solving Eq. 13.

The main difficulty is to determine the values of m and EI to be used, since the tower has distributed mass and elasticity, i.e., the structure is non-uniform. Nevertheless, this structure can be modeled as a generalized SDOF system and provide an approximate solution. This procedure is called SDOF reduction and consists in creating a SDOF-equivalent system with distributed mass and stiffness, where according to the principle of virtual work, the generalized mass M^* and stiffness K^* can be obtained [6, 13, 14],

$$M^* = M_{tip} + \int_0^H m(z) \Phi^{*2}(z) dz \quad (14)$$

$$K^* = \int_0^H EI(z) \left[\frac{\partial^2 \Phi^*(z)}{\partial z^2} \right]^2 dz - \int_0^H N(z) \left[\frac{\partial \Phi^*(z)}{\partial z} \right]^2 dz \quad (15)$$

Paz [5] recommends the Eq. 16 as a simplified mode shape of the tower,

$$\Phi^*(z) = 1 - \cos\left(\frac{\pi z}{2H}\right) \quad (16)$$

On the other hand, an alternative method to establish the stiffness of the structure is through the linear relationship between the force and displacement Eq.17. But the difficulty with this procedure is that one must know the force and the displacement caused by that force.

$$F = Kx \rightarrow K = \frac{F}{\delta} \quad (17)$$

The displacement can be determined by theoretical calculations or by structural analysis software. Balagopal *et al.* [14] present a simplified model for calculating the displacement at the top considering the application of a unit force on the structure. The procedure defined the cross sectional area of the tower and the moment of inertia are calculated based on ASCE 48-11 [15].

$$K = \frac{1}{\delta_{unit}} \quad (18)$$

$$\delta_{unit} = \delta_{lat} + \delta_{vert} \quad (19)$$

$$I = C d_m^3 e \quad C = 0,403 \quad d_m = (d_t + d_b)/2 \quad (20)$$

$$A = 3,19 d_m e \quad (21)$$

The displacement δ_{unit} is calculated using the following set of equations,

$$\delta_{lat} = \int_0^H \frac{z^2}{E C e (d_t + s_p z)^3} dz \quad (22)$$

$$\delta_{vert} = \int_0^H \frac{M z}{E C e (d_t + s_p z)^3} dz \quad (23)$$

$$M = \delta_{lat} V = \delta_{lat} M_{tip} * g \quad (24)$$

$$s_p = \left(\frac{d_b - d_t}{H} \right) \quad (25)$$

When the law of conservation of energy is used to obtain the differential equation of motion for an undamped system in free vibration, the so-called Rayleigh's method is derived to find the natural frequency, by equalizing the maximum kinetic energy to the maximum potential energy (at different specific instants); but for this, it is necessary to assume a deformed shape. Usually, the shape is determined as that produced by the gravitational loads acting in the direction of the expected displacements [5, 6]. The natural frequency is expressed as,

$$f = \frac{1}{2\pi} \sqrt{\frac{g \sum_i W_i \delta_i}{\sum_i W_i \delta_i^2}} \quad (26)$$

where δ_i is deflection at the coordinate i and W_i is the concentrated weight at this coordinate.

Holmes [2] uses a semi empirical formula for cantilevered tapered circular tower, that was also recommended by the European Convention for Structural Steelwork in 1978, given by

$$f = \frac{\lambda}{2\pi H^2} \sqrt{\frac{E I_b}{m_b}} \quad (27)$$

$$\lambda = 1,9 * \exp\left(\frac{-4d_t}{d_b}\right) + \frac{6,65}{0,9 + (e_t/e_b)^{0,666}} \quad (28)$$

Another simplified expression is presented in the Annex F of EN 1991-1-4 [3],

$$f = \frac{1}{2\pi} \sqrt{\frac{g}{\delta_{w,max}}} \quad (29)$$

where $\delta_{w,max}$ is the maximum displacement (expressed in meters) due to self-weight applied in the vibration direction.

3 TOWER AND INVESTIGATION DESCRIPTION

To determine the natural frequency of a structure, there are three main approaches: theoretical calculation, application of the finite element method (FEM) using robust computational software, and experimental determination on the real structure. In general, the FEM method and the experimental determination show more accurate results, but they are also more expensive to achieve and perform.

To analyze the accuracy of the simplified models in determining the first natural frequency of conical hollow towers, the results of the formulations presented in the literature review are compared to the numerical FEM model and the experimental results.

3.1 Description of the tower

A metal tower 17.8 m height located at the School of Technology and Management of the Polytechnic Institute of Bragança (Portugal), consists of a steel S275 structure with a hexadecagonal section with an outside diameter of 0.5890 m at the base and 0.1954 m at the top, with a constant wall thickness of 4 mm. The tower is fixed to the gravity-base foundation by 16 anchor bolts connected to a flange at the base; the flange has an external diameter of 0.7960 m and a thickness of 20 mm. The main properties of the tower are presented in Table 1, and the geometric plan view configuration is shown in Figure 1.

Density	7850.000	[kg/m ³]
Young's modulus	210.000	[GPa]
Poisson's ratio	0.300	--
Yield strength	275.000	[MPa]
H	17.800	[m]
d_t	0.195	[m]
d_b	0.589	[m]
d_m	0.392	[m]
s_p	22.135x10 ⁻³	
$d(z)$	0.589 – 22.135x10 ⁻³ z	[m/m]
$e_b = e_t = e$	0,004	[m]
$A(z)$	0,765(9,36 – 0,35376z)10 ⁻³	[m ² /m]
$m(z)$	6,008(9,36 – 0,35376z)	[kg/m]
$I(z)$	(2,987 – 0,339z + 0,013z ² – 1,612x10 ⁻⁴ z ³)10 ⁻⁴	[m ⁴ /m]
M_{tip}	75,000	[kg]
M_{tower}	664,277	[kg]

Table 1: Tower properties

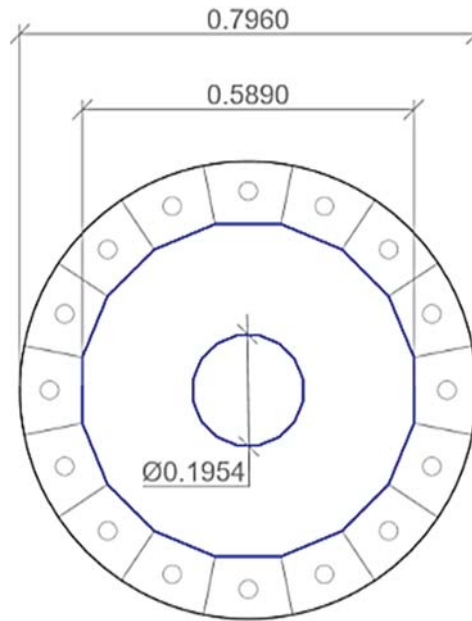


Figure 1 : Tower geometries.

3.2 Numerical model

The analysis of the structure using the finite element method is performed using the SAP2000 Software. The tower is modeled with the geometry presented above, considering the bottom boundary condition of the type BC1f (CEN, 2010) [3] for the location of the 16 anchor bolts; the top boundary is considered free with the action of a tip mass of 75 kg that corresponds to the weight of the wind turbine. The simulation is performed considering the linear behavior of the material.

3.3 Experimental analysis

To determine the dynamic characteristics of the structure, the experimental modal analysis was carried out using: a data acquisition system composed of NI USB-4431 data acquisition board with 4 input channels, 24-bit ACD resolution, sampling rate from 1 kS/s to 102.4 kS/s, resolution 2.10 mS/s; piezoresistive accelerometer ICP® with a frequency range from 0.5 to 2000 Hz; and a laptop with SignalExpress © software.

Two accelerometers are placed at 1.41 meters high in two distinct perpendicular directions (x and y). The input force is caused by the impact hammer PCB 086b20. The first (and others, if required) natural frequency is defined by the peak-picking technique.

3.4 Summary of analysis

In Table 2 are synthesized the methodologies used in this work for the determination of the WTT fundamental frequency, ranging from several simplified formulations presented in the literature to the numerical model and experimental analysis; some formulas require the use of a software to find the displacement, in which case the FTOOL software was use.

Equation	Stiffness parameters	General parameters	Name/reference
$f = \frac{1}{2\pi} \sqrt{\frac{K_L}{M_{tip} + \alpha M_{tower}}}$	$K_L = \frac{3EI_m}{H^3}$	$\alpha = 0,25$	DNV-OS-J101
		$\alpha = 0,5$	IEC 61400-1
		$\alpha = 33/140$	Blevins, 1979
$f = \frac{1}{2\pi} \frac{\lambda^2}{H^2} \sqrt{\frac{EI}{m}}$	$I = I_m$	$1 + \cos \lambda \cosh \lambda$ $m = m_m$	Characteristic equation
		$1 + \cos \lambda \cosh \lambda + \frac{\lambda M_{tip}}{mH} [\cos \lambda \sinh \lambda - \sin \lambda \cosh \lambda]$ $m = m_m$	Characteristic equation + M_{tip}
$f = \frac{1}{2\pi} \sqrt{\frac{K^*}{M^*}}$		$N(z) = g M_{tip}$	SDOF reduction
$f = \frac{1}{2\pi} \sqrt{\frac{K}{M}}$	$K = \frac{1}{\delta_{unit}}$	$\delta_{unit} = \delta_{lat} + \delta_{vert}$ $M = 3,19 d_m e H \rho$	Balagopal, 2018
		δ_{unit} – Ftool 1 segments d_m $M = M_{tip} + M_{tower}$	
$f = \frac{1}{2\pi} \sqrt{\frac{g \sum_i W_i \delta_i}{\sum_i W_i \delta_i^2}}$		δ_i – Ftool 10 segments $d_{m,i}$	Rayleigh's method
$f = \frac{\lambda}{2\pi H^2} \sqrt{\frac{EI_b}{m_b}}$		$\lambda = 1,9 * \exp\left(\frac{-4d_t}{d_b}\right) + \frac{6,65}{0,9 + (e_t/e_b)^{0,666}}$	Holmes, 2011
$f = \frac{1}{2\pi} \sqrt{\frac{g}{\delta_{w,max}}}$		$\delta_{w,max}$ – Ftool 1 segments d_m	EN 1991-1-4
f		FEM	SAP2000
f		Experimental	EMA – Hammer impact

Table 2: Analysis summary

4 RESULTS AND DISCUSSION

The advantage of using a finite element model is the determination of the mode shapes of the structure, as the fundamental or 1st mode shape shown in Figure 2(a). As mentioned in Paz and Kim [5], the accurate determination of the mode shapes is one of the crucial points for the correct calculation of the frequency by the application of SDOF reduction [5]. Figure 2 (b) compares the FEM mode shape and the approximate mode shape given by Eq. 16.

In relation to the results of the experimental analysis, the power spectra density is presented in Figure 3 (a) for the x-direction and in Figure 3 (b) for the y-direction. As shown, the first natural frequency is coherently evaluated as 1.610 Hz.

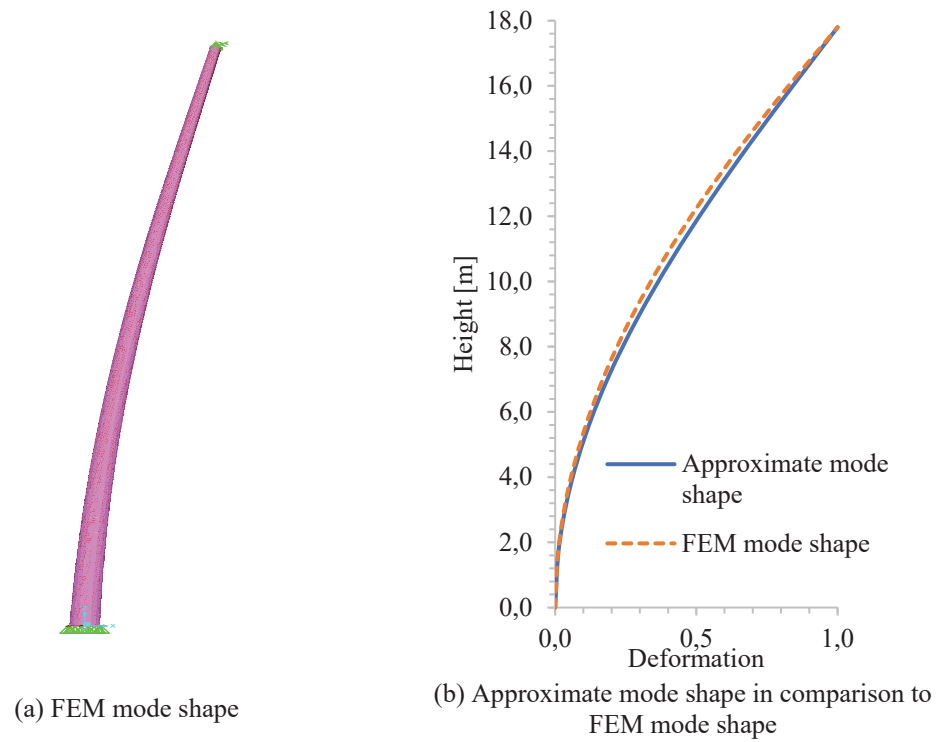


Figure 2: Tower mode shapes

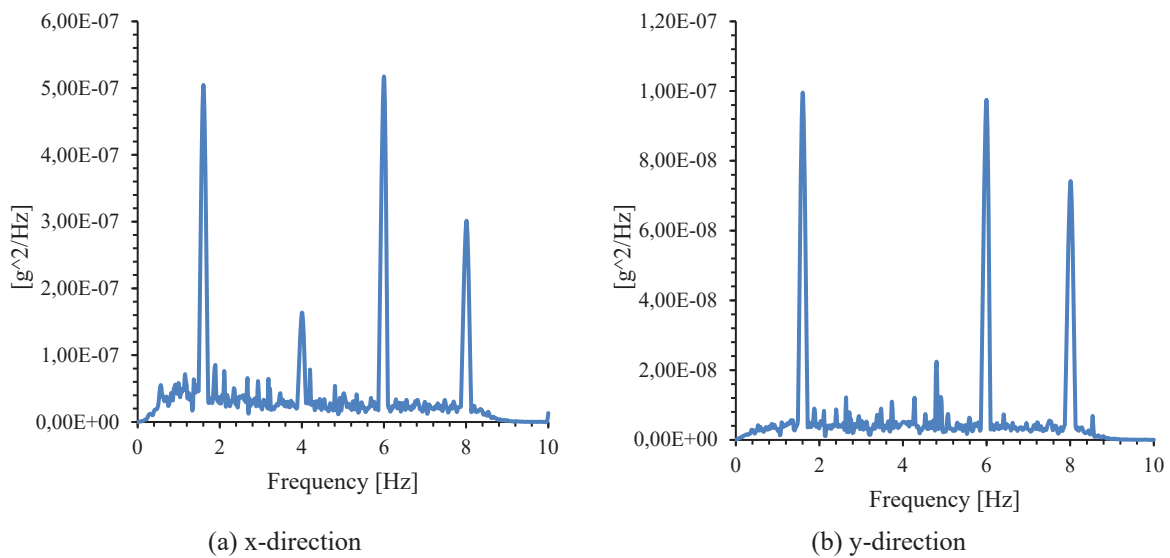


Figure 3: Power spectral density

The values obtained by the different methods for the first natural frequency are shown in Figure 4. It is possible to observe a large dispersion of results with relative differences in the order of 50%, in comparison with the experimental value; this is due to the fact that most of the formulations are established for a tower of constant mass and constant inertia per unit length. Although they are simplifications, the problem lies mainly in the definition of the inertia to be used, since it varies cubically.

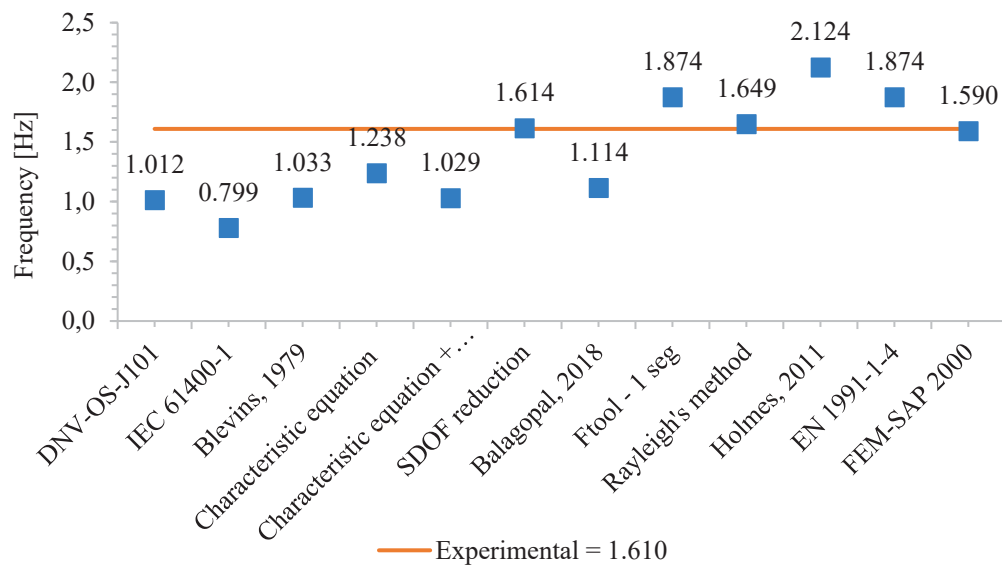


Figure 4: First natural frequency, by different methodologies

It is observed that the simplified models that present the results closest to the experimental value are the FEM model, the Rayleigh method and the SDOF reduction method; however the first two methods require the use of software, and are more time consuming. The difficulty in applying the SDOF reduction method consists in solving the integrals, but they are easily solved with a graphic scientific calculator; in fact this method presents the best results when analyzing the frequency value and the time taken to calculate it.

Notice that the vast majority of results by different methods underestimate the value of the fundamental frequency, that is, consider the structure more flexible than it really is. This is mainly due to consider the inertia and the mass defined in the first half of the structure (up to $H/2$), and because the tower having a conical or tapered shape its mass is more concentrated near the base. Also the results of the expressions using the displacement value at the top distributed by a simplified model of average diameter in the FTOOL, overestimate the frequency value by about 16%.

5 CONCLUSIONS

The metallic hollow cantilever tapered tower analyzed has the first natural frequency of 1.61 Hz. This frequency can be accurately evaluated by the application of the finite-element model, even though this method is time consuming. The Rayleigh's method also shows accurate result for the WTT analyzed; but the single degree of freedom reduction method is the simplified method that has the best performance, since it is simple and the result is accurate.

The analysis shows that the main difficulty of simplified formulas is the determination of the moment of inertia and mass, which significantly affect the results. The results show large difference between the frequencies analytically evaluated by different methods (with values in a range of 0.8 to 2.12 Hz), some of them with a significant difference from the real natural frequency, and the majority of them underestimate the value of the frequency.

The dispersion of the results reflects the importance of accurate assessment of the structural inertia and mass on the use of simplified methods, for tapered tower with tip mass; nevertheless further investigation, on the accurate estimation of mass and inertia for the tapered towers, should be carried out.

ACKNOWLEDGEMENTS

This paper is within the scope of the first author's Ph.D. degree in progress, financially supported by the Portuguese Foundation for Science and Technology (FCT) through the PhD grant reference SFRH/BD/147789/2019 under the programme POCH (N2020 – P2020) and subsidized by the European Social Fund (FSE) and national funds from MCTES. This work was financially supported by: Base Funding - UIDB/04708/2020 of the CONSTRUCT - Instituto de I&D em Estruturas e Construções - funded by national funds through the FCT/MCTES (PIDDAC).

REFERENCES

- [1] Y. Y. Ko, A simplified structural model for monopile-supported offshore wind turbines with tapered towers. *Renewable Energy*, vol. 156, 777–790, 2020, doi: 10.1016/j.renene.2020.03.149.
- [2] J. Holmes, *Wind Loading of Structures (Third Edition)*. 2015.
- [3] CEN, Eurocode 1: Actions on structures - Part 1-4: General actions - Wind actions, 2010.
- [4] R. C. Barros, Dimensionamento estrutural de mastros metálicos. *Revista Internacional de Métodos Numéricos Para Cálculo y Diseño En Ingeniería*, vol. 18, 3, 351–365, 2002.
- [5] M. . Paz, Y. H. Kim, *Structural dynamics: theory and computation*, 6th ed., vol. 38, 10. Springer, 1985.
- [6] W. T. Thomson, *Teoria da vibração*. Rio de Janeiro: Editora Interciência, 1978.
- [7] DNV, DNV-OS-J101 Design of Offshore Wind Turbine Structures. 212–214, 2014.
- [8] IEC, Wind turbines – Part 1: Design requirements, IEC 61400-1. *IEC*, Geneva, Switzerland, 2014.
- [9] R. D. Blevins, *Formulas for natural frequency and mode shape*. 1979.
- [10] J. Genov, B. Gilev, Y. Slavchev, and G. Venkov, “Modeling and control of wind Turbine tower vibrations,” *AIP Conference Proceedings*, vol. 1293, 30–38, 2010, doi: 10.1063/1.3515600.
- [11] M. D. Greenberg, *Advanced Engineering Mathematics*, 2nd ed. Upper Saddle River, NJ: Prentice Hall, 1998.
- [12] A. Erturk, D. J. Inman, Appendix C: Modal Analysis of a Uniform Cantilever with a Tip Mass. *Piezoelectric Energy Harvesting*, 353–366, 2011, doi: 10.1002/9781119991151.app3.
- [13] R. W. Clough, J. Penzien, *Dynamics of structures*, 3rd Edition. Berkeley: Computers & Structures, Inc., 2003.
- [14] R. Balagopal, N. Prasad Rao, R. P. Rokade, Simplified Model to Predict Deflection and Natural Frequency of Steel Pole Structures. *Journal of The Institution of Engineers Ser. A*, vol. 99, 3, 595–607, 2018, doi: 10.1007/s40030-018-0298-3.
- [15] ASCE, *Design of steel transmission pole structures*, no. 48–11. 2011.

FINITE ELEMENT MODEL CALIBRATION EFFECTS ON THE STATIC AND DYNAMIC RESPONSE OF A METALLIC HOLLOW TOWER

Dick Anelise¹, Carneiro-Barros Rui¹, and Braz-César T. Manuel²

¹ CONSTRUCT, Faculdade de Engenharia, Universidade do Porto
FEUP, Porto, Portugal
{anelise.dick, rcb}@fe.up.pt

² CONSTRUCT, Instituto Politécnico de Bragança
IPB, Bragança, Portugal
brazcesar@ipb.pt

Abstract

Analysis and modeling of structures, under the influence of dynamic loads, is usually carried out through the application of the finite element method (FEM). These analyses are intrinsically dependent on the parameters considered in the model, and the parameters must translate the real properties of the structure so that the model's behavior is reliable as compared with the physical behavior of the structure; for these purposes the model calibration using experimental data aims to improve the uncertainty of model parameters or inaccuracies in modeling.

In the present work a numerical analysis was carried out, on a small wind turbine metallic hollow tower with hexa-decagon section and 17.80m high, applying the finite element theory with SAP2000® software. The FEM model was updated with the frequency results of in-situ vibration tests; to compare the results, two methods Experimental Modal Analysis (EMA) and the Operational Modal Analysis (OMA) were applied in the experimental tests to evaluate the dynamic properties of the tower.

It is noticed that the first frequency of the model without calibration has a value of 2.129 Hz that is 32,2% above the real measured 1.610 Hz; after calibration update, the first frequency of the tower has a value of 1.590 Hz consistent with the results of the vibration tests. The static response of the structure to loading at the top, also shows a significant difference between the uncalibrated and the calibrated model: after calibration there is a 25% increase in displacement at the top of the structure; the compression force is the one with the smaller differences, while the base shear and base moments increased tremendously but maintained the location of points of maximum stresses.

Keywords: Finite element model calibration; Ambient vibration test; Impact hammer test; hollow tapered tower; Small wind turbine tower.

1 INTRODUCTION

Developing and improving sustainable and affordable energy production systems is one of today's engineering concerns. Wind energy is one of the sources of renewable energy that has been recently continuously studied, also with the purpose of optimizing the costs of installation and production. The wind turbine tower WTT is a part of the system that affects production efficiency and is usually a slender and flexible structure; it is considered the critical part of the wind turbine, since it should support the dead loads of equipment and additional loads caused by wind. The wind turbine tower has two crucial functions: supports in the height the rotor nacelle system in the height and transfer the loads' action on the structure to the foundation.

The analysis and modeling of these type of structures, under the influence of dynamic loads, is usually achieved through analytical computational modeling techniques, on the application of the finite element method (FEM). These analyses are intrinsically dependent on the values chosen for the parameters considered in the model, which must translate the real properties of the structure so that the model's behavior is reliable as the physical behavior of the structure.

In complex structures, the model generally consists of some simplification of the structure, but it must adequately represent the real structure; so there is a need to validate the numerical model with test results in real structures, to adjust the parameters used. Adjusting the analytical model using experimental data is known as model calibration in structural dynamics, and aims to improve the uncertainty of model parameters or inaccuracies in modeling.

To determine the dynamic characteristics of a structure, there are two experimental methods accessible: Experimental Modal Analysis (EMA) and Operational Modal Analysis (OMA); and the main difference between these methods, is the need or not for a controlled excitation source. In EMA, it is necessary to know the excitation force and the response of the structure; on the other hand, in OMA only the response of the structure is measured. In fact, for general structures OMA is largely more applied -- as in bridges [1]–[7], tall or quite specific buildings [8]–[11] and towers [12]–[14] – for example through structural health monitoring associated with series of ambient vibration measurements.

In the case of dynamic excitations in towers of major wind turbines, there are several studies in the bibliography that compared analytical and experimental results [15]–[18]; for such it is common to use the NREL 5MW wind turbine as the object of study [19]–[22], and then apply different techniques of dynamic tests and structural monitoring.

However, when it comes to small wind turbines, those that have a rotor swept area smaller than 200 m², comparative studies are limited. Castellani et al. [23] calibrated and updated the parameters of a small wind turbine using the power spectra density, function of major excited frequencies, evaluated with an impact hammer test in a prototype tower for wind tunnel test; but in his work, the main objective was the study of the wind turbine. In the present work a numerical analysis was carried out, on a small wind turbine metallic hollow tower with hexa-decagonal section and 17.80 meters high, applying the finite element method with SAP2000 software and using the results of dynamic vibration tests in the real tower to calibrate the model.

2 DESCRIPTION OF THE TOWER

The analyzed metal tower is located at the School of Technology and Management of the Polytechnic Institute of Bragança (Portugal), consists of a steel structure with the height of 17.81 m, having a hexa-decagonal section with an outside diameter of 0.5890 m at the base and 0.1954 m at the top, and with constant wall thickness of 4 mm. The tower is fixed to the gravity-base foundation by 16 anchor bolts connected to a flange at the base; the flange has an external diameter of 0.7960 m and a thickness of 20 mm.

The designed tower structure has a straight geometric configuration as shown in Fig. 1 (a); but the real tower structure presents an initial out-of-straightness with a total offset of 0.122 m at the top in relation to the axis of the tower, as shown in Fig. 1 (b). The tower is produced from S275 steel whose properties and design characteristics were established in accordance with the Eurocode 3 [24]; considering the thickness $t \leq 4$ mm, the properties are shown in Table 1. The computational simulations using FEM considered the linear behavior of the material.

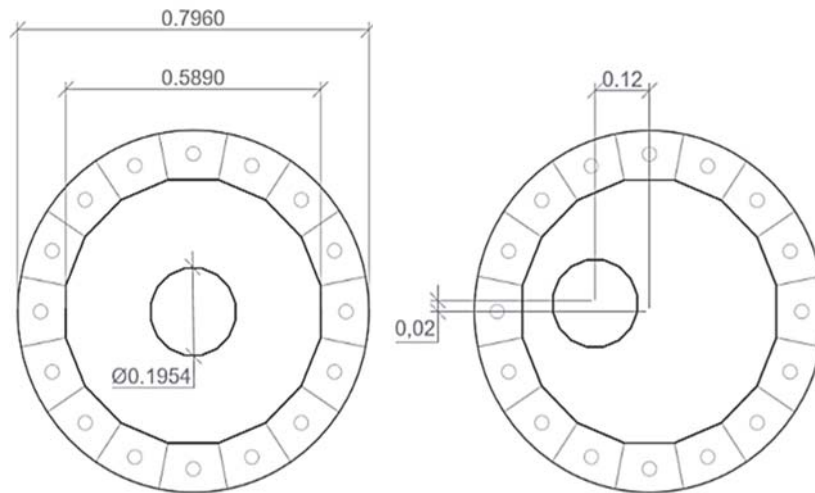


Figure 1. Tower geometries. (a) Straight tower, (b) Crooked tower.

	Linear	
Density	7850	[kg/m ³]
Young's modulus	210	[GPa]
Poisson's ratio	0.3	--
Yield strength	275	[MPa]
Ultimate strength	430	[MPa]

Table 1 : Steel S275 properties.

2.1 In situ vibration measurement

To determine the dynamic characteristics of the structure two methods were applied in the studied tower: EMA and OMA.

Measurements associated with the experimental modal analysis were carried out using: a data acquisition system composed of NI USB-4431 data acquisition board with 4 input channels, 24-bit ACD resolution, sampling rate from 1 kS/s to 102.4 kS/s, resolution 2.10 mS/s; piezoresistive accelerometer ICP® with a frequency range from 0.5 to 2000 Hz; and a laptop with SignalExpress © software.

Firstly, the dynamic load test was performed with two accelerometers placed at 1.41 meters high in two distinct perpendicular directions (x and y). The input excitation force is caused by the impact hammer PCB 086b20. The first (and others, if required) natural frequency is defined by the peak-picking technique.

The power spectra density (PSD) functions associated with this EMA is presented in Figure 2(a) for the x-direction and in Figure 2(b) for the y-direction.

The average values of the first three eigenfrequencies, in one direction, were obtained: 1.610 Hz for the first natural vibration frequency, 5.990 Hz for the second natural frequency, and 8.010 Hz for the third natural frequency.

As the structure is mainly symmetric, these frequencies for the two measured directions (x and y) are practically considered the same, as is possible to verify in the given PSD's.

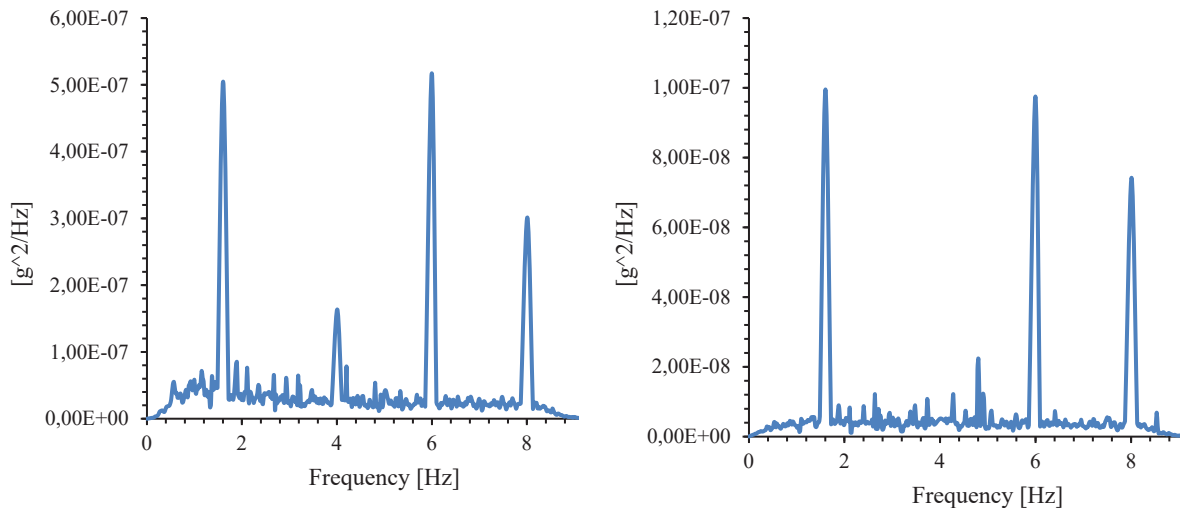


Figure 2 : PSD -- EMA. (a) x-direction, (b) y-direction

The ambient vibration testing associated with OMA was carried out for 20 minutes records, with the same location of the two accelerometers, and was executed three times. During the test, the average wind speed was 1.333 m/s in the SWW direction, with a peak velocity of 4.92 m/s in the S direction. As it is possible to verify in the PSD's presented in Figure 3, the external excitation was not capable to excite all the range of structural frequencies, so it is only possible to determine the first frequency that is congruent with the EMA results.

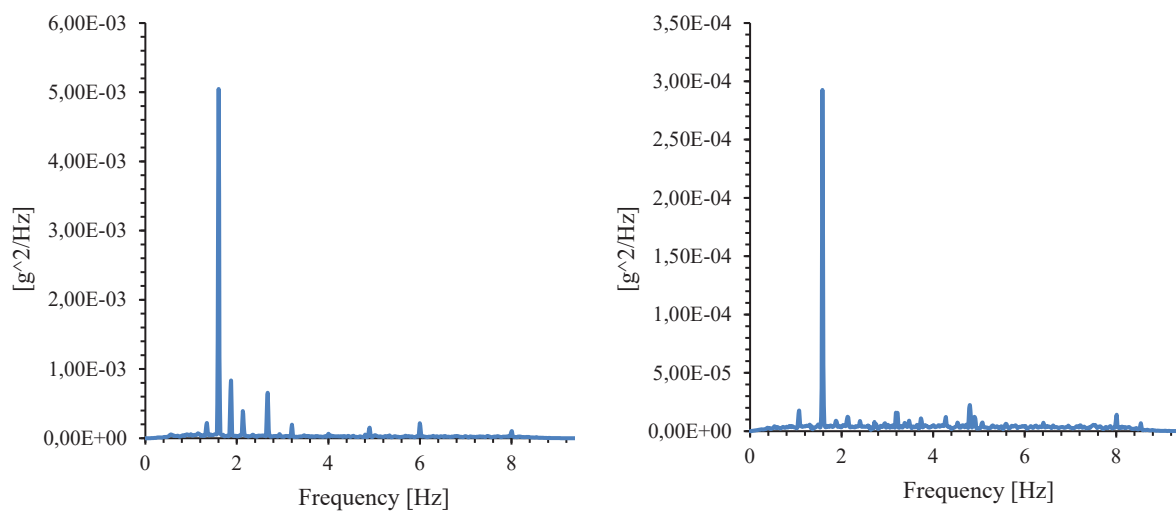


Figure 3 : PSD -- OMA. (a) x-direction, (b) y-direction

3 NUMERICAL MODEL

The analysis of the structure using the Finite Element Method (FEM) is performed using the SAP2000 software. Initially, the model consists of a straight tower with the geometry presented above, including wind turbine's weight as a static boundary condition corresponding to a concentrated mass at the top of the tower. The boundary conditions assumed in the analysis must be chosen in such a way as to guarantee and achieve a realistic or conservative model of the actual structure. According to Eurocode 3 - Part 1-6 [3] the upper extremity is a free boundary condition (type BC3), and for the first model the lower extremity boundary condition is considered rigid (type BC1r, infinity support for which any type of movement is prevented).

Although FEM is a powerful tool for engineers, some aspects need to be verified carefully and the refinement of the mesh should be checked to avoid unrealistic local behavior; also the mesh should satisfy the so-called patch test. Figure 4 displays the frequency convergence of the model according to the number of elements, so the ideal mesh for the first FEM model divides the tower into 76800 elements; for such first model the converged fundamental frequency was evaluated as 2.12965 Hz.

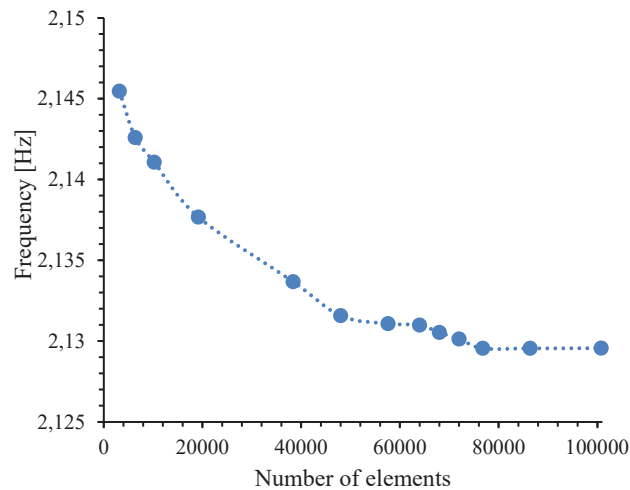


Figure 4 : Frequency convergence

3.1 Finite element method model updating procedure

The FEM model generally consists of a simplification of the structure, corresponding to some assumptions made, but it must adequately represent the real structure; so there is a need to validate the numerical model with test results in real structures, to adjust the parameters used. The procedure of adjusting the analytical or computational model using experimental data is known as a model calibration or model updating in structural dynamics; it aims to improve the uncertainty of model parameters or inaccuracies in modeling, that originate the uncertainties in simplifying assumptions of the structural geometry, materials, and even of inaccurate boundary conditions [25].

The comparison between the results of the experimental dynamic tests (EMA-OMA), the initial FE model and the updated FE models, are shown in Table 2.

	Experimental	Initial FEM	1 st update	2 nd update	3 rd update
First frequency [Hz]	1.610	2.129	1.732	1.724	1.590
Second frequency [Hz]	5.990	8.881	7.668	6.898	6.330

Table 2 : Results of experimental and analytical modal identification and modification of structure parameters

As the first frequency of the model 2.12965 Hz does not match with the measured 1.61 Hz frequency, the first model update was the inclusion of the flange and the change of the lower boundary condition, applying boundary condition of the type BC1f [26] (only rotation is free) in the location of the 16 bolts. The second updating was the consideration of the out-of-straightness of the tower and the eccentricity of the wind turbine. Even though the frequency is still above the real one, as the structure presents a service ladder and its equivalent mass was not considered in the numerical model, it is responsible for altering the inertia of the structure; so the last change or third updating, was to consider that equivalent mass through a factor. Now the first frequency of the model is the same as the measured one, and the model is considered calibrated. Even though the second frequency is not exact, it is very close and the final upgrade of the initial FE model produced a quite good agreement with the experimental results. The first frequency value shows a reduction about 25% from de non calibrated model to the calibrated one, and in Figure 5 it is possible to observe the change in the form of the mode shapes.

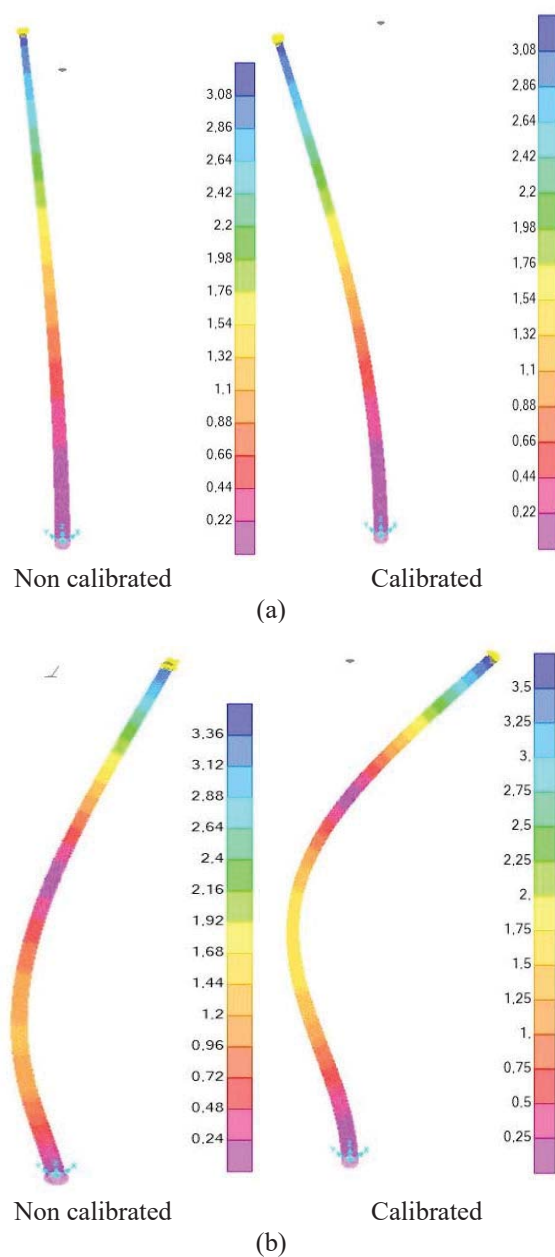


Figure 5 : Changed form of the mode shapes. (a) first mode, (b) second mode

3.2 Static analysis

To evaluate the effects of the calibration upgrading in a static analysis, the external forces acting on the top of the tower that are induced by the wind turbine were determined according to DNV guidelines [27]. For simplification, the wind force acting laterally on the tower was not considered in this analysis.

The aerodynamic drag force produced by the blades on the top of the tower can be predicted by simplified calculations based on the projected area perpendicular to the flow. The rotor loads are expressed by three load quantities: static horizontal airflow (Eq. 1), driving torque (Eq.2) and weight of the rotor.

$$F_0 = 300 \cdot A \quad (1)$$

$$M_{e,nom} = \frac{P_{nom}}{2\pi n_l \eta} \quad (2)$$

where A is the swept area of the rotor in (m^2), P_{nom} is the nominal power of the wind turbine, n_l is the rotor frequency and η the nominal efficiency.

The wind turbine supported by the tower is a Fortis Passat (1.4 kW) and the characteristics are presented in Table 3 including static loads predicted on top of the tower.

Fortis Passat (1.4 kW)			
Gravitational acceleration	g	9.8066	[m/s ²]
Rotor blade radius	r	1.5	[m]
Area of rotor	A	7.65	[m ²]
Rotor mass	m	75	[kg]
Rotor frequency	n_l	3	[Hz]
Nominal power of wind turbine	P_{nom}	1400	[W]
Nominal efficiency	η	0.7	
Calculations			
Static horizontal airflow load	F_0	2295.000	[N]
Driving torque	$M_{e,nom}$	106.103	[N.m]
Eccentricity	e	0.250	[m]
Static load			
Moment about horizontal axis rotor plane	M_x	573.750	[N.m]
Horizontal force along rotor axis	F_y	2295.000	[N]
Moment about axis rotor	M_y	137.934	[N.m]
Vertical force	F_z	-735.495	[N]
Moment about vertical axis	M_z	573.750	[N.m]

Table 3 : Simplified load calculations on top of the tower

The structural analysis results shown in Table 4 for top displacements and generalized stress resultants, before and after model calibration updating and upgrading, indicate the differences between the correct calibrated model and the initial model; the most important differences occur for the maximum base shear force and the maximum and minimum base moments.

	Initial FEM	Final FEM	Difference (%)
First frequency [Hz]	2.129	1.590	-25.32
Top displacement [m]	0.146683	0.196223	25.25
Fmax [kN]	1156.488	1323.539	14.44
Fmin [kN]	-1213.27	-1430.88	17.94
Vmax [kN]	5.676	488.543	8507.17
Mmax [kN.m]	0.101	17.997	17718.81
Mmin [kN.m]	-0.096	-19.497	20209.38

Table 4 : Comparison of results before and after model calibration updating

Figure 6 shows that the points of maximum stresses are the same in both models, however, the intensity of the stress is much larger in the calibrated model.

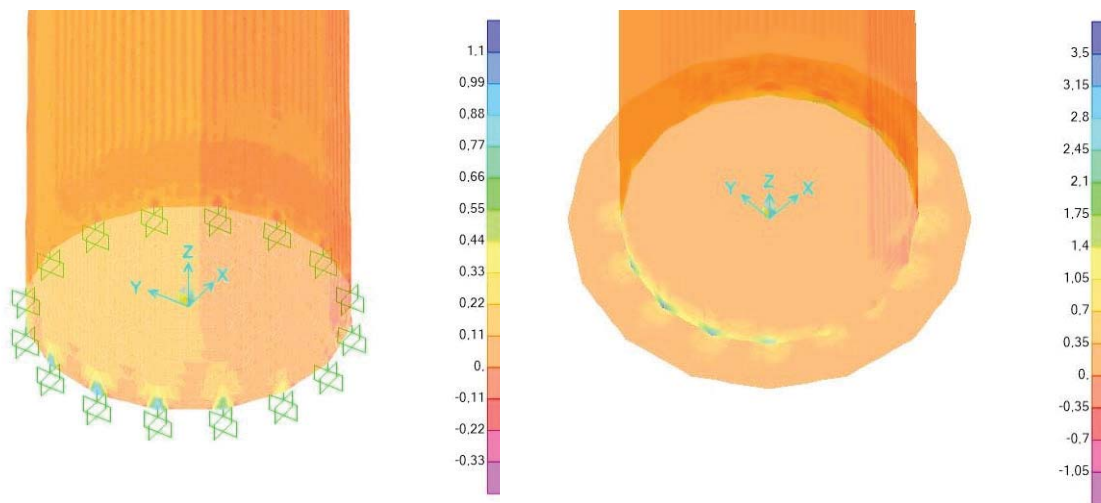


Figure 6 : Normalized maximum stress. (a) non calibrated, (b) calibrated model.

4 CONCLUSIONS

In this paper, modal testing and finite element model updating of a steel hollow tapered tower were presented. A 3D finite element model of the tower was developed using the SAP2000 software. Dynamic tests were performed using the impact hammer technique and also ambient vibration testing, in order to extract the natural frequencies of the tower. The FEM model was calibrated changing the boundary conditions, but also including some geometric characteristics complemented by better detailing of some uncertain modeling parameters.

Based on the results of this study, the following conclusions can be made with respect to differences in dynamic characteristics: reduction of 25% in the first natural frequency of the tower from the initial FEM model to the final calibrated model, and a reduction of 29% for the second natural frequency; considerable changes in the form of the 1st and 2nd mode shapes. With respect to differences in the static behavior of the structure, results showed: a 25% increase in tower top displacement; the compression force is the one with the smaller differences, with an increase of around 14% to 18% in maximum and minimum values; the major differences in calculated values occur in the base shear and the base moment values, with increases ranging from 8500% to 20200% but maintaining the location of the points of maximum stresses.

These results show the importance and the need of calibrating FEM numerical models to properly represent the real dynamic behavior of the steel structures.

ACKNOWLEDGEMENTS

This paper is within the scope of the first author's Ph.D. degree in progress, financially supported by the Portuguese Foundation for Science and Technology (FCT) through the PhD grant reference SFRH/BD/147789/2019 under the programme POCH (N2020 – P2020) and subsidized by the European Social Fund (FSE) and national funds from MCTES. This work was financially supported by: Base Funding - UIDB/04708/2020 of the CONSTRUCT - Instituto de I&D em Estruturas e Construções - funded by national funds through the FCT/MCTES (PIDDAC).

REFERENCES

- [1] I. Roselli, M. Malena, M. Mongelli, N. Cvalagli, M. Giofrè, G. Canio, G. Felice, Health assessment and ambient vibration testing of the 'Ponte delle Torri' of Spoleto during the 2016–2017 Central Italy seismic sequence, *Journal of Civil Structural Health Monitoring*, Vol. 8, 2, 199–216, 2018, doi: 10.1007/s13349-018-0268-5..
- [2] A. Brencich, D. Sabia, Experimental identification of a multi-span masonry bridge: The Tanaro Bridge. *Construction and Building Materials*, Vol. 22, 10, 2087–2099, 2008, doi: 10.1016/j.conbuildmat.2007.07.031.
- [3] H. Wang, A. Q. Li, J. Li, Progressive finite element model calibration of a long-span suspension bridge based on ambient vibration and static measurements, *Engineering and Structures*, vol. 32, 9, 2546–2556, 2010, doi: 10.1016/j.engstruct.2010.04.028.
- [4] G. Boscato, A. Dal Cin, Experimental and numerical evaluation of structural dynamic behavior of Rialto Bridge in Venice. *Journal of Civil Structures and Health Monitoring*, vol. 7, 4, p 557–572, 2017, doi: 10.1007/s13349-017-0242-7.
- [5] D. Ribeiro, P. Jorge, C. Costa, R. Silva, A. Arêde, and R. Calçada, Calibração experimental de modelos numéricos de pontes ferroviárias em alvenaria de pedra. *XXXVII Iberian Latin American Congress on Computational Methods in Engineering*, 20, 2016
- [6] B. Sevim, A. Bayraktar, A. C. Altuniik, S. Atamtürktür, F. Birinci, Finite element model calibration effects on the earthquake response of masonry arch bridges. *Finite Element Analysis and Design*, vol. 47, 7, 621–634, 2011, doi: 10.1016/j.finel.2010.12.011.
- [7] A. C. Altunişik, A. Bayraktar, B. Sevim, F. Birincia, Vibration-based operational modal analysis of the mikron historic arch bridge after restoration. *Civil Engineering and Environmental Systems*, vol. 28, 3, 247–259, 2011, doi: 10.1080/10286608.2011.588328.
- [8] C. E. Ventura, J.F. Lord, and R. D. Simpson, Effective Use of Ambient Vibration Measurements for Modal Updating of a 48 Storey Building in Vancouver, Canada. *International Conference on Structural Dynamics Modeling–Test, Analysis, Correlation and Validation*, 1–10, 2002.
- [9] M. Baptista, P. Mendes, A. Costa, A. Afilhado, P. Silva, C. Oliveira, Análise experimental para a obtenção das características dinâmicas do edifício da Portugal Telecom no Parque das Nações, *6º Congresso Nacional de Sismologia e Engenharia Sísmica - Sísmica 2004*, Aveiro, Portugal, vol. 2, 1–9, 2004.

- [10] M. Pieraccini, D. Dei, M. Betti, G. Bartoli, G. Tucci, N. Guardini, Dynamic identification of historic masonry towers through an expeditious and no-contact approach: Application to the ‘Torre del Mangia’ in Siena (Italy). *Journal of Cultural Heritage*, vol. 15, 3, 275–282, 2014, doi: 10.1016/j.culher.2013.07.006.
- [11] A. Demir, H. Nohutcu, E. Ercan, E. Hokelekli, G. Altintas, Effect of model calibration on seismic behaviour of a historical mosque. *Structural Engineering and Mechanics*, vol. 60, 5, 749–760, 2016, doi: 10.12989/sem.2016.60.5.749.
- [12] M. Pavlovic, S. Trevisani, A. Cecchi, A Procedure for the Structural Identification of Masonry Towers, *Journal of Nondestructive Evaluation*, vol. 38, 2, 1–12, 2019, doi: 10.1007/s10921-019-0575-8.
- [13] M. Girardi, C. Padovani, D. Pellegrini, L. Robol, A finite element model updating method based on global optimization. *Mechanical Systems and Signal Processing* 107372, 2020, doi: 10.1016/j.ymssp.2020.107372.
- [14] G. Saudi, Structural assessment of a guyed mast through measurement of natural frequencies. *Engineering Structures*, vol. 59, 104–112, 2014, doi: 10.1016/j.engstruct.2013.09.049.
- [15] A. F. Mensah, L. Dueñas-Osorio, Improved reliability of wind turbine towers with tuned liquid column dampers (TLCDs). *Structural Safety*. vol. 47, 78–86, 2014, doi: 10.1016/j.strusafe.2013.08.004.
- [16] M. A. Lackner, M. A. Rotea, Passive structural control of offshore wind turbines. *Wind Energy*, vol. 14, 373–388, 2011, doi: 10.1002/we.
- [17] G. Oliveira, F. Magalhães, A. Cunha, E. Caetano, Dynamic monitoring system for utility-scale wind turbines: damage detection and fatigue assessment. *Journal of Civil Structures and Health Monitoring*, vol. 7, 5, 657–668, 2017, doi: 10.1007/s13349-017-0250-7.
- [18] B. Fitzgerald, B. Basu, Active tuned mass damper control of wind turbine nacelle/tower vibrations with damaged foundations. *Key Engineering Materials*, vol. 569–570, 660–667, 2013, doi: 10.4028/www.scientific.net/KEM.569-570.660.
- [19] H. Zuo, K. Bi, H. Hao, Using multiple tuned mass dampers to control offshore wind turbine vibrations under multiple hazards. *Engineering Structures*, vol. 141, 303–315, 2017, doi: 10.1016/j.engstruct.2017.03.006.
- [20] T. Gentils, L. Wang, A. Kolios, Integrated structural optimisation of offshore wind turbine support structures based on finite element analysis and genetic algorithm. *Applied Energy*, vol. 199, 187–204, 2017, doi: 10.1016/j.apenergy.2017.05.009.
- [21] Y. Y. Ko, A simplified structural model for monopile-supported offshore wind turbines with tapered towers. *Renewable Energy*, vol. 156, 777–790, 2020, doi: 10.1016/j.renene.2020.03.149.
- [22] Z. Zhang, A. Staino, B. Basu, S. R. K. Nielsen, Performance evaluation of full-scale tuned liquid dampers (TLDs) for vibration control of large wind turbines using real-time hybrid testing. *Engineering Structures*, vol. 126, 417–431, 2016, doi: 10.1016/j.engstruct.2016.07.008.

- [23] F. Castellani, D. Astolfi, M. Becchetti, F. Berno, F. Cianetti, A. Cetrini, Experimental and numerical vibrational analysis of a horizontal-axis micro-wind turbine. *Energies*, vol. 11, 2, 2018, doi: 10.3390/en11020456.
- [24] CEN, Eurocódigo 3 – Projecto de estruturas de aço Parte 1-1: Regras gerais e regras para edificios. 2010.
- [25] M. E. Arslan, A. Durmuş, Modal testing and finite element model calibration of in-filled reinforce concrete frames. *JVC/Journal Vibration and Control*, vol. 20, 13, 1946–1959, 2014, doi: 10.1177/1077546313480545.
- [26] CEN, Eurocode 3 - Design of steel structures - Part 1-6: Strength and Stability of Shell Structures, 2007.
- [27] DNV/Risø, *Guidelines for Design of Wind Turbines*. Denmark, 2002.

PARAMETRIC STUDY OF LATTICE TOWERS ON THE INFLUENCE OF WIND ACTION FOR DIFFERENT TYPOLOGIES OF BRACING

Carneiro-Barros Rui¹, and Barros R.G. Luís²

¹ CONSTRUCT, Faculdade de Engenharia, Universidade do Porto
FEUP, Porto, Portugal
rcb@fe.up.pt

² BSSE, Lda. – Porto, Portugal
luis.guimaraes.barros@gmail.com

Abstract

The telecommunications sector is a fundamental pillar of today's society. The answer to the need for constant communication is based on a network of structures, that allows the uninterrupted functioning of the communication system. Among these structures of the communication infrastructure are the so-called telecommunications towers, which are fundamental elements for the functioning of the system. Therefore, given the importance and actual demand for these structures, there is a great need for a deep knowledge of their behaviour, to find more economically viable and safer solutions. Since the wind action is in fact the most significant and conditioning for the design of this type of structures, this work focusses on the study of different bracing schemes, which were divided into three groups differing by specific parameters or even locations. Starting from a base or initial model of a lattice tower designed according to Eurocodes (EC1 and EC3), five conceptual tower models were redesigned with different lay-out schemes, but without changing the territorial location and their height and width. These models were analysed and compared to understand how different bracing schemes can affected the wind action determination and what are their consequences on the behaviour of the structures and their design.

Keywords: Lattice towers, wind loading action, EN 1991-1-4, EN 1993-3-1, parametric study on bracing.

1 INTRODUCTION

The development of today's society is also strongly linked to the ease and speed of communication and information sharing, and so it is not difficult to understand the importance of telecommunications towers, commonly present in the urban landscape and elsewhere. These structures, normally of great height, have as main objective the placement of transmission equipment on its top that allows the adequate transmission of signals. With an increasing use of mobile phones and the offer of services such as channel television, there is a greater need for the implantation of these structures to guarantee a good quality of all the services provided [1]. But despite the great importance of telecommunications towers to society, these structures exhibit statistically a higher number of failures when compared with many other structures [2]. Thus, it is essential to understand the behaviour of these structures, so that it is possible to design them as economically viable as possible, but still complying with safety criteria.

This work focusses on the study of different bracing schemes, which can be divided into three groups differing by specific parameters or even locations; a change or modification done to a specific tower parameter causes re-sizing of structural members to satisfy the structural design conditions for the tower wind actions at the implantation site [3]. Starting from a base model of a lattice tower designed according to Eurocodes (EC1 and EC3), conceptual tower models were redesigned with different lay-out of bracing schemes, but without changing the territorial location and the tower height and width. These models were analysed and compared to understand how different bracing schemes can affected the wind action determination and what are their consequences on the behaviour of the structures and their design.

2 DESCRIPTION OF CONCEPTUAL TOWER MODELS

2.1 Initial Tower Model for Reference Comparison

The initial model of the tower, predesigned by the industrial partner Metalgalva - Irmãos Silva SA according to this metalo-mechanical company experience on lattice towers and its industrial production characteristics (including delivery and assemblage at specific locations), consists of a self-supporting lattice tower with a triangular section 100 meters high and 15 meters wide at the base.

The tower can be divided into two distinct tower segments: the first or lower segment, from the base to about two thirds of the height, up to 72.5 meters, uses the K-typology scheme as the main bracing system in elevation along the height; the second or upper segment, in the last 27.5 meters, uses lattice diagonal bracing because this tower segment width is much smaller.

The diaphragms, which constitute horizontal stiffening zones or horizontal bracing systems, are spaced 6 meters apart up to 72.5 meters in height of the first tower segment; in the last 27.5 meters, the diaphragms of the second tower segment are spaced 3 meters apart.

Table 1 indicates the characteristics of the initial tower model; and Figure 1 shows the general 3D layout.

Table 1 : Characteristics of the initial tower model

Total height	100 m
Top width	3 m
Base width	15 m
Number of sub-segments (12+10)	22
Type of profile used	Circular
Steel class	S 355
Ultimate stress (f_u)	510 MPa
Yield stress (f_y)	355 MPa
Elasticity modulus (E)	210 000 MPa
Distortion modulus (G)	81 000 MPa
Poisson coefficient (ν)	0.3
Coefficient of thermal expansion (α)	$12 \times 10^{-6} / ^\circ\text{C}$

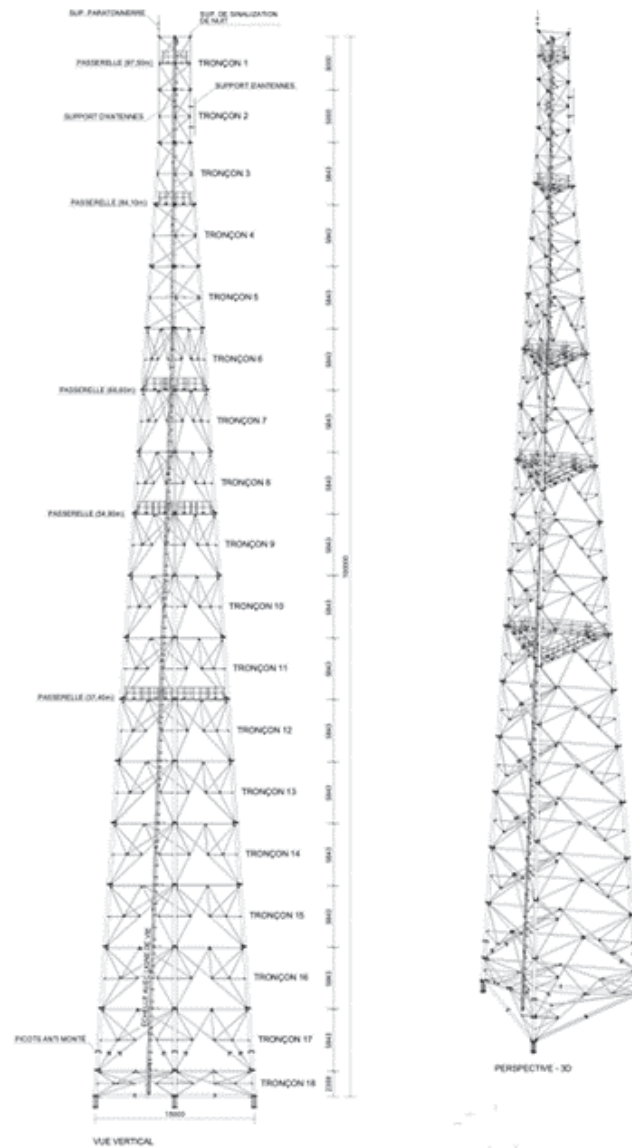


Figure 1 : Initial tower model.

2.2 Tower Model A

This tower model A (shown in Figure 2) is very similar to the initial tower model, the only change occurring in the upper tower segment with a truss system where a new circular profile member was added in the opposite direction to the existing one; therefore, making it a cross (or X) bracing system instead of the diagonal bracing of the initial tower model.

This alteration attributes a greater stiffness to the altered upper tower segment, increasing its torsional stiffness; however, with the addition of the diagonals, the exposure area to wind actions increases.

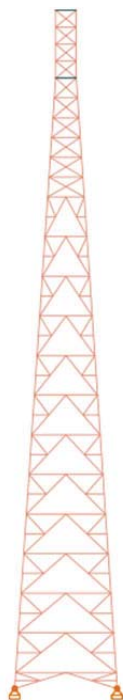


Figure 2 : Tower model A.

2.3 Tower Model B

In tower model B (shown in Figure 3 (a)), the change made consists of varying the spacing between the horizontal diaphragms bracing system. Such change occurred only in the first third part of the structure, up to 37 meters in height, and the spacing chosen between diaphragm levels is 4 meters.

2.4 Tower Model C

The tower model C (shown in Figure 3 (b)) is like tower model B, but now studying the variation of results for a chosen spacing of 5 meters between horizontal diaphragms in the first 37 meters of the tower structure; so, initial tower model has horizontal diaphragm bracing system with 6 meters spacing, while for tower models B and C, such spacing is of 4 meters and 5 meters respectively.

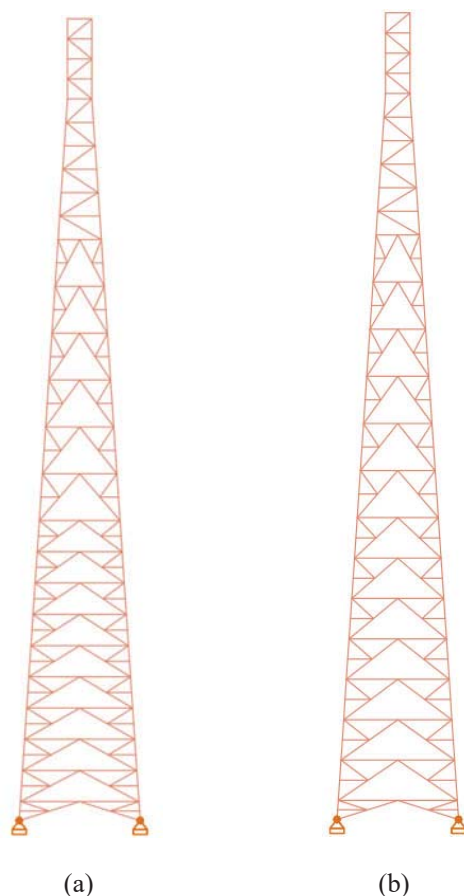


Figure 3 : (a) Tower model B ; (b) Tower model C.

2.5 Tower Model D

The development of the tower model D aims to analyse the structure's behaviour in case the main bracing system in elevation is altered in the first third part of the structure, up to 37 meters in height, from the original “K” bracing system to a discontinuous bracing system; as shown in Figure 4 (a), this tower model D still presents the continuous horizontal diaphragm bracing system at specific horizontal intersections.

2.6 Tower Model E

The tower model E shown in Figure 4 (b), like the tower model D, also aims to study how some alterations of the bracing system influences the operation of the tower, using another variation of discontinuous main bracing system in elevation. In this model tower E, the main “K” bracing system that exists in elevation in the original tower was replaced entirely up to 72.5 meters in height, by a discontinuous bracing locking system in elevation, but still with continuous horizontal diaphragm bracing system at specific horizontal intersections.

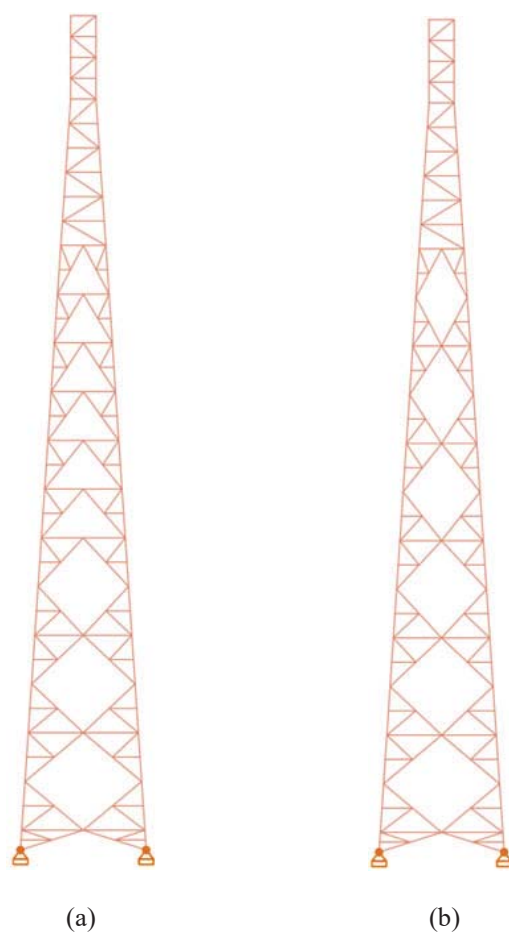


Figure 4 : (a) Tower model D ; (b) Tower model E.

In Table 2 a brief synthesis is given about the six tower models designed and analysed in this parametric study, but still complying with the metal-mechanical company experience on lattice towers and its industrial production characteristics. For each design alternative, emphasis is given to the final total weight of the tower (directly related to costs) and to the exposed area to wind in each tower face or incidence plane to wind.

Table 2 : Final weight and exposed areas, for alternative tower models

Tower label	Total weight of tower (kgf) ; 1 kgf \approx 0.01 kN	Exposed area per face (m ²)
Initial tower model	22354.13	95
Tower model A	23366.31	95.5
Tower model B	29610.04	114
Tower model C	27087.03	108
Tower model D	21928.05	93
Tower model E	21995.66	90

3 WIND ACTIONS ON THE TOWERS

The design guidelines for the regulatory normative of the wind actions on the towers, were the corresponding parts of Eurocodes EC1 and EC3 namely EN 1991-1-4 [4] and 1993-3-1 [5]. Additional comprehensive bibliography used as support were the book chapter of Barros *et al.* [6] and the article of Calostescu [7]. Also the graduation master's thesis of the second co-author [8] details the remaining expressions and calculations.

3.1 Wind velocity and dynamic wind pressure

The tower is located in Zone B mentioned in NP EN1991-1-4/NA [4], to which corresponds a reference wind base velocity of 30 m/s; the adopted orography coefficient was $c_o(z)=1$.

For ground category II, parameters z_0 and z_{min} are respectively $z_0=0.05$ m and $z_{min}=2$ m.

The turbulence coefficient K_f used, was the recommended value of 1. Using specific mass of air $\rho_{air} = 1.25 \text{ kg/m}^3$ – mentioned in clause 4.5 (1) of Eurocode 1 - EN 1991-1-4 [4] – and resorting to the expressions of EC1 [4] and EC3 [5] with respect to characterization of wind actions (by one of the two methodologies in Eurocode annexes), or to the expressions also used in the abovementioned comprehensive bibliography of Barros *et al.* [6] and Calostescu [7], Table 3 can be systematically obtained. The last two columns in this table (calculation procedure of wind actions - step I) present respectively the dynamic wind pressure (in Pa) and the wind peak velocity (in m/s) at 18 section levels (limiting distinct tower panels), in which the towers were discretized along height at specific elevations z (in m) for improving more accurate determination of distributed wind related quantities.

Table 3 : Calculation procedure - step I

Section	z (m)	v_m (m/s)	$C_f(z)$	I_v	q_p (Pa)	V_{peak} (m/s)
1	2,37	21,994	0,733	0,259	850,818	36,895
2	8,21	29,076	0,969	0,196	1253,478	44,783
3	14,06	32,143	1,071	0,177	1447,278	48,121
4	19,9	34,123	1,137	0,167	1578,664	50,258
5	25,756	35,593	1,186	0,1601	1679,394	51,837
6	31,6	36,758	1,225	0,155	1761,169	53,084
7	37,44	37,725	1,258	0,15109	1830,273	54,115
8	43,29	38,553	1,285	0,148	1890,361	54,996
9	49,14	39,275	1,309	0,145129	1943,522	55,764
10	55	39,917	1,331	0,143	1991,32	56,446
11	60,83	40,491	1,349	0,141	2034,501	57,054
12	66,68	41,015	1,36	0,139	2074,216	57,609
13	72,53	41,494	1,383	0,137	2110,888	58,116
14	78,37	41,936	1,398	0,136	2144,913	58,582
15	84,22	42,346	1,411	0,1346	2176,762	59,015
16	90,07	42,729	1,424	0,133	2206,661	59,419
17	95,06	43,036	1,434	0,132	2230,8	59,743
18	100	43,325	1,444	0,131	2253,588	60,047

3.2 Wind force coefficient

The coefficient of wind force of a lattice metallic tower C_f , depends on the index of filled parts φ defined as the ratio between the solid area per panel and the area of the panel if it was completely filled. In this determination of the coefficient of wind force required for the calculation of wind actions, it is conservatively assumed that the tower is subjected to a super-critical wind flow. For lattice towers of triangular cross section, made of equilateral triangles, the wind causes the maximum drag when its direction is normal to the face, as [9]. So it is going to be considered in these analyses a null or zero angle of attack, that is the wind acts normal to the face of the tower ($\theta = 0^\circ$) and then the wind incidence factor $K_\theta = 1$.

Table 4 details for the section levels associated with tower panels, the calculation procedure of wind actions - step II: index of filled parts, and corresponding wind force coefficient.

Table 4 : Calculation procedure - step II

Section	z (m)	φ	C_f
1	2,37	0,156	1,083
2	8,21	0,091	1,088
3	14,06	0,094	1,088
4	19,9	0,096	1,088
5	25,756	0,099	1,087
6	31,6	0,1	1,087
7	37,44	0,105	1,087
8	43,29	0,103	1,087
9	49,14	0,109	1,08
10	55	0,110	1,086
11	60,83	0,117	1,086
12	66,68	0,128	1,085
13	72,53	0,133	1,085
14	78,37	0,144	1,084
15	84,22	0,143	1,084
16	90,07	0,165	1,084
17	95,06	0,153	1,083
18	100	0,153	1,083

3.3 Structural coefficient

For the determination of the structural coefficient $C_s C_d$ the dynamic parameters of the tower were obtained using a finite element method model. The first vibration mode has a frequency very close to unit, so that (in Eurocodes symbology) $n_1=1$; also, for the logarithmic decrement of structural damping, the value $\delta_s = 0.05$ was assumed. The remaining intermediate values necessary for the calculation of the structural coefficients are shown in the following Table 5 through Table 7; for more details, refer to [6] [7] [8].

Table 5 : Calculation procedure - step III (a)

L (z _s)	m_e (Kg/m)	δ_s
209,181	669,5	0,05

Table 6 : Calculation procedure - step III (b)

Section	R_h	R_b	n_h	—————	n_b	S_l	f_l	δ	K_p
1	0,037	0,254	26,771		3,933	0,026	12,174	0,305	3,082
2	0,049	0,355	20,250		2,817	0,032	9,209	0,371	3,176
3	0,055	0,416	18,318		2,405	0,034	8,330	0,385	3,220
4	0,058	0,469	17,255		2,131	0,035	7,847	0,384	3,254
5	0,060	0,522	16,543		1,914	0,036	7,523	0,377	3,283
6	0,062	0,579	16,018		1,728	0,037	7,284	0,364	3,311
7	0,064	0,640	15,608		1,562	0,038	7,097	0,349	3,338
8	0,065	0,709	15,273		1,410	0,038	6,945	0,332	3,365
9	0,067	0,789	14,992		1,267	0,038	6,817	0,313	3,393
10	0,068	0,884	14,750		1,131	0,039	6,708	0,293	3,421
11	0,069	0,997	14,541		1,003	0,039	6,612	0,271	3,451
12	0,070	1,138	14,356		0,879	0,040	6,528	0,249	3,483
13	0,070	1,320	14,190		0,758	0,040	6,453	0,225	3,517
14	0,071	1,562	14,040		0,640	0,040	6,385	0,201	3,553
15	0,072	1,903	13,904		0,526	0,040	6,323	0,177	3,593
16	0,073	2,419	13,780		0,413	0,041	6,266	0,151	3,636
17	0,073	2,436	13,681		0,410	0,041	6,222	0,152	3,637
18	0,074	2,453	13,590		0,408	0,041	6,180	0,153	3,639

Table 7 : Calculation procedure - step III (c)

Section	z (m)	—————	B (m)	B^2	R^2	$C_s C_d$
1	2,37		14,69	0,618	0,004	0,706
2	8,21		13,91	0,618	0,007	0,746
3	14,06		13,13	0,618	0,010	0,761
4	19,9		12,35	0,618	0,012	0,771
5	25,756		11,57	0,618	0,015	0,778
6	31,6		10,79	0,618	0,018	0,784
7	37,44		10,01	0,618	0,022	0,789
8	43,29		9,23	0,618	0,026	0,794
9	49,14		8,45	0,618	0,032	0,798
10	55		7,67	0,618	0,039	0,803
11	60,83		6,9	0,618	0,049	0,807
12	66,68		6,12	0,618	0,062	0,812
13	72,53		5,34	0,618	0,081	0,817
14	78,37		4,56	0,618	0,110	0,823
15	84,22		3,78	0,618	0,155	0,832
16	90,07		3	0,618	0,233	0,849
17	95,06		3	0,618	0,236	0,850
18	100		3	0,618	0,239	0,851

3.4 Wind forces

The wind forces are calculated using the following equation

$$F_w = c_s c_d c_f q_p(z_s) A_{ref} \quad (1)$$

which was shown in detail and with its used explained, in the third chapter of [8].

In Table 8 are presented the quantities used for the calculation of wind force, the wind force value, and the wind force value per node in each panel; again, for more details, refer to [6] [7] [8].

Table 8 : Calculation procedure - step IV

Section	z (m)	$C_s C_D$	$I_v(z)$	q_p (Pa)	A_{ref} (m ²)	F_w (kN)	F_w per node (kN)
1	2,37	0,706	0,259	850,818	5,466	3,56	1,19
2	8,21	0,746	0,196	1253,478	7,646	7,78	2,59
3	14,06	0,761	0,177	1447,278	7,452	8,93	2,98
4	19,90	0,771	0,167	1578,664	7,116	9,42	3,14
5	25,76	0,778	0,160	1679,394	6,938	9,86	3,29
6	31,60	0,784	0,155	1761,169	6,623	9,94	3,31
7	37,44	0,789	0,151	1830,273	6,401	10,05	3,35
8	43,29	0,794	0,148	1890,361	5,787	9,44	3,15
9	49,14	0,798	0,145	1943,522	5,644	9,52	3,17
10	55,00	0,803	0,143	1991,320	5,212	9,05	3,02
11	60,83	0,807	0,141	2034,501	4,968	8,86	2,95
12	66,68	0,812	0,139	2074,216	4,851	8,86	2,95
13	72,53	0,817	0,137	2110,888	4,445	8,31	2,77
14	78,37	0,823	0,136	2144,913	4,169	7,98	2,66
15	84,22	0,832	0,135	2176,762	3,484	6,84	2,28
16	90,07	0,849	0,133	2206,661	3,266	6,62	2,21
17	95,06	0,850	0,132	2230,800	2,298	4,72	1,57
18	100,00	0,851	0,132	2253,588	2,298	4,77	1,59

3.5 Wind forces on equipment auxiliary structures

For the calculation of the forces acting on equipment auxiliary structures, an equipment exposed area of 30 m² was allowed in the last 10 meters from the top of the tower. Account was also taken on the existence of an access staircase throughout the height of the tower, as well as 0.30 m of cablings width across the height.

Table 9 shows the values of wind forces in auxiliary structures, and their section level of actuation.

Table 9 : Wind forces on equipment auxiliary structures

Section	F_W (kN)	F_w per node (kN)
7	1,35	0,45
9	1,20	0,40
16	11,8	3,83
17	11,64	3,88
18	11,72	3,91

3.6 Combinations of actions

The combinations of actions used in this parametric study for the ultimate limit state (ULS) are shown in Tables 10-11-12. Tables 10 and 11, detail the conditioning combinations for the determination of generalized forces; and Table 12 details the conditioning combination for the determination of displacements.

Table 13 details the conditioning combination of actions used in this parametric study for the determination of displacements under the serviceability limit state (SLS).

For a better understanding of the combinations detailed, the nomenclature used and its meaning is the following: PP refers to self-weight; Wind_Y+ refers to wind acting along the direction Y+ ; Wind_Y- refers to wind acting along the direction Y- ; Wind_X refers to wind acting along the direction X ; PLAT SW refers to platform self-weight; PLAT LL refers to platform live load.

Table 10 : Combination of actions for ULS – generalized forces (1st combination)

Factor	Action
1.2	PP
1.2	PLAT SW
1.12	PLAT LL
1.6	Wind_Y+

Table 11 : Combination of actions for ULS – generalized forces (2nd combination)

Factor	Action
1.2	PP
1.2	PLAT SW
1.12	PLAT LL
1.6	Wind_X

Table 12 : Combination of actions for ULS – displacements

Factor	Action
1.2	PP
1.2	PLAT SW
1.12	PLAT LL
1.6	Wind_Y-

Table 13 : Combination of actions for SLS – displacements

Factor	Action
1.0	PP
1.0	PLAT SW
0.64	Wind_Y-

4 ANALYSIS OF RESULTS

Table 14 shows the values of the generalized reactions at the base of the towers, obtained at each tower model analysed in accordance with the ULS combinations of Tables 10 and 11. These generalized reactions are respectively the force reactions in the horizontal base plane (F_x and F_y) and the vertical force reaction F_z ; as well as the two moment reactions M_x and M_y at the base of the towers.

Table 14 : Values of Reactions at the base of the towers for ULS

Tower label	Fx (kN)		Fy (kN)		Fz (kN)		Mx (kNm)	My (kNm)
	Max	Mín	Max	Mín	Max	Mín		
Initial tower model	72	-134	142	-170	1330	-1148	17294	15855
Tower model A	74	-139	148	-176	1401	-1212	18213	16774
Tower model B	77	-142	142	-178	1378	-1144	17914	16041
Tower model C	77	-140	149	-181	1381	-1164	17953	16178
Tower model D	74	-134	144	-171	1321	-1141	17173	15817
Tower model E	71	-131	140	-167	1321	-1141	17173	15772

From the analysis of the results of this parametric study, each tower identity or parameter of change can be easily distinguished. Tower model A has the highest bending moments (M_x and M_y) at the base due to the increase in the wind force because of the increase in the exposure area of this model has been made at the top of the structure, greatly influencing the value of the moments at the base.

In the tower models B and C, the two bending moments at the base are superior to the moments at the base of the initial tower model: for reasons already explained above, and also because the compromise between increased wind action and increased stiffness (due to the resizing) did not prove to be beneficial at this point.

In the tower models D and E, the two bending moments at the base are slightly lower than the moments at the base of the initial tower model: because the action of the wind on these tower models is slightly less than the action of the wind on the original tower, thus generating smaller moments.

Regarding the values of the generalized displacements (lateral displacements and torsional rotation through vertical global axis) in accordance with the SLS combination of Table 13, their results are presented in Table 15 for the top as well as for sections at two-thirds and one-third of the tower height (H).

Table 15 : Values of lateral displacements and rotations, for the SLS

Tower model	Lateral displacement (cm)			Rotation along vertical axis (°)		
	Top	2/3 H	1/3 H	Top	2/3 H	1/3 H
Initial tower	31,1	14,7	3,9	0,526	0,321	0,134
Tower A	32,9	15,6	4,1	0,497	0,351	0,139
Tower B	32	15,2	4,1	0,532	0,327	0,123
Tower C	32	15,1	4	0,531	0,330	0,128
Tower D	31,2	14,8	4	0,523	0,321	0,131
Tower E	32,1	15,5	4	0,529	0,325	0,160

In general, it is observed that the difference in lateral displacements is not significant: of the order of 1 cm in the top section for models A-B-C-E, and 1 mm for model D; much smaller differences at the other tower sections. With regards to rotation along vertical axis, all the tower models have rotation values quite identical, except the top rotation of tower model A; in fact, for this tower model A the maximum rotation is 5% to 7% lower than maximum rotation of the other tower models. This could be expected because the increase of the stiffness of the top third part of the tower structure (above 72.5 m) by adding an additional diagonal member, converting the initial diagonal bracing into a cross X-bracing, leads to an expected reduction of torsional rotations at the top tower levels.

5 CONCLUSIONS

All the proposed tower models were resized or redesigned, leading to changes in the type of circular profile used in various sections and in the total number of elements used. These changes, besides leading to different structural responses when the towers were subject to wind action (as previously explained and analysed), also lead to different costs of the models proposed tower structures. Table 16 shows an estimate of the total weight of each tower and an estimate of the price of each tower, considering a market value for the steel price of around 2.5 euros per kilogram-force of weight.

In view of the foregoing considerations -- both in terms of the generalized reaction values and generalized displacements, and in terms of estimated total cost associated with the studied solutions in this parametric study -- it is thought that, in addition to the original solution associated with the initial tower model structure, the most indicated alternatives may be the tower models D and E.

Table 16 : Cost estimate of the tower models

Tower model	Total weight of tower (kgf) ; 1 kgf \approx 0.01 kN	Cost estimate of tower (Euro)
Initial tower	22354.13	55885.33
Tower A	23366.31	58415.79
Tower B	29610.04	74025.09
Tower C	27087.03	67717.57
Tower D	21928.05	54820.13
Tower E	21995.66	54989.14

ACKNOWLEDGEMENTS

This work was financially supported by: Base Funding - UIDB/04708/2020 of the CONSTRUCT - Instituto de I&D em Estruturas e Construções - funded by national funds through the FCT/MCTES (PIDDAC).

REFERENCES

- [1] S. Sreevidya and N. Subramanian -- "Aesthetic appraisal of antenna towers"; *J. Archit. Eng.*, vol. 9, no. 3, pp. 102–108, 2003; doi: 10.1061/(ASCE)1076-0431(2003)9:3(102).
- [2] B. W. Smith -- *Communication Structures*; Thomas Telford Ltd, London, 2007.
- [3] D. Vieira, and R. Carneiro-Barros -- "Tubular Steel Lattice Telecommunication Towers, Subjected to Wind Loading and Vortex Shedding"; in *COMPdyn 2017 - Proceedings of the 6th International Conference on Computational Methods in Structural Dynamics and Earthquake Engineering*, 2:3154–62. National Technical University of Athens (NTUA); 2017. doi: 10.7712/120117.5635.20402.
- [4] CEN 2010 -- *Eurocódigo 1 – Acções em estruturas – Parte 1-4: Acções gerais – Acções do vento*; NP EN 1991-1-4, Norma Europeia, Portugal: IPQ; 2010.
- [5] CEN 2006 -- *Eurocode 3: Design of Steel Structures - Part 3-1: Towers, Masts and Chimneys*; Brussels; 2005.
- [6] R.C. Barros, N. Ferreira and R. Delgado -- "Effects of Wind in Tall Buildings: a comparison for a real case and its vibration control using a Tuned Mass Damper"; chapter of the book *Tall Buildings: Design Advances for Construction* (edited by J.W. Bull), Saxe-Coburg Publications - UK, ISBN: 978-1-874672-25-8, 2014.
- [7] I. Çalostescu -- "Wind Loads on Structures: Software Application II. Towers"; *Buletinul Institutului Politehnic Din IASI*, Tomul LIX (LXIII), Fasc. 5, pp. 49-61, Secția: Construcții Arhitectura; 2013.
- [8] L.M.R.G. Barros -- "Estudo Paramétrico de Torres Treliçadas (Comparação de Esquemas de Contraventamento)"; *M.Sc. thesis in structural engineering* supervised by Prof. Rui Carneiro Barros, FEUP, Porto-Portugal, October 2020 (in Portuguese).
- [9] P. Sachs -- *Wind Forces in Engineering*, 2nd Ed.; Pergamon Press, Oxford, New York; 1978.s, *Wind Forces in Engineering*. 1978.

EXPERIMENTAL IN-PLANE LATERAL RESPONSE OF A FULL-SCALE ADOBE MASONRY WALL WITH OPENING

Paolino Cassese¹, Luigi Fenu², Domenico Asprone³ Antonio Occhiuzzi^{4,5} and
Fulvio Parisi³

¹ National Research Council (CNR), Construction Technologies Institute (ITC)
c/o Polo Tecnologico di San Giovanni a Teduccio, Naples, Italy - paolino.cassese@itc.cnr.it

² University of Cagliari, Department of Civil Engineering, Environment Engineering and Architecture
Via Marengo 2, Cagliari, Italy - lfenu@unica.it

³ University of Naples Federico II, Department of Structures for Engineering and Architecture
Via Claudio 21, Naples, Italy - d.asprone@unina.it, fulvio.parisi@unina.it

⁴ National Research Council (CNR), Construction Technologies Institute (ITC)
Viale Lombardia, 49, San Giuliano Milanese, Italy - occhiuzzi@itc.cnr.it

⁵ University Parthenope, Department of Engineering
Centro Direzionale Isola C4, 80143 Naples, Italy - antonio.occhiuzzi@uniparthenope.it

Abstract

A large amount of world population lives nowadays in earthen buildings, often constructed only based on construction practice and within earthquake-prone regions. In the recent history, several strong earthquakes had dramatic consequences on these structures, highlighting their significant seismic vulnerability due to multiple reasons, such as poor mechanical properties, poor detailing, and large inertia mass. Several aspects of seismic performance of existing earthen constructions need to be investigated through full-scale experimental testing. In this regard, the present study aims at contributing to the investigation by testing a full-scale adobe masonry wall with a central door-type opening under in-plane lateral loading with cyclic fashion. The mechanical behaviour of materials, specimen's design, loading protocol and instrumentation setup are described. The experimental response curves, observed damage evolution and failure mode are discussed, especially focusing on dissipation capacity of the wall.

Keywords: Full-scale tests; Adobe masonry; Walls; Cyclic tests; Seismic capacity.

1 INTRODUCTION

Unreinforced masonry (URM) structures represented the most popular solution for buildings adopted in many countries up to the last century, when other construction technologies became progressively more common [1]. Thus, a large portion of the existing building stock around the world is made of URM structures, often within high-seismicity regions such as Europe and Pacific Rim countries [2]. Among URM typologies, adobe masonry (AM) represents one of the most ancient and widespread for historical construction as well as currently still used for construction of low-cost dwellings in less developed areas of the world [3-4]. Recently, several reconnaissance missions after strong earthquakes [5-9] revealed the considerable vulnerability of existing URM structures, with severe damages and frequent global collapses resulting in significant losses.

This framework led researchers in increasing interest on the seismic assessment and retrofitting of URM members during last few decades, resulting in numerous experimental investigations. Firstly, these studies were mainly focused on the mechanical behaviour of URM walls representative of masonry piers, on the basis that these latter governed seismic response of the structure, whereas spandrel panels were considered secondary elements [10-11, among many others]. Then, several studies established the key role of spandrel panels in load-carrying capacity under lateral actions [12-13], thus several testing programs were performed on both reduced-scale full-buildings and spandrels. Benedetti et al. [14] presented the experimental results of 24 shaking-table tests on 1:2 scaled models of two-story masonry buildings before and after cracks-repairing and strengthening of spandrels. The as-built specimens were characterized by severe cracks localized on spandrel-panels and showed higher capacity than strengthened ones for which critical damage occurred in the piers resulting in premature collapse. A full-scale prototype of two-story URM building was tested under increasing cyclic lateral load in both as-built and strengthened conditions by Moon and his co-authors [2, 15]. A combined strengthening system was applied to the structure, made of fibre reinforced plastic e post-tensioning devices, proving to be considerably effective in improving original seismic capacity. Bothara et al. [1] performed a shaking-table test on a half-scale model of an existing New Zeland URM structure with two stories, gable walls, inclined roof and slightly eccentricity. The unreinforced test-building was prior shacked along longitudinal direction, then repaired and tested in the opposite direction. Intense rocking and out-of-plane phenomena were observed, especially on gable walls and experimentally-based fragility curves were derived. The results of an experimental campaign on URM spandrels were presented in [16-18]. Specific testing setups were realized in order to reproduce piers constraint effects and properly apply the cyclic lateral loading. Different spandrel configurations were tested showing that their strength and failure modes were governed by the axial load acting along the member. Chourasia et al. [19] carried out quasi-static cyclic tests on full-scale single-room URM building composed of four orthogonal walls connected to a reinforced concrete (RC) slab on top, before and after strengthening by means of RC bands. Typical Indian materials were adopted for masonry. Brittle failure was observed for the unreinforced specimen, with huge diagonal cracks and sliding of RC roof, whereas the repaired one showed substantial strength improvement.

A first example of in-plane cyclic testing on full-sized URM wall with door-opening representative of a structural sub-assembly was reported in [20]. Firstly, monotonically increasing lateral load was applied until damage occurred in the spandrel. Then, this latter was strengthened by means of inorganic reinforced matrix and further cyclic tests were carried out on the wall. Experimental evidence showed that most of the observed damage was localized in the spandrel-panel, whereas rocking of piers governed the hysteretic response, and the

strengthening system was effective in improving lateral response. Knox and his co-authors presented two experimental studies [21-22] focusing on the influence of spandrel panels on the mechanical response of URM structures under in-plane cyclic lateral loads. Pier-spandrel sub-assemblages were tested in [21] in which different failure modes of the whole structure were observed depending on different spandrel's aspect-ratio (namely, height-to-width ratio). The experimental outcomes derived from testing a half-scale two-story perforated (i.e., with multiple door- and window-type openings) URM wall were provided in [22]. The shallow spandrels behaved as coupling beams for masonry piers which were governed by rocking mechanism resulting in an elastic-perfectly plastic response with notable displacement ductility. More recently, an experimental and numerical study was carried out by Choudhury et al. [23] on typical Indian URM buildings. Specifically, the Authors performed cyclic in-plane tests on three different full-scale walls (respectively, with a door in the middle, a window in the centre and a solid wall) and a single-story one-room building, observing combined flexural action and sliding shear. Finally, Howlader et al. [24] experimentally investigated in-plane cyclic response of eight full-scale URM walls with semi-circular arched openings and materials typical of Australian last-century constructions. Specimens were different in terms of dimensions of spandrels and piers as well as imposed vertical loads. The observed lateral load capacity and failure modes were governed by changes in wall geometry.

The experimental study presented in this paper fits in this line of research focusing on the mechanical response of a perforated adobe masonry wall, with a central door-type opening, under quasi-static in-plane cyclic loading. Notice that, currently, no similar experimental studies are available in literature. A proper experimental characterization carried out for the adopted materials, i.e. adobe bricks and mud mortar representative of existing Italian earthen buildings and largely widespread in Sardinia island [25-26], is described according to a multiscale approach. Then, geometry of the wall specimen and details of the experimental program are illustrated. Then, test results are presented and discussed in terms of both observed damage and response curves.

2 EXPERIMENTAL PROGRAM

A full-scale AM wall with a central door-type opening was constructed within the structural laboratory at the University of Naples Federico II. The wall specimen was tested into place under cyclically increasing lateral displacements and constant vertical loading. In the following, a detailed description of material properties is reported according to a multiscale approach, from constituents to the behaviour of the adobe masonry under uniaxial compression and shear. Then, the geometry of the wall specimen, test set-up and monitoring instrumentation along with loading protocol are described.

2.1 Material properties

The wall specimen was made of adobe bricks and mud mortar. Bricks were obtained by reproducing the non-industrial manufacturing process, mainly based on the worker's experience, in compliance with Sardinian construction practice. Local soil, classified as clayey-silty sand, was mixed with water and straw fibres by volume. Specifically, randomly oriented straw fibres with different dimensions were added to a first soil/water mixture. Subsequently, some water or soil was added based on the mixture appearance evaluated by the manufacturer. Then, the final form was achieved by filling a prismatic wood formwork characterized by internal grooved surface and the wet brick was left to dry to the sun. On average, straw fibres had diameter equal to 3 mm, 70 mm length and 0.64% percentage by weight. Density and water content were 2.68 g/cm³ and 27%, respectively. Each adobe bricks was 200×400×100 mm³ in

size. The resulting mean unit weight was equal to 16.80 kN/m^3 with a very limited coefficient of variation ($\text{CoV} = 2\%$). Mud mortar used for masonry joints had same particle size of earth bricks, but no fibres were added to the mixture as typical of Sardinian adobe masonry [25, 27]. Nevertheless, a different amount of water was added during the mixing operations until a 20% optimal water content by volume was reached, in tune with trend from literature [28]. More detailed description of the production process and physical properties can be found in [26].

Mechanical properties of both adobe bricks and mud mortar were derived through uniaxial compression and three-point bending tests. Overall, compressive standard tests [29] were performed on 6 and 36 cubic specimens, respectively for mortar and bricks, from which mean values of compressive strength (f_c) equal to 0.50 MPa ($\text{CoV} = 14\%$) and 1.08 MPa ($\text{CoV} = 36\%$) were derived. Standard three-point bending tests on specimens $40 \times 40 \times 160 \text{ mm}^3$, in compliance with the European standard EN 1015-11 [30], were carried out for assessing tensile properties. In this case, for the adobe bricks test-specimens were extracted from original units, whereas for mortar characterization they were moulded into standard formwork. A total of 8 tests were performed on mud mortar and 36 on adobe bricks. Notice that higher number of experimental tests were systematically conducted for bricks in order to properly taking into account the further source of variability in mechanical response due to straw fibres with respect to mud mortar. On average, tensile strength (f_t) of adobe bricks was 0.56 MPa ($\text{CoV} = 36\%$) whereas a lower value ($f_t = 0.45$) was obtained for mud mortar, as expected due to absence of fibres reinforcement, with CoV equal to 20%. Typical observed failure modes of tested specimens in tension and compression are shown in Figure 1. Furthermore, main materials mechanical properties are summarized in Table 1.

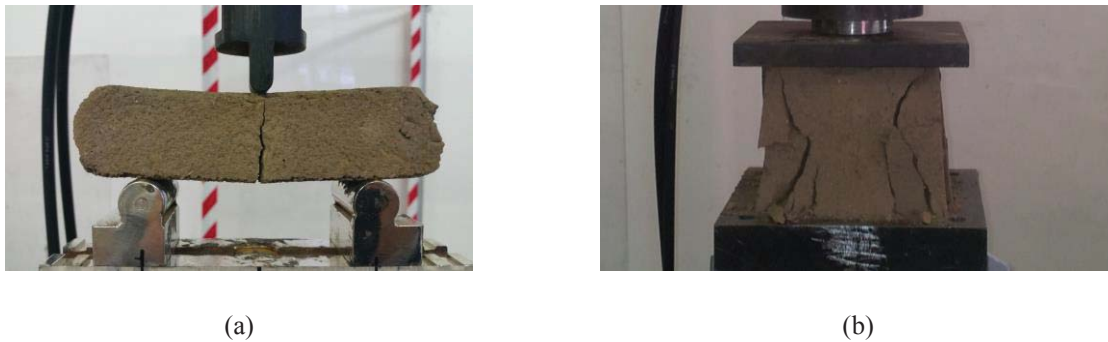


Figure 1: Typical failure modes of material test specimens in tension (a) and compression (b).

Material	f_c [MPa]	f_t [MPa]	E_c [MPa]	E_t [MPa]
Bricks	1.08 (36%)	0.56 (36%)	143 (40%)	69 (29%)
Mortar	0.50 (14%)	0.45 (20%)	47.5 (35%)	20.5 (33%)

* Coefficient of variation reported in round brackets.

Table 1: Main mechanical properties of AM constituents*.

2.2 Experimental characterization of adobe masonry under uniaxial compression and shear

In addition to base materials, associated to bricks and mortar, the mechanical behaviour of the adobe masonry used for construction of the wall specimen was furtherly investigated by testing at the level of the elementary sub-assembly. Specifically, mechanical properties of adobe masonry wallets under compression and shear, respectively, were assessed by means of uniaxial compression and diagonal compression tests.

Uniaxial compression tests were carried out on 8 adobe masonry single-leaf running-bond wallets with size $610 \times 650 \times 200 \text{ mm}^3$, composed of six horizontal courses and 10-mm-thick mud mortar joints. Wallets were subjected to monotonically increasing vertical displacement by means of a universal electro-hydraulic testing machine with a 2000 kN force capacity and total stroke of $\pm 150 \text{ mm}$. In order to achieve uniform distribution of axial stress a rigid steel beam was interposed between machine loading head and top of masonry prism. A load cell was used to measure applied force acting on specimen, whereas the deformations were measured by means of a specific monitoring-system composed of linear variable displacement transducers (LVDTs) installed vertically in the middle of the panel and horizontally along specimen's thickness to monitor splitting phenomena at failure. Normal stress (σ) was derived considering the gross cross-section of the wallet whereas vertical strain (ε) was computed from records of vertical LVDTs.

For all specimens, failure mode was characterized by cracks along compressive isostatic lines, involving both bricks and joints (see Figure 2a,b), and considerable splitting observed within specimen thickness. Resulting stress-strain (σ - ε) curves are reported in Figure 2c. Compressive strength of the adobe masonry ($f_{c,am}$) was equal to 1.32 MPa, on average, slightly higher than bricks, with low dispersion (CoV = 8%). Conversely, larger scatter was recorded for Young's modulus ($E_{c,m}$), evaluated at half peak-stress, the mean value of which was 425.4 MPa with CoV = 25%.

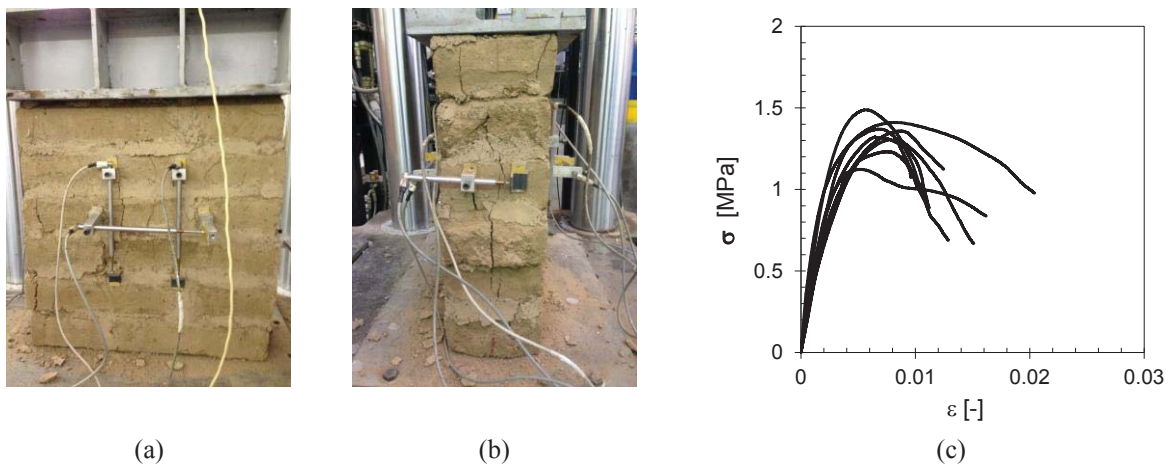


Figure 2: Typical damage state corresponding to compression failure (a,b) and stress-strain response curves (c).

Shear response of AM masonry was assessed by means of diagonal compression tests on seven wallets of total size of $410 \times 1230 \times 1230 \text{ mm}^3$ and running bond configuration. Such specimens were built on specific supports in order to allow for the execution of testing by means of the portable loading set-up depicted in Figure 3a. This latter was composed of a steel closed reaction-system acting as contrast to ejection of the hydraulic-jack interposed on the specimen. The adopted testing set-up was able to reduce either disturbance of wallets due

to transportation to laboratory and preparation time. The testing machine reached maximum load of 500 kN and total stroke equal to ± 75 mm. Double pair of linear variable differential transformers (LVDTs), with 400 mm gauge length, were installed in the middle of masonry external panels to monitoring the deformations along specimen's diagonal. Experimental records were processed according to the American standard ASTM E519-15 [31] in order to derive shear stress and strain (τ - γ). Typical final damage state is reported in Figure 3b. Diagonal-tension failure mode occurred with cracking patterns characterized by wide passing-through diagonal cracks generally involving both joints and bricks. Response τ - γ curves of all tested wallets are shown in Figure 3c. AM specimens were characterised by a pseudo-elastic branch up to peak shear stress followed by limited softening until collapse occurred. Post-peak softening response was considerably different among specimens. Peak shear stress ($\tau_{max,m}$) equal to 0.107 MPa was obtained on average, with limited dispersion (CoV = 7%), whereas the mean value of the initial shear modulus (G_i), assumed as secant at $\tau_{max}/4$, was equal to 185 MPa (CoV = 33%).

Table 2 summarizes strength and stiffness mean properties obtained for elementary AM sub-assembly under axial compression and shear along with their CoV.

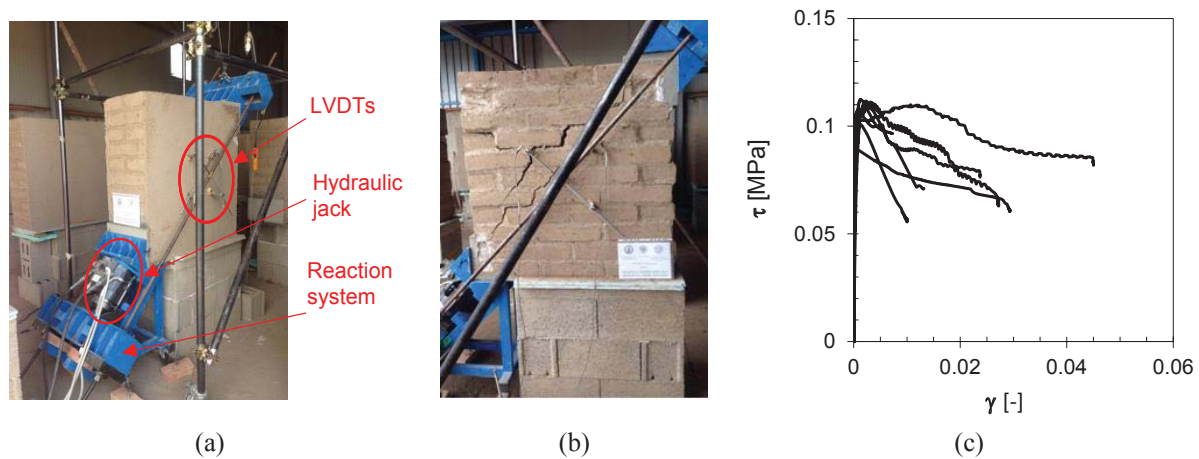


Figure 3: Diagonal compression tests on AM wallets: test set-up (a), typical failure mode (b), τ - γ curves (c).

Statistic	Compressive properties		Shear properties	
	$f_{c,m}$ [MPa]	$E_{c,m}$ [MPa]	$\tau_{max,m}$ [MPa]	G_i [MPa]
Mean	1.32	425.4	0.107	185
CoV	(8%)	(25%)	(7%)	(33%)

* Coefficient of variation reported in round brackets.

Table 2: Mean values of mechanical properties of adobe masonry*.

2.3 Geometry of the specimen

The AM specimens was a full-scale single-leaf masonry wall with a door-type opening in the middle-length (Figure 4). The latter was 1.70 m-long and 2.00 m-high. The two adjacent masonry piers had same opening's dimensions and were interconnected by a spandrel panel with height of 1.00 m. Three masonry layers were built above the piers in order to ensure proper vertical-load distribution. At the spandrel-panel intrados a wooden lintel was installed

with 150 mm anchorage-length within the piers. Therefore, the wall had total height and length equal to 3.60 m and 5.10 m, respectively, and 400 mm thickness.

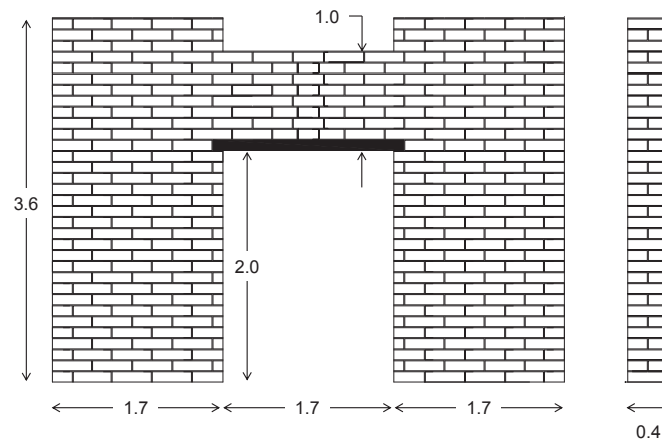


Figure 4: Frontal and lateral views of the adobe wall specimen (dimensions in m).

2.4 Test set-up and instrumentation

The specimen was erected on a rigid reinforced concrete (RC) beam, acting as wall-foundation. Such basement was anchored to the strong floor of the testing laboratory by means of pre-tensioned high-strength steel rebars. Vertical load on piers, kept constant during the test, was applied by means of two hydraulic jacks (one for each pier). Each hydraulic jack pushed against a steel reaction closed-system made of a rigid short beam, perpendicular to the wall, to which two steel rebars were connected. These latter were hinged to both ends so that any parasite contribution of the test set-up to the overall response of the specimen was prevented. Similarly, spherical hinges were introduced in-between hydraulic jack and the overlying beam. In order to uniformly distributing the vertical load, two rigid I-beam were interposed between hydraulic-jacks and pier tops, on which levelled mortar layers were priorly realized. Horizontal cyclic displacement was applied to the wall top by means of a servo-hydraulic actuator, with a nominal capacity of 1250 kN and ± 25 cm stroke, anchored to a vertical RC contrast. The actuator was equipped with a hinged head, with the aim to accommodate the actual deformed shape of the wall, fixed to a steel collar made of a couple of rigid plates located on the opposite sides of the wall and interconnected each-other by means of six steel bars, slightly pre-tensioned.

Main deformation sources were monitored during the test by means of a proper instrumentation system installed on both front and back sides of the wall specimen. Specifically, on the front side, a total of eight linear variable differential transformers (LVDTs) were installed at the location of critical end sections of the piers and central spandrel element, in order to measure axial displacements due to bending. On the backside, specific vertical LVDTs were mounted piers/foundation interface in order to measure the width of rocking-induced cracks. Those displacement transducers were complemented by two couples of vertical wire potentiometers (PTs) that measured the axial and bending deformations of each pier. Additional PTs were arranged along diagonals of piers and spandrel panel with the aim of monitoring shear deformations. Finally, a horizontal PT was installed at the same elevation of the actuator (i.e., $y = 3055$ mm) and connected to a wall edge.



Figure 5: Test set-up and instrumentation installed on the adobe wall specimen before testing.

2.5 Loading protocol

Load application was performed in two consecutive stages. Firstly, vertical loads were applied on top of piers under force control in order to simulate gravity loads transferred by an ideal floor. After that effective contrast between jacks and piers were obtained, the axial load on piers was monotonically increased according to a force rate equal to 1 kN/s until load value of 88 kN was reached (corresponding to 10% of the mean ultimate load of pier cross sections). Then, such value was kept constant during the second stage of the test when in-plane horizontal cyclic displacement was applied to the wall corresponding to the top of the spandrel, reproducing slab/wall transfer. The cyclic displacement history was composed of increasing displacement blocks of three cycles at a given amplitude peak until failure was observed. The amplitude was increased between consecutive blocks of 5.6 mm. The displacement rate was set at 0.70 mm/s. The cyclic displacement history is shown in Figure 6. A sampling rate equal to 5 Hz was of all instruments to ensure a proper monitoring of deformations during the entire test. The positive orientation was assumed as associated to a pushing action of the actuator. A total number of twelve displacement cycles were imposed on the specimen for a maximum displacement reached equal to 33.6 mm.

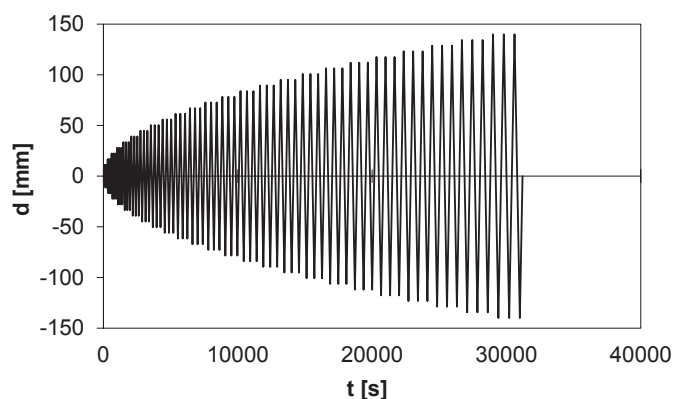


Figure 6: Cyclic displacement time history.

3 OBSERVED DAMAGE AND FAILURE MODE

Figure 7 shows the damage occurred to the specimen at the end of the experimental test. Horizontal cracks were observed on both sides of the spandrel panel along different bed joints and extended to the whole length. On the lower part of the spandrel, in the proximity of the lintel, a partially inclined crack was observed towards the left-hand side end. Such a crack pattern is representative of shear failure mode. Overall, a quite moderate damage was observed on the spandrel. Conversely, both piers suffered large cracks on the bottom part. Specifically, sub-horizontal cracks concentrated in the first six/seven masonry layers from the base were firstly observed, subsequently evolving along inclined directions, mainly developed along mortar-joints. Corresponding to peak load condition, vertical cracks were observed within piers thickness due to failure of masonry in the compressed zone. Therefore, bending failure was experienced by the piers. Beyond the peak load, the wide cracks located at the base of the piers caused piers buckling and the experimental test was arrested when significant out-of-plane deformations were identified.



Figure 7: Damages observed on the specimen at the end of the experimental test.

4 RESPONSE CURVES

The horizontal load recorded by the actuator load-cell is plotted against the horizontal displacement measured by the PT positioned at the same height in Figure 8. Globally, the hysteresis curve appears quite symmetrical both in force and displacement for the first three cycles, whereas the fourth group of cycles was slightly asymmetrical due to onset of vertical cracks widening and piers buckling. The maximum horizontal force was reached in the positive orientation and was equal to 86.4 kN, whereas 81.4 kN peak force was recorded in the opposite orientation. By assuming the lateral resisting force as the average of such values ($F_{max} = 83.9$ kN), a load-capacity value equal to approximately 31% of vertical load (apart from the effect of self-weight) was reached by the AM wall. Therefore, an in-plane acceleration-capacity of 0.31g can be assumed for the specimens. The experimental test was stopped during the first cycle of the fifth loading block when a horizontal force of 61.4 kN was attained on the last positive displacement cycle, evidencing approximately a 25% reduction in lateral resistance, for which evident out-of-plane deformations were observed. Regarding the deformation ca-

capacity of the adobe wall, the maximum horizontal displacements reached in the positive and negative orientations of lateral loading were respectively equal to 31.81 mm and 34.50 mm.

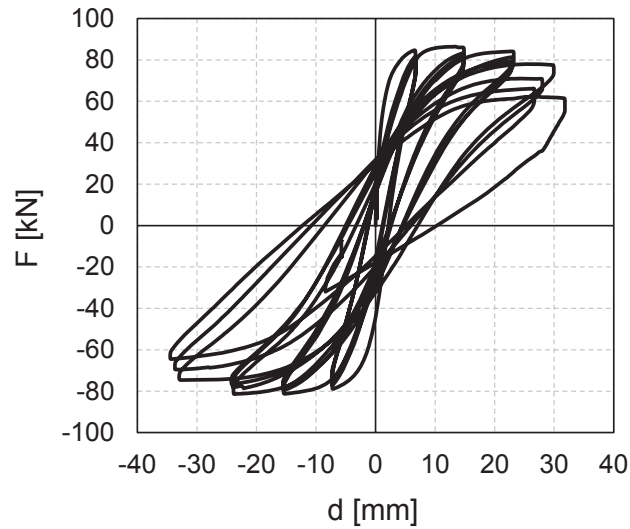


Figure 8: Force-displacement (F - d) curve recorded during the experimental test.

The experimental response curve of the AM wall is reported in Figure 9 as backbone of the hysteresis cycles expressed in terms of lateral force versus inter-storey drift ratio (F - IDR), the latter assumed as the measured lateral displacement normalized to the height of the horizontal loading line from the base of the piers. Within the framework of seismic performance-based assessment of masonry structures, establishing a relationship between limit states and observed damage appears crucial for response assessment as well as repair costs. Therefore, on the envelope curve, three performance levels (PLs) were identified representative of significant limit states of the wall:

- elastic limit (PL1), corresponding to diffuse cracks on wall members and herein associated to $0.6F_{\max}$;
- peak condition (PL2), related to lateral peak-load attainment and for which severe damage was observed on the wall (such as, vertical cracks due to rupture of masonry under compression);
- ultimate limit state (PL3), identified when a drop in lateral force equal to $0.2F_{\max}$ was recorded and representative of incipient loss of load-bearing capacity for the wall.

Mean values, between positive and negative directions, of force (F) and inter-storey drift ratio (IDR) corresponding to the above-defined PLs are summarized in Table 3. The AM specimen reached a IDR value higher than 1.00% at failure, significant for a masonry structures, whereas peak condition was attained at about $IDR = 0.61\%$. Finally, the elastic behaviour was overcome at very early stage ($IDR = 0.02\%$).

PL1		PL2		PL2	
IDR	F	IDR	F	IDR	F
[%]	[kN]	[%]	[kN]	[%]	[kN]
0.023	50.3	0.606	83.9	1.043	67.1

Table 3: Forces and inter-storey drift ratios associated with different performance limit states.

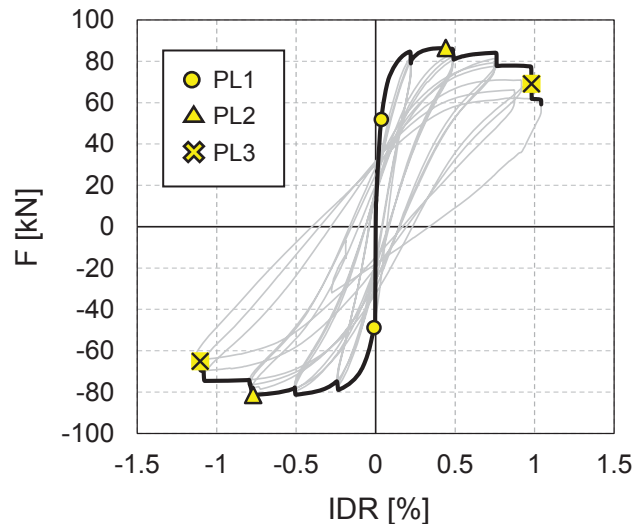


Figure 9: Experimental envelope in terms of force versus inter-storey drift ratio (F -IDR).

5 CONCLUSIONS

In this study, the nonlinear response of a full-scale adobe masonry wall with a central door-type opening to cyclic lateral loading and constant vertical loading has been described. A detailed experimental characterization of masonry constituents, i.e. adobe bricks and mud mortar with peculiarities of existing Sardinian earthen dwellings, and of adobe masonry as a whole was carried out according to a multiscale approach. The geometry of the wall specimen, test set-up, measuring system and loading protocol have been described. Preliminary experimental results on the wall specimen have been discussed. Specifically, observed crack patterns and failure modes have been firstly described; then, damage states were related to the force-drift response by identifying specific performance levels. Based on such discussion, the following remarks can be pointed out:

- The wall specimen reached its lateral strength due to bending failure of masonry piers associated with extensive toe crushing at the base of piers.
- The spandrel panel suffered a relatively moderate damage, mainly due to shear action.
- The ultimate limit state of the wall was characterized by incipient loss of wall load-bearing capacity with visible out-of-plane deformations.
- The in-plane response of the wall was defined by premature cracking and relatively large ultimate inter-storey drift ratio, which was slightly larger than 1%.

REFERENCES

- [1] J.K. Bothara, R.P. Dhakal, J.B. Mander, Seismic performance of an unreinforced masonry building: an experimental investigation. *Earthquake Engineering & Structural Dynamics*, **39**(1), 45-68, 2010.
- [2] F.L. Moon, T. Yi, R.T. Leon, L.F. Kahn, Testing of a full scale unreinforced masonry building following seismic strengthening. *Journal of Structural Engineering*, **133**(9), 1215–1226, 2007.

- [3] E.L. Tolles, E.E. Kimbro, F.A. Webster, W.S. Ginell, *Seismic stabilization of historic adobe structures: Final report of the Getty seismic adobe project*. Los Angeles: Getty Publications, 2000.
- [4] M. Blondet, J. Vargas, N. Tarque, Available low-cost technologies to improve the seismic performance of earthen houses in developing countries. In: *Proceedings of 14th World Conference on Earthquake Engineering*, Beijing, 2008.
- [5] N. Augenti, F. Parisi, Learning from construction failures due to the 2009 L'Aquila, Italy, earthquake. *Journal of Performance of Constructed Facilities*, **24**(6), 536-555, 2010.
- [6] D.F. D'Ayala, S. Paganoni, Assessment and analysis of damage in L'Aquila historic city centre after 6th April 2009. *Bulletin of Earthquake Engineering*, **9**(1), 81-104, 2011.
- [7] L. Moon, D. Dizhur, I. Senaldi, H. Derakhshan, M. Griffith, G. Magenes, J. Ingham, The demise of the URM building stock in Christchurch during the 2010–2011 Canterbury earthquake sequence. *Earthquake Spectra*, **30**(1), 253-276, 2014.
- [8] D. Dizhur, R.P. Dhakal, J. Bothara, J.M. Ingham, Building typologies and failure modes observed in the 2015 Gorkha (Nepal) earthquake. *Bulletin of New Zealand Society for Earthquake Engineering*, **49**(2), 211-232, 2016.
- [9] L. Sorrentino, S. Cattari, F. Da Porto, G. Magenes, A. Penna, Seismic behaviour of ordinary masonry buildings during the 2016 central Italy earthquakes. *Bulletin of Earthquake Engineering*, **17**(10), 5583-5607, 2019.
- [10] D.P. Abrams, N. Shah, *Cyclic load testing of unreinforced masonry walls. Advanced Construction Technology Centre Report No. 92-26-10*. University of Illinois at Urbana-Champaign, IL, 1992.
- [11] A.D. Mahmoud, A.A. Hamid, S.A. El Magd. Lateral response of unreinforced solid masonry shear walls: an experimental study. In: *Proceedings of the 7th Canadian Masonry Symposium*, Hamilton, 1995.
- [12] K. Shahzada, A.N. Khan, A.S. Elnashai, M. Ashraf, M. Javed, A. Naseer, B. Alam, Experimental seismic performance evaluation of unreinforced brick masonry buildings. *Earthquake Spectra*, **28**(3), 1269-1290, 2012.
- [13] G. Magenes, G.M. Calvi, In-plane seismic response of brick masonry walls. *Earthquake Engineering and Structural Dynamics*, **26**(11), 1091-1112, 1997.
- [14] D. Benedetti, P. Carydis, P. Pezzoli, Shaking table tests on 24 masonry buildings. *Earthquake Engineering and Structural Dynamics*, **27**(1), 67–90, 1998.
- [15] T. Yi, F.L. Moon, R.T. Leon, L.F. Kahn, Lateral load tests on a two-story unreinforced masonry building. *Journal of Structural Engineering*, **132**(5), 643–652, 2006.
- [16] N. Gattesco, I. Clemente, L. Macorini, S. Noè, Experimental investigation of the behavior of spandrels in ancient masonry buildings. In: *Proceedings of the 14th World Conference on Earthquake Engineering*, Beijing, China.
- [17] F. Graziotti, G. Magenes, A. Penna, *Progetto di una sperimentazione su elementi di fascia muraria, Rapporto Reluis, Allegato 4.3-UR01-1*. Università di Pavia and EUCENTRE, Pavia, Italy.
- [18] K. Beyer, A. Dazio, Quasi-static cyclic tests on masonry spandrels. *Earthquake Spectra*, **28**(3), 907-929, 2012.

- [19] A. Chourasia, S.K. Bhattacharyya, N. M. Bhandari, P. Bhargava, Seismic performance of different masonry buildings: full-scale experimental study. *Journal of Performance of Constructed Facilities*, **30**(5), 04016006, 2016.
- [20] N. Augenti, F. Parisi, A. Prota, G. Manfredi, In-plane lateral response of a full-scale masonry subassemblage with and without an inorganic matrix-grid strengthening system. *Journal of Composites for Construction*, **15**(4), 578-590, 2011.
- [21] C.L. Knox, D. Dizhur, J.M. Ingham, Experimental cyclic testing of URM pier-spandrel substructures. *Journal of Structural Engineering*, **143**(2), 04016177, 2017.
- [22] C.L. Knox, D. Dizhur, J.M. Ingham, Two-story perforated URM wall subjected to cyclic in-plane loading. *Journal of Structural Engineering*, **144**(5), 04018037, 2018.
- [23] T. Choudhury, G. Milani, H.B. Kaushik, Experimental and numerical analyses of unreinforced masonry wall components and building. *Construction and Building Materials*, **257**, 119599, 2020.
- [24] M.K. Howlader, M.J. Masia, M.C. Griffith, In-plane response of perforated unreinforced masonry walls under cyclic loading: Experimental study. *Journal of Structural Engineering*, **146**(6), 04020106, 2020.
- [25] C. Atzeni, Stone masonry in rural Sardinian building. Evolution of the traditional building techniques between XIX and XX Century. In: *Proceedings of the First International Congress on Construction History*, Madrid, 2003.
- [26] F. Parisi, D. Asprone, L. Fenu, A. Prota, Experimental characterization of Italian composite adobe bricks reinforced with straw fibers. *Composite Structures*. **122**, 300-307, 2015.
- [27] A. Caporale, F. Parisi, D. Asprone, R. Luciano, A. Prota, Micromechanical analysis of adobe masonry as two-component composite: Influence of bond and loading schemes. *Composite Structures*; **112**, 254-263, 2014.
- [28] F. Wu, G. Li, H.N. Li, Q. Jia, Strength and stress-strain characteristics of traditional adobe block and masonry. *Materials and Structures*, **46**(9), 1449-1457, 2013.
- [29] EN 1926. Natural stone test methods – determination of compressive strength. Brussels: Comité Européen de Normalisation; 1999.
- [30] EN 1015-11. Methods of test for mortar for masonry – Part 11: Determination of flexural and compressive strength of hardened mortar. Brussels: Comité Européen de Normalisation; 1999.
- [31] ASTM. ASTM E 519-15. Standard test method for diagonal tension (shear) in masonry assemblages. ASTM International, West Conshohocken, PA, USA; 2015.

INFLUENCE OF BEAM-TO-COLUMN CONNECTIONS IN SEISMIC VULNERABILITY ASSESSMENT OF STEEL STRUCTURES

G. Gabbianelli¹, D. Perrone^{1,2}, and E. Brunesi³

¹ University School for Advanced Studies IUSS Pavia
Piazza della Vittoria 15, 27100, Pavia, Italy
giammaria.gabbianelli@iusspavia.it, daniele.perrone@iusspavia.it

² Department of Engineering for Innovation, University of Salento
Via per Monteroni, 73100, Lecce, Italy
daniele.perrone@unisalento.it

³ European Centre for Training and Research in Earthquake Engineering (EUCENTRE)
Via Ferrata 1, 27100, Pavia, Italy
emanuele.brunesi@eucentre.it

Abstract

It is worldwide recognized the importance of assessing the vulnerability of structures in seismic prone zones. Focusing on steel structures, it is well-known that the behavior of beam-to-column connections plays a key role in the seismic response of any moment-resisting frame system. Recently, a research project funded by European Commission investigated the seismic performance of pre-qualified connections through numerical analyses and pseudo-static cyclic testing. From a designer perspective, it is, however, necessary to understand the efficiency of such connections in terms of building performance to take a rational and conscious decision when designing a building. With this in mind, this paper investigates the influence of different beam-to-column connections on the seismic response and vulnerability of medium-rise steel frame structures. The behavior of these structures has been investigated by means of non-linear dynamic analysis for increasing seismic intensity levels using the OpenSeesPy finite element software. The record selection has been carried out through the Average Sa-based method. The building performance has been assessed computing both maximum and residual interstory drifts, as well as fragility curves and absolute acceleration floor response spectra. The last mentioned enables to evaluate the likely damages experienced by acceleration sensitive non-structural elements, giving an additional point-of-view for estimating the building content performance. The outcomes of this study provide useful information for practitioners and designers interested in adopting the new set of pre-qualified connections, clarifying their effects on performance of common buildings and their content.

Keywords: Beam-to-Column Connections, Steel Structures, Seismic Vulnerability, Fragility Curves, Non-structural Elements.

1 INTRODUCTION

The importance of explicit modeling for beam-to-column connections is well-known and recognized in literature with unanimous consensus [1]. The stiffness and strength of beam-of-column connections could affect both the static and dynamic response of structures, leading to unrealistic or unconservative results if their behavior is not adequately considered. To deal with such an issue, experimental data is necessary in order to study the hysteretic response of the connections and to calibrate numerical models that have to be accurate and computationally efficient at the same time. However, analyzing data available in literature, it appears evident that exhaustive test results on the cyclic response of different typologies of beam-column connections are still missing, which could call for further efforts towards standardization.

Following damage observed after the 1994 Northridge (CA, USA) earthquake to steel structures, some significant efforts have been done by US researchers to investigate the response of a wide set of selected joints, commonly adopted in moment-resisting frames (MRFs). The research outcomes allowed to conceive a specific standard [2] that describes criteria for design, detailing, fabrication, and quality of the set of pre-qualified connections.

Regarding the European context, a recent research project [3] tried to fulfill such gaps. The EQUALJOINTS project [3], funded by the European Commission, aimed at providing a qualification of European beam-to-column joints adopted for seismic design. In order to accomplish such a goal, this project selected a set of common joint configurations and focused on the standardization of design and manufacturing procedures. In particular, bolted haunched, bolted extended stiffened end-plate, bolted extended unstiffened end-plate and welded dog-bone joints were experimentally and numerically studied. From the results of the project, it is possible to obtain the cyclic hysteretic response curves, in terms of moment-rotation relationships, which are useful for the explicit modeling of the behavior of connections when integrated in steel MRFs.

Recent studies also focused on the evaluation of the seismic response of steel MRFs considering the influence of joint behavior by means of numerical analyses [4] and shake-table tests [5].

The present study is meant to provide a further contribution on the evaluation of the influence of the explicit modeling of beam-to-column connections in the seismic vulnerability assessment of steel MRFs; in addition, the results of the undertaken nonlinear dynamic analyses are used here to estimate the seismic demand on non-structural elements (NSEs) via floor absolute acceleration spectra [6].

The consideration of NSEs in performance-based earthquake engineering is of paramount importance since they significantly contribute to economic losses and buildings' functionality issues [7-9]. Indeed, recent earthquakes have shown that earthquake-induced direct (i.e., structural and non-structural damages, deaths) and indirect (i.e., downtime and business disruption) losses might be socio-economically arduous [7].

Regarding the seismic performance assessment, several studies dealt with the selection of the most suitable parameter for measuring the damage of steel MRFs due to seismic actions. Generally, the choice bias for the interstory drift [10,11]. Besides, further studies comprised the computation of performance and fragility functions [12-17] or robustness [18] for steel MRFs.

This study aims to evaluate the influence of beam-column connections in the performance of a MRF steel building by employing fragility curves and interstory drift profiles; moreover, for a non-structural perspective, the connections' influence in the seismic demand on NSEs was assessed through acceleration profiles and floor absolute acceleration response spectra.

2 NUMERICAL MODEL OF THE CASE-STUDY BUILDING

The case-study building is a medium-rise steel MRF structure. The structural layout is presented in Figure 1. The building has 6-floor levels, with an interstory height of 3.0 m and a total height of 18 m. In the X-direction, the lateral stability is provided by a 4-bay MRF (Figure 1a) with all the beams spanning 6 m; contrariwise, the lateral support system in the Y direction is offered by diagonal braces (Figure 1b), located in the two end frames (Figure 1c). In this direction, the bay length is equal to 5 m.

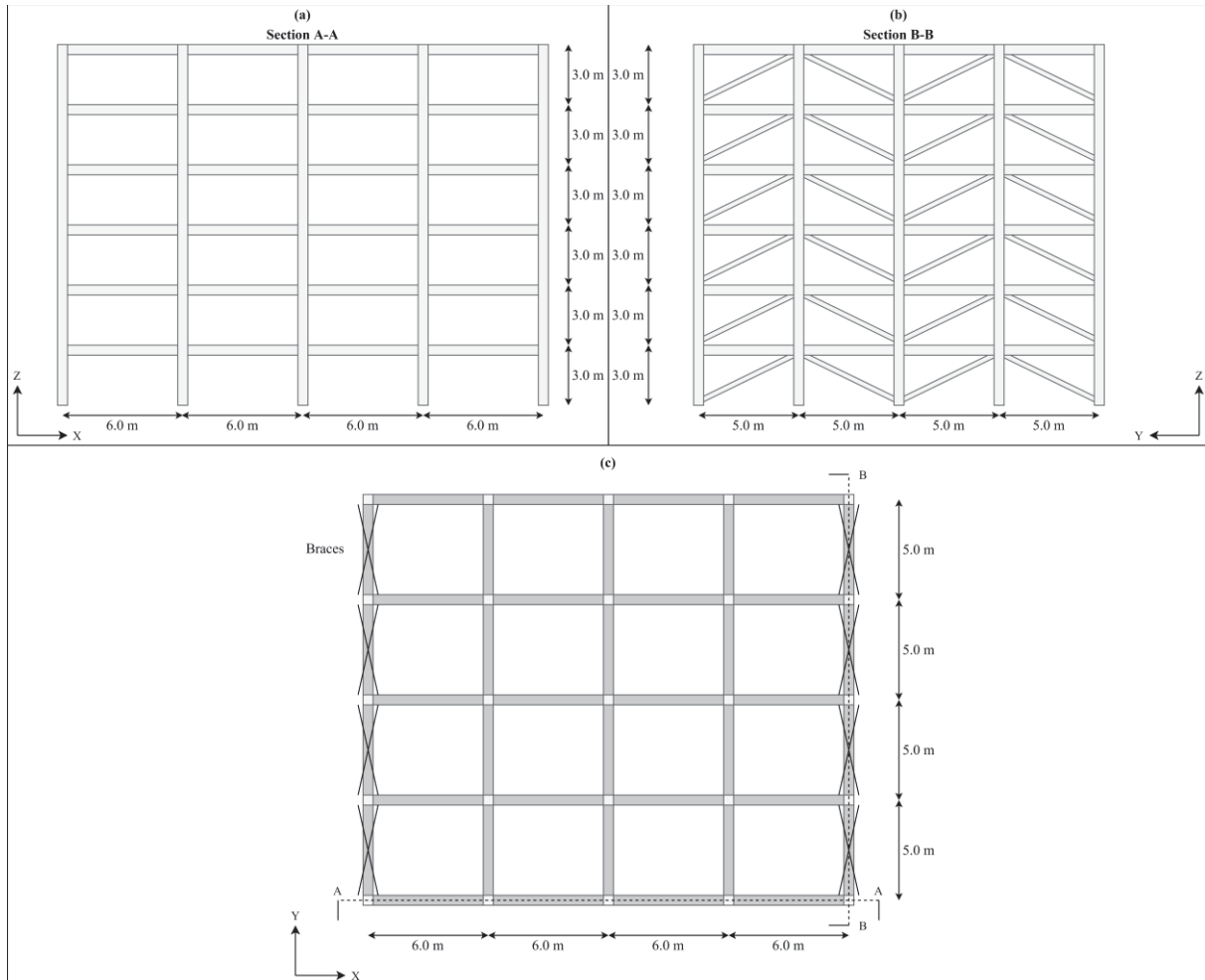


Figure 1: Structural layout: a) moment-resisting frame, b) concentric braced frame, c) plan-view of the building.

The structure was designed in compliance with European standards [19,20] for steel structures under seismic actions. Table 1 reports the profiles assumed for both beams and columns. It should be noted that all the sections are composed of an S355 material, the behavior of which has been simulated by means of a Menegotto-Pinto material model [21]. The choice of the sections and the bay length in the X-direction was made according to the available data from the experimental tests conducted in [3]. The diagonal braces are composed of hollow square sections with a width of 100 mm and a thickness of 10 mm. Following the load analysis, a uniform load equal to 40.5 kN/m and 30.25 kN/m was applied to the main internal and external beams (parallel to X-direction), respectively. At the roof level, the loads applied to the beams are equal to 33.25 kN/m and 16.78 kN/m for internal and external beams, respectively. Secondary external beams (parallel to Y-direction) are supposed to carry infills' weight,

computed and turned into a uniform load equal to 10 kN/m; the same beams at the roof are instead subjected to a load equal to 0.15 kN/m due to the parapet.

From a numerical point of view, the MRF connections were modeled following two different approaches: 1) full-rigid beam-to-column connections, namely Rigid (R) model and 2) explicit modeling of connections. This latter modeling option makes use of the outcomes of EQUALJOINTS [3], and in particular of results corresponding to the bolted extended stiffened end-plate connections, thus leading to the nomenclature of Extended Stiffened (ES) model. It should be noted that the bolted extended stiffened end-plate joint, in practical design, is generally assumed as rigid; therefore, the comparison between the two modeling approaches is consistent and is meant to shed light into the effects produced by basic modeling assumptions made at the design level. To deal with the geometry of the building, and the selected beams and columns, four connections tested in the EQUALJOINTS project were selected. Using the experimental results, the numerical models simulating the beam-column connections were developed using the pinching4 material model [22] available in OpenSeesPy. For illustrative purposes, and to demonstrate the good prediction capability of the calibrated numerical models, Figure 2 reports the numerical-experimental comparison of the hysteretic curves. Assuming the nomenclature adopted in EQUALJOINTS [3], the joint E1-TB-E-C1 (Figure 2a) and E1-XW-P-C1 (Figure 2a) refer to the HEB280-IPE360 and HEB340-IPE360 connection, respectively.

Floor level	Internal column	External column	Internal beam	External beam	Brace
1	HEB500	HEB340	IPE450	IPE360	100x100x10
2	HEB500	HEB340	IPE450	IPE360	100x100x10
3	HEB340	HEB280	IPE450	IPE360	100x100x10
4	HEB340	HEB280	IPE450	IPE360	100x100x10
5	HEB340	HEB280	IPE450	IPE360	100x100x10
6	HEB340	HEB280	IPE450	IPE360	100x100x10

Table 1: Selected sections for columns, beams, and braces.

The beam-to-column connections in the frames along the Y-direction were modeled as pinned. In this direction, only the braces act as lateral load-bearing elements. These members were modeled as truss elements, i.e., they sustain only tension and compression loads. However, due to their propensity for buckling, the braces were modeled with an asymmetric material, which offers a full-strength for the tension load and a partial-strength for the compression load. It should be noted that the partial strength was calibrated in order to permit the brace to reach its critical load.

The three-dimensional numerical models were developed by the finite-element software OpenSeesPy [23]. Both columns and beams were modeled by force-based beam-column elements with two-point Gauss integration for the interior element and two-point Gauss-Radau integration over each plastic hinge length at the element ends [24]. Such an approach permits to capture the material nonlinearity by discretizing the sections in fibers (about 100 fibers, in this study).

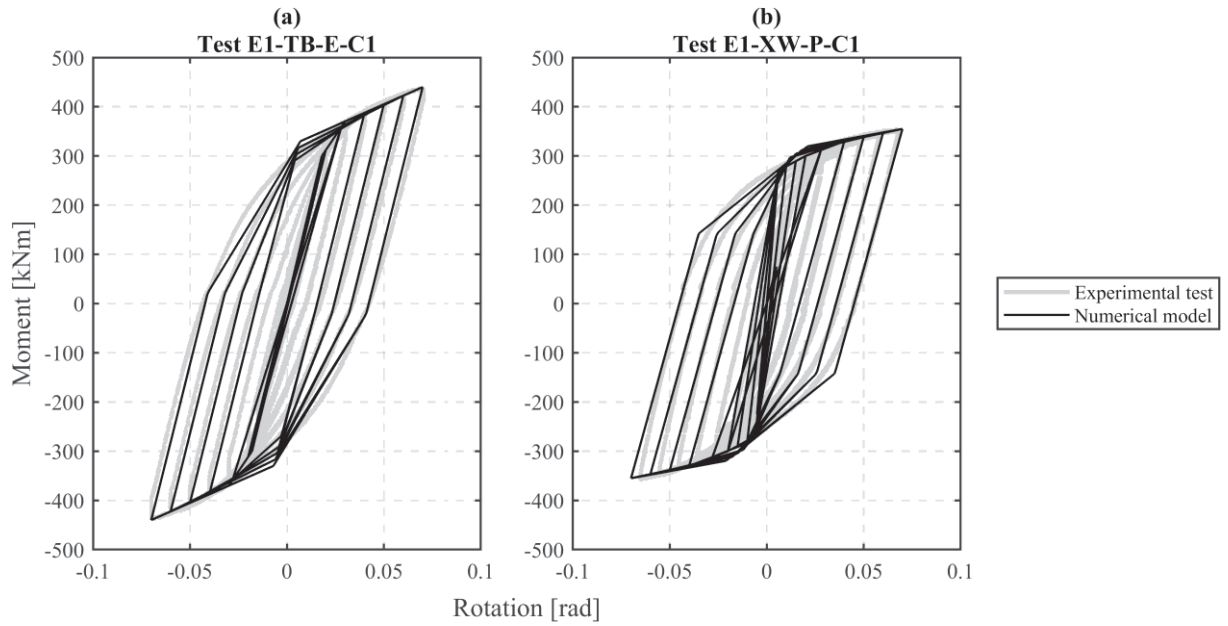


Figure 2: Calibration of the beam-column connection models with the test results provided by EQUALJOINTS [3].

Finally, a modal analysis was performed in order to capture both the free-vibration modes of the building with the two different modeling approaches and obtain essential information for the PSHA and record selection procedure, described in Section 3. Table 2 shows the first six periods of the building obtained from the two modeling approaches. The first, fourth, fifth, and sixth mode are predominantly translational in the X-direction; the second mode is translational in the Y-direction, while the third mode is torsional. Note that these considerations are valid for both R and ES models. As can be observed in Table 2, the actual connections' effect increases the first period by approximately 41%, while minor changes were obtained for the other periods.

Mode	R-model	ES-model	Mode shape
1 st	1.24 s	1.75 s	Translational, X-direction
2 nd	0.96 s	0.96 s	Translational, Y-direction
3 rd	0.71 s	0.77 s	Torsional
4 th	0.60 s	0.60 s	Translational, X-direction
5 th	0.49 s	0.54 s	Translational, X-direction
6 th	0.41 s	0.49 s	Translational, X-direction

Table 2: Free-vibration periods for the R- and ES-model.

In the nonlinear dynamic analyses, a Rayleigh damping model with 2% of critical damping was set for the first and third modes of vibration resulting from each eigenvalue analysis performed.

3 PSHA AND RECORD SELECTION

To obtain a suitable seismic threat for a specific location, a probabilistic seismic hazard analysis (PSHA) should be performed. As it is well-known, the PSHA gives the earthquake rate causing exceedance of any arbitrary ground-motion Intensity Measure (IM) at the site [25]. Therefore, the PSHA provides the seismic actions necessary to perform the structural design and assessment. In this study, the PSHA was performed with the assistance of the

OpenQuake platform [26]. The chosen location to perform the PSHA is the city of L'Aquila, a high seismicity zone in Italy, also tragically known for the catastrophic 2009 earthquake. An average seismic shear-wave velocity from the surface to a depth of 30 m (V_{s30}) equal to 200 m/s was selected, corresponding to a class soil C in accordance with the soil classification proposed in Eurocode 8 [20]. Note that for the PSHA, an appropriate ground motion prediction equation (GMPE) should be selected; in this study, the GMPE proposed by Lanzano et al. [27] has been used, since such equation is the latest revision for shallow crustal earthquakes in Italy.

Return Period [years]	Probability of Exceedance	Limit state
30	81% in 50 years	SLO – Immediate Occupancy
50	63% in 50 years	SLD – Damage Control Range
475	10% in 50 years	SLV – Life Safety
975	5% in 50 years	SLC – Collapse Prevention
2475	2% in 50 years	
4975	1% in 50 years	

Table 3: Return period of the record selection.

The Multiple-Stripe Analysis (MSA) [28] has been used to perform the seismic vulnerability assessment. Therefore, for each stripe, a PSHA has to be performed, varying the IM increasing the return periods. In Table 3, the six return periods (RPs) selected are reported, together with the probability of exceedance and the limit state associated in accordance with the Italian standard [29].

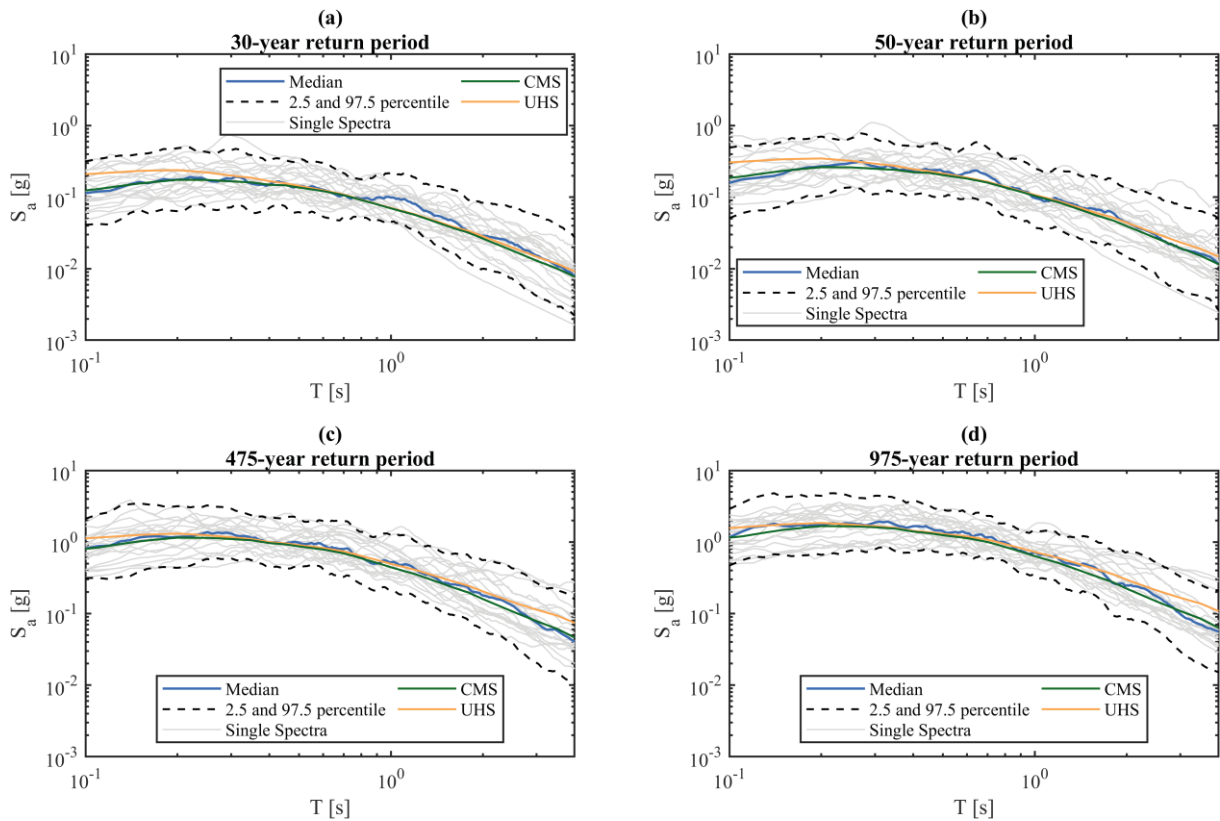


Figure 3: Ground motion spectra for the four selected limit states.

Regarding the choice of the IM and the calculation of the conditional mean spectra (CMS) necessary for the record selection, the average spectral acceleration (AvgSA) was adopted [30]. The AvgSA permits to consider spectral accelerations in a wide range of periods; as suggested by Kohrangi and Bazzurro [30], the calculation of the mean of the log spectral accelerations should be approximately in the range of $0.2T_1$ and $1.5T_1$, where T_1 is the first vibration period of the building. Since in this study there are two models with different first vibration periods, the computation of the range was performed considering the lower first period (1.24s) for the lower bound and the higher first period (1.75s) for the upper bound, leading to a range equal to 0.2s – 2.6s.

For each RP 20 ground motions were selected and, for the return periods associated to the limit state in accordance with the Italian standard [29], depicted in Figure 3 together with Uniform Hazard Spectrum (UHS), the CMS, the median of the selected records, and the median plus/minus the standard deviation, i.e., the 2.5% and 97.5% percentile.

4 STRUCTURAL RESPONSE RESULTS

The MSA is a powerful tool to assess the seismic performance of a structure and, in this case, to investigate the effects of the two considered modeling approaches. The main performance metric considered for steel structures is the interstory drift. Besides, this measure can be discerned in two parts, namely the transient drift and the residual (or permanent) drift. The former one represents the drift experienced during the analysis, and generally, from a performance metric perspective, it corresponds to the maximum drift reached during the whole analysis. Instead, the latter represents the drift in which the structure lies after the dynamic analysis due to permanent deformations caused by the nonlinear behavior of the buckled or yielded components. Therefore, for the sake of completeness, both maximum and residual interstory drifts were recorded.

Moreover, after collecting the accelerations experienced by the case study structures, the floor absolute acceleration response spectra were computed to offer an overview of the differences between the two modeling approaches (R and ES model) in terms of seismic demand on NSEs.

4.1 Interstory drift profiles

The maximum peak interstory drift profiles, for each record, were recorded and are plotted in Figure 4. In particular, Figure 4 shows all the outcomes derived from the six RPs selected and for the two considered configurations. It is worth mentioning that only the results in the X-directions are reported because in the Y-direction pinned connections are assumed. The results in the Y-direction are not discussed also because, from the eigenvalue analysis, it was observed that the different modeling approaches adopted in the two configurations modified the vibration periods but did not affect the global behavior of the structure in terms of modal shapes.

As a general remark, for both R and ES models and for all the RPs, the median peaks drift along the height are concentrated at the fourth and fifth floors. For instance, in the case of life safety limit state (i.e., 475-year RP), the median peak drift occurs at the fourth floor and it is equal to 1.83% for the R model and to 2.61% for the ES model. Similar considerations can be conceived for the other RPs.

As far as the seismic behavior for higher RPs is concerned, both modeling techniques revealed a soft-story mechanism activated between the second and third floors. Therefore, one may deduce that explicit modeling of connections does not change the overall seismic behavior of the structure when subjected to high seismic input.

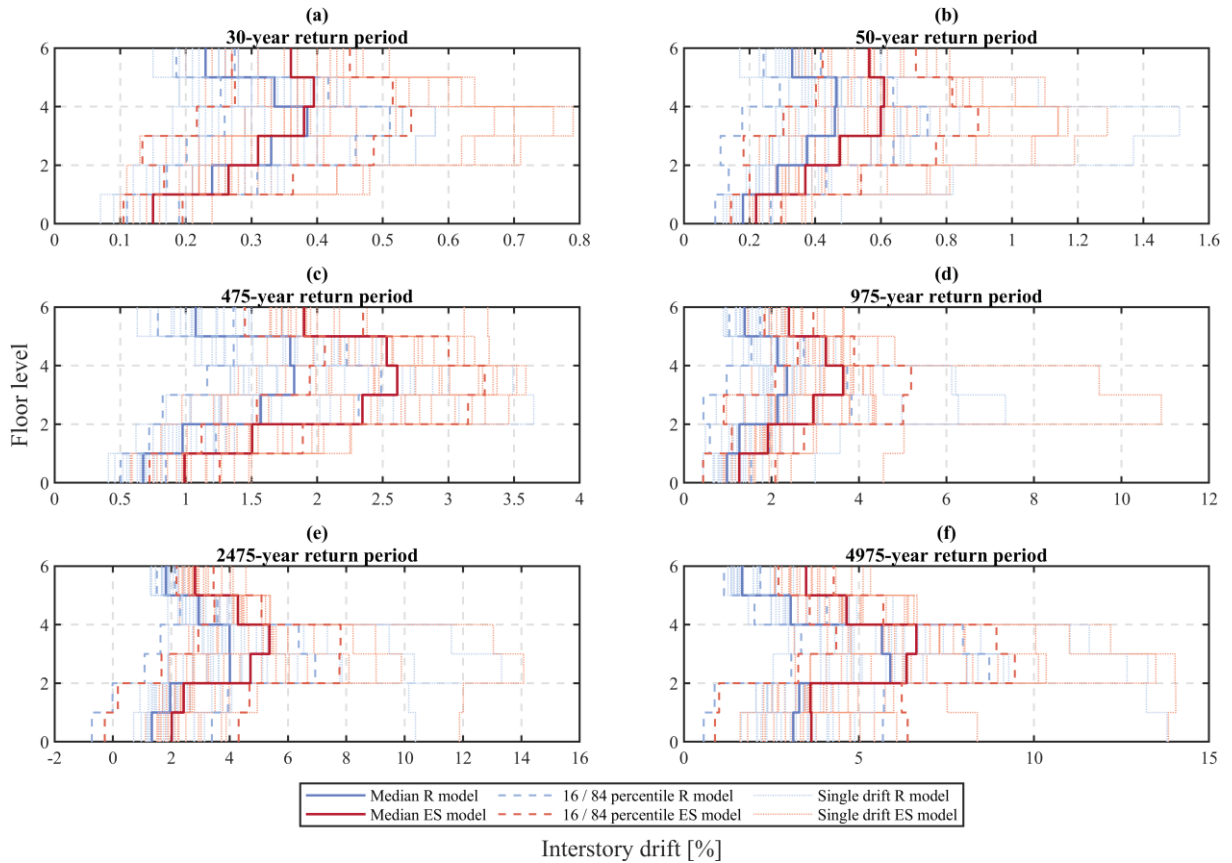


Figure 4: Interstory drift peak profiles for each RP in the X-direction.

However, although the drift trends are quite similar, the inclusion of the actual connections significantly increased the experienced drift values. This is especially true if medium-high RPs are considered. For the 475-year RP an increase of the peak drift equal to 43% is recorded, while for the 975-year RP an increase of 55% is observed. Lower percentage increases of the drifts are instead estimated for the 2475-year and 4975-year RPs, since the experienced drifts present a significant increment of 34% and 17%, respectively. The lower difference of the peak for the two higher RPs (2475-year and 4975-year) is due to the fact that both models, with these RPs, are subjected to large displacements, which induced significant plastic deformation in joints and elements, reducing in turn the stiffness and flattening the dissimilarity between the two structural models. Considering the FEMA-356 [31] interstory drift limitations, the two models behaved quite well. In fact, according to FEMA-356 [31], the maximum drifts are equal to 0.7%, 2.5% and 5% for the immediate occupancy (30-year RP), life safety (475-year RP) and collapse prevention (975-year RP) performance levels, respectively. Only in the case of life safety (Figure 8c) such limits are exceeded since, for the ES model, a maximum peak interstory drift of 2.61% located at the fourth floor is assessed. It is worth mentioning that, although the structure was designed according to EC8 [20], the comparison in terms of maximum interstory drift has been conducted considering the thresholds provided by FEMA-356 [31] because the EC8 [20] only provides some indications for the serviceability limit states.

4.2 Residual drift profiles

The median residual interstory drifts, together with the 16% and 84% percentile and the single drift profiles for each record, are reported in Figure 5. At first glance, it can be noted

that the higher differences between the R and ES models can be appraised for the lower RPs, namely 30- and 50-year RP. In these cases, the increase in terms of residual drifts is around 125% and 280% for the 30- and 50-year RP, respectively. However, considering the first four RPs, it can be noted that the record-to-record variability is considerably higher for the ES model; nevertheless, for the 475- and 975-year RPs, this discrepancy is due to few records with very large residual drift demands.

Overall, both structures behave well with respect to the FEMA-356 [31] limitations. Regarding the immediate occupancy limit state (30-year RP), FEMA-356 [31] indicates a negligible residual drift; in this context, a negligible maximum median value of 0.09% was obtained for the ES model, while an even smaller value was estimated for the R model, i.e., 0.04%. In the case of the life safety limit state (475-year RP), the limitation coincides with 1.0% of residual drift. Again, both models experienced smaller values, i.e., 0.39% and 0.3% for the ES and R models, respectively. Finally, concerning the collapse prevention performance level (975-year RP), a limit of 5% is defined, while the two models did not reach such value, since the maximum median residual drifts corresponded to 0.53% and 0.39% for the ES and R model, respectively.

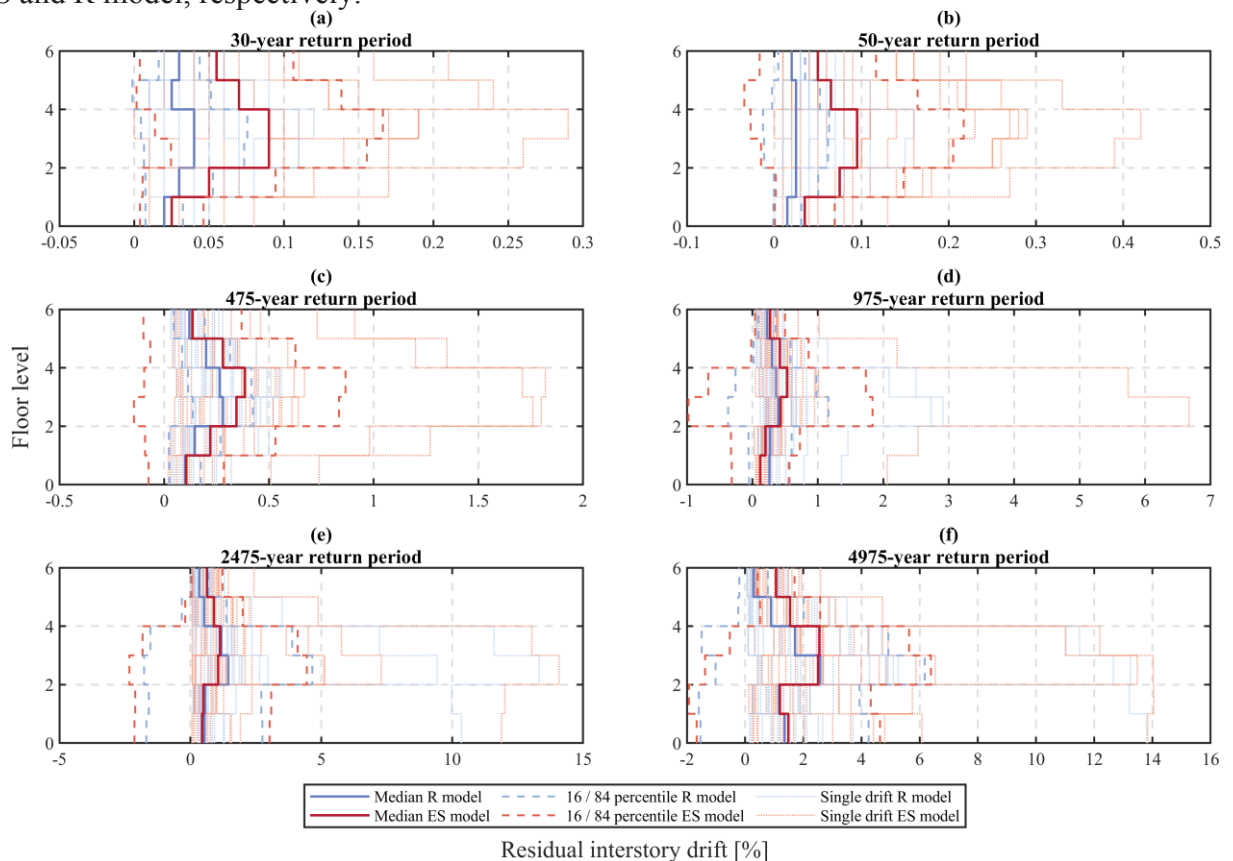


Figure 5: Residual interstory drift peak profiles for each RP in the X-direction.

4.3 Floor acceleration response spectra

Although floor response spectra are generally not considered to assess the structural performance, their evaluation could provide useful information regarding the dynamic response of the building and could also give an insight about the seismic demand at which the NSE installed in the building are prone.

Floor absolute acceleration response spectra were computed for each floor and RP. Figure 6 shows the absolute acceleration floor response spectra related to the roof floor for all the

RPs under investigation. In the first two RPs, namely the 30-year and 50-year RP, distinct peaks can be observed in proximity to the first and fifth (R-model) or sixth (ES-model) free-vibration periods (Figure 6a and 6b). Note that the spectra collected in Figure 6 are related to the X-direction; hence, a peak at the second free-vibration period, which involves masses in Y-direction, is not expected. Considering the differences between the two modeling approaches, it can be inferred that the median peaks in proximity to the sixth and fifth period for the R and ES model reached quite similar values (i.e., 0.8g and 0.66g for the 30-year RP and 1.23g and 1.24g for the 50-year RP, considering the R and ES models, respectively).

As regards the peaks at the first period, the differences are remarkable both in terms of spectral acceleration (0.74g and 0.25g for the 30-year RP and 1.0g and 0.49g for the 50-year RP, referring to R and ES models) and in terms of period shifting. Obviously, the first period elongation was expected for the ES model, as confirmed by the outcomes of the modal analyses performed prior to NLTHAs. For higher RPs, a flattening effect in the first periods can be observed; this phenomenon is quite common and it is due to the nonlinear response of the structures. In all RPs, the absolute acceleration response spectra present significant peaks in proximity to the structures' higher modes. Again, this outcome is not surprising since it is well-known that, in some circumstances, the floor acceleration response spectra are high-mode dominated [32-34]. This behavior is also the consequence of the high fundamental period of the structure, which is associated with lower ground spectral accelerations with respect to the higher modes, although the associated seismic masses are lower.

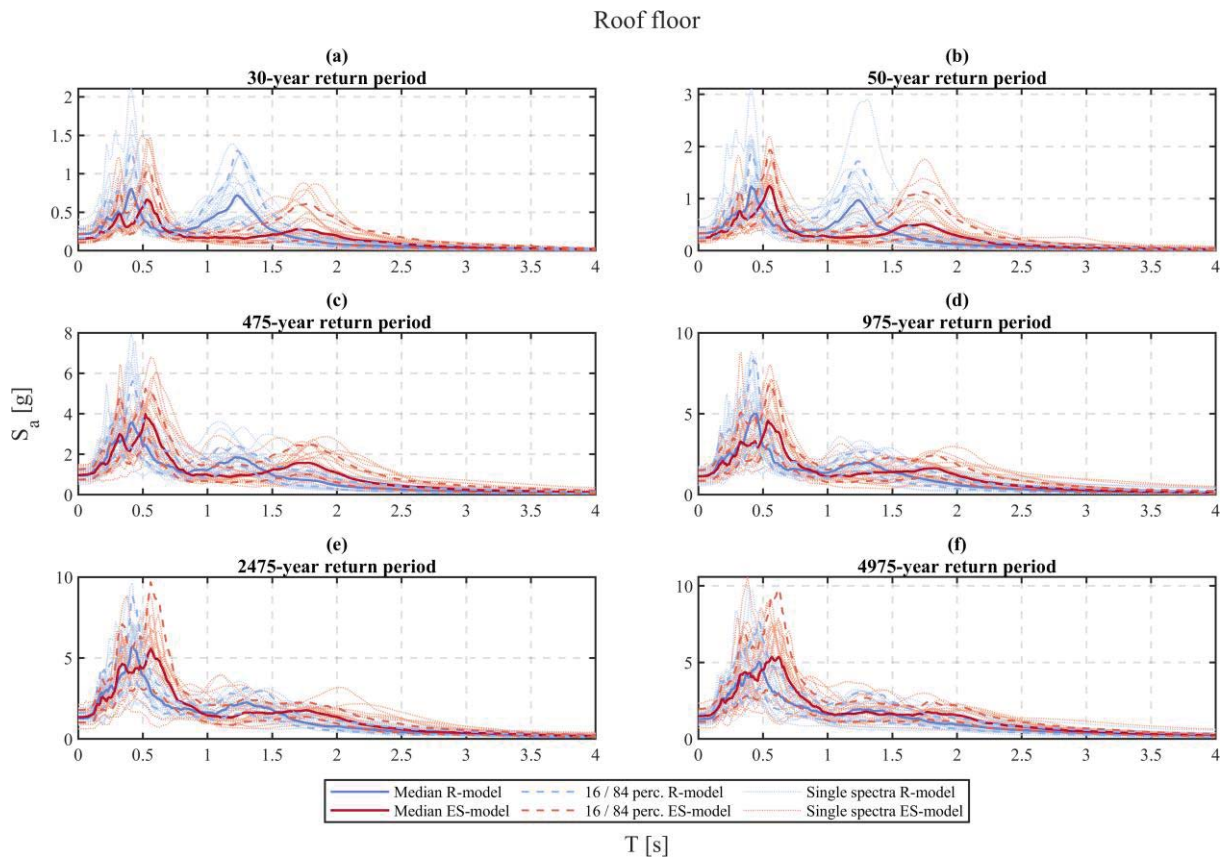


Figure 6: Absolute acceleration floor response spectra at the roof floor for each RP in the X-direction.

5 FRAGILITY CURVES

The calculation of fragility functions was carried out in accordance with the indications provided by Baker [35], in which the fitting technique of the maximum likelihood was suggested. Fragility curves obtained from the NLTHAs are shown in Figure 7; median and dispersion for each curve are also reported.

The limit states were defined following the indications provided by FEMA-356 [31] and already mentioned in the previous sections. FEMA-356 [31], concerning the steel MRFs, suggests adopting a 0.7% transient interstory drift and negligible residual drift for the immediate occupancy limit state; 2.5% transient and 1% residual drift for the life safety limit state and 5% transient or residual drift for the collapse prevention limit state. In addition, a further limit state was considered, namely collapse limit state, in which a limit of 10% transient or residual interstory drift was defined. Therefore, such parameters and thresholds were considered in the fragility curves computation for both models (R and ES model). Note that the curves constructed only refer to the X-direction of the structure.

As can be clearly seen from Figure 7, the ES model (dashed lines) presents a higher seismic vulnerability for most of the limit states. In particular, the median for the attainment of the life safety limit state is equal to 0.34g against a higher value for the R model, i.e., 0.48g. The same applies to the collapse prevention (0.77g versus 0.83g) and collapse (2.06g versus 2.14g) limit states. Only in the case of the immediate occupancy, the median presents identical values (0.09g), although the dispersion is different.

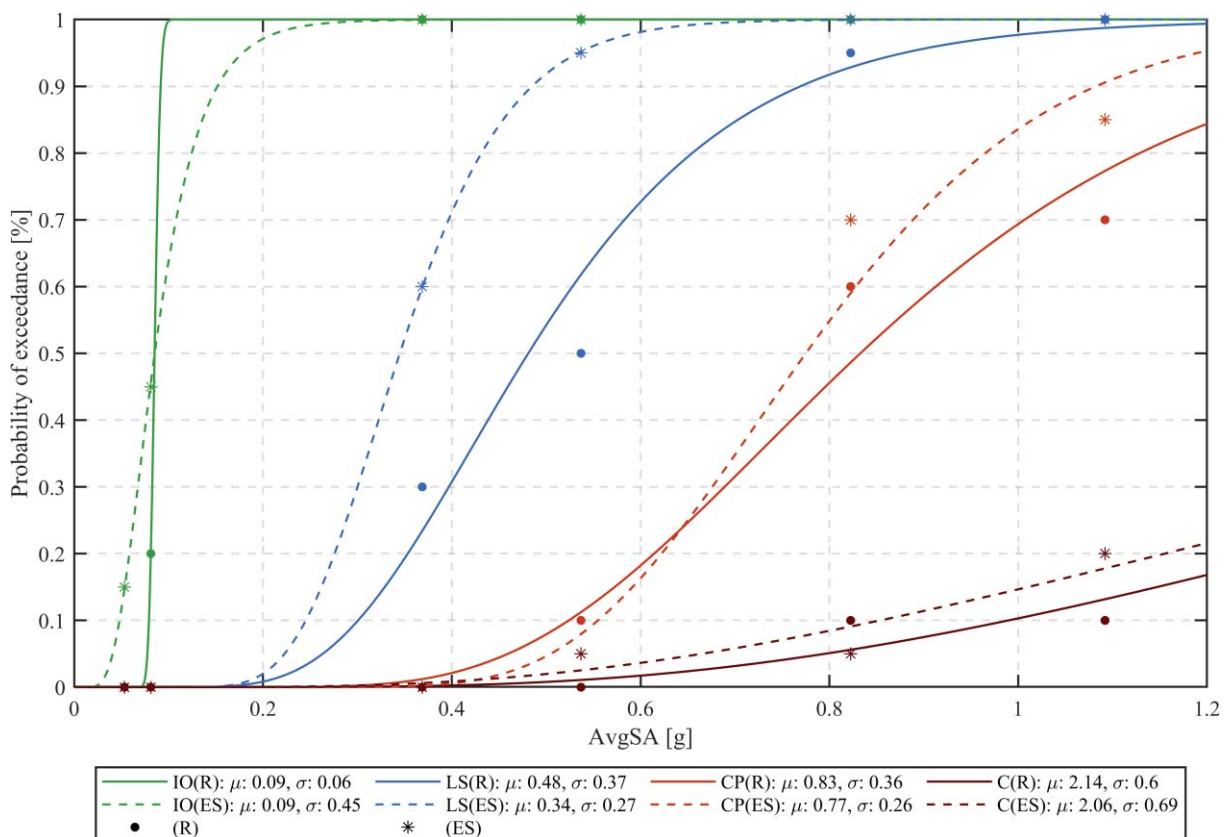


Figure 7: Fragility curves of the case study structure in the X-direction.

A straightforward conclusion can be done from a structural seismic performance perspective, adopting concepts similar to the collapse margin ratio (CMR), i.e. the ratio between the median collapse intensity and the intensity at the collapse limit state. The seismic intensities

(i.e., the AvgSA) for each limit state are 0.05g, 0.37g and 0.54g for the immediate occupancy, life safety and collapse prevention limit states. Therefore, the ratios between the median of each fragility curve and these last intensities are 1.8 (both models) for the immediate occupancy, 1.3 and 0.92 (R and ES model) for the life safety, and 1.54 and 1.43 (R and ES model) for the collapse prevention limit state, respectively. Reflecting the outcomes related to the maximum peak interstory drifts, only in the ES model case for the life safety limit state the ratio fell behind the unity, indicating a dangerous probability of reaching such limit state. This consideration also provides further insights into the importance of an accurate numerical modeling of the beam-column connections.

6 CONCLUSIONS

Past earthquakes demonstrated that, although less attention is generally paid to the seismic performance assessment of steel buildings with respect to, for instance, reinforced concrete and masonry structures, this structural typology could suffer significant damages, both from a structural and non-structural point of view. For this reason, it is of paramount importance to determine suitable models and methods to define the seismic performance correctly. As such, recent researches and projects focused on closing those gaps. In a European context, accurate investigations on pre-qualified joints' seismic behavior for steel buildings were missing until the very last years. Therefore, this study focused on evaluating the influence of the explicit modeling of joints in the structure's seismic performance. The performance metrics considered glanced at both structural and NSEs. Outlining that further research is necessary to define general conclusions for different steel buildings typologies and for all the pre-qualified joints, the outcomes of the analyses conducted in this study are listed in the following:

- The explicit modeling of a rigid joint reduced the structure's overall stiffness; therefore, a significant increment of the interstory drift can be observed. Similar considerations can be made referring to the residual interstory drift.
- The evaluation of the fragility functions, for different performance limit states, pointed out a high vulnerability of the structure if the actual behavior of the joints is explicitly modeled. For the case study structure, only in the case of life safety limit state, for the configuration in which the joints' behavior is modeled, the minimum requirements were not met.
- The shape of the floor absolute acceleration response spectra is significantly affected by the modeling of the joints, in particular for lower return periods. This consideration is of particular interest because the variation of the periods at which the maximum spectral accelerations are observed could significantly modify demand on and, thus, design of NSEs installed in the structure.

REFERENCES

- [1] G. Della Corte, G. De Matteis, R. Landolfo, F.M. Mazzolani, Seismic analysis of MR steel frames based on refined hysteretic models of connections. *Journal of Constructional Steel Research*, **58**, 1331-1345, 2002. [https://doi.org/10.1016/S0143-974X\(02\)00014-7](https://doi.org/10.1016/S0143-974X(02)00014-7)

- [2] ANSI/AISC 358, *Prequalified Connections for Special and Intermediate Steel Moment Frames for Seismic Applications, including Supplements No. 1 (2018) and No. 2 (2020)*. American Institute of Steel Construction (AISC), CHICAGO, IL, 60601, 2016.
- [3] R. Landolfo et al., European pre-qualified steel joints (EQUALJOINTS). *Research fund for coal and steel (RFCS)*, Grant agreement RFSR-CT-2013-00021, 2013-2016.
- [4] S. Costanzo, M. D'Aniello, R. Landolfo, The influence of moment resisting beam-to-column connections on seismic behavior of chevron concentrically braced frames. *Soil Dynamics and Earthquake Engineering*, **113**, 136-147, 2018. <https://doi.org/10.1016/j.soildyn.2018.06.001>
- [5] R. Tartaglia, M. D'Aniello, R. Landolfo, Numerical simulations to predict the seismic performance of a 2-story steel moment-resisting frame. *Materials*, **13**, 4831, 2020. <https://doi.org/10.3390/ma13214831>
- [6] I. González, A. Silva, L. Macedo, R. Monteiro, J.M. Castro, Critical assessment of estimation procedures for floor acceleration demands in steel moment-resisting frames. *Frontiers in Built Environment*, **5:139**, 2019. <https://doi.org/10.3389/fbuil.2019.00139>
- [7] A. Silva, L. Macedo, R. Monteiro, J.M. Castro, Earthquake-induced loss assessment of steel buildings designed to Eurocode 8. *Engineering Structures*, **208**, 110244, 2020. <https://doi.org/10.1016/j.engstruct.2020.110244>
- [8] G. Cantisani, G. Della Corte, T.J. Sullivan, R. Roldan, Displacement-based simplified seismic loss assessment of steel buildings. *Journal of Earthquake Engineering*, **24:sup1**, 146-178, 2020. <https://doi.org/10.1080/13632469.2020.1713932>
- [9] A. Silva, J.M. Castro, R. Monteiro, Brace-to-frame connection modelling effects on seismic loss assessment of steel concentrically-braced frames. *Journal of Constructional Steel Research*, **172**, 106230, 2020. <https://doi.org/10.1016/j.jcsr.2020.106230>
- [10] A. Gupta, H. Krawinkler, Estimation of seismic drift demands for frame structures. *Earthquake Engineering and Structural Dynamics*, **29**, 1287-1305, 2000. [https://doi.org/10.1002/1096-9845\(200009\)29:9<1287::AID-EQE971>3.0.CO;2-B](https://doi.org/10.1002/1096-9845(200009)29:9<1287::AID-EQE971>3.0.CO;2-B)
- [11] J. Ruiz-García, J.C. Negrete-Manriquez, Evaluation of drift demands in existing steel frames under as-recorded far-field and near-fault mainshock-aftershock seismic sequences. *Engineering Structures*, **33(2)**, 621-634, 2011. <https://doi.org/10.1016/j.engstruct.2010.11.021>
- [12] R.J. Merino Vela, E. Brunesi, R. Nascimbene, Seismic assessment of an industrial frame-tank system: development of fragility functions. *Bulletin of Earthquake Engineering*, **17(5)**, 2569-2602, 2019. <https://doi.org/10.1007/s10518-018-00548-2>
- [13] E. Brunesi, R. Nascimbene, G.A. Rassati, Seismic fragility analysis of MRFs with PR bolted connections using IDA approach. *Key Engineering Materials*, **763**, 678-685, 2018. <https://doi.org/10.4028/www.scientific.net/KEM.763.678>
- [14] F. Gutiérrez-Urzuá, F. Freddi, L. Di Sarno, Comparative analysis of code-based approaches for seismic assessment of existing steel moment resisting frames, *Journal of Constructional Steel Research*, **181**, 106589, 2021. <https://doi.org/10.1016/j.jcsr.2021.106589>
- [15] G. Gabbianelli, F. Cavalieri, R. Nascimbene, Seismic vulnerability assessment of steel storage pallet racks, *Ingegneria Sismica*, **37(2)**, 18-40, 2020.

- [16] A. Silva, Y. Jiang, L. Macedo, J.M. Castro, R. Monteiro, N. Silvestre, Seismic performance of composite moment-resisting frames achieved with sustainable CFST members. *Frontiers of Structural and Civil Engineering*, **10(3)**, 312-332, 2016. <https://doi.org/10.1007/s11709-016-0345-y>
- [17] A. Silva, Y. Jiang, L. Macedo, J.M. Castro, R. Monteiro, N. Silvestre, Monotonic and cyclic flexural behaviour of square/rectangular rubberized concrete-filled steel tubes. *Journal of Constructional Steel Research*, **139**, 385-396, 2017. <https://doi.org/10.1016/j.jcsr.2017.09.006>
- [18] D. Rodríguez, E. Brunesi, R. Nascimbene, Fragility and sensitivity analysis of steel frames with bolted-angle connections under progressive collapse. *Engineering Structures*, **228**, 111508, 2021. <https://doi.org/10.1016/j.engstruct.2020.111508>
- [19] EN 1993-1-1, *Eurocode 3: Design of steel structures - Part 1-1: General rules and rules for buildings*. European Committee for Standardisation, Brussels, Belgium, 2014.
- [20] E N 1998-1, *Eurocode 8: Design of structures for earthquake resistance - Part 1: General rules, seismic actions and rules for buildings*. European Committee for Standardisation, Brussels, Belgium, 2011.
- [21] K. Kolozvari, K. Orakcal, J. W. Wallace, *Shear-flexure interaction modeling for reinforced concrete structural walls and columns under reversed cyclic loading*, PEER 2015/12. Pacific Earthquake Engineering Research Center, 2015.
- [22] L.N. Lowes, N. Mitra, A. Altoontash, *A beam-column joint model for simulating the earthquake response of reinforced concrete frames*, PEER 2003/10. Pacific Earthquake Engineering Research Center, 2004.
- [23] M. Zhu, F. McKenna, M.H. Scott, OpenSeesPy: Python library for the OpenSees finite element framework. *SoftwareX*, **7**, 6-11, 2018. <https://doi.org/10.1016/j.softx.2017.10.009>
- [24] M.H. Scott, G.L. Fenves, Plastic hinge integration methods for force-based beam-column elements. *Journal of Structural Engineering*, **132(2)**, 244-252, 2006. [https://doi.org/10.1061/\(ASCE\)0733-9445\(2006\)132:2\(244\)](https://doi.org/10.1061/(ASCE)0733-9445(2006)132:2(244))
- [25] C.A. Cornell, Engineering seismic risk analysis. *Bulletin of the Seismological Society of America*, **58(5)**, 1583-1606, 1968.
- [26] M. Pagani, D. Monelli, G. Weatherill, L. Danciu, H. Crowley, V. Silva, P. Henshaw, L. Butler, M. Nastasi, L. Panzeri, M. Simionato, D. Vigano, OpenQuake Engine: An Open Hazard (and Risk) Software for the Global Earthquake Model. *Seismological Research Letters*, **85(3)**, 692-702, 2014. <https://doi.org/10.1785/0220130087>
- [27] G. Lanzano, L. Luzi, F. Pacor, C. Felicetta, R. Puglia, S. Sgobba, M. D'Amico, A revised ground-motion prediction model for shallow crustal earthquakes in Italy, *Bulletin of Seismological Society of America*, **109(2)**, 525-540, 2019. <https://doi.org/10.1785/0120180210>
- [28] F. Jalayer, C.A. Cornell, Alternative non-linear demand estimation methods for probability-based seismic assessments, *Earthquake Engineering and Structural Dynamics*, **38(8)**, 951-972, 2009. <https://doi.org/10.1002/eqe.876>
- [29] NTC18, *Norme Tecniche per le Costruzioni*, DM 17/1/2018. Gazzetta Ufficiale della Repubblica Italiana, Italian Ministry of Infrastructure and Transport, Rome, Italy, 2018.

- [30] M. Kohrangi, P. Bazzurro, D. Vamvatsikos, A. Spillatura, Conditional spectrum-based ground motion record selection using average spectral acceleration, *Earthquake Engineering and Structural Dynamics*, **46(10)**, 1667-1685, 2017. <https://doi.org/10.1002/eqe.2876>
- [31] FEMA-356, *Prestandard and commentary for the seismic rehabilitation of buildings*. Federal Emergency Management Agency, Washington, DC 20472, 2000.
- [32] G. Gabbianelli, D. Perrone, E. Brunesi, R. Monteiro, Seismic acceleration and displacement demand profiles of non-structural elements in hospital buildings, *Buildings*, **10(12)**, 243, 1-19, 2020. <https://doi.org/10.3390/buildings10120243>
- [33] V. Vukobratović, S. Ruggieri, Floor acceleration demands in a twelve-storey RC shear wall building, *Buildings*, **11(2)**, 38, 1-20, 2021. <https://doi.org/10.3390/buildings11020038>
- [34] R. Merino, D. Perrone, A. Filiatrault, Consistent floor response spectra for performance-based seismic design of non-structural elements, *Earthquake Engineering and Structural Dynamics*, **49(3)**, 261-284, 2021. <https://doi.org/10.1002/eqe.3236>
- [35] J.W. Baker, Efficient analytical fragility function fitting using dynamic structural analysis, *Earthquake Spectra*, **31(1)**, 579-599, 2015. <https://doi.org/10.1193/021113EQS025M>

ASSESSMENT OF RC HOLLOW-PIERS FOR SEISMIC LIMIT STATE OF DAMAGE - DIRECT REPAIR COSTS

Pedro Delgado^{1,3}, Naiara Silva², Mário Marques³ and António Arêde³

¹ PROMETHEUS, Instituto Politécnico de Viana do Castelo,
Rua Escola Industrial e Comercial de Nun'Álvares, 4900-347, Viana do Castelo, Portugal,
pdelgado@estg.ipv.pt, ORCID 0000-0002-4024-0442

² Instituto Politécnico de Viana do Castelo
Rua Escola Industrial e Comercial de Nun'Álvares, 4900-347, Viana do Castelo, Portugal
naiaalexandrep@gmail.com

³ CONSTRUCT-LESE, Faculdade de Engenharia (FEUP) Universidade do Porto
R. Dr. Roberto Frias, s/n 4200-465 Porto, Portugal
mario.marques@fe.up.pt; aarede@fe.up.pt

Abstract

Due to the vulnerability of reinforced concrete hollow piers subjected to seismic actions, it becomes urgent to assess the expected shear damage and its evolution with the increase of the intensity level. Additionally, the focus of the scientific research dedicated to seismic behaviour of these elements is still reduced, in particular with regard to the limit states of damage and to the economic consequences of repairing and retrofitting the physical damages existing in RC hollow piers subjected to the seismic action. This information is deemed crucial when cost-benefit analysis is concerned for the definition of measures for repair and retrofit of seismic damage.

This paper focus on the issue of damage to hollow piers due to the seismic action, proposing a methodology to characterize the limit states of damage under the perspective of the physical behaviour. It also intends to discuss adequate strengthening strategies and their direct costs, associated with each seismic physical limit state of damage. An extensive review of numerous cyclic experimental works on RC hollow piers will be performed, and in liaison with specialized construction companies, the direct repair costs will be estimated.

Keywords: Repair cost; Shear limit state damage, RC hollow-piers, Non-linear cyclic behaviour.

1. INTRODUCTION

The hollow section piers are often used in high-rise bridges, particularly when it is necessary to ensure high stiffness and simultaneously low weight, thus leading to a more economical construction. Hollow piers can be compared to reinforced concrete walls, however when such components are subjected to high intensity seismic actions can, in certain circumstances, evidence a significant vulnerability associated mainly to the low shear capacity.

Due to the expected vulnerability of these piers, when subjected to seismic actions, it becomes urgent to assess the expected damage and its evolution with the increase of the intensity level. Additionally, it is noted that the focus of the scientific research devoted to seismic behaviour of these elements is still reduced, in particular with regard to damage and to the limit states of damage. This paper focus on the analysis of damages on hollow piers due to the seismic action, proposing a methodology to characterize the limit states of damage under the perspective of the physical behaviour. To establish a correspondence between physical damage states and structural parameters, a set of results of quasi-static experimental tests was analysed, in hollow piers of reinforced concrete subject to cyclic loading [1-3].

An experimental test campaign was conducted in the Laboratory of Earthquake and Structural Engineering (LESE), located at the Faculty of Engineering of University of Porto, where a test setup was developed and that served to several research works on this field of study.

This experimental test campaign consisted of 12 piers, 6 with a squares cross section (PO1) and 6 with a rectangular section (PO2). The square piers have a section of 0.45x0.45m and a wall thickness of 7.5cm. The rectangular piers have a section of 0.90x0.45m also with a wall thickness of 7.5cm. All piers are 1.40m tall and were built with 1/4 scale from the original size. All the piers have different characteristics of materials, arrangement of shear reinforcement or cross areas of reinforcement. Table 1 shows these characteristics of the piers [1-3] and Figure 1 illustrate the reinforcement details. An axial load of 250 kN was considered, that corresponds to a normalized axial force of 0.08.

Designation	Geometry	f_{cm} (Mpa)	Longitudinal Reinforcement		Shear Reinforcement		
			area	f_{sy} (Mpa)	\emptyset (mm)	f_{sy} (Mpa)	Type
PO1-N1	Square	19,8	40 ϕ 8	625	3,8	390	2 legs
PO2-N1	Rectangular	19,8	64 ϕ 8	625	3,8	390	2 legs
PO1-N2	Square	27,9	40 ϕ 8	435	2,6	437	2 legs
PO1-N3	Square	27,9	40 ϕ 8	435	2,6	437	2 legs
PO2-N2	Rectangular	27,9	64 ϕ 8	435	2,6	437	2 legs
PO2-N3	Rectangular	27,9	64 ϕ 8	435	2,6	437	2 legs
PO1-N4	Square	28,5	40 ϕ 8	560	2,6	443	2 legs
PO1-N5	Square	28,5	40 ϕ 8	560	2,6	443	2 legs (EC8)
PO1-N6	Square	28,5	40 ϕ 8	560	2,6	443	4 legs (EC8)
PO2-N4	Rectangular	28,5	64 ϕ 8	560	2,6	443	2 legs
PO2-N5	Rectangular	28,5	64 ϕ 8	560	2,6	443	2 legs (EC8)
PO2-N6	Rectangular	28,5	64 ϕ 8	560	2,6	443	4 legs (EC8)

Table 1 : Properties of tested piers.

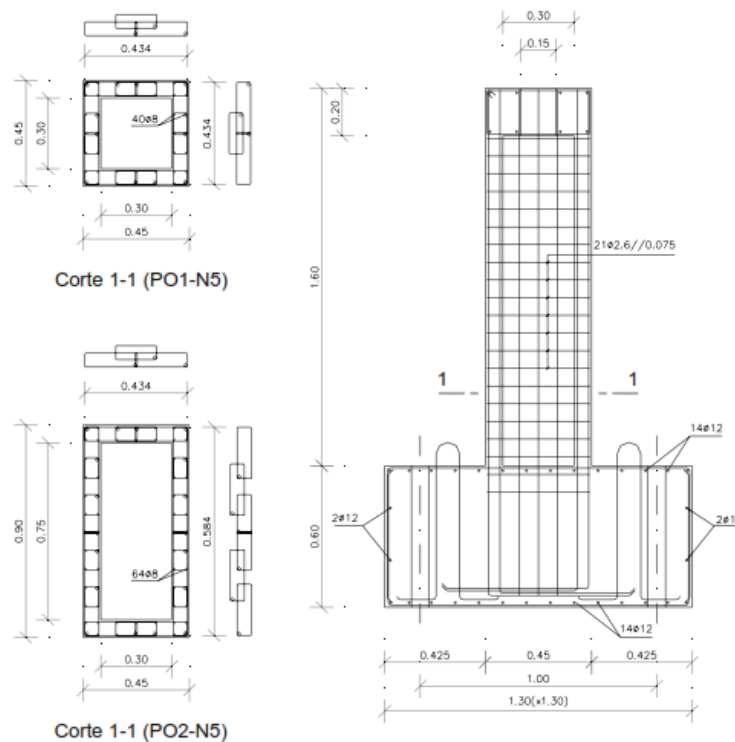


Figure 1: Piers PO1-N5 and PO2-N5 reinforcement details [1].

2. LIMIT STATES OF SEISMIC DAMAGE

With the analysis of the experimental test it was possible to perform an evaluation of the damages in the columns. The types of damages that were observed correspond to: concrete cracking, concrete spalling and concrete crushing. After quantifying and analysing the damages due to the displacement applied on the top of the column, it was possible to identify several response levels corresponding to the seismic damage limit states. The seismic damage limit states chosen for the present study were those defined by Delgado *et al.* [4]. These seismic damage limit states are in line with other studies and documents, e.g. [5] and [6].

The methodology proposed by Delgado *et al.* [4] defines a total of four damage limit states. The first state of damage corresponds to slight damage. In this state, the damage is barely visible and does not compromise the structural stability. The visible damages are essentially the beginning of cracking, in a small extension and density, concentrated on the lower third of the columns. The second state of damage, referred to as moderate damage, is distinguished from the previous state limit by the increase in cracking. The cracks have reduced openings, smaller than 1mm, being a large part of the typical cracks, shear cracking, which reach a maximum of 1mm of opening. The third state of damage is the state of extensive damage. When a pier reaches this level of damage the element already requires attention and a significant repair. The most visible damages in the piers are the appearance of cracks openings of up to 3 mm and with a high density. In this state of damage the cracks are essentially due to shear in the webs and to bending in the flanges also noting the effect of "shear lag effect". The cracks are evenly distributed over the entire section of the pier. It is also possible to observe some concrete spalling. The ultimate damage state is the collapse. When damage to the pier reaches this level, it is no longer economically and feasible to repair the structural element and its structural safety is seriously compromised. Between this state and the state of extensive damage, there is a significant evolution of damages, with emphasis on the concrete

crushing and an increase of the detachment of the concrete cover. Numerically, this state is defined when the shear stress is higher than the theoretical resistant value or the conventional shear occurs. Figure 2 illustrates the evolution of damage, in the various limit states of damage.

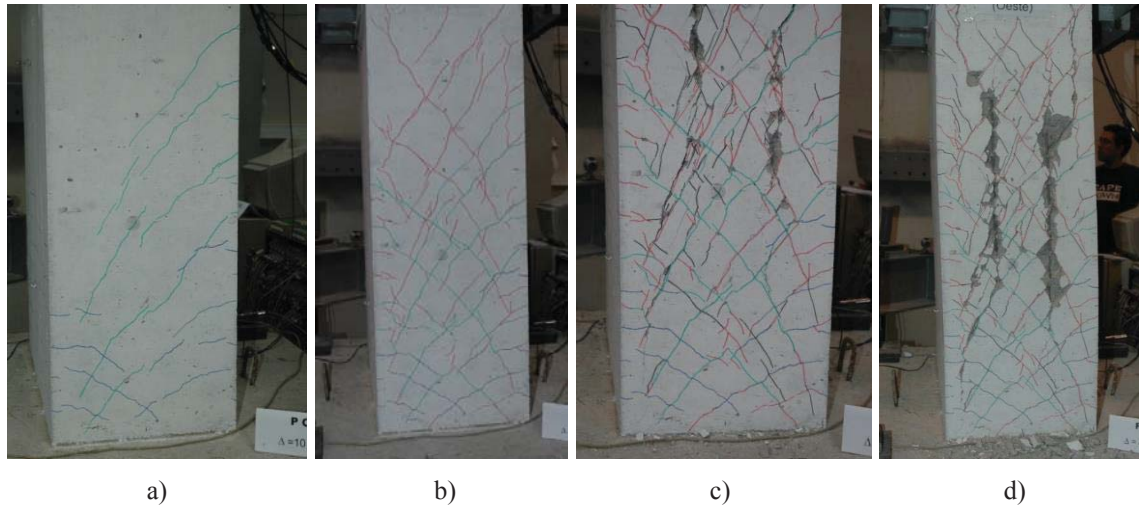


Figure 2: a) Slight damage, b) Moderate damage, c) Extensive damage, d) Collapse.

After defining the several damage states, it is necessary to identify a response parameter capable to translate the evolution of the physical damages of the column in each of the above limit states. Thus, and with the purpose of using a single structural parameter for all limit states, which can be easily evaluated in any numerical model, the drift response parameter was selected. The correspondence between the four previously defined limited states of damage and the drift values was established from the analysis of the experimental tests of the hollow piers, and considering a description of each boundary state. Table 2 translates the drift limit values associated with each physical damage state.

Limit State	Drift (%)
Slight	0.6
Moderate	1.3
Extensive	2.0
Collapse	3.0

Table 2 :Limit states and corresponding drift value.

3. SEISMIC REHABILITATION TECHNIQUES

Currently, there are several techniques for the repair and strengthening of structures, with the aim to ensure the replacement or improving of seismic behaviour and capacity. This study was followed by the approach and characterization of repair techniques proposed in the research project "PRISE - Evaluation of Losses and Seismic Risk of Buildings in Portugal" [7], funded by the Portuguese Foundation for Science and Technology, in which the authors of this study were involved, and as presented in the work conducted by Delgado *et al.* [4]. In this project was built a database of unit repair costs for each repair technique, which includes materials and labour costs, obtained from surveys collected from several construction companies existing in Portugal and specialized in repairing/strengthening these damages. In this study, the costs of the access to the pier to be repaired and other works, were considered.

3.1. Slight Damage

This limit state is characterized by minor or irrelevant, and almost imperceptible visualized damages, with very small cracks, up to 0.5mm of opening. For such pattern, with crack width less than or equal to 0.1mm, three possible repair techniques are identified and may or may not occur together, namely: surface painting; Surface plaster of the piers; Scrub surface with epoxy resin. If the environmental conditions of aggression are zero, no repair is necessary. For crack width between 0.1mm and 0.5mm, the most appropriate repair technique is the injection of epoxy resin.

The painting of the concrete surfaces of the piers must be carried out through water-based monolayer paint scheme. This painting should be done in two coats, with a smooth finish, resistant to the alkalis of the hydraulic binders and complying with the minimum requirements of EN 1504-2 [8]. This painting should be done with elastic paints to prevent further fissure of the piers. The surface plater repair technique consists of a generalized treatment of the cracks at an unspecified location. The same plastering should be done with an adjuvant mortar. The last repair technique, applied on crack width lower than 0.1mm is to scrub the surface with epoxy resin. This technique consists on the application of impregnation product with one coat, resistant to the alkali of the hydraulic binders and fulfilling the minimum requirements of EN 1504-2, [8].

3.2. Moderate Damage

The state of moderate damage is characterized by small cracks in the abutment faces, corresponding to an opening between 0.5mm and 1.0mm. Structural stability is not compromised, and any type of structural intervention is unnecessary. To repair crack openings, the most appropriate repair technique is the injection of epoxy resin, which must comply with EN 1504-5 [9], regarding injections in reinforced concrete structures

3.3. Extensive Damage

In the limit state of extensive damages the crack width is, approximately, between 2mm to 3 mm, and is visible some concrete spalling. When a pier reaches this state of damage it already requires some attention, and needs to be repaired in a short term in order not to compromise the structural stability. For this reason, it is necessary to proceed with a structural reinforcement of the element. The repair technique for the cracks consists of the injection of epoxy resin, respecting EN 1504-5 [9], as previously mentioned. When the pier has cracks and some spalling, it is necessary to proceed with the reconstruction of the piers. With respect to the structural reinforcement of the element this can be realized in three distinct ways: increase of the section with the use of reinforced concrete; Bonding of metal sheets and Pier engagement with carbon fibre blankets (CFRP).

When the piers have some concrete spalling, it is necessary to replace this same concrete. It is first necessary to remove the damaged concrete, to clean and to perform a surface treatment with a needle hammer. Once the degraded concrete has been cleaned, it is necessary to place a new concrete in compliance with EN 1504-2 [8].

One of the most used strengthening techniques is the jacketing with carbon fibre blankets (CFRP). This technique has the advantage of causing a minimal increase of the section and greatly increasing the strength. This technique consists of bonding carbon fibre blankets using epoxy resins and then finishing with a self-adhesive mortar. In this type of strengthening, it is necessary to ensure that the ends are well bonded. Figure 3 illustrates the result of a CFRP-reinforced piers. All of these glues referred to in the previous reinforcements must comply with EN 1504-4 [10].



Figure 3: Pier reinforced with CFRP.

3.4. Collapse

As previously mentioned, the damage limit state corresponding to the collapse is characterized by a large concrete spalling and in which the theoretical resistance is exceeded. Thus, when a pier reaches this state of damage, it becomes economically impracticable to repair. If the demolition operation is not possible, there is no feasible repair techniques and only structural reinforcement is possible, using the reinforcement techniques described above.

4. DIRECT REPAIR COSTS ESTIMATION

After identifying the unit costs associated with the tasks and resources required for each rehabilitation and strengthening technique of the piers, the evolution of the cost according to the response of the structural element was quantified. The pier behavior develops according to its material and geometric characteristics, and the level of seismic action. The drift was considered as the response parameter, thus allowing to estimate the cost of piers rehabilitation for each seismic damage limit state [7]. The quality of the cost estimate for repair or strengthening is very important in the identification of the technique to be adopted. In the case of rehabilitation works, construction presents several sources of uncertainty, due, for example, to the difficulty in performing some of the tasks, making it difficult to quantify the necessary resources, such as man cost and equipment needed in the intervention. However, in this work an estimate of the average costs of the pier rehabilitation was carried out according to its damage limit state and separating the cost by type of work to be carried out, that is, the cost of materials, the cost of labor and cost of access to the pier area to be repaired and other additional works.

4.1. Slight Damage

For the limit state of slight damage, if the cracks have openings less than 0.5mm, the cracked surface must be repaired, corresponding to the pier bottom, in this case approximately equal to the dimension of the cross section. Table 3 illustrates the separation of repair costs according to the type of work to be carried out.

	Average Cost (€)
Material	77
Labors	49
Accessibility and other works	21
Total	154

Table 3 :Pier repair costs for limit state of slight damage.

4.2. Moderate Damage

For the limit state of moderate damage with cracks between 0.5mm and 1mm, the injection of epoxy resin should be used. In this case, about 2/3 of the pier surface is cracked, including the repair costs associated with each task in Table 4.

	Average Cost (€)
Material	112
Labors	98
Accessibility and other works	49
Total	259

Table 4 :Pier repair costs for limit state of moderate damage.

4.3. Extensive Damage

The limit state of extensive damage is characterized by the deteriorating of the state of the structure, with the appearance of large cracks, with openings that can vary between 1 mm and 3 mm, distributed on all sides of the pier, and it is also possible to verify the spalling of the concrete cover. When the pier reaches this state of damage, the surface treatment is not sufficient to guarantee the necessary minimum requirements, thus it is necessary to proceed with a structural reinforcement of the element. Table 5 represents the different costs by type for repair, taking into account an average estimate of the three structural reinforcement techniques namely: increase in section with reinforced concrete, reinforcement with the addition of metallic profiles and reinforcement with carbon fiber blankets (CFRP).

	Average Cost (€)
Material	245
Labors	252
Accessibility and other works	105
Total	602

Table 5 :Pier repair costs for limit state of extensive damage.

4.4. Collapse

Finally, for the limit state of collapse, which is characterized by a large detachment of the covering concrete, its repair is economically unfeasible. Thus, the demolition and construction of a new pier corresponds to the work to be applied in this case. The total cost will reflect all the demolition work on the pier, involving the recycling of all materials, loading, transport

and unloading, as well as the auxiliary tasks necessary for cleaning the site. The cost of building a new pier includes the execution of an identical reinforced concrete pier, including the supply, placement, compaction and curing of the concrete. The total price for demolition and construction of this reinforced concrete pier is around € 699. Table 6 shows the costs separated according to the type of work to be carried out. Unit costs were estimated and validated through contact with specialized construction companies.

	Average Cost (€)
Material	209
Labors	280
Accessibility and other works	210
Total	699

Table 6 : Pier repair costs for limit state of collapse.

4.5. Evolution of structural intervention costs

After analysing the costs of each structural repair and strengthening technique, it is necessary to understand how the cost evolution occurs as a function of the structural response, considering in this case the drift as a response parameter. Thus, it will be possible to quantify the economic weight of each state limit for the repair or strengthening of the piers.

In order to make this analysis more global, it was adopted to represent the evolution of the ratio between the cost of repair and the cost of replacing the pier as a function of the drift, as illustrated in Figure 4, for each Limit State of Damage (LSD). This transfer evolution of damage into costs, provides an important indicator for any cost estimate in hollow section reinforced concrete piers. Additionally, it also allows to assess the impact and efficiency of each repair or strengthening technique. Figure 4 reveals that the repair costs associated with the extensive and collapse damage levels mean that the repair of the structural element is not viable. However, even in the case of slight and moderate damages the respective costs are already quite significant.

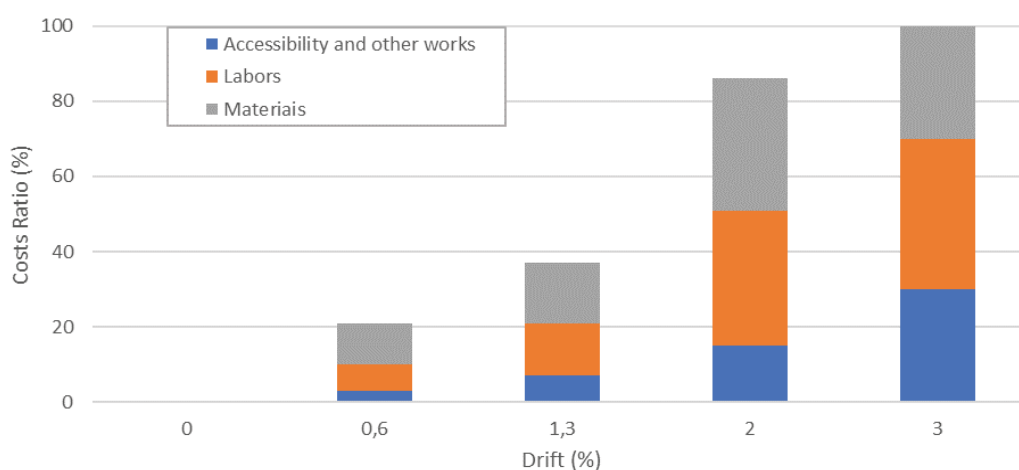


Figure 4: Evolution of the repair cost ratio (%) for each LSD/drift.

In the case of this study, for structures that suffered from the impact of an earthquake and therefore in need of rehabilitation, factors such as the type, size of the bridge and how it will be made accessible must be taken into account. The places where structures are found that are damaged by earthquakes are usually difficult to access, and the debris on the site and the size of the structure contribute to a considerable increase in the budget. The piers previously studied are usually implemented in different types of bridges, with different dimensions and which, in terms of accessibility, can vary between easy access, moderately difficult access and difficult access.

5. CONCLUSIONS

In the present study, the evolution of structural damage in hollow reinforced concrete piers (whose behaviour is also representative of reinforced concrete walls) due to the action of earthquakes, with the purpose of defining limit states of damage (LSD), is based on a previous study of the authors of this study Delgado *et al.* [4]. This information was associated with repair and strengthening techniques, which are commonly applied in Portugal. Finally, the respective costs were estimated, which allowed to characterize the evolution of the costs of piers repair and strengthening as a function of the structural response. This work uses the construction techniques and their unit costs established under the PRISE project.

In this study, it was intended to obtain a methodology that is capable of predicting an assessment of the damage to the different piers, and the cost estimation of piers repair and strengthening, allowing to assess, in a simplified way, the cost estimate of the piers rehabilitation with insufficient shear capacity for each limit state of seismic damage. The proposed methodology allows to conclude that the repair of hollow reinforced concrete piers has significant costs even for moderate damage, and the replacement costs for collapse and extensive damage are practically identical. Thus, both from the point of view of costs and seismic safety, this study identifies the urgency of verifying the shear capacity of bridge piers and, in case it is insufficient, proceed to strengthening it in order to avoid the most severe LSD or collapse.

6. ACKNOWLEDGMENTS

This work was developed within the scope of the project proMetheus – Research Unit on Materials, Energy and Environment for Sustainability, FCT Ref. UID/05975/2020, financed by national funds through the FCT/MCTES.

This work was also financially supported by: Financiamento Base - UIDB/04708/2020 e Financiamento programático - UIDP/04708/2020 - CONSTRUCT - Institute of R&D In Structures and Construction funded by national funds through FCT - Fundação para a Ciência e a Tecnologia/MCTES (PIDDAC).



REFERENCES

- [1] Delgado, R., Delgado, P., Vila Pouca, N., Arêde, A., Rocha, P., Costa, A. Shear effects on hollow section piers under seismic actions: experimental and numerical analysis, *Bulletin of Earthquake Engineering*, **7**, 377-389, 2009. (DOI: 10.1007/s10518-008-9098-x).
- [2] Delgado, P., Monteiro, A., Arêde, A., Vila Pouca, N., Delgado R., & Costa, A. Numerical Simulations of RC Hollow Piers Under Horizontal Cyclic Loading. *Journal of Earthquake Engineering*, **15**:6, 833-849, 2011.
- [3] Delgado, P., Arêde, A., Vila Pouca, N., Rocha, P., Costa, A., Delgado, R. Retrofit of RC Hollow Piers with CFRP Sheets, *Composite Structures*, **94**, 1280–1287, doi:10.1016/j.compstruct.2011.11.032, 2012.
- [4] Delgado, P., Sá, N., Marques, M. & Arêde, A., Methodology for the characterization of seismic limit states of damage in RC hollow piers experiment. 16WCEE – *16th Conference on Earthquake*, Chile, 9-13 January, 2017.
- [5] Rodrigues, H., Arêde, A., Varum, H. & Costa, A., Damage evolution in reinforced concrete columns subjected to biaxial loading. *Bull Earthquake Eng*, pp. 1517-1540, 2013.
- [6] FEMA, HAZUS MR4. Washington DC: National Institute of Building Sciences, 2003.
- [7] PRISE, “Avaliação de Perdas e Risco Sísmico dos Edifícios em Portugal”, projeto financiado pela Fundação para a Ciência e a Tecnologia, 2013-2015 (<http://prise.fe.up.pt>)
- [8] CEN, NP EN 1504-2. Produtos e sistemas para a protecção e reparação de estruturas de betão - Definições, requisitos, controlo da qualidade e avaliação da conformidade. Parte 2: Sistemas de protecção superficial do betão. Brussels: European Standard, 2006.
- [9] CEN, NP EN 1504-5. Produtos e sistemas para a protecção e reparação de estruturas de betão - Definições, requisitos, controlo da qualidade e avaliação da conformidade. Parte 5: Injeção do betão. Brussels: European Standard, 2006.
- [10] CEN, NP EN 1504-4. Produtos e sistemas para a protecção e reparação de estruturas de betão - Definições, requisitos, controlo da qualidade e avaliação da conformidade. Parte 4: Colagem estrutural. Brussels: European Standard, 2006.

OPTIMIZATION OF THE SLIP FORCE IN A NOVEL FRICTION-BASED CONNECTION FOR THE E-CLT TECHNOLOGY

A. Aloisio¹, F. Boggian², R. Tomasi³

¹ Department of Civil, Construction-Architectural and Environmental Engineering, Università degli Studi dell'Aquila, L'Aquila, Italy, e-mail: angelo.aloisio1@univaq.it

² Department of Civil, Environmental and Mechanical Engineering, University of Trento, Trento Italy, Faculty of Science and Technology, Norwegian University of Life Sciences, Ås, Norway, e-mail: francesco.boggian@unitn.it , francesco.boggian@nmbu.no

³ Faculty of Science and Technology, Norwegian University of Life Sciences, Ås, Norway, e-mail: roberto.tomasi@nmbu.no

Keywords: Seismic retrofitting, friction-based dissipation, Cross-Laminated Timber panels, Reinforced Concrete structures, Sustainability.

Abstract. *The European Union has sponsored the development of a new friction dissipating system, for improving seismic behaviour of existing buildings. The proposed system consists of CLT-elements connected to the external beams of existing reinforced concrete building using steel profiles. Each of the steel profiles consists of two separate plates connected by a friction connection made by preloaded bolts in elongated holes. The authors carried out the experimental testing of the friction connection by estimating the corresponding hysteresis curve. A Duhem-like mechanical model, matching with the experimental results, simulates the cyclic response of the connection. The authors investigate the seismic performance of a structural archetype, a plane RC frame with CLT shear walls equipped with this sort of friction dampers. It is assessed the optimum preload condition to achieve an optimal seismic performance according to the Italian seismic scenario by the fragility assessments. A selected suite of earthquakes is the basis of Incremental Dynamic Analysis (IDA) of the structural archetype, without and with the friction device. The optimum preload of the dissipating systems descends by optimizing the structural performance: maximizing the dissipated energy by preventing damage to the CLT panel and the reinforced concrete frame.*

1 INTRODUCTION

The vulnerability of the existing building entails developing non-invasive retrofitting approaches, based on passive devices [1, 2, 3].

The use of passive devices could be advantageous due to low-invasiveness and reduced installation time [4, 5], compared to more traditional seismic retrofitting strategies [6, 7, 8].

Among them, friction-based dampers have shown great potential, compared to the most diffuse buckling restrained braces and fluid viscous dampers [9, 10]. The performance of friction-based systems is sensitive to dampers' location and the value of the slip forces. The first studies about friction dampers directed on experimental tests and technological development of the friction-based devices with the hysteresis loop's rectangular shape [11], as the Slotted Bolted Connection (SBC) discussed by [12, 13, 14]. Lately, several researchers proposed alternative friction dampers featured by nonrectangular hysteresis curves. Among the others, Clifton et al. [15] introduced the asymmetric sliding hinge joint (SHJ) for steel moment-resisting frames with a nonrectangular hysteresis.

A few investigations dealt with applications of friction devices on timber shear walls. Filiatrault et al. [16] proved the advantage in using friction sliders in timber sheathed shear walls. Loo et al. [17] confirmed the findings by [16]: they applied symmetric slip friction connections to replace the traditional nail plate hold-downs for timber Laminated-Veer-Lumber (LVL) walls. Hashemi et al. [18] extended the study by [17] to Cross-Laminated Timber (CLT) coupled walls and hybrid timber–steel core walls. Recently, Hashemi et al. [19] developed an innovative, resilient slip friction joint (RSFJ) characterized by a nonrectangular hysteresis shape.

The current research focuses on the e-CLT technology, developed on the ongoing multidis-

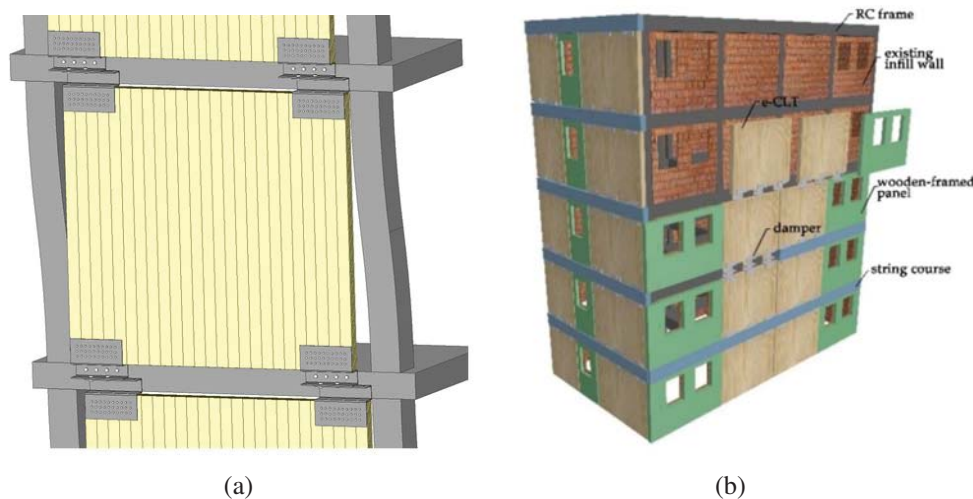


Figure 1: (a) Proposed friction energy dissipating system; (b) Illustration of a working application.

ciplinary Horizon 2020 research project e-SAFE (Energy and Seismic Affordable rEnovation solutions): an application of Asymmetric Friction Connection (AFC) dampers and CLT panels on existing reinforced concrete structures for seismic retrofitting purposes.

The AFC is an arrangement of five plates, three steel plates and two thinner plates, named shims, assembled using high strength bolts. The AFC were studied by [15]. Primary attempts used brass shims based on the energy dissipation mechanism proposed by [14] for slotted bolted connections. Succeeding studies carried out by [20] extended the SHJ idea to mild steel and aluminium shims. Fresh studies carried out by [21] introduced bisalloy grades 80 and 400 shims.

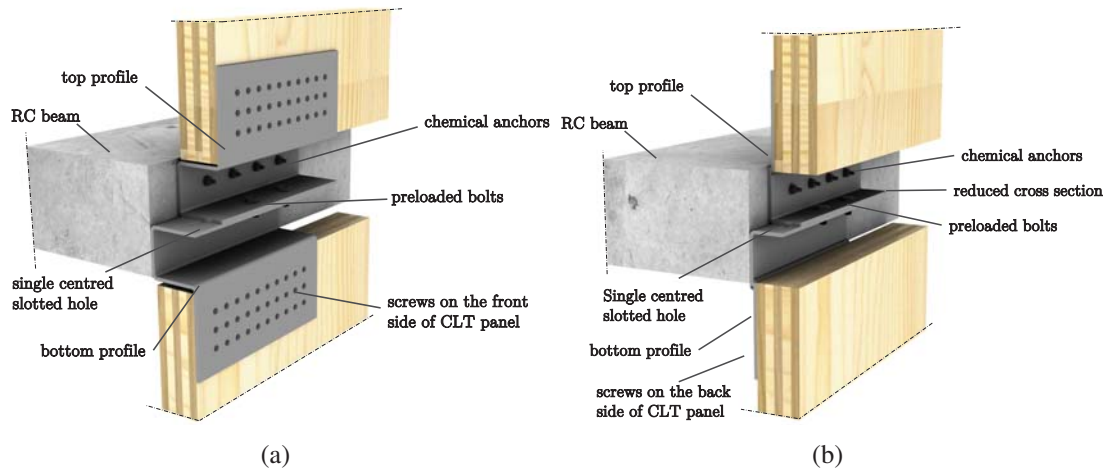


Figure 2: (a) Possible profile design with front mounted CLT panel; (b) Possible profile design with back mounted CLT panel.

The e-CLT technology consists of the external application of prefabricated Cross-Laminated Timber (CLT) [22, 23, 24] structural panels by connecting them to the RC beams through AFC, see Fig.1 and 2. If moderate earthquakes occur, the dampers rigidly connect the CLT panels to the RC structure, by enhancing the lateral stiffness and strength. During strong ground motions, the friction dampers activate with possible significant energy dissipation. The e-CLT system aims at reducing the storey drift demand and the damage to nonstructural and structural components. The presented retrofitting intervention may combine the e-CLT technology with nonstructural pre-assembled panels made of wooden frames and provided with high-performing windows to replace the existing ones. Not secondarily, structural and nonstructural panels integrate bio-based insulation materials and the desired finishing layer to improve the energy performance and the architectural image of the renovated building [25].

The e-CLT technology comprises the installation of AFC, whose response is mostly driven by Columbian forces. The damper consists of a contacting friction interface clamped by pretension high strength bolts: the friction interface sliding guarantees energy dissipation. The device has two cold-bent steel profiles that connect the CLT panels of two consecutive storeys with the existing interposed RC beam. The upper profile is connected to the RC beam by anchor bolts. The bottom profile is provided with slotted holes and is connected to the upper one by pre-tensioned high strength bolts. Standard timber screws connect both the upper and bottom profile to the CLT panels. The authors present the experimental cyclic response of the considered AFC by addressing the slip force's role for its optimum design.

To the authors' knowledge, a few studies focused on the optimum design of friction-based dampers. The most recent researches examine the optimum design of friction-based dampers installed on structural archetypes through nonlinear dynamic analysis driven by optimization algorithms [26].

So far the most significant achievements about the optimum design of friction-based dampers are:

- Optimum distribution of the friction device and optimum selection of the slip force value can lead to a more than 50% reduction of the inter-storey drift in RC frames. Additionally, a nonuniform distribution of the total slip force along the building's height can further reduce the inter-storey drift [27, 28].

- The optimum slip load values are more affected by the amplitude and frequency of the input earthquakes (e.g. peak ground acceleration) rather than the characteristics of the structure [16].
- [29] derived an empirical equation which predicts the optimum slip load:

$$R = 1.12 e^{-0.11n} \quad (1)$$

where R is the ratio between the average of the slip loads with uniform cumulative distribution and the average shear strengths of the storeys, n is the number of storeys.

The mentioned studies, focused on optimizing slip-forces in friction dampers, required extensive parametric studies, which involved modelling a large variety of structural archetypes. However, the analyses' main drawback stood in the adoption of simplified constitutive models for concrete and the dampers and the modelling of the frames without the infill. The use of an elementary Coulomb-like friction model may be inadequate due to the possible higher slip force during the first cycles. The stability of the hysteresis loop and the magnitude of the friction forces developed by AFC specimens are directly related to the shim material hardness [30]. The presence of the masonry infill affects the seismic performance of RC frames significantly by increasing both the stiffness and resistance, as well as the ductility and pinching phenomena [31].

This paper investigates the performance of the e-CLT technology on an RC frame with masonry infill, which is the primary unit of many existing RC buildings. The main novelties of the research are:

- Discussion of the experimental cyclic response of a novel AFC, included in the e-CLT technology, and presentation of an enhanced Coulomb-like model.
- Investigation of the seismic response of an elementary RC frame equipped with the AFC using the Atan model calibrated on the experimental cyclic response of an RC frame with clay infill. Estimation of the optimum slip-force in the considered system, which yields the minimum displacement drift.
- Comparison between the optimization results with existing empirical formulations useful for preliminary design.

The paper has the following organization. The second section formulates the optimization problem, while the third presents and discusses the experimental tests on the friction-based dampers. The fourth section addresses the modelling choices and the calibration of the hysteresis models for simulating the RC frame and the friction damper. The fifth section discusses the first results obtained from the coupled system, while the sixth section deals with the optimization problem's solution. The last section compares the obtained results to the existing formulations by proposing alternative design approaches.

2 ACTIVATION CONDITION

The preliminary design of friction-based dampers may descend from the definition of their activation condition. The activation identifies the phase when the inertial forces win the connection's slip resistance, and the device starts dissipating energy.

The activation condition definition is crucial: a precocious activation may lead to a non-optimum

exploit of the structure's elastic energy. A late activation determines the safety margin's erosion: the damper may start dissipating when the system has already suffered extensive and critical damage. Therefore, the activation phase must occur just in time to yield the maximum benefits to the structure.

Likely, the activation is not contemporary between all devices, since the structural deformation is not uniform within the structure. Therefore, the activation condition's optimum design is the most crucial task in designing a retrofitting intervention based on friction dampers. The practitioner must design both the slip force and the distribution of the dampers inside the structure.

Let us consider an elementary structural archetype, a plane frame, representing the primary structural unit in an RC frame building. The dampers' activation at the i -th storey occurs when the inter-storey drift exceeds a given threshold.

The authors will focus on estimating the slip force associated with a structural archetype's optimum seismic performance and will neglect to determine the dampers' optimum distribution, which can be the object of future investigations.

Why is the design of the slip resistance a minimum problem? Let us consider the maximum inter-story drift, which is an acknowledged indicator of the damage level in both structural and non-structural elements of RC structures [32]. The displacement drift depends on multiple factors. The authors will consider the sole slip resistance of the damper:

$$d_{\max} = f(F_{s,R}, \mathbf{x}) \quad (2)$$

where d_{\max} denotes the maximum displacement demand, $F_{s,R}$ is the damper slip resistance and \mathbf{x} collects additional variables affecting the maximum drift demand (structural stiffness, e.g.). The following paragraphs explain the presumed evolution of the maximum displacement demand as a function of the slip resistance, qualitatively illustrated in Fig.3.

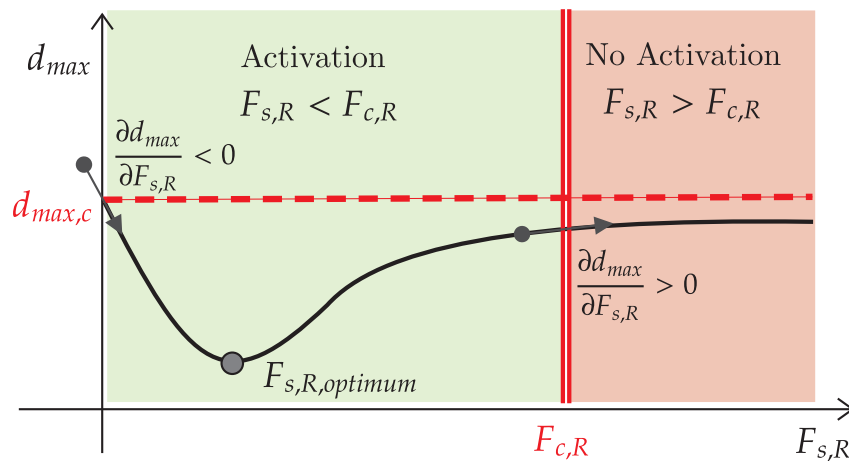


Figure 3: Qualitative illustration of the trend of the maximum displacement d_{\max} as a function of the slip resistance of the AFC.

The displacement drift is related to the dissipated energy during the seismic excitation. If the damper's slip resistance tends to zero, the structure behaves as if no damper is installed.

$$\lim_{F_{s,R} \rightarrow 0} d_{\max} = d_{\max,c} \quad (3)$$

where d_{\max} is the maximum displacement demand, and $d_{\max,c}$ is the maximum displacement demand of the RC structure without dampers. If the slip resistance tends to infinity (Eq.4), the damper does not activate, and the structure behaves as if no damper is installed and the CLT panel behaves as an additional stiffening element reducing the maximum displacement demand: the slip resistance would be higher than the shear resistance of the RC structure, expressed by a double vertical line in Fig.3.

$$\lim_{F_{s,R} \rightarrow \infty} d_{\max} = d_{\max,c} - d_{CLT} \quad (4)$$

where d_{CLT} is a contribution which lowers the displacement demand due to the additional stiffness of the CLT panel. If the slip resistance increases from the zero value, see Fig.3, the dissipated energy increases. The damper activates when there are low inertial forces. Still, the friction-based device must endure significant displacement to obtain a meaningful energy dissipation. However, the drift should reduce, and the following derivative would be negative:

$$\lim_{F_{s,R} \rightarrow 0} \frac{\partial d_{\max}}{\partial F_{s,R}} < 0 \quad (5)$$

If the slip force is lower than the shear resistance of the structure, the damping device can activate, green region in Fig.3. However, if the slip resistance reduces from the value corresponding to the structure's shear resistance (red area in Fig.3), the expected drift should reduce. The damper may start dissipating when the system did not attain the maximum displacement capacity, thus increasing the dissipated energy and possibly lowering the drift demand. The AFC has larger displacement margin for dissipation. Therefore, the following derivative would be positive:

$$\lim_{F_{s,R} \rightarrow F_{c,R}} \frac{\partial d_{\max}}{\partial F_{s,R}} > 0 \quad (6)$$

where $F_{c,R}$ is the shear resistance of the RC frame. The design of the slip force resembles a minimum problem. Likely, there is a force value which may minimize the drift demand during seismic excitation. The mathematical problem cannot have a closed-form formulation. The optimum performance depends on the expected seismic scenario. Therefore, the authors followed an *a posteriori* approach, conventional in earthquake engineering. They select a set of earthquakes, matching a given design spectrum. Then, they estimated the nonlinear dynamic response of a specific structural archetype by varying the slip resistance in a given range—the minimum of these values obtained from the considered list of earthquakes identifies the optimum solution.

$$F_{s,R,optimum} = \arg \min_{F_{R,s}} d_{\max}(F_{R,s}, a_g) \quad (7)$$

where a_g represents a seismic scenario. The paper aims to solve the minimum problem in a specific structural configuration, representing the anatomical unit of the e-CLT technology.

3 Experimental tests

The authors investigated the cyclic behaviour of the AFC devised for e-CLT technology. The considered setup focuses on the friction damper and does not include CLT elements. The experimental setup consists of a rigid steel frame, namely the columns have a 12.5mm thickness and 100×200mm rectangular section, the bottom profile of the specimen is attached to the right

column, while the top profile is in the central part of the frame and is free to slide, being connected to the actuator of the press. An additional steel cap plate and two aluminium shim layers were inserted between the profiles, to obtain an asymmetrical friction connection. The goal of

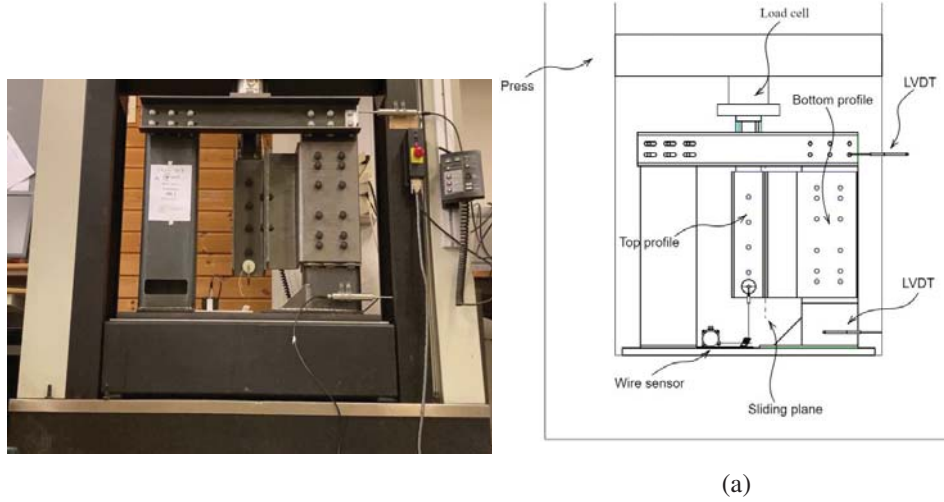


Figure 4: (a) Setup with all measuring instruments mounted; (c) illustration of the setup

the friction connection in the current setup is to have a 30kN sliding force, this threshold originates from the working limit of the press machine and previous FEM models [33]. The preload force in the bolt was set to $F_{P,c} = 36\text{kN}$, which resulted in an experimental slip resistance $F_{s,R} = 29.57\text{kN}$, calculated as [17]. The experimental friction coefficient is calculated as:

$$\mu = \frac{F_{s,R}}{n_s n_b F_{P,C}} = \frac{29.57}{2 \cdot 2 \cdot 36} = 0.21 \quad (8)$$

where $F_{s,R}$ is the experimental slip resistance, $n_s = 2$ is the number of shear surfaces, $n_b = 2$ is the number of the preloaded bolts and $F_{P,c}$ is the preload force in the bolts. Interestingly, the

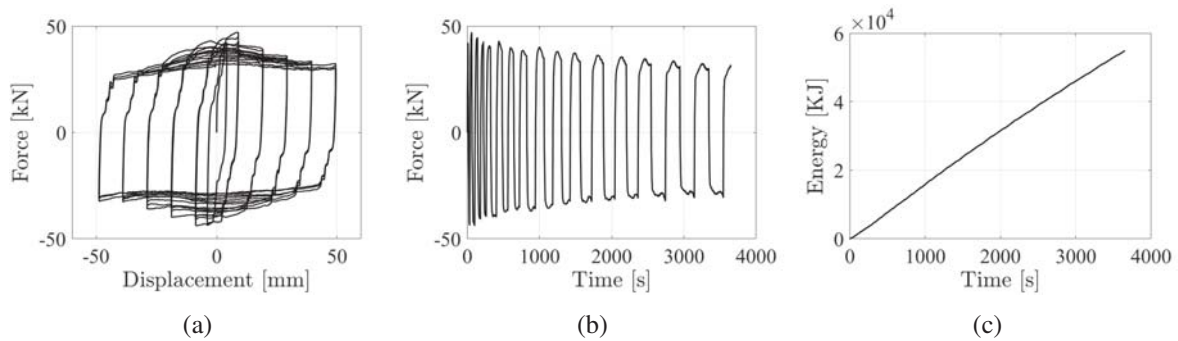


Figure 5: (a) Experimental hysteresis loop; (b) Force-Time function; (c) Dissipated Energy-time function.

estimation of resistant slip force is not unmistakable. The hysteresis loop does not display an expected rectangular shape. There is a significant increment of the slip resistance in the first few cycles at lower displacements, while it stabilizes at higher displacement to an almost constant value equal to 30kN, as seen in Fig.5. This effect is not negligible, since there is an approximate 56% increment of the peak to the stable value at higher deformations. The modelling of this

phenomenon is mandatory to achieve a reliable prediction of the performance of this system. This aspect is in full accordance with the experimental tests reported by [30]. Specifically, the adoption of an aluminium plate, characterised by low hardness, causes moderately stable loops. The friction coefficient corresponding to the peak force value is, in fact:

$$\mu = \frac{F_{peak}}{n_s n b F_{p,C}} = \frac{47.03}{2 \cdot 2 \cdot 36} = 0.33 \quad (9)$$

This value is in accordance with the findings by [30], who, in the case of aluminium shims, obtained a static friction coefficient of 0.34 and a dynamic of 0.21.

4 MODELLING OF THE COUPLED SYSTEM: RC FRAME, CLT PANEL AND AFC CONNECTION

The authors modelled the hysteretic response of the RC frame in Fig.6(a). Fig.6(b) shows the experimental cyclic response by increasing the displacement at each cycle up to a drift of 2.5 %. The authors reproduced the hysteretic response in Fig.6(b) using the Atan model, presented

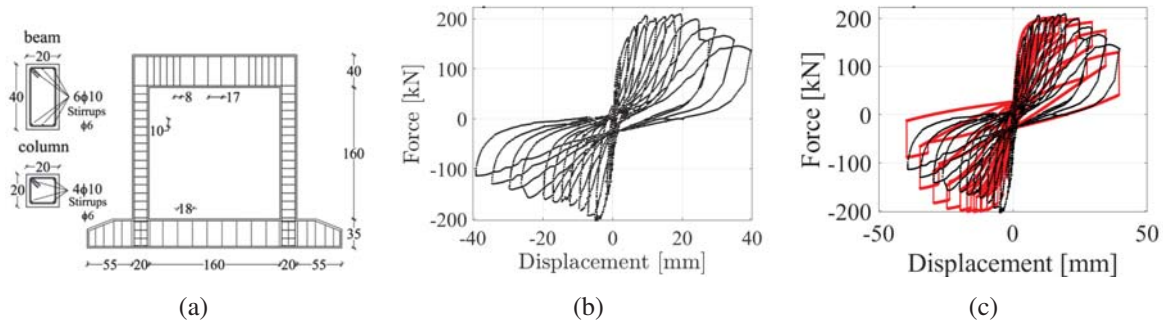


Figure 6: (a) RC frame subject to cyclic loading after [31]; (b) Experimental hysteresis loop; (c) Comparison with the Atan model.

by [34], which suits the simulation of mechanical systems with pinching, and both strength and stiffness degradation. It is a hysteresis model based on the arctangent function characterized by the following piece-wise definition:

$$\begin{aligned} 1 - a_1 \arctan(b_1 x - |c_1|) & \text{ if } \{ \dot{x} > 0, x > 0, |x| > q \max(|x(t)|) \forall t \in [0, t] \} \\ 2 - a_2 \arctan(b_2 x - |c_2|) & \text{ if } \{ \dot{x} < 0, x > 0 \} \\ 3 - a_3 \arctan(b_3 x + |c_3|) & \text{ if } \{ \dot{x} < 0, x < 0 \} \\ 4 - a_4 \arctan(b_4 x - |c_4|) & \text{ if } \{ \dot{x} > 0, x > 0, |x| < q \max(|x(t)|) \forall t \in [0, t] \} \\ 5 - a_5 \arctan(b_5 x + |c_5|) & \text{ if } \{ \dot{x} > 0, x < 0, |x| \leq q \max(|x(t)|) \forall t \in [0, t] \} \\ 6 - a_6 \arctan(b_6 x + |c_6|) & \text{ if } \{ \dot{x} < 0, x < 0, |x| \leq q \max(|x(t)|) \forall t \in [0, t] \} \end{aligned} \quad (10)$$

where the six conditional statements identify the transition between the different parts of the hysteresis. A set of three parameters define the arctangent function in each section of the loop: a_i characterise the amplitude of the force, b_i the x axis resolution and c_i the residual displacement. The subscript i varies between 1 and 6. The strength and stiffness degradation descend from the use of an exponential function, like in [35, 36]. The exponential function expresses the force and stiffness degradation as a function of the dissipated hysteretic energy (ϵ). The energy-dependent definition of a_i and b_i is:

$$a_i(\epsilon) = e^{(-\xi_{a_i} \epsilon)} a_0 \quad (11)$$

$$b_i(\epsilon) = e^{(-\xi_{b_i}\epsilon)} b_{0,i} \quad (12)$$

where ξ_{a_i} and ξ_{b_i} are properly calibrated to the degradation of the strength and stiffness respectively. The parameters are $a_0 = \frac{2F_u}{\pi}$ and $b_{0,i} = \frac{k_{0,i}}{a_0}$, where $k_{0,i}$ is the tangent stiffness, and F_u is the ultimate resistance.

Fig.6(c) displays the superposition between the experimental cyclic response of the RC frame and the simulated one using the Atan model with the parameters in Tab.1. The model satis-

Table 1: Parameters of the Atan model for the simulation of the cyclic response of the RC frame in Fig.6.

Parameter	Value
a_0	140.12
$b_{0,1}, b_{0,4}$	0.71
$b_{0,2}, b_{0,3}$	0.32
$b_{0,5}, b_{0,6}$	0.25
c_{1-6}	0.20
ξ_{a_i}, ξ_{b_i}	0.00005
q	0.80

factorily follows the experimental data by exhibiting the expected degradation behaviour. The model's significant stability under dynamic excitation endorsed this model's adoption: it was explicitly conceived to enhance the stability of hysteresis models with pinching, which present several convergence issues due to the stiffness boost in the pinched branches.

Columbian friction mainly drives the cyclic response of the AFC. Therefore, the authors adopted the following definition of the slip force:

$$F_s(\epsilon) = \mu(\epsilon) F_{p,C} \text{sign}(\dot{x}) \quad (13)$$

where $F_s(\epsilon)$ is the slip force, $F_{p,C}$ is the absolute value of the preload force, \dot{x} the velocity of deformation, ϵ is the dissipated hysteretic energy. The definition of the friction coefficient is:

$$\mu(\epsilon) = \mu_0 [\exp(-\xi\epsilon(i)) + 1] \quad (14)$$

where the μ_0 and ξ from an ordinary least squares optimization are 0.33 and 0.00005 respectively. The authors noticed that an exponential function closely follows the strength evolution

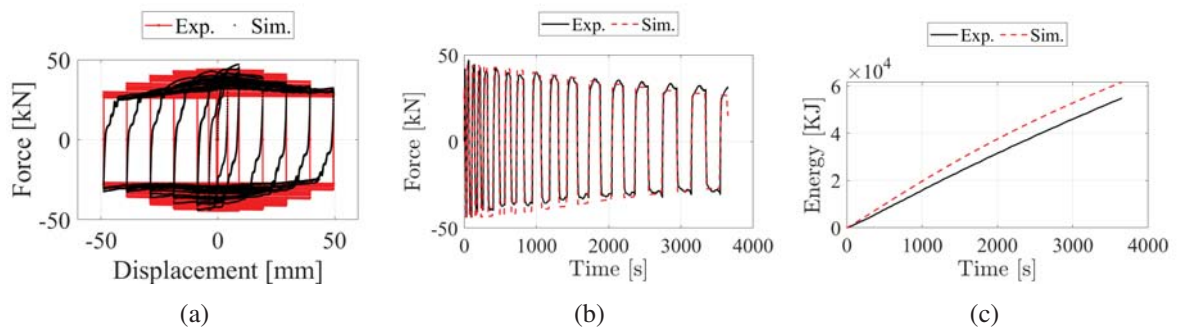


Figure 7: Comparison between the experimental data and the Coulomb-like friction model: (a) Hysteresis loop; (b) Force-Time function; (c) Dissipated Energy-time function.

of the AFC. Fig.7 presents the comparison between the experimental data and the Coulomb-like friction model. The model seizes the experimental response, but it exhibits an energy dissipation higher than expected due to the loop's non-rectangular shape due to the corner chirping effect. The authors neglect this phenomenon in the current investigation due to its limited influence on the dissipated hysteretic energy.

4.1 Modeling the coupled system

The assemblage of the RC frame with masonry infill, a CLT wall panel and the AFC represents the structural unit of the e-CLT technology. In the considered system, the CLT panel's in-plane resistance must be higher than the slip resistance of the AFC. The CLT panel increases the RC frame's strength and stiffness, but the sole AFC provides the extra dissipation capacity. Accordingly, a linear elastic behaviour of the CLT is assumed for the modelling of the panel. In the current case, the structural unit consists of the RC frame equipped with a 90mm thick CLT panel, circumscribed by the frame. Likely, the CLT panel behaves like a clamped-clamped beam. Therefore, the lateral stiffness is:

$$k_{CLT} = \frac{1}{\frac{h^3}{12EI} + \frac{1.2h}{GA}} \quad (15)$$

where k_{CLT} is the lateral stiffness, h the panel's height, E the longitudinal elastic modulus, I the cross-section inertia, G the shear modulus, A the cross-section area. The authors adopted the following parameters $E = 11600\text{MPa}$ and $G = 450\text{MPa}$. The assemblage's lateral resistance, F_T , is the summation of the three contributes, conditional of the exceeding of the slip resistance: the resistance of the RC frame F_c , the slip resistance of the AFC F_s and the CLT panel contribute F_{CLT} .

$$F_T(x, \dot{x}, \max(|x(t)|), t, \epsilon) = F_c(x, \dot{x}, \max(|x(t)|), t, \epsilon) + F_{CLT}(x) \quad \text{if } F_T \leq F_s \quad (16)$$

$$F_T(x, \dot{x}, \max(|x(t)|), t, \epsilon) = F_c(x, \dot{x}, \max(|x(t)|), t, \epsilon) + F_{CLT}(x) + F_s(\dot{x}, \epsilon) \quad \text{if } F_T > F_s \quad (17)$$

where x is the top displacement of the frame, F_c is described by the Atan model, F_s by Eqs.(13)-(14), and $F_{CLT} = k_{CLT}x$. Likely, the combination of Eqs.(16)-(17) would simulate the lateral response of the structural unit obtained by assembling the RC frame, the CLT panel and the AFC connection.

5 SEISMIC PERFORMANCE OF THE STRUCTURAL ARRANGEMENT

The inelastic restoring force in Eqs.(16)-(17) participates to the equilibrium of single-degree-of-freedom oscillator (SDOF), representative of the RC frame dynamic response. The equilibrium of a lumped mass above the frame yields the following ordinary differential equation under earthquake excitation:

$$m\ddot{x} + F_T = -m\ddot{x}_g \quad (18)$$

where m is the mass, x the displacement, \ddot{x} the double derivative of x with respect to time, F_T the resisting inelastic force defined in Eqs.(16)-(17), and \ddot{x}_g the ground acceleration. A SDOF system is the most elementary structure. Nevertheless, it is the most meaningful, and the results obtained from this basic structure have universal application. The SDOF model is used to assess the slip force, which guarantees the lowest inter-storey drift. An RC frame represents any

storey distinguished by a prevalent shear-type response. Accurately, any structure is a stand-alone case, but an elementary model's accurate analysis supports a mindful assessment of the optimum ranges to be expected in more complicated structures. In contrast with the previous section, the displacement is unknown and must descend from the numerical integration of the ODE. Precisely, the authors used the explicit fourth-order Runge–Kutta method for the temporal discretization of the approximate solution of the ODE. The optimization of the slip force in AFC descends from an indirect approach. The authors simulated the response of an RC frame equipped with the AFC to a set of 41 earthquakes by varying the value of the slip force in a given range. A list of 41 Italian earthquake records with magnitude M_L ranging between 5 and 6.5, reported in [37, 38], represented the base for generating 41 artificial earthquakes, scaled to the same PGA and optimized to match a given design spectrum. The design spectrum corresponds to the seismic scenario expected in L'Aquila, Italy, according to the National Seismic Code. The algorithm presented by [39] is used to scale the accelerograms to a 0.3PGA, and carry out the analyses based on coherent inputs. The algorithm modifies the frequency content without producing substantial shape modifications. The force slip varied in the range 0-100kN, with a 1kN step. Fig.8 displays the results of the analyses. Fig.8(a) reports the maximum displacement drift due to a single earthquake. Maximum inter-story drift is widely used to evaluate the level of damage to both structural and non-structural elements in RC structures [32]. Fig.8(b) superposes the curves in Fig.8(a) by considering the responses to the 41 earthquakes. The mean and variance of the minima of the curves in Fig.8(b) leads to the normal distribution pictured in Fig.8(c).

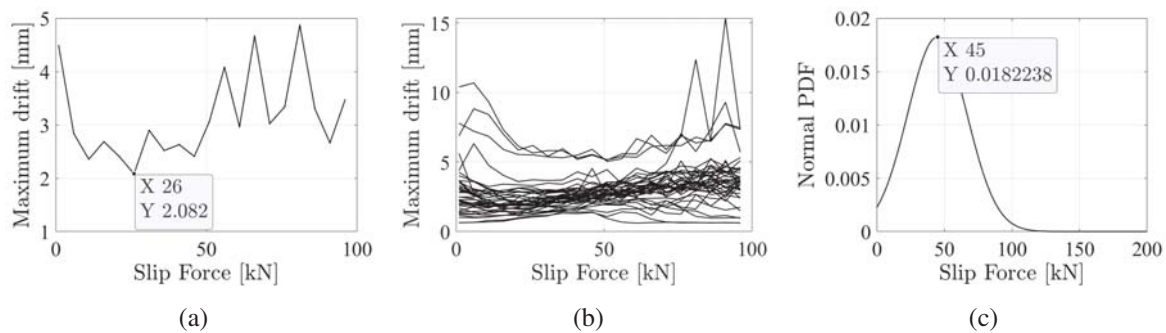


Figure 8: (a) Maximum drift of the RC frame from the response to the El Centro earthquake as a function of the slip force; (b) Superposition of the maximum drifts of the considered system under the earthquakes in Tab.??; (c) Half-Normal distribution of the slip force vales corresponding to the minimum drift.

The curves do not exhibit a smooth trend: they are very jagged. Still, despite the oscillation, each curve has a minima range with a concave shape by the minima. Hence, the authors picked the argument corresponding to the lowest value, considered representative of the optimum slip force. There are considerable differences between the curves obtained from different earthquakes. This evidence agrees with the findings by [16]. They observed that the optimum slip load values are more affected by the amplitude and frequency of the input earthquakes (e.g. peak ground acceleration) rather than the structure's characteristics.

Interestingly, the range of local minima gathers by the lower values of the slip force.

Also [29], [40] and [41] observed that the use of friction dampers leads to an optimum range of slip load ratios that, on average, leads to lower inter-story drifts. According to [29], the slip load ratio is the ratio between the slip value and the resistance of the structure without the

passive device. They found the following empirical function for the prediction of the optimum slip force as a function of the number of storeys n :

$$R = 1.12 e^{-0.11n} \quad (19)$$

If there is one storey, the R ratio is almost one. As the number of storeys grows, the R ratio reduces to 0.12. This empirical equation does not agree with the outcomes of this investigation. The R ratio in the considered configuration is $R \approx 0.23$.

According to [29], in the considered case, the optimum slip resistance should be approximately equal to 200kN. Numerous factors are affecting the optimum value of the slip force. Both the RC frame and the AFC dissipate the seismic energy. The energy dissipated by the friction dampers is proportional to both the slip force and the mutual drift. If the slip force is kept low, the dissipated energy increment must descend from the increment in displacement. If the slip force is higher, a lower displacement can generate the same dissipation. However, higher forces cause the device activates when the RC frame has already experienced a significant displacement drift. In the considered system, characterized by strength and stiffness degradation, if the slip force was equal to 200kN, the AFC's benefit was reduced by its tardy intervention.

Still, the RC frame with masonry infill can exhibit more the 50% strength increment to the same structure without infill. If R is the ratio between the slip resistance and the RC lateral capacity without the infill, the findings of this research and those by [29] become coherent, R will approximate one. The masonry infill is determinant for the correct assessment of the optimum slip force.

6 Conclusions

The paper addresses the seismic performance of the e-CLT technology via nonlinear dynamic analysis on an elementary RC frame with masonry infill. The e-CLT technology is a seismic retrofitting solution of existing RC building based on the use of cross-laminated timber (CLT) panels and asymmetric friction connectors (AFC). In an RC frame, one end of the CLT panel is fixed on the lower beam, while the other end is equipped with an AFC, connected to the RC frame's upper beam. The slip force's exceeding in the AFC activates the dissipating device, which possibly contributes to the seismic energy absorption and the reduction of the displacement drift demand. The authors experimented the cyclic behaviour of the AFC and proposed a Coulomb-like model with a friction coefficient dependent on the dissipated hysteretic energy. The experimental data are used to simulate a frame's coupled response with masonry infill equipped with the AFC. The Atan model, which is an empirical hysteresis model proposed by [34], simulates the experimental cyclic response of an RC frame with masonry infill, tested by [31]. The authors tested the frame's response, represented by an SDOF oscillator with a lumped mass on the top, under a set of 41 earthquakes by varying the slip force in a given range. Interestingly, there is a range of minima where the slip force is associated with a significant reduction of the storey drift. The displacement reduction can be higher than 50%. However, as observed by [16], seismic input's nature significantly affects the optimum slip force's value, which exhibits a significant scatter. The mean value of the optimum slip forces found in the considered structure is 45kN, which is approximately the 21% of the shear resistance of the frame. This evidence does not match the findings by [29], who predicted higher optimum slip force values in bare RC structural archetypes with friction dampers; while in the analyses of this paper the RC frame was modelled with its real behaviour including the masonry infill. The masonry infill can add more than 50% increment in strength and stiffness to the same RC frame without infill, in which case the results from this paper would align with [29].

Funding

This paper was carried out in the framework of the "Energy and seismic affordable renovation solutions" (e-SAFE) project, which has received funding from the European Union's Horizon 2020 research and innovation programme under grant agreement No.893135. Neither the Executive Agency for Small and Medium-sized Enterprises (EASME) nor the European Commission is in any way responsible for any use that may be made of the information it contains.

REFERENCES

- [1] M. H. Milman and C.-C. Chu, "Optimization methods for passive damper placement and tuning," *Journal of Guidance, Control, and Dynamics*, vol. 17, no. 4, pp. 848–856, 1994.
- [2] R. Levy and O. Lavan, "Fully stressed design of passive controllers in framed structures for seismic loadings," *Structural and Multidisciplinary Optimization*, vol. 32, no. 6, pp. 485–498, 2006.
- [3] I. Takewaki, *Building control with passive dampers: optimal performance-based design for earthquakes*. John Wiley & Sons, 2011.
- [4] S. Jaisee, F. Yue, and Y. H. Ooi, "A state-of-the-art review on passive friction dampers and their applications," *Engineering Structures*, vol. 235, p. 112022, 2021.
- [5] S. Pagliaro, A. Aloisio, R. Alaggio, and A. Di Egidio, "Rigid block coupled with a 2 dof system: Numerical and experimental investigation," *Coupled systems mechanics*, vol. 9, no. 6, pp. 539–562, 2020.
- [6] A. Aloisio, L. D. Battista, R. Alaggio, E. Antonacci, and M. Fragiaco, "Assessment of structural interventions using bayesian updating and subspace-based fault detection methods: the case study of s. maria di collemaggio basilica, l'aquila, italy," *Structure and Infrastructure Engineering*, pp. 1–15, 2020.
- [7] A. Aloisio, I. Capanna, R. Cirella, R. Alaggio, F. Di Fabio, and M. Fragiaco, "Identification and model update of the dynamic properties of the san silvestro belfry in l'aquila and estimation of bell's dynamic actions," *Applied Sciences*, vol. 10, no. 12, p. 4289, 2020.
- [8] Y. Qie, F. Barbagallo, E. M. Marino, C. Du, and T. Wang, "Full-scale hybrid test for realistic verification of a seismic upgrading technique of rc frames by brbs," *Earthquake Engineering & Structural Dynamics*, vol. 49, no. 14, pp. 1452–1472, 2020.
- [9] A. S. Pall, C. Marsh, *et al.*, "Response of friction damped braced frames," *Journal of Structural Engineering*, vol. 108, no. 9, pp. 1313–1323, 1982.
- [10] M. Nakashima, K. Saburi, and B. Tsuji, "Energy input and dissipation behaviour of structures with hysteretic dampers," *Earthquake engineering & structural dynamics*, vol. 25, no. 5, pp. 483–496, 1996.
- [11] C.-G. Cho and M. Kwon, "Development and modeling of a frictional wall damper and its applications in reinforced concrete frame structures," *Earthquake engineering & structural dynamics*, vol. 33, no. 7, pp. 821–838, 2004.

- [12] T. Fitzgerald, T. Anagnos, M. Goodson, and T. Zsutty, "Slotted bolted connections in aseismic design for concentrically braced connections," *Earthquake spectra*, vol. 5, no. 2, pp. 383–391, 1989.
- [13] E. P. Popov, C. E. Grigorian, and T.-S. Yang, "Developments in seismic structural analysis and design," *Engineering structures*, vol. 17, no. 3, pp. 187–197, 1995.
- [14] C. E. Grigorian, T.-S. Yang, and E. P. Popov, "Slotted bolted connection energy dissipators," *Earthquake Spectra*, vol. 9, no. 3, pp. 491–504, 1993.
- [15] G. Clifton, G. MacRae, H. Mackinven, S. Pampanin, and J. Butterworth, "Sliding hinge joints and subassemblies for steel moment frames," in *Palmerston North, New Zealand: Proc of New Zealand Society for Earthq Eng Conf*, 2007.
- [16] A. Filiatrault and S. Cherry, "Seismic design spectra for friction-damped structures," *Journal of Structural Engineering*, vol. 116, no. 5, pp. 1334–1355, 1990.
- [17] W. Y. Loo, C. Kun, P. Quenneville, and N. Chouw, "Experimental testing of a rocking timber shear wall with slip-friction connectors," *Earthquake engineering & structural dynamics*, vol. 43, no. 11, pp. 1621–1639, 2014.
- [18] A. Hashemi, P. Zarnani, R. Masoudnia, and P. Quenneville, "Experimental testing of rocking cross-laminated timber walls with resilient slip friction joints," *Journal of Structural Engineering*, vol. 144, no. 1, p. 04017180, 2018.
- [19] A. Hashemi, H. Bagheri, S. M. M. Yousef-Beik, F. M. Darani, A. Valadbeigi, P. Zarnani, and P. Quenneville, "Enhanced seismic performance of timber structures using resilient connections: full-scale testing and design procedure," *Journal of structural engineering*, vol. 146, no. 9, p. 04020180, 2020.
- [20] H. Mackinven, "Sliding hinge joint for steel moment frames experimental testing," *Unpublished ENCI493 Project Report. Department of Civil Engineering*, 2006.
- [21] H.-H. Khoo, C. Clifton, J. Butterworth, G. MacRae, and G. Ferguson, "Influence of steel shim hardness on the sliding hinge joint performance," *Journal of Constructional Steel Research*, vol. 72, pp. 119–129, 2012.
- [22] A. Sandoli, C. D'Ambra, C. Ceraldi, B. Calderoni, and A. Prota, "Sustainable cross-laminated timber structures in a seismic area: Overview and future trends," *Applied Sciences*, vol. 11, no. 5, p. 2078, 2021.
- [23] A. Aloisio, D. Pasca, R. Tomasi, and M. Fragiaco, "Dynamic identification and model updating of an eight-storey clt building," *Engineering Structures*, vol. 213, p. 110593, 2020.
- [24] A. Aloisio and M. Fragiaco, "Reliability-based overstrength factors of cross-laminated timber shear walls for seismic design," *Engineering Structures*, vol. 228, p. 111547, 2021.
- [25] G. Margani, G. Evola, C. Tardo, and E. M. Marino, "Energy, seismic, and architectural renovation of rc framed buildings with prefabricated timber panels," *Sustainability*, vol. 12, no. 12, p. 4845, 2020.

- [26] L. Moreschi and M. Singh, “Design of yielding metallic and friction dampers for optimal seismic performance,” *Earthquake engineering & structural dynamics*, vol. 32, no. 8, pp. 1291–1311, 2003.
- [27] N. Nabid, I. Hajirasouliha, and M. Petkovski, “Performance-based optimisation of rc frames with friction wall dampers using a low-cost optimisation method,” *Bulletin of Earthquake Engineering*, vol. 16, no. 10, pp. 5017–5040, 2018.
- [28] L. F. F. Miguel, L. F. F. Miguel, and R. H. Lopez, “Simultaneous optimization of force and placement of friction dampers under seismic loading,” *Engineering Optimization*, vol. 48, no. 4, pp. 582–602, 2016.
- [29] N. Nabid, I. Hajirasouliha, and M. Petkovski, “A practical method for optimum seismic design of friction wall dampers,” *Earthquake Spectra*, vol. 33, no. 3, pp. 1033–1052, 2017.
- [30] J. C. Golondrino, G. MacRae, and C. Clifton, “Behaviour of asymmetrical friction connections using different shim materials,” in *Proceedings of the New Zealand Society for Earthquake Engineering Conference*, 2012.
- [31] L. Cavaleri and F. Di Trapani, “Cyclic response of masonry infilled rc frames: Experimental results and simplified modeling,” *Soil Dynamics and Earthquake Engineering*, vol. 65, pp. 224–242, 2014.
- [32] I. Hajirasouliha, P. Asadi, and K. Pilakoutas, “An efficient performance-based seismic design method for reinforced concrete frames,” *Earthquake engineering & structural dynamics*, vol. 41, no. 4, pp. 663–679, 2012.
- [33] C. Tardo, F. Boggian, M. Hatletveit, E. Marino, G. Margani, and R. Tomasi, “Mechanical characterization of energy dissipation devices in retrofit solution of reinforced concrete frames coupled with solid wood panels,” in *Proceedings of the 12th International Conference on Structural Analysis of Historical Constructions*, 2020.
- [34] A. Aloisio, P. Sejkot, A. Iqbal, and M. Fragiaco, “An empirical transcendental hysteresis model for structural systems with pinching and degradation,” *Earthquake Engineering & Structural Dynamics*.
- [35] G. C. Foliente, “Hysteresis modeling of wood joints and structural systems,” *Journal of Structural Engineering*, vol. 121, no. 6, pp. 1013–1022, 1995.
- [36] A. Aloisio, R. Alaggio, J. Köhler, and M. Fragiaco, “Extension of generalized bouc-wen hysteresis modeling of wood joints and structural systems,” *Journal of Engineering Mechanics*, vol. 146, no. 3, p. 04020001, 2020.
- [37] A. Aloisio, R. Alaggio, and M. Fragiaco, “Fragility functions and behavior factors estimation of multi-story cross-laminated timber structures characterized by an energy-dependent hysteretic model,” *Earthquake Spectra*, p. 8755293020936696, 2020.
- [38] A. Aloisio, R. Alaggio, and M. Fragiaco, “Equivalent viscous damping of cross-laminated timber structural archetypes,” *Journal of Structural Engineering*, vol. 147, no. 4, p. 04021012, 2021.

- [39] F. Ferreira, C. Moutinho, Á. Cunha, and E. Caetano, “An artificial accelerogram generator code written in matlab,” *Engineering Reports*, vol. 2, no. 3, p. e12129, 2020.
- [40] M. Petkovski and P. Waldron, “Optimum friction forces for passive control of the seismic response of multi-storey buildings,” *Proc. of the 40 years of European Earthquake Engineering SE40EEE*, 2003.
- [41] N. Fallah and S. Honarparast, “Nsga-ii based multi-objective optimization in design of pall friction dampers,” *Journal of Constructional Steel Research*, vol. 89, pp. 75–85, 2013.

EXPERIMENTAL AND NUMERICAL INVESTIGATION OF INNOVATIVE DUCTILE AND REPLACEABLE ANCHORING SYSTEMS FOR WOOD SHEAR WALLS UNDER SEISMIC LOADS

Georgios Balaskas¹, Vera Wilden¹, Benno Hoffmeister¹

¹ Institute of Steel Construction, RWTH Aachen University
 {g.balaskas, v.wilden, hoff}@stb.rwth-aachen.de

Abstract

Recently, timber has gained increasing importance as a structural material, as it offers competitive structural performance and efficient production combined with a significant reduction of the environmental impact. Light-weight timber frames provide an efficient structural solution for wooden multi-storey buildings, in which the wall elements - acting as diaphragms - provide lateral stiffness and resistance to wind and earthquake loads. Light-weight timber frame elements are built up of several components (sheeting, fasteners, frame, support and anchorages), each of them contributing to the total performance of the structure. The current paper presents the outcome of experimental and numerical investigations on a ductile and replaceable supporting and anchoring system for wood shear walls. The aim of the examined novel system is two-fold: (i) to limit the damage of the superstructure under seismic loads by concentrating plastic deformations on the anchoring elements, placed at the base of the building and (ii) to be replaced after getting damaged because of a significant earthquake. The supporting and anchoring detail is made of steel and designed appropriately to behave nonlinear in a ductile manner under severe seismic loads and thus to provide additional energy dissipation. The damage is concentrated on the steel part, which acts as a dissipative mechanism limiting the forces transferred into the timber building. Consequently, the timber members remain undamaged for moderate earthquakes and slightly damaged in case of strong seismic events. A parametric study, using FE models validated based on experimental results, was conducted with the objective to investigate the influence of the geometrical characteristics of the anchorage. Moreover, a built-up anchoring configuration optimized for replaceability was developed and analyzed. Finally, recommendations for applications are provided, as well as the main conclusions of the study.

Keywords: timber shear walls, ductile and replaceable anchoring system, experimental tests, FE-investigation

1 INTRODUCTION

Recently, timber has gained increasing importance as a structural material, as it offers competitive structural performance and efficient production combined with a significant reduction of the environmental impact. Light-weight timber frames provide an efficient structural solution for wooden multi-storey buildings, in which the wall elements - acting as diaphragms - provide lateral stiffness and resistance to wind and earthquake loads. Light-weight timber frame elements are built up of several components (sheeting, fasteners, frame, support and anchorages); each of them contributes to the total performance of the structure.

Rising demand for multi-storey timber buildings leads to new challenges regarding stiffness, strength and ductility - properties responsible for the seismic performance. On the one hand, because of their relatively low structural mass, timber buildings are exposed to lower seismic loads compared to other structural materials. On the other hand, the anisotropic and naturally scattering characteristics of wood material settle the design of timber structures for dissipative behavior a challenging process. Fundamental for the dissipation is the capacity design, which guarantees a reliable and accurate prediction of the nonlinear response of the dissipative elements. Therefore, an innovative support and anchoring system acting as a dissipative element was developed, aiming at improving the seismic performance of light-weight timber frame structures.

Currently, tension ties made of galvanized flat steel represent the common solution for anchoring timber frames to the foundation. These ties are designed for uplift forces only; they are connected to the timber studs by means of screws or nails and to the foundations by anchor bolts. In [1][2], tension ties were investigated and it was found that, although the tested specimens can resist adequate tensile forces and provide ductility redundancies, they are susceptible to sudden failures. The limited predictability of the governing failure mode of the tension ties was confirmed by own tests (Figure 8 b & c). Tlustochowicz [3], compared two different alternative techniques for the transmission of shear and tension forces: either through nailing plates welded to a foundation steel plate or via a HEB profile, which was connected to the studs of the timber wall by glued rods and anchored in the foundation. The specimens with glued rods failed suddenly in the glued interface [4]. The alternative with nailing plates is widely used in timber structures. Sufficient ductility can be provided by adequate number and strength of nails, but sudden block failure of the connectors must be prevented.

In light-weight timber frames, the key component governing the ductility (stiffness and strength as well) is the shear connection between sheathing and frame. The investigated anchoring detail was developed to enhance the ductility and dissipation capability of the structure by adding a dissipative mechanism at the base of the timber wall. The development of the novel anchorage targeted at eliminating the drawbacks of existing solutions, by providing a simple, reliable and replaceable element which, to some extent, also prevents damages to the main timber structure. To this end, the anchorage must provide a stable hysteretic performance in the plastic domain. Additionally, the opportunity to strengthen or substitute the anchorage after a significant seismic event resulting in plastic deformations limited to the anchor system was also taken into account. This concept allows for a rapid restoration of the occupancy of the building after an earthquake.

The novel anchorage examined within the current study is made of steel and is integrated into the corner studs of a timber wall, as shown in Figure 1. It consists of a steel rectangular hollow section (RHS) and a steel plate, welded to the upper flange of the hollow section. The steel plate is used for transferring vertical forces from the slitted timber stud by means of a double shear connection with steel dowels or bolts. The anchoring device is designed to transfer

vertical loads (tension and compression) only. Shear forces are transferred by separate shear keys or angle profiles to the foundation.

The response of the structure to seismic loads can be “controlled” through definition of different performance levels for the proposed anchorages. Following the principles of the modern codes [6], three main performance levels are considered: damage limitation, significant damage and near collapse. By adjusting the elastic limit of the examined anchorage, the performance of the total building can be subdivided into: (i) damage limitation performance level: both superstructure and anchorage respond elastic, (ii) the significant damage performance level (or ultimate limit state): the anchoring device behaves nonlinear and dissipates energy, the timber superstructure remains undamaged or slightly damaged and (iii) near collapse level, damages (nonlinear response) are expected both at the anchorage and at the superstructure.

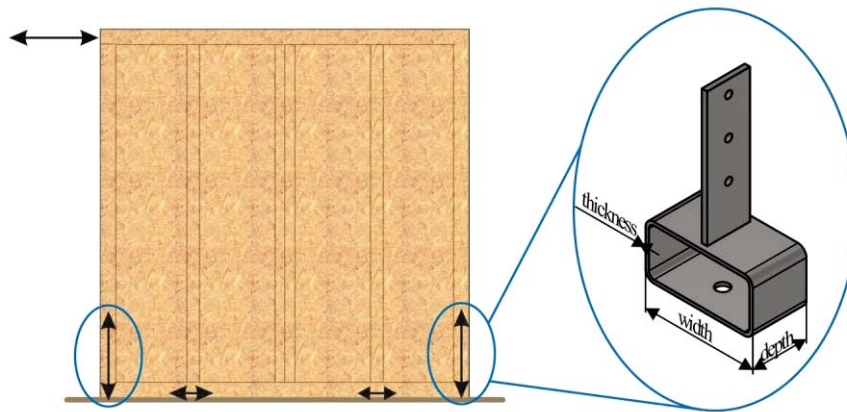


Figure 1: Innovative ductile and replaceable anchorage for timber shear walls

Crucial point of the developed concept is the capacity design of the detailing. The non-dissipative elements should be designed appropriately to remain elastic, permitting yielding and nonlinear response of the dissipative elements. Material hardening and overstrength of the dissipative elements must be considered. Concerning the tested subassemblies, fasteners, internal steel plate and timber studs were considered as non-dissipative elements. Regarding global systems, depending on the desired performance level, shear walls can also be considered as non-dissipative for specific scenarios.

The reliability of the novel ductile anchorage was investigated experimentally and validated numerically by the Institute of Steel Construction of RWTH University in Aachen, Germany. The investigation was part of a national funded research project (HOLZBEBEN), in which the seismic response of light-weight timber frames was holistically examined including tests on connections details, on wall elements and on a reference structure [7].

2 EXPERIMENTAL INVESTIGATIONS

Two series of experimental tests both monotonic and cyclic were carried out. The aim of the first series (S1) was the investigation of the principle of the novel anchorage and the validation of the numerical models, whereas the target of the following tests (S2) was to examine the performance of the anchorages as parts of a realistic building, including the interaction with the timber members. For comparison reasons also tests on commercial tension ties were executed. Table 1 provides an overview of the tested specimens and their characteristics.

Series	Specimen	Anchorage	Dimensions (b x t x h x d) in mm	Material	Connectors Ø in mm	Loading
S1	M01	novel anch.	200x100x100x6.3	S235	3 x threaded rods 12-8.8	monotonic tension
S1	M01*	novel anch.	200x100x100x6.3	S235	3 x threaded rods 12-8.8	monotonic compression
S1	Z01	novel anch.	200x100x100x6.3	S235	3 x threaded rods 12-8.8	cyclic (ECCS)
S1	Z02	novel anch.	200x100x100x6.3	S235	3 x threaded rods 12-8.8	cyclic (ECCS)
S1	Z03	novel anch.	200x100x100x6.3	S235	3 x threaded rods 12-8.8	cyclic (ECCS)
S2	A01	novel anch.	200x100x100x12.5	S355	14 x dowels 12- S355	monotonic tension
S2	A02	tension tie	HTT31 [9]	S350GD	49 screws 5.0x80 + 1 bolt 24-8.8	monotonic tension
S2	A03	tension tie	HTT31 [9]	S350GD	49 screws 5.0x80 + 1 bolt 24-8.8	monotonic tension

Table 1: Overview of experimental tests

2.1 Investigation of Series 1

2.1.1. Test set-up and instrumentation

The tests of this series were conducted on a ZwickRoell Z100 testing machine. The specimens were fixed through a bolt on a steel plate, which was rigidly clamped at the testing machine. The loads were transmitted from the machine jack through the timber element using a steel to timber connection.

Firstly, a monotonic tensile test (M01) was performed, in order to define the yield displacement, according to ECCS testing procedure [8]. The determination of the yield displacement is necessary to define the amplitudes for the following cyclic tests (Z01-Z03).

During the tests, the machine jack displacement and the applied load were recorded by the testing machine. In addition, the vertical displacement in the middle of the hollow cross-section (W1), the vertical displacement at the upper corner of the hollow profile (W2) and the relative displacement between the inner steel plate and the timber member (W3) were measured by displacement transducers. During the cyclic tests (Z01-Z03), the inclination of the right and left part of the hollow steel member flange were recorded by inclinometers (N1 and N2). The monotonic and the cyclic tests were conducted in displacement control with a constant speed rate of 0.1 mm/s. The instrumentation configuration is presented in Figure 2.

2.1.1. Results

Regarding the monotonic (M01 and M01*) tests, it was observed, that: (i) the novel anchorage presented significantly different stiffness in tension $K_t = 2.69 \text{ kN/mm}$ and in compression $K_c = 23.92 \text{ kN/mm}$, (ii) in tension the behavior was ductile and a remarkable amount of energy could be dissipated, (iii) no brittle failure occurred despite extreme tensile displacement, and (iv) the high compression stiffness is present, when the system anchorage-stud returns to the initial position and the compression load was transferred by contact between the timber stud

and the flange of the RHS. The response of the anchorage is displayed in Figure 3, whereas the initial stiffness, the yield point (according to ECCS [8]), the dissipated energy and the damping ratio are depicted in Table 2.

Concerning the cyclic tests, it was observed, that the envelope curve is very close to the monotonic curve. Moreover, the anchorage was proved to be capable of dissipating energy and resisting a large number of loading cycles, without significant strength reduction (less than 7.5% as illustrated in Figure 4). In addition, the measurements of inclinometers confirmed, that the anchoring device responded in a symmetric way.



Figure 2: Series 1 test set-up

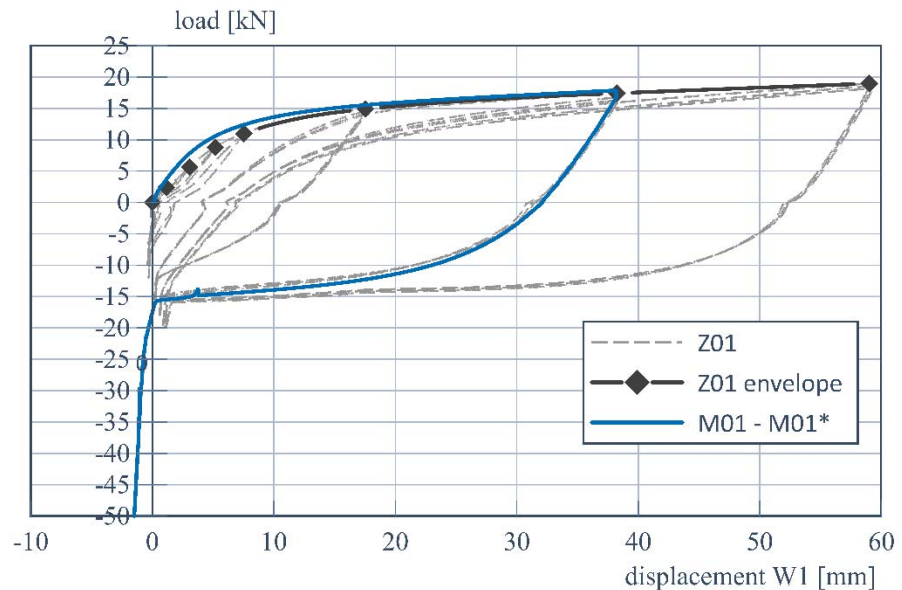


Figure 3: Load displacement curves M01 - M01* and Z01

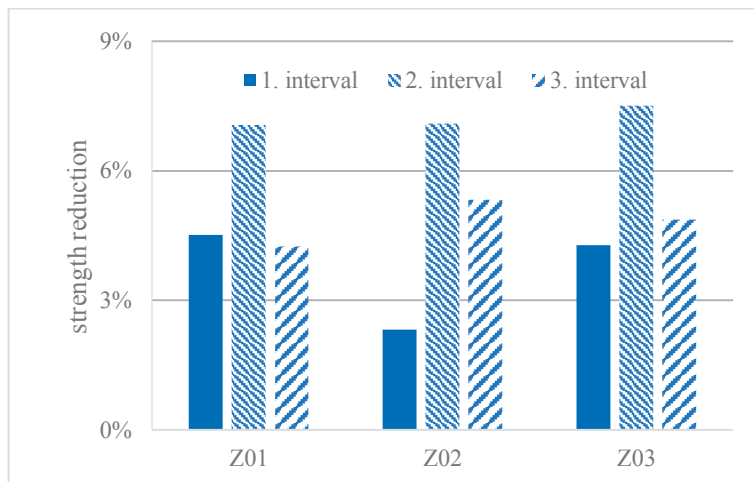


Figure 4: Strength reduction between 1. & 3. cycle of each interval



Figure 5: Deformed shapes of the specimen

Test results	Values
Initial stiffness in tension	2.69 kN/mm
Stiffness in compression	23.92 kN/mm
Yield force	12.30 kN
Yield displacement	4.48 mm
Dissipated energy	865 J
Equiv. damping ratio	7 %

Table 2: Series 1; results M01-M01*

2.2 Investigation of Series 2

2.2.1. Test set-up and instrumentation

After the applicability of the novel anchoring devices was experimentally proven in test-series S1, the anchorages were designed for the shear walls of a multi-storey timber building. In addition, commercial tension ties (HTT31, Simpson Strong Tie [9]), which could be used as a conventional solution for the same building, were selected as reference anchorages. Tensile tests were carried out on one specimen of the innovative anchorage and on two HTT31 specimens. The innovative anchorage was made of steel S355 and its thickness was $t=12.5\text{ mm}$. HTT31 anchoring elements are made of galvanized steel S350GD. According to [9], they can resist $R_{t,c} = 85.1\text{ kN}$ characteristic tensile load. They are considered to be very ductile and capable of dissipating energy and are assumed to provide sufficient dissipation capability for ductility classes DCM or even DCH.

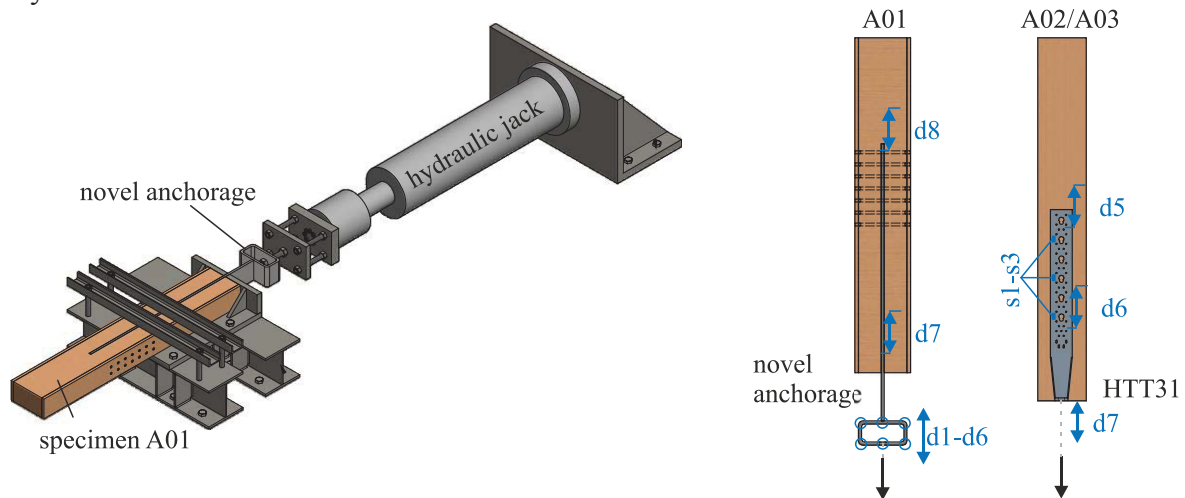


Figure 6: Series 2, test set-up and instrumentation configuration

For the test-series S2 a new test set-up was used, accounting for the increased dimensions and expected loads. The test configuration, the specimens and the instrumentation system are depicted in Figure 6. The instrumentation of the novel anchorage consisted of eight displacement transducers, two of them (d7 and d8) measuring the relative displacement between the internal steel plate and the timber stud. The other sensors (d1 ÷ d6) were measuring the response of the anchorage in terms of displacement at three points (left, right, middle) at the upper and at the lower flange of the hollow profile. The instrumentation of the tension ties included measurement of the relative displacement between steel plate and timber member by displacement transducers d5 and d6 and measuring of the displacement in the middle of the bottom angle part by the transducer d7. In addition, the strains at three characteristic positions along flat steel part

of the ties were measured ($s1 \div s3$), in order to determine, the load distribution to the connectors. In all tests the hydraulic jack load and displacement were measured too.

2.2.2. Results

In Figure 7, the experimental results are presented. The novel device displays no failure until a load of 230 kN (max. load capacity of the hydraulic jack) with a corresponding displacement of about 90 mm . It is obvious, that such displacements are not considered as accepted under seismic loads. The maximum accepted displacement depends on the requirements of each building. Regarding the specimen, it is to underline, that after a displacement of about 40 mm , membrane effects appear and are responsible for the change of inclination. Concerning the HTT31 tension ties, it is to be noted, that their stiffness, calculated according to [14], was close to the suggested values and their capacity about 27% higher than characteristic strength provided in the approval [9]. The results of the experiments are included in Table 3. In addition, it is worth mentioning, that the two HTT31 specimens presented different failure modes (Figure 8: b & c). The first one exposed net cross-section failure in tension, while the second one failed in the bottom part responsible for the connection to the foundation. Both failure mechanisms provided some plastic ductility followed by a sudden drop of resistance. Measurements by strain gauges showed a non-uniform force distribution along the HTT31 and the corresponding fasteners. The measured force decreases from 1 kN (point s3) to 0.67 kN (point s2) and 0.25 kN (point s3) (the values are normalized). Comparing the test configuration of the novel anchorage with the reference anchorage, the main conclusions are: (i) the novel anchorage is slightly stiffer and presents higher strength, (ii) the yield point is clearly identifiable and is about 50% higher (96.01 kN to 62.65 kN), (iii) both anchors are very ductile in monotonic tension however, the novel anchorage has the potential to dissipate significantly more seismic energy by developing stable

Test results	Novel A01	HTT31 A03
Initial stiffness	29.63 kN/mm	27.39 kN/mm
Yield load	96.01 kN/mm	62.65 kN
Yield displacement	3.14 mm	2.42 mm
Max. load	>230 kN	109.17 kN
Max. displacement	>90 mm	19.62 mm
Ductility factor	-	8.1

Table 3: Series 2; results A01, A03

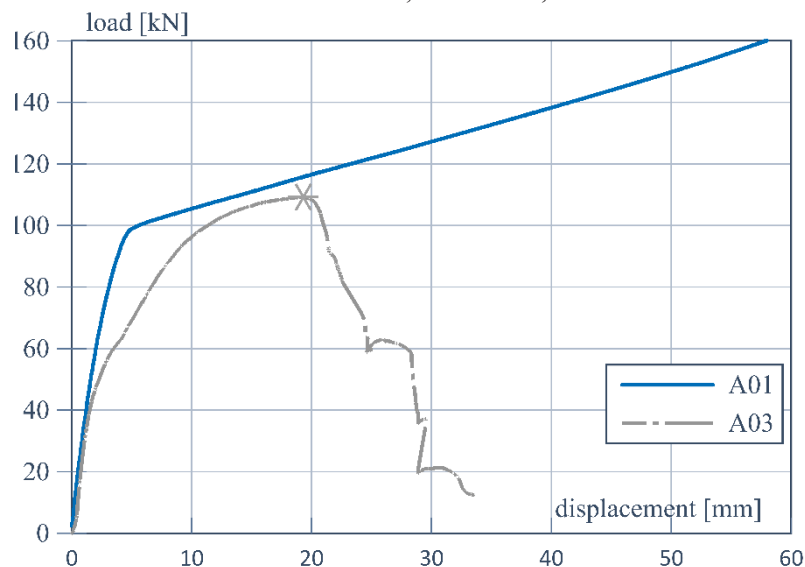


Figure 7: Test results A01 (novel anchorage) and A03 (HTT31)

hysteresis in tension and compression. In general, the examined novel anchorage shows an excellent performance, regarding the decisive properties for the seismic design – stiffness, strength and ductility - compared with a very effective reference tension tie (HTT31).

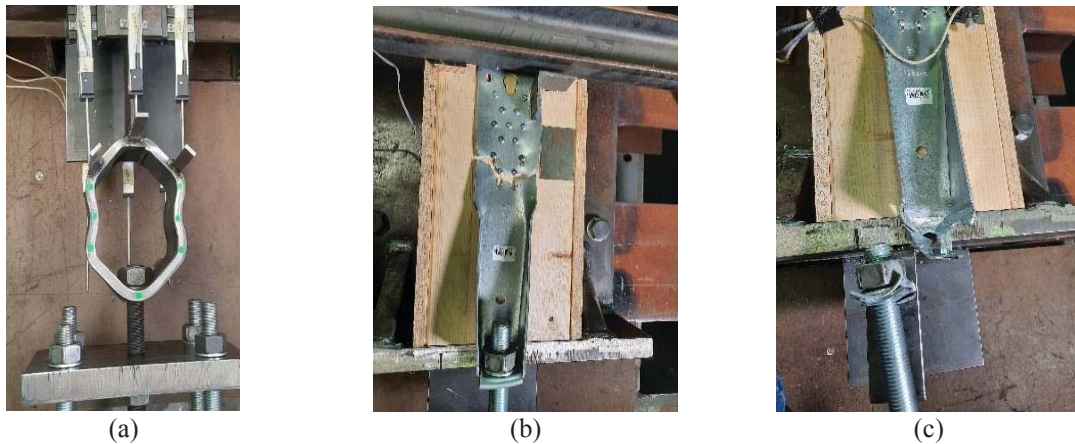


Figure 8: (a) Novel anchorage after loading with 230 kN and 94 mm deformation, (b) Failure mode of HTT31- (A2) specimen, (c) Failure mode of HTT31 - (A3) specimen

3 NUMERICAL AND ANALYTICAL INVESTIGATION

Numerical simulations were used to verify and to predict the behavior (load transfer, plastic hinges) of the examined specimens and to extend the study to other parameters (geometry, material properties) allowing for an adjustment of the anchorage to the design situation. The numerical investigations in this study were developed using the FEM software Abaqus Simulia 2018 [12].

3.1 FEM modeling procedure

The numerical models consisted of solid elements and included the rectangular hollow section (RHS), the steel plate, a foundation plate and the connectors, as depicted in Figure 9. The RHS, the steel plate and the foundation plate were modeled with a simplified isotropic bilinear material law for steel S235 and S355, according to the minimum requirements for steel as proposed by Eurocode 3[11]. The material law for the steel to timber connectors is taken from experimental results published in [10]. The timber element was modeled assuming elastic behavior, based on observations from the tests. Regarding the interactions and boundary conditions, the following options were applied: (i) “tie constraint” – for the welded connection between internal steel plate and hollow profile, (ii) “contact interaction” – for the interaction of different model components (bolts-timber, timber - RHS, RHS – foundation plate) in contact. The ‘normal hard contact’ used in the model, allows for separation between the parts and the ‘friction/penalty contact’ for considering friction effects. Sensitivity study for penalty values between 0.01 and 0.25 exposed that the penalty value does not influence the results. Regarding the boundary conditions, the foundation plate was fixed on both transverse edges, which approaches very close the real boundary conditions of the testing machine. The external loading was applied as imposed vertical displacement on the upper surface of the timber stud. For convergence reasons ‘Dynamic Explicit Analysis’, with a smooth step amplitude was selected, considering geometrical and material nonlinearities. The kinetic energy at all stages of the analyses (monotonic and cyclic) remained negligible. Regarding the discretization method, the mesh was adapted to the different components (4 mm for the timber stud and the hollow profile, 1.5 mm for the connectors and 1 mm at the areas of the RHS, where plastic strains were

expected). The element type was linear hexahedral elements type C3D8R. The size of the mesh elements was adapted until the results were independent of the mesh.

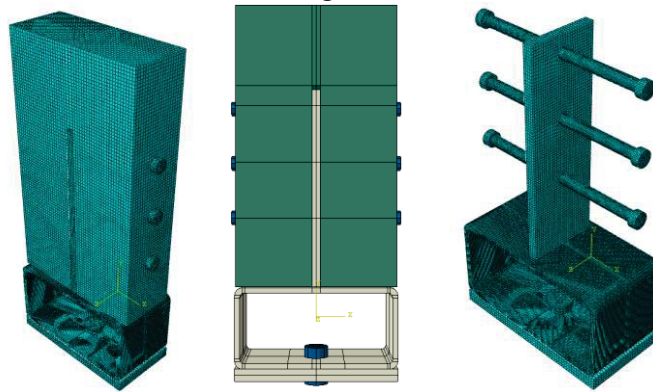


Figure 9: Assembled finite element model and discretization

3.2 Calibration of the model

The numerical model was developed with the characteristics described above and was calibrated with the monotonic and pseudo cyclic load – displacement curve from the tests A01 and M01 - M01*. In Figure 10, the results of the test and of the numerical simulation both in tension and compression are compared.

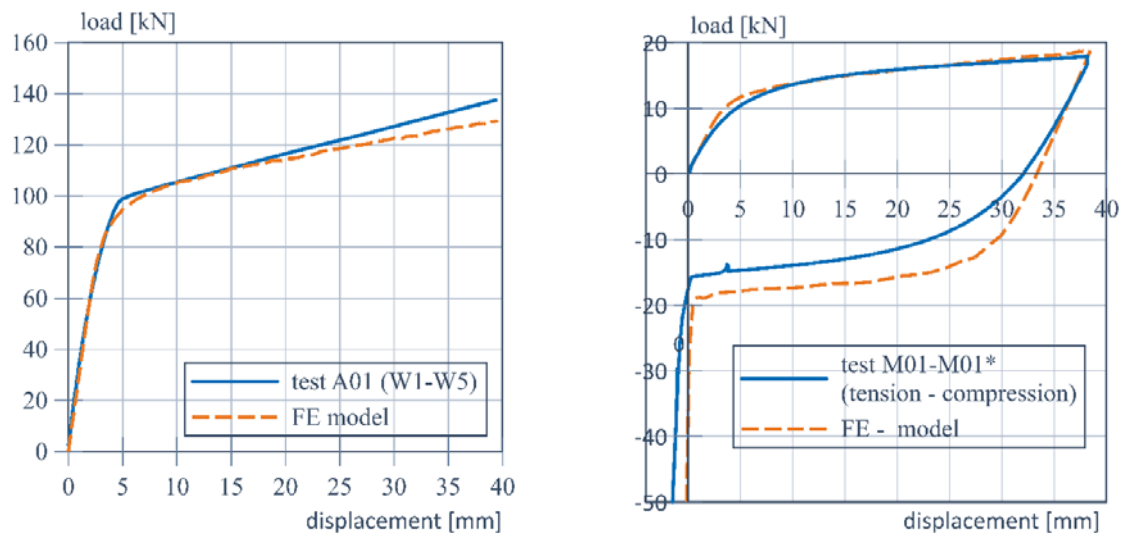


Figure 10: Comparison of response curves: test versus numerical reference model

Taking into consideration the simplified material law, the numerical and experimental results are in good agreement. The differences between the numerical and the experimental results are within an acceptable range for the intended application. In detail, the following deviations between A1 test and simulation are observed: (i) 1.0 % at yield force, (ii) 1.8 % at initial stiffness. Between M01-M01* test and FE model the deviations are: (i) 5.6 % at yield, (ii) 9.49 % at initial stiffness, (iii) 2.9 % at maximum load and (iii) 13.2 % at dissipated energy. The stress and stain distribution of the numerical model, that represented the specimen M01-M01* are displayed at the image series of Figure 11. The distribution of stresses and equivalent strain (PEEQ) illustrates the symmetric response of the anchoring and the sequential formation of plastic zones in the RHS, initially, near the foundation connector and at the sides of the vertical plate and afterwards at both ends of the webs.

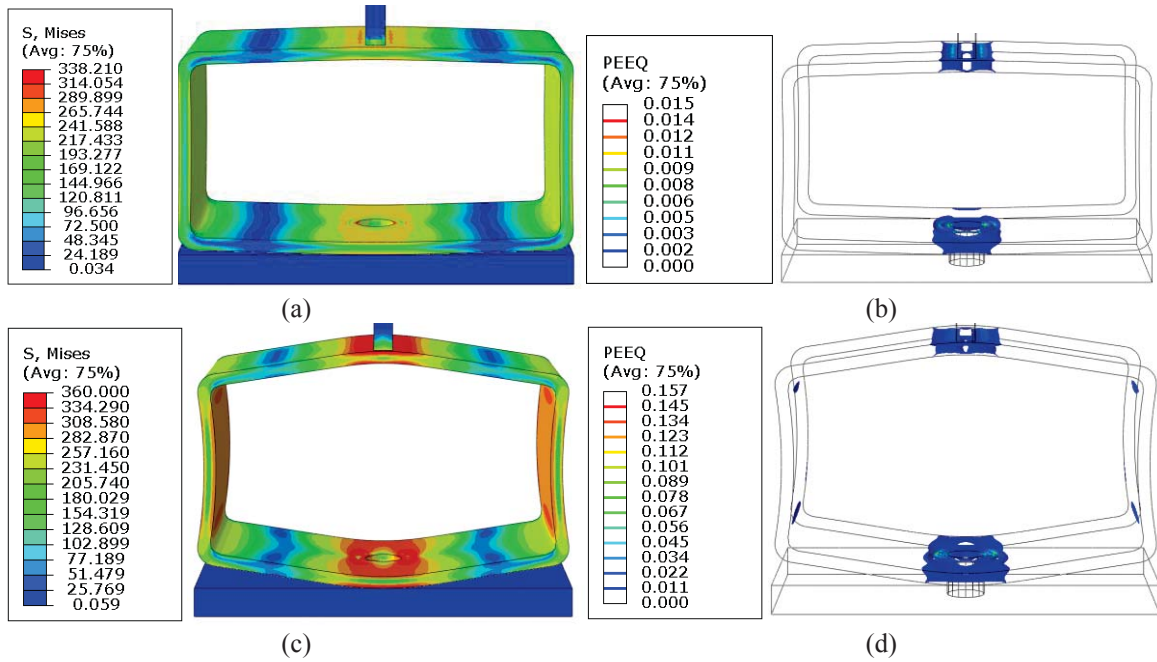


Figure 11: (a) stress distribution $U_2 = 5$ mm, (b) plastic strains at $U_2 = 5$ mm, (c) stress distribution $U_2 = 25$ mm, (d) plastic strains at $U_2 = 25$ mm

3.3 Parametric Study

After the calibration of the numerical models based on the experimental results, a parameter study was performed, in order to investigate the influence of the geometrical characteristics of the novel anchorage. The influence of wall thickness (t), width (w) and depth (d) of RHS was examined by varying separately these parameters in numerical models. As reference the anchorage with the properties as tested in first experimental series is used. The load-displacement curves in tension for various values of (t), (w) and (d) determined by FEM are presented in Figure 13. Furthermore, a simple analytical approach for the determination of the

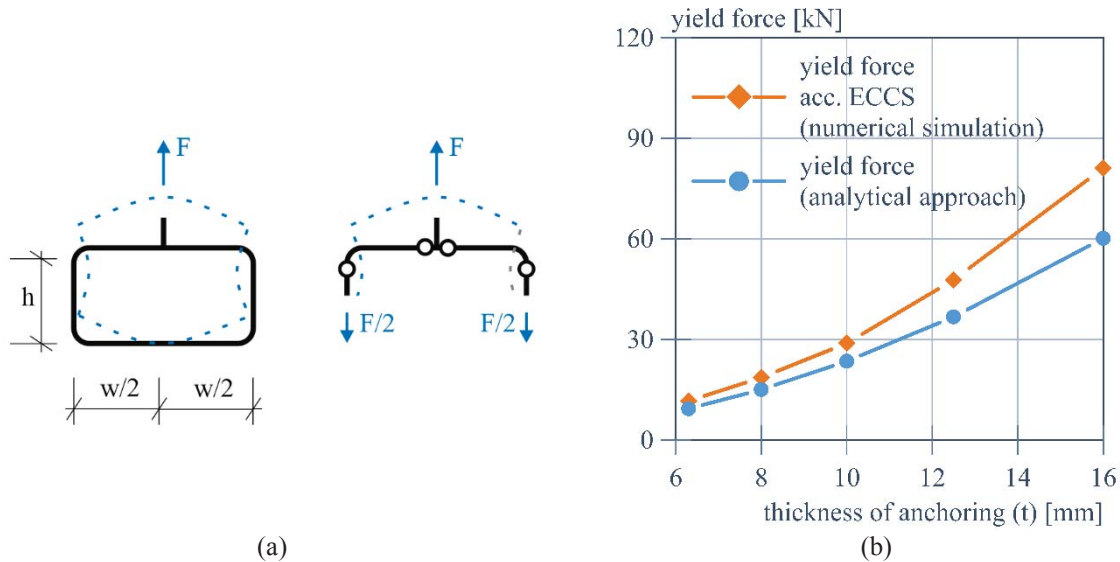


Figure 12: (a) Simplified model for analytical investigation, (b) Influence of thickness on yield force according to numerical and analytical approach

yield force was developed. For the analytical approach, the plastic zones are reduced to plastic hinges Figure 12a. The influence of the thickness on the yield force by the analytical and the

numerical approach is illustrated in the Figure 12b. For the upper part of the plastic mechanism with four plastic hinges, the following equations apply:

$$M_{ex} = F_y \cdot \frac{w}{2} \quad (1)$$

$$M_{ex} = 4 \cdot M_{pl} \quad (2)$$

$$M_{pl} = \left(d \cdot \frac{t}{2} \cdot f_y \right) \cdot \frac{t}{2} \quad (3)$$

Combining the equations (1÷3) allows the calculation of the yield force F_y as function of thickness t , depth d , width w and material (f_y):

$$F_y = \frac{2 \cdot f_y \cdot d \cdot t^2}{w} \quad (4)$$

Parametric studies have shown, that the thickness t has the strongest influence on the initial stiffness, the yield load and the dissipation capacity. The influence of the depth and width variation is less significant, but changes of these parameters allow for a fine-tuning of the anchors, according to the specific structure and loading situation. Finally, the dependency of the dissipated energy on thickness, depth and width of the RHS was examined by FE-analysis. To this end, each of these values was increased by 20% compared to the reference dimensions. The dissipated energy was determined for a loading cycle with a deformation amplitude of 30 mm in tension. It was found that 20% thickness increase ($t = 7.5\text{mm}$) leads to 53% more energy dissipation, 20% increase depth ($d = 120\text{ mm}$) absorbs 19.8% more energy and a 20% wider RHS dissipated 29.3% less energy.

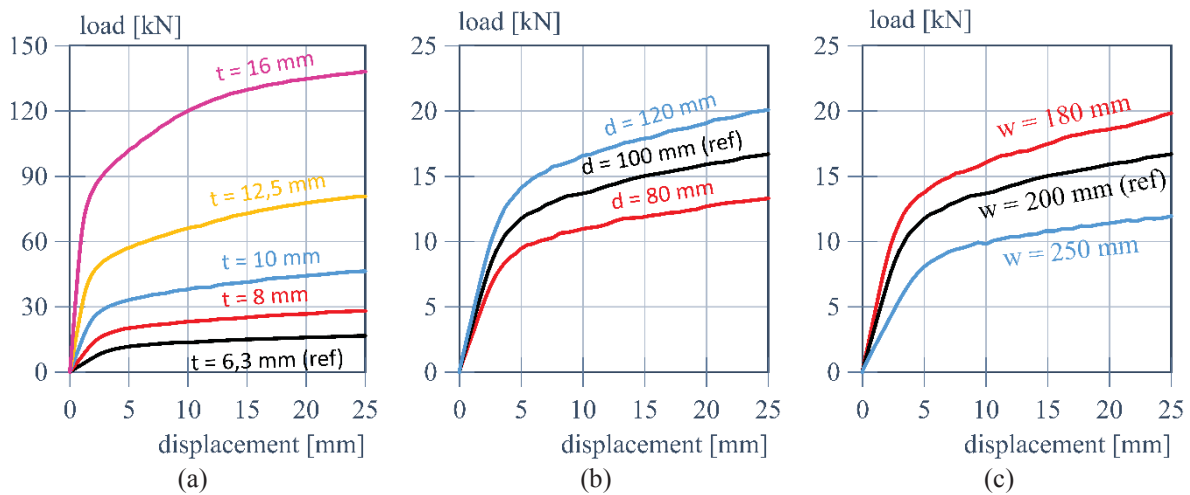


Figure 13: Load-displacement parametric curves of the anchorage (a) wall thickness varying between 6.3 mm to 16 mm, (b) depth varying between 80 mm to 120 mm and (c) width varying between 180 mm to 250 mm

3.4 Optimization for replaceability

One of major aims of the development of the novel anchorage was its replaceability after a significant earthquake. The substitution of dissipating structural parts is always a great challenge, as the existing structure should be temporarily supported and residual forces in the members or details are expected [15][16]. On the other hand, considering the concept of

replaceability in the design and detailing of a structure inherently includes the option of recentering the main structure, under condition that the residual (plastic) deformations are limited to the specific dissipative objects. The introduced innovative anchoring solution can be also designed for disassembling and replacing, as long as the connection of the anchor to the timber studs remains elastic. Also, the main timber structure shall not suffer significant damages. Using the validated numerical models, different alternatives following this concept were investigated. The research focused on built-up members, in which one part only (the lower one in particular) is considered to be dissipative and needs to be replaced. The upper (non-dissipative) part must remain robust and undamaged. After investigating several alternatives, the configuration illustrated in Figure 14a, was selected as the most efficient one. It enables the transfer of gravity forces by contact and simultaneously the lower part (dissipative part) is activated only when uplift forces are present. The investigated hybrid built-up member consists of an outer profile with thickness $t = 16 \text{ mm}$ and width $w = 200 \text{ mm}$. Regarding the internal profile, the dissipative flange was selected as $t = 6.3 \text{ mm}$; the webs are $t = 16 \text{ mm}$ thick as well. The total height of the anchorage remains 100 mm, the steel material is S235 for both the lower and the upper part. The connecting bolts are M16-10.9.

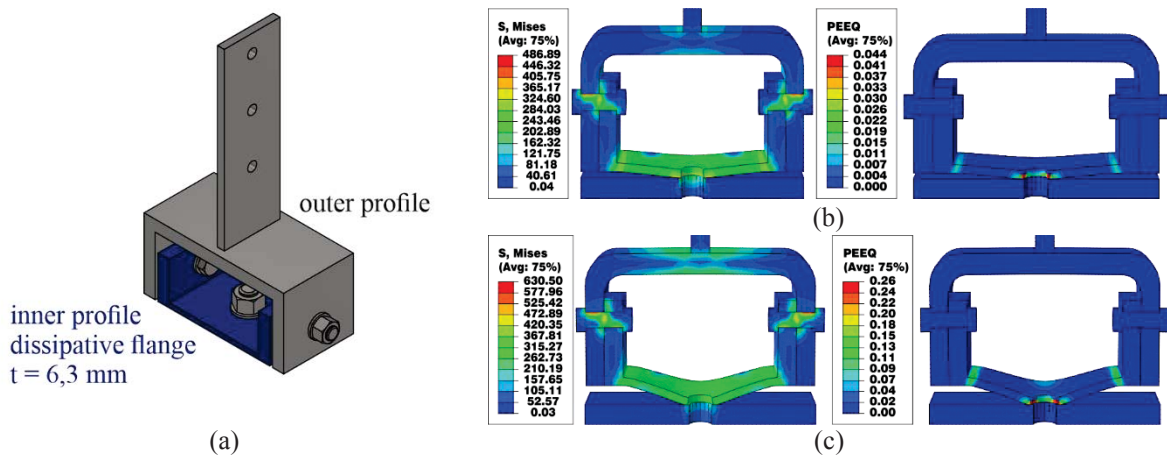


Figure 14: (a) Built up optimized anchoring device, (b) Stress and plastic strain distribution, $U2 = 5 \text{ mm}$, (c) Stress and plastic strain distribution, $U2 = 15 \text{ mm}$

The results of the numerical simulation, plotted in Figure 15, are very encouraging, as the optimized configuration presents a similar initial stiffness to the RHS anchoring configuration with $t = 10 \text{ mm}$ thickness ($K_{t=10} = 14.57 \text{ kN/mm}$) and a performance (yield force and plastic behaviour), which corresponds to the novel RHS anchorage with a thickness between $t = 8 \text{ mm}$ and $t = 10 \text{ mm}$. The plastic hinges form in three regions (around the foundation bolt and at both ends of the dissipative flange), as illustrated in Figure 14 (b & c: plastic strains). The performance limit was estimated to be at an uplift deformation of about 26 mm, where the concentration of strains is significantly beyond those in the reference configuration (RHS). Nevertheless, the ratio between ultimate displacement ($d_u = 26 \text{ mm}$) and yield displacement ($d_y = 1.4 \text{ mm}$) combined with the stable cyclic response without pitching effects (Figure 15b) indicate that the optimized configuration is also capable of dissipating considerable amount of seismic energy. In order to keep the lower part replaceable, the webs of the lower profile must remain elastic, to enable unscrewing the connecting bolts.

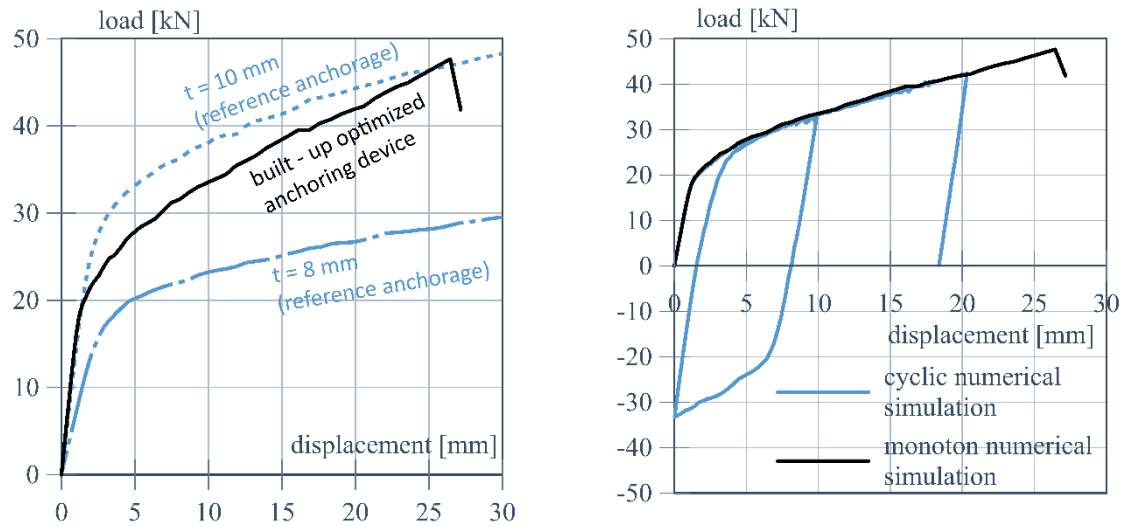


Figure 15: Load – displacement curves of the optimized anchoring configuration

4 APPLICATION

For the application of the novel anchors in timber buildings, the stiffness and strength characteristics and relations of the timber superstructure and the anchors need to be considered. The anchors have different stiffness properties in pure compression (e.g., gravity loads govern the force) and if uplift forces (overturning moment governs) are present. In pure compression the elastic stiffness of the anchors is very high, thus having limited influence on the stiffness of the building. The plastic deformations and cyclic energy dissipation are activated as soon as uplift forces appear. In order to avoid damages to the timber building, it needs to be designed using the lateral seismic actions corresponding to the yield force of the anchors. This shall comprise material overstrength and hardening effects of the dissipative part. Also, the transfer of the base shear force to the foundation and of the shear force between the storeys must follow this principle. If designing for deformations on top of the building, the whole horizontal displacement shall be determined considering two components:

- (i) the displacement Δ_1 , which is the sum of the horizontal head displacement of the wall on each floor due to shear loads and depends on the applied shear force on each floor and on the stiffness of the wall and
- (ii) the displacement Δ_2 , which is the result of the rocking effect due to usage of the novel ductile anchorage and depends on the presence of uplift forces and the corresponding stiffness of the anchoring

In order to achieve an optimum seismic performance in combination with limited damage to the building, the following aspects shall be considered:

- anchorage should be equipped with sufficient strength to remain elastic under moderate earthquakes (local damage limitation);
- light timber shear walls should be designed appropriately according to capacity design as non-dissipative elements for the design earthquake, in order to concentrate the damages in the ductile anchoring device;
- the inherently available ductility of the light timber shear walls should be activated only for a near collapse seismic scenario. In such case, lateral deformations may become critical (inter-storey drift, theory 2nd order effects). This can be controlled either by selecting stiffer profiles or by using additional tension ties, which get activated after a certain, pre-defined uplifting displacement.

As horizontal displacements and drifts are decisive for the design of the ductile anchorage, a pushover analysis is recommended for the evaluation of the different performance levels. Finally, the novel anchorage is designed to transfer vertical loads only (uplifting and compression). In order to prevent unintended transfer of base shear forces, slotted holes for the innovative anchorage should be used. Additional shear keys preferably at the middle of the wall, are suggested.

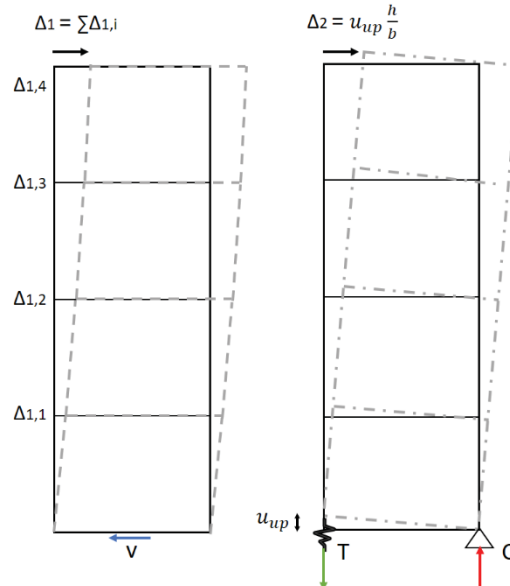


Figure 16: Shear displacements (left), displacement due to rocking effects at the base (right)

5 CONCLUSIONS

The current paper described the results of experimental and numerical investigations of an innovative, ductile and replaceable anchorage for timber shear walls. Aim of the developed device is the protection of the timber superstructure. One additional advantage of the investigated system is its replaceability. The monotonic experimental tests have shown that the anchoring device behaves in a very ductile manner, when uplift forces are present; in pure compression the loads are transferred by contact and the anchor behaves elastically with a high stiffness. Buckling effects under compressive loads should also be taken into consideration. Cyclic tests have proved, that the investigated anchoring can withstand many loading cycles even of high amplitude, without any significant reduction of its strength. Simultaneously a reasonable amount of seismic energy can be absorbed. After validating the numerical models based on experimental results, a parametric study was conducted and proved that the governing parameter for the behavior of the introduced anchorage is the thickness of the profile. Thicker profiles have an increased stiffness, yield force and dissipation capacity. Finally, the examined anchorage was optimized aiming at its replaceability. The most effective solution among several investigated cases was a built-up member, in which only the lower part is dedicated to dissipate energy and must be replaced after a significant earthquake. The achievement of the intended plastic mechanism requires the application of capacity design rules, in order to prevent plastic deformations or damages in the connections to the timber studs and to the parts of the anchorage, which are supposed to remain in the structure.

ACKNOWLEDGEMENTS

The authors are grateful for the financial support by BMWI, which funded the ZIM research project.

REFERENCES

- [1] T. Vogt, J. Hummel, M. Schick, and W. Seim, “Experimentelle Untersuchungen für innovative erdbebensichere Konstruktionen im Holzbau,” *Bautechnik*, vol. 91, no. 1, pp. 1–14, 2014, doi: 10.1002/bate.201300083
- [2] M. Schick, T. Vogt, and W. Seim, “Connections and anchoring for wall and slab elements in seismic design,” 2013
- [3] G. Tlustochowicz, *Racking behaviour of stabilising walls and the anchorage systems for beam and post system in timber: Test report*. Luleå: Luleå tekniska universitet, 2010.
- [4] G. Parida, M. Fragiaco, and H. Johnsson, “Prefabricated timber walls anchored with glued-in rod connections: racking tests and preliminary design,” *Eur. J. Wood Prod.*, vol. 71, no. 5, pp. 635–646, 2013, doi: 10.1007/s00107-013-0726-z.
- [5] CEN (European Committee for Standardization): Eurocode 5: Design of Timber Structures - Part 1-1: General - Common rules and rules for buildings (EN 1995-1-1: 2004). CEN, Brussels, Belgium.
- [6] CEN (European Committee for Standardization): Eurocode 8: Design of structures for earthquake resistance - Part 3: Assessment and retrofitting of buildings (EN 1998-3:2005). CEN, Brussels, Belgium.
- [7] V. Wilden and B. Hoffmeister, “Experimental analyses of innovative wood-shear walls under seismic loads,” IABSE Congress - Resilient Technologies for sustainable infrastructure, September 2-4, Christchurch, New Zealand, 2020.
- [8] European Convention for Constructional Steelwork, Technical Committee 1 TWG 1.3 – Seismic Design, No. 45, 1986, “Recommended testing procedures for assessing the behavior of structural elements under cyclic loads”.
- [9] European Technical Assessment ETA 072/0285: Simpson Strong Tie Hold Downs and Post Bases,” May. 2020.
- [10] R. Don, A. Ciutina, C. Vulcu, and A. Stratan, “Seismic resistant slim-floor beam-to-column joints: experimental and numerical investigations,” *Steel and Composite Structures*, 37 (3), pp. 307–321, 2020. [Online]. Available: <https://doi.org/10.12989/SCS.2020.37.3.307>
- [11] CEN (European Committee for Standardization). (2005). “Eurocode 3: Design of steel structures—Part 1-1: General rules and rules for buildings.” EN 1993-1-1, Brussels, Belgium.
- [12] Abaqus v2018 (2018), Dassault Systemes, Waltham, USA.
- [13] Abaqus-docs: Solid (continuum) elements. Online verfügbar unter <https://abaqus-docs.mit.edu/2017/English/SIMACAEELMRefMap/simaelm-c-solidcont.htm>, zuletzt geprüft am 18.01.2021

- [14] EN12512:2001 2001 Timber structures – Test methods – Cyclic testing of joints made with mechanical fasteners European Committee for Standardisation (Brussels).
- [15] I. Vayas, P. Karydakis, D. Dimakogianni, G. Dougka, C. A. Castiglioni, and A. Kanyilmaz, *Dissipative devices for seismic-resistant steel frames (Fuseis): Final report*. Luxembourg: Publications Office of the European Union, 2013. [Online]. Available: <http://dx.doi.org/10.2777/88177>
- [16] I. Vayas, D. Vamvatsikos, and P. Thanopoulos, “I.11.00: Innovative systems for seismic resistance: The INNNOSEIS Project,” *ce/papers*, vol. 1, 2-3, pp. 3375–3384, 2017, doi: 10.1002/cepa.392

ANALYTICAL AND NUMERICAL MODELLING OF THE IN-PLANE RESPONSE OF TIMBER DIAPHRAGMS RETROFITTED WITH PLYWOOD PANELS

Michele Mirra¹, Marianthi Sousamli², Michele Longo², Geert Ravenshorst¹

¹ Faculty of Civil Engineering and Geosciences – Section of Bio-Based Structures and Materials
Delft University of Technology
Stevinweg 1, 2628 CN Delft, The Netherlands
e-mail: m.mirra@tudelft.nl, g.j.p.ravenshorst@tudelft.nl

² Faculty of Civil Engineering and Geosciences – Section of Applied Mechanics
Delft University of Technology
Stevinweg 1, 2628 CN Delft, The Netherlands
e-mail: m.sousamli@tudelft.nl, m.longo@tudelft.nl

Abstract

In the region of Groningen (NL), human-induced earthquakes initiated by gas extraction are causing structural damage. In that area, the building stock is mainly composed of unreinforced masonry (URM) buildings with light and flexible timber floors and roofs. Thus, an experimental campaign was arranged for assessing the in-plane response of these diaphragms, and a retrofitting method was developed, consisting of an overlay of plywood panels screwed to the existing sheathing around their perimeter. This light, reversible stiffening measure showed a great increase in the in-plane strength, stiffness, and energy dissipation of the floors. Subsequently, an analytical model was developed, showing very good agreement with experimental results, and enabling the design of retrofitting interventions with this technique. Starting from the formulated model, a user-supplied subroutine was implemented in the finite element software DIANA FEA, allowing to represent the in-plane response of the diaphragms, including their energy dissipation. Finally, the impact of this retrofitting intervention on a case study of an existing building was evaluated by means of nonlinear time-history analyses. The results of numerical analyses show that the user-supplied subroutine accurately describes the in-plane behaviour of the retrofitted timber floors. Besides, the proposed retrofitting technique greatly increases the global seismic performance of the building, compared with both its as-built configuration and to stiffer and less reversible strengthening measures.

Keywords: Timber floors, Seismic Rehabilitation, Retrofitting, Seismic capacity, Masonry.

1 INTRODUCTION

In-plane response of timber diaphragms greatly influences the seismic response of existing unreinforced masonry (URM) buildings. As-built floors are often too flexible to withstand in-plane loads without causing the out-of-plane collapse of the walls. Hence, a proper retrofitting of the diaphragms, as well as an improvement of their connections to the walls, have to be performed. In this framework, several strengthening techniques have been investigated in the recent years [1]-[14], aiming at enhancing the seismic properties of the existing diaphragms. Among these techniques, reversible ones are usually preferred when they are applied to monumental structures, because of their lower impact [15].

Retrofitting interventions on timber diaphragms appear to be urgent and delicate in the region of Groningen, in the northern part of the Netherlands, where earthquakes induced by gas extraction are causing structural damage. The seismic events up to now have been light and have not caused collapses, but according to probabilistic studies, more intense events might occur. In that area, the building stock is mainly composed of URM low-rise buildings with light and flexible timber floors and roofs. This construction typology is widely present and very vulnerable to horizontal loads, because the buildings were not designed to withstand earthquakes, since seismic events were absent until recently. Thus, in 2018-19 a full-scale test campaign, recalled in Section 2, was arranged at Delft University of Technology for assessing the in-plane response of as-built and strengthened timber diaphragms typical of the Groningen area. The retrofitting measure consisted of an overlay of plywood panels screwed to the existing sheathing around their perimeter. This light, reversible strengthening measure showed a great increase in the in-plane strength, stiffness, and energy dissipation of the floors [14].

In this work, the analytical and numerical modelling of the refurbished floors is presented. An analytical model was firstly developed to enable a detailed design of the retrofitting intervention with the proposed strengthening technique. The formulated model, presented in detail in [16] and recalled in Section 3, estimates well the floors' strength, stiffness and energy dissipation, including pinching behaviour.

After these first steps, the impact of this retrofitting intervention in a case study of an existing building was evaluated by means of nonlinear time-history analyses. Three configurations were studied: an as-built one with flexible floors; one where a stiff and not reversible retrofitting intervention was applied, such as the cast of a concrete slab on the existing diaphragms; one where the proposed strengthening method was applied. For the latter case, given the high amount of energy dissipation of floors already at limited in-plane deflection, and their characteristic pinching behaviour, it was important to model in detail their seismic response for fully evaluating the impact of this retrofitting method. For this purpose, starting from the developed analytical model, a user-supplied subroutine was implemented in the finite element software DIANA FEA [17], allowing to represent the global in-plane response of the diaphragms. In this way, it was possible to simulate the nonlinear behaviour of both masonry (already featured by the software) and timber floors. The subroutine implementation is presented in Section 4, while results from the analyses on the case-study building are discussed in Section 5.

2 IN-PLANE EXPERIMENTAL TESTS ON TIMBER DIAPHRAGMS

To gain more insight into the in-plane behaviour of timber diaphragms with Dutch features, an experimental campaign was arranged at Delft University of Technology [14]. The floors were initially tested in their as-built configuration, and then retested after being strengthened with an overlay of plywood panels screwed along their perimeter to the existing sheathing. Prior to testing, portions of diaphragms were extracted from existing buildings in the Groningen area, so that the material properties of the tested samples could be accurately replicat-

ed and representative for the actual floors. Five full-scale samples representing half of a floor were tested in a vertical configuration (Fig. 1): two specimens were tested parallel to the joists (*DFpar-1*, *DFpar-2*) and two perpendicular to them (*DFper-3*, *DFper-4*), the last represented a roof pitch (*DRpar-5*). For the strengthened samples, the same nomenclature was adopted, adding the letter *s* at the end of each specimen name. As can be noticed from Fig. 1, the retrofitted floors exhibited a great improvement in strength, stiffness, and energy dissipation. To facilitate a detailed design of retrofitting interventions by adopting the proposed strengthening technique, an analytical model was formulated, which is presented in the next section. For further details on this experimental campaign, the reader can refer to [14].

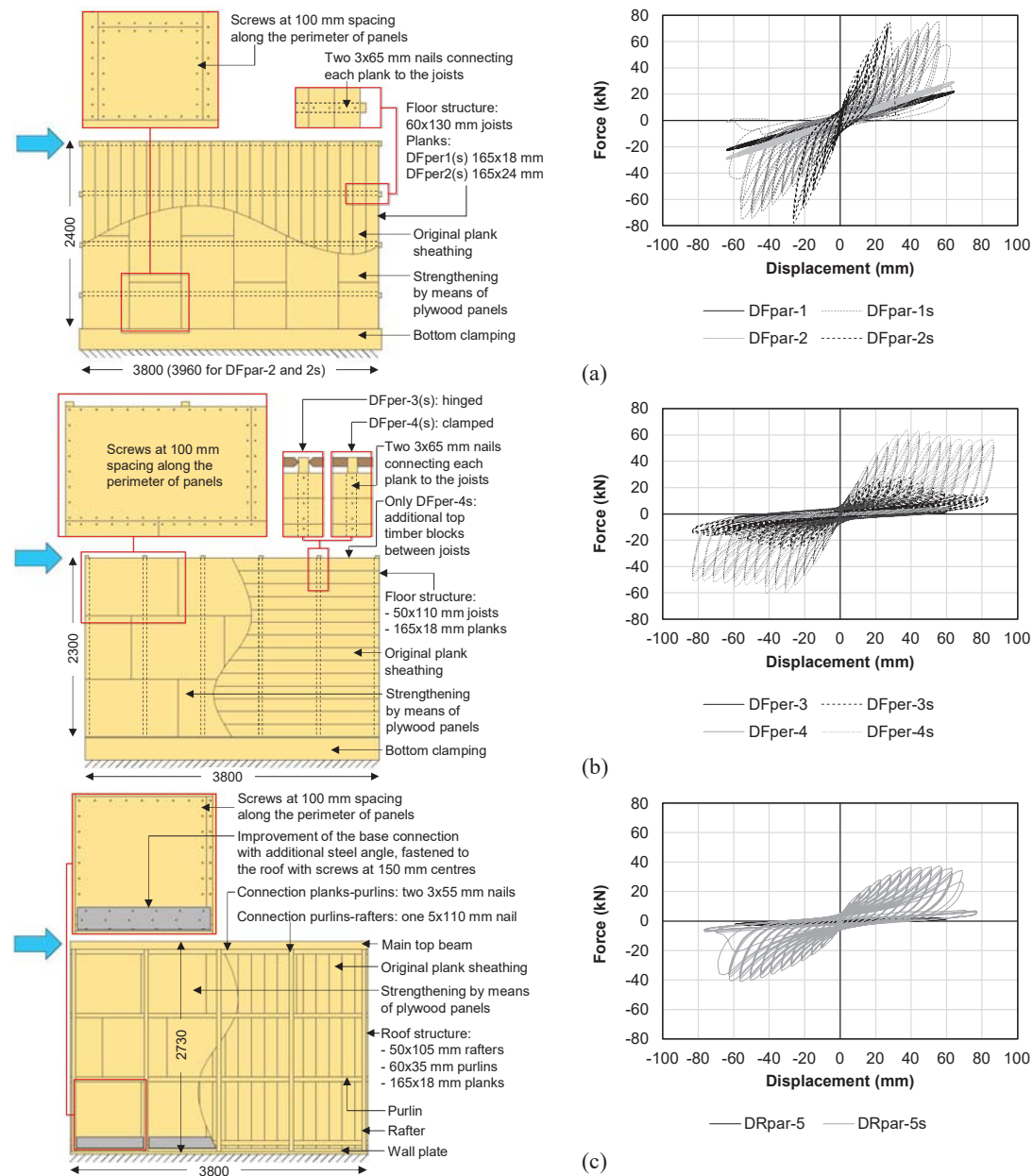


Figure 1: Main characteristics and cyclic in-plane response of the timber diaphragms; floors tested parallel (a) and perpendicular to the joists (b), roof pitch (c) [14].

3 ANALYTICAL MODELLING OF THE STRENGTHENED DIAPHRAGMS

3.1 General

The starting point for the formulation of the model was the evaluation of the load-slip behaviour of the screws fastening planks and plywood panels (Section 3.2). Based on their response, the global in-plane response of the diaphragm was then derived analytically (Section 3.3). The developed calculation model enables a good prediction of the diaphragms' in-plane behaviour [16], as shown in Section 3.4.

3.2 Evaluation of the load-slip behaviour of the fasteners

Besides the experimental campaign on full-scale floors, tests were also performed on fourteen small-size replicates for evaluating the response of the screws connecting plywood panels and planks. These specimens were composed of a plank and a plywood panel portion fastened together by means of two screws (Fig. 2). The samples were tested in shear, under the quasi-static reversed-cyclic loading protocol of ISO 16670 [18]: seven replicates were tested parallel to the main direction of the plank, and the other seven orthogonal to it (Fig. 2a). Similar load-slip curves were obtained between the two loading directions (Fig. 3).

Based on the obtained results, the load-slip response was modelled by means of a combination of a linear and a parabolic branch, representing the initial stiffness and the global behaviour, respectively [16]. A continuous curve was created with an extension of Foschi's load-slip model for nails [19]. With the proposed model, both post-yielding and softening behaviour of the fasteners can be described. The equation of the curve was defined as follows:

$$F_s = (F_0 + a d_s + b d_s^2)[1 - \exp(-K_0 d_s/F_0)] \geq 0; \text{ with } a > 0, b < 0 \quad (1)$$

In Eq. 1, F_s and d_s are the force and displacement of the screw, respectively; F_0 , a and b are the coefficients of the parabola representing the global behaviour, while K_0 is the slope of the line representing the initial stiffness. This curve fits the experimental points with $R^2 = 0.83$ when the panel is loaded parallel to the plank, and with $R^2 = 0.95$ if the force is applied perpendicular to it (Fig. 3). As a failure criterion, the ultimate displacement was considered as the one for which the transferred load drops below 80% of the peak strength during the softening phase, in agreement with the provisions of ISO 16670 [18] and EN 12512 [20]. As a last consideration, a scatter is present in the data points and the backbones, as it is usually observed when analysing tests on timber joints. Yet, since a large number of screws is used in the whole floor, the global behaviour will approach the average trend.

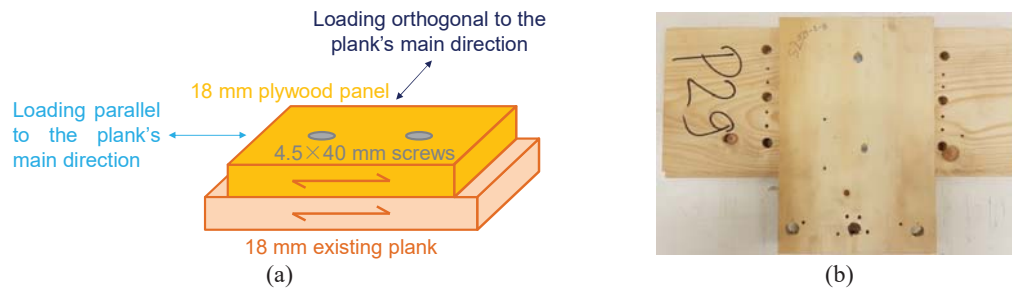


Figure 2: Samples prepared for testing the screws fastening the plywood panels to the existing sheathing: schematic description (a) and example of specimen (b) [16].

With the aforementioned procedure, it is possible to construct the load-slip curve starting from experimental tests, but in order to further generalize the proposed model, a fully analytical estimation of the curve was proposed as well [16]. This generalization was also necessary because some of the full-scale strengthened floors had different characteristics from the small-size replicates: sample *DFpar-2s* featured 24 mm planks, and in specimens *DFpar-2s*, *DFper-3s*, *DFper-4s* screws with a 5 mm diameter were used [14]. Therefore, the parameters K_0 , F_0 , a and b were also estimated according to formulations from standards or literature.

The initial stiffness K_0 was found to be well predicted with the expression provided in [21] for non-predrilled nails, thus $K_0 = 50 d^{1.7}$, with d nominal diameter of the screw.

F_0 can be predicted starting from the knowledge of the maximum force F_{max} determined according to EN 1995 [22] and Johansen's theory [23] for timber-to-timber joints, and with a screw sufficiently slender to develop two plastic hinges. Then, F_0 can be estimated as $F_{max}/8$ (Fig. 4).

To determine the parameters a and b , three points crossed by the parabola have to be identified. The last quantity to be estimated is thus the slip d_{max} of the screw at F_{max} . To this end, firstly the expression of EN 409 [24] can be used for determining the angle α at which the screws' bending moment is evaluated, and adopting for its calculation the shank or inner diameter d_1 of the screw. Secondly, the distance $(b_1 + b_2)$ between the two plastic hinges according to Johansen's theory [23] is determined. By combining these two quantities, the slip at F_{max} can be estimated as $d_{max} = (b_1 + b_2) \tan(\alpha)$ (Fig. 4). The parabola is thus now identified by the three points $(0, F_0)$, (d_{max}, F_{max}) , and $(2d_{max}, F_0)$. Further details on the analytical derivation of the proposed load-slip curve can be found in [16].

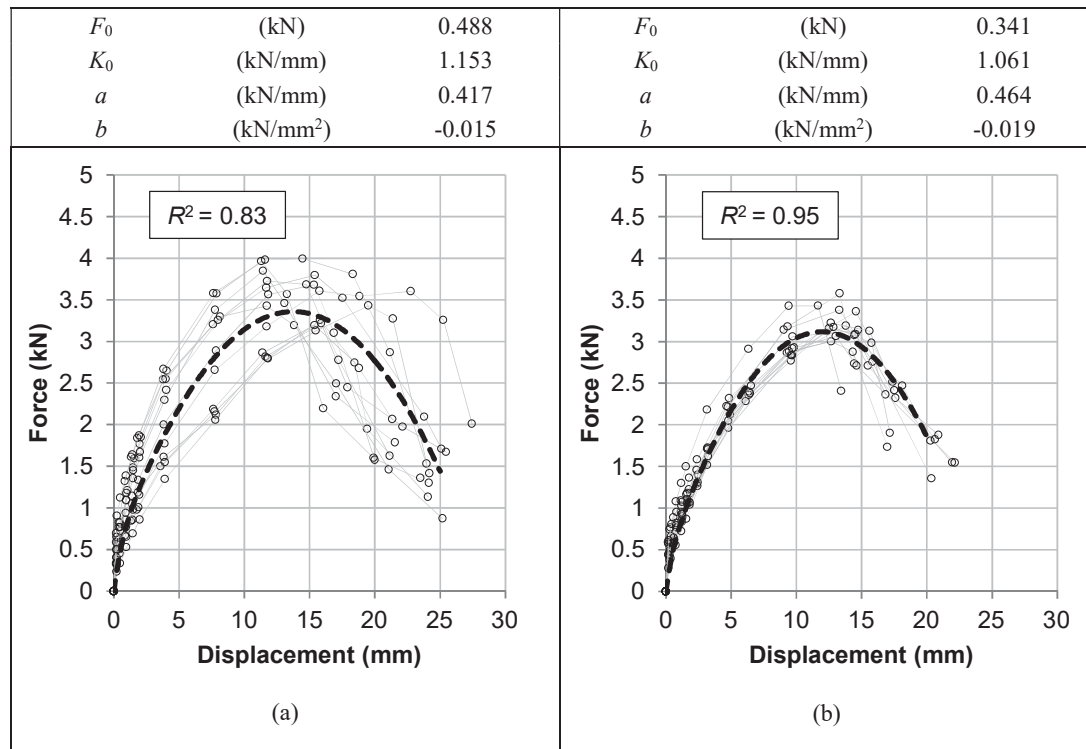


Figure 3: Proposed load-slip curve (dashed) in comparison to experimental data points and backbones for the direction parallel (a) and perpendicular to planks (b). The main parameters of the equation are also reported [16].

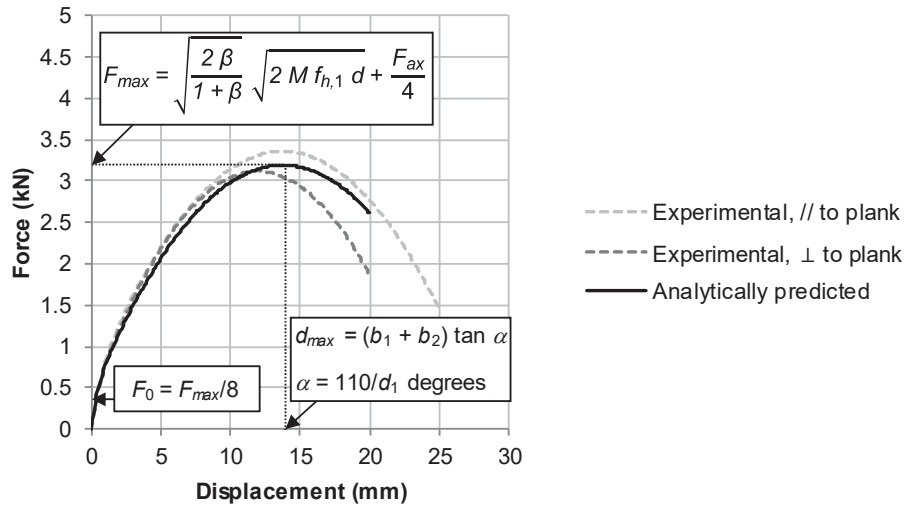


Figure 4: Comparison between the analytically derived curve and the ones obtained from the experimental data [16]. In the reported equations, the same notation as in EN 1995 [22] and EN 409 [24] is used.

3.3 Prediction of the global response of the retrofitted diaphragms

The floors were retrofitted by screwing plywood panels along their perimeter to the existing sheathing. This type of refurbishment is particularly advantageous, because the screws are placed in such a way that it is possible to identify their specific contribution to the overall resisting mechanism. With reference to Fig. 5, when the strengthened floor is subjected to a horizontal load and the panels are vertically arranged, the force is subdivided among the columns of panels, and the screws are opposing to it with their stiffness. Each column of panels is subjected to rotation and sliding: the rocking behaviour is taken into account by considering the vertical screws, while the (very limited) slip is evaluated through the horizontal screws (Fig. 5). In general, the diaphragms retrofitted with this method can be regarded as very similar to timber shear walls. Therefore, once the load-slip response of the single screw is known, the global behaviour can be predicted by considering equilibrium relations [16].

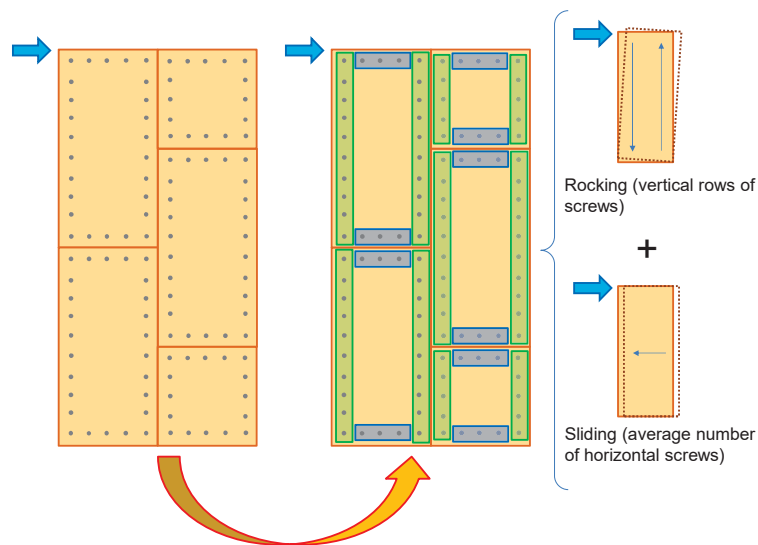


Figure 5: Determination of the global floors' response from single screws through equilibrium relations [16].

Additionally, the evaluation of energy dissipation was essential, because the strengthened diaphragms proved to provide significant values of equivalent hysteretic damping, of approximately 14-15% [25]. In order to consider this potentially beneficial effect in numerical modelling, an analytical formulation for determining the evolution of pinching cycles was proposed [16].

The pinching behaviour implies the presence of a residual force at zero displacement: this load approximately corresponds to the force causing the very first yielding of the tested sample. In the analytical curve equation, F_0 is the intercept on the y -axis (force) of the parabola representing the global response of the specimens. To capture the very first yielding on the analytical curve, the intercept on the y -axis assumed for the pinching cycle was $2/3F_0$, a value around which the initial slope of the curve starts to change.

Starting from this first intercept, the pinching cycle can be estimated for a certain amplitude identified by a point $(\delta_c, F_c(\delta_c))$ on the curve. As a first step, two lines are determined: one joining the points $(0, 2/3F_0)$ and $(\delta_c, F_c(\delta_c))$, and one crossing the point $(\delta_c, F_c(\delta_c))$ with slope K_0 (Fig. 6, step 1). Then, the bisector of these two lines is found (step 2). In step 3, the remaining part of the cycle is defined: firstly, the line joining $(0, 2/3F_0)$ and the point on the bisector having x -coordinate equal to $\delta_c/2$ is determined; secondly, a line parallel to the former one intersects the branch having slope K_0 , starting from the point $(0, -2/3F_0)$.

In step 4, the whole multilinear cycle is determined, and could already be used for software implementation, as it was exemplified in [16]. The negative part of the pinching cycle (points B', C', D' of Fig. 6) is antisymmetric to the positive one, as is assumed for the backbone curve equation. For a more refined evaluation of both pinching and damping properties of the diaphragms, this multilinear cycle is used in step 5 to construct four exponential branches, smoothening the straight lines, again similarly to Foschi's formulation. The equations of these branches are reported in Section 4.3, in which the implementation of the user-supplied subroutine is presented. A graphical representation of them is given in step 6 of Fig. 6, showing the pinching cycles evolution.

3.4 Comparison between analytical and experimental results

By combining the derived analytical curve and the pinching cycles estimation, the cyclic response of the tested diaphragms was predicted: the reliability of the developed model can now be evaluated by comparing the analytical results with experimental ones. Therefore, this section presents a comparison of the analytical backbone (always depicted in red) and an estimated representative pinching cycle (always shown in dark blue), with the experimental hysteretic cycles (light blue). The results are shown in Figs. 7-9 for a diaphragm tested parallel to the joists (sample *DFpar-1s*, Fig. 7), a floor tested perpendicular to the joists (sample *DFper-4s*, Fig. 8), and the roof pitch (Sample *DFper-5s*, Fig. 9); both the global behaviour and the initial response (up to 20 mm displacement) are displayed. For a more detailed comparison and overview, the reader is referred to [16]. As can be noticed, the analytical model proves to well predict the in-plane behaviour of all diaphragms, also when variations are present with respect to the reference tests on plank-plywood panel joints. In general, the initial stiffness and pinching response are accurately captured by the model, along with strength and displacement at failure of the specimens.

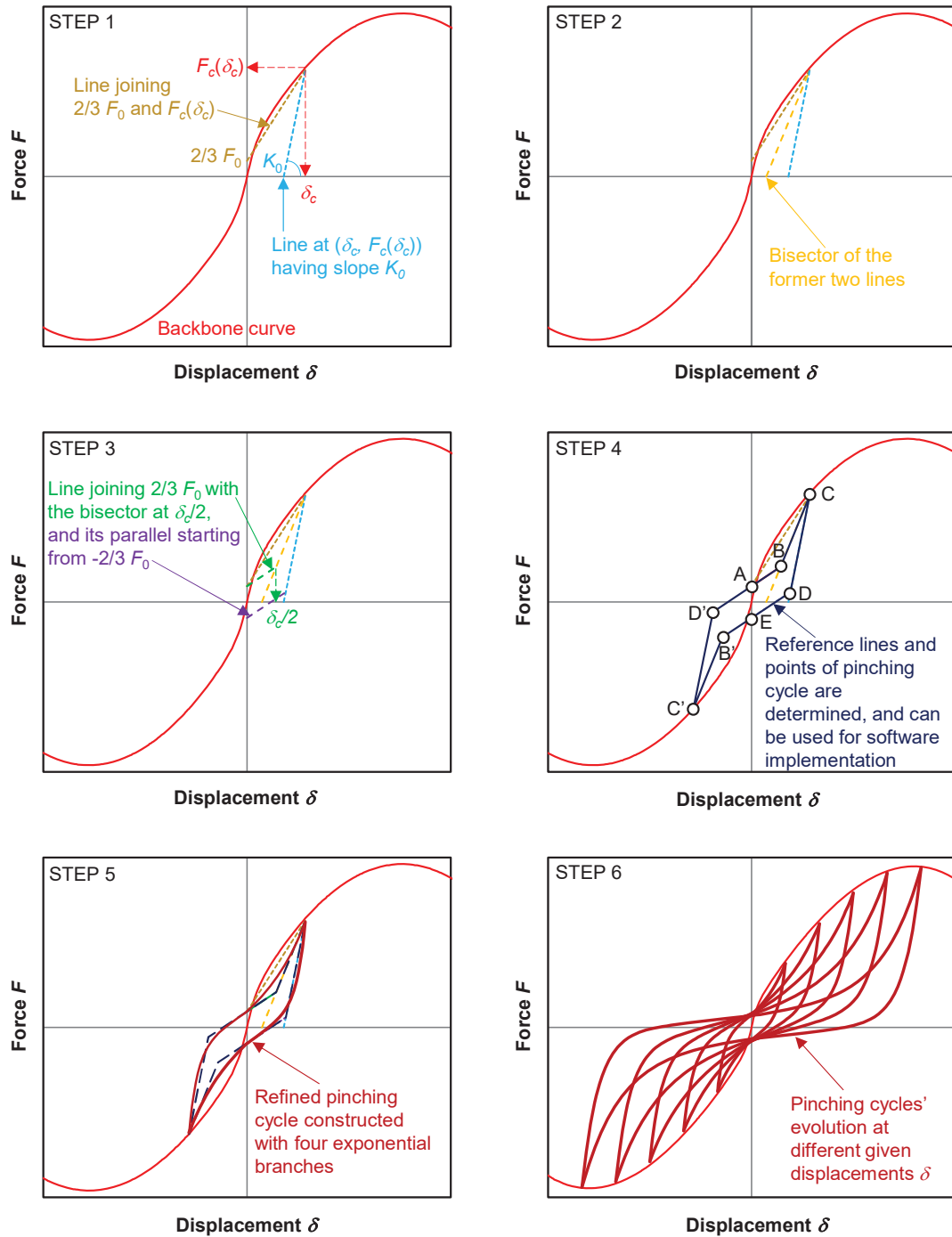


Figure 6: Procedure for the determination of the pinching cycles from the analytical backbone curve [16].

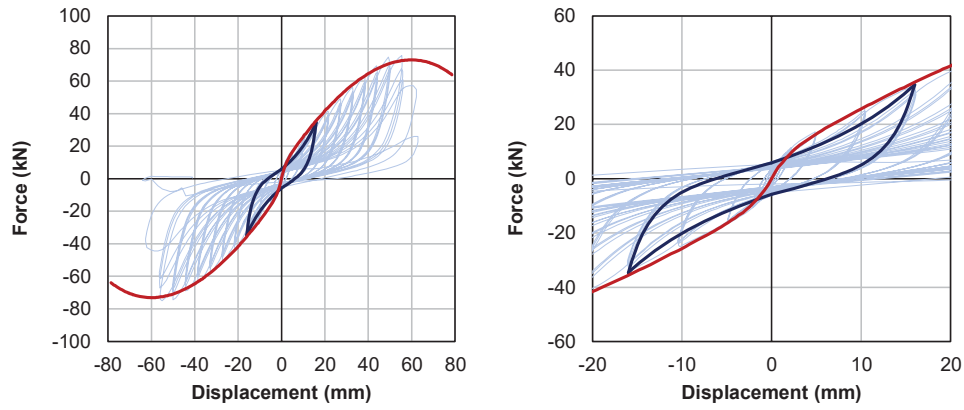


Figure 7: Comparison between analytical backbone (red) and a representative pinching cycle (dark blue) with the experimental hysteretic response (light blue) for sample *DFpar-1s*: global (left) and initial (right) response [16].

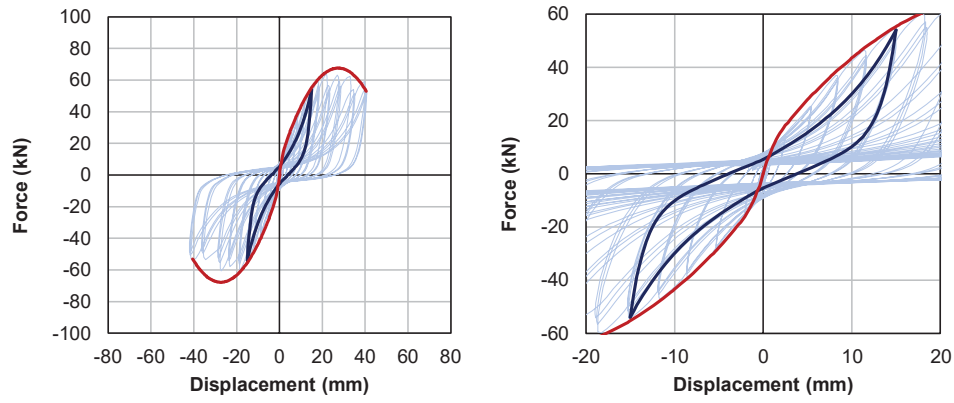


Figure 8: Comparison between analytical backbone (red) and a representative pinching cycle (dark blue) with the experimental hysteretic response (light blue) for sample *DFper-4s*: global (left) and initial (right) response [16].

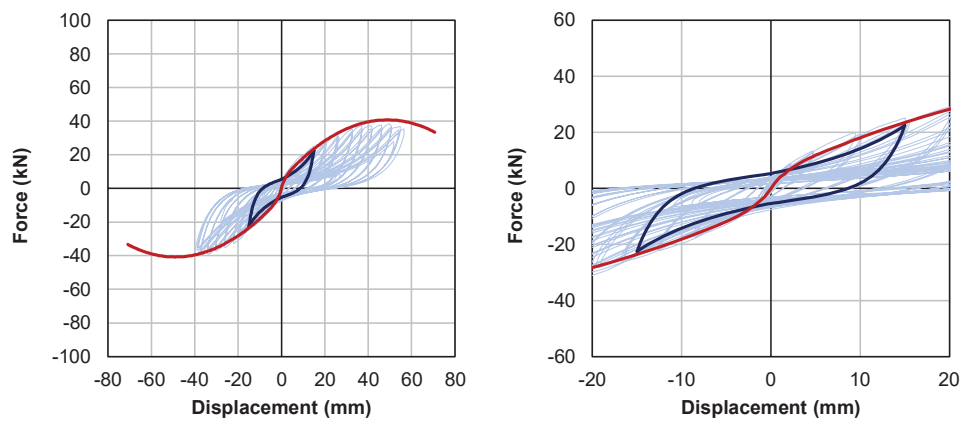


Figure 9: Comparison between analytical backbone (red) and a representative pinching cycle (dark blue) with the experimental hysteretic response (light blue) for sample *DFpar-5s*: global (left) and initial (right) response [16].

4 NUMERICAL MODELLING OF THE STRENGTHENED DIAPHRAGMS

4.1 General

Given the great improvement in relevant seismic properties of the retrofitted timber diaphragms, it was important to properly model their in-plane response. In this way, the potentially beneficial effect of their energy dissipation, provided at an already limited deflection, could be described. Yet, when considering existing URM buildings with timber floors, the behaviour of the diaphragms is usually simplified in numerical models. Existing or not stiff diaphragms are often modelled as (very flexible) linear elastic orthotropic slabs [26], while after retrofitting them the hypothesis of infinitely stiff diaphragms is frequently assumed, given its compliance with the pushover method [27].

Therefore, the potential energy dissipation of the floors is neglected, and their global in-plane response is not fully considered. However, if it is possible to properly account for both, then an optimized design of the retrofitted diaphragms could be achieved, so that the floors can become an additional source of energy dissipation for the buildings in which they are present. In order to further investigate these aspects, the aforementioned analytical model was implemented in a user-supplied subroutine to be imported in the software DIANA FEA, version 10.4 [17]. This software already featured an advanced nonlinear model for masonry, but lacked suitable materials and constitutive laws for modelling timber floors. In the following sections, the adopted modelling strategy, the subroutine implementation, and its validation are discussed.

4.2 Modelling strategy for timber floors

In order to properly capture the in-plane and out-of-plane behaviour of the diaphragms, while simultaneously implementing the analytical model, a macro-element strategy was adopted (Fig. 10). The floors were modelled by combining linear elastic shell elements, for representing the out-of-plane behaviour under static vertical loads, and nonlinear macro-elements overlapped to them for describing the in-plane behaviour.

These macro-elements consisted of six trusses: four rigid trusses connected to form a quadrilateral, and two nonlinear trusses placed diagonally (Fig. 10), in which the nonlinear in-plane behaviour of the floor was implemented adopting the proposed analytical model. This modelling strategy proved to be accurate and efficient, and was also adopted in past research studies [28], [29]. For the linear elastic orthotropic shells, the flexural characteristics were assigned considering an equivalence between the actual inertial properties of the joists, and those of the slab, so that the same vertical deflection could be achieved.

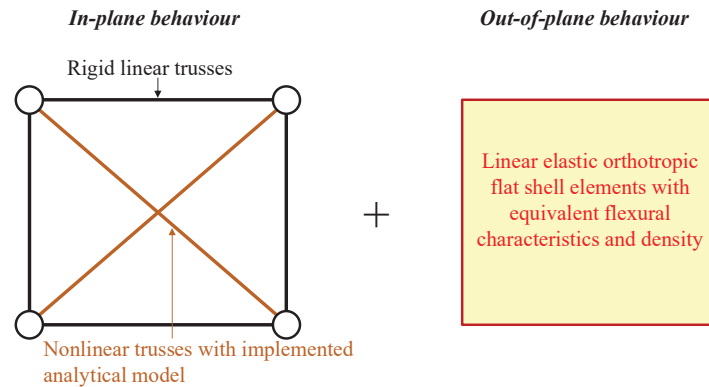


Figure 10: Adopted strategy for modelling in-plane and out-of-plane behaviour of timber diaphragms.

4.3 Implementation of the user-supplied subroutine

In order for the user-supplied subroutine to be compatible with the DIANA FEA environment, the constitutive laws for the diagonal trusses of the macro-elements were implemented adopting the FORTRAN 90 programming language. Two types of input variables are required by the software: user-specified initialization parameters (not changing within the subroutine calculations), and initial state variables (varying during subroutine calculations, e.g. for determining loading and unloading points). As output, DIANA FEA requires user-supplied subroutines to provide the stress-strain relation, to be adopted at every calculation step.

Three relevant parameters for initialization were chosen: the strain ε_{max} at peak stress σ_{max} , the peak stress σ_{max} itself, and the initial elastic modulus K_0 (Fig. 11). These parameters are known, once the retrofitting of the diaphragm is designed through the analytical model, according to the expected seismic loads. Besides, ten initial state variables were adopted, necessary for describing all loading and unloading branches, and their initial value was set to 0. With reference to Fig. 11, these variables are the maximum strains ever reached in tension and compression ($\varepsilon_{t,max}$ and $\varepsilon_{c,max}$, respectively), and the stress-strain coordinates identifying the end of the loading and unloading branches in tension (points $(\varepsilon_{t,l}, \sigma_{t,l})$ and $(\varepsilon_{t,ul}, \sigma_{t,ul})$, respectively) and compression (points $(\varepsilon_{c,l}, \sigma_{c,l})$ and $(\varepsilon_{c,ul}, \sigma_{c,ul})$, respectively). Through these variables, the pinching behaviour during unloading and reloading can be defined. The constitutive laws implemented through the user-supplied subroutine are now presented for the tensile branch only, since the compressive one follows antisymmetric relations.

The material follows the tensile loading branch as long as $\varepsilon > 0$ and $\varepsilon > \varepsilon_{t,max}$, with the constitutive law of Eq. 2 (Fig. 12, blue branch):

$$\sigma = (\sigma_y + a \varepsilon + b \varepsilon^2)[1 - \exp(-K_0 \varepsilon / \sigma_y)] \quad (2)$$

In Eq. 2, $\sigma_y = \sigma_{max}/8$, following the analytical derivation presented in Section 3.2.

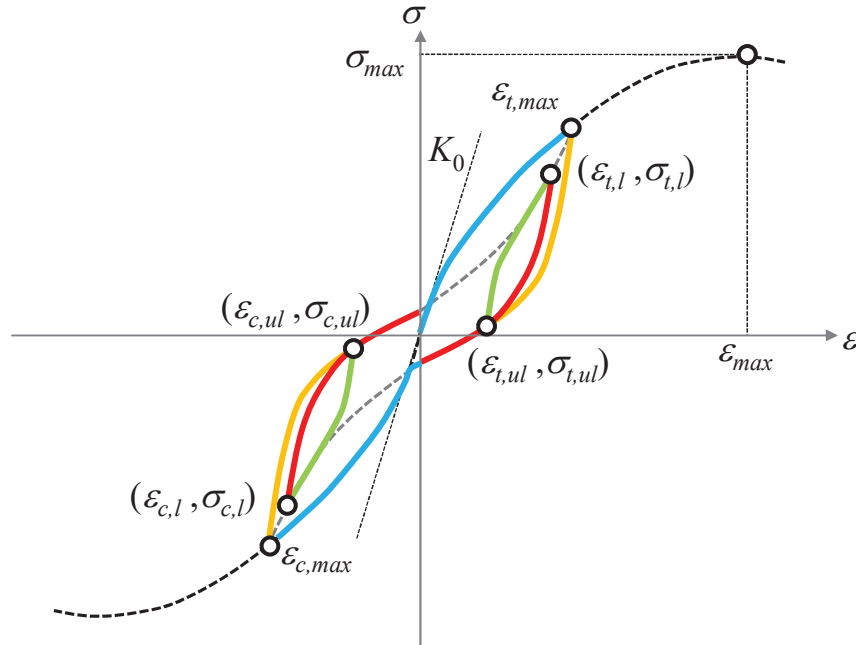


Figure 11: Representation of the input parameters for the user-supplied subroutine.

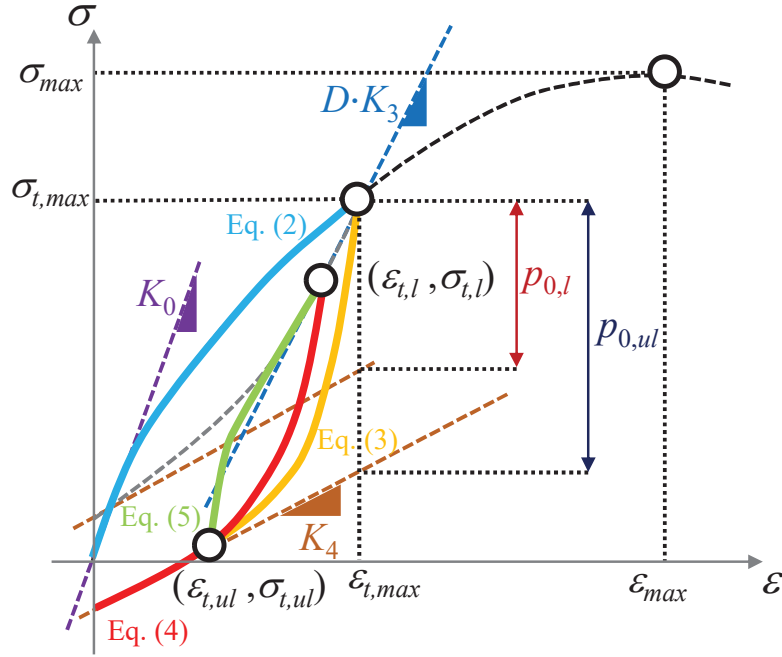


Figure 12: Loading, unloading and reloading branches implemented in the user-supplied subroutine.

After reaching $\varepsilon_{t,max}$, the tensile unloading phase is defined if $\varepsilon > 0$, $\varepsilon < \varepsilon_{t,max}$, and $\varepsilon < \varepsilon_0$, with ε_0 initial strain at the beginning of the current step. In this case, the response is distinguished between the case in which the unloading starts from the envelope curve (at $\varepsilon_{t,max}$, yellow branch of Fig. 12), and when the unloading occurs after a reloading phase (red branch of Fig. 12). In the first case, $\varepsilon_{t,l} \equiv \varepsilon_{t,max}$, and the constitutive law is formulated as (see Fig. 12 for the meaning of the various parameters):

$$\sigma = f_{t,ul} = \sigma_{t,max} - [\sigma_{t,max} - p_{0,ul} - K_4(\varepsilon - \varepsilon_{t,max})] \{1 - \exp[2K_0(\varepsilon - \varepsilon_{t,max})/(\sigma_{t,max} - p_{0,ul})]\} \quad (3)$$

In the second case, instead, the relation is ($\varepsilon_{t,l} \neq \varepsilon_{t,max}$):

$$\sigma = \sigma_{t,l} - (\sigma_{t,l} - f_{t,ul}) \{1 - \exp[2K_0(\varepsilon - \varepsilon_{t,l})/(\sigma_{t,l} - f_{t,ul})]\} \quad (4)$$

Finally, the tensile reloading phase is defined if $\varepsilon > 0$, $\varepsilon < \varepsilon_{t,max}$, and $\varepsilon > \varepsilon_0$, according to the constitutive law of Eq. 5:

$$\sigma = \sigma_{t,ul} + (f_{t,l} - \sigma_{t,ul}) \{1 - \exp[-2K_0(\varepsilon - \varepsilon_{t,ul})/(f_{t,l} - \sigma_{t,ul})]\} \quad (5)$$

with:

$$f_{t,l} = \sigma_{t,max} - [\sigma_{t,max} - p_{0,l} - K_4(\varepsilon - \varepsilon_{t,max})] \{1 - \exp[D \cdot K_3(\varepsilon - \varepsilon_{t,max})/(\sigma_{t,max} - p_{0,l})]\} \quad (6)$$

and:

$$D = 1 + (\varepsilon_{t,max}/\varepsilon_{max})^3 \quad (7)$$

With reference to Eq. 7, the parameter D is a factor accounting for the progressive degradation of the pinching cycles, becoming progressively less stiff when the floor drift increases (Fig. 6, step 6).

4.4 Validation of the user-supplied subroutine

As already presented in section 3.4, the analytical model proved to be accurate for predicting the global in-plane response of the retrofitted timber diaphragms. Since the model was implemented in the user-supplied subroutine, very close results were expected, useful to validate both the subroutine itself, and the adopted modelling strategy for timber diaphragms.

As validation example, a retrofitted timber diaphragm with similar characteristics to sample *DFpar-1s* was modelled. A 4×6 m floor was considered, supported on the long sides, having as in-plane properties an initial stiffness of 10 kN/mm, and a strength of 150 kN activated at 60 mm displacement. The floor featured 60×130 mm joists at a heart-to-heart distance of 500 mm, while the thickness of both plywood panels and planks was 18 mm. The elastic modulus of timber was assumed to be 10000 MPa. On the basis of these characteristics, equivalent input properties were determined for the elements in the numerical model.

The modelled diaphragm consisted of a mesh of 1×1 m macro-elements (capturing the in-plane response), overlapped to flat shell elements (accounting for the out-of-plane behaviour), as shown in Fig. 13. The three initial parameters, required by the user-supplied subroutine for determining the constitutive law of the nonlinear diagonal trusses, can be derived from geometrical considerations. Starting from the whole floor deflection u , the displacement δ of a truss is given by:

$$\delta = (u \cos \alpha)/m \quad (8)$$

where α is the angle between the truss and the loading direction (Fig. 13), and m the number of macro-elements rows parallel to the applied load in half of the floor (in this case, $m = 2$). The shear force $F/2$ is then subdivided among the s trusses in one macro-elements row, and transformed into an axial force N on a single one:

$$N = F/(2 s \cos \alpha) \quad (9)$$

From the knowledge of the geometrical relations for N and δ , also the initial stiffness of the diagonal trusses can be calculated. For convenience, a unitary section was adopted for the truss elements, so that force and stress could be coincident in their values.

The properties of the shell elements were derived by considering an equivalence in flexural properties between the joists and the slab, defining an equivalent elastic modulus E_{eq} :

$$E_{eq} = E_{timber} I_{joists} / I_{slab} \quad (10)$$

where I_{joists} is the sum of the moments of inertia of the single joists, and I_{slab} is the moment of inertia of the slab, defined by attributing to the shell elements a thickness of 36 mm (planks and plywood panels). According to the reference system of Fig. 13, the elastic modulus E_{eq} was assigned to all directions, while the shear moduli were different: a value of 0.1 MPa was assigned to G_{xy} , because the in-plane behaviour was already described by the macro-elements, while $G_{xz} = G_{zy} = E_{eq}/16$ (similarly to an actual timber material). The main material properties assigned to the model are summarized in Table 1. Hinged supports were placed to the two lateral edges parallel to the application of the in-plane load (Fig. 13).

The floor was firstly subjected to a linear static analysis to verify the equivalence in flexural properties between the slab and the joists (Fig. 14a). Both the self-weight and a vertical load of 1.5 kN/m² were applied. Then, two in-plane cyclic analyses were performed, one to assess the global cyclic behaviour (Fig. 14b), and one in which local loops were imposed (Fig. 14c). These analyses were displacement-based, and the displacement was applied at the floor midspan (Fig. 13). Finally, a time-history analysis was conducted (Fig. 14d), subjecting the floor to a scaled seismic signal, representative for the Groningen area.

As can be noticed (Fig. 14), both out-of-plane and in-plane behaviour of the floor are properly captured by the adopted modelling strategy and the implemented subroutine. The deflection under vertical loads proved the correct application of the flexural properties to the shell elements: the obtained displacement was practically coincident with the one calculated analytically by considering the floor joists. With regard to the in-plane response, strength, stiffness, energy dissipation and pinching behaviour are well described in all in-plane analyses, with a response quite close to that of reference sample *DFpar-1s* (Fig. 7a).

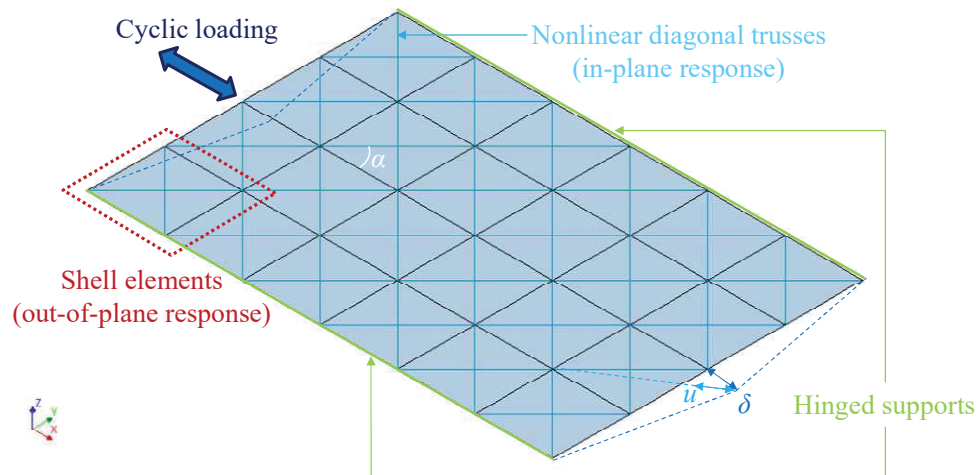


Figure 13: Model of the retrofitted diaphragm for the validation of the user-supplied subroutine.

Table 1: Properties adopted in the floor model.

Function	Element type	Property	Value
Macro-elements representing the in-plane behaviour of the floor	Rigid trusses	Elastic modulus E_t (MPa)	10^{10}
		ϵ_{max}	0.01
	Diagonal trusses	σ_{max} (MPa)	12000
		K_0 (MPa)	5520000
Shell elements describing the out- of-plane response of the floor	Shell elements	Elastic moduli E_x, E_y, E_z (MPa)	62000
		In-plane shear modulus G_{xy} (MPa)	0.1
		Shear moduli G_{xz}, G_{zy} (MPa)	3880

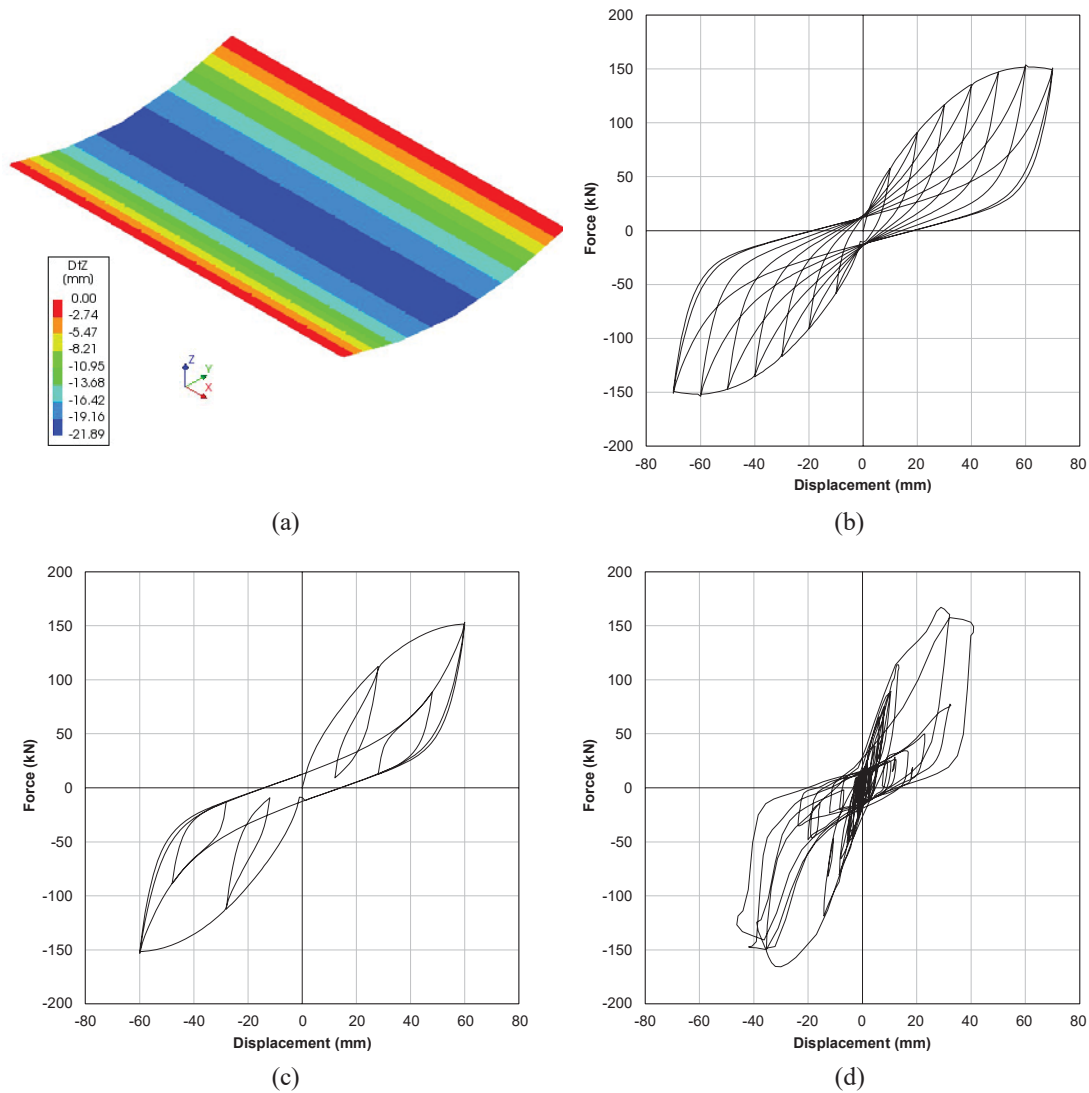


Figure 14: Results from the analyses conducted for the validation of the user-supplied subroutine and the overall modelling strategy for timber floors: out-of-plane static analysis under vertical loads (a); complete displacement-based in-plane cyclic analysis (b); displacement-based in-plane cyclic analysis with local loops (c); in-plane time-history analysis under an induced Groningen earthquake accelerogram (d).

5 CASE STUDY: A MASONRY DETACHED HOUSE WITH TIMBER FLOORS

5.1 Introduction

The implemented user-supplied subroutine opened up the opportunity to analyse the beneficial impact of a dissipative retrofitting of timber diaphragms in an existing URM building. The effect of floors strengthened with plywood panels, and thus with a light, reversible technique, was compared to that of the as-built configuration, and of another not reversible retrofitting measure, widely applied also in the past, and namely the cast of a reinforced concrete slab on the existing diaphragms. Several studies have already shown that the latter retrofitting measure could be detrimental for masonry buildings [28]-[30], and not advisable if the construction is protected or part of the architectural heritage of a certain context [15]. Yet, the

need of stiffening in their plane the existing, inadequate floors, combined with design rules based on the hypothesis of infinitely stiff diaphragms [27], could often result in realizing a concrete slab. This intervention undoubtedly increases the overall seismic masses, but contemporarily improves the static out-of-plane behaviour of the floor, and also the in-plane capacity of walls. After applying these retrofitting measures, or similar ones making the floors almost infinitely stiff, the contribution that is missing is the potential energy dissipation that the floors could provide. If, instead, the diaphragms are strengthened with a dissipative technique, allowing efficient shear transfer and horizontal loads redistribution, and at the same time a controlled deflection, then their role can be quite beneficial. With the adopted retrofitting solution, this advantageous effect can be obtained, and through the user-supplied subroutine it can be evaluated through numerical analyses, fully accounting for the nonlinear in-plane response of the floors.

5.2 Characteristics of the analysed building

A detached house typical of the Groningen area was selected as the case-study building (Fig. 15). This URM low-rise house has a relatively simple structure, but some irregularities are present, such as the position and shape of wall openings, and the thickness of the walls, not constant along the height, with gables featuring a single-leaf wall (100 mm thick) instead of the ground floor double-leaf walls (210 mm thick). Besides, one more single-leaf wall was present, supporting one of the floors approximately at midspan, in correspondence to the staircase (Fig. 15). Three configurations were studied: one represented the as-built house with flexible diaphragms; in the other two, the floors were retrofitted with plywood panels or with a concrete slab. The properties of masonry, reported in Table 2, were assumed to be the same for the three configurations. The adopted values are in line with the characteristics of medium-low quality masonry: these material properties fall on the conservative side with respect to experimental tests performed on both existing and replicated Dutch masonry [31], [32], and were also defined according to calibration studies [33]. Shell elements with the implemented DIANA FEA Engineering Masonry Model [34] were used for modelling the masonry.

For all configurations, nonlinear incremental dynamic analyses were performed, by subjecting the house to seven accelerograms of induced earthquakes retrieved from the seismic database of the Netherlands Normalisatie-instituut (NEN) [35]. The main loading directions x and y were studied separately, therefore a total of 42 analyses were performed. The signals were referred to an average peak ground acceleration (PGA) of 0.17g, and are shown in Fig. 16; a Rayleigh damping of 2% was considered in the analyses. While for walls a density of 2000 kg/m³ was assumed, for the diaphragms the density values included the self-weight of structural elements, a dead load of 1.00 kN/m² (accounting for further elements such as non-structural walls, finishes, plants, pipes), and 30% of the live load, equal to 1.75 kN/m² for Dutch residential buildings [36].

The as-built configuration featured flexible diaphragms: the 4.0×4.6 m floor presented 75×180 mm joists at a heart-to-heart distance of 800 mm; the 4.6×6.8 m floor had 60×160 mm joists arranged at 750 mm heart-to-heart distance; the roof presented 50×105 mm rafters at 900 mm heart-to-heart distance; all diaphragms had 18 mm thick planks. These structural properties were translated in the numerical model by following the modelling strategy for shell elements described in Section 4.2. In this case, because of the very small energy dissipation observed from tests on replicated as-built floors [14], the diaphragms were modelled with linear elastic orthotropic shell elements (thus without overlapping the nonlinear macro-elements), whose properties are reported in Table 3. The in-plane shear moduli of the diaphragms were derived by considering the flexural properties of the planks or the joists [14]. These values would correspond to equivalent shear stiffnesses of 108 to 216 kN/m, and are

thus in line with other similar stiffness estimations for existing floors from literature [3], [4], [7], [8], [11]-[14]. From an in-situ inspection, it was noticed that a timber wall plate surrounded the whole roof, and the floor joists were also connected to this structure. Therefore, a continuous hinged connection was assumed between diaphragms and walls at the floors supports. A continuous connection among masonry walls was assumed as well. In general, the main elements of vulnerability due to the diaphragms flexibility, are related to the lack of seismic load redistribution among the walls in the x direction, and to the very low stiffness of the roof structure in the y direction, with possible local collapses of the north and south wall gables. These issues were confirmed by the observed failures, as discussed in the next section.

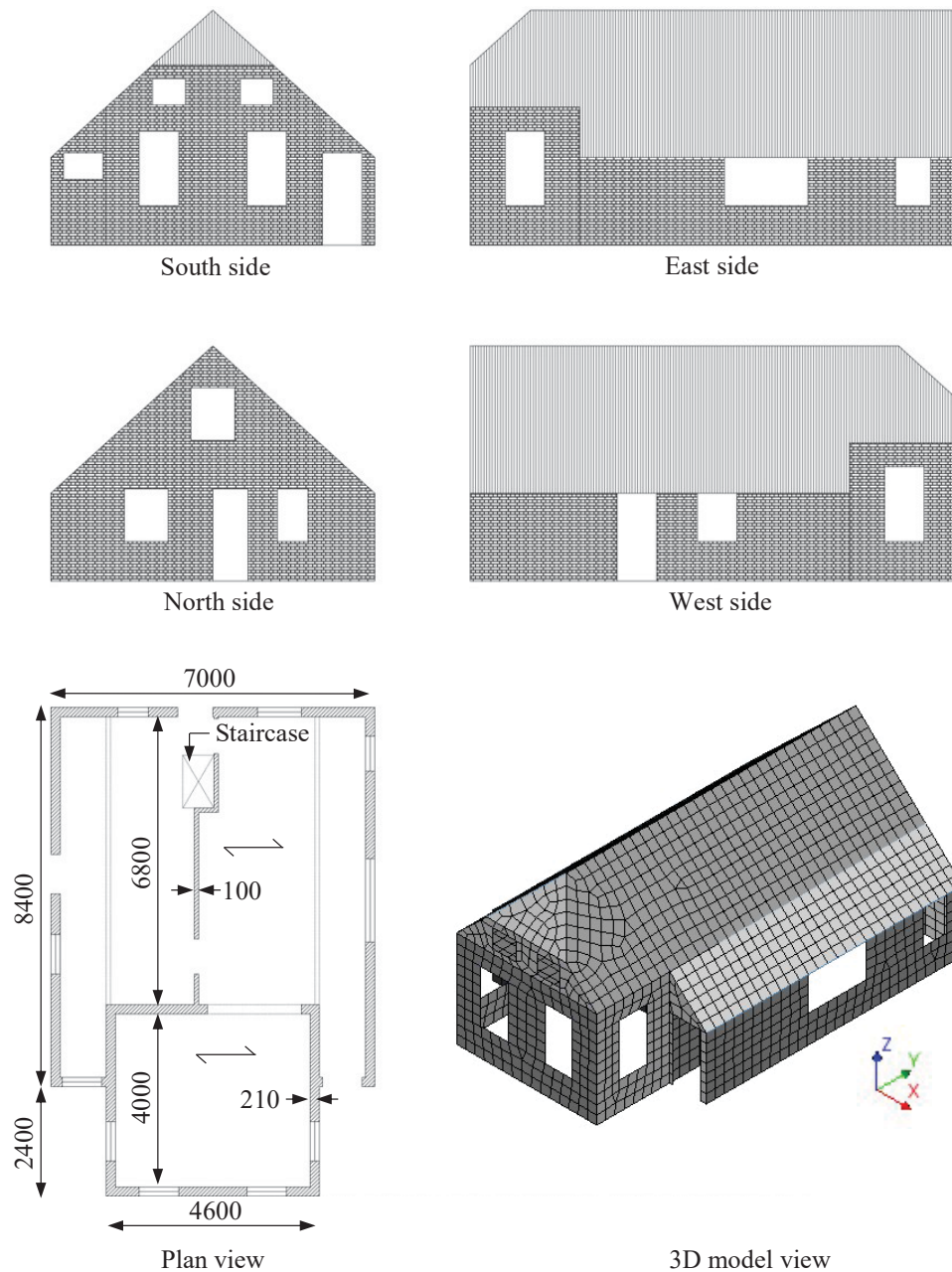


Figure 15: Main properties and geometry of the case-study building.

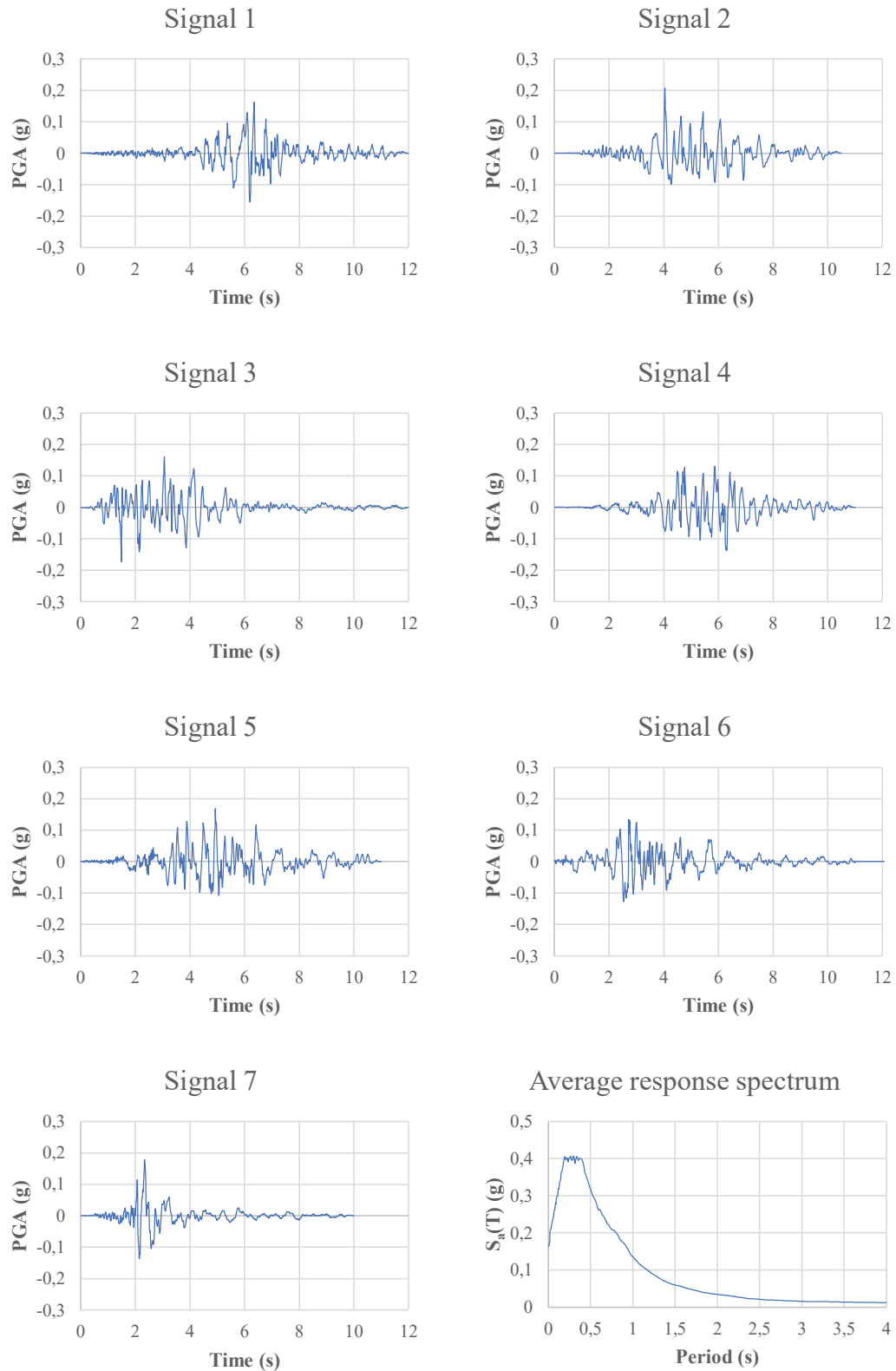


Figure 16: Adopted signals for time-history analyses; their average response spectrum is also reported. Data from NPR 9998 Webtool [35].

The following modelling strategies were adopted for the building with retrofitted floors:

- In the configuration with diaphragms retrofitted by casting a concrete slab on them, the floors were also modelled with linear elastic orthotropic shell elements, having the properties of structural reinforced concrete (Table 4). The thickness of the slab was 50 mm, as it would commonly be realized in practice [1], [6], [27]-[30].
- For the configuration featuring floors retrofitted with plywood panels, the modelling strategy discussed in section 4.2 was adopted: besides the linear elastic orthotropic shell elements, also the nonlinear macro-elements were present. The retrofitting interventions on the diaphragms were designed according to the global in-plane capacity of the piers, and conservative out-of-plane drift limits for the walls. The maximum base shear of the house (approximately 450 kN) was evaluated through a preliminary pushover analysis applied to the configuration with stiff diaphragms, and then the loads at floor and roof level were estimated through the lateral force method. The retrofitting intervention was designed accordingly, providing sufficient strength to activate in-plane failure mechanisms, but at the same time deflection capacity. With regard to this latter aspect, to prevent out-of-plane walls failure, the maximum midspan displacement, at which the diaphragms reached their strength, was fixed at 2% of the out-of-plane walls (or gables, for the roof) height. This value is in line with the 2.5% global drift suggested by New Zealand standards [37], which includes, however, also the displacement contribution of the in-plane walls. The potential stiffening effect of the out-of-plane walls was conservatively not taken into account, also because of the presence of large openings. Besides, use of dry screed made of loose material was assumed. Table 5 reports the properties of the retrofitted diaphragms adopted as input for the numerical model.

Table 2: Properties adopted for masonry shell elements based on [31]-[33].

Property	Value
Young modulus E_x parallel to bed joint (MPa)	1500
Young modulus E_y perpendicular to bed joint (MPa)	2000
Shear modulus G_{xy} (MPa)	800
Mass density ρ (kg/m ³)	2000
Bed joint tensile strength f_t (MPa)	0.15
Fracture energy in tension G_{F1} (N/mm)	0.01
Compressive strength f_c (MPa)	14
Fracture energy in compression G_c (N/mm)	30
Friction angle (°)	34
Cohesion (MPa)	0.2
Fracture energy in shear (N/mm)	0.1

Table 3: Properties adopted for the shell elements (thickness = 18 mm) representing the flexible diaphragms.

Property	Value		
	4.0×4.6 m floor	4.6×6.8 m floor	Roof
Young moduli E_x, E_y, E_z (MPa)	978000	620000	405000
In-plane shear modulus G_{xy} (MPa)	12	7	6
Shear moduli G_{xz}, G_{zy} (MPa)	61125	38750	25312
Mass density ρ (kg/m ³)	9440	9270	6170

Table 4: Properties adopted for the shell elements (thickness = 68 mm) representing the concrete slabs.

Property	Value		
	4.0×4.6 m floor	4.6×6.8 m floor	Roof
Young moduli E_x, E_y, E_z (MPa)	30000	30000	30000
Shear moduli G_{xy}, G_{xz}, G_{zy} (MPa)	12500	12500	12500
Mass density ρ (kg/m ³)	4336	4290	4250

Table 5: Properties adopted for the macro-elements and shell elements (thickness = 36 mm) representing the diaphragms retrofitted with plywood panels.

Property	Value		
	4.0×4.6 m floor	4.6×6.8 m floor	Roof
<i>Macro-elements</i>			
ϵ_{max}	0.027	0.019	0.012
σ_{max} (MPa)	12700	21200	13700
K_0 (MPa)	2490000	5980000	5980000
<i>Shell elements</i>			
Young moduli E_x, E_y, E_z (MPa)	122000	77500	50700
In-plane shear modulus G_{xy} (MPa)	0.1	0.1	0.1
Shear moduli G_{xz}, G_{zy} (MPa)	7640	4840	3170
Mass density ρ (kg/m ³)	4940	4860	3310

5.3 Results of the time-history analyses and discussion

The three configurations of the house were subjected to the seven signals shown in Fig. 16, by progressively scaling them until collapse. The results in terms of PGA at collapse of the configurations are presented in Fig. 17. The reference design response spectrum (2475 years return period) for the location of the house (Godlinze) corresponded to an expected maximum PGA of 0.17g; as can be noticed, the as-built configuration already collapsed at this level of intensity under almost all signals, making a retrofitting intervention necessary to increase the seismic performance of the house. Instead, the floors stiffened with a concrete slab greatly improve the capacity of the building, but the best performance is obtained with the plywood panels overlay, in both directions. The latter retrofitting intervention is easily applicable, light, reversible, and provides a beneficial energy dissipation to the diaphragms, improving even more the seismic capacity of the house.

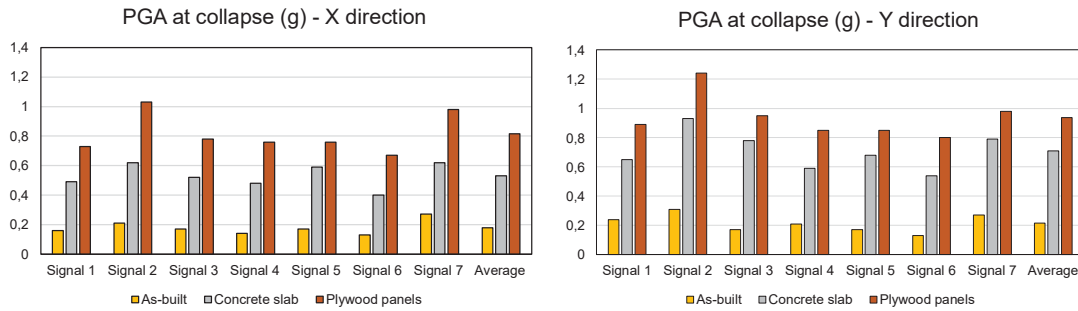


Figure 17: PGA at collapse for the three configurations in the x (left) and y direction (right).

The effect of the diaphragms on the response of the building is represented in Fig. 18: the base shear-displacement curves are reported at collapse, and refer, as a representative example, to signal 1 applied in the x direction (the weakest); the control node for displacement corresponds to the centre of mass of the roof. The as-built configuration shows a very flexible response: the floors undergo large displacements at an already limited signal amplitude, and the in-plane walls are not brought into play. Besides, the crack pattern (Fig. 18a) shows a partial out-of-plane collapse of the 100 mm thick central wall, and of the north gable, probably due to torsional effects.

A very different situation is noticeable with the floors retrofitted with concrete slabs. In this case, the failure of the building is fully related to the in-plane walls, and a beneficial redistribution of horizontal loads is achieved among the various walls; the force-displacement graph also confirms a typical in-plane failure of masonry (Fig. 18b).

A hybrid response between the first two configurations is obtained when the floors are retrofitted with plywood panels: a larger displacement capacity of the diaphragms together with an in-plane failure of the walls is noticeable (Fig. 18c). The crack pattern is similar to that observed for the concrete slab configuration, with a slightly higher amount of damage in the out-of-plane walls, because of the lower stiffness of the floors. Yet, the beneficial dissipative effect of the diaphragms leads to a 30% higher performance of the building in terms of PGA.

The possibility of withstanding more intense earthquakes does not only depend on the lower seismic mass provided by the reversible retrofitting intervention, but also because of its energy dissipation capacity. In fact, first of all, the higher mass of the concrete slab has a beneficial effect on the in-plane capacity of the wall, which is increased due to the larger vertical precompression applied. Secondly, by performing a modal analysis, the fundamental period of the house retrofitted with concrete slabs resulted as 0.1 s, while for the configuration with diaphragms strengthened with plywood panels it was 0.14 s. In both cases, the structure in the elastic phase is stiff, as expected when studying a low-rise masonry building; however, the plateau of the design average response spectrum starts at a period of 0.19 s (Fig. 16). Since the displacement capacity of the diaphragms retrofitted with plywood panels immediately brings into play their nonlinearity (including pinching cycles and energy dissipation), this configuration has a rapid increase of its period, and becomes quickly subjected to the maximum spectral acceleration. When concrete slabs are present, the diaphragms can be regarded as infinitely stiff, thus the response is approximately linear elastic until the in-plane capacity of the weakest wall is reached. The combination of a higher precompression on the walls (and therefore a higher in-plane strength) with a limited displacement capacity, compared to the floors retrofitted with plywood panels, implies a slower evolution of the period due to nonlinearities, and the spectral plateau is reached at a later stage. Nevertheless, the reversible retrofitting still shows a higher capacity, confirming its beneficial dissipative role.

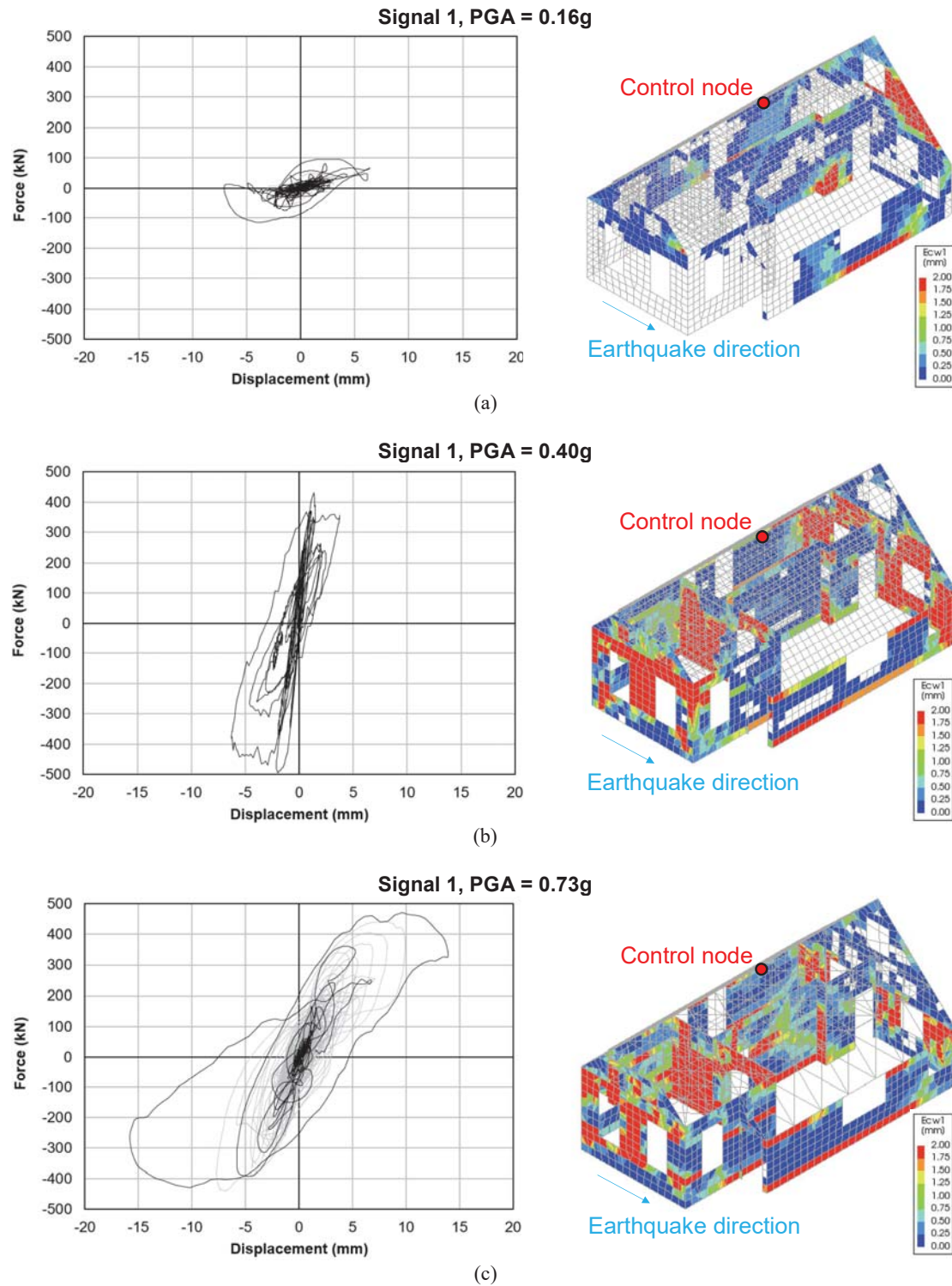


Figure 18: Base shear vs. roof displacement response and crack opening (Ecw1) pattern of the three configurations: as-built (a), floors strengthened with concrete slabs (b), diaphragms retrofitted with plywood panels (c).

The dissipation provided by the floors is further highlighted by Figs. 19 and 20, both showing the positive effect of the plywood panels retrofitting on the response of the building. Fig. 19 compares the in-plane behaviour of the most solicited wall at the collapse PGA for the concrete slab configuration, and the same response with the plywood panels overlay. As can be noticed, in the latter case the wall has not yet reached its capacity, but has just started to behave nonlinearly. Fig. 20 shows the total hysteretic energy dissipated by the structural components of the house: the amount of energy dissipated by the floors is relevant and, especially in the early phase of an earthquake, this can helpfully reduce in-plane loads on the walls.

As last consideration, in [25] a value of equivalent hysteretic damping ratio $\xi = 15\%$ was determined for the diaphragms retrofitted with plywood panels. The difference in PGA at collapse between the configuration with stiff floors and that with the dissipative diaphragms was on average 30% (Fig. 17). This result appears to confirm the obtained 15% damping ratio: if the floors were retrofitted with plywood panels, and for a simplified modelling (e.g. a pushover analysis) they were assumed as stiff, their dissipative contribution could be taken into account by considering an overdamped spectrum reduced by the factor $\eta = [10/(5+\xi)]^{1/2}$ [38]. It is interesting to notice that $\eta = 0.71$ for $\xi = 15\%$, a value suggesting that the collapse response spectrum could indeed correspond to approximately 30% higher spectral acceleration when a dissipative retrofitting of the floors is designed, and in addition to the further nonlinear contribution of the in-plane masonry walls.

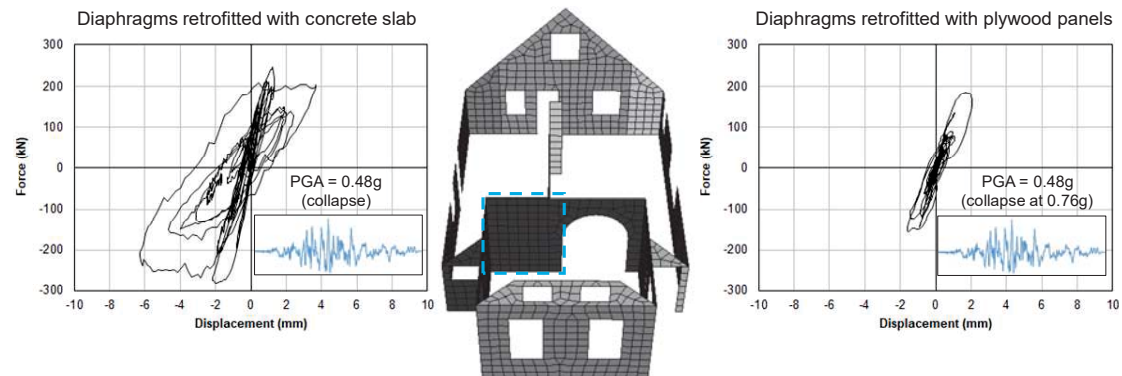


Figure 19: Comparison between the in-plane response of the most solicited wall under the application of signal 4 in the configuration having floors strengthened with concrete slabs (left) and with plywood panels (right).

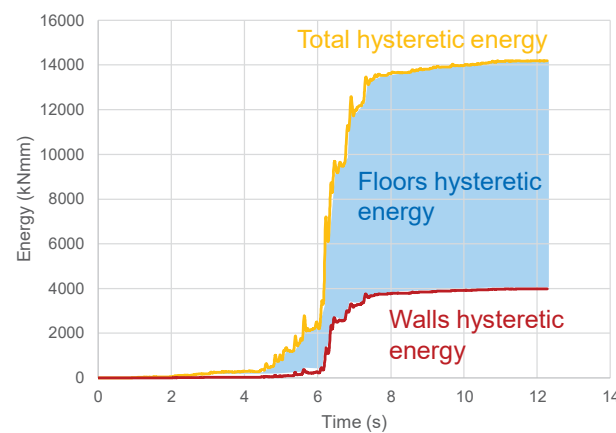


Figure 20: Hysteretic energy vs. time response under seismic signal 1 for the building having floors retrofitted with plywood panels: the dissipative role of the diaphragms is evident.

6 SUMMARY AND CONCLUSIONS

In this work, starting from an experimental campaign on as-built and strengthened timber diaphragms, the analytical and numerical modelling of the retrofitted floors was presented, including an application to a case-study existing building.

The strengthening technique, consisting of an overlay of plywood panels screwed along their perimeter to the existing sheathing, showed a great improvement in strength, stiffness and energy dissipation of the diaphragms. In order to enable the design of the proposed retrofitting method, and to account for the nonlinear and dissipative response of the floors, an analytical model was formulated, starting from the load-slip behaviour of the single screws fastening plywood panels and planks. The analytical model shows good agreement with the experimental results, and can be adopted to determine the relevant seismic properties of the retrofitted diaphragms.

The formulated model opened up the opportunity to implement a user-supplied subroutine in the software DIANA FEA: the subroutine validation demonstrated that an accurate numerical modelling of the in-plane response of the floors can be achieved. Then, the proposed retrofitting intervention was applied to the case-study of an existing building, and the seismic response was compared to both that of the as-built house, and that of a configuration in which the floors were stiffened with concrete slabs. The numerical time-history analyses showed that the diaphragms retrofitted with plywood panels can greatly improve the seismic capacity of the building, mainly because high energy dissipation is provided, and already at limited deflections. This allows to beneficially dampen the in-plane loads on the walls, obtaining the best performance, even in comparison to the configuration retrofitted with concrete slabs.

Therefore, the choice of light, reversible and dissipative retrofitting like the proposed one could be not only a more suitable technique for seismic strengthening of buildings belonging to architectural heritage, but also more beneficial in improving seismic capacity compared to stiffer, not reversible, and less sustainable techniques.

REFERENCES

- [1] M. Piazza, C. Baldessari, R. Tomasi, The Role of In-Plane Floor Stiffness in the Seismic Behaviour of Traditional Buildings. *14th World Conference on Earthquake Engineering*, Beijing, 2008.
- [2] C. Modena, M.R. Valluzzi, E. Garbin, F. da Porto, A strengthening technique for timber floors using traditional materials. *Proceedings of the Fourth International Conference on Structural Analysis of Historical Constructions SAHC 04*, Padua, Italy, 10–13 November 2004, pp. 911–921, 2004.
- [3] M.R. Valluzzi, E. Garbin, M. Dalla Benetta, C. Modena, In-Plane Strengthening of Timber Floors For The Seismic Improvement Of Masonry Buildings. *11th World Conference on Timber Engineering*, Riva del Garda, 2010.
- [4] M.R. Valluzzi, E. Garbin, M. Dalla Benetta, C. Modena, Experimental Assessment and Modelling of In-Plane Behaviour of Timber Floors. D. D’Ayala and E. Fodde (Eds.), *Proceedings of the VI International Conference on Structural Analysis of Historic Construction, SAHC 08*, 2–4 July 2008, Bath, UK, 2008, pp. 755-762.
- [5] N. Gattesco, L. Macorini, High reversibility technique for in-plane stiffening of wooden floors. D. D’Ayala and E. Fodde (Eds.), *Proceedings of the VI International Conference*

- on *Structural Analysis of Historic Construction, SAHC 08*, 2–4 July 2008, Bath, UK, 2008, pp. 1035–1042.
- [6] M. Corradi, E. Speranzini, A. Borri, A. Vignoli, In-Plane Shear Reinforcement of Wood Beam Floors With FRP. *Composites: Part B* **37**, 310-319, 2006.
 - [7] J.M. Branco, M. Kekeliak, P.B. Lourenço, In-Plane Stiffness of Timber Floors Strengthened with CLT. *European Journal of Wood Products* **73**, 313-323, 2015.
 - [8] A. Gubana, M. Melotto, Experimental tests on wood-based in-plane strengthening solutions for the seismic retrofit of traditional timber floors, *Construction and Building Materials* **191**, 290–299, 2018.
 - [9] E. Rizzi, M. Capovilla, M. Piazza, I. Giongo, In-plane behaviour of timber diaphragms retrofitted with CLT panels. Chapter in book: R. Aguilar et al. (Eds.): *Structural Analysis of Historical Constructions*, RILEM Bookseries 18, pp. 1613-16222, 019
 - [10] D.F. Peralta, M.J. Bracci, M.B.D. Huete, Seismic Behavior of Wood Diaphragms in Pre-1950s Unreinforced Masonry Buildings. *Journal of Structural Engineering* **130**, 2040-2050, 2004.
 - [11] A. Brignola, S. Pampanin, S. Podestà, Experimental Evaluation of the In-Plane Stiffness of Timber Diaphragms. *Earthquake Spectra*, Volume 28, No. **4**, 1–23, 2012.
 - [12] A. Wilson, P.J.H. Quenneville, J.M. Ingham, In-Plane Orthotropic Behavior of Timber Floor Diaphragms in Unreinforced Masonry Buildings. *Journal of Structural Engineering* **140**, 2014.
 - [13] E. Rizzi, I. Giongo, J. Ingham, D. Dizhur D., Testing and Modeling In-Plane Behavior of Retrofitted Timber Diaphragms. *Journal of Structural Engineering*, vol. 146, **2**, 2020.
 - [14] M. Mirra, G. Ravenshorst, J.W. van de Kuilen, Experimental and analytical evaluation of the in-plane behaviour of as-built and strengthened traditional wooden floors. *Engineering Structures* **211**, 2020.
 - [15] A. Gubana, State-of-the-Art Report on high reversible timber to timber strengthening interventions on wooden floors. *Construction and Building Materials* **97**, 25-33, 2015.
 - [16] M. Mirra, G. Ravenshorst, P. de Vries, J.W. van de Kuilen, An analytical model describing the in-plane behaviour of timber diaphragms strengthened with plywood panels. *Engineering Structures* **235**, 2021.
 - [17] D. Ferreira, ed., DIANA – Finite element analysis. User’s manual release 10.4. DIANA FEA BV, Delft, The Netherlands, 2020.
 - [18] ISO 16670:2003. Timber structures — Joints made with mechanical fasteners — Quasi-static reversed-cyclic test method. ISO (International Organization for Standardization)
 - [19] R.O. Foschi, Load-Slip Characteristics of Nails. *Wood Science* **17**, 69-77, 1974.
 - [20] EN 12512:2001. Timber Structures – Test Methods – Cyclic Testing of Joints Made with Mechanical Fasteners. CEN (European Committee for Standardization).
 - [21] P. Dubas, E. Gehri, T. Steurer, Einführung in die Norm SIA 164 (1981) – Holzbau. Publication No. 81-1, Baustatik und Stahlbau, ETH Zürich, Switzerland, 1981.

- [22] EN 1995-1-1:2004+A2:2014. Eurocode 5: Design of timber structures - Part 1-1: General - Common rules and rules for buildings. CEN (European Committee for Standardization).
- [23] K.W. Johansen, Theory of timber connections. Publ. 9 Bern. International Association of Bridge and Structural Engineering, 1949.
- [24] EN 409:2009. Timber structures - Test methods - Determination of the yield moment of dowel type fasteners. CEN (European Committee for Standardization).
- [25] M. Mirra, G. Ravenshorst, J.W. van de Kuilen, Dissipative properties of timber diaphragms strengthened with plywood panels. *Proceedings of the 16th World Conference on Timber Engineering*, Santiago, Chile, 9-12 August 2021. (submitted)
- [26] S. Lagomarsino, A. Penna, A. Galasco, S. Cattari, TREMURI program: An equivalent frame model for the nonlinear seismic analysis of masonry buildings. *Engineering Structures* 56, 1787-1799, 2013.
- [27] I. Giongo, M. Piazza, R. Tomasi, Pushover analysis of traditional masonry buildings: influence of refurbished timber-floors stiffness. *SHATIS'11 International Conference on Structural Health Assessment of Timber Structures* - Lisbon, Portugal, June 2011.
- [28] R. Scotta, D. Trutalli, L. Marchi, L. Pozza, M. Mirra, Seismic response of masonry buildings with alternative techniques for in-plane strengthening of timber floors. *Revista Portuguesa de Engenharia de Estruturas*. Ed. LNEC. Série III, no 4, 2017
- [29] R. Scotta, D. Trutalli, L. Marchi, L. Pozza, M. Mirra, Non-linear time history analyses of unreinforced masonry buildings with in-plane stiffened timber floors. *Proceedings of the 17th ANIDIS Conference*, Pistoia, Italy, 2017.
- [30] D. Trutalli, L. Marchi, R. Scotta, L. Pozza, Dynamic simulation of an irregular masonry building with different rehabilitation methods applied to timber floors. M. Papadrakakis, M. Fragiadakis (eds.), *Proceedings of the 6th ECCOMAS Thematic Conference on Computational Methods in Structural Dynamics and Earthquake Engineering*, Rhodes Island, Greece, 15-17 June 2017.
- [31] F. Messali, G. Ravenshorst, R. Esposito, J.G. Rots, Large-scale testing program for the seismic characterization of Dutch masonry walls. *Proceedings of 16th World Conference on Earthquake (WCEE)*, Santiago, Chile, 9-13 January 2017.
- [32] S. Jafari, J.G. Rots, R. Esposito, F. Messali, *Characterizing the Material Properties of Dutch Unreinforced Masonry*. *Procedia Engineering* **193**, p. 250-257, 2017.
- [33] F. Messali, M. Longo, Influence of dormers on the seismic performance of a detached house: case study Kwelder 1, Loppersum. Report number B2B-R04, Version 01, Delft University of Technology, 21 January 2021.
- [34] G.M.A. Schreppers, A. Garofano, F. Messali, J.G. Rots. DIANA validation report for masonry modelling. DIANA FEA BV and Delft University of Technology, 2017
- [35] Webtool NPR 9998 (<https://seismischekrachten.nen.nl>). Nederlands Normalisatie-instituut (NEN), 2021.
- [36] NEN-EN 1990:2002+A1:2019+NB:2019. Grondslagen van het constructief ontwerp (Dutch national version of Eurocode 0). Nederlands Normalisatie-instituut (NEN).

- [37] NZS 1170.5. Structural design actions, Part 5: Earthquake actions – New Zealand, Standards New Zealand, Wellington, 2004.
- [38] EN 1998-1:2004. Eurocode 8: Design of structures for earthquake resistance – Part 1: General rules, seismic actions and rules for buildings. CEN (European Committee for Standardization).

MOMENT-CURVATURE DIAGRAMS FOR CLT PANELS ACCOUNTING FOR ORTHOGONAL TO GRAIN COMPRESSION TIMBER PROPERTIES

A. Sandoli¹, C. D'Ambra¹, M. Lippiello¹, C. Ceraldi¹, B. Calderoni¹, and A. Prota¹

¹Dept. of Structures for Engineering and Architecture
via Claudio 21, 80125, Naples, Italy

e-mail: antonio.sandoli@unina.it, claudio.dambra@unina.it, maria.lippiello@unina.it,
ceraldi@unina.it, calderon@unina.it, apota@unina.it

Abstract

Typically, panel-to-panel and panel-to-foundation connection zones in Cross-Laminated Timber (CLT) walls consist of steel-to-timber mechanical connections (hold-downs and angle-brackets) and timber-to-timber contact. While hold-downs and angle brackets are extensively studied in literature, the role of timber-to timber contact is underestimated. The platform constructional technology used for build CLT walls requires that the vertical timber panels compresses the horizontal CLT floors, engaging the orthogonal to grain timber properties in the seismic response.

This paper discusses a new development concerning a theoretical sectional model for CLT panels proposed by the authors in a recent work, where strength of the panels subjected to combined axial force and bending moment was studied accounting for orthogonal to grain timber properties. As advancement, a theoretical moment-curvature model for CLT panels is proposed in this paper and the displacement capacity (i.e., ductility) is investigated. The main parameters which affect the ductile behavior of the panels have been studied by means of parametric analyses, i.e. varying cross-section dimensions, amount of axial force, and hold-downs resistance.

Theoretical results have been also compared with numerical ones derived from a bi-dimensional finite element model developed by the authors and a good matching between the results has been highlighted.

Keywords: CLT panels, Orthogonal to grain compression, Connection Modelling, Theoretical model, Moment-Curvature diagrams.

1 INTRODUCTION

Cross-Laminated Timber (CLT) represents a high efficient engineered mass timber product originated in Austria in the early 1990s. In Europe, CLT panels are one of the most diffused mass timber product used for low and mid-rise residential and non-residential buildings in seismic prone area. It has been estimated that the global annual production of CLT is growing exponentially in Europe, from 25.000 m³ in 1996, up to 1.2 million of m³ in 2020 [1]. Nevertheless, a significant annual increase of the manufactured CLT has been also recorded in the United States, Canada, Australia, Japan and New Zealand [2-4].

Shake-table tests demonstrated the satisfactory seismic behavior of multi-story CLT buildings. They resisted seismic accelerations up to 0.82g for a seven story building [5] and up to 1.52g for a two-story building [6] thanks to their good dissipative behavior. The dissipation is mainly concentrated in the panel-to-panel and in panel-to-foundation mechanical connection zones, generally composed by thin-walled steel plates nailed or screwed to the vertical panels and bolted in foundation, named as Hold-Downs (HDs) and Angle-Brackets (ABs). HDs are devoted to withstand tensile forces produced by the overturning moments, while ABs resist to shear forces. Compression forces, instead, are faced by timber-to-timber or timber-to-foundation contact.

Experimental local tests on mechanical connections aimed at investigating their cyclic behavior highlighted that ductile failure mechanisms can be achieved when properly designed [7, 8]. Contrariwise, brittle failure mechanisms could occur if the requirements for end and edge distances are not respected [9]. Commonly, in timber practice it is assumed that ductile mechanisms are those respecting the Johansen's failure modes [10] also included in Eurocode 5 [10]. Although provided of an appreciable dissipative behavior, such mechanisms entail significant damaging of vertical timber panels making them unusable after the seismic event [12].

In addition to the seismic resistance, modern seismic design approaches based on the Performance-Based Design require that also damaging of structural (and non-structural) components should be prevented or reduced as far as possible. Thus, alternative connection systems based on the 'plug and play' concept have been introduced by researchers [13-15]. They consist of replaceable steel fuses, or other steel-based material, fastened to timber panels which dissipate energy through the cyclic plasticization of the steel parts only, while timber parts remain elastic. Steel parts, which can be substituted after the seismic event, are devoted to prevent the damaging of timber CLT panels and consequently to reduce economical losses for their repairing.

To date, theoretical models for evaluating flexural load-bearing capacity of CLT panels subjected to combined bending and axial force are presented in literature, taking into account the contribution of the HDs and ABs at the base of the panels [16, 17]. Two are the main shortcomings that characterize such methods: *a)* the role of timber-to-timber contact is under evaluated, *b)* no formulation for evaluating the ductility are presented.

Usually, the timber-to-timber contact is modelled considering the parallel to grain direction timber properties [19]. Contrariwise, due to the platform constructional technology used to realize CLT buildings, the perpendicular to grain timber properties (i.e., Young's modulus, ultimate compression strength and strain) are unavoidably involved in the seismic behavior of the panel. In fact, at each story the horizontal CLT floor panels are inserted between two consecutive vertical CLT panels, while at ground level a horizontal timber beam is commonly interposed between vertical panel and foundation (Fig. 1). Conversely, if interposed timber beams are not used and the vertical panels are directly placed on the reinforced concrete foundation, the parallel to grain timber properties must be employed in the calculations.

Nowadays, no specific information relative to the orthogonal to grain compressive behavior of CLT elements are provided in the European standards (with exception for the Austrian National Annex [20]), as well as limited experimental and numerical results can be found in literature [20-22].

This paper deals with a new development of a theoretical sectional model for CLT panels subjected to combined axial force and bending moment, presented by the authors in a recent paper [23]. The method presented in [23] permitted to define the flexural load-bearing capacity of the panels through axial force-bending moment interaction domains. As advancement, a theoretical moment-curvature ($M-\chi$) model for CLT panels is herein presented.

A parametric study aimed at investigating the influence of different factors on the post-elastic displacement capacity of the panels - such as percentage of reinforcement ratio (intended as the contribution provided by HDs in tension), the amount of axial force and the length-to-width ratios of the panel cross-section - has been carried out. Due to the absence of experimental tests, the validity of the proposed $M-\chi$ diagrams has been assessed by comparison with a finite element numerical model of the CLT panels developed by the authors.

The results allowed to investigate the role of the mechanical connections and timber-to-timber contact on the ductile behavior of the panels, highlighting a good matching between theoretical and numerical results. Moreover, the comparative analyses permitted to develop a design-oriented approach for evaluating the ultimate curvature and the ultimate bending moment of the panels through closed-formulas, useful in engineering practice.

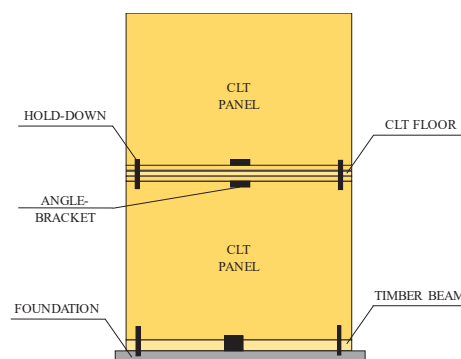


Figure 1: Platform constructional technology for CLT buildings.

2 CONNECTIONS MECHANICAL MODEL

With aim of calculating the flexural load-carrying capacity of CLT panels under gravity and horizontal loads, different methods for schematizing the panel to panel and the panel to foundation connection zone are proposed in literature. These methods, extensively compared in [17] and in [12], are mainly based on static equilibrium equations. They assume the hypothesis that CLT panel behaves as a rigid-body with deformations concentrated in the mechanical connections: the overturning moments are faced by HDs (tension) and timber-to-timber contact (compression), while shear forces are resisted by ABs exclusively. Due to buckling, the contribution of HDs under compression is generally disregarded.

Recently, a mechanical model to schematize the connections has been proposed by the authors in [23]. The goal of the method was that of determining the flexural load-bearing capacity of CLT panels and deriving the axial force-bending moment interaction domains. The same model has been employed for deriving moment-curvature diagrams in the present paper, allowing to investigate the post-elastic displacement capacity of the CLT panels with mechanical connections at the base.

The proposed model could be considered as an advancement with respect to the method presented in [16], in which the behavior of panel-to-panel and panel-to-foundation connection zone has been modelled in analogy with Reinforced Concrete (RC) cross-sections: HDs are considered as the tensile-resistant elements which yield in tension, while timber-to-timber contact is assimilated to compressed concrete whose behavior is limited to the elastic field. For timber-to-timber contact, the maximum compression strength is assumed equal to that in parallel to grain direction, while the Young's modulus is that in orthogonal to grain direction. Conversely, for timber-to-RC foundation contact the parallel to grain Young's modulus is considered (while the compression strength remains that in parallel direction).

In the proposed method, instead, both orthogonal or parallel to grain timber properties for panel-to-foundation connections can be used, as a function of constructional technology used at the ground level (i.e., if interposed timber beam between vertical panel and foundation is used or not). While, only the orthogonal to grain contact is assumed for panel-to-panel connections at upper storey.

2.1 Orthogonal to grain compression behavior

Orthogonal to grain compression situations are a direct consequence of the platform constructional technology used to build CLT structures. Under seismic actions, the vertical panel rocks around a pivot point - often not coincident with the corner of the panel - loading in orthogonal to grain direction the CLT timber floors at upper storey or the timber beams at ground floor when present [24] (Fig. 2).

This phenomenon cannot be neglect in evaluating the load-carrying capacity of the panel, because:

- (i) the orthogonal to grain compressive strength $f_{c,90}$ is less than that in parallel to grain direction $f_{c,0}$ ($f_{c,90}/f_{c,0} \sim 1/10$);
- (ii) the Young's modulus in perpendicular direction E_{90} is much less than that in parallel direction E_0 ($E_{90}/E_0 \sim 1/30$);
- (iii) the orthogonal to grain ultimate strain $\varepsilon_{c,90}$ is much higher than in parallel direction $\varepsilon_{c,0}$ ($\varepsilon_{c,0}/\varepsilon_{c,90} \sim 1/10-1/15$).

Although the orthogonal to grain compressive behavior for mono-dimensional elements has been extensively studied and tests procedures codified [25, 26], few are the results available for CLT specimens. Some experimental results on CLT specimens subjected to perpendicular to grain compression loads, with different loads configurations, are presented in [20-22]. Experimental stress (σ)-strain (ε) diagrams are characterized by a first nonlinear elastic branch, followed by a significant perfectly-plastic branch with hardening at the end.

By a theoretical point of view, the shape of the σ - ε diagram can be described by parabola-rectangle constitutive law (Fig. 3). The shape is similar to that of concrete subjected to compression and then, by analogy, the same constitutive law suggested for concrete in the Eurocode 2 [27] has been adopted to describe the orthogonal to grain compressive behavior of timber. The parabolic and the constant branch are described by the following equations, respectively:

$$\sigma = \eta(2 - \eta)f_{c,90,d} \quad 0 \leq \eta \leq 1 \quad (1)$$

$$\sigma = f_{c,90,d} \quad 1 \leq \eta \leq \varepsilon_{c,90,u} / \varepsilon_{c,90,el} \quad (2)$$

where $\eta = \varepsilon / \varepsilon_{c,90,el}$ represents the ratio between the values of strain (ε) included into the interval $[0; \varepsilon_{c,90,el}]$ for eq. (1) and into the interval $[\varepsilon_{c,90,el}; \varepsilon_{c,90,u}]$ for eq. (2); while $\varepsilon_{c,90,el}$ and $\varepsilon_{c,90,u}$ represent the limit elastic and ultimate strain of timber, respectively.

Contrarily to the maximum perpendicular compression strength, whose values are codified also by Eurocode 5 [11], for orthogonal to grain ultimate strain no values are suggested by codes. Experimental studies conducted by Serrano and Enquist [20] and by Brandner [22] on CLT panels under compression shown significant plastic strains, greater than 15-20% at the end of tests.

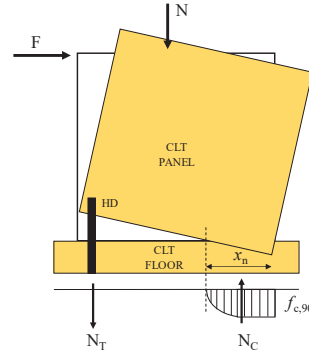


Figure 2: Orthogonal to grain crushing of CLT floors due to rocking of the vertical panel.

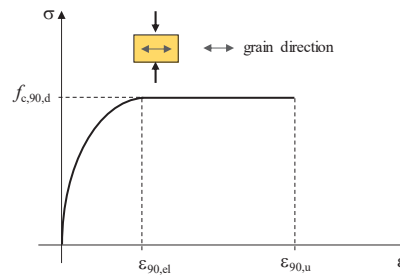


Figure 3: Constitutive stress-strain behavior for timber compressed in orthogonal to grain direction.

2.2 Cross-sectional behavior modelling

In this paper, a model for describing the cross-sectional behavior of CLT panels developed by analogy with RC cross-sections is presented. The term ‘section’ indicates the timber-to-timber contact area defined between the vertical and the horizontal timber panels.

In this model, tensile-resistant contributions are provided by hold-downs (*HDs*) exclusively, or combining hold-downs and angle brackets (*ABs*) if both are assumed able to resist tensile forces [7, 9, 28]. Instead, compression forces are totally faced by timber-to-timber or by timber-to-RC foundation contact.

By analogy with RC, three different behavioral stages for the cross-section have been defined (Fig. 4): stage *I*, in which both timber-to-timber contact and tensile-resistant elements behave elastically both in compression and in tension; stage *II*, when the maximum strength into timber-to-timber compressed corner is reached, whereas tensile-resistant elements still work in linear-elastic field (or vice versa); stage *III*, when the orthogonal to grain ultimate strain at compressed corner is attained, while tensile-resistant elements are ‘yielded’.

It should to be highlighted that the proposed theoretical method is of general validity. In fact, failure mechanisms based on (*A*) timber embedding combined with metal fasteners [10, 11] or on (*B*) yielding of metal steel elements (steel plates, steel fuses based on ‘plug and play’ concept, etc.) with timber in elastic field can be both implemented. As already noted in Sect. 1, the failure mechanisms (*B*) are far preferred to avoid permanent damage into timber panels in case of earthquakes and represents a new frontier for low-damage and more sustainable CLT buildings [12, 13].

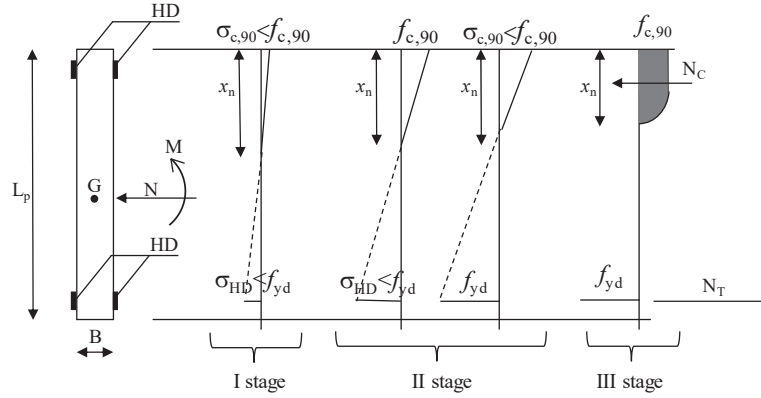


Figure 4: Normal stress diagrams for the three behavioral stages.

3 THEORETICAL MOMENT-CURVATURE DIAGRAMS

Moment-curvature diagrams represent a useful tool for evaluating the ductile behavior of CLT panels subjected to combined horizontal seismic actions and gravity loads.

The $M-\chi$ cross-sectional behavior has been investigated based on the Euler-Bernoulli hypothesis concerning the conservation of plain transversal cross-sections after the deformation. Moreover, it has been assumed that the mechanical connections fail according to the mechanism type-B only, thus maximum yielding strength and ultimate strain in tension of thin-steel plates (e.g., HDs) are involved in the plastic mechanism. In other terms, a mechanical connection based on a ‘plug and play’ system, or having innovative dog-bone shaped hold-downs presented in [23] has been herein considered. While for the compressed timber the orthogonal to grain direction properties have been taken into account.

On the other side, also failure mechanisms type-A (Johansen’s mechanisms) can be implemented in the proposed model, but with the disadvantage that it is more complex to establish a suitable and reliable value of ultimate strain (axial elongation) due timber-to-steel interaction. In fact, available experimental tests provided only maximum values of axial displacement in timber-to-steel interaction because it is difficult to evaluate the corresponding strain.

Constitutive stress-strain behaviors adopted for timber (Fig. 5a) and steel (Fig. 5b) in this paper are represented in Fig. 5. For timber the parabola-rectangle constitutive behavior has been obtained by using the eqs. (1) and (2), with $\varepsilon_{c,90,u}=5\%$ (assumed as a reasonable value by the authors), $\varepsilon_{c,90,el}=0.75\%$ and design perpendicular to grain compression strength $f_{c,90,d}=2.90$ MPa. The latter has been evaluated considering the spatial dispersion of locally applied compression perpendicular to grain stresses: the increasing coefficient $k_{c,90}$ (in this case equal to 1.50) has been multiplied for the perpendicular compression strength according to [11]. Note that the material properties of the 3-ply CLT panels have been derived from ETA-14/0349 [29], as those corresponding to solid wood of class C24.

For steel, instead, an elastic-perfectly plastic constitutive stress-strain behavior has been adopted, considering steel-type S275 (as defined in Eurocode 3 [30]) with design yielding strength $f_{yd}=261.9$ MPa, yielding strain $\varepsilon_{HD,y}=0.12\%$ and ultimate strain $\varepsilon_{HD,u}=7\%$.

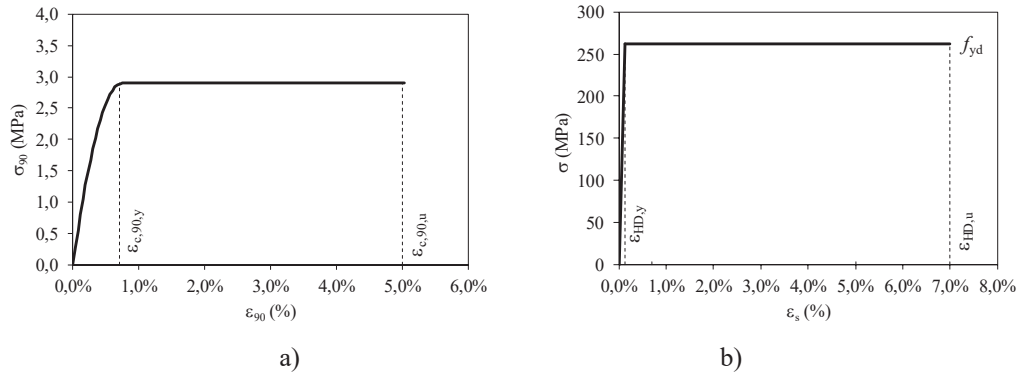


Figure 5: Constitutive stress-strain behavior for (a) timber compressed in orthogonal to grain direction, (b) steel in tension.

3.1 Methodology

Moment-curvature diagrams have been obtained by means of an iterative procedure, schematically represented in the flowchart reported in Fig. 6. The procedure consists of assigning a pair of first attempt values (χ , x_n) - where χ represents the curvature of and x_n the neutral axis depth - for panel to panel or panel to foundation contact cross-section and of verifying, by means of equilibrium conditions, that such assumption is right. In the following is summarized step-by-step the procedure:

- (i) assign attempt values of (χ , x_n);
- (ii) calculation of values of strains (ε) corresponding to the couple (χ , x_n) in each point of the cross-section thanks Euler-Bernoulli hypothesis;
- (iii) calculation of normal stresses associated to these strains from the constitutive stress-strain constitutive behavior adopted for both CLT and HD;
- (iv) determination of both internal compression and the tension resultant forces by integrating the stresses diagram over the cross-sections;
- (v) the supposed values of χ and x_n are right if the translation equilibrium over the cross-section among the internal forces and the applied axial force is satisfied. If it is not satisfied, the procedure must be reiterated by choosing another couple of values (χ , x_n); if it is satisfied, the corresponding moment (M) can be determined through the equilibrium rotation (with respect to the center-of-gravity of the section).

To obtain the entire M - χ diagram, the procedure must be developed for the interval between $\chi=0$ and the ultimate curvature χ_u .

3.2 Parametric analyses results

Based on the iterative procedure, theoretical M - χ diagrams have been obtained. In particular, parametric analyses considering different factors which influence the cross-sectional behavior have been conducted. The investigated parameters are listed in the following:

1. geometrical 'reinforcement' percentage ratio:

$$\rho = \frac{A_{HD}}{A_{CLT}} (\%) \quad (3)$$

where A_{HD} represent the cross-section area of HDs involved in the plastic mechanism, while A_{CLT} is the cross-section area of the CLT panel.

2. Cross- section slenderness ratio:

$$\lambda = \frac{L_p}{B} \quad (4)$$

where L_p represents the panel length, while B the panel width.

3. Dimensionless axial force ratio:

$$\nu = \frac{N_{Ed}}{N_{Rd}} (\%) \quad (5)$$

where N_{Ed} is the acting axial force and N_{Rd} the ultimate strength of the fully compressed section.

In Figure 7 are represented the $M-\chi$ diagrams obtained by varying the geometrical ‘reinforcement’ percentage ratios, from $\rho=0\%$ to $\rho=0.30\%$. To obtain these diagrams, a CLT panel having a slenderness ratio $\lambda=18$ (cross-section with $L_p=2500$ mm and $B=135$ mm) and an axial force ratio $\nu=20\%$ has been considered as representative and however realistic for CLT buildings. As it can be noted in Figure 7, for increasing value of ρ the ultimate moments of the panel increases, whereas the ductility reduces more than 50% passing from $\rho=0\%$ to $\rho=0.30\%$. This means that higher reinforcement percentages (i.e., several HDs) lead the panel toward brittle behavior, in the face of increase of flexural resistance.

On the same diagrams, squared blue dots indicate the curvature corresponding to the HDs which yield in tension ($\epsilon_{HD,y}$), green dots the points in which the timber-to-timber contact attains its yielding strain ($\epsilon_{c,90,y}$), while red triangles the achievement of the ultimate strain of timber compressed in orthogonal to grain direction ($\epsilon_{c,90,u}$). It can be observed that for a wide range of ρ (from 0 to 0.24%) the yielding of HDs in tension precede that of timber in compression, while for ρ greater than 0.24% timber yield before than HD. Moreover, as ρ increases the interval of the first yielding curvature between HDs and compressed timber reduces.

In Figure 8 are represented the $M-\chi$ diagrams for slenderness ratios ranging from $\lambda=10$ to $\lambda=38$, relative to a panel having constant width (B) equal to 135 mm while the panel length (L_p) varies from 150 to 500 mm. The $M-\chi$ diagrams show that as λ increases the ductility decreases, while ultimate moment increases. Also in these diagrams the yielding in tension of the HDs anticipates that of timber stressed in orthogonal to grain compression, whilst the ultimate curvature is attained when the compressed timber reaches the its ultimate strain at the compressed edge.

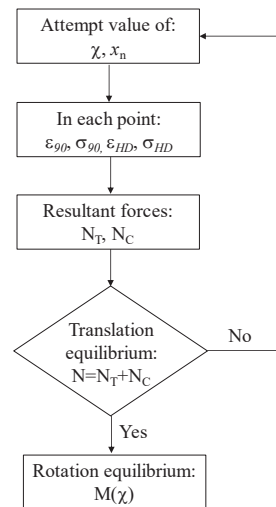


Figure 6: Flowchart of the iterative procedure developed for obtaining the $M-\chi$ diagrams.

In Figure 9 instead are reported the $M-\chi$ diagrams for dimensionless axial forces ratios varying from 0% (pure bending) to 40%. Again, the yielding of HDs precedes that of compressed timber, except for the case having $v=40\%$. This latter finding is convincing, because high values of the applied axial force involves significant orthogonal to grain compression stresses on the cross-section which lead to a 'yielding' of timber before of HDs. For the sake of simplicity, the curve with $v=50\%$ has not been reported in the Figure because resulted quite superimposed with the curve having $v=40\%$: This is reasonable observing the N-M interaction domains: about $v=40-50\%$ the domain varies smooth, such that ultimate moment (which is reached at $v=50\%$) varies little from $v=40\%$ to $v=50\%$ [23]. On the contrary, passing from $v=40\%$ to 50% the ductility reduces further.

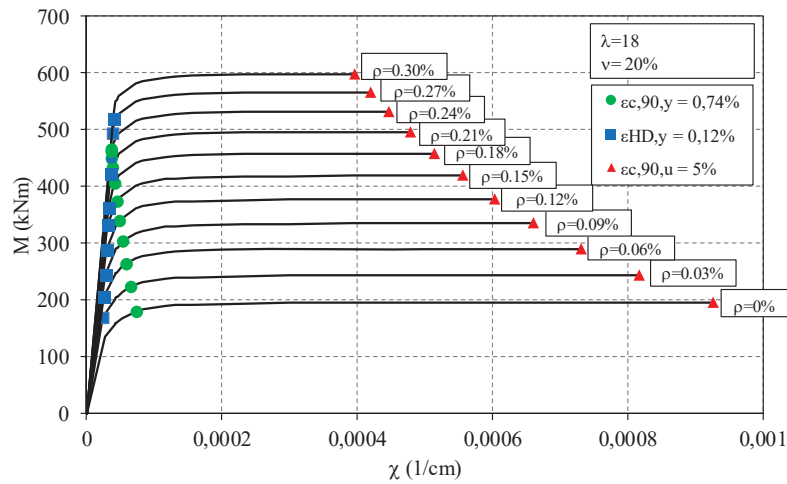


Figure 7: Moment-curvature diagrams obtained varying the 'reinforcement' area ratio.

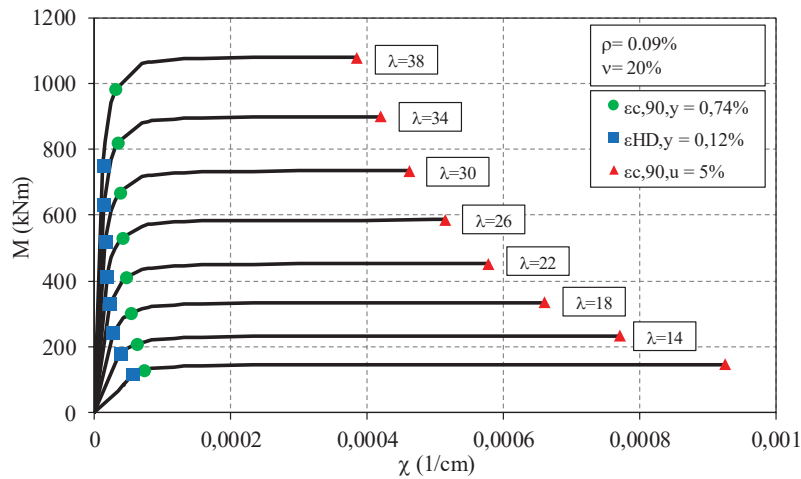


Figure 8: Moment-curvature diagrams obtained varying the cross-section slenderness ratio.

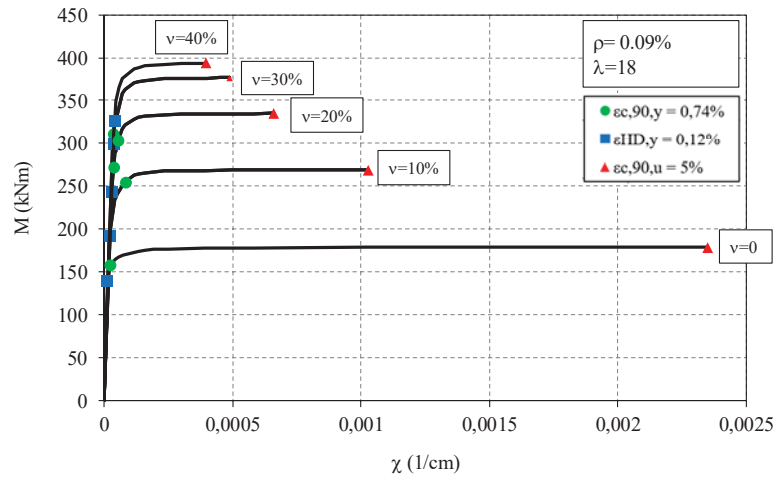


Figure 9: Moment-curvature diagrams obtained varying the dimensionless axial force.

4 COMPARISON WITH THE NUMERICAL MODEL

To assess their effectiveness, theoretical $M-\chi$ diagrams have been compared with those obtained through a numerical Finite Element Model (FEM) developed with the software SAP 2000 v.18 [31]. This required to model both CLT ‘material’ and mechanical connections and to carry-out nonlinear static analysis (e.g., pushover analyses).

4.1 Material modelling

CLT panels have been modelled through a two-dimensional FEM consisting of squared shell elements provided by in-plane shear and flexural stiffness, with a mesh 125x125 mm and thickness equal to those of the panel.

Due to its cross-layered nature, the in-plane behavior of CLT panels has been simulated through an equivalent (indefinitely) elastic orthotropic material. In other terms, only the layers of boards capable of withstanding the internal forces have been assumed as effective with regards to both flexural and shear elastic stiffness (i.e., two external layers for 3-ply vertical panels). Then, Young’s moduli of CLT have been obtained as it in the following:

$$E_L = \frac{n_l}{n_{tot}} E_0 \quad (6)$$

$$E_T = \frac{n_t}{n_{tot}} E_0 \quad (7)$$

where E_L and E_T represent the reduced Young’s moduli in longitudinal and transversal direction, respectively; E_0 the Young’s modulus of raw material, n_l and n_t the number of layer in longitudinal and transversal direction, respectively; n_{tot} the total number of layer of the panel. The same reduction has been also applied to the tangential modulus (G) in both longitudinal and transversal direction. This material modelling gives back an acceptable representation of the material elastic properties, and is frequently adopted in literature [9, 18, 24, 32].

4.2 Connections modelling

Mechanical connections are usually modelled using links, trusses or frame elements having uniaxial or biaxial behavior [9, 18, 23, 33]. In the uniaxial case, HDs and ABs resist only in their primary direction (e.g., HDs in tension and ABs in shear only). In the biaxial case, both HDs and ABs resist to axial and shear forces simultaneously.

In this paper, vertical truss elements are used to model the HDs and the timber-to-timber contact, while frame elements are used for the ABs [23]. Three different elements have been defined to model the connection zones (Fig. 10):

1. HD element, consists of a no-compression truss element devoted to face the tensile forces at the bottom of the CLT panel;
2. AB element, consists of a no-compression frame element devoted to face the shear forces at the bottom of the CLT panel;
3. C element, consists of a no-tension truss element devoted to face the compression at the bottom of the panel.

The nonlinear behavior of the connection elements has been simulated through a lumped plasticity model. An elastic-perfectly plastic axial force (N)-displacement (Δ) behavior for both HD and C elements and an elastic-perfectly plastic shear (V)-displacement (Δ) behavior for ABs have been assumed (Fig. 8). Concerning HDs and ABs, this modelling approach has been considered suitable also in other literature works and then effectively used to perform nonlinear analyses [16, 34]. While for C elements, the elastic-perfectly plastic behavior represents an acceptable approximation of the parabola-rectangle behavior (see Fig 5a).

Due to buckling phenomenon which interests the HDs loaded in compression, their contribution has been disregarded in the model; while both hold-downs and angle brackets have been modelled with biaxial behavior but neglecting the reduction of strength due to axial-shear force interaction [9].

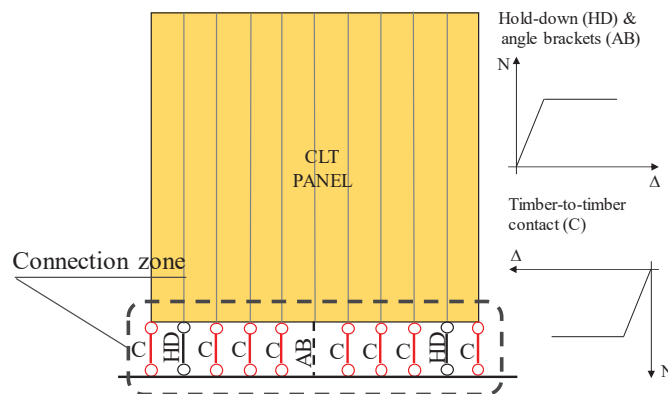


Figure 10: Representative scheme of the connection model.

4.3 Comparisons

In this Section the theoretical M - χ diagrams are compared with the numerical ones. At this stage of the research, only two cases have been analysed and compared: M - χ diagrams obtained by varying reinforcement area ratio (ρ) and the dimensionless axial force ratio (v).

Fig. 11 reports the comparison in terms of reinforcement area ratios. On the graphs are indicated the points corresponding to the first yielding of both HDs and compressed timber and those indicating the attainment of ultimate strain by timber. Numerical curves fit the theoretical ones satisfactorily: the curvature corresponding to first yielding of steel or

compressed timber are best quantified, while ultimate curvature provided by the numerical model resulted greater than the theoretical one.

In Fig. 12, instead, theoretical and numerical $M-\chi$ curves obtained by varying the dimensionless axial force ratios are compared. Also in this case, a good matching between the curves in terms of yielding curvature (provided by steel in tension) is resulted, while ultimate curvature provided by the numerical model is greater than theoretical.

In general, the numerical results confirm the trend that (i) the yielding curvature is ruled by steel in tension, because it precede the ‘yielding’ of timber under compression and that (ii) the ultimate curvature depends on ultimate strain in orthogonal to grain direction of compressed timber.

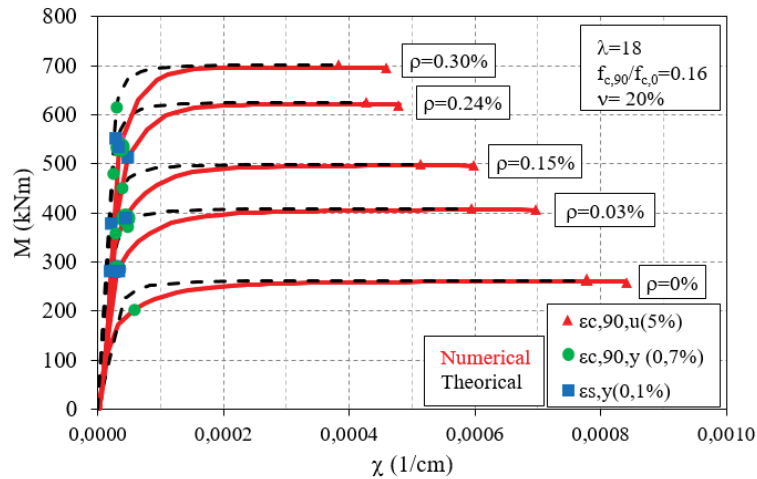


Figure 11: Comparison between theoretical and numerical $M-\chi$ diagrams by varying the reinforcement area ratios.

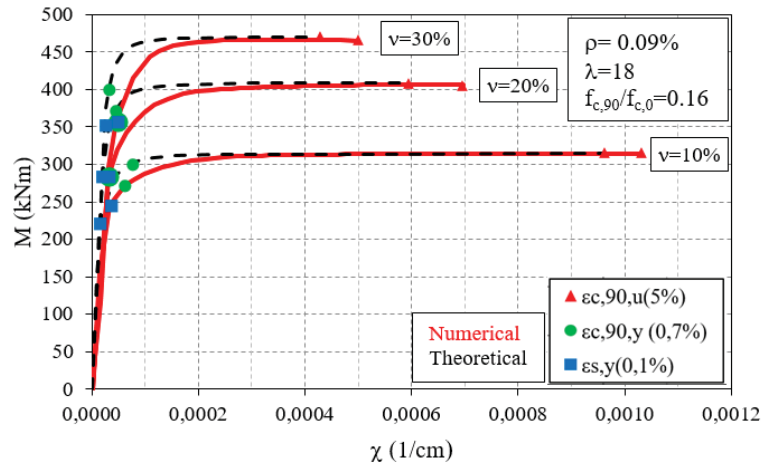


Figure 12: Comparison between theoretical and numerical $M-\chi$ diagrams by varying the dimensionless axial force ratios.

4.4 Design-oriented formulas for estimating the ultimate curvature

Both theoretical and numerical analyses proved that yielding in tension of HDs precedes those in compression of timber, and that ultimate curvature of the cross-section is ruled by the ultimate strain of the compressed timber.

In the light of this, it is reasonable to assume as optimal *failure condition* at Ultimate Limit State (ULS) for timber-to-timber contact cross-section those corresponding to HDs yielded in

tension and timber at its ultimate strain ($\varepsilon_{c,90,u}$) in compression (Fig. 13). Based on this assumption, *design-oriented* formulas for evaluating both ultimate curvature and the corresponding ultimate moment of the cross-section have been defined in the following.

With regards the ultimate curvature, a closed- form formula has been obtained starting from a translation equilibrium condition on cross-section between the applied axial force (N_{Ed}) and tensile and compression internal resultants:

$$\beta B x_{n,u} f_{c,90,d} - \sum_{HD=1}^n (A_{HD} \sigma_{HD})_i = N_{Ed} \quad (8)$$

where β represents the filling coefficient of the adopted parabola rectangle normal stress distribution, assumed equal to 0.810 for rectangular cross-section (also according to Refs. [29,36]), B the panel width, $f_{c,90,d}$ the design compression strength of timber in orthogonal to grain direction, A_{HD} the cross-section area of the tensile-resistant element and σ_{HD} the associated normal stress.

The maximum (or ultimate) axial force of the cross-section subjected to pure compression is:

$$N_{Rd} = B L_p f_{c,90,d} \quad (9)$$

where L_p represents the panel length.

Dividing the eq. (8) by eq. (9) the equilibrium translation becomes:

$$\beta \frac{x_{n,u}}{L_p} - \frac{\sum_{HD=1}^n (A_{HD} \sigma_{HD})_i}{B L_p f_{c,90,d}} = \frac{N_{Ed}}{B L_p f_{c,90,d}} \quad (10)$$

They have been defined with the symbols ω and ν the mechanical reinforcement percentage and the dimensionless axial force, respectively:

$$\omega_i = \frac{(A_{HD} \sigma_{HD})_i}{B L_p f_{c,90,d}} \quad (11)$$

$$\nu = \frac{N_{Ed}}{B L_p f_{c,90,d}} \quad (12)$$

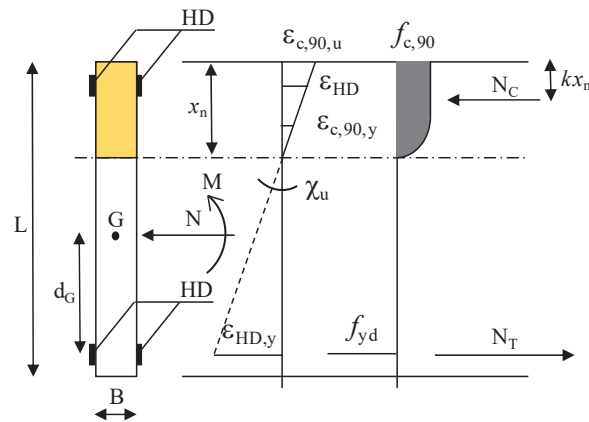


Figure 13: Failure condition for the timber-to-timber cross-section at ULS (i.e., stage III).

By introducing ω and ν , the equilibrium translation equation can be written as:

$$\beta \frac{x_{n,u}}{L_p} = \sum_{HD=1}^n \omega_i + \nu \quad (13)$$

In general, the ultimate curvature is given by:

$$\chi_u = \frac{\varepsilon_{c,90,u}}{x_{n,u}} \quad (14)$$

where $\varepsilon_{c,90,u}$ represents the ultimate strain of timber at compressed edge and $x_{n,u}$ the ultimate neutral axis depth. By substituting the eq. (14) in the eq. (13) the ultimate curvature of the cross-section can be expressed with the closed formula:

$$\chi_u = \beta \frac{\varepsilon_{c,90,u}}{L_p \left(\sum_{HD=1}^n \omega_i + \nu \right)} \quad (15)$$

As it can be noted, the eq. (15) is easy of use. It allows to determine the ultimate curvature as a function of mechanical parameters which define the timber-to-timber connection zones without any other additional calculation. Furthermore, the eq. (15) confirms all the findings proved through the Figures 7, 8 and 9: when ω , ν and L_p increase the ultimate curvature decreases. While, if the ultimate strain ($\varepsilon_{c,90,u}$) of compressed timber reduces (increases) also the ultimate curvature reduces (increases) proportionally.

The ultimate moment of the cross-section associated to χ_u is determined through the equilibrium rotation around the center-of-gravity of the cross-section:

$$M_{Rd}(N_{Ed}) = \beta B x_{n,u} f_{c,90,d} (L_p / 2 - k x_{n,u}) + \sum_{HD=1}^n (A_{HD} \sigma_{HD} d_G)_i \quad (16)$$

where $k x_{n,u}$ represent the distance of the internal compression resultant of timber with respect to the compressed edge, with $k=0.40$ and d_G the distance of the i -th tensile resistant element with respect to the center-of-gravity of the section (Fig. 13).

Case	$\chi_{u, th}$ (1/cm)	ω (-)	ν (-)	$\chi_{u, CF}$ (1/cm)	$\Delta(\chi_u)$ (%)
$\rho=0.00\%$	0.00092	0.000	0.20	0.00081	12
$\rho=0.03\%$	0.00081	0.027	0.20	0.00071	12
$\rho=0.06\%$	0.00073	0.053	0.20	0.00064	12
$\rho=0.09\%$	0.00066	0.080	0.20	0.00057	14
$\rho=0.12\%$	0.00060	0.107	0.20	0.00052	13
$\rho=0.15\%$	0.00055	0.137	0.20	0.00048	13
$\rho=0.18\%$	0.00051	0.161	0.20	0.00044	14
$\rho=0.21\%$	0.00048	0.187	0.20	0.00042	12
$\rho=0.24\%$	0.00044	0.220	0.20	0.00039	11
$\rho=0.27\%$	0.00042	0.240	0.20	0.00037	12
$\rho=0.30\%$	0.00039	0.267	0.20	0.00035	10

Table 1: Comparisons among ultimate curvature derived by theoretical and closed-form formula obtained by varying the percentage reinforcement area ratio.

In Table 1 and 2 are summarized and compared the values of the ultimate curvature obtained from theoretical model (indicated as $\chi_{u,th}$) with those derived the proposed closed-form formula described by the eq. (15) (indicated as $\chi_{u,CF}$). In particular, Table 1 refers to the ultimate curvature obtained by varying the reinforcement percentage ratios, while Table 2 refers to ultimate curvature obtained by varying the dimensionless axial force ratios. In the same Tables, the percentage differences between $\chi_{u,th}$ and $\chi_{u,CF}$, indicated with the symbol $\Delta(\chi_u)$, are also reported. The results proved that the percentage deviations $\Delta(\chi_u)$ are quite constant and included in the interval 10-15%, thus confirming that the closed-form formula gives acceptable results.

Case	$\chi_{u, th}$ (1/cm)	ω (-)	ρ (%)	$\chi_{u, CF}$ (1/cm)	$\Delta(\chi_u)$ (%)
$v=0.0\%$	0.00235	0.080	0.09	0.00200	15
$v=10\%$	0.00102	0.080	0.09	0.00090	12
$v=20\%$	0.00066	0.080	0.09	0.00058	12
$v=30\%$	0.00049	0.080	0.09	0.00042	14

Table 2: Comparisons among ultimate curvature derived by theoretical and closed-form formula obtained by varying the dimensionless axial force ratio.

5 CONCLUSIONS

Despite that CLT constructional technology is widely diffused in many countries, a unified approach for evaluating the flexural load-bearing and displacement capacity of the panel subjected to seismic and gravity loads has not been yet defined. Different theoretical methods are proposed in literature, whose main shortcomings consist of under evaluating the role of compressed timber in the timber-to-timber contact zone and its influence on the ductile behavior of the panels.

This paper presents a novel moment-curvature ($M-\chi$) theoretical model for CLT panels. The method, based on an iterative procedure, allowed to develop the entire $M-\chi$ diagrams and to investigate the ductile behavior of CLT accounting for the orthogonal to grain properties of compressed timber.

The influence of different parameters on the post-elastic displacement capacity of the panels has been investigated through a parametric study. The obtained results proved that: (i) CLT panels are provided of good ductile behavior; (ii) increments of percentage reinforcement ratios, as well as of slenderness cross-section ratios and amount of axial force, induce significant reductions of the panels' ductility, whereas the ultimate moment increases simultaneously; (iii) the yielding curvature is ruled by HDs in tension, while the ultimate curvature depends on timber compressed in perpendicular to grain direction.

To assess the validity of the theoretical $M-\chi$ diagrams, a comparison with a finite element numerical model has been carried out. Theoretical vs numerical results showed a good matching, thus confirming the validity of the theoretical method.

Finally, based on the results achieved with the parametric study, a design-oriented approach for evaluating the ultimate curvature (together with the associate ultimate moment) through a closed-form formula has been presented in the paper. Comparison of the results shown a good accordance of the closed-form formula with the theoretical approach.

REFERENCES

- [1] R. Brandner, G. Flatscher, A. Ringhofer, G. Schickhofer, A. Thiel. Cross laminated timber (CLT): Overview and development. *Eur J Wood Prod*, **74**, 331–351, 2016.
- [2] A. Iqbal. Cross Laminated Timber in New Zealand: Introduction, prospects and challenges. *New Zealand Timb Design J*, **22**, 3–8, 2018.
- [3] S. Pei, D. Rammer, M. Popovski, T. Williamson, P. Line, J.W. van de Lindt. An overview of CLT research and implementation in North America. *16th World Conference on Timber Engineering* (WCTE 2016), Wien, Austria, August 11–25, 2016.
- [4] Y. Goto, R. Jockwer, K. Kobayashi, Y. Karube, H. Fukuyama. Legislative background and building culture for the design of timber structures in Europe and Japan. *17th World Conference on Timber Engineering* (WCTE 2018), Seoul, Korea, 20–23 August 2018.
- [5] A. Ceccotti, C. Sandhaas, M. Okabe, M. Yasumura, C. Minowa, N. Kawai. SOFIE project—3D shaking table test on a seven-storey full-scale cross-laminated timber building. *Earth Eng Struct Dyn*, **42**, 2003–2021, 2013.
- [6] J.W. van de Lindt, J. Furley, M.O. Amini, S. Pei, G. Tamagnone, A.R. Barbosa, D. Rammer, P. Line, M. Fragiaco, M. Popovski. Experimental seismic behaviour of a two-story CLT platform building. *Eng. Struct.* **183**, 408–422, 2019.
- [7] I. Gavric, M. Fragiaco, A. Ceccotti, Cyclic behaviour of typical metal connectors for cross-laminated (CLT) structures, *Materials and Structures* **48**, 1841–1857, 2015.
- [8] R. Tomasi, I. Smith. Experimental characterization of monotonic and cyclic loading response of CLT panel-to-foundation angle bracket connection. *J Mater Civ Eng*, **27** (6), 2015.
- [9] M. Izzi, D. Casagrande, S. Bezzi, D. Pasca, M. Follesa, R. Tomasi. Seismic behavior of Cross-Laminated Timber structures: A state-of-the-art review. *Eng Struct* **170**, 45–52, 2018.
- [10] K.W. Johansen. Theory of timber connections. *Int Ass for Bridge and Struct Eng* **9**, 249–262, 1949.
- [11] EN 1995-1-1: 2004. Eurocode 5: Design of timber structures – Part-1-1: general rules and rules for buildings. European Committee for Standardization (CEN), Brussels, Belgium; 2003.
- [12] A. Sandoli, C. D'Ambra, C. Ceraldi, B. Calderoni, A. Prota. Sustainable Cross-Laminated Timber Structures in a Seismic Area: Overview and Future Trends. *Applied Science*, **11**, 2078, 2021. doi.org/10.3390/app11052078.
- [13] F. Sarti, A. Palermo, S. Pampanin. Quasi static cyclic testing of two-thirds scale unbonded posttensioned rocking dissipative timber walls. *J. Struct Eng* **142**, E40115005, 2016.
- [14] Latour, M.; Rizzano, G. Seismic behavior of cross-laminated timber equipped with traditional and innovative connectors. *Arch Civ Mech Eng* **17**, 382–399, 2017.
- [15] R. Scotta, L. Marchi, D. Trutalli, L. Pozza. A dissipative connector for CLT buildings: Concept, design and testing. *Materials* **9**, 139, 2016.
- [16] G. Tamagnone, G. Rinaldin, M. Fragiaco. A novel method for nonlinear design of CLT wall systems. *Eng Struct* **167**, 760–771, 2018.

- [17] I. Lukacs, A. Bjornfot, R. Tomasi. Strength and stiffness of cross laminated timber (CLT) shear walls: State-of-art of analytical approaches. *Eng Struct* **178**, 136-147, 2019.
- [18] D. Vassallo, M. Follesa, M. Fragiaco. Seismic design of a six-storey CLT buildings in Italy. *Eng Struct* **175**, 322-338, 2018.
- [19] ONORM B 1995-1-1, Eurocode 5: Design of Timber Structures – Part 1-1: General Common Rules and Rules for Buildings – National Specification for the Implementation of ONORM EN 1995-1-1, National Comments and National Supplements, Austrian Standards Institute (ASI), 2015 (in German).
- [20] E. Serrano, B. Enquist. Compression strength perpendicular to grain in cross-laminated timber (CLT). 11th *World Conference on Timber Engineering* (WCTE 2010), Riva del Garda, Italy, 2010.
- [21] E. Gasparri, F. Lam, Y. Liu. Compression perpendicular to grain behaviour for the design of a prefabricated CLT façade horizontal joint. 16th *World Conference on Timber Engineering* (WCTE 2016), Wien, Austria, August 11-25, 2016.
- [22] R. Brandner. Cross laminate timber (CLT) in compression perpendicular to plane: testing, properties, design and recommendations for harmonizing design provisions for structural timber products. *Eng Struct* **17**, 944-960, 2018.
- [23] A. Sandoli, C. D'Ambra, C. Ceraldi, B. Calderoni, A. Prota. Role of perpendicular to grain compression properties on the seismic behaviour of CLT walls. *Journal of Building Engineering*, **34**, 101889, 2021.
- [24] A. Sandoli, D. Moroder, S. Pampanin, B. Calderoni. Simplified analytical models for coupled CLT walls. 16th *World Conference on Timber Engineering* (WCTE 2016), Wien, Austria, August 11-25, 2016.
- [25] EN 338, Structural Timber - Strength Classes, European Committee for Standardization (CEN), 2016.
- [26] EN14080, Timber Structures - Glued Laminated Timber and Glued Solid Timber- Requirements, European Committee for Standardization (CEN), 2013.
- [27] European Committee for Standardization (CEN) Eurocode 2: Design of concrete structures –Part a-a: General rules and rules for buildings; 2004.
- [28] L. Franco, L. Pozza, A. Saetta, D. Talledo, Enhanced N-V interaction domains for the design of CLT shear wall based on couple interaction models. *Eng Struct* **231**, 111607, 2021.
- [29] ETA-14/0349. (2019). European Technical Assessment, issued in accordance with Regulation EU n° 305/2011.
- [30] EN 1993-1. Eurocode 3: Design of steel structures - Part 1-1 general rules and rules for buildings. European Committee for Standardization (CEN), Brussels, Belgium; 2003
- [31] SAP 2000 (v.18). Structural Analysis Program, CSI.
- [32] A. Sandoli, B. Calderoni. The rolling shear influence on the out-of-plane behavior of CLT panels: A comparative analysis. *Buildings*, 10(3), **42**, 2020.
- [33] S. Pei, J. van de Lindt, M. Popovski. Approximate R-factor for cross-laminated timber (CT) shear walls: state-of-art of analytical approaches. *Eng Struct* **178**, 136-147, 2019.

- [34] L. Embury-Williams, E. Karakabey (Eds.), Application of Analysis Tools from NEW Buildings Research Network in Design of a High-Rise Wood Building. NSERC: Strategic Research Network on Innovative Wood Products and Building Systems (New Buildings), 2014.

REINFORCING STOP-SPLAYED SCARF JOINTS WITH TIMBER PEGS: ROLE OF SLENDERNESS

C. Ceraldi¹, C. D'Ambra¹, M. Lippiello¹, A. Sandoli¹ and A. Prota¹

¹ Department of Structure for Engineering and Architecture, University of Naples "Federico II"
via Claudio 21, 80125, Naples
e-mail: {carla.ceraldi,claudio.dambra,maria.lippiello, antonio.sandoli,andrea.prota}@unina.it

Abstract

Repairing stop-splayed scarf-joints in beams or truss-rods is a frequent occurrence in restoring ancient timber structures. Reinforcement of carpentry joints by means of metallic elements as well as unconventional materials is extensively investigated in literature, while timber pegs in timber to timber connections are studied referring mainly to new timber structures.

In the present paper, authors' previous research analysing the mechanical behaviour of stop-splayed scarf joints reinforced with timber pegs has been carried on, focusing on the evaluation of ductility which can be achieved by reinforcement with timber pegs. Moreover, the role of slenderness, the rate between jointed timber thickness and peg diameter is analysed.

An experimental program has been carried out testing in axial tension two samples of fir scarf joints with an ash key: one sample constituted of two simple scarf joints, and one constituted of three scarf joints reinforced with two ash pegs of 20 mm of diameter. Comparing experimental results has allowed to better understand the role played by timber pegs in reinforcement and to evaluate the influence of reinforcement on ductility of reinforced scarf joints behaviour.

Experimental results have also been compared with those obtained in a previous experimental study where an analogous experimental program has been made on smaller scarf joints reinforced with two ash pegs of 8 mm of diameter. So, the role played by slenderness has been focused.

The evaluation of the attained results, even if not exhaustive for a reliable theoretical formulation of timber peg behaviour in reinforcing stop-splayed joints, has allowed the identification of some interesting features, that is stiffness and reinforcement due to timber pegs.

Keywords: stop-splayed scarf joint, reinforcement, timber peg, ductility, slenderness, timber structures.

1 INTRODUCTION

In the field of ancient timber structures restoration, the need of substituting rotten portions of structural elements, preserving the original spatial configuration without modifying their structural behavior is advisable. At this aim, when total or partial substitution of an element is needed, the employment of traditional carpentry joints normally leads to a more conservative approach. In particular, in ancient trusses and floors, taking off the end portions of rafters or beams, damaged by biotic agents often due to high moisture content inside the masonry walls, is sometimes inevitable.

A quite speared methodology of restoration envisages the introduction of new timber elements connected to the standing structure. This connection is generally realized with metallic bolted plates, steel pins, or epoxy resin adhesives. According to their arrangement and geometry, common traditional carpentry joints can be divided in four main types: a) tenon and mortise joints; b) notched joints; c) lap joints and d) scarf joints. These connections are generally fixed or reinforced with metallic connectors, or epoxy resin adhesive, even if some disadvantages may occur such as (i) moisture condensing problems in the interface between timber and steel elements, (ii) questionable aesthetic output in uncovered structures, and (iii) the difficult reversibility of the intervention with resin adhesives [1, 2]. Nowadays an efficient alternative is the use of timber pegs in timber to timber connections. In literature, reinforcement of carpentry joints by means of metallic elements, as well as unconventional materials, is extensively investigated, while fewer papers can be found regarding the employment of timber pegs. In a review paper by Branco and Descamps [3] a state of art is described where many interesting references are quoted concerning the main themes as modelling and simulation of analysis and strengthening of carpentry joints. Moreover, several papers focusing on birds mouth joint [1, 2], mortise and tenon joint [4-6], and dowel joint [7, 8] can be found. A general overview regarding lapped scarf joints is presented by Kunecký et al. [9] in which the stiffness assessment of jointed structural elements for different joint positions and element sizes is investigated. Arciszewska-Kędzior et al. [10] performed both experimental and numerical analyses to study the mechanical behavior of a lapped scarf joint with inclined contact faces and four oak dowels. Sangree and Schafer [11] presented an experimental study on the mechanical behavior of a stop-splayed scarf joint with transverse key. Mechanical tests on four specimens simulating real joints have been performed and the study has been completed using a three-dimensional finite element model created using ABAQUS. Ceraldi et al. [12] analyze the mechanical behavior of stop-splayed scarf joints unreinforced and reinforced with timber pegs and with steel pins, subjected to tension test, to assess the reliability of employing timber fasteners. The role of the fastener inside this tensile-resistant carpentry joint and its contribution in yield strength and stiffness have been investigated. Aira et al. [13] experimentally analyze the structural behavior of halved and tenoned scarf joint subjected to tensile stresses in order to describe the different failure modes. In Perria et al. [14] results of an experimental campaign and an analytical model for the behavior of the halved under-squinted scarf joint are presented. Different aspects that influence the behavior of the connection subjected to pure compression, pure bending and combined compression and bending are analyzed. The stiffness of scarf joints with keys and timber pegs has been investigated and modelled by Fajman and Măca [15], including the role of friction forces, already studied in [16]. An experimental evaluation of traditional scarf joinery behavior in bending can be found in Hirst et al. [17]. More recently, in Karolak et al. [18] a more in-depth analysis on the current state of knowledge related to scarf and splice carpentry joints in flexural elements as well as selected examples of tensile elements is presented.

The rheological behavior of timber to timber joints connected by timber pegs, its modelling and the formulation of corresponding design rules, can be more extensively found in literature

referred to new structures, such as timber frames. Generally, research about timber peg behaviour in simple and double shear plane joints fastened with timber pegs and its theoretical and numerical interpretation aims to the identification of codified design rules, usually starting from those derived from Johansen's theory [19] prescribed for calculating strength capacity of steel fasteners [20-23]. Design rules validated for mortice and tenon joints have been proposed in [24, 25]. Many research, instead, have investigated the role of the different parameters influencing the joint behavior: rate of diameter and timber board thickness [21]; dowel bearing strength [22, 26, 27, 28]; shear and bending of the peg [19, 29, 30, 31]; direction of the load [32]; ductility [21, 33, 34, 35].

In the present paper, authors' previous research analyzing the mechanical behaviour of stop-splayed scarf joints reinforced with timber pegs has been carried on, focusing on the evaluation of ductility which can be achieved by reinforcement with timber pegs.

Ductility describes the ability of a structure to attain large deformation in the plastic range before its collapse. In timber structures, it may predominantly be supplied by plastic behaviour of the connections which are the critical regions for load transfer. There are several definitions of ductility, all related to stress, strain or energy, which may be useful in different situations [34]. For connection design, definitions referring to absolute values of rotation and displacement may be the most applicable [33]. Also, ductility may further be divided into static ductility for constant loads, and dynamic ductility for cyclic loads [33]. Commonly, it is defined as the ratio between ultimate and yield displacement, according to the European code EN 12512 [36] and the Swiss code SIA 265 [37] for timber structures.

Since knowledge of the yield point and ductility of a structure is important in seismic design, their investigation has become more and more of interest within recent years. From structural engineering point of view in general and for timber engineering, there is not a unified definition of the ductility term, nor is there a common understanding on how ductility shall be used in structural design. As a result, several methods have been developed in order to determinate the point of yield and, consequently several measures for evaluating of the ductility of timber structures and connections are obtained. In Northern America is widely used the equivalent energy elastic-plastic method (EEEP); in the European code EN 12512 (CEN method) the 1/6 method is adopted [36]; the 0.5 F_{max} method so as deduced from Karacabeyli and Ceccotto and finally, according to Yasamura and Kawei, the 10-40-90 method are also employed. A detailed description and discussion of those different methods can be found in [33]. According to these approaches, the evaluation of ductility can be carried out on the analysis of the load-displacements diagrams resulting from experimental tests or, alternatively, on approximating curves. This paper is focused on comparing two analysis methods commonly used in determination of yield load and deformation and of failure load and deformation, respectively.

An experimental program has been carried out testing in axial tension two samples of fir scarf joints with an ash key: one sample constituted of two simple scarf joints, and one constituted of three scarf joints reinforced with two ash pegs of 20 mm of diameter. Comparing experimental results has allowed to better understand the role played by timber pegs in reinforcement and to evaluate the influence of reinforcement on ductility of reinforced scarf joints.

Experimental results have also been compared with those obtained in a previous experimental study where an analogous experimental program has been made on smaller scarf joints reinforced with two ash pegs of 8 mm of diameter. So, the role played by slenderness has been focused.

The evaluation of the attained results, even if not exhaustive for a reliable theoretical formulation of timber peg behaviour in reinforcing stop-splayed joints, has allowed the identification of some interesting features, that is stiffness and reinforcement due to timber pegs.

2 EXPERIMENTAL PROGRAM

2.1 Samples and test set-up

The experimental program concerns two samples of stop splayed scarf joints made of fir, (*Abies alba*) with a key made of ash, (*Fraxinus excelsior*), whose dimensions and geometry are illustrated in Figure 1.

Sample A_D20 consists of two unreinforced joints, while sample B_D20 is constituted by three specimens of the same type of sample A_D20 but reinforced with two ash pegs with diameter of 20 millimeters (Figure 1).

Proportions and limit dimensions recommended for traditional configuration of scarf joints, with length three times the height of the cross section, have been assumed in their design.

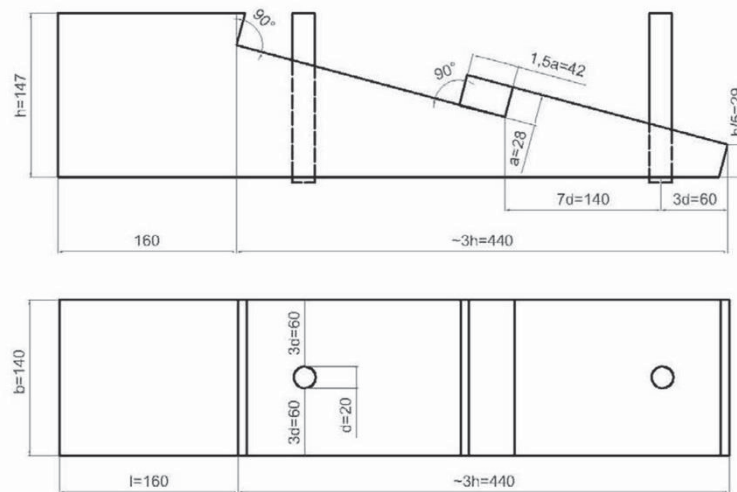


Figure 1: Specimen geometry of samples A_D20 e B_D20 (dimensions in mm)

Density and parallel to grain compression strength ($\sigma_{c,0}$) of the two employed essences quoted in Table 1 have been experimentally determined in previous research [22, 31] with an average moisture content approximately equal to 12%.

Timber	Density (kg/m ³)	$\sigma_{c,0}$ (MPa)
Ash	652	56.3
Fir	472	39.2

Table 1: Mean values of density and parallel-to-grain compression strength.

Samples have been tested in tension with a universal electromechanical test machine with hydro pump LOSENHAUSENWERK, Mod: UHP 60, electronic control with control unit Zwick Roell, (Figure 2), in displacement control, at a speed of 0.8 mm/min, until a complete loss of bearing capacity was reached.



Figure 2: Test set-up

2.2 Unreinforced sample (Sample A_D20)

Final collapse of an unreinforced scarf joint with a key loaded in tension [32], can occur on the following critical surfaces: (i) compression failure at key contact inclined surface (notch area), (ii) shear failure through the horizontal plane in the heel surface, (iii) combined tension and bending failure at the reduced section above the notch and (iv) compression failure perpendicular to grain of the key (Figure 3).

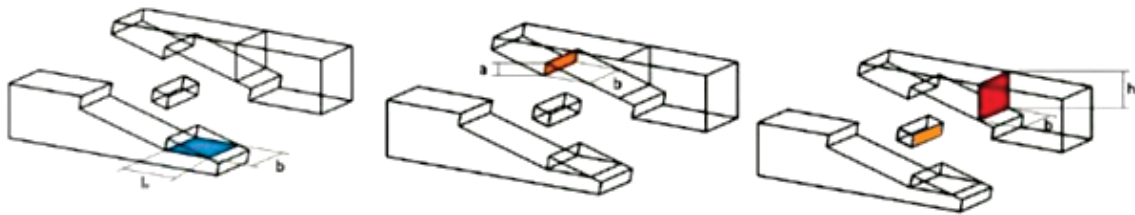


Figure 3: Failure surfaces of an unreinforced scarf joint with a key

Both specimens of sample A_D20 have failed due to shear stresses through the heel area (Figure 4). Force-displacement diagrams (Figure 5) show that the observed behavior can be schematized with two linear steps: the elastic one, and, after the yielding point, the plastic one, with a relevant hardening. Stiffness, which is governed only by the level of confinement of the key, increases in the plastic phase, due to the enforcement of the key, which has shown no deformation at all after collapse of both unreinforced joints. In specimen 1A_D20 this increase is more than in specimen 2A_D20 as its elastic stiffness is 26% of the plastic one, while that of test 2A_D20 is 35%.



Figure 4: Failure mode of specimens 1A_D20 e 2A_D20

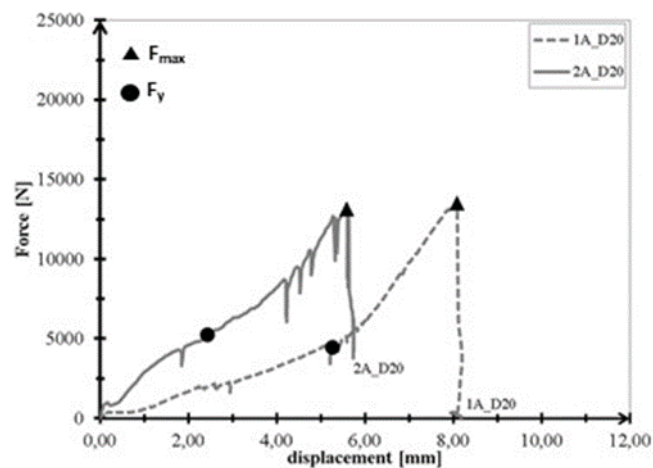


Figure 5: Force-displacement diagrams of sample A_D20

2.3 Sample reinforced with pegs (Sample B_D20)

In addition to the failure mode on the critical surfaces of a scarf joint with key, the reinforced joint can collapse in the single plane shear joint for embedment of the connected parts or failure of the peg in bending or “effective peg shear” failure mode, which is a combination of peg shearing, peg bending and embedding of timber boards [31].

Specimens 1B_D20 e 2B_D20 have both failed due to shear stresses through the heel area, while bending of the peg and embedding in the connected zone have been of little intensity in the first test and absent in the second. The key hasn't shown deformations (Figure 6).

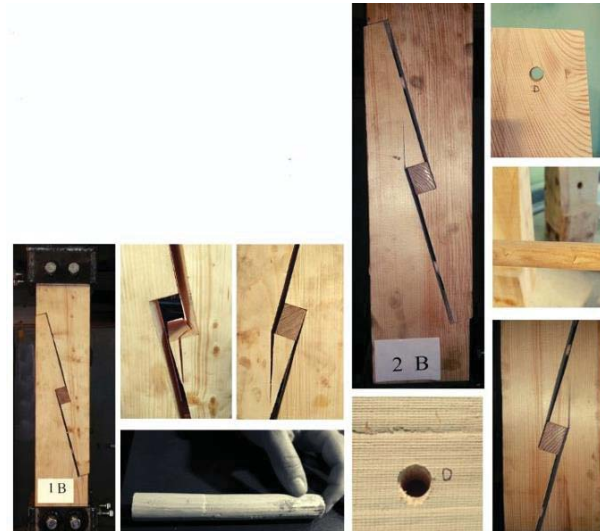


Figure 6: Failure mode of specimens 1B_D20 e 2B_D20

Specimen 3B_D20 has shown a different failure mode as collapse has been determined by embedding of the lower connection, with scarce deformation in the pegs, while the key has been undeformed (Figure 7).

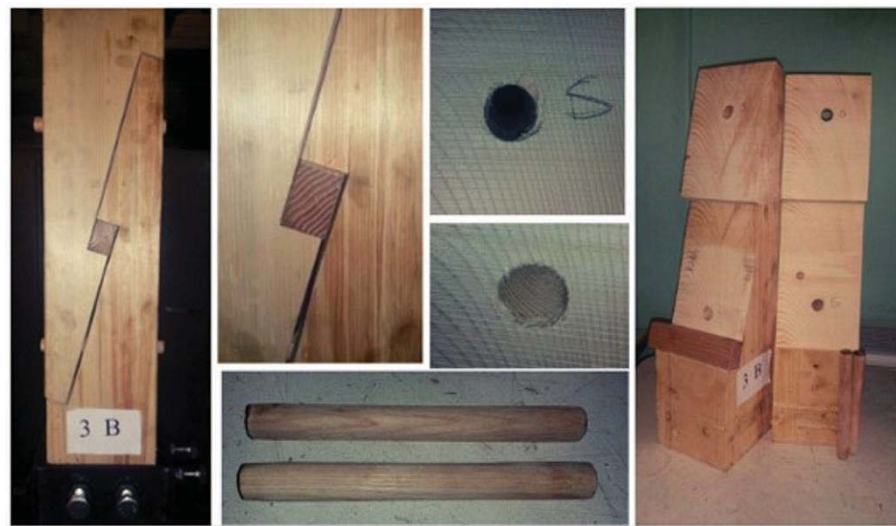


Figure 7: Failure mode of specimen 3B_D20

Comparing force-displacement diagrams for sample B_D20, quoted in Figure 8, it can be noted that only the specimen 2B_D20 doesn't have the ductile phase expected for the presence of the pegs [12], as collapse has been attained without deformations in the peg connection. Nonetheless, while specimens 2B_D20 and 3B_D20 present the same behaviour until the rupture of the first, specimen 1B_D20 differs from both. During the test of specimen 1B_D20, an initial crack developed in the notch area, parallel to the grain. This splitting due to tension perpendicular to the grain induced by compression parallel to the grain of the fibres, has generated a little crack which has not extended to the edge of the joint, as the presence of the peg connections delayed this occurrence, which at the end has induced shear collapse in the heel area.

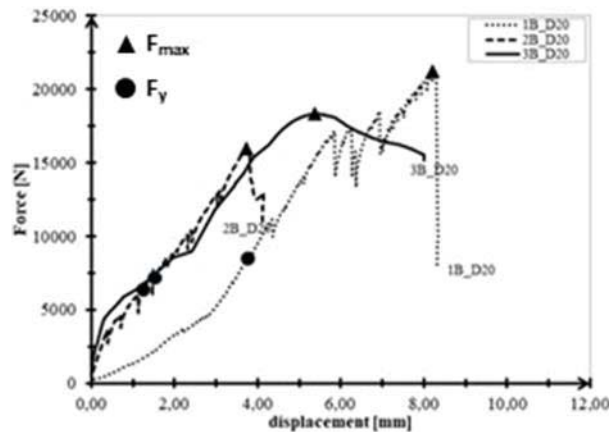


Figure 8: Force-displacement diagrams of sample B_D20

2.4 Discussion of experimental results

In Table 2 yielding force F_y and maximum force F_{max} values are summarized, together with corresponding displacement. In sample B_D20, due to the presence of the peg, the yielding point has been determined following the American procedure ASTM 5764 [38], consisting in choosing as yield point the intersection of the load-displacement curve with a straight line parallel to the linear phase of the diagram shifted to a distance equal to 5% of fastener diameter.

Specimen	d mm	F_y (N)	u_y mm	F_{max} (N)	u_f mm
1A_D20	20	11664.1	8.1	13514	8.1
2A_D20	20	10025.0	5.6	13129	5.6
1B_D20	20	16507.5	8.3	21227	8.2
2B_D20	20	14701.3	3.8	15959	3.7
3B_D20	20	16590.3	4.4	18340	5.4

Table 2: Force and displacement values for sample A_D20 e B_D20

The reduced number of performed tests doesn't allow choosing a diagram fully representative of each sample behavior; so, with aim of comparing the rheological behavior of the two samples, all the diagrams are together compared in Figure 9.

The reinforcement with timber pegs is resulted efficient as it has induced a considerable increase of yielding and maximum forces values with respect to the unreinforced sample. In fact, sample B_D20 mean values $F_{y,mean}=15933$ N and $F_{max,mean}=18509$ N are 47% and 39% larger than the corresponding values of sample A_D20 $F_{y,mean}=10845$ N and $F_{max,mean}=13322$ N. This enforcement can be ascribed to the interaction between the timber peg and the joint, which has delayed the failure along the typical critical surfaces of the scarf joint. So, a reliable prediction of load-bearing capacity of the reinforced stop-splayed scarf joint depends upon evaluating the amount of load transferred to the joint, inducing the collapse of critical surfaces, as observed in [12].

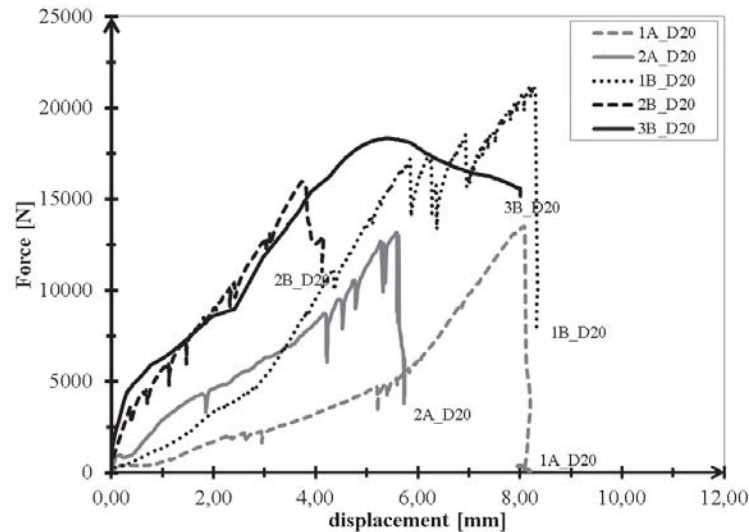


Figure 9: Comparison of force-displacement diagrams of samples A_D20 and B_D20

The observed rheological behaviors are quite different both in elastic and plastic range. While sample A_D20 shows a linear response in the elastic as well as in the plastic phase, sample B_D20, when deformation appears in the simple shear plane joint constituted by the timber peg connection, shows a stiffer behavior in the elastic phase and a more ductile behavior, in the plastic one. In fact, the overall behavior of the reinforced joint is conditioned by the force distribution among the resisting elements, i.e., the ash key and the added fasteners, which act as damping elements in transferring loads. Moreover, the stiffening effect can be related to the friction forces generated by the contact between the two timber elements, which help hold tight the connection and enhance the level of confinement of the key. The presence of no negligible friction forces when timber pegs are used and the influence of the key on the joint axial stiffness have been already noticed and measured in [11, 15, 16], highlighting that the more the key is confined, the stiffer is the joint behavior.

3 INFLUENCE OF SLENDERNESS ON DUCTILITY

3.1 Ductility

Ductility is related to the ability of a structure to attain large deformations in the plastic range before its collapse and without substantial reduction in strength in specimen loaded in displacement control. There are several definitions of ductility, all related to stress, strain, or energy, which may be useful in different situations. For connection design, definitions referring to absolute values of rotation and displacement may be the most applicable (see [33]).

Commonly, ductility ratio is defined as the proportion of the displacement at failure u_f to the displacement at yielding u_y , so as deduced in the European and Swiss codes [36,37], which is given by:

$$D_f = \frac{u_f}{u_y} \quad (1)$$

An additional definition of the ductility ratio is also based on the displacement u_u at ultimate load F_u and it is represented by the following equation:

$$D_u = \frac{u_u}{u_f} \quad (2)$$

These parameters can be determined from the analysis of the load-displacements graphs resulting from experimental tests. The displacement at yield u_y , with the corresponding yielding load F_y , describes the point where the elastic behavior passes into a plastic behavior. So, in order to estimate ductility, the identification of yield point is necessary and as a yield criterion for timber connections is not well defined, several methods for its determination have been developed [36,37,39,40,41].

In the present paper, Eqs (1) (2) have been used to estimate the level of ductility of the two stop splayed scarf joints samples tested: sample A_D20, unreinforced, and sample B_D20 reinforced with timber pegs. In figure 10, referring to a graph for a specimen of sample B_D20, are identified: F_y as the force at the yield point, determined by the method based on a 5% diameter offset, F_{max} as the maximum value registered and F_u as the ultimate force at the failure point.

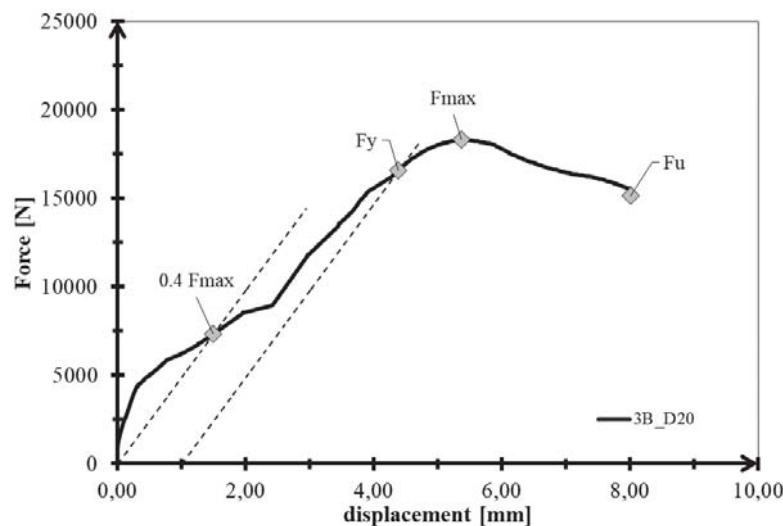


Figure 10: Identification of force values for samples B_D20

A summary of load and displacements at the yield and failure points, for the two samples under consideration is given in Table 3.

Specimen	d mm	F_y (N)	u_y mm	F_{max} (N)	u_f mm	F_u (N)	u_u mm	D_f -	D_u -
1A_D20	20	11664.1	8.1	13514	8.1	3593.8	8.21	1.00	1.01
2A_D20	20	10025.0	5.6	13129	5.6	5669.5	5.74	1.00	1.02
1B_D20	20	16507.5	8.3	21227	8.2	9807.7	8.35	0.99	1.00
2B_D20	20	14701.3	3.8	15959	3.7	12944.1	4.15	0.97	1.08
3B_D20	20	16590.3	4.4	18340	5.4	15163.5	8.01	1.23	1.83

Table 3: Determination of the displacements at point of yielding (u_y) and failure (u_f) and ductility ratio based on Eqs (1) and (2).

As can be seen from Table 3, the ductility values show a uniformity of results in unreinforced and reinforced samples, respectively. Also, the mean value of ductility, at the yield point, in-

creases by approximately 6% in the reinforced joint compared to the unreinforced one. Furthermore, the mean ductility value increases if the ultimate displacement is considered. As can be easily seen, in this case the increase in ductility is about 30%. However, evaluating the plastic displacement ($u_f - u_y$) only the reinforced specimen 3B_D20 shows a definite ductile behavior.

3.2 Role of slenderness

The present experimental results have also been compared with those obtained in a previous study [12], where an analogous experimental program has been made on smaller scarf joints, unreinforced sample A_D8, and reinforced with two ash pegs of 8 mm of diameter, sample B_8D (see Figure 11).

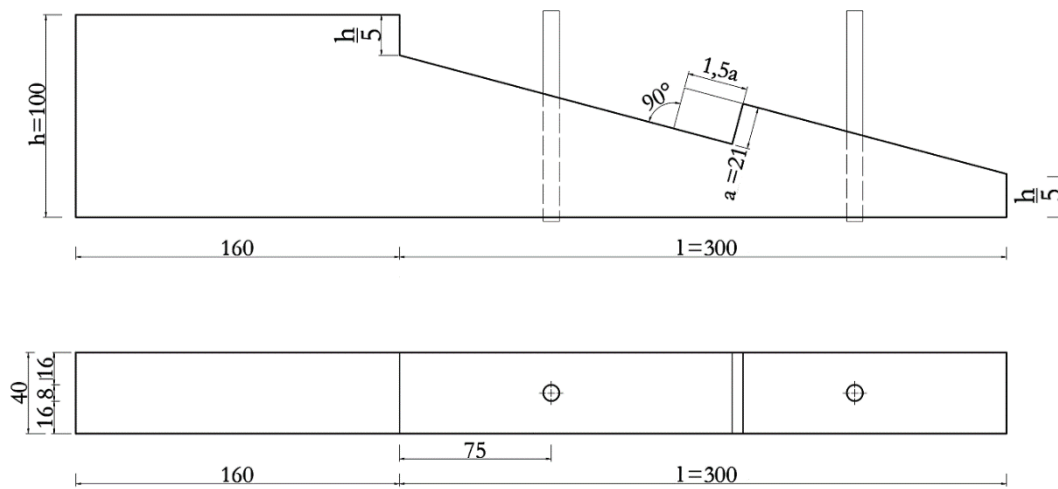


Fig. 11. Specimen geometry of samples A_D8 and B_D8 [12] (dimensions in *mm*)

So, the role played by slenderness in reinforcement with timber pegs has been evaluated. In that regard, the slenderness λ is defined as follows:

$$\lambda = \frac{s}{d} \quad (3)$$

where “s” is the smallest thickness of the pegged joint and “d” is the diameter of peg.

The slenderness values of B_D20D and B_D8 are quoted in Table 4:

Specimen	h cm	s cm	d cm	λ
B_D20	140	48	20	2.4
B_D8	100	44	8	5.5

Table 4: Slenderness values for samples B_20D and B_D8

Speci- men	d mm	F _y (N)	u _y mm	F _{max} (N)	u _r mm	F _u (N)	u _u mm	D _f -	D _u -
1A_D20	20	11664.1	8.1	13514	8.1	3593.8	8.21	1.00	1.01
2A_D20	20	10025.0	5.6	13129	5.6	5669.5	5.74	1.00	1.02
1B_D20	20	16507.5	8.3	21227	8.2	9807.7	8.35	0.99	1.00
2B_D20	20	14701.3	3.8	15959	3.7	12944.1	4.15	0.97	1.08
3B_D20	20	16590.3	4.4	18340	5.4	15163.5	8.01	1.23	1.83
1A_D8	8	5849.7	5.9	6070.5	6.7	6058.9	6.72	1.14	1.15
2A_D8	8	6837.6	6.4	7504.61	8.6	4772.2	15.41	1.34	2.42
1B_D8	8	6955.6	4.5	8678.9	12.7	6918.3	14.10	2.83	3.13
2B_D8	8	9264.8	6.9	9486	8.8	9327.0	9.01	1.28	1.31
3B_D8	8	6969.1	4.9	8770	8.5	7945.0	14.73	1.74	3.03

Table 5: Comparison of samples_D8 and samples_D20

Also, the ductility gain obtained reinforcing the scarf joint with timber pegs is larger for the slenderer samples. In fact, for samples_D8, D_f and D_u increase of 57% and 40% respectively with the reinforcement, while for samples_D20 they increase only of 6% and 30%, respectively.

4 CONCLUSION

The reduced dimensions of the tested samples in this step of the research do not allow definitive conclusions about the influence of reinforcing stop-played scarf joints with timber pegs on ductility. Nonetheless, some interesting remarks have been deduced with can guide modeling the reinforced joint behavior.

First of all, the reinforcement with timber pegs is resulted efficient as it has induced a considerable increase of yielding and maximum forces values with respect to the unreinforced sample and it leads to a ductility increase. A fundamental question is given by the reference point: the European code and Swiss code for timber structures set the reference to the displacement at failure, whereas other methods consider the displacement at ultimate load to evaluate the ductility ratio.

Moreover, the observed rheological behaviors are quite different both in elastic and plastic range. While sample A_D20 shows a liner response in the elastic as well as in the plastic phase, sample B_20, when deformation appears in the simple shear plane joint constituted by the timber peg connection, shows a stiffer behavior in the elastic phase and a more ductile behavior, in the plastic one.

Finally, a more sensitive gain in ductility can be observed when the slenderness is low. In particular, according the Eqs (1-2) for samples_D8, D_f and D_u increase of 57% and 40% respectively with the reinforcement, while for samples_D20 they increase only of 6% and 30%, respectively. So, in designing reinforcement with timber pegs checking slenderness is necessary, as one of the parameters orienting the choice of peg diameter to be employed.

REFERENCES

- [1] M.A. Parisi, M. Piazza, Mechanics of plain and retrofitted traditional timber connections. *Journal of Structures Engineering*, **126** (12), 1395–1403, 2000.

- [2] J.M. Branco, M. Piazza, P.J.S. Cruz, Experimental evaluation of different strengthening techniques of traditional timber connections. *Engineering Structures*, **33**, 2259–2270, 2011.
- [3] J.M. Branco, T. Descamps, Analysis and strengthening of carpentry joints. *Construction and Building Materials*, **97**, 34–47, 2015.
- [4] R. Aman, H. West, D. Cormier, An evaluation of loose tenon joint strength. *Forest Products Journal*, **58**(3), 61–64, 2008.
- [5] J. Judd, F. Fonseca, C. Walker, P. Thorley. Tensile strength of varied-angle mortise and tenon connections in timber frames. *Journal of Structures Engineering*, **137**(5), 636–644, 2012.
- [6] E. Likos, E. Haviarova, C. Eckelman, Y. Erdil, A. Ozcifci. Effect of tenon geometry, grain orientation, and shoulder on bending moment capacity and moment rotation characteristics of mortise and tenon joints. *Wood Fiber Science*, **44**(4), 1–8, 2012.
- [7] M. Dorn, K. De Borst, J. Eberhardsteiner. Experiments on dowel-type timber connections. *Engineering Structures*, **47**, 67–80, 2013.
- [8] B.H. Xu, M. Taazount, A. Bouchair, P. Racher. Numerical 3D finite element modelling and experimental tests for dowel-type timber joints. *Construction and Building Materials*, **23**, 3043–3052, 2009.
- [9] J. Kunecký, H. Hasníková, M. Kloiber, J. Milch, V. Sebera, J. Tippner. Structural assessment of a lapped scarf joints applied to historical timber constructions in central Europe. *International Journal of Architectural Heritage*, **12**, 666–682, 2018.
- [10] A. Arciszewska-Kêdzior, J. Kunecký, H. Hasníková, V. Sebera. Lapped Scarf Joint with Inclined Faces and Wooden Dowels: Experimental and Numerical Analysis. *Engineering Structures*, **94**, 1–8, 2016.
- [11] R.H. Sangree, B.W. Schafer. Experimental and numerical analysis of a stop-splayed traditional timber scarf joint with key. *Construction and Building Materials*, **23**, 376–385, 2009.
- [12] C. Ceraldi, C. D'Ambra, M. Lippiello, A. Sandoli, A. Prota. Structural behaviour of stop-splayed scarf joint reinforced with timber pegs. *Construction and Building Materials*, **269**, 121330–, 2021.
- [13] J. R. Aira, F. Arriaga, G. Iniguez-Gonzalez, M. Guaita. Failure modes in halved and tenoned timber scarf joints by tension test. *Construction and Building Materials*, **96**, 360–367, 2015.
- [14] E. Perria, M. Paradiso, M. Kessel. Experimental verification of the static model for the characterization of the halved and undersquinted scarf connection. Van Balen & Verstrynghe eds. *10th International Conference on Structural Analysis of Historic Construction*, Leuven, Belgium, September 13–15, 2016.
- [15] P. Fajman, J. Maca. Stiffness of scarf joints with dowels. *Computers and Structures*, **207**, 194–199, 2018.
- [16] P. Fajman. A Scarf Joint for Reconstructions of Historical Structures. *Advanced in Materials Research*, **969**, 9–15, 2014.

- [17] E. Hirst, A. Brett, A. Thomson, P. Walker, R. Harris. The structural performance of traditional oak tension & scarf joints. 10th *World Conference on Timber Engineering (WCTE)*, Miyazaki, Japan, June 2-5, 2008.
- [18] A. Karolak, J. Jasienko, K. Raszczuk. Historical scarf and splice carpentry joints: state of the art. *Heritage Science*, **8**, 105, 2020.
- [19] K.W. Johansen. Theory of timber connections. *International Association for Bridge and Structural Engineering Publications*, **9**, 249-262, 1949.
- [20] R.J. Schmidt, R.B. MacKey. Timber Frame Tension Joinery. *Research. Report*, University of Wyoming, Dep. of Civil and Architectural Eng, 1997.
- [21] C. Ceraldi, V. Mormone, E. Russo Ermolli. Restoring of timber structures: connections with timber pegs. D. D'Ayala and E. Fodde eds. 6th *International Conference on Structural Analysis of Historic Construction*, Bath, England, July 2-4, 2008.
- [22] C. Ceraldi, C. D'Ambra, M. Lippiello, A. Prota. The Influence of Dowel-Bearing Strength in Designing Timber Pegged Timber Joints. *International Journal of Architectural Heritage*, **12**, 3362-375, 2018.
- [23] I. Teodorescu, B. Pereira, C.D. Aquino, J.M. Branco. Experimental evaluation of dowel-type timber joints with wooden dowels. *Proceedings of the Institution of Civil Engineers – Structures and Buildings*, <https://doi.org/10.1680/jstbu.20.00021>.
- [24] R.J. Schmidt. Timber Pegs – Considerations for Mortise and Tenon Joint Design. *Structural Magazine*, **3**, 44-47, 2006.
- [25] J.F. Miller, R.J. Schmidt, W.M. Bulleit. New Yield Model for Wood Dowel Connections. *Journal of Structural Engineering*, **10**, 1255-126, 2010.
- [26] R.J. Schmidt, G.F. Scholl. Load Duration and Seasoning Effects on Mortise and Tenon Joints. *Research Report*, University of Wyoming, Dep. of Civil and Architectural Eng, 2000.
- [27] C. Ceraldi, M. Lippiello, E. Russo Ermolli. Connections with timber pins: the influence of dowel-bearing strength. *Proceedings of International Conference on Structural Health Assessment of Timber Structures*, Lisbon, June 16-17, 2011.
- [28] C. Ceraldi, C. D'Ambra, M. Lippiello, A. Prota. The Influence of Dowel-Bearing Strength in Designing Timber Pegged Timber Joints. K. Van Balen and E. Verstrynghe eds. 10th *International Conference on Structural Analysis of Historic Construction*, Leuven, Belgium, September 13–15, 2016.
- [29] R.J. Schmidt, J.F. Miller. Capacity of Pegged Mortise and Tenon Joinery. *Research Report*, University of Wyoming, Dep. of Civil and Architectural Eng, 2004.
- [30] C. Ceraldi, M. Lippiello, E. Russo Ermolli. Timber pins connections: reliability of bolted joints design rules. J. Jasieński ed. 8th *International Conference on Structural Analysis of Historic Construction*, Wrocław, Poland, October 15-17, 2012.
- [31] C. Ceraldi, C. D'Ambra, M. Lippiello, A. Prota. Restoring of timber structures: connections with timber pegs. *European Journal of Wood and Wood Products*, **75**(6), 957-971, 2017.
- [32] J. Milch, J. Tippner, M. Brabec, V. Sebera. Experimental Verification of Numerical Model of Single and Double-Shear Dowel-Type Joints in Wood. H. M. Barnes and V. L.

- Herian eds. *57th International Convention of Society of Wood Science and Technology*. Zvolen Slovakia Technical University, 2014.
- [33] A. Jorissen, M. Fragiaco. General notes on ductility in timber structures. *Engineering Structures*, **33**, 2987-2997, 2011.
- [34] K. A. Malo, J. Siem, P. Ellingsbø. Quantifying ductility in timber structures. *Engineering Structures*, **33**, 2998-3006, 2011.
- [35] H. J. Blaß, P. Schädle. Ductility aspects of reinforced and non-reinforced timber joints. *Engineering Structures*, **33**, 3018-3026, 2011.
- [36] EN 12512-2001: Timber structures – test methods-cyclic testing of joints made with mechanical fasteners.
- [37] SIA 265:2012 Holzbau. Schweizerischer Ingenieur-und Architektenverein, 2012.
- [38] ASTM D 5764 – 97a: Standard Test Method for Evaluating Dowel-Bearing Strength of Wood and Wood-Based Products. ASTM International.
- [39] E. Karacabeyli, A. Ceccotti. Nailed Wood-Frame Shear Walls for Seismic Loads: Test Results and Design Considerations. *Proceedings, Structural Engineering World Wide*, Paper Reference T207-6, 1-9, 1999.
- [40] M. Yasumura, N. Kawai N. Estimating seismic performance of Wood-framed structures. *Proceedings of 5th World Conference on Timber Engineering*, **2**, 564-571, 1998.
- [41] C. G. Foliente. Issues in seismic performance testing and evaluation of timber structural systems. *International Wood Engineering Conference*, October 28-31, New Orleans, USA, 1996.

IMPACT OF RETROFIT OF RC FRAMES BY CLT PANELS AND FRICTION DAMPERS

F. Barbagallo¹, G. Margani¹, E.M. Marino¹, A. Moretti², C. Tardo¹

¹ Department of Civil Engineering and Architecture, University of Catania,
Via S. Sofia 64, 95125 Catania, Italy
e-mail: fbarbaga@dica.unict.it, margani@unict.it, emarino@dica.unict.it, carola.tardo@unict.it

² Advenco s.r.l.,
Via Monte Guglielmo 61, 25060 Cogozzo di Villa Carcina (BS), Italy
e-mail: alberto@advenco.com

Abstract

In Italy, as well as in other earthquake-prone countries, most buildings have been erected without considering the effects of seismic excitation or according to obsolete seismic design provisions. Furthermore, they also suffer from significant structural deficiencies because of the low mechanical characteristics or the natural decay of the materials. The seismic vulnerability of the existing building stock is a serious economic and social concern and the need for retrofitting or rebuilding grows as time progresses. In this framework, this study investigates a newly developed retrofit technique for buildings with RC framed structure. The intervention is realized by means of Cross-Laminated Timber (CLT) panels placed over the exterior walls and connected to the RC structure by friction dampers. The CLT panels provide the existing structure with additional lateral stiffness and strength. The role of the friction dampers is twofold. On one hand they cap the internal forces of CLT panels, thus controlling the reaction forces transmitted to the existing structure and avoiding the failure of CLT panels themselves. On the other, friction dampers dissipate part of the input earthquake energy. The effect of these multiple features could reduce the storey drifts demanded by the earthquake to values compatible with the structure capacity. This paper aims at sounding the impact of the proposed retrofit solution on the response of the RC framed structure to be upgraded. To this end, a one storey RC frame representative of existing RC framed structures designed considering only gravity loads is upgraded by a CLT panel and friction dampers of usual size. The impact of the retrofit intervention is investigated in terms of the achieved increase of stiffness, strength and energy dissipation capacity. The bare RC frame and the frame equipped with CLT panel and friction dampers are modelled in OpenSEES environment. Hence, the nonlinear responses of the two frames are assessed by monotonic and cyclic pushover analyses and the comparison between the results obtained for the bare and the upgraded frame quantifies the expected impact of the proposed retrofit intervention.

Keywords: Existing buildings, RC framed structure, seismic retrofit, CLT, friction dampers.

1 INTRODUCTION

In European seismic countries – such as Italy, Greece, Bulgaria, Turkey, Romania and the Balkan peninsula [1] – the building stock designed without anti-seismic criteria or according to old seismic standards is extremely wide, including mainly masonry or Reinforced Concrete (RC) framed buildings. For instance, in Italy, over 55% of the existing residential buildings was built before the 1970s [2], when seismic regulations were not in force and only gravity loads were considered at the design stage. Moreover, these buildings are over 50 years old, which means that they have reached their nominal service life, exhibiting structural deficiencies mainly due to the naturally decay of the materials originally used.

In this framework, seismic upgrading of the existing buildings is strongly needed, in order to ensure a higher level of safety for inhabitants, meanwhile to reduce the economic losses and environmental harm which could be caused by the damage or collapse of buildings in the event of earthquakes.

With reference to RC framed structures, the current seismic upgrading techniques are aimed at increasing the strength, stiffness, and ductility capacity of the structure and/or reducing the seismic demand. The most common techniques include the strengthening of the existing structural members by traditional materials (i.e. steel, concrete) or innovative ones (fibre-reinforced polymer, textile-reinforced mortar), as well as the addition of new RC shear walls or steel-braced frames. Other techniques include the installation of base isolators or energy dissipation devices. The main drawbacks that limit the wide applicability of these techniques are the excessive costs and time for implementation as well as the high occupants' disturbance. In fact, common strengthening techniques require the temporary downtime of the building and considerable demolition and reconstruction actions, which may affect up to 70-75% of the total construction costs in a new building [3]. Instead, the addition of a new seismic-resistant system requires relevant enlargements and reinforcement of the foundations and is not always possible if located externally to the building.

In order to overcome these drawbacks, newly seismic retrofit techniques need to be investigated, which can be able to meet the current needs of cost-effectiveness, quick installation and reduced users' disturbance. To this purpose, the use of Cross Laminated Timber (CLT) has been recently investigated as an alternative and sustainable solution to increase the seismic performance of the existing buildings, thanks to its high mechanical performance [4]. CLT is a plate-like engineered timber product, commonly composed of an uneven number of timber board layers, which are arranged crosswise to each other at an angle of 90° and quasi rigidly connected by adhesive bonding. The crosswise build-up provides the material high capacity of bearing loads both in-plane and out-of-plane, allowing its use for structural purpose [5].

Strengthening technique based on coupling the infill outer walls of the existing RC framed buildings by CLT panels has been investigated by Sustersic e Dujic [6-7], in view of an integrated retrofitting approach aimed also at increasing the energy efficiency of the buildings. Specifically, they proposed to realize the connection between the panels and the structure through special steel brackets, provided of ductility and energy dissipation capacity. The external application of CLT panels has been recently investigated also within the AdESA project [8], resulting in a real application on a case study characterized by a prefabricated RC structure. Stazi et al. [9] proposed CLT shear walls in replacement of the existing masonry infill walls. In particular, the results of preliminary numerical studies proved that CLT infills allows the RC frame to reach higher lateral stiffness and peak load values compared to common masonry infills. CLT infilled shear walls have been also analysed by Haba et al. [10], who investigated narrow CLT elements bonded to each other and onto the RC frame with epoxy resin, with po-

tential results in terms of stiffness and ductility capacity according to the experimental activities conducted. Then, the use of post-tensioned, dissipative, and re-centering rocking CLT walls located in the external perimeter of the building has been investigated by Sandoli et al. [11]. In this work, nonlinear analyses on a case study showed the considerable effectiveness of this intervention in terms of seismic capacity increase, even using a small number of CLT walls with limited size.

The research on the topic of seismic upgrading of RC frame structures through strengthening CLT panels is still ongoing, and further studies are needed. Additional investigations on connection systems between the CLT panels and the existing structure are also required, in order to make this renovation solution concretely and widely applicable [12]. In this framework, this study investigates an innovative seismic retrofit technology (named e-CLT) for RC framed buildings based on the use of CLT panels placed over the exterior walls and connected to the structure by means of friction dampers [13]. This solution is currently under development within the ongoing multidisciplinary Horizon 2020 innovation project, called e-SAFE (energy and Seismic AFFordable rEnovation solutions), aimed at investigating innovative and combinable integrated retrofitting interventions. In this work, the impact of the e-CLT retrofit intervention on the response of the RC framed building structures is investigated, referring to existing structures designed considering only gravity loads. In the following sections, first the proposed retrofitting system is presented focusing on its components, mechanics, and installation. Hence, a RC frame is designed according to old building regulations and from this a set of single-storey frames with and without e-CLT is derived. The aim is to analyse the seismic response of RC frames upgraded by the e-CLT system, considering the number of CLT panels and friction dampers applied, as well as the contribution/presence of infill walls.

2 SEISMIC UPGRADING BY e-CLT SYSTEM

The e-CLT system is aimed at reducing the drifts demanded by earthquakes and improving the seismic performance of the building for the expected levels of seismic excitation. It consists in the application of CLT panels on the outer side of the existing walls, by connecting them to the RC structure through friction dampers (Figure 1a). The system is conceived so that in occurrence of moderate ground motions, the dampers rigidly connect CLT panels to the RC structure, thus making available additional lateral stiffness and strength that reduce drifts and may protect non-structural elements. Conversely, dampers activate in occurrence of stronger ground motions, thus dissipating part of the input seismic energy. This further resource of the system activated at this seismic excitation level, after cracking of non-structural elements, reduces the damage of structural components and protect the building from collapse. Furthermore, the activation of the dampers defines an upper bound to the force sustained by the CLT panels, thus preventing their failure even under strong ground motions. The installation of CLT panels from the outside of the building minimizes the occupants' disturbance, while maintaining the building operativity.

The mechanical characterization of the proposed friction damper is currently under investigation within the e-SAFE project [14]. The damper is basically made by two steel profiles, which connect the CLT panels of two consecutive floors to the existing interposed RC beam (Figure 1a). One profile (named "anchor profile") is connected to the RC beam by anchor bolts and to the other profile (named "free profile") by slotted holes and pretensioned high-strength bolts. Common timber screws connect both the steel profiles to the CLT panels. The shear force is transmitted from the free to the anchor profile by means of the friction exerted in the contact surface. During an earthquake, when the force transmitted by the damper attains the value

of the friction force, the free profile slides on the anchor one and thus dissipates seismic energy (Figure 1b).

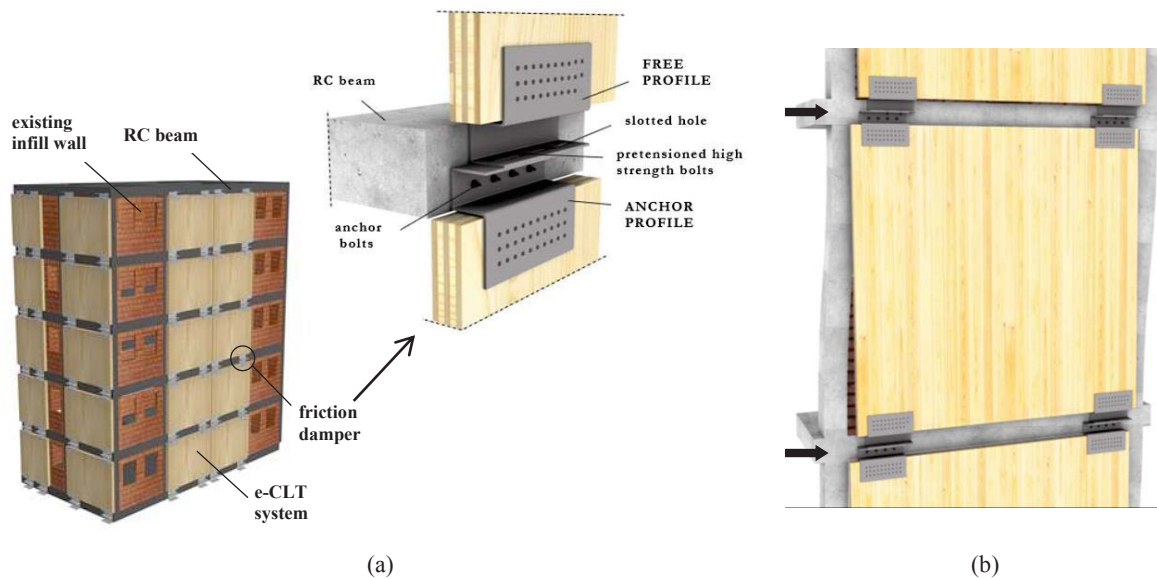


Figure 1: (a) e-CLT system and (b) behaviour of e-CLT system under seismic loads

The e-CLT system is designed also to allow a quick and easy external installation, which can be performed by means of a mobile lifting equipment (cranes, aerial platforms, etc.), proceeding to apply panels from the ground floor to the top of the building. In particular, the anchor profiles of each damper can be pre-assembled on the top of CLT panels off-site, in order to connect directly the panels to the existing RC beams through chemical anchors.

Moreover, the e-CLT system is designed to be combined with energy-efficient solutions, in view of an integrated (seismic and energy) approach to the buildings renovation. More details can be found in [15].

3 CASE STUDY

The case study is a one storey, three-bay RC frame having net height and net width of 3.2 m and 11.1 m, respectively. The columns have cross-section of 30x30 cm and are reinforced by four rebars with diameter of 14 mm, while the beams have cross-section of 30x50 cm and are reinforced by nine rebars with the 14 mm diameter. Both columns and beams have been designed according to the regulations in force in Italy during the 1970s, as well as the construction practices of that period. In particular, the cross-sections size and the steel reinforcements area of the frame members have been designed by means of the allowable stress method [16], considering gravity loads only. Columns have been designed to resist only to axial force, that was evaluated on the assumption of a 4-storey RC frame.

Steel grade Feb38K with a characteristic yield stress $f_{yk}=375$ MPa is assumed for rebars, while the characteristic compressive cubic strength R_{ck} of concrete is assumed equal to 20 MPa (corresponding to cylinder strength f_{ck} equal to 17 MPa).

The case study frame has been analysed considering both the bare and the infilled configuration. Specifically, the infill wall has been assumed made of two leaves of hollow clay bricks (8-cm and 12-cm thick, internally and externally respectively, with an intermediate air cavity), according to the construction techniques used in Southern Italy between the 1950s and 1980s.

Window openings in the infill walls have been considered according to two layouts. In the first and the second layout, openings are assumed in the two lateral bays and in the central one, respectively.

The impact of the e-CLT system on the seismic response of both bare and infilled case study frame has been investigated, considering two different configurations of the seismic retrofit system (configurations 1 and 2 in Figure 2). Specifically, configuration 1 (Figures 2a, c) involves the application of a single CLT panel to the central bay of the frame, while in configuration 2 (Figures 2b, d) the RC frame is retrofitted by 2 CLT panels applied to the lateral bays of the frame.

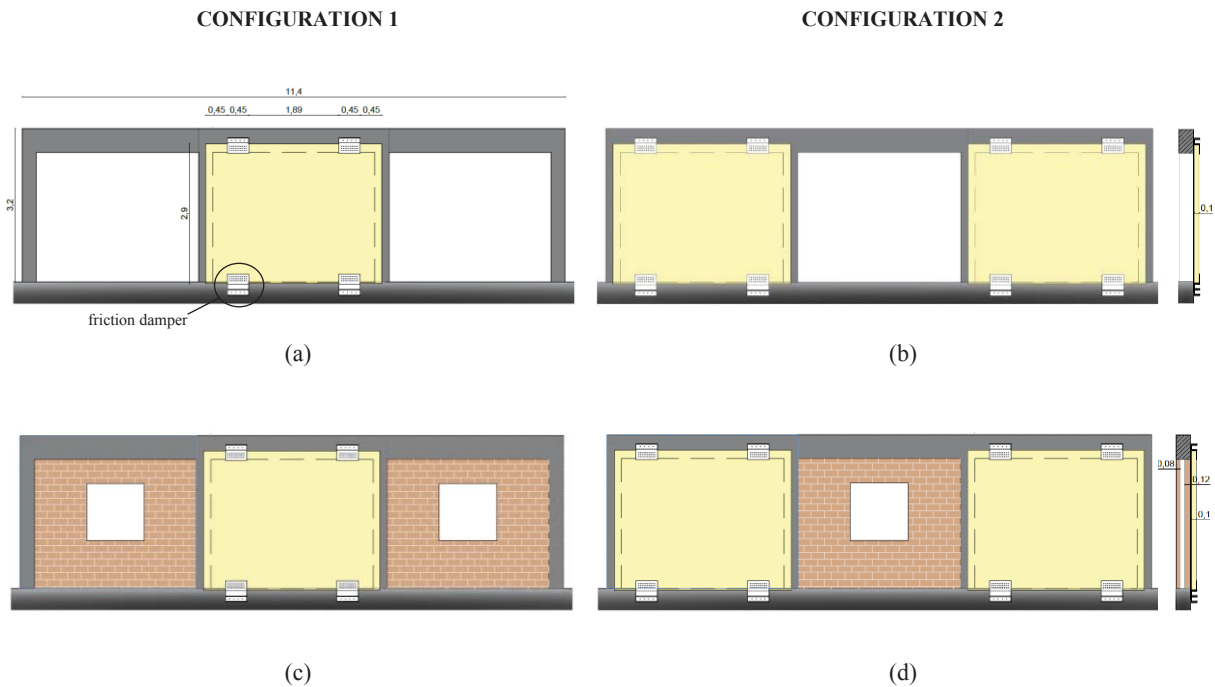


Figure 2: Investigated configurations of the e-CLT retrofitting intervention on the case study frame: (a) bare and (c) infilled frame with e-CLT in configuration 1; (b) bare and (d) infilled frame with e-CLT in configuration 2.

In both configurations, 10-cm thick, 3-ply CLT panels made of C24-class boards are assumed. Each CLT panel is 2.9-m high and 3.7-m wide and is connected to the RC beam by means of two anchor profiles arranged on its top. Two friction dampers connect the bottom of each CLT panel to the foundation of the RC frame. The friction dampers are 450-mm wide and 8-mm thick and are arranged symmetrically each other, at a distance of 0.45 m from the side edge of the panel.

4 NUMERICAL MODELLING

A numerical model has been implemented in OpenSees environment, in order to analyse the nonlinear response of the investigated RC frame at pre- and post-intervention state, considering the configurations described in Section 3.

Figure 3 shows the numerical model schema, referring to a single infilled bay of the case study frame, equipped with CLT panel and friction dampers. The detailed description of the parts the numerical model (RC frame, CLT panel, friction damper and infill) is reported in the following Sections.

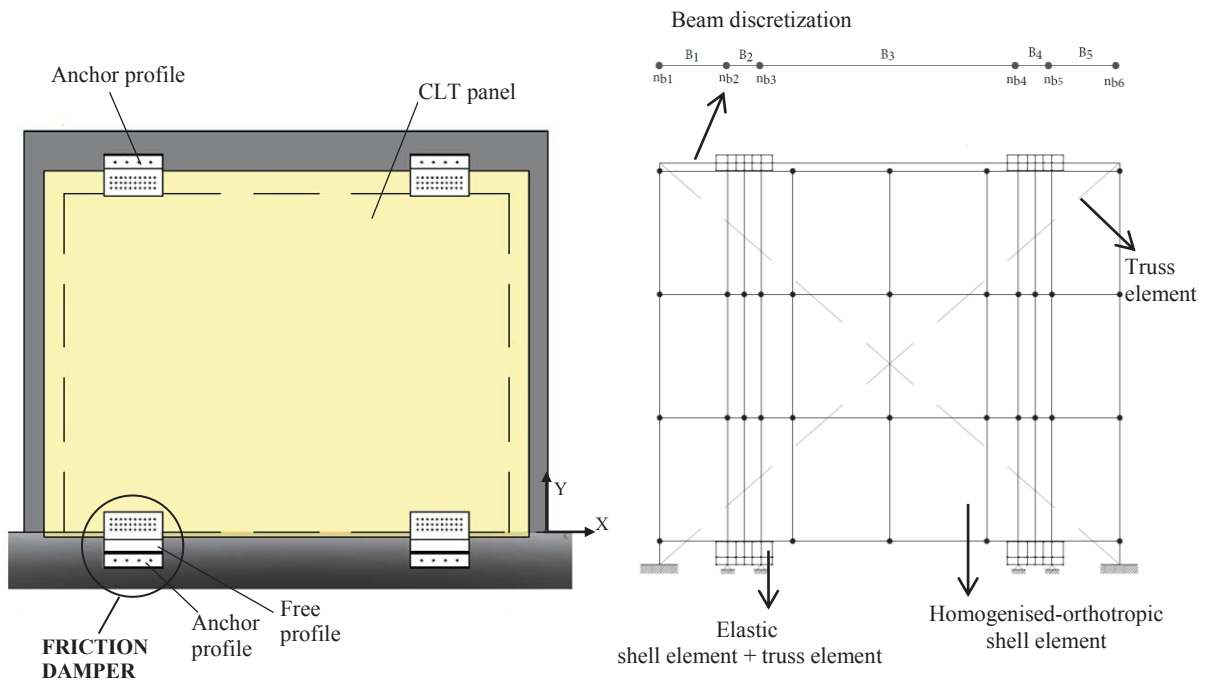


Figure 3: Numerical model schema, referring to a single infilled bay of the case study frame at post-intervention state.

4.1 RC frame

Beams and columns of the RC frame have been modelled differently. Specifically, the “beamWithHinges Element” is used for columns. This element consists in a member with a linear-elastic region in the middle and plastic hinges at its ends. The length of the plastic hinges is equal to the depth of the column cross section. Instead, beams where the CLT panels are fixed at post-intervention state are discretized in five elements (elements B₁-B₅ in Figure 3). The intent was to locate along each beam four intermediate nodes (nodes nb₂, nb₃, nb₄ and nb₅ in Figure 3) to connect the beam and the two anchor profiles. The two lateral beam portions (elements B₁ and B₅) and the central one (element B₃) are modelled by the “nonlinear-BeamColumn Element”, a nonlinear force-based beam-column element able to replicate the spread of plasticity along the member. Three and five Gauss integration points are assigned to the lateral and central portions of the beam, respectively. Whereas, the “elasticBeamColumn Element” is used to model the beam portions B₂ and B₄, assuming that plastic hinges form outside of the damper length. Instead, the beams belonging to the span without CLT panels are modelled by nonlinear force-based beam-column elements, with five Gauss integration points.

A fibre cross section is assigned to each plastic zones of nonlinear RC members, considering both the concrete part and steel rebars. The concrete part is divided into fibres having constant 5-mm depth, to which the Mander constitutive law (“Concrete 04” uniaxial material) is assigned. Instead, single fibres enclosed in the cross section are used to model the steel rebars. In particular, an elastic-plastic material with isotropic strain hardening (“Steel 02” uniaxial material) is assigned to steel rebars. The parameters used for the two materials are summarized in Table 1.

Concrete	
Average compressive strength	25 MPa
Strain at maximum strength	0.002
Strain at crushing strength	0.0035
Young's modulus	31,500 MPa
Rebars	
Average yielding strength	380 MPa
Young's modulus	200,000 MPa

Table 1: Material properties of RC frame members.

4.2 CLT panel

The 3-ply CLT panel (layers thickness: 30-40-30 mm) is modelled as an assembly of 10-cm thick “MITC4 Shell Elements”, as shown in Figure 3. In order to model the multi-layer panel layout, an orthotropic and homogenized material is assigned to the cross section of each shell element, according to the reduced cross section method proposed in [17]. This method is based on the reduction of a multi-layer material into a single-layer one by means of specific composition factors, assuming a plane stress state of the timber panel. This assumption is widely adopted to define the material properties of CLT for the needs of seismic modelling, when building nonlinear behaviour is mostly localized in connections [6,18].

The material properties of the homogenized CLT material are reported in Table 2 and are based on the mechanical characteristics of C24-class spruce wood, according to EN 338 [19]. The value of shear modulus was reduced to 500 MPa since generally CLT panels are not glued on their narrow face. For the same reason, the value of Poisson's ratio has been set equal to 0.0 [20].

CLT	
Perpendicular-to-grain Young's modulus (E_{wx})	4622 MPa
Parallel-to-grain Young's modulus (E_{wy})	6748 MPa
Perpendicular-to-grain Young's modulus (E_{wz})	370 MPa
Shear modulus	500 MPa
Poisson's ratios	0.0
Density	420 kg m ⁻³

Table 2: Material properties of CLT panel.

4.3 Friction damper and connection elements

As shown in Figure 1a, the proposed friction damper is made by two steel profiles (i.e. anchor and free profile), which mainly consist of a middle web and two side flanges. The “ShellMITC4 Element” and the “Truss Element” are used to model both these components. Specifically, the web of each profile is modelled by five 8-mm thick shell elements (Figure 3), while the flanges are modelled by truss elements (8-mm thick and 100-mm depth) which connect the edge nodes of the above-mentioned shell elements. An elastic material is assigned to web and flanges of the steel profiles, assuming that they do not yield. The Young modulus of steel ($E_s=210.000$ MPa) is considered for the assigned material.

A “zeroLength Element” is used to connect the adjacent nodes of the anchor profile and “free profile” of each friction damper. In the X direction, an elasto-plastic material with strain kinematic hardening constitutive law (“Steel01” uniaxial material) is assigned to each element, in order to model the sliding movement of the upper profile when the shear force attains the

value of 30 kN. In the Y direction, two of these elements are characterized by a large stiffness, in order to simulate the pretensioned high strength bolts that connect the two steel profiles.

Then, “Two Node Link Elements” are used to model the connection between the friction damper and CLT panel by means of timber screws. An elastic material is assigned to each element, whose stiffness is calculated in accordance with the Eurocode 5 [21] assuming the use of 30 screws for each damper.

The same modeling is used for the anchor profiles on the top of each CLT panel, using “zeroLength Elements” with large stiffness to connect the web to the RC beams, in order to simulate the connection by means of chemical anchors.

4.4 Infill wall

The infill walls are modelled by a pair of diagonal “Truss Elements”, which connect the top of each column with the bottom of the subsequent one (Figure 3). These elements are supposed to have no tension resistance and their force-displacement relationship is calibrated to replicate the shear force-drift relationship of the infill panel, as proposed by Panagiotakos and Fardis [22] and Celarec et al. [23]. This relationship consists of four branches: a first elastic branch up to the first cracking of panel, a second branch with a lower stiffness up to the complete cracking of panel, a degrading branch and a last branch with a residual resistance. The stiffness and the value of the maximum force of each branch are determined according to the equations proposed in [23]. The multi-linear force-displacement relationship thus obtained is then converted into an equivalent stress-strain relationship. The values of stress and strain corresponding to the three corners of the envelope are assigned to the truss member by means of the “Hysteretic” uniaxial material implemented in OpenSees. The force-displacement relationship is first determined for the infill without openings assuming that it is 20-cm thick, as reported in Section 3, the shear cracking strength is equal to 0.28 MPa, while Young modulus and shear modulus are equal to 4130 and 1240 MPa, respectively. The ordinates of this force-displacement relationship have been reduced to 50% for the infill with openings. These relationships define a layout of infills with high mechanical properties. Other two infill layouts are defined reducing the ordinates of the force-displacement relationships of the first layout to 80% and 60%, in order to represent infills with lower mechanical properties and/or window openings having larger size.

5 ANALYSES AND RESULTS

Monotonic and cyclic pushover analyses in displacement control have been carried out both on bare and infilled RC frame at pre- and post-intervention state (Figure 4a). First, a vertical load of 292.5 kN has been applied at the top of the two central columns, a vertical load of 146.25 kN at the top of the two lateral ones, and a uniformly distributed load of 26 kN has been applied on each beam. These loads are consistent with those used to design the frame.

The top horizontal displacement corresponding to the near collapse limit state of the bare RC frame is determined by monotonic pushover analysis. In this case, the top horizontal displacement is increased until in one column the chord rotation has attained its ultimate value determined according to Eurocode 8 – part 1-3 [24]. The cyclic pushover analysis is performed for all the considered frames. The applied top horizontal displacement is cycled according to the loading protocol reported in Figure 4b, where the maximum amplitude is equal to the top displacement corresponding to the near collapse limit state of the bare RC frame. The hysteretic responses of bare and infilled frame are shown in Figures 5 and 6, respectively. Specifically, the seismic response of the masonry infilled frame has been investigated assum-

ing the three different levels of quality of masonry infill, i.e. mechanical properties equal to 100%, 80% and 60% of the reference infill defined in Section 4.4.

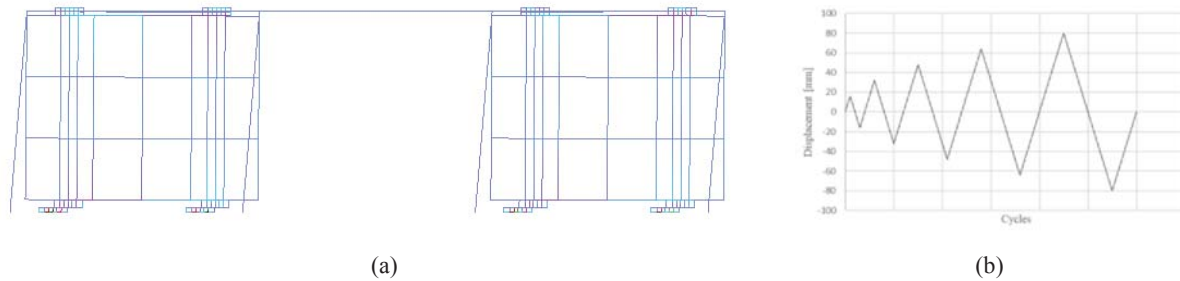


Figure 4: (a) Cyclic pushover analysis on bare RC frame equipped with e-CLT in configuration 2 and (b) cycling loading protocol.

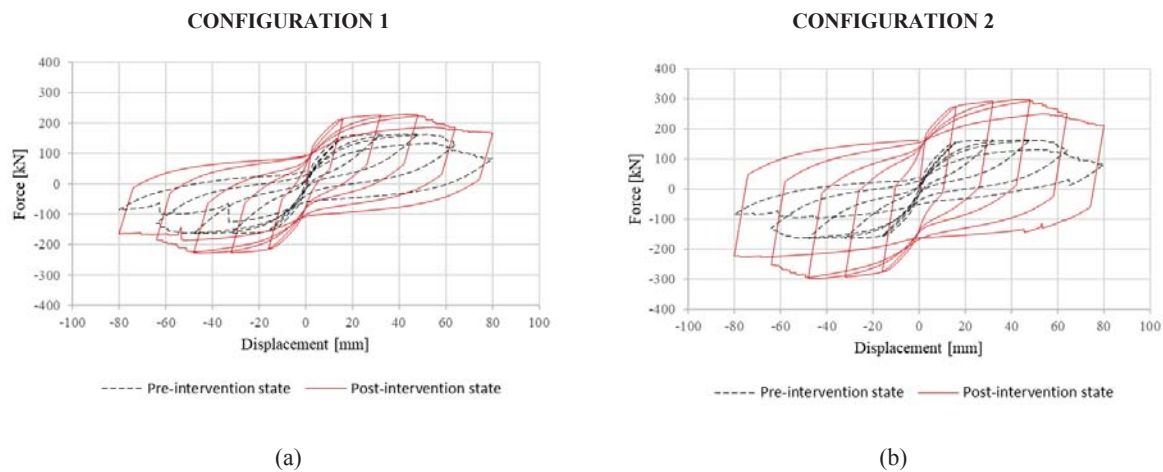


Figure 5: Hysteretic responses of the investigated bare frame at pre- and post-intervention state, with e-CLT system in (a) configuration 1 and (b) configuration 2.

The impact of the retrofit by e-CLT system on the seismic capacity of the case study frames has been investigated in terms of the achieved increase of lateral strength, stiffness, and energy dissipation capacity. The lateral strength is assumed equal to the maximum horizontal force sustained by the system during cyclic loading. The lateral stiffness is calculated as the ratio of the lateral strength to the corresponding displacement. Finally, energy dissipation capacity is quantified as the energy dissipated during cyclic loading, which is calculated as the area enclosed by the hysteresis loops.

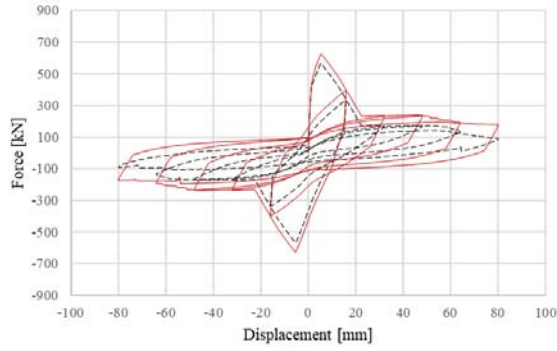
The hysteretic responses of the bare frame at pre- and post-intervention state (Figures 5a, b) show a considerable increase of the seismic capacity after the application of the e-CLT system. In particular, the lateral resistance of the structure upgraded by the e-CLT in configurations 1 and 2 reaches the values of 231 kN and 300 kN. Compared to the lateral strength of 165 kN at pre-intervention state, the achieved percentage increase is 40% and 82% for configurations 1 and 2, respectively. Furthermore, the application of a single CLT panel equipped with two friction dampers (configuration 1) provides the RC frame with an increase of lateral stiffness and energy dissipation capacity of 93% and 128%, respectively. Instead, by adding

two CLT panels and four friction dampers (configuration 2) the stiffness of the structure increases of 165%, while the energy dissipation capacity of 275%.

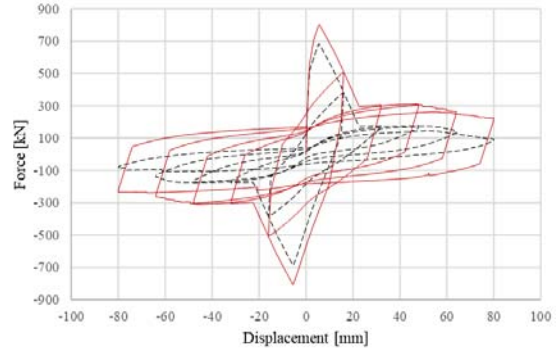
CONFIGURATION 1

CONFIGURATION 2

Values of masonry infill at 100%, high mechanical properties

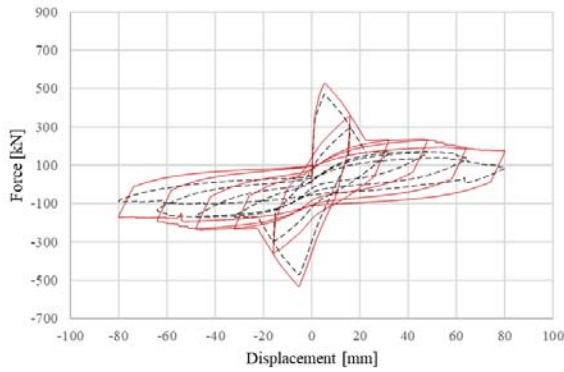


(a)

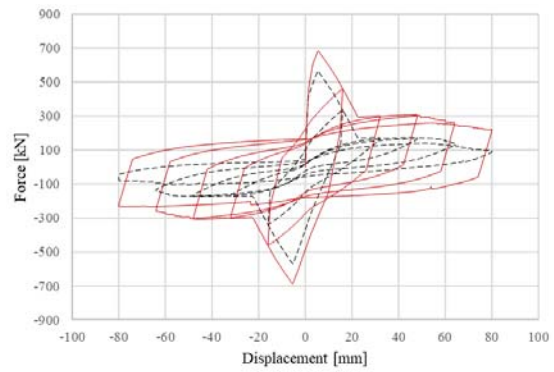


(b)

Values of masonry infill at 80%, intermediate mechanical properties

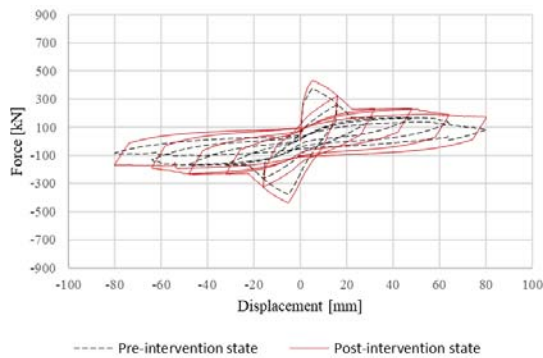


(c)

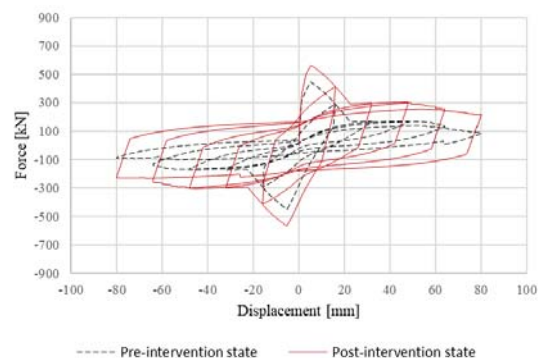


(d)

Values of masonry infill at 60%, low mechanical properties



(e)



(f)

Figure 6: Hysteretic responses of the investigated infilled frame at pre- and post-intervention state, with e-CLT system in (a-c-e) configuration 1 and (b-d-f) configuration 2, assuming the mechanical characteristic values of the masonry infill at: (a,b) 100%; (c,d) 80%; (e,f) 60%.

The impact of the e-CLT system on the capacity of infilled frames (Figure 6) is less remarkable, because the infills make the frame stiffer and stronger, and significantly depends on the capacity parameter. As showed by the comparison of the hysteretic responses of the infilled frame at pre- and post- intervention state, the application of CLT panels determines a negligible increase of the lateral stiffness, regardless of the mechanical properties of infills.

The increase of lateral strength is also low, with higher percentage increase for infills with low mechanical properties (increase of 16% and 26.3% in configuration 1 and 2, respectively). However, the introduction of the e-CLT still leads to a significant increase of the lateral residual strength of the RC frame after the infill failure and even a more remarkable increase of energy dissipation capacity. The percentage increase of lateral residual strength achieved by the retrofit with e-CLT in configuration 1 and 2 is about 38% and 77%, respectively. Finally, the percentage increase of energy dissipation capacity achieved for infills with high, intermediate and low mechanical properties is 82%, 89.5% and 98.5% after the application of the e-CLT in configuration 1 and 146%, 162.7% and 182.6% in configuration 2.

6 CONCLUSIONS

This paper investigates the potential impact of an innovative seismic retrofit technology on the response of RC framed structures. This technology, named e-CLT system, consists in the application of CLT panels on the outer side of the existing walls, by connecting them to the RC structure through innovative friction dampers. The friction damper is still under development and here it is idealised with a connection with rigid-plastic cyclic behaviour. The results reported in this work evidence the potential of the e-CLT system in enhancing the seismic performance of existing RC framed buildings considering different features of the buildings to be upgraded (with and without infill walls) and different importance of the retrofit solution (one or two CLT panels with dampers for the one storey, three-bay RC frame considered as case study).

Even the configuration with the single CLT panel, if applied to the bare RC frame, leads to a significant improvement of all the seismically relevant features of the building: lateral strength, stiffness and energy dissipation capacity. In this case, the largest impact is on energy dissipation capacity. Significant is also the impact on lateral stiffness. However, when the e-CLT system is applied to infilled frames, even considering the solution with two CLT panels, the impact on the lateral stiffness is minor. Instead, the improvement achieved in terms of increase of energy dissipation capacity remains significant: for instance, even in the case of the stiffest and strongest considered infill, it was found equal to 82% and 146% for the configurations with one or two CLT panels, respectively. The increase of lateral strength of the infilled frame provided by the e-CLT system is fair.

Based on these results, the e-CLT system appears to be a promising tool for seismic upgrading of RC framed buildings. Its effectiveness is expected to be great in fulfilling the Near Collapse performance objective, which relies mostly on energy dissipation capacity of the structure. Instead, when the improvement of seismic performance is mainly related to the increase of lateral stiffness, as in the case of damage limitation performance objective, the effectiveness of the e-CLT system could be limited when it is applied to infilled frames. In the future, more comprehensive investigation will be performed, based on the experimental mechanical characterization of the proposed friction damper. Furthermore, the effectiveness of the e-CLT system will be also investigated by multi-storey numerical models.

ACKNOWLEDGEMENTS

This paper was carried out in the framework of the “Energy and seismic affordable renovation solutions” (e-SAFE) project, which has received funding from the European Union's Horizon 2020 research and innovation programme under grant agreement No. 893135. Neither the Executive Agency for Small-and-Medium-sized Enterprises (EASME) nor the European Commission is in any way responsible for any use that may be made of the information it contains

REFERENCES

- [1] Seismic Hazard Harmonization in Europe (SHARE). *European seismic hazard map*. Available online: http://www.share-eu.org/sites/default/files/SHARE_Brochure_public.web_.pdf
- [2] Italian National Statistical Institute (ISTAT). Population Housing 2011 Census. Available online: <http://dati-censimentopopolazione.istat.it/Index.aspx?lang=en&SubSessionId=f51c00689a7d-42c5-abe4-9c3ef54656a0&themetreeid=-200>
- [3] European Commission. *Technology options for earthquake resistant, eco-efficient buildings in Europe: Research needs*. Publications Office of the European Union: Luxembourg: 2014, ISBN 978-92-79-35424-3.
- [4] A. Björnfort, F. Boggian, A. Nygård, R. Tomasi. Strengthening of traditional buildings with slim panels of cross-laminated timber (CLT). 4th international conference on structural health assessment of timber structures (SHATIS'17), Istanbul, 20-22 September, 2017.
- [5] R. Brandner, G. Flatscher, A. Ringhofer, G. Schickhofer, A. Thiel. Cross laminated timber (CLT): overview and development. *Eur. J. Wood Prod.*, **74**, 331–351, 2016.
- [6] I. Sustersic, B. Dujic. Seismic strengthening of existing URM and RC structures using Xlam timber panels. *International conference on Earthquake Engineering*, Skopje, Macedonia, 2013.
- [7] I. Sustersic, B. Dujic. Seismic shaking table testing of a reinforced concrete frame with masonry infill strengthened with cross laminated timber panels. *World Conference on Timber Engineering*, Quebec City, Canada, August 10-14, 2014.
- [8] J. Zanni, S. Cademartori, A. Marini, A. Belleri, E. Giuriani, P. Riva, B. Angi, G. Franchini, A.L. Marchetti, P. Odorizzi, G. Luitprandi. Riquilificazione integrata e sostenibile di edifici esistenti con esoscheletri a guscio prefabbricati: il caso studio AdESA. *Proceedings of Artec Conference - Colloqui.AT.e 2020*, Catania, Italy, 9-12 December 2020 (In Italian).
- [9] F. Stazi, M. Serpilli, G. Maracchini, A. Pavone. An experimental and numerical study on CLT panels used as infill shear walls for RC buildings retrofit. *Constr. Build. Mater.* **211**, 605–616, 2019.
- [10] R. Haba, A. Kitamori, T. Mori, T. Fukuhara, T. Kurihara, H. Isoda. Development of clt panels bond-in method for seismic retrofitting of RC frame structure. *J. Struct. Constr. Eng.* **81**, 1299–1308, 2016 (In Japanese).

- [11] A. Sandoli, M. Pinto, S. Pampanin, B. Calderoni. Protezione sismica di edifici esistenti in c.a. mediante l'utilizzo di pareti lignee post-tese. Proceedings of 17th Conference ANIDIS –L'ingegneria sismica in Italia, Pistoia, Italy, 2017 (In Italian).
- [12] M. Stepinac, I. Sustersic, I. Gavric, V. Rajcic; V. Seismic design of timber buildings: highlighted challenges and future trends. *Appl. Sci.* 10, 1380, 2020.
- [13] G. Margani, G. Evola, C. Tardo, E. M. Marino. Energy, seismic, and architectural renovation of RC framed buildings with prefabricated timber panels. *Sustainability* 12, 12, 4845, 2020.
- [14] C. Tardo, F. Boggian, M. Hatletveit, E. M. Marino, G. Margani, R. Tomasi. Mechanical characterization of energy dissipation devices in retrofit solution of reinforced concrete frames coupled with solid wood panels. *12th International Conference on Structural Analysis of Historical Constructions*, 2020 (in press).
- [15] e-SAFE project (energy and Seismic AFFordable rEnovation solutions) <http://esafe-buildings.eu/en/project/>
- [16] Italian Ministry of Public Works: Ministry Decree, 30/05/1974, Norme tecniche per l'esecuzione delle opere in cemento armato normale e precompresso e per le strutture metalliche (Technical regulations for constructions with reinforced concrete, prestresses concrete and steel structure), *Gazzetta Ufficiale Serie generale*, 29/07/1974, Rome (In Italian).
- [17] H. Blass, P. Fellmoser. Design of solid wood panels with cross layers. *World Conference on Timber Engineering*. Lahti, Finland, June 14-17, 2004.
- [18] M. Fragiaco, B. Dujic, I. Sustersic, Elastic and ductile design of multi-storey cross-lam massive wooden buildings under seismic actions, *Eng. Struct.* 33, 11, 3043–3053, 2011.
- [19] EN 338:2016. Structural timber - Strength classes.
- [20] C. Aranha, J. Branco, P. Lourenço, G. Flatscher, G. Schickhofer. Finite element modelling of the cyclic behaviour of CLT connectors and walls. *World Conference on Timber Engineering*, Vienna, Austria, August 22-25, 2016.
- [21] CEN. Eurocode 5: Design of timber structures. Part 1-1: General – Common rules and rules for buildings. European Committee for Standardization, Brussels; 2004.
- [22] T. B. Panagiotakos, M.N. Fardis, Seismic response of infilled RC frame structures. *11th world conference on earthquake engineering*, Acapulco, Mexico, June 23-28 1996.
- [23] D. Celarec, P. Ricci, M. Dolšek, The sensitivity of seismic response parameters to the uncertain modelling variables of masonry-infilled reinforced concrete frames, *Engineering Structures* 35, 165-177, 2012.
- [24] CEN. Eurocode 8: Design of structures for earthquake resistance. Part 1-3: Assessment and retrofitting of buildings. European Committee for Standardization, Brussels; 2005.

SEISMIC STRENGTHENING OF EXISTING URM STRUCTURES THROUGH CLT ELEMENTS: NUMERICAL ANALYSIS OF THE APPLICATION OF A NOVEL INTERVENTION TECHNIQUE

M. Salvalaggio¹, M. Pegoraro¹, E. Saler², U. Turrini³ and M.R. Valluzzi¹

¹ Department of Cultural Heritage, University of Padova
Piazza Capitaniato 7, 35139 Padova, Italy
matteo.salvalaggio@unipd.it, marco.pegoraro@dicea.unipd.it, mariarosa.valluzzi@unipd.it

² Department of Geosciences, University of Padova
via Gradenigo 6, 35131 Padova, Italy
elisa.saler@unipd.it

³ Department of Civil, Environmental and Architectural Engineering, University of Padova
via Marzolo 9, 35131 Padova, Italy
umberto.turrini@unipd.it

Abstract

The retrofit of existing masonry buildings plays a relevant role in the Italian building context, both for preservation and requalification of the cultural and architectural heritage. Historically, timber has been widely used in unreinforced masonry (URM) buildings, mainly for horizontal structures. In recent years, the use of timber in the retrofit of existing buildings has gained an increasing interest for the improvements of both structural and energetic performances. Indeed, wooden elements present good hygrothermal properties and, thanks to their lightweight and stiffness, they are suitable for the seismic improvement of masonry buildings. The aim of this paper is to numerically investigate the seismic strengthening of existing URM structures by means of cross laminated timber (CLT) panels, evaluating the coupling degree of the timber-masonry integrated system. The investigation was carried out through a finite element modelling. First a parametric local model of a CLT-masonry coupled wall was calibrated with literature experimental data. Then, the study was extended to a XVII-century URM building located in the Italian Alpine region (Roana, Vicenza province). Non-linear static analyses were carried out in order to assess the local and global behavior of the URM-CLT system and its potential benefits. Results suggested a seismic capacity improvement due to shear strength increase and global weight reduction.

Keywords: masonry building, CLT, seismic retrofitting, integrated intervention technique, FEM.

1 INTRODUCTION

The seismic retrofit of existing buildings has gained more and more interest in the Italian context due to the necessity of protecting the cultural and architectural heritage. The great variability of the building typologies and the sustainability requirements lead to the necessity of finding alternative solutions to invasive interventions. As a matter of fact, massive replacements of the wooden floors with RC elements, insertion of RC curbs, etc., within unreinforced masonry (URM) buildings aimed at activating an ideal ‘box-like behavior’, proved to be damaging, by excessively weighing down the structure and leading to local collapses of vulnerable portions of the buildings [1].

These observations led to the need for a more accurate study on the effects of the interventions and the search for innovative methods. Timber structural elements, which were historically used in masonry buildings even for seismic purposes [2][3], present favorable characteristics for some of the problems that characterize conventional reinforcement interventions, such as reduced weight, which permits widespread intervention in the structure with a limited variation of the total seismic mass, and good mechanical properties, often more compatible with URM historical structures. Furthermore, the rapidly evolving of timber technology in recent decades developed more efficient materials, e.g., Cross Laminated Timber - CLT, widening its application field and possibilities.

The intervention described in this paper is addressed to existing URM buildings which need an improvement in terms of structural-seismic capacity, functionality and energetic performances. Based on the effectiveness of URM-CLT coupling walls for shear capacity [4][5] and energetic performances improvement [6], such as the benefits of stiffened timber diaphragms [7][8], an integrated intervention aimed at the insertion of a CLT endoskeleton within a URM structure was designed.

The intervention consists in inserting a CLT structure inside the perimeter walls, substituting the un-strengthened existing floors and inner partitions and assembling a inner core able to bear part of the static and eventual seismic loads. The paper presents the procedure implemented to simulate the intervention. First, a coupled URM-CLT wall was modeled within finite element (FE) software (i.e., DIANA FEA [8]): the model was validated through the comparison with literature studies [10][11] and the influence of FEM parameters involved in the system were evaluated. Following, global models of an existing URM structure and the proposed integrated CLT-URM were created. The CLT nest was designed through a specific software for timber structures ([12]), defining the structural properties such as panel thickness and connection types. Modal and non-linear static analyses were performed, and the results compared.

1.1 State of Art

The CLT technology consists of layered panels of solid timber, in which each layer is oriented perpendicular to adjacent ones. This configuration permits the use of the material for the realization of large boards that can be used for both wall and floor elements, being able to bear both in-plane and out-of-plane loads. Those characteristics make the CLT an efficient and versatile element, which use has spread largely in recent years. CLT products are widely used for new buildings, but in recent years are also gaining attention for the retrofit of existing buildings [4][10][13][14].

One of the most acknowledged intervention consists in coupling CLT panels to masonry walls, thus providing benefits on structural, energetical and architectural fields [6][15]. In this

framework, two main approaches can be adopted, depending on the location of CLT reinforcement panels, at the exterior or interior of walls [4][14], as shown in Figure 1.

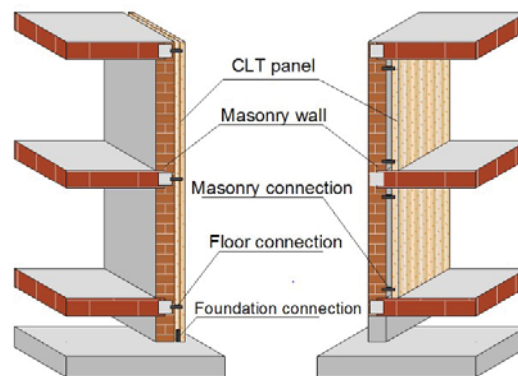


Figure 1: Approaches for CLT intervention on existing structures [6]

Particular attention has to be paid to connection systems among the existing structure and CLT elements. Different approaches can be adopted, such as connection at floor levels, taking advantage of existing RC curbs [14], or distributed URM-to-CLT connections realized with screwed joints [16]. The connection system plays a crucial role in the intervention, having to transmit actions from one system to the other and to provide ductility and resistance. However, studies proved that coupling at floors levels, without specific URM-CLT diffused connectors, is enough for shear and displacement capacities improvement of a URM wall [4].

1.2 Case Study

The case-study belongs to a building system known as “Cattedra”, risen in Canove di Roana (Vicenza), in the North-East Italian Alps. The intervention is limited to this original building which dates back to the XVII century. It's a three-story building with a rectangular plan (10m x 13m)(Figure 2). The structure is composed of stone masonry (SB) walls in the lower section, and hollow clay brick (HCB) masonry in the upper one (due to an elevation intervention), while floor and roof structures are RC based.

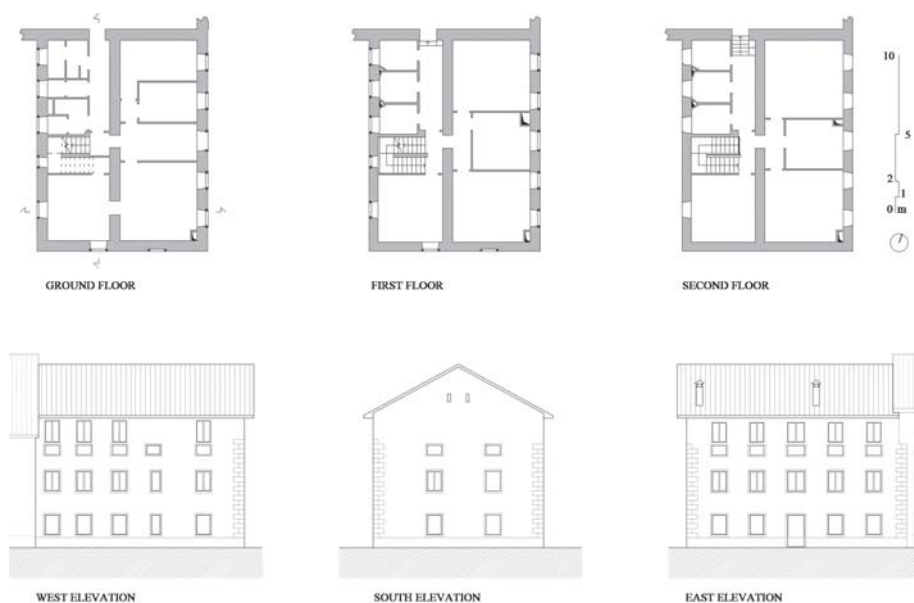


Figure 2: Plans and elevations of the case study.

The intervention concerned the upper stories of the building, excluding the first floor, due to the toned of preserving the existing conditions at this level (Figure 3). Indeed, the intervention consisted of removing the existing floors and roof structures and inserting a CLT nest, connected with the existing URM structure at floor levels. No direct connections were provided between CLT panels and URM walls.

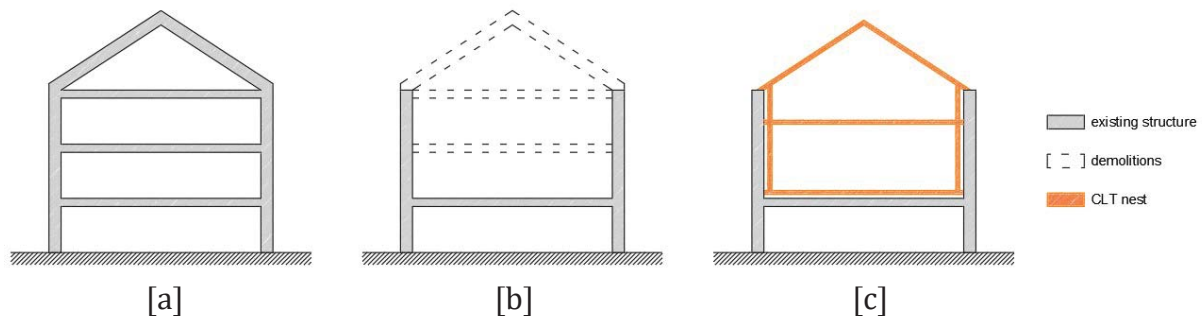


Figure 3: Intervention scheme: a) existing structure, b) demolished parts, c) new CLT nesting structure.

2 COUPLED WALL SIMULATION

The FE modeling of the global structure had to be preceded by the study of a local model, consisting of a 40 cm-thick masonry wall retrofitted with three 6 cm-thick CLT panels (Figure 4). The model was compared and validated with a literature example provided by [10], since the same FE code was used and later subjected to a parametric analysis involving both masonry and CLT systems.

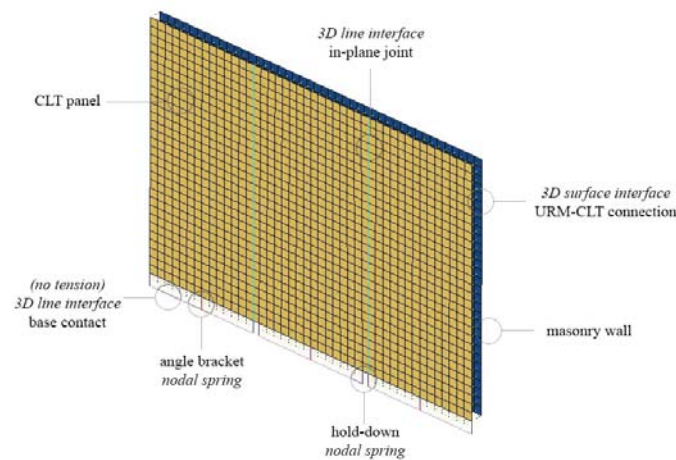


Figure 4: Local FEM model for URM-CLT interaction

2.1 Model Generation

The FEM model was realized with DIANA FEA software [8]. The masonry panel was modeled with 4-noded quadrilateral linear flat shell elements: a macro-modeling approach for material behavior was implemented, and units and mortar properties were merged into a continuum homogeneous material [17]. Physical non-linearities follow the smeared crack approach (*Total Strain Based Crack* in DIANA), in which tensile and compressive behaviors are described by stress-strain curves. Specifically, a linear softening behavior in tension and a parabolic behavior in compression were chosen. CLT panels were modeled with 4-noded quadrilateral linear curved shell. The layered structure of CLT was simplified into a homoge-

neous linear orthotropic material, which elastic properties were calculated according to the analytical approach for composite sections suggested by Eurocode 5 [18]. Table 1 reports the material parameters.

Masonry		CLT	
Elastic Properties		Material Properties	
E	2500 MPa	E_x	9000 MPa
ν	0.25	E_y	4500 MPa
W_{URM}	14 kN/m ³	E_z	1000 MPa
Total Strain Parameters		G_{xy}	821 MPa
f_t	0.01 MPa	G_{xz}	370 MPa
G_t	0.00135 N/mm	G_{yz}	121 MPa
f_c	3 MPa		
G_c	4.8 N/mm		
β	0.01	W_{CLT}	4.5 kN/m ³

Table 1: FEM parameters for masonry and CLT material models (Young's and shear moduli E and G , Poisson's ratio ν , specific weight W , compressive and tensile strength f_c and f_t , compressive and tensile fracture energy G_c and G_t , shear retention factor β).

The panels were externally connected via nodal springs, which represent the tension and shear connections (i.e., hold-down and angle bracket), while 3D line interface elements were introduced to simulate in-plane joints between panels. The CLT panels were connected to the URM wall through 3D surface interface elements. At last, a no-tension non-linear 3D line interface element was modeled, which represents the contact interactions at the base of the panel; this was to simulate base compression and neglect tensile retention during shear loads. Table 2 shows the FE parameters implemented for the connection elements.

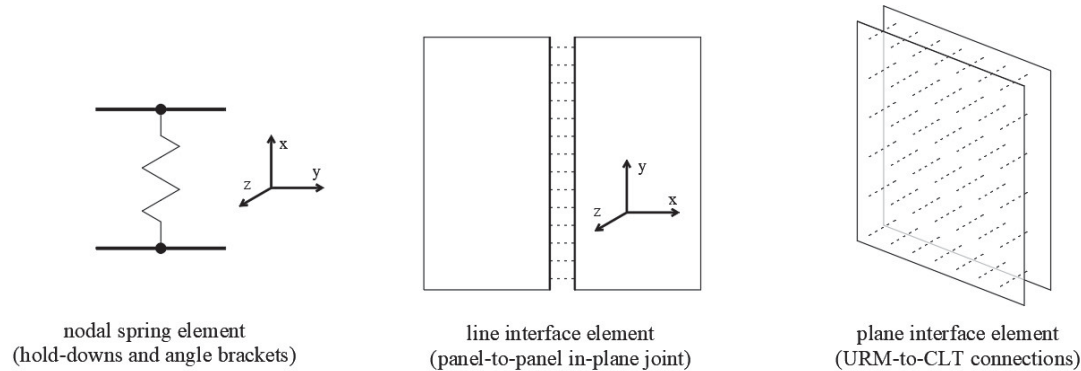


Figure 5: Local reference axes for connection elements in FE model.

Connection	Typology	$k_{s,x}$ [N/mm]	$k_{s,y}$ [N/mm]	$k_{s,z}$ [N/mm]
Hold-down	<i>nodal spring</i>	50000	0	0
Angle brackets	<i>nodal spring</i>	0	50000	50000
		$k_{i,x}$ [N/mm ³]	$k_{i,y}$ [N/mm ³]	$k_{i,z}$ [N/mm ³]
in-plane joints	<i>3D line interface</i>	10	0.16	0.16
URM-CLT connection	<i>3D surface interface</i>	1	0.05	0.05

Table 2: FEM parameters for connections: linear spring stiffness k_s and interface stiffness k_i along x , y and z local axes [4].

Pushover analyses were carried out on the URM wall and on the coupled one to evaluate the in-plane response of both systems.

By comparing the capacity curves (Figure 6), no significant differences can be noticed on the elastic branch [4]; this suggests that, in this phase, the response of the reinforced system was still determined by the masonry characteristics. When cracking occurred, an increase both in post-elastic stiffness (and consequently maximum shear) and in the ultimate displacement capacity was observed in the coupled model. These results suggest that the CLT system is more effective in the masonry damaged conditions, leading to a significant increase of system ductility (almost doubled with the CLT panels reinforcement).

The capacity curves compared to the ones provided by the reference case resulted in a good match both in terms of maximum shear resistance and ultimate displacement capacity was detected.

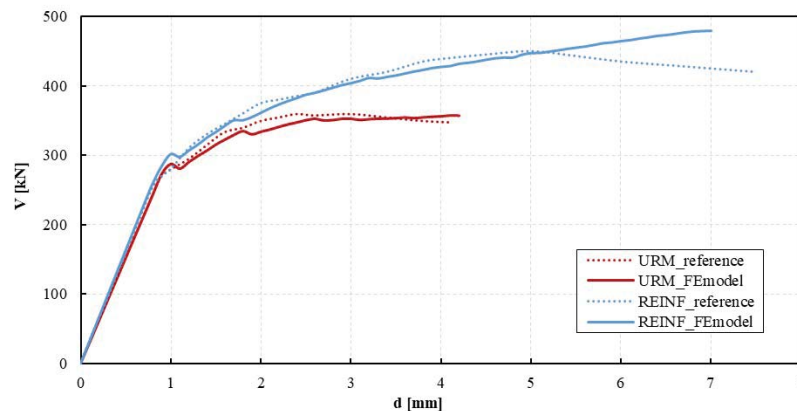


Figure 6: Comparison between FE models of URM and retrofitted walls compared to Giongo et al. [4]

2.2 Parametric Study

A parametric study was performed to assess input parameters and evaluate the incidence of various characteristics on the wall behavior. The investigated parameters involved both masonry and CLT systems, starting from the reference values used in the previously described model. In the *Total Strain Based Crack* model used for masonry, the main uncertainties concern tensile and compressive energy fracture and shear behavior (*rotating crack* and *fixed crack* models); therefore, these parameters were taken in account for the parametric analyses carried out on the URM model (Table 3), which led to the analysis of 9 cases.

			1	2	3
Parameter	G_t [N/mm]	GT	0.012	0.005	0.00135
	G_c [N/mm]	GC	4.8	3.6	2.5
	Shear behavior	S	<i>rotating</i>	<i>fixed</i> $\beta = 0.01$	<i>fixed</i> $\beta = 0.05$

Table 3: Parameters for masonry analyses. Reference parameters cells, used for the previously validated model, are filled in grey.

The obtained pushover curves (Figure 7) revealed that the G_c parameter had low impact on global behavior, presumably because compressive strength of masonry is way higher than tensile one, which play the major role in shear failure. The differences observed for G_t parameter are more evident, as a higher value provided a much higher displacement capacity (+71% on the reference one). An even major influence was noticed for the shear behavior. In particular,

rotating crack model provided a higher ideal yielding point and, consequently, higher shear resistance, while the two fixed crack model curves presented equal elastic branch. However, the higher shear retention factor β led to both higher post-elastic stiffness and ultimate displacement values.

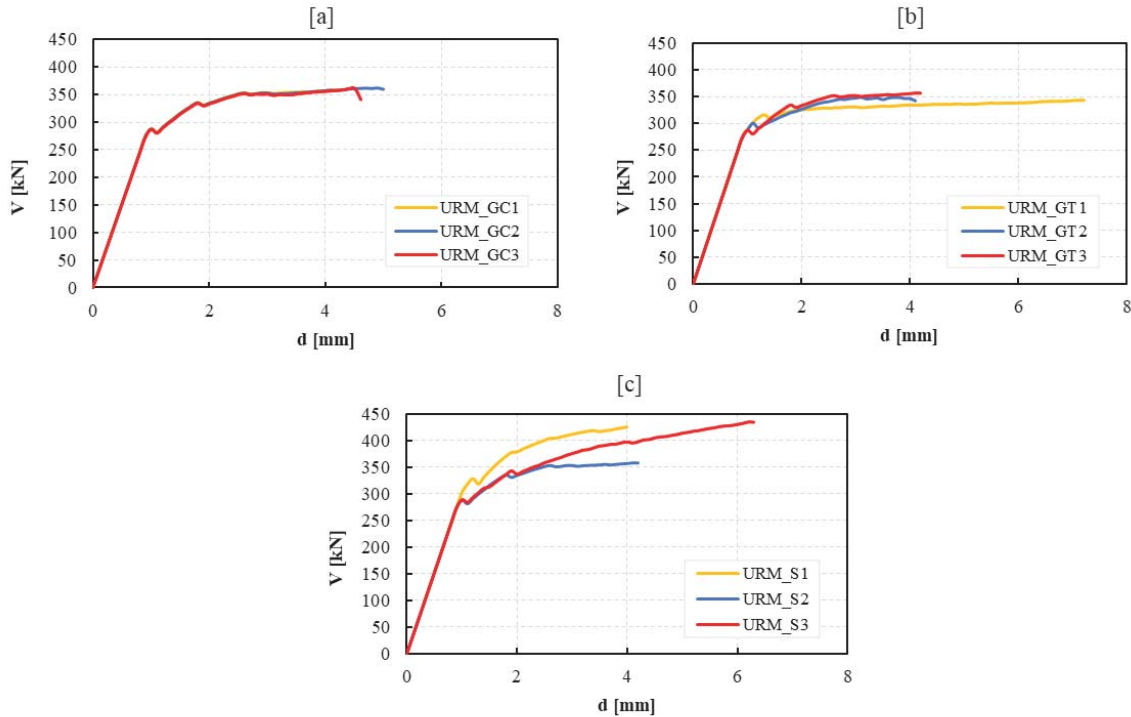


Figure 7: Pushover curves by variation of a) compressive fracture energy G_c , b) tensile fracture energy G_t , and c) shear behavior model

The parameters of the CLT system, i.e., hold-down stiffness, in-plane joints stiffness and panel's thickness (Table 4), were evaluated through 9 cases on the reinforced model.

			1	2	3
Parameter	HD $k_{s,x}$ [N/mm]	HD	10000	20000	50000
	in-plane $k_{i,y}$ [N/mm ³]	K	0.05	0.16	1.5
	panel thickness [mm]	T	60	90	140

Table 4: Parameters for CLT system. Reference parameters cells, used for the previously validate model, are filled in grey.

By comparing the obtained capacity curves (Figure 8), small dissimilarities can be noticed by changing connection type, as both for hold-downs and in-plane joints, with slightly higher shear values reached by the system as elements' stiffness increases. However, differences are not very significant, which suggest that relevant improvements could be achieved by intervening on both connection systems. No major differences were observed with the variation of CLT panel thickness, since the shear behavior of the panel is still ruled by connections in the range of the measured displacements.

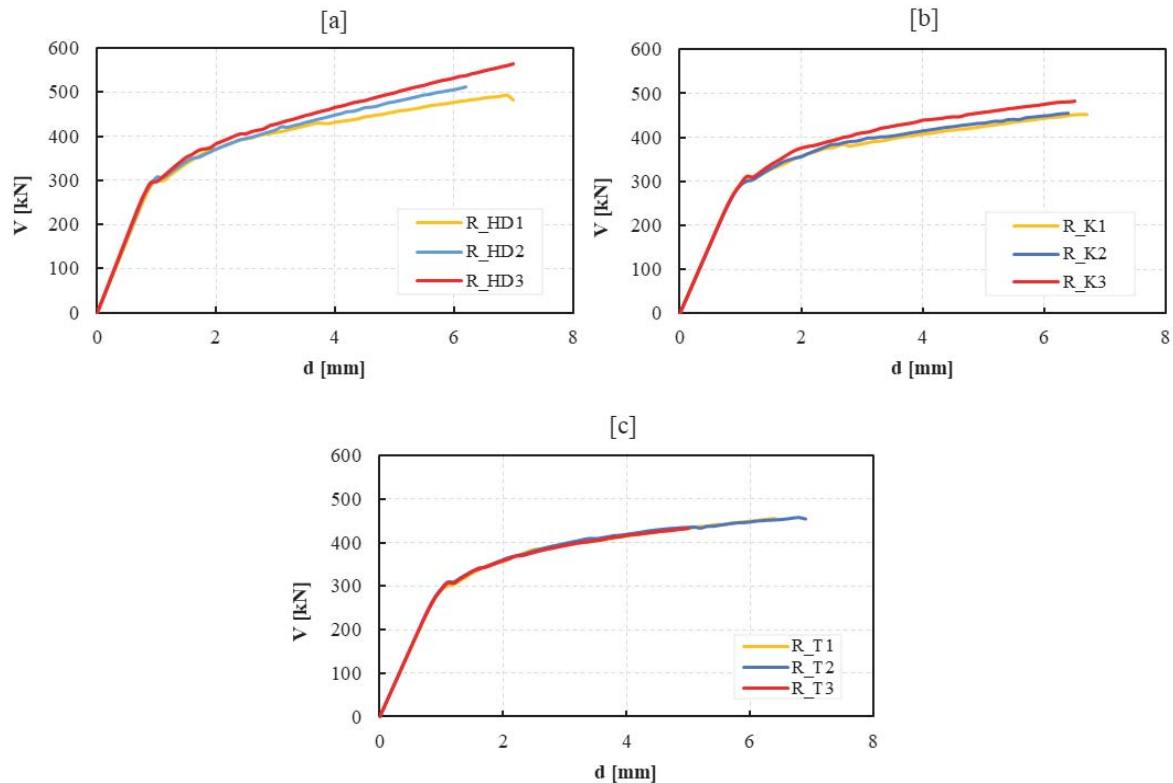


Figure 8: Pushover curves by variation of a) hold-down stiffness, b) in-plane joints stiffness, and c) panel's thickness.

3 MODELING OF THE INTEGRATED INTERVENTION

The extension of the local simulation to a real-scale structure was carried out by assessing a URM case study and then its retrofitted configuration with the endoskeleton integrated solution. FE models within DIANA FEA environment were generated, preceded by the preliminary design and dimensioning of the CLT inner structure.

3.1 Preliminary design of CLT nest

The internal CLT nest was sized by the means of TimberTech Buildings software [12], by assuming the CLT nest as independent from the URM structure. The numerical model was based on the definition of a macro-element for CLT system, which considers the different contributions in deformation and resistance provided by panels and connection elements. The software allows to easily design the structure through pre-defined elements and to verify it by means of linear static and dynamic analyses, for both vertical and horizontal loads. The process led to the definition of three-layered 10 cm panels for walls and five-layered 14 cm and 16 cm panels for the first and the second floor, respectively. Table 5 reports the details of the panels' types.

Element	Material	n. of layers	Thickness [mm]	Layers' thickness [mm]
Walls	Spruce C24	3	100	30 - 40 - 30
First floor	Spruce C24	5	160	40 - 20 - 40 - 20 - 40
Second floor	Spruce C24	5	140	40 - 20 - 20 - 20 - 40

Table 5: CLT panels typology

Tensile and shear connections were sized with reference to the most common commercial typologies. Three types of hold-down and one type of angle bracket were used (Table 6), depending on their location in the structure.

Furthermore, panels were connected through in plane joints, consisting in 6 mm x 80 mm screws, spaced 150 mm and coupled with a 27 mm Laminated Veneer Lumber (LVL) board.

Element	Typology	Connector	n. connectors
HD340	Hold-Down	Nail 4x60mm	20
HD440	Hold-Down	Nail 4x60mm	30
HD540	Hold-Down	Nail 4x60mm	45
AB240	Angle Bracket	Nail 4x60mm	36

Table 6: Hold-down and angle brackets types.

3.2 Global FE model generation

The overall FE study was carried out with DIANA FEA [8]. Firstly, a URM model of the existing structure was created. As in the local model, masonry walls were modeled as 4-noded linear flat shell elements. A *Total Strain Based Crack* material model was chosen, which properties are reported in Table 7. Tensile and compressive strength values were obtained from the Italian seismic code [19][20] following the results of IQM (masonry quality index) analyses carried out for walls [21]. The fracture energy values were chosen by the previous local modal and from multiple values suggested by scientific literature [22], assuming a conservative low tensile fracture energy, close to the brittle behavior.

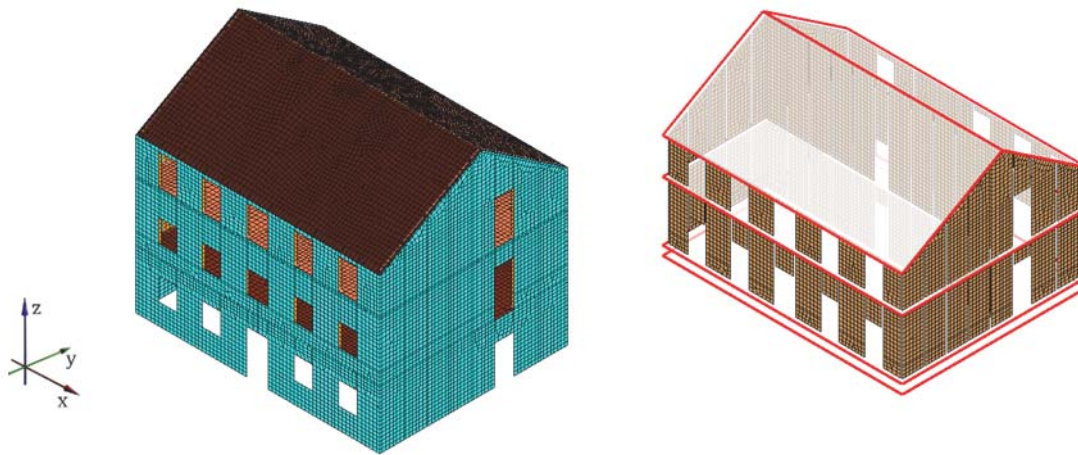


Figure 9: FEM model of a) URM building and b) CLT nest.

Masonry properties of the retrofitted model did not change since no intervention was provided for masonry, in order to assess directly the benefits of the endoskeleton addition. The CLT structure was modeled in reference to the preliminary design. CLT material properties and connection elements were the same of those of the local FE model (Table 1), i.e., nodal springs for hold-downs and angle brackets and linear interface elements for in-plane joints.

Masonry		
Parameter	SB Masonry	HCB Masonry
E [MPa]	1740	4550
ν	0.25	0.25
w [kN/m ³]	20	14
Tens. function	Linear softening	Linear softening
f _t [MPa]	0.018	0.037
G _t [N/mm]	0.00135	0.0045
Comp. function	Parabolic	Parabolic
f _c [MPa]	1.12	1.85
G _c [N/mm]	4.8	5
β	0.01	0.01

Table 7: Mechanical parameter for masonry type (SB: stone blocks; HCB: hollow clay bricks).

The values for the connections' stiffness were analytically identified according to the European regulations for steel-to-timber fasteners and connectors [18]. As the project did not provide for any connection between the masonry walls and the CLT panels, the 3D surface interface elements were not considered, likewise the layout in [4]. At last, non-linearities were located in the masonry material model only.

Modal and pushover analyses were performed on the URM and the URM-CLT models. Uniform loads in both principal directions were considered for pushover analysis.

3.3 Results

The modal analyses results (Table 8) showed an increase in modal frequencies due to nesting intervention, partly due to the decrease of total mass for the reinforced model (about 25%). The modal participation mass factor also decreases to around 65% for the first two bending modes, in each principal direction. This could be due to the difference in terms of masses and stiffnesses distributions generated by the presence of the endoskeleton only at the second and third floors, whereas the first one remained unchanged.

Mode	URM model			Reinforced model		
	f [Hz]	% mx	% my	f [Hz]	% mx	% my
1	6.147	0.00%	75.55%	7.298	0.09%	66.89%
2	8.052	76.15%	0.00%	8.491	65.66%	0.10%
3	9.787	2.21%	0.01%	10.845	0.56%	0.01%

Table 8: Frequencies and mass participation factors for the first three modes: URM and reinforced (URM+CLT) models.

Pushover analyses results were evaluated in terms of equivalent acceleration at the base, thus normalizing the results to the mass of the model to obtain comparable curves (Figure 10). This comparison shows an increase in maximum equivalent acceleration for the retrofitted model. Differences were more pronounced for Y direction analyses than X direction's ones; this suggests that the intervention could be more effective on the shear capacity of the weaker direction. Ultimate displacement capacity does not get significantly affected instead.

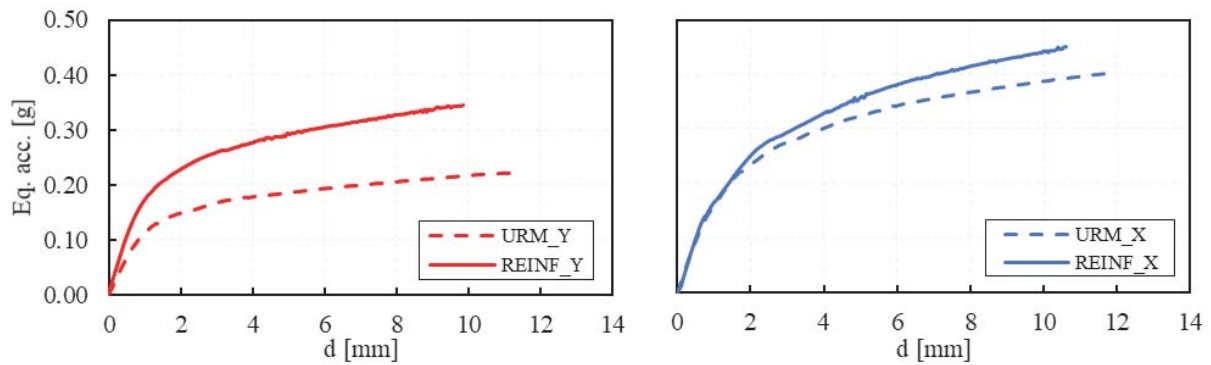


Figure 10: Pushover curves for X e Y directions analyses

Further observations can be made from the contour of tensile strain, where cracks should rise. On the URM model (Figure 11a), damage is mainly located on the piers of the ground floor, while upper levels are less damaged. With the intervention (Figure 11b), the damage involves all stories, thus exploiting the resistant elements along the entire height. Moreover, in the URM model, tensile strains significantly spread in piers and lintels, whereas in the URM-CLT model strains are lumped in piers, i.e., the resistant elements of masonry structures.

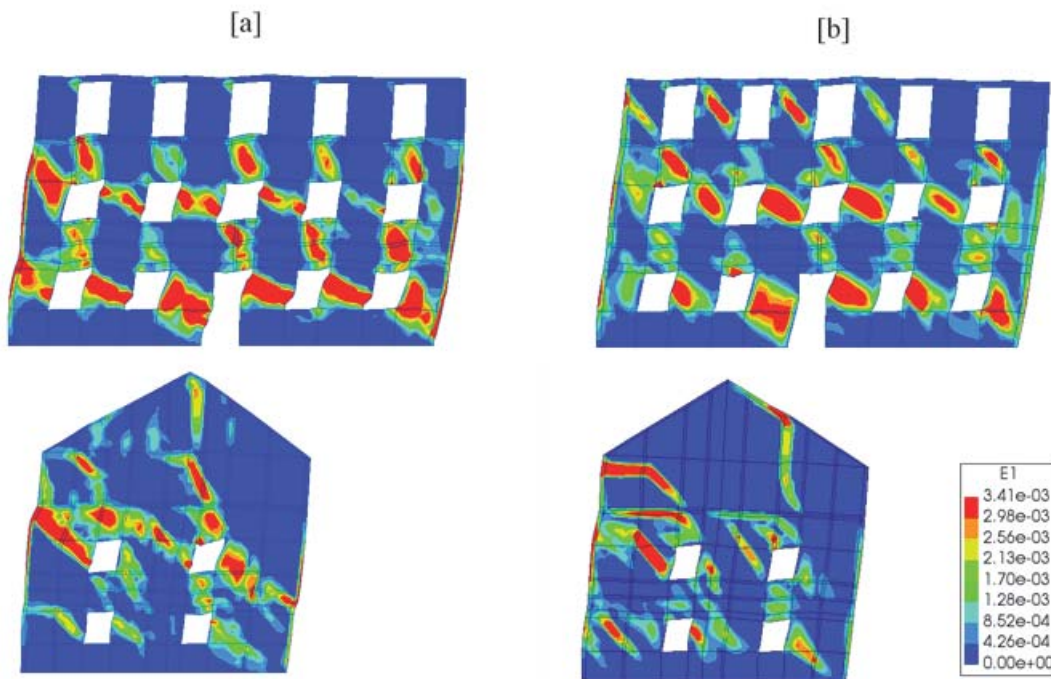


Figure 11: Damage patterns for a) URM and b) retrofitted models.

At last, to measure the intervention benefits, seismic safety verifications were carried out according to the Italian code [19], by comparing PGA (peak ground acceleration) values for derived from the capacity curves. The results showed an improvement on the global behavior of the building thanks to the intervention, with an increase of +8.6% and +19.8% in X and Y directions, respectively (Table 9). Further improvements can be obtained, taking into consideration that, currently: i) the intervention is lumped at second and third stories, whereas the first one is the most solicited by uniform mass distribution and, ii) no improving interventions such as injections or joints rebars were adopted for masonry walls.

Direction	URM	URM+CLT	
	PGA _C [g]	PGA _C [g]	Δ PGA _C [%]
+X	0.222	0.241	8.6%
+Y	0.187	0.224	19.8%

Table 9: Near-collapse PGA capacities (PGA_C) and percentage variation between un-strengthened and retrofitted cases.

4 CONCLUSIONS

The modelling of a novel intervention technique for URM buildings was discussed in this paper. The study was carried out both at local and overall scale. The local model, on which parametric analyses were performed showed that:

- the CLT reinforcement is effective on the post-elastic phase of masonry, when cracking occurs and cause a loss in masonry stiffness;
- the timber connections (i.e., hold-down and angle brackets) play a fundamental role in the effectiveness of the system, since they affect its stiffness more than CLT panel thickness.

The local FE model allowed the connections of timber (both panel-to-panel and floor-to-panel) to be calibrated and to be implemented within a global FE model of an existing URM building. Modal and pushover analyses were carried out, on both as-built and retrofitted models. Results suggested that:

- mass reduction due to substitution of RC floors with lighter timber panels induced the increment in mode frequencies;
- retrofitted configuration can bear a higher equivalent acceleration than as-built one;
- the intervention led to a more homogeneous damage pattern, involving more resistant elements than the un-strengthened case;
- the intervention was effective, taking into consideration that it is limited to the second and third floor (demolition of two RC floors and RC roof), and provided an improvement in terms of PGA_C up to 20%.

The results showed that the CLT endoskeleton proposed here is a promising technique to improve the seismic performances of URM buildings. However, further studies need to be carried out to better clarify the effectiveness of the intervention and to extend its field of application.

ACKNOWLEDGEMENTS

This work was supported by the CORE-WOOD (COmpetitive REpositioning of WOOD sector) Italian project, in the framework of POR-FESR 2014–2020 Line 1 Action 1.1.4 of the Veneto Region.

REFERENCES

- [1] F. Celano, M. Cimmino, O. Coppola, G. Magliulo, P. Salzano, Report dei danni registrati a seguito del terremoto del Centro Italia del 24 Agosto 2016, *Reluis Report (Release 1)*, 2016, [Online]. Available: <http://www.reluis.it>. (in Italian)

- [2] R. Cardoso, M. Lopes, R. Bento, Earthquake Resistant Structures of Portuguese Old ‘Pombalino’ Buildings, *13th World Conference Earthquake Engineering Vancouver, B.C., Canada*, 918, 2004.
- [3] S. Tonna, N. Ruggieri, C. Chesi, Comparison between Two Traditional Earthquake-Proof Solutions: Borbone and Lefkada Timber-Frame Systems, *Journal of Architectural Engineering*, 24, 4, 2018.
- [4] L. Pozza, L. Marchi, D. Trutalli, R. Scotta, In-plane strengthening of masonry buildings with timber panels, *Proceedings of the Institution of Civil Engineers – Structures and Buildings*, 1–15, 2021. <https://doi.org/10.1680/jstbu.19.00121>.
- [5] L. Pozza, F. Evangelista, R. Scotta, CLT used as seismic strengthener for existing masonry walls, *Atti del XVII convegno ANIDIS L’Ingegneria sismica in Italia*, pp. 210–220, 2017.
- [6] M.R. Valluzzi, E. Saler, A. Vignato, M. Salvalaggio, G. Croatto, G. Dorigatti, U. Turrini, Nested buildings: An innovative strategy for the integrated seismic and energy retrofit of existing masonry buildings with CLT panels, *Sustainability* **13**, 1–19, 2021. <https://doi.org/10.3390/su13031188>.
- [7] R. Scotta, D. Trutalli, L. Marchi, L. Pozza, Seismic performance of URM buildings with in-plane non-stiffened and stiffened timber floors, *Engineering Structures*, **167**, 683–694, 2018. <https://doi.org/10.1016/j.engstruct.2018.02.060>.
- [8] TNO Building and Construction Research, *DIANA – Finite Element Analysis User’s Manual - Release 10.4*, 2020
- [9] M. Salvalaggio, L. Sbrogiò, M. Pavanetto, M.R. Valluzzi, Evaluation of the effect of compatible interventions applied to horizontal components of URM buildings with EFM and FEM models. The case of palazzo Carraro in Noale (Italy), *COMPDYN Proc.* 1 (2019) 1472–1481. <https://doi.org/10.7712/120119.7012.19513>.
- [10] I. Giongo, G. Schiro, M. Piazza, On the Use of Timber-Based Panels for the Seismic Retrofit of Masonry Structures, *3rd Int. Conf. on Protection of Historical Construction*, pp. 12–15, 2017.
- [11] S. Churilov, E. Dumova-Jovanoska, In-plane shear behaviour of unreinforced and jacketed brick masonry walls, *Soil Dynamics and Earthquake Engineering*, **50**, 85–105, 2013. <https://doi.org/10.1016/j.soildyn.2013.03.006>.
- [12] TimberTech, *TimberTech Buildings*, ver.77.
- [13] J.M. Branco, M. Kekeliak, P.B. Lourenço, In-plane stiffness of timber floors strengthened with CLT, *Eur. J. Wood Wood Prod.* **73**, 313–323, 2015. <https://doi.org/10.1007/s00107-015-0892-2>.
- [14] I. Sustersic, B. Dujic, Seismic Strengthening of Existing Concrete and Masonry Buildings with Crosslam Timber Panels, *Materials and Joints in Timber Structures*, 713–723, 2014.

- [15] A. Lucchini, E. S. Mazzucchelli, S. Mangialardo, M. Persello, Façadism and Clt Technology : an Innovative System for Masonry Construction Refurbishment, *40th IAHS World Congress Hous.*, December 2014.
- [16] D. Riccadonna, I. Giongo, G. Schiro, E. Rizzi, M. A. Parisi, Experimental shear testing of timber-masonry dry connections for the seismic retrofit of unreinforced masonry shear walls, *Construction and Building Materials*, vol. **211**, 52–72, 2019.
- [17] P. B. Lourenço, “Structural Masonry Analysis: Recent Developments and Prospects,” *J. Chem. Inf. Model.*, vol. 53, no. 2004, p. 160, 2008.
- [18] European Committee for Standardization, “Eurocode 5: Design of Timber Structure” *BSI*, 1994.
- [19] C.S.LL.PP, Circolare 21 gennaio 2019, n. 7, “Circolare applicativa delle nuove Norme Tecniche per le Costruzioni approvate con D.M. 17 gennaio 2018”, 2019. (In Italian)
- [20] Ministero delle Infrastrutture e dei Trasporti, D.M. 17 gennaio 2018, “Aggiornamento delle «Norme tecniche per le Costruzioni»”, 2018. (in Italian)
- [21] A. Borri, A. De Maria, Indice di Qualità Muraria (IQM): correlazione con le caratteristiche meccaniche e livelli di conoscenza, *ReLuis 2015 - Linea Costruzioni in. Muratura*, 45–63, 2015. (in Italian)
- [22] L. Bejarano-Urrego, E. Verstrynge, G. Giardina, K. Van Balen, Crack growth in masonry: Numerical analysis and sensitivity study for discrete and smeared crack modelling, *Engineering Structures*, **165**, 471–485, 2018.

POST-TENSIONED LOW DAMAGE TIMBER WALLS WITH DISSIPATIVE DEVICES BEHAVIOR: NUMERICAL PREDICTION

Valentina Tomei^{1*}, Maria Zucconi¹, and Barbara Ferracuti¹

¹ Department of Engineering “Niccolò Cusano”
via Don Carlo Gnocchi 3, 00166 Rome, Italy
{[valentina.tomei](mailto:valentina.tomei@unicusano.it), [maria.zucconi](mailto:maria.zucconi@unicusano.it), [barbara.ferracuti](mailto:barbara.ferracuti@unicusano.it)}@unicusano.it

Abstract

In the last decades, low-damage post-tensioned technologies have been introduced in the field of timber constructions, with the aim to obtain structural solutions able to guarantee, in case of seismic events, not only the safeguarding of human life, but also the rapid re-use of the buildings without permanent damage. To this aim, structural systems based on rocking dissipative timber walls have been conceived, which rocking behaviour is due to the presence of post-tensioning cables, and the dissipative contribution is provided by steel dampers, easily replaceable after an intense seismic event. The paper presents a numerical non-linear model to predict the response of PT-timber walls, particularly useful to support the design. In particular, the geometrical non-linearity due to the rocking behavior of the walls and material non linearities that characterize the dampers, are specifically taken into account. The post-tensioned systems characterized by the single wall configuration with axial dampers are analyzed by considering different initial post-tensioning levels. The proposed numerical modeling strategy has been validated with experimental literature tests, demonstrating its effectiveness in predicting the behavior of post-tensioned walls subjected to cyclic loads.

Keywords: post-tensioning timber walls, dissipative dampers, numerical modelling.

1 INTRODUCTION

In the last two decades, the employment of timber buildings is increasing in seismic prone areas, thanks to the significant evolution of performances of these constructions against seismic actions, mainly due to the development of new technologies [1]. The most common timber buildings are composed of engineered timber walls, i.e. Cross Laminated Timber (CLT) or Laminated Veneer Lumber (LVL), connected to each other and to the foundation through steel connectors, such as angle-brackets, hold-downs, nails, and screws. During a seismic event, the energy dissipation is mainly devoted to connectors, which could be severely damaged [2-5]. Moreover, both internal and external timber walls are load bearing elements, leading to an excessive use of the material and to the impossibility of moving the internal walls, so their position constitutes an architectural constraint. In order to avoid these drawbacks, low-damage post-tensioned (PT) technologies have been introduced [6], which entrust the energy dissipation to rocking timber walls equipped with dampers, whose main advantages are: the re-centering of walls at the end of the seismic motion, additional energy dissipation, and easy replacement of dampers. Since this system is predominantly employed in seismic prone zones, the assessment of a numerical modelling strategy to predict the cyclic behavior of post-tensioned timber walls assumes significant importance within the structural engineering field. Downstream of this brief discussion, the paper presents numerical models to predict the response of PT-timber walls, particularly useful to support the design. In particular, the geometrical non-linearity due to the partial uplift of the walls and material non-linearities that characterize the dissipaters, are specifically taken into account. The responses in terms of horizontal load-displacement curves and post-tensioning (PT) force-displacement curves are presented. The post-tensioned systems characterized by the single wall configuration with axial dampers are analyzed by considering different initial post-tensioning levels. The proposed numerical modelling strategy has been validated with literature experimental tests, demonstrating its effectiveness in predicting the behavior of post-tensioned walls subjected to cyclic loads.

2 LOW DAMAGE TIMBER SYSTEMS

Low damage timber systems arise from the need to guarantee, in case of a critical seismic event, not only the safeguarding of human life, but also the rapid re-use of the buildings without permanent damage. Laboratory tests and numerical investigations highlight that CLT traditional buildings can resist high intensity seismic actions [7]; however, a high-permanent damage in connection steel elements and on timber panels is generally observed. From these observations comes the idea of conceiving a system able to prevent damage to the load-bearing structural elements. In this regard, low damage timber systems were thought to be constituted of timber elements destined to remain in the elastic field during a seismic event, and steel dampers, destined to be severely damaged and then easily replaced. It deals with rocking dissipative walls, which rocking behaviour is due to the presence of post-tensioning cables placed inside cavities in the wall, fixed at the base and anchored at the top of the wall, while the dissipative contribution is due to steel dampers. The dampers can work as axial dampers, positioned at the base of the walls, and/or shear dampers, i.e. connecting adjacent rocking timber elements along elevation [6, 8–12]. The contribution of post-tensioning cables and steel dampers could be simply recognizable by observing a typical flag-shape force-displacement curve of a post-tensioning wall subjected to cycling loading (Figure 1), in which the bilinear envelope is mainly due to the rocking behaviour, controlled by the post-tensioning cables, and the amplitude of the flag is mainly due to the dissipative contribution of the steel dampers. This system takes inspiration from precast post-tensioned concrete elements that

were firstly developed by Stone et al. [13], and then investigated by Priestley *et al.* [14] within a five-story building.

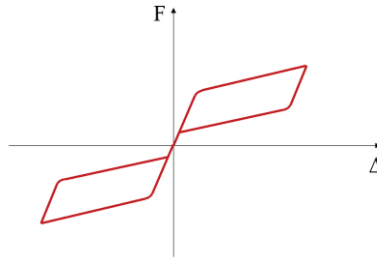


Figure 1: Typical flag-shape force- top displacement (F-Δ) curve of a PT- wall subjected to cycling loading.

To confirm the validity and the growing diffusion of this structural idea, some buildings are recently constructed in New Zealand adopting this innovative solution. Furthermore, it is important to underline that the design of post-tensioned timber buildings is also proposed in the Australian and New Zealand design guidelines [15].

3 LITERATURE EXPERIMENTAL CAMPAIGNS

The firsts experimental campaigns have been performed on Laminated Veneer Lumber (LVL) PT- walls, in reference to single-wall [9] and double [6] systems. In particular, these configurations have been tested with and without dampers to highlight their benefits in terms of dissipative contribution. The dampers employed for the single wall systems are fuse-type dampers [8, 16, 17], which connect the PT wall to the foundation and works along the axial direction. These are characterized by a mild steel round bar placed inside a confining tube, and the space between them is filled with grout or epoxy, which act as a buckling restraint. Instead, the dampers employed for the double-wall systems are U-shape dampers [18, 19] connecting the walls along elevation.

Similarly, Ganey et al. [10] carried out an experimental campaign on single PT- wall systems without damping, and on double walls connected by U-shape dampers, while Massari et al. [11] conducted experimental tests on a single PT-wall system provided by fuse-type dissipaters, but using CLT walls.

Some authors have also proposed a configuration in which the PT- walls are connected to boundary columns by means of dampers [20], ensuring the support to the inter-floor beams connected to the diaphragm. This system avoids the vertical uplift generated by the rocking behaviour that causes vertical displacements incompatible with the diaphragm system, leading to unexpected damage.

In the present paper, the results of the experimental campaign conducted by Sarti et al. [9] was employed to validate the proposed numerical model, which will be presented in the next section. The experimental campaign concerns single wall systems, made of LVL characterized by a modulus of elasticity E_t of 11 GPa. The rocking behavior is entrusted to two post-tensioned steel bars characterized by a diameter of 32 mm, a Young modulus of E_p of 170 GPa, and a yield strength f_{py} of 835 MPa. The dissipative contribution is due to fuse-type dampers characterized by a diameter of 14 mm, a mild steel with a Young modulus of E_s of 200 GPa, and yield stress f_{sy} of 400 MPa. The single wall system has been tested in the various configuration:

- post-tensioned configuration (no dampers), with initial post-tensioning levels of 200 kN, 400 kN, and 600 kN;

- post-tensioned configuration with two couple of fuse-type dampers, with initial post-tensioning levels of 400 kN and 600 kN;
- post-tensioned configuration with four couple of fuse-type dampers, with initial post-tensioning level of 400 kN.

Figure 2 shows the geometric and mechanical characteristics of the experimental setup.

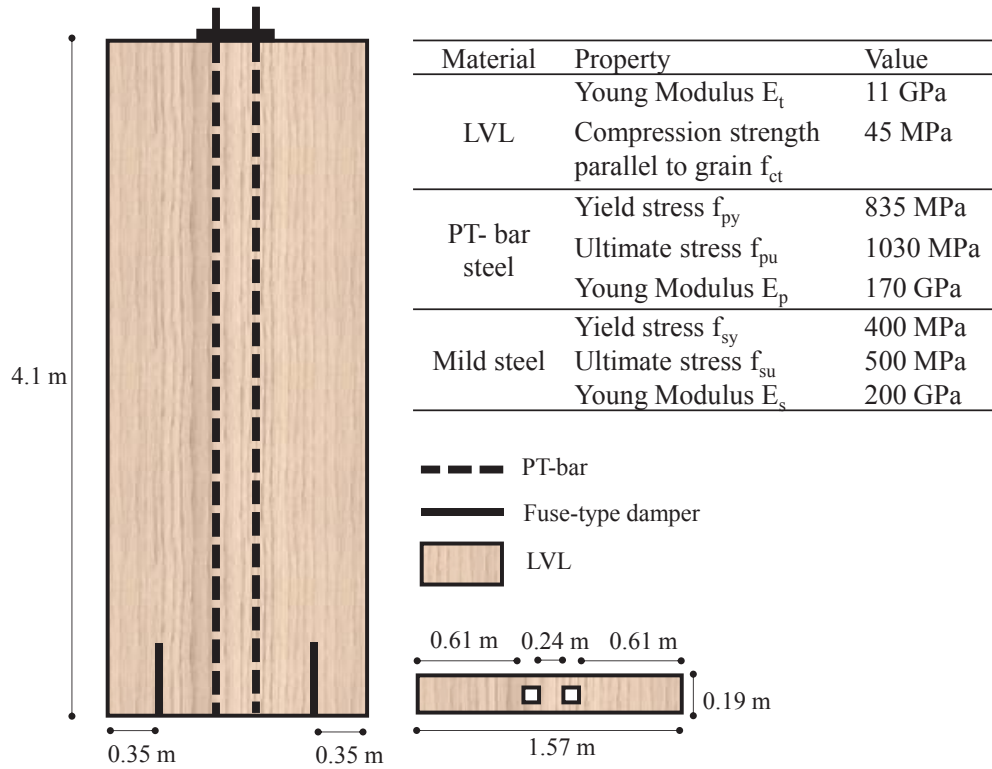


Figure 2: Geometric and mechanical characteristics of the reference experimental setup.

4 NUMERICAL MODELING

In order to predict the response of PT-timber walls, a numerical model was developed, particularly useful to support the design of the described system. The proposed numerical model has been validated on the experimental campaign results conducted by Sarti et al. [9] described in section 3. For the sake of brevity, the comparison between experimental and numerical results will be shown for post-tensioned configurations with two couple of fuse-type dampers, and initial post-tensioning levels of 400 kN and 600 kN.

4.1 Description of the numerical model

The proposed numerical model has been developed in the OpenSees [21], a software framework for simulating the seismic response of structural and geotechnical systems, realized by the Pacific Earthquake Engineering Research Center.

The numerical model of the structural system, shown in Figure 3, accounts for the geometrical and mechanical non-linearities. In particular, the first is due to the rocking behaviour of the system allowed by introducing unilateral constraints at the base, the second is mainly due to the presence of axial dampers simulated by non-linear springs. LVL walls and columns have been schematized with 2D Quadrilateral elements (Quad) associated with an elastic orthotropic material, supposing that timber elements remain in the elastic range.

The PT- bars have been modelled with truss elements, which is associated with an elastic-plastic force-displacement response with an initial imposed strain that simulates the initial post-tensioning level. Furthermore, to capture the rocking behaviour of LVL panels, the unilateral constraints at the base have been represented by inserting zero-length elements, characterized by an elastic no-tension material (gap elements).

For the simulation of the test performed with axial dampers, non-linear springs that simulate their behaviour are included in the model. The two pairs of axial dampers, placed at the base, are simulated with non-linear springs using zero-length elements.

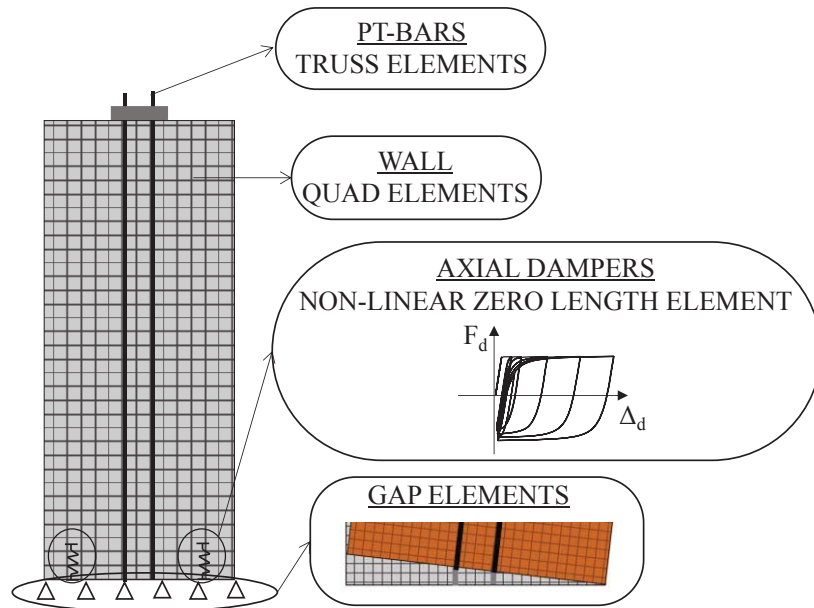


Figure 3: Numerical model.

4.2 Validation of the proposed numerical model

In this section, a comparison between experimental results and numerical simulations is reported in terms of horizontal load/ drift curves and PT-force/ drift curves, by considering the post-tensioned configuration with two couple of fuse-type dampers, with initial post-tensioning levels of 400 kN and 600 kN. The horizontal load/ drift curves are shown in Figure 4(a) and Figure 4 (b) for initial post-tensioning levels of 400 kN and 600 kN, respectively. The monotonic envelopes are characterized by a well-defined bilinear curve, in which the transition point between the first branch and the second one, corresponds to the drift at which the first cable is subjected to an increment of tension due to the wall rocking. The comparison shows a good agreement between experimental and numerical results, in terms of initial stiffness, strength and cyclic behaviour. In this regard, the predicted cyclic behaviour is slightly underestimated, because of the presence of frictional dissipations not included in the numerical model. It is interesting observing that the model is able to capture also the effect of increasing the initial post-tensioning level on the global response of the system: a greater strength characterizes the configuration with the higher PT-level, and it shows a greater re-centering capacity, recognizable by the typical flag shape. Focusing on the behaviour of the PT-bars, these are subjected to an axial deformation make the PT force increase with respect to the initial imposed load, due to the wall uplift. This variation will be higher for the cable close to the wall edge that is uplift. To clarify this behaviour, the numerical wall base uplifts, evaluated at 20 cm from the base, are reported in Figure 5 for various drift levels, where the

position of the cables is drawn in order to perceive their increasing deformation as the drift of the wall increases. It is interesting to highlight that the base uplifts for fixed values of drift are similar for both the post-tensioning levels of 400 kN (Figure 5(a)) and 600 kN (Figure 5(b)), suggesting that the kinematic of the system is almost independent from the initial post-tensioning level. However, it affects the lateral strength of the wall (Figure 4). The good agreement between experimental tests results and numerical simulations is well confirmed also by the comparison in terms of PT force-drift response of the walls for both the initial post-tensioning levels of 400 kN (200 kN for each cable) and 600 kN (300 kN for each cable) reported in Figure 6(a) and (b), respectively. For both the post-tensioning levels, graphs show that the numerical model well captures the PT force variation in both the loading and unloading phases, showing a slight difference for the cable further from the uplifted wall corner.

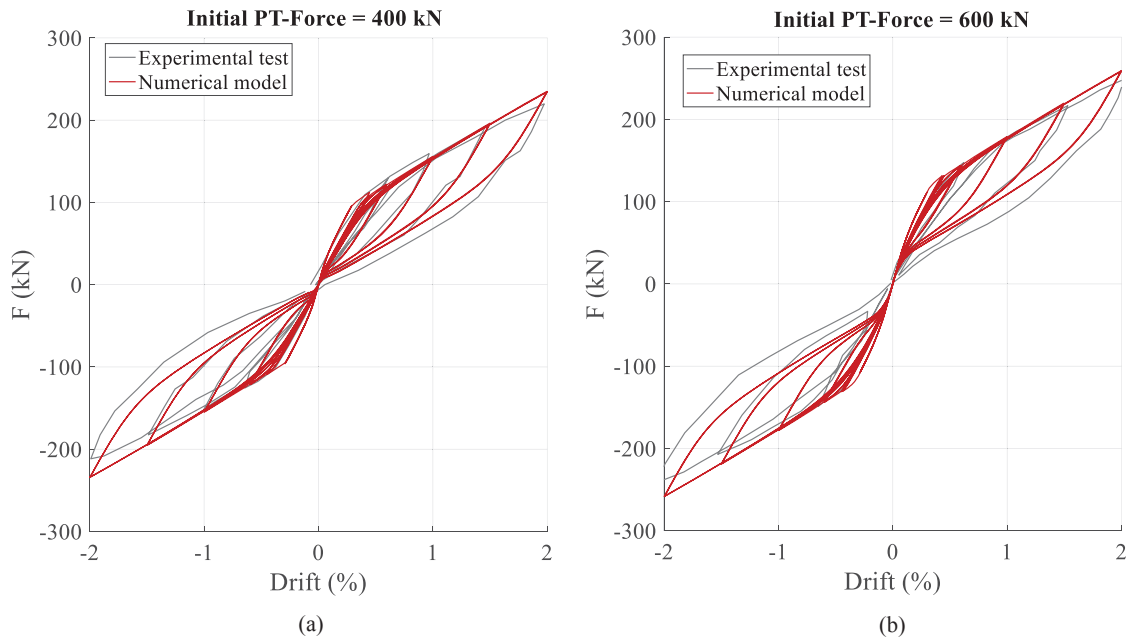


Figure 4: Horizontal load/ drift curves: (a) initial PT-force of 400 kN and (b) initial PT-force of 600 kN.

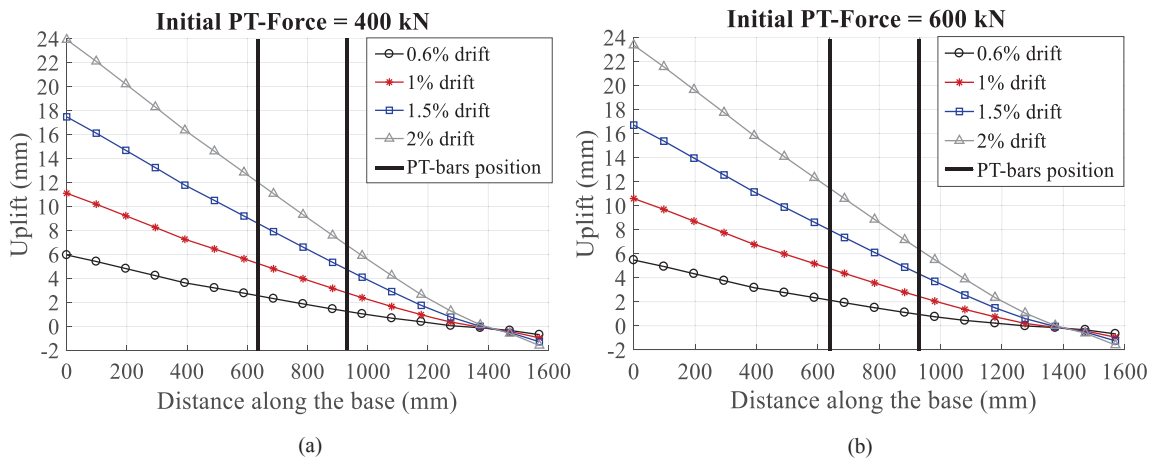


Figure 5: Numerical wall base uplift for various drift levels, evaluated at 20 cm from the base: (a) initial PT-force of 400 kN and (b) initial PT-force of 600 kN.

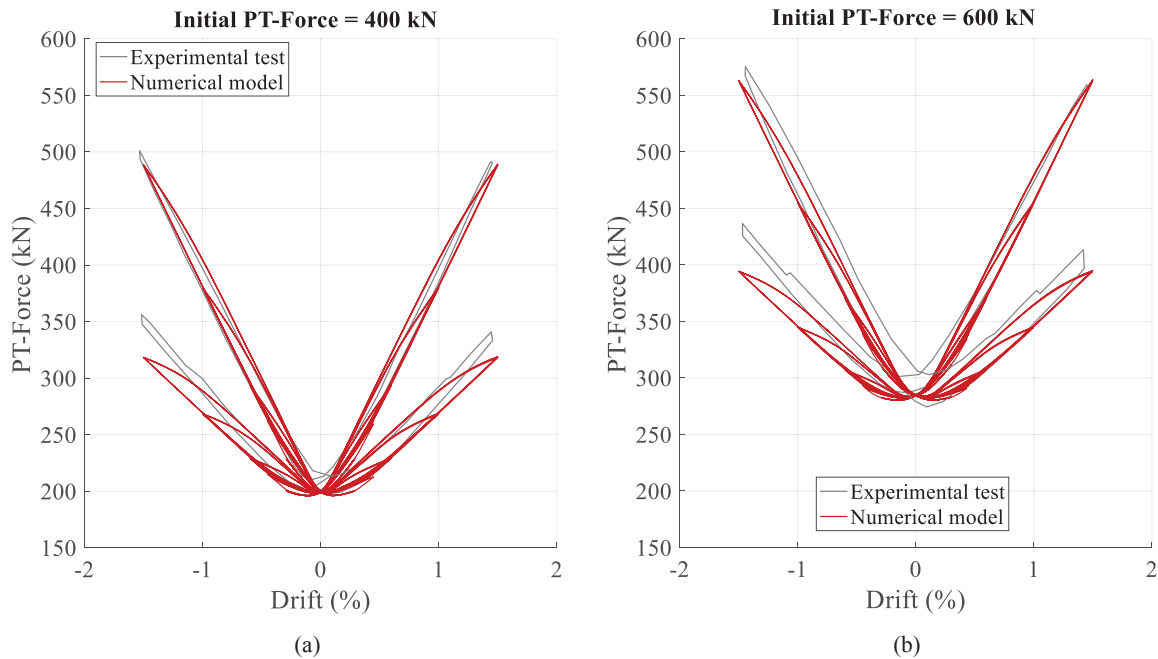


Figure 6: PT-force/ drift curves: (a) initial PT-force of 400 kN and (b) initial PT-force of 600 kN.

CONCLUSIONS

The paper deals with a proposal for a non-linear numerical model, developed in the OpenSees framework, for the prediction of the cyclic response of rocking dissipative timber walls, by virtue of the fact that in the last decade, a diffusion of low damage systems have been observed, so it is particularly important to develop numerical models that can support the design phase. The proposed numerical model specifically considers geometric and material non-linearities associated with the rocking behavior and the entry into the plastic field of the dampers, respectively. A first validation with experimental results from literature is presented here. In particular, the global response in terms of horizontal load-displacement curves and post-tensioning force-drift curves has been investigated, demonstrating its effectiveness in predicting the behavior of post-tensioned walls subjected to cyclic loads with different levels of post-tensioning force.

Further developments will be to verify the numerical model's capability to predict the non-linear response of different experimental tests on various PT wall configurations, also including shear dampers. After the proper validation of the rocking wall numerical model, it will be employed for design purpose in a more complex framework, together with the timber frame structure designed for gravital loading.

ACKNOWLEDGEMENT

The financial support of TIRISICO Project (POR FESR 2014-2020 – Regione Emilia Romagna) is gratefully acknowledged.

REFERENCES

- [1] M. Fragiaco, B. Dujic, and I. Sustersic, Elastic and ductile design of multi-storey crosslam massive wooden buildings under seismic actions. *Engineering Structures*, **33** (1), 3043-3053, 2011.
- [2] L. Pozza, A. Saetta, M. Savoia, and D. Talledo, Coupled axial-shear numerical model

- for CLT connections, *Construction and Building Material*, **150**, 568–582, 2017.
- [3] L. Pozza, B. Ferracuti, M. Massari, and M. Savoia, Axial – Shear interaction on CLT hold-down connections – Experimental investigation, *Engineering Structures*, **160**, 95–110, 2018.
 - [4] D. Trutalli, L. Marchi, R. Scotta, and L. Pozza, Capacity design of traditional and innovative ductile connections for earthquake-resistant CLT structures, *Bulletin of Earthquake Engineering*, 2018.
 - [5] J. Liu and F. Lam, Experimental test of coupling effect on CLT hold-down connections, *Engineering Structures*, **178**, 586-602, 2019.
 - [6] A. Iqbal, S. Pampanin, A. Palermo, and A. H. Buchanan, Performance and design of LVL walls coupled with UFP dissipaters, *Journal of Earthquake Engineering*, **19**(3), 383-409, 2015.
 - [7] A. Ceccotti, C. Sandhaas, M. Okabe, M. Yasumura, C. Minowa, and N. Kawai, SOFIE project – 3D shaking table test on a seven-storey full-scale cross-laminated building, *Earthquake Engineering Structural Dynamics*, **42** (13), 2013.
 - [8] D. Marriott, S. Pampanin, D. Bull, and A. Palermo, Dynamic testing of precast, post-tensioned rocking wall systems with alternative dissipating solutions, *Bulletin of the New Zealand Society of Earthquake Engineering*, 2008.
 - [9] F. Sarti, A. Palermo, and S. Pampanin, Quasi-Static Cyclic Testing of Two-Thirds Scale Unbonded Posttensioned Rocking Dissipative Timber Walls, *Journal of Structural Engineering*, **142**, 2016.
 - [10] R. Ganey *et al.*, Experimental Investigation of Self-Centering Cross-Laminated Timber Walls, *Journal of Structural Engineering*, **143** (10), 2017.
 - [11] M. Massari, M. Savoia, and A. R. Barbosa, Experimental and Numerical Study of Two-Story Post-Tensioned Seismic Resisting CLT Wall with External Hysteretic Energy Dissipaters, in *Atti del XVII Convegno ANIDIS L'ingegneria Sismica in Italia*, 2017.
 - [12] A. Sandoli, V. Tomei, B. Ferracuti, and M. Zucconi, Challenges on clt structures seismic response: Traditional vs low-damage systems, in *16th European Conference on Earthquake Engineering*, 2018.
 - [13] W. C. Stone, G. S. Cheok, and J. F. Stanton, Performance of Hybrid Moment-Resisting Precast Beam-Column Concrete Connections Subjected to Cyclic Loading, *ACI Structural Journal*, **92** (2), 1995.
 - [14] M. J. N. Priestley, S. S. Sritharan, J. R. Conley, and S. Pampanin, Preliminary results and conclusions from the PRESSS five-story precast concrete test building, *PCI Journal*, **44** (6), 42-67, 1999.
 - [15] STIC, Design guide Australia and New Zealand – Post-tensioned timber buildings. Structural Timber Innovation Company, Christchurch, New Zealand., 2013.
 - [16] F. Sarti, A. Palermo, and S. Pampanin, Fuse-Type External Replaceable Dissipaters: Experimental Program and Numerical Modeling, **142** (12), *Journal of Structural Engineering*, 2016.
 - [17] T. Smith, S. Pampanin, A. Buchanan, and M. Fragiacomio, Feasibility and Detailing of Post-tensioned Timber Buildings for Seismic Areas, in *2008 NZSEE Conference*, 2008.
 - [18] J. M. Kelly, R. I. Skinner, and A. J. Heine, Mechanisms of energy absorption in special devices for use in earthquake resistant structures, *Bulletin of the New Zealand Society of Earthquake Engineering*, 1972.
 - [19] A. Baird, T. Smith, A. Palermo, and S. Pampanin, Experimental and numerical Study of U-shape Flexural Plate (UFP) dissipaters, *NZSEE Conference*, 2014.
 - [20] F. Sarti, A. Palermo, and S. Pampanin, Development and Testing of an Alternative

- Dissipative Posttensioned Rocking Timber Wall with Boundary Columns, *Journal of Structural Engineering*, **142** (4), 2016.
- [21] F. McKenna, M. H. Scott, and G. L. Fenves, Nonlinear finite-element analysis software architecture using object composition, *J. Computing in Civil Engineering*, **24** (91), 2010.

MASONRY-INFILLED RC FRAMES STRENGTHENED WITH CROSS-LAMINATED TIMBER PANELS

Zabih Mehdipour¹, Jorge M. Branco¹, Iztok Sustersic², Leonardo G. Rodrigues¹, Paulo B. Lourenço¹

¹ University of Minho, ISISE, Department of Civil Engineering, Guimarães, Portugal
zabih.mehdipour@gmail.com, jbranco@civil.uminho.pt, leonardofgrodrigues@gmail.com,
pbl@civil.uminho.pt

² InnoRenew CoE, Izola, Slovenia
iztok.sustersic@innorenew.eu

Abstract

Southern regions of Europe are characterized by presenting a large number of existing buildings with reinforced concrete (RC) structures with masonry infills. From a structural point of view, they are characterized by one-way RC frames, with poor structural details and masonry infills, contributing to the high seismic vulnerability of these constructions.

Current retrofitting technologies, such as reinforced concrete jacketing of columns, concrete shear walls or FRP wrapping, could be effective but require the occupants' relocation, available perimetral space and legislative constraints. The use of CLT panels, as an innovative retrofitting technique, seems to be a reasonable alternative for existing buildings given their easy and fast assembly, high performance and reversibility.

This paper presents a numerical analysis to evaluate the seismic behavior of masonry-infilled RC portal frames strengthened by an external CLT panel. The 20 cm thick masonry wall was represented by two nonlinear diagonal elements with a multi-linear plastic constitutive law, including a Pivot hysteresis type in the axial direction. On the other hand, the 100 mm thick CLT panel was modeled through an orthotropic elastic shell-element. The study comprises four different connections between the RC frame and CLT panels. These connections are modeled through nonlinear Pivot links in both uplift and lateral directions. Their cyclic response, including degradation parameters, effective stiffness and force-deformation envelope curve, was calibrated based on previous experimental results. Numerical results confirm that CLT panels can be an efficient strengthening solution to increase the initial stiffness, as well as energy dissipation, while decreasing the impact of strength degradation on the response of masonry-infilled RC frames against in-plane quasi-static cyclic loading.

Keywords: RC Frame; Masonry infills; Cross Laminated Timber; Quasi-static Analysis

1 INTRODUCTION

Masonry-infilled reinforced concrete (RC) buildings constitute a significant part of the existing building stock across southern regions of Europe [1]. Consequently, many studies have been conducted to analyze the properties of infilled RC frames, in order to improve their weaknesses and prevent their failure under cyclic loading [2][3].

The presence of infill walls on the bare frame can induce unexpected force distributions that can lead to local failures during intense ground shaking [4]. The main failure modes in masonry-infilled RC frames that have been shown in experimental, analytical, and numerical research works are: corner crushing mode; sliding shear mode; diagonal cracking mode; diagonal compression mode; and the failure of the RC frame [5]. Furthermore, when subjected to seismic loads, RC frames are susceptible to non-ductile failure modes, particularly the frames built according to previous codes and standards [6]. Therefore, seismic retrofitting seems inevitable. Some of the available retrofitting techniques aim to directly strengthen the masonry infill, besides an improvement of the RC frame structure. Indeed, there is a wide range of retrofitting techniques that are divided into two general approaches: structure-level retrofit and member-level retrofit [7].

Cross-laminated timber (CLT) panels are a combination of several crosswise-stacked lumber boards that confer high in-plane stiffness. These panels allow fastening the construction work and can contribute to meet societal goals in terms of environmental sustainability, improving the energy performance of buildings, while reducing CO₂ emissions of construction. Sustersic et al. [8] introduced CLT as a seismic retrofitting method for infilled RC buildings by developing a three-step over strengthened connection. This study showed that longer CLT panels are more efficient than shorter segments under seismic forces for a better bending behavior.

On the other hand, Stazi et al. [9] showed that RC frames strengthened by CLT can reach higher lateral stiffness and peak load values than masonry-infilled RC frames. In both cases, the use of prefabricated timber panels improves the energy efficiency of the building by reducing global energy demand up to nearly 60% [10].

Experimental evaluations have shown that the connection used to connect panels and the main RC structures play a crucial role in the overall seismic response, given their nonlinear behavior that promotes energy dissipation [11][12]. Considering this fact, special attention should be given to their design and assessment.

The present work studies the response of strengthened RC frame under cyclic loadings with a special focus on strength degradation, stiffness deterioration, ductility and energy dissipation. A one-story one-bay infilled reinforced RC frame is used as a case study, where its seismic response is improved through a collaborative CLT panel. Four different connections between the CLT panel and RC frame, are evaluated by adopting distinct properties to nonlinear link connection elements. It is worth noting that these properties were defined based on tests results obtained through previous experimental campaigns [13][14][15]. The masonry infill is represented by an equivalent diagonal element, consisting on a macro-modeling procedure that exploits the multi-linear plastic link element with Pivot hysteresis law, available in SAP2000 NL software [16]. Moreover, the CLT panel is represented by the Homogenized-Orthotropic-plane stress-reduced cross-section (HOBS) approach [17].

2 DESCRIPTION OF THE INFILLED RC FRAME

The RC frame employed here, representing the actual building practice in Portugal, was built and tested at the University of Minho's laboratory in the 2/3 scale RC frame by Silva et al. [13]. Figure 1 shows the geometry and reinforcement scheme.

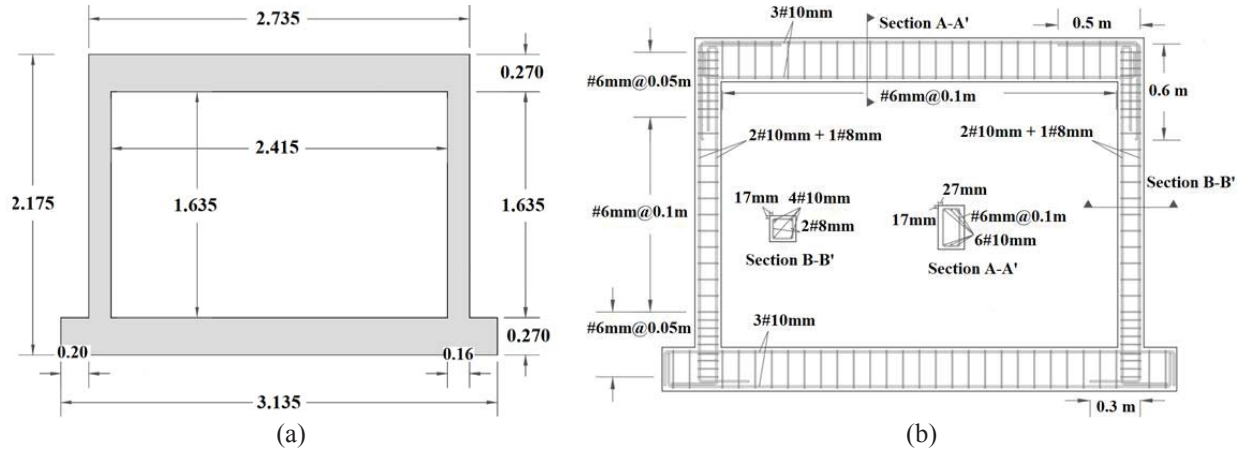


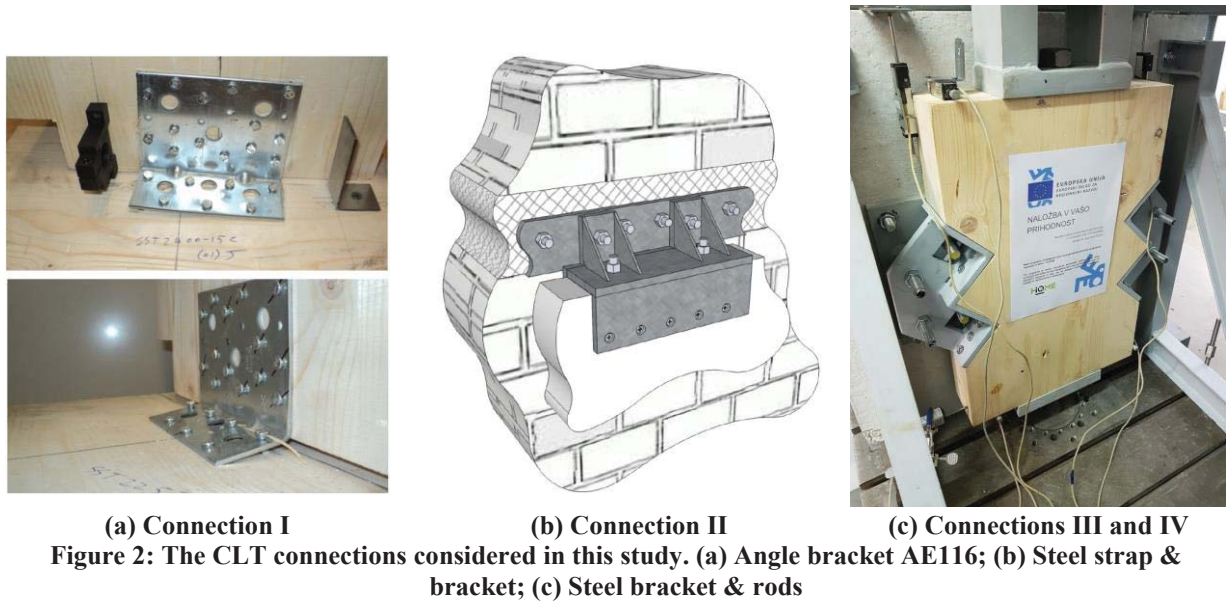
Figure 1: RC frame used in this study, (a) Geometry, (b) Reinforcement scheme (Silva et al. [13])

The frame length and height are 2575 mm and 1770 mm, respectively. Beam and column sections are 270×60 mm and 160×160 mm, respectively. The masonry infill was built with 294x187x140mm bricks with vertical perforation, using murfor RND 0.5 100 reinforcement in every two rows, and murfor L +100 anchors to connect the infill to the RC frame at the same level of reinforcements. The rebars used in the RC frame and masonry infill are an A400NR, and A500NR, respectively. The concrete of the RC elements is from the C55/67 class. For laying of masonry units, an M10 mortar is employed. The thickness of the horizontal joints is assumed to be 0.5 cm. More details can be found in Silva et al. [18].

3 CLT PANEL AND CONNECTIONS

The CLT panel has a thickness of 97 mm, comprising three layers with thicknesses 35, 27, and 35 mm. The panel's mechanical properties, including moduli of elasticity and shear modulus, are determined according to standard EN 338 [19] and DIN 1052 [20], while the Poisson coefficients are obtained according to Bodig et al. [21].

Four different connections were considered in this study. The first (Figure 2 (a)) consists of a prefabricated mechanical connector, angle bracket AE116, widely used in the CLT structures [14]. The second one, Figure 2 (b), comprises three parts: a steel strap and steel threaded rods connecting to the beams, a steel bracket connected to the panel through self-tapping screws, and a steel plate connecting the steel strap with the steel bracket. The first two are designed to behave essentially elastic, whereas the last part is designed with a controlled failure, ductility and energy dissipation. This connection was developed and characterized by Sustersic [15]. The third and fourth connections, developed by Sustersic [15], adopt a newly designed angle bracket and two steel threaded rods with a length of 50 mm and grade rods of 4.6 and 8.8, respectively (Figure 2 (c)). The connections of Figure 2 (a) were selected because they represent a common in CLT buildings, while the remaining ones have presented an adequate response under cyclic loading both for sliding (shear) and uplift (tension) motions [15]. It is important to mention that the availability of experimental tests [14][15] allows calibrating numerical models, increasing the reliability of their results.



4 MODELLING METHODOLOGY

4.1 Characteristics of RC plastic hinges

The RC frame is represented through linear elastic frame elements with plastic hinges at their ends that concentrate the nonlinear behavior of the beam-column joints. These plastic hinges whose properties are obtained according to Eurocode 8 (part 3) provisions [22] are governed by the Pivot hysteresis model, available in SAP2000 NL software [16]. The Pivot's coefficients are then adjusted in order to obtain an agreement between the numerical model and the test results from Silva et al. [13], in terms of the envelope curve, as shown in Figure 3.

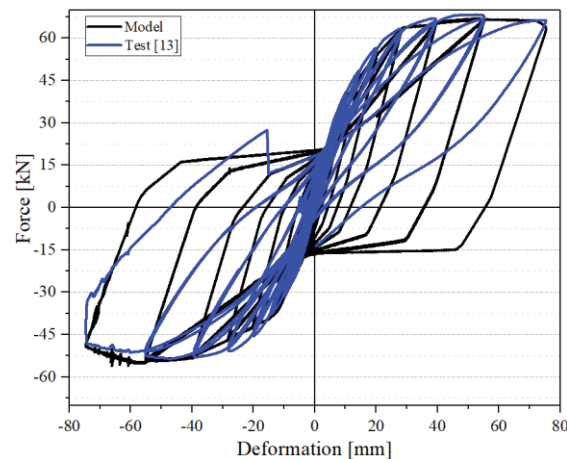


Figure 3: Experimental/analytical cyclic response of the selected RC frame from Silva et al. [13]

4.2 Characteristics of the masonry infill

The confined masonry infill is represented with two diagonal multi-linear link elements following the Pivot hysteresis law. The parameters of the links, including Pivot coefficients and Force-Deformation envelope definition, along with plastic hinges assigned to RC joints, are obtained after a calibration process based on the test data available in Silva et al. [10]. Figure 4 allows evaluating the response of the masonry infilled RC frame under cyclic loading

and verifying the agreement between the numerical model and the experimental data in terms of force-displacement curves. The accuracy of the method is satisfactory in terms of the envelope curve, while the model is not accurate enough in terms of unloading stiffness.

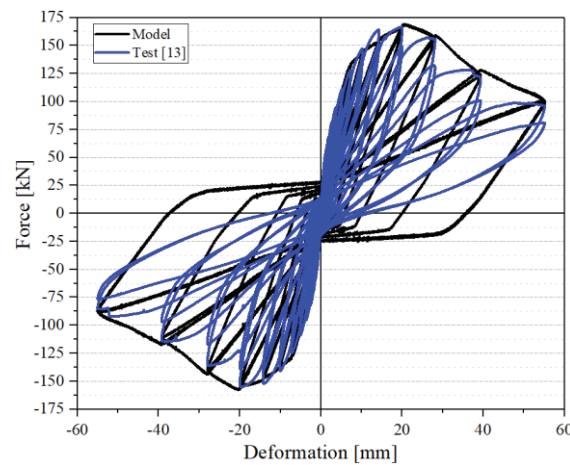


Figure 4: Experimental/analytical cyclic response of the selected infilled RC frame from Silva et al. [13]

4.3 Characteristics of connections between the CLT and frame

The connections between the CLT panel and the RC frame are represented by multi-linear plastic link elements that are governed by the Pivot hysteresis law. The force-deformation definition and Pivot's coefficients are obtained by a calibration process based on the experimental campaign developed by Matos et al. [14]. For connection I (angle bracket AE116), Figure 5 allows the numerical and experimental results of cyclic tests, for both lateral (a) and uplift (b) motions, in terms of force-deformation curves. In turn, Figure 6 presents the tension and shear response of an over strengthened connection (II), according to the experimental results obtained by Šušteršič [15]. The connections III and IV, presented in Figure 2 (c), were tested for loads applied in horizontal and vertical directions. In this regard, Figure 7 shows the behavior in shear for both numerical and experimental responses under cyclic loads for connections III (4.6 grade rods) and IV (8.8 grade rods).

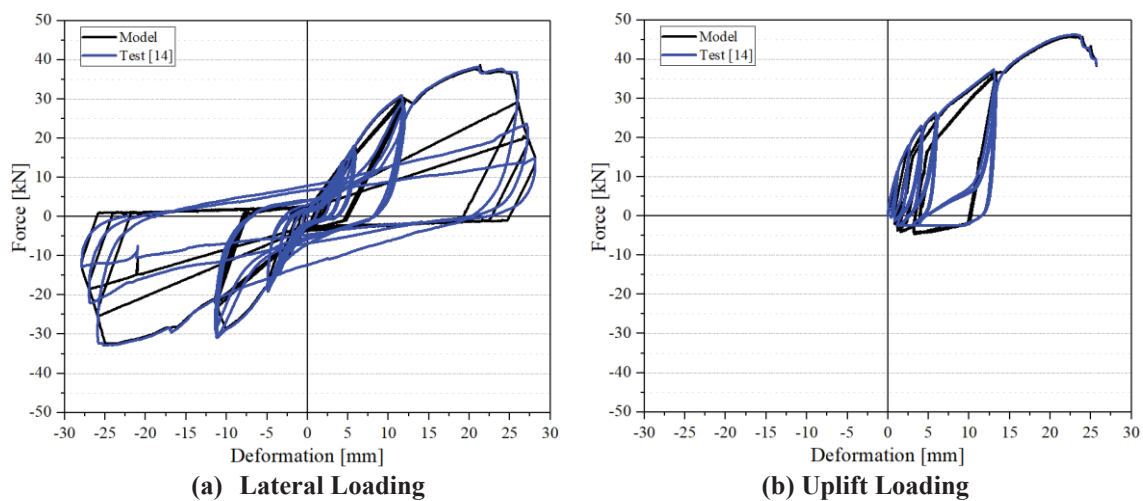


Figure 5: Experimental/analytical cyclic response of the first connection I

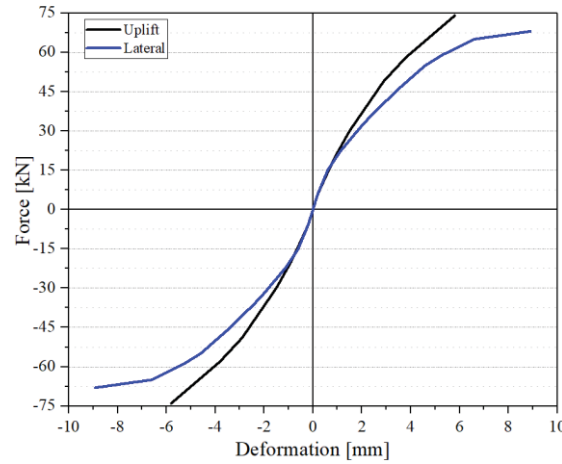


Figure 6: Uplift and Lateral force versus deformation in connection II [15]

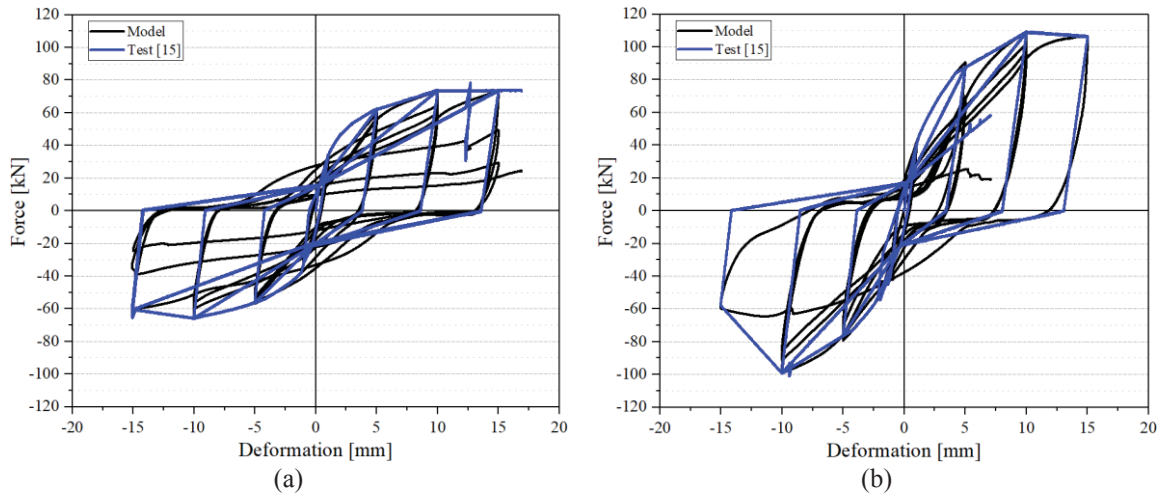


Figure 7: Experimental/analytical cyclic response, (a) Connection III, (b) Connection IV

4.4 Simulation of the infilled frame strengthened by CLT

The CLT panel and connections are simulated separately in this study. The panel is discretized according to the homogenized-orthotropic-plane stress-reduced cross-section method. The modeling approach adopted considered the three-layered panel as a single-layer shell element [17], based on reduction coefficients that result in a simplification, which requires less computational efforts, where most of the attention must be paid to connections modeling. Their correspondent links, divided into two sliding and uplift springs, can be distributed along panels' borders (beams and columns) or concentrated in four positions (corners). Considering the latter, in which the upper and lower beams corners are linked to the panel so that the end of connections is set to the end of beams, all springs are attributed by multi-linear plastic link elements.

The loading pattern applied in the experimental campaign [10] followed FEMA 461 [14], in which the displacement is applied throughout 16 steps, starting from 0.5 mm, and ending in 75 mm. Each step is repeated two times except for the first one, which is repeated six times. The numerical study adopts the same loading pattern as the experimental work.

5 NUMERICAL RESULTS

In this section, one can evaluate the structural responses, under cyclic loading, obtained through the numerical modes used to represent the distinct connection schemes under study. The behavior is evaluated in terms of base shear versus top displacement, dissipated energy, and ductility factor.

5.1 Force-displacement response of frames

Figures 8-11 present the force-displacement responses of the bare frame, the bare frame strengthened by CLT, infilled frame, and infilled frame strengthened by CLT, subjected to cyclic loading considering the four CLT connections.

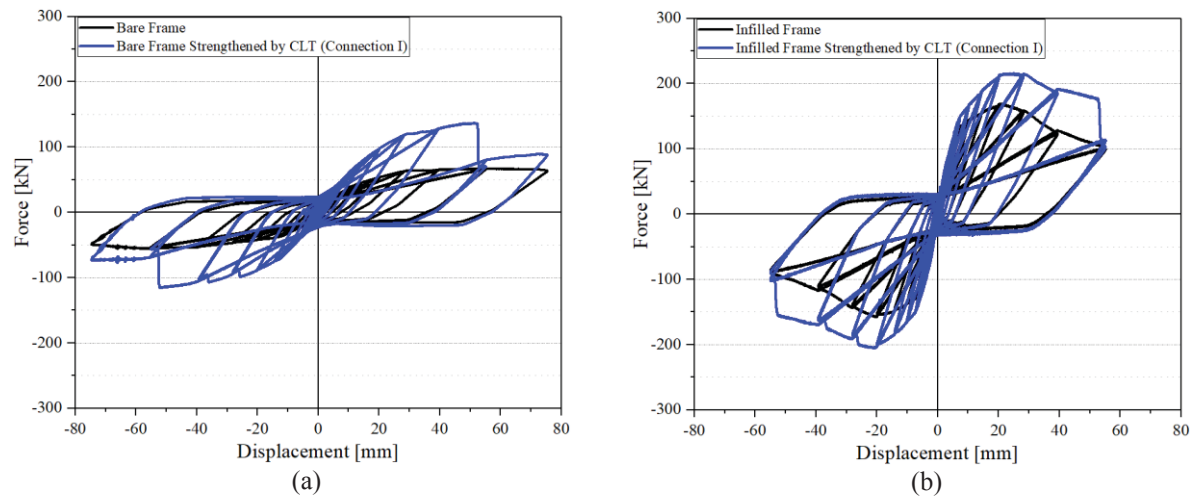


Figure 8: Force-displacement response considering connection I: (a) Bare frame and bare frame strengthened by CLT; (b) Infilled frame and infilled frame strengthened by CLT

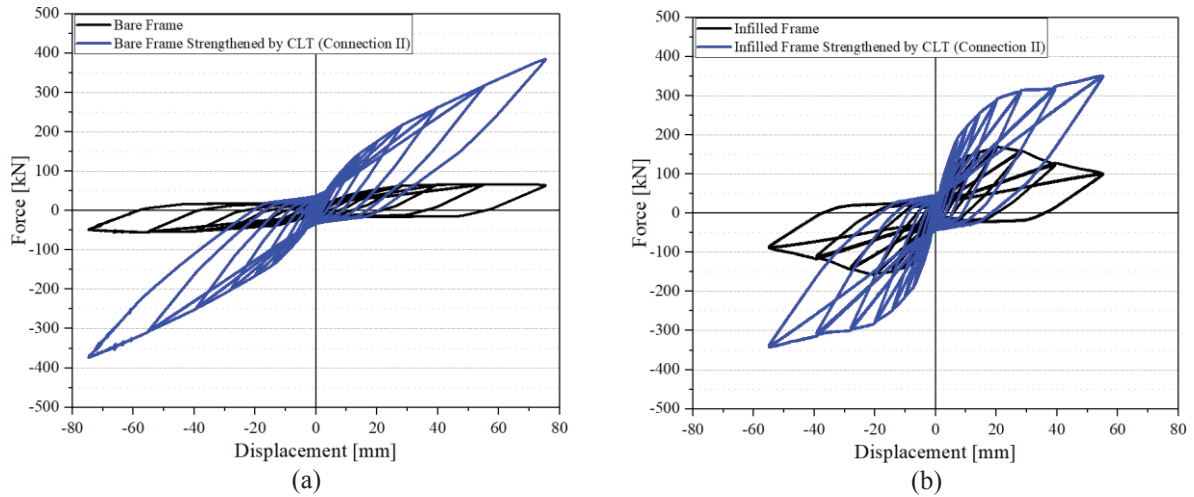


Figure 9: Force-displacement response considering connection II: (a) Bare frame and bare frame strengthened by CLT; (b) Infilled frame and infilled frame strengthened by CLT

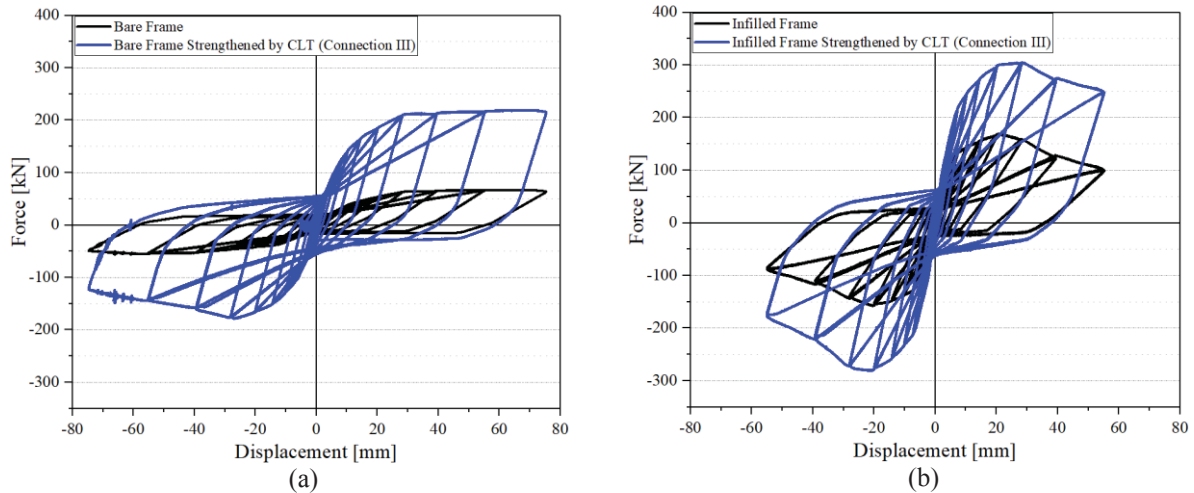


Figure 10: Force-displacement response considering connection III: (a) Bare frame and bare frame strengthened by CLT; (b) Infilled frame and infilled frame strengthened by CLT

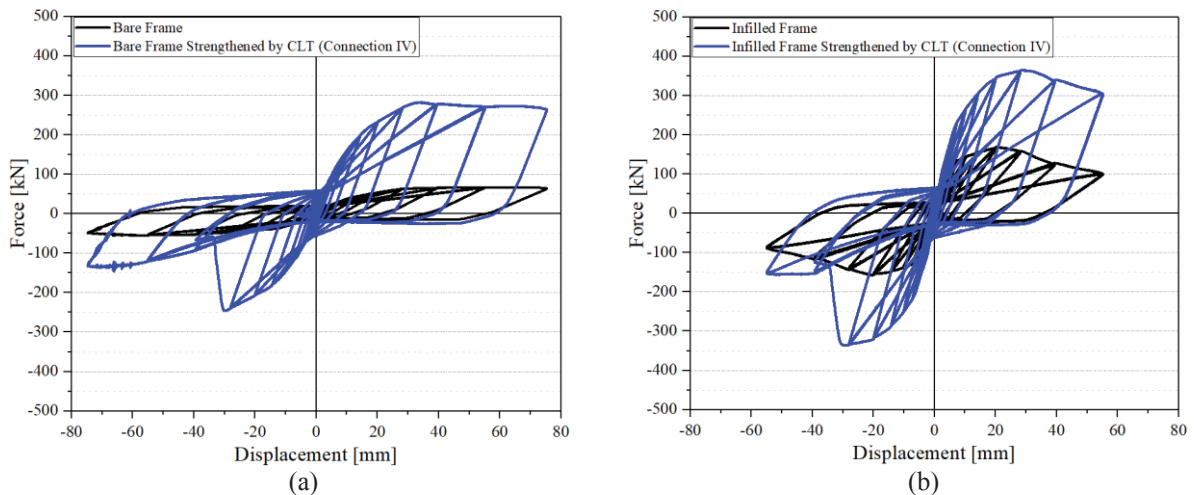


Figure 11: Force-displacement response considering connection IV: (a) Bare frame and bare frame strengthened by CLT; (b) Infilled frame and infilled frame strengthened by CLT

The oversized connection II makes 473% and 107% improvement in the maximum capacity of the bare frame and infilled frame, respectively. In this joint, unlike others, no strength degradation is observed for both bare and infilled frame strengthened. On the other hand, connection I has an increase of 104% and 27% in the strength capacity of the bare and infilled frame, respectively, which seems negligible compared to connection II, while the pinching effect as an index for evaluating energy dissipation is the same as previous. Figures 10 and 11 show the substantial ability of connections III and IV to dissipate energy, even more than connection II, although these connectors are simpler and then cheaper than three-part connection II, indicating that more efficient joints associating seismic reliability are possible at a lower cost. Connection IV shows about 30% and 15% improvement in strength capacity for bare and infilled frames, respectively, which is not satisfactory enough based on the differences in their rod strength. In other words, it proves that the geometry of connection, such as plate's thickness, number of rods and their size, makes a more contribution to modifying seismic properties of structures.

With regards to Figures 8-11, it is proved again that infills generally improve the post-elastic behavior of bare frames with increasing maximum strength and dissipating more seismic energy despite the fact that the ultimate strength stays almost unchanged. Comparing the

results of the bare frame strengthened by CLT panel and those of infilled frame, a result is that the bare frame strengthened by CLT has higher seismic performance than the infilled frame due to the considerable potential shown to increase the energy dissipated, the initial stiffness, unloading and reloading stiffness, load carrying capacity, and decreasing strength/stiffness degradation.

It should be pointed out irregular responses in two opposite loading directions, as shown in Figure 11, due to unequal inelastic behavior in tension and compression.

In summary, Figure 12, through the backbone curves obtained from the cyclic analysis, compares the strengthening effect of the CLT panel connected to the RC frame considering four different connections. The comparisons are divided into two cases: bare frame (Figure 12 (a)) and masonry-infilled frame (Figure 12 (b)).

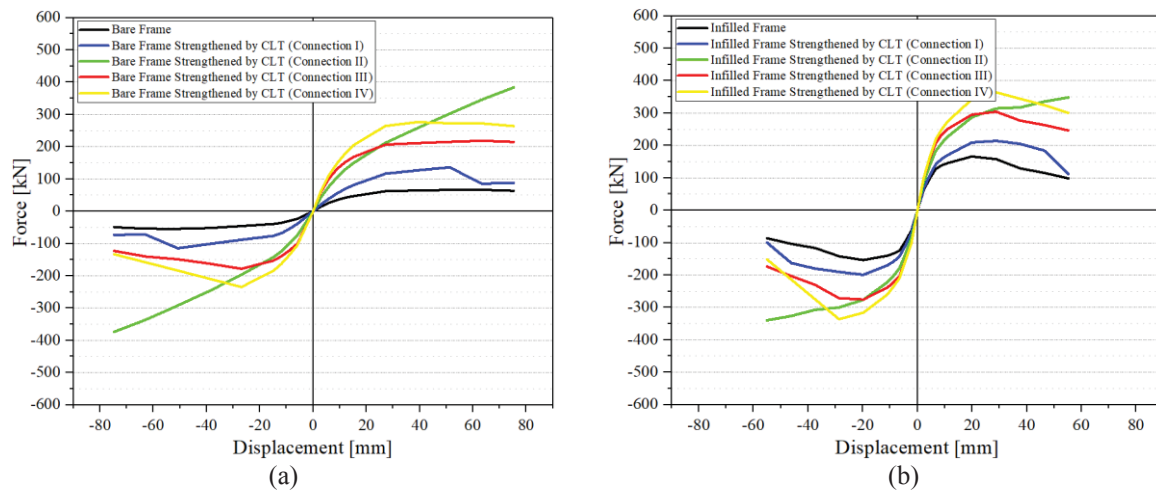


Figure 12: Pushover curves considering all connections, (a) Bare frame and bare frame strengthened by CLT; (b) Infilled frame and infilled frame strengthened by CLT

Figure 12 shows that connection II, which presents a higher strength capacity than the remaining ones, did not achieve its post-peak strength, while other connections underwent that region. Furthermore, connection III presented higher peak strength per rod strength in comparison with connection IV; maybe referring to that strength itself is not a priority in the seismic design of connections. It should be stated that the CLT strengthening using connection I (AE116), which has a small contribution to the frame, has about the same peak capacity as the infilled frame (~160 kN).

5.2 Structural ductility

Having extracted the Pushover curves from the cyclic curves, the structural ductility factor (R), according to FEMA 2004 [23], is computed for all cases as:

$$R = \Delta_m / \Delta_y \quad (1)$$

In which, Δ_y and Δ_m indicate the yield displacement and the displacement associated with the structure's maximum shear capacity, respectively. These amounts are achieved by calculating the equivalent bilinear curve, which has the same area as the envelope curve, as shown below.

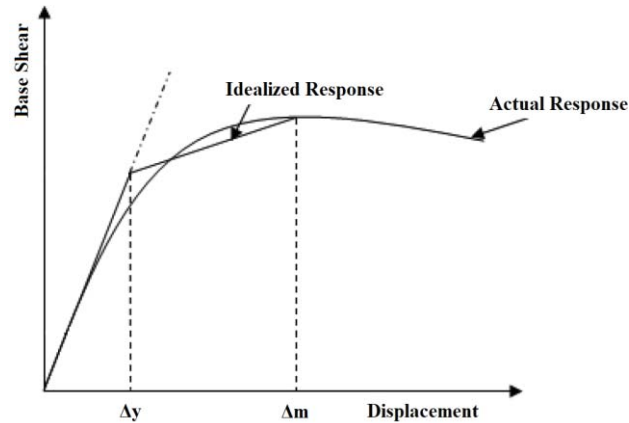


Figure 13: Definition of yield and maximum displacement

Therefore, all envelope curves in Figure 12 are transformed to equivalent bilinear curves, and then the ductility factor is calculated for the bare frame, infilled frame, and infilled frame strengthened by adding a CLT panel, considering the four selected connections (Table 1).

Table 1: Structural Ductility Factor

Bare Frame	Bare Frame Strengthened by CLT			
	Connection I	Connection II	Connection III	Connection IV
14.29	18.87	11.63	15.63	10.00
Infilled Frame	Infilled Frame Strengthened by CLT			
	Connection I	Connection II	Connection III	Connection IV
7.04	15.63	9.17	9.09	9.01

As shown in the above table, the infilled frame and infilled frame strengthened by CLT have mostly a lower ductility factor than the bare frame and bare frame strengthened by CLT, respectively, owing to failures of masonry that usually happens before the frame or connections. In addition, adding CLT led to an enhanced ductility in the infilled frame strengthened by CLT compared to the infilled frame due to transferring a part of loading from the masonry infill to the CLT panel. However, regarding the bare frame, adding CLT panels might not result in ductility increment, as shown in the case of the bare frame strengthened by CLT with connection II and IV. Nevertheless, there are other definitions for ductility that may be accompanied by increasing these amounts.

5.3 Energy dissipation

In order to have better comparisons between all frames under cyclic loading, in terms of energy dissipation, the accumulated energy versus displacement was calculated from base shear versus top displacement (Figure 8-11) and presented in Figure 14. According to Figure 14 (a), energy dissipation of the bare frame strengthened by CLT with connections I-IV is 1.6, 4.4, 3.1, and 3.4 times higher than that of the bare frame, respectively. In addition, Figure 14 (b) shows that energy dissipation of infilled frame strengthened by CLT with connections I-IV is respectively 1.3, 2.2, 1.9, and 2 times of infilled frame. The direct result is the seismic efficacy of CLT panels as a renovation of infilled RC frames. On the other hand, for comparing the effect of masonry infill in dissipation, energy dissipation of infilled frame and infilled frame strengthened with CLT with connections I-IV (Figure 14 (b)) are, respectively, 95%, 57%, 0%, 18%, and 15% larger than those of bare frame in Figure 14 (a). As a matter of fact,

while masonry infills contribute to increasing energy dissipation of bare frames, there are not as efficient as adding CLT panels to bare frames.

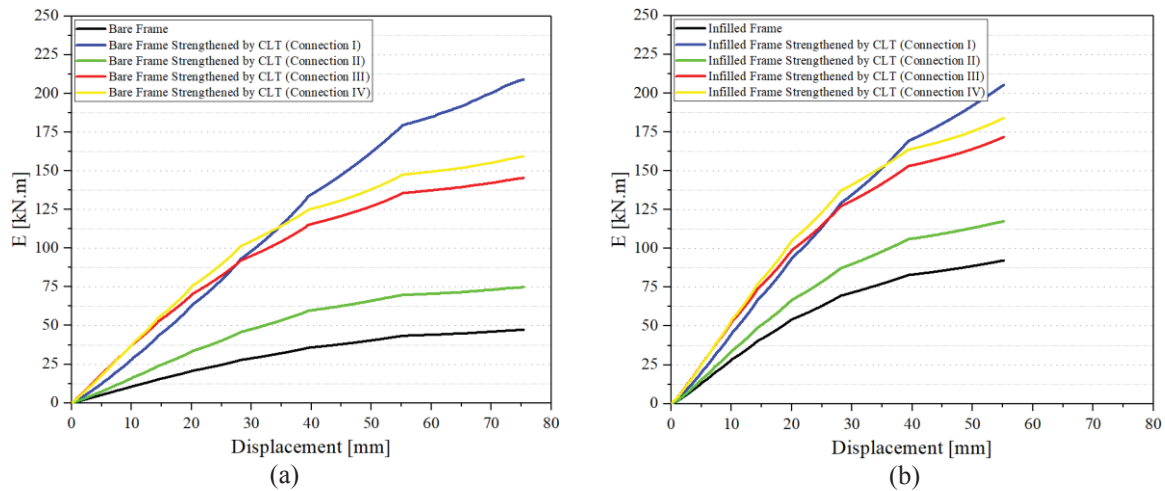


Figure 14: Accumulated dissipated energy considering all connections, (a) Bare frame and bare frame strengthened by CLT; (b) Infilled frame and infilled frame strengthened by CLT

6 CONCLUSIONS

In the present study, the seismic resistance of masonry-infilled RC frames retrofitted with CLT panels was evaluated. A collection of previous experimental tests on RC frame, masonry infills and connections was considered for calibrating finite element models that comprise four distinct connection techniques. The numerical simulations performed allowed to draw the following remarks:

- Adding a CLT panel increases the frame's load-carrying capacity, accompanied by an increment of the initial stiffness and post-yielding stiffness. However, in spite of the lessening pinching effect, stiffness and strength degradation, which is widely found in masonry-infilled frames, does not change considerably;
- Connections play a critical role in the post-yielding behavior of frames. An essential part of energy in cyclic loading is dissipated by these joints. The simulations showed a connection with lower load-carrying capacity and cheaper might result in better seismic behavior, mainly depending on joints' geometry;
- Regarding the ductility factor, defined by FEMA 2004, adding CLT panels does not always result in a ductility increment for bare frames, in opposition to what was expected. However, the ductility of infilled frames might be increased by adding CLT.
- Due to the first nonlinearity and failure observed in the structure by infill, along with the elastic behavior of CLT panels and high load-carrying capacity of connections in the post-elastic range, it can be concluded that CLT panels make much more contribution than masonry infills to energy dissipation under cyclic loadings.

Finally, it seems clear that CLT panels can be used as a strengthening measure that improves the seismic response of RC structures. However, it is crucial to develop connections able to ensure accurate performance, as the existing ones were not designed for this particular application.

ACKNOWLEDGMENT

This work was partly financed by FEDER funds through the Competitivity and Internationalization Operational Programme COMPETE, Portugal 2020, and by national funds through ‘FCT – Foundation for Science and Technology’ within the scope of the project POCI-01-0145-FEDER-032031. Iztok Sustersic also gratefully acknowledges receiving funding from programme Horizon 2020 Framework Programme of the European Union; H2020 WIDESPREAD-2-Teaming: (#739574) and the Republic of Slovenia.

REFERENCES

- [1] M. Polese, M. Di Ludovico, M. Gaetani d’Aragona, A. Prota, and G. Manfredi, “Regional vulnerability and risk assessment accounting for local building typologies,” *Int. J. Disaster Risk Reduct.*, vol. 43, 2020, doi: 10.1016/j.ijdr.2019.101400.
- [2] A. B. Mehrabi, P. Benson Shing, M. P. Schuller, and J. L. Noland, “Experimental Evaluation of Masonry-Infilled RC Frames,” *J. Struct. Eng.*, vol. 122, no. 3, 1996, doi: 10.1061/(asce)0733-9445(1996)122:3(228).
- [3] M. F. Paulo, M. F. Neto, J. E. Dias, and P. B. Lourenço, “Behavior of masonry infill panels in RC frames subjected to in plane and out of plane loads,” 7th Int. Conf. amcm2011, 2011.
- [4] P. G. Asteris, D. M. Cotsovos, C. Z. Chrysostomou, A. Mohebkah, and G. K. Al-Chaar, “Mathematical micromodeling of infilled frames: State of the art,” *Eng. Struct.*, vol. 56, 2013, doi: 10.1016/j.engstruct.2013.08.010.
- [5] T. Nicola, C. Leandro, C. Guido, and S. Enrico, “Masonry infilled frame structures: State-of-the-art review of numerical modelling,” *Earthq. Struct.*, vol. 8, no. 1, 2015, doi: 10.12989/eas.2015.8.1.225.
- [6] H. Varum, A. G. da Costa, and P. V. Real, “Seismic assessment, strengthening and repair of existing buildings,” 2003.
- [7] JW. Bai and M. B. Hueste, “Seismic Retrofit for Reinforced Concrete Building Structures,” *Consequence based engineering (CEB) Institute Final Report*, Texas University, 2003.
- [8] I. Sustersic and B. Dujic, “Seismic shaking table testing of a reinforced concrete frame with masonry infill strengthened with cross laminated timber panels,” 2014.
- [9] F. Stazi, M. Serpilli, G. Maracchini, and A. Pavone, “An experimental and numerical study on CLT panels used as infill shear walls for RC buildings retrofit,” *Constr. Build. Mater.*, vol. 211, 2019, doi: 10.1016/j.conbuildmat.2019.03.196.
- [10] G. Margani, G. Evola, C. Tardo, and E. M. Marino, “Energy, seismic, and architectural renovation of RC framed buildings with prefabricated timber panels,” *Sustain.*, vol. 12, no. 12, 2020, doi: 10.3390/SU12124845.
- [11] J. M. Branco, P. J. S. Cruz, and M. Piazza, “Experimental analysis of laterally loaded nailed timber-to-concrete connections,” *Constr. Build. Mater.*, vol. 23, no. 1, 2009, doi: 10.1016/j.conbuildmat.2007.11.011.
- [12] I. Gavric, M. Fragiaco, and A. Ceccotti, “Cyclic behaviour of typical metal

- connectors for cross-laminated (CLT) structures,” *Mater. Struct. Constr.*, vol. 48, no. 6, 2015, doi: 10.1617/s11527-014-0278-7.
- [13] L. M. Silva, G. Vasconcelos, P. B. Lourenço, and F. Akhoundi, “Seismic performance of Portuguese masonry infill walls: From traditional systems to new solutions,” in *COMPdyn Proceedings*, 2019, vol. 2, doi: 10.7712/120119.7063.19702.
- [14] F. T. Matos, J. M. Branco, P. Rocha, T. Demschneider, and P. B. Lourenço, “Quasi-static tests on a two-story CLT building,” *Eng. Struct.*, vol. 201, 2019, doi: 10.1016/j.engstruct.2019.109806.
- [15] I. Sustersic, “Strengthening of Buildings with Cross-laminated Timber Plates,” University of Ljubljana, 2017.
- [16] SAP 2000 14.2.2 [Computer software]. Computer & Structures, Berkeley, CA.
- [17] H. Blass and P. Fellmoser, “Design of solid wood panels with cross layers,” in *8th World Conference on Timber Engineering*, 2004, vol. 14.
- [18] L. M. Silva, G. Vasconcelos, and P. B. Lourenço, “Innovative systems for earthquake-resistant masonry infill walls: Characterization of materials and masonry assemblages,” *J. Build. Eng.*, vol. 39, 2021, doi: 10.1016/j.jobbe.2021.102195.
- [19] European Committee for Standardization (CEN). EN 338:2003. Structural timber. Strength classes.
- [20] DIN 1052:2008 Entwurf, Berechnung und Bemessung von Holzbauwerken – Allgemeine Bemessungsregeln und Bemessungsregeln für den Hochbau. .
- [21] J. Bodig and B. Jayne, *Mechanics of Wood and Wood Composites*. New York, USA: Van Nostrand Reinhold, 1982.
- [22] EN 1998-3:2005 - Eurocode 8: Design of structures for earthquake resistance - Part 3: Assessment and retrofitting of buildings. European Committee for Standardization.
- [23] Federal Emergency Management Agency (FEMA). NEHRP recommended provisions for seismic regulations for new buildings and other structures. Washington, DC: FEMA 450, 2004.

INFLUENCE OF PERPENDICULAR WALLS ON THE LATERAL STIFFNESS OF CLT SHEAR WALLS

E. Ruggeri¹, G. D'Arenzo², M. Fossetti³ and W. Seim⁴

¹ Faculty of Engineering and Architecture, Kore University of Enna, Italy
e-mail: elisabettamaria.ruggeri@unikorestudent.it

² Timber Engineering and Building Rehabilitation, University of Kassel, Germany
e-mail: giuseppe.darenzo@uni-kassel.de

³ Faculty of Engineering and Architecture, Kore University of Enna, Italy
e-mail: marinella.fossetti@unikore.it

⁴ Timber Engineering and Building Rehabilitation, University of Kassel, Germany
e-mail: wseim@uni-kassel.de

Keywords: CLT shear walls, wall-to-wall connections, perpendicular walls interaction, mechanical models, parametric analyses

Abstract. *Cross-Laminated Timber (CLT) walls are used in CLT buildings to carry both vertical and horizontal loads. The mechanical behaviour of CLT shear walls for lateral loads is typically assumed to be governed from the base connections, which transfer the horizontal loads from the upper storeys to the foundations. However, in a CLT building, other connection typologies, such as the connection between shear walls and perpendicular walls, can contribute to the mechanical performances of the CLT shear walls. This paper presents a study on the effects of the perpendicular walls on the lateral stiffness of Cross-Laminated Timber shear walls. An analytical model for the calculation of the lateral stiffness of CLT shear walls connected at the base with typical hold-downs and angle brackets and to perpendicular walls by means of wall-to-wall connections is presented. The analytical model is compared with different models taken from the literature and validated against a numerical model developed in SAP2000. The analytical model is used to perform a parametric study in which the geometry and the connections are varied while different assumptions on the mechanical behaviour of the perpendicular walls are considered. Results of the parametric analyses showed that the perpendicular walls increase the lateral stiffness of CLT shear walls. The increase of lateral stiffness depends on the stiffness of the wall-to-wall connections, position and assumption on the behaviour of the perpendicular walls. Results of this study represent a basis for future studies in which the contribution of the perpendicular walls is investigated at building level.*

1. INTRODUCTION

1.1. Background

The wooden structures sector has been growing strongly in recent decades due to a combination of different factors, such as the sustainability of the material, the fact that the structures are made of prefabricated elements which permit a fast erection of buildings and their good mechanical performances in case of seismic actions. In this context, Cross-Laminated Timber (CLT) structures play an important role that strongly contributes to the growth of the sector.

CLT structures are realized by means of CLT panels, which are mutually connected with metal fasteners and mechanical anchors. The Lateral Load Resisting System (LLRS) of this structural typology is composed of the CLT shear walls, which are connected to foundations by steel brackets, such as hold-downs and angle brackets, using small diameter fasteners like screws and nails. The CLT panels have a stiff behaviour if compared to that of the mechanical connections, therefore in a CLT building most of the structural flexibility is provided from the connections, which consequently play the most important role in terms of stiffness, strength and ductility of the structure.

The seismic performance of CLT structures has been the central topic of several experimental research projects that were carried out on wall systems and full-scale buildings. In Europe several experimental campaigns were performed to investigate the seismic behaviour of CLT shear walls, see for instance [1-3]. The results of these studies showed that the layout of connections influence the cyclic behaviour of shear walls and that the CLT panels act as rigid bodies with low in-plane deformations. One of the largest experimental research activities on the seismic behaviour of low-and-medium-rise CLT buildings was carried out within the SOFIE Project [4], in which shake table tests on a three- and a seven-story CLT building were performed. The outcomes of tests on the buildings showed that the CLT panels remained undamaged and failures were observed only locally in joints and connections.

In CLT buildings, the lateral deformation mechanisms of the shear walls are considered when determining their lateral stiffness and resistance. CLT shear walls subjected to lateral loads typically deform with a combined mechanism of rocking and sliding. Regarding the lateral resistance, a global failure mechanism related to rocking behaviour is typically observed in CLT shear walls with a low width-to-height aspect ratios, while sliding failures occur in CLT shear walls with high width-to-height aspect ratios [3, 5]. Regarding the lateral stiffness, several analytical models are available in literature to calculate the shear wall lateral stiffness and some of these analytical studies are discussed in the next sections.

Knowing the lateral stiffness of CLT shear walls is important for determining the distribution of the lateral loads among the shear walls of CLT buildings. If a rigid behaviour can be assumed for the floor diaphragms, the distribution of the lateral loads among the shear walls can be assumed – in elastic analyses – proportional to their lateral stiffness. The load undertaken from each shear wall can be then used for designing the wall base connections, unless capacity design strategies are adopted. The overall lateral stiffness and capacity of the CLT building is therefore calculated as the sum of the capacities of the individual shear walls, which work as an in-parallel system.

However, the lateral stiffness of CLT shear walls can be influenced from other connections typologies that are present in CLT buildings, such as the connections between the shear walls and perpendicular walls, see Fig.1. Such connections can contribute to variate the lateral stiffness of CLT shear walls and contribute mostly to the so-called box-behaviour of the CLT buildings.

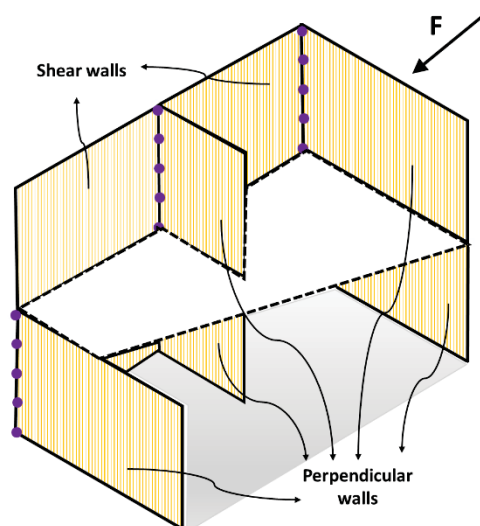


Fig.1: Representation of a typical CLT building with shear and perpendicular walls.

1.2. Effect of perpendicular walls

The behaviour of shear walls can be influenced from the three-dimensional behaviour of the building. In this respect, the perpendicular walls and the connections to the shear walls can play an important role. However, the research on the effects of perpendicular walls on seismic performance of CLT shear walls is limited.

The effects of perpendicular walls was found in several experimental campaigns on full-size Light Frame Timber (LFT) platform buildings [6, 7]. Such effects were found also from Popovski and Gavric [8], who investigated the three-dimensional performance of a two-story CLT building under lateral cyclic loads. In this experimental study, uplift of the perpendicular walls, which contributed to the overall building capacity, were detected. Such result highlighted that perpendicular walls may act as a hold-down system and have a significant effect on the lateral-load resistance and deformability of CLT structures. In a subsequent study [9] the same authors calculated the building lateral capacity and found an additional contribution to the lateral resistance given from the perpendicular walls. In the study, the authors concluded that the influence of perpendicular walls shall be included in the analytical design of CLT shear walls.

The influence of the perpendicular walls on the lateral stiffness and capacity of CLT buildings was found also in analytical and numerical studies.

Shahnewaz et al.[10], presented closed-form equations to estimate the deflection of single and coupled CLT shear walls under lateral loading considering the influence of wall-to-wall and floor-to-wall connections. Parametric analyses showed that the presence of perpendicular wall reduces the deflections as a function of the stiffness of the connections.

Hummel et al. [11] considered the influence of the perpendicular walls in seismic analyses of CLT buildings, to evaluate the q -factor. From this study, it is emerged that connecting shear walls to perpendicular walls provides an increase of the lateral resistance and of the deformation capacity of the building.

Tamagnone et al. [12], proposed a simplified non-linear procedure for seismic design of CLT wall systems that was validated against two- and three-dimensional numerical models. While acceptable accuracy was obtained in the comparison with two-dimensional numerical models, larger errors were detected in comparisons with three-dimensional models due to the box effect of the CLT building provided from the connection between perpendicular walls. In this study,

the authors concluded that the box behaviour has a stiffening influence on the response of shear walls, which decreases the sliding and rocking deformations of the shear walls.

Typically, in the practical design, the influence of the perpendicular walls on the mechanical behaviour of CLT buildings is not taken into account. Although this approach simplifies the seismic design procedure, from the other side it neglects the effects of the perpendicular walls and the box behaviour of the building, which was found in several studies to be significative.

With the aim to quantify these effects, this paper proposes an analytical model for the evaluation of the elastic horizontal stiffness of CLT shear walls connected to perpendicular walls through wall-to-wall connections.

2. HORIZONTAL STIFFNESS OF CLT SHEAR WALLS

2.1. Analytical models from the literature

Analytical models for the design of CLT shear walls are based on the different contributions of the shear wall deformations.

The evaluation of lateral stiffness of CLT shear walls is carried out with analytical models that consider the kinematic behaviour of the wall. Typically, three displacement contributions take place in CLT shear walls under lateral loads: rigid-body rotation (rocking), rigid-body translation (sliding), and panel deformation which has a shear and a bending contribution, see Fig.2.

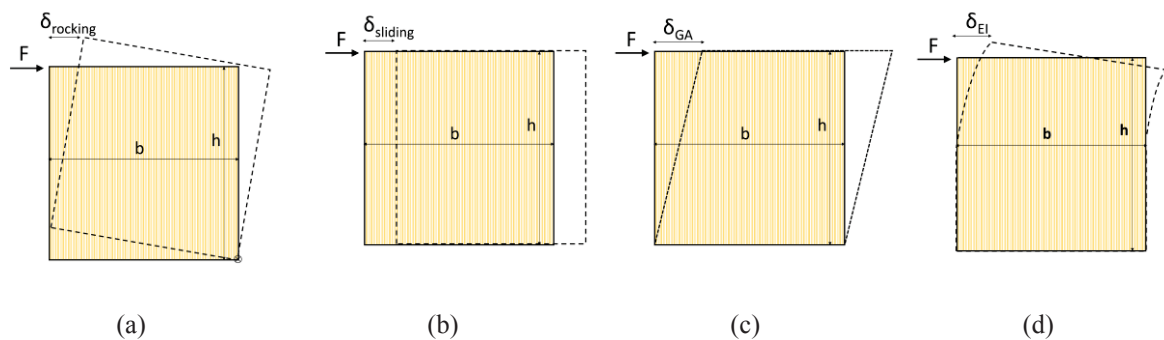


Fig. 2: CLT shearwall deformation mechanisms: rocking (a), sliding (b), in plane shear deformation (c), in plane bending deformation (d).

The total displacement of CLT shear wall, δ_{wall} , subject to a horizontal force F , can be written as shown in equation Eq.(1):

$$\delta_{wall} = \delta_{rocking} + \delta_{sliding} + \delta_{GA} + \delta_{EI} \quad (1)$$

Eq.(1) is valid for a single CLT shear wall, while in the case of multi-storey shear wall assemblies the contribution of the cumulated rotation should be also taken into account.

Several models for calculating the horizontal displacement of a CLT shear wall, which are based on different assumptions regarding the deformation mechanisms, are available in literature, see for instance [3, 5, 13-15]. In the next, three of these models are discussed to report a short state-of-the-art. The models are reported by considering the effect of the lateral loads and neglecting the contribution of the vertical loads, as not of interest for the scope of this work.

2.1.1. Casagrande et al. [5]

Casagrande et al. [5] presented a simplified analytical method to evaluate the horizontal displacement of a CLT shear wall. Three deformation mechanisms are considered: rigid-body rotation, rigid-body translation and in plane shear panel deformation. In this model, the bending deformation of panel is neglected.

The contribution of rocking deformation depends on the stiffness of the hold-down and on the wall geometry, according to Eq.(2):

$$\delta_{rocking} = \left(\frac{Fh^2}{K_{HD}(\tau b)^2} \right) \quad (2)$$

In which:

F is the horizontal force,

h is height of the CLT shear wall,

(τb) is the distance of hold-down from the point of rotation of the CLT panel,

K_{HD} is the stiffness of the hold-down

The horizontal sliding contribution depends on the angle bracket's stiffness, see Eq.(3):

$$\delta_{sliding} = \frac{F}{n_{AB}k_{AB}} \quad (3)$$

In which:

n_{AB} is the number of angle brackets,

k_{AB} is the stiffness of one angle bracket.

The shear panel deformation depends on the geometry and the shear modulus of the CLT panel, see Eq.(4):

$$\delta_{GA} = \frac{Fh}{G_{CLT}A_{eff}} \quad (4)$$

In which:

G_{CLT} and A_{eff} are the shear modulus and the effective shear area of the CLT panel.

2.1.2. Hummel et al. [13]

Hummel et al. [13] proposed a method that takes into account the four deformation contributions shown in Fig.2.

Two cases are considered for the rocking deformation: a rigid foundation (for instance, concrete foundation) and an elastic foundation (for instance, CLT floor). While in case of rigid foundation, the rocking contribution is the same of Eq.(2), in case of elastic foundation, the rocking contribution is given in Eq.(5):

$$\delta_{rocking} = \frac{h^2}{l^* - \frac{l_c}{3}} \cdot \frac{2F}{K_D l_c^2} \quad (5)$$

In which K_D is the stiffness of elastic foundation and l^* is the distance between the centre of rotation of the wall and the furthest hold-down and l_c is the length of zone in compression. The stiffness of elastic foundation can be calculated as $K_D = \frac{E_s b_s}{t_s}$, where b_s and t_s define the wall width and thickness, respectively, and E_s is the modulus of elasticity of the elastic foundation.

The contributions due to sliding and shear deformation can be calculated with Eq.(3) and (4) respectively.

The contribution due to the bending deformation can be calculated with Eq.(6):

$$\delta_{EI} = \frac{Fh^3}{3E_{CLT}I_{eff}} \quad (6)$$

In which:

E_{CLT} and I_{eff} are the elastic modulus and the effective inertia of the CLT panel.

2.1.3. Gavric et al. [3]

The model proposed from Gavric et al. [3] takes into account the whole load-displacement curve of the connectors and it is able to predict the entire elasto-plastic behaviour of the shear wall, by means of a step-by-step analysis. In this paper, only the part related to elastic displacements is presented. The difference between the model proposed from Gavric et al. [3] and the previous two models regards the behaviour of angle brackets for tensile loads. The analytical model from Gavric et al. [3] assumes that all wall base connections react with vertical tensile loads.

This model considers the four shear wall deformation contributions given in Fig.2. The lateral displacement due to rigid-body rotation is given by the rotational equilibrium considering the tensile force in the generic connection. The contribution of rocking deformation can be calculated with Eq.(7)

$$\delta_{rocking} = \left(\frac{Fh^2}{\sum_{i=1}^n K_i x_i^2} \right) \quad (7)$$

In which:

K_i and x_i are the vertical stiffness and the distances from the point of rotation of the CLT panel of the i^{th} wall base connection.

The contributions due to sliding, shear and bending panel deformations can be calculated with Eq.(3), (4) and (6), respectively.

2.2. CLT shear walls connected to perpendicular walls

In the next, an analytical model of laterally loaded CLT that considers the contribution of the wall base connections and the contribution of the connection between the shear wall and the perpendicular wall is presented. The model is defined with the aim to quantify the additional contribution of the connection between the shear wall and the perpendicular wall on the lateral stiffness of the shear wall.

The model, shown in Fig.3, is based on the following assumptions: only the wall-base connections and the wall-to-wall connections between the shear wall and perpendicular wall are considered. The monodirectional behaviour of the wall base connection is considered, therefore hold-downs are modelled as vertical elastic springs whereas angle brackets as horizontal elastic springs. It is assumed that the CLT walls behave as rigid bodies, hence the deformations due to CLT panels are not taken into account.

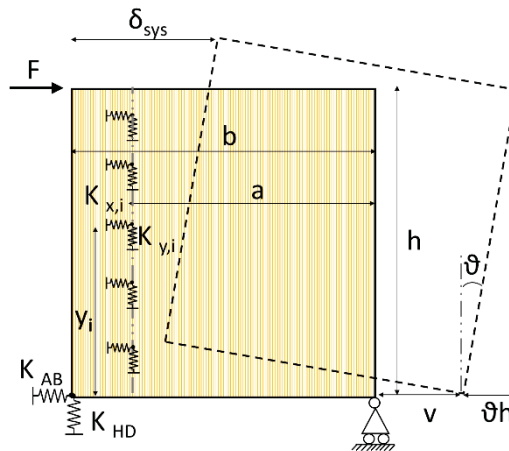


Fig. 3: Mechanical system of CLT shear wall connected to a perpendicular wall.

Consider the kinematic variables of the mechanical system shown in Fig.3, v and ϑ , whose meaning is given in Fig.3 and the substitutions shown in Eq.8.

$$\delta_{rocking} = \vartheta h \quad (a)$$

$$\delta_{sliding} = v \quad (b)$$

$$\delta_{sys} = \vartheta h + v \quad (9)$$

The total potential energy principle is used for defining the equilibrium equations of the system shown in Fig.3, with the aim to define the horizontal displacement of the model as function of the stiffness of the connections. The total potential energy of the mechanical system can be evaluated as the difference between the elastic energy of the system and the energy associated to the external horizontal force, see Eq.(10).

$$E_{tot} = \frac{1}{2}K_{AB}v^2 + \frac{1}{2}K_{HD}(\vartheta b)^2 + \frac{1}{2} \sum_{i=1}^{n_{w-w}} K_x (v + \vartheta y_i)^2 + \frac{1}{2} n_{w-w} K_y (\vartheta a)^2 - F(v + \vartheta h) \quad (10)$$

In which K_{AB} represents the sum of the horizontal stiffness of the angle brackets, K_{HD} represents the vertical stiffness of the hold-down, K_x and K_y are the stiffness of the wall-to-wall connections in the horizontal and vertical direction, respectively, and n_{w-w} is the number of wall-to-wall connections.

According to the total potential energy principle, the equilibrium condition of the mechanical system shown in Fig.3 can be found by equating the first derivative of the total potential energy respect to the kinematic variables of the system to zero.

$$\frac{\partial E_{tot}}{\partial v} = K_{AB}v + n_{w-w}K_x v + K_x \sum_{i=1}^{n_{w-w}} y_i \vartheta + F = 0 \quad (11)$$

$$\frac{\partial E_{tot}}{\partial \vartheta} = K_{HD}b^2\vartheta + K_x \sum_{i=1}^{n_{w-w}} y_i^2 \vartheta + K_x \sum_{i=1}^{n_{w-w}} y_i v + n_{w-w}K_y a^2 \vartheta + Fh = 0 \quad (12)$$

Eq.(11) and Eq.(12) represent the system of two equations, one of translational equilibrium and one of rotational equilibrium, which describe the analytical model shown in Fig.3.

$$\begin{cases} F = (K_{AB} + n_{w-w}K_x)v + \left(K_x \sum_{i=1}^{n_{w-w}} y_i \right) \vartheta \\ Fh = \left(K_x \sum_{i=1}^{n_{w-w}} y_i \right) v + \left(K_{HD}b^2 + K_x \sum_{i=1}^{n_{w-w}} y_i^2 + n_{w-w}K_y a^2 \right) \vartheta \end{cases} \quad (13)$$

2.3. Comparison of elastic stiffness matrix

The different wall displacement contributions described in the previous sections represent equilibrium equations of different elastic systems. On this basis, the displacement contributions of the CLT wall system can be written in the form shown in Eq.(14).

$$\{F\} = [K] \cdot \{\delta\} \quad (14)$$

In which F is the vector of the forces, K is the elastic stiffness matrix of the system and δ is the vector of the displacements.

The analytical model of Casagrande et al. [5], described in section 2.1.1, can be written as shown in Eq.(15).

$$\begin{Bmatrix} F \\ Fh \end{Bmatrix} = \begin{bmatrix} n_{AB}k_{AB} & 0 \\ 0 & K_{HD}\tau^2b^2 \end{bmatrix} \begin{Bmatrix} v \\ \vartheta \end{Bmatrix} \quad (15)$$

The analytical model of Hummel et al. [13] can be written as in Eq.(15) in case of rigid foundation, whereas in case of elastic foundation can be written as shown in Eq.(16).

$$\begin{Bmatrix} F \\ Fh \end{Bmatrix} = \begin{bmatrix} n_{AB}k_{AB} & 0 \\ 0 & \frac{1}{2}K_Dl_c^2 \left(l^* - \frac{l_c}{3} \right) \end{bmatrix} \begin{Bmatrix} v \\ \vartheta \end{Bmatrix} \quad (16)$$

The analytical model of Gavric et al. [3], described in section 2.1.3, can be written as shown in Eq.(17).

$$\begin{Bmatrix} F \\ Fh \end{Bmatrix} = \begin{bmatrix} n_{AB}k_{AB} & 0 \\ 0 & \sum_{i=1}^n K_i x_i^2 \end{bmatrix} \begin{Bmatrix} v \\ \vartheta \end{Bmatrix} \quad (17)$$

The analytical model presented in this work, described at the Section 2.2, can be written as shown in Eq.(18).

$$\begin{Bmatrix} F \\ Fh \end{Bmatrix} = \begin{bmatrix} (K_{AB} + n_{w-w}K_x) & \left(K_x \sum_{i=1}^{n_{w-w}} y_i \right) \\ \left(K_x \sum_{i=1}^{n_{w-w}} y_i \right) & \left(K_{HD}b^2 + K_x \sum_{i=1}^{n_{w-w}} y_i^2 + n_{w-w}K_ya^2 \right) \end{bmatrix} \begin{Bmatrix} v \\ \vartheta \end{Bmatrix} \quad (18)$$

It is possible to observe that, the equations (15) to (17) describe diagonal matrices, in which sliding and rocking of a single shear wall are independent. In these cases, the stiffness of rocking ($K_{rocking}$) and the stiffness of sliding ($K_{sliding}$) depend on terms in the diagonal of the stiffness matrix.

The new model of shear wall with wall-to-wall connections given in Eq.(18) describes an elastic stiffness matrix in which sliding and rocking are mutually influenced. Shear wall connected to perpendicular wall model constitute a system, which is statically indeterminate, differently from the shear wall models without wall-to-wall connections between perpendicular walls.

From the resolution of the system described with Eq.(18), it is possible to obtain the horizontal contribution of deformation due to rocking ($\delta_{rocking}$), see Eq.8(a), and sliding ($\delta_{sliding}$), see Eq.8(b), which depend on the stiffness of hold-down, angle brackets and wall-to-wall connections. As consequence, the rocking stiffness ($K_{rocking}$) and the sliding stiffness ($K_{sliding}$) of the system depend on hold-down, angle brackets and wall-to-wall connections, and can be calculated with Eq.19(a) and (b).

$$K_{rocking} = \frac{F}{\delta_{rocking}} \quad (a)$$

$$K_{sliding} = \frac{F}{\delta_{sliding}} \quad (b) \quad (19)$$

Since the CLT walls deform under lateral load as an in-series system, the overall stiffness of the system can be calculated with Eq.(20). According to Casagrande et al. [5], Eq.(20) can

schematized as shown in Figure 4(a) in the case of shear wall without the wall-to-wall connections. Considering the effect of the wall-to-wall connections the system can be modified as shown in Figure 4(b), from which is possible to observe that the sliding and rocking stiffness continue to work as in-series system. However in this case, the mutual influence of the connections system contribute to increase their magnitude working as an internal in-parallel system.

$$K_{sys} = \left(\frac{1}{K_{rocking}} + \frac{1}{K_{sliding}} \right)^{-1} \quad (20)$$



Fig. 4: Scheme of two elastic in-series springs for single shear wall (a) and for shear wall connected to perpendicular wall (b).

The horizontal elastic displacement of the CLT shear wall can be calculated as function of the overall stiffness of the system as shown in Eq.(21):

$$\delta_{sys} = \frac{F}{K_{sys}} \quad (21)$$

3. NUMERICAL MODEL

To validate the correctness of the analytical model presented in the previous section, an analogous numerical model of CLT shear wall anchored with wall base and wall-to-wall connections is presented in this section. The numerical model, developed in the FE software SAP2000 [16], is a two-dimensional model composed of shell elements and elastic springs, see Fig.5.

To simulate the assumption of wall panel rigid behaviour, the CLT panel was modelled as isotropic shell element from SAP2000 library with a high elastic modulus equal to 200.000 MPa. Analogously to the analytical model, hold-downs and angle brackets were considered effective along their primary direction. Hold-downs were modelled as 1-joint vertical elastic springs connected to the tense side of the wall end. Angle brackets were modelled as a unique lumped 1-joint horizontal elastic springs connected to the wall end. The compressed corner of the CLT shear wall was modelled with a vertical support that allowed horizontal translation and rotation. The wall-to-wall connections were modelled with a series of 1-joint elastic springs acting in the vertical and horizontal direction, z and x according to Fig.5.

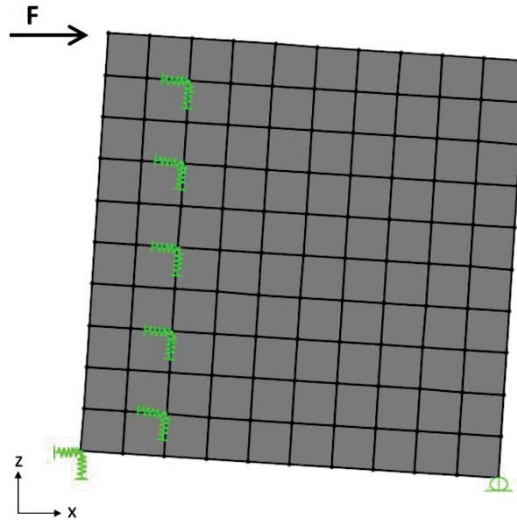


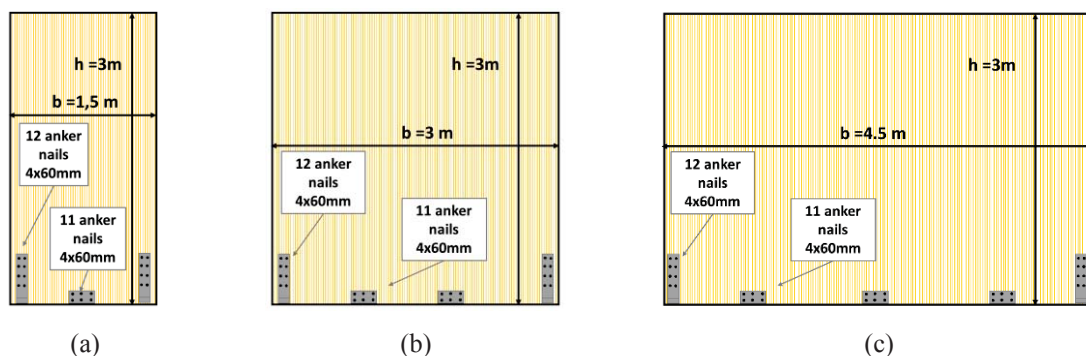
Fig. 5: FEM model of CLT shear wall and connections.

The values of stiffness of the elastic springs representing the different CLT connections were taken from experimental campaigns from the literature. Such values and the wall geometries are given in the next section, in which a parametric analysis is presented with the aim to check the correctness of the analytical model and to investigate the stiffening effect of the wall-to-wall connections in different geometrical and mechanical conditions.

4. PARAMETRIC ANALYSIS

The analytical model presented in section 2.2 and the numerical model presented in the previous sections are used in this chapter to perform a parametric analysis in which different geometrical and mechanical properties of CLT walls are considered.

Since the lateral behaviour of a CLT shear wall strongly depends on the wall aspect ratio three different wall aspect ratio equal to $b/h=0.5$, $b/h=1.0$ and $b/h=1.5$ were analysed in the parametric analysis, see Fig.6.

Fig. 6: Aspect ratio of the shear walls: $b/h=0.5$ (a), $b/h=1$ (b) and $b/h=1.5$ (c).

The parametric analysis was carried out by considering mechanical properties of wall base connections based on experimental results from Gavric et al. [3]. In this study, hold-downs with twelve 4×60 mm nails, and angle brackets with eleven 4×60 mm nails were tested under tension and shear loads, respectively. Based on these experimental results, the values of stiffness of hold-downs and one angle bracket used in the parametric analysis were set equal to 4.59 kN/mm and 1.96 kN/mm, respectively. As shown in Fig.6, one, two and three angle brackets were considered for the three different wall aspect ratios $b/h=0.5$, $b/h=1.0$ and $b/h=1.5$, respectively.

The stiffness of the wall-to-wall connections was assigned based on experimental results from [17], in which wall-to-wall connections between perpendicular walls with self-tapping screws 10×180 mm, installed with an inclination of 90° respect to the plane of the shear wall, were tested. A stiffness equal to 1.53 kN/mm was considered for the wall-to-wall connections in both vertical and horizontal direction. The spacing between each connection was set equal to 300 mm that for a wall height of 3 m led to a number of wall-to-wall connections equal to $n_w=10$.

As shown in Fig. 1, perpendicular walls can be connected to shear walls in different positions.

Such positions can differently influence the mechanical behaviour of the shear wall. To evaluate such aspect, three different position of the wall-to-wall connections were considered in this study, as shown in Fig. 7:

- i. Perpendicular wall on tense side of the shear wall,
- ii. Perpendicular wall on central side of the shear wall,
- iii. Perpendicular wall on compressed side of the shear wall.

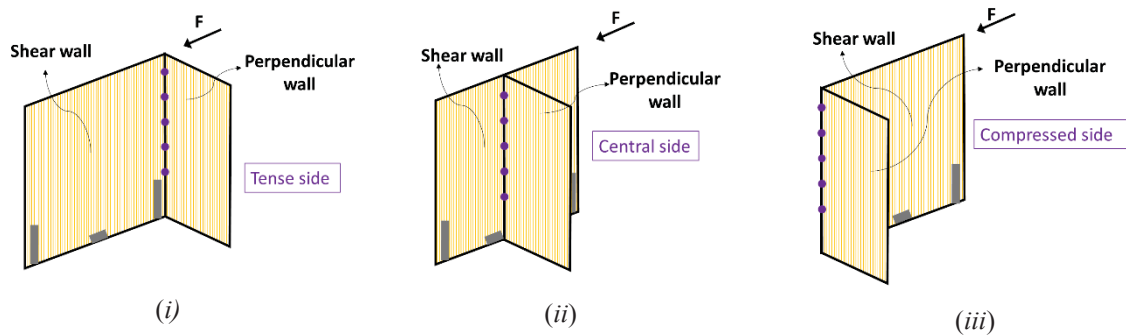


Fig. 7: Position of perpendicular wall respect to shear wall: tense side (i), central side (ii) and compressed side (iii).

It should be mentioned that the stiffening contribution of the perpendicular walls on the lateral stiffness of the shear wall depends on the wall-to-wall connections as well as on the stiffness of the wall base connections of the perpendicular wall. From Fig. 8(a), it is possible to observe that the rocking mechanism of the shear wall is influenced from the vertical stiffness of the wall-to-wall connections and on the vertical stiffness of the hold-downs of the perpendicular wall. On the other hand, the sliding mechanism is differently influenced from the perpendicular walls, which cannot undertake the horizontal load of the wall-to-wall connections since their wall base connections mostly have a hinge behaviour in the direction out of the plane, which do not permit the transfer of such forces, see Fig. 8(b). To investigate such aspects, the parametric analysis was performed in three different conditions:

- iv. Both vertical and horizontal stiffness considered with $K_y=K_x=1.53$ kN/mm;
- v. Only the vertical stiffness considered with $K_y=1.53$ kN/mm and $K_x=0$;
- vi. Only the vertical stiffness considered with $K_y=0.35$ kN/mm and $K_x=0$;

While the condition iv is representative of the potential condition in which the lateral load can be transfer to the perpendicular wall by means of both rocking and sliding mechanism, the conditions v and vi represent the realistic conditions in which only the rocking mechanism contributes to transfer the lateral load to the perpendicular walls. The condition v represents the case of perpendicular wall connected at the base with highly rigid hold-downs whereas in the condition vi represents the case of perpendicular wall connected at the base with flexible hold-

downs. In the case vi the stiffness K_y is calculated assuming an in-series behaviour of wall-to-wall connections and hold-down of the perpendicular wall.

The parameters used for the parametric analyses are summarized in Table 1.

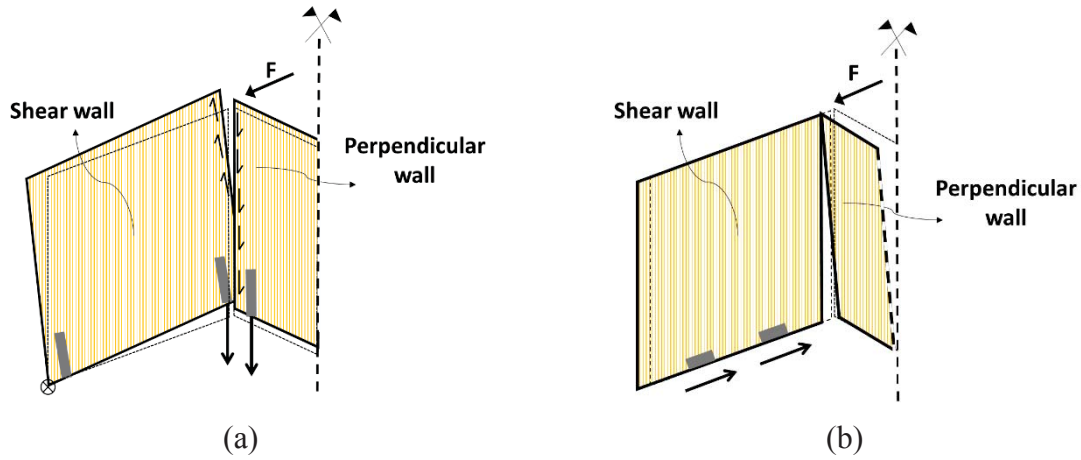


Fig. 8: Rocking (a) and sliding (b) mechanism of shear wall connected to perpendicular wall.

Perp. wall Position	h [m]	h/b [-]	K_{HD} [kN/mm]	K_{AB} [kN/mm]	K_y [kN/mm]	K_x [kN/mm]	n_{w-w} [-]
Tense side		0.5		1.96	$1.53^{(iv,v)}$	$1.53^{(iv)}$	
Central side	3	1.0	4.59	3.92	$0.35^{(vi)}$	$0^{(v,vi)}$	10
Compressed side		1.5		5.88			

Tab. 1: Parameters used for the parametric analyses.

5. RESULTS AND DISCUSSION

To evaluate the influence of the wall-to-wall connection on the lateral stiffness of the shear walls, the parametric analysis was carried out considering the conditions given in Table 1 and the benchmark condition in which the wall-to-wall connections are not considered. Such analyses were performed by using the equations of the analytical model given in Section 2.2 and the numerical model presented in Section 3. Results in terms of wall stiffness from the analytical and numerical models showed differences smaller than 1% for all the conditions analysed.

The results of parametric analysis are reported in Fig.9, Fig.10 and Fig.11, for the cases iv , v and vi described in the previous section, respectively. The figures show graphs organized in matrix form representing the different wall aspect ratios and perpendicular wall positions. Each graph reports the lateral stiffness and the rocking and sliding displacement contributions of the shear wall. The rocking and sliding displacement contributions were calculated as the ratio between the rocking and sliding displacement, calculated from Eq.8(a) and (b), and the total displacement, calculated from Eq.9.

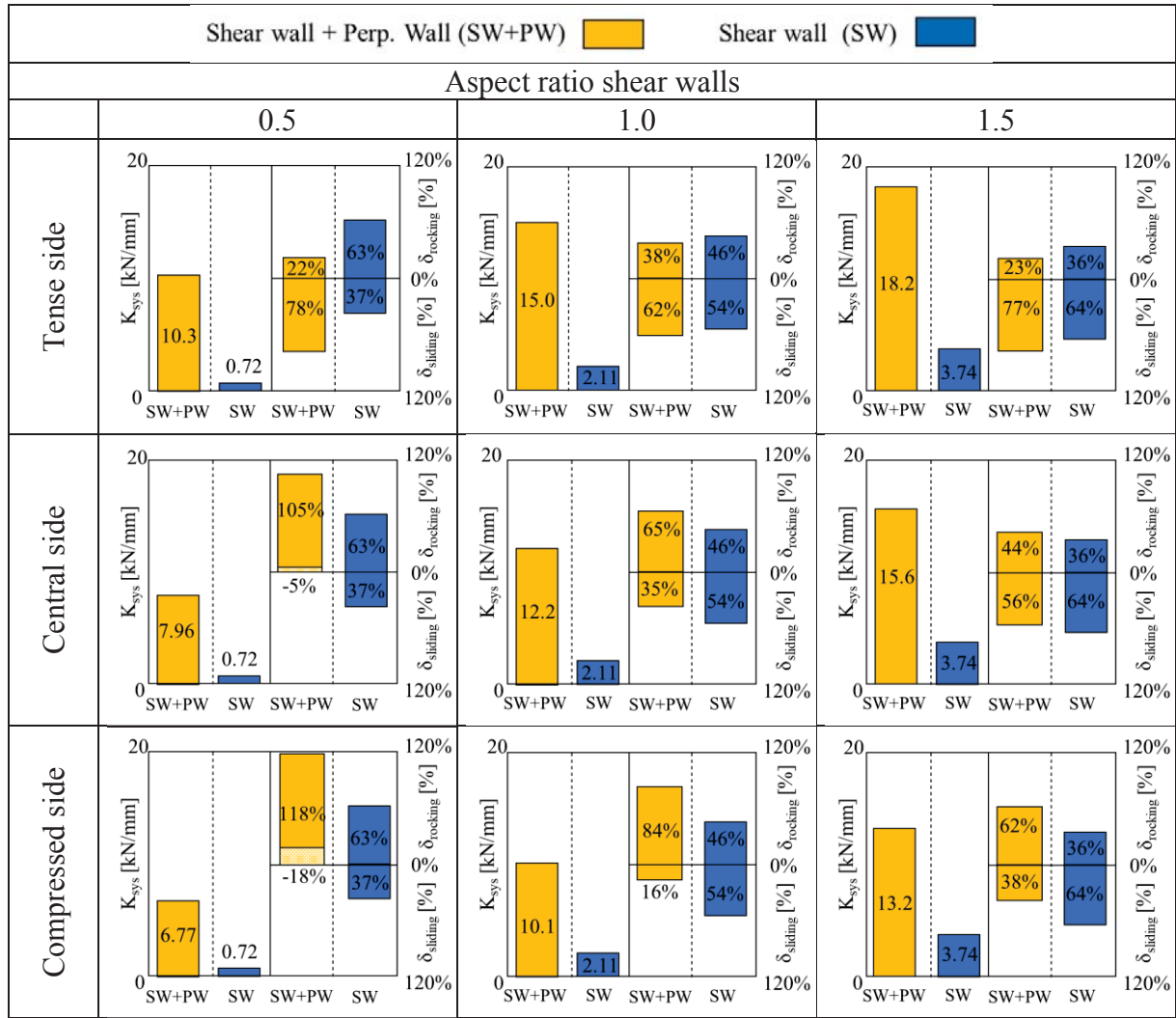


Fig. 9: Results of parametric analysis for the case *iv*.

It is possible to observe that there is an increase of the lateral stiffness in all cases analysed, due to the effect of the wall-to-wall connections. Such effect is always larger in the case of the perpendicular wall is anchored to the tense side of the shear wall and reduces as the perpendicular wall is moved toward the compressed side of the shear wall. The highest increases of stiffness are observed for wall aspect ratios equal to $b/h=0.5$ and such stiffening effect decreases as the wall aspect ratio b/h increases.

In the case *iv*, in which the shear walls can potentially transfer both uplift and lateral forces to the perpendicular walls, the highest increases of stiffness are observed. In this case, increases of the lateral stiffness up to 14 times respect to the case without the wall-to-wall connections can be observed. The results in terms of increase of lateral stiffness of the case *iv* show the potential effect of the wall-to-wall connections on the stiffness of the shear wall.

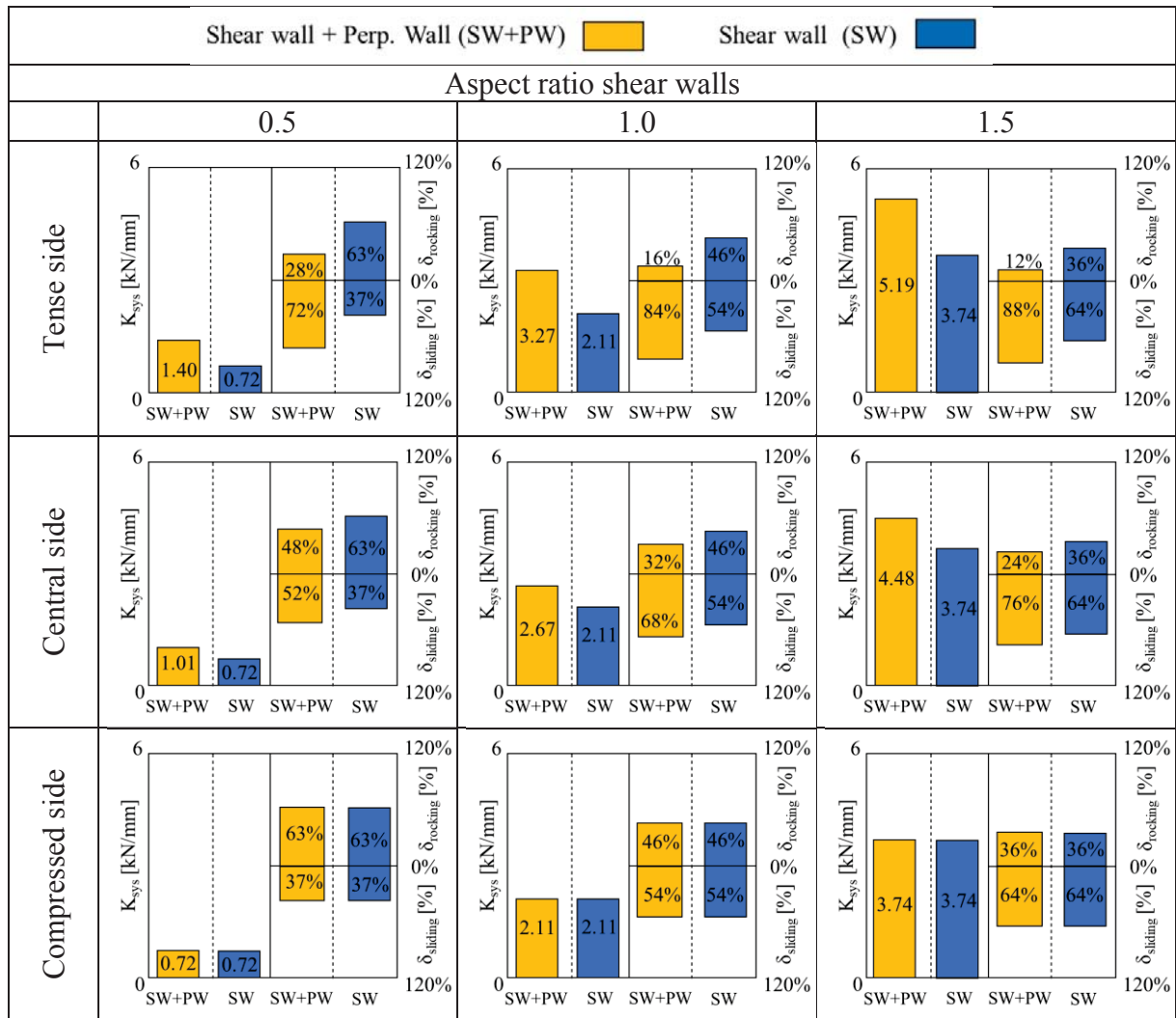


Fig. 10: Results of parametric analysis for the case *v*.

In the case *v*, in which the shear walls transfer only uplift forces to the perpendicular walls and the latter are anchored with stiff hold-downs, great reductions of the increase of lateral stiffness in comparison to the case *iv* are observed. In this case, increases of the lateral stiffness up to 2 times respect to the case without the wall-to-wall connections can be observed. Such result is due to the absence of the stiffening contribution for the sliding mechanism, which consequently become the predominant deformation mechanism. Such aspect can be observed also from the deformation mechanism contributions: in the cases where there are the highest increases of lateral stiffness there are also the greatest change in the deformation mechanisms of the shear wall.

In the case *vi*, in which the shear walls transfer only uplift forces to the perpendicular walls and the latter are anchored with flexible hold-downs, further reductions of the increase of lateral stiffness in comparison to the case *v* are observed. In this case, increases of the lateral stiffness up to 1.4 times respect to the case without the wall-to-wall connections can be observed.

In both cases *v* and *vi*, it is interesting to note the when the perpendicular wall is placed on the compressed side of the shear wall, none increase of stiffness is detected.

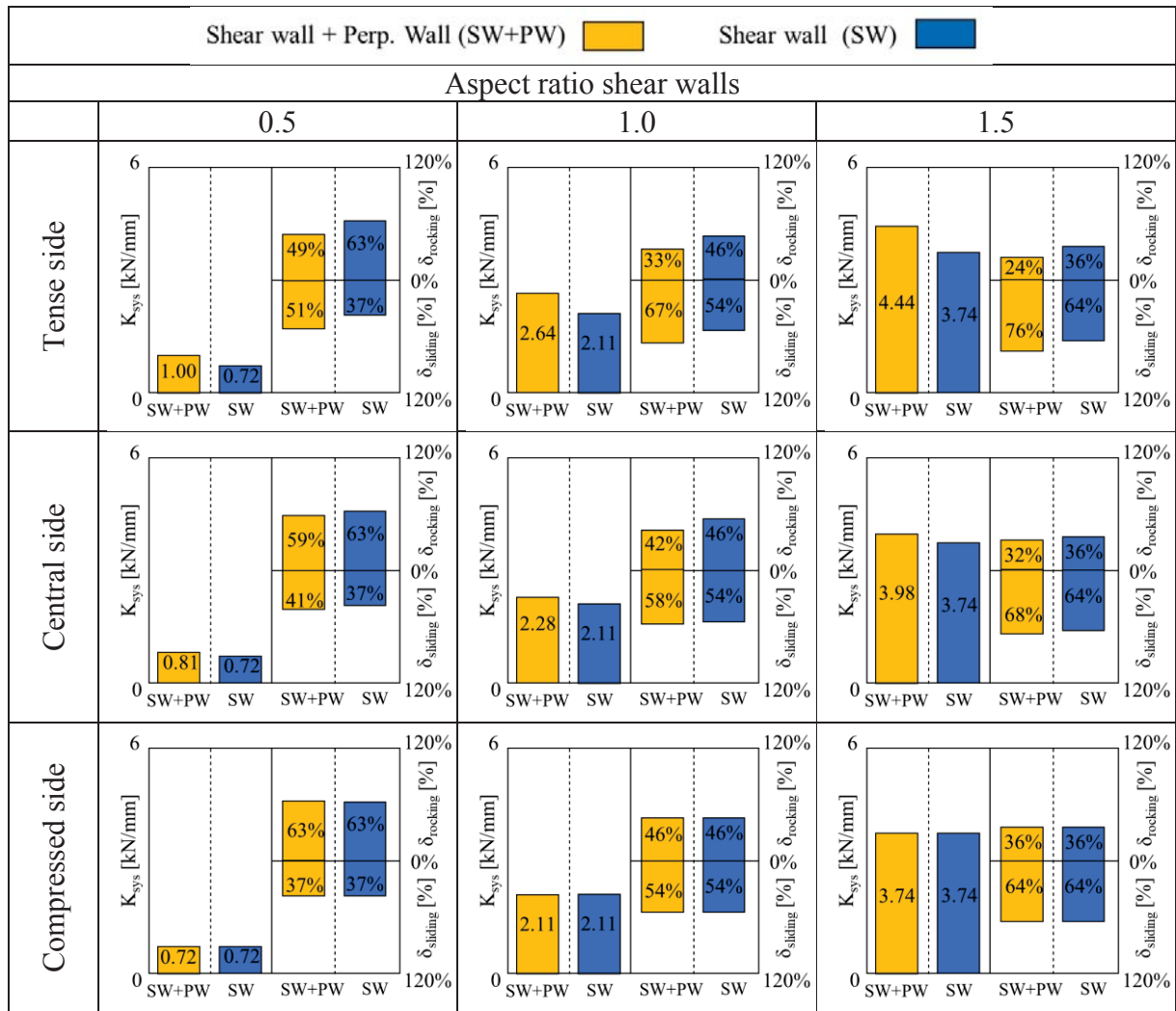


Fig. 11: Results of parametric analysis for the case vi.

CONCLUSIONS

In this paper, a study on the effect of the perpendicular walls on the lateral stiffness of CLT shear walls is presented. A new analytical model capable of calculating the stiffness of CLT shear walls connected to perpendicular walls through wall-to-wall connections is presented. The new analytical model is compared with several analytical models taken from the literature and the differences among the models are described through their stiffness matrices.

The analytical model was validated against numerical models developed in SAP2000 and used to perform a parametric analysis in which different wall geometries, anchoring configurations, position of the perpendicular walls and assumptions of the load transfer from the shear wall to the perpendicular walls were considered. The results of the parametric analysis showed that considering the effect of the perpendicular walls increase the lateral stiffness of the shear walls and modifies the contributions of rocking and sliding displacement of the shear walls in comparison to the cases in which the perpendicular walls are not taken into account. It was also shown that stiffening effect of the perpendicular walls strongly depends on the capability of their wall base connections to undertake the uplift and out-of-the-plane forces transferred from the shear walls. With current connection technologies available on the market, the perpendicular walls can contribute to increase up two times the lateral stiffness of shear walls.

Future studies of the authors will focus on the contribution of the perpendicular walls on the lateral capacity and ductility of the shear walls and on the effects of the box-behaviour at building level.

REFERENCES

- [1] J. Hummel, *Displacement-based seismic design for multi-storey cross laminated timber buildings. Dissertation.* University of Kassel, 2017.
- [2] B. Dujic, S. Aicher, and R. Zarnic, Investigations on in-plane loaded wooden elements – influence of loading and boundary conditions. *Otto Graf J.*, vol. **16**, pp. 259–272, 2005.
- [3] I. Gavric, M. Fragiaco, and A. Ceccotti, Cyclic Behavior of CLT Wall Systems : Experimental Tests and Analytical Prediction Models. *J. Struct. Eng.* vol. **141**, no. 5, pp. 1–14, 2015.
- [4] A. Ceccotti, C. Sandhaas, M. Okabe, M. Yasumura, SOFIE project-3D shaking table test on a seven-storey full-scale cross-laminated building. *Earthq. Eng. Struct. Dyn.*, vol. **13**, pp. 2003–2021, October, 2013.
- [5] D. Casagrande, S. Rossi, T. Sartori, and R. Tomasi, Proposal of an analytical procedure and a simplified numerical model for elastic response of single-storey timber shear-walls. *Constr. Build. Mater.*, vol. **102**, pp. 1101–1112, 2016.
- [6] J. W. van de Lindt, S. Pei, S. E. Pryor, H. Shimizu, H. Isoda, Experimental seismic response of a full-scale six-story wood apartment building. *11th World Conf. Timber Eng. 2010, WCTE 2010*, vol. **4**, October, pp. 3158–3165 2010.
- [7] R. Tomasi, T. Sartori, D. Casagrande, and M. Piazza, Shaking table testing of a full-scale prefabricated three-story timber-frame building. *J. Earthq. Eng.*, vol. **19**, no. 3, pp. 505–534, 2015.
- [8] M. Popovski and I. Gavric, Performance of a 2-Story CLT House Subjected to Lateral Loads. *J. Struct. Eng.*, vol. **142**, no. 4, pp. 1–12, 2016.
- [9] I. Gavric and M. Popovski, Design models for CLT shearwalls and assemblies based on connection properties. *Proc. Meet. 47, INTER- Int. Netw. Timber Eng. Res.*, no. January, pp. 269–280, 2014.
- [10] M. Shahnewaz, M. Popovski, and T. Tannert, Deflection of cross-laminated timber shear walls for platform-type construction. *Eng. Struct.*, vol. **221**, no. August 2019, p. 111091, 2020.
- [11] J. Hummel and W. Seim, Displacement-based design approach to evaluate the behaviour factor for multi-storey CLT buildings. *Eng. Struct.*, vol. **201**, December, 2019.
- [12] G. Tamagnone, G. Rinaldin, and M. Fragiaco, A novel method for non-linear design of CLT wall systems. *Eng. Struct.*, vol. **167**, no. January 2019.
- [13] J. Hummel, W. Seim, and S. Otto, Steifigkeit und Eigenfrequenzen im mehrgeschossigen Holzbau. *Bautechnik*, vol. **93**, no. 11, pp. 781–794, 2016.
- [14] M. Wallner-Novak, J. Koppelhuber, and K. Pock, *pro:Holz Brettsper Holz Bemessung Grundlagen für Statik und Konstruktion nach Eurocode.* 2013.
- [15] G. Flatscher, *Evaluation and approximation of timber connection properties for displacement-based analysis of CLT wall systems Dissertation.* Graz University of Technology, 2017.
- [16] CSI, CSI Analysis Reference Manual. *I Berkeley (CA, USA) Comput. Struct. INC*, 2013.
- [17] I. Gavric, M. Fragiaco, and A. Ceccotti, Cyclic behavior of typical screwed connections for cross-laminated (CLT) structures. *European Journal of Wood and Wood Products*, vol. **73**, pp. 179–191, 2015.

POST-TENSIONED LOW DAMAGE CLT WALLS WITH REPLACEABLE HYSTERETIC DEVICES – CONCEPT, EXPERIMENTAL AND NUMERICAL CHARACTERIZATION

Luca Pozza¹, Luca Benedetti², Valentina Tomei³, Barbara Ferracuti³, Maria Zucconi³,
Claudio Mazzotti¹

¹ Department of Civil, Chemical, Environmental and Material Engineering (DICAM), University of
Bologna

Viale Risorgimento 2, 40136, Bologna, Italy
{[luca.pozza2](mailto:luca.pozza2@unibo.it), [claudio.mazzotti](mailto:claudio.mazzotti@unibo.it)}@unibo.it

² CIRI Buildings and Construction (CIRI-EC), University of Bologna

Via del Lazzaretto 15/5, 40131, Bologna, Italy
{[luca.benedetti12](mailto:luca.benedetti12@unibo.it)}@unibo.it

³ Department of Engineering “Niccolò Cusano”

Via Don Csrlo Gnocchi 3, 00166 Rome, Italy
{[valentina.tomei](mailto:valentina.tomei@unicusano.it), [barbara.ferracuti](mailto:barbara.ferracuti@unicusano.it), [maria.zucconi](mailto:maria.zucconi@unicusano.it)}@unicusano.it

Abstract

This paper deals with the conception, the experimental and numerical characterization of an innovative post-tensioned CLT wall system equipped with external and replaceable hysteretic devices. The cyclic behavior of the post-tensioned walls was firstly investigated at the mechanical laboratory of CIRI-EC of University of Bologna by means of experimental tests on single component of the structural system and on the full-scale post-tensioned CLT walls prototypes. Results from experimental tests demonstrate the capability of the conceived post-tensioned wall systems to withstand significant drift without damage on the main timber and steel components. A good dissipative capacity of the wall configurations equipped with dissipaters was also observed. A nonlinear Finite Element model capable of reproducing the wall system hysteretic behavior was developed in the OpenSees framework. Implemented FE numerical model demonstrated a good capability of reproducing the experimental response.

Keywords: CLT walls, Experimental test, Hysteretic devices, Numerical Model, Post-tension

1 INTRODUCTION

The growing diffusion of timber buildings in seismic areas drawn the scientific community's attention to this kind of structures [1–4], leading to the conception of structural solutions able to preserve the buildings after a seismic event. To this aim, low damage post-tensioned technologies were introduced [5–8], which entrust the horizontal load to rocking dissipative timber walls. The rocking behavior is mainly controlled by PT (Post-Tensioned) bars positioned into cavities in the walls, fixed at the base and connected at the top of the wall, that control the re-centering of the system. The dissipative contribution is devoted to hysteretic dampers, simply replaceable after a seismic event, connecting the base wall to the foundation [9,10] or adjacent timber elements along elevation [10,11]. This paper deals with the experimental characterization, and numerical investigation of an innovative post-tensioned CLT wall system, equipped with external and replaceable hysteretic dampers. The investigated wall system was conceived referring to previous experience on GluLam and LVL post-tensioned technology available in literature [5,6,12] and then improved adapting the system to the use of CLT panel [7,8] and external replaceable hysteretic dampers [9].

The cyclic behaviour of the post-tensioned walls was investigated at the mechanical laboratory of CIRI-EC of University of Bologna by means of experimental tests on a single component of the structural system and on the full-scale post-tensioned CLT walls prototypes. Results from experimental tests demonstrated the capability of the conceived post-tensioned wall system to withstand significant drift without damage to the timber elements. A good dissipative capacity was also observed, mainly due to the entering into the plastic field of the dampers, which result severely damaged and easily replaceable.

A nonlinear Finite Element model capable of reproducing the wall system cyclic behaviour was developed in the OpenSees framework. The implemented FE numerical model demonstrated a good capability to reproduce the experimental response, resulting in an efficient tool for simulating the response of the entire building realized using the developed technology.

2 EXPERIMENTAL CAMPAIGN

The analyzed configuration is characterized by a single dissipative rocking wall connected to GluLam boundary columns. The GluLam columns are assumed to be part of a timber frame aiming to resist to vertical loads, while the CLT PT-wall system preserves the building against the horizontal action. The boundary columns were thought to be connected to the inter-floor beams, to avoid their direct connection with the rocking wall, that could lead to vertical displacements incompatible with the diaphragm system, as suggested by previous authors [12].

The rocking behavior is entrusted to the PT-bar and the dissipative contribution is devoted to hysteretic dampers. In particular, two pairs of dampers are placed along the base of the wall, working predominantly in the axial direction (axial dampers), and two pairs of dampers are positioned at the wall/column interfaces, working predominantly in the transversal direction (shear dampers). In addition, a post-tensioned only configuration (with no dampers) was considered, to highlight the dissipative and resistant contribution of the dampers. The PT-bars are also positioned in columns to simulate the presence of axial load.

The adopted hysteretic dampers are the so-called X-brackets [10,13], which was conceived to be employed both as axial and shear dampers. At the component level, tests were conducted to characterize the connection system developed for the fastening of the hysteretic dampers to the CLT panel adopting a superficial FRP reinforcement [14]. Results demonstrated the effectiveness of the fastening system, especially with regard to the replaceability of the hysteretic dampers. At the system level, the single wall configuration with boundary columns was considered with an initial post-tension load of 350 kN. Figure 1 reports the test setup, the sample's geometry,

and the cyclic protocol used to impose the top displacement to the wall, evaluated according to UNI EN 12512 [15], reaching 1.5% drift. The CLT panel was realized with C24 wood layers, while the initial PT (Post-Tensioned)- Force was conferred through a dywidag steel bar (“www.dywidag-systems.com/emea”) of 32 mm, characterized by a modulus of elasticity of 205 GPa and a yielding stress of 950 MPa. In addition, the X-Brackets are characterized by steel S275 and a thickness of 8 mm.

The horizontal cyclic displacement was applied to the system by means of an hydraulic actuator with a capacity of 1000 kN, positioned at 3.1 from the wall base, while the initial PT force was applied to the PT-bars by means of a hydraulic jack. Furthermore, the horizontal loads were measured during the test together with the PT forces. These records are essential for the reconstruction of the global response of the system. Moreover, in order to obtain information on the local response of the system, Linear Variable Displacement Transducers (LVDTs) were employed to measure displacements in crucial points of the system, as shown in Figure 1. In particular, one LVDT was positioned in correspondence of the actuator, to record the displacements imposed to the system; two LVDTs measured the slip between the wall and the steel foundation; eight LVDTs measured the base uplifts of the wall and columns, in order to derive the neutral axis depths; two LVDTs measured the vertical slip between column to wall interfaces.

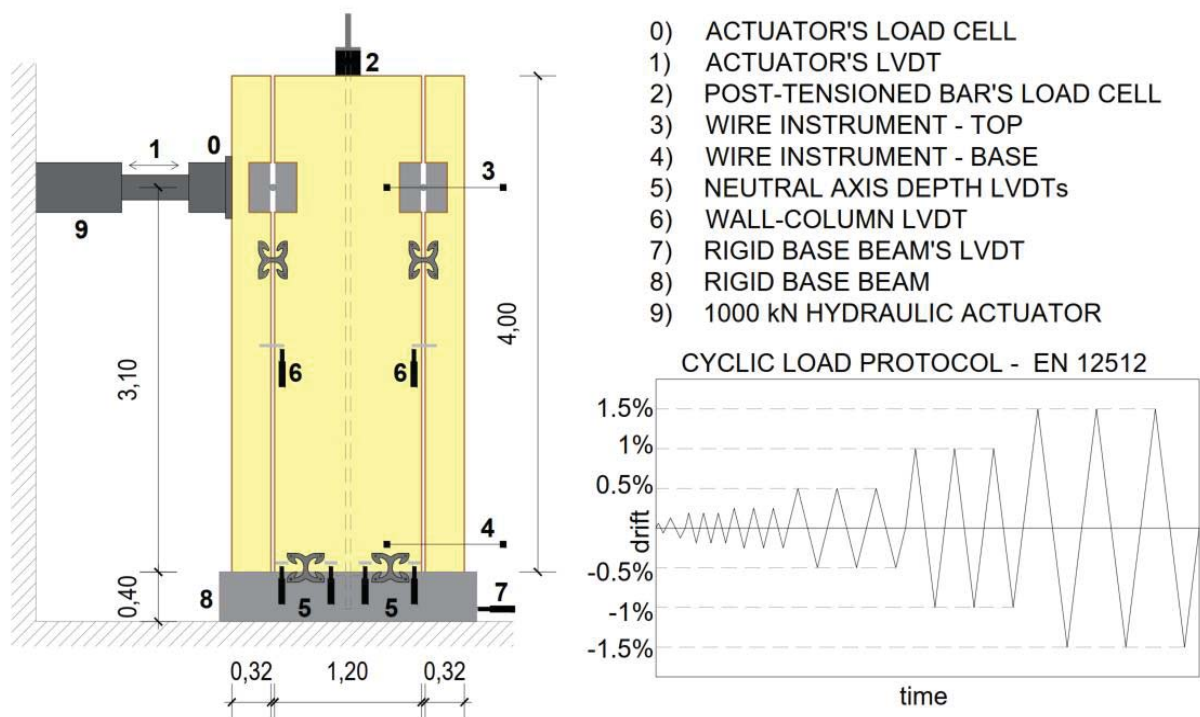
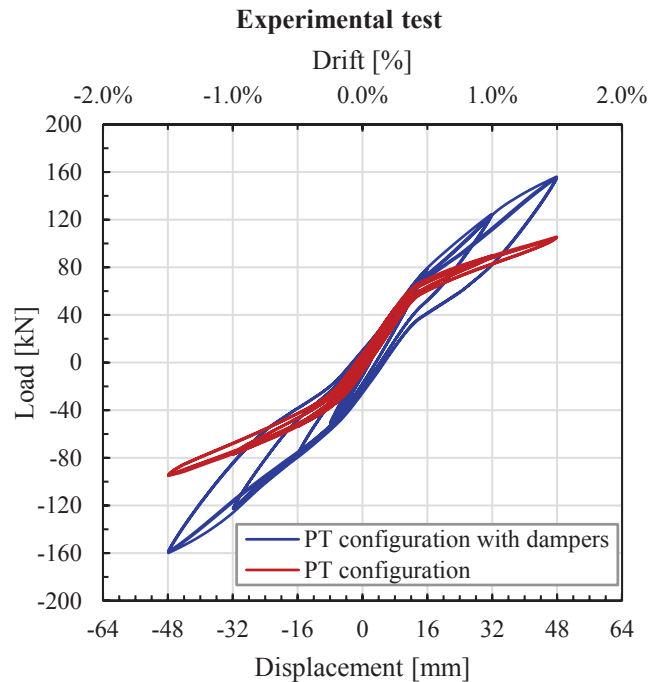


Figure 1: Column-wall-column test setup and adopted load protocol.

At tile of example, Figure 2 (a) show the view of the PT configuration equipped with both axial dampers (framed in red) and shear dampers (framed in blue). In Figure 2(b), global results in terms horizontal load/ drift curves are shows for the PT configuration (red) and for the PT configuration with dampers (blue). The two curves show an almost bilinear trend, more evident for the PT configuration, which transition point represents the drift at which the PT bar in the wall starts to deform. From the comparison between the two curves, it clearly emerges the contribution of dampers in terms of energy dissipation and strength, appreciable through the amplitude of the cycles and the horizontal load values reached with the same drift, respectively.



(a)



(b)

Figure 2: (a) View of the setup and (b) Experimental Horizontal load - Drift curves.

3 EXPERIMENTAL AND NUMERICAL RESULTS

In order to design, and then to simulate, the experimental campaign, a non-linear numerical model was developed in the OpesSees frame work[17]. The model took into account both geometrical and material non-linearities, the former due to the rocking behaviour of the system, and the latter due to the presence of axial and shear dampers. In particular, the behaviour of axial and shear dampers were calibrated on the base of experimental results obtained on the single components.

In this section, the main results of the experimental campaign are shown, compared with outputs of the numerical simulations. In particular, results obtained for the PT configuration (no dampers) and for the PT configuration equipped with axial and shear dampers are shown. Figure 3(a) and (b) report the horizontal load/ drift curves for the PT configuration and for the PT configuration equipped with dampers, respectively, highlighting their benefits in terms of energy dissipation and strength. The comparison between experimental and numerical results shows a good agreement in terms of initial stiffness, strength and cyclic behaviour. However, a slight underestimation of the cyclic behavior can be observed in the numerical simulations, mainly due to some frictional dissipation neglected in the numerical model.

The good agreement between experimental and numerical results is also confirmed by comparing the local behavior of the system, particularly on the wall uplifts measured along the base at the height of 20 cm shown in Figure 4. Furthermore, this plot helps to understand the behavior of the PT-bars, which, during the wall rocking, was subjected to elongation, and so to a PT-force increase, to accommodate the kinematic of the system. Figure 5 (a) shows the comparison between the experimental and numerical column to wall vertical slip versus drift, in which the left column, the wall and the right column are denoted as C1, W and C2, respectively. This comparison show a good agreement between results, even if the numerical model slightly overestimated vertical slips. These results are of particular interest, since the dissipative contribution of the shear dampers maily depends on the colum to wall vertical slip; it is therefore possible

to find information on the behavior of dampers even if it is not directly investigated from an experimental point of view. In this regard it is also useful to analyze some results carried out by the numerical model: as an example, the Figure 5 (b) shows numerical vertical slip/ shear force curves of the pair of shear dampers connecting the left column with the wall. In particular, it is evident that the shear dampers work in the plastic field ensuring a strong contribution in terms of energy dissipation; furthermore, it was predominantly exploited in one direction. In fact, due to the rocking behavior, when the system is pulled, the vertical slips between the left column and the wall is reduced, due to the limited width of the column, compared to that observed when it is pushed. The opposite is observed for the vertical slips between the wall and the right column.

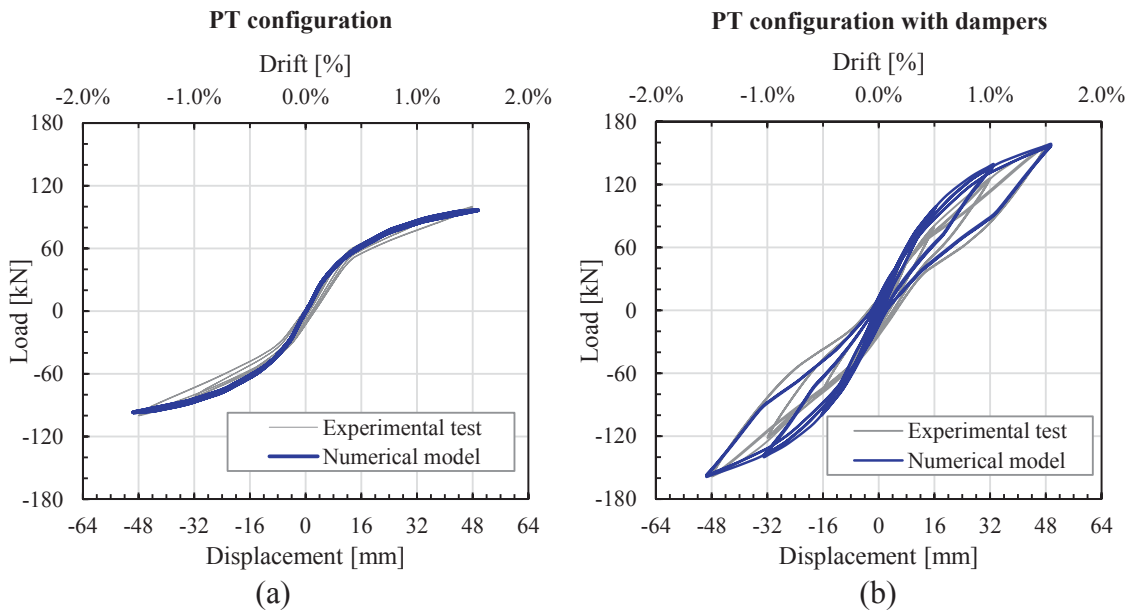


Figure 3: Horizontal Load-Drift curves: (a) PT configuration; (b) PT configuration with dampers.

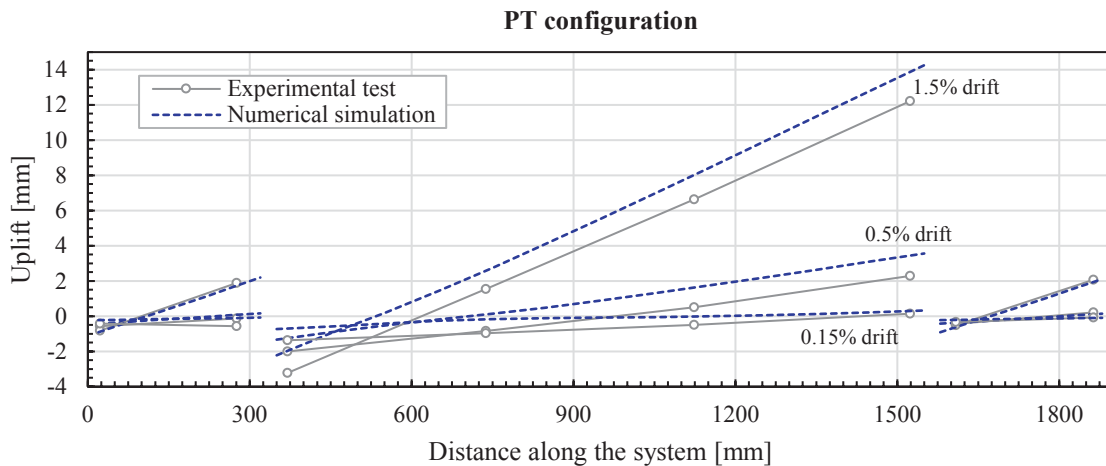


Figure 4: Base vertical uplifts: PT configuration.

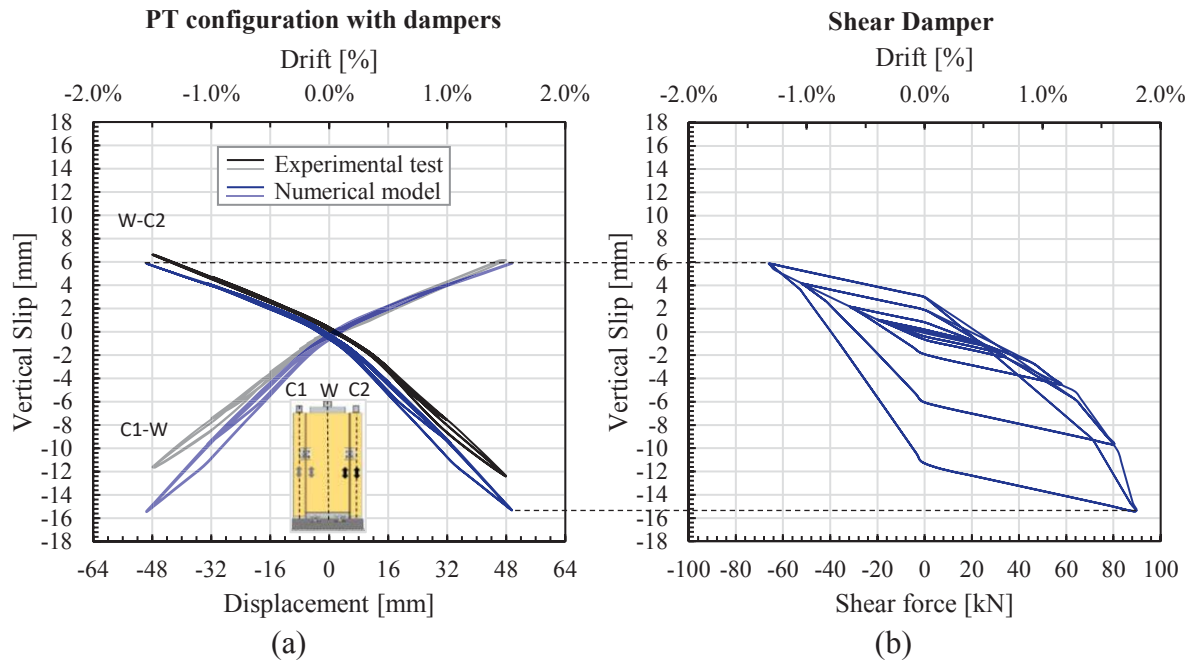


Figure 5: (a) Vertical slip/ Drift curves for the PT configuration with damper; (b) numerical vertical slip/ dampers' shear force.

CONCLUSIONS

Results of an experimental campaign on post-tensioned CLT wall system equipped with external and replaceable hysteretic devices were reported in this paper, demonstrating the capability of the developed system to withstand significant drift, until 1.5%, without damage in the structural timber elements and the principal connection systems. Moreover, a good dissipative capacity of the wall configuration equipped with both axial and shear dampers was observed, and the replaceability of the hysteretic dampers was also proved during the experimental campaign. Furthermore, a numerical model was specifically developed to predict the response of the proposed systems', considering the geometric and material non-linearities mainly due to the wall rocking behavior and to the hysteretic dampers. The proposed numerical model demonstrated a good capability of reproducing the experimental response both at global and local levels, and the ability to provide reliable prediction on behaviors not directly investigated during the experimental tests on the PT-wall system, such as the response of the hysteretic dampers. Therefore, it can be employed for the modelling of similar PT-wall systems supporting the design phase.

ACKNOWLEDGEMENT

The financial support of TIRISICO Project (POR FESR 2014-2020 – Regione Emilia Romagna) and of (Italian) Department of Civil Protection (ReLUIS 2019-2021 Grant – Innovative Materials) are gratefully acknowledged. The Authors would like also to thank the partner companies Vibro-Bloc S.p.A., Fibrenet S.p.A. and Rothoblass S.r.l. for their support and Dr. Gianluca Ussia and Dr. Francesco Grandi for the kind cooperation.

REFERENCES

- [1] A. Ceccotti, C. Sandhaas, M. Okabe, M. Yasumura, C. Minowa, and N. Kawai, SOFIE project – 3D shaking table test on a seven-storey full-scale cross-laminated building,

- Earthquake Engineering Structural Dynamics*, **42** (13), 2013.
- [2] I. Gavric, M. Fragiaco, and A. Ceccotti, Cyclic behavior of CLT wall systems: Experimental tests and analytical prediction models, *Journal of Structural Engineering*, 2015.
 - [3] F. Asdrubali, B. Ferracuti, L. Lombardi, C. Guattari, L. Evangelisti, and G. Grazieschi, A review of structural, thermo-physical, acoustical, and environmental properties of wooden materials for building applications, *Building and Environment*, 2017.
 - [4] A. Sandoli, V. Tomei, B. Ferracuti, and M. Zucconi, Challenges on clt structures seismic response: Traditional vs low-damage systems, in *16th European Conference on Earthquake Engineering*, 2018.
 - [5] A. Iqbal, S. Pampanin, A. Palermo, and A. H. Buchanan, Performance and design of LVL walls coupled with UFP dissipaters, *Journal of Earthquake Engineering*, 2015.
 - [6] F. Sarti, A. Palermo, and S. Pampanin, Quasi-Static Cyclic Testing of Two-Thirds Scale Unbonded Posttensioned Rocking Dissipative Timber Walls, *Journal of Structural Engineering*, 2016.
 - [7] R. Ganey *et al.*, Experimental Investigation of Self-Centering Cross-Laminated Timber Walls, *Journal of Structural Engineering*, 2017.
 - [8] M. Massari, M. Savoia, and A. R. Barbosa, Experimental and Numerical Study of Two-Story Post-Tensioned Seismic Resisting CLT Wall with External Hysteretic Energy Dissipaters, in *Atti del XVII Convegno ANIDIS L'ingegneria Sismica in Italia*, 2017.
 - [9] F. Sarti, A. Palermo, and S. Pampanin, Fuse-Type External Replaceable Dissipaters: Experimental Program and Numerical Modeling, *Journal of Structural Engineering*, 2016.
 - [10] R. Scotta, L. Marchi, D. Trutalli, and L. Pozza, A dissipative connector for CLT buildings: Concept, design and testing, *Materials (Basel)*, 2016.
 - [11] J. M. Kelly, R. I. Skinner, and A. J. Heine, Mechanisms of energy absorption in special devices for use in earthquake resistant structures., *Bulletin of the New Zealand Society for Earthquake Engineering*, 1972.
 - [12] F. Sarti, A. Palermo, and S. Pampanin, Development and Testing of an Alternative Dissipative Posttensioned Rocking Timber Wall with Boundary Columns, *Journal of Structural Engineering*, 2016.
 - [13] D. Trutalli, L. Marchi, R. Scotta, and L. Pozza, Capacity design of traditional and innovative ductile connections for earthquake-resistant CLT structures, *Bulletin of Earthquake Engineering*, 2018.
 - [14] A. Bellini, L. Benedetti, L. Pozza, and C. Mazzotti, Experimental characterization of monotonic and cyclic behavior of steel-to-CLT nailed joints strengthened with composite plies, *Construction and Building Materials*, 2020.
 - [15] UNI EN 12512, Timber structures. Test methods. Cyclic testing of joints made with mechanical fasteners. UNI. 2006. 2006.
 - [16] www.dywidag-systems.com/emea.
 - [17] F. McKenna, M. H. Scott, and G. L. Fenves, Nonlinear finite-element analysis software architecture using object composition, *Journal of Computing in Civil Engineering*, 2010.

TIMBER BEAM-TO-COLUMN JOINT WITH STEEL LINK: DESIGN AND MECHANICAL CHARACTERIZATION THROUGH NUMERICAL INVESTIGATION

G. Iovane, B. Faggiano *

University of Naples Federico II, Dept. Structures for Engineering and Architecture
Via Claudio 21, 80125, Naples, Italy
giacomo.iovane@unina.it, faggiano@unina.it

Abstract

For the design of dissipative heavy timber frame structures, in the context of modern seismic design approach based on the mechanical triad of strength, stiffness and ductility, brittle timber failure modes can be avoided by integrating hybrid timber-steel system into modern timber connection technology. Thus, the overall seismic performance of timber structures can be improved, entrusting the dissipation function to ad hoc conceived devices, like steel links. With reference to the structural type of Moment Resisting Frames (MRF), steel links located at the ends of the beams are able to provide a significant dissipative capacity, by means of cycles of plastic deformations, while timber members and steel connections, to be designed with an adequate overstrength as respect to the link, behave in elastic field. In this regards, the paper presents the capacity design and the mechanical characterization through monotonic numerical analyses of two different timber beam-to-column joint with steel link for MRF structures, consisting of a timber beam and a steel link connected each other by means of a stiffened end-plate and glued-in steel rods. The proposed design criteria of the joint are validated through the evaluation of performance, by means of nonlinear pushover analyses on the joint refined FEM models, in terms of key parameters, such as ultimate resistance, stiffness, rotation capacity and failure modes. The numerical results confirm the plastic deformation of the link, which large dissipative capacity of the joint corresponds to.

Keywords: Seismic resistant timber structures, beam-to-column joints for dissipative timber moment resisting frames, steel link, component method for timber joints, capacity design for timber structures, FEM analysis of beam-to column joints for timber MRFs.

1 INTRODUCTION

Toward the dissipative seismic resistant timber structures design, steps must be taken to overcome the seismic deficiencies related to the inherent fragility of wood. Since timber is a material with an elastic-fragile behavior, in the present anti-seismic regulations, such as in Europe the Eurocode 8 [1], it is indicated that the joints could dissipate through the plastic deformations of metallic connectors. However, joints are structural elements with an important role in bearing the design loads. In view of the development of heavy timber seismic resistant structures, in the context of modern seismic design approach based on the mechanical triad of strength, stiffness and ductility, the dissipative capabilities should be delegated to specific devices [2]. In fact, by integrating modern steel connection technology into timber system, brittle wood failure modes can be avoided and the overall seismic performance of timber structures can be improved. Some recent research has focused on the development of hybrid timber-steel, instead of relying on an all-timber structure, showing good potential for improving the behaviour of seismic resistant timber structures [2-4]. Very efficient solutions are steel links, to be located in timber members depending on the seismic resistant structural type, which are able to provide a significant dissipative capacity, by means of cycles of deformations in plastic field, if designed with adequate strength, stiffness and ductility.

It is therefore possible to take advantage of the knowhow on steel constructions related to the seismic design criteria, according to the approach based on the ductile and dissipation requirements (capacity design), adopting necessary adaptations corresponding to the peculiarities of timber, which should be based on the calibration of the fundamental parameters. With reference to the structural types of Moment Resisting Frames (MRF), steel links located at the ends of the beams [5-12] have the function of ductile fuses, where the plastic hinge in bending is concentrated, while the timber members should be designed with an adequate overstrength, to remain in elastic field. Recently Montuori and Sagarese [9] have applied the steel reduced beam sections, commonly proposed for steel MR frames [10, 11], to timber beams.

The crucial aspect is the design of joints. In timber structures engineering this issue is certainly innovative, it requiring a significant detailed study aimed at characterizing the mechanical behavior of connections in terms of stiffness, strength and ductility.

In this regards the paper focuses on the design of two beam to column timber joints, with the same configuration, equipped with different steel links, for dissipative heavy timber MRF. It illustrates a part of a wider study, including both numerical and experimental investigations on either joints or whole structural systems.

The joints are designed through the capacity design approach, by applying the component method, with the aim to allow the plastic hinge formation in the steel links, while the timber member and the connections are designed to remain elastic, with adequate overstrength.

The mechanical characterization of the joints is carried out through monotonic numerical analyses, on refined FE models, already calibrated upon past experimental tests [8], by means of the structural calculation program ABAQUS FEA (2019). As a result, the numerical F-u (vertical force-displacement) and M- θ (bending moment-rotation) curves obtained are compared to evaluate the capabilities of the joints and the adequacy of the proposed design criteria.

2 DISSIPATIVE JOINTS DESIGN

2.1 Design criteria of the joint

The detail of the configuration of the beam-to-column joint with steel link under study is shown in Figure 1a. In particular the steel link is connected to the timber members by means of bolted endplates stiffened by triangular plates. The capacity design is applied on two levels

[12]: for macro-components, they being timber beam and column, steel link, connection between link and timber members, so that timber members and connections have an over strength as respect to the steel link; for sub-components, they being timber members, steel link, connection elements, such as, end-plate, stiffeners and steel bars, imposing a collapse hierarchy of components for achieving an overall ductile failure of the joint (Fig. 1).

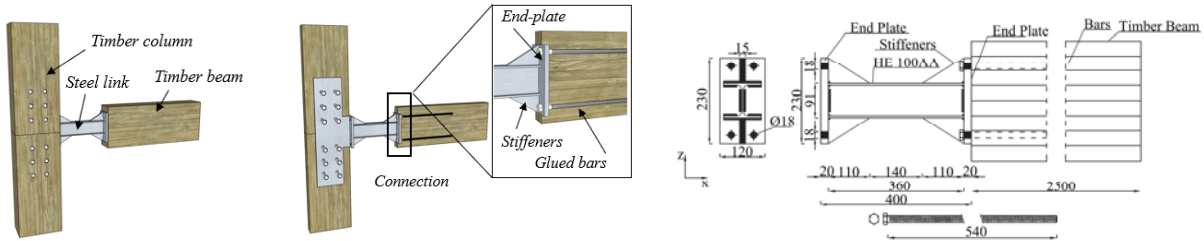


Figure 1: a) Identification of the joint components; b) the reference joint [mm; 12].

With regards to the capacity design for macro-components, the dissipative link should be designed in order to achieve a pure bending behavior, so that the full plastic bending resistance and the rotation capacity of the dissipative link should be not affected by axial and shear forces (Eurocode 3 (EC3) part 1-1[13]. At the same time, the link cross sections should have high ductility, according to EC8 [1]. For non-dissipative elements, such as timber beams and columns, the capacity design criterion should be satisfied, according to EC8 [1].

With regards to the capacity design for sub-components, according to the component method (EC3 part 1-8 [13]) the joint is assumed as an assembly of components, whose mechanical behavior is studied separately, taking into consideration the contribution of each one in terms of strength, stiffness and rotation. The link to column connection is assumed as rigid.

The design bending resistance of the joint is determined as it follows [12]:

$$M_{i,Rd} = F_{i,Rd} \cdot z \quad (1)$$

where z is the lever arm of the resistant bending moment (Fig. 2) and $F_{i,Rd}$ is the resistance of the weakest joint component, such as the smallest value among the following ones, where the stiffened endplate is studied as an equivalent T-stub (Fig. 2b, c; EC3 part 1-8 [13]).

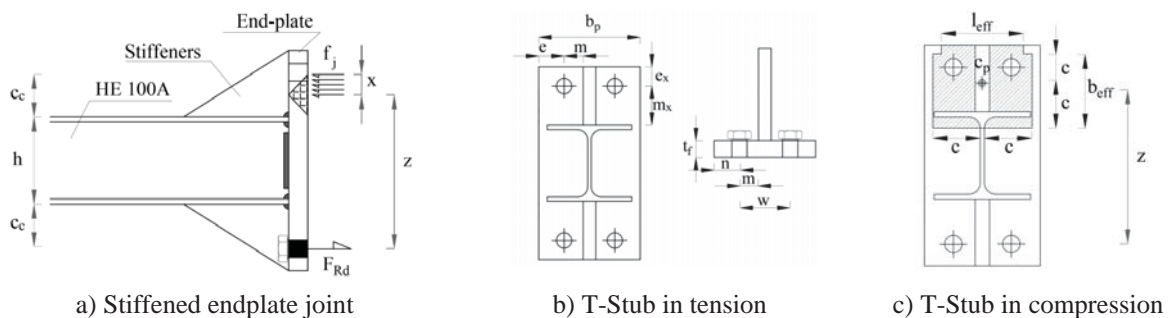


Figure 2: Joint models [13].

For the T-stub in tension (Fig. 2b), $F_{t,T-stub,Rd}$ is the minimum contribution provided by the following possible failure modes (EC3 part 1-8 [13]: 1) complete yielding of the flange; 2) bars failure with yielding of the flange in presence of prying forces; 3) bar failure in tension.

For the T-stub in compression (Fig. 2c; EC3 part 1-8 [13], $F_{c,T-stub,Rd}$ is evaluated with reference to an effective compression area, assuming the compression centre (c_p) approximately located at the centroid of the T section identified by the stiffener and the steel link flange.

For the steel stiffeners, $F_{s,Rd}$ is determined through the equivalent truss model [14], which defines the equivalent strut area of the stiffener, with a possible yielding failure mode.

For the glued-in steel bars in tension (pull-out; CNR-DT 206 R1/2018 [15]), $F_{ax,Rd}$ is evaluated with reference to the following possible failure modes: a) bar failure in tension; b) failure for debonding at the adhesive to timber interface; c) failure of timber in tension; d) failure of timber for splitting in the bar direction. The latter can be avoided by respecting the minimum distances from the edge and minimum spaces between the glued bars in tension [15].

2.2 The joints studied

The reference joint [12] is shown in Figure 1b. New link devices are here adopted, such as HE100A (Fig. 3a) and IPE100 (Fig. 3b) steel profiles. The hierarchy resistance criteria are applied to design the joints components (timber beam, end-plate, stiffeners, bars). Definitely the two study joints have the features shown in Figure 3, they also differ for the endplates thickness, they being 20 and 15 mm thick, respectively. Material grades are given in Figure 4.

In Table 3 the results of the joints design are presented. The outputs are provided for the joint components in terms of design resistance $F_{i,Rd}$, bending resistance $M_{i,Rd}$ (eq. 1) and over-strength (OS_i), evaluated as the ratio $M_{i,Rd}/M_{i,pl,Rd}$, where $M_{i,pl,Rd}$ is the bending design resistance of the link. It is apparent that the dissipative link is the first component to reach the elastic limit (yielding). Moreover the overstrength coefficient of the timber beam as respect to the link is larger for the IPE100 device and the collapse hierarchy changes for the two cases.

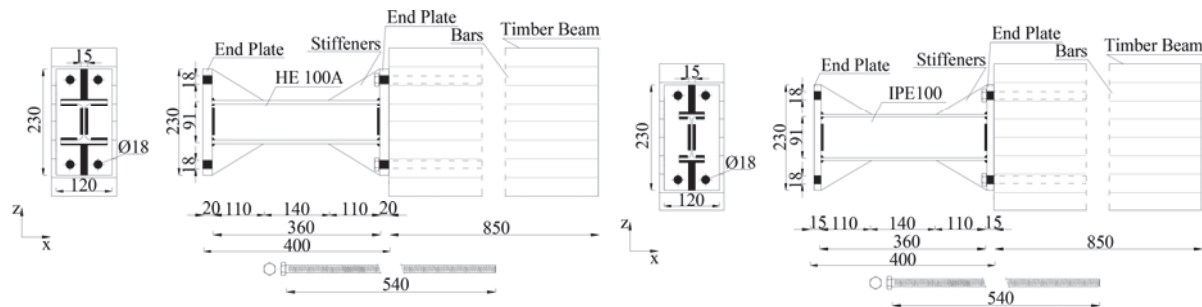


Figure 3: Geometrical features: a) HE100A and b) IPE100 joints.

HE100A				IPE100			
Collapse hierarchy	$F_{i,Rd}$ [kN]	$M_{i,Rd}$ [kNm]	OS_i [%]	Collapse hierarchy	$F_{i,Rd}$ [kN]	$M_{i,Rd}$ [kNm]	OS_i [%]
Link yielding	/	26	1,00	Link yielding	/	12	1
Pull-out (Mode d)	137	27	1,04	Stiffeners yielding	89	17	1,43
Stiffeners yielding	183	35	1,35	T-stub in tension (Mode 1)	132	26	2,12
Pull-out (Mode c)	208	40	1,53	Pull-out (Mode d)	137	27	2,19
T-stub in tension (Mode 1)	219	42	1,61	T-stub in compression	165	32	2,64
T-stub in compression	220	42	1,62	Pull-out (Mode c)	208	40	3,39
Bar failure in tension	226	43	1,66	Bar failure in tension	226	43	3,62
Timber beam in bending	/	50	1,95	Timber beam in bending	/	50	4,16

Table 3: Study joints: collapse hierarchy, design force ($F_{i,Rd}$) and bending resistance ($M_{i,Rd}$), over-strength (OS_i).

3 MECHANICAL CHARACTERIZATION OF THE JOINTS

3.1 Monotonic numerical analysis

The mechanical behavior of the HE100A and IPE100 joints is examined through a mono-

tonic nonlinear numerical analysis through the software ABAQUS FEA (2019). The implicit dynamic analysis is performed applying a load history in displacement control. The displacement is imposed at the end of the cantilever beam, with increment of 20mm up to collapse, corresponding to the test speed of 0,2 mm/s [16]. The F-u and M- θ curves are drawn to evaluate the global and local behavior of the joints. In particular, the bending moment at the joint (M) and the corresponding rotation (θ) are evaluated at the mid section of the link; the displacement (u) in z-direction is evaluated at the applied force (F) section (Fig. 4a).

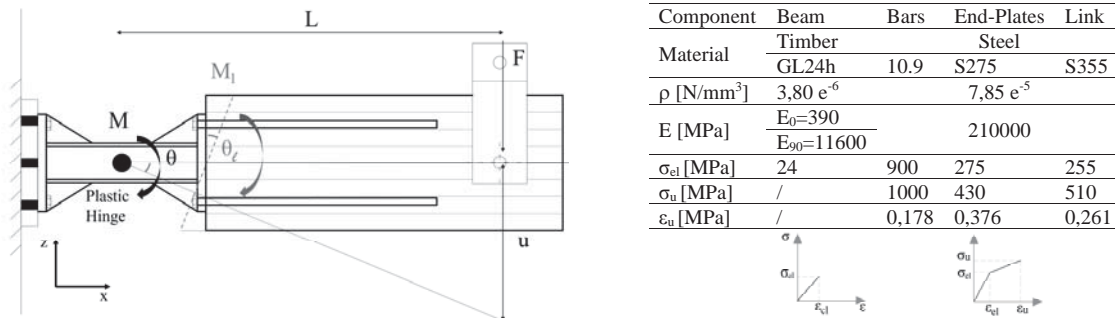


Figure 4: a) Geometric model and performance parameters of the joint; b) Materials features: density (ρ), elastic modulus (E), elastic (σ_{el}) and ultimate resistance (σ_u) resistance, elastic (ϵ_{el}) and ultimate (ϵ_u) strains.

With regard to the material models, timber is assumed with an elastic fragile behavior, while for end-plate, bolts and link steels an isotropic hardening model is adopted, according to EC3 part 1-1 ([13] Fig. 4b), and true stress-true strain equations.

In Figure 5 the Force-displacement (F-u) and Moment-rotation (M- θ) curves of the HE100A and IPE100 joints are presented and compared. Specific performance points are evidenced, corresponding to the link yielding (P_Y), full plasticization (P_P) and ultimate strength (P_C), as collapse condition and the end of the numerical analysis, it corresponding to the buckling of the link web (HE100A) or flange (IPE100).

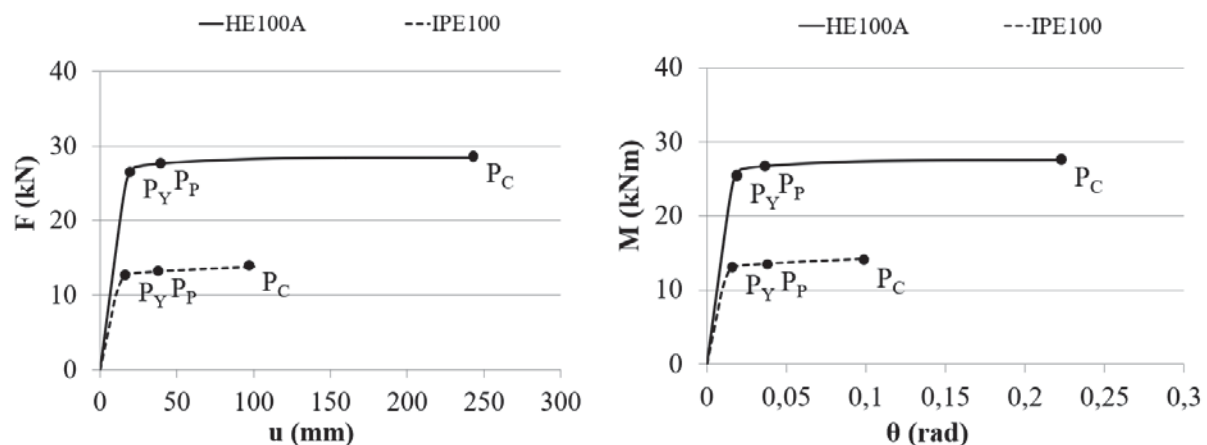


Figure 5: F-u and M- θ curves; performance points: Y-yielding, P- plasticization, C- collapse.

It is observed that the HE100A joint has greater stiffness, strength and ductility as respect to the IPE100 joint thanks to the link steel profile and the larger end-plate thickness. In both joints the plastic deformation of the link occurs, achieving the formation of the plastic hinge.

3.2 Analysis of results

The stress distribution in the joint and the AC yield (Actively Yielding) distribution that

identifies the attainment of yield stresses in the joint are shown in Table 5 at the collapse condition, where the maximum stress value (σ_{\max}) of each joint component is also given.

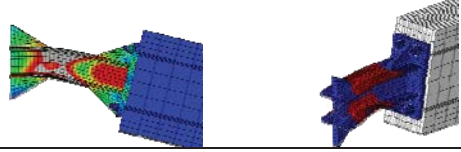

HE100A						IPE100				
										
	Link	End Plate	Threaded Bars	Timber beam	Stiffeners	Link	End Plate	Threaded Bars	Timber beam	Stiffeners
σ_{\max}	438	260	537	11,9	299	402	222	308	7,5	289

Table 5: Stress [MPa] distributions and maximum value in the joint components at collapse P_c .

For each i -th component (end-plate, stiffeners, threaded bars or timber beam) of the joints, the demand capacity ratio ($DCR_{i,j,el} = \sigma_{i,j} / \sigma_{i,el}$) between the maximum stress value evaluated at P_c point ($\sigma_{i,Pc}$) and the stress value at the elastic limit P_y point ($\sigma_{i,el}$) is provided in Table 6.

[%]	Link		End Plate		Thread Bars		Timber beam		Stiffeners	
	HE100A	IPE100	HE100A	IPE100	HE100A	IPE100	HE100A	IPE100	HE100A	IPE100
$DCR_{i,el}$	123	113	95	81	60	34	50	31	109	105

Table 6: DCR [%] at P_c for HE100A and IPE 100 joints.

The following collapse hierarchy of the joint components is evidenced: Link web (HE100A) or flange (IPE100) buckle, thus inducing the joint collapse, stiffeners undergoes plastic deformation, while end-plate, bars and timber beam are still in elastic field.

4 CONCLUSIVE REMARKS

The paper focuses on beam to column joints with dissipative steel link in the beam for seismic moment resistant heavy timber framed structures. In particular, the capacity design is applied through the component method, defining a collapse hierarchy on two levels, macro-components and sub-components. For both the joints, the numerical non linear pushover analysis has confirmed both the formation of the plastic hinge in the link which dissipates the energy through plastic deformation and the collapse hierarchy of the joint components, validating both the efficiency of the system and the proposed design method.

Future developments include the numerical evaluation of the cyclic behavior of the joints. Moreover, experimental tests will allow to check the accuracy of the proposed design criteria and the calibration of the design parameters.

The topic is noteworthy, as background for the development of the chapter on seismic-resistant timber structures of the technical standards for constructions.

ACKNOWLEDGEMENT

The study is object of the Reluis/DPC 2019-2021 (WP3, Task 1) project.

REFERENCES

- [1] EN 1998-1: 2004: Eurocode 8: Design of structures for earthquake resistance – Part 1: General rules, seismic actions and rules for buildings (CEN: Comité Européen de Nor-

malisation).

- [2] Faggiano B., Iovane G.. First considerations on the design approach and criteria for seismic resistant moment resisting and bracings timber frames. J. Eberhardsteiner, W. Winter, A. Fadaei, M. Pöll eds. *World Conference on Timber Engineering, (WCTE2016)*, Full paper ID1094, Vienna, Austria, August 22-25, 2016.
- [3] Humbert J., Lee S.J., Park J.-S., Park M.-J.. Moment resistance of post-and-beam joints with concealed metallic connectors. A. Salenikovitch ed., *World Conference on Timber Engineering (WCTE 2014)*, Quebec City, Canada, August 10-14, 2014.
- [4] Komatsu K., Kitamori A., Mori T.. Evaluation on dynamic performance of glulam frame structure composed of slotted bolted connection system. A. Salenikovitch ed., *World Conf. on Timber Engin.(WCTE 2014)*, Quebec City, Canada, August 10-14, 2014.
- [5] Tomasi R., Zandonini R., Piazza M., Andreolli M.. Ductile end connections for glulam beams. *Structural Engineering International*, 18, 290-296, 2008.
- [6] Andreolli M., Piazza M., Tomasi R., Zandonin R.. Ductile moment-resistant steel-timber connections. *Structures and Buildings*, 164 (SB2), 65-78, 2011.
- [7] Gohlich R., Erochko J., Woods J.E.. Experimental testing and numerical modelling of a heavy timber moment-resisting frame with ductile steel links. *Earthquake Engineering & Structural Dynamics*, 47,1460-1477, 2018.
- [8] Faggiano B., Iovane G., Tartaglia R., Ciccone G., Landolfo R., Mazzolani F.M., Andreoli M., Tomasi R., Piazza M.. Numerical simulation of monotonic tests on beam-column timber joints equipped with steel links for heavy timber seismic resistant MRF. *16th International Conference of Numerical Analysis and Applied Mathematics (ICNAAM 2018)*, doi.org/10.1063/1.5114268.
- [9] Montuori R. and Sagarese V.. The use of steel RBS to increase ductility of wooden beams. *Engineering Structures*, 169, 154-161. 2018.
- [10] Faggiano B., De Cesbron De La Grennelais E., Landolfo R.. Design criteria for RBS in MR frame retrofitting. *4th International Conference Behaviour of steel structures in seismic areas (STESSA 2003)*, 683-690, 2003.
- [11] Montuori R.. The influence of gravity loads on the seismic design of RBS connections. *The Open Construction and Building Technology Journal*, 8, 248-261, 2014.
- [12] Iovane G., Noviello C., Mazzolani F.M., Landolfo R., Faggiano B.. Beam-to-column joint with steel link for timber structures: system optimization through numerical investigations and design criteria. *World Conference on Timber Engineering (WCTE2021)*, Santhiago del Chile, Chile, August 9-10, 2021.
- [13] EN 1993: 2005: Eurocode 3: Design of steel structures. Part 1-1: General rules and rules for buildings, Part 1-8: Design of joints (CEN: Comité Européen de Normalisation).
- [14] Lee C.H. Seismic Design of Rib-Reinforced Steel Moment Connections based on Equivalent Strut Model. *Structural Engineering*, 128 (9), 1121-1129, 2002.
- [15] CNR DT 206–R1/2018,. Instructions for the Design, Execution and Control of Timber Structures. Technical document CNR (National Research Council), 2018.
- [16] EN 12512: 2001/A1: 2005: Timber Structures - Test methods - Cyclic testing of joints made with mechanical fasteners (CEN, French: Comité Européen de Normalisation).

A NUMERICAL STUDY ON A TIMBER-BASED SEISMIC RETROFIT INTERVENTION FOR MASONRY INFILLED CONCRETE FRAMES

F. Smioldo¹, D. Viel², I. Giongo¹, and M. Piazza¹

¹ University of Trento
Via Mesiano 38123, Trento (Italy)
 {francesco.smioldo, ivan.giongo, maurizio.piazza}@unitn.it

² University of Trento
Via Mesiano 38123, Trento (Italy)
davide.viel@alumni.unitn.it

Abstract

The paper focuses on a retrofit strategy applicable to existing reinforced concrete (RC) frame structures to reduce their seismic vulnerability. The intervention strategy, for the sake of brevity named RC-TP (Reinforced Concrete-Timber Panels), consists in the removal of the existing masonry infills and in their replacements with Cross Laminated Timber (CLT) panels fixed to the concrete elements by means of a timber subframe and a dissipative connection comprised of metal dowel-type fasteners. The analyses were performed via finite element modelling by adopting numerical strategies with different levels of refinement. In particular, refined 3-dimensional models (created using the software Abaqus) and simpler 2-dimensional models (created using the software SAP2000) were used. At first, the refined modelling approach was validated on experimental evidence on timber and concrete connectors available from the literature. Then, such 3-dimensional models were used to investigate the connection system of the proposed retrofit strategy paying particular attention to possible out-of-plane effects that cannot be directly observed with 2-dimensional models. The obtained results were used to calibrate the 2-dimensional models so that these “secondary” effects could be accounted for even in the simplified modelling. Subsequently, both modelling approaches were used to analyse an isolated one-storey one-bay frame via nonlinear static analyses that addressed the a) bare, b) original masonry infilled, and c) retrofitted configurations. The two alternative numerical strategies showed consistent results, both suggesting that the proposed intervention can significantly improve the seismic behaviour of existing RC frames.

Keywords: Structural rehabilitation; Seismic engineering; Concrete structures; Timber panels; Finite-element modelling; Nonlinear analyses.

1 INTRODUCTION

Reinforced concrete (RC) buildings represent a large percentage of the built heritage stock of many countries. Over the last decade, numerous studies have shown that, even in the case of minor earthquakes, past construction practices often led to vulnerabilities that resulted in extensive damage and collapse of the RC structure or portions of it [1], [2]. Examples of such vulnerabilities are the collapse of the masonry infills, the brittle shear failure of the RC elements or the activation of soft-storey mechanisms. Most of these buildings, indeed, were designed using codes that when they did not neglect the seismic action, accounted for it only partially. In addition, the presence of masonry infills was often disregarded in the modelling phase although nowadays it is well-known that their presence has a strong influence on the seismic behaviour of the structure [3], [4].

As a consequence, the interest of the scientific community towards such issues has grown over the years, with new solutions to improve the seismic behaviour of RC structures being proposed more and more frequently. Among these, the solutions that see the use of timber elements are gaining attention (e.g., [5]-[8]). In this regard, a retrofit intervention presented by Smioldo et al. [9], [10] is being developed at the University of Trento (Italy). Such intervention strategy aims at mitigating the seismic vulnerability of existing RC structures without modifying the original structural system. The intervention, named RC-TP (Reinforced Concrete-Timber Panels), consists in the removal of the existing masonry infills and in their replacement with Cross Laminated Timber (CLT) structural panels connected to the existing RC frame so as to redistribute the stresses due to the seismic action in order to avoid the development of brittle collapses and to favour the development of ductile mechanisms.

In this paper, the RC-TP retrofit strategy was studied via finite element modelling by adopting numerical strategies with two different levels of refinement: a 3-dimensional (3D), refined modelling approach was developed by using the finite element software Abaqus [11], while a 2-dimensional (2D), simpler approach was developed using the software SAP2000 [12]. In the first phase, the refined approach was calibrated on experimental evidence from the literature [13]-[15] concerning concrete-to-timber and timber-to-timber connections. Then, the 3D approach was used to reproduce the connection details implemented in the proposed intervention. Starting from the outcomes of the refined 3D models and focusing on the observed out-of-plane secondary effects that could have not been explicitly reproduced by 2-dimensional models, the 2D approach was tweaked to take implicitly into account such effects. Subsequently, the analyses were extended to more complex models of multiple-fastener connections and then to complete one-storey, one-bay RC frames retrofitted with the RC-TP intervention. The frame was analysed also considering the “bare frame” and “original masonry-infilled” configurations. Both in the refined and in the simplified approach, the masonry infills were simulated with modelling strategies adapted from the literature [16]-[18].

In all the configurations analysed, the alternative modelling approaches led to consistent results and confirmed the ability of the proposed intervention system to enhance the seismic behaviour of existing RC frames.

2 PRE-INTERVENTION RC FRAME

The intervention system presented in this paper is designed to be applied to existing structures. Consequently, the geometry, the detailing and the material properties of the case-study RC frame and masonry infill were selected so as to reflect the typical characteristics of buildings belonging to the existing stock. Table 1 reports the mechanical properties assumed for concrete (frame elements), steel (rebars and confinement reinforcement) and masonry (infills) in the numerical models.

Concrete		Steel		Masonry		
f_c	E_c	f_y	E_s	f_m	$f_{v,0}$	E_m
[MPa]	[MPa]	[MPa]	[MPa]	[MPa]	[MPa]	[MPa]
16,73	25673	440	21000	6,00	0,25	3000

Table 1: Mechanical properties of existing materials

Table 2 reports the geometrical and load characteristics of the RC frame used in the numerical analyses, where n is the number of longitudinal rebars, Φ is the diameter of rebars in millimetres and @ is the stirrup spacing in millimetres.

Pre-intervention characteristics		Value
Concrete frame	Length l [mm]	5000
	Height h [mm]	3000
	Column section (base \times height) [mm]	300 \times 300
	Beam section (base \times height) [mm]	300 \times 500
Reinforcements	Column longitudinal rebars	$n3+3 \Phi16$
	Column confinement reinforcement (2-legged stirrups)	$\Phi6 @150$
	Beam longitudinal rebars at ends (top – bottom side)	6 $\Phi14$ – 4 $\Phi14$
	Beam longitudinal rebars at mid-span (top – bottom side)	2 $\Phi14$ – 4 $\Phi14$
	Beam confinement reinforcement (2-legged stirrups)	$\Phi6 @200$
Masonry infill	Thickness [mm]	200
Loads	Vertical distributed (upper beam) [kN/m]	10
	Vertical concentrated (each column) [kN]	100

Table 2: Geometrical and load pre-intervention characteristics

3 INTERVENTION SYSTEM

Because the proposed intervention strategy has been fully illustrated in [9] and [10], in the present paper, only a brief description is reported. Starting from the masonry-infilled original configuration (Figure 1a), the first step is the removal of the masonry infill (Figure 1b).

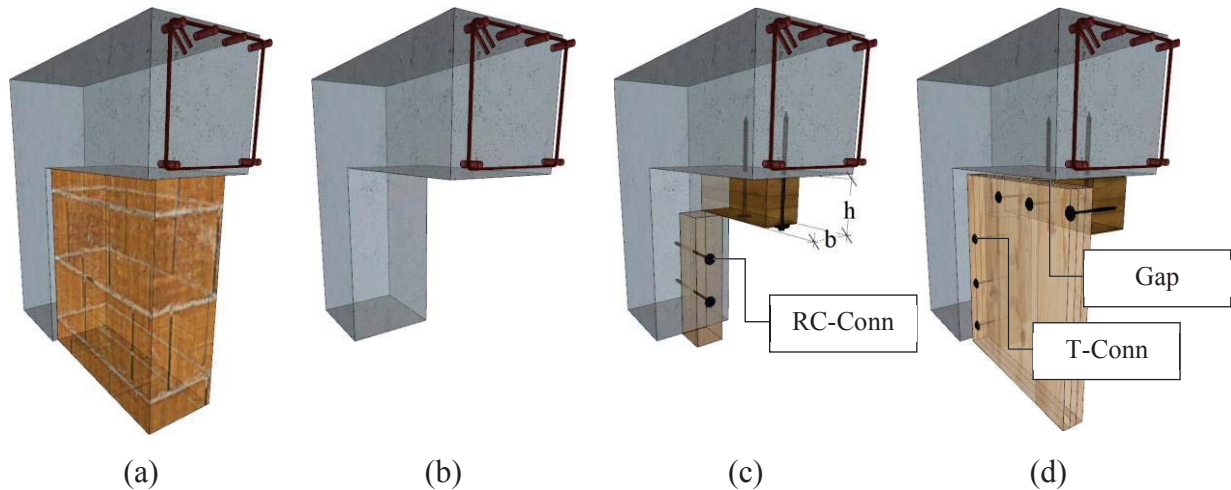


Figure 1: Intervention procedure

Subsequently, a timber subframe is connected to the RC elements through metal screw fasteners (Figure 1c). This connection is reported in Figure 2 and is named “RC-Conn” for the sake of brevity. It comprises partially-threaded concrete screws (named RC-F), inserted with washers (RC-W). The fasteners are regularly spaced at 15 cm and are designed not to exceed the elastic range when the structure is subjected to design-intensity earthquakes.

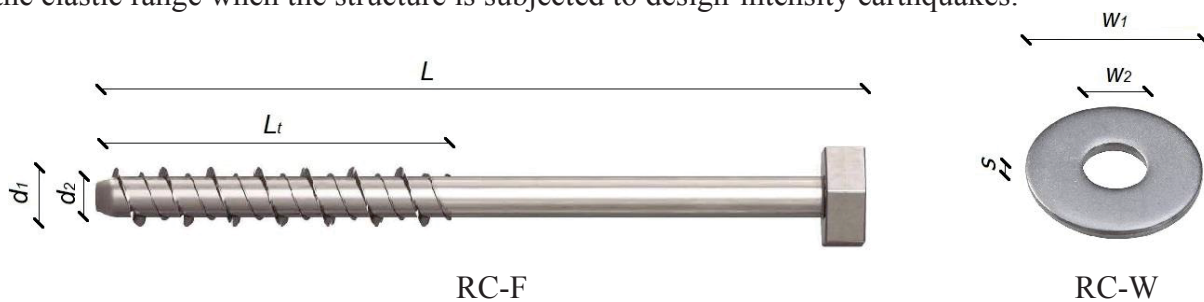


Figure 2: RC frame – timber subframe connection (RC-Conn)

In the last step of the implementation procedure (Figure 1d), a timber panel is inserted inside the RC frame and is connected to the timber subframe by using partially threaded timber screws (CLT-F) and washers (CLT-W) as those represented in Figure 3. This connection is named “T-Conn”. In the models described in the present paper, the screws were spaced at 10 cm. The role of the T-Conn is that of transferring the stresses from the timber subframe to the CLT panel and of dissipating seismic energy by engaging the post-elastic behaviour of the fasteners.

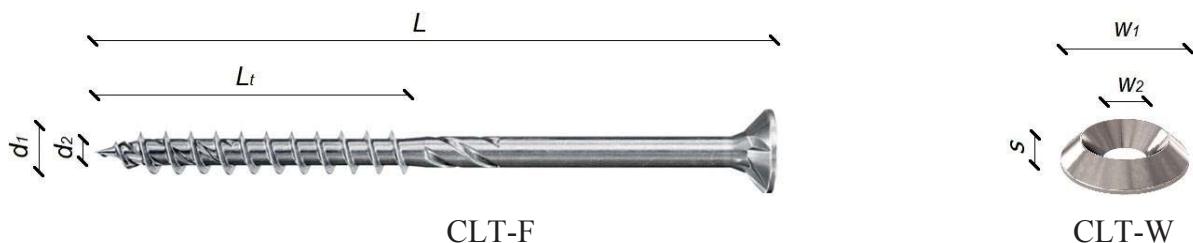


Figure 3: Timber subframe – CLT panel connection (T-Conn)

Table 3 and Table 4 give the geometrical characteristics of screws and washers, respectively.

	L [mm]	L_t [mm]	d_1 [mm]	d_2 [mm]
RC-F	200	80	12,0	8,8
CLT-F	120	60	10,0	6,4

Table 3: Geometrical properties for screws

	W_1 [mm]	W_2 [mm]	s [mm]
RC-W	44,0	13,5	4,0
CLT-W	30,0	10,8	6,4

Table 4: Geometrical properties for washers

At the perimeter of the CLT panel, between the panel edges and the internal faces of the RC frame there is a gap (visible in Figure 1d). This gap creates the necessary space for the insertion of the panel into the frame and, above all, ensures that the transfer of stress between the frame and the panel is governed by the T-Conn rather than by direct contact. In this way, it is possible to optimize the force-transfer mechanism so as to favour the development of ductile mechanisms (bending) instead of brittle failures (shear).

In the present study, the timber subframe is made of Glued Laminated Timber (grade class GL24h according to [19]) with $b \times h$ dimensions equal to 100×120 mm (Figure 1c), while the CLT panel (grade class C24 according to [20]) is 3-layered and 60 mm thick. The mechanical properties and the density of the timber elements are reported in Table 5 and were defined considering the relative Standard Codes [19], [20], and the studies of Bogensperger et al. (2011) [21], Harris et al. (2013) [22] and Gečys et al. (2015) [23].

	Bending f_m [MPa]	Tension $f_{t,0}$ [MPa]	$f_{t,90}$ [MPa]	Compression $f_{c,0}$ [MPa]	$f_{c,90}$ [MPa]	Shear f_v [MPa]	Density ρ [kg/m ³]
GL24h	24,0	19,2	0,5	24,0	2,5	3,5	420
C24	24,0	14,5	0,4	21,0	2,5	4,0	420

	Elastic modulus			Shear modulus			Poisson ratio		
	E_L [MPa]	E_R [MPa]	E_T [MPa]	G_{RL} [MPa]	G_{TL} [MPa]	G_{TR} [MPa]	ν_{RL}	ν_{TL}	ν_{RT}
GL24h	11500	300	300	650	650	65	0,00894	0,00894	0,538
C24	11000	370	370	690	690	69	0,0420	0,0270	0,602

Table 5: Mechanical properties and density for the timber elements

Additionally, in case of damage or collapse of the RC frame the use of structural CLT panel leads to a “bearing capacity reserve” for vertical actions. For this reason, the external layers of the CLT panel are oriented along the vertical axis.

4 NUMERICAL MODELS

In the present work, two different modelling approaches were used to investigate the RC-TP intervention system. The software Abaqus was used to develop 3-dimensional (3D) refined models (Figure 4a), while the software SAP2000 was used to develop 2-dimensional (2D) simplified models (Figure 4b). Specifically, the refined approach was calibrated based on experimental evidence available from the literature. Subsequently, it was used to investigate the connections implemented in the RC-TP intervention by reproducing them singularly. Furthermore, by using the 3D refined model it was possible to study possible secondary out-of-plane effects that could not have been directly observed with 2D models. The results obtained permitted to calibrate the simpler 2D models to account for the secondary effects with smaller computational effort than that required by the refined models.

Both the refined and the simpler models were used to analyse the above-mentioned RC frame under monotonic in-plane loading considering the bare, the masonry infilled and the retrofitted configurations.

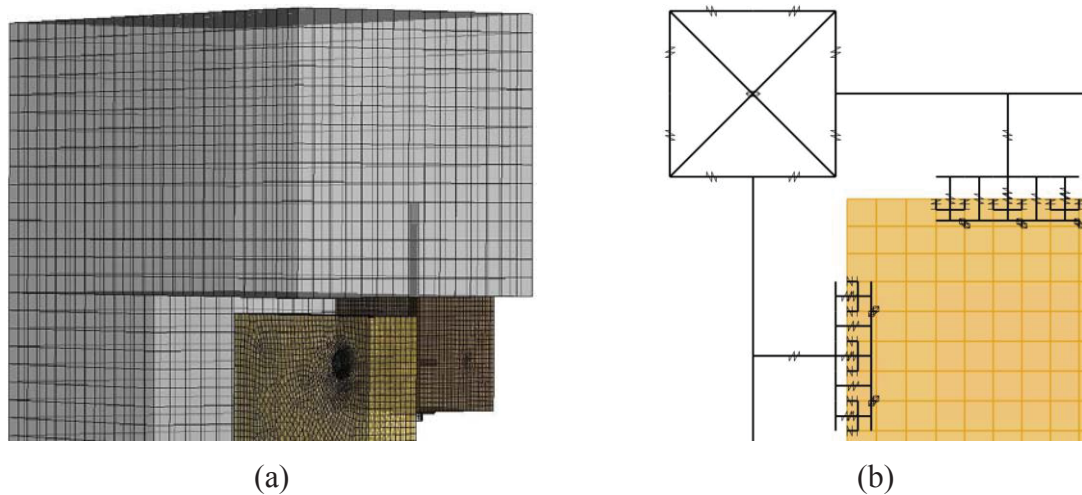


Figure 4: Alternative numerical approaches: a) Refined 3D Abaqus model; b) Simplified 2D SAP2000 model

4.1 3D modelling

The present chapter focuses on the refined 3D modelling strategy used to reproduce the RC-TP intervention system previously described. This strategy was developed using the software Abaqus/Explicit and adopted to perform nonlinear dynamic quasi-static analyses under displacement-control.

In the definition of the analysis steps, the “target time increment” coefficient was calibrated through a sensitivity analysis so as to reduce the processing time to the minimum without affecting the quality of the numerical results.

With the purpose of verifying the absence of dynamic effects, and hence confirm the acceptability of the results, the ratio between internal and kinematics energy was checked a posteriori. As suggested by [24] and [25], this ratio should not exceed 10%. Thanks to the selection of an adequate “time step” and the application of a “smooth” displacement with a sufficiently small initial slope, it was possible to limit the dynamic effects within the predetermined range.

The refined 3D model is represented in Figure 5a. It was obtained by assembling the individual elements that compose the system (a few of these elements are visible in Figure 5b). The geometry of each element was carefully designed and then imported from a 3D CAD [26] environment.

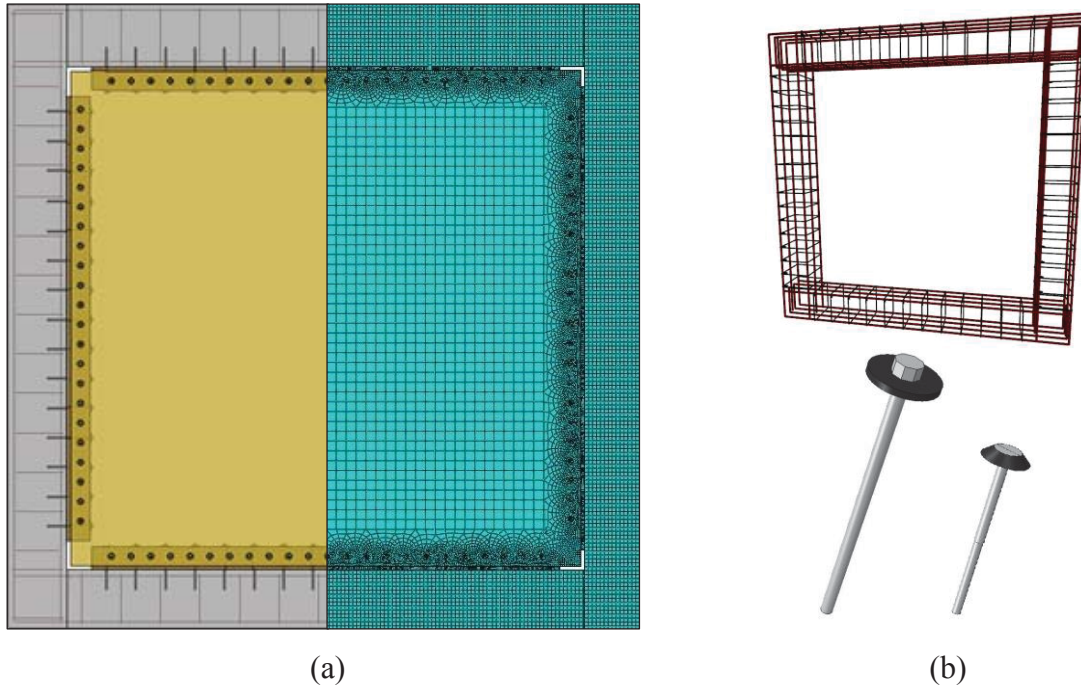


Figure 5: Intervention system – refined 3D finite element model

Concrete frame, CLT panel, timber subframe, fasteners and washers were all modelled as three-dimensional solid elements (*3D solid part*) with a homogeneous solid section. Steel bars and stirrups, instead, were modelled as one-dimensional elements (*3D wire part*).

Regarding the definition of the materials, the steel elements (bars, stirrups, fasteners and washers) were simulated as isotropic elastic-plastic elements. The three layers that compose the CLT panel were obtained from the division of a single homogeneous solid element and are oriented alternately. Each layer was modelled as an elastic orthotropic material with Hill plasticity, as recommended by [27], where the failure surface was defined with reference to the $f_{c,0}$, $f_{c,90}$ and f_v strength values reported in Table 5. Because of the failure surface symmetry, the positive (tension) stress limit for each principal direction was assumed as identical to the related negative (compression) limit. It was therefore decided to refer to the values associated with the compression parallel and perpendicular to the grain. This choice is justified by the fact that the expected collapse mechanism sees the local bearing failure of the wood material in the proximity of the screw fasteners, which depends almost exclusively on the compressive strength parameters.

The timber subframe was modelled similarly to the layers of the CLT panel (i.e. elastic orthotropic material with Hill plasticity).

The concrete elements were simulated as homogeneous and isotropic, with a post-elastic behaviour based on the “Concrete Damage Plasticity” constitutive law available from the software library, which relies on the material fracture energy for governing the post-peak softening (for more details see [11]). The tension and compression curves for uniaxial loading are reported in Figure 6, where: $\sigma_t - \varepsilon_t$ and $\sigma_c - \varepsilon_c$ are the stress – strain values associated to tension and compression; E_0 is the initial elastic modulus; $\sigma_{t0} - \sigma_{c0}$ are the elastic stresses for tension – compression; σ_{cu} is the maximum compression stress.

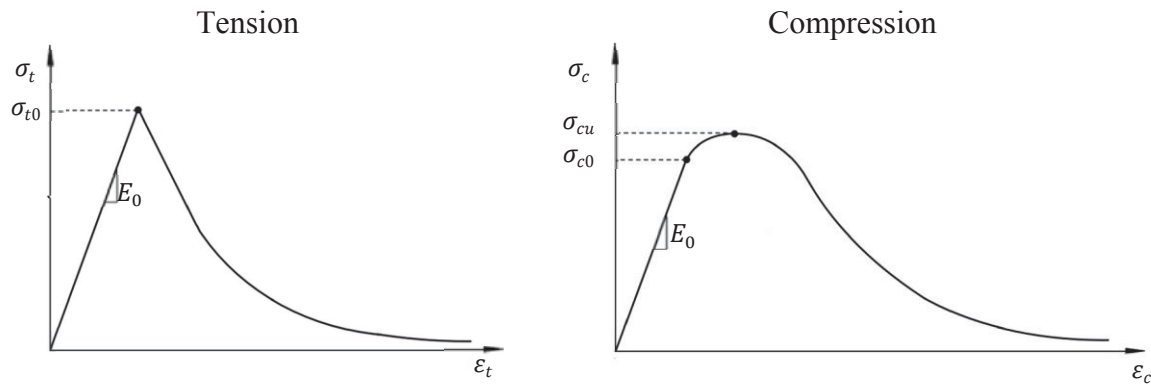


Figure 6: “Concrete Damage Plasticity” behaviour

The interaction between steel reinforcements and frame elements was reproduced with an “Embedded region” constraint (Figure 7). This constraint implies a perfect adherence between the constrained elements.

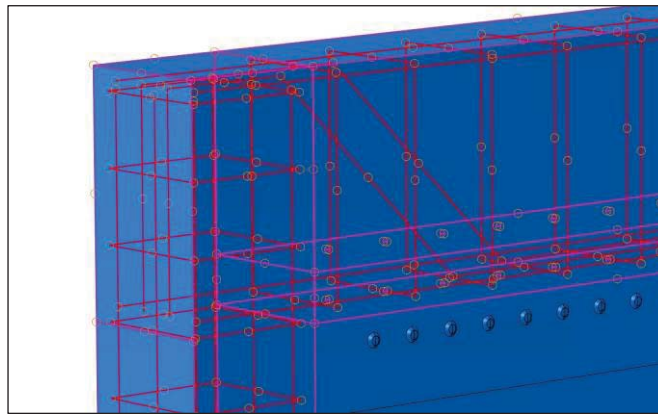


Figure 7: Refined modelling approach – “Embedded region” constraint between concrete and the steel reinforcements

A general “Hard” contact was applied to all the solid elements of the model to avoid unrealistic material penetrations. Additional interaction properties were assigned to the surfaces between the elements (“Individual property assignments”) to reproduce the overall behaviour of the system. In particular, a “tangential behaviour” with penalty friction formulation was assigned to the contact surfaces (fasteners-washer, CLT panel-timber subframe, CLT panel-washer, timber subframe-washer, timber subframe-RC frame) using diversified frictional coefficients for the various surface types (e.g., Figure 8 shows the in-contact surfaces between metal fasteners and connected elements).

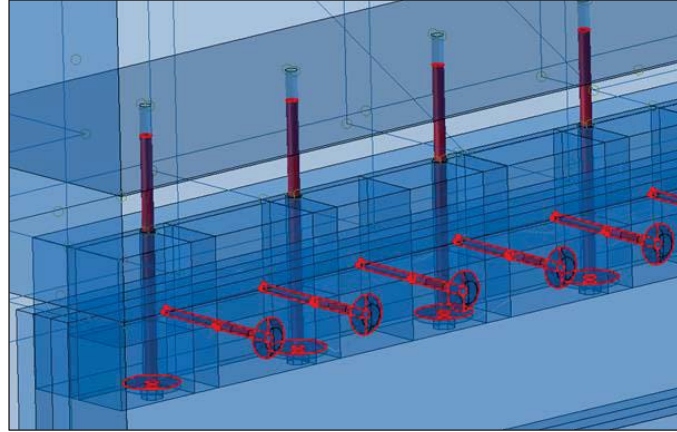


Figure 8: Refined modelling approach – Individual property assignments: fastener cylindrical contact-surfaces

The pull-out mechanisms associated with the threaded portion of the screw fasteners were modelled through a cohesive contact with an elastic uncoupled behaviour depending on K_n , K_s , K_t (stiffness associated respectively to the normal and the two shear-directions) for which, once the design strength is reached, a damage function reduces the tangential resistance (Figure 9).

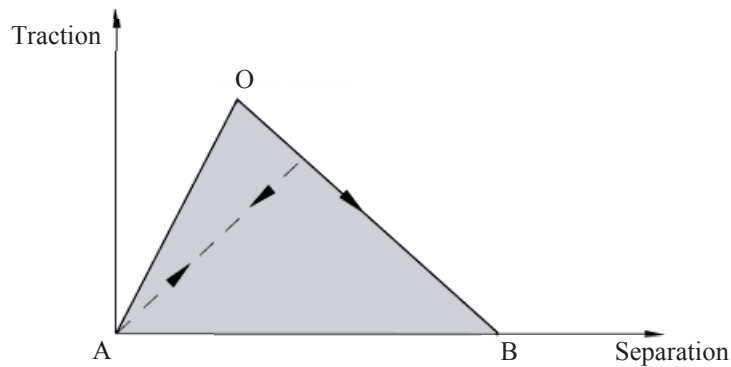


Figure 9: Cohesive fracture energy – damage evolution

To obtain the above mentioned behaviour the "maximum nominal stress" (MAXS) option was selected [27]. As a consequence, the pull-out mechanism activates when Equation 1, which depends on the parameters t_n , t_s , t_t (normal and shear stresses) and t_n^0 , t_s^0 , t_t^0 (corresponding reference strength values), is satisfied.

$$\max \left\{ \frac{t_n}{t_n^0}; \frac{t_s}{t_s^0}; \frac{t_t}{t_t^0} \right\} = 1 \quad (1)$$

For the modelling of the contacts, the interacting surfaces were categorized into "master" and "slave" surfaces. The mesh characteristics played a fundamental role in the process of attributing the master/slave categories. For all solid components, prismatic "C3D8" elements were preferred to linear tetrahedral elements "C3D4" (which might lead to less reliable results) or quadratic tetrahedral elements "C3D10" (which imply longer analysis durations).

Because the solid models of the RC frame, CLT panel and timber subframe present numerous holes due to presence of the fasteners, it was necessary to partition the geometry to facilitate meshing. Sensitivity analyses were performed and meshes with diverse levels of refinement were adopted for different elements and for different areas in the same element. For example, in the CLT panel, the areas around the fastener holes required a more refined mesh with respect to the rest of the element (Figure 10).

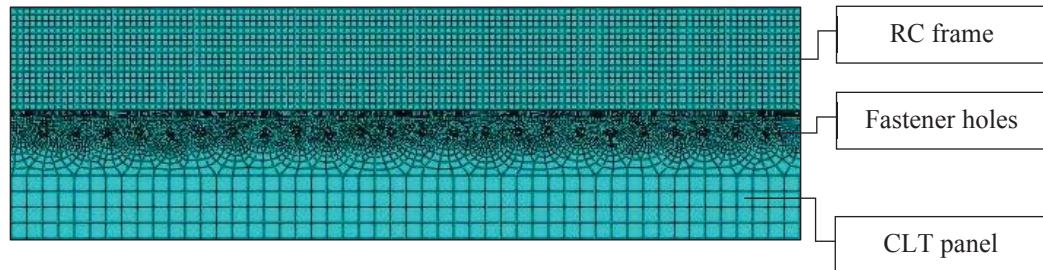


Figure 10: RC-TP refined model – mesh

Once the main aspects of the model were defined, preliminary small-scale analyses were conducted with the aim of calibrating and validating the modelling parameters. The shear and pull-out behaviours of the fasteners were studied separately, considering both the connection with concrete and timber. The numerical results obtained were compared with experimental evidence available from the literature. As an example, Figure 11a and Figure 11b give the comparison between numerical results (red curves) and experimental results taken from [13] (for concrete pull-out) and from [15] (for timber shear) respectively.

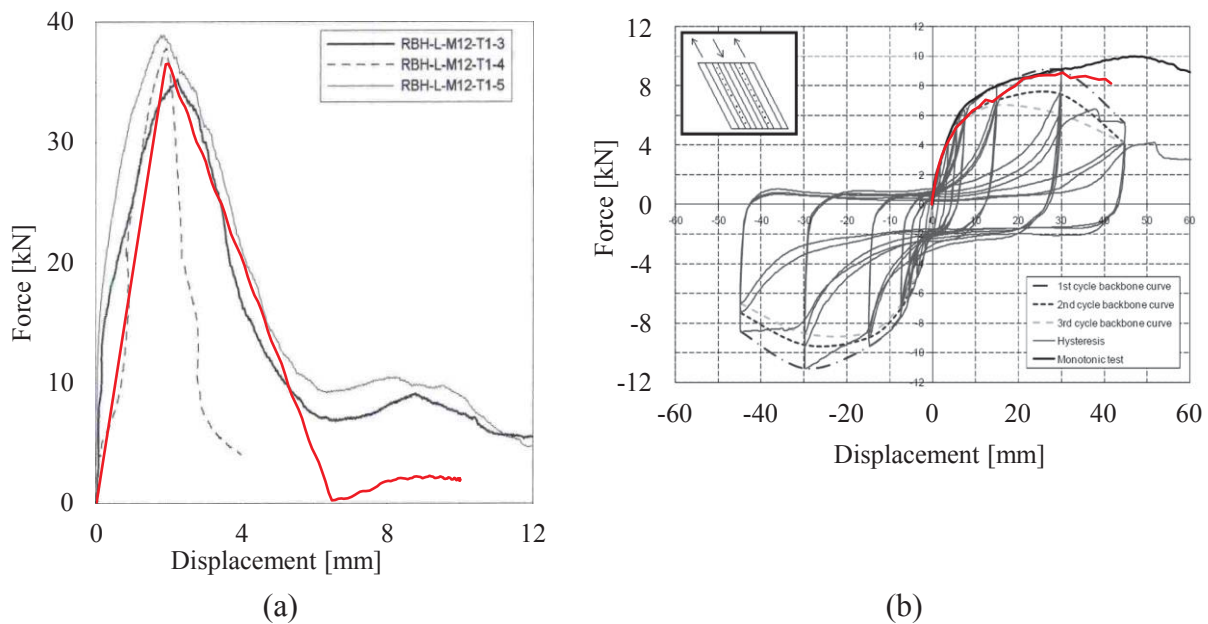


Figure 11: Numerical calibration and validation of the connection behaviour in the refined model (red curves) – comparison with experimental evidence: a) concrete pull-out, b) timber shear

For the original pre-intervention frame configuration, the masonry infill was treated similarly to the concrete elements. Specifically, the infill was modelled with a macro-modelling approach (Figure 12a) where mortar and bricks were represented by an equivalent homogeneous isotropic material (Figure 12b). The post-elastic behaviour was simulated by adopting the “Concrete Damage Plasticity” constitutive model (Figure 6) as suggested by [16]. With this

modelling strategy, it is possible to account for both rocking and diagonal shear failure mechanisms. The contact interaction between masonry and concrete is reproduced by a general “Hard” contact and a frictional “tangential behaviour”.

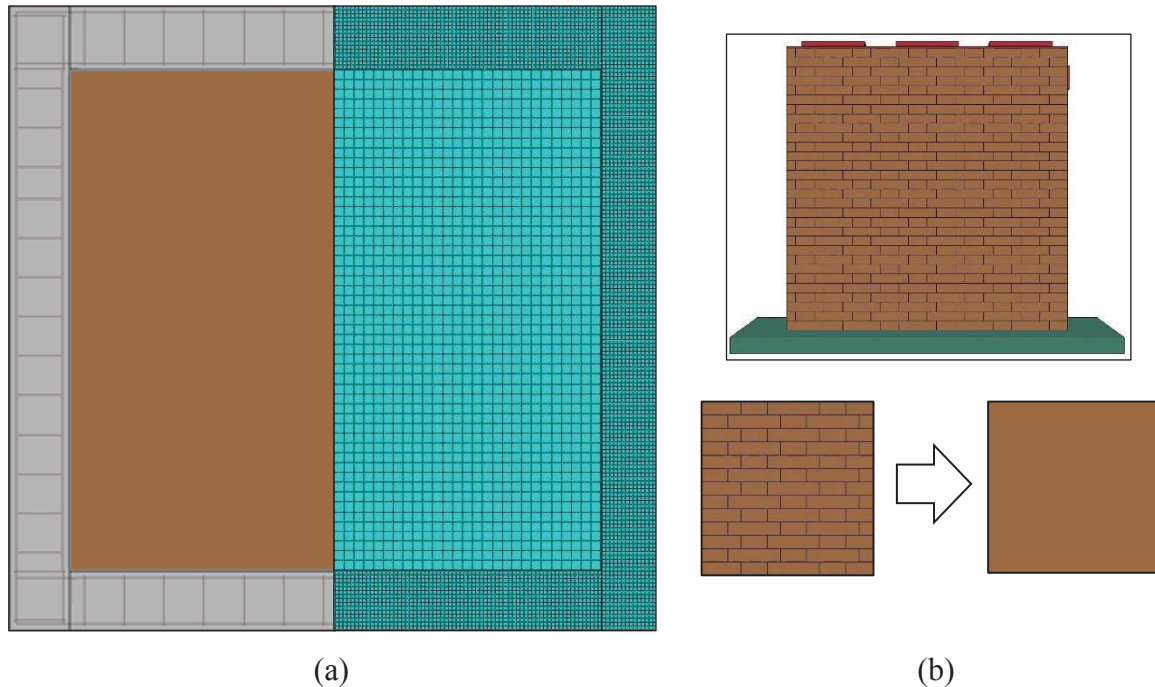


Figure 12: Refined modelling approach: a) masonry infilled frame; b) mortar and bricks represented as an equivalent homogeneous material

4.2 2D modelling

The present chapter focuses on the 2D modelling approaches adopted to simulate the bare frame, the original masonry-infilled frame and the retrofitted frame.

Regarding the retrofitted frame, the modelling strategy presented in this section Figure 13a) is an updated version of that exposed in detail in [9] and [10]. The main upgrades consist in an improved characterization of the non-linear properties of the elements and in an improved definition of the behaviour of the connections. By relying on the findings of the 3D refined models, the 2D approach was calibrated to account for possible out-of-plane secondary effects. The main characteristics of the 2D models are summarized in the following paragraphs.

The concrete frame was modelled by using *frame elements* capable of accounting for the nonlinear behaviour of concrete and steel. Deformation-controlled and force-controlled *hinge elements* were assigned at the extremities of columns and beams to consider respectively bending and shear collapse.

The nonlinear response of the beam-column joint was simulated by using two cross *nonlinear links* connected to the extremities of columns and beams. The joint model adopted herein has been proposed by Sung et al. (2013) [28] and it permits to account for the failure of the joints with small computational effort.

The CLT panel was modelled via *layered orthotropic nonlinear shell elements* where each of the three layers was assumed to be “inactive” along its weak direction.

The timber subframe was an *elastic frame element*. The validity of the elastic-behaviour assumption was confirmed a posteriori by investigating the subframe stress state.

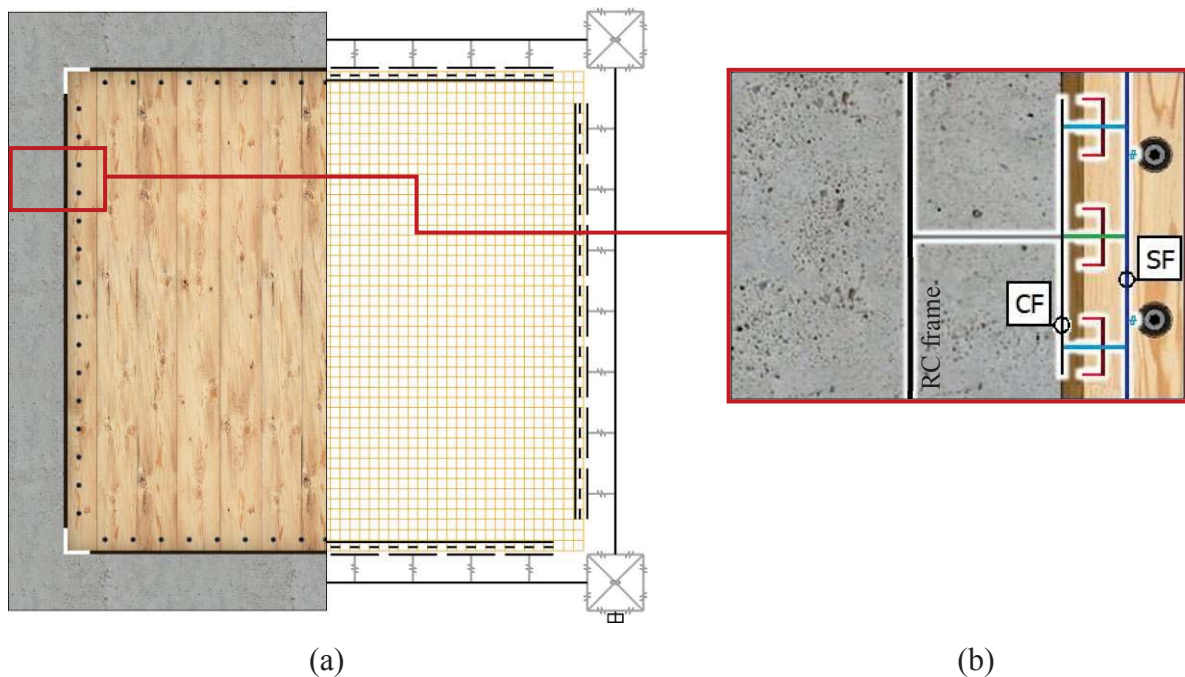


Figure 13: Simplified finite element model: a) Complete intervention system; b) Interaction system

As extensively described in [10], an “interaction system” reproduces the interaction between RC frame, timber subframe and CLT panel. In Figure 13b, it is possible to observe the frame elements that represent the middle line of the column “RC frame”, the internal face of the column “CF” and the middle line of the timber subframe “SF”.

The interaction system (Figure 13b and Figure 14a) is obtained from the overlap of a “connection system” and a “contact system”.

The connection system (Figure 14b) simulates the RC-Conn (represented by the *link elements* “CL”) and the T-Conn (represented by the *link elements* “TL”). In addition, this system simulates the contact-interaction between the timber subframe “SF” and the internal face of the concrete frame “CF”. This contact is governed by *gap link elements* “GL”.

The contact system (Figure 14c) replicates the direct contact between CLT panel and RC frame. This contact occurs when the gap between the CLT panel and the internal face of the RC frame (CF) goes to zero and it is reproduced by using *hook link elements* “HL”.

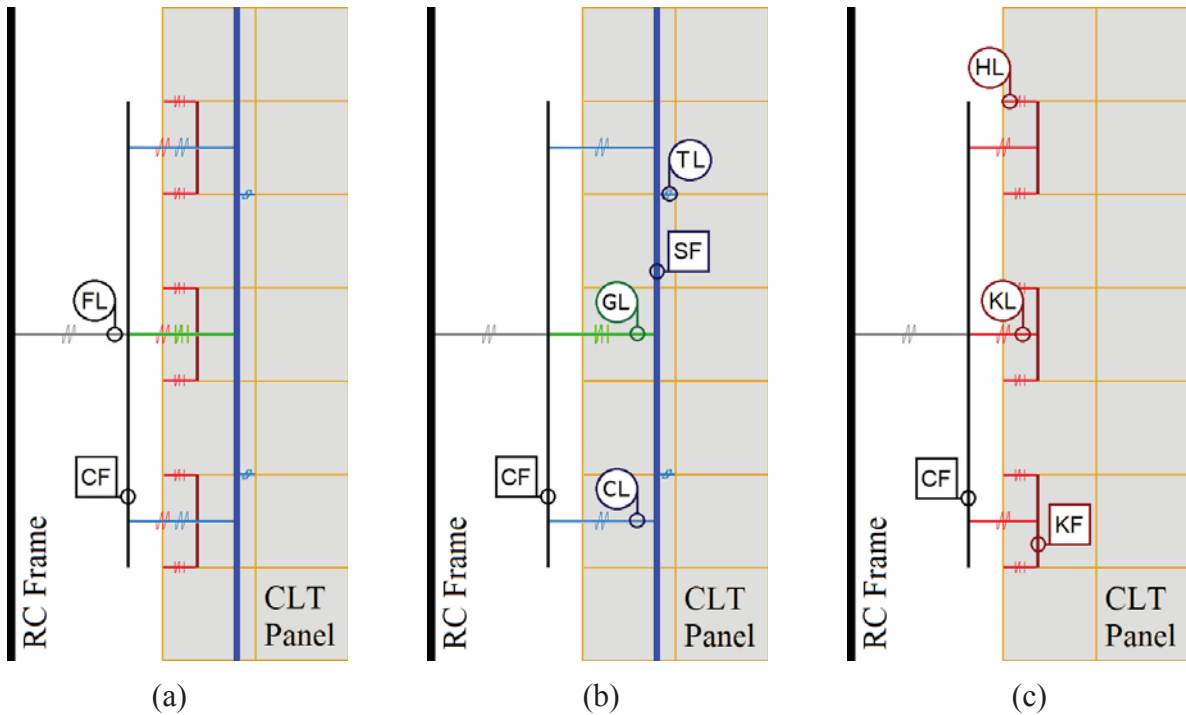


Figure 14: Interaction system between RC frame, timber subframe and CLT panel: (a) Complete interaction system; (b) connection system; (c) contact system

Table 6 reports a summary of the abbreviations used for the main elements and a brief description of the relative functions.

ID	Name	Functions
CF	Concrete Frame	<ul style="list-style-type: none"> - Massless rigid frame. - Represents the internal surface of the RC elements.
KF	Fake Frame	<ul style="list-style-type: none"> - Massless rigid frame. - Used as a support element in the contact system.
SF	Subframe Frame	<ul style="list-style-type: none"> - Elastic frame. - Geometrical characteristics of the timber subframe. - Positioned on the middle line of the timber subframe.
CL	Concrete fastener Link	<ul style="list-style-type: none"> - Nonlinear link. - Represents the RC-Conn.
FL	Frame-thickness Link	<ul style="list-style-type: none"> - Rigid link - Represents the in-plane semi-thickness of column and beams.
GL	Gap Link	<ul style="list-style-type: none"> - Nonlinear gap link. - Reproduces the contact between RC frame and timber subframe.
HL	Hook Link	<ul style="list-style-type: none"> - Nonlinear hook link. - Reproduces the contact between timber subframe and CLT panel.
KL	Fake Link	<ul style="list-style-type: none"> - Rigid link. - Used as a support element in the contact system.

TL	Timber fastener Link	- Nonlinear link. - Represents the T-Conn..
----	-------------------------	--

Table 6: Interaction system – Abbreviations used and main functions

The nonlinear behaviour of CLs and TLs was defined based on the results obtained from the refined Abaqus 3D models because such models account for possible effects due to the out-of-plane eccentricity associated with the physical thickness of the various components. The details of the curves assigned to the CLs and TLs are given in the next section.

The response of the original masonry infilled system was simulated by using an equivalent diagonal struts model (Figure 15). This model was defined starting from the approaches proposed by Al-Chaar (2002) [17] and Liberatore et al. (2018) [18]. Specifically, the proposed masonry model consists of two eccentric diagonal rods, whose location in the RC frame is given by the provisions of [17], while the compression behaviour of the rods is defined according to [18]. The tensile strength of the diagonal elements reproduces the tensile strength of the masonry. Consequently, if a lateral force is applied as shown in Figure 15a, the two links work as strut and tie. The behaviour of each diagonal link is reported in Figure 15b, where the blue branch and the red branch represent the compression and the tension response respectively.

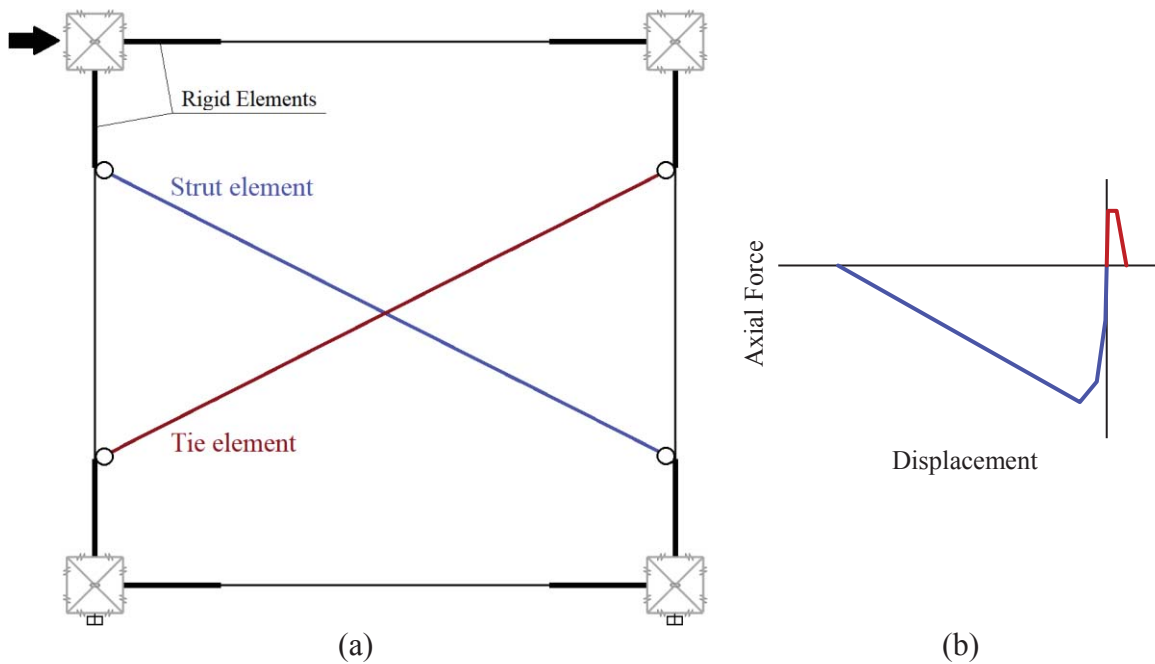


Figure 15: Original masonry-infilled system: a) Equivalent diagonal “strut and tie” model; b) Force-displacement response

According to [17], in order to consider the confinement produced by the masonry infill, the portions of beams and columns between the joints and the diagonal links are modelled as *rigid elements* (Figure 15a). Only the intermediate sections of columns and beams can therefore develop nonlinear responses.

5 NUMERICAL ANALYSES AND RESULTS

5.1 Preliminary analyses

The first step of the numerical study presented herein saw the simulation of isolated RC-Conn and T-Conn connections under pull-out and shear loading conditions. Several configurations were considered (e.g., pull-out tests carried out by pulling the screw directly or by pulling the subframe, or shear and pull-out tests performed “with and without” washers). Figure 16 shows the most relevant results: a) RC-Conn - push-out; b) RC-Conn - shear parallel to the subframe; c) T-Conn - shear perpendicular to the subframe; d) T-Conn - shear parallel to the subframe.

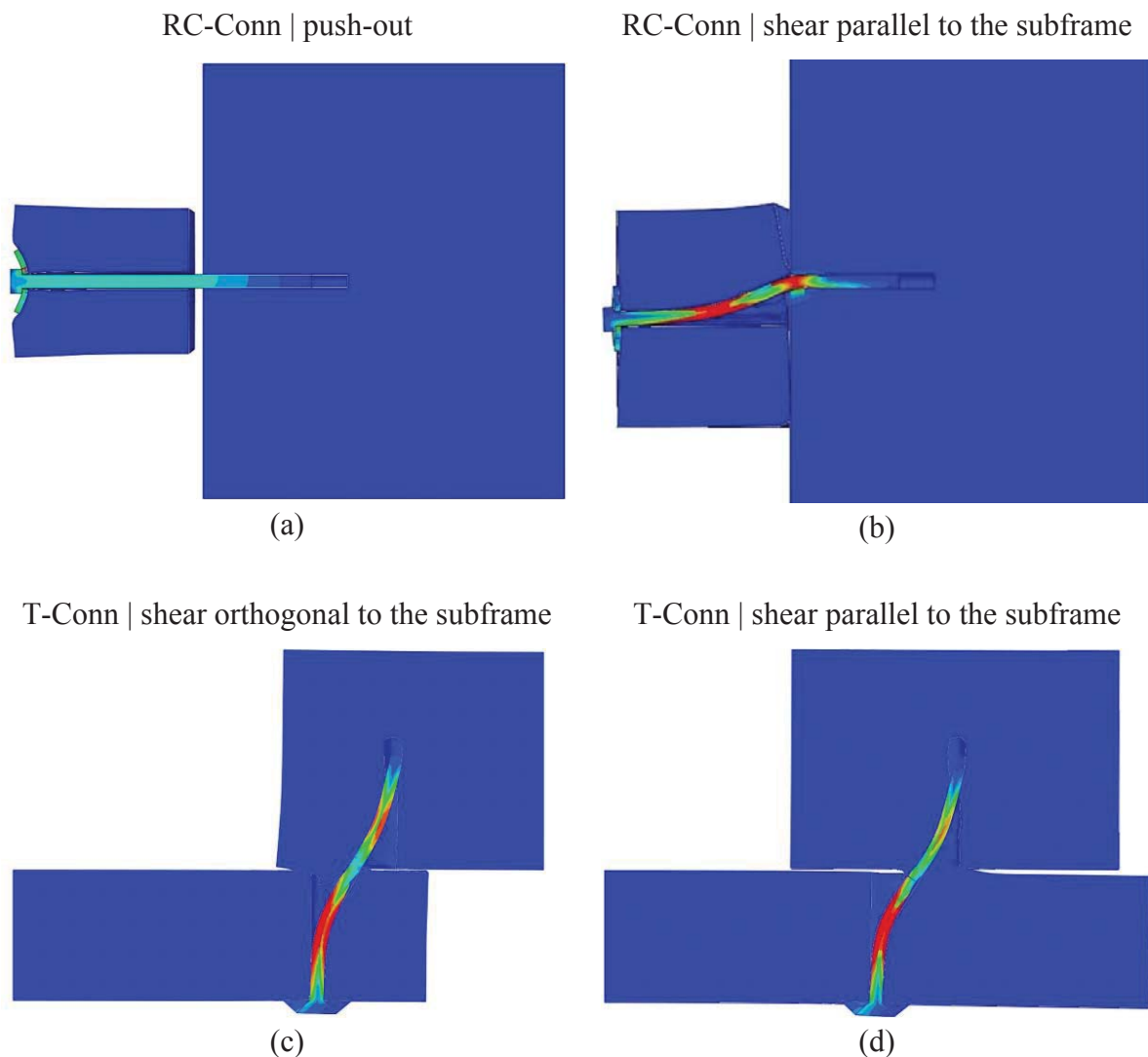


Figure 16: Tests on RC-Conn and T-Conn – stress contour

Subsequently, in order to account for possible out-of-plane displacements due to the eccentric interaction between RC frame – timber subframe – CLT panel, a test structure (referred to as "Test-Module") was defined (Figure 17). The size of the Test-Module was selected so as to replicate the “base-unit” of the retrofit system. Because the RC-Conns have a 15 cm spacing and the T-Conns have a 10 cm spacing, the Test-Module comprise two RC-Conn and three T-Conn fasteners.

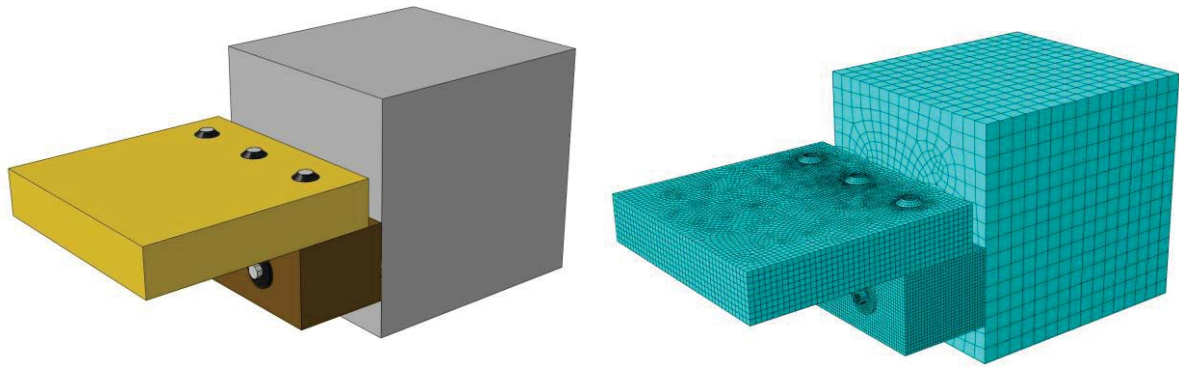


Figure 17: “Test-Module”

The out-of-plane effects observed from the analysis of the Test-Module were included in the simplified 2D models through the response-curve attributed to the TL and the CL elements (for labelling details please see Table 6). In particular, such secondary effects were found to be non-negligible when the force was applied in the Z-direction (Figure 18a).

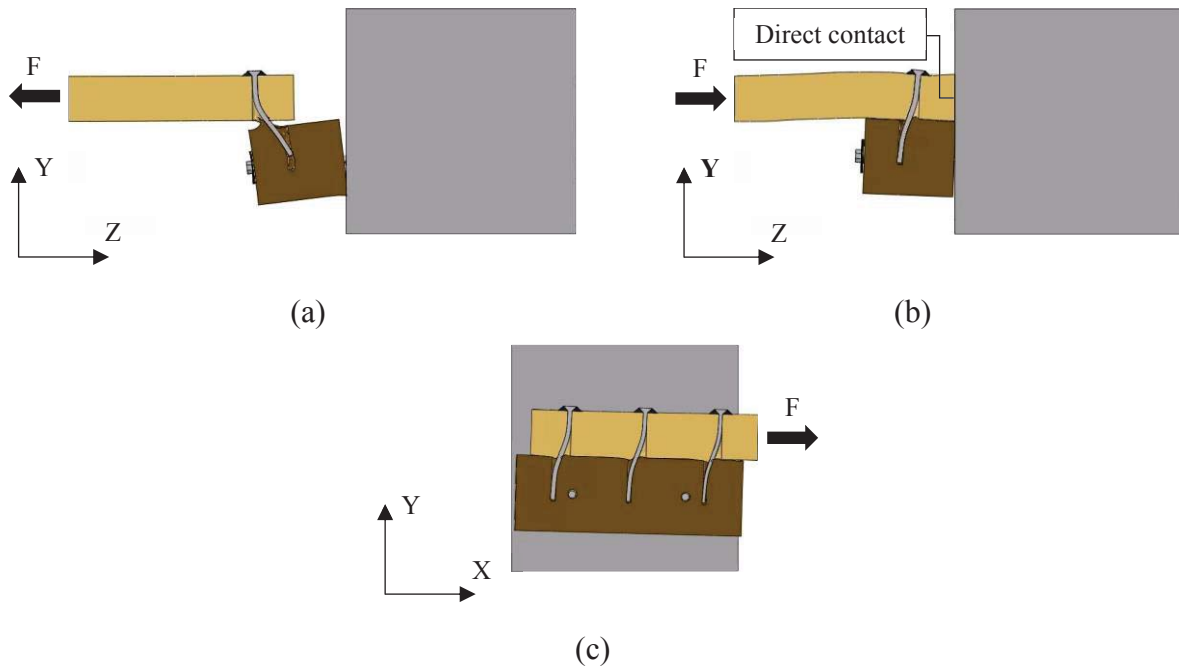


Figure 18: “Test-Module” – out-of-plane secondary effects

Figure 19 shows the backbone curves of the T-Conn shear tests (Figure 19a) and RC-Conn pull-out tests (Figure 19b). The green curves were obtained from the 3D model neglecting the secondary effects by restraining the out-of-plane movements. The blue curve obtained with the refined model considering the secondary effects. The red curves, which are the idealized versions of the blue curves, were subsequently implemented in the 2D model to account for the secondary effects.

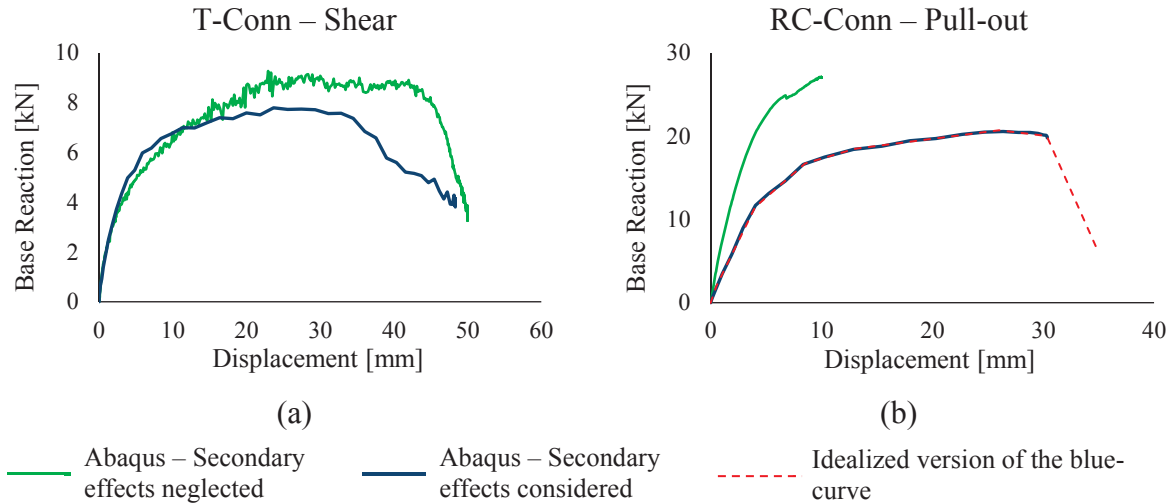


Figure 19: Backbone curves from single-connection tests: a) T-Conn shear; b) RC-Conn pull-out

Figure 20 shows the response of the Test-Module obtained by using the 3D refined modelling approach and the 2D modelling approach (with secondary effect accounted for). In particular, in Figure 20a, the force applied to the panel was parallel to the X-direction (Figure 18c), while in Figure 20b the panel was pulled and pushed in the Z-direction (see Figure 18a and Figure 18b).

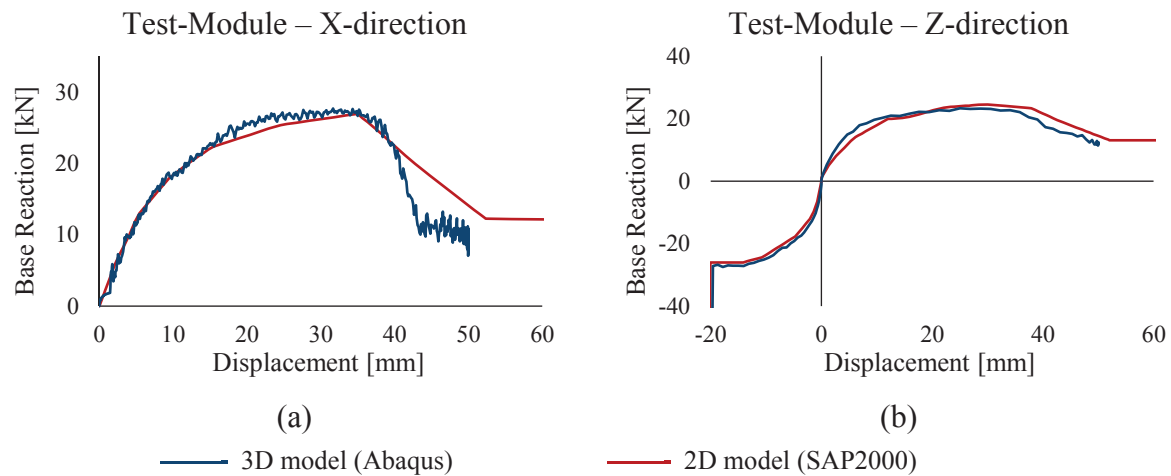


Figure 20: Behaviour of the Test-Module obtained with the 3D (blue) and the 2D (red) approach: a) X direction; b) Y direction

As it is possible to observe from the graphs, the outcomes of the two modelling approaches are consistent for both test configurations. When including the out-of-plane secondary effects in the 2D model, it was possible to match closely the curves from the 3D model at a much smaller computational effort. As visible from Figure 20b, it is interesting to notice that both the 3D and the 2D models experienced a sudden stiffness increase at a negative displacement close to -20 mm. This increase is due to the gap between the CLT panel and the RC frame (represented by the HL elements in the 2D model) that goes to zero involving a direct contact (observable from Figure 18b).

5.2 Full-scale one-storey one-bay frame

After having calibrated the 2D modelling approach on the results from the connection tests studied with the 3D approach, and having proof-checked the correspondence between the approaches through the analysis of the Test-Module, the case-study frame described in section 2 was modelled.

The one-storey, one-bay frame was analysed considering three alternative configurations: Bare frame (Figure 21a), Masonry infilled frame (Figure 21b) and RC-TP retrofitted frame (Figure 21c). Based on the findings reported in [9] and [10], the optimal RC-TP configuration for the case-study frame was assumed to be that having a GAP of 20 mm and T-Conns arranged only along the beams.

The three frame configurations were analysed with both modelling approaches via nonlinear static analysis. In the first step, the vertical loads (values reported in Table 2) were applied to the columns and the upper beam. Then, the in-plane horizontal force was introduced at the top joint level and was incremented until the collapse of any of the structural elements was reached.

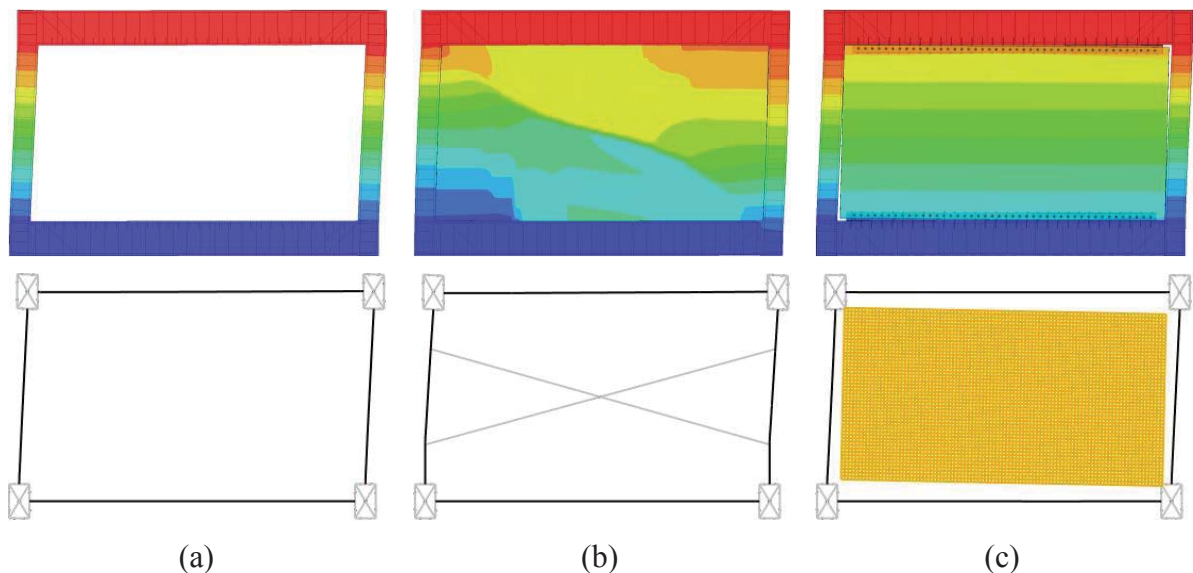


Figure 21: 3D and 2D models of the case-study frame configurations: a) Bare frame; b) Masonry infilled frame; RC-TP retrofitted frame

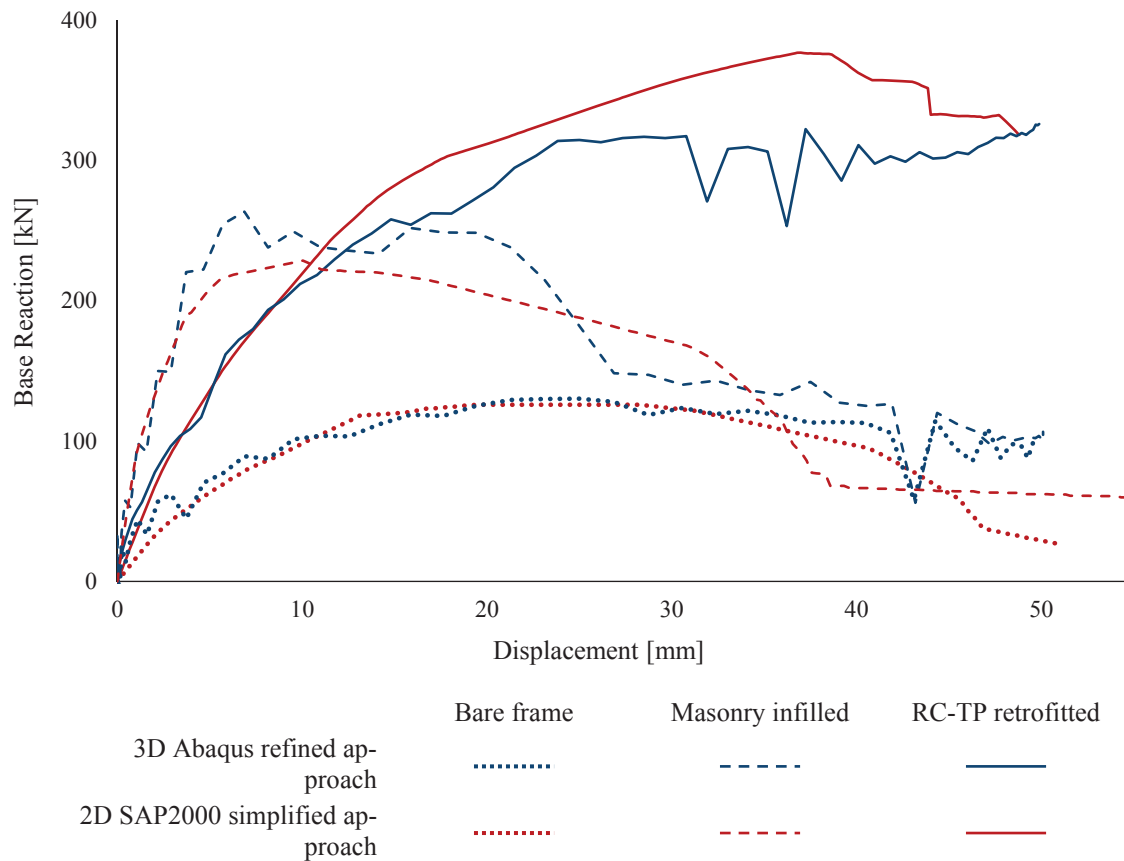


Figure 22: Isolated frame backbone curves – comparison between the 3D and the 2D modelling approach

Figure 22 reports the results obtained by performing the nonlinear static analyses of the isolated frame in the three configurations and using both modelling approaches. Both numerical strategies produced consistent results, showing similar behaviours for all the analysed configurations in terms of stiffness, strength and failure mechanism.

For all three configurations the frame collapsed due to the bending failure of the concrete column. However, for the masonry infilled frame, the column failure was preceded by the collapse of the infill which caused an evident reduction in the load bearing capacity at a displacement level close to 20 mm. The retrofitted frame, instead, showed a remarkable increase in the bearing capacity, with the peak capacity at a displacement of approximately 40 mm. The bending failure of the concrete columns in the retrofitted frame occurred at displacement values similar to those observed in the bare frame, attesting that the proposed intervention does not impede the full development of the column flexural ductility.

6 CONCLUSIONS

The present paper reports the results of a numerical study on a retrofit intervention for existing RC masonry infilled structures. The intervention, named RC-TP, is aimed at reducing the seismic vulnerability of this kind of structure by replacing the masonry infills with timber panels connected to the RC-frame with screw-fasteners. The present research focused on the modelling of the pre- and post- intervention system via two alternative numerical strategies with different levels of refinement. In particular, a 3D refined modelling approach and a 2D simpler modelling approach were investigated. Preliminary analyses on isolated connections permitted

both to validate the 3D modelling approach on experimental evidence available from the literature, and to calibrate the 2D models to account for secondary effects that cannot be directly observed by two-dimensional models. Consequently, an isolated one-storey one-bay concrete frame representative of the built stock of many Countries was modelled using both strategies and considering the “bare”, the “masonry infilled” and the “retrofitted” configurations. The RC frame was subjected to nonlinear static analyses until the collapse of any of the structural elements was reached. The analysis outcomes showed that the proposed retrofit system can effectively reduce the seismic vulnerability of existing masonry infilled RC frames, consistently with the findings of preliminary studies previously published. By virtue of the good correspondence between the refined 3D approach and the less refined but computationally far more efficient 2D approach, future steps of the research will be devoted to using the 2D models for extensive parametric studies on all the details affecting the performance of the timber-panel strengthening technique discussed herein.

7 ACKNOWLEDGEMENTS

The research work was carried out within the framework of the 2019-2021 ReLUIS-DPC network (Italian University Network of Seismic Engineering Laboratories and Italian Civil Protection Agency).

REFERENCES

- [1] S. Kadysiewski and K.M. Mosalam KM. Modeling of Unreinforced Masonry Infill Walls Considering In-Plane and Out-of-Plane Interaction. Pacific Earthquake Engineering Research Center, University of California, Berkeley, California, 2009
- [2] M. Gaetani d'Aragona, M. Polese, M. Di Ludovico, A. Prota. Seismic vulnerability for RC infilled frames: simplified evaluation for as-built and retrofitted building typologies. *Buildings*, 8(10):137, 2018
- [3] D. Perrone, M. Leone, M.A. Aiello. Non-linear behaviour of masonry infilled RC frames: influence of masonry mechanical properties. *Eng Struct*, 150 (2017), pp. 875-891, 2017
- [4] N. Ning, Z. John Ma, P. Zhang, D. Yu, and J. Wang. Influence of masonry infills on seismic response of RC frames under low frequency cyclic load. *Engineering Structures*, vol. 183, pp. 70–82, 2019
- [5] I. Sustersic and B. Dujic. Seismic strengthening of existing buildings with cross laminated timber panels. *World Conference on Timber Engineering*. Auckland, New Zeland, 16-19 July, 2012.
- [6] J. Suga, M. Ono, K. Aoki, T. Fukuhara, T. Kurihara, T. Maeda. Timber Shear Walls for Seismic Retrofit of Reinforced Concrete Buildings. *World Conference on Timber Engineering*. Seoul, Republic of Korea, 20-23 August; 2018
- [7] F. Staz, M. Serpilli, G. Maracchini, A. Pavone. An experimental and numerical study on CLT panels used as infill shear walls for RC buildings retrofit. *Construction and Building Materials*, 211: 605-616. <https://doi.org/10.1016/j.conbuildmat.2019.03.196>, 2019
- [8] G. Margani, G. Evola, C. Tardo, and E.M. Marino. Energy, Seismic, and Architectural Renovation of RC Framed Buildings with Prefabricated Timber Panels. *Sustainability*, 12, p. 4845, 2020
- [9] F. Smirolto, I. Giongo, M. Piazza. Seismic retrofit of masonry infilled frames by using timber panels. *17th World Conference on Earthquake Engineering, 17WCEE*, Sendai, Japan, 2020.
- [10] F. Smirolto, I. Giongo, M. Piazza. Use of timber panels to reduce the seismic vulnerability of concrete frame structures. *Engineering Structures*, 2021.
- [11] Dassault Systèmes: Abaqus analysis users' manual, Simulia Corp., Providence, RI, USA, 2011
- [12] SAP 2000 Integrated Software for Structural Analysis and Design, Computers and Structures Inc., Walnut Creek, California, USA.
- [13] M. Madeddu. Preliminary tests on Screw Anchor. *Polytechnic University of Milan – Department of Structural Engineering - Testing Material Laboratory – CE Marking Section*, 2006.
- [14] R. Tomasi, A. Crosatti, M. Piazza M. Theoretical and experimental analysis of timber-totimber joints connected with inclined screws, *Constr Build Mater*, 24:1560–71, 2010
- [15] I. Gavric, M. Fragiaco, A. Ceccotti. Strength and deformation characteristics of typical CLT connections. *Proceeding of the 12th World Conference on Timber Engineering*, Auckland, New Zealand, 2012

- [16] P. Lourenco, Structural masonry analysis: recent developments and prospects. *Proceedings of the 15th International brick & brick masonry conference*, Sydney, Australia, 1341-1356, 17-20 February 2008.
- [17] G. Al-Chaar, Evaluating Strength and Stiffness of Unreinforced Masonry Infill Structures, *407 US Army Corps of Engineers, Engineer Research and Development Center*, ERDC/CERL TR-408 02-1, Illinois, 2002
- [18] L. Liberatore, F. Noto, F. Mollaioli and P. Franchin. In-plane response of masonry infill walls: Comprehensive experimentally-based equivalent strut model for deterministic and probabilistic analysis. *Engineering Structures*, 167: 533-548. <https://doi.org/10.1016/j.engstruct.2018.04.057>, 2018
- [19] EN 14080:2013. Timber Structures – Glued laminated timber and glued solid timber – Requirements, *European Committee for Standardization*, Brussels.
- [20] EN 338:2016. Structural timber – Strength classes, *BSI Standards Publication*, London, UK.
- [21] T. Bogensperger, M. Augustin, G. Schickhofer, *Properties of CLT-panels exposed to compression perpendicular to their plane*. 44th CIB-W18 Meeting, Alghero, 2011
- [22] R. Harris, A. Ringhofer and G. Schickhofer. Focus Solid Timber Solutions – European Conference on Cross Laminated Timber (CLT). *Institute of Timber Engineering and Wood Technology (2 676 080)*, University of Bath, UK, 2013.
- [23] T. Gečys, A. Daniūnas, T.K. Bader, L. Wagner, J. Eberhardsteiner, 3D finite element analysis and experimental investigations of a new type of timber beam-to-beam connection. *Engineering Structures*, 86, 134–145, 2015
- [24] Y. Hu, L. Shen, S. Nie, B. Yang, W. Sha. FE simulation and experimental tests of high-strength structural bolts under tension. *Journal of Constructional Steel Research*, 2016
- [25] A. Al-Rifaie, Z.W. Guan, S.W. Zones. Quasi-Static Analysis of End Plate Beam-to-Column Connections. *Engineering and Technology, International Journal of Civil and Environmental Engineering*, Vol:11, No:7, 2017
- [26] AutoCAD, Autodesk, Inc., California, USA.
- [27] C. Bedon, M. Fragiocomo, Numerical analysis of timber-to-timber joints and composite beams with inclined self-tapping screws. *Composite Structures* 207, 13–28, 2019
- [28] Y.C. Sung YC, T.K. Lin, C.C. Hsiao and M.C. Lai, Pushover analysis of reinforced concrete frames considering shear failure at beam-column joints. *Earthquake Engineering and Engineering Vibration*, 12 (3), 373-383, 2013

COMPREHENSIVE NONLINEAR ANALYSIS OF FAILURES OF A FIRE-SPRINKLER SYSTEM BASED ON FINITE ELEMENT MODELLING AND AMBIENT VIBRATION TESTS

Shakhzod M. Takhirov¹ and Amir S. Gilani²

¹ Department of Civil and Environmental Engineering, University of California, Berkeley
337 Davis Hall, Berkeley, CA 94720, USA
e-mail: takhirov@berkeley.edu

² Miyamoto International
1450 Halyard Dr., West Sacramento, CA 95691, USA
e-mail: agilani@miyamotointernational.com

Abstract

In the aftermath of the 2014 South Napa Earthquake, several failures of fire-sprinkler systems were observed. The failures were related to excessive displacements of these systems leading to an uncontrolled interaction with the surrounding nonstructural components, e.g., suspended ceiling systems, light fixtures, and ventilation ducts. The large displacements of the fire-sprinkler system can be related to the support elements with under-designed flexibility and/or failures of the support elements in which demand exceeded capacity. In addition to the excessive interaction with the surrounding nonstructural components, the large displacements can result in failures of the joints that are designed to accommodate only a limited rotation. To investigate the seismic performance of a typical fire-sprinkler system, a building in Napa, California (USA) was selected. A fire-sprinkler system in this building was damaged by the 2014 South Napa Earthquake and the damages were captured in 3D with high accuracy by a laser scanner. A finite element model of this building was generated and studied earlier but was limited to elastic models of both the building and the fire-sprinkler system. Artificially large amplifications of the seismic excitation over the elevation of the building were observed. The building's model was evaluated based on the ambient vibration tests. Amplification of the seismic excitation over the elevation was estimated from an instrumented building with a similar design and resonant frequencies. The amplified seismic impact was imposed on the fire-sprinkler system, which was modelled as a system with nonlinear behavior.

Keywords: Fire-sprinkler System, Seismic Performance, Nonstructural Components, Ambient Vibration Study, Nonlinear Modelling.

1 INTRODUCTION

A fire-sprinkler system represents a complex piping system suspended from the ceiling that spreads out in space and consists of many joints. To investigate the seismic performance of a typical fire-sprinkler system, a building in Napa, California (USA) was selected. The fire-sprinkler system in this building was damaged by the 2014 South Napa Earthquake and the damages were captured in 3D with high accuracy by a laser scanner. A finite element model of this building was generated and studied earlier [1] but it was limited to elastic models of both the building and the fire-sprinkler system. In this study, artificially large amplifications of the seismic excitation over the elevation of the building were observed. To address this shortcoming, a new model of the building and the fire-sprinkler system was generated. The building's model was calibrated based on the ambient vibration tests. Amplification of the seismic excitation over the elevation was estimated from an instrumented building with a similar design and resonant frequencies.

2 AFTERMATH ANALYSIS BY LASER SCANNING

Immediately after the 2014 South Napa Earthquake, the parking structure with a failed fire-sprinkler system was laser scanned by means of a C10 ScanStation from Leica Geosystems [2]. A global view of the building taken from Google Earth is shown in Figure 1a. The overall view of the point cloud collected during this scanning project is presented in Figure 1b. The point cloud presented in Figure 1b is a registration of point clouds collected from more than 14 stations throughout the structure. The point cloud registration was conducted in Cyclone from Leica Geosystems [3].

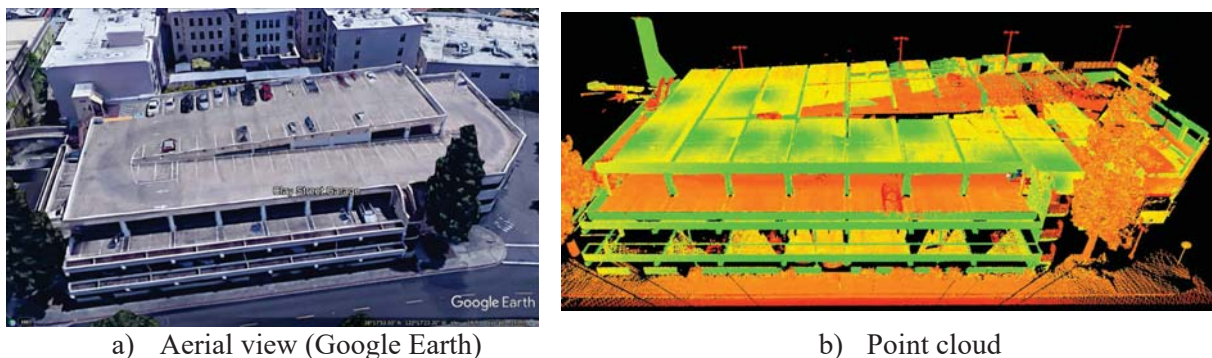


Figure 1: Overall view of the parking structure.

As was discussed in the earlier paper [1], most failures of the fire-sprinkler system were observed on the 3rd floor of the structure, the structure's highest elevation, where the suspended fire-sprinkler system was located. In other words, this was the highest floor with a ceiling from which the system can be suspended. Therefore, this elevation was studied in more detail and 13 stations of the laser scanning project were conducted on this floor. As a result, all failures of the fire-sprinkler system were documented within a few millimeters of accuracy. In addition, the failures were captured from many points by the still imaging camera built into the scanner. A detailed discussion of the failures was provided in [1].

3 RESULTS OF AMBIENT VIBRATION STUDY

A solid element model of the parking structure was generated earlier. It was based on the geometry captured by the laser scanner and a few assumptions about the materials used in the structure's construction. To access the actual performance characteristics of the structure, an

ambient vibration study was conducted. It was conducted on the top floor of the parking structure from which the fire-sprinkler system was suspended as presented in Figure 2a.

A portable data acquisition system (PI-6008U from Pacific Instruments [4]) was used in this study. The system has a flexibility in its power supply and as one of the available options it can be powered by a car battery. This power supply option was used in this study. The acceleration of the ambient vibrations was recorded.

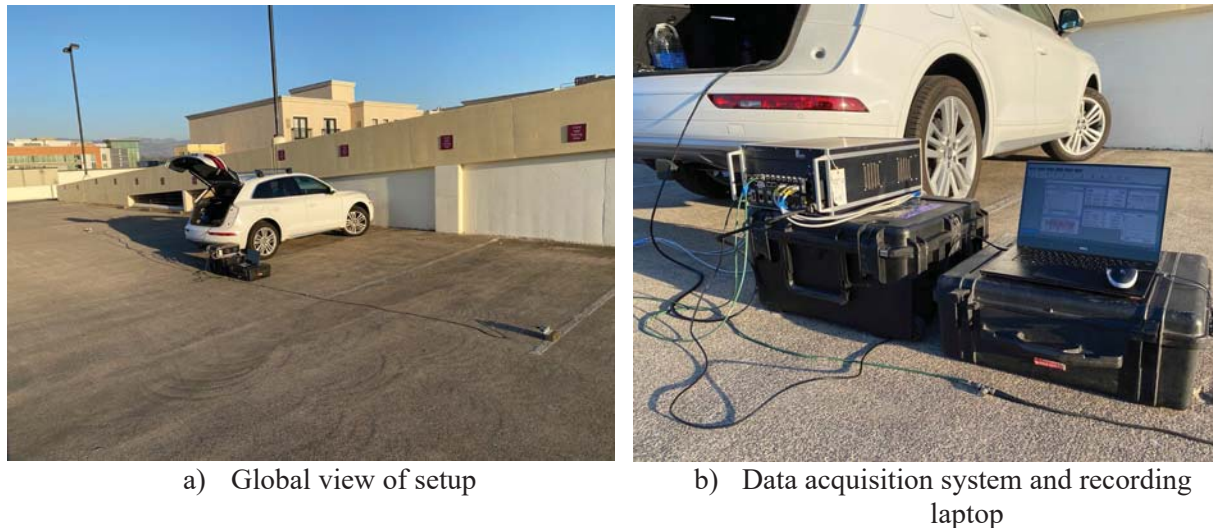


Figure 2: Setup of ambient vibration study.

Three different models of accelerometers were used. Two of them were of a piezoelectric type and the third one was a MEMS accelerometer. The results for one of the piezoelectric accelerometers discussed herein. The MEMS accelerometer was triaxial, therefore only the orientation of the piezoelectric accelerometers was changed to measure the structure's response in all three principal directions. The orientations of the piezoelectric accelerometer in Z and X are shown in Figure 3. The orientation of the accelerometer to measure the response in Y direction is presented in Figure 4a. The latter shows an example of another piezoelectric accelerometer. For comparative analysis of the MEMS and the piezoelectric accelerometer, both were installed on the same block as presented in Figure 4b.

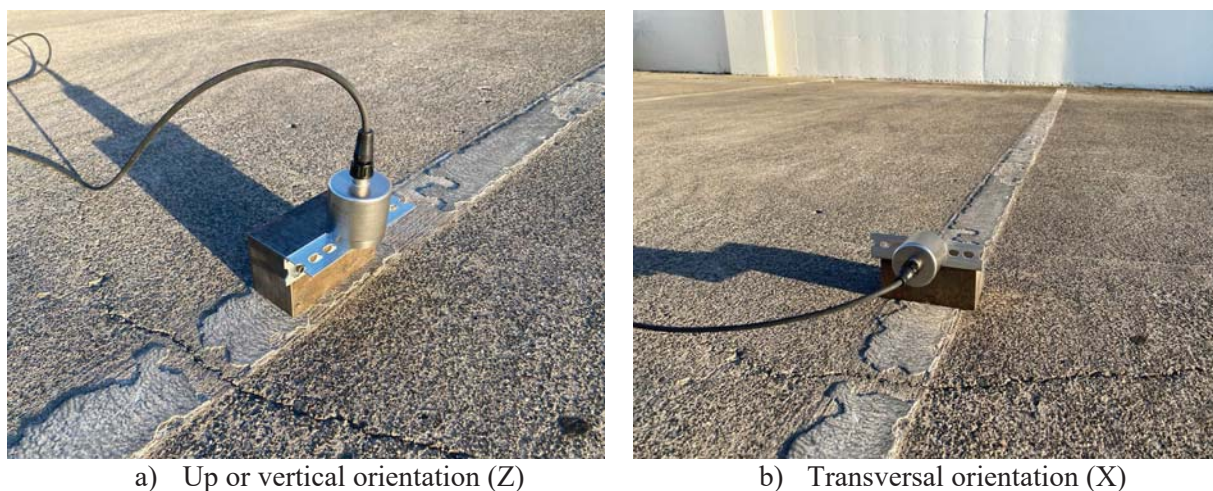


Figure 3: Orientations of accelerometer to measure response in Z and X.

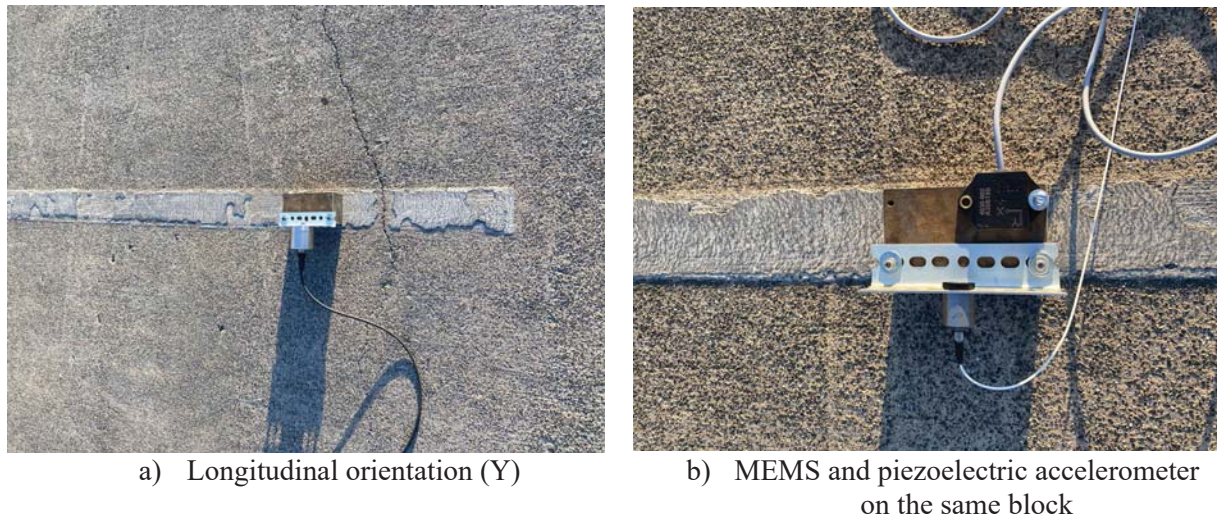


Figure 4: Orientation of accelerometer in Y and two accelerometers sharing at the same location for a comparative study.

Typical results of the ambient vibration study are presented in Figure 5. Both plots show Fast Fourier Transforms of the acceleration records. The plot on the left is obtained for the orientation in the transversal axis of the structure and the plot on the right corresponds to the records obtained for the longitudinal orientation of the accelerometer. Based on these plots, the lowest resonant frequencies of the structure are 4.8 Hz and 6.9 Hz in the transversal and longitudinal directions, respectively.

It is worth noting that both resonant frequencies of the structure are located within the frequency range of the AC156's spectral plateau [5].

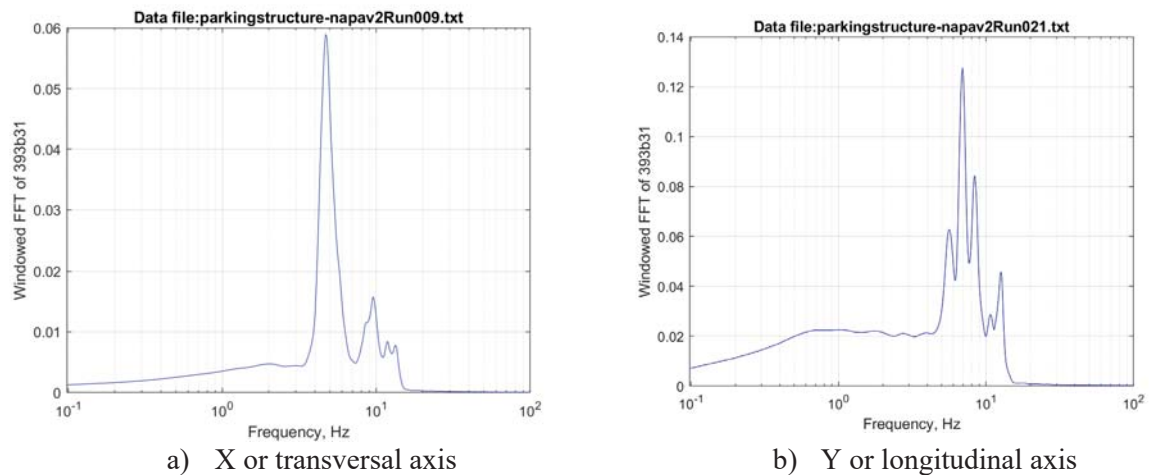


Figure 5: Results of ambient vibration study.

4 TIME HISTORY BASED ON AC156 SPECTRA

A selection of a time history for the finite element analysis was based on requirements of AC156. The hazard level at the site was taken from the USGS's maps [6]. The S_s values for California are presented in Figure 6a. In this figure the legend shows the correlation between the color and range of S_s expressed in percent of g. Figure 6b shows the close-up view of

these maps with the city of Napa shown in the magenta box. A tri-axial time history satisfying the requirements of AC156 was developed earlier [7] and had been utilized for the non-structural testing at the Pacific Earthquake Engineering Center (PEER) – UC Berkeley for quite some time. It was scaled accordingly, assuming a maximum value of S_S for Napa.

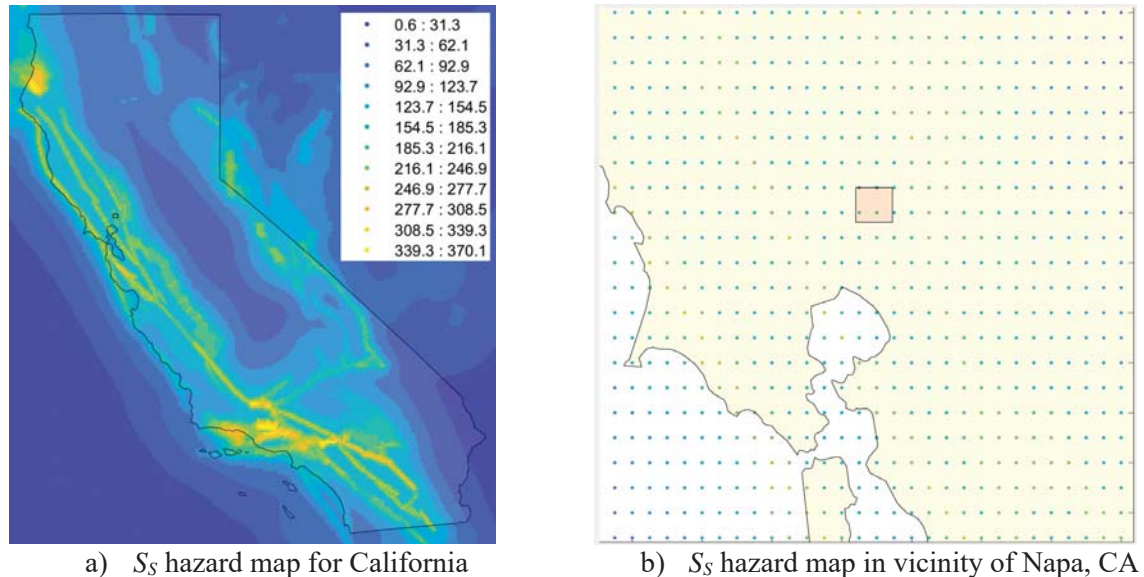


Figure 6: Hazard maps

5 FINITE ELEMENT MODEL

All modelling was conducted in SAP2000 [8]. The finite element model of the piping system is presented in Figure 7. It was generated based on the laser scans. It consists of the main supply constructed of a 114-mm pipe that branches out to a 50-mm pipe with sprinkler heads at the very end. The 114-mm pipeline consists of 3 major sections. Section 1 of the main supply runs along the length of the structure and is parallel to the horizontal ceiling or the third floor. Section 2 is shorter and runs across the width of the structure. Section 3 also runs along the structure's length, but it is inclined to accommodate the sloped ceiling of the ramped section of the floor as opposed to Section 1.

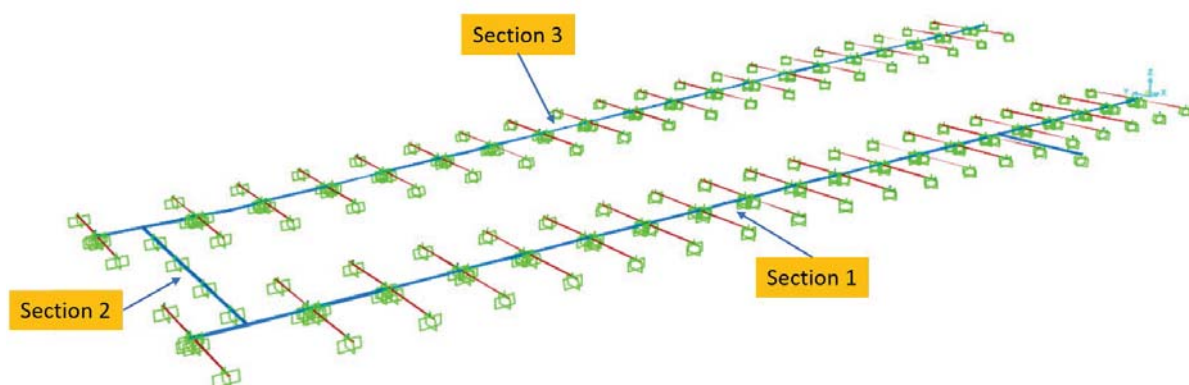


Figure 7: Finite element model of fire-sprinkler system.

All pipes were modelled as frames in SAP2000 terminology. The intersection points between the beams and the 114-mm pipelines were modelled as frictionless rollers allowing the

pipe to move along its longitudinal axis and restraining the pipe in both the vertical and transverse directions. The effective mass of the pipelines was increased to account for the weight of the water inside the pipes.

Typical installations of rods used for suspending the piping system from the ceiling are shown in Figure 8. The supporting rods were modelled as rods with rigid connections to the pipes and the ceiling. Since the actual installation used the threaded rods, the effective diameter of the rods was reduced accordingly, and they were also modelled as elastic frames in the first stage of analysis.

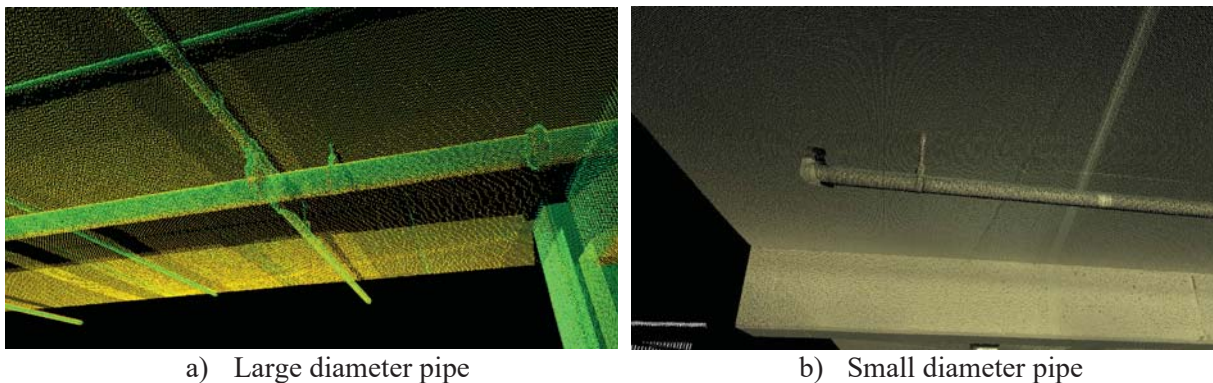


Figure 8: Typical installation of supporting rods.

Based on the results of the time history analysis of the elastic FE element model, it was concluded that the bending stress in a few supporting rods is below the yielding stress of mild steel. Nevertheless, failures of the supporting rods were observed as presented in Figure 9.

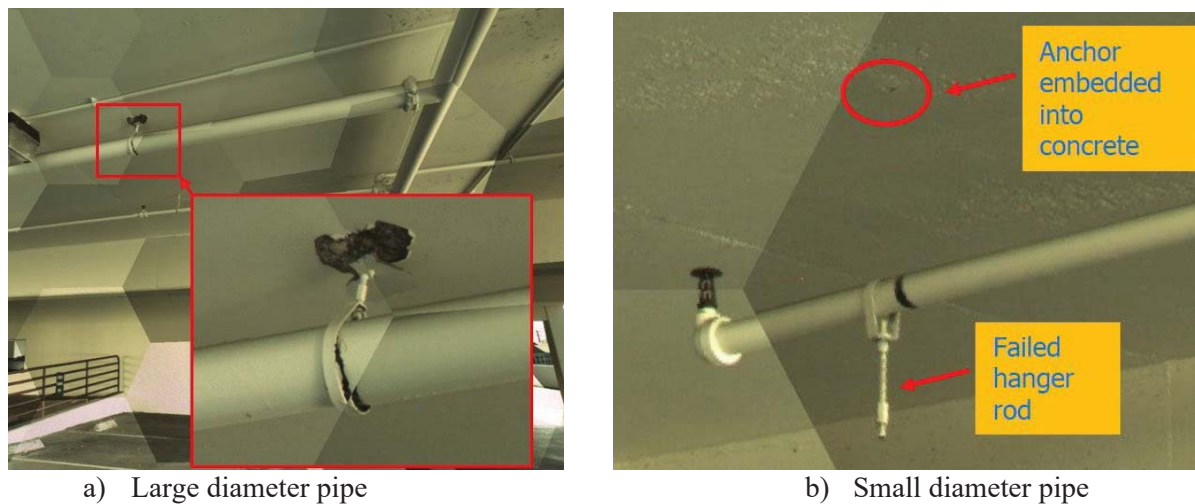


Figure 9: Typical failures of supporting rods [1].

The failure in the right image is related to the low-cycle fatigue capacity of the smaller rods in bending. As opposed to that, the left image shows a failure of the larger supporting rod that resulted from the failure of the anchoring part of the rod. The anchor's depth was not sufficient to avoid a failure of the concrete. These nonlinear effects will be modelled in the next stage of the finite element modelling. This part of the finite element modelling is ongoing. In this stage a number of component tests will be performed to generate a realistic model.

6 ACKNOWLEDGMENTS

The laser scans were collected during operations of nees@berkeley which was supported by the National Science Foundation (NSF). Special thanks are due to Smart Scanning Solutions, LLC (Tashkent, Uzbekistan) for the extensive work on converting the point cloud into solids. The authors would like to acknowledge Sensor Fusion and Monitoring Technologies, LLC (USA) for providing access to the portable data acquisition system. Special thanks are due to Holly Halligan of UC Berkeley for editing the paper.

7 CONCLUSIONS

- Based on the laser scans of a parking structure a finite element model of the fire-sprinkler piping system was generated.
- To estimate the dominant frequencies of the structure it was studied via ambient vibration tests.
- A few assumptions were made for the first stage of modelling. The resulting simplified model was studied in a linear time history analysis.
- The results of the first stage clearly show larger stresses as the locations of the observed failures, although they were below the yielding stress of mild steel.
- The first stage analysis shows a strong need for non-linear analysis based on component testing of typical connections. This part of the study is ongoing.

REFERENCES

- [1] S. Takhirov, K.M. Mosalam, F. Cakir, S. Günay (2017). ‘Performance of Fire Sprinkler Systems in the 2014 South Napa Earthquake: Numerical Modelling with Validation by Laser Scans of Aftermath’. The 16th World Conference on Earthquake Engineering. January 7-13, 2017 Santiago, Chile.
- [2] Leica Geosystems AG (2011). Leica ScanStation C10. https://w3.leica-geosystems.com/downloads123/hds/hds/ScanStation%20C10/brochures-datasheet/Leica_ScanStation_C10_DS_en.pdf.
- [3] Leica Geosystems (2018). Cyclone Version 9.2.1.
- [4] Pacific Instruments, Inc. (2017). http://catalog.pacificinstruments.com/Asset/6008U_Enclosure%204-slot%2012V%20DC%20USB%20Control%20&%20Data%20Interface.pdf last retrieved on 11/23/20.
- [5] International Code Council Evaluation Service Inc. (ICC-ES), 2015. ‘Acceptance Criteria for Seismic Qualification by Shake-Table Testing of Nonstructural Components and Systems, AC156’, ICC-ES.
- [6] The United States Geological Survey (USGS). <https://www.usgs.gov/natural-hazards/earthquake-hazards/hazards> (last accessed on 04/16/2021).

- [7] Amir Gilani and Shakhzod Takhirov. 'Current U.S. practice of seismic qualification of suspended ceilings by means of shake table tests', *INGEGNERIA SISMICA* journal, Italy: Vol. XXVIII, No. 1, pp. 26-42, 2011.
- [8] Computers and Structures, Inc., CSI (2014): SAP2000 Ultimate Version 16.1.1. Structural Analysis Program.

IMPROVEMENT OF DYNAMIC AND SEISMIC BEHAVIOUR OF CABINETS THROUGH CONTROLLED DEFORMATION

S. Pagliaro¹, A. Di Egidio², and A. Contento³

¹University of L'Aquila - DICEAA
via G. Gronchi 19, 64100 L'Aquila - Italy
e-mail: stefano.pagliaro@graduate.univaq.it

²University of L'Aquila - DICEAA
via G. Gronchi 19, 64100 L'Aquila - Italy
e-mail: angelo.diegidio@univaq.it

³University of L'Aquila - DICEAA
via G. Gronchi 19, 64100 L'Aquila - Italy
e-mail: alessandro.contento@univaq.it

Keywords: Deformable rocking model, overturning, rocking maps, one-sine impulse, seismic excitation.

Abstract. *In this paper the possibility to improve the dynamic and seismic response of cabinets that can exhibit rocking dynamics is investigated. The generic cabinet is modelled as an assembly of rigid components and can undergo a change of configuration. The scope of the research is to verify if the allowed deformation could protect the cabinet by preventing the overturning or reducing the amplitude of rocking oscillations. The control of the deformation is obtained by using linear visco-elastic devices, whose mechanical characteristics are at the base of the parametric analysis performed in the paper. An extensive parametric analysis is carried out by numerically integrating the equations of motion. The effectiveness of this protection method is analyzed by comparing the behaviour of rigid and deformable cabinets under one-sine pulse and seismic excitations. For the one-sine pulse excitation, the comparison is made with overturning spectra that provide the amplitude of the excitation able to overturn the cabinets versus its circular frequency. For the seismic excitation, the comparison is performed by using different registered earthquakes and comparing the maximum rocking angle reached during the motion. The results show that the ability of cabinets to change their configuration improves the dynamical and seismic performances compared to those of the equivalent rigid cabinets.*

1 Introduction

The protection of rigid blocks from the overturning is a fascinating argument in the scientific literature. Most of the studies on the protection of rigid blocks from overturning are focused on the use of external devices such as base isolation [1, 2, 3, 4, 5] and base anchorages [6, 7]. Several authors used mass-dampers, that have been modeled either in the shape of a pendulum [8, 9, 10, 11] or as a single degree of freedom mass running on the top of the rigid body [12, 13, 14]. Some researchers studied the use of semi-active anchorages [15, 16] or base active control systems [17, 18, 19] to increase the amplitude of base excitation required to topple a rigid body.

This paper investigates the dynamic and seismic response of cabinets that are constituted by four external panels, hinged to each other in the four vertexes of the body. Four linear visco-elastic devices of equal characteristics are associated with these hinges. Due to this particular configuration, the body can deform as an articulated quadrilateral. Additionally, it is assumed that the body can undergo a rocking motion but cannot slide. The equations of motion are obtained by a Lagrangian approach. Two different impacts are considered in the paper: the classical impact of the base of the body with the support during the rocking motion and the impact on security stops, needed to limit the maximum angular deformation.

The model presented here is conceptually similar to the flexible rocking body models presented in [20, 21, 22] or [23], where the flexible rocking model was used to interpret the experimental response of tuff walls. However, the novelty of the paper is not in the description of a flexible rocking structure but in the investigation of the behaviour of a structure where specific devices are added to guide its deformation with the aim of reducing the amplitude of the rocking oscillation and preventing the overturning.

An extensive parametric analysis is performed by numerically integrating the equations of motion. The effectiveness of this protection method is analyzed by comparing the behaviour of rigid (i.e., with fixed connections) and deformable cabinets under one-sine pulse and seismic excitations. For the one-sine pulse excitation, the comparison is made with overturning spectra that provide the amplitude of the excitation able to overturn the cabinets versus its circular frequency. For the seismic excitation, the comparison is performed by building rocking maps that are contour plots of the maximum rocking angle in a specific parameter plane. Different recorded earthquakes have been used in the simulations.

2 Mechanical model of the cabinet

The mechanical system used to schematize the cabinet is shown in Fig. 1a. The perimeter panels are connected through hinges and four equal Kelvin-Voight devices in the vertexes of the cabinet (see Fig. 1a). With this particular structure, the mechanical system can deform as an articulated quadrilateral and its kinematics would be undetermined without the Kelvin-Voight devices. The vertical distance h between two consecutive shelves is constant so the total height of the cabinet is $4h$. The base of the cabinet has a dimension $2b$ and its depth (i.e., the dimension orthogonal to the plane of Fig. 1) is $d = 1.0\text{m}$.

All panels have a thickness $s = 0.02\text{m}$ and a bulk density $\rho = 650\text{kg/m}^3$ (i.e., chipboard wood). The cabinet may contain additional masses placed on the shelves. Such masses are quantified multiplying a bulk density $\rho_{fill} = 130\text{kg/m}^3$ for the volume between two consecutive horizontal panels and are added to the mass of the panel on which they are placed. Considering also the additional masses M , the masses of the seven panels m_j ($j = 1, \dots, 7$) are evaluated as

$$\begin{aligned} m_{1,3} &= \rho \cdot d \cdot s \cdot 4h \\ m_{2,4-7} &= \rho \cdot d \cdot s \cdot 2b + M \end{aligned} \quad (1)$$

It is assumed that the additional mass M is located in the same mass centre of the panel on which it is placed and that there is no inertia moment associated to these masses. Since the sliding of the cabinet is prevented, the motion of the body can be divided into two different phases: (i) the full-contact phase, where the body deforms as an articulated quadrilateral (Fig. 1b), and (ii) the rocking phase, where the body rotates alternatively around one of its base corners and deforms at the same time (Fig. 1c). The Lagrangian parameter $\theta(t)$ describes the deformation of the cabinet, whereas the parameter $\psi(t)$ describes the rocking motion.

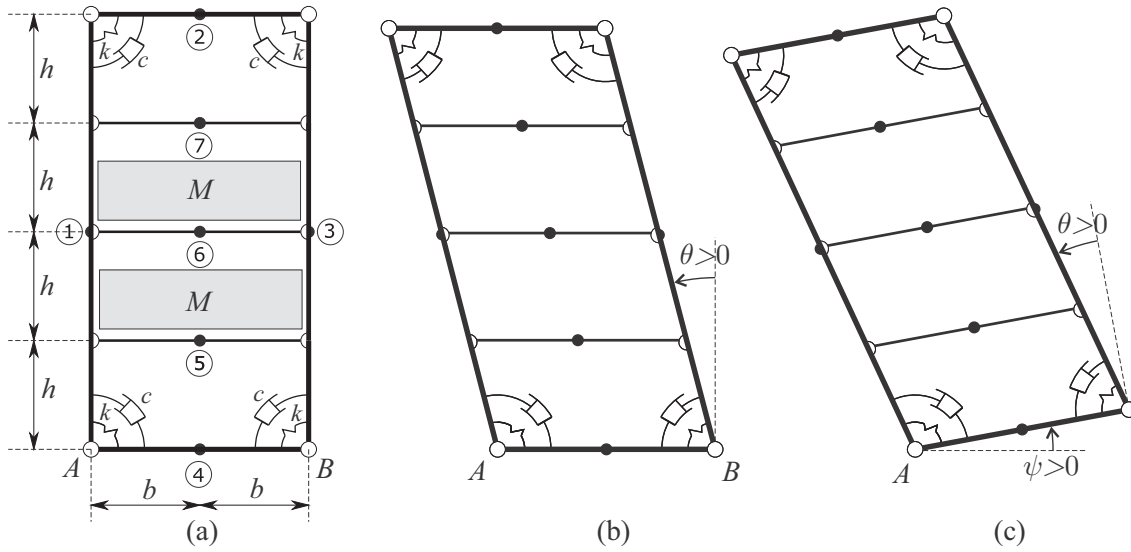


Figure 1: Model: (a) Geometrical characterization; (b) Full-contact deformed configuration; (c) Rocked and deformed configuration.

2.1 Equations of motion

The equations of motion are obtained through a Lagrangian approach. For brevity, only the equations of the rocking phase around the left corner A are presented in this section. The equations of the full-contact phase can be obtained by those of the rocking phase by neglecting the angle $\theta(t)$ and its time-derivatives ($\theta(t) = \dot{\theta}(t) = \ddot{\theta}(t) = 0$). The two equations of motion of the body that rocks around the left base corner read:

$$\begin{aligned} & h^2 (4m_1 + 16m_2 + 4m_3 + m_5 + 4m_6 + 9m_7) [\psi''(t) + \theta''(t)] - \\ & bh (4m_2 + 4m_3 + m_5 + 2m_6 + 3m_7) \{ \psi''(t) \sin[\theta(t)] - \psi'(t)^2 \cos[\theta(t)] \} - \\ & h (2m_1 + 4m_2 + 2m_3 + m_5 + 2m_6 + 3m_7) g \sin[\theta(t) + \psi(t)] - \\ & h (2m_1 + 4m_2 + 2m_3 + m_5 + 2m_6 + 3m_7) x_{gr}''(t) \cos[\theta(t) + \psi(t)] + \\ & (J_1 + J_3) \theta''(t) + 4c\theta'(t) + 4k\theta(t) = 0 \end{aligned} \quad (2)$$

$$\begin{aligned}
 & (J_1 + J_2 + J_3 + J_4 + J_5 + J_6 + J_7)\psi''(t) + \\
 & b^2 (m_2 + 4m_3 + m_4 + m_5 + m_6 + m_7) \psi''(t) - \\
 & 2bh (4m_2 + 4m_3 + m_5 + 2m_6 + 3m_7) \psi''(t) \sin [\theta(t)] - \\
 & 2bh (4m_2 + 4m_3 + m_5 + 2m_6 + 3m_7) \psi'(t) \theta'(t) \cos [\theta(t)] + \\
 & h^2 (4m_1 + 16m_2 + 4m_3 + m_5 + 4m_6 + 9m_7) [\psi''(t) + \theta''(t)] + \\
 & b (m_2 + 2m_3 + m_4 + m_5 + m_6 + m_7) \{g \cos [\psi(t)] - \sin [\psi(t)] x''_{gr}(t)\} - \\
 & bh (4m_2 + 4m_3 + m_5 + 2m_6 + 3m_7) \{\theta''(t) \sin [\theta(t)] + \theta'(t)^2 \cos [\theta(t)]\} - \\
 & h (2m_1 + 4m_2 + 2m_3 + m_5 + 2m_6 + 3m_7) g \sin [\theta(t) + \psi(t)] - \\
 & h (2m_1 + 4m_2 + 2m_3 + m_5 + 2m_6 + 3m_7) x''_{gr}(t) \cos [\theta(t) + \psi(t)] = 0
 \end{aligned} \tag{3}$$

Eq. 2 models the deformation of the body and Eq. 3 models the rocking motion. In the remaining of the paper, the dependence of θ , ψ , and x_{gr} on t is omitted.

2.2 Uplift conditions

The uplift acceleration a_{UP}^A , able to uplift the body around A coincides with the expression of x''_{gr} obtained from Eq. 3 when $\dot{\psi} = \ddot{\psi} = 0$

$$\begin{aligned}
 a_{UP}^A = & \{bg (m_2 + 2m_3 + m_4 + m_5 + m_6 + m_7) - \\
 & bh (4m_2 + 4m_3 + m_5 + 2m_6 + 3m_7) [\theta'' \sin (\theta) - \theta'^2 \cos (\theta)] - \\
 & gh (2m_1 + 4m_2 + 2m_3 + m_5 + 2m_6 + 3m_7) \sin (\theta) + \\
 & h^2 (4m_1 + 16m_2 + 4m_3 + m_5 + 4m_6 + 9m_7) \theta''\} / \\
 & [h(2m_1 + 4m_2 + 2m_3 + m_5 + 2m_6 + 3m_7) \cos (\theta)]
 \end{aligned} \tag{4}$$

The uplift acceleration a_{UP}^A depends on the geometry of the cabinet and on its deformation during the full-contact phase (i.e., depend on θ , $\dot{\theta}$ and $\ddot{\theta}$).

2.3 Impact conditions

The model presented in this paper considers two different kinds of impact: (i) the impact between the base of the cabinet and the support during the rocking motion and (ii) the impact on security stops that are used to limit the deformation of the cabinet.

The impact conditions referring to a cabinet that after an impact re-uplifts around the left corner A are obtained assuming that the cabinet position after the impact remains unchanged, the angular momentum of the whole cabinet around the re-uplifting corner A is preserved, and the horizontal momentum of the cabinet is also preserved. Under such assumptions, it is possible to evaluate the post-impact angular velocities $\dot{\theta}^+$ and $\dot{\psi}^+$ as functions of the pre-impact angular velocities $\dot{\theta}^-$ and $\dot{\psi}^-$

$$\dot{\theta}^+ = \dot{\theta}^- + r_{\theta}(\theta) \dot{\psi}^-; \quad \dot{\psi}^+ = s_{\theta}(\theta)(\dot{\theta}^- - \dot{\theta}^+) + s_{\psi}(\theta) \dot{\psi}^- \tag{5}$$

where

$$r_{\theta}(\theta) = \frac{\left[4b^2 (2m_1 + m_2 + m_4 + m_5 + m_6 + m_7) - 2bh (2m_1 + 4m_2 + 3m_3 + m_5 + 2m_6 + 2m_7) \theta \right]}{\left[b^2 (m_2 + 4m_3 + m_4 + m_5 + m_6 + m_7) - bh (8m_2 + 8m_3 + 2m_5 + 4m_6 + 6m_7) \theta + h^2 (4m_1 + 16m_2 + 4m_3 + m_5 + 4m_6 + 9m_7) \theta^2 + 4h^2 (m_1 + m_3) + J_2 + J_4 + J_5 + J_6 + J_7 \right]} \tag{6}$$

$$s_\theta(\theta) = \frac{h^2(16m_2 + m_5 + 4m_6 + 9m_7) + J_1 + J_3}{\left[\frac{J_A - bh(8m_1 + 8m_2 + 2m_5 + 4m_6 + 6m_7)\theta + h^2(4m_1 + 16m_2 + 4m_3 + m_5 + 4m_6 + 9m_7)\theta^2}{h^2(4m_1 + 16m_2 + 4m_3 + m_5 + 4m_6 + 9m_7)\theta^2} \right]} \quad (7)$$

$$s_\psi(\theta) = \frac{\left[\frac{J_A - 2bS_{yB} + bh(4m_1 - 4m_3)\theta + h^2(4m_1 + 16m_2 + 4m_3 + m_5 + 4m_6 + 9m_7)\theta^2}{J_A - bh(8m_1 + 8m_2 + 2m_5 + 4m_6 + 6m_7)\theta + h^2(4m_1 + 16m_2 + 4m_3 + m_5 + 4m_6 + 9m_7)\theta^2} \right]}{\left[\frac{J_A - bh(8m_1 + 8m_2 + 2m_5 + 4m_6 + 6m_7)\theta + h^2(4m_1 + 16m_2 + 4m_3 + m_5 + 4m_6 + 9m_7)\theta^2}{h^2(4m_1 + 16m_2 + 4m_3 + m_5 + 4m_6 + 9m_7)\theta^2} \right]} \quad (8)$$

The quantities $r_\theta(\theta)$, $s_\theta(\theta)$, and $s_\psi(\theta)$ play the role of restitution coefficients and depend on the deformed configuration of the system. Inside their expressions, J_A is the polar inertia of the whole cabinet with respect to A and S_{yA} is the static moment of the system with respect a vertical axis passing through A .

Security stops are introduced to limit the deformation (i.e., the maximum value of θ) during the motion. By referring to an impact on security stops during a rocking motion around the base corner A , it is possible to obtain the post-impact velocities $\dot{\theta}^+$ and $\dot{\psi}^+$ as functions of the pre-impact angular velocities $\dot{\theta}^-$ and $\dot{\psi}^-$ through the following relationships:

$$\dot{\theta}^+ = -\eta\dot{\theta}^-; \quad \dot{\psi}^+ = \dot{\psi}^- + p(\theta, \psi)\dot{\theta}^- \quad (9)$$

where

$$p(\theta, \psi) = \frac{(\eta + 1)h(2m_1 + 4m_2 + 2m_3 + m_5 + 2m_6 + 3m_7)}{\left[\frac{b(m_2 + 2m_3 + m_4 + m_5 + m_6 + m_7)\sin(\psi) - h(2m_1 + 4m_2 + 2m_3 + m_5 + 2m_6 + 3m_7)\theta\sin(\psi) + h(2m_1 + 4m_2 + 2m_3 + m_5 + 2m_6 + 3m_7)\cos(\psi)}{h(2m_1 + 4m_2 + 2m_3 + m_5 + 2m_6 + 3m_7)\cos(\psi)} \right]} \quad (10)$$

It is assumed that after an impact on security stops the value of $\dot{\theta}$ changes its sign and is reduced to a fraction of the value before the impact. The restitution coefficient η depends on the characteristics of the security stops and $\eta \leq 1$. The angular velocity $\dot{\psi}^+$ is obtained by assuring the conservation of the horizontal momentum of the cabinet.

3 Numerical simulations

An extensive parametric analysis is performed by numerically integrating the equations of motion. Such analyses are performed varying the oscillation period T of the cabinet in the full-contact phase and the dimensions (i.e., base $2b$ and slenderness $\lambda = 2h/b$) of the cabinet. All the other quantities are fixed: damping ratio of the cabinets $\xi = 0.05$, restitution coefficient of the security stops $\eta = 0.5$, maximum angle allowed by the security stops $\theta_{max} = 0.1\text{rad}$, and the cabinet is considered to be full (i.e., the additional mass M is added to the mass of the shelves from 4 to 7, see Fig. 1a).

3.1 One-sine impulsive excitation

In the analyses performed in this section, the cabinet is excited by a one-sine pulse excitation:

$$\ddot{x}_g(t) = \begin{cases} A_s \sin\left(\frac{2\pi}{T_s}t\right) & 0 \leq t \leq T_s \\ 0 & T_s < t \leq t_{max} \end{cases} \quad (11)$$

where T_s is the period of the one-sine cycle, $\Omega = 2\pi/T_s$ is the circular frequency of the excitation, A_s is its amplitude, and t_{\max} is the maximum time used in the numerical integrations ($t_{\max} = 10T_s$). The results are arranged in overturning spectra, that provide the amplitude of the excitation that generates the first overturning occurrence versus the circular frequency of the excitation.

An initial parametric analysis is performed to investigate the sensitivity of the dynamics of the cabinet to T . In such an analysis the geometrical characteristics of the cabinet are fixed, $2b = 0.6\text{m}$, $4h = 2.6\text{m}$. Figure 2a presents the results obtained with a model that does not include security stops, whereas Fig. 2b shows the corresponding results obtained by including the security stops. In the two figures, dashed lines refer to a rigid cabinet, whereas solid lines refer to a deformable cabinet. The spectra are labelled with the value of the period T used in the analysis. Such labels are surrounded by an ellipse if, during the motion, the cabinet impacts on security stops or by a rectangle otherwise. In Fig. 2a, since the security stops are not considered, the labels are all rectangular. Such a convention that shows the occurrence of impacts on security stops is used in all the figures of this section. In Figs. 2a and 2b, the overturning spectra of the deformable cabinets with periods $T \geq 1.0\text{s}$ are above the curves of the rigid cabinets in a wide range of the values of Ω . This means that the amplitude of the excitation A_s required to overturn a deformable cabinet is higher than amplitude needed to overturn the corresponding rigid cabinet. Moreover, the comparison between Fig. 2a and 2b shows that, when impacts on security stops occur (e.g., cabinet with $T = 1.5\text{s}$), the presence of the security stops significantly affects the dynamics of the cabinet. Nevertheless, the overturning spectrum obtained for $T = 1.5\text{s}$ in Fig. 2b is still above the curve of rigid cabinet in most of the considered range of Ω . In general all the overturning spectra in Fig. 2 present a jump. As it occurs in rigid blocks ([24, 25]), also in deformable rocking bodies such a jump is associated to a change of the overturning mode. Specifically, before the jump the body overturns hitting once the ground, whereas after the jump the body overturns without hitting the ground. The deformability of the cabinet shifts the jump on the left leading to a general improvement of the behaviour of the cabinet.

In the following analysis the dimensions of the cabinet, $2b$ and $4h$, are considered as variable parameters. In Fig. 3, the results of the analysis are arranged in matrix form. Each row refers to a different base dimension, whereas each column refers to a different height of the cabinet. As expected, the dimensions of the cabinet significantly affect the overturning spectra of the rigid body. In general, the deformable cabinets are less prone to overturn than the equivalent rigid cabinets, especially for more slender cabinets (i.e., those in the upper row). In Fig. 3, the left graph on the first row and the middle graph on the second row refer to cabinets with $\lambda = 3$ and different scale size. The comparison of the two graphs shows that the improvement in the dynamics of the deformable cabinets (solid lines) with respect to the correspondent rigid case (dashed lines) is smaller in the cabinet with larger scale.

3.2 Seismic excitation

A parametric analysis is performed to assess if the deformation of the cabinet can reduce the amplitude of the rocking oscillations and eventually avoid the overturning of the cabinet during a seismic event. For this analysis, seismic events with different characteristics are selected. Fig. 4 shows the time-histories of the seismic records that are listed in the following:

- Kobe, Takarazuka-000 station, ground motion recorded during the 1995 Japan earthquake;

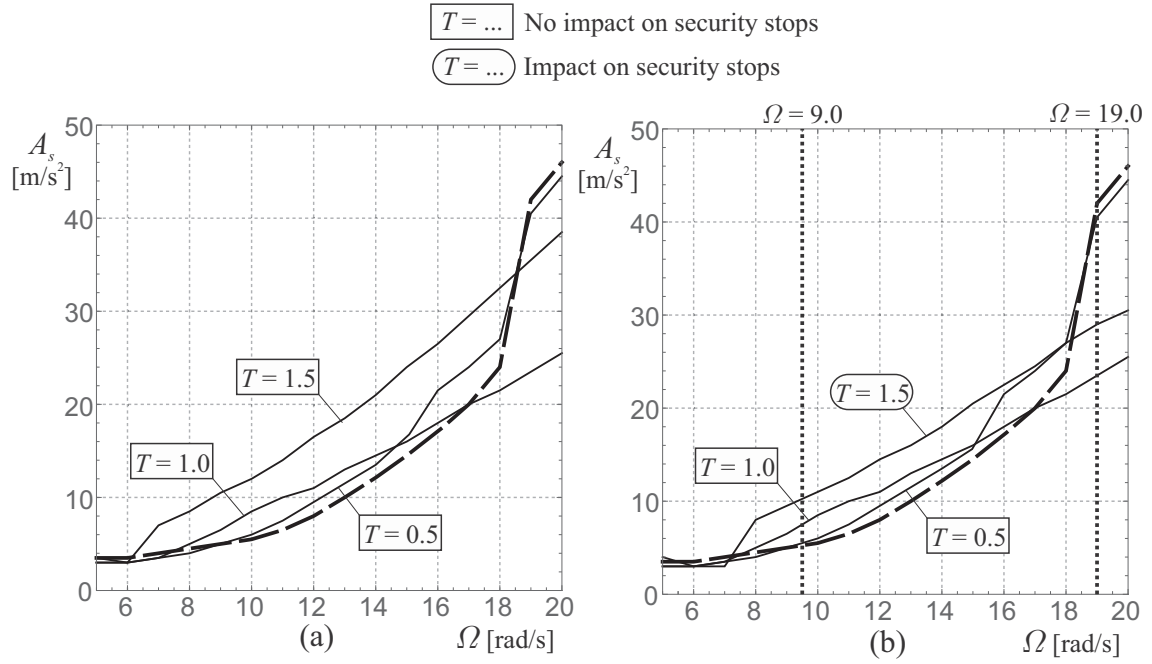


Figure 2: Overturning curves for different period T : (a) Overturning curves without security stops; (b) Overturning curves with security stops ($\xi = 0.05$, $\eta = 0.5$, $\theta_{max} = 0.1$, $2b = 0.6\text{m}$, $4h = 2.6\text{m}$, cabinet full).

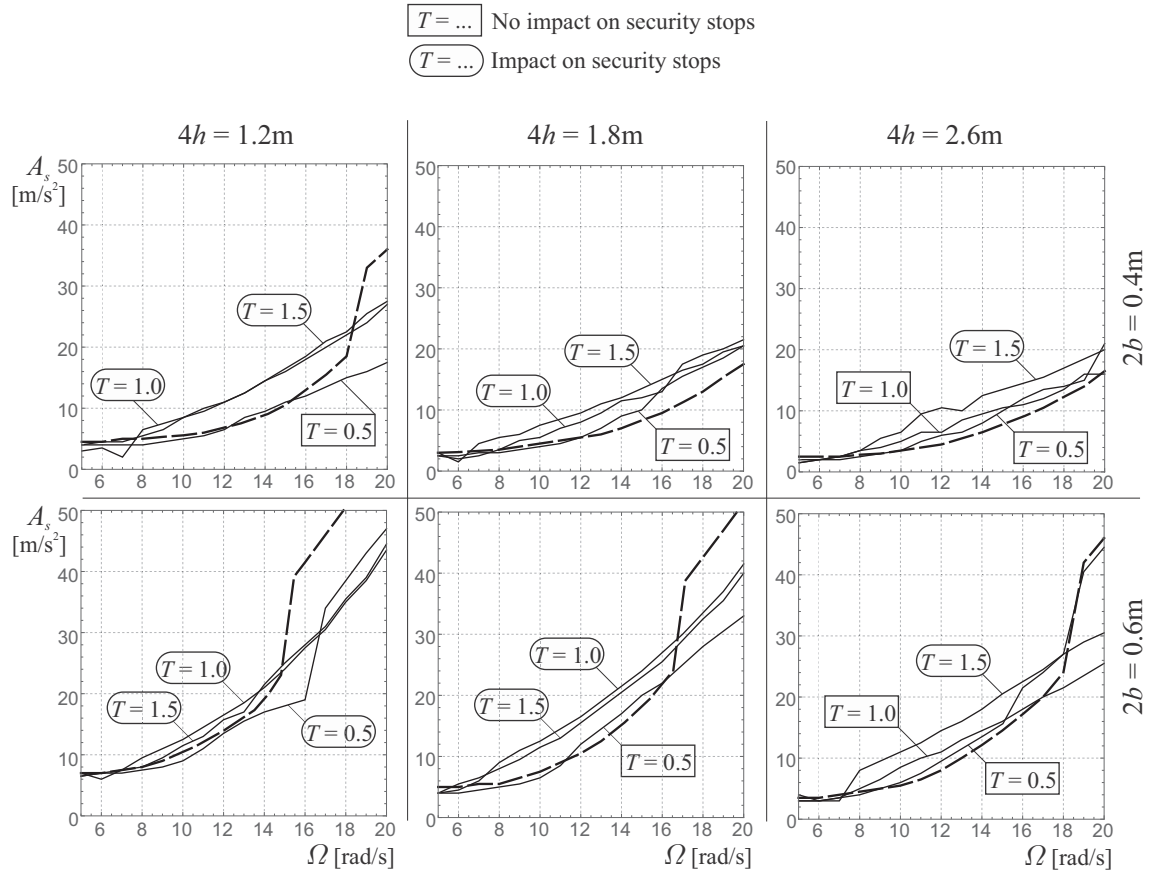


Figure 3: Overturning curve for different geometrical characteristics of the cabinet ($\xi = 0.05$, $\eta = 0.5$, $\theta_{max} = 0.1$, cabinet full).

- Newhall, Newhall-360 station, ground motion recorded during the 1994 Northridge, California earthquake;
- San José, Fremont Mission San Jose motion recorded during the October 17, 1989, Lorna Prieta earthquake.

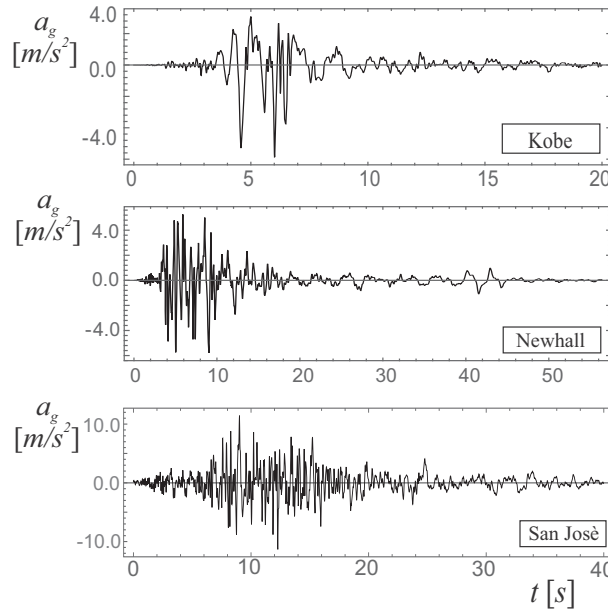


Figure 4: Time-histories of the recorded earthquakes.

The results of the parametric analysis performed with seismic excitation are arranged in rocking maps. Such rocking maps are contour plots of the maximum rocking angle in the parameter plane $2b-\lambda$. The rocking maps obtained for rigid and deformable cabinets are compared to assess if the deformation improves the seismic behaviour of the cabinets.

In Fig. 5 the rocking maps are organized in matrix form where each column refers to a different earthquake (Kobe, Newhall, and San José). The first row shows the maps of the rigid cabinet, rows two and three refer to deformable cabinets with $T = 1.0$ s and $T = 1.5$ s, respectively. In the maps, the light grey regions (rocking regions) are those where the cabinet undergoes rocking motion. The contour levels inside these regions refer to the maximum rocking angle reached during the motion. The dark grey regions (overturning regions) are those where the cabinet overturns. The first row of Fig. 5 shows that the rigid cabinet overturns in almost all the parameter plane except that in the right lower part of the maps that correspond to combinations of larger values of the base and lower slenderness of the cabinet. Rows two and three of Fig. 5 show that deformable cabinets have smaller overturning regions that generally tend to shrink as T increases. As an exception, for the Newhall seismic event, the cabinet with $T = 1.0$ s does not overturn in the whole parameter plane, whereas the cabinet with $T = 1.5$ s overturns only in a small portion of the parameter space. Finally, the contour levels inside the light grey regions show a general reduction of the maximum rocking angle when the period T increases.

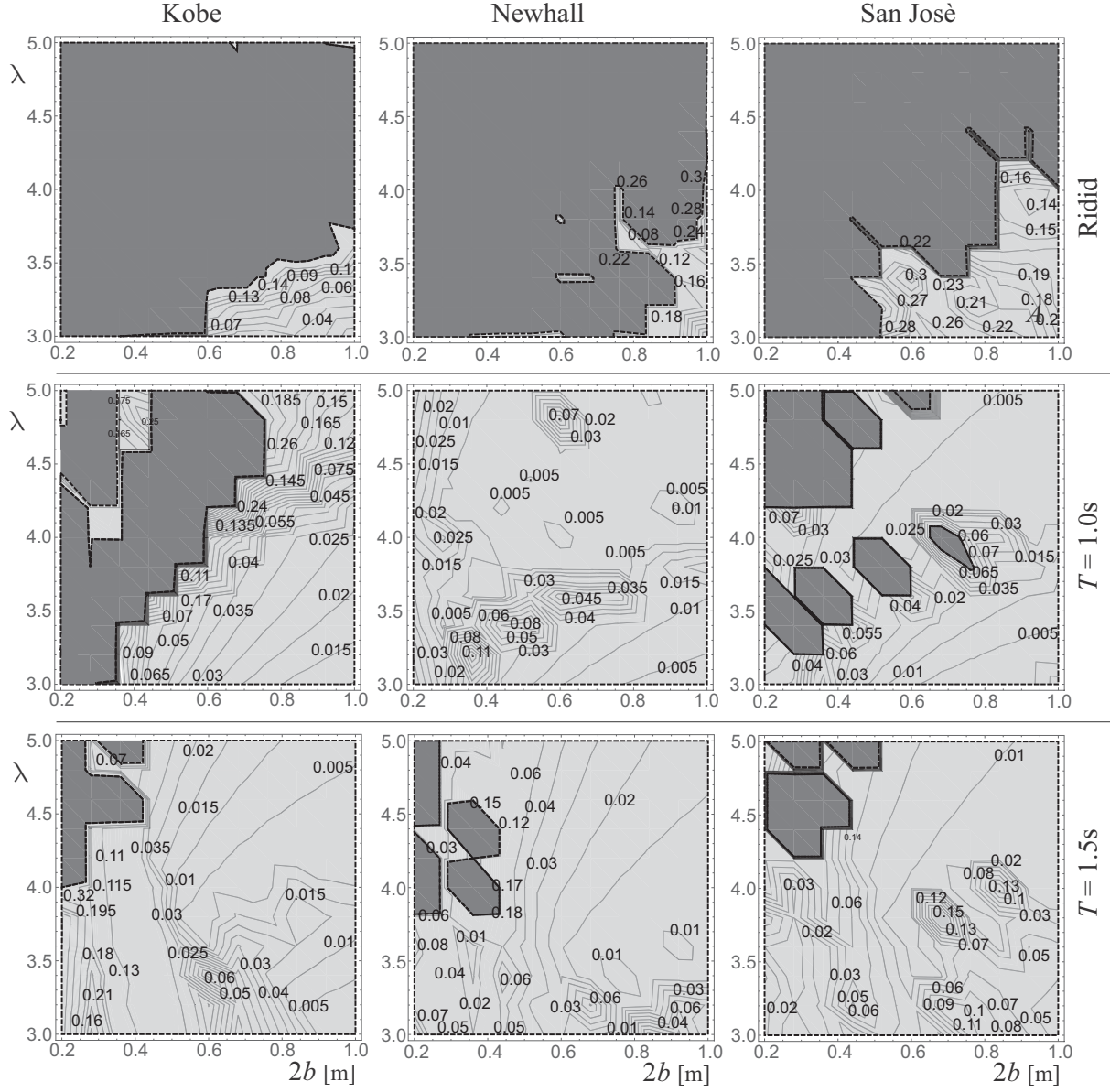


Figure 5: Rocking maps for three different earthquakes (Kobe, Newhall, San José) ($\xi = 0.25, \eta = 0.5, \theta_{max} = 0.1$, cabinet full).

4 Conclusions

This paper presents the model of a cabinet that can undergo a guided deformation. This model has been used to investigate the possibility to improve the dynamic and seismic behaviour of cabinets and racks by providing them of the ability to change their geometrical configuration during the rocking motion. The kinematic related to the change of geometrical configuration is specific to the model studied in this paper but can be easily generalized to other models representing cabinets and racks, both for civil and industrial use.

It has been assumed that the body can undergo only rocking motion, without sliding. The equations of motion have been obtained through a Lagrangian approach. The classical impact of the body base with the support during the rocking motion and the impact on security stops needed to limit the maximum angular deformation have been considered to describe the motion of the system.

An extensive parametric analysis has been performed by numerically integrating the equations of motion. The improvement in the dynamics has been analyzed by comparing the behaviour of rigid and deformable cabinets under one-sine pulse and seismic excitations. For the one-sine pulse excitation, the comparison has been made with overturning spectra that provide the amplitude of the excitation able to overturn the cabinets versus its circular frequency. For the seismic excitation, the maximum rocking angle reached during the motion under different recorded earthquakes have been arranged in rocking maps and compared.

The results shows that the ability of a cabinet to change its geometrical configuration before and after the start of the rocking motion significantly improves its dynamical and seismic performance compared to the performance of an equivalent rigid cabinet.

References

- [1] A. Di Egidio and A. Contento. Base isolation of sliding-rocking non-symmetry rigid blocks subjected to impulsive and seismic excitations. *Engineering Structures*, 31:2723–2734, 2009.
- [2] A. Di Egidio and A. Contento. Seismic response of a non-symmetric rigid block on a constrained oscillating base. *Engineering Structures*, 32:3028–3039, 2010.
- [3] A. Contento and A. Di Egidio. On the use of base isolation for the protection of rigid bodies placed on a multi-storey frame under seismic excitation. *Engineering Structures*, 62-63:1–10, 2014.
- [4] I. Calìo and M. Marletta. Passive control of the seismic response of art objects. *Engineering Structures*, 25:1009–1018, 2003.
- [5] M.F. Vassiliou and N. Makris. Analysis of the rocking response of rigid blocks standing free on a seismically isolated base. *Earthquake engineering and structural dynamics*, 41(2):177–196, 2012.
- [6] N. Makris and J. Zhang. Rocking response of anchored blocks under pulse-type motions. *Journal of Engineering Mechanics*, 127(5):484–493, 2001.
- [7] E.G. Dimitrakopoulos and M.J. DeJong. Overturning of retrofitted rocking structures under pulse-type excitations. *Journal of Engineering Mechanics*, 138:963–972, 2012.

- [8] L. Collini, R. Garziera, K. Riabova, M. Munitsyna, and A. Tasora. Oscillations control of rocking-block-type buildings by the addition of a tuned pendulum. *Shock and Vibration*, 2016:Article ID 8570538, 2016.
- [9] P. Brzeski, T. Kapitaniak, and P. Perlikowski. The use of tuned mass absorber to prevent overturning of the rigid block during earthquake. *International Journal of Structural Stability and Dynamics*, 6(10):Article ID 1550075, 2016.
- [10] A. de Leo, G. Simoneschi, C. Fabrizio, and A. Di Egidio. On the use of a pendulum as mass damper to control the rocking motion of a non-symmetric rigid block. *Meccanica*, 51:2727–2740, 2016.
- [11] A. Di Egidio, R. Alaggio, A. Aloisio, A.M. de Leo, A. Contento, and M. Tursini. Analytical and experimental investigation into the effectiveness of a pendulum dynamic absorber to protect rigid blocks from overturning. *Int. Journal of Non-Linear Mechanics*, 115:1–10, 2019.
- [12] G. Simoneschi, A. de Leo, and A. Di Egidio. Effectiveness of oscillating mass damper system in the protection of rigid blocks under impulsive excitation. *Engineering Structures*, 137:285–295, 2017.
- [13] G. Simoneschi, A. Geniola, A. de Leo, and A. Di Egidio. On the seismic performances of rigid blocks coupled with an oscillating mass working as tmd. *Earthquake Engineering and Structural Dynamics*, 46:1453–1469, 2017.
- [14] A. Di Egidio, A. de Leo, and G. Simoneschi. Effectiveness of mass-damper dynamic absorber on rocking block under one-sine pulse ground motion. *International Limits of Non-Linear Mechanics*, 98:154–162, 2018.
- [15] R. Ceravolo, M.L. Pecorelli, and L. Zanotti Fragonara. Semi-active control of the rocking motion of monolithic art objects. *Journal of Sound and Vibration*, 374:1–16, 2016.
- [16] R. Ceravolo, M.L. Pecorelli, and L. Zanotti Fragonara. Comparison of semi-active control strategies for rocking objects under pulse and harmonic excitations. *Mechanical Systems and Signal Processing*, 90:175–188, 2017.
- [17] A. Di Egidio, G. Simoneschi, C. Olivieri, and A.M. de Leo. Protection of slender rigid blocks from the overturning by using an active control system. In *Proceedings of the XXIII Conference The Italian Association of Theoretical and Applied Mechanics*, 2014.
- [18] G. Simoneschi, C. Olivieri, A.M. de Leo, and A. Di Egidio. Pole placement method to control the rocking motion of rigid blocks. *Engineering Structures*, 167:39–47, 2018.
- [19] A. Di Egidio, C. Olivieri, and A.M. de Leo. Protection from overturning of rigid block-like objects with linear quadratic regulator active control. *Structural Control and Health Monitoring*, 27, 2020.
- [20] M. Michalis Vassiliou, K.R. MackieBozidar, and B. Stojadinovic. Dynamic response analysis of solitary flexible rocking bodies: Modeling and behavior under pulse-like ground excitation. *Earthquake Engineering and Structural Dynamics*, 43(10):1463–1481, 2014.

- [21] R. Thiers-Moggia and C. Málaga-Chuquitaype. Seismic control of flexible rocking structures using inerters. *Earthquake Engineering and Structural Dynamics*, 49(14):1519–1538, 2020.
- [22] S. Acikgoz and M.J. DeJong. The interaction of elasticity and rocking in flexible structures allowed to uplift. *Earthquake Engineering and Structural Dynamics*, 41(15):2177–2194, 2012.
- [23] E. Cappelli, A. Di Egidio, and F. Vestroni. Analytical and experimental investigation into the behavior of a rocking masonry tuff wall. *Journal of Engineering Mechanics*, 146(6), 2020.
- [24] J. Zhang and N. Makris. Rocking response of free-standing blocks under cycloidal pulses. *Journal of Engineering Mechanics*, 127(5):473–483, 2001.
- [25] A. Di Egidio, A.M. de Leo, and A. Contento. The use of a pendulum dynamic mass absorber to protect a trilithic symmetric system from the overturning. *Mathematical Problems in Engineering*, 2019, article Id: 4843738:14, 2019.

NUMERICAL MODELING OF A ROCKING AND SLIDING CYLINDRICAL COLUMN UNDER SEISMIC EXCITATION

Antonios A. Katsamakas ¹ and Michalis F. Vassiliou ²

¹ Ph.D. Candidate, Chair of Seismic Design and Analysis, IBK, ETH Zurich
Stefano-Franscini-Platz 5
8093 Zürich
Switzerland
e-mail: katsamakas@ibk.baug.ethz.ch

² Assistant Professor, Chair of Seismic Design and Analysis, IBK, ETH Zurich
Stefano-Franscini-Platz 5
8093 Zürich
Switzerland
e-mail: vassiliou@ibk.baug.ethz.ch

Abstract

This paper presents a finite element (FE) modeling approach for simulating the 3D response of a free-standing cylindrical column. The model is validated against experimental results, which involved testing of the cylindrical steel column under a set of 100 bidirectional ground motions. The specimen was free-standing and allowed to slide and rock in all directions. Both the tested specimen and the shake table platen were stiff enough to be modeled as rigid. The contact surface was modeled using Coulomb friction for the tangential behavior and stiff contact for the normal direction. Two energy dissipation mechanisms were modelled; friction and radiation damping. Since Rayleigh damping is not directly linked to the physical problem, it was set equal to zero.

It has been proven that the response of a single column to an individual ground motion is a chaotic and unpredictable problem. Therefore, a statistical approach was utilized to compare the numerical to the experimental results, using the cumulative distribution function (CDF) for the main response quantities (i.e., maximum displacement at the top of the column and residual displacement), demonstrating satisfying agreement.

The influence of the friction coefficient was assessed through an extensive sensitivity analysis using non-linear time-history analyses. Results proved that the statistics of the response only smoothly depend on the exact value of the friction coefficient even though the response to an individual ground motion seems chaotic.

Keywords: *Rocking Columns, Finite Elements, Statistical Validation, Sensitivity Analysis, Free-Standing Equipment*

1 INTRODUCTION

Rocking structures are the ones that are allowed to uplift. Under ground motion, uplifting occurs when:

$$\ddot{u}_g > g \tan \alpha \quad (1)$$

where \ddot{u}_g is the ground acceleration, g is the gravity acceleration, and α is the slenderness of the block (Figure 1). It is assumed that the sliding surface is sufficiently rough to prevent sliding. This uplifting effect acts as a fuse, limiting the inertial forces transmitted to the superstructure. After uplift, a rocking oscillator demonstrates negative stiffness, making the description of such systems significantly different to the conventional ones.

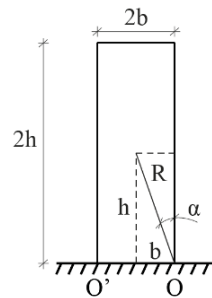


Figure 1. Geometric properties of a rocking block.

The first analytical study of this phenomenon is dated back to 1885 [1,2]. However, rocking structures have been systematically studied after 1963, when Housner published his seminal paper [3] where two main properties of the rocking structures were elucidated: i) out of two geometrically similar rocking blocks (same α) the larger one (larger R) can survive an excitation which will topple the smaller one ii) longer period ground motions have a higher overturning potential [3].

The rocking oscillator has been used to describe the dynamic behavior of free-standing equipment [4-16], masonry structures [17-26] and ancient temples [27-34]. Rocking is also a promising seismic response modification technique, both for bridges and buildings, with practical applications in the former USSR and New Zealand. Applications in buildings may comprise a soft-rocking-story mechanism [35-37], or a rocking wall [38, 39], whereas in bridges, rocking piers [40-56]. Several analytical studies investigated the response of rocking structures combined with external dampers or restraining tendons [57-60]. The influence of the flexibility of the rocking body was also studied, both analytically and experimentally [61-65].

The analytical model proposed by Housner describes the planar response of a rigid rocking body when subjected to one-directional excitation. However, under seismic excitation, rocking structures are subjected to bidirectional (or three-directional when the vertical acceleration is considered) excitation [66-69]. Under these conditions, an unanchored body may rock in 3D dimensions (wobble). When it is not restrained, it may also slide out of its initial position or completely detach from the support.

This study aims at developing a practical three-dimensional finite element model to predict the response of free-standing cylindrical rocking columns. The validity of the proposed model is assessed by statistically comparing numerical and experimental results. The experimental results comprise 100 shake table tests, using a cylindrical steel column with a slenderness (α) of 0.2. The number of tests performed is large enough to create an experimental benchmark

dataset, which could be used for a statistical comparison. The specimen was subjected to two-dimensional excitation, and it was free to slide, rock and wobble in all directions. As the column is free to slide and wobble out of its original position, it serves for validation of numerical models used for the description of the seismic behavior of unanchored equipment, rather than of structures that use rocking as a seismic isolation strategy, where the rocking members would not be allowed to slide.

2 STATISTICAL VALIDATION

Rocking is often characterized as “chaotic”, in the sense that the response of rocking objects is sensitive to the initial conditions [70], often making tests non-repeatable. Therefore, validating numerical models in a deterministic way does not even make sense.

Bachmann et al. [71] and Del Giudice et al. [72,73] claimed that validating a numerical model using a single ground motion is a sufficient but not necessary validation procedure. The seismic response is inherently stochastic since the excitation is stochastic. Therefore, a statistical (and not a deterministic) validation of the numerical model is proposed. During this statistical validation, the statistical distributions of the main response quantities of the model and the experiments are compared. This procedure requires an experimental benchmark dataset, where the same (or identical specimens) are excited by an ensemble of ground motions. Afterwards, a numerical model is used to create another dataset, using the same ensemble of excitations. The validity of the numerical model is assessed by comparing the Cumulative Distribution Function (CDF) of these two datasets for the same response quantities (i.e., maximum displacement at the top and residual displacement). This validation test is weaker (and easier to pass), yet sufficient for earthquake engineering applications.

3 NUMERICAL STUDIES OF ROCKING STRUCTURES: RESULTS OF A BLIND PREDICTION CONTEST

During the last decade, both FEM and DEM numerical models were developed to predict the rocking problem [74-79]. A recent blind prediction contest organized by ETH Zurich, the University of Bristol and the Pacific Earthquake Engineering Research (PEER) Center, shed light on the efficiency of numerical models used to describe the statistical response of a rocking podium structure [80,81]. Unlike the tests discussed in this paper, the tests of [80,81] concerned a rocking podium structure that was restrained not to slide or wobble out of its original position. Thirteen contestants participated, using FEM, DEM, and analytical rigid-body models [80,82-83]. One of the important outcomes of this contest is that there is no basis for recommending FEM or DEM to model the response of wobbling structures; the accuracy of these models depends on the modeling assumptions. Moreover, it was proven that even though the winning models precisely captured the Cumulative Distribution Function of the maxima of the responses to each set of excitations, they were unable to accurately predict the response to each individual ground motion.

4 EXPERIMENTAL PROCEDURE

This section briefly presents an experimental investigation designed at ETH Zurich and carried out at EQUALS Lab, University of Bristol [84]. This investigation includes 115 shake table tests of cylindrical free-standing rocking bodies, which were free to slide and rock in all directions. More details about the tests can be found in [84]. From the various free-standing columns which were experimentally tested (Figure 2), this paper utilizes the results of one cylindrical column to assess the efficiency of the proposed FE model (Figure 3, right). The ex-

perimental results from [84] served as an experimental (benchmark) dataset, to assess the proposed FE model.

The experimental results of [84] serve for model validation and were not chosen to represent specific free-standing rocking equipment. The specimens were designed to remain elastic after each test, so the same specimen could be excited with a large number of earthquake excitations to create a database suitable for a statistical validation. The specimens were made of round steel pipes, with different dimensions and slenderness.

The rocking response was induced by a di-directional dynamic excitation using a shake table. The applied ground motions were synthesized using a spectral version of the Rezaeian and Der Kiureghian stochastic ground motion model [85-86]. The 1989 Loma Prieta UCSC Lick Observatory ground motion record was used as a seed ground motion to generate an ensemble of 100 ground motions. The ground motions were scaled, with the frequency of ground motions increased by 2 without changing the amplitude. Therefore, in the prototype scale, the columns are 4 times larger.

5 NUMERICAL MODEL

The finite element software ABAQUS [87] was utilized to perform the analysis. The model comprised the cylindrical rocking body and a moving flat base-slab. The moving flat base emulates the top surface of the shake table. Both the rocking column and the flat base were modeled as rigid, since they were stiff enough and demonstrated no damage after testing. The flat base-slab was vertically supported by a spring-dashpot system to simulate the vertical stiffness of the shake-table platform and the radiation/impact damping mechanism (Figure 3, Left). Its rotation was constrained and set equal to zero. This approach was previously used in [88] in an effort to model radiation/impact damping, and it was shown that that in the planar case it leads to Housner's solution, as long as the stiffness of the spring is relatively high. Therefore, the spring constant was set to 10^9 N/m so that the pre-uplift vertical eigenperiod of the system is 0.001 sec. All rotations of the base were fixed. To apply the ground motion, the base moved parallel to x and y axis.

A uniform mesh with a size of 5 mm was utilized in all analyses. A 4-node 3D rigid quadrilateral finite element was used both for the rocking column and the flat base. The motion of the specimen was monitored with a reference point at the top of the column. The contact surface was simulated using Coulomb friction for the tangential behavior and ABAQUS stiff contact [87] for the normal direction. An explicit scheme with a fixed time increment of 10^{-6} sec was used in all cases.

The developed numerical model considers two main damping mechanisms; friction and radiation/impact damping. Inherent Rayleigh damping is set to zero since this energy dissipation mechanism is inconsistent with the physical problem. Energy dissipation through friction is considered through the friction coefficient, whereas radiation damping through the utilized dashpot. Neither the friction (μ) nor the dashpot (ζ) coefficient was known a priori; the influence of the friction coefficient was assessed through an extensive parametric analysis employing non-linear time history analysis.



Figure 2. Free-standing rocking column specimens on the shake table at EQUALS lab, University of Bristol.

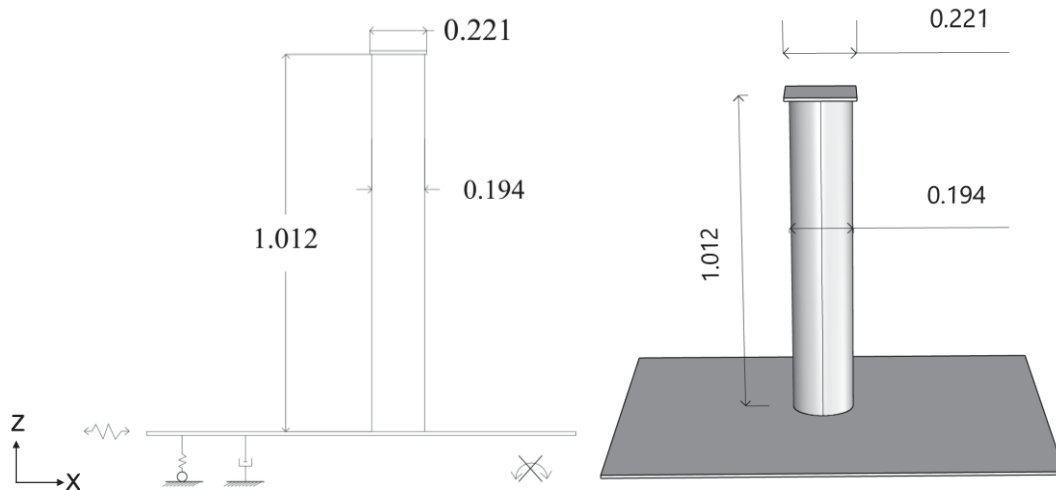


Figure 3. Left: Schematic representation of the rocking column, the constraint of the flat base and the spring-dashpot system below the base; Right: Dimensions (in m) of the tested specimen.

In this parametric analysis, the coefficient of friction μ was varied from 0.3 to 2. Not all the above values are realistic, but the analysis explores the influence of extreme values of the modelling parameters on the rocking response. The damping ratio ζ corresponding to the vertical vibration mode (i.e. radiation damping) was set to $\zeta=1\%$. This damping should not be confused with Rayleigh, which was equal to zero in all tests.

6 RESULTS

6.1. Deterministic Comparison

Figure 4 presents scatter plots that compare the experimental to the numerical results for different values of the critical modeling parameter (i.e., friction coefficient). The investigated response parameters are the maximum displacement (u_{\max}) at the top of the rocking column,

and the residual displacement after the end of the excitation (u_{res}), both measured in meters. In the following plots, “OT” denotes overturning of the specimen. In all scatter plots, the horizontal axis corresponds to the experimental results, whereas the vertical to the numerical ones.

It is evident that the numerical results are moderately correlated to the experimental ones. Moreover, similarly to previous studies, the numerical model often fails to predict overturning. However, the relevant question in earthquake engineering is not whether the model is accurate but whether it is biased and whether it induces more uncertainty than the ground motion. Comparing the results of individual ground motions, it is not possible to identify clear patterns of the influence of the coefficient of friction on the maximum response of the body. Most importantly, minor changes in the coefficient of friction, lead to very large changes in the response.

6.2 Statistical Comparison

When the numerical results are statistically assessed, clear trends emerge (Figure 5), similarly to what was observed for the planar rocking model by Yim et al [89] as early as in 1980. An increase of the friction coefficient leads to an increase of the maximum displacement of the rocking column (Figure 5, left). The residual displacement does not seem to depend on the coefficient of friction, provided that there is no overturn. Hence, neglecting sliding (i.e. using a very high value for μ) is a conservative modelling approach, at least in terms of maximum displacement and prediction of overturning probability.

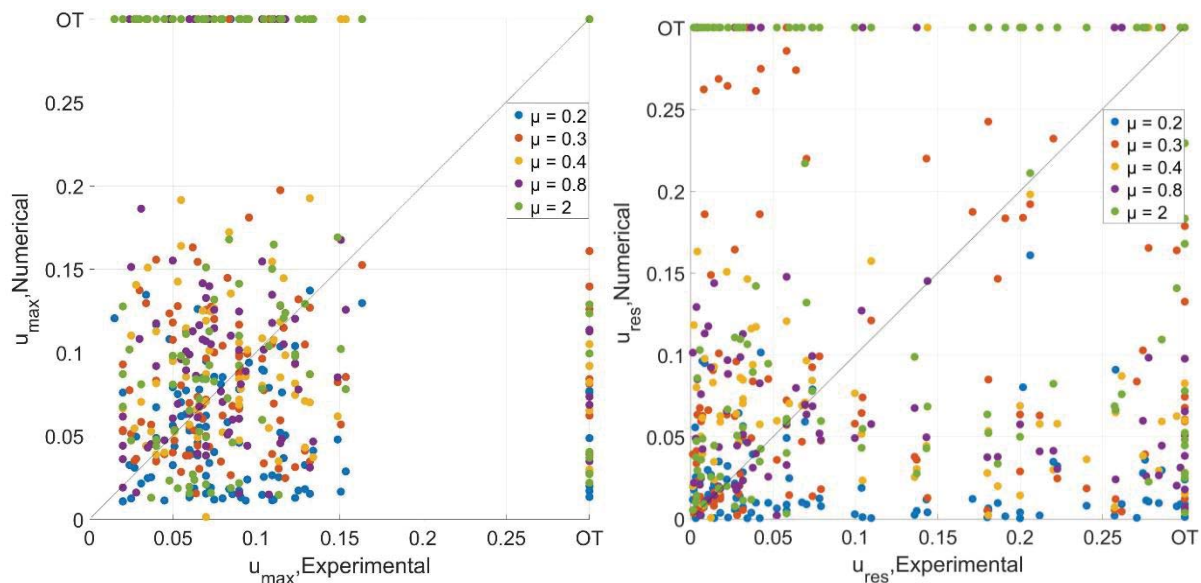


Figure 4. Deterministic comparison for experimental and numerical results of the columns. Sensitivity analysis for friction coefficient. Left: Maximum Displacement, Right: Residual Displacement

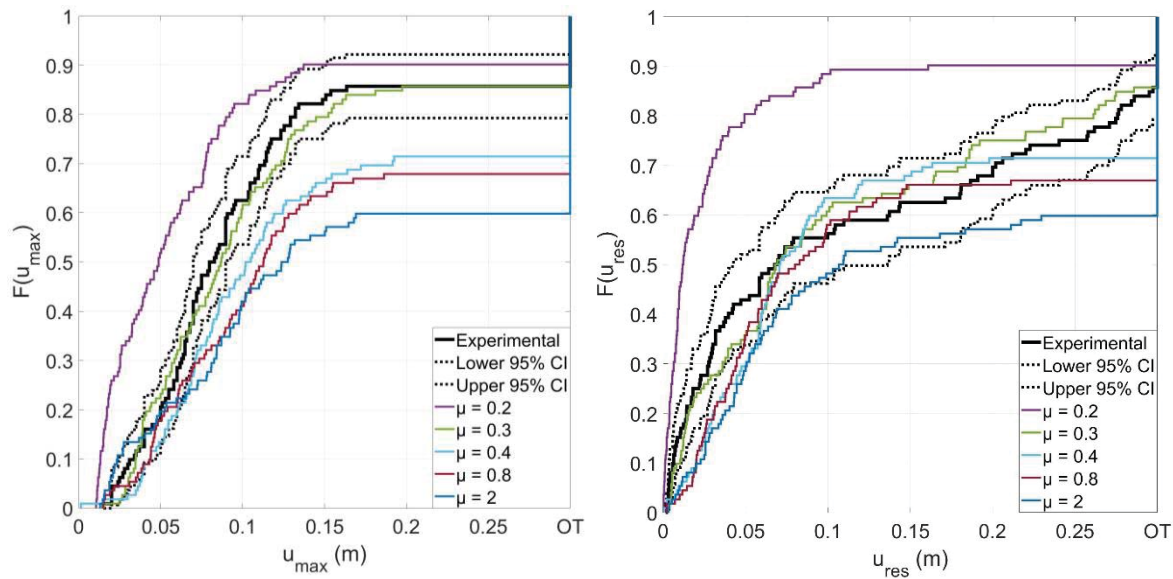


Figure 5. Statistical comparison for experimental and numerical results of the columns. Sensitivity analysis for friction coefficient. Left: Maximum Displacement, Right: Residual Displacement

7. CONCLUSIONS

The presented numerical model simulates the response of a free-standing cylindrical column. The column had a slenderness ratio of $\alpha = 0.2$, and, during testing, it was free to slide and rock in all directions. It is shown that the model performs poorly when it is deterministically assessed based on its ability to predict the maximum displacement at the top of the column. However, it can perform well, when it is evaluated based on its ability to predict the CDF of the maxima of the response to a set of ground motions.

The friction coefficient between the rocking block and the supporting surface was varied numerically and its influence was assessed with a large number of non-linear time-history analyses. Even though the exact value of the friction coefficient significantly influences the deterministic response, it affects the statistical response only moderately. The CDF curves show that an increase of the friction coefficient amplifies uplifting and leads to larger maximum rocking displacements, thus making the model more conservative. A friction coefficient equal to $\mu = 0.3$ and a radiation damping equal to $\zeta = 1\%$ leads to the optimal match between experimental and numerical results.

REFERENCES

- [1] Milne, J. (1885): Seismic experiments. *Trans. Seismol. Soc. Jpn.*, 8, 1-82
- [2] Makris, N. (2014): A half-century of rocking isolation. *Earthquakes and Structures*, 7(6), 1187–1221.
- [3] Housner, GW. (1963): The behavior of inverted pendulum structures during earthquakes. *Bull Seismol Soc Am*. 53(2): 403 - 417.
- [4] Konstantinidis, D., Makris, N. (2009): Experimental and analytical studies on the response of free-standing laboratory equipment to earthquake shaking. *Earthquake Engng Struct. Dyn.* 38:827–848. DOI: 10.1002/eqe.871

- [5] Konstantinidis, D., Makris, N. (2010): Experimental and analytical studies on the response of $\frac{1}{4}$ -scale models of free-standing laboratory equipment subjected to strong earthquake shaking. *Bull Earthquake Eng.* 8:1457–1477 DOI 10.1007/s10518-010-9192-8
- [6] Di Sarno, L., Magliulo, G., D'Angela, D., Cosenza, E. (2019): Experimental assessment of the seismic performance of hospital cabinets using shake table testing. *Earthq Eng Struct Dyn.* 48(1):103-123.
- [7] Fragiadakis, M, Diamantopoulos, S. Fragility and risk assessment of freestanding building contents. *Earthquake Engng Struct Dyn.* 2020; 49: 1028 - 1048. <https://doi.org/10.1002/eqe.3276>
- [8] Di Sarno, L., Petrone, C., Magliudo, G., Manfredi, G. (2015) Dynamic properties of typical consultation room medical components. *Engineering Structures*, Volume 100, 1 October 2015, Pages 442-454, <https://doi.org/10.1016/j.engstruct.2015.06.036>
- [9] Cosenza, E., Di Sarno, L., Maddaloni, G., Magliulo, G., Petrone, C., and Prota, A. (2014), Shake table tests for the seismic fragility evaluation of hospital rooms, *Earthquake Engng Struct. Dyn.*, 44, 23– 40, doi: 10.1002/eqe.2456
- [10] Wittich CE, Hutchinson TC. Shake table tests of stiff, unattached, asymmetric structures. *Earthq Eng Struct Dyn.* 2015; 44(14): 2425– 2443.
- [11] Bao, Y., & Konstantinidis, D. (2020). Dynamics of a sliding - rocking block considering impact with an adjacent wall. *Earthquake Engineering & Structural Dynamics*, 49(5), 498-523.
- [12] D'Angela, D., Magliulo, G., & Cosenza, E. (2021). Towards a reliable seismic assessment of rocking components. *Engineering Structures*, 230, 111673.
- [13] Cocuzza Avellino, G., Cannizzaro, F., Di Martino, A., Valenti, R., Paternò, E., Calì, I., & Impollonia, N. (2021). Numerical and Experimental Response of Free-Standing Art Objects Subjected to Ground Motion. *International Journal of Architectural Heritage*, 1-16.
- [14] Voyagaki, E., Kloukinas, P., Dietz, M., Dihoru, L., Horseman, T., Oddbjornsson, O., ... & Steer, A. (2018). Earthquake response of a multiblock nuclear reactor graphite core: experimental model vs simulations. *Earthquake Engineering & Structural Dynamics*, 47(13), 2601-2626.
- [15] Bao, Y., & Konstantinidis, D. (2020). Dynamics of a sliding - rocking block considering impact with an adjacent wall. *Earthquake Engineering & Structural Dynamics*, 49(5), 498-523.
- [16] Linde, S. A., Konstantinidis, D., & Tait, M. J. (2020). Rocking response of unanchored building contents considering horizontal and vertical excitation. *Journal of Structural Engineering*, 146(9), 04020175.
- [17] Stefanou, I., Psycharis, I., Georgopoulos, IO. (2011): Dynamic response of reinforced masonry columns in classical monuments. *Construct Build Mater* 25(12):4325 - 4337.
- [18] DeJong MJ. (2012): Seismic response of stone masonry spires: analytical modeling. *Eng Struct.* 40:556 - 565.

- [19] Tondelli M, Beyer K, DeJong M. (2016): Influence of boundary conditions on the out-of-plane response of brick masonry walls in buildings with RC slabs. *Earthq Eng Struct Dynam.* 45(8):1337 - 1356.
- [20] Casapulla, C., Giresini, L., Lourenço, PB. (2017): Rocking and kinematic approaches for rigid block analysis of masonry walls: state of the art and recent developments. *Buildings.* 7(3):69
- [21] Kalliontzis D, Schultz AE. (2017): Characterizing the in-plane rocking response of masonry walls with unbonded posttensioning. *J Struct Eng.* 143(9):04017110.
- [22] Mehrotra A, DeJong MJ. (2018): The influence of interface geometry, stiffness, and crushing on the dynamic response of masonry collapse mechanisms. *Earthq Eng Struct Dynam.* 47(13):2661 - 2681.
- [23] Giresini, L., Sassu, M., & Sorrentino, L. (2018). In situ free-vibration tests on unrestrained and restrained rocking masonry walls. *Earthquake Engineering & Structural Dynamics*, 47(15), 3006-3025.
- [24] Čeh, N., Jelenić, G., & Bićanić, N. (2018). Analysis of restitution in rocking of single rigid blocks. *Acta Mechanica*, 229(11), 4623-4642.
- [25] Jaimes, M. A., Chávez, M. M., Peña, F., & García-Soto, A. D. (2021). Out-of-plane mechanism in the seismic risk of masonry facades. *Bulletin of Earthquake Engineering*, 19(3), 1509-1535.
- [26] Ma, Q. T., Parshottam, S., & Montalla, M. (2018, June). Modelling Rocking Behaviour using Physics Engine Simulation. In *Eleventh US National Conference on Earthquake Engineering*. Earthquake Engineering Research Institute.
- [27] Mouzakis HP, Psycharis IN, Papastamatiou DY, Carydis PG, Papantonopoulos C, Zambas C. (2002): Experimental investigation of the earthquake response of a model of a marble classical column. *Earthq Eng Struct Dynam.* 31(9):1681 - 1698.
- [28] Funari, M. F., Spadea, S., Lonetti, P., Fabbrocino, F., & Luciano, R. (2020). Visual programming for structural assessment of out-of-plane mechanisms in historic masonry structures. *J. Build. Eng.* , 31, 101425.
- [29] Papantonopoulos C, Psycharis IN, Papastamatiou DY, Lemos JV, Mouzakis HP. (2002): Numerical prediction of the earthquake response of classical columns using the distinct element method. *Earthq Eng Struct Dynam.* 31(9):1699 - 1717.
- [30] Vassiliou MF, Makris N. (2012): Analysis of the rocking response of rigid blocks standing free on a seismically isolated base. *Earthq Eng Struct Dynam.* 41(2):177 - 196.
- [31] Drosos, V.A., Anastasopoulos, I. (2015): Experimental investigation of the seismic response of classical temple columns. *Bull Earthquake Eng* 13, 299–310. <https://doi.org/10.1007/s10518-014-9608-y>
- [32] Drosos V, Anastasopoulos I (2014): Shaking table testing of multi-drum columns and portals. *Earthquake Engineering & Structural Dynamics*, 43(11):1703-1723.
- [33] Psycharis IN, Fragiadakis M, Stefanou I. Seismic reliability assessment of classical columns subjected to near-fault ground motions. *Earthquake Eng Struct Dyn.* 2013; 42(14): 2061– 2079.

- [34] Sarhosis, V., Baraldi, D., Lemos, J.V., Milani, G. (2019). Dynamic behaviour of ancient freestanding multi-drum and monolithic columns subjected to horizontal and vertical excitations. *Soil Dynamics and Earthquake Engineering*, Volume 120, May 2019, Pages 39-57, <https://doi.org/10.1016/j.soildyn.2019.01.024>
- [35] Bantilas, KE., Kavvadias, IE., Vasiliadis, LK. (2020): Seismic response of elastic multidegree of freedom oscillators placed on the top of rocking storey. *Earthquake Engng Struct Dyn*.1– 19. <https://doi.org/10.1002/eqe.3400>
- [36] Bachmann, JA., Vassiliou, MF., Stojadinović, B. (2017): Dynamics of rocking podium structures. *Earthquake Engng Struct. Dyn.*, 46: 2499– 2517. doi: 10.1002/eqe.2915.
- [37] Bachmann, JA, Vassiliou, MF, Stojadinovic, B. (2019): Rolling and rocking of rigid uplifting structures. *Earthquake Engng Struct Dyn.* 2019 48: 1556– 1574. <https://doi.org/10.1002/eqe.3213>
- [38] Makris, N., Aghagholizadeh, M. (2017): The dynamics of an elastic structure coupled with a rocking wall. *Earthquake Engng Struct. Dyn.*, 46: 945– 962. doi: 10.1002/eqe.2838.
- [39] Di Egidio, A., Pagliaro, S., Fabrizio, C., & de Leo, A. M. (2020). Seismic performance of frame structures coupled with an external rocking wall. *Engineering Structures*, 224, 111207.
- [40] Makris, N., Vassiliou, MF. (2013): Planar rocking response and stability analysis of an array of free - standing columns capped with a freely supported rigid beam. *Earthq Eng Struct Dyn*. 42(3): 431 - 449.
- [41] Makris, N., Vassiliou, MF. (2012): Are some top-heavy structures more stable? *Journal of Structural Engineering*. [https://doi.org/10.1061/\(ASCE\)ST.1943-541X.0000933](https://doi.org/10.1061/(ASCE)ST.1943-541X.0000933)
- [42] Makris, N., Vassiliou, MF. (2014): Dynamics of the rocking frame with vertical restrainers. *J Struct Eng*. 141(10):04014245.
- [43] Dimitrakopoulos EG, Giouvanidis AI. (2015): Seismic response analysis of the planar rocking frame. *J Eng Mech*. 2015; 141(7):04015003.
- [44] Giouvanidis AI, Dimitrakopoulos EG. (2017): Seismic performance of rocking frames with flag - shaped hysteretic behavior. *J Eng Mech*. 143(5):04017008.
- [45] Reggiani Manzo, N, Vassiliou, MF. Displacement - based analysis and design of rocking structures. *Earthquake Engng Struct Dyn*. 2019; 48: 1613 - 1629. <https://doi.org/10.1002/eqe.3217>
- [46] Reggiani Manzo, N, Vassiliou, MF. (2021): Simplified analysis of bilinear elastic systems exhibiting negative stiffness behavior. *Earthquake Engng Struct Dyn*. 2021; 50: 580– 600. <https://doi.org/10.1002/eqe.3347>
- [47] Thomaidis, IM., Kappos, AJ., Camara, A. (2020): Dynamics and seismic performance of rocking bridges accounting for the abutment - backfill contribution. *Earthquake Engng Struct Dyn* 49:1161-1179
- [48] Giouvanidis, A. I., & Dong, Y. (2020). Seismic loss and resilience assessment of single-column rocking bridges. *Bulletin of earthquake engineering*, 18, 4481-4513.

- [49] Kashani, M. M., Gonzalez-Buelga, A., Thayalan, R. P., Thomas, A. R., & Alexander, N. A. (2018). Experimental investigation of a novel class of self-centring spinal rocking column. *J. Sound. Vib.*, 437, 308-324.
- [50] Giouvanidis, A. I., & Dimitrakopoulos, E. G. (2018). Rocking amplification and strong-motion duration. *Earthquake Engineering & Structural Dynamics*, 47(10), 2094-2116.
- [51] Thiers-Moggia, R., & Málaga-Chuquitaype, C. (2019). Seismic protection of rocking structures with inerters. *Earthquake Engineering & Structural Dynamics*, 48(5), 528-547.
- [52] Aghagholizadeh, M. (2020). A finite element model for seismic response analysis of vertically-damped rocking-columns. *Engineering Structures*, 219, 110894.
- [53] Thiers-Moggia, R., & Málaga-Chuquitaype, C. (2020). Seismic control of flexible rocking structures using inerters. *Earthquake Engineering & Structural Dynamics*, 49(14), 1519-1538.
- [54] Zhou, Y., Zhang, J., Cheng, S., He, H., Dong, Z., & Qiang, H. (2020, January). Seismic Response of Rocking Double-Column Bridge Bents with External Hysteretic Dissipaters. In *2020 International Conference on Intelligent Transportation, Big Data & Smart City (ICITBS)* (pp. 353-357). IEEE.
- [55] Xie, Y., Zhang, J., DesRoches, R., & Padgett, J. E. (2019). Seismic fragilities of single-column highway bridges with rocking column-footing. *Earthquake Engineering & Structural Dynamics*, 48(7), 843-864.
- [56] Xia, X., Wu, S., Shi, J., Jia, J., Chen, X., & Ma, H. (2020). Seismic response of rocking isolated railway bridge piers with sacrificial components. *Earthquake Engineering and Engineering Vibration*, 19(4), 1005-1015.
- [57] Thiers-Moggia, R., & Málaga-Chuquitaype, C. (2020). Dynamic response of post-tensioned rocking structures with inerters. *International Journal of Mechanical Sciences*, 187, 105927.
- [58] Makris, N., Vassiliou, MF. (2015): Dynamics of the rocking frame with vertical restrainers. *Journal of Structural Engineering* [https://doi.org/10.1061/\(ASCE\)ST.1943-541X.0001231](https://doi.org/10.1061/(ASCE)ST.1943-541X.0001231)
- [59] Vassiliou, MF., Makris, N. (2015): Dynamics of the vertically restrained rocking column. *Journal of Engineering Mechanics* [https://doi.org/10.1061/\(ASCE\)EM.1943-7889.0000953](https://doi.org/10.1061/(ASCE)EM.1943-7889.0000953)
- [60] Makris, N., Aghagholizadeh M. (2019): Effect of supplemental hysteretic and viscous damping on rocking response of free-standing columns. *Journal of Engineering Mechanics* [https://doi.org/10.1061/\(ASCE\)EM.1943-7889.0001596](https://doi.org/10.1061/(ASCE)EM.1943-7889.0001596)
- [61] Acikgoz, S., DeJong, M. (2012): The interaction of elasticity and rocking in flexible structures allowed to uplift *Earthquake Engng Struct. Dyn.* 41:2177–2194 DOI: 10.1002/eqe.2181
- [62] Vassiliou, MF., Mackie KR., Stojadinović B. (2014): Dynamic response analysis of solitary flexible rocking bodies: modeling and behavior under pulse-like ground excitation *Earthquake Engng Struct. Dyn.* 43:1463–1481 DOI: 10.1002/eqe.2406

- [63] Vassiliou, MF., Truniger, R., Stojadinović, B. (2015): An analytical model of a deformable cantilèver structure rocking on a rigid surface: development and verification *Earthquake Engng Struct. Dyn.* 44:2775–2794 DOI: 10.1002/eqe.2608
- [64] Truniger, R., Vassiliou, MF., Stojadinović, B. (2015): An analytical model of a deformable cantilèver structure rocking on a rigid surface: experimental validation *Earthquake Engng Struct. Dyn* 44:2795–2815 DOI: 10.1002/eqe.2609
- [65] Avgenakis, E., & Psycharis, I. N. (2020). An integrated macroelement formulation for the dynamic response of inelastic deformable rocking bodies. *Earthquake Engineering & Structural Dynamics*, 49(11), 1072-1094.
- [66] Chatzis, MN., Smyth, AW. (2012): Modeling of the 3D rocking problem. *International Journal of Non-linear Mechanics*. 47(4):85–98.
- [67] Chatzis MN, Smyth AW. (2012): Three-dimensional dynamics of a rigid body with wheels on a moving base. *Journal of Engineering Mechanics* 2012; 139(4):496–511.
- [68] Vassiliou, MF., Burger, S., Egger, M., Bachmann, J., Broccardo, M., Stojadinović, B. (2017): The three-dimensional behavior of inverted pendulum cylindrical structures during earthquakes. *Earthquake Engng Struct. Dyn.*, 46: 2261– 2280. doi: 10.1002/eqe.2903.
- [69] Vassiliou, MF. (2018): Seismic response of a wobbling 3D frame. *Earthquake Engng Struct Dyn*. 47: 1212– 1228. <https://doi.org/10.1002/eqe.3013>
- [70] Messina, E., Chioccarelli, E., Baltzopoulos, G., & Vecchio, A. (2020). Numerical analysis of the dynamics of rigid blocks subjected to support excitation. *Applied Numerical Mathematics*, 155, 29-37.
- [71] Bachmann, J.A., Strand, M., Vassiliou, M.F., Broccardo, M., Stojadinović, B. (2017): Is rocking motion predictable? *Earthquake Engng Struct Dyn*.47: 535–552. DOI: 10.1002/eqe.2978
- [72] Del Giudice, L., Vassiliou, MF. (2020): Mechanical properties of 3D printed material with binder jet technology and potential applications of additive manufacturing in seismic testing of structures. *Additive Manufacturing*. <https://doi.org/10.1016/j.addma.2020.101714>
- [73] Del Giudice, L., Wrobel, R., Leinenbach, C., & Vassiliou, M. F. (2020). Static testing of additively manufactured microreinforced concrete specimens for statistical structural model validation at a small scale. In *8th International Conference on Advances in Experimental Structural Engineering (8AESE)*.
- [74] Agalianos, A., Psychari, A., Vassiliou, MF., Stojadinović, B., Anastasopoulos, I. (2017): Comparative assessment of two rocking isolation techniques for a motorway overpass bridge *Front. Built Environ*. <https://doi.org/10.3389/fbuil.2017.00047>
- [75] Thomaidis, IM., Camara, A., Kappos, AJ. (2018): Simulating the rocking response of rigid bodies using general-purpose finite element software. *16th European conference on Earthquake Engineering*
- [76] Pappas, A., Sextos, A., da Porto, F., Modena, C. (2017): Efficiency of alternative intensity measures for the seismic assessment of monolithic free-standing columns. *Bull Earthquake Eng* 15:1635–1659

- [77] Sextos, A.G., Manolis, G.D., Athanasiou, A., Ioannidis, N. (2017): Seismically induced uplift effects on nuclear power plants. Part 1: Containment building rocking spectra, *Nuclear Engineering and Design*, <https://doi.org/10.1016/j.nucengdes.2016.12.035>
- [78] Sextos, A.G., Manolis, G.D., Athanasiou, A., Ioannidis, N. (2017): Seismically induced uplift effects on nuclear power plants. Part 2: Demand on internal equipment, *Nuclear Engineering and Design*, <https://doi.org/10.1016/j.nucengdes.2016.12.036>
- [79] Sieber, M, Klar, S, Vassiliou, MF, Anastasopoulos, I. (2020) Robustness of simplified analysis methods for rocking structures on compliant soil. *Earthquake Engng Struct Dyn*. 2020; 49: 1388– 1405. <https://doi.org/10.1002/eqe.3294>
- [80] Vassiliou, MF, Broccardo, M, Cengiz, C, et al (2020): Shake table testing of a rocking podium: Results of a blind prediction contest. *Earthquake Engng Struct Dyn*. 1– 20. <https://doi.org/10.1002/eqe.3386>
- [81] Vassiliou, M. F., Cengiz, C., Dietz, M., Dihoru, L., Broccardo, M., Mylonakis, G., ... & Stojadinovic, B. (2020). Dataset from the shake table tests of a rocking podium structure. *Earthquake Spectra*, 8755293020988017.
- [82] Zhong, C, Christopoulos, C. (2020): Finite element analysis of the seismic shake-table response of a rocking podium structure. *Earthquake Engng Struct Dyn*. 1– 8. <https://doi.org/10.1002/eqe.3397>
- [83] Malomo, D, Mehrotra, A, DeJong, MJ. (2020): Distinct element modeling of the dynamic response of a rocking podium tested on a shake table. *Earthquake Engng Struct Dyn*. 1-7. <https://doi.org/10.1002/eqe.3404>
- [84] Vassiliou, MF., Cengiz, C., Dietz, M. et al. (2021) Dataset from shake table tests of free-standing rocking bodies. *Earthquake Spectra* (under review)
- [85] Rezaeian S, Der Kiureghian A. (2008): A stochastic ground motion model with separable temporal and spectral nonstationarities. *Earthq Eng Struct Dyn*. 2008;37(13):1565-1584.
- [86] Broccardo M, Dabaghi M. (2017) A spectral-based stochastic ground motion model with a non-parametric time-modulating function. In: 12th International Conference on Structural Safety and Reliability; Vienna; 2017:1-10.
- [87] ABAQUS 2019 (2019). *Standard User's Manual*. Providence, RI: Dassault Systèmes Simulia Corp.,
- [88] Vassiliou, M. F., Mackie, K. R., and Stojadinović, B. (2017): A finite element model for seismic response analysis of deformable rocking frames. *Earthquake Engng Struct. Dyn.*, 46: 447– 466. doi: 10.1002/eqe.2799.
- [89] Yim, C. S., Chopra, A. K., & Penzien, J. (1980). Rocking response of rigid blocks to earthquakes. *Earthquake Engineering & Structural Dynamics*, 8(6), 565-587.

SEISMIC RISK ASSESSMENT OF ROCKING BUILDING CONTENTS

Michalis Fragiadakis¹, Spyridon Diamantopoulos¹

¹ School of Civil Engineering, National Technical University of Athens
9 Iroon Polytechniou 15780, Zografou Campus, Athens, Greece
e-mail: mfrag@mail.ntua.gr; sdiamadop@central.ntua.gr

Keywords: building contents, Incremental Dynamic Analysis, fragility, nonstructural, rocking, freestanding.

Abstract. *The paper presents a fully performance-based seismic reliability and risk assessment framework for freestanding structural components and contents that can be modelled as rocking rigid blocks. It is shown that a drift-driven Incremental Dynamic Analysis approach can be adopted in order to obtain the floor timehistories which are then used as input for the response history analysis of the contents. Therefore, first the demand at the storey level is obtained and then the response of the contents is calculated using the storey acceleration response history. An alternative methodology where the fragility of the building and of the freestanding contents are derived separately is also examined and its limitations are discussed. The seismic response of building contents depends on several parameters such as the geometry of the object, the dynamic characteristics of the building and the storey that the object is located.*

1 INTRODUCTION

Earthquake losses may be due to structural damage, damage of non-structural components (e.g. infills, piping system) and also due to the damage of the structure's contents. Non-structural damage can be due to damage of components attached, or anchored, to the hosting building, or due to damage on the freestanding inventory of the building. In the latter case, there is a huge variability of systems and configurations hampering the systematic study of the problem and the recommendation of generally-applicable guidelines. The risk assessment of building contents is a complicated task since the response of the contents depends also on the behaviour of the hosting structure. As a result, there may be cases where a strong earthquake does not overturn an object but strongly damages the structure, while more benign ground motions may leave the structure intact however causing losses due to damage on the building's contents.

The paper focuses on the seismic performance, fragility and risk assessment of freestanding building contents. Freestanding building contents are treated as rocking rigid blocks and are modelled using Housner's theory [1]. A specifically tailored version of the Incremental Dynamic Analysis (IDA) method is proposed in order to assess the structure and its contents considering that the structural collapse implies also collapse/overturning of the contents [2]. A second point of interest is the derivation of fragility curves and the calculation of the Mean Annual Frequency (MAF) of building contents.

Despite the significance of the problem, there are relatively few past studies on the seismic response assessment of freestanding contents, especially compared to the case of anchored non-structural components and anchored building equipment. The paper presents a performance-based seismic fragility and risk assessment framework for freestanding building contents. Contrary to previous works on the seismic fragility assessment of rocking contents, the proposed methodology discusses how the response of the hosting building and that of the contents are coupled and also the effect of different stories and different block geometries. In order to consistently study the effect of increasing seismic intensity in a performance-based setting, a modified version of the well-known Incremental Dynamic Analysis (IDA) method is presented. It is shown that the EDP that should "drive" the IDA simulations is that of the building rather than that of the contents and also that the collapse of the building should not be neglected. Moreover, the calculation of fragility and risk are discussed. Existing fragility assessment methodologies are adopted showing that the IM of the building should be adopted (instead of that of the contents), while a procedure that uses the total probability theorem in order to calculate the MAFs combining fragilities that were separately generated for the structure and for the contents is investigated. Overall it is shown that the problem is not as simple, as it may initially seem, and that various tools should be appropriately combined in order to accurately and efficiently calculate the risk of freestanding contents.

2 Theory of the rocking block

In order to study the seismic response of freestanding bodies to an earthquake ground motion, it is assumed that the bodies are orthogonal blocks. Following the pioneering work of Housner [1], the problem of rocking and overturning of freestanding blocks to earthquakes has been the subject of intense analytical and experimental research. Despite its apparent simplicity, the rocking problem has been proven difficult, since the blocks behave nonlinearly and also due to the occurrence of many impacts between the rocking bodies and their base. The fundamentals of rocking theory are briefly summarized in order to allow studying the seismic behaviour of

freestanding rocking blocks. A rigid block of dimensions $2b \times 2h$ that oscillates about pivot point A (or A'). The block has weight W and moment of inertia I_0 about point A. Assuming that the block is homogeneous and thus the center of gravity is located at height h , the block's slenderness angle is equal to $\alpha = \text{atan}(b/h)$. The slenderness angle α together with the size parameter $R = \sqrt{b^2 + h^2}$ define fully the geometry of the block. Consequently, the equation of motion of the rocking block is [1]:

$$I_0 \ddot{\theta}(t) + mgR \sin[\alpha \text{sgn}(\theta(t) - \theta(t))] = -m\ddot{u}_g(t) R \cos[\alpha \text{sgn}(\theta(t) - \theta(t))] \quad (1)$$

where the angle of rotation θ is the only degree of freedom. The sign function is used to define the pivot point (A or A'), i.e. when A' is the pivot point, the angle θ is negative. The above Eq. 1 can be solved either with the aid of an Ordinary Differential Equation (ODE) solver or using simple Finite Element models (e.g. Diamantopoulos and Fragiadakis[3]).

3 Seismic response assessment of building contents

The procedure followed for the seismic response assessment of freestanding building contents is relatively easy. The building is subjected to an acceleration timehistory and the total acceleration response history of the storey of interest is stored. The stored storey acceleration response history is used as the input acceleration time history for the rigid block assessment. This conceptually simple cascading procedure requires two models, one for simulating the building and a second for simulating the freestanding contents. Moreover, after every building simulation the complete acceleration, or velocity, response history has to be stored for every storey. This workflow is used also for developing the fragility curves of the rocking objects of interest.

Seismic response assessment requires to define pertinent Intensity Measures (IM) and Engineering Demand Parameters (EDP) for both the structure and the contents. This step is also important for the fragility assessment. IMs represent seismic intensity, while the EDPs are used to measure the demand, or the "damage". In order to distinguish the quantities that refer to the "structure" and the "block", the superscripts "s" and "b" are used, respectively. Therefore, $EDP^{(s)}$ and $IM^{(s)}$ are the IM and the EDP of the structure, while $EDP^{(b)}$ and $IM^{(b)}$ refer to the rigid block. For a block at storey j , $IM^{(b)}$ will coincide with (or be derived from) the structure's $EDP_j^{(s)}$, or, simply, the peak floor acceleration of the storey is the peak ground acceleration for the rocking body. Therefore, the selection of $EDP_j^{(s)}$ and $IM^{(b)}$ should be consistent.

For moderate-period structures with no near-fault activity, an appropriate choice for the intensity measure of the building $IM^{(s)}$, is the 5%-damped, first-mode spectral acceleration, $S_a(T_1, 5\%)$. Moreover, the most common EDP for moment frames is the maximum interstorey drift. However, since our focus is on freestanding components, instead of the maximum interstorey drift, a consistent quantity should be chosen as the $EDP^{(s)}$, while the intensity measure $IM^{(s)}$ is always $S_a(T_1, 5\%)$, although other measures are also possible.

For a rocking block, the most intuitive IM choice is the peak ground acceleration (PGA), since it is the parameter that defines the maximum overturning moment, while according to $\ddot{u}_g \geq \tan \alpha$ and $\ddot{u}_g \geq \mu \tan \alpha$ the PGA defines whether rocking and sliding respectively or none of the two will occur. Although it is not necessary, the PGA is normalized with $g \tan \alpha$ and thus the block's IM is $IM^{(b)} = PGA / g \tan \alpha$, where $IM^{(b)} \leq 1$ implies that the block does not start rocking. Furthermore, past research[4, 5] has shown that the PGV is also an important response parameter that provides a good correlation between seismic demand and block overturning. For simplicity, we choose not to normalize the PGV , but researchers[?] have

also proposed the normalized quantity $pPGV/g\tan\alpha$ as an IM suitable for rocking blocks. Our results have shown that the PGV (or PFV) performs well as an IM and hence we have chosen the simplest IM possible. Therefore, the $IM^{(b)}$ for a rocking block at storey j considered, is either the normalized peak floor acceleration PFA_j , or the peak floor velocity PFV_j ; the parameter chosen will be also used as the demand parameter of the building $EDP_j^{(s)}$. The most suitable engineering demand parameter $EDP^{(b)}$ for the rocking block is the rotation angle θ normalized by slenderness angle α , i.e. $EDP^{(b)} = |\theta|/\alpha$.

In order to assess a system's capacity, meaningful performance objectives related with the system's modes of failure or damage have to be identified. For rocking systems, overturning is the primary limit-state of interest, while rocking initiation is also of interest but it can be easily identified from the PGA . Depending on the freestanding component, (e.g. its purpose, its material, etc), "limited" damage can be identified for normalized rotation values $\theta/\alpha \approx 0.1 \div 0.3$, "moderate" damage for $\theta/\alpha \approx 0.3 \div 0.5$ and "overturning" is assumed for $\theta/\alpha \geq 1$. Recommendations of limit-state thresholds for rocking bodies can be found in various publications, e.g. Dimitrakopoulos and Paraskeya[6], Psycharis *et al.*[7] and Kavvadias *et al.*[8]. In practice, these limits vary considerably and it is not possible to decide threshold values that are generally applicable. For example, for sensitive mechanical equipment a rotation $\theta/\alpha \geq 0.1$ may result to permanent damage and thus in terms of loss the outcome will be the same with overturning. Another important aspect is the geometry of the block. Slender blocks start rocking for smaller acceleration values, while stocky blocks require higher acceleration values to start rocking and are more stable.

4 Fragility and risk calculations

The seismic risk assessment of building contents requires the prior knowledge of their fragility. As fragility, or "fragility function", we refer to the cumulative distribution function of the capacity of an asset to resist an undesirable limit-state [9]. For building contents, the fragility provides the probability of overturning as a function of the seismic excitation. Although often in the literature the terms "fragility" and "vulnerability" are used interchangeably, in this work we assume that fragility refers to the overturning probability as function of seismic intensity, while vulnerability is used to measure loss. Past research on fragility assessment focuses on the risk assessment of the structure itself[10], while the contents are examined separately and, usually, neglecting the effect of the hosting structure. Independent, and often generic, fragility curves for various building contents can be found in guidelines (e.g. FEMA P-58[11]) and the literature. Such fragility curves are empirical and are targeted to specific component types (e.g. cladding panels, masonry parapets). The direct fragility calculation that is here proposed through simulations allows to consider additional sources of uncertainty (e.g. related to the shape of the object, its mass distribution) and hence is preferable.

The fragility function is the conditional limit-state exceedance probability, given by the expression:

$$F_R = P(EDP > edp|IM) \quad (2)$$

The structure is first examined. There will be simulations that the building collapses (denoted as "C") and simulations where no collapse occurs (denoted as "NC"). Making this separation and dropping the conditioning term in order to simplify the notation, i.e.: $P(EDP) = P(EDP > edp|IM)$, the probability of Eq. 2 is calculated using the total probability theorem (TPT) as follows:

$$F_R^{(s)} = P(EDP^{(s)}|NC)P_{NC} + P(EDP^{(s)}|C)P_C \Leftrightarrow$$

$$F_R^{(s)} = P(EDP^{(s)}|NC)(1 - P_C) + P_C \quad (3)$$

where $P(EDP > edp^{(s)}|C)$ is equal to 1 since the inequality is always satisfied and $P_{NC} = 1 - P_C$.

Focusing on the rocking body, when an object is subjected to a seismic ground motion there are three possible types of response: (i) the object may not rock and remain at rest, (ii) it may rock, or (iii) it may overturn. Using the total probability theorem for the block, the fragility function becomes:

$$F_R^{(b)} = P(EDP^{(b)}|NoRock)P_{NoRock} + P(EDP^{(b)}|Rocking)P_{Rocking} + P(EDP^{(b)}|Ovtn)P_{Ovtn} \quad (4)$$

where $P(EDP^{(b)}|NoRock)$, $P(EDP^{(b)}|Rocking)$ and $P(EDP^{(b)}|Ovtn)$ are the probabilities that $EDP^{(b)} = \theta/\alpha$ exceeds a threshold value $edp^{(b)}$ and P_{NoRock} , $P_{Rocking}$ and P_{Ovtn} are the corresponding probabilities of no rocking, rocking and overturning, respectively. Blocks that will not rock, will not exceed any $edp^{(b)}$ value and thus $P(EDP|NoRock) = 0$, while the overturning blocks always exceed the limit-state threshold and thus $P(EDP|Ovtn) = 1$. The conditional limit-state probability (fragility) is further simplified to:

$$F_R^{(b)} = P(EDP^{(b)} \geq edp|Rocking)(1 - P_{Ovtn} - P_{NoRock}) + P_{Ovtn} \quad (5)$$

The calculation of Eq. 5 is discussed in the sections that follow. A fundamental assumption of our derivation is that *the simulations that collapse the building also overturn/collapse the freestanding contents* [2].

The risk is expressed as the mean annual frequency (MAF) of a limit-state being exceeded. Adopting the PEER's formula, the limit-state MAF for the structure and for a rigid block are calculated with the aid of the following expressions: where $\lambda_{EDP}^{(s)}$, $\lambda_{EDP}^{(b)}$ is the mean annual frequency of the engineering demand parameter ($EDP^{(s)}$ or $EDP^{(b)}$) exceeding threshold level and $d\lambda_{IM}^{(s)}$, $d\lambda_{IM}^{(b)}$ is the slope of the seismic hazard curve. The limit-state MAFs are easily obtained convolving the site hazard curve, expressed as function of the IM, with the fragility curve obtained with respect to any of the EDPs of interest. For the structure, the IM of interest is always available, e.g. spectral acceleration $S_a(T_1, 5\%)$, but for the block this information is available only at the ground floor. For assets located at a storey, the calculation of $d\lambda_{IM}^{(b)}$ has no meaning and thus their fragility should be calculated as function of $IM^{(s)}$ instead of $IM^{(b)}$:

$$\lambda_{EDP}^{(b)} = \int_{IM^{(s)}} P(EDP^{(b)}|IM^{(s)}) |d\lambda_{IM}| \quad (6)$$

Conditioning the block's fragility to $IM^{(s)}$, i.e. using Eq. 6 is also conceptually preferable since the MAF is directly calculated from the site's hazard. Note that we have dropped the superscript "s" from $d\lambda_{IM^{(s)}}$, since $d\lambda_{IM}$ always refers to the site and thus the structure.

A simplified and more generic methodology for the seismic risk of structure's contents is possible if we apply the total probability theorem (TPT), using the block's intensity measure $IM^{(b)}$ as an intermediate variable. This allows to expand Eq. 6 and obtain the MAF using the expression:

$$\lambda_{EDP}^{(b)} = \int_{IM^{(s)}} \int_{IM^{(b)}} P(EDP^{(b)}|IM^{(b)}) dP(IM^{(b)}|IM^{(s)}) |d\lambda_{IM}| \quad (7)$$

where $P(IM^{(b)}|IM^{(s)}) = P(EDP^{(s)}|IM^{(s)})$ is the building's fragility curve. Eq. 7 can be used in order to calculate separately the fragilities thus bypassing the need for performing building simulations and storing the response acceleration histories for the stories of interest.

5 Incremental Dynamic Analysis for freestanding components

The Incremental Dynamic Analysis (IDA) method is used for calculating the limit-state fragilities for both the structure and its contents. IDA involves subjecting the structure, or the block, to a suite of ground motion records, each scaled to multiple levels of intensity. After incrementally scaling every ground motion, single record capacity curves are produced in terms of demand versus seismic intensity. IDA has conceptual similarities to the Multiple Stripe Analysis (MSA) method [12, 13], where instead of scaling separately all ground motions, every record is scaled to the same IM level. Since for every scaling level the ground motions have the same IM value, the EDP values form a “stripe” which allows to directly calculate the median (50% percentile) and the 16% and 84% percentile capacity curves conditional on the IM. Strictly speaking, in IDA the scaling factors will be different, but stripped data can be easily obtained with interpolation. For the sake of simplicity, in this work MSA was performed (i.e. scaling the records to a common IM level), but loosely speaking the “term” IDA is used since it is more widespread and difference is merely a matter of implementation. Below we first discuss how the IDA method is applied for the cascading problem at hand. We first examine the structure since the ground motions are applied at the base of the building and in the subsection that follows we discuss how the fragilities of the freestanding contents are obtained from the floor response histories.

5.1 Hosting structure

For the four-storey RC building considered [2], every IDA curve is plotted in the EDP-IM plane as shown in Figure 1. The median curve (50% percentile) provides an estimate of the expected value and the fractile curves can be used to measure the dispersion [14]. The IDA capacity curve of Figure 1 is not the most common form of IDA where $EDP^{(s)}$ is the maximum interstorey drift ratio. A different EDP has to be adopted for studying building contents which leads to the representation of Figure 1, where the $EDP^{(s)}$ is either the normalised peak floor acceleration (PFA), or the peak floor velocity (PFV). The summarized EDP-IM plots (Fig. 1a or b) allow to directly calculate $P(EDP_j^{(s)}|NC)$ and P_C (Eq. 3) for every IM stripe. If the $EDP_j^{(s)}$ values are lognormally distributed, the buildings fragility for the j^{th} storey is calculated as follows:

$$P(EDP^{(s)} \geq edp^{(s)}) = 1 - P(EDP^{(s)} < edp^{(s)}) = \Phi \left(\frac{\mu_{\log EDP} - edp^{(s)}}{\sigma_{\log EDP}} \right) \quad (8)$$

where $\mu_{\log EDP}$ and $\sigma_{\log EDP}$ are the mean and the standard deviation of the logarithm of the demand, always conditional on the $IM^{(s)}$. Regardless the IM, the fragility of the building should be obtained combining Eq. 8 with Eq. 3:

$$F_R^{(s)} = \Phi \left(\frac{\mu_{\log EDP} - edp^{(s)}}{\sigma_{\log EDP}} \right) (1 - P_C) + P_C \quad (9)$$

where P_C is the percentage of collapsed simulations. Obviously different fragilities will be obtained depending on the EDP of interest.

Based on Figure 1 and Eq. 8 it is understood that the calculation of Eq. 8 is not efficient when the drift is used as the EDP. This is understood looking at Figure 1 where it is evident that the median (or the 16, 84% fractile) curves, conditional on the IM, cannot be calculated above the IM level where more than 50% (or the 16, 84% fractile, respectively) of the single-record

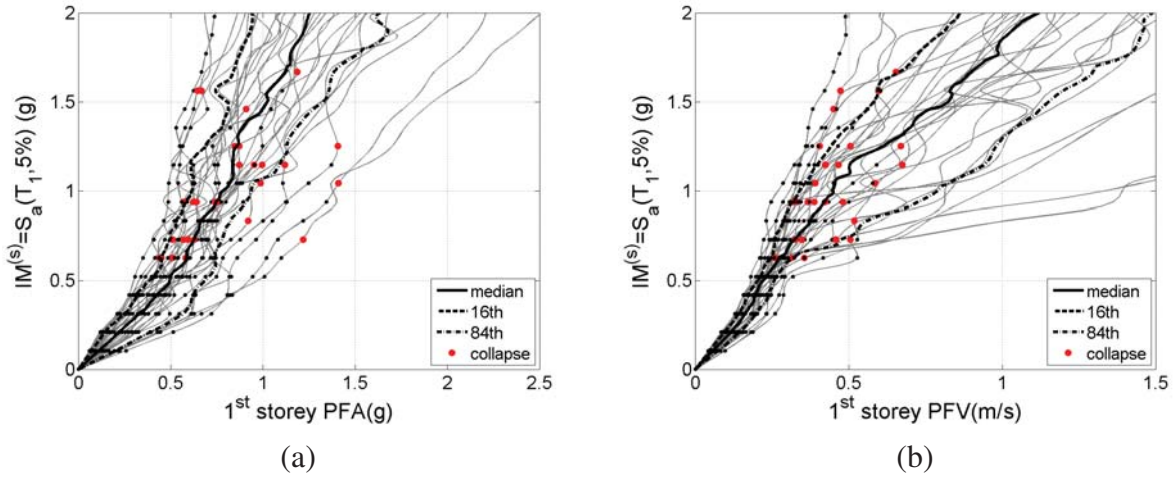


Figure 1: Storey capacity curves for the four-storey RC building considered, using as EDP: (a) the Peak Floor Acceleration (PFA), and (b) the Peak Floor Velocity (PFV).

IDAs become horizontal. On the contrary, when the PFA , or the PFV , is adopted, the median and the 16, 84% fractiles can be easily calculated due to the practically monotonic increase of the IDA curves.

Moreover, although the drift is not the primary EDP of interest, the IDAs should be driven by the drift, or any other EDP that is related with the structural damage. This is because when structural collapse occurs, the freestanding contents are also considered collapsed (overturned). In the single-record capacity curves of Figure 1, the solid dots indicate when the building collapses, i.e. either when the analysis structurally fails, or when the maximum drift threshold is exceeded. The dots are transferred in Figure 1 indicating the occurrence of structural failure. This is done merely for visualization purposes since all simulations after the dots are assumed collapsed. This visualization shows that even for relatively low PFA , or PFV values, structural damage may have already occurred.

5.2 Rocking contents

Figure 2 shows the EDP-IM plots of a freestanding block with $R = 1.0m$ and $\alpha = 0.2$. The hosting structure was subjected to the IDA simulations of Figures 1 and 3 and then the simulations (shown as black dots in Fig. 1) are transferred to the $EDP^{(b)} - IM^{(b)}$ (Fig. 2a), or the $EDP^{(b)} - IM^{(s)}$ plane (Fig. 2b). In both plots the collapsed simulations appear as dots just right to the vertical line at $EDP^{(b)} = 1$. The dots below the horizontal line at $IM^{(b)} = 1$ (Fig. 2a) correspond to the no rocking simulations. As already discussed in a previous section, the $EDP^{(b)} - IM^{(b)}$ representation is the natural EDP-IM choice, but is not the easiest choice when it comes to the calculation of MAF $\lambda_{EDP}^{(b)}$. Moreover, as shown in Figure 2a, the data in the $EDP^{(b)} - IM^{(b)}$ form a cloud, while if they are plotted in the $EDP^{(b)} - IM^{(s)}$ place they are already conditional on the $IM^{(s)}$.

Both EDP-IM representations allow to calculate the fragility of the blocks, but with respect to a different IM. Defining the fragility conditional on the IM of the structure, i.e. $F_R^{(b)} = P(EDP^{(b)}|IM^{(s)})$ can be used for directly calculating the MAF using Eq. 6. On the other hand, the intuitive definition $F_R^{(b)} = P(EDP^{(b)}|IM^{(b)})$ provides the storey fragilities with respect to the block's IM and always for the storey of interest. Another major difference is that when $IM^{(b)}$ is adopted, the EDP-IM data appear as a “cloud” (Fig. 2a), while when $IM^{(s)}$

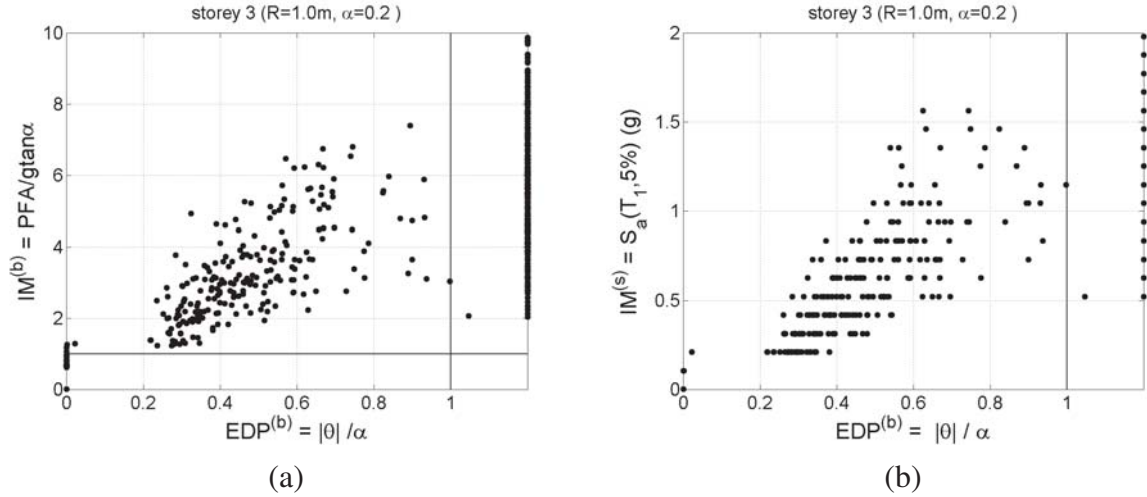


Figure 2: Seismic response of a freestanding building object with $R = 1.0m$ and $\alpha = 0.2$: (a) plotting $EDP^{(b)} - IM^{(b)}$ results to cloud data, (b) plotting $EDP^{(b)} - IM^{(s)}$ results to data in stripes.

is adopted instead, they appear in stripes (Fig. 2b). The IDA method can be directly applied to the striped data, while the cloud data require a different post-processing in order to derive the fragility curve. In the case of Figure 2b, the data form stripes and hence they can be post processed as was already shown in Section 5.1 for the building:

$$F_R^{(b)} = \Phi \left(\frac{\mu_{\log EDPb} - edp^{(b)}}{\sigma_{\log EDPb}} \right) (1 - P_{Ovtn} - P_{NoRock}) + P_{Ovtn} \quad (10)$$

Since the $F_R^{(b)}$ is calculated at every stripe P_{NoRock} , P_{Ovtn} are simply obtained as the percentage of simulations where no-rocking and overturning was observed, respectively. An alternative efficient way is to fit the cumulative distribution function (CDF) of a lognormal distribution on the striped EDP-IM data as discussed by Baker [15]. If the data are not stripped, as in Figure 2a, the cloud analysis method should be used instead.

6 Numerical Results

The acceleration and the velocity response spectra [2] allow to understand how the structure filters the record, i.e. they show the modes that are amplified and those that are filtered out. However, rocking structures do not have modes of vibration in the classical sense, i.e. like an elastically deforming body. For this reason, Figure 3 shows the mean rotation demand for two rigid blocks with the same size parameter $R = 1m$ and varying slenderness angle α . A smaller slenderness α value implies a more slender block, hence the block is more sensitive to overturning and keen to larger rotations. Having set overturning simulations to $\theta/\alpha = 1$, very interesting findings are offered by Figure 3. At $S_a(T_1, 5\%) = 0.4g$ (Fig. 3), the mean rotations of the scaled ground motions are very close to that of the top storey, while the demand is considerably smaller at lower stories. When the building is inelastic ($S_a(T_1, 5\%) = 1.0g$, Fig. 3b), the blocks that are subjected to the storey response histories have smaller rotation demand compared to the “ground” records. Therefore, regardless of the $S_a(T_1, 5\%)$ level, the building alters the frequency content of the ground motions reducing the fragility of the block for any slenderness angle α .

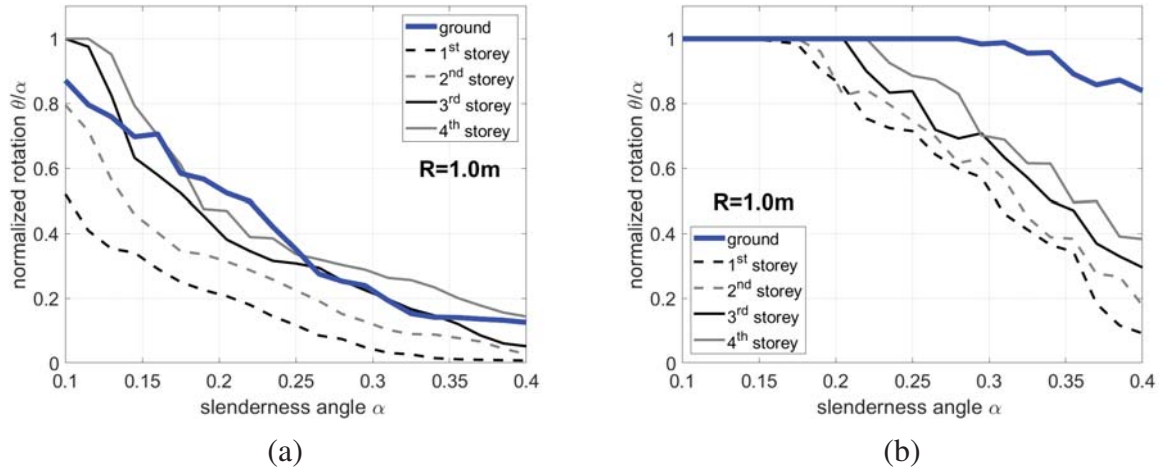


Figure 3: Mean rotation demands for rigid blocks with $R = 1m$ as function of the slenderness angle. The spectra were produced for building response histories scaled at: (a) $IM^{(s)} = 0.4g$ (elastic structure), and (b) $IM^{(s)} = 1.0g$ (inelastic structure).

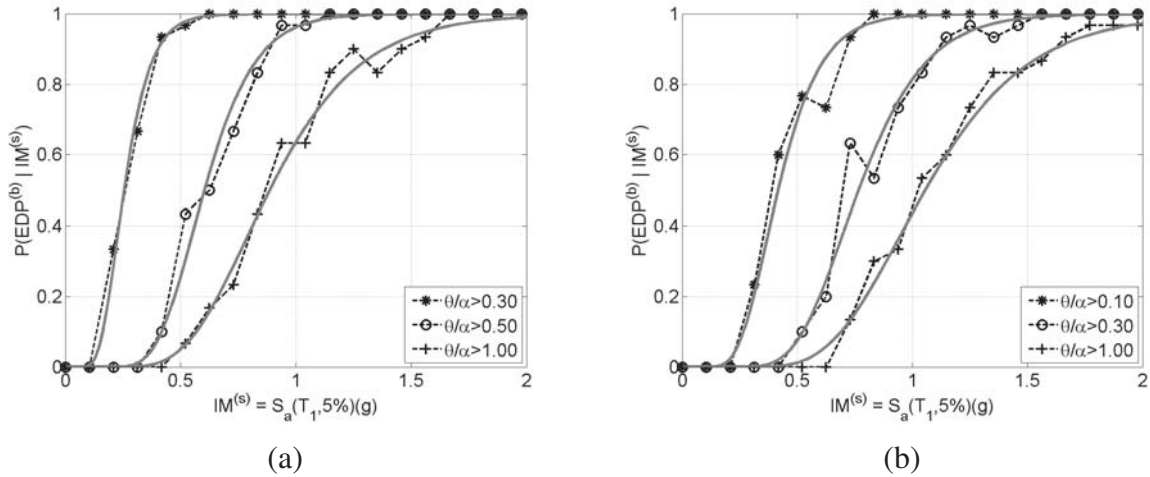


Figure 4: Fragility curves for a block located at the 3rd storey of the building: (a) slender block ($R = 1.0m$, $\alpha = 0.2$), (b) stocky block ($R = 1.0m$, $\alpha = 0.35$).

The remaining of the paper is focused on the seismic fragility assessment of the freestanding contents. We isolate two freestanding rocking blocks with $R = 1m$. The first has a slenderness angle $\alpha = 0.20$ and is considered as “slender”, while the second has $\alpha = 0.35$ and is referred as “stocky”. Three limit-states are identified for each block. For the slender block, the corresponding $EDP^{(b)} = \theta/\alpha$ threshold values are assumed as 0.3, 0.5 and 1, respectively, while for the stocky block the values are 0.1, 0.3 and 1. Different threshold values are used for each block due to their very different dynamic behaviour (e.g. see Fig 3). For example, $\theta/\alpha = 0.1$ is easily exceeded for the slender block and thus it is not a reasonable threshold, while for a stocky block the limit-state fragility of $\theta/\alpha = 0.5$ will, practically, coincide with that of overturning ($\theta/\alpha \geq 1$).

Figure 5 shows the block overturning fragilities using PFA as the intensity measure $IM^{(b)}$ of the block. The solid lines refer to the block subjected to the original ground motions, while the dashed lines were obtained using the response history of the fourth storey. Also, the dark

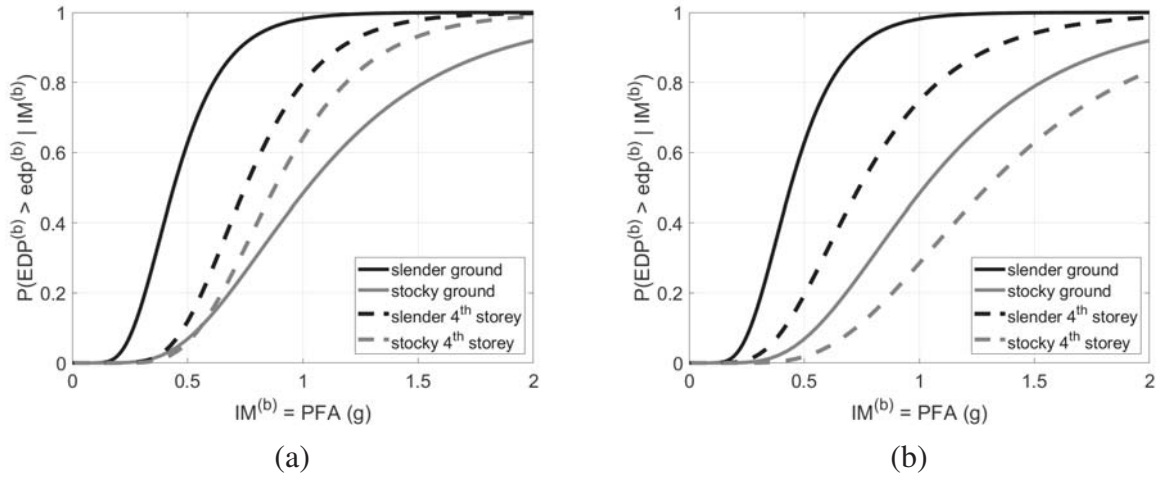


Figure 5: Overturning fragility curves of a slender ($R = 1.0m$, $\alpha = 0.2$) and a stocky block ($R = 1.0m$, $\alpha = 0.35$) assuming $IM^{(b)} = PFA$: (a) the block is considered overturned when the structure collapses, (b) the collapse of the structure is omitted.

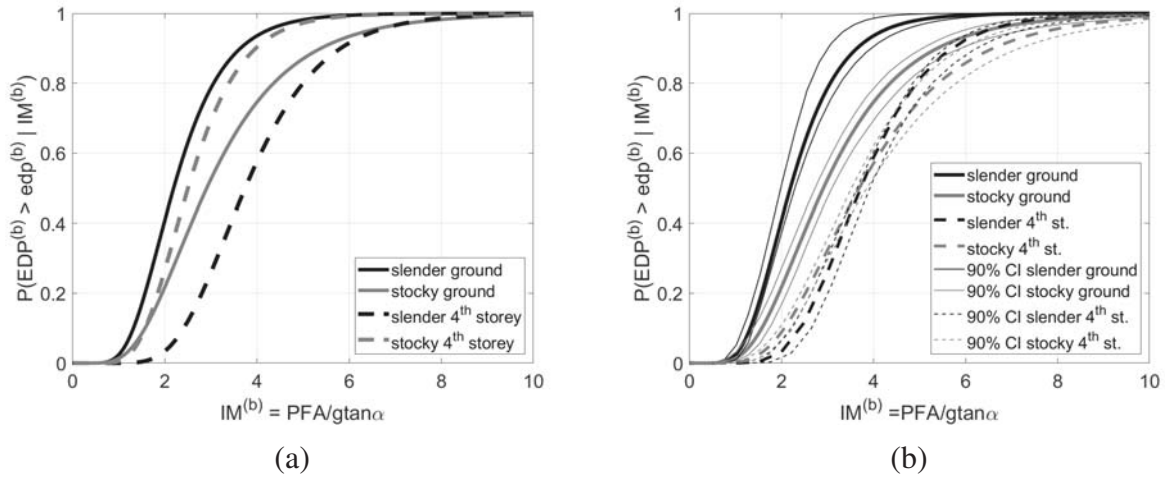


Figure 6: Overturning fragility curves of a slender ($R = 1.0m$, $\alpha = 0.2$) and a stocky block ($R = 1.0m$, $\alpha = 0.35$) assuming $IM^{(b)} = PFA/g \tan \alpha$: (a) the block is considered overturned when the structure collapses, (b) the collapse of the structure is omitted.

lines correspond to the slender block and the grey to the stocky. As expected, the slender block is always more vulnerable, while the building reduces its fragility (Fig. 5a). On the contrary, the building fragility overall increases for the stocky block. This is in agreement with the rocking spectra of Figure 3. In order to better understand the importance of considering the collapse of the structure, Figure 5b, repeats the fragility curves of Figure 5a, but this time ignoring the coupling between the structure and the block. In other words, in Figure 5b, we do not assume that the block overturns when structural collapse occurs. As before, for the slender block the fragilities are only slightly affected, but for the stocky block the fragility is very different. According to Figure 5a and b, when the coupling is neglected, the building is beneficial also for the stocky block.

The results of Figure 5 are repeated in Figure 6 but with $IM^{(b)} = PFA/g \tan \alpha$, instead of PFA . Since the blocks have a different slenderness angle α , the normalized $IM^{(b)}$ affects the

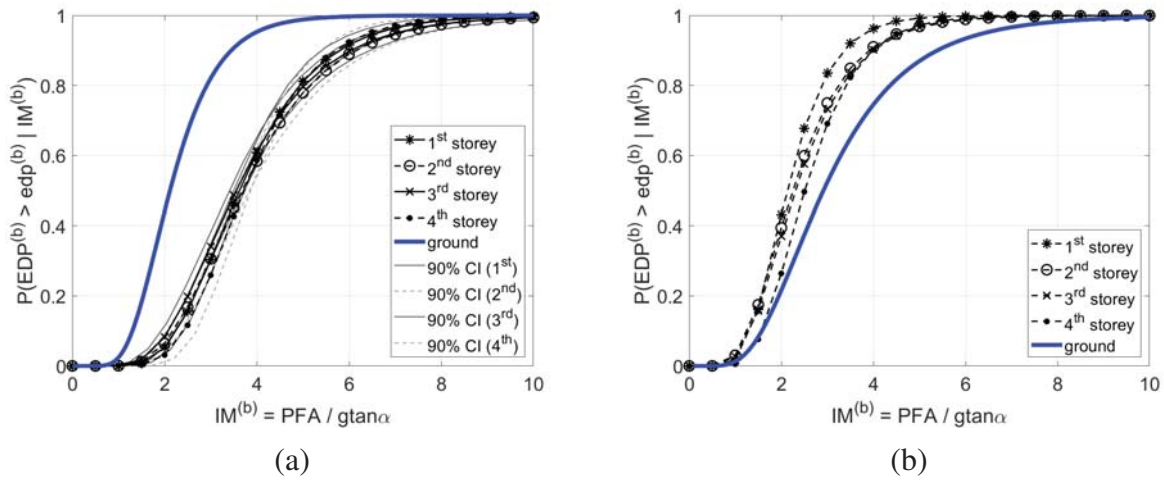


Figure 7: Storey overturning fragility curves: (a) slender block ($R = 1.0m$, $\alpha = 0.2$), (b) stocky block ($R = 1.0m$, $\alpha = 0.35$).

fragilities obtained. Qualitatively the results are the same compared to those of Figure 5a and b, but the fragilities curves are less dispersed, bringing closer the slender and the stocky block fragilities. Figure 6b also shows the 90% bootstrap confidence intervals around each fragility curve. The narrow confidence intervals obtained, verify that the comparison is statistically significant.

Figure 7 presents for all stories of the structure the block overturning fragilities assuming $IM^{(b)} = PGA/g \tan \alpha$. For both blocks, the storey fragilities practically coincide, while the “ground” fragilities differ considerably from those of the four stories. In principle, the fragility curves should coincide since they provide a property of the system that should not be sensitive to the ground motion set. However, due to the substantially different frequency content of the ground motions this is not the case here. Of interest is also to show the fragilities obtained using as $IM^{(b)}$ the PGV (or PFV) instead of the PGA (Fig. 8). Adopting the PGV , the storey fragilities appear more dispersed compared to the $PFA/g \tan \alpha$, which is more profound for the stocky block. Quantitatively, as before, the stocky block is more vulnerable on the ground, while the slender block is less affected by the structure compared Figure 5a. As a general conclusion, although qualitatively our conclusions are not affected by the $IM^{(b)}$, the fragility curves will differ and their interpretation requires attention. Furthermore, Figures 7a and 8a show the 90% confidence intervals which again verify the statistical significance of the fragilities obtained.

In order to calculate the limit-state mean annual frequencies (MAF) of the block, we adopt the hazard curve that corresponds to a site in the island of Crete, Greece. As discussed in a previous section, the limit-state MAFs are “exactly” calculated with Eq. 6. Alternatively, the MAFs can be calculated with Eq. 7 finding separately the fragility of the block and of the structure. The calculation of Eq. 7 requires the derivative of the block’s fragility, which essentially is the probability density function (PDF) for a number of discrete limit-states. For the example considered, the MAFs of Eq. 6 and Eq. 7 are shown in Table 1 for the first and the fourth storey of the RC building considered. In Eq. 7 two $IM^{(b)}$ were considered, $PGA/g \tan \alpha$ and PFV . Sufficient accuracy between the MAFs of the two approaches is achieved when the PFV is used as the intermediate variable in Eq. 7, while significant errors are observed for $IM^{(b)} = PFA/g \tan \alpha$. Although not shown, poor results were observed when the PFA was

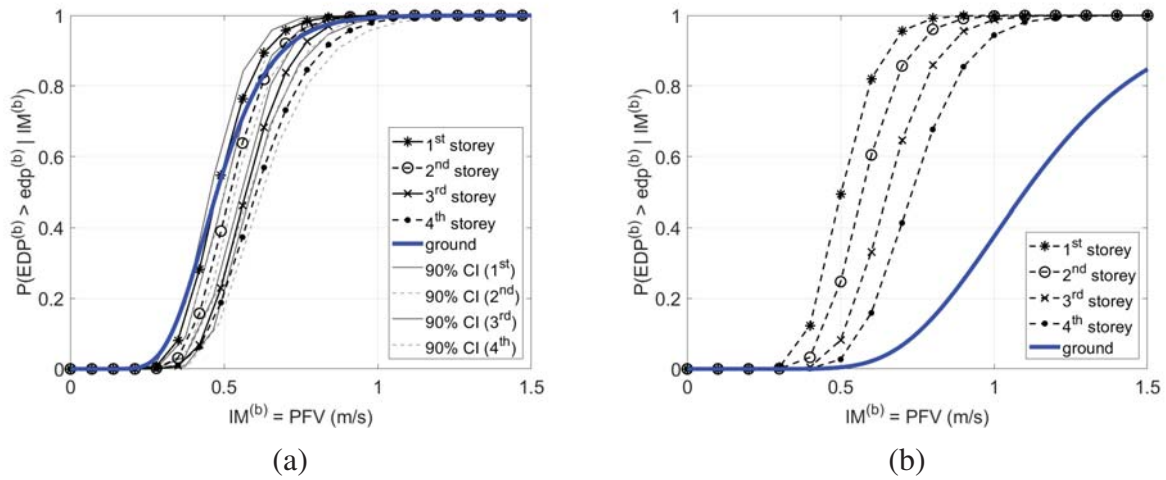


Figure 8: Storey overturning fragility curves using PFV as the IM of the block: (a) slender block ($R = 1.0m, \alpha = 0.2$), (b) stocky block ($R = 1.0m, \alpha = 0.35$).

used as $IM^{(b)}$. Moreover, the simplified method of Eq. 7 produces slightly better estimates for the slender block. The cloud data should be handled carefully, since the associated dispersion is naturally large. The main reason for the large variation of the MAFs in Table 1 is the biased fragilities of the blocks when the IM considered is the PFA. However, we have observed that using the PFV as IM, the approximate evaluation tends to produce smaller errors.

Table 1: Limit-state MAFs obtained for a rocking block using the exact (Eq. 6) and the simplified approach (Eq. 7) with either $PFA/gtan\alpha$ or PFV as the intermediate variables.

Slender block				
storey	$IM^{(b)}$	$(\theta/\alpha \leq 0.3)$	$(\theta/\alpha \leq 0.5)$	$(\theta/\alpha \leq 1.0)$
1 st storey	exact	7.389×10^{-4}	2.918×10^{-4}	1.894×10^{-4}
	simpl. PFA	13.304×10^{-4}	6.843×10^{-4}	5.760×10^{-4}
	simpl. PFV	5.470×10^{-4}	2.427×10^{-4}	1.940×10^{-4}
4 th storey	exact	58.502×10^{-4}	12.372×10^{-4}	4.035×10^{-4}
	simpl. PFA	40.966×10^{-4}	21.168×10^{-4}	12.938×10^{-4}
	simpl. PFV	33.753×10^{-4}	11.930×10^{-4}	4.959×10^{-4}
Stocky block				
storey	$IM^{(b)}$	$(\theta/\alpha \leq 0.1)$	$(\theta/\alpha \leq 0.3)$	$(\theta/\alpha \leq 1.0)$
1 st storey	exact	3.328×10^{-4}	1.831×10^{-4}	1.661×10^{-4}
	simpl. PFA	5.556×10^{-4}	4.534×10^{-4}	4.395×10^{-4}
	simpl. PFV	2.753×10^{-4}	1.903×10^{-4}	1.822×10^{-4}
4 th storey	exact	53.987×10^{-4}	7.115×10^{-4}	1.661×10^{-4}
	simpl. PFA	30.435×10^{-4}	11.557×10^{-4}	6.623×10^{-4}
	simpl. PFV	31.043×10^{-4}	6.180×10^{-4}	2.269×10^{-4}

The comparison of the MAF estimates is better understood looking at the fragilities of Figure 9. The fragility $P(EDP^{(b)} | IM^{(s)})$ is compared with the direct calculation and is calculated as $P(EDP^{(b)} | IM^{(s)}) = \int_{IM^{(b)}} P(EDP^{(b)} | IM^{(b)}) dP(IM^{(b)} | IM^{(s)})$. Essentially the calculation

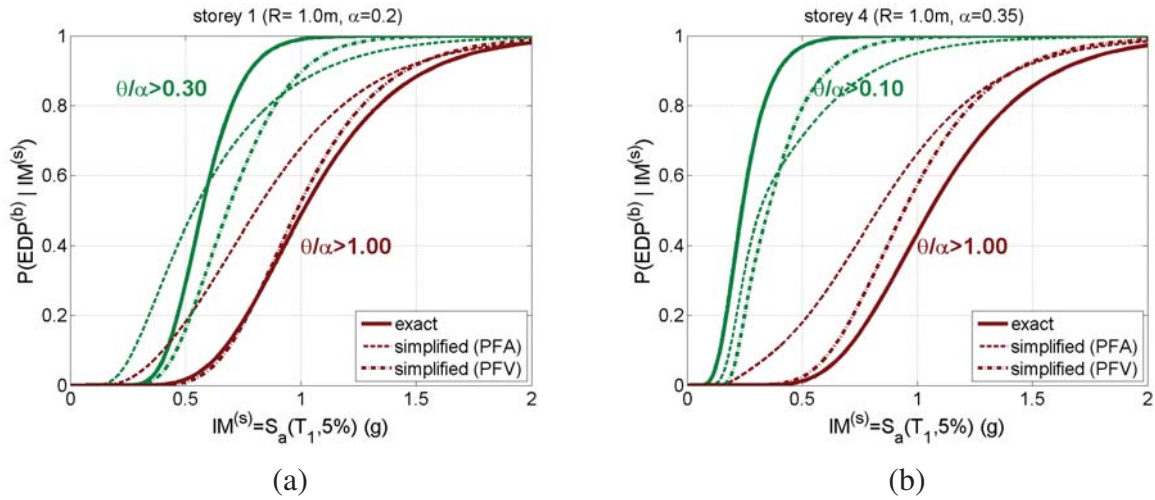


Figure 9: Fragility curves using the exact (Eq. 6) and the simplified approach (Eq. 7) for the slender block ($R = 1.0m, \alpha = 0.2$) and the stocky block ($R = 1.0m, \alpha = 0.35$): (a) first storey, (b) forth storey, respectively.

of Eq. 7 is repeated leaving out the slope of the hazard curve $d\lambda_{IM^{(s)}}$, which is common for both MAF equations. Figure 9 shows the good performance of *PFV* as opposed to *PFA*/ $gtan\alpha$, while better agreement is shown for the overturning limit-state and for the slender block.

Accepting that the choice of the $IM^{(b)}$ is important, it is necessary to investigate where do the errors shown in Figure 9 come from. This is understood comparing Figure 7 and Figure 9. Figure 7 shows that the fragility curves of the block at the building and at the ground will differ for the stocky block but not for the slender block. Since the collapse of the building does not affect the overturning fragility of the slender block (Fig. 7a), the overturning fragility of the slender block is almost the same regardless, if the structure's collapse is neglected or not, hence the overturning MAF of Figure 9 is closely estimated. On the other hand, for the slender block, the building and the ground fragilities differ and this is transferred to Figure 9b. However, even for the stocky block, the solution provided is acceptable given the many sources of uncertainty on the problem at hand. Another important remark is that the block used in this example were obtained including the building's collapse. Therefore, when the building's collapse does affect the fragilities, as in the case of the slender block, Eq. 7 is accurate. This hampers the use of Eq. 7 when generic fragility curves are to be adopted.

7 CONCLUSIONS

The fragility assessment of freestanding building contents has been discussed. The building contents were modelled as rigid blocks and it was assumed that they are hosted in a four-storey RC building. It has been shown that the problem addressed is complicated since the response of the structure and the contents are coupled. The findings of the study have been obtained using a single two-dimensional, four-storey building and hence cannot be always generalized. For this reason, further research is required in order to fully understand the effect of the structure on the fragility of freestanding contents. Nevertheless, the work presented should be considered as an attempt to offer some first guidelines on how the rocking problem can be handled for freestanding objects that are hosted in a building.

REFERENCES

- [1] G.W. Housner, The behavior of inverted pendulum structures during earthquakes. *Bulletin of the Seismological Society of America*, **53**(2), 404–417, 1963.
- [2] M. Fragiadakis, S. Diamantopoulos, Fragility and risk assessment of freestanding building contents. *Earthq Eng Struct Dyn*, **49**(10), 1028–1048, 2020.
- [3] S. Diamantopoulos, M. Fragiadakis, Seismic response assessment of rocking systems using single degree-of-freedom oscillators. *Earthq Eng Struct Dyn*, **48**(7), 689–708, 2019.
- [4] Y. Ishiyama, Motions of rigid bodies and criteria for overturning by earthquake excitations. *Earthq Eng Struct Dyn*, **10**, 635–650, 1982.
- [5] E.G. Dimitrakopoulos, A.I. Giouvanidis, Seismic response analysis of the planar rocking frame. *Journal of Engineering Mechanics*, **141**(7), 04015003, 2015.
- [6] E.G. Dimitrakopoulos, T.S. Paraskeva, Dimensionless fragility curves for rocking response to near-fault excitations. *Earthq. Eng. Struct. Dyn*, **44**(12), 2015–2033, 2015.
- [7] I. Psycharis, M. Fragiadakis, I. Stefanou, Seismic reliability assessment of classical columns subjected to near-fault ground motions. *Earthq. Eng. Struct. Dyn*, **42**(14), 2061–2079, 2013.
- [8] I. Kavvadias, L. Vasiliadis, Ar. Elenas, Seismic Response Parametric Study of Ancient Rocking Columns. *International Journal of Architectural Heritage*, **11**(6), 791–804, 2017.
- [9] K. Porter, K. Farokhnia, D. Vamvatsikos, I. Cho, *Guidelines for component-based analytical vulnerability assessment of buildings and nonstructural elements*. Technical Report, 2015.
- [10] M. Fragiadakis, D. Vamvatsikos, M.G. Karlaftis, N.D. Lagaros, M. Papadrakakis, Seismic assessment of structures and lifelines. *Journal of Sound and Vibration*, **334**, 29–56, 2015.
- [11] FEMA, *FEMA P-58-1: Seismic Performance Assessment of Buildings - Volume 1, Methodology elements*. 2012.
- [12] F. Jalayer, *Direct probabilistic seismic analysis: Implementing non-linear dynamic assessments*. Department of Civil and Environmental Engineering, Stanford University, CA, 2003.
- [13] J.W. Baker, Efficient Analytical Fragility Function Fitting Using Dynamic Structural Analysis. *Earthquake Spectra*, **31**(1), 579–599, 2015.
- [14] D. Vamvatsikos, M. Fragiadakis Incremental dynamic analysis for estimating seismic performance sensitivity and uncertainty. *Earthq. Eng. Struct. Dyn*, **39**(2), 141–163, 2010.
- [15] J.W. Baker, Efficient analytical fragility function fitting using dynamic structural analysis. *Earthq Spectra*, **31**(1), 579–599, 2015.

SOME RECENT ADVANCES ON THE MODELING OF THE HYSTERETIC BEHAVIOR OF RATE-INDEPENDENT PASSIVE ENERGY DISSIPATION DEVICES

Nicolò Vaiana, Ciro Napolitano, and Luciano Rosati

Department of Structures for Engineering and Architecture, University of Naples Federico II
via Claudio, 21, 80124 Naples, Italy
e-mail: nicolo.vaiana@unina.it

Keywords: Energy Dissipation Device, Hysteretic Behavior, Nonlinear Dynamic Analysis, Phenomenological Model, Shear Link.

Abstract. *Structures with passive energy dissipation systems are characterized by a complex dynamic behavior due to the hysteretic nature governing the response of the adopted devices. Mathematically speaking, the hysteretic models currently available to simulate the behavior of rate-independent devices, such as metallic and friction dampers, are much more complicated than those developed for rate-dependent devices, such as viscous fluid and viscoelastic solid dampers. To allow for a straightforward, accurate and efficient modeling of rate-independent energy dissipation devices in practice, we introduce a novel phenomenological model suitable for both metallic and friction dampers. Such a model offers the advantage of requiring an easy calibration procedure since it is based on a set of only four parameters having a clear mechanical significance. The proposed model is employed to simulate the actual behavior of some metallic dampers, denominated Shear Links, that have been experimentally tested at the University of Naples Federico II. In addition, numerical simulations are performed to show the capability of such devices in protecting structures from earthquake excitations.*

1 INTRODUCTION

Passive energy dissipation represents one of the most effective techniques for the seismic protection of buildings and bridges [1, 2, 3, 4]. This technique requires the use of special devices, called *dampers*, that are characterized by a high energy dissipation capacity and are generally incorporated in the external frames of a structure thus dissipating energy throughout its entire height [5].

Dampers typically exhibit a complex hysteretic behavior. In particular, such a behavior is referred to as *rate-independent* if the device restoring force depends on the device displacement, whereas it is defined *rate-dependent* when the device restoring force is a function of the device velocity. Clearly, there may exist some dampers showing both types of behavior at the same time [6].

Examples of rate-independent passive energy dissipation devices, commonly used for seismic protection of structures, are *metallic dampers* and *friction dampers*, whereas examples of rate-dependent devices are *viscous fluid dampers* and *viscoelastic solid dampers*.

Several hysteretic models have been proposed in the literature for simulating the complex behavior occurring in dampers [7]. Typically, rate-independent hysteretic models are much more complex than the rate-dependent ones from a mathematical point of view [8].

Among existing rate-independent models, the Bouc-Wen model [9, 10] and its modified versions [7] seem to be the most suitable ones since they allow for an accurate prediction of the hysteretic response of both metallic and friction dampers by using a relatively small number of parameters. Unfortunately, these models require parameters with no clear mechanical meaning thus involving the use of complex and time-consuming identification procedures. In addition, due to their differential nature, they are not computationally efficient since they require the numerical solution of a first-order nonlinear ordinary differential equation for the evaluation of the hysteretic variable at each time step of a nonlinear dynamic analysis.

To foster the use of accurate and efficient rate-independent models in practice, this paper proposes a novel phenomenological model able to predict the hysteretic behavior generally displayed by metallic and friction dampers. Compared to the celebrated Bouc-Wen model or its modified versions, the proposed model, belonging to a more general class formulated in [11, 12, 13], is based on a set of only four parameters having a clear mechanical significance. For such a reason, it needs a straightforward calibration procedure and, consequently, it may be easily adopted in practice.

The paper is organized into three parts. In the first part (Sections 2 and 3), we first derive the nonlinear equilibrium equations of a typical building frame equipped with energy dissipation devices and subjected to earthquake excitation. Subsequently, we briefly describe, for the reader's convenience, the three main categories of dampers with particular emphasis on the description of their hysteretic behavior.

In the second part (Section 4), we present a preliminary formulation of the proposed hysteretic model suitable for rate-independent dampers, such as metallic and friction devices, and then we illustrate the influence of the four parameters on the hysteresis loop size and/or shape.

Finally, in the third part (Section 5), we adopt the proposed hysteretic model to simulate the experimental behavior of a particular class of metallic dampers, denominated Shear Links, and we perform several nonlinear dynamic analyses on a building frame equipped with such devices to show their capability in reducing both floor relative displacements and absolute accelerations.

2 NONLINEAR EQUILIBRIUM EQUATIONS

The response of a Multi-Degree-Of-Freedom (MDOF) system is generally governed by the following system of coupled second-order nonlinear Ordinary Differential Equations (ODEs):

$$\mathbf{M}\ddot{\mathbf{u}}(t) + \mathbf{C}\dot{\mathbf{u}}(t) + \mathbf{K}\mathbf{u}(t) + \mathbf{f}_n(t) = \mathbf{p}(t), \quad (1)$$

in which $\mathbf{u}(t)$, $\dot{\mathbf{u}}(t)$, and $\ddot{\mathbf{u}}(t)$ are the generalized displacement, velocity, and acceleration vectors, respectively, whereas \mathbf{M} , \mathbf{C} , and \mathbf{K} represent the generalized constant mass, damping, and elastic stiffness matrices, respectively; in addition, $\mathbf{f}_n(t)$ is the generalized nonlinear force vector, which may have rate-independent and/or rate-dependent hysteretic nature, whereas $\mathbf{p}(t)$ represents the generalized external force vector depending on time t .

In this work, we specialize such nonlinear equilibrium equations to the structural model of a typical building frame equipped with energy dissipation devices, each mounted in combination with two diagonal braces. In particular, we introduce a 3-story two-dimensional (2D) structural model whose geometry is defined in a global, right-handed Cartesian coordinate system (O , Y , Z), as shown in Figure 1.

For simplicity, we assume that: a) frame elements, such as beams, columns, and braces, deform within their linear elastic range during the earthquake excitation, whereas the hysteretic devices exhibit nonlinear behavior; b) columns are axially inextensible; c) beams and braces are axially inextensible and flexurally rigid. We observe that these assumptions, typically introduced in the literature [14], can be removed without any influence on the proposed results.

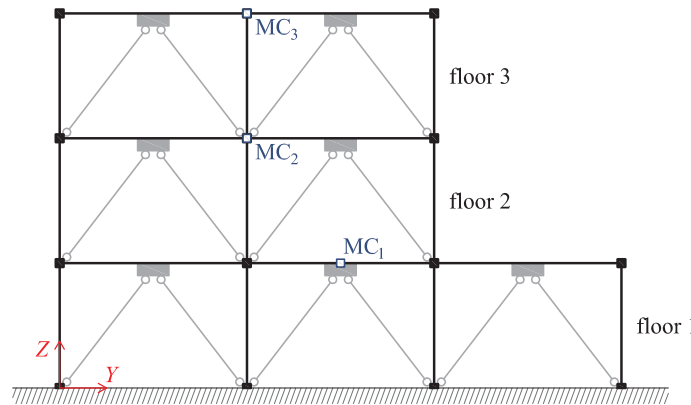


Figure 1: 2D structural model of a typical building frame with added dampers.

The above-described structural idealization allows us to write the displacement, velocity, and acceleration vectors of the 2D structural model, relative to the ground, as follows:

$$\mathbf{u} = \begin{Bmatrix} u^{(1)} \\ u^{(2)} \\ u^{(3)} \end{Bmatrix}, \quad \dot{\mathbf{u}} = \begin{Bmatrix} \dot{u}^{(1)} \\ \dot{u}^{(2)} \\ \dot{u}^{(3)} \end{Bmatrix}, \quad \ddot{\mathbf{u}} = \begin{Bmatrix} \ddot{u}^{(1)} \\ \ddot{u}^{(2)} \\ \ddot{u}^{(3)} \end{Bmatrix}, \quad (2)$$

where $u^{(i)}$, $\dot{u}^{(i)}$, $\ddot{u}^{(i)}$ represent, respectively, the displacement, velocity, and acceleration along the Y -axis of the i -th floor.

On account of that, the constant mass, damping, and elastic stiffness matrices become:

$$\mathbf{M} = \begin{bmatrix} M^{(1)} & 0 & 0 \\ 0 & M^{(2)} & 0 \\ 0 & 0 & M^{(3)} \end{bmatrix}, \quad \mathbf{C} = \begin{bmatrix} C^{(1)} + C^{(2)} & -C^{(2)} & 0 \\ -C^{(2)} & C^{(2)} + C^{(3)} & -C^{(3)} \\ 0 & -C^{(3)} & C^{(3)} \end{bmatrix}, \quad (3)$$

$$\mathbf{K} = \begin{bmatrix} K^{(1)} + K^{(2)} & -K^{(2)} & 0 \\ -K^{(2)} & K^{(2)} + K^{(3)} & -K^{(3)} \\ 0 & -K^{(3)} & K^{(3)} \end{bmatrix},$$

where $M^{(i)}$ is the i -th floor mass, $C^{(i)}$ is the i -th floor damping coefficient, whereas $K^{(i)}$ is the i -th floor elastic stiffness, obtained by summing the elastic stiffnesses of the i -th floor columns.

Finally, the nonlinear force vector and the external force vector are given by:

$$\mathbf{f}_n = \begin{Bmatrix} f_n^{(1)} \\ f_n^{(2)} \\ f_n^{(3)} \end{Bmatrix}, \quad \mathbf{p} = - \begin{bmatrix} M^{(1)} & 0 & 0 \\ 0 & M^{(2)} & 0 \\ 0 & 0 & M^{(3)} \end{bmatrix} \begin{Bmatrix} 1 \\ 1 \\ 1 \end{Bmatrix} \ddot{u}_g, \quad (4)$$

where $f_n^{(i)}$ represents the nonlinear force of the i -th floor, whereas \ddot{u}_g is the ground acceleration applied along the Y -axis. In particular, if the vector \mathbf{f}_n is a function of the displacement vector \mathbf{u} , its three components are computed as:

$$\begin{aligned} f_n^{(1)} &= \sum_{j=1}^3 f_j^{(1)}(u^{(1)}) - \sum_{j=1}^2 f_j^{(2)}(u^{(2)} - u^{(1)}), \\ f_n^{(2)} &= \sum_{j=1}^2 f_j^{(2)}(u^{(2)} - u^{(1)}) - \sum_{j=1}^2 f_j^{(3)}(u^{(3)} - u^{(2)}), \\ f_n^{(3)} &= \sum_{j=1}^2 f_j^{(3)}(u^{(3)} - u^{(2)}), \end{aligned} \quad (5)$$

where $f_j^{(i)}$ is the *rate-independent hysteretic force* exhibited by the j -th damper of the i -th floor.

Conversely, if the vector \mathbf{f}_n is a function of the velocity vector $\dot{\mathbf{u}}$, the displacement $u^{(i)}$, appearing in Equation 5, has to be substituted with the velocity $\dot{u}^{(i)}$; in such a case, $f_j^{(i)}$ would represent the *rate-dependent hysteretic force* displayed by the j -th damper of the i -th floor.

3 ENERGY DISSIPATION DEVICES

Several types of passive energy dissipation devices have been adopted worldwide to protect structures from earthquake excitations. According to the nature of their hysteretic behavior, such devices may be classified into three categories [7]:

1. *rate-independent hysteretic devices*: dampers whose restoring force does not depend on the rate of variation of the displacement (i.e., velocity) but only upon the displacement amplitude and the sign of the velocity (i.e., direction of the motion). Some examples are represented by *metallic dampers* and *friction dampers*.
2. *rate-dependent hysteretic devices*: dampers whose restoring force depends, partially or totally, on the rate of variation of the displacement (i.e., velocity). Examples of such devices are *viscous fluid dampers* and *viscoelastic solid dampers*.

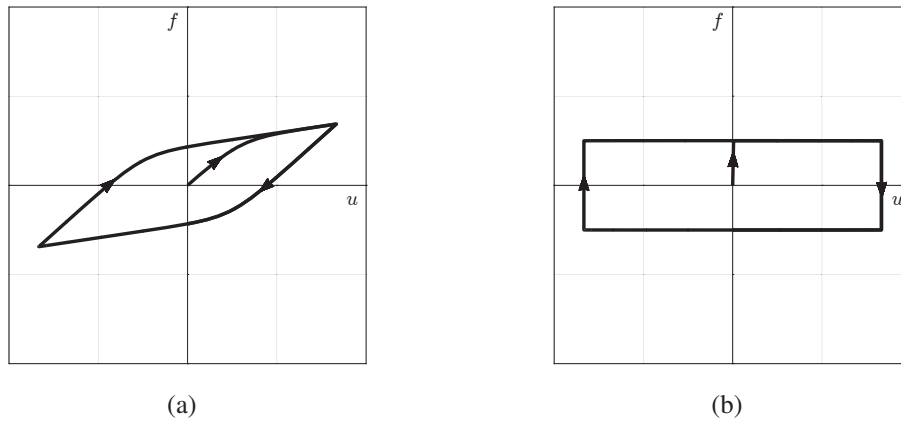


Figure 2: Typical hysteresis loop of (a) metallic and (b) friction dampers.

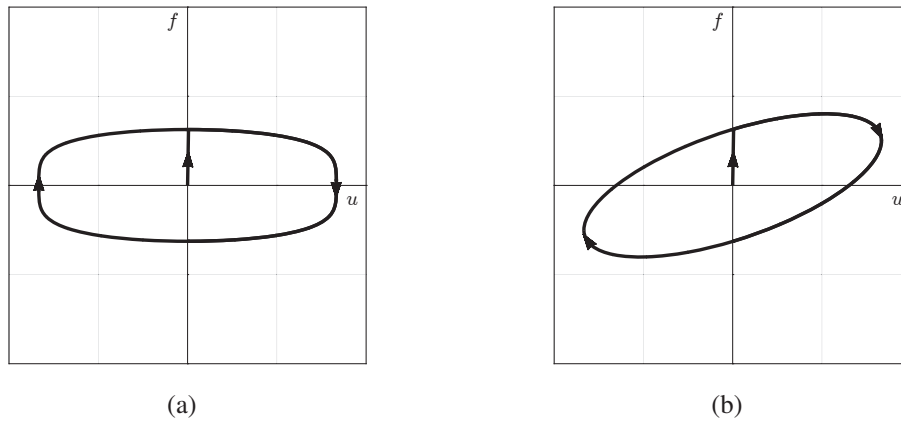


Figure 3: Typical hysteresis loop of (a) viscous fluid and (b) viscoelastic solid dampers.

3. *further devices*: dampers which cannot be classified by one of the above-described basic types. Some examples are friction-spring devices with re-centering capability and fluid restoring force-damping devices.

Figure 2a (b) illustrates the typical force-displacement hysteresis loop of a metallic (friction) damper, whereas Figure 3a (b) shows the hysteresis loop which generally characterizes a viscous fluid (viscoelastic solid) damper.

Clearly, the hysteresis phenomena observed in these devices are induced by different types of mechanisms. As a matter of fact, in metallic dampers such a nonlinear behavior is associated with yielding of mild steel, whereas in friction dampers it is due to the sliding friction across the interface between two solid bodies.

Furthermore, in viscous fluid dampers the energy dissipation is due to the friction between fluid particles and the piston head, whereas in viscoelastic solid dampers it is related to the deformation of solid elastomeric pads.

4 PROPOSED HYSTERETIC MODEL

In this Section, we focus on the modeling of rate-independent hysteretic devices which, differently from the rate-dependent ones, require much more complex hysteretic models.

In particular, we first summarize the formulation of a novel uniaxial phenomenological

model belonging to a more general class introduced by Vaiana et al. [11, 12, 13, 15]; subsequently, we illustrate the influence of the four model parameters on the size and/or shape of the restoring force-displacement hysteresis loops.

4.1 Model Formulation

In the Proposed Hysteretic Model (PHM), u (f) represents the damper axial/transverse displacement (restoring force), whereas \dot{u} is the damper axial/transverse velocity.

The restoring force, during the generic loading case ($\dot{u} > 0$), is evaluated as:

$$f(u, u_j^+) = \begin{cases} c^+(u, u_j^+) & u \in [u_j^+ - 2u_0, u_j^+] \\ c_u(u) & u \in [u_j^+, \infty) \end{cases} \quad (6a)$$

$$(6b)$$

whereas, during the generic unloading case ($\dot{u} < 0$), it is computed as:

$$f(u, u_j^-) = \begin{cases} c^-(u, u_j^-) & u \in [u_j^-, u_j^- + 2u_0] \\ c_l(u) & u \in (-\infty, u_j^-] \end{cases} \quad (7a)$$

$$(7b)$$

In Equations 6 and 7, c^+ and c^- represent, respectively, the generic loading and unloading curves:

$$c^+(u, u_j^+) = k_b u + f_0 + \frac{k_a - k_b}{c_1} \left[+u - u_j^+ - \alpha_1 \log \left(c_1 + e^{\frac{+u - u_j^+ + 2u_0 - \alpha_2}{\alpha_1}} \right) + c_2 \right], \quad (8)$$

$$c^-(u, u_j^-) = k_b u - f_0 - \frac{k_a - k_b}{c_1} \left[-u + u_j^- - \alpha_1 \log \left(c_1 + e^{\frac{-u + u_j^- + 2u_0 - \alpha_2}{\alpha_1}} \right) + c_2 \right], \quad (9)$$

whereas c_u and c_l are, respectively, the upper and lower limiting curves:

$$c_u(u) = k_b u + f_0, \quad (10)$$

$$c_l(u) = k_b u - f_0. \quad (11)$$

The internal variable u_j^+ (u_j^-), that represents the displacement value where the generic loading (unloading) curve intersects the upper (lower) limiting curve, is given by:

$$u_j^+ = +\alpha_1 \log \left\{ c_1^{-1} \left[e^{+\frac{u_P + c_2 - c_1(k_a - k_b)^{-1}(f_P - k_b u_P - f_0)}{\alpha_1}} - e^{\frac{+u_P + 2u_0 - \alpha_2}{\alpha_1}} \right] \right\}, \quad (12)$$

$$u_j^- = -\alpha_1 \log \left\{ c_1^{-1} \left[e^{-\frac{u_P - c_2 - c_1(k_a - k_b)^{-1}(f_P - k_b u_P + f_0)}{\alpha_1}} - e^{\frac{-u_P + 2u_0 - \alpha_2}{\alpha_1}} \right] \right\}, \quad (13)$$

in which u_P and f_P are the coordinates of a generic point P belonging to c^+ or c^- .

As regards the internal parameters f_0 and u_0 , they are evaluated as:

$$f_0 = \frac{k_a - k_b}{2c_1} (2u_0 - c_2), \quad (14)$$

$$u_0 = \frac{1}{2} \left[\alpha_2 + \alpha_1 \log \left(\frac{k_a - k_b}{\delta_k} - c_1 \right) \right], \quad (15)$$

where δ_k is a numerical parameter set equal to 10^{-20} , whereas k_a , k_b , α_1 and α_2 represent the four model parameters to be calibrated from experimental or numerical data, with $k_a > k_b$, $k_a > 0$, $\alpha_1 > 0$, $\alpha_2 > 0$. Finally, c_1 and c_2 are two constants whose expressions, depending on the four model parameters and omitted for brevity, will be illustrated in detail in a future work.

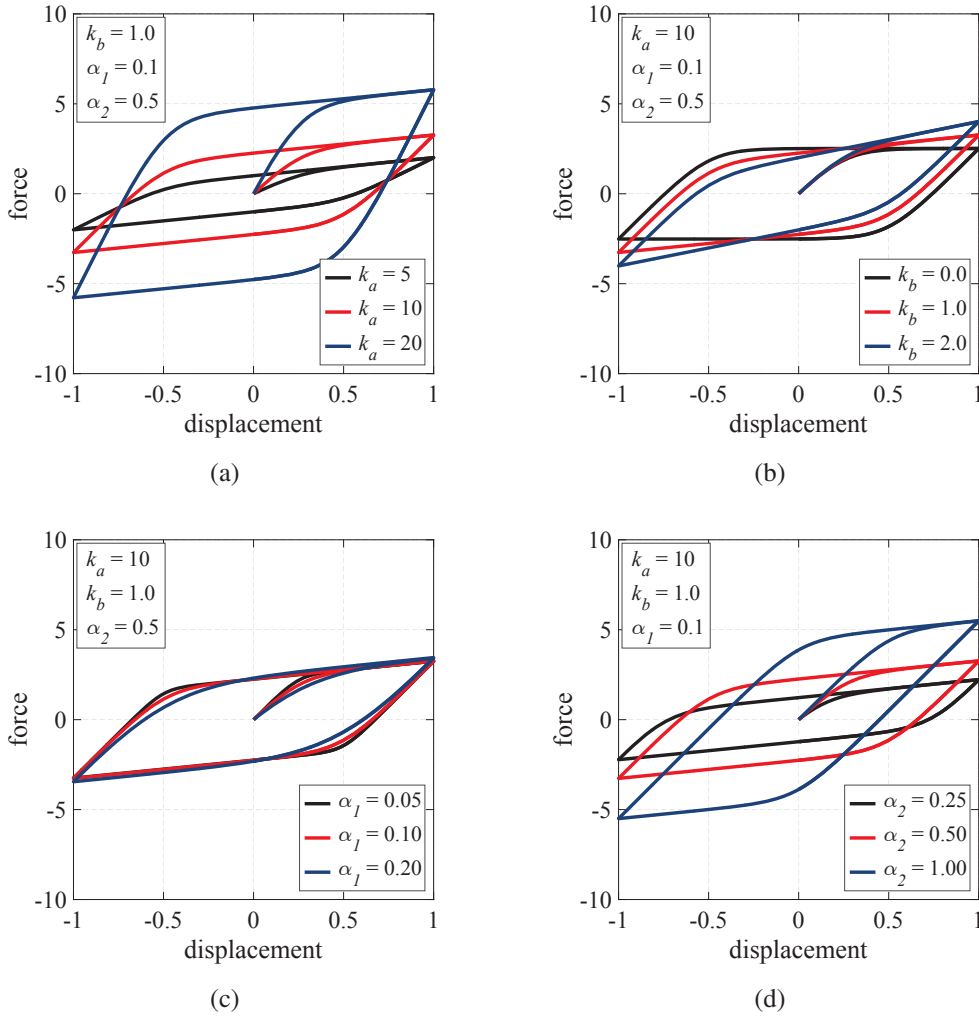


Figure 4: Influence of the PHM parameters variation on the hysteresis loop size and/or shape: (a) k_a , (b) k_b , (c) α_1 , and (d) α_2 .

4.2 Parameter Sensitivity Analysis

Figure 4 shows how the size and (or) the shape of hysteresis loops, obtained by imposing a full sinusoidal cycle of displacement having unit amplitude and frequency, change(s) due to the variation of each PHM parameter, namely k_a , k_b , α_1 and α_2 .

5 NUMERICAL EXPERIMENTS

This Section illustrates the results of several nonlinear time history analyses performed on a building frame equipped with energy dissipation devices and subjected to earthquake excitation. In order to demonstrate the effectiveness of the adopted passive control system and its capability to significantly decrease both floor relative displacements and absolute accelerations, the numerical results are compared with those obtained by analyzing the same building frame, having linear elastic behavior, without using the hysteretic devices.

To carry out the nonlinear dynamic analyses, the proposed hysteretic model, described in Section 4, is employed to simulate the behavior of each damper adopted in the passive control system. Furthermore, an accurate and computationally efficient explicit time integration method, described in [8], is adopted to numerically integrate the system of nonlinear equilib-

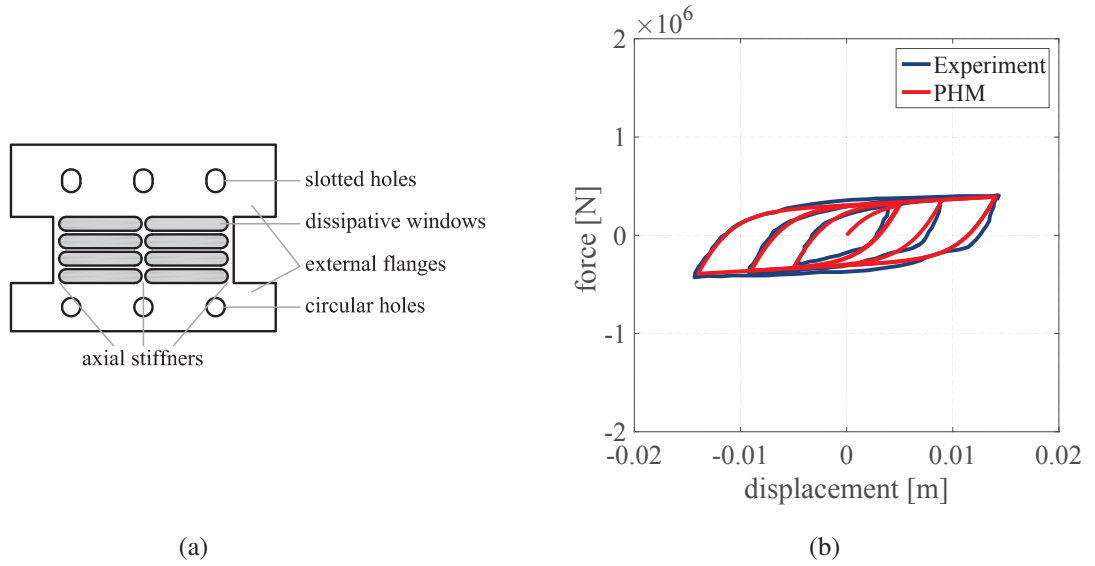


Figure 5: Shear Link: (a) typical lateral view and (b) comparison between experimental and analytical hysteresis loops of device *SL_30_3*.

rium equations. Due to its explicit nature, such a method offers the advantage of performing nonlinear dynamic analyses without adopting iterative procedures.

Both the hysteretic model and the numerical method have been implemented in the computer program MATLAB.

5.1 Structure Properties

Figure 1 shows the 2D structural model of the building frame selected to perform the numerical experiments. In particular, it is a three-story, three-bay reinforced concrete structure whose beams (columns) have a length of 6.0 m (3.2 m) and are characterized by a rectangular section with size 0.3 m x 0.4 m (0.5 m x 0.5 m).

The masses of the first, second, and third floor are equal to $85200 \text{ N s}^2 \text{ m}^{-1}$, $57400 \text{ N s}^2 \text{ m}^{-1}$, and $42600 \text{ N s}^2 \text{ m}^{-1}$, respectively, and are assumed to be lumped in the respective floor mass center, namely MC_1 , MC_2 , and MC_3 .

As a result of the assumptions made in Section 2, the total number of Degrees-Of-Freedom (DOFs) is equal to 3, whereas the three natural periods, evaluated without taking into account dampers and steel braces, are $T_1 = 0.2220 \text{ s}$, $T_2 = 0.0916 \text{ s}$, and $T_3 = 0.0630 \text{ s}$. As typically done with reinforced concrete structures, it is assumed that each mode has a damping ratio of 5% [14].

The passive control system consists of 7 dampers which are mounted between the steel braces and the upper beam, as illustrated in Figure 1. The adopted devices, denominated *Shear Links*, are metallic dampers, having rate-independent hysteretic behavior, that are manufactured from a I-shaped laminated steel plate [16, 17]. As shown in Figure 5(a), this type of device is typically made up of a) vertical stiffeners, that ensure the device stability, b) external flanges, that allow for the device connection to structural elements, and c) dissipative windows, that are capable of dissipating energy. Bolted connections are employed to facilitate the installation process; in particular, slotted holes are used for the upper connection in order to avoid axial forces on the device.

The Shear Links employed in this paper have been experimentally tested by Nuzzo et al. [18]

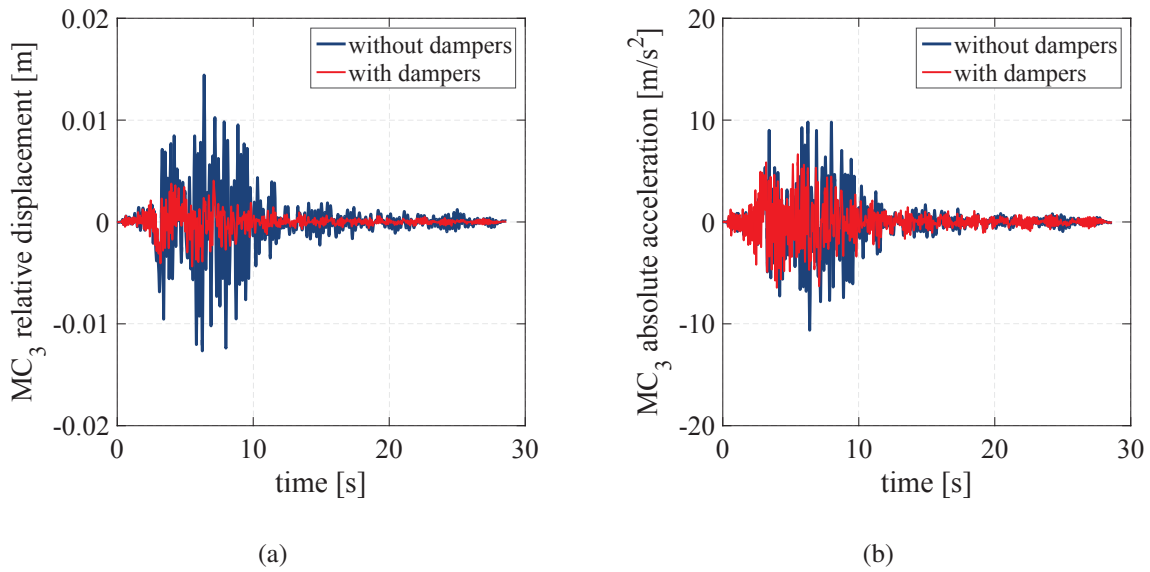


Figure 6: Time histories of the MC_3 (a) relative displacement and (b) absolute acceleration obtained with (red line) and without (blue line) metallic dampers.

at the laboratory of Department of Structures for Engineering and Architecture of the University of Naples Federico II (Italy). In particular, the device adopted in the numerical simulation, denominated SL_{30_3} , exhibits the restoring force-displacement hysteresis loops of Figure 5(b) when subjected to a displacement time history having increasing amplitude [18].

5.2 Applied earthquake excitation

The analyses are performed by imposing, along the Y -axis, the component SN of the 1994 Northridge motion, and by adopting a ground acceleration record time step of 0.005 s.

5.3 Hysteretic model parameters

The complex behavior of each Shear Link is simulated with the novel phenomenological model, presented in Section 4, whose 4 parameters have been calibrated on the basis of the experimental hysteresis loops obtained by Nuzzo et al. [18]. In particular, the values identified for such parameters are: $k_a = 2 \times 10^8$ N/m, $k_b = 6 \times 10^6$ N/m, and $\alpha_1 = \alpha_2 = 0.002$ m.

Figure 5(b) compares the experimental hysteresis loops of the device SL_{30_3} with those predicted by means of the proposed hysteretic model thus demonstrating a satisfactory agreement between them.

5.4 Numerical results

Figure 6(a) illustrates the time histories of the MC_3 displacement, relative to the ground, obtained with (red line) and without (blue line) metallic dampers; similarly, Figure 6(b) shows the time histories of the MC_3 absolute acceleration obtained with (red line) and without (blue line) Shear Links. Looking at such comparisons, it is evident that the adopted passive protection system is capable of limiting potential damages induced by seismic events since it allows for the reduction of both floor relative displacements and absolute accelerations.

6 CONCLUSIONS

We have presented a preliminary formulation of a novel uniaxial phenomenological model that is capable of simulating the complex behavior of both metallic and friction dampers by employing four parameters having a clear mechanical significance.

The proposed model has been calibrated on the basis of some experimental hysteresis loops obtained by Nuzzo et al. [18] during an experimental campaign performed on Shear Link devices. In particular, the accuracy of the model has been verified by comparing the simulated restoring force-displacement hysteresis loops with those obtained from the experimental tests.

In addition, the proposed model has been employed to analyze a building frame equipped with Shear Links. The numerical results obtained by applying an earthquake ground acceleration have demonstrated the capability of the adopted dampers in controlling excessive floor displacements and accelerations.

REFERENCES

- [1] T.T. Soong, B.F. Spencer Jr, Supplemental energy dissipation: State-of-the-art and state-of-the-practice. *Engineering structures*, **24**(3), 243–259, 2002.
- [2] A. Calabrese, D. Losanno, M. Spizzuoco, S. Strano, M. Terzo, Recycled Rubber Fiber Reinforced Bearings (RR-FRBs) as base isolators for residential buildings in developing countries: The demonstration building of Pasir Badak, Indonesia. *Engineering Structures*, **192**, 126–144, 2019.
- [3] D. Losanno, M. Spizzuoco, G. Serino, Design and retrofit of multistory frames with elastic-deformable viscous damping braces. *Journal of Earthquake Engineering*, **23**(9), 1441–1464, 2019.
- [4] D. Losanno, I.E. Madera Sierra, M. Spizzuoco, J. Marulanda, P. Thomson, Experimental performance of unbonded polyester and carbon fiber reinforced elastomeric isolators under bidirectional seismic excitation. *Engineering Structures*, **209**, 110003, 2020.
- [5] M.C. Constantinou, M.D. Symans, Seismic response of structures with supplemental damping. *The Structural Design of Tall Buildings*, **2**(2), 77–92, 1993.
- [6] M.C. Constantinou, T.T. Soong, G.F. Dargush, *Passive energy dissipation systems for structural design and retrofit*. MCEER Monograph No. 1, State University of New York, Buffalo, NY, USA, 1998.
- [7] M.D. Symans, F.A. Charney, A.S. Whittaker, M.C. Constantinou, C.A. Kircher, M.W. Johnson, R.J. McNamara, Energy dissipation systems for seismic applications: Current practice and recent developments. *Journal of Structural Engineering*, **134**(1), 3–21, 2008.
- [8] N. Vaiana, S. Sessa, F. Marmo, L. Rosati, Nonlinear dynamic analysis of hysteretic mechanical systems by combining a novel rate-independent model and an explicit time integration method. *Nonlinear Dynamics*, **98**(4), 2879–2901, 2019.
- [9] R. Bouc, Modele mathematique d’hysteresis. *Acustica*, **24**(1), 16–25, 1971.
- [10] Y.K. Wen, Method for random vibration of hysteretic systems. *Journal of the Engineering Mechanics Division*, **102**(2), 249–263, 1976.

- [11] N. Vaiana, S. Sessa, F. Marmo, L. Rosati, A class of uniaxial phenomenological models for simulating hysteretic phenomena in rate-independent mechanical systems and materials. *Nonlinear Dynamics*, **93**(3), 1647–1669, 2018.
- [12] N. Vaiana, S. Sessa, L. Rosati, A generalized class of uniaxial rate-independent models for simulating asymmetric mechanical hysteresis phenomena. *Mechanical Systems and Signal Processing*, **146**, 106984, 2021.
- [13] N. Vaiana, D. Losanno, N. Ravichandran, A novel family of multiple springs models suitable for biaxial rate-independent hysteretic behavior. *Computers and Structures*, **244**, 106403, 2021.
- [14] A.K. Chopra, *Dynamics of structures: Theory and applications to earthquake engineering*, 4th Edition. Prentice Hall, 2012.
- [15] S. Sessa, N. Vaiana, M. Paradiso, L. Rosati, An inverse identification strategy for the mechanical parameters of a phenomenological hysteretic constitutive model. *Mechanical Systems and Signal Processing*, **139**, 106622, 2020.
- [16] I. Nuzzo, D. Losanno, N. Caterino, Seismic design and retrofit of frame structures with hysteretic dampers: A simplified displacement-based procedure. *Bulletin of Earthquake Engineering*, **17**(5), 2787–2819, 2019.
- [17] I. Nuzzo, D. Losanno, F. Cilento, N. Caterino, Analytical and numerical modelling of shear-link device for seismic energy dissipation in frame structures. *Engineering Structures*, **214**, 110630, 2020.
- [18] I. Nuzzo, D. Losanno, N. Caterino, G. Serino, L.M. Bozzo Rotondo, Experimental and analytical characterization of steel shear links for seismic energy dissipation. *Engineering Structures*, **172**, 405–418, 2018.

SEISMIC PROTECTION OF CULTURAL HERITAGE ARTEFACTS BY MEANS OF ELASTOMERIC ISOLATORS: A CASE STUDY

**Davide Pellecchia¹, Stefania Lo Feudo², Nicolò Vaiana¹, Jean-Luc Dion², and
Luciano Rosati¹**

¹Department of Structures for Engineering and Architecture, University of Naples Federico II
via Claudio 21, 80125 Naples, Italy
davide.pellecchia@unina.it

² QUARTZ-SUPMÉCA – Institut Supérieur de Mécanique de Paris
3 rue Fernand Hainaut, 93407 Saint-Ouen, France
stefania.lofeudo@supmeca.fr

Keywords: Seismic Protection; Art Objects; Elastomeric Isolators; Lead Rubber Bearings; Hysteretic Model.

Abstract. *We investigate the rocking response of a Caryatid from the Erechtheion, modelled as a rigid body freestanding on an isolation system made of Lead Rubber Bearings. An efficient uniaxial phenomenological model belonging to a recently developed class is used to simulate the strongly nonlinear response typically exhibited by elastomeric devices. The algebraic nature of the proposed hysteretic model allows one to obtain the device restoring force by solving an algebraic equation, thus reducing the computational effort of the nonlinear dynamic analyses that have been carried out on the above-mentioned Caryatid statue. In order to establish the effective performances of the proposed isolation system the isolated and non-isolated rocking responses of the statue are derived and compared.*

1 INTRODUCTION

Nowadays the large majority of statues contained in museums are not equipped to resist oscillations induced by earthquakes. For this reason, seismic protection of artefacts belonging to the cultural heritage is a topic that has received significant interest over the last years [1, 2, 3, 4, 5, 6, 7, 8]. In particular, researchers focused on the study of the rocking behaviour of rigid bodies since the statues, which are simply supported on the floor or a pedestal, could overturn under seismic excitation. Moreover, their overturning and damage is potentially associated with significant human and economic losses [9, 10].

Base isolation represents one of the most adopted strategies for the seismic protection of artefacts belonging to the cultural heritage. In fact, such a technique has been used for the protection of some statues in Italy, such as the Riace bronzes exhibited in the Archaeological Museum in Reggio Calabria [11], the Dancing Satyr at the Dancing Satyr Museum in Mazara del Vallo, and the Imperatore Germanico at the Edilberto Rosa Museum in Amelia [12].

The most used isolation device - mostly for the seismic protection of buildings and bridges - are the Elastomeric and Sliding isolators. The formers provide energy dissipation by using an elastomeric material, whereas the latter display an energy dissipation capacity due to the friction damping occurring at the sliding interface. Both seismic isolation bearings display a force-transverse displacement relationship of hysteretic nature.

The dynamics of a base-isolated rigid body strictly depends on the interaction between the complex nonlinear behaviour of the isolation devices and the rocking behaviour of the rigid body. Consequently, it is very important to adopt a hysteretic model able to accurately predict the seismic isolators response.

In this paper, we investigate the rocking response of a Caryatid from the Erechtheion, modelled as a rigid body freestanding on an isolation system made of Lead Rubber Bearings, i.e. one of the most popular elastomeric isolators used in Civil Engineering applications.

The behaviour of the elastomeric devices is predicted by using an efficient uniaxial phenomenological model belonging to a recently developed class [13, 14, 15]. Since the model has an algebraic nature, the device restoring force is computed by solving an algebraic equation so that the numerical solution of a first-order nonlinear ordinary differential equation at each time step of the analysis is not required. Moreover, the model is based on a small set of parameters having a clear mechanical significance.

Nonlinear dynamic analyses are carried out on the above-mentioned Caryatid statue, with and without isolation, in order to establish the performance of the latter in protecting the analysed art object from seismic excitations.

2 SEISMICALLY ISOLATED RIGID BODY MODEL

The Caryatid from the Erechtheion under investigation has been modelled as a symmetric rigid body freestanding on an isolation system made of elastomeric bearings. We supposed that the friction between the statue and the isolated base is high enough to avoid the sliding.

The geometrical parameters of the model are shown in Fig. 1(a), namely the distance R between the centre of gravity and the centre of rotation, and the slenderness γ measured as the tilt angle relative to the vertical axis when the body is at rest. Their values are taken from a paper by Constantinides et al. [16] who studied the seismic response of six statues belonging to a collection shown at the University of California, Berkeley.

The Caryatid's mass m , equal to 3 172.05 kg, has been obtained supposing that the density of Caryatid's material is equal to 2 650 kg m⁻³. Hence, the Caryatid's fundamental angular

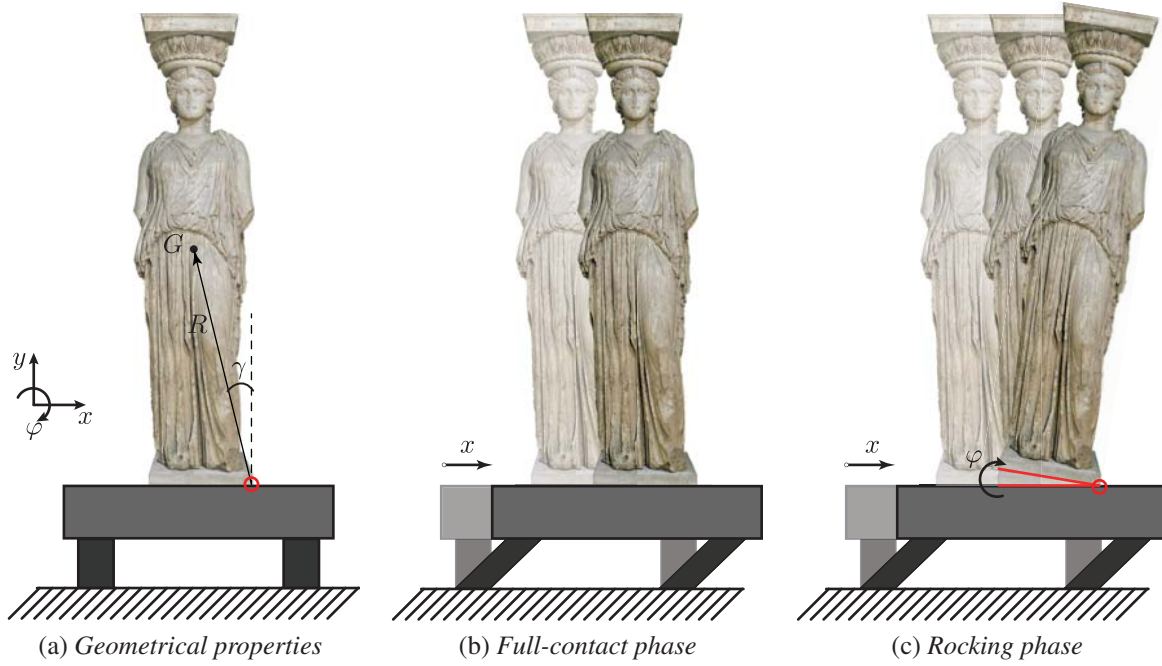


Figure 1: The Caryatid from the Erechtheion.

rocking frequency is given by

$$\omega_r = \sqrt{\frac{m g R}{J_O}} \approx 2.60 \text{ rad s}^{-1}, \quad (1)$$

where g is the gravity acceleration and J_O is the polar inertia around one of the two Caryatid's centre of rotation.

Finally, the mass of the isolated base m_b is supposed to equal to 212 kg.

2.1 Kinematic phases

There are two phases of motion that can occur, namely the full-contact and the rocking motion. The former is described by one degree of freedom, i.e. the horizontal movement of the base $x(t)$, whereas in the latter there are two degrees of freedom activated: one is the horizontal movement and the other measures the tilt angle of the body $\varphi(t)$.

The equations of motion change depending on the phase of motion that the rigid body undergoes.

2.2 The full-contact motion

In the full-contact phase, the Caryatid does not rock while the isolated base moves as shown in Fig. 1(b).

The equation of motion that describes this phase is

$$(m + m_b) (\ddot{x}_g + \ddot{x}) + n_d f = 0, \quad (2)$$

where \ddot{x}_g is the ground acceleration, n_d is the number of devices that support the isolated base and the statue, and f is the generalised restoring force of the elastomeric isolator.

2.3 The rocking motion

Fig. 1(c) illustrates the rocking motion. In this phase, the Caryatid rocks while the isolated base moves; thus there are two degrees of freedom activated.

By using the signum function $\text{sgn}(\cdot)$, as shown in [3], this phase can be described by just one set of two equations, regardless of the centre of rotation around which the Caryatid rocks. Hence, we have

$$m(\ddot{x}_g + \ddot{x} + \ddot{x}_\varphi) + m_b(\ddot{x}_g + \ddot{x}) + n_d f = 0, \quad (3)$$

$$J_O \ddot{\varphi} + m(\ddot{x}_g + \ddot{x}) R \cos(\text{sgn}(\varphi) \gamma - \varphi) = -m g R \sin(\text{sgn}(\varphi) \gamma - \varphi), \quad (4)$$

in which \ddot{x}_φ is the acceleration of the centre of mass relative to the ground. This acceleration depends on the rocking angle φ , since

$$x_\varphi = \text{sgn}(\varphi) R \sin(\gamma) - R \sin(\text{sgn}(\varphi) \gamma - \varphi). \quad (5)$$

Consequently, the second derivative with respect to the time of (5) is:

$$\ddot{x}_\varphi = R \sin(\text{sgn}(\varphi) \gamma - \varphi) \dot{\varphi}^2 + R \cos(\text{sgn}(\varphi) \gamma - \varphi) \ddot{\varphi}. \quad (6)$$

2.4 Collisions

As usual in the specialised literature, we assume that when the Caryatid collides with the isolated base, the linear (angular) momentum remains unchanged whereas the linear (angular) kinetic energy decreases. Accordingly, the angular and the linear coefficients of restitution obtained by the law of momentum conservation are [2]:

$$e_\varphi = 1 + \frac{2 R^2 \sin^2(\gamma) m}{R^2 \cos^2(\gamma) m \tilde{m} - J_O}, \quad (7)$$

and

$$e_x = \frac{2 R^4 \sin^2(\gamma) \cos^2(\gamma) m \tilde{m}}{R^2 \cos^2(\gamma) m \tilde{m} - J_O}, \quad (8)$$

where $\tilde{m} = m/(m + m_b)$.

3 LEAD RUBBER BEARINGS AND THEIR MATHEMATICAL MODEL

Elastomeric isolators are one of the most popular devices used for the protection of mechanical and civil systems from seismic events. They are characterised by layers of elastomeric materials and thin reinforcing elements. Elastomers provide energy dissipation and flexibility, whereas the reinforcing elements avoid the lateral expansion of the elastomer due to the axial compressive load.

In this Section, the main characteristics of Lead Rubber Bearings (LRBs) - one of the most used types of elastomeric isolators - are illustrated. In addition, the proposed hysteretic model, able to predict the complex hysteretic behaviour of such isolators, is described.

3.1 Lead Rubber Bearings

Lead Rubber Bearings have a circular or square transverse cross-section and are connected with the superstructure and the substructure by means of two steel plates bounded to the top and the bottom surfaces of the devices, see Fig. 2(a). Additionally, they are characterised by one or more lead cores that provide high values of horizontal stiffness and energy dissipation. In particular, the damping factor of such devices can reach a value up to $\xi \approx 15 \div 35\%$. Fig. 2(b) shows the typical hysteresis loop shape displayed by LRBs.

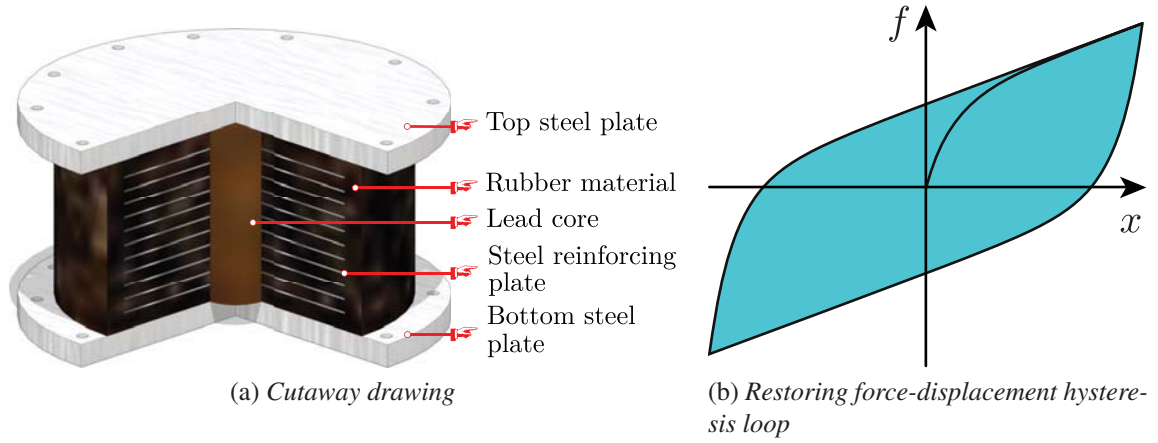


Figure 2: Lead Rubber Bearing.

3.2 Proposed hysteretic model

In this Section, we present the proposed hysteretic model able to predict the complex behaviour of the LRBs isolators. The accuracy and the computational efficiency of such a model have been demonstrated in previous papers [13, 17], by comparison with the celebrated Bouc-Wen model [18, 19]. In fact, the latter model requires the numerical solution of a differential equation to compute the restoring force of the device, what increases the overall computational effort. On the contrary, the proposed hysteretic model is of algebraic nature, i.e. the restoring force can be computed by means of algebraic equations; moreover, the model is based on just three constitutive parameters that can be calibrated from experimental tests [20] or by means of a design procedure described in [21].

Making reference to [22] for further details, the generic hysteresis loop is modelled by four types of curves, namely the upper (lower) limiting curve c_u (c_l) and the generic loading (unloading) curve c^+ (c^-), as shown in Fig. 3. The point of intersection between the upper (lower) limiting curve and the axis of ordinate is denoted as f_0 ($-f_0$). In addition, the starting and the ending points of the generic loading (unloading) limiting curve have abscissa x_i^+ and x_j^+ (x_i^- and x_j^-), respectively. The model assumes that the horizontal distance between the starting and the ending points for both loading and unloading curves is constant and equal to $2x_0$, where x_0 is an internal model parameter.

The restoring force in the generic loading case is equal to $f = c^+$ when $x_i^+ < x < x_j^+$ and $f = c_u$ when $x > x_j^+$; whereas $f = c^-$ when $x_j^- < x < x_i^-$ and $f = c_l$ when $x < x_j^-$.

The expressions of the upper (lower) and the loading (unloading) limiting curves used for predicting the hysteretic behaviour of LRBs are

$$c_u = k_b x + f_0, \quad (9)$$

$$c_l = k_b x - f_0, \quad (10)$$

and

$$c^+ = k_b x + (k_a - k_b) \left[\frac{(1 + x - x_j^+ + 2x_0)^{(1-\alpha)}}{1-\alpha} - \frac{(1 + 2x_0)^{(1-\alpha)}}{1-\alpha} \right] + f_0, \quad (11)$$

$$c^- = k_b x + (k_a - k_b) \left[\frac{(1 + x - x_j^- + 2x_0)^{(1-\alpha)}}{\alpha - 1} - \frac{(1 + 2x_0)^{(1-\alpha)}}{\alpha - 1} \right] - f_0, \quad (12)$$

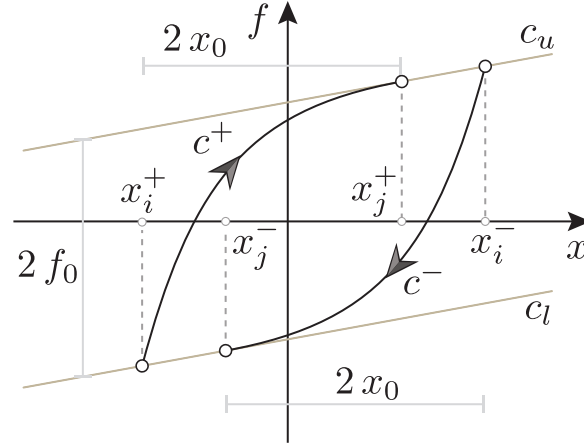


Figure 3: Proposed hysteretic model.

where k_a , k_b and α are the model's constitutive parameters. The mechanical significance of these parameters is illustrated in [22].

Finally, the internal model parameters x_0 and f_0 are computed as follows:

$$x_0 = \frac{1}{2} \left[\left(\frac{k_a - k_b}{\delta_k} \right)^{\frac{1}{\alpha}} - 1 \right], \quad (13)$$

$$f_0 = \frac{k_a - k_b}{2} \left[\frac{(1 + 2x_0)^{(1-\alpha)} - 1}{1 - \alpha} \right], \quad (14)$$

in which δ_k may be set equal to 10^{-20} , as shown in [13].

4 APPLICATION TO A CARYATID FROM THE ERECHTHEION

In this Section, we show the results obtained from some nonlinear time history analyses on the Caryatid from the Erechtheion described in Sec. 2. The East-West component of ground acceleration recorded at the AL011_DZC station during the Düzce earthquake (Turkey), that occurred on the 12th of November 1999, is used as seismic input. Such an acceleration, displayed in Fig. 4(a), has been taken from the Engineering Strong Motion (ESM) database [23]. The rocking response of the non-isolated Caryatid subjected to the above-mentioned acceleration is shown in Fig. 4(b). As a result, the Caryatid needs to be protected since, due to the assumed excitation, it overturns after approximately thirty-five seconds.

Firstly, we built the Caryatid's rocking spectrum when it is subjected to the Düzce earthquake acceleration, see Fig. 5(a), where T_r refers to the rocking period. We observe that the Caryatid is vulnerable to such an excitation when its rocking period is less than four seconds. Hence, the base isolation will be efficient if it increases the Caryatid rocking period above four seconds.

Fig. 5(b) shows the horizontal displacement spectrum referred to the isolated Caryatid with LRBs devices by increasing the viscous damping factor, where T_{bi} is the isolation period. This spectrum allows one to infer the isolation period and the equivalent viscous damping factor providing a displacement less than the device's maximum allowed displacement, x_{\max} .

Fig. 6 illustrates the time histories of the rocking angle (a) and displacement (b) of the base-isolated Caryatid characterised by the properties shown in Tab. 1(a). The adopted constitutive parameters of the model are shown in Tab. 1(b). Such parameters have been obtained from the design procedure described in [21].

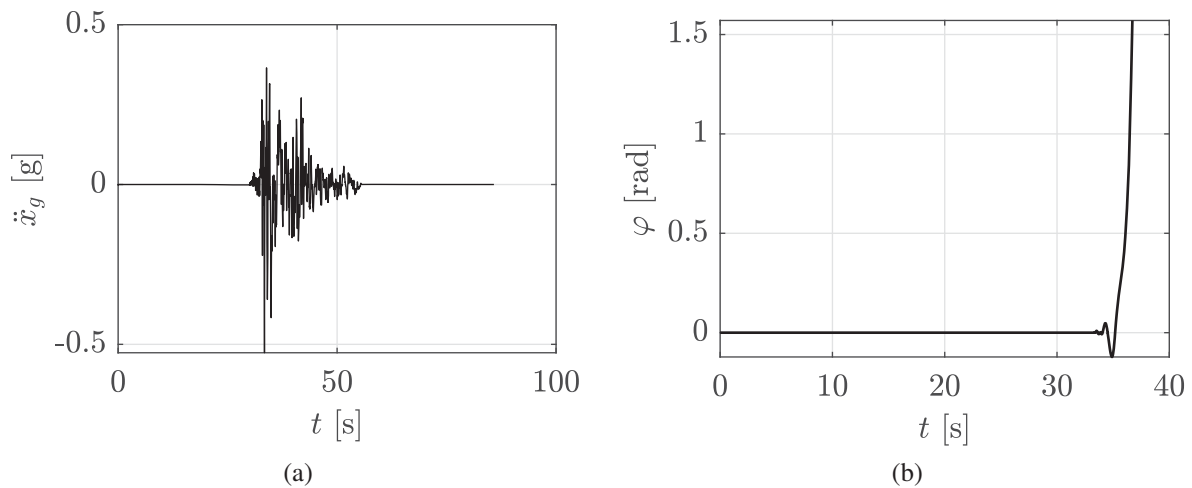


Figure 4: The East-West component of the Düzce earthquake acceleration recorded on the 12th of November 1999 (a); Non-isolated Caryatid's rocking response (b).

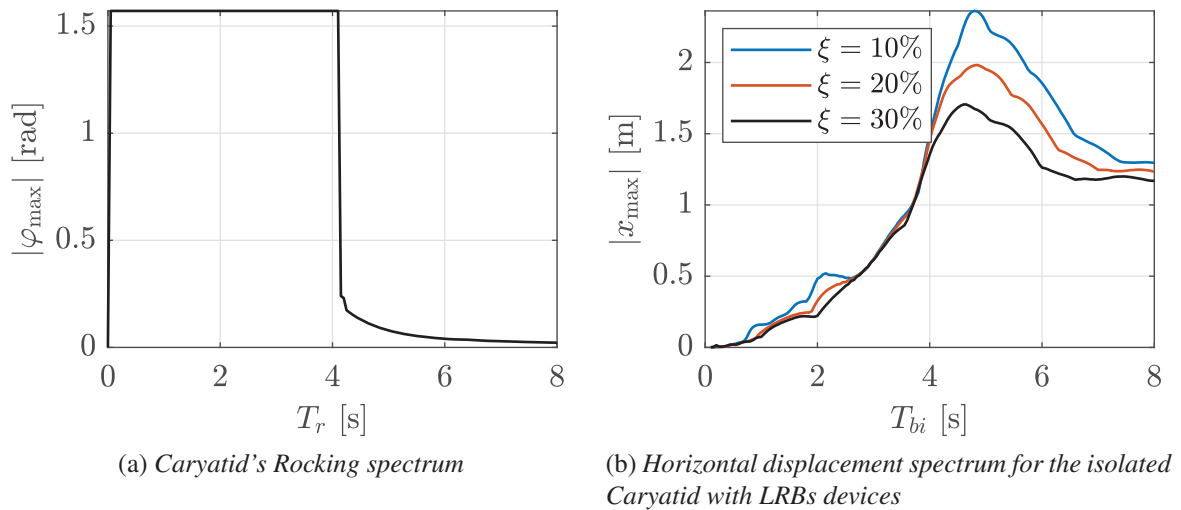


Figure 5: Response spectra obtained from the Düzce earthquake acceleration.

The results are very satisfactory, given that the base-isolated Caryatid does not rock, removing the possibility of damage due to collisions. Moreover, the attained displacements are much smaller than the device's maximum assumed displacement whose value is shown in Tab. 1(a).

Table 1: LRBs' properties (a); The model constitutive parameters of the model (b).

n_d [-]	T_{bi} [s]	x_{\max} [m]	ξ [%]	k_a [N m ⁻¹]	k_b [N m ⁻¹]	α [-]
4	2	0.30	30	6.22×10^4	6.22×10^3	44.69

(a)
(b)

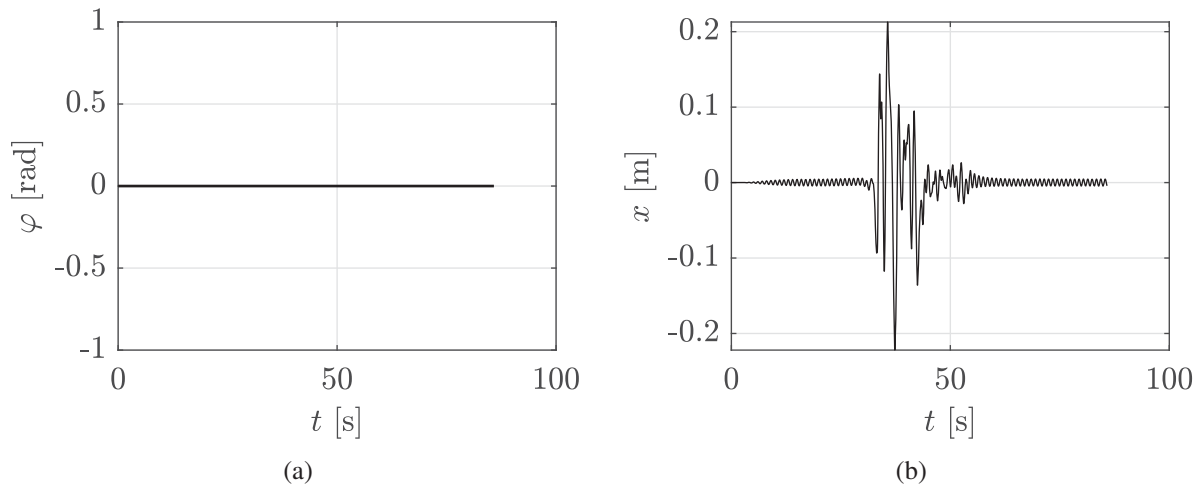


Figure 6: The rocking (a) and horizontal displacement (b) responses of the seismically base-isolated Caryatid.

5 CONCLUSIONS

The rocking behaviour of a Caryatid from the Erechtheion subjected to the 1999 Düzce earthquake (Turkey) has been investigated. After approximately thirty-five seconds the statue overturns. Consequently, a base isolation supported on four Lead Rubber Bearings as seismic protection system has been considered. We modelled the Caryatid object under study as a symmetric rigid body able to rock about one of the two bottom corners and assuming that sliding was prevented. Regarding the collisions, we applied the laws of conservation of linear and angular momentum in order to evaluate the angular and linear coefficients of restitution.

The complex hysteretic behaviour of the assumed elastomeric devices has been predicted by an innovative uniaxial phenomenological model of algebraic nature. As a consequence, the computational effort is drastically reduced, since there is no need to solve any differential equation to evaluate the device's restoring force as in the well-known Bouc-Wen model. In addition, the algebraic nature makes the model suitable for a design procedure able to provide the required constitutive parameters. The related procedure will be illustrated in a forthcoming paper [21].

Numerical assessments have been carried out on the Caryatid statue, with and without isolation. Firstly, we computed the rocking and horizontal displacement response spectra of the statue subjected to seismic excitation, in order to establish the isolation period and the device's maximum displacement to utilise. The results have shown that the Lead Rubber Bearings isolation system not only avoids overturning of the Caryatid, but it completely removes the rocking motion; hence, any kind of damage due to collision is avoided. Moreover, the horizontal displacements attained by the base-isolated are less than the maximum displacement allowed for the adopted device.

In future papers, further types of rate-independent hysteretic devices [24, 25, 26, 27, 28] will be employed to evaluate their capability in protecting rigid bodies from earthquake excitations.

REFERENCES

- [1] F. Vestroni, S. Di Cinto, Base isolation for seismic protection of statues. *Proceedings of 12th World Conference of Earthquake Engineering (WCEE 2000)*, Auckland, New

Zealand, 30 January - 4 February, 2000.

- [2] P. C. Roussis, E. A. Pavlou, E. C. Pisiara, Base-isolation technology for earthquake protection of art objects. *Proceedings of 14th World Conference on Earthquake Engineering (WCEE 2008)*, Beijing, China, October 12-17, 2008.
- [3] M. F. Vassiliou, N. Makris, Analysis of the rocking response of rigid blocks standing free on a seismically isolated base. *Earthquake Engineering & Structural Dynamics*, **41**(2), 177–196, 2012.
- [4] S. Sorace, G. Terenzi, Seismic performance assessment and base-isolated floor protection of statues exhibited in museum halls. *Bulletin of Earthquake Engineering*, **13**(6), 1873–1892, 2015.
- [5] S. Baggio, L. Berto, T. Favaretto, A. Saetta, R. Vitaliani, Seismic isolation technique of marble sculptures at the Accademia Gallery in Florence: numerical calibration and simulation modelling. *Bulletin of Earthquake Engineering*, **13**(9), 2719–2744, 2015.
- [6] A. Gesualdo, A. Iannuzzo, M. Monaco, F. Penta, Rocking of a rigid block freestanding on a flat pedestal. *Journal of Zhejiang University-SCIENCE A*, **19**(5), 331–345, 2018.
- [7] I. E. Kavvadias, L. Vasiliadis, A. Elenas, K. Koutsoupakis, Fragility assessment of base isolated free standing museum artifacts. *Proceedings of 6th Conference on Computational Methods in Structural Dynamics and Earthquake Engineering (COMPDYN 2019)*, Crete, Greece, 24–26 June, 2019.
- [8] D. Pellecchia, S. Sessa, N. Vaiana, L. Rosati, Comparative Assessment on the Rocking Response of Seismically Base-Isolated Rigid Blocks. *Procedia Structural Integrity*, **29**, 95–102, 2020.
- [9] D. D’Angela, G. Magliulo, E. Cosenza, Towards a reliable seismic assessment of rocking components. *Engineering Structures*, **230**, 111673, 2021.
- [10] G. Zuccaro, F. Dato, F. Cacace, D. de Gregorio, S. Sessa, Seismic collapse mechanisms analyses and masonry structures typologies: A possible correlation. *Ingegneria Sismica*, **34**(4), 121–149, 2017.
- [11] G. De Canio, Marble devices for the Base isolation of the two Bronzes of Riace: a proposal for the David of Michelangelo. *Proceedings of 15th World Conference on Earthquake Engineering (WCEE 2012)*, Lisbon, Portugal, September 24-28, 2012.
- [12] I. Calì, M. Marletta, On the mitigation of the seismic risk of art objects: case-studies. *Proceedings of 13th World Conference on Earthquake Engineering (WCEE 2004)*, Vancouver, British Columbia, Canada, August 1-6, 2004.
- [13] N. Vaiana, S. Sessa, F. Marmo, L. Rosati, A class of uniaxial phenomenological models for simulating hysteretic phenomena in rate-independent mechanical systems and materials. *Nonlinear Dynamics*, **93**(3), 1647–1669, 2018.
- [14] N. Vaiana, S. Sessa, L. Rosati, A generalized class of uniaxial rate-independent models for simulating asymmetric mechanical hysteresis phenomena. *Mechanical Systems and Signal Processing*, **146**, 106984, 2021.

- [15] N. Vaiana, D. Losanno, N. Ravichandran, A novel family of multiple springs models suitable for biaxial rate-independent hysteretic behavior. *Computers and Structures*, **244**, 106403, 2021.
- [16] M. Constantinides, N. Makris, S. G. Miller. *Seismic Response Analysis of Plaster Cast Sculptures on the University of California, Berkeley Campus, Report No. EERC 2003-07*. Earthquake Engineering Research Center, 2003.
- [17] N. Vaiana, S. Sessa, F. Marmo, L. Rosati, Nonlinear dynamic analysis of hysteretic mechanical systems by combining a novel rateindependent model and an explicit time integration method. *Nonlinear Dynamics*, **98**(4), 2879–2901, 2019.
- [18] R. Bouc, Modele mathematique d’hysteresis. *Acustica*, **24**(1), 16–25, 1971.
- [19] Y. K. Wen, Method for random vibration of hysteretic systems. *Journal of the Engineering Mechanics Division*, **102**(2), 249–263, 1976.
- [20] S. Sessa, N. Vaiana, M. Paradiso, L. Rosati, An inverse identification strategy for the mechanical parameters of a phenomenological hysteretic constitutive model. *Mechanical Systems and Signal Processing*, **139**, 106622, 2020.
- [21] D. Pellecchia, Elastomeric bearings-based isolation for seismic protection of art objects. *To be submitted*, 2021.
- [22] N. Vaiana, S. Sessa, F. Marmo, L. Rosati, An accurate and computationally efficient uniaxial phenomenological model for steel and fiber reinforced elastomeric bearings. *Composite Structures*, **211**, 196–212, 2019.
- [23] L. Luzi, G. Lanzano, C. Felicetta, M. C. D’Amico, E. Russo, S. Sgobba, F. Pacor, & ORFEUS Working Group 5. *Engineering Strong Motion Database (ESM) (Version 2.0)*. Istituto Nazionale di Geofisica e Vulcanologia (INGV), 2020.
- [24] D. Losanno, M. Spizzuoco, G. Serino, Optimal design of seismic isolation systems for simply supported bridges. *Earthquakes and Structures*, **7**(6), 969–999, 2014.
- [25] D. Losanno, H. A. Hadad, G. Serino, Seismic behavior of isolated bridges with additional damping under far-field and near fault ground motion. *Earthquakes and Structures*, **13**(2), 119–130, 2017.
- [26] D. Losanno, H. A. Hadad, G. Serino, Design charts for Eurocode based design procedure of elastomeric seismic isolation systems. *Soil Dynamics and Earthquake Engineering*, **119**, 488–498, 2018.
- [27] D. Losanno, M. Spizzuoco, A. Calabrese, Bidirectional shaking table tests of unbonded recycled rubber fiber reinforced bearings (RR-FRBs). *Structural Control and Health Monitoring*, e2386, 2019.
- [28] D. Losanno, I. E. Madera Sierra, M. Spizzuoco, J. Marulanda, P. Thomson, Experimental Performance of Unbonded Polyester and Carbon Fiber Reinforced Elastomeric Isolators under Bidirectional Seismic Excitation. *Engineering Structures*, **209**, 110003, 2020.

TUNING THE LATERAL RESPONSE OF UNBONDED FIBER REINFORCED ELASTOMERIC ISOLATORS (U-FREIS): EXPERIMENTAL – NUMERICAL FINDINGS

Simone Galano^{1,2}, Andrea Calabrese², Daniele Losanno¹

¹, Department of Structures for Engineering & Architecture, University of Naples Federico II
Napoli, via Claudio 21, Naples 80125, Italy
{simone.galano,daniele.losanno}@unina.it

², Department of Civil Engineering & Construction Engineering Management, California State University
Long Beach
Long Beach, CA, USA
{Simone.Galano,Andrea.Calabrese}@csulb.edu

Abstract

Fiber-reinforced elastomeric isolators (FREIs) are elastomeric devices which have been introduced as a low-cost alternative to the well-known steel-reinforced elastomeric isolators (SREIs). As common in rubber-based devices, the application of FREIs to lightweight structures is challenging: when the mass is limited, the resulting slender bearings tend to become unstable under large horizontal displacements. On the basis of numerical and experimental findings, this research work aims to demonstrate a simple to implement and low-cost approach to extend the application of FREIs to lightweight structures. The technique here discussed allows (i) to reduce the horizontal stiffness of FREIs, (ii) to increase the stability range of the bearings, and (iii) to obtain a desired hardening response for large lateral deformations, with no instability.

Keywords: seismic isolation, elastomeric isolators, fiber-reinforced elastomeric isolators, low-cost seismic isolation, finite element analysis.

1. INTRODUCTION

Fiber-reinforced elastomeric isolators (FREIs) are made by bonding together layers of elastomer and layers of carbon or glass fibers. These bearings were introduced as a low-cost alternative to common steel-reinforced elastomeric isolators (SREIs) [1]. Several studies have shown the advantages of using FREIs in common base isolation applications. In particular, it has been proved that FREIs can be made using a cold vulcanization process, which is less expensive than the vulcanization process used for SREIs [2]. With the same process it is possible to manufacture eco-friendly and low-cost devices using elastomeric layers of recycled rubber and readily available fiber fabrics [3, 4].

FREIs are generally used in unbonded applications (U-FREIs). In this configuration, the imposed shear load is transferred through friction [5]. U-FREIs show a unique rollover deformation when they are displaced under lateral loads ([1], [6]): the top and bottom sides of the bearings detach from the horizontal subgrades, while the lateral surfaces of the bearings rotate until they touch the horizontal plates [7]. Depending on the aspect ratio of the bearing and the applied axial load, the lateral response of a FREI can become unstable for a lateral displacement larger than half of its base ([8], [9]). Analytical models for the static and dynamic response of rubber bearings have been

proposed ([10, 11, 12, 13, 14]). But the challenging lateral response of the bearings has prompted several experimental ([15], [16], [17], [18], [19], [20]) and numerical studies ([21, 22]).

For elastomeric base isolation systems, the period of isolation is function of the applied vertical load ([23], [24]). Ideally, a rubber-based device should be flexible, stable under large lateral deformations, and should show hardening for very large displacements to contain the deformation of the bearing and to prevent damage. With this aim in mind, different geometric configurations have been tested, most of which have been obtained by creating vertical holes in FREIs to reduce their horizontal stiffness, with a minimal impact on the stability of the bearing under lateral loads ([25], [26], [27], [28]). A different concept for the modification of the response of U-FREIs is discussed in the present work. In particular, the effects of horizontal holes on the lateral response of rubber-based devices, introduced by the authors earlier [29], are discussed. Results of experimental and numerical analyses are presented to show that by changing the geometry of a FREI, it is possible to obtain:

- a controlled reduction of the horizontal stiffness.
- hardening under large lateral deformations.
- a wide range of stable response.

2. EXPERIMENTAL TESTS

2.1. Description of the tested samples

The bearings tested in this study were manufactured by Kirkhill Manufacturing Company, Downey, CA following Caltrans specifications [30]. As per specifications, laminated pads were made by bonding together elastomeric layers and fabric reinforcements. Each of the tested bearings was cut from a pad of bigger dimensions. Each sample was made by bonding 9 layers of neoprene to 8 layers of bidirectional glass fiber reinforcements.

A total of 4 bearings were tested; Table 1 gives an overview of the main geometric characteristics of the bearings. In Table 1: $2b$ is the side of the bearing perpendicular to the holes, $2a$ is the side parallel to the holes; $A = 4ab$ is the plan area of the bearing; H is its total height; $V = A \cdot H$ is the volume of the bearing; \emptyset is the diameter of the single hole; V_{holes} is the total volume of the holes.

Figure 1 is a schematic of the tested samples, with dimensions. The four samples have the same geometry (130(2a)x60(2b)x52(H) mm) and an increasing number of holes (0, 4, 12, 20).

Table 1: Description of the tested bearings.

N. test	Elastomer	Fabric	Modifies	2a [mm]	2b [mm]	A [mm ²]	H [mm]	V [mm ³]	n° holes	Ø holes [mm]	V _{holes} [mm ³]	V _{holes} /V	Name
[-]	[-]	[-]	[-]	[]	[]	[]	[]	[mm ³]	[-]	[mm]	[]	[mm ³]	[-]
1	Neoprene	Glass	Unmodified	130	60	7800	52	40560	0	6	0.0	0.00%	130x60 U
2	Neoprene	Glass	4 holes Ø6	130	60	7800	52	40560	4	6	67856	1.67%	130x60 4H
3	Neoprene	Glass	12 holes Ø6	130	60	7800	52	40560	12	6	20357	5.02%	130x60 12H
4	Neoprene	Glass	20 holes Ø6	130	60	7800	52	40560	20	6	33929	8.37%	130x60 20H

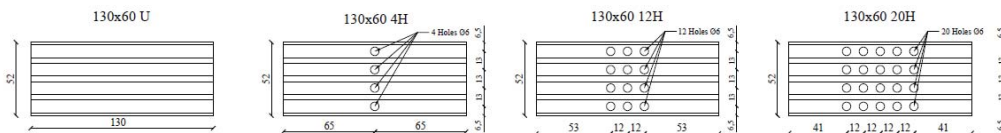


Figure 1: Bearing: a) 130x60 U, b) 130x60 4H, c) 130x60 12H, d) 130x60 20H. All the bearings have 52 mm height.

The holes are made using a drill press (Figure 2), while clamping the sample between two steel plates for alignment. As clear from Table 1, the percentage of removed volume is rather low, being always less than 10% of the total volume of the bearing.



Figure 2: Creation of the pattern of holes in a FREI.

2.2. Description of the tests

The shear tests were performed using the test frame shown in Figure 3a. and applying the quasi-static lateral displacement of Figure 3b (strain rate of 1%/s). During testing, a vertical load of 18.8 kN was imposed on the bearings. Additional information on the testing apparatus are available in literature [31].

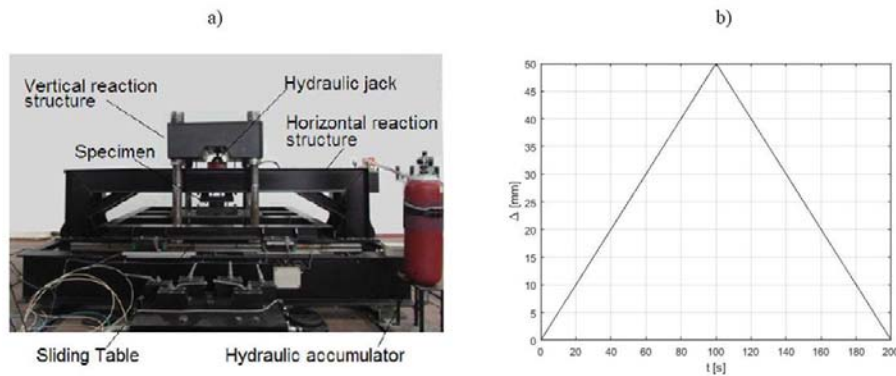


Figure 3: a) Testing frame, b) Time-history of the imposed lateral displacement.

2.3. Experimental test results

Figure 4 shows the deformed shape of the bearing during testing. Each column shows three different steps:

- Column 1 - full vertical load and zero lateral displacement.
- Column 2 - full vertical load at a shear deformation of 50%.
- Column 3 - full vertical load at a shear deformation of 100%.

The four rows of the Figure show the four test pieces described in Table 1: Description of the tested bearings. Table 1 (first row: no modification; last row: 20 holes). As intuition suggests, a greater vertical

deformation corresponds to a larger number of holes. Nevertheless, this variation is minor because of the very low volume of the rubber removed during drilling. All the samples show the onset of a stable roll-over deformation well before $\gamma_H = 50\%$.



Figure 4: Tested samples at $\gamma_H = 0\%$ with full compression, $\gamma_H = 50\%$ and $\gamma_H = 100\%$: a) 130x60 U, b) 130x60 4H, c) 130x60 12H, d) 130x60 20H

Figure 5 shows the horizontal force-displacement curves obtained from the experimental tests and the comparison between specimens with the same geometry (130x60x52 mm) and variable number of holes. As clear from this plot, while the peak horizontal load is substantially reduced by the holes, the curve of the bearing with 20 holes shows a positive tangent stiffness, with no instability of the rubber device. Table 2 reports the numerical value of the secant stiffness for each of the samples.

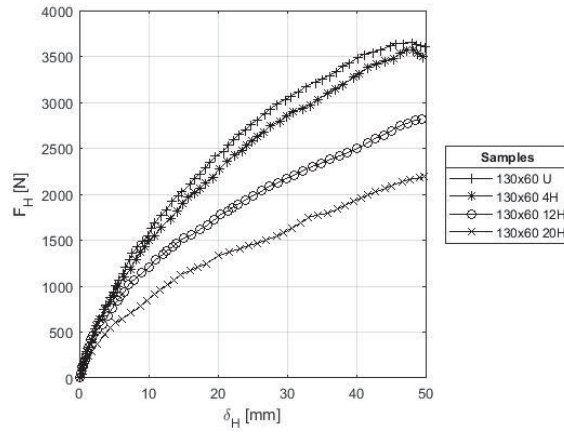


Figure 5: Lateral force displacement response of the tested bearings.

As clear from Figure 5, the sample 130x60 U (top line with + markers) shows a large initial stiffness, with an initial linear response. As the displacement increases past the initial deformation, the bearing shows softening and a peak of the response for a lateral deformation of 45 mm ($\gamma_H = 86\%$). A similar result is obtained for the sample with one column of holes (130x60 4H, second curve from the top). The curve differs very little from the one of the unmodified 130x60 U, which is not surprising considering the low percentage of removed volume (1.67%, see Table 1). The lateral secant stiffness differs no more than 7% from that of the unmodified sample (Table 2). Again, the response shows negative horizontal stiffness starting from a lateral displacement value of 48 mm ($\gamma_H = 96\%$) that is the peak of the lateral force. Compared to the bearing with no holes, an improvement in the lateral response of the sample with 4 holes is evident, as this device has a large range of stable deformations. Because the peak of the response was reached during testing, by increasing the lateral displacement, the bearing 130x60 4H would show instability. By increasing the number of holes, the lateral response of the sample changes significantly. For the bearing with 20 holes, the lateral stiffness is largely reduced. In general, the reduction of stiffness is proportional to the percentage of volume removed from the sample (Table 2).

Table 2: Lateral secant stiffness at different imposed deformations, for the tested bearings.

Δ [mm]	130x60 U		130x60 4H		130x60 12H		130x60 20H	
	K_H		K_H	$1 - \%K_H^U$	K_H	$1 - \%K_H^U$	K_H	$1 - \%K_H^U$
	[N/mm]		[N/mm]	[N/mm]	[N/mm]	[N/mm]	[N/mm]	[N/mm]
5	200		188	6.20%	159	20.5%	124	37.9%
10	156		150	3.52%	118	23.9%	91	41.5%
15	136		128	5.44%	104	23.6%	77	43.0%
20	122		114	6.51%	87	29.0%	67	45.1%
25	111		103	7.30%	79	29.1%	58	47.9%
30	102		97	5.03%	73	27.8%	54	46.9%
35	93		87	6.50%	66	29.7%	51	45.3%
40	87		83	4.22%	63	27.7%	48	44.5%
45	81		77	4.27%	60	25.8%	47	41.7%
50	72		71	1.37%	55	23.2%	43	40.1%

For the bearing with 20 holes, the most significant improvement concerns the overall response of the sample: as can be seen in Figure 5, when the lateral displacement increases, the response remains stable. The bearing shows no softening and the lateral stiffness is always positive: by creating holes in a bearing, it is possible to modify an unstable device to obtain a stable response. This modification of the response is only possible when a larger volume of rubber is removed. If the volume of removed rubber is less than 5%, the modification of the response is not appreciable. Figure 6 is a plot of the tangent stiffness of each bearing as function of the imposed deformation. As clear from the figure, the first two samples show a softening response with a stable peak around 25 mm of lateral displacement ($\gamma_H = 50\%$); for the unmodified sample, the tangent stiffness then becomes negative around 45 mm as mentioned above, while the sample with 4 holes shows a negative tangent stiffness for large deformation. The samples with 12 and 20 holes, show a decreasing stiffness up to $\gamma_H \approx 65\%$, with hardening past this level of deformation.

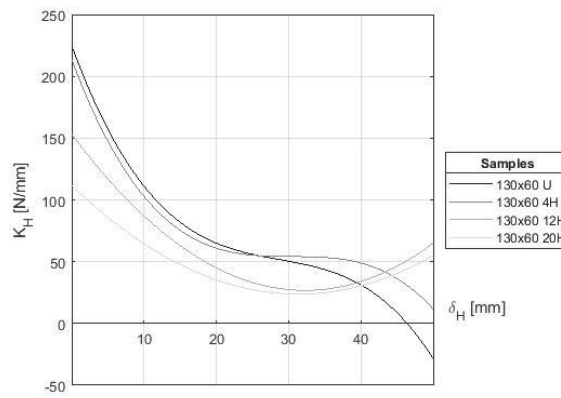


Figure 6: Tangent stiffness vs imposed displacement for the tested devices.

3. FINITE ELEMENT ANALYSIS

3.1. Analysis setting

The numerical analysis were performed using MSC Marc [32], a general-purpose finite element analysis software. Marc is designed to perform complex non-linear analyses in one, two or three dimensions. This characteristic, combined with the ability to perform complex contact analyses at large strains and the wide choice of hyperelastic material models suitable for elastomers, makes MARC a good choice for numerical analysis of rubber-based devices such as FREIs. Two-dimensional plain strain analyses were used for this study. In all the FEAs, the elastomer was modeled using a Neo-Hookean hyperelastic material fully defined by two constants C_1 and C_2 , where [33]:

$$C_1 = \frac{G}{2} \quad (3.1)$$

$$C_2 = \frac{\lambda}{2} = \frac{K}{2} - \frac{G}{3} = \frac{K}{2} - \frac{2C_1}{3}$$

with K being the bulk modulus of the rubber. The fiber reinforcement layers were modeled using a linear elastic material. The layers are fully defined by three parameters: the elastic modulus E_f , the Poisson's ratio ν_f and the equivalent thickness of the fiber layer t_f . All the parameters used for FEAs are detailed in Table 3.

Table 3: Parameters of the numerical model defined in MARC.

C_1	C_2	E_f	ν_f	t_f
[MPa]	[MPa]	[MPa]	[-]	[mm]
0.55	1000	70000	0.1	0.1

The elastomeric layers were modeled using a four-node, isoparametric, quadrilateral element, written for plane strain incompressible applications [34]. The reinforcement layers were modeled using an isoparametric, plane strain, 2-node element [34]. The top and bottom supports were modeled using rigid contact lines. The interface between the bearing and the rigid supports has been set as "contact" in MARC with a friction coefficient of 1 ([5], [6]).

3.2.FEA results: lateral load-displacement curves

Figure 7a shows the horizontal force-displacement curves obtained from FEAs. As clear from Table 4, the variations of horizontal stiffness when holes are made in the bearings are the same as those obtained from the experimental tests (see Table 2). The FEAs results are consistent with the experimental findings. Starting from the basic 130x60 geometry, the horizontal stiffness is reduced on by 6%, 27% and 45%, by drilling 4 holes on one column, 12 holes on three columns and 20 holes on 4 columns respectively.

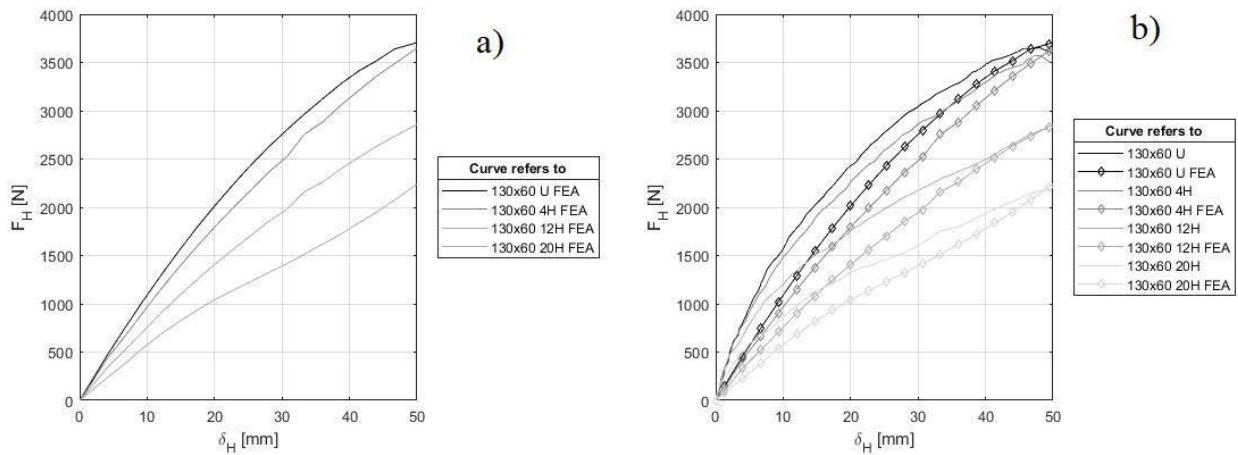


Figure 7: Lateral load-displacement curves: a) 130x60 FEA with variable number of holes, b) comparison of experimental vs FEAs results.

Figure 7a, shows a FEAs response of the bearing similar to that determined with experimental tests.

From the lateral response, it is clear that the stable range for bearing 130x60 12H is larger than that of bearing 130x60 U, as the latter reaches a peak of the response for a displacement of only 50mm. Moreover, the bearing with 20 holes shows hardening, with no softening.

Table 4: Lateral secant stiffness at different imposed displacements from FEAs.

130x60 U							
Δ	FEA	130x60 4H FEA		130x60 12H FEA		130x60 20H FEA	
[mm]	K_H	K_H	$1-\%K_H^U$	K_H	$1-\%K_H^U$	K_H	$1-\%K_H^U$
	[N/mm]	[N/mm]	[N/mm]	[N/mm]	[N/mm]	[N/mm]	[N/mm]
5	92	85.23	7.0%	66.82	27.1%	46.06	49.8%
10	102	90.54	11.5%	70.99	30.6%	54.09	47.1%

15	103	91.57	11.1%	71.79	30.3%	54.17	47.4%
20	101	89.71	10.9%	70.34	30.1%	52.13	48.2%
25	89	79.59	10.7%	62.40	30.0%	45.49	49.0%
30	87	78.80	9.9%	61.78	29.4%	44.15	49.5%
35	85	78.81	7.0%	61.79	27.1%	43.25	49.0%
40	82	76.35	6.8%	59.86	26.9%	42.96	47.6%
45	78	74.60	4.6%	58.49	25.2%	43.27	44.6%
50	74	72.31	2.1%	56.69	23.2%	44.14	40.2%

3.3.FEA results: stress distribution in the bearings

Figure 8 shows the Von Mises stress contours at three levels of lateral deformation for each of the tested bearings. From left to right, a snapshot is given for $\gamma_H = 0$, $\gamma_H = 50\%$ and $\gamma_H = 100\%$ under the same axial load of 18 kN. As clear from Figure 8, the holes change the stress distribution in the device, with the bearing becoming mostly unloaded in the central area, with a large increase of stress in the confined regions of the elastomer. Compared to the unmodified bearing, under pure compression and zero lateral displacement, there is an increase in peak stress in the bearings with 12 holes and 20 holes. These devices show an increase of stress of 27% and 42% respectively.

Under large lateral displacements, as the holes in the bearings tend to collapse under the imposed deformation, a stress redistribution happens. For the bearing with one column of holes, at $\gamma_H = 100\%$, the stress level is very similar to that of the unmodified device (Figure 8c, Figure 8f), with a difference of only 3%. The percentage of removed volume with a single column of holes is too low to induce significant changes in the lateral response of the device. By removing at least 5% of the initial volume, a controlled reduction of the initial stiffness at low deformations can be obtained. Due to the presence of the holes, a redistribution of the stresses at the edge of the bearing is induced. Under large imposed deformations, the small holes created in the samples collapse on themselves, with the bearing showing hardening.

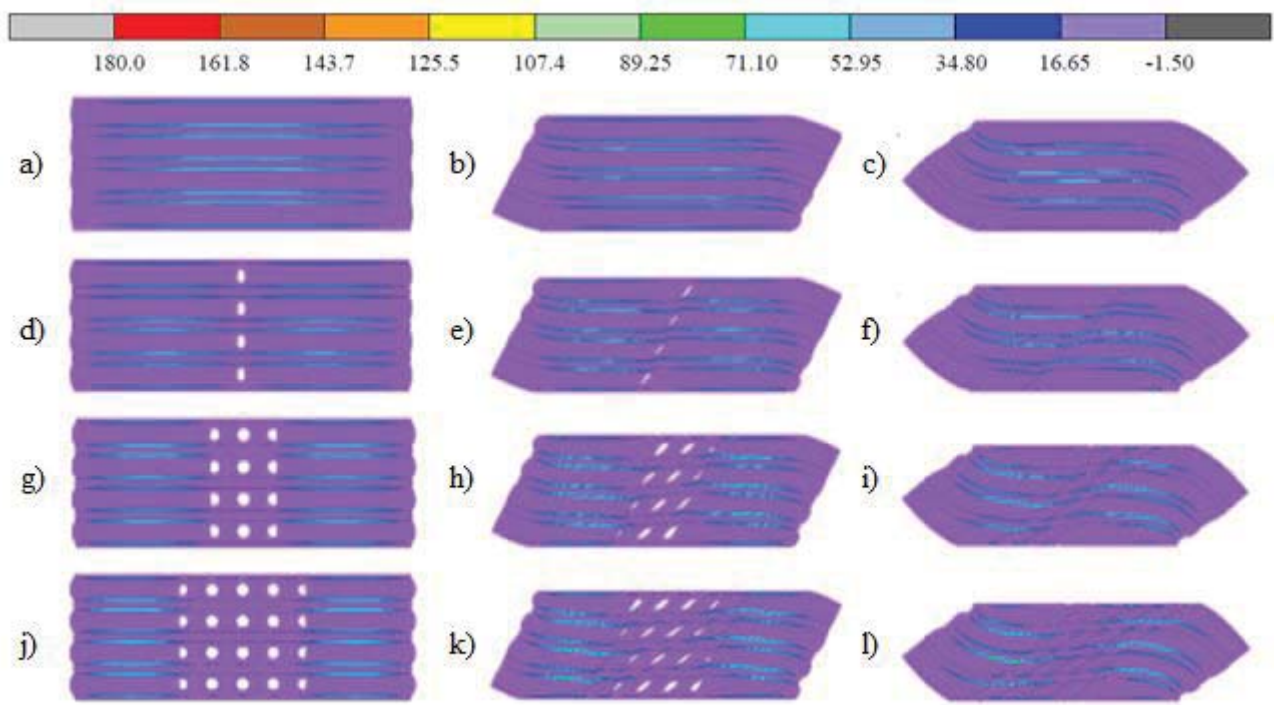


Figure 8: Equivalent Von Mises stresses: a) compression and zero lateral displacement, 130x60 U; b) 50% γ 130x60 U; c) 100% γ 130x60 U; d) compression and zero lateral displacement, 130x60 4H; e) 50% γ 130x60 4H; f) 100% γ 130x60 4H; g) compression and zero lateral displacement, 130x60 12H; h) 50% γ 130x60 12H; i) 100% γ 130x60 12H; j) compression and zero lateral displacement, 130x60 20H; k) 50% γ 130x60 20H; l) 100% γ 130x60 20H.

4. CONCLUSIONS

This study aims to introduce a new rubber-based technology for base isolation of lightweight structures. Experimental and FEAs show that it is possible to obtain an improvement in the response of FREIs by creating simple patterns of holes in the elastomer. It was found that by removing at least 5% of the initial volume of rubber an improvement in the lateral response of the device can be obtained, to get:

- i. a controlled reduction of the horizontal stiffness (6%, 27% and 45% reduction with 4, 12 and 20 holes respectively),
- ii. an extension of the stable range of deformation of the bearing. With imposed deformations up to $\gamma_H = 100\%$, the bearing always showed a positive horizontal stiffness. Devices which are unstable beyond a deformation of $\gamma_H \approx 90\%$ show a larger stable range when modified with lateral holes.

FEAs confirmed the experimental results. The stress analysis of the bearing helps understanding the behavior of the modified FREIs under combined axial and shear loads. As the number of holes (columns of holes) increases, the area close to the holes becomes stress free. Under large imposed deformations, the small holes created in the bearing collapse, and a redistribution of stresses occurs in the device. Additional studies are needed to investigate the effect of the aspect ratio of the bearing, of different materials and geometries on the lateral and vertical response of the devices when pattern of holes of different sizes and shapes are created.

5. REFERENCES

- [1] J. M. Kelly, "Analysis of Fiber-Reinforced Elastomeric Isolators," *Journal of Seismology and Earthquake Engineering*, vol. 2, no. 1, 1999.
- [2] B. Y. Moon, G. J. Kang, B. S. Kang and J. M. Kelly, "Design and manufacturing of fiber reinforced elastomeric isolator for seismic isolation," *Journal of Materials Processing Technology*, vol. 130, no. 131, pp. 145-150, 2002.
- [3] A. Calabrese, D. Losanno, M. Spizzuoco, S. Strano and M. Terzo, "Recycled Rubber Fiber Reinforced Bearings (RR-FRBs) as base isolators for residential buildings in developing countries: The demonstration building of Pasir Badak, Indonesia," *Engineering Structures*, no. 192, pp. 126-144, 2019.
- [4] D. Losanno, A. Calabrese, I. E. Madera Sierra, M. Spizzuoco, J. Marulanda, P. Thomson and G. Serino, "Recycled Versus Natural-Rubber Fiber-Reinforced Bearings For base Isolation: Review of the Experimental Findings," *Journal of Earthquake Engineering*, 2020.
- [5] J. M. Kelly and D. Konstantinidis, "Effect of Friction on Unbonded Elastomeric Bearings," *Journal of Engineering Mechanics*, vol. 135, no. 9, pp. 953-960, 2009.
- [6] H. Toopchi-Nezhad, M. J. Tait and R. G. Drysdale, "Testing and modeling of square carbon fiber-reinforced elastomeric seismic isolators," *Structural Control and Health Monitoring*, vol. 15, pp. 876-900, 2007.
- [7] H. Toopchi-Nezhad, M. J. Tait and R. G. Drysdale, "Bonded versus unbonded strip fiber reinforced elastomeric isolators: Finite element analysis," *Composite Structures*, vol. 93, pp. 850-859, 2011.
- [8] J. M. Kelly and A. Calabrese, "Mechanics of fiber reinforced bearings," PEER Report 101, Pacific Earthquake Engineering Research Center, College of Engineering, University of California Berkeley, 2012.
- [9] N. C. Van Engelen, M. J. Tait and D. Konstantinidis, "Model of the Shear Behavior of Unbonded Fiber-Reinforced Elastomeric Isolators," *Journal of Structural Engineering*, vol. 141, no. 7, 2015.
- [10] N. Vaiana, R. Capuano, S. Sessa, F. Marmo and L. Rosati, "Nonlinear dynamic analysis of seismically base-isolated structures by a novel OpenSees hysteretic material model," *Applied Sciences*, vol. 11, no. 3, p. 900, 2021.
- [11] N. Vaiana, D. Losanno and N. Ravichandran, "A novel family of multiple springs models suitable for biaxial rate-independent hysteretic behavior," *Computers & Structures*, vol. 244, p. 106403, 2021.
- [12] N. Vaiana, S. Sessa and L. Rosati, "A generalized class of uniaxial rate-independent models for simulating asymmetric mechanical hysteresis phenomena," *Mechanical Systems and Signal Processing*, vol. 146, p. 106984, 2021.
- [13] N. Vaiana, S. Sessa, M. Paradiso, F. Marmo and L. Rosati, "An efficient computational strategy for nonlinear time history analysis of seismically base-isolated structures," in *Proceedings of XXIV AIMETA Conference 2019*, 2019.
- [14] F. Marmo, S. Sessa, N. Vaiana, D. De Gregorio and L. Rosati, "Complete solutions of three dimensional problems in transversely isotropic media," *Continuum Mechanics and Thermodynamics*, vol. 32, no. 3, pp. 775-802, 2020.

- [15] D. Losanno, I. E. Madera Sierra, M. Spizzuoco, J. Marulanda and P. Thomson, "Experimental performance of unbonded polyester and carbon fiber reinforced elastomeric isolators under bidirectional seismic excitation," *Engineering Structures*, no. 209, 2020.
- [16] D. Losanno, F. Palumbo, A. Calabrese, T. Barrasso and N. Vaiana, "Preliminary investigation of aging effects on Recycled Rubber Fiber Reinforced Bearings (RR-FRBs)," *Journal of Earthquake Engineering*, 2021.
- [17] D. Losanno, I. E. Sierra Madera, M. Spizzuoco, J. Marulanda and P. Thomson, "Experimental assessment and analytical modeling of novel fiber-reinforced isolators in unbounded configuration," *Composite Structures*, no. 212, pp. 66-82, 2019.
- [18] D. Losanno, N. Ravichandran, F. Parisi, A. Calabrese and G. Serino, "Seismic performance of a Low-Cost base isolation system for unreinforced brick Masonry buildings in developing countries," *Soil Dynamics and Earthquake Engineering*.
- [19] D. Losanno, M. Spizzuoco and A. Calabrese, "Bidirectional shaking-table tests of unbonded recycled-rubber fiber-reinforced bearings (RR-FRBs)," *Wiley*, 2019.
- [20] I. E. Madera Sierra, D. Losanno, S. Strano, J. Marulanda and P. Thomson, "Development and experimental behavior of HDR seismic isolators for low-rise residential buildings," *Engineering Structures*, no. 183, pp. 894-906, 2019.
- [21] A. Calabrese, M. Spizzuoco, S. Galano, N. Tran, S. Strano and M. Terzo, "A Parametric Study on the Stability of Fiber Reinforced Rubber Bearings Under Combined Axial and Shear Loads," *Engineering Structures*, vol. 227, p. 111441, 2020.
- [22] S. Galano, D. Losanno and A. Calabrese, *Stability Analysis of Unbonded Fiber Reinforced Isolators of Square Shape*, In proceeding, 2020.
- [23] F. Naeim and J. M. Kelly, *Design of seismic isolated structures*, John Wiley & Sons, Inc., 1999.
- [24] J. M. Kelly and D. Konstantinidis, *Mechanics of Rubber Bearings for Seismic Isolation and Vibration Isolation*, John Wiley and Sons, Ltd, 2011.
- [25] N. C. Van Engelen, M. J. Tait and D. Konstantinidis, "Vertical response behaviour of stable unbonded fiber reinforced elastomeric isolators (SU-FREIs) with holes in the loaded surface," in *Canadian society for civil engineering annual general conference*, Edmonton, Canada, 2012.
- [26] N. C. Van Engelen, M. J. Tait and D. Konstantinidis, "Horizontal Behaviour of Stable Unbonded Fiber Reinforced Elastomeric Isolators (SU-FREIs) with Holes," in *World Conference on Earthquake Engineering*, Lisboa, 2012.
- [27] N. C. Van Engelen, P. M. Osgooei, M. J. Tait and D. Konstantinidis, "Experimental and finite element study on the compression properties of Modified Rectangular Fiber-Reinforced Elastomeric Isolators (MR-FREIs)," *Engineering Structures*, no. 74, pp. 52-64, 2014.
- [28] P. M. Osgooei, N. C. Van Engelen, D. Konstantinidis and M. J. Tait, "Experimental and finite element study on the lateral response of modified rectangular fiber-reinforced elastomeric isolators (MR-FREIs)," *Engineering Structures*, no. 85, pp. 293-303, 2015.

- [29] C. Tran, A. Calabrese, M. F. Vassiliou and S. Galano, "A simple strategy to tune the lateral response of unbonded Fiber Reinforced Elastomeric Isolators (FREIs)," *Engineering Structures*, no. 222, pp. 111-129, 2020.
- [30] Caltrans, Caltrans Standard Plans, State of California: California Department of Transportation, 2018.
- [31] G. Palli, S. Strano and M. Terzo, "A novel adaptive-gain technique for high-order sliding-mode observers with application to electro-hydraulic systems," *Mechanical Systems and Signal Processing*, no. 106875, 2020.
- [32] MSC.Software Corporation, Volume A: Theory and User Information, Santa Ana, CA, USA, 2017.
- [33] MSC.Software Corporation, MAR103 Experimental Elastomer Analysis, Santa Ana, CA, USA, 2017.
- [34] MSC.Software Corporation, Volume B: Element Library, Santa Ana, CA, USA, 2017.

ON THE VERTICAL RESPONSE OF FIBER REINFORCED ELASTOMERIC ISOLATORS (FREIs) UNDER COMBINED VERTICAL AND LATERAL LOADING

Simone Galano^{1,2}

¹, Department of Structures for Engineering & Architecture, University of Naples Federico II
Napoli, via Claudio 21, Naples 80125, Italy
simone.galano@unina.it

², Department of Civil Engineering & Construction Engineering Management, California State University
Long Beach,
Long Beach, CA, USA
Simone.Galano@csulb.edu

Abstract

The vertical behavior of Fiber Reinforced Elastomeric Isolators (FREIs) is controlled by geometric and mechanical parameters, such as primary and secondary shape factors, shear modulus of the rubber and effective compressive modulus of the rubber-reinforcements compound. Several studies dealt with the vertical properties of the bearings, deriving analytical formulations in function of the bearing geometry and materials' properties. These relations have been derived under pure compression, considering the interaction between single rubber layers and flexible reinforcements. As of today, few works have been proposed on the influence of the horizontal displacement imposed on the bearing, i.e. no interaction between vertical pressure and horizontal displacement on the vertical stiffness and the compressive modulus has been accounted for. In this paper, a numerical study on the influence of the primary and secondary shape factor, the shear modulus of the rubber and the vertical pressure on the vertical properties of the FREIs is presented. In a first stage the behavior of square shaped FREIs under pure compression is examined and relative outcomes are presented. Then the influence of the horizontal displacement on the vertical response of the bearings is considered. Interesting results on the trend of the vertical stiffness and compressive modulus are obtained and useful considerations on the stability of FREIs are provided.

Keywords: Fiber-Reinforced Elastomeric Isolators, Vertical Properties, Elastomeric Seismic Isolators, Rubber bearings, Seismic Isolation.

1. INTRODUCTION

Fiber-reinforced elastomeric isolators (FREIs) were introduced as alternative seismic isolation devices to steel-reinforced elastomeric isolators (SREIs). Several advantages in cost and manufacturing result replacing steel reinforcements with fiber fabrics such as:

- Fiber fabrics are much lighter than steel, despite having similar elastic mechanical properties. With the same volume of reinforcement, fiber-reinforced bearings are therefore lighter than steel-reinforced ones [1].
- Fiber-reinforced bearings can be produced in a cheaper and faster manufacturing process, i.e. cold vulcanization process [2].

- From larger sized pads, it would be possible to cut bearings of the required size and different shapes (i.e. strip-shaped) [1, 3, 4].

Using fiber-reinforced bearings in unbonded configuration, i.e. allowing the marginal areas of the bearing to detach from the supports during horizontal displacement resulting in the rollover deformation, further advantages can be achieved.

- As the marginal portions of the bearing gradually detach from the supports during horizontal displacement, the contact area reduces and consequently the lateral stiffness of the bearing, increasing the efficiency of the isolation system [5].
- The tensile stresses that would develop in the marginal area of the bearing in bonded configuration are greatly reduced when these marginal portions can detach from the supports [6].
- The rollover deformation proceeds until the initial vertical faces of the bearing fully touch the supports becoming horizontal and increasing the lateral stiffness of the bearing. As this occurs at large deformations, the isolation system acquires greater stability at large displacements [5, 6].

The response of fiber reinforced elastomeric isolators has been studied in several works. Analytical formulations for vertical ([1, 7, 8, 9]) and horizontal stiffness ([10, 11, 12, 13]) have been proposed, and a number of other studies have investigated the mechanical properties of bearings through experimental tests ([4, 3, 14, 15, 16, 17, 18, 19, 20, 21]) and finite element analysis ([22, 23, 24, 25]). Furthermore, analytical models for static and dynamic response have been proposed ([26, 27, 28, 29, 30]).

The vertical stiffness of an elastomeric bearing is primarily controlled by two parameters [31]: primary shape factor S_1 (defined as the ratio between the loaded area and the area free to bulge) and effective compressive modulus E_c (defined as the instantaneous elastic modulus of the rubber-reinforcements compound). The lateral response of an unbonded FREIs can be stable or unstable (Figure 1). In the first case, the bearing shows a positive tangent lateral stiffness throughout the lateral deformation; in the second case the horizontal tangent stiffness of the bearing could decrease until becoming equal or less than zero. The horizontal response is mainly controlled by the secondary shape factor [32], that is the ratio between the base side in the horizontal displacement direction and the total height of the bearing ($S_2 = B / H$). Current codes require stable behavior to bearings [33, 34, 35], i.e. a sufficiently high secondary shape factor. Several experimental and numerical studies have shown that a stable behavior is ensured if S_2 is at least equal to 2.5 [36, 37, 36, 38].

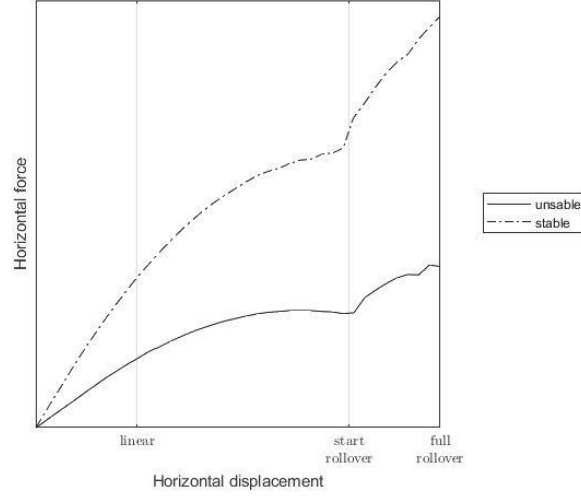


Figure 1: Stable vs unstable lateral behavior of U-FREIs under combined axial and shear load.

Elastomeric bearings require larger vertical stiffness than horizontal one (e.g. at least two order of magnitude) to support the weight of the superstructure and avoid potential rocking motions [39, 31]. Comparing the vertical stiffness under pure compression and the secant horizontal stiffness of a generic bearing with a sufficiently large primary shape factor, this requirement is easily met. However, during the rollover of the lateral displacement, the contact area between the bearing and the supports is reduced, which also reduces the vertical stiffness of the bearing. It is therefore necessary to take this reduction into account when comparing vertical and horizontal stiffness. In a safety evaluation, the vertical and horizontal stiffnesses could be compared at a given level of horizontal displacement.

However, few studies have considered the reduction of vertical stiffness with increasing horizontal displacement [40] and there is a lack of knowledge on the influence of the main geometric and mechanical parameters on the interaction between vertical and horizontal response. This work proposes a large number of finite element analysis on square shaped FREIs, varying different mechanical and numerical parameters. The influence of the primary and secondary shape factor on the combined vertical and horizontal response is taken into account.

2. FINITE ELEMENT ANALYSIS: OVERVIEW

Several different values for two combinations of geometric and mechanical parameters were considered:

- Geometric: base dimensions $B = 2a = 2b$ and thickness of the elastomeric layers t_e ;
- Mechanical: shear modulus G of the elastomer and vertical applied pressure σ_v .

In addition, four parameters were also kept constant: the total height of the bearing $H = nt_e + (n-1)t_f$, the equivalent thickness of the fiber reinforcement t_f , Young's modulus E_f of the fiber fabric and its Poisson's ratio ν_f . All the considered parameters are listed in Table 1. By permuting the parameters shown in Table 1, a total of 240 numerical models were obtained, with 9 different secondary shape factors, ranging from 1 to 5, and 16 primary shape factors, from 5 to 62.5.

Table 1: Variable parameters considered in the finite element analysis.

$2a = 2b = B$	H	t_e	G	σ_v	E_f	t_f	ν_f
[mm]	[mm]	[mm]	[MPa]	[MPa]	[MPa]	[mm]	[-]
100	100	2	0.4	2	70000	0.1	0.1
150		5	0.8	4			
200			1.2	6			
250				8			
300							
350							
400							
450							
500							

All the finite element analyses were carried out using MSC Marc [41], a general purpose FEA software optimized for non-linear analyses. This software allows careful modeling of nonlinear behavior, with a wide choice of hyperelastic material models for elastomers.

The elastomer was modeled using a Neo-Hookean hyperelastic material. When the compressibility of the elastomer is taken into account, the strain energy density function can be obtained as [42]:

$$W = C_1(I_1 - 3 - 2 \ln J) + C_2(J - 1)^2 \quad (2.1)$$

where C_1 and C_2 are material constants, $I_1 = \lambda_1^2 + \lambda_2^2 + \lambda_3^2$ the first invariant of the right Cauchy-Green deformation tensor and $J = \lambda_1 \lambda_2 \lambda_3$ the determinant of the deformation gradient.

The strain energy density function for an incompressible Neo-Hookean material is given by:

$$W = C_1(I_1 - 3) \quad (2.2)$$

obtained from (2.1) when $J = 1$. The two constants C_1 and C_2 can be correlated to the Lamè constants:

$$\begin{aligned} C_1 &= \frac{G}{2} \\ C_2 &= \frac{\lambda}{2} = \frac{K}{2} - \frac{G}{3} = \frac{K}{2} - \frac{2C_1}{3} \end{aligned} \quad (2.3)$$

The fiber reinforcement layers were modeled using a linear elastic model, with each layer is fully defined by the three parameters shown in Table 1 (E_f , ν_f and t_f). The elastomeric layers were modeled using a four-node, isoparametric, quadrilateral elements, implemented for plane-strain incompressible applications [43]. The reinforcement layers were modeled using an isoparametric, plane-strain, 2-node rods or cords (*i.e.* rebars), in conjunction with the 4-node plane strain continuum elements used for the rubber layers [43]. Top and bottom supports were modeled using rigid contact curves. A “touch” type of contact between the bearing and the rigid supports has been set, with a friction coefficient of 1, a reasonable value to describe the friction at the rubber-steel interface [44].

2D models were used for this study, taking into account the out of plane dimension of the bearing, resulting in equivalent 3D models (Figure 2).

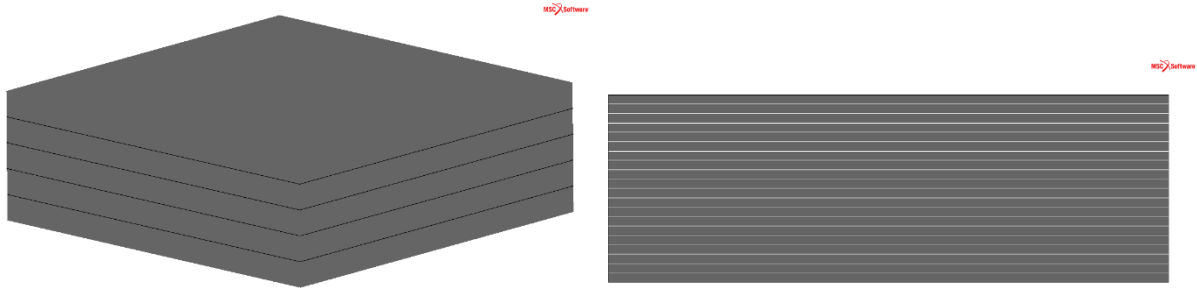


Figure 2: Full 3D numerical model vs equivalent 3D FEA model.

3. FINITE ELEMENT ANALYSIS RESULTS: VERTICAL STIFFNESS

3.1 – Pure compression

The trend of vertical stiffness under four different values of vertical pressure (from 2 to 8 MPa) and for different values of the shear modulus is shown in Figure 3 and Figure 4 for $t_e = 2$ mm and $t_e = 5$. In each graph, the vertical stiffness is plotted with respect to the vertical displacement (primary axes, black curves) and to the primary shape factor (secondary axes, gray curves); for each curve, each marker stands for a different secondary shape factor, i.e. one of the bases listed in Table 1 being the total height constant. This representation allows to simultaneously monitor the interaction between mechanical and geometric parameters on the vertical stiffness of the bearings.

The significant role of the primary shape factor S_1 is confirmed, i.e. an approximately quadratic relationship with the vertical stiffness is found. The vertical stiffness does not vary appreciably with the vertical pressure applied as S_1 varies. With the same S_1 , even if the vertical pressure is four times higher, the vertical stiffness is almost constant. A clear change of response is appreciable in vertical displacements. The vertical response may be split into two ranges of S_2 ; for a generic G modulus and a generic vertical pressure σ_v :

- If $S_2 > 2.5$: the vertical displacement varies slightly between one bearing and another, varying less and less and tending to a vertical asymptote as S_2 increases, regardless of mechanical parameters (pressure and shear modulus).
- If $S_2 \leq 2.5$: displacements under vertical load vary more and more as S_2 decreases..

The transition value $S_2 = 2.5$ agrees with previous findings from literature regarding the stability of bearings subjected to simultaneous vertical and horizontal load: bearings with a larger value of S_2 have a more stable behavior and are less dependent on mechanical parameters ([37, 38]).

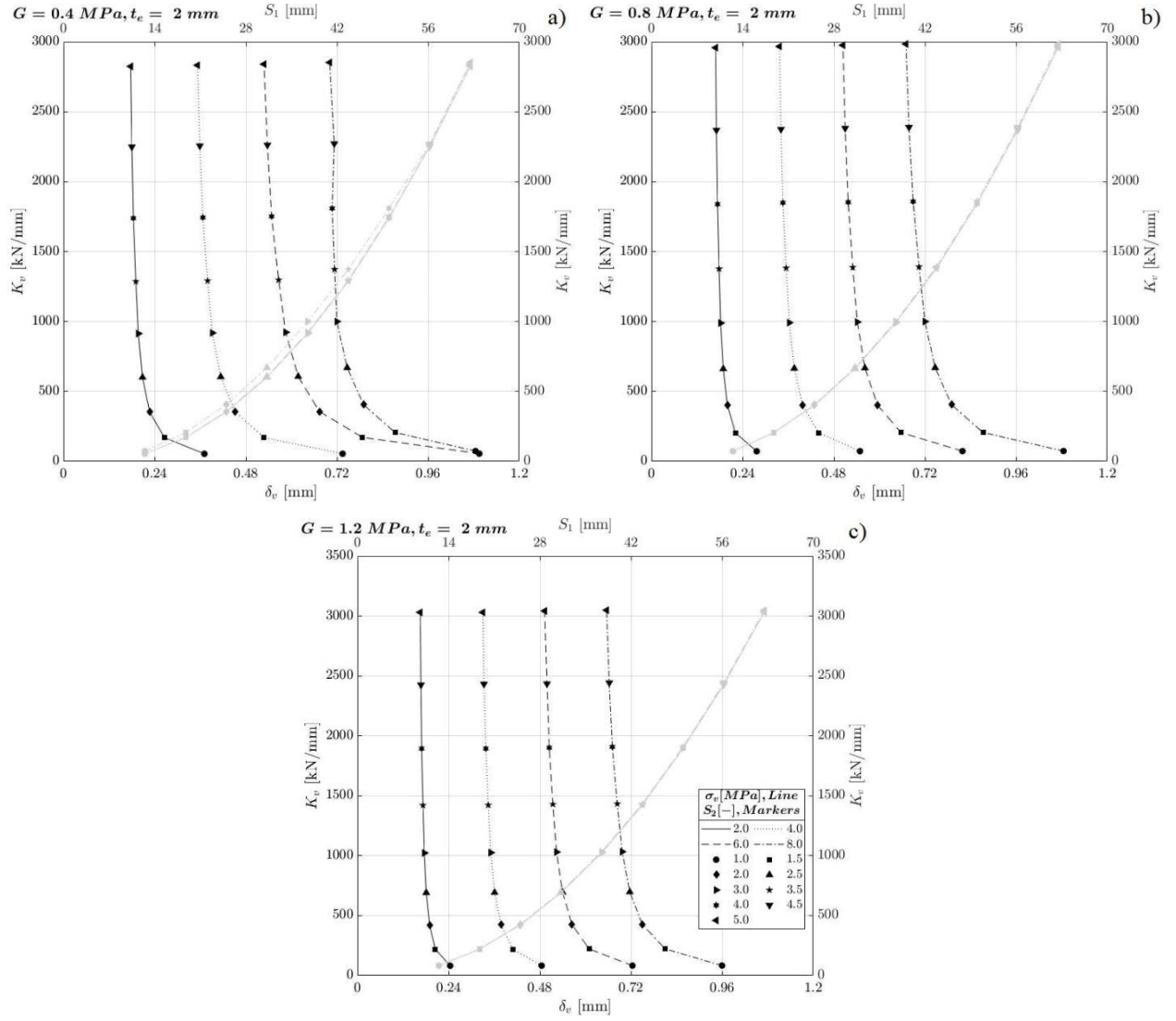


Figure 3: Vertical stiffness under pure compression for different vertical pressure, primary and secondary shape factor, $t_e = 2$ mm: a) $G = 0.4$ MPa, b) $G = 0.8$ MPa, c) $G = 1.2$ MPa

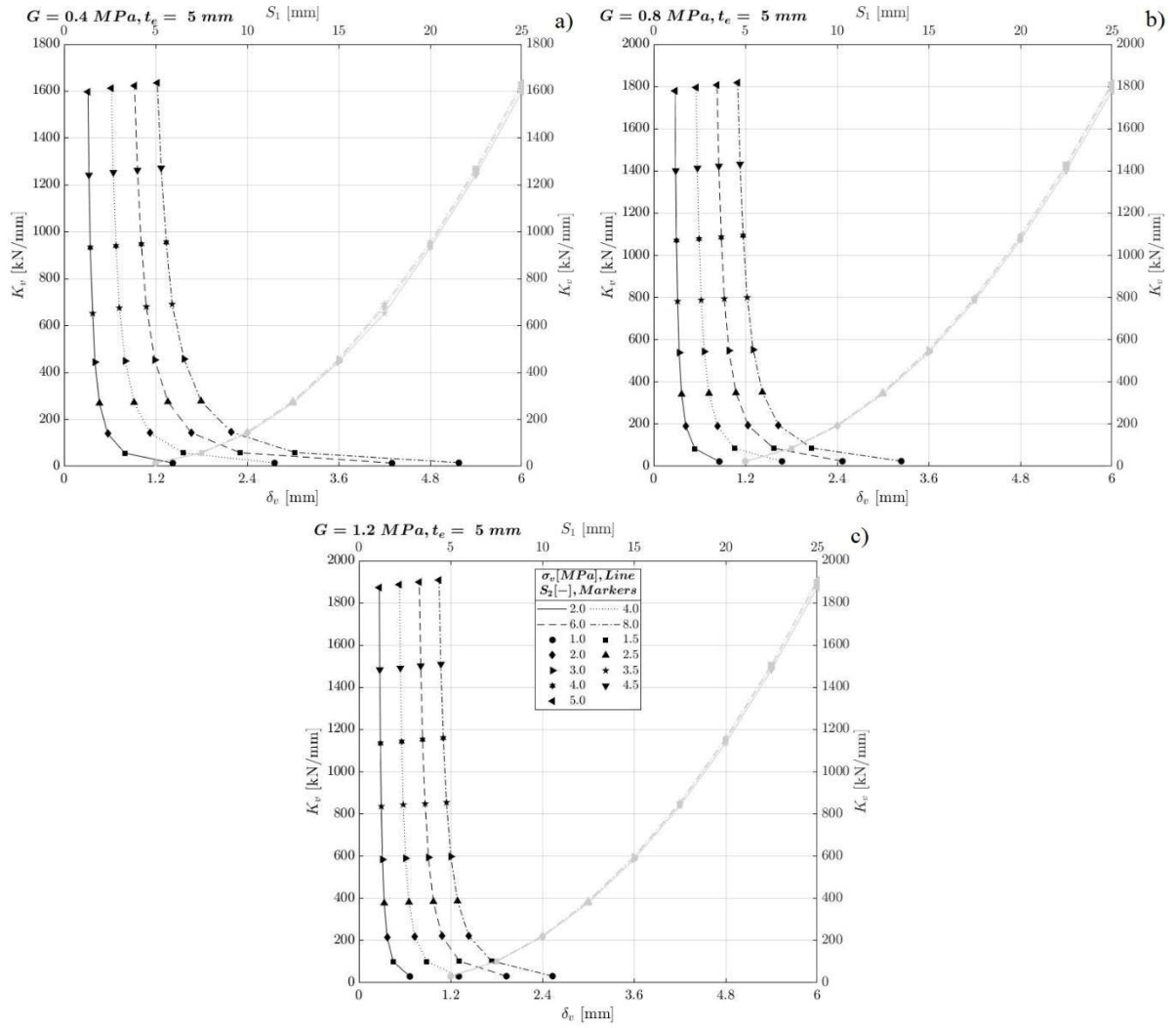


Figure 4: Vertical stiffness under pure compression for different vertical pressure and secondary shape factor, $t_e = 5$ mm: a) $G = 0.4$ MPa, b) $G = 0.8$ MPa, c) $G = 1.2$ MPa

3.2 – Combined vertical and horizontal load

The vertical stiffness of bearings under combined vertical and horizontal load is reduced due to the rollover: the marginal areas of the bearing detach from the supports, the contact area is reduced and consequently the vertical stiffness. The reduction of vertical stiffness involves an increase in the axial compressibility of the bearing. Figure 5 and Figure 6 show the trends of vertical stiffness with vertical and horizontal displacement, for $t_e = 2$ mm and $t_e = 5$ mm. The left columns of the figures show the $K_v - \delta_v$ trends, while those on the right show the $K_v - \delta_H$ trends; each row refers to a different value of the shear modulus G .

As from Figure 3 and from Figure 4 it can be deduced that the trend of the vertical stiffness does not depend on the applied pressure (its effect is to increase the compression and, therefore, the vertical displacements), e.g. $\sigma_v = 8$ MPa was considered in Figure 5 and Figure 6.

Compared to the vertical displacement, the stiffness is constant in a first part, where the horizontal displacement is zero. The horizontal extension of the constant stiffness section is smaller as S_2 increases, because the vertical stiffness increases.

Vertical stiffness is always decreasing as the horizontal displacement increases with an almost linear trend; this decrease is smaller for the higher values of S_2 . Table 2 shows the average on the pressures and on the G modulus of the ratios between the vertical stiffness at the generic level of horizontal displacement (K_v) and that under pure compression ($K_v^{(0)}$). Again, there is a difference in vertical response between bearings with S_2 lower and higher than 2.5:

- If $S_2 > 2.5$: the vertical stiffness, even at large displacements, still anyway around the 50% of that under pure compression. This reduction tends to zero as S_2 increases, with a vertical stiffness at $\gamma_H = 2.00$ for $S_2 = 5.00$ on average 17% lower than the stiffness under pure vertical load.
- If $S_2 \leq 2.5$: as S_2 decreases, the bearings is unstable before one of the selected thresholds of horizontal displacement and the computation of the vertical stiffness is meaningless. For bearings that reach full rollover, the vertical stiffness almost drops to zero.

As mentioned, the vertical stiffness must be sufficiently higher than the horizontal stiffness. Their ratio must have at least two orders of magnitude of difference. Considering a ratio between vertical stiffness under pure compression and horizontal stiffness equal to 500, this ratio is reduced under combined vertical and horizontal action according to Table 2. The numerical values are shown in Table 3. As can be seen, only where S_2 is at least equal to 2.5 this ratio remains greater than 100 up to full rollover.

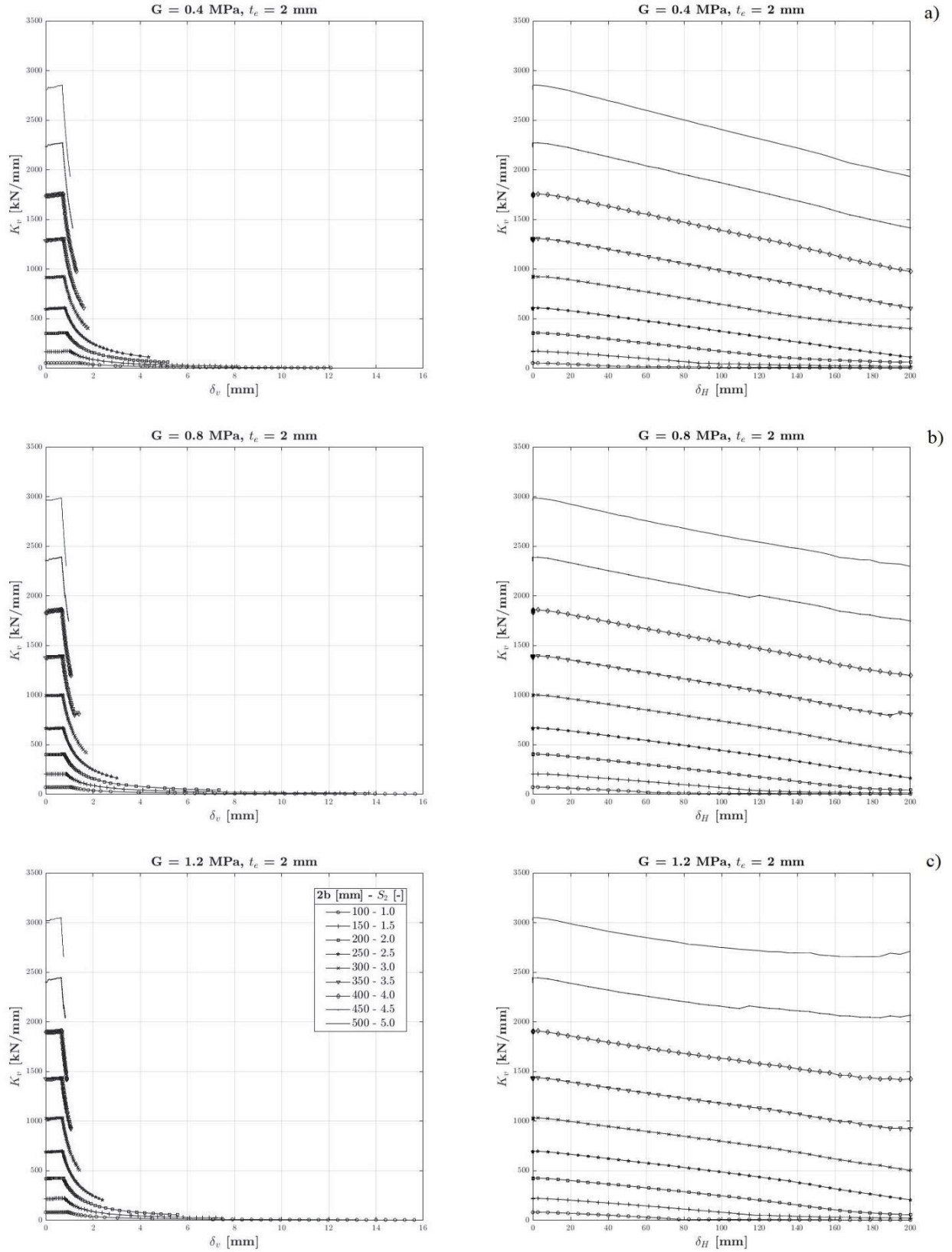


Figure 5: Vertical stiffness variable with vertical and horizontal displacement, $t_e = 2$ mm: a) $G = 0.4$ MPa, b) $G = 0.8$ MPa, c) $G = 1.2$ MPa.

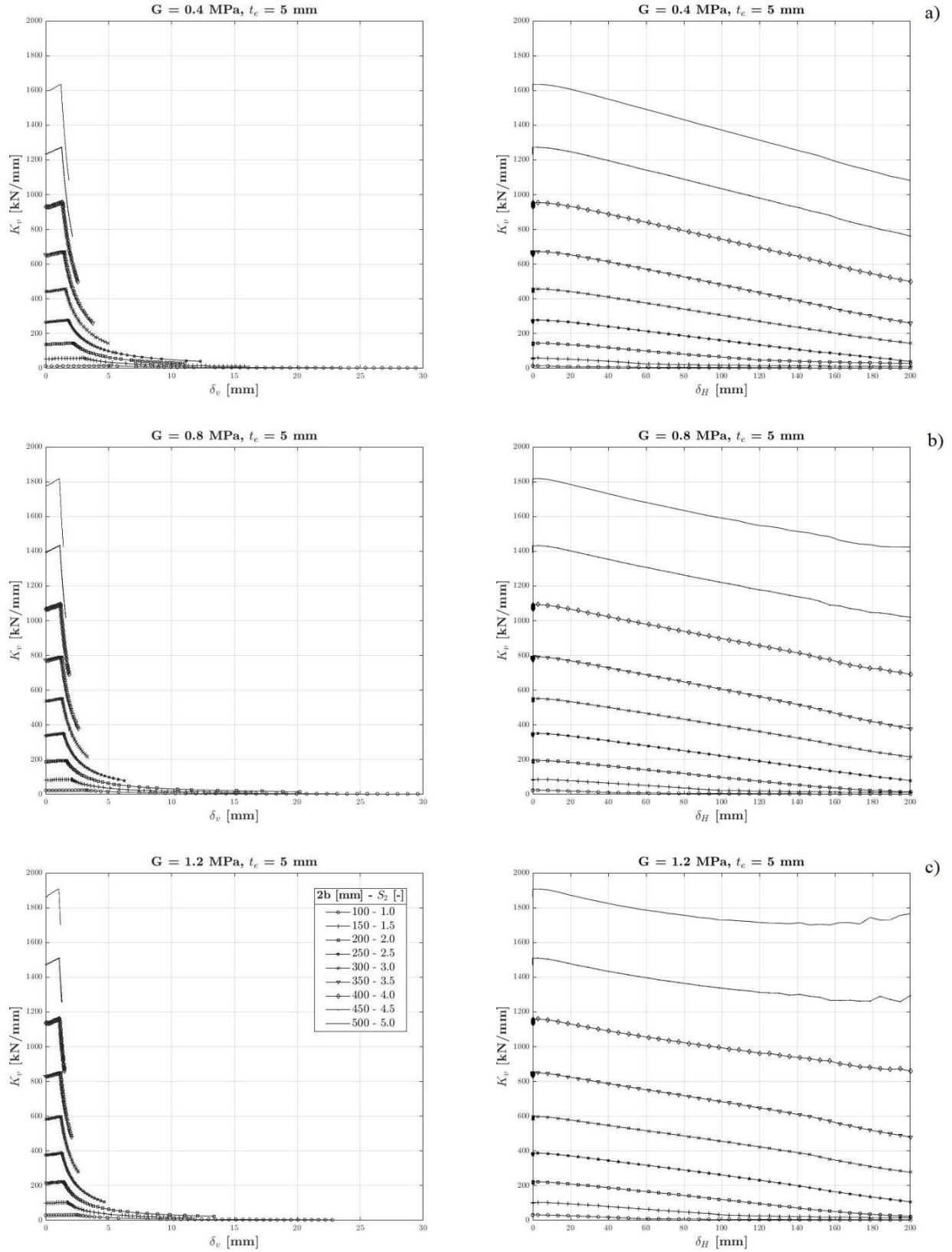


Figure 6: Vertical stiffness variable with vertical and horizontal displacement, $t_e = 5$ mm: a) $G=0.4$ MPa , b) $G=0.8$ MPa . c) $G=1.2$ MPa .

Table 2: Average $K_v / K_v^{(0)}$ ratios for different horizontal displacement levels.

γ_H	S_2								
	1.00	1.50	2.00	2.50	3.00	3.50	4.00	4.50	5.00
	$K_v / K_v^{(0)}$								
0.00	1.00	1.00	1.00	1.00	1.00	1.00	1.00	1.00	1.00
0.50	0.51	0.72	0.82	0.87	0.90	0.91	0.93	0.94	0.95
1.00	-	0.28	0.54	0.67	0.75	0.80	0.84	0.86	0.89
1.50	-	-	0.27	0.47	0.60	0.68	0.76	0.81	0.85
2.00	-	-	0.03	0.25	0.43	0.56	0.69	0.76	0.83

Table 3: Examples of K_v / K_H ratios for different horizontal displacement levels.

γ_H	S_2								
	1.00	1.50	2.00	2.50	3.00	3.50	4.00	4.50	5.00
	K_v / K_H								
0.00	500	500	500	500	500	500	500	500	500
0.50	238	356	406	430	445	454	463	468	472
1.00	-	111	262	325	365	389	412	427	437
1.50	-	-	118	224	290	327	368	396	413
2.00	-	-	33	116	209	260	320	364	392

4. FINITE ELEMENT ANALYSIS RESULTS: COMPRESSIVE MODULUS

4.1 – Pure compression

The compressive modulus E_c under pure compression depends solely on the mechanical and geometric properties of the bearing. Starting from the vertical stiffness obtained in §3.1, it is therefore possible to obtain the E_c modulus under pure compression by varying both the geometry (S_1 , S_2) and the mechanical parameters (G , σ_v), as follows:

$$E_c(\delta_H = 0) = \frac{K_v \cdot t_r}{A_c} \quad (4.1)$$

where t_r is the total rubber height and A_c the contact area between bearing and support. Figure 7 and Figure 8, as done for vertical stiffness, show the trends of the compressive modulus under pure compression as the vertical pressure, secondary shape factor (primary axes, black curves) and primary shape factor vary (secondary axes, gray curves). Again, the vertical pressure does not affect the shape of the curves, making these translate horizontally (black curves) or vertically (gray curves). The secondary shape factor affects the response under pure compression only for low values ($S_2 < 2.5$), while for high values the compressive modulus seems to converge to a common value for a fixed G and σ_v . Finally, the G modulus clearly affects the compressibility of the bearing, more significantly when the thickness of the elastomeric layer is greater.

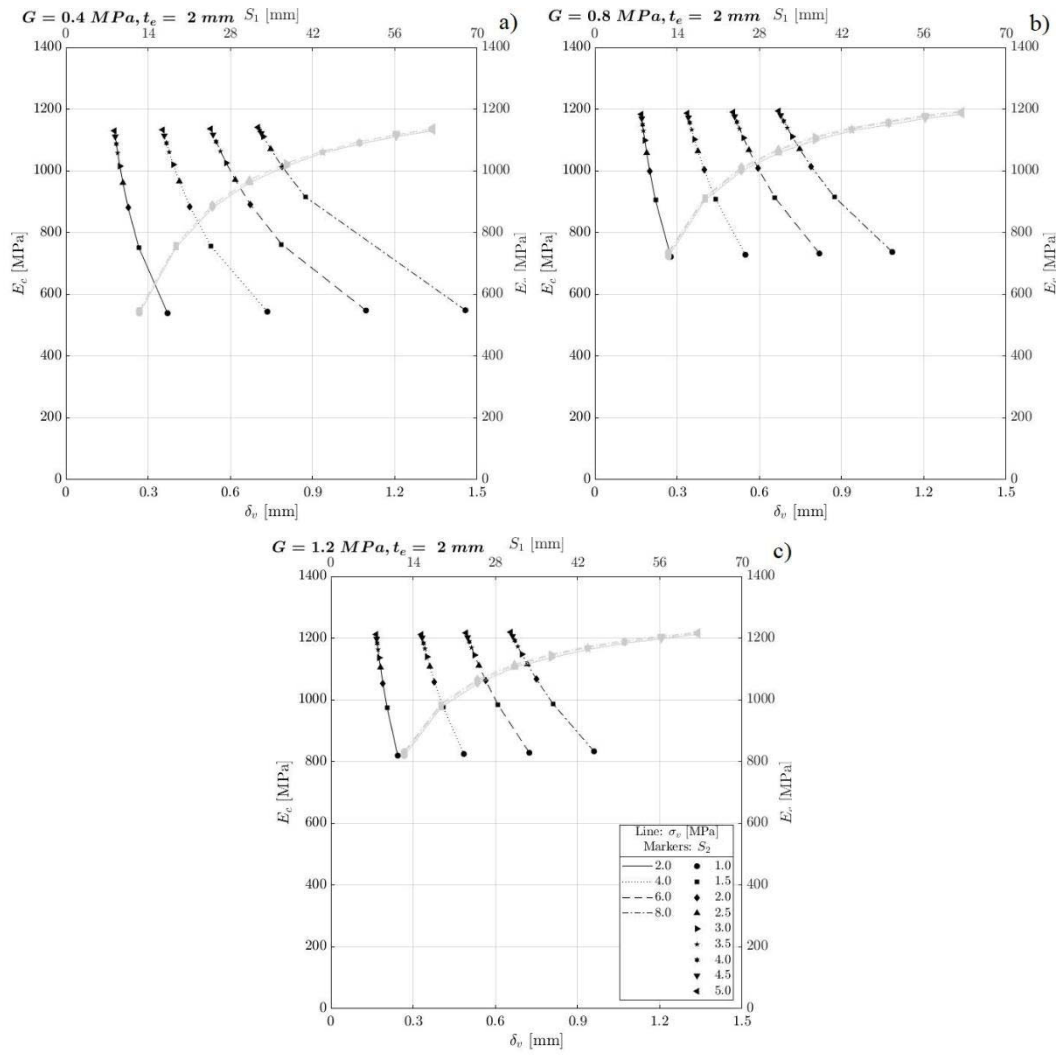


Figure 7: Effective compressive modulus under pure compression for different vertical pressure, primary and secondary shape factor, $t_e = 2$ mm: a) $G = 0.4$ MPa, b) $G = 0.8$ MPa, c) $G = 1.2$ MPa

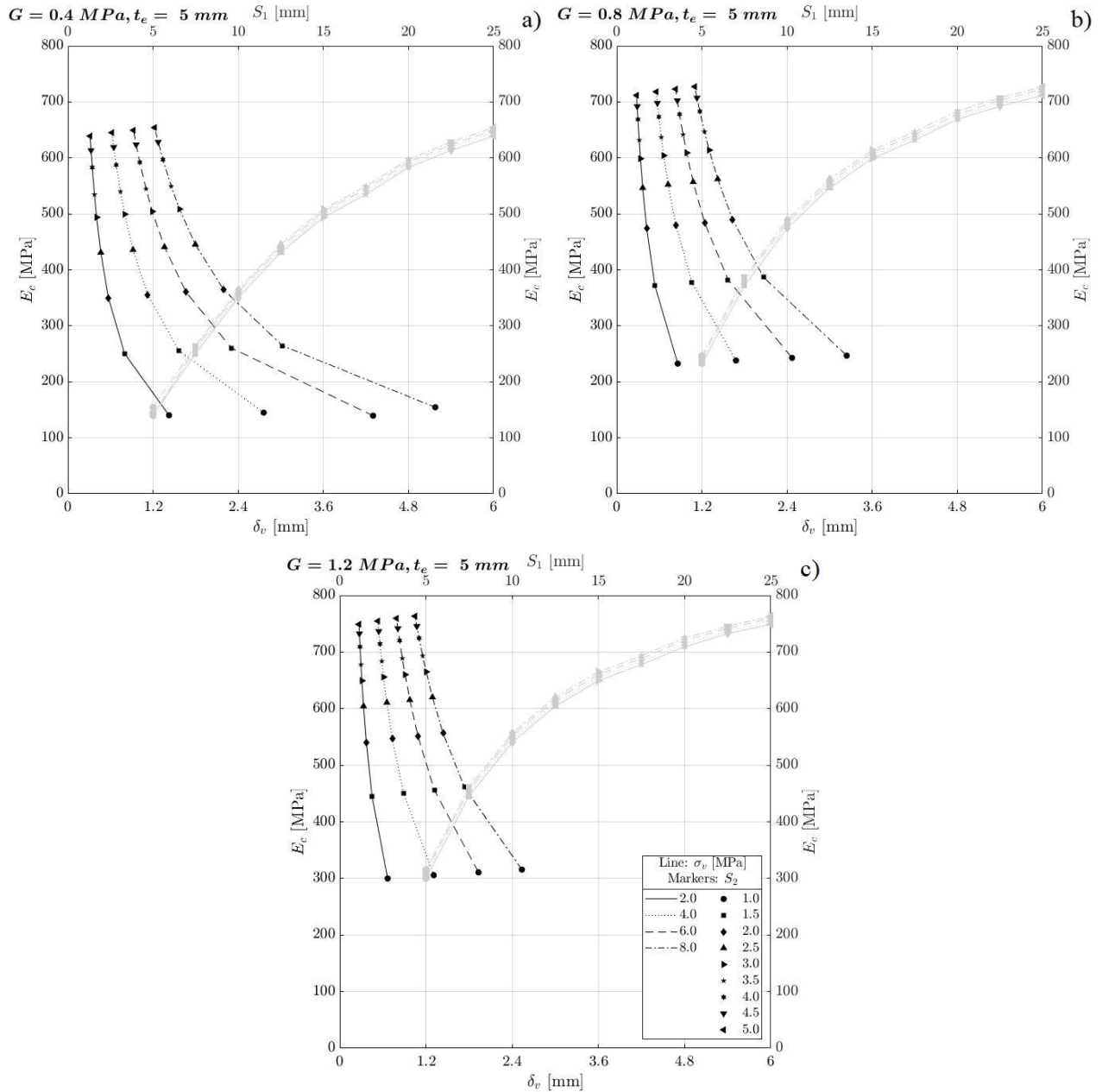


Figure 8: Effective compressive modulus under pure compression for different vertical pressure, primary and secondary shape factor, $t_e = 5$ mm: a) $G = 0.4$ MPa, b) $G = 0.8$ MPa, c) $G = 1.2$ MPa

4.2 – Combined vertical and horizontal load

The effective compressive modulus E_c of the bearings under combined axial and shear load was determined as follow:

$$E_c(\delta_H) = \frac{K_v \cdot t_r}{A_c(\delta_H)} = \frac{F_v \cdot t_r}{\delta_v(\delta_H) \cdot A_c(\delta_H)} \quad (4.2)$$

being $F_v = \sigma_v \cdot A$ the vertical applied force and δ_v the total vertical displacement at the top of the bearing. During horizontal displacement, the total vertical displacement and the contact area vary, increasing and decreasing respectively, resulting functions of the horizontal displacement. Since the

vertical displacement increases as the horizontal displacement increases while the contact area decreases, the E_c modulus can either decrease or increase.

Figure 9 and Figure 10 show the trends of the E_c modulus with the horizontal displacement. Again, a dual range can be defined by the secondary shape factor:

- If $S_2 \leq 2.5$: the modulus has a strictly decreasing trend with the horizontal displacement, the more marked the lower is S_2 . This is because the vertical displacement in formula (4.2) increases faster than the contact area decreases.
- If $S_2 > 2.5$: the E_c modulus is constant in a first section up to a horizontal displacement around 150 mm, then E_c rapidly decreases. In the first section, the variations in vertical displacement and contact area are almost equivalent, so the modulus varies little noticeably. In the second section, due to the full rollover, the contact area increases and the E_c modulus can only decrease.

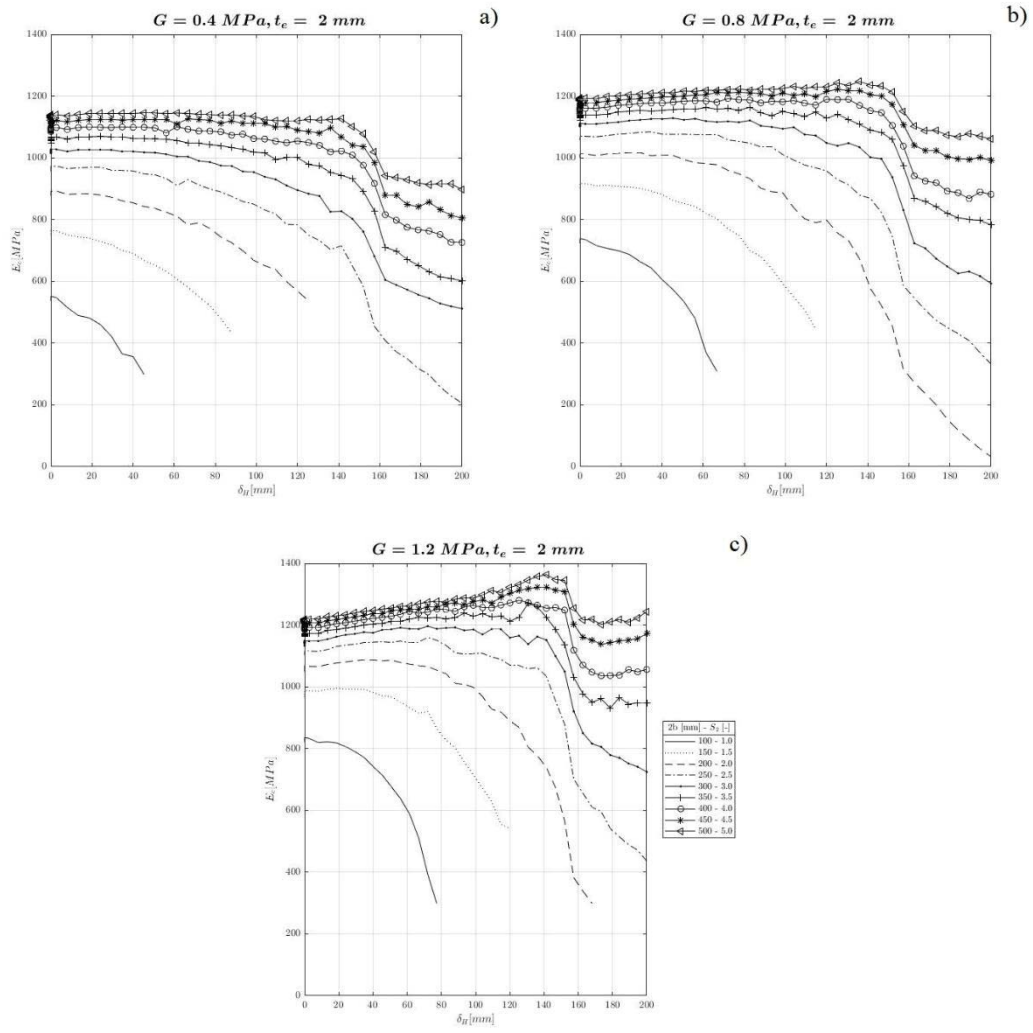


Figure 9: Effective compressive modulus vs horizontal displacement, $t_e = 2$ mm: a) $G = 0.4$ MPa, b) $G = 0.8$ MPa . c) $G = 1.2$ MPa .

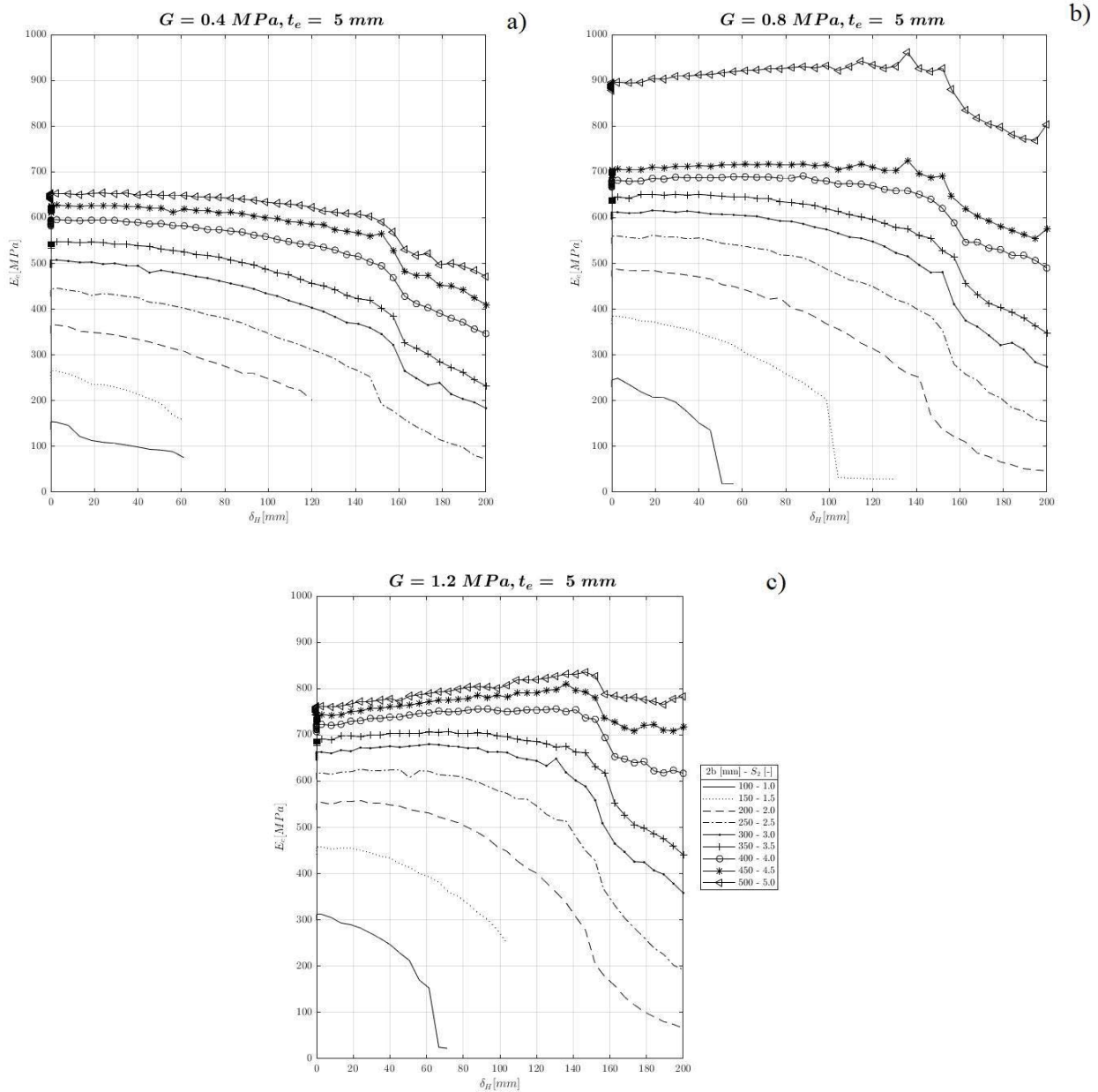


Figure 10: Effective compressive modulus vs horizontal displacement, $t_e = 5$ mm: a) $G = 0.4$ MPa, b) $G = 0.8$ MPa. c) $G = 1.2$ MPa.

5. CONCLUSIONS

The vertical response of a large number of fiber-reinforced elastomeric isolators was analyzed in this paper, i.e. vertical stiffness and effective compressive modulus have been studied into details. Two conditions of variation of the vertical properties were considered: vertical properties both under pure compression and combined vertical and horizontal load. The geometric and mechanical factors considered allowed to draw general conclusions on the variability of the vertical response. The bearings exhibit a response mainly dependent on geometry rather than on applied pressure; the mechanical parameters influence the magnitude of the response but not the shape, which is preserved. The main role of the primary shape factor S_1 on the vertical response of a single bearings under pure compression is confirmed. When the bearing is subjected to simultaneous

vertical and horizontal action, the secondary shape factor S_2 plays a key role, particularly affecting the stability of the bearing. A transition value approximately equal to 2.5 can be found, which separates the response of stable from unstable bearings. Unstable bearings show a rapid decrease in vertical stiffness and effective compressive modulus; in stable bearings the vertical response parameters decrease less noticeably as the lateral stiffness increases. It is essential that the vertical stiffness tends to be higher than horizontal stiffness even under lateral deformation: this requirement tends to be met by bearings with a secondary shape factor greater than 2.5.

6. REFERENCES

- [1] J. M. Kelly, "Analysis of Fiber-Reinforced Elastomeric Isolators," *Journal of Seismology and Earthquake Engineering*, vol. 2, no. 1, 1999.
- [2] B. Y. Moon, G. J. Kang, B. S. Kang and J. M. Kelly, "Design and manufacturing of fiber reinforced elastomeric isolator for seismic isolation," *Journal of Materials Processing Technology*, vol. 130, no. 131, pp. 145-150, 2002.
- [3] B. Y. Moon, G. J. Kang, B. S. Kang, G. S. Kim and J. M. Kelly, "Mechanical properties of seismic isolation system with fiber-reinforced bearing of strip type," *International Applied Mechanics*, vol. 39, no. 10, pp. 1231-1239, 2003.
- [4] J. M. Kelly and M. S. Takhirov, "Analytical and experimental study of fiber-reinforced elastomeric isolators," PEER Report 11, Pacific Earthquake Engineering Research Center, College of Engineering, University of California Berkeley, 2001.
- [5] H. Toopchi-Nezhad, M. J. Tait and R. G. Drysdale, "Testing and modeling of square carbon fiber-reinforced elastomeric seismic isolators," *Structural Control and Health Monitoring*, vol. 15, pp. 876-900, 2007.
- [6] H. Toopchi-Nezhad, M. J. Tait and R. G. Drysdale, "Bonded versus unbonded strip fiber reinforced elastomeric isolators: Finite element analysis," *Composite Structures*, vol. 93, pp. 850-859, 2011.
- [7] H. C. Tsai and J. M. Kelly, "Stiffness analysis of fiber-reinforced elastomeric isolators," PEER Report 05, Pacific Earthquake Engineering Research Center, College of Engineering, University of California Berkeley, 2001.
- [8] H. C. Tsai, "Compression stiffness of infinite-strip bearings of laminated elastic material interleaving with flexible reinforcements," *International Journal of Solids and Structures*, vol. 41, pp. 6647-6660, 2004.
- [9] H. C. Tsai, "Compression stiffness of circular bearings of laminated elastic material interleaving with flexible reinforcements," *International Journal of Solids and Structures*, vol. 43, pp. 3484-3497, 2006.
- [10] H. C. Tsai and J. M. Kelly, "Buckling of short beams with warping effect included," *International Journal of Solids and Structures*, no. 42, pp. 239-253, 2005.

- [11] H. C. Tsai and J. M. Kelly, "Buckling load of seismic isolators affected by flexibility of reinforcement," *International Journal of Solids and Structures*, no. 42, pp. 255-269, 2005.
- [12] G. Russo, M. Pauletta and A. Cortesia, "A study on experimental shear behavior of fiber-reinforced elastomeric isolators with various fiber layouts, elastomers and aging conditions," *Engineering Structures*, vol. 52, pp. 422-433, 2013.
- [13] N. C. Van Engelen, M. J. Tait and D. Konstantinidis, "Model of the Shear Behavior of Unbonded Fiber-Reinforced Elastomeric Isolators," *Journal of Structural Engineering*, vol. 141, no. 7, 2015.
- [14] A. Calabrese, G. Serino, S. Strano and M. Terzo, "Experimental investigation of a low-cost elastomeric anti-seismic device using recycled rubber," *Meccanica*, no. 50, pp. 2201-2218, 2015.
- [15] D. Losanno, M. Spizzuoco and A. Calabrese, "Bidirectional shaking-table tests of unbonded recycled-rubber fiber-reinforced bearings (RR-FRBs)," *Structural Control and Health Monitoring*, vol. 26, no. 9, p. e2386, 2019.
- [16] D. Losanno, I. E. Sierra Madera, M. Spizzuoco, J. Marulanda and P. Thomson, "Experimental assessment and analytical modeling of novel fiber-reinforced isolators in unbounded configuration," *Composite Structures*, no. 212, pp. 66-82, 2019.
- [17] D. Losanno, A. Calabrese, I. E. Madera Sierra, M. Spizzuoco, J. Marulanda, P. Thomson and G. Serino, "Recycled Versus Natural-Rubber Fiber-Reinforced Bearings for Base Isolation: Review of the Experimental Findings," *Journal of Earthquake Engineering*, 2020.
- [18] D. Losanno, I. E. Madera Sierra, M. Spizzuoco, J. Marulanda and P. Thomson, "Experimental performance of unbonded polyester and carbon fiber reinforced elastomeric isolators under bidirectional seismic excitation," *Engineering Structures*, no. 209, p. 110003, 2020.
- [19] I. E. Madera Sierra, D. Losanno, S. Strano, J. Marulanda and P. Thomson, "Development and experimental behavior of HDR seismic isolators for low-rise residential buildings," *Engineering Structures*, no. 183, pp. 894-906, 2019.
- [20] D. Losanno, F. Palumbo, A. Calabrese, T. Barrasso and N. Vaiana, "Preliminary investigation of aging effects on Recycled Rubber Fiber Reinforced Bearings (RR-FRBs)," *Journal of Earthquake Engineering*, no. DOI: 10.1080/13632469.2021.1871683, 2021.
- [21] A. Calabrese, D. Losanno, M. Spizzuoco, S. Strano and M. Terzo, "Recycled Rubber Fiber Reinforced Bearings (RR-FRBs) as base isolators for residential buildings in developing countries: The demonstration building of Pasir Badak, Indonesia," *Engineering Structures*, no. 192, pp. 126-144, 2019.
- [22] J. M. Kelly and A. Calabrese, "Analysis of Fiber-Reinforced Elastomeric Isolators Including Stretching of Reinforcement and Compressibility of Elastomer.," *Ingegneria Sismica*, vol. 30, no. 3, pp. 5-14, 2013.
- [23] Y. Al-Anany and M. J. Tait, "A numerical study on the compressive and rotational behavior of fiber reinforced elastomeric isolators (FREI)," *Composite Structures*, no. 133, pp. 1249-1266,

2015.

- [24] A. Calabrese, M. Spizzuoco, S. Galano, N. Tran, S. Strano and M. Terzo, "A Parametric Study on the Stability of Fiber Reinforced Rubber Bearings Under Combined Axial and Shear Loads," *Engineering Structures*, vol. 227, p. 111441, 2020.
- [25] D. Losanno, N. Ravichandran, F. Parisi, A. Calabrese and G. Serino, "Seismic performance of a Low-Cost base isolation system for unreinforced brick Masonry buildings in developing countries," *Soil Dynamics and Earthquake Engineering*, no. 141, p. 106501, 2021.
- [26] N. Vaiana, S. Sessa, M. Paradiso and L. Rosati, "Accurate and efficient modeling of the husteretic behavior of sliding bearings," in *Proceedings of the 7th ECCOMAS thematic conferenc on Computational Methods in Structural Dunamics and Earthquake Engineering*, Compdyn 2019, 2019.
- [27] S. Sessa, N. Vaiana, M. Paradiso and L. Rosati, "An inverse identification strategy for the mechanical parameters of a phenomenological hysteretic constitutive model," *Mechanical Systems and Signal Processing*, vol. 139, p. 106622, 2020.
- [28] F. Marmo, S. Sessa, N. Vaiana, D. De Gregorio and L. Rosati, "Complete solutions of three dimensional problems in transversely isotropic media," *Continuum Mechanics and Thermodynamics*, vol. 32, no. 3, pp. 775-802, 2020.
- [29] N. Vaiana, S. Sessa and L. Rosati, "A generalized class of uniaxial rate-independent models for simulating asymmetric mechanical hysteresis phenomena," *Mechanical Systems and Signal Processing*, vol. 146, p. 106984, 2021.
- [30] N. Vaiana, D. Losanno and N. Ravichandran, "A novel family of multiple springs models suitable for biaxial rate-independent hysteretic behavior," *Computers & Structures*, vol. 244, p. 106403, 2021.
- [31] J. M. Kelly and D. Konstantinidis, *Mechanics of Rubber Bearings for Seismic Isolation and Vibration Isolation*, John Wiley and Sons, Ltd, 2011.
- [32] H. Toopchi-Nezhad, M. J. Tait and R. G. Drysdale, "Lateral Response Evaluation of Fiber-Reinforced Neoprene Seismic Isolators Utilized in an Unbonded Application," *JOURNAL OF STRUCTURAL ENGINEERING*, vol. 10, no. 134, pp. 1627-2637, 2008.
- [33] *ASCE-7. Minimum design loads for buildings and other structures*, ASCE/SEI 7–, 2010.
- [34] *UNI EN 1998-1:2013 Part 1*, 2013.
- [35] *Aggiornamento delle «Norme tecniche per le costruzioni»*, 2018.
- [36] H. Toopchi-Nezhad, R. G. Drysdale and M. J. Tait, "Parametric Study on the Response of Stable Unbonded-Fiber Reinforced Elastomeric Isolators (SU-FREIs)," *Journal of Composite Materials*, vol. 43, no. 15, 2009.
- [37] M. G. De Raaf, M. J. Tait and H. Toopchi-Nezhad, "Stability of fiber-reinforced elastomeric bearings in an unbonded application," *Journal of Composite Materials*, vol. 45, no. 18, pp.

1873-1884, 2011.

- [38] S. Galano, D. Losanno and A. Calabrese, *Stability Analysis of Unbonded Fiber Reinforced Isolators of Square Shape*, Under review. Submitted to Engineering Structures, 2021.
- [39] F. Naeim and J. M. Kelly, Design of seismic isolated structures, John Wiley & Sons, Inc., 1999.
- [40] P. M. Osgooei, D. Konstantinidis and M. J. Tait, "Variation of the vertical stiffness of strip-shaped fiber-reinforced elastomeric isolators under lateral loading," *Composite Structures*, vol. 144, pp. 177-184, 2016.
- [41] MSC.Software Corporation, MSC.Marc Mentat release guide, Santa Ana, CA, USA, 2005.
- [42] MSC.Software Corporation, MAR103 Experimental Elastomer Analysis, Santa Ana, CA, USA, 2017.
- [43] MSC.Software Corporation, Volume B: Element Library, Santa Ana, CA, USA, 2017.
- [44] J. M. Kelly and D. Konstantinidis, "Effect of Friction on Unbonded Elastomeric Bearings," *Journal of Engineering Mechanics*, vol. 135, no. 9, pp. 953-960, 2009.

SEISMIC ISOLATION OF LIGHTWEIGHT STRUCTURES THROUGH WIRE ROPE DEVICES: PRELIMINARY EXPERIMENTAL RESULTS AND SIMULATION

Mariacristina Spizzuoco¹, and Giorgio Serino¹

¹Department of Structures for Engineering & Architecture, University of Napoli Federico II
Via Claudio 21, 80125 Naples, Italy
e-mail: spizzuoc@unina.it

Abstract

The work presents some preliminary results of experimental tests performed on a Helical Wire Rope Isolator (HWRI), to the aim of describing the dynamic behavior of the metal isolation device, without pre-load and under the effect of a vertical pre-load, for different displacement amplitudes. During the dynamic tests, the testing machine allows to apply a vertical displacement or load history to the tested device, subjected to a constant vertical pre-load. The dynamic behavior of the tested device depends on the applied displacement amplitude: the HWRI displays an asymmetric behaviour, i.e. a different response when it is subjected to compression or tension; in the latter case, it shows an hardening effect for larger displacements. Moreover, the experimental tests make clear that the application of a vertical pre-load determines a different behaviour in Compression vs. Tension, with slightly variable damping properties. In order to simulate the dynamic behavior of the HWRI in Compression-Tension direction, a nonlinear model is proposed, that is validated by comparing the experimental hysteresis loops obtained during cyclic tests with those predicted analytically.

Keywords: Base Isolation, Experimental Dynamic Characterization, Wire-Rope Isolators.

1 INTRODUCTION

Helical Wire Rope Isolators (HWRI) are metal devices which are effective in protecting sensitive equipment from shock and vibration [1], so that they are frequently used as devices for the earthquake protection of that equipment installed in buildings [2] and for the reduction of seismic vibration induced on high voltage ceramic circuit breakers [3-6]. But, they have been also adopted as vertical isolators under the basement of the two statues known as “Bronzes of Riace” [7].

HWRI are made of a stainless steel cable embedded into two aluminum alloy or steel retainer bars. They can deform in both vertical and horizontal directions and they have a significant dissipation capacity caused by the inner sliding friction and rubbing among the various strand's wires and among the intertwined strands [1]. The mechanical behavior of HWRI depends on their geometrical characteristics: the height to width ratio, the device's diameter, the number of strands, the cable length and twist, the number of cables per section and the number of loops [2].

A HWR Isolator, manufactured by Powerflex s.r.l (Limatola, Italy), has been experimentally investigated in its vertical direction, named Compression/Tension. The aim of the experimental tests was to study the dynamic behaviour of the considered device in a quite large displacements range, by assigning four different values to the vertical pre-load. Literature shows the results of experimental tests performed within a relatively small displacements range [2, 6, 8].

The experimental investigation of the tested HWRI has been carried out by operating a testing machine available at the Laboratory of Department of Structures for Engineering and Architecture of the University of Naples Federico II. Its dynamic behavior has been studied by analyzing the values assumed by two parameters computed from the experimental hysteresis loops: the average effective (or secant) stiffness in both Compression and Tension, and the average equivalent viscous damping ratio.

2 HELICAL WIRE ROPE ISOLATOR UNDER TESTING

HWRI are metal devices that are obtained by wounding a wire rope in the form of a helix and embedding into two drilled metal retainer bars. The rope is given by the layering of several strands around a central one. The HWRI manufactured by Powerflex S.r.l (Limatola, Italy), have a rope that is composed by six strands, each consisting in 25 wires, and a central strand with 49 wires. The cable is made of stainless steel type 316, whereas the material of the retainer bars is an aluminum alloy.

Figure 1 shows the geometrical characteristics of the tested HWRI and the indication of the tested vertical direction: Compression/Tension.

Table 1 lists the geometrical characteristics (cable's diameter, length, width and height of the device) of the tested devices: HWRI PWHS16010 and HWRI PWHS16040.

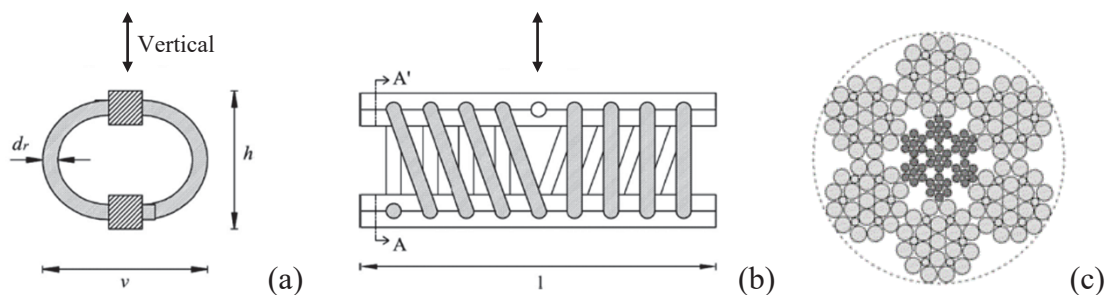


Figure 1: Mount of a wire rope (a); helical configuration of the cable (b); stranded cable's cross section (c).

HWRI	l [mm]	h [mm]	v [mm]	h/v	d_r [mm]
PWHS 16010	267	100	110	0.90	16
PWHS 16040	267	125	150	0.83	16

Table 1: Geometrical characteristics of the HWRIs selected for experimental tests.

3 TESTING MACHINE FOR COMPRESSION/TENSION TESTS

The dynamic experimental tests on the selected HWRIs in Compression/Tension direction have been carried out through a testing machine (Figure 2) available at the Department of Structures for Engineering and Architecture of the University of Naples Federico II (Italy): an MTS Series 370 Servohydraulic Load Frame. The load frame is suitable to perform tests in compression and tension. It includes an axial hydraulic actuator with a maximum capacity of 250 kN and a stroke of 150 mm. Both displacement and force controlled procedures can be followed. In the configuration shown in Figure 2, the dynamic actuator is mounted on the upper crosshead, while a load cell is mounted below the lower hydraulic wedge. The data acquisition system along with the control of the hydraulic actuator are performed with a software running on a personal computer. For Compression/Tension tests, the steel retainer bars of the isolator are gripped by the upper and lower rigid steel parts of the machine. All tests were conducted by imposing vertical displacements at room temperature and the data were sampled at 102.4 Hz. The relative vertical displacement and vertical load time histories have been measured.



Figure 2: Testing machine and the HWRI mounted in vertical direction.

4 EXPERIMENTAL CHARACTERIZATION TESTS

Cyclic tests have been carried out in order to understand the influence of displacement amplitude and vertical pre-load on the dynamic behavior of the selected HWRIs in vertical (Compression/Tension) direction. Nine different displacement amplitudes, four vertical pre-

load values and a testing frequency of 0.1 Hz have been assumed, where the maximum amplitude has been chosen to prevent damage to the aluminum alloy retainer bars. The testing protocol consisted in applying ten fully reversed sinusoidal cycles of vertical displacement, having specified amplitude A and frequency f , while a constant vertical pre-load was applied to the device. The dynamic displacement-controlled tests are listed in Table 2.

No. of Tests	Frequency [Hz]	Amplitude [mm]	Vertical Load [kN]
HWRI PWHS 16010			
6	0.1	2.5, 5, 7.5, 10, 12.5, 15	0
6	0.1	2.5, 5, 7.5, 10, 12.5, 15	2
HWRI PWHS 16040			
6	0.1	5, 10, 15, 20, 25, 30	0
6	0.1	5, 10, 15, 20, 25, 30	1.2
6	0.1	5, 10, 15, 20, 25, 30	2
6	0.1	5, 10, 15, 20, 25, 30	3

Table 2: Dynamic tests in vertical direction.

5 EXPERIMENTAL TESTS OUTCOMES

The results of the dynamic experimental tests performed on the investigated HWRI PWHS 16040 are presented in this paragraph. The dynamic parameters evaluated from the asymmetric experimental force-displacement hysteresis loops are the average effective (or secant) stiffness values in Compression and Tension, and the average equivalent viscous damping ratio. The effective stiffnesses in Compression and in Tension, corresponding to each load cycle of a dynamic test, have been evaluated based on the peak vertical load and displacement [10], both on Compression side and on Tension side:

$$k_{eff,T} = \frac{f_{max}}{u_{max}} \quad k_{eff,C} = \frac{f_{min}}{u_{min}} \quad (1)$$

where f_{max} , f_{min} , u_{max} , and u_{min} are the peak values of vertical load and displacement, respectively, at the extremes of the cyclic displacement range. The average effective stiffnesses $k_{eff,T,a}$ and $k_{eff,C,a}$ have been calculated as mean values of those obtained from seven of the ten experimental loading cycles. The equivalent viscous damping ratio of the device at each cycle has been evaluated as [11, 12]:

$$\xi_{eq} = \frac{1}{\pi} \frac{E_d}{(A_{sT} + A_{sC} + A_{rect})} \quad (2)$$

where E_d represents the dissipated energy, that is, the area within the asymmetric hysteresis loop, and A_{sT} , A_{sC} and A_{rect} are the following areas:

$$A_{sT} = \frac{1}{2} k_{eff,T} u_{max}^2, \quad A_{sC} = \frac{1}{2} k_{eff,C} u_{min}^2, \quad A_{rect} = u_{max} \cdot f_{min} \quad (3)$$

with $u_{max} = u_{min}$ the positive and negative maximum displacements, and f_{min} the negative peak value of vertical load. The average equivalent viscous damping ratio $\xi_{eq,a}$ has been calculated as mean value of those obtained from seven of the ten loading cycles applied to the device.

Regarding the influence of the displacement amplitude on the dynamic behavior of the tested HWRI, Table 3 presents the values of the average effective stiffnesses and the equivalent viscous damping ratio obtained for six different amplitudes without the effect of the vertical pre-load. It can be observed that the tested metal device displays higher effective

stiffnesses and equivalent damping ratio at smaller displacements. The effective stiffness in Compression and the equivalent damping ratio decrease with increasing displacement amplitude, whereas the effective stiffness in Tension increases dramatically at the largest amplitudes. Figure 3 shows the asymmetric force-displacement hysteresis loops obtained in Compression/Tension direction (compression and tension are assumed, respectively, negative and positive) for all six different values of amplitude, for $f = 0.1$ Hz and without the effect of the vertical pre-load. It is worth to note that the shape of the hysteresis loops changes according to the displacement amplitude: at the smallest amplitude the hysteresis loops display a softening stiffness in Compression and a slightly hardening stiffness in Tension, whereas at the highest amplitude the experimental cycles exhibit a stronger nonlinear stiffening behavior only on Tension side.

$P_v = 0$ kN, $f = 0.1$ Hz	Amplitude [mm]	k_{eff,C_a} [N/m]	k_{eff,T_a} [N/m]	$\xi_{eq,a}$ [%]
Compression/Tension	5	859659	1238110	22.7
Compression/Tension	10	576639	1038541	17.5
Compression/Tension	15	454733	999633	15.0
Compression/Tension	20	386610	1023578	13.5
Compression/Tension	25	341244	1114642	12.4
Compression/Tension	30	305053	1343628	11.4

Table 3: Influence of displacement amplitude.

As regards to the effect of the vertical pre-load on the dynamic behavior of the tested metal device, Tables 4 and 5 show the results obtained in Compression/Tension direction for four different values of vertical pre-load, by applying a sinusoidal harmonic motion having frequency of 0.1 Hz and amplitude equal to 15 mm and 30 mm, respectively. From the examination of the outcomes, it can be deduced that, in the case of an intermediate displacement amplitude (15 mm), an increase in the pre-load produces a reduction in the average effective stiffnesses and an approximately constant equivalent viscous damping ratio (Table 4).

$A = 15$ mm, $f = 0.1$ Hz	Vertical Load [kN]	k_{eff,C_a} [N/m]	k_{eff,T_a} [N/m]	$\xi_{eq,a}$ [%]
Compression/Tension	0.0	454733	999633	15.0
Compression/Tension	1.2	406447	864757	14.6
Compression/Tension	2.0	410924	878796	15.0
Compression/Tension	3.0	413397	894691	14.7

Table 4: Influence of vertical load for $A = 15$ mm.

On the other hand, in the case of a larger displacement amplitude (30 mm), an increase in the vertical pre-load produces a strong increase of the average effective stiffness in Tension while the variation of the stiffness in Compression is negligible, and determines a slight decrease of the equivalent viscous damping ratio (Table 5).

$A = 30$ mm, $f = 0.1$ Hz	Vertical Load [kN]	k_{eff,C_a} [N/m]	k_{eff,T_a} [N/m]	$\xi_{eq,a}$ [%]
Compression/Tension	0.0	305453	1343628	11.4
Compression/Tension	1.2	304997	1693672	10.6
Compression/Tension	2.0	305366	1736038	10.0
Compression/Tension	3.0	307147	1943828	9.5

Table 5: Influence of vertical load for $A = 30$ mm.

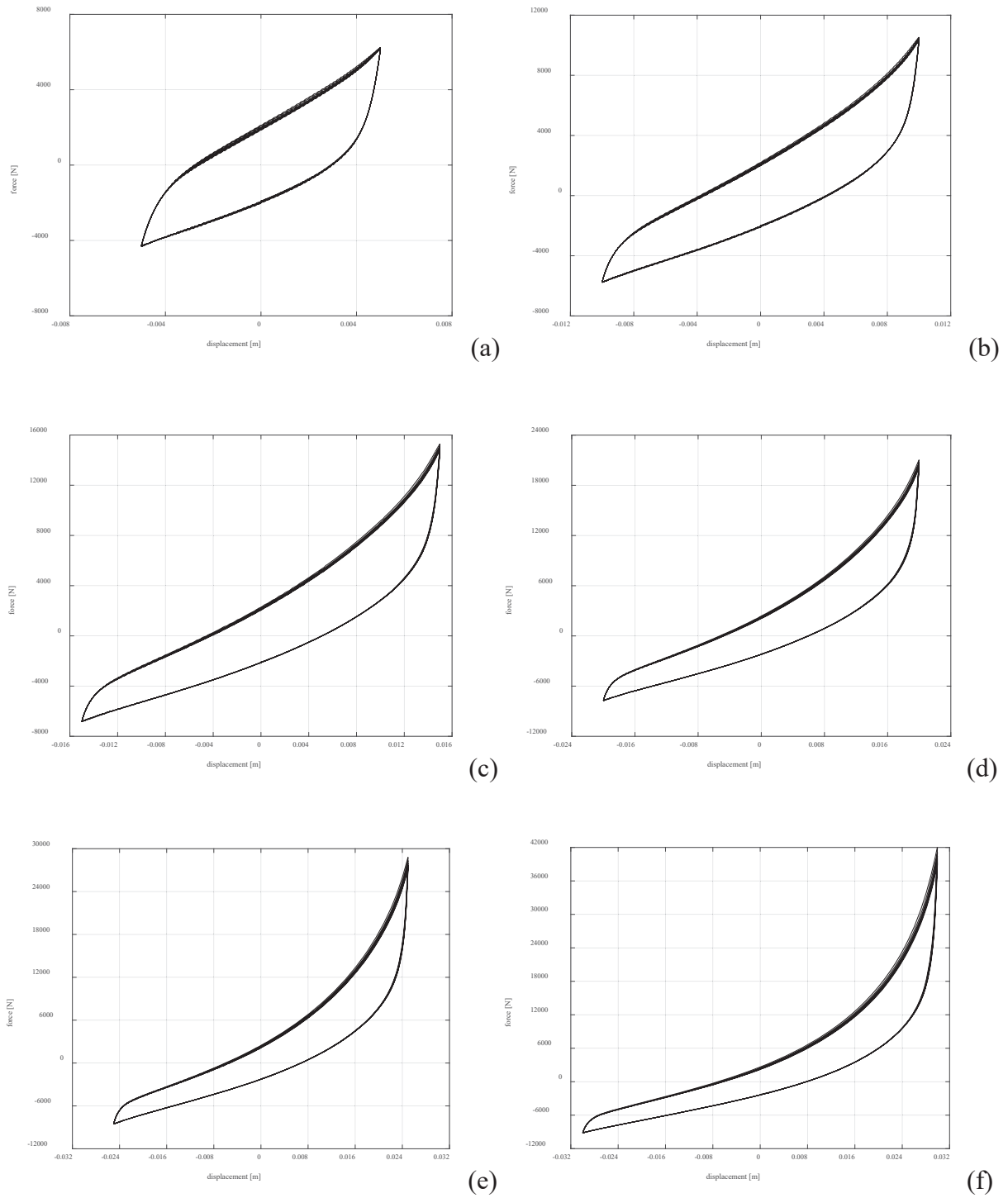


Figure 3: Force-displacement hysteresis loops of HWRI PWHS 16040 at different displacement amplitudes in C/T direction, for $P_v = 0$ kN and $f = 0.1$ Hz: (a) ± 5 , (b) ± 10 , (c) ± 15 , (d) ± 20 , (e) ± 25 , (f) ± 30 .

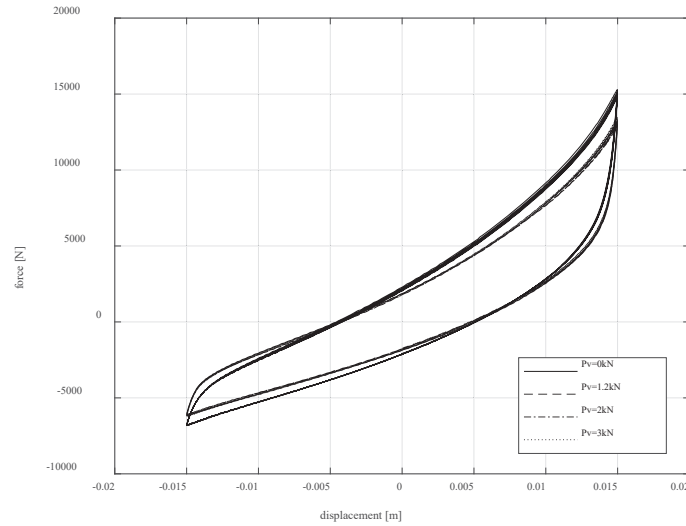


Figure 4: HWRI PWHS 16040: Influence of vertical pre-load at $A = 15$ mm in Compression/Tension direction.

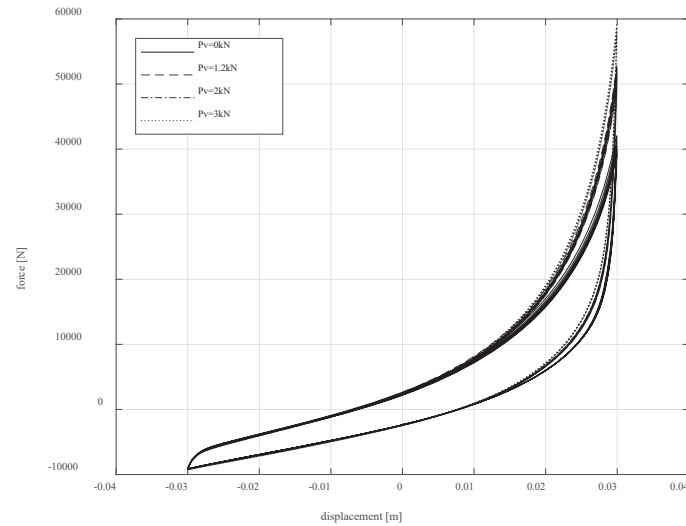


Figure 5: HWRI PWHS 16040: Influence of vertical pre-load at $A = 30$ mm in Compression/Tension direction.

Figures 4 and 5 show the asymmetric force-displacement hysteresis loops obtained in Compression/Tension direction, under the effect of different values of vertical pre-load, at the displacement amplitudes $A = 15$ mm (Figure 4) and $A = 30$ mm (Figure 5). It can be observed that at the largest displacements, the applied vertical pre-load affects much less the dynamic response of the metal device only on Compression side.

6 NUMERICAL SIMULATION OF THE EXPERIMENTAL BEHAVIOUR

As far as the modeling of the dynamic behavior of HWRI in the vertical direction is concerned, a Modified Bouc-Wen Model (MBWM) is proposed to predict their response. This analytical model is obtained by modifying the expression of the generalized force (Eq. (4)) of the Bouc-Wen Model (depending on five parameters k_2 , k_d , β , γ , ϵ):

$$f_u = k_2 u + z(u) \quad (4)$$

where u is the generalized relative displacement, and $z(u)$ is the hysteretic variable given by solving the following first order differential equation:

$$\dot{z} = \left\{ k_d - [\gamma + \beta \cdot \text{sgn}(z \cdot \dot{u})] |z|^n \right\} \dot{u} \quad (5)$$

The proposed modification of the generalized force:

$$f = -(\lambda_1 + \lambda_2)u + e^{(\lambda_1 u)} - e^{(-\lambda_2 u)} + e^{(\eta u)} (k_2 u + z) \quad (6)$$

allows to simulate the asymmetric behaviour in Compression/Tension direction. The proposed model depends by eight parameters k_2 , k_d , n , β , γ , λ_1 , λ_2 and η , where the latter λ_1 , λ_2 and η are those determining the asymmetry of the loops.

The experimental hysteresis loops, obtained by the dynamic tests performed on the different HWRI, are compared to those derived by the application of the proposed numerical model: the values of the above eight parameters are calibrated in order to simulate the experimental response for a certain vertical pre-load and all the different displacement amplitudes. In particular, such values are: $k_2 = 1100000$, $k_d = 8500000$, $n = 1$, $\beta = 3000$, $\gamma = 0$, $\lambda_1 = 775$, $\lambda_2 = 630$ and $\eta = 55$.

Figure 6 shows the analytical versus experimental comparison for the HWRI PWHS 16010, subjected to a pre-load of 2 kN, with varying the displacement amplitude as described in Table 2. It demonstrates that the proposed mathematical model can satisfactorily predict the dynamic response in a wide displacement range. This satisfying agreement is achieved by all the tested devices, under the different vertical pre-loads.

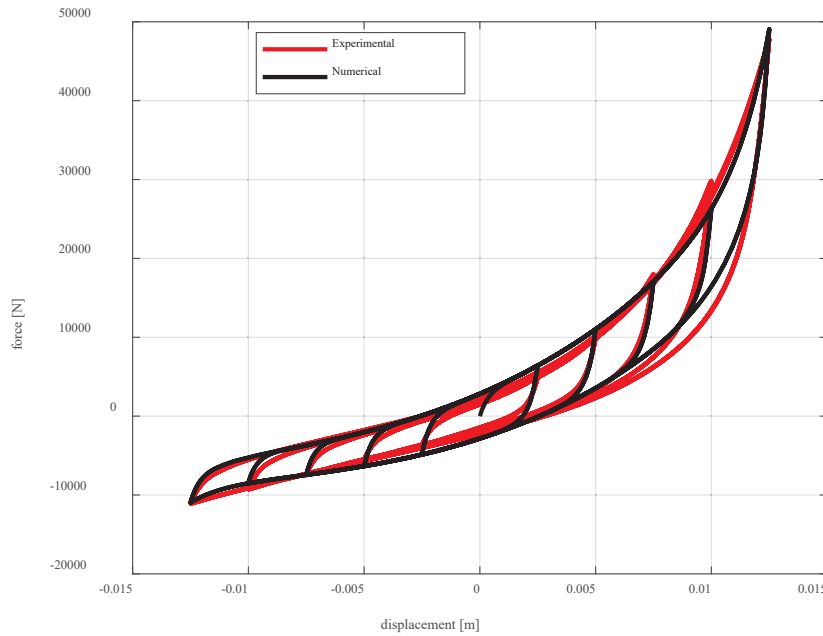


Figure 6: HWRI PWHS 16010: experimental versus numerical hysteresis loops, under a pre-load of 2 kN.

7 CONCLUSIONS

The experimental investigation of the dynamic response of HWRI, manufactured by Powerflex S.r.l (Limatola, Italy), has been carried out by adopting a testing machine available at the Department of Structures for Engineering and Architecture of the University of Naples Federico II, which allows to impose vertical displacement or load histories to the tested device with a constant vertical pre-load.

Each test consisted in imposing ten cycles of sinusoidal displacement having specified amplitude and frequency, under four different values of vertical pre-load. Six amplitude values have been chosen with the maximum one selected in order to avoid damages to the two alu-

minum alloy retainer bars of the device during the experimental tests. The most investigated loading frequency was assumed equal to 0.1 Hz.

According to the experimental tests results, the tested device is characterized by high effective stiffnesses and equivalent damping ratio in the case of very small imposed displacement amplitudes. These parameters decrease with increasing displacement amplitude, except for the effective stiffness in Tension that dramatically increase towards the largest amplitudes. The shape of the hysteresis loops changes according to the displacements amplitude: at the smallest imposed displacements, the hysteresis loops display a softening stiffness in Compression and a slight hardening in Tension, whereas, at the largest imposed displacements, the device exhibits a hardening stiffness in Tension.

Regarding the effect of the vertical pre-load on the dynamic behavior of the tested HWRI, the experimental outcomes reveal a reduction in the effective stiffness in Compression and an approximately constant equivalent viscous damping ratio due to the increase of the vertical load, while the effective stiffness in Tension increases for the largest amplitudes.

In order to simulate the dynamic behavior of the HWRI in Compression-Tension direction, a nonlinear model has been proposed, accurately calibrated, and validated by comparing the experimental hysteresis loops provided by cyclic tests with those predicted mathematically. In future papers, it will be necessary to identify a more suitable hysteretic model among those already available in the literature [13-20].

REFERENCES

- [1] M.L. Tinker, M.A. Cutchins, Damping phenomena in a wire rope vibration isolation system. *Journal of Sound and Vibration*, **157** (1), 7-18, 1992.
- [2] G.F. Demetriades, M.C. Constantinou, A.M. Reinhorn, Study of wire rope systems for seismic protection of equipment in buildings. *Engineering Structures*, **15** (5), 321-334, 1993.
- [3] G. Serino, F. Bettinali, G. Bonacina, Seismic base isolation of gas insulated electrical substations: comparison among different solutions. *Proceedings of the 4th US Conference on Lifeline Earthquake Engineering*, San Francisco, California, 1995.
- [4] G. Serino, G. Bonacina, F. Bettinali, Passive protection devices for high-voltage equipment: design procedures and performance evaluation. *Proceedings of the 4th US Conference on Lifeline Earthquake Engineering*, San Francisco, California, 1995.
- [5] M. Di Donn, G. Serino, Base isolation of high-voltage equipment: comparison between two different solutions. *Proceedings of the 7th International Conference on Probabilistic Methods Applied to Power Systems*, Napoli, Italy, 2002.
- [6] S. Alessandri, R. Giannini, F. Paolacci, M. Malena, Seismic retrofitting of an HV circuit breaker using base isolation with wire ropes. Part 1: Preliminary tests and analyses. *Engineering Structures*, **98**, 251-262, 2015.
- [7] G. De Canio, Marble devices for the base isolation of the two bronzes of Riace: a proposal for the David of Michelangelo. *Proceedings of the 15th World Conference on Earthquake Engineering*, Lisbon, Portugal, 2012.
- [8] S. Alessandri, R. Giannini, F. Paolacci, M. Amoretti, A. Freddo, Seismic retrofitting of an HV circuit breaker using base isolation with wire ropes. Part 2: Shaking-table test validation. *Engineering Structures*, **98**, 263-274, 2015.

- [9] S. Pagano, M. Russo, S. Strano, M. Terzo, A mixed approach for the control of a testing equipment employed for earthquake isolation systems. *Journal of Mechanical Engineering Science*, **228** (2), 246-261, 2014.
- [10] A.K. Chopra, *Dynamics of Structures: Theory and Applications to Earthquake Engineering, 4th Edition*. Englewood Cliffs, NJ: Prentice Hall, 2012.
- [11] P. Chakraborty, A.R. Roshan, A. Das, Evaluation of dynamic properties of partially saturated sands using cyclic triaxial tests. *Indian Geotechnical Journal*, Pune, Maharashtra, India, 2015.
- [12] S.S. Kumar, A.M. Krishna, A. Dey, Cyclic response of sand using stress controlled cyclic triaxial tests. *Proceedings of the 50th Indian Geotechnical Conference*, **50**, 948-962, 2020.
- [13] N. Vaiana, D. Losanno, N. Ravichandran, A novel family of multiple springs models suitable for biaxial rate-independent hysteretic behavior. *Computers & Structures*, **244**, 106403, 2021.
- [14] N. Vaiana, R. Capuano, S. Sessa, F. Marmo, L. Rosati, Nonlinear dynamic analysis of seismically base-isolated structures by a novel OpenSees hysteretic material model. *Applied Sciences*, **11** (3), 900, 2021.
- [15] N. Vaiana, S. Sessa, L. Rosati, A generalized class of uniaxial rate-independent models for simulating asymmetric mechanical hysteresis phenomena. *Mechanical Systems and Signal Processing*, **146**, 106984, 2021.
- [16] N. Vaiana, S. Sessa, F. Marmo, L. Rosati, A class of uniaxial phenomenological models for simulating hysteretic phenomena in rate-independent mechanical systems and materials. *Nonlinear Dynamics*, **93** (3), 1647-1669, 2018.
- [17] D. Pellicchia, S. Sessa, N. Vaiana, L. Rosati, Comparative assessment on the rocking response of seismically base-isolated rigid blocks. *Procedia Structural Integrity*, **29**, 95-102, 2020.
- [18] N. Vaiana, S. Sessa, M. Paradiso, F. Marmo, L. Rosati, An efficient computational strategy for nonlinear time history analysis of seismically base-isolated structures. *Proceedings of XXIV AIMETA Conference 2019. Lecture Notes in Mechanical Engineering*, 2020. https://doi.org/10.1007/978-3-030-41057-5_108
- [19] N. Vaiana, S. Sessa, M. Paradiso, L. Rosati, Accurate and efficient modeling of the hysteretic behavior of sliding bearings. *Proceedings of the 7th ECCOMAS Thematic Conference on Computational Methods in Structural Dynamics and Earthquake Engineering (COMPDYN 2019)*, 2019. <https://doi.org/10.7712/120119.7304.19506>
- [20] S. Sessa, N. Vaiana, M. Paradiso, L. Rosati, An inverse identification strategy for the mechanical parameters of a phenomenological hysteretic constitutive model. *Mechanical Systems and Signal Processing*, **139**, 106622, 2020.

REAL-TIME HYBRID SIMULATION OF A STRUCTURE WITH CIRCULAR FIBER REINFORCED ISOLATORS

Carlos Riascos¹, Semion Klopov², Johannio Marulanda², Peter Thomson² & Giorgio Serino³

¹ Program of Civil Engineering, Universidad del Quindío, Armenia, Colombia
cariascos@uniquindio.edu.co

² School of Civil Engineering and Geomatics, Universidad del Valle, Cali, Colombia
{semen.klopov, johannio.marulanda, peter.thomson}@correounivalle.edu.co

³ Università degli Studi di Napoli Federico II, Naples, Italy
giorgio.serino@unina.it

Abstract

More than 87% of the Colombian population lives in zones of intermediate and high seismic hazard, which has generated an increasing interest toward base isolated structures. Nowadays, this technique has been mainly applied to hospitals and bridges. However, it is necessary to expand the action field of isolators to diverse kind of structures in countries with high seismic hazard. In this direction, the performance of circular unbounded fiber reinforced elastomeric isolators (U-FREI) was studied in a two degrees-of-freedom (DoF), medium scale structure, under seismic excitation. This evaluation was achieved employing a Real-Time Hybrid Simulation (RTHS), which is defined as a modern cyber-physical technique used for the experimental evaluation of complex systems, that treats the system components with predictable behavior as a numerical substructure, and the components that are difficult to model as an experimental substructure. In this case, the main structure was considered as the numerical substructure and a couple of U-FREI was treated as the experimental substructure. The RTHS was evaluated using a set of Current Assessment Measurements, where an accurate tracking of the transfer system was determined. Furthermore, the experimental results were compared with Shaking Table Tests (STT) developed at University of Naples Federico II. Particularly, peak and RMS comparison of force and acceleration signals showed a similar behavior of the RTHS according to the STT results. Overall, both approaches demonstrated that the U-FREI were able to reduce more than the 70% of the structural drift with respect to the fixed structure, and the applied RTHS methodology was verified.

Keywords: structural control, real-time hybrid simulation, unbounded circular fiber reinforced elastomeric isolator, current assessment measurements.

1 INTRODUCTION

Earthquakes are one of the main natural hazards in countries of the Pacific zone such as Colombia, Mexico, Ecuador, Chile and Japan. To counteract the effect of the earthquake, there are two widely accepted and implemented alternatives. The first consists in isolating the structure at the base, thus reducing the energy input of the earthquake to the building [1–3]. While the second one concentrates in mitigating, through auxiliary devices, the energy that has been transmitted by the earthquake to the structure [4–6]. In a conventional design, the building will dissipate this energy through vibrations that can lead to the generation of damage in its structural and non-structural elements.

In response to this issue, one of the alternatives for structural control that became popular in Japan was the seismic isolation, due to its great performance during the Kobe earthquake of 1995 [7]. De la Llera et al. in [8] has shown the positive experience of the base isolation application with budget limitation and other technological constraints. A cost reduction alternative consists of simplifying the isolator installation process, due to it can be located between the foundation and the structure without bonding at the contact surfaces. This simplified installation method is named ‘unbonded application’ which has been recently investigated on Fiber Reinforced Elastomeric Isolators (FREI) [9].

Unfortunately, to validate the performance of such systems in civil structures would be necessary to implement full-scale experimental tests. These tests require enormous resources that can be prohibitive for some projects. In contrast, the evaluation of non-conventional and earthquake-prone structures is currently being promoted using Real-Time Hybrid Simulation (RTHS). These simulations allow the study of complex systems by classifying components that are easy to model as numerical substructure and components whose behavior is difficult to predict as experimental substructure [10–12]. Thus, the numerical substructure is represented computationally, while the experimental substructure is constructed and tested physically [13–15]. Therefore, RTHS technique involves advantages as low cost, small space, low loading capacity requirements [12, 16].

This study addressed this issue developing a RTHS for a structure with unbounded seismic isolators U-FREI (Unbounded Fiber Reinforced Elastomeric Isolators).

2 SHAKING TABLE TEST (STT)

2.1 Main structure

Losanno et al. [17] conducted a series of Shaking Table Tests (STT) with an experimental two degrees-of-freedom (DoF) base isolated system. This structure was installed at the Department of Structures for Engineering and Architecture (DiST) of the University of Naples Federico II in Italy. A cylindrical U-FREI was used below each column. Also, previously in the research [18] both polyester and carbon reinforcement were considered, where their characterization was developed through uniaxial shear and compression tests. In this case, the results obtained by Losanno et al. in [17] are used as the reference data, with the aim of validating the RTHS results achieved in this application. The reference structure consists of a steel frame, with a total height of 2.9 m and plan dimensions of 2.65x2.15 m², as shown in Figure 1. The total weight of the structure is 77 kN, with a base load of 36 kN and a top load of 41 kN. Additionally, the structural response was measured through 3-axis accelerometers (PCB356A17) and displacement sensors (Micro-epsilon ILD1402-600, Wenglor CP35MHT80) in each level.

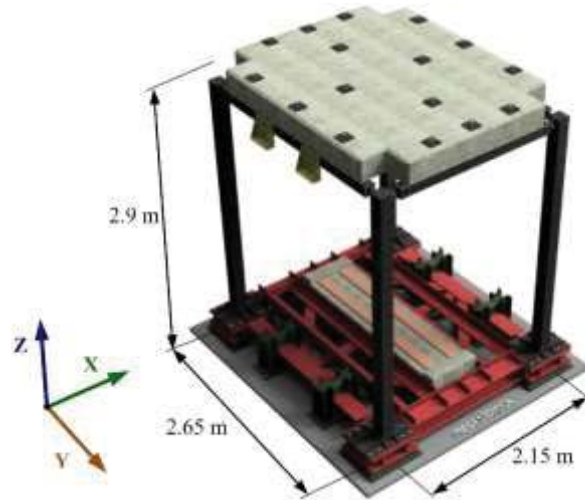


Figure 1: Scheme of the reference structure.

The dynamic characteristics of the main structure in fixed-based configuration were identified through shaking table tests in [19], and masses, natural frequency and damping ratio are presented in Table 1.

$m_{bottom}(kg)$	$m_{top}(kg)$	$f_n(Hz)$	$\zeta(\%)$
3675	4180	3.81	1.00

Table 1: Dynamic properties of the main structure.

2.2 Circular unbounded fiber reinforced elastomeric isolators

The main structure was supported by four cylindrical U-FREI, as shown in Figure 2. These isolators have a diameter of 80 mm and total height of 44 mm. Particularly, these U-FREIs are composed of 15 rubber layers with a thick of 2 mm, which were reinforced by 14 polyester fiber layers with a thick of 1 mm. The total height of rubber is $H_r = 30$ mm. The same manufacturing process is also described in Madera Sierra et al. [20].

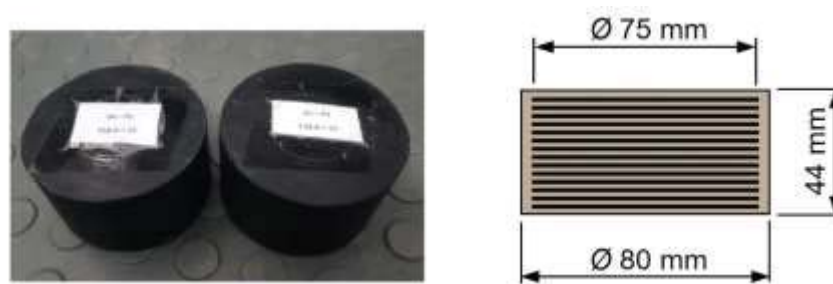


Figure 2: U-FREI.

The U-FREIs employed in the STT were characterized using a cyclic test with a maximum displacement of 9 cm, i.e. 300% shear strain. The hysteretic behavior of two set of these isolators is shown in Figure 3, as references T1a and T1b. In this study, two set of isolators, with the same geometry of those used at University of Naples, were analyzed in the LINSE Laboratory at Universidad del Valle, Cali, Colombia. These isolators were characterized with an equivalent cyclic test that presents a maximum displacement of 5 cm, whose results are

indicated in Figure 3 as LINSE (Sp1) and LINSE (Sp2). A challenging non-linear behavior is exhibited by U-FREIs as recently confirmed by several attempts to develop accurate hysteretic models [21–23].

The effective lateral stiffness $K_{h,i}$ of the devices was calculated based on the peak-to-peak lateral response for each deformation cycle, as shown in Eq. (1), where $F_{max,i}$ and $F_{min,i}$ are the maximum and minimum values of the force during the i -th cycle, and $D_{max,i}$ and $D_{min,i}$ are the corresponding for the displacement. The equivalent damping ratio β_i was estimated as a function of the dissipated area, $E_{d,i}$, during each deformation cycle, as shown in Eq. (2). Both parameters are shown in Figure 4.

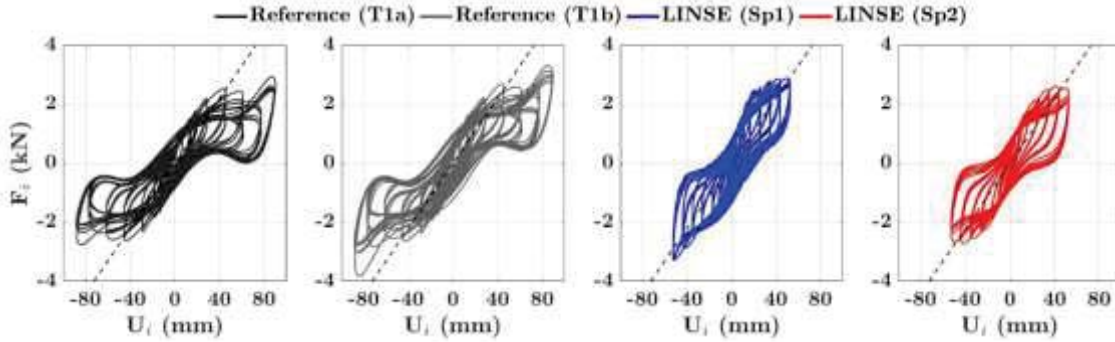


Figure 3: Hysteresis loops from cyclic tests for (a) Reference specimen T1a; (b) Reference specimen T1b; (c) LINSE specimen 1; (d) LINSE specimen 2.

$$K_{h,i} = \frac{F_{max,i} - F_{min,i}}{D_{max,i} - D_{min,i}} \quad (1)$$

$$\beta_i = \frac{E_{d,i}}{2 \cdot \pi \cdot K_{h,i} \cdot (D_{max,i})^2} \quad (2)$$

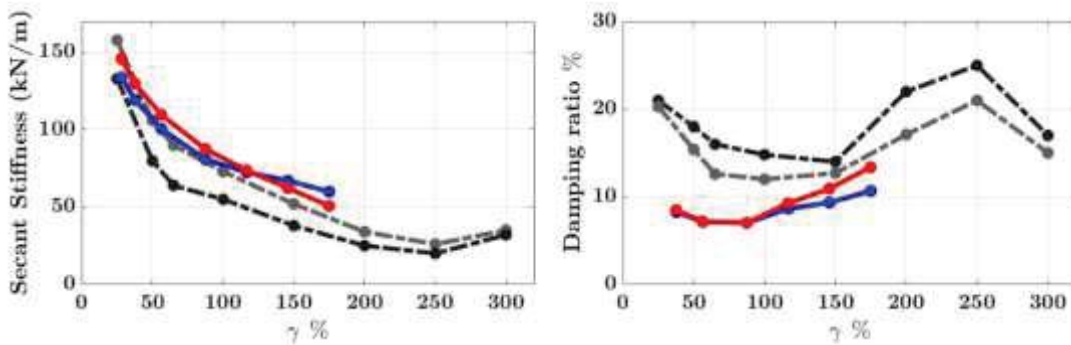


Figure 4: Comparison for the LINSE's and Federico II specimens of the (a) Secant stiffnesses and (b) Damping coefficients.

Even if secant stiffness of LINSE prototypes lightly exceeds the values from previous ones, it can be noted that a significantly lower damping is obtained especially at low deformation levels. This is probably due to a different rubber compound assumed in the manufacturing.

3 REAL-TIME HYBRID SIMULATION

Real-time hybrid simulation (RTHS) is a modern cyber-physical technique used for the experimental evaluation of complex systems, which treats the components with predictable behavior of the system as numerical substructure and the components that are difficult to model as experimental substructure. In this implementation, the structural system (without isolators) is considered as the numerical substructure since it can be modeled with a high level of accuracy, whilst the isolators are considered as the experimental substructure.

One of the main challenges of the RTHS is the generation of the boundary conditions in the experimental substructure. This process demands a detailed knowledge of the actuators that apply the information obtained from the numerical integration. These actuators are known as transfer systems. In this implementation two decentralized transfer systems are included. One of them is focused on the normal force, which is directly applied to the isolator specimens, and the other reproduces the horizontal displacement at the base of the numerical substructure through a shear force.

The input of the RTHS is the base acceleration caused by the Campano-Lucano (CAM 50%) earthquake scaled to the 50%, $a_g(t)$, which corresponds to the first input of the numerical substructure model (see, Figure 6). The horizontal displacement of the numerical substructure at the isolator location was taken as the reference signal of the horizontal transfer system, $x_{i,d}(t)$. This process generates physically a displacement in the experimental substructure that corresponds to the measured displacement, $x_{i,m}(t)$, as shown in Figure 5. Furthermore, the vertical transfer system induces a normal force, $F_v(t)$, with a reference value of 19 kN, being this value, the structural weight supported by each isolator during the STT. In this direction, the shear force produced by the experimental substructure is the feedback force, $F_{i,fb}(t)$, and this signal is assigned as the second input of the numerical substructure.

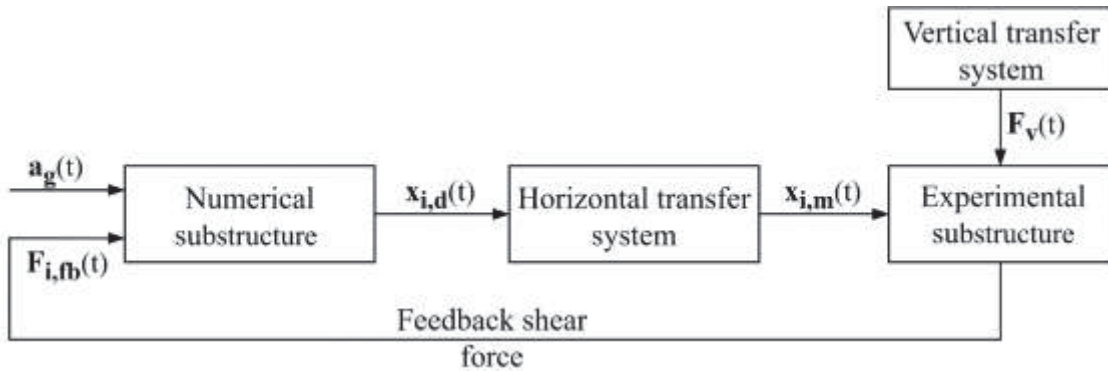


Figure 5: RTHS scheme.

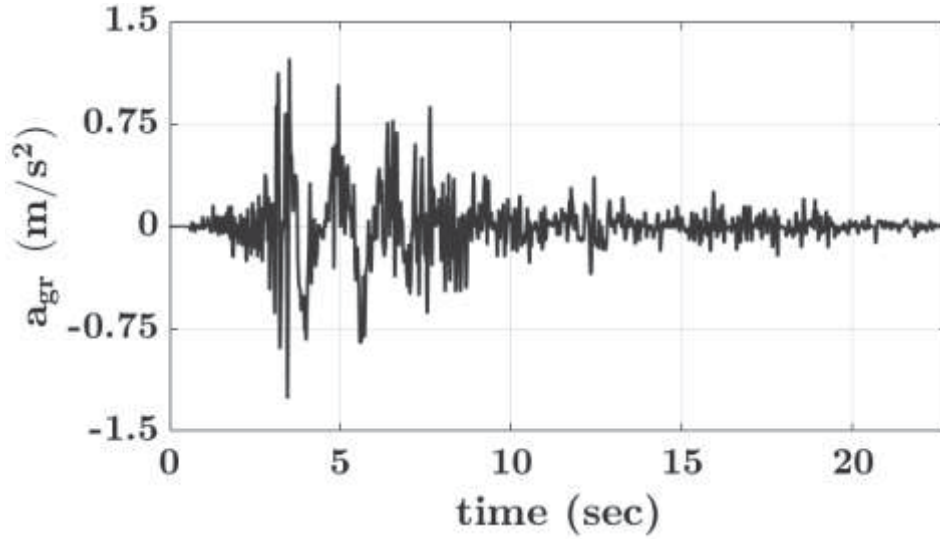


Figure 6: Ground acceleration of the CAM50% earthquake.

3.1 Numerical substructure

The main structure was modeled as a two DoF system, as shown in Eq. (3). In this state space representation m_1 and m_2 are the bottom and top structural masses, as indicates in Figure 7. k_s and c_s are the stiffness and damping of the main structure, respectively. Moreover, $u_i(t)$ and $u_s(t)$ are the displacement of the isolators and the structural displacement. The four system states correspond to the isolator displacement, x_1 , the structural displacement, x_2 , the isolator velocity, x_3 , and the structural velocity, x_4 . As mentioned above, the system inputs are the ground acceleration, $a_g(t)$, and the isolator shear force, $F_{i,fb}$, which is measured during the RTHS. It is important to mention that the system output is the first state of the numerical model.

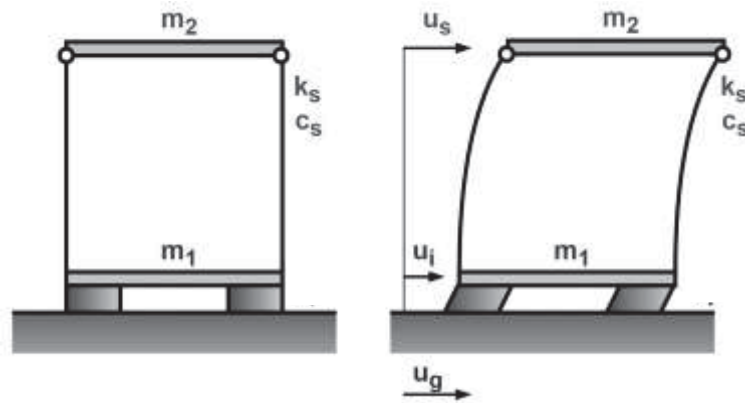


Figure 7: Main structure scheme.

$$\begin{Bmatrix} \dot{x}_1 \\ \dot{x}_2 \\ \dot{x}_3 \\ \dot{x}_4 \end{Bmatrix} = \begin{bmatrix} 0 & 0 & 1 & 0 \\ 0 & 0 & 0 & 1 \\ -k_s/m_1 & k_s/m_1 & -c_s/m_1 & c_s/m_1 \\ k_s/m_2 & -k_s/m_2 & c_s/m_2 & -c_s/m_2 \end{bmatrix} \begin{Bmatrix} x_1 \\ x_2 \\ x_3 \\ x_4 \end{Bmatrix} + \begin{bmatrix} 0 & 0 \\ 0 & 0 \\ -1 & -1/m_1 \\ -1 & 0 \end{bmatrix} \begin{Bmatrix} a_g(t) \\ F_{i,fb}(t) \end{Bmatrix} \quad (3)$$

3.2 Experimental substructure

The behavior of the isolators in unbounded configuration is highly complex: because of the variation of the contact area [14, 18], it tends to decrease the horizontal stiffness and increase the energy dissipation. Also, U-FREI performs a phenomenon denominated roll-over as mentioned previously. A complete roll-over takes place when the original vertical face of the isolator is approaching the horizontal support [9, 18, 24, 25]. It is shown that after the initial point of roll-over, a gradual softening of the isolators is produced, and after the end point of full roll-over, it can be observed an effect of stiffness hardening. Thus, in this study the U-FREIs are considered as the experimental substructure. For this purpose, an experimental setup was developed to couple the experimental substructure with the cybernetic component of the RTHS.

The experimental setup involves a moving plate, which is released in the vertical direction to allow the movement associated with the compression of the isolators. In addition, this plate is supported on linear bearings, which are oriented in the horizontal direction. In this configuration, two isolators are disposed in the experimental setup as shown in Figure 8. Thus, the opposition force of the isolators was measured by a load cell Optima OP-312-3. The normal force was set to 19 kN during the simulation, which is applied by a vertical hydraulic actuator. The compression load cell Omega LPCH-5-M12 was used to control the vertical compression.

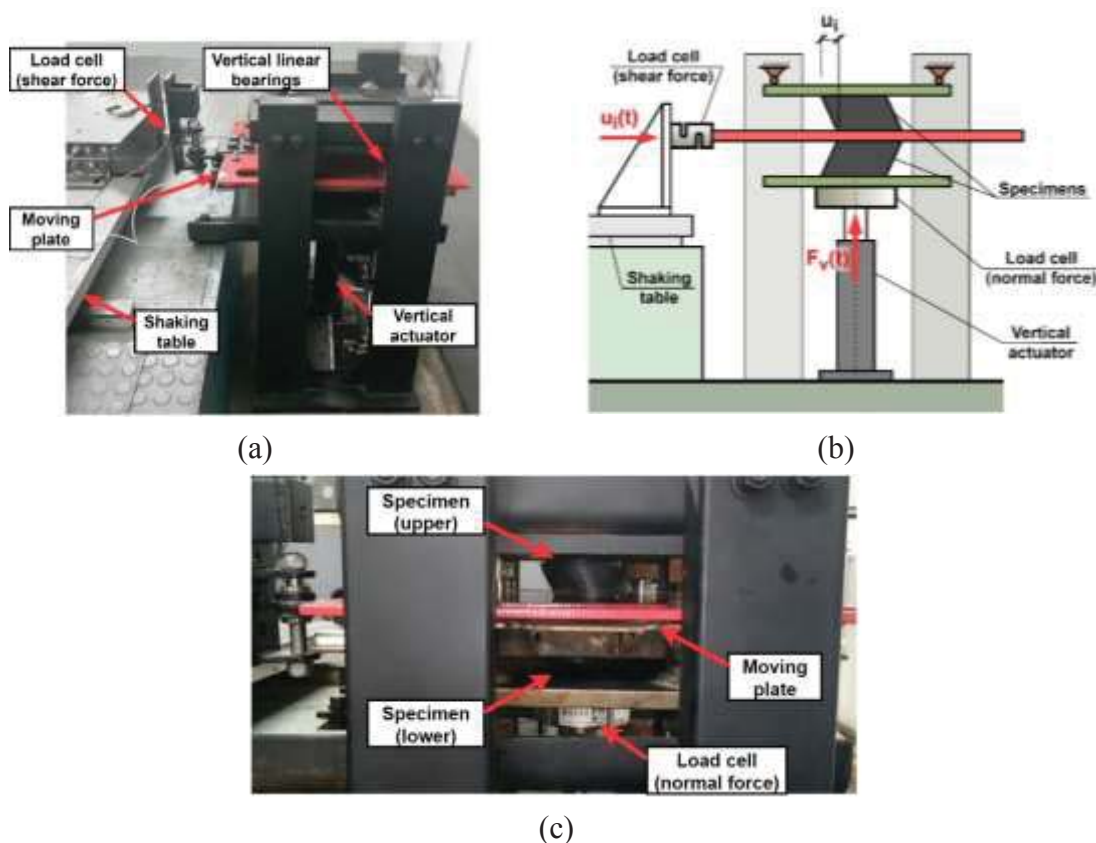


Figure 8: (a) Experimental setup, (b) Experimental setup scheme, and (c) Deformed U-FREI.

3.3 Transfer systems

The RTHS control scheme is shown in Figure 9, where the horizontal control displacement is achieved through an actuator Shore Wester 911D, which has a linear variable differential transformer (LVDT). This LVDT allows to measure the displacement of the actuator piston with higher precision. This actuator is activated by a hydraulic pump that presents a maximum flow of 13.2 liters per minute. Particularly, the system pump-actuator or plant was modeled as a continuous system with one pole at the origin, without zeros, a nominal gain of 14, and a delay of 33 milliseconds. Due to the considerable noise in the LVDT measure, a Kalman filter was designed to obtain an adequate signal, according to the RTHS scope. As shown in Figure 9, the plant was feed-back using the filtered actuator displacement, $x_{m,f}[kT]$, and a unit delay. This close loop generates a stable system, in contrast to the marginal stability of the plant in open loop. Moreover, the internal loop can filter the high frequency components of the controller output, $v[kT]$. Nevertheless, the adequate tracking characteristics (amplitude and angle phase) of the horizontal transfer system were achieved using an optimal control technique in the external loop. In this case, a H_∞ controller was employed, which Riascos et al. in [26–28] designed using the hinfstruc Matlab function, where the optimization was developed for minimizing the error signal, $e[kT]$, and the operational voltage signal, $u[kT]$.

On the other hand, the vertical control force consists of three components. The first component is a linear function expressed as $a F_{v,d} + b$, which determines the nominal voltage required by a Power Unity to apply a force, $F_{v,d}$, in the actuator. The second component is a term based on a hysteretic loop between the actuator force and the power unity voltage. This term depends on the error sign, as described in Figure 9. The third component consists of a proportional-integral (PI) controller, which fits the voltage to achieve a measured force close to the reference despite of the isolator deformation.

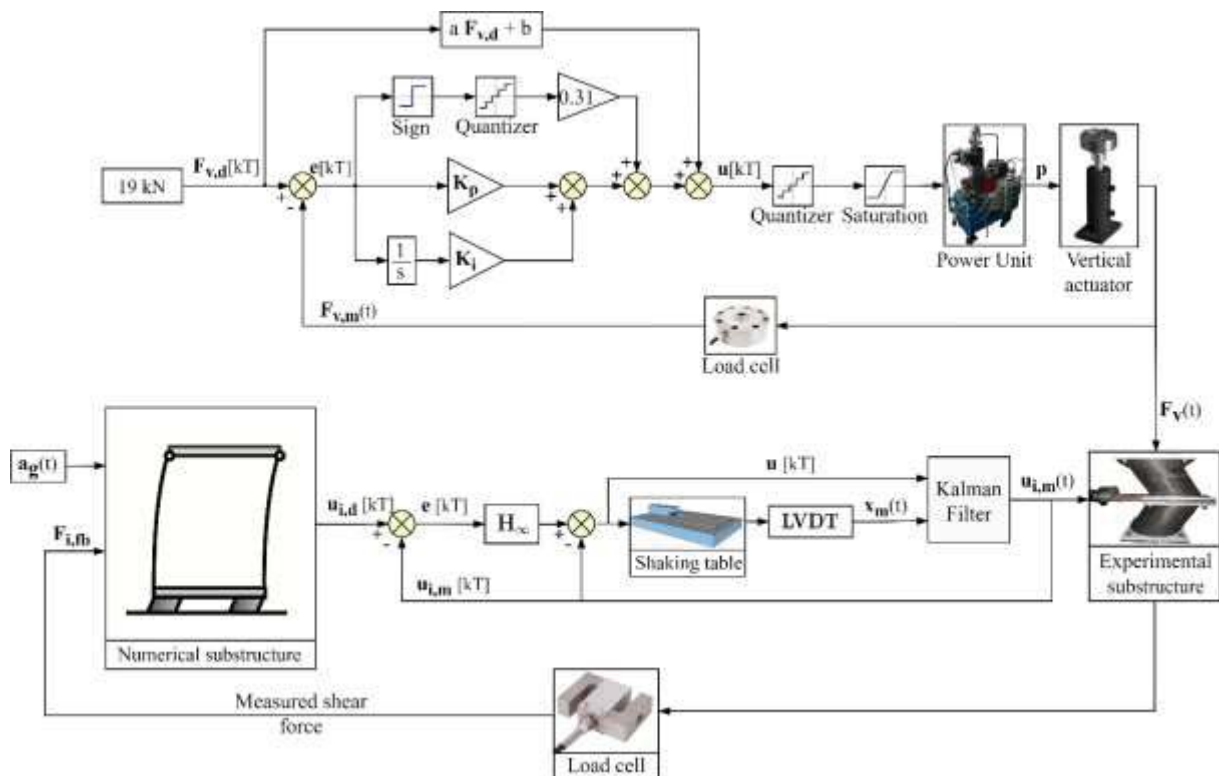


Figure 9: RTHS scheme.

4 RTHS IMPLEMENTATION

This RTHS was implemented with a high-speed executing computer (SpeedGoat target machine). For this task, a host computer with Matlab's Xpc protocol and a sampling frequency of 1024 Hz was used. The SpeedGoat has high processing capacity to guarantee real-time evaluation of the hybrid simulation. For the CAM 50% earthquake, a comparison between STT and RTHS approaches is presented in Figure 10.

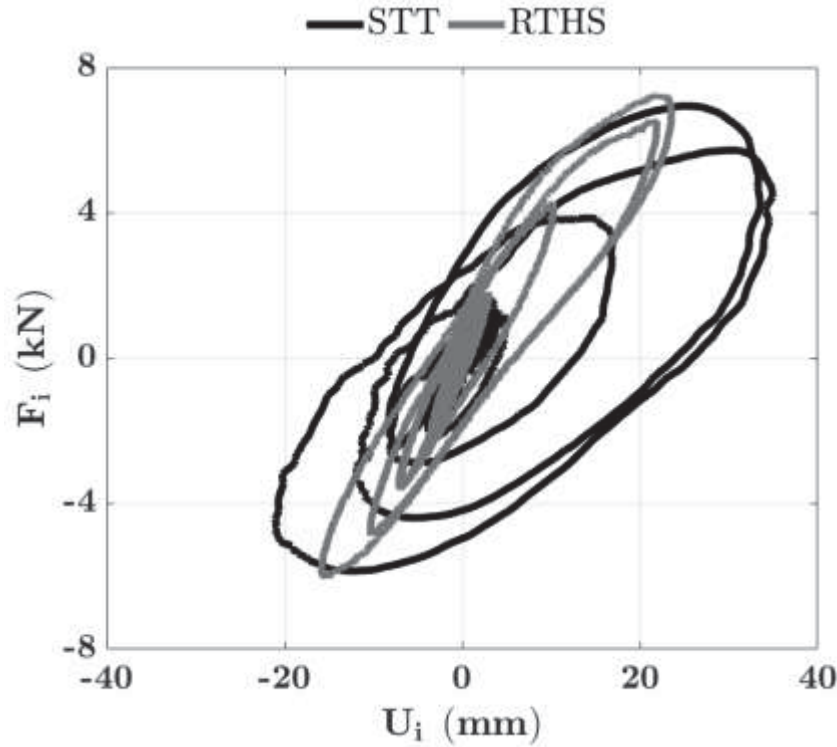


Figure 10: RTHS implementation.

4.1 RTHS performance

Assessment measures are adopted to determine the accuracy of the RTHS. The parameters selected in this study focused especially on the tracking accuracy of the main transfer system. These parameters involve time or frequency domains. For example, the difference of maximum error and the maximum difference errors are calculated in time domain, as given in Eqs. (4) and (5). The frequency evaluation index (FEI) compares the target and measured signals in the frequency domain using the fast Fourier transform (FFT), and the equivalent frequency (f^{eq}) identifies the cycle frequency where there is the most energy of the signal, as given in Eqs. (6) and (7), respectively. The generalized amplitude, A_0 , and generalized angle, ϕ , depend on the FEI as expressed in Eqs. (8)-(9). Further, the delay, δ , between the target and measured signals is determined in function of FEI, which is the opposite value of the FEI argument over the equivalent angular frequency, as given by Eq. (10).

$$e_{DM} = \frac{||x_t|^{max} - |x_m|^{max}|}{|x_m|^{max}} \quad (4)$$

$$e_{MD} = \frac{|x_t - x_m|^{max}}{|x_m|^{max}} \quad (5)$$

$$FEI = \sum_{j=1}^N \left\{ \frac{y_m(j)}{y_c(j)} \cdot \frac{\|y_c(j)\|^l}{\sum_{i=1}^p \|y_c(j)\|^l} \right\} \quad (6)$$

$$f^{eq} = \frac{\sum_{j=1}^N \{\|y_c(j)\|^l \cdot f_j\}}{\sum_{j=1}^N \|y_c(j)\|^l} \quad (7)$$

$$A_0 = \|FEI\| \quad (8)$$

$$\emptyset = \arctan[Im(FEI)/Re(FEI)] \quad (9)$$

$$\delta = -\frac{\emptyset}{2\pi f^{eq}} \quad (10)$$

FEI	$f^{eq}(Hz)$	A_0	$e_{DM}(\%)$	$e_{MD}(\%)$	δ (ms)
1.000 – 0.009 i	0.52	1.00	0.27	2.25	2.87

Table 2: Assessment measures.

4.2 RTHS Comparison

To validate the RTHS results some comparison indexes were proposed. These indexes allow to determine the peak and Root Mean Square (RMS) coherence between the force, acceleration, or displacement, of the RTHS (y_{RTHS}), with respect to those obtained with the STT (y_{STT}). Both indexes are defined in Eqs. (11)-(12). The comparison index results are listed in Table 3, where can be observed the adequate correspondence between the force and acceleration signals obtained with the RTHS in comparison with those of the STT. However, the displacement signal between both approaches presented considerable differences. These differences indicate that the isolator displacement in the RTHS technique was approximately only 66% of the STT response. This was caused by the higher stiffness of the specimens used in this study, which also present lower damping for small deformations. In addition, the upper structure presented a maximum inter-story drift of 0.109% through the STT, whilst a drift of 0.179% was achieved with the RTHS approach. This drift difference was caused by the high stiffness of the U-FREIs employed during the RTHS, since these isolators transmit more seismic energy to the upper structure in comparison with those implemented in the STT.

$$J_{peak} (\%) = 100 \frac{\max(y_{RTHS})}{\max(y_{STT})} \quad (11)$$

$$J_{RMS} (\%) = 100 \frac{RMS(y_{RTHS})}{RMS(y_{STT})} \quad (12)$$

Signal	J_{peak} (%)	J_{RMS} (%)
Force	104	105
Acceleration	91	95
Displacement	67	66

Table 3: Indexes of comparison between responses for RTHS and STT.

5 CONCLUSIONS

The main findings of this study can be listed as follows:

- Experimental results show that the horizontal transfer system was able to generate the isolator displacement obtained from the numerical integration with good accuracy.
- The equivalent frequency of the RTHS reported an operational frequency at 0.52 Hz, which allowed to the transfer system achieving an excellent tracking with respect to the desired displacement, where generalized amplitude of 1.00 and delay lower than 3 milliseconds were obtained.
- The RTHS achieved an adequate prediction of the peak and RMS force and acceleration of the isolated structure, despite of using a simplified model of the main structure and an experimental substructure with different mechanical characteristics in terms of stiffness and damping, with respect to that presented during the STT.
- In the RTHS technique, the isolator displacement was approximately a fraction, i.e. 66% of the STT response. This was caused by the higher stiffness that presents the specimens used in this study, which present poor damping for small deformations.
- Overall, both approaches demonstrated that the U-FREIs were able to reduce considerably the structural drift with respect to the fixed structure, and the applied RTHS methodology was verified.
- As a further development the authors will improve the numerical models of the structure in order to improve the accuracy of the RTHS.

ACKNOWLEDGEMENTS

The authors would like to acknowledge the financial support granted by the postdoctoral project with contract 80740-159-2020 (OCONT-189) (OCONT-98), from the Administrative Ministry of Science and Technology of Colombia MINCIENCIAS and the Universidad del Quindío, and the technical support provided through the project 21115 financed by MINCIENCIAS and the Universidad del Valle.

REFERENCES

- [1] D. Losanno, H. A. Hadad, and G. Serino, “Design charts for eurocode-based design of elastomeric seismic isolation systems,” *Soil Dyn. Earthq. Eng.*, vol. 119, pp. 488–498, 2019.
- [2] D. Losanno, H. A. Hadad, and G. Serino, “Seismic behavior of isolated bridges with additional damping under far-field and near fault ground motion,” *Earthquakes Struct.*,

- vol. 13, no. 2, pp. 119–130, 2017.
- [3] D. Losanno, M. Spizzuoco, and G. Serino, “Optimal design of the seismic protection system for isolated bridges,” *Earthquakes Struct.*, vol. 7, no. 6, pp. 969–999, 2014.
- [4] D. Losanno, M. Spizzuoco, and G. Serino, “Design and retrofit of multistory frames with elastic-deformable viscous damping braces,” *J. Earthq. Eng.*, vol. 23, no. 9, pp. 1441–1464, 2019.
- [5] I. Nuzzo, D. Losanno, and N. Caterino, “Seismic design and retrofit of frame structures with hysteretic dampers: a simplified displacement-based procedure,” *Bull. Earthq. Eng.*, vol. 17, no. 5, pp. 2787–2819, 2019.
- [6] I. Nuzzo, D. Losanno, F. Cilento, and N. Caterino, “Analytical and numerical modelling of shear-link device for seismic energy dissipation in frame structures,” *Eng. Struct.*, vol. 214, p. 110630, 2020.
- [7] P. T. Daniel Gomez, Johannio Marulanda, “SISTEMAS DE CONTROL PARA LA PROTECCIÓN DE ESTRUCTURAS CIVILES SOMETIDAS A CARGAS DINÁMICAS,” *Dyna*, vol. 155, pp. 77–89, 2008.
- [8] J. C. De la Llera, C. Lüders, P. Leigh, and H. Sady, “Analysis, testing, and implementation of seismic isolation of buildings in Chile,” *Earthq. Eng. Struct. Dyn.*, vol. 33, no. 5, pp. 543–574, 2004.
- [9] H. Toopchi-Nezhad, M. J. Tait, and R. G. Drysdale, “Shake table study on an ordinary low-rise building seismically isolated with SU-FREIs (stable unbonded-fiber reinforced elastomeric isolators),” *Earthq. Eng. Struct. Dyn.*, vol. 38, no. 11, pp. 1335–1357, 2009.
- [10] G. Mosqueda, B. Stojadinovic, and S. A. Mahin, “Real-time error monitoring for hybrid simulation. Part I: methodology and experimental verification,” *J. Struct. Eng.*, 2007.
- [11] Y. Qian, G. Ou, A. Maghareh, and S. J. Dyke, “Parametric identification of a servo-hydraulic actuator for real-time hybrid simulation,” *Mech. Syst. Signal Process.*, 2014.
- [12] F. Lin, A. Maghareh, S. J. Dyke, and X. Lu, “Experimental implementation of predictive indicators for configuring a real-time hybrid simulation,” *Eng. Struct.*, vol. 101, pp. 427–438, 2015.
- [13] S. Strano and M. Terzo, “Implementation and validation of a hybrid testing procedure for base-isolated structures,” in *Lecture Notes in Engineering and Computer Science*, 2016.
- [14] A. Calabrese, S. Strano, and M. Terzo, “Real-time hybrid simulations vs shaking table tests: Case study of a fibre-reinforced bearings isolated building under seismic loading,” *Struct. Control Heal. Monit.*, vol. 22, no. 3, pp. 535–556, 2015.
- [15] R. Zhang, B. M. Phillips, S. Taniguchi, M. Ikenaga, and K. Ikago, “Shake table real-time hybrid simulation techniques for the performance evaluation of buildings with inter-story isolation,” *Struct. Control Heal. Monit.*, vol. 24, no. 10, pp. 1–19, 2017.
- [16] D. Gomez, S. J. Dyke, and A. Maghareh, “Enabling role of hybrid simulation across NEES in advancing earthquake engineering,” *Smart Struct. Syst.*, vol. 15, no. 3, pp. 913–929, 2014.
- [17] D. Losanno, I. E. M. Sierra, M. Spizzuoco, J. Marulanda, and P. Thomson, “Experimental performance of unbonded polyester and carbon fiber reinforced elastomeric isolators under bidirectional seismic excitation,” *Eng. Struct.*, vol. 209, p. 110003, 2020.
- [18] D. Losanno, I. E. M. Sierra, M. Spizzuoco, J. Marulanda, and P. Thomson, “Experimental assessment and analytical modeling of novel fiber-reinforced isolators in unbounded configuration,” *Compos. Struct.*, vol. 212, pp. 66–82, 2019.
- [19] G. Magliulo *et al.*, “Shake table tests on infill plasterboard partitions,” *Open Constr. Build. Technol. J.*, vol. 6, no. 1, 2012.

- [20] I. E. M. Sierra, D. Losanno, S. Strano, J. Marulanda, and P. Thomson, “Development and experimental behavior of HDR seismic isolators for low-rise residential buildings,” *Eng. Struct.*, vol. 183, pp. 894–906, 2019.
- [21] N. Vaiana, S. Sessa, F. Marmo, and L. Rosati, “A class of uniaxial phenomenological models for simulating hysteretic phenomena in rate-independent mechanical systems and materials,” *Nonlinear Dyn.*, vol. 93, no. 3, pp. 1647–1669, 2018.
- [22] N. Vaiana, D. Losanno, and N. Ravichandran, “A novel family of multiple springs models suitable for biaxial rate-independent hysteretic behavior,” *Comput. Struct.*, vol. 244, p. 106403, 2021.
- [23] N. Vaiana, S. Sessa, and L. Rosati, “A generalized class of uniaxial rate-independent models for simulating asymmetric mechanical hysteresis phenomena,” *Mech. Syst. Signal Process.*, vol. 146, p. 106984, 2021.
- [24] D. Losanno *et al.*, “Recycled versus natural-rubber fiber-reinforced bearings for base isolation: review of the experimental findings,” *J. Earthq. Eng.*, pp. 1–20, 2020.
- [25] D. Losanno, M. Spizzuoco, and A. Calabrese, “Bidirectional shaking-table tests of unbonded recycled-rubber fiber-reinforced bearings (RR-FRBs),” *Struct. Control Heal. Monit.*, vol. 26, no. 9, p. e2386, 2019.
- [26] C. Riascos, J. Marulanda Casas, and P. Thomson, “Semi-active tuned liquid column damper implementation with real-time hybrid simulations,” in *Active and Passive Smart Structures and Integrated Systems 2016*, 2016, vol. 9799, p. 979919.
- [27] C. A. Riascos-González, P. Thomson, and S. Dyke, “Performance evaluation of a non-linear tuned mass damper through real-time hybrid simulation,” *INGE CUC*, vol. 15, no. 2, pp. 11–22, 2019.
- [28] C. Riascos, J. Marulanda, and P. Thomson, “Structural control of a grandstand using a semi-active pressurized tuned liquid column damper considering effects of passive crowds,” *Struct. Control Heal. Monit.*, 2019.

A COMPARATIVE STUDY ON THE ACCURACY AND EFFICIENCY OF TWO BIAXIAL HYSTERETIC MODELS SUITABLE FOR ELASTOMERIC BEARINGS

Nagavinothini Ravichandran¹

¹ Department of Structures for Engineering and Architecture, University of Naples Federico II, Via
Claudio 21, 80125, Napoli, Italy
e-mail: nagavinothini.ravichandran@unina.it

Abstract

In common practice, uncoupled hysteretic models, that is, models that do not consider the biaxial interaction between the restoring forces along two generic orthogonal transverse directions, are typically employed to perform nonlinear time history analyses of base isolated structures. However, such models do not suitably reproduce the exact response of the structure when the system is subjected to external excitation in two orthogonal directions. Thus, the selection of suitable phenomenological model and the time integration method is important while carrying out nonlinear time history analysis (NLTHA) of base isolated structures. In the present study, a detailed investigation is carried out to assess the effectiveness of two hysteretic models to reproduce the hysteretic behaviour of the elastomeric bearings. A three-dimensional base-isolated reinforced concrete building is analysed under earthquake excitations, by employing a novel biaxial phenomenological model denominated Multiple Springs Exponential Model (MSEM) and Biaxial Bouc-Wen model (BBWM). Numerical accuracy and the computational efficiency of these methods are assessed through NLTHA. The results show that the novel method is advantageous and computationally efficient in comparison with BBWM.

Keywords: Hysteresis model, base isolated structure, phenomenological model, multiple springs, nonlinear time history analysis.

1 INTRODUCTION

Base isolation is one of the effective response control technologies that helps in reducing the seismic response of structures by introducing isolation bearings between the foundation and superstructure of the building [1,2,3,4]. The continuous development in the base isolation technology and innovative isolation devices [5,6,7,8] lead to a significant increase in the base isolated structures in the recent years. The behaviour of base isolated structures is highly influenced by the base isolation system, which need to be carefully investigated [9,10,11]. Due to the difficulties associated with the development of detailed finite element models of isolation bearings, several studies were carried out to identify a hysteresis model to reproduce the most realistic behaviour of the bearings [12].

In addition, the isolation bearings display a coupled behaviour when subjected to external excitation in two orthogonal directions [13]. Several phenomenological models are widely used to reproduce the biaxial rate-independent behaviour of seismic isolation bearings obtained from cyclic experimental tests. Biaxial differential models are mostly employed to reproduce the hysteresis phenomena, due to its accuracy and requirement of a smaller number of model parameters [14]. However, the computational efficiency of such models are affected due to the physical insignificance of the model parameters. Also, they demand a numerical solution of a differential vector equation to obtain the response of the building at each time step of a Nonlinear Time History Analysis (NLTHA).

One of the most commonly used models is the Bouc-Wen model (BWM), but the nonlinear time history analysis of a structural model using BWM demands increased computational effort. Further, the interpretation of BWM parameters is not straightforward due to its peculiar formulation [15]. The recently formulated Biaxial Bouc-Wen model (BBWM) is capable of reproducing the biaxial behaviour of the isolation bearings. Despite its reported accuracy, the physical interpretation of model parameters and the computational time remains as a major difficulty during the response analyses of base isolated buildings.

Considering the assessment of base-isolated building response, the accuracy of the nonlinear analyses depends on the selection of suitable phenomenological model and the time integration method to solve the nonlinear equilibrium equations. In this context, the present study aims at investigating the novel coupled phenomenological model developed by Vaiana et al. [14] to simulate the rate-independent hysteretic behaviour of isolation bearings of a base isolated structure. Multiple Springs Exponential Model (MSEM), formulated from the general class of novel phenomenological model, is considered for the study. The obtained results are compared with the BBWM results in order to check the accuracy and computational efficiency of the MSEM. Further, Nonlinear Time History Analyses (NLTHAs) of a two-story base-isolated reinforced concrete building is also carried out using MSEM and BBWM to model the behaviour of isolation bearings. Considering the importance of time integration method in the NLTHA of base-isolated buildings, the widely used Newmark's constant acceleration method is used along with the BBWM model. In case of base isolated building with MSEM mode, Chang's explicit method is used for NLTHA due to reduced computational effort and the results obtained from this novel methodology is compared with the conventional procedure.

2 HYSTERESIS MODELS

The response of a base-isolated structure is highly influenced by the dynamic properties of the isolation devices. Hence, the selection of a suitable hysteresis model plays a major role in the nonlinear analysis of such structures. Hysteresis models, ranging from simple bilinear models to complex models and developed for particular applications, are available in the liter-

ature [16,17]. In the present study, a novel biaxial phenomenological model, denominated Multiple Springs Exponential Model (MSEM) and formulated by Vaiana et al. [14], is considered along with the celebrated BBWM. The hysteresis models used to represent the behaviour of isolation bearings are presented in the following subsections.

2.1 Bouc-Wen model

BWM is governed by a first-order nonlinear Ordinary Differential Equation (ODE) characterized by six parameters that govern the shape and size of the hysteresis loops. The model is based in the Duhem hysteresis operator and simulates a smooth transition between elastic and post-elastic states [18,19]. Park et al. [20] extended the uniaxial model to simulate the biaxial rate-independent hysteretic behaviour of systems and materials. Finally, the generalized biaxial formulation of the model is proposed by Harvey and Gavin [21], and the components of the generalized force vector are given by:

$$\begin{Bmatrix} f_x(u_x) \\ f_y(u_y) \end{Bmatrix} = a k \begin{Bmatrix} u_x \\ u_y \end{Bmatrix} + (1 - a) k d \begin{Bmatrix} z_x \\ z_y \end{Bmatrix} \quad (1)$$

where k and d are parameters with dimensions of stiffness and displacement, respectively, u_x and u_y are the generalized displacements along X-axis and Y-axis, respectively, a is a dimensionless parameter, and z_x and z_y are dimensionless variables which can be obtained from the following system of two coupled first-order nonlinear ODEs:

$$\dot{z}_x = d^{-1} \left[A \dot{u}_x - z_x (b |\dot{u}_x z_x| + c \dot{u}_x z_x + b |\dot{u}_y z_y| + c \dot{u}_y z_y) (z_x^2 + z_y^2)^{\frac{e-2}{2}} \right] \quad (2)$$

$$\dot{z}_y = d^{-1} \left[A \dot{u}_y - z_y (b |\dot{u}_x z_x| + c \dot{u}_x z_x + b |\dot{u}_y z_y| + c \dot{u}_y z_y) (z_x^2 + z_y^2)^{\frac{e-2}{2}} \right] \quad (3)$$

where A , b , and c are dimensionless parameters that control the shape of the hysteresis loops. Thus, BBWM requires the calibration of seven parameters to simulate the exact hysteresis behaviour of isolation bearings through experiments. BWM is used along with Newmark's constant average acceleration method to solve the nonlinear equilibrium equations. This method is unconditionally stable and also allows the use of large time steps while fulfilling the requirement for accuracy [22,23]. However, the computational efficiency of the method is highly affected by the convergence issues due to the conjunction of the method along with the iterative procedure [24].

2.2 Multiple Springs Exponential Model

The novel family of biaxial models proposed by Vaiana et al. [14] is capable of simulating the typical bidirectional kinematic rate-independent hysteretic behaviour displayed by mechanical systems and materials. The biaxial model is formulated by employing the multiple springs model [25] in conjunction with the uniaxial phenomenological models developed by Vaiana et al. [26,27]. The model was developed by introducing n evenly spaced springs in a circular configuration around the origin of the adopted coordinate system as shown in Figure 1(a). Each spring is made up of two different springs in parallel such as the elastic spring with generalized tangent stiffness k_e , and a rate-independent hysteretic spring with generalized tangent stiffness k_b , as shown in Figure 1(b). The generalized tangent stiffness k_t is obtained by summing k_e and k_b .

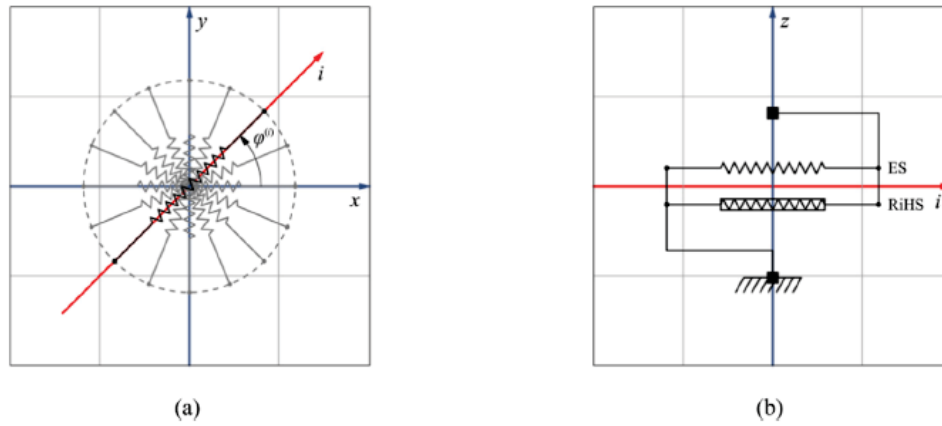


Figure 1: (a) Plan view of the multiple springs model, and (b) i-th spring [14].

The generalized force-displacement hysteresis loops characterizing the i-th spring of the proposed model may be limited to two parallel straight lines (curves), as shown in Figure 2. The integration of the general expression of the generalized tangent stiffness functions yields the expressions for the generic loading (unloading) curve and for the upper (lower) limiting curve. The integration constants are obtained by considering the intersection of generic loading (unloading) curve and upper (lower) limiting curve. The abscissa of the intersection point is represented as the generalized history variable.

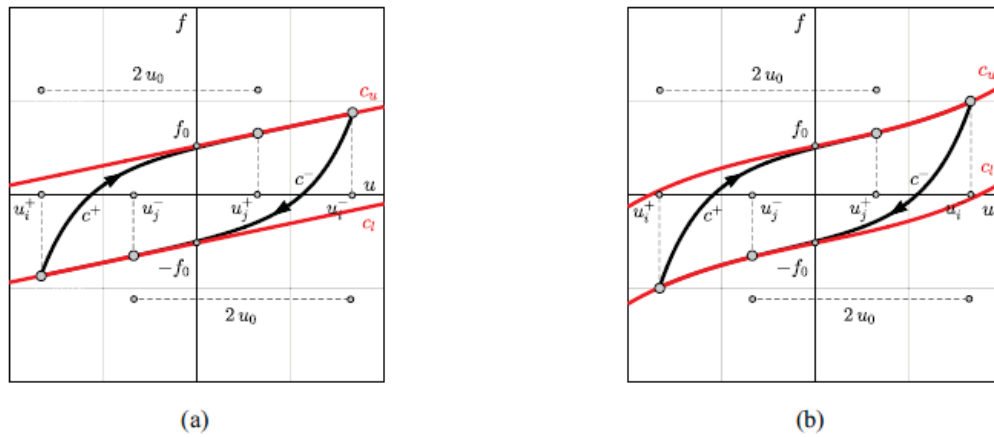


Figure 2: Hysteresis loop limited by two parallel (a) straight lines, and (b) curves [14].

Multiple Springs Exponential Model (MSEM) considered in the present study belongs to this family of biaxial models, which is obtained by selecting a suitable generalized tangent stiffness functions and then by deriving the particularized expression of the generalized force, history variable, and internal constant parameters. For simplicity, same properties are assigned for all the springs in the model, thus obtaining an isotropic model. MSEM is a more sophisticated model where the typical generalized force-displacement hysteresis loop of the i-th spring is limited by two parallel straight lines or curves. This model requires four parameters to simulate the complex biaxial hysteresis phenomena. The general expression of the generalized tangent stiffness functions can be obtained from the sum of following expressions of k_e and k_h :

$$k_e(u) = -2\beta + \beta(e^{\beta u} + e^{-\beta u}) \quad \text{on } (-\infty, \infty) \quad (4)$$

$$k_h(u, u_j^+) = \begin{cases} k_b + (k_a - k_b)e^{-\alpha(u - u_j^+ + 2u_0)} & \text{on } [u_j^+ - 2u_0, u_j^+ [\\ k_b & \text{on }]u_j^+, \infty), \end{cases} \quad (5)$$

$$k_h(u, u_j^-) = \begin{cases} k_b + (k_a - k_b)e^{-\alpha(-u + u_j^- + 2u_0)} & \text{on }]u_j^-, u_j^- + 2u_0] \\ k_b & \text{on } (-\infty, u_j^- [\end{cases} \quad (6)$$

where k_a , k_b , α , and β are the four model parameters that fulfill the following conditions: $k_a > k_b$, $k_a > 0$, $\alpha > 0$, whereas β is real.

The general expression of the i -th spring generic loading and unloading curves can be written as follows:

$$c^+(u, u_j^+) = -2\beta u + e^{\beta u} - e^{-\beta u} + k_b u - \frac{(k_a - k_b)}{\alpha} \left[e^{-\alpha(u - u_j^+ + 2u_0)} - e^{-2\alpha u_0} \right] + f_0 \quad (7)$$

$$c^-(u, u_j^-) = -2\beta u + e^{\beta u} - e^{-\beta u} + k_b u + \frac{(k_a - k_b)}{\alpha} \left[e^{-\alpha(-u + u_j^- + 2u_0)} - e^{-2\alpha u_0} \right] - f_0 \quad (8)$$

Further, the expressions of the upper and lower limiting curves are given by:

$$c_u(u) = -2\beta u + e^{\beta u} + e^{-\beta u} + k_b u + f_0 \quad (9)$$

$$c_l(u) = -2\beta u + e^{\beta u} - e^{-\beta u} + k_b u - f_0 \quad (10)$$

The general equations used to evaluate the generalized history variable for the generic loading and unloading cases are as follows:

$$u_j^+ = u_p + 2u_0 + \frac{1}{\alpha} \ln \left[+ \frac{\alpha}{k_a - k_b} \left(-2\beta u_p + e^{\beta u_p} - e^{-\beta u_p} + k_b u_p + \frac{(k_a - k_b)}{\alpha} e^{-2\alpha u_0} + f_0 - f_p \right) \right] \quad (11)$$

$$u_j^- = u_p - 2u_0 - \frac{1}{\alpha} \ln \left[- \frac{\alpha}{k_a - k_b} \left(-2\beta u_p + e^{\beta u_p} - e^{-\beta u_p} + k_b u_p - \frac{(k_a - k_b)}{\alpha} e^{-2\alpha u_0} - f_0 - f_p \right) \right] \quad (12)$$

The expression of the constant parameter u_0 can be derived by assuming that the upper (lower) limiting curves and generic loading (unloading) curves have the same generalized tangent stiffness functions at their intersection point. It can be given by:

$$u_0 = -\frac{1}{2\alpha} \ln \left(\frac{\delta_k}{k_a - k_b} \right) \quad (13)$$

Further, the expression for the constant parameter f_0 is obtained as follows:

$$f_0 = \frac{k_a - k_b}{2\alpha} (1 - e^{-2\alpha u_0}) \quad (14)$$

In the present study, this novel coupled phenomenological model is used along with an explicit unconditionally stable time integration method. This strategy avoids the use of iterative procedures for solving nonlinear equilibrium equations and it is useful when complex prob-

lems need to be addressed [28,29]. The explicit time integration method considered in the study represents a specific algorithm developed by Chang [30] and adopted by Vaiana et al. [31] for base-isolated structures. In case of non-stiffening systems, this method tends to be unconditionally stable and has a second-order accuracy. Further, the method does not suffer from numerical damping and displays only a small relative period error.

3 NUMERICAL MODEL

A three dimensional (3D) structural model with two substructures such as the n -story superstructure and a base isolation system is considered to assess the accuracy and computational efficiency of the proposed model. The 3D model defined in global, right-handed cartesian coordinate system attached to the mass centre of the base isolation system is shown in Figure 3. The nonlinear analysis of the base isolated structure is carried out considering the following assumptions: (a) the deformation of the superstructure is within the linear elastic range during the earthquake excitation, (b) the floor diaphragm is infinitely rigid in its own plane, (c) the columns are axially inextensible, (d) the beams are flexurally rigid and axially inextensible, (e) the base isolation bearings are axially inextensible.

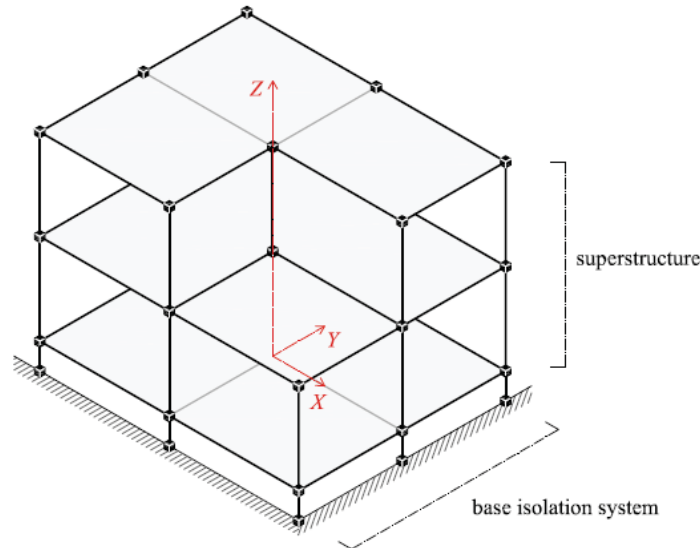


Figure 3: Three-dimensional model of base isolated structure.

The superstructure of the base isolated structure is a two-story reinforced concrete structure with vertical geometrical irregularity. The plan dimension of the building is 10.0 m x 8.0 m with a story height of 3.50 m. The weight of the superstructure is 1802.90 kN. The first three natural periods of the superstructure are 0.15 s, 0.14 s and 0.10 s. The total weight of base isolation system with 9 elastomeric bearings is 914.90 kN. The bearings are placed between the superstructure columns full diaphragm. The base isolation system is designed to provide an effective isolation period of 2.25 s and an effective viscous damping of 15% at the design displacement 0.50 m. As per the assumptions considered for the nonlinear analysis of the structure, the number of degrees-of-freedom of the super structure and the isolation system are equal to 6 and 3, respectively.

The nonlinear equilibrium equation considered for the analysis of the Multi-Degree-Of-Freedom (MDOF) base isolated structure is given by:

$$M\ddot{u}(t) + C\dot{u}(t) + Ku(t) + f_n(t) = p(t) \quad (15)$$

where, $u(t)$, $\dot{u}(t)$, and $\ddot{u}(t)$ are the generalized displacement, velocity, acceleration vectors, respectively, M , C , and K are the generalized constant mass, damping and elastic stiffness matrices, respectively, $f_n(t)$ is the generalized nonlinear force vector, and $p(t)$ is the generalized external force vector at time t .

For the adopted base isolated structure idealization, the motion vectors of the model relative to the ground can be written as follows:

$$u = \begin{Bmatrix} u_b \\ u_s \end{Bmatrix}, \quad \dot{u} = \begin{Bmatrix} \dot{u}_b \\ \dot{u}_s \end{Bmatrix}, \quad \ddot{u} = \begin{Bmatrix} \ddot{u}_b \\ \ddot{u}_s \end{Bmatrix} \quad (16)$$

where, $u_b, \dot{u}_b, \ddot{u}_b$ ($u_s, \dot{u}_s, \ddot{u}_s$) are the displacement, velocity and acceleration vectors of base isolation device (superstructure) of size 3×1 ($3n \times 1$), respectively.

The force vectors are given by:

$$f_n = \begin{Bmatrix} f_{nb} \\ 0 \end{Bmatrix}, \quad p = - \begin{bmatrix} M_b & 0^T \\ 0 & M_s \end{bmatrix} \begin{Bmatrix} R_b \\ R_s \end{Bmatrix} \ddot{u}_g \quad (17)$$

where, f_{nb} is the nonlinear force vector of the base isolation system with dimension 3×1 , $R_b(R_s)$ is the influence matrix of base isolation system (superstructure), and \ddot{u}_g is the ground acceleration vector of dimension 3×1 .

4 HYSTERESIS MODEL PARAMETERS

The parameters of the biaxial Bouc-Wen model adopted to simulate the behaviour of the elastomeric bearings are shown in Table 1. MSEM requires calibration of four parameters (k_a, k_b, α, β) and 'n' number of springs. MSEM model parameters are identified using Particle Swarm Optimization (PSO) algorithm [32] which is a computational technique with easy implementation and convergence properties. In the algorithm, a set of random parameters are first initialized, and the value of each parameter is iteratively modified. The optimization is performed by considering the interaction among the parameters and the objective function is minimized. MSEM parameters are calibrated in the present study by minimizing the following objective function:

$$\Theta = \sum_j \sqrt{(f_j^{MSEM} - f_j)^2} \quad \text{with } j = x, y \quad (18)$$

where, f_j^{MSEM} is the j-th component of the generalized force vector computed using MSEM and f_j is the j-th component of the generalized force vector describing the behaviour of the isolation bearings using BWM. The following PSO parameters are used to avoid premature convergence of the solution in the local optimum points:

- population size: 100,
- number of iterations: 200,
- acceleration factors: $c_1 = c_2 = 2$,
- maximum and minimum inertia weights: $w_{\max} = 0.9$ and $w_{\min} = 0.4$.

The adopted MSEM parameters are listed in Table 2. The comparison of hysteresis loops of BWM and MSEM model with the calibrated parameters are shown in Figure 4. The plots are obtained by imposing eight-shaped displacement orbit given by $u_x = a_o \sin \omega t$ and $u_y = a_o \sin 2\omega t$, with $a_o = 0.5$ m and $\omega = 2\pi$ rad/s. It can be clearly seen that the MSEM model is capable of representing the hysteresis behaviour of the isolation bearing with reduced number of parameters, in comparison with BWM.

K [N/m]	A	a	b	c	d [m]	e
1.83e6	1	0.10	1.00	0.00	0.017	1.00

Table 1: BWM parameters used in the NLTHAs.

n	k_a [N/m]	k_b [N/m]	α [m ⁻¹]	β [N/m]
16.00	5.78e8	1.83e5	1.04e4	0

Table 2: MSEM parameters used in the NLTHAs.

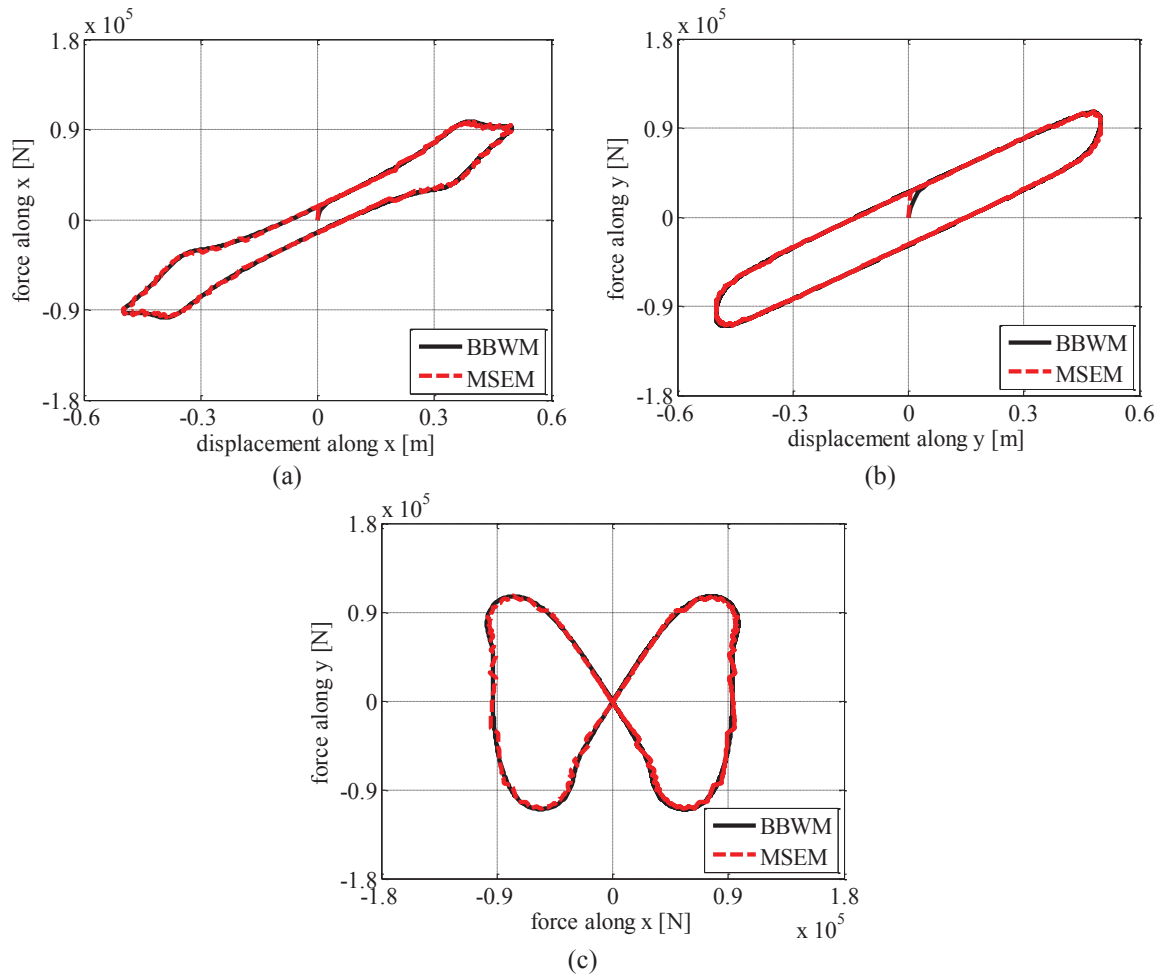


Figure 4: Comparison between BBWM and MSEM hysteresis loops along (a) X-axis, (b) Y-axis, and (c) generalized force paths by applying eight-shaped generalized displacement orbit.

The numerical model has been programmed in MATLAB and run on a computer with Intel® Core™ i5-5200U processor and a CPU at 2.20GHz with 8.00 GB RAM. The computational time of BBWM is 20.97 s, whereas the MSEM model required only 0.53s, which is about 2.50% of the BBWM computational time. Along with the computational time, the model also exhibits acceptable accuracy with reduced number of model parameters, making the calibration process easier.

5 NUMERICAL ANALYSES OF A BASE-ISOLATED STRUCTURE

The response of the base isolated structure under bidirectional earthquake excitation is presented in this section. In the analyses, the BBWM and MSEM are used to reproduce the dynamic behaviour of the isolation bearings of the base isolated structure. Further, conventional time integration method is used along with BBWM to numerically integrate the nonlinear equilibrium equations, whereas Chang's explicit method is used along with the novel MSEM. The NLTHA of the base isolated structure is performed by imposing Northridge earthquake acceleration time history along X-axis and Y-axis as shown in Figure 5.

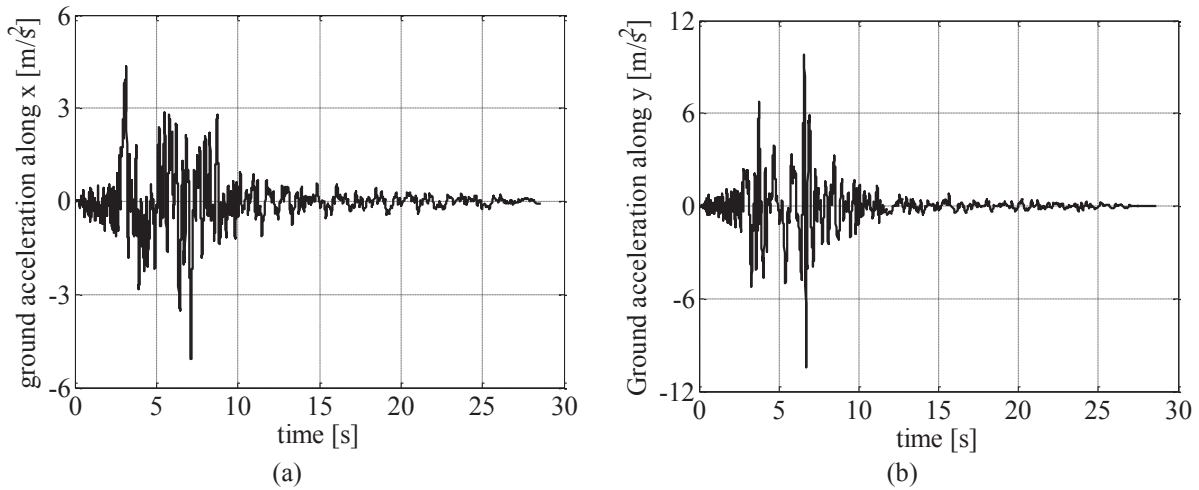


Figure 5: Ground acceleration time histories of Northridge earthquake along (a) X-axis and (b) Y-axis.

The numerical results and computational time are compared to assess the accuracy and computational efficiency of the solution strategies. The first order nonlinear ODE in the BWM is solved using the unconditionally stable semi-implicit Range-Kutta method with 50 number of steps [33]. The results of the NLTHAs are listed in Table 3. It can be clearly seen that the maximum and minimum values of the base isolation system mass centre displacements (\mathbf{u}), velocities ($\dot{\mathbf{u}}$) and accelerations ($\ddot{\mathbf{u}}$) obtained using BBWM and MSEM are almost equal. In addition to the seismic response of the base isolated structure, the total computational time tct required to perform NLTHAs by BBWM and MSEM are also given in Table 3. It can be clearly seen that the MSEM reduces the computational time drastically. Since, the obtained computational time highly depends on the CPU speed, relevant memory and background process running on the computer, an additional parameter $tctp$ which is the total computational time percentage is also evaluated as follows:

$$\text{MSEM } tctp [\%] = \frac{\text{MSEM } tct}{\text{BBWM } tct} \cdot 100 \quad (19)$$

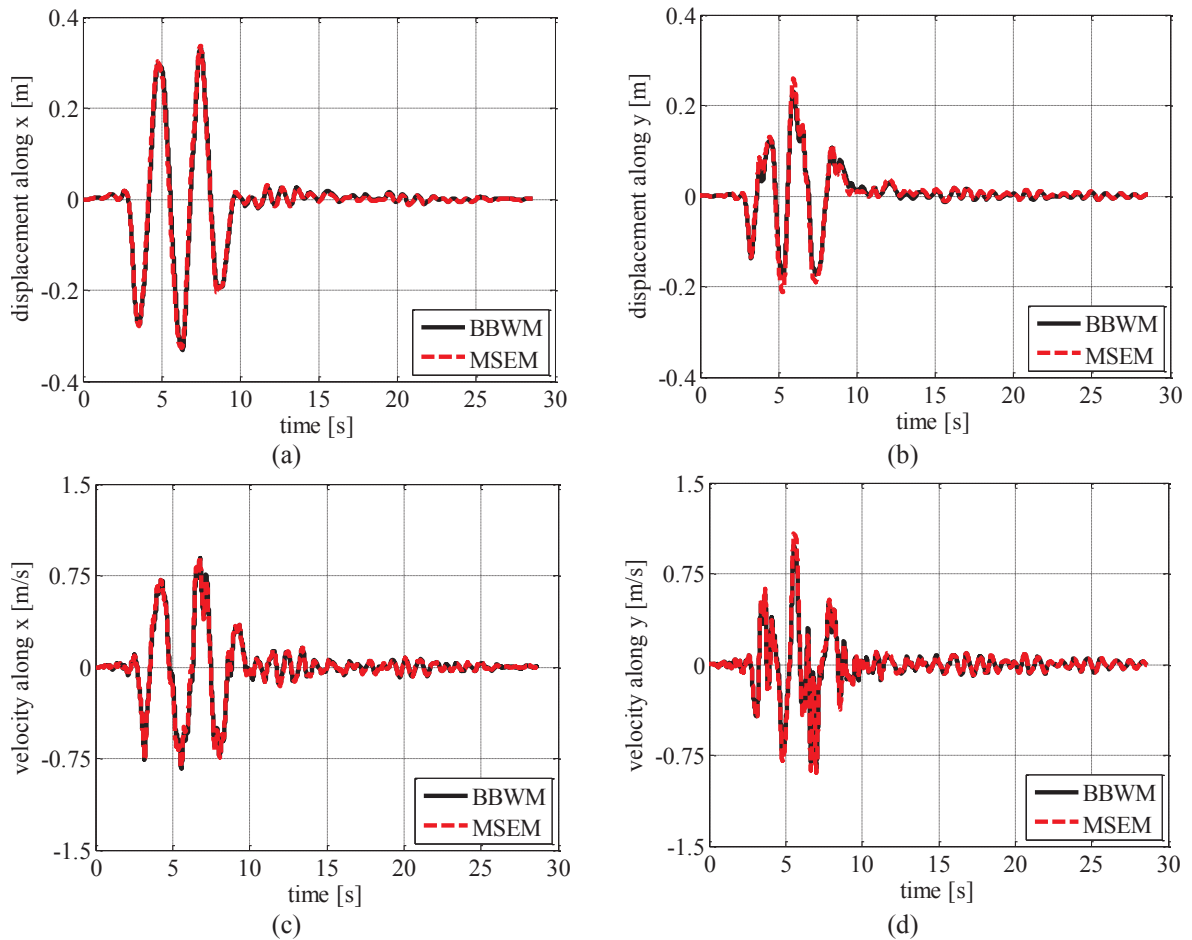
This parameter provides a more meaningful measure of the computational benefits associated with MSEM, in comparison with BBWM. The value of the $tctp$ in the order of 0.87% highlights the advantages of implementing this model in structural analysis tools and commercial computer programs.

Further, the comparison of displacement, velocity and acceleration response measured at the base isolation system mass centre obtained using BBWM and MSEM models are shown in Figure 6(a) to 6(f). The results clearly highlight the accuracy of the novel biaxial phenomenological model in comparison with the BBWM. A minor difference arises in terms of hysteresis

etic response of the isolation bearings in Figure 6(g) and 6(h) due to different formulations of the models to be properly calibrated on experimental tests.

		BBWM	MSEM	ϵ [%]
t_{ct} [s]		12104	105	
t_{ctp} [%]		-	0.87	
u_x [m]	Max	0.33	0.33	0.00
	Min	-0.33	-0.33	0.00
u_y [m]	Max	0.23	0.25	8.00
	min	-0.18	-0.21	14.29
\dot{u}_x [ms ⁻¹]	Max	0.89	0.90	1.11
	min	-0.83	-0.82	-1.20
\dot{u}_y [ms ⁻¹]	Max	0.98	1.08	9.26
	min	-0.85	-0.89	1.12
\ddot{u}_x [ms ⁻²]	Max	5.16	4.90	-5.04
	min	-3.93	-3.83	-2.54
\ddot{u}_y [ms ⁻²]	Max	10.37	10.47	0.96
	min	-10.55	-10.30	-2.37

Table 3: NLTHAs results under Northridge excitation.



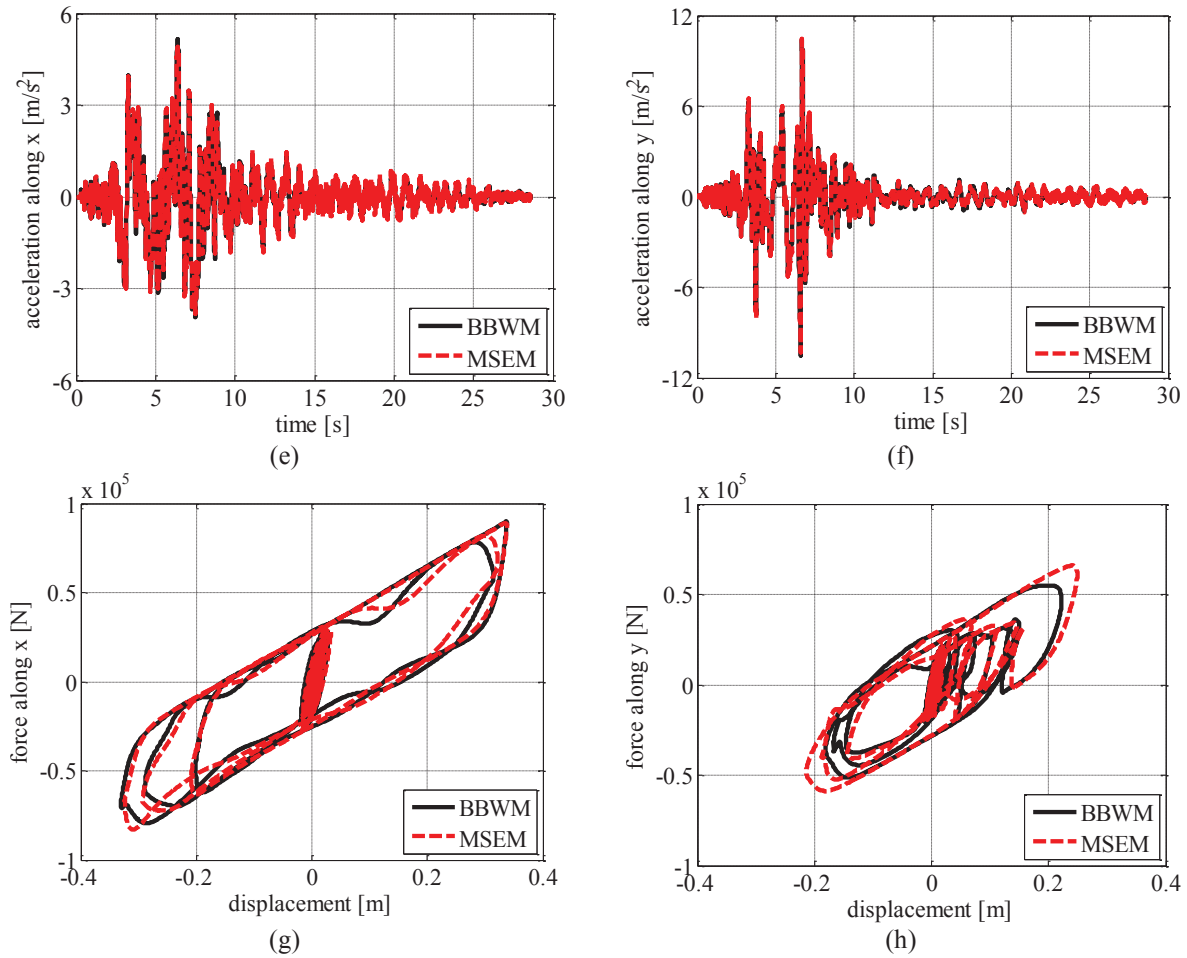


Figure 6: Seismic response of the base isolated structure (a) displacement along X-axis, (b) displacement along Y-axis, (c) velocity along X-axis, (d) velocity along Y-axis, (e) acceleration along X-axis, (f) acceleration along y-axis, (g) hysteresis loops along X-axis, and (h) hysteresis loops along Y-axis.

6 CONCLUSIONS

In the present study, the accuracy and computational efficiency of the two biaxial hysteretic models to reproduce the behaviour of elastomeric bearings is assessed. A novel biaxial phenomenological model denominated Multiple Springs Exponential Model is compared with the commonly used Biaxial Bouc-Wen Model. The novel model is found to be advantageous in comparison with BBWM due its reduced number of model parameters, physical interpretation of parameters, easier calibration, and reduced computational time.

Further, NLTHA of a three-dimensional base isolated reinforced concrete building is also carried out. Considering the importance of time integration methods employed in NLTHA of base isolated structures, Newmark's constant average acceleration method and Chang's explicit method are used along with BBWM and MSEM, respectively. The dynamic response of the base isolated structure obtained using the MSEM model and Chang's explicit method closely matches with the results from the conventional procedure using BBWM and Newmark's method. Further, the total computational time percentage of the novel method is only around 0.87% which highlights the computational efficiency and suitability of this model for implementation in structural analysis tools.

REFERENCES

- [1] D. Losanno, H.A. Hadad, G. Serino, Seismic behavior of isolated bridges with additional damping under far-field and near fault ground motion. *Earthquakes and Structures*, 13(2), 119-130, 2017.
- [2] D. Losanno, H.A. Hadad, G. Serino, Design charts for eurocode-based design of elastomeric seismic isolation systems. *Soil Dynamics and Earthquake Engineering*, 119, 488-498, 2019.
- [3] D. Losanno, M. Spizzuoco, A. Calabrese, Bidirectional shaking-table tests of unbonded recycled-rubber fiber-reinforced bearings (RR-FRBs). *Structural Control and Health Monitoring*, 26(9), e2386, 2019.
- [4] N. Vaiana, R. Capuano, S. Sessa, F. Marmo, L. Rosati, Nonlinear Dynamic Analysis of Seismically Base-Isolated Structures by a Novel OpenSees Hysteretic Material Model. *Applied Sciences*, 11(3), 900, 2021.
- [5] A. Calabrese, D. Losanno, M. Spizzuoco, S. Strano, M. Terzo, Recycled Rubber Fiber Reinforced Bearings (RR-FRBs) as base isolators for residential buildings in developing countries: The demonstration building of Pasir Badak, Indonesia. *Engineering Structures*, 192, 126-144, 2019.
- [6] N. Vaiana, S. Sessa, M. Paradiso, L. Rosati, Accurate and efficient modeling of the hysteretic behavior of sliding bearings. In *7th International Conference on Computational Methods in Structural Dynamics and Earthquake Engineering (COMPDYN 2019)*, Crete, Greece, June, 2019. doi: 10.7712/120119.7304.19506
- [7] D. Losanno, A. Calabrese, I.E. Madera-Sierra, M. Spizzuoco, J. Marulanda, P. Thomson, G. Serino, Recycled versus natural-rubber fiber-reinforced bearings for base isolation: review of the experimental findings. *Journal of Earthquake Engineering*, 1-20, 2020.
- [8] D. Losanno, F. Palumbo, A. Calabrese, T. Barrasso, N. Vaiana, Preliminary Investigation of Aging Effects on Recycled Rubber Fiber Reinforced Bearings (RR-FRBs). *Journal of Earthquake Engineering*, 1-18, 2021.
- [9] D. Losanno, I.E.M. Sierra, M. Spizzuoco, J. Marulanda, P. Thomson, Experimental assessment and analytical modeling of novel fiber-reinforced isolators in unbounded configuration. *Composite Structures*, 212, 66-82, 2019.
- [10] D. Losanno, N. Ravichandran, F. Parisi, A. Calabrese, G. Serino, Seismic performance of a Low-Cost base isolation system for unreinforced brick Masonry buildings in developing countries. *Soil Dynamics and Earthquake Engineering*, 141, 106501, 2021.
- [11] I.E.M. Sierra, D. Losanno, S. Strano, J. Marulanda, P. Thomson, Development and experimental behavior of HDR seismic isolators for low-rise residential buildings. *Engineering Structures*, 183, 894-906, 2019.
- [12] N. Ravichandran, A comparative study of phenomenological hysteretic models with application to recycled rubber-fibre reinforced bearings. *Journal of Vibroengineering*, 22(8), 1798-1813, 2020.
- [13] D. Losanno, I.E.M. Sierra, M. Spizzuoco, J. Marulanda, P. Thomson, P. Thomson, Experimental performance of unbonded polyester and carbon fiber reinforced elastomeric isolators under bidirectional seismic excitation. *Engineering Structures*, 209, 110003, 2020.

- [14] N. Vaiana, D. Losanno, N. Ravichandran, A novel family of multiple springs models suitable for biaxial rate-independent hysteretic behavior. *Computers & Structures*, 244, 106403, 2021.
- [15] A.E. Charalampakis, V.K. Koumoussis, Identification of Bouc–Wen hysteretic systems by a hybrid evolutionary algorithm. *Journal of Sound and Vibration*, 314(3-5), 571-585, 2008.
- [16] J. Lubliner, *Plasticity theory*. Courier Corporation, 2008.
- [17] C.S. Tsai, T.C. Chiang, B.J. Chen, S.B. Lin, An advanced analytical model for high damping rubber bearings. *Earthquake engineering & structural dynamics*, 32(9), 1373-1387, 2003.
- [18] Y.K. Wen, Method for random vibration of hysteretic systems. *Journal of the engineering mechanics division*, 102(2), 249-263, 1976.
- [19] Y.K. Wen, Equivalent linearization for hysteretic systems under random excitation. *Journal of applied mechanics*, 47(1), 150-154, 1980.
- [20] Y.J. Park, Y.K. Wen, A.H.S. Ang, Random vibration of hysteretic systems under bi-directional ground motions. *Earthquake engineering & structural dynamics*, 14(4), 543-557, 1986.
- [21] P.S. Harvey Jr, H.P. Gavin, Truly isotropic biaxial hysteresis with arbitrary knee sharpness. *Earthquake engineering & structural dynamics*, 43(13), 2051-2057, 2014.
- [22] K.J. Bathe, *Finite element procedures*. Klaus-Jurgen Bathe, 2006.
- [23] F. Greco, R. Luciano, G. Serino, N. Vaiana, A mixed explicit–implicit time integration approach for nonlinear analysis of base-isolated structures. *Annals of Solid and Structural Mechanics*, 10(1-2), 17-29, 2018.
- [24] R. Clough, J. Penzien, *Dynamics of structures*. McGraw-Hill, New York, 1993.
- [25] A. Wada, M. Kinoshita, Elastic plastic dynamic 3-dimensional response analysis by using multiple shear spring model Part1 and Part2. In *Summaries of Technical Papers of Annual Meeting* (pp. 313-316). 313–316 (in Japanese) Tokai, Japan, 1985.
- [26] N. Vaiana, S. Sessa, F. Marmo, L. Rosati, A class of uniaxial phenomenological models for simulating hysteretic phenomena in rate-independent mechanical systems and materials. *Nonlinear Dynamics*, 93(3), 1647-1669, 2018.
- [27] N. Vaiana, S. Sessa, L. Rosati, A generalized class of uniaxial rate-independent models for simulating asymmetric mechanical hysteresis phenomena. *Mechanical Systems and Signal Processing*, 146, 106984, 2021.
- [28] S. Sessa, F. Marmo, N. Vaiana, L. Rosati, A computational strategy for Eurocode 8-compliant analyses of reinforced concrete structures by seismic envelopes. *Journal of Earthquake Engineering*, 1-34, 2018.
- [29] F. Marmo, S. Sessa, N. Vaiana, D. De Gregorio, L. Rosati, Complete solutions of three-dimensional problems in transversely isotropic media. *Continuum Mechanics and Thermodynamics*, 32(3), 775-802, 2020.
- [30] S.Y. Chang, Family of structure-dependent explicit methods for structural dynamics. *Journal of Engineering Mechanics*, 140(6), 06014005, 2014.

- [31] N. Vaiana, S. Sessa, M. Paradiso, F. Marmo, L. Rosati, An Efficient Computational Strategy for Nonlinear Time History Analysis of Seismically Base-Isolated Structures. In *Conference of the Italian Association of Theoretical and Applied Mechanics* (pp. 1340-1353). Springer, Cham, September, 2019.
https://doi.org/10.1007/978-3-030-41057-5_108
- [32] J. Kennedy, R. Eberhart, Particle swarm optimization. In *Proceedings of ICNN'95-international conference on neural networks* (Vol. 4, pp. 1942-1948). IEEE, November, 1995.
- [33] H.H. Rosenbrock, Some general implicit processes for the numerical solution of differential equations. *The Computer Journal*, 5(4), 329-330, 1963.

LABORATORY CHARACTERIZATION OF A RECLAIMED RUBBER COMPOUND FOR LOW-COST ELASTOMERIC ISOLATORS

Fabrizia Cilento¹, Daniele Losanno¹, Luigi Piga²

¹ Department of Structures for Engineering and Architecture, University of Naples, Federico II, Via Claudio 21, Naples, Italy
{fabrizia.cilento, daniele.losanno}@unina.it

² Italgum srl, Via Vegri 27, Zanè (VI), Italy
luigi_piga@italgum.com

Abstract

Although seismic isolation devices are effective in protecting structures during an earthquake, they are generally large, heavy, and expensive, making their application prohibitive for housing buildings. In the last few years, different strategies have been investigated to make seismic isolators cheaper and lighter for housing buildings in developing countries. Lower costs can be obtained at different scales: simplifying the installation process of devices, reducing energy consumption during manufacturing, and using recycled materials. Both weight and cost of isolators could be reduced by adopting flexible reinforcements in place of steel reinforcing plates, also allowing easier installation without bolted connections in unbounded configuration. Costs can be further reduced by replacing natural rubber with a recycled elastomer. It has been demonstrated that trying to give a second life to rubber is challenging, since devulcanization process, capable of breaking chemical bonds between rubber and sulphur, is highly polluting and requires high consumption of energy. In the present work, a recycled compound has been preliminary developed with mechanical properties not significantly lower than virgin rubber. Obtained parameters are satisfactory for use in unbounded isolators with flexible internal reinforcement where internal stresses are significantly reduced. In particular, a novel compound has been properly formulated in order to be lower cost in comparison to traditional one. Mechanical characterization of the material showed excellent properties including shear modulus and hardness similar to those of a soft rubber, even if a reduced ultimate deformation capacity is achieved. Furthermore, rubber adhesion with different fabrics has been investigated. Preliminary results are very promising and pave the way for the development of high-performance and low-cost rubber isolators.

Keywords: Base isolation, fibre reinforced elastomeric rubber isolators, recycled rubber

1 INTRODUCTION

Base isolation is one of the most effective technologies in seismic protection of structures [1]. Its objectives are the protection of human life and the reduction of damage caused to buildings during earthquakes. Despite all, the system is rarely used in emerging countries due to its relatively high cost and features of the design codes. In fact, classical steel-reinforced elastomeric isolators (SREIs) are generally large, heavy, and expensive due to the highly labor-intensive manufacturing process, making their application prohibitive in the case of housing buildings. In the last years, many efforts have been done trying to develop novel low-cost seismic devices, in order to expand the market of seismic protection systems also to ordinary housing buildings, particularly in high seismicity areas of developing countries [2,3]. Lower costs can be obtained by: (i) simplifying the installation process of the devices, (ii) reducing energy consumption during manufacturing process and (iii) using waste and recycled materials. The first approach was aimed to replace steel plates with fibre sheets [4]. In comparison with rigid reinforcements, flexible reinforcements are lighter and can be easily introduced in the manufacturing process of elastomeric rubber bearing to be installed under the structure in an unbonded configuration [5,6]. In fact, in masonry buildings, these devices are placed directly under the foundations of the structure, with no need for additional transfer elements, leading to a significant reduction of the construction costs [3]. These new devices are known as fiber reinforced elastomeric isolators (FREIs) [7]. Costs can be further reduced by replacing virgin rubber with a recycled low-cost elastomer, mitigating, at the same time, the threat of rubber scraps increasing all over the world. However, recycling rubber is challenging, due to its chemical structure and composition, which make it an insoluble and infusible material that cannot be easily reprocessed. One of the major methods of sustainable management of used tyres is grinding them and use the rubber particles to produce a new environmental-friendly polymer. The fabrication process of these material consists in grinding rubber into particles of different shape and dimensions, mixing them with a low amount of polyurethane and then hot pressing or cold forging the material in order to obtain recycled rubber pads. This material is characterized by density low and low mechanical properties [8]. Another method to obtain a 100% recycled rubber material consists in compression moulding of rubber granules at elevated temperature and pressure, necessary to break the crosslink bond, without the addition of any binder [9–11]. This material exhibits good mechanical properties and high density [12]. Some studies have shown the possibility of using rubber pads to produce recycled rubber isolators reinforced with carbon fibres (RU-FREI) avoiding the vulcanization process [13]. In fact, manufacturing cost of one RU-FREI is of a few Euros and about 1/10 of the cost of a traditional SREI. Shaking table tests, performed by Losanno et al. [14,15] confirmed the effectiveness of the RU-FREI isolation systems in reducing the accelerations and inter-story drifts along the height of the building. However, RU-FREI could be employed as seismic isolation system for heavy structures, such as masonry buildings, because when designed for a lightweight frame, these bearings end up having a low aspect ratio, becoming unstable under large lateral deformations [7]. In the present work, the authors introduce a new compound whose characteristics are in between virgin natural rubber and recycled rubber. For this purpose, a novel compound has been formulated and the physical and mechanical properties have been investigated. The material has shown excellent mechanical properties compared to that of natural rubber, in terms of both shear modulus and hardness, even if a reduced ultimate deformation capacity is achieved. Most importantly, the material exhibited excellent adhesion both with metal and synthetic fabric, preventing debonding which characterized RU-FREI. Thus, the cost savings for raw materials combined with satisfactory mechanical performance could pave the way to a novel low-cost isolation system. Finally, the preliminary design of

seismic isolator reinforced with nylon and polyester fabric is presented as prototypes to be tested in the near future.

2 DEVELOPMENT OF THE COMPOUND

Both physical and mechanical properties of the compound are investigated to assess hardness, stiffness, equivalent viscous damping, deformation, and durability properties of the compound.

The rheometric behaviour of the material has been investigated according to ISO 3417 [16]. Two moulding temperatures, 140°C and 177°C, are considered in order to find the optimal combination of curing temperature and time. This test describes precisely and quickly curing and processing characteristics of vulcanizable rubber compounds. A test piece of rubber compound is contained in a sealed test cavity under positive pressure and maintained at a specified elevated temperature. A rotor biconical disc is embedded in the test piece and is oscillated through small specified rotary amplitude. A complete cure in terms of applied torque versus cure time is obtained.

Shore Durometer A (UNI EN ISO 868 [17]) and international rubber hardness degrees (IRHD) (ISO 48 Method N [18]) were evaluated. The hardness is evaluated by inducing reversible, elastic deformation by means of a specially shaped indenter. Five samples of 35 mm diameter and 6 mm thick, with smooth, flat surface are tested for 3 sec in case of Shore A and 30 sec for IRHD, and the average values of hardness are computed. Tests are conducted both on samples cured at 140°C for 25 minutes and 170°C for 9 minutes.

Tensile tests are conducted on dumb-bells specimens, according to ISO 37 [19], using tensile tester, equipped with 10 kN loadcell. Six samples of thickness 2 mm, width 4 mm and length 20 mm were tested and the average value was computed for the only rubber compound moulded at 140°C for 25 minutes. Test are conducted with a strain rate of 500 mm/min up to failure.

Tear tests are conducted following ISO 34-1 [20], using the trouser test pieces. It is preferred to other methods since providing information about the fundamental tear properties of the material and less sensitive to the length of the cut. The tearing force is applied by means of a tensile testing machine, which operates continuously at 100 mm/min until the test piece breaks. Five samples of thickness 2 mm, width 15 mm and length 100 mm were considered and a cut of length 40 mm was applied in the longitudinal direction.

Shear tests are conducted with a quadrupole setup. The test pieces consist of four rectangular rubber pads 4 mm thick, 25 mm long and 20 mm wide, bonded on four rigid plates of the same width. This system is connected to an actuator, which applies shear deflection with a strain rate of 5mm/min. Samples are subjected to four static half-cycles of shear amplitude 20%, 40%, 60%, 80% and then 100%. Also dynamic properties are estimated considering a frequency of 0,5 Hz.

Rubber aging behaviour is also investigated by performing accelerated aging, according to ISO 188 [21]. Samples are conditioned at 70°C for 168h (7 days).

Finally, the adhesion of rubber with different supports (steel, nylon, polyester) is investigated performing peeling tests, according to ISO 813 [22]. A strip of rubber is bonded to a single plate of rigid material and peeled with an angle of 90° with a strain rate of 50 mm/min. The applied force required to tear the rubber from the support is measured. The standard test piece consists of a strip 6 mm thick, 25 mm wide and 125 mm long, bonded to a square area of size 25 mm on the surface of a metal plate and of the fiber textiles bonded on a rigid support.

3 CHARACTERIZATION TESTS

3.1 Tyre rubber crumb

Use of tyre rubber crumb provides advantages during the moulding process due to the bonds that are activated during the grinding. In particular, styrene butadiene rubber (SBR) and natural rubber (NR), unlike butyl rubber, ensure good compatibility not only with the virgin rubber compound, but also with the fabric providing good adhesion. For this purpose, a rubber crumb composed by SBR and NR was chosen.

TGA analysis are performed by considering the temperature ramp of Figure 1a and the weight loss percentages are reported in Figure 1b and summarized in Table 1. A first weight loss of 14 wt% is observed at around 350°C due to the plasticizers, followed by significant weight loss of 54 wt% at around 545°C, which corresponds to SBR and NR. Residuals are attributed to other fillers, such as silica, typical of tyre compounds, or other additives.

Table 1. Reclaimed rubber composition

<i>Components</i>	<i>T [°C]</i>	<i>wt %</i>
Absorbed water	70	0.47
Plasticizer (oil, volatile components)	350	13.63
Polymers (NR and SBR)	545	54.96
Carbon black	700	25.13
Ash, inorganic components (ZnO, SiO ₂ ,...)	>700	5.85

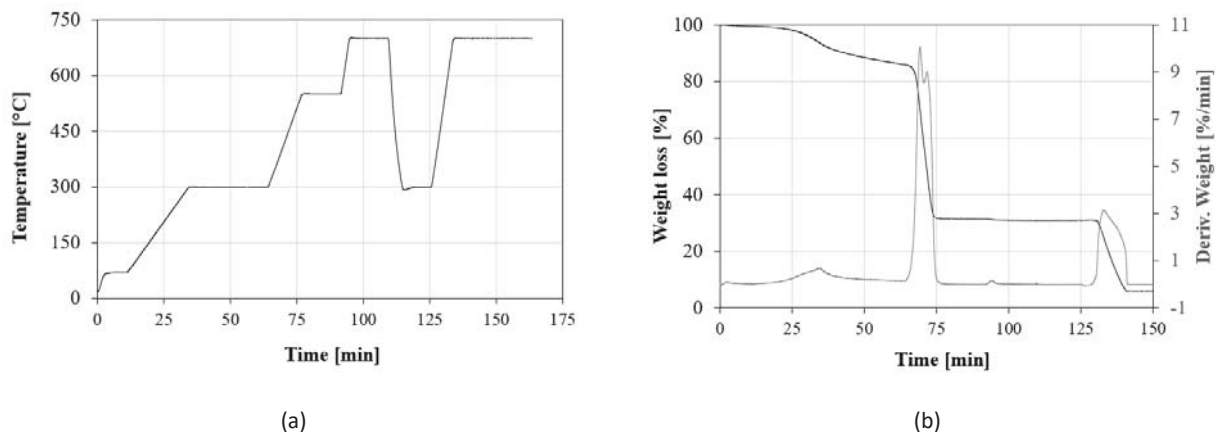


Figure 1. TGA analysis of tyre reclaimed rubber: (a) Temperature-Time procedure; (b) Weight loss

3.2 Novel rubber compound investigation

The vulcanization process of the compound at different temperature was investigated. Rheometric curves at 140°C and 177°C are reported in Figure 2. Curing is governed by activators, catalysts, cross-linking agents, hardeners, and accelerators. The time required to obtain the curing curve is a function of the test temperature and the vulcanization characteristics of the rubber compound [23]. By increasing the testing temperature from 140°C to 177°C, the time to achieve the 90% of cure decreases of about 8 times. The material also shows a stable behaviour at 140°C, since the curve reaches a plateau, without experiencing a reversion of torque [24].

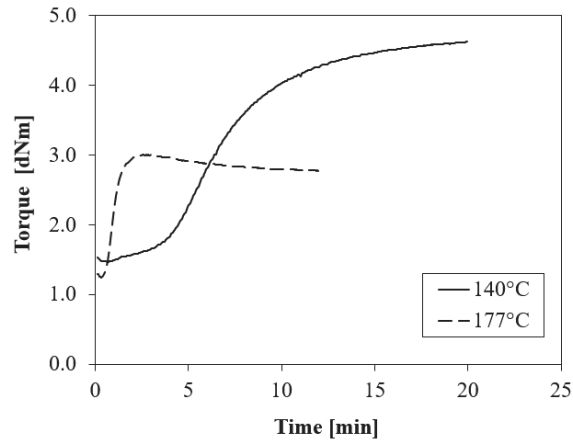


Figure 2. Rheometric curves of the novel rubber compound at 140°C and 177°C

Average values of hardness are reported in Table 2, for samples cured at both 140°C and 170°C. Durometer values are typical of a soft vulcanized rubber [17]. These results indicate that hardness is sensitive to the vulcanization process. In particular, the curing cycle of sample moulded at 140°C is longer than that of samples moulded at 170°C. In fact, slower vulcanization processes at lower temperature allow the formation of stronger networks, which results in higher hardness of the material.

Table 2. Hardness values

	Shore A		IRHD	
<i>Test temperature</i>	140°C	170°C	140°C	170°C
<i>Average value</i>	47.4	45.1	41.32	34.65

Tensile and tear tests on rubber specimens cured at 140°C for 25 min, revealed an excellent behaviour of rubber compound (Figure 3a-b). The maximum average stress and strains are 2.6 MPa and 330%, respectively. Even if these values are lower than virgin rubber compounds, they are significantly higher than previously adopted reclaimed compounds for RU-FREIs [8,12]. A tear resistance of 6.94 N/mm was measured, which is lightly lower than the minimum requirements, i.e. 8 N/mm [20]. However, these results are highly promising for applicability to elastomeric seismic isolators in unbonded configuration. Unlike isolators in bolted configuration, in unbonded application rubber ends are not constrained by steel plates and are free to strain with very limited internal stress. With increasing shear deformations, the ends at contact with the supports tend to roll-off and vertical faces rotate in a roll-over mechanism [25]. This also results in a significantly lower internal peeling stress at rubber-fibre interface.

Hardness and mechanical properties of the material are also investigated after accelerated aging. In particular, after conditioning rubber at 70°C for 7 days a hardness and tensile strength increase of 9% and 36% were measured, while elongation at break decreased of 8.5%.

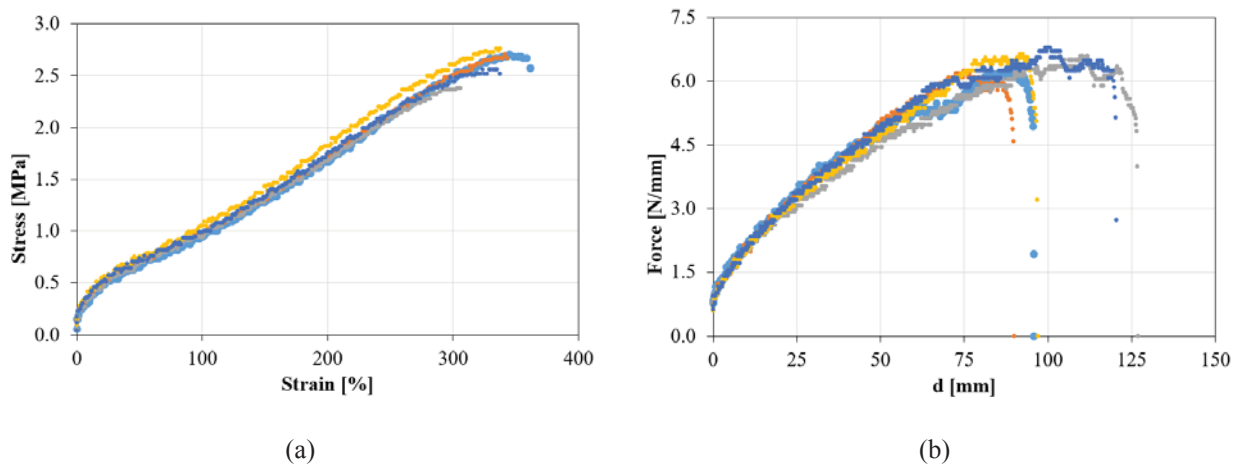


Figure 3. (a) Tensile test and (b) tear test

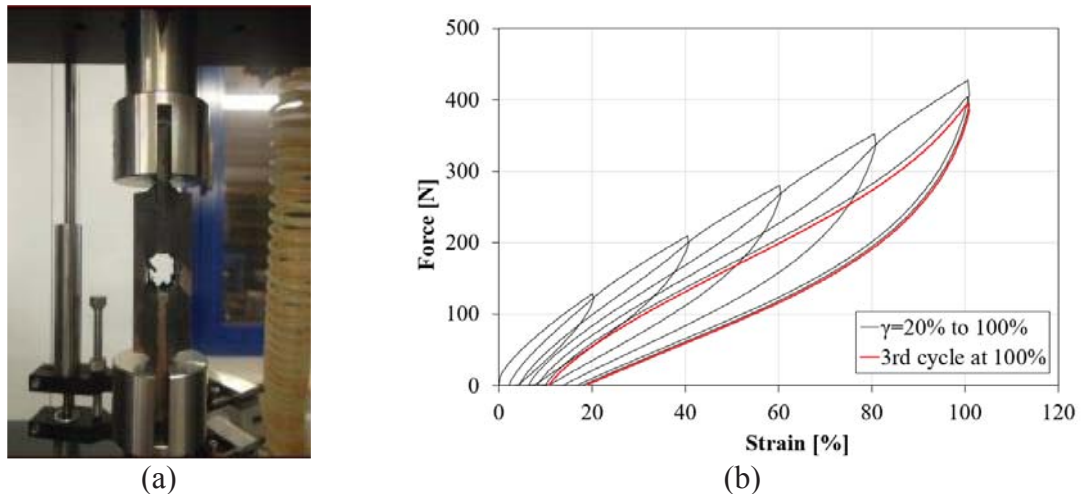


Figure 4. Shear test on rubber: (a) Setup of quadrupole test; (b) Results

Shear modulus and damping were evaluated for a shear strain $\gamma=100\%$ being 0.39 MPa and 4.9% respectively, while dynamic properties were estimated around 0.52 MPa and 10.4 %, respectively. A low shear modulus of the compound, combined with a higher shear strain capacity, can lead to design of seismic isolators with higher shape factors, thus preventing lateral instability which strongly limited previous investigations on RU-FREIs.

In FREIs, the bonding between layers is of paramount importance since it may govern the failure of the bearing. Tests showed an excellent adhesion of rubber with metal. For all samples rubber tearing occurred before any debonding from the support (Figure 5), providing optimal adhesion between the two materials. For nylon and polyester fabric, a proper adhesive was introduced to impregnate the textiles in order to promote the adhesion. Also in this case, tests showed an excellent behaviour with the tearing of the rubber from the support both for nylon and polyester (Table 3).

Table 3. Strength of adhesion of steel vs synthetic fabric (nylon and polyester)

	<i>Steel</i>	<i>Nylon</i>	<i>Polyester</i>
d_{\max} [mm]	181	170	181
F_{\max} [N/mm]	7.46	7.01	7.46

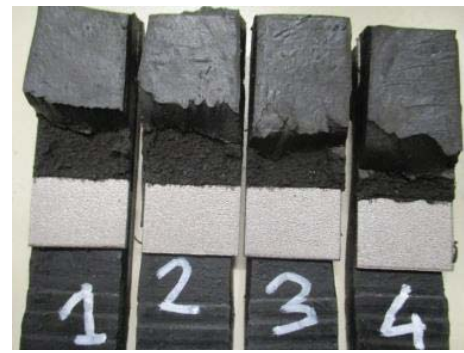
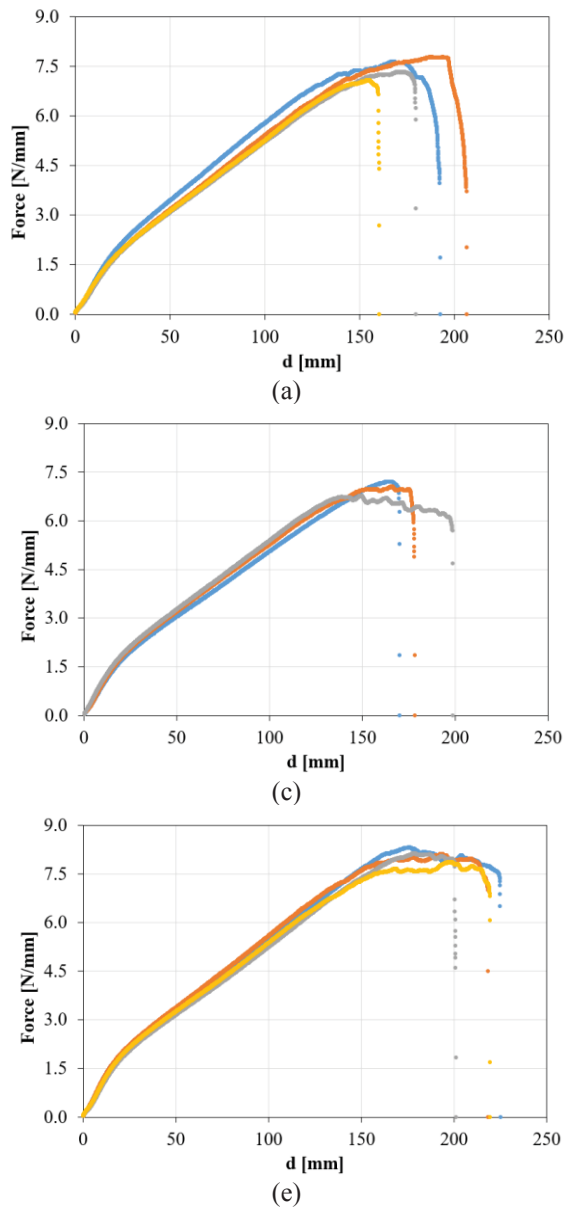


Figure 5. Quality of adhesion between rubber and (a-b) steel, (c-d) nylon; (e-f) polyester

Table 4. Technical datasheet of novel rubber compound

<i>Properties</i>	<i>Value</i>	<i>Specification</i>
Hardness (Shore A)	47.4	ISO 868
Hardness (IRHD)	41.3	ISO 48
Tensile strength	2.6 N/mm ²	ISO 37 Type 2
Elongation at break	330%	ISO 37 Type 2
Tear resistance	6.5 N/mm	ISO 34-1
Specific gravity	1.18 g/cm ³	ISO 1183-1
Shear modulus	0.52 MPa	UNI 1827
Damping	10.40%	UNI 1827
Adhesion to metal	7.5 N/mm	ISO 813
Adhesion to nylon	7.0 N/mm	ISO 813
Adhesion to polyester	7.5 N/mm	ISO 188

4. PRELIMINARY DESIGN OF ISOLATORS

On the basis of the preliminary characterization of the novel rubber compound whose main properties are summarised in Table 4, prototype isolators reinforced with polyester and nylon fabric have been designed. Nylon fabric and Polyester fabric coated with graphene were adopted as reinforcement. These are balanced fabrics with a very low cost with respect to conventional steel shims. The geometry of the devices is summarized in Table 5 and sketched in Figure 6.

Table 5. Geometry of rubber isolator reinforced with polyester/nylon fabrics

Device	n° of rubber layers	D [mm]	H [mm]	t _r [mm]	t _f [mm]	S [-]
<i>RR - Nylon</i>	8	200	49.5	5.17	1.16	9.7
<i>RR - Polyester</i>	9	200	49.5	5.02	0.54	10.0

Compared to RU-FREIs from literature [13–15], these prototypes are characterized by a higher shape factor roughly equal to 10. These values are consistent with those of FREI devices fabricated with virgin rubber. Differently, in case of RU-FREIs, the relatively large shear modulus of the rubber and the limited shear strain ($\gamma=50\%$), resulted in a slender geometry with an aspect ratio close to 1. Consequently, the use of softer compound with higher deformation capacity allows to design more squat geometry thus preventing instability issues [26]. Lateral stability will be investigated up to complete roll-over of the vertical faces under shear tests. In addition to this, vertical behavior will be tested in order to assess the compressibility of the bearing and the influence of limited elastic modulus of the reinforcement in comparison to conventional steel plates and carbon fibers.

Finally, it will be necessary to select the most suitable hysteretic model, among those introduced in the literature [27–31], to allow for an accurate simulation of their nonlinear response.

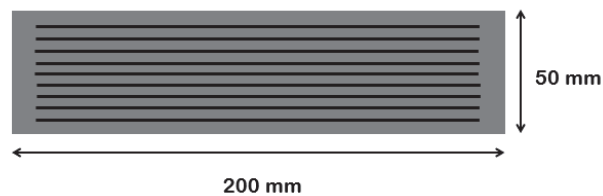


Figure 6. Elastomeric rubber isolator reinforced with polyester/nylon fabrics

4 5 CONCLUSIONS

A new recycled compound with promising mechanical properties has been developed. The material has been extensively characterized and its physical and mechanical properties have been investigated and properly calibrated.

The shear properties of the material are in between natural rubber and totally-recycled rubber pads, exhibiting shear strain up to 100%, i.e. around two times higher than the latters. Also, tensile strength is satisfactory for use in unbounded configuration with flexible internal reinforcement where internal stresses are significantly released.

In addition to this, the novel compound has shown excellent adhesion not only with steel but also with different fabrics such as nylon and polyester. These are very common, cheap textiles commonly used for industrial application such as conveyor belt or work clothes. They can be easily purchased and inserted in the manufacturing process. Devices can be produced

by direct molding, overlaying rubber layers and flexible reinforcements. Consequently, not only the weight of the devices is significantly reduced, but also the efforts associated to their fabrication.

The lower shear modulus and the higher shear strain of the compound compared to that of recycled rubber pads allow the fabrication of devices with higher shape factors. This can significantly increase the stability limits that were poorly investigated in previous investigations.

The next step of the study is aimed to develop prototype of isolators to be experimentally tested. The proposed technology is very promising and could pave the way for the development of high-performance and low-cost rubber isolators.

REFERENCES

- [1] J.M. Kelly, D.A. Konstantinidis, *Mechanics of Rubber Bearings for Seismic and Vibration Isolation*, 2011. <https://doi.org/10.1002/9781119971870>.
- [2] A. Calabrese, D. Losanno, M. Spizzuoco, S. Strano, M. Terzo, Recycled Rubber Fiber Reinforced Bearings (RR-FRBs) as base isolators for residential buildings in developing countries: The demonstration building of Pasir Badak, Indonesia, *Eng. Struct.* 192 (2019) 126–144. <https://doi.org/10.1016/j.engstruct.2019.04.076>.
- [3] D. Losanno, N. Ravichandran, F. Parisi, A. Calabrese, G. Serino, Seismic performance of a Low-Cost base isolation system for unreinforced brick Masonry buildings in developing countries, *Soil Dyn. Earthq. Eng.* 141 (2021) 106501. <https://doi.org/10.1016/j.soildyn.2020.106501>.
- [4] D. Konstantinidis, J.M. Kelly, Advances in low-cost seismic isolation with rubber, NCEE 2014 - 10th U.S. Natl. Conf. Earthq. Eng. Front. Earthq. Eng. (2014). <https://doi.org/10.4231/D36M33449>.
- [5] P. Tan, K. Xu, B. Wang, C.M. Chang, H. Liu, F.L. Zhou, Development and performance evaluation of an innovative low-cost seismic isolator, *Sci. China Technol. Sci.* 57 (2014) 2050–2061. <https://doi.org/10.1007/s11431-014-5662-6>.
- [6] D. Losanno, I.E. Madera Sierra, M. Spizzuoco, J. Marulanda, P. Thomson, Experimental assessment and analytical modeling of novel fiber-reinforced isolators in unbounded configuration, *Compos. Struct.* 212 (2019) 66–82. <https://doi.org/10.1016/j.compstruct.2019.01.026>.
- [7] D. Losanno, A. Calabrese, I.E. Madera-Sierra, M. Spizzuoco, J. Marulanda, P. Thomson, G. Serino, Recycled versus Natural-Rubber Fiber-Reinforced Bearings for Base Isolation: Review of the Experimental Findings, *J. Earthq. Eng.* 00 (2020) 1–20. <https://doi.org/10.1080/13632469.2020.1748764>.
- [8] G. Serino, C. Onorii, Mi.S.E. ICE CRUI Project 2008, (2008).
- [9] J.E. Morin, D.E. Williams., R.J. Farris, A Novel Method To Recycle Scrap Tires :, *Rubber Chem. Technol.* 75 (2002) 955–968.
- [10] E. Bilgili, A. Dybek, H. Arastoopour, B. Bernstein, A new recycling technology: Compression molding of pulverized rubber waste in the absence of virgin rubber, *J. Elastomers Plast.* 35 (2003) 235–256. <https://doi.org/10.1177/0095244303035003004>.
- [11] A. Guglielmotti, C. Lucignano, F. Quadrini, Production of rubber pads by tyre recycling, *Int. J. Mater. Eng. Innov.* 1 (2009) 91–106. <https://doi.org/10.1504/IJMATEI.2009.024029>.
- [12] F. Quadrini, L. Santo, E. Musacchi, A sustainable molding process for new rubber products from tire recycling, *Prog. Rubber, Plast. Recycl. Technol.* 35 (2019) 41–55. <https://doi.org/10.1177/1477760618798274>.
- [13] M. Spizzuoco, A. Calabrese, G. Serino, Innovative low-cost recycled rubber-fiber reinforced isolator: Experimental tests and Finite Element Analyses, *Eng. Struct.* 76 (2014) 99–111. <https://doi.org/10.1016/j.engstruct.2014.07.001>.
- [14] D. Losanno, M. Spizzuoco, A. Calabrese, Bidirectional shaking-table tests of unbonded recycled-rubber fiber-reinforced bearings (RR-FRBs), *Struct. Control Heal. Monit.* 26 (2019) 1–14. <https://doi.org/10.1002/stc.2386>.
- [15] D. Losanno, I.E. Madera Sierra, M. Spizzuoco, J. Marulanda, P. Thomson, Experimental performance of unbonded polyester and carbon fiber reinforced elastomeric isolators under bidirectional seismic excitation, *Eng. Struct.* 209 (2020) 110003. <https://doi.org/10.1016/j.engstruct.2019.110003>.

- [16] ISO 3417 Rubber — Measurement of vulcanization characteristics with the oscillating disc curemeter, Int. Stand. (2008).
- [17] ISO 868 - Shore hardness, 61010-1 © Iec2001. 2014 (2014) 13.
- [18] ISO 48 Rubber, vulcanized or thermoplastic — Determination of hardness (hardness between 10 IRHD and 100 IRHD), Int. Stand. (2010) 13.
- [19] ISO 37 Rubber, vulcanized or thermoplastic — Determination of tensile stress-strain properties, Int. Stand. 2017 (2017).
- [20] ISO 34 -1. Rubber, vulcanized or thermoplastic — Determination of tear strength, Int. Stand. 2015 (2015).
- [21] ISO 188 Rubber, vulcanized or thermoplastic — Accelerated ageing and heat resistance tests, Int. Stand. (2007) 13.
- [22] ISO 813 Rubber, vulcanized or thermoplastic — Determination of adhesion to a rigid substrate — 90° peel method, Int. Mater. Rev. 2010 (2010).
- [23] R. Ding, A.I. Leonov, A.Y. Coran, A Study of the Vulcanization Kinetics of an Accelerated-Sulfur SBR Compound, Rubber Chem. Technol. 69 (1996) 81–91. <https://doi.org/10.5254/1.3538360>.
- [24] P. Ghosh, S. Katare, P. Patkar, J.M. Caruthers, V. Venkatasubramanian, K.A. Walker, Sulfur vulcanization of natural rubber for benzothiazole accelerated formulations: From reaction mechanisms to a rational kinetic model, Rubber Chem. Technol. 76 (2003) 592–693. <https://doi.org/10.5254/1.3547762>.
- [25] P.M. Ajayan, T.W. Ebbesen, T. Ichihashi, S. Iijima, K. Tanigaki, H. Hiura, Opening carbon nanotubes with oxygen and implications for filling, Nature. 362 (1993) 522–525.
- [26] D. Losanno, H.A. Hadad, G. Serino, Design charts for eurocode-based design of elastomeric seismic isolation systems, Soil Dyn. Earthq. Eng. 119 (2019) 488–498. <https://doi.org/10.1016/j.soildyn.2017.12.017>.
- [27] N. Vaiana, R. Capuano, S. Sessa, F. Marmo, L. Rosati, Nonlinear Dynamic Analysis of Seismically Base-Isolated Structures by a Novel OpenSees Hysteretic Material Model, Appl. Sci. . 11 (2021). <https://doi.org/10.3390/app11030900>.
- [28] N. Vaiana, S. Sessa, L. Rosati, A generalized class of uniaxial rate-independent models for simulating asymmetric mechanical hysteresis phenomena, Mech. Syst. Signal Process. 146 (2021) 106984. <https://doi.org/https://doi.org/10.1016/j.ymssp.2020.106984>.
- [29] S. Sessa, F. Marmo, N. Vaiana, L. Rosati, A Computational Strategy for Eurocode 8-Compliant Analyses of Reinforced Concrete Structures by Seismic Envelopes, J. Earthq. Eng. (2018) 1–34. <https://doi.org/10.1080/13632469.2018.1551161>.
- [30] N. Vaiana, S. Sessa, M. Paradiso, F. Marmo, L. Rosati, An Efficient Computational Strategy for Nonlinear Time History Analysis of Seismically Base-Isolated Structures BT - Proceedings of XXIV AIMETA Conference 2019, in: A. Carcaterra, A. Paolone, G. Graziani (Eds.), Springer International Publishing, Cham, 2020: pp. 1340–1353.
- [31] N. Vaiana, S. Sessa, M. Paradiso, L. Rosati, Accurate and efficient modeling of the hysteretic behavior of sliding bearings, COMPDYN Proc. 3 (2019) 5291–5303. <https://doi.org/10.7712/120119.7304.19506>.

EFFECT OF EXTREMELY LOW TEMPERATURE ON MECHANICAL PROPERTIES OF A LARGE SIZE LRB

G. Ozdemir¹, E. Cavdar¹, and V. Karuk¹

¹ESQUAKE Seismic Isolator Test Laboratory, Eskisehir Technical University
Eskisehir, Turkey
e-mail: gokhan_ozdemir@eskisehir.edu.tr

{esengulcavdar, volkankaruk}@eskisehir.edu.tr

Abstract

The most important demand parameter for a seismically isolated structure is the maximum displacement at the isolation level. Currently, the most accurate way to estimate both the maximum isolator displacement and the isolator shear force is to perform bounding analyses. Accordingly, in bounding analyses, the lower and upper bound characteristics of isolator units are used in order to consider the change in isolator properties due variation in loading history, aging and environmental factors such as climatic conditions that the isolator is exposed during its lifetime. The objective of this study is to experimentally investigate the change in mechanical properties of a lead rubber bearing under very low ambient temperature. For this purpose, a lead rubber bearing with a total height of 361 mm, a diameter of 1020 mm and a lead core diameter of 190 mm is subjected to displacement-controlled loading at different ambient temperatures. The seismic isolator unit was first kept in room condition (20°C) for 24 hours in ESQUAKE Seismic Isolator Test Laboratory established in Eskisehir Technical University and then tested under cyclic motion. Then, the isolator unit which was conditioned at -30°C for 24 hours, was subjected to the same cyclic loading. Recorded force-displacement curves for both ambient temperatures are compared. In the loading protocol, the amount of axial load was 4500 kN (6 MPa normal stress), the amplitude of the horizontal motion was 280 mm (100% shear strain), the number of cycles was 3 and the frequency of motion was 0.1 Hz. Based on the test results conducted for both ambient temperatures, post-yield stiffness, effective stiffness, energy dissipated per cycle and equivalent damping ratios of the isolator were calculated for each cycle and compared with each other. Results showed that mechanical properties of lead rubber bearing significantly changed under low ambient temperature when compared to those obtained at laboratory conditions. When the ambient temperature drops down to -30°C from 20°C, the amplifications in post yield stiffness and characteristic strength are 10% and 50%, respectively.

Keywords: Seismic Isolation, Ambient Temperature, Cyclic Loading, Lead Rubber Bearing.

1 INTRODUCTION

Seismic isolation is an earthquake resistant design strategy which is adopted to protect structures against adverse effects of ground motions. It relies on lengthening of natural period of structure by introducing systems, that possess low horizontal stiffness, between the superstructure and substructure. Accordingly, in case of a seismic excitation, rather than the seismically isolated structure, seismic isolators will undergo large deformations and dissipate energy. Among various seismic isolation systems, lead rubber bearing (LRB) is one of the most widely used seismic isolators. They are composed of alternate layers of rubber and steel plates with a lead core at the center that passes through the height of the bearing. Rubber layers are responsible for the lateral stiffness of the bearing whereas lead core provides the required lateral strength. Since it was invented by Robinson in the 1970s, LRBs have been used in several structures (bridges, hospitals, data centers etc.) around the world [1-3]. In parallel, several research has been conducted to determine performance of LRBs under the effect of different parameters [4-10]. One of these parameters is the change in ambient temperature.

Mechanical properties of LRBs, mainly post yield stiffness and characteristic strength, are related to properties of rubber and lead, respectively. Although there are numerous studies that focused on the change in rigidity of rubber at low temperatures [11-17], very few experimental data are available for modification of LRB properties at low temperatures [18-20]. The LRB tested by Hasegawa et al. [18] was 250 mm in diameter with a lead core diameter of 38 mm. Displacement controlled LRB tests were conducted at temperatures of 40, 20, 0 and -20°C for a shear strain of 100% at 0.3 Hz. It was reported that the exposure time of the bearing to these temperatures is 5hrs. Similarly, Constantinou et al. [7] conducted tests with an LRB having rubber and lead core diameters of 381 mm and 70 mm, respectively. Isolator tests were carried out at a shear strain of 58% and loading frequency was 0.35 Hz. Constantinou et al. [7] stated that LRB was conditioned at -26°C and 20°C for 48 hrs prior to tests. Compared to LRBs used in experimental studies of Hasegawa et al. [18] and Constantinou et al. [7], LRB tested by Cho et al. [19] was a large size bearing with rubber and lead core diameters of 860 mm and 170 mm, respectively. The total rubber thickness was 288 mm and tested at a shear strain of 15%. Temperatures considered by Cho et al. [19] were -20, -10, 0 and 23°C. It is to be mentioned that 15% shear strain is very low to be representative of seismic behavior of an LRB designed to undergo large deformations. Accordingly, variation in mechanical properties of a large size LRB exposed to low temperature was revisited by Park et al. [20]. Rubber and lead core diameters of the LRB were 800 mm and 180 mm, respectively and tested at a shear strain of 100%.

The objective of this study is to determine the effect of low ambient temperature on mechanical properties of a lead rubber bearing. Accordingly, first, a large-size LRB was tested at both room (20°C) and low (-30°C) temperatures under dynamic conditions. The tested seismic isolator is subjected to displacement-controlled loading cycles that corresponds to 100% shear strain. Test results obtained for two distinct ambient temperatures are used to construct force-displacement curves for both conditions. Variation in characteristic strength (Q), post yield stiffness (K_d), effective stiffness (K_{eff}), dissipated energy per cycle (EDC) and equivalent damping ratio (ξ_{eff}) computed for both conditions are compared with each other.

2 TESTED LEAD RUBBER BEARING

The bearing tested in this study is a large-size LRB with rubber and lead core diameters of 1020 mm and 190 mm, respectively. Height of the bearing is 436 mm including the top and bottom plates together with the end shim at the top. It is composed of 28 layers of rubber each of which has 10 mm thickness with a total rubber height of 280 mm. Geometrical properties of the tested LRB is presented in Figure 1.

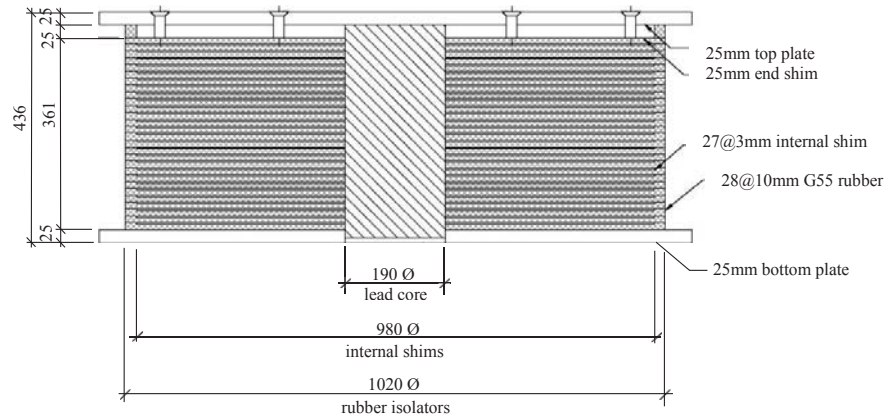


Figure 1: Section cut of test specimen.

3 ISOLATOR TESTS AT ROOM AND LOW AIR TEMPERATURE

In order to determine the mechanical properties of the specimen, its hysteretic response in shear was recorded under a constant compressive load. Accordingly, the LRB was subjected to three cycles of sinusoidal motion with amplitude equals to 280 mm that corresponds to 100% shear strain. Frequency of the motion was 0.1 Hz where the maximum velocity is 176 mm/s. The axial force acting on the bearing was 4500 kN which result in 6 MPa normal stress. The LRB was first tested at a temperature of 20°C after conditioning for 24 hours inside the laboratory and tested again at a temperature of -30°C after conditioning for 24 hours inside the air-conditioned room (Figure 2.a). Tests were conducted at ESQUAKE Seismic Isolator Test Laboratory of Eskisehir Technical University. The test setup of ESQUAKE shown in Figure 2.b is capable of applying dynamic motions in both horizontal and vertical directions. Table 1 presents the loading capacities of ESQUAKE test setup. Horizontal force-displacement curves obtained from tests for 20°C and -30°C are given in Figure 3.



(a)



(b)

Figure 2: (a) Air-conditioned room and (b) seismic isolator test setup of ESQUAKE

Max. Vertical Load:	20.000 kN
Max. Horizontal Load:	2.000 kN
Max. Horizontal Stroke:	±600 mm
Max. Velocity:	1.000 mm/s

Table 1: Properties of ESQUAKE test setup.

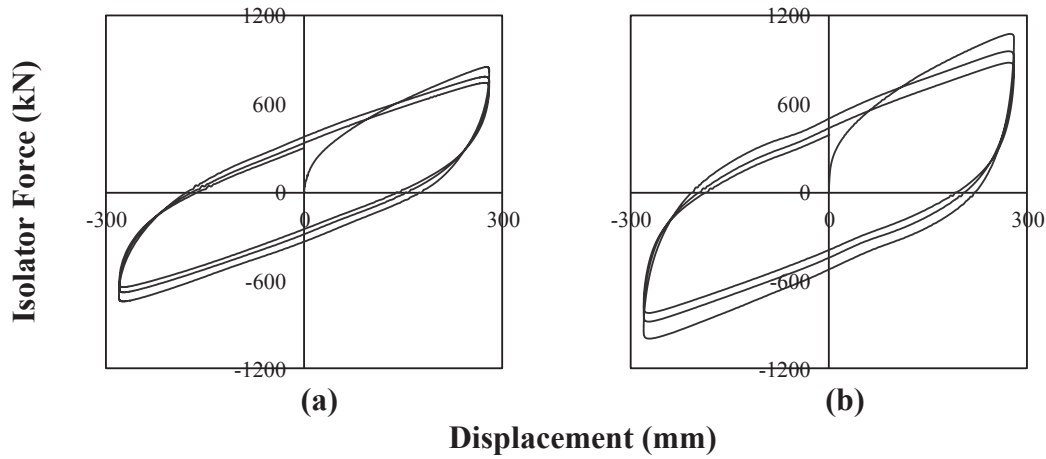


Figure 3: Force-displacement curves of LRB tested at a) 20°C and b) -30°C.

4 MECHANICAL PROPERTIES OF LRB

Mechanical properties of the tested LRB such as post-yield stiffness (K_d), characteristic strength (Q_d), effective stiffness (K_{eff}), energy dissipation capacity (EDC) and effective damping ratio (ζ_{eff}) for temperatures of 20°C and -30°C are presented in Table 2. Data given in Table 2 are computed by means of Equations (1)-(4) and Figure 4. In Equations (1) and (2), Q_1' , Q_1'' , Q_2' and Q_2'' are the isolator forces at 50% of the maximum positive and negative horizontal displacements d_{max} and d_{min} as per ISO 22762-1 [21]. Q_1 and Q_2 of Equation (3) are the isolator forces at d_{max} and d_{min} , respectively (see Figure 4).

Temperature	Cycle	Q_d (kN)	K_d (kN/m)	K_{eff} (kN/m)	EDC (kN·m)	ζ_{eff} (%)
-30°C	1	489	2020	3441	504	0.29
	2	414	1919	3100	433	0.28
	3	372	1864	2913	382	0.26
20°C	1	324	1833	2706	335	0.25
	2	286	1796	2510	297	0.24
	3	260	1766	2392	264	0.22

Table 2: Mechanical properties of LRB at 20°C and -30°C

In order to better understanding of change in mechanical properties of LRB isolator at low temperature, Figure 5 is depicted. In this figure amount of variation in isolator properties with respect to the room temperature is presented for all considered features. Accordingly, comparison of test results obtained for temperatures of 20°C and -30°C reveals the following conclusions. Characteristic strength (force intercept at zero displacement) Q_d of the tested LRB increases when the temperature drops down to -30°C. The amount of amplification in Q_d is 50% for the first cycle whereas it is 45% and 43% for the second and third cycles,

respectively. Similarly, post-yield stiffness K_d of the LRB increases as the temperature decreases. However, the amount of variations in K_d , which are 10%, 7% and 6% for first, second and third cycles, are relatively small compared to those computed for Q_d . Based on the data presented in Table 2, the amount of change in effective stiffness K_{eff} due to temperature decrease is 27% for the first cycle and reduced to 24% and 22% for the second and third cycles, respectively. According to Table 2, energy dissipation capacity EDC , defined as the area under force-displacement curve at each cycle, increases as the temperature decreases. Amplification in EDC at first, second and third cycles are computed as 50%, 46% and 44% in the same order. In parallel, reducing the temperature from 20°C to -30°C contributes to an increase in effective damping ratio ξ_{eff} equal to 17% for the first cycle. The amplifications are 19% and 18% for the second and third cycles, respectively. Considering the test results, it is evident that amount of variation in mechanical properties of LRB is not constant at all loading cycles and the trend is to decrease with increasing number of cycles.

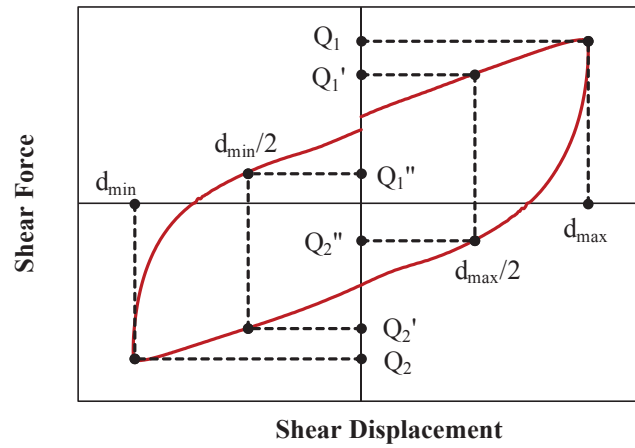


Figure 4 - Force-displacement definitions for LRBs.

$$Q_d = \left[\frac{Q_1'' d_{\max}/2 - Q_1' d_{\min}/2}{(d_{\max} - d_{\min})/2} - \frac{Q_2' d_{\max}/2 - Q_2'' d_{\min}/2}{(d_{\max} - d_{\min})/2} \right] / 2 \quad (1)$$

$$K_d = \left[\frac{Q_1' - Q_1''}{(d_{\max} - d_{\min})/2} + \frac{Q_2'' - Q_2'}{(d_{\max} - d_{\min})/2} \right] / 2 \quad (2)$$

$$K_{eff} = \left[\frac{Q_1 - Q_2}{d_{\max} - d_{\min}} \right] \quad (3)$$

$$\xi = \left[\frac{EDC}{\pi(F_{\max} D_{\max} + F_{\min} D_{\min})} \right] \quad (4)$$

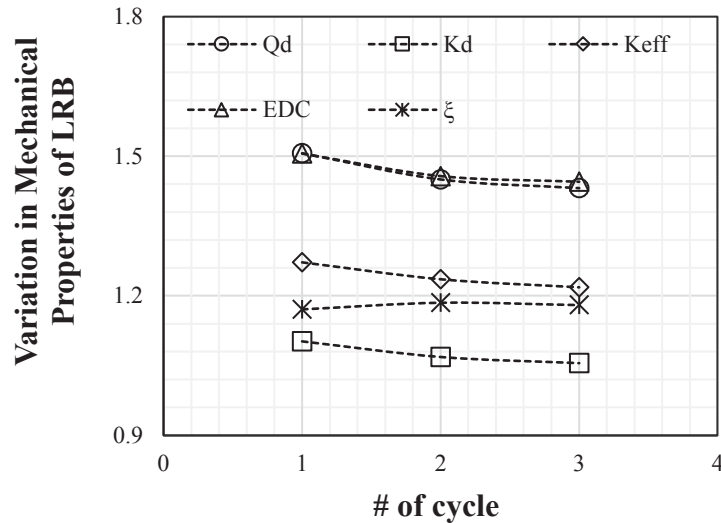


Figure 5: Amount of variation in mechanical properties of LRB isolator per cycle with respect to room temperature.

5 CONCLUSIONS

This study quantifies the variation in mechanical properties of an LRB isolator under the effect of very low ambient temperatures. For this purpose, an experimental investigation was performed at 20°C to -30°C. Recorded force-displacement curves for both considered temperatures are compared. Results showed that characteristic strength and post-yield stiffness of bilinear force-displacement curve of the tested LRB increases when the temperature drops from 20°C to -30°C. The amplifications in strength and stiffness are observed to be in the order of 50% and 10%, respectively. As the number of cycles increases, these values decrease gradually.

REFERENCES

- [1] R.I. Skinner, W.H. Robinson, G.H. McVerry, *An Introduction to Seismic Isolation*. Chichester: John Wiley & Sons, 1993.
- [2] F. Naeim, J. Kelly, *Design of Seismic Isolated Structures: From Theory to Practice*. New York: John Wiley & Sons, 1999.
- [3] M.C. Kunde, R.S. Jangid, Seismic Behavior of Isolated Bridges: A-state-of-the-art review, *Electronic Journal of Structural Engineering*, 3, 140–170, 2003.
- [4] W.H. Robinson, Lead Rubber Hysteretic Bearings Suitable for Protecting Structures During Earthquake, *Earthquake Engineering and Structural Dynamics*, 10(4), 593–604, 1982.
- [5] S. Nagarajaiah, X. Sun, Response of Base Isolated USC Hospital Building in Northridge Earthquake, *Journal of Structural Engineering (ASCE)*, 126(10), 1177–1186, 2000.
- [6] C.W. Roeder, Proposed Design Method for Thermal Bridge Movements, *Journal of Bridge Engineering*, 8(1), 12–19, 2003.

- [7] M.C. Constantinou, A.S. Whittaker, Y. Kalpakidis, D.M. Fenz, G.P. Warn, Performance of Seismic Isolation Hardware Under Service and Seismic Loading, *Technical report, NY: MCEER=07-2012*, Buffalo, 2007.
- [8] G. Benzoni, C. Casarotti, Effects of Vertical Load, Strain Rate and Cycling on The Response of Lead-Rubber Seismic Isolators, *Journal of Earthquake Engineering*, 13(3), 293-312, 2009.
- [9] H. Erdoğan, E. Çavdar, G. Özdemir, Türk Deprem Yönetmelikleri (DBYBHY ve TBDY) Spektrum Tanımlarının Deprem Yalıtım Sistemi Tasarımı Özelinde Karşılaştırılması, *Teknik Dergi*, 32(5), 2021.
- [10] S. Pinarbasi, U. Akyuz, Sismik İzolasyon ve Elastomerik Yastık Deneyleri. *İMO Teknik Dergi*, 237, 3581-3598, 2005.
- [11] C.W. Roeder, J.F. Stanto, A.W. Taylor, *Performance of Elastomeric Bearings* (No. 298). Washington, DC: National Cooperative Highway Research Program, Transportation Research Board, 1987.
- [12] D.F. Ritchie, *Neoprene Bridge Bearing Pads, Gaskets and Seals*. Rubber World, Lippincott & Petto Inc. 200(2), 27–31, 1989.
- [13] R. Eyre, A. Stevenson, Performance of Elastomeric Bridge Bearings at Low Temperatures, *Proceedings 3rd World Congress on Joint Sealing and Bearing Systems for Concrete Structures*, 736-762. Toronto, Canada, 1991.
- [14] A. Yakut, J.A. Yura, Evaluation of Low-Temperature Test Methods for Elastomeric Bridge Bearings, *Journal of Bridge Engineering*, 7(1), 50-56, 2002(a).
- [15] A. Yakut, J.A. Yura, Parameters Influencing Performance of Elastomeric Bearings at Low Temperatures, *Journal of Structural Engineering*, 128(8), 986–994., 2002(b).
- [16] K.N.G. Fuller, J. Gough, A.G. Thomas, The Effect of Low-Temperature Crystallization on The Mechanical Behavior of Rubber, *Journal of Polymer Science: Part B: Polymer Physics*, 42(11), 2181-2190, 2004.
- [17] D. Cardone, G. Gesualdi, D. Nigro, Effects of Air Temperature on The Cyclic Behavior of Elastomeric Seismic Isolators, *Bulletin of Earthquake Engineering*, 9(4), 1227–55, 2011.
- [18] O. Hasegawa, I. Shimoda, M. Ikenaga, Characteristic of Lead Rubber Bearing by Temperature. *Summaries of Technical Papers of Annual Meeting Architectural Institute of Japan*, B-2, Structures II, Structural Dynamics Nuclear Power Plants, Architectural Institute of Japan, pp: 511-512, 1997.
- [19] C.B. Cho, I.J. Kwahk, Y.J. Kim, An Experimental Study for The Shear Property and The Temperature Dependency of Seismic Isolation Bearings, *Journal of the Earthquake Engineering Society of Korea*, 12(1), 67-77, 2008.
- [20] J.Y. Park, K.S. Jang, H.P. Lee, Y.H. Lee, H. Kim, Experimental Study on The Temperature Dependency of Full-Scale Low Hardness Lead Rubber Bearing, *Journal of Computational Structural Engineering*, 25(6), 533-540, 2012.
- [21] ISO (International Organization for Standardization). ISO 22762-1:2005: Elastomeric seismic-protection isolators – Part 1: Test methods, 2005.

STIFF DYNAMIC ABSORBERS FOR THE VERTICAL SEISMIC PROTECTION OF STRUCTURES

M. E. Kalogerakou^{2*}, K. A. Kapasakalis¹, I. A. Antoniadis², E. J. Sapountzakis¹

¹ Institute of Structural Analysis and Antiseismic Research
School of Civil Engineering, National Technical University of Athens
Zografou Campus, GR-157 80 Athens, Greece
kostiskapasakalis@hotmail.com, cvsapoun@central.ntua.gr

² Dynamics and Structures Laboratory
Mechanical Design and Control Systems Section
Mechanical Engineering Department, National Technical University of Athens
Zografou Campus, GR-157 80 Athens, Greece
marina.e.kalogerakou@gmail.com, antogian@central.ntua.gr

Abstract

The majority of the existing seismic protection systems and techniques are related to horizontal ground motions, while there are only a few vertical seismic protection systems. The main reason is due to the conflict concerning the demand for isolation stiffness. More specifically, a vertical isolated system must have sufficient vertical rigidity to sustain the weight of the isolated object/system and retain the static vertical deflection in reasonable limits. On the other hand, the isolated system must also have enough flexibility to isolate the accelerations. In order to overcome this difficulty, a novel vertical seismic absorber system is proposed, that combines a Quasi-Zero Stiffness (QZS) design including negative stiffness elements, an enhanced Tuned Mass Damper (TMD) and an inerter. The QZS oscillator manages to maintain the vertical rigidity of the structure, the inerter manages to reduce the frequency of the system, without weakening the structure or increase the seismic load and the TMD is responsible for absorbing the external excitations, significantly increasing the effective damping. This way, the dynamic behavior of the system is improved, in terms of absolute accelerations, and simultaneously, the static settlements are retained at any desired level. The design is based on engineering criteria, and the excitation input is selected according to the seismic design codes.

Keywords: Vertical Seismic Protection, Negative Stiffness, KDamper, Damping, Vibration Absorption.

1. INTRODUCTION

Earthquakes consist one of the major environmental hazards. During 2011 e.g., over 20,000 people died and about a million people lost their homes globally, due to earthquakes and their effects. Moreover, a wide class of ground vibrations generated by heavy and high-speed vehicles such as trains and trucks, construction activities (i.e., dynamic compaction, roadbed compaction, pile driving, blasting) or blasts, present a frequency spectrum in the order of a few Hz. Together with other sources inside the building, (e.g., impact noise between floors), noise pollution is their major effect.

The conventional design approach to address such loads consists of stiff and highly damped structures. Apart from technical (and financial) constraints in their realization, (e.g., current unavailability of large sized dampers, cases of heavy structures, etc.), such designs may result to reverse effects concerning certain aspects of their desired dynamic behavior. For example, stiff and highly damped structures can enhance the transfer of base acceleration excitations to the main structure. This may result to damaging effects in the interior of the structure relating e.g., to the secondary loads (machines, sensitive equipment, etc.) in the case of earthquakes.

Isolation appears to be a promising alternative, as it is based on the concept of altering the dynamics of the system and to reduce the vibration, rather than increasing the resistance capacity of the structure. The concept of isolation relies on a flexible layer between the structure and its base. This way, the fundamental natural period of the base isolated system is significantly longer, and thus, the structure can absorb less energy from the broad base excitation frequency spectrum. However, in order to isolate the building from its base, large displacements are required due to the fundamental dynamic behavior of the system, which can be even in the range of tenths of centimeters for certain earthquakes. These displacements can be hardly acceptable for numerous reasons, such as structural pounding, sensitivity in horizontal loads, proper connection for utilities, and more, rendering this concept inadequate for retrofitting.

The above comments have motivated the development of alternative vibration control strategies, which among others, include: (i) Tuned Mass Dampers (TMDs), (ii) Inerters, (iii) Negative Stiffness Devices (NSD) and “Quazi Zero Stiffness” (QZS) oscillators, and (iv) Negative Stiffness driven Absorbers/KDampers. (Figure 1)

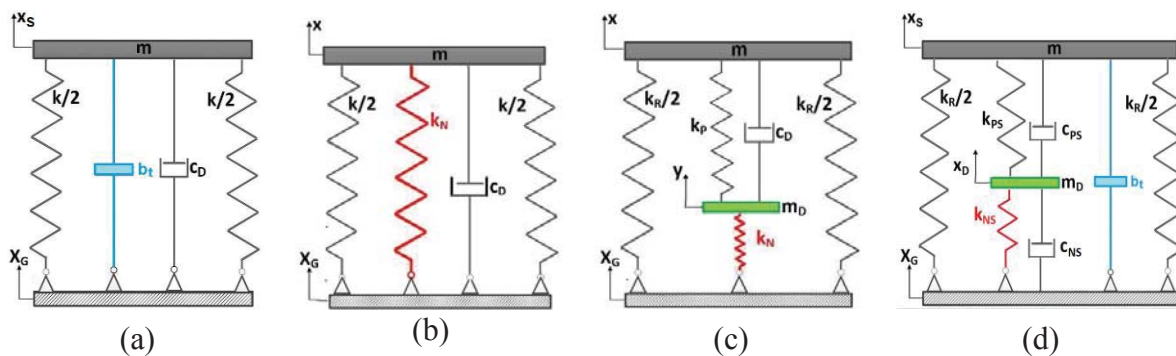


Figure 1 (a) Inerters; (b) Negative Stiffness Absorbers/QZS oscillators; (c) KDamper concept; (d) Proposed Stiff Dynamic Absorbers

The Tuned Mass Damper (TMD) has a long history, with applications in several types of engineering structures, such as high-rise buildings and skyscrapers [1,2,3], bridges [4], wind and wave excitation in wind turbines [5], etc. In addition, the TMD can be used as a possible supplement to the conventional base isolation approaches, implemented within the bases of structures, aiming to reduce the displacement demand [6–8]. The main disadvantages of

vibration absorption techniques that use a TMD-related approach are associated with the requirement for large additional masses in order for the TMD to be effective, and with the fact that a slight alteration of its parameters can alter the TMD tuning and consequently reduce the system's performance significantly [9].

In an attempt to reduce the requirements for heavy oscillating masses under the TMD concept, the inerter has been introduced in the early 2000s [10,11]. The inerter is a two-terminal element (Figure 1.a), which has the property of generating at its ends a force that is proportional to the relative acceleration of its terminals. The main advantage of the inerter lies in the fact that it does not need to have large mass in order to achieve the same inertia effect as the additional mass required under the TMD approach. The essential limitation of the inerter is the complex and elaborate mechanical design configurations needed for its implementation, and the reduction of the effective damping of the system due to the increase of the effective mass. Moreover, the major disadvantage of the TMD in base isolation applications, is that enhances the transfer of base acceleration excitations to the main structure, even more significantly than a damper of a high value. As mentioned, this can result to damaging effects in the interior of the structure.

A parallel direction to the various TMD approaches is the concept of introducing negative stiffness (NS) elements for vibration absorption (Figure 1.b). The use of negative stiffness elements (or “anti-springs”) for vibration isolation was first introduced in the pioneering works of Molyneaux [12], and of Platus [13]. The central concept of these approaches is the significant reduction of the isolator's stiffness, which, consequently, leads to the decrease of the natural frequency of the system even at almost zero levels. Towards this direction, the so called “Quasi-Zero Stiffness” (QZS) oscillators have been proposed [14]. An initial comprehensive review of such designs can be found in [15]. Nagarajaiah et. al [16] introduced a new structural modification approach for the seismic protection of structures using an adaptive negative stiffness device that resulted to the decrease of the dynamic forces imposed on the structure. The QZS oscillators are designs of an essentially non-linear stiffness, combining a positive spring in parallel with a non-linear spring, which exhibits a negative stiffness region under nominal load. In this way, QZS oscillators combine a high static stiffness, capable of maintaining the structural load, with a low dynamic stiffness, enabling a low isolation frequency. However, QZS oscillators offer a low damping capacity. In addition, even small load disturbances around the static equilibrium point of the QZS designs can significantly affect their response.

Extending the concept of the traditional Tuned Mass Dampers, a novel passive vibration absorption and damping concept (the KDamper) is introduced [17]. Compared to the TMD, the KDamper uses an additional negative stiffness spring (Figure 1.c). connecting the additional mass to the ground. This negative stiffness spring generates a force in phase with the acceleration response, acting essentially as an inertial force of the additional mass. In this way, the performance of the KDamper can be drastically increased, just by increasing the value of the negative stiffness spring and without the need to increase the value of the additional mass. Thus, the KDamper has been shown to present extraordinary damping/absorption properties, with relatively small (even minimal) values of the additional mass.

Although the KDamper incorporates a negative stiffness element, it is designed to be both statically and dynamically stable. Thus, the KDamper can be designed to present the same overall (static) stiffness as a traditional reference original oscillator, while simultaneously offering drastically increased damping properties. Since the presence of a negative stiffness spring in series with a positive stiffness spring can result to a negative stiffness value, the static behavior of the KDamper can be controlled to be similar to that of a QZS oscillator, ensuring both high static stiffness and low dynamic stiffness.

A number of KDamper designs [18] and extensions [19] have been applied as seismic absorbers in the bases of structures. Their overall static stiffness is allowed to vary, ranging from low values that are similar to that of seismic isolation systems, up to values corresponding to a significantly higher stiffness. In the former case, the KDamper presents a behavior similar to that of a base isolated system, combined however with a drastically increased damping. In the latter case, the KDamper has shown the ability to drastically reduce the structure base displacements relative to the ground in the range of few centimeters, while maintaining the absolute structure accelerations within reasonable limits. This aforementioned result implies that the KDamper can be used as an alternative method to conventional base isolation systems, enabling its implementation (under certain conditions) even for retrofitting existing structures.

Quite recently, the extended KDamper has been used in parallel to an inerter (Figure 1.d). [20] for vertical seismic protection. Under a proper optimization procedure, this combination has shown to result to configurations offering a stiff vertical static stiffness (and thus an acceptable vertical static displacement of the structure) with an acceptable level of reduction of the vertical accelerations induced to the structure. This concept is the underlying notion and configuration of the Stiff Dynamic Absorbers.

The first key difference between the proposed design and the one proposed in [20], is that the static loading is now borne only by the external k_R (Figure 1.d) spring element of the SDA, and not by the overall static stiffness of the assembly. The rest of the spring elements k_N , k_P (Figure 1.d) need to participate only in the dynamic response of the excited system, similarly to the concept of the QZSs.

The second key difference is the fact that a new more general objective function is introduced for the optimization procedure. It is thus shown that a unique optimal SDA design can be used, not only for the vertical seismic protection of the structures, but also for a range of important vertical dynamic absorption applications, including low frequency machine mounts and impact noise insulation.

2. STIFF BASE ABSORBER WITH EXTENDED KDAMPER AND INERTER

2.1. Conventional SDoF damping system

The fundamental aim of seismic isolation is to decrease the natural frequency of the system, f , below the dominant energy-containing frequencies of ground motion excitation, thus allowing reduced peak accelerations of the structure. A major constraint with this approach lies in the weakened static loading capacity of the structure as a result decreasing its overall stiffness, k , leading to large static displacements. Denoting with the X_{VSD} vertical static deflection of the conventional spring-mass system in Figure 2:

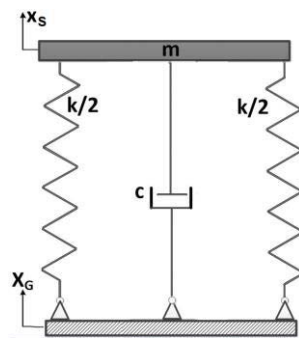


Figure 2. Conventional vibration damper

$$X_{VSD} = \frac{mg}{k} = \frac{g}{(2\pi f)^2} \quad (1)$$

The equation of motion of this system is:

$$m\ddot{u}_S + c\dot{u}_S + ku_S = -m_S\ddot{X}_G, \quad (2)$$

where $u_S = X_S - X_G$. Assuming a harmonic base excitation in the form of $\ddot{X}_G(t) = A_G e^{j\omega t}$, the steady-state response will be:

$$u_S(t) = \tilde{U}_S e^{j\omega t} \quad (3)$$

where \tilde{U}_S denotes the complex amplitude. The equation of motion of the SDoF system can be written in the following form:

$$-\omega^2 m \tilde{U}_S + j\omega c \tilde{U}_S + k \tilde{U}_S = -m A_G \quad (4)$$

The Transfer Functions of the system are calculated as:

$$\tilde{H}_{US} = \tilde{U}_S / A_G = -\tilde{H}^{-1} m \quad (5)$$

where:

$$\tilde{H} = [-\omega^2 m + j\omega c + k] \quad (6)$$

$$\tilde{H}_{AS} = A_S / A_G = -\omega^2 \tilde{X}_S / A_G = 1 - \omega^2 \tilde{H}_{US} \quad (7)$$

The natural frequency and the damping ratio of the SDoF isolated system are:

$$f = \frac{1}{2\pi} \sqrt{\frac{k}{m}} \quad (8)$$

$$\zeta = c / (2\sqrt{mk}) \quad (9)$$

2.2. Proposed extension of KDamper equipped with inerter

This paper proposes a seismic protection system based on the combination of a Tuned Mass Damper (TMD) and a Quasi-Zero Stiffness (QZS) design introducing negative stiffness elements, accompanied by an inerter (Figure 1.d). The first component of the proposed system (combination of a TMD with a QZS design) is essentially based on the KDamper concept [17], whereby the introduction of the negative stiffness element reduces transmissibility of the system by lowering the natural frequency while increasing the effective damping of a conventional TMD. The introduction of an inerter between the structure and the ground results to an increased effective mass of the system without the need for additional weight, further improving its dynamic behavior. The proposed design is based on the one proposed by [20], with several differentiations. The positive stiffness element k_P connects the structure to the additional mass m_D , which in turn is connected to the ground through the NS element k_N , as per the initial KDamper design [17]. The k_R spring element connects the structure directly to the ground, accompanied by the inerter (b_R).

The overall stiffness of the system can be calculated as:

$$k_{tot} = k_R + \frac{k_P k_N}{k_P + k_N} \quad (10)$$

A key difference between the proposed design and the one proposed by [20], 2020 is that the static loading is now borne by the k_R element only (which is equal to the stiffness of the initial structure, k_S) and not the overall k_{tot} , while the k_N , k_P elements participate only in the dynamic response of the excited system. As the static capacity of the system is fully maintained, the system can be designed for larger absolute magnitudes of the NS element k_N , while the static deflection X_{VSD} remains at acceptable levels. This enables better seismic isolation and reduced transmissibility of the system, while maintaining its static rigidity.

Denoting the relative displacement between the structure and the ground as $u_s = X_S - X_G$, the equations of motion for the two masses are:

$$(m_S + b_R)\ddot{u}_S + c_P(\dot{u}_S - \dot{u}_D) + k_R u_S + k_P(u_S - u_D) = -m_S \ddot{X}_G \quad (11)$$

$$m_D \ddot{u}_D + c_P(\dot{u}_D - \dot{u}_S) + c_N \dot{u}_D + k_N u_D + k_P(u_D - u_S) = -m_D \ddot{X}_G \quad (12)$$

The steady state responses of the system are:

$$u_S(t) = \tilde{U}_S e^{j\omega t} \quad (13)$$

$$u_D(t) = \tilde{U}_D e^{j\omega t} \quad (14)$$

where \tilde{U}_S, \tilde{U}_D , denote the response complex amplitudes. The abovementioned equations of motion of the system hence become:

$$-\omega^2(m_S + b_R)\tilde{U}_S + j\omega c_P(\tilde{U}_S - \tilde{U}_D) + k_R \tilde{U}_S + k_P(\tilde{U}_S - \tilde{U}_D) = -m_S A_G \quad (15)$$

$$-\omega^2 m_D \tilde{U}_D + j\omega c_P(\tilde{U}_D - \tilde{U}_S) + j\omega c_N \tilde{U}_D + k_N \tilde{U}_D + k_P(\tilde{U}_D - \tilde{U}_S) = -m_D A_G \quad (16)$$

The resulting transfer functions (TFs) can be derived:

$$\begin{bmatrix} \tilde{H}_{US} \\ \tilde{H}_{UD} \end{bmatrix} = \begin{bmatrix} \tilde{U}_S/A_G \\ \tilde{U}_D/A_G \end{bmatrix} = H^{-1} \begin{bmatrix} m_S \\ m_D \end{bmatrix} \quad (17)$$

where:

$\tilde{H} =$

$$\begin{bmatrix} -\omega^2(m_S + b_R) + j\omega c_P + (k_R + k_P) & -(j\omega c_P + k_P) \\ -(j\omega c_P + k_P) & -\omega^2 m_D + j\omega(c_P + c_N) + (k_N + k_P) \end{bmatrix} \quad (18)$$

$$\tilde{H}_{AS} = A_S/A_G = 1 - \omega^2 \tilde{H}_{US} \quad (19)$$

$$\tilde{H}_{AD} = A_D/A_G = 1 - \omega^2 \tilde{H}_{UD} \quad (20)$$

The following quantities represent the area under the transfer functions of the system (scaled by the factor $d\omega$) and are indicators of the transmissibility of the system within the frequency range of interest (ω_1 to ω_2).

$$Q_{US} = \frac{1}{d\omega} \int_{\omega_1}^{\omega_2} |H(\omega)_{US}|^2 \quad (21)$$

$$Q_{UD} = \frac{1}{d\omega} \int_{\omega_1}^{\omega_2} |H(\omega)_{UD}|^2 \quad (22)$$

$$Q_{AS} = \frac{1}{d\omega} \int_{\omega_1}^{\omega_2} |H(\omega)_{AS}|^2 \quad (23)$$

Denoting by S_A the PSD of the ground motion acceleration, the response power spectral densities can be calculated:

$$S_{US}=|H_{US}|^2 S_A \quad (24)$$

$$S_{UD}=|H_{UD}|^2 S_A \quad (25)$$

$$S_{AS}=|H_{AS}|^2 S_A \quad (26)$$

The root mean square (RMS) values of the responses are finally defined as the root under the area of the PSD curve, which can be used as indicators of the actual energy content of the response:

$$R_{US}=\sqrt{\int_{-\infty}^{+\infty} S_{US}(\omega)d\omega} \quad (27)$$

$$R_{UD}=\sqrt{\int_{-\infty}^{+\infty} S_{UD}(\omega)d\omega} \quad (28)$$

$$R_{AS}=\sqrt{\int_{-\infty}^{+\infty} S_{AS}(\omega)d\omega} \quad (29)$$

Next, the following quantities concerning the system configuration are introduced:

$$m_D=\mu_D m_S \quad (30)$$

$$b_R=\mu_R m_S \quad (31)$$

$$\zeta_N= c_N/(2\sqrt{m_S k_R}) \quad (32)$$

$$\zeta_P= c_P/(2\sqrt{m_S k_R}) \quad (33)$$

3. OPTIMISATION METHOD FOR THE CONFIGURATION OF THE VERTICAL EXTENDED KDAMPER & INERTER SYSTEM

3.1. Objective function

The quantity Q_{AS} as defined in equation (23) is selected as the primary objective function for the reference optimization of the structure under the proposed approach. Q_{AS} represents the area under the acceleration transfer function of the system and is a measure of the transmissibility of the system. Hence, this quantity can be a good indicator of the portion of energy that is transferred to the structure as absolute acceleration, and consequently for the magnitude of the expected force reactions borne by the structure during the earthquake. It is noted that this approach does not require the use of a specific excitation power spectrum or time history excitation, leading to an optimized design that depends solely on the characteristics of the structure and can be used across a range of low-frequency excitations.

As a secondary approach, and for the purposes of comparison and verification of the proposed method, the quantity R_{AS} as defined in equation (29) is used as an alternative objective function. R_{AS} is an indicator of the actual energy content of the response to a specific excitation PSD. Section 4.2 explores the extent to which the response results derived from solving the problem with either of the two objective functions are equivalent.

3.2. Fixed parameters

The following are considered as fixed parameters of the system with regards of the optimization problem:

- X_{VSD} : The static deflection of the structure depends on the initial stiffness of the structure and its mass, or, in other words, its natural frequency, f_0 :

$$X_{VSD} = \frac{m_S g}{k_S} \quad (34)$$

As mentioned in section 2.2, a highlight in the proposed system is the fact that the static vertical deflections are determined by the initial vertical stiffness elements of the structure, hence:

$$k_R = k_S \quad (35)$$

This way, the static vertical deflections of the system are maintained at the desired level, while the negative stiffness element participates only in the dynamic response of the system. The static settlement of the rigid mass X_{VSD} (or, alternatively the initial stiffness of the structure (k_S) or its initial natural frequency (f_0)) is therefore the first fixed design variable of the system. X_{VSD} is taken equal to 2cm in the reference problem. The impact of X_{VSD} is also explored in section 4.2 where results of the optimization are shown for the range 1-3cm.

- m_S, m_D : The reference structure mass m_S is taken 1000kg. The small oscillating mass m_D is determined through (30) where μ_D is taken equal to 5%.
- $\varepsilon_N, \varepsilon_P$ and ε_R : Variations from the design values of the various stiffness can occur due to many factors such as temperature variations, manufacturing tolerances, or nonlinear behavior. The values of $\varepsilon_N, \varepsilon_P$ and ε_R are taken equal to 10%, 5% and 5% respectively.

3.3. Optimized parameters

The four parameters that are optimized under the proposed method are:

- k_N : The value of the NS element. The NS element maximum (absolute) value is equal to -100 N/m per kg of structure mass, as presented in [17]; the minimum value is equal to -800 N/m per kg
- c_N and c_P : The damping factors related to the stiffness elements k_P, k_N . In the reference problem, the upper limit of the damping ratios ζ_N, ζ_P is set 1.0%.
- μ_R : The inertance ratio of the main structure inerter, b_R . The upper limit of μ_R is set to 2.0.

3.4. Dependent variables

Positive stiffness element K_p derived from the static stability limit case:

To ensure that potential loss of the static stability is prevented, the possible variations of k_N, k_P, k_R should be taken into consideration in the design and optimization of the system. The stiffness parameters of the system may present significant fluctuations since almost all NS designs result from unstable non-linear configurations [21]. Consequently, an increase of the absolute value of k_N and/or a decrease of the values of k_P and k_R by a factor $\varepsilon_N, \varepsilon_P$ and

ε_R respectively, may result in the system being unstable. In the limit case that the total overall stiffness k_{tot} as calculated by equation (10) is equal to zero, the system is unstable:

$$k_{tot}=0 \Leftrightarrow (1 - \varepsilon_R)k_R + \frac{(1 - \varepsilon_P)k_P(1 + \varepsilon_N)k_N}{(1 - \varepsilon_P)k_P + (1 + \varepsilon_N)k_N} = 0 \quad (36)$$

$$\Rightarrow k_P = - \frac{(1 - \varepsilon_R)(1 + \varepsilon_N)}{(1 - \varepsilon_P) [(1 - \varepsilon_R) + (1 + \varepsilon_N)(k_N/k_R)]} k_N \quad (37)$$

Equation (36) shows the dependance of k_P on k_N , ε_N , ε_P and ε_R . The values of ε_N , ε_P and ε_R are fixed design parameters (paragraph 3.2), and k_N is obtained through the optimization (paragraph 3.3); hence the value of k_P can be derived from the above.

4. OPTIMIZATION RESULTS AND ANALYSIS

4.1. Reference optimization problem and results

The extended KDamper & inerter system is configured to control vibrations of a rigid mass of $m_s=1000$ kg. The optimal parameters are selected according to the optimization procedure described in section 3, using the interior-point optimization method. The results are presented for different values of the fixed parameter X_{VSD} within the allowable range of [1 3] (cm). The full set of parameters is presented in Table 1. The transfer functions H_{AS} , H_{US} , and the response PSDs S_{AS} , S_{US} are presented in Figure 3 and Figure 4 for different values of the design parameter X_{VSD} in order to evaluate the sensitivity of the TFs and response PSDs to the parameter X_{VSD} . The acceleration response spectrum utilized in this paper is the one used in [20] and it is based on a database of 50 artificial accelerograms, generated to match the EC8 spectrum with characteristics: Type 1 with spectral acceleration $\text{avg}(g)=0.9*0.36$.

It can be observed from Figure 3 that the maximum values of acceleration H_{AS} and S_{AS} are not substantially affected by the X_{VSD} . The relative displacement H_{US} is affected in the low-frequency range, while the S_{US} is less affected.

	μ_D	μ_b	k_N (kN/m)	k_R (kN/m)	k_P (kN/m)	ζ_N (%)	c_N (kNs/m)	ζ_P (%)	c_P (kNs/m)
$X_{VSD}=1\text{cm}$	0.05	0.60	-164.31	981.00	236.03	1.00	0.626	1.00	0.626
$X_{VSD}=2\text{cm}$	0.05	0.43	-86.45	490.50	125.76	1.00	0.442	1.00	0.442
$X_{VSD}=3\text{cm}$	0.05	0.36	-59.10	327.00	86.55	1.00	0.362	1.00	0.362

Table 1: Full set of the system parameters in the range of the design parameter $X_{VSD}=[1\ 3]$ (cm).

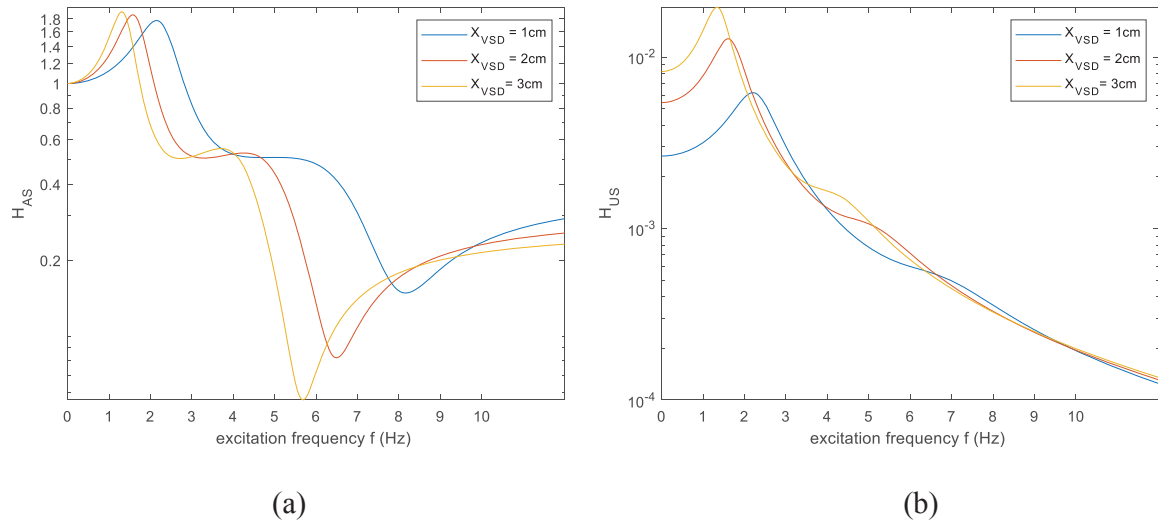


Figure 3. Transfer Functions of the optimized system with X_{VSD} varying in the range [1 3] (cm). (a) Structure absolute acceleration H_{AS} ; (b) structure relative displacement H_{US} .

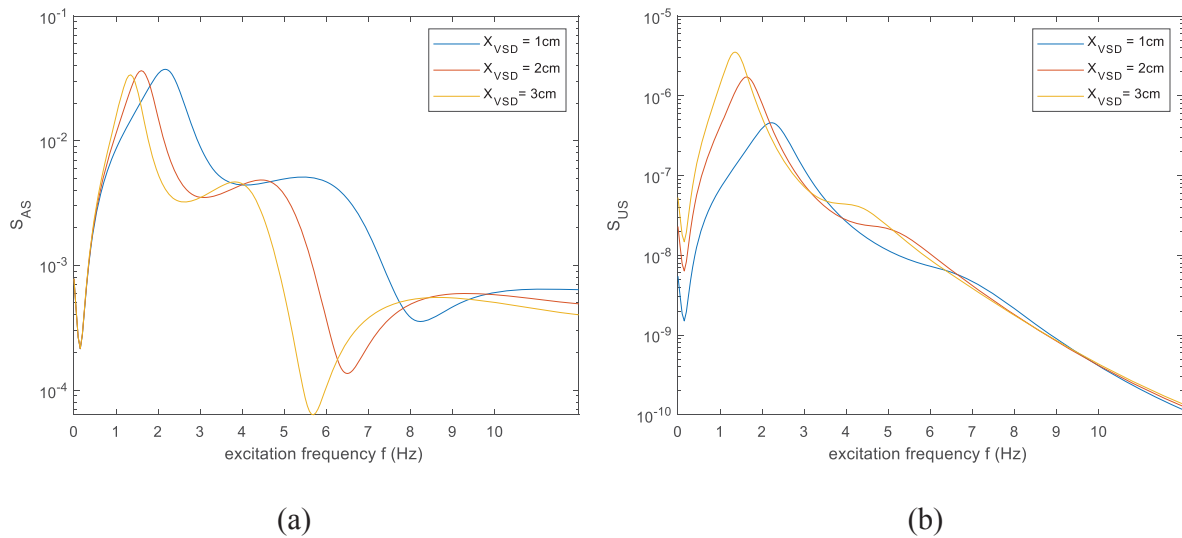


Figure 4. Response PSDs considering the ground motion acceleration excitation PSD, S_A , (a) Structure absolute acceleration S_{AS} ; and (b) relative displacement S_{US} .

The following section explores the impact of the selection of objective function to the optimization problem. This is evaluated in terms of response to excitation PSD and time history response to the sample of 50 artificial accelerograms. In order to better observe the effectiveness of the proposed configuration, in the next sections the responses are compared with a highly damped ($\zeta=15\%$) conventional damper (CD) as described in paragraph 2.1.

4.2. Effect of objective function (Q_{AS} , R_{AS})

As discussed in paragraph 3, the optimization approach considers the area under the acceleration transfer function of the system (scaled by a factor $d\omega$) as the primary objective function for this problem, Q_{AS} as defined in equation (23). One of the motivations of this paper is to explore its equivalency vs. the more conventional approach of using a measure of the actual content of the response (such as R_{AS} defined in equation (29)) as the objective function.

The results are shown for a ground motion acceleration excitation PSD and subsequently verified through time history analyses. An acceleration response indicator r_{AS} is defined as:

$$r_{AS,CD} = \frac{R_{AS,CD}}{\sqrt{\int_{-\infty}^{+\infty} S_{AS}(\omega) d\omega (= PGA)}} \quad (38)$$

$$r_{AS,KD,Opt} = \frac{R_{AS,KD,Opt}}{\sqrt{\int_{-\infty}^{+\infty} S_{AS}(\omega) d\omega (= PGA)}} \quad (39)$$

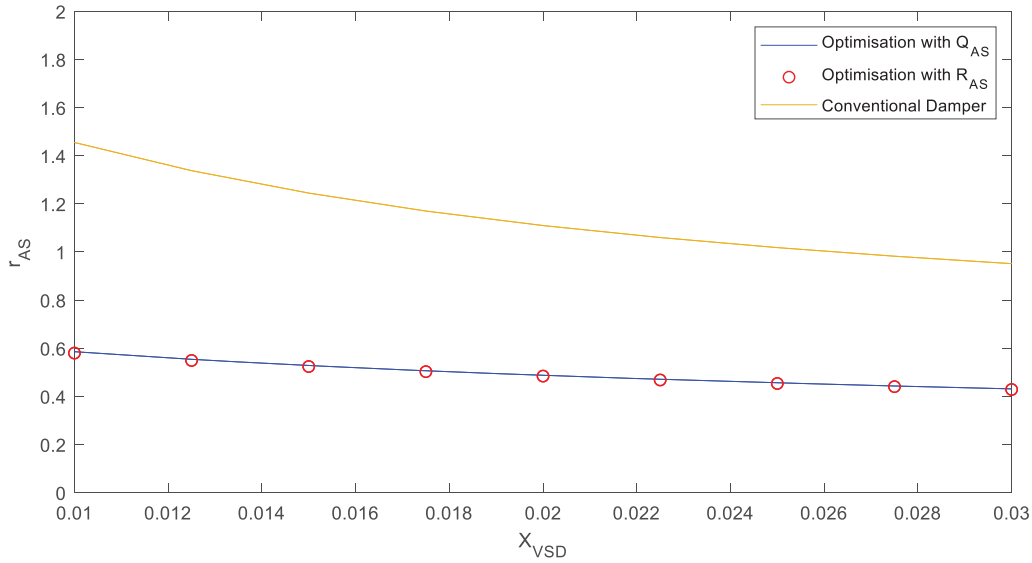


Figure 5. Variation of the acceleration response indicator r_{AS} over the X_{VSD} , of the conventional damping system and proposed configuration, for the two objective functions examined.

Figure 5 above presents the response indicators with respect to varying X_{VSD} in the cases of: (i) the Ext. KDamper & inerter system optimized via Q_{AS} as the objective function (blue line), (ii) the Ext. KDamper & inerter system optimized via R_{AS} as the objective function (red circles), (iii) the conventional damper (yellow line). It is evident that the two optimization methods coincide.

The PSD response results are subsequently verified with time history analyses from the 50 accelerograms. Below are the cumulative results showing the peak values of the quantities of interest (structure absolute acceleration a_S , structure relative displacement u_S , and oscillating mass relative displacement u_D) for X_{VSD} in the range of [1 3] (cm). Blue color corresponds to the reference optimization of the extended KDamper & inerter system, as described in Table 1. Red color shows the optimization using the same fixed parameters and constraints, but using R_{AS} as the objective function (instead of Q_{AS}). Finally, the orange bar represents the conventional damping system. Figure 6(a) shows the peak a_S averaged over the 50 accelerograms, while Figure 6(b)-(d) show the overall maxima of the peak quantities. It can be verified that the two objective functions yield very similar results across all quantities of interest. Moreover, it is observed that the proposed optimized system can reduce the structure peak acceleration up to more than 50% when compared to a conventional damping system, while maintaining the displacement within a satisfactory range.

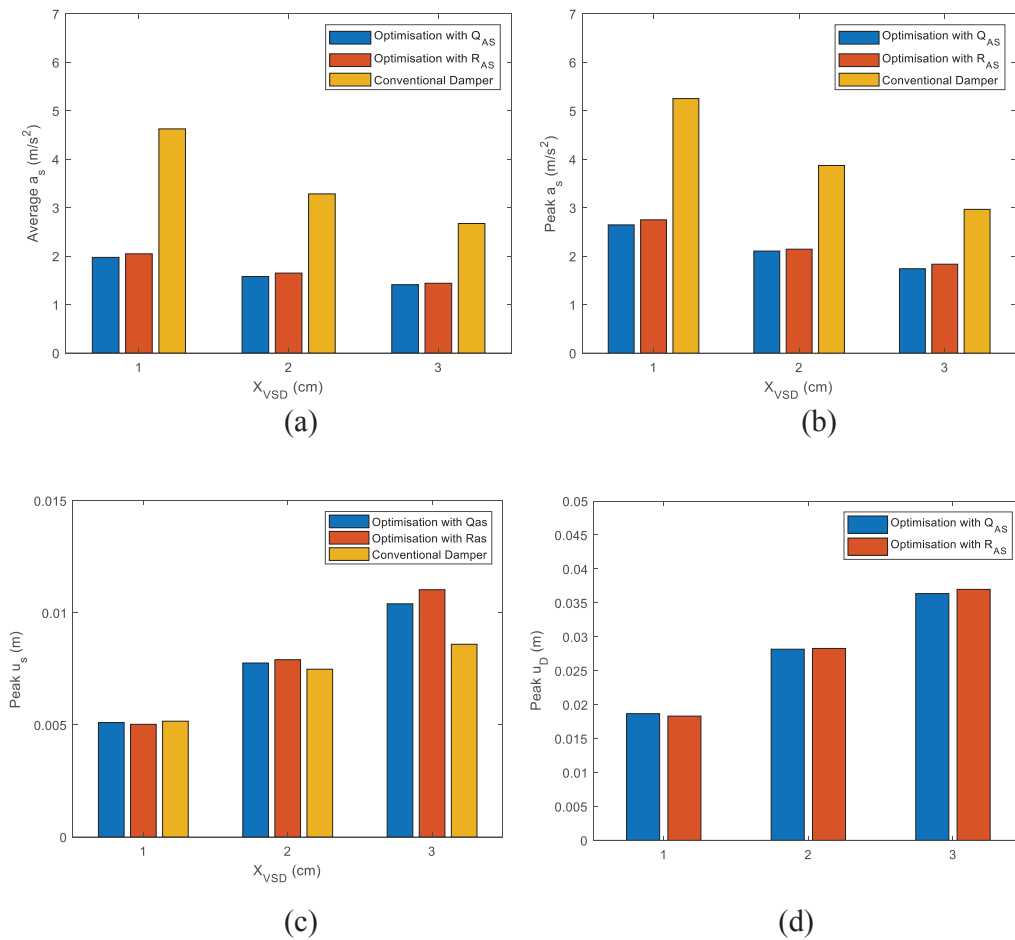


Figure 6. Results from the time history responses over 50 artificial accelerograms with the system optimized for the two different objective functions, and for the conventional damper. (a) Peak absolute acceleration averaged over the 50 accelerograms; (b) Overall maximum of the peak absolute acceleration; (c) Overall maximum of the peak relative structure displacement absolute accelerations; (d) Overall maximum of the peak relative oscillating mass displacement.

5. CONCLUSIONS

This paper proposes a stiff dynamic absorber, combining a negative stiffness element, a tuned-mass damper and an inerter. The system is configured under a proper optimization procedure, and the results are subsequently verified with an excitation PSD, generated from a database of artificial accelerograms designed to match the EC8 vertical spectrum as well as with time history results from the individual accelerograms.

Results indicate that the proposed system can drastically reduce structure accelerations (>50% reduction compared to a conventional damping system), while the vertical displacement remains at satisfactory levels. The proposed system thus demonstrates an enhanced dynamic behavior while maintaining suitable vertical stiffness. A key highlight of the proposed system in relation to previous works is the fact that the initial static stiffness is retained, since the negative stiffness elements participate only in the dynamic response.

Moreover, a new optimization approach is utilized through the introduction of a more general objective function which depends solely on the characteristics of the structure and not the excitation parameters. The suitability of this method is tested using response spectra and time history analyses for the abovementioned excitations, and verified through a comparison with previous optimization strategies that depend on a specific spectral excitation. The comparison

results confirm that a unique optimal stiff dynamic absorber design can be used across a wide range of important vertical dynamic absorption applications, as well as structure seismic protection.

6. ACKNOWLEDGMENTS

Marina Kalogerakou has been financed by the European Union's Horizon 2020 research and innovation programme under the Marie Skłodowska-Curie grant (grant agreement No INSPIRE-813424, "INSPIRE - Innovative Ground Interface Concepts for Structure Protection").

7. REFERENCES

1. Luft RW. Optimal Tuned Mass Dampers for Buildings. *Journal of the Structural Division* 1979; 105(12): 2766–2772.
2. Qin L, Yan W, Li Y. Design of frictional pendulum TMD and its wind control effectiveness. *Journal of Earthquake Engineering and Engineering Vibration* 2009; 29(5): 153–157.
3. Ramezani M, Bathaei A, Ghorbani-Tanha AK. Application of artificial neural networks in optimal tuning of tuned mass dampers implemented in high-rise buildings subjected to wind load. *Earthquake Engineering and Engineering Vibration* 2018; 17(4): 903–915. DOI: 10.1007/s11803-018-0483-4.
4. Debnath N, Deb SK, Dutta A. Multi-modal vibration control of truss bridges with tuned mass dampers under general loading. *JVC/Journal of Vibration and Control* 2016; 22(20): 4121–4140. DOI: 10.1177/1077546315571172.
5. Chen JL, Georgakis CT. Spherical tuned liquid damper for vibration control in wind turbines. *Journal of Vibration and Control* 2015; 21(10): 1875–1885. DOI: 10.1177/1077546313495911.
6. Taniguchi T, Der Kiureghian A, Melkumyan M. Effect of tuned mass damper on displacement demand of base-isolated structures. *Engineering Structures* 2008; 30(12): 3478–3488. DOI: 10.1016/j.engstruct.2008.05.027.
7. Xiang P, Nishitani A. Optimum design for more effective tuned mass damper system and its application to base-isolated buildings. *Structural Control and Health Monitoring* 2014; 21(1): 98–114. DOI: 10.1002/stc.1556.
8. Hashimoto T, Fujita K, Tsuji M, Takewaki I. Innovative base-isolated building with large mass-ratio TMD at basement for greater earthquake resilience. *Future Cities and Environment* 2015. DOI: 10.1186/s40984-015-0007-6.
9. Weber B, Feltrin G. Assessment of long-term behavior of tuned mass dampers by system identification. *Engineering Structures* 2010; 32(11): 3670–3682. DOI: 10.1016/j.engstruct.2010.08.011.

10. Smith MC. Synthesis of mechanical networks: The inerter. *IEEE Transactions on Automatic Control* 2002. DOI: 10.1109/TAC.2002.803532.
11. Chen MZQ, Smith MC. Restricted complexity network realizations for passive mechanical control. *IEEE Transactions on Automatic Control* 2009; 54(10): 2290–2301. DOI: 10.1109/TAC.2009.2028953.
12. Molyneaux W. Supports for Vibration Isolation. G. Britain: ARC/CP-322, Aer Res Council; 1957.
13. Platus DL, L.Platus D. Negative-stiffness-mechanism vibration isolation systems. *Proc. of SPIE*, vol. 1619, 1992.
14. Carrella A, Brennan MJ, Waters TP. Static analysis of a passive vibration isolator with quasi-zero-stiffness characteristic. *Journal of Sound and Vibration* 2007; 301(3–5): 678–689. DOI: 10.1016/j.jsv.2006.10.011.
15. Ibrahim RA. Recent advances in nonlinear passive vibration isolators. *Journal of Sound and Vibration* 2008; 314(3–5): 371–452. DOI: 10.1016/j.jsv.2008.01.014.
16. Nagarajaiah S, Pasala DTR, Reinhorn A, Constantinou M, Sirilis AA, Taylor D. Adaptive Negative Stiffness: A New Structural Modification Approach for Seismic Protection. *Advanced Materials Research* 2013; 639–640: 54–66. DOI: 10.4028/www.scientific.net/amr.639-640.54.
17. Antoniadis IA, Kanarachos SA, Gryllias K, Sapountzakis IE. KDamping: A stiffness based vibration absorption concept. *JVC/Journal of Vibration and Control* 2018; 24(3): 588–606. DOI: 10.1177/1077546316646514.
18. Kapasakalis K, Antoniadis I, Sapountzakis E. Performance Assessment of the KDamper as a Seismic Absorption Base. *Structural Control and Health Monitoring* 2019. DOI: 10.1002/stc.2482.
19. Kapasakalis KA, Antoniadis IA, Sapountzakis EJ. Constrained optimal design of seismic base absorbers based on an extended KDamper concept. *Engineering Structures* 2021; 226. DOI: 10.1016/j.engstruct.2020.111312.
20. Kapasakalis K, Antoniadis I, Sapountzakis E, Stiff Vertical Seismic Absorbers, *Journal of Vibration and Control*, to appear.
21. Li H, Li Y and Li J (2020) Negative stiffness devices for vibration isolation applications: A review. *Advances in Structural Engineering*; DOI: 10.1177/1369433219900311.

ACCURATE COLLAPSE CAPACITY QUANTIFICATION FOR INFILLED RC FRAME BUILDINGS

Al Mouayed Bellah Nafeh¹, Gerard J. O'Reilly¹

¹ Centre for Training and Research on Reduction of Seismic Risk (ROSE Centre), Scuola
Universitaria Superiore IUSS Pavia
Palazzo del Broletto, Piazza della Vittoria 15, Pavia 27100, Italy
e-mail: {mouayed.nafeh, gerard.oreilly}@iusspavia.it

Abstract

The seismic assessment of reinforced concrete (RC) structures with masonry infills is an important issue in modern earthquake engineering. This typology is prevalent in the southern-Mediterranean region and represents a large percentage of the Italian building stock. A pertinent aspect in their seismic assessment entails the quantification of structural performance up to global collapse. Collapse capacity can be quantified through a fragility function, which relates the probability of collapse to seismic intensity and is typically generated through computationally expensive non-linear dynamic analyses. However, simplified methodologies exist, offering a trade-off between accuracy and extensive analyses through empirical relationships derived from large analyses databases, and are typically referred to as $R-\mu-T$ relationships. To this end, this paper explores a simplified methodology for collapse assessment of infilled RC frames using such $R-\mu-T$ relationships, incorporating the general response of the structural typology and employing average spectral acceleration AvgSa as a more accurate and appropriate intensity measure (IM). Such an approach can be of great assistance to practitioners, stakeholders and decision-makers in quantifying the collapse capacity of structures, as it removes the need for large computational analysis whilst still maintaining a high level of accuracy. This paper illustrates the robustness of the developed $R-\mu-T$ relationships for infilled RC frames in quantifying median collapse intensities and dispersions and compares the outcome with traditional non-linear dynamic analyses for several archetypical 3D buildings, representative of the aforementioned typology found in Italy.

Keywords: infilled; assessment; collapse quantification; average spectral acceleration; performance-based.

1 INTRODUCTION

Italian and European reinforced concrete (RC) frame buildings with masonry infill panels comprise a significant portion of the Mediterranean building stock (Figure 1). Before the 1970s (i.e. before the introduction of suitable seismic provisions), buildings in Italy in specific, and also across Southern Europe, were generally designed and constructed to resist gravity loads only [1,2]. In Italy, these were designed according to Regio Decreto (RD2229/1939) [3]. This design approach entails the use of the allowable stress method for the detailing of structural sections. Structural elements designed this way were typically characterised with inadequate seismic detailing. For example, the use of smooth rebars, low compressive strengths for concrete, and no consideration for a ductile failure mechanism (i.e. capacity design, strong column-weak beam formulation). Furthermore, unreinforced clay brick masonry infills were typically used as partitioning and façade elements based on their thermal and acoustic insulation, fire retarding and moisture control behaviour. These elements, however, were not considered in the structural design and therefore their effects on the structural response were neglected. Experimental and analytical studies, however, have outlined the effects of masonry infills on the global lateral response of the structural system [4–11]. These effects are characterised by a significant addition in lateral stiffness and a sudden drop in lateral strength with the rupture of infills on one or several storeys.

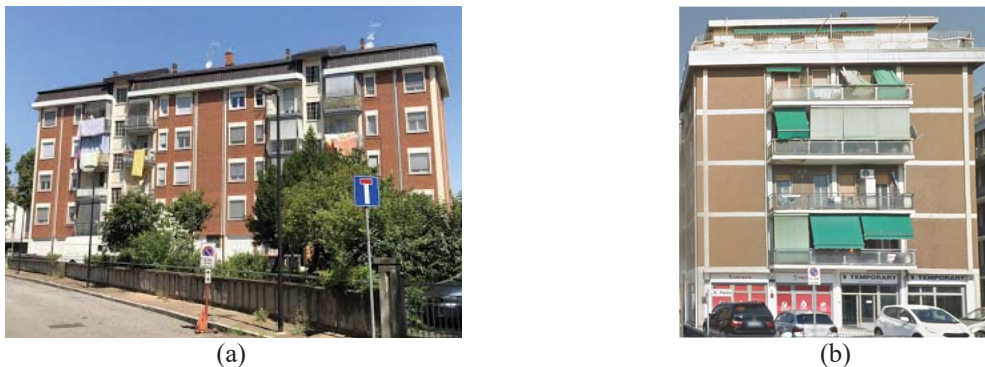


Figure 1: Typical Italian residential housing using infilled frame structures

Moreover, assessing the structural performance of structures requires accurate quantification of the exceedance of any structural demand-based performance level. The latter is typically quantified using fragility curves, which link the probability of exceeding predefined thresholds of demand for a given intensity level of ground-shaking. These are usually the end-result of extensive numerical analysis (i.e. numerical modelling, ground-motion selection, nonlinear dynamic analyses). To reduce the computational effort and time required by such analyses, simplified tools and methodologies for the assessment of RC frame structures have emerged, with the introduction of the SPO2IDA [12], SPO2FRAG [13] and other simplified methodologies [14–16]. These simplified approaches utilise $R-\mu-T$ for a direct estimation of the seismic demand and capacity. The aim of these tools is to supply users with aid in the quantification and mitigation of seismic risk compatible with different guidelines [17,18]. For example, the inclusion of SPO2IDA within the FEMA P-58 guidelines [19] can be considered a testimony to the added value of simplified tools in performance-based earthquake engineering (PBE) [20]. To this end, the aim of the study is to present and further develop a simplified methodology previously introduced as ExtendedSPO2IDA [21], which had been tailored specifically for infilled RC frame structures. Previously, the $R-\mu-T$ relationships used in this tool were fitted considering the 5% damped spectral acceleration at the fundamental period,

$Sa(T_1)$. Therefore, subsequent sections will revisit the issue of a suitable IM choice for the characterisation of seismic demand in infilled RC frames. Subsequently, a refitting of the aforementioned tool is then conducted with reference to the selected IM. Two case study buildings are then presented to verify and evaluate the refitted tool in terms of median collapse intensities in comparison with results obtained from a non-linear dynamic analysis with a rigorous ground-motion selection and fully detailed numerical models.

2 SUITABLE CHOICE OF INTENSITY MEASURE

Average spectral acceleration ($AvgSa$) has been observed in several studies [22–24] to be a more advantageous intensity measure (IM) when compared to spectral acceleration at the fundamental period ($Sa(T_1)$) and particularly for the quantification of the collapse intensity for RC frames [25–27]. Efficiency and sufficiency are often the metrics used when comparing IMs. The former represents the capability of a selected IM to accurately predict a designated EDP, while the latter examines the level of independence of the structural response value from seismological properties (e.g. magnitude, rupture distance).

The definition of $AvgSa$ thus incorporates spectral acceleration intensities at periods around T_1 , which can consider the elongation effects of a structural system up to collapse and also the higher mode contributions at periods shorter than T_1 . This definition has rendered it a better predictor in terms of reduced dispersion (i.e. increased efficiency) when large deformations and non-linearities start occurring in the structural model. This comparison is highlighted in Figure 2, in terms of incremental dynamic analysis (IDA) results on two single-degree-of-freedom (SDOF) systems studied previously in Nafeh et al. [21]. IDA is conducted using the FEMA P695 [28] far-field record set and is presented in terms of the median, 16th and 84th percentiles with $Sa(T_1)$ and $AvgSa$ as IMs. From these IDA results, one can notice a noticeable change in the dispersion of the results reflected in the quantiles at each intensity measure level. IDA curves for two SDOF systems are presented herein in Figure 2. It can be observed that for both cases, when employing $AvgSa$, the dispersion at collapse decreased by 46.9% ($\beta_{IM=Sa(T_1)} = 0.35$, $\beta_{IM=AvgSa} = 0.18$) and 41.5% ($\beta_{IM=Sa(T_1)} = 0.34$, $\beta_{IM=AvgSa} = 0.20$) as opposed to using $Sa(T_1)$ for the two respective cases.

Eads et al. [25] noted relatively stable collapse risk estimates across various ground motions sets for steel MRFs and shear wall structures when employing $AvgSa$. O'Reilly [29] infers similar conclusions on the beneficial use of $AvgSa$ and the limitations of $Sa(T_1)$ in the collapse assessment of non-ductile infilled RC frames, of interest to this study. Following the above remarks, $AvgSa$ has been seen to be an advantageous IM for assessing the collapse capacity of infilled RC frames and will be explored herein for the development of simplified collapse assessment tools.

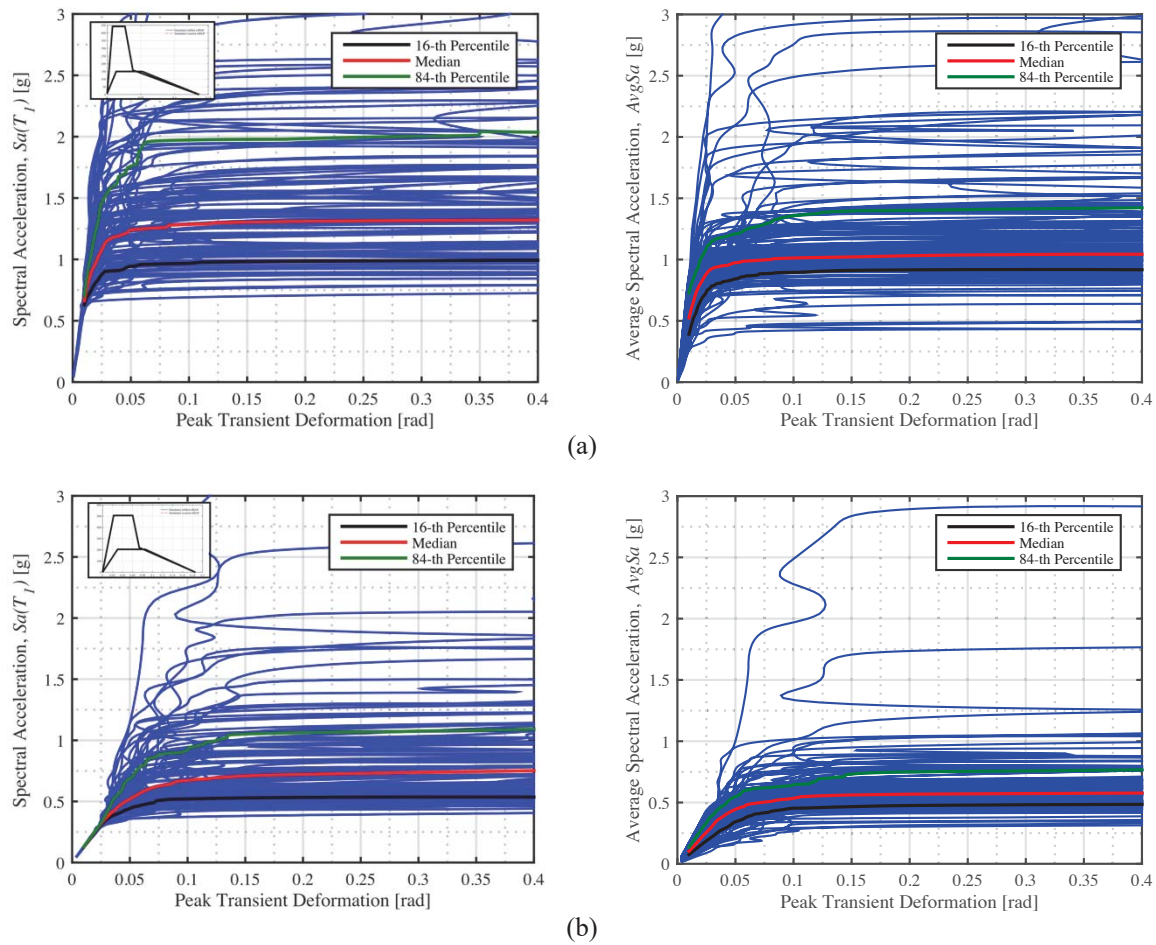


Figure 2. Comparison of IDA quantiles (16th, 50th and 84th) for two SDOF systems (a-b) considering $AvgSa$ (left) and $Sa(T_1)$ (right) as IMs using FEMA P695 Far-Field record set

3 DEVELOPMENT OF A SIMPLIFIED TOOL FOR COLLAPSE ASSESSMENT

The fundamental concept behind the development [12] and extension [21] of the SPO2IDA tool is to relate the force-deformation capacity of a given frame structure (obtained through non-linear static, or static pushover (SPO), analysis) to its dynamic counterpart, typically illustrated using IDA [30]. The extension of SPO2IDA was developed to incorporate the behaviour of infilled RC frames whose behaviour was not properly represented in the original version. This behaviour is characterised by a significant addition in lateral stiffness followed by a sudden loss of lateral strength capacity due to the localisation of damage on one or several storeys (i.e. formation of a soft-storey mechanism due to the sudden rupture of infill panels) shown in Figure 3.

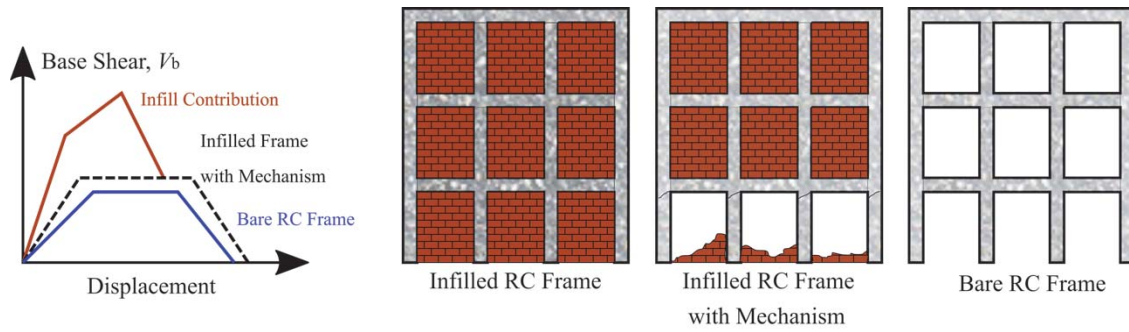


Figure 3: Illustration of the contribution of infill panels on the stiffness and strength of the global system before period elongation due to the formation of a non-ductile mechanism.

For the development of the tool, a large dataset of SDOF systems with varying backbone parameters is required. IDA then subjects the set of SDOF systems to increasing levels of intensity until numerical collapse is achieved. This forms a library of seismic demand-capacity models for various SDOF with distinct features. The library can then be utilised for a direct estimation of the seismic demand and capacity through interpolation and fitted closed-form expressions. This is done using results from SPO and eigenvalue (modal) analyses to relate a multi-degree-of-freedom (MDOF) system to an SDOF oscillator (presented in Figure 4). Then, the median collapse intensity and dispersion associated with the collapsing intensity are estimated using the results of the extensive numerical analysis (i.e. IDAs) and a set of R - μ - T relationships relating the SPO backbone characteristics with the medians and dispersions obtained.

The two ground motion record sets from INNOSIS [31] that are representative of European seismicity (i.e. medium and high seismicity) were utilised for the IDA related to this study. Subsequent sections will highlight the methodology proposed in this study, which incorporates the use of SDOF systems representative of the response of infilled RC typology, quantifying the dynamic response through IDA and fitting closed-form expression at each response branch up to global collapse.

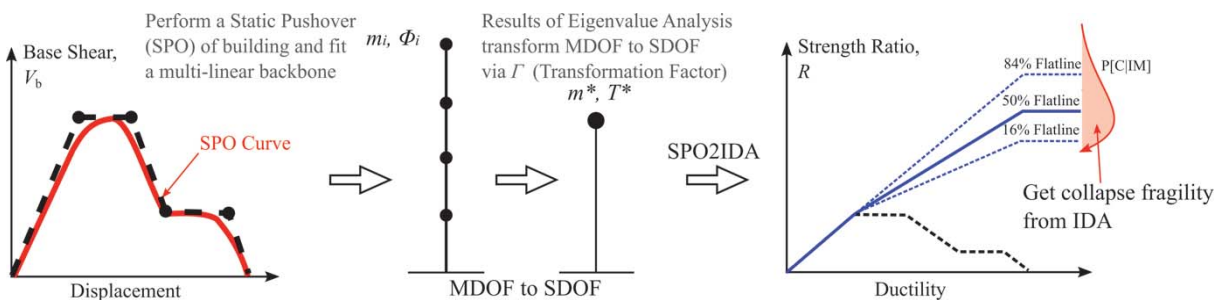


Figure 4: Direct estimation of seismic demand-capacity of a multi-degree-of-freedom system using single-degree-of-freedom systems through extendedSPO2IDA via results of pushover and eigenvalue analysis.

3.1. Methodology

This section introduces the methodology employed for analysing a set of equivalent SDOF oscillators to analyse the dynamic capacity properties of infilled RC frames. The methodology is as follows:

- 1) Perform IDAs on SDOFs whose capacity curve parameters are known *a priori* (from a previously generated set accounting for the variability in the backbone parameters) to relate the IM (i.e. $AvgSa$) to the engineering demand parameter (EDP) of the system.

- 2) Find the static response parameters corresponding to each SDOF analysis ($R_{st,i}$, $\mu_{st,i}$) defined in Equations 1.1 and 1.2, where i corresponds to the response branch (i.e. elastic, post-capping, softening, residual strength (plateau) and strength degradation), $V_{b,st,i}$ and $V_{b,y}$ are respectively the base shear values at the response branch and the nominal yield force, $\Delta_{r,st,i}$ and $\Delta_{r,y}$ are respectively the roof displacement values at the response branch and displacement corresponding to the nominal yield force.

$$R_{st,i} = V_{b,st,i}/V_{b,y} \quad \text{Equation 1.1}$$

$$\mu_{st,i} = \Delta_{r,st,i}/\Delta_{r,y} \quad \text{Equation 1.2}$$

- 3) Process the IDA results and convert the median and fractile quantities (i.e. 16th and 84th percentiles) IM-EDP IDA curves to the corresponding dynamic response parameters ($R_{dyn,i}$, $\mu_{dyn,i}$) defined in Equations 2.1 and 2.2. Sa_y is the yield spectral acceleration, Γ is the transformation factor obtained from eigenvalue analysis. T^* , m^* , Δ_y^* and V_y^* are respectively the period, effective mass, deformation capacity at yield and the nominal yielding force of the SDOF system. Sa_{ratio} is the ratio of the spectral shape introduced by Eads et al. [26]. The steps presented herein were only performed during the processing of the IDAs and will not be later required by the user as input.

$$R_{dyn,i} = \frac{Sa(T^*)_i}{Sa_y} \quad \text{Equation 2.1}$$

$$\mu_{dyn,i} = \frac{\Delta_{dyn,i}}{\Delta_{dyn,y}} \quad \text{Equation 2.2}$$

$$Sa_{ratio} = \frac{Sa(T^*)}{AvgSa(T^*[a, b])} \quad \text{Equation 2.3}$$

From Equations 2.1 and 2.3:

$$Sa_{ratio} AvgSa(T^*[a, b]) = Sa(T^*) = R_{dyn,i} Sa_y \quad \text{Equation 2.4}$$

$$\frac{AvgSa(T^*[a, b])}{Sa_y} = \frac{R_{dyn,i}}{Sa_{ratio}} = \rho \quad \text{Equation 2.5}$$

$$\widehat{AvgSa} = \rho Sa_y \Gamma \quad \text{Equation 2.6}$$

where the transformation factor is introduced in Equation 2.6 to estimate the AvgSa for the MDOF system. It is also noted that:

$$Sa_y = \frac{4\pi^2 * \Delta_y^*}{T^{*2}} = \frac{V_y}{m^*} \quad \text{Equation 2.7}$$

$$T^* = 2\pi \sqrt{\frac{m^* * \Delta_y^*}{V_y^*}} \quad \text{Equation 2.8}$$

- 4) Interpolate the dynamic response parameters ($R_{dyn,i}$, $\mu_{dyn,i}$) corresponding to the former (as highlighted in Figure 5) for each static response branch of every SDOF system. The step herein populates a database of static vs dynamic response parameters which will be further utilised to fit the expressions in Table 1 via two-step regression analysis.

- a) 1st step: obtain a functional form expressing the median and fractile quantities (i.e. $R_{dyn,i}$, $\mu_{dyn,i}$) of the IDA in function of the static parameters ($R_{st,i}$, $\mu_{st,i}$) obtained from static pushover analyses.
- b) 2nd step: relate the functional form coefficients in step (a) to the fundamental period and other relevant capacity parameters.

3.2. Fitting of Functions

For the two-step regression analysis conducted herein, the Least Absolute Residuals (LAR) and the Bisquare weights methods were employed to increase the robustness of the fitting routine. The LAR method finds a curve that minimises the absolute difference of the residuals, rather than the squared differences. Therefore, extreme values have a lesser influence on the fit. The Bisquare weights method minimises a weighted sum of squares, where the weight given to each data point depends on how far the point is from the fitted line. Points near the line get full weight and points farther from the line get reduced weight. The LAR method has been used herein.

The resulting R - μ - T relationships from two-step regression analysis are presented in Table 1, whereas Figure 5 illustrates the strength and ductility factors figuring in the Equations for each response branch. A simple linear functional form is attributed to the relationship between the dynamic strength factors and the ductilities at each response branch threshold. A more complex functional form is used for the introduction of the fundamental period, reduction in strength due to the rupture of infills, and the corresponding residual strength capacity of the structure (i.e. as seen in the 2nd step regression). Previous work in Nafeh et al. [21] opted for the use of more complex functional forms to characterise the relationship between the static and dynamic response parameters presented in the previous section. Moreover, the reduction in strength and residual capacity of the global system was not incorporated in past work.

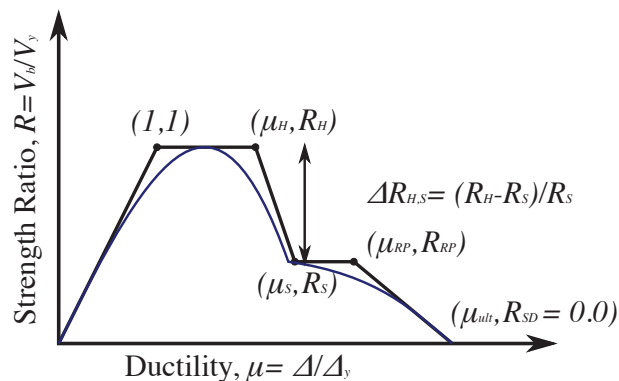


Figure 5: Illustration of the normalized static pushover curve and the response branch parameters noted in the Equations in Table 1

Table 1: Closed-form expression denoting R - μ - T relationships for infilled RC frames for each response branch using two-step regression analysis and implemented in extendedSPO2IDA

Response Branch	1 st Step Regression	2 nd Step Regression
Hardening (H)	$R_{dyn,H} = \alpha_{1,qt}\mu_H + \beta_{1,qt}$	$\alpha_{1,16} = -0.5563T^{*2} + 0.711T^* + 0.0115$ $\beta_{1,16} = 0.5563T^{*2} - 0.711T^* + 0.9885$ $\alpha_{1,50} = -0.634T^{*2} + 0.9239T^* + 0.08742$ $\beta_{1,50} = 0.634T^{*2} - 0.9239T^* + 0.9126$ $\alpha_{1,84} = -1.053T^{*2} + 1.509T^* + 0.1239$ $\beta_{1,84} = 1.053T^{*2} - 1.509T^* + 0.8761$
	Where $\mu_H \in (1; \mu_H]$	
Softening (S)	$R_{dyn,S} = \alpha_{2,qt}\mu_S + \beta_{2,qt}$	$\alpha_{2,16} = 0.2186\left(\frac{T^*}{\Delta R_{H,S}}\right)^{0.34}$ $\beta_{2,qt} = 0.7782\left(\frac{T^*}{\Delta R_{H,S}}\right)^{-0.08327}$ $\alpha_{2,50} = 0.377\left(\frac{T^*}{\Delta R_{H,S}}\right)^{0.2951}$ $\beta_{2,50} = 0.6189\left(\frac{T^*}{\Delta R_{H,S}}\right)^{-0.1445}$ $\alpha_{2,84} = 0.5857\left(\frac{T^*}{\Delta R_{H,S}}\right)^{0.2825}$ $\beta_{2,84} = 0.4087\left(\frac{T^*}{\Delta R_{H,S}}\right)^{-0.3045}$
	Where $\mu_S \in (\mu_H; \mu_S]$	
Residual Plateau (RP)	$R_{dyn,RP} = \alpha_{3,qt}\mu_{RP} + \beta_{3,qt}$	$\alpha_{3,16} = 0.07401T^{*2} + 0.04584T^* - 0.00548$ $\beta_{3,16} = -2.158R_{RP}^2 + 2.196R_{RP} + 0.9244$ $\alpha_{3,50} = 0.04537T^{*2} + 0.08579T^* - 0.01045$ $\beta_{3,50} = -1.549R_{RP}^2 + 1.754R_{RP} + 1.288$ $\alpha_{3,84} = 0.06217T^{*2} + 0.2534T^* - 0.0286$ $\beta_{3,84} = -2.174R_{RP}^2 + 2.179R_{RP} + 1.552$
	Where $\mu_{RP} \in (\mu_S; \mu_{RP}]$	
Strength Degradation (SD)	$R_{dyn,SD} = \alpha_{4,qt}\mu_{SD} + \beta_{4,qt}$	$\alpha_{4,16} = 0.01552T^* - 0.001861$ $\beta_{4,16} = -1.662T^{*2} + 2.049T^* + 1.173$ $\alpha_{4,50} = 0.02035T^* - 0.002569$ $\beta_{4,50} = -2.008T^{*2} + 2.541T^* + 1.405$ $\alpha_{4,84} = 0.02875T^* - 0.003179$ $\beta_{4,84} = -3.886T^{*2} + 4.641T^* + 1.553$
	Where $\mu_{SD} \in (\mu_{RP}; \mu_{ult}]$	

3.3. Verification of extendedSPO2IDA using SDOF validation set

An additional set of 40 equivalent SDOFs was employed as a test set for the functions previously fitted. IDA was again carried out using the INNOSIS record set. Subsequently, the median collapse intensity of the SDOF systems and their corresponding dispersions were extracted. Consequently, the verification of the developed tool refers to the comparison of the extracted values, obtained via traditional IDA and the values obtained from applying extendedSPO2IDA. The median intensity and associated dispersion for the collapsing cases are illustrated in Figure 6. The observations show a relatively good agreement when comparing the two analysis methods (i.e. extensive IDA and simplified SPO2IDA). Additionally, Figure 6 reports the comparison of the median collapse intensities and dispersions obtained using the original version of the extendedSPO2IDA tool (i.e. calibrated on the spectral acceleration at the fundamental period $Sa(T_1)$). The comparison shows the capability of the original version in predicting the response of the system. However, the main difference and benefit of the $AvgSa$ -based tool are noted in the dispersion at collapse, where higher values for $IM = Sa(T_1)$ can be

clearly seen when compared to *AvgSa*, indicating a reduction in uncertainty and increased efficiency and accuracy of the tool.

Further validation of the $R-\mu-T$ relationships is conducted on two case study structures by considering two distinct locations, where records differing from the INNOSEIS record set will be selected based on the seismicity of the said locations.

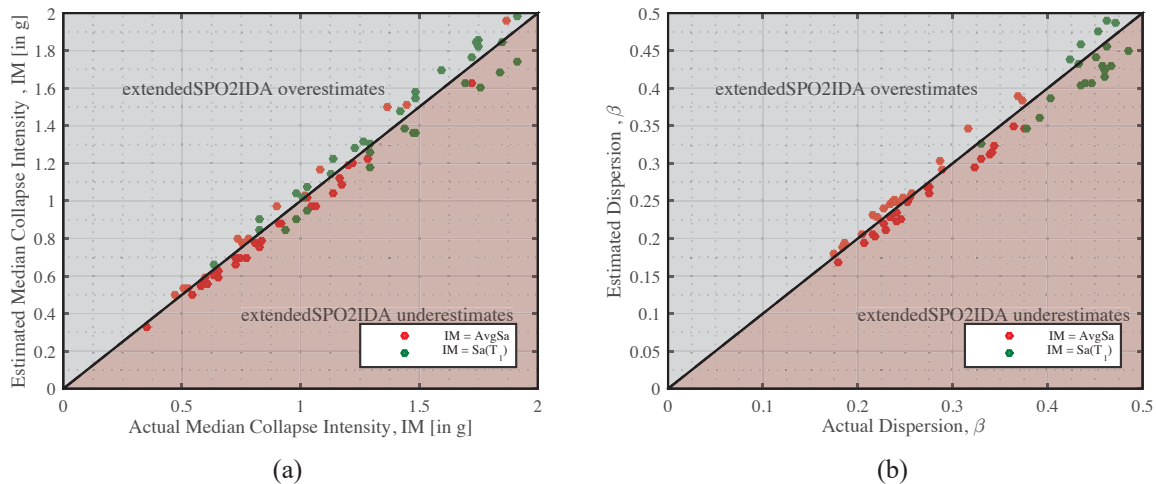


Figure 6. Comparison of the estimated (using extendedSPO2IDA) vs actual (using IDA) (a) median collapse intensity given in terms of *AvgSa* and *Sa(T₁)* [in g] and (b) dispersion at collapsing runs considering an SDOF validation set.

4 CHARACTERISATION AND NUMERICAL MODELLING OF CASE STUDY BUILDINGS

The development of archetype numerical models characterising a particular building class forms the basis of structural performance quantification. To this end, population and housing statistics provide important information related to the prevalence of a structural typology as part of the regional building stock. Additional information concerning the architectural features of the built environment can be extracted from databases like ISTAT [32] to further characterise the building class.

Moreover, geographical specifications and conditions (i.e. building material, design methodology specific for a region, etc.) need to be accounted for. Generally, before the introduction of seismic provisions (i.e. before the 1970s), southern European RC residential buildings with masonry infills were designed to resist gravity loads only (termed GLD herein) with no consideration to ductile detailing. For the specific case of Italian structures, said buildings were designed to Regio Decreto 39 (RD2229/39) [3] with complementary references [33,34]. Design features include: frames span in one direction only, the use of smooth plain rebars and concrete with respectively low yield and compressive strengths; poor transverse detailing and shear reinforcement; inadequate detailing of the beam-column joints.

The two archetypes described herein form a subset of a larger database of RC buildings with masonry infill panels. They comprise two and six-storey structures with dimensioning of the span widths and space designations presented in Figure 7. The latter elements are representative of the Italian architectural definition at the construction period of interest. Applied permanent loads were defined as 500 and 450 kg/m² for typical floors and roofs respectively, whereas accidental loads of 200 and 150 kg/m² were applied. Allowable stresses equal to 5 N/mm² for concrete and 140 N/mm² for reinforcing steel were considered, as per RD2229/39. These values correspond to 29.2% and 33.3% of the maximum stresses for concrete and steel respectively.

The corresponding sections and detailing found when conducting a simulated design for the two GLD archetype buildings are presented in Table 2.

The numerical modelling of the case study buildings was performed in OpenSees [35] using a 3D lumped-plasticity model. “*forceBeamColumn*” elements with a finite plastic hinge length were used to describe the structural response of beam-column elements. The latter elements are then coupled with *zero-length* elements at the plastic hinge locations utilising a “*Pinching4*” hysteretic material model based on the force-deformation relationships for non-conforming structures [4,36]. Interior and exterior beam-column joints with poor detailing and smooth bars with end-hooks were modelled using *zero-length* elements using a “*Hysteretic*” model elements to capture both flexural and axial behaviour accordingly with the recommendations of O'Reilly and Sullivan and De Risi et al. [4,37]. Rigid offsets were accounted for in the element transformation. Furthermore, the in-plane behaviour of masonry infill panels was modelled using the equivalent strut approach following the recommendations of Verderame et al. [36]. The difference in infill strength (weak, medium and strong) parameters used herein depends on the characterisation performed in Hak et al. [38]. Staircase elements were modelled similarly to the beam-column elements, accounting for the inclination through assigning adequate geometric transformations in both directions. Additionally, shear hinges were also implemented to account for the shear behaviour caused due to the short column effect typically observed in stairs elements. The architectural plan layouts and the corresponding numerical model of the case study buildings are presented in Figure 7.

Table 2. Structural detailing and material properties for the gravity-load designed archetypes #1 and #2.

ID	Number of Frames	Column Sections (mm)	Beam Sections (mm)	Longitudinal Reinforcement Ratios (%)	Transverse Reinforcement (diameter/spacing)	Material Characteristics
GLD#1	Exterior	2	500x300mm	C: 0.89% - 0.98% ($\phi 14 - \phi 16$) B: 0.21% - 0.31% ($\phi 14$)	C: $\phi 6 @ 150\text{mm}$ B: $\phi 6 @ 200\text{mm}$	Smooth Rebars (Aq42, $\sigma=140$ MPa); Concrete ($\sigma=5$ MPa);
	Dir-X	2				
	Interior	2				
	Exterior	2				
GLD#2	Interior	0	500x300mm	C: 0.89% - 0.98% ($\phi 14 - \phi 16$) B: 0.40% - 0.67% ($\phi 16$)	C: $\phi 6 @ 150\text{mm}$ B: $\phi 6 @ 200\text{mm}$	
	Dir-X	2				
	Interior	2				
	Exterior	2				
	Dir-Y	0	300x300mm			

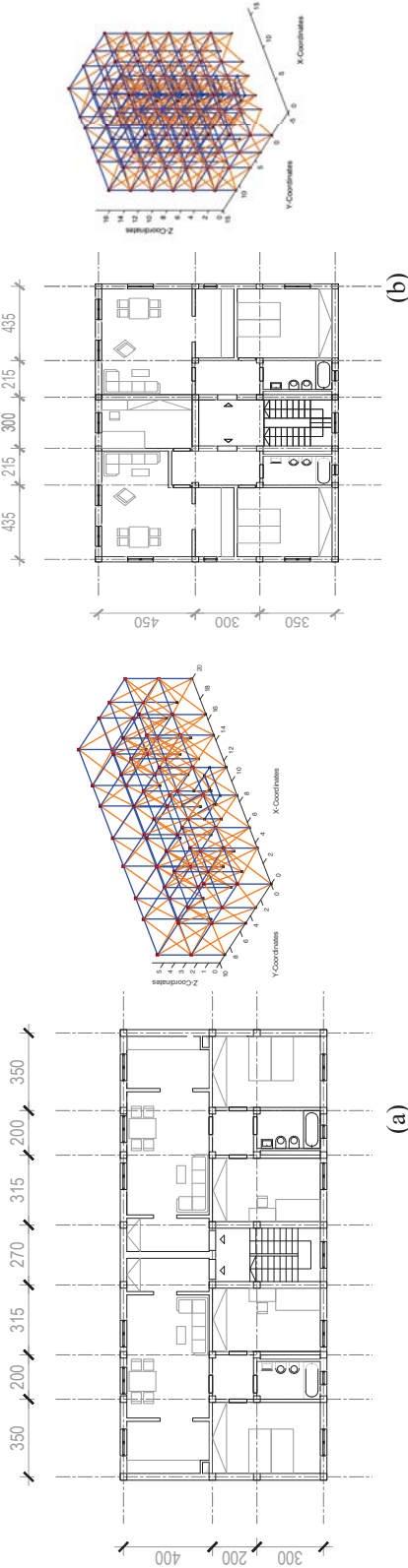


Figure 7. Architectural plan layout and OpenSees numerical model of (a): 2-storey and (b): 6-storey infilled RC archetype buildings.

5 APPLICATION OF EXTENDED SPO2IDA

Considering the application of extendedSPO2IDA, Monteleone di Spoleto and San Severo located in Central Italy were selected as case study locations for the archetypes GLD#1 and GLD#2, respectively, and correspond to high and medium seismicity. Subsequently, hazard analysis for record selection (as shown in Figure 8) was conducted using the OpenQuake engine [39] considering *AvgSa* as the IM and the site characteristics presented in Mori et al. [40]. The period range $[T_{lower}, T_{upper}]$ was defined as outlined for non-ductile infilled RC frames in O'Reilly [29] with a spacing of 0.1s and are shown in Table 3. Records were then selected from the NGA database using the conditional mean spectrum method [41] with the modifications suggested by Kohrangi et al. [23] for *AvgSa*. The correlation model by Baker and Jayaram [42] was used in all cases and the geometric mean of the two components was used in the selection. Six intensity measure levels (IMLs) were investigated for the characterization of the structural response covering initial damage of the masonry infill panels up to global structural collapse.

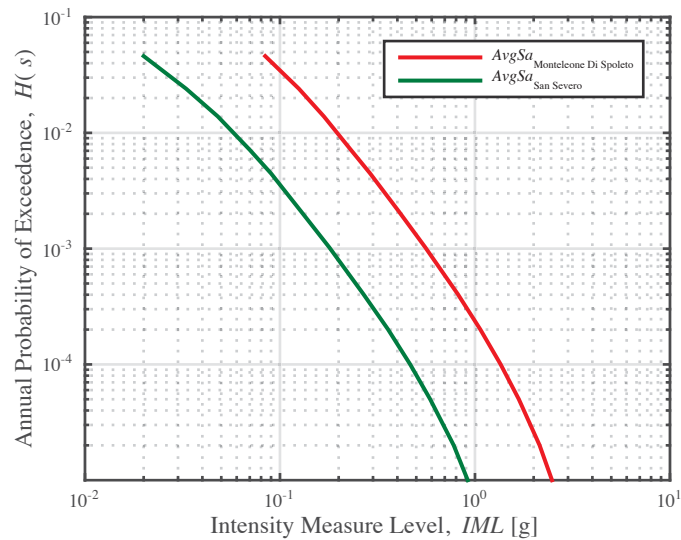


Figure 8: Hazard curves of Monteleone di Spoleto and San Severa highlighting the annual probability of exceedance of increasing intensity measure levels corresponding to *AvgSa*

Table 3: Modal properties of the case study buildings

ID	Direction	Period, T	Modal Mass, M	$AvgSa$	
				T_{lower}	T_{upper}
1	X ₁	0.19s	81.6%	0.09s	0.60s
	Y ₁	0.21s	84.3%		
	X ₂	0.07s	11.5%		
	Y ₂	0.08s	10.6%		
2	X ₁	0.48s	82.0%	0.30s	1.50s
	Y ₁	0.52s	83.4%		
	X ₂	0.16s	11.0%		
	Y ₂	0.35s	10.4%		

First, a static pushover (SPO) analysis was conducted, where an inverse triangular load was applied laterally to the two principal directions of the case study structures. The results are presented in Figure 9(a), which when combined with the modal analysis output (i.e. the modal masses at each floor and the modal shape corresponding to the first-mode), can be used as input

for the extendedSPO2IDA tool by considering the SPO analysis results in both directions and then linearizing the curves as suggested in Nafeh et al. [21] for the earlier versions of the tool. The median collapse intensity and dispersions are then directly extracted from the tool.

Second, a multiple stripe analysis (MSA) was conducted in OpenSees at increasing levels of intensity. The ground-motion pairs were applied simultaneously in both principal directions of the three-dimensional case study buildings. The results of the analysis in terms of $AvgSa$ and maximum peak storey drift θ_{max} are illustrated in Figure 9(b). The median collapse intensity and dispersion due to the record-to-record variability were obtained using the maximum likelihood method. The collapse fragility curves obtained from MSA and extendedSPO2IDA are illustrated and compared in Figure 10.

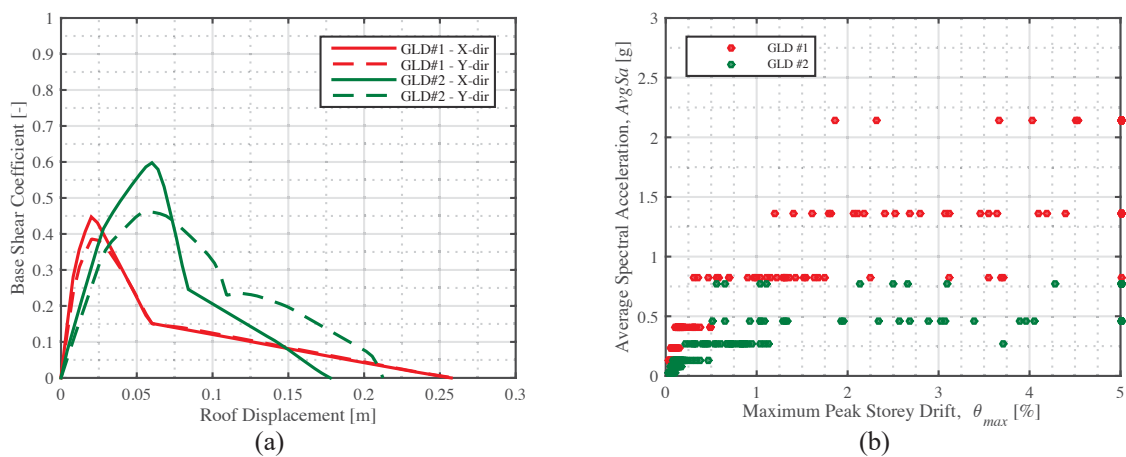


Figure 9: (a) Static pushover analysis curves for GLD#1 and #2 in both principal directions (b) Multiple stripe analysis results of GLD#1 and #2

Subsequently, the collapse fragility functions were obtained considering a lognormal distribution with median collapse intensities and dispersions obtained from the MSA analysis and the simplified relationships developed herein. The comparison is illustrated in Figure 9, where the collapse fragilities for both case study buildings were plotted. Comparing the fragility functions, an excellent match is observed between the two sets in both locations and in the two principal directions of the numerical models. This is true both in terms of the median intensity required to exceed each of these performance limit states and also the level of dispersion. The median collapse intensities reported from the MSA and the associate dispersions pair were respectively 1.58g and 0.36 for GLD#1 and 0.61g and 0.39 for GLD#2. Considering extendedSPO2IDA, the values reported for GLD#1 in the X-direction are 1.53g and 0.29, whereas for the Y-direction, a median collapse intensity of 1.64g and an associated dispersion of 0.31 were estimated. Similarly for GLD#2, collapse intensities of 0.63g and 0.53g with dispersion values of 0.20 and 0.23 were predicted for the X and Y directions, respectively.

This comparison illustrates the accuracy of the proposed tool to be generally employed for such typologies of different building height and period range across different seismicity types. Moreover, other aspects of the tool not discussed herein but worth mentioning are: (1) the inclusion of the period elongation effect by considering an SDOF system aggregating the backbones of the infill contribution and the frame with the critical storey mechanism formed [21]; (2) the consideration of the sudden rupture of infills on the dynamic stability of the global system.

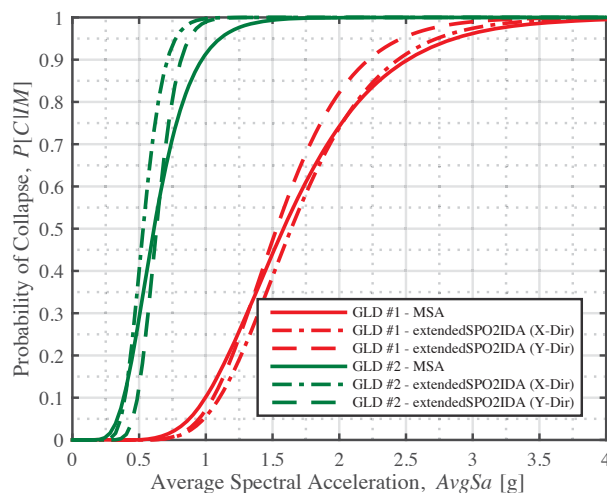


Figure 10: Collapse fragility functions of GLD#1 and #2 considering the median collapse intensities and dispersion obtained from MSA and extendedSPO2IDA.

6 CONCLUSIONS

The seismic assessment of RC structures with masonry infills is an important issue in modern earthquake engineering considering the prevalence of such typology in the southern European building stock. The characterisation of their behaviour up to global collapse is essential when performing risk-based analyses associated with performance-based earthquake engineering. Non-linear dynamic analyses such as IDA or MSA are computationally expensive in terms of time and effort. To this end, R - μ - T relationships, incorporating the general response of the structural typology were developed herein. The latter was developed here in terms of $AvgSa$, which demonstrated itself as a more accurate and appropriate IM. From the results of the study developed herein, the following can be noted considering the benefits of the developed tool:

- The consideration of $AvgSa$ as an intensity measure for infilled RC frames is characterised with low dispersions, rendering it a good predictor for collapse estimation.
- The ease of applicability of the tool by simplifies the estimation of collapse capacity and reduces the need for non-linear dynamic analyses by employing eigenvalue and non-linear static procedures as inputs.
- The accuracy of the tool in terms of its ability to predict the median collapse intensity and dispersion for two case study buildings and two different site hazards has been illustrated.

7 ACKNOWLEDGEMENTS

The work presented in this paper has been developed within the framework of the project “Dipartimenti di Eccellenza”, funded by the Italian Ministry of Education, University and Research at IUSS Pavia. The authors would like to acknowledge the contribution of Arch. Ing. Tereza Nádeníková and Arch. Ing. Barbara Ferma during the conception of the case study buildings presented in this study.

REFERENCES

- [1] Masi A. Seismic vulnerability assessment of gravity load designed R/C frames. Bull Earthq Eng 2003. <https://doi.org/10.1023/B:BEEE.0000021426.31223.60>.
- [2] Repapis C, Zeris CA. Seismic Assessment of Non-conforming Infilled RC Buildings Using IDA

- Procedures. *Front Built Environ* 2019;4. <https://doi.org/10.3389/fbuil.2018.00088>.
- [3] Decreto R. Norme per la esecuzione delle opere in conglomerato cementizio semplice ed armato. 1939.
- [4] O'Reilly GJ, Sullivan TJ. Modeling Techniques for the Seismic Assessment of the Existing Italian RC Frame Structures. *J Earthq Eng* 2019;23:1262–96. <https://doi.org/10.1080/13632469.2017.1360224>.
- [5] O'Reilly GJ, Sullivan TJ. Probabilistic seismic assessment and retrofit considerations for Italian RC frame buildings. *Bull Earthq Eng* 2018;16:1447–85. <https://doi.org/10.1007/s10518-017-0257-9>.
- [6] Fardis MN, Calvi GM. Effects of infills on the global response of reinforced concrete frames. 10th Eur. Conf. Earthq. Eng., Balkema, Rotterdam: 1995, p. 2893–2898.
- [7] Dolšek M, Fajfar P. The effect of masonry infills on the seismic response of a four-storey reinforced concrete frame — a deterministic assessment. *Eng Struct* 2008;30:1991–2001. <https://doi.org/10.1016/j.engstruct.2008.01.001>.
- [8] Dolšek M, Fajfar P. The effect of masonry infills on the seismic response of a four storey reinforced concrete frame-a probabilistic assessment. *Eng Struct* 2008. <https://doi.org/10.1016/j.engstruct.2008.04.031>.
- [9] Dolšek M, Fajfar P. Mathematical modelling of an infilled RC frame structure based on the results of pseudo-dynamic tests. *Earthq Eng Struct Dyn* 2002;31:1215–30. <https://doi.org/10.1002/eqe.154>.
- [10] Morandi P, Hak S, Magenes G. Performance-based interpretation of in-plane cyclic tests on RC frames with strong masonry infills. *Eng Struct* 2018. <https://doi.org/10.1016/j.engstruct.2017.11.058>.
- [11] Fardis MN, Negro P, Bousias SN, Colombo A. Seismic design of open-storey infilled RC buildings. *J Earthq Eng* 1999. <https://doi.org/10.1080/13632469909350344>.
- [12] Vamvatsikos D, Cornell CA. Direct estimation of seismic demand and capacity of multidegree-of-freedom systems through incremental dynamic analysis of single degree of freedom approximation. *J Struct Eng* 2005;131:589–99. [https://doi.org/10.1061/\(ASCE\)0733-9445\(2005\)131:4\(589\)](https://doi.org/10.1061/(ASCE)0733-9445(2005)131:4(589)).
- [13] Baltzopoulos G, Baraschino R, Iervolino I, Vamvatsikos D. SPO2FRAG: software for seismic fragility assessment based on static pushover. *Bull Earthq Eng* 2017;15:4399–425. <https://doi.org/10.1007/s10518-017-0145-3>.
- [14] Dolšek M, Fajfar P. Inelastic spectra for infilled reinforced concrete frames. *Earthq Eng Struct Dyn* 2004;33:1395–416. <https://doi.org/10.1002/eqe.410>.
- [15] Dolšek M, Fajfar P. Simplified non-linear seismic analysis of infilled reinforced concrete frames. *Earthq Eng Struct Dyn* 2005. <https://doi.org/10.1002/eqe.411>.
- [16] Guerrini G, Graziotti F, Penna A, Magenes G. Improved evaluation of inelastic displacement demands for short-period masonry structures. *Earthq Eng Struct Dyn* 2017. <https://doi.org/10.1002/eqe.2862>.
- [17] FEMA. Prestandard and Commentary for the Seismic Rehabilitation of Buildings. *Rehabil Requir* 2000:1–518.
- [18] ATC. Improvement of Nonlinear Static Seismic Analysis Procedures. FEMA 440, Fed Emerg Manag Agency, Washingt DC 2005.
- [19] Federal Emergency Management Agency P-58-1. Seismic Performance Assessment of Buildings. *Fema P-58-1* 2012.
- [20] Cornell CA, Krawinkler H. Progress and Challenges in Seismic Performance Assessment. *PEER Cent News* 2000.
- [21] Nafeh AMB, O'Reilly GJ, Monteiro R. Simplified seismic assessment of infilled RC frame structures. vol. 18. Springer Netherlands; 2020. <https://doi.org/10.1007/s10518-019-00758-2>.
- [22] Kohrangi M, Kotha SR, Bazzurro P. Ground-motion models for average spectral acceleration in a period range: direct and indirect methods. *Bull Earthq Eng* 2018;16:45–65. <https://doi.org/10.1007/s10518-017-0216-5>.
- [23] Kohrangi M, Bazzurro P, Vamvatsikos D, Spillatura A. Conditional spectrum-based ground motion record selection using average spectral acceleration. *Earthq Eng Struct Dyn* 2017. <https://doi.org/10.1002/eqe.2876>.
- [24] Kohrangi M, Vamvatsikos D, Bazzurro P. A Record Selection Methodology for Vulnerability Functions Consistent with Regional Seismic Hazard for Classes of Buildings. 16th World Conf Earthq Eng 2017.
- [25] Eads L, Miranda E, Lignos DG. Average spectral acceleration as an intensity measure for collapse risk assessment. *Earthq Eng Struct Dyn* 2015. <https://doi.org/10.1002/eqe.2575>.
- [26] Eads L, Miranda E, Lignos D. Spectral shape metrics and structural collapse potential. *Earthq. Eng. Struct. Dyn.*, 2016. <https://doi.org/10.1002/eqe.2739>.
- [27] O'Reilly GJ, Kohrangi M, Bazzurro P, Monteiro R. Intensity Measures for the Collapse Assessment of Infilled RC Frames. 16th Eur Conf Earthq Eng 2018.
- [28] FEMA P695. Quantification of building seismic performance factors. Washington, DC: 2009.
- [29] O'Reilly GJ. Limitations of $S_a(T_1)$ as an intensity measure when assessing non-ductile infilled RC frame structures. *Bull Earthq Eng* 2021. <https://doi.org/10.1007/s10518-021-01071-7>.

- [30] Vamvatsikos D, Cornell CA. Incremental dynamic analysis. *Earthq Eng Struct Dyn* 2002;31:491–514. <https://doi.org/10.1002/eqe.141>.
- [31] Vamvatsikos D, Bakalis K, Kohrangi M, Pyrza S, Castiglioni CA, Kanyilmaz A, et al. A risk-consistent approach to determine EN1998 behaviour factors for lateral load resisting systems. *Soil Dyn Earthq Eng* 2020;131. <https://doi.org/10.1016/j.soildyn.2019.106008>.
- [32] ISTAT. Censimento della popolazione e delle abitazioni 2011,” Censimento Popolazione Abitazioni 2011.
- [33] Pagano M. Teoria degli edifici – Edifici in cemento armato. Edizione L. 1968.
- [34] Santarella L. Il cemento armato – Le applicazioni alle costruzioni civili ed industriali. Edizione H. 1968.
- [35] McKenna F. OpenSees: A framework for earthquake engineering simulation. *Comput Sci Eng* 2011. <https://doi.org/10.1109/MCSE.2011.66>.
- [36] Verderame GM, Ricci P, De Risi MT, Del Gaudio C. Experimental Assessment and Numerical Modelling of Conforming and Non-Conforming RC Frames with and without Infills. *J Earthq Eng* 2019. <https://doi.org/10.1080/13632469.2019.1692098>.
- [37] De Risi MT, Verderame GM. Experimental assessment and numerical modelling of exterior non-conforming beam-column joints with plain bars. *Eng Struct* 2017. <https://doi.org/10.1016/j.engstruct.2017.07.039>.
- [38] Hak S, Morandi P, Magenes G, Sullivan TJ. Damage control for clay masonry infills in the design of RC frame structures. *J Earthq Eng* 2012;16:1–35. <https://doi.org/10.1080/13632469.2012.670575>.
- [39] Pagani M, Monelli D, Weatherill G, Danciu L, Crowley H, Silva V, et al. Openquake engine: An open hazard (and risk) software for the global earthquake model. *Seismol Res Lett* 2014. <https://doi.org/10.1785/0220130087>.
- [40] Mori F, Mendicelli A, Moscatelli M, Romagnoli G, Peronace E, Naso G. A new Vs30 map for Italy based on the seismic microzonation dataset. *Eng Geol* 2020. <https://doi.org/10.1016/j.enggeo.2020.105745>.
- [41] Baker JW. Conditional Mean Spectrum: Tool for Ground-Motion Selection. *J Struct Eng* 2011;137:322–31. [https://doi.org/10.1061/\(asce\)st.1943-541x.0000215](https://doi.org/10.1061/(asce)st.1943-541x.0000215).
- [42] Baker JW, Jayaram N. Correlation of spectral acceleration values from NGA ground motion models. *Earthq Spectra* 2008;24:299–317. <https://doi.org/10.1193/1.2857544>.

DEVELOPMENT OF A PYTHON-BASED STOREY LOSS FUNCTION GENERATOR

Davit Shahnazaryan¹, Gerard J. O'Reilly¹, and Ricardo Monteiro¹

¹ Centre for Training and Research on Reduction of Seismic Risk (ROSE), Scuola Universitaria
Superiore IUSS Pavia
Palazzo del Broletto, Piazza della Vittoria 15, Pavia 27100, Italy
e-mail: {davit.shahnazaryan,gerard.oreilly,ricardo.monteiro}@iusspavia.it

Abstract

With the development of performance-based earthquake engineering (PBEE) for mitigating seismic risk, significant work has been carried out to implement risk-based design and assessment frameworks. However, the probabilistic nature and computationally heavy implementation of the PBEE framework when using a component-based loss assessment approach, made it less desirable for practitioners. As a consequence, methods employing storey loss functions (SLFs), which ease the computational cost of the component-based approach, have emerged. The use of predefined SLFs, especially at a design stage, is desirable where component information is likely missing. This article describes an object-oriented toolbox, recently developed in Python, for the estimation of SLFs. The step-by-step implementation is described along with a comparative demonstration of its application to a case study existing building versus the more rigorous component-based approach described in FEMA P-58. The attained loss metrics demonstrate the quality and prove that the SLF-based approach, while being more simplistic in nature, achieves accurate results with relative ease across all levels of seismic response.

Keywords: PBEE, seismic assessment, loss estimation, storey loss function.

1 INTRODUCTION

Over the years, it has become paramount to characterize seismic risk using terms more meaningful to stakeholders and practitioners. These performance measures can be characterised by losses, downtime and casualties/fatalities. To avoid describing performance at discrete hazard levels, as typically prescribed in design codes (e.g. [1]–[3]), probabilistic frameworks have been developed to include uncertainties for hazard, structural response, damage and monetary loss. One of these frameworks is the performance-based earthquake engineering (PBEE) proposed by the Pacific Earthquake Engineering Research (PEER) Center [4]. However, due to its probabilistic nature and computationally expensive implementation, it has become popular primarily within academic research or specialized reports, such as FEMA P-58 [5], rather than a widespread code-based implementation for practitioners. While existing structures might offer easily-accessible information regarding their component inventory, the opposite is the case for newly designed structures and practitioners may be hesitant to carry out a full loss-driven design consisting of many trials and iterations. Over the years, many risk-targeted design methods have been developed, where many of them ([6]–[13]) are risk-targeted approaches using collapse risk as their primary design objective, while others ([9], [11], [14]) explore the possibility of using economic loss as well. To simplify the codification of these approaches, alternatives to component-based probabilistic loss estimation are sought.

Ramirez and Miranda [15] looked into simplifying the PEER's building-specific loss estimation methodology by creating so-called engineering demand parameters versus decision variable (EDP-DV) functions, where the structural response parameters, or EDPs, are directly related to economic losses, or DVs. These functions typically define monetary loss at a storey level hence are termed storey loss functions (SLF). They provide readymade loss functions describing the repair costs over a predefined building inventory of damageable components in a simplified manner, thus reducing the amount of data required to be handled for the building's inventory during loss assessment. As mentioned earlier, during the design phase of new buildings, the complete component inventory of the building might not be fully known, therefore generic SLFs will potentially help avoid the issue of having excessive computations required in component-based driven approaches. These SLFs have been recently implemented in Silva *et al.* [16] for steel buildings in a European context, for example, although options for reinforced concrete (RC) buildings are generally lacking.

Based on the storey loss estimation framework by Ramirez and Miranda [15], a toolbox for creating generic user-based SLFs has been developed. Component quantities, fragility and consequence functions are used as input elements to generate FEMA P-58 compatible SLFs [5]. While the framework by Ramirez and Miranda [15] uses cost distributions for different RC building occupancies in California, Papadopoulos *et al.* [17] developed SLFs for steel buildings in Greece. Similarly, SLFs were developed for URM buildings by Ottonelli *et al.* [18] and masonry infill walls by other researchers [19]–[21]. Additionally, recent studies on loss estimation ([22], [23]) highlighted the need for developing SLFs to cover a wide range of building characteristics, such as its storey-wise functionality, typology of structure, and occupancy. Sullivan [23] presented a simplified loss assessment approach to calculate expected annual loss, EAL, however, a limitation was mentioned, whereby the knowledge of quantity, distribution, and characteristics of all damageable components within the building inventory might not always necessarily be readily available and, to address it, SLFs may be used. On the contrary, Perrone *et al.* [22] proposed a method for estimating the EAL of Italian RC buildings using suitable SLFs, further highlighting the need for developing simplified alternatives.

This paper describes the development of a toolbox that allows the automated production of SLFs through regression analysis using the results of random sampling of component damage

states and costs, including damage correlation among components. Contrary to past research, the aim is not to create generic readymade loss functions for a specific building category, but to develop a tool for any user to create their own functions, based on an existing database of components, such as FEMA P-58 or expert opinion, without being limited to existing SLF libraries. The framework implemented within the toolbox is described herein. The main decisions encompassing the use of the toolbox include: the building characterisation through the definition of component inventory, defined by component quantities, fragility and consequence functions; performance grouping of components based on EDP sensitivity; identification of possible interactions among different components; choosing the number of simulations for the sampling of damage states; and selecting a regression fitting type. The latter may be extended by adding more regression options. Finally, the framework is validated with a case-study application to a generic RC building, and the results are compared with a component-based loss assessment of the same building (Figure 1) following FEMA P-58.

2 STOREY LOSS FUNCTION ESTIMATION TOOLBOX

As previously mentioned, the framework implemented within the SLF estimation toolbox consists of the following steps:

1. Building characterisation;
2. Component inventory definition;
3. Component grouping;
4. Consideration of correlations between components;
5. Monte Carlo Simulation of damage states;
6. Repair cost computation;
7. Storey loss function fitting.

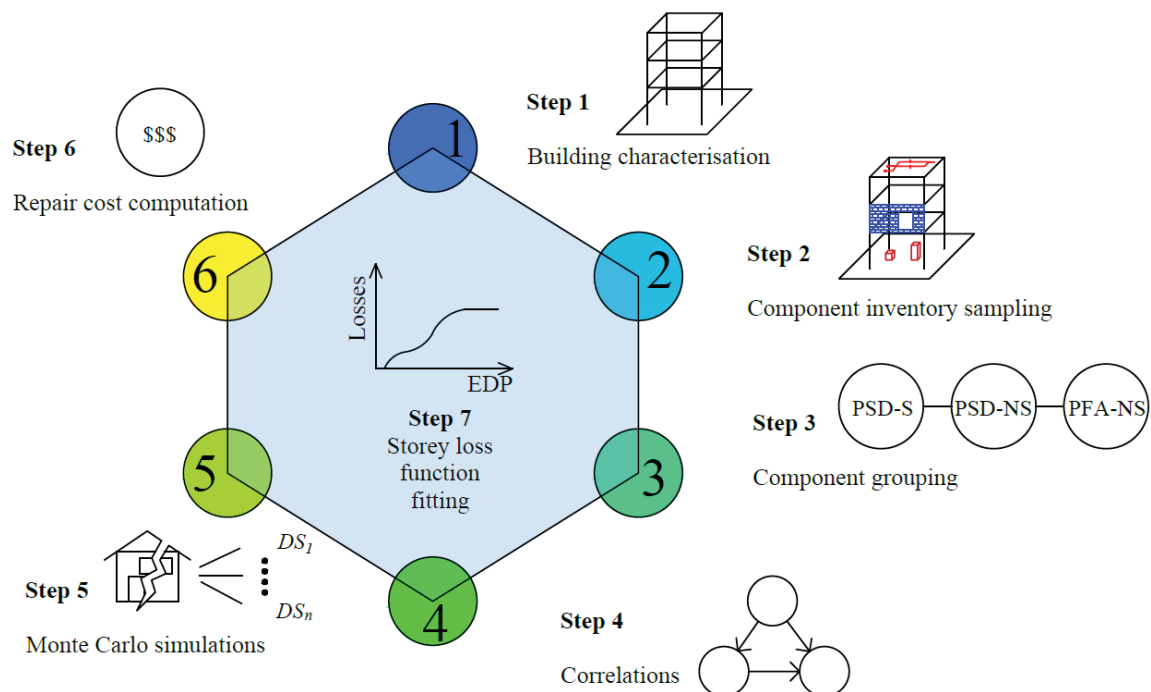


Figure 1: Flowchart of storey loss function generation framework.

The first step of the framework is the identification of the building's characteristics including the number of storeys, global dimensions, occupancy type and usage. However, if those are yet

to be identified, SLFs may still be identified for a desired reference area and extrapolated to a specific building configuration through the actual building area. Once the building characteristics have been identified, or the reference area selected, a damageable component inventory may be created. Building occupancy type and structural typology will play a key role in gaining insight into possible distributions of components if they are not preliminary known, as is common for new designs. The distributions (mean and uncertainty) of those components may be obtained from empirical and statistical data, collected from existing buildings and surveys, or based on expert opinion or personal judgment. The inventory consists of structural, non-structural components, and building contents likely to be damaged, all of which contribute to the economic losses deriving from required repair costs following seismic damage.

Typically, the component inventory has information on item types, component quantities, EDP sensitivity and typology (structural or non-structural) of each component. Three performance groups are identified unless otherwise specified, and fragility and consequence functions for the components should be provided. To compile the component database, damage states and associated fragility and consequence functions may be adapted from the FEMA P-58 database or other similar sources. Additionally, it needs to be specified whether the component will be affected by the EDP of the floor slab above the current storey or by the supporting floor slab at the current storey. For example, water distribution piping systems connected to the ceiling in a storey will be sensitive to the peak floor acceleration (PFA) of the above floor, while contents, such as electronic equipment will usually be sensitive to the PFA of the supporting floor. To account for this, a simplifying assumption is made within the toolbox, whereby the component losses in storey i , but affected by the upper floor, are computed as part of, or moved to, storey $i+1$. Even though the physical location of costs with respect to which storey the loss will be assigned is not quite correct, it will still lead to a correct total cost in the building.

In order to utilize the framework for 3D buildings, it needs to be applied to both directions of the building separately. Additionally, each direction will include components oriented along that direction. Essentially, the analyst would need to identify, for each damageable component at each storey level, in which principal direction of the building it is sensitive to damage. This way, the components can be grouped and analysed separately using the structural demands in the two orthogonal directions. To what pertains non-directional components, the framework is applied only once. In this case, both directions of seismic action are of importance, and the maximum value of two demand parameters in both directions may be multiplied by a non-directional conversion factor, as suggested in FEMA P-58, and used for a single SLF in the analysis. However, interactions of seismic effects in two orthogonal directions on a given component are not accounted for in cases where such interaction is expected to be significant, more advanced methods of loss assessment should be adopted.

Once the component inventory is identified, components may be classified into groups depending on the type of the component (i.e. structural or non-structural) and their EDP (e.g. peak storey drift (PSD) or PFA). Components within a performance group will be assessed together for a mutual demand and subsequent losses will be summed up to estimate the group's SLF. In other words, losses from all components within a performance group will be tied to the same EDP.

Similar to past studies ([15], [17]), the effects of such EDPs, such as vertical acceleration or building torsion, are not accounted for within the framework. Additionally, as discussed in O'Reilly *et al.* [24], torsion could be better dealt with by adopting a component-based approach. However, if one is to provide the toolbox with fragility and consequence functions associated with components other than PSD- or PFA-sensitive (e.g. peak floor velocity), the toolbox will still be capable of producing the appropriate SLFs. This classification of components into

different performance groups allows the disaggregation of losses at later stages to identify the main contributors to the economic losses, which can be useful in deciding which type of retrofitting strategies should be adopted as demonstrated by Carofilis *et al.* [25].

Similar to the studies of Ramirez and Miranda [15], structural and non-structural components sensitive to the same EDP may be grouped to allow for the consideration of possible correlations between the damage states. For example, a specific intensity level may not result in damage to a specific non-structural component, but it may affect a different component connected to it that does suffer a degree of damage. To repair this damaged component, access should be first granted, which foresees the removal of the portion or the entirety of the undamaged non-structural component. Essentially, for any independent component i , all damage states (DSs) are assumed to have an independent sequential occurrence unless otherwise specified and each DS is assumed to be mutually exclusive. A probability of occurrence is assigned to mutually exclusive DSs, which sum up to 100%. In contrast, if DS j of component i is dependent on the occurrence of a DS d of a component m , then the DS of component i is assumed independent of component m unless component m is in DS d or higher (i.e. DS d in component m triggers DS j in component i). As illustrated in Figure 2, for an EDP of edp , if component m is in DS3, then even if there is no indication of damage for component i , the latter component is assumed to be in DS2.

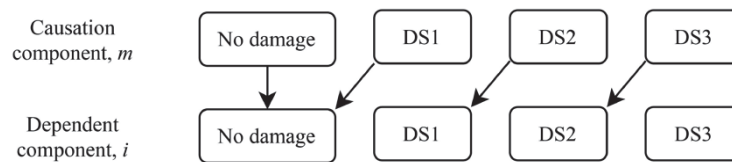


Figure 2: Relationship between causation and dependent components.

With a component inventory identified along with possible correlations among the damage states of different components, Monte Carlo simulations are performed. For each simulation, damage and repair costs are sampled for each component within the performance group, where all costs are added to obtain the performance group's total loss for a given EDP. Essentially, the algorithm samples damage states for each component at a given EDP level and for a specified number of simulations. A random value is generated within 0 and 1 and a DS is assigned to a component based on its fragility functions. An example describing the relationship between causation and dependent components is illustrated in Figure 3. At an EDP level of 0.02 (point 1 in Figure 3), if the sampled probability for the causation component is 0.3, then DS3 is assigned to the component. At the same EDP level, a sampled probability of 0.8 is assigned to the dependent component, which sets it in DS1. Following the relationship of the components described in Figure 2, the DS of the dependent component is modified to DS2.

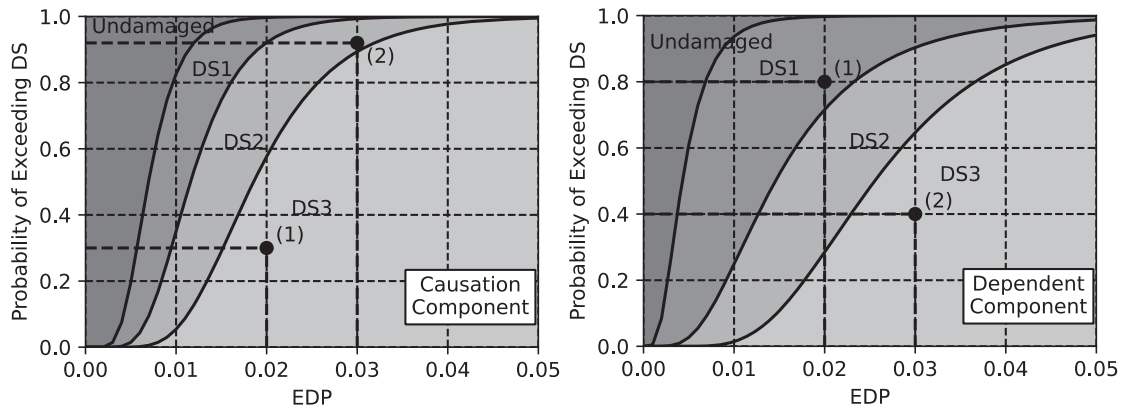


Figure 3: Damage states and fragility functions of a sample: (left) causation component and (right) dependent component.

Once damage states for all components have been sampled, repair costs may be evaluated. For each component, at each sampled DS, the repair cost is assigned based on the provided consequence function. If the consequence function is represented only by the mean value, then the mean value is assigned, while if a distribution is provided, then a value as the repair cost is sampled from the repair cost distribution.

Finally, SLFs for component groups may be identified through regression analysis on sampled repair costs. More than one analytical expression may be used within the toolbox at <https://github.com/davitshahnazaryan3/SLFGenerator> (Figure 4), while possible addition of new functions may be considered, as future research identifies better alternatives. The Weibull cumulative distribution function may be used to perform the regression, described in Equation 1:

$$y = \alpha \left(1 - \exp \left(- \left(\frac{x}{\beta} \right)^\gamma \right) \right) \quad (1)$$

where, α , β and γ are the fitting coefficients, x is the EDP value and y is the fitted loss value. Alternatively, the regression model proposed by Papadopoulos *et al.* [17], defined in Equation 2, may be used:

$$y = \varepsilon \frac{x^\alpha}{\beta^\alpha + x^\alpha} + (1 - \varepsilon) \frac{x^\gamma}{\beta^\gamma + x^\gamma} \quad (2)$$

where, α , β , γ , δ and ε are the fitting coefficients, x is the EDP value and y is the fitted loss value.

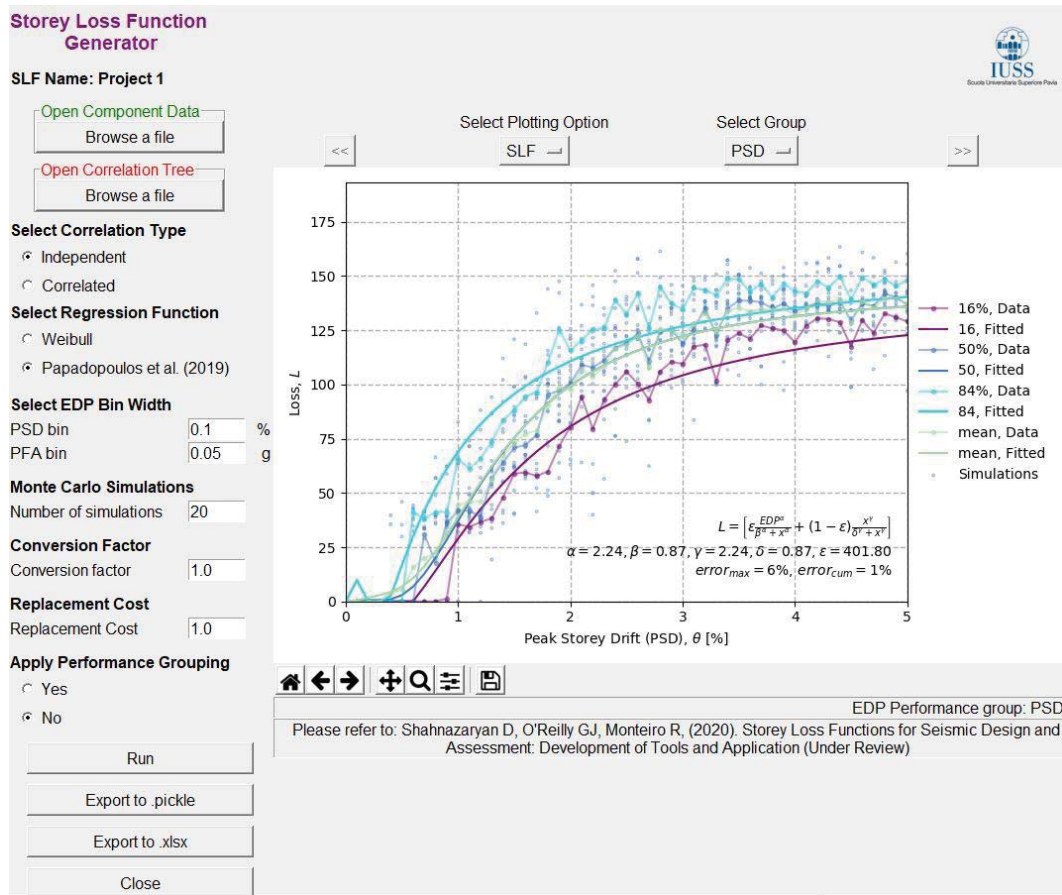


Figure 4: Overview of the storey loss function generator interface.

3 EXAMPLE APPLICATION

To demonstrate the capabilities of the toolbox for generating SLFs, a generic case-study RC building of 3 storeys and a reference area of 432 m² (Figure 5) is designed according to Eurocode 2 [26] and Eurocode 8, EC8, [27] provisions. Based on the design, a three-dimensional non-linear numerical model was created using OpenSees [28] and incremental dynamic analysis [29] was carried out. Finally, using the generated SLFs, loss assessment was carried out and compared with the component-based assessment following the FEMA P-58 guidelines. It is important to note that the results are not meant to be indicative of typical RC building performance, but more as a comparative exercise between the two approaches. The building is assumed to be located in the city of L'Aquila, Italy on a stiff clay site according to EC8's site classification. The gravity loads, including imposed and dead loads, were assumed as 8.06 kN/m² and 6.56 kN/m² at the general floor and roof level, respectively. The building has two seismic frames along its perimeter in each of the principal directions. The material properties used in the design and detailing were 25 MPa for the concrete compressive strength and 415 MPa for the steel yield strength. No plan or elevation irregularities are present. The replacement cost of the building was assumed as 1572000€.

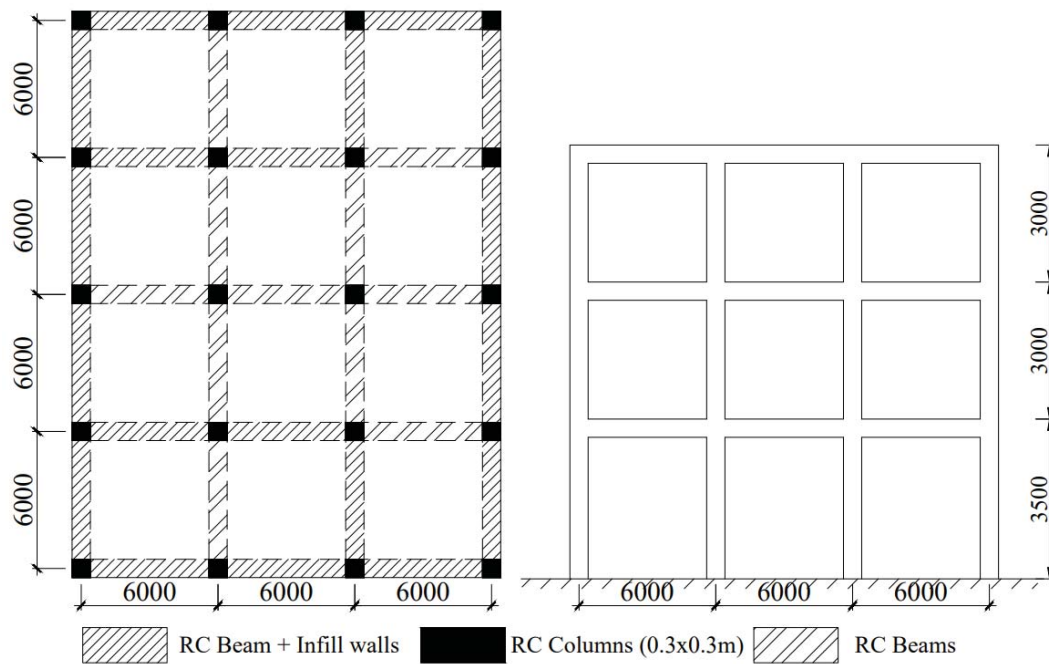


Figure 5: Plan and elevation view of the structural configuration of the case study building.

PFA and PSD sensitive components were considered within the component inventory of the case study building. Components with sensitivity towards one direction of seismic action and having the same EDP sensitivity were grouped, while non-directional components were classified into a different performance group. Moreover, PFA-sensitive components were grouped depending on the location within a storey and to which EDP they were sensitive. For example, components such as piping systems located in a storey j but sensitive to the EDP of the above storey were tied to the PFA of storey $j+1$, while electronic devices in storey j were tied to the PFA of storey j , as described previously. Table 1 to Table 3 summarise the mean structural, PSD-sensitive and PFA-sensitive non-structural component quantities.

Table 1: Mean quantities for the damageable PSD-sensitive non-structural components of the case-study RC building in X (Y) direction.

ID	Component	Unit	Quantity per storey		
			Storey 1	Storey 2	Storey 3
B101	Exterior masonry infill with windows	per m ²	84(63)	72(54)	72(54)
B102	Internal masonry partition		67.75 (32.3)	59.8 (24.2)	59.8 (24.2)
B103	Internal gypsum partition		105(75)	95(62)	95(62)
B104	Non-monolithic precast concrete stairs		1(-)	1(-)	1(-)
B105	Door	per unit	6(4)	6(4)	6(4)
B106	Small window		2(2)	2(2)	2(2)
B107	Medium window		7(0)	7(0)	7(0)
B108	Large window		3(0)	3(0)	3(0)
B109	Very large window		1(0)	1(0)	1(0)
B110	Office chair		2(-)	2(-)	2(-)
B111	Basic chair		12(-)	12(-)	12(-)
B112	Armchair		4(-)	4(-)	4(-)
B113	Oven with cooker		2(-)	2(-)	2(-)
B114	Fridge		2(-)	2(-)	2(-)
B115	Washing machine		2(-)	2(-)	2(-)

Table 2: Mean quantities for the damageable PSD-sensitive structural components of the case study RC building in X (Y) direction.

ID	Component	Unit	Quantity per storey		
			Storey 1	Storey 2	Storey 3
A101	Exterior beam-column joint (end-hooks)	per unit	4(-)	4(-)	4(-)
A102	Interior beam-column joint (weak columns)		6(4)	6(4)	6(4)
A103	Gravity column		6(-)	6(-)	6(-)

Table 3: Mean quantities for the damageable PFA-sensitive non-directional non-structural components of the case-study RC building.

ID	Component	Above EDP	Unit	Quantity per storey		
				Storey 1	Storey 2	Storey 3
C101	Fancoil	1	per unit	8	8	8
C102	Ceiling systems		per m ²	418.5	418.5	432
C103	Lighting systems			20	20	20
C104	Piping systems – water distribution (pipe)		per 250m	0.879	0.879	0.879
C105	Piping systems – heating distribution (pipe)			0.927	0.927	0.927
C106	Sanitary waste piping			0.879	0.879	0.879
C107	Small bookshelf			2	2	2
C108	Large bookshelf			2	2	2
C109	Luxurious bookshelf			2	2	2
C110	Small wardrobe			2	2	2
C111	Medium wardrobe			4	4	4
C112	Large wardrobe			2	2	2
C113	Small sofa			1	1	1
C114	Medium sofa			3	3	3
C115	Small table		per unit	6	6	6
C116	Medium table			2	2	2
C117	3 compartment shelves			6	6	6
C118	4 compartment shelves			3	3	3
C119	5 compartment shelves			2	2	2
C120	Singe bed	0		2	2	2
C121	Double bed			4	4	4
C122	Kitchen equipment			2	2	2
C123	Computers and notebooks			8	8	8
C124	TV equipment	1		4	4	4
C125	Fire sprinklers water piping		per 250m	0.753	0.753	0.753
C126	Fire sprinklers drop			12	12	12
C127	Distribution panel for fire sprinkler	0		1	1	1
C128	Hydraulic elevator		per unit	1	0	0
C129	Battery rack			1	0	0
C130	Battery charger			1	0	0
C131	Distribution panel for the elevator			1	0	0

Knowing the quantities at each storey, creating SLFs necessitates the definition of fragility and consequence functions for all components within the inventory. Table 4 to Table 6 summarise the damage descriptions, the sources for the function definitions and the fragility parameters for structural, PSD-sensitive and PFA-sensitive non-structural components, respectively. For the majority of the components, fragility and consequence functions were adopted from the available literature ([19], [30], [31]), while for the remaining components, mean repair costs were based on typical costs expected in Italy. To what pertains the fragility functions of the latter components, they were primarily tied to fragilities of other components. This is a correlation assumption between two components, even though it was not directly implemented. In the absence of fragility functions for some non-structural components, some assumptions were made using engineering judgment. While many components (e.g. doors, chairs, fridges, washing machines) were assumed damaged when the interior masonry partitions have reached collapse DS, others (e.g. windows) were assumed damaged when the exterior masonry walls have reached collapse DS, considering that collapse of walls or partitions would damage the adjacent chairs, doors and windows. Similarly, TV and computers were considered damaged once there was 30% damage and falling of ceiling tiles and many other components (e.g. bookshelves, wardrobes, sofas, tables, shelves, beds and kitchen equipment) were damaged once there was large leakage of piping systems.

Table 4: Fragility function parameters and repair costs for PSD-sensitive non-structural components.

ID	Damage states	Source	Fragility function parameters		Mean repair cost €
			Median (% for PSD, g for PFA)	Dispersion	
B101	DS1 Light cracking	Cardone & Perone [19]	0.10	0.5	62
	DS2 Extensive cracking		0.30	0.5	117
	DS3 Corner crushing		0.75	0.4	234
	DS4 Collapse		1.75	0.35	234
B102	DS1 Light cracking		0.15	0.5	62
	DS2 Extensive cracking		0.40	0.5	117
	DS3 Collapse		1.00	0.4	234
B103	DS1 Operational	Sassun <i>et al.</i> [31]	0.18	0.52	34
	DS2 Damage limitation		0.46	0.54	62
	DS3 Significant damage		1.05	0.4	1243
	DS4 Near collapse limit state		1.88	0.38	
B104	DS1 Non-structural damage	FEMA P-58 [32]	0.50	0.6	918
	DS2 Structural damage		1.70	0.6	4852
	DS3 Loss of live load capacity		2.80	0.45	30097
B105			1.88	0.38	220
B106			1.75	0.35	134
B107			1.75	0.35	212
B108			1.75	0.35	298
B109			1.75	0.35	449
B110	DS1 Damaged	Personal judgment	1.88	0.38	199
B111			1.88	0.38	49
B112			1.88	0.38	199
B113			1.88	0.38	569
B114			1.88	0.38	649
B115			1.88	0.38	349

Table 5: Fragility function parameters and repair costs for PFA-sensitive non-structural components.

ID	Damage states	Source	Fragility function parameters		Mean repair cost €
			Median (% for PSD, g for PFA)	Dispersion	
C101	DS1 Falls	FEMA P-58 [32]	0.80	0.4	1035
	DS1 5% damaged		0.55	0.4	49
C102	DS2 30% damaged		1.00	0.4	69
	DS3 50% damaged		1.50	0.4	99
C103	DS1 Disassembly of rod system at connections		1.00	0.4	583
C104	DS1 Small leakage		0.55	0.4	307
	DS2 Large leakage		1.10	0.4	2302
C105	DS1 Isolated support failure		0.55	0.4	307
			1.10	0.4	2302
C106	DS2 Multiple supports failure		1.20	0.4	525
			2.40	0.4	3737
C107		Personal judgement			35
C108					80
C109					140
C110					70
C111					126
C112					199
C113					179
C114			1.10	0.4	399
C115	DS1 Damaged				20
C116					159
C117		FEMA P-58 [32]			80
C118					90
C119					99
C120					169
C121					349
C122					962
C123			1.00	0.4	1220
C124					610
C125	DS1 Spraying and dripping leakage		1.10	0.4	252
			2.40	0.5	1911
C126	DS2 Joints break – major leakage	FEMA P-58 [32]	0.75	0.4	43
			0.95	0.4	43
C127	DS1 Damaged		3.05	0.4	7298
C128	DS1 Damaged		0.50	0.3	10753
C129	DS1 Batteries spill acid		1.11	0.6	10032
C130	DS1 Damaged		1.07	0.4	9560
C131	DS1 Anchorage failure		3.05	0.4	7298

Consideration was already given here for correlations among damage states of different components in the case study building. Components like doors, windows, chairs were tied to the DS of causation component due to the absence of fragility functions in the literature. However, additional logical correlations based on engineering judgment were assigned among other components within the same EDP-sensitivity group. Table 7 describes the damage of the causation component, as well as its effect on the correlated component. It is important to note that this set of correlations will not be considered within the component-based loss assessment framework hence some difference in results should be expected a priori should this aspect have

a notable impact. However, a demonstration of variation of including such correlations with respect to ignoring them in an SLF-based approach will be commented on later.

Table 6: Fragility function parameters and repair costs for structural components.

ID	Damage states	Source	Fragility function parameters		Mean repair cost €
			Median (% for PSD, g for PFA)	Dispersion	
A101	DS1 Light cracking	FEMA P-58 [32] for fragility functions and Cardone [33] for costs	2.00	0.4	2090
A102	DS2 Concrete spalling		2.75	0.3	3026
	DS3 Concrete crushing		5.00	0.3	4093
A103					1744
					2861
					4488

Table 7: Correlations between DSs component of the case study building.

Causation Component ID	Damage de- scription of causation component	Dependant Component ID	Effect on the dependent component	DS of a de- pendent component
C104	DS1 Small leakage	C102	30% damaged	DS2
		C103	Disassembly of rod system at connections	DS1

4 RESULTS

The toolbox was applied at each storey of the building and SLFs were derived based on the component data provided previously. Correlations among dependent component DSs were considered as described in Table 7. For PSD-sensitive components, a set of three SLFs were derived for both principal directions and the non-directional components, corresponding to each of the three storeys of the building. For PFA-sensitive components, loss functions for four floors were derived, based on whether the component was sensitive to the PFA of the above floor or the floor upon which it is placed. The PACT software [32] provided with FEMA P-58 was used to conduct the component-based loss estimation, where a non-directional conversion factor was assumed to be 1.2. Apart from record-to-record variability, no epistemic uncertainty was considered for simplicity, as this study acts as a comparative study between two methodologies.

To attain the SLFs, performance grouping was applied and Equation 2 was used to carry out regression and identify mean curves. Sample SLFs for the 2nd storey and 2nd floor of the building are provided in Figure 6 and regression parameters are provided in Table 8. Losses of non-structural (NS) components start accumulating at low values of PSD, which is particularly due to low capacities of interior and exterior infills (Table 4). In contrast, losses of structural (S) components start accumulating once a certain threshold of PSD value is reached, which could be attributed to the high capacities of well-designed ductile columns. The toolbox was also applied assuming component correlations. Figure 6(b) demonstrates the SLFs of PFA-sensitive components on the 2nd floor of the case study building. The consideration of correlation among some of the components as detailed in Table 7, has an impact on the losses within PFA values of 0.5 to 2.5g. The inclusion of correlations results in an increase in vulnerability through the curves shifting to the left in Figure 6(b).

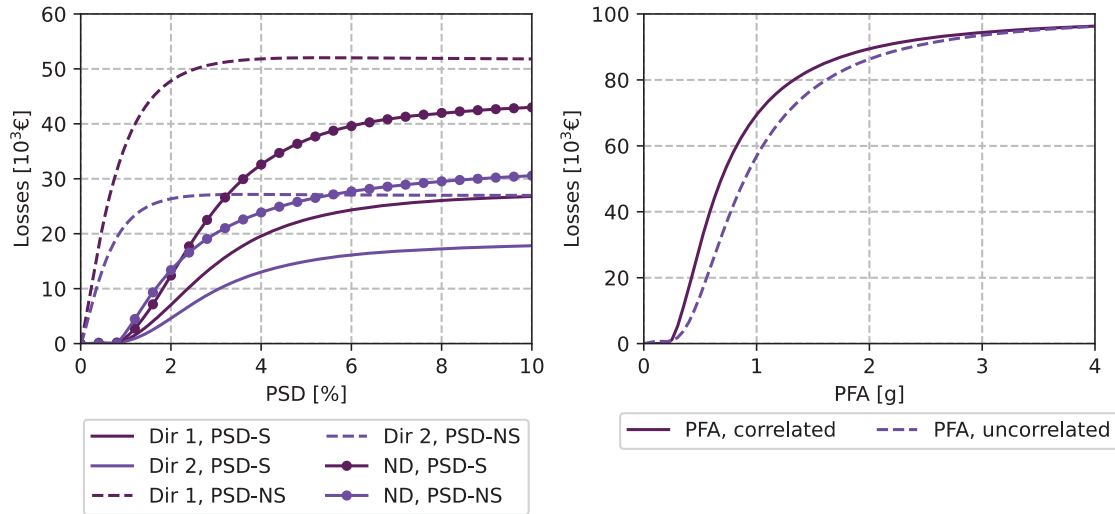


Figure 6: SLFs for the case-study building intermediate (2nd) storey level and 2nd floor (Equation 2). (a) PSD-sensitive components, (b) PFA-sensitive non-structural components.

Table 8: Regression parameters for the fitted SLFs at the 2nd storey of the case study building using Equation 2.

Performance group	Direction 1					Direction 2				
	α	β	γ	δ	ε	α	β	γ	δ	ε
PSD S	2.435	2.285	5.300	0.970	1.333	2.020	1.676	2.936	0.978	2.168
PSD NS	1.348	1.892	1.351	1.908	138.3	1.402	1.563	1.406	1.574	174.7
PFA NS, correlated	2.003	0.271	2.010	0.270	176.7	-	-	-	-	-
PFA NS, uncorrelated	2.112	0.410	2.115	0.408	259.7	-	-	-	-	-

Probabilistic seismic hazard analysis (PSHA) was performed using OpenQuake [34] with the SHARE hazard model [35]. A set of 30 ground motion record pairs were selected from the NGA West-2 database [36] with each record's soil type being consistent with that of the site. Hazard curves obtained from PSHA were used to carry out the loss assessment. Figure 7 illustrates the hazard curve for the selected case study location. The intensity measure (IM) selected was the spectral acceleration, $Sa(T^*)$, at a conditioning period, T^* . Since the building has two principal modes of vibration in two orthogonal directions, following the suggestion of FEMA P58 [5], a T^* of 1.1s corresponding to the arithmetic mean of two orthogonal modal periods was selected. Non-linear response-history analyses were conducted and the results were used to carry out loss assessment using the PACT software for a component-based approach and using the SLFs generated via the proposed toolbox for the SLF-based approach.

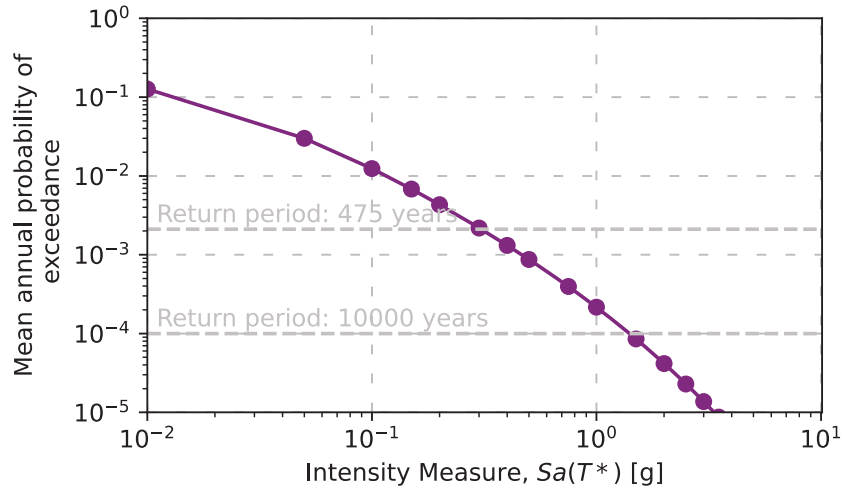


Figure 7: Hazard curve for the site considered in L'Aquila, Italy at a period of 1.1s.

The approach proposed by Ramirez and Miranda [37] was used to perform an SLF-based loss assessment. Residual deformations are accounted for to compute the probability of the building being demolished after an earthquake. The economic loss computed consists of the following terms: losses due to building collapsing; repair costs due to the building's structural and non-structural components being damaged; and losses resulting from the demolition of the building if excessive residual drifts were recorded. For the case-study building, probability of the building being demolished due to excessive residual drifts is assumed to be lognormally distributed with a median of 0.015 and a logarithmic standard deviation of 0.3 [37].

Based on the loss assessment results, the expected annual loss (EAL) was computed for the case study building by integrating the vulnerability curve, expressed in terms of expected direct economic loss as a function of IM, with the site hazard curve defined according to Equation 3.

$$EAL = \int E[L_r | IM] \left| \frac{dH}{dIM} \right| dIM \quad (3)$$

where dH/dIM is the mean annual frequency of the ground motion IM. EAL disaggregated by cost type and vulnerability curves are presented in Figure 8. The EAL computed using SLFs was 0.63%, which is slightly lower when compared to the one computed via the FEMA P-58 component-based approach, which amounted to 0.66%. As observed, the main contribution to the EAL comes from non-structural components, while structural components represent the lowest proportion. This demonstrates how structural components designed following seismic code provisions have larger capacities against damage. The similarity of vulnerability curves, as well as the proportions of contributions towards EAL, enforce the quality of a more simplistic SLF-based approach in ensuring proper assessment of losses when compared to the more rigorous component-based approach.

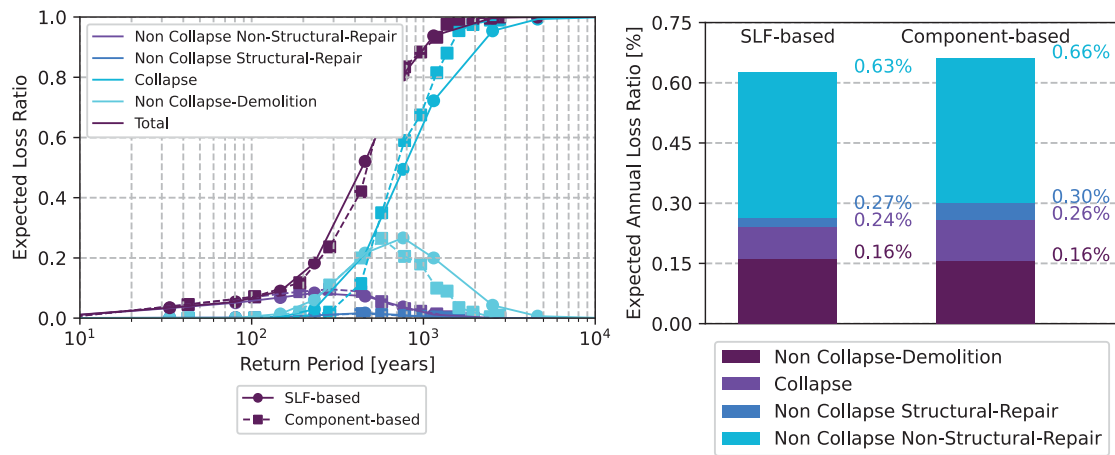


Figure 8: (left) Vulnerability curves and (right) expected annual loss showing the breakdown of different contributors in a comparative assessment between an SLF-based and component-based loss assessment approach.

Finally, Figure 9 provides the relative contributions to the vulnerability curves as a function of the return period. As observed, the main contributors at low hazard levels are the non-structural repair costs. With increasing return period, the costs from collapse and demolition start increasing, with collapse taking a significant portion of the costs at higher return periods. Cost contributions from demolition losses are quite high at high return periods, where in the absence of collapse the building needs to be demolished. Essentially, even though one might expect for structural component repair costs to increase with increasing return period, as they undergo damage, it precedes by the building needing demolition or collapse, therefore loss contributions from structural repair costs are inexistent at higher return periods as well.

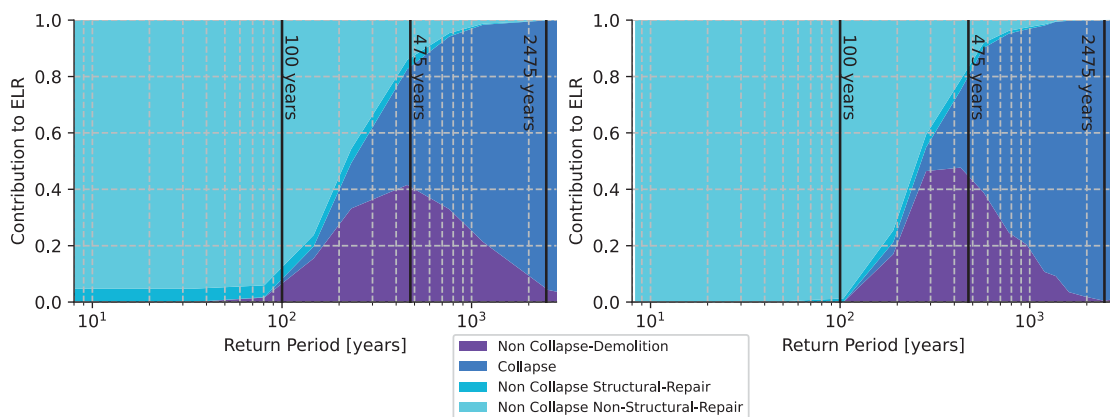


Figure 9: Relative contribution to expected loss with respect to increasing return period for a (left) SLF-based approach and (right) component-based approach. As reference points, the 100, 475 and 2475-year return periods have been annotated on each plot.

5 SUMMARY AND CONCLUSIONS

With the lack of available tools to develop storey loss functions (SLFs) to fit specific needs, this article aims to fill the gap by introducing an SLF generation toolbox for seismic design and assessment of buildings. A description of the toolbox is presented, and it was validated through an application to a case study building in a comparative study with the more rigorous component-based loss assessment described in FEMA P-58. Additionally, the toolbox was

applied to compare the effects of assumptions where component damage states were considered independent and where the dependency of damage states of different components was assumed. The main observations from the study are as follows:

- The toolbox can consider component correlations. An example at the 2nd floor of the building considering peak floor acceleration sensitive components demonstrated that inclusion of dependencies and interactions of various components may impact the vulnerabilities avoiding potential underestimations in costs;
- SLFs were developed for the entire case study reinforced concrete building accounting for the response in both directions and a subsequent loss assessment was carried out. Results were compared to a component-based loss assessment approach with a good match in EAL between the two approaches;
- A close match of SLF-based loss estimates to the detailed component-based loss assessment was observed in the distribution of losses among performance groups per intensity highlighting the validity of the developed tool and its accurate applicability for the intended scopes initially outlined;
- While important for loss assessment on existing buildings, the SLF generation toolbox may be even more of an important tool for new designs within new risk-based design approaches.

ACKNOWLEDGEMENTS

The work presented in this paper has been developed within the framework of the project “Dipartimenti di Eccellenza”, funded by the Italian Ministry of Education, University and Research at IUSS Pavia.

REFERENCES

- [1] ASCE 7-16, “Minimum Design Loads for Buildings and Other Structures,” Reston, VA, USA, 2016.
- [2] CEN, *Eurocode 8: design of structures for earthquake resistance, Part 1, General Rules, Seismic Actions and Rules for Buildings*. Brussels, Belgium: European Committee for Standardization (CEN), 2004.
- [3] NZS 1170.5:2004, *Structural design actions part 5: Earthquake actions*. Wellington, New Zealand, 2004.
- [4] K. A. Porter, “An Overview of PEER’s Performance-Based Earthquake Engineering Methodology,” *9th Int. Conf. Appl. Stat. Probab. Civ. Eng.*, vol. 273, no. 1995, pp. 973–980, 2003, doi: 10.1.1.538.4550.
- [5] FEMA, “FEMA P-58-1: Seismic Performance Assessment of Buildings: Volume 1 - Methodology,” Washington, DC, 2012.
- [6] M. Aschheim and E. F. Black, “Yield point spectra for seismic design and rehabilitation,” *Earthq. Spectra*, vol. 16, no. 2, pp. 317–335, May 2000, doi: 10.1193/1.1586115.
- [7] C. A. Cornell, “Calculating building seismic performance reliability: a basis for multi-level design norms,” in *11th World Conference on Earthquake Engineering*, 1996, p. 8.
- [8] R. C. Kennedy and S. A. Short, “Basis for seismic provisions of DOE-STD-1020,” Livermore, California, 1994.

- [9] H. Krawinkler, F. Zareian, R. A. Medina, and L. F. Ibarra, "Decision support for conceptual performance-based design," *Earthq. Eng. Struct. Dyn.*, vol. 35, no. 1, pp. 115–133, 2006, doi: 10.1002/eqe.536.
- [10] N. Luco, B. R. Ellingwood, R. O. Hamburger, J. D. Hooper, J. K. Kimball, and C. A. Kircher, "Risk-targeted versus current seismic design maps for the conterminous United States," 2007.
- [11] G. J. O'Reilly and G. M. Calvi, "Conceptual seismic design in performance-based earthquake engineering," *Earthq. Eng. Struct. Dyn.*, vol. 48, no. 4, pp. 389–411, Apr. 2019, doi: 10.1002/eqe.3141.
- [12] D. Vamvatsikos and M. A. Aschheim, "Performance-based seismic design via yield frequency spectra \ddagger ," *Earthq. Eng. Struct. Dyn.*, vol. 45, no. 11, pp. 1759–1778, Sep. 2016, doi: 10.1002/eqe.2727.
- [13] J. Žižmond and M. Dolšek, "Formulation of risk - targeted seismic action for the force - based seismic design of structures," no. January, pp. 1–23, 2019, doi: 10.1002/eqe.3206.
- [14] D. Shahnazaryan and G. J. O'Reilly, "Integrating expected loss and collapse risk in performance-based seismic design of structures," *Bull. Earthq. Eng.*, vol. 19, no. 2, pp. 987–1025, Jan. 2021, doi: 10.1007/s10518-020-01003-x.
- [15] C. M. Ramirez and E. Miranda, "Building specific loss estimation methods & tools for simplified performance-based earthquake engineering," *Blume Cent. Rep.*, no. 171, 2009.
- [16] A. Silva, L. Macedo, R. Monteiro, and J. M. Castro, "Earthquake-induced loss assessment of steel buildings designed to Eurocode 8," *Eng. Struct.*, vol. 208, p. 110244, Apr. 2020, doi: 10.1016/j.engstruct.2020.110244.
- [17] A. N. Papadopoulos, D. Vamvatsikos, and A. Kazantzi, "Development and application of FEMA P-58 compatible story loss functions," *Earthq. Spectra*, vol. 35, no. 1, pp. 39–60, Feb. 2019, doi: 10.1193/020518EQS033M.
- [18] D. Ottonelli, S. Cattari, and S. Lagomarsino, "Displacement-Based Simplified Seismic Loss Assessment of Masonry Buildings," *J. Earthq. Eng.*, vol. 24, no. sup1, pp. 23–59, 2020, doi: 10.1080/13632469.2020.1755747.
- [19] D. Cardone and G. Perrone, "Developing fragility curves and loss functions for masonry infill walls," *Earthq. Struct.*, vol. 9, no. 1, pp. 257–279, 2015, doi: 10.12989/eas.2015.9.1.257.
- [20] A. Chiozzi and E. Miranda, "Fragility functions for masonry infill walls with in-plane loading," *Earthq. Eng. Struct. Dyn.*, vol. 46, no. 15, pp. 2831–2850, 2017, doi: 10.1002/eqe.2934.
- [21] C. Del Gaudio *et al.*, "Empirical fragility curves for masonry buildings after the 2009 L'Aquila, Italy, earthquake," *Bull. Earthq. Eng.*, vol. 17, no. 11, pp. 6301–6330, 2019, doi: 10.1007/s10518-019-00683-4.
- [22] G. Perrone, D. Cardone, G. J. O'Reilly, and T. J. Sullivan, "Developing a Direct Approach for Estimating Expected Annual Losses of Italian Buildings," *J. Earthq. Eng.*, vol. 00, no. 00, pp. 1–32, 2019, doi: 10.1080/13632469.2019.1657988.
- [23] T. J. Sullivan, "Use of Limit State Loss versus Intensity Models for Simplified Estimation of Expected Annual Loss," *J. Earthq. Eng.*, vol. 20, no. 6, pp. 954–974, 2016, doi: 10.1080/13632469.2015.1112325.

- [24] G. J. O'Reilly, T. J. Sullivan, and A. Filiatrault, "Implications of a More Refined Damage Estimation Approach in the Assessment of RC Frames," *16th World Conf. Earthq. Eng.*, no. February, 2017.
- [25] W. Carofilis, G. Gabbianelli, and R. Monteiro, "Assessment of Multi-Criteria Evaluation Procedures for Identification of Optimal Seismic Retrofitting Strategies for Existing RC Buildings," *J. Earthq. Eng. In-press*, vol. 00, no. 00, pp. 1–34, 2021, doi: 10.1080/13632469.2021.1878074.
- [26] CEN, *EN 1992-1-1 Eurocode 2: Design of concrete structures - Part 1-1: General rules and rules for buildings*. Brussels. Brussels, Belgium: European Committee for Standardization (CEN), 2004.
- [27] CEN, "Eurocode 8: Design of Structures for Earthquake Resistance - Part 1: General Rules, Seismic Actions and Rules for Buildings (EN 1998-1:2004)," Brussels, Belgium, Comité Européen de Normalisation, 2004.
- [28] S. Mazzoni, F. McKenna, M. H. Scott, and G. L. Fenves, "OpenSees Command Language Manual," 2006.
- [29] D. Vamvatsikos and C. A. Cornell, "Applied incremental dynamic analysis," *Earthq. Spectra*, vol. 20, no. 2, pp. 523–553, 2004, doi: 10.1193/1.1737737.
- [30] Applied Technology Council, "FEMA P-58-2: Seismic Performance Assessment of Buildings. Volume 2 – Implementation Guide," *Fema P-58*, vol. 2, no. December 2018, p. 378, 2018, [Online]. Available: <https://www.fema.gov/media-library/assets/documents/90380>.
- [31] K. Sassun, T. J. Sullivan, P. Morandi, and D. Cardone, "Characterising the in-plane seismic performance of infill masonry," *Bull. New Zeal. Soc. Earthq. Eng.*, vol. 49, no. 1, pp. 98–115, 2016, doi: 10.5459/bnzsee.49.1.98-115.
- [32] FEMA, "FEMA P58-3. Seismic Performance Assessment of Buildings Volume 3 - Performance Assessment Calculation Tool (PACT)," Washington, D.C., 2012.
- [33] D. Cardone, "Fragility curves and loss functions for RC structural components with smooth rebars," *Earthq. Struct.*, vol. 10, no. 5, pp. 1181–1212, 2016, doi: 10.12989/eas.2016.10.5.1181.
- [34] M. Pagani *et al.*, "OpenQuake Engine : An Open Hazard (and Risk) Software for the Global Earthquake Model," no. September, 2014, doi: 10.1785/0220130087.
- [35] R. W. Musson *et al.*, "The 2013 European Seismic Hazard Model: key components and results," *Bull. Earthq. Eng.*, vol. 13, no. 12, pp. 3553–3596, 2015, doi: 10.1007/s10518-015-9795-1.
- [36] T. D. Ancheta *et al.*, "NGA-West2 database," *Earthq. Spectra*, vol. 30, no. 3, pp. 989–1005, 2014, doi: 10.1193/070913EQS197M.
- [37] C. M. Ramirez and E. Miranda, "Significance of residual drifts in building earthquake loss estimation," *Earthquake Engineering and Structural Dynamics*, vol. 41, no. 11, pp. 1477–1493, 2012, doi: 10.1002/eqe.2217.

ASSESSMENT OF POST-EARTHQUAKE DAMAGES ON ITALIAN SCHOOL BUILDING PORTFOLIOS OVER THE LAST 50 YEARS

Sergio Ruggieri¹, Chiara Tosto¹, Daniele Perrone^{2,3}, Giuseppina Uva¹, Maria Antonietta Aiello²

¹ Polytechnic University of Bari
Via Amendola, 70126 Bari, Italy
{sergio.ruggieri, chiara.tosto, giuseppina.uva}@poliba.it

² University of Salento
Via per Monteroni, 73100 Lecce, Italy
{daniele.perrone, antonietta.aiello}@unisalento.it

³ University School for Advanced Studies IUSS Pavia
Piazza della Vittoria, 27100 Pavia, Italy
daniele.perrone@iusspavia.it

Abstract

The Italian peninsula has been subjected to several destructive earthquakes over the last 50 years which denoted the high vulnerability of the existing building stock. In this context, the analysis of post-earthquake damages is of paramount importance for manifold reasons, such as the management of the emergency phase for establishing the usability of buildings and the identification of the main sources of vulnerability for future risk mitigation plans. Since about 50 years, the post-earthquake usability of buildings is assessed through simplified forms filled by experts and practitioners during extensive in-situ inspections. The data collected during the post-earthquake inspections have been recently catalogued in the Observed Damage Database (DA.D.O), which is a freely available platform for the scientific community. Starting from the data available in the DA.D.O platform, the damage reported by Italian school buildings have been analyzed in order to elaborate a proper school buildings database. The results of this statistical investigation are used for identifying the main sources of vulnerability characterizing the Italian school buildings and assuming a key role for the empirical calibration of reliable procedures of large-scale seismic risk assessment, mapping and reduction.

Keywords: Risk Assessment, School Buildings, Post-Earthquake Damages, DA.D.O platform.

1 INTRODUCTION

The post-earthquake inspections made after major earthquakes in the Mediterranean area highlighted the high vulnerability of building portfolios, especially with regard to existing structures built before the introduction of seismic provisions in national and international building codes. In Italy, the damages observed after the major seismic events occurred over the last 50 years raised the awareness of public institutions, researchers and practitioners about the vulnerability of existing buildings and the need for a large-scale seismic risk assessment to promote seismic risk mitigation programs [1-6]. Within this framework, the scientific community has developed several empirical and analytical procedures to define vulnerability curves for different building typologies, e.g. reinforced concrete (RC) buildings [7-11], masonry buildings [12-13], precast buildings [14], based on post-earthquake damage observations. Specific studies dealing with the seismic vulnerability assessment of relevant building typologies, such as schools [15-17], hospitals [18] and ecclesiastic heritage [19-22] are also available. Among the most common approaches adopted to assess and mitigate seismic risk, it is worthwhile mentioning also mechanical-based approaches [23-25], rapid visual screening (RVS) methodologies [26-27] and hybrid methods.

Empirical methods consist in the statistical processing of data about damages observed after past earthquakes. The data analysis allows to estimate the probability of occurrence of a certain damage state for increasing seismic intensities. The final output is represented by fragility curves, which can be considered vulnerability curves if a certain quantification of the expected losses is taken into account in the adopted intensity measure (IM). Over the years, several empirical-based vulnerability functions have been developed by referring to different building typologies. Qualitative and quantitative measures have been adopted to define the IM used in the vulnerability curves. In particular, the most widely adopted quantitative measure is the peak ground acceleration (PGA), while for the qualitative measures, some macro-seismic scales are defined, such as the Modified Mercalli Intensity (MMI), Medvedev–Sponheuer–Karnik (MSK) and Mercalli–Cancani–Sieberg (MCS). Qualitative and quantitative measures are often freely available online for different seismic events [28-29].

The damage probability matrix (DPM) proposed by Braga et al. [30] was one of the first empirical methods to be developed. It consists in the definition of the discrete probability that a certain damage - measured according to a macro-seismic scale - occurs in the total sample of investigated buildings. Braga et al. adopted the MSK scale to apply the DPM method to RC buildings damaged by the Irpinia earthquake (1980). Rossetto and Elnashai [31] proposed empirical fragility curves for RC buildings using a database of about 350.000 units. Di Pasquale et al. [32] developed a loss model based on the damage observed during past earthquakes in Italy. Lagomarsino and Giovinazzi [33] proposed, for several building typologies in the Mediterranean area, a methodology for relating macro-seismic and mechanical models for vulnerability assessment, basing on post-earthquake observations. Recent works [6-22] have refined the empirical methodologies and the related vulnerability and fragility curves by using large samples of buildings damaged by recent earthquakes. A useful tool for analyzing the damage occurred after Italian earthquakes has been recently developed by the Italian Department of Civil Protection: the Observed Damage Database (DA.D.O) web-gis platform, which collects the results of post-earthquake inspections made after the major Italian earthquakes.

Using the data available in DA.D.O. platform, the present study focuses on the assessment of damages occurred in Italian school buildings after the main Italian seismic events over the last 50 years. All data have been firstly extracted from DA.D.O. platform and then processed by taking into account some typological parameters, such as construction typology, year of construction, number of storeys, area and structural regularity. Once all data have been orga-

nized in a specific database, they have been processed for a twofold scope: (a) providing a statistical quantification of the damaged school buildings and their main typological features; (b) providing vulnerability curves, according to the defined building classification.

2 DA.D.O. PLATFORM: A DATA COLLECTION OF EARTHQUAKE RELATED DAMAGE OVER THE LAST 50 YEARS IN ITALY

The Da.D.O. web-gis platform has been conceived with the specific purpose to collect, catalogue and compare data related to damage and structural characteristics of buildings inspected after earthquakes occurred in Italy over the last 50 years. Data from ten seismic events characterized by a high seismic intensity are provided [34]: Friuli 1976; Irpinia 1980; Abruzzi 1984; Umbria-Marche 1997; Pollino 1998; Molise 2002; Emilia 2003; L'Aquila 2009; Emilia 2012, Garfagnana 2013. A summary of the general information present in the database is provided in Del Gaudio et al. [8], which reports that the total number of inspected buildings amounts to 320.000, subdivided among 78% of masonry buildings, 8% of RC buildings and 14% for other construction typologies. Since the survey forms have been modified over the years, the information available for each seismic event can vary. Presently, post-earthquake inspections are carried out by using the AeDES form [36], which was firstly introduced following the Umbria-Marche 1997 event. Previously, different survey forms were adopted (former versions of the AeDES form). For each seismic event collected in the Da.D.O. platform, Table 1 reports the key information accessible for each building. In particular, the information available in each survey form can be summarized in five macro-sections:

1. Building registry: general information and location of the buildings (e.g. year of construction, latitude and longitude, municipality, census code);
2. Geometry: main typological and geometrical features (e.g. number of storeys, qualitative estimate of area, inter-storey height);
3. Use destination: information about the use of the building from stakeholders (e.g. building use, number of occupants, strategic destination);
4. Position in urban context: information about the position of the building (e.g. reference with the position of near buildings, soil and topography);
5. Construction typology: main structural features (e.g. construction material, presence of retrofit devices, regularity).

The level of completeness and the quality of the data depends on the seismic events, more detailed information being available for more recent earthquakes. Table 1 reports a general indication about the level of detail of the recorded information distinguishing between: complete (C), incomplete (I) and absent (A) information. Regarding the building registry, all survey forms contain some details, however, for the first three considered events (Friuli 1976, Irpinia 1980 and Abruzzi 1984), the latitude and longitude are referred to the municipality in which the buildings are located and not to the specific location of the analyzed building. Concerning the geometry, the survey forms used after the first three events only report the plan dimension, while from the Irpinia 1980 earthquake the number of storeys and inter-storey height are also available. Only the data about the Abruzzi 1984 earthquake do not report the inter-storey height. The forms used in the first three events did not provide details about the use of the buildings, while for the Umbria-Marche 1997 and the Pollino 1998 earthquakes this information is reported, allowing to classify the buildings also based on their strategic importance. With regard to the position in the urban context, the form used in the Friuli 1976 earthquake reports if the building is isolated, outer-edge or in the corner of other building complexes. Only in the case of the Irpinia 1980 and the Abruzzi 1984 earthquakes, this data is

not reported. Lastly, with reference to the construction typology, complete information is provided for all seismic events but for the first three events only the construction material is reported.

Seismic event	Building registry	Geometry	Use destination	Position in urban context	Construction typology
Friuli 1976	I	I	A	I	I
Irpinia 1980	I	C	A	A	I
Abruzzi 1984	I	I	A	A	I
Umbria-Marche 1997	C	C	I	C	C
Pollino 1998	C	C	I	C	C
Molise 2002	C	C	C	C	C
Emilia 2003	C	C	C	C	C
L'Aquila 2009	C	C	C	C	C
Emilia 2012	C	C	C	C	C
Garfagnana 2013	C	C	C	C	C

Table 1: Summary of the key information reported in the survey forms adopted after the Italian seismic events occurred over the last 50 years (information about damage data are herein excluded)

As for the details related to the identification of the building's features, also the damage classification is related to the survey form adopted for the post-earthquake inspections. The forms used for the first three considered seismic events (Friuli 1976, Irpinia 1980 and Abruzzi 1984) do not allow to identify the damage extension [8]. The form adopted following the Friuli 1976 earthquake only allowed to classify buildings based on their global damage state, while more detailed information was introduced in the forms adopted during the following earthquakes. In particular, starting from the Pollino 1998 earthquake, it was possible to collect details about the damage state of five building components (vertical structures, horizontal structures, stairs, roofs and infill panels or non-structural elements). Table 2 reports the damage levels adopted in each survey form by grouping the different damage states in four main sub-categories. More in detail, the survey form adopted after the Friuli 1976 earthquake provides a synthetic judgement about observed damages (from destroyed to undamaged) subdivided in five damage levels (L0-L4). The survey form adopted after the Irpinia 1980 earthquake presents eight damage levels (L0-L7), while in the case of Abruzzi 1984 earthquake, the damage state was classified distinguishing between five damage levels (L1-L5) defined according to the EMS98 scale. From the Umbria-Marche 1997 earthquake, the AEDS survey form was introduced and the damage levels were classified according to damage states (D) defined according to the EMS98 scale.

It is worth mentioning that in the DA.D.O platform the details provided by the Institute of Geophysics and Vulcanology (INGV) for the characterization of the seismic events are also reported. This data includes: shake maps [37], date, magnitude, distance, geographic position (epicentre and hypocentre) and macro-seismic intensities in terms of Mercalli-Cancani-Sieberg scale (IMCS) [38].

Seismic event	Damage levels	Heavy damages	Medium damages	Light damages	Null damage
Friuli 1976	5	L3-L4	L2	L1	L0
Irpinia 1980	8	L5-L6-L7	L3-L4	L1-L2	L0
Abruzzi 1984	5	L4-L5	L2-L3	L1	/
Umbria-Marche 1997	3	D4-D5	D2-D3	D0-D1	/

Pollino 1998	4	D4-D5	D2-D3	D1	D0
Molise 2002	4	D4-D5	D2-D3	D1	D0
Emilia 2003	4	D4-D5	D2-D3	D1	D0
L'Aquila 2009	4	D4-D5	D2-D3	D1	D0
Emilia 2012	4	D4-D5	D2-D3	D1	D0
Garfagnana 2013	4	D4-D5	D2-D3	D1	D0

Table 2: Summary of the damage classification in the survey forms used after the main Italian seismic events, considering 4 macro-sections of damage: heavy, medium, light and null.

3 SCHOOL BUILDINGS DAMAGED BY ITALIAN EARTHQUAKES: STATISTICAL ANALYSIS ON THE SPECIFIC-CLASS PARAMETERS

Using the data available in the DA.D.O platform, all the school buildings damaged following the selected seismic events have been classified and statistically analysed. As reported in Table 1, the usage of the buildings was not available for seismic events occurred before 2002. In order to identify the school buildings for all considered seismic events, the information provided by DA.D.O platform has been compared with the Open Data about Italian schools provided by Italian Ministry of University and Research (MIUR) [39]. For each damaged building, DA.D.O provides the latitude and the longitude, while the MIUR database provides the address and the municipality of all Italian school buildings. Using reverse geocoding algorithm [40], latitude and longitude of all Italian school buildings have been found and matched with latitude and longitude of the damaged buildings, by imposing a tolerance -in absolute value- to the fourth decimal place. The summary of the identified school buildings, subdivided for construction typology, is provided in Table 3.

Seismic event	Number of school buildings extracted by DA.D.O.	RC [%]	Masonry [%]	Other typologies [%]
Friuli 1976	/	/	/	/
Irpinia 1980	/	/	/	/
Abruzzi 1984	3	0.0	100.0	0
Umbria-Marche 1997	153	15.0	79.5	5.5
Pollino 1998	25	12.0	64.0	24.0
Molise 2002	248	48.8	35.1	16.1
Emilia 2003	17	0.0	88.2	11.8
L'Aquila 2009	616	54.7	27.8	17.5
Emilia 2012	577	34.9	44.7	20.4
Garfagnana 2013	/	/	/	/

Table 3: Number of school buildings damaged by Italian seismic events over the last 50 years, accounting for the construction typology.

For Friuli 1976 earthquake, for the fixed tolerance, the matching procedure has not provided any useful results. The Irpinia 1980 earthquake, although several data are available, has been discarded because for this event the coordinates available are referred to the municipality and not to the specific location of the building. For Abruzzi 1984, Umbria-Marche 1997 and Pollino 1998 earthquakes, several units have been identified, as reported in Table 3. Although the adopted identification procedure can be affected by uncertainty, some random checks have been performed, observing a good level of accuracy. The distribution of the selected school buildings along the entire territory can be displayed using the extracted data. Figures 1 and 2

report the identified school buildings for Pollino 1998 and Emilia 2013 earthquakes and, additionally, the I_{MCS} for each municipality.

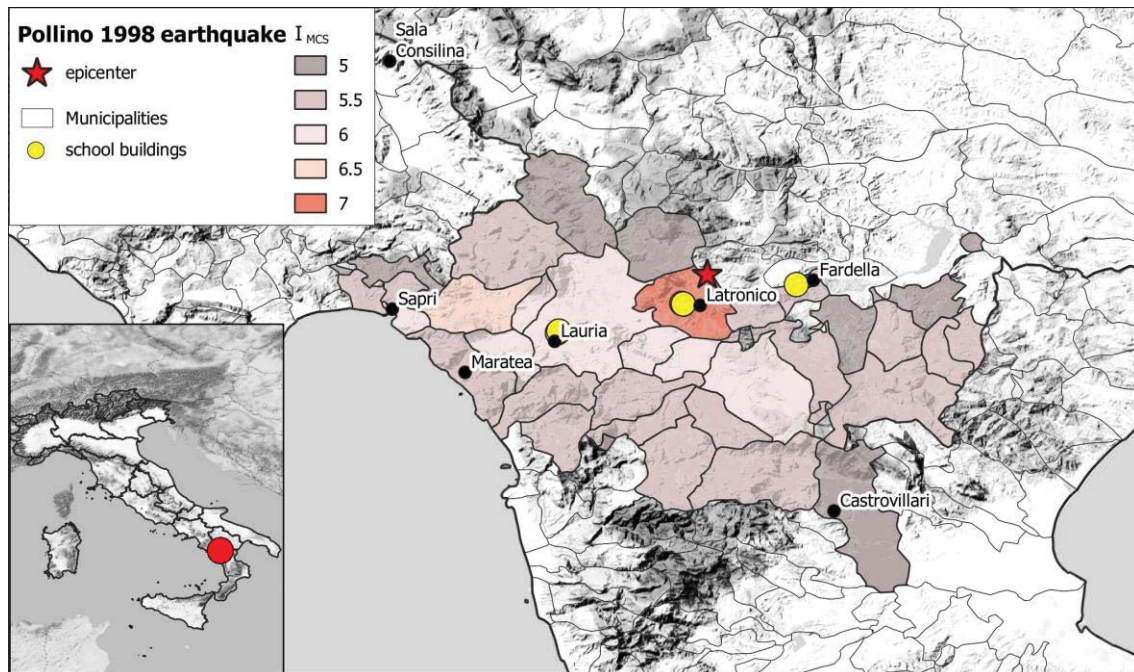


Figure 1: Distribution of school buildings damaged by Umbria-Marche 1997 earthquakes, with indication of I_{MCS} for each municipality.

Based on the defined school building database, several observations can be made on damaged masonry and RC school buildings, with the aim to evaluate the entire school building portfolio damaged by recent Italian earthquakes. Firstly, the year of construction for masonry and RC school buildings has been analyzed (Figure 3) NC indicates the school for which this information was not available. As expected, about 75% of masonry units were built before 1961 and about 90% before 1980. A different situation is observed for RC school buildings, where about 60% of the units were built before 1980. In 1980, the first seismic building code was released in Italy. This aspect suggests that the greater part of masonry and RC school buildings was not designed according to seismic details, which highlight a high seismic vulnerability of the building portfolio.

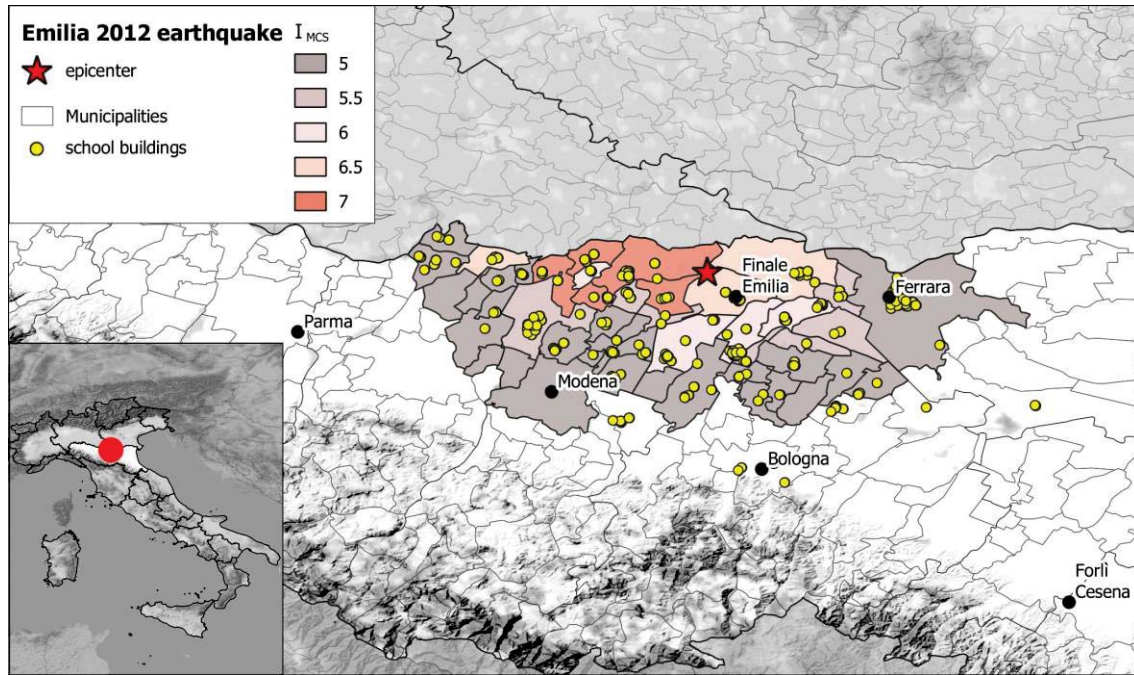


Figure 2: Distribution of school buildings damaged by Emilia 2013 earthquakes, with indication of I_{MCS} for each municipality.

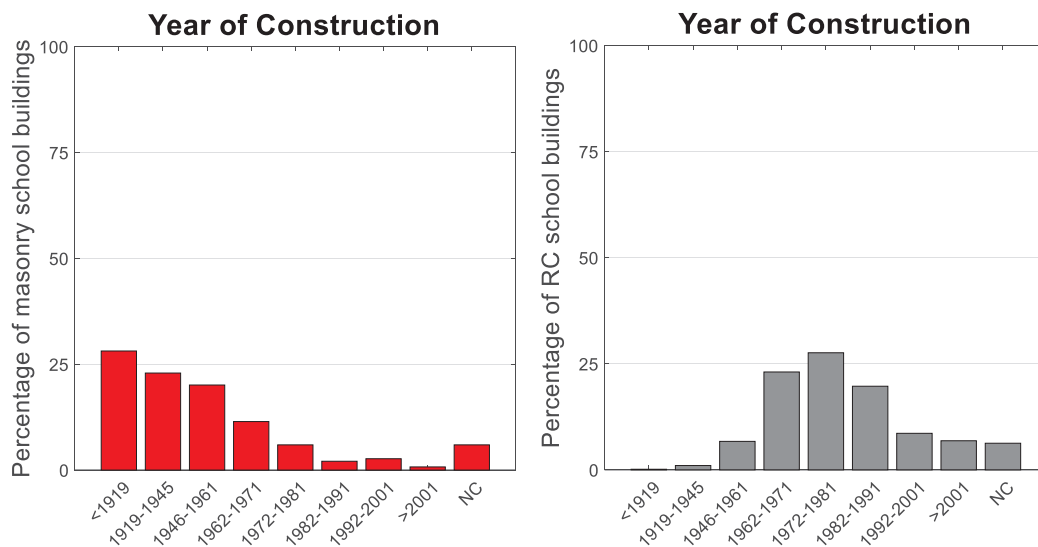


Figure 3: Percentage of masonry and RC school buildings, subdivided for year of construction parameter.

Figure 4 reports the number of storeys by distinguishing between masonry and RC buildings. Approximately 75% of the masonry and RC school buildings have three or fewer storeys. This observation implies that most of the damaged Italian school buildings can be classified as low-rise buildings (this evidence is also reported in several scientific works, e.g. [25, 27]). No particular evidence can be extracted from the inter-storey height parameter: about 85% of the RC school buildings presents values that range from 2.50 m and 3.50 m, while the remaining 15% presents higher values. The inter-storey height is more discretized for masonry buildings; higher inter-storey heights are observed in the schools built before 1920 (> 5.00 m), while inter-storey heights ranging from 3.50 m to 5.00 m have been observed for more recent buildings.

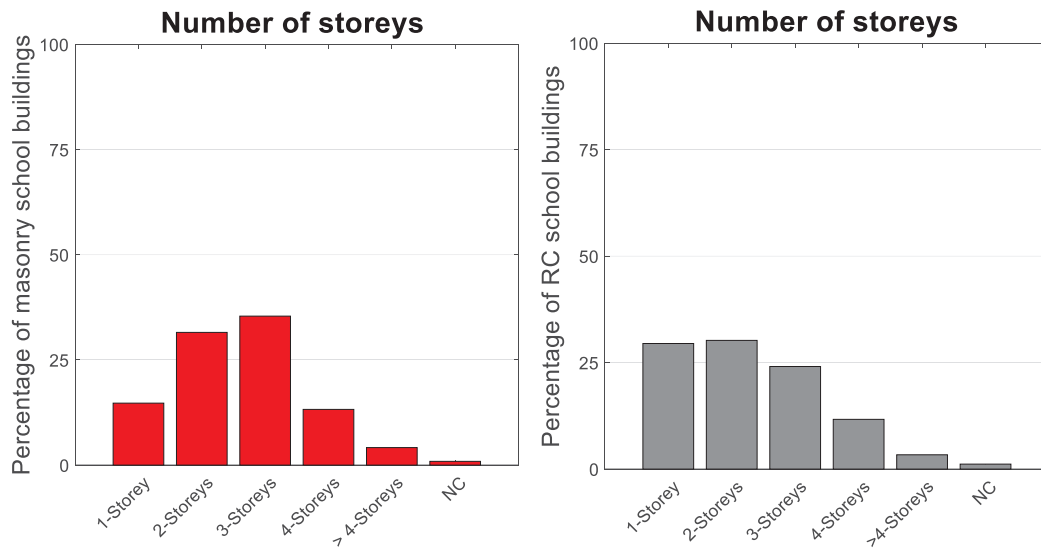


Figure 4: Percentage of masonry and RC school buildings, subdivided for number of storeys parameter.

Less homogenous is the distribution of the area parameter. As shown in Figure 5, about 40% of masonry school buildings and 25% of RC school buildings have an area ranging from 50 m² to 300 m², while about 50% of masonry and RC school buildings presents an area comprised from 300 m² to 1200 m². The high percentage of buildings characterized by large plan dimensions might suggests that this parameter can influence the seismic behavior.

As for the area parameter, also the structural regularity is an important parameter for defining the seismic vulnerability. This information is not available for all the units. In particular, the data available for school buildings damaged by Abruzzi 1984 and Umbria-Marche 1997 earthquakes do not report information on regularity and then they have been classified as NC. Looking at the percentage of regular and irregular school buildings, Figure 5 reports a summary for all the units. It is evident that about 50% of masonry and RC buildings presents structural irregularities. This aspect needs to be taken into account, considering that the structural irregularity assumes a key role in the seismic response of buildings.

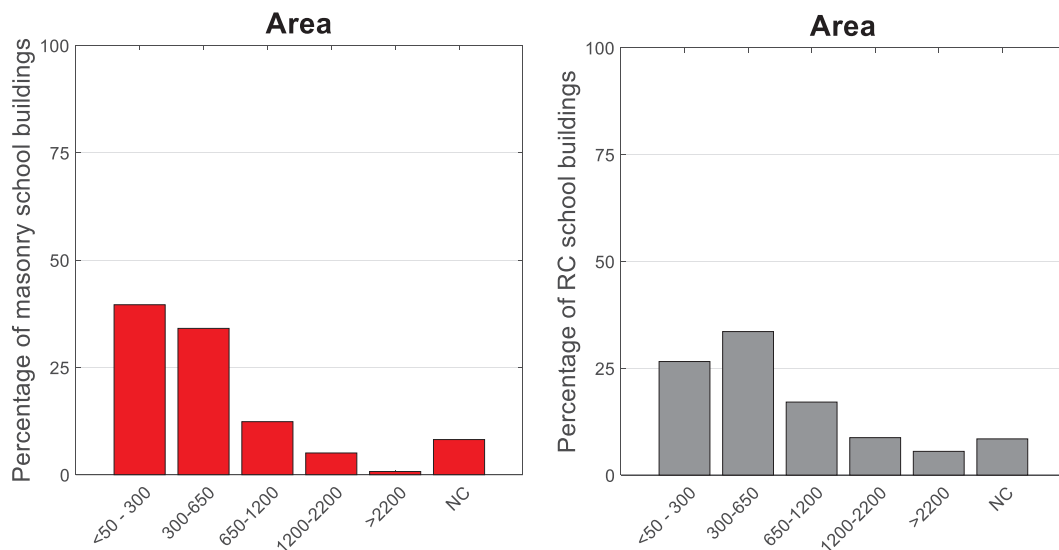


Figure 5: Percentage of masonry and RC school buildings, subdivided for area parameter.

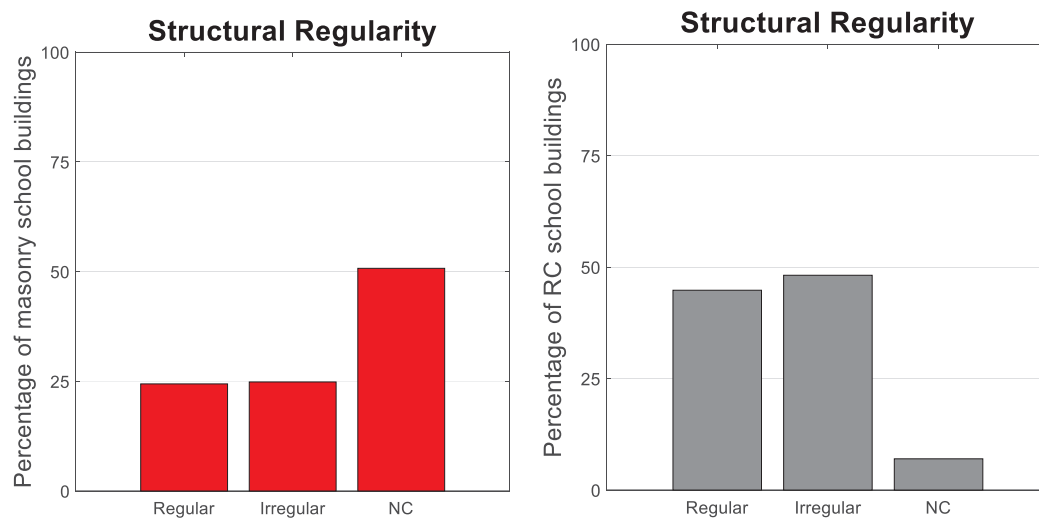


Figure 6: Percentage of masonry and RC school buildings, subdivided for structural regularity parameter.

4 EMPIRICAL ESTIMATION OF THE SEISMIC BEHAVIOUR OF ITALIAN SCHOOL BUILDINGS: DAMAGE DISTRIBUTION AND VULNERABILITY CURVES

The data collected in the DA.D.O. platform reports the results of the inspections made by practitioners and researchers rushed to the scene in the days after the earthquakes. As for rapid visual screening procedures, the definition of the damage state is based on the surveyors' experience, although some guidelines describing the different damage states are available. As previously discussed, it is worth mentioning that the survey forms adopted over the years can differ both in terms of investigated structural elements and damage classification. The survey form adopted in the Abruzzi 1984 earthquake contains judgments only about vertical and horizontal structures, while the one employed in the Umbria-Marche 1997 earthquake also considers damage to stairs. A complete information is provided for the Irpinia 1980 earthquake and for earthquakes after the Pollino 1998 and the Molise 2002 earthquake (AeDES form), in which damage data about vertical and horizontal structures, stairs, roofs and non-structural elements (such as infill panels for RC buildings) are present.

Basing on the developed school buildings database, it is possible to provide a critical discussion on the damages reported by school buildings after the selected earthquakes, by means of DPMs. Since the damages in AeDES form are classified according to the EMS98 scale, it is necessary to convert the damage levels reported for those earthquakes in which the AeDES form was not adopted (see Table 2) into the EMS98 measure scale. The methodology proposed by Del Gaudio et al. [8] has been adopted for the conversion into the EMS98 measure scale. Then, DPMs can be elaborated, as shown in Figures 7 and 8, accounting for horizontal structures, stairs, roofs and non-structural elements and by separating the RC and masonry school building samples.

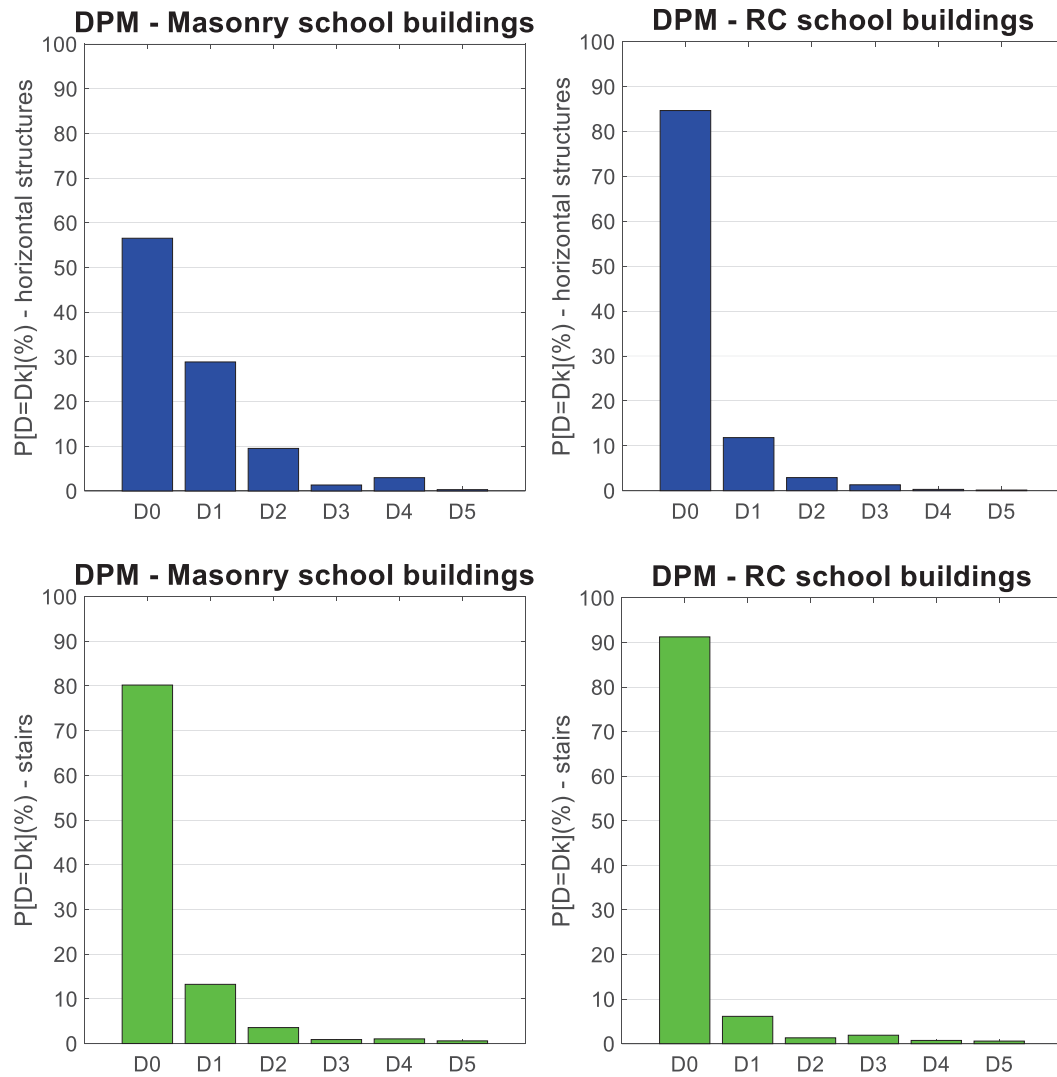


Figure 7: DPM for masonry and RC school buildings, accounting for damages on horizontal structures and stairs.

The results of the statistical analysis show that about 85-90% of the RC buildings have a damage level D0 and 10% have a damage level D1, with regard to horizontal structures, stairs and roofs. Despite the sample was not sorted for year of construction, few damages were detected. Different evidence is shown for non-structural elements (e.g. masonry infill panels and partitions), which show about 40% of units having damage level D1 and about 20% having damage levels ranging from D2 to D5. For non-structural elements, similar percentages are reported for masonry school buildings, for which non-structural elements present damage levels greater than D0 for about 55% of the units. Again for masonry buildings, DPMs show several damages on horizontal structures (about 45% of buildings have a damage level greater than D0), whereas few units present damages to stairs and roofs.

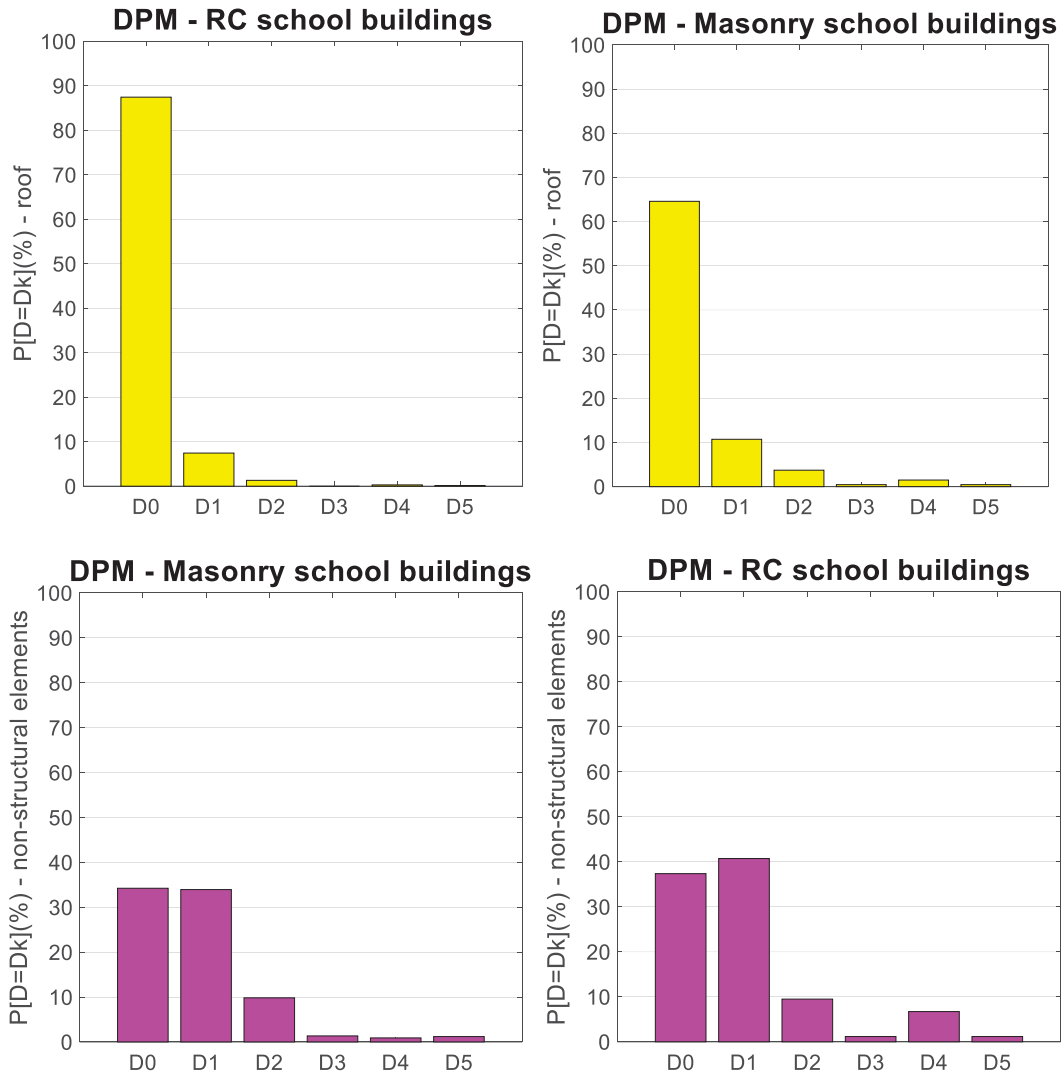


Figure 8: DPM for masonry and RC school buildings, accounting for damages on roofs and non-structural elements.

With regard to vertical structural elements, data can be processed by means of vulnerability curves. In particular, the entire set of school buildings has been subdivided into three samples: (a) Masonry school buildings, (b) RC school buildings designed before 1980 (pre 1980), (c) RC school buildings designed after 1980 (post 1980), by assuming 1980 as the threshold year that separate the buildings with and without seismic details. To this scope, for each unit of the three samples (N_{units}), damage data are reported in Figure 9, in which the abscissa reports the I_{MCS} identified for each municipality and the ordinate reports the mean damage (μ_D), evaluated as the weighted average of the buildings having a certain damage “DS” equal to an assigned value of damage “ds”. This formulation, as proposed in [8], is reported in the following:

$$\mu_{D,j} = \frac{1}{5} \frac{\sum_{ds=0}^5 N_{units}(DS=ds) * ds}{\sum N_{units}} \quad (1)$$

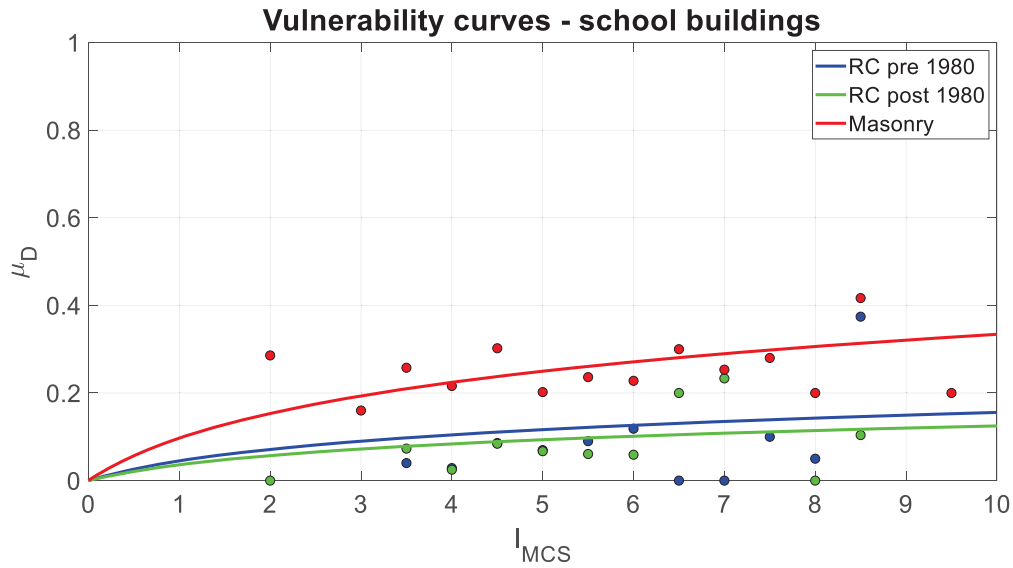


Figure 9: Vulnerability curves of RC and masonry school buildings damaged by Italian earthquakes.

Three points have been obtained for each value of I_{MCS} and all points have been fitted by lognormal cumulative functions and by optimizing the problem, assuming the minimum of the sum of squared errors between the set of points and the proposed curve. The result shows that RC buildings designed after 1980 present lower damages also for the highest values of the IM assumed, while the trend increases for RC buildings designed before 1980. Masonry buildings present substantial damages for high values of I_{MCS} , also arriving at values of μ_D equal to 0.4. Overall, the obtained vulnerability curves present a safer scenario for RC buildings than masonry ones. The observed low values of μ_D , also for higher values of IM, requires to better investigate the vulnerability of this typology of buildings, also considering other damage sources. As a matter of fact, it seems that the RC school buildings did not suffer damages.

5 CONCLUSIONS AND FUTURE DEVELOPMENTS

This study has analyzed the effects of earthquakes occurred over the last 50 years on the Italian school building portfolio. The data collected in the DA.D.O. platform have been used to perform this investigation. A database including information about masonry and RC school buildings surveyed after Italian earthquakes has been created. A critical discussion of the key features of Italian school buildings, accounting for construction typology, year of construction, number of storeys, area and structural regularity is provided. In addition, a post-processing of the damages suffered after the selected seismic events has been carried out, by providing damage probability matrices for damages on horizontal structures, stairs, roofs and non-structural elements and vulnerability curves accounting for damages on vertical structural elements.

The results of the statistical investigations have provided a basic idea about the seismic performance of Italian school buildings. The database will be used for future investigations aimed at defining a taxonomy of Italian school building and identifying the main vulnerability sources, basing on the damages suffered during past seismic events. The elaboration of the information collected in the database can assume a key role for future empirical procedures, aimed at investigating the seismic risk at regional scale for school buildings and at providing strategies of seismic risk mapping and reduction.

REFERENCES

- [1] G. Nicodemo, M. Pittore, A. Masi, V. Manfredi, Modelling exposure and vulnerability from post-earthquake survey data with risk-oriented taxonomies: AeDES form, GEM taxonomy and EMS-98 typologies. *International Journal of Disaster Risk Reduction*, **50**, 101894, 2020.
- [2] V. Silva, D. Amo-Oduro, A. Calderon, J. Dabbeek, V. Despotaki, L. Martins, A. Rao, M. Simionato, D. Viganò, C. Yepes, A. Acevedo, N. Horspool, H. Crowley, K. Jaiswal, M. Journeay, M. Pittore, Global earthquake model (GEM) seismic risk map (version 2018.1), 2018. <https://doi.org/10.13117/gem-global-seismic-risk-map-2018.1>
- [3] T. Rossetto, I. Ioannou, D. Grant, Existing empirical fragility and vulnerability functions: compendium and guide for selection, *GEM Technical Report 2013-X*, GEM Foundation, Pavia, 2013.
- [4] V. Silva, S. Akkar, J.W. Baker, P. Bazzurro, J.M. Castro, H. Crowley, M. Dolsek, C. Galasso, S. Lagomarsino, R. Monteiro, D. Perrone, K. Pitilakis, D. Vamvatsikos, Current challenges and future trends in analytical fragility and vulnerability modelling. *Earthquake Spectra*, **35(4)**, 1927-1952, 2019.
- [5] V. Cerchiello, P. Ceresa, R. Monteiro, N. Komendantova, Assessment of social vulnerability to seismic hazard in Nablus, Palestina. *International Journal of Disaster Risk Reduction*, **28**, 491-506, 2018.
- [6] G.J. O'Reilly, R. Monteiro, A.M.B. Nafeh, T.J. Sullivan, G.M. Calvi, Displacement-based framework for simplified seismic loss assessment. *Journal of Earthquake Engineering*, 2020, doi.org/10.1080/13632469.2020.1730272.
- [7] A. Masi, L. Chiauuzzi, G. Santarsiero, V. Manfredi, S. Biondi, E. Spacone, C. Del Gaudio, P. Ricci, G. Manfredi, G.M. Verderame, Seismic response of RC buildings during the Mw 6.0 August 24, 2016 Central Italy earthquake: the Amatrice case study. *Bulletin of Earthquake Engineering*, **17**, 5631-5654, 2017. <https://doi.org/10.1007/s10518-017-0277-5>
- [8] C. Del Gaudio, P. Ricci, G.M. Verderame, G. Manfredi, Observed and predicted earthquake damage scenarios: the case study of Pettino (L'Aquila) after the 6th April 2009 event. *Bulletin of Earthquake Engineering*, **14(10)**, 2643-2678, 2016.
- [9] C. Del Gaudio, M. Di Ludovico, M. Polese, G. Manfredi, A. Prota, P. Ricci, G.M. Verderame, Seismic fragility for Italian RC buildings based on damage data of the last 50 years. *Bulletin of Earthquake Engineering*, **18(5)**, 2023-2059, 2020.
- [10] M. Rota, A. Penna, C.L. Strobbia, Processing Italian damage data to derive typological fragility curves. *Soil Dynamics and Earthquake Engineering*, **28(10-11)**, 933-947, 2008.
- [11] A. Rosti, C. Del Gaudio, M. Rota, P. Ricci, M. Di Ludovico, A. Penna, G.M. Verderame, Empirical fragility curves for Italian residential RC buildings. *Bulletin of Earthquake Engineering*, 2020, <https://doi.org/10.1007/s10518-020-00971-4>
- [12] G. Zuccaro, F.L. Perelli, D. De Gregorio, F. Cacace, Empirical vulnerability curves for Italian masonry buildings: evolution of vulnerability model from the DPM to curves as a function of acceleration. *Bulletin of Earthquake Engineering*, 2020, <https://doi.org/10.1007/s10518-020-00954-5>.

- [13] A. Rosti, M. Rota, A. Penna, Empirical fragility curves for Italian URM buildings. *Bulletin of Earthquake Engineering*, 2020. <https://doi.org/10.1007/s10518-020-00845-9>
- [14] M. Savoia, N. Buratti, L. Vincenzi, Damage and collapses in industrial precast buildings after the 2012 Emilia earthquake. *Engineering Structures*, **137**, 162–180, 2017.
- [15] M. Di Ludovico, A. Digriolo, C. Moroni, F. Graziotti, V. Manfredi, A. Prota, M. Dolce, G. Manfredi, Remarks on damage and response of school buildings after the Central Italy earthquake sequence. *Bulletin of Earthquake Engineering*, **17**, 5679-5700, 2019, <https://doi.org/10.1007/s10518-018-0332-x>
- [16] B. Borzi, P. Ceresa, M. Favarelli, E. Fiorini, M. Onida, Definition of a prioritization procedure for structural retrofitting of Italian school buildings. *COMPADYN 2011 III ECCOMAS Thematic Conference on Computational Methods in Structural Dynamics and Earthquake Engineering: An IACM Special Interest Conference, Programme*. Papadrakakis M., Fragiadakis, M., Plevris, V. Corfù, Greece.
- [17] D.H. Lang, M.I. Verbicaro, Y. Singh, Seismic vulnerability assessment of hospitals and schools based on questionnaire survey. Kjeller, Norway, 2009.
- [18] D. Perrone, G.J. O'Reilly, R. Monteiro, A. Filiatrault, Assessing seismic risk in typical Italian school buildings: From in-situ survey to loss estimation. *International journal of disaster risk reduction*, **44**, 101448, 2020.
- [19] M. Morici, C. Canuti, A. Dall'Asta, G. Leoni, Empirical predictive model for seismic damage of historical churches. *Bulletin of Earthquake Engineering*, **18(13)**, 6015-6037, 2020.
- [20] G. De Matteis, G. Brando, V. Corlito, Predictive model for seismic vulnerability assessment of churches based on the 2009 L'Aquila earthquake. *Bulletin of Earthquake Engineering*, **17**, 4909–36, 2019, doi:10.1007/s10518-019-00656-7.
- [21] S. Lagomarsino, Damage assessment of churches after L'Aquila earthquake. *Bulletin of Earthquake Engineering*, **10 (1)**, 73–92, 2021, doi:10.1007/ s10518-011-9307-x.
- [22] S. Ruggieri, C. Tosto, G. Rosati, G. Uva, G.A. Ferro, Seismic Vulnerability Analysis of Masonry Churches in Piemonte after 2003 Valle Scrivia Earthquake: Post-event Screening and Situation 17 Years Later. *International Journal of Architectural Heritage*, 1-29, 2020, doi:10.1080/15583058.2020.1841366.
- [23] B. Borzi, R. Pinho, H. Crowley, Simplified pushover-based vulnerability analysis for large scale assessment of RC buildings. *Engineering Structures*, **30(3)**, 804–820, 2008.
- [24] M.A. Aiello, P.L. Ciampoli, A. Fiore, D. Perrone, G. Uva, Influence of infilled frames on seismic vulnerability assessment of recurrent building typologies. *Ingegneria Sismica*, **34(4)**, 58–80, 2017.
- [25] S. Ruggieri, F. Porco, G. Uva, D. Vamvatsikos, Two frugal options to assess class fragility and seismic safety for low-rise reinforced concrete school buildings in Southern Italy. *Bulletin of Earthquake Engineering*, 2010, DOI: 10.1007/s10518-020-01033-5.
- [26] D. Perrone, M.A. Aiello, M. Pecce, F. Rossi F, Rapid visual screening for seismic evaluation of RC hospital buildings, *Structures*, **3**, 57–70, 2015.
- [27] S. Ruggieri, D. Perrone, M. Leone, G. Uva, M.A. Aiello, A prioritization RVS methodology for the seismic risk assessment of RC school buildings. *International Journal of Disaster Risk Reduction*, **51**, 101807, 2020, doi.org/10.1016/j.ijdr.2020.101807

- [28] Italian National Institute of geophysics and volcanology (INGV), Website, <http://www.ingv.it/it/>.
- [29] L. Faenza, A. Michelini, Regression analysis of MCS intensity and ground motion parameters in Italy and its application in ShakeMap. *Geophysical Journal International*, **180**(3), 1138–1152, 2010, doi:10.1111/j.1365-246X.2009.04467.x.
- [30] F. Braga, M. Dolce, D. Liberatore, A statistical study on damaged buildings and an ensuing review of the MSK-76 scale. In: *Proceedings of the 7th European conference on earthquake engineering*, Athens, Greece, 431–450, 1982.
- [31] G. Di Pasquale, G. Orsini, R.W. Romero, New developments in seismic risk assessment in Italy. *Bulletin of Earthquake Engineering*, **3**(1), 101–128, 2005.
- [32] T. Rossetto, A. Elnashai, Derivation of Vulnerability Functions for European-Type RC Structures Based on Observational Data. *Journal of Engineering Structures*, **25**, 1241–1263, 2003.
- [33] S. Lagomarsino, S. Giovinazzi, Macroseismic and mechanical models for the vulnerability and damage assessment of current buildings. *Bulletin of Earthquake Engineering*, **4**(4), 415–443, 2006.
- [34] M. Dolce, A. Goretti, Building damage assessment after the 2009 Abruzzi earthquake. *Bulletin of Earthquake Engineering*, **13**, 2241–2264, 2015.
- [35] M. Dolce, E. Speranza, F. Giordano, B. Borzi, F. Bocchi, C. Conte, A. Di Meo, M. Favarelli, V. Pascale, Observed damage database of past Italian earthquakes: the Da. DO WebGIS. *Bollettino di Geofisica Teorica ed Applicata*, **60**(2), 141–164, 2019.
- [36] C. Baggio, A. Bernardini, R. Colozza, S. Coppari, L. Corazza, M. Della Bella, G. Di Pasquale, M. Dolce, A. Goretti, A. Martinelli, G. Orsini, F. Papa, G. Zuccaro, Field manual for post-earthquake damage and safety assessment and short term countermeasures. In: Pinto A, Taucer F (eds) Translation from Italian: Goretti A, Rota M, JRC Scientific and Technical Reports, EUR 22868 EN-2007, 2007.
- [37] <http://shake map.rm.ingv.it/shake /archive/>
- [38] A. Sieberg, Scale MCS (Mercalli-Cancani-Sieberg). *Geologie der Erdbeben, Handbuch der Geophysik*, **2**, 552–55, 1930.
- [39] Italian Ministry of University and Research (MIUR), Portale unico della scuola (2019) Website: <https://dati.istruzione.it/> (In Italian).
- [40] <https://github.com/anhelus/reverse-geocoding>

SEISMIC RISK ASSESSMENT FOR THE ITALIAN RESIDENTIAL MASONRY BUILT STOCK AND EFFECTIVENESS OF DIFFERENT MITIGATION STRATEGIES

Pietro Carpanese¹, Veronica Follador¹, Elisa Saler¹ and Francesca da Porto¹

¹ Depart. of Geosciences - University of Padova
Via G. Gradenigo, 6, 35131 Padova, Italy
pietro.carpanese@phd.unipd.it, {veronica.follador, elisa.saler, francesca.daporto}@unipd.it

Abstract

Italy is one of the countries most subject to seismic risk, not only because of high seismicity, but also because of its significant exposure and vulnerability. These aspects can determine very high social and economic costs for the country. In order to have a good estimate of risk indicators such as economic losses, casualties and usability of buildings in the aftermath of an earthquake, some computation tools that perform damage and risk assessments can be utilized. Particularly, this work uses the Italian Risk MAPs (IRMA) platform developed by Eucentre, which can produce maps of conditional damage (with a selected return period) or unconditional damage (with an observation time window) to evaluate seismic risk in Italy. IRMA allows the combination of hazard and exposure data included in the platform with vulnerability models. In this case, a vulnerability model for residential masonry is implemented within the platform to obtain the as-built risk evaluation. Moreover, a retrofitted vulnerability model is also derived, obtaining fragility curves that consider the main seismic retrofit interventions that can be performed on masonry buildings. By comparing the as-built risk evaluations with the mitigated ones, it is possible to highlight the entity of the benefit after a retrofit and compare it to its cost, at territorial scale. This analysis allows the assessment of the economic effectiveness of different seismic mitigation strategies.

Keywords: Residential Masonry Buildings, Seismic Risk Assessment, Cost-benefit analysis, Retrofit Interventions, Mitigation strategies

1 INTRODUCTION

Seismic risk assessment is an essential task for countries with intense seismic activity, such as Italy. To carry out seismic risk analyses, it is necessary to deepen the knowledge about the various components of this risk at national scale, starting from the vulnerability assessment of the built heritage. Particular attention should be paid to historical buildings, as they usually represent the most vulnerable component of the built stock.

Not only is it important to correctly assess the seismic vulnerability of the buildings as they currently are (i.e., as-built configuration), but it is also essential to plan possible retrofit intervention strategies, in order to mitigate seismic vulnerability and reduce the losses due to seismic events. In order to do so, simulations of intervention strategies should be performed, and the mitigated vulnerability should be compared with the “as-built” one.

Seismic vulnerability is often expressed by fragility curves. In literature, several methods to derive fragility curves are available [1]: empirical methods, that calibrate fragility curves from damage data collected after seismic events [2, 3]; mechanical methods, based on numerical or simplified models that simulate the seismic behavior of buildings [4, 5]; and hybrid methods, characterized by features of both empirical and analytical methods [6].

In this study, the simplified mechanical method proposed by Donà et al. [7-9] was followed. Specifically, a database of 205 buildings dating from before 1919 was considered, and the seismic vulnerability for this typology was evaluated with the software *Vulnus vb 4.0* [10, 11], described at §2.1. Different vulnerability models were thus obtained, for the as built configuration and for eight retrofit solutions, considered suitable for the construction period under consideration.

As a final elaboration, the vulnerability models were used to produce seismic risk maps of Italy through the IRMA platform [12, 13], highlighting the differences in terms of benefit that each intervention can bring in different parts of the country.

The maps presented in this paper may reach very practical outcomes, and they can be used by risk management institutions (such as the Department of Civil Protection) as guidelines to prioritize anti-seismic actions. The results may suggest where to take action and with which strategies, in order to move towards a targeted risk mitigation at a national level.

2 FRAGILITY CURVES FOR ITALIAN MASONRY BUILDINGS

2.1 Elaboration of fragility sets: tools and methodology

In this work, the elaboration of fragility curves is carried out with *Vulnus vb 4.0*. *Vulnus* is a software developed by the University of Padova, which analyzes load-bearing masonry structures in a simplified way. It uses few geometrical, structural, and qualitative information to calculate three fragility curves representative of the overall response of buildings to horizontal actions. The three fragility curves represent the mean (White curve) and the extreme (Lower-Bounds and Upper-Bounds curves) probabilities of reaching or exceeding the acceleration value that triggers in-plane or out-of-plane mechanisms. For this reason, they are associated to a medium-severe damage state (DS2-3, intermediate between DS2 and DS3 of the EMS98 scale [14]).

The aim of the procedure presented in Donà et al. [8] is to define a fragility curve describing the behavior of an entire building macro-typology (i.e., of a category of masonry buildings belonging to the same construction period). For this reason, when applying the *Vulnus* procedure to a database of buildings, the curves obtained for every building have to be eventually combined. The first step of the procedure consists of averaging the single curves by municipality and by number of floors. Then, weighted means between the curves belonging to

buildings of 1 and 2 stories and between the curves of 3, 4 and 5 stories are calculated. The weights are selected following the real distribution of the different typologies in Italy, using ISTAT 2001 census data [15]. The results are two sets of DS2-3 fragility curves representative of Low Rise (1 and 2 stories) and Mid Rise (3, 4 and 5 stories) buildings.

In order to represent seismic fragility over the five damage states (from DS1 to DS5), the fragility model of Lagomarsino and Cattari [16] is calibrated on the DS2-3 mechanical fragility curves previously obtained.

Lastly, the White, Upper- and Lower-Bounds sets are combined. The average fragility defined by the White curves is maintained (mean value of the lognormal fragility curve), whereas the dispersion parameter is adapted to the extreme probabilities range. In this way, the single fragility set derived for each building typology is more suitable to represent large-scale vulnerability.

For more detailed explanations on how the procedure is implemented, please refer to Donà et al. [8].

2.2 Retrofit interventions for Pre-1919 buildings

The first goal of this study is to compare different retrofit strategies and their ability to reduce seismic risk. To do so, the most adequate retrofit interventions for the building typology under investigation were studied.

As said before, this work focuses on Pre-1919 buildings. This typology of buildings is usually characterized by stone (mainly random) and solid brick masonry, timber floors and roofs, and absence of retaining elements. The consequence is usually an inadequate response to the seismic actions, making strengthening interventions necessary.

A considerable number of studies has been published on retrofit interventions for seismic vulnerability reduction. In particular, the most effective interventions for historical ordinary buildings are the following: interventions that increase strength and compactness of walls [17-20], interventions that improve connections [21-23], and interventions of stiffening of floors and roofs [24-27].

For the construction period Pre-1919, four individual retrofit interventions and four combined ones were selected on the basis of field experiences in past works [28-30]. The final eight interventions are shown in Table 1.

<i>individual interventions</i>			<i>combined interventions</i>	
<i>MSN1</i>	1 st stage of masonry strengthening	→	<i>MSN1+TR</i>	1 st stage of masonry strengthening + addition of tie-rods
<i>MSN2</i>	2 nd stage of masonry strengthening		<i>MSN1+FLR</i>	1 st stage of masonry strengthening + stiffening of floors
<i>TR</i>	addition of tie-rods		<i>MSN2+TR</i>	2 nd stage of masonry strengthening + addition of tie-rods
<i>FLR</i>	stiffening of floors (light interventions)		<i>MSN2+FLR</i>	2 nd stage of masonry strengthening + stiffening of floors

Table 1: Individual and combined retrofit interventions considered significant for Pre-1919 buildings

Specifically, masonry strengthening consists in the application of light or single interventions for the 1st stage (MSN1), while more phases of interventions or a single overall heavy intervention are associated to the 2nd stage (MSN2). Usually, masonry interventions for Pre-1919 buildings depend on type and quality of masonry. When the masonry is inconsistent

(i.e., random rubble and multi-leaf masonry), injections of mortar are often considered, whereas FRCM-TRM reinforced plaster (Fiber/Fabric Reinforced Cementitious Matrix/Mortar – Textile Reinforced Mortars) is taken into account in presence of stone ashlar or brick masonry.

The insertion of tie-rods (TR) is another typical intervention for masonry buildings. It improves (or even creates) the connections between structural elements (wall-to-wall and wall-to-floor) and prevents the activation of out-of-plane mechanisms.

As regards to floor interventions (FLR), the most efficient solutions for historical buildings are the insertion of bracing systems or the installation of double timber planks, in order to increase the stiffness without excessively affecting the loads. In addition, connection elements anchored to the masonry and to the bearing elements of the floor must be placed to ensure the effectiveness of the intervention.

Lastly, the combined application of different interventions can improve even more the seismic response of the building.

Since Vulnus performs simplified vulnerability analyses of masonry buildings, even the interventions were implemented in a simplified way [31]. In fact, it is possible to implement some interventions directly through the options allowed by the software (insertion of tie-rods), whereas others have to be implemented indirectly, using corrective coefficients (masonry strengthening) or reproducing the effect of the intervention on the overall behavior of the building (stiffening of floors).

2.3 Fragility curves for the as-built configuration and the intervention strategies

The Donà et al. [8] methodology was implemented for Pre-19 buildings, firstly for the as-built configuration and then for each intervention presented in §2.2. Therefore, the fragility sets related to the two building sub-typologies analyzed (Pre-1919 Low-Rise - 1, 2 stories, and Pre-1919 Mid-Rise - 3, 4, 5 stories) were obtained. In Table 2 the means (μ) and standard deviations (β) of the resulting model are reported, and in Figure 1 the values of μ for each DS are compared for Low-Rise and Mid-Rise buildings.

As expected, the results show that the interventions of masonry strengthening are overall more effective than the insertion of tie-rods or the intervention on floors. In addition, combined interventions are more effective than single ones. Moreover, it should be noticed that the reduction of vulnerability deriving from a combination of two interventions is not simply the sum of the reductions of vulnerability deriving from the two interventions performed individually.

<i>Interventions</i>		DS1		DS2		DS3		DS4		DS5	
		μ [g]	β [-]	μ [g]	β [-]	μ [g]	β [-]	μ [g]	β [-]	μ [g]	β [-]
AS-BUILT	$n \leq 2$	0.097	0.693	0.172	0.709	0.278	0.720	0.450	0.750	0.820	0.793
	$n \geq 3$	0.074	0.743	0.131	0.768	0.212	0.777	0.342	0.776	0.620	0.809
FLR	$n \leq 2$	0.126	0.735	0.224	0.757	0.361	0.747	0.584	0.751	1.062	0.756
	$n \geq 3$	0.094	0.675	0.168	0.704	0.270	0.711	0.437	0.743	0.796	0.782
TR	$n \leq 2$	0.112	0.746	0.198	0.774	0.320	0.761	0.518	0.775	0.950	0.807
	$n \geq 3$	0.079	0.739	0.140	0.750	0.227	0.758	0.366	0.766	0.663	0.804
MSN1	$n \leq 2$	0.131	0.709	0.233	0.736	0.376	0.727	0.608	0.729	1.104	0.722
	$n \geq 3$	0.112	0.758	0.199	0.788	0.321	0.774	0.519	0.788	0.951	0.814
MSN2	$n \leq 2$	0.153	0.689	0.271	0.723	0.438	0.733	0.709	0.755	1.290	0.683
	$n \geq 3$	0.129	0.739	0.229	0.770	0.370	0.761	0.597	0.766	1.086	0.757
MSN1 + FLR	$n \leq 2$	0.206	0.700	0.366	0.703	0.589	0.681	0.947	0.673	1.689	0.667
	$n \geq 3$	0.153	0.662	0.271	0.689	0.437	0.704	0.707	0.729	1.286	0.679

MSN1 + TR	$n \leq 2$	0.168	0.693	0.299	0.718	0.483	0.737	0.783	0.780	1.432	0.699
	$n \geq 3$	0.120	0.738	0.213	0.762	0.344	0.748	0.556	0.753	1.015	0.776
MSN2 + FLR	$n \leq 2$	0.263	0.739	0.467	0.738	0.755	0.724	1.217	0.652	2.161	0.612
	$n \geq 3$	0.188	0.692	0.334	0.699	0.540	0.700	0.872	0.742	1.569	0.707
MSN2 + TR	$n \leq 2$	0.191	0.732	0.339	0.738	0.548	0.729	0.884	0.760	1.586	0.708
	$n \geq 3$	0.144	0.696	0.255	0.725	0.412	0.730	0.665	0.745	1.208	0.691

Table 2: Means (μ) and standard deviations (β) of the fragility model for Pre-1919 buildings in as-built condition and after the analyzed interventions (where n is number of stories).

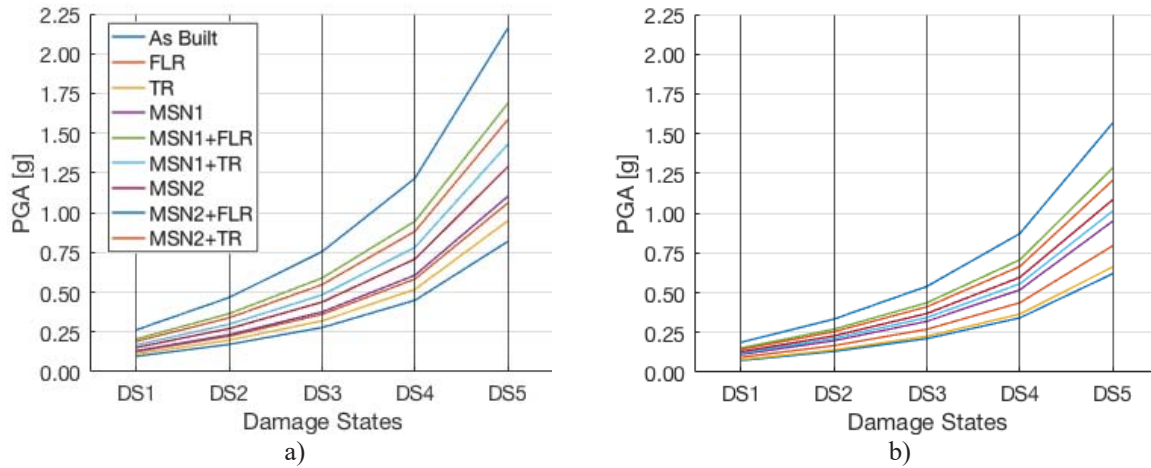


Figure 1: Comparison of the means (μ) of the fragility curves for each damage state DS, for each intervention, and for: a) Low-Rise buildings ($n \leq 2$); b) Mid-Rise buildings ($n \geq 3$)

3 RISK MAPS

Once the fragility curves for the as-built configuration and the intervention strategies are defined, they can be implemented in the IRMA platform. IRMA is a tool developed by Eucentre (*European centre for training and research in earthquake engineering*) for the Italian Department of Civil Protection: it elaborates seismic hazard, vulnerability and exposure data in Italy, in order to produce damage and risk maps. The hazard used in the platform is the MPS04 hazard model, developed by the National Institute of Geophysics and Volcanology [32]. The exposure for residential buildings derives from the Italian census data (ISTAT) and is presented in terms of number of buildings, dwellings or their total floor area at municipality level. Lastly, vulnerability can be customized and has to be given as an input by the user. In this work, the fragility models defined in §2.3 were used.

Combining these three components, IRMA can elaborate maps of conditional damage and risk (i.e., the return period is selected), as well as maps of unconditional damage and risks (i.e., an observation time window is selected).

In this work, mainly the direct economic losses caused by earthquakes were taken into account. Table 3 shows the percentages of the repair (or replacement) cost as a function of building damage. In IRMA, the default reconstruction cost is 1350 €/m², and this value was kept throughout all the simulations. The parameters proposed in IRMA were calibrated on the actual repair costs incurred after the Italian earthquake of L'Aquila 2009 [33, 34].

The analyses carried out in the following §3.1 and §3.2 refer to an unconditional time window of 50 years, and are related to a type A soil (rocks or very rigid soils). Also, since the vulnerability models described in §2.3 only refer to buildings belonging to Pre-1919, all the

maps and results shown in this paper are related only to the Italian built stock from that construction period.

For further explanations about how the platform works, please refer to [13].

	<i>DS1</i>	<i>DS2</i>	<i>DS3</i>	<i>DS4</i>	<i>DS5</i>
% of total cost (1350 €/m ²)	2%	10%	30%	60%	100%

Table 3: Percentages used by the IRMA platform for computation of economic losses

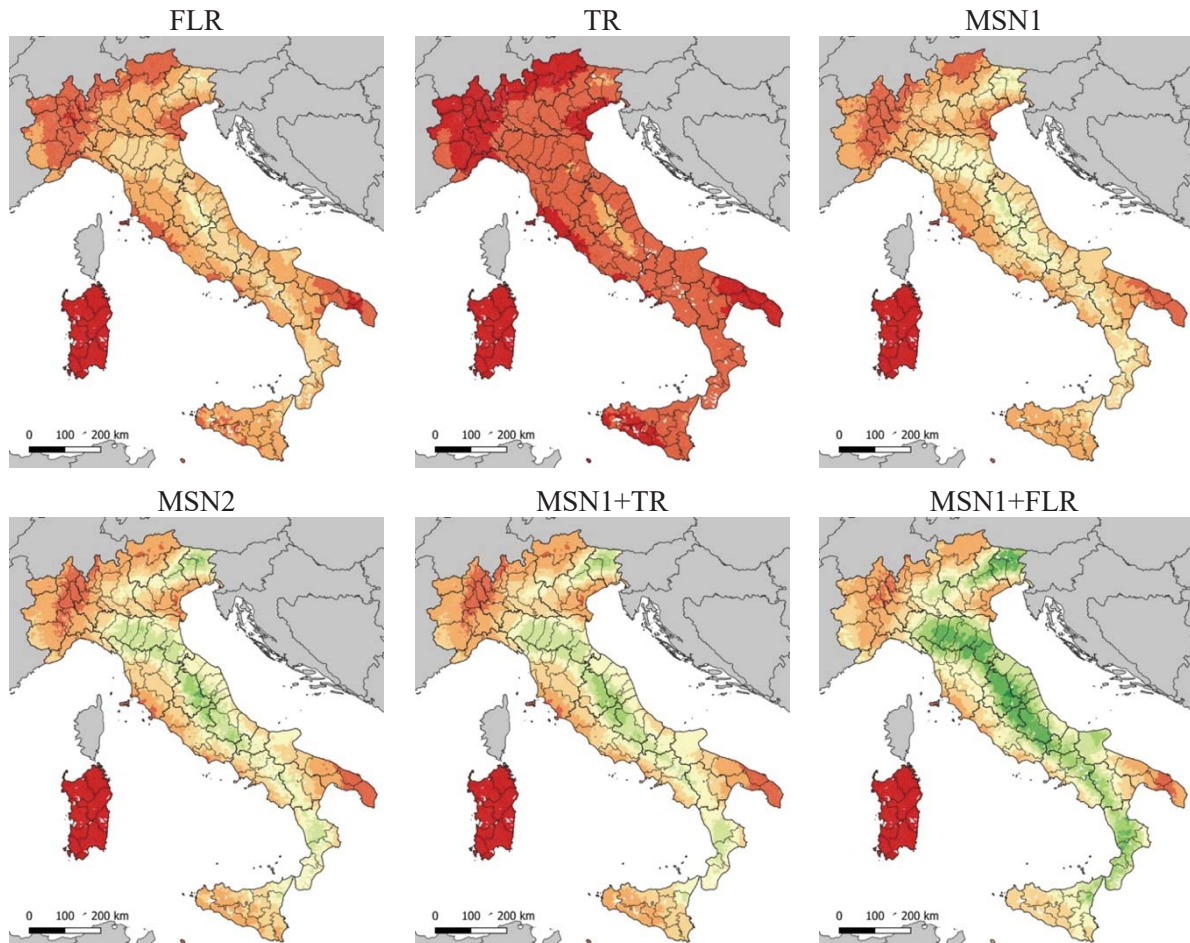
3.1 Benefit and normalized benefit

As a first step, it is useful to compute the benefit (B) expected in a time window of 50 year. B is defined as the difference between economic losses for a scenario where all the buildings are in the as-built configuration ($EL_{as-built}$) and the economic losses in case an intervention strategy is extensively implemented at national level (EL_{int}), according to equation (1):

$$B = EL_{as\ built} - EL_{int} \quad (1)$$

Of course, benefit is deeply influenced by exposure, as higher losses are expected in bigger towns with higher exposure. For this reason, it can be useful to visualize the results in terms of normalized benefit (NB): to obtain this variable, the benefit in each municipality is divided by its Pre-1919 exposure.

Figure 2 shows the maps with the NB results for all Italian municipalities, and for each possibility of intervention presented in §2.2 (both individual and combined interventions).



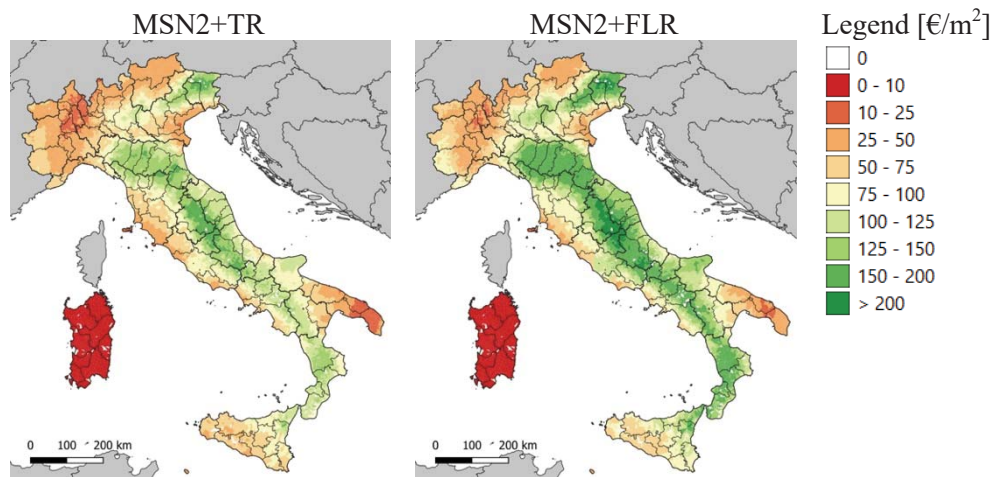


Figure 2: Normalized benefit (NB) maps of Italy for the retrofit interventions considered

It should be notice how some combined strategies lead to the same overall results as some individual ones (for example, the map for $MSN1+TR$ is very similar to the one for $MSN2$). This consideration could be significant when planning mitigation actions at territorial scale.

3.2 Cost-benefit analysis

In order to assess the real economic effectiveness of the interventions analyzed, the benefit B has to be compared with the cost C of these interventions. In particular, B is divided by C , thus obtaining an index I .

When I is equal to or greater than 1, this means that the benefit exceeds the cost, making the initial investment economically reasonable. The lower the value of I , the less economically justified the intervention will be. Table 4 shows the costs per square meter that were estimated for each intervention [35].

INTERVENTIONS	COST [€/m²]
FLR	185
TR	
<i>Low-Rise buildings (1-2 stories)</i>	110
<i>Mid-Rise buildings (3-4-5 stories)</i>	45
MSN1	140
MSN1 + FLR	330
MSN1 + TR	
<i>Low-Rise buildings (1-2 stories)</i>	250
<i>Mid-Rise buildings (3-4-5 stories)</i>	190
MSN2	210
MSN2 + FLR	395
MSN2 + TR	
<i>Low-Rise buildings (1-2 stories)</i>	320
<i>Mid-Rise buildings (3-4-5 stories)</i>	255

Table 4: Costs in €/m² for each intervention considered

In this work, the aim of the cost-benefit analysis is to identify the most convenient retrofit strategy in different Italian locations.

In this procedure, each Italian municipality will have eight indices I (one for each intervention proposed). The group of eight indices I for each municipality will match one of the following cases:

1. if some or all of them are greater than 0.5 (i.e., more than 50% of the initial cost will be totally recovered in 50 years): among the ones that meet this condition, the most performing intervention is chosen (i.e., the one that gives the greatest benefit B);
2. if some or all of them are lower than 0.5 but greater than 0.3 (i.e., between 30 and 50% of the initial cost will be totally recovered in 50 years): among the ones that meet this condition, the cheapest intervention is chosen (i.e., the ones with the lowest cost C);
3. if all the indices are less than 0.3 (i.e., less than 30% of the initial cost will be totally recovered in 50 years): no intervention strategy is considered effective enough.

As can be noticed, the value $I=0.5$ sets a decision boundary: in case interventions have $I>0.5$, their performance is taken into account, while when $I<0.5$ their affordability will be considered first. This choice can be explained remembering that the values here calculated only take into consideration the direct losses; if all the other costs were included, the values of I would approximately double [36].

Figure 3 shows the results of this calculation for each Italian municipality.

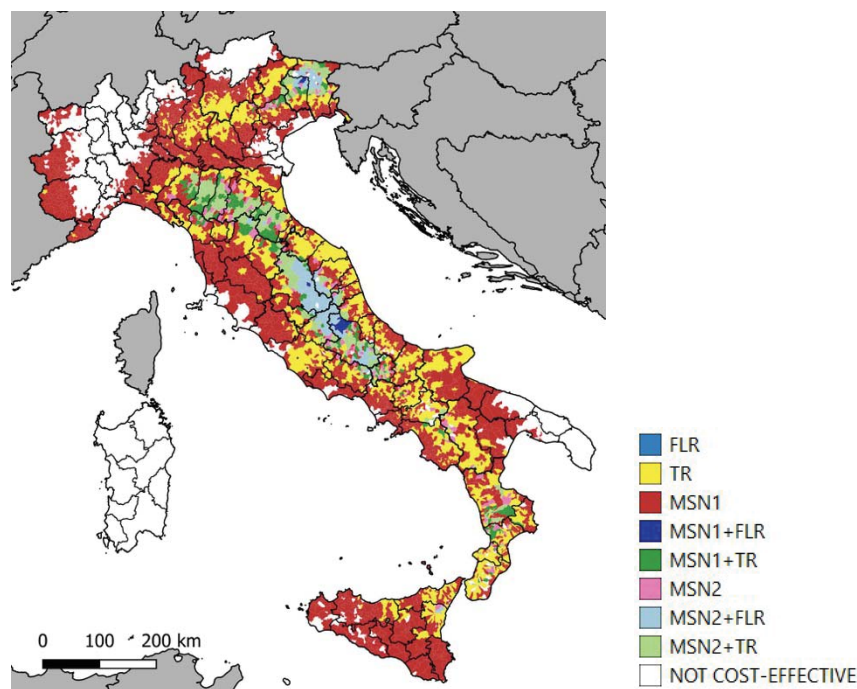


Figure 3: Cost-effectiveness map, derived from the cost-benefit analysis

Firstly, the map shows how more invasive interventions (as, for example, combined ones) are economically effective in areas with a higher seismic hazard (Central Italy, North-East Italy). The choice of which specific intervention should be implemented often derives from the exposure in the specific analyzed municipality. In zones with a medium-low seismic hazard, usually individual interventions are considered sufficient. Where seismic hazard is very low, no retrofit intervention seems economically effective in a time window of 50 years.

3.3 Recovery time of the initial cost of interventions

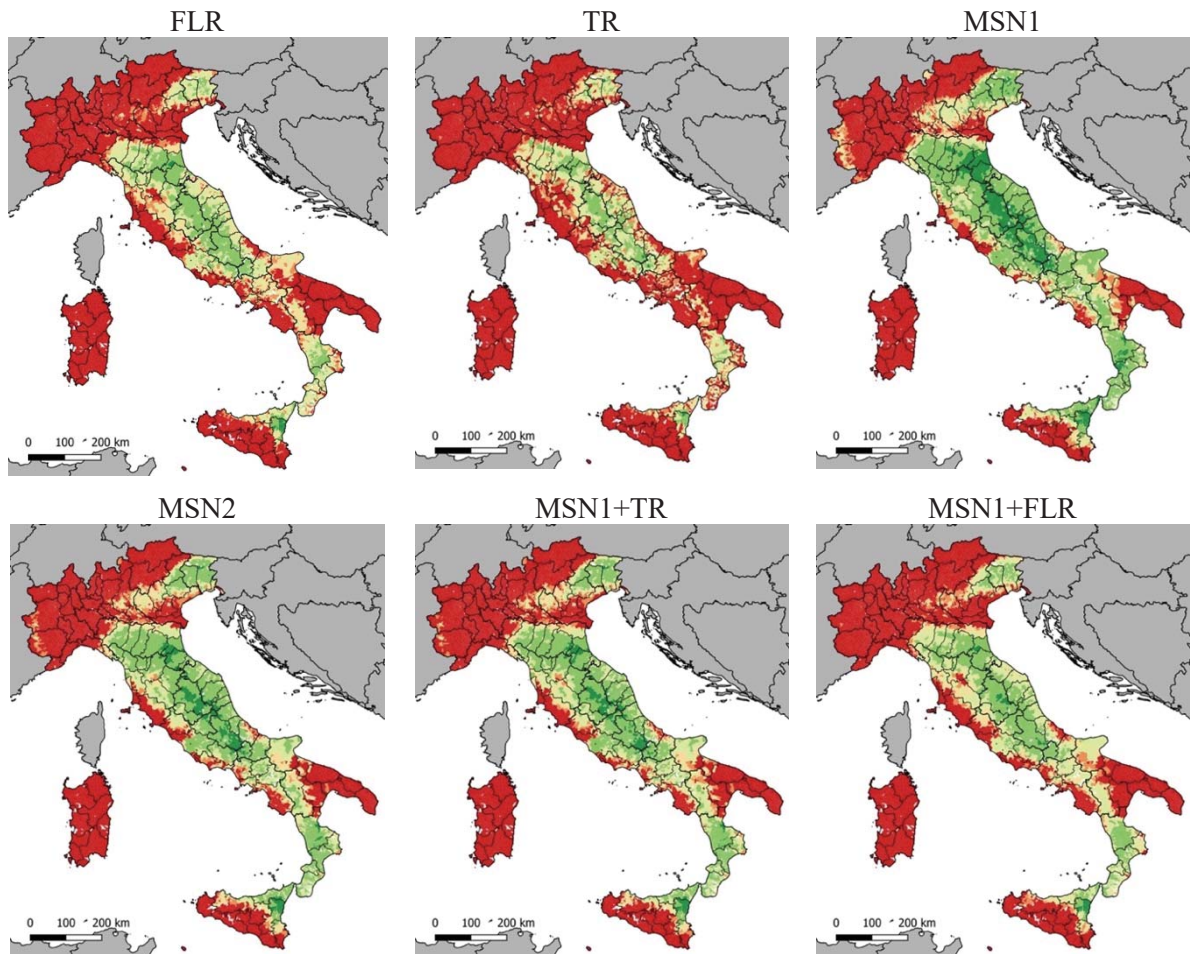
Other than the choice of the most effective intervention strategy, it is interesting to evaluate in how many years the cost of interventions can be recovered, i.e., in what year t , from the date on which the intervention was implemented, the benefit B fully recovers the initial cost C . In order to do so, the benefit is initially calculated for a time window of 1 year, and then updated year by year to obtain a gross present value (GPV), according to equation (2):

$$GPV(t) = B_{1\text{ year}} \cdot \sum_{t=1}^T \frac{(1+f)^t}{(1+r)^t} \quad (2)$$

where f is the inflation rate, and r is the discount rate. For this work, $f=0.01$ and $r=0.02$ were assumed [37].

By updating the benefit B , there will be a year t when the benefit B reaches or overcomes the initial cost C . This represents indeed the recovery time of an intervention. The maps in Figure 4 show the recovery time of the interventions considered.

The single light intervention on masonry (MSN1) results to have the shortest recovery time in large part of the national area, due to its well-balanced benefits and costs of intervention. Other types of light retrofit strategies instead, such as tie-rods, are surely less expensive, but the provided benefit appears to be insufficient to effectively recover the cost (albeit limited) of intervention.



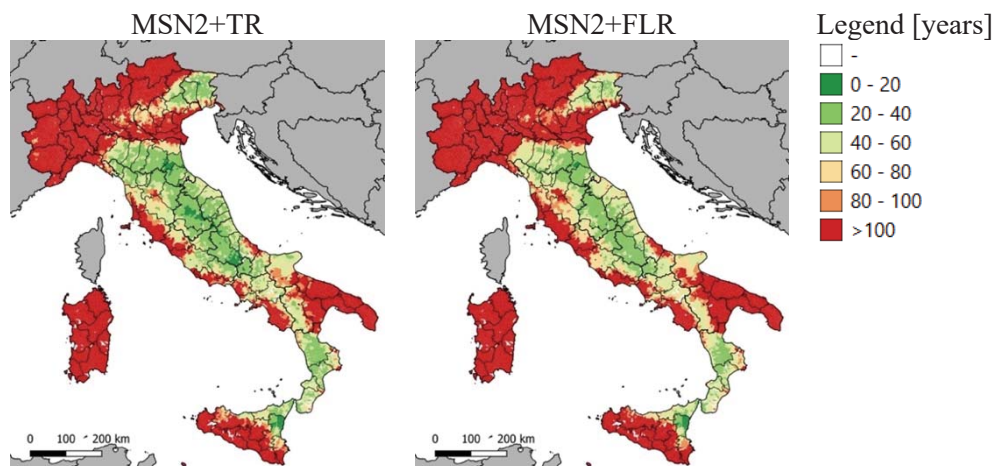


Figure 4: Recovery time of the initial cost of each intervention strategy

4 CONCLUSIONS

- A simplified mechanical method was used to create fragility curves for Pre-1919 buildings, both in their as-built configuration and with simulated retrofit interventions.
- Some applications of these fragility curves have been shown in terms of risk maps. Mitigated risk maps were created, showing the difference between the as-built configuration and the retrofitted one. Through a cost-benefit analysis, the cost-effectiveness of the retrofit interventions was evaluated. For each Italian municipality, a specific intervention strategy was considered more convenient, depending on seismic hazard and exposure. A calculation for estimating the recovery time of the interventions was also proposed.
- The maps presented in this paper can be essential tools for authorities and decision-makers, when planning risk mitigation strategies at territorial or even national scale.
- The results provided in this paper only take into account the masonry historical built stock in Italy (i.e., built before 1919). The final aim of this work is to obtain a vulnerability model (both as-built and retrofitted) also for more recent building typologies. In this way, the seismic risk analyses and the mitigation assessments will consider the whole exposure in Italy. Then, a natural progression of the present work is to carry out more detailed risk analyses in terms of economic losses (including the estimation of indirect losses), which would lead to the selection of intervention strategies in a more sophisticated way. In addition, possible casualties (in terms of injuries and victims) will have to be taken into account in order to make these estimations more valid.

ACKNOWLEDGEMENTS

Special thanks are due to the Italian Department of Civil Protection (DPC), which funded this study in the framework of the *ReLUIS-DPC Project 2019-2021 – Work Package 4: MARS (Maps of Risk and Scenarios of seismic damage) – Task 6: Preventive strategies: comparative analysis in terms of risk at national scale (Strategie preventive: analisi comparata in termini di rischio a scala nazionale)*.

We would also like to thank Eucentre (*European centre for training and research in earthquake engineering*) for creating the IRMA platform and giving access to our research unit.

REFERENCES

- [1] G.M. Calvi, R. Pinho, G. Magenes, J.J. Bommer, L.F. Restrepo-Veléz, H. Crowley, The development of seismic vulnerability assessment methodologies for variable geographical scales over the past 30 years. *ISET Journal of Earthquake Technology*, **43**, 75–104, 2006.
- [2] T. Rossetto, I. Ioannou, D.N. Grant, Existing empirical fragility and vulnerability functions: Compendium and guide for selection. GEM Technical Report 2013-X, GEM Foundation, Pavia, Italy, 2013.
- [3] A. Rosti, M. Rota, A. Penna, Empirical fragility curves for Italian URM buildings. *Bulletin of Earthquake Engineering*, 2020.
- [4] D. D'Ayala, A. Meslem, D. Vamvatsikos, K. Porter, T. Rossetto, V. Silva, Guidelines for analytical vulnerability assessment of low/mid-rise buildings, Vulnerability Global Component Project. *GEM Technical Report*, 2015.
- [5] B. Borzi, M. Faravelli, A. Di Meo, Application of the SP-BELA methodology to RC residential buildings in Italy to produce seismic risk maps for the national risk assessment. *Bulletin of Earthquake Engineering*, 2020.
- [6] A.J. Kappos, G. Panagopoulos, C. Panagiotopoulos, G. Penelis, A hybrid method for the vulnerability assessment of RC and URM buildings. *Bulletin of Earthquake Engineering*, **4**, 391-413, 2006.
- [7] M. Donà, P. Carpanese, V. Follador, F. da Porto, Derivation of mechanical fragility curves for macro-typologies of Italian masonry buildings. M. Papadrakakis, M. Fragiadakis eds. *7th ECCOMAS Thematic Conference on Computational Methods in Structural Dynamics and Earthquake Engineering (COMPDYN 2019)*, Crete, Greece, June 24-26, 2019.
- [8] M. Donà, P. Carpanese, V. Follador, L. Sbrogio, F. da Porto, Mechanics-based fragility curves for Italian residential URM buildings. *Bulletin of Earthquake Engineering*, 2020.
- [9] M. Vettore, M. Donà, P. Carpanese, V. Follador, F. da Porto, M.R. Valluzzi, A Multilevel Procedure at Urban Scale to Assess the Vulnerability and the Exposure of Residential Masonry Buildings: The Case Study of Pordenone, Northeast Italy. *Heritage*, **3**(4), 1433–1468, 2020.
- [10] A. Bernardini, M. Gori, C. Modena, Application of coupled analytical models and experimental knowledge to seismic vulnerability analyses of masonry buildings, A. Koridze ed. *Earthquake damage evaluation and vulnerability analysis of Building structures*, INEEC, Omega Scientific, Ozon, 161-180, 1990.
- [11] M.R. Valluzzi, Manuale d'uso del programma Vulnus 4.0, programma originario di A. Bernardini, R. Gori, C. Modena, versione Vb a cura di M.R. Valluzzi, contributi di G. Benincà, E. Barbetta, M. Munari, 2009. (*in Italian*)
- [12] F. da Porto, M. Donà, A. Rosti, M. Rota, S. Lagomarsino, S. Cattari, B. Borzi, M. Onida, D. De Gregorio, F.L. Perelli, C. Del Gaudio, P. Ricci, E. Speranza. Comparative analysis of the fragility curves for Italian residential masonry and RC buildings. *Bulletin of Earthquake Engineering, Special Issue: Seismic Risk Assessment in Italy*, 2021.

- [13] B. Borzi, M. Onida, M. Faravelli, D. Polli, M. Pagano, D. Quaroni, A. Cantoni, E. Speranza, C. Moroni. IRMA platform for the calculation of damages and risks of Italian residential buildings. *Bulletin of Earthquake Engineering*, 2020.
- [14] G. Grünthal, European Macroseismic Scale. *Chaiers du Centre Européen de Géodynamique et de Séismologie*, vol. 15. Luxembourg, 1998.
- [15] Italian National Institute of Statistics (ISTAT 2001) Website and data warehouse, 2001. <https://www.istat.it/it/censimenti-permanenti/censimenti-precedenti/popolazione-e-abitazioni/popolazione-2001>
- [16] S. Lagomarsino, S. Cattari, Fragility functions of masonry buildings, (Chapter 5), K. Pitilakis, H. Crowley, A.M. Kaynia eds. *SYNER-G: Typology Definition and Fragility Functions for Physical Elements at Seismic Risk, Vol. 27*, 111- 156, Springer 2014.
- [17] MR. Valluzzi, F. da Porto, C. Modena, Behavior and modeling of strengthened three-leaf stone masonry walls. *Materials and Structures*, **37**, 184–192, 2004.
- [18] N. Mazzon, MR. Valluzzi, T. Aoki, E. Garbin, G. De Canio, N. Ranieri, C. Modena, Shaking table tests on two multi-leaf stone masonry buildings. *11th Canadian Masonry Symposium*, Toronto, Canada, May 31–June 3, 2009.
- [19] B. Silva, M. Dalla Benetta, F. da Porto, MR. Valluzzi, Compression and Sonic Tests to Assess Effectiveness of Grout Injection on Three-Leaf Stone Masonry Walls. *International Journal of Architectural Heritage*, **8**, 408-435, 2014.
- [20] M. Giaretton, D. Dizhur, E. Garbin, J. Ingham, F. da Porto, In-plane strengthening of clay brick and block masonry walls using textile-reinforced mortar. *Journal of Composites for Construction*, **22**(5), 2018.
- [21] C. Modena, F. Casarin, F. da Porto, E. Garbin, N. Mazzon, M. Munari, M. Panizza, MR. Valluzzi, Structural interventions on historical masonry buildings: review of Eurocode 8 provisions in the light of the Italian experience. E. Cosenza ed. *Eurocode 8 Perspectives from the Italian Standpoint*, 225 – 236, Napoli, Doppiavoce, 2009.
- [22] C. Modena, MR. Valluzzi, F. da Porto, F. Casarin, Structural Aspects of The Conservation of Historic Masonry Constructions in Seismic Areas: Remedial Measures and Emergency Actions. *International Journal of Architectural Heritage*, **5**, 539-558, 2011.
- [23] F. da Porto, MR. Valluzzi, M. Munari, C. Modena, A. Arêde, AA. Costa, Strengthening of Stone and Brick Masonry Buildings. AA. Costa, A. Arêde, H. Varum (eds) *Strengthening and Retrofitting of Existing Structures. Building Pathology and Rehabilitation*, vol 9. Springer, Singapore, 2018.
- [24] MR. Valluzzi, E. Garbin, M. Dalla Benedetta, C. Modena, In-plane strengthening of timber floors for the seismic improvement of masonry buildings. *World Conference on Timber Engineering (WCTE)*, Curran Associates, Red Hook, NY, 2010.
- [25] MR. Valluzzi, E. Garbin, M. Dalla Benedetta, C. Modena, Experimental assessment and modelling of in-plane behaviour of timber floors. *VI Int. Conf. on Structural Analysis of Historical Constructions (SAHC08)*, Bath, United Kingdom, July 2nd-4th, 2008.
- [26] D. Dizhur, M. Giaretton, J. Ingham, URM wall-to-diaphragm and timber joist connection testing. *10th International Masonry Conference – IMC*, Milan, Italy, July 2018.

- [27] M. Giaretton, I. Giongo, D. Dizhur, Field testing of unreinforced masonry wall-to-diaphragm connection via through-bolt plate anchors and timber blocking. *Masonry International*, **32**, 63–71, 2019.
- [28] Y. Saretta, L. Sbrogio, M.R. Valluzzi, Seismic response of masonry buildings in historic centres struck by the 2016 Central Italy earthquake. Calibration of a vulnerability model for strengthened conditions, *Constr. Build. Mater.* (in print).
- [29] M. Vettore, Y. Saretta, L. Sbrogio, M.R. Valluzzi, A New Methodology for the Survey and Evaluation of Seismic Damage and Vulnerability Entailed by Structural Interventions on Masonry Buildings: Validation on the Town of Castelsantangelo sul Nera (MC), Italy. *Int. J. Archit. Herit.*, 1–26, 2020.
- [30] M.R. Valluzzi, L. Sbrogio, Y. Saretta, H. Wenliuhan, Seismic response of masonry buildings in historical centres struck by the 2016 Central Italy earthquake. Impact of building features on damage evaluation. *Int. J. Archit. Herit.* (in print).
- [31] V. Follador, M. Donà, P. Carpanese, F. da Porto, Fragility curves for Italian residential masonry buildings with retrofit interventions. *8th ECCOMAS Thematic Conference on Computational Methods in Structural Dynamics and Earthquake Engineering (COMPDYN 2021)*, Athens, Greece, June 27–30, 2021. (under review)
- [32] M. Stucchi, C. Meletti, V. Montaldo, Seismic hazard assessment (2003-2009) for the Italian building code. *Bulletin of the Seismological Society of America*, **101**(4), 1885-1911, 2011.
- [33] M. Di Ludovico, A. Prota, C. Moroni, Reconstruction process of damaged residential buildings outside historical centres after the L’Aquila earthquake: part I – “light damage” reconstruction. *Bulletin of Earthquake Engineering*, **15**, 667–692, 2017.
- [34] M. Di Ludovico, A. Prota, C. Moroni, Reconstruction process of damaged residential buildings outside historical centres after the L’Aquila earthquake: part II – “heavy damage” reconstruction. *Bulletin of Earthquake Engineering*, **15**, 693–729, 2017.
- [35] DEI, Prezzi informativi dell’edilizia, *DEI - Tipografia del genio civile*, 2019. (in italian)
- [36] M. Dolce, D. Di Bucci, Comparing recent Italian earthquakes. *Bulletin of Earthquake Engineering*, **15**(2), 497–533, 2017.
- [37] M. Donà, L. Bizzaro, F. Carturan, F. da Porto, Effects of business recovery strategies on seismic risk and cost-effectiveness of structural retrofitting for business enterprises. *Earthquake Spectra*, **35**(4), 1795–1819, 2019.

THE USE OF STICK-IT MODEL FOR EDP ASSESSMENT IN EXISTING RC INFILLED TYPOLOGIES

M. Gaetani d'Aragona¹, M. Polese¹, M. Di Ludovico¹, and A. Prota¹

¹ Department of Structures for Engineering and Architecture, University of Naples Federico II

Via Claudio 21, 80125, Naples, Italy

e-mail: {marco.gaetanidaragona, maria.polese, marco.diludovico, andrea.prota}@unina.it

Abstract

The estimation of expected seismic losses at regional scale represents a critical issue for the assessment of the seismic risk and for the evaluation of the seismic resilience of large communities. As a basic step, the assessment of economic losses requires the computation of the building performances in terms of engineering demand parameters such as interstorey drift ratios and peak floor accelerations in order to assess the distribution and the extent of the damage experienced by various building components. The Stick-IT model (Stick for Infilled frames Typologies) was recently proposed to predict the response, in terms of engineering demand parameters, for infilled RC building typologies. Stick-IT is a MDOF system consisting of a series of lumped masses connected by nonlinear shear link elements. The model parameters can be defined for building typologies starting from low level information that can be easily retrievable at the large scale via image-based processing techniques integrated with generic information about typical construction features, such as in plan dimensions, the number of stories or the percentage of infills openings and considering the infills consistency. This paper adopts the Stick-IT model to predict damage and expected losses for a set of RC infilled buildings located in L'Aquila town. The application shows the advantages and the potentiality of the proposed model when adopted for large scale loss assessments.

Keywords: nonlinear response history analysis; IDR; PFA; Stick model.

1 INTRODUCTION

The PEER framework [1] allows estimating the expected losses in the aftermath of damaging earthquakes involving a four-step procedure: hazard analysis, structural analysis, damage, and loss analysis. In this context, the structural analysis is required to calculate the building performances expressed in terms of engineering demand parameters (EDPs) such as inter-story drift ratios (IDRs) and peak floor accelerations (PFAs). The EDPs may be used to predict the distribution and the extent of the damage in structural, non-structural components and building contents and then, relying on suitable cost functions, are often adopted to quantify the economic losses.

At the building level, the most complete procedure to assess building structural performances consists of performing Nonlinear Response History Analyses (NRHA) on refined finite element models (e.g., [2]). However, the structural modeling and computational effort required for the analysis at the single building level are not suitable also for large-scale analyses. To overcome this issue, faster and simpler approaches are required. In this sense, different approaches were proposed in the last years relying on static analysis performed on refined [3] or simplified models [4]-[6], or on NRHAs performed on simplified models (e.g., shear models [7]). The latter models have been demonstrated to describe the non-linear characteristics and failure modes of multi-story buildings with sufficient accuracy both at the building scale and at the regional scale, enabling to capture the story-level damage concentration due to seismic loads [8]-[10]. Further, appropriate calibration of the simplified MDOF model, depending on specific features of the building typologies to be assessed, improves the accuracy of response prediction [7]. Recently, in Gaetani d'Aragona et al. [11] a simplified multi-degree of freedom (MDOF) model, named Stick-IT, was proposed to evaluate the response of building typologies representative of RC infilled moment resisting frames. The model was calibrated to represent the behavior of infilled Italian typologies and has been demonstrated to reliably predict the building response and direct economic losses when compared to more refined finite element models [12].

In Gaetani d'Aragona et al. [11] simplified formulas based on few geometrical and structural parameters are proposed to define the structural model. The formulations require assumptions in defining the infill consistency which may affect structural behavior and the assessment of repair costs [7]. The definition of these properties can be of difficult when dealing with the assessment of the behavior of a large building portfolio and need to be hypothesized on the basis of specific considerations based on construction techniques in force in the analyzed region also depending on the construction time. For this reason, in this paper, the impact of these assumptions on the assessment of repair costs is analyzed.

Following, the Stick-IT model is first briefly introduced. Next, the adopted methodology to evaluate expected seismic losses is described and an application of the model for L'Aquila town is presented.

2 STICK-IT FOR RAPID EDP ASSESSMENT

In Gaetani d'Aragona et al. [7], building typologies representative of RC infilled moment resisting frames are modeled with simplified Stick model (Stick-I), which is a MDOF Non-Linear Shear Model consisting of a series of masses lumped at the story level and connected in series by means of nonlinear shear springs; the Stick-I model is developed for each direction of the building (see Figure 1).

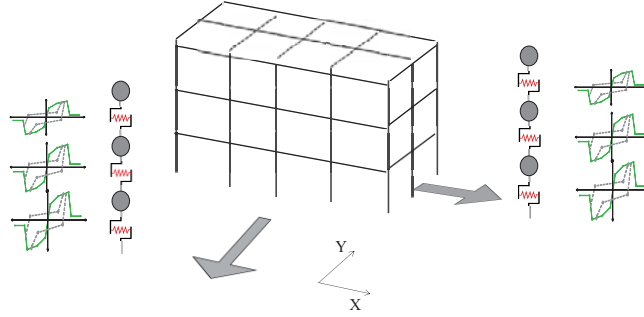


Figure 1: Simplified Stick model for infilled RC frames.

The story-level backbone of such spring is approximated by a four-linear backbone curve which can be defined based on 7 parameters (Figure 2). To simulate the hysteretic behavior, and in particular the pinched response and the strength and stiffness cyclic degradation of the story-level spring link element, the Pinching4 material available in OpenSees [13] is adopted. In general, such material requires the definition of 21 parameters governing the pinching response as well as stiffness and strength deterioration.

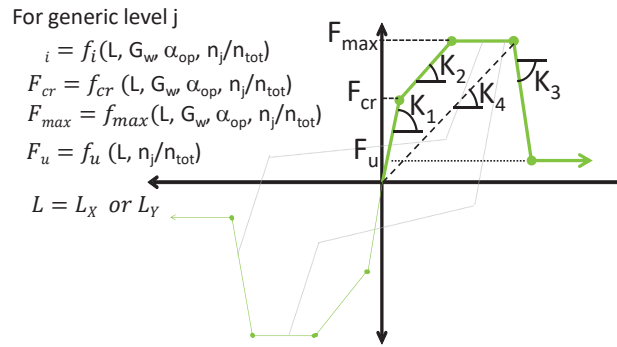


Figure 2: Definition of Stick-IT parameters for envelope curves.

In Gaetani d'Aragona et al. [11] an evolution of the stick model to predict the response of existing infilled RC typologies was introduced. The latter, denominated Stick-IT (i.e. Stick-I referred to a building Typology), is characterized by suitable parameters enabling to describe the backbone and hysteretic behavior at the generic story of the typology. In order to derive the story-level backbone and hysteretic parameters of Stick-IT, in [11] a regression study was performed on a large database, comprising 5632 Stick-I models. The database of Stick-I models was obtained with the following procedure: (a) assemble a large portfolio of building FE models with simulated design procedure; (b) determine the backbone (depending on 7 model parameters) for stick-I referring to longitudinal and transversal directions for all the building models in the generated portfolio; (c) perform calibration of the hysteretic behavior for stick-I model adopting a generic algorithm GA procedure and determine hysteretic model parameters (7 model parameters for the pinching4 material).

The regression study was finalized to describe the Stick-IT model as a function of few variables, mainly those ones that could be easily retrieved for large scale studies, e.g. from rapid on-site surveys or remote sensing procedures. As a result of the regression study performed in [11], given the building storey class n_s , the Stick-IT backbone curve at each story can be derived by the following parameters: dimension of the building in the analyzed direction ($L=L_x$ or L_y depending if longitudinal or transversal direction is considered), the normal-

ized storey number for the generic i^{th} level $n_{\text{nsi}} (=i/n_s)$ and the opening percentage α_{op} , representing the area of openings for the infills with respect to of the infill area for each panel. In addition, the infill elastic shear modulus G_w is considered to represent the infills consistency.

The model parameters for envelope curves are expressed with an exponential type formulation as in Eq. (1), that expresses the generic parameter $P_{b,i}$ of the backbone curve at the i^{th} storey:

$$P_{b,i} = a_1 + a_2 \cdot L^{a_3} \cdot G_w^{a_4} \cdot (1 - \alpha_{\text{op}})^{a_5} \cdot n_{\text{nsi}}^{a_6} \quad (1)$$

In Eq. (1) L is the dimension of the building in the analyzed direction ($L=L_x$ or L_y depending if longitudinal or transversal direction is considered), while other parameters are explained above.

Concerning the parameters defining the hysteretic behavior, a simplified approach was adopted in Gaetani d'Aragona et al. [11], assuming that the pinched behavior is symmetric in both the positive and the negative direction and neglecting the strength deterioration mode. This way the number of parameters defining the hysteretic behavior of the spring is limited to 3 pinching parameters and 4 degradation parameters depending on energy. Eq. (2) expresses the stiffness deterioration index (δk_i) as a function of n_{cyc} depending on two parameters g_{K2} and g_{K4} :

$$\delta k_i = g_{K2} (n_{\text{cyc}})^{g_{K4}} \leq g_{K_{\text{lim}}} \quad (2)$$

Similar expression can be adopted for deterioration of reloading stiffness. For further details, please refer to Gaetani d'Aragona et al. [11].

3 APPLICATION TO L'AQUILA TOWN

3.1 Building inventory

In the aftermath of L'Aquila earthquake, the Italian government fully funded the reconstruction process of damaged buildings. In Del Vecchio et al. [14] the repair costs for a database composed of 120 residential buildings damaged and repaired after L'Aquila earthquake is analyzed. The repair costs were defined and calculated, after suitable design, by practitioners during the reconstruction process. In this paper, the repair costs by Del Vecchio et al. [14] are adopted as a reference for comparison of repair cost predictions.

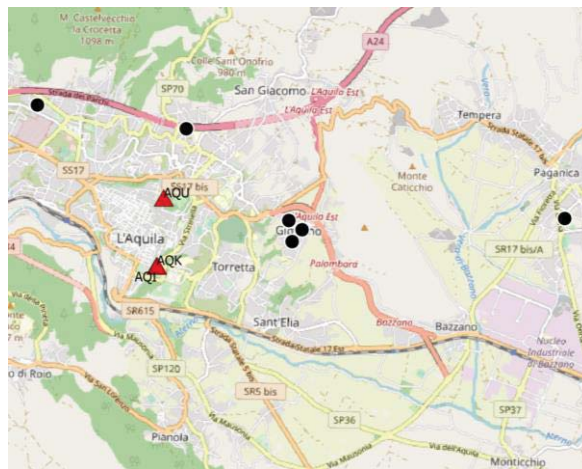


Figure 3: Location of selected buildings (black dot) and accelerometric stations (AQU, AQK).

Generally, damage and loss assessment of large building portfolios is carried by grouping buildings with similar characteristics (e.g., [15]). However, the method analyzed in this paper lend itself to be applied considering more specific building features as explained above.

For this application, a subset of 6 buildings from the database analyzed in Del Vecchio [14] was selected (see Figure 3). The buildings were selected to be close to the accelerometric station and to have approximately a rectangular shape in plan, to be representative typical height distributions in the town (3,4, and 5 stories). In Table 1, the main geometrical features for the analyzed buildings are reported, including the angle of orientation with respect to North, the number of stories (n_s), the Surface Area (SA), and the longitudinal and transverse building dimensions (L_x , L_y).

id	Angle to N(°)	n_s	SA (m ²)	L_x (m)	L_y (m)
1	5	5	274	23.60	11.60
2	30	5	256	18.00	14.20
3	45	4	90	12.70	7.10
4	45	4	170	17.00	10.00
5	30	3	210	20.40	10.30
6	35	3	193	16.60	11.65

Table 1: Geometry of the selected buildings.

3.2 Seismic hazard

The 2009 L'Aquila earthquake was characterized by a magnitude $M_w=6.3$ and a fault-normal mechanism at about 9 km depth and an epicentral distance from L'Aquila city of about 6 km. For the analysis, the acceleration time-histories recorded for the L'Aquila earthquake by two different accelerometric stations (AQU, AQK) located in proximity with the analyzed buildings were analyzed. Both ground motion records were recorded on soil class B, with a PGA ranging between 0.25-0.35g, and were extracted from the Italian Accelerometric Archive (ITACA 3.1, <http://itaca.mi.ingv.it/>). Figure 4 represents the 5%-damped Pseudo-acceleration spectrum for both records in the N-S and E-W directions.

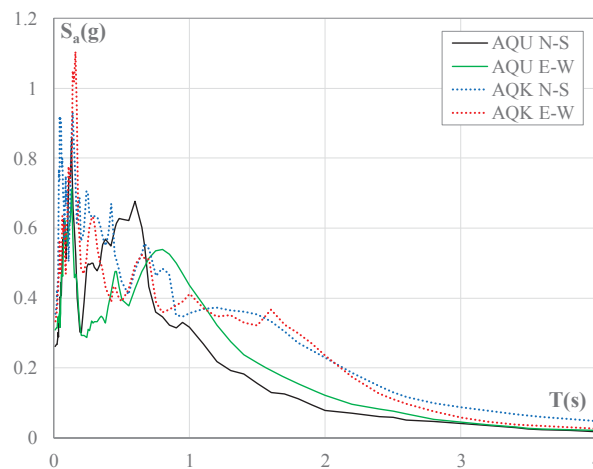


Figure 4: 5%-damped Pseudo-acceleration spectrum for AQU and AQK ground motion records.

The horizontal components of the selected records were suitably scaled in order to account for the local amplification at the building site, and rotated according to the orientation of the principal directions of the structure [16].

3.3 Model and Structural Analysis

The structural analysis is performed via NTHA for each selected building, considering the simplified Stick-IT model generated according to the procedure described in §2 and by adopting median parameters for regression parameters. The building geometry (i.e., approximate longitudinal and transversal dimensions as well as number of stories) necessary to retrieve model features can be obtained with rapid image-based processing techniques (e.g., [17]-[18]). However, in this study, such features were derived from the original building database [14]. The analyzed buildings are assumed approximately regular both in plan and in elevation. Finally, the storey mass is obtained multiplying the surface area $SA(=L_x \cdot L_y)$ by unit load of 1.1 tons/m². For the upper story the unit load is assumed equal to 0.9 tons/m².

The infill panel consistency, represented by the infill thickness, shear modulus, and opening percentage are considered as a variable parameter to quantify its influence on the building response and assessment of repair costs. To this end, three different thicknesses for the infill panels are considered, 20cm-24cm-30cm, corresponding to weak, medium and strong infill, respectively, according to Hak et al. [19]. To simulate different infill thicknesses, the procedure proposed in [12] is adopted. The opening percentage is considered constant and equal to 20% of the area of the infill panel. The adoption of different opening percentages along the height also significantly influences the building response and the distribution of lateral deformations (e.g., [21]-[22]). However, this effect is not investigated in this study.

For each one of the two ground motion records in §3.2, each model was analyzed by rotating and scaling the ground motion components in the two separate directions (longitudinal and transverse).

The Stick-IT model is able to predict the intensity and distribution of Engineering Demand Parameters such as Interstory Drift Ratios (IDRs) and Peak Floor Accelerations (PFAs). However, in this study only IDRs are evaluated, since only damage experienced by drift-sensitive components is considered.

As an example, Figure 5 depicts the maximum IDR profiles obtained for the Stick-IT model of the building with 'id 1' (see Table 1) subjected to the two records AQU and AQR and analyzed in the two orthogonal directions. As an assumption, the longitudinal direction is the direction of maximum extension of the building in plan. For this reason, due to the largest amount of infill panels, it represents the direction characterized by higher capacity to withstand to lateral loads, and with lower deformability. In particular, due to the lower excursion in the nonlinear range for the longitudinal direction, the IDRs for AQU and AQR are much closer than those obtained in the transverse direction, where the two records may lead to significantly different IDR (due to concentration of damage) and the maximum IDR may be localized in a different story.

In particular, the Figure 5(a)-(c) depicts the shape of IDR for varying infill thicknesses. Obviously, the higher the infill panel thickness, the lower the maximum experienced IDR. However, while for the transverse direction this effect is evident, in the longitudinal direction this effect is negligible. Further, by keeping as a reference the panels with $t_w=24\text{cm}$, the maximum scatter between different thicknesses is obtained for the AQR record in the transverse direction, at the third story, where a scatter of 76% in IDR value is achieved. The effect of infill thickness produces a significant variation of IDR [22], and thus of the potential damage experienced by drift-sensitive components.

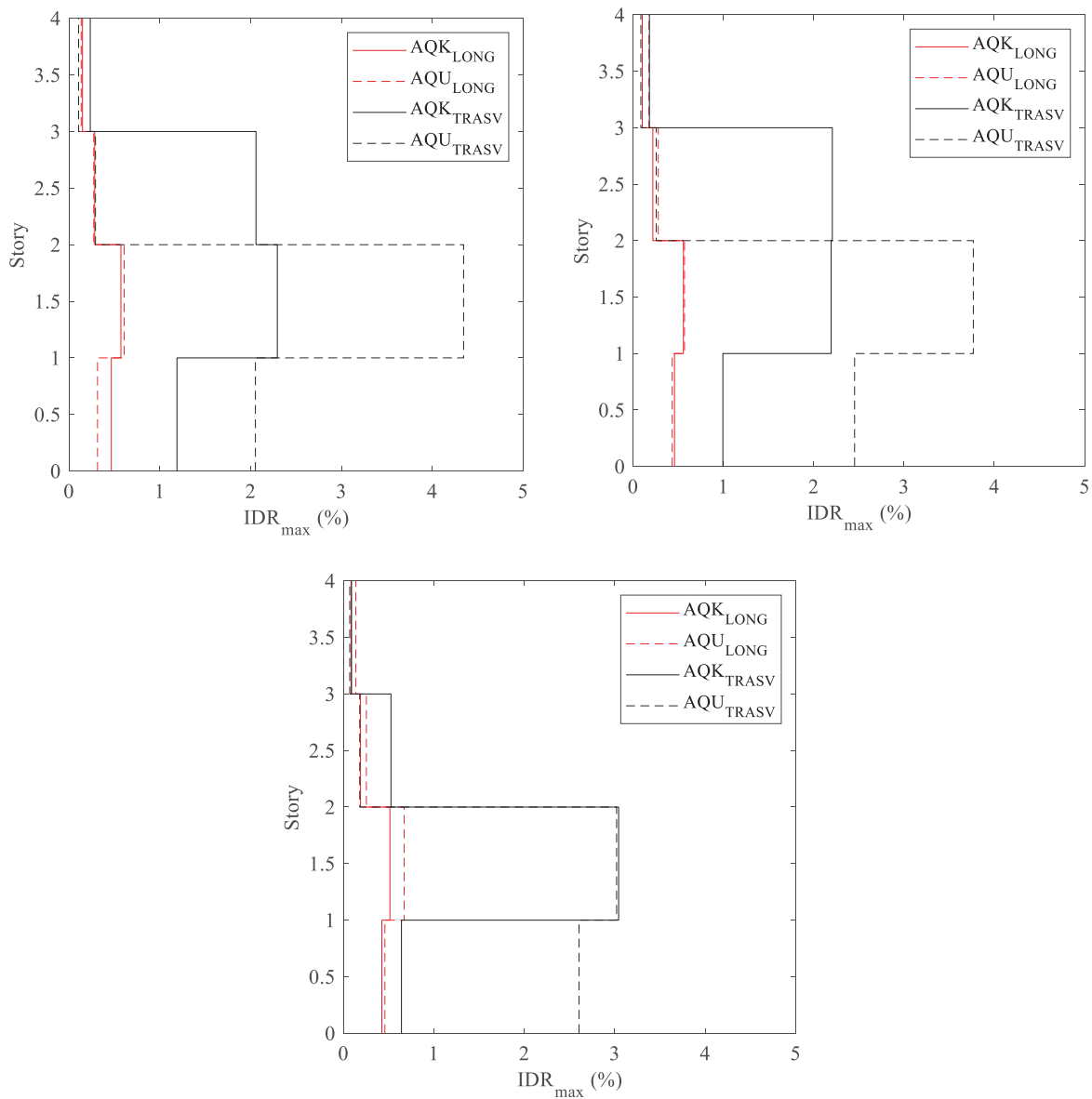


Figure 5: Distribution of maximum IDRs for (a) $t_w=20\text{cm}$, (b) $t_w=24\text{cm}$ and (c) $t_w=30\text{cm}$ for building 'id 1'.

3.4 Damage and Loss assessment

In this section the damage and loss assessment is performed adopting global indicators (i.e., EDPs) as a proxy for damage prediction. To this end, suitable EDP-dependent damage functions for both structural and nonstructural components specifically calibrated for typical Italian standard components need to be adopted. For residential buildings the largest amount of repair costs mainly depends on damage to infills and partitions [14]. For this reason, this paper limits the assessment of repair costs only referring to the costs related to repair of infill, partitions and integrated components (i.e., plumbing and electrical system, doors and windows).

With reference to the infill walls and interior partitions, Del Gaudio et al. [23] recently proposed damage fragility functions for typical Italian hollow clay infills, with and without

openings, based on the analysis of a large experimental dataset. The proposed values were adopted to capture the observed damage experienced by exterior and interior infills at different stories.

Direct losses associated to infills, partitions and integrated components are calculated by adopting the cost function developed in Del Vecchio et al. [14] for Italian standards. The functions include the cost of all the repair actions needed to restore the building to its pre-event conditions depending on the presence/absence of openings, the damage state experienced, and the extension of the damaged components.

The extent of damageable components need to be quantified based on a simulated architectural layout that can be obtained based on the procedure reported in [12]. In particular, the procedure assumes that infill wall panels extend along the whole exterior perimeter of the building, while partitions are located along each bay in each building direction. Further, it is considered that the 50% of exterior infill panels has openings while the 50% has no openings, and interior partitions are always classified as elements with openings. The simulation of the architectural layout, significantly influences the prediction of repair costs, while it has no influence on the building structural response. Thus, in this section the extent of partitions will be also varied in order to quantify the influence of this assumption. In particular, it will be considered the 100% of the extension of the simulated layout and then, the 50% and the 150% of the extension obtained for interior partitions. For instance 50% means that only the one half the bays in the longitudinal and transverse direction of the building, the number and extension of which depends on the simulated design, are filled with partitions. Finally 150% of the extension of the simulated layout means that there is the 50% more of partitions with respect to those simulated. Instead, the extension of perimeter infills is considered invariant.

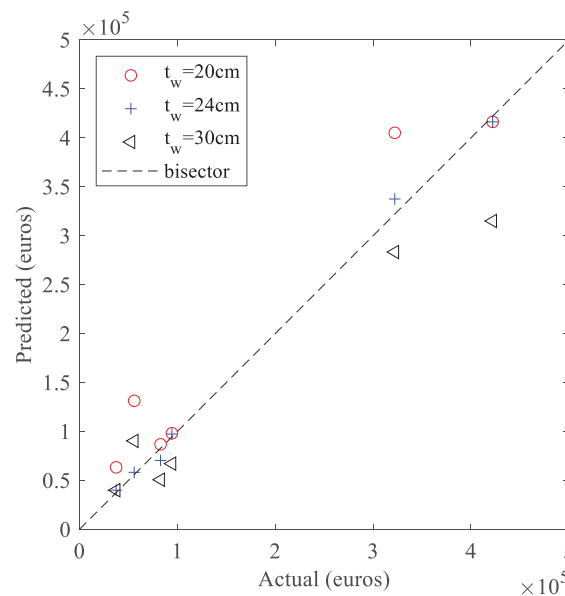


Figure 6: Actual vs Predicted repair costs to infill panels, partitions and integrated components for $t_w=20\text{cm}$ - 24cm - 30cm .

The damage level was calculated by adopting as input parameters the IDR for each story and direction obtained in §3.3. The maximum repair cost between those obtained considering the records AQU and AQK is assumed as a reference. By summing up the repair cost between each story and direction, the total repair cost for infills, partitions and integrated components is calculated. For each story, it is assumed that the level of damage for the generic type of

component (i.e., infill/partition with openings or without openings) is the same throughout the story, but may be different between orthogonal directions. Figure 6 depicts the comparison between the actual and the predicted repair cost obtained by adopting different infill wall thicknesses (and 100% of the extension of infill/partitions obtained via simulated architectural layout). It can be noted that the prediction is in general acceptable, and it is most approximated when adopting $t_w=24\text{cm}$.

In particular, for $t_w=20\text{cm}$ the mean (median) ratio between the predicted and the actual repair cost for infills, partitions and integrated components is 1.39 (1.15). For $t_w=24\text{cm}$ these ratios reduces to 1.00 (1.04), and for $t_w=30\text{cm}$ to 0.93 (0.81). The maximum scatter between predicted and actual repair cost is achieved for $t_w=20\text{cm}$ and is of 134%. Thus, the mean consistency for infill panel seems to lead to more reliable predictions for repair costs. However, this assumption should be validated on a larger building database.

Another assumption regards the extension of damageable components. This is expected to be an influential parameter in terms of estimation of repair cost, characterized by a larger dispersion due to extreme variability of the possible configurations of the interior architectural layout. Obviously, the incidence on the total repair cost due to the different architectural layout of interior partitions mainly depends on the surface area of the building.

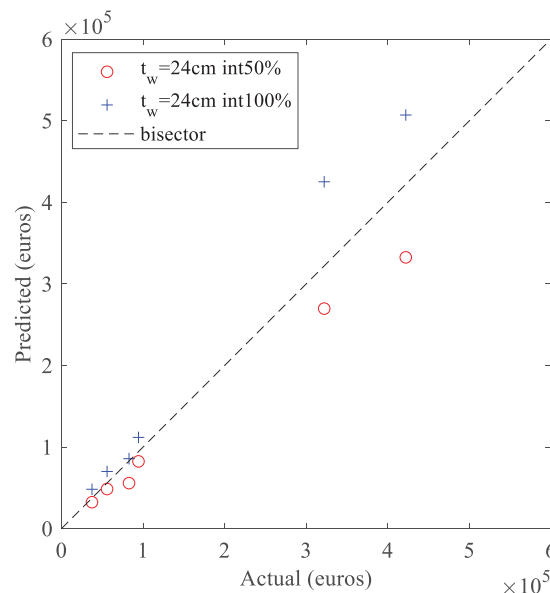


Figure 7: Actual vs Predicted repair costs to infill panels, partitions and integrated components for $t_w=24\text{cm}$ and considering 50% and 150% of simulated architectural layout for interior partitions.

As evidenced in Figure 7, which depicts the comparison between the actual and predicted repair cost considering different extensions for interior partitions (architectural layout), accounting for lower extension leads to underprediction or repair costs, while larger extension to overprediction of repair costs. In this case, by adopting the IDRs obtained considering the mean infill consistency for the model, the adoption of 50% of initial simulation of partition layout leads to a median (and median) underestimation of repair costs with respect to the actual ones of 15% and to an overestimation of 23% if a 150% of the initial layout is adopted, suggesting that the original simulated layout leads to the best prediction of repair costs. Finally, the maximum scatter between predicted and actual repair cost of $\pm 30\%$ is obtained for the single building.

4 CONCLUSIONS

This study presents the first comparisons of a simplified loss assessment procedure to evaluate expected seismic losses at the large scale.

The procedure is based on the adoption of a simplified multi degree of freedom MDOF Stick-IT model introduced in [11], which allows to rapidly calculate the performance of infilled RC buildings in terms of engineering demand parameters EDP such as interstory drift ratios, IDRs, and peak floor accelerations, PFAs, using Nonlinear Response History Analyses.

The loss assessment procedure was tested on a set of 6 buildings damaged and repaired after the 2009 L'Aquila earthquake. Firstly, main building features such as in plan dimensions and story number were retrieved, and a building inventory defined. Then, the Stick-IT model were defined for each one of the considered building. Next, after rotating and scaling two ground motion records for the L'Aquila earthquake, NRHA were performed by adopting the Stick-IT models. The response for each typology was expressed in terms of maximum IDR along building height. Finally, by adopting suitable cost functions, the repair costs for infills, partitions and integrated components are calculated and compared to the actual repair costs for these components.

In this study the validity of some assumptions to be adopted for large scale assessment purposes were tested. Firstly, the model requires the definition of the consistency of infill panels that contribute to the resistance and deformability against lateral loads. While this parameter is easy to define at the building level, it is of difficult definition for a large building portfolio for which only low-level information are available. By considering three possible consistencies according to the technical literature (weak, medium and strong), it has been found that the 'mean' consistency for infill panels generally leads to the best prediction for repair costs of infill, partitions and integrated components, while the other generally leads to an overestimation or underestimation of repair costs due to a different prediction of lateral deformations that is about 40% in terms of mean error for the considered building set, while a maximum scatter of 135% may be achieved for the single building.

Further, also the simulated design procedure adopted to quantify of the extension of damageable components was tested. This is characterized by a large dispersion due to extreme variability of the possible configurations of the interior architectural layout. The influence of this quantification alter the prediction of repair cost of about 20% in mean terms for the considered building set, while it led to a maximum scatter of about 30% for the single building. However, it is expected that the influence of this parameter is conditioned on the in plane shape ratio and the surface area of the building, and further studies are required to quantify the effect of these hypotheses.

In this proposed study, median values for definition of Stick-IT model parameters as proposed in [11] were employed. However, due to the large amount of uncertainties in the Stick-IT model definition, a fully probabilistic framework application would allow a more realistic assessment of repair costs. Moreover, time-based assessment of expected seismic losses could be performed by repeating the evaluation at various level of earthquake intensity according to the seismic hazard of the area. Future studies will address these issues.

Despite this application is limited to the assessment of infills, it shows the possibility to easily implement the proposed methodology for rapid estimation of expected losses at the large scale. Other cost-functions could be adopted, suitably accounting, e.g. for costs of acceleration sensitive components.

REFERENCES

- [1] Porter KA. An overview of PEER's performance-based earthquake engineering methodology. Proceedings of 9th International Conference on Applications of Statistics and Probability in Civil Engineering, 2003.
- [2] Gaetani d'Aragona M, Polese M, Prota A. Effect of Masonry Infill Constitutive Law on the Global Response of Infilled RC Buildings, *Buildings*; 11(2), 57; <https://doi.org/10.3390/buildings11020057>.
- [3] Gaetani d'Aragona M, Polese M, Di Ludovico M, Prota A. Simplified assessment of expected seismic losses for as built and retrofitted RC buildings, proceedings of COMPDYN 2017 6th ECCOMAS Thematic Conference on Computational Methods in Structural Dynamics and Earthquake Engineering, Rhodes Island, Greece, 15–17 June 2017.
- [4] Gaetani d'Aragona M, Polese M, Cosenza E, Prota A. Simplified Assessment of Maximum Interstory Drift for RC buildings with Irregular Infills Distribution Along the Height, *Bull Earthquake Engineering*, 2019; 17(2), 707-736. <https://dx.doi.org/10.1007/s10518-018-0473-y>.
- [5] Gaetani d'Aragona M, Polese M, Di Ludovico M, Prota A. Seismic vulnerability for RC infilled frames: Simplified evaluation for as-built and retrofitted building typologies. *Buildings*, 2018; 8(10): 137. <https://doi.org/10.3390/buildings8100137>.
- [6] Polese M, Gaetani d'Aragona M, Di Ludovico M, Prota A. Sustainable selective mitigation interventions towards effective earthquake risk reduction at the community scale. *Sustainability*, 2018; 10, 2894. <https://doi.org/10.3390/su10082894>.
- [7] Gaetani d'Aragona, M, Polese, M, Prota, A. Simplified model calibration for dynamic response assessment of infilled RC buildings. In Proceedings of the 7th ECCOMAS Thematic Conference on Computational Methods in Structural Dynamics and Earthquake Engineering, Crete, Greece, 24-26 June 2019.
- [8] Xiong C, Lu XZ, Lin XC, Xu Z, Ye LP. Parameter determination and damage assessment for THA-based regional seismic damage prediction of multi-story buildings. *J. Earthq. Eng.* 2017; 21(3): 461–485.
- [9] Lu XZ, Lu B, Xu Z, Xiong C, & Zeng X. High performance computing for regional building seismic damage simulation. *Procedia Engineering*. 2017; 198: 836-844.
- [10] Dao ND, Ryan KL, & Nguyen - Van H. Evaluating simplified models in predicting global seismic responses of a shake table – test building isolated by triple friction pendulum bearings. *Earthquake Engineering & Structural Dynamics*. 2019; 48(6):594-610.
- [11] Gaetani d'Aragona, M, Polese, M, Prota, A. Stick-It: A simplified model for rapid estimation of IDR and PFA for existing low-rise symmetric infilled RC building typologies. *Engineering Structures*, 2020; 223, 111182. <https://doi.org/10.1016/j.engstruct.2020.111182>.
- [12] Gaetani d'Aragona, M, Polese, M, Di Ludovico, M, Prota, A. The use of Stick-It model for the prediction of direct economic losses. *Earthquake Engineering and Structural Dynamics*, 2021. <https://doi.org/10.1002/eqe.3429>.

- [13] OpenSees. Open system for earthquake engineering simulation OpenSees framework-Version 3.2.2. Pacific Earthquake Engineering Research Center, Univ. of California, Berkeley, 2021.
- [14] Del Vecchio C, Di Ludovico M, & Prota A. Repair costs of reinforced concrete building components: from actual data analysis to calibrated consequence functions. *Earthquake Spectra*, 2020; 36(1):353–377-
- [15] Polese M, Di Ludovico M, Gaetani d'Aragona M, Prota A, Manfredi G. Regional vulnerability and risk assessment accounting for local building typologies, *International Journal of Disaster Risk Reduction*, 2020; 43:101400. <https://doi.org/10.1016/j.ijdrr.2019.101400>
- [16] Somerville P. Characterizing near fault ground motion for the design and evaluation of bridges, in *Proceedings of the Third National Seismic Conference and Workshop on Bridges and Highways* 01/2002, 28 April–1 May 2002, Portland, OR.
- [17] Gaetani d'Aragona M, Polese M, Tocchi G, Prota A. Application of a simplified nonlinear model to predict seismic losses for infilled RC buildings at the territorial scale. In *Proceedings of the 17th Conference on Earthquake Engineering*, Sendai, Japan, September 13th to 18th 2020.
- [18] Polese M, Gaetani d'Aragona M. Seismic event scenarios, pp 67-110, in *Study of the seismic risk scenarios in support of Civil Protection Plans for the town of Pozzuoli*, DoppiaVoce ed. (in Italian).
- [19] Hak S, Morandi P, Magenes G, & Sullivan TJ. Damage control for clay masonry infills in the design of RC frame structures. *Journal of Earthquake Engineering*, 2012; 16(1): 1-35.
- [20] Gaetani d'Aragona M, Polese M, Cosenza E, Prota A. Simplified Assessment of Maximum Interstory Drift for RC Buildings with Irregular Infills Distribution Along the Height, *Bull Earthquake Engineering*, 2019; 17(2), 707-736. <https://dx.doi.org/10.1007/s10518-018-0473-y>.
- [21] Gaetani d'Aragona M, Polese M, Prota A. Influence factors for the assessment of maximum lateral seismic deformations in Italian multistorey RC buildings, *proceed-ings of COMPDYN 2017 6th ECCOMAS Thematic Conference on Computational Methods in Structural Dynamics and Earthquake Engineering*, Rhodes Island, Greece, 15–17 June 2017.
- [22] Gaetani d'Aragona M, Polese M, Prota A. Effect of Masonry Infill Constitutive Law on the Global Response of Infilled RC Buildings. *Buildings*, 2021; 11(2), 57; <https://doi.org/10.3390/buildings11020057>
- [23] Del Gaudio C, De Risi MT, Ricci P, & Verderame GM. Empirical drift-fragility functions and loss estimation for infills in reinforced concrete frames under seismic loading. *Bulletin of Earthquake Engineering*, 2019; 17(3):1285-1330.

APPLICATION OF THE EMPIRICAL PREDICTIVE DAMAGE MODEL OF HISTORICAL CHURCHES

C. Canuti¹, M. Morici¹, A. Dall'Asta¹, G. Leoni¹

¹SAAD, University of Camerino
Viale della Rimembranza 9, 63100, Ascoli Piceno, Italy
{claudia.canuti, michele.morici, andrea.dallasta, graziano.leoni}@unicam.it

Abstract

Strong seismic events are the main cause of serious damage to cultural heritage, especially to historical churches characterized by a lack of efficient resisting mechanisms and by high vulnerability due to their structural systems peculiarities. Their poor seismic performance is demonstrated by the recurrence of specific seismic damage mechanisms. In this paper, an empirical probabilistic damage predictive model recently presented in the literature is used to provide a scenario dependent risk assessment in a seismic prone area in Italy. In this response model, the damage is expressed by a continuous index and the seismic action is described by a scalar intensity measure. For the illustrative case study, a sample of churches falling into a limited area of Marche Region, hit by the Central Italy 2016 seismic sequence, has been chosen. The sample includes all the historical churches belonging to the Archdiocese of Camerino-San Severino. The damage scenario following a seismic event of magnitude 5.8, generated by the Camerino fault, has been evaluated to illustrate the capability of this model in the prediction of post-earthquake situation. Risk maps obtained by means of the method presented in the paper, can provide a notable support to the organization of post-event emergency actions and to the planning of preventive actions for the risk mitigation.

Keywords: Historical churches; Seismic damage; Predictive empirical model; Shear-wave velocity.

1 INTRODUCTION

The Italian territory is popular for its high number of historical churches constituting a very dominant part of the cultural heritage for the country. Unfortunately, most of the Italian territory is characterized by high seismicity and the effects of seismic events on the cultural heritage may be destructive, as demonstrated over the last years by seismic sequences, such as Irpinia earthquake (1980), Umbria Marche earthquake (1997), Molise earthquake (2002), L'Aquila earthquake (2009), Emilia Romagna earthquake (2012), Central Italy seismic sequence (2016).

Churches are characterized by structural and typological vulnerabilities higher than vulnerabilities of ordinary masonry buildings [1]. This bad seismic performance is caused by specific architectural configurations, such as large halls, absence of internal diaphragms, and presence of vaults and arches.

Studies carried out after seismic events, highlighted that the seismic response of churches is featured by a set of macro-elements, such as façade, transept, nave, apse, characterized by independent dynamic behaviors [2]; this is also confirmed by different analytical studies on the vulnerability assessment of single churches (e.g. [3-5]) and of groups of churches (e.g. [6-8]). In addition, the analysis of the observed damage after past seismic events, such as the Umbria-Marche 1997 earthquake [9-11], the Molise 2002 earthquake [12], L'Aquila 2009 earthquake [13-15], the Emilia 2012 earthquake [16,17], and Central Italy 2016 seismic sequence [18-23] demonstrated that damage mechanisms have constant characteristics, in spite of the uniqueness of each structure.

Starting from the damage observed after the seismic events, it is possible to define empirical predictive models relating damage with intensity measure. In literature, studies on this topic provided statistical analyses of the damages and models based on a discrete description of damage (damage limit states) [10, 13, 15, 18, 21, 23, 24, 25, 26].

Moreover, thanks to the enhancement of the seismographic network in recent years, recorded ground motions allow to develop more accurate relationships between ground motion intensity measure and observed damage. Indeed, recent works avoided the approximate description provided by macro-seismic scales and preferred a description based on objective measures of the ground motion, such as the Peak Ground Acceleration (PGA) [18, 21, 23, 26].

A probabilistic response model based on the analysis of data coming from post-earthquake surveys of historical churches has been defined in [27]. This empirical probabilistic damage model relates the measure of the ground motion intensity to the overall damage index, defined in a continuous range.

In this paper, an application of this predictive probabilistic damage model has been developed, considering a strong event generated by the main local seismogenetic source that struck 514 historical churches (Archdiocese of Camerino-San Severino) located in this seismic prone area. A damage scenario following an event of magnitude 5.8 generated by the Camerino fault has been considered and the intensity measure at the site of each church has been evaluated using the Ground Motion Prediction Equations of Sabetta and Pugliese [28]. In addition, the effects of local site amplification due to soil type is taken into account by means of the specific values of the time-averaged shear-wave velocity $V_{s,30}$. The application depicts the potentialities of the model in the prediction of post-earthquake damage scenarios model, and the potential use of this risk assessment in the decision-making process by simulating a problem often arising in the post-event emergency phase, regarding the selection of those historical churches that may have suffered the highest damage levels.

2 EMPIRICAL DAMAGE PROBABILISTIC MODEL

In this section, a brief introduction of the damage probabilistic model proposed by Morici et al. [27] and used in the following, is reported.

The model assumes that the damage index is a continuous random variable D , and the values d are in the domain $[0,1]$ while the seismic intensity is described by a positive scalar random variable I , in the domain $i \in (0, \infty)$. The boundary value $d = 0$ represents the case of marginal damage while $d = 1$ represents the case of collapsed church.

The probability to observe a damage level lower than an assigned value d , given the seismic intensity, defines the system response, described by the following Cumulative Density Function (CDF)

$$F_{D|I}(d|i) = P[D < d|i] \quad (1)$$

where $d \in [0,1]$. The conditional CDF of damage, given i , can be expressed in the form:

$$F_{D|I}(d|i) = F_0(i)H(d) + (1 - F_0(i) - F_1(i))F_{D|I}^*(d|i) + F_1(i)H(d-1) \quad (2)$$

since the expected conditional Probability Density Function (PDF) is expressed by a continuous function in the open interval $(0,1)$, and discontinuities are awaited at the boundaries $d = 0$ (no damage) and $d = 1$ (collapse).

In Equation 2, $F_0(i)$ provides the probability of observing $d = 0$, $F_1(i)$ the probability of observing a damage $d = 1$, and the function $F_{D|I}^*(d|i; \Theta_d)$ is a conditional CDF describing the distribution of damage probability for the range $0 < d < 1$. $H(x)$ is the Heaviside step function, such that $H(x) = 1$ for $x \geq 0$ and it is 0 elsewhere.

The associated conditional PDF has the form

$$f_{D|I}(d|i) = F_0(i)\delta(d) + (1 - F_0(i) - F_1(i))f_{D|I}^*(d|i) + F_1(i)\delta(d-1) \quad (3)$$

where δ is the delta Dirac function that expresses the derivative of the Heaviside function, while $f_{D|I}^*(d|i)$ is the derivative of $F_{D|I}^*(d|i)$ with respect to d . Figure 1 shows the conditional CDF $F_{D|I}(d|i)$ and PDF $f_{D|I}(d|i)$ adopted in the model.

The functions $F_0(i; \Theta_0)$ and $F_1(i; \Theta_1)$ are selected from the exponential family according with the available data and model discussed in [27]. In particular, the functions assume the forms $F_0(i) = e^{-6.32i}$ and $F_1(i) = 1 - e^{-0.076i}$. The conditional PDF $f_{D|I}^*(d|i; \Theta_d)$ consists of a combination of two Exponential Distribution Functions (EDF), $f_{D|I}^*(d|i) = \frac{1}{A(i)} \left(e^{-(4.9111-9.2474i)d} - e^{-(4.9111-9.2474i)} \right) \left(e^{-(4.5176+12.4867i)(1-d)} - e^{-(4.5176+12.4867i)} \right)$ where the

term $A(i)$ is a normalization coefficient $A(i) = \int_0^1 f_{D|I}^*(d|i) dd$. Finally, in the model, the measurement of the seismic intensity is described by means of the Peak Ground Acceleration (PGA).

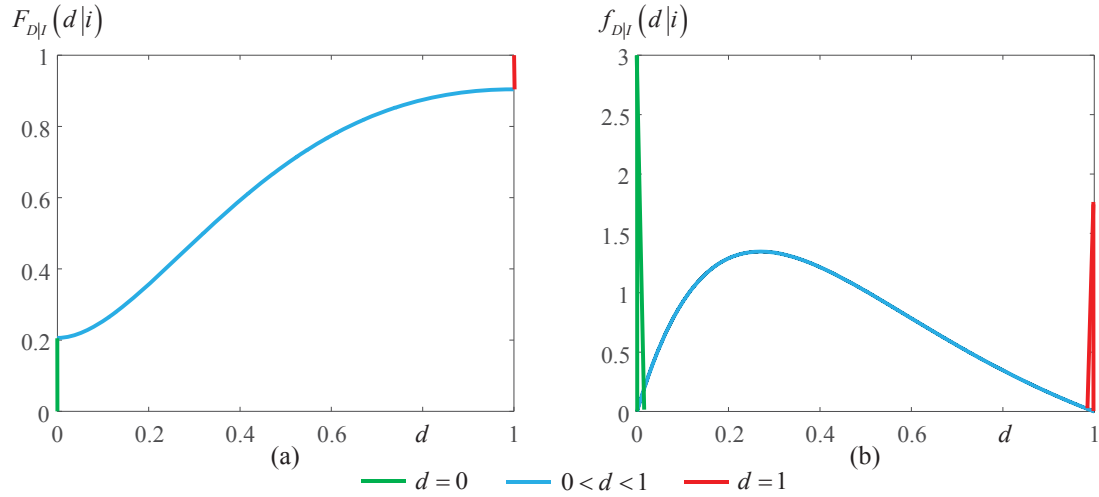


Figure 1: (a) Conditional CDF and (b) conditional PDF assumed in the [27] model.

3 APPLICATION OF THE PROBABILISTIC DAMAGE MODEL

3.1 Seismic scenario

In this paragraph, the evaluation of a damage scenario is presented, the Camerino fault has been considered as the seismic source and the damage expected in the set of historical churches belonging to Archdiocese of Camerino-San Severino, has been evaluated.

The Fault is located to a depth of 9-15 km (Figure 2b) and it is characterized by a potential magnitude $M_w=5.8$, testified by the seismic event of 1799 that had a complex, and probably multiple, source that produced two separate areas of maximum damage [29]. The fault belongs to the Central Apennines fault system, where the active faults consist of arrays of distinct overlapping segments which may be unconnected or linked into a single continuous fault surface [30] as illustrated in Figure 2c. In addition, unconnected adjacent faults may interact each other through their stress fields, activating different earthquake sequences [30]. However, according with [31], it is possible to assume that the surface faults, belonging to each seismogenic zone responsible for generating single seismic events with multiple ruptures, are the surface manifestations of earthquake-related deformation.

Figure 2a reports the geographic location of Camerino fault, and Figure 2b shows the distribution of the historical and recent seismic activity of the region and the areas mainly damaged after the event of 1799, identified with light blue rectangles [29]. Finally, Figure 2c displays the Central Apennines Fault System where measured active surface faults and related deep seismogenic structures are also shown [30].

The distribution of intensity measure $f_I(i)$ in terms of PGA, given the epicentral distance r and the magnitude M , is evaluated by using Ambraseys et al. Ground Motion Prediction Equation (GMPE) [28] that assumes the form

$$\log_{10}(I) = C_1 + C_2 M_S + C_4 \log_{10} \rho + C_A S_A + C_S S_S + \varepsilon(\sigma) \quad (4)$$

where $\varepsilon(\sigma)$ is a 0-mean Gaussian random variable with standard deviation σ that represent the inter-event residual, S_A and S_S are dummy variables depending on superficial soil category (rock, stiff, soft and very soft soil), $\rho = \sqrt{r^2 + h_0^2}$ contains the epicentral distance r and the fictitious depth h , and C_1, C_2, C_4, C_A, C_S are the model constants.

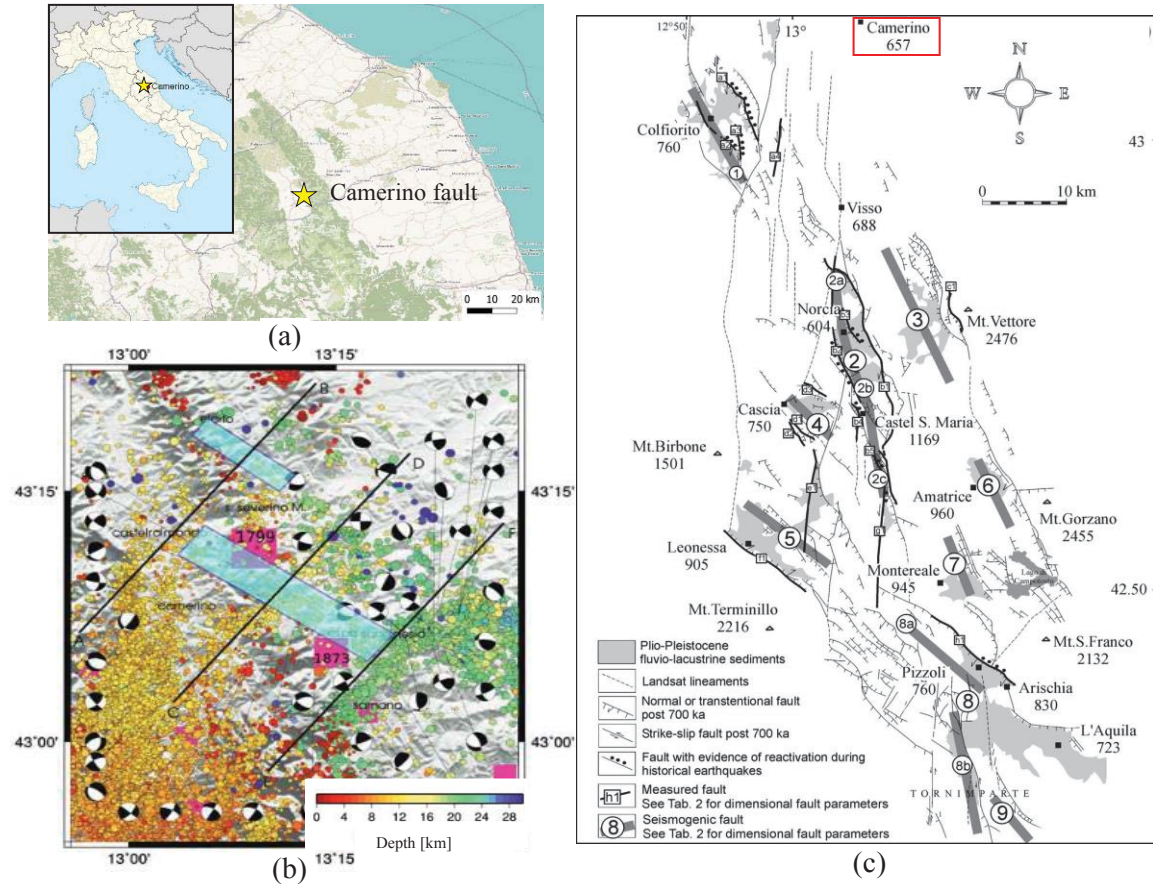


Figure 2: (a) Geographic location of Camerino fault; (b) Distribution of the historical and recent seismicity of the area with the areas mainly damaged after the 1799 earthquake [29]; (c) the Central Apennines Fault System [30].

In this study, parameters of the Eq. (4) are evaluated from the work [28] and the following values are assumed: $C_1 = -1.48$, $C_2 = 0.266$, $C_4 = -0.922$, $C_A = 0.117$, $C_S = 0.124$ and $h_0 = 3.5$, while the standard deviation of ε is equal to 0.25. The dummy variables S_A and S_S refer to the site classification: for $V_{s,30} < 180 \text{ m/s}$, $S_A = 0$ and $S_S = 1$ (very soft soil), for $180 \text{ m/s} \leq V_{s,30} < 360 \text{ m/s}$, $S_A = 0$ and $S_S = 1$ (soft soil), for $360 \text{ m/s} \leq V_{s,30} < 750 \text{ m/s}$, $S_A = 1$ and $S_S = 0$ (stiff soil), and for $V_{s,30} > 750 \text{ m/s}$, $S_A = 0$ and $S_S = 0$ (rock).

The possible effects of local amplification caused by the local geology of the site and identified by the category of soil, are evaluated by means of the $V_{s,30}$ parameter. The $V_{s,30}$ value represents the time-averaged shear-wave velocity to 30 m depth, and it is representative of the soil deformability. The specific $V_{s,30}$ of each church site has been selected on the basis of the studies of USGS [32-33].

Figure 3 shows the distribution of the $V_{s,30}$ at each church site derived from the USGS $V_{s,30}$ Map Viewer. The table reports the number of historical churches placed in sites with different range of $V_{s,30}$. Figure 4a shows the distribution of the mean value of intensity measure for each k^{th} church ($k = 1, \dots, 514$) where the index has been assigned after the churches have been ordered according to the expected intensity measure. Figure 4b reports the PDF of the intensity $f_i^k(i)$ expected at each k^{th} church, considering their epicentral distance and the relevant $V_{s,30}$.

It can be observed that the seismic intensity is mainly related to the epicentral distance while the local amplification related to $V_{s,30}$ plays a secondary role.

The distribution of damage can be evaluated by combining the damage model with the distribution of seismic intensity:

$$F_D^k(d) = \int_{\mathbb{R}^+} F_D(d) f_I^k(i) di \quad (5)$$

where $F_D^k(d)$ is the CDF of the damage relative to the k^{th} church.

Figure 5 reports the CDF $F_D^k(d)$ and the related PDF $f_D^k(d)$ of damage for each church. It can be noticed that the probability of observing undamaged churches ($d = 0$) increases with the reduction of the seismic intensity.

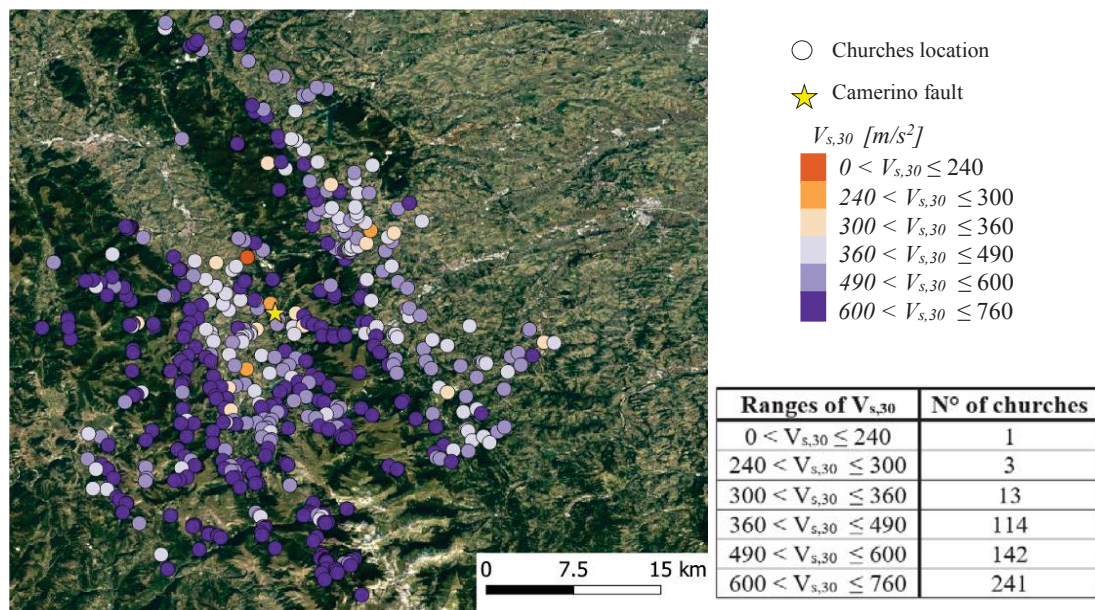


Figure 3: $V_{s,30}$ distribution over the territory for the churches of the Archdiocese of Camerino San-Severino.

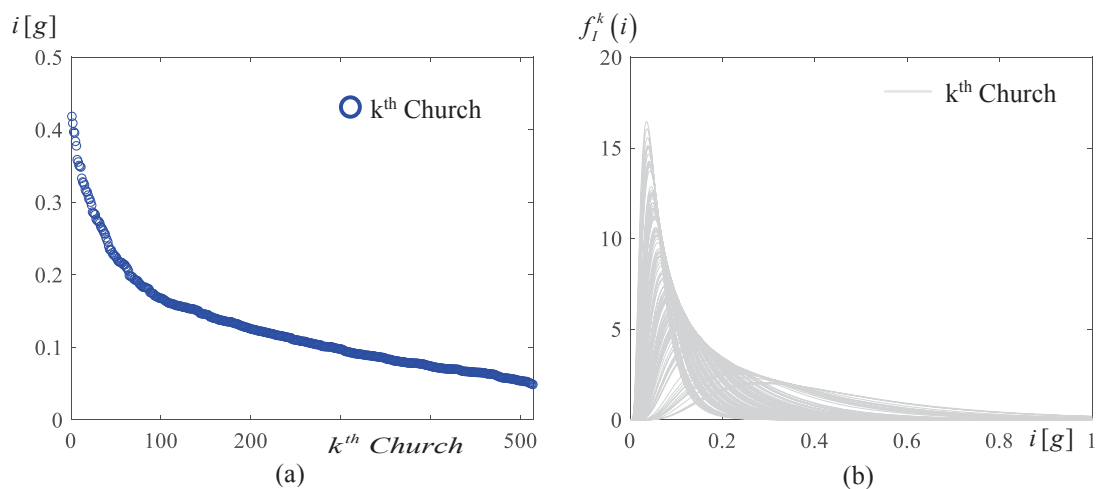


Figure 4: (a) mean expected intensity measure of seismic hazard; (b) distribution of intensity given epicentral distance

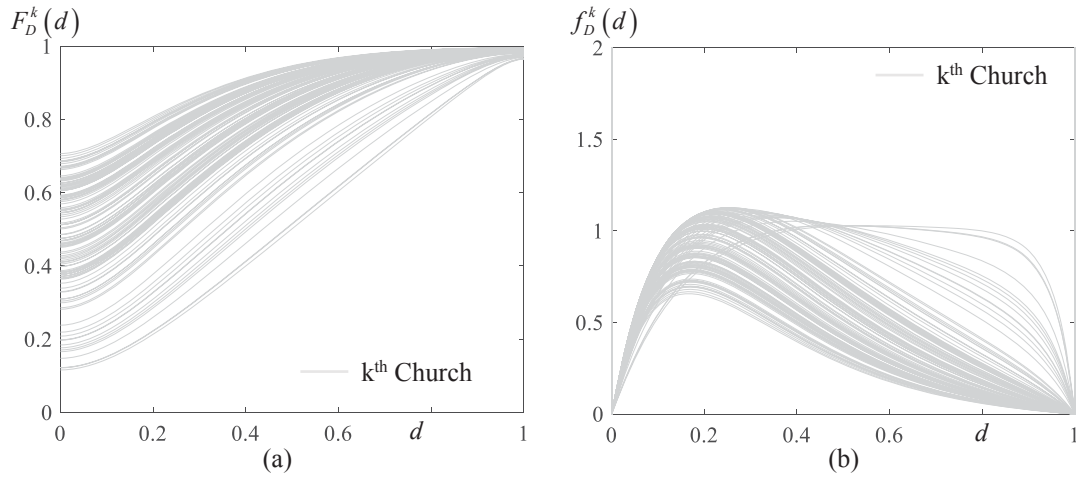


Figure 5: Damage distribution given epicentral distance and $V_{S,30}$: (a) CDF $F_D^k(d)$ and (b) PDF $f_D^k(d)$.

Figure 6a shows the distribution of the mean damage μ_D^k and $\mu_D^k \pm \sigma_D^k$ where σ_D^k is the standard deviation of each church, over the seismic intensity. Figure 6b reports the 25th percentile, the median, and the 75th percentile for the damage of each church. Moreover, also the extreme values corresponding to the 5 and 95 percentiles are reported.

Finally, Figure 7 describes the overall damage scenario expected for the churches of the Archdiocese of Camerino- San Severino, by combining results obtained from the damage models with the location of the historical churches. In details, the expected mean value of d of each church is illustrated by a red color scale and the table reports the number of historical churches suffering of different levels of damage.

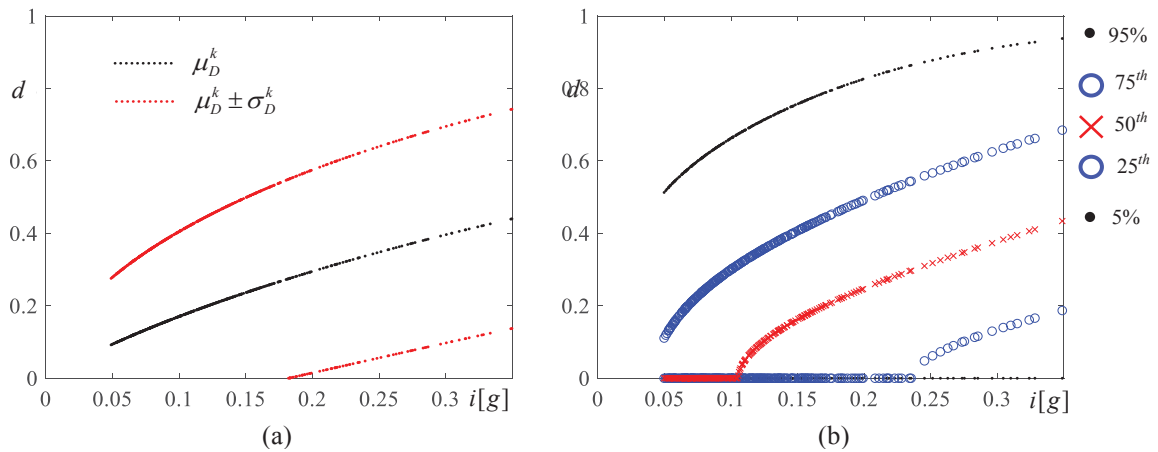


Figure 6: Damage distribution given seismic intensity (a) mean damage and (b) percentiles of damage.

3.2 Decision making

The damage scenario, that represents the combination between the response model and the seismic hazard, may be used to take decisions concerning specific actions oriented to mitigate the seismic risk or to improve the emergency management.

In particular, the following decision problem concerning the emergency management is considered to illustrate the potentialities of the methodology presented for the risk assessment.

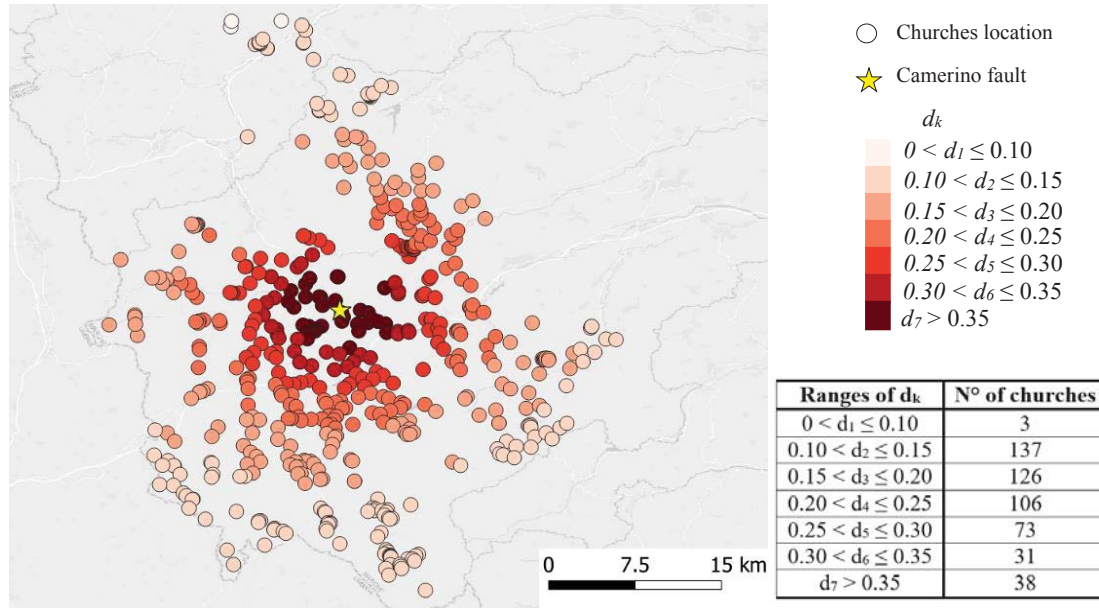


Figure 7: Damage distribution over the territory for the churches of the Archdiocese of Camerino San-Severino.

After a seismic event, the total set of churches must be divided into two subsets where, in one case, a damage larger than an assigned threshold is expected while, in the other case a damage lower than this threshold is expected. The sub-division is based on the location of the churches. A percentage of misclassification is expected in both the subsets, and the study wants to divide the total set in such a way that the misclassification is minimized.

The churches have been classified considering the median value of the seismic intensity at their site. This is an information usually available after the seismic event and it depends on the church location only, so that a classification based on the geographical position is possible. The median value of the intensity can be evaluated by Eq. 4, neglecting the last term related to the uncertainties. A threshold i_0 is chosen to divide the total set into two subsets where the median value of the expected intensity is lower or higher than i_0 .

The number of churches falling in the set where the median value of the intensity is lower than i_0 is denoted by $n_0(i_0)$. It can be concluded that the total probability to observe the event E_0 in this subset can be obtained by combining the probability to observe a damage lower than the threshold \bar{d} with the probability of selecting a church in this subset

$$P_E[E_0|i_0] = \frac{1}{n_0(i_0)} \sum_0^{n_0(i_0)} \int_0^{\bar{d}} f_D^k(d) dd \quad (6)$$

while $P_E[E_1|i_0] = 1 - P_E[E_0|i_0]$ provides the probability to observe the event E_1 within the same subset.

In this analysis, two threshold damage values $\bar{d} = 0.1$ and $\bar{d} = 0.2$ have been considered. Figure 8 shows the trends of $P_E[E_0|i_0]$ and $P_E[E_1|i_0]$, the value of seismic intensity i_0 that minimizes the probability of misprediction is highlighted by the dashed line. The optimal values of the seismic intensities i_0 are 0.1240g for $\bar{d} = 0.1$, and 0.1708g for $\bar{d} = 0.2$, respectively.

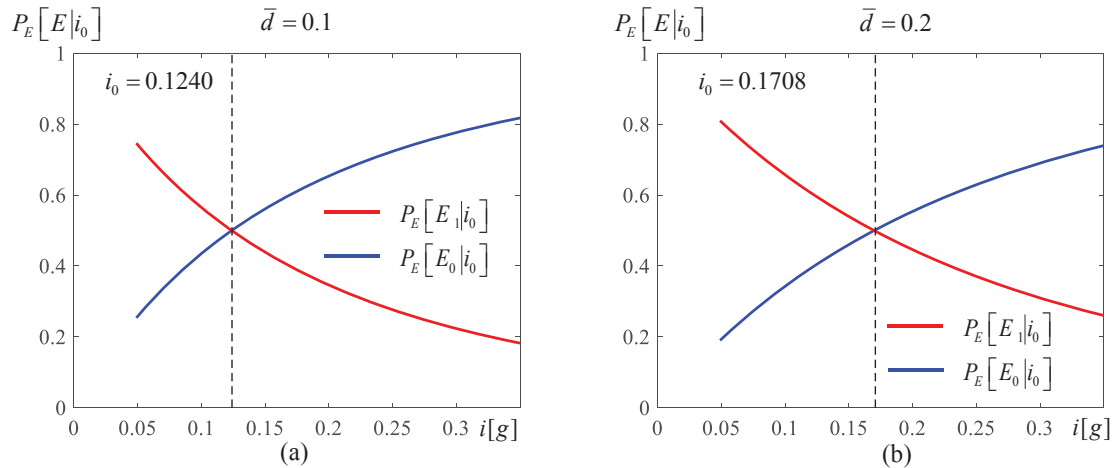


Figure 8: Probability of the two events E_0 and E_1 for different threshold of the intensity, for $\bar{d} = 0.1$ and $\bar{d} = 0.2$.

4 CONCLUSIONS

An illustrative application, starting from the empirical predictive model for the seismic damage of historical churches recently presented in the technical literature, has been proposed in this paper. In this empirical probabilistic model, the damage is expressed by a continuous index and the seismic action is described by a scalar intensity measure. A sample of churches falling into a limited area of Marche Region hit by the Central Italy 2016 seismic sequence has been chosen for the illustrative case study.

A specific scenario has been considered, assuming a seismic event of magnitude 5.8 generated by the Camerino fault. The probability distribution of damage has been evaluated for 514 historical churches, according to their locations and the mechanical properties of the soil. Results have been discussed and risk maps have been presented.

Potential use of this risk assessment methodology in the decision-making process has been illustrated by simulating a problem often arising in the post-event emergency phase: the selection of those historical churches that may have suffered the highest damage levels.

ACKNOWLEDGMENTS

The authors acknowledge the sponsorship of the Italian Civil Protection, through the RELUIS Project - WP4: MAppe di Rischio e Scenari di danno sismico (MARS) (2019).

REFERENCES

- [1] L. Sorrentino, S. Cattari, F. Da Porto, G. Magenes, A. Penna, Seismic behaviour of ordinary masonry buildings during the 2016 central Italy earthquakes. *Bulletin of Earthquake Engineering* <https://doi.org/10.1007/s10518-018-0370-4>, 2019.
- [2] F. Doglioni, A. Moretti, V. Petrini, P. Angeletti, Le Chiese e il Terremoti: Dalla Vulnerabilità Constatata nel Terremoto del Friuli al Miglioramento Antisismico nel Restauro, Verso una Politica di Prevenzione. Edizioni Lint, Trieste, Italy, 1994.
- [3] E. Mele, A. De Luca, A. Giordano, Modelling and analysis of a basilica under earthquake loading. *Journal of Cultural Heritage*. 4 (4):355–67. <https://doi.org/10.1016/j.culher.2003.03.002>, 2003.

- [4] F. Casarin, C. Modena, Seismic assessment of complex historical buildings: application to Reggio Emilia Cathedral, Italy. *International Journal of Architectural Heritage*. 2 (3):304–27. [https://doi: 10.1080/15583050802063659](https://doi.org/10.1080/15583050802063659), 2008.
- [5] G. De Matteis, F.M. Mazzolani, The Fossanova Church: seismic vulnerability assessment by numeric and physical testing. *International Journal of Architectural Heritage*. 4 (3):222–45. [https://doi: 10.1080/15583050903078903](https://doi.org/10.1080/15583050903078903), 2010.
- [6] M. D'Amato, M. Laterza, D. Diaz Fuentes, Simplified seismic analyses of ancient churches in Matera's Landscape. *International Journal of Architectural Heritage*, Article Published on line, 1–20, [https://doi: 10.1080/15583058.2018.1511000](https://doi.org/10.1080/15583058.2018.1511000), 2018.
- [7] F. Fabbrocino, G. Vaiano, A. Formisano, Parametric analysis on local collapse mechanisms of masonry churches. *Proceedings of AIP Conference*, Rhodes, Greece, 2018.
- [8] D.D. Fuente, M. D'Amato, M. Laterza, Seismic vulnerability and risk assessment of historic constructions: the case of masonry and adobe churches in Italy and Chile. *11th International Conference on Structural Analysis of Historical Constructions*, Cusco, Perú, pp. 1127–37, 2019.
- [9] S. Lagomarsino, S. Podestà, Seismic vulnerability of ancient churches I. Damage assessment and emergency. *Earthquake Spectra*. 20 (2):377–94. [https://doi:10.1193/1.1737735](https://doi.org/10.1193/1.1737735), 2004a.
- [10] S. Lagomarsino, S. Podestà, Seismic vulnerability of ancient churches II. Statistical analysis of surveyed data and methods for risk analysis. *Earthquake Spectra*. 20 (2):395–412. [https://doi:10.1193/1.1737736](https://doi.org/10.1193/1.1737736), 2004b.
- [11] S. Giovinazzi, S. Lagomarsino, A macroseismic method for the vulnerability assessment of buildings. *13th World Conference on Earthquake Engineering*, 2004.
- [12] S. Lagomarsino, S. Podestà, Damage and vulnerability assessment of churches after the Molise earthquake 2002. *Earthquake Spectra*. 20(S1):S271–S283, 2004c.
- [13] S. Lagomarsino, Damage assessment of churches after L'Aquila earthquake (2009), *Bulletin of Earthquake Engineering*. <https://doi.org/10.1007/s10518-011-9307-x>, 2012.
- [14] F. Da Porto, B. Silva, C. Costa, C. Modena, Macro-Scale Analysis of Damage to Churches after Earthquake in Abruzzo (Italy) on April 6, 2009, *Journal of Earthquake Engineering*. 16:6, 739–758, [https://doi: 10.1080/13632469.2012.685207](https://doi.org/10.1080/13632469.2012.685207), 2012.
- [15] G. De Matteis, G. Brando, V. Corlito, Simplified Assessment of the Seismic Vulnerability of Churches After the 2009 L'Aquila Earthquake, *Structural Analysis of Historical Constructions. Bulletin Earthquake Engineering*. 17: 4909. <https://doi.org/10.1007/s10518-019-00656-7>, 2019.
- [16] M. Indirli, G. Marghella, A. Marzo, Damage and collapse mechanisms in churches during the Pianura Padana Emiliana earthquake. *Energia Ambiente Innovazione*. 11/2012; 4/5:69–94, 2012.
- [17] L. Sorrentino, L. Liberatore, L.D. Decanini, D. Liberatore, The performance of churches in the 2012 Emilia earthquakes. *Bulletin of Earthquake Engineering*. 12, 2299–2331, 2014.
- [18] C. Canuti, S. Carbonari, A. Dall'Asta, L. Dezi, F. Gara, G. Leoni, M. Morici, E. Petrucci, A. Prota, A. Zona, Post-Earthquake Damage and Vulnerability Assessment of Churches in the Marche Region Struck by the 2016 Central Italy Seismic Sequence. *International Journal of Architectural Heritage*, [https://doi: 10.1080/15583058.2019.1653403](https://doi.org/10.1080/15583058.2019.1653403), 2019.

- [19] S. Carbonari, A. Dall'Asta, L. Dezi, F. Gara, G. Leoni, M. Morici, A. Prota, A. Zona, First analysis of data concerning damage occurred to churches of the Marche region following the 2016 central Italy earthquakes. *Bollettino di Geofisica Teorica ed Applicata*, 60 (2):183-96, 2019.
- [20] A. Penna, C. Calderini, L. Sorrentino, C. Carocci, E. Cescatti, R. Sisti, A. Borri, C. Modena, A. Prota, Damage to churches in the 2016 central Italy earthquakes. *Bulletin of Earthquake Engineering*. [https://doi: 10.1007/s10518-019-00594-4](https://doi.org/10.1007/s10518-019-00594-4), 2019.
- [21] E. Cescatti, P. Salzano, C. Casapulla, F. Ceroni, F. da Porto, A. Prota, Damages to masonry churches after 2016–2017 Central Italy seismic sequence and definition of fragility curves. *Bulletin of Earthquake Engineering*, [https://doi: 10.1007/s10518-019-00729-7](https://doi.org/10.1007/s10518-019-00729-7), 2019.
- [22] M. Di Ludovico, G. De Martino, A. Santoro, A. Prota, G. Manfredi, C. Calderini, C. Carocci, F. Da Porto, A. Dall'Asta, S. De Santis, G. Fiorentino, A. Digrisolo, M. Dolce, C. Moroni, B. Ferracuti, D. Ferretti, F. Graziotti, A. Penna, A. Mannella, L. Sorrentino, Usability and damage assessment of public buildings and churches after the 2016 Central Italy earthquake. *Earthquake Geotechnical Engineering for Protection and Development of Environment and Constructions*. Volume: Silvestri & Moraci (Eds), 2019.
- [23] G. De Matteis, M. Zizi, Seismic Damage Prediction of Masonry Churches by a PGA-based Approach, *International Journal of Architectural Heritage*. 13:7, 1165-1179, [https://doi: 10.1080/15583058.2019.1597215](https://doi.org/10.1080/15583058.2019.1597215), 2019.
- [24] S. Lagomarsino, On the vulnerability assessment of monumental buildings. *Bulletin of Earthquake Engineering*. 4. 445-463. [10.1007/s10518-006-9025-y](https://doi.org/10.1007/s10518-006-9025-y), 2006.
- [25] G. De Matteis, E. Ciber, G. Brando, Damage Probability Matrices for Three-Nave Masonry Churches in Abruzzi After the 2009 L'Aquila Earthquake. *International Journal of Architectural Heritage*, 10:2-3, 120-145. <http://dx.doi.org/10.1080/15583058.2015.1113340>, 2016.
- [26] L. Hofer, P. Zampieri, M.A. Zanini, F. Faleschini, C. Pellegrino, Seismic damage survey and empirical fragility curves for churches after the August 24, 2016 Central Italy earthquake. *Soil Dynamics and Earthquake Engineering*, 111, 98-109, 2018.
- [27] M. Morici, C. Canuti, A. Dall'Asta, G. Leoni, Empirical predictive model for seismic damage of historical churches. *Bulletin of Earthquake Engineering*. doi:10.1007/s10518-020-00903-2, 2020.
- [28] N.N Ambraseys, K. Simpson, A. Bommer, Prediction of horizontal response spectra in Europe. *Earthquake Engineering & Structural Dynamics*, 25:4, 371-400, 1996.
- [29] Quaderni di Geofisica, ISSN 1590-2595, Numero 138, In Italian, 2016
- [30] E. Tondi, G. Cello, Spatiotemporal evolution of the Central Apennines fault system (Italy), *Journal of Geodynamics*, Volume 36, Issues 1–2, Pages 113-128, ISSN 0264-3707, [https://doi.org/10.1016/S0264-3707\(03\)00043-7](https://doi.org/10.1016/S0264-3707(03)00043-7), 2003.
- [31] E., Tondi, Geological analysis and seismic hazard in the Central Apennines. In: Cello, G., Tondi, E. (Eds.), The resolution of geological analysis and models for earthquake faulting studies. *Journal of Geodynamics* 29 (3–5), 517– 534, 2000.
- [32] Vs30 Map Viewer: Topographic Slope as a Proxy for Seismic Site-Conditions (VS30) and Amplification around the Globe, Trevor I. Allen and David J. Wald, Website. <https://usgs.maps.arcgis.com>. Accessed 15 March 2021

- [33] D. Heath, D.J. Wald, C.B. Worden, E.M. Thompson, G. Scmocyk, A Global Hybrid VS30 Map with a Topographic-Slope-Based Default and Regional Map Insets”, *Earthquake Spectra*, vol. 36, 3: pp. 1570-1584, 2020.

A SEISMIC RISK ASSESSMENT FRAMEWORK FOR LOSS ESTIMATION OF CRITICAL INFRASTRUCTURE – HOSPITALS CASE

Basso P.¹, Osmani S.¹, Scolari M.² and Valsecchi R.²

RINA Consulting

¹ Via Antonio Cecchi 6, Genova - Italy

e-mail: paolo.basso@rina.org – saimir.osmani@rina.org

² Via Gran S. Bernardo, Strada 7, Palazzo R, Rozzano (MI) - Italy

e-mail: matteo.scolari@rina.org– ruben.valsecchi@rina.org

Abstract

In this paper, a framework developed for the seismic risk assessment and loss estimate of the Health-Care sector is described. The methodology herein presented derived from a wider study that refers to a multi-hazard (earthquake, hurricane, flood, landslide, rockfall, avalanche) and multi-asset (healthcare and energy infrastructure).

The loss estimate is based on the probabilistic modelling of hazards and asset vulnerability and an overall assessment of the impact generated from the suffered damage treated as a deterministic consequence of it.

Specifically, the total impact computation is based on the combined analysis of different aspects, such as physical damages, service reduction, and social impact. For the sake of completeness also the impact is evaluated per each aftermath level. It must be pointed out that in so doing the loss computed per each impact can be ensured as hazard independent.

An important role in the impact evaluation is also played by resilience. A simplified evaluation of preparedness and resourcefulness at asset and local level is performed to originate a set of resilience-based coefficients which, in turn, are used to influence the evaluation of the loss per each impact component and level of damage.

Finally, the Expected Annual Loss (EAL) is provided as the exponential relation between the probability of damage occurrence expressed as mean annual frequency, and the loss, expressed in economic terms. So, this relation can define the properties of damage occurrence and loss of each possible event. Thanks to the quantitative approach of the framework it can be seen how each risk aspect influence the curve properties, such as the horizontal stretch due to resilience influence on the loss degree and the vertical stretch due to vulnerability effect on the damage occurrence.

Keywords: Asset Integrity Management, Loss assessment, Probabilistic assessment, Expected Annual Loss, Territorial scale, Decision Support System

1 INTRODUCTION

When assessing the risk posed by a certain hazard the first parameter to be qualified is its frequency of occurrence. The definition is deeply related to the relevant historical data for a given geographic reference. The determination of the hazard alone cannot be directly used if not correctly correlated in space and time.

The determination of the hazard starts from the qualitative depiction of a plausible threat scenario for which the occurring frequency is determined. The definition of exposure calls into play the time and spatial correlation as some areas might be more prone to a certain hazard rather than others (e.g. the threat of an earthquake is deeply correlated to the geographic location of an asset and the surrounding context).

Along with the determination of possible threats and relevant frequencies, the vulnerability of the asset shall be determined as well using a structural and logistics assessment. The impact could be evaluated for different kind of assets as well as for different kind of targets. The weighted average of all the estimated impacts (damages) arising from the execution of a threat is called Impact.



Figure 1: Key elements of Risk Assessment

2 HAZARD ASSESSMENT

In the proposed methodologies the Hazard is considered through the definition of the Hazard curves (Figure 2). They describe the frequency of occurrence of the Intensity Measure (IM) of a certain hazard (e.g. PGA for earthquake), allowing in this way extended and detailed analyses. For the Hazard data collection, it will be possible to consider the following sources:

- Literature Databases;
- National Codes (it provides the procedure to obtain the hazard curve, if available);
- Websites Databases;
- Thematic maps on hazard distribution produced at the national level.

In the case of Literature databases and National Codes, besides having the entire hazard curve, we can obtain a limited number of IMs with the associated frequency/probability of occurrence. In this case, the few data available (IMs) can be used to build up the hazard curve through a fitting process through power or exponential laws, following the procedure presented hereafter.

2.1 Hazard curve definition

The Peak Ground Acceleration (PGA), expressed in g, are commonly given for 4 different percentage of exceedance in 50 years, which are commonly 2%, 10%, 50%, and 68%.

The hazard is often expressed in terms of exceedance probability, rather than in terms of exceedance rate (number of events per unit time). The exceedance probability is the probability that a certain intensity will occur at least once in a given period.

The two can be related using a concept called a Poisson process, which is a stochastic process that counts the number of events and the number of times in which they occur in a given interval. The relationship is explained in the following formula:

$$G = -\ln(1 - P)/t \quad (1)$$

In which G is the occurrence rate (i.e. events per unit time) that is expressed as the inverse of the return period Tr , while P is the probability of occurrence of at least one event in the considered period t .

Based on this formulation the occurrence rate, Mean Annual Frequency (MAF), and the return periods (Tr) can be calculated considering a reference period $t=50$ years:

$$\begin{aligned} MAF &= -\ln(1 - P) / 50 \\ Tr &= 50 / \ln(1 - P) \end{aligned} \quad (2)$$

Therefore, The Mean Annual Frequency (MAF) and the return period (Tr) can be computed by the 4-given percentage of exceedance in 50 years (Table 1).

Probability in 50 years	Tr	MAF
%	y	1/y
2	2475	0.0004
10	475	0.0021
50	72	0.0138
68	40	0.0228

Table 1: Mean Annual Frequency values (MAF) – Earthquake case

For each site is possible, by using the IMs (e.g. PGA for the earthquake) of the different return periods and the MAF, to define the hazard curve (Figure 2) by fitting the 4 points.

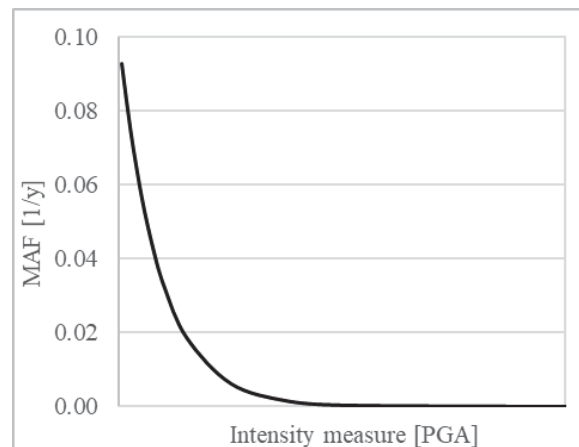


Figure 2: Typical Hazard curves for Earthquake

3 VULNERABILITY DEFINITION

Vulnerability is a measure of asset damage/failure due to a hazardous event. As an alternative, it could be also defined as the target's inability to deter and withstand the specific disaster. The assessment can be defined considering three different factors: Geographical location; Hazard response; Target hardness.

The vulnerability assessment is made by an exhaustive Database generated through the knowledge from literature, internal resources or by directly inputting the fragility curves parameters, in case of ad hoc developed fragility curves.

For each asset category, 4 damage states are selected (DS1, DS2, DS3, DS4), defined to represent the most important probability of exceedance, following the *Hazus* [5] subdivision of damage levels.

DS1 (Slight)	Flexural or shear type hairline cracks in some beams and columns near joints or within joints
DS2 (Moderate)	Most beams and columns exhibit hairline cracks. In ductile frames, some of the elements have reached yield capacity, showing larger flexural cracks and spalling. Nonductile frames may exhibit larger shear cracks and spalling
DS3 (Extensive)	Some of the elements have reached the ultimate capacity. In ductile frames large flexural cracks, spalled concrete and buckled reinforcement occur. The nonductile elements may experience shear or bond failures at reinforcement splices, or broken ties or buckled reinforcement in columns, leading to a partial collapse
DS4 (Complete)	The structure is collapsed or in imminent danger of collapse due to brittle failure of nonductile elements or loss of frame stability. Approximately 13%(low-rise), 10%(mid-rise) or 5%(high-rise), respectively for low/mid/high-rise, of the area of buildings, is expected to be collapsed

Table 2: Limit states description [5]

As can be seen in Figure 3 and Table 3, for each asset category is set 4 levels of damage, which represent 4 levels of criticality. For each damage state is defined:

- Percentage of damage, per each level and asset, which are stored in an internal database;
- The description of the visible effect on the facility per each damage level (Table 2).

This subdivision in 4 levels is useful to check out the probability of damaging and to know also the damage level that can be reached with this value of probability. The 4 levels are used in this analysis to reach a desirable level of simplicity, without losing the minimum level of accuracy required. Therefore, this kind of subdivision gives the possibility to set, among the different subsectors, different criticality levels depending on the specific asset considered.

In the following tables, characteristics (structural and temporal) and parameters (mean values and standard deviation) used respectively to select and define the fragility curves are listed.

Asset	Parameter 1	Parameter 2	Mean values [g]				Standard deviation			
			DS1	DS2	DS3	DS4	DS1	DS2	DS3	DS4
Hospital	1-3 storeys	pre-1950	0.09	0.18	0.30	0.42	0.78	0.74	0.73	0.73
	4-7 storeys	pre-1950	0.02	0.15	0.24	0.29	0.97	0.69	0.67	0.67
	8+ storeys	pre-1950	0.07	0.19	0.37	1.24	0.74	0.66	0.64	0.64
	1-3 storeys	post-1950	0.12	0.29	1.67	2.17	0.75	0.71	0.70	0.70
	4-7 storeys	post-1950	0.10	0.21	0.86	1.70	0.66	0.64	0.64	0.62
	8+ storeys	post-1950	0.10	0.27	1.58	4.26	0.63	0.60	0.59	0.53

Table 3: Limit states description [7]

For the selection of the appropriate Fragility curve (Figure 3) many parameters are considered, such as the principal construction material, construction typology, year of construction, the presence or not of codes during the design phase of the asset, dimensions of the asset (e.g. footprint, ground floors, n° of stories etc.).

A specific database is built with standardized unitary value to overcome the potential lack of information. So, starting from the main characteristics of the asset, the fragility function can be selected. In Figure 3 an example is shown.

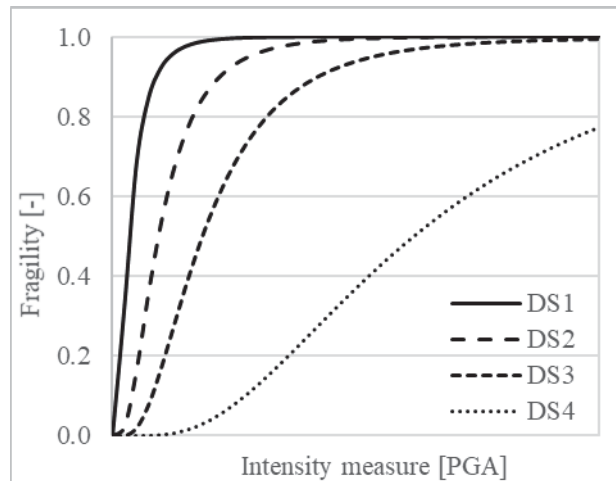


Figure 3: Example of fragility curves

4 IMPACT ANALYSIS

The Impact is defined as the presence of people, livelihoods, species or ecosystems, environmental functions, services, and resources, infrastructure, or economic, social, or cultural assets in places and settings that could be adversely affected by a hazard. Therefore, it can be seen as the scale of the consequences of a hazard.

The impact is normally quantified in the determination of damages and losses caused to stakeholders, environment and human life. In this particular study case, the analysis of the impact is based on the analysis of three different categories:

- Impacts on People (fatalities/injuries);
- impacts on the Physical System/Infrastructure (damages on the structures);
- impacts on Service continuity (interruptions/downtime).

The evaluation of each component is also provided in economic terms; in such a way the combination of the three is possible, providing a unique impact value.

4.1 Impacts on People

The analysis of the impact on the people (IP_{DSi}) is based on the evaluation of the number of fatalities and injuries [6] due to the occurrence of a certain hazard. The methodology used is based on the definition of three categories: Death, Slightly injured, and Severe injured.

The evaluation is provided according to the relation carried out by *Cimellaro et al.* [1], in the paper the percentage of death and injured people is related to the damage state that occurred after the hazardous event.

	U.M.	DS1	DS2	DS3	DS4
Death _{DSi}	%	0.000	0.000	0.0015	12.500
Injury _{DSi}	%	0.000	0.030	0.1005	22.500

Table 4: Normalized human losses ratios for different damage state [1]

The number of deaths can be obtained by multiplying the death loss ratio shown above (Table 4) with the number of people inside the hospital:

$$Death_{DSi} = Death_{DSi}(\%) \cdot \delta_t \cdot People_in_hospital \quad (3)$$

In which $Death_{DSi}(\%)$ is the percentage derived from Table 4, $People_in_hospital$ is the number of people in the hospital, and δ_t is the coefficient of reduction that consider the effect of the asset preparedness on the people evacuation (section 5.1).

Furthermore, thanks to the *Syner-G* [2] a further distinction could be made on the injury. They are divided into slightly and severely injured through the severity injured ratio ζ that typically varies between 1/3 and 1/2 (in the evaluation 1/3 is used).

It must be pointed out that some further consideration must be performed on the analysis of the severely injured. They are assumed to be the people which need surgical treatment, thus they are considered as the Hospital Treatment Demand, HTD, which must be compared with the Hospital Treatment Capacity per hours, HTC [2].

$$HTD_{DSi} = People \cdot (1 - \delta_p) \cdot Severe_injured_{DSi}(\%) \quad (4)$$

In which δ_p is the percentage of people evacuated within the due time (section 5.2).

The people affected are obtained by the district density and the analyzed area:

$$People = density_{distric} \cdot Area \quad (5)$$

The area used for this evaluation should be selected as the minor between the influence area of the hospital and the hazard area:

- Influence Area: A rough area of influence per each hospital is evaluated simply implementing the Voronoi Diagram using the hospitals as discrete points;
- The hazard area rather is defined as the one on which the considered hazard produces the selected damage. It can be defined considering the attenuation function of the hazard intensity, starting from the studied point. In literature several examples can be found, e.g. for the earthquake, this area is defined according to the empirical attenuation formula for the PGA [8]:

$$\log(a) = \alpha + \beta \cdot M - \log(r) + b \cdot r \quad (6)$$

$$r = \sqrt{d^2 + h^2}$$

Where d is the distance from the source which can be computed per each damage state through a solver algorithm. The other parameters are: a is in g, α is -1.09, β is 0.238, b is -0.0005, and h is 6.0 for horizontal PGA [8].

	U.M.	DS1	DS2	DS3	DS4
Severe injured	%	0.00	$\zeta \cdot 0.03$	$\zeta \cdot 0.1005$	$\zeta \cdot 22.50$
Hazard area	km ²	Empirical evaluation of affect area			
Hospital influence area	km ²	Voronoi Diagram			

Table 5: Hospital Treatment Demand evaluation

The hospital Capacity per one day is computed considering the operative functionalities decay after the hazardous event [2].

$$HTC_{DSi} = \frac{1}{\delta_{int}} \cdot \frac{\gamma_{1,DSi} \gamma_2}{t_m} \cdot 24h \quad (7)$$

Where $\gamma_{1,DSi}$ is the number of operating theatres which remain operative after the hazardous event, γ_2 is a Boolean function (equal to 1 if the system “survives” and to 0 otherwise), t_m is the mean duration of a surgical operation, measured in hours (in this study this value is assumed equal to 2h according to [2]), and δ_{int} is the coefficient that considers goodness of the internal coordination among facilities and department (section 5.4).

The number of operating theatres (γ_1) is evaluated by considering the decay of the capacity of the hospital:

$$\gamma_{1,DSi} = OT \cdot (1 - Service_{DSi}) \quad (8)$$

In which OT is the number of operating theatres and $Service_{DSi}$ represent the percentage decrease of the hospital service, which can be derived from literature per each damage state.

The economic loss due to the impact on the people (IPDSi) can be evaluated by considering two different aspect:

- The “direct” death due to the event (computed by people inside the hospital).
- If $HTD > HTC$, the “indirect” death is determined as the severely injured people that cannot have access to the surgical treatment (computed using the people inside the so-called influence area) [2].

Therefore, the number of human life losses can be multiplied by the mean value of human life.

$$IP_{DSi} = \{Death_{DSi} + [(HTD_{DSi} - \delta_{E2} \cdot Share_P \cdot N_Hospital) - HTC_{DSi}]\} \cdot Life\ Value \quad (9)$$

In which *Life value* is expressed in k\$/person and δ_{E2} represents the coefficient related to hospital redistribution capacity during an emergency (section 5.6).

Share_P represent the sharing capacity between two hospitals, calibrated considering the average number of patients that can be relocated during an emergency. It sets equal to 35, based on the experience derived from the Italian 2020 healthcare crisis due to Covid-19 [13].

$N_Hospital$ is the number of hospitals within the sharing distance, which in first approximation is set to 30km. Such value is computed by the hospital influence area, according to the following formulation:

$$N_Hospital = 2 \left[\left(\frac{30km}{2\sqrt{A_{inf}/\pi}} \right) + 2 \right] \quad (10)$$

To have a better understanding of the approach a simplified scheme is listed below.

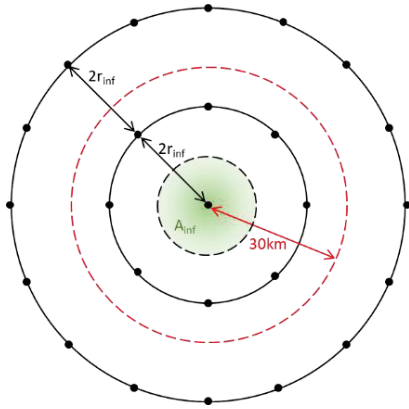


Figure 4: Hypothetic sharing scheme

- The points in this scheme represent the hospitals.
- A_{inf} , which is drawn in green is the area of influence of each hospital. It can be computed as the mean of the district/province.
- r_{inf} is consequently the radius of influence.
- 30km, as said before, represents the distance over which the sharing is no more feasible.

Therefore, the value inside the round bracket should be rounded down. Since inside the square bracket, an integer number must be used, because it represents the number of rings of hospitals inside the sharing distance.

4.2 Impacts on Physical system

The impact on the physical system (ID_{DSi}) can be defined as the impact cost due to the direct damage experienced by the facility [6]. The economic loss can be ease defined as follow:

$$ID_{DSi} = Damage_{DSi}(\%) \cdot Reconstruction_Cost \quad (11)$$

In which $Damage_{DSi}(\%)$ is the damage value associated with each damage state, that can be derived from literature per each damage state [3], while $Reconstruction_Cost$ is the expected cost to take back the asset to full operation, comprehensive of both structural and equipment cost. It can be calculated in two different way: directly calculated from the construction cost or indirectly derived from dimension and the unitary cost, taken from the literature [4].

4.3 Impacts on Service continuity

The impact on service continuity (IR_{DSi}) can be related to the effects on the population, of the reduction of the service due to damage [6]. The evaluation is based on the information on the mean recovery time and service reduction per each damage state, according to the relation carried out by *Cimellaro et al.* [1].

The additional time that the people need to get access to the health care facilities is the base of the economic loss evaluation. As can be seen in the following formula the recovery is considered as a linear function:

$$IR_{DSi} = \delta_{rec} \cdot t_{r,DSi} [Service_{DSi}(\%) \cdot (Size - \delta_{E1} \cdot Mobile_P \cdot Gr)] (2t_{dist} \cdot Value_{time}) \quad (12)$$

Where $Service_{DSi}(\%)$ is the percentage of service reduction per each damage state, that can be derived from literature per each damage state, $t_{r,DSi}$ is the recovery time, that can be derived from literature per each damage state, t_{dist} is the time needed to reach the nearest facility per each damage state, $Size$, it must be expressed by the characteristic unit of measure (number of people), $Value_{time}$, it is the value of the people time, δ_{E1} represents the coefficient related to the accessibility to the eventual mobile health care post (section 5.5), δ_{rec} is the coefficient that considers how the recovery is carried out (section 5.3), $Mobile_P$ represent the number of patients that can be endorsed by this mobile healthcare post, that usually has a capacity of 25 beds [14], and Gr represents the ratio among bed capacity and the average people inside the hospital.

Total impact

The total impact ($I_{TOT,DSi}$) is evaluated by summing the different economic losses categories per each damage state, as shown in the following formula:

$$I_{TOT,DSi} = IP_{DSi} + ID_{DSi} + IR_{DSi} \quad (13)$$

In which IP_{DSi} is the Impact on People economic loss, ID_{DSi} is the Impact on Physical System economic loss, and IR_{DSi} is the Impact on Service Continuity economic loss.

5 RESILIENCE

The term resilience means the ability to prepare for and adapt to changing conditions and withstand and recover rapidly from disruptions, it includes the ability to withstand and recover from occurring threats or incidents.

The resilience is evaluated using a score index (from 0 to 3). Three main categories are considered for its definition:

- Preparation (planning in advance), which consider the existence/status of emergency plans (P1) and the frequency of training courses/exercise (P2), the existence of insurance cover (P3), the existence of backup systems (P4), the community experience on the hazardous event (P5), and the warning time before the hazardous event (P6).
- Internal resourcefulness considers the effectiveness and availability of resources, such as early warning system and/or specific countermeasure (Int1), materials to offset the loss (Int2), and coordination with facilities/department of Hospitals (Int3).
- External resourcefulness in which are considered the existence of the external agreement and coordination plants with other subjects: institution and/or organizations (Ext1), public units and/or local government institutions (Ext2), provincial health directorate institutions (Ext3), and special treatment units of hospitals (Ext4).

Resilience is considered in the risk assessment through the evaluation of resilience (I_{Res}). The score of each asset is therefore evaluated developing a resilience matrix (Table 6), in which the score can be obtained for every single hazard or as the total one. The final value of the resilience index is computed by a weighted average [9]:

$$I_{Res} = \sum_{i=1}^3 RC_i \cdot W_i \quad (14)$$

Where RC_i is the resilience component score and W_i is the weight of each component.

Earthquake	Preparation	Internal Resourcefulness	External Resourcefulness	I_{Res}
Score [0 to 3]	1.76	3.00	3.00	84%
Weight	0.38	0.316	0.304	1

Table 6: Resilience analysis matrix (example of compilation)

It is important to note that the Resilience Index is a way to compare the levels of resilience of critical infrastructures and to help the prioritization of investment [9] together with the just explained Expected Annual Loss.

This resilience, beyond the assignment of the so-called resilience indicator, are also used to affect the impact analysis. Some resilience coefficients are defined to consider these resilience factors also into the impact analysis, as can be seen in the following table.

Resilience Indicators	Preparation						Resourcefulness							
							Internal				External			
	P1	P2	P3	P4	P5	P6	Int1	Int2	Int3	Int4	Ext1	Ext2	Ext3	Ext4
IP	δ_t	δ_t			δ_p	δ_p			δ_{int}				δ_{E2}	δ_{E2}
ID														
IS				δ_{rec}			δ_{rec}	δ_{rec}			δ_{E1}	δ_{E1}		

Table 7: Resilience indicators dependency on the resilience aspects and their influence on the impact on people (IP), on the physical system (ID), and service continuity (IS)

5.1 δ_t : Preparedness - Evacuation efficiency inside the asset

The evaluation of the casualties should consider the capacity of the people inside the asset to evacuate in the best way. Usually, this capacity can be related to the existence or not of the emergency plan and also its quality. The second aspect is the training. Also, in this case, this can be asses analyzing not only its occurrence or not, but also the frequency at which it is set.

In the work done by *Li et al.* [10] the evacuation efficiency is assessed through two factors:

- k_s is defined as the attraction capacity of the exit to the people inside the asset;
- k_D is related to the people evacuation behaviour and its coordination.

In so doing the planning and training can be used to build a matrix that describes the preparedness effect on the number of deaths.

		Training (k_D)		
		Yearly	Yes	No
Plan (k_s)	No	0.35	0.73	1.00
	Yes	0.15	0.15	0.15
	Detailed	0.15	0.15	0.15

Table 8: δ_t evaluation

5.2 δ_p : Preparedness - Evacuation efficiency around the asset

The second aspect of preparedness that is considered is related to the around community preparedness. This resilience coefficient is very important to fit the real number of people heated by a hazardous event. It is known from the literature that exists a relation between the warning time and the percentage of people evacuated from a certain area.

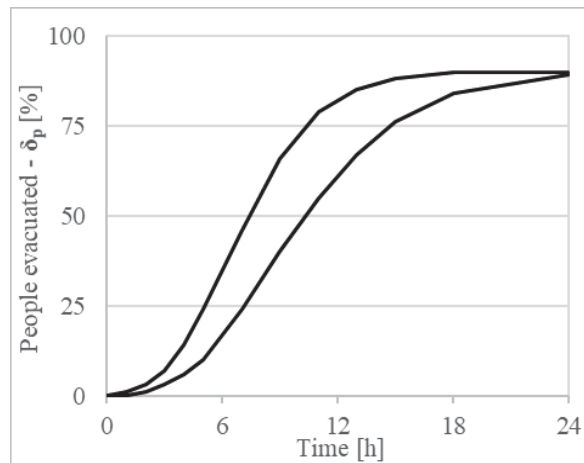
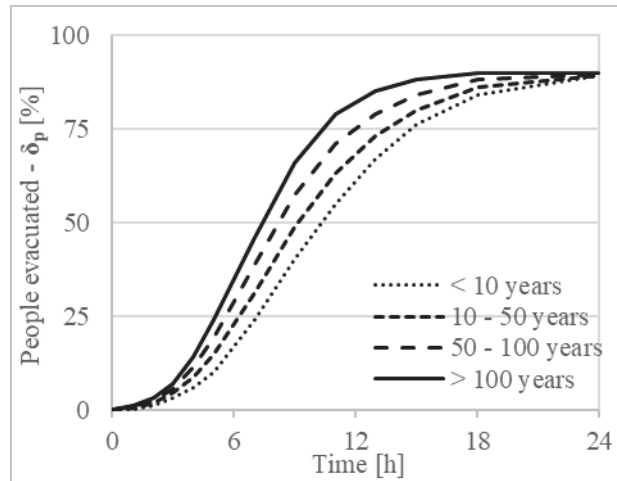


Figure 5: Example of evacuation curves

This quite wide range can be attributed to the community capacity to react to a determined hazardous event. This aspect can be related to the so-called community experience. A community that has already experienced a certain event should have a better reaction capacity.

Therefore, the two boundaries find in literature [11] can be associated with ones of the community experience, namely less than 10 years and more the 100 years. Successively the other values can be included in the just mentioned two boundaries.

	δ_p	Community experience			
		> 100 years	< 100 years	< 50 years	< 10 years
Warning time	< 1 hour	0.003	0.007	0.010	0.007
	< 12 hours	0.615	0.680	0.746	0.824
	< 1 day	0.885	0.891	0.897	0.900
	> 1 day	0.900	0.900	0.900	0.900

Table 9: δ_p evaluationFigure 6: δ_p evaluation

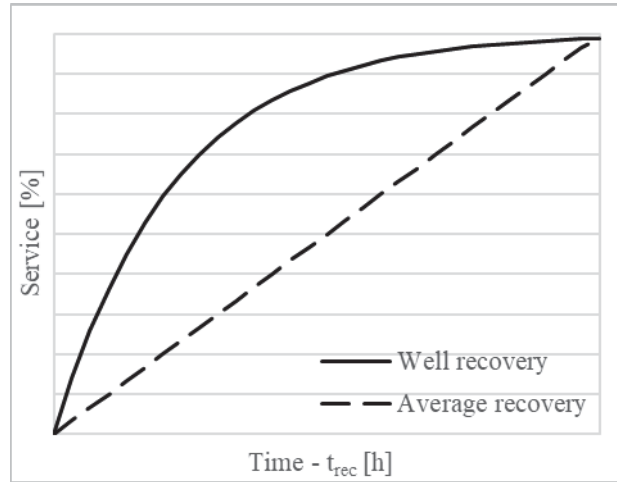
5.3 δ_{rec} : Recovery efficiency

During the aftermath of the event impact, an important role is played by the recovery efficiency. This efficiency has an important role in the way in which the recovery is carried out.

The recovery coefficient is set to consider the changing recovery performance during the aftermath period. This variation is related to the internal resourcefulness and preparedness of the assets according to *Cimellaro et al.*[1].

Since the recovery economic loss is related to the unserved characteristic in a certain period. Therefore, the coefficient is simply evaluated as the reciprocal of the area under the recovery function.

$$\delta_{rec,i} = \int 1 - f_{rec}(t) dt \quad (15)$$

Figure 7: δ_{rec} evaluation

Two different values of $\delta_{rec,i}$ are defined, which are the lower 0.19 (well) and upper 0.5 (average and not-well) bound. The coefficient varies linearly between these two limits. To obtain the exact value, the average score of the above-mentioned question should be computed, the scoring value varies from 0 to 3.

$$\delta_{rec} = \delta_{rec,up} - \frac{Avg.Score}{3} \cdot (\delta_{rec,up} - \delta_{rec,down}) \quad (16)$$

As shown in the following table an average scoring can be computed.

Internal resourcefulness & preparedness	Material to offset the loss	Backup system	Warning System / Measures
No	0	0	0
Yes Partly	1	3	3
Yes Full	3	3	3

Table 10: δ_{rec} evaluation

5.4 δ_{int} : Internal resourcefulness

In the specific case of the analysis on the event impact on the hospital another coefficient should be considered. More precisely the internal resourcefulness should be considered.

This coefficient is called δ_{int} and it considers the goodness of the internal coordination among facilities and department. This coefficient is the merge of two different factors α and β that describe the organizational and the human component during emergencies, according to *Syner-G* [2]. The coefficient represents the capacity of the hospital system to increase its treatment capacity during the emergency.

Since in the treatment capacity formula is inserted as $1/\delta_{int}$, the lowest in the value, the highest is the capacity. Therefore, if the increased capacity is not ensured then the coefficient is set equal to 1, while it is equal to 0.57. This value is carried out according to Italian increase capacity in terms of treatment capacity during the Italian 2020 healthcare crisis, according to the data given by the *Italian Ministry of Health* [12]. Such a document underlined the increasing treatment capacity of 75% in the most affected regions. The value can be defined as follow:

- Existence of coordination with facilities/departments of the hospital - $\delta_{int} = 0.57$.
- Not existence of coordination with facilities/departments of the hospital - $\delta_{int} = 1$.

5.5 δ_{E1} : External resourcefulness – Institution efficiency

An important aspect that should be considered is the external resourcefulness, especially related to the institution efficiency. The coefficient, in this case, can be related to the accessibility to the eventual mobile healthcare post, which can ensure a certain level of treatment capacity despite the service reduction due to the damage experienced. Therefore, δ_{E1} can be set according to the scheme shown in the following table.

δ_{E1}		Agreements with organization/institutions	
		Yes	No
Local government coordination	Yes	1	0.5
	No	0.5	0

Table 11: δ_{E1} evaluation

The value of this parameter is defined initially as a Boolean function if both the question leads to a positive effect leads is equal to 1, or 0 otherwise. If the two questions have opposite answered the half is taken.

5.6 δ_{E2} : External resourcefulness – Care system efficiency

An important aspect that should be considered is the external resourcefulness, especially related to the health care system efficiency, at the interhospital level. The coefficient, in this case, can be related to hospital redistribution capacity during an emergency. Therefore, δ_{E2} can be set according to the scheme shown in the following table.

δ_{E2}		Health directorate coordination	
		Yes	No
Coordination among hospitals	Yes	1	0.5
	No	0.5	0

Table 12: δ_{E2} evaluation

The value of this parameter is defined initially as a Boolean function if both the question leads to a positive effect leads is equal to 1, or 0 otherwise. If the two questions have opposite answered the half is taken.

6 PROBABILITY OF DAMAGE OCCURRENCE

In this paragraph, the hazard and vulnerability properties are combined to obtain the value of the probability of occurrence of a certain damage state. The results of this combination are representing the probability of occurrence of the impact.

The Damage probability per each damage state (P_D) can be computed as the convolution integral between the Hazard curve, if available, and the fragility curves of the limit state DS.

$$P_{D,DSi} = \int_0^{+\infty} F_{R,DSi}(IM) * H_S(IM) d(IM) \quad (17)$$

Where F_R represents the fragility curve and H_S the hazard curve, both expressed as a function of IM (PGA [g] for earthquake).

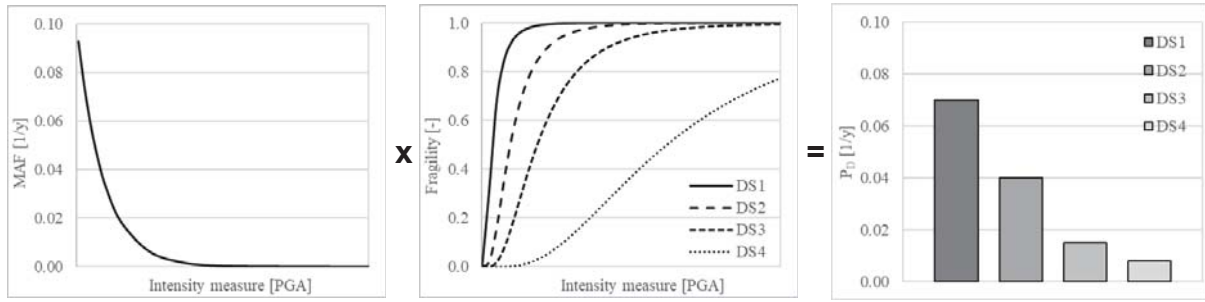


Figure 8: Damage probability per each DS

If the hazard curve is not available, which means that is unknown the occurrence probability of all the intensity measures but only of some of them, the approach is the one shown below.

$$P_D = \sum_{i=1}^n F_{i-1} MAF_{i-1} (1 - \exp(m_i \Delta IM_i)) - \frac{\Delta F_i}{\Delta IM_i} MAF_{i-1} (\exp(m_i \Delta IM_i) \left(\Delta IM_i - \frac{1}{m_i} \right) + \frac{1}{m_i}) \quad (18)$$

In which:

- $\Delta IM_i = IM_i - IM_{i-1}$;
- $F_i = F_i - F_{i-1}$, in which $F(s)$ is the fragility cumulative lognormal distribution function;
- $m_i = \frac{\ln\left(\frac{MAF_i}{MAF_{i-1}}\right)}{\Delta IM_i}$, that is the angular coefficient of the MAF curve;
- $a_i = MAF_{i-1} (1 - \exp(m_i \Delta IM_i))$;
- $b_i = \frac{MAF_{i-1}}{\Delta IM_i} \left(\exp(m_i \Delta IM_i) \left(\Delta IM_i - \frac{1}{m_i} \right) + \frac{1}{m_i} \right)$.

7 EXPECTED ANNUAL LOSS

The last step of this study consists of the definition of the Expected Annual Loss (EAL). EAL is used in this methodology as the quantification of the risk level. This final value considers all the different component of the risk assessment theory, such as the probability of damage occurrence (Hazard and Vulnerability) and the total impact (Impact and Resilience).

The EAL, which can be built using the total impact and the damage (Figure 9).

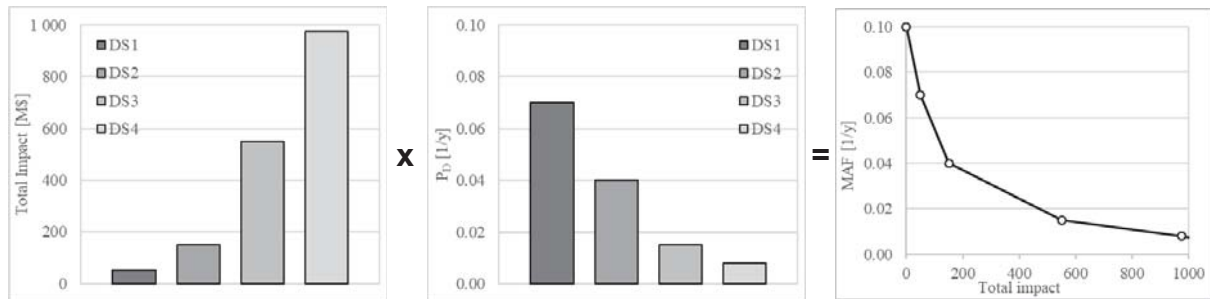


Figure 9: EAL evaluation

Finally, the area under the EAL curve is computed. This kind of results gives a unique value representing the loss of the assets per year for the considered hazard.

$$EAL = \sum_{i=1}^n \frac{(I_{TOT,DS(i+1)} - I_{TOT,DSi})(P_{D,DS(i+1)} + P_{D,DSi})}{2} \quad (19)$$

In which P_D is the Mean Annual Frequency (MAF) and I_{TOT} is the impact loss. Therefore, the EAL is the final measure of the risk per a certain asset, subjected to an earthquake.

8 CONCLUSIONS

A procedure for the seismic risk assessment of hospital buildings has been presented. The following advantages are worth to be highlighted:

- The framework can be extended to the assessment of different hazards. This is mainly related to the fact that the approach used in the hazard evaluation can be used for whichever kind of natural hazard that can be expressed as an intensity measure (i.e. acceleration for earthquake, wind speed for a hurricane, water height for flood etc...) as a function of a probability of occurrence.
- This procedure is capable to compare different assets, thanks to the computation of the economic value of the risk, known as the expected annual loss (EAL) which is derived from the calculated total impact and the probability of damage occurrence (hazard + vulnerability). The result is a scalar value, computed as the area under the loss curve (Figure 9), that should be used to compare the risk among the different assets.
- The Impact is defined by considering the presence of people, livelihoods, species or ecosystems, environmental functions, services, and resources, infrastructure, or economic, social, or cultural assets in places and settings that could be adversely affected by a seismic hazard. Thus impact is normally quantified as the consequence of damages and losses caused to stakeholders, to the environment and human life. The analysis of the impact is consequently based on the definition of 3 loss categories: Impacts on People, impacts on the Physical System/Infrastructure, and Impacts on Service continuity. The consideration of all these different aspects of the impact leads to a real representation of the current value of the critical infrastructure sectors.
- The already mentioned criticality level should be defined uniquely. In so doing each level, labelled DS1, DS2, DS3, and DS4, represent always the same damage state, per each asset analysed.
- The losses are evaluated as a function of time as can be appreciated in the impact analysis. This is mainly related to the concept of damage and service which can be recovered in a certain time, called recovery time. How the impact is assessed permit also to take into account the resilience as a coefficient able to affect the recovery function.

REFERENCES

- [1] G.P. Cimellaro, A.M. Reinhorn, M. Bruneau. "Seismic resilience of a hospital system". *Structure and Infrastructure Engineering*, Vol.6, 2010.
- [2] Syner-G. "D6.7 Application and validation study to a hospital facility (Italy)". *Systemic Seismic Vulnerability and Risk Analysis for Buildings, Lifeline Networks and Infrastructures Safety Gain*, 2012.

- [3] A.J. Kappos, G. Panagopoulos, C. Panagiotopoulos, G. Penelis. “A hybrid method for the vulnerability assessment of R/C and URM buildings”. *Bulletin of Earthquake Engineering*, 4:391-413. 2006
- [4] World Bank Group. “How Power Investments Contribute to Jobs and Economic Growth in Turkey”. 2017.
- [5] FEMA. “Hazardus-MH2.1 - Multihazard Loss Estimation Methodology - Earthquake - Model Technical Manual”. 2013.
- [6] M.L. Sousa, G. Tsionis. “Recommendation for a National Risk Assessment for Disaster Risk Management in EU - Approaches for identifying, analysing and evaluating risk”. *JRC Science for policy report*. Version 0. Cap.9, 56-67. 2019.
- [7] Syner-G. “D3.1 – Fragility functions for common RC building types in Europe”. *Systemic Seismic Vulnerability and Risk Analysis for Buildings, Lifeline Networks and Infrastructures Safety Gain*. 2011.
- [8] E. Ulutas, M.F. Ozer. “Empirical attenuation relationship of peak ground acceleration for eastern Marmara region in Turkey”. *The Arabian Journal for Science and Engineering*, 35, 1°, 187-203. 2010.
- [9] R. E. Fisher, G. W. Bassett, W. A. Buehring, M. J. Collins, D.C. Dickinson, L.K. Eaton, D.J. Millier. “Constructing a resilience index for the enhanced critical infrastructure protection program”. *Argonne Decision and Information Sciences*. 2010.
- [10] S. Li, C. Zhai, L. Xie. “Occupant evacuation and casualty estimation in a building under earthquake using cellular automata”. *Physica A: Statistical Mechanics and its Applications*, 424, 152-167. 2015.
- [11] S. N. Jonkman. “Loss of life estimation in flood risk assessment; theory and applications”. 2007.
- [12] Italian Ministry of Health. 0007865-25/03/2020-DGPROGS-MDS-P, Aggiornamento delle linee di indirizzo organizzative dei servizi ospedalieri e territoriali in corso di emergenza COVID-19. 2020. (in Italian)
- [13] <https://www.ilsole24ore.com/art/coronavirus-1865-nuovi-contagi-e-76-morti-lombardia-AD40iMD> Last accessed 28/07/2020. (in Italian)
- [14] <https://www.naffco.com/uae/en/products/mobile-medical-units> Last accessed 21/05/2020.

CAESAR II: AN ITALIAN DECISION SUPPORT TOOL FOR THE SEISMIC RISK. THE CASE STUDY OF TORRE PELLICE, VILLAR PELLICE AND PINEROLO MUNICIPALITIES

Giulio Zuccaro, Francesca Linda Perelli, Daniela De Gregorio, Daniele Masi

PLINIVS Study Centre
University of Naples Federico II
via Toledo 402, 80134, Naples
zuccaro@unina.it, francescalinda.perelli@unina.it,
daniela.degregorio@unina.it, daniele.masi@unina.it,

Abstract

Italy is a country with high seismic risk; however, a broad seismic classification of the national territory has been introduced only in the last twenty years. Therefore, most of the existing buildings stock do not comply with the current anti-seismic codes. In recent years, the seismic events that occurred in Italy have highlighted the complexity of emergency management and the great challenge for public authorities called to answer to the post-event reconstruction and the planning of effective risk prevention and mitigation measures implemented in "peacetime".

In this perspective, the CAESAR II project (Controlling, Mitigating and Managing Earthquake Emergency: Cost-Benefit and Multi-criteria Analysis of Impact Scenarios for Risk Reduction and Increased Resilience) has been developed as a decision support system for public authorities engaged in the development of seismic disaster risk reduction plans. CAESAR II includes a module for the simulation of retrofitting measures applied at the municipal scale, integrating different categories of anti-seismic and energy improvement measures based on the vulnerability analysis of the existing buildings stock. The CAESAR II tool's core is the module for evaluating "seismic impact scenarios" based on the end-users' hazard. The output of the model includes information on expected damage levels for buildings (from D0-no damage to D5- total collapse) and population (dead, injured and homeless). Impact scenarios can be customised according to the minimum unit of analysis assumed (municipality or 250x250m square mesh grid) and the availability of exposure data (from national census data or survey on the spot building by building according to the PLINIVS form). Scenarios include geo-referenced data managed by geo-servers to exchange data in a format compliant with OGC (Open Gis Consortium) standards and the European INSPIRE Directive. Simulation results can be further processed through the Multi-Criteria and Cost-Benefit Analysis modules to support the comparative assessment of alternative seismic and energy measurements.

In this work, the procedures included in CAESAR II are described and a case study is reported. It concerns the analysis of the expected damage assessment on buildings and population for three municipalities in northern Italy, Torre Pellice, Villar Pellice and Pinerolo (Piedmont Region).

1. INTRODUCTION

Effective planning and programming in seismic emergencies require preliminary assessments of the effects on the territory. Due to the different objectives, it is possible to distinguish two types of assessments based on risk analysis and scenario analysis.

Risk is the probability that a prefixed level of damage (on people, buildings, infrastructures, economy, etc.) caused by seismic events will occur within a given period in a specific geographical area. Therefore, the risk should be intended as a cumulative assessment, which considers the total potential damage in the same area generated by different events in a fixed time frame. Scenario, instead, represents the probabilistic distribution, in a particular geographical area, of the damage induced by a single seismic event with an assigned probability of occurrence (assumed as the reference scenario).

In both types of analyses, three random variables come into question: hazard, exposure, and vulnerability. The “hazard” is the probability of occurrence, in a specific area and a specific period, of all possible seismic events, for risk analysis, or of a single event, in the case of scenario analysis. The “exposure” is the geographic distribution in quantitative and qualitative terms of the different elements at risk that characterise the area under consideration (people, buildings, infrastructure, activities and movable property). The conditions and/or operation may be damaged, altered or destroyed due to the occurrence of the natural event. The “vulnerability” is the sensitivity of an exposed element to a natural event. It can be evaluated as the probability that the exposed element will suffer a certain level of damage or change of state, concerning an appropriate scale, because of a seismic event of assigned intensity.

In emergency planning, both risk and scenario analyses can be used in response to the different goals that are to be pursued. Risk analyses allow comparative evaluations of areas subject to planning both for decisions on intervention strategies (e.g. evacuation priorities, etc.) and the definition of damage mitigation interventions. Scenario analyses, through the identification of the extension of the area of interest and the evaluation of the territorial impact, help quantify the resources necessary for the emergency planning and the organisation of the operative intervention.

In the literature, there are many works related to risk analysis in a broad sense or to some specific factor. Some specific studies on the vulnerability can be found in [1], [2], [3] and [4], and the exposure in [5], [6] and [7]. About the costs analyses some works are reported in [8] and [9] and on the multi-criteria there are [10] and [11].

In recent years, research has focused on creating comprehensive tools for every aspect of the process. One of the newcomers is the IRMA (Italian Risk MAPs) platform [12], developed by the Department of Italian Civil Protection (DPC). It integrates tools for calculating damage scenarios and risk maps for the Italian territory. The IRMA platform is designed for the scientific community and allows to create and load different exposure/vulnerability databases and different sets of fragility curves. The hazard for calculating risk maps is instead preloaded and is the hazard model developed by INGV (National Institute of Geophysics and Volcanology) and adopted at the national level.

In this framework, the CAESAR II project (Controlling, Mitigating and Managing Seismic Emergencies: Cost-Benefit and Multi-Criteria Analysis of Impact Scenarios for Risk Reduction and Increased Resilience) is born. It is a web-service procedure conceived as a decision support system for public authorities engaged in the development of disaster risk reduction plans, with the possibility to plan medium and long-term investments, as well as to define customised financial support mechanisms and fiscal incentives.

The project, developed as a follow-up to the CRISMA EU-FP7 (http://www.protezionecivile.gov.it/resources/cms/documents/CRISMA_locandina.pdf) and CAESAR I projects (a seismic impact model developed for the Campania region operations room in 2005), is funded by the Agenzia per la Coesione Territoriale (National Territorial Cohesion Agency), within the framework of the PON (National Operative Project) Governance and Institutional Capacities 2014-2020, as an intervention aimed at the transfer, evolution and dissemination of best practices among Public Administrations. CAESAR II includes a module for the simulation of

retrofitting measures applied at the municipal scale, integrating different categories of anti-seismic and energy improvement measures based on analysing the existing building stock's vulnerability.

The CAESAR II tool's core is the 'seismic impact scenarios' evaluation module, based on the hazard assumed by the end-users. The output of the model includes information on the expected damage levels for buildings (from D0- no damage to D5- total collapse) and population (deaths, injuries and homelessness). Impact scenarios can be customised according to the minimum unit of analysis assumed (municipality or 250x250m square mesh grid) and the availability of exposure data. The exposure is estimated by exploiting the ISTAT (National Institute of Statistics) Census 2011 [13], an Italian database that provides, for census zones, aggregated information on the buildings and the number of residents.

The scenarios include geo-referenced data managed by geo-servers capable of exchanging data in a format compliant with OGC standards and the European INSPIRE Directive. Simulation results can be further processed through the Multi-Criteria and Cost-Benefit Analysis modules to support the comparative evaluation of alternative seismic and energy measures. One of the CAESAR II tool's main strengths is that it does not require specific technical or engineering skills from the user, as it is offered as a complete package that needs some input data.

The paper has been structured in two main sections: the former one describes the calculation models and assumptions on which the CAESAR II procedure is based and the format of the information that is requested from the user; the latter one shows an application example on three Piedmontese municipalities (Pinerolo, Torre Pellice and Villar Pellice) made possible thanks to the data provided by the RISVAL project (<https://www.interreg-alcotra.eu/it/decouvrir-alcotra/les-projets-finances/risvalrischio-sismico-e-vulnerabilita-alpina>).

2. THE CAESAR II MODEL

Caesar II is a web-service procedure developed for the Territorial Cohesion Agency, producing scenario and seismic risk analyses in terms of economic, building and human life losses and evaluating their possible reduction through cost-benefit and multi-criteria analyses to support decisions. The application works on municipalities on a grid of 250x250m for which hazard and exposure factors are defined. CAESAR II is based on three models of analysis, described below:

1. Seismic Impact Risk and Scenario Analysis Model;
2. Post-seismic economic loss forecasting Model;
3. Multi-Criteria Analysis Model.

The three models have been synergistically implemented in as many modules within the so-called reuse kit.

2.1. Seismic Impact Risk and Scenario Analysis Model

Hazard

The seismic hazard adopted in CAESAR II is a function of the type of analysis to be developed. In the case of "risk" analysis, the primary seismic hazard is adopted, i.e. the maximum value of horizontal ground acceleration (PGA, peak ground acceleration), calculated by the INGV. The PGA values are given in correspondence of a grid of 10.751 points, defined by latitude and longitude coordinates, covering the whole national territory (**Figure 1**).

For each node in the geographic grid, parameters are provided at specified return periods, TR (30, 50, 72, 101, 140, 201, 475, 975, and 2,475 years). PGA maps are calculated for different exceedance probabilities over 50 years (9 in total, ranging from 2% to 81%). For each estimation, the 50th percentile distribution (median map, which is the reference map for each exceedance probability) and the 16th and 84th percentile distributions are available, indicating the variability of the estimates.

In the case of "scenario" analysis, the seismic event taken as a reference can be assumed through: 1) an attenuation law as a function of some seismic parameters, such as the coordinates of the hypocenter and the magnitude value, or 2) a shaking map (ShakeMap). The distribution over the territory of the parameters that define the extent of a seismic event (e.g., the PGA) can be derived

through the adoption of an attenuation law, as a function of other seismic parameters (usually the magnitude) and epicentral (or hypocentral) coordinates. CAESAR II adopts, as attenuation law, the relation of Blake [14], which assumes a decimal logarithmic decay, and the conversion law determined by Faenza and Michelini [15], [16] between the observed shaking parameters and the MCS intensity scale. In Italy, shaking maps are provided by INGV for all earthquakes with magnitude $M \geq 3.0$ occurring in the national territory and surrounding areas. They are published on the website <http://shakemap.rm.ingv.it>. When new information or additional earthquake data become available (e.g., the size of the earthquake fault -extended fault-, new data from networks operated by other agencies), the maps are updated to improve the definition of ground shaking, particularly in epicentral areas. They provide an immediate visualisation of the level of shaking of an area affected or interested by an earthquake, reporting the peak values recorded by accelerometers and seismometers, mainly provided by the National Accelerometric Network (RAN) of the Department of Civil Protection and the National Seismic Network (RSN) of INGV, present in the area of the earthquake. If there are no observed values, an ad hoc software interpolates the data using, for example, the attenuation laws of the shaking with the distance available for the centre of each cell of the grid belonging to the area under examination.

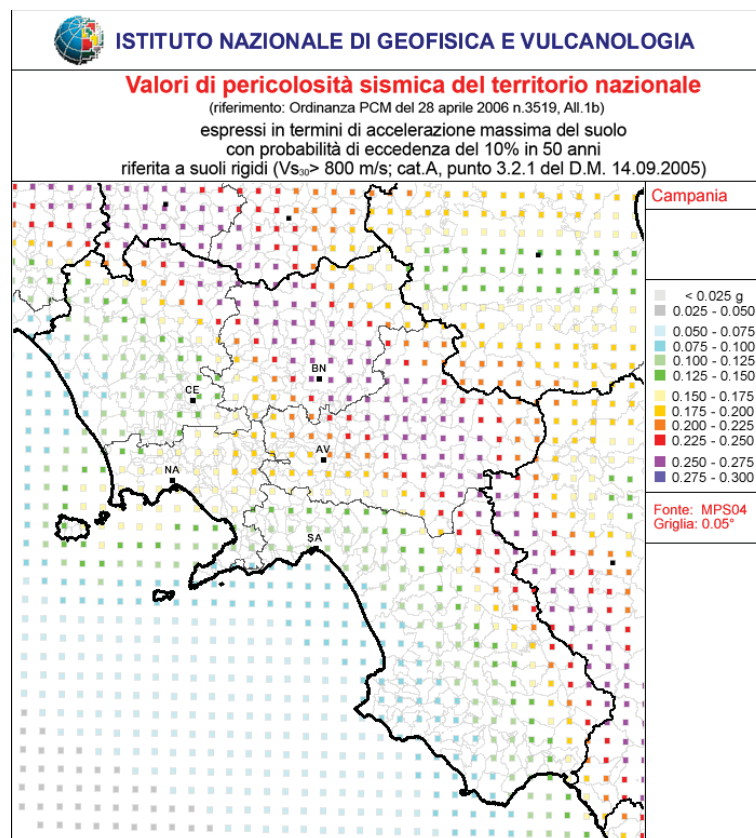


Figure 1. Seismic hazard values of the national territory expressed in terms of maximum ground acceleration with a probability of exceeding 10% in 50 years, referred to rigid soils.

Exposure

Exposure and vulnerability are closely related factors. For each category of elements at risk, the estimate of vulnerability to the seismic event must be accompanied by "a qualitative and quantitative analysis of the exposed property" (exposure), in order to identify the spatial distribution, and possibly temporal, of typological classes of elements at risk, called classes of vulnerability, each of which is a set of elements that for characteristics present similar behaviour (Vulnerability) concerning the earthquake. In other words, it is necessary to identify the salient characteristics of the element at risk (vulnerability factors), to which a specific capacity to respond to the natural phenomenon is attributed.

CAESAR II refers to two types of elements at risk: ordinary buildings and their occupants. The estimation of the buildings in the area under examination can be based on a statistical analysis, which

evaluates the percentage distribution of the different classes of vulnerability of the buildings (A, B, C, D for decreasing vulnerability) based on their different behaviour towards the natural event. A similar procedure is adopted to estimate the population and the distribution of occupants for buildings divided by class of vulnerability.

The exposure model uses a procedure that can take into account both the ISTAT data only and the ISTAT data combined with information coming from a data collection activity on the investigated area. These input data are processed by the tools S.A.V.E. [17] and B.I.N.C. [7], two procedures developed by the PLINIVS Study Centre which aim to characterise the seismic vulnerability of specific building typologies (S.A.V.E.) and to evaluate a probable geographical distribution of these building typologies according to their recurrence in the ISTAT census data (B.I.N.C.).

In particular, the S.A.V.E. model is used to assign vulnerability classes to single buildings, detected in the data collection campaigns on the territory, according to their typological and structural characteristics. The B.I.N.C. model exploits the S.A.V.E. method and defines a probable distribution of the ISTAT buildings on the vulnerability classes, starting from the population density of the considered municipality and from the ages of construction of the buildings identified on each census section.

The distribution of vulnerability classes (exposure) is defined for each minimum reference unit of the model (250x250m cell of a regular square-mesh grid). However, ISTAT data on buildings refer to individual census sections, which may also contain a large number of cells, so a criterion for assigning census data to each cell was adopted, following relations (1) and (2), having defined "zones" as the areas of intersection between census sections and the grid (**Figure 2**):

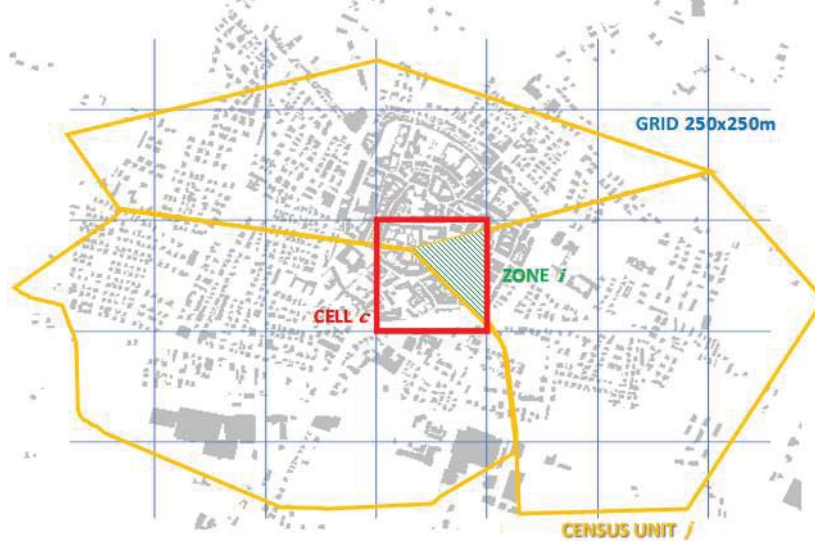


Figure 2. Illustrative representation of the "zones" (green), defined as the areas of intersection between the ISTAT census sections (yellow) and the 250x250m cells (red) of the model's reference grid (blue).

The number of buildings in zone i of census section j of vulnerability class k are estimated as in the equation (1); the number of buildings in cell c of vulnerability class k are obtained by the relation (2):

$$E_{i,j}^k = \begin{cases} E_{i,j}^{k,R} & \text{se: } E_j^{ISTAT} / E_j^R \leq 1 \\ E_{i,j}^{k,R} + E_{i,j}^{k,R} = E_{i,j}^{k,R} + E_j^k / E_j^{ISTAT} \cdot (E_{i,j} - E_{i,j}^R) & \text{se: } E_j^{ISTAT} / E_j^R > 1 \end{cases} \quad (1)$$

$$E_c^k = \sum_{i=1}^n E_{i,j}^k \quad (2)$$

Where:

c is the cell

j is the census section

i is the zone, intersection of the reference grid and census section

k is the vulnerability class ($k = A, B, C, D$)

n is the number of zones constituting cell i

E_j^{ISTAT} is the number of buildings in census section j

E_j^k is the number of buildings of census section j of vulnerability class k (BINC)

E_j^R is the number of buildings of census section j surveyed

$E_{i,j}^k$ is the number of buildings in zone i of census section j of vulnerability class k

$E_{i,j}^{k,R}$ is the number of buildings detected of zone i of census section j of vulnerability class k

(S.A.V.E.)

$E_{i,j}^{k,R}$ is the number of undetected buildings of zone i of census section j of vulnerability class k

E_c^k is the number of buildings in cell c of vulnerability class k .

Regarding the occupants' exposure, the CAESAR II model considers the assumption that the population is uniformly distributed over the homes. The data collected by the PLINIVS Study Centre and processed with the SAVE method have allowed to define a correlation between the number of houses present in a building and the vulnerability class to which the building belongs (**Table 1**).

average of dwellings	Vulnerability class of the building			
	A	B	C	D
M_{Ab}	2.0	2.7	3.45	6.90

Table 1. average of dwellings for buildings related to the vulnerability class

Therefore, the population distribution over the vulnerability classes is calculated as in equation (3).

$$N_{P_k} = \frac{E_k \cdot M_{Ab_k}}{\sum_{t=A, \dots, D} E_t \cdot M_{Ab_t}} P^{ISTAT} \quad (3)$$

Where

E_k is the number of buildings of vulnerability class k ,

M_{Ab_k} is the average of dwellings for the buildings of vulnerability class k ,

E_t is the number of buildings of vulnerability class t ,

M_{Ab_t} is the average of dwellings for the buildings of vulnerability class t ,

P^{ISTAT} is the population indicated in the ISTAT data

Finally, the average number of occupants as the seismic class k (N_{O_k}) of each cell in the reference grid varied was evaluated using relation (4).

$$N_{O_k} = N_{P_k} \cdot Q_{m,o} \quad (4)$$

Where:

N_{P_k} is the number of people per seismic class k estimated, cell by cell, based on ISTAT data;

$Q_{m,o}$ is the average percentage of occupants, assumed to be 65%, of the total population.

Vulnerability

A building's vulnerability is the probability that the system (entire building), subsystems (walls, framing, roofs, etc.), or components of the system (beams, columns, infill panels, windows, doors, etc.) will be damaged as a result of an assigned action to which they are subjected. The concept of vulnerability requires to define unambiguously the level of "damageability" of the exposed asset due to the natural event. The damage scale adopted in CAESAR II refers to the six levels of damage of the: D0: no damage; D1: not structural damage; D2: light structural damage; D3: structural damage; D4: partial collapse; D5: total collapse.

The propensity of a building to sustain damage is a function of its constituent elements. The strength and technological aspects of structural (walls, beams, columns, floors, roofs, etc.) and non-structural (infill panels, openings, protective panels, etc.) elements strongly influence the vulnerability of the building itself [18].

The vulnerability of a building to an earthquake can be assessed through the so-called vulnerability curves. For an assigned class of vulnerability, they express the probability of exceeding a certain level of damage as the hazard measurement parameter varies, which may be the peak seismic acceleration, spectral intensity, macroseismic intensity, etc..

CAESAR II uses the model of vulnerability curves for ordinary buildings. These curves were calibrated on data from damage probability matrices produced through a statistical analysis of observed damage following earthquakes that have occurred in Italy since 1980, and converted to PGAs via Margottini's law [19]. The mean and standard deviation parameters of the vulnerability curves are shown in **Table 2**.

The vulnerability of the population to the earthquake is determined with reference to the damage suffered by the buildings occupied by the people. In **Table 3**, the percentages of dead QD and injured QI are reported as a function of the building's level of damage. The values shown were calibrated based on data collected from past earthquake events [20].

CLASS	PERCENTILE	D1		D2		D3		D4		D5	
		μ	σ	μ	σ	μ	σ	μ	σ	μ	σ
A	16%	-3,50	0,80	-2,70	0,80	-1,95	0,70	-1,35	0,60	-0,75	0,60
A	50%	-3,35	0,80	-2,60	0,80	-1,74	0,80	-0,95	0,75	-0,40	0,75
A	84%	-3,25	0,80	-2,25	0,80	-1,65	0,80	-1,00	0,80	-0,15	0,80
B	16%	-2,80	1,20	-1,55	1,10	-0,70	1,10	0,00	0,80	0,50	0,55
B	50%	-2,45	1,20	-1,20	1,00	-0,45	0,90	0,10	0,70	0,40	0,70
B	84%	-1,90	1,00	-0,90	0,80	-0,35	0,70	0,20	0,40	0,45	0,40
C	16%	-2,60	1,60	-1,20	1,20	-0,35	0,90	0,20	0,70	0,55	0,45
C	50%	-2,10	1,30	-0,80	1,00	-0,15	0,80	0,40	0,80	0,70	0,70
C	84%	-1,50	1,20	-0,50	0,80	-0,03	0,60	0,20	0,45	0,55	0,40
D	16%	-1,40	1,40	-0,10	1,00	0,40	0,60	0,70	0,55	1,30	0,60
D	50%	-1,00	1,20	0,00	0,80	0,60	0,60	0,80	0,50	1,50	0,60
D	84%	-0,40	1,00	0,40	0,70	1,10	0,80	1,20	0,60	1,70	0,60

Table 2. logarithmic mean and logarithmic standard deviation of the vulnerability curves

Percentage of death (Q _D) and injured (Q _I)	Level of damage						Vulnerability Class
	D0	D1	D2	D3	D4	D5	
Q _D	0	0	0	0	0.03	0.14	A, B, C
Q _D	0	0	0	0	0.06	0.28	D
Q _I	0	0	0	0	0.10	0.56	A, B, C
Q _I	0	0	0	0	0.12	0.42	D

Table 3. Percentage of death and injured regarding the levels of damage and vulnerability class

Finally, The EASE model (Zuccaro et al., 2008; Zuccaro and Cacace, 2010), developed and engineered by the PLINIVS centre for DPC, was adopted to estimate the effects of risk related to the chosen reference period. The model discretises the territory through a square-mesh grid of size 250x250m. To each cell is assigned: hazard data, in terms of PGA; and exposure data, in terms of the number of buildings for each structural vulnerability class and the number of occupants. Combining these data with seismic vulnerability (percentiles 16, 50, and 84%), the model yields the following products on a cell-by-cell basis:

- Number of collapsed buildings, as the sum of buildings with D4 and D5 damage.
- Number of uninhabitable buildings, as the sum of buildings with D4 and D5 damage and 60% of buildings with D3 damage.
- Number of deaths N_D and injuries N_I , as assessed through the equations (5) and (6):

$$N_D = (1 + TI_c) \cdot \sum_{t=1}^4 \sum_{j=1}^5 N_{t,j} \cdot NO_t \cdot Q_{Dt,j} \quad (5)$$

$$N_I = (1 + TI_c) \cdot \sum_{t=1}^4 \sum_{j=1}^5 N_{t,j} \cdot NO_t \cdot Q_{It,j} \quad (6)$$

Where:

- t is the seismic class of the building (A, B, C, D);
- j is the damage level of the building (D1, D2, D3, D4, D5);
- $N_{t,j}$ is the number of buildings, per cell, of seismic class t having damage level j ;
- NO_t is the average number of occupants per building of seismic class t ;
- TI_c is the tourism index of the city [0-100%];
- $Q_{Dt,j}$ is the percentage of deaths per seismic class t and damage level j ;
- $Q_{It,j}$ is the percent injured per seismic class t and damage level j .
- Number of homeless assessed through the relationship (7):

$$N_H = \sum_{t=1}^4 [(0.5 \cdot N_{t,D3} + N_{t,D4} + N_{t,D5}) - N_D] \quad (7)$$

Where:

- $N_{t,D3}$ is the number of buildings, per cell, of seismic class t having damage level D3;
- $N_{t,D4}$ is the number of buildings, per cell, of seismic class t having damage level D4;
- $N_{t,D5}$ is the number of buildings, per cell, of seismic class t having damage level D5.

2.2. A post-seismic economic loss forecasting model

Seismic emergency management requires specific programs for identifying the objectives to organise an adequate and quick response. They manage a complex workforce, equipment and resources arranged and coordinated by local administrations both in space and time.

The introductory knowledge basis, necessary to allocate resources, is represented by damage scenarios, useful to predict possible damages due to an earthquake impact and following population involvement in the affected area [21]. Such scenarios contain data like territorial seismic vulnerability with particular attention to the built environment. Moreover, they can provide valuable information about the extension of the most seriously affected area, working of transport infrastructures, roads and service networks, damage on buildings and the expected casualties, as well as the corresponding financial burden.

Within this dense framework, an earthquake can be described as a phenomenon characterised by a two-phases temporal sequence, each of which has direct and indirect economic consequences. For what that concerns the directly related ones, it is possible to find all those connected to protection, improvement, and structural seismic adaptation to reduce the general vulnerability of ordinary buildings. Equation (8) can assess these mitigation costs (MTC). In **Table 4** the Average cost of mitigation interventions from a vulnerability class to another (€/m²) are summarized.

$$MTC = \sum_{j=A}^D emc_j \cdot sm_{emc_j} \cdot cm_{emc_j} + \sum_{j=A}^D emc_j \cdot cman_{emc_j} \quad (8)$$

Where:

- emc_j is the number of j -th vulnerability class buildings to be mitigated;

sm_{emc_j} is the average area of the j -th vulnerability class building to be mitigated;
 cm_{emc_j} is the average mitigation cost for the j -th vulnerability class building (Table 4);
 $cman_{emc_j}$ is the average maintenance cost for the j -th vulnerability class building ($cman_{emc_A} = 1.500$ €/year; $cman_{emc_B} = 1.800$ €/year; $cman_{emc_C} = 2.000$ €/year; $cman_{emc_D} = 2.600$ €/year).

Class	B	C	D
A	360	510	624
B	-	390	540
C	-	-	378

Table 4. Average cost of mitigation interventions from a vulnerability class to another (€/m²)

Inside the area hit by an earthquake of a given magnitude, all post-event operations can be immediately translated into costs directly linked to the buildings' damage and affected population. As part of the post-event costs, those related to reconstruction, on-site or in a new different location, involve buildings irreversibly damaged by the earthquake (damage level D4-D5 under the EMS'98 classification). The relation (9) can assess these reconstruction costs (RC).

$$RC = \sum_{i=4}^5 edl_i \cdot sm_{edl_i} \cdot crl + \sum_{i=4}^5 edd_i \cdot sm_{edd_i} \cdot crd \quad (9)$$

Where:

sm_{edl_i} is the average area of the i -th damage level building to be rebuilt on-site;
 crl is the reconstruction cost for a residential building on-site (1.235,94 €/m²);
 edd_i is the number of i -th damage level buildings to be rebuilt delocalised;
 sm_{edd_i} is the average area of the i -th damage level building to be rebuilt delocalised;
 crd is the reconstruction cost for a residential building delocalised (1.250 €/m²).

The Restoration costs (RT) are, instead, connected to the activities planned for recovery buildings and infrastructures damaged in a non-irreversible way by the earthquake (damage level D1-D2-D3 under the EMS'98 classification) and can be calculated as in the formula (10).

$$RT = \sum_{i=1}^3 ed_i \cdot sm_{ed_i} \cdot cr_{ed_i} \quad (10)$$

Where:

ed_i : number of i -th damage level buildings to be restored;
 sm_{ed_i} : average area of the i -th damage level building to be restored;
 cr_{ed_i} : restoration cost for a residential building as a function of damage level ($cr_{ed1}=360$ €/m²; $cr_{ed2}=458$ €/m²; $cr_{ed3}=545$ €/m²).

At this stage, all those costs related to the *demolition and rubble removal (DR)* of lost buildings are certainly not negligible, as well as the management cost for specialised landfills. The formula (11) can assess these efforts:

$$DR = \sum_{i=4}^5 ed_i \cdot vm_{ed_i} \cdot cd + \sum_{i=4}^5 ed_i \cdot vm_{ed_i} \cdot ct \cdot dm + \sum_{i=4}^5 ed_i \cdot vm_{ed_i} \cdot cg \quad (11)$$

where:

ed_i is the number of i -th damage level buildings to be demolished;
 vm_{ed_i} is the average volume of the i -th damage level building to be demolished;
 cd is the demolition cost for a lost building as a function of vulnerability class ($cd_{A-B}=12$ €/m³; $cd_C=14$ €/m³; $cd_D=16$ €/m³);
 ct is the cost of rubble transportation to the landfill (0,6 €/m);

dm is the average site distance from the landfill (300 m);

cg is the average landfill management cost (1,4682 €/m²).

As part of the costs associated with safeguarding the population affected by the earthquake, it is possible to include *health care* costs (HT) for establishing medical equipment, strengthening existing local public facilities, as well as physical and psychological support. These costs can be calculated as in the equation (12).

$$HT = f \cdot cm \cdot tm \quad (12)$$

where:

f is the number of people in need of medical care;

cm is the unit cost of medical care operations (200 €);

tm is the average time for medical care (10 days).

The formula (13) calculates the *evacuation* costs (EV) of the population, split up according to the destination and the means of transport employed:

$$EV = s_{nm} \cdot cm_t + cm_c \cdot \frac{s_t}{s_c} + cm_{pc} \cdot tu_c + cm_{kp} \cdot s_t + cg_{at} \cdot \frac{st_t}{sm_t} \cdot tu_c + cg_t \cdot s_{te} + cg_h \cdot s_h \quad (13)$$

Where:

s_{nm} is the number of homeless people with no vehicle;

cm_t is the total cost of public transport (15.599 €);

cm_c is the cost of checkpoints set-up (7.050 €);

s_t is the total number of homeless people;

s_c is the number of homeless people evacuated at checkpoints;

cm_{pc} is the daily cost of checkpoints staff (5.930 €);

tu_c is the checkpoints' time usage;

cm_{kp} is the unit cost of the emergency kit (10 €);

cg_{at} is the daily depreciation cost per tent set up (20,55 €);

st_t is the number of homeless people evacuated in tents;

sm_t is the average number of people for each tent set up;

cg_h is the daily cost for the stay in the hotel (45 €);

s_h is the number of homeless people accommodated in hotels;

cg_t is the daily cost for accommodation in the tent;

s_{te} is the number of homeless people placed in tents.

The last cost item estimated is related to *emergency management* (EM) activities following an earthquake, which includes the construction of operational structures and the deployment of vehicles and employees to prepare equipped areas. The formula (14) is used to this purpose.

$$EM = pg_{pc} \cdot cm_{cc} + c_r + cp_{gpc} \cdot tp_{pc} + cp_{gpo} \cdot tp_{po} + cp_{gmo} \cdot tp_{mo} + cm_{pv} \cdot tp_{pv} \quad (14)$$

Where:

pg_{pc} is the average daily presence of Department of Italian Civil Protection staff;

cm_{cc} is the unit cost for coordination centre set-up (3.000 €);

c_r is the cost of communication networks and IT services (5.000.000 €);

cp_{gpc} is the cost for daily presence of Department of Italian Civil Protection staff (126.18 €/day);

tp_{pc} is the presence of the Department of Italian Civil Protection staff;

cp_{gpo} is the cost for daily presence of operating structures staff (130 €/day);

tp_{po} is the presence of operating structures staff;

cp_{gmo} is the cost for daily presence of operating structures means of transport (20 €/day);

tp_{mo} is the presence of operating structures means of transport;

cm_{pv} is the cost for daily presence of volunteer staff (100 €/day);

tp_{pv} is the presence of volunteer staff.

All the parametric costs showed are from the Department of Italian Civil Protection's elaborations about the L'Aquila 2009's earthquake.

2.3. The multi-criteria analysis model

The amount of damage caused by earthquakes can be minimised by adopting systematic measures of emergency management. Within this context, it is crucial to intervene immediately by making decisions that result as accurate and objective as possible, by recognising all the viable alternatives and analysing their consequences. Decision-making problems framed into this background involve a multiplicity of relevant aspects and the presence of various goals and constraints, often not explicit or even contrasting. These items can be inserted in a so-called *decision tree* with a general objective at the top and at least a decision-maker. Such models can keep account of the conflicting nature of uncommonly complex situations and explain the criteria for selecting the alternatives in terms of specific targets to reach.

The multi-criteria analysis' main point is not a pursuit for objectively optimal solutions but the support to rationalise the decision-making process and optimise a set of criteria weighted according to the decision-makers' preferences. This new kind of evaluation scheme identifies alternatives that satisfy a certain number of explicitly defined standards. It is possible to sort the elements of a decision tree as:

- Objectives: statements regarding the condition to achieve, made operational by allocating one or more qualitative and quantitative attributes;
- Criteria: standards of judgment or rules useful to test the worth of decision alternatives, including both the concept of goal and attribute;
- Alternatives: elements of evaluation and choice that must be ordered based on dominance scores representing the entries of the decision matrix.

One of multi-criteria's most powerful tool is undoubtedly the *Analytic Hierarchy Process* [22]. Such a complex algorithm makes it possible to evaluate the priority of actions, programs, intervention strategies, plans and projects by applying mathematical concepts to decision-making, as well as quantitative methodologies to evaluate mostly intangible and subjective judgments. They oppose the classic single-criterion linear analysis models suitable only to straightforward cases and under enough simplified hypotheses. The main advantage is now the flexibility in solving difficult problems by adopting a typical human mind's cognitive model.

It is possible to obtain reliable scales by only using personal judgments, identifying all the single elements of a problem, placing them inside homogeneous sets and sorting each set at a different level. In hierarchies, intricate schemes are top-down analysed in their basics, simulating how the human brain analyses complexity and breaks down the objects perceived by the senses into categories and sub-categories, building a so-called dominance hierarchy (**Figure 3**).

The first level contains the general objective, while the second level contains its further specifications. A possible third level can add more details to the upper level and so on. Finally, alternatives are placed at the base of the dominance hierarchy. Once completed this initial phase, pairwise comparisons are performed for each element of a certain level, with reference to the element placed at that immediately higher. According to the hierarchy shown in Figure 1, second-level criteria are pairwise compared with reference to the overall objective. Third-level sub-criteria are pairwise compared with reference to each second-level criterion until the alternatives are compared according to each third-level sub-criterion, each second-level criterion and, finally, the overall objective.

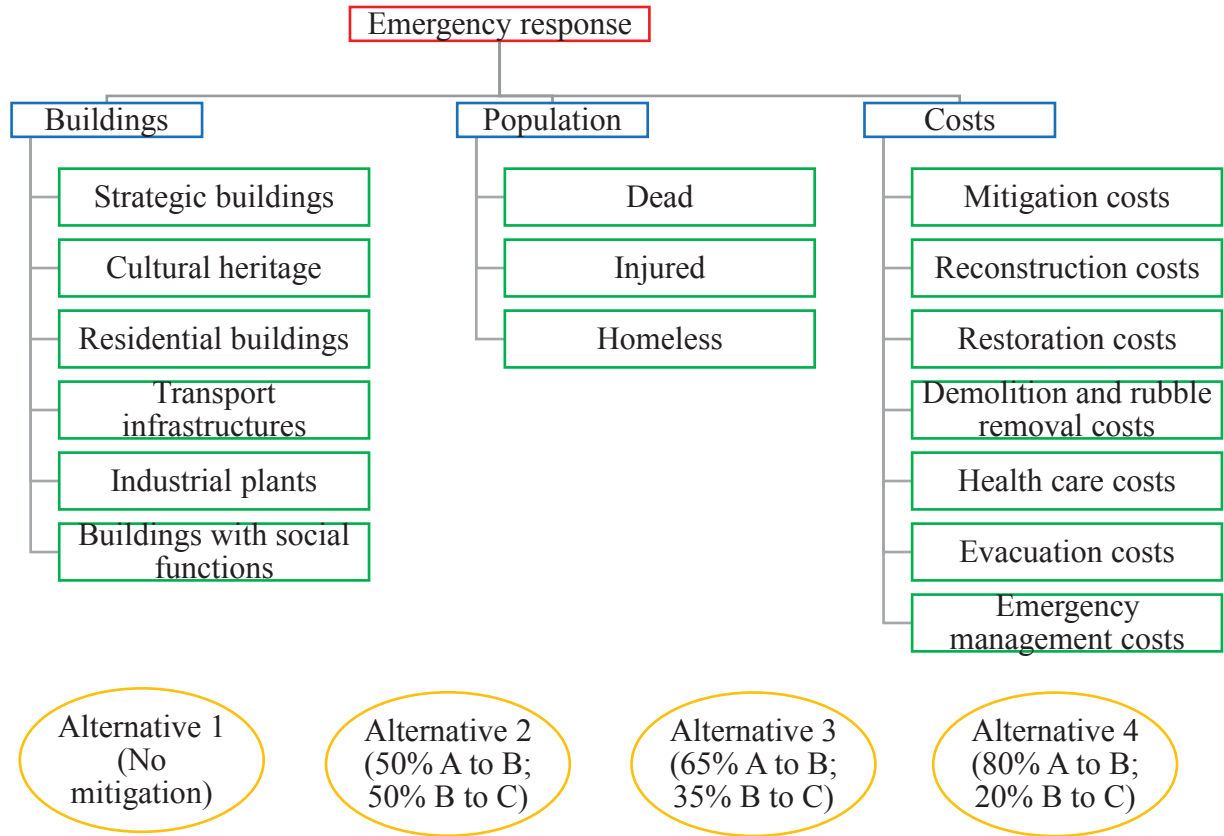


Figure 3. The dominance hierarchy

These operations provide a series of comparison coefficients placed into a so-called dominance matrix and a priority vector that measures all the alternatives' relative reasonability. When the use of judgments is necessary, these can be expressed via the semantic scale of Saaty (Table 5). Such a scheme links natural numbers to qualitative linguistic variables making it possible to answer the crucial question behind all pairwise comparisons: "How much does an element dominate another with reference to a specific criterion or attribute? ".

Intensity of dominance (a_{ij})	Judgement
1	Equal importance
3	Weak predominance
5	Moderate predominance
7	Strong predominance
9	Absolute predominance
2 4 6 8	Values of compromise

Table 5. The semantic scale of Saaty

Denoting by n the number of criteria to be considered, the dominance matrix A^k , built by an individual decision-maker, will be square and symmetrical (Equation (15):

$$A^k = \begin{bmatrix} a_{11}^k & a_{12}^k & \dots & a_{1n}^k \\ a_{21}^k & a_{22}^k & \dots & a_{2n}^k \\ \dots & \dots & \dots & \dots \\ a_{n1}^k & a_{n2}^k & \dots & a_{nn}^k \end{bmatrix} \quad (15)$$

where a_{ij}^k denotes the k -th preference of the generic decision-maker, referred to the i -th criterion concerning the j -th one. If there are more than one decision-makers, individual preferences are averaged and inserted into a new dominance matrix A (Equation (16))

$$A = \begin{bmatrix} a_{11} & a_{12} & \dots & a_{1n} \\ a_{21} & a_{22} & \dots & a_{2n} \\ \dots & \dots & \dots & \dots \\ a_{n1} & a_{n2} & \dots & a_{nn} \end{bmatrix} \quad (16)$$

Following the Analytic Hierarchy Process, every criterion's normalised weight w_{Ni} is calculated as in the (17).

$$w_{Ni} = \frac{(\prod_{j=1}^n a_{ij})^{\frac{1}{n}}}{\sum_{i=1}^n w_i} \quad i = 1, \dots, n \quad (17)$$

The eigenvalue for each row of the dominance matrix A is computed as in the (18).

$$\lambda_i = w_i \left(\frac{\sum_{j=1}^n a_{ij}}{\sum_{i=1}^n w_i} \right) \quad i, j = 1, \dots, n \quad (18)$$

and so the maximum eigenvalue is calculated as in (19), that represents the limit value that n must take in order for the (20).

$$\lambda_{max} = \sum_{i=1}^n \lambda_i \quad (19)$$

$$w_i = \frac{\sum_{j=1}^n a_{ij} w_j}{(\lambda_{max} = n)} \rightarrow \sum_{j=1}^n a_{ij} w_j = \lambda_{max} w_i \quad (20)$$

The following *consistency index* CI measures the deviation of A from the coherence and allows to measure the overall difference between the two sets of values, as in the (21).

$$CI = \frac{\lambda_{max} - n}{n - 1} \quad (21)$$

Impossibility to make reliable judgments, lack of data and inexperience can drive inconsistency. However, it is crucial to establish its maximum admissible value to avoid having completely erroneous data, so the consistency index is compared with arbitrary *random index* RI . The ratio between CI and RI provides the *consistency ratio* CR expressed in the (22).

$$CR = \frac{CI}{RI} \leq 0.10 \quad (22)$$

3. A CASE STUDY: PINEROLO, TORRE PELLICE AND VILLAR PELLICE MUNICIPALITIES

This section shows the application of CAESAR II system on three municipalities in the Piedmont Region: Pinerolo, Torre Pellice and Villar Pellice.

First of all, the impact model requires the choice of the kind of analysis (risk or scenario). In case of risk, the return period must be defined, while in case of scenario a shakemap has to be uploaded or coordinates and depth of the epicentre have to be provided

The analyses proposed for the Piedmontese municipalities have been done considering the area's risk, with reference to a seismic hazard expressed in acceleration (ag) and a probability of exceedance in 50 years of 10% (return period of 475 years). The hazard value is almost homogeneous on the three municipalities.

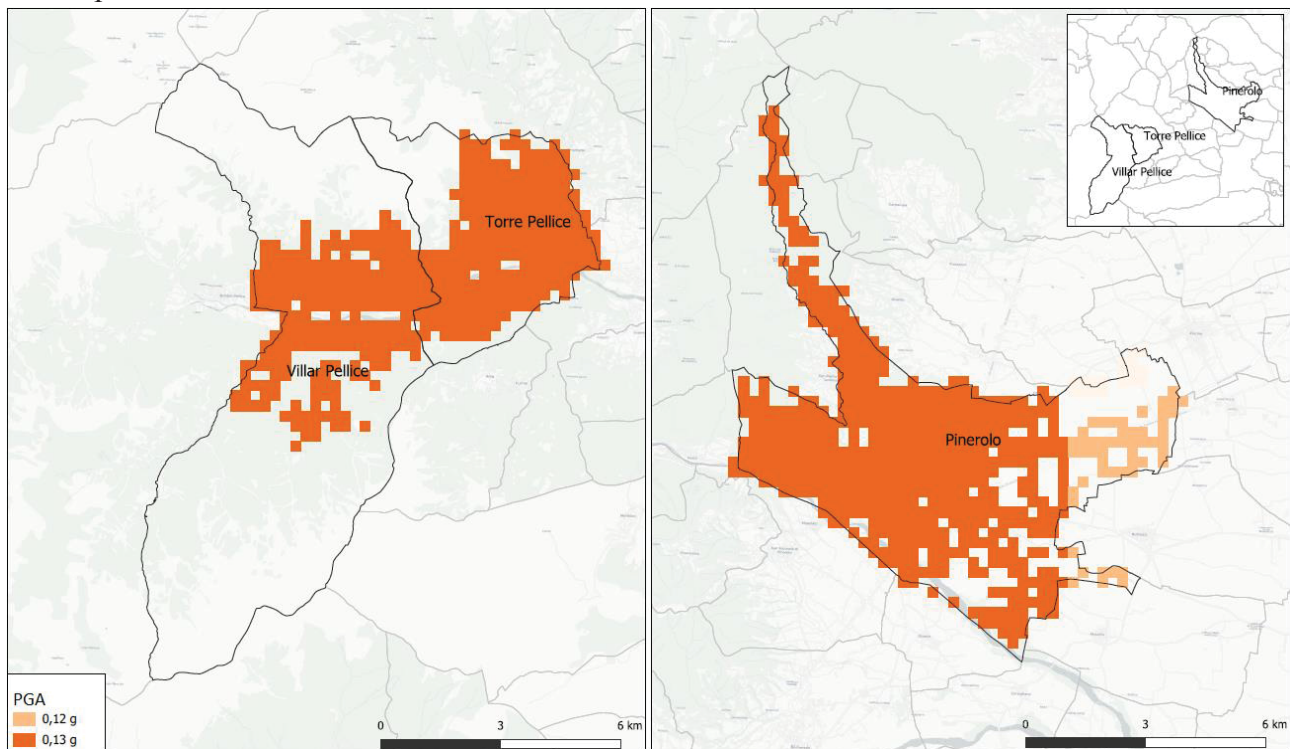


Figure 4. Hazard distribution on the cells of the investigated municipalities

Also, a dataset of 1,642 detected buildings has been provided by the Piedmont Region. With reference to the exposure model, estimated based on equations (1) and (2), the buildings distribution on the vulnerability classes summarised in the **Table 6** has been obtained. It is shown that all the investigated municipalities have a high percentage of buildings in class A (Villar Pellice 66%, Torre Pellice 52 % and Pinerolo 41%). With reference to class D, the high percentage is found in Pinerolo (28%), followed by Torre Pellice (21%) and, at the end, Villar Pellice (11%). The intermediated classes have similar values: class B occurs with a frequency of 18% in Pinerolo and Torre Pellice, and 17% in Villar Pellice; instead class C is manifested by a percentage of 13% in Pinerolo, 10% in Torre Pellice and 6% in Villar Pellice.

municipality	buildings	VULNERABILITY CLASS							
		A		B		C		D	
		n°	%	n°	%	n°	%	n°	%
Pinerolo	4211	1723	41	750	18	543	13	1195	28
Torre Pellice	1180	616	52	207	18	114	10	243	21
Villar Pellice	802	533	66	134	17	50	6	85	11

Table 6. Buildings distribution on the vulnerability classes for each investigated municipality

municipality	buildings	COLLAPSED BUILDINGS						UNHABITABLES BUILDINGS					
		min		med		max		min		med		max	
		n°	%	n°	%	n°	%	n°	%	n°	%	n°	%
Pinerolo	4211	93	2	196	5	357	8	295	7	502	12	764	18
Torre Pellice	1180	33	3	69	6	125	11	103	9	174	15	262	22

Villar Pellice	802	28	3	59	7	106	13	88	11	147	18	219	27
----------------	-----	----	---	----	---	-----	----	----	----	-----	----	-----	----

Table 7. Impact on the buildings

municipality	population	DEATH						INJURED						HOMELESS					
		min		med		max		min		med		max		min		med		max	
		n°	%	n°	%	n°	%	n°	%	n°	%	n°	%	n°	%	n°	%	n°	%
Pinerolo	34854	11	0,03	25	0,07	49	0,14	38	0,11	89	0,26	180	0,52	284	1	477	1	715	2
Torre Pellice	4573	2	0,04	5	0,11	9	0,20	7	0,15	17	0,37	34	0,74	101	2	169	4	253	6
Villar Pellice	1120	1	0,09	2	0,18	3	0,27	3	0,27	6	0,54	12	1,07	87	8	145	13	216	19

Table 8. Impact on the population

The impact estimated by the CAESAR II model with reference to the buildings and the population have been summarised in the Table 7 and Table 8 respectively, on the basis of the vulnerability model in the Table 2. The minimum values has been obtained with the vulnerability parameters related to the 16%, the medium values with the ones related to the 50% and the maximum values with the ones related to the 84%.

Although Pinerolo is the municipality with a high impact on the buildings and the population in total terms, it has a low percentage term. Contrary, Villar Pellice shows the low impact in full terms and the high impact in percentage terms. These results are perfectly consistent with the input data. The three municipalities are affected by an almost homogeneous hazard, so the exposure model dictates the differences. As shown, Villar Pellice is the most fragile municipality (high percentage of class A buildings), while Pinerolo has higher percentages of class C and D buildings. However, the buildings and inhabitants in Villar Pellice are 19% and 3% respectively of those in Pinerolo, so in total terms, the incidence is much lower.

The cost analysis model does not require information; the input data are the impact model's casualties and losses. In **Table 9** the costs analyses for each municipality, with reference to minimum, medium and maximum values, have been summarised. Since there are no hypotheses of mitigations in this phase, in all the cases, this value is equal to zero. The higher costs are always related to the restoration that in each case represent more than the 50% of the total costs.

The multi-criteria analysis's input data are provided by the casualties and economic losses resulting from some possible scenarios. In the case study four scenarios have been considered: the first one (SCENARIO 0) is related to the actual state while the remaining three are obtained by assuming forms of mitigation on existing buildings (SCENARIO 1: 50% of class A buildings are transformed into class B buildings and 50% of class B buildings are transformed into class C buildings; SCENARIO 2: 65% of class A buildings are transformed into class B buildings and 35% of class B buildings are transformed into class C buildings; SCENARIO 3: 80% of class A buildings are transformed into class B buildings and 20% of class B buildings are transformed into class C buildings). For each scenario have been considered the data estimated with the vulnerability model at 50%.

	PINEROLO			TORRE PELLICE			VILLAR PELLICE		
	MIN	MED	MAX	MIN	MED	MAX	MIN	MED	MAX
mitigation	-	-	-	-	-	-	-	-	-
reconstruction	76 MLN€	162 MLN€	298 MLN€	27 MLN€	56 MLN€	102 MLN€	23 MLN€	47 MLN€	87 MLN€
restoration	695 MLN€	862 MLN€	977 MLN€	218 MLN€	258 MLN€	282 MLN€	164 MLN€	185 MLN€	195 MLN€
demolition and rubble removal	1.84 MLN€	3.76 MLN€	6.57 MLN€	0.66 MLN€	1.32 MLN€	2.28 MLN€	0.55 MLN€	1.12 MLN€	1.93 MLN€
health	0.07 MLN€	0,17 MLN€	0.36 MLN€	0.01 MLN€	0.03 MLN€	0.07 MLN€	0.01 MLN€	0.01 MLN€	0.02 MLN€
evacuation	0.20 MLN€	0.21 MLN€	0.23 MLN€	0.19 MLN€	0.19 MLN€	0.20 MLN€	0.18 MLN€	0.19 MLN€	0.19 MLN€
emergency management	252 MLN€	252 MLN€	252 MLN€	252 MLN€	252 MLN€	252 MLN€	252 MLN€	252 MLN€	252 MLN€
TOTAL	1,026 MLN€	1,281 MLN€	1,534 MLN€	498 MLN€	568 MLN€	640 MLN€	439 MLN€	486 MLN€	535 MLN€

Table 9. Costs analyses for each municipality, with reference to minimum, medium and maximum values

In **Table 10** the impact (on the buildings and on the population) and costs of each scenario has been resumed. Also, the percentage of the impact aspects of each hypothesised scenario with reference to the actual case (SCENARIO 0) has been indicated.

		scenario 0	scenario 1		scenario 2		scenario 3	
human losses	death	49	26	53%	21	43%	15	31%
	injured	107	56	52%	43	40%	30	28%
	homeless	703	384	55%	306	44%	230	33%
buildings losses	uninhabitable	824	510	62%	429	52%	346	42%
	collapsed	324	181	56%	142	44%	101	31%
costs	mitigation	- MLN€	501 MLN€	n.e.	456 MLN€	n.e.	321 MLN€	n.e.
	reconstruction	267 MLN€	155 MLN€	58%	122 MLN€	45%	89 MLN€	33%
	restoration	1,306 MLN€	1,283 MLN€	98%	1,284 MLN€	98%	1,284 MLN€	98%
	demolition and rubble removal	6.20 MLN€	3.55 MLN€	57%	2.76 MLN€	44%	1.99 MLN€	32%
	health	0.22 MLN€	0.11 MLN€	52%	0.08 MLN€	39%	0.06 MLN€	27%
	evacuation	0,58 MLN€	0.56 MLN€	96%	0.56 MLN€	95%	0.55 MLN€	94%
	emergency management	756 MLN€	756 MLN€	100%	756 MLN€	100%	756 MLN€	100%
	TOTAL	2,221 MLN€	2,620 MLN€	118%	2,553 MLN€	115%	2,394 MLN€	108%

Table 10. Impact (on the buildings and the population) and costs of each scenario and percentage of the impact aspects of each hypothesised scenario with reference to the actual case (SCENARIO 0)

The objective of this case study is to draw up an adequate response to a seismic emergency. Such a program represents a dynamic tool open to updates and revisions, subject to the identification and definition of multiple criteria articulated on different levels and configured to anticipate, prevent or deal with an earthquake that hits territory and social community

The dominance hierarchy proposed for this case identifies an objective O represented by the *emergency response* and three criteria C_i that specify the contents and meanings of the objective. *Buildings*, *population* and *costs* represent these first-level criteria. Sixteen second-level sub-criteria S_i further characterising the criteria in the higher level are expressed by *strategic buildings*, *cultural heritage*, *residential buildings*, *transport infrastructures*, *industrial plants*, *buildings with social functions*, *dead*, *injured*, *homeless*, *mitigation costs*, *reconstruction costs*, *restoration costs*, *demolition and rubble removal costs*, *health care costs*, *evacuation costs* and *emergency management costs*. The four decision alternatives A_i are described by the four scenarios derived from the two impact models already mentioned.

The first phase of the decision-making process is the composition of a team in which each member involved has specific skills within disciplines related to the strategic resolution of the problem. Based on the semantic scale of Saaty, every opinion expressed by the single decision-maker on an explanatory and simplified questionnaire represents the intensity of dominance to each pairwise comparison between elements belonging to the same hierarchical level. Results are averaged to take account of the multidisciplinary nature of the problem and transferred into the Analytic Hierarchy Process in the form of matrices of pairwise comparisons.

The first matrix of pairwise comparisons contains the criteria *buildings* C_1 , *population* C_2 and *costs* C_3 that are compared with each other regarding the objective *emergency response* O . Consequently, the normalised weight of each criterion is calculated.

O	C_1	C_2	C_3
C_1	1	1/5	3
C_2	5	1	6
C_3	1/3	1/6	1

Table 11. Matrix of pairwise comparison of criteria regarding the objective O

The second matrix of pairwise comparisons contains the sub-criteria *strategic buildings* S_1 , *cultural heritage* S_2 , *residential buildings* S_3 , *transport infrastructure* S_4 , *industrial plants* S_5 and *buildings with social functions* S_6 that are mutually compared regarding the criterion *buildings* C_1 . The third matrix of pairwise comparisons contains the sub-criteria *dead* S_7 , *injured* S_8 and *homeless* S_9 that are mutually compared regarding the criterion *population* C_2 . The fourth matrix of pairwise comparisons contains the sub-criteria *mitigation costs* S_{10} , *reconstruction costs* S_{11} , *restoration costs* S_{12} , *demolition and rubble removal costs* S_{13} , *health care* S_{14} , *evacuation costs* S_{15} and *emergency management costs* S_{16} that are mutually compared regarding the criterion *costs* C_3 . Therefore, all the weights are calculated and inserted into specific vectors.

Finally, sixteen matrices of pairwise comparisons are assembled: the alternatives *seismic vulnerability condition 1* A_1 , *seismic vulnerability condition 2* A_2 , *seismic vulnerability condition 3* A_3 and *seismic vulnerability condition 4* A_4 are compared with each other concerning the various sub-criteria S_i by an automatic algorithm able to assign a value from the semantic scale of Saaty to every ratio. All the matrices so calculated can provide the weight of each alternative with reference to each sub-criterion.

These decision alternatives are subsequently weighted in relation to the criteria *buildings* C_1 , *population* C_2 , *costs* C_3 and, ultimately, with reference to the objective *emergency response* O . The decision alternative *seismic vulnerability condition 4* A_4 turns out to be the best compromise between expected losses and economic burden for the community.

O	C_1	C_2	C_3	w_{Ai}
w_{Si}	0,195	0,717	0,088	
A_i				
w_{A1}	0,230	0,045	0,419	0,114
w_{A2}	0,238	0,143	0,126	0,160
w_{A3}	0,252	0,248	0,164	0,242
w_{A4}	0,280	0,563	0,291	0,484

Table 12. Calculation of the weights of the alternatives regarding the objective O

4. CONCLUSIONS

CAESAR II is a web-service procedure conceived as a decision support system for public authorities engaged in disaster risk reduction plans. The platform gives the possibility to plan medium and long-term investments and define customised financial support mechanisms and fiscal incentives. The 'seismic impact scenarios' evaluation module estimates the impact on the buildings and the population based on the user's few values on the hazard and, eventually, on the exposure. Simulation results can be further processed through the Multi-Criteria Cost-Benefit Analysis modules to support the comparative evaluation of alternative seismic and energy measures.

This paper described the procedure and the parameters included in each module of the tool and shows an application on three municipalities of the Pedimont region: Pinerolo, Villar Pellice and Torre Pellice. It is shown that CAESAR II requires few and easy data to the user, although it is able to provides a complete package of outcomes useful to support the emergency management and the mitigation decisions.

REFERENCES

- [1] Perelli, F. L., De Gregorio, D, Cacace, F. Zuccaro, G. - Empirical vulnerability curves for Italian Masonry Buildings – COMPDYN 2019. 7th ECCOMAS Thematic Conference on Computational Methods in Structural Dynamics and Earthquake Engineering, Crete, Greece, 24–26 June 2019.
- [2] Zuccaro, G., Perelli, F. L., De Gregorio, D., Cacace, F. - Empirical vulnerability curves for Italian masonry buildings: evolution of vulnerability model from the DPM to curves as a function of acceleration, Bulletin of Earthquake Engineering (2020) <https://doi.org/10.1007/s10518-020-00954-5>
- [3] Zuccaro G., Albanese V., Cacace F., Mercuri C. and Papa F., (2008). Seismic Vulnerability Evaluations within the Structural and Functional Survey Activities of the COM bases in Italy, AIP Conference, 2008.
- [4] Lagomarsino, S., Cattari, S. & Ottonelli, D. - The heuristic vulnerability model: fragility curves for masonry buildings. Bull Earthquake Eng (2021). <https://doi.org/10.1007/s10518-021-01063-7>
- [5] Zuccaro, G., Dolce, M., De Gregorio, D., Speranza, E., Moroni, C. (2015). La scheda CARTIS per la caratterizzazione tipologico- strutturale dei comparti urbani costituiti da edifici ordinari. Valutazione dell'esposizione in analisi di rischio sismico. 34° Convegno Nazionale GNGTS, Trieste, 17-19 novembre 2015, p.281-287
- [6] Zuccaro G., Cacace F., De Gregorio D. (2012). Buildings inventory for seismic vulnerability assessment at National and regional scale", In: 15th World Conference on Earthquake Engineering, 15th WCEE 2012, Lisbon (Portugal), 24–28 September 2012. Paper no 2829, 2012.

- [7] Cacace, F., Zuccaro, G., De Gregorio, D., Perelli, F. L. - Building Inventory at National scale by evaluation of seismic vulnerability classes distribution based on Census data analysis: BINC procedure International Journal of Disaster Risk Reduction Volume 28, June 2018, Pages 384-393
- [8] Zuccaro and Cacace (2011). Seismic casualty evaluation: The Italian model, an application to the L'Aquila 2009 event. Human casualties in earthquakes, 171-184.
- [9] Zuccaro G., Leone M. F., Del Cogliano D., Sgroi A. (2013). Economic impact of explosive volcanic eruptions: A simulation-based assessment model applied to Campania region volcanoes. JOURNAL OF VOLCANOLOGY AND GEOTHERMAL RESEARCH, vol. 266, p. 1-15, ISSN: 0377-0273, doi: 10.1016/j.jvolgeores.2013.09.002.
- [10] Leone, M.F., Zuccaro, G. (2016) Seismic and energy retrofiting of residential buildings: a simulation-based approach, *UPLanD – Journal of Urban Planning, Landscape & environmental Design*, 1(1), 11-25
- [11] Malczewski J. (1999). GIS and Multicriteria Decision Analysis. Wiley & Sons INC.
- [12] Borzi B, Faravelli M, Onida M, Polli D, Quaroni D, Pagano M, Di Meo A. (2018) Piattaforma IRMA (Italian Risk MAPs). GNGTS, pp 382–388.
- [13] ISTAT (2001) 14° censimento della popolazione e delle abitazioni.
- [14] Blake A. (1941). On the estimation of focal depth from macroseismic data. Bull. Seismol. Soc. Am., 31, 225-231.
- [15] Faenza L. and Michelini A. (2011). Regression analysis of MCS intensity and ground motion spectral accelerations (SAs) in Italy. Geophysical Journal International 186 (3), 1415-1430.
- [16] Faenza L. and Michelini A. (2010). Regression analysis of MCS intensity and ground motion parameters in Italy and its application in ShakeMap. Geophysical Journal International 180 (3), 1138-1152.
- [17] Zuccaro G, Cacace F (2015) Seismic vulnerability assessment based on typological characteristics. First level procedure S.A.V.E. Soil Dyn Earthquake Eng, pp 262–269
- [18] Zuccaro G. and De Gregorio D., (2013). Time and Space dependency in impact damage evaluation of a sub- Plinian eruption at Mount Vesuvius. Natural Hazard (2013) 68:1399–1423. DOI: 10.1007/s11069-013-0571-8, 2013.
- [19] C. Margottini, D. Molin and L. Serva (1992). Intensity versus ground motion: A new approach using Italian data, Engineering Geology, 33, 1, 45-58.
- [20] Contributo in volume (Capitolo o Saggio). Zuccaro Giulio, De Gregorio Daniela (2015). Scenario di impatto da evento idrogeologico nella pianificazione di emergenza. In: Caruso Antonio;Di Benedetto Antonio;Giulivo Italo;Santo Antonio;Zuccaro Giulio. (a cura di): Santo Antonio, Prevenzione dei rischi naturali ed antropici. Il presidio idrogeologico del territorio in Campania. p. 142-152, Dragoni:Edistampa Sud s.r.l., ISBN: 978-88-909754-1-7
- [21] Zuccaro and Cacace (2011). Seismic casualty evaluation: The Italian model, an application to the L'Aquila 2009 event. Human casualties in earthquakes, 171-184.
- [22] Saaty, T. L. (1980) The analytic hierarchy process: planning, priority setting, resource allocation, *McGraw-Hill*.

OPEN MODELS AND SOFTWARE FOR ASSESSING THE VULNERABILITY OF THE EUROPEAN BUILDING STOCK

Helen Crowley¹, Vitor Silva², Luis Martins², Xavier Romão³ and Nuno Pereira³

¹ EUCENTRE
Via Ferrata 1, Pavia 27100, Italy
e-mail: helen.crowley@eucentre.it

² GEM Foundation
Via Ferrata 1, Pavia 27100, Italy
vitor.silva@globalquakemodel.org, luis.martins@globalquakemodel.org

³ University of Porto
Rua Dr. Roberto Fria, 4200-465 Porto, Portugal
xnr@fe.up.pt, nmisp@fe.up.pt

Abstract

Reproducibility and transparency have become standard practice in earthquake loss modelling following a growing demand from both the public and private sectors for understandable and accessible risk model input data, software and results. Since the 1990's the European scientific community has worked together on many aspects of seismic hazard and risk modelling. These advances have led to the 2020 European Seismic Risk Model (ESRM20), which has been computed with open source software and is now being openly released to the wider scientific community. This paper presents the recently released input models and software to assess the vulnerability of the European building stock within ESRM20.

Keywords: Vulnerability, Fragility, European Exposure, Open-Source, Open Data.

1 INTRODUCTION

Reproducibility and transparency have become standard practice in earthquake loss modelling following a growing demand from both the public and private sectors for understandable and accessible risk model input data, software and results. Since the 1990's the European scientific community has worked together on many aspects of seismic hazard and risk modelling. These advances have led to the 2020 European Seismic Risk Model (ESRM20), which has been computed with open source software and is now being openly released to the wider scientific community (Crowley et al., 2019 [1]). This paper summarises the recently released input models and software to assess the vulnerability of the European building stock within ESRM20.

2 CAPACITY CURVES FOR EUROPEAN BUILDING STOCK

Capacity curves provide a description of the lateral strength and deformation capacity of buildings or building classes, and are often transformed to the ADRS (acceleration displacement response spectrum) format for the purposes of developing fragility functions.

For ESRM20, capacity curves for a large range of building classes are needed to cover the varying construction types in Europe (as included within the European exposure model: Crowley et al., 2020a [2]; Crowley et al., 2020b [3]). The GED4ALL Building Taxonomy has been used to classify the vulnerability of European buildings (Brzev et al., 2021 [4]) with the attributes summarised below:

- **Materials.** CR: reinforced concrete, MR: reinforced masonry, MCF: confined masonry, MUR: unreinforced masonry, MUR-ADO: adobe, MUR-CB99: concrete block masonry, MUR-CL99: clay brick masonry, MUR-STDRE: dressed stone masonry, MUR-STRUB: rubble stone masonry, S: steel, W: wood/timber.
- **Lateral load resisting systems.** LDUAL: dual frame-wall system, LFINF: infilled frame, LWAL: load bearing wall, LFM: moment frame, LFBR: braced frame.
- **Code Level or Ductility.** CDN: absence of seismic design, CDL: low code level (designed for lateral resistance using allowable stress design), CDM: moderate code level (designed for lateral resistance with modern limit state design), CDH: high code level (designed for lateral resistance coupled with target ductility requirements and capacity design), DNO: non-ductile, DUL: low ductility, DUM: moderate ductility, DUH: high ductility.
- **Height.** H: number of storeys.
- **Lateral Force Coefficient.** The value of the lateral force coefficient, i.e. the fraction of the weight that was specified as the design lateral force in the seismic design code (see Code Level), expressed in % (applied to reinforced concrete moment and infilled frames only).

Following their use in the calculation of their Global Seismic Risk Map (GEM, 2018), the GEM Foundation has released a global database of capacity curves (Martins and Silva, 2020 [5]) which have been derived through the compilation of data coming from research studies and experimental campaigns. These capacity curves have been used to represent the European CR_LDUAL, CR_LWAL, MCF, MR, MUR, S and W typologies with different heights and ductility, for a total of 217 building classes.

As part of the European SERA project (www.sera-eu.org), a detailed set of capacity curves for European reinforced concrete infilled frames (CR_LFINF) and moment frames (CR_LFM) has been recently developed (Romão et al., 2019 [6]). A total of 264 reinforced concrete classes have been identified by combining different numbers of storeys (1 to 6), seismic design code levels (no code: CDN, low code: CDL, moderate code: CDM, high code: CDH) and lateral force coefficient levels (0, 5, 10, 15, 20, 25, 30 % of the weight of the structure). Buildings of

design class CDN were typically designed to older codes (from before the 1960's) that used allowable stresses and very low material strength values and considered predominantly the gravity loads. Buildings of design class CDL were designed considering the seismic action by enforcing values of the seismic coefficient, β (referred to herein as lateral force coefficient). Structural design for these codes was typically based on material-specific standards that used allowable stress design or a stress-block approach. Seismic design including modern concepts of ultimate capacity and partial safety factors (limit state design) was the basis of the CDM category of codes. The seismic action was also accounted for in the design by enforcing values for the lateral force coefficient, β . Finally, the CDH class refers to modern seismic design principles that account for capacity design and local ductility measures, similar to those available in Eurocode 8 (CEN, 2004 [7]). Seismic zonation maps associated with the seismic design codes employed in Europe over the last century can be used to identify the lateral force coefficient (i.e. the fraction of the weight that was specified as the design lateral force in the seismic design code, expressed in %) (see Crowley et al., 2021 [2] and Crowley et al., 2020c [9]).

The capacity curves for the 264 building classes were developed through simulated design of prototype frames (see e.g. Borzi et al., 2008 [10]; Verderame et al., 2010 [11]) and then nonlinear analysis has been undertaken to obtain the backbone capacity curves of these frames. Up to 300 capacity curves have been simulated per class by modifying the geometrical and material properties of the prototype frames, and thus accounting for the building-to-building variability in the simulated design. Figure 1 shows the median capacity curves for reinforced concrete frames with masonry infills not designed with seismic loads (CDN).

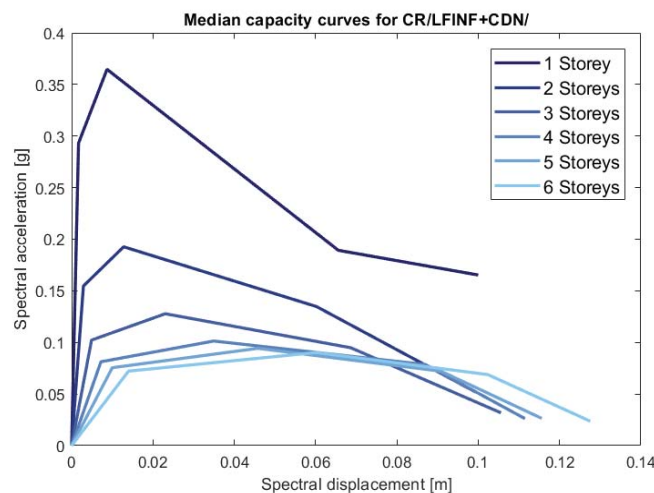


Figure 1: Median capacity curves from Romão et al. (2020) [12] for reinforced concrete frames with masonry infills (CR/LFINF) not designed with seismic loads (CDN)

All of the median capacity curves for the 481 building classes are publicly available on a GitLab repository (Romão et al. 2020 [12]).

3 VULNERABILITY MODELLING

3.1 Vulnerability Modellers' Toolkit (VMTK)

The fragility functions of these European building classes have been computed using the Vulnerability Modeller's Toolkit, a resource that has been developed and released by the GEM Foundation in collaboration with members of the European risk community (Martins et al., 2021 [13]). This toolkit is a set of Python scripts that read the capacity curves, produce SDOF

hysteretic models, launch OpenSeesPy¹ to run nonlinear dynamic analysis, apply linear censored regression to the cloud of nonlinear responses, and compute fragility functions for different damage states, based on the user-defined damage state thresholds. A graphical user interface is included with the toolkit and includes a set of default assumptions, allowing less experienced users to interact with the VMTK (Figure 2). Experienced users are instead encouraged to make use of Python's scripting capabilities to explore all the features of the VMTK source code and to contribute to future releases of the toolkit. The complete toolkit, including source code and GUI, is currently hosted in a publicly available GitHub repository².

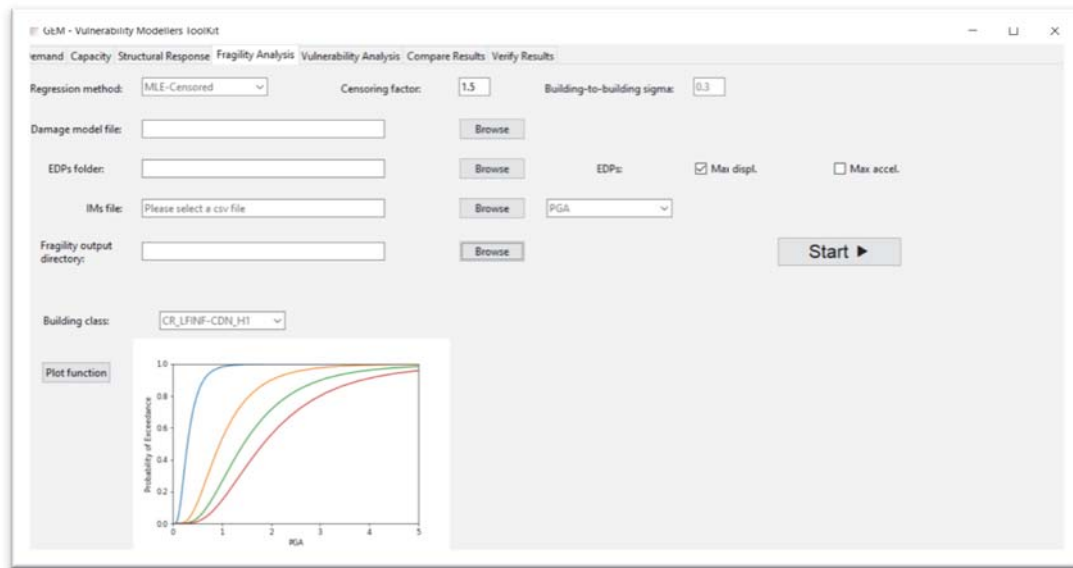


Figure 2: Graphical user interface of the fragility module of the VMTK (Martins et al., 2021 [13])

3.2 Fragility Functions

The median capacity curves in Romão et al. 2020 [12] have been read by the VMTK's 'nlth_on_s dof.py' script which has been used to produce SDOF models using the Pinching4 hyseresis curve of OpenSeesPy. Pinching4 is a uniaxial material that represents a 'pinched' load-deformation response and exhibits degradation under cyclic loading. In addition to the response envelope (taken from the capacity curves), the hysteretic properties given in Table 1 have been assumed for the SDOF models for the different material types. Cyclic degradation of the strength and stiffness is modelled for the CR, MUR, MCF and MR typologies through unloading stiffness degradation, reloading stiffness degradation, and strength degradation. Mass proportional damping is used with different damping ratios for each typology. Typically, masonry is assigned 10% damping, reinforced concrete and wood is 5%, and steel is 3%. The 'nlth_on_s dof.py' script runs nonlinear dynamic analysis using each SDOF and a set of records. A database of recordings has been compiled for the nonlinear dynamic analyses using records with PGA above 0.05g in the Engineering Strong Motion (ESM, Luzi *et al* 2016 [14]; Luzi *et al.* 2020 [15]) and NGA (Chiou et al. 2008 [16]) databases. Records have then been selected from this database to match a range of intensity measure bins with a maximum scaling factor of 2.

¹ <https://openseespydoc.readthedocs.io/en/latest/index.html>

² <https://github.com/GEMScienceTools/VMTK-Vulnerability-Modellers-ToolKit>

The SDOF properties reported above are currently being further tested and modifications might still be incorporated in the final European fragility models. The final scripts used to develop the models will be made available on the aforementioned GitLab repository (Romão et al. 2020 [12]) so that are final assumptions are transparent and it will be possible to easily reproduce the models.

Table 1: Adopted parameters of the Pinching4 hysteresis model

Parameters of Pinching4*	CR, MUR, MCF, MR	W, S
rdispP/N, fForceP/N, uForceP/N	0.5, 0.25, 0.05	0.5, 0.25, 0.5
gK1 gK2 gK3 gK4 gKLim	0, 0.1, 0, 0, 0.2	0,0,0,0,0
gD1 gD2 gD3 gD4 gDLim	0, 0.1, 0, 0, 0.2	0,0,0,0,0
gF1 gF2 gF3 gF4 gFLim	0, 0.4, 0, 0.4, 0.9	0,0,0,0,0
gE	10	10
dmgType	energy	energy

* See <https://openseespydoc.readthedocs.io/en/latest/src/Pinching4.html?highlight=pinching4> for definition of the parameters

The ‘fragility_censored_cloud_analysis.py’ script in the VMTK uses the nonlinear response outputs from each dynamic analysis together with damage thresholds to apply linear censored regression, and this is then used to compute fragility functions (lognormal distributions) for different damage states, based on the user-defined damage state thresholds. For the European fragility functions, the damage thresholds presented in Figure 3 have been assumed.

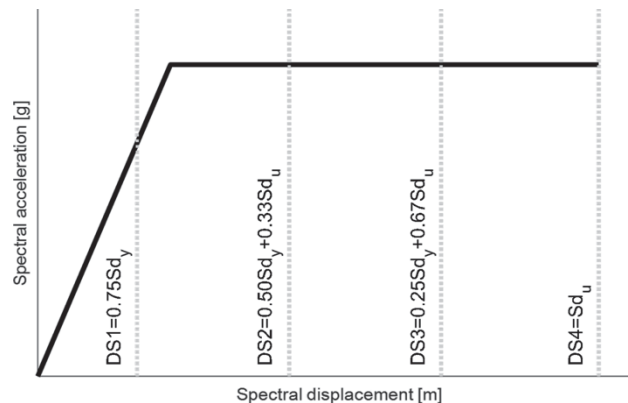


Figure 3: Damage thresholds assumed in the development of the fragility functions (Martins and Silva, 2020 [8])

Four different intensity measure types have been used in the censored regression: PGA, Sa(0.3), Sa(0.6) and Sa(1.0). An average spectral acceleration (see e.g. Baker and Cornell (2006) [17]; Eads et al., 2015 [18]) with 20 intervals between 0.05 and 3 seconds is also currently being investigated. The final intensity measure for each building typology is taken as that with the lowest lognormal dispersion in the fragility function given that this is related to efficiency (i.e. low dispersion in the nonlinear response, given the intensity measure), and it has been found by checking the sufficiency (i.e. conditional independence of the distribution of nonlinear response, given IM, on other parameters of the ground motion) of the different intensity measures that the most efficient is typically also sufficient. Some recent studies have shown that the higher the efficiency, the higher the sufficiency of the intensity measure (e.g. Bradley et al. 2010 [19]). Others have cautioned that the typical checks for sufficiency (e.g. Luco and Cornell, 2007 [20]) only provide evidence rather than proof of sufficiency and that it should be ensured

that the intensity measure is also efficient to ensure that the additional parameters really are having a significant influence on the response (Kazantzi and Vamvatsikos, 2015 [21]). For illustration purposes, Figure 4 shows the fragility functions in terms of $S_a(0.3s)$ that have been obtained with the capacity curves presented in Figure 1.

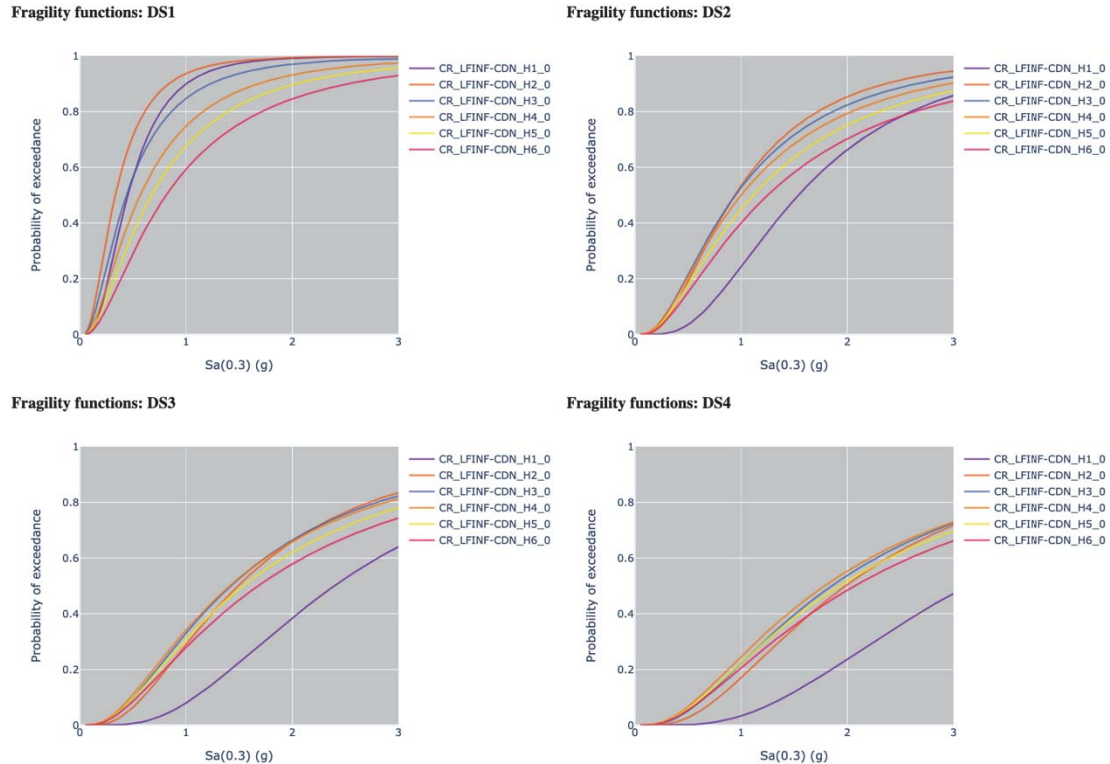


Figure 4: Fragility functions calculated using the capacity curves presented in Figure 1, where DS1 = slight damage, DS2 = moderate damage, DS3 = extensive damage and DS4 = complete damage

3.3 Vulnerability functions for cost of repair/replacement

The fragility functions are converted into vulnerability models using damage-loss models which provide damage ratios for each damage state (slight, moderate, extensive and complete). For losses due to the repair of damage, the damage ratios (which represent the ratio of cost of repair to cost of replacement) from HAZUS (FEMA, 2004 [22]) are being adopted, i.e. 0.02 (slight damage), 0.1 (moderate damage), 0.5 (extensive damage), 1.0 (complete damage). These values are being further tested and calibrated using the results of the tests described in Section 4 and may be adapted before the final release of ESRM20. For a range of intensity measure levels, the probability of occurrence of each damage state is obtained from the fragility functions, multiplied by the damage ratios and summed leading to a mean loss ratio. A lognormal cumulative distribution function has then been fit to the vulnerability data to obtain the median and lognormal standard deviation (dispersion).

In order to account for the building-to-building variability, which is not accounted for given the use of the median capacity curves, a separate study to produce vulnerability functions using all available capacity curves for the CR/LFINF and CR/LFM typologies has been undertaken. This study showed that the mean vulnerability function based on all of the capacity curves of a given typology had a very similar median to the vulnerability function based on the median capacity curves. However, the dispersion was, as expected, slightly higher. It was found that the additional dispersion required to account for building-to-building variability was around 0.3,

and this is therefore combined with the dispersion obtained with the median capacity curves through the square-root-sum-of-squares to produce the final vulnerability functions.

3.4 Vulnerability functions for loss of life

For loss of life, the model uses a number of factors obtained from both past observations and expert judgment, including the likelihood that a completely damaged building will collapse to the extent that it could cause loss of life (currently taken as 1.5% based on the data from recent earthquakes: Antonios Pomonis, personal communication), the probability of entrapment given collapse (Reinoso et al. 2017 [23]), and the probability of loss of life given entrapment (Reinoso et al. 2017 [23]). Different entrapment ratio for day and night are assumed, with higher values for the latter given the increased time required for people to wake up and escape from the collapsing building. Also, an increase in the entrapment ratio with number of storeys has been implemented for the day-time entrapment rates. The loss of life given entrapment has been obtained from the data in Table 2 of Reinoso et al. (2017 [23]) with a clear distinction between buildings with less than and more than 5 storeys being observed and thus applied. Table 2 presents all of the assumed values.

Table 2: Adopted fatality model input parameters

Number of storeys	P-entrapment (day)	P-entrapment (night)	P-loss-life entrapment
1	0.25	0.95	0.4
2	0.5	0.95	0.4
3-4	0.75	0.95	0.4
>5	0.95	0.95	0.7

The fatality vulnerability models are obtained by multiplying the complete damage fragility functions by 1.5% and the factors presented in Table 2. A lognormal function is then fit to the data and the dispersion is increased to account for building-to-building variability (as presented in the previous section).

3.5 Vulnerability Viewer

A Dash App is currently under development to allow users to view and compare the fragility and vulnerability functions for all of building classes and for all the available intensity measure types. A prototype that presents the vulnerability functions in terms of $S_a(0.3)$ is currently available at <http://vulncurves.eu-risk.eucentre.it/> (see Figure 5).

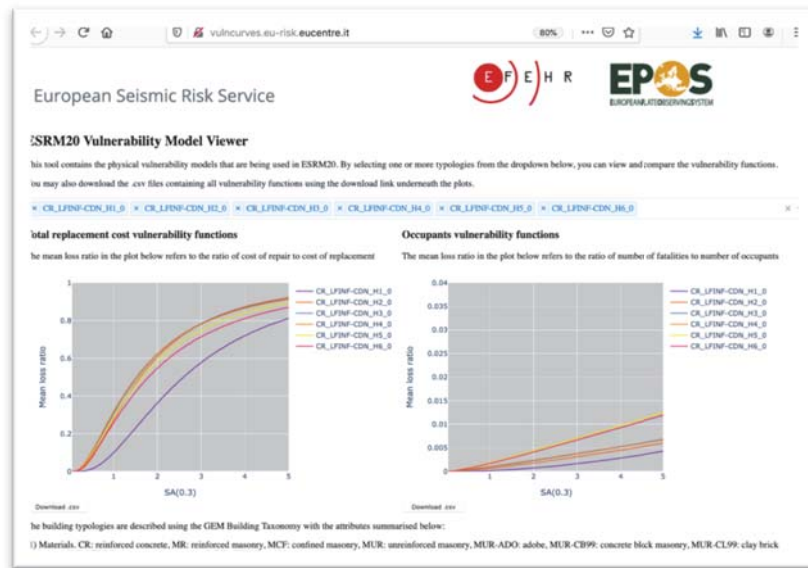


Figure 5: Screenshot of the vulnerability viewer currently under development

4 VULNERABILITY TESTING

Extensive testing of the resulting fragility and vulnerability models has been undertaken by comparing the modelled damage/losses with empirical models as well as with observations from a large number of past European earthquake scenarios (Crowley et al. 2020d [24]).

Simple sanity checks, so-called ‘unit tests’ are undertaken to ensure the median and dispersion values are within sensible ranges, and to compare with existing functions from the literature. The VMTK includes a module that allows users to test their model’s against GEM’s global vulnerability models, which have been calibrated or tested using past earthquake damage and loss data. Useful, and openly available, data for this purpose includes the empirical vulnerability models developed by PAGER (Jaiswal et al., 2009 [25]; Jaiswal and Wald, 2013 [26]), as well as fatality, economic loss and damage data from various databases including the Centre for Research on the Epidemiology of Disasters (CRED)’s EMDAT data-base (EMDAT, 2019 [27]), the Italian Department of Civil Protection’s Da.D.O. data-base (Dolce et al., 2019 [28]), NOAA’s Significant Earthquake Database (NGDC/WGS), and the Cambridge Earthquake Impact Database (www.ceqid.org).

Figure 6 shows two examples of tests that have been undertaken with the European vulnerability model. In the first example, a mean vulnerability function calculated through an exposure-weighted combination of all the building classes in the country has been produced and compared with the empirical models developed by PAGER, following conversion of the spectral ordinates to macroseismic intensity (with the associated uncertainty in the conversion shown by the mean and ± 1 standard deviation vulnerability curves). In the second example, ground motion fields (modelled using scenario rupture models and the latest European ground motion and site amplification models) have been developed for over 30 damaging historical events above magnitude 5 in Europe since the 1980’s. These ground motions are then combined with the current exposure and vulnerability models to estimate direct economic losses. These are then compared in a statistical sense with the reports on economic losses (that are corrected to today’s value). Similar tests can also be undertaken for fatalities. These tests provide a check to ensure that probabilistic losses predicted by the risk model are not biased.

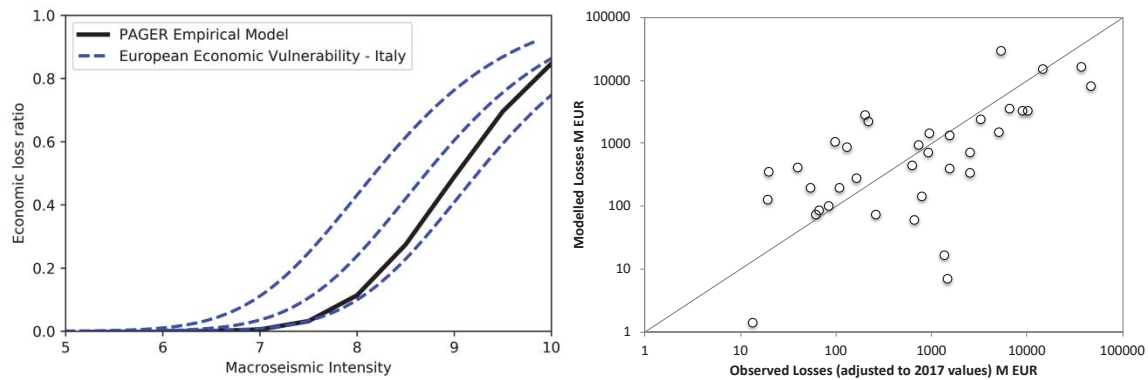


Figure 6: Example tests of the European vulnerability model: (left) comparison with the PAGER vulnerability model, where the three blue dashed lines represent the mean and \pm sigma, (right) comparison of estimated and observed losses for damaging European events since 1980

These tests will continue to be undertaken until the finalization and release of ESRM20 which is expected in October 2021. As mentioned previously, all of the scripts and input data described herein will then be released on the dedicated vulnerability GitLab repository (Romão et al. 2020 [12]).

REFERENCES

- [1] H. Crowley, D. Rodrigues, V. Silva, V. Despotaki, L. Martins, X. Romão, J.M. Castro, N. Pereira, A. Pomonis, A. Lemoine, A. Roullé, B. Tourlière, G. Weatherill, K. Pitilakis, L. Danciu, A.A. Correia, S. Akkar, U. Hancilar, P. Covi, The European Seismic Risk model 2020 (ESRM20). *2nd International Conference on Natural Hazards and Infrastructure*, ICONHIC, Chania, Crete, Greece, 2019.
- [2] H. Crowley, V. Despotaki, D. Rodrigues, V. Silva, D. Toma-Danila, E. Riga, A. Karatzetzou, S. Fotopoulou, Z. Zugic, L. Sousa, S. Ozcebe, P. Gamba, Exposure model for European seismic risk assessment, *Earthquake Spectra*, DOI: <https://doi.org/10.1177/8755293020919429>, 2020a.
- [3] H. Crowley, V. Despotaki, D. Rodrigues, V. Silva, C. Costa, D. Toma-Danila, E. Riga, A. Karatzetzou, S. Fotopoulou, L. Sousa, S. Ozcebe, P. Gamba, J. Dabbeek, X. Romão, N. Pereira, J. M. Castro, J. Daniell, E. Velu, H. Bilgin, C. Adam, M. Deyanova, N. Ademović, J. Atalic, B. Bessason, V. Shendova, A. Tiganescu, D. Toma-Danila, Z. Zugic, S. Akkar, U. Hancilar, Exposure Contributors, European Exposure Model Data Repository (Version 0.9) [Data set]. Zenodo. DOI: <http://doi.org/10.5281/zenodo.4062044>, 2020b.
- [4] S. Brzev, V. Silva, L. Allen, C. Scawthorn, C. Yepes, J. Dabbeek, H. Crowley, A building classification scheme for multi-hazard risk assessment. *Submitted to Natural Hazards and Earthquake System Sciences*, 2021.
- [5] GEM, Global earthquake maps. Available at: www.globalquakemodel.org/gem (accessed 21 March 2021), 2018.
- [6] X. Romão, N. Pereira, J. M. Castro, F. De Maio, H. Crowley, V. Silva, L. Martins, *European physical vulnerability models*. SERA Deliverable D26.5, Available from URL: http://static.seismo.ethz.ch/SERA/JRA/SERA_D26.5_Physical_Vulnerability.pdf, 2019.

- [7] CEN, *Eurocode 8: Design of structures for earthquake resistance - Part 1: General rules, seismic actions and rules for buildings*. Comité Européen de normalization, Brussels, Belgium, 2004.
- [8] L. Martins, V. Silva, Development of a fragility and vulnerability model for global seismic risk analyses. *Bulletin of Earthquake Engineering*, <https://doi.org/10.1007/s10518-020-00885-1>, 2020.
- [9] H. Crowley, V. Despotaki, V. Silva, J. Dabbeek, X. Romão, N. Pereira, J.M. Castro, J. Daniell, E. Velu, H. Bilgin, C. Adam, M. Deyanova, N. Ademović, J. Atalic, E. Riga, A. Karatzetzu, B. Bessason, V. Sendova, D. Toma-Danila, Z. Zugic, S. Akkar, U. Hancilar, Model of Seismic Design Lateral Force Levels for the Existing Reinforced Concrete European Building Stock. *Bulletin of Earthquake Engineering*, in press, 2020d.
- [10] B. Borzi, H. Crowley, R. Pinho, Simplified pushover-based vulnerability analysis for large-scale assessment of RC buildings. *Engineering Structures*, 30, 804-820, 2008.
- [11] G.M. Verderame, M. Polese, C. Marinello, G. Manfredi, A simulated design procedure for the assessment of seismic capacity of existing reinforced concrete buildings. *Advances in Engineering Software*, 41(2), 323- 335, 2010.
- [12] X. Romão, N. Pereira, J. M. Castro, F. De Maio, H. Crowley, V. Silva, L. Martins, European Building Vulnerability Data Repository (Version v1.1) [Data set]. Zenodo. <http://doi.org/10.5281/zenodo.4087810>, 2020.
- [13] L. Martins, V. Silva, H. Crowley, F. Cavalieri, Vulnerability Modeller's Toolkit, an Open-Source Platform for Vulnerability Analysis. *Computers & Structures*, submitted.
- [14] L. Luzi, R. Puglia, E. Russo, M. D'Amico, C. Felicetta, F. Pacor, G. Lanzano, U. Çeken, J. Clinton, G. Costa, L. Duni, E. Farzanegan, P. Gueguen, C. Ionescu, I. Kalogeras, H. Özener, D. Pesaresi, R. Sleeman, A. Strollo, M. Zare, The Engineering Strong-Motion Database: A Platform to Access Pan-European Accelerometric Data. *Seismological Research Letters*, 87(4): p. 987-997. DOI: 10.1785/0220150278, 2016.
- [15] L. Luzi, G. Lanzano, C. Felicetta, M.C. D'Amico, E. Russo, S. Sgobba, F. Pacor, ORFEUS Working Group 5, Engineering Strong Motion Database (ESM) (Version 2.0). Istituto Nazionale di Geofisica e Vulcanologia (INGV) DOI: <https://doi.org/10.13127/ESM>, 2020.
- [16] B. Chiou, R. Darragh, N. Gregor, W. Silva, NGA project strong-motion database. *Earthquake Spectra*, 24, 23-44, 2008.
- [17] J.W. Baker, C.A. Cornell, Spectral shape, epsilon and record selection. *Earthquake Engineering & Structural Dynamics*, 35(9), 1077-1095, DOI: <https://doi.org/10.1002/eqe.571>, 2006.
- [18] L. Eads, E. Miranda, D.G. Lignos, Average spectral acceleration as an intensity measure for collapse risk assessment. *Earthquake Engineering & Structural Dynamics*, 44(12), 2057-2073, DOI: doi:10.1002/eqe.2575, 2015.
- [19] B.A. Bradley, R.P. Dhakal, G.A. MacRae, M. Cubrinovski, Prediction of spatially distributed seismic demands in specific structures: Ground motion and structural response. *Earthquake Engineering and Structural Dynamics*, 39, 501-520, 2010.
- [20] N. Luco, A. Cornell, Structure-Specific Scalar Intensity Measures for Near-Source and Ordinary Earthquake Ground Motions. *Earthquake Spectra*, 23(2), 357-392, 2007.

- [21] A.K. Kazantzi, D. Vamvatsikos, Intensity measure selection for vulnerability studies of building classes. *Earthquake Engineering and Structural Dynamics*, 44, 2677-2694, 2015.
- [22] FEMA, *HAZUS-MH Technical Manual*, Federal Emergency Management Agency, Washington DC, 2004.
- [23] E. Reinoso, M.A. Jaimes, L. Esteva, Estimation of life vulnerability inside buildings during earthquakes. *Structure and Infrastructure Engineering*, DOI: 10.1080/15732479.2017.1401097, 2017.
- [24] H. Crowley, V. Silva, P. Kalakonas, L. Martins, G. Weatherill, K. Pitilakis, E. Riga, B. Borzi, M. Faravelli, Verification of the European Seismic Risk Model (ESRM20). *Proceedings of 17th World Conference on Earthquake Engineering*, Sendai, Japan, 2020d.
- [25] K. Jaiswal, D. Wald, M. Hearne, *Estimating casualties for large worldwide earthquakes using an empirical approach*. US Geological Survey Open-File Report 1136, 2009.
- [26] K. Jaiswal, D. Wald, Estimating Economic Losses from Earthquakes Using an Empirical Approach. *Earthquake Spectra*, 29(1), 309-324, 2013.
- [27] EMDAT, International Disasters Database of the Centre for Research on the Epidemiology of Disasters. Available at <https://www.emdat.be/> 2019.
- [28] M. Dolce, E. Speranza, F. Giordano, B. Borzi, F. Bocchi, C. Conte, A. Di Meo, M. Faravelli, V. Pascale, Observed damage database of past Italian earthquakes: the Da.D.O WebGIS. *Bollettino di Geofisica Teorica ed Applicata*, 60(2), 141-164, DOI: 10.4430/bgta0254, 2019.

PELL-SCHOOLS A STANDARDIZED AND INTEROPERABLE PLATFORM FOR THE SEISMIC VULNERABILITY AND ENERGY EFFICIENCY DATA MANAGEMENT OF ITALIAN SCHOOLS

L. Blaso¹, S. Giovinazzi¹, S. Bianchi², L. Pedone², C. Ormando¹, P. Clemente¹, S. Pampanin², N. Gozo¹, G. Giuliani¹, M. Pollino¹

¹ ENEA, National Agency for New Technologies, Energy and Sustainable Economic Development
Lungotevere Thaon di Revel, 76 00196 Rome, Italy
e-mail: (laura.blaso, paolo.clemente, sonia.giovinazzi, giuseppina.giuliani, nicoletta.gozo, maurizio.pollino)@enea.it

² Sapienza University of Rome
Department of Structural and Geotechnical Engineering, Via Eudossiana 18, 00184 Rome, Italy
(simona.bianchi, stefano.pampanin, livio.pedone)@uniroma1.it

Abstract

PELL, Public Energy Living Lab, is a platform conceived to support the Public Administration in Italy towards the definition and implementation of interventions on public buildings, aiming to jointly pursue their seismic safety, energy efficiency and environmental certification. This paper presents the on-going activities for the development of the platform PELL-Schools, focusing, in particular, on the “Seismic-Response” module that aims to become a standardized and interoperable database for the collection and collation of relevant data for the seismic vulnerability assessment and for the seismic monitoring of Italian schools. In order to test, tune and modify, if necessary, the proposed PELL-School Seismic-Response module and to contribute to its implementation on Italian school buildings a Working Group has been set up involving several Italian municipalities and stakeholders. The paper concludes with a call to action inviting researchers working on the seismic vulnerability assessment and monitoring of strategic buildings to join the Working Group to contribute their knowledge towards the common goal of guarantying the seismic safety of schools and other strategic buildings in Italy.

Keywords: School Buildings; Geodatabase; Standardization; Interoperability, Seismic Vulnerability Assessment; Seismic Risk; Public Administration; Energy Efficiency

1 INTRODUCTION

The Italian Ministry of Education and Research (MIUR) permanently guarantees the access and reusability of the data of the national education and training system, making accessible in open format, among others, the data from the National School Building Registry System (SNAES). According to SNAES data, the portfolio of Italian schools includes 40.151 actively operating buildings belonging to local authorities, out of which: about 50% were built before 1970; 46.8% do not hold a static safety certificate; 59.5% do not hold the fire prevention certificate; and 53.8% do not hold the certificate of viability/habitability. The situation is indeed critical. As far as the seismic vulnerability of school is concerned, the situation is possibly even worse despite the several initiatives undertaken by the Italian Government. After the 2002 earthquake in Puglia and Molise, the directive of the President of the Council of Ministers (PCM) n. 3274 of 20 March 2003, referred hereafter as OPCM 3274 [1], reclassified the entire national territory into four areas with different level of hazards (removing the non-seismic areas) and introduced the obligation for the owners to proceed with the seismic verification of strategic buildings and of buildings relevant for civil protection purposes, including school buildings. Specific funds for extraordinary interventions, including seismic checks and first urgent interventions, were made available¹, and were allocated by the Civil Protection Department - through the Regions – for financing the seismic checks of about 2.300 school buildings (out of the 40.151 building patrimony). Furthermore, the Regions and Municipalities carried out further seismic checks of school buildings with their own funds. At the moment the Italian Civil Protection Department is digitizing the summary data of the checks carried out in order to establish a centralized database associated with ARES, the *Regional Registry of School Building* (in Italian, “*Anagrafe Regionale Edilizia Scolastica*”)².

To support this process, ENEA intends to make available all the technologies and experience gained, thanks to the PELL experience, to contribute to build an interoperable database of Italian school buildings throughout the national territory. PELL, Public Energy Living Lab, is a platform conceived to: a) achieve a minimum standard of building knowledge; b) monitor and evaluate the state of art of buildings and performances; and c) support the Public Administration (PA) in Italy towards the definition and implementation of interventions on public buildings, aiming to jointly pursue their seismic safety, energy management efficiency [2]. PELL-IP, the platform for the census and monitoring of Public Lighting at national scale, is already a successful reality in Italy (since 2019).

This paper presents the on-going activities for the development of the *PELL-School* platform, focusing, in particular, on the “Seismic-Response” module, referred hereafter as *PELL-School-RS* that aims to become a standardized and interoperable database for the collection and collation of relevant data for the seismic vulnerability assessment and for the seismic monitoring of Italian schools. As far as the seismic vulnerability assessment is concerned, *PELL-Schools-RS* will faithfully replicate and build on the data structure of the official form [3] defined by the Italian Presidency of the Council of Ministers (PdCM), Department of Civil Protection, for the seismic vulnerability assessment of strategic buildings. The inclusion in *PELL-Schools* of additional input data, aimed at identifying critical vulnerabilities and at estimating a risk class and the expected average annual loss (EAL), before and after seismic retrofitting interventions, is proposed in line with the approach officially adopted in Italy for the classification of the seismic risk of residential buildings [4].

¹ The Fund of 200 million euros was implemented through the opcm n. 3362 of 8 July 2004 and no. 3505 of 9 March 2006

² Quoting from - <http://www.protezionecivile.gov.it/attivita-rischi/rischio-sismico/attivita/sicurezza-scuole>

The paper also presents the Key Performance Indicators (KPIs) indicators included in *PELL-School-RS*, namely: *Static KPIs*, providing a measure of the building seismic vulnerability and expected “nominal” risk (Section 4.1), and *dynamically computed KPIs* (Section 4.2) that aim to provide a quasi-real time estimation of the extent of earthquake-induced damage. The KPI assessment is performed in *PELL-School-RS*, at different level of reliability, Tiered approaches, based on the state-of-the-art methodologies and via a simplified analytical-mechanical approach referred to as SLAMA method [5], [6] depending on the level of knowledge achievable and on the information available for each school.

In summary, as showcased in the paper *PELL-School* aims to become a national database/cadaster of school buildings, working as:

1. a standardized and homogeneous geospatial repository of identity, consumption and seismic vulnerability data of Italian school buildings, where data are structured according to ad-hoc technical specifications from AgID³ the Agency for Digital Italy, a technical agency of the *PdCM*;
2. an interoperable platform that, thanks to the development of appropriate communication protocols and webservices, allows for a two way data exchange and update with other existing DBs;
3. a tool for monitoring the service performance and the residual functionality of schools for both business-as-usual and post-disaster times.

2 PELL PUBLIC BUILDINGS – ENERGY AND SEISMIC RESPONSE LIVING LAB

Since several years ENEA has been promoting and boosting the digitization of data and information related to the public administration assets. Particular focus has been given to energy-intensive infrastructures (such as street Public Lighting) and to the strategic infrastructures (e.g. school buildings, hospital systems among others) and/or critical for the smart management of cities and territories.

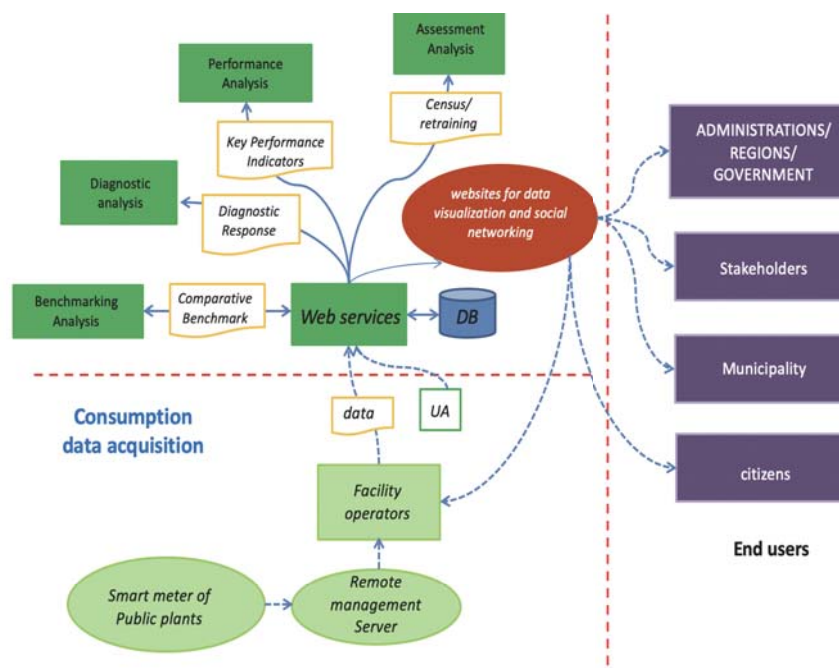


Figure 1. PELL Platform, ICT layout.

³ Agenzia per l'Italia Digitale (<https://www.agid.gov.it/>)

The goal is to promote a more efficient and effective management of these infrastructures and associated services, through the development and adoption of new methodological and technological solutions, allowing to provide to the stakeholders a set of management tools, embedded in the PELL platform, that can support and inform their decision-making processes about the adoption of targeted development goals.

Towards that the idea is to automatically and constantly assess, in a uniform and standardized way, at both national and local level, both the physical conditions of the structure or infrastructure under analysis as well as the functional ones, the latter by monitoring the quality level of the service provided.

The PELL platform, developed thanks to the System Research Program Agreement under the Italian Minister of Economic Development, MISE, is made available free of charge by ENEA. The vertical PELL platform is a smart city as-a-service platform, whose general architecture defines the retrieval of data from different infrastructures and managers and the creation of a series of services for end users (Figure 1). The PELL platform is structured to operate both a static mode, to support the census of the identity data of the infrastructure, and in a dynamic mode, to support the continuous monitoring of the structure/infrastructure functioning.

3 PELL-School-RS DATA STRUCTURE

Figure 2 presents the data structure proposed for the *PELL-School-RS* module.

<ul style="list-style-type: none"> ✓ Seismic and hydrogeological hazard (ES) ✓ Year of construction; original and current use (ES) ✓ Interventions and their compliance with standards (ES) ✓ Dimensional characteristics (ES) ✓ State of conservation (ES)
<ol style="list-style-type: none"> 1. Identification of Structural Unit (US) 2. Dimensional data, Age of construction/renovation, Description of any structural intervention performed. Technical regulations for design, construction and subsequent interventions (US) 3. Intended Use and Exposure of people and content (US) 4. Hazard events suffered and geomorphological data (US) 5. Main structural material of vertical structure (US) 6. Type and organization of the resistant system (US) (for CA, Masonry and Steel) 7. Horizontal Diaphragms (US) 8. Roofing systems (US) 9. Distribution of infill panels for Reinforced Concrete (US) 10. Foundations (US) 11. Additional data needed for the 1 and 2 level PdCM assessment (US) 12. Seismic classification (US) 13. Subsoil category and site morphological conditions (microzonation) (US) 14. Prediction of possible seismic improvement interventions (US) 15. Data Source and Acquisition of available architectonical and structural design (US) 16. Geometric criticalities: regularity / irregularity and mass / stiffness distribution in plan and elevation (US) 17. Constructive and material-related criticalities (US) 18. Structural Details or presence of Improvement Technologies (including vernacular ones) critical to the building seismic response (US)

Figure 2. Main group of data included in the *PELL-School-RS* module.

In line with the structure of the ARES DB, some group of data (i.e. those included in the grey box in Figure 2) are acquired at building level, while all the others (fields from 1 to 18 in the blue box in Figure 2) refer to the Structural Unit (US, i.e. *Unità Strutturale* in Italian) and therefore need to be collected and collated for each one of the US identified within the school building.

A *Structural Unit*, *US* (Figure 3b), is identifiable by the homogeneity of the structural characteristics and therefore distinguishable from the adjacent buildings by these characteristics and also by the difference in height and/or age of construction and/or staggered floors, etc. The US is also the reference survey unit for *PdCM Level 1 and Level 2 forms* [3].

A full presentation of the data included in *PELL-School-RS* is out of the scope of the paper.

In the following a brief overview is provided on:

- 1) ARES DB, *PdCM Level 0* and *PdCM Level 1-2 forms* [3], and other “institutional” forms such as [4] and [7], that have been taken as a reference to build the data structure of *PELL-School-RS* module;
- 2) the proposal of additional data to be collected in order to identify the constructive, material and geometric criticalities and peculiarities that might significantly affect the seismic response of a building.

3.1 Data sourced from existing institutional forms

As mentioned *PELL-School* is interoperable with ARES Database (*Anagrafe Regionale Edilizia Scolastica*) that is part of the National School Building Registry System, SNAES. ARES is managed by the Italian Regions and is continuously updated by Municipalities, Provinces and Metropolitan Cities through a user-friendly graphical user interface (Figure 3).

ARES includes two different data structure, namely: a *Building* and *US* (Structural Unit) *Form* dedicated to the survey of data related to the conditions of the school building; and a *PES Form* (i.e. *Punto di Erogazione del Servizio Scolastico*, in Italian) dedicated to the collection of data relevant to the school consistency and functionality (one school building might have multiple PES, e.g. Figure 3a).

The *ARES Building Form* and *US Form* have to be filled in by the local authority owning/responsible for the school. The *ARES PES Form* has to be filled in by the headmaster. Figure 3 shows an overview of the ARES Platform dashboard and of some images extracted from an ARES manual.

ARES Building and *US Form* includes 8 sections. *PELL-School-RS* sources data from the first three of them, namely:

- *Section A*, including: identifier data of the school building, comprising a unique ID;
- *Section B*, including: identifier data of each Structural Unit, US; structural information of the US, i.e. material and typology of the main vertical and horizontal structural systems and their peculiar constructive techniques; design code; any strengthening and seismic retrofit interventions, and related risk indicator assessed according to the legislation in force at the time of the design and execution of the work;
- *Section C*, including: data on the use of the US; some geometrical and dimensional features (number of storeys, area floor, etc.); constructive techniques of non-structural elements, such as infills, facade/claddings; information on maintenance/retrofitting interventions if any, for both structural and non-structural element, (e.g. beams, columns, floors, infills, facade/cladding; hydraulic and electrical systems).

Not all the *ARES DB* is included in the *PELL-School* platform, as the aims of the two platforms are indeed different. *PELL-School* will acquire only ARES data relevant for the identification of the school building and of its structural units, and for performing their seismic

vulnerability assessment as well as their energy efficiency assessment. Any data included in ARES that is judged to be relevant for the aforementioned aims is directly acquired in PELL-School automatically sourcing it from ARES, thus avoiding any replication of data request to the Public Administrations, PAs.

This is possible thanks to the interoperability between *ARES DB* and *PELL-School-RS*, meaning that all the relevant data collected and collated in ARES will be available in PELL-School; after an initial acquisition of the data already included in ARES and relevant to PELL a webservice will be established between ARES and PELL-Schools allowing to periodically check for and to periodically acquire newly uploaded data and/or updated data.

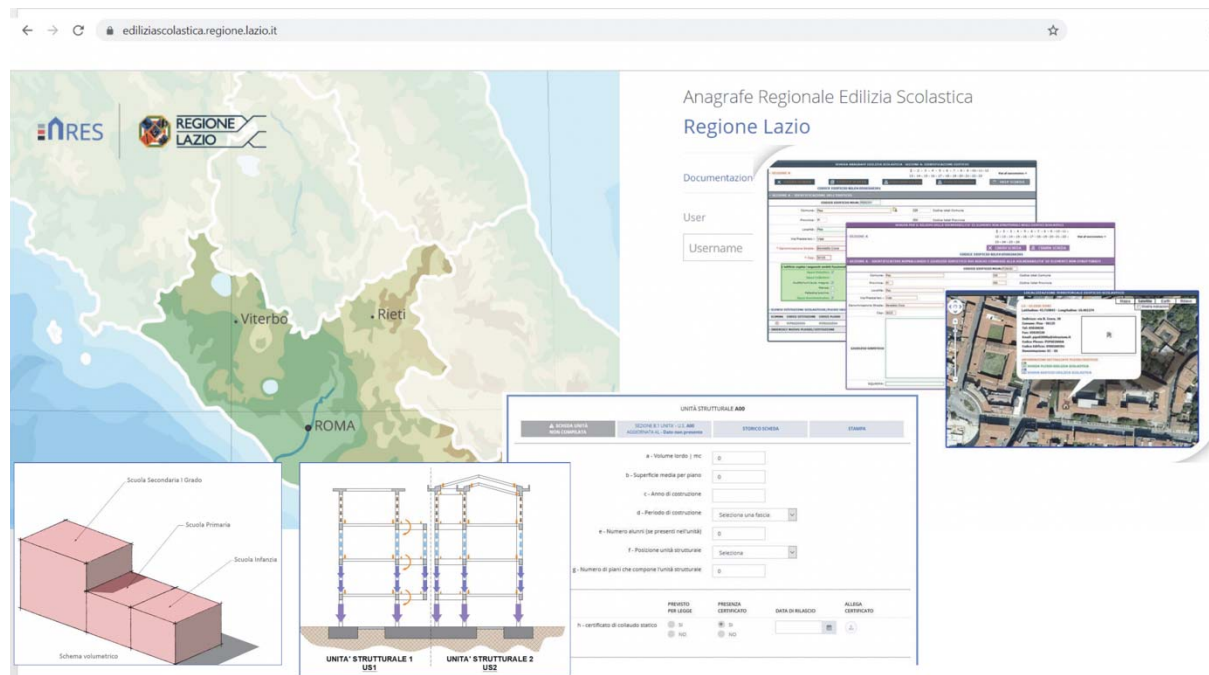


Figure 3. ARES Platform: Layout of the dashboard and GUI interfaces and pictures from ARES manual that clarifies the concept of PES and of US, Structural Unit.

PELL-School replicates in its data structure (Figure 2) the two seismic vulnerability assessment forms established by OPCM n. 3274 2003 [1], namely: *PdCM Level 0 Form*, and *PdCM Level 1-2 Form*. *PdCM Level 0 Form* aimed to support a first-step screening of the structures whose seismic vulnerability should have been assessed according to OPCM n. 3274 and to support a prioritization for their thorough seismic vulnerability assessment and identification of any required seismic retrofit intervention. Several data requested by *PdCM Level 0 Form* are already included in the ARES DB, namely: identifying data, geometrical data, construction period, material of the main vertical structural system, use of the building and presence of retrofitting interventions.

PdCM Level 1-2 Form, collect the necessary information to perform an engineering assessment of the seismic vulnerability, according to the codified methodology in the current Italian seismic code, NTC 2018 [8], to assess the a Risk Indicators (α), defined as US Capacity vs. Demand ratios; a brief summary on the concept underpinning the assessment of the seismic Capacity for US in terms of its performance at the various Limit States, according to [8], is provided in section 4.1. *PdCM Level 1-2 Form* includes 30 different sections where data are collected either as unique or multiple choice questions or by fill-in boxes where written or numerical information have to be provided, as appropriate. Data included in *PdCM Level 1-2 Form* have been replicated in the *PELL-School RS* module, as follow: sections from 1 to 20 and

section from 29 to 30 have been replicated and expanded (as briefly mentioned in the following); sections from 21 to 28 included have been grouped in the field 11 of the *PELL-School RS* module (see Figure 2) and faithfully replicated with no proposed addition.

For both *PdCM Level 0* and *Level 1-2 Forms*, that were originally conceived in paper format, data digitization is allowed through an ad-hoc software that the Department of Civil Protection, DPC, has prepared and made available to the Italian Regions⁴. Provided DPC approval already digitalized data, available as *.mdb files will be acquired by the *PELL-School RS* module and interoperability between the DPC repository and *PELL-School* will be established.

Further institutional forms/approaches, that have been taken as a reference and from where some data were sourced for inclusion in the *PELL-School RS* module include: “*Guidelines for the Seismic Risk Classification of Buildings*” so-called “*SismaBonus*” [4] and “*CLE, Limit Condition in Emergency*”⁵ form [6].

“*SismaBonus*” approach (Figure 4), that is briefly described in section 4.1, uses EMS-98 [8] typological classification to attribute a typological seismic vulnerability class to a building (Figure 4, step 1) and provides a list of constructive and geometric criticalities/peculiarities (Figure 4, step 2) to be surveyed and accounted for towards refining the assessment. Retracing the macroseismic approach proposed by [7], “*SismaBonus*” approach [4] establishes that a building can be judged to belong to a worse or better seismic vulnerability class, on respect to the one attributed simply by a typological identification, once considered respectively any anti-seismic peculiarities or criticalities that can be recognised in the building.

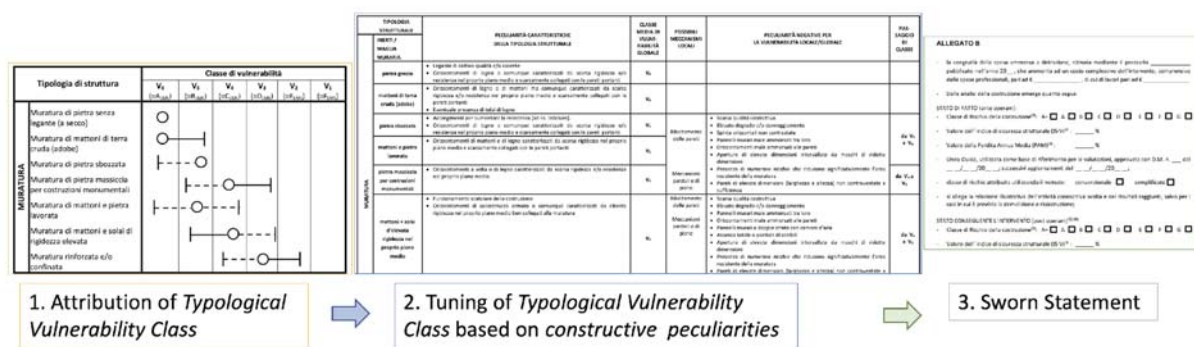


Figure 4. Schematic representation of the simplified “*SismaBonus*” approach for masonry building typologies.

As an example, for the definition of field 5 of the *PELL-School RS* module, namely “*Main structural material of vertical structures*”, as far as masonry buildings are concerned, the masonry typologies recognized by “*SismaBonus*” (indeed the same recognized by EMS-98) were integrated in *PELL-School RS* module with the ones considered by the *PdCM Level 1-2* form and with the ones included in the *ARES DB* (Figure 5); as a matter of fact the three aforementioned forms/approaches refer to a different classification system for masonry buildings and *PELL-School* aims to be inclusive and interoperable with them all and avoid data replication as said (Section 1). Furthermore several geometric criticalities/peculiarities (Figure 4, step 2) included in “*SismaBonus*” have been included in the fields from 16 to 18 of the *PELL-School-RS* module (Figure 5).

⁴ DPC circular /SISM/0092847 of 09/12/2010 rules the digitization *PdCM Level 0* and *Level 1-2 Forms* through the software “DPC Liv1-2.msi” prepared by DPC and available at <http://www.fileserve.com/file/CUkc9mM>

⁵ <http://www.protezionecivile.gov.it/en/risk-activities/seismic-risk/activities/analysis-limit-condition-emergency>

A	E	F	G	I	J
Classe	Attributo	Tipologia	Campi da compilare	Descrizione	Note interne
DENOMINAZIONE	Nome Edificio Scolastico	String (500)		Indica il nome dell'edificio scolastico	Versione 1 scheda PdCM
US	Codice Edificio Scolastico	String (10)		Indica il codice dell'edificio scolastico	da ARES
US	Codice Unità Strutturale	String (10)		Indica il codice dell'unità strutturale	da ARES
US	Anno di costruzione	Num		Anno di costruzione dell'unità strutturale	da ARES
US	Periodo di costruzione	Enum		Periodo di costruzione dell'unità strutturale	da ARES
FD	Fonte dei Dati - Giudizio esperto	Boolean	SI	Fonte dei Dati - Giudizio esperto	NUOVO
FD	Fonte dei Dati - Interviste	Boolean	SI	Fonte dei Dati - Interviste	NUOVO
FD	Fonte dei Dati - Ispezione diretta	Boolean	SI	Fonte dei Dati - Ispezione diretta	NUOVO
FD	Fonte dei Dati - Disegni Digitali Architettonici	Boolean	SI	Disegni Digitali Architettonici (piante architettoniche, prospetti, sezioni, planimetria generale) (formato .dwg - C)	NUOVO
FD	Fonte dei Dati - Disegni Digitali Strutturali	Boolean	SI	Disegni Digitali Strutturali (piante strutturali, sezioni, carpenterie) (formato .dwg - CAD)	NUOVO
FD	Fonte dei Dati - Disegni cartacei originali	Boolean	SI	Disegni cartacei originali: architettonici e/o strutturali	NUOVO
FD	Fonte dei Dati - Documentazione storica di progetti	Boolean	SI	Documentazione storica di progetto	NUOVO
FD	Fonte dei Dati - Relazioni di vulnerabilità sismica	Boolean	SI	Relazioni di vulnerabilità sismica: Relazione generale, Relazione di calcolo, Relazione geologica, Relazione prove	NUOVO
FD	Fonte dei Dati - Documentazione fotografica	Boolean	SI	Documentazione fotografica	NUOVO
FD	Fonte dei Dati - Riferimento	String (500)		Indicare l'archivio cartaceo e/o digitale presso il quale tale documentazione è reperibile (e/o ufficio di riferimento)	NUOVO
FD	Fonte dei Dati - Note	String (500)		Note	NUOVO
US-CA-Pes	Posizione strutturale	Enum	Isolati	Posizione dell'unità strutturale	ARES
US-M-SV	Tipologia muratura portante	Boolean	SI	muratura portante in laterizi	da ARES equiparato campo 12 opzione (8) e (9) scheda PdCM
US-M-SV	Tipologia muratura portante	Boolean	SI	muratura portante in pietrame irregolare	da ARES equiparato campo 12 opzione (1) scheda PdCM
US-M-SV	Tipologia muratura portante	Boolean	SI	muratura portante in pietrame regolare/tufo	da ARES equiparato campo 12 opzione (4) scheda PdCM
US-M-SV	Tipologia muratura portante	Boolean	SI	muratura portante in blocchi di calcestruzzo	da ARES equiparato campo 12 opzione (10) e (11) scheda PdCM
US-M-SV	Tipologia muratura portante	Boolean	SI	muratura portante in muratura a sacco	da ARES equiparato campo 12 opzione (7) scheda PdCM
US-M-SV	Tipologia muratura portante	Boolean	SI	muratura in mattoni di terra cruda (adobe)	campo presente del DM65 del 07-03-17 "Sismabonus"
US-M-SV	Tipologia muratura portante	Boolean	SI	muratura in pietre a spacco con buona tessitura	campo 12 opzione (3) scheda PdCM
US-M-SV	Tipologia muratura portante	Boolean	SI	muratura a blocchi lapidei squadriti	campo 12 opzione (5) scheda PdCM
US-M-SV	Tipologia muratura portante	Boolean	SI	muratura in mattoni pieni e malta di calce	campo 12 opzione (6) scheda PdCM
US-M-SV	Tipologia muratura portante	Boolean	SI	muratura in mattoni semipieni con malta cementizia (es.: doppio UNI)	campo 12 opzione (7) scheda PdCM
US-M-SV	Tipologia muratura portante	Boolean	SI	muratura in pietra rinfasciata per costruzioni monumentali	campo presente del DM65 del 07-03-17 "Sismabonus"
US-M-SV	Tipologia muratura portante	Boolean	SI	muratura armata e/o confinata	campo presente del DM65 del 07-03-17 "Sismabonus"
US-M-Costr	Criticità Costruttiva - scarsa qualità costruttiva	Boolean	SI	Scarsa qualità costruttiva	campo presente del DM65 del 07-03-17 "Sismabonus"
US-M-Costr	Criticità Costruttiva - aperture di elevata dimensione	Boolean	SI	Aperture di elevate dimensioni intervallate da maschi di ridotte dimensioni	campo presente del DM65 del 07-03-17 "Sismabonus"
US-M-Costr	Criticità Costruttiva - presenza di nicchie	Boolean	SI	Presenza di numerose nicchie che riducono significativamente l'area resistente della muratura	campo presente del DM65 del 07-03-17 "Sismabonus"
US-M-Costr	Criticità Costruttiva - pareti non controventate	Boolean	SI	Pareti di elevate dimensioni (larghezza e altezza) non controventate a sufficienza	campo presente del DM65 del 07-03-17 "Sismabonus"
US-M-Costr	Criticità Costruttiva - spinte orizzontali non contrastate	Boolean	SI	Spinte orizzontali (da tetti sporgenti e/o anelli e volte) non contrastate a sufficienza	campo presente del DM65 del 07-03-17 "Sismabonus"
US-M-Mat	Criticità Materiali - scarsa qualità	Boolean	SI	Scarsa qualità dei materiali	campo presente del DM65 del 07-03-17 "Sismabonus"
US-M-Mat	Criticità Materiali - deterioramento, disgregazione	Boolean	SI	Presenza di fenomeni di deterioramento materiali /disgregazione malte	campo presente del DM65 del 07-03-17 "Sismabonus"
US-M-Danno	Danno pregresso - presenza di lesioni e/o fuoripiani	Boolean	SI	Presenza di lesioni e/o fuoripiani pareti	campo presente del DM65 del 07-03-17 "Sismabonus"

Figure 5. Screenshot of some of the data included in *PELL-School RS* for masonry building typologies where in (last column of the table) is clarified the origin of the data field: ARES (green rows); newly proposed (white); Sismabonus (yellow); PdCM (light blue).

As far as the “*CLE, Limit Condition in Emergency*” approach⁶ is concerned that included 5 forms (namely: Strategic Building, ES; Emergency Area, AE; Infrastructure Accessibility/Connection, AC; Structural Aggregate, AS; Structural Unit, US), *PELL-School RS* is including in fields from 16 to 18 the *CLE AS Form* data structure that collect relevant data on the possible negative interaction between adjacent US due to, for instance: the misalignment between roofs, slabs or façade walls; the misalignment in interior spaces; juxtaposition or structurally poorly connected elements (such as stairwells, canopies, balconies); incongruous punching system; isolated pillars, arcades, piloty floors; the presence of terraces, towers, chimneys. Data-structure of the further *CLS Forms* will be included in the near future development of *PELL-School-RS* as the aim would be to assess *PELL-School KPI*, not only for the school in itself but also for all the essential structures and services whose functionality are strongly influential, if not vital, for the functioning of the school.

As a matter of fact the final goal of the *PELL-School* should be to collect data and assess KPI towards a continuous monitoring of the school resilience both in business as usual time and in consideration of possible crises event. For the latter point, as far as seismic events are concerned, the idea is to include in *PELL-School* data relevant to all the Disaster Risk Management, DRM, cycle. In Figure 6 are showcased, as an example, forms currently used by the National and Regional Civil Departments and relevant to school buildings as well as to other strategic buildings for the three phases of DRM, namely before, during and after disaster:

a) Before disaster: *PCdM Level 0* and *Level 1-2* forms (already fully included in *PELL-School-RS*) and *CLE Forms* (partially included in *PELL*, only *CLE AS* data at the time being);

⁶ The analysis of the CLE of the urban settlement is carried out using standards of storage and cartographic representation of data, collected through a special form prepared by the Technical Commission for the studies of MS, established by OPCM 3907/2010 (art. 5 paragraphs 7 and 8), and issued by a special decree of the Head of the Department of Civil Protection.

b) During disaster: *FAST Form* for the synthetic assessment of post-earthquake usability (all the structural, geometrical and typological data of the *FAST form* are already included in *PELL-School-RS*; to be included data on the FAST 4 levels usability scale, i.e.: usable; non usable; non usable because of external risks; inspection non performed for causes to be specified.

c) After disaster: *AeDES Form*⁷ for post-earthquake damage and safety assessment and short term countermeasures identification; and form used by Region for post-disaster reconstruction reconnaissance as the ones used after 2009 L'Aquila (Italy) earthquake and stored in an ad-hoc created repository, i.e. *School Building Information System (in Italian Sistema Informatico Edilizia Scolastico, SIES)* with whom, needless to say *PELL-School-RS* will try to establish interoperability and data exchange.

AeDES form include 8 sections plus a note section. *PELL-School-RS* includes already data of 4 of those sections related to building identification, description, typology, soil and foundation. Still to be included in *PELL-School-RS* is the *AeDES* data structure related to damage assessment (i.e., damage to main structural components; damage to non-structural elements; external risk and existing short term countermeasures) and usability assessment.

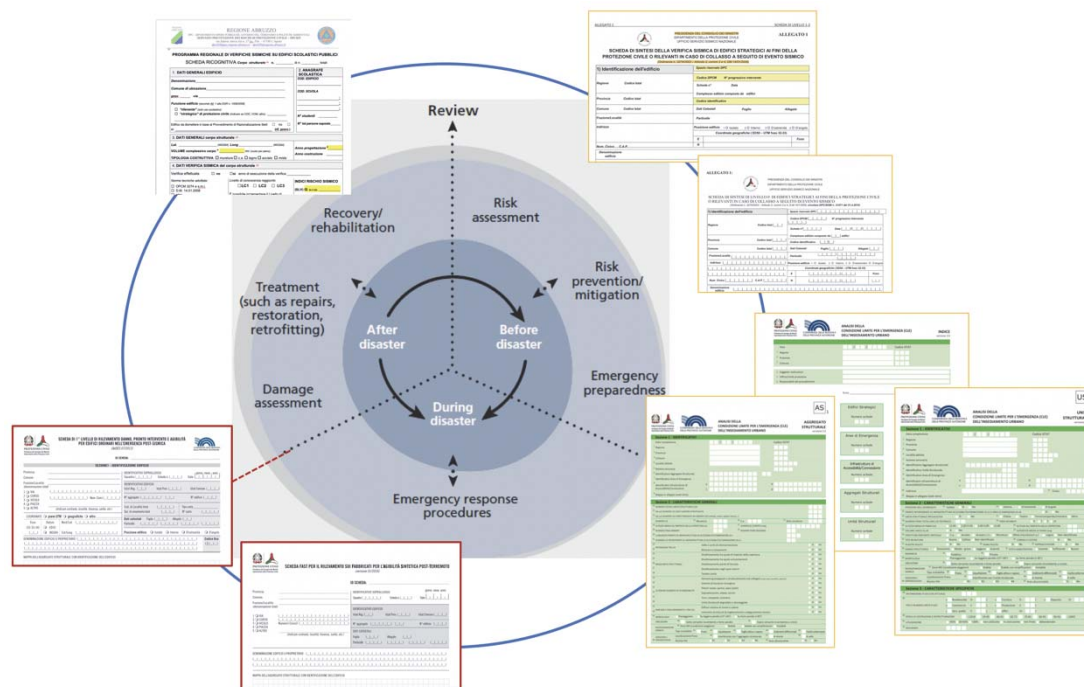


Figure 6. Some of the institutional forms used in Italy in the different phases of the Disaster Risk Management cycle, namely: before disaster PdCM and CLE forms; during disaster FAST form; post disaster AeDES and

It is worth highlighting that:

- more than 50% of the information that are usually collected and collated in post-disaster circumstances with the *FAST Form* and the *AeDES Form* would be already available in *PELL-School-RS*; this will significantly speed up the post-disaster operations of damage and usability assessment;
- *PELL-School-RS* dynamically assessed KPI can support and inform post-disaster operations of damage and usability assessment;
- It is also worth highlighting that on the other hand it will be important to include in *PELL-School-RS* the additional fields comprised in the *FAST Form* and *AeDES Form*, as those

⁷ <https://core.ac.uk/download/pdf/38619561.pdf>

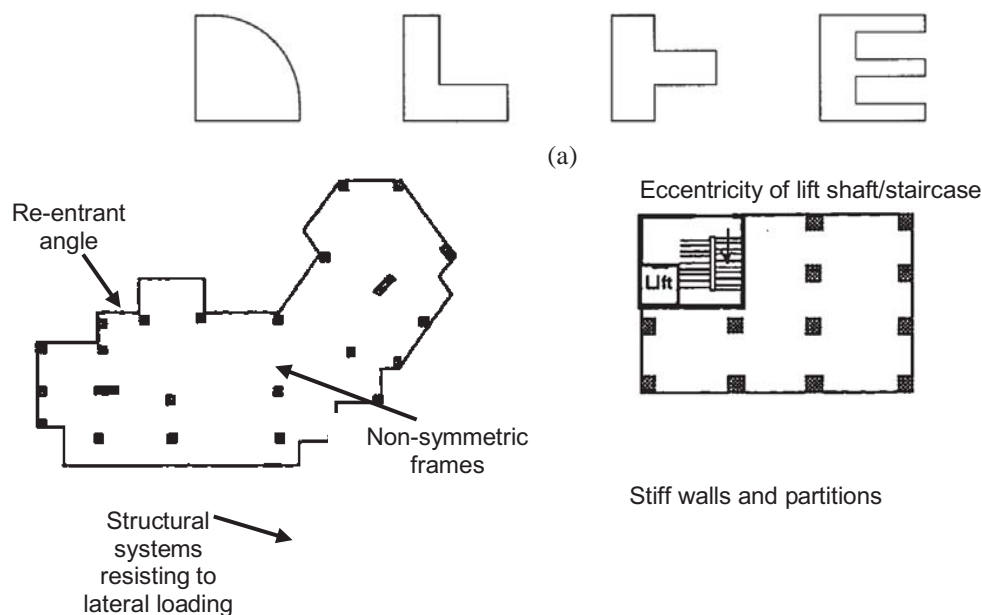
data will be a vital source of information to validate and tune, if necessary, dynamically calculated KPIs.

3.2 Newly proposed data

When assessing the earthquake prone status of buildings, initial screenings are needed to identify any weakness in the structure that could potentially influence its capacity, consequently reducing the building seismic performance thereby increasing the life safety risks to occupants and/or having a negative effect on neighbouring buildings. In order to collect key vulnerabilities without going through the length of an extensive analysis, new defined data/information have been proposed and included in *PELL-School-RS*. These data can be easily collected from available architectural and structural drawings (digital files and/or original paper documents), photographic records and technical reports on the building seismic vulnerability.

Focusing on Reinforced Concrete (RC) buildings, general information on the building position (isolated, internal, edge), type of structural system resisting to lateral loads (frame, wall, combination of both) as well as warping and typology of flooring system (e.g. heavy/light) are added to the existing data, as crucial aspects to determine the structural capacity in earthquakes and potential impacts on adjacent buildings. As an example, a brief explanation is provided for the newly proposed data included in the data groups from 16 to 18 (Figure 2), in particular:

16. Geometric Criticalities: Data collected here are related to the possible presence of: both plan and vertical irregularities. Plan irregularities might include non-symmetrical plan shapes, e.g. L-, T-, E- (Figure 7a) and non-symmetrical structural systems; large spacing of lateral systems in case of long-narrow buildings; non-uniform and eccentric distribution of weights (as well as ramps, stairs, walls, stiff partitions); the presence of torsional effects in case of corner buildings. Vertical irregularities concern the possible presence of soft stories, mass variation, vertical discontinuity of structural systems (Figure 7b). Moreover, geometrical weaknesses might also include the presence and dimensions of structural gaps (building separation), that can lead to pounding effects.



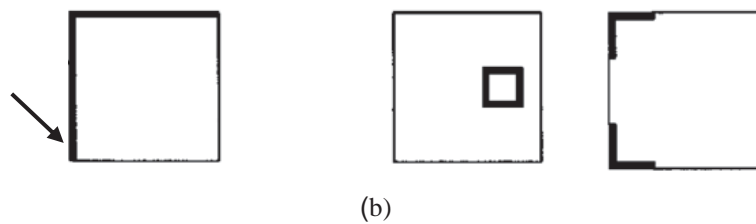


Figure 7. Schematic illustration of: a) plan irregularities; b) vertical irregularities.

17. Constructive and Material-related Criticalities: Constructive criticalities for RC building mainly relate to the peculiar plan and vertical distribution of infill walls (that severely interact with the primary structure system during earthquakes, possibly contributing to the increase of both stiffness and strength or to brittle global collapse mechanisms such as soft story mechanisms), the presence of short columns, the absence of measures able to mitigate brittle collapse mechanisms and out-of-plane expulsions. Material-related criticalities for RC buildings refers to: low quality concrete and/or degraded concrete; low quality steel bars, or presence of plain round bars, corrosion. Poor materials and deterioration might lower even considerably the capacity of structural members.

18 Structural Details critical to the seismic response: These comprise indications on the detailing of beam-column joints, the steel reinforcement ratios, longitudinal and transverse steel spacing and detailing of structural members, the location of lap splices and anchorage of longitudinal bars, the detailing in the critical dissipative zones, as well as the absence of hierarchy of strengths (capacity design) principles. Structural deficiencies are in fact a consequence of incorrect design methods adopted in the past, based on gravity loading only and not accounting for seismic forces. Therefore, structural details are required as additional data in order to identify possible failure modes of the building structural elements.

In addition to the judgment on each structural weakness, the provision on numerical dimensional data is requested, specifically: the length and number of spans in both structural directions; the section geometry (width, height) and reinforcement quantities (longitudinal, transverse) for beams, columns, walls, the beam-column joint details (w/ or w/o stirrups, type of bar anchorage in the joints); the thickness of the floor slab and its reinforcement details. These quantities allow to estimate the local and global capacity of the building by simple analytical calculations, as briefly explained in the following section.

4 PELL-SCHOOL-RS KEY PERFORMANCE INDICATORS, KPI

PELL platform assess both static KPI, providing a measure of the building seismic vulnerability and expected “nominal” risk index through the estimation or evaluation of capacity/demand ratio with reference to a nominal/code design earthquake intensity (Section 4.1), and dynamically computed KPI (Section 4.2) that in the occurrence of a seismic event aim to provide a quasi-real time estimation of the extent of damage occurred and of the expected level of safety and functionality of the school building. This is done through comparison with the engineering demand parameter thresholds associated to various limit states: i.e. Operational (SLO), Damage Control (SLD), Life Safety (SLV) and Collapse Prevention (SLC).

As far as the monitoring of the seismic response is concerned, *PELL-School-RS* conveys continuous Key Performance Indicators, as a ratio between the recorded engineering demand parameters, EDP, (actual demand) and the estimated/calculated EDP capacity thresholds associated to the various Limit/Damage States, calculated after the automatic processing of data

recorded from MEMS- based accelerometers. The final aim is to derive an objective, prompt and quantitative indication of the damage state and level of safety and functionality of the school building in the aftermath of a seismic event.

4.1 Static KPI

As discussed in the previous section, the collection of additional input data in the *PELL-School-RS* aims at identifying the critical weaknesses/vulnerabilities of buildings. Moreover, these data allow to assess the Seismic Risk Class, including both the Safety Index (IS-V, ζ_E) and Expected Annual Losses (EAL) before and after seismic retrofitting interventions. The estimation of these safety and (economic) performance indicators is proposed in the *PELL-School-RS* by adopting the methodology currently adopted in Italy for the classification of the seismic risk of residential buildings [4].

Referring to the official forms provided by the Italian Presidency of the Council of Ministers (PCM), according to the OPCM n. 3274, 2003, namely *Levels 1-2* assessment for strategic structures, Risk Indicators (α) are defined as Capacity vs. Demand ratios in terms of both Peak Ground Acceleration (PGA) - PGA_C/PGA_D - and Return Period (T_R) - TR_C/TR_D -. The α values are computed at the four different seismic intensity levels or Limit States, namely: Operational (SLO), Damage Control (SLD), Life Safety (SLV) and Collapse Prevention (SLC). The seismic Demand (PGA_D , TR_D) represents the design demand in acceleration/period for a new building located in the same site. The seismic Capacity in terms of acceleration (PGA_C) depends on the building performance at the various Limit States and is evaluated according to the codified methodology in the current Italian seismic code, NTC 2018 [9], considering both brittle and ductile failure modes. On the other hand, the Capacity in terms of Return Period (TR_C) can be computed from the PGA_C by using the seismic hazard maps provided by the Italian seismic code. It is worth noting that, typically, the seismic hazard curves have a concave shape. Therefore, in order to provide a T_R -based risk scale similar to the PGA-based scale and according to the PCM approach, the Return Period ratio (TR_C/TR_D) is raised to the power of 0.41 (value obtained from statistics on hazard curves at national level). Referring to these Risk Indicators (T_R , PGA ratios), low α values clearly mean high seismic risk, while values of around 1 indicate a safety level comparable to new buildings.

Similarly, in the “*Guidelines for the Seismic Risk Classification of Buildings*”, DM 65 2017 [4], a Safety Index (IS-V) of the building is proposed and defined as the Capacity vs Demand ratio in terms of PGA at SLV intensity level (same as the Risk Indicator defined in the PCM).

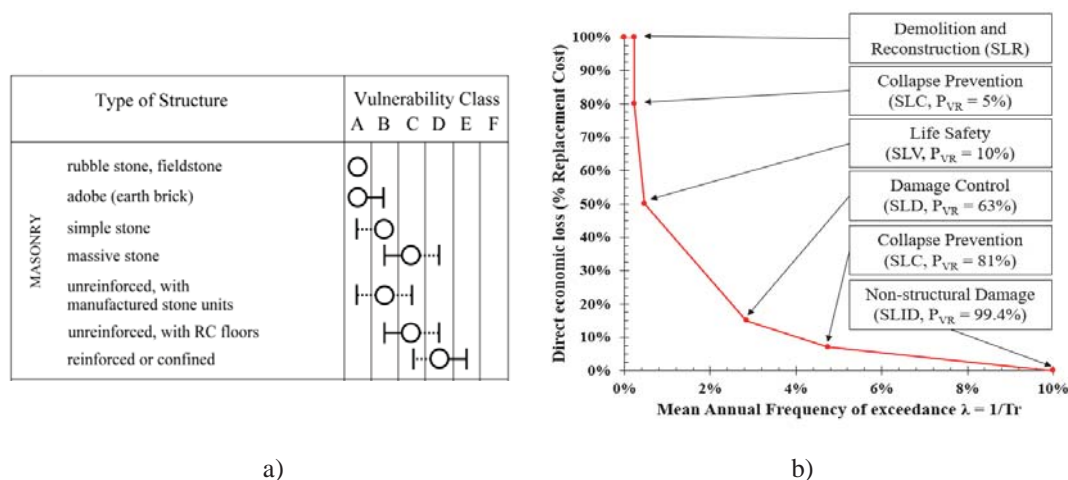


Figure 7. a) Evaluation grid based on the European Macroseismic Scale EMS-98 [8] for masonry buildings (adopted in the simplified method); b) PAM curve as defined in the SismaBonus guidelines [4].

These guidelines, so-called “*Sisma Bonus*”, define a general framework to identify the Seismic Risk Class of buildings as well as the rules to access significant financial incentives (from 75% to 110% in the form of tax deductions in 5 years) when implementing seismic retrofitting interventions. The Risk Class can be assessed by two alternative approaches: 1) the so-called “*simplified*” approach, applicable to masonry structures only and based on the qualitative and archetype-based classification provided by the European Macroseismic Scale (EMS-98 [8], Figure 7a); 2) the “*conventional*” approach, based on the quantification of the capacity and demand, through the implementation of the current code provisions, NTC2018 for the estimation of both the Safety Index (IS-V or ζ_E) and the Expected Annual Losses index (EAL, or PAM in the Italian guidelines). In the latter approach, the Seismic Risk Class of the building is defined as the minimum between the two classes associated with the two mentioned indicators (from A+ to F for IS-V, from A+ to G for PAM, where A+ indicates higher performance).

The EAL (or PAM) index is evaluated by assessing the seismic performance in terms of Mean Annual Frequency of exceedance (MAF or $\lambda = 1/T_R$) at different Limit States (SLO, SLD, SLV, SLC, plus SLDI, SLR, i.e. Non-structural Damage, Demolition and Reconstruction, respectively). Then, a direct economic loss, expressed as a percentage of the Reconstruction Cost of the building (%RC), is associated with each Limit State. Hence, the EAL index is defined as the area under the curve obtained by connecting the λ -RC points, as shown in Figure 7b.

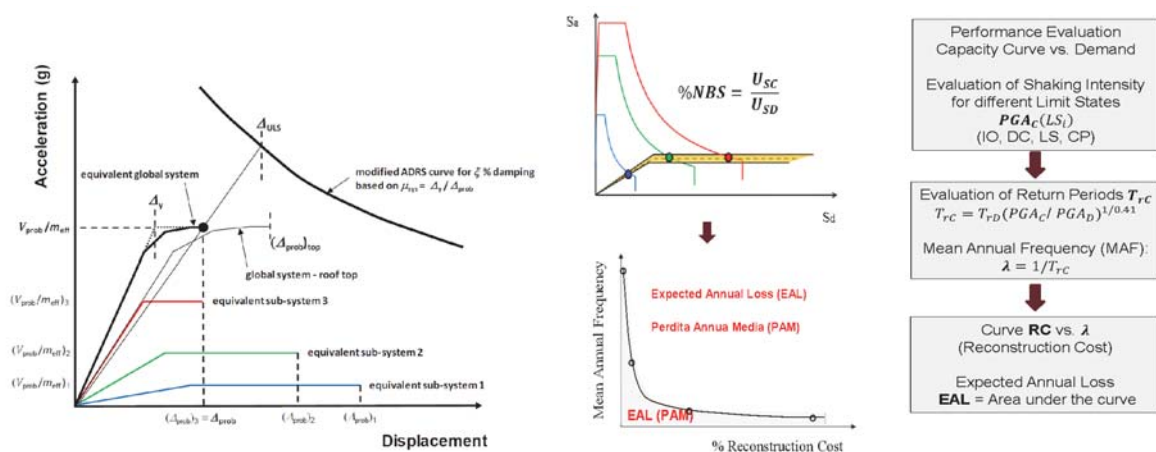


Figure 8. Evaluation of the Safety Index α /IS-V (left) and EAL (right) through the SLaMa Method

The data included in the PELL form allow to compute these key performance indicators (α /IS-V/ ζ_E and EAL/PAM). More specifically, as a further step of this research, the building data can be used to implement a simplified analytical-mechanical seismic assessment of the structure, referred to as SLaMA method (Simple Lateral Analysis Mechanism), developed and introduced in the NZSEE2017 Seismic Assessment Guidelines and fully compatible with, and applicable within, the framework of the Italian NTC2018 code provisions. Following this method, a rapid estimation of the safety level of existing buildings as well as of the expected annual losses can be analytically computed, without any need for a computer/numerical model. In fact, SLaMA allows to determine the force-displacement (pushover) capacity curve and the sequence of local and global mechanisms of a structure by simple analytical (by “hand”) calculations. Therefore, SLaMA results can be used to determine the α /IS-V and EAL classes

(Figure 8) according to the state-of-the-art methodologies available for non-linear static analysis (pushover curve, Capacity) in combination with the Demand within a ADRS, Acceleration-Displacement Response Spectrum (i.e., Capacity Spectrum Method, ATC 1996 [10], or N2 method, Fajfar 2000 [11]).

Overall, four levels of vulnerability assessment evaluation are envisaged (Table 1) for the assessment of static KPI, (Tiers Sn, n from 1 to 4) including a vulnerability-index based analysis as a Tier 0S, plus three Tier level based on either static and dynamic analyses, and on either analytical or numerical models, namely:

- *Tier S0*, vulnerability-index based analysis that envisages the attribution of a vulnerability class and vulnerability index, V, according to [4] and [7] respectively to be adopted for screening and prioritization purposes;
- *Tier S1*, dynamic elastic (modal, response spectrum) analysis - numerical model;
- *Tier S2*, a) non-linear static (pushover) analysis - analytical model (SLaMa method), b) non-linear static (pushover) analysis - numerical model (SLaMa method);
- *Tier S3*, non-linear dynamic (time-history) analysis – numerical model.

	Required information	Demand Parameter	Approach	Risk or damage KPI
Tier S0	<i>PELL-School RS</i> Data groups 5, 16, 17, 18	PGA	Macroseismic Sisma Bonus	V
Tier S1	<i>PELL-School RS</i> Static Data (All)	Design Spectra (T_R , PGA for SLO, SLD, SLV and SLC level)	Numerical Model	α /IS-V and EAL
Tier S2a Non Linear Static Analytical (Simplified)	<i>PELL-School RS</i> Static Data (mandatory only)*	Design Spectra (T_R , PGA for SLO, SLD, SLV and SLC level)	SLaMA analytical method	α /IS-V and EAL
Tier S2b Static Numerical (Conventional)	<i>PELL-School RS</i> Static Data (All)	Design Spectra (T_R , PGA for SLO, SLD, SLV and SLC level)	Numerical Model	α /IS-V and EAL
Tier S3 Dynamic	<i>PELL-School RS</i> - Static Data - Dynamically collected data from SHM	Spectrum compatible accelerograms	Numerical Model +SHM	KPI

*Exclusion made for the Data group 11 (Figure 2), i.e. “Additional data needed for the PdCM Level 1-2 assessment”

Table 1. *PELL-School-RS* Tiered approach for static KPI assessment.

Each approach allows to evaluate, with difference level of trade-off between complexity of the analysis, accuracy, effort/cost and engineering judgement (Figure 9), the expected performance of the school building both in terms of Safety Index and Expected Annual Losses, under various levels of earthquake intensities, i.e. represented by design spectra or spectrum compatible input ground motions (accelerograms).

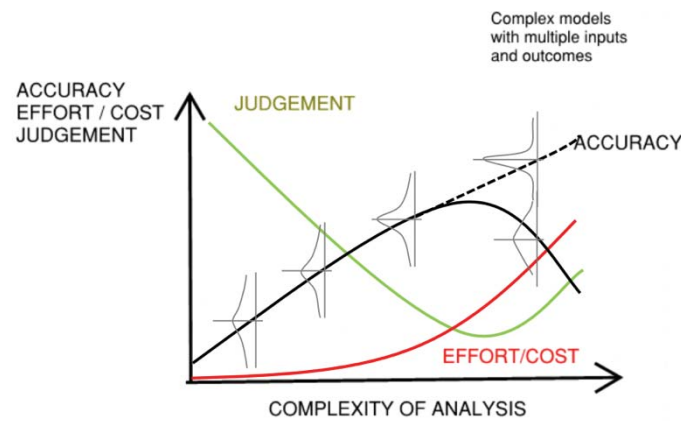


Figure 9. Trade-off and relationship between complexity of the analysis and accuracy, effort/cost, engineering judgement (Kam and Jury, 2015, NZSEE2017)

4.2 Dynamically assessed KPIs

The seismic monitoring is of fundamental importance to assess the post-event response, performance and actual EDPs and expected damage and validate/integrate the model prediction with the observed damage and actual response of the instrumented buildings.

Similarly to what proposed for the static KPI, *PELL-School-RS* will follow a tiered approach for dynamically assessing KPIs post-event including two Tiers (Table 2), namely:

- *Tier D1*, Dynamic Simplified analysis - analytical model;
- *Tier D2*, Dynamic Simplified analysis - numerical model.

	Required information	Demand Parameter	Approach	Risk or damage KPI
Tier D1 Dynamic Simplified	PELL-Building RS Static Data (mandatory only)* Dynamically collected data from SHM	T_R , PGA for SLO, SLD, SLV and SLC Limit States using response Spectra from recorded event accelerogram	SLaMA method +SHM	Limit States KPIs
Tier D2 Dynamic	PELL-Building RS <ul style="list-style-type: none"> • Static Data (ALL) • Dynamically collected data from SHM 	Recorded accelerogram and actual EDP from SHM monitoring	Numerical Model +SHM	Limit States KPIs

Table 2: *PELL-School-RS* Post-event Tiered approach for dynamically assessed KPI assessment.

As far as the Tier D2 approach is concerned, the idea is to adopt the procedure set-up by Mori et al. [12] that includes four steps, namely: i) collecting basic data on the foundation soil and on the building; ii) in situ experimental measurements on the foundation soil and on the building; iii) Operational Modal Analysis (OMA) analysis and modeling through the SMAV software; iv) evaluation of the structural and operational performance of the building.

With reference to the data collection (i), the required basic data include the structural and architectural plans, the floor heights, the type of structural elements and the volume mass of materials; all these data are already collected as part of the *PELL-School-RS* module (Figure 2).

As for the experimental measures (ii), polygons with rigid behavior are identified within each floor of the building, and sensors are deployed at all the building floors and at least at two locations within each polygon using, if possible, the same configuration for all the floors.

As for the OMA (iii) the SMAV software is used: the translational and rotational mass of each identified polygon is considered concentrated in its center of gravity), the participation coefficients and the modal masses are calculated starting from the mass matrix and the experimental deformations defined in terms of translations and rotations of the polygons. From the identified frequencies and modal shapes for each configuration, and after a suitable check for their independency, the global modal shapes of the entire building are obtained.

As for the evaluation of the structural and operational performance of the building (iv) the SMAV software implements the "frequency drop-drift" literature curves and updates the natural frequencies identified with the OMA by means of an iterative algorithm, which recalculates accelerations, displacements and inter-story drift up to convergence. This equivalent linear dynamic analysis allows to follow the variation of natural frequencies up to the drift thresholds which represent the beginning of the structural damage, including in this damage also the non-structural elements interacting with the structure.

5 CONCLUSIONS

This paper presents the on-going activities for the development of the *PELL-School* platform. With the *PELL-School* platform ENEA aims to introduce a shared minimum standard of building knowledge among stakeholders, governance, municipalities and all the involved operators in order to reach a national knowledge and updated evaluation of a very important strategic infrastructure and patrimony, which includes approximately 45.000 public schools in Italy.

In order to test, tune and modify, if necessary, the proposed *PELL-School Seismic-Response* module and to contribute to its implementation on Italian school buildings a Working Group has been set up. The *PELL-School Seismic-Response* Working Group led by ENEA is involving several Municipalities and stakeholders to share and promote the test of the *PELL-School-RS* form (Figure 5) and to contribute to its implementation. The process is also engaging Italian Regions who are in charge of the ARES platform.

Thanks to Municipalities and stakeholders who first joined the Working Group, it has been possible to discuss and test the proposed form on different public schools and so doing, to customize it to the different building peculiarities and to the application capability of the operators. Following the test phase, the *PELL-School-RS* form will be digitized following AgID specifications for data models and will be embedded in the PELL platform, which should be ready by the end of 2022.

Although significant effort have been dedicated by the authors to ensure that the data and KPIs proposed for inclusion in the *PELL-School Seismic-Response* module are aligned and best

represent the scientific and professional advancements in the fields of seismic engineering, seismic vulnerability assessment and seismic monitoring of buildings in Italy, that Italy can boast thanks to the work of professional associations, universities, networks of laboratories, research institutions and research foundations, the collaboration of such experts in the Working Group would be welcome and much appreciated.

All the interest experts are therefore warmly invited to take part in the activities of the *PELL-School Seismic-Response Working Group* towards the common goal of guarantying in the short run the seismic safety of schools and other strategic buildings in Italy.

PELL Schools, is a further step towards the digitization and automation of the information, management and evaluation processes of the strategic infrastructure aiming to renovate streets, districts, towns and territories in order to make them more sustainable, resilient and sharply managed.

ENEA's goal is to make available the *PELL-School* by 2023 for operational use by municipalities and stakeholders.

ACKNOWLEDGEMENTS

The activities of the *PELL Public Energy Living Lab*, research are funded under the Project 1.7 “*Technologies for the efficient penetration of the electric vector in the final uses*” within the “*Electrical System Research*” Programme Agreements 19-21 between ENEA and the Ministry of Economic Development

REFERENCES

- [1] OPCM 3274, Primi elementi in materia di criteri generali per la classificazione del territorio nazionale e di normative tecniche, Ordinance of 20/03/2003, G.U. n.105 of 08/05/2003, 2003.
- [2] M. Annunziato, L. Blaso, G. Buffarini, P. Clemente, S. Giovinazzi, C. Meloni, S. Pampanin, S. Pizzuti, M. Pollino, V. Rosato. PELL-Seismic School: piattaforma integrata, standardizzata ed interoperabile per supportare la valutazione della vulnerabilità sismica delle scuole italiane. *Proceeding of XVIII Congresso Nazionale "L'Ingegneria Sismica in Italia"* (Ascoli Piceno, 15-19 sei 2019). SS13-110. No. 3735, ANIDIS, Roma. 2019.
- [3] Scheda di Sintesi di Edifici Strategici ai Fini di Protezione Civile o Rilevanti in Caso di Collasso a Seguito di Evento Sismico, Ordinance n. 3274/2003 - Ministerial Decree n. 3274/2003 of 14/01/2008.
- [4] DM 65 2017, Guidelines for the Classification of Seismic Risk of Buildings, Annex A, Ministerial Decree n.65 of 07/03/2017, 2017, also referred to as “Sisma Bonus”.
- [5] NZSEE, The seismic assessment of existing buildings - technical guidelines for engineering assessments. *New Zealand Society for Earthquake Engineering*, 2017.
- [6] M., Dolce, E. Speranza, F. Bocchi and C. Conte, Probabilistic assessment of structural operational efficiency in emergency limit conditions: the I.OPà.CLE method. *Bull. Earthquake Eng.*, **16**:3791, 2018, doi:10.1007/s10518- 018-0327-7.
- [7] S. Lagomarsino, S. Giovinazzi, Macroseismic and Mechanical Models for the Vulnerability assessment of current buildings. *Bulletin of Earthquake Engineering*, **4**(4), 415-443, 2006.

- [8] G. Grunthal, European Macroseismic Scale. European Seismological Commission. Conseil de l'Europe, Cahiers du Centre Européen de Géodynamique et de Séismologie, Vol. 15, Luxembourg, 1998.
- [9] NTC 2018, Aggiornamento delle Norme Tecniche per le Costruzioni, Ministero delle Infrastrutture, Suppl. ordinario n°8 alle G.U. n° 42 del 20/02/2018, (in Italian) serie generale, Rome, Italy, 2018.
- [10] Applied Technology Council, Seismic evaluation and retrofit of concrete buildings. ATC 40, Redwood City, CA, USA, 1996.
- [11] P. Fajfar, A nonlinear analysis method for performance-based seismic design. *Earthquake Spectra*, **16**(3), 573-592, 2000.
- [12] F. Mori, D. Spina. Vulnerability assessment of strategic buildings based on ambient vibrations measurements. *Struct. Monit. Maint*, **2**(2), 115-132, 2015.

EFFECT OF BUILDING SAMPLE SELECTION ON SEISMIC FRAGILITY CURVES FOR RC BUILDINGS AT TERRITORIAL SCALE

Maria Zucconi¹, Fabio Romano¹, Barbara Ferracuti¹

¹ Niccolò Cusano University

Via Don Carlo Gnocchi 3, Rome, Italy

{fabio.romano, maria.zucconi, barbara.ferracuti}@unicusano.it

Abstract

A reliable estimate of the seismic vulnerability of building typological classes is a crucial issue to understand how to manage the limited funds available for the reduction of the social and economic losses caused by seismic events. In this context, the goal of this paper is to develop typological empirical fragility curves for reinforced concrete building classes at different damage states. The vulnerability probabilistic assessment is deduced starting from the damage scenario observed after the 2012 Emilia earthquake, available from the Da.D.O. platform. The element-level damage information for the different structural elements is used to define a global building damage state according to a damage index available in the literature. A single value of seismic demand is estimated for each locality and is associated with each building in that locality. Census data have been added to the detected typological building sample with the aim to account for uninspected buildings, and the effect on fragility curves due to the increased dataset is evaluated. Moreover, a completeness ratio is defined for each locality, and lower bounds on the locality seismic demand and completeness ratio are introduced to discard irrelevant damage data and evaluate the consequent effect on the damage state fragility curves.

Keywords: Vulnerability assessment; post-earthquake damage data; Emilia earthquake; Census data; completeness ratio.

1 INTRODUCTION

The increasing interest of national governments in social and economic losses caused by seismic events over the years is demonstrated by the large number of research projects and guidelines that are developing worldwide, dealing with risk or vulnerability predictive models [1, 2]. Predicting losses from future earthquakes at territorial scale requires the development of robust frameworks and procedures [3–7]. Empirical methods have been the first methods developed for the seismic vulnerability assessment starting from the early 70's, because based on the statistical analysis of the observed damage collected after a seismic event. The results are represented in terms of Damage Probability Matrix (DPM), which expresses in a discrete form the conditional probability of reaching a damage level for a given IM value, or in terms of vulnerability or fragility curves. In particular, fragility curves are one of the most effective representations of the buildings seismic vulnerability at territorial scale for specific typological building classes, expressing the probability of exceeding discrete building damage states [8–10]. In general, the results of empirical vulnerability methods have always been affected by a great variety of features [11–13], because directly based on the damage scenarios observed during post-earthquake surveys. The selection of a statistically relevant building sample is a critical issue in the development of fragility curves, because in general only municipalities closer to the earthquake epicenter are completely surveyed, whereas buildings with no damage or very low damage far away from the epicentral area are often not surveyed [14–18]. Such incompleteness of damage dataset could introduce a certain level of bias in the estimation of damage state relative frequencies, consequently in the shape of the fitted damage state fragility curves.

This paper first reports a brief review on main features concerning the seismic vulnerability assessment methods, then the work focuses on the development of sets of empirical fragility curves for RC frame buildings class. The goal is to evaluate the influence on the fragility curve parameters of the building sample selection and the addition of Census data. Fragility curves are calibrated on the damage scenario data observed after the 2012 Emilia earthquake, surveyed via the AeDES post-earthquake damage assessment form [19]. The damage scenarios are obtained from the database Da.D.O. (Observed Damage Database) [20]. The IM is expressed in terms of PGA and estimated at locality-level. Moreover, a completeness ratio is computed for each hit locality, to assess the completeness rate of surveys in post-earthquake emergency.

2 DAMAGE SCALE, DAMAGE FORMS AND BUILDING CLASSIFICATION

2.1 Damage state scales

The definition of a qualitative damage scale is fundamental to obtain a meaningful estimate of the seismic vulnerability. Damage onset and evolution is a continuous process but describing the actual damage condition of a single element or the entire building requires the detection of discrete damage states, incorporated in a damage scale. They can be related to the damage condition of the entire building or of structural and nonstructural elements. In the description of RC buildings global damage, both the damage to RC frames and infill walls is considered, as reported in the damage scales provided by the European Macroseismic Scale (EMS-98) [21] and ASCE/SEI 41-06 [22], underlying the relevant role of infill panels on the RC buildings seismic response.

Different damage indices have been proposed in the literature to trace back the element damage level to one of the five damage states of the EMS-98 damage scale [23–25]. In the present work the damage index proposed by De Martino et al. [26] has been adopted.

2.2 Damage assessment forms

Both at global and element level, the damage described in damage scales is fundamental to properly detect the damage observed in post-earthquake surveys. The damage datasets thereby collected constitutes the statistical basis to develop empirical vulnerability predictive models. Rapid damage assessment forms are very useful instruments to gather standardized and organized information on the damage at building level or at element level, together with the essential geometrical and mechanical features of the building [19, 27, 28]. To be employed in the vulnerability assessment of different building types, the data required in a damage assessment form should be sufficiently detailed and at the same time easily identifiable during a rapid visual inspection. Moreover, they should be reported in a standardized manner, in this way understandable and usable by all researchers worldwide. In fact, the quality and reliability of vulnerability assessment results increase at the increasing of the damage statistical dataset. Unfortunately, damage data collected after different earthquakes are not directly comparable to each other, due to the different forms used in post-earthquake surveys, varying over the years and from country to country, and preliminary activities are necessary to homogenize the different datasets [20, 29]. Moreover, observational data can be affected by errors due to the inspector judgment, hence further effort is necessary to avoid a different interpretation of similar damage conditions by inspector operating in post-earthquake surveys. Much progress has been made over the years trying to reduce the uncertainties in the collection of data from post-earthquake surveys and to homogenize their interpretation, such as the updating of the damage forms or creating training programs for the inspectors. In the present paper, the data collected using the updated Italian form is analyzed.

2.3 Typological building classification

The results of seismic vulnerability assessment methods should represent in a realistic way the actual building damage under a specific seismic action. The building vulnerability however depends on a great number of specific characteristics, such as the quality of materials, the correct application of construction technologies, or the level of in-plan and elevation regularity. The presence of pre-existing damage or strengthening interventions can also influence the structural seismic response. However, the development of specific fragility curve sets for each single building would be unpractical, requiring a great number of information, and a so elevate level of accuracy probably would not even be necessary in a context of vulnerability assessment at territorial scale. In order to regroup together facilities with a similar expected seismic behavior, a suitable classification of building typologies is hence required, based on a limited number of relevant information easily accessible.

Among the various constructive features that affect the building response and performance under seismic action, those generally adopted are the earthquake-resistant structural system, the number of stories, N , and the level of seismic design, the latter strictly related to the age of construction and the site seismicity. Within the European context, different guidelines and research groups proposed a typological building classification based on the number of stories and the seismic design level. For what concern the number of stories classification, i) two building classes or ii) three building classes are generally detected: i) Low-rise and Mid-High-rise buildings, [9, 30] or ii) Low-rise, Mid-rise, and High-rise buildings [31–33]. Low-rise buildings are mostly up to 3-story buildings ($N \leq 3$) while the threshold separating Mid-rise and High-rise buildings is generally 7 stories.

Regarding the seismic design level typological classification, EMS-98 guidelines [21] considered three building classes based on the site seismicity defined at the building time of construction, while Lagomarsino and Giovinazzi [32] defined four classes based on the level of ductility prescriptions and the site seismicity level. More recently, and specifically to the Italian context, the seismic design level has been related to the age of construction, in general distinguishing two building classes composed of non-compliant or compliant buildings to modern design seismic codes [30, 33, 34]. The year threshold adopted to separate the two classes depends on the building stock employed for the vulnerability assessment, influenced by the introduction of regional or national seismic codes and the changes in site seismicity over the years. It is worth noting that, within each abovementioned proposal, the earthquake-resistant structural system does not affect the thresholds selected to distinguish the different story-based or seismic-design-level-based building classes.

3 BUILDING SAMPLE SELECTION AND COMPLETENESS RATIO

In this paper, the damage scenario surveyed after the 2012 Emilia earthquake is employed to assess the probabilistic vulnerability of the regional RC frames building stock. Two main shocks stroke the Emilia territory over late May 2012, May 20th event, with momentum magnitude $M_w = 5.9$, and the May 29th event, $M_w = 5.6$. Starting from the whole dataset of surveyed buildings available from the web platform Da.D.O. (Observed Damage Database) [20], the RC frame subsets of 1,993 is first extracted. Then, the subset of precast RC buildings is discarded from the RC frame subset, in order to restrict the probabilistic vulnerability assessment to sample of RC moment-resisting frames. In order to remove such constructions typology from the dataset, the one-story buildings with interstory height $H \geq 5.0$ m and floor area $A_{floor} \geq 130$ m² are discarded. According to these criteria, a total amount of 362 buildings is discarded, reducing the subset to 1,631 RC moment-resisting frames.

The characteristics of the RC frames subset are presented in Figure 1. Figure 1(a) shows a strong increase of new RC frames starting from the 1960s of the last century, with the timespans 1972 – 1981 and 1982 – 1991 be the most populated, whereas Figure 1(b) underlines a prevalence of buildings having less than 4 stories.

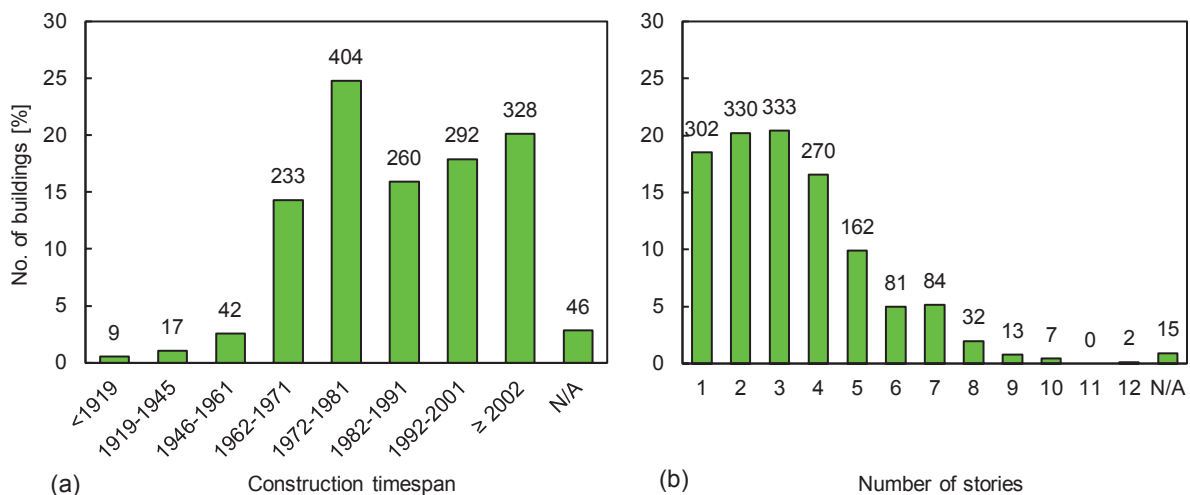


Figure 1: Relative frequency distribution of the RC frames: (a) construction timespan; (b) number of stories. Total number of the buildings: 1,631

In order to obtain fragility curve sets representative of a homogeneous buildings vulnerability to the seismic action, the building sample was separated into two typological classes based on the number of stories: Low-rise = 1 – 3 stories; Mid-High-rise ≥ 4 stories. Because of the selected typological classification, the surveyed buildings for which the information on the number of stories is missing have been discarded, hence the final building sample is composed of 1,616 RC frames.

In general, only the most damaged areas close to the earthquake epicenter are completely surveyed after a seismic event. Such lack of information, mainly related to the undamaged buildings, produce errors in the estimation of a given damage state probability of exceedance. Because of this reason, in the present work a completeness ratio, r , is defined for each locality hit by the Emilia earthquake as the number of buildings surveyed after the seismic event and the total number of buildings in that locality from Census database. It is assumed that buildings added from Census were not surveyed because not exhibiting damage, hence they are assumed to be undamaged. Table 1 summarizes the population of the surveyed RC frames sample and the number of added Census buildings, both separated into the two building classes; the results reveal for the Emilia earthquake a very low average completeness ratio of only 7.3%, probably because the surveys for the Emilia earthquake were performed only on owners' request.

Building samples	$N \leq 3$	$N \geq 4$	Total
Buildings from surveys (Da.D.O.)	965	651	1,616
Added Census buildings (ISTAT)	14,504	5,897	20,401
Total category RC frames	15,469	6,548	22,017

Table 1: Number of RC frames for the selected sample and number of added Census buildings

4 SEISMIC DEMAND AND DAMAGE SCENARIO

In this work, the earthquake IM is expressed in terms of peak ground acceleration (PGA). In particular, a specific value of PGA is estimated in correspondence of the urban center of each locality involved during the seismic events, starting from the PGA values provided by the INGV for the spatial square grid with nodes every 1 km. Since the Emilia earthquake is characterized by two mainshocks, the PGA value is estimated as the maximum between the two mainshocks. Then, the surveyed RC buildings and those added from Census for each locality are regrouped into 0.05 g PGA bins.

For what concern the damage scenario collected from the post-earthquake surveys, the damage was obtained through the Italian AeDES form [19] that defines three damage levels (D1: Light, D2-D3: Medium-Severe, and D4-D5: Very Heavy) to estimate the damage of structural components. Table 2 reports the normalized damage distribution for the different structural elements. The comparison shows that masonry infill walls are the most damaged components (around 70% of buildings), while only 30% of RC frames presents damage; such percentage is approximately 15% for the remaining structural elements. In all the cases, the damaged elements mainly present a slight damage level.

Structural element	AeDES damage state			
	Null	D1: Slight	D2-D3: Medium-heavy	D4-D5: Very heavy
RC frames	72%	14%	8%	6%
Masonry infill walls	32%	43%	17%	8%
Floors	86%	10%	2%	1%
Stairs	86%	10%	2%	2%
Roof	87%	8%	3%	3%

Table 2: Percentage distribution of buildings according to AeDES form damage scale and type of damageable structural element. Total number of RC frames: 1,616.

In order to develop fragility curves, the damage at element level is summarized as a unique damage state for each RC building in the sample via a damage index. The damage index proposed by De Martino et al. [26] estimates the global building damage, as defined according to the EMS-98 scale [21], considering the damage contribution from all the structural elements considered by the AeDES damage form.

5 FRAGILITY CURVES

The effect of adding Census data, treated as undamaged buildings, to the sample of surveyed buildings is here reported in terms of fragility curves. The Maximum Likelihood Estimation (MLE) method is used for the calibration of the typological damage states fragility curves

$$\text{Likelihood} = \prod_{j=1}^m \binom{n_j}{z_j} P(DS \geq DS_i | PGA_j)^{z_j} \left(1 - P(DS \geq DS_i | PGA_j)\right)^{n_j - z_j} \quad (1)$$

where the damage data in each j -th PGA interval are binomially distributed and $P(DS \geq DS_i | PGA_j)$ is the probability of exceeding a the i -th damage state for a given j -th PGA interval. The lognormal distribution is the model assumed for the damage state fragility curves, the most used in the recent literature [35, 36].

Figure 2 shows the sets of fragility curves obtained considering only the surveyed buildings and those obtained adding undamaged buildings from Census; the low-rise building class is selected for the comparison because is the most populated class. Figure 2(a) shows that the set of fragility curves obtained using only the surveyed buildings presents a very flat trend, probably due to the high incompleteness level of the surveys at lowest PGA intervals. The comparison between Figure 2(a) and Figure 2(b) shows a strong reduction of the probability of exceeding the different EMS-98 damage states when undamaged buildings from Census data are introduced, especially at lower PGA bins. It is worth noting that a great number of undamaged buildings is added also in the areas at highest PGA values, hence for the Emilia earthquake the surveys completeness ratio is low also for municipalities close to the epicenter.

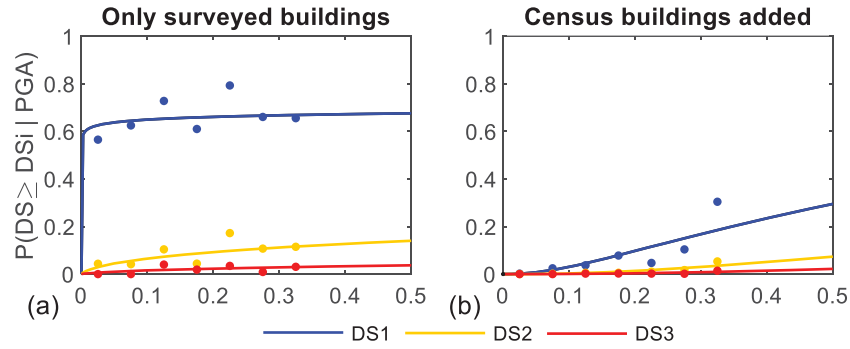


Figure 2. Influence of including Census data (undamaged buildings) on damage state fragility curves for low-rise buildings.

In this work, a completeness ratio, r , is computed for each locality and a unique PGA value is assigned to the selected buildings within each locality. It is comprehensible to recognize that the localities very distant from the epicenter or scarcely surveyed can introduce a bias in the fragility curve shape, hence a $0.05g$ minimum threshold is applied to the PGA range and a 5% minimum threshold on the locality completeness ratio, in order to discard the localities presenting values lower than such thresholds. Figure 3 shows neglectable changes in the set of fragility curves both for low-rise buildings and mid-high-rise buildings, only an increases of the probability of exceeding $DS1$ is appreciable, probably because the influence of the Census undamaged buildings is prevalent for the fragility curves shape. It is worth noting that the curves shown in Figure 3(a) are the same of Figure 2(b).

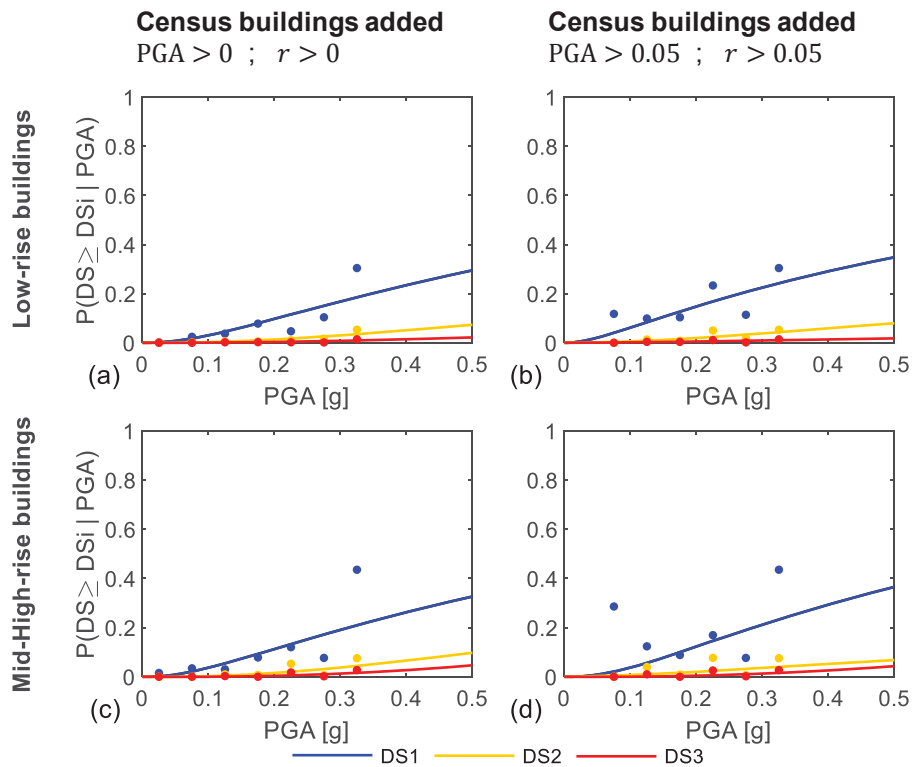


Figure 3. Influence of different criteria for buildings sample selection on damage state fragility curves developed for low-rise buildings.

6 CONCLUSIONS

In the present paper, fragility curves are calibrated for RC frame buildings, based on the observational damage data collected after the 2012 Emilia earthquake and available from the damage database Da.D.O. In particular, the influence of uninspected buildings added to the starting damage datasets have been evaluated. A statistical sample composed of 1,616 RC frames is selected, divided into two typological building classes. The surveyed buildings sample is hence increased by RC frames from Census database, the latter assumed undamaged, and new sets of fragility curves are calibrated. A unique PGA value is estimated for all the RC frames in a specific locality, and a completeness ratio of post-earthquake surveys is computed for each locality.

The vulnerability assessment results show the great influence of added Census data on the fragility curves shape, especially for the first damage state at lower PGA bins. Moreover, the comparison reveals that the survey completeness ratio is low also for municipalities close to the epicenter. On the contrary, neglectable differences are observed between the seismic vulnerability of low-rise and mid-high-rise building classes, and the fragility curve parameters are scarcely affected by the lower bounds on the seismic demand and the completeness ratio parameter.

7 ACKNOWLEDGMENTS

The authors wish to acknowledge the financial support received by the Italian Department of Civil Protection (ReLUIS 2019-2021 Grant – Inventory of existing structural and building types-CARTIS).

REFERENCES

- [1] M. Di Ludovico, A. Digrisolo, F. Graziotti, C. Moroni, A. Belleri, S. Caprili, C. Carocci, A. Dall'Asta, G. De Martino, S. De Santis, B. Ferracuti, D. Ferretti, G. Fiorentino, A. Mannella, A. Marini, C. Mazzotti, A. Sandoli, A. Santoro, S. Silvestri, L. Sorrentino, G. Magenes, A. Masi, A. Prota, M. Dolce, G. Manfredi, The contribution of ReLUIS to the usability assessment of school buildings following the 2016 central Italy earthquake. *Bollettino di Geofisica Teorica ed Applicata*, **58**, 353–376, 2017.
- [2] A. Masi, S. Lagomarsino, M. Dolce, V. Manfredi, D. Ottonelli, *Towards the updated Italian seismic risk assessment: exposure and vulnerability modelling*. Springer Netherlands, 2021.
- [3] M. Dolce, A. Kappos, A. Masi, G. Penelis, M. Vona, Vulnerability assessment and earthquake damage scenarios of the building stock of Potenza (Southern Italy) using Italian and Greek methodologies. *Engineering Structures*, **28**, 357–371, 2006.
- [4] F. Romano, M. Faggella, R. Gigliotti, M. Zucconi, B. Ferracuti, Comparative seismic loss analysis of an existing infilled RC building based on element fragility functions proposals. *Engineering Structures*, **177**, 707–723, 2018.
- [5] M. Dolce, A. Prota, B. Borzi, F. da Porto, S. Lagomarsino, G. Magenes, C. Moroni, A. Penna, M. Polese, E. Speranza, G.M. Verderame, G. Zuccaro, *Seismic risk assessment of residential buildings in Italy*. Springer Netherlands, 2020.

- [6] B. Ferracuti, M. Savoia, M. Zucconi, RC frame structures retrofitted by FRP-wrapping: A model for columns under axial loading and cyclic bending. *Engineering Structures*, **207**, 110243, 2020.
- [7] F. Romano, M.S. Alam, M. Zucconi, M. Faggella, A.R. Barbosa, B. Ferracuti, Seismic demand model class uncertainty in seismic loss analysis for a code-designed URM infilled RC frame building. *Bulletin of Earthquake Engineering*, **19**, 429–462, 2021.
- [8] T. Rossetto, A. Elnashai, Derivation of vulnerability functions for European-type RC structures based on observational data. *Engineering Structures*, **25**, 1241–1263, 2003.
- [9] M. Rota, A. Penna, C.L. Strobbia, Processing Italian damage data to derive typological fragility curves. *Soil Dynamics and Earthquake Engineering*, **28**, 933–947, 2008.
- [10] N. Buratti, F. Minghini, E. Ongaretto, M. Savoia, N. Tullini, Empirical seismic fragility for the precast RC industrial buildings damaged by the 2012 Emilia (Italy) earthquakes. *Earthquake Engineering & Structural Dynamics*, **46**, 2317–2335, 2017.
- [11] G.M. Calvi, R. Pinho, G. Magenes, J.J. Bommer, L.F. Restrepo-Vélez, H. Crowley, Development of seismic vulnerability assessment methodologies over the past 30 years. *ISET Journal of Earthquake Technology*, **43**, 75–104, 2006.
- [12] F. Romano, M. Zucconi, B. Ferracuti, Comparative analysis of seismic vulnerability assessment methodologies for RC buildings at territorial scale. *Proceedings of the 16th European Conference on Earthquake Engineering*, 2018.
- [13] F. Romano, M. Zucconi, B. Ferracuti, Seismic fragility curves for RC buildings at territorial scale. M. Papadrakakis, M. Fragiadakis eds. *COMPDYN 2019 -7th ECCOMAS Thematic Conference on Computational Methods in Structural Dynamics and Earthquake Engineering*, National Technical University of Athens, 2019.
- [14] M. Zucconi, L. Sorrentino, R. Ferlito, Principal component analysis for a seismic usability model of unreinforced masonry buildings. *Soil Dynamics and Earthquake Engineering*, **96**, 64–75, 2017.
- [15] M. Zucconi, R. Ferlito, L. Sorrentino, Simplified survey form of unreinforced masonry buildings calibrated on data from the 2009 L’Aquila earthquake. *Bulletin of Earthquake Engineering*, **16**, 2877–2911, 2018.
- [16] M. Zucconi, R. Ferlito, L. Sorrentino, Validation and extension of a statistical usability model for unreinforced masonry buildings with different ground motion intensity measures. *Bulletin of Earthquake Engineering*, 2020.
- [17] C. Del Gaudio, M. Di Ludovico, M. Polese, G. Manfredi, A. Prota, P. Ricci, G.M. Verderame, *Seismic fragility for Italian RC buildings based on damage data of the last 50 years*. Springer Netherlands, 2020.
- [18] A. Rosti, M. Rota, A. Penna, Empirical fragility curves for Italian URM buildings. *Bulletin of Earthquake Engineering*, 2020.
- [19] C. Baggio, A. Bernardini, R. Colozza, L. Corazza, M. Della Bella, G.D.I. Pasquale, M. Dolce, A. Goretti, A. Martinelli, G. Orsini, F. Papa, G. Zuccaro, *Field Manual for post-earthquake damage and safety assessment and short term countermeasures (AeDES)*. In: Pinto A, Taucer F (eds) Translation from Italian: Goretti A, Rota M, JRC Scientific and Technical Reports, EUR 22868 EN-2007, 2007.

- [20] M. Dolce, E. Speranza, F. Giordano, B. Borzi, F. Bocchi, C. Conte, D. Meo, M. Faravelli, V. Pascale, Da.D.O - A web-based tool for analyzing and comparing post-earthquake damage database relevant to national seismic events since 1976. *Proceedings of the XVII National Conference ANIDIS*, 17-21 September, Pistoia, Italy, 2017.
- [21] G. Grünthal, *European Macroseismic Scale 1998*. Cahiers du Centre Européen de Géodynamique et de Séismologie, 1998.
- [22] ASCE/SEI, *ASCE 41-06 Seismic Rehabilitation of Existing Buildings*. American Society of Civil Engineers, 2007.
- [23] A. Goretti, G. Di Pasquale, Building inspection and damage data for the 2002 Molise, Italy, earthquake. *Earthquake Spectra*, **20**, S167–S190, 2004.
- [24] C. Del Gaudio, G. De Martino, M. Di Ludovico, G. Manfredi, A. Prota, P. Ricci, G.M. Verderame, Empirical fragility curves from damage data on RC buildings after the 2009 L'Aquila earthquake. *Bulletin of Earthquake Engineering*, **15**, 1425–1450, 2017.
- [25] M. Dolce, A. Goretti, Building damage assessment after the 2009 Abruzzi earthquake. *Bulletin of Earthquake Engineering*, **13**, 2241–2264, 2015.
- [26] G. De Martino, M. Di Ludovico, A. Prota, C. Moroni, G. Manfredi, M. Dolce, Estimation of repair costs for RC and masonry residential buildings based on damage data collected by post-earthquake visual inspection. *Bulletin of Earthquake Engineering*, **15**, 1681–1706, 2017.
- [27] ATC, *ATC-45 Field Manual: Safety Evaluation of Buildings after Windstorms and Floods*. Applied Technology Council, 2004.
- [28] MBIE, *Rapid post disaster building usability assessment – earthquake*. Ministry of Business Innovation and Employment, 2014.
- [29] M. Dolce, E. Speranza, F. Giordano, B. Borzi, F. Bocchi, C. Conte, A. Di Meo, M. Faravelli, V. Pascale, Observed damage database of past Italian earthquakes: The da.D.O. WebGIS. *Bollettino di Geofisica Teorica ed Applicata*, **60**, 141–164, 2019.
- [30] C. Del Gaudio, P. Ricci, G.M. Verderame, G. Manfredi, Development and urban-scale application of a simplified method for seismic fragility assessment of RC buildings. *Engineering Structures*, **91**, 40–57, 2015.
- [31] Z. V Milutinovic, G.S. Trendafiloski, WP4: Vulnerability of current buildings. *Contract: EVK4-CT-2000-00014, WP4: Vulnerability of Current Buildings*, 110, 2003.
- [32] S. Lagomarsino, S. Giovinazzi, Macroseismic and mechanical models for the vulnerability and damage assessment of current buildings. *Bulletin of Earthquake Engineering*, **4**, 415–443, 2006.
- [33] V. Silva, H. Crowley, R. Pinho, H. Varum, Extending displacement-based earthquake loss assessment (DBELA) for the computation of fragility curves. *Engineering Structures*, **56**, 343–356, 2013.
- [34] M. Rota, A. Penna, C. Strobbia, G. Magenes, Typological Seismic Risk Maps for Italy. *Earthquake Spectra*, **27**, 907–926, 2011.
- [35] A.B. Liel, K.P. Lynch, Vulnerability of Reinforced-Concrete-Frame Buildings and Their Occupants in the 2009 L'Aquila, Italy, Earthquake. *Natural Hazards Review*, **13**, 11–23, 2012.

- [36] U. Hancilar, F. Taucer, C. Corbane, Empirical Fragility Functions based on Remote Sensing and Field Data after the 12 January 2010 Haiti Earthquake. *Earthquake Spectra*, **29**, 1275–1310, 2013.

COMPDYN 2021

**Proceedings of the
8th International Conference on
Computational Methods in Structural Dynamics and Earthquake Engineering**

M. Papadrakakis, M. Fragiadakis (Eds.)

First Edition, September 2021

ISBN (set): 978-618-85072-5-8

ISBN (vol I): 978-618-85072-3-4



**Institute of Structural Analysis and Antiseismic Research
National Technical University of Athens, Greece**